南方科技大学
SOUTHERN UNIVERSITY OF SCIENCE AND TECHNOLOGY

2024 >> 5月10-12日 May 10-12
中国·深圳 Shenzhen, China

Proceedings of the 3rd Conference on Fully Actuated System Theory and Applications

Organizing Institutions

Southern University of Science and Technology

Technical Committee on Fully Actuated System Theory and Applications, Chinese Association of Automation

Hosts

School of System Design and Intelligent Manufacturing, Southern University of Science and Technology

Shenzhen Key Laboratory of Control Theory and Intelligent Systems

Guangdong Provincial Key Laboratory of Fully Actuated System Control Theory and Technology

National Key Laboratory of Complex System Control and Intelligent Agent Cooperation

Proceedings of FASTA 2024

- **IEEE Catalog Number:**CFP24DM5-ART
- **ISBN:**979-8-3503-7369-1

Welcome Address

The 3rd Conference on Fully Actuated System Theory and Applications (FASTA2024) will be held on May 10-12, 2024 at Haide Hotel, Shenzhen, Guangdong. The General Chair of the conference is Professor Guangren Duan, an Academician of the Chinese Academy of Sciences from the Southern University of Science and Technology, and the Program Committee Chair is Professor Minyue Fu, a Fellow of the Chinese Association of Automation, from the Southern University of Science and Technology. The conference aims to provide an academic exchange platform for domestic and foreign experts, scholars, and engineering and technical personnel engaged in the research field related to the theory and applications of fully actuated systems, to better publicize the research results in the field of fully actuated system theory and applications, and to promote the development of research on fully actuated system theory and applications. The conference takes the form of plenary lectures, semi-plenary lectures, oral sessions, and poster sessions. The working languages of the conference are Chinese and English. The accepted English papers will be submitted to the IEEE Xplore database after the conference.



Guangren Duan
General Chair



Minyue Fu
Program Committee Chair

On behalf of the conference Program Committee, we would like to express our heartfelt thanks and warmest welcome to all the contributors and participants!

The conference is co-sponsored by the Southern University of Science and Technology and the Technical Committee on Fully Actuated System Theory and Applications, CAA, hosted by the School of System Design and Intelligent Manufacturing, Southern University of Science and Technology, and co-organized by IEEE Industrial Electronics Society, IEEE Guangzhou Section, Harbin Institute of Technology (Shenzhen), Tsinghua Shenzhen International Graduate School, Shenzhen University, and Sun Yat-Sen University.

A total of 353 papers are submitted from 12 countries and regions, including China, France, Australia, Singapore, Canada, America, Japan, Switzerland, etc. After a strict and careful review process, 308 papers (including 27 extended abstracts) are accepted by the conference. During the conference, 8-10 conference rooms are assigned for 4 rounds of oral presentation, including 33 oral sessions that cover a total of 241 papers. Two poster sessions, including a total of 60 papers, are also scheduled during the conference.

We are honored to invite three internationally famous scholars to deliver Plenary Lectures. They are Professor Zhong-Ping Jiang (New York University, USA), Professor Guo-Ping Liu (Southern University of Science and Technology, China), and Professor Michael V. Basin (Autonomous University of Nuevo Leon, Mexico). We also organize 8 Semi-plenary Lectures and they are delivered by Prof. Zhiyun Lin from Southern University of Science and Technology, Prof. Keyou You from Tsinghua University, Prof. Jianbin Qiu from Harbin Institute of Technology, Prof. Dan Ma and Prof. Tengfei Liu from Northeastern University, Prof. Bo Yang from Shanghai Jiao Tong University, Prof. Ai-Guo Wu from Harbin Institute of Technology (Shenzhen), and Prof. Qingkai Yang from Beijing Institute of Technology. In order to create an academic atmosphere, encourage more young scientists and students to devote themselves to the research of fully actuated system control theory and applications, and further improve the quality of academic papers and the influence of the conference, the conference set up the “FASTA Outstanding Youth Paper Award” and “FASTA Best Student Paper Award”, with 6 papers shortlisted respectively. The conference aims to reward outstanding young scholars to promote the cultivation of high-end talents in the discipline and further promote the development of automatic control theory and applications.

We would like to express our most sincere gratitude to all those who contributed to the successful convening of this conference! Thanks to the reviewers and members of the Program Committee for their rigorous review of the submitted papers! Thank the organizing committee and volunteers for their warm service! We would like to thank the plenary speakers and the semi-plenary speakers for accepting the conference invitation and sharing their latest research findings with us! Finally, on behalf of the Program Committee, we would like to thank all contributors and participants for their support of the 3rd Conference on Fully Actuated System Theory and Applications!

Welcome to the 3rd Conference on Fully Actuated System Theory and Applications!

Guangren Duan
General Chair

Minyue Fu
Program Committee Chair

Conference Committees

Organizing Institutions

Southern University of Science and Technology
Technical Committee on Fully Actuated System Theor y and Applications, Chinese Association of Automation

Host

School of System Design and Intelligent ManufacturingSouthern University of Science and Technology

Technical Co-Sponsors

IEEE Guangzhou Section
IEEE Industrial Electronics Society
Harbin Institute ofTechnology (Shen Zhen)
Tsinghua Shenzhen International Graduate School
Shenzhen University
Sun Yat-Sen University

Advisory Committee

Weimin Bao	China Aerospace Science and Technology Corporation
Xibin Cao	Harbin Institute of Technology
Jie Chen	Tongji University
Xiaohong Guan	Xi'an Jiaotong University
Weihua Gui	Central South University
Hong Qiao	Institute of Automation, CAS
Tieniu Tan	Nanjing University
Yaonan Wang	Hunan University
Yiyin Wei	China Aerospace Science and Industry Corporation Ltd
Dengyun Yu	China Aerospace Science and Technology Corporation
Nanning Zheng	Xi'an Jiaotong University
Lei Guo	Beihang University

General Chairman

Guangren Duan	Southern University of Science and Technology /Harbin Institute of Technology

Program Committee Chairman

Minyue Fu	Southern University of Science and Technology

Region Chairman

Yang Shi	University of Victoria
Huijun Gao	Harbin Institute of Technology

Program Committee Vice-Chairs

Guoping Liu	Southern University of Science and Technology
Wanquan Liu	Sun Yat-Sen University

Program Committee General Secretaries

Wei Zhang	Southern University of Science and Technology
Ying Zhang	Harbin Institute of Technology (Shen Zhen)

Program Deputy General Secretaries

He Kong	Southern University of Science and Technology
Kemi Ding	Southern University of Science and Technology
Liangming Chen	Southern University of Science and Technology

Organizing Committee Chair

Zhiyun Lin	Southern University of Science and Technology
Xiang Xu	Southern University of Science and Technology

Organizing Vice-Chairs

Li Qiu	Southern University of Science and Technology
Derong Liu	Southern University of Science and Technology
Haoqian Wang	Tsinghua SIGS
Zongze Wu	Shenzhen University

Organizing Committee General Secretary

Zaiyue Yang	Southern University of Science and Technology

Organizing Deputy General Secretaries

Jian Chen	Southern University of Science and Technology
Weijie Yuan	Southern University of Science and Technology
Fan Liu	Southern University of Science and Technology

Poster Session Chairman

Chenxiao Cai	Nanjing University of Science and Technology

Award Paper Chair

Bin Zhou	Harbin Institute of Technology

Publication Committee Chair

Aiguo Wu	Harbin Institute of Technology (Shen Zhen)

Publication Vice-Chairs

Yuan Chen	Southern University of Science and Technology
Zhenkun Wang	Southern University of Science and Technology

IPC Members

Xiaojun Ban	Harbin Institute of Technology
Bo Cai	Harbin Institute of Technology
He Cai	South China University of Technology
Ci Chen	Guangdong University of Technology
Liheng Chen	Harbin Engineering University
Yangyang Chen	Southeast University
Yang Cui	Liaoning University of Science and Technology
Yukang Cui	Shenzhen University
Zhiyuan Dong	Harbin Institute of Technology(Shenzhen)
Junfang Fan	Beijing Information Science and Technology University
June Feng	Shandong University
Fangzhou Fu	Sun Yat-sen University
Youmin Gong	Harbin Institute of Technology(Shenzhen)
Dake Gu	Tohoku Electric Power University
Guoxiang Gu	Louisiana State University
Fei Han	Shanghai Institute of Aerospace Control Technology
Mingrui Hao	Beijing Institute of Mechanical and Electrical Engineering
Wangli He	East China University of Science and Technology
Liang He	Northwestern Polytechnical University
Mingzhe Hou	Harbin Institute of Technology
Changchun Hua	Yanshan University
Ling Huang	Harbin Engineering University
Xiuwei Huang	Jihua Laboratory
Bin Jiang	Nanjing University of Aeronautics and Astronautics
Huaiyuan Jiang	Harbin Institute of Technology
Shuilin Jin	Harbin Institute of Technology
Bin Li	Sichuan University
Chaoyan Li	Harbin Institute of Technology
Huiping Li	Northwestern Polytechnical University
Ping Li	Southern University of Science and Technology
Rui Li	University of Electronic Science and Technology of China
Tieshan Li	University of Electronic Science and Technology of China
Xuefang Li	Sun Yat-sen University
Zhibin Li	Shandong University of Science and Technology
Jianxing Liu	Harbin Institute of Technology
Lu Liu	City University of Hong Kong
Ming Liu	Harbin Institute of Technology
Wei Liu	South China University of Technology
Yang Liu	Beihang University
Lingling Lv	North China University of Water Conservancy and Electric Power
Dan Ma	Northeastern University
Lei Ma	China University of Mining and Technology
Lifeng Ma	Nanjing University of Science and Technology
Jie Mei	Harbin Institute of Technology(Shenzhen)
Deshan Meng	Sun Yat-sen University
Deyuan Meng	Beihang University
Wei Meng	Guangdong University of Technology
Zibo Miao	Harbin Institute of Technology(Shenzhen)
Zhiqiang MIiao	Hunan University
Huixiu Peng	Nanjing University of Aeronautics and Astronautics

Hongsheng Qi	Chinese Academy of Sciences
Wenhai Qi	Qufu Normal University
Jianbin Qiu	Harbin Institute of Technology
Li Qiu	Shenzhen University
Jun Shang	Tongji University
Mouquan Shen	Nanjing Tech University
Shenmin Song	Harbin Institute of Technology
Guanghui Sun	Harbin Institute of Technology
Huijie Sun	Sun Yat-sen University
Yang Tong	East China University of Science and Technology
Xiongbo Wan	China University of Geosciences
Long Wang	Peking University
Peng Wang	Shanghai Jiaotong University
Qian Wang	Hangzhou University of Electronic Science and Technology
Shenquan Wang	Changchun University of Technology
Wei Wang	Shandong University
Zhuo Wang	Beihang University
Caisheng Wei	Central South University
Guanghui Wen	Southeast University
Jie Wen	Harbin Institute of Technology (Shenzhen)
Xuyang Wu	Southern University of Science and Technology
Yuyao Wu	Sun Yat-sen University
Feng Xiao	North China Electric Power University
Xiaochen Xie	Harbin Institute of Technology (Shenzhen)
Juanjuan Xu	Shandong University
Shengyuan Xu	Nanjing University of Science and Technology
Wenying Xu	Southeast University
Jianan Yang	Harbin Institute of Technology
Xuebo Yang	Harbin Institute of Technology
Ziwen Yang	Shanghai Jiao Tong University
Xiuming Yao	Beijing Jiaotong University
Wenwu Yu	Southeast University
Baoyong Zhang	Nanjing University of Science and Technology
Chengxi Zhang	Jiangnan University
Dan Zhang	Zhejiang University of Technology
Feng Zhang	China Academy of Launch Vehicle Technology University
Hongwei Zhang	Harbin Institute of Technology (Shenzhen)
Kai Zhang	Sichuan University
Ke Zhang	Nanjing University of Aeronautics and Astronautics
Lixian Zhang	Harbin Institute of Technology
Liu Zhang	Jilin University
Shijie Zhang	Henan University of Technology
Zhongcai Zhang	Qufu Normal University
Bo Zhao	Beijing Normal University
Guanglei Zhao	Yanshan University
Qianchuan Zhao	Tsinghua University
Kai Zheng	Dalian Maritime University
Shanying Zhu	Shanghai Jiao Tong University
Yanzheng Zhu	Shandong University of Science and Technology
Yun Zou	Nanjing University of Science and Technology

Plenary Lectures

Plenary Lecture 1

Zhong-Ping Jiang
New York University, USA

Small-Gain Theory for Stability and Control of Interconnected Systems

Chair: Li Qiu, Southern University of Science and Technology, China

Abstract: The world is nonlinear and linked. Small-gain theory is one of the most important tools to tackle fundamentally challenging control problems for interconnected nonlinear systems. In this talk, I will first review our early work in nonlinear small-gain theorems and associated nonlinear control design. Then, I will present recent developments in network small-gain theorems for complex large-scale nonlinear systems, with applications to networked and event-triggered control under communications and computation constraints. Finally, I will discuss how small-gain methods can be integrated with reinforcement learning techniques to solve real-time decision-making problems when the system model is completely unknown. Autonomous driving and human motor control will be used to illustrate our recent research in learning-based control, a new direction in control theory.



Zhong-Ping Jiang received the M.Sc. degree in statistics from the University of Paris XI, France, in 1989, and the Ph.D. degree in automatic control and mathematics from ParisTech-Mines (formerly called the Ecole des Mines de Paris), France, in 1993, under the direction of Prof. Laurent Praly. Currently, he is a Professor of Electrical and Computer Engineering at the Tandon School of Engineering, New York University. His main research interests include stability theory, robust/adaptive/distributed nonlinear control, robust adaptive dynamic programming, reinforcement learning, and their applications to information, mechanical, and biological systems. In these fields, he has written six books and is the author/co-author of about 600 peer-reviewed journal and conference papers.

Prof. Jiang is a recipient of the prestigious Queen Elizabeth II Fellowship Award from the Australian Research Council, CAREER Award from the U.S. National Science Foundation, JSPS Invitation Fellowship from the Japan Society for the Promotion of Science, Distinguished Overseas Chinese Scholar Award from the NSF of China, and several best paper awards. He has served as Deputy Editor-in-Chief, Senior Editor and Associate Editor for numerous journals. Prof. Jiang is a Fellow of the IEEE, IFAC, CAA, and AAIA, a foreign member of the Academia Europaea (Academy of Europe), and is among the Clarivate Analytics Highly Cited Researchers and Stanford' s Top 2% Most Highly Cited Scientists. In 2022, he received the Excellence in Research Award from the NYU Tandon School of Engineering.

Plenary Lecture 2

Guo-Ping Liu
Southern University of Science and Technology, China

High-order Fully Actuated Predictive Control for Networked Systems

Chair: Lei Guo, Beihang University, China

Abstract: The rapid development of network technology accelerates the development of networked systems, such as the Internet of Things and industrial Internet systems. This talk mainly introduces the high-order fully actuated predictive control for networked systems. A generic high-order fully actuated model in the discrete-time domain is employed to describe the control problem of both networked linear and nonlinear systems with communication constraints. Based on this model, various high-order fully actuated predictive control schemes are discussed, which actively compensate for communication constraints and simultaneously achieve the required stability and performance. Those schemes greatly simplify the design of networked control systems with communication constraints and significantly make them have a similar control performance to networked systems without communication constraints. The closed-loop high-order fully actuated predictive control systems are analysed and the criteria on their stability are derived. Various simulations and experiments successfully demonstrate the effectiveness of the high-order fully actuated predictive control schemes.



Guo-Ping Liu received the BEng degree in industrial automation and MEng degree in control engineering from the Central South University of Technology in China and the PhD degree in control systems from the University of Manchester in the UK. He was a professor with the Institute of Automation in the Chinese Academy of Sciences, University of South Wales, Harbin Institute of Technology, and Wuhan University. He is now a chair professor with the Southern University of Science and Technology. Prof Liu's research interests include networked control systems, multi-objective optimal control and intelligent decision, nonlinear identification and intelligent control, and industrial advanced control applications. He was named a highly cited researcher by Thomson Reuters, Clarivate Analytics, and Elsevier, and was awarded the Alexander von Humboldt research fellowship. He received the second prize of Chinese National Science and Technology Awards twice. Prof. Liu was the general chair of the 2007 IEEE International Conference on Networking, Sensing and Control, 2011 International Conference on Intelligent Control and Information Processing, and 2012 UKACC International Conference on Control. He is a member of the Academy of Europe and a fellow of IEEE, IET, and CAA.

Plenary Lecture 3

Michael V. Basin
Autonomous University of Nuevo Leon, Mexico & Ningbo University of Technology, China

Predefined-Time Convergent Continuous Controllers: Design and Applications

Chair: Donghua Zhou, Tsinghua University, China

Abstract: This talk presents predefined-time convergent continuous controller design for scalar and multidimensional systems with incompletely measured states and matched/unmatched disturbances. The theoretical design principles are outlined and applied to stabilization problems for full-scale 4D permanent-magnet synchronous motor (PMSM) and brushed direct current (DC) motor systems. Three cases have been considered: disturbance-free, in presence of matched/unmatched deterministic disturbances satisfying Lipschitz condition, and in presence of both matched/unmatched stochastic white noises and deterministic disturbances satisfying Lipschitz condition. A predefined-time convergent observer is designed to reconstruct unmeasurable system states and provide the controller feedback. Numerical simulations are conducted to validate the obtained theoretical results in each of the three considered cases. The simulation results demonstrate that the employed values of the predefined-time convergent control inputs are applicable in practice and verify the algorithm efficiency in each considered case. Finally, some ideas for designing predefined-time convergent continuous controllers based on the concept of fully actuated systems are discussed.



Michael V. Basin received his Ph.D. degree in Physical and Mathematical Sciences with major in Automatic Control and System Analysis from the Moscow Aviation University (MAI) in 1992. He is currently Full Professor with the Autonomous University of Nuevo Leon, Mexico, and the Ningbo University of Technology, China. Starting from 1992, Dr. Basin published more than 400 research papers in international referred journals and conference proceedings. He is the author of the monograph "New Trends in Optimal Filtering and Control for Polynomial and Time-Delay Systems," published by Springer. His works are cited more than 8000 times (h-index = 48). Dr. Basin has supervised 17 doctoral and 10 master's theses. He has served as the Editor-in-Chief and serves as the Co-Editor-in-Chief of Journal of The Franklin Institute, the Senior Editor of IEEE/ASME Transactions on Mechatronics and IEEE Transactions on Systems, Man and Cybernetics: Systems, an Associate Editor of Automatica, IET-Control Theory and Applications, International Journal of Systems Science, Neural Networks. Dr. Basin was awarded a title of Highly Cited Researcher by Thomson Reuters,the publisher of Science Citation Index, in 2009, and listed in "100 000 Leading Scientists in the World"; he is a regular member of the Mexican Academy of Sciences and a recipient of the Kimura Best Paper Award from Asian Control Association. Prof. Basin has been honored as a Fellow of Prominent Talent (Qian Ren) Program of Zhejiang Province, China. His research interests include optimal filtering and control problems, stochastic systems, time-delay systems, identification, sliding mode control and variable structure systems, applications to mechatronic and transportation systems.

Table of Contents

H∞Consensus Control for High-Order Fully Actuated Multi-Agent Systems with External Disturbances ..... ZHANG Qinghao, LU Jun-Guo 1
Adaptive Stabilization Control for Fully Actuated Systems with Unknown Measurement Sensitivity ..... WU Xueqi, SUN Wei 7
Coordinated Control for Incomplete Controllable Systems over Finite Fields ..... QIN Ao, GAO Zhe, FENG Jun-e 13
On Full-Actuation of Linear Boolean Control Networks ..... DING Yuanpeng, FENG Jun-e, YU Yongyuan 19
Adaptive Dynamic Event-Triggered Tracking Control for Uncertain High-Order Fully Actuated Systems ..... LI Zhaoyang, CHEN Zhongyu, NIU Yichun, SHENG Li 25
Event-Triggered Robust Control for a Class of Nonlinear Systems with Uncertainty: A HOFA System Approach .... ZHANG Luhan, WANG Lou, ZHANG Cui-Hua, HUA Changchun, ZHANG Ying, LI Li 31
Event-Triggered Tracking Control for High-Order Fully Actuated Strict-Feedback Systems ..... LIU Yang, ZHANG Jiaming 37
Adaptive Control for Active Suspension System Based on the High-order Fully Actuated System Theory ..... ZHAO Haohan, ZHANG Yahui, JIAO Xiaohong 42
Observer-Based Control for Fully Actuated Systems with Time-Varying Delays: A Fully Actuated System Approach ..... CHEN Zhijun, ZHANG Shiyu, DUAN Guangren 48
Tracking Control of Unmanned Surface Vessels Based on Fully Actuated System Approaches ..... LI Zijing, ZHU Jing, ZHAI Xiangping, ZHANG Hongwei 54
Optimal Control and Stabilization for NCS over Multi-Hop Relay Networks ..... ZHAO Qinglun, HAN Chunyan 60
Distributed Recursive Filter for 2-D Markov Jump Systems with Stochastic Communication Protocol and Nonlinearities ..... GE Fengying, HAN Chunyan 66
Output Tracking Based on Reduced-Order Observer for Fully Actuated Systems ..... JIANG Hong, DUAN Guangren 72
Enhancing Frequency Emergency Control with Battery Energy Storage Systems in Low-Inertia Power Grid ..... YUXIN Weng, GENG Guangchao, JIANG Quanyuan, WANG Heng 78
Explicit Solution to Quasi-Polynomial Matrix Right Coprime Factorization with Application in Establishment of Time-Delay Fully Actuated System ..... ZHANG Xujie, DUAN Guangren 86
Adaptive Control for Fully Actuated Systems with Input Quantization .... LIU Lin, DUAN Guangren 92
Optimal Filtering for NCSs with Amplify-and-forward Relays ..... LIU Xiaohan, HAN Chunyan 97
Finite-Time Command Filtered Backstepping Design for High-Order Fully Actuated Strict-Feedback Systems ..... LIU Weizhen, DUAN Guang-Ren, TIAN Guangtai, GOLESTANI Mehdi, KONG He 103
Operational Flexibility Enhancement with Aggregated Electric Vehicles Based on Virtual Energy Storage Model .... SHIWEI Chen, LANG Hongfei, WAN Muchun, DU Junjun, BAO Feng, GENG Guangchao 110
Robotic Manipulator Control Based on Disturbance Observer: A High-Order Fully Actuated System Approach ..... YUEBIN Qiu, ZHANG Shijie, WU Xiang, ZHANG Hui, YANG Tianle 116
Design and Modeling of A Trapezoidal Leaf Spring-Based Actuators with Valid Arm Length and Bending Deformation for Stiffness Adjustment. ..... YANG Tianle, ZHANG Hui, ZHANG Shijie, WU Xiang, YUEBIN Qiu, ZHANG Jing 121
Adaptive Fuzzy Fault-Tolerant Control of High-Order Nonlinear Time-Varying Delay Systems with Dead-Zone Inputs: A Fully Actuated System Approach ..... ZHENG Sen, CUI Yang 127

Event-triggered Fuzzy Adaptive Fault-Tolerant Control of High-Order Nonlinear Systems: A Fully Actuated System Approach ..... ZHAO Qingyi, CUI Yang 134
Global Prescribed-Time Control Fully Actuated Nonlinear Systems
..... NING Pengju, HUA Changchun, LI Hao 141
Consensus Analysis and Control for Second-Order Fully Actuated Multi-agent Systems
..... YANG Xin-Rong, ZHONG Zefeng 147
Practical Prescribed Time Control for Space Manipulators Based on Fully Actuated System Approach
..... TIAN Guangtai, DUAN Guangren, LIU Weizhen, GOLESTANI Mehdi, KONG He 152
Adaptive Tracking Control for Random High-Order Fully Actuated Systems with Unknown Drift Nonlinearity and Diffusion Coefficient ..... CHEN Yunqi, DUAN Guangren 158
An Observer-based Robust Sliding Mode Control for the System with Actuator Saturation and False Data Injection Attack ..... WANG Qian, WANG Xinyuan, JIN Yan 165
A Fully Actuated System Approach for Robust Control of a Type of Feedback Linearizable System
..... GUO Xiaomeng, GU Dake, LIU Yin-Dong 171
High Precision Trajectory Tracking Control for a Kind of Novel Cable-driven Space Manipulator
..... ZOU Xiangxiang, MENG Deshan, SUN Hui-Jie, WU Yuyao, TAN Lining 177
Predictor-based Sliding Mode Control for Systems with Input Delays
..... ZHANG Xinyu, WANG Yu, HAO Jun 183
Fully Actuated Behavioral Control for Multiple Omnidirectional Mobile Robots System with Uncertain Dynamics ..... MO Zhibin, LIU Wanquan, WU Yuyao, SUN Hui-Jie 189
Adaptive Neural-networks Control for Uncertain Second-order Fully Actuated Strict-feedback Systems without Over-parametrization ..... QI Wennian, WU Aiguo, ZHANG Jie 195
Dynamics Modeling of Soft Robots Based on Attention-enhanced Lagrangian Deep Neural Networks
..... WEI Yeqi, SHAO Xiangyu, LIU Jingyue, ZHANG Shaojie, XU Linke 200
Robust LPV System Identification with Asymmetric Measurement Noise
..... XIN Liu, YANG Hai, DAI Wei 208
Event-Triggered Prescribed Performance Control for Multi-Input Multi-Output Nonlinear Systems
..... CUI En-Yuan, ZHANG Jin-Xi 216
Time-Optimal and Jerk-Continuous Trajectory Planning and Tracking Control for 6-DOF Manipulator Based on High-Order Fully Actuated System Control Theory
..... ZOU Die, HUANG Likun, WANG Wei, LIN Mengying, HUANG Zixin 222
H∞Voltage Control of Islanded Microgrid Three-phase Inverter: a Model-free Integral Reinforcement Learning Approach ..... ZHOU Linna, LI Fuxing, LI Gonghe, LIU Xiaomin, YANG Chunyu 226
On Designing Interval Observer for Discrete-time Positive Fuzzy Markov Jump Systems with Bounded Disturbance Input ..... WANG Shujia, ZHU Shuqian, ZHANG Dawei 232
Robust Sequential Covariance Intersection Fusion Kalman Filters with Noise Variances Uncertainties
..... SONG Yangyi, QI Wenjuan 238
Time-varying Filters for Uncertain Singular System with Random D-step Measurement Delay and Packet Dropout ..... ZHANG Xinyu, RAN Chenjian 243
PMSM Speed Control Based on Fully Actuated Systems Theory
..... QUAN Fangyi, FAN Jun-fang, ZHANG Sixing, JI Yi, CHEN Shiwei 249
Observer-based Sliding Mode Control for Internal Oxygen Supply of PEM Fuel Cell
..... LIU Li, LI Jisen, ZHAO Dongqi, CHEN Qihong 254
A Differentiable QP-based Learning Framework for Safety-Critical Control of Fully Actuated AUVs
..... JIANG Yongchao, WANG Chenggang, HE Ziqi, SONG Lei 259

Construction of Barrier Surfaces in Mutual Attack-Defense Games
. . . . . XU Jingwen, HE Qiyong, MENG Min, LI Xiuxian 265
Finite-horizon Security-guaranteed Non-fragile H∞Estimation under Integral Measurements
. . . . . LUO Zongjie, YANQIN Wang, DAI Dongyan, HOU Nan, LI Weijian 271
Design of Coordinated Path Tracking Controller for Underactuated Multiple Unmanned Ships
. . . . . WANG Yiyang, ZHANG Yi, WANG Chenqi 279
Fuzzy-based Dynamic Event-triggered Control for Uncertain Nonlinear Systems
. . . . . YAXIN An, LIU Yongchao 284
The Autonomous Flight of an Indoor Quadrotor Using Onboard Vision
. . . . . SHI Ying Jing, LI Rui, ZHOU Chen 290
Output Feedback Predictive Steering Control in Autonomous Driving : an Interval Type-2 T-S Fuzzy-Model-Based Approach . . . . . HU Jinfei, DING Shengsi, ZHANG Changzhu 296
A New BRB-Based Fault Diagnosis Method for Leader-Following Multi-Agent Systems with Communication Interferences . . . . . WANG Ziyi, JI Wenqiang, YANG Ruohan 302
Finite-Time Controller Design for Continuous-Time T–S Fuzzy Systems with Partly Measurable Premise Variables . . . . . ZHANG Shanfeng, ZHANG Kai, WU Yue, CHEN Siyuan, WANG Yang 308
Response Estimation and Reference Model-free Controller Design Approach for 2-DOF Control Systems
. . . . . YANG Ruirui, YUBAI Kazuhiro, KOMADA Satoshi, YASHIRO Daisuke, REN Weijie 314
Optimized State Estimation for Complex Networks with Sensor Fault and Probability-Based Quantization
. . . . . CHU Hongchun, JIA Chaoqing, CHEN Cai, CHI Kun, LEI Tao 319
Fuzzy-based Filtering of Autonomous Vehicle System via Memory-based Event-triggered Mechanism
. . . . . GU Yaxin, ZHAO Weiyi, LIU Xinxin, SU Xiaojie, LIU Jianxing 325
Adaptive Cloaking Region Obfuscation in Road Networks
. . . . . MA Baihe, WANG Xu, JIANG Yanna, LIN Xiaojie 331
Air Supply Control for PEM Fuel Cells under Hamiltonian Framework: A Segmentation Approach
. . . . . KUMAR Lalitesh, CHEN Jian, LI Xinyu, LI Zhongliang 337
Finite-time Shifting Control for LPV Systems with Parametervarying Time Delays via State Feedback
. . . . . HU Yanmei, ZHANG Dandan, LI Shaoyuan 343
Coordination Control of Networked Robotic Systems via A Fully-Actuated System Approach
. . . . . WANG Jiange, TONG Zhang, LI Xiaolei, WEI Yan-Qiao, WANG Yuzhong 349
A Distributed Fixed-Time Optimal Consensus Algorithm over Second-Order Multi-Agent Systems
. . . . . SHI Xiasheng, SUI Tianju 355
Event-Triggered Control of High-Order Fully Actuated Nonlinear Multi-Agent Systems
. . . . . CUI Hailong, ZHAO Guanglei 359
Integral Adaptive Sliding Mode Control for Vehicle Platoon with Disturbance Observer
. . . . . YANG Xin, LIU Cheng-Lin 365
Fixed-time Funnel Sliding Mode Control for Dual-motor Driving System
. . . . . WU Jiameng, LIU Cheng-Lin 371
Specified-time Dynamic Target Autonomous Surrounding Formation for Multi-agent Network: A General Exploring Relationship . . . . . XUE Hao Liang, ZHOU Yuan, ZHAO Yu 377
ADMM-based Privacy-Preserving Peer-to-Peer Energy Trading Negotiation Mechanism
. . . . . GUO Zhenwei, ZHU Jiajian, LI Haoran, ZHENG Haibin, WANG Yujue 383
Formation Control of Discrete-time Multi-agent Systems Based on Distributed Filter Observer
. . . . . GAO Huanli, LI Wei, QIU Ming, CAI He 389

Safety Deep Reinforcement Learning Approach to Voltage Control in Flexible Network Topologies ..... DENG Yaoming, YANG Zaiyue 395
Robust Operation of Distribution Systems with Uncertain Renewable Generation via Energy Sharing ..... YANG Meng, CHEN Yue 401
Influence of Algebraic Connectivity and Out-degree of Leader on Distributed Observer ..... ZHANG Xiaobo, LI Peng 407
Truncated Predictive Containment Control of Input Delay Multi-agent Systems with Coding-Decoding Communication Protocol ..... MING Wu, SUO Jinghui 414
Dynamic Event-triggered Model-free Adaptive Heading Consensus Tracking Control for Unmanned Surface Vehicles ..... ZHAO Huarong, SHAN JINJUN, LI Xing, XIE Linbo 420
Robust Containment Control of Heterogeneous Uncertain Multi-Agent Systems under Markovian Switching Topologies ..... GUO Haihua, BI Cong, XU Xiang 426
Fully Distributed Adaptive State Estimation and Consensus Control of Multi-agent Systems: A Reduced-order Observer-based Approach ..... HUANG Jiazhu, LI Yan, LV Yuezu, JIALING Zhou 432
Method of Spacecraft Cluster Orbital Pursuit-evasion Game Based on the Hierarchical Theory Structure ..... FENG Haolong, WU Songtai, LIU ShengYang, SONG Ting, HAN Fei 438
Distributed Entire State Estimation and Consensus Control for Lipschitz Nonlinear Multi-agent Systems ..... LI Yan, HUANG Jiazhu, LV Yuezu, JIALING Zhou 443
Distributed Air-Assisted Coverage Control for Sensing-Limited Multi-Robot Systems in Time-Varying Environment ..... ZHANG Hang, ZHENG Ronghao, LU Lingxia, ZHANG Senlin, LIU Meiqin 449
Incorporating Steering Constraints in AGV Path Planning Through Graph Augmentation ..... ZHANG Liming, HAN Zhimin, WANG Bo, LIN Zhiyun, XU Xiangdong 455
Containment Control of Fractional-order Nonlinear Multi-agent Systems with Time Delay ..... LI Yanqiu, ZHU Wei, CHEN Bo 460
Dual Filtering Based Decentralized Learning Against Byzantine Attack ..... QING Jiansong, ZHANG Lizong, ZHOU Dongcheng, WAN Jianjun, ZHEN Wei, HE Qiang, LIN Yanjun 466
Relative-Based Finite-Time Formation Stabilization for Multi-Agent Systems via Asynchronous Event-Triggered Approach ..... LUAN Fan, LIN Yanjun 471
Research on Reliability Control for Nonlinear Multi-Agent Systems with Time Delays ..... XING Yang, LIU YiMin 476
Dynamic Gain Scheduling Laplacian-like Output Feedback Control of Linear Multiagent Systems with Input Saturation ..... GAO Xiangyu, CHEN Anlong, WANG Jian-Qiao 482
Multi-Agent Clusters Flocking Control via High-Order Fully Actuated System Approach .... HOU Qimin, WANG Zhenhuan, GAO Yabin, SHANG Hanjun, JIYUAN Kuang, ZHUANG Liu 488
A Blockchain-Enhanced Secure and Reliable Data Transaction Scheme in MAS via HTLC ..... YU Boyuan, GUAN Yichun, GENG Shiyao, MIAO Linlong, ZHANG Yue, GONG Yi 494
Cross-Multi-Agent Systems Identity Authentication Framework on Decentralized Identity ..... XU Zixin, ZUO YuXin, YU Boyuan, ZHANG Yue, GONG Yi 500
A High-Order Fully Actuated Consensus Approach for Strict-feedback Nonlinear Multi-Agent Systems ..... TIAN Congcong, MEI Jie, MA Guangfu 506
Finite-time Consensus for Third-Order Multi-Agent Systems with Directed Communication Networks ..... ZHANG Xirui, ZHAO Zhiliang, LIU Tengteng, JIANG Zhong-Ping 511
Extended Dissipative Sliding Mode Control for T-S Fuzzy Polynomial Singular System ..... LIU Jiarui, LI Jiangrong, ZHU Jiming 517

Actuator Faults Tolerance for Stochastic High-order Fully Actuated Systems
..... LIU Xueqing, SHENG Li, ZHOU Donghua 523
Neural-Network-Based Fault-Tolerant Control for Unknown High-Order Fully Actuated Systems
..... CAI Miao, HE Xiao, ZHOU Donghua 529
Practical Prescribed Time Fault-Tolerant Tracking Control for a Quadrotor UAV: A Solution Based on FASA ..... MA Yonghao, JIANG Bin, ZHANG Ke 534
Fault-Tolerant Control for Uncertain Sub-Fully Actuated Systems
..... GONG Mengtong, SHENG Li, ZHOU Donghua 540
Multidimensional Fault Characterization Model Based Fault Identification for New Type Dissimilar Redundant Actuation System ..... WANG Jun, HUANG Jian, LI Weikang, FENG Yongxing 546
Distributed Observer-Based Failure Compensation Load Frequency Control of Multi-Area Power Systems
.. WEI Jiayu, LIU Jing, HUANG Xin, ZHANG Siyuan, HAN Xinyu, SUN Anping, CHANG Chenxu 552
Design of Hypersonic Vehicle Tracking Controller Based on High-order Fully Actuated System Theory
..... ZHOU Yirong, QI Ruiyun 558
Neural Observer-Based Intelligent Fault-Tolerant Control of Multi-Helicopters under Actuator Faults: A Fully Actuated System Approach ..... MIAO Qiyang, XIA Jingping, JIANG Bin, ZHANG Ke 565
A Fully Actuated System Approach for Interval Observer Design and Fault Detection
..... REN Weijie, DUAN Guangren, KONG He 571
A Novel Trajectory Replanning Method for Autonomous Robots under Actuator Faults
..... LIU Fuqiang, LUO Cheng, NCUBE Sisindisiwe Nomalanga, LI Aoshen, BAI Xiaoshan 577
Fault-tolerant Pursuit-evasion Games for Quadrotor Helicopters Based on a Fully-actuated System Approach ..... XU Jianfeng, XU Yuhang, JIANG Bin 583
Fault-Tolerant Model Predictive Load Frequency Control for Power Systems with Electrolytic Aluminum Load under New Event-triggered Mechanism ..... ZHOU Shisen, WANG Ziqian, WAN Xiongbo 589
Forecasting Method of Process Pump Equipment Based on Grey Theory
..... CHENG Nie, LIU YiMin, CHENG Wen 595
Finite-Time Fault Detection for T-S Fuzzy Systems under Encoding-Decoding Mechanism
..... MA Siteng, HU Jun, WU Zhihui, YU Hui, YU Tianze 603
An Attention-LSTM-based Fault Diagnosis Method for Satellite Attitude Control System
..... MA Siyuan, GAO Sheng, ZUO Xiaozhong, LV Zhengyang, ZOU Chenyang 609
Fault Diagnosis of Rotating Equipment Bearings Based on VMD-MSGWO-SVM
..... DENG Jibao, LIU YiMin, LI Zixuan 614
Fault Estimation and Fault-Tolerant Compensation Tracking Control for Autonomous Underwater Vehicles ..... ZENG Deyu, WANG Limin, CHEN ShouYan 620
A Projection-based Binary Classiffcation Method for Fault Detection of T-S Fuzzy Systems with Multiplicative Faults ..... ZHANG Haili, LI Linlin, YU Qianxiang 626
Distributed Detection for Plantwide Processes with Randomly Occurring Faults
..... SONG Jian, LI Wangyan, BAO Jie 632
Remaining Useful Life Prediction Based on Improved Transformer Network for Pneumatic Control Valve
..... CHENG Yu, CHEN Jianliang 638
Adaptive Event-Triggered Fault Detection of Nonlinear Lipschitz Systems in Finite Frequency Domain
..... CHENG Peng, CAI Chenxiao, LIU Jason Jinrong 644
Fault Detection Based on Operational State Recognition for Wind Turbine Gearbox
..... LIN Wei, DOU Jinzhou, YUAN Linsong, ZHANG Kai 650

Structure and Thrust Fault Detection and Diagnosis for Hypersonic Aircrafts via a Data-Driven Approach ..... ZHANG Chaoyue, HU Qinglei, HAN Tuo 656
Intelligent Decision-Making for Maintenance Assurance Throughout the Lifetime of Helicopter Swarms ..... WANG Yanan, ZHANG Ke, JIANG Bin 662
Robust Control of Single-Link Flexible-Joint Manipulators with Perturbed Inertia Based on Fully Actuated System Approach ..... ZHANG Shiyu, DUAN Guangren 668
Robust Bounded-H∞Control for High-Order Fully Actuated Systems Based on FAS Approaches ..... HU Liyao, DUAN Guangren 674
Differentiator-Based Adaptive H∞Tracking Control of Fully Actuated Systems ..... FENG Yuxin, LI Zhiqiang, LIU Yang, HE Zhaoshui, LI Hongyi 680
Active Disturbance Rejection Control of Hydraulic Turbine Based on Fully Actuated System Theory ..... LV Lingling, YANG Delong 685
Sampled-Data H_∞ Control for High-Order Fully Actuated Systems Based on A Local Lipschitz Condition ..... WANG Tingrui, GAO Zifan, ZHANG Dawei 691
Tracking Control and Obstacle Avoidance of Quad-rotor UAV Based on High-Order Fully Actuated System Approach ..... SHI Yankui, WANG Runze, TONG Ruizhi, ZENG Yi 695
Adaptive Deep Neural Network Sliding Mode Control for UAVs ..... CHEN Zhang, XU Jing, LI Fanbiao, NIU Yugang 701
Robust Control for DC-DC Buck Converters Based on Fully Actuated System Theory ... LI Fangyuan, LIU Guangxin, SHEN Xiaoning, LI Cheng, LIN Xinpo, GAO Yabin, LIU Jianxing 707
Disturbance Observer-Based High-Order Fully Actuated Robust Control of Uncertain Robotic Systems ..... ZHU Fuxing, ZHAO Yue, ZHUANG Liu, YAN Fei, LIU Jianxing 713
Finite-time Stability Analysis of Switched Systems under Time-dependent Switchings ..... WU Jie, YANG Rongni 719
Preview Tracking Control of the SIR Model with Saturation Incidence Rate ..... WANG Chenqi, LI Yuan, ZHANG Yi 725
Exponential Stability and Asynchronous Stabilization of Impulsive Switched Systems with Admissible Edge-dependent Average Dwell Time ..... LI Mengjie, QU Menghao, LIJUN Gao 731
A Brief Survey on Complex Networks Synchronization Control with Limited Bandwidth ..... GUO Jing, HUANG Ling 737
Event-triggered Bounded Synchronization Control for Heterogeneous Complex Networks ..... WANG Zhentao, HUANG Ling, WANG Yunfei, LI Bing 743
Reachable Set Estimation of Singular Markovian Jump Systems via State Decomposition Method ..... WANG Qingxiang, GUOWEI Zhao, FENG Zhiguang 749
Observer-based Stabilization for Networked Interval Type-2 Fuzzy Semi-Markov Jump Systems with Cyber Attacks ..... LI Runkun, QI Wenhai 753
Coding-Decoding-Based Sliding Mode Control for Discrete Uncertain T-S Fuzzy Systems with Time-Varying Delays ..... ZUO Zhiyuan, HU Jun, ZHANG Hongxu, LIN Na, ZHOU Aozhan 758
The Reachable Set Estimation for Continuous-time Delayed Nonlinear Switched Systems with Impulsive Perturbation ..... GUO Qingzheng, FENG Zhiguang 764
A Real-time Event-Based Learning Approach for Input-Output Sensitivity Analysis ..... SHE Xingjing, GENG Hang, GOU Xuan, CHEN Kai 770
An INS/GNSS Localization Method Based on Set-Membership Filter for Unmanned Aerial Vehicles ..... QIN XuJie, LAI Jun, CONG Yirui, WANG Xiangke 775

Robust Kalman Predictor under Linearly Correlated Noise and Mixed Uncertainties of Noise Variances and Multiple Networked-inducements ..... ZHAO Ying, YANG Chunshan, ZHENG Liu, WANG Jianqi, WANG Xuemei, TAO Guili 780
Distributed Fusion Estimator for Networked Multi-rate Multi-sensor Systems with Unknown Inputs ..... LIU Qiang, LIN Honglei 786
A Novel Particle Filter Based on One-Step Smoothing for Nonlinear System with Missing Measurements ..... YANG Zhenrong, ZHANG Xing, XIAO YuShan 792
Obervability Analysis for Space Target Sequential-Image Relative Navigation System with Fully-Actuated System Control ..... HOU Bowen, WANG Dayi, DONG Tianshu, WANG Jiongqi 798
Energy-aware Trajectory Optimization for UAV-enabled Wireless Powered WSN ..... QIU Feihang, GUO Jing, DIAO Huineng, ZHANG Xu 804
Innovation-trigger-based Sequential Fusion Kalman Filter for CPSs with Multiplicative Noises Against Deception Attacks ..... ZHENG Baifu, ZHANG Xuenan, GAO Yuan, LIU Jinfang 809
Optimal Reduced-order Filter for Systems with Deterministic Observations and Stochastic Observations ..... GAO Yuan, SUN Shuli, GAO Yuan 815
Prompt Engineering Approach Study for Supervised Fine-Tuned (SFT) Large Language Models (LLMs) in Spacecraft Fault Diagnosis ..... XIA Qing, ZHAO Haotian, LIU Ming 819
Optimal Fuel Solution to the Lambert Problem under Complex Perturbation Conditions Based on BP Neural Network ..... WU Wenbin, ZHANG Qian, TAN Minglang, ZHONG Yini, YUAN Ronghao 825
Synchronization for Singular Neural Networks with Finite Time Characteristic under Event-triggered Scheme ..... WU Yifan, ZHU Jingjuan, PANG Yujing, FU Yanran, HAO Mengjuan, MENG Yanan, ZHUANG Guangming 831
State-of-Health Estimation of Lithium-ion Batteries Based on CNN-LSTM-Attention ..... DING Dong, MAO Songheng, FAN Yuan 837
Backdoor Attack and Defense in Asynchronous Federated Learning for Multiple Unmanned Vehicles ..... WANG Kehao, ZHANG Hao 843
Traffic Signal Control for Large-Scale Road Networks Based on Deep Reinforcement with PSR ..... ZHOU Zhicheng, ZHANG Hui, ZHANG Ya 848
A Multi-scale Adaptive Label Assignment Neural Network Architecture for Brake Disc Surface Defect Detection ..... WANG Shaoquan, ZHANG Guoshan, GUAN Bin 854
Depth Guided Fast Rendering Neural Radiance Field ..... ZHANG Tao, WANG HAOQIAN 860
Navigating the Accuracy-Privacy Dilemma in Load Forecasting with Noisy Data ..... GUO Cheng 868
A Parameter Correction Method of Motor System Based on Particle Swarm and Convolutional Neural Network ZENG Depeng, HONG Junjie, HAN Liangheng, ZHANG Kun, REN Yueru, WANG ZunHeng 873
Deep Reinforcement Learning-Based Scheduling Optimization of a Wind-solar Coupled CHP Unit System Considering Source-load Uncertainty ..... WANG Baohua, GAO Xinglong, WANG Xianlian, WANG Zhixiao, SUN Li, HUA Shan 879
Interpretable Fourier Neural Ordinary Differential Equations ..... BIAN Hanlin, ZHU Wei, CHEN Zhang, LI Jingsui, PEI Chao 885
Trajectory Tracking Control of CNC System Based on RBF Neural Network Composite Learning Control ..... HU Zhiyu, XU Juncheng, LI Jiangang 891
Dynamic Region Detection and Removal Based on Deep Learning and Optical Flow ..... FAN ShiXiong, QIAN Mengmeng, MAO Songheng, LIU Aoqiang, FAN Yuan 897
A Shape Reconstruction Method for Space Continuum Robot Based on Neural Network ..... WANG Guopeng, YAN Yuchao, LI Zuan, LI Yuntao, XIONG Liang, FEI Han, XINPENG Di 903

A Research on Rapid Assessment of Cross-Domain Perceptual Fidelity for Practical Applications ..... TAO Wenguang, WANG Xiaotian, YAN Tian, LI Guodong, ZENG Qingjie, LU Ruitao 909
Adaptive Neural Network Control for Uncertain Strict-feedback Nonlinear Systems with Unknown Control Coefficients: A Fully Actuated System Approach ..... YE Yueyao, FAN Debao, ZHANG Xianfu 915
Static Output Feedback Control Design for Nonlinear Descriptor Systems with Actuator Saturation ..... ZHANG Yabo, SUN Liying 921
Disturbance Observer-based Nonlinear Control for Underactuated Bridge Cranes: High-order Fully Actuated System Approach ..... ZHOU Xiaoshuang, YANG Yana, HUA Changchun, LIU Guopin 926
Formation Control of Under-actuated Multi-robot Vehicle Systems Based on High-order Fully Actuated Systems Approach ..... ZHAO Guanglei, LUO Lu, WANG Peng, HUA Changchun 932
Aircraft Middle and Final Stage Attitude Control on Fully Actuated System Theory ..... LIU Xinyu, HAO Mingrui, FAN Yu, ZHEN Yan, SUN Wendi 938
Global Prescribed Performance Control for Nonlinear Interconnected Systems: A High-order Fully Actuated System Approach ..... ZHANG Yu, LIU Guopin, HUA Changchun, YANG Yana 945
ESO-based Trajectory Tracking Control of a 7-DOF Manipulator: A High-Order Fully Actuated System Approach ..... LIU Yanling, ZHANG Jialong, ZHANG Yahui, TAN Zhao, SUN Yingbing, ZHAO Haohan, WEN Guilin 951
Algebraic Differentiator Based Fractional Order Controller by High-order Fully Actuated System Approach ..... WEI Yan-Qiao, WANG YanHai, LIU Da-Yan, HUA Changchun 957
Angle Attitude Control for Motion Platform Driven by Pneumatic Muscle Actuators ..... CAO Yipeng, LI Li, LIU Chao, QIANG Jiaping, ZHANG Cui-Hua 962
Observed State-Dependent Adaptive Control for Thermoacoustic Instability in Aeroengine Oscillating Combustion with Unknown Thermal Inertia ..... ZHAO Yuzhuo, MA Dan 968
Robust Prescribed-Time Global Control for the Elliptical Orbital Rendezvous System: A Fully Actuated System Approach ..... LI Shunli, DUAN Guangren 974
Fully Actuated System Approach-Based Adaptive Event-Triggered Control for Nonlinear Switched Systems ..... YAN Chengyuan, XIA Jianwei, SUN Wei 980
Adaptive Fixed-Time Control for High-Order Fully Actuated System with Input Saturation ..... WANG Ping, DUAN Guang-Ren 986
DC-Link Voltage Control of Three-Phase AC/DC Converters with Current Constraints ..... FU Cheng, ZHANG Zicheng, CHANG Le, ZHANG Guanguan 993
Integrated Guidance and Control Design Subject to Actuator Saturation Based on Fully Actuated System Approach ..... YANG Lin, LI Yuanlong 998
Planned Fully Actuated Attitude Control Strategy for Flexible Spacecraft ..... WANG Dian, WU Yunhua, MA Song 1004
Robust Multi-mobile Robot Formation Control: A Fully Actuated System Control Approach ..... LIU Zhihao, LI Peng 1011
Sliding Mode Control for Tower Crane with Double Spherical Pendulum and Variable Cable Length ..... LI Gang, MA Xin, LI Jing, LI Yibin 1017
Dynamic Modeling and Analysis of Wafers in Near-field Acoustic Levitation ..... WANG Lipeng, JIANG Wu, PAN Chengqi 1023
An FASA Based Fixed-Time Sliding Mode Control for Robotic Manipulator ..... ZHANG Yu, MENG Fan-wei, LI Bin 1029
The Robust PI Control of A Magnetically Levitated Planar Motor with Output Constrains ..... CHEN Xiang, NA Tuopu, MA Chenglong, NING Lei, ZHAO Bo 1035

Wave Motion Compensation Controller Design for a Catamaran Upper Platform in the Presence of External Disturbances ..... SHEN Junyu, YIN Rongji, YU Yao, ZENG Rijie, HU Zhihuan, ZHANG Weidong, LU Jinhui, XIE Wei 1041
Adaptive Tracking Control for State-Constrained Fully Actuated Systems And Its Application to Overhead Cranes ..... GAO Yang, ZHANG Zhongcai, HUANG Peng, WU Yuqiang 1046
Prescribed-Time Stabilization of Switched Nonholonomic Systems with Asymmetric Constraints ..... LI Siquan, MAO Xujing, SHANG Yanling, GAO Fangzheng, HUANG Jiacai 1050
Sliding Mode Based Incremental Tracking Control of High-Order Fully Actuated Systems with Application ..... YU Miao, HOU Mingzhe, TAN Feng 1055
High-Order Sliding Mode Control for Flexible Servo Systems Using Fully Actuated System Approaches ..... WANG Yuzhong, DUAN Guangren, LI Ping 1061
A Fully Actuated System Approach to Control of the 3D Cubli: Theory and Experiments ..... LIU Zhijie, YAO Fuxing, DUAN Guangren, KONG He 1066
Stabilization Control of Second-order Nonholonomic System with High-Order Fully Actuated System Approach ..... PAN Qi, PENG Xiuhui, WANG Xueyan 1072
Fully-Actuated Sliding Mode Synchronization Control for H-type Linear Motor System ..... LI Xiaolei, TANG Feilong, LIU Jiawei, XIANG Zhihua 1078
Prescribed-Time Tracking Control for Autonomous Underwater Vehicles ..... JIANG Shihui, FANG Jing, LIU Xing, YANG Jinhong, HAO Liming 1084
Stackelberg Differential Game-based Hierarchical Approximate Optimal Interaction Control of Human-Centered Reconfigurable Robot Manipulator Systems ..... AN Tianjiao, YAN Haoyu, MA Bing, HUCHENG Jiang, DONG Bo 1089
Tracking Ability of High-Order Fully Actuated Iterative Learning Control ..... ZHANG Zeyi, JIANG Hao, SHEN Dong 1095
Robust Adaptive Control for a Class of Nonlinear Uncertain HOFA Systems with Actuator Attacks ..... QIN CunFu, WANG Xiao, ZHAO Ping 1101
Adaptive Iterative Learning Control for Permanent Magnet Synchronous Motors with Uncertainties ..... KE Yang, LI Xuefang 1107
Hierarchical Robust Control for Unmanned Quadrotor Transportation Systems: Exploiting Beneficial State-Coupling ..... HAN Lincong, ZHANG Menghua 1113
Model Reference Adaptive Control for Multi-variable Systems Using Available Signal for Feedback ..... SANG Yingli, ZHANG Zhengqiang 1118
Mitigation of Distribution Transformer Overloading with Rolling-Horizon Optimization of Vehicle-to-Grid Resource ..... XIA Lin, HONG Xiao, SUN Xiaowei, LI Qingxue, WU Hao, HUO Yingning, GENG Guangchao 1123
A Learning Controller for Periodic Disturbance Rejection of Uncertain Nonholonomic Systems ..... LIU Li, ZHAO Yan, YU Jiangbo, WANG Chunxiao, YU Xiao 1129
Adaptive Fixed-time Fault-tolerant Control of Nonstrict-Feedback Nonlinear Systems ..... WU Jing, XING Lantao 1134
Bias-Policy Iteration Based Adaptive Dynamic Programming for Linear Fully Actuated Systems ..... JIANG Huaiyuan, YANG Xuefei, XU Chuanchuan, ZHANG Kangkang 1140
UUV Trajectory Tracking Control Based on Gaussian Process Model Predictive Control ..... YAN Xiaoming, LIU Yang 1146
Low-cost adaptive obstacle avoidance trajectory control for express delivery drone ..... ZHANG Yanhui, ZHANG Yi Fan, TONG Zheyu, YANG Hua, WEI Caisheng, CHEN Weifang 1152

Adaptive Dynamic Programming-based Self-triggered Optimal Control for Nonzero-sum Games of Nonlinear Systems with Constrained State ..... ZHI Gan, SU Hanguang, WANG Rui, MA Dazhong 1158
Reinforcement Learning Control for a 2-DOF Flight Attitude Simulator
..... CAI Yu, BAN Xiao Jun, ZHOU Chengbao 1164
Adaptive Iterative Learning Control for Underactuated Systems with Unknown Input Distribution Matrices: Ensuring Input Continuity ..... YIN Mali, LI Xuefang 1170
Adaptive Neural Network Sliding Mode Vibration Control for Clamped Beam Systems with Input Saturation and Model Uncertainties ..... LI Shilun, LIN Xiaohan, WANG Jun, QU ChuanKun 1176
Adaptive Dynamic Programming and Blockchain Technique-Based Smart Home Energy Management
..... ZENG Chujian, ZHAO Bo, LIU Derong 1182
Dynamic SLAM Based on Neural Network and Depth Information
..... LIU Aoqiang, YANG Shu, FAN Yuan 1187
High-order Fully Actuated Approach for Output Position Control of Two Mass Systems Based on Extended State Observer ..... LI Ping, DUAN Guang-Ren, ZHANG Bi, WANG Yuzhong 1193
Tracking Control of Motion Control Systems with Disturbance Observer Based on High-order Fully Actuated System Approach ..... LI Rongmei, HUO Xin, WU Aijing, LIU Weizhen 1199
Gait Stability Control of Quadruped Robot by Composite Nonlinear Feedback and Model Predictive Control ..... XU Jiang, PENG Xiafu, YU Xiao, LAN Weiyao 1204
Attitude Control of a Three-Cable-Driven Parallel Robot for Full-Mode Chattering Wind Tunnel Tests
..... ZHAN Lei, QI Lin, LAN Weiyao 1210
Modeling, Simulation and Experiment of an Origami Robot with a Coupled Bar-hinge Mechanism
..... MAI Junpeng, SHAO Hanzhao, LIU Shaojie, ZHANG Yuan Zhuo, CHEN Liangming, FENG Huijuan 1216
Fault Estimation for Unmanned Surface Vehicles Based on Adaptive Observer
..... GAO Feng, CHEN Liheng 1222
Research on Unmanned Surface Vessel Intrusion Evasion Strategy Based on Deep Reinforcement Learning
..... WU Chang Mao, CHEN Liheng 1228
Path-following Control of Autonomous Tugs Based on Gaussian Process Regression and Arithmetic Optimization Algorithm ..... LI Shijie, LI Yang, HU Xinjue, LIU Jialun, WEI Muheng 1234
Development and Verification of Semi-physical In-loop Real-time Control Experimental Platform for Harsh Sea Condition Floating Body Salvage
..... ZHAO Xiaoning, SUN Yougang, ZHIQIANG Xu, HE Zhenyu 1242
Trajectory Tracking of Differential Driven AGV Based on Kalman Filter and Model Predictive Control
..... XU Zhihao, JIANG Yue, PENG Kai, WANG Hongxia 1247
Robust H_∞ Synchronization for Networked Re-Entrant Manufacturing Systems
..... LIU Chenguang, GAO Qing, WANG Wei, LU Jinhu 1253
Structural Design and Kinematic Analysis of Fully Automated Material Handling Robots for Warehouse Logistics ..... ZHAO Runchen, DU Haibo, SUN Xunhong, ZHU Wenwu 1259
Identification Algorithm of Industrial Dryers Based on Subspace
..... DING Ning, MA Jianwei, LI Jiangrong 1265
Model Predictive Path Integral Control of a Temperature Profile in Tubular Chemical Reactor with Recycle ..... AI Ling, YINGWEI Chen, XU Yang, XUEQIN Chen, TEO Kok Lay 1271
Distributed Fault Detection Scheme for Snake Robot Platoon
..... WANG Qin, HUANG Darong, NA Yuhong, ZHOU Yunhu 1277

Distributed Secondary Control for DC Microgrids Leveraging a Fully Actuated System Approach
..... DAI Xiaoran, LIU Guoping, HU Wenshan, LEI Zhongcheng, ZHOU Hong, JUN Zhang 1283
A Method for Multi-snake-like Robot Formation Control and Cooperative Obstacle Avoidance
..... PANG Yunbo, HUANG Darong, NA Yuhong, ZHOU Yunhu 1288
Ship Energy Efficiency Prediction Method Based on Data Mining Techniques
..... CHENG Nuo, CHEN Liheng, ZENG Depeng 1294
Circular Phased Array Ultrasonic Transducer Design for Internal Inspection of Natural Gas Pipeline
..... QI ZhongWei, LIAO MingYan, SHENG Li, CHEN Zhongyu, NIU Yichun 1299
Intelligent Warehouse Multi-robot Scheduling System Based on Improved A* Algorithm
..... WANG Ao 1305
Intention Recognition Algorithm for Multi-agent Systems Based on High-order Fully Actuated System Approach ..... DU Qinlong, HUO Xin, ZHOU Dianle, ZHENG Kai, LI Rongmei 1311
Optimization Strategy for Wind-Solar Complementary Energy Storage Capacity Leveraging Photovoltaic Virtual Energy Storage ..... JIAHUA Ni, CHEN Yuwei, TONG Wang, JIN Wei 1317
Optimizing Hybrid Energy Storage in Offshore Wind Farms with a Focus on Extending Storage Life
..... CHEN Yuwei 1323
Partially Observed Optimal Control with Correlated Noises
..... LI Zhipeng, FU Minyue, ZHANG Huanshui, ZHANG Zhongcai 1328
Adaptive Coverage Path Planning of Marine Vehicles with Multi-Sensor
..... ZHANG Zheng, WANG Peng 1334
Pricing Frequency Ancillary Services for Low-Inertia Power Systems under Model Nonconvexity
..... LI Zhihao, XU Yinliang 1340
Neural-Network-Based Nonlinear Model Predictive Control of Suspension Gravity Offload System
..... YAN Huixing, LU Hongqian, WANG Hanyu, ZHANG Zhen, HUANG Xianlin 1346
Model Predictive Control for Attitude Tracking of Rehabilitation Exoskeleton Robots
..... WANG Zheming, WANG Bin, ZHOU Yuan, CHEN Ming, CHEN Bo, ZHANG Jiyu 1352
An Improved Model Predictive Control with Neutral-point Voltage Balancing and Common-mode Voltage Suppression for Three-level T-type Converters
..... HAN Xiaomin, ZHANG Hongliang, MA Yuying, WU Huiqing 1358
Simplified Double-vector Finite Control Set Model Predictive Control for LCL-filtered T-type Inverters with Active Damping ..... LIU Bei, XING Xiangyang, LIU Chang 1364
Fully-actuated Robust Predictive Control for Cascaded Under-actuated Systems
..... WANG Xiubo, DUAN Guangren 1370
A Prioritized Replay Safe Soft-actor Critic (PR-sSAC) Deep Reinforcement Learning for Real-time Energy Dispatch of Integrated Energy Systems. ..... ALABI Tobi, YANG Zaiyue 1376
Predictive Path-following Control for Tilt-quadrotor UAV Based on Fully-actuated System Approaches
..... XU Lixue, WANG Xiubo, HE Ping, WANG Yan 1382
Robust Model Predictive Control for Trajectory Tracking of Robotic Manipulators Based on Fully Actuated System Approach ..... YANG Yi Heng, ZHANG Kai, CHEN Zhihua, LI Bin 1388
Fixed-time Attitude Control and Active Vibration Suppression for Flexible Spacecraft Based on the Fully-actuated System Approach ..... LIU Kerun, LIU Ming, LI Huayi 1394
Active Disturbance Rejection Controller with Variable Control Gain for Aero-Engine
..... LIU Shuheng, YU Liang, FEI Zhongyang, ZHANG Wenbo 1400
Multi-Spacecraft Adaptive Tracking Control with Collision Avoidance Based on Fully Actuated System Approach ..... ZHANG Xiaoxiang, GENG Yunhai, WU Baolin 1406

Unwinding-Free Attitude Control via Fully Actuated System Approach
. . . . . XIAO Fu-Zheng, CHEN Li-Qun 1412
Reinforcement Learning-based Three-dimensional Cooperative Guidance Law
. . . . . GU Zhen, ZHANG Zeqi, KANG Honglong, LI Jianfeng, YUE Keyuan, SONG Shenmin 1418
Optimal Control Method for Deployment and Retrieval of Transverse Formation Satellite-Sail Systems
. . . . . ZHONG Yini, TAN Minglang, ZHANG Qian, WU Wenbin, YUAN Ronghao 1424
Research on Algorithm Design and Code Automatic Generation for Satellite Attitude Planning
. . . . . LUO Zhouhuai, YUAN Ronghao, XIAOKUN Liu, ZHANG Qian, JIN Yang 1430
Non-Cooperative Target Approach Strategy Design Based on Bearing-only Measurement
. . . . . LI Yinkang, LIU Weixing, XIAOKUN Liu, CHEN Xiaoran, JIN Yang 1435
An Status-deformation Cooperative Control for Morphing Vehicle
. . . . . ZHENG Wenquan, TIAN Ye, YE Saixian, JIN Yihuan, LIU Lu 1441
A Method of Lunar Autonomous Driving Perception Planning Based on Hybrid A*
. . . . . HU Tao, CAO Tao, ZHENG Bo, QIAN Zhouyuan, HAN Fei, HE Liang 1447
Robust Tracking Control for A Type of Combined Spacecraft: A Discrete-Time FAS Approach
. . . . . CUI Kaixin, DUAN Guangren 1453
Sliding-Mode Disturbance Observer-Based HOFA Predictive Control of Spacecraft Flying-Around
. . . . . ZHANG Da-Wei, LIU Guoping 1459
Safety-Critical Control in Multi-Spacecraft Specific Tracking of Rotating Target Based on Fully Actuated System Models . . . . . LIN Zijie, WU Baolin, CHEN Junyu, SUN Zhaobo 1465
Longitudinal Active Load Relief Control of Launcher Based on Fully-Actuated System Approach
. . . . . ZHANG Feng, CHEN Haipeng, WU Shengbao 1471
Predefined-time Based Tracking Control and Formation Control for Hypersonic Flight Vehicles
. . . . . WANG Dinghua, WANG Jie, YUAN Jicheng 1475
Disturbance Separation-Based Antidisturbance Attitude Control for Flexible Liquid-Filled Spacecrafts
. . . . . ZHU Baopeng, TENG Hao, MENG Yan, ZHU Yukai 1480
Research on Fixed-Time Convergence of Multi-Missile Cooperative Terminal Guidance Law
. . . . . LIN Jiakuo, CHENG Pengfei, SI YuJIe, WANG Changqing, GUO Yong 1486
Data-driven Control Design for UAV Autolanding: a Pitch-only Case Study . . . . . HU Tianjiang 1493
Sliding Mode Control for Helicopter Systems Based on Fully Actuated Method
. . . . . LI Yankai, XU Jinyu, XUE Xiaohui, YI Yingmin, SHAO Shuyi 1498
Attitude Control of Hypersonic Vehicle Based on Reinforcement Learning
. . . . . LIU Jingwen, FAN Hongdong, FAN Yong Hua, CAI Guang-Bin 1503
Global Stabilization of Circular Orbit Rendezvous by Bounded Linear Feedback
. . . . . LUO Weiwei, FU Wenbo, ZHU Song, XU Chuanchuan 1508
Fault-tolerant Attitude Tracking Control of Combined Spacecraft with Actuator Saturation Based on Fully-actuated System Approach . . . . . HUANG Xiuwei, YANG Peng, LIU Zhen, AN Li, WANG Hao 1513
A Novel Rolling Takeoff Flight Control for Fixed-Wing Unmanned Aerial Vehicle
. . . . . LIU Wangkui, WANG Xiangyu, SHUI Zunshi, CHEN Zhihua, QIU Huabing, YANG Xuefei 1520
Input Saturation Control of Manipulator Based on Fully Actuated System Approach
. . . . . XIAO Yongqiang, CAI Guang-Bin, HOU Mingzhe, YAN Xunliang 1526
Adaptive Attitude Tracking Control of Spacecraft Based on High-Order Fully Actuated System Approach
. . . . . JIN Dongyan, HOU Mingyu, WANG Tong, QIU Jianbin 1532
Robust Attitude Control of a Tilt Trirotor in VTOL Mode
. . . . . LIN Zemin, LIAN Shikang, MENG Wei 1538

High-order Fully-actuated System Approach Based Fault-tolerant Attitude Tracking Control via Extended State Observer ..... JIA Shixiang, JIN Yang, WANG Tong, QIU Jianbin 1543
Fully Actuated Control for Directional Accuracy in Multiaxis Antennas Utilizing Sliding Mode and STESO Observers ..... GAO Feng, LI Jiayang, DENG Heng, SUN Guanghui 1549
High-order Fully Actuated System Approach for a 3-DOF Quadrotor Control Based on Extended State Observers ..... LU Shi, TSAKALIS Konstantinos, CHEN Yan 1555
A Practical Method for Quadrotor Modeling and Parameter Identification ..... LING Tianwei, LI Rui, SHI Ying Jing 1561
High-order Fully-actuated Controller Design for a Dual-Quadrotor Suspension System ..... JIANG Zhipeng, LI Xianwei 1568
Terminal Angle Constrained Three-Dimensional Disturbance Rejection Guidance via an Incremental Twisting Algorithm ..... HU Jintao, HU Qinglei, HAN Tuo 1574
Predefined Time Sliding Mode Attitude Tracking Control for Rigid Spacecraft Based on Fully Actuated System Method ..... ZHENG Yin, ZHANG He, WANG Yan 1579

Proceedings of the 3rd Conference on Fully Actuated System Theory and Applications
May 10-12, 2024, Shenzhen, China

H_∞ Consensus Control for High-Order Fully Actuated Multi-Agent Systems with External Disturbances

Qing-Hao Zhang[1,2,3], Jun-Guo Lu[1,2,3,*]

1. Department of Automation, Shanghai Jiao Tong University, Shanghai, 200240, China

2. Key Laboratory of System Control and Information Processing, Ministry of Education of China, Shanghai, 200240, China

3. Shanghai Engineering Research Center of Intelligent Control and Management, Shanghai, 200240, China
E-mail: zhangqinghao@sjtu.edu.cn, jglu@sjtu.edu.cn

Abstract: This paper investigates the problems of H_∞ consensus control for high-order fully actuated multi-agent systems (HOFAMASs) with external disturbances. By utilizing the characteristics of high-order fully actuated systems (HOFASs), the distributed control protocols are designed, eliminating all nonlinear characteristics of open loop systems while establishing new closed-loop dynamic characteristics. Then, the H_∞ consensus problems of HOFAMASs are addressed. The corresponding parameters to be designed in the distributed control protocols are given by using linear matrix inequalities (LMIs). A novel multi-spacecraft attitude model is proposed based on HOFASs. An illustrative example of the multi-spacecraft attitude model is given, in order to demonstrate the effectiveness and application of the results proposed in this paper.

Key Words: High-order fully actuated system, multi-agent system, H_∞ consensus control, multi-spacecraft attitude model

1 Introduction

With the rapid development of industrial demand, modern control systems are becoming more and more complex and highly distributed. In this promotion, the multi-agent system (MAS), which consists of a set of connected agents, is regarded as a powerful system architectural to deal with these challenging problems. The MASs have attracted considerable research attention and have been widely applied in multi-spacecraft systems, multi-AUV systems, battery systems and so on [1–3].

Consensus control is one of the important topics in the cooperative control field of MASs. Moreover, owing to the modeling and measurement errors [4, 5], external disturbances widely exist in MASs [6]. For MASs with simultaneous actuator and sensor faults, the H_∞ control protocol is proposed by applying the static output-feedback design technique in [7]. When MASs are with simultaneous communication delay, random packet dropout and external disturbances, sufficient conditions for the H_∞ consensus are developed in terms of LMI form in [8]. In order to tackle the satellite attitude tracking filtering problems, the distributed H_∞ consensus filters are given to to ensure the optimal H_∞ consensus disturbance rejection attenuation performance in [9]. For guaranteed-cost H_∞ consensus problems for nonlinear MASs, a distributed event-triggered controller is designed in [10] by using the Lyapunov function method. For discrete-time fractional order MASs with external disturbance, different consensus protocols involving finite-dimensional memory for state and output feedback are given in [11] based on the Lyapunov function and Q-learning approach.

However, most of the aforementioned significant developments in the consensus control, especially H_∞ consensus control, of MASs are based on the first-order state-space approach [12]. When the first-order state-space approach is used to model the agents of MASs, the physical background information of the agents is lost because most practical systems are essentially second-order or high-order models after modeling using physical laws such as Theorem of Linear and Angular Momentum, Newton's Law, and so on. Recently, HOFASs have drawn great attention. HOFASs become general models for control systems if this concept is mathematically generalized [13–16]. Most nonlinear systems can be naturally modelled or converted into HOFASs as long as they satisfy a certain kind of controllability property [17, 18]. For the control design of nonlinear systems, the type of HOFASs is relatively simple because the controllers can be immediately written out for HOFASs and eventually obtain the constant linear closed-loop systems. Thus, applying HOFASs to model the agents of MASs can not only truly reflect the background information of MASs, but also be more convenient for designing consensus control protocols. In [19], the coordinated control of discrete-time HOFAMASs is investigated and a predictive control strategy is proposed to realize the simultaneous stability and output consensus. However, the external disturbances are not considered in [19] and the H_∞ consensus of continuous-time HOFAMASs is one of the important problems urgent to be studied.

Motivated by the above facts, the H_∞ consensus of continuous-time HOFAMASs is researched in this paper and the main contributions can be summarized as follows:

(1) The H_∞ consensus problems of continuous-time HOFAMASs are addressed based on the bounded real lemmas and inequality techniques. For HOFAMASs with the undirected graph, the sufficient and necessary condition for the H_∞ consensus is given and the distributed control protocol is established.

(2) Inspired by [20], the second-order fully actuated continuous-time system is applied to model spacecraft attitude control systems and extended to multi-spacecraft attitude nonlinear systems. Then, the HOFAMASs are obtained and the H_∞ consensus distributed control protocols are given based on the proposed methods in this paper.

The work of this paper is supported by the National Natural Science Foundation of China (No. 62303309 and No. 62073217).

* Corresponding author

The rest of this paper is as follows. The description of HOFAMASs and some preliminaries are given in Section 2. The distributed control protocol is established in Section 3d. In Section 4, a numerical example is given. Section 5 concludes this paper.

2 Preliminaries and Problem Formulation

Notations: $\mathcal{G}_u = (\mathcal{V}, \epsilon, \mathcal{A})$ represents the undirected graph, in which $\mathcal{V} = \{1, 2, \cdots, N\}$ is the nodes set of N agents, $\epsilon \subseteq \mathcal{V} \times \mathcal{V}$ is the edges set and $\mathcal{A} = [a_{ij}] \in \mathbb{R}^{n\times n}$ is the adjacent matrix. (i, j) is an edge of $\mathcal{G}_u$. $\mathscr{N}_i$ is the neighbor of node i. For the undirected graph $\mathcal{G}_u$, $(i, j) \in \epsilon$ is equivalent to $a_{ij} = a_{ji} = 1$, otherwise $a_{ij} = 0$. If $i = j, \forall i \in \mathcal{V}$, then $a_{ii} = 1$ if the node i knows its own state information; $a_{ii} = 0$, otherwise. $\mathscr{L} = [l_{ij}] \in \mathbb{R}^{n\times n}$ represents the Laplacian matrix of $\mathcal{G}_u$ and $l_{ii} = a_{ii} + \sum_{j\in\mathscr{N}_i} a_{ij}$, $l_{ij} = -a_{ij}$, for $i \neq j$. For a node i in the undirected graph $\mathcal{G}_u$, if there exists at least a path such that this node could reach any other node, then the graph $\mathcal{G}_u$ is connected. $\otimes$ is the Kronecker product. Λ^T represents the transpose of matrix Λ. $\bar{\sigma}(\Lambda)$ is the maximum singular value of matrix Λ. $\mathrm{Sym}\{\Lambda\}$ represents $\Lambda^T + \Lambda$. $\det(\Lambda)$ is the determinant of matrix Λ.

Assumption 1. *Assume that the undirected graph $\mathcal{G}_u$ is connected and has at least one node knowing its own state information.*

Consider the following HOFAMAS

$$\begin{aligned} x_i^{(n)} =& f_i(x_i^{(0\sim n-1)}) + G_i(x_i^{(0\sim n-1)})u_i + Bw_i, \\ z_i =& Cx_i^{(0\sim n-1)},\ i = 1, 2, \cdots N, \end{aligned} \tag{1}$$

where $x_i \in \mathbb{R}^r$, $u_i(t) \in \mathbb{R}^r$, $w_i(t) \in \mathbb{R}^p$, $z_i(t) \in \mathbb{R}^q$ are the state vector, the control input, the exogenous input and the measured output of $i-$th agent, respectively. $f_i \in \mathbb{R}^r$ represents a continuous vector function. $G_i \in \mathbb{R}^{r\times r}$ represents a continuous matrix function satisfying $\det(G_i) \neq 0$. $B \in \mathbb{R}^{r\times p}$, $C \in \mathbb{R}^{q\times nr}$ are real constant matrices. n is an integer and $n \geq 1$. $x_i^{(0\sim n-1)} = \begin{bmatrix} x_i & \dot{x}_i & \cdots & x_i^{n-1} \end{bmatrix}^T$.

Remark 1. *The condition $\det(G_i) \neq 0$ implies that each agent in system (1) is a HOFAS. It should be emphasized that the HOFAS is a general model for control systems if this concept is extended in mathematics [13–16]. Many typical systems, such as affine systems, strict feedback systems and interconnected systems, can be converted into HOFASs as long as they satisfy a certain kind of controllability property [17, 18]. Compared with the first-order state-space models, one of the improvements of HOFASs is that they are directly established by physical laws without model reduction. Another improvement of HOFASs is that it makes the control design for nonlinear systems more concise. Controllers can be immediately proposed based on HOFASs.*

For HOFAMAS (1), a distributed control protocol is designed

$$\begin{aligned} u_i &= G_i^{-1}(x_i^{(0\sim n-1)})(g_i + s_i), \\ g_i &= -f_i(x_i^{(0\sim n-1)}) - A_{0\sim n-1}x_i^{(0\sim n-1)} + v_i, \\ s_i &= cK\Big(\sum_{j\in\mathscr{N}_i} a_{ij}(x_i^{(0\sim n-1)} - x_j^{(0\sim n-1)}) + a_{ii}x_i^{(0\sim n-1)}\Big), \end{aligned} \tag{2}$$

in which $A_{0\sim n-1} = \begin{bmatrix} A_0 & A_1 & \cdots & A_{n-1} \end{bmatrix}$, $A_0,\ A_1,\ \cdots,\ A_{n-1}$ and K are control protocol gain matrices, v_i is some external signal, $c > 0$ represents the coupling strength. With the distributed control protocol (2), HOFAMAS (1) can be transformed into:

$$\begin{aligned} x_i^{(n)} =& -A_{0\sim n-1}x_i^{(0\sim n-1)} + v_i + Bw_i \\ &+ cK\Big(\sum_{j\in\mathscr{N}_i} a_{ij}(x_i^{(0\sim n-1)} - x_j^{(0\sim n-1)}) + a_{ii}x_i^{(0\sim n-1)}\Big), \\ z_i =& Cx_i^{(0\sim n-1)}. \end{aligned} \tag{3}$$

System (3) is equivalent to

$$\begin{aligned} \dot{x}_i^{(0\sim n-1)} =& \phi(A_{0\sim n-1})x_i^{(0\sim n-1)} + B_c v_i + B_c B w_i \\ &+ cB_cK\Big(\sum_{j\in\mathscr{N}_i} a_{ij}(x_i^{(0\sim n-1)} - x_j^{(0\sim n-1)}) \\ &+ a_{ii}x_i^{(0\sim n-1)}\Big), \\ z_i =& Cx_i^{(0\sim n-1)}, \end{aligned} \tag{4}$$

in which $B_c = \begin{bmatrix} 0_{r\times r} & 0_{r\times r} & \cdots & I_r \end{bmatrix}^T \in \mathbb{R}^{nr\times r}$, and

$$\phi(A_{0\sim n-1}) = \begin{bmatrix} 0 & I_r & & \\ & & \ddots & \\ & & & I_r \\ -A_0 & -A_1 & \cdots & -A_{n-1} \end{bmatrix} \in \mathbb{R}^{nr\times nr}.$$

Denote the follow variables

$$\begin{aligned} x^{(0\sim n-1)} &= \begin{bmatrix} (x_1^{(0\sim n-1)})^T & (x_2^{(0\sim n-1)})^T & \cdots & (x_N^{(0\sim n-1)})^T \end{bmatrix}^T, \\ v &= \begin{bmatrix} v_1 & v_2 & \cdots & v_N \end{bmatrix}^T,\ w = \begin{bmatrix} w_1 & w_2 & \cdots & w_N \end{bmatrix}^T, \\ z &= \begin{bmatrix} z_1 & z_2 & \cdots & z_N \end{bmatrix}^T, \end{aligned}$$

with which system (4) is equivalent to

$$\begin{aligned} \dot{x}^{(0\sim n-1)} =& \left(I_N \otimes \phi(A_{0\sim n-1}) + c\mathscr{L} \otimes B_cK\right) x^{(0\sim n-1)} \\ &+ \left(I_N \otimes B_c\right) v + \left(I_N \otimes (B_cB)\right) w, \\ z =& (I_N \otimes C)x^{(0\sim n-1)}. \end{aligned} \tag{5}$$

It can be seen that HOFAMAS (1) with nonlinear terms could be transformed into closed-loop linear system (5) by applying the distributed control protocol (2), which is one of the advantages of HOFASs as stated in Remark 1. Then, some necessary definitions and lemmas can be given.

Definition 1. *[21] For HOFAMAS (1) and a given real scalar $\gamma > 0$, a distributed control protocol (2) is said to address the H_∞ consensus problem if*

1) system (5) with $w_i = 0$ and $v_i = 0$ realizes consensus satisfying $\lim_{t\to\infty} ||x_i - x_j|| = 0,\ \forall i, j = 1, 2, \cdots, N$;

2) the transfer function from w to z of system (5) satisfies $||T_{wz}(s)||_\infty < \gamma$, where $||T_{wz}(s)||_\infty = \sup_{w\in\mathbb{R}} \bar{\sigma}(T_{wz}(\boldsymbol{j}w))$ is the H_∞ norm of $T_{wz}(s)$, $\boldsymbol{j}$ is a imaginary unit.

Based on Definition 1, the H_∞ consensus problem of HOFAMAS (1) can be addressed if the H_∞ control problem of system (5) is solved. The definition of the H_∞ control problem of system (5) is as follows.

Definition 2. *For a given real scalar $\gamma > 0$, the H_∞ control problem of system (5) is solved if*

1) system (5) *is asymptotically stable when* $v = 0,\ w = 0$*;*

2) the transfer function from w *to* z *of system* (5) *satisfies* $||T_{wz}(s)||_\infty < \gamma$*, where* $||T_{wz}(s)||_\infty = \sup_{w\in\mathbb{R}} \bar{\sigma}(T_{wz}(\boldsymbol{j}w))$ *is the* H_∞ *norm of* $T_{wz}(s)$*,* $\boldsymbol{j}$ *is a imaginary unit.*

Lemma 1. *[22] For the undirected graph* $\mathcal{G}_u$*, if* $\mathcal{G}_u$ *is connected and at least one node knows its own state information, all the eigenvalues of* $\mathscr{L}$ *are real and positive.*

The objective is as follows: For a given real scalar $\gamma > 0$, under the Assumption 1, design the corresponding distributed control protocol (2) such that the H_∞ consensus problems of HOFAMAS (1) are solved.

3 Main Results

In this section, Theorems 1 and 2 are derived to solve the H_∞ consensus problem of HOFAMAS (1) with the undirected graph.

Theorem 1. *For a given real scalar* $\gamma > 0$ *and undirected graph* $\mathcal{G}_u$*, system* (5) *is asymptotically stable and* $||T_{wz}||_\infty < \gamma$ *iff the following* N *systems are concurrently asymptotically stable and* $||T_{\tilde{w}_i\tilde{z}_i}||_\infty < \gamma$*, where* $T_{\tilde{w}_i\tilde{z}_i}$ *is the transfer function of the following* N *systems*

$$\begin{aligned}\dot{\tilde{x}}_i^{(0\sim n-1)} =& (\phi(A_{0\sim n-1}) + c\lambda_i B_c K)\,\tilde{x}_i^{(0\sim n-1)} \\ &+ B_c\tilde{v}_i + B_cB\tilde{w}_i, \\ z_i =& C\tilde{x}_i^{(0\sim n-1)},\ i = 1, 2, \cdots, N.\end{aligned} \tag{6}$$

Proof. Since $\mathcal{G}_u$ is undirected and connected and has at least one node knowing its own state information, there exists a unitary matrix $\mathscr{H}$ satisfying

$$\mathscr{H}^T\mathscr{L}\mathscr{H} = \Gamma = \mathrm{diag}\{\lambda_1, \lambda_2, \cdots, \lambda_N\}, \tag{7}$$

in which $0 < \lambda_1 \le \lambda_2 \le \cdots \le \lambda_N$ based on Lemma 1. Let

$$\begin{aligned}\tilde{x}_i^{(0\sim n-1)} &= (\mathscr{H}^T \otimes I_N)x_i^{(0\sim n-1)},\ \tilde{w} = (\mathscr{H}^T \otimes I_N)w, \\ \tilde{v} &= (\mathscr{H}^T \otimes I_N)v,\ \ \tilde{z} = (\mathscr{H}^T \otimes I_N)z.\end{aligned} \tag{8}$$

Substituting (8) into system (5) yields

$$\begin{aligned}\dot{\tilde{x}}^{(0\sim n-1)} =& (I_N \otimes \phi(A_{0\sim n-1}) + c\Gamma \otimes B_cK)\,\tilde{x}^{(0\sim n-1)} \\ &+ (I_N \otimes B_c)\,\tilde{v} + (I_N \otimes (B_cB))\,\tilde{w}, \\ \tilde{z} =& (I_N \otimes C)\tilde{x}^{(0\sim n-1)}.\end{aligned} \tag{9}$$

Denote

$$\begin{aligned}\tilde{x}^{(0\sim n-1)} &= \left[(\tilde{x}_1^{(0\sim n-1)})^T \quad (\tilde{x}_2^{(0\sim n-1)})^T \quad \cdots \quad (\tilde{x}_N^{(0\sim n-1)})^T\right]^T, \\ \tilde{v} &= \begin{bmatrix}\tilde{v}_1 & \tilde{v}_2 & \cdots & \tilde{v}_N\end{bmatrix}^T,\ \tilde{w} = \begin{bmatrix}\tilde{w}_1 & \tilde{w}_2 & \cdots & \tilde{w}_N\end{bmatrix}^T, \\ \tilde{z} &= \begin{bmatrix}\tilde{z}_1 & \tilde{z}_2 & \cdots & \tilde{z}_N\end{bmatrix}^T.\end{aligned} \tag{10}$$

Then, system (9) can be transformed into system (6). The transfer function of system (5) is

$$\begin{aligned}T_{wz}(s) =& (I_N \otimes C)(s(I_N \otimes I_r) - (I_N \otimes \phi(A_{0\sim n-1}) \\ &+ cL \otimes B_cK))^{-1}\,(I_N \otimes (B_cB)).\end{aligned} \tag{11}$$

The transfer function of system (9) is

$$\begin{aligned}T_{\tilde{w}\tilde{z}}(s) =& (I_N \otimes C)(s(I_N \otimes I_r) - (I_N \otimes \phi(A_{0\sim n-1}) \\ &+ c\Gamma \otimes B_cK))^{-1}\,(I_N \otimes (B_cB)).\end{aligned} \tag{12}$$

The transfer function of system (6) is

$$T_{\tilde{w}_i\tilde{z}_i}(s) = C(sI_r - (\phi(A_{0\sim n-1}) + c\lambda_i B_cK))^{-1}(B_cB). \tag{13}$$

From (11)-(13), one can find that $T_{wz}(s) = (\mathscr{H}^T \otimes I_r)T_{\tilde{w}\tilde{z}}(s)(\mathscr{H}^T \otimes I_r)$ and

$$\begin{aligned}||T_{wz}(s)||_\infty = ||T_{\tilde{w}\tilde{z}}(s)||_\infty =& \max\{||T_{\tilde{w}_i\tilde{z}_i}(s)||_\infty\}, \\ & i = 1, 2, \cdots, N.\end{aligned} \tag{14}$$

The proof is completed. □

Based on Theorem 1, the H_∞ consensus problem of HOFAMAS (1) with the undirected graph is solved and the distributed control protocol is developed as follows.

Theorem 2. *For a given real scalar* $\gamma > 0$ *and undirected graph* $\mathcal{G}_u$*, system* (5) *is asymptotically stable and* $||T_{wz}||_\infty < \gamma$ *iff there exist matrices* $P \in \mathbb{R}^{nr\times nr}$*,* $P > 0$*,* $T \in \mathbb{R}^{r\times nr}$*, real scalar* $\tau > 0$ *such that*

$$\begin{bmatrix}\mathrm{Sym}\{\phi(0_{0\sim n-1})P + B_cT\} - \tau B_cB_c^T & B_cB & PC^T \\ B^TB_c^T & -\gamma I_p & 0 \\ CP & 0 & -\gamma I_q\end{bmatrix} < 0, \tag{15}$$

where $\phi(0_{0\sim n-1}) = \begin{bmatrix}0 & I_r & & \\ & & \ddots & \\ & & & I_r \\ 0_{r\times r} & 0_{r\times r} & \cdots & 0_{r\times r}\end{bmatrix}$*. Then, the gain matrices in the distributed control protocol* (2) *can be designed as* $A_{0\sim n-1} = -TP^{-1}$*,* $K = -0.5B_c^TP^{-1}$ *and the coupling strength can be chosen as* $c \ge \frac{\tau}{\min\{\lambda_i\}}$*, where* $\lambda_i (i = 1, 2, \cdots, N)$ *are the eigenvalues of* $\mathscr{L}$ *.*

Proof. **Sufficiency:** Substituting $A_{0\sim n-1} = -TP^{-1}$ into inequality (15) and applying Schur complement lemma, one has

$$\begin{aligned}&\mathrm{Sym}\{\phi(0_{0\sim n-1})P - B_cA_{0\sim n-1}P\} - \tau B_cB_c^T \\ &\quad + \gamma^{-1}B_cBB^TB_c^T + \gamma^{-1}PC^TCP < 0.\end{aligned} \tag{16}$$

Note that $c \ge \frac{\tau}{\min\{\lambda_i\}}$, which implies that $c\lambda_i \ge \tau > 0$. From inequality (16), the following inequality holds

$$\begin{aligned}&\mathrm{Sym}\{\phi(0_{0\sim n-1})P - B_cA_{0\sim n-1}P\} - c\lambda_i B_cB_c^T \\ &\quad + \gamma^{-1}B_cBB^TB_c^T + \gamma^{-1}PC^TCP < 0.\end{aligned} \tag{17}$$

By substituting $K = -0.5B_c^TP^{-1}$, there holds

$$\begin{aligned}&\mathrm{Sym}\{\phi(0_{0\sim n-1})P - B_cA_{0\sim n-1}P\} + c\lambda_iB_cKP \\ &\quad + c\lambda_iPK^TB_c^T + \gamma^{-1}B_cBB^TB_c^T + \gamma^{-1}PC^TCP \\ &= \mathrm{Sym}\{\phi(0_{0\sim n-1})P - B_cA_{0\sim n-1}P\} - c\lambda_iB_cB_c^T \\ &\quad + \gamma^{-1}B_cBB^TB_c^T + \gamma^{-1}PC^TCP < 0.\end{aligned} \tag{18}$$

Using Schur complement lemma, one has

$$\begin{bmatrix}\mathrm{Sym}\{(\phi(A_{0\sim n-1}) + c\lambda_iB_cK)P\} & B_cB & PC^T \\ B^TB_c^T & -\gamma I_p & 0 \\ CP & 0 & -\gamma I_q\end{bmatrix} < 0. \tag{19}$$

From Theorem 1 and the Bounded Real Lemma in [23], system (5) is asymptotically stable and $||T_{wz}||_\infty < \gamma$.

Necessity: If system (5) is asymptotically stable and $||T_{wz}||_\infty < \gamma$, a matrix $X > 0$ can be found such that

$$\begin{bmatrix} \mathrm{Sym}\{(\phi(A_{0\sim n-1}) + c\lambda_i B_c K)X\} & B_c B & XC^T \\ B^T B_c^T & -\gamma I_p & 0 \\ CX & 0 & -\gamma I_q \end{bmatrix} < 0, \tag{20}$$

namely,

$$\begin{aligned} &\mathrm{Sym}\{\phi(0_{0\sim n-1})X - B_c A_{0\sim n-1}X\} + c\lambda_i B_c KX \\ &+ c\lambda_i XK^T B_c^T + \gamma^{-1} B_c B B^T B_c^T + \gamma^{-1} XC^T CX < 0. \end{aligned} \tag{21}$$

Since $c > 0$ and $\lambda_i > 0$, there exists a real scalar τ_1 satisfying $0 < \tau_1 < c\lambda_i$. Denote $Y = KX$ and then the following inequality holds

$$\begin{aligned} &\mathrm{Sym}\{\phi(0_{0\sim n-1})X - B_c A_{0\sim n-1}X\} + \tau_1 B_c Y \\ &+ \tau_1 Y^T B_c^T + \gamma^{-1} B_c B B^T B_c^T + \gamma^{-1} XC^T CX < 0. \end{aligned} \tag{22}$$

From Finsler Lemma [24], there exists a real scalar $\tau_2 > 0$ satisfying

$$\begin{aligned} &\mathrm{Sym}\{\phi(0_{0\sim n-1})X - B_c A_{0\sim n-1}X\} - \tau_2\tau_1 B_c B_c^T \\ &+ \gamma^{-1} B_c B B^T B_c^T + \gamma^{-1} XC^T CX < 0. \end{aligned} \tag{23}$$

Denote $T = A_{0\sim n-1}X$, $\tau = \tau_1\tau_2$, $P = X$ and then inequality (15) holds. The proof is completed. □

Remark 2. *For the H_∞ consensus problem of HOFAMAS* (1)*, the necessary and sufficient condition is given and the distributed control protocol is developed by introducing the coupling strength parameter and using the LMI approach. It should be emphasized that one only needs to solve one LMI in Theorem 2, and does not need to substitute each eigenvalue of the Laplacian matrix $\mathscr{L}$ into the LMI to find the common solution set. By comparison, the methods in [10, 25, 26] need to substitute each eigenvalue of the Laplacian matrix $\mathscr{L}$ into the LMI to find the common feasible solution set and address consensus problems of MASs with the undirected graph, which could increase the computational complexity when the number of the agents increases.*

4 Numerical Example

In this section, a multi-spacecraft attitude model is proposed and converted into a HOFAMAS. Then, the H_∞ control protocol of this multi-spacecraft attitude model is given.

4.1 The Multi-Spacecraft Attitude Model

The commonly used models to analyze the spacecraft attitude include the Euler angle, quaternion, Classical Rodrigues Parameter (CRP) and Modified Rodrigues Parameter (MRP) [27–29]. The Euler angle is the most widely used attitude description method in engineering practice, which has clear physical meanings and can be directly obtained by attitude sensors [30]. Therefore, the Euler angle is used in this paper. The dynamics for the attitude motion of the ith rigid spacecraft can be written as follows [31]:

$$\boldsymbol{J}\dot{\boldsymbol{\omega}}_i + \boldsymbol{\omega}_i \times (\boldsymbol{J}\boldsymbol{\omega}_i) = \boldsymbol{T}_{ci} + \boldsymbol{T}_{gi} + \boldsymbol{T}_{di},\ i = 1, 2, 3, \cdots, N, \tag{24}$$

where $\boldsymbol{J} = \boldsymbol{J} = \mathbb{R}^{3\times 3}$ is the inertia matrix, $\boldsymbol{\omega}_i$, $\boldsymbol{T}_{ci}$, $\boldsymbol{T}_{gi}$, $\boldsymbol{T}_{di}$ denote the angular velocity, control input torque, gravity gradient torque and the external disturbance torque of the ith rigid spacecraft, respectively.

Similar to the results in [31], the following equations can be obtained

$$\begin{cases} J_x\ddot{\varphi}_i + 4(J_y - J_z)\omega_0^2\varphi_i + (J_y - J_z - J_x)\omega_0\dot{\psi}_i = T_{cxi} + T_{dxi}, \\ J_y\ddot{\theta}_i + 3\omega_0^2(J_x - J_z)\theta_i = T_{cyi} + T_{dyi}, \\ J_z\ddot{\psi}_i + (J_y - J_x)\omega_0^2\psi_i + (J_x + J_z - J_y)\omega_0\dot{\varphi}_i = T_{czi} + T_{dzi}, \end{cases} \tag{25}$$

where J_x, J_y and J_z are the three components of inertia matrix; φ_i, θ_i and ψ_i are the roll, pitch and yaw attitude angles; T_{dxi}, T_{dyi} and T_{dzi} are the three components of the external disturbance torque; T_{cxi}, T_{cyi} and T_{czi} are the three components of the control input torque; ω_0 is the orbital angular velocity.

Let $x_i = \begin{bmatrix}\varphi_i & \theta_i & \psi_i\end{bmatrix}^T$, $z_i = \begin{bmatrix}\varphi_i & \theta_i & \psi_i\end{bmatrix}^T$, $u_i = \begin{bmatrix}T_{cxi} & T_{cyi} & T_{czi}\end{bmatrix}^T$, $w_i = \begin{bmatrix}T_{dxi} & T_{dyi} & T_{dzi}\end{bmatrix}^T$. System (25) can be written as

$$\begin{aligned} \ddot{x}_i &= \xi_i(x, \dot{x}) + B_1 u_i + B_2 w_i, \\ z_i &= C_1 x_i,\ i = 1, 2, 3, \cdots, N, \end{aligned} \tag{26}$$

where

$$\xi_i(x,\dot{x}) = \begin{bmatrix} -4J_x^{-1}(J_y - J_z)\omega_0^2\varphi_i + J_x^{-1}(J_x + J_z - J_y)\omega_0\dot{\psi}_i \\ -3J_y^{-1}\omega_0^2(J_x - J_z)\theta_i \\ -J_z^{-1}(J_y - J_x)\omega_0^2\psi_i - J_z^{-1}(J_x + J_z - J_y)\omega_0\dot{\varphi}_i \end{bmatrix},$$

$$B_1 = B_2 = \begin{bmatrix} J_x^{-1} & 0 & 0 \\ 0 & J_y^{-1} & 0 \\ 0 & 0 & J_z^{-1} \end{bmatrix},\ C_1 = \begin{bmatrix} 1 & 0 & 0 \\ 0 & 1 & 0 \\ 0 & 0 & 1 \end{bmatrix}.$$

Considering the nonlinear dynamics $g_i = \sin(\dot{\theta})$ of pitching systems, system (26) is transformed into

$$\begin{aligned} \ddot{x}_i &= f_i(x, \dot{x}) + B_1 u_i + B_2 w_i, \\ z_i &= C_1 x_i,\ i = 1, 2, 3, \cdots, N, \end{aligned} \tag{27}$$

where

$$f_i(x,\dot{x}) = \begin{bmatrix} -4J_x^{-1}(J_y - J_z)\omega_0^2\varphi_i + J_x^{-1}(J_x + J_z - J_y)\omega_0\dot{\psi}_i \\ -3J_y^{-1}\omega_0^2(J_x - J_z)\theta_i + g_i \\ -J_z^{-1}(J_y - J_x)\omega_0^2\psi_i - J_z^{-1}(J_x + J_z - J_y)\omega_0\dot{\varphi}_i \end{bmatrix}.$$

Remark 3. *Note that many spacecraft attitude models are based on the the state-space approach [9, 29, 31], where the model is reduced to a first order system. From* (25)*, it can be seen that the spacecraft attitude model is a second order system in nature. Thus, a novel multi-spacecraft attitude model is obtained in* (27)*, which is the second order fully actuated multi-agent system, i.e. a typical case of HOFAMAS* (1)*.*

4.2 H_∞ Consensus Control for The Multi-Spacecraft Attitude Model

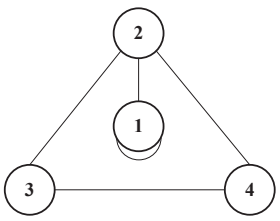

Fig. 1: Communication topology graph $\mathcal{G}_u$.

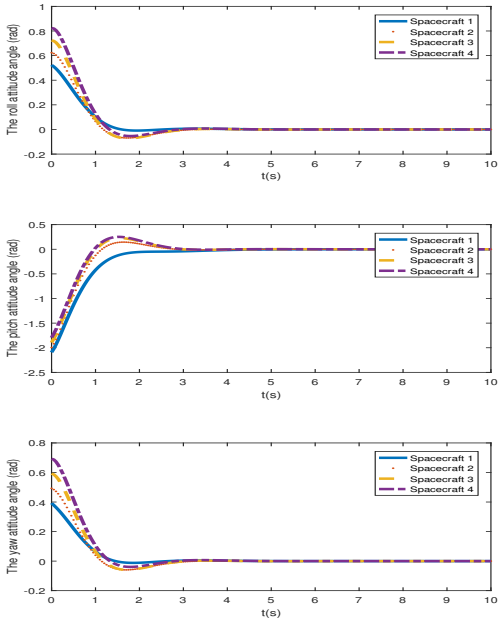

Fig. 2: The state evolution of the attitude angles.

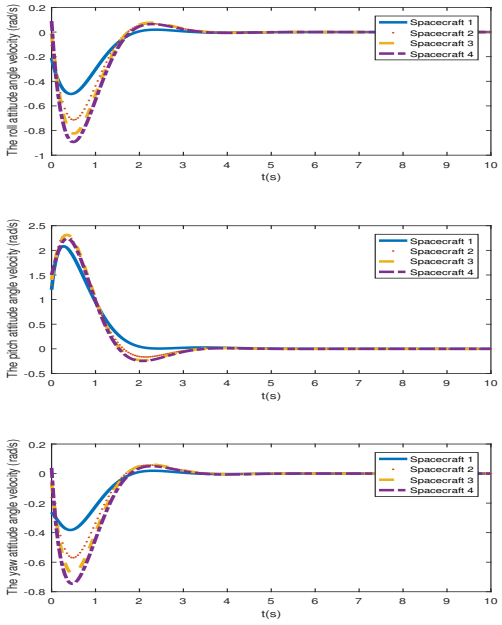

Fig. 3: The state evolution of the attitude angular velocities.

Consider the multi-spacecraft attitude model with the moments of inertia $J_x = 18,\ J_y = 21,\ J_z = 24$ [20] and the undirected graph $\mathcal{G}_u$, which is shown in Fig. 1. The aim is to design the distributed control protocol (2) such that system (27) with $\mathcal{G}_u$ achieves the H_∞ consensus. The Laplacian matrix of the undirected graph $\mathcal{G}_u$ is $L = \begin{bmatrix} 2 & -1 & 0 & 0 \\ -1 & 3 & -1 & -1 \\ 0 & -1 & 2 & -1 \\ 0 & -1 & -1 & 2 \end{bmatrix}$. By applying Theorem 2 with $\gamma = 1$, there exist feasible solutions $P = \begin{bmatrix} P_1 & P_2 \\ P_2 & P_3 \end{bmatrix}$, $T = \begin{bmatrix} T_1 & T_2 \end{bmatrix}$, $\tau = 1.2977$, where $P_1 = \text{diag}\{0.4327, 0.4327, 0.4327\}$, $P_2 = \text{diag}\{-0.3246, -0.3246, -0.3246\}$, $P_3 = \text{diag}\{1.2978, 1.2978, 1.2978\}$, $T_1 = \text{diag}\{-1.2977, -1.2977, -1.2977\}$, $T_2 = \text{diag}\{-1.2979, -1.2979, -1.2979\}$. Then, the gain matrices to be determined in the distributed control protocol (2) can be designed as $A_{0\sim1} = \begin{bmatrix} \Pi_1 & \Pi_2 \end{bmatrix}$, $K = \begin{bmatrix} K_1 & K_2 \end{bmatrix}$, where $\Pi_1 = \text{diag}\{-4.6144, -4.6144, -4.6144\}$, $\Pi_2 = \text{diag}\{-2.1541, -2.1541, -2.1541\}$, $K_1 = \text{diag}\{-0.3557, -0.3557, -0.3557\}$, $K_2 = \text{diag}\{-0.4742, -0.4742, -0.4742\}$. The coupling strength parameter $c \geq \frac{\tau}{\min\{\lambda_i\}} = 9.3226,\ i = 1, 2, 3, 4$. Then, the coupling strength parameter c can be taken as 10.

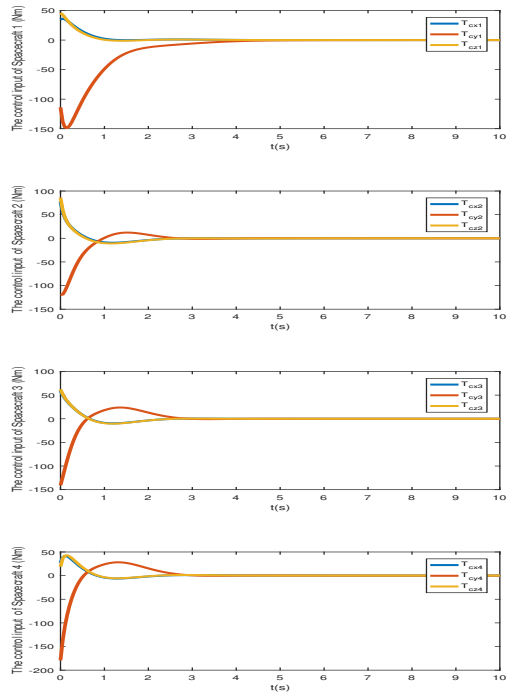

Fig. 4: The control inputs of the spacecrafts.

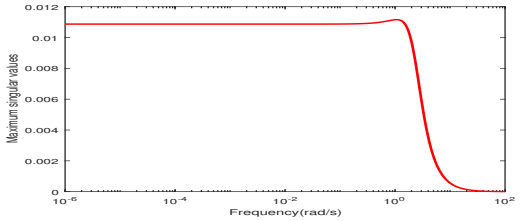

Fig. 5: The values of $\bar{\sigma}(T_{wz}(jw)$.

In order to show the effectiveness of the proposed distributed control protocol, consider the following initial values of attitude angles and attitude angular velocities of the multi-spacecraft model: $\varphi_1(0) = 0.5236,\ \theta_1(0) = -2.0944,\ \psi_1(0) = 0.3927,\ \dot{\varphi}_1(0) = -0.2104,\ \dot{\theta}_1(0) = 1.2000,\ \dot{\psi}_1(0) = -0.2618,\ \varphi_2(0) = 0.6236,\ \theta_2(0) = -1.9944,\ \psi_2(0) = 0.4927,\ \dot{\varphi}_2(0) = -0.1104,\ \dot{\theta}_2(0) = 1.3000,\ \dot{\psi}_2(0) = -0.1618,\ \varphi_3(0) = 0.7236,\ \theta_3(0) = -1.8944,\ \psi_3(0) = 0.5927,\ \dot{\varphi}_3(0) = -0.0104,\ \dot{\theta}_3(0) = 1.4000,\ \dot{\psi}_3(0) = -0.0618,\ \varphi_4(0) = 0.8236,\ \theta_4(0) = -1.7944,\ \psi_4(0) = 0.6927,\ \dot{\varphi}_4(0) = 0.0896,\ \dot{\theta}_4(0) = 1.5000,\ \dot{\psi}_4(0) = 0.0382$. The state evolutions of attitude angles and attitude angular velocities are shown in Fig. 2 and 3, respectively, where it can be seen that both attitude angles and attitude angular velocities realize consensus. The values of $\bar{\sigma}(T_{wz}(jw))$ are shown in Fig. 5, where the maximum peak value is about $0.0112 < 1$. It can be seen that

the H_∞ consensus of the multi-spacecraft attitude model has been realized under the distributed control protocol (2). The corresponding control inputs of the spacecrafts are shown in Fig. 4. One can find that during the initial phase, the control inputs are large but gradually decrease as the the multi-spacecraft attitude tends to achieve consensus.

5 Conclusions

For HOFAMASs with external disturbances, the H_∞ distributed control protocols have been designed, which can eliminate all nonlinear characteristics of open loop systems and establish new closed-loop dynamic characteristics. For the H_∞ consensus of HOFAMASs with the undirected graph, the necessary and sufficient condition has been given and the gain matrices in the distributed control protocol have been developed. Finally, a multi-spacecraft attitude model has been proposed based on the HOFAS and a numerical example has been given to show the effectiveness of the results.

References

[1] B. Cui, L. Zhang, Y. Xia, and J. Zhang, "Continuous distributed fixed-time attitude controller design for multiple spacecraft systems with a directed graph," *IEEE Trans. Circuits Syst. II, Exp. Briefs*, vol. 69, no. 11, pp. 4478–4482, 2022.

[2] W. Sui, G. Duan, M. Hou, and M. Zhang, "Distributed fixed-time attitude coordinated tracking for multiple rigid spacecraft via a novel integral sliding mode approach," *J. Franklin Inst.*, vol. 357, no. 14, pp. 9399–9422, 2020.

[3] B. Chen, J. Hu, Y. Zhao, and B. K. Ghosh, "Finite-time velocity-free rendezvous control of multiple AUV systems with intermittent communication," *IEEE Trans. Syst., Man, Cybern. Syst.*, vol. 52, no. 10, pp. 6618–6629, 2022.

[4] Q.-H. Zhang and J.-G. Lu, "Bounded real lemmas for singular fractional-order systems: The $1 < \alpha < 2$ case," *IEEE Trans. Circuits Syst. II, Exp. Briefs*, vol. 68, no. 2, pp. 732–736, 2021.

[5] Q.-H. Zhang, J.-G. Lu, J. Xu, and Y.-Q. Chen, "Solution analysis and novel admissibility conditions of SFOSs: The $1 < \alpha < 2$ case," *IEEE Trans. Syst., Man, Cybern. Syst.*, vol. 52, no. 8, pp. 5056–5067, 2022.

[6] Y. Jiang, W. Gao, J. Wu, T. Chai, and F. L. Lewis, "Reinforcement learning and cooperative H_∞ output regulation of linear continuous-time multi-agent systems," *Automatica*, vol. 148, p. 110768, 2023.

[7] C. Chen, F. L. Lewis, S. Xie, H. Modares, Z. Liu, S. Zuo, and A. Davoudi, "Resilient adaptive and H_∞ controls of multi-agent systems under sensor and actuator faults," *Automatica*, vol. 102, pp. 19–26, 2019.

[8] A. Elahi, A. Alfi, and H. Modares, "H_∞ consensus control of discrete-time multi-agent systems under network imperfections and external disturbance," *IEEE/CAA J. Autom. Sinica*, vol. 6, no. 3, pp. 667–675, 2019.

[9] H. Qu, F. Yang, Q.-L. Han, and Y. Zhang, "Distributed H_∞ consensus filtering for attitude tracking using ground-based radars," *IEEE Trans. Cybern.*, vol. 51, no. 7, pp. 3767–3778, 2021.

[10] Y. Luo, W. Zhu, J. Cao, and L. Rutkowski, "Event-triggered finite-time guaranteed cost H_∞ consensus for nonlinear uncertain multi-agent systems," *IEEE Trans. Netw. Sci. Eng.*, vol. 9, no. 3, pp. 1527–1539, 2022.

[11] C. An, H. Su, and S. Chen, "H_∞ consensus for discrete-time fractional-order multi-agent systems with disturbance via Q-learning in zero-sum games," *IEEE Trans. Netw. Sci. Eng.*, vol. 9, no. 4, pp. 2803–2814, 2022.

[12] Q.-H. Zhang, J.-G. Lu, Y.-D. Ma, and Y.-Q. Chen, "Time domain solution analysis and novel admissibility conditions of singular fractional-order systems," *IEEE Trans. Circuits Syst. I, Reg. Papers*, vol. 68, no. 2, pp. 842–855, 2021.

[13] G. Duan, "High-order fully actuated system approaches: Part I. Models and basic procedure," *Int. J. Syst. Sci.*, vol. 52, no. 2, pp. 422–435, 2021.

[14] ——, "High-order fully actuated system approaches: Part II. Generalized strict-feedback systems," *Int. J. Syst. Sci.*, vol. 52, no. 3, pp. 437–454, 2021.

[15] ——, "High-order fully actuated system approaches: Part III. Robust control and high-order backstepping," *Int. J. Syst. Sci.*, vol. 52, no. 5, pp. 952–971, 2021.

[16] ——, "High-order system approaches: I. Fully-actuated systems and parametric designs," *Acta Automatica Sinica*, vol. 46, no. 7, pp. 1333–1345, 2020.

[17] ——, "High-order system approaches: II. Controllability and fully-actuation," *Acta Automatica Sinica*, vol. 46, no. 8, pp. 1571–1581, 2020.

[18] ——, "High-order system approaches: III. Observability and observer design," *Acta Automatica Sinica*, vol. 46, no. 9, pp. 1885–1895, 2020.

[19] D.-W. Zhang, G.-P. Liu, and L. Cao, "Proportional integral predictive control of high-order fully actuated networked multiagent systems with communication delays," *IEEE Trans. Syst., Man, Cybern. Syst.*, vol. 53, no. 2, pp. 801–812, 2023.

[20] G. Duan, "High-order fully actuated system approaches: Part VIII. Optimal control with application in spacecraft attitude stabilisation," *Int. J. Syst. Sci.*, vol. 53, no. 1, pp. 54–73, 2022.

[21] Z. Li and Z. Duan, *Cooperative Control of Multi-Agent Systems: A Consensus Region Approach*. CRC press, 2017.

[22] Y. Hong, J. Hu, and L. Gao, "Tracking control for multi-agent consensus with an active leader and variable topology," *Automatica*, vol. 42, no. 7, pp. 1177–1182, 2006.

[23] G.-R. Duan and H.-H. Yu, *LMIs in Control Systems: Analysis, Design and Applications*. CRC press, 2013.

[24] T. Iwasaki and R. E. Skelton, "All controllers for the general H_∞ control problem: LMI existence conditions and state space formulas," *Automatica*, vol. 30, no. 8, pp. 1307–1317, 1994.

[25] S. Zhang, Z. Li, and X. Wang, "Robust H_2 consensus for multi-agent systems with parametric uncertainties," *IEEE Trans. Circuits Syst. II, Exp. Briefs*, vol. 68, no. 7, pp. 2473–2477, 2021.

[26] H. Pan, X. Yu, G. Yang, and L. Xue, "Robust consensus of fractional-order singular uncertain multi-agent systems," *Asian J. Control*, vol. 22, no. 6, pp. 2377–2387, 2020.

[27] B. Zhou, "On stability and stabilization of the linearized spacecraft attitude control system with bounded inputs," *Automatica*, vol. 105, pp. 448–452, 2019.

[28] H. Jiang, B. Zhou, D. Li, and G. Duan, "Data-driven–based attitude control of combined spacecraft with noncooperative target," *Int J Robust Nonlinear Control.*, vol. 29, no. 16, pp. 5801–5819, 2019.

[29] B. Wang, W. Chen, B. Zhang, P. Shi, and H. Zhang, "A nonlinear observer-based approach to robust cooperative tracking for heterogeneous spacecraft attitude control and formation applications," *IEEE Trans. Automat. Control*, vol. 68, no. 1, pp. 400–407, 2023.

[30] C. Zhong, Z. Chen, and Y. Guo, "Attitude control for flexible spacecraft with disturbance rejection," *IEEE Trans. Aerosp. Electron. Syst.*, vol. 53, no. 1, pp. 101–110, 2017.

[31] X. Liang, Q. Wang, C. Hu, and C. Dong, "Observer-based H_∞ fault-tolerant attitude control for satellite with actuator and sensor faults," *Aerosp. Sci. Technol.*, vol. 95, p. 105424, 2019.

Proceedings of the 3rd Conference on Fully Actuated System Theory and Applications
May 10-12, 2024, Shenzhen, China

Adaptive Stabilization Control for Fully Actuated Systems with Unknown Measurement Sensitivity

Xueqi Wu[1], Wei Sun[1]
1. Liaocheng University, Liaocheng 252000, P. R. China
E-mail: wuxq2025@163.com, sunwei@lcu.edu.cn

Abstract: This study addresses the adaptive control problem of uncertain high-order fully actuated systems with unknown measurement sensitivity. Sensitivity is a crucial metric for assessing sensor performance, directly influencing the effectiveness of sensor applications. Considering sensitivity as an unknown constant, this paper employs the theory of fully actuated systems. An adaptive controller is designed based on the actual measurement values of the system state, aiming to achieve stable control performance and bounded signals within the closed-loop system. Finally, the proposed control approach is applied to a 2-DOF robotic arm, validating the effectiveness of the proposed methodology.

Key Words: Fully actuated systems, adaptive control, unknown measurement sensitivity.

1 Introduction

The state space method provides an intuitive way to describe the dynamic behavior of linear systems, providing a common framework for analyzing and designing linear systems. However, with the continuous development of modern industry, the state space method has become insufficient to meet the control needs of nonlinear systems. For example, for many practical control systems, applying the state space method to design globally stable control laws is a highly challenging task. In recent years, Professor Duan proposed a revolutionary new theory parallel to the state space method–the fully actuated system (FAS) theory. This method can effectively describe almost all nonlinear control systems. The full-actuation characteristic allows us to cancel out all the dynamic characteristics of the open loop system (whether linear or non-linear), while establishing new and promising closed-loop dynamic characteristics. Even in the case of nonlinear systems, A desired time-invariant linear closed-loop system can also be obtained [1–3].

The FAS theory, once proposed, received a lot of attention from many scholars because it was based on the full-actuation system model and completely freed from the state space method. It has shown extremely strong advantages in dealing with a series of complex problems such as nonlinearity, time-varying, and lag characteristics. The fully actuated system theory provides a new framework for studying nonlinear system control. Since the proposal of this theory, academic research on full-actuation system control has emerged successively. In [4], the adaptive control problem of a class of time-delay systems based on the high order full drive system method is studied, and a continuous adaptive controller is designed. It is proved that the controller can make the system reach asymptotic stability. A proposed optimal controller is presented in [5] for FASs, with the aim of achieving attitude and orbit stabilization control for combined spacecraft. In [6], a model for the six-degree-of-freedom spacecraft motion, specifically employing a FAS framework, is initially developed through variable elimination from the state-space model. Subsequently, a tracking controller is crafted based on the principles of the FAS approach.

It is pertinent to highlight that, owing to technological constraints, sensors are unable to capture all state variables. Consequently, the actual values of the output function unavoidably deviate from their nominal counterparts. In the magnetic bearing suspension system, there is a sensitivity error of 10% in the displacement sensor [7]. In [8], the problem of global finite-time output feedback stabilization for uncertain nonlinear systems with unknown measurement sensitivity is investigated. Diao et al. [9] address the tracking control problem for flexible joint robots with unknown measurement sensitivity in multi-input multi-output Euler-Lagrange systems, regardless of the complete uncertainty in system dynamics.

In summary, this paper investigates the adaptive control problem of a high-order fully actuated system with unknown measurement sensitivity. The contributions of this paper are as follows:

(1) The use of the FAS method to address the challenges of high-order systems with unknown measurement sensitivity, eliminating the need for conversion into first-order systems and thereby reducing computational complexity.

(2) The design of an adaptive controller based on unreal state values measured by sensors, ensuring that all signals within the closed-loop system remain bounded.

Notations: For ease of description, several symbols are used in this paper. The upcoming section will simplify the notation of the functions. Specifically, functions like $f_i(\cdot)$ will be represented as f_i. I is the identity matrix, and I^* is the inverse identity matrix,

$$p^{(0\sim n)} = \left[\begin{array}{cccc} p^T, & \dot{p}^T, & \ldots, & p^{(n)T} \end{array} \right]^T,$$

$$p_{i\sim j}^{(0\sim n)} = \left[\begin{array}{cccc} p_i^{(0\sim n)}, & p_{i+1}^{(0\sim n)}, & \ldots, & p_j^{(0\sim n)} \end{array} \right]^T, \ j \geq i,$$

$$B^{0\sim n-1} = \left[\begin{array}{cccc} B_0 & B_1 & \ldots & B_{n-1} \end{array} \right],$$

$$\phi(B^{0\sim n-1}) = \left[\begin{array}{cc} 0 & I \\ -B^{0\sim n-1} & \end{array} \right].$$

This work is supported by Guangyue Young Scholar Innovation Team of Liaocheng University under Grant LCUGYTD2022-01, Liaocheng University Major Vertical Project Cultivation Plan Project under Grant 318062305 and the Science Center Program of National Natural Science Foundation of China under Grant 62188101.

2 Problem Statement and Preliminaries

2.1 Problem Statement

Examine a category of uncertain nonlinear high-order FASs:

$$\begin{cases} p_i^{(m_i)} = f_i(p_{1\sim i}^{(0\sim m_i-1)}) + g_i(p_{1\sim i}^{(0\sim m_i-1)})p_{i+1}, \\ \qquad\qquad\qquad\qquad i = 1,\ldots,n-1, \\ p_n^{(m_n)} = f_n(p_{1\sim n}^{(0\sim m_n-1)}) + g_n(p_{1\sim n}^{(0\sim m_n-1)})u, \\ w_i = \eta_i p_i, \qquad\qquad i = 1,\ldots,n, \end{cases} \tag{1}$$

where $p_i \in \mathbb{R}^r$ represents the state variables, m_i is a set of positive integers, $f_i(p_{1\sim i}^{(0\sim m_i-1)})$ denotes a set of sufficiently smooth vector functions, $g_i(p_{1\sim i}^{(0\sim m_i-1)}) \in \mathbb{R}^{r\times r}$ is a collection of sufficiently smooth matrix functions, $\eta_i \in \mathbb{R}$ signifies the untrue system state value measured by sensors, utilized for feedback control, where $\eta_i \neq 0$ denotes the measurement sensitivity and is characterized as an unknown parameter. Assuming, under the assumption of generality, that the unknown measurement sensitivity η_i is positive. Additionally, $u \in \mathbb{R}^r$ is the control input.

The control objective of this paper is to achieve stability for the system (1) and ensure that all signals within the closed-loop system remain bounded.

2.2 Preliminaries

Assumption A1: The control distribution matrix $g_i(p_{1\sim i}^{(0\sim m_i-1)})$ satisfies the full-actuation condition $\det g_i(p_{1\sim i}^{(0\sim m_i-1)}) \neq 0, i = 1,\ldots,n$.

Lemma 1 [10]: Radial basis function neural networks have the capability to approximate any continuous function $\chi(x)$ over a compact set Ω_x with arbitrary precision $e > 0$, as demonstrated below:

$$k(x) = \psi^T S(x) + r(x),$$

satisfying

$$\sup_{x\in\Omega_x} |\chi(x) - k(x)| \leq e,$$

where $r(x)$ denotes the estimation error, ψ represents the weight vector, and $S(x)$ corresponds to the basis function vector.

Lemma 2 [11]: If matrix $B^{0\sim n-1}$ is chosen to guarantee the stability of matrix $\phi(B^{0\sim n-1})$, then there exists a positive definite matrix $E(B^{0\sim n-1})$ that fulfills the equation

$$\phi^T(B^{0\sim n-1})E(B^{0\sim n-1}) + E(B^{0\sim n-1})\phi(B^{0\sim n-1}) \leq -I,$$

where I denotes identity matrix.

Lemma 3 [12]: For any positive constant o and any variable $\omega \in R$, the ensuing inequality prevails:

$$0 \leq |\omega| - \frac{\omega^2}{\sqrt{\omega^2 + o^2}} \leq o.$$

The following section encompasses preparatory work, excluding assumptions and lemmas. Initially, introduce an array of matrices $B_i^{0\sim m_i-1} \in R^{r\times nr}, i = 1,2,\ldots,n$ that ensures the stability of $\phi(B_i^{0\sim m_i-1}) \in R^{nr\times nr}$. Assuming the unique existence of the solution P to the following Lyapunov inequality,

$$\phi^T(B_i^{0\sim m_i-1})E_i(B_i^{0\sim m_i-1}) + E_i(B_i^{0\sim m_i-1})\phi(B_i^{0\sim m_i-1}) \leq -I_{nr}$$

for $i = 1,2,\ldots,n$, among them,

$$E_i(B_i^{0\sim m_i-1}) = \left[\ E_{iF}(B_i^{0\sim m_i-1}),\cdots,\ E_{iL}(B_i^{0\sim m_i-1})\ \right] \in R^{nr\times nr},$$

where $E_{iF}(B_i^{0\sim m_i-1})$ and $E_{iL}(B_i^{0\sim m_i-1}) \in R^{nr\times r}$. In addition to that, we have to define

$$\tilde{E}_i(B_i^{0\sim m_i-1}) = I_i^* E_i^T(B_i^{0\sim m_i-1}),\ i = 1,2,\ldots,n,$$

$$\begin{aligned} &\tilde{E}_i^{-1}(B_i^{0\sim m_i-1}) \\ &= \begin{bmatrix} J_{i1}(B_i^{0\sim m_i-1}) \\ J_{i2}(B_i^{0\sim m_i-1}) \end{bmatrix} \\ &= \begin{bmatrix} J_{i1}(B_i^{0\sim m_i-1}) \\ J_{iF}(B_i^{0\sim m_i-1})\ J_{iM}(B_i^{0\sim m_i-1})\ J_{iL}(B_i^{0\sim m_i-1}) \end{bmatrix}, \end{aligned}$$

where $J_{iF}(B_i^{0\sim m_i-1})$ and $J_{iL}(B_i^{0\sim m_i-1})$ are two constant matrices. Next, define the constant Θ as:

$$\Theta = \max\{\| W_i \|^2, \frac{\eta_i^2}{\eta_{i+1}^2}, i = 1,...,n\},$$

where $\tilde{\Theta} = \Theta - \hat{\Theta}$, $\hat{\Theta}$ is an estimate of Θ, $\tilde{\Theta}$ is the estimated error.

3 Controller design

Step 1: First, define

$$\zeta_1^{(0\sim m_1-1)} = w_1^{(0\sim m_1-1)} \tag{2}$$

and

$$E_2(B_2^{0\sim m_2-1})\zeta_2^{(0\sim m_2-1)} = w_2^{(0\sim m_2-1)} - \begin{bmatrix} \alpha_1 \\ 0 \end{bmatrix}. \tag{3}$$

Considering the symmetry property of E_2, divide the above equation into

$$E_{2L}^T(B_2^{0\sim m_2-1})\zeta_2^{(0\sim m_2-1)} = w_2 - \alpha_1, \tag{4}$$

Then, write $\dot{\zeta}_1^{(0\sim m_1-1)}$ in state space form

$$\dot{\zeta}_1^{(0\sim m_1-1)} = \phi(B_1^{0\sim m_1-1})\zeta_1^{(0\sim m_1-1)} + \begin{bmatrix} \mathbf{0}_{(m_1-1)} \\ \Xi \end{bmatrix}.$$

where $\Xi = \eta_1 f_1 + \frac{\eta_1}{\eta_2} g_1(\alpha_1 + E_{2L}^T\zeta_2^{(0\sim m_2-1)}) + B_1^{0\sim m_1-1}\zeta_1^{(0\sim m_1-1)}$. Introduce $F_1(P_1) = W_1^T\psi_1(P_1) + \epsilon_1(P_1)$, where $\epsilon_1(P_1)$ is approximation error and $\| \epsilon_1(P_1) \| \leq \bar{\epsilon}_1$. Let $F_1(P_1) = \eta_1 f_1$, where $P_1 = [p_1^{(0\sim m_1-1)}]$. Construct $\bar{V}_1 = (\zeta_1^{(0\sim m_1-1)})^T E_1 \zeta_1^{(0\sim m_1-1)}$,

$$\begin{aligned} \dot{\bar{V}}_1 =& \frac{1}{2}(\zeta_1^{(0\sim m_1-1)})^T(\phi^T E_1 + E_1\phi)\zeta_1^{(0\sim m_1-1)} \\ &+ (\zeta_1^{(0\sim m_1-1)})^T E_{1L}(W_1^T\psi_1 + \epsilon_1 + \frac{\eta_1}{\eta_2} g_1\alpha_1 \\ &+ \frac{\eta_1}{\eta_2} g_1 E_{2L}^T\zeta_2^{(0\sim m_2-1)} + B_1^{0\sim m_1-1}\zeta_1^{(0\sim m_1-1)}). \end{aligned}$$

By using Young's inequality, one obtains

$$
\begin{aligned}
&(\zeta_1^{(0\sim m_1-1)})^T E_{1L} W_1^T \psi_1 \\
&\quad \leq \frac{1}{2b_1^2}(\zeta_1^{(0\sim m_1-1)})^T E_{1L} E_{1L}^T \zeta_1^{(0\sim m_1-1)} \Theta \psi_1^T \psi_1 + \frac{1}{2} b_1^2, \\
&(\zeta_1^{(0\sim m_1-1)})^T E_{1L} \epsilon_1 \\
&\quad \leq \frac{1}{2}(\zeta_1^{(0\sim m_1-1)})^T E_{1L} E_{1L}^T \zeta_1^{(0\sim m_1-1)} + \frac{1}{2}\bar{\epsilon}_1^2, \\
&\frac{\eta_1}{\eta_2}(\zeta_1^{(0\sim m_1-1)})^T E_{1L} g_1 E_{2L}^T \zeta_2^{(0\sim m_2-1)} \\
&\quad \leq \frac{1}{2}\Theta(\zeta_1^{(0\sim m_1-1)})^T E_{1L} E_{1L}^T \zeta_1^{(0\sim m_1-1)} g_1^2 \\
&\qquad + \frac{1}{2}(\zeta_2^{(0\sim m_2-1)})^T E_{2L} E_{2L}^T \zeta_2^{(0\sim m_2-1)}.
\end{aligned}
$$

Let $V_1 = \bar{V}_1 + \frac{1}{2a_1}\tilde{\Theta}^2 + \frac{\eta_1}{2a_2\eta_2}\tilde{v}_1^2$, the virtual controller and the adaptive laws are designed based on Assumption 1 as follows

$$
\begin{cases}
\bar{\alpha}_1 = g_1^{-1}(\dfrac{\hat{\Theta}}{2b_1^2} E_{1L}^T \zeta_1^{(0\sim m_1-1)} \psi_1^T \psi_1 + \dfrac{1}{2} E_{1L}^T \zeta_1^{(0\sim m_1-1)} \\
\qquad + \dfrac{\hat{\Theta}}{2} g_1^2 E_{1L}^T \zeta_1^{(0\sim m_1-1)} + B_1^{0\sim m_1-1} \zeta_1^{(0\sim m_1-1)}), \\
\alpha_1 = -\dfrac{g_1 E_{1L}^T \zeta_1^{(0\sim m_1-1)} \bar{\alpha}_1^T \bar{\alpha}_1 \hat{v}_1^2}{\sqrt{\| g_1 E_{1L}^T \zeta_1^{(0\sim m_1-1)} \bar{\alpha}_1 \|^2 \hat{v}_1^2 + \varepsilon_1^2}}, \\
\dot{\hat{v}}_1 = a_2(\zeta_1^{(0\sim m_1-1)})^T E_{1L} g_1 \bar{\alpha}_1 - a_2 c_1 \hat{v}_1, \\
\tau_1 = \dfrac{a_1}{2}(\zeta_1^{(0\sim m_1-1)})^T E_{1L} g_1^2 E_{1L}^T \zeta_1^{(0\sim m_1-1)} - a_1 c_0 \hat{\Theta} \\
\qquad + \dfrac{a_1}{2b_1^2}(\zeta_1^{(0\sim m_1-1)})^T E_{1L} E_{1L}^T \zeta_1^{(0\sim m_1-1)} \psi_1^T \psi_1.
\end{cases}
$$

Furthermore, it is possible to obtain

$$
\begin{aligned}
\dot{V}_1 =& \dot{\bar{V}}_1 - \frac{1}{a_1}\tilde{\Theta}\dot{\hat{\Theta}} - \frac{\eta_1}{a_2\eta_2}\tilde{v}_1\dot{\hat{v}}_1 \\
\leq& -\frac{1}{2}\| \zeta_1^{(0\sim m_1-1)} \|^2 + \frac{\tilde{\Theta}}{a_1}(\tau_1 - \dot{\hat{\Theta}}) + \frac{1}{2}b_1^2 + \frac{1}{2}\bar{\epsilon}_1^2 \\
&+ \frac{1}{2}(\zeta_2^{(0\sim m_2-1)})^T E_{2L} E_{2L}^T \zeta_2^{(0\sim m_2-1)} + \frac{\eta_1}{\eta_2}\varepsilon_1 \\
&+ c_0\tilde{\Theta}\hat{\Theta} + \frac{\eta_1}{a_2\eta_2} c_1 \tilde{v}_1 \hat{v}_1.
\end{aligned}
$$

Step i **(**$2 \leq i \leq n-1$**):** By utilizing Equation (3), we can obtain

$$
\zeta_i^{(0\sim m_i-1)} = \tilde{E}_i^{-1}\left(w_i^{(0\sim m_i-1)} - \begin{bmatrix} \alpha_{i-1} \\ 0 \end{bmatrix} \right),
$$

which gives

$$
\begin{aligned}
\zeta_i^{(m_i-1)} =& J_{iF}(w_i - \alpha_{i-1}) + J_{iM} w_i^{(1\sim m_i-2)} \\
&+ J_{iL} w_i^{(m_i-1)},
\end{aligned}
$$

taking the derivative of it,

$$
\zeta_i^{(m_i)} = J_{iF}(\dot{w}_i - \dot{\alpha}_{i-1}) + J_{iM} w_i^{(2\sim m_i-1)} + J_{iL} w_i^{(m_i)}
$$

Let $F_i(P_i) = W_i^T \psi_i(P_i) + \epsilon_i(P_i), P_i = [(p_1^{(0\sim m_1-1)})^T, \ldots, (p_i^{(0\sim m_i-1)})^T, \hat{\Theta}]^T$, where $\| \epsilon_i(P_i) \| \leq \bar{\epsilon}_i$ is approximation error. Define $F_i(P_i) = J_{iF}(\dot{w}_i - \dot{\alpha}_{i-1}) + J_{iM} w_i^{(2\sim m_i-1)} + J_{iL}\eta_i f_i$. Let $V_i = V_{i-1} + (\zeta_i^{(0\sim m_i-1)})^T E_i \zeta_i^{(0\sim m_i-1)} + \frac{\eta_i}{2a_i\eta_{i+1}}\tilde{v}_i^2$, designing virtual controllers and adaptive laws

$$
\begin{cases}
\bar{\alpha}_i = (J_{iL} g_i)^{-1}(\dfrac{\hat{\Theta}}{2b_i^2} E_{iL}^T \zeta_i^{(0\sim m_i-1)} \psi_i^T \psi_i + E_{iL}^T \zeta_i^{(0\sim m_i-1)} \\
\qquad + \dfrac{\hat{\Theta}}{2}(J_{iL} g_i)^2 E_{iL}^T \zeta_i^{(0\sim m_i-1)} + B_i^{0\sim m_i-1} \zeta_i^{(0\sim m_i-1)}), \\
\alpha_i = -\dfrac{J_{iL} g_i E_{iL}^T \zeta_i^{(0\sim m_i-1)} \bar{\alpha}_i^T \bar{\alpha}_i \hat{v}_i^2}{\sqrt{\| J_{iL} g_i E_{iL}^T \zeta_i^{(0\sim m_i-1)} \bar{\alpha}_i \|^2 \hat{v}_i^2 + \varepsilon_i^2}}, \\
\dot{\hat{v}}_i = a_2(\zeta_i^{(0\sim m_i-1)})^T E_{iL} g_i \bar{\alpha}_i - a_2 c_i \hat{v}_i, \\
\tau_i = \tau_{i-1} + \dfrac{a_1}{2b_i^2}(\zeta_i^{(0\sim m_i-1)})^T E_{iL} E_{iL}^T \zeta_i^{(0\sim m_i-1)} \psi_i^T \psi_i \\
\qquad + \dfrac{a_1}{2} J_{iL}^2 (\zeta_i^{(0\sim m_i-1)})^T E_{iL} g_i^2 E_{iL}^T \zeta_i^{(0\sim m_i-1)}.
\end{cases}
$$

Thus,

$$
\begin{aligned}
\dot{V}_i \leq& -\sum_{j=1}^{i}\frac{1}{2}\| \zeta_j^{(0\sim m_j-1)} \|^2 + \sum_{j=1}^{i}\frac{\eta_i}{\eta_{i+1}} c_i \tilde{v}_i \hat{v}_i + \frac{1}{2}\sum_{j=1}^{i}\bar{\epsilon}_j^2 \\
&+ \frac{\tilde{\Theta}}{a_1}(\tau_i - \dot{\hat{\Theta}}) + c_0\tilde{\Theta}\hat{\Theta} + \sum_{j=1}^{i}\frac{\eta_j}{\eta_{j+1}}\varepsilon_j + \frac{1}{2}\sum_{j=1}^{i} b_j^2 \\
&+ \frac{1}{2}(\zeta_{i+1}^{(0\sim m_{i+1}-1)})^T E_{i+1,L} E_{i+1,L}^T \zeta_{i+1}^{(0\sim m_{i+1}-1)}.
\end{aligned}
$$

Step n**:** Based on the previous $n-1$ steps, we can immediately obtain

$$
\zeta_n^{(m_n)} = J_{nF}(\dot{w}_n - \dot{\alpha}_{n-1}) + J_{nM} w_n^{(2\sim m_n-1)} + J_{nL} w_n^{(m_n)}.
$$

Let $F_n(P_n) = W_n^T \psi_n(P_n) + \epsilon_n(P_n), P_n = [(p_1^{(0\sim m1-1)})^T, \ldots, (p_n^{(0\sim m_n-1)})^T, \hat{\Theta}]^T$, where $\| \epsilon_n(P_n) \| \leq \bar{\epsilon}_n$ is approximation error. Define $F_n(P_n) = J_{nF}(\dot{w}_n - \dot{\alpha}_{n-1}) + J_{nM} w_n^{(2\sim m_n-1)} + J_{nL}\eta_n f_n$. Construct $V_n = V_{n-1} + (\zeta_n^{(0\sim m_n-1)})^T E_L \zeta_n^{(0\sim m_n-1)} + \frac{\eta_i}{2a_i\eta_{i+1}}\tilde{v}_n^2$, designing the controller and adaptive gains is outlined below

$$
\begin{cases}
\bar{\alpha}_n = (J_{nL} g_n)^{-1}(\dfrac{\hat{\Theta}}{2b_n^2} E_{nL}^T \zeta_n^{(0\sim m_n-1)} \psi_n^T \psi_n \\
\qquad + E_{nL}^T \zeta_n^{(0\sim m_n-1)} + B_n^{0\sim m_n-1} \zeta_n^{(0\sim m_n-1)}), \\
\alpha_n = -\dfrac{J_{nL} g_n E_{nL}^T \zeta_n^{(0\sim m_n-1)} \bar{\alpha}_n^T \bar{\alpha}_n \hat{v}_n^2}{\sqrt{\| J_{nL} g_n E_{nL}^T \zeta_n^{(0\sim m_n-1)} \bar{\alpha}_n \|^2 \hat{v}_n^2 + \varepsilon_n^2}}, \\
\dot{\hat{v}}_n = a_2(\zeta_n^{(0\sim m_n-1)})^T E_{nL} g_n \bar{\alpha}_n - a_2 c_n \hat{v}_n, \\
\tau_n = \dfrac{a_1}{2b_n^2}(\zeta_n^{(0\sim m_n-1)})^T E_{nL} E_{nL}^T \zeta_n^{(0\sim m_n-1)} \psi_n^T \psi_n \\
\qquad + \tau_{n-1}.
\end{cases}
\tag{5}
$$

As a consequence,

$$
\begin{aligned}
\dot{V}_n \leq& -\sum_{j=1}^{n}\frac{1}{2}\| \zeta_j^{(0\sim m_j-1)} \|^2 + \eta_n c_n \tilde{v}_n \hat{v}_n + \frac{1}{2}\sum_{j=1}^{n}\bar{\epsilon}_j^2 \\
&+ \sum_{j=1}^{n-1}\frac{\eta_j}{\eta_{j+1}} c_j \tilde{v}_j \hat{v}_j + \sum_{j=1}^{n-1}\frac{\eta_j}{\eta_{j+1}}\varepsilon_j + \frac{1}{2}\sum_{j=1}^{n} b_j^2 \\
&+ \frac{\tilde{\Theta}}{a_1}(\tau_n - \dot{\hat{\Theta}}) + c_0\tilde{\Theta}\hat{\Theta} + \eta_n\varepsilon_n
\end{aligned}
$$

4 Stability Analysis

Theorem 1: For high-order FASs (1), the design of controllers and adaptive laws (6) guarantee the stabilization of the systems, and all signals of the closed-loop system remain bounded.

Proof: Given that $\tilde{\Theta} = \Theta - \hat{\Theta}$, one has

$$\eta_n c_n \tilde{v}_n \hat{v}_n \leq -\frac{1}{2}\eta_n c_n \tilde{v}_n^2 + \frac{1}{2}\eta_n c_n v_n^2,$$

$$\sum_{j=1}^{n-1} \frac{\eta_j}{\eta_{j+1}} c_j \tilde{v}_j \hat{v}_j \leq -\frac{1}{2}\sum_{j=1}^{n-1} \frac{\eta_j}{\eta_{j+1}} c_j \tilde{v}_j^2 + \frac{1}{2}\sum_{j=1}^{n-1} \frac{\eta_j}{\eta_{j+1}} c_j v_j^2,$$

$$c_0 \tilde{\Theta}\hat{\Theta} \leq -\frac{1}{2}c_0 \tilde{\Theta}^2 + \frac{1}{2}c_0 \Theta^2.$$

Hence,

$$\begin{aligned}\dot{V}_n \leq & -\sum_{j=1}^{n} \frac{1}{2} \parallel \zeta_j^{(0\sim m_j-1)} \parallel^2 - \frac{1}{2}\sum_{j=1}^{n-1} \frac{\eta_j}{\eta_{j+1}} c_j \tilde{v}_j^2 + \eta_n \varepsilon_n \\ & - \frac{1}{2}\eta_n c_n \tilde{v}_n^2 + \frac{1}{2}\eta_n c_n v_n^2 + \sum_{j=1}^{n-1} \frac{\eta_j}{\eta_{j+1}} \varepsilon_j + \frac{1}{2}\sum_{j=1}^{n} b_j^2 \\ & + \frac{1}{2}\sum_{j=1}^{n-1} \frac{\eta_j}{\eta_{j+1}} c_j v_j^2 - \frac{1}{2}c_0 \tilde{\Theta}^2 + \frac{1}{2}\sum_{j=1}^{n} \bar{\epsilon}_j^2 + \frac{1}{2}c_0 \Theta^2 \\ \leq & -cV_n + \Gamma,\end{aligned}$$

where $c = min\{\lambda_{min}^{-1}(E), a_1 c_0, a_2 c_i\}$, $\Gamma = \sum_{j=1}^{n-1} \frac{\eta_j}{\eta_{j+1}} \varepsilon_j + \frac{1}{2}\sum_{j=1}^{n} b_j^2 + \eta_n \varepsilon_n + \frac{1}{2}\sum_{j=1}^{n-1} \frac{\eta_j}{\eta_{j+1}} c_j v_j^2 + \frac{1}{2}\eta_n c_n v_n^2 + \frac{1}{2}\sum_{j=1}^{n} \bar{\epsilon}_j^2 + \frac{1}{2}c_0 \Theta^2$. Therefore,

$$0 \leq V(t) \leq \frac{\Gamma}{c} + (V(0) - \frac{\Gamma}{c})e^{-ct},$$

which means that all signals are bounded.

5 Simulation examples

To verify the effectiveness of the proposed method, we apply it to 2-DOF robot manipulators. The dynamic equation of the system is given by [13]

$$D(x)\ddot{x} + R(x, \dot{x})\ddot{x} + H(x) = \tau,$$

where $x \in R^2$ is the vector of joint position, $D(x) \in R^{2\times 2}$ is the inertia matrix, $R(x, \dot{x}) \in R^{2\times 2}$ is the centrifugal and Coriolis matrix, $H(x) \in R^2$ is the gravitational forces vector, $\tau(t) \in R^2$ is the input torque vector. In this context, each vector or matrix can be further decomposed into the following forms:

$$D(x) = \begin{bmatrix} (s_1 + m_2)d_1^2 + s_2 d_2^2 + 2s_2 d_1 d_2 \cos(x_2) + I_1 & s_2 d_2^2 + s_2 d_1 d_2 \cos(x_2) \\ s_2 d_2^2 + d_1 d_2 \cos(x_2) & s_2 d_2^2 + I_2 \end{bmatrix},$$

$$R(x, \dot{x}) = \begin{bmatrix} -s_2 d_1 d_2 \sin(x_2)\dot{q}_1 & -2s_2 d_1 d_2 \sin(x_2)\dot{q}_1 \\ 0 & s_2 d_1 d_2 \sin(x_2)\dot{q}_2 \end{bmatrix},$$

$$H(x) = \begin{bmatrix} (s_1 + s_2)g d_1 \cos(x_2) + s_2 g d_2 \cos(x_1 + x_2) \\ s_2 g d_2 \cos(x_1 + x_2) \end{bmatrix},$$

where m_ι represents the mass of link ι, d_ι signifies the length of link ι, and I_ι stands for the moment of inertia of link ι, $\iota = 1, 2$.

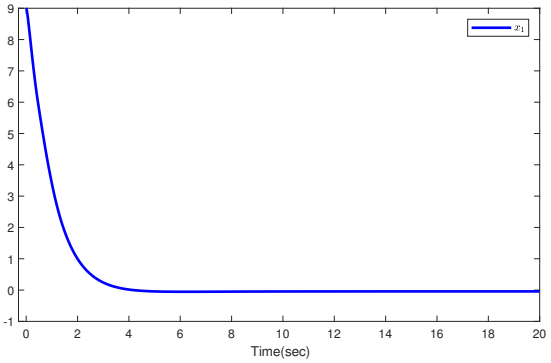

Fig. 1. Trajectory of x_1.

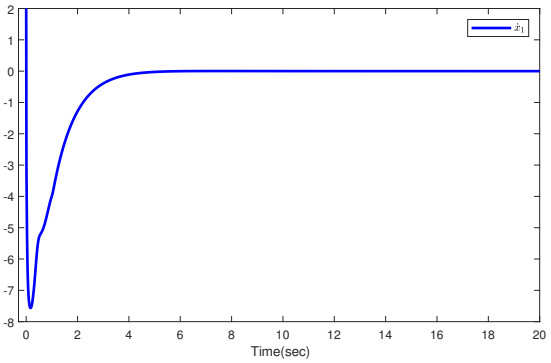

Fig. 2. Trajectory of $\dot{x}_1$.

$$E = \begin{bmatrix} 2.6329 & -0.1366 & 0.7878 & -1.0756 \\ -0.1366 & 1.3488 & -0.1366 & 0.3488 \\ 0.7878 & -0.1366 & 0.4465 & -0.5159 \\ -1.0756 & 0.3488 & -0.5156 & 0.9707 \end{bmatrix},$$

$$B_0 = \begin{bmatrix} 2 & 4 \\ 1 & 3 \end{bmatrix}, \quad B_1 = \begin{bmatrix} 3 & 4 \\ 0.1 & 3 \end{bmatrix}$$

The system parameters are chosen as $s_1 = 4, s_2 = 1, d_1 = 0.5, d_2 = 1, I_1 = 1, I_2 = 0.5, \varepsilon = 0.01, \eta = 0.75$. The initial values are $x_1(0) = 9$, $\dot{x}_1(0) = 2$, $x_2(0) = -6$, $\dot{x}_2(0) = 2$, $\hat{\Theta}(0) = 2$, $\hat{v}(0) = 5$, $b = 0.4, a_1 = 0.5, a_2 = 0.5, c_0 = 0.5, c_1 = 3$. The trajectories of the motion variables x_1, $\dot{x}_1$, x_2 and $\dot{x}_2$ are depicted in Figs. 1-4. Additionally, Fig. 5 and Fig. 6 illustrate that the adaptive parameters eventually become bounded, while Fig. 7 and Fig. 8 display the trajectories of the inputs u_1 and u_2.

6 Conclusion

This paper addresses the adaptive stabilization control of a class of high-order fully actuated systems with unknown measurement sensitivity. Drawing upon the theory of fully actuated systems, the approach directly tackles high-order systems, circumventing the computational complexity introduced by system reduction. Leveraging the state values measured by sensors, the system is brought to stability with all signals within the closed-loop system bounded. Finally, the proposed control scheme is applied to a 2-DOF robotic arm, substantiating the feasibility of the algorithm.

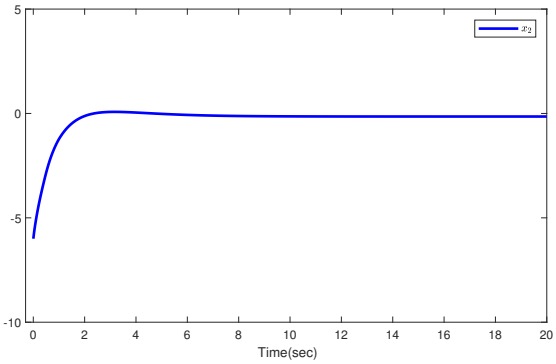

Fig. 3. Trajectory of x_2.

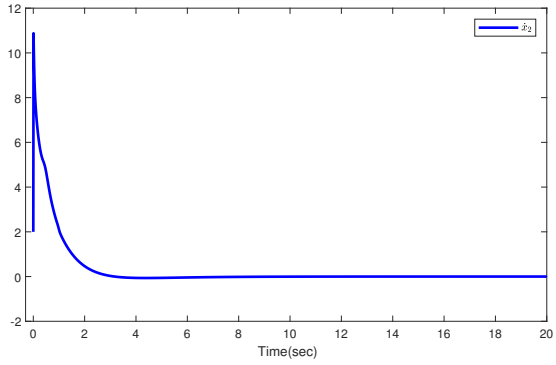

Fig. 4. Trajectory of $\dot{x}_2$.

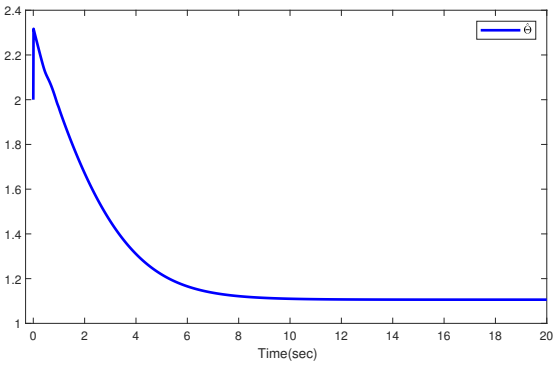

Fig. 5. Trajectory of $\hat{\Theta}$.

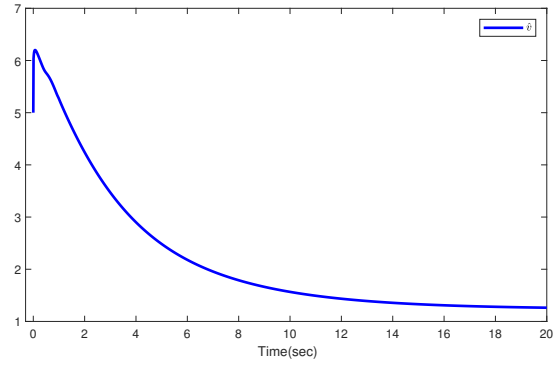

Fig. 6. Trajectory of $\hat{v}$.

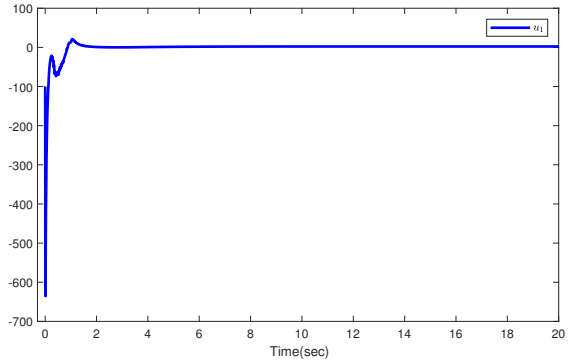

Fig. 7. Trajectory of u_1.

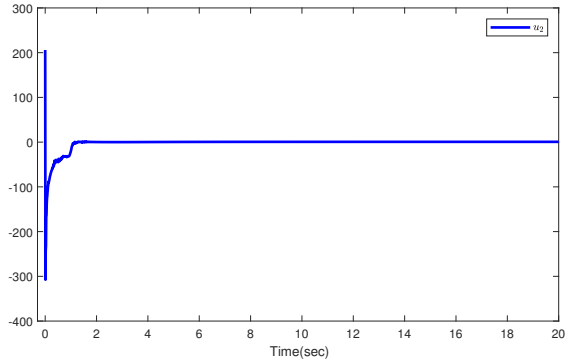

Fig. 8. Trajectory of u_2.

References

[1] G. R. Duan, High-order system approaches–I. Full-actuation and parametric design," *Acta Automatica Sinica*, 2020, 46(7): 1333–1345.

[2] G. R. Duan, High-order system approaches–II. Controllability and fully-actuatio," *Acta Automatica Sinica*, 2020, 46(8): 1571–1581.

[3] G. R. Duan, High-order fully actuated system approaches: Part I. Models and basic procedure. *International Journal of Systems Science*, 2021, 52(2): 422–435.

[4] P. J. Ning, C. C. Hua , R. Meng. Adaptive control for a class of nonlinear time-delay system based on the fully actuated system approaches. *Journal of Systems Science and Complexity*, 2022, 35(2): 522–534.

[5] G. R. Duan , G. P. Liu. Attitude and orbit optimal control of combined spacecraft via a fully-actuated system approach. *Journal of Systems Science and Complexity*, 2022, 35(2): 623–640.

[6] Q. Zhao, G. R. Duan. Fully actuated system approach for 6D-OF spacecraft control based on extended state observer. *Journal of Systems Science and Complexity*, 2022, 35(2): 604–622.

[7] C. C. Chen, C. J. Qian, Z. Y. Sun, and Y. W. Liang, Global output feedback stabilization of a class of nonlinear systems with unknown measurement sensitivity. *IEEE Transactions on Automatic Control*, 2018, 63(7): 2212–2217.

[8] Z. Y. Sun, C. Liu, S. F. Su, W. Sun, "Global Finite-Time Stabilization for Uncertain Systems With Unknown Measurement Sensitivity," in IEEE Transactions on Cybernetics, vol. 52, no. 8, pp. 7602-7611, Aug. 2022.

[9] S. Z. Diao, W. Sun, S. F. Su, X. D. Zhao, N. Xu, "Novel Adaptive Control for Flexible-Joint Robots With Unknown Measurement Sensitivity," in IEEE Transactions on Automation

Science and Engineering, Doi: 10.1109/TASE.2023.3248178.

[10] M. Y. Li, T. T. Yang, and S. C. Tong, Adaptive Neural Networks Finite-Time Optimal Control for a Class of Nonlinear Systems. *IEEE Transactions on Neural Networks and Learning Systems*, 2020, 31(11): 4451–4460.

[11] G. R. Duan, High-order fully actuated system approaches: Part IV. Adaptive control and high-order backstepping. *International Journal of System Sciences*, 2020, 52(5): 972–989.

[12] C. C. Hua, K. Li, and X. P. Guan, Decentralized event-triggered control for interconnected time-delay stochastic nonlinear systems using neural networks. *Neurocomputing*, 2018, 272: 270–278.

[13] M. Boukattaya, H. Gassara ,and T. Damak, A global time-varying sliding-mode control for the tracking problem of uncertain dynamical systems. *ISA Transactions*, 2020, 97: 155–170.

Proceedings of the 3rd Conference on Fully Actuated System Theory and Applications
May 10-12, 2024, Shenzhen, China

Coordinated Control for Incomplete Controllable Systems over Finite Fields

Qin Ao[1], Gao Zhe[1], Feng Jun-e[1]
1. School of Mathematics, Shandong University, Jinan 250100, P. R. China
E-mail: fengjune@sdu.edu.cn

Abstract: Controller design is discussed for coordinated control problems of incomplete controllable systems over finite fields. Generalized types of consensus and synchronization are proposed, respectively. Combined with high-order fully actuated system approaches, incomplete controllable systems are decoupled. Under some circumstances, suitable controllers are given to achieve consensus or synchronization in the general context. Finally, a numerical example about camera light network is shown to verify our results.

Key Words: Incomplete controllable Systems, Coordinated control, Finite fields, High-order fully actuated system

1 Introduction

Networks over finite fields have gained significant attention in recent years due to their applications in various areas, including control, coordination, communication, etc [1].

Pasqualetti et al. [2] presented an analysis of consensus networks over finite fields. Xu and Hong [3] further explored leader-following consensus in multi-agent systems with directed acyclic graph topology. Time-delayed consensus networks were investigated by Li et al. [4], and the discussion of switching topology on consensus networks was explored in their subsequent work [5]. Yu et al. [6] highlighted the importance of finite-field networks in achieving coordinated output behavior in leader-follower structures.

Synchronization, a more common case of consensus, was investigated by Meng et al. [7] and Wang et al. [8], who extended results in [2] to synchronization networks. Zhu et al. [9] looked into synchronization with time delays with the help of linear recursion theory.

There are many explorations of synchronization in specialized networks. Zhang et al. [10] investigated synchronization in networks with switching multiple communication channels. Lin et al. [11] provided insights into synchronization under uncertain conditions by analyzing stochastic networks through finite fields. Cluster synchronization, a concept crucial for large-scale networks, was explored by Lin et al. [12], by means of semi-tensor product. Chen and Zhu [13] contributed by conducting a synchronization analysis of Boolean networks, which also used semi-tensor product. Zhao et al. [14] extended this work by studying the synchronization of drive-response singular Boolean networks, providing valuable insights into the synchronization behavior of specialized Boolean networks.

The literature reviewed demonstrates the versatility and applicability of finite-field networks in diverse scenarios. However, their discussions are more or less based on special topology structure of the multi-agent network, or based on semi-tensor product, which has the disadvantage of computing.

High-order fully actuated (HOFA) systems have become a focal point in control theory and engineering applications due to their relevance in addressing complex dynamical systems. [15] provided a foundational understanding of HOFA systems, outlining models and basic procedures. The series begin with an exploration of fully actuated systems and parametric designs [16], followed by discussions on controllability and full actuation [17]. Subsequent articles delve into robust control and high-order backstepping [18], adaptive control and high-order backstepping [19], robust adaptive control [20], disturbance attenuation, and decoupling [21], showcasing a comprehensive approach to control design.

The application of HOFA systems extends to specific domains. The work [22] on optimal control, particularly in spacecraft attitude stabilization, the introduction of discrete-time systems [23], as well as discrete time delay systems [24], demonstrate the adaptability of HOFA system approaches to different contexts. Researchers such as Liu [25] and Zhang et al. [26] have extended HOFA system approaches to networked multi-agent systems. Yang et al. [27] explored the controllability of multi-agent systems over finite fields using HOFA system approaches. HOFA system approaches have shown a suitable method for problems of multi-agent systems, which may also be helpful in the coordinated control problems.

For linear systems, they can be converted to HOFA systems if and only if they are controllable [17]. Under the framework of linear systems over finite fields, coordinated problems of incomplete controllable systems will be discussed in this paper, by using HOFA system approaches. The main contributions of this paper can be summarized as follows:

(i) The concept of v-consensus and v-synchronization is introduced, which is a generalized concept of the original ones, with corresponding properties and conditions.

(ii) For both consensus and synchronization problems of incomplete controllable systems, proper controllers are given to achieve consensus and synchronization in the general context under certain circumstances.

The rest of our paper are organized as follows. Section 2 introduces some basic knowledge about finite fields and HOFA systems. Section 3 is the main section, including the concept of v-consensus and v-synchronization, the analysis of incomplete controllable systems, and the controller design. Section 4 is a numerical example, and Section 5 concludes this paper briefly.

This work was supported in part by the Science Center Program of National Natural Science Foundation of China under Grant 62188101, 62273201, and the Research Fund for the Taishan Scholar Project of Shandong Province of China (TSTP20221103).

2 Preliminaries

2.1 Finite Fields

Define the finite field $\mathbb{F}_p = \{0, 1, \ldots, p-1\}$ with two operations $(+, \times)$, where p is a prime number, and the calculations use modular arithmetic. For example, in $\mathbb{F}_5$, $3 + 4 = 7 \ mod \ 5 = 2$, and $3 \times 4 = 12 \ mod \ 5 = 2$. For simplicity, the symbol "$\times$" will be omitted. Fields defined in this way are called Galois fields, and they are extensively applied in multi-agent problems.

Unless otherwise specified, all operations in this paper are carried out in the finite field $\mathbb{F}_p$.

In finite fields, the concept of "order" is frequently used, which is defined as follows:

Definition 1 ([28]). *For $\alpha \in \mathbb{F}_p$, where $\alpha \neq 0$, the order denoted as $ord(\alpha) = s$ is defined as the smallest positive integer s that satisfies $\alpha^s = 1$.*

Next, we will discuss the basic form of systems over finite fields. The coordination control problems over finite fields are discussed in the context of the following system

$$x(k+1) = Ax(k) + Bu(k), \tag{1}$$

where $x(k) = [x_1(k), x_2(k), \ldots, x_n(k)]^\top \in \mathbb{F}_p^n$, $A \in \mathbb{F}_p^{n\times n}$, $B \in \mathbb{F}_p^{n\times m}$, $rank[B] = m$, and $u(k) = [u_1(k), u_2(k), \ldots, u_m(k)]^\top \in \mathbb{F}_p^m$ is the control vector, with k starting from 0.

Discussing linear systems over finite fields has its unique advantage. For example, the requirement for consensus in the real field demands that the norm of the state difference tends to zero as time approaches infinity, whereas in a finite field, it is sufficient for the states to be equal within a finite time, given the limited range of possible state values.

2.2 HOFA System Approaches

This subsection provides a brief introduction to the HOFA system approaches. First, we present the definition of fully actuated systems over a finite field. Although the original definition is on the real field $\mathbb{R}$ [23], it is applicable to finite fields as well.

Definition 2 ([23]). *For system* (1)*, if $det(B) \neq 0$, then system* (1) *is fully actuated.*

The importance of Definition 2 is reflected in the following lemma.

Lemma 1 ([15]). *Given a matrix $A_0 \in \mathbb{F}_p^{n\times n}$. If* (1) *is fully actuated, then with the control law $u(k) = B^{-1}(-Ax(k) + A_0x(k) + v(k))$, system $x(k+1) = A_0x(k) + v(k)$ can be obtained.*

This method eliminates all open loop characteristics of the original system, replacing them with the desired system characteristics, which is beneficial for controller design. This method will be used in the issues related to finite fields.

For linear systems over finite fields, the following lemma holds.

Lemma 2 ([27]). *System* (1) *is controllable if and only if it can be equivalently transformed into a step forward HOFA system or a step backward HOFA system.*

Using the method from [27], we can transform a controllable system into both the the forward and backward HOFA systems. The step forward HOFA system is represented in this paper as

$$\tilde{z}_1(k+1) = L(\tilde{z}_1(k)) + \tilde{B}u(k), \tag{2}$$

and the step backward HOFA system is written as

$$\tilde{z}_2(k+1) = L(\tilde{z}_2(k)) + \tilde{B}u(k), \tag{3}$$

where $\tilde{B}$ is the same, with diagonal elements as 1 [29].

Systems (2) and (3) are equivalent forms of system (1) when it is controllable. Although the controllers designed in the following sections is for (2) and (3), they can also be applied to (1). In fact, under the inverse transformation $x(k) = Q^{-1}z(k)$, we can obtain the corresponding states (trajectories) of original system (1) .

3 Analysis of Incomplete Controllable Systems

In the multi-agent network over a finite field, both consensus and synchronization describe the behavior of individual agents. Therefore, after a coordinate transformation of the states (system), certain behavioral patterns can be obtained. We will start with nonsingular coordinate transformation, introduce new features of consensus and synchronization, and analyze the consensus and synchronization issues of incomplete controllable systems.

3.1 Analysis of v-consensus

Consensus in a finite-field network requires that, for all initial values $x(0)$, there exists a finite time $T \in \mathbb{N}$ such that

$$x(T) = x(T+\tau) = \alpha\mathbb{1} \tag{4}$$

holds for all $\tau \in \mathbb{N}$, where $\alpha \in \mathbb{F}_p$, and $\mathbb{1}$ represents $[1, \ldots, 1]^\top$ of proper dimensions. Here we introduce a nonsingular coordinate transformation $z(k) = Vx(k)$ and define $v = V\mathbb{1} \neq \mathbb{0}$, where $\mathbb{0}$ represents a vector or matrix with its elements all 0 of proper dimensions. Then (4) can be rewritten as

$$z(T) = z(T+\tau) = Vx(T) = \alpha V\mathbb{1} = \alpha v. \tag{5}$$

Comparing (5) with (4), (5) only replaces $\mathbb{1}$ with v. Since the coordinate transformation is nonsingular, consensus features of the original system can be obtained by the inverse transformation $x(T) = V^{-1}z(T)$. The form of (5) has certain generalizations compared to the consensus, especially when the conditions for the transformation matrix are unclear, allowing for characteristics of system consensus to be obtained in a similar way. The following definition is provided for this type of consensus.

Definition 3. *For all initial values $z(0) \in \mathbb{F}_p^n$, system*

$$z(k+1) = A_z z(k), \ A_z \in \mathbb{F}_p^{n\times n} \tag{6}$$

achieves v-consensus, if there exists a finite time $T \in \mathbb{N}$ such that $z(T) = z(T+\tau) = \alpha v$ holds for all $\tau \in \mathbb{N}$, where $\alpha \in \mathbb{F}_p$ and $v \in \mathbb{F}_p^n$.

Similar to the general consensus situation, a necessary condition can be readily obtained.

Proposition 1. *Consider finite-field system* (6) *under nonsingular coordinate transformation* $z(k) = Vx(k)$. *If it achieves* v*-consensus, then matrix* A_z *should satisfy*

$$A_z v = v, \quad v \neq \mathbb{0}, \tag{7}$$

or matrix A_z *is nilpotent.*

Proof. Since system (6) achieves v-consensus, according to Definition 3, for all $z(0)$, there exists $T \in \mathbb{N}$, when $t \geq T$, $A_z^t z(0) = A_z^{t+1} z(0) = \alpha v$. This implies $A_z \alpha v = \alpha v$, which leads to either $A_z v = v$ or, for all $z(0)$, $\alpha = 0$, i.e., matrix A_z is nilpotent. □

It should be noted that, the propositions presented below shares some similarities with conclusions related to general consensus in the literature. These propositions can be directly interpreted through the invariance of coordinate transformation, and the results and proof process are basically the same as in literature [2].

Proposition 2. *Consider system* (6)*, and let* A_z *satisfy* (7)*,* V *is a nonsingular matrix. The necessary and sufficient condition for* (6) *to achieve* v*-consensus is* $P_{A_z}(s) = s^{n-1}(s-1)$*, where* $P_{A_z}(s)$ *is the characteristic polynomial of* A_z*, and* $v = V\mathbb{1}$.

Proposition 3. *Consider system* (6)*, and let* A_z *satisfy* (7)*,* V *is a nonsingular matrix. Suppose* (6) *achieves* v*-consensus, where* $v = V\mathbb{1}$. *Let* $z(0) \in F_p^n$ *be the initial state. Assume* $T < n$ *represents the maximum dimension of the Jordan block associated with the eigenvalue 0. Let* $\pi \in F_p^{1\times n}$ *be the unique eigenvector satisfying* $\pi A_z = \pi$, $\pi v = 1$. *Then* $A_z^T = v\pi$, *and it takes* T *iterations to achieve* v*-consensus with value* $v\pi z(0)$.

3.2 Analysis of v-synchronization

Synchronization in a network over a finite field requires that for all initial values $x(0)$, there exists a finite time $T \in \mathbb{N}$ such that all states satisfy $x_1(t) = x_2(t) = \cdots = x_n(t)$, i.e.,

$$x(t) \in \{\alpha\mathbb{1} | \alpha \in \mathbb{F}_p\}, \tag{8}$$

and this holds for all $t \geq T$. If we also introduce a nonsingular coordinate transformation $z(k) = Vx(k)$, then (8) can be rewritten as $v(t) \in \{\alpha v | \alpha \in \mathbb{F}_p\}$. Similar to the case of v-consensus, we can define the concept of v-synchronization.

Definition 4. *For all initial values* $z(0) \in \mathbb{F}_p^n$*, system* (6) *achieves* v*-synchronization, if there exists a finite time* $T \in \mathbb{N}$ *such that* $z(t) \in \{\alpha v | \alpha \in \mathbb{F}_p\}$ *holds for all* $t \geq T$, $v \in \mathbb{F}_p^n$.

Similar to the case of v-consensus, we can clearly obtain a necessary condition:

Proposition 4. *If system* (6) *achieves* v*-synchronization,* V *is a nonsingular matrix, then the matrix* A_z *should satisfy*

$$A_z v = \alpha v, \ \alpha \neq 0, v \neq \mathbb{0}, \tag{9}$$

or the matrix A_z *is nilpotent.*

Clearly, when $\alpha = 1$, the result of Proposition 4 reduces to the conclusion of Proposition 1.

Next, we present the necessary and sufficient conditions for v-synchronization. The basic idea is similar to the previous subsection on v-consensus, and the related conclusions for v-synchronization can be degenerated into those for v-consensus. The proof refers to [7].

Proposition 5. *If* A_z *satisfies* (9)*,* V *is a nonsingular matrix, then system* (6) *achieves* v*-synchronization if and only if* $P_{A_z}(s) = s^{n-1}(s-\alpha)$*, where* $v = V\mathbb{1}$.

The time needed and values for synchronization can be analogous to Proposition 3 and are stated as follows.

Proposition 6. *Consider* (6)*. Suppose* A_z *satisfies* (9)*, and let the initial state be* $z(0) \in \mathbb{F}_p^n$*. Assume that* (6) *achieves* v*-synchronization, where* $v = V\mathbb{1}$*,* V *is a nonsingular matrix. Let* $T < n$ *represents the maximum dimension of the largest Jordan block associated with the eigenvalue 0. Let* $\pi \in \mathbb{F}_p^n$ *be the unique eigenvector satisfying* $\pi v = 1$. *Then it takes* T *iterations to achieve* v*-synchronization, and the state vector is in the cycle* $\{v\pi z(0) \to v\pi\alpha z(0) \to \cdots \to v\pi\alpha^{s-1} z(0) \to v\pi z(0) \to \dots\}$, $s = ord(\alpha) \bmod p$*, or the state vector is merely* $\mathbb{0}$.

Remark 1. *The definitions of* v*-consensus and* v*-synchronization extend the coordinated behavior of agents. Specifically,* (4) *and* (8) *both require that the states of one agent must be the same at one time, which are actually* $\mathbb{1}$*-consensus and* $\mathbb{1}$*-synchronization, respectively. However,* v*-consensus and* v*-synchronization do not require so. Besides, they also show a coordinated behavior, and thus further extend the original concepts of consensus and synchronization.*

In fact, the propositions above can be further extended to a general vector v, other than merely from a nonsingular transformation, the proof is omitted here for limited space. The next subsection directly applies these results to specific scenarios.

3.3 Controller Design for Incomplete Controllable Systems

For a general linear system with control inputs over a finite field, there may exist a state pair (x_i, x_j) such that there is no control input sequence allowing the system to transit from state x_i to x_j. Systems exhibiting this behavior are referred to as incomplete controllable systems.

Similar to linear systems over the real field $\mathbb{R}$, consider a system described by

$$x(k+1) = Ax(k) + Bu(k), \ x \in \mathbb{F}_p^n, \ B \neq \mathbb{0}. \tag{10}$$

System (10) is incomplete controllable, i.e., $\text{rank}(B) = m < n$, and the order of non-controllable part is denoted by $\bar{n} \geq 1$. The controllable part has the order $n - \bar{n}$, meaning there are $n - \bar{n}$ linearly independent vectors in the controllability matrix. These vectors can be written in the form

$$\begin{aligned} M_1 = [&b_1, Ab_1, \dots, A^{c_1-1}b_1, \\ &b_2, Ab_2, \dots, A^{c_2-1}b_2, \dots, A^{c_m-1}b_m], \end{aligned}$$

where $\sum_{i=1}^{m} c_i = n - \bar{n}$, $M_1 \in \mathbb{F}_p^{n\times(n-\bar{n})}$.

Literature [30] provides a synthesis method to obtain the standard form of incomplete controllable systems and their

transformations over finite fields. The method is listed as follows.

Firstly, extend M_1 to a reversible matrix $M = [M_1, M_2]$, where $M_2 \in \mathbb{F}_p^{n\times\bar{n}}$ is chosen such that its rank is $\bar{n}$ and $M_2^\top M_1 = 0$.

Next, compute M^{-1}. Denote $\sigma_i = \sum_{j=1}^{i} c_j$, $i = 1, \ldots, m$, and $(\bar{l}_i)^\top = Row_{\sigma_i}(M^{-1})$. Choose a nonsingular transformation matrix as $R = [(R^1)^\top, (R^2)^\top]^\top$, where

$$R^1 = [(\bar{l}_1)^\top, (\bar{l}_1 A)^\top, \ldots, (\bar{l}_1 A^{c_1-1})^\top, (\bar{l}_2)^\top, (\bar{l}_2 A)^\top, \ldots, (\bar{l}_2 A^{c_2-1})^\top, \ldots, (\bar{l}_m A^{c_m-1})^\top]^\top,$$

$$R^2 = [Row_{(n-\bar{n}+1)}(M^{-1})^\top, \ldots, Row_n(M^{-1})^\top]^\top.$$

Then under the transformation $y(k) = Rx(k)$, system (10) becomes

$$y(k+1) = Ey(k) + Fu(k), \tag{11}$$

where

$$E = \begin{bmatrix} E_1 & E_2 \\ \mathbb{0} & E_3 \end{bmatrix}, F = \begin{bmatrix} F_1 \\ \mathbb{0} \end{bmatrix}.$$

The forms of each block are as follows, $E_1 = [E_{ij}^c]$, where

$$E_{ii}^c = \begin{bmatrix} \mathbb{0}_{(c_i-1)\times 1} & I_{(c_i-1)\times(c_i-1)} \\ e_{c_i 1}^{ii} & e_{c_i 2}^{ii} \; e_{c_i 3}^{ii} \; \cdots \; e_{c_i c_i}^{ii} \end{bmatrix},$$

$$E_{ij}^c = \begin{bmatrix} \mathbb{0}_{(c_i-1)\times c_i} \\ e_{c_i 1}^{ij} \; e_{c_i 2}^{ij} \; e_{c_i 3}^{ij} \; \cdots \; e_{c_i c_j}^{ij} \end{bmatrix}, \; i \neq j,$$

$$E_2 = \left[(E_1^c)^\top, \ldots, (E_m^c)^\top\right]^\top,$$

$$E_i^c = \begin{bmatrix} \mathbb{0}_{(c_i-1)\times \bar{n}} \\ e_{c_i 1} \; e_{c_i 2} \; e_{c_i 3} \; \cdots \; e_{c_i \bar{n}} \end{bmatrix},$$

$$F_1 = \left[(F_1^c)^\top, \ldots, (F_m^c)^\top\right]^\top,$$

$$F_i^c = \begin{bmatrix} \mathbb{0}_{(c_i-1)\times m} \\ 0 \; \cdots \; f_{c_i i} \; f_{c_i i+1} \; \cdots \; f_{c_i m} \end{bmatrix}.$$

$E_{ij}^c \in \mathbb{F}_p^{c_i\times c_j}$, $F_i^c \in \mathbb{F}_p^{c_i\times m}$, $i, j = 1, \ldots, m$. $f_{c_i i} = 1$ is the element in the c_i-th row and i-th column of F_i^c. $E_1 \in \mathbb{F}_p^{(n-\bar{n})\times(n-\bar{n})}$, $F_1 \in \mathbb{F}_p^{(n-\bar{n})\times m}$, $E_2 \in \mathbb{F}_p^{(n-\bar{n})\times\bar{n}}$, $E_3 \in \mathbb{F}_p^{\bar{n}\times\bar{n}}$, and (E_1, F_1) is in the controllable canonical form [30].

Rewriting (11) into the form of two subsystems,

$$y_1(k+1) = E_1 y_1(k) + E_2 y_2(k) + F_1 u(k), \tag{12}$$

$$y_2(k+1) = E_3 y_2(k), \tag{13}$$

where $y_1(k) \in \mathbb{F}_p^{(n-\bar{n})}$, $y_2(k) \in \mathbb{F}_p^{\bar{n}}$, it can be observed that (13) is an autonomous system, not influenced by external control, while (12) is a coupled system where $y_1(k+1)$ is influenced by $y_1(k)$, $y_2(k)$, and external control.

Let $R\mathbb{1} = [(R^1\mathbb{1})^\top, (R^2\mathbb{1})^\top]^\top = [(r^1)^\top, (r^2)^\top]^\top$, $r^1 = [r_{11}^1, \ldots, r_{1c_1}^1, \ldots, r_{m1}^1, \ldots, r_{mc_m}^1]^\top$, $r^2 = [r_{b1}^2, \ldots, r_{b\bar{n}}^2]^\top$, $y_1(k)$ and $y_2(k)$ are also divided this way. The next part will use the theory of HOFA systems to decouple (11) and write it in the form of an HOFA system.

Subsystem (12) contains items related to $y_1(k)$ and $y_2(k)$. The key to decoupling (12) is to eliminate $A_{12}y_2(k)$ in (12). In other words, we need to find a suitable controller $u(k)$ satisfying $E_2 y_2(k) + F_1 u(k) = \mathbb{0}$. Literature [30] provides an approach using state feedback $u(k) = Kx(k)$ to decouple.

In the transformed system, suppose the feedback matrix is $\bar{K}$, which is further divided into $\bar{K} = [\bar{K}_1, \bar{K}_2]$. Thus, $u(k) = \bar{K}_1 y_1(k) + \bar{K}_2 y_2(k)$. It is sufficient to reach the condition $F_1\bar{K}_2 = -E_2$, and it can always be satisfied.

Lemma 3 ([30]). *The uncontrollable part can always be decoupled from* (12) *in the form of linear state feedback.*

The discussion above is from literature [30]. Inspired by this lemma, we will use the theory of HOFA systems to further illustrate. Observing the structural features of E_2, we can directly rewrite (12) using the methods from the [29] as the following step forward HOFA system

$$\tilde{y}_1(k+1) = L(\tilde{y}_1(k)) + L^{'}(y_2(k)) + \tilde{B}u(k), \tag{14}$$

where

$$\tilde{y}_1(k) = (y_{11}(k+c_1-1), y_{21}(k+c_2-1), \ldots, y_{m1}(k+c_m-1))^\top,$$

$$L(\tilde{y}_1(k)) = (L_1(\tilde{y}_1, k), L_2(\tilde{y}_1, k), \ldots, L_m(\tilde{y}_1, k))^\top,$$

$$L_i(\tilde{y}_1, k) = \sum_{j=1}^{c_i} e_{c_i j}^{ii} y_{i1}(k+j-1) + \gamma_i(k),$$

$$\gamma_i(k) = \sum_{j=1, j\neq i}^{m} \sum_{l=1}^{c_j} e_{c_i l}^{ij} y_{j1}(k+l-1),$$

$$L^{'}(y_2(k)) = (L_1^{'}(y_2(k)), L_2^{'}(y_2(k)), \ldots, L_m^{'}(y_2(k)))^\top,$$

$$L_i^{'}(y_2(k)) = \sum_{j=1}^{\bar{n}} e_{c_i j} y_{2j}(k), \; i = 1, \ldots, m,$$

and $\tilde{B}$ is a upper triangular matrix with diagonal elements being 1.

It can be observed that the terms related to $y_2(k)$ in (12) can be directly incorporated into the form of the HOFA system. This allows for the elimination of the uncontrollable parts using the controller from Lemma 1, and its form can be rewritten in the state feedback form. This is the content of Lemma 3.

The above lemma indicates that a general incomplete controllable system can be decoupled into two identical subsystems. In the problem of consensus, it is only necessary to discuss each part separately. But first we have to introduce a lemma that gives a direct way to design coordinated controllers for controllable systems.

Lemma 4 ([29]). *Suppose system* (1) *is controllable, it achieves synchronization with trajectory*

$$\beta\mathbb{1} \to \alpha\beta\mathbb{1} \to \cdots \to \alpha^{s-1}\beta\mathbb{1} \to \beta\mathbb{1} \to \alpha\beta\mathbb{1} \to \cdots,$$

where $\alpha, \beta \in F_p - \{0\}$, $s = ord(\alpha) \bmod p$, *if and only if* Q *satisfies*

$$q_{ij} = \alpha^{j-1} q_{i1}, i = 1, \ldots, m, j = 1, \ldots, c_i > 1, \tag{15}$$

under control law

$$u(k) = -\tilde{B}^{-1}(L(\tilde{z}_1(k)) + \alpha(k)\beta\bar{q}^{\urcorner}), \tag{16}$$

for system (2)*, where* $\alpha(k) = [\alpha^{k+c_1}, \alpha^{k+c_2}, \ldots, \alpha^{k+c_m}]^\top$, Q *is the transformation matrix, and* $q_{ij} = Q_{ij}\mathbb{1}$, Q_{ij} *is the* $(\sigma_{i-1}+j)$*-th row of* Q, $\sigma_0 = 0$, $\bar{q}^{\urcorner} = [q_{11}, q_{21}, \ldots, q_{m1}]^\top$.

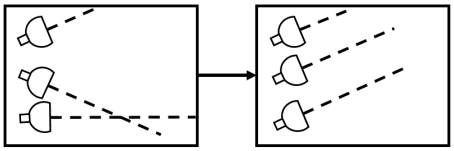

Fig. 1: The camera light network

Lemmas 3 and 4 lead to the conclusions below.

Theorem 1. *Incomplete controllable system* (10) *can achieve consensus under control if and only if, for system* (11) *via the transformation* $y(k) = Rx(k)$*, the following two conditions are satisfied simultaneously:*

(i) Subsystem (13) *achieves* r^2*-consensus;*

(ii) r^1 *satisfies* $r^1_{ij} = r^1_{i1}$, $i = 1, \ldots, m$, $j = 1, \ldots, c_i$.

Proof. The consensus of incomplete controllable system (10) is equivalent to the $(R\mathbb{1})$-consensus of system (11). Thus, we will directly discuss (11).

For subsystem (13), since it achieves r^2-consensus, assume it converges to $\alpha(y_2(0))r^2 \in \mathbb{F}_p^n$ after $\bar{n}^{'}$ steps, where $\bar{n}^{'}$ corresponds to the dimension of the largest Jordan block of E_3, and $\alpha(y_2(0)) \in \mathbb{F}_p$ is dependent on the initial value. For subsystem (12), the goal is to use the controller to bring the state trajectory into a sequence that achieves r^1-consensus. Using Lemma 4, and taking the following controller

$$u(k) = -\tilde{B}^{-1}(L(\tilde{y}_1(k)) + L^{'}(y_2(k)) + \alpha(y_2(0))r_1^{\urcorner}), \quad (17)$$

where $r_1^{\urcorner} = [r^1_{11}, r^1_{21}, \ldots, r^1_{m1}]^{\top}$, $\alpha(y_2(0)) \in \mathbb{F}_p$, $k \geq 0$, system (14) is transformed into $\tilde{y}_1(k+1) = \alpha(y_2(0))r_1^{\urcorner}$. Combined with condition (ii) and Lemma 4, subsystem (13) achieves r^1-consensus. Along with condition (i), system (11) achieves $(R\mathbb{1})$-consensus. □

Utilizing Lemma 3 and the characteristics of system (14), a generally incomplete controllable system can be decoupled into two subsystems. In addressing the consensus problem of the system, it is only necessary to separately discuss the two parts to obtain the conclusions mentioned above. Similar results can also be obtained for the synchronization.

Theorem 2. *Incomplete controllable system* (10) *can achieve synchronization under control, if and only if, for system* (11) *via the transformation* $y(k) = Rx(k)$*, the following two conditions are satisfied simultaneously:*

(i) Subsystem (13) *achieves* r^2*-synchronization,* $E_3 r^2 = \alpha r^2$, $\alpha \in F_p$*;*

(ii) r^1 *satisfies* $r^1_{ij} = \alpha^{j-1} r^1_{i1}, i = 1, \ldots, m, j = 1, \ldots, c_i > 1$.

Proof. It is equivalent to consider system (11). Using the conclusions of Proposition 6, without loss of generality, we can assume that subsystem (13) achieves r^2-synchronization after $\bar{n}^{'}$ steps, where $\bar{n}^{'}$ corresponds to the dimension of the largest Jordan block of E_3, and assume $y_2(\bar{n}^{'} + k) = \alpha^k \beta(y_2(0))r^2$, $k \geq 0$, $\beta(y_2(0)) \in F_p$ depends on the initial value.

Using Lemma 4, we can adopt the following form of the controller:

$$u(k) = -\tilde{B}^{-1}(L(\tilde{y}_1(k)) + L^{'}(y_2(k)) + \alpha_1(k)\beta(y_2(0))\bar{r}^{\urcorner}), \quad (18)$$

where $\alpha_1(k) = \alpha^{-\bar{n}^{'}}[\alpha^{k+c_1}, \alpha^{k+c_2}, \ldots, \alpha^{k+c_m}]^{\top}$, $r_1^{\urcorner} = [r^1_{11}, r^1_{21}, \ldots, r^1_{m1}]^{\top}$, $\beta(y_2(0)) \in F_p$. The system (14) is then transformed into $\tilde{y}_1(k+1) = \alpha_1(k)\beta(y_2(0))\bar{r}^{\urcorner}$, Combining Lemma 4 and condition (ii), we obtain that when $c_{max} < \bar{n}^{'}$, where $c_{max} = \max\limits_{i \in \{1,\ldots,m\}} \{c_i\}$

$$\begin{aligned} y_1(\bar{n}^{'} + k) =& \alpha^k \beta(y_2(0))[r^1_{11}, \alpha r^1_{11}, \ldots, \alpha^{c_1 - 1} r^1_{11}, \ldots, \\ & r^1_{m1}, \alpha r^1_{m1}, \ldots, \alpha^{c_m - 1} r^1_{m1}]^{\top} \\ =& \alpha^k \beta(y_2(0)) R^1 \mathbb{1}, \end{aligned}$$

and consequently, $y(\bar{n}^{'} + k) = \alpha^k \beta(y_2(0))R\mathbb{1}$, $k \geq 0$.

When $c_{max} \geq \bar{n}^{'}$,

$$\begin{aligned} y_1(c_{max} + k) &= y_1(\bar{n}^{'} + k + c_{max} - \bar{n}^{'}) \\ &= \alpha^{k + c_{max} - \bar{n}^{'}} \beta(y_2(0)) R^1 \mathbb{1}, \end{aligned}$$

and $y_2(c_{max} + k) = \alpha^{k + c_{max} - \bar{n}^{'}} \beta(y_2(0)) r^2$. Thus, we also have $y(c_{max} + k) = \alpha^{k + c_{max} - \bar{n}^{'}} \beta(y_2(0))R\mathbb{1}$, $k \geq 0$, and under both two situations, system (11) can achieve $(R\mathbb{1})$-synchronization. □

c_{max} in the proof above indicates the convergence time of the controller in Lemma 4, this can be found in [29], whereas $\bar{n}^{'}$ is the convergence time of the uncontrollable part (13). It can be deduced that after $max\{c_{max}, \bar{n}^{'}\}$ steps, under controller (18), system (11) achieves $(R\mathbb{1})$-synchronization. Exactly, $max\{c_{max}, \bar{n}^{'}\}$ is the convergence time for controller (18), which is also the convergence time for controller (17).

4 Numerical Example

We use a camera light network to illustrate the results mentioned above. Let $\theta_i(k) : \mathbb{N}_{\geq 0} \to \mathbb{F}_p$ denote the angle of the i-th camera light with respect to time, where $\mathbb{F}_p$ represents the set of azimuth angles $\{j\frac{2\pi}{p} \mid j \in \mathbb{F}_p\}$, and $i \in \{1, \ldots, n\}$. A camera light network can be represented by the following incomplete controllable system over F_2: $\theta(k+1) = A\theta(k) + Bu(k)$, where

$$A = \begin{bmatrix} 1 & 1 & 0 & 1 & 0 \\ 0 & 1 & 1 & 1 & 0 \\ 0 & 0 & 1 & 0 & 0 \\ 0 & 0 & 0 & 1 & 0 \\ 1 & 0 & 0 & 0 & 0 \end{bmatrix}, \quad B = \begin{bmatrix} 0 \\ 0 \\ 0 \\ 1 \\ 0 \end{bmatrix}.$$

For A, its row sums are all 1, and the characteristic polynomial is $s^5 + s$, which does not satisfy Proposition 2. The problem is to find a control law to make the angle of all camera lights the same, in other words, to achieve consensus for the camera light network via control inputs, also shown in Fig 1.

Decomposing the controllable system, we get

$$y(k+1) = \begin{bmatrix} 0 & 1 & 0 & 0 & 0 \\ 0 & 0 & 1 & 0 & 0 \\ 1 & 1 & 1 & 1 & 1 \\ 0 & 0 & 0 & 1 & 0 \\ 0 & 0 & 0 & 1 & 0 \end{bmatrix} y(k) + \begin{bmatrix} 0 \\ 0 \\ 1 \\ 0 \\ 0 \end{bmatrix} u(k),$$

where the transformation $y(k) = R\theta(k)$ is applied with

$$R = \begin{bmatrix} 0 & 0 & 0 & 0 & 1 \\ 1 & 0 & 0 & 0 & 0 \\ 1 & 1 & 0 & 1 & 0 \\ 1 & 1 & 0 & 0 & 1 \\ 0 & 0 & 1 & 0 & 0 \end{bmatrix}.$$

The controllability index is $c_1 = 3$, and the row sums of R are all 1. The uncontrollable subsystem reaches a consensus sequence after one iteration. Fig 2 shows the trajectory of $\theta(k)$ with initial values $\theta(0) = [0, 0, 0, 1, 1]^\top$ ($y(0) = [1, 0, 1, 1, 0]^\top$), applying Theorem 1 with $r_1^\urcorner = 1$ and $\alpha(y_2(0)) = 1$. It can be observed that $\theta(k)$ eventually enters a consensus trajectory.

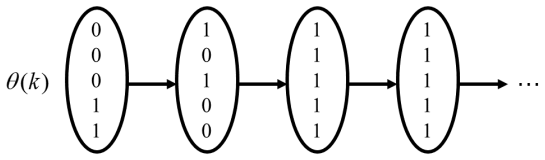

Fig. 2: The trajectory of $\theta(k)$

5 Conclusion

In this paper, controller design was extended to incomplete controllable systems. The concept of v-consensus and v-synchronization was proposed, which generalized the usual consensus and synchronization. For incomplete controllable systems, by means of nonsingular transformation, the controller design was available. Using HOFA system approaches with properties of v-consensus and v-synchronization, proper controllers were designed. Our future research will continue to concentrate on applying HOFA system approaches to more complex situations.

References

[1] Y. Yang, J. Feng, and L. Jia, Recent advances of finite-field networks. *Mathematical Modelling and Control*, 2023, 3(3): 244–255.

[2] F. Pasqualetti, D. Borra, and F. Bullo, Consensus networks over finite fields. *Automatica*, 2014, 50(2): 349–358.

[3] X. Xu and Y. Hong, Leader-following consensus of multi-agent systems over finite fields, in *IEEE Conference on Decision and Control*, 2014: 2999–3004.

[4] X. Li, H. Su, and M. Chen, Consensus networks with time-delays over finite fields. *International Journal of Control*, 2016, 89(5): 1000–1008.

[5] X. Li, M. Chen, H. Su, and C. Li, Consensus networks with switching topology and time-delays over finite fields. *Automatica*, 2016, 68: 39–43.

[6] M. Yu, J. Xia, J. Feng, S. Fu, and H. Shen, Leader-follower output consensus of multiagent systems over finite fields. *Neurocomputing*, 2023, 550: 126495.

[7] M. Meng, X. Li, and G. Xiao, Synchronization of networks over finite fields. *Automatica*, 2020, 115: 108877.

[8] J. Wang, J. Feng, Y. Yu, and H. Huang, Synchronous networks over finite fields. *IEEE Transactions on Automatic Control*, 2023, 68(11): 6907-6912.

[9] W. Zhu, J. Cao, X. Shi, and L. Rutkowski, Synchronization of finite-field networks with time delays. *IEEE Transactions on Network Science and Engineering*, 2022, 9(2): 347–355.

[10] J. Zhang, J. Lu, M. Xing, and J. Liang, Synchronization of finite field networks with switching multiple communication channels. *IEEE Transactions on Network Science and Engineering*, 2021, 8(3): 2160–2169.

[11] L. Lin, J. Cao, S. Zhu, and P. Shi, Synchronization analysis for stochastic networks through finite fields. *IEEE Transactions on Automatic Control*, 2022, 67(2): 1016–1022.

[12] L. Lin, J. Cao, X. Liu, G. Lu, and M. Abdel-Aty, Cluster synchronization of finite-field networks. *IEEE Transactions on Cybernetics*, 2024, 54(1): 635–640.

[13] C. Chen and W. Zhu, Synchronization analysis of Boolean network. *Applied Mechanics and Materials*, 2013, 432: 528–532.

[14] R. Zhao, B. Wang, and J. Feng, Synchronization of drive-response singular Boolean networks. *Nonlinear Analysis - Hybrid Systems*, 2022, 44: 101141.

[15] G. Duan, High-order fully actuated system approaches: Part I. Models and basic procedure. *International Journal of Systems Science*, 2021, 52(2): 422–435.

[16] G. Duan, High-order system approaches: I. Fully-actuated systems and parametric designs. *Acta Automatica Sinica*, 2020, 46(7): 1333–1345.

[17] G. Duan, High-order system approaches: II. Controllability and full-actuation. *Acta Automatica Sinica*, 2020, 46(8): 1571–1581.

[18] G. Duan, High-order fully actuated system approaches: Part III. Robust control and high-order backstepping. *International Journal of Systems Science*, 2021, 52(5): 952–971.

[19] G. Duan, High-order fully actuated system approaches: Part IV. Adaptive control and high-order backstepping. *International Journal of Systems Science*, 2021, 52(5): 972–989.

[20] G. Duan, High-order fully actuated system approaches: Part V. Robust adaptive control. *International Journal of Systems Science*, 2021, 52(10): 2129–2143.

[21] G. Duan, High-order fully-actuated system approaches: Part VI. Disturbance attenuation and decoupling. *International Journal of Systems Science*, 2021, 52(10): 2161–2181.

[22] G. Duan, High-order fully actuated system approaches: Part VIII. Optimal control with application in spacecraft attitude stabilisation. *International Journal of Systems Science*, 2022, 53(1): 54–73.

[23] G. Duan, High-order fully actuated system approaches: Part X. Basics of discrete-time systems. *International Journal of Systems Science*, 2022, 53(4): 810–832.

[24] G. Duan, Discrete-time delay systems: Part 1. Global fully actuated case. *Science China Information Sciences*, 2022, 65(8): 182–201.

[25] G. Liu, Coordination of networked nonlinear multi-agents using a high-order fully actuated predictive control strategy. *IEEE/CAA Journal of Automatica Sinica*, 2022, 9(4): 615–623.

[26] D. Zhang, G. Liu, and L. Cao, Proportional integral predictive control of high-order fully actuated networked multiagent systems with communication delays. *IEEE Transactions on Systems, Man, and Cybernetics: Systems*, 2023, 53(2): 801–812.

[27] Y. Yang, J. Feng, and Z. Gao, Controllability of multi-agent systems over finite fields based on high-order fully actuated system approaches, in *2nd Conference on Fully Actuated System Theory and Applications*, 2023: 283–289.

[28] S. Lang, *Algebra*, Springer Science & Business Media, 2012.

[29] A. Qin, Y. Yu, Z. Gao, J. Feng, Controller design of coordinated control problems over finite fields via fully actuated approach. *Franklin Open*, 2024, 7:100091.

[30] J. Reger, Linear systems over finite fields–modeling, analysis, and synthesis. *at-Automatisierungstechnik*, 2005, 53(1): 45.

Proceedings of the 3rd Conference on Fully Actuated System Theory and Applications
May 10-12, 2024, Shenzhen, China

On Full-Actuation of Linear Boolean Control Networks

Yuanpeng Ding, Jun-e Feng, Yongyuan Yu
School of Mathematics, Shandong University, Jinan, 250100, China
E-mail: yyyu@sdu.edu.cn

Abstract: This paper investigates fully actuated linear Boolean networks. Firstly, using semi-tensor product of matrices, necessary and sufficient conditions are provided to determine whether a Boolean (control) network is linear. Furthermore, a suitable algorithm is established to calculate corresponding coefficient matrices if the considered Boolean control network is linear. Then, the definition of the fully actuated discrete linear systems is generalized to that of Boolean networks for the first time. On the basis of equivalent condition obtained to determine the full-actuation of Boolean control networks, it is revealed that two definitions of full actuation, which are respectively for linear systems and Boolean networks, are consistent. Finally, effectiveness of obtained results is shown by an illustrative example.

Key Words: Fully actuated systems, Linear Boolean networks, Feedback, Semi-tensor product

1 Introduction

In 1969, Kauffman first proposed Boolean networks (BNs) [1]. Subsequently, the discrete dynamic model with variables taking values in $\{0, 1\}$, began to be widely used to describe gene networks [2–4]. To account for the influence of the external environment, BNs were extended to Boolean control networks (BCNs) by adding control inputs. With the rapid development of systems biology and medical science, BNs have played an increasingly important role in gene regulatory networks [5].

For a long time, there was no convenient method for dealing with BNs until the emergence of semi-tensor product (STP) [6, 7], which broke the dimension limit of traditional matrix product. With the help of this tool, many fruitful results about BCNs have emerged, such as controllability [8–10], observability [8, 11], stabilizability [12–14], detectability [15] and so on.

The stability and stabilization of BNs are two fundamental problems, in which significant progress has been made. Under the framework of STP, stability and stabilization of BNs were first discussed in [12]. In [13], necessary and sufficient conditions for the existence of global stable state feedback controllers, along with a general design method, were provided. The investigation into set stability and set stabilization of BNs began in [14], where some necessary and sufficient conditions were established based on invariant subsets.

The traditional state space model of dynamic systems may be the optimal method for solving response analysis problems, but it is improvable in controller design. Recently, the fully actuated system approach, has been used as a universal model for a majority of physical systems [16]. In fully actuated systems (FASs), as long as the nonlinear term is measurable, the full-actuation property enables the elimination of all nonlinear dynamics, facilitating the implementation of control in a straightforward way [17]. This systematic approach can also be applied to robust control [18], adaptive control [19], disturbance attenuation and decoupling [20] and so on.

Linear automata based on XOR ($\bar{\vee}$) operations have considerable logical functionality and have been widely applied in practical problems, such as the reading and writing circuits of memory and the implementation of automatic error-correcting codes [21]. In addition, synchronization of linear Boolean networks (LBNs) that are also linear automata were discussed in [22]. Recently, feedback shaping for BNs was investigated via Koopman representation in [23]. However, generally speaking, BNs are nonlinear, so solving control problems is often challenging. We always hope that BCNs can achieve the desired closed-loop system through feedback control. Therefore, studying the feedback capability of BCNs can help in analyzing and designing BCNs. Notably, to the best of our knowledge, there were fewer results on fully actuated BNs. Motivated by these, fully actuated LBNs will be discussed in this paper.

The main contributions of this paper are listed as follows:

- Necessary and sufficient conditions for determining whether a BCN (BN) is linear, and the algorithm to calculate the coefficient matrices are given.
- The definition of fully actuated Boolean networks (FABNs) is introduced for the first time along with a necessary and sufficient algebraic condition.
- The relationship is revealed between two kinds of definitions on full-actuation of linear Boolean control networks (LBCNs).

The rest of this paper is organized as follows. Section 2 recommends useful notations and preliminaries. Section 3 provides the necessary and sufficient conditions for determining whether a BCN (BN) is linear. Section 4 proposes the definition of FABNs and proves the equivalence of two types of definitions on full-actuation in LBCNs. An illustrative example is provided in Section 5, followed by a brief conclusion.

2 Preliminaries

In this section, we give some useful notations and definitions about STP, BNs, BCNs and FASs, which will be used in the sequel.

2.1 Notations

- $\mathbb{N} := \{0, 1, 2, \dots\}$, the set of natural numbers.

This work was supported by the National Natural Science Foundation of China (62273201, 62203264, 72134004, 12326425), the Taishan Scholar Project of Shandong Province of China (tstp20221103), Science Center Program of National Natural Science Foundation of China (62188101) and the Natural Science Foundation of Shandong Province (ZR2022QF061), the Support Plan for Youth Innovation Team in Shandong Higher Education Institutions (2022KJ022).

- $[i, j] := \{i, i+1, \ldots, j\}$, if $i, j \in \mathbb{N}$ and $i < j$.
- $\mathbb{R}^{m\times n}$: the set of $m \times n$ real matrices.
- $\mathcal{D} := \{1, 0\}$, and $\mathcal{D}^n := \underbrace{\mathcal{D} \times \cdots \times \mathcal{D}}_{n}$.
- δ_n^i : the i-th column of the identity matrix I_n.
- $\Delta_n := \{\delta_n^i | 1 \le i \le n\}$. For convenience, $\Delta := \Delta_2$.
- $\mathbf{1}_{n\times m}$ is an $n \times m$ matrix whose components are all 1.
- Matrix $L \in \mathbb{R}^{n\times m}$ is called a logical matrix, if $L = [\delta_n^{i_1}, \delta_n^{i_2}, \ldots, \delta_n^{i_m}]$, where $i_k \in [1, n]$, $k \in [1, m]$, denoted by $L = \delta_n[i_1, i_2, \ldots, i_m]$.
- $\mathcal{L}^{n\times m}$: the set of all $n \times m$ logical matrices.
- $Col_i(A)$: the i-th column of matrix A.
- $Row_i(A)$: the i-th row of matrix A.
- $[A]_{i,j}$: the (i, j)-th element of A.
- $A \ge B$: $[A]_{i,j} \ge [B]_{i,j}, \forall\, i, j$.
- $A \bar{\vee} B$: Exclusive OR operation between A and B. For two matrices A and B of the same dimension, $[A \bar{\vee} B]_{i,j} := [A]_{i,j} \bar{\vee} [B]_{i,j}$.
- $|X|$: the cardinality of set X, i.e., the number of elements in set X.
- The Kronecker product of matrices $A = (a_{ij}) \in \mathbb{R}^{m\times n}$ and $B \in \mathbb{R}^{p\times q}$ is

$$A \otimes B = \begin{pmatrix} a_{11}B & a_{12}B & \ldots & a_{1n}B \\ a_{21}B & a_{22}B & \ldots & a_{2n}B \\ \vdots & \vdots & \vdots & \vdots \\ a_{m1}B & a_{m2}B & \ldots & a_{mn}B \end{pmatrix}.$$

Definition 1. [6] The semi-tensor product of two matrices $A \in \mathbb{R}^{m\times n}$ and $B \in \mathbb{R}^{p\times q}$ is

$$A \ltimes B = (A \otimes I_{\frac{\alpha}{n}})(B \otimes I_{\frac{\alpha}{p}}), \tag{1}$$

where $\alpha = lcm(n, p)$ is the least common multiple of n and p.

Remark 1. STP retains almost all the properties of the traditional matrix product. It reduces to the traditional matrix product when $n = p$. In this paper, we omit the symbol "$\ltimes$" if there is no confusion.

Proposition 1. [6] The following properties about STP hold.

1) Let $X \in \mathbb{R}^{m\times 1}$ and $Y \in \mathbb{R}^{n\times 1}$ be two column vectors. Then,
$$Y \ltimes X = W_{[m,n]} \ltimes X \ltimes Y, \tag{2}$$
where $W_{[m,n]}$ is the swap matrix defined as
$$[\delta_n^1\delta_m^1, \ldots, \delta_n^n\delta_m^1, \ldots, \delta_n^1\delta_m^m, \ldots, \delta_n^n\delta_m^m]. \tag{3}$$
2) Let $X \in \mathcal{L}^{m\times 1}$ be a logical vector. Then,
$$X \ltimes X = M_r \ltimes X, \tag{4}$$
where $M_r := \mathrm{Diag}\{\delta_m^1, \delta_m^2, \ldots, \delta_m^m\}$ is the power reducing matrix.

2.2 Algebraic Representation of BCNs

A BCN with n state nodes $\{\bar{x}_1, \bar{x}_2, \ldots, \bar{x}_n\}$ and m control nodes $\{\bar{u}_1, \bar{u}_2, \ldots, \bar{u}_m\}$ can be described as

$$\begin{cases} \bar{x}_1(t+1) = f_1(X(t), U(t)) \\ \bar{x}_2(t+1) = f_2(X(t), U(t)) \\ \qquad\vdots \\ \bar{x}_n(t+1) = f_n(X(t), U(t)). \end{cases} \tag{5}$$

where $X(t) = [\bar{x}_1(t), \bar{x}_2(t), \ldots, \bar{x}_n(t)]^\top, \bar{x}_i \in \mathcal{D}, i = 1, 2, \ldots, n$ and $U(t) = [\bar{u}_1(t), \bar{u}_2(t), \ldots, \bar{u}_m(t)]^\top, \bar{u}_i \in \mathcal{D}, i = 1, 2, \ldots, m$ are Boolean variables, and $f_i : \mathcal{D}^{n+m} \mapsto \mathcal{D}, i = 1, 2, \ldots, n$ are Boolean functions. It can be rewritten in the following form:

$$X(t+1) = f(X(t), U(t)). \tag{6}$$

Eliminating the influence of control in BCNs, a BN with n state nodes $\{\bar{x}_1, \bar{x}_2, \ldots, \bar{x}_n\}$ can be described as

$$\begin{cases} \bar{x}_1(t+1) = f_1(X(t)) \\ \bar{x}_2(t+1) = f_2(X(t)) \\ \qquad\vdots \\ \bar{x}_n(t+1) = f_n(X(t)). \end{cases} \tag{7}$$

Moreover, it can also be expressed as the following concise form:

$$X(t+1) = f(X(t)). \tag{8}$$

By denoting $1 \sim \delta_2^1$ and $0 \sim \delta_2^2$, we have $\Delta \sim \mathcal{D}$, where "$\sim$" indicates two different forms of the same object.

Lemma 1. [6] Let $f(\bar{x}_1, \bar{x}_2, \ldots, \bar{x}_n) : \mathcal{D}^n \mapsto \mathcal{D}$ be a Boolean function. Then, there exists a unique matrix $M_f \in \mathcal{L}^{2\times 2^n}$, called the structure matrix of f, such that

$$\delta_2^{2-f(\bar{x}_1,\bar{x}_2,\ldots,\bar{x}_n)} = M_f \ltimes_{i=1}^n x_i, \tag{9}$$

where $x_i = \delta_2^{2-\bar{x}_i} \in \Delta$.

Specially, we give the structure matrices of two basic logical operators, which will be used later.

- Negation $(\neg)$: $M_n = \delta_2[2, 1]$;
- Exclusive OR $(\bar{\vee})$: $M_p = \delta_2[2, 1, 1, 2]$.

Lemma 2. [6] Assume that $y = M_y \ltimes_{i=1}^n x_i, z = M_z \ltimes_{i=1}^n x_i$, where $x_i \in \Delta, i = 1, 2, \ldots, n, M_y \in \mathcal{L}^{2\times 2^n}$ and $M_z \in \mathcal{L}^{2\times 2^n}$. Then

$$yz = (M_y * M_z) \ltimes_{i=1}^n x_i, \tag{10}$$

where $M_y * M_z = [Col_1(M_y) \otimes Col_1(M_z), \ldots, Col_{2^n}(M_y) \otimes Col_{2^n}(M_z)]$ is the K-R product of M_y and M_z.

Using Lemma 1, there exist structure matrices $L_i \in \mathcal{L}^{2\times 2^{m+n}}$ of $f_i, i = 1, 2, \ldots, n$, such that BCN (5) can be converted into

$$x_i(t+1) = L_i u(t) x(t),\ i = 1, 2, \ldots, n, \tag{11}$$

where $x(t) = \ltimes_{i=1}^n x_i(t), u(t) = \ltimes_{i=1}^m u_i(t) = \ltimes_{i=1}^m \delta_2^{2-\bar{u}_i}$. Then, the algebraic representation of BCN (5) can be expressed by Lemma 2 as follows:

$$x(t+1) = Lu(t)x(t), \tag{12}$$

where $L = L_1 * L_2 * \cdots * L_n \in \mathcal{L}^{2^n\times 2^{m+n}}$.

Similarly, under the framework of STP, (7) can be rewritten as

$$x_i(t+1) = F_i x(t),\ i = 1, 2, \ldots, n, \tag{13}$$

where $F_i \in \mathcal{L}^{2\times 2^n}$ is the structure matrix of f_i, $x(t) = \ltimes_{i=1}^n x_i(t)$, and

$$x(t+1) = Fx(t), \tag{14}$$

where $F = F_1 * F_2 * \cdots * F_n \in \mathcal{L}^{2^n \times 2^n}$.

For ease of expression, this paper discusses general form of BNs. In other words, in (5) or (7), f_i formally depends on all variables, but in reality, it may contain virtual redundant variables. Therefore, Lemma 3 is introduced to analyze redundant variables.

Lemma 3. [8] For a BN with algebraic form (13), the value of node i is not influenced by the value of node j if and only if F_i satisfies

$$F_i W_{[2,2^{j-1}]}(M_n - I_2) = 0, \tag{15}$$

where M_n, $W_{[2,2^{j-1}]}$ are the structure matrix of negation $\neg$ and the swap matrix, respectively.

Moreover, as long as the equation above holds, $x_i(t+1) = F_i x(t)$ can be replaced by

$$x_i(t+1) = F_i' x_1(t) \dots x_{j-1}(t) x_{j+1}(t) \dots x_n(t), \tag{16}$$

where $F_i' = L_i W_{[2,2^{j-1}]} \delta_2^1$.

2.3 Fully Actuated System

In this subsection, we briefly introduce the fully actuated system.

Definition 2. [24] Let $A, B \in \mathbb{R}^{n\times n}$, if B is nonsingular, then the discrete-time linear system

$$X(t+1) = AX(t) + BU(t), \tag{17}$$

is called a fully actuated system.

For FASs, one can design control in an extremely simple way, since the full-actuation property allows us to eliminate the original dynamics. For example, we can design the controller as $U(t) = B^{-1}(-AX(t) + A_0X(t) + V(t))$, where $V(t)$ is an external signal. Then we can obtain a desired closed-loop system $X(t+1) = A_0X(t) + V(t)$.

Although the definition above is based on linear systems over $\mathbb{R}$, it is applicable to linear systems over the finite fields.

3 Linear Boolean Control Networks

In this section, we give definitions of LBCNs and LBNs. By introducing a matrix sequence, we formulate procedures to determine the linearity of BCNs and BNs, respectively. Additionally, methods to obtain the coefficient matrices of LBCNs and LBNs are presented. We first give the definition of linear Boolean function.

Definition 3. Boolean function $f_0 : \mathcal{D}^p \mapsto \mathcal{D}$ is called a linear Boolean function, if $\forall\, X, Y \in \mathcal{D}^p$, f_0 satisfies

$$f_0(X \bar{\vee} Y) = f_0(X) \bar{\vee} f_0(Y). \tag{18}$$

Definition 4. Vector valued Boolean function $f = [f_1, f_2, \dots, f_q]^\top : \mathcal{D}^p \mapsto \mathcal{D}^q$ is called a linear vector valued Boolean function if all component Boolean functions f_i are linear Boolean functions.

Definition 5. BCN (6) (resp. BN (8)) is called a linear Boolean control network (resp. linear Boolean network), if its iterative function f is a linear vector valued Boolean function.

Remark 2. The definition of linear Boolean networks according to equation (18), as stated in [22], is consistent with Definition 5.

From the definitions above, we have the following proposition directly.

Proposition 2. BCN (6) (resp. BN (8)) is linear if and only if each Boolean function f_i in (5) (resp. (7)) is linear Boolean function.

The following lemma shows the property of linear Boolean functions.

Lemma 4. The Exclusive OR $\bar{\vee}$ of two linear Boolean functions results in a Boolean function that is still linear.

Proof. Assume $h_1, h_2 : \mathcal{D}^n \mapsto \mathcal{D}$ are two linear Boolean functions. Denote $h = h_1 \bar{\vee} h_2$. Next, we prove that h is also a linear Boolean function.

In term of Definition 3, we have

$$h_i(X \bar{\vee} Y) = h_i(X) \bar{\vee} h_i(Y), \forall X, Y \in \mathcal{D}^n, i = 1, 2. \tag{19}$$

Substituting (19) into $h(X \bar{\vee} Y) = h_1(X \bar{\vee} Y) \bar{\vee} h_2(X \bar{\vee} Y)$, we have $h(X \bar{\vee} Y) = h_1(X) \bar{\vee} h_1(Y) \bar{\vee} h_2(X) \bar{\vee} h_2(Y)$. Then, $h(X \bar{\vee} Y) = h(X) \bar{\vee} h(Y), \forall X, Y \in \mathcal{D}^n$, which implies h is a linear Boolean function. Hence, the conclusion holds. □

Based on Lemma 4, we present a necessary and sufficient condition to determine the linearity of linear Boolean functions.

Theorem 1. Boolean function $f : \mathcal{D}^n \mapsto \mathcal{D}$ is a linear Boolean function if and only if it always equals to 0 or there exists a Boolean function g with $\bar{\vee}$ as its unique logical operator, such that $f(X) = g(X), \forall X \in \mathcal{D}^n$.

Proof. (Necessity) Assume Boolean function $f : \mathcal{D}^n \mapsto \mathcal{D}$ is a linear Boolean function. Denote $X_i = Col_i(I_n) \in \mathcal{D}^n$, and $f^i = f(X_i)$. Next, we prove that f equals to the following Boolean function:

$$g(X) = \bar{\bigvee_{i=1}^{n}} (x_i \wedge f^i), \tag{20}$$

where $X = [\bar{x}_1, \bar{x}_2, \dots, \bar{x}_n]^\top \in \mathcal{D}^n$.

Note that any $X \in \mathcal{D}^n$ can be represented by a combination of elements in $\{X_i\}_{i=1}^n$ connected by $\bar{\vee}$, and each element in $\{X_i\}_{i=1}^n$ appears at most once. In addition, except for the order, this representation is unique. For any $X \in \mathcal{D}^n$, we may suppose $X = \bar{\bigvee}_{j=1}^{k} X_{i_j}$. Since f is a linear Boolean function, we have

$$f(X) = f(\bar{\bigvee_{j=1}^{k}} X_{i_j}) = \bar{\bigvee_{j=1}^{k}} f(X_{i_j}) = \bar{\bigvee_{j=1}^{k}} f^{i_j}. \tag{21}$$

Notice that, in (20), $x_i \wedge f^i = f^i$ when $x_i = 1$, and $x_i \wedge f^i = 0$ when $x_i = 0$. Then, one can obtain that $g(X) = \bar{\bigvee}_{j=1}^{k} f^{i_j}$, which implies $f(X) = g(X), \forall X \in \mathcal{D}^n$.

For Boolean function g, $x_i \wedge f^i = x_i$ when $f^i = 1$, and $x_i \wedge f^i = 0$ when $f^i = 0$. Then, g consists $\bar{\vee}$ as its unique logical operator. Specially, when all f^i are equal to 0, f always equals to 0. Thus, the necessity holds.

(Sufficiency) When f always equals to 0, it is evident that f is linear. Consider that f equals to a Boolean function g

that consists $\bar{\vee}$ as its unique logical operator, and suppose $g(\bar{x}_1, \bar{x}_2, \ldots, \bar{x}_n) = \bar{\vee}_{j=1}^{k} \bar{x}_{i_j}$.

Let $g_j(\bar{x}_1, \bar{x}_2, \ldots, \bar{x}_n) = \bar{x}_{i_j}$, $j = 1, 2, \ldots, k$. Easy to verify that all g_i are linear Boolean functions. Through Lemma 4, we conclude that g is a linear Boolean function. Then, f is also a linear Boolean function. Thus, the sufficiency holds. □

Through the definitions and theorem above, we can easily obtain the following proposition.

Proposition 3. If (6) (resp. (8)) is an LBCN (resp. LBN), then there exist $A \in \mathcal{D}^{n\times n}$ and $B \in \mathcal{D}^{n\times m}$ (resp. $A \in \mathcal{D}^{n\times n}$), such that (6) (resp. (8)) can be equivalently expressed as (22) (resp. (23)), where the matrix operations are performed in F_2, listed as follows:

$$X(t+1) = AX(t) + BU(t), \tag{22}$$
$$X(t+1) = AX(t). \tag{23}$$

In term of the propositions above, we will present a matrix-based approach to determine whether a BCN (resp. BN) is an LBCN (resp. LBN) and obtain its coefficient matrices (A, B) (resp. A) effectively.

Now, we elucidate how to determine whether BCN (11) is an LBCN by using the aforementioned lemmas, while providing the coefficient matrices.

According to Proposition 2, determining whether a BCN is an LBCN is equivalent to verify whether all f_i are linear Boolean functions. In order to address this issue, we construct a matrix sequence as follows:

$$E_{i+1} = [M_n E_i, E_i],\ i = 1, 2, \cdots, \tag{24}$$

where $E_1 = I_2$ and $M_n = \delta_2[2, 1]$ is the structure matrix of negation $\neg$.

Proposition 4. The structure matrix of $f_0(\bar{x}_1, \bar{x}_2, \ldots, \bar{x}_i) = \bar{x}_1 \bar{\vee} \bar{x}_2 \bar{\vee} \cdots \bar{\vee} \bar{x}_i$ is E_i, $i = 1, 2, \cdots$.

Proof. We prove it by mathematical induction.

When $i = 1$, it is trivial that the statement holds. Then, assume conclusion holds for $i = k$, and consider Boolean function $g(\bar{x}_1, \bar{x}_2, \ldots, \bar{x}_{k+1}) = \bar{x}_1 \bar{\vee} \bar{x}_2 \bar{\vee} \cdots \bar{\vee} \bar{x}_{k+1}$.

Denote $h(\bar{x}_2, \bar{x}_3, \ldots, \bar{x}_{k+1}) = \bar{x}_2 \bar{\vee} \bar{x}_3 \bar{\vee} \cdots \bar{\vee} \bar{x}_{k+1}$. Then, $g(\bar{x}_1, \bar{x}_2, \ldots, \bar{x}_{k+1}) = \bar{x}_1 \bar{\vee} h(\bar{x}_2, \bar{x}_3, \ldots, \bar{x}_{k+1})$. According to the induction hypothesis, the structure matrix of h is E_k. Moreover, we obtain $g = \neg h$ when x_1 takes 1, and $g = h$ when x_1 takes 0, which implies the structure matrix of f is $E_{k+1} = [M_n E_k, E_k]$. Hence, the conclusion is true for $i = k + 1$.

By induction, the conclusion holds for any i. □

Since not all nodes impact the value of node i, we need to obtain the simplified form of the structure matrix for f_i after removing all redundant dummy variables via Lemma 3.

Thus, in (11), we define the unrelated control set

$$N_i^u = \{j | L_i W_{[2,2^{j-1}]}(M_n - I_2) = 0 \text{ and } j \in [1, m]\},$$

and unrelated state set

$$N_i^x = \{j | L_i W_{[2,2^{j-1}]}(M_n - I_2) = 0 \text{ and } j \in [m+1, m+n]\}$$

of node i. Denote $N_i = N_i^u \cup N_i^x$, and assume $N_i = \{i_1, i_2, \ldots, i_{|N_i|}\}, i_1 < i_2 < \cdots < i_{|N_i|}$. For convenience, we denote $u_i(t)$ and $x_i(t)$ as $y_i(t)$ and $y_{i+m}(t)$, respectively. Then we obtain:

$$\begin{aligned}
x_i(t+1) &= L_i u_1(t) \cdots u_m(t) x_1(t) \cdots x_n(t) \\
&= L_i y_1(t) y_2(t) \cdots y_{m+n}(t) \\
&= L_i W_{[2,2^{i_1-1}]} y_{i_1}(t) \underset{k\neq i_1}{\ltimes} y_k(t) \\
&= L_i W_{[2,2^{i_1-1}]} W_{[2,2^{i_2-1}]} y_{i_2}(t) y_{i_1}(t) \underset{k\neq i_1,i_2}{\ltimes} y_k(t) \\
&\vdots \\
&= \bar{L}_i y_{i_{|N_i|}}(t) \cdots y_{i_1}(t) \underset{k\neq i_1,i_2\ldots i_{|N_i|}}{\ltimes} y_k(t),
\end{aligned}$$

where $\bar{L}_i = L_i \ltimes_{j=1}^{|N_i|} W_{[2,2^{i_j-1}]}$. Thus, matrix $\widetilde{L}_i = \bar{L}_i \delta^1_{2^{|N_i|}}$ is the simplified structure matrix after removing all redundant dummy variables.

However, there is another special case where a node is not influenced by any other nodes, i.e., there exists i_0 such that $N_{i_0} = [1, m+n]$. In this case, f_{i_0} is a linear Boolean function if and only if the structure matrix $L_{i_0} = \delta_2[2, \ldots, 2]$. In addition, for an LBCN, its coefficient matrix under (22) can also be easily obtained through the unrelated control sets and the unrelated state sets. The discussion above can be summarized as the following theorem and algorithm.

Theorem 2. BCN (11) is an LBCN if and only if for any i, $L_i = \delta_2[2, 2, \ldots, 2]$ or its simplified structure matrix satisfies $\widetilde{L}_i = E_{m+n-|N_i|}$, where $N_i = N_i^u \cup N_i^x$, N_i^u and N_i^x are the unrelated control set and unrelated state set of node i, respectively.

Algorithm 1. Given the structure matrices $L_i \in \mathcal{L}^{2\times 2^{m+n}}$, $i = 1, 2, \ldots, n$.

Step 1: For $i = 1$ to n, if $L_i = \delta_2[1, 1, \ldots, 1]$, go to step 6. Else, go to the next step.

Step 2: Determine the unrelated control set N_i^u and the unrelated state set N_i^x. Assume $N_i = N_i^u \cup N_i^x = \{i_1, i_2, \ldots, i_{|N_i|}\}, i_1 < i_2 < \cdots < i_{|N_i|}$. If $N_i = [1, m+n]$, go to step 5. Else, go to the next step.

Step 3: Obtain the simplified structure matrix:

$$\widetilde{L}_i = L_i \underset{j=1}{\overset{|N_i|}{\ltimes}} W_{[2,2^{i_j-1}]} \ltimes \delta^1_{2^{|N_i|}}. \tag{25}$$

Step 4: Check whether $\widetilde{L}_i$ satisfies the following equation:

$$\widetilde{L}_i = E_{m+n-|N_i|}. \tag{26}$$

If $\widetilde{L}_i$ fails to satisfy (26), go to step 6. Else, go to the next step.

Step 5: $Row_i(B, A)^\top = \mathbf{1}_{(m+n)\times 1} - \sum_{k=1}^{|N_i|} \delta^{i_k}_{m+n}$, $i = i + 1$. If $i \leq n$, go to step 1. Else, go to the next step.

Step 6: If $i = n + 1$, this BCN is an LBCN and return matrices (B, A), stop. Else, it is not, stop.

BNs are special BCNs with constant input. The procedure to determine whether BN (13) is an LBN is similar to the discussion above, except that there are no unrelated control

sets, only unrelated state sets $N_i^x = \{j | F_i W_{[2,2^{j-1}]}(M_n - I_2) = 0\}, i = 1, 2, \cdots, n$. We obtain the following corollary.

Corollary 1. BN (13) is an LBN if and only if for any i, $F_i = \delta_2[2, \ldots, 2]$ or its simplified structure matrix satisfies $\widetilde{F}_i = E_{n-|N_i^x|}$, where N_i^x is the unrelated state set of node i.

If (13) is an LBN, then its coefficient matrix A in (23) can be obtained as follows:

$$[A]_{i,j} = \begin{cases} 0, & \text{if } j \in N_i^x, \\ 1, & \text{otherwise.} \end{cases} \tag{27}$$

4 Fully Actuated Boolean Networks

In this section, we present the definition of FABNs. Additionally, we clarify that, the full-actuation of LBCNs are equivalent under two definitions.

FASs allow us to eliminate all the original dynamics, and a desired closed-loop systems can be obtained, which helps us to efficiently analyze and design systems. Furthermore, with the help of the full-actuation feature, many control problems such as stabilization, disturbance decoupling, robust control, and optimal control can be easily addressed. Moreover, many systems in the world can be transformed into high order fully actuated systems, including controllable linear systems, controllable canonical forms of nonlinear systems, and strict-feedback nonlinear systems. Inspired by this innovation, we present the definition of FABNs below, which similarly allows the design of closed-loop systems as desired.

Definition 6. BCN (12) is called a fully actuated Boolean network, if for any given logical matrix $F \in \mathcal{L}^{2^n \times 2^n}$, there exists a state feedback control $u(t) = Kx(t)$, $K \in \mathcal{L}^{2^m \times 2^n}$ such that the system can be converted into the following closed-loop system

$$x(t+1) = Fx(t). \tag{28}$$

Since not all BCNs are LBCNs, the definition above generalizes the full-actuation definition of linear systems over finite field F_2 to arbitrary systems, including nonlinear ones.

Lemma 5. [25] For two given matrices $L \in \mathcal{L}^{2^n \times \omega 2^n}$ and $F \in \mathcal{L}^{2^n \times 2^n}$, there exists a matrix $K \in \mathcal{L}^{\omega \times 2^n}$ such that $LKM_r = F$, if and only if $L\mathbf{1}_{\omega \times 1} \geq F$.

Through the lemma about logical matrix equations, we obtain the following theorem.

Theorem 3. BCN (12) is an FABN if and only if $L\mathbf{1}_{2^m \times 1} \geq \mathbf{1}_{2^n \times 2^n}$.

Proof. Substituting $u(t) = Kx(t)$ into (12), yields

$$x(t+1) = LKx(t)x(t). \tag{29}$$

Then, we obtain $x(t+1) = LKM_r x(t)$ via the power reducing matrix. In view of Lemma 5, BCN (12) is an FABN, if and only if $L\mathbf{1}_{2^m \times 1} \geq F$, for all $F \in \mathcal{L}^{2^n \times 2^n}$, which implies $L\mathbf{1}_{2^m \times 1} \geq \mathbf{1}_{2^n \times 2^n}$. □

It is obvious to see, a necessary condition for a BCN to be an FABN is that the number of its control nodes is greater than or equal to the number of its state nodes, i.e., $m \geq n$.

Now, we clarify the relationship between Definition 2 and Definition 6 for LBCNs with n state nodes and n control nodes.

Theorem 4. When $m = n$, LBCN (12) is an FABN if and only if linear system (22) obtained through Algorithm 1 is an FAS.

Proof. (Necessity) Suppose that $x(t+1) = Lu(t)x(t)$ is an LBCN with n state nodes and n control nodes, and it is an FABN, which implies $L\mathbf{1}_{2^n \times 1} = \mathbf{1}_{2^n \times 2^n}$. It can be transformed into the following linear system using Algorithm 1:

$$X(t+1) = AX(t) + BU(t). \tag{30}$$

Next, we will prove that B is nonsingular, i.e., invertible. Split L into 2^n blocks as

$$L = [L\delta_{2^n}^1, L\delta_{2^n}^2, \ldots, L\delta_{2^n}^{2^n}]. \tag{31}$$

Using the representation above, $L\mathbf{1}_{2^n \times 1} = \mathbf{1}_{2^n \times 2^n}$ implies $\forall\, j = 1, 2, \ldots, 2^n$,

$$\{Col_j(L\delta_{2^n}^i) | i = 1, 2, \ldots, 2^n\} = \Delta_{2^n}. \tag{32}$$

It is not difficult to see that $Col_j(L\delta_{2^n}^i) = L\delta_{2^n}^i \delta_{2^n}^j$, this means that state $\delta_{2^n}^j$ is driven to state $Col_j(L\delta_{2^n}^i)$ by control input $\delta_{2^n}^i$.

Through the analysis above, equation (32) implies that, for any given initial state $x_0 = \delta_{2^n}^j$, it reaches different states under different controls

In linear system (22), for any given initial state $X_0 \in \mathcal{D}^n$, driving it under different controls leads to different states. This implies

$$\{AX_0 + BU | U \in \mathcal{D}^n\} = \mathcal{D}^n, \forall\, X_0 \in \mathcal{D}^n. \tag{33}$$

Since the invertibility of B is equivalent to the statement that the equation $BU = 0$ has only the trivial solution, assuming B is singular, then there exist $U_1 \neq U_2$ such that $BU_1 = BU_2$, which contradicts to (33). Thus, B is nonsingular, which implies that the necessity holds.

(Sufficiency) Suppose linear system (22) is fully actuated. Then, B is nonsingular, which indicates equation $BU = 0$ has only the trivial solution, i.e., $\forall\, U_1 \neq U_2$, $BU_1 \neq BU_2$. Moreover, we have

$$\{AX_0 + BU | U \in \mathcal{D}^n\} = \mathcal{D}^n, \forall\, X_0 \in \mathcal{D}^n. \tag{34}$$

Retracing the proof of necessity, sufficiency holds. □

The theorem above indicates, for LBCNs, the definitions of full-actuation under the two different forms are equivalent.

5 An Illustrative Example

In this section, we provide an illustrative example to demonstrate our algorithm and verify the equivalence of Definitions 2 and 6 in LBCNs.

Example 1. Consider BCN (11) with

$$L_1 = \delta_2[1, 2, 2, 1, 2, 1, 1, 2, 1, 2, 2, 1, 2, 1, 1, 2];$$
$$L_2 = \delta_2[2, 1, 2, 1, 2, 1, 2, 1, 1, 2, 1, 2, 1, 2, 1, 2].$$

Then, via Lemma 2, one can obtain its structure matrix:

$$L = \delta_4[2, 3, 4, 1, 4, 1, 2, 3, 1, 4, 3, 2, 3, 2, 1, 4].$$

It is observed that $L\mathbf{1}_{4\times 1} = \mathbf{1}_{4\times 4}$, thus this BCN is fully actuated.

Next, we use Algorithm 1 to determine whether it is an LBCN. If it is, we transform it into a linear system and verify that the transformed linear system is also fully actuated.

By examining the value of $L_i W_{[2,2^{j-1}]}(M_n - I_2)$, $i = 1, 2$, $j = 1, 2, 3, 4$, we can derive the unrelated control set N_i^u, $i = 1, 2$ and the unrelated control set N_i^x, $i = 1, 2$. Through straightforward calculations, we obtain

$$N_1^u = \{1\},\ N_1^x = \varnothing;\ N_2^u = \{2\},\ N_2^x = \{3\}.$$

It follows that the unrelated sets of the two nodes are $N_1 = \{1\}$ and $N_2 = \{2, 3\}$, respectively. Therefore, the simplified structure matrix are:

$$\widetilde{L}_1 = L_1 W_{[2,1]} \ltimes \delta_2^1 = \delta_2[1, 2, 2, 1, 2, 1, 1, 2];$$
$$\widetilde{L}_2 = L_2 W_{[2,2]} W_{[2,4]} \ltimes \delta_4^1 = \delta_2[2, 1, 1, 2].$$

Direct verification yields $\widetilde{L}_1 = E_3$ and $\widetilde{L}_1 = E_2$, which implies that this BCN is an LBCN, and the corresponding coefficient matrices are:

$$A = \begin{bmatrix} 1 & 1 \\ 0 & 1 \end{bmatrix}, \quad B = \begin{bmatrix} 0 & 1 \\ 1 & 0 \end{bmatrix}.$$

As B is nonsingular, this indicates that under Definition 2, the transformed linear system $X(t+1) = AX(t) + BU(t)$ is fully actuated.

6 Conclusion

In this paper, utilizing STP as a tool, we have presented a mechanical algorithm to determine whether a BCN or BN can be "linearized", i.e., transformed into a linear system over finite field F_2. Additionally, by the unrelated sets, a method to calculate the corresponding coefficient matrices has been presented. Inspired by the work in [24], the definition of FABNs has been proposed for the first time, allowing for the design of desired closed-loop systems through state feedback control. Furthermore, a necessary and sufficient algebraic condition for determining full-actuation has been provided. Finally, the equivalence of two definitions of full-actuation for LBCNs, has been established.

In the future, we will leverage the concept of full-actuation to explore the control problems of general BCNs. These are networks that cannot be transformed into linear systems over finite field F_2. We will also investigate cases where the number of state nodes is not equal to the number of control nodes. The full-actuation of arbitrary logical networks will also be explored in the near future. Additionally, the relationship between controllability and high-order full-actuation in arbitrary logical networks will be investigated.

References

[1] S. A. Kauffman, Metabolic stability and epigenesis in randomly constructed genetic nets. *Journal of Theoretical Biology*, 1969, 22(3): 437–467.

[2] S. A. Kauffman, E. D. Weinberger, The NK model of rugged fitness landscapes and its application to maturation of the immune response. *Journal of Theoretical Biology*, 1989, 141(2): 211–245.

[3] R. Albert, H. G. Othmer, The topology of the regulatory interactions predicts the expression pattern of the segment polarity genes in Drosophila melanogaster. *Journal of Theoretical Biology*, 2003, 223 (1): 1–18.

[4] M. Chaves, R. Albert, E. D. Sontag, Robustness and fragility of Boolean models for genetic regulatory networks. *Journal of Theoretical Biology*, 2005, 235(3): 431–449.

[5] N. Bof, E. Fornasini, M. E. Valcher, Output feedback stabilization of Boolean control networks. *Automatica*, 2015, 57: 21–28.

[6] D. Cheng, H. Qi, *Semi-Tensor Product of Matrices Theory and Applications*, Science Press, Beijing, 2007.

[7] D. Cheng, H. Qi, Z. Li, *Analysis and Control of Boolean Networks: A Semi-Tensor Product Approach*, Springer Science & Business Media, 2010.

[8] D. Cheng, H. Qi, Controllability and observability of Boolean control networks. *Automatica*, 2009, 45(7): 1659–1667.

[9] Y. Zhao, H. Qi, D. Cheng, Input-state incidence matrix of Boolean control networks and its applications. *Systems & Control Letters*, 2010, 59(12): 767–774.

[10] Y. Yu, J. Feng, B. Wang, P. Wang, Sampled-data controllability and stabilizability of Boolean control networks: Nonuniform sampling. *Journal of the Franklin Institute*, 2018, 355(12): 5324–5335.

[11] Y. Yu, M. Meng, J. Feng, Observability of Boolean networks via matrix equations. *Automatica*, 2020, 111: 108621.

[12] D. Cheng, H. Qi, Z. Li, J. Liu, Stability and stabilization of Boolean networks. *International Journal of Robust and Nonlinear Control*, 2011, 21(2): 134–156.

[13] R. Li, M. Yang, T. Chu, State feedback stabilization for Boolean control networks. *IEEE Transactions on Automatic Control*, 2013, 58(7): 1853–1857.

[14] Y. Guo, P. Wang, W. Gui, C. Yang, Set stability and set stabilization of Boolean control networks based on invariant subsets. *Automatica*, 2015, 61: 106–112.

[15] B. Wang, J. Feng, H. Li, Y. Yu, On detectability of Boolean control networks. *Nonlinear Analysis: Hybrid Systems*, 2020, 36: 100859.

[16] G. Duan, High-order fully actuated system approaches: Part I. Models and basic procedure. *International Journal of Systems Science*, 2020, 52(2): 422–435.

[17] G. Duan, High-order fully actuated system approaches: Part II. Generalized strict-feedback systems. *International Journal of Systems Science*, 2020, 52(3): 437–454.

[18] G. Duan, High-order fully actuated system approaches: Part III. Robust control and high-order backstepping. *International Journal of Systems Science*, 2020, 52(5): 952–971.

[19] G. Duan, High-order fully actuated system approaches: Part IV. Adaptive control and high-order backstepping. *International Journal of Systems Science*, 2020, 52(5): 972–989.

[20] G. Duan, High-order fully-actuated system approaches: Part VI. Disturbance attenuation and decoupling. *International Journal of Systems Science*, 2020, 52(10): 2161–2181.

[21] X. Qian, J. Song, *Engineering Control Theory*, Science Press, Beijing, 2011.

[22] J. Wang, J. Feng, Y. Yu, H. Huang, Synchronous networks over finite fields, *IEEE Transactions on Automatic Control*, 2023, 68(11): 6907–6912.

[23] H. Qi, M. E .Valcher, G. Shi, Feedback shaping for Boolean networks. *IFAC-PapersOnLine*, 2023, 56(2): 6684–6689.

[24] G. Duan, High-order fully actuated system approaches: Part X. Basics of discrete-time systems. *International Journal of Systems Science*, 2021, 53(4): 810–832.

[25] Y. Yu, Logical Matrix Equation and Its Applications in Boolean Networks. Shandong University, 2019, chapter 7.

Proceedings of the 3rd Conference on Fully Actuated System Theory and Applications
May 10-12, 2024, Shenzhen, China

Adaptive Dynamic Event-Triggered Tracking Control for Uncertain High-Order Fully Actuated Systems

Zhaoyang Li[1], Zhongyu Chen[1], Yichun Niu[2], Li Sheng *[1]

1. College of Control Science and Engineering, China University of Petroleum (East China), Qingdao 266580,P. R. China
E-mail: shengli@upc.edu.cn

2. College of Electrical Engineering and Automation, Shandong University of Science and Technology, Qingdao 266590, P. R. China
E-mail: niuyichun123@163.com

Abstract: This paper proposes an adaptive dynamic event-triggered tracking control scheme for a class of uncertain high-order fully actuated (HOFA) systems with input saturation. To address the issue of uncertainties in the system, parameter adaption technology is adopted in the control scheme. Then, a dynamic event-triggered mechanism is proposed in order to mitigate the communication frequency between the controller and the actuator. In contrast to the conventional static event-triggered mechanism, the proposed dynamic event-triggered mechanism enables a more efficient utilization of communication resources. Additionally, based on Lyapunov stability theory, it is strictly proven that the designed controller guarantees the boundedness of all signals within the closed-loop system and prevents the occurrence of Zeno behavior. Finally, the efficacy of the proposed control scheme is substantiated through a numerical simulation case study.

Key Words: High-order fully actuated (HOFA) systems, adaptive control, input saturation, dynamic event-triggered mechanism

1 Introduction

In the development of control area, first-order state-space models have traditionally dominated. However, the focus in these models is primarily on state variables rather than control variables, which cause challenges in addressing control problems. Then, the corresponding control approaches often transformed these systems into first-order models through state augmentation, thereby resulting in a increased complexity and losing the fully actuated property. Recently, the concept of high-order fully actuated (HOFA) system was initially proposed in [1], providing a simplified framework for controller design once HOFA system models can be obtained. Subsequently, for a certain category of HOFA systems characterized by parameter uncertainties, both adaptive stabilization and tracking control strategies were developed in [2]. Furthermore, the author in [3] presented two design schemes for adaptive robust stabilization controller and adaptive robust tracking controller of HOFA systems with parametric uncertainties and nonlinear uncertainties. However, it is important to acknowledge that the aforementioned control strategies are designed based on a time-triggered approache without considering the communication burden.

To decrease the transmission frequency, in recent years, an event-triggered mechanism (ETM) has been widely employed in network control systems. As an aperiodic transmission control strategy, the control input with ETM is updated exclusively upon the occurrence of the specified conditions, thereby mitigating energy expenditure and reducing wear on actuators [4]. This process also improves the resource utilization efficiency. However, there are few works available for nonlinear HOFA systems that take the transmission efficiency into account. In [5], a dual-channel event-triggered control strategy based on the HOFA theory was designed for a category of nonlinear strict-feedback systems. In [6] an adaptive ETM was presented for the control design of uncertain HOFA systems with uncertain controller gain matrices. However, it should be noted that the design approaches mentioned above only focuse on the conventional static event-triggered mechanism (SETM), which fails to adequately alleviate communication pressure. Keeping this in consideration, the dynamic event-triggered mechanism (DETM), as an improved iteration of SETM, was proposed in [7] for the first time. As a result of the incorporation of dynamic variables, the DETM is more flexible in the systems where fast change of signals are required, and the average inter-event interval can be extended, thereby further resulting in a reduction in terms of communication resource consumption [8]. Nonetheless, the aforementioned results cannot be directly extended to the dynamic event-triggered control design considering input saturation due to the uncertainty of actuator dynamics.

In many practical control systems, the output of actuators is often subject to threshold limitations which may causes deteriorated control performance or even leads to instability. Therefore, the input saturation is an important issue that needs to be solved. In [9], an asymmetric saturation model based on the Gaussian error function was employed to address the issue of asymmetric saturation nonlinearity. In [10], an adaptive fault-tolerant controller with input saturation was designed by introducing a smooth hyperbolic tangent function. Additionally, the issue of actuator saturation was addressed by adjusting the reference signal using an explicit reference governor [11]. Nevertheless, based on a thorough survey of existing works, the problem of adaptive dynamic event-triggered tracking control for uncertain HOFA systems with input saturation has not been studied, which motivates our current research.

Inspired by the preceding discussions in this paper, we propose an adaptive dynamic event-triggered tracking control framework for uncertain HOFA systems with input saturation. The key contributions can be summarized as follows:

1) In this paper, the dynamic event-triggered tracking con-

This work was supported by the National Natural Science Foundation of China under Grants 62073339, 62173343, and the Postdoctoral Program for Innovative Talents of Shandong Province of China under Grant SDBX2023021. *: Corresponding author.

trol problem for a class of uncertain HOFA systems with input saturation is addressed initially. The control scheme puts forward in this paper results in significant savings in communication resources, and the negative influence caused by the actuator saturation can be conquered.

2) Compared with the conventional SETM, the DETM introduced in this paper achieves lower transmission frequency, which declines the frequency of communication effectively.

Notations: In the following discussion, some variables are abbreviated if there is no ambiguity, e.g., P stands for matrix $P(A^{0\sim n-1})$, $\lambda_{\max}(\cdot)$ and $\lambda_{\min}(\cdot)$ represent the maximum and minimum eigenvalues of a matrix respectively. Additionally, $A^{0\sim n-1}=[A_0,A_1,\ldots,A_{n-1}]$, $x^{(n)}$ signifies the n-th derivative of x, $t_k=[t_{1,k},\ldots,t_{r,k}]^T\in R^r$,

$$\Phi\left(A^{0\sim n-1}\right)=\begin{bmatrix}0_{r\times r} & I_{r\times r} & & \\ & & \ddots & \\ & & & I_{r\times r}\\ -A_0 & -A_1 & \cdots & -A_{n-1}\end{bmatrix}\in R^{nr\times nr},$$

where $0_{r\times r}$ and $I_{r\times r}$ stand for the $r\times r$ null matrix and identity matrix respectively.

2 Preliminaries and Problem Description

Consider the uncertain HOFA system with disturbances, input saturation and unknown nonlinearities as:

$$\begin{aligned}x^{(n)}=&f(\bar{x})+\Delta f(\bar{x})+H^T(\bar{x})\theta\\&+G(\bar{x})u(v)+D(\bar{x})d\end{aligned}\tag{1}$$

where $x\in R^r$ is the system state vector; $\bar{x}=[x,\dot{x},\ldots,x^{(n-1)}]^T\in R^{nr}$; $f(\bar{x})\in R^r$ is a known sufficiently smooth nonlinear vector function; $H(\bar{x})\in R^{m\times r}$ and $D(\bar{x})\in R^{r\times r}$ are known sufficiently smooth matrix functions; $G(\bar{x})\in R^{r\times r}$ denotes the unknown control gain matrix function; $\Delta f(\bar{x})\in R^r$ and $\theta\in R^m$ denote the nonlinear uncertainty and the parameter uncertainty, respectively; $d\in R^r$ is an unknown disturbance input vector; $u(v)=[u_1(v_1),\ldots,u_r(v_r)]^T\in R^r$ denotes the actual input signal, which can be mathematically described by the following equation:

$$u_i(v_i)=\begin{cases}u_{i,UB}, & v_i\geq u_{i,UB}\\ v_i, & u_{i,LB}<v_i<u_{i,UB}\\ u_{i,LB}, & v_i\leq u_{i,LB}\end{cases}\tag{2}$$

where $i=1,\ldots,r$, v_i is the input signal, $u_{i,UB}>0$ and $u_{i,LB}<0$ denote the upper bound and lower bound of the actuator respectively, and there are $u_{UB}=[u_{1,UB},\ldots,u_{r,UB}]^T\in R^r$, $u_{LB}=[u_{1,LB},\ldots,u_{r,LB}]^T\in R^r$. In order to ensure the smoothness of $u(v)$, a saturation model is taken into account to describe the saturation nonlinearity:

$$sat(v_i)=u_{i,m}\times\operatorname{erf}\left(\frac{\sqrt{\pi}}{2u_{i,m}}v_i\right)\tag{3}$$

where $u_{i,m}=(u_{i,UB}+u_{i,LB})/2+(u_{i,UB}-u_{i,LB})\operatorname{sgn}(v_i)/2$, $\operatorname{sgn}(\cdot)$ and $\operatorname{erf}(\cdot)$ represent a sign function and a Gaussian error function respectively [12].

To facilitate subsequent controller analysis and design, the saturation approximation error is defined as follows:

$$\Delta=u(v)-pv\tag{4}$$

where $\Delta=[\Delta_1,\ldots,\Delta_r]^T\in R^r$ is bounded, $v(t)=[v_1(t),\ldots,v_r(t)]^T\in R^r$, p is a positive constant. Then, the saturation model (3) can be represented by the following manner:

$$u(v)=pv+\Delta.\tag{5}$$

Therefore, the uncertain HOFA system (1) can be expressed in forms of

$$\begin{aligned}x^{(n)}=&f(\bar{x})+\Delta f(\bar{x})+H^T(\bar{x})\theta\\&+G(\bar{x})(pv+\Delta)+D(\bar{x})d.\end{aligned}\tag{6}$$

Considering y_d as the desired reference signal, the tracking error z and its derivatives are expressed as follows:

$$\begin{aligned}z=&x-y_d\\ z^{(j)}=&x^{(j)}-{y_d}^{(j)},j=1,2,\ldots,n.\end{aligned}\tag{7}$$

Then, the system (6) can be converted into an uncertain HOFA tracking error system as follows:

$$\begin{aligned}z^{(n)}=&f(\bar{z})+\Delta f(\bar{z})+H^T(\bar{z})\theta+G(\bar{z})(pv+\Delta)\\&+D(\bar{z})d-{y_d}^{(n)}\end{aligned}\tag{8}$$

where $\bar{z}=[z,\dot{z},\ldots,z^{(n-1)}]^T\in R^{nr}$.

The primary goal of this study is to develop an adaptive event-triggered tracking controller with the input saturation (3), such that y_d can be tracked accurately by the state x and the boundedness of all signals within the closed-loop system is guaranteed. To this end, the relevant assumptions and lemmas are given below.

Assumption 1 *There exists unknown constants $\underline{g}$ and $\overline{g}$ satisfying $0<\underline{g}\leq\overline{g}$ and*

$$\underline{g}\leq\lambda_{\min}(G(\bar{x}))\leq\lambda_{\max}(G(\bar{x}))\leq\overline{g}.$$

Assumption 2 *The uncertain nonlinearity $\Delta f(\bar{x})$ of the system (1) is constrained by the product of a know non-negative continuous function $f'(\bar{x})$ and an unknown constant s, i.e.*

$$\|\Delta f(\bar{x})\|\leq sf'(\bar{x}).$$

Assumption 3 *There exists positive constants $\overline{\Delta}$, $\overline{d}$ that satisfie $\|\Delta\|\leq\overline{\Delta}$, $\|d\|\leq\overline{d}$,*

Assumption 4 *The desired reference signal y_d and ${y_d}^{(n)}$ are continuous, bounded and available.*

Remark 1 *Assumption 1 ensures the controllability of the HOFA system (1); Assumption 2 is a commonly used assumption when dealing with unknown nonlinear functions, which guarantees the uncertainty and nonlinearity of the function $\Delta f(\bar{x})$; Assumption 3 shows the disturbance term $D(\bar{x})d$ satisfies the norm-bounded condition.*

Lemma 1 *[2] Let $A \in R^{n\times n}$ satisfies $\mathrm{Re}\lambda_i(A) < -\frac{\mu}{2}$, where $i = 1, 2, \ldots, n$, $\mu > 0$. Then there exists a positive definite matrix $P \in R^{n\times n}$ that satisfies*

$$A^T P + PA \le -\mu P.$$

Lemma 2 *[2] For any positive constant μ, there exists a set of matrices $A_i \in R^{r\times r}, i = 0, 1, \ldots, n-1$ that satisfies*

$$\mathrm{Re}\lambda_i\left(\Phi\left(A^{0\sim n-1}\right)\right) < -\frac{\mu}{2}, \quad i = 1, 2, \ldots, nr.$$

Lemma 3 *[13] For any positive constant μ and any variable $h \in R$, there is an inequality satisfies*

$$0 \le |h| - \frac{h^2}{\sqrt{h^2+\mu^2}} < \mu.$$

Remark 2 *Lemma 2 shows that the eigenvalues can be freely designed by properly choosing $A_i \in R^{r\times r}, i = 0, 1, \ldots, n-1$ for matrix $\Phi\left(A^{0\sim n-1}\right)$. When the condition in Lemma 2 holds, it can be inferred that a positive definite matrix $P(A^{0\sim n-1}) = [P_1, P_2, \ldots, P_n]$, $P_i \in R^{nr\times r}$ exists according to Lemma 1, for which the following inequality holds:*

$$\begin{aligned}&\Phi^T(A^{0\sim n-1})P(A^{0\sim n-1}) + P(A^{0\sim n-1})\Phi(A^{0\sim n-1})\\ &\quad\le -\mu P(A^{0\sim n-1}).\end{aligned} \tag{9}$$

3 Controller Design and Stability Analysis

In order to obtain the HOFA closed-loop system, an auxiliary signal $\overline{u}$ is introduced as follows [6]:

$$\overline{u} = A^{0\sim n-1}\bar{z} + f(\bar{z}) + \Psi^T(\bar{z})\hat{\Theta} - y_d^{(n)} \tag{10}$$

where $\hat{\Theta} = [\hat{\theta}, \hat{s}]^T \in R^{m+1}$ is the estimate of $\Theta = [\theta, s]^T \in R^{m+1}$ in which $\hat{\theta}$, $\hat{s}$ are the estimated values of θ, s, respectively. Then there exist $\tilde{\Theta}(t) = \Theta - \hat{\Theta}(t)$, $\tilde{\theta}(t) = \theta - \hat{\theta}(t)$, $\tilde{s}(t) = s - \hat{s}(t)$. $\Psi(\bar{z})$ is an augmentation of $H(\bar{z})$ and $\zeta^T(\bar{z})$, which are given as fellows:

$$\begin{aligned}\Psi(\bar{z}) =& \left[H^T(\bar{z}), \zeta(\bar{z})\right]^T\\ \zeta(\bar{z}) =& \frac{f'^2 P_n^T \bar{z}}{\sqrt{f'^2\left\|\bar{z}^T P_n\right\|^2 + \varepsilon_2^2}}\end{aligned}$$

where ε_2 is a positive constant.

Then, according to the auxiliary signal (10), the above uncertain HOFA tracking error model (8) can be converted to a HOFA standard closed-loop system form:

$$z^{(n)} + A^{0\sim n-1}\bar{z} = \phi(\bar{z}). \tag{11}$$

where

$$\begin{aligned}\phi(\bar{z}) =& \Delta f(\bar{z}) + H^T(\bar{z})\tilde{\theta} + D(\bar{z})d - \zeta(\bar{z})\hat{s}\\ &+ G(\bar{z})(pv + \Delta) + \overline{u}.\end{aligned}$$

Further, (11) can be converted into the form of state-space model:

$$\dot{\bar{z}} = \Phi\left(A^{0\sim n-1}\right)\bar{z} + \begin{bmatrix}0_{(n-1)r}\\ \phi(\bar{z})\end{bmatrix} \tag{12}$$

In order to minimize the frequency of triggers, a DETM is introduced, which includes dynamic event-triggered condition and definition of dynamic variable ρ_i:

$$t_{i,k+1} = \min\left\{t \ge t_{i,k} : \rho_i + \left(\overline{B}_i - |u_{di} - v_i|\right) \le 0\right\} \tag{13}$$

$$\dot{\rho}_i = -\eta_i\rho_i + \left(\overline{B}_i - |u_{di} - v_i|\right), \rho_i(0) = 0 \tag{14}$$

where $\overline{B}_i$, η_i are the designed positive constants, $u_d = [u_{d1}, \ldots, u_{dr}]^T \in R^r$ is the control law to be designed subsequently, $\rho = [\rho_1, \ldots, \rho_r]^T \in R^r$, $\overline{B} = \left[\overline{B}_1, \ldots, \overline{B}_r\right]^T \in R^r$.

The dynamic event-triggered control is now presented as:

$$v_i(t) = u_{di}(t_{i,k}), t \in [t_{i,k}, t_{i,k+1}). \tag{15}$$

Lemma 4 *For dynamic variable ρ_i, there exists $0 \le \rho_i \le \frac{\overline{B}_i}{\eta_i}$ for all $t \in [0, t_\infty)$ under the event-triggered condition (13) and the dynamic variable (14).*

Proof: According to (13), it can be inferred that

$$\rho_i + \left(\overline{B}_i - |u_{di} - v_i|\right) > 0, t \in [t_{i,k}, t_{i,k+1}). \tag{16}$$

Bringing the above equation into the definition of dynamic variable (14), that

$$\dot{\rho}_i \ge -\eta_i\rho_i - \rho_i. \tag{17}$$

Based on comparison lemma, there exists $\rho_i > 0$ when $t \in [t_{i,k}, t_{i,k+1})$.

From (14) the following inequality can be obtained:

$$\dot{\rho}_i \le -\eta_i\rho_i + \overline{B}_i. \tag{18}$$

For $\rho_i(0) = 0$, there exists $\rho_i(t) \le \frac{\overline{B}_i}{\eta_i}(1 - e^{-\eta_i t})$ by solving the differential equation of (17). Therefore, ρ_i has upper bound of $\frac{\overline{B}_i}{\eta_i}$ for all $t \in [0, t_\infty)$.

In conclusion, ρ_i is bounded by $0 \le \rho_i \le \frac{\overline{B}_i}{\eta_i}$. The proof is complete. □

When $A_i \in R^{r\times r}$ satisfies Lemma 2, a positive definite matrix $P(A^{0\sim n-1})$ can be found. Now, choose the Lyapunov function as

$$V = \frac{1}{2p}\bar{z}^T P\bar{z} + \frac{\underline{g}\tilde{\gamma}^2}{2} + \frac{1}{2p}\tilde{\Theta}^T\Gamma^{-1}\tilde{\Theta} + \frac{\underline{g}\tilde{b}^2}{2} \tag{19}$$

where $\Gamma \in R^{(m+1)\times(m+1)}$ stands for a gain matrix which is positive definite; $\tilde{\gamma}(t) = \gamma - \hat{\gamma}(t) \in R$, in which $\hat{\gamma}$ represents the estimated value of γ with $\gamma = \frac{1}{p\underline{g}}$; $\tilde{b}(t) = b - \hat{b}(t) \in R$, in which $\hat{b}$ represents the estimated value of b with $b = \frac{\overline{g}}{\underline{g}}$.

Then, we have

$$\begin{aligned}\dot{V} \le& -\frac{\mu}{2p}\bar{z}^T P\bar{z} + \frac{1}{p}\bar{z}^T P_n\Big(\Delta f(\bar{z}) + H^T(\bar{z})\tilde{\theta}\\ &+ D(\bar{z})d - \zeta(\bar{z})\hat{s} + G(\bar{z})(pv + \Delta) + \overline{u}\Big)\\ &- \underline{g}\tilde{\gamma}\dot{\hat{\gamma}} - \frac{1}{p}\tilde{\Theta}^T\Gamma^{-1}\dot{\hat{\Theta}} - \underline{g}\tilde{b}\dot{\hat{b}}.\end{aligned} \tag{20}$$

According to Assumption 2 and lemma 3, it can be obtained that

$$\frac{1}{p}\bar{z}^T P_n\Delta f(\bar{z}) \le \frac{1}{p}s\bar{z}^T P_n\zeta(\bar{z}) + \frac{1}{p}s\varepsilon_2. \tag{21}$$

By applying Young's inequality, the subsequent relationships are established:

$$\begin{aligned}\frac{1}{p}\bar{z}^T P_n D(\bar{z})\, d &\le \frac{1}{p}\left\|\bar{z}^T P_n\right\| \|D(\bar{z})\|\, \overline{d} \\ &\le \frac{1}{2p}\left\|\bar{z}^T P_n\right\|^2 \|D(\bar{z})\|^2 + \frac{1}{2p}\overline{d}^2\end{aligned} \tag{22}$$

$$\begin{aligned}\frac{1}{p}\bar{z}^T P_n G(\bar{z})\, \Delta &\le \frac{1}{p}\left\|\bar{z}^T P_n\right\| \overline{g}\overline{\Delta} \\ &\le \frac{1}{2p}\left\|\bar{z}^T P_n\right\|^2 + \frac{1}{2p}\overline{g}^2\overline{\Delta}^2.\end{aligned} \tag{23}$$

Bringing (21)-(23) into (20), there exists

$$\begin{aligned}\dot{V} \le & -\frac{\mu}{2p}\bar{z}^T P\bar{z} + \frac{1}{p}\bar{z}^T P_n\Big(\overline{u} + C + \Psi^T(\bar{z})\,\tilde{\Theta} \\ & + G(\bar{z})\, pv\Big) - \underline{g}\tilde{\gamma}\dot{\hat{\gamma}} - \frac{1}{p}\tilde{\Theta}^T\Gamma^{-1}\dot{\hat{\Theta}} - \underline{g}\tilde{b}\dot{\hat{b}} \\ & + \frac{1}{p}s\varepsilon_2 + \frac{1}{2p}\overline{d}^2 + \frac{1}{2p}\overline{g}^2\overline{\Delta}^2\end{aligned} \tag{24}$$

where $C = \frac{1}{2}P_n^T\bar{z}\left[1 + \|D(\bar{z})\|^2\right] \in R^r$.

According to (13), we have $\rho_i + \left(\overline{B}_i - |u_{di} - v_i|\right) \ge 0$, i.e., $|u_{di} - v_i| \le \rho_i + \overline{B}_i$, $t \in [t_{i,k}, t_{i,k+1})$. Hence, the following equation can be derived:

$$v = u_d - \lambda(t)\left(\overline{B} + \rho\right) \tag{25}$$

where $\lambda(t)$ represents a time-varying function satisfying the conditions $|\lambda(t)| \le 1$ with $\lambda(t_{\dot{\kappa}}) = 0$, $\lambda(t_{\dot{\kappa}+1}) = 1$.

Taking (25) into (24) yields

$$\begin{aligned}\dot{V} \le & -\frac{\mu}{2p}\bar{z}^T P\bar{z} + \frac{1}{p}\bar{z}^T P_n\Big(\overline{u} + C + \Psi^T(\bar{z})\,\tilde{\Theta} \\ & + G(\bar{z})\, p\left(u_d - \lambda(t)\left(\overline{B} + \rho\right)\right)\Big) - \underline{g}\tilde{\gamma}\dot{\hat{\gamma}} \\ & - \frac{1}{p}\tilde{\Theta}^T\Gamma^{-1}\dot{\hat{\Theta}} - \underline{g}\tilde{b}\dot{\hat{b}} + \frac{1}{p}s\varepsilon_2 + \frac{1}{2p}\overline{d}^2 + \frac{1}{2p}\overline{g}^2\overline{\Delta}^2.\end{aligned} \tag{26}$$

Based on Lyapunov stability theory, the adaptive event-triggered tracking controller u_d is designed as

$$\begin{cases} u_d = -r_1 - \hat{b}r_2 \\ r_1 = \dfrac{\hat{\gamma}^2(\overline{u}+C)\left((\overline{u}+C)^T P_n^T\bar{z}\right)}{\sqrt{\left(\hat{\gamma}\bar{z}^T P_n(\overline{u}+C)\right)^2 + \varepsilon_1^2}} \\ r_2 = \dfrac{W\left(W^T P_n^T\bar{z}\right)}{\sqrt{\left(\bar{z}^T P_n W\right)^2 + \varepsilon_1^2}} \end{cases} \tag{27}$$

where $W = \overline{B} + \rho \in R^r$, ε_1 is a positive constant.

Considering $\bar{z}^T P_n G(\bar{z})\, u_d \le 0$ and Lemma 1, substituting (27) into (26), there exists:

$$\begin{aligned}&\frac{1}{p}\bar{z}^T P_n G(\bar{z})\, p\left(u_d - \lambda(t)\left(\overline{B} + \rho\right)\right) \\ =&\bar{z}^T P_n G(\bar{z})\, u_d - \bar{z}^T P_n G(\bar{z})\left(\lambda(t)\left(\overline{B} + \rho\right)\right) \\ \le&\underline{g}\bar{z}^T P_n u_d + \overline{g}\bar{z}^T P_n r_2 + \varepsilon_1\overline{g} \\ \le& -\underline{g}\hat{\gamma}\bar{z}^T P_n(\overline{u} + C) + \varepsilon_1\underline{g} - \underline{g}\hat{b}\bar{z}^T P_n r_2 \\ & + \overline{g}\bar{z}^T P_n r_2 + \varepsilon_1\overline{g} \\ \le& -\frac{1}{p}\bar{z}^T P_n(\overline{u} + C) + \underline{g}\tilde{\gamma}\bar{z}^T P_n(\overline{u} + C) \\ & + \underline{g}\tilde{b}\bar{z}^T P_n r_2 + \varepsilon_1\underline{g} + \varepsilon_1\overline{g}.\end{aligned} \tag{28}$$

Bringing (28) back to (26) yields:

$$\begin{aligned}\dot{V} \le & -\frac{\mu}{2p}\bar{z}^T P\bar{z} + \varepsilon_1\underline{g} + \varepsilon_1\overline{g} + \frac{1}{p}s\varepsilon_2 + \frac{1}{2p}\overline{d}^2 \\ & + \frac{1}{2p}\overline{g}^2\overline{\Delta}^2 - \underline{g}\tilde{\gamma}\left(\dot{\hat{\gamma}} - \bar{z}^T P_n(\overline{u} + C)\right) \\ & - \frac{1}{p}\tilde{\Theta}^T\Gamma^{-1}\left(\dot{\hat{\Theta}} - \Gamma\Psi P_n^T\bar{z}\right) - \underline{g}\tilde{b}\left(\dot{\hat{b}} - \bar{z}^T P_n r_2\right).\end{aligned} \tag{29}$$

Thus, the adaptive laws can be intuitively designed as

$$\begin{cases} \dot{\hat{\gamma}} = \bar{z}^T P_n(\overline{u} + C) - \tau_1\hat{\gamma} \\ \dot{\hat{\Theta}} = \Gamma\Psi P_n^T\bar{z} - \tau_2\Gamma\hat{\Theta} \\ \dot{\hat{b}} = \bar{z}^T P_n r_2 - \tau_3\hat{b} \end{cases} \tag{30}$$

where τ_1, τ_2, τ_3 are the designed positive constants.

Finally, substituting (30) into (29) yields:

$$\begin{aligned}\dot{V} \le & -\frac{\mu}{2p}\bar{z}^T P\bar{z} - \frac{\tau_1\underline{g}}{2}\tilde{\gamma}^2 - \frac{\tau_2}{2p}\tilde{\Theta}^T\tilde{\Theta} \\ & - \frac{\tau_3\underline{g}}{2}\tilde{b}^2 + \frac{\tau_1\underline{g}}{2}\gamma^2 + \frac{\tau_2}{2p}\Theta^T\Theta + \frac{\tau_3\underline{g}}{2}b^2 \\ & + \varepsilon_1\underline{g} + \varepsilon_1\overline{g} + \frac{1}{p}s\varepsilon_2 + \frac{1}{2p}\overline{d}^2 + \frac{1}{2p}\overline{g}^2\overline{\Delta}^2 \\ \le & -aV + w\end{aligned} \tag{31}$$

where

$$\begin{aligned}a =& \min\left\{\mu, \tau_1, \tau_2/\lambda_{\max}\left(\Gamma^{-1}\right), \tau_3\right\} \\ w =& \frac{\tau_1\underline{g}}{2}\gamma^2 + \frac{\tau_2}{2p}\Theta^T\Theta + \frac{\tau_3\underline{g}}{2}b^2 + \varepsilon_1\underline{g} + \varepsilon_1\overline{g} \\ & + \frac{1}{p}s\varepsilon_2 + \frac{1}{2p}\overline{d}^2 + \frac{1}{2p}\overline{g}^2\overline{\Delta}^2.\end{aligned}$$

Theorem 1 *Considering the uncertain HOFA system (1) satisfying Assumptions 1, 2, 3, 4, the adaptive event-triggered tracking controller (27) designed with adaptive laws (30) guarantee the boundedness of all signals within the closed-loop system. There is no occurrence of Zeno behavior under the controller and adaptive laws designed above.*

Proof: It can be obtained $V \le e^{-at}(V(0) - \frac{w}{a}) + \frac{w}{a}$ by solving the differential equation of (31). When $t \to +\infty$, it is easy to conclude $V \to \frac{w}{a}$, which in turn gives the boundness of $\bar{z}$, $\hat{\gamma}$, $\hat{\Theta}$ and $\hat{b}$. Then, we can obtain that $f'(\bar{z})$ and $\Psi(\bar{z})$ are bounded. According to (10), the boundedness of $\overline{u}$

can be obtained. Since $0 \leq \rho_i \leq \frac{\overline{B}_i}{\eta_i}$ was proved in Lemma 4, then u_d, v and u are bounded due to the boundedness of $\overline{u}$, ρ and p. Thus, it is guaranteed that all signals within the closed-loop system remain bounded.

Next it is shown that the event-triggered control scheme proposed above avoids Zeno behavior, i.e., there exists a minimum inter-execution time $t^* = [t_1^*, \ldots, t_r^*]^T \in R^r$ satisfying $t_{i,k+1} - t_{i,k} \geq t_i^*$ with $\forall k \in Z^+$. Letting $e_i = u_{di} - v_i$, obviously, for $\forall t \in [t_{i,k}, t_{i,k+1})$ it holds that

$$\frac{d}{dt}|e_i| = \frac{d}{dt}(e_i * e_i)^{\frac{1}{2}} = \frac{e_i \dot{e}_i}{|e_i|} = \text{sign}(e_i)\dot{e}_i \leq |\dot{u}_{di}| \quad (32)$$

where u_d is differentiable and $\dot{u}_d$ is a function comprised of all bounded signals. Therefore, there must exist a positive constant m_i such that the inequality $|\dot{u}_{di}| \leq m_i$ holds. Integrating (32) from t_k to t_{k+1} with $e_i(t_k) = 0$ and $\lim_{t \to t_{k+1}} e_i(t) = \lim_{t \to t_{k+1}} [\rho_i(t) + \overline{B}_i] = \rho_i(t_{k+1}) + \overline{B}_i > 0$, thus yields $\overline{B}_i \leq \rho_i(t_{k+1}) + \overline{B}_i \leq m_i(t_{k+1} - t_k)$, i.e., there exists

$$t_{k+1} - t_k \geq t^* = \frac{\overline{B}_i}{m_i} > 0.$$

Therefore, no Zeno behavior is exhibited. □

4 Simulation Studies

In this subsection, a simulation example is presented to illustrate the efficacy of the proposed adaptive dynamic event-triggered tracking controller. Consider the following uncertain fourth-order fully actuated system as

$$\begin{aligned} x^{(4)} =& f(\bar{x}) + \Delta f(\bar{x}) + H^T(\bar{x})\theta \\ &+ G(\bar{x})u(v) + D(\bar{x})d \end{aligned} \quad (33)$$

where $\bar{x} = [x, \dot{x}, x^{(2)}, x^{(3)}]^T$, $f(\bar{x}) = \sin(x) + \cos(x + \dot{x}) + \sin(x^{(2)}x^{(3)}) + x\dot{x}$, $\Delta f(\bar{x}) = \cos(x\dot{x} + x^{(2)})\sin(x^{(3)})$, $H(\bar{x}) = [0.25\sin(x), 0.5\dot{x}\cos(x^{(2)}), x + x^{(3)}]^T$, $\theta = [1, 0.5, 0.5]^T$, $G(\bar{x}) = 0.1\sin(x + \dot{x} + x^{(2)} + x^{(3)}) + 0.5$, $D(\bar{x}) = \cos(x + x^{(3)}) + \dot{x}$, $d = 0.1\sin(2t)$. Choose the desired reference signal as $y_d = 1.5\sin(t)$ and the saturation input is defined with $u_{UB} = 60$ and $u_{LB} = -30$ as its upper and lower bounds, respectively. The dynamic parameters set as $\eta = 0.3$, $\overline{B} = 18$. According to Assumption 2, Lemma 1 and Lemma 2, we choose $f'(\bar{x}) = \sin(x\dot{x}) + \sin(x^{(2)}x^{(3)})$, $A^{0\sim3} = [36, 60, 37, 10]$, $P_4 = [0.1124, 0.1464, 0.0637, 0.0091]^T$. The initial conditions are selected as $[x(0), \dot{x}(0), x^{(2)}(0), x^{(3)}(0)] = [0.5, 1.5, 0.75, 0.25]$, $[\hat{\gamma}(0), \hat{\Theta}^T(0), \hat{b}(0)] = [0.1, 0.1, 0.1, 0.1, 0.1, 0.1]$ and $\rho(0) = 0$ is designed based on Lemma 4. The remaining parameters are presented as $\Gamma = \textbf{diag}\{5, 5, 5, 5\}$, $\varepsilon_1 = \varepsilon_2 = 0.01$, $\tau_1 = 0.1$, $\tau_2 = 0.2$, $\tau_3 = 0.5$.

The simulation results are illustrated in Figs. 1-7. The tracking performance of the designed algorithm is demonstrated in Fig. 1, which illustrates that the algorithm is capable of tracking the reference signal effectively. Fig. 2 indicates that the tracking error eventually converge to zero. Fig. 3 illustrates the actual control signal of the system with asymmetric saturation. Fig. 4 demonstrates the boundedness of the adaptive parameters $\hat{\gamma}$, $\hat{\Theta}$ and $\hat{b}$, thereby implying that the estimation errors are also bounded. Fig. 5 displays that the dynamic variable ρ is bounded within the range of 0 to $\frac{\overline{B}}{\eta}$, which corroborates Lemma 4 mentioned earlier. Fig. 6 shows the interval times between two consecutive triggers. Fig. 7 compares the numbers of transmissions between DETM and SETM, indicating that additional communication resources can be can conserved by the proposed DETM compared to conventional SETM.

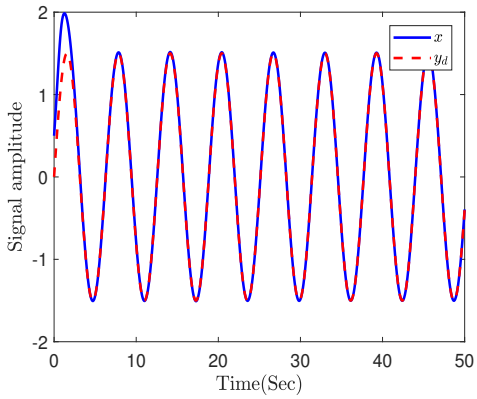

Fig. 1: Tracking trajectory.

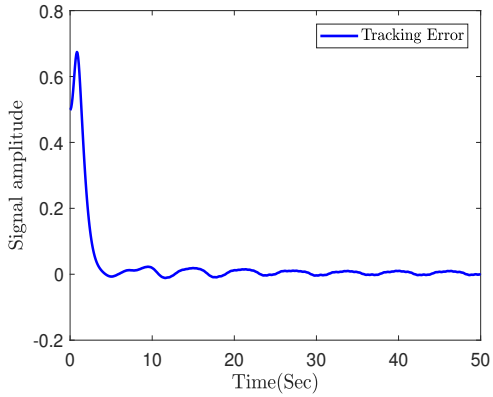

Fig. 2: Tracking error.

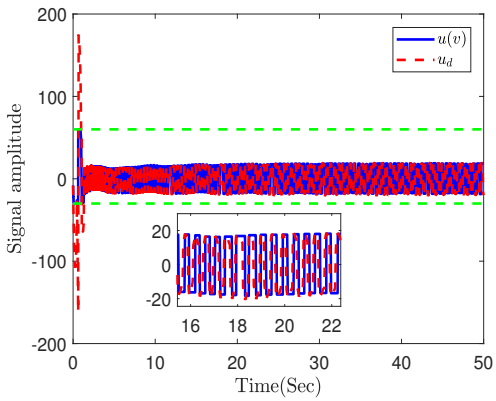

Fig. 3: The actual control signal.

5 Conclusion

This paper has explored the adaptive dynamic event-triggered tracking control problem for a class of uncertain HOFA nonlinear systems containing actuator saturation. In

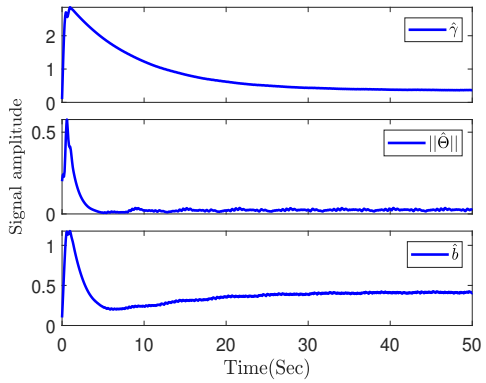

Fig. 4: Adaptive updating parameters $\hat{\gamma}$, $\hat{\Theta}$ and $\hat{b}$.

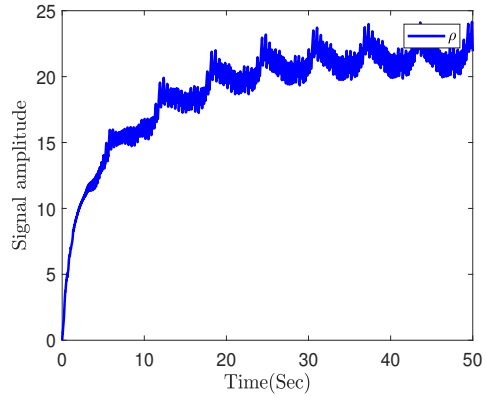

Fig. 5: The dynamic variable ρ.

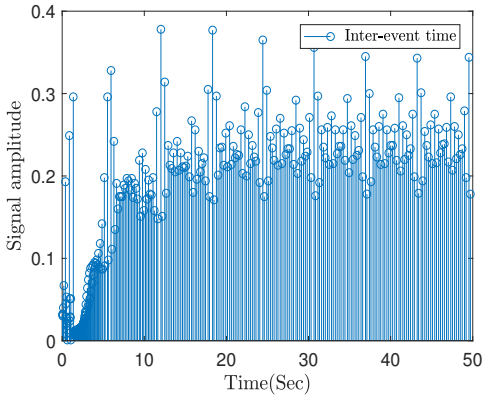

Fig. 6: Triggering instants and inter-event times.

this study, the uncertainty nonlinearities presented in the system are converted to adaptive estimation problems of unknown parameters. Then the proposed controller has effectively mitigated the impact of input saturation. Moreover, the introduced DETM has further improved the communication efficiency compared to the conventional SETM. Finally, the efficacy of the designed control strategy has been rigorously verified through theoretical proofs and simulations.

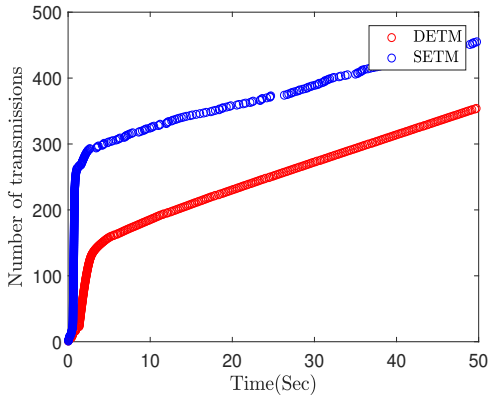

Fig. 7: The number of transmitted events by DETM and SETM.

References

[1] G. Duan. High-order fully actuated system approaches: Part i. models and basic procedure. *International Journal of Systems Science*, 2021, 52(2): 422–435.

[2] G. Duan. High-order fully actuated system approaches: Part iv. adaptive control and high-order backstepping. *International Journal of Systems Science*, 2021, 52(5): 972–989.

[3] G. Duan. High-order fully actuated system approaches: Part v. robust adaptive control. *International Journal of Systems Science*, 2021, 52(10): 2129–2143.

[4] Y. Li and G. Yang. Model-based adaptive event-triggered control of strict-feedback nonlinear systems. *IEEE transactions on neural networks and learning systems*, 2017, 29(4): 1033–1045.

[5] Z. Chen, L. Sheng, and M. Gao. Event-triggered control for nonlinear systems: A high-order full-actuation approach, in *2023 2nd Conference on Fully Actuated System Theory and Applications (CFASTA)*, 2023: 71–76.

[6] R. Meng, C. Hua, K. Li, and P. Ning. Adaptive event-triggered control for uncertain high-order fully actuated system. *IEEE Transactions on Circuits and Systems II: Express Briefs*, 2022, 69(11): 4438–4442.

[7] A. Girard. Dynamic triggering mechanisms for event-triggered control. *IEEE Transactions on Automatic Control*, 2014, 60(7): 1992–1997.

[8] X. Ge, Q. Han, L. Ding, Y. Wang, and X. Zhang. Dynamic event-triggered distributed coordination control and its applications: A survey of trends and techniques. *IEEE Transactions on Systems, Man, and Cybernetics: Systems*, 2020, 50(9): 3112–3125.

[9] J. Ma, S. S. Ge, Z. Zheng, and D. Hu. Adaptive nn control of a class of nonlinear systems with asymmetric saturation actuators. *IEEE transactions on neural networks and learning systems*, 2014, 26(7): 1532–1538.

[10] L. Wang, H. Gong, and C. Liu. Disturbance observer-based adaptive fault-tolerant dynamic surface control of nonlinear system with asymmetric input saturation. *International Journal of Control, Automation and Systems*, 2019, 17: 617–629.

[11] L. Yang and Y. Li. Tracking control for high-order fully actuated system with input constraints by explicit reference governor, in *2023 2nd Conference on Fully Actuated System Theory and Applications (CFASTA)*, 2023: 769–774.

[12] Z. Chen, B. Niu, L. Zhang, J. Zhao, A. M. Ahmad, and M. O. Alassafi. Command filtering-based adaptive neural network control for uncertain switched nonlinear systems using event-triggered communication. *International Journal of Robust and Nonlinear Control*, 2022, 32(11): 6507–6522.

[13] C. Wang and Y. Lin. Decentralized adaptive tracking control for a class of interconnected nonlinear time-varying systems. *Automatica*, 2015, 54: 16–24.

Proceedings of the 3rd Conference on Fully Actuated System Theory and Applications
May 10-12, 2024, Shenzhen, China

Event-Triggered Robust Control for a Class of Nonlinear Systems with Uncertainty: A HOFA System Approach

Lu-Han Zhang, Lou Wang, Cui-Hua Zhang, Chang-Chun Hua, Ying Zhang and Li Li
Yanshan University, Qinhuangdao 066004, P. R. China
E-mail: zhangluhan1216@163.com; wanglou120516@163.com; cuihuazhang@ysu.edu.cn; cch@ysu.edu.cn; yzhang@ysu.edu.cn; lili@ysu.edu.cn

Abstract: This paper focuses on addressing the event-triggered control problem for a specific class of nonlinear systems that involve unknown terms. To tackle this issue, the paper employs the recursive design method of "ascending dimension and descending order" to transform the cascade system into a high-order fully actuated (HOFA) model. The control law is then obtained using HOFA system approaches. Furthermore, a robust control technique is applied to handle the unknown terms and improve system stability and control accuracy. To reduce computation and energy consumption in signal transmission, a relative threshold event-triggered mechanism (ETM) is designed. By utilizing Lyapunov stability theory, the stability of the closed-loop system is examined. The analysis confirms that all signals within the closed-loop system exhibit ultimate boundedness. Finally, the proposed approach is validated through a simulation example, showcasing its effectiveness in achieving the desired control objectives.

Key Words: Robust control, High-order fully actuated systems, Event-triggered control, Nonlinear systems

1 Introduction

Significant progress has been made in control theory over the last few decades. Although linear system theory is mature and widely used in theory, linear feedback control is often difficult to meet various practical requirements with the development of science and technology and the continuous improvement of control system performance requirements. Most actual control systems are often nonlinear, so it is necessary to study the nonlinear system [1], [2], [3]. Extensive research and optimization on the control theory of nonlinear systems have been conducted by many experts and scholars in recent years, such as robust control [4], adaptive control [5, 6], neural network theory [7], [8], fuzzy control [9], [10] and so on.

Although the state-space model is widely used and has a good theoretical basis in the modeling and control of nonlinear systems, it still has some inherent defects [11]. Fortunately, there exists another system model called the high-order fully actuated (HOFA) mode [12], in addition to the state-space techniques. Regardless of their complexity, the nonlinear terms in the HOFA model could be conveniently eliminated by converting them into measurable forms using the full-actuation structure. The HOFA system methods are combined with robust control [13], optimal control [14] and adaptive control [16] and so on.

In the process of designing controllers, it is crucial to consider model uncertainties as they can have a detrimental impact on the performance of control systems. Robust control can maintain in the system containing unknown term stability and robustness, and simplify the design and adaptive [17]. However, when dealing with systems with unknown terms, robust control may not be able to completely eliminate uncertainties and perturbations. The combination of HOFA system approaches can further improve the robustness and control performance of the system, make up for the limitations of robust control, and ensure that the system has better control effects. Therefor, the paper research using robust control method to deal with the uncertainties of the system to ensure the stability.

Event-triggered control strategies were proposed [15, 18] as an alternative method to deal with the traditional periodic execution control problems [19], considering the limited communication resources of communication channels and the ability of sending channels. Reference [20] explored the event-triggered output feedback control law to achieve robust output regulation of linear systems. The problem's solvability was summarized via internal model design, and a triggered mechanism based on the system output was proposed to reduce steady-state tracking error. For a class of uncertain nonlinear systems in [21], the authors of the paper addressed the problem of global finite-time stabilization for uncertain nonlinear systems with event-triggered inputs.

After comprehensive design, the innovation points of this paper are as follows:

- This paper introduces the utilization of HOFA system approaches as an alternative to the traditional backstepping method [22]. To convert the cascade system into the HOFA model, the paper employs the recursive design method known as "ascending dimension reduction". This approach eliminates the need for complex coordinate transformations and significantly reduces computational complexity.
- In this paper, the robust controllers and the ETM [23] are synthetically designed. The use of HOFA system approaches can boost system response prediction accuracy and simplify the creation of more efficient ETM with relative thresholds. This design saves network resources during signal transmission and avoids the constant updating of the controller [24]. The control strategy employed ensures that all signals within the closed-loop system exhibit ultimate boundedness.

This work was supported in part by the Funds of the National Natural Science Foundation of China (Grant No. 62203377), the Hebei Natural Science Foundation (Grant No. F2022203097), the S&T Program of Hebei (Grant Nos. 236Z1603G and 236Z2002G), the Science Research Project of Hebei Education Department (Grant No. QN2022077), and the Fund of Innovation Capability Improvement Plan Project of Hebei Province (Grant No. 22567619H). *(Corresponding author: Cui-Hua Zhang.)*

Notations. The set of real numbers is denoted by $\mathbb{R}$, the set of positive numbers is denoted by $\mathbb{Z}_+$, $c \in \mathbb{C}$ means that c is c constant. $G_i(\cdot)$, $(i = 1,2,...,n)$, are continuously differentiable functions, which can be simply expressed as G_i. $H_i(\cdot)$, $(i = 1,2,...,n)$is the continuous partial derivative symbol, which can be simply expressed as H_i. $\Delta f_i(x_{1\sim n})$ is the system uncertainty. Q is a real symmetric matrix that is positive definite, and the last row of the matrix Q is denoted by Q_L. For $x_k \in \mathbb{R}$, $c_k \in \mathbb{C}$, we set

$$x^{(0\sim k)} = \begin{pmatrix} x \\ \dot{x} \\ \ddot{x} \\ \vdots \\ x^{(k)} \end{pmatrix}, x_{1\sim k} = \begin{pmatrix} x_1 \\ x_2 \\ \vdots \\ x_k \end{pmatrix},$$

$$c_{0\sim k}x^{(0\sim k)} = (c_0, c_1, ..., c_k)(x, \dot{x}, \ddot{x}, ..., x^{(k)})^T,$$

$$k = 1,2,...,n.$$

2 Problem Formulation and Preliminaries

2.1 Problem Formulation

This paper focuses on a specific class of nonlinear system with unknown terms:

$$\begin{cases} \dot{x}_i = f_i(x_{1\sim i+1}), \quad i = 1,2,...,n-1, \\ \dot{x}_n = u + \Delta f_n(x_{1\sim n}) + f_n(x_{1\sim n}), \end{cases} \tag{1}$$

where $x_i \in \mathbb{R}$, $(i = 1,2,...,n)$ are the state variables, $u \in \mathbb{R}$ is the control input, $f_i(\cdot)$, $(i = 1,2,...,n)$ are the differentiable functions, $\Delta f_n(x_{1\sim n})$ is the system uncertainty.

The main purpose of this paper is to co-design a robust controller and event-triggered mechanism that ensure the ultimate boundedness of all signals in the considered systems. In the case of cascading systems, the conventional approach involves using backstepping, which can be cumbersome and challenging. This paper utilizes the novel approach of employing HOFA system techniques to address the stabilization problem of these systems.

2.2 Preliminaries

To provide a controller for systems with dynamic uncertainties, it is necessary to present the preliminary results.

Lemma 2.1 [13]: Assuming the existence of a nonnegative continuous scalar function $\rho(x_{1\sim n})$, it can be guaranteed $\Delta f(x_{1\sim n}) \in \mathbb{R}^r$ satisfies the following conditions:

$$\|H_{n-1}\Delta f(x_{1\sim n})\| \leq \rho(x_{1\sim n}). \tag{2}$$

Lemma 2.2 [15]: Let B $\in \mathbb{R}^{r\times r}$ satisfy:

$$\mathrm{Re}\lambda_i(B) \leq -\frac{\alpha}{2}, i = 1,2,...,n, \tag{3}$$

where $\alpha > 0$. Satisfying the above given conditions, there is a positive definite matrix $C \in \mathbb{R}^{r\times r}$ satisfying:

$$B^T C + CB \leq -\alpha C. \tag{4}$$

Lemma 2.3 [15]: There exist a set of matrices $C_i \in \mathbb{R}^{r\times r}$, $(i = 0,1,2,...,n-1)$ for any $\lambda > 0$, satisfying:

$$\mathrm{Re}\lambda_i(C) \leq -\frac{\lambda}{2}, i = 1,2,...,n, \tag{5}$$

by properly selecting C_i, $(i = 0,1,2,...,n-1)$, the eigenvalues of C can be arbitrarily assigned, thereby confirming the validity of the conclusion.

According to Lemma 2.2, if the condition in (5) is met for some $\lambda > 0$, then there exists a positive definite matrix Q.

$$C^T Q + QC \leq -\lambda Q. \tag{6}$$

Lemma 2.4 [16]: For two real numbers m and n, where $n > 0$, the following relation holds:

$$m - \frac{m^2}{4n} \leq n. \tag{7}$$

3 Event-Triggered Control Design

3.1 HOFA System Model

This section designs the control law of the system. To accomplish this, the cascading system (1) is transformed into the HOFA system model using a mathematical induction technique.

To facilitate subsequent derivations, coordinate transformation processing is performed. Where x_2 can be expressed as a function of $\dot{x}_1$, and $\dot{x}_1$ can be substituted into the equation for x_2. Also, x_3 can be expressed as a function of x_1, x_2, $\dot{x}_1$, $\dot{x}_2$, which means x_3 can be expressed as a function of x_1, $\dot{x}_1$, $\ddot{x}_1$. Therefore, the law of coordinate transformation is summarized as follows:

$$x_{i+1} = m_i(x_1^{(0\sim i)}), i = 1,2,...,n-1, \tag{8}$$

where $m_i(\cdot)$, $(i = 1,2,...,n-1)$ are the continuous differentiable functions.

Therefore, in the later no longer described in the derivation of coordinate transformation.

For system (1), when i =1,2 that is

$$\begin{cases} \dot{x}_1 = f_1(x_1, x_2), \\ \dot{x}_2 = f_2(x_1, x_2, x_3). \end{cases} \tag{9}$$

Taking the derivatives of the first equation in (9), it can be obtained that

$$\begin{aligned} \ddot{x}_2 &= \frac{\partial f_1}{\partial x_1}\dot{x}_1 + \frac{\partial f_1}{\partial x_2}\dot{x}_2 \\ &= G_1 + H_1 f_2, \end{aligned} \tag{10}$$

where

$$G_1(x_1^{(0\sim 1)}) = \frac{\partial f_1}{\partial x_1}\dot{x}_1,$$

$$H_1(x_1^{(0\sim 1)}) = \frac{\partial f_1}{\partial x_2}.$$

Then take the derivative of both sides of (10) and get the following result

$$\begin{aligned} x^{(3)} &= \dot{G}_1 + (H_1 f_2)^{(1)} - H_1\frac{\partial f_2}{\partial x_3}\dot{x}_3 + H_1\frac{\partial f_2}{\partial x_3}\dot{x}_3 \\ &= G_2 + H_2 f_3, \end{aligned} \tag{11}$$

where

$$\begin{aligned} G_2(x_1^{(0\sim 2)}) &= \dot{G}_1 + (H_1 f_2)^{(1)} - H_1 \frac{\partial f_2}{\partial x_3}\dot{x}_3 \\ &= \dot{G}_1 + (H_1 f_2)^{(1)} - H_2 \dot{x}_3 \\ &= \dot{G}_1 + (H_1 f_2)^{(1)} - H_2 f_3, \\ H_2(x_1^{(0\sim 2)}) &= H_1 \frac{\partial f_2}{\partial x_3}. \end{aligned}$$

When $i = k$, it follows

$$x_1^{(k)} = G_{k-1} + H_{k-1} f_k, \tag{12}$$

where

$$\begin{aligned} G_{k-1} &= (G_{k-2})^{(1)} + (H_{k-2} f_{k-1})^{(1)} - H_{k-1} f_k, \\ H_{k-1} &= H_{k-2} \frac{\partial f_{k-1}}{\partial x_k}. \end{aligned}$$

Once again, by taking the derivatives of both sides of equation (12), we can obtain the following expression:

$$x_1^{(k+1)} = G_k + H_k f_{k+1}, \tag{13}$$

where

$$\begin{aligned} G_k &= (G_{k-1})^{(1)} + (H_{k-1} f_k)^{(1)} - H_k f_{k+1}, \\ H_k &= H_{k-1} \frac{\partial f_k}{\partial x_{k+1}}, \end{aligned}$$

it can be seen that this is the case for $i = k+1$.

From the above inference, it can be seen that the following equation is always valid for system (1):

$$x_1^{(i)} = G_{i-1} + H_{i-1} f_i, \tag{14}$$

where $i = 1, 2, ..., n-1$

$$\begin{aligned} G_i &= (G_{i-1})^{(1)} + (H_{i-1} f_i)^{(1)} - H_i f_{i+1}, \\ H_i &= H_{i-1} \frac{\partial f_i}{\partial x_{i+1}}. \end{aligned}$$

Especially, the initial values are set to $G_0 = f_1(x_1, x_2)$, $H_0 = 0$.

When $i = n-1$, it can be deduced from equation (14) that:

$$x_1^{(n-1)} = G_{n-2} + H_{n-2} f_{n-1}. \tag{15}$$

The derivation of both sides of (15), get

$$\begin{aligned} x_1^{(n)} =& G_{n-1} + H_{n-1}\dot{x}_n \\ =& G_{n-1} + H_{n-1}(u + \Delta f_n(x_{1\sim n}) + f_n(x_{1\sim n})), \end{aligned} \tag{16}$$

where

$$\begin{aligned} G_{n-1} &= (G_{n-2})^{(1)} + (H_{n-2} f_{n-1})^{(1)} - H_{n-2} \frac{\partial f_{n-1}}{\partial x_n}\dot{x}_n, \\ H_{n-1} &= H_{n-2} \frac{\partial f_{n-1}}{\partial x_n}. \end{aligned}$$

In fact, the expression in (16) represents the HOFA model, which serves as the basis for designing the event-triggered robust controller.

3.2 Robust Control

The following theorem can be stated regarding the robust stabilization of the high-order system (16) with nonlinear uncertainties:

Theorem 1: Suppose that system (16) satisfies Lemma 2.1. Let ε and λ be two arbitrarily given positive numbers, and let $C_i \in \mathbb{R}^{r\times r}$, $(i = 1, 2, ..., n-1)$ be a set of matrices that satisfy (5). For ease of presentation, denote $x_1^{(0\sim n-1)}$ as $\bar{X}_1$.

For the uncertain system (16), the following control law is then applied.

$$\begin{aligned} u =& -f_n(x_{1\sim n}) - H_{n-1}^{-1}(c^{0\sim n-1}\bar{X}_1 + G_{n-1} \\ &+ \frac{1}{4\varepsilon}\rho^2(x_{1\sim n}) Q_L \bar{X}_1), \end{aligned} \tag{17}$$

converging to the ellipsoid centered at the origin is guaranteed by this control law for the state $\bar{X}_1$, as follows:

$$\Xi_{\lambda,\varepsilon}(0) = \left\{ \bar{X}_1 \,\middle|\, (\bar{X}_1)^T Q \bar{X}_1 \le \frac{\varepsilon}{\lambda} \right\}. \tag{18}$$

Proof: Substituting the control law (17) into system (16), then the HOFA model can convert to

$$x_1^{(n)} = -c^{0\sim n-1}\bar{X}_1 + \Psi(\bar{X}_1), \tag{19}$$

where

$$\Psi(\bar{X}_1) = -\frac{1}{4\varepsilon}\rho^2(x_{1\sim n}) Q_L^T x_1^{(0\sim n-1)} + H_{n-1}\Delta f(x_{1\sim n}).$$

It can easily obtain that:

$$(\bar{X}_1)' = C\bar{X}_1 + \begin{bmatrix} 0_{(n-1)\times 1} \\ \Psi(\bar{X}_1) \end{bmatrix}. \tag{20}$$

Then for system (20), can choose the following Lyapunov function:

$$V = \frac{1}{2}(\bar{X}_1)^T Q \bar{X}_1. \tag{21}$$

In view of (6), (20), we have

$$\begin{aligned} \dot{V} =& \frac{1}{2}((\bar{X}_1)')^T Q \bar{X}_1 + \frac{1}{2}(\bar{X}_1)^T Q (\bar{X}_1)' \\ =& \frac{1}{2}(\bar{X}_1)^T (C^T Q + QC)\bar{X}_1 + (\bar{X}_1)^T Q \begin{bmatrix} 0_{(n-1)\times 1} \\ \Psi(\bar{X}_1) \end{bmatrix} \\ \le& -\frac{\lambda}{2}(\bar{X}_1)^T Q(\bar{X}_1) + (\bar{X}_1)^T Q_L \Psi(\bar{X}_1) \\ =& -\lambda V + (\bar{X}_1)^T Q_L \Psi(\bar{X}_1). \end{aligned} \tag{22}$$

Next, we will examine the final term in the above equation. According to Lemma 2.1 and Lemma 2.4, the last term of (22) is:

$$\begin{aligned} & (\bar{X}_1)^T Q_L \Psi(\bar{X}_1) \\ =& -\frac{\rho^2(x_{1\sim n})}{4\varepsilon}\|Q_L\bar{X}_1\|^2 + (\bar{X}_1)^T Q_L H_{n-1}\Delta f(x_{1\sim n}) \\ \le& -\frac{\rho^2(x_{1\sim n})}{4\varepsilon}\|Q_L\bar{X}_1\|^2 + \|H_{n-1}\Delta f(x_{1\sim n})\|\,\|Q_L\bar{X}_1\| \\ \le& -\frac{\rho^2(x_{1\sim n})}{4\varepsilon}\|Q_L\bar{X}_1\|^2 + \rho(x_{1\sim n})\|Q_L\bar{X}_1\| \\ \le& \varepsilon. \end{aligned} \tag{23}$$

Taking (22) and (23) together, it can be obtained:

$$\dot{V} \leq -\lambda V + \varepsilon. \tag{24}$$

According to the Comparison Theorem [25] can be obtained

$$V \leq V(0)e^{-\lambda t} + \frac{\varepsilon}{\lambda}(1-e^{-\lambda t}), \tag{25}$$

which gives

$$V \leq (V(0) - \frac{\varepsilon}{\lambda})e^{-\lambda t} + \frac{\varepsilon}{\lambda} \to \frac{\varepsilon}{\lambda}, t \to \infty. \tag{26}$$

In conclusion, the state $\bar{X}_1$ ultimately converges to the ellipsoid $\Xi_{\lambda,\varepsilon}(0)$, which completes the proof.

Module $\Psi(\bar{X}_1)$ plays a crucial role in the control law by integrating HOFA and ETM, thereby streamlining the system's communication load.

There are two ways to adjust the ellipsoid radius $\Xi_{\lambda,\varepsilon}(0)$: increasing the stability threshold of the linear part λ and decreasing the value of the ε. The adjustment of these two methods will directly affect the size of the ellipsoid.

3.3 Relative Threshold Event-triggered Robust Control

This section primarily focuses on the design of a robust event-triggered controller:

$$\begin{aligned}\omega(t) &= (\sigma+\delta)\times\omega_1\tanh(\frac{Q_L\bar{X}_1\omega_1}{\eta}) \\ &+ (\rho(x_{1\sim n})+m_1)\tanh(\frac{Q_L\bar{X}_1(\rho(x_{1\sim n})+m_1)}{\eta}),\end{aligned} \tag{27}$$

$$u(t) = \omega(t_s), \tag{28}$$

$$t_{s+1} = \inf\{t\in\mathbb{R}\,||e(t)|\geq M\}, \tag{29}$$

where $M = \delta|u(t)|+m, t\in[t_s,t_{s+1}), \delta, \eta, m_1, m$ are positive parameters, $\sigma<-1, m_1>m/(1-\delta)$, the measurement error $e(t)=\omega(t)-u(t)$, $t_s, s\in\mathbb{Z}_+$ is the update time. According to (17), settings $\omega_1 = u$.

Considering the design of the controller and the given conditions of event-triggered, we can obtain the following theorem.

Theorem 2: The event-triggered controller designed by equations (27), (28), and (29) for the HOFA model (16) obtained from the transformation of the cascade system (1) is proven to ensure that all signals of the closed-loop system are ultimately bounded.

Proof: From (29), we get $\omega(t) = (1+\varphi_1(t)\delta)u(t) + \varphi_2(t)m_1$ in the interval $[t_s,t_{s+1}]$, where time-varying parameters $\varphi_1(t)$ and $\varphi_2(t)$ satisfy that the absolute value is less than or equal to 1. Thus, we can obtain $u(t) = \omega/(1+\varphi_1\delta) - (\varphi_2 m_1/(1+\varphi_1\delta))$. Then for the Lyapunov function designed by equation (21), there is

$$\begin{aligned}\dot{V} &\leq -\lambda V \\ &+ (\bar{X}_1)^T Q_L(H_{n-1}\Delta f_n(x_{1\sim n}) + \omega_1 - \frac{\omega-\varphi_2 m_1}{1+\varphi_1\delta}),\end{aligned} \tag{30}$$

the last term in (30) is shown as follows

$$\begin{aligned}&(\bar{X}_1)^T Q_L\left(H_{n-1}\Delta f_n(x_{1\sim n}) + \omega_1 - \frac{\omega-\varphi_2 m_1}{1+\varphi_1\delta}\right) \\ =&(\bar{X}_1)^T Q_L H_{n-1}\Delta f_n(x_{1\sim n}) + (\bar{X}_1)^T Q_L\omega_1 \\ &- (\bar{X}_1)^T Q_L\frac{\omega-\varphi_2 m_1}{1+\varphi_1\delta} \\ \leq&\left|(\bar{X}_1)^T Q_L(\rho+m_1)\right| \\ &- (\bar{X}_1)^T Q_L(\rho+m_1)\tanh(\frac{Q_L\bar{X}_1(\rho+m_1)}{\eta}) \\ &+\left|(\bar{X}_1)^T Q_L\omega_1\right| - (\bar{X}_1)^T Q_L\omega_1\tanh(\frac{Q_L\bar{X}_1\omega_1}{\eta}).\end{aligned} \tag{31}$$

One of the properties of a hyperbolic tangent function $\tanh(\cdot)$ is as follows [25]:

$$0 \leq |\xi| - \xi\tanh(\frac{\xi}{\kappa}) \leq 0.2785\kappa, \tag{32}$$

based on equation (32), at the same time, condition $\sigma<-1$ is used for inequality reduction, the final equation (30) can be obtained

$$\dot{V} \leq -\lambda V + 0.557\eta. \tag{33}$$

Through standard analysis, it can be concluded that all signals in the closed-loop system are ultimately bounded.

Now, there exists $\hat{t}>0$ such that $\forall s\in\mathbb{Z}_+$, $\{t_{s+1}-t_s\}\geq\hat{t}$. By calling $e(t)=\omega(t)-u(t)$, $\forall t\in[t_s,t_{s+1})$, we have

$$\frac{d}{dt}|e| = \frac{d}{dt}(e\times e)^{\frac{1}{2}} = sign(e)\dot{e} \leq |\dot{\omega}|. \tag{34}$$

From equation (27), it can be derived that both ω and $\dot{\omega}$ must be continuous. Since$\dot{\omega}$ is a function of the signal x, and all the closed-loop signals are ultimately bounded, there exists a constant $\zeta>0$ such that $|\dot{\omega}|\leq\zeta$.

By considering that $e(t_s)=0$ and $\lim_{t\to t_{s+1}} e(t)=m$, we can conclude that the lower bound of inter-execution intervals $\hat{t}$ must satisfy $\hat{t}\geq M/\zeta$ to avoid Zeno-behavior.

Remark 1: In comparison to the traditional relative threshold strategy [26], this technical note introduces an additional constant term m in equation (29). By employing the presented approach, we can ensure that the inter-execution time $\hat{t}$ of the relative threshold strategy is always bounded from below. Specifically, when the control signal $u(t)$ is zero, the value of m determines the minimum duration between executions. Setting the value of m too small will cause the controller to fire frequently and make the ETM ineffective.

Remark 2: Under the current framework, we can only get the result that all signals are ultimately bounded. This is due to the uncertainty of the combination makes the system stability and ETM are different from the traditional system, at the same time the introduction of ETM also increases the complexity of the system. Therefore, future work need to be further collaboration and optimization of this aspect.

4 Simulation Result

This section provides a simulation example to illustrate the effectiveness of the robust controller triggered by relative threshold events.

Consider the following system

$$\begin{cases} \dot{x}_1 = x_1^2 + x_2, \\ \dot{x}_2 = x_1 + \sin\Delta x + u. \end{cases} \tag{35}$$

The following HOFA model can be easily derived from the system transformation.

$$\ddot{x}_1 = 2x_1(x_1^2 + x_2) + x_1 + \sin\Delta x + u. \tag{36}$$

In this case, the parameters in C are set as $c_0 = c_1 = 1$, $C = \begin{pmatrix} 0 & 1 \\ -1 & -1 \end{pmatrix}$. Then the positive definite matrix Q can be designed as $Q = \begin{pmatrix} 2 & 1 \\ 1 & 2 \end{pmatrix}$. It is easy to obtain that $Q_L x_1^{(0\sim1)} = x_1 + 2\dot{x}_1$. Then the controller is designed as

$$\begin{aligned} \omega(t) = (\sigma+\delta)[(\omega_1 \tanh(\frac{(x_1+2\dot{x}_1)\omega_1}{\eta})) \\ + (\rho+m_1)\tanh(\frac{(x_1+2\dot{x}_1)(\rho+m_1)}{\eta}). \end{aligned} \tag{37}$$

The parameters of the above equation are designed as: $x_1(0) = 0$, $x_2(0) = 0$, $\sigma = -2.76$, $\delta = 0.5$, $\eta = 6.7$, $m_1 = 1.37$, $m = 2$, and take $\rho(x_{1\sim n}) = 1$.

Figs. 1-4 show the simulation results of the designed relative threshold event-triggered controller. The trajectory of the state variables is shown in Figs. 1-2. Fig. 3 shows the trajectory of the control signal. The trigger time is shown in Fig. 4. The simulation results show the effectiveness of the designed relative threshold event trigger controller. The simulation results demonstrate that the HOFA system approach is very simple and efficient.

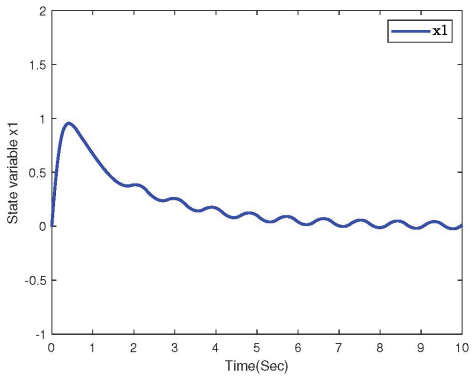

Fig. 1: The trajectory of x_1.

5 Conclusion

A class of nonlinear systems problem with unknown terms in this paper is solved by application an event triggers a robust control strategy. By adopting HOFA system method, the cascaded system is transformed into HOFA model. At the same time, for the uncertain items the robust control method is adopted to ensure the stability of the system. The relative threshold event-triggered mechanism is designed to update the controller based on the system state and a predetermined threshold, aiming to minimize computation and energy consumption during signal transmission. This paper proves that

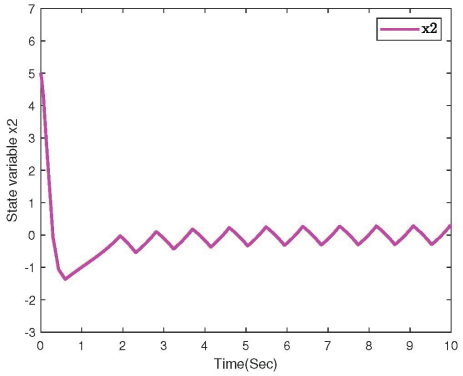

Fig. 2: The trajectory of x_2.

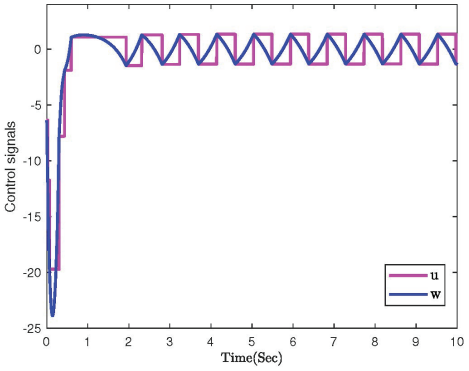

Fig. 3: The trajectory of u and w.

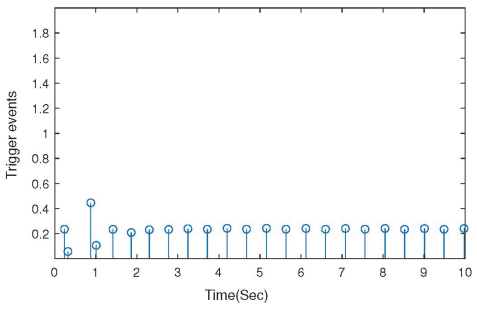

Fig. 4: Triggering events.

all signals are ultimately bounded by utilizing Lyapunov stability theory to analyze the stability of the closed-loop system. Finally, the performance of the designed controller is verified by a simulation example. The results show that the control system has good stability and robustness, and can achieve high control accuracy and efficiency.

References

[1] K. Li, C. C. Hua, X. You, X. P. Guan, Distributed Output-Feedback Consensus Control of Multiagent Systems with Unknown Output Measurement Sensitivity, *IEEE Transactions on Automatic Control*, 2021, 66(7): 3303–3310.

[2] N. Pang, X. Wang, Z. Wang, Event-Triggered Adaptive Control of Nonlinear Systems With Dynamic Uncertainties: The Switching Threshold Case, *IEEE Transactions on Circuits and Systems II: Express Briefs*, 2022, 69(8): 3540–3544.

[3] C. Hua, L. Zhang, X. Guan, Decentralized Output Feedback Adaptive NN Tracking Control for Time-Delay Stochastic Nonlinear Systems With Prescribed Performance, *IEEE Transactions on Neural Networks and Learning Systems*, 2015, 26(11): 2749–2759.

[4] J. Ting, S. Basyal, B. C. Allen, Robust Control of a Nonsmooth or Switched Control Affine Uncertain Nonlinear System Using a Novel RISE-Inspired Approach, in *2023 American Control Conference (ACC)*, 2023: 4253–4257.

[5] C. H. Zhang, G. H. Yang, Adaptive disturbance attenuation for a class of uncertain nonlinear systems: A double-gain nonlinear observer method. *Journal of the Franklin Institute*, 2019 356158890–8905.

[6] S. Zhou, X. Wang, Robust Adaptive Control for Nonlinear Strict-feedback Systems with Function Constraints on States, in *2022 34th Chinese Control and Decision Conference (CCDC)* ,2022:5172–5177.

[7] C. H. Zhang, G. H. Yang, Event-Triggered Adaptive Output Feedback Control for a Class of Uncertain Nonlinear Systems With Actuator Failures, *IEEE Transactions on Cybernetics*, 2020 50(1): 201–210.

[8] D. Chen, X. Li, S. Li, A Novel Convolutional Neural Network Model Based on Beetle Antennae Search Optimization Algorithm for Computerized Tomography Diagnosis, *IEEE Transactions on Neural Networks and Learning Systems*, 2023, 34(3): 1418–1429.

[9] Y. J. Li, S. X. Li, C. H. Zhang, C. C. Hua, Switched-Threshold Event-Triggered Fixed-Time Control for Nonlinear Uncertain Systems with Full-States Constraints, in *2023 IEEE 13th International Conference on CYBER Technology in Automation, Control, and Intelligent Systems (CYBER)*, 2023: 811–816.

[10] M. Li, S. Li, C. K. Ahn, Z. Xiang, Adaptive Fuzzy Event-Triggered Command-Filtered Control for Nonlinear Time-Delay Systems, *IEEE Transactions on Fuzzy Systems*, 2022, 30(4):1025–1035.

[11] X. Min, S. Tong, Y. Li, W. Wu, Fuzzy output-feedback control for nonlinear stochastic systems with unknown-time-delays, in *2018 Chinese Control And Decision Conference (CCDC)*, 2018: 5435–5438.

[12] G. R. Duan, High-order fully actuated system approaches: Part i. models and basic procedure, *International Journal of Systems Science*, 2021, 52(2): 422–435.

[13] G. Duan, "High-order fully actuated system approaches: Part iii. robust control and high-order backstepping, *International Journal of Systems Science*, vol. 52, no. 5, pp. 952–971, 2021.

[14] G. R. Duan, High-order fully actuated system approaches: Part iii. robust control and high-order backstepping, *International Journal of Systems Science*, 2022, 53(1): 54–73.

[15] L. Wang, Y. X. Liu, C. H. Zhang, C. C. Hua, Y. Q. Wei, Adaptive Event-Triggered Control for the Nonlinear Cascade Systems: A HOFA System Approach, in *2023 IEEE 13th International Conference on CYBER Technology in Automation, Control, and Intelligent Systems (CYBER)*, 2023: 356–361.

[16] G. R. Duan, High-order fully actuated system approaches: Part iv. adaptive control and high-order backstepping, *International Journal of Systems Science*, 2021, 52(5): 972–989.

[17] B. Ren, Q. C. Zhong, J. Chen, Robust Control for a Class of Nonaffine Nonlinear Systems Based on the Uncertainty and Disturbance Estimator, *IEEE Transactions on Industrial Electronics*, 2015, 62(9): 5881–5888.

[18] C. H. Zhang, Y. J. Li, C. C. Hua, Y. Zhang, A New Event-Triggered Adaptive Fixed-Time Control Design for Uncertain Nonlinear Systems, *IEEE Transactions on Cybernetics*, 2024: 1–12.

[19] M. Mazo, P. Tabuada, Decentralized Event-Triggered Control Over Wireless Sensor/Actuator Networks, *IEEE Transactions on Automatic Control*, 2011, 56(10): 2456–2461.

[20] D. Liang, J. Huang, Practical Robust Output Regulation of Linear Systems by Event-Triggered Dynamic Output Feedback Control, in *2018 37th Chinese Control Conference (CCC)* 2018: 5116–5121.

[21] C. H. Zhang, G. H. Yang, Event-Triggered Global Finite-Time Control for a Class of Uncertain Nonlinear Systems *IEEE Transactions on Automatic Control*, 2020, 65(3): 1340–1347.

[22] M. Merei, J. K. Tar, Adaptive Backstepping Control Design for Nonlinear System, in *2023 IEEE 17th International Symposium on Applied Computational Intelligence and Informatics (SACI)*, 2023: 000147–000152.

[23] N. Pang, X. Wang, Z. Wang, Event-Triggered Adaptive Control of Nonlinear Systems With Dynamic Uncertainties: The Switching Threshold Case, *IEEE Transactions on Circuits and Systems II: Express Briefs*, 2022, 69(8): 3540–3544.

[24] C. H. Zhang, G. H. Yang, Event-Based Remote State Estimation for Nonlinear Systems: A Box Particle Filtering Method, *IEEE Transactions on Cybernetics*, 2024, 54(4): 2472–2482.

[25] L. Xing, C. Wen, Z. Liu, H. Su, J. Cai, Event-triggered adaptive control for a class of uncertain nonlinear systems, *IEEE Transactions on Automatic Control*, 2016, 62(4): 2071–2076.

[26] Z. Liu, G. Lai, Y. Zhang, C. L. P. Chen, Adaptive Fuzzy Tracking Control of Nonlinear Time-Delay Systems With Dead-Zone Output Mechanism Based on a Novel Smooth Model, *IEEE Transactions on Fuzzy Systems*, 2015,23(6): 1998–2011.

Proceedings of the 3rd Conference on Fully Actuated System Theory and Applications
May 10-12, 2024, Shenzhen, China

Event-Triggered Tracking Control for High-Order Fully Actuated Strict-Feedback Systems

Yang Liu, Jiaming Zhang
Seventh Research Division and Center for Information and Control, School of Automation Science and Electrical Engineering, Beihang University (BUAA), Beijing 100191, P. R. China
E-mail: ylbuaa@163.com; zhangjiaming96@163.com.

Abstract: In this paper, event-triggered tracking control scheme is proposed for a class of high-order strict-feedback systems with uncertain nonlinear system functions. The structure of the subsystems in high-order nonlinear strict-feedback systems satisfies the high-order fully actuated (HOFA) system model and the order of each subsystem is not necessarily the same. The system meets the fully actuacted property, that is, the control gain matrix is reversible. Therefore, a relatively simple controller designed by using the HOFA system approach can convert the closed-loop system into a constant linear system with the desired characteristic structure. Based on the backstepping method, a switched threshold event-triggered control method is constructed to realize the tracking control, meanwhile reduce the update frequency of controllers. In addition, the robust controller constructed using the switched threshold event-triggered strategies can guarantee that all signals in the whole closed-loop system are bounded and violate the Zeno behavior. Finally, the simulation results illustrate the validity of the proposed schemes by a practical example.

Key Words: High-order fully actuated system, mixed-order system, event-triggered strategy, uncertain system function.

1 Introduction

During the past decades, the event-triggered control mechanism has been studied by widely scholars, and resulting plentiful literature due to its application in practical engineering (see typically in [1–4]). Different from the time-triggered control strategy based on periodic sampling, the event-triggered control strategy is proposed in which the sampling condition is determined by the system states or the set threshold. Hence, compared with traditional control methods, the event-triggered strategy can save communication resources and reduce controller update frequency.

In detail, [5] proposed a fixed threshold strategy under which the controllers were updated based on the occurrence of an fixed event (this fixed event typically takes the form of a constant). In [6], a relative threshold strategy was developed to install a relatively variational event. The event of the relative threshold strategy is time-varying and dependent on the size of the sampling object. However, both the above-mentioned strategies have the following drawbacks: for the fixed threshold strategy, when the size of the sampling object is small, the fixed threshold in this case is a large value and will not trigger the events; for the relative threshold strategy, when the size of the sampling object is big, an enormous pulse at every trigger moment will create and destroy the system performance. Therefore, a switching threshold strategy was presented by combining the fixed threshold strategy and the relative threshold strategy in [6]. The key to setting up a switching domain is to use the fixed threshold strategy outside the predefined domain and use the relative threshold strategy inside the predefined domain. The switching threshold strategy can centralize the advantages of the other two ETC strategies, but very few works used this strategy.

In 2020, Duan proposed the control theory of high-order fully actuated (HOFA) system. Based on the fully actuated system model, this method completely gets rid of the bondage of state-space model and shows strong advantages in dealing with a series of complex problems such as nonlinearity. Traditional nonlinear control methods based on the state-space model often require some strong assumptions and the controller design is rather complicated. The HOFA method has greater advantages in the universality of the actual system, the simplicity and flexibility of the controller design. Enlightened by Duan's work ([7–12]), the HOFA system approach has emerged in control field, and attracted plenty of scholars' research interests (see [13–16]). In the control design of nonlinear HOFA systems, the main strategy is to design controller to eliminate the nonlinearities and obtain a linear closed-loop system [14]. In [15] and [16], by using HOFA systems approach, fault-tolerance control and output-feedback control are proposed for nonlinear HOFA systems with parameter uncertainties, actuator faults, and measurement noises. Then, the coordination of networked nonlinear multi-agents was studies by using HOFA system approach and predictive control strategy in [17]. As a significant problem in the field of nonlinear system control, the research on the control of nonlinear strict-feedback system is always a hot issue. Therefore, we are stimulated to use the HOFA method to solve the tracking control problem of nonlinear high-order strict-feedback systems.

Inspired by the above-mentioned challenges, this paper concentrates upon the event-triggered tracking control for a class of nonlinear high-order strict-feedback systems with uncertain nonlinear system functions. The structure of the subsystems in high-order nonlinear strict-feedback systems satisfies the HOFA system model and the order of each subsystem is not necessarily the same. The proposed event-triggered control strategy can ensure that all signals in the closed-loop system are bounded,the output tracks the reference signal and non-Zeno behavior simultaneously. Specially, we summarize the main contributions as follows.

(1) By using HOFA system approach, the constructed controller can directly eliminate the nonlinearities and obtain a linear closed-loop system. Further, most of the actual physical systems can be directly modeled by nonlinear HOFA system instead of the state-space model.

(2) Compared with the traditional backstepping method

This work is supported by NSFC (62073020, 62133001, 62227810).

for the nonlinear strict-feedback systems [18, 19], the design process of controller in this paper is more simplified when the order of system is extremely high. Hence, the proposed scheme reduces the number of derivative of the virtual controllers, such that reduces the computational burden.

(3) A switched threshold event-triggered control strategy is introduced to construct the controller. The proposed event-triggered control strategy combines the advantages of the fixed threshold event-triggered control strategy and the relative threshold event-triggered control strategy. Moreover, the value of the switch domain can be determined by user, which makes the strategy more practical and flexible.

Notation: $\|\cdot\|$ denotes the Euclidean norm; $\lambda_i(\cdot)$, $\lambda_{min}(\cdot)$, $\lambda_{max}(\cdot)$, respectively, represent the i-th eigenvalue, the minimum and the maximum eigenvalues of a matrix; for a vector $x \in R^m$, $x^{[n-1]}= [x, \dot{x}, \cdots, x^{(n-1)}]^T \in R^{nm}$ with $x^{(n)}$ the n-th derivative of x; for matrices $K_i \in R^{m\times m}$ with $i = 0, 1, ..., n-1$, let $K^{<n-1>} = [K_0, K_1, \cdots, K_{n-1}] \in R^{m\times nm}$, and $\Phi(K^{<n-1>}) = \begin{bmatrix} 0_{m\times m} & I_{m\times m} & & \\ & & \ddots & \\ & & & I_{m\times m} \\ -K_0 & -K_1 & \cdots & -K_{n-1} \end{bmatrix} \in R^{nm\times nm}$ with $I_{m\times m}$ the $m \times m$ identity matrix. Without loss of generality, the description of variables will be omitted to simplify if there is no confusion.

2 Preliminaries and problem formulation

2.1 HOFA system

The dynamic of the nonlinear HOFA system is described by the following structure:

$$x^{(n)} = L(x^{[n-1]}, t)u + F(x^{[n-1]}, t), y = x, \qquad (1)$$

where $x \in R^m$, $u \in R^m$ and $y \in R^m$ denote the state, the input and the output of the system, respectively. $F \in R^m$ and $L \in R^{m\times m}$ represent the nonlinear vector function and the control gain matrix function, respectively. The HOFA system usually contains the following assumption and lemmas:

Assumption 1 [7, 16]: The control gain matrix function L satisfies $det\ L \neq 0$ for $\forall x^{(k)} \in R^m, k = 0, 1, ..., n-1$.

Lemma 1 [9]: For any $\mu > 0$, if there exist a matric $K \in R^{m\times nm}$ satisfying $Re\lambda(\Phi(K)) < -\frac{\mu}{2}$, then there exists a positive definite matrix $Q_i(K) = [Q_{i1}\ Q_{i2}\ \cdots\ Q_{in}]$, $Q_{ij} \in R^{nm\times m}$, satisfying $\Phi(K)^T Q(K) + Q(K)\Phi(K) < -\mu Q(K)$.

According to [7], a general controller which can achieve asymptotic stability for the system (1) is presented as

$$u = -L^{-1}(F + K^{<n-1>}x^{[n-1]}). \qquad (2)$$

2.2 High-order nonlinear strict-feedback system

In this paper, the following uncertain high-order nonlinear strict-feedback system is considered [10]:

$$\begin{cases} x_1^{[m_1]} = g_1\left(x_1^{[m_1-1]}\right)x_2 + f_1\left(x_1^{[m_1-1]}\right) \\ \qquad + \Delta f_1\left(x_1^{[m_1-1]}\right) \\ x_2^{[m_2]} = g_2\left(x_i^{[m_i-1]}|_{i=1\sim 2}\right)x_3 + f_2\left(x_i^{[m_i-1]}|_{i=1\sim 2}\right) \\ \qquad + \Delta f_2\left(x_i^{[m_i-1]}|_{i=1\sim 2}\right) \\ \qquad \vdots \\ x_n^{[m_n]} = g_n\left(x_i^{[m_i-1]}|_{i=1\sim n}\right)u + f_n\left(x_i^{[m_i-1]}|_{i=1\sim n}\right) \\ \qquad + \Delta f_n\left(x_i^{[m_i-1]}|_{i=1\sim n}\right) \end{cases} \qquad (3)$$

where for $i = 1, 2, ..., n$, $x_i \in R$, $g_i \in R^{m\times m}$ and $f_i \in R^m$ represent the nonlinear vector functions and the control gain matrix functions, $m_i \in Z^+$ is the order of subsystem state. For convenience, define notations $p_i = m_1 + m_2 + ... + m_i$ and $p = p_n$. $\Delta f_i \in R^m$ is a set of sufficiently smooth unknown vector functions for $i = 1, 2, ..., n$, and there exists a non-negative continuous scalar function $\gamma_i\left(x_j^{[m_j-1]}|_{j=1\sim i}\right)$ such that Δf_i satisfies $\|\Delta f_i\| \leq \gamma_i$. The objective of this paper is to present event-triggered controllers for the mixed-order nonlinear strict-feedback system (3), such that the system output can asymptotically track the reference signal $y_d(t)$. The control gain matrix function g_i satisfies $det\ g_i \neq 0$. Some necessary assumption and lemma are given as follows.

Remark 1: Note that the order of subsystems cannot be necessarily the same. For example, the single-link flexible-joint robot system consists of two second-order fully actuated subsystems [4], while the electromechanical system in [13] consists of one-order and second-order fully actuated subsystems. Hence, nonlinear high-order strict-feedback systems with arbitrary order subsystems are more practical and general.

Lemma 2 (Young's inequality): For any $x \in R^n$, $y \in R^n$, there always holds

$$x^T y \leq \frac{1}{p}|x|^p + \frac{1}{q}|y|^q, \qquad (4)$$

where $p > 0$ and $q > 0$ are real numbers satisfying $\frac{1}{p} + \frac{1}{q} = 1$.

Lemma 3 [2, 14]: Given $\varepsilon > 0$ and $z \in R$. The following relationships hold:

$$|z| - z\tanh\left(\frac{z}{\varepsilon}\right) \leq \kappa\varepsilon,$$
$$|z| - \frac{z^2}{\sqrt{z^2+\varepsilon^2}} \leq \varepsilon, \qquad (5)$$

where κ is a constant and $\kappa = e^{-(\kappa+1)}$, κ=0.2785.

Assumption 2 [18]: The reference signal y_d and its time derivatives up to the n-th order are continuous and bounded.

3 Main result

3.1 Switched Threshold Event-Triggered Control Design through Backstepping Process

In this part, we provide the backstepping design process for the system (3) based on switched threshold event-

triggered control strategy.

Step 1: Firstly, define the tracking errors

$$z_1 = x_1 - y_d, z_i = x_i - \alpha_{i-1},\ for\ i = 2, 3, ..., n, \quad (6)$$

where α_{i-1} is the virtual controller.

From (3) and (6), we have

$$\begin{aligned} z_1^{(m_1)} =& x_1^{(m_1)} - y_d^{(m_1)} = g_1 x_2 + f_1 + \Delta f_1 - y_d^{(p_1)} \\ =& g_1(z_2 + \alpha_1) + f_1 + \Delta f_1 - y_d^{(m_1)}, \end{aligned} \quad (7)$$

where the virtual control law α_1 is constructed as

$$\begin{aligned} \alpha_1 =& - g_1^{-1}(K_1^{<m_1-1>} z_1^{[m_1-1]} + f_1 - y_d^{(m_1)} + \Omega_1) \\ =& \alpha_1(z_1^{[m_1-1]}, y_d^{(p_1)}) \end{aligned} \quad (8)$$

with $\Omega_1 = \frac{\gamma_1^2 Q_{1n}^T z_1^{[m_1-1]}}{\sqrt{\gamma_1{}^2 \left\| Q_{1n}^T z_i^{[m_1-1]} \right\|^2 + \varepsilon^2}}$ and ε is chosen such as $\int_0^\infty \varepsilon(\tau) d\tau \leq \varepsilon_M < \infty$, ε_M is a positive constant, Q_{1n} is a positive definite matrix defined in Lemma 1. Then, (7) becomes

$$z_1^{(m_1)} + K_1^{<m_1-1>} z_1^{[m_1-1]} = g_1 z_2 + \Delta f_1 - \Omega_1. \quad (9)$$

Then, choose the Lyapunov function candidate as

$$V_1 = V_{10} = \frac{1}{2} z_1^{[m_1-1]T} Q_1 z_1^{[m_1-1]}, \quad (10)$$

where Q_1 is a positive definite matrix defined in Lemma 1. The time derivative of V_1 can be calculated as

$$\begin{aligned} \dot{V}_1 =& \frac{1}{2} z_1^{[m_1-1]T} \left(\Phi_1^T Q_1 + Q_1 \Phi_1 \right) z_1^{[m_1-1]} \\ &+ Q_{1n}^T z_1^{[m_1-1]} g_1 z_2 + Q_{1n}^T z_1^{[m_1-1]} (\Delta f_1 - \Omega_1) \\ \leq& - \left(\mu_1 - 2\lambda_{\max}(Q_1) \right) V_{10} + Q_{1n}^T z_1^{[m_1-1]} (\Delta f_1 - \Omega_1) \\ &+ \frac{\|g_1\|^2}{4\lambda_{\min}(Q_2)} \left(z_2^{[m_2-1]T} Q_2 z_2^{[m_2-1]} \right). \end{aligned} \quad (11)$$

Using the definition of Δf_1, we get

$$\begin{aligned} Q_{1n}^T z_1^{[m_1-1]} \Delta f_1 \leq& \left\| Q_{1n}^T z_1^{[m_1-1]} \right\| \gamma_1 \\ \leq& \frac{\gamma_1^2 \left\| Q_{1n}^T z_1^{[m_1-1]} \right\|^2}{\sqrt{\gamma_1^2 \left\| Q_{1n}^T z_1^{[m_1-1]} \right\|^2 + \varepsilon^2}} + \varepsilon. \end{aligned} \quad (12)$$

Applying (12) to (11) yields

$$\begin{aligned} \dot{V}_1 \leq& - \left(\mu_1 - 2\lambda_{\max}(Q_1) \right) V_{10} \\ &+ \frac{\|g_1\|^2}{4\lambda_{\min}(Q_2)} \left(z_2^{[m_2-1]T} Q_2 z_2^{[m_2-1]} \right) + \varepsilon. \end{aligned} \quad (13)$$

Step i: It can be deduced that $\alpha_{i-1}^{(m_i)} = h_{i-1}(z_j^{[m_j-1]}|_{j=1\sim i}, y_d^{[p_i]}) + \Delta h_{i-1}(z_j^{[m_j-1]}|_{j=1\sim i}, y_d^{[p_i]})$, such that

$$\begin{aligned} z_i^{(m_i)} =& x_i^{(m_i)} - \alpha_{i-1}^{(m_i)} = g_i x_{i+1} + f_i - h_{i-1} - \Delta h_{i-1} \\ =& g_i(z_{i+1} + \alpha_i) + f_i - h_{i-1} - \Delta h_{i-1}, \end{aligned} \quad (14)$$

where $\|\Delta h_i\| \leq \bar{\gamma}_i$ with $\bar{\gamma}_i$ a known non-negative continuous scalar function, then the virtual control law α_i is designed as

$$\begin{aligned} \alpha_i =& - g_i^{-1}(K_i^{<m_i-1>} z_i^{[m_i-1]} + f_i - h_{i-1} + \Omega_i) \\ =& \alpha_i(z_j^{[m_j-1]}|_{j=1\sim i}, y_d^{[p_i]}) \end{aligned} \quad (15)$$

and $\Omega_i = \frac{(\gamma_i + \bar{\gamma}_i)^2 Q_{in}^T z_i^{[m_i-1]}}{\sqrt{(\gamma_i + \bar{\gamma}_i)^2 \left\| Q_{in}^T z_i^{[m_i-1]} \right\|^2 + \varepsilon^2}}$ with Q_{in} is a positive definite matrix defined in Lemma 1.

Take the Lyapunov function candidates as

$$V_i = V_{i-1} + V_{i0} = V_{i-1} + \frac{1}{2} z_i^{[m_i-1]T} Q_i z_i^{[m_i-1]}, \quad (16)$$

where Q_i is a positive definite matrix defined in Lemma 1. The first-order derivative of V_i along the trajectory of system (3) is

$$\begin{aligned} \dot{V}_i \leq& - \sum_{j=1}^{i} \left(\mu_j - 2\lambda_{\max}(Q_j) - \frac{\|g_{j-1}\|^2}{2\lambda_{\min}(Q_j)} \right) V_{j0} \\ &+ \frac{\|g_i\|^2}{4\lambda_{\min}(Q_{i+1})} \left(z_{i+1}^{[m_{i+1}-1]T} Q_{i+1} z_{i+1}^{[m_{i+1}-1]} \right) + i\varepsilon. \end{aligned} \quad (17)$$

Step n: Design the switched threshold event-triggered controller as

$$u^*(t) = - \alpha_n \tanh\left(\frac{\alpha_n g_n Q_{nn}^T z_n^{[m_n-1]}}{\varepsilon} \right) \quad (18)$$

$$u(t) = u^*(t_k), \forall t \in [t_k, t_{k+1}), \quad (19)$$

$$t_{k+1} = \begin{cases} \inf\{ t > t_k \,||u^*(t) - u(t)| \geq \delta |u(t)| + q_1 \}, \\ if\ |u(t)| \leq D, \\ \inf\{ t > t_k \,||u^*(t) - u(t)| \geq q_2 \}, \\ if\ |u(t)| > D, \end{cases} \quad (20)$$

where D, q_1 and q_2 are positive parameters to be designed, Q_{nn} is a positive definite matrix defined in Lemma 1. Consider the Lyapunov function as

$$V_n = V_{n-1} + V_{n0} = V_{n-1} + \frac{1}{2} z_n^{[m_n-1]T} Q_n z_n^{[m_n-1]}, \quad (21)$$

where Q_n is a positive definite matrix defined in Lemma 1.

3.2 Stability Analysis

Theorem 1: Consider the high-order nonlinear strict-feedback system (3) with uncertainties. Under the switched threshold event-triggered controller (19), if for $i = 1, 2, ..., n$, the matrix Q_i are chosen to satisfy the following inequalities:

$$\left(\mu_i - 2\lambda_{\max}(Q_i) - \frac{\|g_{i-1}\|^2}{2\lambda_{\min}(Q_i)} \right) > 0, \quad (22)$$

then the global uniformly ultimately bounded tracking performance can be realized without Zeno behavior.

Proof:

From (19), it can be proved that

$$u^*(t) - u(t) = \begin{cases} \lambda_1(t) (\delta |u(t)| + q_1), if\ |u(t)| \leq D, \\ \lambda_2(t) q_2, if\ |u(t)| > D, \end{cases} \quad (23)$$

where $\lambda_1(t)$ and $\lambda_2(t)$ are time-varying parameters satisfying $|\lambda_1(t)| \leq 1$ and $|\lambda_2(t)| \leq 1$.

By (23) one can get

$$u(t) = M(t)u^*(t) + \nu(t), \tag{24}$$

where $M(t) = \begin{cases} \frac{1}{1+\lambda_1(t)sign(u(t))\delta}, if\ |u(t)| \leq D, \\ 1, if\ |u(t)| > D \end{cases}$ and $\nu(t) = \begin{cases} \frac{-\lambda_1(t)q_1}{1+\lambda_1(t)sign(u(t))\delta}, if\ |u(t)| \leq D, \\ -\lambda_2(t)q_2, if\ |u(t)| > D. \end{cases}$

From (3) and (24), we can obtain that

$$\begin{aligned} z_n^{(m_n)} =& x_n^{(m_n)} - \alpha_{n-1}^{(m_n)} \\ =& g_n u + f_n + \Delta f_n - h_{n-1} - \Delta h_{n-1} \\ =& g_n M u^* - g_n \alpha_n + g_n \alpha_n + f_n + \Delta f_n - h_{n-1} \\ & - \Delta h_{n-1}, \end{aligned} \tag{25}$$

where $\alpha_n = -g_n^{-1}(K_n^{<m_n-1>} z_n^{[m_n-1]} + f_n - h_{n-1} + \Omega_n)$ with $\Omega_n = \frac{(\gamma_n+\bar{\gamma}_n)^2 Q_{nn}^T z_n^{[m_n-1]}}{\sqrt{(\gamma_n+\bar{\gamma}_n)^2 \left\| Q_{nn}^T z_n^{[m_n-1]} \right\|^2 + \varepsilon^2}}$.

Subsequently, take the Lyapunov function as $V = V_n$. According to (25), the time derivative of V is

$$\begin{aligned} \dot{V} \leq & -\sum_{i=1}^{n} \left(\mu_i - 2\lambda_{\max}(Q_i) - \frac{\|g_{i-1}\|^2}{2\lambda_{\min}(Q_i)} \right) V_{i0} + n\varepsilon \\ & + Q_{nn}^T z_n^{[m_n-1]} g_n M u^* - Q_{nn}^T z_n^{[m_n-1]} g_n \alpha_n \\ & + Q_{nn}^T z_n^{[m_n-1]} g_n \nu. \end{aligned} \tag{26}$$

Using lemma 2 and 3, it calculates

$$\begin{aligned} & Q_{nn}^T z_n^{[m_n-1]} g_n M u^* - Q_{nn}^T z_n^{[m_n-1]} g_n \alpha_n \\ & = -Q_{nn}^T z_n^{[m_n-1]} g_n M \alpha_n \tanh\left(\frac{\alpha_n g_n Q_{nn}^T z_n^{[m_n-1]}}{\varepsilon} \right) \\ & - \|Q_{nn}^T z_n^{[m_n-1]} g_n \alpha_n\| \leq \kappa\varepsilon, \\ & Q_{nn}^T z_n^{[m_n-1]} g_n \nu \leq 2\lambda_{max}(Q_n) V_{n0} + \frac{1}{4}\bar{\nu}^2 \|g_n\|^2, \end{aligned} \tag{27}$$

where $\bar{\nu} \geq \sup\{|\nu|\}$.

Combine (27), (26) becomes

$$\dot{V} \leq -aV + b, \tag{28}$$

where $a = \min\left\{ \left(\mu_i - 2\lambda_{\max}(Q_i) - \frac{\|g_{i-1}\|^2}{2\lambda_{\min}(Q_i)} \right), \left(\mu_n - 4\lambda_{\max}(Q_n) - \frac{\|g_{n-1}\|^2}{2\lambda_{\min}(Q_n)} \right) \right\}$ and $b = (n+\kappa)\varepsilon + \frac{1}{4}\bar{\nu}^2\|g_n\|^2$. Conclusions can be drawn from (28) that $V(t)$ is bounded, which implies the tracking error is bounded.

Then, we illustrate there exists a $\bar{t} > 0$ such that $t_{k+1} - t_k > \bar{t}$ for $\forall k$. Define the trigger error by $r(t)$, we have $r(t) = u(t) - u^*(t)$, then

$$\frac{d}{dt}|r(t)| = sign(r(t))\dot{r}(t) \leq |\dot{u}^*|. \tag{29}$$

There exists a positive constant U such that $|\dot{u}^*| \leq U$. Using the mean value theorem and $r(t_k) = 0$, $\lim_{t \to t_{k+1}} r(t_{k+1}) \geq \min\{q_1, q_2\}$, we obtain that the lower bound of $\bar{t}$ will not be less than $\frac{\min\{q_1,q_2\}}{U}$. It is worthy to note that under our design, even if the control input u converges to zero, we still ensure $\bar{t}$ is not zero. Hence, the Zeno phenomenon will not appear.

4 Simulation

To show the superiority of the theoretical results, the examples of the single-link flexible-joint robot system is applied to conduct simulation results.

Fig. 1. The single-link flexible-joint robot.

The single-link flexible-joint robot system. The dynamic of the actual single-link flexible-joint robot system (Fig. 1) is given as

$$\begin{aligned} ml^2\ddot{q}_1 + mgl\sin(q_1) + F(\dot{q}_1) + Kq_1 =& Kq_2, \\ J\ddot{q}_2 + B\dot{q}_2 + K(q_2 - q_1) =& u, \end{aligned} \tag{30}$$

where $F(\dot{q}_1) = cos(\dot{q}_1)$. The values of m, l, g, J, K, B are $m = 0.5$kg, $l = 7.5$m, $g = 9.8$m/s^2, $J = 0.35$m/s^2, $K = 140$N·m/rad, $B = 0.95$.

In the simulation, we set the output signals of the leaders as $y_d = 1 + e^{-t}$. The initial states are set as $q_1(0) = 1$, $\dot{q}_1(0) = 0.1$, $q_2(0) = 0.1$, $\dot{q}_2(0) = 0.1$. Next, according to [10], the solution of control parameters are taken as $K_i^{<1>} = \begin{bmatrix} 120 & 22 \end{bmatrix}$ with $i = 1, 2$. The design parameters in switched threshold event-triggered control strategy are chosen as $D = 50$, $q_1 = 1$, $q_2 = 4$, $\delta = 0.5$. Moreover, the uncertainties are set as $\Delta f_1 = 0$, $\Delta f_2 = 0.1\sin(q_1) + \dot{q}_2^2$, the following conclusion can be observed that $|\Delta f_2| \leq 0.1 + \dot{q}_2^2 = \gamma_2$. Other parameter is chosen as $\varepsilon = 1$.

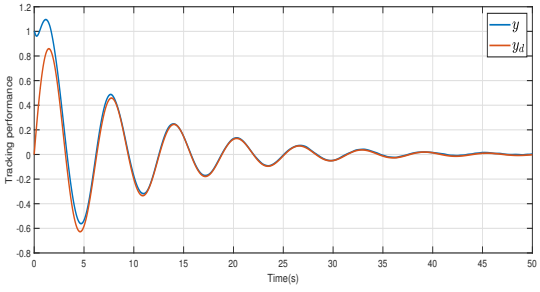

Fig. 2. The profiles of output and reference trajectories.

Under the proposed event-triggered control protocols, the simulation results are displayed in Figs. 2-5. Figs. 2-3 show that the outputs of the system track the reference signal and the tracking errors are bounded. The profiles of inter-event times and the controller are shown in Fig. 4 and Fig. 5, respectively.

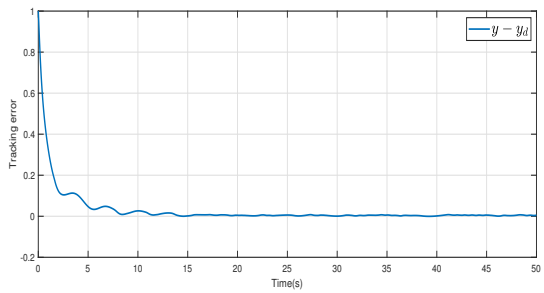

Fig. 3. The profile of tracking error trajectory.

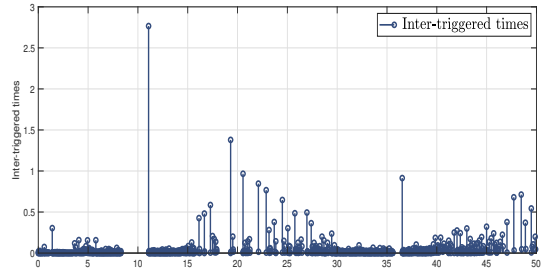

Fig. 4. The profile of inter-event times.

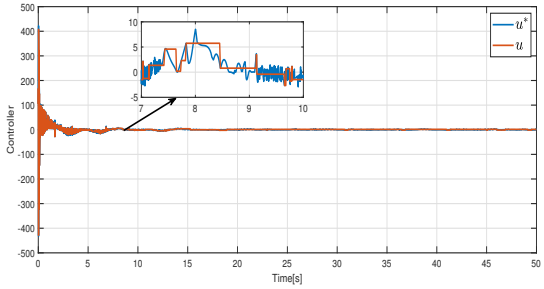

Fig. 5. The profile of controller.

5 Conclusion

In this paper, the event-triggered control strategy for high-order nonlinear strict-feedback systems has been presented for the first time. The structure of the subsystems in high-order nonlinear strict-feedback systems satisfies the HOFA system model and the order of each subsystem can be different. A robust controller is constructed based on the backstepping method to eliminate the effects of uncertainties. Moreover, a switched threshold event-triggered strategy is proposed to reduce the update frequency of the controller. It is proved that the designed event-triggered robust controller can ensure global uniformly ultimately bounded tracking performance and violate Zeno behavior. For future exploration, we will extend our control framework to the cooperative control of HOFA multi-agent systems.

References

[1] Y. Liu and Y. Chen, "Dynamic memory event-triggered adaptive control for a class of strict-feedback nonlinear systems," *IEEE Transactions on Circuits and Systems II: Express Briefs*, vol. 69, no. 8, pp. 3470–3474, 2022.

[2] L. Xing and C. Wen, "Dynamic event-triggered adaptive control for a class of uncertain nonlinear systems," *Automatica*, vol. 158, p. 111286, 2023.

[3] X.-M. Zhang, Q.-L. Han, and B.-L. Zhang, "An overview and deep investigation on sampled-data-based event-triggered control and filtering for networked systems," *IEEE Transactions on Industrial Informatics*, vol. 13, no. 1, pp. 4–16, 2017.

[4] S. Diao, W. Sun, S.-F. Su, and J. Xia, "Adaptive fuzzy event-triggered control for single-link flexible-joint robots with actuator failures," *IEEE Transactions on Cybernetics*, vol. 52, no. 8, pp. 7231–7241, 2022.

[5] E. Garcia and P. J. Antsaklis, "Model-based event-triggered control with time-varying network delays," *2011 50th IEEE CDC-ECC*, pp. 1650–1655, 2011.

[6] L. Xing, C. Wen, Z. Liu, H. Su, and J. Cai, "Event-triggered adaptive control for a class of uncertain nonlinear systems," *IEEE Transactions on Automatic Control*, vol. 62, no. 4, pp. 2071–2076, 2017.

[7] G. Duan, "High-order fully actuated system approaches: Part i. models and basic procedure," *International Journal of Systems Science*, vol. 52, no. 2, pp. 422–435, 2021.

[8] G. Duan, "High-order fully actuated system approaches: Part ii. generalized strict-feedback systems," *International Journal of Systems Science*, vol. 52, no. 3, pp. 437–454, 2021.

[9] G. Duan, "High-order fully actuated system approaches: Part iii. robust control and high-order backstepping," *International Journal of Systems Science*, vol. 52, no. 5, pp. 952–971, 2021.

[10] G. Duan, "High-order fully actuated system approaches: Part iv. adaptive control and high-order backstepping," *International Journal of Systems Science*, vol. 52, no. 5, pp. 972–989, 2021.

[11] G. Duan, "High-order fully actuated system approaches: Part v. robust adaptive control," *International Journal of Systems Science*, vol. 52, no. 10, pp. 2129–2143, 2021.

[12] G. Duan, "High-order fully-actuated system approaches: Part vi. disturbance attenuation and decoupling," *International Journal of Systems Science*, vol. 52, no. 10, pp. 2161–2181, 2021.

[13] W. Liu, G. Duan, and M. Hou, "Concurrent learning adaptive command filtered backstepping control for high-order strict-feedback systems," *IEEE Transactions on Circuits and Systems I: Regular Papers*, vol. 70, no. 4, pp. 1696–1709, 2023.

[14] R. Meng, C. Hua, K. Li, and P. Ning, "Adaptive event-triggered control for uncertain high-order fully actuated system," *IEEE Transactions on Circuits and Systems II: Express Briefs*, vol. 69, no. 11, pp. 4438–4442, 2022.

[15] M. Cai, X. He, and D. Zhou, "Low-power fault-tolerant control for nonideal high-order fully actuated systems," *IEEE Transactions on Systems, Man, and Cybernetics: Systems*, vol. 53, no. 8, pp. 4875–4887, 2023.

[16] M. Cai, X. He, and D. Zhou, "An active fault tolerance framework for uncertain nonlinear high-order fully-actuated systems," *Automatica*, vol. 152, p. 110969, 2023.

[17] G.-P. Liu, "Coordination of networked nonlinear multi-agents using a high-order fully actuated predictive control strategy," *IEEE/CAA Journal of Automatica Sinica*, vol. 9, no. 4, pp. 615–623, 2022.

[18] B. Chen, X. Liu, K. Liu, and C. Lin, "Direct adaptive fuzzy control of nonlinear strict-feedback systems," *Automatica*, vol. 45, no. 6, pp. 1530–1535, 2009.

[19] Y. Li, S. Liang, and M. Hou, "Asymptotic tracking control for uncertain strict-feedback nonlinear systems with delayed full-state constraints," *International Journal of Robust and Nonlinear Control*, vol. 30, no. 18, pp. 8174–8191, 2020.

Proceedings of the 3rd Conference on Fully Actuated System Theory and Applications
May 10-12, 2024, Shenzhen, China

Adaptive Control for Active Suspension System Based on the High-order Fully Actuated System Theory

Haohan Zhao[1], Yahui Zhang[1], Xiaohong Jiao[2]

1. School of Mechanical Engineering, Yanshan University, Qinhuangdao 066004, P. R. China
E-mail: zhangyahui@ysu.edu.cn

2. School of Electrical Engineering, Yanshan University, Qinhuangdao 066004, P. R. China

Abstract: Active suspension systems are key in improving vehicle comfort and handling stability. However, designing controllers more effectively remains a challenge. Most existing methods are based on the state-space method to design the controller, and each control method has shortcomings. To enhance suspension control performance and damping efficacy under road surface excitation, this paper proposed a novel adaptive control strategy for active suspensions based on the high-order fully actuated (HOFA) approach, anchored in the continuous damping control shock absorber actuator. Firstly, we formulated the dynamical model for active suspension based on Newton's second law and transformed it into a fully actuated physical model. Subsequently, we proposed a novel controller grounded in high-order fully actuated theory. Through simulation in MATLAB/Simulink, the results demonstrate significant enhancements in ride comfort and road handling using the proposed approach while ensuring robust performance against sinusoidal road excitation. In conclusion, the proposed control method exhibits superior effectiveness to other controllers discussed in this paper.

Key Words: Active suspension; High-order fully actuated theory; Road excitation; Adaptive control

1 Introduction

Active suspension, a pivotal component within the vehicle chassis, is crucial in effectively mitigating vertical vibrations and enhancing overall vehicle ride comfort [1-3]. In tandem with advancements in vehicle technology, an increasing number of premium vehicles are now equipped with an active suspension system, incorporating features such as the continuous damping control (CDC) shock absorber. The CDC shock absorber achieves adjustable damping in the active suspension by regulating the open-shut operation of the internal solenoid valve [4]. As is well-established, vehicle suspension systems are broadly categorized into three types: passive, semi-active, and active. Numerous studies on suspension systems have consistently concluded that active suspension systems offer substantial performance improvements over passive suspensions when vehicles encounter vibrations on diverse road surfaces. However, the widespread adoption of active suspension systems is hindered by their high energy consumption and cost [5]. Consequently, despite these challenges, active suspension systems are gaining popularity due to their exceptional shock absorption and actuation capabilities.

With the development of control theory, some advanced control methods are applied in the active suspension systems, which can effectively improve the vehicle ride comfort and handling stability. Thus, the active suspension control system design has been developed by some automakers over the past decades. For example, $Audi$ and BMW have implemented the active body control strategy to improve suspension performance and vehicle ride comfort. In modern control theory, many control methods are usually based on the state-space representation to further design controllers. In recent years, many researchers have proposed control methods for active suspension systems. Even preview control has been applied to active suspension systems using road recognition technology [6]. For example, Shao. $et\ al.$ [7] proposed the output feedback H_∞ control for active suspension of in-wheel motor-driven electric vehicle considering the control faults and input delay. Zhang. $et\ al.$ [8] proposed the bioinspired nonlinear dynamics-based adaptive neural network control for vehicle suspension systems with uncertain/unknown dynamics and input delay. The effectiveness of the proposed method has been verified through experiments. Besides, there are also lots of control methods applied in the active suspension system, for example: model predictive control [9], sliding mode control [10], and active disturbance rejection control [11] $et\ al.$

During the past several decades, state-space approaches have dominated the control field in an absolute state. In 2020, G. R. Duan [12-15] proposed the high-order fully actuated (HOFA) system approach. HOFA is directly proposed for control objects by transforming the control system into a high-order full-actuated system model and directly designing controllers and control laws. The HOFA systems widely exist in practical systems, and their remarkable feature is that the control matrix function is reversible. In recent years, the HOFA method has been applied in the space manipulator, the vehicle system, and the UAVs $et\ al.$ Active suspension controls input variables and state variables. So, we can convert the suspension dynamic model into the HOFA model. Then, the control law about the active suspension system will be directly designed through the HOFA method. In this paper, we choose the adaptive control method based on the HOFA theory applied in the active suspension system.

The remainder of this paper is organized as follows: Section 2 mainly describes the fixed expression of the formula. Section 3 illustrates the active suspension modeling, problem formulation, road excitation, and HOFA models. Section 4 mainly explains the controller design method. Section

This work has been partially supported by the Foundation of National Natural Science Foundation of China (52302482), the Foundation of Central government guided local science and Technology Development (236Z2202G), the Natural Science Foundation of Hebei Province (E2021203079), Science and Technology Foundation of Hebei Education Department (QN2022176), and Scientific Research Foundation of Hebei Province for the Returned Overseas Chinese Scholars (C20210323).

5 compares the simulation results and analysis with different controllers. The last section mainly concludes this paper.

2 Preliminaries

Firstly, we recall some commonly used notations in [12-15]. In this paper, I_n represents the identity matrix, and the following symbols are used in this paper:

$$K_{0\sim n} = \begin{bmatrix} K_0 & K_1 & \cdots & K_n \end{bmatrix}$$

$$A^{0\sim n-1} = \begin{bmatrix} A_0 \\ A_1 \\ \cdots \\ A_{n-1} \end{bmatrix}$$

$$x^{0\sim n} = \begin{bmatrix} x \\ \dot{x} \\ \vdots \\ x^n \end{bmatrix}$$

$$\Phi(A^{0\sim n-1}) = \begin{bmatrix} 0 & I & & \\ & & \ddots & \\ & & & I \\ -A_0 & -A_1 & \cdots & -A_{n-1} \end{bmatrix}$$

3 Modeling and analysis

3.1 Active suspension modeling

The quarter vehicle model always represents the one corner of a vehicle for which only the vertical dynamics are considered. From the Fig. 1, we can know the sample structure of the active suspension. The actuator is the CDC shock absorber. we have ignored it because it has a complex dynamic and action mechanism [16]. The sprung mass represents the vehicle body mass, where the vehicle's body is denoted by the sprung mass M_b. The unsprung mass represents the tire mass, where the vehicle's tire is denoted by the unsprung mass M_u. u is the active suspension control force input. Z_s and Z_u respectively represent the travel between the sprung and unsprung mass. z_r represents the road profile. The model of the active suspension system can be represented as the equation (1):

$$\begin{cases} m_b\ddot{z}_s + c_s(\dot{z}_s - \dot{z}_u) + k_s(z_s - z_u) = u \\ m_u\ddot{z}_u - c_s(\dot{z}_s - \dot{z}_u) - k_s(z_s - z_u) + k_t(z_u - z_r) = -u \end{cases} \tag{1}$$

If we use the traditional control method, the controller design is based on the state-space representation. So we can convert equation (1) to the state-space representation equation (2):

$$\begin{cases} x_1 = \dot{x}_2 \\ \dot{x}_2 = -\frac{c_s}{m_b}(\dot{z}_s - \dot{z}_u) - \frac{k_s}{m_b}(z_s - z_u) + \frac{1}{m_b}u \\ x_3 = \dot{x}_4 \\ \dot{x}_4 = \frac{c_s}{m_u}(\dot{z}_s - \dot{z}_u) + \frac{k_s}{m_u}(z_s - z_u) - \frac{k_t}{m_u}(z_u - z_r) - \frac{1}{m_u}u \end{cases} \tag{2}$$

According to the state-space representation equation, the active suspension system is modeled as a fourth-order system with a single control input and two state outputs, indicative of its characteristic as a typical under-actuated system. Consequently, in our initial investigation, the imperative is to transform this under-actuated system into a fully actuated counterpart.

3.2 Problem formulation

The control object is to suppress the vibration of the vehicle body and the suspension travel space within the range of safety. Some assumptions are required to facilitate the controller design.

Assumption 1: For the convenience of research, it is assumed that the system operates in an ideal environment without external interference. So we think that the $\hat{d} = 0$.

Assumption 2: The travel of the suspension z_u and the travel of the vehicle body z_s are all bounded.

Assumption 3: However, the spring damping has nonlinear characters. We should segment research or numerical fitting to apply it. But, we don't consider it to simplify this research.

Assumption 4: The actuator doesn't have to produce the delay, dead input, and fault $et\ al.$ phenomenon.

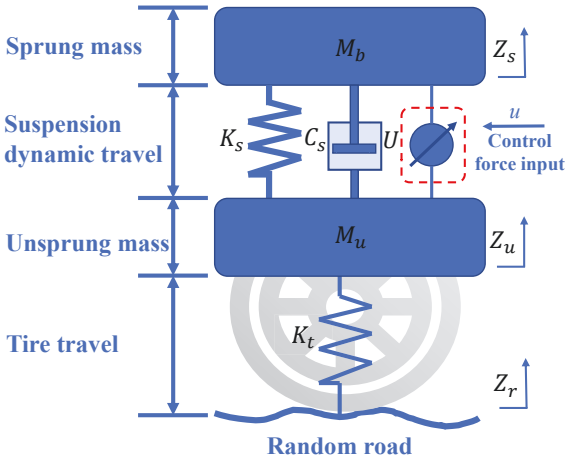

Fig. 1: Physical model of active suspension

3.3 Road model

The road excitation is the input signal into the suspension system. In the research, we can choose different roads, for example, the random road disturbance, bump road disturbance, and sine road disturbance $et\ al.$ In this paper, we choose the sine road as the input signal. The equation (3) represents the road sine signal. As shown in fig.2, which is the sine road pavement map. The road excitation signal will input the active suspension system to action the actuator.

$$z_r = 0.02sin(2\pi t), (t \geq 0) \tag{3}$$

3.4 HOFA model

According to the equation (1), we can define that z_s and z_u are the state variables, and u is the control input variable. We can define that: $x_1 = z_s, x_2 = z_u, z_r = \xi$, The vehicle travel is the x_1, and the suspension travel is the x_2, ξ is the road

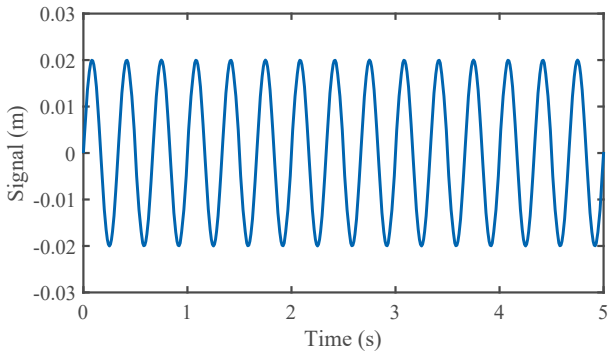

Fig. 2: Road excitation signal.

signal. The equation (1) can be converted to the equation (4):

$$\begin{cases} m_b\ddot{x}_1 + c_s(\dot{x}_1 - \dot{x}_2) + k_s(x_1 - x_2) = u \\ m_u\ddot{x}_2 - c_s(\dot{x}_1 - \dot{x}_2) - k_s(x_1 - x_2) + k_t(x_2 - \xi) = -u \end{cases} \tag{4}$$

According to equation (4), we can get equation (5) by adding the two sub-formulas. In the equation (5), the control input u has been eliminated.

$$m_b\ddot{x}_1 + m_u\ddot{x}_2 + k_t(x_2 - \xi) = 0 \tag{5}$$

To convert to a high-order fully actuated model, the intermediate variables z are constructed as equation (6). Z expresses the coupling relationship between the two state variables.

$$\ddot{z} = m_b\ddot{x}_1 + m_u\ddot{x}_2 \tag{6}$$

Substituting (6) into (5) yields. Therefore, we can get the following equation (7).

$$\ddot{z} + k_t(x_2 - \xi) = 0 \tag{7}$$

Based on its physical background, we can get the relationship of z and x_1, z_2. Respectively: $\dot{z} = m_b\dot{x}_1 + m_u\dot{x}_2$ and $z = m_bx_1 + m_ux_2$. According to the equation (4) and equation (5), we can get the equation (8).

$$c_s(\dot{x}_1 - \dot{x}_2) + k_s(x_1 - x_2) - m_u\ddot{x}_2 - k_t(x_2 - \xi) = u \tag{8}$$

According to the equation (7), we can get the relationship of z and x_2.

$$\begin{cases} x_2 = \xi - \frac{1}{k_t}\ddot{z} \\ \dot{x}_2 = \dot{\xi} - \frac{1}{k_t}z^{(3)} \\ \ddot{x}_2 = \ddot{\xi} - \frac{1}{k_t}z^{(4)} \end{cases} \tag{9}$$

Based on the equation (9), we can get the equation (10).

$$\dot{x}_1 = \frac{\dot{z} - m_u\dot{x}_2}{m_b} \tag{10}$$

Substituting $\dot{x}_2$ into the equation (9), we can get the equation (11) and equation (12).

$$\ddot{x}_1 = \frac{\dot{z} - m_u\left(\ddot{\xi} - \frac{1}{k\,t}z^{(4)}\right)}{m_b} \tag{11}$$

$$x_1 = \frac{z - m_u\left(\xi - \frac{1}{k_t}\ddot{z}\right)}{m_b} \tag{12}$$

Finally, by transforming and iterating the abovementioned equations, we can get the HOFA expression about the active suspension system in equation (13). In the equation, only one control input is u, and one state variable is z.

$$\begin{aligned} &\frac{m_u}{k_t}z^{(4)} + \frac{m_uc_s + m_bc_s}{m_bk_t}z^{(3)} + \frac{m_uk_s + m_bk_s + m_bk_t}{m_bk_t}\ddot{z} \\ &+ \frac{c_s}{m_b}\dot{z} + \frac{k_s}{m_b}z - m_u\ddot{\xi} - \frac{c_s(m_u + m_b)}{m_b}\dot{\xi} \\ &- \frac{k_s(m_u + m_b)}{m_b}\xi = u \end{aligned} \tag{13}$$

4 Controller designing and analysis

The HOFA controller design mainly includes the adaptive control law design process, the parametric design process, and the controller stability analysis. We will explain these parts in detail in the following sections.

4.1 Adaptive control law design process

In this research, we have considered the following HOFA system with an unknown parameter vector. According to the references [12-16], we can learn the standard style of HOFA, such as in equation (14).

$$z^{(n)} = H^T\left(z^{(0\sim n-1)}\right)\theta + q\left(z^{(0\sim n-1)}\right) + L\left(z^{(0\sim n-1)}\right)u \tag{14}$$

where the z and u are the state vector and the control input vector, respectively, θ is an unknown constant vector, q is a sufficiently smooth vector function, H and L are two sufficiently smooth matrix functions, and L satisfies the full-actuation condition.

According to equation (2), the active suspension system is a fourth-order system, so we can think that the system order $n = 4$. And we can get the equation (15).

$$z^{(4)} = H^T\left(z^{(0\sim3)}\right)\theta + q\left(z^{(0\sim3)}\right) + L\left(z^{(0\sim3)}\right)u \tag{15}$$

Because we don't consider the external disturbances θ, the external disturbances $\theta = 0$. We can write the equation (16) and convert the equation (14).

$$\begin{aligned} z^{(4)} &= \frac{k_t}{m_u}u - \left(\frac{m_uc_s + m_bc_s}{m_bm_u}\right)z^{(3)} \\ &- \left(\frac{m_uk_s + m_bk_s + m_bk_t}{m_bm_u}\right)z^{(2)} - \frac{c_sk_t}{m_bm_u}\dot{z} - \frac{k_sk_t}{m_bm_u}z \\ &+ k_t\ddot{\xi} + \left(\frac{c_sk_t(m_u + m_b)}{m_bm_u}\right)\dot{\xi} + \left(\frac{k_sk_t(m_u + m_b)}{m_bm_u}\right)\xi \end{aligned} \tag{16}$$

From the equation (16), we can get the equation (17) compared with the equation (15).

$$\begin{cases} z^{(4)} = x^{(4)}, \\ L(x^{(0\sim3)}) = \frac{k_t}{m_u}, \\ H^T(x^{0\sim3})\theta = 0, \\ q^{(0\sim3)} = \left(\frac{m_u c_s + m_b c_s}{m_b k_t}\right) z^{(3)} + \left(\frac{m_u k_s + m_b k_s + m_b k_t}{m_b k_t}\right) z^{(2)} \\ + \left(\frac{c_s k_t}{m_b m_u}\right) \dot{z} + \left(\frac{k_s k_t}{m_b m_u}\right) z - k_t \ddot{\xi} - \left(\frac{c_s k_t (m_u + m_b)}{m_b m_u}\right) \dot{\xi} \\ - \left(\frac{k_s k_t (m_u + m_b)}{m_b m_u}\right) \xi \end{cases} \tag{17}$$

To establish the control law of the HOFA system (15) with unknown parameters, we need the following preparations.

Lemma 1 : We can assume that $A \in R^{r\times r}$ satisfies [14]

$$Re\lambda_i \leq -\frac{\mu}{2}, i = 1, 2, 3 \ldots, n, \tag{18}$$

where $\mu > 0$, then there exists a matrix $P > 0$ such that

$$\begin{aligned} \Phi^T(A^{0\sim n-1})P(A^{0\sim n-1}) + (A^{0\sim n-1})\Phi(A^{0\sim n-1}) \\ \leq -\mu P(A^{0\sim n-1}) \end{aligned} \tag{19}$$

Theorem 1 : The next step is to design the controller based on the previous work. We can reference the paper [12-16]. The expression of the controller is as follows in the equation (20).

$$\begin{cases} u = -L^{-1}x^{(0\sim n-1)}\left(A^{(0\sim n-1)}x^{(0\sim n-1)} + u^*\right) \\ u^* = H^T x^{(0\sim n-1)}\hat{\theta} + q\left(x^{(0\sim n-1)}\right) \end{cases} \tag{20}$$

From the function (20), we can get the $u^* = q^{(0\sim3)}$. The HOFA controller can be expressed as the equation (19).

$$\begin{aligned} u = -\frac{m_u}{k_t}[A^{0\sim3}z^{(0\sim3)} + A_{11}\ddot{\xi} + A_{12}\dot{\xi} + A_{13}\xi + A_{14}z^{(3)} \\ + A_{15}z^{(2)} + A_{16}\dot{z} + A_{17}z] \end{aligned} \tag{21}$$

In equation (21), the relationship can be defined as:

$$\begin{cases} A_{11} = k_t \\ A_{12} = \frac{c_s(m_u + m_b)}{m_b m_u} \\ A_{13} = \frac{k_s(m_u + m_b)}{m_b m_u} \\ A_{14} = \frac{m_u c_s + m_b c_s}{m_b m_u} \\ A_{15} = \frac{m_u k_s + m_b k_s + m_b k_t}{m_b m_u} \\ A_{16} = \frac{c_s k_t}{m_b m_u} \\ A_{17} = \frac{k_s k_t}{m_b m_u} \end{cases} \tag{22}$$

Then, we analyze the controller's stability [12-16]. Substituting the control law (20) into (15), the controller close-loop system is shown in the equation (23).

$$x^{(4)} + A^{0\sim3}x^{(0\sim3)} = 0 \tag{23}$$

The part of closed-loop system (23) can be expressed in the following state-space form:

$$\dot{x}^{0\sim3} = \Phi(x^{0\sim3})x^{0\sim3} + \begin{bmatrix} 0_{3\times1} \\ 0 \end{bmatrix} \tag{24}$$

Since $A_i \in \mathbb{R}^{r\times r}$,$i = 0, 1, ..., n-1$ satisfy the condition (18), there exists a positive definite matrix $P(A^{0\sim n-1})$ satisfying (19). Then the following Lyapunov function can be chosen for the system (25):

Proof: Therefore, the following Lyapunov function can be selected for the system (25).

$$V = (x^{(0\sim n-1)})^T P(A^{0\sim n-1})x^{(0\sim n-1)} \tag{25}$$

Because $n = 4$, the Lyapunov function also is the:

$$V = (x^{(0\sim3)})^T P(A^{0\sim3})x^{(0\sim3)}$$

We have

$$\begin{aligned} \dot{V} =& (\dot{x}^{(0\sim3)})^T P x^{(0\sim3)} + (x^{(0\sim3)})^T P \dot{x}^{(0\sim3)} \\ =& (\Phi x^{(0\sim3)})^T P x^{(0\sim3)} + (x^{(0\sim3)})^T P(\Phi x^{(0\sim3)}) \\ =& (x^{(0\sim3)})^T(\Phi^T P + P\Phi)x^{(0\sim3)} + 2(x^{0\sim3})^T P(A^{(0\sim3)}[0] \\ =& (x^{(0\sim3)})^T(\Phi^T P + P\Phi)x^{(0\sim3)} \\ \leq& -\mu V \end{aligned}$$

It thus follows from the Comparison Theorem that

$$V \leq V(0)e^{(-\mu t)} \to 0, t \to \infty.$$

A comprehensive stability analysis has established that the designed active suspension HOFA controller is indeed stable.

4.2 Parametric design process

For an arbitrarily chosen $F \in \mathbb{R}^{nr\times nr}$, all the matrix $A^{0\sim n-1}$, and the nonsingular matrix $V \in \mathbb{R}^{nr\times nr}$ satisfying the equation (26) [15].

$$\Phi(A^{0\sim n-1}) = VFV^{-1} \tag{26}$$

are given by

$$A^{0\sim n-1} = -ZF^nV^{-1}(Z, F) \tag{27}$$

In this paper, with $n = 4$, the subsequent function is derived.

$$A^{0\sim3} = -ZF^4V^{-1}(Z, F) \tag{28}$$

and

$$V(Z, F) = \begin{bmatrix} Z \\ ZF \\ ZF^2 \\ ZF^3 \end{bmatrix} \tag{29}$$

Where $Z \in \mathbb{R}^{r\times nr}$ is an arbitrary parameter matrix satisfying

$$detV(Z, F) \neq 0 \tag{30}$$

$$F = \begin{bmatrix} -a & -b & 0 & 0 \\ b & -a & 0 & 0 \\ 0 & 0 & -c & 0 \\ 0 & 0 & 0 & -d \end{bmatrix} \tag{31}$$

We can set the a, b, c, and d as four positive scalars, included as a diagonal block in F. In the matrix F, we choose the $a = 1, b = 8, c = 12, d = 40$ and $Z = \begin{bmatrix} 1 & 1 & 1 & 1 \end{bmatrix}$. The a, b, c, and d are adjustable and are very important for the convergence of the system.

5 Simulation results and analysis

The parameters of the quarter-vehicle model in the simulation framework are delineated in Table 1 [18]. The HOFA control model is incorporated into the control module of the suspension system. Then, we simulate and analyze key performance indicators such as vehicle body acceleration, vehicle body travel, and vehicle tire travel $et\ al.$. For comparative analysis, we choose the passive suspension (no control) and Fuzzy PID control as the comparison object. In the simulation, the PID controller gain has been chosen ($K_p = 5000$, $K_i = 500$, $K_d = 10$) [19]. The ensuing section presents the simulation results and their corresponding analysis.

Table 1: Active suspension system parameters

Vehicle body mass (kg)	m_b	2.45
Vehicle wheel mass (kg)	m_u	1
Suspension spring stiffness (N/m)	k_s	900
Suspension damping coefficient (Ns/m)	c_s	7.5
Wheel stiffness (Ns/m)	k_t	2500

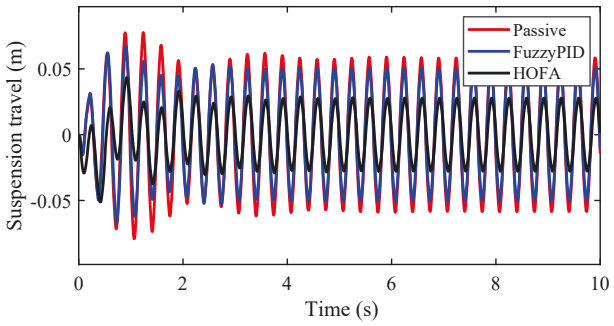

Fig. 3: Active suspension travel.

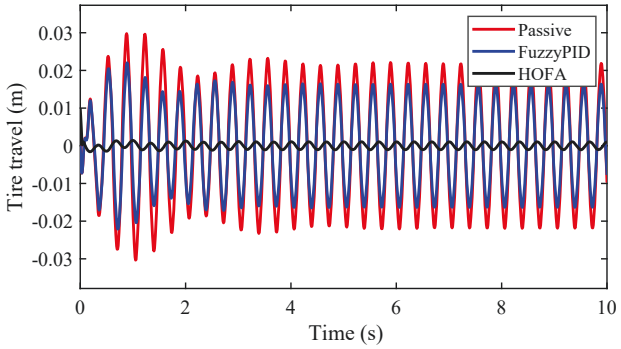

Fig. 4: Vehicle tire travel.

Table 2: Comparison of RMS values of different control modes under the sine road surface

Controller model	Suspension travel	Tire travel	Vehicle body acceleration	Vehicle body travel
Passive	0.014	0.009	8.523	0.024
FuzzyPID	0.011	0.007	6.566	0.018
HOFA	**0.001**	**0.001**	**1.093**	**0.002**

As shown in Figure 3-6, in the case of the time domain, the Suspension travel, Vehicle tire travel, Vehicle body acceleration, and Vehicle body travel under HOFA controller are respectively reduced by 92 %, 88%, 87% and 91% compared with the no control. HOFA control is respectively reduced by 90 %, 85%, 83%, and 88% compared with the Fuzzy PID control. The comparison of RMS values of different control modes under the sine road surface can be shown in Table 2. These results show that the proposed algorithm is effective and the vehicle ride comfort is improved in the vertical direction.

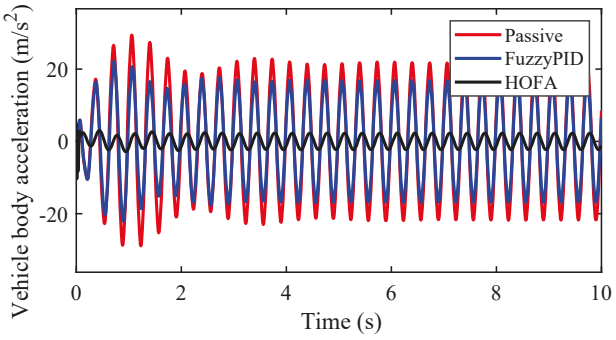

Fig. 5: Vehicle body acceleration.

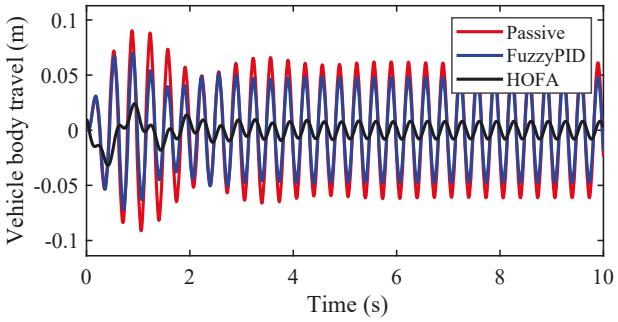

Fig. 6: Vehicle body travel.

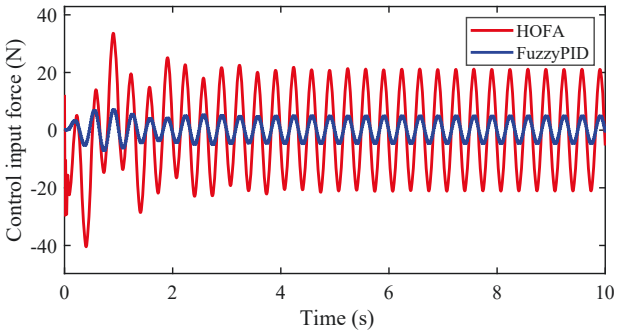

Fig. 7: System control input force.

As shown in Figure 7, the control input force signal is under the HOFA controller and the Fuzzy PID controller. According to section 4, the control force has stability and convergence in finite time. From the result, the HOFA controller provides a higher control input force.

6 Conclusion

In practice, the HOFA system model is regarded as a novel system representation rather than a novel system. HOFA system can maintain the full actuation characteristic of original systems. This paper introduces the HOFA control for active suspension systems. The proposed adaptive algorithm demonstrates efficacy in significantly reducing the performance index and enhancing ride comfort. The application

of the HOFA algorithm in the active suspension system has been successfully validated through simulation.

In addition to the significant findings presented in this paper. There are also numerous questions necessitating further exploration in future research. For example, several modeling assumptions and simplifications have been employed in this paper, and the external disturbances have been omitted. In future research, we aim to construct a comprehensive vehicle model as the research object, and the road identification techniques also need to be considered. The external disturbances of the system have a huge impact on the control effectiveness of the controller [20]. Subsequently, observation and estimation of external uncertain disturbances will be carried out, and the disturbance signal in the controller will be compensated to improve the control effectiveness further. To validate the efficacy of the proposed algorithm, we also plan to design the hardware experiments for verification.

References

[1] T. L. Huang, J. Wang, H. H. Pan, Approximation-Free Prespecified Time Bionic Reliable Control for Vehicle Suspension. *IEEE Transactions on Automation Science and Engineering*, 2023, DOI: 10.1109/TASE.2023.3310335.

[2] B. Q. Zhang, H. H. Zhao, X. Zhang, Adaptive variable domain fuzzy PID control strategy based on road excitation for semi-active suspension using CDC shock absorber. *Journal of Vibration and Control*, 2023, 10775463231152287.

[3] H. Wang, P. K. Wang, J. Zhao, Observer-based robust gain-scheduled control for semi-active air suspension systems subject to uncertainties and external disturbance. *Mechanical Systems and Signal Processing*, 2022, 173, 109045.

[4] J. H. Zhang, J. Liu, F. Ding, Collaborative optimization design framework for hierarchical filter barrier control suspension system with projection adaptive tracking hydraulic actuator. *Nonlinear Dynamics*, 2022, 108(4): 3417–3434.

[5] M. H. Zhang, X. J. Jing, Energy-saving robust saturated control for active suspension systems via employing beneficial nonlinearity and disturbance. *IEEE Transactions on Cybernetics*, 2021, 52(10): 10089-10100.

[6] T. L. Huang, J. Wang, H. H. Pan, Adaptive Bioinspired Preview Suspension Control With Constrained Velocity Planning for Autonomous Vehicles. *IEEE Transactions on Intelligent Vehicles*, 2023.

[7] X. X. Shao, F. Naghdy, P. H. Du, H. Y. Li, Output feedback H∞ control for active suspension of in-wheel motor driven electric vehicle with control faults and input delay. *ISA transactions*, 2019, 92: 94-108.

[8] M. H. Zhang, X. J. Jing, G. Wang, Bioinspired nonlinear dynamics-based adaptive neural network control for vehicle suspension systems with uncertain/unknown dynamics and input delay. *IEEE Transactions on Industrial Electronics*, 2020, 68(12): 12646-12656.

[9] T. Johan, S. Aldo, G. Patrick, Regionless explicit model predictive control of active suspension systems with preview.*IEEE Transactions on Industrial Electronics*, 2019, 67(6): 4877-4888.

[10] H. Cong Minh, T. Duc Thien, A. Kyoung Kwan, Adaptive sliding mode control based nonlinear disturbance observer for active suspension with pneumatic spring.*Journal of sound and vibration*, 2021, 509: 116241.

[11] H. Faried, F. Waleed F, D. Fadly Jashi, and A. Mohammad. Ride comfort performance of a non-linear full-car using active suspension system with active disturbance rejection control and input decoupling transformation.*International Journal of Heavy Vehicle Systems*, 2019, 26(2): 188-224.

[12] G. R. Duan, High-order fully actuated system approaches: Part I. Models and basic procedure.*International Journal of Systems Science*, 2021, 52(5): 422-435.

[13] G. R. Duan, High-order fully actuated system approaches: Part II. Generalized strict-feedback systems.*International Journal of Systems Science*, 2021, 52(3): 437-454.

[14] G. R. Duan, High-order fully actuated system approaches: Part III. Robust control and high-order backstepping.*International Journal of Systems Science*, 2021, 52(5): 952-971.

[15] G. R. Duan, High-order fully actuated system approaches: Part IV. Adaptive control and high-order backstepping.*International Journal of Systems Science*, 2021, 52(5): 972-989.

[16] G. R. Duan, High-order fully actuated system approaches: Part V. Robust adaptive control. *International Journal of Systems Science*, 2021, 52(10):2129-2143.

[17] T. L. Huang, J. Wang, H. H. Pan, Adaptive bioinspired preview suspension control with constrained velocity planning for autonomous vehicles. *IEEE Transactions on Intelligent Vehicles*, 2023, 8(7): 3925-3935.

[18] J. Wu, H. L. Zhou, Z. Y. Liu, M. Q. Gu, Ride comfort optimization via speed planning and preview semi-active suspension control for autonomous vehicles on uneven roads. *International Journal of Systems Science*, 2020, 69(8): 8343-8355.

[19] X. J. Guo, J. H. Zhang, W. C. Sun, Robust saturated fault-tolerant control for active suspension system via partial measurement information. *Mechanical Systems and Signal Processing*, 2023, 191, 110116.

[20] G. Wang, M. Chadli, M. V. Basin, Practical terminal sliding mode control of nonlinear uncertain active suspension systems with adaptive disturbance observer. *IEEE/ASME Transactions On Mechatronics*, 2020, 26(2): 789-797.

Proceedings of the 3rd Conference on Fully Actuated System Theory and Applications
May 10-12, 2024, Shenzhen, China

Observer-Based Control for Fully Actuated Systems with Time-Varying Delays: A Fully Actuated System Approach

Zhijun Chen[1], Shiyu Zhang[1], Guangren Duan[1,2]

1. Center for Control Theory and Guidance Technology, Harbin Institute of Technology, Harbin 150001, P. R. China
E-mail: chenzj1998@126.com, zsy13436552937@163.com

2. Shenzhen Key Laboratory of Control Theory and Intelligent Systems, Southern University of Science and Technology, Shenzhen 518055, P. R. China
E-mail: g.r.duan@hit.edu.cn

Abstract: Inspired by the fully actuated system (FAS) approach, this paper proposes an observer-based control method for a class of FASs with time-varying delays. Firstly, an observer-based controller is designed and the corresponding augmented system is derived. The uniformly exponential stability of the augmented system is then demonstrated by means of Lyapunov stability analysis. Finally, the effectiveness of the proposed method is demonstrated by the simulation of the thermoacoustic instability system. The parameters to be designed for the controller are determined using a parametric approach which provides a rich degree of design freedom.

Key Words: Observer-Based Control, Fully Actuated System Approach, Nonlinear Control, Thermoacoustic Systems

1 Introduction

The observer-based control design for the general nonlinear systems is quite difficult, and there is currently no universal and effective method. Different from the linear cases, the separation principle is not usually guaranteed due to the complex structure of nonlinear systems. Most of the existing results are obtained in a local sense for systems with special forms under some certain assumptions [1–3]. Recently, aiming to develop a unified architecture for the control design of general nonlinear systems, Duan has heuristically proposed a so-called mathematical fully actuated system (FAS) approach [4–6]. The full-actuation feature of the FAS systems allows us to directly cancel the nonlinearity of the system, resulting in a linear time invariant closed-loop system with an arbitrarily assignable eigenstructure, when the full state is measurable. However, if only partial states are measurable, designing a state observer is an intuitive idea to circumvent this barrier in practical applications.

It is vital how much convenience the FAS approach provides for observer design and observer-based control. As outlined in [7, 8], the separation principle is still effective in the FAS theory, and thus we can directly design state observers for linear closed-loop systems, which significantly reduces the complexity of the problem. Zhao et al. introduced the concept of an exponentially stable observer and further proposed an observer-based control method for the attitude control of flexible spacecraft with nonlinear inertia for the output feedback case [7]. Under the same Lipschitz condition, a generalized proportional-integral observer for single-order FASs was presented by using the linear matrix inequality (LMI) technique in [8]. Also, a practical application for the twelve-input overactuated tiltrotor was reported in [9].

Furthermore, considering the FASs with external disturbances, an extended state observer (ESO) is applied to estimate the state and total disturbance of the 6DOF spacecraft motion [10]. Different from the above traditional ESO, Cai et al. presented a fully-actuated fault-tolerant control technique in conjunction with an ESO involving the sign function [11], but the chattering phenomenon became an inevitable problem. In the same year, the similar structure of ESO was utilized to estimate unknown state variables of a proton exchange membrane fuel cell air feed system [12]. Besides, benefiting from the simple structure of the FAS model, fruitful results regarding disturbance observers can be found in the references [13–17].

Based on the above analyses, this paper proposes an observer-based control method for a class of FASs with time-varying delays. The model of FASs with time-varying delays is proposed, which represents a complex and general control model. An observer-based controller is given for the FAS and the augmented system is also derived. The uniformly exponential stability of this augmented system is strictly proved by applying Lyapunov stability analysis. Finally, the proposed method is applied to the control of a thermoacoustic instability system and the simulation results show the effectiveness.

The paper is divided into 6 sections. The next section provides the problem formulation. Some preliminaries are introduced in Section 3. Section 4 is the solution to the problem, where the augmented system is proven to be uniformly exponentially stable. In Section 5, we select a thermoacoustic instability system to illustrate the effectiveness of our proposed approach, followed by a brief conclusion in Section 6.

The standard notations are used: the maximum and minimum eigenvalues of a matrix $P \in \mathbb{R}^{n\times n}$ are denoted by $\lambda_{\max}(P)$ and $\lambda_{\min}(P)$, respectively, $\|P\|$ is its spectral norm, $\mathrm{Re}(z)$ denotes the real part of a complex number z, and the Euclidean norm of a vector x is denoted by $\|x\|$. Furthermore, we introduce the following symbols frequently used in the FAS theory:

$$x^{(0\sim n-1)} = \left[x^{\mathrm{T}} \quad \dot{x}^{\mathrm{T}} \quad \cdots \quad (x^{(n-1)})^{\mathrm{T}}\right]^{\mathrm{T}},$$

$$A_{0\sim n-1} = \left[A_0 \quad A_1 \quad \cdots \quad A_{n-1}\right],$$

This work is supported by the Science Center Program of the National Natural Science Foundation (NNSF) of China under Grant 62188101.

$$\Phi\left(A_{0\sim n-1}\right)=\begin{bmatrix} 0 & I & & \\ & & \ddots & \\ & & & I \\ -A_0 & -A_1 & \cdots & -A_{n-1} \end{bmatrix},$$

$$\Phi\left(0_{0\sim n-1}\right)=\begin{bmatrix} 0 & I & & \\ & & \ddots & \\ & & & I \\ 0 & 0 & \cdots & 0 \end{bmatrix}, B_c=\begin{bmatrix} 0 \\ 0 \\ \vdots \\ I \end{bmatrix}.$$

2 Problem Statements

2.1 Problem Formulation

Consider the system

$$\begin{cases} x^{(n)}=f\left(x^{(0\sim n-1)},\zeta_x,t\right)+B\left(y,\zeta_y,t\right)u \\ y=C_{0\sim n-1}x^{(0\sim n-1)}, \end{cases} \tag{1}$$

where $x\in\mathbb{R}^r$ and $u\in\mathbb{R}^r$ are the system elementary state vector and the system input vector, respectively, $y\in\mathbb{R}^m$ is the output vector, and $C_{0\sim n-1}\in\mathbb{R}^{m\times nr}$ is a known constant matrix, ζ_x and ζ_y are the delay terms in the system and are defined as

$$\zeta_x\triangleq\begin{bmatrix} x^{(0\sim n-1)}\left(t-\tau_{x1}\left(t\right)\right) \\ x^{(0\sim n-1)}\left(t-\tau_{x2}\left(t\right)\right) \\ \vdots \\ x^{(0\sim n-1)}\left(t-\tau_{x\gamma_x}\left(t\right)\right) \end{bmatrix}, \tag{2}$$

$$\zeta_y\triangleq\begin{bmatrix} y\left(t-\tau_{y1}\left(t\right)\right) \\ y\left(t-\tau_{y2}\left(t\right)\right) \\ \vdots \\ y\left(t-\tau_{y\gamma_y}\left(t\right)\right) \end{bmatrix}, \tag{3}$$

with $\tau_{xi}\left(t\right),i=1,2,...,\gamma_x$, and $\tau_{yi}\left(t\right),i=1,2,...,\gamma_y$, being sets of nonnegative scalar functions. Furthermore, $f\left(x^{(0\sim n-1)},\zeta_x,t\right)$ is a nonlinear function, and $B\left(y,\zeta_y,t\right)$ is a matrix function satisfying the following assumptions.

Assumption 2.1. $\det B\left(y,\zeta_y,t\right)\neq 0$ or ∞, for all $y\in\mathbb{R}^m$, $\zeta_y\in\mathbb{R}^{m\gamma_y}$, and $t\geq 0$.

Assumption 2.2. There exist a scalar $\rho>0$ and a convex subset $\Omega\subseteq\mathbb{R}^{nr}$ containing the origin such that:

$$\begin{aligned} &\left\|f\left(x_1^{(0\sim n-1)},\zeta_{x_1},t\right)-f\left(x_2^{(0\sim n-1)},\zeta_{x_2},t\right)\right\| \\ \leqslant\ &\rho\left\|x_1^{(0\sim n-1)}-x_2^{(0\sim n-1)}\right\|, \end{aligned} \tag{4}$$

holds for $\forall x_1^{(0\sim n-1)},x_2^{(0\sim n-1)}\in\Omega$.

The observer-based dynamical output controller for system (1) can be designed as

$$\begin{cases} u=-B^{-1}\left(\cdot\right)\left(f\left(\hat{x}^{(0\sim n-1)},\hat{\zeta}_x,t\right)+v\right) \\ v=A_{0\sim n-1}\hat{x}^{(0\sim n-1)} \\ \dot{\hat{x}}^{(0\sim n-1)}=\Phi\left(A_{0\sim n-1}\right)\hat{x}^{(0\sim n-1)} \\ \qquad\qquad -L\left(y-C_{0\sim n-1}\hat{x}^{(0\sim n-1)}\right), \end{cases} \tag{5}$$

where $\hat{x}^{(0\sim n-1)}$ is the estimation of $x^{(0\sim n-1)}$, and $A_{0\sim n-1}\in\mathbb{R}^{r\times nr}$ and $L\in\mathbb{R}^{nr\times m}$ are matrices to be designed.

With the above controller, system (1) becomes

$$x^{(n)}=-A_{0\sim n-1}\hat{x}^{(0\sim n-1)}+\Delta f\left(\cdot\right), \tag{6}$$

where

$$\begin{aligned} \Delta f\left(\cdot\right) &\triangleq \Delta f\left(x^{(0\sim n-1)},\hat{x}^{(0\sim n-1)},\zeta_x,\hat{\zeta}_x,t\right) \\ &= f\left(x^{(0\sim n-1)},\zeta_x,t\right)-f\left(\hat{x}^{(0\sim n-1)},\hat{\zeta}_x,t\right). \end{aligned} \tag{7}$$

Note that the state-space form of (6) is

$$\begin{aligned} \dot{x}^{(0\sim n-1)} &= \Phi\left(0_{0\sim n-1}\right)x^{(0\sim n-1)} \\ &\quad +B_c\left(\Delta f\left(\cdot\right)-A_{0\sim n-1}\hat{x}^{(0\sim n-1)}\right). \end{aligned} \tag{8}$$

The closed-loop system is obviously composed of

$$\begin{aligned} \dot{\hat{x}}^{(0\sim n-1)} &= \Phi\left(A_{0\sim n-1}\right)\hat{x}^{(0\sim n-1)} \\ &\quad -LC_{0\sim n-1}\left(x^{(0\sim n-1)}-\hat{x}^{(0\sim n-1)}\right), \end{aligned} \tag{9}$$

and

$$\begin{aligned} \dot{x}^{(0\sim n-1)} &= \Phi\left(0_{0\sim n-1}\right)x^{(0\sim n-1)} \\ &\quad +B_c\left(\Delta f\left(\cdot\right)-A_{0\sim n-1}\hat{x}^{(0\sim n-1)}\right). \end{aligned} \tag{10}$$

Then, we impose the following assumption, which plays a role in the subsequent stability analysis.

Assumption 2.3. The matrix pair $\left(\Phi\left(0_{0\sim n-1}\right),C_{0\sim n-1}\right)$ is observable.

Based on the above preparation, we can now state the problem to be solved in this paper as follows.

Problem 2.4. Under Assumptions 2.1-2.3, find a dynamical output controller in the form of (5) such that the closed-loop system (9)-(10) is uniformly exponentially stable.

3 Preliminaries

For observer-based control of FAS (1), the following preliminary results proposed in [18] are needed.

Lemma 3.1 ([18])**.** Let $A\in\mathbb{R}^{n\times n}$ satisfy

$$\mathrm{Re}\ \lambda_i\left(A\right)\leq-\frac{\gamma}{2},\ i=1,2,\cdots,n, \tag{11}$$

where $\gamma>0$, then there exists a positive definite matrix $P\in\mathbb{R}^{n\times n}$ satisfying

$$A^{\mathrm{T}}P+PA\leq-\gamma P. \tag{12}$$

Lemma 3.2 ([18])**.** For any $\mu_c>0$, there exist a set of matrices $A_i\in\mathbb{R}^{r\times r},\ i=0,1,\cdots,n-1$, satisfying

$$\mathrm{Re}\ \lambda_i\left(\Phi\left(A_{0\sim n-1}\right)\right)\leq-\frac{\mu}{2},\ i=1,2,\cdots,nr. \tag{13}$$

It is known from Lemma 3.1 that, when the condition in (13) holds for some $\mu_c>0$, there exists a positive definite matrix $P^{\mathrm{c}}\triangleq P^{\mathrm{c}}(A_{0\sim n-1})$ satisfying

$$\Phi^{\mathrm{T}}\left(A_{0\sim n-1}\right)P^{\mathrm{c}}+P^{\mathrm{c}}\Phi\left(A_{0\sim n-1}\right)\leq-\mu_{\mathrm{c}}P^{\mathrm{c}}. \tag{14}$$

Similarly, due to Assumption 2.3, there exists a $L \in \mathbb{R}^{nr\times m}$ satisfying

$$\mathrm{Re}\ \lambda_i\left(\Phi\left(0_{0\sim n-1}\right)+LC_{0\sim n-1}\right)\leq -\frac{\mu_{\mathrm{o}}}{2},\ i=1,2,\cdots,nr. \tag{15}$$

Then it follows Lemma 3.1 again that there exists a positive definite matrix P^{o} satisfying

$$\begin{aligned}&\left(\Phi\left(0_{0\sim n-1}\right)+LC_{0\sim n-1}\right)^{\mathrm{T}}P^{\mathrm{o}}+P^{\mathrm{o}}\left(\Phi\left(0_{0\sim n-1}\right)\right.\\&\quad\left.+LC_{0\sim n-1}\right)\leq -\mu_{\mathrm{o}}P^{\mathrm{o}}.\end{aligned} \tag{16}$$

4 Solution to Problem

This section treats the observer-based control design. Firstly, we convert the closed-loop system (9)-(10) to obtain an augmented system. Then we discuss the stability of the augmented system.

4.1 The Augmented System

Define the observation error vector

$$\tilde{x}^{(0\sim n-1)}=x^{(0\sim n-1)}-\hat{x}^{(0\sim n-1)}. \tag{17}$$

Then by Assumption 2.2, we have

$$\begin{aligned}&\left\|f\left(x^{(0\sim n-1)},\zeta_x,t\right)-f\left(\hat{x}^{(0\sim n-1)},\hat{\zeta}_x,t\right)\right\|\\\leqslant\ &\rho\left\|\tilde{x}^{(0\sim n-1)}\right\|,\end{aligned} \tag{18}$$

and the second equation of (5) can be written as

$$\begin{aligned}\dot{\hat{x}}^{(0\sim n-1)}&=\Phi\left(A_{0\sim n-1}\right)\hat{x}^{(0\sim n-1)}\\&\quad -LC_{0\sim n-1}\tilde{x}^{(0\sim n-1)}.\end{aligned} \tag{19}$$

Since

$$\Phi\left(A_{0\sim n-1}\right)=\Phi\left(0_{0\sim n-1}\right)-B_cA_{0\sim n-1}, \tag{20}$$

the observer equation (19) can be rewritten as

$$\begin{aligned}\dot{\hat{x}}^{(0\sim n-1)}&=\Phi\left(0_{0\sim n-1}\right)\hat{x}^{(0\sim n-1)}\\&\quad -LC_{0\sim n-1}\tilde{x}^{(0\sim n-1)}\\&\quad -B_cA_{0\sim n-1}\hat{x}^{(0\sim n-1)}.\end{aligned} \tag{21}$$

Meanwhile, it follows from (8) and (21) that

$$\begin{aligned}\dot{\tilde{x}}^{(0\sim n-1)}&=\left(\Phi\left(0_{0\sim n-1}\right)+LC_{0\sim n-1}\right)\tilde{x}^{(0\sim n-1)}\\&\quad +B_c\Delta f\left(\cdot\right).\end{aligned} \tag{22}$$

By combining the above with (19), we obtain the following closed-loop system

$$\begin{cases}\dot{\hat{x}}^{(0\sim n-1)}=\Phi\left(A_{0\sim n-1}\right)\hat{x}^{(0\sim n-1)}-LC_{0\sim n-1}\tilde{x}^{(0\sim n-1)}\\ \dot{\tilde{x}}^{(0\sim n-1)}=\left(\Phi\left(0_{0\sim n-1}\right)+LC_{0\sim n-1}\right)\tilde{x}^{(0\sim n-1)}\\ \qquad\qquad +B_c\Delta f\left(\cdot\right).\end{cases} \tag{23}$$

Define

$$X=\left[\begin{array}{c}\hat{x}^{(0\sim n-1)}\\ \tilde{x}^{(0\sim n-1)}\end{array}\right], \tag{24}$$

then we can obtain the following augmented system

$$\begin{aligned}\dot{X}&=\left[\begin{array}{cc}\Phi\left(A_{0\sim n-1}\right)&-LC_{0\sim n-1}\\0&\Phi\left(0_{0\sim n-1}\right)+LC_{0\sim n-1}\end{array}\right]X\\&\quad+\left[\begin{array}{c}0\\B_c\Delta f\left(\cdot\right)\end{array}\right],\end{aligned} \tag{25}$$

where $\Delta f\left(\cdot\right)$ satisfies (18).

4.2 Uniformly Exponential Stability

Regarding the stability of the above system (25), we have the following result.

Theorem 4.1. Suppose that Assumptions 2.1-2.3 hold. Let
1. μ_{c} and μ_{o} be two positive numbers;
2. $A_{0\sim n-1}\in\mathbb{R}^{r\times nr}$ and $L\in\mathbb{R}^{nr\times m}$ be two matrices satisfying (13) and (15), respectively; and
3. P^{c} and P^{o} be two matrices satisfying (14), (16) and

$$\begin{cases}\mu_{\mathrm{c}}-\lambda_{\max}\left(P^{\mathrm{c}}\right)>0\\ \mu_{\mathrm{o}}-\dfrac{2\rho\left\|P^{\mathrm{o}}B_c\right\|}{\lambda_{\min}\left(P^{\mathrm{o}}\right)}-\dfrac{\left\|LC_{0\sim n-1}\right\|^2}{\lambda_{\min}\left(P^{\mathrm{o}}\right)}>0.\end{cases} \tag{26}$$

Then, the observer-based controller (5) guarantees that system (25) is uniformly exponentially stable.

Proof. Since $A_{0\sim n-1}\in\mathbb{R}^{r\times nr}$ and $L\in\mathbb{R}^{nr\times m}$ respectively satisfy (13) and (15), there exist two positive definite matrices P^{c} and P^{o} satisfying (14) and (16), respectively. Then the following Lyapunov function can be chosen for the system (25):

$$V=V_1+V_2, \tag{27}$$

where

$$V_1=\frac{1}{2}\left(\hat{x}^{(0\sim n-1)}\right)^{\mathrm{T}}P^{\mathrm{c}}\hat{x}^{(0\sim n-1)}, \tag{28}$$

and

$$V_2=\frac{1}{2}\left(\tilde{x}^{(0\sim n-1)}\right)^{\mathrm{T}}P^{\mathrm{o}}\tilde{x}^{(0\sim n-1)}. \tag{29}$$

In view of (14) and (19), we have

$$\begin{aligned}\dot{V}_1&=\frac{1}{2}\left(\hat{x}^{(0\sim n-1)}\right)^{\mathrm{T}}\left(\Phi^{\mathrm{T}}\left(A_{0\sim n-1}\right)P^{\mathrm{c}}\right.\\&\quad\left.+P^{\mathrm{c}}\Phi\left(A_{0\sim n-1}\right)\right)\hat{x}^{(0\sim n-1)}\\&\quad-\left(\hat{x}^{(0\sim n-1)}\right)^{\mathrm{T}}P^{\mathrm{c}}LC_{0\sim n-1}\tilde{x}^{(0\sim n-1)}\\&\leq-\frac{\mu_{\mathrm{c}}}{2}\left(\hat{x}^{(0\sim n-1)}\right)^{\mathrm{T}}P^{\mathrm{c}}\hat{x}^{(0\sim n-1)}+W,\end{aligned} \tag{30}$$

where

$$W=-\left(\hat{x}^{(0\sim n-1)}\right)^{\mathrm{T}}P^{\mathrm{c}}LC_{0\sim n-1}\tilde{x}^{(0\sim n-1)}.$$

Using Young's inequality, and the following relations

$$\begin{aligned}&\left(\hat{x}^{(0\sim n-1)}\right)^{\mathrm{T}}P^{\mathrm{c}}\left(P^{\mathrm{c}}\right)^{\mathrm{T}}\hat{x}^{(0\sim n-1)}\\\leq\ &\lambda_{\max}\left(P^{\mathrm{c}}\right)\left(\hat{x}^{(0\sim n-1)}\right)^{\mathrm{T}}P^{\mathrm{c}}\hat{x}^{(0\sim n-1)},\end{aligned} \tag{31}$$

$$\begin{aligned}&\lambda_{\min}\left(P^{\mathrm{o}}\right)\left(\tilde{x}^{(0\sim n-1)}\right)^{\mathrm{T}}\tilde{x}^{(0\sim n-1)}\\\leq\ &\left(\tilde{x}^{(0\sim n-1)}\right)^{\mathrm{T}}P^{\mathrm{o}}\tilde{x}^{(0\sim n-1)},\end{aligned} \tag{32}$$

we can obtain

$$\begin{aligned}W&\leq\frac{1}{2}\left(\hat{x}^{(0\sim n-1)}\right)^{\mathrm{T}}P^{\mathrm{c}}\left(P^{\mathrm{c}}\right)^{\mathrm{T}}\hat{x}^{(0\sim n-1)}\\&\quad+\frac{1}{2}\left\|LC_{0\sim n-1}\tilde{x}^{(0\sim n-1)}\right\|^2\\&\leq\frac{1}{2}\lambda_{\max}\left(P^{\mathrm{c}}\right)\left(\hat{x}^{(0\sim n-1)}\right)^{\mathrm{T}}P^{\mathrm{c}}\hat{x}^{(0\sim n-1)}\\&\quad+\frac{\left\|LC_{0\sim n-1}\right\|^2}{2\lambda_{\min}\left(P^{\mathrm{o}}\right)}\left(\tilde{x}^{(0\sim n-1)}\right)^{\mathrm{T}}P^{\mathrm{o}}\tilde{x}^{(0\sim n-1)}\end{aligned} \tag{33}$$

Then it follows from (30) that

$$\begin{aligned}\dot{V}_1 &\leq -\frac{1}{2}\left(\mu_{\mathrm{c}}-\lambda_{\max}\left(P^{\mathrm{c}}\right)\right)\left(\hat{x}^{(0\sim n-1)}\right)^{\mathrm{T}}P^{\mathrm{c}}\hat{x}^{(0\sim n-1)}\\ &\quad+\frac{1}{2}\frac{\left\|LC_{0\sim n-1}\right\|^2}{\lambda_{\min}\left(P^{\mathrm{o}}\right)}\left(\tilde{x}^{(0\sim n-1)}\right)^{\mathrm{T}}P^{\mathrm{o}}\tilde{x}^{(0\sim n-1)}. \quad (34)\end{aligned}$$

In view of (16), (18), (22), and (32), we have

$$\begin{aligned}\dot{V}_2 &= \frac{1}{2}\left(\tilde{x}^{(0\sim n-1)}\right)^{\mathrm{T}}\left(\left(\Phi\left(0_{0\sim n-1}\right)+LC_{0\sim n-1}\right)^{\mathrm{T}}P^{\mathrm{o}}\right.\\ &\quad\left.+P^{\mathrm{o}}\left(\Phi\left(0_{0\sim n-1}\right)+LC_{0\sim n-1}\right)\right)\tilde{x}^{(0\sim n-1)}\\ &\quad+\left(\tilde{x}^{(0\sim n-1)}\right)^{\mathrm{T}}P^{\mathrm{o}}B_c\Delta f\left(\cdot\right)\\ &\leq -\frac{\mu_{\mathrm{o}}}{2}\left(\tilde{x}^{(0\sim n-1)}\right)^{\mathrm{T}}P^{\mathrm{o}}\tilde{x}^{(0\sim n-1)}\\ &\quad+\rho\left\|P^{\mathrm{o}}B_c\right\|\left\|\tilde{x}^{(0\sim n-1)}\right\|^2\\ &\leq -\frac{\mu_{\mathrm{o}}}{2}\left(\tilde{x}^{(0\sim n-1)}\right)^{\mathrm{T}}P^{\mathrm{o}}\tilde{x}^{(0\sim n-1)}\\ &\quad+\frac{\rho\left\|P^{\mathrm{o}}B_c\right\|}{\lambda_{\min}\left(P^{\mathrm{o}}\right)}\left(\tilde{x}^{(0\sim n-1)}\right)^{\mathrm{T}}P^{\mathrm{o}}\tilde{x}^{(0\sim n-1)}. \quad (35)\end{aligned}$$

Combining (34) and (35), gives

$$\begin{aligned}\dot{V} &\leq -\frac{1}{2}\left(\mu_{\mathrm{c}}-\lambda_{\max}\left(P^{\mathrm{c}}\right)\right)\left(\hat{x}^{(0\sim n-1)}\right)^{\mathrm{T}}P^{\mathrm{c}}\hat{x}^{(0\sim n-1)}\\ &\quad+\frac{1}{2}\frac{\left\|LC_{0\sim n-1}\right\|^2}{\lambda_{\min}\left(P^{\mathrm{o}}\right)}\left(\tilde{x}^{(0\sim n-1)}\right)^{\mathrm{T}}P^{\mathrm{o}}\tilde{x}^{(0\sim n-1)}\\ &\quad-\frac{\mu_{\mathrm{o}}}{2}\left(\tilde{x}^{(0\sim n-1)}\right)^{\mathrm{T}}P^{\mathrm{o}}\tilde{x}^{(0\sim n-1)}\\ &\quad+\frac{\rho\left\|P^{\mathrm{o}}B_c\right\|}{\lambda_{\min}\left(P^{\mathrm{o}}\right)}\left(\tilde{x}^{(0\sim n-1)}\right)^{\mathrm{T}}P^{\mathrm{o}}\tilde{x}^{(0\sim n-1)}\\ &= -\frac{1}{2}\left(\mu_{\mathrm{c}}-\lambda_{\max}\left(P^{\mathrm{c}}\right)\right)\left(\hat{x}^{(0\sim n-1)}\right)^{\mathrm{T}}P^{\mathrm{c}}\hat{x}^{(0\sim n-1)}\\ &\quad-\frac{1}{2}\varpi\left(\tilde{x}^{(0\sim n-1)}\right)^{\mathrm{T}}P^{\mathrm{o}}\tilde{x}^{(0\sim n-1)}, \quad (36)\end{aligned}$$

where

$$\varpi=\mu_{\mathrm{o}}-\frac{2\rho\left\|P^{\mathrm{o}}B_c\right\|}{\lambda_{\min}\left(P^{\mathrm{o}}\right)}-\frac{\left\|LC_{0\sim n-1}\right\|^2}{\lambda_{\min}\left(P^{\mathrm{o}}\right)}.$$

If (26) holds, then we have

$$\dot{V}\leq -kV, \quad (37)$$

where

$$k=\min\left\{\mu_{\mathrm{c}}-\lambda_{\max}\left(P^{\mathrm{c}}\right),\varpi\right\}>0. \quad (38)$$

Based on the Comparison Theorem, we have from (37) that

$$V\leq V\left(0\right)e^{-kt},$$

thus the conclusion is easily obtained. Then the proof is completed. □

Remark 4.2. If Assumption 2.2 is assumed to be globally satisfied, then the closed-loop system is uniformly globally exponentially stable, which is distinct from other reported boundedness in various senses such as semi-global boundedness [21] and global ultimately uniformly boundedness [11].

5 An Illustrative Example

The following thermoacoustic instability system in [19], that is, a Rijke tube, is used to illustrate the effectiveness of the proposed observer-based controller.

$$\begin{cases}\ddot{\eta}_1=f_1\left(\eta_{1\sim 2}^{(0\sim 1)}\left(t-\tau\right)\right)+q_1\left(\eta_1^{(0\sim 1)}\left(t\right)\right)+u_1\\ \ddot{\eta}_2=f_2\left(\eta_{1\sim 2}^{(0\sim 1)}\left(t-\tau\right)\right)+q_2\left(\eta_2^{(0\sim 1)}\left(t\right)\right)+u_2,\end{cases} \quad (39)$$

where $\eta=\left[\begin{array}{cc}\eta_1 & \eta_2\end{array}\right]^{\mathrm{T}}$, with $\eta_i,\dot{\eta}_i$ denoting the amplitude of velocity and pressure fluctuation of the i-th order acoustic mode, respectively, u_1,u_2 are the control inputs, and

$$\begin{cases}f_i\left(\eta_{1\sim 2}^{(0\sim 1)}\left(t-\tau\right)\right)=-2i\pi\left(\gamma-1\right)\dot{Q}_{si}\left(t-\tau\right)\sin\left(i\pi x_f\right)\\ q_i\left(\eta_i^{(0\sim 1)}\left(t\right)\right)=-\left[\begin{array}{cc}\left(i\pi\right)^2 & \epsilon_i\end{array}\right]\eta_i^{(0\sim 1)},\ i=1,2,\end{cases}$$

with γ being the specific heat ratio of the medium, x_f being the location of the heat source, ϵ_i, $i=1,2$ denoting the damping coefficient, and τ representing the dimensionless time delay between heat transfer and flow field velocity. We assume the output of system (39) to be

$$\begin{cases}y=C_{0\sim 1}\eta^{(0\sim 1)}\\ C_{0\sim 1}=\left[\begin{array}{cccc}1&0&0&0\\0&1&0&0\end{array}\right].\end{cases}$$

Additionally, $\dot{Q}_{si}\left(t-\tau\right)$, $i=1,2$, are the nondimensional heat release rates in the following form of

$$\begin{aligned}\dot{Q}_{si}\left(t-\tau\right) &= \frac{2L_\omega\left(T_\omega-\bar{T}_0\right)}{\sqrt{3\upsilon_0}\gamma P_0 S}\sqrt{\pi\lambda C_\upsilon\rho_0\frac{d_\omega}{2}}\\ &\quad\times\left(\sqrt{\left|\frac{1}{3}+\upsilon_{fi}\left(t-\tau\right)\right|}-\sqrt{\frac{1}{3}}\right), \quad (40)\end{aligned}$$

where L_ω, d_ω and T_ω are the dimensionless length, diameter and temperature of the heating coil, respectively, $\bar{T}_0$ is the average temperature of the surrounding air, υ_0,P_0 are the mean value of velocity and pressure, C_υ is the specific heat capacity, S denotes the cross-sectional area of the tube, ρ_0 represents the average density of the gas, and λ is the thermal conductivity of air.

As pointed out in [20], if $\left|\upsilon_{fi}\left(t-\tau\right)\right|<0.3$, we have

$$\begin{aligned}\upsilon_{fi}\left(t-\tau\right) &\approx \upsilon_{fi}\left(t\right)-\tau\dot{\upsilon}_{fi}\left(t\right)\\ &= \eta_i\cos\left(\pi x_f\right)-\tau\dot{\eta}_i\cos\left(\pi x_f\right),\end{aligned}$$

and (40) can be rewritten as

$$\begin{aligned}\dot{Q}_{si}\left(t-\tau\right) &= \frac{2L_\omega\left(T_\omega-\bar{T}_0\right)}{\sqrt{3\upsilon_0}\gamma P_0 S}\sqrt{\pi\lambda C_\upsilon\rho_0\frac{d_\omega}{2}}\\ &\quad\times\left(\sqrt{\frac{1}{3}+\eta_i\cos\left(\pi x_f\right)-\tau\dot{\eta}_i\cos\left(\pi x_f\right)}\right.\\ &\quad\left.-\sqrt{\frac{1}{3}}\right). \quad (41)\end{aligned}$$

It can be easily verified that the matrix pair $\left(\Phi\left(0_{0\sim 1}\right),C_{0\sim 1}\right)$ is observable and Assumption 2.2 also holds.

In the simulation, the physical parameters listed in Table 1 are considered [20]. Applying Theorem 4.1, we choose the following control parameters

$$\begin{cases} A_{0\sim1} = \begin{bmatrix} 3 & 0 & 4 & 0 \\ 0 & 8 & 0 & 6 \end{bmatrix} \\ L = \begin{bmatrix} -17 & 0 & -70 & 0 \\ 0 & -8 & 0 & -15 \end{bmatrix}^{\mathrm{T}}. \end{cases}$$

Besides, the initial values are selected as $\eta^{(0\sim1)}(0) = \begin{bmatrix} 0.5 & 0.2 & 0.05 & -0.1 \end{bmatrix}^{\mathrm{T}}$ and $\hat{\eta}^{(0\sim1)}(0) = \begin{bmatrix} 0 & 0 & 0 & 0 \end{bmatrix}^{\mathrm{T}}$.

The results are shown in Figs. 1-3. Figs. 1-2 depict the time responses of velocity amplitude and pressure amplitude, where $\hat{\eta}^{(0\sim1)}$ is the estimation of $\eta^{(0\sim1)}$. Commensurate with the aforementioned analysis, the proposed observer-based controller ensures that $\hat{\eta}^{(0\sim1)}$ tracks exponentially the actual state, and $\eta^{(0\sim1)}$ converges exponentially to zero in about 5 seconds without overshoot. Also, it is seen from Fig. 3 that the control magnitudes required are still in a reasonable range.

Table 1: Physical parameters

Parameter	Value	Parameter	Value
L_ω	2.5 m	S	0.00156 m^2
d_ω	0.0005 m	ρ_0	1.225 kg/m
T_ω	1680 K	x_f	0.25 m
T_0	295 K	λ	0.0328 W/(mK)
v_0	0.3 m/s	τ	0.2 s
P_0	86900 Pa	ϵ_1	0.044
C_v	719 J/(kgK)	ϵ_2	0.1657
γ	1.4		

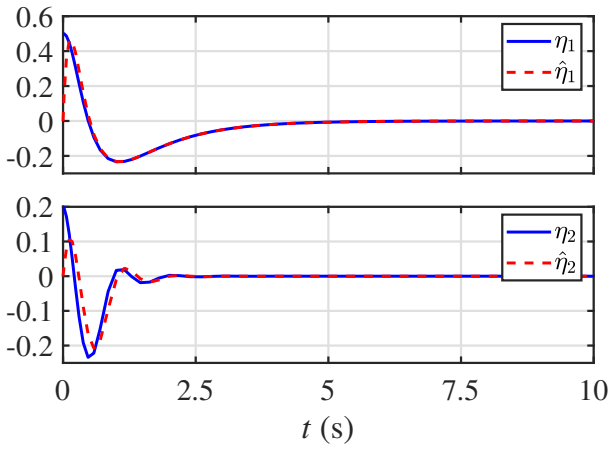

Fig. 1: Response of η and $\hat{\eta}$

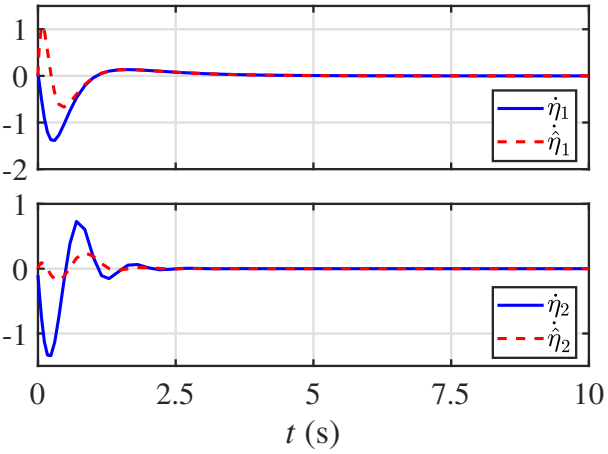

Fig. 2: Response of $\dot{\eta}$ and $\dot{\hat{\eta}}$

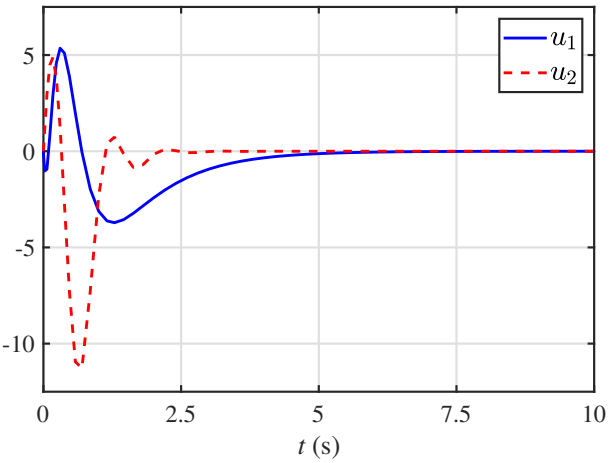

Fig. 3: Control inputs

6 Conclusion

In this paper, an observer-based control method is proposed for FASs with time-varying delays. The control scheme consists of an observer equation using output information and a feedback controller with full-actuation property. The application of the parametric approach provides rich design degrees of freedom for the selection of control parameters. The effectiveness of the proposed method is demonstrated by stability analysis and simulations of the thermoacoustic system. In future work, we will consider the observer-based control of continuous-time systems with both state delays and input delays and try to make assumptions required more relax. Furthermore, the corresponding results could also be extended to multi-order FASs, even sub-FASs, which only partially satisfy the full-actuation condition.

References

[1] Y. G. Sun, J. Q. Xu, G. B. Lin, W. Jin, and L. K. Wang, RBF neural network-based supervisor control for maglev vehicles on an elastic track with network time delay, *IEEE Transactions on Industrial Informatics*, 2022, 18(1): 509–519.

[2] Y. G. Sun, J. Q. Xu, C. Chen, and W. Hu, Reinforcement learning-based optimal tracking control for levitation system of maglev vehicle with input time delay, *IEEE Transactions on Instrumentation and Measurement*, 2022, 71: 7500813.

[3] H. Katayama, Design of reduced-order observers for nonlinear sampled-data strict-feedback systems with actuator dynamics and disturbances, *International Journal of Control*, 2019, 92(9): 2112–2122.

[4] G. R. Duan, High-order system approaches: III. Observability and observer design, *ACTA Automatica Sinica (in Chinese)*, 2020, 46(9): 1885–1895.

[5] G. R. Duan, Robust stabilization of time-varying nonlinear systems with time-varying delays: A fully actuated system approach, *IEEE Transactions on Cybernetics*, DOI: 10.1109/TCYB.2022.3217317.

[6] G. R. Duan, High-order fully actuated system approaches: Part I. Models and basic procedure, *International Journal of Systems Science*, 2020, 52(2): 422–435.

[7] T. Y. Zhao, G. R. Duan, and W. Q. Xin, Observer-based control for high-order fully actuated systems, *IEEE ACCESS*, 2023, 11: 132239–132253.

[8] H. Jiang and G. R. Duan, Output tracking based on generalized proportional-integral observer for fully actuated systems, in *2023 2nd Conference on Fully Actuated System Theory and Applications*, 2023: 117–121.

[9] Y. P. Yang, X. H. Yu, Y. Li, S. C. Yang, Z. Li, and H. J. Gao, Angular acceleration observer design for Jerk-level control of tiltrotors based on the high-order fully actuated system approaches, in *Proceedings of 2022 Chinese Automation Congress*, 2022: 3750–3755.

[10] Q. Zhao and G. R. Duan, Fully actuated system approach for 6DOF spacecraft control based on extended state observer, *Journal of Systems Science and Complexity*, 2022, 35(2): 604–622.

[11] M. Cai, X. He, and D. H. Zhou, Fault-tolerant tracking control for nonlinear observer-extended high-order fully-actuated systems, *Journal of the Franklin Institute*, 2023, 360: 136–153.

[12] C. Li, X. N. Shen, F. Yan, Y. B. Gao, and J. X. Liu, Observer-based control of PEMFC air feed systems via high-order fully actuated system approaches, in *2023 2nd Conference on Fully Actuated System Theory and Applications*, 2023: 711–716.

[13] G. Q. Liu, K. Zhang, and B. Li, Fully-actuated system approach based optimal attitude tracking control of rigid spacecraft with actuator saturation, *Journal of Systems Science and Complexity*, 2022, 35(2): 688–702.

[14] D. W. Zhang and G. P. Liu, Predictive control for networked high-order fully actuated systems subject to communication delays and external disturbances, *ISA Transactions*, 2023, 139: 425–435.

[15] S. W. Chen, W. Wang, J. F. Fan, and Y. Ji, Impact angle constraint guidance law using fully-actuated system approach, *Aerospace Science and Technology*, 2023, 136: 108220.

[16] F. Adiguzel and Y. Yalcin, Immersion and invariance disturbance observer-based nonlinear discrete-time control for fully actuated mechanical systems, *International Journal of Systems Science*, 2022, 53(2): 388–401.

[17] K. X. Cui and G. R. Duan, Adaptive disturbance observer design for discrete-time high-order fully actuated systems based on LMI and its application to combined spacecrafts, in *2023 2nd Conference on Fully Actuated System Theory and Applications*, 2023: 12-17.

[18] G. R. Duan, High-order fully actuated system approaches: Part III. Robust control and high-order backstepping, *International Journal of Systems Science*, 2020, 52(5): 952–971.

[19] Y. Z. Zhao, D. Ma, and Y. W. Zhang, Adaptive asymptotic stabilization of uncertain nonstrict feedback nonlinear HOFA systems with time delays, *Nonlinear Dynamics*, 2023, 11: 14139–14153.

[20] Y. Z. Zhao, D. Ma, and H. Ma, Adaptive neural network control of thermoacoustic instability in rijke tube: A fully actuated system approach, *Journal of Systems Science and Complexity*, 2022, 35(2): 586–603.

[21] B. Chen, H. G. Zhang, and C. Lin, Observer-based adaptive neural network control for nonlinear systems in nonstrict-feedback form, *IEEE Transactions on Neural Networks and Learning Systems*, 2016, 27(1): 89–98.

Proceedings of the 3rd Conference on Fully Actuated System Theory and Applications
May 10-12, 2024, Shenzhen, China

Tracking Control of Unmanned Surface Vessels Based on Fully Actuated System Approaches

Zijing Li[1], Jing Zhu[1], Xiangping Zhai[2], Hongwei Zhang[3]

1. College of Automation Engineering, Nanjing University of Aeronautics and Astronautics, Nanjing 211106, China
E-mail: drzhujing@nuaa.edu.cn

2. College of Computer Science and Technology, Nanjing University of Aeronautics and Astronautics, Nanjing 211106, China
E-mail: blueicezhaixp@nuaa.edu.cn

3. School of Mechanical Engineering and Automation, Harbin Institute of Technology, Shenzhen, Guangdong 518055, P.R. China
E-mail: hwzhang@hit.edu.cn

Abstract: Considering the complication and high requirements of controller design in unmanned surface vessels (USVs) from the perspective of under-actuated model, this paper investigates the tracking control of USVs in terms of fully actuated system approaches (FASA). We firstly propose a high-order fully actuated (HOFA) model of USV for path tracking. Then, using the idea and method of FASA controller design, a control law is proposed to make the closed-loop system obtain the dynamic characteristics we expect and decouple it into two linear systems, which can be achieved with simple and easy computation. The proposed USV path tracking control law achieves global asymptotic stability without continuous angular and forward velocity excitations. The effectiveness of this method is verified through MATLAB simulation.

Key Words: FASA, USVs, HOFA, model transformation

1 Introduction

Unmanned surface vessels (USVs) are water-body working systems without on board crew, which have been widely used in large applications, ranging from military to civilian in reconnaissance, patrol, surveillance, search and rescue, just to name a few [1]. Therefore, more and more attentions have been drawn on the fully autonomous capabilities for USVs to realize operations in various complex environments.

Control system is fundamental and crucial for the autonomy in USVs [2]. However, the designing of control system for most USVs can be quite challenging. Firstly, the dynamic model of USVs is rather special. For a conventional USV, the propulsion device is either a propeller with a rudder or water jets, which means there is no device applying force for side motion. The above configuration is embodied as only two independent control inputs therein the three-degree-of-freedoms (3-DOF) mathematical model for USVs. Thus, the dynamic model for USV is typically described as a 3-DOF under-actuated first-order system with second-order nonholonomic acceleration constraints. Additionally, various uncertainties such as modeling inaccuracy, unmodeled dynamics, modification in physical parameters as well as external disturbance caused by wind, waves, and currents affect the performance of the control system.

Path tracking control is one of the typical application scenarios for USVs [3] with a control target of following a desired 2-D path and stabilize the heading dynamics [4]. Different control strategies and algorithms have been proposed [5,6,7,8,9,10,11,12] to solve the path following issue for USVs at present by adding diffeomorphism transformation, taking backstepping method, sliding mode method, adaptive method [13,14], artificial neural network and other methods on the basis of Lyapunov direct method [15]. However, applying these methods to the controller design process can be rather complicated: it is often necessary to do proper subsystem division and set up multiple virtual control quantities. Besides, some of the above controllers are designed under the persistent excitation condition of yaw velocities in USVs, which means that the control system can only complete the working condition of curve path tracking. Additionally, the problem of external interference is not considered or only be considered under the assumption of constant interference.

In this paper, a newly proposed control theory-fully actuated system approaches (FASA) is considered to be applied on the path tracking issue of under-actuated USVs, since its property of controller-oriented enables us to avoid hierarchical design for controller and its fully-actuated property enables the controller designed without the assumption of persistent excitation for surge or yaw velocities at the same time. The FASA demands establishing a high-order fully actuated (HOFA) model firstly, and then, it is easy to design the control law to eliminate the dynamic characteristics (including nonlinear ones) of the open loop system and a new expected closed loop system with arbitrarily assignable eigenstructures can be achieved by properly selecting parameters in the control law.

This paper is structured as follows. High-order fully actuated system approaches is briefly reviewed and the conventional under-actuated USV model is addressed in Section 2. A forth-order fully actuated system for USVs and a HOFA controller design approach for the path tracking of USVs, which does not require hierarchical design and

*This work is supported in part by the Science Center Program of National Natural Science Foundation of China under Grant 62188101, in part by the Natural minimize the completion time and mission latency respectively 61 Science Foundation of Jiangsu Province of China under Grants BK20222012 and BK20231439, and in part by the Fundamental Research Funds for the Central Universities under Grant NS2023052.

persistent excitation for surge or yaw velocities is proposed in Section 3. Numerical simulations for two working conditions of USV path tracking control-linear and curved path tracking, are presented to demonstrate the effectiveness of the proposed HOFA controller in Section 4, and this paper is concluded in Section 5.

The contribution of this paper is applying a novel control theory-fully actuated system to path tracking control issue of USVs, which effectively simplifies the controller design process and relaxes the controller design condition as well.

2 Preliminaries

This section briefly reviews modeling and control of HOFA systems with some definitions and lemmas, then introduces the first-order USV model prepared for the HOFA model transforming.

2.1 Modeling and control of HOFA systems

Definition 1 [17]: For a general nonlinear system in the affine form shown as following,

$$x^{(m)} = f(x,\dot{x},\cdots,x^{(m-1)},t) + B(x,x,\dot{x},\cdots,x^{(m-1)},t)u \tag{1}$$

where $x \in \mathbb{R}^n$ is the state vector, $u \in \mathbb{R}^r$ is the system input vector, $f(x,\dot{x},\cdots,x^{(m-1)},t) \in \mathbb{R}^n$ is a sufficiently differentiable vector function, and $B(x,x,\dot{x},\cdots,x^{(m-1)},t) \in \mathbb{R}^{n\times r}$ is a matrix function, if

$$\begin{cases} n = r \\ rank(B(x,x,\dot{x},\cdots,x^{(m-1)},t)) = r \end{cases} \tag{2}$$

system (1) is called fully actuated.

Lemma 1 [18]: Let $A_i \in \mathbb{R}^{r\times r}, i = 0,1,\cdots,m-1$, be a series of matrixes which can be designed in need, then the following controller

$$u = -B^{-1}(\cdot)[f(\cdot) + \sum_{i=0}^{m-1} A_i x^{(i)} - z]$$

for fully actuated system (1) will generate the following constant linear closed-loop system,

$$x^{(m)} + A_{m-1}x^{(m-1)} + \cdots + A_1\dot{x} + A_0 x = z \tag{3}$$

where $z \in \mathbb{R}^n$ is the external input vector.

According to the characteristics shown in Lemma 1, by selecting A_i matrixes for controller, the engenstructures of closed-loop system (3) can be set arbitrarily.

Lemma 2 [19]: It can be guaranteed to get the solution of $A_{0\sim m-1} = [A_0 \quad A_1 \quad \cdots \quad A_{m-1}]$ for (3) as

$$A_{0\sim m-1} = -Q \cdot P^m \cdot V_e^{-1}(P,Q),$$

if and only if $\exists P \in \mathbb{R}^{mn\times mn}$ and $Q \in \mathbb{R}^{n\times mn}$ satisfy that

$$\det V_e(P,Q) \neq 0,$$

where $V_e = \begin{bmatrix} Q & Q\cdot P & \cdots & Q\cdot P^{m-1} \end{bmatrix}^T$ is the eigenvector matrix and P is the corresponding Jordon matrix of eigenvalues.

Corollary 1: The closed-loop system (3) in Lemma 1 can be decoupled and globally asymptotically stable if P and Q in Lemma 2 be selected as follows:

$$P = diag\{\begin{bmatrix} -\alpha_1 & \beta_1 \\ -\beta_1 & -\alpha_1 \end{bmatrix} \cdots \begin{bmatrix} -\alpha_{nm/2} & \beta_{nm/2} \\ -\beta_{nm/2} & -\alpha_{nm/2} \end{bmatrix}\}$$

where $\alpha_i > 0, \beta_i > 0, i = 1,2\cdots,mn/2$, and

$$Q = \begin{bmatrix} I_{1\times m} & & \\ & \ddots & \\ & & I_{1\times m} \end{bmatrix}_{n\times nm}.$$

Proof: Since $\alpha_i > 0$ in P, all the eigenvalues of system (3) are set in the left-half plane of the complex plane, that is the system (3) achieves globally asymptotically stable. It is trivial to get that $\det V_e(P,Q) \neq 0$, and therefore according to Lemma 2, $A_i \in \mathbb{R}^{r\times r}, i = 0,1,\cdots,m-1$ can be calculated as diagonal matrixes, making system (3) decoupled for each dimension of the state vector x. ■

2.2 Preparation for HOFA model transforming

Given the simple and effective property for control design of FASA as described in section 2.1, modeling a HOFA system for USV becomes the first step we should take.

The commonly used first-order 3-DOF USV model in [16] is simplified to design the tracking controller based on FASA by applying the following assumptions:

Assumption 1: The off-diagonal terms of inertial and drag matrixes are small compared to main diagonal terms, and can be ignored.

Assumption 2: The hydrodynamic added mass m_{11}, m_{22} of USVs relative to the x, y axis is very small compared with the ship body mass m, and can be simplified as $m_{11} = m_{22} = m$.

In this way, the first-order 3-DOF USV model with under-actuated form is expressed as

$$\begin{cases} \dot{x} = u\cos\varphi - v\sin\varphi \\ \dot{y} = u\sin\varphi + v\cos\varphi \\ \dot{\varphi} = r \\ m\dot{u} = mvr - d_{11}u + F \\ m\dot{v} = -mur - d_{22}v \\ m_{33}\dot{r} = -d_{33}r + T \end{cases} \tag{4}$$

where x, y stand for the position coordinates, φ denotes yaw angle in the inertial frame. u, v, r corresponds to the surge, sway and yaw velocities of the vessel in the body-fixed reference frame. The parameters m_{33} and $d_{ii}(i = 1,2,3)$ denote the vessel inertia including added mass effects and hydrodynamic damping. m is the mass of USV and the available control inputs denoted by F and T are the surge thrust and yaw moment.

3 Main Results

This section shall address our two main results. The first one is the HOFA system we established for under-actuated USVs through model transformation from (4). The second one is the controller we designed for HOFA system by applying FASA.

3.1 HOFA system of USVs

According to Definition 1, before transformation, state vector $x \in \mathbb{R}^n$ and input vector $u \in \mathbb{R}^r$ for HOFA system, should be selected from the first-order 3-DOF USV model (4). Given that path tracking control of USVs aims to make the vessel travel along the expected 2-D path with a stabilized forward heading yaw angle along the path, we consider the direct tracking control for USVs, which means

the (x,y) position coordinates of USVs in (4) are selected as a 2-D state vector $Z=[x \quad y]^T$ for HOFA system to be controlled to follow the desired path coordinates (x_d, y_d). And since under-actuated USVs only have two available control inputs F and T, the input vector is selected as a 2-D vector $U=[\ddot{F} \quad T]^T$.

Theorem 1: The first-order under-actuated USV system (4) is equivalent to the HOFA system (7) if the input F satisfies

$$F \neq (d_{11}-d_{22})u \tag{5}$$

Remark 1: Assumption (8) is the embodiment of the fully-actuated property for HOFA system and also the prerequisite to ensure the effectiveness of controller design based on FASA. It is worth noticing that the assumption of persistent excitation for surge or yaw velocities of USVs can be pretty hard to guarantee during the path tracking process, whereas, assumption (5) can be much easier to be satisfied by designing the control input F.

Proof: Considering the state vector and input vector for HOFA system has been selected as $Z=[x \quad y]^T$ and $U=[\ddot{F} \quad T]^T$, the HOFA system is therefore a 2-D system. That is to say two equations should be obtained for $x,y,\ddot{F}$ and T after transformation. Since the number of equations can be reduced by raising the order of the system, we take derivative of the first two equations, which are for x,y in (4), continuously to get the high order expressions of x and y. Substituting the corresponding derivatives of u,v,r,φ into the high order expressions of x and y, the third to sixth equations in (4) can be thus reduced. By this means, the fourth derivatives of x and y meet the condition that $x,y,\ddot{F}$ and T appear simultaneously, so the transformed high order system of under-actuated USVs is shown as

$$\begin{cases} x^{(4)} = \dfrac{\cos\varphi}{m}\ddot{F} - \dfrac{1}{m}(\cos\varphi\dfrac{d_{11}-d_{22}}{m_{33}}v + \sin\varphi\dfrac{F-d_{11}u+d_{22}u}{m_{33}})T + f_1 \\ y^{(4)} = \dfrac{\sin\varphi}{m}\ddot{F} - \dfrac{1}{m}(\sin\varphi\dfrac{d_{11}-d_{22}}{m_{33}}v - \cos\varphi\dfrac{F-d_{11}u+d_{22}u}{m_{33}})T + f_2 \end{cases} \tag{6}$$

with

$$f_1 = [\frac{\cos\varphi}{m}(\frac{d_{11}^{\ 2}}{m^2}-r^2) + \sin\varphi\frac{d_{11}-d_{22}}{m^2}r]F - (\frac{d_{11}}{m^2}\cos\varphi + \frac{2r\sin\varphi}{m})\dot{F}$$
$$-\frac{\cos\varphi}{m}(p_1ur^2+p_2vr+p_3u) - \frac{\sin\varphi}{m}(p_1vr^2-p_4ur-p_5v-p_6r),$$
$$f_2 = [\frac{\sin\varphi}{m}(\frac{d_{11}^{\ 2}}{m^2}-r^2) - \cos\varphi\frac{d_{11}-d_{22}}{m^2}r]F - (\frac{d_{11}}{m^2}\sin\varphi - \frac{2r\cos\varphi}{m})\dot{F}$$
$$-\frac{\sin\varphi}{m}(p_1ur^2+p_2vr+p_3u) + \frac{\cos\varphi}{m}(p_1vr^2-p_4ur-p_5v-p_6r),$$

where $p_i\,(i=1\sim 6)$ are parameters, specifically expressed as

$$p_1 = 2d_{22}-2d_{11}$$
$$p_2 = \frac{2d_{22}^2-d_{11}d_{22}-d_{11}^2}{m} + \frac{(d_{22}-d_{11})d_{33}}{m_{33}}$$
$$p_3 = d_{11}^3/m^2$$
$$p_4 = \frac{(d_{22}-d_{11})(2d_{11}+d_{22})}{m}$$
$$p_5 = d_{22}^{\ 3}/m^2$$
$$p_6 = d_{33}/m_{33}.$$

To simplify the expression, let

$$B = \begin{bmatrix} \dfrac{\cos\varphi}{m} & -\dfrac{1}{m}(\cos\varphi\dfrac{d_{11}-d_{22}}{m_{33}}v + \sin\varphi\dfrac{F-d_{11}u+d_{22}u}{m_{33}}) \\ \dfrac{\sin\varphi}{m} & -\dfrac{1}{m}(\sin\varphi\dfrac{d_{11}-d_{22}}{m_{33}}v - \cos\varphi\dfrac{F-d_{11}u+d_{22}u}{m_{33}}) \end{bmatrix}, \tag{7}$$

$f=[f_1 \quad f_2]^T$, such that system (4) can be rewritten as

$$Z^{(4)} = B\cdot U + f. \tag{8}$$

According to Definition 1, (8) satisfies the form of (1) with $m=4$, $n=r=2$. Calculate the determinate of B from (7), we have

$$|B| = \frac{F+(d_{22}-d_{11})u}{m^2\cdot m_{33}},$$

Substituting (8), we can get $|B|\neq 0$, which is equivalent to $rank(B_{2\times 2})=2$ based on the knowledge of linear algebra. From (2) in Definition 1, it turns out that the 4-order system (8) is a HOFA system. The proof is completed. ■

3.2 Controller Design Based on FASA

In this section, we shall design a virtual control law for HOFA system (8) we proposed in Section 3.1 based on FASA, and then combining the condition (5), transform the virtual control input to one for the original under-actuated USV system (4).

According to the theory of FASA, we can design $A_{0\sim 3}$ to get the closed-loop dynamic characteristic we expect for position error e, that are the eigenvalues and eigenvectors of the closed-loop system.

Theorem 2: The path tracking error e of HOFA USV system (8) is globally asymptotically stable if the following control law is adopted.

$$U = -B^{-1}[f + A_{0\sim 3}\cdot E^{(0\sim 3)} - d]$$

where $A_{0\sim 3} = \begin{bmatrix} 1.57 & 0 & 7.51 & 0 & 11.5 & 0 & 6 & 0 \\ 0 & 1.57 & 0 & 7.51 & 0 & 11.5 & 0 & 6 \end{bmatrix}$.

Proof: According to Lemma 1, the virtual control law for HOFA model (8) can be designed as follows:

$$U = -B^{-1}[f + A_{0\sim 3}\cdot E^{(0\sim 3)} - d] \tag{9}$$

where $A_{0\sim 3}=[A_0 \quad A_1 \quad A_2 \quad A_3]$, and $A_i(i=0,1,2,3)$ are all 2×2 real matrixes waiting to be designed, $E^{(0\sim 3)} = [e_x \quad e_y \quad \dot{e}_x \quad \dot{e}_y \quad \ddot{e}_x \quad \ddot{e}_y \quad e_x^{(3)} \quad e_y^{(3)}]^T$, with $e_x = x - x_d$ and $e_y = y - y_d$ denote the position errors, and $d = [x_d^{(4)} \quad y_d^{(4)}]^T$.

Combined with (9), the closed-loop system of (8) can be expressed as follows:

$$Z^{(4)} - d + A_{0\sim 3}\cdot E^{(0\sim 3)} = 0$$

that is

$$e^{(4)} + A_3e^{(3)} + A_2\ddot{e} + A_1\dot{e} + A_0e = 0 \tag{10}$$

where $e=[e_x \quad e_y]^T$.

According to Corollary 1, we can choose P and Q in the form shown in Corollary 1, and construct the appropriate performance index function below:

$$J(P) = \|V_e\|\|V_e^{-1}\|$$

then combining the assumption (5), the matrix P can be obtained by solving the following optimization problem:

$$\begin{cases} \min & J(P) \\ s.t. & F \neq (d_{11} - d_{22})u \\ & \alpha_i > 0, \beta_i > 0, i = 1,2,3,4 \end{cases} \quad (11)$$

So, we finally get the matrix P, Q as follows:

$$P = \begin{bmatrix} -2.5 & 0.04 & 0 & 0 & 0 & 0 & 0 & 0 \\ -0.04 & -2.5 & 0 & 0 & 0 & 0 & 0 & 0 \\ 0 & 0 & -0.5 & 0.04 & 0 & 0 & 0 & 0 \\ 0 & 0 & -0.04 & -0.5 & 0 & 0 & 0 & 0 \\ 0 & 0 & 0 & 0 & -2.5 & 0.04 & 0 & 0 \\ 0 & 0 & 0 & 0 & -0.04 & -2.5 & 0 & 0 \\ 0 & 0 & 0 & 0 & 0 & 0 & -0.5 & 0.04 \\ 0 & 0 & 0 & 0 & 0 & 0 & -0.04 & -0.5 \end{bmatrix}$$

$$Q = \begin{bmatrix} 1 & 1 & 1 & 1 & 0 & 0 & 0 & 0 \\ 0 & 0 & 0 & 0 & 1 & 1 & 1 & 1 \end{bmatrix}$$

and then we can get

$$A_{0\sim3} = \begin{bmatrix} 1.57 & 0 & 7.51 & 0 & 11.5 & 0 & 6 & 0 \\ 0 & 1.57 & 0 & 7.51 & 0 & 11.5 & 0 & 6 \end{bmatrix}. \quad (12)$$

Substituting (12) into (10), the decoupled two closed-loop linear systems can be derived as

$$\begin{cases} e_x^{(4)} + 6e_x^{(3)} + 11.5\ddot{e}_x + 7.51\dot{e}_x + 1.57e_x = 0 \\ e_y^{(4)} + 6e_y^{(3)} + 11.5\ddot{e}_y + 7.51\dot{e}_y + 1.57e_y = 0, \end{cases}$$

and the parameters in each system satisfied Hurwitz condition, making the path tracking error e_x and e_y globally asymptotically stable. The proof is completed. ■

4 Simulation

In this section, the validation of the proposed control scheme is exhibited. Numerical simulations for two working conditions of USV path tracking control-linear and curved path tracking are conducted in MATLAB/Simulink and the corresponding parameters for first-order 3-DOF USV model are as follows,

$m = 200kg$, $m_{33} = 80kg \cdot m^2$, $d_{11} = 70kg \cdot s^{-1}$, $d_{22} = 100kg \cdot s^{-1}$, $d_{33} = 50kg \cdot s^{-1}$ [20].

Our first simulation considers the working condition of linear path tracking and the desired straight path is selected and expressed as $x_d(t) = 2.3t$, $y_d(t) = 2.3t$. The initial states of the USV are set as $x(0) = 20m, y(0) = -20m, \varphi(0) = 90^\circ$, $u(0) = 0$ m/s, $v(0) = 0$ m/s, $r(0) = 0$ rad/s and the initial value of the controller is set as $F_0 = 1N$.

The real tracking path of the vessel and the desired straight path are shown in Fig. 1, where N and E refer to the x and y position coordinates in the inertial frame. It can be seen from Fig.1 that with the use of the proposed controller, the USV can achieve accurate straight path tracking. Fig.2 displays the real yaw angle during the tracking process and the desired heading, which can be calculated from the desired path as $\varphi_d = a\tan(\dot{y}_d / \dot{x}_d) = 45\deg$ and it demonstrates that the yaw angle of the vessel is able to reach the desired heading and remain stable. Fig.3 further shows the change of surge, sway and yaw velocities of the vessel while tracking the straight path and they all become stable, which indicates that the vessel sails at a steady speed along the desired path. The surge force and yaw torch forced on the vessel during the tracking control are shown in Fig.4, which demonstrates a stable performance of the control inputs.

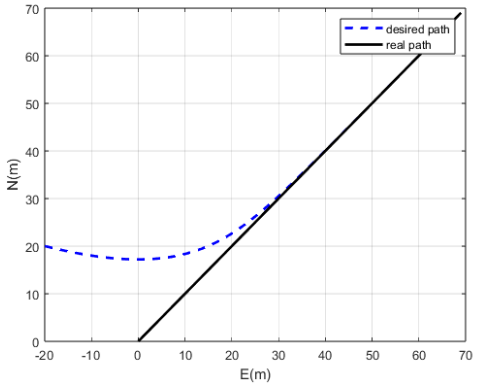

Fig. 1: The straight tracking path of USV

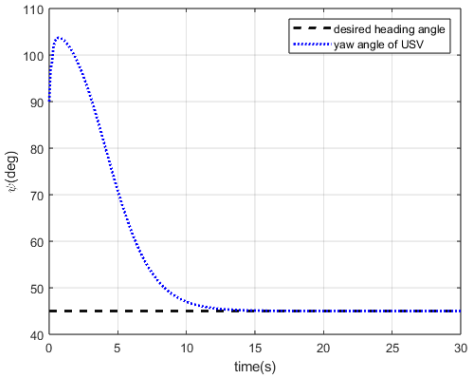

Fig. 2: The yaw angle of USV

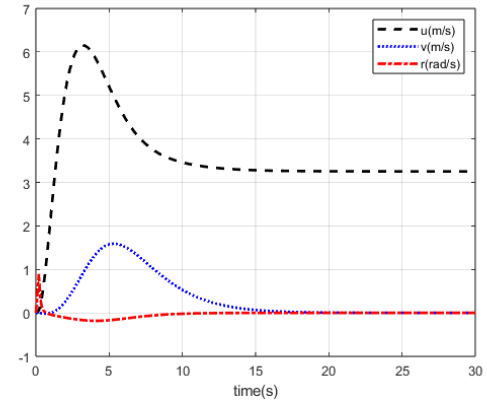

Fig. 3: The surge, sway and yaw velocities of USV

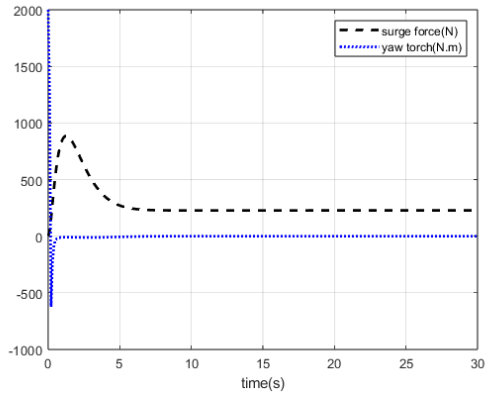

Fig. 4: Surge force and yaw torch for USV

For the second simulation, we consider the case of curved path tracking. The expected curved path we selected is expressed as $x_d(t) = 150 \cdot \cos(0.1t)$, $y_d(t) = 150 \cdot \sin(0.1t)$, that is a circle with a radius of 150 m. Initial states of the vessel are set as follows,

$x(0) = 200m, y(0) = -50m, \varphi(0) = 60^\circ$, $u(0) = 0$ m/s, $v(0) = 0$ m/s, $r(0) = 0$ rad/s and the initial value of the controller is set as $F_0 = 1N$.

The real tracking path of the USV and the expected circled path are shown in Fig. 5 and it can be seen from Fig.5 that the USV can achieve accurate curved path tracking under the control of the proposed controller. Fig.6 displays the real yaw angle during the tracking process and the desired heading, which can be calculated from the desired path as $\varphi_d = a\tan(\dot{y}_d / \dot{x}_d)$ and Fig.6 demonstrates that the yaw angle of the vessel is able to follow the change of the desired heading with an acceptable error of about 2 deg. Fig.7 further shows the change of surge, sway and yaw velocities of the vessel while tracking the curved path and they all become stable, which indicates that the vessel sails at a steady speed along the desired path in the end. The surge force and yaw torch forced on the vessel during the curved tracking control are shown in Fig.8, which demonstrates a stable performance of the control inputs.

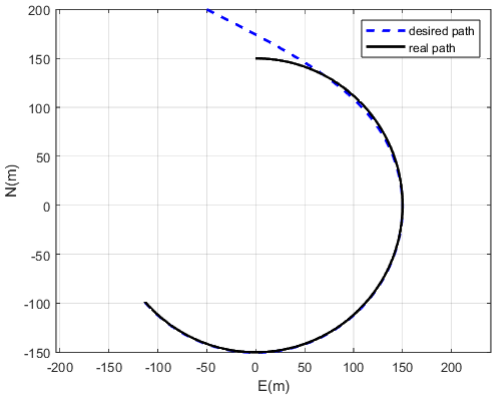

Fig. 5: The curved path tracking of USV

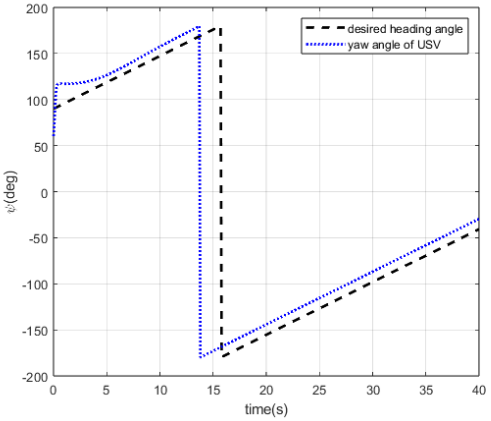

Fig. 6: The yaw angle of USV

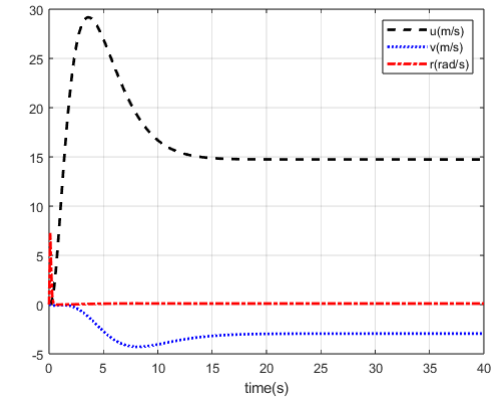

Fig. 7: The surge, sway and yaw velocities of USV

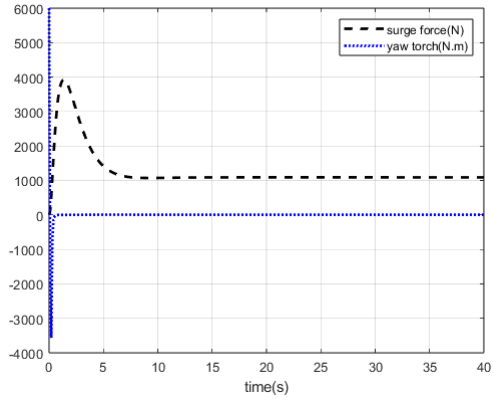

Fig. 8: Surge thrust and yaw moment forced on the USV

5 Conclusion

Based on the FASA, this paper proposes a four-order 2-D HOFA model for first-order 3-DOF USV model with under-actuated form. Then, applying the controller design idea and method for HOFA system on our HOFA USV system, we propose a controller which enables the closed-loop four-order system to obtain the desired dynamic characteristics, decouple the 2-D system, and thus effectively simplify the design process of USV path tracking controller by translating it to the selecting of eigenstructure for high-order linear system. The USV path tracking controller

we proposed in this paper achieves global asymptotic stabilization for the tracking position errors and relaxes the assumption of continuous excitation for angular and forward velocity in previous path tracking control laws to one assumption for control input (surge thrust F). Finally, simulations are conducted to verify the control effectiveness of the proposed HOFA controller and the results show that it performs good for both two tracking cases for USV: straight and curved path tracking. Our next work shall concern on the uncertainties such as modeling inaccuracy, unmodeled dynamics, modification in physical parameters as well as external disturbance caused by wind, waves, and currents for path tracking control.

References

[1] R. Wang, C. Si, H. Ma, and C. Hao, Global event-triggered inner–outer loop stabilization of under-actuated surface vessels, *Ocean Engineering*, 218: 108228, 2020.

[2] X. Y. Kong, X. Q. Xia, R. Hu, et al, Trajectory Tracking Control for Under-Actuated Hovercraft Using Differential Flatness and Reinforcement Learning-Based Active Disturbance Rejection Control, *Journal of systems science & complexity*, 35(2): 502-521, 2022.

[3] Y. Zhao, X. Qi, Y. Ma, Z. Li, R. Malekian, and M. A. Sotelo, Path following optimization for an underactuated USV using smoothly-convergent deep reinforcement learning, *IEEE Transactions on Intelligent Transportation Systems*, 22(10): 6208-6220, 2020.

[4] N. Hung, F. Rego, J. Quintas, et al, A review of path following control strategies for autonomous robotic vehicles: Theory, simulations, and experiments, *Journal of Field Robotics*, 40(3): 747-779, 2023.

[5] C. Karnani, S. A. Raza, M Asif, et al. Adaptive Control Algorithm for Trajectory Tracking of Underactuated Unmanned Surface Vehicle (UUSV), *Journal of Robotics*, 2023.

[6] K. L. Fetzer, S. Nersesov, H. Ashrafiuon, Full-state nonlinear trajectory tracking control of underactuated surface vessels, *Journal of Vibration and Control*, 26(15-16): 1286-1296, 2020.

[7] L. Li, K. Dong, G. Guo, Trajectory tracking control of underactuated surface vessel with full state constraints, *Asian Journal of Control*, 23(4): 1762-1771, 2021.

[8] J. Qin, J. Du, Adaptive fast nonsingular terminal sliding mode control for underactuated surface vessel trajectory tracking, *2019 19th International Conference on Control, Automation and Systems*, 2019: 1365-1370.

[9] X. He, Z. Geng, Point stabilization and trajectory tracking of underactuated surface vessels: A geometric control approach, *Journal of the Franklin Institute*, 358(14): 7119-7141, 2021.

[10] Z. Zwierzewicz, Robust and adaptive path-following control of an underactuated ship, *IEEE Access*, 8: 120198-120207, 2020.

[11] Z. Liu, Practical backstepping control for underactuated ship path following associated with disturbances, *IET Intelligent Transport Systems*, 13(5): 834-840, 2019.

[12] W. Caharija, A. J. Sørensen, K. Y. Pettersen, et al, Path following control of underactuated surface vessels in the presence of multiple disturbances, *2019 18th European Control Conference*, 2019: 2551-2558.

[13] Z. Jia, Z. Hu, W. Zhang, Adaptive output-feedback control with prescribed performance for trajectory tracking of underactuated surface vessels, *ISA transactions*, 95: 18-26, 2019.

[14] D. Cabecinhas, C. Silvestre, Trajectory tracking control of a nonlinear autonomous surface vessel, *2019 American Control Conference*, 2019: 4380-4385.

[15] J. Li, J. Du, Y. Sun, et al, Robust adaptive trajectory tracking control of underactuated autonomous underwater vehicles with prescribed performance, *International Journal of Robust and Nonlinear Control*, 29(14): 4629-4643, 2019.

[16] D. Gu, S. Wang, A high-order fully actuated system approach for a class of nonlinear systems, *Journal of Systems Science & Complexity*, 35(2): 714-730, 2022.

[17] G. Duan, High-order fully actuated system approaches: Part I. Models and basic procedure, *International Journal of Systems Science*, 52(2): 422-435, 2021.

[18] G. Duan, High-order fully actuated system approaches: Part II. Generalized strict-feedback systems, *International Journal of Systems Science*, 52(3): 2161-2181, 2021.

[19] G. Duan, High-order fully-actuated system approaches: Part VI. Disturbance attenuation and decoupling, *International Journal of Systems Science*, 52(10):437-454, 2021.

[20] Z. Li, R. Bu, Trajectory tracking of under-actuated ships based on optimal sliding mode control with state observer, *Ocean Engineering*, 233: 109186, 2021.

Proceedings of the 3rd Conference on Fully Actuated System Theory and Applications
May 10-12, 2024, Shenzhen, China

Optimal Control and Stabilization for NCS over Multi-Hop Relay Networks

Qinglun Zhao[1], Chunyan Han[1]*
1. School of Electrical Engineering, University of Jinan, Jinan 250022, P. R. China
E-mail: cyhan823@hotmail.com

Abstract: This paper is concerned with the optimal control for networked control systems over multi-hop relay networks. In the transmission process, there exist package losses which lead to heavy damage. To overcome the multi-hop relay package losses, we introduce the relay code and a new Markov chain which convert the optimal control with series of packet losses into the general Markovian jumping parameter system. Based on the converted system, a modified maximum principle is developed, which is actually a forward-backward jumping parameter difference equation. In the finite horizon, the key step is to reveal the relationship between the system state and optimal costate. The optimal controller as well as the optimal performance is deduced via the solutions to the optimal costate and one type of coupled difference Riccati equation. In the infinite horizon, a new type of Lyapunov function is defined, by which a necessary and sufficient stabilization condition is obtained, and an infinite optimal controller is developed.

Key Words: Optimal Control; Stabilization; Multi-Hop Relay Network; Packet Loss

1 Introduction

A networked control system (NCS) is a closed-loop system, in which the individual components including plant, sensor, controller, and actuator are connected through a wireless communication network. In the past few decades, NCS is widely used in the computer networks fields, burgeoning iot devices, automated highway systems, and unmanned aerial vehicles [1]. This is because of its high security, flexibility, expansibility and auto-tuning optimization. At present, many research achievements have been given on optimal control [2], H_∞ control [3], guaranteed performance control [4] and stabilization [5] of NCSs.

However, because of data collisions, network congestion and so on, there is inevitably existed packet losses in the data transmission line, which will deteriorate the system performance. Generally, there are two types of packet loss models: the independent and identically distributed (i.i.d.) Bernoulli model and the Markov model. In [6], the optimal control and stabilization of the NCSs with two-way Markov packet dropouts, i.e., from the sensor to the estimator and from the controller to the actuator, was considered. By the Maximum principle, the optimal controller as well as its existence condition was given. Also, the infinite horizon stabilization condition was supplied by the solution to an algebraic Riccati equation.

On the other hand, there exists a situation that the packet losses and transmission delays occured simutaneouly. As for the NCSs both with transmission delays and scalar Bernoulli type packet losses, a necessary and sufficient condition for stabilizing the NCSs based on the unique positive solution to a certain algebraic equation was presented in [7]. For the NCSs with scalar Markovian packet loss and transmission delay, the finite horizon optimal control and stabilization condition were supplied by the stochastic Markovian maximum principle method in [8]. The solution to the finite horizon optimal controller and infinite horizon stabilization condition were given in terms of two coupled difference/algebraic Riccati equations. In [9], a sufficient condition with an H_∞ disturbance attenuation level for NCSs with Markovian packet losses was derived.

Up to now, some researches have been made on the filtering of relay network systems, but less attention has been paid to the optimal control and stabilization of relay networks. The use of relay networks could significantly enhance the propagation distance of wireless communication with high quality communication performance [10]. However, most of the previous works focused on single-hop communication [11], [12], [13], [14]. To balance the computation capability and energy consumption, we introduce the relay code strategy in the NCSs, which would reduce the forwarding times and gurantee the transmission accuracy.

In this paper, we investigate the optimal control and stabilization for NCS over multi-hop relay networks. The main contributions are as below: (1) Multiple relay nodes are introduced in the transmission line from the controller to the actuator, and a higher reliable NCS model is proposed. (2) A new multi-state Markov chain is defined, by which the optimal control and stabilization over multi-relay NCSs is transformed into the optimal control and stabilization for the Markovian jumping parameter systems. (3) The finite horizon optimal controller is designed by employing the stochastic Markovian maximum principle. And the necessary and sufficient stabilization condition is given by applying a new type of coupled Lyapunov function.

The structure is listed as below. Section 2 gives the problem formulation of finite horizon optimal control and supplies the optimal solution and its existence condition by the stochastic maximum principle. Section 3 is concerned with the infinite horizon optimal control and stabilization. The conclusion is drawn in Section 4.

Notation: R^n stands for the n dimensional Euclidean space, R^{m*n} stands for the set of all $m*n$ real matrices. $A > 0 (\geq 0)$ means that A is a positive definite (positive semi-definite) matrix. A^T,$A^{'}$ are the transpose matrix and inverse matrix of A, respectively. $P(A|B)$ is the conditional probability.

This work is supported by the Natural Science Foundation of Shandong Province (No. ZR2021MF069).

*Corresponding author

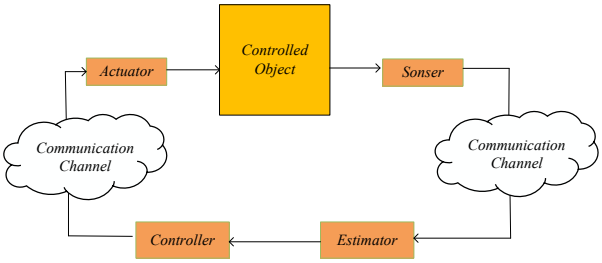

Fig. 1: A block diagram of NCS

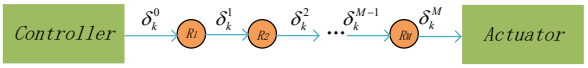

Fig. 2: A structure of multi-hop relay network

$E[.]$ represents the mathematical expectation. I represents an identity matrix of appropriate dimension. $\{\mathcal{G},\mathcal{G}_k,P,\Omega\}$ is the stochastic basis and $\mathcal{G}_k$ represents the random variables $\{\gamma(k), k = 1, 2\}$

2 Finite Horizon Optimal Control

2.1 Problem statement

A block diagram of NCS is given in Figure 1 and a structure of multi-hop relay network is given in Figure 2.

Now consider the following NCS with multi-hop relay nodes

$$x(k+1) = Ax(k) + Bu^{\alpha}(k), x(0) = x_0, \tag{1}$$

where $x(k) \in R^n$ is the system state, $u^{\alpha}(k) \in R^m$ is the actuator signal, A, B are matrices of appropriate dimensions, and

$$u^{\alpha}(k) = \gamma(k)u(k), \tag{2}$$

where $u(k)$ is the controller signal, $\gamma(k)$ characterizes the multistage pocket losses from the controller to the actuator in the procedure of data transmission

$$\gamma(k) = \prod_{i=0}^{M} \delta_k^i, \tag{3}$$

Supposed that the controller signal $u(k)$ is transmitted from the remote controller to the actuator via wireless medium with successive M relay nodes at time k, k= 0, 1, ... , T. The current relay node will receive data from its last node and then forward data to the adjoining node. We denote the arrival process of the observation at time k by a binary stochastic variable δ_k^i, $k = 0, 1, \ldots, T$, where $\delta_k^i = 1$ represents that i-th relay node successfully receives the adjoining data at the time k , otherwise $\delta_k^i = 0$.

In this part, each δ_k^i is depicted as a two-state Markov chain (See in Figure 3) with the transition probablity matrix

$$\Lambda^i = \begin{bmatrix} \lambda_{00}^i & \lambda_{01}^i \\ \lambda_{10}^i & \lambda_{11}^i \end{bmatrix}, \ i = 1, 2, \cdots, M, \tag{4}$$

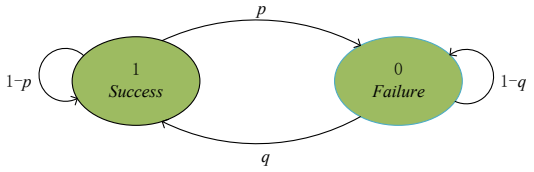

Fig. 3: Markov packet loss model

Baseed on the definition (3), we know that the transition probability of $\gamma(k)$ satisfies

$$\begin{aligned} \lambda_{00} &= Prob\{\gamma(k+1) = 0 | \gamma(k) = 0\} \\ &= 1 - \tfrac{1}{2^{M+1}-1}[\prod_{i=0}^{M}(\lambda_{01}^i + \lambda_{11}^i) - \prod_{i=0}^{M}\lambda_{11}^i], \end{aligned} \tag{5}$$

$$\begin{aligned} \lambda_{01} &= Prob\{\gamma(k+1) = 1 | \gamma(k) = 0\} \\ &= \tfrac{1}{2^{M+1}-1}[\prod_{i=0}^{M}(\lambda_{01}^i + \lambda_{11}^i) - \prod_{i=0}^{M}\lambda_{11}^i], \end{aligned} \tag{6}$$

$$\begin{aligned} \lambda_{10} &= Prob\{\gamma(k+1) = 0 | \gamma(k) = 1\} \\ &= \prod_{i=0}^{M}(\lambda_{10}^i + \lambda_{11}^i) - \prod_{i=0}^{M}\lambda_{11}^i, \end{aligned} \tag{7}$$

$$\begin{aligned} \lambda_{11} &= Prob\{\gamma(k+1) = 1 | \gamma(k) = 1\} \\ &= \prod_{i=0}^{M}\lambda_{11}^i, \end{aligned} \tag{8}$$

Based on the above analysis, systems (1) is transmitted as

$$x(k+1) = Ax(k) + G_{\gamma(k)}u(k), x(0) = x_0, \tag{9}$$

where

$$G_{\gamma(k)} = B\gamma(k), \tag{10}$$

The performance index subject to finite horizon optimal control is given by

$$\begin{aligned} J_T = E\{ &[\sum_{k=1}^{T}[x(k)^{'}Qx(k) + u(k)^{'}Ru(k)] + \\ &x(T+1)^{'}P(T+1)x(T+1)\}, \end{aligned} \tag{11}$$

where Q and R are both positive semi-definite matrices, $P(T+1)$ reflects the penalty on the terminal state.

Problem 1 (Finite Horion Optimal Control) Find a $\mathcal{G}_k$-measurement controller $u(k)$, such that the performance index (11) is minimized subject to system (1).

2.2 Solution to problem 1

Definition 1. Problem 1 is called solvable if there exists an admissible control $(u^*(0), ..., u^*(T))$ such that (11) is minimized for any x_0.

The modified maximum principle is established as follows.

Lemma 1 (Modified Maximum Principle). According to

system (1) and cost function (11), if the linear quadratic problem min J_T is solvable, then the optimal $\mathcal{G}_k$-measurable control $u(k)$ satisfies the following equilibrium equation

$$0 = E[G_{\gamma(k)}^{'}\eta_k + Ru(k)|\mathcal{G}_k] \quad k = 0, \ldots, T, \tag{12}$$

and the costate η_k satisfies

$$\eta_T = P(T+1)x(T+1), \tag{13}$$

$$\eta_{k-1} = E[A^{'}\eta_k + Qx(k)|\mathcal{G}_k]. \tag{14}$$

Proof. The derivation process can be implemented along the similar line in [9], and is therefore omitted for conciseness. (1), (12), (13) and (14) form the forward-backward stochastic Markovian difference equations (FBSMDEs). Now we give the main result of this section.

Therom 1. Problem 1 has a unique solution if and only if the following coupled difference Riccati equation

$$P_i(k) = A^{'}(\sum_{j=1}^{2}\lambda_{i,j}P_j(k+1))A+Q-M_i(k)^{'}\Gamma_i(k)^{-1}M_i(k), \tag{15}$$

$$\Gamma_i(k) = G_i^{'}(\sum_{j=1}^{2}\lambda_{i,j}P_j(k+1))G_i + R, \tag{16}$$

$$M_i(k) = G_i^{'}(\sum_{j=1}^{2}\lambda_{i,j}P_j(k+1))A, \tag{17}$$

are well defined for $k = T, ..., 0$, $i = 1, 2$, that is, $\Gamma_i(k)(k = T, \ldots, 0, i = 1, 2)$ are all invertible. In this situation, the analytical solution to the finite-horizon optimal control is given as

$$u^*(k) = -\Gamma_{\gamma_{(k)}}(k)^{-1}M_{\gamma_{(k)}}(k)x(k), \quad i = 1, 2, \tag{18}$$

for $k = T, \ldots, 0$.

Moreover, the optimal costate is given by

$$\eta_{k-1} = P_{\gamma_{(k)}}(k)x(k), \tag{19}$$

and the optimal performance satisfies

$$J_T^* = E[x(0)^{'}P_{\gamma(0)}(0)x(0)]. \tag{20}$$

Proof. See Appendiex A.

3 INFINITE-HORIZON OPTIMAL CONTROL

In this section, we will seek for the infinite horizon optimal control and stabilization condition for system (1).

3.1 Problem statement

Firstly, we consider a time-invariant version of the system (1) and the infinite horizon performance index

$$J = E\{\sum_{k=0}^{\infty}[x(k)^{'}Qx(k) + u(k)^{'}R(k)u(k)]\}. \tag{21}$$

Before proceeding further, we will introduce some definitions which will be used in the latter derivation of our results.

Definition 2. System (1) is mean-square stabilizable (MSS) if there is a $\mathcal{G}_k$-measurement controller $u(k) = F_{\gamma(k)}x(k)$ satisfying $\lim_{k\to\infty} = E[u(k)^{'}u(k)] = 0$, such that system (1) is asymptotically mean-square stable.

Definition 3. The following system

$$x(k+1) = Ax(k) + G_{\gamma(k)}u(k),\ y(k) = Cx(k), \tag{22}$$

is said to be exactly observable, if for any $T \geq 0$,

$$y(k) = 0, a.s., \forall k \in [0, T] \Longrightarrow x_0 = 0. \tag{23}$$

For convenience of description, denote $A = (A, A)$, $G = (G_1, G_2)$, $C = (C, C)$. If system (1) is mean squre stabilizable and exactly observable, we say that the pair (A, G) is mean square stabilizable and (C, A) is exactly observable.

Problem 2. Find the $\mathcal{G}_k$-measurable controller $u(k) = F_{\gamma(k)}x(k)$, $k \geq 0$, such that the closed loop system is asymptotically stable in the mean-sequare sense, which also minimizes the performance index (21).

3.2 Soluton to problem 2

Without loss of generality, we assume the terminal weight matrix $P(T+1)$ in (11) to be zero and define the following coupled algebraic Riccati equations

$$P_i = A^{'}\big(\sum_{j=1}^{2}\lambda_{i,j}P_j\big)A + Q - M_i^{'}\Gamma_i^{-1}M_i, \quad i = 1, 2, \tag{24}$$

$$\Gamma_i = G_i^{'}\big(\sum_{j=1}^{2}\lambda_{i,j}P_j\big)G_i + R, \quad i = 1, 2, \tag{25}$$

$$M_i = G_i^{'}\big(\sum_{j=1}^{2}\lambda_{i,j}P_j\big)A, \quad i = 1, 2, \tag{26}$$

Theorem 2. If system (1) is mean-square stabilizable, then $P_i^T(k)(i = 1, 2)$ is convergent when $T \to \infty$, i.e. $\lim_{T\to\infty} P_i^T(k) = P_i(i = 1, 2)$, where $P_i(i = 1, 2)$ satisfies (24), (25), (26) and $P_i > 0$.

Proof. See Appendix B.

Theorem 3. Consider Assumptions 1 and 2, system (1) is stabilizable in the mean squre sense if and only if there exists a unique solution to (24)-(26) such that $P_i > 0$ for $i = 1, 2$. In this situation, the optimal controller is given by

$$u(k) = \Gamma_{\gamma(k)}M_{\gamma(k)}x(k), k \geq 0, \tag{27}$$

which stabilizes (1) in the mean-square sense and minimizes performance (21) simutaneously. The infinite horizon optimal performance is given as

$$J^* = E\{x(0)^{'}P_{\gamma(0)}x(0)\}. \tag{28}$$

Proof. The derivation process is similar to that of Theorem 3 in [15], and thus is omitted here.

4 Numerical Example

In this section, we will give numerical examples to illustrate the right of the results above.

4.1 Finite-horizon example

In this part ,we consider the NCS with the following specific matrices

$$A = \begin{bmatrix} 0.8 & 0.1 \\ -0.2 & 0.7 \end{bmatrix}, B = \begin{bmatrix} 0.2 & 0.7 \\ -0.05 & 1.4 \end{bmatrix},$$

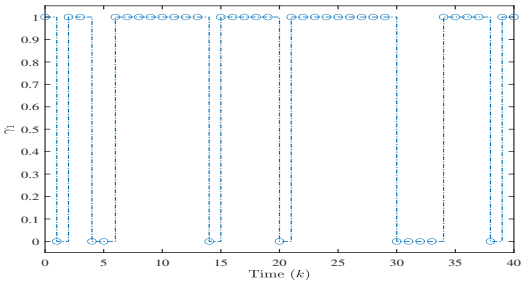

Fig. 4: The path of $\gamma(k)$

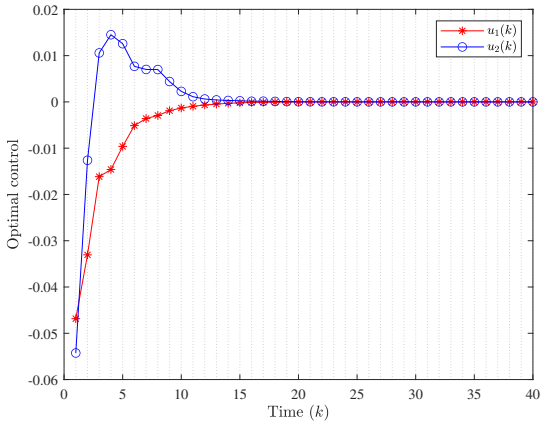

Fig. 5: the trajectories of the optimal controllers

while the weight matrices of the cost function (11) are given by

$$Q = \begin{bmatrix} 0.8 & 0 \\ 2 & 1.1 \end{bmatrix}, B = \begin{bmatrix} 0.7 & 0 \\ 0 & 0.5 \end{bmatrix}, P(T+1) = \begin{bmatrix} 1 & 0 \\ 0 & 1 \end{bmatrix}$$

. Let T= 40 and the initial value $x(0) = \begin{bmatrix} 0.55 \\ 0.35 \end{bmatrix}$, $u^{\alpha} = \begin{bmatrix} 0.1 \\ 0.3 \end{bmatrix}$. And we set the transition probability matrices below

$$\Lambda_1 = \begin{bmatrix} 0.3 & 0.7 \\ 0.15 & 0.85 \end{bmatrix}, \Lambda_2 = \begin{bmatrix} 0.1 & 0.9 \\ 0.25 & 0.75 \end{bmatrix}.$$

Implementing 100 Monte Carlo simulations from k = 0 to k = 40 and in terms of T = 40, we obtain the simulation results as below. In accordance with Theorem 1, Figure 4 is depicted as the transitions of the Markov chain $\lambda(k)$, Figure 5 is used to represent the trajectories of the optimal controllers and Figure 6 is used to represent the trajectories of the state $x(k)$.

5 conclusion

In this paper, we have investageted the optimal control and stabilization for NCSs over multi-hop relay networks. A new packet loss model has been established to describe the unreliable charicteristic of the relay comunication line. The relationship between the costate and system state has been revealed, and the finite horizon optimal controller was supplied. Addtionally, the necessary and sufficient stabilization condition has been developed according to the solution to an algebraic Riccati equation.

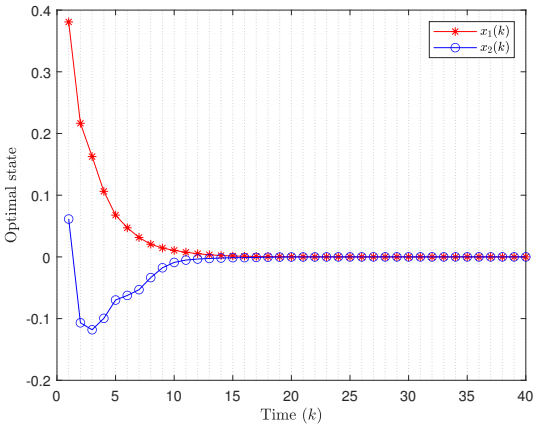

Fig. 6: The trajectories of the state $x(k)$.

Appendiex A (Proof of Theorem 1)

Proof. (Necessary) Assume that Problem 1 is solvable, we will prove $\Gamma_i(k)$ is invertible for all $k = T, \ldots, 0$ such that $u(k)$ satifies (19). By the induction method, we first define

$$J(k) = E\{ [\sum_{k=1}^{T} [x(k)^{'} Q x(k) + u(k)^{'} R u(k)] + x(T+1)^{'} P(T+1) x(T+1) | \mathcal{G}_k] \quad \}, \tag{29}$$

for $k = T, ..., 0$. When $k = T$, (29) can be rewritten as

$$J(T) = E\{[x(T)^{'} Q x(T) + u(T)^{'} R u(T)] + x(T+1)^{'} P(T+1) x(T+1) | \mathcal{G}_T\}. \tag{30}$$

Let $x(T) = 0$ and substitute (1) into (30), we have

$$\begin{aligned} J(T) &= E\{[x(T)^{'} Q x(T) \\ &\quad + [Ax(T) + G_{\gamma(T)} u(T)]^{'} P(T+1) [Ax(T) \\ &\quad + G_{\gamma(T)} u(T)] | \mathcal{G}_T]\} \\ &= u(T)^{'} \Gamma_i(T) u(T), \end{aligned} \tag{31}$$

in which

$$\Gamma_i(T) = R + G_i^{'} \big(\sum_{j=1}^{2} \lambda_{i,j} P(T+1) \big) G_i. \tag{32}$$

Since $J(T) > 0$, we get $\Gamma_i(T) > 0$.
Now, we concentrate on the derivation of the optimal controller $u(T)$. In view of (15)-(17), we have

$$\begin{aligned} 0 &= G_i^{'} \big(\sum_{j=1}^{2} \lambda_{i,j} P(T+1) \big) A x(T) \\ &\quad + [G_i^{'} \big(\sum_{j=1}^{2} \lambda_{i,j} P(T+1) \big) G_i + R] u(T). \end{aligned} \tag{33}$$

In view of (33), one yields

$$u(T) = -\Gamma_i(T)^{-1} M_i(T) x(T), \tag{34}$$

in which Γ_i(T) is the same as (32) and M_i(T) is as below

$$M_i(T) = G_i^{'} \big(\sum_{j=1}^{2} \lambda_{i,j} P(T+1) \big) A. \tag{35}$$

Based on (1), (16) and (A3), we have

$$\begin{aligned}\eta(T-1) &= E[A^{'}\eta_T + Qx(T)|\mathcal{G}_T] \\ &= \{A^{'}\big(\sum_{j=1}^{2}\lambda_{i,j}P_j(T+1)\big)A + Q \\ &- M_i(T)^{'}\Gamma_i(T)^{-1}M_i(T)\}x(T) \\ &= P_i(T)x(T), \end{aligned} \tag{36}$$

where

$$\begin{aligned}P_i(T) &= A^{'}\big(\sum_{j=1}^{2}\lambda_{i,j}P(T+1)\big)A + Q \\ &- M_i(T)^{'}\Gamma_i(T)^{-1}M_i(T). \end{aligned} \tag{37}$$

Taking any k with $1 \le k \le T$, for any $t \ge k+1$, we assume that $\Gamma_i(t)(i = 1, 2)$ is invertible and the optimal controller and the optimal costate are satisfied, respectively. By the inductive method, we will prove these conditions are satisfied for $t = k$. Let $x(k) = 0$ and on the basis of (1), (12), (13) and (14), we have

$$\begin{aligned}&E\{x(t)^{'}\eta_{t-1} - x(t+1)^{'}\eta_t|\mathcal{G}_{k+1}\} \\ &= E\{x(t)^{'}Qx(t) + u(t)^{'}Ru(t)|\mathcal{G}_{k+1}\}. \end{aligned} \tag{38}$$

Taking addition from $t = k+1$ to $t = T$ on both sides of (38), we get

$$\begin{aligned}&E\{x(k+1)^{'}\eta_k - x(T+1)^{'}\eta_T|\mathcal{G}_{k+1}\} \\ &= \sum_{t=k+1}^{T} E\{x(t)^{'}Qx(t) + u(t)^{'}Ru(t)|\mathcal{G}_{k+1}\}. \end{aligned} \tag{39}$$

So we can obtain from (39) and (16) that

$$J(k) = E\{u(k)^{'}Ru(k) + u(k)^{'}G^{'}_{\gamma(k)}\eta_k|\mathcal{G}_k\}. \tag{40}$$

Note that

$$\begin{aligned}\eta_k &= P_{\gamma(k)}(k+1)x(k+1) \\ &= P_{\gamma(k)}(k+1)[Ax(k) + G_{\gamma(k)}u(k)], \end{aligned} \tag{41}$$

we have

$$\begin{aligned}J(k) &= E\{u(k)^{'}Ru(k) \\ &+ u(k)^{'}G_i^{'}\sum_{j=1}^{2}\lambda_{i,j}P_j(k+1)G_iu(k)|\mathcal{G}_k\} \\ &= u(k)^{'}[R + G_i^{'}\sum_{i=1}^{2}\lambda_{i,j}P_j(k+1)G_i]u(k) \\ &= u(k)^{'}\Gamma_i(k)u(k), \quad i = 1, 2. \end{aligned} \tag{42}$$

Based on the uniqueness of the optimal controller, we know that $J(k)$ must be positive for any $u(k) \neq 0$. Thus we can say $\Gamma_i > 0$ for $i = 1, \ldots, M$. In order to obtain $u(k)$, substituting (41) into (16) yields

$$\begin{aligned}0 &= E[G^{'}_{\gamma(k)}\eta_k + Ru(k)|\mathcal{G}_k] \\ &= G_i^{'}(\sum_{j=1}^{2}\lambda_{i,j}P(T+1))Ax(T) \\ &+ [G_i^{'}(\sum_{j=1}^{2}\lambda_{i,j}P(T+1))G_i + R]u(T) \\ &= M_i(k)x(k) + \Gamma_i(k)u(k). \end{aligned} \tag{43}$$

In light of (43), we get

$$u(k) = -\Gamma_i(k)^{-1}M_i(k)x(k), \tag{44}$$

which

$$\Gamma_k(k) = G_i^{'}(\sum_{j=1}^{2}\lambda_{i,j}P_j(k+1))G_i + R, \tag{45}$$

$$M_i(k) = G_i^{'}(\sum_{j=1}^{2}\lambda_{i,j}P_i(k+1))A. \tag{46}$$

Based on (12), (41) and (43) , we have

$$\begin{aligned}\eta_{k-1} &= E[A^{'}\eta_T + Qx(T)|\mathcal{G}_k] \\ &= P_i(k)x(k), \end{aligned} \tag{47}$$

where

$$P_i(k) = [Q + A^{'}P_i(k+1)A] - M_i(k)^{'}\Gamma_i(k)^{-1}M_i(k). \tag{48}$$

(Sufficiency) Suppose $\Gamma_i(k)$ for $i = 1, 2$, we focus on proving that there exists a unique solution for Problem 1. Define

$$V_T(k, x(k)) = E[x(k)^{'}P_{\gamma(k)}(k)x(k)]. \tag{49}$$

Based on above (49) and (15)-(17), we can obtain

$$\begin{aligned}&V_T\big(k, x(k)\big) - V_T\big(k+1, x(k+1)\big) \\ &= E\{x(k)^{'}Q_{\gamma(k)}(k)x(k) + u(k)^{'}Ru(k) \\ &- [u(k) + \Gamma^{-1}_{\gamma(k)}(k)M_{\gamma(k)}(k)x(k)]^{'}\Gamma_{\gamma(k)}(k)[u(k) \\ &+ \Gamma^{-1}_{\gamma(k)}(k)M_{\gamma(k)}(k)x(k)]\}. \end{aligned} \tag{50}$$

Adding from $k = 0$ to $k = T$, the performance index (11) is rewritten as

$$\begin{aligned}J_T =& E\{x(0)^{'}Qx(0) + \sum_{k=0}^{T}[u(k) \\ &+ \Gamma_{\gamma(k)}(k)^{-1}M_{\gamma(k)}(k)x(k)]^{'}\Gamma_{\gamma(k)}(k)[u(k) \\ &+ \Gamma_{\gamma(k)}(k)^{-1}M_{\gamma(k)}(k)x(k)]\}. \end{aligned} \tag{51}$$

Problem 1 has a unique solution, and the optimal controller is

$$u(k) = -\Gamma_{\gamma(k)}(k)^{-1}M_{\gamma(k)}(k)x(k). \tag{52}$$

The optimal performance index is

$$J_T = E[x(0)^{'}P_{\gamma(0)}(0)x(0)]. \tag{53}$$

This completes the proof of Theorem 1.

Appendiex B (Proof of Theorem 2)

Proof. In term of $J_T \leq J_{T+1}$, we get $J_T^* \leq J_{T+1}^*$ for any initial value x_0. From (26), we have

$$E\{x_0^{'} P^T(0) x_0\} \leq E\{x_0^{'} P^{T+1}(0) x_0\}. \tag{54}$$

Because of the arbitrary of x_0, we have $P^T(0) \leq P^{T+1}(0)$, it means that $P^T(0)$ is increasing with respect to T.
In the sequel, we will prove that $P^T(0)$ is bounded. If system (1) is stabilizable in the mean-square sense, there exists $u(k) = F_{\gamma(k)} x(k)$ satisfying

$$\lim_{k\to\infty} E[x(k)^{'} x(k)] = 0. \tag{55}$$

So one yields

$$\begin{aligned} J^* \leq J &= E\sum_{k=0}^{\infty}[x(k)^{'} Q x(k) + u(k)^{'} R u(k)] \\ &\leq \lambda E\sum_{k=0}^{\infty}[x(k)^{'} x(k)] \leq \lambda c E[x(k)^{'} x(k)], \end{aligned} \tag{56}$$

where λ denotes the maximum eigenvalue of $(Q + F_{\gamma(k)}^{'} R F_{\gamma(k)})$ and c is a positive constant. In view of (56), we have

$$E[x(0)^{'} P(0) x(0)] \leq \lambda c E[x(k)^{'} x(k)], \tag{57}$$

that is

$$P^T(0) \leq \lambda c I. \tag{58}$$

Therefore, $P^T(0)$ is bound. On the account of $P^T(0)$ is monotonous, we can say that $P^T(0)$ is convergent. As is stated above, the variables given in (15)-(17) are time invariant for T because of $P_j(T+1) = 0, (j = 1, 2)$, thus we have

$$\lim_{k\to\infty} P_i^T(k) = \lim_{k\to\infty} P_i^{T-k}(k) = P_i, \tag{59}$$

At the same time, we get

$$\lim_{k\to\infty} \Gamma_i^T(k) = \Gamma_i, \lim_{k\to\infty} M_i(k) = M_i. \tag{60}$$

Next, we will show $P_i > 0$. Because of $J^* \geq 0$, we have $P^T(0) \geq 0$ for the arbitrary of x_0. We will prove that there exists a positive intenger T_0 that make $P^T(0) \geq 0\ (T \geq T_0)$. If not, there exists a nonempty set

$$X_T = \{x \in R_n : x \neq 0, x' P_{\gamma_0}^T(0) = 0\}. \tag{61}$$

Owing to $P_T(0)$ is monotonically increasing, we have that if $E\{x^{'} P^{T+1}(0) x\} = 0$, then $E\{x^{'} P^T(0) x\} = 0$, that is, $X_{T+1} \subseteq X_T$. As X_T is a nonempty finite dimensional set, so we get

$$1 \leq \cdots \leq dim(X_2) \leq dim(X_1) \leq dim(X_0) \leq k. \tag{62}$$

So, there exists a positive intenger T_0, such that

$$dim(X_T) = dim(X_{T_0}). \tag{63}$$

For any $T > T_0$. That is $X_{T^{'}} = X_{T_0}$. Thus , there exists a nonzero $x \in X_T$ satisfying $x^{'} P_T(0) x = 0$. Set $x_0 = x$, we can obtain

$$\begin{aligned} J_T^* &= E\{\sum_{k=0}^{\infty}[x^*(k)^{'} Q x^*(k) + u^*(k)^{'} R u^*(k)]\} \\ &= E[x^{'}(0) P_{\gamma(k)}^T(0) x(0)] = 0. \end{aligned} \tag{64}$$

Since $Q \geq 0$, $R > 0$, we have $u^*(k) = 0, Cx^*(k) = 0$, that is,

$$x^*(k+1) = Ax^*(k), C_{\gamma(k)} x^*(k) = 0. \tag{65}$$

Note that (C, A) is exactly observable, so we get $x = 0$. This contradicts with $x \neq 0$. Thus, there must exist a positive integer T_0, such that $P(0) \geq 0$. Therefore

$$P_i \geq \lim_{T\to\infty} P_i^T(k) \geq P_i^{T_0}(k) > 0. \tag{66}$$

This completes the proof.

References

[1] X. Cao, P. Cheng, J. Chen, et al, An online optimization approach for control and communication codesign in networked cyber-physical systems, IEEE Transactions on Industrial Informatics, 2012, 9(1): 439-450.

[2] C. Han, H. Li, and H. Zhang, Optimal control for discrete-time Markov jump linear system with control input delay, arXiv preprint arXiv:1808.06228, 2018.

[3] Z. Wang, F. Yang, et al, Robust H_∞ control for networked systems with random packet losses, IEEE Transactions on Systems, Man, and Cybernetics, Part B (Cybernetics), 2007, 37(4): 916-924.

[4] S. Xie, L . Xie, Y. Wang, et al, Decentralised control of multimachine power systems with guaranteed performance, IEE Proceedings-Control Theory and Applications, 2000, 147(3): 355-365.

[5] H. Gao, X. Meng, T. Chen, Stabilization of networked control systems with a new delay characterization, IEEE Transactions on Automatic Control, 2008, 53(9): 2142-2148.

[6] X. Lu, Y. Cai, H. Wang, et al, Necessary and Sufficient Condition of Optimal Control for Networked Control Systems with Markovian Packet Dropouts, International Journal of Control, Automation and Systems, 2023, 21(5): 1485-1492.

[7] C. Tan, L. Li, H. Zhang, Stabilization of networked control systems with both network-induced delay and packet dropout, Automatica, 2015, 59: 194-199.

[8] H. Li, C. Han, H. Zhang, et al. Optimal control and stabilization for networked systems with input delay and Markovian packet losses, IEEE Transactions on Systems, Man, and Cybernetics: Systems, 2019, 51(7): 4453-4465.

[9] D. Wang, J. Wang, W. Wang, H_∞ controller design of networked control systems with Markov packet dropouts, IEEE transactions on systems, man, and cybernetics: Systems, 2013, 43(3): 689-697.

[10] Y. Han, M. Cui, S. Liu, Optimal sensor and relay nodes power scheduling for remote state estimation with energy constraint, Sensors, 2020, 20(4): 1073.

[11] B. Sinopoli, L. Schenato, M. Franceschetti, et al, Kalman filtering with intermittent observations, IEEE transactions on Automatic Control, 2004, 49(9): 1453-1464.

[12] K. You, M. Fu, L. Xie, Mean square stability for Kalman filtering with Markovian packet losses, Automatica, 2011, 47(12): 2647-2657.

[13] L. Shi, P. Cheng, J. Chen, Sensor data scheduling for optimal state estimation with communication energy constraint, Automatica, 2011, 47(8): 1693-1698.

[14] J. Wu, QS. Jia, KH. Johansson, et al, Event-based sensor data scheduling: Trade-off between communication rate and estimation quality, IEEE Transactions on automatic control, 2012, 58(4): 1041-1046.

[15] C. Han, H. Li, H. Zhang, et al, Optimal control and stabilization for discrete-time Markov jump linear systems with input delay, SIAM Journal on Control and Optimization, 2021, 59(5): 3524-3551.

Proceedings of the 3rd Conference on Fully Actuated System Theory and Applications
May 10-12, 2024, Shenzhen, China

Distributed recursive filter for 2-D Markov jump systems with stochastic communication protocol and nonlinearities

Fengying Ge[1], Chunyan Han[1]*
1. School of Electrical Engineering, University of Jinan, Jinan 250022, P.R.China
E-mail: cyhan823@hotmail.com; gefy_g@163.com

Abstract: This paper investigates the distributed filtering for a class of two-dimensional Markov jump parameter systems with communication protocols and nonlinearity. The system is described by the FM-II model and the random communication protocol is characterized by a set of mutually uncorrelated random processes with known probability distributions, which determines the transmission order of each sensor data. The objective is to develop a recursive distributed filter for the two-dimensional systems. Firstly, an upper bound of the local estimation error variance is established through the mathematical induction method and the stochastic analysis approach. Then, by the complete mean square method, the filter gains are derived by optimizing the upper bound of the estimation error variance. Subsequently, a distributed filter based on covariance intersection (CI) fusion algorithm is developed, which exhibits higher accuracy and reliability. Finally, a numerical example is provided to demonstrate that the fusion estimator exhibits higher estimation accuracy compared to the local one.

Key Words: CI fusion estimation; Markov jump linear system; two-dimensional system; stochastic nonlinearity; Riccati equation

1 INTRODUCTION

Over the past few years, two-dimensional (2-D) systems have gradually become a research hotpot, owing mainly to the 2-D systems can effectively describe real-world systems with multiple variables in practical processes. The applications of 2-D systems can be found in various areas which include, but are not limited to signal and image processing, iterative learning tracking, water stream heating, and environmental monitoring [1]-[2]. It is worth noting that compared to the traditional one-dimensional (1-D) state-space model where signals evolve along a single direction, the 2-D systems possess the feature that the system states are transmitted along two independent directions. This means that existing theories for 1-D systems may become inapplicable in the 2-D settings. Accordingly, a host of researchers focus on the investigation of the recursive filtering problem for 2-D systems, yielding some representative results [3]-[4].

With the increasing prevalence of sensor networks, the distributed filtering problem has garnered heightened research interest, primarily attributed to its extensive prospective applications in the fields of communication, control, and signal processing [5]-[7]. It is well acknowledged that, in the distributed systems, the sensors or nodes collaborate among each others through communication links to estimate the systems state, enhancing the filtering performance collectively. In response to the popularity of sensor networks, significant efforts have been devoted to the distributed filtering. In general, the distributed Kalman filter consists of two strategies: the distributed consistency strategy [8]- [10] and the distributed fusion strategy [11]- [14]. These strategies differ in the processes of information fusion and sharing pattern. In [14], the consensus distributed H_∞ filtering for 2-D systems based on Rosser models was investigated. The aim was to ensure the stability of the filtering error systems by the satisfactions of a set of linear matrix inequality form conditions. In [13], a distributed recursive filter was designed for the 2-D systems with constraints on random communication protocols. Based on the given topology, the local real state of the system was estimated by utilizing available information from individual nodes and adjacent nodes in the sensor network. Finally, the filter parameters to be designed were determined through the vector augmentation method and the centralized fusion approach.

On the other hand, with the development of modern technology and communication techniques, the construction of communication protocols plays a significant role in the distributed filtering research, which involves several issues such as the timing of information exchange between nodes, the triggering conditions, and the reliability of data transmission. It is worth noting that a reasonable communication protocol not only reduces the communication overhead and improves the real-time performance of the system, but also enhances the robustness of the system against noise and uncertainty. Consequently, the problem of filtering based on communication protocols has attracted much attention by researchers [15]. In [13], a communication protocol characterized by mutually uncorrelated random variables with known probability distributions was proposed, which determined the transmission order of each sensors data packet. In the context of given topology, a distributed filter was designed in the 2-D framework. By employing the mathematical induction and matrix simplification techniques, the minimum upper bound on the estimation error variance was established, along with the determination of the required filter gains. So far, there have been some preliminary research results on the filtering the 1-D network systems with stochastic communication protocols. Yet, the distributed filtering problem for 2-D Markov jump parameter systems subject to stochastic communication protocols and nonlinearities has been seldom studied.

Inspired by the discussions above, this study focuses on the investigation of the distributed recursive filter for a 2-D Markov jump parameter system with the influence of random communication protocols and nonlinearity. The main

This work is supported by the Natural Science Foundation of Shandong Province (No. ZR2021MF069).
*Corresponding author

contributions of this paper are as follows: (1) The random communication protocol is described by an independent random sequence with known probability distribution, which is to determine the order of the packets received by each sensor. (2) A class of Riccati difference equations is defined to derive the local upper bound of the filtering error variance matrix by mathematical induction method. The filter gain is then determined by the complete mean square method. (3) Utilizing the distributed CI fusion estimation algorithm, we derive the information fusion estimator for the multi-sensor scenario. This approach effectively avoids the computational burden associated with the cross-covariance matrix of the estimation error.

This paper is organized as follows: Section II provides the problem description and preliminaries. Section III outlines local estimators, and then develops a distributed fusion estimator by the CI fusion method. Section IV presents a simulation example to shown the efficiency of the proposed algorithm. Section V draws the conclusion in the final part.

Notations: $\mathbb{R}^n$ represents the n-dimensional real-valued vector. The superscript "T" denotes the transpose of the matrix and $tr\{\cdot\}$ indicates the trace of the matrix. '$\circ$' stands for the Hadamard product. $diag\{\cdot\}$ denotes the block diagonalization operation. $E[\cdot]$ and $P_r\{\cdot\}$ serve as the expectation operator and the probability of the random variable, respectively.

2 PROBLEM DESCRIPTION AND PREPARATION

The stochastic 2-D Markov jump system is considered on $i, j \in [0, N]$,

$$\begin{aligned} &x(i+1,j+1) \\ &= A^1_{\theta(i+1,j)}x(i+1,j) + A^2_{\theta(i,j+1)}x(i,j+1) \\ &+ B^1_{\theta(i+1,j)}w(i+1,j) + B^2_{\theta(i,j+1)}w(i,j+1) \\ &+ \alpha^1_{\theta(i+1,j)}f(x(i+1,j)) + \alpha^2_{\theta(i,j+1)}f(x(i,j+1)), \quad (1) \\ &y_l(i,j) = C^l_{\theta(i,j)}x(i,j) + \beta^l_{\theta(i,j)}h^l(x(i,j)) + v^l(i,j), \quad (2) \end{aligned}$$

where $x(i,j) \in \mathbb{R}^{n_x}$ represents the system state, $y_l(i,j) \in \mathbb{R}^{n_y}$ represents the output of the l th sensor. We set $A^r_{\theta(i,j)}$, $B^r_{\theta(i,j)}$ $(r = 1, 2)$ and $C^l_{\theta(i,j)}$ $(l = 1, 2, \cdots, m)$ for the coefficient matrices of systems (1) and (2), which are functions of $\theta(i,j)$. $\theta(i,j)$ is a discrete time Markov chain with finite state space $\theta(i,j) \in \{1, 2, \ldots, N_\theta\}$ and transition probability $p_{ez} = P\{\theta(i+1,j) = z|\theta(i,j) = e\} = P\{\theta(i,j+1) = z|\theta(i,j) = e\}$, $e, z \in \{1, 2, \ldots, N_\theta\}$. Let $\pi_z(i,j) = P(\theta(i,j) = z)$. $f(x(i,j))$ and $h^l(x(i,j))$ indicates the nonlinear functions. $w(i,j)$ and $v^l(i,j)$, respectively stands for the zero-mean process noise and measurement noises with covariances $Q(i,j)$ and $R^l(i,j)$. $\alpha^r_{\theta(i,j)}$ and $\beta^l_{\theta(i,j)}$ are random variables with mean zero and covariances $\sigma^r_{\theta(i,j)}$ and $\gamma^l_{\theta(i,j)}$, respectively.

We set the initial conditions of the system to be,

$$\begin{aligned} \mathcal{E}\{x(i,0)\} &= u_1(i), \\ \mathcal{E}\{x(0,j)\} &= u_2(j), \\ \mathrm{cov}\{x(i,0), x(s,0)\} &= P(i,0)\delta(i,s), \\ \mathrm{cov}\{x(0,j), x(0,t)\} &= P(0,j)\delta(j,t), \\ \mathrm{cov}\{x(i,0), x(0,j)\} &= P(0,0)\delta(i,0), \delta(0,j), \quad (3) \end{aligned}$$

where $u_1(i), u_2(j), P(i,0)$ and $P(0,j)$ are known parameters with appropriate dimensions and $u_1(0) = u_2(0)$.

As for the stochastic nonlinear functions $f(x(i,j)) \in \mathbb{R}^{n_x}$ and $h^l(x(i,j)) \in \mathbb{R}^{n_y}$, the following properties are satisfied

$$\begin{aligned} f(0) = 0, h^l(0) = 0, \\ (f(x) - f(s))^T(f(x) - f(s)) \le \lambda(x-s)^T(x-s), \\ (h_l(x) - h_l(s))^T(h_l(x) - h_l(s)) \le \tau_l(x-s)^T(x-s), \end{aligned}$$

where x, s are the state vectors, λ, τ_l are known positive scalars.

The information obtained from the sensor is subsequently organized through a stochastic communication protocol. Each sensor is with limited capacity, allowing only n_y packets to be simultaneously observed during network transmission. To ensure the signal integrity, it is assumed that each sensor can only transmit a single data packet at any given time. Thus, the random variable $\zeta_l(i,j)$ $(l = 1, 2, \cdots, m)$ is introduced, where $\zeta_l(i,j) \in \{1, 2, \ldots, n_y\}$ denotes the transmission characteristic of the l th sensor at the instant (i,j) and $\zeta_1(i,j), \zeta_2(i,j), \ldots, \zeta_m(i,j)$ are mutually uncorrelated random variables. The event $\zeta_l(i,j) = t$ signifies that the l-th sensor transmits the observed tth packet to the estimator. The probability distribution of $\zeta_l(i,j)$ is given as below

$$prob\{\zeta_l(i,j) = t\} = \rho_{lt}. \quad (4)$$

here, ρ_{lt} is a known positive scalar that satisfies $\rho_{l1} + \rho_{l2} + \cdots + \rho_{ln_y} = 1$.

For short, denote the observed output of the lth sensor as below

$$y_l(i,j) = [\ y_{l1}(i,j) \quad y_{l2}(i,j) \quad \cdots \quad y_{ln_y}(i,j)\ ]^T.$$

Since each sensor can only send one data packet through the shared network at each transmission time, then the aforementioned communication protocol is employed for scheduling. And the received observation for the l-th sensor can be written as

$$\bar{y}_l(i,j) = \begin{bmatrix} \delta(\zeta_l(i,j),1)y_{l1}(i,j) \\ \delta(\zeta_l(i,j),2)y_{l2}(i,j) \\ \vdots \\ \delta(\zeta_l(i,j),n_y)y_{ln_y}(i,j) \end{bmatrix}.$$

So it can be converted as,

$$\bar{y}_l(i,j) = H_{\zeta_l(i,j)}y_l(i,j), \quad (5)$$

where $\mathrm{H}_{\zeta_l(i,j)} \triangleq diag_{1\le t\le n_y}\{\delta(\zeta_l(i,j),t)\}$, which satisfies the following statistical properties,

$$E\{H_{\varsigma_l(i,j)}\} = \bar{\Phi}_l,$$

with $\bar{\Phi}_l = diag_{1\le l\le m}\{\rho_{lt}\} \in \mathbb{R}^{n_y\times n_y}$. Based on the function of $\delta(\cdot,\cdot)$, the following equalities hold for $l, k \in [1, m]$, $s, t \in [1, n_y]$

$$\begin{aligned} E\{\delta^2(\zeta_k(i,j),s)\} = \rho_{ks}, \\ E\{\delta(\zeta_k(i,j),s)\delta(\zeta_k(i,j),t)\} = 0, s \ne t, \\ E\{\delta(\zeta_k(i,j),s)\delta(\zeta_l(i,j),t)\} = \rho_{ks}\rho_{lt}, k \ne l. \end{aligned}$$

Then, for any matrix Y, the following equality holds

$$\begin{aligned} &E\{H_{\varsigma_l(i,j)} Y H^T_{\varsigma_l(i,j)}\} = \hat{\Phi}_l^{\circ} Y, \\ &\tilde{\Phi}_l^{\circ} Y = \hat{\Phi}_l^{\circ} Y - \bar{\Phi}_l Y \bar{\Phi}_l^T, \end{aligned} \tag{6}$$

where $\tilde{\Phi}_l = (\tilde{\Phi}_{l,st})_{n_y \times n_y}$ satisfies

$$\tilde{\Phi}_{l,st} = \begin{cases} \rho_{ls}(1-\rho_{ls}), & s = t \\ -\rho_{ls}\rho_{lt}, & s \neq t \end{cases}. \tag{7}$$

Now, we make the following assumption.

Assumption 1 For the random sequences $\zeta_l(i,j)$, $w^T(i,j)$, $v_l^T(i,j)$, $\alpha_s(i,j)$ and $\beta_l(i,j)$ are mutually uncorrelated for $i,j \in [0,N]$ and $s,l \in [1,m]$.

The problem investigated in this paper is to design a distributed filter based on the CI fusion algorithm for (1) and (2).

3 MAIN RESULTS

This section aims to develop a distributed recursive estimator of 2-D systems with jumping parameters. The initial step is to design a local filter based on the lth measurement

$$\begin{aligned} \hat{x}_p^l(i,j) &= A^1_{\theta(i,j-1)} \hat{x}_u^l(i,j-1) \\ &\quad + A^2_{\theta(i-1,j)} \hat{x}_u^l(i-1,j), \end{aligned} \tag{8}$$

$$\begin{aligned} \hat{x}_u^l(i,j) &= \hat{x}_p^l(i,j) + K^l_{\theta(i,j)} (\bar{y}_l(i,j) \\ &\quad - H_{\varsigma_l(i,j)} C^l_{\theta(i,j)} \hat{x}_p^l(i,j)), \end{aligned} \tag{9}$$

where $\hat{x}_p^l(i,j)$ and $\hat{x}_u^l(i,j)$ represents the local one-step prediction and local state estimation of the lth sensor state $x(i,j)$, respectively. $K^l_{\theta(i,j)}$ is the filter gain.

According to (1), (2), (8) and (9), the local one-step prediction error $\tilde{x}_p^l(i,j) \triangleq x(i,j) - \hat{x}_p^l(i,j)$ and the local filtering error $\tilde{x}_u^l(i,j) \triangleq x(i,j) - \hat{x}_u^l(i,j)$ are respectively defined as below

$$\begin{aligned} &\tilde{x}_p^l(i,j) = A^1_{\theta(i,j-1)} \tilde{x}_u^l(i,j-1) + A^2_{\theta(i-1,j)} \tilde{x}_u^l(i-1,j) \\ &+ B^1_{\theta(i,j-1)} w(i,j-1) + B^2_{\theta(i-1,j)} w(i-1,j) \\ &+ \alpha^1_{\theta(i,j-1)} f(x(i,j-1)) + \alpha^2_{\theta(i-1,j)} f(x(i-1,j)), \end{aligned} \tag{10}$$

$$\begin{aligned} &\tilde{x}_u^l(i,j) = [I - K^l_{\theta(i,j)} H_{\varsigma_l(i,j)} C^l_{\theta(i,j)}] \tilde{x}_p^l(i,j) \\ &- K^l_{\theta(i,j)} H_{\varsigma_l(i,j)} [\beta^l_{\theta(i,j)} h^l(x(i,j)) + v^l(i,j)]. \end{aligned} \tag{11}$$

Subsequently, a 2-D distributed CI fusion estimator $\hat{x}_u^{CI}(i,j)$ can be obtained recursively based on the local predictors and filters by the CI fusion algorithm.

For simplicity, we denote the second moments of the above variables as below,

$$\begin{aligned} X_z(i,j) &\triangleq E\{x(i,j)x^T(i,j)1_{\theta(i,j)=z}\}, \\ P_p^{lz}(i,j) &\triangleq E\{\tilde{x}_p^l(i,j)\tilde{x}_p^l(i,j)^T 1_{\theta(i,j)=z}\}, \\ P_u^{lz}(i,j) &\triangleq E\{\tilde{x}_u^l(i,j)\tilde{x}_u^l(i,j)^T 1_{\theta(i,j)=z}\}, \\ X_e(i,j-1;i-1,j) &\triangleq E\{x(i,j-1)x^T(i-1,j) \\ &\quad \times 1_{\theta(i,j-1)=e} 1_{\theta(i-1,j)=e}\}, \\ P_p^{le}(i,j-1;i-1,j) &\triangleq E\{\tilde{x}_p^l(i,j-1)(\tilde{x}_p^l(i-1,j))^T \\ &\quad \times 1_{\theta(i,j-1)=e} 1_{\theta(i-1,j)=e}\}, \\ P_u^{le}(i,j-1;i-1,j) &\triangleq E\{\tilde{x}_u^l(i,j-1)(\tilde{x}_u^l(i-1,j))^T \\ &\quad \times 1_{\theta(i,j-1)=e} 1_{\theta(i-1,j)=e}\}. \end{aligned}$$

The upper bounds of the aforementioned second moments are provided in the following lemmas, which are conducive to the subsequent inference of results.

Lemma 1 Consider the 2-D jumping parameter system (1), (2) and the local estimator (9), (10), under the condition that there exists a set of positive definite matrix sequences $\{\bar{X}_z(i,j)\}_{i,j=1}^N$ satisfying the following recursive equation for any given positive scalar μ, then $\bar{X}_z(i,j)$ forms the upper bound for the second moments of the system state,

$$\begin{aligned} &\bar{X}_z(i,j) \\ &= \sum_{e=1}^{N_\theta} p_{ez} \{(1+\mu) A^1_e(i,j-1) \bar{X}_e(i,j-1) A^1_e(i,j-1)^T \\ &+ (1+\mu^{-1}) A^2_e(i-1,j) \bar{X}_e(i-1,j) A^2_e(i-1,j)^T \\ &+ \pi_e B^1_e(i,j-1) Q(i,j-1) (B^1_e(i,j-1))^T \\ &+ \pi_e B^2_e(i-1,j) Q(i-1,j) (B^2_e(i-1,j))^T \\ &+ \lambda \sigma^1_e tr\{\bar{X}_e(i,j-1)\} I \\ &+ \lambda \sigma^2_e tr\{\bar{X}_e(i-1,j)\} I\}. \end{aligned} \tag{12}$$

Proof. In light of the nonlinear properties, we have

$$\begin{aligned} &E\{f(x(i,j))f^T(x(i,j))1_{\theta(i,j)=z}\} \\ &\leq \lambda E\{x^T(i,j)x(i,j)1_{\theta(i,j)=z}\} I \\ &\leq \lambda tr\{X_z(i,j)\} I. \end{aligned} \tag{13}$$

On the basis of (1) and in view of the statistical property of the random variables, the recursive equation for the second moments $X(i,j)$ can be expressed as

$$\begin{aligned} &X_z(i,j) = E\{x(i,j)x^T(i,j)1_{\theta(i,j)=z}\} \\ &= \sum_{e=1}^{N_\theta} p_{ez} [A^1_e(i,j-1) X_e(i,j-1) (A^1_e(i,j-1))^T \\ &+ A^2_e(i-1,j) X_e(i-1,j) (A^2_e(i-1,j))^T \\ &+ \pi_e B^1_e(i,j-1) Q(i,j-1) (B^1_e(i,j-1))^T \\ &+ \pi_e B^2_e(i-1,j) Q(i-1,j) (B^2_e(i-1,j))^T \\ &+ \sigma^1_e E\{f(x(i,j-1)) f^T(x(i,j-1))\} \\ &+ \sigma^2_e E\{f(x(i-1,j)) f^T(x(i-1,j))\} \\ &+ A^1_e(i,j-1) X_e(i,j-1;i-1,j) (A^2_e(i-1,j))^T \\ &+ A^2_e(i-1,j) X_e(i-1,j;i,j-1) (A^1_e(i,j-1))^T] \\ &\leq \sum_{e=1}^{N_\theta} p_{ez} \{(1+\mu) A^1_e(i,j-1) X_e(i,j-1) \\ &\times (A^1_e(i,j-1))^T + (1+\mu^{-1}) A^2_e(i-1,j) \\ &\times X_e(i-1,j) (A^2_e(i-1,j))^T \\ &+ \pi_e B^1_e(i,j-1) Q(i,j-1) (B^1_e(i,j-1))^T \\ &+ \pi_e B^2_e(i-1,j) Q(i-1,j) (B^2_e(i-1,j))^T \\ &+ \lambda \sigma^1_e tr\{X_e(i,j-1)\} I \\ &+ \lambda \sigma^2_e tr\{X_e(i-1,j)\} I\}. \end{aligned} \tag{14}$$

Based on (12), (14), one yields

$$\begin{aligned}X_z(i,j)-\bar{X}_z(i,j)\le&\sum_{e=1}^{N_\theta}p_{ez}\{(1+\mu)A_e^1(i,j-1)\\&\times(X_e(i,j-1)-\bar{X}_e(i,j-1))(A_e^1(i,j-1))^T\\&+(1+\mu^{-1})A_e^2(i-1,j)(X_e(i-1,j)\\&-\bar{X}_e(i-1,j))(A_e^2(i-1,j))^T\\&+\lambda\sigma_e^1tr\{(X_e(i,j-1)-\bar{X}_e(i,j-1))\}I\\&+\lambda\sigma_e^2tr\{(X_e(i-1,j)-\bar{X}_e(i-1,j))\}I\}.\end{aligned}\tag{15}$$

According to the initial conditions $\bar{X}_z(i,0)=X_z(i,0)$, $\bar{X}_z(0,j)=X_z(0,j)$, one has (12) for $(i,j)\in\{(i_1,j_1)|i_1,j_1>0;i_1+j_1=1\}$. Next, assume $(i,j)\in\{(i_1,j_1)|i_1,j_1>0;i_1+j_1=k\}$, $X_z(i,j)\le\bar{X}_z(i,j)$ is true. By the mathematical induction method, we obtain $X_z(i,j)\le\bar{X}_z(i,j)$ for $(i,j)\in\{(i_1,j_1)|i_1,j_1>0;i_1+j_1=k+1\}$. This completes the proof of Lemma 1.

Lemma 2 Consider (10) and (11), the recursive form for the local error covariance matrices $P_p^{lz}(i,j)$ and $P_u^{lz}(i,j)$ are respectively given as below

$$\begin{aligned}P_p^{lz}(i,j)=&\sum_{e=1}^{N_\theta}p_{ez}\{A_e^1(i,j-1)P_u^{le}(i,j-1)\\&\times(A_e^1(i,j-1))^T+A_e^1(i,j-1)\\&\times P_u^{le}(i,j-1;i-1,j)(A_e^2(i-1,j))^T\\&+A_e^2(i-1,j)P_u^{le}(i-1,j;i,j-1)\\&\times(A_e^1(i,j-1))^T\\&+A_e^2(i-1,j)P_u^{le}(i-1,j)(A_e^2(i-1,j))^T\\&+\pi_eB_e^1(i,j-1)Q(i,j-1)(B_e^1(i,j-1))^T\\&+\pi_eB_e^2(i-1,j)Q(i-1,j)(B_e^2(i-1,j))^T\\&+\lambda\sigma_e^1E\{f(x(i,j-1))f^T(x(i,j-1))\}\\&+\lambda\sigma_e^2E\{f(x(i-1,j))f^T(x(i-1,j))\}\},\end{aligned}\tag{16}$$

$$\begin{aligned}P_u^{lz}(i,j)=&E\{\tilde{x}_u^l(i,j)(\tilde{x}_u^l(i,j))^T1_{\theta(i,j)=z}\}\\=&E\{[I-K_z^l(i,j)H_{\varsigma_l(i,j)}C_z^l(i,j)]P_p^{lz}(i,j)\\&\times[I-K_z^l(i,j)H_{\varsigma_l(i,j)}C_z^l(i,j)]^T\}\\&+E\{K_z^l(i,j)H_{\varsigma_l(i,j)}[\beta_z^l(i,j)h^l(x(i,j))\\&\times(h^l(x(i,j))^T)(\beta_z^l(i,j))^T+R^l(i,j)]\\&\times(K_z^l(i,j)H_{\varsigma_l(i,j)})^T\}.\end{aligned}\tag{17}$$

Proof. Based on (10), (11), and by the definition of $f(x(i,j))$, $h^l(x(i,j))$ under Assumption 1, this lemma can be obtained straightly. Thus, the proof is omitted for simplicity.

Remark 1 Lemmas 1 and 2 provide the recursive equations for the prediction and filter error variances. It is evident that, due to the presence of nonlinear terms in the covariance matrix of the state estimation errors, direct calculation of the filter gains are not feasible. Therefore, our subsequent step is to seek for an upper bound of the covariance matrix of the state estimation error.

Theorem 1 Assume that there exist two sets of positive definite matrix sequences $Y_p^{lz}(i,j)$, $Y_u^{lz}(i,j)$ satisfying the following recursive equations

$$\begin{aligned}Y_p^{lz}(i,j)=&\sum_{e=1}^{N_\theta}p_{ez}[(1+\mu)A_e^1(i,j-1)Y_u^{le}(i,j-1)\\&\times(A_e^1(i,j-1))^T+(1+\mu^{-1})A_e^2(i-1,j)\\&\times Y_u^{le}(i,j-1)(A_e^2(i-1,j))^T\\&+\pi_eB_e^1(i,j-1)Q(i,j-1)(B_e^1(i,j-1))^T\\&+\pi_eB_e^2(i-1,j)Q(i-1,j)(B_e^2(i-1,j))^T\\&+\lambda(\sigma_e^1tr\{\bar{X}_e(i,j-1)\}\\&+\sigma_e^2tr\{\bar{X}_e(i-1,j)\})I],\end{aligned}\tag{18}$$

$$\begin{aligned}Y_u^{lz}(i,j)=&(I-K_z^l(i,j)\bar{\Phi}_lC_z^l(i,j))Y_p^{lz}(i,j)\\&\times(I-K_z^l(i,j)\bar{\Phi}_lC_z^l(i,j))^T\\&+K_z^l(i,j)[\hat{\Phi}_l^\circ\bar{R}(i,j)+\tilde{\Phi}_l^\circ(C_z^l(i,j))\\&\times Y_p^{lz}(i,j)(C_z^l(i,j))^T)+\kappa I]\\&\times(K_z^l(i,j))^T,\end{aligned}\tag{19}$$

for $i,j\in[1,N]$, where λ and k are the given positive scalars and the initial conditions obey

$$Y_u^{lz}(i,0)=P_u^{lz}(i,0),Y_u^{lz}(0,j)=P_u^{lz}(0,j),i,j\in[1,N],$$

then the covariance matrices of prediction and filter errors are with the following upper bounds

$$P_p^{lz}(i,j)\le Y_p^{lz}(i,j),P_u^{lz}(i,j)\le Y_u^{lz}(i,j).\tag{20}$$

Proof. According to (19), we obtain

$$\begin{aligned}&E\{f(x(i,j))f^T(x(i,j))1_{\theta(i,j)=z}\}\\&\le\lambda tr\{\bar{X}_z(i,j)\}I_{n_x}.\end{aligned}\tag{21}$$

Similarly, one yields

$$\begin{aligned}&E\{h^l(x(i,j))(h^l(x(i,j)))^T1_{\theta(i,j)=z}\}\\&\le\tau_ltr\{\bar{X}_z\{i,j\}\}I_{n_y}.\end{aligned}\tag{22}$$

Substituting (21) into (16), we have

$$\begin{aligned}P_p^{lz}(i,j)\le&\sum_{e=1}^{N_\theta}p_{ez}\{(1+\mu)A_e^1(i,j-1)\\&\times P_u^{le}(i,j-1)(A_e^1(i,j-1))^T\\&+(1+\mu^{-1})A_e^2(i-1,j)P_u^{le}(i-1,j)\\&\times(A_e^2(i-1,j))^T\\&+\pi_eB_e^1(i,j-1)Q(i,j-1)(B_e^1(i,j-1))^T\\&+\pi_eB_e^2(i-1,j)Q(i-1,j)(B_e^2(i-1,j))^T\\&+\lambda(\sigma_e^1tr\{\bar{X}_e(i,j-1)\}\\&+\sigma_e^2tr\{\bar{X}_e(i-1,j)\})I\}.\end{aligned}\tag{23}$$

According to (22), we have

$$\begin{aligned}&E\{H_{\varsigma_l(i,j)}[\beta_{\theta(i,j)}^lh^l(x(i,j))(h^l(x(i,j)))^T\\&\times(\beta_{\theta(i,j)}^l)^T+R^l(i,j)](H_{\varsigma_l(i,j)})^T1_{\theta(i,j)=z}\}\\&\le\hat{\Phi}_l\circ[\gamma_z^l\tau_ltr\{\bar{X}_z(i,j)\}I+R^l(i,j)].\end{aligned}\tag{24}$$

And in light of (6), (17) and (24), one yields

$$\begin{aligned}P_u^{lz}(i,j) \le\ & P_p^{lz}(i,j) - K_z^l(i,j)\bar{\Phi}_l C_z^l(i,j)P_p^{lz}(i,j)\\ & - P_p^{lz}(i,j)(C_z^l(i,j))^T\bar{\Phi}_l^T(K_z^l(i,j))^T\\ & + K_z^l(i,j)[\hat{\Phi}_l \circ C_z^l(i,j)P_p^{lz}(i,j)(C_z^l(i,j))^T\\ & + \bar{R}(i,j)](K_z^l(i,j))^T\\ =\ & (I - K_z^l(i,j)\bar{\Phi}_l C_z^l(i,j))P_p^{lz}(i,j)\\ & \times (I - K_z^l(i,j)\bar{\Phi}_l C_z^l(i,j))^T\\ & + K_z^l(i,j)[\hat{\Phi}_l \circ \bar{R}^l(i,j) + \tilde{\Phi}_l\\ & \circ (C_z^l(i,j)P_p^{lz}(i,j)(C_z^l(i,j))^T)]\\ & \times (K_z^l(i,j))^T, \end{aligned} \tag{25}$$

where

$$\bar{R}^l(i,j) = \gamma_z^l\tau_l tr\{\bar{X}_z(i,j)\}I + R^l(i,j).$$

Remark 2 Theorem 1 supplies the upper bounds of the estimation error variances. The next step is to design the filter gains by minimizing the trace of the upper bound matrix for the estimation error variances.

Theorem 2 Consider the local estimator defined in (8) and (9), the estimator gain $K_z^l(i,j)$ that minimizes the trace of the upper bound for the estimation error variance $Y_u^{lz}(i,j)$ is given by

$$K_z^l(i,j) = Y_p^{lz}(i,j)(C_z^l(i,j))^T\bar{\Phi}_l^T(\hat{R}^l(i,j))^{-1}. \tag{26}$$

Proof. In view of (6) and (19), the upper bound of the estimation error variance can be expressed as

$$\begin{aligned}Y_u^{lz}(i,j) =\ & Y_p^{lz}(i,j) - K_z^l(i,j)\bar{\Phi}_l C_z^l(i,j)Y_p^{lz}(i,j)\\ & - Y_p^{lz}(i,j)(C_z^l(i,j))^T\bar{\Phi}_l^T(K_z^l(i,j))^T\\ & + K_z^l(i,j)[\bar{\Phi}_l C_z^l(i,j)Y_p^{lz}(i,j)(C_z^l(i,j))^T\bar{\Phi}_l^T\\ & + \hat{\Phi}_l \circ \bar{R}^l(i,j) + \tilde{\Phi}\circ C_z^l(i,j)Y_p^{lz}(i,j)(C_z^l(i,j))^T\\ & + \kappa I](K_z^l(i,j))^T\\ =\ & Y_p^{lz}(i,j) + [K_z^l(i,j) - \bar{K}_z^l(i,j)]\\ & \times \hat{R}^l(i,j)[K_z^l(i,j) - \bar{K}_z^l(i,j)]^T\\ & - \bar{K}_z^l(i,j)\hat{R}^l(i,j)(\bar{K}_z^l(i,j))^T. \end{aligned} \tag{27}$$

By minimizing the upper bound of the local estimation error covariance, the filter gain $K_z^l(i,j)$ is to be determined based on the complete square method, where

$$\hat{R}^l(i,j) = \hat{\Phi}_l \circ (\bar{R}^l + C_z^l(i,j)Y_p^{lz}(i,j)(C_z^l(i,j))^T) + \kappa I,$$

$$K_z^l(i,j) = Y_p^{lz}(i,j)(C_z^l(i,j))^T\bar{\Phi}_l^T(\hat{R}^l(i,j))^{-1}.$$

If select $K_z^l(i,j) = \bar{K}_z^l(i,j)$, $Y_u^{lz}(i,j)$ would be minimized. So the local minimum upper bound for the estimation error variance is obtained,

$$Y_u^{lz}(i,j) = Y_p^{lz}(i,j) - K_z^l(i,j)\bar{\Phi}_l C_z^l(i,j)Y_p^{lz}(i,j). \tag{28}$$

This completes the proof of Theorem 2.

On the basis of the local state estimators, a distributed state fusion estimator based on the CI fusion algorithm will be presented in the following result.

Theorem 3 Consider the 2-D systems (1) and (2), a distributed CI fusion estimator is given by

$$\begin{aligned}\hat{x}_u^{CI}(i,j) =\ & \sum_{l=1}^m \omega_z^l(i,j)Y_u^{CIz}(i,j)\\ & \times [Y_u^{lz}(i,j)]^{-1}\hat{x}_u^l(i,j), \end{aligned} \tag{29}$$

$$Y_u^{CIz}(i,j) = [\sum_{l=1}^m \omega_z^l(i,j)[Y_u^{lz}(i,j)]^{-1}]^{-1}, \tag{30}$$

where $Y_u^{CIz}(i,j)$ is the upper bound for the variance of the distributed state fusion estimator, $\omega_z^l(i,j)$ is the weight coefficients satisfying $0 \le \omega_z^l(i,j) \le 1$, $\omega_z^1(i,j) + \omega_z^2(i,j) + \cdots + \omega_z^m(i,j) = 1$, which can be calculated as follows

$$\omega_z^l(i,j) = \frac{tr[Y_u^{lz}(i,j)^{-1}]}{\sum_{l=1}^m tr[Y_u^{lz}(i,j)^{-1}]}. \tag{31}$$

Proof. In view of (9), Theorem 2 and the CI fusion estimation algorithm, the CI fusion estimator can be obtained straightforwardly, and therefore is omitted here.

Remark 3 In Theorem 3, a distributed CI based estimation algorithm is developed, which avoids computing the error covariance matrix of local estimators and effectively reduces the computational complexity.

4 NUMERICAL EXAMPLE

In this section, we present a simple example of a 2-D jumping parameter system to illustrate the feasibility of the design scheme. Consider a 2-D system with two observation channels, as described in (1), (2) and (5). The system parameters are provided as below.

If $\theta(i,j) = 1$,

$$A_1^1(i,j) = \begin{bmatrix} 0.4 & 0.05 \\ 0 & 0.4 \end{bmatrix}, A_1^2(i,j) = \begin{bmatrix} 0.35 & 0.2 \\ 0.1 & 0.45 \end{bmatrix},$$

$$B_1^1(i,j) = \begin{bmatrix} 0.3 & 0.2 \end{bmatrix}^T, B_1^2(i,j) = \begin{bmatrix} 0.3 & 0.25 \end{bmatrix}^T,$$

$$C_1^1(i,j) = \begin{bmatrix} 0.3 & 0.5 \\ 0.6 & 0.8 \end{bmatrix}, C_1^2(i,j) = \begin{bmatrix} 0.32 & 0.5 \\ 0.55 & 0.8 \end{bmatrix},$$

If $\theta(i,j) = 2$,

$$A_2^1(i,j) = \begin{bmatrix} 0.4 & 0.04 \\ 0 & 0.4 \end{bmatrix}, A_2^2(i,j) = \begin{bmatrix} 0.35 & 0.1 \\ 0 & 0.45 \end{bmatrix},$$

$$B_2^1(i,j) = \begin{bmatrix} 0.3 & 0.35 \end{bmatrix}^T, B_2^2(i,j) = \begin{bmatrix} 0.3 & 0.24 \end{bmatrix}^T,$$

$$C_2^1(i,j) = \begin{bmatrix} 0.3 & 0.6 \\ 0.5 & 0.8 \end{bmatrix}, C_2^2(i,j) = \begin{bmatrix} 0.32 & 0.4 \\ 0.5 & 0.8 \end{bmatrix}.$$

The transition probabilities between different modes satisfy

$$P = \begin{bmatrix} 0.5 & 0.5 \\ 0.6 & 0.4 \end{bmatrix},$$

where $\mu = 0.9$, $\lambda = 0.9$, $\kappa = 0.01$, $\tau_l = 0.3$, $N = 50$ and $l = 2$. $w(i,j)$, $v^l(i,j)$ are mutually independent zero-mean Gaussian white noises with variances of $Q = 0.16$,

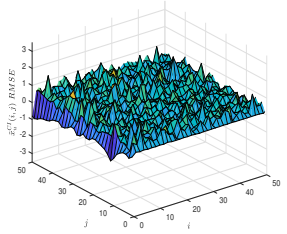

Fig. 1: The first component of the Root Mean Square Error of CI Fusion Estimation.

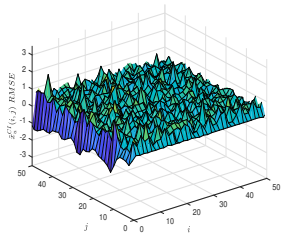

Fig. 2: The second component of the Root Mean Square Error of CI Fusion Estimation.

$R^1(i,j) = 0.09I$ and $R^2(i,j) = 0.09I$, respectively. The random variables $\alpha^l_{\theta(i,j)}$ and $\beta^l_{\theta(i,j)}$ are zero-mean Gaussian white noises with variances of $\sigma^l_{\theta(i,j)} = 0.04$ and $\gamma^l_{\theta(i,j)} = 0.125$. $\theta(i,j)$ is a Markov chain taking in a finite set $\{1,2\}$, and the initial distribution of $\theta(i,j)$ is (0.5, 0.5). The probability distribution of the random variables depicting the communication protocol are $prob(\zeta_l(i,j) = 1) = 0.5$ and $prob(\zeta_2(i,j) = 1) = 0.5$. Here, the nonlinear functions satisfy $f(x(i,j)) = 0.3|x(i,j)|$ and $h^l(x(i,j)) = 0.3|x(i,j)|$. The initial conditions are $x(0,j) = x(i,0) = 0$, $P(0,j) = P(i,0) = I$.

The simulation results are shown in Figures 1-3. Figure 1 displays the first component of the root mean square error of the CI Fusion Estimation and Figure 2 shows the second component of the root mean square error of the CI Fusion Estimation. Figure 3 shows the trace of the covariance for the CI fusion estimate error. It can be seen that the CI fusion estimator can estimate the state of the system effectively.

5 CONCLUSION

In this paper, a recursive distributed filter has been designed for a 2-D Markov jump parameter system with communication protocols and nonlinearity. The system utilizes a set of mutually uncorrelated random sequences to characterize the random communication protocols. Through the mathematical induction method and the stochastic analysis approach, the upper bounds on the local estimation error variances have been established. The filter gains were designed by minimizing the upper bounds on the estimation error variances obtained at each moment. Finally, a CI fusion algorithm has been applied to address the optimal state fusion estimation problem, demonstrating its high precision and reliability.

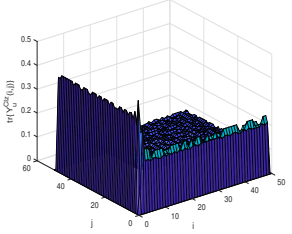

Fig. 3: Trace of the covariance matrix of the CI fusion estimation error $Y_u^{CIz}(i,j)$.

References

[1] Y. Ran, The Kalman filtering of 2-D systems in Fornasini-Marchesini model, 2008 27th Chinese Control Conference. IEEE, 2008, 49(10): 736-740.

[2] C. K. Ahn, P. Shi, M. V. Basin, Two-dimensional peak-to-peak filtering for stochastic Fornasini-Marchesini systems, IEEE Transactions on Automatic Control, 2017, 63(5): 1472-1479.

[3] Y. Zou, M. Sheng, N. Zhong, et al, A generalized Kalman filter for 2D discrete systems, Circuits, Systems and Signal Processing, 2004, 23: 351-364.

[4] F. Wang, Z. Wang, J. Liang, et al, Recursive state estimation for two-dimensional shift-varying systems with random parameter perturbation and dynamical bias, Automatica, 2020, 112: 108658.

[5] J. Hu, Z. Wang, G. P. Liu, et al, A prediction-based approach to distributed filtering with missing measurements and communication delays through sensor networks, IEEE Transactions on Systems, Man, and Cybernetics: Systems, 2020, 51(11): 7063-7074.

[6] X. Ge, Q. L. Han, Distributed event-triggered H_∞ filtering over sensor networks with communication delays, Information Sciences, 2015, 291: 128-142.

[7] R. Olfati-Saber, Kalman-consensus filter: Optimality, stability, and performance, Proceedings of the 48h IEEE Conference on Decision and Control (CDC) held jointly with 2009 28th Chinese Control Conference. IEEE, 2009: 7036-7042.

[8] S. Das, J. M. F. Moura, Distributed Kalman filtering with dynamic observations consensus, IEEE Transactions on Signal Processing, 2015, 63(17): 4458-4473.

[9] J. Wang, P. Dong, Z. Jing, et al, Consensus-based filter for distributed sensor networks with colored measurement noise, Sensors, 2018, 18(11): 3678.

[10] W. Li, Y. Jia, J. Du, Distributed filtering for discrete-time linear systems with fading measurements and time-correlated noise, Digital Signal Processing, 2017, 60: 211-219.

[11] J. Feng, M. Zeng, Optimal distributed Kalman filtering fusion for a linear dynamic system with cross-correlated noises, International Journal of Systems Science, 2012, 43(2): 385-398.

[12] L. Liu, L. Ma, Y. Wang, et al, Distributed set-membership filtering for time-varying systems under constrained measurements and replay attacks, Journal of the Franklin Institute, 2020, 357(8): 4983-5003.

[13] F. Wang, Z. Wang, J. Liang, et al, Recursive distributed filtering for two-dimensional shift-varying systems over sensor networks under stochastic communication protocols, Automatica, 2020, 115: 108865.

[14] H. Yu, Y. Zhuang, W. Wang, Distributed H_∞ filtering with consensus in sensor networks: a two-dimensional system-based approach, International Journal of Systems Science, 2011, 42(9): 1543-1557.

[15] L. Zou, Z. Wang, J. Hu, et al, On H_∞ Finite-Horizon Filtering Under Stochastic Protocol: Dealing With High-Rate Communication Networks, IEEE Transactions on Automatic Control, 2017, 62(9): 4884-4890.

Proceedings of the 3rd Conference on Fully Actuated System Theory and Applications
May 10-12, 2024, Shenzhen, China

Output Tracking Based on Reduced-Order Observer for Fully Actuated Systems

Hong Jiang[1], Guangren Duan[1,2]

1. Center for Control Theory and Guidance Technology, Harbin Institute of Technology, Harbin 150001, P. R. China
E-mail: jiang_hong1993@163.com, g.r.duan@hit.edu.cn

2. Center for Control Science and Technology, Southern University of Science and Technology, Shenzhen 518055, P. R. China
E-mail: duangr@sustech.edu.cn

Abstract: In this paper, an output tracking control scheme based on the reduced-order observer is proposed for fully actuated systems. First, to make more use of the output information, a reduced-order observer is designed, and a linear matrix inequality condition is given to solve the observer gain. The estimated values of the observer can converge to the true values exponentially. Second, taking advantage of the full-actuation property, an output tracking controller based on the above observer is designed such that the system output tracks a given signal, and the condition for exponential convergence of the tracking error is also given. An example is provided to show the effectiveness of the proposed approach.

Key Words: Reduced-Order Observer, Fully Actuated System, Linear Matrix Inequality, Full-Actuation Property, Output Tracking Controller

1 Introduction

Actual physical systems are often nonlinear, which makes the controllers design enormously difficult and the form of controllers complex. For this reason, Duan proposed the full-actuated system (FAS) approach to deal with the controller design problem for nonlinear systems [1–3]. By means of ascending the system order, the original system is transformed into a higher-order system, whose number of states is equal to the number of control inputs and the control input matrix is invertible. Then we can utilize the full-actuation property to eliminate the nonlinearity of the system and obtain a high-order linear closed-loop system. Duan also illustrates that many systems can be converted to FASs [4, 5], meaning that FASs are widespread. Due to the great advantages of the FAS approach in controller design, the method has also been extended to complex nonlinear systems such as discrete-time systems [6], time-delay systems [7], and nonholonomic systems [8], as well as to engineering applications [9–11].

However, the above results are based on state-feedback control, which is the only way to eliminate the nonlinearity in the system. In actual engineering systems, the states are not always measurable, in which case we need use observers to estimate the states and use estimations to design the controller. For example, Zhao designed an exponentially convergent observer using the linear parameter varying (LPV) approach and an observer-based state stabilization controller to make the closed-loop system exponentially stable [12]. Jiang devised a generalized proportional-integral (PI) observer and applied it to the output tracking problem [13]. In addition, the extended state observer (ESO) has been introduced for FASs with disturbances, and satisfactory results have been obtained [14–16].

For the observer design of FASs, all of them currently observe the full state of the system, which does not make maximal use of the output information. In order to further utilize the output information and reduce the dimension of the observer, one generally designs a reduced-order observer. For instance, Zhu provided a design method for reduced-order observer of nonlinear systems using Riccati equation, and proved that the existence of the full- and reduced-order observers are equivalent [17]. Trin derived the reduced-order observer gain for the nonlinear systems based on the LMI method [18]. Furthermore, the reduced-order observer is also extended to discrete-time systems [19] and many engineering systems [20–22]. It can be seen that in the framework of state-space model, the reduced-order observer has been well applied for nonlinear systems.

In this paper, a reduced-order observer-based output tracking controller is designed for FASs. The contribution includes two parts. First, a reduced-order observer is designed for FASs, which makes full use of the output information and reduces the dimensionality of the observer compared to existing work of FASs. Second, on the basis of the full-actuation property, a reduced-order observer-based controller is proposed to make output tracking a reference signal. Also, we show that for the tracking error to be exponentially convergent, the nonlinear function needs to satisfy an additional condition.

In the subsequent sections, I_r denotes the r-order identity matrix. $0_{n\times m}$ and 0_n both denote the zero matrix. $\lambda_{\max}(A)$ and $\lambda_{\min}(A)$ denote the maximum and minimum eigenvalues of A. In order to keep consistent with the FAS series papers, we continue to use the following symbols

$$x^{(0\sim n-1)}=\begin{bmatrix} x \\ \dot{x} \\ \vdots \\ x^{(n-1)} \end{bmatrix},\ B_r=\begin{bmatrix} 0 \\ \vdots \\ 0 \\ I_r \end{bmatrix},$$

$$A_{0\sim n-1}=\begin{bmatrix} A_0 & A_1 & \cdots & A_{n-1} \end{bmatrix},$$

$$\Phi(A_{0\sim n-1})=\begin{bmatrix} 0 & I_r & \cdots & 0 \\ 0 & 0 & \ddots & \vdots \\ \vdots & \vdots & \cdots & I_r \\ A_0 & A_1 & \cdots & A_{n-1} \end{bmatrix}.$$

This work is supported by Science Center Program of the National Natural Science Foundation of China under Grant 62188101.

This paper contains 5 sections. In the next section, we design a reduced-order observer for FASs, and give the LMI condition for exponential convergence of the observation error. Then, we apply the observer to the output tracking in Section 3. Section 4 is a numerical example for the effect of our approach. The last section is a brief conclusion.

2 Observer Design

In this paper, we consider the following general FAS

$$\begin{cases} x^{(n)} = f(x^{(0\sim n-1)}) + B(y)u \\ y = Cx^{(0\sim n-1)}, \end{cases} \tag{1}$$

where $u \in \mathbb{R}^r$ and $y \in \mathbb{R}^m$ are the input and output vectors, respectively, $x \in \mathbb{R}^r$ is the state vector, $f(\cdot) \in \mathbb{R}^r$ and $B(y) \in \mathbb{R}^{r\times r}$ are vector and matrix functions, and $C \in \mathbb{R}^{m\times nr}$ is a constant full-row matrix.

Assumption 1. $\det(B(y)) \neq 0$ *or* ∞*, for all* $y \in \mathbb{R}^m$.

Assumption 2. $f(x)$ *is* α_1*-Lipschitz for all* $x \in \mathbb{R}^{nr}$*, that is,* $\|f(x_1) - f(x_2)\| \leq \alpha_1\|x_1 - x_2\|$.

The system (1) can be rewritten as

$$\begin{aligned} \dot{x}^{(0\sim n-1)} =& \Phi(0_{0\sim n-1})x^{(0\sim n-1)} \\ &+ B_r f(x^{(0\sim n-1)}) + B_r B(y)u. \end{aligned} \tag{2}$$

For the observer design, it is natural to have the observability assumption.

Assumption 3. *The matrix pair* $(\Phi(0_{0\sim n-1}), C)$ *is observable.*

Since C is full-row, then there exists a matrix $M \in \mathbb{R}^{(nr-m)\times nr}$, such that $T = \begin{bmatrix} C \\ M \end{bmatrix}$ is non-singular. Denote

$$Q = T^{-1} = \begin{bmatrix} Q_1 & Q_2 \end{bmatrix},$$

where $Q_1 \in \mathbb{R}^{nr\times m}$ and $Q_2 \in \mathbb{R}^{nr\times(nr-m)}$, then

$$CQ_1 = I_m,\ CQ_2 = 0,\ MQ_1 = 0,\ MQ_2 = I_{n-m}.$$

Define

$$z = Tx^{(0\sim n-1)},$$

then, the derivative of z is

$$\begin{aligned} \dot{z} =& T\dot{x}^{(0\sim n-1)} \\ =& T\Phi(0_{0\sim n-1})x^{(0\sim n-1)} + TB_r f(x^{(0\sim n-1)}) \\ &+ TB_r B(y)u \\ =& T\Phi(0_{0\sim n-1})T^{-1}z + TB_r f(x^{(0\sim n-1)}) \\ &+ TB_r B(y)u \\ =& \begin{bmatrix} C\Phi(0_{0\sim n-1})Q_1 & C\Phi(0_{0\sim n-1})Q_2 \\ M\Phi(0_{0\sim n-1})Q_1 & M\Phi(0_{0\sim n-1})Q_2 \end{bmatrix} z \\ &+ \begin{bmatrix} C \\ M \end{bmatrix} B_r f(x^{(0\sim n-1)}) + \begin{bmatrix} C \\ M \end{bmatrix} B_r B(y)u. \end{aligned} \tag{3}$$

Block z as

$$z = \begin{bmatrix} z_1 \\ z_2 \end{bmatrix},$$

where $z_1 \in \mathbb{R}^m$ and $z_2 \in \mathbb{R}^{nr-m}$. Then, we have

$$\begin{cases} \dot{z}_1 = C\Phi(0_{0\sim n-1})Q_1 z_1 + C\Phi(0_{0\sim n-1})Q_2 z_2 \\ \qquad + CB_r f(x^{(0\sim n-1)}) + CB_r B(y)u \\ \dot{z}_2 = M\Phi(0_{0\sim n-1})Q_1 z_1 + M\Phi(0_{0\sim n-1})Q_2 z_2 \\ \qquad + MB_r f(x^{(0\sim n-1)}) + MB_r B(y)u, \end{cases} \tag{4}$$

and

$$\begin{aligned} y =& CT^{-1}z \\ =& C\begin{bmatrix} Q_1 & Q_2 \end{bmatrix} z \\ =& \begin{bmatrix} I_m & 0_{m\times(nr-m)} \end{bmatrix} \begin{bmatrix} z_1 \\ z_2 \end{bmatrix} \\ =& z_1. \end{aligned} \tag{5}$$

Thus, we we can only estimate z_2 by the following reduced-order observer

$$\begin{aligned} \dot{\hat{z}}_2 =& M\Phi(0_{0\sim n-1})Q_1 z_1 + M\Phi(0_{0\sim n-1})Q_2 \hat{z}_2 \\ &+ MB_r f(\hat{x}^{(0\sim n-1)}) + MB_r B(y)u \\ &- L[\dot{z}_1 - C\Phi(0_{0\sim n-1})Q_1 z_1 - C\Phi(0_{0\sim n-1})Q_2 \hat{z}_2 \\ &\quad - CB_r f(\hat{x}^{(0\sim n-1)}) - CB_r B(y)u], \end{aligned} \tag{6}$$

where $L \in \mathbb{R}^{(nr-m)\times m}$ is the gain matrix, and $\hat{x}^{(0\sim n-1)}$ is the estimation of $x^{(0\sim n-1)}$. We can define the estimations of z and $x^{(0\sim n-1)}$ as

$$\hat{z} = \begin{bmatrix} z_1 \\ \hat{z}_2 \end{bmatrix}, \tag{7}$$

and

$$\hat{x}^{(0\sim n-1)} = T^{-1}\hat{z} = \begin{bmatrix} Q_1 & Q_2 \end{bmatrix} \begin{bmatrix} z_1 \\ \hat{z}_2 \end{bmatrix} = Q_1 y + Q_2 \hat{z}_2. \tag{8}$$

Since the derivative of z_1 contains the unavailable state z_2, we define the following auxiliary vector

$$w = \hat{z}_2 + Ly, \tag{9}$$

then, combining with (6), we have

$$\begin{aligned} \dot{w} =& \dot{\hat{z}}_2 + L\dot{y} \\ =& (M + LC)[\Phi(0_{0\sim n-1})Q_1 y + \Phi(0_{0\sim n-1})Q_2 \hat{z}_2 \\ &+ B_r f(Q_1 y + Q_2 \hat{z}_2) + B_r B(y)u]. \end{aligned} \tag{10}$$

Therefore, the observer (6) is rewritten as

$$\begin{cases} \dot{w} = (M + LC)[\Phi(0_{0\sim n-1})Q_1 y + \Phi(0_{0\sim n-1})Q_2 \hat{z}_2 \\ \qquad + B_r f(Q_1 y + Q_2 \hat{z}_2) + B_r B(y)u] \\ \hat{z}_2 = w - Ly, \end{cases} \tag{11}$$

Define the estimation error as

$$e_z = z_2 - \hat{z}_2, \tag{12}$$

then

$$x^{(0\sim n-1)} - \hat{x}^{(0\sim n-1)} = Q_2 e_z.$$

Taking the derivative of (12), we have the following state-space model

$$\begin{aligned} \dot{e}_z =& [M\Phi(0_{0\sim n-1})Q_2 + LC\Phi(0_{0\sim n-1})Q_2]e_z \\ &+ (M + LC)B_r \Delta f(\cdot), \end{aligned} \tag{13}$$

with

$$\Delta f(\cdot) = f(x^{(0\sim n-1)}) - f(\hat{x}^{(0\sim n-1)}). \tag{14}$$

Now, we have the following theorem.

Theorem 1. *If there exist a symmetric positive definite matrix P, a constant matrix R with appropriate dimensions, and a positive real number μ, such that*

$$\begin{bmatrix} H_1 + \varepsilon\alpha\|Q_2\|^2 I + \mu P & H_2 \\ H_2^{\mathrm{T}} & -\varepsilon I \end{bmatrix} < 0, \tag{15}$$

where ε is an any given positive real number, and

$$\begin{cases} H_1 = PM\Phi(0_{0\sim n-1})Q_2 + Q_2^{\mathrm{T}}\Phi^{\mathrm{T}}(0_{0\sim n-1})M^{\mathrm{T}}P \\ \qquad + RC\Phi(0_{0\sim n-1})Q_2 + Q_2^{\mathrm{T}}\Phi^{\mathrm{T}}(0_{0\sim n-1})C^{\mathrm{T}}R^{\mathrm{T}} \\ H_2 = PMB_r + RCB_r. \end{cases} \tag{16}$$

The estimation error of observer (11) is exponential convergent, and the observer gain is

$$L = P^{-1}R. \tag{17}$$

Proof. Choose the following Lyapunov function

$$V(t) = e_z^{\mathrm{T}} P e_z. \tag{18}$$

Taking the derivative of (18), and combining with (16) and (17), give

$$\begin{aligned} \dot{V} &= e_z^{\mathrm{T}} P\dot{e}_z + \dot{e}_z^{\mathrm{T}} P e_z \\ &= e_z^{\mathrm{T}} H_1 e_z + e_z^{\mathrm{T}} H_2 \Delta f(\cdot) + \Delta f^{\mathrm{T}}(\cdot) H_2^{\mathrm{T}} e_z \\ &= \begin{bmatrix} e_z \\ \Delta f(\cdot) \end{bmatrix}^{\mathrm{T}} \begin{bmatrix} H_1 & H_2 \\ H_2^{\mathrm{T}} & 0 \end{bmatrix} \begin{bmatrix} e_z \\ \Delta f(\cdot) \end{bmatrix}. \end{aligned} \tag{19}$$

In view of (15), we have

$$\begin{aligned} \dot{V} &< \begin{bmatrix} e_z \\ \Delta f(\cdot) \end{bmatrix}^{\mathrm{T}} \begin{bmatrix} -\varepsilon\alpha\|Q_2\|^2 I - \mu P & 0 \\ 0 & \varepsilon I \end{bmatrix} \begin{bmatrix} e_z \\ \Delta f(\cdot) \end{bmatrix} \\ &= -\varepsilon\alpha\|Q_2\|^2\|e_z\|^2 - \mu e_z^{\mathrm{T}} P e_z + \varepsilon\|\Delta f(\cdot)\|^2 \\ &< -\varepsilon\alpha\|Q_2\|^2\|e_z\|^2 - \mu e_z^{\mathrm{T}} P e_z + \varepsilon\alpha\|Q_2 e_z\|^2 \\ &< -\mu V. \end{aligned}$$

It is obvious that

$$V(t) \le V(0)\mathrm{e}^{-\mu t}. \tag{20}$$

According to the definition of the Lyapunov function, we obtain

$$\begin{aligned} \|e_z(t)\|^2 &\le \lambda_{\min}^{-1}(P)V(t) \le \lambda_{\min}^{-1}(P)V(0)\mathrm{e}^{-\mu t} \\ &\le \frac{\lambda_{\max}(P)}{\lambda_{\min}(P)}\|e_z(0)\|^2\mathrm{e}^{-\mu t} \\ &= c_1\|e_z(0)\|^2\mathrm{e}^{-\mu t}, \end{aligned} \tag{21}$$

where

$$c_1 = \frac{\lambda_{\max}(P)}{\lambda_{\min}(P)}.$$

Furthermore, on the basis of (13), we know

$$\begin{aligned} \|\dot{e}_z\| \le& \|M\Phi(0_{0\sim n-1})Q_2 + LC\Phi(0_{0\sim n-1})Q_2\|\|e_z\| \\ &+ \alpha_1\|(M+LC)B_r\|\|e_z\| \\ \le& c_2\|e_z(0)\|^2\mathrm{e}^{-\mu t}, \end{aligned} \tag{22}$$

where

$$\begin{aligned} c_2 =& c_1\|M\Phi(0_{0\sim n-1})Q_2 + LC\Phi(0_{0\sim n-1})Q_2\|\|e_z\| \\ &+ c_1\alpha_1\|(M+LC)B_r\|. \end{aligned}$$

□

3 Output Tracking

In control theory, the main target of a control system is to achieve state stabilization. Furthermore, output tracking is also a fundamental control objective. In this section, we will present the output tracking controller design based on the reduced-order observer (11). First, let us introduce the following assumption.

Assumption 4. *$f(x) \in \mathbb{R}^m$ is a differentiable Lipschitz function satisfying $\|f(x)-f(y)\| \le \alpha_1\|x-y\|$ and $\|\dot{f}(x)-\dot{f}(y)\| \le \alpha_2\|x-y\|$.*

Compared to the Lipschitz condition, the above assumptions seem more strict, but most Lipschitz functions also meet the above condition, such as the trigonometric function. For output tracking, similar to state-feedback [23], on the basis of the full-actuation property, utilizing the estimation of nonlinear function to counteract nonlinearity in the system, the following controller is designed

$$u = B^{-1}(y)[-f(\hat{x}^{(0\sim n-1)}) + v]. \tag{23}$$

Define

$$q(t) = \int_0^t [y(\tau) - y_{\mathrm{r}}]\,\mathrm{d}\tau. \tag{24}$$

Using the controller (23), and combining with (4) and (6), give

$$\begin{cases} \dot{z}_1 =& C\Phi(0_{0\sim n-1})Q_1 z_1 + C\Phi(0_{0\sim n-1})Q_2\hat{z}_2 \\ & + CB_r v + C\Phi(0_{0\sim n-1})Q_2 e_z + CB_r\Delta f(\cdot) \\ \dot{\hat{z}}_2 =& M\Phi(0_{0\sim n-1})Q_1 z_1 + M\Phi(0_{0\sim n-1})Q_2\hat{z}_2 \\ & + MB_r v - L_1[C\Phi(0_{0\sim n-1})Q_2 e_z + CB_r\Delta f(\cdot)]. \end{cases} \tag{25}$$

From (8), the derivative of $\hat{x}^{(0\sim n-1)}$ is

$$\begin{aligned} &\dot{\hat{x}}^{(0\sim n-1)} \\ &= Q_1\dot{z}_1 + Q_2\dot{\hat{z}}_2 \\ &= \begin{bmatrix} Q_1 & Q_2 \end{bmatrix} \begin{bmatrix} C\Phi(0_{0\sim n-1})Q_1 & C\Phi(0_{0\sim n-1})Q_2 \\ M\Phi(0_{0\sim n-1})Q_1 & M\Phi(0_{0\sim n-1})Q_2 \end{bmatrix} \times \\ &\quad \begin{bmatrix} C \\ M \end{bmatrix} \hat{x}^{(0\sim n-1)} + \begin{bmatrix} Q_1 & Q_2 \end{bmatrix} \begin{bmatrix} C \\ M \end{bmatrix} B_r v \\ &\quad + (Q_1 - Q_2L_1)(C\Phi(0_{0\sim n-1})Q_2 e_z + CB_r\Delta f(\cdot)) \\ &= \Phi(0_{0\sim n-1})\hat{x}^{(0\sim n-1)} + B_r v + \Psi_1 e_z + \Psi_2\Delta f(\cdot), \end{aligned} \tag{26}$$

and the output can be rewritten as

$$y = C\hat{x}^{(0\sim n-1)} + CQ_2 e_z, \tag{27}$$

with

$$\begin{cases} \Psi_1 = (Q_1 - Q_2L_1)C\Phi(0_{0\sim n-1})Q_2 \\ \Psi_2 = (Q_1 - Q_2L_1)CB_r. \end{cases} \tag{28}$$

The extended system is

$$\begin{bmatrix}\dot{\hat{x}}^{(0\sim n-1)}\\ \dot{q}\end{bmatrix}=\begin{bmatrix}\Phi(0_{0\sim n-1}) & 0\\ C & 0_m\end{bmatrix}\begin{bmatrix}\hat{x}^{(0\sim n-1)}\\ q\end{bmatrix}+\begin{bmatrix}B_r\\ 0\end{bmatrix}v+\begin{bmatrix}\Psi_1 e_z+\Psi_2\Delta f(\cdot)\\ CQ_2e_z-y_{\mathrm{r}}\end{bmatrix}. \tag{29}$$

Let

$$A=\begin{bmatrix}\Phi(0_{0\sim n-1}) & B_r\\ C & 0\end{bmatrix}, \tag{30}$$

and

$$A_o=\begin{bmatrix}\Phi(0_{0\sim n-1}) & 0\\ C & 0_m\end{bmatrix},\ B_o=\begin{bmatrix}B_r\\ 0\end{bmatrix}. \tag{31}$$

It is obvious that (A_o, B_o) is controllable if and only if $\mathrm{rank}(A)=n+m$. The proof is similar to Lemma 3.1 in [23].

At this point, we can give the following theorem to illustrate the asymptotic convergence of tracking error.

Theorem 2. *For the extended system* (29) *under Assumption 4, if* $\mathrm{rank}(A)=n+m$*, we can find a control variable*

$$v=A_{0\sim n-1}\hat{x}^{(0\sim n-1)}+Kq, \tag{32}$$

such that A_c *is Hurwitz, where*

$$A_c=\begin{bmatrix}\Phi(A_{0\sim n-1}) & B_rK\\ C & 0_m\end{bmatrix}, \tag{33}$$

then the following equation holds

$$\lim_{t\to\infty}\dot{q}=\lim_{t\to\infty}y(t)-y_{\mathrm{r}}=0. \tag{34}$$

Proof. Since $\mathrm{rank}(A)=n+m$, it follows that (A_o, B_o) is controllable. Then we can find a set of matrices $A_{0\sim n-1}$ such that A_c is Hurwitz. There exist a positive real number μ and a symmetric positive definite matrix P such that

$$PA_c+A_c^{\mathrm{T}}P\le-\mu P.$$

The closed-loop system is

$$\begin{bmatrix}\dot{\hat{x}}^{(0\sim n-1)}\\ \dot{q}\end{bmatrix}=A_c\begin{bmatrix}\hat{x}^{(0\sim n-1)}\\ q\end{bmatrix}+\begin{bmatrix}\Psi_1 e_z+\Psi_2\Delta f(\cdot)\\ CQ_2e_z-y_{\mathrm{r}}\end{bmatrix}.$$

Taking the derivative of the above equation, gives

$$\begin{bmatrix}\ddot{\hat{x}}^{(0\sim n-1)}\\ \ddot{q}\end{bmatrix}=A_c\begin{bmatrix}\dot{\hat{x}}^{(0\sim n-1)}\\ \dot{q}\end{bmatrix}+\begin{bmatrix}\Psi_1\dot{e}_z+\Psi_2\Delta\dot{f}(\cdot)\\ CQ_2\dot{e}_z\end{bmatrix}. \tag{35}$$

Define

$$X=\begin{bmatrix}\dot{\hat{x}}^{(0\sim n-1)}\\ \dot{q}\end{bmatrix},$$

and choose the Lyapunov function as

$$V=X^{\mathrm{T}}PX.$$

Block P as

$$P=\begin{bmatrix}P_1 & P_2\end{bmatrix},$$

where $P_1\in\mathbb{R}^{(n+m)\times n}$ and $P_2\in\mathbb{R}^{(n+m)\times m}$. The derivative of Lyapunov function is

$$\begin{aligned}\dot{V}=&X^{\mathrm{T}}(PA_c+A_c^{\mathrm{T}}P)X\\&+2X^{\mathrm{T}}\begin{bmatrix}P_1 & P_2\end{bmatrix}\begin{bmatrix}\Psi_1\dot{e}_z+\Psi_2\Delta\dot{f}(\cdot)\\ CQ_2\dot{e}_z\end{bmatrix}\\\le&-\mu V+2X^{\mathrm{T}}P_1(\Psi_1\dot{e}_z+\Psi_2\Delta\dot{f}(\cdot))\\&+2X^{\mathrm{T}}P_2CQ_2\dot{e}_z\\\le&-\mu V+2\alpha_2\|X\|\|P_1\Psi_2\|\|e_z\|\\&+2\|X\|\left(\|P_2CQ_2\|+\|P_1\Psi_1\|\right)\|\dot{e}_z\|\\\le&-\mu V+\alpha_2\|P_1\Psi_2\|\left(\varepsilon_1\|X\|^2+\frac{1}{\varepsilon_1}\|e_z\|^2\right)\\&+\left(\|P_2CQ_2\|+\|P_1\Psi_1\|\right)\left(\varepsilon_2\|X\|^2+\frac{1}{\varepsilon_2}\|\dot{e}_z\|^2\right)\\\le&-\mu V+\varepsilon_1\alpha_2\|P_1\Psi_2\|\lambda_{\min}^{-1}(P)X^{\mathrm{T}}PX\\&+\varepsilon_2\left(\|P_2CQ_2\|+\|P_1\Psi_1\|\right)\lambda_{\min}^{-1}(P)X^{\mathrm{T}}PX\\&+\frac{c_1}{\varepsilon_2}\left(\|P_2CQ_2\|+\|P_1\Psi_1\|\right)\|e_z(0)\|^2\mathrm{e}^{-\mu t}\\&+\frac{c_1\alpha_2}{\varepsilon_1}\|P_1\Psi_2\|\|e_z(0)\|^2\mathrm{e}^{-\mu t}\\=&-\sigma V+\beta\|e_z(0)\|^2\mathrm{e}^{-\mu t},\end{aligned}$$

with

$$\begin{cases}\sigma=\mu-\varepsilon_1\alpha_2\|P_1\Psi_2\|\lambda_{\min}^{-1}(P)\\\qquad-\varepsilon_2\left(\|P_2CQ_2\|+\|P_1\Psi_1\|\right)\lambda_{\min}^{-1}(P)\\\beta=\dfrac{c_1\alpha_2}{\varepsilon_1}\|P_1\Psi_2\|+\dfrac{c_1}{\varepsilon_2}\left(\|P_2CQ_2\|+\|P_1\Psi_1\|\right).\end{cases}$$

Since ε_1, ε_2 can be arbitrarily small, we can find two real positive numbers such that $\sigma>0$. Based on the Comparison Theorem, we have

$$V(t)\le\left(V(0)-\frac{\beta\|e_z(0)\|^2}{\sigma-\mu}\right)\mathrm{e}^{-\sigma t}+\frac{\beta\|e_z(0)\|^2}{\sigma-\mu}\mathrm{e}^{-\mu t}.$$

$V(t)$ converges to zero, then X also converges to zero. That is, (34) holds. □

Remark 1. In this section, the output tracks a constant signal, but our method can also be used to track a time-varying signal, such as the signal generated by a linear system, for which the readers can combine our approach with the literature [23].

4 Example

In this section, a numerical simulation is given respectively to verify the validity of the proposed method. The system is described as

$$\begin{cases}\dot{x}_1=x_2\\ \dot{x}_2+x_2=x_3\\ \dot{x}_3+x_2-x_3+\sin x_2=u\\ y=x_1.\end{cases}$$

From the first two equation of above equation, we have

$$x_2=\dot{x}_1,\ \dot{x}_2=\ddot{x}_1,\ x_3=\dot{x}_1+\ddot{x}_1.$$

Taking the third-order derivative of x_1, yields

$$\begin{aligned} x_1^{(3)} &= \ddot{x}_2 = -\dot{x}_2 + \dot{x}_3 \\ &= -\dot{x}_2 - x_2 + x_3 - \sin x_2 + u \\ &= -\ddot{x}_1 - \dot{x}_1 + \dot{x}_1 + \ddot{x}_1 - \sin \dot{x}_1 + u \\ &= -\sin \dot{x}_1 + u. \end{aligned}$$

Reviewing the design process of the reduced-order observer, we can obtain

$$M = \begin{bmatrix} 0 & 1 & 0 \\ 0 & 0 & 1 \end{bmatrix}, \; Q_1 = \begin{bmatrix} 1 \\ 0 \\ 0 \end{bmatrix}, \; Q_2 = \begin{bmatrix} 0 & 0 \\ 1 & 0 \\ 0 & 1 \end{bmatrix},$$

and define

$$z_1 = x_1, \; z_2 = \begin{bmatrix} \dot{x}_1 & \ddot{x}_1 \end{bmatrix}^{\mathrm{T}}, \; f(z_1, \hat{z}_2) = \sin z_{21}.$$

Solving the LMI (15), gives

$$L = \begin{bmatrix} -3.5 \\ -3.5 \end{bmatrix}.$$

The simulation result is shown in Fig. 1 with initial values and input signal being

$$\begin{cases} x_1(0) = -1, \; x_2(0) = -1, \; x_3 = 1, \; w = [0 \;\; 0]^{\mathrm{T}} \\ u = 0.1 \sin 10t. \end{cases}$$

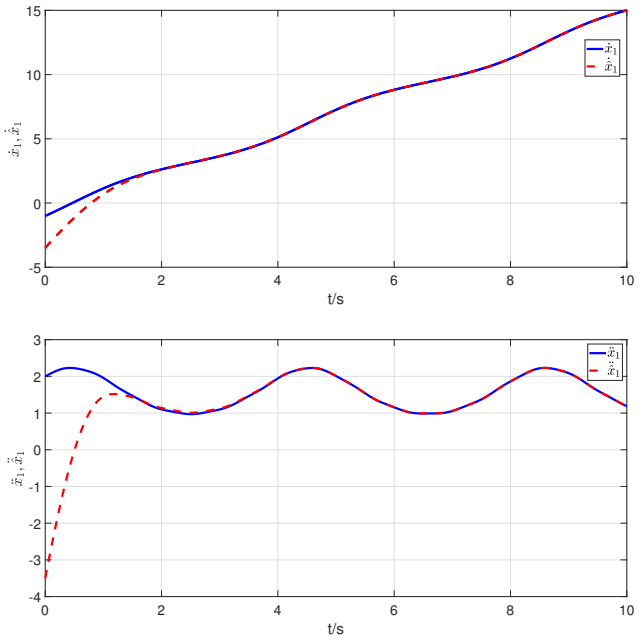

Figure 1: Simulation results of observer

According to Theorem 2, the control matrices are chosen as

$$A_{0\sim 2} = \begin{bmatrix} -18.8 & -18.3 & -6.8 \end{bmatrix}, \; K = -8.5,$$

and the tracking result is shown in Fig. 2. It can be seen that the system output can track the reference signal eventually, which is consistent with Theorem 2.

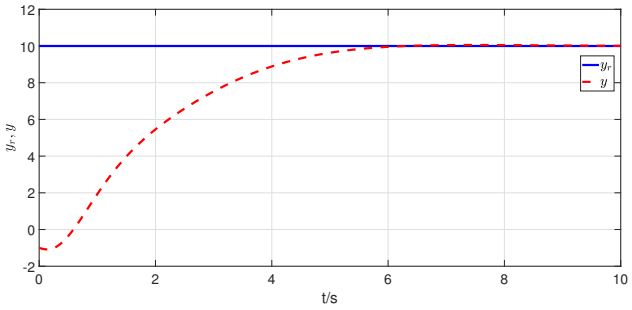

Figure 2: Simulation results of output tracking

5 Conclusion

This paper designs a reduced-order observer and an output tracking controller based on the proposed observer. It can be seen that for the tracking error to converge to zero exponentially, we need to give not only the design condition for the controller, but also additional constraint that need to be satisfied by the nonlinearity. Therefore, the exponential convergence of the observation error also does not guarantee that the tracking error exponentially converge to zero.

References

[1] G. R. Duan, High-order fully actuated system approaches: Part I. Models and basic procedure, *International Journal of Systems Science*, 52(2): 422–435, 2021.

[2] G. R. Duan, High-order fully actuated system approaches: Part II. Generalized strict-feedback systems, *International Journal of Systems Science*, 52(3): 437–454, 2021.

[3] G. R. Duan, High-order fully actuated system approaches: Part III. Robust control and high-order backstepping, *International Journal of Systems Science*, 52(5): 952–971, 2021.

[4] G. R. Duan, High-order System Approaches: I. Fully-actuated Systems and Parametric Designs, *ACTA Automatica Sinica* (in Chinese), 46(7): 1333-1345, 2020.

[5] G. R. Duan, High-order System Approaches: II. Controllability and Full-actuation, *ACTA Automatica Sinica* (in Chinese), 46(8): 1571-1581, 2020.

[6] G. R. Duan, High-order fully actuated system approaches: Part X. Basics of discrete-time systems, *International Journal of Systems Science*, 53(4): 810–832, 2022.

[7] L. L. Zhang, P. Wang, and C. C. Hua, Adaptive control of time-delay nonlinear HOFA systems with unmodeled dynamics and unknown dead-zone input, *International Journal of Robust and Nonlinear Control*, 33(4): 2615–2628, 2023.

[8] G. R. Duan, Brockett's first example: An fas approach treatment, *Journal of Systems Science & Complexity*, 35(2): 441–456, 2022.

[9] G. T. Tian, B. Li, Q. Zhao, and G. R. Duan, High-precision trajectory tracking control for free-flying space manipulator subject to multiple constraints and system uncertainty, *IEEE Transaction on Aerospace and Electronic System*, 2023, early access.

[10] G. P. Liu, Attitude and orbit optimal control of combined spacecraft via a fully-actuated system approach, *IEEE/CAA Journal of Automatica Sinica*, 9(4): 615–623, 2022.

[11] G. Q. Liu, K. Zhang, and B. Li, Fully-actuated system approach based optimal attitude tracking control of rigid spacecraft with actuator saturation, *Journal of Systems Science & Complexity*, 35(2): 688–702, 2022.

[12] T. Y. Zhao, Parametric design of observer-based control sys-

tem and its application, Ph.D. dissertation, Harbin Institute of Technology, Harbin, China, 2022.

[13] H. Jiang and G. R. Duan, Output tracking based on generalized proportional-integral observer for fully actuated systems, in *Proceedings of 2nd Conference on Fully Actuated System Theory and Applications*, 2023: 117–121.

[14] S. W. Chen, W. Wang, J. F. Fan, and Y. Ji, Impact angle constraint guidance law using fully-actuated system approach, *Aerospace Science and Technology*, 136, 2023, early access.

[15] X. Q. Liu, M. Y. Chen, L. Sheng, and D. H. Zhou, Adaptive fault-tolerant control for nonlinear high-order fully-actuated systems, *Neurocomputing*, 495: 75–85, 2022.

[16] Z. Y. Feng, M. Liu, and X. B. Cao, A fully-actuated system approach for spacecraft attitude control with input saturation, in *Proceedings of 2nd Conference on Fully Actuated System Theory and Applications*, 2023: 705–710.

[17] F. L. Zhu and Z. Z. Han, A note on observers for Lipschitz nonlinear systems, *IEEE Transactions on Automatic Control*, 47(10): 1751–1754, 2002.

[18] H. Trinh, T. Fernando, and S. Nahavandi, Partial-state observers for nonlinear systems, *IEEE Transactions on Automatic Control*, 51(11): 1808–1812, 2006.

[19] M. Benallouch, M. Boutayeb, and M. Zasadzinski, Observer design for one-sided Lipschitz discrete-time systems, *Systems & Control Lettere*, 61(9): 879–886, 2012.

[20] M. Homayounzade and M. Keshmiri, A note on a reduced-order observer based controller for a class of Lipschitz nonlinear systems, *Journal of Dynamic Systems, Measurement, and Control*, 135(1): 014 505:1–014 505:4, 2012.

[21] Z. X. Liu, Y. B. Li, F. Y. Wang, and Z. Q. Chen, Reduced-order observer-based leader-following formation control for discrete-time linear multi-agent systems, *IEEE/CAA Journal of Automatica Sinica*, 8(10): 1715–1723, 2021.

[22] A. Cristofaro and A. De Luca, Reduced-order observer design for robot manipulators, *IEEE Control & Systems Letters*, 7: 520–525, 2023.

[23] G. R. Duan, High-order fully-actuated system approaches: Part IX. Generalised PID control and model reference tracking, *International Journal of Systems Science*, 53(3): 652–674, 2022.

Proceedings of the 3rd Conference on Fully Actuated System Theory and Applications
May 10-12, 2024, Shenzhen, China

Enhancing Frequency Emergency Control with Battery Energy Storage Systems in Low-Inertia Power Grid

Yuxin Weng[1], Guangchao Geng[1], Quanyuan Jiang[1], Heng Wang[2]

1. College of Electrical Engineering, Zhejiang University, Hangzhou 310027
E-mail: 22210016@zju.edu.cn

2. State Grid Xinjiang Electric Power Co., Ltd., Urumqi 830002

Abstract: The high penetration of renewable energy into the power grid results in a reduction of system inertia. Consequently, in the event of faults like DC blocking fault, low-inertia systems exhibit severe frequency fluctuations, thereby triggering the activation of stability control devices and resulting in substantial economic losses. Frequency emergency control is of great significance for ensuring the safe and stable operation after large disturbances. This paper combines energy storage control with frequency emergency control. Specifically, it integrates the actual output of the energy storage into the generation tripping tuning process, thereby reducing the amount of generation tripping, optimizing the frequency intervals and delays of generation tripping. This paper constructs an optimization model for the coordinated operation of energy storage systems, consisting of two stages: optimization tuning and simulation verification. The optimization tuning module includes a scenario selection process considering system inertia and a generator tripping tuning process, which combines the energy storage output to obtain an optimized generator tripping scheme. The verification module consists of an energy storage control model based on MPC-MHE (Model Predictive Control and Moving Horizon Estimation) and an energy storage virtual inertia control process, verifying the effectiveness of energy storage control under the proposed generator tripping scheme. Finally, a provincial-level power grid is taken as a case study to validate the effectiveness of the proposed energy storage control strategy.

Key words: Energy storage system, Frequency emergency control, Low-inertia system and Model predictive control

1 Introduction

In response to the carbon peak and carbon neutrality goals, China has vigorously promoted the development of new energy generation in various provinces and cities in recent years. The northwestern region, as an important new energy base in China, has witnessed rapid growth in the development of new energy [1]. As of December 30, 2022, the proportion of new energy installed capacity in the northwestern power grid has increased to 45%, surpassing coal-fired power and becoming the largest power source [2]. The large-scale connection of new energy has reduced the system inertia, posing significant challenges to the frequency stability operation of the northwestern sending-end grid.

Frequency emergency control, as an important measure to maintain the stable operation of power systems, is also a significant component of the second and third lines of defense. Its primary function is to ensure the system's stable operation or prevent further escalation of system faults when the system cannot maintain stability in its original state[3], [4]. This is achieved by shedding a portion of the load or units. Energy Storage System (ESS), with its fast response and effective regulation, has emerged as a key research focus for its involvement in frequency emergency control[5]. Many experts and scholars have devoted their attention to studying the ways in which energy storage can participate in frequency emergency control.

There are currently two main control strategies for energy storage: 1) Measurement-based strategies [6], [7], including Proportional-Derivative (PD) control, fuzzy logic control, power-frequency characteristic curve control, etc. 2) Model-based strategies [8], [9]. This paper primarily adopts a model-based control strategy, which has the advantage of considering system constraints comprehensively and establishing more accurate models for energy storage control.

In terms of frequency emergency control, many scholars have conducted research in this area. Reference [10] performed sensitivity analysis using a binary table to optimize high-frequency generator tripping schemes. In [11] a scheme is proposed for the construction of a secure and stable defense system for wind-solar-bundled multi-terminal HVDC transmission networks, ensuring frequency stability in the northwest transmission network of China. Reference [12] suggested that shedding wind power units is beneficial for reducing transient frequency deviations and facilitating system frequency recovery.

However, there is currently limited research on the ways in which energy storage can participate in frequency emergency control. Therefore, this paper proposes a two-stage optimization model. Firstly, a high-frequency generator tripping scheme is established considering the energy storage output curve. By taking into account the scenario with the most severe inertia deficiency, the generator tripping scheme that minimizes system losses is determined, considering factors such as frequency intervals and time delays for generator tripping. Secondly, a model-based control strategy is developed using Model Predictive Control with Moving Horizon Estimation (MPC-MHE) for energy storage. By incorporating energy storage virtual inertia control, the optimization of energy storage output is achieved.

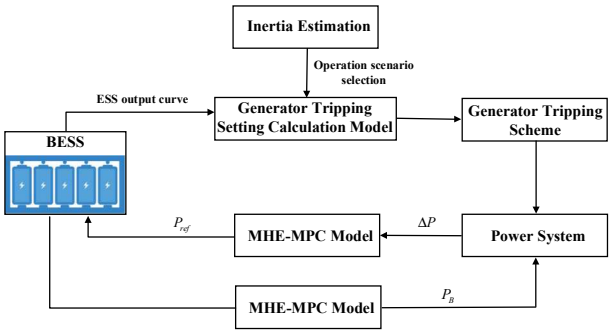

Fig.1 The overall control strategy.

The main innovations of this paper are as follows:

(1) A frequency emergency control strategy for ESS participation based on MPC-MHE has been constructed, which can enable ESS to cooperate with frequency emergency control strategy and accelerate frequency recovery speed;

(2) A tuning method for emergency frequency control of the second line of defense in power systems involving energy storage has been proposed. This method significantly reduces system downtime by configuring energy storage through offline calculation.

2 Energy Storage Control Model

The energy storage control model constructed in this paper mainly consists of three parts: Model Predictive Control, Moving Horizon Estimation, and virtual inertia control. MHE provides the predicted grid frequency deviation for MPC control, while MPC control provides the energy storage reference output to the ESS. The actual ESS output is obtained by the ESS through virtual inertia control.

2.1 MPC Model

The basic principle of MPC is: At sampling time k, based on the current measurement information obtained, an open-loop optimization problem is solved online over a finite time horizon. The first element of the resulting control sequence is then applied to the controlled object. At sampling time k+1, the process is repeated by refreshing the optimization problem with new measurements and solving it again.

For the ESS control system, at each sampling time k, the MPC model utilizes the measured actual grid frequency f_k and the grid active power imbalance ΔP_k to solve for a control sequence containing power control signals for the energy storage system over the next H time steps. The first set of control signals, denoted as $P_{B,k}^{ch*}$ or $P_{B,k}^{dis*}$ (all symbolic variables defined in this article are real numbers), is then applied to the system. At the next sampling time, the optimization problem is solved again based on the latest measurement information at that time.

1) Objective function:

In the energy storage participation frequency emergency control strategy proposed in this paper, the controller aims to meet the following requirements: to find the optimal control inputs that make the predicted curve of the grid frequency as close as possible to the reference curve of the grid frequency, while minimizing the control cost. Therefore, the objective function is defined as follows:

$$\begin{aligned} J_k\left(\left\{P_{B,k+h|k}^{ch}\right\},\left\{P_{B,k+h|k}^{dis}\right\}\right) &= \alpha\sum_{h=1}^{H}\left(f_{k+h|k}-f_0\right)^2 \\ &+\beta\sum_{h=0}^{H-1}\left[\left(P_{B,k+h|k}^{ch}\right)^2+\left(P_{B,k+h|k}^{dis}\right)^2\right] \end{aligned} \tag{1}$$

where $k+h|k$ represents the estimated value of the parameters at time k based on the information available at time k. The coefficients α and β are weighting factors where larger values indicate a higher penalty for the corresponding term. $P_{B,k}^{ch}$ and $P_{B,k}^{dis}$ represent the charging and discharging amounts of the energy storage system at time k, respectively. f_k and f_0 represent the predicted frequency and the reference frequency of the system at time k, respectively.

2) Constraints:

The considered constraint conditions mainly include system frequency constraints and energy storage constraints. The system frequency constraints are set as follows:

When the number of time points within the prediction time horizon H where the system frequency deviation exceeds the action threshold of the second and third defense lines exceeds N (indicating a significant predicted system frequency deviation that would trigger the action of the second and third defense lines), no frequency constraint conditions are imposed.

Otherwise, the frequency constraint conditions are set as follows:

$$\Delta f^{t+k\cdot\Delta t} \geq \Delta f_{HFGT}+\delta \tag{2}$$

where δ represents the frequency error, Δf_{HFGT} represents the High Frequency Generator Tripping frequency (HFGT).

The energy storage system constraints mainly include power constraints, charge-discharge constraints, and State of Charge (SOC) constraints, as follows:

$$\begin{cases} 0 < P_{B,k+h|k}^{ch} \leq P_{B,\max} \\ 0 < P_{B,k+h|k}^{dis} \leq P_{B,\max} \end{cases} \quad h=1,2,\cdots,H \tag{3}$$

where $P_{B,\max}$ represents the maximum output of ESS.

$$P_{B,k+h|k}^{ch}P_{B,k+h|k}^{dis}=0 \quad h=1,2,\cdots,H \tag{4}$$

$$S_{\min} \leq E_{B,k+h|k} \leq S_{\max} \quad h=1,2,\cdots,H \tag{5}$$

where $S_{\min}$ represents the set lower limit of the SOC, and $S_{\max}$ represents the set upper limit of the SOC.

Up to now, this paper has established a controller model based on MPC, which is a quadratic programming problem with formula (1) as the objective function and (2) ~ (5) as the

constraint conditions. This formulation makes it convenient to use commercial solvers for solving the optimization problem.

2.2 MHE Model

MHE (Moving Horizon Estimation) algorithm, similar to MPC, is also based on the system's dynamic model and involves solving an online optimization problem. It allows the direct representation of time-domain constraints and nonlinear characteristics of the system in the optimization problem formulation. Unlike other estimation methods such as Kalman Filtering (KF), MHE is capable of handling constraints, resulting in more accurate and reliable estimation results.

MHE can be categorized into full information MHE and approximate MHE. To reduce the computational burden of the online optimization problem, the Approximate MHE approach is commonly adopted [13].

In the context of power grid applications, considering the availability of measurements for the power imbalance, the estimation of the system frequency deviation Δf can be achieved using ΔP . The specific relationship can be expressed as follows:

$$\dot{f} = \frac{\Delta P}{2H} f_0 = \frac{-P_L + P_G + P_R + P_W}{2H} f_0 \tag{6}$$

where f represents the actual grid frequency, ΔP denotes the grid active power imbalance, f_0 corresponds to the rated frequency of the system, H represents the grid inertia time constant, P_L represents the load power, P_G and P_R represent the generated power and the reserve power provided by thermal power units, P_W represents the wind power output.

The further discretization of equation (6) yields:

$$f_{k+1} = f_k + \frac{T_s f_0}{2H} \Delta P_k \tag{7}$$

where T_s representing the discrete time constant.

The state-space model of the system in discrete time can be formulated as follows:

$$\begin{cases} x_{k+1} = A_e x_k + b_e \omega_k \\ y_k = c_e x_k \end{cases} \tag{8}$$

where the state vector $x_k = \left[x_{1,k} \; x_{2,k} \right]^T = \left[f_k \; \Delta P_k \right]^T$, the process noise $\omega_k = \delta_{V,k}$, and the measurement output $y_k = f_k$. The parameter definitions for each matrix are as follows:

$$\boldsymbol{A}_{\mathrm{e}} = \begin{bmatrix} 1 & \frac{T_{\mathrm{s}} f_0}{2H} \\ 0 & 1 \end{bmatrix} \quad \boldsymbol{b}_{\mathrm{e}} = \begin{bmatrix} 0 \\ T_{\mathrm{s}} \end{bmatrix} \quad \boldsymbol{c}_{\mathrm{e}} = \begin{bmatrix} 1 & 0 \end{bmatrix} \tag{9}$$

The estimation problem for the system frequency deviation can be defined as follows: at time instant k, using the N+1 latest measurement data $\left\{ \Delta \tilde{P}_{k-N}, \Delta \tilde{P}_{k-N+1}, \cdots, \Delta \tilde{P}_k \right\}$ from the past N time instants, estimate the system frequency f_k at time instant k. The optimization objective is defined as follows:

$$J_k = \sum_{i=k-N}^{k} (\Delta f_i - \Delta \hat{f}_i)^2 \tag{10}$$

where Δf_i represents the actual system frequency deviation, and $\Delta \hat{f}_i$ represents the predicted system frequency deviation.

To enhance the accuracy of the prediction results, noise sequence is incorporated into the equation (7), then we get:

$$f_{k+1} = f_k + \frac{T_s f_0}{2H} \Delta P_k + \omega_{\mathrm{k}} \tag{11}$$

Equation (12) can be obtained by (10):

$$J = \sum_{i=k-N}^{k} (\Delta f_i - \Delta \hat{f}_i)^2 + \sum_{i=k-N}^{k} (\omega_{\mathrm{k}})^2 \tag{12}$$

In summary, the frequency deviation prediction model constructed in this paper, based on MHE, simultaneously optimizes the frequency deviation Δf_{k-N} and the compensation sequence $\{\omega_k\}_{k-N}^{N}$. It estimates the frequency deviation at time instant k, and the obtained results are used in the MPC model.

2.3 Virtual Inertia Control

The energy storage device's virtual inertia control module generates active power reference value and power response by introducing the grid frequency differential signal [14] and considering the effects of frequency rate of change and inertia control gain. A typical energy storage virtual inertia control model is shown in Fig.2. With reference to the control model depicted in Fig.2, the active power output P_B^{fin} of the energy storage device can be represented as [15]:

$$P_B^{fin} = \frac{\Delta f K_{df} s}{1 + T_1 s} \tag{13}$$

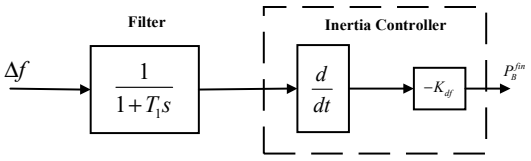

Fig.2 Energy storage virtual inertia control module.

The magnitude of the virtual inertia provided by the energy storage can be calculated based on SOC of the energy

storage. The specific derivation process can be found in reference [15]. The expression is as follows:

$$\begin{aligned} H_{BESS}(t) &= \frac{K_{df}u_N\omega_N}{Ku_dS_{N_BESS}}L^{-1}[\frac{s}{T_1T_2s^2+(T_1+T_2)s+1}] \\ &= K_{df}K'L^{-1}\left(\frac{K_1}{s+\alpha_1}+\frac{K_2}{s+\alpha_2}\right) \\ &= K_{df}K'(K_1e^{-\alpha_1 t}+K_2e^{-\alpha_2 t}) \end{aligned} \tag{14}$$

where K represents the conversion coefficient, $K'=\frac{u_N\omega_N}{Ku_dS_{N_BESS}}$, u_N and u_d represent the DC components of the grid voltage, ω_N represents the rated angular velocity of the synchronous generator, S_{N_BESS} represents the rated capacity of the energy storage system, K_1 and K_2 represents the coefficient of the quadratic term expansion, α_1 and α_2 are the two roots of the denominator polynomial.

2.4 Generator Tripping Model

The method proposed in this paper for setting the generator tripping is an offline calculation. Firstly, the minimum inertia requirement of the system is considered. By taking into account the system frequency Rate of Change of Frequency (RoCoF) limit, frequency minimum/maximum limits, and considering different renewable energy output scenarios and generator combinations under different operating conditions, a genetic algorithm is employed to find the minimum inertia required by the system under various scenarios. Subsequently, by establishing the relationship between the virtual inertia provided by energy storage and the generator tripping, the role of energy storage in reducing the generator tripping is demonstrated. The process of setting the generator tripping involves using the optimized power output of the energy storage as input and combining it with the minimum inertia requirement in each scenario to determine the optimal governor droop setting.

2.5 Inertia Estimation

The inertia of a power system refers to its resistance to frequency changes caused by external disturbances. It helps to slow down the rate of frequency variations and is a crucial safeguard for maintaining system frequency stability [16]. System inertia is a quantitative measure of system inertia and can be expressed in various forms, such as inertia time constant *M*, inertia time *H*, rotational inertia *J*, etc. In this paper, the inertia time *H* is used to describe and calculate the critical inertia requirement of the system. The calculation method is described by the following equation:

$$H_{\text{sys}} = E_{\text{sys}} / S_{sys} \tag{15}$$

where H_{sys} represents the system inertia time, E_{sys} represents the rotational kinetic energy of thermal power units, hydroelectric units, and wind power units in the system, and S_{sys} represents the total rated capacity of the system.

The stability constraints of the grid frequency at the sending end mainly consider the limits on the maximum RoCoF and the maximum frequency deviation. The maximum frequency deviation constraint can be obtained by [17]:

$$\frac{2\Delta P}{\pi T_s}\sum_{i=1}^{n}u_{i,t}k_{Gi}\left[t_m-T_{Gi}+T_{Gi}e^{-t_m/T_{Gi}}\right]-k_D\Delta f_m \geq \Delta P \tag{16}$$

where k_G represents the power frequency characteristic coefficient, T_G represents the integrated time constant of generator governor and prime mover, ΔP represents the power deviation, t_m represents the time to reach the nadir frequency, u_i represents the start/stop status of the *i*-th generating unit, k_D represents the the load frequency response coefficient.

The maximum RoCoF constraint is as follows:

$$RoCoF^{\min} \leq \frac{\Delta P_L}{2H} \leq RoCoF^{\max} \tag{17}$$

where $RoCoF^{\max}$ and $RoCoF^{\min}$ represents the maximum and minimum RoCoF tolerance capacity of the generating units.

Due to the limited adjustable power of thermal power units, it is necessary to consider the maximum power limit and the minimum technical output of the units:

$$-\Delta P_{Gmi}^{D}-\Delta P_{Bi}^{D} \leq \Delta P_{Gmi} \leq \Delta P_{Gmi}^{U}+\Delta P_{Bi}^{U}, i=1,2,\cdots,n \tag{18}$$

where ΔP_{Gmi}^{D} represents the minimum technical output of generator *i*, and ΔP_{Gmi}^{U} represents the maximum power limit of generator *i*. ΔP_{Bi}^{D} and ΔP_{Bi}^{U} represent the additional power allowed by the ESS installed for generator *i*.

In conclusion, the calculation of critical inertia for the system can be described as the following optimization problem:

$$\begin{aligned} &\min H \\ s.t.\ &\frac{2\Delta P}{\pi T_s}\sum_{i=1}^{n}u_{i,t}k_{Gi}\left[t_m-T_{Gi}+T_{Gi}e^{-t_m/T_{Gi}}\right]-k_D\Delta f_m \geq \Delta P \\ &RoCoF^{\min} \leq \frac{\Delta P_L}{2H} \leq RoCoF^{\max} \\ &-\Delta P_{Gmi}^{D}-\Delta P_{Bi}^{D} \leq \Delta P_{Gmi} \leq \Delta P_{Gmi}^{U}+\Delta P_{Bi}^{U}, i=1,2,\cdots,n \end{aligned} \tag{19}$$

This paper adopts a genetic algorithm to solve the global optimization problem defined by equation (19). The process is shown in Fig.3:

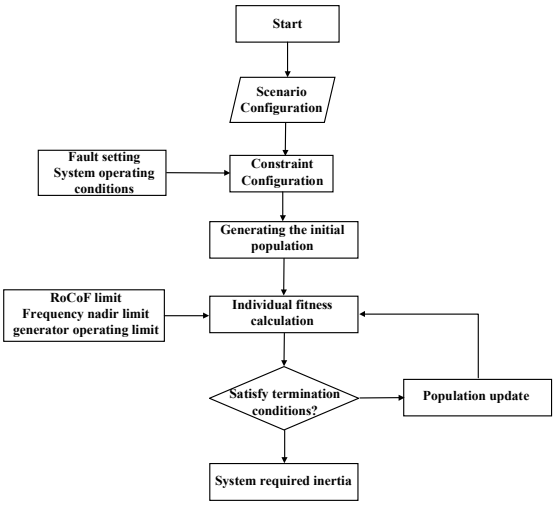

Fig.3 Genetic Algorithm Flowchart

In this algorithm, the fitness of the population corresponds to the system inertia time *H*. The individuals in the population must satisfy constraints such as frequency deviation, RoCoF, and generator operating constraints. If any individual fails to meet these constraints, the iteration process is repeated. Eventually, the algorithm determines the minimum critical inertia required by the system.

2.6 Generator tripping adjustment model

3) Total setting of generator tripping

The problem of total generator tripping calculation can be defined as the following optimization problem:

$$\begin{cases} \min \Delta P_{trip} \,\&\, \max \Delta P_{trip} \\ \text{s.t.} \quad f_{\min} > f_{\text{UFLS, sct1}} \\ \qquad f_{\max}, f_{\text{OPC, set}} \\ \qquad \Delta P_{\text{trip}}, P_{\text{dist,max}} \end{cases} \tag{20}$$

where ΔP_{trip} represents the actual total generator tripping, $P_{\text{dist,max}}$ represents the maximum system power disturbance, $f_{UFLS,set1}$ represents the tuning value for the frequency of the first round of system low-frequency load shedding, and $f_{OPC,set}$ represents the tuning value for the over speed protect (OPC) controller action of the generator units.

The calculations for $f_{\min}$ and $f_{\max}$ are obtained using the following equation:

$$\Delta f = \frac{1}{2Hs + D_L} \cdot \left(\Delta P_G + \Delta P_W + \Delta P_E - \Delta P_L \right) \tag{21}$$

where D_L represents the frequency regulation coefficient of the system load, ΔP_G represents the total output of conventional generating units, ΔP_W represents the wind power output, ΔP_E represents the output of ESS, ΔP_L represents the system load.

By solving equation (20), we can obtain the maximum and minimum values of ΔP_{trip}. The total generator tripping can be calculated by taking the average value:

$$\Delta P_{trip} = \frac{\Delta P_{trip,\max} + \Delta P_{trip,\min}}{2} \tag{22}$$

where $\Delta P_{trip,\max}$ and $\Delta P_{trip,\min}$ represents the maximum and minimum value of ΔP_{trip}.

4) Each Round of Generator Tripping Quantity Distribution

In order to optimize the generator tripping in each round, it is necessary to incorporate ESS output in the optimization problem. Additionally, to prevent excessive generator tripping in each round that may trigger low-frequency load shedding, it is important to ensure that the generator tripping in each round remains within a certain range around the average total generator tripping. The tuning of generator tripping in each round can be formulated as the following optimization problem:

$$\begin{cases} \min \ \Delta P_{trip,i} \\ s.t. \dfrac{\Delta P_{trip}}{n} - \delta \le \Delta P_{trip,i} \le \dfrac{\Delta P_{trip}}{n} + \delta \\ f_{\min} \ge f_{HFGT} \\ f^{t+\Delta t} = f^{t} + \dfrac{T_s f_0}{2H} \Delta P_k - \Delta P_E \end{cases} \tag{23}$$

where $\Delta P_{trip,i}$ represents the generator tripping in the *i*-th round of the system, δ represents the maximum power deviation, and ΔP_E represents the size of the energy storage output.

By solving equations (20), (22), and (24), we can obtain the final tuning for the total generator tripping as well as the generator tripping in each round.

3 Case Study

This paper uses a provincial power grid in the western region of China as a case study. The unit parameters are based on the BPA 2021 summer biggest operating mode. The total installed capacity of the provincial power grid is 76,324 MVA, which includes 119 thermal power units. Under stable conditions, the total power generation in the entire grid is 65,347 MW, the provincial load is 25,743 MW, and the power transmitted through AC and DC interconnections is approximately 39,604 MW.

3.1 Generation loss

This section primarily focuses on low-frequency faults that occur in the system due to generator failures. These faults are relatively mild, and they are used to validate the advantages of the proposed control strategy. The generation loss in the system is simulated by disconnecting a thermal power generator, resulting in a loss of 498MW of active power. This event triggers a low-frequency fault in the system, which may lead to low-frequency load shedding.

After incorporating energy storage, both droop control and the proposed control strategy are implemented. The resulting system frequency response curve and energy storage output curve are as follows:

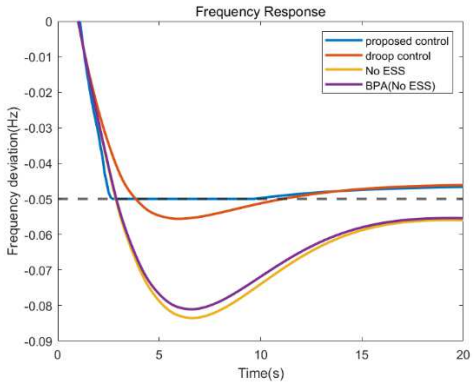

Fig.4 Frequency curve under different methods

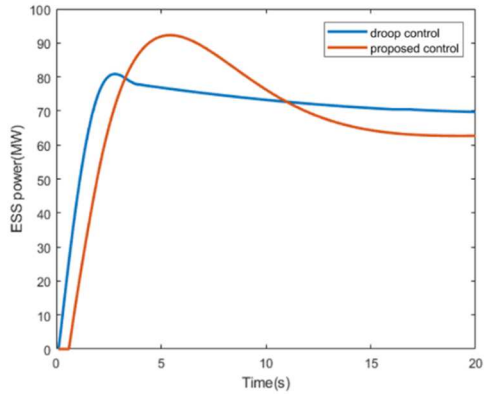

Fig.5 ESS power curve under two methods

From the Fig.4 above, it can be observed that the proposed strategy effectively reduces the maximum frequency deviation after system faults to below 0.05Hz, thereby preventing low-frequency load shedding. On the other hand, although traditional droop control also reduces system frequency deviation, it does not incorporate frequency constraints and therefore cannot guarantee the avoidance of low-frequency load shedding. Additionally, as shown in Fig.5, the proposed strategy exhibits a maximum increase of only 11.9% in energy storage output compared to traditional energy storage control methods, demonstrating its economic feasibility.

3.2 DC fault

Firstly, the inertia of each scenario was assessed based on the load and power output data during summer daytime, summer nighttime, winter daytime, and winter nighttime. The results are as follows:

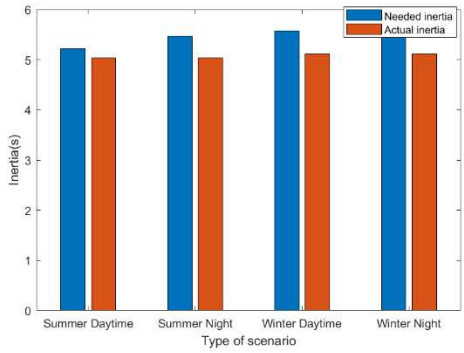

Fig.6 The inertia deficiency in different scenarios

From the above figure, it can be observed that the most severe inertia deficiency occurs during winter daytime. Winter daytime exhibits the highest required inertia, which is 5.57 seconds. Additionally, during winter, due to high load levels and limited renewable energy output, the system already has a relatively small inertia time of only 4.81 seconds, which clearly does not meet the system's inertia requirements.

Taking the scenario with the most severe inertia deficiency as an example, the ESS output curve obtained using the proposed energy storage control strategy, along with the system frequency response curve, is shown below:

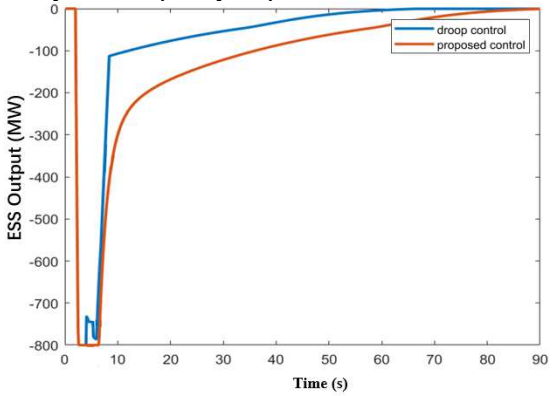

Fig.7 ESS output under different control strategies

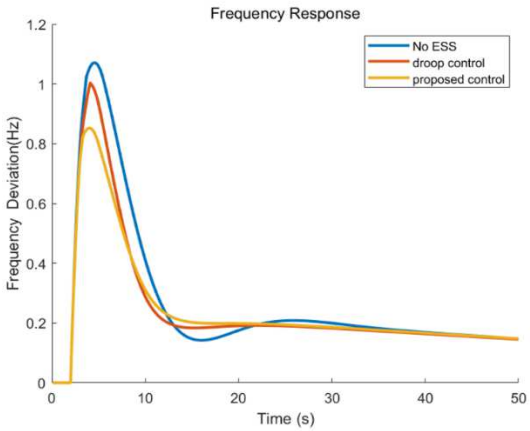

Fig.8 Frequency deviation under different control strategies

Without energy storage configuration, the maximum frequency deviation in the system will exceed 1Hz. By incorporating energy storage, the maximum frequency deviation can be reduced to around 0.85Hz. Fig.7 illustrates the power output throughout the ESS process. It can be observed that the proposed strategy effectively combines the process of generator tripping. After the first round of generator tripping is triggered, the energy storage power output is reduced to prevent the system frequency from dropping too rapidly, which could result in an excessive RoCoF. After the last round of generator tripping is triggered, the ESS output is increased again to allow the system frequency to quickly recover. Once the generator tripping process is completed, the ESS output reduce rapidly to further conserve the ESS power.

The comparison of the system generator tripping schemes with 800MW ESS capacity after tuning is as follows:

Table 1: Different trippings

	No ESS	**ESS**	**ESS With Proposed Strategy**
First round	f>50.6Hz; tripping generators 2024.5MW	f>50.6Hz; tripping generators 2031MW	f>50.6Hz; tripping generators 2024.5MW
Second round	f>50.8Hz; tripping generators 2024.5MW	f>50.8Hz; tripping generators 2031MW	f>50.7Hz; tripping generators 1984.4MW
Third round	f>51Hz; tripping generators 2024.5MW	f>51Hz; tripping generators 2031MW	f>50.8Hz; tripping generators 1916.1MW
Final round	f>52Hz; tripping generators 2024.5MW	/	/

By incorporating energy storage and adopting the proposed tuning strategy, the system can reduce one round of generator tripping. Moreover, compared to conventional methods of ESS configuration, the proposed tuning strategy can further reduce the amount of generator tripping and, at the same time, decrease the frequency interval between each round of generator tripping. This leads to an accelerated frequency recovery process.

The virtual inertia support effect of ESS is shown as follows:

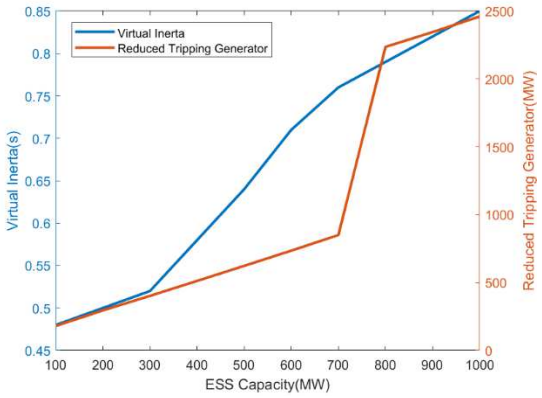

Fig.9 Relationship between ESS capacity with its virtual inertia and reduction in generator tripping

From Fig.9, it can be observed that as the capacity of the ESS increases, it provides a higher level of virtual inertia. When the ESS capacity reaches 800MW, the system's inertia level meets the requirements, leading to a significant reduction in the amount of generator tripping required.

4 Conclusion

This paper proposes a two-stage optimization model for energy storage participation in frequency emergency control. The energy storage control module consists of Model Predictive Control, Moving Horizon Estimation, and virtual inertia control components. It can provide emergency frequency support and compensate for the system's inertia deficiency during system frequency disturbances. The paper primarily focuses on high-frequency generator tripping in frequency emergency control and incorporates ESS output in the tuning process to further optimize generator tripping time interval and the total amount of generator tripping. Finally, the effectiveness of the proposed method is demonstrated through a case study conducted on a provincial power grid.

References

[1] J. Hu, G. Yang, Z. Song, and C. Kang, “Preliminary discussion on the supporting policies and the China’s development model of the new energy storage,” *Power System Technology*, pp. 1–11.

[2] “Renewable Energy Surpasses Coal Power, Becomes the Largest 'Power Source' in Northwestern China - Xinhua News.” Accessed: Jan. 20, 2024. [Online]. Available: http://www.news.cn/politics/2022-12/31/c_1129246951.htm

[3] Y. Liu, Y. Song, Z. Wang, and C. Shen, “Optimal Emergency Frequency Control Based on Coordinated Droop in Multi-Infeed Hybrid AC-DC System,” *IEEE Trans. Power Syst.*, vol. 36, no. 4, pp. 3305–3316, Jul. 2021.

[4] W. Ni, T. Liu, and S. Chen, “Rapid Generation of Emergency Response Plans for Unconventional Emergencies,” *IEEE Access*, vol. 8, pp. 181036–181048, 2020.

[5] Z. Shi, Y. Xu, Y. Wang, J. He, G. Li, and Z. Liu, “Coordinating Multiple Resources for Emergency Frequency Control in the Energy Receiving-End Power System With HVDCs,” *IEEE Trans. Power Syst.*, vol. 38, no. 5, pp. 4708–4723, Sep. 2023.

[6] D.-I. Stroe, V. Knap, M. Swierczynski, A.-I. Stroe, and R. Teodorescu, “Operation of a Grid-Connected Lithium-Ion Battery Energy Storage System for Primary Frequency Regulation: A Battery Lifetime Perspective,” *IEEE Trans. Ind. Appl.*, vol. 53, no. 1, pp. 430–438, Jan. 2017.

[7] V. Knap, S. K. Chaudhary, D.-I. Stroe, M. Swierczynski, B.-I. Craciun, and R. Teodorescu, "Sizing of an Energy Storage System for Grid Inertial Response and Primary Frequency Reserve," *IEEE Trans. Power Syst.*, vol. 31, no. 5, pp. 3447–3456, Sep. 2016.

[8] G. Delille, B. Francois, and G. Malarange, "Dynamic Frequency Control Support by Energy Storage to Reduce the Impact of Wind and Solar Generation on Isolated Power System's Inertia," *IEEE Trans. Sustain. Energy*, vol. 3, no. 4, pp. 931–939, Oct. 2012.

[9] M. A. Torres L., L. A. C. Lopes, L. A. Morán T., and J. R. Espinoza C., "Self-Tuning Virtual Synchronous Machine: A Control Strategy for Energy Storage Systems to Support Dynamic Frequency Control," *IEEE Trans. Energy Convers.*, vol. 29, no. 4, pp. 833–840, Dec. 2014.

[10] Y. Xie, H. Zhang, and C. Li, "Orderly Over-frequency Generator Tripping Strategy for Sending-end Power Grid Considering Wind," *Automation of Electric Power System*, vol. 45, no. 9, pp. 153–161, 2021.

[11] T. Han, B. Li, and Z. Zhang, "Security and stability defense system for power grid with wind-photovoltaic-thermal power bundling and multi-DC weak sending-end," *Electric Power Engineering Technology*, vol. 39, no. 3, pp. 15–22, 2020.

[12] H. Yuan, F. Liu, and Y. Hou, "A tuning method for high-frequency protection program of fans considering emergency reserve and coordination with emergency control," *Power System Protection and Control*, vol. 45, no. 7, pp. 77–83, 2017.

[13] X. Hu, D. Cao, and B. Egardt, "Condition Monitoring in Advanced Battery Management Systems: Moving Horizon Estimation Using a Reduced Electrochemical Model," *IEEEASME Trans. Mechatron.*, vol. 23, no. 1, pp. 167–178, Feb. 2018.

[14] J. Pahasa, P. Potejana, and I. Ngamroo, "MPC-Based Virtual Energy Storage System Using PV and Air Conditioner to Emulate Virtual Inertia and Frequency Regulation of the Low-Inertia Microgrid," *IEEE Access*, vol. 10, pp. 133708–133719, 2022.

[15] S. Li, R. Deng, and Z. Xue, "Virtual Inertia Compensation Control Method for Energy Storage Device Based on Calculation of Virtual Inertia," *Proceedings of the CSU-EPSA*, vol. 35, no. 11, pp. 114–121, 2023.

[16] J. Zhao, Y. Tang, and V. Terzija, "Robust Online Estimation of Power System Center of Inertia Frequency," *IEEE Trans. Power Syst.*, vol. 34, no. 1, pp. 821–825, Jan. 2019.

[17] H. Lin *et al.*, "Unit Commitment of Power System With High Proportion of Wind Power Considering Frequency Safety Constraints," *Power System Technology*, vol. 45, no. 1, pp. 1–13, 2021.

Proceedings of the 3rd Conference on Fully Actuated System Theory and Applications
May 10-12, 2024, Shenzhen, China

Explicit Solution to Quasi-Polynomial Matrix Right Coprime Factorization with Application in Establishment of Time-Delay Fully Actuated System

Xujie Zhang[1], Guangren Duan[1,2*]

1. Shenzhen Key Laboratory of Control Theory and Intelligent Systems, Southern University of Science and Technology, Shenzhen 518055, China
E-mail: zhangxujie1208@outlook.com

2. Center for Control Theory and Guidance Technology, Harbin Institute of Technology, Harbin 150001, China
E-mail: duangr@sustech.edu.cn / g.r.duan@hit.edu.cn

Abstract: We investigate the right coprime factorization of the transfer function matrix of a linear time-delay system considering constant state and input delays. This transfer function matrix is a quasi-polynomial matrix, and its right coprime factorization can be explicitly obtained by solving a series of linear equations once a user-specified Pseudo-Controllability Indices (PCI) set is selected. Besides, we determine the condition for the PCI set such that the denominator matrix in the right coprime factorization is column reduced. We then utilize these results to transform the original time-delay system into a fully actuated one. Finally, an example demonstrates the effectiveness of our method.

Key Words: Right coprime factorization, quasi-polynomial matrix, time-delay fully actuated systems, Pseudo-Controllability Indices (PCI), column reduced

1 Introduction

Time delays play an important role in various engineering systems such as underwater vehicles, industrial processes, and communication networks since they inherently exist in the process of communication, computation, and execution [1]. The majority of the contributions are devoted to stabilizing time-delay systems [2, 3]. Among numerous methods, the fully actuated system (FAS) approach can eliminate all the dynamic characteristics of the open-loop system and achieve a linear time-invariant closed-loop system with an arbitrarily assignable eigenstructure [4, 5]. This provides a novel idea for the controller design of time-delay systems.

The control problem of FASs with nonlinearity and multiple time-varying state delays is solved thanks to the FAS approach [6]. The time-delay sub-FASs (namely, the time-delay systems that do not completely but partially satisfy the full actuation) are investigated [7], and a region of exponential attraction (ROEA) is defined for the constraint of initial values to achieve exponential stability. When initial values are outside the ROEA, a globally stabilizing controller or pre-controller should be deployed [8, 9]. Additionally, a time-varying nonlinear uncertain system with state delays is presented [10], and a robust controller is developed for this system by the FAS approach. However, these studies merely consider state delays. Based on [6], both state and input delays are considered in [11] where the FAS approaches for systems with time-varying state delays and a constant input delay are proposed. A prediction scheme is also introduced for such systems. Besides, researchers utilize the FAS approach to stabilize discrete-time nonlinear systems with multiple input delays [12], but this investigation does not consider state delays. Notably, the potential of the FAS approach is elucidated for the stabilization of time-delay systems. Meanwhile, further explorations of the FAS approach to general systems with both state and input delays are required.

For time-delay systems, we can concisely design a stabilizing control law by the FAS approach provided that a time-delay FAS model is given. However, the existing studies usually use manual variable elimination to derive time-delay FAS models, leading to non-uniform results. Moreover, this manual deployment is cumbersome and entails in-depth skills for high-order systems. To overcome these obstacles, the polynomial matrix description (PMD) is employed to establish a FAS model for a linear controllable system from the frequency domain perspective [13]. More specifically, this method requires not only a right coprime factorization of the system's transfer function matrix but also a column reduced denominator matrix in the factorization. The study [13], however, is restricted to the treatment of a non-delayed case. To the best of our knowledge, an implementable approach is still missing for converting time-delay systems to the corresponding FAS models.

In this paper, a linear system with both state and input delays is considered, and its FAS model is established. Inspired by the procedure of the polynomial matrix right coprime factorization in [14] that analyzes a non-delayed system, we further use the Pseudo-Controllability Indices (PCI) set to attain the right coprime factorization of the transfer function matrix of the considered time-delay system. Besides, different from [13] employing elementary column operations to reduce the column degree of the matrix, we *directly* attain a column reduced denominator matrix in the right coprime factorization. With the obtained solution, the original time-delay system can be transformed into a fully actuated one. Our work provides insight into a procedural

* Corresponding author: Guangren Duan. This work was supported by the Science, Technology, and Innovation Commission of Shenzhen Municipality, China, under Grant No. ZDSYS20220330161800001, and the Shenzhen Science and Technology Program under Grant No. KQTD20221101093557010. This work was also supported by the Science Center Program of the National Natural Science Foundation of China (NSFC) under Grant No. 62188101.

way to obtain time-delay FAS models.

2 Problem Formulation

We consider the following linear time-delay system:

$$\dot{\boldsymbol{x}}(t)=\boldsymbol{A}\boldsymbol{x}(t-\tau)+\boldsymbol{B}\boldsymbol{u}(t-h) \tag{1}$$

where $\boldsymbol{x}(t)\in\mathbb{R}^n$ and $\boldsymbol{u}(t)\in\mathbb{R}^r$ are respectively the state and input vectors; $\boldsymbol{A}\in\mathbb{R}^{n\times n}$ and $\boldsymbol{B}\in\mathbb{R}^{n\times r}$ are constant coefficient matrices; $\tau\in\mathbb{R}$ and $h\in\mathbb{R}$ are constant state and input delays, respectively.

We then obtain the following PMD model of the system (1) by taking the Laplace transformation of (1) with the zero initial condition:

$$\boldsymbol{P}(s)\boldsymbol{X}(s)=\boldsymbol{Q}(s)\boldsymbol{U}(s) \tag{2}$$

where s is the Laplace variable; $\big(\boldsymbol{P}(s),\boldsymbol{Q}(s)\big)=\left(s\mathbf{I}_n-\boldsymbol{A}e^{-\tau s},\boldsymbol{B}e^{-hs}\right)$; $\boldsymbol{X}(s)=\mathcal{L}\big(\boldsymbol{x}(t)\big)$; $\boldsymbol{U}(s)=\mathcal{L}\big(\boldsymbol{u}(t)\big)$.

Definition 1 (Fully actuated PMD model)**.** The PMD model (2) is said to be fully actuated if $n=r$ and $\boldsymbol{Q}(s)$ is a nonsingular matrix.

Besides, the transfer function matrix of (1) is

$$\boldsymbol{G}(s)=\left(s\mathbf{I}_n-\boldsymbol{A}e^{-\tau s}\right)^{-1}\boldsymbol{B}e^{-hs}. \tag{3}$$

We assume that two matrices $\boldsymbol{N}(s)\in\mathbb{R}^{n\times r}$ and $\boldsymbol{D}(s)\in\mathbb{R}^{r\times r}$ factorize (3) into the following form:

$$\left(s\mathbf{I}_n-\boldsymbol{A}e^{-\tau s}\right)^{-1}\boldsymbol{B}e^{-hs}=\boldsymbol{N}(s)\boldsymbol{D}(s)^{-1}. \tag{4}$$

We then introduce the following definitions given in [15].

Definition 2 (Right coprime factorization of $\boldsymbol{G}(s)$)**.** For controllable (1), $\boldsymbol{N}(s)\in\mathbb{R}^{n\times r}$ and $\boldsymbol{D}(s)\in\mathbb{R}^{r\times r}$ satisfying (4) are right coprime iff

$$\deg\Big(\det\big(\boldsymbol{D}(s)\big)\Big)=\dim(\boldsymbol{A})=n. \tag{5}$$

Definition 3 (Column reduction of $\boldsymbol{D}(s)$)**.** $\boldsymbol{D}(s)$ is column reduced if

$$\deg\Big(\det\big(\boldsymbol{D}(s)\big)\Big)=\sum_{i=1}^{r}\upsilon_i \tag{6}$$

where υ_i, $i=1,2,...,r$ is the degree of the ith column of $\boldsymbol{D}(s)$.

The objective of this paper is threefold: i) Obtain a right coprime pair $\big(\boldsymbol{N}(s),\boldsymbol{D}(s)\big)$ satisfying (4); ii) Determine the condition for a column reduced $\boldsymbol{D}(s)$ in the obtained factorization; iii) Apply the above results to establish a time-delay FAS of (1).

3 Solution to Quasi-Polynomial Matrix Right Coprime Factorization

We first denote $\boldsymbol{D}(s)=\big[\boldsymbol{D}_{ij}(s)\big]$ and $t=\max_{1\le i,j\le r}\Big(\deg\big(\boldsymbol{D}_{ij}(s)\big)\Big)$. With these, we can express $\boldsymbol{N}(s)$ and $\boldsymbol{D}(s)$ as

$$\begin{aligned}\boldsymbol{N}(s)&=\sum_{i=0}^{t-1}\boldsymbol{N}_i\left(e^{\tau s}\right)s^i,\ \boldsymbol{N}_i\in\mathbb{R}^{n\times r},\\ \boldsymbol{D}(s)&=\sum_{i=0}^{t}\boldsymbol{D}_i\left(e^{\tau s},e^{hs}\right)s^i,\ \boldsymbol{D}_i\in\mathbb{R}^{r\times r}.\end{aligned} \tag{7}$$

We then substitute (7) into (4) and obtain

$$\boldsymbol{B}e^{-hs}\sum_{i=0}^{t}\boldsymbol{D}_i s^i=\sum_{i=0}^{t-1}\boldsymbol{N}_i s^{i+1}-\boldsymbol{A}e^{-\tau s}\sum_{i=0}^{t-1}\boldsymbol{N}_i s^i. \tag{8}$$

We can rewrite (8) as

$$\begin{cases}-\boldsymbol{A}\boldsymbol{N}_0e^{-\tau s}=\boldsymbol{B}\boldsymbol{D}_0e^{-hs}\\ \boldsymbol{N}_{i-1}-\boldsymbol{A}\boldsymbol{N}_ie^{-\tau s}=\boldsymbol{B}\boldsymbol{D}_ie^{-hs},\ i=1,2,...,t-1\\ \boldsymbol{N}_{t-1}=\boldsymbol{B}\boldsymbol{D}_te^{-hs}.\end{cases} \tag{9}$$

The following lemma is extended from Lemma 2 in [14]:

Lemma 1. *Given* $\boldsymbol{N}_i$, $i=0,1,...,t-1$ *and* $\boldsymbol{D}_i$, $i=0,1,...,t$ *in (7), (4) holds iff* $\boldsymbol{D}_i$, $i=0,1,...,t$ *satisfy*

$$\begin{bmatrix}\boldsymbol{B} & \boldsymbol{A}\boldsymbol{B} & \cdots & \boldsymbol{A}^{t-1}\boldsymbol{B} & \boldsymbol{A}^t\boldsymbol{B}\end{bmatrix}\begin{bmatrix}\boldsymbol{D}_0\\ \boldsymbol{D}_1e^{-\tau s}\\ \vdots\\ \boldsymbol{D}_{t-1}e^{-(t-1)\tau s}\\ \boldsymbol{D}_te^{-t\tau s}\end{bmatrix}e^{-hs}=\boldsymbol{0} \tag{10}$$

and $\boldsymbol{N}_i$, $i=0,1,...,t-1$ *satisfy*

$$\begin{bmatrix}\boldsymbol{N}_0 & \boldsymbol{N}_1 & \cdots & \boldsymbol{N}_{t-2} & \boldsymbol{N}_{t-1}\end{bmatrix}=\boldsymbol{Q}(t)\boldsymbol{S}\left(e^{-\tau s},t\right)e^{-hs} \tag{11}$$

where

$$\boldsymbol{Q}(t)=\begin{bmatrix}\boldsymbol{B} & \boldsymbol{A}\boldsymbol{B} & \cdots & \boldsymbol{A}^{t-2}\boldsymbol{B} & \boldsymbol{A}^{t-1}\boldsymbol{B}\end{bmatrix}$$

and

$$\boldsymbol{S}\left(e^{-\tau s},t\right)=\begin{bmatrix}\boldsymbol{D}_1 & \boldsymbol{D}_2 & \cdots & \boldsymbol{D}_{t-1} & \boldsymbol{D}_t\\ \boldsymbol{D}_2e^{-\tau s} & \boldsymbol{D}_3e^{-\tau s} & \cdots & \boldsymbol{D}_te^{-\tau s} & \\ \vdots & \vdots & \iddots & & \\ \boldsymbol{D}_{t-1}e^{-(t-2)\tau s} & \boldsymbol{D}_te^{-(t-2)\tau s} & & & \\ \boldsymbol{D}_te^{-(t-1)\tau s} & & & & \end{bmatrix}$$

is an upper block matrix.

Proof. We first demonstrate how to get (10) and (11) from (9), i.e., the proof of sufficiency. Multiplying both sides of the ith, $i=0,1,...,t$ equation in (9) by $\boldsymbol{A}^ie^{-i\tau s}$ on the left yields

$$\begin{cases}-\boldsymbol{A}\boldsymbol{N}_0e^{-\tau s}=\boldsymbol{B}\boldsymbol{D}_0e^{-hs}\\ \boldsymbol{A}^i\boldsymbol{N}_{i-1}e^{-i\tau s}-\boldsymbol{A}^{i+1}\boldsymbol{N}_ie^{-(i+1)\tau s}\\ \qquad\qquad=\boldsymbol{A}^i\boldsymbol{B}\boldsymbol{D}_ie^{-(i\tau+h)s},\ i=1,2,...,t-1\\ \boldsymbol{A}^t\boldsymbol{N}_{t-1}e^{-t\tau s}=\boldsymbol{A}^t\boldsymbol{B}\boldsymbol{D}_te^{-(t\tau+h)s}.\end{cases} \tag{12}$$

We then sum both sides of the obtained $t+1$ equations in (12), leading to

$$\boldsymbol{0}=\left(\boldsymbol{B}\boldsymbol{D}_0+\boldsymbol{A}\boldsymbol{B}\boldsymbol{D}_1e^{-\tau s}+\cdots+\boldsymbol{A}^t\boldsymbol{B}\boldsymbol{D}_te^{-t\tau s}\right)e^{-hs}, \tag{13}$$

the matrix form of which is (10).

Note that substituting $\boldsymbol{N}_{t-1}$ in the tth equation of (9) into the $(t-1)^{\text{th}}$ equation results in

$$\begin{aligned}\boldsymbol{N}_{t-2}&=\boldsymbol{A}\boldsymbol{N}_{t-1}e^{-\tau s}+\boldsymbol{B}\boldsymbol{D}_{t-1}e^{-hs}\\ &=\boldsymbol{A}\boldsymbol{B}\boldsymbol{D}_te^{-(\tau+h)s}+\boldsymbol{B}\boldsymbol{D}_{t-1}e^{-hs}.\end{aligned} \tag{14}$$

Furthermore, we can obtain $\boldsymbol{N}_i$, $i=0,1,...,t-1$ written in (11) by repeating the above procedure.

We then explain how to derive (9) according to (10) and (11), i.e., the proof of necessity. With (10) and (11) at hand, we obtain

$$\begin{aligned}&\boldsymbol{A}\boldsymbol{N}_0e^{-\tau s}+\boldsymbol{B}\boldsymbol{D}_0e^{-hs}\\&=\boldsymbol{A}\left(\boldsymbol{B}\boldsymbol{D}_1+\cdots+\boldsymbol{A}^{t-1}\boldsymbol{B}\boldsymbol{D}_te^{-(t-1)\tau s}\right)e^{-hs}e^{-\tau s}\\&\quad-\left(\boldsymbol{A}\boldsymbol{B}\boldsymbol{D}_1e^{-\tau s}+\cdots+\boldsymbol{A}^{t}\boldsymbol{B}\boldsymbol{D}_te^{-t\tau s}\right)e^{-hs}\\&=\boldsymbol{0},\end{aligned}\tag{15}$$

$$\begin{aligned}&\boldsymbol{A}\boldsymbol{N}_ie^{-\tau s}-\boldsymbol{N}_{i-1}\\&=\boldsymbol{A}\left(\boldsymbol{B}\boldsymbol{D}_{i+1}+\cdots+\boldsymbol{A}^{t-i-1}\boldsymbol{B}\boldsymbol{D}_{t-i+1}e^{-(t-i-1)\tau s}\right)e^{-hs}e^{-\tau s}\\&\quad-\left(\boldsymbol{B}\boldsymbol{D}_i+\cdots+\boldsymbol{A}^{t-i}\boldsymbol{B}\boldsymbol{D}_{t-i+1}e^{-(t-i)\tau s}\right)e^{-hs}\\&=-\boldsymbol{B}\boldsymbol{D}_ie^{-hs},\ i=1,2,...,t-1,\end{aligned}\tag{16}$$

and

$$\boldsymbol{B}\boldsymbol{D}_te^{-hs}-\boldsymbol{N}_{t-1}=\boldsymbol{0}.\tag{17}$$

Equations (15), (16), and (17) are equivalent to (8). That completes the proof. □

We then introduce the following definitions mentioned in [14] and [16].

Definition 4 (Pseudo-Controllability Indices (PCI))**.** The set of PCI, denoted by $\{h_1,h_2,\cdots,h_r\}$, is any of integers h_i, $i=1,2,\cdots,r$ satisfying $0\le h_i\le n,\ i=1,2,\cdots,r$ and $\Sigma_i^r h_i=n$.

Definition 5 (Admissibility of the PCI set)**.** Given that the sets $\boldsymbol{\varphi}_i=\{\boldsymbol{b}_i,\boldsymbol{A}^1\boldsymbol{b}_i,\cdots,\boldsymbol{A}^{h_i-1}\boldsymbol{b}_i\}$, $h_i\ge1,\ i=1,2,\cdots,r$, the set of PCI is admissible if

$$\{\boldsymbol{\varphi}_1,\boldsymbol{\varphi}_2,\cdots,\boldsymbol{\varphi}_r\}\tag{18}$$

form a set of linearly independent columns.

The following theorem is then presented.

Theorem 1. *For controllable (1) where $\boldsymbol{A}\in\mathbb{R}^{n\times n}$ and $\boldsymbol{B}\in\mathbb{R}^{n\times r}$, an admissible PCI set $\{h_1,h_2,\cdots,h_r\}$ exists such that*

$$\boldsymbol{A}^{h_k}\boldsymbol{b}_k=\sum_{i=1}^{r}\sum_{j=0}^{h_i-1}\alpha_{jik}\boldsymbol{A}^j\boldsymbol{b}_i,\ h_i\ge1,\ k=1,2,\cdots,r\tag{19}$$

where $\alpha_{jik}\in\mathbb{R}$. Then, $\boldsymbol{N}(s)$ and $\boldsymbol{D}(s)$ in (4) are right coprime if $\boldsymbol{D}(s)$ is determined below and $\boldsymbol{N}(s)$ is subsequently calculated by (11):

$$\boldsymbol{D}(s)=\left[\boldsymbol{D}_{ik}(s)\right]=\left[\sum_{j=0}^{t}\beta_{jik}s^je^{j\tau s}\right]\tag{20}$$

where $t=\max(h_i)$, $1\le i\le r$ and

$$\beta_{jik}=\begin{cases}1, & j=h_k\\-\alpha_{jik}, & j\le h_k-1,\ i,k=1,2,\cdots,r\\0, & j>h_k.\end{cases}\tag{21}$$

Proof. Instead of a general proof, we use an example to illustrate the philosophy behind our theorem. We take $\boldsymbol{A}\in\mathbb{R}^{6\times6},\boldsymbol{B}=\left[\boldsymbol{b}_1\ \boldsymbol{b}_2\ \boldsymbol{b}_3\right]\in\mathbb{R}^{6\times3}$ and choose an admissible PCI set as $\{h_1,h_2,h_3\}=\{2,3,1\}$. Thus, a unique combination of α_{jik} satisfying (19) exists since the n columns defined in (18) are linearly independent. Besides, the matrices $\boldsymbol{D}_i\in\mathbb{R}^{r\times r},i=0,1,\cdots,t$ satisfy (10) as per Lemma 1, leading to

$$\left[\boldsymbol{b}_1\ \boldsymbol{b}_2\ \boldsymbol{b}_3\ \cdots\ \boldsymbol{A}^3\boldsymbol{b}_1\ \boldsymbol{A}^3\boldsymbol{b}_2\ \boldsymbol{A}^3\boldsymbol{b}_3\right]\begin{bmatrix}\boldsymbol{D}_0\\\boldsymbol{D}_1e^{-\tau s}\\\boldsymbol{D}_2e^{-2\tau s}\\\boldsymbol{D}_3e^{-3\tau s}\end{bmatrix}e^{-hs}=\boldsymbol{0}\tag{22}$$

where

$$\boldsymbol{D}_0=-\begin{bmatrix}\alpha_{011}&\alpha_{012}&\alpha_{013}\\\alpha_{021}&\alpha_{022}&\alpha_{023}\\\alpha_{031}&\alpha_{032}&\alpha_{033}\end{bmatrix}e^{hs},$$

$$\boldsymbol{D}_1=-\begin{bmatrix}\alpha_{111}&\alpha_{112}&\alpha_{113}\\\alpha_{121}&\alpha_{122}&\alpha_{123}\\0&0&-1\end{bmatrix}e^{(\tau+h)s},$$

$$\boldsymbol{D}_2=-\begin{bmatrix}-1&0&0\\\alpha_{221}&\alpha_{222}&\alpha_{223}\\0&0&0\end{bmatrix}e^{(2\tau+h)s},$$

$$\boldsymbol{D}_3=-\begin{bmatrix}0&0&0\\0&-1&0\\0&0&0\end{bmatrix}e^{(3\tau+h)s}.$$

According to (7), $\boldsymbol{D}(s)$ can then be calculated as

$$\begin{aligned}\boldsymbol{D}(s)&=\sum_{i=0}^{3}\boldsymbol{D}_i\left(e^{\tau s},e^{hs}\right)s^i\\&=\begin{bmatrix}s^2e^{2\tau s}-\sum_{i=0}^{1}\alpha_{i11}s^ie^{i\tau s}&-\sum_{i=0}^{1}\alpha_{i12}s^ie^{i\tau s}&-\sum_{i=0}^{1}\alpha_{i13}s^ie^{i\tau s}\\-\sum_{i=0}^{2}\alpha_{i21}s^ie^{i\tau s}&s^3e^{3\tau s}-\sum_{i=0}^{2}\alpha_{i22}s^ie^{i\tau s}&-\sum_{i=0}^{2}\alpha_{i23}s^ie^{i\tau s}\\-\alpha_{031}&-\alpha_{032}&se^{\tau s}-\alpha_{033}\end{bmatrix}e^{hs},\end{aligned}$$

which satisfies $\deg\left(\det\left(\boldsymbol{D}(s)\right)\right)=\Sigma_{i=1}^{3}h_i=\dim(\boldsymbol{A})=6$. Therefore, $\boldsymbol{N}(s)$ and $\boldsymbol{D}(s)$ in (4) are right coprime according to Definition 2. Furthermore, $\boldsymbol{D}(s)$ can be described by (20) after defining (21). □

Note that Theorem 1 achieves the right coprime factorization of (3). However, it does not ensure a column reduced $\boldsymbol{D}(s)$. Specifically, the summation of the column degree of the obtained $\boldsymbol{D}(s)$ is 7, indicating that $\boldsymbol{D}(s)$ is not column reduced as per Definition 3. The following corollary then presents a way to obtain a column reduced $\boldsymbol{D}(s)$ in the right coprime factorization by appropriately choosing the admissible PCI set.

Corollary 1. *$\boldsymbol{D}(s)$ and $\boldsymbol{N}(s)$ determined by Theorem 1 are not only right coprime but also $\boldsymbol{D}(s)$ is column reduced when the admissible PCI set is chosen as*

$$\{h_1,\cdots,h_r\}=\underbrace{\{\lambda,\cdots,\lambda\}}_{r-\varphi},\underbrace{\{\lambda+1,\cdots,\lambda+1\}}_{\varphi}\tag{23}$$

where $\lambda=n//r$ and $\varphi=n\%r$ represent the quotient and remainder of n divided by r, respectively.

Proof. We still take $\boldsymbol{A}\in\mathbb{R}^{6\times 6},\boldsymbol{B}=\left[\boldsymbol{b}_1\ \boldsymbol{b}_2\ \boldsymbol{b}_3\right]\in\mathbb{R}^{6\times 3}$ as an illustration. We choose another admissible PCI set as $\left\{h_1,h_2,h_3\right\}=\left\{2,2,2\right\}$ according to (23), and $\boldsymbol{D}(s)$ is then obtained as

$$\begin{aligned}\boldsymbol{D}(s)&=\sum_{i=0}^{2}\boldsymbol{D}_i\left(e^{\tau s},e^{hs}\right)s^i\\&=\begin{bmatrix}s^2e^{2\tau s}-\sum_{i=0}^{1}\alpha_{i11}s^ie^{i\tau s} & -\sum_{i=0}^{1}\alpha_{i12}s^ie^{i\tau s} & -\sum_{i=0}^{1}\alpha_{i13}s^ie^{i\tau s}\\ -\sum_{i=0}^{1}\alpha_{i21}s^ie^{i\tau s} & s^2e^{2\tau s}-\sum_{i=0}^{1}\alpha_{i22}s^ie^{i\tau s} & -\sum_{i=0}^{1}\alpha_{i23}s^ie^{i\tau s}\\ -\sum_{i=0}^{1}\alpha_{i31}s^ie^{i\tau s} & -\sum_{i=0}^{1}\alpha_{i32}s^ie^{i\tau s} & s^2e^{2\tau s}-\sum_{i=0}^{1}\alpha_{i33}s^ie^{i\tau s}\end{bmatrix}e^{hs},\end{aligned}$$

whose column degree summation is $6=n$, indicating that $\boldsymbol{D}(s)$ is column reduced according to Definition 3. □

Remark 1. For an admissible PCI set $\left\{h_1,h_2,\cdots,h_r\right\}$, the column degree summation of $\boldsymbol{D}(s)$, denoted by $\Sigma_{\deg}$, can be calculated as

$$\Sigma_{\deg}=\begin{cases}n, & \text{PCI set determined by (23)}\\ t+(t-1)\times(r-1), & \text{other admissible PCI sets}\end{cases}$$

where $t=\max\left(h_i\right),\ 1\le i\le r$.

The subsequent section will establish the time-delay FAS model of (1) with the help of Corollary 1.

4 Application in Establishment of Time-Delay FAS

For a column reduced $\boldsymbol{D}(s)$ obtained by Corollary 1, it can be written as

$$\boldsymbol{D}(s)=\tilde{\boldsymbol{D}}_0\boldsymbol{\Delta}\left(s,e^{\tau s},e^{hs}\right)+\boldsymbol{L}\left(s,e^{\tau s},e^{hs}\right)\tag{24}$$

where $\tilde{\boldsymbol{D}}_0\in\mathbb{R}^{r\times r}$ is nonsingular [15] and the degree of each column of $\boldsymbol{L}\left(s,e^{\tau s},e^{hs}\right)\in\mathbb{R}^{r\times r}$ is correspondingly smaller than that of $\boldsymbol{D}(s)$. Besides,

$$\boldsymbol{\Delta}\left(s,e^{\tau s},e^{hs}\right)=\begin{bmatrix}s^{\lambda}e^{\lambda\tau s} & & & & & & \\ & \ddots & & & & & \\ & & s^{\lambda}e^{\lambda\tau s} & & & & \\ & & & s^{\lambda+1}e^{(\lambda+1)\tau s} & & & \\ & & & & \ddots & & \\ & & & & & s^{\lambda+1}e^{(\lambda+1)\tau s}\end{bmatrix}e^{hs},$$

$$\underbrace{\qquad\qquad}_{r-\varphi}\ \underbrace{\qquad\qquad\qquad\qquad}_{\varphi}$$

in which λ and φ are defined in (23). Furthermore, we can factorize $\boldsymbol{\Delta}\left(s,e^{\tau s},e^{hs}\right)$ as

$$\boldsymbol{\Delta}\left(s,e^{\tau s},e^{hs}\right)=\bar{\boldsymbol{\Delta}}_1\left(s,e^{-\tau s}\right)\bar{\boldsymbol{\Delta}}_2\left(s,e^{\tau s},e^{hs}\right)\tag{25}$$

where

$$\bar{\boldsymbol{\Delta}}_1\left(s,e^{-\tau s}\right)=\underbrace{\begin{bmatrix}e^{-\tau s} & & & & \\ & \ddots & & & \\ & & e^{-\tau s} & & \\ & & & 1 & \\ & & & & \ddots \\ & & & & & 1\end{bmatrix}}_{r-\varphi}\ \underbrace{\qquad}_{\varphi},$$

$$\bar{\boldsymbol{\Delta}}_2\left(s,e^{\tau s},e^{hs}\right)=\underbrace{\begin{bmatrix}s^{\lambda}e^{(\lambda+1)\tau s} & & & & & & \\ & \ddots & & & & & \\ & & s^{\lambda}e^{(\lambda+1)\tau s} & & & & \\ & & & s^{\lambda+1}e^{(\lambda+1)\tau s} & & & \\ & & & & \ddots & & \\ & & & & & s^{\lambda+1}e^{(\lambda+1)\tau s}\end{bmatrix}}_{r-\varphi}\ \underbrace{\qquad\qquad}_{\varphi}e^{hs}.$$

When the transfer function matrix $\boldsymbol{G}(s)$ in (3) is strictly proper [15], we can express $\boldsymbol{D}(s)$ and $\boldsymbol{N}(s)$ in (4) as

$$\begin{aligned}\boldsymbol{D}(s)=&\tilde{\boldsymbol{D}}_0\bar{\boldsymbol{\Delta}}_1\left(s,e^{-\tau s}\right)\bar{\boldsymbol{\Delta}}_2\left(s,e^{\tau s},e^{hs}\right)\\&+\left[\tilde{\boldsymbol{D}}_1\boldsymbol{l}_1(s)\ \tilde{\boldsymbol{D}}_2\boldsymbol{l}_2(s)\ \cdots\ \tilde{\boldsymbol{D}}_r\boldsymbol{l}_r(s)\right],\end{aligned}\tag{26}$$

$$\boldsymbol{N}(s)=\left[\tilde{\boldsymbol{N}}_1\boldsymbol{l}_1(s)\ \tilde{\boldsymbol{N}}_2\boldsymbol{l}_2(s)\ \cdots\ \tilde{\boldsymbol{N}}_r\boldsymbol{l}_r(s)\right]\tag{27}$$

where $\left(\tilde{\boldsymbol{D}}_i,\tilde{\boldsymbol{N}}_i\right)\in\left(\mathbb{R}^{r\times h_i},\mathbb{R}^{n\times h_i}\right),\ i=1,2,\cdots,r$ and

$$\boldsymbol{l}_i(s)=\left[1\quad s\quad\cdots\quad s^{h_i-1}\right]^{\mathrm{T}}\in\mathbb{R}^{h_i},\ i=1,2,\cdots,r.$$

The following theorem is then presented.

Theorem 2. *For the controllable system (1) whose transfer function matrix is strictly proper, let $\boldsymbol{D}(s)$ and $\boldsymbol{N}(s)$ satisfying (4) be determined by Corollary 1. Furthermore, let $\boldsymbol{D}(s)$ and $\boldsymbol{N}(s)$ be expressed by (26) and (27), respectively. Then, the fully actuated PMD of (1) can be represented as*

$$\begin{aligned}&\left\{\bar{\boldsymbol{\Delta}}_2+\left(\tilde{\boldsymbol{D}}_0\bar{\boldsymbol{\Delta}}_1\right)^{-1}\left[\tilde{\boldsymbol{D}}_1\boldsymbol{l}_1\ \tilde{\boldsymbol{D}}_2\boldsymbol{l}_2\cdots\tilde{\boldsymbol{D}}_r\boldsymbol{l}_r\right]\right\}\boldsymbol{Z}(s)e^{-[(\lambda+1)\tau+h]s}\\&=\left(\tilde{\boldsymbol{D}}_0\bar{\boldsymbol{\Delta}}_1\right)^{-1}\boldsymbol{U}(s)e^{-[(\lambda+1)\tau+h]s}\end{aligned}\tag{28}$$

where $\boldsymbol{Z}(s)$ is the Laplace transformation of $\boldsymbol{z}(t)\in\mathbb{R}^r$ that is referred to as a generalized state vector. Additionally, $\boldsymbol{Z}(s)$ can be uniquely determined by

$$\boldsymbol{Z}(s)=\begin{bmatrix}\boldsymbol{e}_1^{\mathrm{T}} & & & \\ & \boldsymbol{e}_2^{\mathrm{T}} & & \\ & & \ddots & \\ & & & \boldsymbol{e}_r^{\mathrm{T}}\end{bmatrix}\left[\tilde{\boldsymbol{N}}_1\ \tilde{\boldsymbol{N}}_2\ \cdots\ \tilde{\boldsymbol{N}}_r\right]^{-1}\boldsymbol{X}(s)\tag{29}$$

where

$$\boldsymbol{e}_i=\left[1\quad 0\quad\cdots\quad 0\right]^{\mathrm{T}}\in\mathbb{R}^{h_i},\ i=1,2,\cdots,r.$$

Proof. The dimensions of $\boldsymbol{z}(t)$ and $\boldsymbol{u}(t)$ are identical to r. Meanwhile, the matrix $\left(\tilde{\boldsymbol{D}}_0\bar{\boldsymbol{\Delta}}_1\right)^{-1}$ is nonsingular. Thus, the PMD model (28) is fully actuated according to Definition 1. Besides, we can obtain $\boldsymbol{Z}(s)=\boldsymbol{D}(s)^{-1}\boldsymbol{U}(s)$ as per (26) and (28). Thus,

$$\begin{aligned}\boldsymbol{X}(s)&=\boldsymbol{G}(s)\boldsymbol{U}(s)=\boldsymbol{N}(s)\boldsymbol{D}(s)^{-1}\boldsymbol{U}(s)\\&=\boldsymbol{N}(s)\boldsymbol{Z}(s)\\&=\left[\tilde{\boldsymbol{N}}_1\boldsymbol{l}_1\ \tilde{\boldsymbol{N}}_2\boldsymbol{l}_2\ \cdots\ \tilde{\boldsymbol{N}}_r\boldsymbol{l}_r\right]\boldsymbol{Z}(s)\\&=\left[\tilde{\boldsymbol{N}}_1\ \tilde{\boldsymbol{N}}_2\ \cdots\ \tilde{\boldsymbol{N}}_r\right]\begin{bmatrix}\boldsymbol{l}_1Z_1(s)\\\boldsymbol{l}_2Z_2(s)\\\vdots\\\boldsymbol{l}_rZ_r(s)\end{bmatrix}.\end{aligned}\tag{30}$$

Since the matrix $\left[\tilde{\boldsymbol{N}}_1\ \tilde{\boldsymbol{N}}_2\ \cdots\ \tilde{\boldsymbol{N}}_r\right]$ is invertible [Lemma 4.4 in 13], (30) can be converted to

$$\begin{bmatrix}\boldsymbol{l}_1Z_1(s)\\\boldsymbol{l}_2Z_2(s)\\\vdots\\\boldsymbol{l}_rZ_r(s)\end{bmatrix}=\left[\tilde{\boldsymbol{N}}_1\ \tilde{\boldsymbol{N}}_2\ \cdots\ \tilde{\boldsymbol{N}}_r\right]^{-1}\boldsymbol{X}(s).\tag{31}$$

Notice that

$$\boldsymbol{Z}(s)=\begin{bmatrix}Z_1(s)\\Z_2(s)\\\vdots\\Z_r(s)\end{bmatrix}=\begin{bmatrix}\boldsymbol{e}_1^{\mathrm{T}}\boldsymbol{l}_1Z_1(s)\\\boldsymbol{e}_2^{\mathrm{T}}\boldsymbol{l}_2Z_2(s)\\\vdots\\\boldsymbol{e}_r^{\mathrm{T}}\boldsymbol{l}_rZ_r(s)\end{bmatrix}.\tag{32}$$

Substituting (31) into (32) then yields (29). □

Remark 2. With Theorem 2 at hand, we can derive the time-delay FAS model of (1) and the generalized state vector $\boldsymbol{z}(t)$ by deploying the Laplace inverse transformation of (28) and (29), respectively.

5 Case study

We consider the system (1) with the following parameters:

$$\boldsymbol{A}=\begin{bmatrix}0&1&0&2&-1\\1&1&0&1&0\\1&-1&0&1&0\\-1&0&-1&-1&-1\\-2&-1&0&1&2\end{bmatrix},\boldsymbol{B}=\begin{bmatrix}1&0&1\\0&0&0\\0&1&0\\0&1&1\\1&0&-1\end{bmatrix}.\tag{33}$$

5.1 Solution to Right Coprime Factorization of $\left(s\mathbf{I}_n-\boldsymbol{A}e^{-\tau s}\right)^{-1}\boldsymbol{B}e^{-hs}$

Given $(\boldsymbol{A},\boldsymbol{B})$ in (33), we verify that the system (1) is controllable and its transfer function matrix is strictly proper. For a column reduced $\boldsymbol{D}(s)$, an admissible PCI set is chosen as $\{h_1,h_2,h_3\}=\{1,2,2\}$ according to (23), leading to a set of linearly independent columns as

$$\{\boldsymbol{b}_1,\boldsymbol{b}_2,\boldsymbol{A}\boldsymbol{b}_2,\boldsymbol{b}_3,\boldsymbol{A}\boldsymbol{b}_3\}.\tag{34}$$

As per Corollary 1, we have

$$\boldsymbol{D}(s)=\begin{bmatrix}se^{\tau s}-1&0&0\\se^{\tau s}&s^2e^{2\tau s}+3se^{\tau s}+2&4se^{\tau s}+4\\-se^{\tau s}+3&-2se^{\tau s}+4&s^2e^{2\tau s}-4se^{\tau s}+1\end{bmatrix}e^{hs}$$

and

$$\boldsymbol{N}(s)=\begin{bmatrix}0&0&se^{2\tau s}-e^{\tau s}\\0&e^{\tau s}&2e^{\tau s}\\e^{\tau s}&se^{2\tau s}+4e^{\tau s}&6e^{\tau s}\\0&se^{2\tau s}-e^{\tau s}&se^{2\tau s}-e^{\tau s}\\2e^{\tau s}&3e^{\tau s}&-se^{2\tau s}+e^{\tau s}\end{bmatrix},$$

which is a solution to the right coprime factorization of the transfer function $\boldsymbol{G}(s)=\left(s\mathbf{I}_n-\boldsymbol{A}e^{-\tau s}\right)^{-1}\boldsymbol{B}e^{-hs}$.

5.2 Establishment of Time-Delay FAS

According to (26) and (27), we rewrite the obtained $\boldsymbol{D}(s)$ and $\boldsymbol{N}(s)$ in Section 5.1 as

$$\boldsymbol{D}(s)=\tilde{\boldsymbol{D}}_0\bar{\boldsymbol{\Delta}}_1\bar{\boldsymbol{\Delta}}_2+\left[\tilde{\boldsymbol{D}}_1\ \tilde{\boldsymbol{D}}_2\begin{bmatrix}1\\s\end{bmatrix}\ \tilde{\boldsymbol{D}}_3\begin{bmatrix}1\\s\end{bmatrix}\right],\tag{35}$$

$$\boldsymbol{N}(s)=\left[\tilde{\boldsymbol{N}}_1\ \tilde{\boldsymbol{N}}_2\begin{bmatrix}1\\s\end{bmatrix}\ \tilde{\boldsymbol{N}}_3\begin{bmatrix}1\\s\end{bmatrix}\right]\tag{36}$$

where

$$\bar{\boldsymbol{\Delta}}_1=\begin{bmatrix}e^{-\tau s}&&\\&1&\\&&1\end{bmatrix},\ \bar{\boldsymbol{\Delta}}_2=\begin{bmatrix}se^{2\tau s}&&\\&s^2e^{2\tau s}&\\&&s^2e^{2\tau s}\end{bmatrix}e^{hs},$$

$$\tilde{\boldsymbol{D}}_0=\begin{bmatrix}1&0&0\\1&1&0\\-1&0&1\end{bmatrix},\ \tilde{\boldsymbol{D}}_1=\begin{bmatrix}-1\\0\\3\end{bmatrix}e^{hs},$$

$$\tilde{\boldsymbol{D}}_2=\begin{bmatrix}0&0\\2&3e^{\tau s}\\4&-2e^{\tau s}\end{bmatrix}e^{hs},\ \tilde{\boldsymbol{D}}_3=\begin{bmatrix}0&0\\4&4e^{\tau s}\\1&-4e^{\tau s}\end{bmatrix}e^{hs},$$

$$\tilde{\boldsymbol{N}}_1=\begin{bmatrix}0\\0\\e^{\tau s}\\0\\2e^{\tau s}\end{bmatrix},\ \tilde{\boldsymbol{N}}_2=\begin{bmatrix}0&0\\e^{\tau s}&0\\4e^{\tau s}&e^{2\tau s}\\-e^{\tau s}&e^{2\tau s}\\3e^{\tau s}&0\end{bmatrix},\ \tilde{\boldsymbol{N}}_3=\begin{bmatrix}-e^{\tau s}&e^{2\tau s}\\2e^{\tau s}&0\\6e^{\tau s}&0\\-e^{\tau s}&e^{2\tau s}\\e^{\tau s}&-e^{2\tau s}\end{bmatrix}.$$

As per (29), if we choose the generalized state vector

$$\begin{aligned}\boldsymbol{z}(t)&=\mathcal{L}^{-1}\left(\boldsymbol{Z}(s)\right)\\&=\mathcal{L}^{-1}\left(\begin{bmatrix}1&&&\\&1&0&\\&&&1&0\end{bmatrix}[\tilde{\boldsymbol{N}}_1\ \tilde{\boldsymbol{N}}_2\ \tilde{\boldsymbol{N}}_3]^{-1}\boldsymbol{X}(s)\right)\\&=\begin{bmatrix}-1&9&-3&3&2\\1&-6&2&-2&-1\\-0.5&3.5&-1&1&0.5\end{bmatrix}\boldsymbol{x}(t-\tau),\end{aligned}\tag{37}$$

we can obtain the following fully actuated PMD model of (1) according to (28):

$$\begin{aligned}&\left(\begin{bmatrix} se^{2\tau s} & & \\ & s^2e^{2\tau s} & \\ & & s^2e^{2\tau s}\end{bmatrix}e^{hs}\right.\\&\left.+\begin{bmatrix} -e^{\tau s} & 0 & 0 \\ 1 & 3se^{\tau s}+2 & 4se^{\tau s}+4 \\ 2 & -2se^{\tau s}+4 & -4se^{\tau s}+1\end{bmatrix}e^{hs}\right)\boldsymbol{Z}(s)e^{-(2\tau+h)s} \quad (38)\\&=\begin{bmatrix} e^{\tau s} & 0 & 0 \\ -1 & 1 & 0 \\ 1 & 0 & 1\end{bmatrix}\boldsymbol{U}(s)e^{-(2\tau+h)s}.\end{aligned}$$

Furthermore, the time-delay FAS model of (1) can be determined by taking the Laplace inverse transformation of (38), which is described by the following two subsystems:

$$\dot{z}_1(t)=z_1(t-\tau)+u_1(t-\tau-h), \quad (39a)$$

$$\begin{aligned}\begin{bmatrix}\ddot{z}_2(t)\\ \ddot{z}_3(t)\end{bmatrix}&=\begin{bmatrix}0 & 0 & -3 & 0 & -4\\ 0 & 0 & 2 & 0 & 4\end{bmatrix}\begin{bmatrix}z_1(t-\tau)\\ z_2(t-\tau)\\ \dot{z}_2(t-\tau)\\ z_3(t-\tau)\\ \dot{z}_3(t-\tau)\end{bmatrix}\\&+\begin{bmatrix}-1 & -2 & 0 & -4 & 0\\ -2 & -4 & 0 & -1 & 0\end{bmatrix}\begin{bmatrix}z_1(t-2\tau)\\ z_2(t-2\tau)\\ \dot{z}_2(t-2\tau)\\ z_3(t-2\tau)\\ \dot{z}_3(t-2\tau)\end{bmatrix} \quad (39b)\\&+\begin{bmatrix}-1 & 1 & 0\\ 1 & 0 & 1\end{bmatrix}\begin{bmatrix}u_1(t-2\tau-h)\\ u_2(t-2\tau-h)\\ u_3(t-2\tau-h)\end{bmatrix}.\end{aligned}$$

The second subsystem (39b) is over-actuated, which can be regarded as a fully actuated case in terms of control [Remark 2.1 in 4]. Furthermore, stabilizing controllers for (39) can be designed in two steps. We first design $u_1(t)$ for (39a). Then, $u_2(t)$ and $u_3(t)$ are designed after substituting $u_1(t)$ into (39b). Note that both of these steps can be accomplished through the FAS approach.

6 Conclusion

For a linear time-delay system where both state and input delays are considered, we obtain an explicit solution to the right coprime factorization of its transfer function matrix. Furthermore, we provide a technique to directly determine a column reduced denominator matrix in the right coprime factorization. The proposed results are then deployed to transform the considered time-delay system into a fully actuated one, which provides a valuable reference for establishing time-delay FASs through a procedural approach. Future work includes establishing time-delay fully actuated systems with multiple state and input delays.

References

[1] Q. C. Zhong, *Robust Control of Time-Delay Systems* (no. 2009). Springer, 2006.

[2] K. Gu, J. Chen, and V. L. Kharitonov, *Stability of Time-Delay Systems*. Springer Science & Business Media, 2003.

[3] R. Sipahi, S. I. Niculescu, C. T. Abdallah, W. Michiels, and K. Gu, "Stability and stabilization of systems with time delay," *IEEE Control Systems Magazine*, vol. 31, no. 1, pp. 38-65, 2011.

[4] G. R. Duan, "High-order fully actuated system approaches: Part I. Models and basic procedure," *International Journal of Systems Science*, vol. 52, no. 2, pp. 422-435, 2021.

[5] G. R. Duan, "High-order fully actuated system approaches: Part VII. Controllability, stabilisability and parametric designs," *International Journal of Systems Science*, vol. 52, no. 14, pp. 3091-3114, 2021.

[6] G. R. Duan, "Fully actuated system approaches for continuous-time delay systems: Part 1. Systems with state delays only," *Science China Information Sciences*, vol. 66, no. 1, 2023, Art. no. 112201.

[7] G. R. Duan, "Substability and substabilization: Control of subfully actuated systems," *IEEE Transactions on Cybernetics*, vol. 53, no. 11, pp. 7309-7322, 2023.

[8] G. R. Duan, "Stabilization via fully actuated system approach: A case study," *Journal of Systems Science and Complexity*, vol. 35, no. 3, pp. 731-747, 2022.

[9] G. R. Duan, "Brockett's first example: An FAS approach treatment," *Journal of Systems Science and Complexity*, vol. 35, no. 2, pp. 441-456, 2022.

[10] G. R. Duan, "Robust stabilization of time-varying nonlinear systems with time-varying delays: A fully actuated system approach," *IEEE Transactions on Cybernetics*, vol. 53, no. 12, pp. 7455-7468, 2023.

[11] G. R. Duan, "Fully actuated system approaches for continuous-time delay systems: Part 2. Systems with input delays," *Science China Information Sciences*, vol. 66, no. 2, 2023, Art. no. 122201.

[12] A. G. Wu, J. Zhang, and Y. Ji, "A fully actuated system approach for stabilization of discrete-time multiple-input nonlinear systems with distinct input delays," *Journal of Systems Science and Complexity*, vol. 35, no. 2, pp. 670-687, 2022.

[13] G. R. Duan and B. Zhou, "Fully actuated system approach for linear systems control: A frequency-domain solution," *Journal of Systems Science and Complexity*, vol. 35, no. 6, pp. 2046-2061, 2022.

[14] B. Zhou and G. R. Duan, "An explicit solution to polynomial matrix right coprime factorization with application in eigenstructure assignment," *Journal of Control Theory and Applications*, vol. 4, pp. 147-154, 2006.

[15] T. Kailath, *Linear Systems*. Prentice-Hall, Englewood Cliffs, NJ, 1980.

[16] S. Bingulac and N. F. Al. Muthairi, "On the equivalence between MFD models and pseudo-observable forms of MIMO systems," *Computers & Electrical Engineering*, vol. 24, no. 5, pp. 295-314, 1998.

Proceedings of the 3rd Conference on Fully Actuated System Theory and Applications
May 10-12, 2024, Shenzhen, China

Adaptive Control for Fully Actuated Systems with Input Quantization

Lin Liu[1], Guangren Duan[1,2]

1. Center for Control Theory and Guidance Technology, Harbin Institute of Technology, Harbin 150001, P. R. China
E-mail: liulin@stu.hit.edu.cn, g.r.duan@hit.edu.cn

2. Shenzhen Key Laboratory of Control Theory and Intelligent Systems, Southern University of Scienceand Technology, Shenzhen 518055, P. R. China
E-mail: duangr@sustech.edu.cn

Abstract: In this paper, we study the fully actuated systems (FASs) with unknown parameters where the control input takes quantized values. It is shown that, compared with early works, the adaptive control law is much easier to design and no longer limited to the single-input systems by utilizing the full-actuation property. The system state can converge to an arbitrarily small neighborhood of the origin with a hysteretic quantizer which can be very coarse. An illustrative example demonstrates the effectiveness of the given method.

Key Words: Adaptive Control, Fully Actuated Systems, Quantization

1 Introduction

Quantized control has attracted a great deal of attention [1, 2] due to the fact that it plays an important role in modern engineering such as the control of network systems, hybrid systems, and multi-agent systems. In these systems, quantizers are usually placed after the controller or the sensors to reduce communication burden. However, at the same time, the quantization error may affect the performance of the closed-loop systems. Two types of quantizers were mainly concerned in the existing literature: dynamic quantizers [3, 4] and static logarithmic (or hysteresis) quantizers [5, 6]. Recently, adaptive quantized control schemes have been developed in [7–10], in which the researchers considered the control of single-input strict-feedback systems based on the state-space approach.

In recent years, a novel philosophy of control called fully actuated system (FAS) approach, which was first proposed in the series of papers [11–13], has attracted many researchers to study. This new control theory no longer depends on the conventional state-space models, and it mathematically generalized the concept of the physical fully actuated systems [14], proving that many control systems (including some underactuated systems) essentially have the full-actuation property [15]. On the basis of this discovery, this newly established approach, which focuses on the FASs, has more simplicity for nonlinear system design, since the dynamics of the open-loop system can be eliminated directly. This control strategy has shown great superiority in many control problems. In [16, 17] and [18–20], authors studied robust and adaptive control for FASs, respectively, while in [21], the model reference tracking controller was proposed.

So far, to the best of the authors' knowledge, there is still no result available for adaptive control for FASs with input quantization. The main contribution of this paper is that we provide a solution to the quantized adaptive control for FASs. Utilizing the adaptive control scheme proposed in [18], we only need to add an additional part to the control input to overcome the influence of the quantization error. Compared with the previous research depending on the state-space models, our control design is much simpler and can be extended to the multi-input systems, the complicated backstepping method is no longer necessary. Meanwhile, the control scheme proposed in this paper does not have any requirements for the density of the quantizer, which means it is still effective when the quantizer is very coarse.

The remaining part of the paper is organized in the following way. Section 2 introduces the system description and preliminary results. Section 3 proposes our adaptive controller for FASs with input quantization. Section 4 studies an illustrative example and shows simulation results. The concluding remarks follow in Section 5.

Through out this paper, we use A^{T} and $\lambda_i(A)$ to denote the transpose and the ith eigenvalue of the matrix A. For a vector a, $\|a\|$ denotes its Euclidean norm. For a complex number s, we use $\mathrm{Re}(s)$ to represent its real part. I_n denotes the $n \times n$ identity matrix. Moreover, for $x \in \mathbf{R}^r$, and $A_i \in \mathbf{R}^{r\times r}$, $i = 0, 1, \ldots, p$, the following symbols are used in this paper:

$$x^{(0\sim p)} = \begin{bmatrix} x \\ \dot{x} \\ \vdots \\ x^{(p)} \end{bmatrix}, \; A_{0\sim p-1} = \begin{bmatrix} A_0 & A_1 & \cdots & A_{p-1} \end{bmatrix},$$

$$\Phi(A_{0\sim p-1}) = \begin{bmatrix} 0 & I_r & & \\ & & \ddots & \\ & & & I_r \\ -A_0 & -A_1 & \cdots & -A_{p-1} \end{bmatrix}.$$

2 System Description and Preliminaries

In this paper, the following high-order system with an unknown parameter is investigated:

$$\begin{aligned} x^{(p)} = {} & f\left(x^{(0\sim p-1)}\right) + \Omega^{\mathrm{T}}\left(x^{(0\sim p-1)}\right)\theta \\ & + B\left(x^{(0\sim p-1)}\right) q(u), \end{aligned} \tag{1}$$

This paper is partially supported by the Science Center Program of the National Natural Science Foundation of China under grant No. 62188101, the Major Program of National Natural Science Foundation of China (61690210, 61690212), and also supported by the National Natural Science Foundation of China (61333003).

where $x \in \mathbf{R}^r$ is the state vector, $u = [u_1, u_2, \ldots, u_r]^{\mathrm{T}} \in \mathbf{R}^r$ is the input vector, $f(\cdot) \in \mathbf{R}^r$, $\Omega(\cdot) \in \mathbf{R}^{n\times r}$ and $B(\cdot) \in \mathbf{R}^{r\times r}$ are known sufficiently smooth vector or matrix functions. $\theta \in \mathbf{R}^n$ is an unknown constant vector. $q(u) = [q_1, q_2, \ldots, q_r]^{\mathrm{T}}$, q_i is the quantization of u_i, $1 \le i \le r$. System (1) is fully actuated, if the following assumption is satisfied.

Assumption A1: $\det B\left(x^{(0\sim p-1)}\right) \neq 0 \text{ or } \infty$, $\forall x^{(j)} \in \mathbf{R}^r, j = 0, 1, \ldots p-1$.

In this paper, same as [7], we use the hysteresis quantizer to avoid chaterring. For $j = 1, 2, \ldots, r$, we have:

$$q_j = \begin{cases} \xi_i \mathrm{sgn}(u_j), & \frac{\xi_i}{1+\delta} < |u_j| \le \xi_i, \dot{u}_j < 0, \text{or} \\ & \xi_i < |u_j| \le \frac{\xi_i}{1-\delta}, \dot{u}_j > 0 \\ \xi_i(1+\delta)\mathrm{sgn}(u_j), & \xi_i < |u_j| \le \frac{\xi_i}{1-\delta}, \dot{u}_j < 0, \text{or} \\ & \frac{\xi_i}{1-\delta} < |u_j| \le \frac{\xi_i(1+\delta)}{1-\delta}, \dot{u}_j > 0 \\ 0, & 0 \le |u_j| < \frac{u_{\min}}{1+\delta}, \dot{u}_j < 0, \text{or} \\ & \frac{u_{\min}}{1+\delta} \le u_j \le u_{\min}, \dot{u}_j > 0 \\ q_j(t^-), & \dot{u}_j = 0 \end{cases} \tag{2}$$

where $\xi_i = \eta^{(1-i)} u_{\min}$, $i = 1, 2, \ldots$, with parameters $u_{\min} > 0$ and $\eta = \frac{1-\delta}{1+\delta}$. $u_{\min}$ denotes the size of the deadzone for the quantizer, while $\eta \in (0, 1)$ determines the quantization density. Parameter δ satisfies:

$$0 < \delta < 1. \tag{3}$$

Our control objective is to design a quantized control law for system (1) to ensure that closed-loop state variables of converge to some neighborhood of the origin whose size is arbitrarily small.

Remark 1. *When systems modeled by many existing physical laws, for example, Lagrangian equation and Kirchhoff's law, a set of high-order differential equations, which constitute the system (1), are naturally obtained. Meanwhile, it has been proven that the system (1) can be converted equivalently from a variety of control systems by using the order-increase method.*

In order to propose our control scheme, we need some preparations. Firstly, we decompose the quantizer $q(u)$ into two parts:

$$q(u) = u + d, \tag{4}$$

where d is the quantization error. And the following lemma holds:

Lemma 1. *The quantization error d satisfies the following inequality:*

$$\|d\| \le \delta \|u\| + \sqrt{r} u_{\min}. \tag{5}$$

Proof. From Lemma 1 of [7], we have the following inequalities:

$$\begin{aligned} d_j^2 &\le \delta^2 u_j^2, \quad \forall |u_j| \ge u_{\min}, \\ d_j^2 &\le u_{\min}^2, \quad \forall |u_j| \le u_{\min}, \end{aligned}$$

d_j is the jth component of d. Then we have:

$$\sum_{j=1}^{r} |d_j|^2 \le \delta^2 \sum_{j=1}^{r} |u_j|^2 + r u_{\min}^2,$$

which implies that the property (5) holds. □

Secondly, the following lemmas are also needed.

Lemma 2 ([16])**.** *Suppose that matrices $A_i \in \mathbf{R}^{r\times r}$, $i = 1, 2, \ldots, p-1$, with $\Phi(A_{0\sim p-1}) \in \mathbf{R}^{pr\times pr}$ satisfy*

$$\mathrm{Re}\lambda_i(\Phi) < -\frac{\mu}{2}, \quad i = 1, 2, \ldots, pr, \tag{6}$$

where μ is a positive constant. Then a positive definite matrix $\mathcal{P} \in \mathbf{R}^{pr\times pr}$ satisfying (7) exists.

$$\Phi^{\mathrm{T}}(A_{0\sim p-1})\mathcal{P} + \mathcal{P}\Phi(A_{0\sim p-1}) \le -\mu\mathcal{P}. \tag{7}$$

Lemma 3 ([16])**.** *Suppose that a, b are two real numbers, and $b > 0$. Then we have:*

$$a - \frac{a^2}{4b} \le b. \tag{8}$$

At last of this section, we introduce the following notation:

$$\mathcal{P}_L = \mathcal{P}\begin{bmatrix} 0_{(pr-r)\times r} \\ I_r \end{bmatrix}. \tag{9}$$

3 Main Results

In this section, we deal with the adaptive control for the nonlinear system (1) with parametric uncertainties. Inspired by the control scheme proposed in [18] and [19], we design the adaptive stabilizing control law as follows:

$$u = -B^{-1}\left(x^{(0\sim p-1)}\right)u_a - u_b, \tag{10}$$

where

$$\begin{cases} u_a = & f\left(x^{(0\sim p-1)}\right) + A_{0\sim p-1}x^{(0\sim p-1)} \\ & + \Omega^{\mathrm{T}}\left(x^{(0\sim p-1)}\right)\vartheta \\ \dot{\vartheta} = & \gamma\Omega\left(x^{(0\sim p-1)}\right)\mathcal{P}_L^{\mathrm{T}}x^{(0\sim p-1)} - \mu\vartheta, \end{cases} \tag{11}$$

is the part to eliminate the nonlinearity, assign the stable eigenstructure, and estimate the unknown vector; while

$$u_b = \frac{1}{4\varepsilon}\psi^2 B^{\mathrm{T}}\left(x^{(0\sim p-1)}\right)\mathcal{P}_L^{\mathrm{T}}x^{(0\sim p-1)}, \tag{12}$$

with

$$\psi = \frac{1}{\sqrt{1-\delta}}\left(\delta\left\|B^{-1}\left(x^{(0\sim p-1)}\right)u_a\right\| + \sqrt{r}u_{\min}\right), \tag{13}$$

is the part to handle the quantization error. $\gamma > 0$ and $\varepsilon > 0$ are two selected real numbers. Then we have the following theorem.

Theorem 1. *Under Assumption A1, let $A_{0\sim p-1} \in \mathbf{R}^{r\times pr}$ be a matrix such that $\Phi(A_{0\sim p-1})$ satisfies (6)–(7), and $\mathcal{P}_L$ be given by (9). Then, the control law given by (10)–(12) guarantees that the closed-loop state variables of (1) can be steered to within an arbitrarily small neighborhood of the origin by properly choosing the design parameters.*

Proof. Substituting control law (10)–(12) into system (1) and using the decomposition (4) gives the closed-loop system as

$$\begin{aligned} x^{(p)} = & -A_{0\sim p-1}x^{(0\sim p-1)} + \Omega^{\mathrm{T}}(\cdot)(\theta - \vartheta) \\ & + B(\cdot)(d - u_b). \end{aligned} \tag{14}$$

We denote

$$\phi_a = \Omega^{\mathrm{T}}(\cdot)\,\overline{\theta} + B(\cdot)\,(d - u_b),$$

where $\overline{\theta} = \theta - \vartheta$. Then we have

$$\dot{\overline{\theta}} = -\dot{\vartheta}, \quad 2\vartheta^{\mathrm{T}}\overline{\theta} \le -\overline{\theta}^{\mathrm{T}}\overline{\theta} + \theta^{\mathrm{T}}\theta. \tag{15}$$

Obviously, (14) is equivalent to the following form:

$$\dot{x}^{(0\sim p-1)} = \Phi(A_{0\sim p-1})x^{(0\sim p-1)} + \begin{bmatrix} 0_{(pr-r)\times 1} \\ \phi_a \end{bmatrix}. \tag{16}$$

Then we consider the following Lyapunov function candidate:

$$\mathcal{V} = \frac{1}{2}\left(x^{(0\sim p-1)}\right)^{\mathrm{T}}\mathcal{P}x^{(0\sim p-1)} + \frac{1}{2\gamma}\overline{\theta}^{\mathrm{T}}\overline{\theta}.$$

In view of (7) and (16), we have

$$\begin{aligned}
\dot{\mathcal{V}} =& \frac{1}{2}\left(\dot{x}^{(0\sim p-1)}\right)^{\mathrm{T}}\mathcal{P}x^{(0\sim p-1)} \\
&+ \frac{1}{2}\left(x^{(0\sim p-1)}\right)^{\mathrm{T}}\mathcal{P}\dot{x}^{(0\sim p-1)} - \frac{1}{\gamma}\dot{\vartheta}^{\mathrm{T}}\overline{\theta} \\
=& \frac{1}{2}\left(x^{(0\sim p-1)}\right)^{\mathrm{T}}\left(\Phi^{\mathrm{T}}\mathcal{P} + \mathcal{P}\Phi\right)x^{(0\sim p-1)} - \frac{1}{\gamma}\dot{\vartheta}^{\mathrm{T}}\overline{\theta} \\
&+ \left(x^{(0\sim p-1)}\right)^{\mathrm{T}}\mathcal{P}\begin{bmatrix} 0_{(pr-r)\times 1} \\ \phi_a \end{bmatrix} \\
\le& -\frac{\mu}{2}\left(x^{(0\sim p-1)}\right)^{\mathrm{T}}\mathcal{P}x^{(0\sim p-1)} + \left(x^{(0\sim p-1)}\right)^{\mathrm{T}}\mathcal{P}_L\phi_a \\
&- \frac{1}{\gamma}\dot{\vartheta}^{\mathrm{T}}\overline{\theta} \\
=& -\frac{\mu}{2}\left(x^{(0\sim p-1)}\right)^{\mathrm{T}}\mathcal{P}x^{(0\sim p-1)} \\
&+ \left(x^{(0\sim p-1)}\right)^{\mathrm{T}}\mathcal{P}_L B(\cdot)\,(d - u_q) \\
&+ \left[\left(x^{(0\sim p-1)}\right)^{\mathrm{T}}\mathcal{P}_L\Omega^{\mathrm{T}}(\cdot) - \frac{1}{\gamma}\dot{\vartheta}^{\mathrm{T}}\right]\overline{\theta} \\
=& -\frac{\mu}{2}\left(x^{(0\sim p-1)}\right)^{\mathrm{T}}\mathcal{P}x^{(0\sim p-1)} + \frac{\mu}{\gamma}\vartheta^{\mathrm{T}}\overline{\theta} \\
&+ \left(x^{(0\sim p-1)}\right)^{\mathrm{T}}\mathcal{P}_L B(\cdot)\,(d - u_b),
\end{aligned}$$

which, by virtue of (15), can be rewritten as

$$\begin{aligned}
\dot{\mathcal{V}} \le& -\frac{\mu}{2}\left(x^{(0\sim p-1)}\right)^{\mathrm{T}}\mathcal{P}x^{(0\sim p-1)} - \frac{\mu}{2\gamma}\overline{\theta}^{\mathrm{T}}\overline{\theta} + \frac{\mu}{2\gamma}\theta^{\mathrm{T}}\theta \\
&+ \left(x^{(0\sim p-1)}\right)^{\mathrm{T}}\mathcal{P}_L B(\cdot)\,(d - u_b) \\
=& -\mu V + \frac{\mu}{2\gamma}\theta^{\mathrm{T}}\theta \\
&+ \left(x^{(0\sim p-1)}\right)^{\mathrm{T}}\mathcal{P}_L B(\cdot)\,(d - u_b).
\end{aligned}$$

Next, let us consider the last term of the above equation. It follows from (5), (8) and (12) that

$$\begin{aligned}
&\left(x^{(0\sim p-1)}\right)^{\mathrm{T}}\mathcal{P}_L B(\cdot)\,(d - u_b) \\
&\le -\frac{1}{4\varepsilon}\psi^2\left\|B^{\mathrm{T}}(\cdot)\,\mathcal{P}_L^{\mathrm{T}}x^{(0\sim p-1)}\right\|^2 \\
&\quad + \left\|B^{\mathrm{T}}(\cdot)\,\mathcal{P}_L^{\mathrm{T}}x^{(0\sim p-1)}\right\|\|d\| \\
&\le -\frac{1}{4\varepsilon}\psi^2\left\|B^{\mathrm{T}}(\cdot)\,\mathcal{P}_L^{\mathrm{T}}x^{(0\sim p-1)}\right\|^2 + \left\|B^{\mathrm{T}}(\cdot)\,\mathcal{P}_L^{\mathrm{T}}x^{(0\sim p-1)}\right\| \\
&\quad \times\left[\delta\left(\left\|B^{-1}(\cdot)\,u_a\right\| + \|u_b\|\right) + \sqrt{r}u_{\min}\right] \\
&= -\frac{1-\delta}{4\varepsilon}\psi^2\left\|B^{\mathrm{T}}(\cdot)\,\mathcal{P}_L^{\mathrm{T}}x^{(0\sim p-1)}\right\|^2 \\
&\quad + \sqrt{1-\delta}\psi\left\|B^{\mathrm{T}}(\cdot)\,\mathcal{P}_L^{\mathrm{T}}x^{(0\sim p-1)}\right\| \\
&\le \varepsilon.
\end{aligned}$$

The above two inequalities imply

$$\dot{\mathcal{V}} \le -\mu\mathcal{V} + \frac{\mu}{2\gamma}\theta^{\mathrm{T}}\theta + \varepsilon,$$

which yields

$$\mathcal{V}(t) \le \mathcal{V}(0)e^{-\mu t} + \left(\frac{1}{2\gamma}\theta^{\mathrm{T}}\theta + \frac{\varepsilon}{\mu}\right)\left(1 - e^{-\mu t}\right).$$

Furthermore,

$$\begin{aligned}
\mathcal{V}(t) &\le \frac{1}{2\gamma}\theta^{\mathrm{T}}\theta + \frac{\varepsilon}{\mu} + \left(\mathcal{V}(0) - \frac{1}{2\gamma}\theta^{\mathrm{T}}\theta - \frac{\varepsilon}{\mu}\right)e^{-\mu t} \\
&\to \frac{1}{2\gamma}\theta^{\mathrm{T}}\theta + \frac{\varepsilon}{\mu}, \quad t \to +\infty.
\end{aligned}$$

Hence, by choosing the design parameters in (10)–(12) so that γ is large enough and ε is small enough, $x^{(0\sim p-1)}$ can converge to a neighborhood of the origin whose size can be arbitrarily small. □

Based on the above theorem, we can give a direct control design (10)–(12) for the FAS (1) without turning the system into a conventional state-space model. The system considered in [7] actually can be converted into the FAS (1), and we do not need to use the complicated backstepping method proposed in previous papers anymore. Our control law is realised in a simpler way. Meanwhile, our control law theoretically does not have any requirements for the quantization density, in other words, our control law is available for a very coarse quantization.

4 An Illustrative Example

We consider the example in [7] to demonstrate our fully actuated control law:

$$\ddot{x} + \theta\sin(\dot{x}) + \tanh(x) = q(u), \tag{17}$$

where x, $u \in \mathbf{R}$, and $q(u)$ is described by (2), and $\theta \in \mathbf{R}$ is an unknown parameter. The parameters of the control law (10)–(12) is chosen as $\mu = 4$, $\gamma = 2$, $\varepsilon = 0.25$. Then the eigenvalues of the matrix $\Phi(A_{0\sim 1})$ are chosen as $-3 \pm j$, which yields

$$A_{0\sim 1} = \begin{bmatrix} 10 & 6 \end{bmatrix}. \tag{18}$$

Consider the Lyapunov function

$$(\Phi + 2I)^{\mathrm{T}}\mathcal{P} + \mathcal{P}(\Phi + 2I) = 0.2I, \tag{19}$$

which implies that the matrix $A_{0\sim1}$ satisfying (7). We obtain

$$\mathcal{P} = \begin{bmatrix} 2.950 & 0.600 \\ 0.600 & 0.175 \end{bmatrix}. \tag{20}$$

We choose the initial values as: $x(0) = \dot{x}(0) = 0.5,\ \vartheta(0) = 0$. In the simulation, $\theta = 1$, and we consider two quantizers with different density:

Case A $\delta = 0.2,\ u_{\min} = 0.02.$
Case B $\delta = 0.8,\ u_{\min} = 0.02.$

Figures 1 and 2 show the results of the simulation, which are consistent with our theoretical findings. Furthermore, for Case B, the control input has large magnitude, since the quantizer with $\delta = 0.8$ is relatively coarse which means great energy is needed to handle the quantization error.

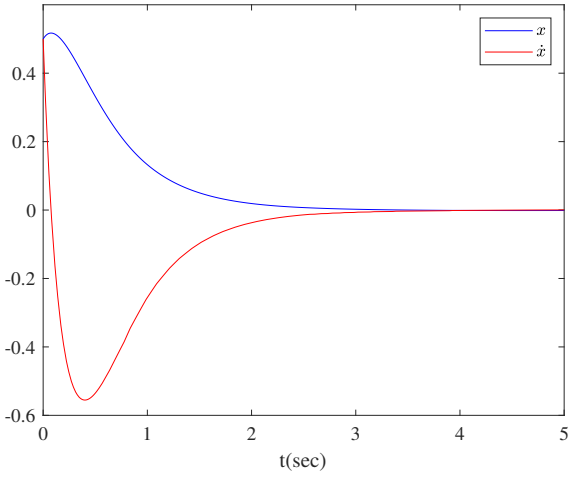

(a) State response

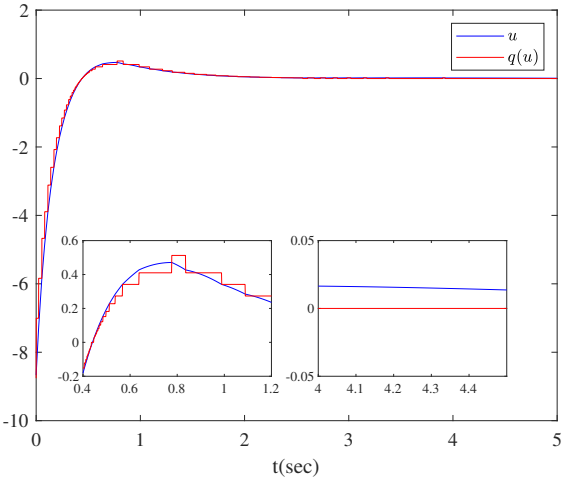

(b) Control input

Fig. 1: Simulation results for Case A

5 Conclusion

In this paper, an adaptive state-feedback stabilization scheme for FASs whose input is quantized by the hysteresis quantizer is developed. By taking advantage of the full-actuation feature of the system, complex nonlinear design methods are no longer necessary, and the proposed controller is still practical for a coarse quantization.

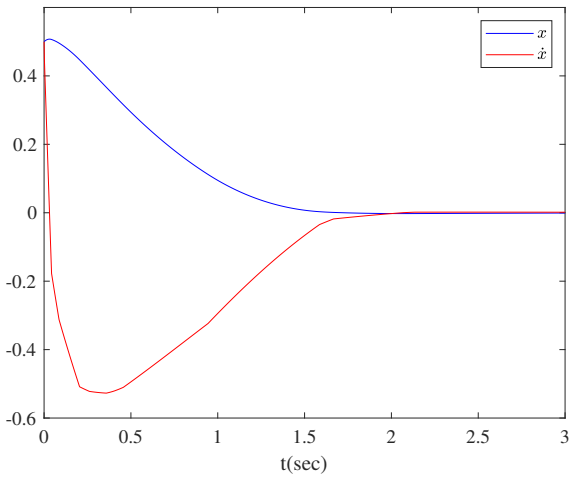

(a) State response

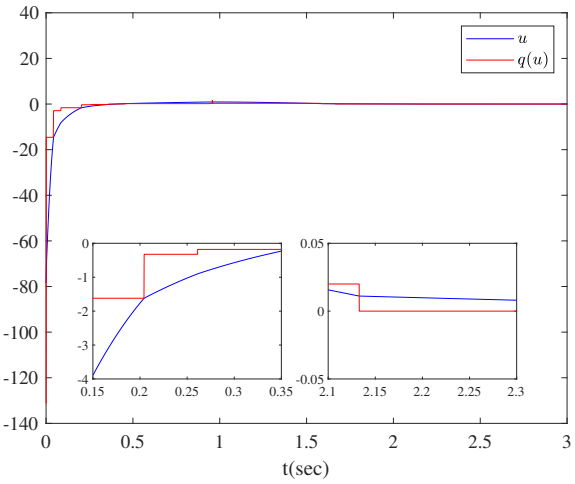

(b) Control input

Fig. 2: Simulation results for Case B

It is worth mentioning that in this paper, only the adaptive control with matching condition is considered, that is, the unknown terms are in the span of the control input. High-order backstepping techique [17, 20] needs to be used, if more general systems are considered. Meanwhile, the controller with state quantization for FASs also deserves future study.

References

[1] S. W. Yun, Y. J. Choi, and P. Park. H_2 control of continuous-time uncertain linear systems with input quantization and matched disturbances. *Automatica*, 45(10):2435–2439, 2009.

[2] L. T. Xing, C. Y. Wen, Y. Zhu, H. Y. Su, and Z. T. Liu. Output feedback control for uncertain nonlinear systems with input quantization. *Automatica*, 65:191–202, 2016.

[3] R. W. Brockett and D. Liberzon. Quantized feedback stabilization of linear systems. *IEEE Transactions on Automatic Control*, 45(7):1279–1289, 2000.

[4] D. Liberzon. Hybrid feedback stabilization of systems with quantized signals. *Automatica*, 39(9):1543–1554, 2003.

[5] M. Y. Fu and L. H. Xie. The sector bound approach to quantized feedback control. *IEEE Transactions on Automatic Control*, 50(11):1698–1711, 2005.

[6] T. F. Liu, Z. P. Jiang, and D. J. Hill. A sector bound approach

to feedback control of nonlinear systems with state quantization. *Automatica*, 48(1):145–152, 2012.

[7] J. Zhou, C. Y. Wen, and G. H. Yang. Adaptive backstepping stabilization of nonlinear uncertain systems with quantized input signal. *IEEE Transactions on Automatic Control*, 59(2):460–464, 2014.

[8] G. Y. Lai, Z Liu, C. L. Philip Chen, and Y. Zhang. Adaptive asymptotic tracking control of uncertain nonlinear system with input quantization. *Systems & Control Letters*, 96:23–29, 2016.

[9] X. W. Yu and Y Lin. Adaptive backstepping quantized control for a class of nonlinear systems. *IEEE Transactions on Automatic Control*, 62(2):981–985, 2017.

[10] X. W. Yu and Y. Lin. Adaptive quantized tracking control for a class of nonlinear systems. *IEEE Transactions on Systems Man Cybernetics-Systems*, 53(4):2554–2559, 2023.

[11] G. R. Duan. High-order system approaches - I. Full-actuation and parametric design. *Acta Automatica Sinica*, 46(7):1333–1345, 2020. (in Chinese).

[12] G. R. Duan. High-order system approaches - II. Controllability and fully-actuation. *Acta Automatica Sinica*, 46(8):1571–1581, 2020. (in Chinese).

[13] G. R. Duan. High-order system approaches - III. Super-observability and observer design. *Acta Automatica Sinica*, 46(9):1885–1895, 2020. (in Chinese).

[14] G. R. Duan. High-order fully actuated system approaches: Part I. Models and basic procedure. *International Journal of Systems Science*, 52(2):422–435, 2021.

[15] G. R. Duan. High-order fully-actuated system approaches: Part II. Generalized strict-feedback systems. *International Journal of Systems Science*, 52(3):437–454, 2021.

[16] G. R. Duan. High-order fully actuated system approaches: Part III. Robust control and high-order backstepping. *International Journal of Systems Science*, 52(5):952–971, 2021.

[17] W. Z. Liu, G. R. Duan, and M. Z. Hou. High-order robust command filtered backstepping design for strict-feedback systems: A high-order fully actuated system approach. *International Journal of Robust and Nonlinear Control*, 32(18, SI):10251–10270, 2022.

[18] G. R. Duan. High-order fully actuated system approaches: Part IV. Adaptive control and high-order backstepping. *International Journal of Systems Science*, 52(5):972–989, 2021.

[19] G. R. Duan. High-order fully actuated system approaches: Part V. Robust adaptive control. *International Journal of Systems Science*, 52(10):2129–2143, 2021.

[20] W. Z. Liu, G. R. Duan, and M. Z. Hou. High-order command filtered adaptive backstepping control for second- and high-order fully actuated strict-feedback systems. *Journal of The Franklin Institute-Engineering and Applied Mathematics*, 360(6):3989–4015, 2023.

[21] G. R. Duan. High-order fully-actuated system approaches: Part IX. Generalised PID control and model reference tracking. *International Journal of Systems Science*, 53(3):652–674, 2022.

Proceedings of the 3rd Conference on Fully Actuated System Theory and Applications
May 10-12, 2024, Shenzhen, China

Optimal filtering for NCSs with amplify-and-forward relays

Xiaohan Liu[1], Chunyan Han[1,*]
1. School of Electrical Engineering, University of Jinan, Jinan 250022, P. R. China
E-mail: cyhan823@hotmail.com

Abstract: This paper is concerned with the optimal Markov jump estimator for wireless networked control system with amplify-and-forward (AF) relay. An AF relay is located in the transmission link between the sensor and the remote estimator to regulate the data transmission. A set of random variables obeying Markov distribution is adopted to model the transmission power of the sensor and relay. By utilising the reorganization Markov chain method, the observation equation with two independent jump processes is transformed into an equivalent one with single jump process. Then, the optimal Markov jump estimator is derived by using the complete square method and the stochastic approximation theory. Further, an optimal stationary Markov jump estimator is developed under the assumption of ergodicity of the associated Markov chain. It is shown that there exists a unique stabilizing solution for the corresponding coupled algebraic Riccati equation, which coincides with the limit of the solution to the corresponding coupled difference Riccati equation for the proposed Markov jump estimator.

Key Words: Amplify-and-forward relay, Transmission power, Reorganization Markov chain method, Markov jump estimator, Stability

1 Introduction

In recent years, benefiting from the burgeoning sensing, computing and communication technologies, networked control systems (NCSs) have been gaining an ever-growing popularity in practical engineering. As an integrated system consisting of network communication media and system components (e.g., sensors, controllers, actuators, and plants), NCSs possess a broad range of applications in a variety of fields including mobile sensor networks [1], smart grids [2], industrial automation systems [3], due to their diverse advantages like easy installation and maintenance, less wiring, lower cost, and more flexibility and maintainability. In particular, one of the fundamental issues for the NCSs is to estimate the system state of the target plant based on a series of measurement sequences observed over the time. Up to now, various types of algorithms have been developed for the state estimation/filtering problems of NCSs, consisting of the Kalman filtering approach [4], the extended Kalman filtering scheme [5], the H_∞ filtering algorithm [6], and etc. In fact, the state estimation problems of NCSs have been acting as a research frontier for almost two decades, and there is already a rich body of literature with respect to this subject [7–9].

For wireless networked systems with relatively long-distance communication, ensuring satisfactory network communication quality is a vitally important issue. Generally, long-distance communication would increase the energy consumption and reduce the received signal strength during the signal transmissions. In order to overcome the disadvantages of the long-distance communication, relay-based transmission technology has been proposed to effectively solve these problems. As one of the essential technologies of 5G mobile networks, relay-based communication has been considered as a promising technology to extend the communication range and improve the transmission link quality [10]. So far, several relaying protocols have been developed in existing literature, such as the amplify-and-forward (AF) protocol [11], the decode-and-forward (DF) protocol [12], the compress-and-forward (CF) protocol [13], and the filter-and-forward (FF) protocol [14], where AF protocol is more popular because of its simplicity and practicality.

It is worth mentioning that, the filtering problem over AF relay network has recently attracted a great deal of attention, see e.g. [11, 15, 16] for some representative results. For example, in [15], a distributed fusion filter was developed for a class of nonlinear time-varying systems in the simultaneous presence of the AF relay communication, the missing measurement, and the dynamic quantization. In [11], the recursive filtering problem was investigated for a class of stochastic uncertain systems over the AF relay protocol, where the transmission power of the sensor and relay transmitting the measurement were described as a set of random variables with certain probability distribution. Despite the fruitful results on the filtering with AF relay, little attention has been paid to the state estimation problem of wireless networked system with both Markov jump parameters and AF relay communication. On the other hand, the filtering problem for sensor system subject to Markov jump parameters has recently drawn much research attention from the fields of control engineering since Markov jump parameters are very appropriate to model random variations resulting from random communication delays [17], packet losses [18], and unpredicted component malfunctions [19]. Therefore, the state estimation problem in the case of the sensor and the AF relay with transmission power of Markov distribution has proven to be both theoretically important and practical significant.

In this article, we endeavor to deal with the optimal Markov jump linear (MJL) estimation problem for wireless networked system over the AF relay strategy. The primary contributions of this paper are highlighted as follows:
(1) The optimal MJL estimator is, for the first time, obtained for the NCSs over the AF relay strategy, where the transmission power of the sensor and the AF relay obey Markov distribution. This is a generalization in previous work [11], since our case brings a challenging issue that the Riccati equation is related with the transition probabilities and probability distributions of the Markov chain.
(2) A sufficient condition is established for the existence and

This work is supported by the Natural Science Foundation of Shandong Province (No. ZR2021MF069).
*Corresponding author

uniqueness of the mean-square stabilizing solution to the associated coupled algebraic Riccati equation.
(3) The stationary case is studied and the proof for the convergence of the solution to the difference Riccati equation for the proposed MJL estimator is obtained, which means that the MJL estimator can be calculated offline.

Notations: Throughout this paper, $\mathbb{R}^n$ stands for the n-dimensional real Euclidean space, $\mathbb{R}^{m\times n}$ denotes the set of all $m\times n$ real matrices. The A^{-1} and A^T represent the inverse and transpose of the matrix A, respectively. As usual, $P>0 (P\geq 0)$ indicates that the real symmetric matrix P is a positive definite (or positive semi-definite) matrix. The $n\times n$ identity matrix is denoted by I_n (or simply I). diag$\{\ldots\}$ denotes a block-diagonal matrix, and E$\{.\}$ represents the expectation of a stochastic variable. $\|.\|$ describes the Euclidean norm of a vector. δ_{ij} means the Kronecker delta function with $\delta_{ij}=1$ if $i=j$, otherwise, $\delta_{ij}=0$. In addition, we denote $\mathbb{H}^{n,m}=\{Q=(Q_1,\ldots,Q_N), Q_i\in\mathbb{R}^{m\times n}\}$ and we adopt, for simplicity, $\mathbb{H}^n=\mathbb{H}^{n,n}$ and $\mathbb{H}^{n*}=\{Q=(Q_1,\ldots,Q_N)\in\mathbb{H}^n; Q_i=Q_i^T, i=1,\ldots,N\}$, $\mathbb{H}^{n+}=\{Q=(Q_1,\ldots,Q_N)\in\mathbb{H}^{n*}; Q_i\geq 0, i=1,\ldots,N\}$. Finally, $1_{\{.\}}$ stands for the indictor function of the event $\{.\}$, and $r_\sigma(.)$ represents the spectral radius of a matrix.

2 Problem formulations

Consider the following linear discrete-time system:

$$x_{k+1}=H_kx_k+B_kw_k \tag{1}$$

$$y_k=F_kx_k+v_k \tag{2}$$

where $x_k\in\mathbb{R}^n$ and $y_k\in\mathbb{R}^m$ stand for the state sequence and the measured output sequence, respectively. $w_k\in\mathbb{R}^p$ and $v_k\in\mathbb{R}^m$ are the white noises with zero mean and covariances E$\{w_kw_l^T\}=Q_k\delta_{kl}$, E$\{v_kv_l^T\}=R_k\delta_{kl}$, respectively. The initial value x_0 is a Gaussian distributed random vector with E$\{x_0\}=\bar{x}_0$ and E$\{(x_0-\bar{x}_0)(x_0-\bar{x}_0)^T\}=P_0$. H_k, B_k, F_k are known matrices of compatible dimensions. The random processes w_k, v_k for all k and the initial state x_0 are mutually independent.

In an ideal condition, the signals from the sensor can be transmitted to the corresponding estimator by arbitrarily long distance. However, this is not always the case due to constrained transmission capability of the sensor. To extend the propagation distance of wireless communication, relay is introduced in the wireless communication link. Motivated by the above discussions, the AF relay node is deployed in this paper to facilitate the signal transmissions between the sensor and the remote estimator, where the transmission power of the sensor and relay obeys Markov distribution and the Markov chains are assumed to be known. The structure diagram of the addressed estimation issue is demonstrated in Fig. 1. It is observed from Fig. 1 that the data transmission channel from the sensor to the estimator can be divided into two parts, including the sensor-to-relay (STR) channel and the relay-to-estimator (RTE) channel. In this paper, only one relay node is introduced between the sensor and the remote estimator, and the design of multi-relay channel filter can be readily obtained based on this algorithm.

The signal received by the relay can be represented as

$$z_k=\sqrt{E_{s,\theta_{s,k}}}C_{s,k}y_k+\varrho_{s,k} \tag{3}$$

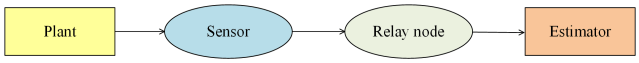

Fig. 1: System model with AF relays

where $E_{s,\theta_{s,k}}$ represents the transmission power of the sensor, $C_{s,k}$ is the known channel gain in STR channel, and $\varrho_{s,k}$ is an additive noise with the statistical characteristics E$\{\varrho_{s,k}\}=0$ and E$\{\varrho_{s,k}\varrho_{s,k}^T\}=S_{s,k}$. In addition, $\theta_{s,k}$ is a discrete-time Markov chain with finite state space $\{1,2,\ldots,\phi\}$ and transition probability $p_{ij}^{(s)}=\Pr\{\theta_{s,k+1}=j|\theta_{s,k}=i\}(i,j=1,2,\ldots,\phi)$, $P^{(s)}=[p_{ij}^{(s)}]$. Denote $\pi_{i,k}^{(s)}=\Pr\{\theta_{s,k}=i\}(i=1,2,\ldots,\phi)$. The transmission power $E_{s,i}(i=1,2,\ldots,\phi)$ is known.

After the signal z_k is received by the AF relay, the relay amplifies and retransmits it to the remote estimator. At the remote estimator, the measurement received from the relay is described as follows

$$r_k=\sqrt{E_{r,\theta_{r,k}}}C_{r,k}z_k+\varrho_{r,k} \tag{4}$$

where $E_{r,\theta_{r,k}}$ represents the transmission power of the relay, $C_{r,k}$ is the known channel gain in RTE channel, and $\varrho_{r,k}$ is an additive noise with the statistical characteristics E$\{\varrho_{r,k}\}=0$ and E$\{\varrho_{r,k}\varrho_{r,k}^T\}=S_{r,k}$. In addition, $\theta_{r,k}$ is a discrete-time Markov chain with finite state space $\{1,2,\ldots,\varphi\}$ and transition probability $p_{ij}^{(r)}=\Pr\{\theta_{r,k+1}=j|\theta_{r,k}=i\}(i,j=1,2,\ldots,\varphi)$, $P^{(r)}=[p_{ij}^{(r)}]$. Denote $\pi_{i,k}^{(r)}=\Pr\{\theta_{r,k}=i\}(i=1,2,\ldots,\varphi)$. The transmission power $E_{r,i}(i=1,2,\ldots,\varphi)$ is known.

Assumption 1. *The noises v_k, $\varrho_{s,k}$, and $\varrho_{r,k}$ are mutually independent.*

Assumption 2. *$\theta_{s,k}$, $\theta_{r,k}$ are known and independent of x_0, w_k, v_k, $\varrho_{s,k}$ and $\varrho_{r,k}$.*

Based on the above statement, the actual measurement received by the estimator at time k can be rewritten as

$$\begin{aligned} r_k=&\sqrt{E_{r,\theta_{r,k}}E_{s,\theta_{s,k}}}C_{r,k}C_{s,k}F_kx_k\\ &+\sqrt{E_{r,\theta_{r,k}}E_{s,\theta_{s,k}}}C_{r,k}C_{s,k}v_k\\ &+\sqrt{E_{r,\theta_{r,k}}}C_{r,k}\varrho_{s,k}+\varrho_{r,k} \end{aligned} \tag{5}$$

Remark 1. *As pointed out in [20], the Markov process is a special random process based on probability statistics. Due to its no memory effect and homogeneity, its widely applied in prediction for power transmission. In this paper, the sensor and the relay transmit the measurements according to the transmission power that they possess. The transmission power is depicted by a homogeneous Markov chain taking different level with different probability distribution. It can be seen that when the current power level is given, the probabilistic law of the future development of power level has nothing to do with the historical state. Note that such a transmission line with Markovian power level has received seldom attention in the filtering investigation field and the main purpose of this paper is to design an optimal filter as well as a stationary filter for the NCSs under such a transmission way.*

The optimal filtering problems in this paper are now stated as follows:

Problem 1 (Optimal MJL estimator)**.** *Given the observation sequences $\{r_0, r_1, \ldots, r_k\}$ and the present-time value of the jumping parameter $\theta_{s,k}$ and $\theta_{r,k}$, find an optimal recursive estimator $\hat{x}_k$ of the state x_k, such that*

$$E\{\|x_k - \hat{x}_k\||r_0, \ldots, r_k; \theta_{s,k}, \theta_{r,k}\} \tag{6}$$

is minimised, while the estimator gain is deterministic.

Problem 2 (Stationary MJL estimator)**.** *Given the observation sequences $\{r_0, r_1, \ldots, r_k\}$ and the present-time value of the jumping parameter $\theta_{s,k}$ and $\theta_{r,k}$, find a stationary MJL estimator $\hat{x}_{e,k}$ of the state x_k, such that*

$$E\{\|x_k - \hat{x}_{e,k}\||r_0, \ldots, r_k; \theta_{s,k}, \theta_{r,k}\} \tag{7}$$

is minimised, while the estimator gain is constant.

Remark 2. *In network-based communication process, the signal transmissions between sensor and estimator is affected by the transmission power of the sensor and the relay. Particularly, a set of Markov distributed variables with known Markov chain is adopted to characterize the transmission power. It is worth noting that the estimation problem with respect to such transmission power has not received sufficient attention, and thus the main purpose of the paper is to design an easy-to-implemented optimal MJL estimator for discrete-time system subject to transmission power from the sensor and relay. Furthermore, a stationary MJL estimator is developed, which means that our optimal MJL estimator can be calculated offline.*

3 Markov jump estimation

The purpose of this section is to design an optimal MJL estimator in the recursive form for systems (1) and (5) by employing the complete square method and the stochastic approximation theory. To be more specific, the reconstruction Markov chain method is adopted to convert the observation equation with jumping parameters $\theta_{s,k}$ and $\theta_{r,k}$ into a new equivalent one with jumping parameter θ_k. Then, we will develop the MJL estimator according to new observation equation.

3.1 Re-organized Markov chain

In what follows, we are going to define the new Markov chains associated with equation (5). For any given time k, let

$$\theta_k = \begin{bmatrix}\theta_{r,k} & \theta_{s,k}\end{bmatrix}^T \tag{8}$$

θ_k is assumed to be a new Markov chain, and takes value from the finite set as follows

$$\begin{aligned} S =& \left\{ \begin{bmatrix}1\\1\end{bmatrix}, \begin{bmatrix}1\\2\end{bmatrix}, \ldots, \begin{bmatrix}1\\\phi\end{bmatrix}, \begin{bmatrix}2\\1\end{bmatrix}, \ldots, \begin{bmatrix}\varphi\\\phi\end{bmatrix} \right\} \\ \triangleq& \{e_1, e_2, \ldots, e_{\varphi\phi}\} \end{aligned} \tag{9}$$

For notational simplicity, denote $N = \varphi\phi$ in the remainder of the paper. The transition probability matrix P can be obtained by

$$P = P^{(r)} \otimes P^{(s)} \triangleq [p_{ij}] \tag{10}$$

where $p_{ij} = \Pr\{\theta_{k+1} = e_j | \theta_k = e_i\}(i, j = 1, 2, \ldots, N)$. The probability to find the jump process in mode $e_i (i = 1, 2, \ldots, N)$ at time $k = 0, 1, 2, \ldots$ is denoted as $\pi_{i,k}$, the vector of the property $\pi_{i,k}$ at time k is denoted as $\pi_k = [\pi_{1,k}, \pi_{2,k}, \ldots, \pi_{N,k}]^T$, which is described as

$$\pi_k = \begin{bmatrix}\pi_{1,k}^{(r)}\\ \pi_{2,k}^{(r)}\\ \vdots\\ \pi_{\varphi,k}^{(r)}\end{bmatrix} \otimes \begin{bmatrix}\pi_{1,k}^{(s)}\\ \pi_{2,k}^{(s)}\\ \vdots\\ \pi_{\phi,k}^{(s)}\end{bmatrix} \tag{11}$$

with the initial value

$$\pi_0 = \left[\pi_{1,0}^{(r)}\pi_{1,0}^{(s)}, \pi_{1,0}^{(r)}\pi_{2,0}^{(s)}, \ldots, \pi_{\varphi,0}^{(r)}\pi_{\phi,0}^{(s)}\right]^T$$

Moreover, π_k and P satisfy the Kolmogorov difference equation, that is

$$\pi_{k+1} = P^T \pi_k \tag{12}$$

which shows the complete description of the jumping parameter θ_k.

In view of the definition of θ_k, the observation equation (5) can be written as

$$r_k = \mathbb{E}_{1,\theta_k} C_{1,k} F_k x_k + \mathbb{E}_{2,\theta_k} C_{2,k} \bar{v}_k \tag{13}$$

where

$$\begin{aligned} \mathbb{E}_{1,\theta_k} =& \sqrt{E_{r,\theta_{r,k}} E_{s,\theta_{s,k}}} \\ \mathbb{E}_{2,\theta_k} =& \begin{bmatrix}\sqrt{E_{r,\theta_{r,k}} E_{s,\theta_{s,k}}} I & \sqrt{E_{r,\theta_{r,k}}} I & I\end{bmatrix} \\ C_{1,k} =& C_{r,k} C_{s,k}, \;\; C_{2,k} = \text{diag}\{C_{r,k} C_{s,k}, C_{r,k}, I\} \\ \bar{v}_k =& \begin{bmatrix}v_k^T & \varrho_{s,k}^T & \varrho_{r,k}^T\end{bmatrix}^T \end{aligned}$$

It can be seen that

$$\begin{aligned} \mathbb{E}_{1,\theta_k} \in& \Big\{ \sqrt{E_{r,1}E_{s,1}}, \ldots, \sqrt{E_{r,1}E_{s,\phi}}, \sqrt{E_{r,2}E_{s,1}}, \ldots, \\ & \sqrt{E_{r,\varphi}E_{s,\phi}} \Big\} \\ \triangleq& \{\mathbb{E}_{1,1}, \ldots, \mathbb{E}_{1,\phi}, \mathbb{E}_{1,\phi+1}, \ldots, \mathbb{E}_{1,N}\} \\ \mathbb{E}_{2,\theta_k} \in& \Big\{ \begin{bmatrix}\sqrt{E_{r,1}E_{s,1}} I & \sqrt{E_{r,1}} I & I\end{bmatrix}, \ldots, \\ & \begin{bmatrix}\sqrt{E_{r,1}E_{s,\phi}} I & \sqrt{E_{r,1}} I & I\end{bmatrix}, \\ & \begin{bmatrix}\sqrt{E_{r,2}E_{s,1}} I & \sqrt{E_{r,2}} I & I\end{bmatrix}, \ldots, \\ & \begin{bmatrix}\sqrt{E_{r,\varphi}E_{s,\phi}} I & \sqrt{E_{r,\varphi}} I & I\end{bmatrix} \Big\} \\ \triangleq& \{\mathbb{E}_{2,1}, \ldots, \mathbb{E}_{2,\phi}, \mathbb{E}_{2,\phi+1}, \ldots, \mathbb{E}_{2,N}\} \end{aligned}$$

Note that the MJL system estimation theory cannot be applied directly since the simultaneous presence of the jump processes $\theta_{s,k}$ and $\theta_{r,k}$. So, we address this issue by reorganisation Markov chain method. From the above discussion, we can know that the next step is to design estimator for MJL system with jumping parameter θ_k.

3.2 Design of the optimal Markov jump estimator

The problem considered here is how to acquire an optimal MJL estimator $\hat{x}_k$ of the state vector x_k by using the new observation equation (13). To begin with, let us give following useful definition.

Definition 1. *Given a time instant k, the optimal MJL filter $\hat{x}_k$ of the state x_k is defined as*

$$\hat{x}_k \triangleq E\{x_k|r_0,\ldots,r_k;\theta_k\} \tag{14}$$

and the optimal MJL one-step predictor $\bar{x}_k$ of the state x_k is defined as

$$\bar{x}_k \triangleq E\{x_k|r_0,\ldots,r_{k-1};\theta_{k-1}\} \tag{15}$$

In addition, define the one-step predictor of the observation

$$\bar{r}_k \triangleq \mathrm{E}\{r_k|r_0,\ldots,r_{k-1};\theta_{k-1}\} \tag{16}$$

and the corresponding innovation sequence is calculated by

$$\varepsilon_k \triangleq r_k - \bar{r}_k \tag{17}$$

Before computing the MJL estimator, we first introduce some notations and derive some preliminary results. Set

$$\begin{aligned}
\tilde{x}_k \triangleq& x_k - \hat{x}_k\\
\bar{\tilde{x}}_k \triangleq& x_k - \bar{x}_k\\
Y_{i,k} \triangleq& \mathrm{E}\{\tilde{x}_k\tilde{x}_k^T 1_{\theta_k=e_i}\},\ \ i=1,2,\ldots,N\\
\bar{Y}_{i,k} \triangleq& \mathrm{E}\{\bar{\tilde{x}}_k\bar{\tilde{x}}_k^T 1_{\theta_k=e_i}\},\ \ i=1,2,\ldots,N\\
W_{i,k} \triangleq& \mathrm{E}\{\varepsilon_k\varepsilon_k^T 1_{\theta_k=e_i}\},\ \ i=1,2,\ldots,N
\end{aligned}$$

Based on the above discussion, we obtain the following main result of this section.

Theorem 1. *Consider the system (1), (13) and given the time k, the predictor $\bar{x}_k$ is given by*

$$\bar{x}_{k+1} = H_k\bar{x}_k + L_{\theta_k,k}\varepsilon_k \tag{18}$$

The innovation sequence ε_k with variance $W_{i,k}$ is calculated by

$$\begin{aligned}
\varepsilon_k =& r_k - \mathbb{E}_{1,\theta_k}C_{1,k}F_k\bar{x}_k &(19)\\
W_{i,k} =& \mathbb{E}_{1,i}C_{1,k}F_k\bar{Y}_{i,k}F_k^TC_{1,k}^T\mathbb{E}_{1,i}^T\\
&+ \pi_{i,k}\mathbb{E}_{2,i}C_{2,k}\bar{R}_kC_{2,k}^T\mathbb{E}_{2,i}^T &(20)
\end{aligned}$$

where

$$\bar{R}_k = diag\{R_k, S_{s,k}, S_{r,k}\}$$

The predictor gain matrix $L_{\theta_k,k}$ is denoted as $L_{i,k}$ for $\theta_k = i(i=1,2,\ldots,N)$, which is determined by

$$L_{i,k} = H_k\bar{Y}_{i,k}F_k^TC_{1,k}^T\mathbb{E}_{1,i}^TW_{i,k}^{-1} \tag{21}$$

The prediction error covariance matrix $\bar{Y}_{i,k}$ for the state satisfies the following equation:

$$\begin{aligned}
\bar{Y}_{j,k+1} =& \sum_{i=1}^{N} p_{ij}\{H_k\bar{Y}_{i,k}H_k^T + \pi_{i,k}B_kQ_kB_k^T\\
&- H_k\bar{Y}_{i,k}F_k^TC_{1,k}^T\mathbb{E}_{1,i}^T[\mathbb{E}_{1,i}C_{1,k}F_k\bar{Y}_{i,k}F_k^TC_{1,k}^T\mathbb{E}_{1,i}^T\\
&+ \pi_{i,k}\mathbb{E}_{2,i}C_{2,k}\bar{R}_kC_{2,k}^T\mathbb{E}_{2,i}^T]^{-1}\mathbb{E}_{1,i}C_{1,k}F_k\bar{Y}_{i,k}H_k^T\}
\end{aligned} \tag{22}$$

with the initial value $\bar{Y}_{j,0} = \pi_{j,0}P_0$.

Proof. From the definition of the innovation sequence, we obtain that

$$\varepsilon_k = \mathbb{E}_{1,\theta_k}C_{1,k}F_k\bar{\tilde{x}}_k + \mathbb{E}_{2,\theta_k}C_{2,k}\bar{v}_k \tag{23}$$

In view of (23), and recalling the notations $W_{i,k}$, we have

$$\begin{aligned}
W_{i,k} =& \mathrm{E}\{\varepsilon_k\varepsilon_k^T 1_{\theta_k=e_i}\}\\
=& \mathrm{E}\{[\mathbb{E}_{1,\theta_k}C_{1,k}F_k\bar{\tilde{x}}_k + \mathbb{E}_{2,\theta_k}C_{2,k}\bar{v}_k]\\
&\times[\mathbb{E}_{1,\theta_k}C_{1,k}F_k\bar{\tilde{x}}_k + \mathbb{E}_{2,\theta_k}C_{2,k}\bar{v}_k]^T 1_{\theta_k=e_i}\}\\
=& \mathbb{E}_{1,i}C_{1,k}F_k\mathrm{E}\{\bar{\tilde{x}}_k\bar{\tilde{x}}_k^T 1_{\theta_k=e_i}\}F_k^TC_{1,k}^T\mathbb{E}_{1,i}^T\\
&+ \mathbb{E}_{2,i}C_{2,k}\mathrm{E}\{\bar{v}_k\bar{v}_k^T 1_{\theta_k=e_i}\}C_{2,k}^T\mathbb{E}_{2,i}^T
\end{aligned} \tag{24}$$

Therefore, we obtain the expression (20).

Next, we have from (1) and (18) that

$$\bar{\tilde{x}}_{k+1} = H_k\bar{\tilde{x}}_k + B_kw_k - L_{\theta_k,k}\varepsilon_k \tag{25}$$

According to the definition of $\bar{Y}_{j,k+1}$, it can be derived as

$$\begin{aligned}
\bar{Y}_{j,k+1} =& \mathrm{E}\{[H_k\bar{\tilde{x}}_k + B_kw_k - L_{\theta_k,k}\varepsilon_k]\\
&\times[H_k\bar{\tilde{x}}_k + B_kw_k - L_{\theta_k,k}\varepsilon_k]^T 1_{\theta_{k+1}=e_j}\}\\
=& \sum_{i=1}^{N} p_{ij}\{H_k\bar{Y}_{i,k}H_k^T - H_k\bar{Y}_{i,k}F_k^TC_{1,k}^T\mathbb{E}_{1,i}^TL_{i,k}^T\\
&+ \pi_{i,k}B_kQ_kB_k^T - L_{i,k}\mathbb{E}_{1,i}C_{1,k}F_k\bar{Y}_{i,k}H_k^T\\
&+ L_{i,k}W_{i,k}L_{i,k}^T\}\\
=& \sum_{i=1}^{N} p_{ij}\{H_k\bar{Y}_{i,k}H_k^T + \pi_{i,k}B_kQ_kB_k^T\\
&+ (L_{i,k} - H_k\bar{Y}_{i,k}F_k^TC_{1,k}^T\mathbb{E}_{1,i}^TW_{i,k}^{-1})W_{i,k}\\
&\times(L_{i,k} - H_k\bar{Y}_{i,k}F_k^TC_{1,k}^T\mathbb{E}_{1,i}^TW_{i,k}^{-1})^T\\
&- H_k\bar{Y}_{i,k}F_k^TC_{1,k}^T\mathbb{E}_{1,i}^TW_{i,k}^{-1}\mathbb{E}_{1,i}C_{1,k}F_k\bar{Y}_{i,k}H_k^T\}
\end{aligned} \tag{26}$$

It can be seen from (26) that $\bar{Y}_{j,k+1}$ will be minimised if $L_{i,k}$ obeys equation (21). Moreover, then (26) becomes (22). The proof is ended here.

Theorem 2. *For system (1), (13), the optimal MJL estimator $\hat{x}_k$ for the state x_k is*

$$\hat{x}_k = \bar{x}_k + K_{\theta_k,k}(r_k - \mathbb{E}_{1,\theta_k}C_{1,k}F_k\bar{x}_k) \tag{27}$$

where the estimator gain $K_{\theta_k,k}$ is denoted as $K_{i,k}$ for $\theta_k = i(i=1,2,\ldots,N)$, and satisfies the following equation:

$$K_{i,k} = \bar{Y}_{i,k}F_k^TC_{1,k}^T\mathbb{E}_{1,i}^TW_{i,k}^{-1} \tag{28}$$

with $\bar{Y}_{i,k}$ is given by (22).

Proof. The proof can be carried out along the similar line to Theorem 1. The detail is omitted to save space.

Remark 3. *In the next section, we consider a scenario that H, B, F, Q, $\bar{R}$, and p_{ij} are time invariant and the Markov chain satisfies the ergodic assumption, so that $\pi_{i,k}$ converges to $\pi_i > 0$ as k goes to infinity, the coupled difference Riccati equations (CDREs) (22) lead to the following coupled algebraic Riccati equations (CAREs)*

$$\bar{Y}_j = \sum_{i=1}^{N} p_{ij}\{H\bar{Y}_iH^T + \pi_iBQB^T - H\bar{Y}_iF^TC_1^T\mathbb{E}_{1,i}^T$$

$$\times [\mathbb{E}_{1,i}C_1F\bar{Y}_iF^TC_1^T\mathbb{E}_{1,i}^T + \pi_i\mathbb{E}_{2,i}C_2\bar{R}C_2^T\mathbb{E}_{2,i}^T]^{-1}$$
$$\times \mathbb{E}_{1,i}C_1F\bar{Y}_iH^T\} \quad (29)$$

Further, we present a sufficient condition for the existence and uniqueness of a positive semi-definite solution $\bar{Y} = (\bar{Y}_1, \ldots, \bar{Y}_N) \in \mathbb{H}^{n+}$ *for (29), and the convergence of* $\bar{Y}_k$ *to* $\bar{Y}$*, so that a stationary estimator would be obtained.*

4 Stationary Markov jump linear estimator

In this section, we assume that all matrices in (1) and (13) are time invariant. Our aim is to show that the asymptotic behaviour of a set of CDREs (22), and the mean square stability of the corresponding estimator under the assumption of ergodicity of the associated Markov chain.

Assume that the Markov chain is ergodic. That is, there exist limit probabilities $\pi_i > 0 (i = 1, 2, \ldots, N)$, with $\sum_{i=1}^N \pi_i = 1$, such that $\lim_{k\to\infty} \pi_{i,k} = \pi_i$ exponentially fast and independent from θ_0. Set $\pi_k = (\pi_{1,k}, \ldots, \pi_{N,k})$, $\pi = (\pi_1, \ldots, \pi_N)$.

We state our stationary estimation problem as: find the estimator gain L_i, $i = 1, 2, \ldots, N$, such that

$$\bar{x}_{e,k+1} = H\bar{x}_{e,k} + L_i[r_k - \mathbb{E}_{1,i}C_1F\bar{x}_{e,k}] \quad (30)$$

is mean square stable and minimizes its corresponding estimation error. The solution of the above proposed problem is closely related to the stabilizing solution for the CAREs (29).

For $\Gamma = (\Gamma_1, \ldots, \Gamma_N) \in \mathbb{H}^n$ and $W = (W_1, \ldots, W_N) \in \mathbb{H}^n$, we define the linear operator $\mathcal{L}(W) = (\mathcal{L}_1(W), \ldots, \mathcal{L}_N(W))$ as

$$\mathcal{L}_j(W) \triangleq \sum_{i=1}^N p_{ij}\Gamma_iW_i\Gamma_i^T \quad (31)$$

Next, to facilitate the subsequent handwriting, let us set $H_i = H$, $B_i = B$, $D_i = \mathbb{E}_{1,i}C_1F$, $G_i = \mathbb{E}_{2,i}C_2$, $i = 1, 2, \ldots, N$, and denote

$$\bar{H} := (H_1, \ldots, H_N) \in \mathbb{H}^n, \ \bar{B} := (B_1, \ldots, B_N) \in \mathbb{H}^{p,n}$$
$$\bar{D} := (D_1, \ldots, D_N) \in \mathbb{H}^{n,m}, \ \bar{G} := (G_1, \ldots, G_N) \in \mathbb{H}^{3m,m}$$

In the following, we will give some definitions, which are the concepts of mean square stabilizability and mean square detectability.

Definition 2 ([21]). *For* $\bar{H} \in \mathbb{H}^n$, $\bar{B} \in \mathbb{H}^{p,n}$*, we say that* $(\bar{H}, \bar{B}, P)$ *is mean square stabilizable if there exists* $M = (M_1, \ldots, M_N) \in \mathbb{H}^{n,p}$ *such that* $r_\sigma(\mathcal{L}) < 1$*, where* $\mathcal{L}$ *is as defined in (31) with* $\Gamma_i = H_i - B_iM_i$*. In this case,* M *is said to stabilize* $(\bar{H}, \bar{B}, P)$*.*

Definition 3 ([21]). *For* $\bar{H} \in \mathbb{H}^n$, $\bar{D} \in \mathbb{H}^{n,m}$*, we say that* $(P, \bar{D}, \bar{H})$ *is mean square detectable if there exists* $M = (M_1, \ldots, M_N) \in \mathbb{H}^{m,n}$ *such that* $r_\sigma(\mathcal{L}) < 1$*, where* $\mathcal{L}$ *is as defined in (31) with* $\Gamma_i = H_i - M_iD_i$*. In this case,* M *is said to stabilize* $(P, \bar{D}, \bar{H})$*.*

Further, for $\bar{Y} = (\bar{Y}_1, \ldots, \bar{Y}_N) \in \mathbb{H}^n$, we define the linear operators $J(\bar{Y}, \pi) = (J_1(\bar{Y}, \pi), \ldots, J_N(\bar{Y}, \pi))$, $M(\bar{Y}, \pi) = (M_1(\bar{Y}, \pi), \ldots, M_N(\bar{Y}, \pi))$, $\Xi(\bar{Y}, \pi) = (\Xi_1(\bar{Y}, \pi), \ldots, \Xi_N(\bar{Y}, \pi))$, $\Phi(M(\bar{Y}, \pi), \pi) = (\Phi_1(M(\bar{Y}, \pi), \pi), \ldots, \Phi_N(M(\bar{Y}, \pi), \pi))$ as

$$J_j(\bar{Y}, \pi) \triangleq \sum_{i=1}^N p_{ij}\{(H_i - M_i(\bar{Y}, \pi)D_i)\bar{Y}_i(H_i - M_i(\bar{Y}, \pi)D_i)^T + \pi_i(M_i(\bar{Y}, \pi)G_i\bar{R}G_i^T(M_i(\bar{Y}, \pi))^T + B_iQB_i^T)\} \quad (32)$$

$$M_i(\bar{Y}, \pi) \triangleq H_i\bar{Y}_iD_i^T(D_i\bar{Y}_iD_i^T + \pi_iG_i\bar{R}G_i^T)^{-1} \quad (33)$$

$$\Phi_j(M(\bar{Y}, \pi), \pi) \triangleq \sum_{i=1}^N p_{ij}\pi_i(M_i(\bar{Y}, \pi)G_i\bar{R}G_i^T(M_i(\bar{Y}, \pi))^T + B_iQB_i^T) \quad (34)$$

$$\Xi_i(\bar{Y}, \pi) \triangleq D_i\bar{Y}_iD_i^T + \pi_iG_i\bar{R}G_i^T \quad (35)$$

In particular, we set $J(\bar{Y}) = J(\bar{Y}, \pi)$, $M(\bar{Y}) = M(\bar{Y}, \pi)$, $\Phi(M(\bar{Y})) = \Phi(M(\bar{Y}, \pi), \pi)$, $\Xi(\bar{Y}) = \Xi(\bar{Y}, \pi)$, then the CAREs (29) can be expressed as

$$\bar{Y}_j = J_j(\bar{Y}), \ \ j = 1, 2, \ldots, N \quad (36)$$

Moreover, we define $\mathbb{X} = \{\bar{Y} = (\bar{Y}_1, \ldots, \bar{Y}_N) \in \mathbb{H}^{n*}; \Xi(\bar{Y}) > 0 \text{ and } -\bar{Y} + J(\bar{Y}) \geq 0\}$.

Now, some useful definitions as for the CAREs (36) and the operator (31) are given as below.

Definition 4 ([22]). *$\bar{Y} = (\bar{Y}_1, \ldots, \bar{Y}_N) \in \mathbb{H}^{n+}$ is a stabilizing solution for the CAREs (36) if it satisfies (36) and $M(\bar{Y}) = (M_1(\bar{Y}), \ldots, M_N(\bar{Y}))$ stabilizes $(P, \bar{D}, \bar{H})$, where $M_i(\bar{Y})(i = 1, 2, \ldots, N)$ is as defined in (33).*

Definition 5 ([21]). *Consider $\mathcal{L}$ as defined in (31). If $r_\sigma(\mathcal{L}) < 1$, then for any $\Phi \in \mathbb{H}^n$, there exists a unique solution $\bar{Y} \in \mathbb{H}^n$ such that $\bar{Y} - \mathcal{L}(\bar{Y}) = \Phi$. Moreover, if $\Phi \in \mathbb{H}^{n+}$, then $\bar{Y} \in \mathbb{H}^{n+}$.*

Lemma 1. *Suppose that $(\bar{H}, \bar{B}, P)$ is mean square stabilizable and $(P, \bar{D}, \bar{H})$ is mean square detectable. Then there exists a unique solution $\tilde{Y} = (\tilde{Y}_1, \ldots, \tilde{Y}_N) \in \mathbb{H}^{n+}$ to the CAREs (36), which will coincide with the mean square stabilizing solution.*

Proof. Along the same line of the proof in [22]. we can prove Lemma 1. The details are omitted to save the space.

Remark 4. *To reduce online computational cost and communication burden, we present a stationary MJL estimator, where the estimator gains can be computed off-line. In this section, conditions for existence, uniqueness, and stability of the stationary MJL estimator is obtained for the case when the system is time invariant.*

Lemma 2. *If $(\bar{H}, \bar{B}, P)$ is mean square stabilizable and $(P, \bar{D}, \bar{H})$ is mean square detectable. Then the solution $\bar{Y}_k = (\bar{Y}_{1,k}, \ldots, \bar{Y}_{N,k})$ of (22) with any initial condition $\bar{Y}_0 \in \mathbb{H}^{n+}$ converges to the unique positive semi-definite solution $\tilde{Y} = (\tilde{Y}_1, \ldots, \tilde{Y}_N)$ as k goes to infinity. In addition, $\tilde{Y} = (\tilde{Y}_1, \ldots, \tilde{Y}_N) \in \mathbb{H}^{n+}$ is the stabilizing solution for the CAREs (29).*

Proof. Similar to Theorem 3 of [23], we can prove Lemma 2. In order to save space, the detailed proof here is omitted.

5 Conclusion

In this paper, the optimal MJL estimator problem has been addressed for wireless networked system with AF relay. The long-distance signal transmission between the sensor and the estimator is implemented by introducing the AF relay node, in which the transmission power of the sensor and the relay is characterized as a set of Markov distributed variables with known Markov chain. Firstly, a new observation equation model is developed by the reorganization Markov chain technique. Then, the MJL estimator has been obtained based on the new observation equation. This is the main novelty of this paper. Secondly, under the hypothesis that ergodicity of the associated Markov chain, the stationary MJL estimator with constant-gain has been explored, and it has been shown that the solution of the CDREs converges to the unique stabilizing solution of the corresponding CAREs.

References

[1] D. Ciuonzo, V. Carotenuto, M. A. De, On multiple covariance equality testing with application to SAR change detection. *IEEE Transactions on Signal Processing*, 2017, 65(19): 5078–5091.

[2] C. Kalalas, L. Thrybom, J. Alonso-Zarate, Cellular communications for smart grid neighborhood area networks: A survey. *IEEE access*, 2016, 4: 1469–1493.

[3] M. Wollschlaeger, T. Sauter, J. Jasperneite, The future of industrial communication: Automation networks in the era of the internet of things and industry 4.0. *IEEE industrial electronics magazine*, 2017, 11(1): 17–27.

[4] D. Liu, Y. Liu, F. E. Alsaadi, Recursive state estimation based-on the outputs of partial nodes for discrete-time stochastic complex networks with switched topology. *Journal of the Franklin Institute*, 2018, 355(11): 4686–4707.

[5] X. Wang, E. E. Yaz, Stochastically resilient extended Kalman filtering for discrete-time nonlinear systems with sensor failures. *International Journal of Systems Science*, 2014, 45(7): 1393–1401.

[6] F. Wang, J. Liang, Constrained H_∞ estimation for time-varying networks with hybrid incomplete information. *International Journal of Robust and Nonlinear Control*, 2018, 28(2): 699–715.

[7] R. Caballero-guila, A. Hermoso-Carazo, J. Linares-Prez, Z. Wang, A new approach to distributed fusion filtering for networked systems with random parameter matrices and correlated noises. *Information Fusion*, 2019, 45: 324–332.

[8] C. Han, H. Zhang, Linear optimal filtering for discrete-time systems with random jump delays. *Signal Processing*, 2009, 89(6): 1121–1128.

[9] J. Xu, G. Gu, V. Gupta, Y. Tang, Optimal stationary state estimation over multiple Markovian packet drop channels. *Automatica*, 2021, 128: 109561.

[10] S. Kiani, S. ShahbazPanahi, M. Dong, G. Boudreau, M. Bavand, Joint Power Allocation and Distributed Equalization Design for OFDM-Based Filter-and-Forward Two-Way Multi-Relay Networks. *IEEE Transactions on Signal Processing*, 2021, 69: 4652–4668.

[11] H. Tan, B. Shen, K. Peng, H. Liu, Robust recursive filtering for uncertain stochastic systems with amplify-and-forward relays. *International Journal of Systems Science*, 2020, 51(7): 1188–1199.

[12] R. Senanayake, S. Atapattu, J. S. Evans, P. J. Smith, Decentralized relay selection in multi-user multihop decode-and-forward relay networks. *IEEE Transactions on Wireless Communications*, 2018, 17(5): 3313–3326.

[13] S. Simoens, O. Munoz-Medina, J. Vidal, A. D. Coso, Compress-and-forward cooperative MIMO relaying with full channel state information. *IEEE Transactions on Signal Processing*, 2009, 58(2): 781–791.

[14] L. Zou, Z. Wang, B. Shen, H. Dong, Moving horizon estimation over relay channels: Dealing with packet losses. *Automatica*, 2023, 155: 111079.

[15] X. Meng, Z. Wang, F. Wang, Y. Chen, Distributed Fusion Filtering for Nonlinear Time-Varying Systems Over Amplify-and-Forward Relay Networks: An H_∞ Quantized Framework. *IEEE Transactions on Network Science and Engineering*, 2023, 10(6): 3597–3608.

[16] Y. Liu, Z. Wang, C. Liu, M. Coombes, W. Chen, Auxiliary particle filtering over sensor networks under protocols of amplify-and-forward and decode-and-forward relays. *IEEE Transactions on Signal and Information Processing over Networks*, 2022, 8: 883–893.

[17] C. Han, H. Zhang, M. Fu, Optimal filtering for networked systems with Markovian communication delays. *Automatica*, 2013, 49(10): 3097–3104.

[18] K. You, M. Fu, L. Xie, Mean square stability for Kalman filtering with Markovian packet losses. *Automatica*, 2011, 47(12): 2647–2657.

[19] Y. Liu, W. Liu, M. A. Obaid, I. A. Abbas, Exponential stability of Markovian jumping CohenCGrossberg neural networks with mixed mode-dependent time-delays. *Neurocomputing*, 2016, 177: 409–415.

[20] H. Ma, H. Lai, M. Wang, Forecasting of dissolved gas in transformer oil by optimized nonlinear Grey bernoulli Markov model, in *Proceedings of 28th Chinese Control and Decision Conference*, 2016: 4168–4173.

[21] O. L. V. Costa, Discrete-time coupled Riccati equations for systems with Markov switching parameters. *Journal of Mathematical Analysis and Applications*, 1995, 194(1): 197–216.

[22] O. L. V. Costa, M. D. Fragoso, R. P. Marques, *Discrete-time Markov jump linear systems*. Springer Science & Business Media, 2005.

[23] C. Han, W. Wang, Optimal filter for MJL system with delayed modes and observations. *IET Control Theory & Applications*, 2018, 12(1): 68–77.

Proceedings of the 3rd Conference on Fully Actuated System Theory and Applications
May 10-12, 2024, Shenzhen, China

Finite-Time Command Filtered Backstepping Design for High-Order Fully Actuated Strict-Feedback Systems

Weizhen Liu[1], Guangren Duan[1,2], Guangtai Tian[1], Mehdi Golestani[1], He Kong[1]

1. Shenzhen Key Laboratory of Control Theory and Intelligent Systems, Southern University of Science and Technology, Shenzhen 518055, China
E-mail: l_weizhen@163.com, gttian_hit@163.com, golestani@sustech.edu.cn, kongh@sustech.edu.cn

2. Center for Control Theory and Guidance Technology, Harbin Institute of Technology, Harbin 150001, China
E-mail: g.r.duan@hit.edu.cn

Abstract: In this paper, we address the challenge of finite-time tracking control for a specific class of high-order fully actuated strict-feedback systems (HOFASFSs). The proposed solution involves the introduction of a finite-time high-order Levant differentiator, which is employed for estimating high-order derivatives to mitigate the "explosion of complexity" problem. Additionally, finite-time error compensation signals are designed to minimize the impact of the unachieved portion between the estimated virtual control and the actual virtual control. The newly developed high-order finite-time command filtered backstepping (HOFTCFB) scheme not only capitalizes on the advantages of reducing backstepping steps through the utilization of high-order fully actuated (HOFA) system approaches but also ensures finite-time convergence. The stability and finite-time convergence properties of the closed-loop system are analyzed using the Lyapunov stability criterion, and the theoretical results are validated through simulation tests.

Key Words: High-order fully-actuated system approach, strict-feedback systems, finite-time convergence, command filtered backstepping

1 Introduction

Even though the fully actuated systems are universal in the second-order mechanical system, it is always neglected and treated as a small proportion of the control system. To be more specific, such inherent fully actuated characteristics of nonlinearities are largely neglected, and almost all the original systems are turned into the first-order form. However, it can be a general model by mathematically generalizing such a concept, and it was named as HOFA system [1]. Ever since the celebrated work of Duan [1, 2], fruitful results have been achieved based on HOFA system approach, e.g., DC microgrids control [3], prescribed time control for strong interconnected nonlinear systems [4], adaptive control [5], weak disturbance decoupling [6], event-triggered control [7].

To study the lower-triangular form nonlinear systems, the seminal backstepping design technique has achieved successful achievement in robust [8] and adaptive nonlinear control design [9]. However, the traditional backstepping technique suffers from the "explosion of complexity" problem that caused by the repeated differentiation of virtual controllers in each step design. Hence, a seminal command filtered backstepping (CFB) is brought out to estimate the derivatives of the virtual control rather than calculate them in detail. Among those CFB approaches, a type of finite-time CFB scheme has gotten great attention since it obtains faster response, higher tracking precision, and better disturbance-rejection ability [10–14]. However, the existing finite-time CFB schemes are restricted to the first-order state-space system framework. Recently, an interesting type of high-order CFB technique has been presented that derives a direct controller design to reduce the backstepping steps. Based on the HOFA system approach, the original HOFA strict-feedback systems (HOFASFSs) need not be converted into the first-order state-space form. The dynamical nonlinear uncertainties and parametric uncertainties are studied in [15] and in [16, 17], respectively. Even though those above high-order CFB schemes do not consider the finite-time convergence, the finite-time convergence propriety is of great significance that can bring out various valuable characteristics for dynamical system, e.g., stronger robustness and rapid transient performance. A natural question arises: Can a novel CFB scheme be devised to tackle the tracking control problem with rapid convergence rates, eliminating the need to transform the original HOFASFS into a first-order state-space form to reduce the number of backstepping steps? This question inspires us to carry out the present work.

In this paper, we developed a high-order finite-time command filtered backstepping (HOFTCFB) scheme. This is a nontrivial task since we need to design high-order differentiators to estimate higher-order derivatives of the virtual control law to avoid the "explosion of complexity" problem. Moreover, the main difficulties lie in guaranteeing the stability and finite-time convergence in this high-order framework. To solve such a problem, we have introduced a finite-time high-order Levant differentiator, which is employed for estimating high-order derivatives to mitigate the "explosion of complexity" problem. Furthermore, we also design finite-time error compensation signals to minimize the impact of the unachieved portion between the estimated virtual control and the actual virtual control.

The paper is organized as follows. Section 2 introduces some preliminaries about the HOFASFSs and the related assumptions. Section 3 formally proposes the designed HOFTCFB scheme for the HOFASFSs, and stability and finite-time convergence properties of the closed-loop system are given. Section 4 provides finite-time trajectory tracking

This work was supported by the Science Center Program of the National Natural Science Foundation of China under Grant No. 62188101, the Program of Heilongjiang Touyan Team, Shenzhen Science and Technology Program under grant No. KQTD20221101093557010, and also by Shenzhen Key Laboratory of Control Theory and Intelligent Systems ZDSYS20220330161800001.

control for an electromechanical system to verify the performance of this scheme. Section 5 ends with some concluding remarks.

For $x \in \mathbb{R}$, and $A_{i,j} \in \mathbb{R},\ i = 1,2,\ldots,n, j = 0,1,\ldots,n-1$, the following symbols, which are frequently used in HOFA systems [2], are also introduced to ease the presentation

$$x^{(0\sim n)} = \begin{bmatrix} x \\ \dot{x} \\ \vdots \\ x^{(n)} \end{bmatrix}, \left\langle x^{(0\sim n)} \right\rangle^{\gamma} = \begin{bmatrix} x^{\gamma} \\ \dot{x}^{\gamma} \\ \vdots \\ \left(x^{(n)}\right)^{\gamma} \end{bmatrix},$$

$$x_{i\sim j}^{(0\sim n)} = \begin{bmatrix} x_i^{(0\sim n)} \\ x_{i+1}^{(0\sim n)} \\ \vdots \\ x_j^{(0\sim n)} \end{bmatrix}, i \le j$$

$$A_i^{0\sim n-1} = \begin{bmatrix} A_{i,0} & A_{i,1} & \cdots & A_{i,n-1} \end{bmatrix},$$

$$\Phi_i\left(A_i^{0\sim n-1}\right) = \begin{bmatrix} 0 & I & & \\ & & \ddots & \\ & & & I \\ -A_{i,0} & -A_{i,1} & \cdots & -A_{i,n-1} \end{bmatrix},$$

where γ is a positive constant and $0 < \gamma < 1$. And $\lambda_{\max}(P)$ and $\lambda_{\min}(P)$ are the largest and smallest eigenvalues of P, respectively.

2 Problem formulation and preliminaries

Consider the following HOFASFSs

$$\begin{cases} x_1^{(q_1)} = f_1\left(x_1^{(0\sim q_1-1)}\right) + g_1\left(x_1^{(0\sim q_1-1)}\right)x_2 \\ x_2^{(q_2)} = f_2\left(x_k^{(0\sim q_k-1)}|_{k=1\sim 2}\right) + g_2\left(x_k^{(0\sim q_k-1)}|_{k=1\sim 2}\right)x_3 \\ \quad\vdots \\ x_{n-1}^{(q_{n-1})} = f_{n-1}\left(x_k^{(0\sim q_k-1)}|_{k=1\sim n-1}\right) \\ \qquad + g_{n-1}\left(x_k^{(0\sim q_k-1)}|_{k=1\sim n-1}\right)x_n \\ x_n^{(q_n)} = f_n\left(x_k^{(0\sim q_k-1)}|_{k=1\sim n}\right) + g_n\left(x_k^{(0\sim q_k-1)}|_{k=1\sim n}\right)u, \end{cases} \tag{1}$$

where $x_i \in \mathbb{R},\ i = 1,2,\ldots,n$ are the state variables, $q_i,\ i = 1,2,\ldots,n$ are a set of positive integers, $f_i\left(x_k^{(0\sim q_k-1)}|_{k=1\sim i}\right) \in \mathbb{R},\ i = 1,2,\ldots,n$ are a set of sufficiently smooth scalar functions. $g_i\left(x_k^{(0\sim q_k-1)}|_{k=1\sim i}\right) \in \mathbb{R},\ i = 1,2,\ldots,n,$ are a group of sufficiently smooth scalar functions. The control objective is to steer the output x_1 of the HOFASFSs (1) from any given initial condition to trace the trajectory y_d in finite-time under the designed control signal u, and also ensures that all the signals of the closed-loop system are uniformly ultimately bounded. Moreover, $g_i,\ i = 1,2,\ldots,n$ satisfy the full-actuation assumption:

Assumption 1

$$g_i\left(x_k^{(0\sim q_k-1)}|_{k=1\sim i}\right) \neq 0,$$
$$\forall\, x_k^{(0\sim q_k-1)} \in \mathbb{R}^{q_k},\ k = 1,2,\ldots,i,\ i = 1,2,\ldots,n.$$

The desired output trajectory y_d are assumed to satisfy the following Assumptions 2.

Assumption 2 *The desired trajectory y_d is available and satisfies that*

$$\begin{bmatrix} y_d & \dot{y}_d & \cdots & y_d^{(2q_1)} \end{bmatrix}^{\top} \in B_{r_0} = \{\begin{bmatrix} z_1 & z_2 & \cdots & z_{2q_1+1} \end{bmatrix}^{\top} : z_1^2 + z_2^2 + \cdots + z_{2q_1+1}^2 \le r_0\}, \tag{2}$$

where r_0 is a positive constant.

Lemma 1 *[18] Consider $A_{i,k} \in \mathbb{R},\ i = 1,2,\ldots,n,\ k = 0,1,\ldots,q_i-1$ and $\Phi_i\left(A_i^{0\sim q_i-1}\right) \in \mathbb{R}^{q_i\times q_i}$ satisfying*

$$\mathrm{Re}\lambda_i\left(\Phi_i\left(A_i^{0\sim q_i-1}\right)\right) < -\frac{\mu_i}{2},\ i = 1,2,\ldots,n, \tag{3}$$

where $\mu_i \in \mathbb{R}_{>0}$. Then, there exist positive definite matrices $P_i\left(A_i^{0\sim q_i-1}\right) \in \mathbb{R}^{q_i\times q_i}$ that satisfy

$$\Phi_i^{\top}\left(A_i^{0\sim q_i-1}\right)P_i\left(A_i^{0\sim q_i-1}\right) + P_i\left(A_i^{0\sim q_i-1}\right)\Phi_i\left(A_i^{0\sim q_i-1}\right) < -\mu_i P_i\left(A_i^{0\sim q_i-1}\right). \tag{4}$$

Assume $A_i^{0\sim q_i-1} \in \mathbb{R}^{1\times q_i},\ i = 1,2,\ldots,n$ are a set of matrices to make $\Phi_i \in \mathbb{R}^{q_i\times q_i},\ i = 1,2,\ldots,n$ Hurwitz and

$$P_i = \begin{bmatrix} P_{iF} & \cdots & P_{iL} \end{bmatrix}, \tag{5}$$

where $P_i \in \mathbb{R}^{q_i\times q_i}$, P_{iF} and P_{iL} are the first and last columns of P_i, respectively.

In the following sections, $\Phi_i\left(A_i^{0\sim q_i-1}\right)$, $P_i\left(A_i^{0\sim q_i-1}\right)$, $g_i\left(x_k^{(0\sim m_k-1)}|_{k=1\sim i}\right)$ and $f_i\left(x_k^{(0\sim q_k-1)}|_{k=1\sim i}\right)$, will be written shortly as Φ_i, P_i, g_i and f_i, respectively.

The high-order Levant differentiator is introduced as follows:

$$\begin{aligned} \dot{\psi}_0 &= \upsilon_0,\ \upsilon_0 = -\lambda_0|\psi_0 - \alpha_\upsilon|^{n/(n+1)}\mathrm{sign}(\psi_0 - \alpha_\upsilon) + \psi_1, \\ \dot{\psi}_1 &= \upsilon_1,\ \upsilon_1 = -\lambda_1|\psi_1 - v_0|^{(n-1)/n}\mathrm{sign}(\psi_1 - \upsilon_0) + \psi_2, \\ &\vdots \\ \dot{\psi}_{n-1} &= \upsilon_{n-1},\ \upsilon_{n-1} = -\lambda_{n-1}|\psi_{n-1} - \upsilon_{n-2}|^{1/2} \\ &\qquad \times \mathrm{sign}(\psi_{n-1} - \upsilon_{n-2}) + \psi_n, \\ \dot{\psi}_n &= -\lambda_n \mathrm{sign}(\psi_n - \upsilon_{n-1}). \end{aligned}$$

where $\psi_i \in \mathbb{R},\ i = 0,1,\ldots,n$ are state variables of the Levant differentiator, α_υ is the input signal, and $\lambda_i, i = 0,1\ldots,n$ are the design parameters. Then, the following Lemma holds:

Lemma 2 *([19]) Let input signal α_υ consists of a bouned noise and an unknown real signal $\alpha_{\upsilon 0}$, and the noise satisfy $|\alpha_\upsilon - \alpha_{\upsilon 0}| \le \varepsilon$. Then, the following real-time robust estimations of $\dot{\alpha}_{\upsilon 0}, \ddot{\alpha}_{\upsilon 0}, \ldots, \alpha_{\upsilon 0}^{(n)}$ satisfy the following inequality in finite time*

$$\left|\psi_i - \alpha_{\upsilon 0}^{(i)}\right| \le \mu_i \varepsilon^{(n-i+1)/(n+1)} = \Delta_i, i = 0,1,\ldots,n.$$

where μ_i and Δ_i are positive constants.

Lemma 3 *([14]) Consider $x_i \in \mathbb{R},\ i = 1,2,\ldots,n,$ and $0 < p < 1$, then*

$$\left(\sum_{i=1}^{n}|x_i|\right)^p \le \sum_{i=1}^{n}|x_i|^p \le n^{1-p}\left(\sum_{i=1}^{n}|x_i|\right)^p. \tag{6}$$

Lemma 4 *([14]) If there exists a continuous function $V(x)$ and parameters $\rho_1 > 0$, $\rho_2 > 0$, $0 < \gamma < 1$, and $0 < c < 1$ for the system $\dot{x} = f(x)$, then the $V(x)$ satisfy that $\dot{V}(x) \leq -\rho_1 V(x) - \rho_2 V^{\gamma}(x) + c$. It can be concluded that the trajectory of the system is practical finite-time stable, and the convergence time is bounded as*

$$T_b \leq \max\left\{t_0 + \frac{1}{\theta_0\rho_1(1-\gamma)}\ln\frac{\theta_0\rho_1 V^{1-\gamma}(t_0)+\rho_2}{\rho_2}, t_0 + \frac{1}{\rho_1(1-\gamma)}\ln\frac{\rho_1 V^{1-\gamma}(t_0)+\theta_0\rho_2}{\theta_0\rho_2}\right\},$$

and $V(x)$ is bounded by

$$\lim_{t\to T_b}\left|V(x) \leq \min\left\{\frac{\eta}{(1-\theta_0)\rho_1}, \left(\frac{\eta}{(1-\theta_0)\rho_2}\right)^{\frac{1}{\gamma}}\right\}\right.$$

where $0 < \theta_0 < 1$.

3 HOFTCFB Design

3.1 Finite-time controller design

The tracking errors for the HOFASFSs (1) are defined as

$$S_i = x_i - x_{ic},\ i = 1,2,\ldots,n, \tag{7}$$

$x_{1c} = y_d$ is the desired trajectory, and x_{ic}, $i = 2,3,\ldots,n$ are derived through a set of high-order Levant differentiators applied to the i-th virtual control function α_i

$$\begin{aligned}
\dot{\psi}_{i,0} =& \upsilon_{i,0},\ \upsilon_{i,0} = -\lambda_{i,0}\left|\psi_{i,0}-\alpha_i\right|^{q_i/(q_i+1)} \\
&\times \operatorname{sign}\left(\psi_{q_i,0}-\alpha_i\right) + \psi_{q_i,1}, \\
\dot{\psi}_{i,1} =& \upsilon_{i,1},\ \upsilon_{i,1} = -\lambda_{i,1}\left|\psi_{i,1}-\upsilon_{i,0}\right|^{(q_i-1)/q_i} \\
&\times \operatorname{sign}\left(\psi_{i,1}-\upsilon_{i,0}\right) + \psi_{i,2}, \\
&\vdots \\
\dot{\psi}_{i,q_i-1} =& \upsilon_{i,q_i-1},\ \upsilon_{i,q_i-1} = -\lambda_{i,q_i-1}\left|\psi_{i,q_i-1}-\upsilon_{i,q_i-2}\right|^{1/2} \\
&\times \operatorname{sign}\left(\psi_{i,q_i-1}-\upsilon_{i,q_i-2}\right) + \psi_{i,q_i}, \\
\dot{\psi}_{i,q_i} =& -\lambda_{i,q_i}\operatorname{sign}\left(\psi_{i,q_i}-\upsilon_{i,q_i-1}\right).
\end{aligned} \tag{8}$$

where $\lambda_{i,k} \in \mathbb{R}_{>0}$, $k = 1,2,\ldots,q_i$, $i = 2,3,\ldots,n$. Furthermore, the outputs of each command filer are expressed as $x_{(i+1)c}^{(k)} = \psi_{i,k}$, $k = 0,1,\ldots,q_i$.

Construct the virtual control function α_i ($i = 1,2,\ldots,n-1$) of the proposed HOFTCFB scheme as follows:

$$\alpha_i = -\frac{1}{g_i}\left(A_i^{0\sim q_i-1}S_i^{(0\sim q_i-1)} + A_i^{0\sim q_i-1}\Phi_i^{-1}\left\langle v_i^{(0\sim q_i-1)}\right\rangle^{\gamma} + f_i - x_{ic}^{(q_i)}\right) \tag{9}$$

and the control law is given as

$$u = -\frac{1}{g_n}\left(A_n^{0\sim q_n-1}S_n^{(0\sim q_n-1)} + A_n^{0\sim q_n-1}\Phi_n^{-1}\left\langle v_n^{(0\sim q_n-1)}\right\rangle^{\gamma} + f_n - x_{nc}^{(q_n)}\right) \tag{10}$$

where $v_i^{(0\sim q_i-1)}$ are the compensated tracking errors that are defined later in (13), and γ is a positive constant that satisfies $0 < \gamma < 1$.

The compensating signals, which aim to remove the effect of $x_{(i+1)c} - \alpha_i$ with $i = 1,2,\ldots,n-1$, are defined as

$$\begin{aligned}
\xi_i^{(q_i)} =& -A_i^{0\sim q_i-1}\xi_i^{(0\sim q_i-1)} + g_i\xi_{i+1} + g_i\left(x_{(i+1)c}-\alpha_i\right) \\
&- \sum_{k=1}^{q_i} l_{i,k}\operatorname{sign}\left(\xi_i^{(k-1)}\right),
\end{aligned} \tag{11}$$

$$\xi_n^{(q_n)} = -A_n^{0\sim q_n-1}\xi_n^{(0\sim q_n-1)} - \sum_{k=1}^{q_n} l_{n,k}\operatorname{sign}\left(\xi_n^{(k-1)}\right). \tag{12}$$

where $l_{i,k}$ are positive constants with $k = 1,2,\ldots,q_i$, $i = 1,2,\ldots,n$.

Define the compensated tracking error signals

$$v_i = S_i - \xi_i. \tag{13}$$

Theorem 5 *Assuming that the HOFASFSs (1) satisfy Assumptions 1-2, consider the proposed scheme comprising the control law (10), the virtual control function (9), and the command filters (8). Given the tuning parameters $A_i^{0\sim q_i-1}$, $i = 1,2,\ldots,n$ that satisfy (3), and positive constants $\lambda_{i,k}$, $k = 1,2,\ldots,q_i$, $i = 2,3,\ldots,n$, $l_{i,k}$, $k = 1,2,\ldots,q_i$, $i = 1,2,\ldots,n$, the proposed HOFTCFB ensures that all states of the closed-loop system remain uniformly ultimately bounded, and the output tracking error can be reduced to a disc region in finite-time.*

Proof. To streamline the presentation and avoid repetitive derivation processes, we initially provide frequently used inequalities. Using Young's inequality, it is clear that

$$\begin{aligned}
&\left(v_i^{(0\sim q_i-1)}\right)^{\top}P_{iL}g_i v_{i+1} \\
=&\left(v_i^{(0\sim q_i-1)}\right)^{\top}P_i\begin{bmatrix}0_{(q_i-1)\times 1}\\ g_i v_{i+1}\end{bmatrix} \\
\leq&\left(v_i^{(0\sim q_i-1)}\right)^{\top}P_iP_i^{\top}v_i^{(0\sim q_i-1)} + \frac{g_i^2}{4}v_{i+1}^2 \\
\leq&\lambda_{\max}(P_i)\left(v_i^{(0\sim q_i-1)}\right)^{\top}P_i v_i^{(0\sim q_i-1)} \\
&+ \frac{g_i^2}{4\lambda_{\min}(P_{i+1})}\left(v_{i+1}^{(0\sim q_{i+1}-1)}\right)^{\top}P_{i+1}v_{i+1}^{(0\sim q_{i+1}-1)},
\end{aligned} \tag{14}$$

and

$$\begin{aligned}
&\left(v_i^{(0\sim q_i-1)}\right)^{\top}P_{iL}\sum_{k=1}^{q_i} l_{i,k}\operatorname{sign}\left(\xi_i^{(k-1)}\right) \\
\leq&\left(v_i^{(0\sim q_i-1)}\right)^{\top}P_iP_i^{\top}v_i^{(0\sim q_i-1)} + \frac{1}{4}\left(\sum_{k=1}^{q_i} l_{i,k}\right)^2 \\
\leq&\left(v_i^{(0\sim q_i-1)}\right)^{\top}P_iP_i^{\top}v_i^{(0\sim q_i-1)} + q_i\sum_{k=1}^{q_i}\frac{l_{i,k}^2}{4} \\
\leq&\lambda_{\max}(P_i)\left(v_i^{(0\sim q_i-1)}\right)^{\top}P_i v_i^{(0\sim q_i-1)} + q_i\sum_{k=1}^{q_i}\frac{l_{i,k}^2}{4}
\end{aligned} \tag{15}$$

The first step: Taking q_1-th differentials of (13) and utilizing (7) with $i = 1$, as well as the first equation in (1), one has

$$\begin{aligned}
v_1^{(q_1)} =& S_1^{(q_1)} - \xi_1^{(q_1)} \\
=& f_1 + g_1(S_2 + x_{2c}) - x_{1c}^{(q_1)} - \xi_1^{(q_1)} \\
=& f_1 + g_1 S_2 + g_1\alpha_1 + g_1(x_{2c}-\alpha_1) - x_{1c}^{(q_1)} - \xi_1^{(q_1)}
\end{aligned}$$

By using the virtual control signal α_1 and the derivative of compensating signal ξ_1, one obtains the closed-loop subsystem

$$\begin{aligned} v_1^{(q_1)} =& -A_1^{0\sim q_1-1} v_1^{(0\sim q_1-1)} - A_1^{0\sim q_1-1}\Phi_1^{-1}\left\langle v_1^{(0\sim q_1-1)}\right\rangle^{\gamma} \\ &+ g_1 v_2 + \sum_{k=1}^{q_1} l_{1,k}\mathrm{sign}\left(\xi_1^{(k-1)}\right) \end{aligned} \tag{16}$$

The above dynamics can be rewritten as

$$\begin{aligned} \dot{v}_1^{(0\sim q_1-1)} =& \Phi_1 v_1^{(0\sim q_1-1)} - \left\langle v_1^{(0\sim q_1-1)}\right\rangle^{\gamma} \\ &+ \begin{bmatrix} 0_{(q_1-1)\times 1} \\ g_1 v_2 + \sum_{k=1}^{q_1} l_{1,k}\mathrm{sign}\left(\xi_1^{(k-1)}\right) \end{bmatrix}. \end{aligned} \tag{17}$$

Then, define

$$V_1 = \frac{1}{2}\left(v_1^{(0\sim q_1-1)}\right)^{\top} P_1 v_1^{(0\sim q_1-1)}.$$

According to the Lemma 1, equations (5) and (17), it follows that

$$\begin{aligned} \dot{V}_1 =& \frac{1}{2}\left(v_1^{(0\sim q_1-1)}\right)^{\top}\left(\Phi_1^{\top}P_1 + P_1\Phi_1\right) v_1^{(0\sim q_1-1)} \\ &- \left(v_1^{(0\sim q_1-1)}\right)^{\top} P_1 \left\langle v_1^{(0\sim q_1-1)}\right\rangle^{\gamma} \\ &+ \left(v_1^{(0\sim q_1-1)}\right)^{\top} P_1 \left(\begin{bmatrix} 0_{(q_1-1)\times 1} \\ g_1 v_2 + \sum_{k=1}^{q_1} l_{1,k}\mathrm{sign}\left(\xi_1^{(k-1)}\right) \end{bmatrix} \right) \\ \leq& -\frac{\mu_1}{2}\left(v_1^{(0\sim q_1-1)}\right)^{\top} P_1 v_1^{(0\sim q_1-1)} \\ &- \left(v_1^{(0\sim q_1-1)}\right)^{\top} P_1 \left\langle v_1^{(0\sim q_1-1)}\right\rangle^{\gamma} \\ &+ \left(v_1^{(0\sim q_1-1)}\right)^{\top} P_{1L}\left(g_1 v_2 - \sum_{k=1}^{q_1} l_{1,k}\mathrm{sign}\left(\xi_1^{(k-1)}\right)\right) \end{aligned}$$

Based on Young's inequality in equations (14) and (15) with $i=1$, the above $\dot{V}_1$ can be reexpressed as

$$\begin{aligned} \dot{V}_1 \leq& -\frac{1}{2}\left(\mu_1 - 4\lambda_{\max}(P_1)\right)\left(v_1^{(0\sim q_1-1)}\right)^{\top} P_1 v_1^{(0\sim q_1-1)} \\ &- \left(v_1^{(0\sim q_1-1)}\right)^{\top} P_1 \left\langle v_1^{(0\sim q_1-1)}\right\rangle^{\gamma} \\ &+ \frac{g_1^2}{4\lambda_{\min}(P_2)}\left(v_2^{(0\sim q_2-1)}\right)^{\top} P_2 v_2^{(0\sim q_2-1)} + q_1\sum_{k=1}^{q_1}\frac{l_{1,k}^2}{4}. \end{aligned}$$

The i-th step: Taking q_i-th differentials of (13) and utilizing (7), as well as the i-th equation in (1), one can deduce the following:

$$\begin{aligned} v_i^{(q_i)} =& S_i^{(q_i)} - \xi_i^{(q_i)} \\ =& f_i + g_i\left(S_{i+1} + x_{(i+1)c}\right) - x_{ic}^{(q_i)} - \xi_i^{(q_i)} \\ =& f_i + g_i S_{i+1} + g_i\alpha_i \\ &+ g_i\left(x_{(i+1)c} - \alpha_i\right) - x_{ic}^{(q_i)} - \xi_i^{(q_i)} \end{aligned} \tag{18}$$

One has the closed-loop subsystem by substituting the virtual control signal α_i and the compensating signal ξ_i into (18)

$$\begin{aligned} \dot{v}_i^{(q_i)} =& -A_i^{0\sim q_i-1} v_i^{(0\sim q_i-1)} - A_i^{0\sim q_i-1}\Phi_i^{-1}\left\langle v_i^{(0\sim q_i-1)}\right\rangle^{\gamma} \\ &+ g_i v_{i+1} + \sum_{k=1}^{q_i} l_{i,k}\mathrm{sign}\left(\xi_i^{(k-1)}\right) \end{aligned} \tag{19}$$

The above dynamics of the tracking errors can be expressed as:

$$\begin{aligned} v_i^{(0\sim q_i-1)} =& \Phi_i v_i^{(0\sim q_i-1)} + \left\langle v_i^{(0\sim q_i-1)}\right\rangle^{\gamma} \\ &+ \begin{bmatrix} 0_{(q_i-1)\times 1} \\ g_i v_{i+1} + \sum_{k=1}^{q_i} l_{i,k}\mathrm{sign}\left(\xi_i^{(k-1)}\right) \end{bmatrix}. \end{aligned} \tag{20}$$

Define

$$V_i = V_{i-1} + \frac{1}{2}\left(v_i^{(0\sim q_i-1)}\right)^{\top} P_i v_i^{(0\sim q_i-1)}.$$

According to the Lemma 1, equations (5) and (20), the above result leads to

$$\begin{aligned} \dot{V}_i =& \dot{V}_{i-1} + \frac{1}{2}\left(v_i^{(0\sim q_i-1)}\right)^{\top}\left(\Phi_i^{\top}P_i + P_i\Phi_i\right) v_i^{(0\sim q_i-1)} \\ &- \left(v_i^{(0\sim q_i-1)}\right)^{\top} P_i \left\langle v_i^{(0\sim q_i-1)}\right\rangle^{\gamma} \\ &+ \left(v_i^{(0\sim q_i-1)}\right)^{\top} P_i \begin{bmatrix} 0_{(q_i-1)\times 1} \\ g_i v_{i+1} + \sum_{k=1}^{q_i} l_{i,k}\mathrm{sign}\left(\xi_i^{(k-1)}\right) \end{bmatrix} \\ \leq& \dot{V}_{i-1} - \frac{\mu_i}{2}\left(v_i^{(0\sim q_i-1)}\right)^{\top} P_i v_i^{(0\sim q_i-1)} \\ &- \left(v_i^{(0\sim q_i-1)}\right)^{\top} P_i \left\langle v_i^{(0\sim q_i-1)}\right\rangle^{\gamma} \\ &+ \left(v_i^{(0\sim q_i-1)}\right)^{\top} P_{iL}\left(g_i v_{i+1} + \sum_{k=1}^{q_i} l_{i,k}\mathrm{sign}\left(\xi_i^{(k-1)}\right)\right) \end{aligned}$$

Based on the equations (14) and (15), it follows that

$$\begin{aligned} \dot{V}_i \leq& -\frac{1}{2}\left(\mu_1 - 4\lambda_{\max}(P_1)\right)\left(v_1^{(0\sim q_1-1)}\right)^{\top} P_1 v_1^{(0\sim q_1-1)} \\ &- \frac{1}{2}\sum_{k=2}^{i}\left(\mu_k - 4\lambda_{\max}(P_k) - \frac{g_{k-1}^2}{2\lambda_{\min}(P_k)}\right)\left(v_k^{(0\sim q_k-1)}\right)^{\top} P_k \\ &\times v_k^{(0\sim q_k-1)} + \frac{g_i^2}{4\lambda_{\min}(P_{i+1})}\left(v_{i+1}^{(0\sim q_{i+1}-1)}\right)^{\top} P_{i+1} v_{i+1}^{(0\sim q_{i+1}-1)} \\ &- \sum_{k=1}^{i}\left(v_k^{(0\sim q_k-1)}\right)^{\top} P_k \left\langle v_k^{(0\sim q_k-1)}\right\rangle^{\gamma} + q_i\sum_{k=1}^{q_i}\frac{l_{i,k}^2}{4} \end{aligned} \tag{21}$$

The n-th step: For brevity, we omit similar steps here, and the n-th step can be derived

$$\begin{aligned} v_n^{(q_n)} =& S_n^{(q_n)} - \xi_n^{(q_n)} \\ =& f_n + g_n u - x_{nc}^{(q_n)} - \xi_n^{(q_n)} \end{aligned} \tag{22}$$

One has the closed-loop subsystem by substituting related control law (10) into (22)

$$\begin{aligned} v_n^{(q_n)} =& -A_n^{0\sim q_n-1} v_n^{(0\sim q_n-1)} - A_n^{0\sim q_n-1}\Phi_n^{-1}\left\langle v_n^{(0\sim q_n-1)}\right\rangle^{\gamma} \\ &+ \sum_{k=1}^{q_n} l_{n,k}\mathrm{sign}\left(\xi_n^{(k-1)}\right). \end{aligned} \tag{23}$$

The dynamics of the system described above can be reformulated as follows:

$$\begin{aligned} \dot{v}_n^{(0\sim q_n-1)} =& \Phi_n v_n^{(0\sim q_n-1)} - \left\langle v_n^{(0\sim q_n-1)}\right\rangle^{\gamma} \\ &+ \begin{bmatrix} 0_{(q_n-1)\times 1} \\ \sum_{k=1}^{q_n} l_{n,k}\mathrm{sign}\left(\xi_n^{(k-1)}\right) \end{bmatrix}. \end{aligned} \tag{24}$$

Define

$$V_n = V_{n-1} + \frac{1}{2}\left(v_n^{(0\sim q_n-1)}\right)^\top P_n v_n^{(0\sim q_n-1)}.$$

According to the Lemma 1, equations (5) and (24), one has

$$\begin{aligned}\dot{V}_n =& \dot{V}_{n-1} - \frac{\mu_n}{2}\left(v_n^{(0\sim q_n-1)}\right)^\top P_n v_n^{(0\sim q_n-1)} \\ &- \left(v_n^{(0\sim q_n-1)}\right)^\top P_n \left\langle v_n^{(0\sim q_n-1)}\right\rangle^\gamma \\ &+ \left(v_n^{(0\sim q_n-1)}\right)^\top P_{nL} \sum_{k=1}^{q_n} l_{n,k}\text{sign}\left(\xi_n^{(k-1)}\right). \end{aligned} \tag{25}$$

By using equation (15), $\dot{V}_n$ is derived as

$$\begin{aligned}\dot{V}_n \leq& \dot{V}_{n-1} - \frac{1}{2}\left(\mu_n - 2\lambda_{\max}(P_n)\right)\left(v_n^{(0\sim q_n-1)}\right)^\top P_n v_n^{(0\sim q_n-1)} \\ &- \left(v_n^{(0\sim q_n-1)}\right)^\top P_n \left\langle v_n^{(0\sim q_n-1)}\right\rangle^\gamma + q_n \sum_{k=1}^{q_n}\frac{l_{n,k}^2}{4} \\ \leq& -\frac{1}{2}\left(\mu_1 - 4\lambda_{\max}(P_1)\right)\left(v_1^{(0\sim q_1-1)}\right)^\top P_1 v_1^{(0\sim q_1-1)} \\ &- \frac{1}{2}\sum_{k=2}^{n-1}\left(\mu_k - 4\lambda_{\max}(P_k) - \frac{g_{k-1}^2}{2\lambda_{\min}(P_k)}\right) \\ &\times \left(v_k^{(0\sim q_k-1)}\right)^\top P_k v_k^{(0\sim q_k-1)} - \frac{1}{2}\left(\mu_n - 2\lambda_{\max}(P_n)\right) \\ &\times \left(v_n^{(0\sim q_n-1)}\right)^\top P_n v_n^{(0\sim q_n-1)} - \sum_{k=1}^{n-1}\left(v_k^{(0\sim q_k-1)}\right)^\top \\ &\times P_k \left\langle v_k^{(0\sim q_k-1)}\right\rangle^\gamma + \sum_{i=1}^{n}\left(q_i\sum_{k=1}^{q_i}\frac{l_{i,k}^2}{4}\right). \end{aligned} \tag{26}$$

Then, the following inequality holds

$$\begin{aligned}&\sum_{i=1}^{n}\left(v_i^{(0\sim q_i-1)}\right)^\top P_i \left\langle v_i^{(0\sim q_i-1)}\right\rangle^\gamma \\ \geq& \sum_{i=1}^{n}\frac{\lambda_{\min}(P_i)}{\lambda_{\max}\left(P_i^{\frac{1+\gamma}{2}}\right)}\left(\left(v_i^{(0\sim q_i-1)}\right)^\top P_i\left(v_i^{(0\sim q_i-1)}\right)\right)^{\frac{1+\gamma}{2}} \\ =& \bar{\lambda}_P \sum_{i=1}^{n}\left(2\frac{1}{2}\left(v_i^{(0\sim q_i-1)}\right)^\top P_i\left(v_i^{(0\sim q_i-1)}\right)\right)^{\frac{1+\gamma}{2}} \\ \geq& 2^{\frac{1+\gamma}{2}}\bar{\lambda}_P\left(\sum_{i=1}^{n}\frac{1}{2}\left(v_i^{(0\sim q_i-1)}\right)^\top P_i\left(v_i^{(0\sim q_i-1)}\right)\right)^{\frac{1+\gamma}{2}} \\ =& 2^{\frac{1+\gamma}{2}}\bar{\lambda}_P V_n^{\frac{1+\gamma}{2}} \end{aligned} \tag{27}$$

where $\bar{\lambda}_P = \min_i \frac{\lambda_{\min}(P_i)}{\lambda_{\max}\left(P_i^{\frac{1+\gamma}{2}}\right)}$ with $i = 1,2,\ldots,n$.

By substituting (27) into (26), it follows that

$$\begin{aligned}\dot{V}_n \leq& -\frac{1}{2}\left(\mu_1 - 4\lambda_{\max}(P_1)\right)\left(v_1^{(0\sim q_1-1)}\right)^\top P_1 v_1^{(0\sim q_1-1)} \\ &- \frac{1}{2}\sum_{k=1}^{n-1}\left(\mu_k - 4\lambda_{\max}(P_k) - \frac{g_{k-1}^2}{2\lambda_{\min}(P_k)}\right) \\ &\times \left(v_k^{(0\sim q_k-1)}\right)^\top P_k v_k^{(0\sim q_k-1)} \\ &- \frac{1}{2}\left(\mu_n - 2\lambda_{\max}(P_n)\right)\left(v_n^{(0\sim q_n-1)}\right)^\top P_n v_n^{(0\sim q_n-1)} \\ &- 2^{\frac{\gamma+1}{2}}\bar{\lambda}_P V_n^{\frac{\gamma+1}{2}} + \sum_{i=1}^{n}\left(q_i\sum_{k=1}^{q_i}\frac{l_{i,k}^2}{4}\right). \\ \leq& -\kappa_1 V_n - \kappa_2 V_n^{\frac{\gamma+1}{2}} + c \end{aligned} \tag{28}$$

where

$$\begin{aligned}\kappa_1 =& \min_{2\leq i\leq n-1}\left(\mu_1 - 4\lambda_{\max}(P_1), \mu_n - 2\lambda_{\max}(P_n),\right. \\ &\left.\mu_i - 4\lambda_{\max}(P_i) - g_{i-1}^2/\left(2\lambda_{\min}(P_i)\right)\right), \\ \kappa_2 =& 2^{\frac{\gamma+1}{2}}\bar{\lambda}_P, \\ c =& \sum_{i=1}^{n}\left(q_i\sum_{k=1}^{q_i}\frac{l_{i,k}^2}{4}\right). \end{aligned}$$

Since the eigenvalues of Φ_i can be arbitrarily assigned by selecting the proper $a_i^{0\sim\eta_i}$, then we can choose a proper μ_i to guarantee that κ_1 is a positive constant. According to Lemma 4, we obtain that v_i converges to

$$v_i \leq \min\left\{\sqrt{\frac{2c}{\lambda_{\min}(P_i)(1-\theta_0)\kappa_1}}, \sqrt{\frac{2}{\lambda_{\min}(P_i)}\left(\frac{c}{(1-\theta_0)\kappa_2}\right)^{\frac{2}{\gamma+1}}}\right\} \tag{29}$$

in finite-time

$$\begin{aligned}T_1 \leq \max\Bigg\{&\frac{1}{\theta_0\kappa_1\left(1-\frac{1+\gamma}{2}\right)}\ln\frac{\theta_0\kappa_1 V^{1-\frac{1+\gamma}{2}}(t_0)+\kappa_2}{\kappa_2}, \\ &\frac{1}{\kappa_1\left(1-\frac{1+\gamma}{2}\right)}\ln\frac{\kappa_1 V^{1-\frac{1+\gamma}{2}}(t_0)+\theta_0\kappa_2}{\theta_0\kappa_2}\Bigg\}. \end{aligned}$$

where $0 < \theta_0 < 1$.

Then, we prove that the compensating signals are bounded and convergent a disc region in finite-time. Define the following Lyapunov function

$$V_\xi = \frac{1}{2}\sum_{i=1}^{n}\left(\xi_i^{(0\sim q_i-1)}\right)^\top P_i \xi_i^{(0\sim q_i-1)}. \tag{30}$$

According to the Lemma 1, equations (11) and (12), it follows that

$$\begin{aligned}\dot{V}_\xi =& -\frac{1}{2}\sum_{i=1}^{n}\mu_i\left(\xi_i^{(0\sim q_i-1)}\right)^\top P_i \xi_i^{(0\sim q_i-1)} \\ &+ \sum_{i=1}^{n}\left(\xi_i^{(0\sim q_i-1)}\right)^\top P_i\begin{bmatrix} 0_{(q_n-1)\times 1} \\ g_i\xi_{i+1} - \sum_{k=1}^{q_i} l_{i,k}\text{sign}\left(\xi_i^{(k-1)}\right)\end{bmatrix} \\ &+ \sum_{i=1}^{n-1}\left(\xi_i^{(0\sim q_i-1)}\right)^\top P_i\begin{bmatrix} 0_{(q_n-1)\times 1} \\ g_i\left(x_{(i+1)c} - \alpha_i\right)\end{bmatrix}. \end{aligned} \tag{31}$$

Based on Young's inequality, one has

$$\begin{aligned}
&\left(\xi_i^{(0\sim q_i-1)}\right)^\top P_i \begin{bmatrix} 0_{(q_n-1)\times 1} \\ g_i\xi_{i+1} \end{bmatrix} \\
\leq&\lambda_{\max}(P_i)\left(\xi_i^{(0\sim q_i-1)}\right)^\top P_i\xi_i^{(0\sim q_i-1)} \\
&+\frac{g_i^2}{4\lambda_{\min}(P_{i+1})}\left(\xi_{i+1}^{(0\sim q_{i+1}-1)}\right)^\top P_{i+1}\xi_{i+1}^{(0\sim q_{i+1}-1)}, \qquad (32)
\end{aligned}$$

$$\begin{aligned}
&\sum_{i=1}^{n-1}\left(\xi_i^{(0\sim q_i-1)}\right)^\top P_i \begin{bmatrix} 0_{(q_n-1)\times 1} \\ g_i\left(x_{(i+1)c}-\alpha_i\right) \end{bmatrix} \\
\leq&\sum_{i=1}^{n-1}\left(\xi_i^{(0\sim q_i-1)}\right)^\top P_i \begin{bmatrix} 0_{(q_n-1)\times 1} \\ |g_i|\Delta_0 \end{bmatrix} \\
\leq&\sum_{i=1}^{n-1}\lambda_{\max}(P_i)\left(\xi_i^{(0\sim q_i-1)}\right)^\top P_i\xi_i^{(0\sim q_i-1)} \\
&+(n-1)\sum_{i=1}^{n-1}\frac{|g_i|^2\Delta_0^2}{4}, \qquad (33)
\end{aligned}$$

and it directly derives that

$$\begin{aligned}
&-\sum_{i=1}^{n}\left(\xi_i^{(0\sim q_i-1)}\right)^\top P_i \begin{bmatrix} 0_{(q_n-1)\times 1} \\ \sum_{k=1}^{q_i} l_{i,k}\mathrm{sign}\left(\xi_i^{(k-1)}\right) \end{bmatrix} \\
=&-\sum_{i=1}^{n}\left(\xi_i^{(0\sim q_i-1)}\right)^\top P_{iL}\begin{bmatrix} l_{i,1} & \cdots & l_{i,q_i} \end{bmatrix} \\
&\times\begin{bmatrix}\mathrm{sign}(\xi_i) & \cdots & \mathrm{sign}\left(\xi_i^{(q_i-1)}\right)\end{bmatrix}^\top \\
\leq&-\sum_{i=1}^{n}\varepsilon_P P_{iL}^\top P_{iL}\frac{1}{\lambda_{\max}\left(P_i^{\frac{1}{2}}\right)}\left(\left(\xi_i^{(0\sim q_i-1)}\right)^\top P_i\left(\xi_i^{(0\sim q_i-1)}\right)\right)^{\frac{1}{2}} \\
\leq&-\tilde{\lambda}_P l_{\min}\sum_{i=1}^{n}\sqrt{2}\left(\frac{1}{2}\left(\xi_i^{(0\sim q_i-1)}\right)^\top P_i\xi_i^{(0\sim q_i-1)}\right)^{\frac{1}{2}} \\
\leq&-\sqrt{2}\tilde{\lambda}_P l_{\min}\left(\sum_{i=1}^{n}\frac{1}{2}\left(\xi_i^{(0\sim q_i-1)}\right)^\top P_i\xi_i^{(0\sim q_i-1)}\right)^{\frac{1}{2}} \\
=&-\sqrt{2}\tilde{\lambda}_P l_{\min}V_\xi^{\frac{1}{2}} \qquad (34)
\end{aligned}$$

where $\varepsilon_P > 0$, $\tilde{\lambda}_P = \min_i \frac{1}{\lambda_{\max}\left(P_i^{\frac{1}{2}}\right)}$, $\varepsilon_P P_{iL} = \begin{bmatrix} l_{i,1} & \cdots & l_{i,q_i}\end{bmatrix}^\top$ and $l_{\min} = \min_i \varepsilon_P P_{iL}^\top P_{iL}$. Above all, it follows that

$$\begin{aligned}
\dot{V}_\xi \leq&-\frac{1}{2}\sum_{i=1}^{n}\mu_i\left(\xi_i^{(0\sim q_i-1)}\right)^\top P_i\xi_i^{(0\sim q_i-1)}-\sqrt{2}\tilde{\lambda}_P l_{\min}V_\xi^{\frac{1}{2}} \\
&-2\lambda_{\max}(P_i)\sum_{i=1}^{n}\left(\xi_i^{(0\sim q_i-1)}\right)^\top P_i\xi_i^{(0\sim q_i-1)}+\sum_{i=1}^{n-1}\frac{|g_i|^2\Delta_0^2}{4} \\
\leq&-\frac{1}{2}\sum_{i=1}^{n-1}\left(\mu_i-4\lambda_{\max}(P_i)\right)\left(\xi_i^{(0\sim q_i-1)}\right)^\top P_i\xi_i^{(0\sim q_i-1)} \\
&-\frac{1}{2}\left(\mu_n-2\lambda_{\max}(P_n)\right)\left(\xi_n^{(0\sim q_n-1)}\right)^\top P_n\xi_n^{(0\sim q_n-1)} \\
&-\sqrt{2}\tilde{\lambda}_P l_{\min}V_\xi^{\frac{1}{2}}+(n-1)\sum_{i=1}^{n-1}\frac{|g_i|^2\Delta_0^2}{4} \\
\leq&-\kappa_{\xi 1}V_\xi-\kappa_{\xi 2}V_\xi^{\frac{1}{2}}+c_\xi \qquad (35)
\end{aligned}$$

where

$$\begin{aligned}
\kappa_{\xi 1}=&\min_{1\leq i\leq n-1}\left(\mu_i-4\lambda_{\max}(P_i),\mu_n-2\lambda_{\max}(P_n)\right), \\
\kappa_{\xi 2}=&\sqrt{2}\tilde{\lambda}_P l_{\min}, \\
c_\xi=&(n-1)\sum_{i=1}^{n-1}\frac{|g_i|^2\Delta_0^2}{4}.
\end{aligned}$$

According to Lemma 4, we obtain that ξ_i convergence to

$$\xi_i\leq\min\left\{\sqrt{\frac{2c_\xi}{\lambda_{\min}(P_i)(1-\theta_0)\kappa_{\xi 1}}},\sqrt{\frac{2}{\lambda_{\min}(P_i)}\left(\frac{c_\xi}{(1-\theta_0)\kappa_{\xi 2}}\right)^2}\right\} \qquad (36)$$

in finite-time

$$\begin{aligned}
T_2\leq\max\Bigg\{&\frac{2}{\theta_0\kappa_{\xi 1}}\ln\frac{\theta_0\kappa_{\xi 1}V^{\frac{1}{2}}(t_0)+\kappa_{\xi 2}}{\kappa_{\xi 2}}, \\
&\frac{2}{\kappa_{\xi 1}}\ln\frac{\kappa_{\xi 1}V^{\frac{1}{2}}(t_0)+\theta_0\kappa_{\xi 2}}{\theta_0\kappa_{\xi 2}}\Bigg\}.
\end{aligned}$$

where $0<\theta_0<1$.

From equation (13), we have

$$|S_1|\leq|v_1|+|\xi_1|, \qquad (37)$$

so we can conclude that the output tracking error can be reduced to a disc region in finite-time. ■

4 Illustrative simulations

Consider the following dynamics of the electromechanical system:

$$\begin{cases} M\ddot{q}+B\dot{q}+N\sin(q)=I \\ L\dot{I}+RI+K_B\dot{q}=V, \end{cases} \qquad (38)$$

where the definitions of q, I, V, L, R, K_B, $\Delta(t)$, M, B, N, and their value are given in [16, 20].

Comparatively, when contrasted with the conventional method that transforms system (38) into a first-order state space, this proposed HOFTCFB scheme offers a direct design approach. We express (38) in the form of (1) by designating $x_1=q$, $x_2=I$, and $u=V$ as follows:

$$\begin{cases} \ddot{x}_1=f_1\left(x_1^{(0\sim 1)}\right)+g_1\left(x_1^{(0\sim 1)}\right)x_2 \\ \dot{x}_2=f_2\left(x_k^{(0\sim q_k-1)}|_{k=1\sim 2}\right)+g_2\left(x_k^{(0\sim q_k-1)}|_{k=1\sim 2}\right)u \end{cases}$$

where $f_1=-\frac{B}{M}\dot{x}_1-\frac{N}{M}\sin(x_1)$, $f_2=-\frac{R}{L}x_2-\frac{K_B}{L}\dot{x}_1$, $g_1=\frac{1}{M}$, and $g_2=\frac{1}{L}$.

This scheme aims to facilitate the tracking of the link angular position to its desired trajectory $x_{1c}=0.5\sin(t)+0.5\sin(0.5t)$ by designing the input control voltage. The simulation parameters are set as follows: $\lambda_{1,0}=450$, $\lambda_{1,1}=8000$, $\psi_{1,0}(0)=\psi_{1,1}(0)=10$, $\gamma=3/5$, $A_1^{0\sim 1}=\begin{bmatrix}120 & 22\end{bmatrix}$, $A_2=60$, $P_1=10^{-5}\times\begin{bmatrix}273558/5 & 31118/91 \\ 31118/91 & 26091/58\end{bmatrix}$, $P_2=1$. Moreover, the simulation is initialized with $x_1(0)=\dot{x}_1(0)=x_2(0)=0.5$, $x_{2c}(0)=10$. The tracking performance and input control voltage of the proposed HOFTCFB scheme are depicted in Figs.1. The first and second subfigure of Fig.1 illustrates that the proposed HOFTCFB scheme fast and accurately achieves the trajectory tracking in finite-time. The third subfigure of Fig.1 shows that only a small control energy is needed to achieve the trajectory tracking.

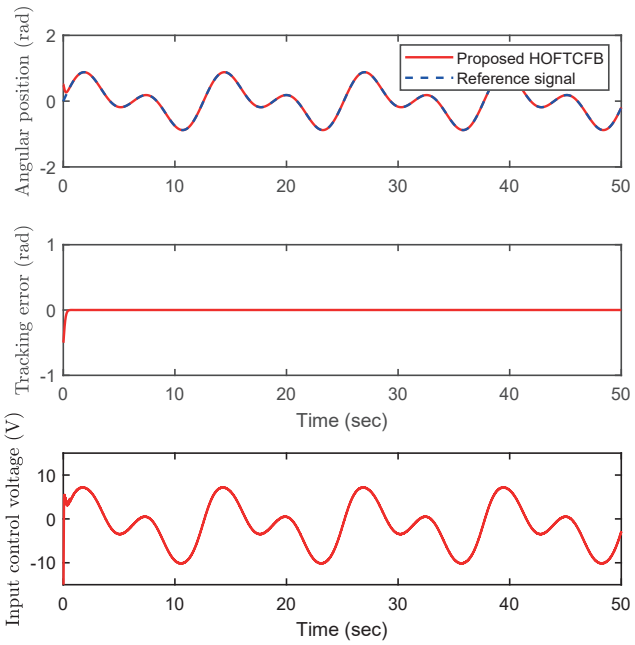

Fig. 1: Tracking performance and input control voltage of the proposed HOFTCFB scheme

5 Conclusion

This paper has proposed a new HOFTCFB scheme for finite-time tracking control of a class of HOFASFSs. The proposed HOFTCFB scheme induces a finite-time high-order Levant differentiator in the control system of each of the subsystems, guaranteeing "explosion of complexity" avoidance by estimating high-order derivatives of the virtual control law. By introducing finite-time error compensation signals, we have derived that the impact of the unachieved portion between the estimated virtual control and the actual virtual control can be minimized. Moreover, we have shown that the proposed scheme achieves the advantages of reducing backstepping steps and finite-time convergence simultaneously based on the HOFA system approaches. The theoretical analysis has shown that the closed-loop system achieves finite-time convergence and uniform ultimate boundedness under the proposed scheme. Future directions will focus on fixed-time or prescribed-time convergence under various uncertainties.

References

[1] G.-R. Duan. High-order fully actuated system approaches: Part I. Models and basic procedure. *International Journal of Systems Science*, 52(2), pp. 422–435, 2021.

[2] G.-R. Duan. Substability and substabilization: Control of sub-fully actuated systems. *IEEE Transactions on Cybernetics*, 53(11), pp. 7309–7322, 2023.

[3] Y. Yu, G.-P. Liu, Y. Huang, and J. M. Guerrero. Coordinated predictive secondary control for DC microgrids based on high-order fully actuated system approaches. *IEEE Transactions on Smart Grid*, 15(1), pp. 19–33, 2024.

[4] L. Zhang, L. Zhu, and C. Hua. Practical prescribed time control based on high-order fully actuated system approach for strong interconnected nonlinear systems. *Nonlinear Dynamics*, 110(4), pp. 3535–3545, 2022.

[5] C. Liu, X. Liu, H. Wang, Y. Zhou, and C. Gao. Adaptive control for unknown hofa nonlinear systems without over-parametrization. *International Journal of Robust and Nonlinear Control*, 33(6), pp. 3640–3660, 2023.

[6] N. Wang, X. Liu, C. Liu, and H. Wang. Weak disturbance decoupling of high-order fully actuated nonlinear systems. *International Journal of Robust and Nonlinear Control*, 34(3), pp. 1971–2012, 2024.

[7] Y. Wang, G. Duan, and P. Li. Event-triggered adaptive sliding mode control of uncertain nonlinear systems based on fully actuated system approach. *IEEE Transactions on Circuits and Systems II: Express Briefs*, 2024.

[8] R. Freeman and P. V. Kokotovic. *Robust Nonlinear Control Design: State-Space and Lyapunov Techniques*. Springer Science & Business Media, 1996.

[9] M. Krstic, P. V. Kokotovic, and I. Kanellakopoulos. *Nonlinear and Adaptive Control Design*. John Wiley & Sons, Inc., 1995.

[10] X. Zheng, X. Yu, J. Jiang, and X. Yang. Practical finite-time command filtered backstepping with its application to DC motor control systems. *IEEE Transactions on Industrial Electronics*, 71(3), pp. 2955–2964, 2024.

[11] C. Xin, Y.-X. Li, and Z. Hou. Finite time adaptive learning for tracking control of constraint nonlinear systems via command filtered output feedback. *International Journal of Robust and Nonlinear Control*, 33(7), pp. 4076–4097, 2023.

[12] W. Yang, G. Cui, Q. Ma, J. Ma, and C. Tao. Finite-time adaptive event-triggered command filtered backstepping control for a quav. *Applied Mathematics and Computation*, 423, p. 126898, 2022.

[13] Y.-X. Li. Finite time command filtered adaptive fault tolerant control for a class of uncertain nonlinear systems. *Automatica*, 106, pp. 117–123, 2019.

[14] J. Yu, P. Shi, and L. Zhao. Finite-time command filtered backstepping control for a class of nonlinear systems. *Automatica*, 92, pp. 173–180, 2018.

[15] W. Liu, G.-R. Duan, and M. Hou. High-order robust command filtered backstepping design for strict-feedback systems: A high-order fully-actuated system approach. *International Journal of Robust and Nonlinear Control*, 32(18), pp. 10251–10270, 2022.

[16] W. Liu, G.-R. Duan, and M. Hou. High-order command filtered adaptive backstepping control for second- and high-order fully actuated strict-feedback systems. *Journal of the Franklin Institute*, 360(6), pp. 3989–4015, 2023.

[17] W. Liu, G.-R. Duan, and M. Hou. Concurrent learning adaptive command filtered backstepping control for high-order strict-feedback systems. *IEEE Transactions on Circuits and Systems I: Regular Papers*, 70(4), pp. 1696–1709, 2023.

[18] G.-R. Duan. High-order fully actuated system approaches: Part III. Robust control and high-order backstepping. *International Journal of Systems Science*, 52(5), pp. 952–971, 2021.

[19] A. Levant. Higher-order sliding modes, differentiation and output-feedback control. *International Journal of Control*, 76(9-10), pp. 924–941, 2003.

[20] Y. Pan and H. Yu. Dynamic surface control via singular perturbation analysis. *Automatica*, 57, pp. 29 – 33, 2015.

Proceedings of the 3rd Conference on Fully Actuated System Theory and Applications
May 10-12, 2024, Shenzhen, China

Operational Flexibility Enhancement with Aggregated Electric Vehicles based on Virtual Energy Storage Model

Shiwei Chen[1], Hongfei Lang[1], Muchun Wan[*2], Junjun Du[1], Feng Bao[1], Guangchao Geng[2]
1. Fuyang Rongda Complete-Set Electric Equipmnent Manufacturing Branch of Hangzhou Power Equipment Manufacturing Co., Ltd., Hangzhou 311400, P. R. China
2. College of Electrical Engineering, Zhejiang University, Hangzhou 310027, P. R. China
E-mail: muchunwan@zju.edu.cn

Abstract: Distribution network (DN) operational flexibility refers to the adaptability of DNs to uncertainties in sources and loads, which is directly related to the reliability and economics of power supply. With the large-scale integration of distributed energy resources (DERs) into DNs, higher requirements are placed on the operational flexibility. As an important load component in DNs, the optimal control of electric vehicles (EVs) is the crucial mean to improve operational flexibility. However, optimizing the charging and discharging power of a large number of EVs requires a significant amount of computation time, making real-time control of EVs difficult. Therefore, this paper aggregates a large number of EVs based on a virtual energy storage model (VESM), and proposes an optimization method for the VESM to obtain its controllable power and capacity limits. In order to reduce computation time, an online tracking method of the controllable power and capacity without re-solving the optimization model is proposed. Finally, the effectiveness of the VESM and proposed online tracking method are verified in both residential and workplace area by case studies.

Key Words: Electric vehicles, Operational flexibility, Online tracking, Virtual energy storage model

1 Introduction

Energy is the everlasting cornerstone of modern society. In recent years, with the gradual depletion of fossil fuels and global advocacy for decarbonization, renewable energy has been vigorously promoted. According to data from [1], the proportion of wind and solar power in the world's total electricity generation has risen from 10% in 2021 to 12% in 2022. Renewable energy has changed the pattern of centralized power supply in traditional power systems, with an increasing number of renewable energy sources being integrated as distributed energy resources (DERs) into low-voltage distribution networks (DNs), with rooftop solar panels being a typical example [2]. According to the "REPowerEU Plan" proposed by the European Union, it is expected that rooftop solar panels can meet nearly 25% of Europe's power consumption in the future [3].

However, as DERs rapidly integrates into DNs, it brings about challenges to the operational flexibility. For DNs, DERs have multiple uncertainties such as power, quantity and location, which may pose new challenges to operational management and safety stability [4]. Electric vehicles (EVs), as an important component of loads in DNs, optimizing and controlling their charging and discharging power is an important mean to improve the operational flexibility of DNs.

In recent years, the development of EVs has been rapid. According to data from [5], EV sales surpassed 10 million in 2022, with an anticipated increase to 14 million by the end of 2023. Against the backdrop of a large number of EVs being connected to the DNs, the uncontrolled peak load caused by their charging behavior is likely to exceed the transformer capacity, posing a threat to the safe operation of the DNs [6]. Therefore, how to aggregate and control the charging and discharging power of EVs has become a key factor in improving the operational flexibility of DNs.

Currently, there are numerous researches on enhancing the operational flexibility of DNs through the aggregated control of EVs. Reference [7] investigated the optimization of EVs charging to improve the voltage distribution in low-voltage DNs and enhance their operational flexibility. Similarly, reference [8] explored the optimization of voltage distribution in medium-voltage DNs by incorporating photovoltaic generators and EVs charging stations. The effectiveness of the approach was demonstrated using the 123-bus test feeder. In the context of large-scale EVs integration into DNs, reference [9] proposed a robust operation method to mitigate the adverse effects brought about by the integration of a large number of EVs, thus improving the operational flexibility of the DNs. Furthermore, reference [10] provided a comprehensive review of EVs' participation in enhancing the operational flexibility of DNs from technical, economic, regulatory and user perspectives. It also presentd a potential value framework for implementation.

However, existing research has proposed optimal control methods for aggregated EVs, but lacks the establishment of a unified aggregated EVs model to enhance the operational flexibility of the DNs, and also lacks consideration for long computation time. To address these issues, this paper proposes an aggregated real-time tracking control method for large numbers of EVs based on virtual energy storage model (VESM). Firstly, a VESM consists of aggregated EVs is proposed to obtain the overall controllable power and capacity. Considering the presence of large numbers of EVs in the VESM, each optimization process takes a significant amount of time, making real-time tracking difficult. Therefore, a online tracking method is proposed. This method allows for online tracking of the controllable power and capacity of the VESM without re-solving the optimization model, thereby reducing the computation time. Finally, the proposed VESM and online tracking method are validated by using real data cases. The results of the case study demonstrate that the

This work is supported by Fuyang Rongda Complete-Set Electric Equipmnent Manufacturing Branch of Hangzhou Power Equipment Manufacturing Co., Ltd. (YF231701)

proposed VESM and online tracking method can effectively calculate the controllable power and capacity while significantly reducing the computation time. The main contribution of this paper are summarized as follows:

- A VESM-based aggregated control optimization model for EVs is proposed, which can accurately calculate the controllable power and capacity under the current state, providing a basis for optimal control of EVs.
- An online tracking method is proposed, which can calculate the real-time controllable power and capacity without re-solving the optimization model, thereby reducing the computation time.

The rest of the paper is organized as follows: Section 2 proposes an aggregated EVs optimization model based on VESM to obtain its controllable power and capacity. Section 3 proposes an online tracking method, which can provide real-time tracking of the controllable power and capacity of the VESM. Section 4 validates the effectiveness of the VESM and online tracking method through real data cases. Section 5 summarizes the paper.

2 Virtual Energy Storage Model

In this section, a VESM consists of aggregated EVs is proposed. According to the mathematical model of VESM, the optimization model can be solved to obtain the upper and lower limits of the controllable power and capacity under the specific time.

2.1 Concept

Under common circumstances, the charging time of EVs probably exceeds their actual charging requirement, allowing for flexible adjustment of the charging load [11]. The emergence of Vehicle-to-Grid (V2G) technology further enables EVs to not only consume energy as a load but also feed energy back into the grid. This dual characteristic of electricity generation and consumption makes EVs capable of being dispatched by the grid, akin to real energy storage, hence referred to as VESM [12].

However, individual EV possesses limited control capabilities over the grid. Therefore, in order to fully utilize the energy storage characteristics of EVs during idle periods, it is necessary to aggregate a large number of EVs through VESM to participate in the grid's macroscopic control such as peak shaving, frequency regulation, load shifting and power supply assurance [13].

In the VESM, EVs are considered as DERs that can function as battery storage devices for storing and releasing electricity. The advantages of the VESM lie in its flexibility and scalability. However, due to the uncontrollability of individual EV's behavior, there are uncertainties regarding the capacity and controllable power of VESM. For a VESM composed of a large number of EVs, the power grid is concerned with the overall controllable power and the state of charge (SOC), rather than individually. The variations in the overall charging and discharging power and SOC of the VESM can be described as (1).

$$C_{ves}^{t} SOC_{ves}^{t} = C_{ves}^{t-1} SOC_{ves}^{t-1} + \left(P_{ch}^{t-1} - P_{dh}^{t-1}\right) \Delta T \quad (1)$$

where, for a VESM, C_{ves}^{t} represents the capacity at time t, SOC_{ves}^{t} represents the SOC at time t, P_{ch}^{t} represents the overall charging power at time t, P_{dh}^{t} represents the overall discharging power at time t, ΔT represents the time interval.

2.2 Mathematical Model

The mathematical model of VESM can be proposed. The VESM consists of two levels of control, namely the overall and individual levels. For the power grid, the overall level is of concern, while for the EV owners, the individual level is of concern. The VESM needs to achieve coordination between the overall and individual levels in order to meet the needs of both parties.

From the overall level, the number of EVs in the VESM may change at any time due to the arrival or departure of EVs. Therefore, the capacity and SOC of the VESM will be updated at time t when an EV arrives or departs. The updating formula can be described as (2) and (3), and the overall charging and discharging power along with SOC changes can be described as (1).

$$C_{ves}^{t} = C_{ves}^{t-1} + \sum_{i=1}^{A^{t-1}} C_{i}^{t-1} - \sum_{j=1}^{D^{t-1}} C_{j}^{t-1} \quad (2)$$

$$\begin{aligned} C_{ves}^{t} SOC_{ves}^{t} =& C_{ves}^{t-1} SOC_{ves}^{t-1} + \sum_{i=1}^{A^{t-1}} C_{i}^{t-1} SOC_{i}^{t-1} \\ & - \sum_{j=1}^{D^{t-1}} C_{j}^{t-1} SOC_{j}^{t-1} \end{aligned} \quad (3)$$

where, C_{i}^{t-1} represents the capacity of individual EV at time $t-1$, SOC_{i}^{t-1} represents the SOC of individual EV at time $t-1$, A^{t-1} represents the arrive car numbers at time $t-1$, D^{t-1} represents the depart car numbers at time $t-1$.

From the individual level, the overall charging and discharging power of the VESM needs to be decomposed into specific power values for each EV, while meeting the usage requirements of each EV owner. Therefore, the power assigned to each EV needs to be calculated based on its specific information. The charging power value for an individual EV can be described as (4) and (5), and the discharging power is similar.

$$P_{ch}^{t} = \sum_{i=1}^{N} P_{ch}^{i,t} \quad (4)$$

$$\min(P_{ch}^{i,t}) \leq P_{ch}^{i,t} \leq \max\left(P_{ch}^{i,t}\right) \quad (5)$$

where, $P_{ch}^{i,t}$ represents the decomposed charging power of individual EV at time t, $\min(P_{ch}^{i,t})$ represents the minimum limit charging power of individual EV at time $t-1$, $\max\left(P_{ch}^{i,t}\right)$ represents the maximum limit charging power of individual EV at time $t-1$.

It is worth noting that the maximum and minimum limit of the charging and discharging power reflect the upper and lower limits of the controllable power for the individual EV at the current time, which can be aggregated to the controllable power and capacity of the overall VESM.

2.3 Controllable Power and Capacity

For the VESM, the controllable power and capacity represent its regulation ability at the moment, which is the most concerned issue for the power grid. The controllable power

and capacity of the VESM can also be divided into two levels: the overall level and individual level.

For the overall level, the controllable power and capacity are aggregated from each EV's. Therefore, obtaining the controllable power and capacity of each individual EV is the key step. For each individual EV, its controllable power and capacity at the current moment, while meeting the EV owner's usage requirements, can be modeled as an optimization problem, which can be mathematically described as (6) and (7). In this model, there are 5 constraints considered, including the SOC safety constraint, the maximum and minimum charging or discharging power limits, the SOC change limit and the owner's target SOC requirement limit.

$$\begin{aligned} F_{low} &= \min \sum_{T=t}^{k} SOC^t \\ F_{up} &= \max \sum_{T=t}^{k} SOC^t \end{aligned} \tag{6}$$

$$s.t. \begin{cases} SOC_{\min} \le SOC^t \le SOC_{\max} \\ P^t_{ch\,\min} \le P^t_{ch\,\max} \le P_{ch\,\max} \\ P^t_{dh\,\min} \le P^t_{dh} \le P^t_{dh\,\max} \\ SOC^t = SOC^{t-1} + (P^{t-1}_{ch} - P^{t-1}_{dh})\Delta T/C \\ SOC^k \ge SOC_{target} \end{cases} \tag{7}$$

where, F_{low} represents the objective function of lower controllable power and capacity of individual EV, while F_{up} represents the upper. t represents the current time, k represents the depart time, SOC_{target} represents the owner's target SOC when departing.

Taking an individual EV at time t as example, the optimization model described above is used to obtain its regulation upper and lower limits that meet the owner's requirements, as shown in Fig 1. By aggregating the regulation upper and lower limit curves of all EVs in the VESM, the overall regulation upper and lower limit curve can be obtained.

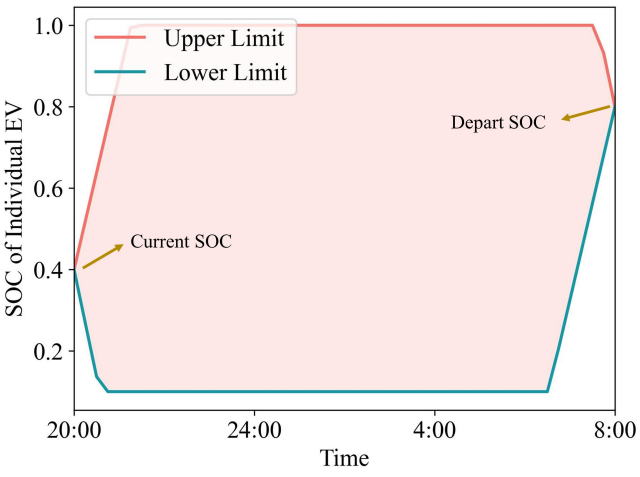

Fig. 1: The regulation limits of individual EV.

3 Online Tracking for Power and Capacity

In Section 2, a VESM consists of aggregated EVs is proposed. However, when there are a large number of EVs in the VESM, solving it requires a significant amount of time, making it impractical to achieve real-time tracking of controllable power and capacity [14]. To address this issue, Section 3 proposes an online tracking method, which can greatly reduce the computation time.

3.1 Theoretical Basis

The VESM is affected by various factors, including the number of EVs, SOC, arrival and departure time. These factors are time variant, which leads to time variant controllable power and capacity of the VESM [15]. When there are a large number of EVs, solving the optimization model at each time step requires a significant amount of time.

To address the issue of long computation time, a novel online tracking method based on optimal sensitivity is proposed. The mathematical model of optimal sensitivity can be referred to in [16]. With the optimal sensitivity $\frac{df}{dx}$, for the time instant $(t + \nabla T)$ in the vicinity of time t, its controllable power and capacity do not need to be resolved, but can be directly estimated by (8).

$$f(x + \Delta x) = f(x) + \frac{df}{dx}\Delta x \tag{8}$$

where, $f(x + \Delta x)$ represents the controllable power or capacity in the time $(t + \nabla T)$, while $f(x)$ represents the value in time t. $\frac{df}{dx}$ represents the optimal sensitivity, Δx represents the change of time variant factors.

By employing this online tracking method based on optimal sensitivity, it is possible to achieve rapid optimization of VESM with a large number of EVs connected, while sacrificing a minimal amount of accuracy.

3.2 Online Tracking Method

Combining the VESM proposed in Section 2 with the optimal sensitivity proposed in Section 3, an online tracking method can be proposed. This method aims to quickly calculate the current controllable power and capacity of the VESM with high accuracy.

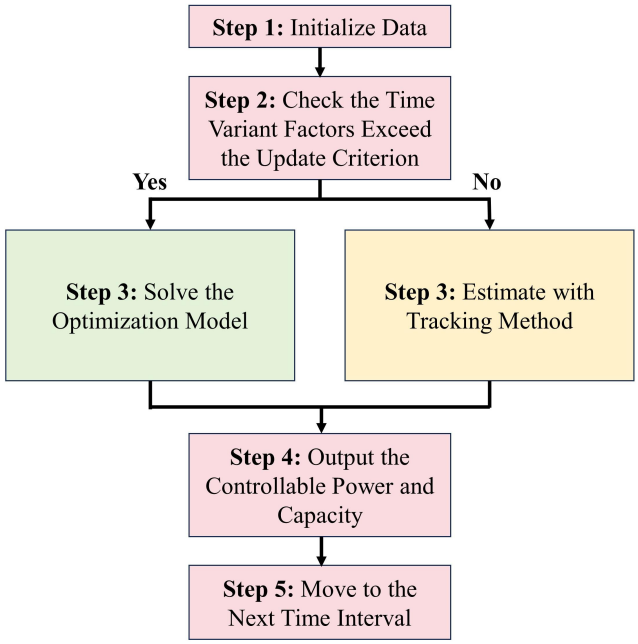

Fig. 2: Online tracking method.

When the time variant factors are below the update criterion, the online tracking method is used for calculation. When the time variant factors exceed the threshold of the update criterion, it is necessary to resolve the optimization model. This method can significantly reduce the number of times the optimization model is solved, thereby reducing computation time. The flowchart of the online tracking method is shown in Fig 2.

4 Case Study

This section validates the proposed VESM from Section 2 and the online tracking method proposed in Section 3 by using real data cases.

4.1 Data Preparation

The data used in this case study is partially provided by the power company of Hangzhou. The data includes the capacity, maximum charging and discharging power, arrival time, departure time, initial SOC and target SOC for each EV. The data consists of 100 EVs and is recorded at a time interval of 15 minutes. This representative dataset can accurately reflects the collective behavior of EVs.

4.2 Aggregated Results using VESM

For the VESM, it is necessary to analyze from both individual and overall levels.

Firstly, the individual level analysis is focused. At any given time t, the state of each EV needs to be solved by an optimization model. Taking the i-th EV as an example, it has a capacity of 60 kWh and a maximum charging and discharging power of ±30 kW. At 20:00, its SOC is 0.4, with an expected departure time the next day at 8:00 and a target SOC of 0.9. Therefore, for this specific time, the controllable power and capacity of the i-th EV are illustrated in Fig 3.

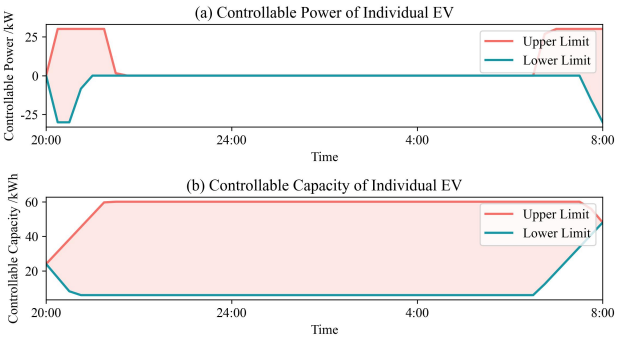

Fig. 3: Controllable power and capacity of individual EV.

It is worth noting that the controllable power and capacity curve in Fig 3 is only applicable to the i-th EV at that particular time 8:00. In subsequent time intervals, recomputing the optimization model based on the actual conditions is necessary. This requirement holds true for each EV and every time interval within the VESM, resulting in a significant computation burden.

Next, the overall level analysis is focused. In fact, the controllable power and capacity at the overall level are similar to the individual level. Considering that the charging and discharging power of each EV can be independently controlled, the controllable power and capacity at the overall level represent the sum of all individual EVs within the VESM. For a specific time interval, the controllable power and capacity for the entire day are illustrated in Fig 4. Similarly, this curve is only valid for that specific time interval, and subsequent time intervals require recalculations.

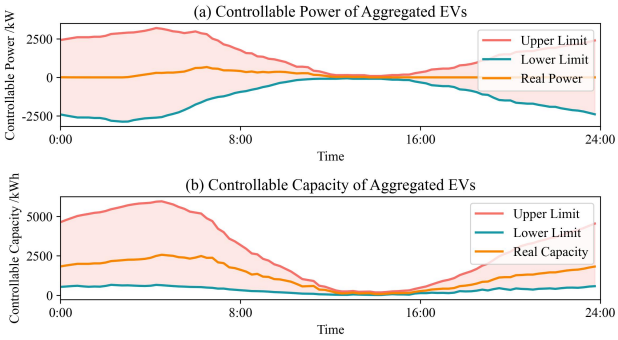

Fig. 4: Controllable power and capacity of aggregated EVs.

The behavior of EVs is closely related to the daily routines of residents. By analyzing Fig 4, it can be observed that the controllable power and capacity of the VESM start to increase around 18:00, reach peak during the early hours of 4:00 and gradually decrease around 8:00 the next day. This pattern can be explained by the fact that this particular day represents a typical workday, and most residents return to their community after 18:00. As a result, the majority of EVs are already fully charged during the early morning hours, leading to the peak in controllable power and capacity. The following morning, when residents have to go to work, a significant number of EVs leave, causing a decrease in controllable power and capacity.

The middle curve in the Fig 4 (a) represents the real control power exerted by the power grid. This control power and capacity are subject to real-time variations, necessitating the real-time solution of an optimization model. In this case study, which involves 100 EVs, the average solving time is 7.82 seconds. However, during the early morning period when a large number of EVs are optimized, the solving time may reach its maximum at 31.27 seconds, posing challenges for real-time tracking of the controllable power and capacity of the VESM.

4.3 Online Tracking Results 1: Residential Area

In order to address the issue of long optimization model solving time in the context of a large number of EVs being connected, an online tracking method, as proposed in Section 3, is employed for analysis by using this case study in residential area.

For this case study, time variant factors include the SOC for each EV in the aggregated model. After multiple experiments, it was determined that a preferable update criterion is $SOC(t+1) - SOC(t) \leq 5\%$. Under this update criterion, the VESM's controllable power and capacity upper or lower limit curves are shown in Fig 5, obtained by using the online tracking method and point-to-point optimization method respectively.

Based on the analysis of Fig 5, it can be observed that the controllable power and capacity upper or lower limit curves obtained from the online tracking method are close to

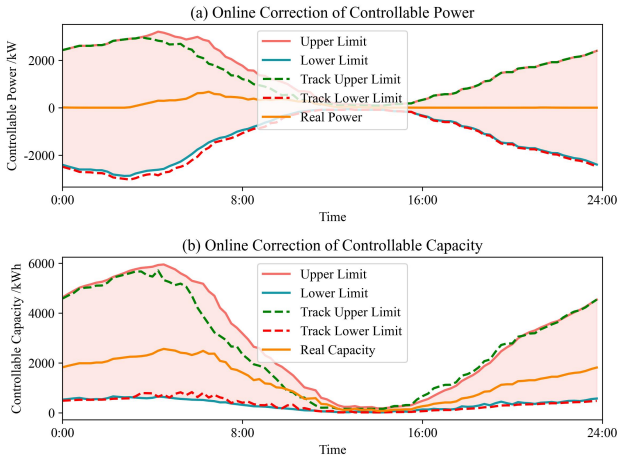

Fig. 5: Online correction results 1.

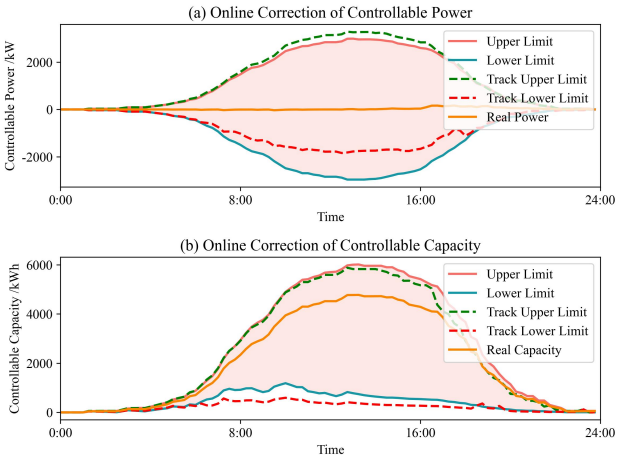

Fig. 6: Online tracking results 2.

those obtained from the point-to-point optimization method, which demonstrates the accuracy of the online tracking method. By employing the online tracking method, the max computation time during the large-scale EVs charging at early morning can be reduced from 31.27 seconds to 7.99 seconds, and the overall computation time can be reduced from 1501.44 seconds to 368.53 seconds, while ensuring the accuracy. The computation time comparison between the online tracking method and the point-to-point optimization method is presented in Table 1.

Table 1: Computation time comparison 1.

Approach	Max Computation Time	Counts	Total Time
Point-to-Point	$31.27s$	4732	$1501.44s$
Online Tracking	$7.99s$	557	$368.53s$

It is evident that the counts for solving the optimization model by using the online tracking method is much less than the point-to-point optimization method, resulting in a 407.88% increase in the overall computation speed.

4.4 Online Tracking Results 2: Workplace Area

The locations where aggregated EVs participate in power grid regulation are diverse. In addition to the residential area mentioned in Section 4.3, the workplace is also a hotspot for idle EVs participation in the VESM. EV owners typically commute to their workplaces in the morning and return home in the evening. In this scenario, EVs also experience long periods of idle time and should therefore be included as case study for analysis.

For this case in the workplace area, the controllable power and capacity of the VESM, as well as the performance of online tracking, are shown in Fig 6. The comparison of computation time between the online tracking method and the point-to-point optimization method is presented in Table 2.

As can be seen, the controllable power and capacity of the VESM increase around 8:00, reach their peak around 12:00, and decrease around 18:00. Similarly, this is closely related to the behavior of EV owners. For the workplace area, EV owners typically commute to work in the morning and return home in the evening.

From Table 2, it can be observed that by employing the online tracking method proposed in Section 3, the maximum computation time of VESM is reduced from 30.68 seconds to 5.08 seconds. The number of solving the optimization model is decreased from 4152 to 175, and the total computation time is reduced from 1248.84 seconds to 116.38 seconds. This case study conducted in the workspace further demonstrate the accuracy and effectiveness of the online tracking method.

Table 2: Computation time comparison 2.

Approach	Max Computation Time	Counts	Total Time
Point-to-Point	$30.68s$	4152	$1248.84s$
Online Tracking	$5.08s$	175	$116.38s$

5 Conclusion

Based on the background that the operation flexibility of the DNs is affected by the large-scale access of DERs, this paper aims to improve the operation flexibility of the DNs by aggregating EVs for regulation.

First, a VESM consists of aggregated EVs is proposed, which is mathematically modeled at both the overall and individual levels to obtain its controllable power and capacity. However, when the number of EVs in VESM is large, the optimization model has long solution time and cannot achieve real-time tracking of the controllable power and capacity.

Furthermore, to address the problem of long computation time, a online tracking method is proposed. Then, the flowchart of online tracking method is presented.

Finally, the effectiveness of the proposed VESM and online tracking method is validated by using real data from both residential area and workplace area. It can achieve online tracking of the controllable power and capacity of the VESM in short time with high accuracy, provide basis for the regulation of DNs, and thus improve the operation flexibility.

References

[1] Małgorzata Wiatros Motyka, "Global electricity review 2023," tech. rep., Ember, 2023.

[2] J. Byrne, J. Taminiau, L. Kurdgelashvili, and K. N. Kim, "A review of the solar city concept and methods to assess rooftop

solar electric potential, with an illustrative application to the city of Seoul," *Renewable and Sustainable Energy Reviews*, vol. 41, pp. 830–844, 2015.

[3] R. Vezzoni, "Green growth for whom, how and why? The REPowerEU Plan and the inconsistencies of European Union energy policy," *Energy Research & Social Science*, vol. 101, p. 103134, 2023.

[4] H. Yu, J. Zhang, J. Ma, C. Chen, G. Geng, and Q. Jiang, "Privacy-preserving demand response of aggregated residential load," *Applied Energy*, vol. 339, p. 121018, 2023.

[5] International Energy Agency, "Global EV outlook 2023," tech. rep., IEA, 2023.

[6] H. Yu, C. Xu, W. Wang, G. Geng, and Q. Jiang, "Communication-free distributed charging control for electric vehicle group," *IEEE Transactions on Smart Grid*, pp. 1–1, 2023. to appear.

[7] K. D., A. S. Bouhouras, I. Skalidi, P. Gkaidatzis, N. Poulakis, and G. Christoforidis, "EV flexibility contribution to distribution network operation," in *The 12th Mediterranean Conference on Power Generation, Transmission, Distribution and Energy Conversion (MEDPOWER 2020)*, vol. 2020, pp. 348–353, 2020.

[8] M. De Santis, A. R. Di Fazio, M. Russo, T. Harighi, and A. Borghetti, "Voltage optimization in distribution networks using EV parking lots and PV systems as flexibility options," in *2023 IEEE International Conference on Environment and Electrical Engineering and 2023 IEEE Industrial and Commercial Power Systems Europe (EEEIC / I&CPS Europe)*, pp. 1–6, 2023.

[9] J. Zhao, J. Qu, H. Ji, J. Xu, H. M. Hasanien, R. A. Turky, and P. Li, "Robust operation of flexible distribution network with large-scale EV charging loads," *IEEE Transactions on Transportation Electrification*, pp. 1–1, 2023.

[10] F. Gonzalez Venegas, M. Petit, and Y. Perez, "Active integration of electric vehicles into distribution grids: Barriers and frameworks for flexibility services," *Renewable and Sustainable Energy Reviews*, vol. 145, p. 111060, 2021.

[11] Y. Tao, M. Huang, Y. Chen, and L. Yang, "Orderly charging strategy of battery electric vehicle driven by real-world driving data," *Energy*, vol. 193, p. 116806, 2020.

[12] J. Mitra and N. Nguyen, "Grid-scale virtual energy storage to advance renewable energy penetration," *IEEE Transactions on Industry Applications*, vol. 58, no. 6, pp. 7952–7965, 2022.

[13] X. Yang and Y. Zhang, "A comprehensive review on electric vehicles integrated in virtual power plants," *Sustainable Energy Technologies and Assessments*, vol. 48, p. 101678, 2021.

[14] T. Mao, X. Zhang, and B. Zhou, "Intelligent energy management algorithms for EV-charging scheduling with consideration of multiple EV charging modes," *Energies*, vol. 12, no. 2, 2019.

[15] A. Alahyari, M. Ehsan, and M. Mousavizadeh, "A hybrid storage-wind virtual power plant (VPP) participation in the electricity markets: A self-scheduling optimization considering price, renewable generation, and electric vehicles uncertainties," *Journal of Energy Storage*, vol. 25, p. 100812, 2019.

[16] K. Zhang, G. Geng, and Q. Jiang, "Online tracking of reactive power reserve for wind farms," *IEEE Transactions on Sustainable Energy*, vol. 11, no. 2, pp. 1100–1102, 2020.

Proceedings of the 3rd Conference on Fully Actuated System Theory and Applications
May 10-12, 2024, Shenzhen, China

Robotic Manipulator Control Based on Disturbance Observer: A High-Order Fully Actuated System Approach

Yuebin Qiu, Shijie Zhang*, Xiang Wu, Hui Zhang, Tianle Yang
1. College of Electrical Engineering, Henan University of Technology, Zhengzhou 450001, P. R. China
E-mail: yuebin. qiu@stu. haut. edu. cn, zhangshijie@haut. edu. cn

Abstract: This paper focuses on the trajectory tracking control of a multi-degree-of-freedom manipulator system. Firstly, the actuator model is introduced into the manipulator system to generate a cascaded system , so as to avoid the negative impact of control for the actuator itself on the tracking accuracy of the system. Then, the trajectory tracking controller is designed based on the high-order fully actuated (HOFA) system approach to make the manipulator reach the desired position with high accuracy. Then, a universal nonlinear disturbance observer (UNDO) designed to compensate for the internal and external uncertainty in practical manipulator systems. Finally, a tracking differentiator (T-D) is employed to obtain the acceleration signal of the manipulator, avoiding the use of expensive acceleration sensors in the construction of the trajectory tracking controller and nonlinear disturbance observer. Simulation results reveal the effectiveness of the proposed method.

Key Words: High-order systems, fully-actuated systems, parametric approaches, fully-measured systems, disturbance observer

1 Introduction

With the development of the robotics industry, robotic manipulators have been applied in various fields, including industrial production, healthcare, military, aerospace, and more[1–3]. However, due to strong coupling, nonlinearity, and the presence of internal and external uncertainties in robotic manipulator systems, it is difficult to build an accurate dynamic model for the manipulator. Consequently, controlling robotic manipulator systems poses a significant challenge. To ensure precise trajectory tracking by robotic manipulators, the development of advanced control methods for robotic manipulator systems is essential.

The trajectory tracking accuracy of a robotic arm reflects its overall performance to a certain extent. In order to enable it to smoothly and precisely track the desired operational trajectory, various relevant control methods have been proposed to address the dynamic and steady-state performance requirements of the robotic manipulator under different conditions. For the trajectory tracking control of robotic arms, commonly used methods include PID control[4], adaptive control[5], sliding mode control[6], neural network control[7], and fuzzy control[8]. PID control is a model-independent control method, which is simple to design, but it is difficult to meet the performance requirements of the robotic manipulator system, whereas the model-dependent control method generally adopts the first-order state-space model as the object of study, and the control accuracy can meet the requirements of the system, but due to the complexity of the dynamics model of the robotic manipulator, the control rate obtained by this type of method may be more complicated. Based on the above considerations, this paper chooses the high-order fully actuated system approach proposed in the recent series of papers[9–18]for the controller design of the robotic manipulator system.

The high-order fully actuated system approach has attracted significant attention since its introduction. For example, the reference [19] studied the attitude tracking control for spacecraft by fully-actuated system approach. In [20], a design method for an angular acceleration observer is proposed based on the high-order fully actuated system approach. In [21], the fully actuated mathematical model of the LCL grid-connected inverter is established, and its control strategy is derived. There is relatively limited research on controlling robotic manipulator based on the fully actuated system approach. Therefore, the main contributions of this paper lie in the design of a universal nonlinear disturbance observer and a trajectory tracking controller within the framework of the high-order fully actuated system approach. This enables the cascaded system composed of the robotic manipulator and the actuator to accurately track the target trajectory. Additionally, a tracking differentiator is introduced to facilitate the acquisition of the acceleration signal in the robotic manipulator system.

The organization of this paper is as follows. The cascaded system model of the actuator and manipulator is given in Section 2. A trajectory tracking controller is designed based on the high-order fully actuated system approach in Section 3. In the following chapter, a universal nonlinear disturbance observer and a tracking differentiator are designed. Section 5 shows the effectiveness of the proposed design method by performing simulations on a two-link robotic manipulator. Finally, the conclusion is presented in the last section.

2 Modeling of Cascaded Systems

In this section, a cascaded model of a n-DOF manipulator is established[22].

2.1 Dynamic Model of the Manipulator

The dynamic model of the n-DOF manipulator is as follows

$$M(q(t))\ddot{q}(t) + C(q(t), \dot{q}(t))\dot{q}(t) + G(q(t)) = \tau(t) + \tau_d(t), \tag{1}$$

where $\tau(t) \in \mathbf{R}^n$ is the control vector produced by the motors at the joint, $q(t) \in \mathbf{R}^n$, $\dot{q}(t) \in \mathbf{R}^n$ and $\ddot{q}(t) \in \mathbf{R}^n$ represent the position, velocity, and acceleration vectors of each joint, respectively. $M(q(t)) \in \mathbf{R}^{n\times n}$ is the symmetric and positive definite robot inertia matrix, $C(q(t), \dot{q}(t)) \in \mathbf{R}^{n\times n}$ comprises the Coriolis and centrifugal effects, and $G(q(t))$ is the gravity vector. The vector $\tau_d(t)$ denotes the unknown bounded disturbance.

2.2 Actuator Model

The model of the actuator can be expressed by the following first-order model

$$\dot{\tau}(t) = f\left(\tau(t), t\right) + u(t), \tag{2}$$

where $\tau(t)$ represents the actuator's output torque vector, $f(\tau(t), t)$ denotes some vector function of dimension n, and $u(t)$ is the driving control vector, which is often a voltage vector. In many cases, the above model can be replaced with the linear one

$$\dot{\tau}(t) = A_a\tau(t) + u(t), \tag{3}$$

with A_a, being coefficient matrice of dimension $n \times n$.

A typical approach to realizing control of the cascaded system is to first reduce the system into a first-order state space form and then apply control techniques to the first-order system. Eventually, a first-order system of dimension $3n$ needs to be dealt with. In contrast to this, in this paper we apply the high-order fully actuated(HOFA) system approach. For simplicity, the first-order linear model (3) is used in this paper.

2.3 Integrated High-order Model

Differentiate the dynamic model (1) of the n-DOF manipulator with respect to both ends and combine Equation (3), we can obtain the following third-order model for the cascaded system:

$$\begin{aligned} &A_3(q,\dot{q},\ddot{q})\dddot{q}(t) + A_2(q,\dot{q},\ddot{q})\ddot{q}(t) + A_1(q,\dot{q},\ddot{q})\dot{q}(t) \\ &\quad + A_0(q,\dot{q},\ddot{q})q(t) = u(t) + d(t), \end{aligned} \tag{4}$$

where

$$A_3(q,\dot{q},\ddot{q}) = M(q(t)), \tag{5}$$

$$A_2(q,\dot{q},\ddot{q}) = \frac{\mathrm{d}M(q(t))}{dt} + C(q(t),\dot{q}(t)) - A_aM(q(t)), \tag{6}$$

$$A_1(q,\dot{q},\ddot{q}) = \frac{\mathrm{d}C(q(t),\dot{q}(t))}{dt} - A_aC(q(t),\dot{q}(t)), \tag{7}$$

$$A_0(q,\dot{q},\ddot{q}) = 0, \tag{8}$$

$$d(t) = \frac{\mathrm{d}\tau_d(t)}{dt} - A_a\tau_d(t) - \frac{\mathrm{d}G(q(t))}{dt} + A_aG(q(t)). \tag{9}$$

According to the theory of the high-order fully actuated system, it can be concluded that the above cascaded system model (4) satisfies the fully-actuated characteristic and can be designed using the direct parameter method for controller.

3 Controller Design

Figure 1 shows the structure diagram of the third-order fully actuated control system for the manipulator. As shown in the figure, we design a controller which is composed of two parts:

$$\begin{cases} u = u_c + u_f, \\ u_c = -d(t), \\ u_f = K_0(q,\dot{q},\ddot{q})q(t) + K_1(q,\dot{q},\ddot{q})\dot{q}(t) \\ \qquad +K_2(q,\dot{q},\ddot{q})\ddot{q}(t) + v, \end{cases} \tag{10}$$

where u_c is used to compensate for the influence of the system modeling uncertainty and disturbance on the cascaded

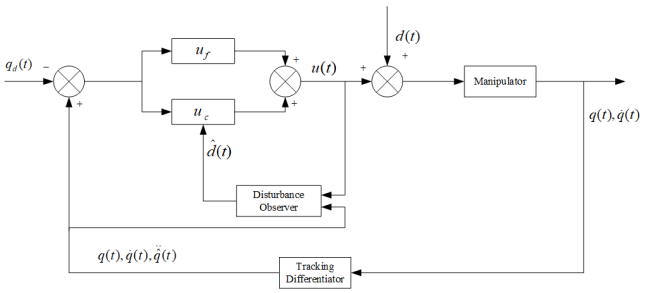

Fig. 1: The structure diagram of the high-order control system for the manipulator.

system, u_f is feedback controller designed by the direct parametric approach, $K_i(q,\dot{q},\ddot{q}) \in \mathbf{R}^{n\times n}, i = 0,1,2$ are the feedback gains to be designed, and v is an external signal.

Applying this controller to the fully-actuated system (4), the closed-loop system can be derived as follows:

$$\begin{aligned} &A_3\left(q,\dot{q},\ddot{q}\right)\dddot{q}\left(t\right) + A_2^c\left(q,\dot{q},\ddot{q}\right)\ddot{q}(t) \\ &\quad + A_1^c\left(q,\dot{q},\ddot{q}\right)\dot{q}(t) + A_0^c\left(q,\dot{q},\ddot{q}\right)q(t) = v, \end{aligned} \tag{11}$$

where

$$A_i^c(q,\dot{q},\ddot{q}) = A_i(q,\dot{q},\ddot{q}) - K_i(q,\dot{q},\ddot{q}), i = 0,1,2. \tag{12}$$

Transform the closed-loop system into first-order form :

$$\dot{X} = A_cX + B_cv, \tag{13}$$

where

$$X = \left[q^{\mathrm{T}} \quad \dot{q}^{\mathrm{T}} \quad \ddot{q}^{\mathrm{T}}\right]^{\mathrm{T}}, \tag{14}$$

$$A_c = \begin{bmatrix} 0 & I_n & 0 \\ 0 & 0 & I_n \\ -A_3^{-1}A_0^c & -A_3^{-1}A_1^c & -A_3^{-1}A_2^c \end{bmatrix}, \tag{15}$$

$$B_c = \begin{bmatrix} 0 \\ 0 \\ A_3^{-1} \end{bmatrix}, \tag{16}$$

and our design purpose is to ensure that the closed-loop system attains the desired Jordan canonical form and characteristic vector matrices.

Therefore, the controller u_f is designed by the direct parametric approach as follows.

Given an arbitrarily chosen matrix $F \in \mathbf{R}^{3n\times 3n}$, there exists a constant nonsingular matrix

$$V = V(Z,F) = \begin{bmatrix} Z \\ ZF \\ ZF^2 \end{bmatrix}, \tag{17}$$

such that,

$$V^{-1}A_cV = F. \tag{18}$$

Where $Z \in \mathbf{R}^{n\times 3n}$ is an arbitrary parameter matrix which makes the matrix $V(Z,F)$ nonsingular.

The feedback gains K_0, K_1, K_2 are given by

$$K_i = A_i(q,\dot{q},\ddot{q}) + G_i(q,\dot{q},\ddot{q}), i = 0,1,2, \tag{19}$$

where $G_i(q,\dot{q},\ddot{q}) \in \mathbf{R}^{n\times n}, i = 0,1,2$,are defined by

$$\begin{aligned} &A_3(q,\dot{q},\ddot{q})ZF^3V^{-1}(Z,F) \\ &= [G_0(q,\dot{q},\ddot{q}) \quad G_1(q,\dot{q},\ddot{q}) \quad G_2(q,\dot{q},\ddot{q})]. \end{aligned} \tag{20}$$

Thus, this direct parametric approach results in a constant linear closed-loop system although the open-loop system is highly nonlinear and the eigenstructure of the constant linear closed-loop system (13) is determined by the matrix F .

4 Universal Nonlinear Disturbance Observer Design

A disturbance observer for the manipulator is proposed as

$$\begin{aligned} \dot{\hat{d}}(t) = -L[&\hat{d}(t) - A_3(q,\dot{q},\ddot{q})\dddot{q}(t) - A_2(q,\dot{q},\ddot{q})\ddot{q}(t) \\ &- A_1(q,\dot{q},\ddot{q})\dot{q}(t) - A_0(q,\dot{q},\ddot{q})q(t) + u(t)] \end{aligned} \tag{21}$$

where $L \in \mathbf{R}^{n\times n}$ is a observer gain to be designed and $\hat{d}(t)$ is the estimated disturbance of the disturbance observer.

According to the equation (21), the implementation of the disturbance observer requires a three-order signal $\dddot{q}(t)$. To avoid the measurement of the third-order signal $\dddot{q}(t)$, it is possible to modify the disturbance observer as follows

$$\begin{cases} z(t) = \hat{d}(t) - LA_3(q,\dot{q},\ddot{q})\ddot{q}(t) \\ \dot{z}(t) = -L\dot{A}_3(q,\dot{q},\ddot{q})\ddot{q}(t) - L[\hat{d}(t) - A_2(q,\dot{q},\ddot{q})\ddot{q}(t) \\ \qquad -A_1(q,\dot{q},\ddot{q})\dot{q}(t) - A_0(q,\dot{q},\ddot{q})q(t) + u(t)]. \end{cases} \tag{22}$$

Define the error of the disturbance observer as

$$\tilde{d}(t) = d(t) - \hat{d}(t), \tag{23}$$

thus the differential equation of estimation error can be expressed as

$$\dot{\tilde{d}}(t) + L\tilde{d}(t) = \dot{d}(t). \tag{24}$$

The solution to Equation (24) is

$$\tilde{d}(t) = e^{-tL}\tilde{d}(0) + e^{-tL}\int_0^t e^{xL}\dot{d}(x)dx, \tag{25}$$

where $e^{(\cdot)}$ represents the exponential function and x represents the integral variable.

The stability of the UNDO is expressed by the following lemma[23]. To simplify the proof for the following lemma, we assume all the elements in L are nonnegative constants.

Lemma 1. Suppose that the derivative of the disturbance for the cascaded system (4) is bounded, that is, $|\dot{d}_i(t)| \le \bar{\dot{d}}_i$ $(i = 1,\ldots,n)$. By using the proposed UNDO (11) and designing a positive definite matrix L, (1) the estimation error $\tilde{d}(t)$ is within the domain $\|\tilde{d}(t)\| \le \min\{\|\tilde{d}(0)\| + \|L^{-1}\dot{d}_{max}\|, \|\hat{d}(0)\| + 2\|d_{max}\|\}$;(2) the estimation error $\tilde{d}(t)$ globally converges into $\|\tilde{\boldsymbol{d}}(t)\| \le \min\{\|\boldsymbol{L}^{-1}\dot{\boldsymbol{d}}_{\max}\|, 2\|d_{max}\|\}$, where $\dot{d}_{\max} = [\bar{\dot{d}}_1,\ldots,\bar{\dot{d}}_n]^{\mathrm{T}}$ and $d_{max} = [\bar{d}_1,\ldots,\bar{d}_n]^{\mathrm{T}}$.

Proof. From equation (24) or (25), we know that the estimator is stable when L is a positive definite matrix. Further, equation (26) can be deduced based on the relationship expressed in equation (25).

$$\begin{aligned} \|\tilde{d}(t)\| &= \|e^{-tL}\tilde{d}(0) + e^{-tL}\int_0^t e^{xL}\dot{d}(x)\,\mathrm{d}x\| \\ &\le \|e^{-tL}\tilde{d}(0)\| + \|e^{-tL}\left[\int_0^t e^{xL}\mathrm{d}xL\right]L^{-1}\dot{d}_{\max}\| \\ &\le \|\tilde{d}(0)\| + \|e^{-tL}\left[\int_0^t e^{xL}\mathrm{d}xL\right]L^{-1}\dot{d}_{\max}\| \\ &= \|\tilde{d}(0)\| + \|(I - e^{-tL})L^{-1}\dot{d}_{\max}\| \\ &\le \|\tilde{d}(0)\| + \|L^{-1}\dot{d}_{\max}\|. \end{aligned} \tag{26}$$

Sometimes the rate of change of disturbance may increase to exceedingly large value, while the value of the disturbance remains relatively small. As a consequence, the upper limit of the disturbance estimation error, calculated based on equation (26), is far greater than the actual value, and it may not be useful in applications. Therefore, this paper derives another upper bound for the disturbance estimation error.

From equation (25), we can obtain

$$\begin{aligned} \tilde{d}(t) &= e^{-tL}\tilde{d}(0) + e^{-tL}\left[e^{xL}d(x)|_0^t - \int_0^t e^{xL}Ld(x)dx\right] \\ &= -e^{-tL}\hat{d}(0) + d(t) - e^{-tL}\int_0^t e^{xL}Ld(x)dx, \end{aligned} \tag{27}$$

and then we can have

$$\begin{aligned} \|\tilde{d}(t)\| &\le \|d(t)\| + \|\hat{d}(0)\| + \|e^{-tL}\int_0^t e^{xL}Ld(x)\,\mathrm{d}x\| \\ &\le \|d(t)\| + \|\hat{d}(0)\| + \|e^{-tL}\int_0^t e^{xL}dxL\|\|d_{\max}\| \\ &\le 2\|d_{\max}\| + \|\hat{d}(0)\|. \end{aligned} \tag{28}$$

Therefore, we can conclude that the upper boundary of the disturbance estimation error are determined by the smaller boundary in equations (26) and (28), which can be expressed as

$$\|\tilde{d}(t)\| \le \min\left\{\|\tilde{d}(0)\| + \|L^{-1}\dot{d}_{\max}\|,\ \left\|\hat{d}(0)\right\| + 2\|d_{\max}\|\right\}. \tag{29}$$

This completes the proof for (1) of Lemma 1.

From equation (25), we have

$$\begin{aligned} \lim_{t\to\infty}\left\|\tilde{d}(t)\right\| &= \lim_{t\to\infty}\|e^{-tL}\int_0^t e^{xL}\dot{d}(x)\mathrm{d}x\| \\ &\le \lim_{t\to\infty}\|e^{-tL}\left[\int_0^t e^{xL}dxL\right]L^{-1}\dot{d}_{\max}\| \\ &= \lim_{t\to\infty}\|e^{-tL}\left[\int_0^t e^{xL}dxL\right]L^{-1}\dot{d}_{\max}\| \\ &= \lim_{t\to\infty}\|(I - e^{-tL})L^{-1}\dot{d}_{\max}\| = \|L^{-1}\dot{d}_{\max}\|. \end{aligned} \tag{30}$$

From equation (27), we can obtain

$$\begin{aligned}\lim_{t\to\infty}\left\|\tilde{d}\,(t)\right\| &= \lim_{t\to\infty}\|d(t)-e^{-tL}\int_0^t e^{xL}Ld(x)\,\mathrm{d}x\| \\ &\le \lim_{t\to\infty}\|d(t)\|+\lim_{t\to\infty}\|e^{-tL}\int_0^t e^{xL}dxL\|\|d_{\max}\| \\ &\le 2\|d_{\max}\|.\end{aligned} \tag{31}$$

Then we can conclude

$$\lim_{t\to\infty}\|\tilde{d}(t)\|\le\min\{\|L^{-1}\dot{d}_{\max}\|,\ 2\|d_{\max}\|\}. \tag{32}$$

This completes the proof for (2) of Lemma 1. The Lemma 1 also indicates that we can enhance the estimation accuracy of disturbance observer (22) by increasing the values of observer gains $l_i(i=1,\ldots,n)$when we choose $L=\mathrm{diag}(l_1,\ldots,l_n)$. However, in practice the observer gains should be selected as a trade-off between the permissible accuracy, model accuracy, the characteristics of noise, and so on[24].

In the design of controllers (10) and disturbance observers (22), the acceleration signal of the manipulator is required. Considering increased system feasibility and reduced system costs, a tracking differentiator(T-D) can be employed in this scenario to avoid the use of expensive acceleration sensors for obtaining the acceleration signal of the manipulator. The T-D is shown as

$$\begin{cases}\dot{x}_1(t)=x_2(t)-\lambda|x_1(t)-\dot{q}(t)|^{\frac{1}{2}}sgn(x_1(t)-\dot{q}(t))\\ \dot{x}_2(t)=-\beta sgn(x_1(t)-\dot{q}(t))\end{cases} \tag{33}$$

where λ and β are adjustable parameters, $\dot{q}(t)$ is the input signal to the tracking differentiator (T-D). The terms $x_1(t)$ and $x_2(t)$ represent the tracking value of the T-D for $\dot{q}(t)$ and its first-order derivative estimation, respectively.

5 Simulations

To validate the effectiveness of the proposed control method and disturbance observer, simulation analysis is conducted using a two-link robot as an example. The specific parameters for the two-link robot and actuator are as follows:

$$M(q)=\begin{bmatrix}a+q_{01}+2q_{02}\cos(q_2) & q_{01}+q_{02}\cos(q_2)\\ q_{01}+q_{02}\cos(q_2) & q_{01}\end{bmatrix}, \tag{34}$$

$$C(q,\dot{q})=\begin{bmatrix}-q_{02}\dot{q}_2\sin(q_2) & -q_{02}(\dot{q}_1+\dot{q}_2)\sin(q_2)\\ q_{02}\dot{q}_1\sin(q_2) & 0\end{bmatrix}, \tag{35}$$

$$G(q)=\begin{bmatrix}15g\cos q_1+8.75g\cos(q_1+q_2)\\ 8.75g\cos(q_1+q_2)\end{bmatrix}, \tag{36}$$

$$A_a=\begin{bmatrix}-1 & 0\\ 0 & -1\end{bmatrix}, \tag{37}$$

where $a=13.33, q_{01}=8.98, q_{02}=8.75, g=9.8$.

The initial angles of each joint in the manipulator system are set to $q_r\,(0)=\begin{bmatrix}5.0 & 3.0\end{bmatrix}^{\mathrm{T}}$ rad, the desired trajectory is $q_d\,(t)=\begin{bmatrix}0.3cos(t) & 0.1cos(5t)\end{bmatrix}^T$ rad. The parameters λ and β for the tracking differentiator are chosen as 5 and 10, respectively.

In addition, according to the desired eigenstructure of the closed-loop system, the parameter F is considered as $F=\mathrm{diag}(-10,-15,-20,-25,-30,-35)$. For simplicity, we just choose $Z=\begin{bmatrix}I_2 & I_2 & I_2\end{bmatrix}$.

The lumped uncertainty of the cascaded system is $d(t)=\begin{bmatrix}5sin(2t) & 2cos(5t)\end{bmatrix}^T$, and the observer gain matrix of UNDO is chosen as $L=\begin{bmatrix}50 & 0\\ 0 & 40\end{bmatrix}$.

When the lumped uncertainty of the cascaded system is zero, the tracking error of the designed trajectory tracking controller is shown in Fig. 2. It can be observed that the trajectory tracking controller designed by the direct parametric approach exhibits excellent performance. Furthermore, the tracking speed can be altered by modifying the eigenstructure of the closed-loop system.

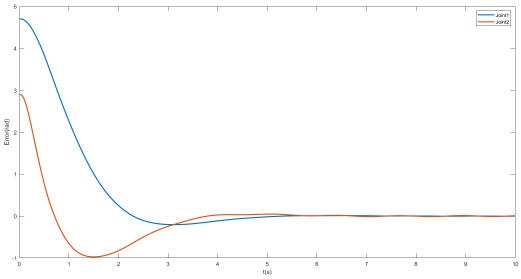

Fig. 2: The tracking error of the designed trajectory tracking controller.

When there are internal and external uncertainties in the system, Figure 3 illustrates the trajectory tracking performance of each joint before and after employing the universal nonlinear disturbance observer. It can be observed that the UNDO effectively enhances the system's disturbance rejection capability.

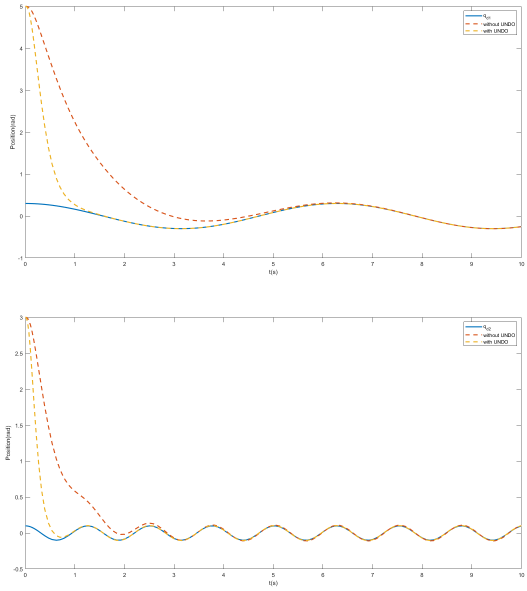

Fig. 3: The trajectory tracking performance of each joint before and after employing the UNDO.

6 Conclusions

This paper presents trajectory tracking control for a multi-degree-of-freedom manipulator system based on the theory of the high-order fully actuated (HOFA) system. To address the internal and external uncertainties in the manipulator system, a universal nonlinear disturbance observer (UNDO) is designed for estimation without requiring a third-order state signal. Combining the actuator model with the dynamic model of the manipulator forms a cascaded system model, aiming to enhance the accuracy of trajectory tracking for the manipulator. A trajectory tracking controller is designed by the direct parametric approach, enabling the system to track the target trajectory within a finite time while meeting performance requirements. Additionally, the use of the tracking differentiator (T-D) addresses challenges in obtaining the acceleration signal of the manipulator, which may be difficult or costly. Finally, simulations are conducted to validate the effectiveness of the proposed theory.

References

[1] Pierre E. Dupont, Bradley J. Nelson, Michael Goldfarb, Blake Hannaford, Arianna Menciassi, Marcia K. O'Malley, Nabil Simaan, Pietro Valdastri, Guang-Zhong Yang, *A decade retrospective of medical robotics research from 2010 to 2020*, *Science Robotics*, vol. 6, no. 60, pp. eabi8017, 2021, American Association for the Advancement of Science.

[2] Andrea Casalino, Davide Bazzi, Andrea Maria Zanchettin, Paolo Rocco, *Optimal proactive path planning for collaborative robots in industrial contexts*, *2019 International Conference on Robotics and Automation (ICRA)*, pp. 6540–6546, 2019, IEEE.

[3] Junling Fu, Massimiliano Poletti, Qingsheng Liu, Elisa Iovene, Hang Su, Giancarlo Ferrigno, Elena De Momi, *Teleoperation control of an underactuated bionic hand: Comparison between wearable and vision-tracking-based methods*, *Robotics*, vol. 11, no. 3, pp. 61, 2022, MDPI.

[4] Victor Santibañez, Karla Camarillo, Javier Moreno-Valenzuela, Ricardo Campa, *A practical PID regulator with bounded torques for robot manipulators*, *International Journal of Control, Automation and Systems*, vol. 8, pp. 544–555, 2010, Springer.

[5] Wei Wang, Bin Xie, Zongyu Zuo, Huijin Fan, *Adaptive backstepping control of uncertain gear transmission servosystems with asymmetric dead-zone nonlinearity*, *IEEE Transactions on Industrial Electronics*, vol. 66, no. 5, pp. 3752–3762, 2018, IEEE.

[6] Brahim Brahmi, Mark Driscoll, Mohamed Hamza Laraki, Abdelkrim Brahmi, *Adaptive high-order sliding mode control based on quasi-time delay estimation for uncertain robot manipulator*, *Control Theory and Technology*, vol. 18, pp. 279–292, 2020, Springer.

[7] Aiqin Liu, Honghua Zhao, Tao Song, Zhi Liu, Haibin Wang, Dianmin Sun, *Adaptive control of manipulator based on neural network*, *Neural Computing and Applications*, vol. 33, pp. 4077–4085, 2021, Springer.

[8] Kshetrimayum Lochan, Binoy Krishna Roy, *Control of two-link 2-DOF robot manipulator using fuzzy logic techniques: a review*, *Proceedings of Fourth International Conference on Soft Computing for Problem Solving: SocProS 2014, Volume 1*, pp. 499–511, 2014, Springer.

[9] Guang-Ren Duan, *High-order fully actuated system approaches: Part I. Models and basic procedure*, *International Journal of Systems Science*, vol. 52, no. 2, pp. 422–435, 2021, Taylor & Francis.

[10] Guang-Ren Duan, *High-order fully actuated system approaches: Part II. Generalized strict-feedback systems*, *International Journal of Systems Science*, vol. 52, no. 3, pp. 437–454, 2021, Taylor & Francis.

[11] Guang-Ren Duan, *High-order fully actuated system approaches: Part III. Robust control and high-order backstepping*, *International Journal of Systems Science*, vol. 52, no. 5, pp. 952–971, 2021, Taylor & Francis.

[12] Guang-Ren Duan, *High-order fully actuated system approaches: Part IV. Adaptive control and high-order backstepping*, *International Journal of Systems Science*, vol. 52, no. 5, pp. 972–989, 2021, Taylor & Francis.

[13] Guang-Ren Duan, *High-order fully actuated system approaches: Part V. Robust adaptive control*, *International Journal of Systems Science*, vol. 52, no. 10, pp. 2129–2143, 2021, Taylor & Francis.

[14] Guang-Ren Duan, *High-order fully-actuated system approaches: Part VI. Disturbance attenuation and decoupling*, *International Journal of Systems Science*, vol. 52, no. 10, pp. 2161–2181, 2021, Taylor & Francis.

[15] Guang-Ren Duan, *High-order fully actuated system approaches: Part VII. Controllability, stabilisability and parametric designs*, *International Journal of Systems Science*, vol. 52, no. 14, pp. 3091–3114, 2021, Taylor & Francis.

[16] Guangren Duan, *High-order fully actuated system approaches: Part VIII. Optimal control with application in spacecraft attitude stabilisation*, *International Journal of Systems Science*, vol. 53, no. 1, pp. 54–73, 2022, Taylor & Francis.

[17] Guangren Duan, *High-order fully-actuated system approaches: Part IX. Generalised PID control and model reference tracking*, *International Journal of Systems Science*, vol. 53, no. 3, pp. 652–674, 2022, Taylor & Francis.

[18] Guangren Duan, *High-order fully actuated system approaches: Part X. Basics of discrete-time systems*, *International Journal of Systems Science*, vol. 53, no. 4, pp. 810–832, 2022, Taylor & Francis.

[19] Guang-Quan Duan, Guo-Ping Liu, *Fully-Actuated System Approach in Attitude Tracking Control for Spacecraft*, *2022 37th Youth Academic Annual Conference of Chinese Association of Automation (YAC)*, pp. 877–881, 2022, IEEE.

[20] Yipeng Yang, Xinghu Yu, Yuan Li, Sichen Yang, Zhan Li, Huijun Gao, *Angular Acceleration Observer Design for Jerk-level Control of Tiltrotors Based on the High-order Fully Actuated System Approaches*, *2022 China Automation Congress (CAC)*, pp. 3750–3755, 2022, IEEE.

[21] Xingyu Zhang, Xuemei Zheng, Zongxuan Liu, Weizhen Liu, *Fully actuated system modeling and control of LCL grid-connected inverter*, *2023 2nd Conference on Fully Actuated System Theory and Applications (CFASTA)*, pp. 857–861, 2023, IEEE.

[22] Guang-Ren Duan, *Direct parametric approach for cascaded systems with application in robot control*, *2014 14th International Conference on Control, Automation and Systems (ICCAS 2014)*, pp. 29–35, 2014, IEEE.

[23] Feilong Zhang, Xin Zhang, Qingxin Li, Hualiang Zhang, *Universal nonlinear disturbance observer for robotic manipulators*, *International Journal of Advanced Robotic Systems*, vol. 20, no. 2, pp. 17298806231167669, 2023, SAGE Publications Sage UK: London, England.

[24] Weiguang Huo, Mohamed Amine Alouane, Yacine Amirat, Samer Mohammed, *Force control of SEA-based exoskeletons for multimode human–robot interactions*, *IEEE Transactions on Robotics*, vol. 36, no. 2, pp. 570–577, 2019, IEEE.

Proceedings of the 3rd Conference on Fully Actuated System Theory and Applications
May 10-12, 2024, Shenzhen, China

Design and Modeling of A Trapezoidal Leaf Spring-Based Actuators with Valid Arm Length and Bending Deformation for Stiffness Adjustment

Tianle Yang[1,*], Hui Zhang[1,*], Shijie Zhang[1,*], Xiang Wu[1], Yuebin Qiu[1], Jing Zhang[2]

1. College of Electrical Engineering, Henan University of Technology, Zhengzhou 450001, P. R. China
E-mail: yangtl2002@stu.haut.edu.cn, huizh2021@haut.edu.cn, zhangshijie@haut.edu.cn

2. Industrial Internet Division, Hitrobot Industry Technology Research Institute Co, LTD, Wuhu 242007, P. R. China

Abstract: This paper proposes a design and modeling of a trapezoidal leaf spring actuator (TLSA) with variable stiffness. The mechanical mechanism of the actuator for stiffness adjustment consists of a flexible trapezoidal leaf spring and two grooved bearing followers (GBFs). The relationship between each GBF and the leaf spring always maintains line contact through the preload generated by the tension spring. Stiffness adjustment is achieved by changing the position of the contact point between the leaf spring and GBF. Such design ensures that only rolling friction ispresent and contributes to the improved stiffness adjustment performance of the actuator. The synchronous belt transmission system is used to change the pivot position accurately and suppress the vibration. Simulation results indicate that the proposed TLSA has the characteristics of a wide stiffness range, rapid stiffness response capability and large maximum load torque value.

Key Words: Actuator, Trapezoidal leaf spring, Stiffness adjustment, Modeling

1 Introduction

With the increasing requirement for robots in the application of various fields, human-robot interaction safety is becoming increasingly important. Flexible robots are developed to fulfil the requirement. Several fixed-flexure devices[1–3] have many beneficial effects in these fields through study and validation. The advanced structure has been the introduction of variable stiffness actuators (VSAs) to maximise efficiency and extend the range of applications. Despite the optimisation of mechanical components through various studies, the use of additional actuators for stiffness control adds complexity, size and weight, affecting the performance of the VSA in terms of torque capacity, stiffness range and adjustment time as well as limiting the VSA applications in robotic systems. Therefore, the more simple and compact VSA is an urgent requirement.

Many existing variable stiffness actuators (VSAs) face trade-offs in order to meet the mechanical requirements of compact size and reduced weight while maintaining energy efficiency, as well as performance requirements such as a large range of stiffness adjustments and high torque capacity[4–7]. Some prioritise small size and light weight, but offer a limited range of stiffness adjustment. Others offer a wide range of stiffness adjustment (from zero to infinite), but at the cost of greater size, weight, and energy consumption.Early implementations of VSAs relied on antagonistic springs or quasi-mechanical devices to regulate stiffness, often consuming significant amounts of energy by adjusting the spring pre-tension[8–11]. The existing technology approach utilises a lever principle to achieve stiffness scaling up and down while saving energy. The lever principle has three specific ways of achieving stiffness adjustment. The first lever principle is implemented by changing the spring position or the effective arm length, as shown in the AwAS[12] and hybrid double actuator devices[13]. The second is to adjust the force applied to the lever position, such as the vsaUT[14], vsaUT-II[15], and sVSA[16]. The third is to modify the pivot position, such as the AwAS-II[17] and CompAct-VSA[18] as well as TSA[19, 20]. It is worth noting that the CompAct-VSA and TSA stands out because it allows the stiffness to transition from zero to full rigidity. However, its mechanical design has some drawbacks. The pivot moves in a sliding groove, which creates significant sliding friction during the energy-intensive stiffness adjustment process. Once the mechanical design is determined, the range of stiffness adjustment depends on the size of the lever structure, which is very sensitive to the pivot position. The use of rack and pinion introduces backlash issues that affect the accuracy of the pivot position, while the use of ball screw drives may introduce control issues due to low response speeds, as well as mechanical design layout issues related to size and weight.

This paper describes a variable stiffness actuator and presents a trapezoidal leaf spring-based actuators with valid arm length and bending. The actuator uses a structure consisting of a trapezoidal leaf spring and two grooved bearing follower (GBF) to adjust the stiffness. Similar to the third lever principle, the structure adjusts the stiffness by changing the pivot position (midpoint between the centers of the two GBFs) on the leaf springs and transitions the stiffness from zero to full rigidity. However, it differs by the use of a trapezoidal leaf spring in the construction and the use of two GBFs in the sliding groove to avoid sliding friction. Rolling friction is used since each GBF has only one point of contact. Since the range of stiffness adjustment is related to the arm length and trapezoidal leaf spring stiffness, for ease of control, the longer the arm length the better as the stiffness increases without increasing the structural dimensions. The proposed TLSA is an improvement in both elastic deflection and elastic energy compared to conventional

This work is supported by the Open Research Fund of Anhui Province Key Laboratory of Machine Vision Inspection under Grant No. KLMVI-2023-HIT-18, the Science Foundation of Henan University of Technology under Grants 2021BS060 and 2020BS059.

designs. The stiffness can be adjusted under normal operating conditions. It not only meets the safety requirement of fast stiffness adjustment from high to low, but also can work normally under variable stiffness. The main purpose of the paper is to present a simple and compact variable stiffness structural model and design.

2 Stiffness Regulation Principle

The TLSA takes the characteristics of a trapezoidal leaf spring to adjust the stiffness by changing the position of the pivot. Designing the trapezoidal leaf spring and two GBFs as shown in the schematic diagram in Fig. 1, where both slant sides of the trapezoidal leaf spring are balanced about the central axis and in contact with the GBFs. δ_1 represents the distance from the joint axis A to the pivot position P. δ_3 and δ_4 are the distances from the starting points of the right-angle side of the trapezoidal leaf spring to the contact points of the slant side with the outer circle of the GBFs, also known as the effective straight arm length. δ_2 is the distance from the joint axis A to the center position of the top vertex of the trapezoidal leaf spring. τ_{11} and τ_{12} represent the torques generated at the joint axis due to the external torque when the trapezoidal leaf spring rotates about the roller. τ_E represents the elastic torque at the joint axis (A), coupled from the torques generated on the two outer edges of the trapezoidal leaf spring by the two grooved rollers. Stiffness adjustment is achieved by moving the center point of the GBF, causing changes in δ_1 , δ_3 , and δ_4 . It is noteworthy that due to the different patterns of contact point changes, the effective lengths of the two outer edges of the trapezoidal leaf spring are not always equal, and stiffness varies with the movement of the pivot position. When point P coincides with point B, the stiffness is infinite, and when point P coincides with point A, the stiffness decreases.

3 Structural Principle

Figure 2 and Figure 3 illustrate the overall structural framework and stiffness adjustment module of the structure. A trapezoidal leaf spring with stiffness X is mounted on the spring bracket, fixed on the input disk, and equipped with two rollers on the roller mechanism. The inner circles of the two rollers can freely rotate about their axes. To ensure that the two grooved rollers (GBFs) are always in contact with the two outer edges of the trapezoidal leaf spring, a sufficient tension needs to be provided beneath the two GBFs, achieved by setting a tension spring pulling towards the center. The tension is small enough to be negligible. The slide rail is placed beneath the output disk, with the slider fixed to the roller frame, capable of sliding in the direction of the conveyor. The stiffness adjustment device is driven by motor M_2 , using a conveyor belt drive. M_2 Motor is a graphite brush DC motor with a rated torque of 30.4 mNm (maxon DC motor 155). The conveyor belt moves around the drive pulley and idle pulley, fixed on the pulley bracket. To prevent component collisions, such as the grooved rollers at the bottom of the trapezoidal leaf spring, a pair of mechanical blocks is placed at the bottom of the trapezoidal leaf spring, limiting the movement of the grooved rollers and preventing detachment from the trapezoidal leaf spring.It is worth noting that the range of angular deflection is influenced not only

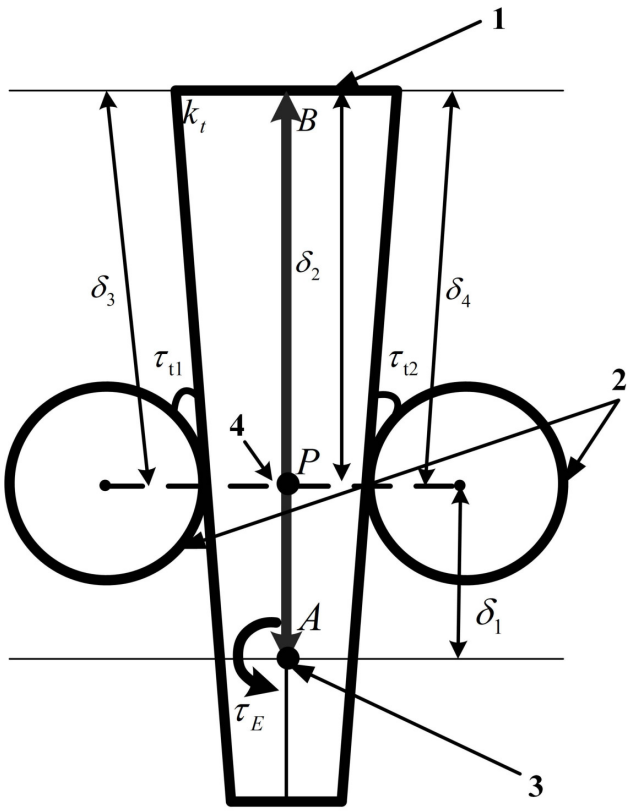

Fig. 1: Schematic of the trapezoidal leaf Spring mechanism with a variable pivot position. 1) Trapezoidal Leaf Sping. 2) Cam bearing follows. 3) Joint Axis. 4) Pivot.

by the components on the output disk but also by the components on the input disk. Specifically, at low stiffness, the components on the output disk have an impact on the deflection range, while at high stiffness, the mechanical blocks on the input disk affect the range of deflection.

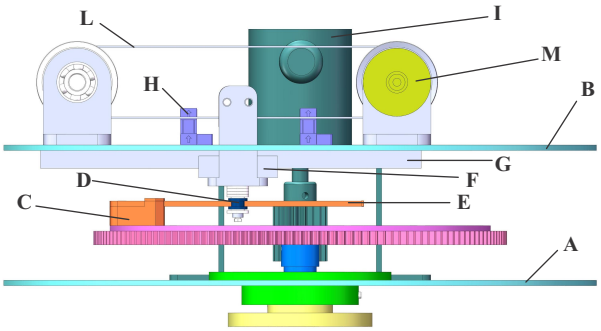

Fig. 2: TLSA assembly in the main view. A) Secondary output panel. B) Main output disk. C) Trapezoidal leaf spring bracket. D) Grooved bearing follower. E) Trapezoidal leaf spring. F) Slide block. G) Slide rail. H) Photoelectric sensors. I) Encoder. L) Drive the pulley. M) MotorM_2.

The stiffness adjustment module is connected to the main actuator. The main motor consists of a 35mNm brushless BLDC motor (ECX FLAT 32 Sϕ32 mm) and a planetary gearbox with a reduction ratio of 103:1 (GPX 32). The sectional view of the overall assembly of the TLSA is shown in

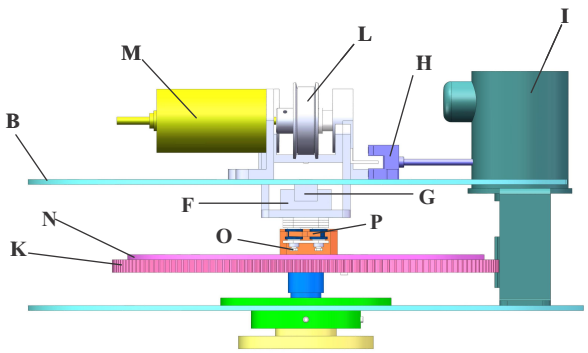

Fig. 3: The reverse side of the main view composed of TLSA. I) Absolute magnetic encoder. H) Photoelectric sensors. L) Drive the pulley. N) Enter the disk. O) Hexagonal screws. P) Limit block. K) Toothed disc.

Fig. 4.

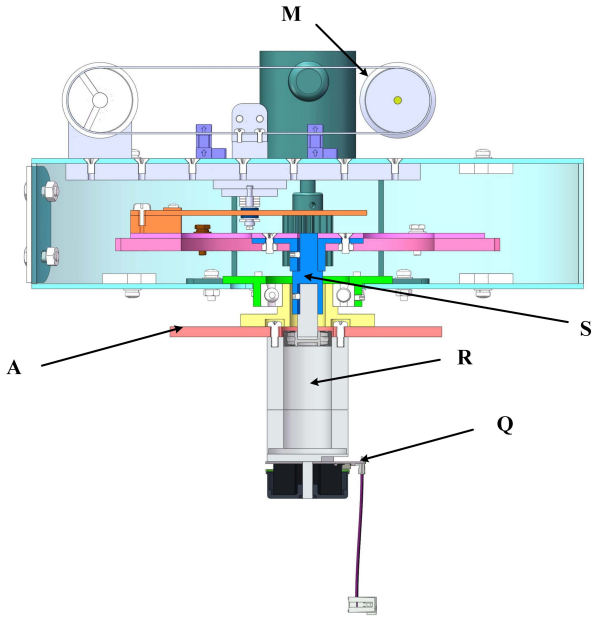

Fig. 4: Sectional view of the total TLSA assembly. A) Pedestal. M) MotorM_2. Q) MotorM_1. R) Planctary gear box. S) Main actuator shaft.

In the TLSA, three position sensors are included to provide feedback on the complete state data. Two incremental encoders are respectively mounted on motor M_1 and motor M_2, with the former used to detect the position of the input disk, and the latter used to detect the position of the roller frame on the conveyor belt. The third sensor is a 12-bit resolution multi-turn absolute encoder (OID-3806D), utilized to measure the angle between the input disk and the output disk.

4 Modeling of the TLSA

The modelling of the TLSA is trapezoidal leaf spring-based characteristics. Figure 5 provides a simplified schematic of the elastic principle. Meanwhile, table 1 gives the meanings expressed by the corresponding parameters. Due to the small gradient of the trapezoidal leaf spring in the actual structure, it is abstracted as a straight leaf spring for study purposes. The figure facilitates a detailed explanation of the modeling process. When the input disk remains stationary and an external torque acts on the output disk, the output disk rotates an angle θ relative to the joint axis. The specific modeling process is as follows:

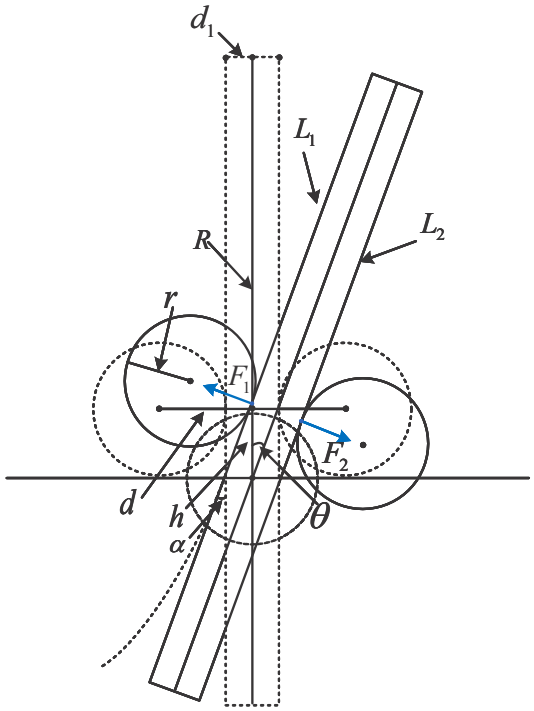

Fig. 5: Schematic of the elastic mechanism.

Table 1: Description of the symbols in Fig. 5

d_1	Half of the upper edge line of the leaf spring
R	Distance from top midpoint of the leaf spring to the joint axis
d	Half distance between two GBF centers
h	Distance between pivot position and the joint axis
θ	Included angle between input disk and output disk
L_1,L_2	Effective straight arm length on both sides of the leaf spring
α	The torsion angle of the leaf spring
r	Radius of GBF

According to the schematic of the elastic principle in Fig. 5 and the symbol descriptions in the table above, the coordinates of the three vertices at the upper end of the leaf spring, from left to right, and the centers of the two GBFs can be given by

$$\begin{cases} x_{t1} = R\sin\theta - d_1\cos\theta \\ y_{t1} = R\cos\theta + d_1\sin\theta \end{cases} \tag{1}$$

$$\begin{cases} x_t = R\sin\theta \\ y_t = R\cos\theta \end{cases} \tag{2}$$

$$\begin{cases} x_{t2} = R\sin\theta + d_1\cos\theta \\ y_{t2} = R\cos\theta - d_1\sin\theta \end{cases} \tag{3}$$

$$\begin{cases} x_{p1} = -d\cos\theta + h\sin\theta \\ y_{p1} = h\cos\theta + d\sin\theta \end{cases} \tag{4}$$

$$\begin{cases} x_{p2} = d\cos\theta + h\sin\theta \\ y_{p2} = h\cos\theta - d\sin\theta \end{cases} \tag{5}$$

where (x_{ti}, y_{ti}) and (x_{pi}, y_{pi}) respectively represent the coordinates of the three vertices at the upper edge of the leaf spring and the center point of the GBF $i \in [1, 2]$. Here, $d = r + d_1$, $[1, 2]$ when considering the subscripts of the left and right sides, and other symbols are represented in the same way. In the context, L_1, L_2 can be expressed as follows:

$$L_1 = \sqrt{(x_{t1} - x_{p1})^2 + (y_{t1} - y_{p1})^2 - r^2} \tag{6}$$

$$L_2 = \sqrt{(x_{t2} - x_{p2})^2 + (y_{t2} - y_{p2})^2 - r^2} \tag{7}$$

According to the principle of cantilever beam, α can be expressed as:

$$\alpha = \frac{FL^2}{2EI} \tag{8}$$

Since here we have approximated the trapezoidal leaf spring by a straight leaf, the angle α, which is the angle of the tangent to the cantilever beam, can be approximately equivalent to θ.

According to the characteristics of the leaf spring, here are the torques, τ_{t1} and τ_{t2}, generated by the leaf spring acting on the two rollers:

$$\tau_{t1} = k_t(\alpha - \alpha_0); \tau_{t2} = k_t(\alpha + \alpha_0) \tag{9}$$

Where k is the stiffness of the leaf spring, and a is the pre-twist angle of the leaf spring. The pre-twist angle ensures that there is a pre-twist angle that keeps the GBF always in a tangential state with the outer edge of the leaf spring. At the point, the forces f1 and f2 generated by the leaf spring at the tangential point can be expressed as:

$$F_1 = \frac{\tau_{t1}}{L_1}, F_2 = \frac{\tau_{t2}}{L_2} \tag{10}$$

At the point, the total elastic torque of the joint can be expressed as:

$$\tau_{_E} = \tau_{E2} - \tau_{E1} \tag{11}$$

Where τ_{E1} and τ_{E2} respectively represent the torque generated by the force of the leaf spring on the rollers, which is translated into torque at the joint axis. It can be expressed using the following formula:

$$\tau_{_{E1}} = F_1\cos\alpha\big(hcos\theta + \mathrm{dsin}\theta\big) \tag{12}$$

$$\tau_{_{E2}} = F_2\cos\alpha\big(hcos\theta - \mathrm{dsin}\theta\big) \tag{13}$$

At the point, the joint stiffness $K = \dfrac{\partial\tau_E}{\partial\theta}$ can be expressed as:

$$K = \frac{\partial(\tau_{E_2} - \tau_{E_1})}{\partial\theta} = \frac{\partial}{\partial\theta}\Big(\frac{k_t(\alpha + \alpha_0)}{L_2}\cos\alpha(hcos\theta - dsin\theta - \frac{k_t(\alpha - \alpha_0)}{L_1}\cos\alpha(hcos\theta + dsin\theta)\Big) \tag{14}$$

From the above equation, it can be seen that the joint stiffness is complex and depends on many parameters. For the sake of convenient analysis, the model has been appropriately simplified as follows:

$$\tau_E = \frac{k_t d\sin(2\theta)}{R - h} \tag{15}$$

The stiffness expression of the structure can be obtained as follows:

$$K = \frac{2k_t d\cos(2\theta)}{R - h} \tag{16}$$

Due to the fact that the position of the pivot is adjusted through the wire rope drive of the motor M_2, the relationship between the position of the pivot h and the angle position of the motor M_2. φ_2 can be expressed as:

$$h = n\varphi_2 \tag{17}$$

In the formula, n is the radius of the transmission wheel, which is called the wire rope transmission ratio. The energy stored in elasticity is very important, and according to (15), it can be expressed as:

$$U_E = \int \tau_E d\theta \tag{18}$$

Through the method, torque resistance can be obtained:

$$\tau_{_R} = \frac{\partial U_{_E}}{\partial\varphi_{_2}} \tag{19}$$

The specific details are as follows:

$$U_{_E} = \frac{k\mathrm{dsin}^2(\theta)}{R - h} \tag{20}$$

$$\tau_{_R} = \frac{k_{,}\,\mathrm{nd}\sin^2(\theta)}{(R - \mathrm{n}\,\varphi_{_2})^2} \tag{21}$$

By deriving the resistive and elastic moments as well as the external moments after the next work-analysis of the dynamics model of the TLSA and the addition of algorithms to achieve the goal simulation experimental purposes.

5 Simulation Analysis

In Fig. 6, the stiffness adjustment of TLSA is represented by the distance relationship between the center point of the roller and the joint axis. Figure 7 shows the stiffness variation of different center point positions with the change of the angle. Both figures provide the relationship between the distance from the center point of the roller to the joint axis and the stiffness when the initial angle is nearly equal to zero. Figure 7 presents the stiffness variation curve for different pivot positions relative to the joint axis under the same angle conditions. In Fig. 6, as the pivot position h increases, the amplitude of the corresponding stiffness variation becomes

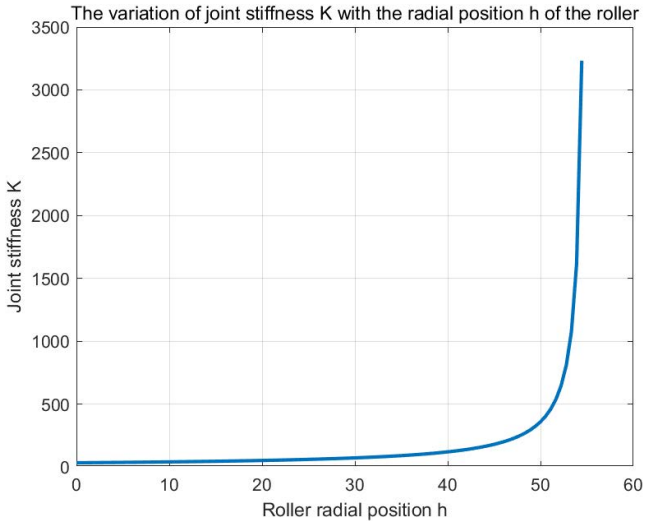

Fig. 6: Stiffness adjustment for the TLSA based on the distance between pivot position and joint axis.

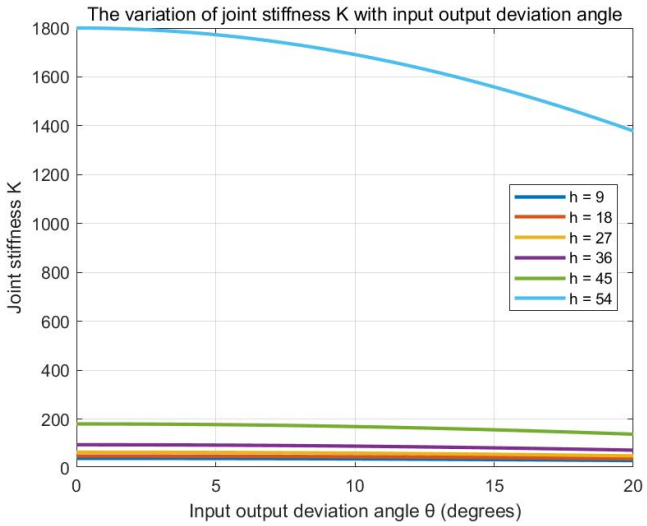

Fig. 7: Stiffness adjustment for the TLSA based on the included angle of the input disk and the output disk.

larger, and the variation speed also accelerates. In Fig. 7, when the pivot position is below 45mm, the range of stiffness adjustment is small, indicating that the stiffness model proposed in the mechanism exhibits good stability at low stiffness. It also maintains relatively stable stiffness when the deflection angle changes within a small range.

Figure 8 shows the τ_E represented by the coordinates of different roller center positions under the same deflection angle. The curve indicates that the structure has relatively good stability performance when adjusting stiffness.

6 Conclusion

This paper presents the design and model approach for a trapezoidal leaf spring-based actuator with variable stiffness. The structure consists of a trapezoidal leaf spring and two grooved bearing follower modules. The advantages of the TLSA are the adoption of a loosely structured and well laid out design concept that prevents component collisions, while also offering a large and precise range of stiffness adjustments, overcoming some of the traditional problems such

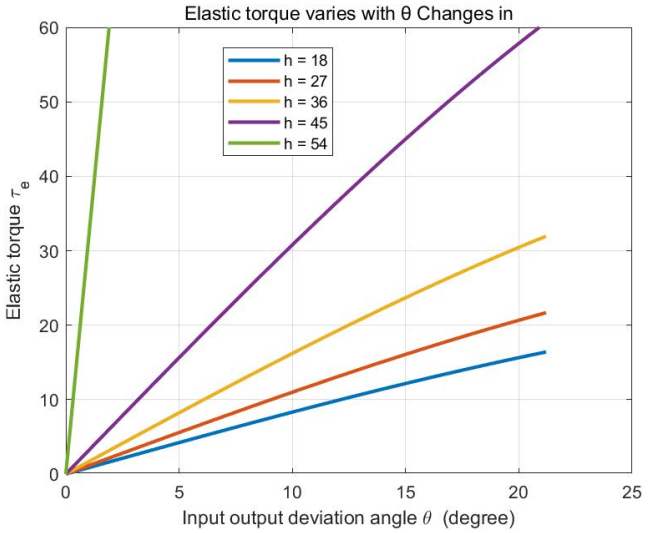

Fig. 8: Elastic torque based on the included angle with different pivot positions.

as small size and high energy consumption. Additionally, the vertical relationship between the trapezoidal leaf spring and the grooved bearing follower further reduces energy consumption. Simulation results show that the structure has good stiffness adjustment range and accuracy as well as large maximum load torque values.

In future research, the structural principle will be further optimised according to the structural characteristics of the trapezoidal leaf spring, and the control algorithm will be further optimised according to the sliding mode control and PID control. In addition, the parameter recognition function of the system will be improved by optimising the structural principle of the trapezoidal leaf spring, and the trajectory tracking performance of the system will be improved by optimising the control algorithm. The ultimate goal is to establish a multi-degree-of-freedom robotic system.

References

[1] Riccardo Schiavi, Giorgio Grioli, Soumen Sen, Antonio Bicchi, "VSA-II: A novel prototype of variable stiffness actuator for safe and performing robots interacting with humans," in *2008 IEEE International Conference on Robotics and Automation*, 2008, pages 2171–2176.

[2] Shane A. Migliore, Edgar A. Brown, Stephen P. DeWeerth, "Biologically inspired joint stiffness control," in *Proceedings of the 2005 IEEE international conference on robotics and automation*, 2005, pages 4508–4513.

[3] Giovanni Tonietti, Riccardo Schiavi, Antonio Bicchi, "Design and control of a variable stiffness actuator for safe and fast physical human/robot interaction," in *Proceedings of the 2005 IEEE international conference on robotics and automation*, 2005, pages 526–531.

[4] Manuel G. Catalano, Giorgio Grioli, Manolo Garabini, Fabio Bonomo, Michele Mancini, Nikolaos Tsagarakis, Antonio Bicchi, "VSA-CubeBot: A modular variable stiffness platform for multiple degrees of freedom robots," in *2011 IEEE international conference on robotics and automation*, 2011, pages 5090–5095.

[5] Dmitry Popov, Igor Gaponov, Jee-Hwan Ryu, "Towards variable stiffness control of antagonistic twisted string actuators," in *2014 IEEE/RSJ International Conference on Intelligent Robots and Systems*, 2014, pages 2789–2794.

[6] Manuel G. Catalano, Giorgio Grioli, Fabio Bonomo, Riccardo Schiavi, Antonio Bicchi, "Vsa-hd: From the enumeration analysis to the prototypical implementation," in *2010 IEEE/RSJ International Conference on Intelligent Robots and Systems*, 2010, pages 3676–3681.

[7] Oliver Eiberger, Sami Haddadin, Michael Weis, Alin Albu-Schäffer, Gerd Hirzinger, "On joint design with intrinsic variable compliance: Derivation of the DLR QA-joint," in *2010 IEEE International Conference on Robotics and Automation*, 2010, pages 1687–1694.

[8] Ludo C. Visser, Raffaella Carloni, Ramazan Ünal, Stefano Stramigioli, "Modeling and design of energy efficient variable stiffness actuators," in *2010 IEEE International Conference on Robotics and Automation*, 2010, pages 3273–3278.

[9] A. Bicchi, G. Tonietti, "Fast and Soft Arm Tactics: Dealing with the Safety-Performance Trade-Off in Robot Arms Design and Control," *Archives De Pédiatrie*, vol. 17, no. 6, pp. 66, 2004.

[10] Aaron M. Dollar, Robert D. Howe, "A robust compliant grasper via shape deposition manufacturing," *IEEE/ASME Transactions on Mechatronics*, vol. 11, no. 2, pp. 154-161, 2006.

[11] K. Kong, J. Bae, M. Tomizuka, "A Compact Rotary Series Elastic Actuator for Human Assistive Systems," *Mechatronics, IEEE/ASME Transactions on*, vol. 17, no. 2, pp. 288-297, 2012.

[12] Amir Jafari, Nikos G. Tsagarakis, Bram Vanderborght, Darwin G. Caldwell, "A novel actuator with adjustable stiffness (AwAS)," in *2010 IEEE/RSJ International Conference on Intelligent Robots and Systems*, 2010, pp. 4201-4206. doi: 10.1109/IROS.2010.5648902.

[13] S. Kajikawa, K. Abe, "Robot Finger Module With Multidirectional Adjustable Joint Stiffness," *IEEE/ASME Transactions on Mechatronics*, vol. 17, no. 1, pp. 128-135, 2012.

[14] S. S. Groothuis, G. Rusticelli, A. Zucchelli, S. Stramigioli, R. Carloni, "The vsaUT-II: A novel rotational variable stiffness actuator," *IEEE*, 2012.

[15] Stefan S. Groothuis, Giacomo Rusticelli, Andrea Zucchelli, Stefano Stramigioli, Raffaella Carloni, "The Variable Stiffness Actuator vsaUT-II: Mechanical Design, Modeling, and Identification," *IEEE/ASME Transactions on Mechatronics*, vol. 19, no. 2, pp. 589-597, 2014.

[16] M. Cempini, M. Fumagalli, N. Vitiello, S. Stramigioli, "A clutch mechanism for switching between position and stiffness control of a variable stiffness actuator," *IEEE*, 2015.

[17] Amir Jafari, Nikos G. Tsagarakis, Darwin G. Caldwell, "AwAS-II: A new Actuator with Adjustable Stiffness based on the novel principle of adaptable pivot point and variable lever ratio," in *IEEE International Conference on Robotics & Automation*, 2011.

[18] Nikos G. Tsagarakis, Irene Sardellitti, Darwin G. Caldwell, "A new variable stiffness actuator (CompAct-VSA): Design and modelling," in *2011 IEEE/RSJ International Conference on Intelligent Robots and Systems*, 2011, pp. 378-383. doi: 10.1109/IROS.2011.6095006.

[19] Decai Yang, Hongzhe Jin, Zhangxing Liu, Jizhuang Fan, Huijuan Dong, "Design and modeling of a torsion spring-based actuator (TSA) with valid straight-arm length adjustable for stiffness regulation," in *IEEE International Conference on Mechatronics & Automation*, 2016.

[20] Hongzhe Jin, Deicai Yang, Hui Zhang, Zhangxing Liu, Jie Zhao, "Flexible Actuator With Variable Stiffness and Its Decoupling Control Algorithm: Principle Prototype Design and Experimental Verification," *IEEE/ASME Transactions on Mechatronics*, vol. PP, no. 99, pp. 1-1, 2018.

Proceedings of the 3rd Conference on Fully Actuated System Theory and Applications
May 10-12, 2024, Shenzhen, China

Adaptive Fuzzy Fault-Tolerant Control of High-Order Nonlinear Time-Varying Delay Systems with Dead-Zone Inputs: A Fully Actuated System Approach

Sen Zheng[1], Yang Cui[1*]

1. School of Electronic and Information Engineering, University of Science and Technology Liaoning, Anshan 114051, China
E-mail: kdcuiyang@163.com

Abstract: This paper investigates adaptive fault-tolerant (FT) tracking control for high-order nonlinear time-varying delay strict-feedback system (SFS) with non-affine nonlinear faults and non-symmetric dead-zone inputs. A novel adaptive fault-tolerant control strategy is developed by combining the theory of high-order fully actuated (HOFA) systems, dynamic surface control techniques, the finite covering lemma, and generalized approximation of fuzzy logic systems (FLSs). Notably, there is no need to reduce the order of high-order systems. Utilizing the finite covering lemma and fuzzy logic systems to address the issue of unknown time-varying delays, this control scheme circumvents the use of Lyapunov-Krasovskii functions, thus removing the condition that the time derivative of the time-varying delay function must be less than one. Through Lyapunov function theory, it is rigorously proved that the designed controller ensures both the stability of the closed-loop system and the convergence of the tracking error to a small neighborhood of the origin. Simulation results are presented to demonstrate the feasibility and effectiveness of the proposed control scheme.

Key Words: Strict-feedback System, Time-varying Delays, Fully Actuated Systems, Fault-tolerant Control, Finite Covering Lemma

1 Introduction

The pursuit of effective tracking control for nonlinear systems has been a prominent area of research, driven by its substantial theoretical and practical relevance in various engineering applications. However, nonlinear systems often exhibit uncertainties, adding complexity to their analysis. The advent of neural networks (NNs) and fuzzy logic systems (FLSs) has invigorated the study of adaptive control in uncertain nonlinear systems, leading to a wealth of discoveries and innovations [1–5]. Specifically, a fuzzy adaptive control problem was investigated for nonlinear systems with unmodelled dynamics, employing finite-time theory in [5].

All the above control methods are based on first-order system approaches in state-space models. However, the majority of practical industrial systems are inherently described by high-order differential equations [6, 7]. Consequently, the utilization of state-space methods requires the conversion of high-order systems into a first-order system format. However, this process can complicate the design of the controller and even compromise the fully-actuated performance of the system. To address these challenges, Professor Guangren Duan introduced the High-Order Fully Actuated (HOFA) system method, which has pioneered an innovative approach to designing controllers for high-order systems [8–10].

It is well known that time delays are a prevalent phenomenon in practical industrial systems. The presence of time delays can adversely affect system performance. In recent years, significant advancements have been made in the study of nonlinear time-delay systems [11–13]. Based on the Lyapunov-Krasovskii methods, the adaptive tracking control approach was proposed for time-delay nonlinear systems with full state constraints in [11]. However, it should be noted that Lyapunov-Krasovskii functionals require that time delays be either constant or that the derivative of time-varying delays does not exceed one. These conditions are not always feasible in practical scenarios. In order to relax the above limitations, a global adaptive control method was proposed for stochastic nonlinear systems in [13], using the Lyapunov-Razumikhin approach. Nevertheless, the Lyapunov-Razumikhin functions tend to be overly conservative and challenging to apply in systems with complex structures. Recently, Duan proposed for the first time the HOFA system controller with time delay in [14]. Building upon this development and leveraging the HOFA theory, significant progress has been achieved in the adaptive control of HOFA systems with time delays [15, 16]. However, strict constraints on time delays are remain crucial. Therefore, it is essential to further investigate adaptive control methods for nonlinear time-varying delay HOFA systems.

In addition to time-varying delays, many mechanical systems exhibit other nonlinear characteristics, such as dead-zone. Various techniques have been developed to counteract the adverse effects of dead-zone [17–19]. For instance, a command-filtered adaptive neural network controller was proposed for non-strict feedback nonlinear systems with dead-zones and input saturation nonlinearity in [19]. Furthermore, faults are an inevitable occurrence in actual industrial systems, and when they do occur, they can lead to severe consequences. Several adaptive control methods for nonlinear systems with faults were investigated in [20–22]. In [22], a fixed-time fuzzy fault-tolerant control method was presented for nonlinear systems with input delays and actuator faults. However, all of the above literature primarily focuses on linear faults or affine nonlinear faults, and the studied systems are often limited to first-order nonlinear systems. Consequently, the development of a direct adaptive controller for high-order nonlinear time-varying delays SFS

This research was supported by the National Natural Science Foundation of China under Grant 61903169, Science Center Program of National Natural Science Foundation of China under Grant 62188101, Liaoning Revitalization Talents Program under Grant XLYC2007182, Education Department Project of Liaoning under Grant LJKMZ20220655.

with non-affine nonlinear faults is an urgent problem.

In comparison to existing literature, this article offers the following major contributions:

1) A novel tracking control method is developed for high-order nonlinear systems with time-varying delays, which simultaneously experience non-affine nonlinear faults and asymmetric nonlinear dead-zones.
2) The method employed in this paper allows for the direct design of controllers for uncertain high-order nonlinear systems without the need for system conversion.

2 Problem description and preliminaries

2.1 Problem formulation

The high-order nonlinear SFS is described as

$$\begin{cases} x_1^{(q_1)} = f_1(x_1^{(0\sim q_1-1)}) + g_1(x_1^{(0\sim q_1-1)})x_2 \\ \qquad + h_1(x_1^{(0\sim q_1-1)}(t-\tau_1(t))), \\ x_2^{(q_2)} = f_2(x_i^{(0\sim q_i-1)}|_{i=1\sim 2}) + g_2(x_i^{(0\sim q_i-1)}|_{i=1\sim 2})x_3 \\ \qquad + h_2(x_i^{(0\sim q_i-1)}(t-\tau_i(t))|_{i=1\sim 2}), \\ \qquad \vdots \\ x_{n-1}^{(q_{n-1})} = f_{n-1}(x_i^{(0\sim q_i-1)}|_{i=1\sim n-1}) \\ \qquad + g_{n-1}(x_i^{(0\sim q_i-1)}|_{i=1\sim n-1})x_n \\ \qquad + h_{n-1}(x_i^{(0\sim q_i-1)}(t-\tau_i(t))|_{i=1\sim n-1}), \\ x_n^{(q_n)} = f_n(x_i^{(0\sim q_i-1)}|_{i=1\sim n}) + g_n(x_i^{(0\sim q_i-1)}|_{i=1\sim n})D(u) \\ \qquad + h_n(x_i^{(0\sim q_i-1)}(t-\tau_i(t))|_{i=1\sim n}) \\ \qquad + l(t-T_0)\nu(x_i^{(0\sim q_i-1)}|_{i=1\sim n}, u), \\ y = x_1, \end{cases} \tag{1}$$

where $x_i \in R$, with $i = 1, 2, \ldots, n$, represents the system state variables, $f_j(x_i^{(0\sim q_i-1)}|_{i=1\sim j}) \in R$ and $h_j(x_i^{(0\sim q_i-1)}(t-\tau_i(t))|_{i=1\sim j}) \in R$, $j = 1, 2 \ldots, n$ denote unknown nonlinear functions, where $\tau_i(t)$ signifies unknown time-varying delays. Known continuous nonlinear functions are denoted by $g_j(x_i^{(0\sim q_i-1)}|_{i=1\sim j}) \in R$. It is assumed that $g_j(x_i^{(0\sim q_i-1)}|_{i=1\sim j}) \neq 0$ and $\left|g_j(x_i^{(0\sim q_i-1)}|_{i=1\sim j})\right| \leq g^*, g^* > 0$. The output and input of the system are represented by $y \in R$ and $u \in R$, respectively. The system is subject to an unknown external disturbance $\nu\left(x_i^{(0\sim q_i-1)}|_{i=1\sim n}, u\right) \in R$ due to a fault. The time profile of the fault occurring at some unknown time is represented by $l(t-T_0) \in R$, described as follows

$$l(t-T_0) = \begin{cases} 0, & t < T_0, \\ 1 - e^{-\delta(t-T_0)}, & t \geq T_0, \end{cases} \tag{2}$$

where $\delta > 0$ is the evolution rate of the unknown fault.

The uncertain asymmetric nonlinear dead-zone $D(u)$ takes the following form:

$$D(u) = \begin{cases} k_r(u)(u-b_r), & u \geq b_r, \\ 0, & b_l < u < b_r, \\ k_l(u)(u-b_l), & u \leq b_l, \end{cases} \tag{3}$$

where $k_r(u)$ and $k_l(u)$ are the unknown smooth slop function of $D(u)$, $b_r > 0$ and $b_l < 0$ denote the unknow breakpoints of $D(u)$.

The reference signal y_r is a smooth function with bounded derivatives up to the q_1th order.

Assumption 1 [23]: For system (1), the inequality

$$\begin{aligned} &|\bar{f}_n + l(t-T_0)\nu\left(x_i^{(0\sim q_i-1)}|_{i=1\sim n}, u\right)| \\ &\leq \eta\left(x_i^{(0\sim q_i-1)}|_{i=1\sim n}, u\right) \end{aligned} \tag{4}$$

holds, where $\bar{f}_n$ represents an unknown nonlinear function, the definition of which will be provided later and $\eta\left(x_i^{(0\sim q_i-1)}|_{i=1\sim n}, u\right)$ is an unknown non-negative function.

Assumption 2 [18]: There exist unknown smooth functions $k_r(u)$ and $k_l(u)$ that satisfy the following conditions:

$$\begin{aligned} &0 < \underline{k}_r \leq k_r(u) \leq \overline{k}_r, \forall u \in [b_r, +\infty), \\ &0 < \underline{k}_l \leq k_l(u) \leq \overline{k}_l, \forall u \in (-\infty, b_l], \end{aligned}$$

with $\underline{k}_r, \underline{k}_l, \overline{k}_r$ and $\overline{k}_l$ are unknown constants, additionally, it is known that $\min\{\underline{k}_r, \underline{k}_l\} \geq k^*$, where k^* is a known positive constant.

As described in [17–19], the dead-zone model (3) can be decomposed into smooth nonlinear terms $k(u)u$ and bounded nonlinear terms $m(u)$.

$$D(u) = k(u)u + m(u), \tag{5}$$

where

$$k(u) = \begin{cases} k_r(u), u \geq 0, \\ k_l(u), u \leq 0, \end{cases}$$

and

$$m(u) = \begin{cases} -k_r(u)b_r, u \geq b_r, \\ -k(u)u, b_l < u < b_r, \\ -k_l(u)b_l, u \leq b_l. \end{cases}$$

Based on this, it can be readily deduced that $m(u)$ is bounded and there exists a positive constant, denoted as m^*, such that $|m(u)| \leq m^*$.

Assumption 3 [24]: $\tau_i(t)$, for $i = 1, 2, \ldots, n$, are contained within a known compact set $[0, \tau_{iM}]$, where τ_{iM} represents the maximum upper bound for each $\tau_i(t)$.

2.2 Preliminaries

For convenience, we introduce the following symbols in this paper to represent commonly used matrices. I_m represents the identity matrix, and

$$x^{(0\sim q)} = \begin{bmatrix} x & \dot{x} & \cdots & x^{(q)} \end{bmatrix}^T,$$

$$x_k^{(q_0\sim q_k)}\Big|_{k=i\sim j} = \begin{bmatrix} x_i^{(q_0\sim q_k)} \\ x_{i+1}^{(q_0\sim q_k)} \\ \vdots \\ x_j^{(q_0\sim q_k)} \end{bmatrix}, j \geq i,$$

$$A^{0\sim q-1} = \begin{bmatrix} A_0 & A_1 & \cdots & A_{q-1} \end{bmatrix},$$

$$\Phi\left(A^{0\sim q-1}\right) = \begin{bmatrix} 0 & I & & \\ & & \ddots & \\ & & & I \\ -A_0 & -A_1 & \cdots & -A_{q-1} \end{bmatrix}.$$

For ensuring the stability of the control system, the following lemmas are essential.

Lemma 1 [24]: Consider a function $h(x)$ defined on a compact set $\Omega_x \to R$. Let $x = x(t - \tau(t))$ be uniformly continuous with respect to t, where $\tau(t) \in [0, \tau_M]$ represents an unknown time-varying delay. The constant τ_M is know. Then, for any constant $\vartheta > 0$, there exists a finite partition of $[0, \tau_M]$, independent of t

$$0 \le t_1 < t_2 < \ldots < t_m \le \tau_M$$

from this partition, time-varying points $\bar{\tau}_{\sigma(t)} \in \{t_1, \ldots, t_m\}$ where $\sigma(t) \in \{1, \ldots, m\}$ can be selected such that:

$$\left| h(x(t - \tau(t))) - h\left(x\left(t - \bar{\tau}_{\sigma(t)}\right)\right) \right| < \vartheta, \forall t \ge 0$$

Lemma 2 [23]: For any continuous function $\bar{f}(x)$ defined on a compact set U, there exists a corresponding FLS $\theta^T \varphi(x)$ such that

$$\sup_{x \in U} \left| \bar{f}(x) - \theta^T \varphi(x) \right| \le \varepsilon, \tag{6}$$

where ε satisfies $|\varepsilon| \le \varepsilon^*$, ε^* is a positive constant.

Proposition 1 [8]-[10]: Given an arbitrarily chosen matrix $F \in R^{q_i \times q_i}$, for all the matrix $A^{0\sim q_i-1}$ and the nonsingular matrix $V \in R^{q_i \times q_i}$ satisfying

$$\Phi\left(A^{0\sim q_i-1}\right) = VFV^{-1}. \tag{7}$$

The matrices $A^{0\sim q_i-1}$ and V are determined as follows:

$$A^{0\sim q_i-1} = -ZF^{q_i}V^{-1}(Z, F), \tag{8}$$

$$V(Z, F) = \left[\begin{array}{cccc} Z & ZF & \cdots & ZF^{q_i-1} \end{array} \right]^T, \tag{9}$$

where $Z \in R^{1 \times q_i}$ is an arbitrary parameter matrix satisfying $\det V(Z, F) \ne 0$.

Then, to solve the matrix $P\left(A_i^{0\sim q_i}\right)$ satisfying the following Lyapunov matrix equation (12), we introduce some notations related to a square matrix $\Phi \in R^{q_i \times q_i}$:

$$\det(sI + \Phi) \triangleq \sum_{i=0}^{q_i} c_i^{\Phi} s^i, \tag{10}$$

$$adj\left(sI + \Phi^T\right) \triangleq \sum_{i=0}^{q_i-1} C_i^{\Phi} s^i. \tag{11}$$

Proposition 2 [10]: If $\Phi \in R^{q_i \times q_i}$ is Hurwitz, then, the following Lyapunov equation

$$\Phi^T P + P\Phi = -I \tag{12}$$

has a unique solution given by $P = \sum_{i=0}^{q_i-1} C_i^{\Phi} P_0^{-1} \Phi^i$ with $P_0 = \sum_{i=0}^{q_i} c_i^{\Phi} \Phi^i$.

3 High-order backstepping controller design

In this section, a direct design approach for the FTC of the high-order nonlinear SFS with time-varying delay(1) is considered.

Consider $A_i^{0\sim q_i-1} \in R^{1 \times q_i}$, for $i = 1, 2, \ldots, n$, are a set of matrices that guarantee the stability of $\Phi(A_i^{0\sim q_i-1}) \in R^{q_i \times q_i}$. Additionally, consider

$$P_i\left(A_i^{0\sim q_i-1}\right) = \left[\begin{array}{ccc} P_{iF}\left(A_i^{0\sim q_i-1}\right) & P_{iM}\left(A_i^{0\sim q_i-1}\right) & P_{iL}\left(A_i^{0\sim q_i-1}\right) \end{array} \right] \in R^{q_i \times q_i}$$

which represents the unique positive definite solution to the Lyapunov equation:

$$\Phi^T\left(A_i^{0\sim q_i-1}\right) P_i\left(A_i^{0\sim q_i-1}\right) + P_i\left(A_i^{0\sim q_i-1}\right) \Phi\left(A_i^{0\sim q_i-1}\right) = -I_{q_i}$$

where $P_{iF}\left(A_i^{0\sim q_i-1}\right) \in R^{q_i \times 1}$ and $P_{iL}\left(A_i^{0\sim q_i-1}\right) \in R^{q_i \times 1}$.

To further simplify the design of the controller, we introduce a first-order filter as follows:

$$l_i \dot{\bar{\alpha}}_i + \bar{\alpha}_i = \alpha_i, i = 2, \ldots, n, \tag{13}$$

where $\bar{\alpha}_i$ denotes the output and the designed virtual controller α_i denotes the input, and l_i is a positive design parameter.

The filter error is defined as $\varpi_i = \bar{\alpha}_i - \alpha_i$, and we can obtain

$$l_i G_i(\cdot) = l_i \dot{\varpi}_i + \varpi_i, \tag{14}$$

where $G_i(\cdot)$ is a continuous function.

According to Lemma 1, we have

$$\begin{aligned} & h_i\left(x_j^{(0\sim q_j-1)}(t - \tau_j(t))\,|_{j=1\sim i}\right) \\ =& h_i\left(x_j^{(0\sim q_j-1)}\left(t - \tau_{j,\sigma(t)}\right)|_{j=1\sim i}\right) + \vartheta_i, \end{aligned} \tag{15}$$

where $|\vartheta_i| \le \vartheta_i^*$, for $i = 1, \ldots, n$, and $\vartheta_i^* \ge 0$ is an unknow constant.

Next, we introduce the following error transformation system

$$\left\{ \begin{array}{l} \xi_1^{(0\sim q_1-1)} = x_1^{(0\sim q_1-1)} - y_r^{(0\sim q_1-1)}, \\ \xi_i^{(0\sim q_i-1)} = x_i^{(0\sim q_i-1)} - \bar{\alpha}_i^{(0\sim q_i-1)}, \end{array} \right. \tag{16}$$

where $i = 2, \ldots, n$.

According to (16), we can extract

$$\xi_i = x_i - \bar{\alpha}_i \tag{17}$$

and

$$\left\{ \begin{array}{l} \xi_1^{(q_1-1)} = x_1^{(q_1-1)} - y_r^{(q_1-1)}, \\ \xi_i^{(q_i-1)} = x_i^{(q_i-1)} - \bar{\alpha}_i^{(q_i-1)}. \end{array} \right. \tag{18}$$

Step 1: By combining (1), (17) and (18), and subsequently substituting (15), we can determine the q_1th derivative of ξ_1 as

$$\xi_1^{(q_1)} = \bar{f}_1 + g_1(x_1^{(0\sim q_1-1)})(\xi_2 + \varpi_2 + \alpha_2) + \vartheta_1 - y_r^{(q_1)}, \tag{19}$$

where $\bar{f}_1 = f_1(x_1^{(0\sim q_1-1)}) + h_1\left(x_1^{(0\sim q_1-1)}\left(t - \tau_{1,\sigma(t)}\right)\right)$.

According to the [24], the unknown nonlinear functions $\bar{f}_i$ can be approximated by FLSs. Then, the virtual control law α_2 and the adaptive law $\dot{\hat{\theta}}_1$ are constructed as follows:

$$\begin{aligned} \alpha_2 = & -g_1^{-1}(x_1^{(0\sim q_1-1)}) \\ & \times \left(A_1^{0\sim q_1-1}\xi_1^{(0\sim q_1-1)} + \hat{\theta}_1^T \varphi_1(z_1) - y_r^{(q_1)}\right), \end{aligned} \tag{20}$$

$$\dot{\hat{\theta}}_1 = \left(\xi_1^{(0\sim q_1-1)}\right)^T P_{1L}\left(A_1^{0\sim q_1-1}\right)\varphi_1(z_1) - \gamma_1\hat{\theta}_1, \quad (21)$$

where $z_1 = \left(x_1^{(0\sim q_1-1)}, x_1^{(0\sim q_1-1)}\left(t-\tau_{1,\sigma(t)}\right)\right)$.

Substituting (20) into (19), it can be further obtained

$$\dot{\xi}_1^{(0\sim q_1-1)} = \Phi_1\left(A_1^{0\sim q_1-1}\right)\xi_1^{(0\sim q_1-1)} + \begin{bmatrix} 0 \\ b_1 \end{bmatrix}, \quad (22)$$

where $b_1 = \tilde{\theta}_1^T\varphi_1(z_1) + \varepsilon_1 + \vartheta_1 + g_1(x_1^{(0\sim q_1-1)})(\xi_2 + \varpi_2)$.

Design the Lyapunov function in the following manner

$$V_1 = \left(\xi_1^{(0\sim q_1-1)}\right)^T P_1\left(A_1^{0\sim q_1-1}\right)\xi_1^{(0\sim q_1-1)} + \tilde{\theta}_1^T\tilde{\theta}_1. \quad (23)$$

Taking the derivative of V_1 and substituting (21) and (22), we obtain

$$\begin{aligned}\dot{V}_1 = &-\left\|\xi_1^{(0\sim q_1-1)}\right\|^2 + 2\gamma_1\tilde{\theta}_1^T\hat{\theta}_1 + 2\left(\xi_1^{(0\sim q_1-1)}\right)^T \\ &\times P_{1L}\left(A_1^{0\sim q_1-1}\right)g_1(x_1^{(0\sim q_1-1)})(\xi_2+\varpi_2) \\ &+ 2\left(\xi_1^{(0\sim q_1-1)}\right)^T P_{1L}\left(A_1^{0\sim q_1-1}\right)(\varepsilon_1+\vartheta_1). \quad (24)\end{aligned}$$

Through the utilization of inequalities, one can derive

$$\begin{aligned}&2\left(\xi_1^{(0\sim q_1-1)}\right)^T P_{1L}\left(A_1^{0\sim q_1-1}\right)g_1(x_1^{(0\sim q_1-1)})(\xi_2+\varpi_2) \\ \le&\frac{1}{4}\left\|\xi_1^{(0\sim q_1-1)}\right\|^2 + 8\left\|P_{1L}\left(A_1^{0\sim q_1-1}\right)\right\|^2 g_1^2(x_1^{(0\sim q_1-1)})\varpi_2^2 \\ &+ 8\left\|P_{1L}\left(A_1^{0\sim q_1-1}\right)\right\|^2 g_1^2(x_1^{(0\sim q_1-1)})\left\|\xi_2^{(0\sim q_2-1)}\right\|^2, \quad (25)\end{aligned}$$

$$\begin{aligned}&2\left(\xi_1^{(0\sim q_1-1)}\right)^T P_{1L}\left(A_1^{0\sim q_1-1}\right)(\varepsilon_1+\vartheta_1) \\ \le&\frac{1}{4}\left\|\xi_1^{(0\sim q_1-1)}\right\|^2 + 8\left\|P_{1L}\left(A_1^{0\sim q_1-1}\right)\right\|^2(\varepsilon_1^{*2}+\vartheta_1^{*2}). \quad (26)\end{aligned}$$

By substituting (25) and (26),(24) can be rewritten as

$$\begin{aligned}\dot{V}_1 \le &-\frac{1}{2}\left\|\xi_1^{(0\sim q_1-1)}\right\|^2 + 2\gamma_1\tilde{\theta}_1^T\hat{\theta}_1 \\ &+ 8\left\|P_{1L}\left(A_1^{0\sim q_1-1}\right)\right\|^2 g_1^2(x_1^{(0\sim q_1-1)})\varpi_2^2 \\ &+ 8\left\|P_{1L}\left(A_1^{0\sim q_1-1}\right)\right\|^2 g_1^2(x_1^{(0\sim q_1-1)})\left\|\xi_2^{(0\sim q_2-1)}\right\|^2 + c_1, \quad (27)\end{aligned}$$

where $c_1 = 8\left\|P_{1L}\left(A_1^{0\sim q_1-1}\right)\right\|^2(\varepsilon_1^{*2}+\vartheta_1^{*2})$.

Step i: Similarly, from (1),(17) and (18), the q_ith derivative of ξ_i can be obtained by substituting (15) as follows :

$$\begin{aligned}\xi_i^{(q_i)} =&\bar{f}_i + g_i(x_j^{(0\sim q_j-1)}|_{j=1\sim i})(\xi_{i+1}+\varpi_{i+1}+\alpha_{i+1}) \\ &+ \vartheta_i - \bar{\alpha}_i^{(q_i)}, \quad (28)\end{aligned}$$

where $\bar{f}_i = h_i\left(x_j^{(0\sim q_j-1)}\left(t-\tau_{j,\sigma(t)}\right)|_{j=1\sim i}\right) + f_i(x_j^{(0\sim q_j-1)}|_{j=1\sim i})$.

The virtual controller α_{i+1} and the adaptive law $\dot{\hat{\theta}}_i$ are chosen as

$$\begin{aligned}\alpha_{i+1} = &-\left(g_i(x_j^{(0\sim q_j-1)}|_{j=1\sim i})\right)^{-1} \\ &\times\left(A_i^{0\sim q_i-1}\xi_i^{(0\sim q_i-1)} + \hat{\theta}_i^T\varphi_i(z_i) - \bar{\alpha}_i^{(q_i)}\right), \quad (29)\end{aligned}$$

$$\dot{\hat{\theta}}_i = \left(\xi_i^{(0\sim q_i-1)}\right)^T P_{iL}\left(A_i^{0\sim q_i-1}\right)\varphi_i(z_i) - \gamma_i\hat{\theta}_i, \quad (30)$$

where $z_i = \left(x_j^{(0\sim q_j-1)}|_{j=1\sim i}, x_j^{(0\sim q_j-1)}(t-\tau_{j,\sigma(t)})|_{j=1\sim i}\right)$.

Combining (28) and (29) yields the updated value of $\xi_i^{(q_i)}$, and furthermore, the state space expression can be obtained

$$\dot{\xi}_i^{(0\sim q_i-1)} = \Phi_i\left(A_i^{0\sim q_i-1}\right)\xi_i^{(0\sim q_i-1)} + \begin{bmatrix} 0 \\ b_i \end{bmatrix}, \quad (31)$$

where $b_i = g_i(x_j^{(0\sim q_j-1)}|_{j=1\sim i})(\xi_{i+1}+\varpi_{i+1}) + \tilde{\theta}_i^T\varphi_i(z_i) + \varepsilon_i + \vartheta_i$.

Choose the Lyapunov function in the following manner

$$V_i = \left(\xi_i^{(0\sim q_i-1)}\right)^T P_i\left(A_i^{0\sim q_i-1}\right)\xi_i^{(0\sim q_i-1)} + \varpi_i^2 + \tilde{\theta}_i^T\tilde{\theta}_i. \quad (32)$$

Differentiating V_i and subsequently replacing (30) and (31) into it yields

$$\begin{aligned}\dot{V}_i = &-\left\|\xi_i^{(0\sim q_i-1)}\right\|^2 + 2\gamma_i\tilde{\theta}_i^T\hat{\theta}_i + 2\left(\xi_i^{(0\sim q_i-1)}\right)^T \\ &\times P_{iL}\left(A_i^{0\sim q_i-1}\right)g_i(x_j^{(0\sim q_j-1)}|_{j=1\sim i})(\xi_{i+1}+\varpi_{i+1}) \\ &+ 2\left(\xi_i^{(0\sim q_i-1)}\right)^T P_{iL}\left(A_i^{0\sim q_i-1}\right)(\varepsilon_i+\vartheta_i) \\ &+ 2\varpi_i\left(G_i(\cdot) - \frac{\varpi_i}{l_i}\right). \quad (33)\end{aligned}$$

By applying the inequality, we conclude that

$$2\varpi_i G_i(\cdot) \le \beta + \frac{G_i^2(\cdot)\varpi_i^2}{\beta}. \quad (34)$$

Substituting (34) into (33) and similar to (25) and (26), (33) can be written as

$$\begin{aligned}\dot{V}_i \le &-\frac{1}{2}\left\|\xi_i^{(0\sim q_i-1)}\right\|^2 + 2\gamma_i\tilde{\theta}_i^T\hat{\theta}_i - \left(\frac{2}{l_i} - \frac{G_i^2(\cdot)}{\beta}\right)\varpi_i^2 \\ &+ 8\left\|P_{iL}\left(A_i^{0\sim q_i-1}\right)\right\|^2 g_i^2(x_j^{(0\sim q_j-1)}|_{j=1\sim i})\left\|\xi_{i+1}^{(0\sim q_{i+1}-1)}\right\|^2 \\ &+ 8\left\|P_{iL}\left(A_i^{0\sim q_i-1}\right)\right\|^2 g_i^2(x_j^{(0\sim q_j-1)}|_{j=1\sim i})\varpi_{i+1}^2 + c_i, \quad (35)\end{aligned}$$

where $c_i = 8\left\|P_{iL}\left(A_i^{0\sim q_i-1}\right)\right\|^2(\varepsilon_i^{*2}+\vartheta_i^{*2}) + \beta$.

Step n: In view of [17], the system (1) together with (15), taking the q_nth derivative of ξ_n yields

$$\begin{aligned}\xi_n^{(q_n)} = &\varrho u + \bar{f}_n(z_n,u) + g_n(x_i^{(0\sim q_i-1)}|_{i=1\sim n})m(u) \\ &+ \vartheta_n - \bar{\alpha}_n^{(q_n)} + l(t-T_0)\nu\left(x_i^{(0\sim q_i-1)}|_{i=1\sim n}, u\right), \quad (36)\end{aligned}$$

where $\bar{f}_n(z_n,u) = \left(g_n(x_i^{(0\sim q_i-1)}|_{i=1\sim n})k(u)-\varrho\right)u + f_n(x_i^{(0\sim q_i-1)}|_{i=1\sim n})+h_n\left(x_i^{(0\sim q_i-1)}\left(t-\tau_{i,\sigma(t)}\right)|_{i=1\sim n}\right)$, $\varrho > 0$ is a design parameter and $z_n = \left(x_i^{(0\sim q_i-1)}|_{i=1\sim n}, x_i^{(0\sim q_i-1)}\left(t-\tau_{i,\sigma(t)}\right)|_{i=1\sim n}\right)$.

The actual controller u and the adaptive law $\dot{\hat{\theta}}_n$ can be constructed as

$$u = -\varrho^{-1}\left(A_n^{0\sim q_n-1}\xi_n^{(0\sim q_n-1)} + \hat{\theta}_n^T\varphi_n(z_n,u_f) - \bar{\alpha}_n^{(q_n)}\right), \tag{37}$$

$$\dot{\hat{\theta}}_n = \left(\xi_n^{(0\sim q_n-1)}\right)^T P_{nL}\left(A_n^{0\sim q_n-1}\right)\varphi_n(z_n,u_f) - \gamma_n\hat{\theta}_n. \tag{38}$$

Substituting (37) into (36), subsequently, it can be transformed into a state-space representation

$$\dot{\xi}_n^{(0\sim q_n-1)} = \Phi_n\left(A_n^{0\sim q_n-1}\right)\xi_n^{(0\sim q_n-1)} + \begin{bmatrix} 0 \\ b_n \end{bmatrix}, \tag{39}$$

where $b_n = \bar{f}_n(z_n,u) + g_n(x_i^{(0\sim q_i-1)}|_{i=1\sim n})m(u) + \vartheta_n - \hat{\theta}_n^T\varphi_n(z_n,u_f) + l(t-T_0)\nu\left(x_i^{(0\sim q_i-1)}|_{i=1\sim n}, u\right)$.

Construct the Lyapunov function in the following manner

$$V_n = \left(\xi_n^{(0\sim q_n-1)}\right)^T P_n\left(A_n^{0\sim q_n-1}\right)\xi_n^{(0\sim q_n-1)} + \varpi_n^2 + \tilde{\theta}_n^T\tilde{\theta}_n. \tag{40}$$

Computing the time derivative of V_n gives

$$\begin{aligned}\dot{V}_n = &\left(\xi_n^{(0\sim q_n-1)}\right)^T\left(\Phi_n^T\left(A_n^{0\sim q_n-1}\right)P_n\left(A_n^{0\sim q_n-1}\right)\right.\\ &\left.+P_n\left(A_n^{0\sim q_n-1}\right)\Phi_n\left(A_n^{0\sim q_n-1}\right)\right)\xi_n^{(0\sim q_n-1)}\\ &+2\left(\xi_n^{(0\sim q_n-1)}\right)^T P_{nL}\left(A_n^{0\sim q_n-1}\right)\left(\bar{f}_n(z_n,u)\right.\\ &\left.+\vartheta_n - \hat{\theta}_n^T\varphi_n(z_n,u_f) + g_n(x_i^{(0\sim q_i-1)}|_{i=1\sim n})m(u)\right.\\ &\left.+l(t-T_0)\nu\left(x_i^{(0\sim q_i-1)}|_{i=1\sim n}, u\right)\right)\\ &+2\varpi_n\left(G_n(\cdot)-\frac{\varpi_n}{l_n}\right) - 2\tilde{\theta}_n^T\dot{\hat{\theta}}_n.\end{aligned} \tag{41}$$

With the application of Assumption 1 and Young's inequality, we can obtain

$$\begin{aligned}&2\left(\xi_n^{(0\sim q_n-1)}\right)^T P_{nL}\left(A_n^{0\sim q_n-1}\right)\left(\bar{f}_n(z_n,u)\right.\\ &\left.+l(t-T_0)\nu\left(x_i^{(0\sim q_i-1)}|_{i=1\sim n}, u\right)\right)\\ \le&2\left|\left(\xi_n^{(0\sim q_n-1)}\right)^T P_{nL}\left(A_n^{0\sim q_n-1}\right)\right||\eta(z_n,u)|\\ \le&\frac{1}{a}\left(\left(\xi_n^{(0\sim q_n-1)}\right)^T P_{nL}\left(A_n^{0\sim q_n-1}\right)\right)^2\eta^2(z_n,u)+a\\ =&2\left(\xi_n^{(0\sim q_n-1)}\right)^T P_{nL}\left(A_n^{0\sim q_n-1}\right)\bar{\eta}(z_n,u)+a,\end{aligned} \tag{42}$$

where $\bar{\eta}(z_n,u) = \frac{1}{2a}\left(\xi_n^{(0\sim q_n-1)}\right)^T P_{nL}\left(A_n^{0\sim q_n-1}\right)\eta^2(z_n,u)$.

Combined with Lemma 2, $\bar{\eta}(z_n,u)$ can be expressed as

$$\bar{\eta}(z_n,u) = \theta_n^T\varphi_n(z_n,u_f) + \varepsilon_n, \tag{43}$$

where $|\varepsilon_n|$ is bounded by ε_n^*, ε_n^* represents a positive constant, u_f is the output of filtered signal

$$u_f = H_L(s)u \approx u \tag{44}$$

with $H_L(s)$ is the Butterworth low-pass filter. Then, (41) can be represented as follows:

$$\begin{aligned}\dot{V}_n \le &-\left\|\xi_n^{(0\sim q_n-1)}\right\|^2 + 2\varpi_n\left(G_n(\cdot)-\frac{\varpi_n}{l_n}\right)\\ &+2\tilde{\theta}_n^T\left(\left(\xi_n^{(0\sim q_n-1)}\right)^T P_{nL}\left(A_n^{0\sim q_n-1}\right)\varphi_n(z_n,u_f) - \dot{\hat{\theta}}_n\right)\\ &+2\left(\xi_n^{(0\sim q_n-1)}\right)^T P_{nL}\left(A_n^{0\sim q_n-1}\right)(\varepsilon_n+\vartheta_n)+a\\ &+2\left(\xi_n^{(0\sim q_n-1)}\right)^T P_{nL}\left(A_n^{0\sim q_n-1}\right)g_n(x_i^{(0\sim q_i-1)}|_{i=1\sim n})m(u).\end{aligned} \tag{45}$$

Based on Yang's inequality,one have

$$\begin{aligned}&2\left(\xi_n^{(0\sim q_n-1)}\right)^T P_{nL}\left(A_n^{0\sim q_n-1}\right)g_n(x_i^{(0\sim q_i-1)}|_{i=1\sim n})m(u)\\ \le&\frac{1}{4}\left\|\xi_n^{(0\sim q_n-1)}\right\|^2 + 4\left\|P_{nL}\left(A_n^{0\sim q_n-1}\right)\right\|^2 g^{*2}m^{*2}.\end{aligned} \tag{46}$$

Substituting (46) into (45) and similar to (26) and (34), we can obtain the following:

$$\dot{V}_n \le -\frac{1}{2}\left\|\xi_n^{(0\sim q_n-1)}\right\|^2 + 2\gamma_n\tilde{\theta}_n^T\hat{\theta}_n - \left(\frac{2}{l_n}-\frac{G_n^2(\cdot)}{\beta}\right)\varpi_n^2 + c_n, \tag{47}$$

where $c_n = 4\left\|P_{nL}\left(A_n^{0\sim q_n-1}\right)\right\|^2\left(2\left(\varepsilon_n^{*2}+\vartheta_n^{*2}\right)+g^{*2}m^{*2}\right)+a+\beta$.

4 Stability analysis

In this section, the main result of the paper is summarised in the following theorem:

Theorem 1: For high-order time-varying delay nonlinear SFS characterized by non-affine nonlinear faults and asymmetric nonlinear dead-zones (1), and subject to Assumptions 1, 2, and 3, the proposed fuzzy adaptive FTC scheme, comprising the virtual control law (20) and (29), the adaptive law (21), (30) and (38), along with the actual controller (37) guarantees the convergence of the tracking error of the closed-loop control system to a small neighborhood around the origin. This holds true for appropriately selected parameters γ_i and l_i, while ensuring the boundedness of all signals.

Proof: The overall Lyapunov function V is selected as $V = \sum_{i=1}^n V_i$.

In light of the inequalities denoted by (27), (35) and (47), we can derive the derivative of V as

$$\begin{aligned}\dot{V} \le &-\sum_{i=1}^n\left(\frac{1}{2}-\eta_i\right)\left\|\xi_i^{(0\sim q_i-1)}\right\|^2 + 2\sum_{i=1}^n\gamma_i\tilde{\theta}_i^T\hat{\theta}_i\\ &-\sum_{i=2}^n\left(\frac{2}{l_i}-\frac{G_i^2(\cdot)}{\beta}-\delta_i\right)\varpi_i^2 + c_0,\end{aligned} \tag{48}$$

where $c_0 = \sum_{i=1}^n c_i$, $\eta_1 = 0$,

$$\eta_i = 8\left\|P_{i-1,L}\left(A_{i-1}^{0\sim q_{i-1}-1}\right)\right\|^2 g_{i-1}^2(x_j^{(0\sim q_j-1)}|_{j=1\sim i-1}), i = 2,\ldots,n.$$

$$\delta_i = 8\left\|P_{i-1,L}\left(A_{i-1}^{0\sim q_{i-1}-1}\right)\right\|^2 g_{i-1}^2(x_j^{(0\sim q_j-1)}|_{j=1\sim i-1}), i = 2,\ldots,n.$$

and $G_i(\cdot)$ satisfy the inequalities $|G_i(\cdot)| \le \bar{G}_i$ with $\bar{G}_i$ being some positive constants.

Based on Young's inequality, one has

$$\tilde{\theta}_i^T\hat{\theta}_i = \tilde{\theta}_i^T\left(\theta_i - \tilde{\theta}_i\right) \le -\frac{1}{2}\tilde{\theta}_i^T\tilde{\theta}_i + \frac{1}{2}\theta_i^T\theta_i. \tag{49}$$

Substituting (49) into (48) gives

$$\begin{aligned}\dot{V} \leq & -\sum_{i=1}^{n}\left(\frac{1}{2}-\eta_i\right)\left\|\xi_i^{(0\sim q_i-1)}\right\|^2-\sum_{i=1}^{n}\gamma_i\tilde{\theta}_i^T\tilde{\theta}_i \\ & -\sum_{i=2}^{n}\left(\frac{2}{l_i}-\frac{\bar{G}_i^2}{\beta}-\delta_i\right)\varpi_i^2+\sum_{i=1}^{n}\gamma_i\theta_i^T\theta_i+c_0 \\ \leq & -bV+c, \end{aligned} \tag{50}$$

where $c = \sum_{i=1}^{n}\gamma_i\theta_i^T\theta_i + c_0$ and $b = \min\left\{\frac{1}{2}-\eta_i, \gamma_i, \frac{2}{l_i}-\frac{\bar{G}_i^2}{\beta}-\delta_i\right\}$.

5 Simulation example

In order to demonstrate the feasibility of the FTC method proposed in this paper, numerical simulations and analyses were conducted using the following the numerical example:

$$\begin{cases}\dot{x}_1 = & f_1(x_1^{(0\sim 1)})+g_1(x_1^{(0\sim 1)})x_2+h_1\left(x_1^{(0\sim 1)}(t-\tau_1(t))\right), \\ \dot{x}_2 = & f_2(x_i^{(0\sim q_i-1)}|_{i=1\sim 2})+g_2(x_i^{(0\sim q_i-1)}|_{i=1\sim 2})D(u) \\ & +h_2\left(x_i^{(0\sim q_i-1)}(t-\tau_i(t))|_{i=1\sim 2}\right) \\ & +l(t-T_0)\nu\left(x_i^{(0\sim q_i-1)}|_{i=1\sim 2}, u\right), \\ y = & x_1, \end{cases}$$

where $f_1(x_1^{(0\sim 2)}) = \sin(\dot{x}_1)e^{-x_1^4}$, $f_2(x_i^{(0\sim q_i-1)}|_{i=1\sim 2}) = \dot{x}_2 e^{0.5x_1\dot{x}_1} + \dot{x}_1\sin(x_1x_2)$, $g_1(x_1^{(0\sim 2)}) = 2+\sin(x_1\dot{x}_1)$, $g_2(x_i^{(0\sim q_i-1)}|_{i=1\sim 2}) = 3+0.5\cos(x_1\dot{x}_1)\sin(x_2\dot{x}_1)$, and the nonlinear time-delay functions are selected as

$$h_1\left(x_1^{(0\sim 1)}(t-\tau_1(t))\right) = \sin\left(x_1(t-\tau_1(t))\dot{x}_1(t-\tau_1(t))\right),$$

$$\begin{aligned}& h_2\left(x_i^{(0\sim q_i-1)}(t-\tau_i(t))|_{i=1\sim 2}\right) \\ & = \cos\left(x_1(t-\tau_1(t))\dot{x}_1(t-\tau_1(t))\right)+x_2(t-\tau_2(t))\dot{x}_2(t-\tau_2(t)).\end{aligned}$$

The time-varying delays are selected as $\tau_1(t) = 1+\sin(t), \tau_2(t) = 1.2(1+\cos(t))$.

The fault function is chosen as $\nu\left(x_i^{(0\sim q_i-1)}|_{i=1\sim 2}, u\right) = 15(x_1\dot{x}_1x_2\dot{x}_2+\sin(u))+15$, and the parameters of the time profile model of the fault are chosen as $\delta = 8$ and $T_0 = 10$s.

And select the dead-zone as

$$D(u) = \begin{cases}(u-2)(0.5-0.3\sin(u)), u > 2 \\ 0, -1.5 \leq u \leq 2 \\ (u+1.5)(0.6-0.2\cos(u)), u < -1.5\end{cases}$$

The Butterworth low-pass filter is chosen as $H_L(s) = \frac{1}{s^2+1.414s+1}$, and the given reference signal is $y_r = 0.5(\sin(t)+\sin(0.5t))$.

Choose $F_1 = \begin{bmatrix}-6 & 1\\ 0 & -6\end{bmatrix}, F_2 = \begin{bmatrix}-5 & -1\\ 1 & -5\end{bmatrix}, Z_1 = \begin{bmatrix}1 & 0\end{bmatrix}$ and $Z_2 = \begin{bmatrix}1 & 1\end{bmatrix}$, by Proposition 1, we have $V_1 = \begin{bmatrix}Z_1\\ Z_1F_1\end{bmatrix} = \begin{bmatrix}1 & 0\\ -6 & 1\end{bmatrix}$, $V_2 = \begin{bmatrix}Z_2\\ Z_2F_2\end{bmatrix} = \begin{bmatrix}1 & 1\\ -4 & -6\end{bmatrix}$, $A_1^{0\sim 2} = -Z_1F_1^2V_1^{-1} = \begin{bmatrix}36 & 12\end{bmatrix}$ and $A_2^{0\sim 2} = -Z_2F_2^2V_2^{-1} = \begin{bmatrix}26 & 10\end{bmatrix}$.

Select the initial values as $x_1(0) = x_2(0) = 0$ and $\theta_1^T(0) = \theta_2^T(0) = [0,0,0,0,0,0,0]$, and choose the design parameters as $\varrho = 80$, $\gamma_1 = \gamma_2 = 60$ and $l_2 = 0.01$.

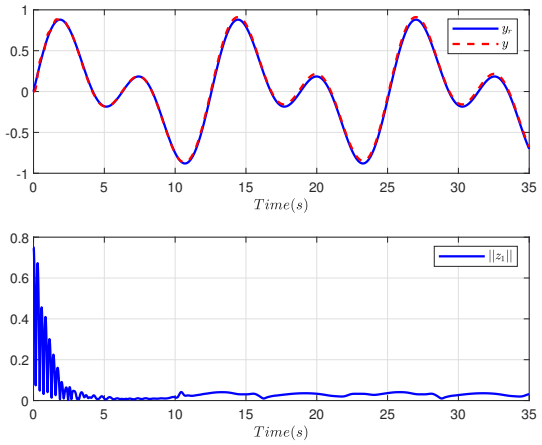

Fig. 1: Tracking performance trajectories

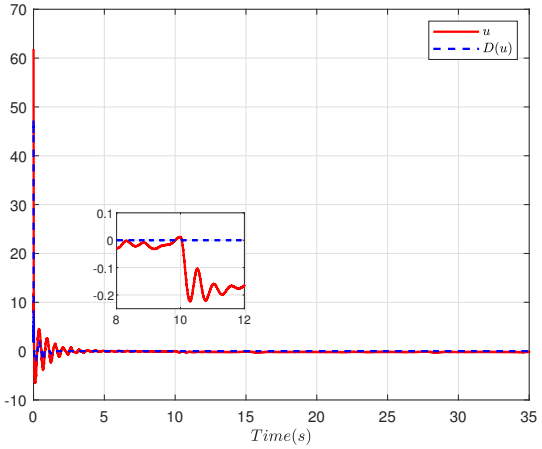

Fig. 2: The trajectories of u and $D(u)$

Simulation results, as shown in Figs. 1-3, clearly demonstrate the effectiveness of the proposed method. It is clear from Fig. 1 that the proposed fuzzy adaptive FTC scheme exhibits excellent control performance. Fig. 2 displays the response of the control input signal. Fig. 3 presents the adaptive laws parameter curves. These results collectively indicate that the control scheme developed in this study not only successfully achieves the specified control objectives but also ensures the stability of the high-order nonlinear SFS.

6 Conclusion

In this study, we have introduced a novel fuzzy adaptive FTC scheme specifically designed for high-order unknown time-varying delay SFS with non-affine nonlinear faults and asymmetric dead-zone inputs. Notably, this approach obviates the requirement for reduced-order processing of high-order systems, enabling a more direct controller design. Furthermore, in dealing with unknown time-varying delays, we relax the condition restrictions by avoiding the use of Lyapunov-Krasovskii functionals, employing combination of the finite coverage lemma and the fuzzy logic systems. And the proposed control method can achieve the control objectives. In future research, we will extend our framework to practical systems such as robotic arm systems,

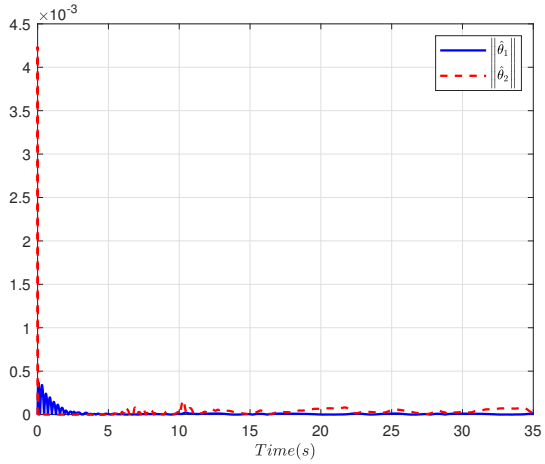

Fig. 3: The trajectories of adaptive parameters

utilizing the theory of fully actuated systems.

References

[1] S. Li, C. K. Ahn, and Z. R. Xiang, Command filter based adaptive fuzzy finite-time control for switched nonlinear systems using state-dependent switching method, *IEEE Transactions on Fuzzy Systems*, 2020, 29(4): 833-845.

[2] Y. M. Li, X. Min, and S. C. Tong, Observer-based fuzzy adaptive inverse optimal output feedback control for uncertain nonlinear systems, *IEEE Transactions on Fuzzy Systems*, 2020, 29(6): 1484-1495.

[3] S. Z. Diao, W. Sun, S. F. Su, and J. W. Xia, Adaptive fuzzy event-triggered control for single-link flexible-joint robots with actuator failures, *IEEE Transactions on Cybernetics*,2021, 52(8): 7231-7241.

[4] G. Zong, Q. Xu, X. Zhao, et al. Output-feedback adaptive neural network control for uncertain nonsmooth nonlinear systems with input deadzone and saturation, *IEEE Transactions on Cybernetics*, 2023, 53(9): 5957-5969.

[5] K. Xu, H. Wang, P. X. Liu, Adaptive fuzzy finite-time tracking control of nonlinear systems with unmodeled dynamics, *Applied Mathematics and Computation*, 2023, 450: 127992.

[6] E. Pereira, S. S. Aphale, V. Feliu, and S. O. R. Moheimani, Integral resonant control for vibration damping and precise tip-positioning of a single-link flexible manipulator, *IEEE/ASME Transactions on Mechatronics*,2010, 16(2): 232-240.

[7] Z. J. Li, Y. Q. Xia, and F. C. Sun, Adaptive fuzzy control for multilateral cooperative teleoperation of multiple robotic manipulators under random network-induced delays, *IEEE Transaction on Fuzzy Systems*, 2013, 22(2): 437-450.

[8] G. R. Duan, High-order fully actuated system approaches: Part II. Generalized strict-feedback systems, *International Journal of Systems Science*, 2021, 52(3): 437-454.

[9] G. R. Duan, High-order fully actuated system approaches: Part III. Robust control and high-order backstepping, *International Journal of Systems Science*,2021, 52(5): 952-971.

[10] G. R. Duan, High-order fully actuated system approaches: Part IV. Adaptive control and high-order backstepping, *International Journal of Systems Science*, 2021, 52(5): 972-989.

[11] Y. Wu, T. Xu, H. Mo, Adaptive tracking control for nonlinear time-delay systems with time-varying full state constraints, *Transactions of the Institute of Measurement and Control*, 2020, 42(12): 2178-2190.

[12] B. Hong, Z. Yu, S. Li, Observer-based adaptive neural control of nonlinear time-delay systems with unknown output function and unknown control directions, *International Journal of Systems Science*, 2021, 52(4): 710-726.

[13] H. Min, S. Xu, B. Zhang, et al. Globally adaptive control for stochastic nonlinear time-delay systems with perturbations and its application, *Automatica*, 2019, 102: 105-110.

[14] G. R. Duan, Fully actuated system approaches for continuous time delay systems: Part 1. Systems with state delays only, *Science China Information Sciences*, 2023, 66(1): 112201.

[15] L. Zhang, P. Wang, C. Hua, Adaptive control of time-delay nonlinear HOFA systems with unmodeled dynamics and unknown dead-zone input, *International Journal of Robust and Nonlinear Control*, 2023, 33(4): 2615-2628.

[16] L. Hu, G. Duan, M. Hou, Adaptive guaranteed cost control for nonlinear systems with unknown parameters and time delays based on fully actuated system approaches, *ISA transactions*, 2024, 145: 112-123.

[17] N. N. Zhao, L. B. Wu, X. Y. Ouyang, et al. Finite-time adaptive fuzzy tracking control for nonlinear systems with disturbances and dead-zone nonlinearities, *Applied Mathematics and Computation*, 2019, 362: 124494

[18] G. Xue, F. Lin, S. Li, et al. Adaptive dynamic surface control for finite-time tracking of uncertain nonlinear systems with dead-zone inputs and actuator faults, *International Journal of Control, Automation and Systems*, 2021, 19(8): 2797-2811.

[19] H. Wang, S. Kang, X. Zhao, et al. Command filter-based adaptive neural control design for nonstrict-feedback nonlinear systems with multiple actuator constraints, *IEEE Transactions on Cybernetics*, 2021, 52(11): 12561-12570.

[20] H. Yang, Y. Jiang, S. Yin, Adaptive fuzzy fault-tolerant control for Markov jump systems with additive and multiplicative actuator faults, *IEEE Transactions on Fuzzy Systems*, 2020, 29(4): 772-785.

[21] D. Yu, M. Yang, Y. J. Liu, et al. Adaptive fuzzy tracking control for uncertain nonlinear systems with multiple actuators and sensors faults, *IEEE Transactions on Fuzzy Systems*, 2022, 31(1): 104-116.

[22] J. Song, Y. Chen, Y. Liu, et al. Fixed-Time Fuzzy Adaptive Fault-Tolerant Control for Strict-Feedback Nonlinear Systems With Input Delay, *IEEE Transactions on Systems, Man, and Cybernetics: Systems*, 2023, 53(11): 6999-7010.

[23] Y. M. Li, K. K. Sun, and S. C. Tong, Observer-based adaptive fuzzy fault-tolerant optimal control for SISO nonlinear systems, *IEEE Transactions on Cybernetics*, 2018, 49(2): 649-661.

[24] D. Zhai, C. Xi, J. Dong, et al. Adaptive fuzzy fault-tolerant tracking control of uncertain nonlinear time-varying delay systems, *IEEE Transactions on Systems, Man, and Cybernetics: Systems*, 2018, 50(5): 1840-1849.

Proceedings of the 3rd Conference on Fully Actuated System Theory and Applications
May 10-12, 2024, Shenzhen, China

Event-triggered Fuzzy Adaptive Fault-Tolerant Control of High-Order Nonlinear Systems: A Fully Actuated System Approach

Qingyi Zhao[1], Yang Cui[1*]

1. School of Electronic and Information Engineering, University of Science and Technology Liaoning, Anshan 114051, China
E-mail: kdcuiyang@163.com

Abstract: In this paper, an event-triggered adaptive tracking control issue is discussed for a class of high-order nonlinear strict-feedback system (SFS). The systems considered involve non-affine nonlinear faults as well as external disturbances. The proposed approach incorporates fuzzy logic systems to handle the unknown nonlinear functions in this system. Additionally, an event-triggered control method is developed using the backstepping technique to conserve network resources. Leveraging the theories of high-order fully actuated (HOFA) systems, dynamic surface control, and event-triggered control, novel adaptive fuzzy fault-tolerant tracking controllers are directly constructed. Importantly, there is no need to convert the high-order system into a first-order one. Theoretical analysis and Lyapunov function theory guarantee the stability of the closed-loop system, ensuring the convergence of the tracking error to a compact neighborhood around zero. The feasibility and effectiveness of the proposed control approach are demonstrated through a simulation example.

Key Words: Fully actuated system approach, Nonlinear systems, Adaptive backstepping control, Fuzzy control, Fault-tolerant control, Event-triggered

1 Introduction

In recent years, the adaptive control problem for uncertain nonlinear systems has garnered significant attention, leading to the proposal of various results [1–3]. With the combination of the backstepping method, the fuzzy control scheme and neural networks has found wide application in practical systems to address uncertainties in nonlinear systems, this approach has been applied to control problems of nonlinear systems, including affine/non-affine nonlinear systems [4, 5] and high-order fully actuated systems [6].

Most of the above control methods are based on the state-space method, which is very effective for dealing with the control problems of nonlinear systems, but it requires that the system must be a first-order differential equation. However, for dealing with control problems of higher-order nonlinear systems, they must be converted to first-order systems, which greatly increases the complexity of the controller design. Many models of real industrial systems often exhibit higher-order differential equations. Therefore, direct controller design for higher-order systems is a great challenge. To address these limitations, a new approach has been introduced—the Fully Actuated System (FAS) approach. Professor Guangren Duan first proposed the High-Order Fully Actuated (HOFA) system method, which was initially proposed and introduced in [7–11]. The above results are extended by incorporating faulty operation conditions to design fault-tolerant controllers for higher-order nonlinear systems in [6]. However, the above article does not consider the problem with event-triggered mechanism for higher-order nonlinear systems.

Event-triggered control has received increasing attention as an effective alternative to traditional time-triggered control. It proves to be efficient in reducing resource waste while ensuring system performance [12–14]. In [14], this brief proposes a fuzzy adaptive event-triggered quantized finite-time control scheme for uncertain strict-feedback nonlinear systems. While there are limited works on event-triggered controllers for fully actuated systems, inspired by the aforementioned results, this study proposes an event-triggered adaptive fuzzy tracking control scheme designed for fully actuated systems.

In real engineering systems, individual components like actuators and sensors may experience abrupt failures during operation. Establishing a fault-tolerant control (FTC) scheme is crucial to address actuator and sensor faults, ensuring the maintenance of a robust system control performance. Several adaptive control methods for nonlinear systems with faults have been investigated in [15–18]. Bias/gain faults, loss of effectiveness faults, and lock-in-place scenarios were considered in previous works [15, 16]. However, these control methods mainly focus on linear faults, most faults are nonlinear functions of both the controller u and state x [17, 18]. However, all the Fault-Tolerant Control (FTC) approaches in the mentioned literature were studied for first-order nonlinear systems. How to directly designing adaptive controllers for higher-order nonlinear SFS with non-affine nonlinear faults has not been studied much. Consequently, this research has significant theoretical and practical value.

The primary contributions of this study are summarized as follows:

1) The proposed high-order backstepping method requires fewer steps compared to the traditional state-space backstepping method. This reduction in steps not only enhances convenience in controller design but also significantly reduces computational complexity.
2) The event-triggered mechanism is designed, which can reduce network resources in signal transmission.
3) Based on the Butterworth low-pass filter, fuzzy logic

This research was supported by the National Natural Science Foundation of China under Grant 61903169, Science Center Program of National Natural Science Foundation of China under Grant 62188101, Liaoning Revitalization Talents Program under Grant XLYC2007182, Education Department Project of Liaoning under Grant LJKMZ20220655.

systems and event-triggered mechanism, we propose an adaptive event-triggered fault-tolerant tracking control law for High-Order Fully Actuated (HOFA) systems with non-affine nonlinear faults and external disturbances.

2 Problem description and preliminaries

2.1 Problem formulation

The high-order nonlinear SFS is considered as

$$\begin{cases} x_1^{(q_1)} = & f_1(x_1^{(0\sim q_1-1)}) + g_1(x_1^{(0\sim q_1-1)})x_2 + d_1(t), \\ x_2^{(q_2)} = & f_2(x_i^{(0\sim q_i-1)}|_{i=1\sim 2}) + g_2(x_i^{(0\sim q_i-1)}|_{i=1\sim 2})x_3 \\ & +d_2(t), \\ & \vdots \\ x_{n-1}^{(q_{n-1})} = & f_{n-1}(x_i^{(0\sim q_i-1)}|_{i=1\sim n-1}) \\ & +g_{n-1}(x_i^{(0\sim q_i-1)}|_{i=1\sim n-1})x_n + d_{n-1}(t), \\ x_n^{(q_n)} = & f_n(x_i^{(0\sim q_i-1)}|_{i=1\sim n}) + g_n(x_i^{(0\sim q_i-1)}|_{i=1\sim n})u \\ & +l(t-T_0)\nu\left(x_i^{(0\sim q_i-1)}|_{i=1\sim n}, u\right) + d_n(t) \\ y = & x_1 \end{cases} \tag{1}$$

where $x_i \in R$, $i = 1, 2, \ldots, n$ are the state variables, $f_j(x_i^{(0\sim q_i-1)}|_{i=1\sim j}) \in R$ and $g_j(x_i^{(0\sim q_i-1)}|_{i=1\sim j}) \in R$, $j = 1, 2 \ldots, n$ denote unknown nonlinear functions and known nonlinear functions, respectively. $y \in R$ and $u \in R$ are the output and input of the considered system. $d_i \in R$, $i = 1, \cdots n$ denotes a bounded external disturbance, and it satisfies that $|d_i(t)| \leq \bar{d}_i$. It is assumed that $g_j(x_i^{(0\sim q_i-1)}|_{i=1\sim j}) \neq 0$. $\nu\left(x_i^{(0\sim q_i-1)}|_{i=1\sim n}, u\right) \in R$ represents an unknown external disturbance induced by a fault. $l(t-T_0) \in R$ signifies the time profile of the fault occurring at an unknown time

$$l(t-T_0) = \begin{cases} 0, & t < T_0 \\ 1 - e^{-\delta(t-T_0)}, & t \geq T_0 \end{cases} \tag{2}$$

where $\delta > 0$ denotes the evolution rate of the unknown fault. The reference signal y_r is a smooth function, and all its derivatives $\dot{y}_r, \ldots, y_r^{(q_1)}$ are bounded.

Assuming that the controller is implemented on a digital platform. We define an increasing sequence $\{t_k\}_{k=0}^{\infty}, t_0 = 0, k \in Z^+$ (Z^+ represents positive integer)to signify the triggering instants of events generated by an event generator. Subsequently, the sample error is expressed as

$$z(t) = \varpi(t) - u(t), t \in [t_k, t_{k+1}) \tag{3}$$

where $\varpi(t)$ is the continuous control input. The sampled control $u(t)$, defined as $u(t) \triangleq \varpi(t_k)$, is obtained at $t = t_k$. The variable $z(t)$ varies randomly and resets to 0 at each t_k, defining a triggering interval $[t_k, t_{k+1})$ as a cycle.

Assumption 1 ([19]): For system (1), the inequality

$$\begin{aligned} &|f_n(x_i^{(0\sim q_i-1)}|_{i=1\sim n}) + l(t-T_0)\nu\left(x_i^{(0\sim q_i-1)}|_{i=1\sim n}, u\right)| \\ \leq &\eta\left(x_i^{(0\sim q_i-1)}|_{i=1\sim n}, u\right) \end{aligned} \tag{4}$$

holds, where $\eta\left(x_i^{(0\sim q_i-1)}|_{i=1\sim n}, u\right)$ is an unknown nonnegative function.

Lemma 1 ([12]): The following inequality holds for any $\rho > 0$ and any $x \in R$:

$$0 \leq |x| - x\tanh\left(\frac{x}{\rho}\right) \leq \kappa\rho \tag{5}$$

where κ is a constant satisfying $\kappa = e^{-(\kappa+1)}$, $\kappa = 0.2785$.

2.2 Preliminaries

In this article, the following symbols are defined to use in the following paper. I_m represents the identity matrix, and

$$x^{(0\sim q)} = \begin{bmatrix} x & \dot{x} & \cdots & x^{(q)} \end{bmatrix}^T$$

$$x_k^{(q_0\sim q_k)}\Big|_{k=i\sim j} = \begin{bmatrix} x_i^{(q_0\sim q_k)} & x_{i+1}^{(q_0\sim q_k)} & \cdots & x_j^{(q_0\sim q_k)} \end{bmatrix}, j \geq i$$

$$A^{0\sim q-1} = \begin{bmatrix} A_0 & A_1 & \cdots & A_{q-1} \end{bmatrix}$$

$$\Phi\left(A^{0\sim q-1}\right) = \begin{bmatrix} 0 & I & & \\ & & \ddots & \\ & & & I \\ -A_0 & -A_1 & \cdots & A_{q-1} \end{bmatrix}$$

Lemma 2 ([19]): Let $f(x)$ be a continuous smooth function defined on a compact set U, for any positive approximation error ε, there exists a Fuzzy Logic System (FLS) $\theta^T\varphi(x)$ such that

$$\sup_{x\in U}\left|f(x) - \theta^T\varphi(x)\right| \leq \varepsilon \tag{6}$$

where ε satisfies $|\varepsilon| \leq \varepsilon^*$, ε^* is a positive constant.

Proposition 1 ([8, 9]): For an arbitrarily chosen $F \in R^{q_i\times q_i}$, all the matrix $A^{0\sim q_i-1}$ and the nonsingular matrix $V \in R^{q_i\times q_i}$ satisfying

$$\Phi\left(A^{0\sim q_i-1}\right) = VFV^{-1}$$

$$A^{0\sim q_i-1} = -ZF^{q_i}V^{-1}(Z, F)$$

$$V(Z, F) = \begin{bmatrix} Z & ZF & \cdots & ZF^{q_i-1} \end{bmatrix}^T$$

where $Z \in R^{1\times q_i}$ is an arbitrary parameter matrix satisfying

$$\det V(Z, F) \neq 0$$

To find the matrix $P\left(A_i^{0\sim q_i}\right)$ that satisfies the Lyapunov matrix equation $\Phi^T P + P\Phi = -I$, we introduce notations related to a square matrix $\Phi \in R^{q_i\times q_i}$: $\det(sI + \Phi) \triangleq \sum_{i=0}^{q_i} c_i^{\Phi} s^i$.

Proposition 2 ([9]): If $\Phi \in R^{q_i\times q_i}$ is Hurwitz, then, the following Lyapunov equation $\Phi^T P + P\Phi = -I$, has a unique solution $P = \sum_{i=0}^{q_i-1} C_i^{\Phi} P_0^{-1}\Phi^i$, where $P_0 = \sum_{i=0}^{q_i} c_i^{\Phi}\Phi^i$.

3 High-order backstepping controller design

Building upon the Higher-Order Fully Actuated (HOFA) theory, the backstepping controller design approach is directly applicable to the high-order nonlinear SFS described by equation (1), eliminating the need to transform the system into a first-order representation.

Consider a set of matrices $A_i^{0\sim q_i-1} \in R^{1\times q_i}$, $i = 1,2,\ldots,n$, these matrices ensure that $\Phi(A_i^{0\sim q_i-1}) \in R^{q_i\times q_i}$, $i = 1,2,\ldots,n$ is stable, and

$$P_i\left(A_i^{0\sim q_i-1}\right)=\left[\begin{array}{ccc} P_{iF}\left(A_i^{0\sim q_i-1}\right) & P_{iM}\left(A_i^{0\sim q_i-1}\right) & P_{iL}\left(A_i^{0\sim q_i-1}\right)\end{array}\right]\in R^{q_i\times q_i} \tag{7}$$

is the unique positive definite solution to the Lyapunov equation:

$$\Phi^T\left(A_i^{0\sim q_i-1}\right)P_i\left(A_i^{0\sim q_i-1}\right)+P_i\left(A_i^{0\sim q_i-1}\right)\Phi\left(A_i^{0\sim q_i-1}\right)=-I_{q_i} \tag{8}$$

where $P_{iF}\left(A_i^{0\sim q_i-1}\right)$, $P_{iL}\left(A_i^{0\sim q_i-1}\right)\in R^{q_i\times 1}$.

This article introduces the following first-order filters:

$$l_i\dot{\bar{\alpha}}_i+\bar{\alpha}_i=\alpha_i, i=2,\ldots,n \tag{9}$$

where $\bar{\alpha}_i$ is the output of filter, α_i is the input of the virtual controller. l_i is a positive design parameter. $\varpi_i=\bar{\alpha}_i-\alpha_i$, denotes the filter error. Then, get

$$l_iG_i(\cdot)=l_i\dot{\varpi}_i+\varpi_i \tag{10}$$

where $G_i(\cdot)$ represents the continuous function.

Step 1: Let

$$\xi_1^{(0\sim q_1-1)}=x_1^{(0\sim q_1-1)}-y_r^{(0\sim q_1-1)}, \tag{11}$$

$$\xi_2^{(0\sim q_2-1)}=x_2^{(0\sim q_2-1)}-\bar{\alpha}_2^{(0\sim q_2-1)}, \tag{12}$$

(12) can be decomposed into $\xi_2=x_2-\bar{\alpha}_2$.

Then, the q_1th derivative of ξ_1 is given by

$$\begin{aligned}\xi_1^{(q_1)}=&f_1(x_1^{(0\sim q_1-1)})+g_1(x_1^{(0\sim q_1-1)})(\xi_2+\varpi_2+\alpha_2)\\&+d_1-y_r^{(q_1)}.\end{aligned} \tag{13}$$

The virtual control α_2 in the design is as follows:

$$\begin{aligned}\alpha_2 =& -g_1^{-1}(x_1^{(0\sim q_1-1)})\left(A_1^{0\sim q_1-1}\xi_1^{(0\sim q_1-1)}\right.\\&\left.+\hat{\theta}_1^T\varphi_1\left(x_1^{(0\sim q_1-1)}\right)-y_r^{(q_1)}\right).\end{aligned} \tag{14}$$

Substituting (14) into (13), (13) can be further expressed as:

$$\dot{\xi}_1^{(0\sim q_1-1)}=\Phi_1\left(A_1^{0\sim q_1-1}\right)\xi_1^{(0\sim q_1-1)}+\left[\begin{array}{cc}0 & b_1\end{array}\right]^T, \tag{15}$$

where $b_1 = \tilde{\theta}_1^T\varphi_1\left(x_1^{(0\sim q_1-1)}\right)+d_1+\varepsilon_1+g_1(x_1^{(0\sim q_1-1)})(\xi_2+\varpi_2)$.

Choosing the Lyapunov function candidate as follows:

$$V_1=\left(\xi_1^{(0\sim q_1-1)}\right)^TP_1\left(A_1^{0\sim q_1-1}\right)\xi_1^{(0\sim q_1-1)}+\tilde{\theta}_1^T\tilde{\theta}_1. \tag{16}$$

The derivative of (16) is

$$\begin{aligned}\dot{V}_1=&\left(\xi_1^{(0\sim q_1-1)}\right)^T\left(\Phi_1^T\left(A_1^{0\sim q_1-1}\right)P_1\left(A_1^{0\sim q_1-1}\right)\right.\\&\left.+P_1\left(A_1^{0\sim q_1-1}\right)\Phi_1\left(A_1^{0\sim q_1-1}\right)\right)\xi_1^{(0\sim q_1-1)}\\&+2\tilde{\theta}_1^T\left(\left(\xi_1^{(0\sim q_1-1)}\right)^TP_{1L}\left(A_1^{0\sim q_1-1}\right)\varphi_1\left(x_1^{(0\sim q_1-1)}\right)-\dot{\hat{\theta}}_1\right)\\&+2\left(\xi_1^{(0\sim q_1-1)}\right)^TP_{1L}\left(A_1^{0\sim q_1-1}\right)g_1(x_1^{(0\sim q_1-1)})(\xi_2+\varpi_2)\\&+2\left(\xi_1^{(0\sim q_1-1)}\right)^TP_{1L}\left(A_1^{0\sim q_1-1}\right)(d_1+\varepsilon_1).\end{aligned} \tag{17}$$

By designing the adaptive law and using the following inequalities:

$$\dot{\hat{\theta}}_1=\left(\xi_1^{(0\sim q_1-1)}\right)^TP_{1L}\left(A_1^{0\sim q_1-1}\right)\varphi_1\left(x_1^{(0\sim q_1-1)}\right)-\lambda_1\hat{\theta}_1 \tag{18}$$

$$\begin{aligned}&2\left(\xi_1^{(0\sim q_1-1)}\right)^TP_{1L}\left(A_1^{0\sim q_1-1}\right)g_1(x_1^{(0\sim q_1-1)})(\xi_2+\varpi_2)\\\le&\frac{1}{4}\left\|\xi_1^{(0\sim q_1-1)}\right\|^2+8\left\|P_{1L}\left(A_1^{0\sim q_1-1}\right)\right\|^2g_1^2(x_1^{(0\sim q_1-1)})\varpi_2^2\\&+8\left\|P_{1L}\left(A_1^{0\sim q_1-1}\right)\right\|^2g_1^2(x_1^{(0\sim q_1-1)})\left\|\xi_2^{(0\sim q_2-1)}\right\|^2\end{aligned} \tag{19}$$

$$\begin{aligned}&2\left(\xi_1^{(0\sim q_1-1)}\right)^TP_{1L}\left(A_1^{0\sim q_1-1}\right)(d_1+\varepsilon_1)\\\le&\frac{1}{2}\left\|\xi_1^{(0\sim q_1-1)}\right\|^2+4\left\|P_{1L}\left(A_1^{0\sim q_1-1}\right)\right\|^2\left(\bar{d}_1^2+\varepsilon_1^{*2}\right)\end{aligned} \tag{20}$$

(17) becomes

$$\begin{aligned}\dot{V}_1\le&-\frac{1}{4}\left\|\xi_1^{(0\sim q_1-1)}\right\|^2+2\lambda_1\tilde{\theta}_1^T\hat{\theta}_1+c_1\\&+8\left\|P_{1L}\left(A_1^{0\sim q_1-1}\right)\right\|^2g_1^2(x_1^{(0\sim q_1-1)})\varpi_2^2\\&+8\left\|P_{1L}\left(A_1^{0\sim q_1-1}\right)\right\|^2g_1^2(x_1^{(0\sim q_1-1)})\left\|\xi_2^{(0\sim q_2-1)}\right\|^2,\end{aligned} \tag{21}$$

where $c_1=4\left\|P_{1L}\left(A_1^{0\sim q_1-1}\right)\right\|^2\left(\bar{d}_1^2+\varepsilon_1^{*2}\right)$.

Step i: Let

$$\xi_i^{(0\sim q_i-1)}=x_i^{(0\sim q_i-1)}-\bar{\alpha}_i^{(0\sim q_i-1)}, \tag{22}$$

(22) can be written as $\xi_i^{(q_i-1)}=x_i^{(q_i-1)}-\bar{\alpha}_i^{(q_i-1)}$.

Utilizing equation (1), yield

$$\begin{aligned}\xi_i^{(q_i)}=&f_i(x_j^{(0\sim q_j-1)}|_{j=1\sim i})+g_i(x_j^{(0\sim q_j-1)}|_{j=1\sim i})x_{i+1}\\&+d_i-\bar{\alpha}_i^{(q_i)}.\end{aligned} \tag{23}$$

Let

$$\xi_{i+1}^{(0\sim q_{i+1}-1)}=x_{i+1}^{(0\sim q_{i+1}-1)}-\bar{\alpha}_{i+1}^{(0\sim q_{i+1}-1)}, \tag{24}$$

(24) can be converted to an equivalent $\xi_{i+1}=x_{i+1}-\bar{\alpha}_{i+1}$.

Substituting $\xi_{i+1}=x_{i+1}-\bar{\alpha}_{i+1}$ into (23) gives

$$\begin{aligned}\xi_i^{(q_i)}=&f_i(x_j^{(0\sim q_j-1)}|_{j=1\sim i})-\bar{\alpha}_i^{(q_i)}+d_i\\&+g_i(x_j^{(0\sim q_j-1)}|_{j=1\sim i})(\xi_{i+1}+\varpi_{i+1}+\alpha_{i+1}).\end{aligned} \tag{25}$$

Designing the virtual controller α_{i+1} as follows:

$$\begin{aligned}\alpha_{i+1}=&-\left(g_i(x_j^{(0\sim q_j-1)}|_{j=1\sim i})\right)^{-1}\left(A_i^{0\sim q_i-1}\xi_i^{(0\sim q_i-1)}\right.\\&\left.+\hat{\theta}_i^T\varphi(x_j^{(0\sim q_j-1)}|_{j=1\sim i})-\bar{\alpha}_i^{(q_i)}\right),\end{aligned} \tag{26}$$

and substituting (26) into (25), (25) can be further rewritten in the state-space form as follows:

$$\dot{\xi}_i^{(0\sim q_i-1)}=\Phi_i\left(A_i^{0\sim q_i-1}\right)\xi_i^{(0\sim q_i-1)}+\left[\begin{array}{cc}0 & b_i\end{array}\right]^T, \tag{27}$$

where $b_i = \tilde{\theta}_i^T \varphi(x_j^{(0\sim q_j-1)}|_{j=1\sim i}) + d_i + \varepsilon_i + g_i(x_j^{(0\sim q_j-1)}|_{j=1\sim i})(\xi_{i+1}+\varpi_{i+1})$.

Select Lyapunov function candidate as follows:

$$V_i = \left(\xi_i^{(0\sim q_i-1)}\right)^T P_i \left(A_i^{0\sim q_i-1}\right) \xi_i^{(0\sim q_i-1)} + \varpi_i^2 + \tilde{\theta}_i^T \tilde{\theta}_i. \tag{28}$$

Taking the derivative of V_i yields

$$\begin{aligned}\dot{V}_i =& \left(\xi_i^{(0\sim q_i-1)}\right)^T \left(\Phi_i^T\left(A_i^{0\sim q_i-1}\right) P_i \left(A_i^{0\sim q_i-1}\right)\right.\\ &\left. + P_i\left(A_i^{0\sim q_i-1}\right)\Phi_i\left(A_i^{0\sim q_i-1}\right)\right)\xi_i^{(0\sim q_i-1)}\\ &+2\tilde{\theta}_i^T\left(\left(\xi_i^{(0\sim q_i-1)}\right)^T P_{iL}\left(A_i^{0\sim q_i-1}\right)\varphi(x_j^{\left(0\sim q_j-1\right)}|_{j=1\sim i})\right.\\ &\left.-\dot{\hat{\theta}}_i\right)+2\left(\xi_i^{(0\sim q_i-1)}\right)^T P_{iL}\left(A_i^{0\sim q_i-1}\right) g_i(x_j^{\left(0\sim q_j-1\right)}|_{j=1\sim i})\\ &(\xi_{i+1}+\varpi_{i+1})+2\left(\xi_i^{(0\sim q_i-1)}\right)^T P_{iL}\left(A_i^{0\sim q_i-1}\right)(d_i+\varepsilon_i)\\ &+2\varpi_i\left(G_i(\cdot)-\frac{\varpi_i}{l_i}\right).\end{aligned} \tag{29}$$

By designing the adaptive law, the following inequality and similar to (19) and (20),

$$\dot{\hat{\theta}}_i = \left(\xi_i^{(0\sim q_i-1)}\right)^T P_{iL}\left(A_i^{0\sim q_i-1}\right)\varphi(x_j^{(0\sim q_j-1)}|_{j=1\sim i}) - \lambda_i\hat{\theta}_i \tag{30}$$

$$2\varpi_i G_i(\cdot) \le \beta + \frac{G_i^2(\cdot)\varpi_i^2}{\beta} \tag{31}$$

(29) becomes

$$\begin{aligned}\dot{V}_i \le& -\frac{1}{4}\left\|\xi_i^{(0\sim q_i-1)}\right\|^2 + 2\lambda_i\tilde{\theta}_i^T\hat{\theta}_i - \left(\frac{2}{l_i}-\frac{G_i^2(\cdot)}{\beta}\right)\varpi_i^2\\ &+8\left\|P_{iL}\left(A_i^{0\sim q_i-1}\right)\right\|^2 g_i^2(x_j^{(0\sim q_j-1)}|_{j=1\sim i})\left\|\xi_{i+1}^{(0\sim q_{i+1}-1)}\right\|^2\\ &+8\left\|P_{iL}\left(A_i^{0\sim q_i-1}\right)\right\|^2 g_i^2(x_j^{(0\sim q_j-1)}|_{j=1\sim i})\varpi_{i+1}^2 + c_i,\end{aligned} \tag{32}$$

where $c_i = 4\left\|P_{iL}\left(A_i^{0\sim q_i-1}\right)\right\|^2\left(\varepsilon_i^{*2}+\bar{d}_i^2\right)+\beta$.

Step n: Similarly, let,

$$\xi_n^{(0\sim q_n-1)} = x_n^{(0\sim q_n-1)} - \bar{\alpha}_n^{(0\sim q_n-1)} \tag{33}$$

which gives $\xi_n^{(q_n-1)} = x_n^{(q_n-1)} - \bar{\alpha}_n^{(q_n-1)}$.

From the system (1), taking the derivative of (33) yields

$$\begin{aligned}\xi_n^{(q_n)} =& f_n(x_i^{(0\sim q_i-1)}|_{i=1\sim n}) + g_n(x_i^{(0\sim q_i-1)}|_{i=1\sim n})u\\ &+d_n + l(t-T_0)\nu\left(x_i^{(0\sim q_i-1)}|_{i=1\sim n}, u\right) - \bar{\alpha}_n^{(q_n)}.\end{aligned} \tag{34}$$

Based on $z(t)$ in (3), the event-triggered mechanism is designed as:

$$\begin{aligned}\varpi(t) =& -(1+\gamma)\left(v\tanh\left(\frac{v}{\rho}\right)+\bar{m}\tanh\left(\frac{\bar{m}}{\rho}\right)\right),\\ u(t) =& \varpi(t_k), \forall t\in[t_k, t_{k+1}),\\ t_{k+1} =& \inf\{t\in R \mid |z(t)| \ge \gamma|u(t)|+m\},\end{aligned} \tag{35}$$

where v is the virtual control input, ρ is a positive constant, $0<\gamma<1$, $m>0$, and $\bar{m} > [m/(1-\gamma)]$ are constants to be designed. From (35), there are two time-varying parameters $r_i(t)$, $i=1,2$, satisfying $|r_i(t)|\le 1$, based on analysis of the relative-threshold scheme in ([20]), such that

$$u(t) = \frac{\varpi(t)}{1+r_1(t)\gamma} - \frac{r_2(t)m}{1+r_1(t)\gamma}. \tag{36}$$

Design the following Lyapunov function

$$V_n = \left(\xi_n^{(0\sim q_n-1)}\right)^T P_n\left(A_n^{0\sim q_n-1}\right)\xi_n^{(0\sim q_n-1)} + \varpi_n^2 + \tilde{\theta}_n^T\tilde{\theta}_n. \tag{37}$$

Combining (34) and (36), V_n derivative is given as

$$\begin{aligned}\dot{V}_n =& \left[\begin{array}{cccc}\dot{\xi}_n & \cdots & \xi_n^{(q_n-1)} & B_1\end{array}\right] P_n\left(A_n^{0\sim q_n-1}\right)\xi_n^{(0\sim q_n-1)}\\ &+\left(\xi_n^{(0\sim q_n-1)}\right)^T P_n\left(A_n^{0\sim q_n-1}\right)\left[\begin{array}{cccc}\dot{\xi}_n & \cdots & \xi_n^{(q_n-1)} & B_1\end{array}\right]^T\\ &+2\varpi_n\left(G_n(\cdot)-\frac{\varpi_n}{l_n}\right)-2\tilde{\theta}_n^T\dot{\hat{\theta}}_n,\end{aligned} \tag{38}$$

where

$$\begin{aligned}B_1 =& f_n(x_i^{(0\sim q_i-1)}|_{i=1\sim n}) + g_n(x_i^{(0\sim q_i-1)}|_{i=1\sim n})\\ &\left(\frac{\varpi(t)}{1+r_1(t)\gamma}-\frac{r_2(t)m}{1+r_1(t)\gamma}\right)+d_n\\ &+l(t-T_0)\nu\left(x_i^{(0\sim q_i-1)}|_{i=1\sim n}, u\right)-\bar{\alpha}_n^{(q_n)}.\end{aligned}$$

In light of $r_1(t)\in[-1,1]$, $r_2(t)\in[-1,1]$, we have

$$\frac{\varpi(t)}{1+r_1(t)\gamma} \le \frac{\varpi(t)}{1+\gamma}, \left|\frac{r_2(t)m}{1+r_1(t)\gamma}\right| \le \frac{m}{1-\gamma}. \tag{39}$$

Substituting (35) and (39) into (38), have

$$\begin{aligned}\dot{V}_n \le& \left[\begin{array}{cccc}\dot{\xi}_n & \cdots & \xi_n^{(q_n-1)} & B_2\end{array}\right] P_n\left(A_n^{0\sim q_n-1}\right)\xi_n^{(0\sim q_n-1)}\\ &+\left(\xi_n^{(0\sim q_n-1)}\right)^T P_n\left(A_n^{0\sim q_n-1}\right)\left[\begin{array}{cccc}\dot{\xi}_n & \cdots & \xi_n^{(q_n-1)} & B_2\end{array}\right]^T\\ &+2\varpi_n\left(G_n(\cdot)-\frac{\varpi_n}{l_n}\right)-2\tilde{\theta}_n^T\dot{\hat{\theta}}_n,\end{aligned} \tag{40}$$

where

$$\begin{aligned}B_2 =& f_n(x_i^{(0\sim q_i-1)}|_{i=1\sim n}) + g_n(x_i^{(0\sim q_i-1)}|_{i=1\sim n})\\ &\left(-v\tanh\left(\frac{v}{\rho}\right)-\bar{m}\tanh\left(\frac{\bar{m}}{\rho}\right)+\left|\frac{m}{1-\gamma}\right|\right)\\ &+d_n+l(t-T_0)\nu\left(x_i^{(0\sim q_i-1)}|_{i=1\sim n}, u\right)-\bar{\alpha}_n^{(q_n)}.\end{aligned}$$

Based on *Lemma 1* and the following inequality:

$$\left|\frac{m}{1-\gamma}\right| - |\bar{m}| < 0. \tag{41}$$

Combining (40), leads to

$$\begin{aligned}\dot{V}_n \le& \left[\begin{array}{cccc}\dot{\xi}_n & \cdots & \xi_n^{(q_n-1)} & B_3\end{array}\right] P_n\left(A_n^{0\sim q_n-1}\right)\xi_n^{(0\sim q_n-1)}\\ &+\left(\xi_n^{(0\sim q_n-1)}\right)^T P_n\left(A_n^{0\sim q_n-1}\right)\left[\begin{array}{cccc}\dot{\xi}_n & \cdots & \xi_n^{(q_n-1)} & B_3\end{array}\right]^T\\ &+2\varpi_n\left(G_n(\cdot)-\frac{\varpi_n}{l_n}\right)-2\tilde{\theta}_n^T\dot{\hat{\theta}}_n,\end{aligned} \tag{42}$$

where

$$B_3 = f_n(x_i^{(0\sim q_i-1)}|_{i=1\sim n}) + g_n(x_i^{(0\sim q_i-1)}|_{i=1\sim n}) (-|v| + 2\kappa\rho) + d_n + l(t-T_0)\nu\left(x_i^{(0\sim q_i-1)}|_{i=1\sim n}, u\right) - \bar{\alpha}_n^{(q_n)}.$$

Designing the virtual controller

$$v = -\left(g_n(x_i^{(0\sim q_i-1)}|_{i=1\sim n})\right)^{-1}\left(A_n^{0\sim q_n-1}\xi_n^{(0\sim q_n-1)} + \hat{\theta}_n^T\varphi(x_i^{(0\sim q_i-1)}|_{i=1\sim n}, u_f) - \bar{\alpha}_n^{(q_n)}\right), \quad (43)$$

(42) can be converted to

$$\dot{V}_n \le \begin{bmatrix} \dot{\xi}_n & \cdots & \xi_n^{(q_n-1)} & B_4 \end{bmatrix} P_n\left(A_n^{0\sim q_n-1}\right)\xi_n^{(0\sim q_n-1)} + \left(\xi_n^{(0\sim q_n-1)}\right)^T P_n\left(A_n^{0\sim q_n-1}\right)\begin{bmatrix} \dot{\xi}_n & \cdots & \xi_n^{(q_n-1)} & B_4 \end{bmatrix}^T + 2\varpi_n\left(G_n(\cdot) - \frac{\varpi_n}{l_n}\right) - 2\tilde{\theta}_n^T\dot{\hat{\theta}}_n, \quad (44)$$

where

$$B_4 = -A_n^{0\sim q_n-1}\xi_n^{(0\sim q_n-1)} + f_n(x_i^{(0\sim q_i-1)}|_{i=1\sim n}) - \hat{\theta}_n^T\varphi(x_i^{(0\sim q_i-1)}|_{i=1\sim n}, u_f) + l(t-T_0)\nu\left(x_i^{(0\sim q_i-1)}|_{i=1\sim n}, u\right) + 2\kappa\rho g_n(x_i^{(0\sim q_i-1)}|_{i=1\sim n}) + d_n.$$

Where, $\begin{bmatrix} \dot{\xi}_n & \cdots & \xi_n^{(q_n-1)} & B_4 \end{bmatrix}^T = \dot{\xi}_n^{(0\sim q_n-1)}$, $\dot{\xi}_n^{(0\sim q_n-1)}$ can be converted into a state-space form

$$\dot{\xi}_n^{(0\sim q_n-1)} = \Phi_n\left(A_n^{0\sim q_n-1}\right)\xi_n^{(0\sim q_n-1)} + \begin{bmatrix} 0 & b_n \end{bmatrix}^T, \quad (45)$$

where $b_n = f_n(x_i^{(0\sim q_i-1)}|_{i=1\sim n}) - \hat{\theta}_n^T\varphi(x_i^{(0\sim q_i-1)}|_{i=1\sim n}, u_f) + l(t-T_0)\nu\left(x_i^{(0\sim q_i-1)}|_{i=1\sim n}, u\right) + 2\kappa\rho g_n(x_i^{(0\sim q_i-1)}|_{i=1\sim n}) + d_n$.

Combining (44) and (45) , we have

$$\dot{V}_n \le \left(\xi_n^{(0\sim q_n-1)}\right)^T\left(\Phi_n^T\left(A_n^{0\sim q_n-1}\right)P_n\left(A_n^{0\sim q_n-1}\right) + P_n\left(A_n^{0\sim q_n-1}\right)\Phi_n\left(A_n^{0\sim q_n-1}\right)\right)\xi_n^{(0\sim q_n-1)} + 2\left(\xi_n^{(0\sim q_n-1)}\right)^T P_{nL}\left(A_n^{0\sim q_n-1}\right)\left(2\kappa\rho g_n(x_i^{(0\sim q_i-1)}|_{i=1\sim n})\right) + 2\left(\xi_n^{(0\sim q_n-1)}\right)^T P_{nL}\left(A_n^{0\sim q_n-1}\right)\left(f_n(x_i^{(0\sim q_i-1)}|_{i=1\sim n}) - \hat{\theta}_n^T\varphi(x_i^{(0\sim q_i-1)}|_{i=1\sim n}, u_f) + l(t-T_0)\nu\left(x_i^{(0\sim q_i-1)}|_{i=1\sim n}, u\right)\right) + 2\left(\xi_n^{(0\sim q_n-1)}\right)^T P_{nL}\left(A_n^{0\sim q_n-1}\right)d_n + 2\varpi_n\left(G_n(\cdot) - \frac{\varpi_n}{l_n}\right) - 2\tilde{\theta}_n^T\dot{\hat{\theta}}_n. \quad (46)$$

By using *Assumption 1* and Young's inequality, one has

$$2\left(\xi_n^{(0\sim q_n-1)}\right)^T P_{nL}\left(A_n^{0\sim q_n-1}\right)\left(f_n(x_i^{(0\sim q_i-1)}|_{i=1\sim n}) + l(t-T_0)\nu\left(x_i^{(0\sim q_i-1)}|_{i=1\sim n}, u\right)\right) \le 2\left(\xi_n^{(0\sim q_n-1)}\right)^T P_{nL}\left(A_n^{0\sim q_n-1}\right)\bar{\eta}\left(x_i^{(0\sim q_i-1)}|_{i=1\sim n}, u\right) + a, \quad (47)$$

where

$$\bar{\eta}\left(x_i^{(0\sim q_i-1)}|_{i=1\sim n}, u\right) = \frac{1}{2a}\left(\xi_n^{(0\sim q_n-1)}\right)^T P_{nL}\left(A_n^{0\sim q_n-1}\right)\eta^2\left(x_i^{(0\sim q_i-1)}|_{i=1\sim n}, u\right). \quad (48)$$

Define the approximation error as

$$\varepsilon_n = \bar{\eta}\left(x_i^{(0\sim q_i-1)}|_{i=1\sim n}, u\right) - \theta_n^T\varphi(x_i^{(0\sim q_i-1)}|_{i=1\sim n}, u_f), \quad (49)$$

where $|\varepsilon_n| \le \varepsilon_n^*$, ε_n^* being a positive constant, u_f is the output of filtered signal

$$u_f = H_L(s)\,u \approx u, \quad (50)$$

and $H_L(s)$ is the Butterworth low-pass filter.

By designing the adaptive law, similar to (20) and (31) and the following inequality:

$$\begin{aligned} & 2\left(\xi_n^{(0\sim q_n-1)}\right)^T P_{nL}\left(A_n^{0\sim q_n-1}\right)\left(2\kappa\rho g_n(x_i^{(0\sim q_i-1)}|_{i=1\sim n})\right) \\ \le\ & \frac{1}{4}\left\|\xi_n^{(0\sim q_n-1)}\right\|^2 + 16\left\|P_{nL}\left(A_n^{0\sim q_n-1}\right)\right\|^2 g_n^2(x_j^{(0\sim q_j-1)}|_{j=1\sim i})\kappa^2\rho^2 \end{aligned} \quad (51)$$

$$\dot{\hat{\theta}}_n = \left(\xi_n^{(0\sim q_n-1)}\right)^T P_{nL}\left(A_n^{0\sim q_n-1}\right)\varphi(x_i^{(0\sim q_i-1)}|_{i=1\sim n}, u_f) - \lambda_n\hat{\theta}_n \quad (52)$$

$\dot{V}_n$ can be obtained as

$$\dot{V}_n \le -\frac{1}{4}\left\|\xi_n^{(0\sim q_n-1)}\right\|^2 + 2\lambda_n\tilde{\theta}_n^T\hat{\theta}_n - \left(\frac{2}{l_n} - \frac{G_n^2(\cdot)}{\beta}\right)\varpi_n^2 + c_n, \quad (53)$$

where $c_n = 4\left\|P_{nL}\left(A_n^{0\sim q_n-1}\right)\right\|^2\left(\varepsilon_n^{*2} + \bar{d}_n^2\right) + a + \beta + 16\kappa^2\rho^2\left\|P_{nL}\left(A_n^{0\sim q_n-1}\right)\right\|^2 g_n^2(x_j^{(0\sim q_j-1)}|_{j=1\sim i})$.

4 Stability analysis

In accordance with the fully actuated system approach, we have developed an adaptive event-triggered tracking Fault-Tolerant Control (FTC) for a high-order nonlinear SFS with non-affine nonlinear faults. Then, a theorem can be summarized as follows.

Theorem 1: For the fuzzy adaptive event-triggered tracking control of the high-order nonlinear SFS with non-affine nonlinear faults described by equation (1), the main components include virtual controllers (14) and (26), the actual controllers (43) and adaptive laws (18), (30) and (52), if there exist the positive design parameters λ_i and l_i satisfy $\frac{1}{4} - \eta_i > 0$ and $\frac{2}{l_i} - \frac{G_i^2}{\beta} - \delta_i > 0$, then all signals in the closed-loop system are bounded.

Proof: Select the whole Lyapunov function V as $V = \sum_{i=1}^n V_i$.

According to the inequalities (21), (32) and (53), the derivative of V can be given as

$$\dot{V} \le -\sum_{i=1}^n\left(\frac{1}{4} - \eta_i\right)\left\|\xi_i^{(0\sim q_i-1)}\right\|^2 + 2\sum_{i=1}^n\lambda_i\tilde{\theta}_i^T\hat{\theta}_i - \sum_{i=2}^n\left(\frac{2}{l_i} - \frac{G_i^2(\cdot)}{\beta} - \delta_i\right)\varpi_i^2 + c_0, \quad (54)$$

where $c_0 = \sum_{i=1}^{n} c_i$, $\eta_1 = 0$,

$$\eta_i = 8\left\|P_{i-1,L}\left(A_{i-1}^{0\sim q_{i-1}-1}\right)\right\|^2 g_{i-1}^2(x_j^{(0\sim q_j-1)}|_{j=1\sim i-1}), i = 2,\ldots,n$$

$$\delta_i = 8\left\|P_{i-1,L}\left(A_{i-1}^{0\sim q_{i-1}-1}\right)\right\|^2 g_{i-1}^2(x_j^{(0\sim q_j-1)}|_{j=1\sim i-1}), i = 2,\ldots,n.$$

and $G_i(\cdot)$ satisfy the inequalities $|G_i(\cdot)| \le \bar{G}_i$ with $\bar{G}_i$ being some positive constants.

Based on Young's inequality, one has

$$\tilde{\theta}_i^T\hat{\theta}_i = \tilde{\theta}_i^T\left(\theta_i - \tilde{\theta}_i\right) \le -\frac{1}{2}\tilde{\theta}_i^T\tilde{\theta}_i + \frac{1}{2}\theta_i^T\theta_i. \tag{55}$$

Substituting (55) into (54) gives

$$\begin{aligned}\dot{V} \le & -\sum_{i=1}^{n}\left(\frac{1}{4}-\eta_i\right)\left\|\xi_i^{(0\sim q_i-1)}\right\|^2 - \sum_{i=1}^{n}\lambda_i\tilde{\theta}_i^T\tilde{\theta}_i \\ & -\sum_{i=2}^{n}\left(\frac{2}{l_i}-\frac{\bar{G}_i^2}{\beta}-\delta_i\right)\varpi_i^2 + \sum_{i=1}^{n}\lambda_i\theta_i^T\theta_i + c_0 \\ \le & -bV + c,\end{aligned} \tag{56}$$

where $c = \sum_{i=1}^{n}\lambda_i\theta_i^T\theta_i + c_0$ and $b = \min\left\{\frac{1}{4}-\eta_i, \lambda_i, \frac{2}{l_i}-\frac{\bar{G}_i^2}{\beta}-\delta_i\right\}$.

It is proved below that the proposed control protocol avoids the Zeno behavior, which is the phenomenon where events are triggered infinitely many times in a finite time interval. It is first shown that there exists a constant $t^* > 0$ satisfying $\forall k \in Z^+$, $\{t_{k+1} - t_k\} \ge t^*$. By (35) and (3), one has

$$\frac{d}{dt}|z| = sign(z)\,\dot{z} \le |\dot{\varpi}| \tag{57}$$

Form (35), it is evident that $\dot{\varpi}$ is a function of α_{n+1}, which is bounded, Additionally, we have established the continuity of $\dot{\varpi}$ in our analysis. Consequently, there exists a constant ω that satisfies $|\dot{\varpi}| \le \omega$. In addition, $z(t_k) = 0$, $\lim_{t_k\to t_{k+1}} z(t_{k+1}) = m$, we can deduce a lower bound t^* satisfy $t^* \ge (m/\omega) > 0$. Thus, this ensures the avoidance of Zeno behavior.

5 Simulation example

To demonstrate the effectiveness of the proposed control approach, we present a numerical example in the following section:

$$\begin{cases}\dot{x}_1 = & f_1(x_1^{(0\sim 2)}) + g_1(x_1^{(0\sim 2)})x_2 + d_1, \\ \dot{x}_2 = & f_2(x_i^{(0\sim q_i-1)}|_{i=1\sim 2}) + g_2(x_i^{(0\sim q_i-1)}|_{i=1\sim 2})u \\ & +l(t-T_0)\,\nu\left(x_i^{(0\sim q_i-1)}|_{i=1\sim 2}, u\right) + d_2 \\ y = & x_1\end{cases} \tag{58}$$

where $f_1(x_1^{(0\sim 2)}) = \sin(\dot{x}_1)e^{-x_1^4}$, $f_2(x_i^{(0\sim q_i-1)}|_{i=1\sim 2}) = \dot{x}_2 e^{0.5x_1\dot{x}_1} + \dot{x}_1\sin(x_1x_2)$, $g_1(x_1^{(0\sim 2)}) = 2 + \sin(x_1\dot{x}_1)$, $g_2(x_i^{(0\sim q_i-1)}|_{i=1\sim 2}) = 3 + 0.5\cos(x_1\dot{x}_1)\sin(x_2\dot{x}_1)$, $d_1 = 0.1\sin(0.2t)$, $d_2 = 0.1\sin(0.5t)$.

Select the fault function as $\nu\left(x_i^{(0\sim q_i-1)}|_{i=1\sim 2}, u\right) = 15(x_1\dot{x}_1x_2\dot{x}_2 + \sin(u)) + 15$, and the time profile of fault as

$$l(t-T_0) = \begin{cases} 0, & t < T_0 \\ 1 - e^{-\delta(t-T_0)}, & t \ge T_0\end{cases}$$

where $\delta = 8$ and $T_0 = 12$s. The Butterworth low-pass filter is chosen as $H_L(s) = \frac{1}{s^2+1.414s+1}$, and the reference signal is chosen as $y_r = \sin(t)$.

Choose $F_1 = \begin{bmatrix}-6 & 1\\ 0 & -6\end{bmatrix}$, $F_2 = \begin{bmatrix}-5 & -1\\ 1 & -5\end{bmatrix}$, $Z_1 = \begin{bmatrix}1 & 0\end{bmatrix}$ and $Z_2 = \begin{bmatrix}1 & 1\end{bmatrix}$, by Proposition 1, we can calculate the value of V_1, V_2, $A_1^{0\sim 2}$ and $A_2^{0\sim 2}$. Select the initial values as $x_1(0) = x_2(0) = 0$ and $\theta_1^T(0) = \theta_2^T(0) = [0,0,0,0,0,0,0,0]$, and choose the design parameters as $\lambda_1 = \lambda_2 = 60$ and $l_2 = 0.01$.

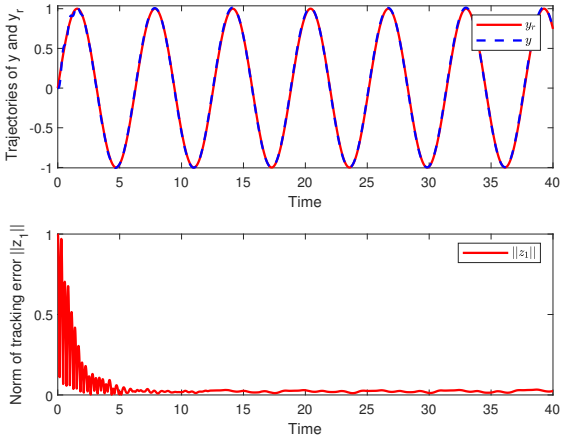

Fig. 1: Tracking performance trajectories

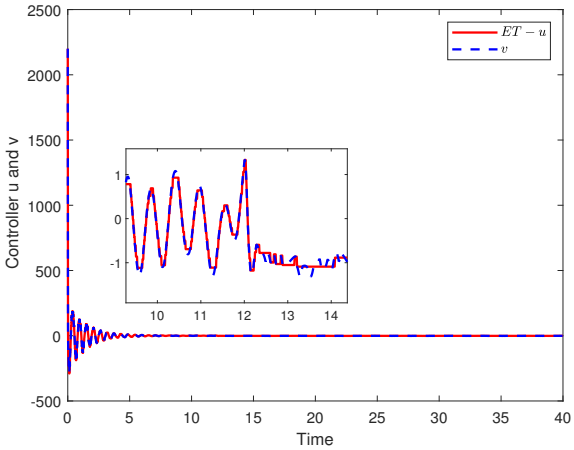

Fig. 2: Trajectory of control signal u

From Fig. 1, the control method proposed in this paper exhibits satisfactory tracking performance. Fig. 2, epicts the response of the adaptive fuzzy tracking controller. The norm of adaptive laws estimation are shown in Fig. 3. The time intervals of the triggering event are illustrated in Fig. 4, the controller minimum triggering time interval $t^* = 0.01 > 0$, which implies the Zeno behavior did not occur. Figs. 1,2,3 and 4 show that our proposed fuzzy adaptive event-triggered tracking control method ensures the stability of the high-order nonlinear SFS. The effectiveness of the proposed algorithm can be obtained from the simulation plots. Compared with Article [6], this paper introduces an event-triggered mechanism in the design of the controller, which consid-

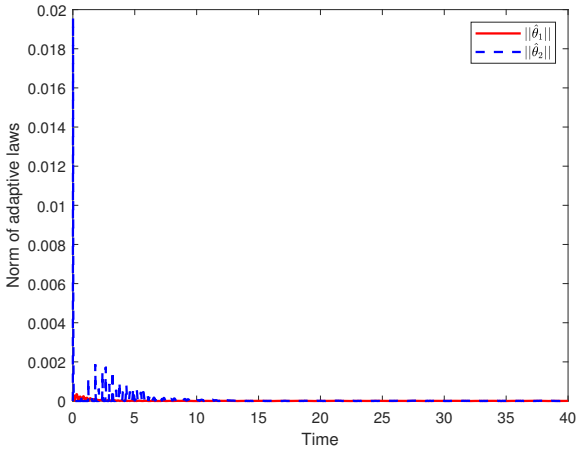

Fig. 3: Trajectories of Norm of adaptive laws estimation $\left\|\hat{\theta}_1\right\|$ and $\left\|\hat{\theta}_2\right\|$

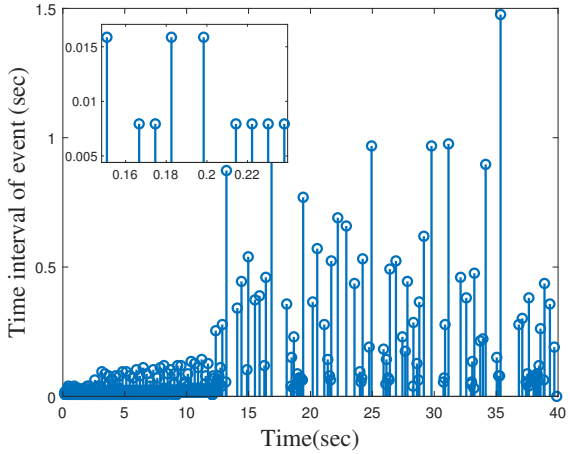

Fig. 4: Time interval of triggering events.

ers the problem of saving the communication resources of the system. Moreover, the fully actuated system method simplifies the controller design compared to the state-space method.

6 Conclusion

We propose a novel event-triggered adaptive fuzzy Fault-Tolerant Control (FTC) method for high-order nonlinear SFS with non-affine nonlinear faults and external disturbances. The fuzzy logic systems serve as approximators for unknown nonlinear functions. The utilization of an event-triggered mechanism contributes to resource conservation on the Internet, and it effectively avoids Zeno behavior. Simulation results for the high-order nonlinear SFS further validate the efficacy of the proposed theoretical approach. Notably, there is no need to convert the high-order system into a first-order one, the controllers are designed directly for the high-order system, and the control performance can be achieved.

References

[1] G Yang, H Wang, J Chen, et al. Command filtered robust control of nonlinear systems with full-state time-varying constraints and disturbances rejection[J]. *Nonlinear Dynamics*, 2020, 101: 2325-2342.

[2] Y Zhang, F Wang, F Yan. Fast finite time adaptive neural network control for a class of uncertain nonlinear systems subject to unmodeled dynamics[J]. *Information Sciences*, 2021, 565: 306-325.

[3] B Li, H Zhang, B Xiao, et al. Fixed-time integral sliding mode control of a high-order nonlinear system[J]. *Nonlinear Dynamics*, 2022, 107: 909-920.

[4] H J Ma, L X Xu, G H Yang. Multiple environment integral reinforcement learning-based fault-tolerant control for affine nonlinear systems[J]. *IEEE transactions on cybernetics*, 2019, 51(4): 1913-1928.

[5] L B Wu, J H Park, X P Xie, et al. Fuzzy adaptive event-triggered control for a class of uncertain nonaffine nonlinear systems with full state constraints[J]. *IEEE Transactions on Fuzzy Systems*, 2020, 29(4): 904-916.

[6] Y Cui, G Duan, X Liu, et al. Adaptive Fuzzy Fault-Tolerant Control of High-Order Nonlinear Systems: A Fully Actuated System Approach[J]. *International Journal of Fuzzy Systems*, 2023: 1-12.

[7] G Duan. High-order fully actuated system approaches: Part II. Generalized strict-feedback systems[J]. *International Journal of Systems Science*, 2021, 52(3): 437-454.

[8] G Duan. High-order fully actuated system approaches: Part III. Robust control and high-order backstepping[J]. *International Journal of Systems Science*, 2021, 52(5): 952-971.

[9] G Duan. High-order fully actuated system approaches: Part IV. Adaptive control and high-order backstepping[J]. *International Journal of Systems Science*, 2021, 52(5): 972-989.

[10] G Duan. High-order fully actuated system approaches: Part V. Robust adaptive control[J]. *International Journal of Systems Science*, 2021, 52(10): 2129-2143.

[11] G Duan. High-order fully actuated system approaches: Part X. Basics of discrete-time systems[J]. *International Journal of Systems Science*, 2022, 53(4): 810-832.

[12] F Li, Y Liu. Adaptive event-triggered output-feedback controller for uncertain nonlinear systems[J]. *Automatica*, 2020, 117: 109006.

[13] R Meng, C Hua, K Li, et al. Adaptive event-triggered control for uncertain high-order fully actuated system[J]. *IEEE Transactions on Circuits and Systems II: Express Briefs*, 2022, 69(11): 4438-4442.

[14] Y Jiang, Z Liu, Z Chen. Fuzzy Adaptive Finite-Time Tracking Control for a Class of Nonlinear Systems: An Event-Triggered Quantized Control Scheme[J]. *IEEE Transactions on Fuzzy Systems*, 2023.

[15] M Liu, D W C Ho, P Shi. Adaptive fault-tolerant compensation control for Markovian jump systems with mismatched external disturbance[J]. *Automatica*, 2015, 58: 5-14.

[16] G Lai, Z Liu, C L P Chen, et al. Adaptive compensation for infinite number of time-varying actuator failures in fuzzy tracking control of uncertain nonlinear systems[J]. *IEEE Transactions on Fuzzy Systems*, 2017, 26(2): 474-486.

[17] W Bai, B Zhang, Q Zhou, et al. Multigradient recursive reinforcement learning NN control for affine nonlinear systems with unmodeled dynamics[J]. *International Journal of Robust and Nonlinear Control*, 2020, 30(4): 1643-1663.

[18] K Sun, L Liu, J Qiu, et al. Fuzzy adaptive finite-time fault-tolerant control for strict-feedback nonlinear systems[J]. *IEEE Transactions on Fuzzy Systems*, 2020, 29(4): 786-796.

[19] Y Li, K Sun, S Tong. Observer-based adaptive fuzzy fault-tolerant optimal control for SISO nonlinear systems[J]. *IEEE transactions on cybernetics*, 2018, 49(2): 649-661.

[20] L Xing, C Wen, Z Liu, et al. Adaptive compensation for actuator failures with event-triggered input[J]. *Automatica*, 2017, 85: 129-136.

Proceedings of the 3rd Conference on Fully Actuated System Theory and Applications
May 10-12, 2024, Shenzhen, China

Global Prescribed-Time Control Fully Actuated Nonlinear Systems

Pengju Ning[1], Changchun Hua*[1], Hao Li[1]

1. The institute of Electrical Engineering, Yanshan University, Qinhuangdao, 066004, China. *Corresponding author: Changchun Hua.
E-mail: pjn-best@foxmail.com;
E-mail: cch@ysu.edu.cn;
E-mail: ysulihao@126.com.

Abstract: This paper studied the problem of prescribed-time control for fully actuated nonlinear system. Utilizing the prescribed-time adjustment function defined herein, along with the solution parameter Lyapunov function, we propose a prescribed-time control scheme for these fully actuated nonlinear systems. Compared to the prescribed-time control scheme based on the backstepping method, the approach presented in this paper offers the benefits of brevity and simplicity in design. Furthermore, we explore the adaptive prescribed-time control for fully actuated nonlinear systems with uncertainties. In this context, we design a novel adaptive time-varying controller to ensure the prescribed-time stability of these uncertain systems. Finally, two simulation examples are givento illustrate the effectiveness of the proposed control scheme.

Key Words: Nonlinear systems, fully actuated system approaches, prescribed-time stability, adaptive control

1 Introduction

Prescribed-time control has been the focus of considerable scholarly interest in recent years, largely due to its characteristics of zero error and expedited convergence. Unlike finite-time and fixed-time control methods, prescribed-time control permits the convergence time to be established independently of the system's initial conditions and control parameters. Furthermore, it allows for the presetting of this time within a practicable range. This unique feature expands the potential applications of prescribed-time control across various fields, including but not limited to, spacecraft rendezvous, telemedicine, emergency braking in automobiles, among other related sectors (see [1]).

The issue of prescribed-time stabilization in high-order nonlinear systems, where nonlinearities and uncertainties are exclusively linked to the control input, was initially explored in [2] using the state-scaling framework. This control framework utilized a time-varying gain function that escalating towards infinity as the settling time nears, serving as a mechanism for state transformation. This innovative approach has since inspired a range of prescribed-time control results, such as [3],[4], [5] and [6]. In [3] and [4], the problems of prescribed-time estimation and output feedback control were addressed for linear systems in observer canonical form and controllable canonical form, respectively. Based on the state-scaling transformation approach, [5] achieved the stabilization of switched nonlinear systems within the prescribed-time. The work of [6] studied the global prescribed-time control problem for strict-feedback nonlinear systems, utilizing the dyncmic gain technique. Different from the state-scaling framework, an innovative method for achieving prescribed-time stabilization of nonlinear systems was developed in [7] using the temporal transformation framework. Building upon this framework, the variable $\tau \in [0, +\infty)$ serves as the mapping for time $t \in [0, T_p)$, thereby transforming the prescribed-time stability problem of the system state with respect to t into an asymptotic stability issue concerning τ.Further, [8] delved into the prescribed-time output feedback control problem for uncertain nonlinear systems. With the aid of two crucial transformations, the adaptive prescribed-time controllers was designed in [9] for strict-feedback nonlinear systems with unknown control directions. Given that the aforementioned methodologies depend on state or temporal transformation, substantial computational resources are essential, particularly for high-order nonlinear systems. To address this limitation, a non-scaling backstepping design methodology was introduced in [10] to achieve prescribed-time stability. This methodology was further extended to address adaptive prescribed-time control for nonlinear time-delay systems and uncertain nonlinear systems with event-trggerring mechanism. The comprehensive details of these extensions can be found in [11], [12], and [13]. In the context of stochastic nonlinear systems with uncertainties, [14] devised prescribed-time state-feedback control strategy, while [15] focused on prescribed-time output-feedback control strategy. In addition, by solving the time-varying parameter Lyapunov equation, [1] accomplished prescribed-time stabilization of linear systems and subsequently extends this approach to nonlinear systems in [16]. However, the current prescribed-time control results rely on the state-space model method, formulated through first-order differential equations, resulting in a relatively intricate controller design.

High-order fully actuated system theory has garnered significant attention in recent years, primarily due to its convenience and effectiveness in addressing control problems. The approaches to high-order fully actuated systems were initially proposed as a methodology in [17], which highlighted the limitations of the first-order system method based on state-space models, introducing the concept of high-order fully actuated systems and emphasizing the advantages in controller design. Based on the Lyapunov stabil-

This work was supported in part by the National Natural Science Foundation of China under Grant U20A20187, in part by the Science Fund for Creative Research Groups of Hebei Province under Grant F2023203100 and Grant F2020203013, in part by the Science and Technology Development Grant of Hebei Province under Grant 20311803D, and in part by the Hebei innovation capability improvement plan project under Grant 22567619H, and in part by the S&T Program of Hebei under Grant No. 236Z1603G.

ity theory, the robust stabilization control scheme and robust tracking control scheme for single high-order fully actuated systems with nonlinear uncertainties were introduced in [18]. Additionally, the work [19] presented an adaptive stabilization control scheme and an adaptive tracking control scheme for high-order fully actuated systems with parametric uncertainties. In [20], the adaptive control problem for uncertain nonlinear time-delay systems was investigated via fully actuated system approaches. In [21], a new active fault-tolerance framework was introduced for uncertain fully-actuated nonlinear systems. The framework established an integration of a fully actuated system adaptive observer and controller. Further, the work [22] presented a linear observer-based fault-tolerant control framework for a class of nonideal time-varying high-order fully actuated systems. The fault-tolerant tracking control problem was studied for fully-actuated nonlinear systems with multiplicative and additive actuator faults in [23]. However, the majority of the aforementioned results can only attain asymptotic stability, signifying that the system state can converge to the equilibrium point only as time approaches infinity.

Building upon the aforementioned discussion, this paper investigates the global prescribed-time control problem for the fully actuated nonlinear system. The main contributions are summarized as follows:

(i) Unlike the prescribed-time control strategy based on the state-space method, the design methodology for the prescribed-time controller proposed in this paper, rooted in the fully actuated system theory, is marked by its straightforwardness and simplicity.

(ii) Contrasting with existing fully actuated system control methods that only achieve asymptotic stability, the control method proposed herein accomplishes prescribed-time stability. This signifies that the system's convergence time remains independent of its initial conditions and other control parameters, and can be determined by the designer within a specified feasible range.

2 Prescribed-Time Control Nonlinear Systems

2.1 Problem formulation

Consider the following fully actuated nonlinear systems

$$\begin{aligned} &x^{(q)}(t) = f(x^{(0\sim q-1)}(t)) + B(x^{(0\sim q-1)}(t))u(t), \\ &u(t) = \nu(t, x^{(0\sim q-1)}(t)), \quad \nu(t,0) = 0, \quad t \geq t_0 \end{aligned} \tag{1}$$

where $t_0 \geq 0$, $x^{(i)}(t) \in \mathcal{R}$, $i = 0, \ldots, q-1$ and $u(t) \in \mathcal{R}$ are the initial time, state and control input of the system, respectively; $\left(x^{(0\sim q-1)}\right)^T = [x, \dot{x}, \cdots, x^{(q-1)}]$, $q \geq 1$ is an integer; $f(\cdot) \in \mathcal{R}$ and $B(\cdot) \in \mathcal{R}_{>0}$ are known continuous functions with $f(0) = 0$. Then $x^{(0\sim q-1)} = 0$ is the equilibrium point of system (1). It should be noted that only x and its derivatives can be obtained and used for controller design.

Let $Z = [x, \dot{x}, \cdots, x^{(q-1)}]^T$, then the system (1) can be transformed into

$$\dot{Z} = AZ + L\left(f\left(x^{(0\sim q-1)}\right) + Bu\right) \tag{2}$$

where $L = [0, 0, \ldots, 0, 1]^T \in \mathcal{R}^q$ and

$$A = \begin{bmatrix} 0 & & & \\ 0 & & I_{(q-1)\times(q-1)} & \\ \vdots & & & \\ 0 & 0 & \cdots & 0 \end{bmatrix} \tag{3}$$

Definition 1 *For an arbitrarily given positive constant T_p, if there exists $u \in \mathcal{R}$, such that the fully actuated system* (1) *is Lyapunov stable, and moreover*

$$x^{(0\sim q-1)}(t) = 0, \ \forall t \geq t_0 + T_p \tag{4}$$

for any $x^{(i)}(t) \in \Omega$, $i = 0, 1 \ldots, q-1$, then the equilibrium point of system (1) *is said to be locally prescribed-time stable, T_p is called the prescribed-time. In particular, if $\Omega = \mathcal{R}$, then the equilibrium point of system* (1) *is called globally prescribed-time stable.*

Definition 2 *([10])* If a continuous function $\mu(t)$ satisfies

$$\begin{aligned} &\mu(t) > 0, \ \ \forall t \in [t_0, t_0 + T_p) \\ &\lim_{t\to(t_0+T_p)^-} \int_{t_0}^{t} \mu(s)\, ds = +\infty \end{aligned} \tag{5}$$

then $\mu(t)$ is called a prescribed-time adjustment (T_p-PTA) function.

Lemma 1 *([16]) Consider the general parametric Lyapunov equation (PLE):*

$$A^T P(\rho) + P(\rho)A - P(\rho)LL^T P(\rho) = -\rho P(\rho) \tag{6}$$

then, we can get that

1) the PLE (6) *has a (unique) positive definite solution $P(\rho) = W^{-1}(\rho)$, which is a polynomial function of ρ, and satisfies the Lyapunov equation*

$$\left(A + \frac{\rho}{2} I_q\right) W + W \left(A + \frac{\rho}{2} I_q\right)^T = LL^T \tag{7}$$

2) $P(\rho)$ has the following properties

$$\frac{dP(\rho)}{d\rho} > 0, \quad \mathrm{tr}(L^T P L) = q\rho \tag{8}$$

3) there exists a constant $\delta \geq 1$, which is independent of ρ, such that

$$\frac{dP(\rho)}{d\rho} \leq \frac{\delta P(\rho)}{q\rho}, \quad \forall \rho > 0 \tag{9}$$

Lemma 2 *([13])* Consider the system (1) with the free control input u, if there exist a continuous differentiable functions $V_1\left(x^{(0\sim q-1)}\right) \in \mathcal{R}_{\geq 0}$, $V_2(t) \in \mathcal{R}_{\geq 0}$ and class $\mathcal{K}_\infty$ functions $\alpha(\cdot)$ satisfying

$$V(t) = V_1(x^{(0\sim q-1)}(t)) + V_2(t) \tag{10}$$

$$\alpha(\|x^{(0\sim q-1)}\|) \leq V_1(x^{(0\sim q-1)}), \ \forall x^{(i)}(t) \in \Omega \tag{11}$$

$$\dot{V}(t) \leq -c\rho(t) V_1(x^{(0\sim q-1)}(t)), \ \forall t \in [t_0, +\infty) \tag{12}$$

where c is a positive constant, $\rho(t) = \mu(t), \ t \in [t_0, t_0 + T_p)$ and $\rho(t) = \varepsilon, \ t \in [t_0 + T_p, +\infty)$ with the T_p-PTA function $\mu(t)$ and the positive constant ε, then the equilibrium point of the system (1) is prescribed-time stable.

The objective of this section is to design a prescribed-time controller for the nonlinear systems (1) based on the fully actuated system approaches, such that the equilibrium point of system (1) is prescribed-time stable.

Remark 1 *The first-order system model within the state-space framework prioritizes the integrity and resolution of the system state, whereas the higher-order fully actuated system model is designed for control development, emphasizing the determination of control variables [1]. On one hand, the derivation of the fully actuated system involves modeling based on fundamental physical principles such as Newton's Law, Momentum (Moment) Theorem, Lagrange's Equation, Kirchhoff's Law, and others [2]. On the other hand, the fully actuated system can be obtained by eliminating and upgrading the underdrive system.*

2.2 Controller design

According to the fully actuated system theory, the controller can be designed as

$$u = -B^{-1}\left(L^T P(\rho) Z + f(x^{(0\sim n-1)})\right), t \in [0, \infty) \quad (13)$$

$$\rho(t) = \begin{cases} \mu(t), & t \in [0, T_p) \\ \varepsilon, & t \in [T_p, +\infty) \end{cases} \quad (14)$$

where $\mu(t) = \frac{\sigma}{T_p - t}$ is a T_p-PTA function, and $\sigma > \frac{\delta}{q} + 1$ is a design parameter. Then, we can obtain that

$$\dot{Z} = AZ - LL^T P(\rho(t)) Z \quad (15)$$

The stability theorem is summarized as follows.

Theorem 1 *For the fully actuated nonlinear systems* (1)*, under the control input* (13)-(14)*, such that the the equilibrium point of system* (1) *is globally prescribed-time stable.*

Proof: First, the Lyapunov function is chosen as

$$V = Z^T P(\rho) Z \quad (16)$$

According to (15), the derivative of Lyapunov function V satisfies

$$\dot{V} = Z^T \left(A^T P + P^T A - 2PLL^T P\right) Z + Z^T \left(\frac{dP}{d\rho}\dot{\rho}\right) Z \quad (17)$$

Then, from (8), (9) and (14), we have

$$0 \le Z^T \left(\frac{dP}{d\rho}\dot{\rho}\right) Z \le \frac{\delta}{\sigma n} \rho Z^T P(\rho) Z \quad (18)$$

since $\sigma > \frac{\delta}{q} + 1$, so $\frac{\delta}{\sigma q} < 1$.

Based on the (6), (17) and (18), we can get that

$$\dot{V} \le -c\rho Z^T P(\rho) Z = -c\rho V \quad (19)$$

where $c = 1 - \frac{\delta}{\sigma q} > 0$ is a constant.

According to (19), we can deduce that

$$V(t) \le V(0)\left(1 - \frac{t}{T_p}\right)^{c\sigma}, \ t \in [0, T_p)$$
$$V(t) = 0, \ t \in [T_p, \infty) \quad (20)$$

where $c\sigma > 1$ is a constant. Let $\rho_0 = \rho(0)$, since

$$V \ge Z^T P(\rho_0) Z \ge \lambda_{min}(P(\rho_0)) \|Z\|^2 \quad (21)$$

we have

$$\|Z(t)\| \le \sqrt{\frac{V(0)}{\lambda_{min}(P(\rho_0))}\left(1 - \frac{t}{T_p}\right)^{c\sigma}}, \ t \in [0, T_p)$$
$$\|Z(t)\| = 0, \ t \in [T_p, \infty) \quad (22)$$

which shows that the equilibrium point $Z = 0$ of system (2) exhibits prescribed-time stability, thereby establishing that the equilibrium point $x^{(0\sim q-1)} = 0$ of system (1) also possesses prescribed-time stability.

In addition, from (8) and (20), one has

$$\begin{aligned} Z^T PLL^T PZ &\le Z^T P^{\frac{1}{2}} \mathrm{tr}\left(P^{\frac{1}{2}} LL^T P^{\frac{1}{2}}\right) P^{\frac{1}{2}} Z \\ &= L^T PLZ^T PZ = n\rho V \\ &\le \frac{nV(0)}{T_p}\left(1 - \frac{t}{T_p}\right)^{\iota}, \ t \in [0, T_p) \\ Z^T PLL^T PZ &= 0, \ t \in [T_p, +\infty) \end{aligned} \quad (23)$$

where $\iota = c\sigma - 1 > 0$ is a constant. Therefore, the controller $u(t)$ is bounded and converges to zero with in the prescribed-time T_p. This proof is finished. ■

Remark 2 *The prior results [17]-[23] based on the full actuated system theory can only achieve bounded stability or asymptotic stability, signifying that the system converges to the origin only as time approaches infinity. In contrast to these works, the prescribed-time control strategy introduced in this article ensures that the system states converge to the origin within a predetermined time, concurrently ensuring boundedness for all state variables. Notably, the settling time of the proposed control strategy is a constant, which is independent of system initial conditions and can be preset according to practical requirements.*

2.3 Simulation example

Consider the fully actuated nonlinear system as follows

$$\ddot{z} = u + 2z\dot{z} + z\sin(\dot{z} - z^2) \quad (24)$$

The controller can be designed as

$$u = -L^T P(\rho) Z - f(\cdot) \quad (25)$$

with $L = [0, 1]^T$, $f(\cdot) = 2z\dot{z} + z\sin(\dot{z} - z^2)$ and

$$P(\rho) = \begin{bmatrix} \rho^3 & \rho^2 \\ \rho^2 & 2\rho \end{bmatrix}, \rho(t) = \begin{cases} \frac{\sigma}{T_p - t}, & t \in [0, T_p) \\ \varepsilon, & t \in [T_p, +\infty) \end{cases} \quad (26)$$

Based on (26), it is easy to verify that

$$\frac{dP(\rho)}{d\rho} \le \frac{3P(\rho)}{\rho} \quad (27)$$

Therefore, the design parameters can be designed as

$$\sigma = 5, \quad \varepsilon = 10, \quad T_p = 5 \quad (28)$$

The initial conditions of the system are given by three different conditions $Z(0) = [1, -1]^T, [-2, 2]^T, [3, 3]^T$. The simulation results are shown in Figs. 1-3.

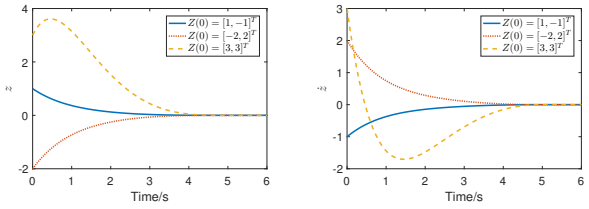

(a) z (b) $\dot{z}$

Fig. 1: The responses of z and $\dot{z}$

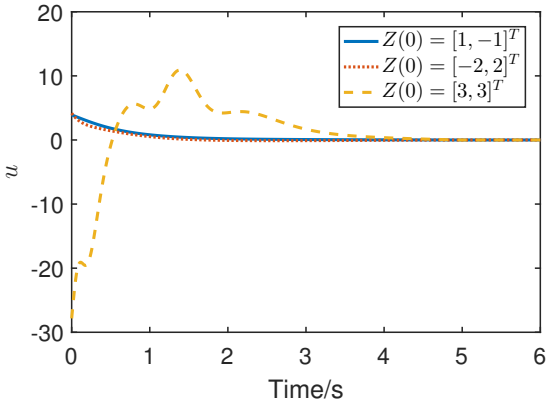

Fig. 2: The responses of u under different initial conditions

The responses of z and $\dot{z}$ are shown in Figs.1-3, from which we can find that the system state converges to the origin within the prescribed-time T_p under different initial conditions. The curves of the controller are shown in Fig. 3, it can be seen from Fig. 3 that the controller is bounded and converges to the origin within the prescribed-time T_p under different initial conditions.

3 Prescribed-time control Uncertain Nonlinear Systems

3.1 Problem formulation

Then fully actuated nonlinear systems with uncertain parameters are considered as follows

$$x^{(q)} = B(x^{(0\sim q-1)})u + f(x^{(0\sim q-1)}) + \theta^T \omega(z^{(0\sim q-1)}) \quad (29)$$

where $\theta \in \mathcal{R}^r$ is an uncertain parameter vector and $\omega \in \mathcal{R}^r$ is a known continuous function with $\omega(0) = 0$.

Similar to Section 2, let $Z = [x, \dot{x}, \cdots, x^{(q-1)}]^T$, then the system (29) can be transformed into

$$\dot{Z} = AZ + L\big(f(x^{(0\sim q-1)}) + \theta^T \omega(x^{(0\sim q-1)}) + Bu\big) \quad (30)$$

where $L = [0, 0, \ldots, 0, 1]^T \in \mathcal{R}^n$ and

$$A = \begin{bmatrix} 0 & & & \\ 0 & & I_{(n-1)\times(n-1)} & \\ \vdots & & & \\ 0 & 0 & \cdots & 0 \end{bmatrix} \quad (31)$$

The objective of this chapter is to design an adaptive controller for the uncertain nonlinear systems (29) based on the fully actuated system approaches, such that the system states $x^{(0\sim q-1)}$ converge to zero within the prescribed-time T_p.

3.2 Controller design

From the fully actuated system theory, the adaptive prescribed-time controller can be designed as

$$u(t) = -B^{-1}\left(L^T P(\rho(t))Z(t) + f(\cdot) + \hat{\theta}^T \omega(\cdot)\right) \quad (32)$$

$$\dot{\hat{\theta}}(t) = \Gamma Z^T P L \omega \quad (33)$$

$$\rho(t) = \begin{cases} \mu(t), & t \in [0, T_p) \\ \varepsilon, & t \in [T_p, +\infty) \end{cases} \quad (34)$$

where $\mu(t) = \frac{\sigma}{T_p - t}$ is a T_p-PTA function with the design parameter $\sigma > \frac{\delta}{q} + 1$ and Γ is positive definite matrix.

Substituting (32)-(34) into (30), we can get that

$$\dot{Z} = AZ - LL^T P(\rho(t))Z + L\tilde{\theta}^T \omega \quad (35)$$

The stability theorem is summarized as follows.

Theorem 2 *For the uncertain fully actuated nonlinear systems* (29)*, under the control input* (32)-(34)*, such that the the equilibrium point of system* (29) *is prescribed-time stable.*

Proof: First, the Lyapunov function is chosen as

$$V = V_1 + V_2$$
$$V_1 = Z^T P(\rho) Z, \quad V_2 = \tilde{\theta}\Gamma^{-1}\tilde{\theta} \quad (36)$$

According to (35) and (36), the derivative of the Lyapunov function V satisfies

$$\dot{V} = Z^T \left(A^T P + P^T A - 2PLL^T P\right) Z + Z^T \left(\frac{dP}{d\rho}\dot{\rho}\right) Z + 2Z^T PL\tilde{\theta}^T \omega - 2\tilde{\theta}\Gamma^{-1}\dot{\hat{\theta}} \quad (37)$$

Then, from (8), (9) and (34), we have

$$0 < Z^T \left(\frac{dP}{d\rho}\dot{\rho}\right) Z \leq \frac{\delta}{\sigma q}\rho Z^T P(\rho) Z \quad (38)$$

since $\sigma > \frac{\delta}{q} + 1$, so $\frac{\delta}{\sigma q} < 1$.

Based on the (6), (33), (37) and (38), we can get that

$$\dot{V} \leq -c\rho Z^T P(\rho) Z = -c\rho V_1 \quad (39)$$

where $c = 1 - \frac{\delta}{\sigma n} > 0$ is a constant.

According to Theorem 1 and (19), we know that

$$\lim_{t\to T_p^-} \|Z\| = \lim_{t\to T_p^-} \sqrt{\frac{V_1}{\lambda_{min}(P(\rho_0))}} = 0 \quad (40)$$

$$\|Z\| = 0, \quad t \in [T_p, +\infty) \quad (41)$$

In addition, from (36) and (39), one has

$$\dot{V}_1 \leq -c\rho V_1 - \dot{V}_2 \quad (42)$$

Based on (42), we can deduce that

$$V_1 \leq V_1(0)\left(1 - \frac{t}{T_p}\right)^{c\sigma} - (T_p - t)^{c\sigma} \int_0^t \frac{\dot{V}_2}{(T_p - s)^{c\sigma}} ds \quad (43)$$

By taking the limits on both sides of (43), we obtain

$$\lim_{t\to T_p^-} \rho V_1 \leq \lim_{t\to T_p^-} -\frac{\sigma}{\iota}\dot{V}_2 \quad (44)$$

where $\iota = c\sigma - 1 > 0$ is a constant.

Then, from (8) and (20), one has

$$Z^T PLL^T PZ \leq Z^T P^{\frac{1}{2}} \mathrm{tr}\left(P^{\frac{1}{2}} LL^T P^{\frac{1}{2}}\right) P^{\frac{1}{2}} Z$$
$$= L^T PLZ^T PZ = n\rho V_1 \tag{45}$$

According to (44) and (45) , we can get that

$$\lim_{t\to T_p^-} Z^T PLL^T PZ \leq \lim_{t\to T_p^-} -\frac{\sigma}{\iota} Z^T PL\omega \tag{46}$$

Since $\omega(0) = 0$, we have

$$\lim_{t\to T_p^-} \|Z^T PL\| \leq \lim_{t\to T_p^-} -\frac{\sigma}{\iota}\omega(\cdot) = 0$$
$$\|Z^T PL\| = 0,\ t \in [0, T_p) \tag{47}$$

Therefore, the controller $u(t)$ is bounded and converges to zero with in the prescribed-time T_p. Furthermore, the equilibrium point $Z = 0$ of system (30) exhibits prescribed-time stability, thereby establishing that the equilibrium point $x^{(0\sim q-1)} = 0$ of system (29) also possesses prescribed-time stability. This proof is finished. ■

Remark 3 *The works [2]-[5] studied the prescribed-time control problem for a class of nonlinear systems; Using adaptive technology, the works of [8]-[13] investigated the prescribed-time control problem of uncertain nonlinear systems. However, the aforementioned results are all based on the state-space approach for designing prescribed-time controllers, which involves relatively complex controller computation and is not easy to implement. In contrast to this methodology, this paper explores the adaptive prescribed-time control problem for uncertain nonlinear systems with unknown parameters based on the fully actuated system theory. The design of the controller is relatively simple and easy to implement.*

3.3 Simulation example

The standard fully actuated uncertain nonlinear system are considered as follows

$$\dddot{z} = u + \theta\ddot{z}^2 + z\sin(\dot{z}) \tag{48}$$

The controller is designed as

$$u = -L^T P(\rho)Z - h(\cdot) - \hat{\theta}^T\omega(\cdot) \tag{49}$$

with $h(\cdot) = z\sin(\dot{z}), \omega = \ddot{z}^2$ and

$$P(\rho) = \begin{bmatrix} \rho^5 & 2\rho^4 & \rho^3 \\ 2\rho^4 & 5\rho^3 & 3\rho^2 \\ \rho^3 & 3\rho^2 & 3\rho \end{bmatrix} \tag{50}$$

From (50), we can get that

$$\frac{dP(\rho)}{d\rho} \leq \frac{5P(\rho)}{\rho} \tag{51}$$

Therefore, the design parameters are selected as

$$\sigma = 8,\ \varepsilon = 10,\ T_p = 5 \tag{52}$$

For simulation, the initial conditions of the system are given by three different conditions $Z(0) = [1,1,1]^T$, $[1,-1,1]^T$, $[-1,-1,-1]^T$. The simulation results are shown in Figs. 6-10.

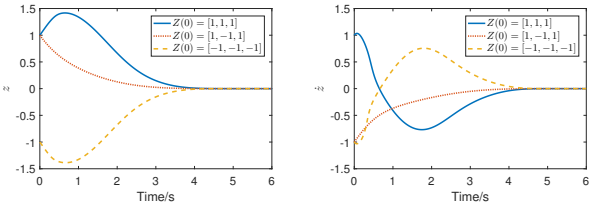

(a) z (b) $\dot{z}$

Fig. 3: The responses of z and $\dot{z}$

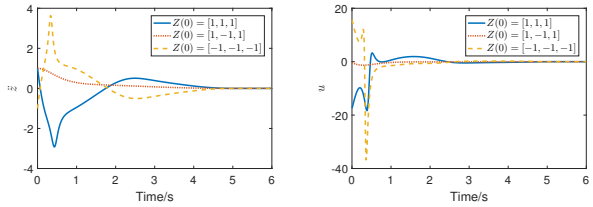

(a) $\ddot{z}$ (b) u

Fig. 4: The responses of $\ddot{z}$ and $\hat{\theta}$

The responses of z, $\dot{z}$, and $\ddot{z}$ are shown in Figs.4-6, from which we can find that the system state converges to the origin within the prescribed-time T_p under different initial conditions. The curves of the controller are shown in Fig. 7, it can be seen from Fig. 7 that the controller is bounded and converges to the origin within the prescribed-time T_p under different initial conditions. The responses of the adaptive parameter are illustrated in Fig. 8, indicating that the adaptive parameter remains bounded.

4 Conclusion

This paper delves into the prescribed-time control problem for fully actuated nonlinear systems. It provides a definition of prescribed-time stability for general fully actuated nonlinear systems. Drawing on the properties of the T_p-PTA function and the solution of the PLE, the paper presents a design methodology for the prescribed-time controller tailored for fully actuated nonlinear systems. Subsequently, for fully actuated uncertain nonlinear systems, the paper outlines the

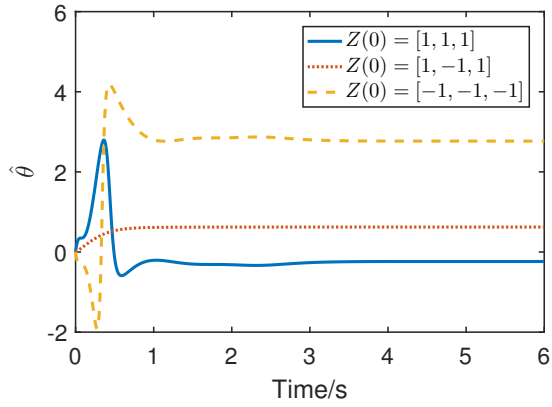

Fig. 5: The responses of $\hat{\theta}$ under different initial conditions

design approach for an adaptive prescribed-time controller. Utilizing the adaptive prescribed-time stability lemma, it is proved that the designed controller can make the system state converge to the origin within the predetermined time. Future research endeavors will focus on addressing the prescribed-time control problem for fully actuated nonlinear time-delay systems.

References

[1] Bin Zhou. Finite-time stability analysis and stabilization by bounded linear time-varying feedback. *Automatica*, 121:109191, 2020.

[2] Yongduan Song, Yujuan Wang, John Holloway, and Miroslav Krstic. Time-varying feedback for regulation of normal-form nonlinear systems in prescribed finite time. *Automatica*, 83:243–251, 2017.

[3] John Holloway and Miroslav Krstic. Prescribed-time observers for linear systems in observer canonical form. *IEEE Transactions on Automatic Control*, 64(9):3905–3912, 2019.

[4] John Holloway and Miroslav Krstic. Prescribed-time output feedback for linear systems in controllable canonical form. *Automatica*, 107:77–85, 2019.

[5] Fangzheng Gao, Yuqiang Wu, and Zhongcai Zhang. Global fixed-time stabilization of switched nonlinear systems: A time-varying scaling transformation approach. *IEEE Transactions on Circuits and Systems II: Express Briefs*, 66(11):1890–1894, 2019.

[6] Pengju Ning, Changchun Hua, Kuo Li, and Rui Meng. Adaptive fixed-time control for uncertain nonlinear cascade systems by dynamic feedback. *IEEE Transactions on Systems, Man, and Cybernetics: Systems*, 53(5):2961–2970, 2022.

[7] Prashanth Krishnamurthy, Farshad Khorrami, and Miroslav Krstic. A dynamic high-gain design for prescribed-time regulation of nonlinear systems. *Automatica*, 115:108860, 2020.

[8] Prashanth Krishnamurthy, Farshad Khorrami, and Miroslav Krstic. Robust adaptive prescribed-time stabilization via output feedback for uncertain nonlinear strict-feedback-like systems. *European Journal of Control*, 55:14–23, 2020.

[9] Caiyun Liu and Yungang Liu. Conditions and synthesis of adaptive prescribed-time controllers. *IEEE Transactions on Automatic Control*, 68(12):8005–8012, 2023.

[10] Changchun Hua, Pengju Ning, and Kuo Li. Adaptive prescribed-time control for a class of uncertain nonlinear systems. *IEEE Transactions on Automatic Control*, 67(11):6159–6166, 2021.

[11] Pengju Ning, Changchun Hua, Kuo Li, and Rui Meng. Event-triggered control for nonlinear uncertain systems via a prescribed-time approach. *IEEE Transactions on Automatic Control*, 2023.

[12] Peng-Ju Ning, Chang-Chun Hua, Kuo Li, and Rui Meng. Event-triggered adaptive prescribed-time control for nonlinear systems with uncertain time-varying parameters. *Automatica*, 157:111229, 2023.

[13] Peng-Ju Ning, Chang-Chun Hua, Kuo Li, and Hao Li. A novel theorem for prescribed-time control of nonlinear uncertain time-delay systems. *Automatica*, 152:111009, 2023.

[14] Wuquan Li and Miroslav Krstic. Stochastic nonlinear prescribed-time stabilization and inverse optimality. *IEEE Transactions on Automatic Control*, 67(3):1179–1193, 2021.

[15] Wuquan Li and Miroslav Krstic. Prescribed-time output-feedback control of stochastic nonlinear systems. *IEEE Transactions on Automatic Control*, 68(3):1431–1446, 2022.

[16] Bin Zhou and Yang Shi. Prescribed-time stabilization of a class of nonlinear systems by linear time-varying feedback. *IEEE Transactions on Automatic Control*, 66(12):6123–6130, 2021.

[17] Guangren Duan. High-order fully actuated system approaches: Part i. models and basic procedure. *International Journal of Systems Science*, 52(2):422–435, 2021.

[18] Guangren Duan. High-order fully actuated system approaches: Part iii. robust control and high-order backstepping. *International Journal of Systems Science*, 52(5):952–971, 2021.

[19] Guangren Duan. High-order fully actuated system approaches: Part v. robust adaptive control. *International Journal of Systems Science*, 52(10):2129–2143, 2021.

[20] Pengju Ning, Changchun Hua, and Rui Meng. Adaptive control for a class of nonlinear time-delay system based on the fully actuated system approaches. *Journal of Systems Science and Complexity*, 35(2):522–534, 2022.

[21] Miao Cai, Xiao He, and Donghua Zhou. An active fault tolerance framework for uncertain nonlinear high-order fully-actuated systems. *Automatica*, 152:110969, 2023.

[22] Miao Cai, Xiao He, and Donghua Zhou. Low-power fault-tolerant control for nonideal high-order fully actuated systems. *IEEE Transactions on Systems, Man, and Cybernetics: Systems*, 53(8):4875–4887, 2023.

[23] Miao Cai, Xiao He, and Donghua Zhou. Fault-tolerant tracking control for nonlinear observer-extended high-order fully-actuated systems. *Journal of the Franklin Institute*, 360(1):136–153, 2023.

Proceedings of the 3rd Conference on Fully Actuated System Theory and Applications
May 10-12, 2024, Shenzhen, China

Consensus Analysis and Control for Second-Order Fully Actuated Multi-agent Systems

Xin-Rong Yang*, Zefeng Zhong
School of Mathematics and Statistics, Guangxi Normal University, Guilin 541004, P. R. China
E-mail: yangxinrong@gxnu.edu.cn

Abstract: Since the consensus problem of first-order multi-agent systems is simple, it has been studied extensively. However, there are few research results for high-order multi-agent systems. This paper concerned with the consensus problem for a class of second-order fully actuated multi-agent systems with directed interaction topology. Based on matrix algebra and graph theory, a fully actuated system theory is adopted to transform second-order nonlinear multi-agent systems into second-order linear multi-agent systems. On this basis, necessary and sufficient conditions are established to design a distributed consensus protocol, which can ensure that the second-order fully actuated multi-agent systems achieve consensus. Moreover, a numerical example is provided to show the effectiveness and feasibility of the proposed control design method.

Key Words: Second-Order Fully Actuated Multi-agent Systems, Distributed Control, Consensus Analysis

1 Introduction

In recent years, consensus of multi-agent systems has become a hot research problem due to its widespread application in spacecraft formation flight, underwater vehicle detection, sensor network design, and other fields [1–3]. The discussions of consensus problems focus on the following points mainly. Firstly, based on the dynamic behavior of individuals in multi-agent systems, establish a model using dynamic equations. Secondly, analyze the factors that affect information communication during system operation. Finally, design appropriate distributed control protocols to ensure that the studied multi-agent systems achieve consensus.

Since various application scenarios of multi-agent systems, many scholars have proposed different dynamic models, including first-order multi-agent systems [4, 5], second-order multi-agent systems [6], and high-order multi-agent systems [7, 8]. A first-order dynamic model is the simplest model for describing the motion of an intelligent agent, which only involves the displacement and velocity of variables. However, when considering acceleration as a control input, the agent needs to be modeled as a second-order model. In addition, there are some systems (such as helicopters) that cannot establish dynamic equations through first-order and second-order models, and high-order integrator models have emerged.

It is worth mentioning that the fully actuated system approaches have been proposed for the control system design problem in recent years [9–11]. In fact, there are many fully actuated systems in the world. And currently available control methods may destroy the full-actuation of the fully actuated systems. Physically, a first-order fully actuated system is of the following form

$$E\dot{x}(t) = f(x,t)x(t) + B(x,t)u(t), \tag{1}$$

where $E \in \mathbb{R}^{n\times n}$ is a constant matrix, which may be identity or singular matrix. $x(t) \in \mathbb{R}^n, u(t) \in \mathbb{R}^n$ are the state and control input, respectively. $f(x,t) \in \mathbb{R}^n$ is a sufficiently differentiable vector function. $B(x,t)$ is a matrix function. System (1) is called a first-order fully actuated system if $B(x,t)$ satisfies the following condition

$$\det[B(x,t)] \neq 0,\ \forall x(t) \in \mathbb{R}^n,\ t \geq 0.$$

However, such a first-order all drive system is rare in reality [12]. Fortunately, there are many second-order fully actuated systems as follows:

$$E\ddot{x}(t) = f(\dot{x},x,t)x(t) + B(\dot{x},x,t)u(t), \tag{2}$$

where matrix $B(\dot{x},x,t)$ satisfies the following fully actuated condition

$$\det[B(\dot{x},x,t)] \neq 0,\ \forall x(t),\dot{x}(t) \in \mathbb{R}^n,\ t \geq 0.$$

In robotics and spacecraft control fields, many practical systems have been described by forms of second-order fully actuated systems

$$M(x,\dot{x},t)\ddot{x}(t) + D(x,\dot{x},t)\dot{x}(t) + K(x,\dot{x},t)x(t) = u(t),$$

where $M(x,\dot{x},t), D(x,\dot{x},t), K(x,\dot{x},t) \in \mathbb{R}^{n\times n}$ are the generalised mass matrix, damping matrix, and stiffness matrix, respectively.

Similarly, we can also define an high-order fully actuated systems. In fact, the second-order fully actuated system (2) is referred in engineering commonly. The first-order and high-order fully actuated systems mentioned above, do not have physical significance generally. They are only abstract mathematical definitions [12].

Based on the previous introduction, for a class of multi-agent systems with agents described by fully actuated multi-agent systems, the research of consensus problem will have important significance and practical value. However, rare works have been published to deal with consensus problems for fully actuated multi-agent systems. [13] has provided a predictive control scheme for the constrained cooperative control for high-order fully actuated multi-agent systems subject to input saturation and prescribed performance. The coordinated control has been investigated for

*Corresponding author.

This work is supported by Natural Science Foundation of Guangxi Province under Grant Guike AD21220062 and Grant 2023GXNSFAA026246, National Natural Science Foundation of China under Grant 62363003 and the Science and technology project of Guangxi under Grant Guike AD21220114.

a class of high-order fully actuated multi-agent systems with a predictive control strategy in [14]. In [13] and [14], the studied systems are only discrete-time systems. In this paper, the continuous-time fully actuated multi-agent systems are considered. The consensus problem is concerned for second-order fully actuated multi-agent systems which agents described by continuous-time second-order fully actuated multi-agent systems.

2 Preliminaries

The networked communication topology of second-order fully actuated multi-agent systems is described by a graph $\mathcal{G} = (\mathcal{N}, \mathcal{E}, \mathcal{A})$, where $\mathcal{N} = \{1, 2, \cdots, N\}$ denotes the agents, a set of directed edges $\mathcal{E} \subseteq \mathcal{N} \times \mathcal{N}$ and a nonnegative weighted adjacency matrix $\mathcal{A} = [a_{ij}] \in \mathbb{R}^{N\times N}$ with $a_{ii} = 0$. The weighted adjacency matrix $\mathcal{A} = [a_{ij}] \in \mathbb{R}^{N\times N}$ is made of nonnegative elements, where $a_{ii} = 0, a_{ij} > 0 \Leftrightarrow j \in N_i,\ N_i = \{j \in \mathcal{N} | (j, i) \in \mathcal{E}\}$, otherwise $a_{ij} = 0$. The Laplacian matrix $\mathcal{L}_{\mathcal{G}} = [l_{ij}] \in \mathbb{R}^{N\times N}$ of $\mathcal{G}$ is defined as

$$l_{ij} = \begin{cases} -a_{ij}, & i \neq j, \\ \sum\limits_{k=1,k\neq i}^{N} a_{ik}, & i = j. \end{cases} \tag{3}$$

Meanwhile, $\mathcal{L}_{\mathcal{G}}$ has the following property.

Lemma 1 *[15] The Laplacian matrix $\mathcal{L}_{\mathcal{G}}$ has at least one zero eigenvalue and all non-zero eigenvalues are in the open right-half plane. Furthermore, $\mathcal{L}_{\mathcal{G}}$ has exactly one zero eigenvalue if and only if $\mathcal{G}$ has a directed spanning tree.*

Before moving on, several definitions and lemmas are introduced as follows.

Definition 1 *[16]Let $\mathbf{E}, \mathbf{A} \in \mathbb{R}^{n\times n}$.*

(i) *$(\mathbf{E}, \mathbf{A})$ is called regular if $\det(s\mathbf{E} - \mathbf{A}) \not\equiv 0$;*

(ii) *$(\mathbf{E}, \mathbf{A})$ is called impulse free if $(\mathbf{E}, \mathbf{A})$ is regular and $\deg\det(s\mathbf{E} - \mathbf{A}) = \mathrm{rank}E$;*

(iii) *$(\mathbf{E}, \mathbf{A})$ is called stable if $\sigma(\mathbf{E}, \mathbf{A}) \subseteq \mathbb{C}^-$;*

(iv) *$(\mathbf{E}, \mathbf{A})$ is called admissible if $(\mathbf{E}, \mathbf{A})$ is impulse free and stable.*

Lemma 2 *[16]Singular system*

$$\mathbf{E}\dot{x}(t) = \mathbf{A}x(t), \tag{4}$$

is admissible (impulse free or stable) if and only if the pair $(\mathbf{E}, \mathbf{A})$ is admissible (impulse free or stable), where $\mathbf{E}, \mathbf{A} \in \mathbb{R}^{n\times n}$, $\mathrm{rank}\mathbf{E} \leq n$.

Lemma 3 *[16] System (4) is impulse free if and only if*

$$\mathrm{rank}\begin{bmatrix} \mathbf{E} & \mathbf{0} \\ \mathbf{A} & \mathbf{E} \end{bmatrix} = n + \mathrm{rank}(\mathbf{E}).$$

Lemma 4 *[16] Let $(\mathbf{E}, \mathbf{A})$ be regular. If there exist $X \geq 0,\ Y > 0$ satisfying*

$$\mathbf{E}^{\mathrm{T}} X\mathbf{A} + \mathbf{A}^{\mathrm{T}} X\mathbf{E} + \mathbf{E}^{\mathrm{T}} Y\mathbf{E} = 0,$$

then singular system (4) is admissible.

3 Problem Formulation

Consider a second-order fully actuated multi-agent system consisting of N agents indexed by $1, 2, \cdots, N$, respectively. The dynamics of the i-th agent is described as follows:

$$E\ddot{x}_i(t) = f(\dot{x}_i, x_i, t) + B(\dot{x}_i, x_i, t)u_i(t),\ i \in \mathcal{N}, \tag{5}$$

where $E \in \mathbb{R}^{n\times n}$ is a constant matrix, which may be identity or singular matrix. $x_i(t) \in \mathbb{R}^n, u_i(t) \in \mathbb{R}^n$ are the state and control input of the ith agent, respectively. $f(\dot{x}_i, x_i, t) \in \mathbb{R}^n$ is a sufficiently differentiable vector function. $B(\dot{x}_i, x_i, t)$ is a matrix function, and $B(\dot{x}_i, x_i, t)$ satisfies the following full-actuation condition:

$$\det[B(\dot{x}_i, x_i, t)] \neq 0,\ \forall x_i(t), \dot{x}_i(t) \in \mathbb{R}^n,\ t \geq 0.$$

The communication topology is described by a directed digraph $\mathcal{G} = (\mathcal{N}, \mathcal{E}, \mathcal{A})$.

Adopt the following control law:

$$\begin{aligned} u_i(t) = &- B^{-1}(\dot{x}_i, x_i, t)[A_1\dot{x}_i(t) + A_0x_i(t) \\ &+ f(\dot{x}_i, x_i, t) - v_i(t)],\ i \in \mathcal{N}, \end{aligned} \tag{6}$$

where $v_i(t)$ is a new control input, $A_1, A_0 \in \mathbb{R}^{n\times n}$ are constant matrices which will be designed.

Thus, the resultant closed-loop system of system (5) via the control law (6) is obtained:

$$E\ddot{x}_i(t) + A_1\dot{x}_i(t) + A_0x_i(t) = v_i(t),\ i \in \mathcal{N}. \tag{7}$$

Let

$$X_i(t) = [x_i^T(t),\ \dot{x}_i^T(t)]^T.$$

$$\bar{E}\dot{X}_i(t) = AX_i(t) + Pv_i(t), \tag{8}$$

where

$$\bar{E} = \begin{bmatrix} I_n & \mathbf{0} \\ \mathbf{0} & E \end{bmatrix},\ A = \begin{bmatrix} \mathbf{0} & I_n \\ -A_0 & -A_1 \end{bmatrix},\ P = \begin{bmatrix} \mathbf{0} \\ I_n \end{bmatrix}. \tag{9}$$

Assume that the i-th agent collects the state information of its neighboring agents. Adopt consensus protocols with the state feedback case. Design the consensus protocol of the i-th agent as follows:

$$\begin{aligned} v_i(t) =& K_1 \sum_{j=1}^{N} [\dot{X}_j(t) - \dot{X}_i(t)] \\ &+ K_2 \sum_{j=1}^{N} a_{ij}[X_j(t) - X_i(t)],\ i = 1, 2, \cdots, N, \end{aligned} \tag{10}$$

where K_1 and K_0 are constant matrices which will be designed.

Thus, the resultant closed-loop system of system (7) via the consensus protocol (10) is obtained:

$$\bar{E}\dot{X}_i(t) = (A + \mathrm{d_{in}}(i)K)\, X_i(t) + PK \sum_{j=1}^{N} a_{ij}X_j(t), \tag{11}$$

where $\mathrm{d_{in}}(i) = \sum\limits_{k=1}^{N} a_{ik}$ and $K = P\begin{bmatrix} K_1 & K_0 \end{bmatrix}$.

Denoting

$$X(t) = [X_1^T(t)\ X_2^T(t)\ \cdots\ X_N^T(t)]^T.$$

Thus, the compact form of system (11) is as follows:

$$(I_N \otimes \bar{E})\dot{\bar{X}}(t) = (I_N \otimes A - \mathcal{L}_{\mathcal{G}} \otimes K)\bar{X}(t). \tag{12}$$

Definition 2 *For the second-order fully actuated multi-agent system (5), consensus protocol (10) is said to solve the consensus problem (or second-order fully actuated multi-agent system (5) achieves consensus via protocol (10) if there exist constant matrices A_1, A_0, K_1 and K_0 such that the resultant closed-loop system (12) is impulse free, and the following condition holds:*

$$\lim_{t\to\infty} \|x_j(t) - x_i(t)\| = 0,$$
$$\lim_{t\to\infty} \|\dot{x}_j(t) - \dot{x}_i(t)\| = 0,\ \forall i, j \in \mathcal{N}.$$

The aim of this paper is to solve the following consensus problem.

Problem 1 *For the second-order fully actuated multi-agent system (5) with a directed topology $\mathcal{G} = (\mathcal{N}, \mathcal{E}, \mathcal{A})$, design the consensus protocol (10) to solve the consensus problem.*

4 Consensus Analysis and Control

Theorem 1 *For the second-order fully actuated multi-agent system (5) with a directed topology $\mathcal{G} = (\mathcal{N}, \mathcal{E}, \mathcal{A})$, protocol (10) solves Problem 1 if and only if there exist constant matrices A_1, A_0, K_1 and K_0 satisfying that the following conditions hold:*

(i) *the matrix pair $[\mathbf{E}, \mathbf{A}]$ is impulse free;*

(ii)

$$\sigma[I_{N-1}\otimes\bar{E}, I_{N-1}\otimes A-(\mathcal{L}_{22}-\mathbf{1}_{N-1}\mathcal{L}_{12})\otimes K] \subset \mathbb{C}^-, \tag{13}$$

where $\bar{E},\ A$ and K are defined as in (9),

$$\mathbf{E} = I_N \otimes \bar{E},\ \mathbf{A} = I_N \otimes A - \mathcal{L}_{\mathcal{G}} \otimes K,$$

$\mathbf{1}_{N-1} = [1\ 1\ \cdots\ 1]^{\mathrm{T}} \in \mathbb{R}^{N-1}$, $\mathcal{L}_{12} \in \mathbb{R}^{1\times(N-1)}$ *and* $\mathcal{L}_{22} \in \mathbb{R}^{(N-1)\times(N-1)}$ *are defined by* $\mathcal{L}_{\mathcal{G}} = \begin{bmatrix} \mathcal{L}_{11} & \mathcal{L}_{12} \\ \mathcal{L}_{21} & \mathcal{L}_{22} \end{bmatrix}$.

Proof Using Lemma 2, it can be concluded that singular system (12) is impulse free if and only if the pair $[I_N \otimes \bar{E},\ I_N \otimes A - \mathcal{L}_{\mathcal{G}} \otimes K]$ is impulse free.

Denote

$$\eta_i(t) = X_i(t) - X_1(t),\ i \in \mathcal{N} \setminus \{1\},$$
$$\eta(t) = [\ \eta_2^{\mathrm{T}}(t) \quad \eta_3^{\mathrm{T}}(t) \quad \cdots \quad \eta_N^{\mathrm{T}}(t)\ ]^{\mathrm{T}}.$$

Thus, it is easy to obtain that the compact form of the state difference system:

$$(I_{N-1}\otimes\bar{E})\dot{\eta}(t) = [I_{N-1}\otimes A-(\mathcal{L}_{22}-\mathbf{1}_{N-1}\mathcal{L}_{12})\otimes K]\eta(t). \tag{14}$$

One has that system (5) via protocol (10) satisfies

$$\lim_{t\to\infty} \|x_j(t) - x_i(t)\| = 0,$$
$$\lim_{t\to\infty} \|\dot{x}_j(t) - \dot{x}_i(t)\| = 0,\ \forall i, j \in \mathcal{N}$$

if and only if $\lim_{t\to\infty} \|\eta(t)\| = 0$ holds, that it is system (14) achieve asymptotically stable, which implies that equation (13) holds. Therefore, according to Definition 2, it can be concluded that protocol (10) solves Problem 1 if and only if there constant matrices A_1, A_0, K_1 and K_0 satisfying that the matrix pair $[\mathbf{E}, \mathbf{A}]$ is impulse free, and equation (13) holds. □

Remark 1 *When $E \in \mathbb{R}^{n\times n}$ is an identity matrix, the conditions (i) and (ii) in Theorem 1 are simplified as the following condition:*

$$\sigma(I_{N-1} \otimes A - (\mathcal{L}_{22} - \mathbf{1}_{N-1}\mathcal{L}_{12}) \otimes K) \subset \mathbb{C}^-.$$

Corollary 1 *For the second-order fully actuated multi-agent system (5) with a directed topology $\mathcal{G} = (\mathcal{N}, \mathcal{E}, \mathcal{A})$, protocol (10) solves Problem 1 if there exist constant matrices $A_1, A_0, K_1, K_0,\ X \geq 0$ and $Y > 0$ satisfying that the following conditions hold:*

(i)

$$\operatorname{rank}\begin{bmatrix} \mathbf{E} & \mathbf{0} \\ \mathbf{A} & \mathbf{E} \end{bmatrix} = nN + \operatorname{rank}(\mathbf{E}); \tag{15}$$

(ii) $(\mathbf{E}, \mathbf{A})$ *is regular;*

(iii) *singular Lyapunov equation*

$$\mathbf{E}^{\mathrm{T}} X \mathbf{A} + \mathbf{A}^{\mathrm{T}} X \mathbf{E} + \mathbf{E}^{\mathrm{T}} Y \mathbf{E} = 0; \tag{16}$$

where $\bar{E},\ A$ and K are defined as in (9), $\mathbf{E},\ \mathbf{A}$, $\mathbf{1}_{N-1}$, $\mathcal{L}_{12}$ and $\mathcal{L}_{22}$ are defined as in Theorem 1.

Proof According to Lemma 3, one obtains that the matrix pair the matrix pair $(\mathbf{E}, \mathbf{A})$ is impulse free if and only if equation (15) holds. Following the proof process of Theorem 1 and Lemma 4, it can be concluded from conditions (ii) and (iii) that equation (13) holds. The proof is completed. □

Remark 2 *When $E \in \mathbb{R}^{n\times n}$ is an identity matrix, the conditions (i) - (iii) in Corollary 1 are simplified as the following condition:*

$$X\mathbf{A} + \mathbf{A}^{\mathrm{T}} X + Y = 0.$$

Corollary 2 *For the second-order fully actuated multi-agent system (5) with a directed topology $\mathcal{G} = (\mathcal{N}, \mathcal{E}, \mathcal{A})$, protocol (10) solves Problem 1 if and only if $\mathcal{G}$ has a directed spanning tree, and there exist constant matrices A_1, A_0, K_1 and K_0 satisfying that the following conditions hold:*

(i)

$$\operatorname{rank}\begin{bmatrix} \bar{E} & \mathbf{0} \\ A & \bar{E} \end{bmatrix} = n + \operatorname{rank}(\bar{E}); \tag{17}$$

(ii) $(\bar{E}, A - \lambda_i K)$ *is admissible,*

where $\lambda_i,\ i \in \mathcal{N}\setminus\{1\}$ are non-zero eigenvalues of $\mathcal{L}_{\mathcal{G}}$, $\bar{E},\ A$ and K are defined as in (9).

Proof

Since $\mathcal{G}$ has a directed spanning tree, it can be concluded from Lemma 1 that $\mathcal{L}_{\mathcal{G}}$ has only one zero eigenvalue. Denote $Q = \begin{pmatrix} 1 & \mathbf{0} \\ \mathbf{1}_{N-1} & I_{N-1} \end{pmatrix}$. Using equation (3), one has

$$Q^{-1}\mathcal{L}_{\mathcal{G}}Q = \begin{pmatrix} \mathbf{0} & \mathcal{L}_{12} \\ 0 & \mathcal{L}_{22} - \mathbf{1}_{N-1}\mathcal{L}_{12} \end{pmatrix}. \tag{18}$$

Let $\lambda_1 = 0, \lambda_i,\ i \in \mathcal{N} \setminus \{1\}$ be all eigenvalues of $\mathcal{L}_{\mathcal{G}}$. From equation (18), it can be obtained that

$$\sigma(\mathcal{L}_{22} - \mathbf{1}_{N-1}\mathcal{L}_{12}) = \{\lambda_2,\ \lambda_3 \cdots,\ \lambda_N\}.$$

Thus, it can be concluded from matrix theory that

$$\sigma[I_{N-1} \otimes \bar{E},\ I_{N-1} \otimes A - (\mathcal{L}_{22} - \mathbf{1}_{N-1}\mathcal{L}_{12}) \otimes K]$$
$$= \bigcup_{i=2}^{N} \sigma(\bar{E},\ A - \lambda_i K).$$

Then one obtains that $[\mathbf{E}, \mathbf{A}]$ is impulse free if and only if $(\bar{E},\ A)$ and $(\bar{E},\ A-\lambda_i K)$ are impulse free for $i \in \mathcal{N}\setminus\{1\}$. Moreover, $[I_{N-1}\otimes\bar{E},\ I_{N-1}\otimes A-(\mathcal{L}_{22}-\mathbf{1}_{N-1}\mathcal{L}_{12})\otimes K]$ is stable if and only if $(\bar{E},\ A-\lambda_i K)$ is stable for $i \in \mathcal{N}\setminus\{1\}$. Using Lemma 3, one obtains that the matrix pair $[\bar{E},\ A]$ is impulse free if and only if equation (17) holds. According to Theorem 1 , it obtains that the second-order fully actuated multi-agent system (5) achieves consensus via protocol (10) if and only if the conditions (i)-(iii) hold. □

Remark 3 *When $E \in \mathbb{R}^{n\times n}$ is an identity matrix, the conditions (i) and (ii) in Corollary 2 are simplified as the following condition:*

$$\sigma(A-\lambda_i K) \subset \mathbb{C}^-,$$

where $\lambda_i,\ i \in \mathcal{N}\setminus\{1\}$ are non-zero eigenvalues of $\mathcal{L}_{\mathcal{G}}$, A, K are defined as in (9).

5 A Numerical Example

Consider a second-order fully actuated multi-agent system consisting of N agents indexed by $1, 2, 3$, respectively. The dynamics of the i-th agent is described as follows:

$$E\ddot{x}_i(t) = f(\dot{x}_i, x_i, t) + B(\dot{x}_i, x_i, t)u_i(t),\ i \in \mathcal{N}, \quad (19)$$

where

$$E = \begin{bmatrix} 1 & 0 \\ 0 & 1 \end{bmatrix},$$

$f(\dot{x}_i, x_i, t)$ is a sufficiently differentiable vector function, $B(\dot{x}_i, x_i, t)$ is a matrix function, and $B(\dot{x}_i, x_i, t)$ satisfies the following full-actuation condition:

$$\det[B(\dot{x}_i, x_i, t)] \neq 0,\ \forall x_i(t), \dot{x}_i(t) \in \mathbb{R}^2,\ t \geq 0.$$

The communication topology is described by a directed digraph $\mathcal{G} = (\mathcal{N}, \mathcal{E}, \mathcal{A})$, where $\mathcal{N} = \{1, 2, 3\}$, $\mathcal{E} = \{(1, 2),\ (2, 1),\ (2, 3),\ (3, 1),\ (3, 2)\}$ and

$$\mathcal{A} = \begin{bmatrix} 0 & 1 & 1 \\ 2 & 0 & 1 \\ 0 & 2 & 0 \end{bmatrix}.$$

Adopt the control law

$$\begin{aligned} u_i(t) =& -B^{-1}(\dot{x}_i, x_i, t)[A_1\dot{x}_i(t) + A_0 x_i(t) \\ &+ f(\dot{x}_i, x_i, t) - v_i(t)],\ i \in \mathcal{N}. \end{aligned} \quad (20)$$

Thus, the resultant closed-loop system of system (5) via the above control law is obtained:

$$E\ddot{x}_i(t) + A_1\dot{x}_i(t) + A_0 x_i(t) = v_i(t),\ i \in \mathcal{N}. \quad (21)$$

According to Corollary 2, the distributed protocol

$$\begin{aligned} v_i(t) =& K_1 \sum_{j=1}^{N} a_{ij}[\dot{X}_j(t) - \dot{X}_i(t)] \\ &+ K_2 \sum_{j=1}^{N} a_{ij}[X_j(t) - X_i(t)],\ i \in \mathcal{N} \end{aligned} \quad (22)$$

is designed by following matrices:

$$A_0 = \begin{bmatrix} 0.2 & 2 \\ 1 & 3 \end{bmatrix},\ A_1 = \begin{bmatrix} -2 & 3 \\ -0.5 & 3 \end{bmatrix},$$

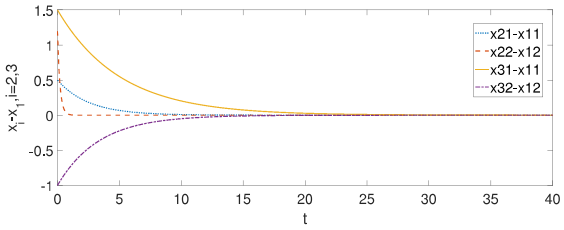

Fig. 1: Trajectories of state difference $x_i - x_1, i = 2, 3$

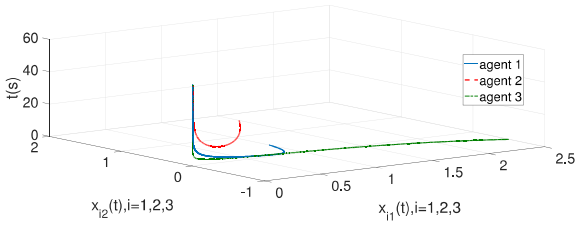

Fig. 2: State trajectories of system (19)

$$K_0 = \begin{bmatrix} 2 & -1 \\ 0.1 & -0.5 \end{bmatrix},\ K_1 = \begin{bmatrix} 0.5 & 2 \\ -1 & 1 \end{bmatrix}.$$

Denote $x_i(t) = \begin{bmatrix} x_{i1}(t) & x_{i2}(t) \end{bmatrix}^T,\ i \in \mathcal{N}$. The simulation results are presented in Fig. 1 and Fig. 2, respectively. It is easy to see that state differences of system (19) all tend to zero from Fig. 1 , which implies that the consensus problem of second-order fully actuated multi-agent system (19) is solved by the designed protocol (22).

6 Conclusion

This research has investigated the consensus problem for a class of second-order fully actuated multi-agent systems. Based on algebra, graph and fully actuated system theory, sufficient and necessary conditions have been proposed to solve the considered problem. The distributed consensus protocol has been proposed to guarantee that the studied second-order fully actuated multi-agent systems achieve consensus. Moreover, the example has been provided to demonstrate effectiveness and feasibility of the proposed control design method.

References

[1] T. Laengle, T. C. Lueth, U Rembold, et al. A distributed control architecture for autonomous mobile robots-implementation of the karlsruhe multi-agent robot architecture. Advanced Robotics, vol. 12, no. 4, pp. 411-431, 1997.

[2] Z. Lin, L. Wang, Z. Han, et al. Distributed formation control of multi-agent systems using complex Laplacian. IEEE Trans. Autom. Control, vol. 59, no. 7, pp. 1765-1777, 2014.

[3] W. Ren. Formation keeping and attitude alignment for multiple spacecraft through local interactions. Journal of Guidance, Control, and Dynamics, vol. 30, no. 2, pp. 633-638, 2007.

[4] S. Chen, D. Ho, L. Li, et al. Fault-tolerant consensus of multi-agent system with distributed adaptive protocol. IEEE Transactions on Cybernetics, vol. 45, no. 10, pp. 2142-2155, 2015.

[5] T. Li and J. Zhang. Consensus conditions of multi-agent system with time-varying topologies and stochastic communication noises. IEEE Trans. Autom. Control, vol. 55, no. 9, pp. 2043-2057, 2010.

[6] Q. Liu, J. Wang. A second-order multi-agent network for

bound-constrained distributed optimization. IEEE Transactions on Automatic Control, vol. 60, no. 12, pp. 3310-3315, 2015.

[7] G. Wen, G. Hu, W. Yu, et al. Consensus tracking for higher-order multi-agent systems with switching directed topologies and occasionally missing control inputs. Systems and Control Letters. vol. 62, no. 12, pp. 1151-1158, 2013.

[8] H. Zhang and F. L. Lewis. Adaptive cooperative tracking control of higher-order nonlinear systems with unknown dynamics. Automatica, vol. 48, no. 7, pp. 1432-1439, 2012.

[9] G. R. Duan, High-order fully actuated systems approaches: Part I. models and basic procedure. Int. J. Syst. Sci., vol. 52, no. 2, pp. 422-435, 2021.

[10] G. R. Duan, High-order system approaches: I fully-actuated systems and parametric designs. ACTA Automatica Sinica, vol. 46, no. 7, pp. 1333-1345, 2020.

[11] G. R. Duan, High-order fully actuated systems approaches: Part VII. controllability, stability and parametric designs. Int. J. Syst. Sci., vol. 52, no. 14, pp. 3091-3114, 2021.

[12] G. R. Duan. High-order system approaches-I. Fully actuated systems and parametric designs. Acta Automatica Sinica, vol. 46, no. 7, pp. 1333-1345, 2020. (in Chinese)

[13] D. W. Zhang, G. P. Liu and L. Gao. Constrained cooperative control for high-order fully actuated multiagent systems with application to air-bearing spacecraft simulators. IEEE/ASME Trans. Mechatronics, vol. 28, no. 3, pp. 1570-1581, 2023.

[14] D. W. Zhang, G. P. Liu and L. Gao. Coordinated control of high-order fully actuated multiagent systems and its application: a predictive control strategy.IEEE/ASME Trans. Mechatronics, vol. 27, no. 6, pp. 4362-4372, 2022.

[15] X. R. Yang and G. P. Liu, Necessary and sufficient consensus conditions of descriptor multi-agent systems. IEEE Trans. Circuits Syst. I: Regular Papers, vol. 59, pp. 2669-2677, 2012.

[16] G. R. Duan, Analysis and Design of Descriptor Linear Systems, New York: Springer, 2010.

Proceedings of the 3rd Conference on Fully Actuated System Theory and Applications
May 10-12, 2024, Shenzhen, China

Practical Prescribed Time Control for Space Manipulators Based on Fully Actuated System Approach

Guangtai Tian[1], Guangren Duan[1,2], Weizhen Liu[1], Mehdi Golestani[1], He Kong[1]

1. Shenzhen Key Laboratory of Control Theory and Intelligent Systems, Southern University of Science and Technology, Shenzhen 518055, P. R. China
E-mail: gttian_hit@163.com, l_weizhen@163.com, golestani@sustech.edu.cn, kongh@sustech.edu.cn

2. Center for Control Theory and Guidance Technology, Harbin Institute of Technology, Harbin 150001, P. R. China
E-mail: duangr@sustech.edu.cn/ g.r.duan@hit.edu.cn

Abstract: This paper proposes a fully actuated system approach (FASA)-based trajectory tracking control strategy for free flying space manipulator, whose pre-assignable tracking performance can be ensured within prescribed time under uncertain dynamics and input saturation. More specifically, the practical prescribed time control is introduced to ensure the convergence time and tracking accuracy regardless of initial condition. Through coordinate transformation, the considered tracking error system is transformed into the fully actuated systems (FASs). Then a FASA-based robust controller is designed to address the uncertain dynamics and system uncertainties. Moreover, an auxiliary system is used for tackling the input saturation. Furthermore, the boundedness of all system signals and global practical prescribed time performance can be ensured. Simulation results are presented to show the effectiveness of the proposed method.

Key Words: Space manipulators, fully actuated system approach (FASA), practical prescribed time performance, input saturation, trajectory tracking.

1 Introduction

Free flying space manipulators are essential for space maneuvering like satellite repairs and debris capture, which have drawed increased attention for precise motion control [2, 3]. However, the complex coupling between the base spacecraft and joints amplifies difficulties in achieving precise trajectory tracking [4, 5]. While advanced control methods aim to enhance tracking performance with complex controller structure [6]. A simpler controller structure can address computational challenges and enhance reliability in engineering applications. Hence, developing a straightforward yet effective control scheme for space manipulators to achieve high-precision trajectory tracking remains an open challenge.

Actually, the precise tracking performance for space manipulators within a short time is highly desirable. Moreover, many control methods, such as finite time control, fixed time control, and predefined time control. However, these methods are restricted to the dependence of controller design parameters, thus the prescribed time control has been developed for mechanical systems [7], networked systems [8], and aerospace systems [9]. In [10], a prescribed time control approach is proposed for high-order uncertain nonlinear systems based on feedback of the scaled system state. In [11], a prescribed time control method is proposed to achieve pre-assignable tracking precision for nonlinear systems in the presence of non-vanishing disturbances and mismatched uncertainties. To address the input saturation problem, a model-free prescribed time control scheme is proposed for robot manipulator subject to input saturation in [12]. In [13], a adaptive prescribed-time control problem is studied for a class of uncertain nonlinear systems.

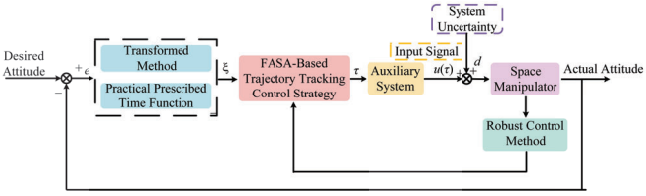

Fig. 1: Structure of the proposed controller.

Actually, space manipulators are naturally modeled as second-order fully actuated systems (FASs) in view of the Newton's Law, the Euler, and Lagrangian equations. However, the aforementioned trajectory tracking control methods have a shortcoming that the original dynamical behavior of space manipulators need to be converted to first-order state-space models, which leading to the increased computational complexity and illconditioned matrices. Recently, a new approach called the FAS approach (FASA) is established [14–19]. The key step of this approach is to design a parametrized controller with special structure. Furthermore, a great advantage of FAS approach is that a controller for a deterministic FAS can be easily designed such that a linear closed-loop system is obtained with an arbitrarily assignable eigenstructure. This efficient tool is well suitable for addressing many nonlinear control problems, such as robust control [15], adaptive control [16], optimal control [18], and tracking control [19]. Recently, [20] investigates the practical prescribed time control problem for strong interconnected nonlinear systems by utilizing the FASA. However, the existing FASA has not been applied to complex space manipulators subject to uncertain dynamics and input saturation to achieve prescribed time control performance.

To solve the aforementioned difficulties, the prescribed

This work has been partially supported by Shenzhen Key Laboratory of Control Theory and Intelligent Systems under grant No. ZDSYS20220330161800001, Shenzhen Science and Technology Program, under grant No. KQTD20221101093557010, Guangdong Basic and Applied Basic Research Foundation under grant No. 2023A1515110761, and also by the Major Program of National Natural Science Foundation of China under grant No. 61690210, 61690212, the National Natural Science Foundation of China under grant No. 61333003, 62203207, and the Science Center Program of the National Natural Science Foundation of China under grant No. 62188101.

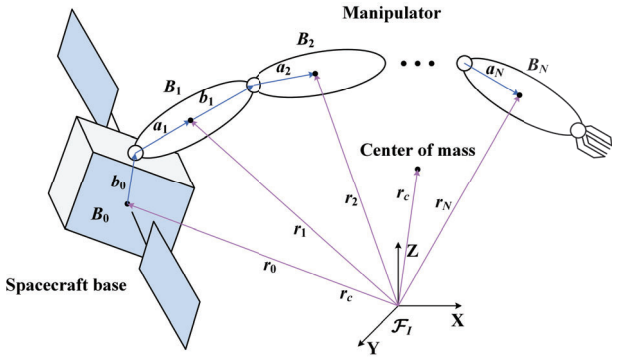

Fig. 2: Structure of the space manipulator.

time control problem for space manipulators with uncertain dynamics, system uncertainties, and input saturation is tackled in this paper. As shown in Fig. 1, the prescribed time control strategy can achieve system nonlinearities compensation, suppressing uncertain dynamics and system uncertainties, and input saturation effect compensation. The main contributions of this paper are summarized as follows: First, a practical prescribed time is designed for the space manipulators to ensure the tracking error within the prescribed bound and achieve a prescribed tracking accuracy within a predefined time independent of initial conditions. Second, a smooth function is introduced to approximate the saturated control input for avoiding sharp change, then an auxiliary system is integrated into the control strategy to compensate the input saturation. Third, different from the back-stepping method, FASA is utilized to design the prescribed time controller, robust control method is used to address the uncertain dynamics and system uncertainties.

In this paper, some frequently used symbols are listed as follows: The matrix transposition is denoted by "T." $\|x\| = \sqrt{x^{\mathrm{T}}x}$ is the Euclidean vector norm. Denote $\xi^{(0\sim1)} = \left[\xi, \dot{\xi}\right]^{\mathrm{T}}$. $\mathrm{diag}\left(\mu_1, \mu_2, ..., \mu_n\right)$ represents a matrix with diagonal elements being μ_1, μ_2,..., μ_n and 0 elsewhere.

2 Problem Formulation

2.1 Space Manipulator Model

As depicted in Fig. 2, a free flying space manipulator is mounted with a movable base spacecraft and a N revolute joints manipulator, the position of the mass center of link i is written as follows:

$$r_i = r_0 + b_0 + \sum_{j=1}^{i-1} l_j + a_i. \tag{1}$$

Taking the differentiate of equation (1), the linear velocity and the angular velocity of body B_i are calculated by

$$\begin{aligned} v_i &= v_0 + w_0 \times (r_i - r_0) + \sum_{j=1}^{i} \left\{k_j \times (r_i - p_j)\right\} \dot{q}_j \\ &= \left[\begin{array}{cc} E_3 & -r_{0i}^{\times} \end{array}\right] \left[\begin{array}{c} v_0 \\ w_0 \end{array}\right] + J_{vi}\dot{q}_m, \end{aligned} \tag{2}$$

$$w_i = w_0 + \sum_{j=1}^{i} k_j \dot{q}_j = w_0 + J_{wi}\dot{q}_m, \tag{3}$$

where w_0 and v_0 are the joint angular velocity and linear velocity of the base spacecraft, respectively. $q_m = [q_1, q_2, ..., q_n]^{\mathrm{T}}$ and $\dot{q}_m = [\dot{q}_1, \dot{q}_2, ..., \dot{q}_n]^{\mathrm{T}}$ are the joint angle and the joint angular velocity, respectively. k_i is a unit vector indicating a rotational axis of joint i. In addition, $r_{0i} = r_i - r_0$, $J_{vi} = \left[\begin{array}{ccccccc} k_1 (r_i - p_1) & k_2 (r_i - p_2) & ... & k_j (r_i - p_j) & 0_3 & ... & 0_3 \end{array}\right]$, $J_{wi} = \left[\begin{array}{ccccccc} k_1 & k_2 & ... & k_j & 0_3 & 0_3 & 0_3 \end{array}\right]$.

In accordance with the principle of linear momentum conservation, the total linear momentum of the space manipulator can be described by

$$\begin{aligned} P_{\mathrm{SM}} &= \sum_{i=0}^{N} m_i v_i \\ &= \sum_{i=0}^{N} \left(m_i \left[\begin{array}{cc} E_3 & -r_{0i}^{\times} \end{array}\right] \left[\begin{array}{c} v_0 \\ w_0 \end{array}\right] + m_i J_{vi}\dot{q}_m \right) \\ &= \left[\begin{array}{cc} mE_3 & -mr_{0c}^{\times} \end{array}\right] \left[\begin{array}{c} v_0 \\ w_0 \end{array}\right] + J_{mv}\dot{q}_m = 0_3, \end{aligned} \tag{4}$$

where $m = \sum_{i=0}^{N} m_i$ is the total mass, $r_{0c} = r_c - r_0$ and $J_{mv} = \sum_{i=0}^{N} m_i J_{vi}$.

The kinetic energy T can be given by

$$T = \frac{1}{2} \sum_{i=0}^{N} \left(w_i^{\mathrm{T}} I_i w_i + m_i v_i^{\mathrm{T}} v_i \right), \tag{5}$$

where I_i and m_i are the moment of inertia and the mass of link i, respectively.

Substituting (2)–(4) into (5), it yields

$$\begin{aligned} T &= \frac{1}{2} \left[\begin{array}{cc} w_0^{\mathrm{T}} & \dot{q}_m^{\mathrm{T}} \end{array}\right] \left[\begin{array}{cc} H_{bb} & H_{bm} \\ H_{bm}^{\mathrm{T}} & H_{mm} \end{array}\right] \left[\begin{array}{c} w_0 \\ \dot{q}_m \end{array}\right] \\ &= \frac{1}{2} \dot{q}^{\mathrm{T}} H(q) \dot{q}, \end{aligned} \tag{6}$$

where H_{bb}, H_{mm} denote the inertia matrix of the base spacecraft and the manipulator, respectively, and H_{bm} is the coupling matrix between the base spacecraft and the manipulator. For more details, please refer to [1].

The rotational motion of the space manipulator is given by

$$H(q)\ddot{q} + C(q, \dot{q})\dot{q} = u(\tau) + d, \tag{7}$$

where $q \in \mathbb{R}^n$ denotes the generalized space manipulator attitude, including the base spacecraft attitude angles and the manipulator joint angles, whose degree of freedom is $n = N + 3$. $H(q)$ and $C(q, \dot{q}) \in \mathbb{R}^{n \times n}$ are the inertia matrix and Coriolis matrix of the space manipulator, respectively. $\tau \in \mathbb{R}^n$ is the control torque and $d \in \mathbb{R}^n$ represents the total system uncertainties and unmodelled dynamics.

Properties 1: [12] For $\forall q \in \mathbb{R}^n$, $\forall x \in \mathbb{R}^n$, the inertia matrix $H(q)$ satisfies $a\|x\|^2 \leq x^{\mathrm{T}} H(q) x \leq b\|x\|^2$, where $a, b > 0$ are the minimum and maximum eigenvalues of H, respectively.

2.2 Control Object

Consider the input saturation, based on the theory in [21], the input saturation effect on $u(\tau)$ can be described by

$$u_i(\tau_i) = \begin{cases} u_{\max i}, & \tau_i > u_{\max i} \\ \tau_i, & u_{\min i} \le \tau_i \le u_{\max i}, \ i = 1, 2, ..., n \\ u_{\min i}, & \tau_i \le u_{\min i} \end{cases}$$

where $u_{\min i}$, $u_{\max i}$ are the control input lower bound and upper bound of joint i, respectively.

Based on the analysis in [21], a smooth function is introduced to approximate the control torque $u(\tau)$

$$\Pi(\tau, \vartheta) = \left[\begin{array}{cccc} \Pi_1(\tau_1, \vartheta_1) & \Pi_2(\tau_2, \vartheta_2) & ... & \Pi_n(\tau_n, \vartheta_n) \end{array} \right]^{\mathrm{T}} \in \mathbb{R}^n,$$

with user-defined parameter and

$$\Pi_i(\tau_i, \vartheta_i) = \begin{cases} \vartheta_i u_{\max i} + \bar{u}_{\max i}, & \tau_i > \vartheta_i u_{\max i} \\ \tau_i, & \vartheta_i u_{\min i} \le \tau_i \le \vartheta_i u_{\max i} \\ \vartheta_i u_{\min i} + \bar{u}_{\min i}, & \tau_i \le \vartheta_i u_{\min i} \end{cases}$$
$$i = 1, 2, ..., n$$

and

$$\bar{u}_{\max i} = (1 - \vartheta_i) u_{\max\ i} \tanh\left(\frac{\tau_i - \vartheta_i u_{\max i}}{(1 - \vartheta_i) u_{\max i}} \right),$$
$$\bar{u}_{\min i} = (1 - \vartheta_i) u_{\min\ i} \tanh\left(\frac{\tau_i - \vartheta_i u_{\min i}}{(1 - \vartheta_i) u_{\min i}} \right),$$

To proceed, the control torque can be written as

$$u(\tau) = \Pi(\tau, \vartheta) + \Delta u,$$

where Δu denotes the control input discrepancy.

Remark 1. *It worth noting that the piecewise function $\Pi(\tau, \vartheta)$ with $\vartheta \in (0, 1)$ possesses second-order differentiability with respect to τ. This property facilitates achieving a smoother control input around the limits by designing a control law τ and substituting it into $\Pi(\tau, \vartheta)$, rather than directly employing $u(\tau)$*

To proceed, space manipulator (7) can be converted to

$$H(q)\ddot{q} + C(q, \dot{q})\dot{q} = \Pi(\tau, \vartheta) + \Delta u + d,$$

where

$$\tau_d^* = d + \Delta u,$$

Define $\Delta\tau = \tau - \Pi(\tau, \vartheta)$, then it follows that

$$H(q)\ddot{q} + C(q, \dot{q})\dot{q} = \tau - \Delta\tau + \tau_d^*,$$

which can be written as

$$\ddot{q} = -H^{-1}(q) C(q, \dot{q})\dot{q} + H^{-1}(q)(\tau - \Delta\tau) + \tau_d,$$

where

$$\tau_d = H^{-1}(q)\tau_d^*.$$

Assumption 1: [2] The total system uncertainty τ_d is bounded by $\|\tau_d\| \le \eta$.

Assumption 2: The desired trajectory q_d with its derivatives are known and bounded.

In this paper, we aim to develop a control strategy to achieve the following control objectives:

(1) All signals of the closed-loop system are bounded;

(2) The tracking error can converge to a pre-assignable bound within a prescribed setting time, which are independent of initial conditions;

(3) The control input is avoided to exceed the limit.

Some necessary lemmas are introduced as follows:

Lemma 1. *([15]) Let $A \in \mathbb{R}^{n\times n}$ satisfy$\mathrm{Re}\,\lambda_i(A) \le -\frac{\gamma}{2}, i = 1, 2, \cdots, n$, where $\gamma > 0$, then there exist a positive definite matrix $P \in \mathbb{R}^{n\times n}$ satisfying$A^{\mathrm{T}}P + PA \le -\gamma P$.*

3 Practical Prescribed Time Control

In this section, a FASA-based control strategy is proposed to guarantee the prescribed time performance for the space manipulator with uncertain dynamics and input saturation. More specifically, a robust method is developed for tackling uncertain dynamics and external disturbances. In addition, an auxiliary system is designed to address the input saturation.

Define the tracking error with its derivatives as follows: $e = q - q_d, \dot{e} = \dot{q} - \dot{q}_d, \ddot{e} = \ddot{q} - \ddot{q}_d$, furthermore, the tracking error e is required to satisfy the following condition:

$$-\rho_i(t) < e_i(t) < \rho_i(t),$$

where $\rho_i(t)$ is the performance function to guarantee the prescribed performance and can be designed as follows:

$$\rho_i(t) = \begin{cases} \left(\frac{1}{t} - \frac{1}{T}\right)^{2p} + \rho_T, & t \in (0, T], \\ \rho_T, & t \in (T, \infty), \end{cases}$$

then we can construct the following compound function $h_i(\gamma(t))$

$$h_i(\gamma_i(t)) = \begin{cases} 1 - \left(\frac{\gamma_i(t)}{a} - 1\right)^{2p}, & 0 < \gamma_i(t) \le a, \\ 1, & \gamma_i(t) > a, \end{cases}$$

where $a > c\rho_T^2$, $\gamma_i(t) = c(\rho_i(t) - e_i(t))(\rho_i(t) + e_i(t))$ with $c > 0$. To proceed, the following transformation can be introduced

$$\xi_i = \frac{e_i}{h_i(\gamma_i(t))},$$

then we have

$$\dot{\xi}_i = \mu_i \dot{e}_i + \upsilon_i, \tag{8}$$

where

$$\mu_i = \begin{cases} \frac{1}{h_i} - \frac{4cp}{ah_i^2}\left(\frac{\gamma_i}{a} - 1\right)^{2p-1} e_i^2 > 0, & 0 < \gamma_i(t) \le a, \\ 1, & \gamma_i(t) > a, \end{cases} \tag{9}$$

and

$$\upsilon_i = \begin{cases} \frac{4cp}{ah_i^2}\left(\frac{\gamma_i}{a} - 1\right)^{2p-1} \rho_i \dot{\rho}_i e_i, & 0 < \gamma_i(t) \le a, \\ 0, & \gamma_i(t) > a, \end{cases} \tag{10}$$

further we have

$$\dot{\mu}_i = \begin{cases} -\frac{\dot{h}_i(\gamma_i(t))}{h_i^2(\gamma_i(t))} - \frac{4cp}{a}\left(\frac{-2\dot{h}_i(\gamma_i(t))}{h_i(\gamma_i(t))^3}\left(\frac{\gamma_i(t)}{a} - 1\right)^{2p-1} e_i^2 \right. \\ + \frac{(2p-1)\dot{\gamma}_i(t)}{ah_i^2(\gamma_i(t))}\left(\frac{\gamma_i(t)}{a} - 1\right)^{2p-2} e_i^2 \\ \left. + \frac{2}{h_i^2}\left(\frac{\gamma_i}{a} - 1\right)^{2p-1} e_i \dot{e}_i \right) > 0, & 0 < \gamma_i(t) \le a, \\ 0, & \gamma_i(t) > a, \end{cases}$$

$$\dot{\upsilon}_i = \begin{cases} \frac{4cp}{a}\left(\frac{-2\dot{h}_i(\gamma_i(t))}{h_i(\gamma_i(t))^3}\left(\frac{\gamma_i}{a}-1\right)^{2p-1}\rho_i\dot{\rho}_i e_i \right. \\ +\frac{(2p-1)\dot{\gamma}_i(t)}{a h_i(\gamma_i(t))^2}\left(\frac{\gamma_i}{a}-1\right)^{2p-2}\rho_i\dot{\rho}_i e_i \\ +\frac{1}{h_i(\gamma_i(t))^2}\left(\frac{\gamma_i}{a}-1\right)^{2p-1}\dot{\rho}_i^2 e_i \\ +\frac{1}{h_i(\gamma_i(t))^2}\left(\frac{\gamma_i}{a}-1\right)^{2p-1}\rho_i\ddot{\rho}_i e_i \\ \left.+\frac{1}{h_i(\gamma_i(t))^2}\left(\frac{\gamma_i}{a}-1\right)^{2p-1}\rho_i\dot{\rho}_i\dot{e}_i\right), & 0<\gamma_i(t)\le a, \\ 0, & \gamma_i(t)>a, \end{cases}$$

Consider system (8), define

$$\begin{aligned} \mu &= \mathrm{diag}\left(\mu_1,\mu_2,...,\mu_n\right)\in\mathbb{R}^{n\times n}, \\ \dot{\mu} &= \mathrm{diag}\left(\dot{\mu}_1,\dot{\mu}_2,...,\dot{\mu}_n\right)\in\mathbb{R}^{n\times n}, \\ \upsilon &= \left[\begin{array}{cccc}\upsilon_1 & \upsilon_2 & ... & \upsilon_n\end{array}\right]^{\mathrm{T}}\in\mathbb{R}^n, \\ \dot{\upsilon} &= \left[\begin{array}{cccc}\dot{\upsilon}_1 & \dot{\upsilon}_2 & ... & \dot{\upsilon}_n\end{array}\right]^{\mathrm{T}}\in\mathbb{R}^n, \end{aligned}$$

then system (8) can be converted to

$$\dot{\xi} = \mu\dot{e} + \upsilon, \tag{11}$$

then it follows that

$$\dot{e} = \mu^{-1}\left(\dot{\xi}-\upsilon\right),$$

to proceed, take derivation of (11), then we have

$$\begin{aligned} \ddot{\xi} =& \dot{\mu}\dot{e}+\mu\ddot{e}+\dot{\upsilon} \\ =& \dot{\mu}\mu^{-1}\left(\dot{\xi}-\upsilon\right)-\mu\left(H^{-1}C\left(\dot{e}+\dot{q}_d\right)+\ddot{q}_d\right) \\ &+\mu\tau_d+\mu H^{-1}\left(\tau-\Delta\tau\right)+\dot{\upsilon}, \end{aligned} \tag{12}$$

further, system (12) can be converted to

$$\ddot{\xi} = \dot{\mu}\dot{e}+\mu\ddot{e}+\dot{\upsilon} = F+D+G\left(\tau-\Delta\tau\right),$$

where

$$\begin{aligned} F =& \dot{\mu}\mu^{-1}\left(\dot{\xi}-\upsilon\right)-\mu H^{-1}C\mu^{-1}\left(\dot{\xi}-\upsilon\right) \\ &-\mu\left(H^{-1}C\dot{q}_d+\ddot{q}_d\right)+\dot{\upsilon}, \\ G =& \mu H^{-1}, \quad D = \mu\tau_d, \end{aligned}$$

To handle the input saturation effect in the stability analysis, the following auxiliary system is introduced:

$$\dot{\varsigma}(t) = -k_2\varsigma(t)-\Delta\tau, \tag{13}$$

further, a FASA-based trajectory tracking controller can be designed as follows:

$$\tau = \underbrace{-G^{-1}F+G^{-1}K_1\dot{\xi}+G^{-1}K_0\xi}_{A}\underbrace{-G^{-1}u_r}_{B}\underbrace{-G^{-1}u_a}_{C}, \tag{14}$$

$$u_r = \frac{\mu^2\eta^2}{4\varepsilon}\left(PB\right)^{\mathrm{T}}\xi^{(0\sim1)}, \quad u_a = k_1\left(B^{\mathrm{T}}PB\right)^{-1}\varsigma, \tag{15}$$

where A is used for system compensation, B is used for suppressing the system uncertainties and external disturbances, C is used for input saturation effect compensation.

Theorem 1. *Consider robotic system (7) with the unknown variable τ_d satisfying Assumption 1. Construct the controller (14) with the auxiliary system (13), if the parameters k_1, k_2, $\mu>0$, $\frac{4k_2}{3}>\frac{3k_1^2}{2\mu\|P\|}$, the control gains K_0, K_1 can be chosen to ensure closed-loop system matrix Hurwitz, then all the signals of the closed-loop system are bounded and the transient performance of tracking error $e(t)$ is maintained within the predefined boundary.*

Proof. Applying controller (14) to system (3), the following closed-loop tracking error system can be derived

$$\ddot{\xi}+K_1\dot{\xi}+K_0\xi = D-u_r-u_a-G\Delta\tau,$$

Denote

$$\xi^{(0\sim1)} = \left[\begin{array}{c}\xi\\ \dot{\xi}\end{array}\right],$$

then it follows that

$$\dot{\xi}^{(0\sim1)} = A\xi^{(0\sim1)}+B\left(D-u_r-u_a\right)-B_G\Delta\tau, \tag{16}$$

where

$$A = \left[\begin{array}{cc}0 & I_n\\ -K_0 & -K_1\end{array}\right], B = \left[\begin{array}{c}0\\ I_n\end{array}\right], B_G = \left[\begin{array}{c}0\\ G\end{array}\right].$$

Considering the tracking error system (16), all eigenvalues of the closed-loop system matrix A can be assigned to lie in the left half-plane by properly choosing K_0 and K_1. In addition, the matrix B is bounded and the estimation error $\tilde{\tau}_d$ is bounded whose bound can be calculated by Theorem 1. Similarly to the proof for the boundedness in above section, the trajectory tracking error is also bounded. This completes the proof.

Define the following Lyapunov function

$$V = \frac{1}{2}\left(\xi^{(0\sim1)}\right)^{\mathrm{T}}P\xi^{(0\sim1)}+\frac{1}{2}\varsigma^{\mathrm{T}}\varsigma,$$

according to the Lemma 1, then we have

$$\begin{aligned} \dot{V} =& \frac{1}{2}\left(\dot{\xi}^{(0\sim1)}\right)^{\mathrm{T}}P\xi^{(0\sim1)}+\frac{1}{2}\left(\xi^{(0\sim1)}\right)^{\mathrm{T}}P\dot{\xi}^{(0\sim1)}+\varsigma^{\mathrm{T}}\dot{\varsigma} \\ =& \frac{1}{2}\left(\xi^{(0\sim1)}\right)^{\mathrm{T}}\left(A^{\mathrm{T}}P+PA\right)\xi^{(0\sim1)} \\ &+\left(\xi^{(0\sim1)}\right)^{\mathrm{T}}PB\left(D-u_r-u_a\right) \\ &-\left(\xi^{(0\sim1)}\right)^{\mathrm{T}}PB_G\Delta\tau-\varsigma^{\mathrm{T}}\left(k_2\varsigma(t)+\Delta\tau\right), \end{aligned}$$

where

$$\begin{aligned} &\left(\xi^{(0\sim1)}\right)^{\mathrm{T}}PB\left(D-u_r\right) \le \left(\xi^{(0\sim1)}\right)^{\mathrm{T}}PBD \\ &-\left(\xi^{(0\sim1)}\right)^{\mathrm{T}}PB\frac{\mu^2\rho^2}{4\varepsilon}\left(PB\right)^{\mathrm{T}}\xi^{(0\sim1)} \\ &\le \left(\xi^{(0\sim1)}\right)^{\mathrm{T}}PB\mu\rho-\left(\xi^{(0\sim1)}\right)^{\mathrm{T}}PB\frac{\mu^2\rho^2}{4\varepsilon}\left(PB\right)^{\mathrm{T}}\xi^{(0\sim1)} \\ &\le ||\mu\rho||\left|\left|\left(PB\right)^{\mathrm{T}}\xi^{(0\sim1)}\right|\right|-\frac{\mu^2\rho^2}{4\varepsilon}\left|\left|\left(PB\right)^{\mathrm{T}}\xi^{(0\sim1)}\right|\right|^2 \\ &\le \varepsilon, \end{aligned}$$

then we have

$$\begin{aligned} \dot{V} \le& -\mu\left(\xi^{(0\sim1)}\right)^{\mathrm{T}}P\xi^{(0\sim1)}-k_2\varsigma^{\mathrm{T}}\varsigma(t)+\varepsilon \\ &-\left(\xi^{(0\sim1)}\right)^{\mathrm{T}}PBu_a-\left(\xi^{(0\sim1)}\right)^{\mathrm{T}}PB_G\Delta\tau-\varsigma^{\mathrm{T}}\Delta\tau \\ \le& -\mu\left(\xi^{(0\sim1)}\right)^{\mathrm{T}}P\xi^{(0\sim1)}-k_2\varsigma^{\mathrm{T}}\varsigma(t)+\varepsilon \\ &-k_1\left(\xi^{(0\sim1)}\right)^{\mathrm{T}}B\varsigma-\left(\xi^{(0\sim1)}\right)^{\mathrm{T}}PB_G\Delta\tau-\varsigma^{\mathrm{T}}\Delta\tau. \end{aligned}$$

With the help of Young's inequalities, we have

$$
\begin{aligned}
-k_1\left(\xi^{(0\sim1)}\right)^{\mathrm{T}} B\varsigma \leq & \frac{\mu\|P\|}{3}\left\|\xi^{(0\sim1)}\right\|^2+\frac{3k_1^2}{4\mu\|P\|}\|\varsigma\|^2 \\
-\left(\xi^{(0\sim1)}\right)^{\mathrm{T}} PB_G\Delta\tau \leq & \frac{\mu\|P\|}{3}\left\|\xi^{(0\sim1)}\right\|^2 \\
& +\frac{3\|P\|}{4\mu}\|B_G\|^2\|\Delta\tau\|^2 \\
-\varsigma^{\mathrm{T}}\Delta\tau \leq & \frac{k_2}{3}\|\varsigma\|^2+\frac{3}{4k_2}\|\Delta\tau\|^2,
\end{aligned}
$$

According to the above results, it follows that

$$
\begin{aligned}
\dot{V} \leq & -\mu\|P\|\left\|\xi^{(0\sim1)}\right\|^2-k_2\varsigma^{\mathrm{T}}\varsigma(t)+\varepsilon \\
& +\frac{\mu\|P\|}{3}\left\|\xi^{(0\sim1)}\right\|^2+\frac{3k_1^2}{4\mu\|P\|}\|\varsigma\|^2 \\
& +\frac{\mu\|P\|}{3}\left\|\xi^{(0\sim1)}\right\|^2+\frac{3\|P\|}{4\mu}\|B_G\|^2\|\Delta\tau\|^2 \\
& +\frac{k_2}{3}\|\varsigma\|^2+\frac{3}{4k_2}\|\Delta\tau\|^2 \\
\leq & -\frac{1}{3}\mu\|P\|\left\|\xi^{(0\sim1)}\right\|^2-\left(\frac{2k_2}{3}-\frac{3k_1^2}{4\mu\|P\|}\right)\|\varsigma\|^2 \\
& +\varepsilon+\left(\frac{3\|P\|}{4\mu}\|B_G\|^2+\frac{3}{4k_2}\right)\|\Delta\tau\|^2,
\end{aligned}
$$

which can be rewritten as

$$
\dot{V} \leq -\gamma V+\Upsilon,
$$

where $\gamma=\min\left\{\frac{2}{3}\mu, \frac{4k_2}{3}-\frac{3k_1^2}{2\mu\|P\|}\right\}$,
$\Upsilon=\varepsilon+\left(\frac{3\|P\|}{4\mu}\|B_G\|^2+\frac{3}{4k_2}\right)\|\Delta\tau\|^2$.

For $k_1, k_2, \mu>0$, $\frac{4k_2}{3}>\frac{3k_1^2}{2\mu\|P\|}$, then we have

$$
V(t) \leq e^{-\gamma t}V(0)+\frac{\Upsilon}{\gamma}\left(1-e^{-\gamma t}\right) \leq V(0)+\frac{\Upsilon}{\gamma}, \quad (17)
$$

which means that $V(t)$ is bounded at $[0,\infty)$ and $V\to\frac{\Upsilon}{\gamma}$ as $t\to\infty$. Thus, $\xi, \dot{\xi}, \varsigma$ are bounded.

Further, we will prove all the singals are bounded. By (17), we can obtain that ξ, $\dot{\xi}$, ς are bounded, which means $|e_i|<{}_i(t)$, and $|e_i|<\rho_T$ after $t>T$. Thus, the system outputs are within the prescribed bounds and converge to the predetermined invariant region in the settling time T regardless of the initial conditions. Meanwhile, it is obvious that μ, $\dot{\mu}$, $\ddot{q}_d$ is bounded, which implies the input torque τ is continuous and bounded regardless of initial condition. Therefore, all the signals in the closed-loop system are bounded. □

4 Simulation Results

Numerical simulations will be performed regarding a two joints planar space manipulator to verify the effectiveness of the proposed FASA-based control strategy. The detailed space manipulator parameters are listed in Table 1, which are available in [22].

The tracking precision and prescribed time are set as $T=2$ s, $\rho_T=0.02$, $a=5$, $c=50$, $p=2$, and the control gain of the robust control method is chosen as $\varepsilon=0.1$. The saturation on the control torque is set as $u_{\max 1}=u_{\max 2}=400$ Nm, and $k_1=0.01$, $k_2=6$. Additionally, the FASA-based control parameters are set as $K_0=\mathrm{diag}(115,126,137)$, $K_1=\mathrm{diag}(21.5,22.5,23.5)$.

Table 1: Parameters of the two joint planar FFSM.

Body No.	$m_i\,(kg)$	$I_i\,(kg\cdot m^2)$	$b_i\,(m)$	$a_i\,(m)$
0	300	27.5000	0.75	0.75
1	6.0	1.125	0.75	0.75
2	5.0	0.9375	0.75	0.75
t	5.0	1.0	0.5	0.75

In this simulation, the space manipulator attitude is driven along a desired trajectory in the inertial frame. The desired trajectory is formulated as $q_r=[0.5\sin(t),0.6\cos(t),0.8\sin(t)]^{\mathrm{T}}$, $\dot{q}_r=[0.5\cos(t),-0.6\sin(t),0.8\cos(t)]^{\mathrm{T}}$. The initial values have been chosen as $q=\left[\frac{\pi}{3},\frac{\pi}{3},\frac{\pi}{6}\right]^{\mathrm{T}}$, $\dot{q}=[0,0,0]^{\mathrm{T}}$. Moreover, $q_t=\frac{\pi}{6}$, and the total uncertain dynaticals and system uncertainties is given by $d=[6\sin(t),3\cos(t),2.5\cos(t)]^{\mathrm{T}}$.

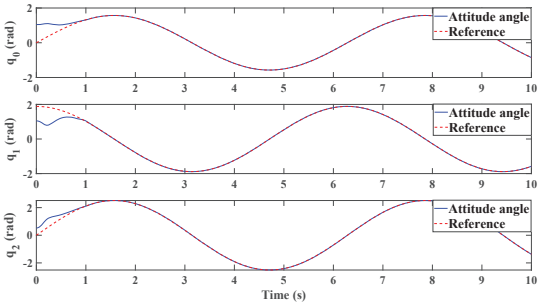

Fig. 3: Space manipulator attitude angles

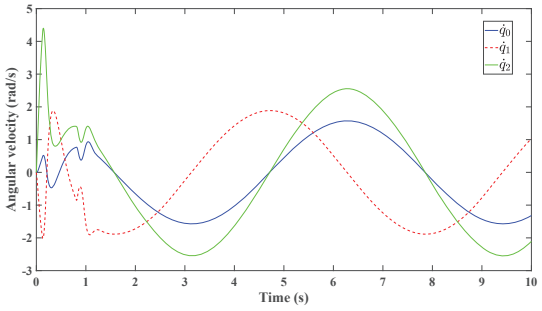

Fig. 4: Space manipulator angular velocities

The space manipulator attitude angles and the reference trajectories are plotted in Figure 3. The space manipulator attitude angular velocities are plotted Figure 4. Figure 5 further gives the tracking error of the space manipulator attitude angles. A shown in the Figure 5, the tracking errors of q_0, q_1 and q_2 converge to the pre-assigned bound 0.03 rad within the prescribed time 2 s. Figure 6 gives the control torques generated by the proposed control method, moreover, the satisfaction of the input torque are ensured. As depicted in Figs. 3–6, the proposed method can effectively control space manipulators under the system uncertainty and

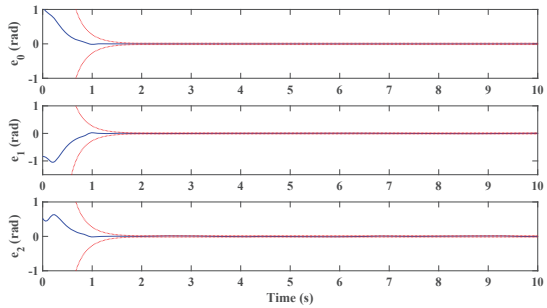

Fig. 5: Tracking errors between the space manipulator and the reference trajectory.

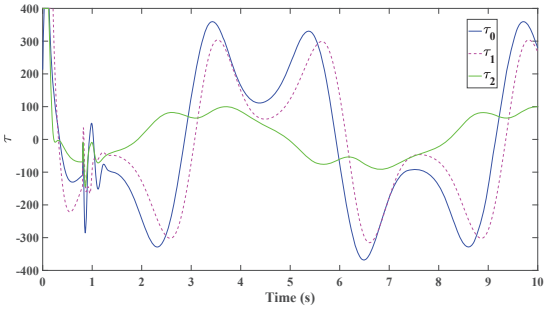

Fig. 6: Response of control torques.

physical constraints with predefined convergence accuracy and convergence time globally.

5 Conclusion

In this paper, we have investigated the prescribed time trajectory tracking control for space manipulators with uncertain dynamics, system uncertainties, and input saturation. A FASA-based control strategy has been designed to guarantee the disturbance rejection and the pre-assignable convergence accuracy within prescribed convergence time globally. Moreover, a smooth function was used to approximate the control input, and the input saturation was compensated by an auxiliary system. Numerical simulations have demonstrated the effectiveness of the proposed control method.

References

[1] Y. Xu, T. Kanade, Space robotics: dynamics and control, Kluwer, Norwell, MA, 1993.

[2] H. Wang, D. Guo, H. Xu, W. Chen, T. Liu, K. K. Leang, Eye-in-hand tracking control of a free-floating space manipulator, *IEEE Transactions Aerospace Electronic Systems*, 53(4): 1855–1865, 2017.

[3] X. Zhang, J. Liu, J. Feng, Y. Liu, Z. Jun, Effective capture of nongraspable objects for space robots using geometric cage pairs, *IEEE-ASME Transactions Mechatronics*, 25(1): 95–107, 2020.

[4] C. Qi, D. Li, W. Ma, Q. Wei, W. Zhang, W. Wang, Y. Hu, F. Gao, Distributed delay compensation for a hybrid simulation system of space manipulator capture, *IEEE-ASME Transactions Mechatronics*, 27(4): 2367–2378, 2022.

[5] J. Qiao, H. Wu, X. Yu, High-precision attitude tracking control of space manipulator system under multiple disturbances, *IEEE Transactions on Systems Man Cybernetics-Systems*, 51(7), 4274–4284, 2021.

[6] X. Shao, G. Sun, W. Yao, X. Li, O. Zhang, Fractional-order resolved acceleration control for free-floating space manipulator with system uncertainty, *Aerospace Science and Technology*, 118, Art. no. 107041, 2021.

[7] Z. Xu, C. Sun, Q. Liu, Output-feedback prescribed performance control for the full-state constrained nonlinear systems and its application to DC motor system, *IEEE Transactions on Systems, Man, and Cybernetics-Systems*, 53(7): 3898–3907, 2023.

[8] X. Guo, H. Zhang, J. Sun, Y. Zhou, Preassigned time adaptive neural tracking control for stochastic nonlinear multiagent systems with deferred constraints, *IEEE Transactions on Neural Networks and Learning Systems*, 2023, early access.

[9] M. Golestani, W. Zhang, Y. Yang, N. Mung, Disturbance observer-based constrained attitude control for flexible spacecraft, *IEEE Transactions on Aerospace and Electronic Systems*, 59(2): 963–972, 2022.

[10] Y. Song, Y. Wang, J. Holloway, M. Krstic, Time-varying feedback for regulation of normal-form nonlinear systems in prescribed finite time, *Automatica*, 83: 243–251, 2017.

[11] Y. Cao, J. Cao, Y. Song, Practical prescribed time tracking control over infinite time interval involving mismatched uncertainties and non-vanishing disturbances, *Automatica*, 136, Art. no. 110050, 2022.

[12] X. W. Huang, Z. Y. Dong, P. Yang, L. H. Zhang, Model-free adaptive trajectory tracking control of robotic manipulators with practical prescribed-time performance, *Nonlinear Dynamics*, 111, Art. no. 21, 2023.

[13] C. Hua, P. Ning, K. Li, Adaptive prescribed-time control for a class of uncertain nonlinear systems, *IEEE Transactions on Automatic Control*, 67(11), Art. no. 11, 2021.

[14] Duan G R, Robust stabilization of time-varying nonlinear systems with time-varying delays: A fully actuated system approach, *IEEE Transactions on Cybernetics*, 53(12), 7455–7468, 2023.

[15] G. Duan, High-order fully actuated system approaches: Part III. Robust control and high-order backstepping, *International Journal of Systems Science*, 52(5): 952–971, 2021.

[16] G. Duan, High-order fully actuated system approaches: Part IV. Adaptive control and high-order backstepping, *International Journal of Systems Science*, 52(5): 972–989, 2021.

[17] G. Duan, High-order fully actuated system approaches: Part VII. Controllability, stabilisability and parametric designs, *International Journal of Systems Science*, 52(14): 3091–3114, 2021.

[18] G. Duan, High-order fully actuated system approaches: Part VIII. Optimal control with application in spacecraft attitude stabilization, *International Journal of System Sciences*, 53(1): 54–73, 2021.

[19] G. Duan, High-order fully-actuated system approaches: Part IX. Generalised PID control and model reference tracking, *International Journal of Systems Science*, 53(3): 652–674, 2021.

[20] L. Zhang, L. Zhu, C. Hua, Practical prescribed time control based on high-order fully actuated system approach for strong interconnected nonlinear systems, *Nonlinear Dynamics*, 110, Art. no. 4, 2022.

[21] C. Yang, D. Huang, W. He, L. Cheng, Neural control of robot manipulators with trajectory tracking constraints and input saturation, *IEEE Transactions on Neural Networks and Learning Systems*, 32(9): 4231–4242, 2020.

[22] T. G. Tian, B. Li, Q. Zhao, G. R. Duan, High-precision trajectory tracking control for free-flying space manipulators with multiple constraints and system uncertainties, *IEEE Transactions on Aerospace and Electronic Systems*, 60(1): 789–801, 2023.

Proceedings of the 3rd Conference on Fully Actuated System Theory and Applications
May 10-12, 2024, Shenzhen, China

Adaptive Tracking Control for Random High-Order Fully Actuated Systems with Unknown Drift Nonlinearity and Diffusion Coefficient

Yunqi Chen[1], Guangren Duan[1,2]

1. Shenzhen Key Laboratory of Control Theory and Intelligent Systems, Southern University of Science and Technology, Shenzhen 518055, China
E-mail: cyq09180@163.com

2. Center for Control Theory and Guidance Technology, Harbin Institute of Technology, Harbin 150001, China
E-mail: duangr@sustech.edu.cn; g.r.duan@hit.edu.cn

Abstract: This paper extends the high-order fully actuated system (HOFAS) theory to the adaptive tracking control of random nonlinear systems disturbed by second-order moment process. Firstly, a random high-order fully actuated system (RHOFAS) with unknown drift nonlinearity and diffusion coefficient is proposed. Secondly, an adaptive tracking controller is designed for this RHOFAS by virtue of the HOFAS theory and a radical basis function neural network (RBFNN). It is proved that the resulting closed-loop system is exponentially noise-to-state practically stable in mean square, the mean square of tracking error can converge to an arbitrarily small neighborhood of zero, and all signals in the closed-loop system is bounded in mean square. Finally, two simulation examples are provided to demonstrate the effectiveness of our proposed controller.

Key Words: Adaptive control, Random systems, High-order fully actuated systems, Unknown nonlinearity, Neural network

1 Introduction

Random noises and nonlinearity are almost inevitable in numerous practical control systems, and hence it is quite necessary to take them into account when modelling control systems. The most celebrated modelling way is the following Itô-type stochastic differential equation (SDE) [1], $\mathrm{d}\boldsymbol{x} = \boldsymbol{f}(\boldsymbol{x},t)+\boldsymbol{G}(\boldsymbol{x},t)\mathrm{d}\boldsymbol{W}_t$ with the initial condition $\boldsymbol{x}(t_0)=\boldsymbol{x}_0$, where $\boldsymbol{x}\in\mathbb{R}^r$ is the system state, $\boldsymbol{f}:\mathbb{R}^r\times\mathbb{R}_+\to\mathbb{R}^r$ and $\boldsymbol{G}:\mathbb{R}^r\times\mathbb{R}_+\to\mathbb{R}^{r\times l}$ are nonlinear functions, and $\boldsymbol{W}_t\in\mathbb{R}^l$ is the Wiener process whose formal derivative $\frac{\mathrm{d}\boldsymbol{W}_t}{\mathrm{d}t}$ is taken as the white noises. Albeit the Itô-type SDE has gained significant success in many science fields, it may not suit very well for describing random noises existing in many control engineering applications. To be specific, in the Itô-type SDE, random noises are modelled by white noises which have infinite mean power. In practical control engineering however, systems are required to run with desired performance under the disturbance of random noises, and thus it is more sensible to model random noises by the second-order moment processes which have finite mean power. This way of modelling random noises corresponds to the so-called random differential equation (RDE) [2]. After a seminal work on the stability analysis of RDE is done by [3], the stability analyses of various types of RDEs are emerging continuously, such as RDEs with time-dependent switch [4, 5], state-dependent switch [6], stochastic impulses [7, 8], and time-varying delay [9, 10]. At the same time, a series of control design problems of RDEs are gradually being solved; see [11] for a detailed overview of the latest progress for stability and control on RDE.

This work is partially supported by the Shenzhen Key Laboratory of Control Theory and Intelligent Systems (ZDSYS20220330161800001), the Shenzhen Science and Technology Program (KQTD20221101093557010), the Major Program of the National Natural Science Foundation of China (61690210, 61690212), the National Natural Science Foundation of China (61333003), and also by the Science Center Program of the National Natural Science Foundation of China under grant No. 62188101.

A common feature of both the Itô-type SDE and RDE is that they are all within the first-order state-space framework, that is, systems are described by one or several first-order differential equations. Even though the state-space framework is convenient for state response analysis and state estimation, it is not the best one for control design. In fact, governed by physical laws including Newton's laws, Lagrange's equations and Kirchhoff's law, many physical systems are originally modelled as high-order differential equations. More importantly, these high-order systems are likely to have the full-actuation property, and this property can greatly simplify the control design as it can be used to eliminate the nonlinearity of systems. However, this charming property would generally no longer exist when these high-order systems are converted into the first-order state-space models via the variable extension method. Inspired by the above facts, Professor Duan recommended to directly model control systems by high-order differential equations and further proposed the corresponding high-order fully actuated system (HOFAS) theory for stability analysis and control design [12, 13]. In the past five years, a series of theoretical results on HOFAS have been done by Duan, such as the generalized strict-feedback system [14], adaptive control [15], robust control [16], optimal control [17], sub-fully actuated systems [18], and nonholonomic systems [19]. Meanwhile, many other researchers have begun to extend the HOFAS theory to several aspects like predictive control [20], cooperative control [21], fault-tolerant control [22] and quadrotor control [23].

Up to now, except for [24–26], almost all the existing research works on the HOFAS theory do not take the influence of random noises into consideration. Moreover, the random noises in [24–26] are described as white noises, which constrains the use of [24–26] in practical control applications. On the basis of the above facts, the motivation of this paper is to extend the HOFAS theory to the random nonlinear systems. Specifically, the main contributions of this paper

consist of the following three aspects:

(1) Different from the existing state-space model (SDE and RDE), a random HOFAS (RHOFAS) is proposed to model the nonlinear control systems disturbed by second-order moment process.

(2) By using the HOFAS theory and a radical basis function neural network (RBFNN) [27], an adaptive tracking controller is designed for the RHOFAS with unknown drift nonlinearity and diffusion coefficient.

(3) The proposed adaptive tracking controller can ensure that: the closed-loop system is exponentially noise-to-state practically stable in mean square; the asymptotic mean squared tracking error can be made as small as possible by properly tuning design parameters; all the closed-loop signals are bounded in mean square.

The remainder of the paper is outlined as follows. In Section 2, some notations and mathematical preliminaries are given. Section 3 introduces the tracking problem of the RHOFAS with unknown drift nonlinearity and diffusion coefficient, and the corresponding adaptive tracking controller is designed and analyzed in Section 4. Simulation examples are provided in Section 5, followed by a concluding remark in Section 6.

2 Notations and mathematical preliminaries

2.1 Notations

Throughout the entire paper, we employ bold characters to denote vectors and matrices, and normal characters are used to represent scalars. $\boldsymbol{I}_n$ is the $n \times n$ identity matrix, and $\mathbf{0}$ is the zero vector or matrix with proper dimension. The n-dimensional vector space and the $m \times n$ dimensional matrix space are represented by $\mathbb{R}^m$ and $\mathbb{R}^{m\times n}$, respectively. For a complex number s, its real part is represented by $\mathrm{Re}\,(s)$. $\mathrm{P}(\cdot)$, $\mathrm{E}[\cdot]$ and $\mathrm{U}[a,b]$ denote the probability, mathematical expectation and the uniform distribution on interval $[a,b]$, respectively. The Frobenius norm of a matrix $\boldsymbol{A}$ is denoted by $\|\boldsymbol{A}\|$. For a square matrix $\boldsymbol{A}$, $\lambda_i(\boldsymbol{A})$, $\lambda_{\max}(\boldsymbol{A})$, $\lambda_{\min}(\boldsymbol{A})$, $\det \boldsymbol{A}$ stand for its i-th, maximum, and minimum eigenvalues and its determinant. $\mathrm{blockdiag}\,(\boldsymbol{A}_i, i=1,2,\ldots,n)$ represents a block diagonal matrix with the i-th diagonal block being $\boldsymbol{A}_i$. $\mathcal{C}^i$ denotes the set of all functions with continuous i-th partial derivatives, and $\mathcal{K}$ represents the set of all functions: $\mathbb{R}_+ \to \mathbb{R}_+$, which are continuous, strictly increasing, and vanishing at zero.

For $\boldsymbol{x} \in \mathbb{R}^m$ and $\boldsymbol{A}_i \in \mathbb{R}^{m\times m}$, $i=1,2,\ldots,n$, the following symbols are used as in [12] for notational convenience:

$$\boldsymbol{x}^{(0\sim n-1)} \triangleq \left[\boldsymbol{x}^{\mathrm{T}}, \dot{\boldsymbol{x}}^{\mathrm{T}}, \cdots, \left(\boldsymbol{x}^{(n-1)}\right)^{\mathrm{T}}\right]^{\mathrm{T}},$$

$$\boldsymbol{A}_{0\sim n-1} \triangleq [\boldsymbol{A}_0, \boldsymbol{A}_1, \ldots, \boldsymbol{A}_{n-1}],$$

$$\boldsymbol{\Phi}(\boldsymbol{A}_{0\sim n-1}) \triangleq \begin{bmatrix} \mathbf{0}_{m(n-1)\times m} & \boldsymbol{I}_{m(n-1)} \\ & -\boldsymbol{A}_{0\sim n-1} \end{bmatrix},$$

where $\boldsymbol{x}^{(i)}$ denotes the i-order derivative of $\boldsymbol{x}$.

2.2 Mathematical preliminaries

Consider the random nonlinear system described by the following RDE:

$$\begin{cases} \dot{\boldsymbol{x}} = \boldsymbol{f}(\boldsymbol{x},t) + \boldsymbol{G}(\boldsymbol{x},t)\boldsymbol{\omega}(t) \\ \boldsymbol{x}(t_0) = \boldsymbol{x}_0, \end{cases} \tag{1}$$

where $\boldsymbol{x} \in \mathbb{R}^r$ and $\boldsymbol{\omega}(t) \in \mathbb{R}^l$ denote the system state and the random noise process, respectively; t_0 and $\boldsymbol{x}(t_0)$ are the initial time and the initial system state, respectively. The underlying complete probability space is represented by the quartet $(\Omega, \mathcal{F}, \mathcal{F}_t, \mathrm{P})$, where Ω, $\mathcal{F}$, $\mathcal{F}_t$, and P are the sample space, sigma-field, filtration, and probability measure, respectively. $\mathcal{F}_t$ is further assumed to satisfy the typical conditions that $\mathcal{F}_t$ is increasing and right continuous while $\mathcal{F}_0$ contains all P-null sets. Nonlinear functions $\boldsymbol{f} : \mathbb{R}^r \times \mathbb{R}_+ \to \mathbb{R}^r$ and $\boldsymbol{G} : \mathbb{R}^r \times \mathbb{R}_+ \to \mathbb{R}^{r\times l}$, called the *drift* and *diffusion* coefficient respectively, are locally Lipschitz in $\boldsymbol{x}$ and piecewise continuous in t, and for all $t \geq t_0$, $\boldsymbol{f}(\mathbf{0},t)$ and $\boldsymbol{G}(\mathbf{0},t)$ are bound almost surely (a.s.). Moreover, $\boldsymbol{\omega}(t)$ is assumed to a second-order random process satisfying the following assumption [11].

Assumption 1. *Random noise process $\boldsymbol{\omega}(t)$ is $\mathcal{F}_t$-adapted and piecewise continuous, and there exist a constant $K > 0$ such that*

$$\sup_{t_0\leq s\leq t} \mathrm{E}\left[\|\boldsymbol{\omega}(s)\|^2\right] \leq K, \forall t \geq t_0. \tag{2}$$

To conduct stability analysis, we adopt the following stability concept and the corresponding stability criterion [28].

Definition 1. *For $m > 0$, system* (1) *is claimed to be exponentially noise-to-state practically stable in the m-th moment (eNSpS-m-M), if there exist constants $a_0 > 0$, $a_1 > 0$, $a_2 \geq 0$ and a class-$\mathcal{K}$ function $\gamma(\cdot)$ such that for $\forall t \in [t_0, +\infty)$,*

$$\mathrm{E}\left[\|\boldsymbol{x}\|^m\right] \leq a_0 \|\boldsymbol{x}_0\|^m \mathrm{e}^{-a_1(t-t_0)} + a_2 + \gamma\left(\sup_{t_0\leq s\leq t} \mathrm{E}\left[\|\boldsymbol{\xi}(s)\|^2\right]\right).$$

Particularly, when $m = 2$, it is also said to be exponentially noise-to-state practically stable in mean square (eNSpS-MS).

Lemma 1. *For system* (1) *under Assumption 1, if there exist constants $m > 0$, $b_1 > b_0 > 0$, $c_0 > 0$, $c_1 > 0$, $c_2 \geq 0$ and a $\mathcal{C}^1$ function $V(\boldsymbol{x},t) : \mathbb{R}^r \times [t_0, +\infty) \to \mathbb{R}_+$ such that*

$$b_0 \|\boldsymbol{x}\|^m \leq V(\boldsymbol{x},t) \leq b_1 \|\boldsymbol{x}\|^m,$$
$$\dot{V}(\boldsymbol{x},t) \leq -c_0 V(\boldsymbol{x},t) + c_1\|\boldsymbol{\omega}(t)\|^2 + c_2.$$

Then system (1) *has a unique global solution for $\forall \boldsymbol{x}_0 \in \mathbb{R}^r$ and is eNSpS-m-M.*

The following lemma about RBFNN is very useful for tackling the control law design of dynamical systems with unknown functions [27].

Lemma 2. *Assume that $\varphi(\boldsymbol{X}) : \mathbb{R}^m \to \mathbb{R}$ is a continuous function over a compact set $\Omega \subset \mathbb{R}$, then the RBFNN can reconstruct $\varphi(\boldsymbol{X})$ as follows:*

$$\varphi(\boldsymbol{X}) = \boldsymbol{W}^{\mathrm{T}}\boldsymbol{S}(\boldsymbol{X}) + \delta_\varphi(\boldsymbol{X}), \forall \boldsymbol{X} \in \mathbb{R}^n,$$
$$|\delta_\varphi(\boldsymbol{X})| \leq \bar{\delta}_\varphi \leq \infty,$$

where $\boldsymbol{W} \in \mathbb{R}^N$ is the ideal weight vector with N being the number of neural network nodes, $\delta_\varphi(\boldsymbol{X})$ is the reconstruction error with $\bar{\delta}_\varphi > 0$ being an unknown constant, and $\boldsymbol{S}(\boldsymbol{X}) = [s_1(\boldsymbol{X}), s_2(\boldsymbol{X}), \ldots, s_N(\boldsymbol{X})]^{\mathrm{T}}$ is the radical basis function (RBF) vector. For $i = 1,2,\ldots,N$,

$s_i(\boldsymbol{X}) = \exp\left[-\left(\boldsymbol{X}-\boldsymbol{\gamma}_i\right)^{\mathrm{T}}\left(\boldsymbol{X}-\boldsymbol{\gamma}_i\right)/\nu_i^2\right]$, *where* ν_i *and* $\boldsymbol{\gamma}_i$ *are the width and center vector respectively.*

In the HOFAS theory, the following lemma plays a vital role in the control law design [16, 22, 29].

Lemma 3. *For any* $\mu > 0$*, there exists a set of matrices* $\boldsymbol{A}_i \in \mathbb{R}^{r\times r}$*,* $i = 0, 1, \ldots, n-1$ *such that*

$$\mathrm{Re}\lambda_i\left(\boldsymbol{\Phi}(\boldsymbol{A}_{0\sim n-1})\right) \leq -\frac{\mu}{2}, \quad i = 1, 2, \ldots, rn. \tag{3}$$

Consequently, there exists a positive definite matrix $\boldsymbol{P} \in \mathbb{R}^{rn\times rn}$ *satisfying*

$$\boldsymbol{\Phi}^{\mathrm{T}}(\boldsymbol{A}_{0\sim n-1})\boldsymbol{P} + \boldsymbol{P}\boldsymbol{\Phi}(\boldsymbol{A}_{0\sim n-1}) \leq -\mu\boldsymbol{P}. \tag{4}$$

3 Problem formulation

In this paper, we consider the following random high-order fully-actuated system (RHOFAS)

$$\begin{aligned}\boldsymbol{x}^{(n)} =& \boldsymbol{f}\left(\boldsymbol{x}^{(0\sim n-1)}\right) + \boldsymbol{G}\left(\boldsymbol{x}^{(0\sim n-1)}\right)\boldsymbol{u} \\ &+ \boldsymbol{\Gamma}\left(\boldsymbol{x}^{(0\sim n-1)}\right)\boldsymbol{\omega}(t),\end{aligned} \tag{5}$$

where $\boldsymbol{x} \in \mathbb{R}^r$ and $\boldsymbol{u} \in \mathbb{R}^r$ are the system state and the control input respectively. The random noise process $\boldsymbol{\omega}(t) \in \mathbb{R}^l$ satisfies Assumption 1. $\boldsymbol{f} : \mathbb{R}^{rn} \to \mathbb{R}^r$ and $\boldsymbol{\Gamma} : \mathbb{R}^{rn} \to \mathbb{R}^{rn}$ are unknown smooth vector and matrix functions respectively, $\boldsymbol{f}(\boldsymbol{0})$ and $\boldsymbol{\Gamma}(\boldsymbol{0})$ are bounded a.s., and moreover, $\boldsymbol{\Gamma}$ satisfies Assumption 2. $\boldsymbol{G} : \mathbb{R}^r \to \mathbb{R}^{r\times l}$ is a known smooth matrix function and satisfies the following fully-actuation Assumption [12].

Assumption 2. $\det \boldsymbol{G}\left(\boldsymbol{x}^{(0\sim n-1)}, t\right) \neq 0$ *or* ∞ *for* $\forall \boldsymbol{x}^{(i)} \in \mathbb{R}^r$*,* $i = 0, 1, \ldots, n-1$*, and* $t \in [t_0, +\infty)$*.*

Objective: For the RHOFAS (5), suppose that there is a desired signal $\boldsymbol{x}_d$ satisfying Assumption 3, the objective of this paper is to design a controller $\boldsymbol{u}$ such that the system state $\boldsymbol{x}$ can track the desired signal $\boldsymbol{x}_d$ as well as possible while maintaining all the closed-loop signals bounded in mean square, regardless of the influence of random noises.

Assumption 3. *The desired signal* $\boldsymbol{x}_d$ *and its first to* n*-th derivatives* $\boldsymbol{x}_d, \dot{\boldsymbol{x}}_d, \ldots, \boldsymbol{x}_d^{(n)}$ *are available and bounded.*

4 Controller design and analysis

4.1 Preparation works

Denote the tracking error by $\boldsymbol{e}(t) = \boldsymbol{x} - \boldsymbol{x}_d$. As a result, $\boldsymbol{e}^{(i)}(t) = \boldsymbol{x}^{(i)} - \boldsymbol{x}_d^{(i)}$, $i = 1, 2, \ldots, n$, and furthermore, the following dynamic equation of the tracking error is obtained

$$\begin{aligned}\boldsymbol{e}^{(n)} =& \boldsymbol{f}\left(\boldsymbol{x}^{(0\sim n-1)}\right) - \boldsymbol{x}_d^{(n)} + \boldsymbol{G}\left(\boldsymbol{x}^{(0\sim n-1)}\right)\boldsymbol{u} \\ &+ \boldsymbol{\Gamma}\left(\boldsymbol{x}^{(0\sim n-1)}\right)\boldsymbol{\omega}(t).\end{aligned} \tag{6}$$

For ease of writing, we shall denote $\boldsymbol{X} \triangleq \boldsymbol{x}^{(0\sim n-1)}$ and $\boldsymbol{\Xi} \triangleq \boldsymbol{e}^{(0\sim n-1)}$ in the remaining context, and moreover, we shall occasionally omit the dependence of $\boldsymbol{f}(\boldsymbol{X})$, $\boldsymbol{G}(\boldsymbol{X})$ and $\boldsymbol{\Gamma}(\boldsymbol{X})$ on $\boldsymbol{X}$ and simply write $\boldsymbol{f}$, $\boldsymbol{G}$ and $\boldsymbol{\Gamma}$ when no confusion can arise.

Now we shall show how to employ the RBFNN to tackle the influence of the two unknown functions $\boldsymbol{f}$ and $\boldsymbol{\Gamma}$.

From Lemma 2 we can get

$$\boldsymbol{f} = \begin{bmatrix} f_1 \\ f_2 \\ \vdots \\ f_r \end{bmatrix} = \begin{bmatrix} \boldsymbol{W}_{1,f}^{\mathrm{T}}\boldsymbol{S}_{1,f}(\boldsymbol{X}) + \delta_{1,f}(\boldsymbol{X}) \\ \boldsymbol{W}_{2,f}^{\mathrm{T}}\boldsymbol{S}_{2,f}(\boldsymbol{X}) + \delta_{2,f}(\boldsymbol{X}) \\ \vdots \\ \boldsymbol{W}_{r,f}^{\mathrm{T}}\boldsymbol{S}_{r,f}(\boldsymbol{X}) + \delta_{r,f}(\boldsymbol{X}) \end{bmatrix}, \tag{7}$$

where for $i = 1, 2, \ldots, r$, $\boldsymbol{W}_{i,f}$ and $\boldsymbol{S}_{i,f}$ are the ideal weight vector and the RBF vector respectively. By letting

$$\begin{aligned}&\bar{\boldsymbol{W}}_{i,f} \triangleq \left[\boldsymbol{W}_{i,f}^{\mathrm{T}}, \delta_{i,f}(\boldsymbol{X})\right]^{\mathrm{T}},\ i = 1, 2, \ldots, r \\ &\bar{\boldsymbol{S}}_{i,f}(\boldsymbol{X}) \triangleq \left[\boldsymbol{S}_{i,f}^{\mathrm{T}}(\boldsymbol{X}), 1\right]^{\mathrm{T}},\ i = 1, 2, \ldots, r, \\ &\bar{\boldsymbol{W}}_f \triangleq \mathrm{blockdiag}\left(\bar{\boldsymbol{W}}_{1,f}, \bar{\boldsymbol{W}}_{2,f}, \ldots, \bar{\boldsymbol{W}}_{r,f}\right), \\ &\bar{\boldsymbol{S}}_f(\boldsymbol{X}) \triangleq \left[\bar{\boldsymbol{S}}_{1,f}^{\mathrm{T}}(\boldsymbol{X}), \bar{\boldsymbol{S}}_{2,f}^{\mathrm{T}}(\boldsymbol{X}), \ldots, \bar{\boldsymbol{S}}_{r,f}^{\mathrm{T}}(\boldsymbol{X})\right]^{\mathrm{T}},\end{aligned} \tag{8}$$

(7) can then be rewritten into the more compact form below

$$\boldsymbol{f} = \bar{\boldsymbol{W}}_f^{\mathrm{T}}\bar{\boldsymbol{S}}_f(\boldsymbol{X}). \tag{9}$$

Further, from Lemma 1 we can also know that

$$\left\|\bar{\boldsymbol{W}}_{i,f}^{\mathrm{T}}\right\|^2 \leq \left\|\left(\boldsymbol{W}_{i,f}^*\right)^{\mathrm{T}}\right\|^2,\ i = 1, 2, \ldots, r, \tag{10}$$

where

$$\boldsymbol{W}_{i,f}^* \triangleq \left[\boldsymbol{W}_{i,f}^{\mathrm{T}}, \delta_{i,f}\right]^{\mathrm{T}}, |\delta_{i,f}(\boldsymbol{X})| \leq \bar{\delta}_{i,f},\ i = 1, 2, \ldots, r, \tag{11}$$

and $\delta_{i,f} > 0$, $i = 1, 2, \ldots, r$ are a set of unknown constants. Using (8)$\sim$(11), yields

$$\|\boldsymbol{f}\|^2 \leq \left\|\bar{\boldsymbol{W}}_f^{\mathrm{T}}\right\|^2 \|\bar{\boldsymbol{S}}_f(\boldsymbol{X})\|^2 \leq \left\|\left(\boldsymbol{W}_f^*\right)^{\mathrm{T}}\right\|^2 \|\bar{\boldsymbol{S}}_f(\boldsymbol{X})\|^2, \tag{12}$$

where we define

$$\boldsymbol{W}_f^* \triangleq \mathrm{blockdiag}\left(\boldsymbol{W}_{1,f}^*, \boldsymbol{W}_{2,f}^*, \ldots, \boldsymbol{W}_{r,f}^*\right). \tag{13}$$

In the following, we will present how to eliminate the impact of unknown function $\boldsymbol{\Gamma}(\boldsymbol{X})$ by RBFNN. For simplicity, we define $h(\boldsymbol{X}) \triangleq \left\|\boldsymbol{\Gamma}^{\mathrm{T}}(\boldsymbol{X})\right\|^2$. Then according to Lemma 2, there exist a ideal weight vector $\boldsymbol{W}_h$ and a RBF vector $\boldsymbol{S}_h(\boldsymbol{X})$ such that

$$h(\boldsymbol{X}) = \boldsymbol{W}_h^{\mathrm{T}}\boldsymbol{S}_h(\boldsymbol{X}) + \delta_h(\boldsymbol{X}),\ |\delta_\varphi(\boldsymbol{X})| \leq \bar{\delta}_h \leq \infty, \tag{14}$$

where $\bar{\delta}_h > 0$ is an unknown constant. Similar to the previous analysis made for $\boldsymbol{f}$, we can obtain the following inequality

$$h(\boldsymbol{X}) \leq |h(\boldsymbol{X})| \leq \left\|\bar{\boldsymbol{W}}_h^{\mathrm{T}}\right\| \left\|\bar{\boldsymbol{S}}_h\right\| \leq \left\|\left(\boldsymbol{W}_h^*\right)^{\mathrm{T}}\right\| \left\|\bar{\boldsymbol{S}}_h\right\|, \tag{15}$$

where

$$\begin{aligned}&\bar{\boldsymbol{W}}_h \triangleq \left[\boldsymbol{W}_h^{\mathrm{T}}, \delta_h(\boldsymbol{X})\right]^{\mathrm{T}}, \\ &\bar{\boldsymbol{S}}_h(\boldsymbol{X}) \triangleq \left[\boldsymbol{S}_h^{\mathrm{T}}(\boldsymbol{X}), 1\right]^{\mathrm{T}}, \\ &\boldsymbol{W}_h^* \triangleq \left[\boldsymbol{W}_h^{\mathrm{T}}, \bar{\delta}_h(\boldsymbol{X})\right]^{\mathrm{T}}.\end{aligned} \tag{16}$$

4.2 Adaptive tracking controller

With the aid of previous preparations, the adaptive tracking controller designed for the RHOFAS (5) can be summarized into the following theorem.

Theorem 1. *Let Assumptions 1∼3 be met. Further let μ be an arbitrary positive number, $\boldsymbol{A}_i \in \mathbb{R}^{r\times r}$, $i = 0, 2, \ldots, n-1$, be a set of matrices satisfying* (3)*, and*

$$\boldsymbol{P}_L = \boldsymbol{P}\begin{bmatrix} \boldsymbol{0}_{r(n-1)\times r} \\ \boldsymbol{I}_r \end{bmatrix}, \tag{17}$$

where the positive definite matrix $\boldsymbol{P} \in \mathbb{R}^{rn\times rn}$ satisfies (4)*. Define unknown parameters $\theta_1 \triangleq \left\|\left(\boldsymbol{W}_f^*\right)^{\mathrm{T}}\right\|^2$ and $\theta_2 \triangleq \left\|(\boldsymbol{W}_h^*)^{\mathrm{T}}\right\|$. Then for the RHOFAS* (5)*, the following controller*

$$\boldsymbol{u} = -\boldsymbol{G}^{-1}\left(\boldsymbol{A}_{0\sim n-1}\boldsymbol{e}^{(0\sim n-1)} - \boldsymbol{x}_d^{(n)} + \boldsymbol{u}_1 + \boldsymbol{u}_2\right), \tag{18a}$$

$$\boldsymbol{u}_1 = \frac{1}{2\varepsilon_1^2}\boldsymbol{P}_L^{\mathrm{T}}\Xi\hat{\theta}_1\|\bar{\boldsymbol{S}}_f(\boldsymbol{X})\|^2, \tag{18b}$$

$$\boldsymbol{u}_2 = \frac{1}{2\varepsilon_2^2}\boldsymbol{P}_L^{\mathrm{T}}\Xi\hat{\theta}_2\|\bar{\boldsymbol{S}}_h(\boldsymbol{X})\|, \tag{18c}$$

and adaptive laws

$$\dot{\hat{\theta}}_1 = \frac{r_1}{2\varepsilon_1^2}\left\|\Xi^T\boldsymbol{P}_L\right\|^2\|\bar{\boldsymbol{S}}_f(\boldsymbol{X})\|^2 - \pi_1\hat{\theta}_1, \tag{19a}$$

$$\dot{\hat{\theta}}_2 = \frac{r_2}{2\varepsilon_2^2}\left\|\Xi^T\boldsymbol{P}_L\right\|^2\|\bar{\boldsymbol{S}}_h(\boldsymbol{X})\| - \pi_2\hat{\theta}_2, \tag{19b}$$

*can guarantee that: the corresponding closed-loop system ((*22*) has a unique solution and is eNSpS-MS; all closed-loop signals are bounded in mean square, and*

$$\lim_{t\to\infty}\mathrm{E}\left[\|\Xi\|^2\right] \le \frac{\varepsilon_2^2 K + 2\varrho}{\lambda_{\min}(\boldsymbol{P})\,c}, \tag{20}$$

where $\varepsilon_1, \varepsilon_2, \pi_1, \pi_2, r_1, r_2 > 0$ and

$$c \triangleq \min(\mu, \pi_1, \pi_2),\ \varrho \triangleq \frac{\varepsilon_1^2}{2} + \frac{\pi_1}{2r_1}\theta_1^2 + \frac{\pi_2}{2r_2}\theta_2^2. \tag{21}$$

Proof. By plugging the controller (18) into system (6), the following closed-loop system is obtained

$$\boldsymbol{e}^{(n)} = -\boldsymbol{A}_{0\sim n-1}\Xi + \boldsymbol{f} - \boldsymbol{u}_1 - \boldsymbol{u}_2 + \boldsymbol{\Gamma}\boldsymbol{\omega}(t),$$

which can be further reformulated into the state-space form

$$\dot{\Xi} = \boldsymbol{\Phi}(\boldsymbol{A}_{0\sim n-1})\Xi + \begin{bmatrix} \boldsymbol{0}_{r(n-1)\times 1} \\ \boldsymbol{f} - \boldsymbol{u}_1 - \boldsymbol{u}_2 + \boldsymbol{\Gamma}\boldsymbol{\omega}(t) \end{bmatrix}. \tag{22}$$

For the system (22), choose the corresponding Lyapunov function as

$$V = \frac{1}{2}\Xi^{\mathrm{T}}\boldsymbol{P}\Xi + \frac{1}{2r_1}\tilde{\theta}_1^2 + \frac{1}{2r_2}\tilde{\theta}_2^2, \tag{23}$$

where $\tilde{\theta}_1 \triangleq \theta_1 - \hat{\theta}_1$ and $\tilde{\theta}_2 \triangleq \theta_2 - \hat{\theta}_2$. Then from (22) we know that the differential of V satisfies

$$\begin{aligned}
\dot{V} &= \frac{1}{2}\dot{\Xi}^{\mathrm{T}}\boldsymbol{P}\Xi + \frac{1}{2}\Xi^{\mathrm{T}}\boldsymbol{P}\dot{\Xi} + \frac{1}{r_1}\tilde{\theta}_1\dot{\hat{\theta}}_1 + \frac{1}{r_2}\tilde{\theta}_2\dot{\hat{\theta}}_2 \\
&= \frac{1}{2}\Xi^{\mathrm{T}}\left(\boldsymbol{\Phi}^{\mathrm{T}}(\boldsymbol{A}_{0\sim n-1})\boldsymbol{P} + \boldsymbol{P}\boldsymbol{\Phi}(\boldsymbol{A}_{0\sim n-1})\right)\Xi \\
&\quad + \Xi^{\mathrm{T}}\boldsymbol{P}\begin{bmatrix} \boldsymbol{0}_{r(n-1)\times 1} \\ \boldsymbol{f} - \boldsymbol{u}_1 - \boldsymbol{u}_2 + \boldsymbol{\Gamma}\boldsymbol{\omega}(t) \end{bmatrix} - \frac{1}{r_1}\tilde{\theta}_1\dot{\hat{\theta}}_1 - \frac{1}{r_2}\tilde{\theta}_2\dot{\hat{\theta}}_2 \\
&\le -\frac{\mu}{2}\Xi^{\mathrm{T}}\boldsymbol{P}\Xi + \Xi^{\mathrm{T}}\boldsymbol{P}_L\boldsymbol{f} - \Xi^{\mathrm{T}}\boldsymbol{P}_L\boldsymbol{u}_1 - \Xi^{\mathrm{T}}\boldsymbol{P}_L\boldsymbol{u}_2 \\
&\quad + \Xi^{\mathrm{T}}\boldsymbol{P}_L\boldsymbol{\Gamma}\boldsymbol{\xi}(t) - \frac{1}{r_1}\tilde{\theta}_1\dot{\hat{\theta}}_1 - \frac{1}{r_2}\tilde{\theta}_2\dot{\hat{\theta}}_2.
\end{aligned} \tag{24}$$

Via Young's inequality and (12), we have

$$\begin{aligned}
\Xi^{\mathrm{T}}\boldsymbol{P}_L\boldsymbol{f} &\leqslant \frac{1}{2\varepsilon_1^2}\left\|\Xi^{\mathrm{T}}\boldsymbol{P}_L\boldsymbol{f}\right\|^2 + \frac{\varepsilon_1^2}{2} \\
&\leqslant \frac{1}{2\varepsilon_1^2}\left\|\Xi^{\mathrm{T}}\boldsymbol{P}_L\right\|^2\|\boldsymbol{f}\|^2 + \frac{\varepsilon_1^2}{2} \\
&\leqslant \frac{1}{2\varepsilon_1^2}\left\|\Xi^{\mathrm{T}}\boldsymbol{P}_L\right\|^2\left\|\left(\boldsymbol{W}_f^*\right)^{\mathrm{T}}\right\|^2\|\bar{\boldsymbol{S}}_f\|^2 + \frac{\varepsilon_1^2}{2}, \\
&= \frac{1}{2\varepsilon_1^2}\left\|\Xi^{\mathrm{T}}\boldsymbol{P}_L\right\|^2\theta_1\|\bar{\boldsymbol{S}}_f\|^2 + \frac{\varepsilon_1^2}{2}
\end{aligned} \tag{25}$$

Substituting (25), (18b) and (19a) into (24) and using the fact $\dot{\tilde{\theta}}_1 = -\dot{\hat{\theta}}_1$, yield

$$\begin{aligned}
\dot{V} \le &-\frac{\mu}{2}\Xi^{\mathrm{T}}\boldsymbol{P}\Xi - \Xi^{\mathrm{T}}\boldsymbol{P}_L\boldsymbol{u}_2 + \Xi^{\mathrm{T}}\boldsymbol{P}_L\boldsymbol{\Gamma}\boldsymbol{\omega}(t) \\
&+ \frac{\pi_1}{r_1}\tilde{\theta}_1\hat{\theta}_1 - \tilde{\theta}_2\dot{\hat{\theta}}_2 + \frac{\varepsilon_1^2}{2}.
\end{aligned} \tag{26}$$

Further, by virtue of Young's inequality and (15), we can obtain

$$\begin{aligned}
\Xi^{\mathrm{T}}\boldsymbol{P}_L\boldsymbol{\Gamma}\boldsymbol{\omega}(t) &\le \frac{1}{2\varepsilon_2^2}\left\|\boldsymbol{\Gamma}^{\mathrm{T}}\boldsymbol{P}_L^{\mathrm{T}}\Xi\right\|^2 + \frac{\varepsilon_2^2}{2}\|\boldsymbol{\omega}(t)\|^2 \\
&\le \frac{1}{2\varepsilon_2^2}\left\|\boldsymbol{\Gamma}^{\mathrm{T}}\right\|^2\left\|\boldsymbol{P}_L^{\mathrm{T}}\Xi\right\|^2 + \frac{\varepsilon_2^2}{2}\|\boldsymbol{\omega}(t)\|^2 \\
&\le \frac{1}{2\varepsilon_2^2}\left\|\boldsymbol{P}_L^{\mathrm{T}}\Xi\right\|^2\left\|(\boldsymbol{W}_h^*)^{\mathrm{T}}\right\|\left\|\bar{\boldsymbol{S}}_h\right\| + \frac{\varepsilon_2^2}{2}\|\boldsymbol{\omega}(t)\|^2 \\
&= \frac{1}{2\varepsilon_2^2}\left\|\boldsymbol{P}_L^{\mathrm{T}}\Xi\right\|^2\theta_2\left\|\bar{\boldsymbol{S}}_h\right\| + \frac{\varepsilon_2^2}{2}\|\boldsymbol{\omega}(t)\|^2.
\end{aligned} \tag{27}$$

By plugging (27), (18c) and (19b) into (26) and by using the fact $\dot{\tilde{\theta}}_2 = -\dot{\hat{\theta}}_2$, it can be obtained that

$$\dot{V} \le -\frac{\mu}{2}\Xi^{\mathrm{T}}\boldsymbol{P}\Xi + \frac{\pi_1}{r_1}\tilde{\theta}_1\hat{\theta}_1 + \frac{\pi_2}{r_2}\tilde{\theta}_2\hat{\theta}_2 + \frac{\varepsilon_1^2}{2} + \frac{\varepsilon_2^2}{2}\|\boldsymbol{\omega}(t)\|^2, \tag{28}$$

Using Young's inequality again, we have

$$\begin{aligned}
\frac{\pi_1}{r_1}\tilde{\theta}_1\hat{\theta}_1 &= -\frac{\pi_1}{r_1}\tilde{\theta}_1^2 + \frac{\pi_1}{r_1}\tilde{\theta}_1\theta_1 \le -\frac{\pi_1}{2r_1}\tilde{\theta}_1^2 + \frac{\pi_1}{2r_1}\theta_1^2, \\
\frac{\pi_2}{r_2}\tilde{\theta}_2\hat{\theta}_2 &= -\frac{\pi_2}{r_2}\tilde{\theta}_2^2 + \frac{\pi_2}{r_2}\tilde{\theta}_2\theta_2 \le -\frac{\pi_2}{2r_2}\tilde{\theta}_2^2 + \frac{\pi_2}{2r_2}\theta_2^2.
\end{aligned} \tag{29}$$

Combining (28) and (29), produces

$$\dot{V} \le -cV + \varrho + \frac{\varepsilon_2^2}{2}\|\boldsymbol{\omega}(t)\|^2. \tag{30}$$

Define $\boldsymbol{Z} \triangleq \left[\boldsymbol{\Xi}^{\mathrm{T}}, \tilde{\theta}_1, \tilde{\theta}_2\right]^{\mathrm{T}}$. Then it can be obtained from (23) that

$$\frac{a_1}{2}\|\boldsymbol{Z}\|^2 \leq V \leq \frac{a_2}{2}\|\boldsymbol{Z}\|^2, \tag{31}$$

where

$$\begin{aligned} a_1 &\triangleq \min\left\{\lambda_{\min}(\boldsymbol{P}), \frac{1}{r_1}, \frac{1}{r_2}\right\}, \\ a_2 &\triangleq \max\left\{\lambda_{\max}(\boldsymbol{P}), \frac{1}{r_1}, \frac{1}{r_2}\right\}. \end{aligned} \tag{32}$$

Consequently, from (30), (31) and Lemma 1, it signifies that the closed-loop system (22) has a unique global solution and is eNSpS-MS.

On the basis of (30), we can further get

$$\frac{\mathrm{d}(\mathrm{E}[V])}{\mathrm{d}t} = \mathrm{E}\left[\dot{V}\right] \leq -c\mathrm{E}[V] + \varrho + \frac{\varepsilon_2^2}{2}\mathrm{E}\left[\|\boldsymbol{\omega}(t)\|^2\right]. \tag{33}$$

Applying the Gronwall inequality to (33) and using Assumption 1, produce

$$\mathrm{E}[V] \leq \mathrm{E}[V(\boldsymbol{Z}(t_0))]\,\mathrm{e}^{-c(t-t_0)} + \frac{\varepsilon_2^2 K + 2\varrho}{2c}. \tag{34}$$

Using (31) and (34), gives

$$\mathrm{E}\left[\|\boldsymbol{Z}\|^2\right] \leq \frac{2\mathrm{E}[V(\boldsymbol{Z}(t_0))]}{a_1}\mathrm{e}^{-c(t-t_0)} + \frac{\varepsilon_2^2 K + 2\varrho}{a_1 c}, \tag{35}$$

which implies the mean-square boundedness of $\boldsymbol{Z} = [\boldsymbol{\Xi}^{\mathrm{T}}, \tilde{\theta}_1, \tilde{\theta}_2]^{\mathrm{T}}$. From Assumption (3) we know that $\boldsymbol{x}_d^{(0\sim n-1)}$ is bounded, and thus $\boldsymbol{x}^{(0\sim n-1)} = \boldsymbol{x}_d^{(0\sim n-1)} + \boldsymbol{\Xi}$ is also bounded. Similarly, the boundedness of $\tilde{\theta}_1$ and $\tilde{\theta}_2$ signifies the boundedness of $\hat{\theta}_1$ and $\hat{\theta}_2$. In addition, by (18), $\boldsymbol{u}$ is also bounded in mean square.

Since

$$\frac{\lambda_{\min}(\boldsymbol{P})}{2}\|\boldsymbol{\Xi}\|^2 \leq V, \tag{36}$$

using (34) and (36), we can get

$$\mathrm{E}\left[\|\boldsymbol{\Xi}\|^2\right] \leq \frac{2\mathrm{E}[V(\boldsymbol{Z}(t_0))]}{\lambda_{\min}(\boldsymbol{P})}\mathrm{e}^{-c(t-t_0)} + \frac{\varepsilon_2^2 K + 2\varrho}{\lambda_{\min}(\boldsymbol{P})\, c}. \tag{37}$$

By taking the limit of both sides of (37) with respect to t, (20) holds. □

Remark 1. *From* (20) *and* (21) *in Theorem 1, it is clear to see that the right hand side of* (20) *can be predesigned arbitrarily small by choosing quite large c and quite small ϱ and ε_2, indicating the asymptotically tracking in the mean square sense. The reason why parameters c and ϱ can be designed satisfactorily is expounded as follows. On the one hand, according to Lemma 3, the eigenvalues of $\boldsymbol{\Phi}(\boldsymbol{A}_{0\sim n-1})$ can always be arbitrarily assigned by selecting proper $\boldsymbol{A}_{0\sim n-1}$ (see [13] for the detailed procedures of how to choose $\boldsymbol{A}_{0\sim n-1}$), and thus μ can be designed as a large value. This fact shows that c can be designed as a large value by designing large μ, π_1 and π_2. On the other hand, ϱ can be designed as a large value by choosing small ε_1 and large r_1 and r_2. Note that even though large π_1 and π_2 may affect ϱ, we can select much larger r_1 and r_2 to eliminate this effect and make the value of ϱ freely tuned.*

5 Simulations

In this section, two examples, including a numerical one and a practical one, are used to testify the performance of the adaptive tracking controller presented in Theorem 1.

5.1 Numerical example

Consider the following RHOFAS

$$x^{(3)} = f(x^{(0\sim 2)}) + G(x^{(0\sim 2)})u + \Gamma(x^{(0\sim 2)})\omega(t), \tag{38}$$

where $f(x^{(0\sim 2)}) = 4\left(\dot{x}^2 + x\ddot{x}\right)$, $G(x^{(0\sim 2)}) = 1$ $\Gamma(x^{(0\sim 2)}) = 0.7x\sin(x)$, and $\omega(t)$ is a colored random disturbance satisfying $\omega(t) = 0.3\sin(t+\phi)$ with $\phi \sim \mathrm{U}[0, 2\pi]$. It is easy to see that $\mathrm{E}\left[\|\omega(t)\|^2\right] \leq 0.09$ for $\forall t \geq 0$, and thus we take $K = 0.09$ in Assumption 1.

To verify the effectiveness of our proposed tracking controller, we assume that $f(x^{(0\sim 2)})$ and $\Gamma(x^{(0\sim 2)})$ are unknown. In the simulation, the desired signal is selected as $x_d(t) = 0.2\sin(0.5t)$. The initial conditions are set to $x^{(0\sim 2)}(0) = [3, 1, -6]^{\mathrm{T}}$, $\hat{\theta}_1(0) = 5$ and $\hat{\theta}_2(0) = 5$, and the designing parameters are chosen as

$$\mu = 1,\ \boldsymbol{A}_{0\sim 2} = [2, 4, 3],\ \boldsymbol{P} = \begin{bmatrix} 0.86 & 0.8 & 0.24 \\ 0.8 & 1.1 & 0.35 \\ 0.24 & 0.35 & 0.16 \end{bmatrix},$$

$\pi_1 = 0.5$, $\pi_2 = 2$, $r_1 = r_2 = 100$, $\varepsilon_1 = \varepsilon_2 = 0.1$.

In RBFNN, the number of neural network nodes is 10, the widths are 2, and the center vectors are located evenly in $[-10, 10] \times [-10, 10] \times [-10, 10]$.

The random disturbance $\omega(t)$, tracking performance and tracking error are shown in Fig. 1, which clearly reflects the mean-square boundedness of random disturbance $\omega(t)$ and the effectiveness of our proposed tracking controller. Fig. 2 exhibits the response curves of control input and parameter estimates $\hat{\theta}_1$ and $\hat{\theta}_2$, and Fig. 3 presents the response curves of the first and second derivatives of e and x. These three figures clearly manifest the (mean-square) boundedness of all the closed-loop signals.

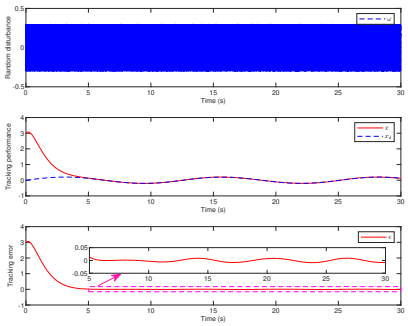

Fig. 1: Random disturbance $\omega(t)$, tracking performance and tracking error e for Example 1.

5.2 Practical example

To further validate the effectiveness of our designed controller, we consider the following one-link manipulator with a stochastic motor dynamics system

$$\begin{cases} A\ddot{\theta} + D\dot{\theta} + M\sin(\theta) = \rho, \\ N\dot{\rho} + F\rho = u - R_m\dot{\theta} + \sigma\rho\omega(t), \end{cases} \tag{39}$$

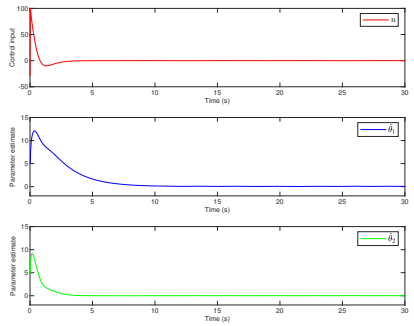

Fig. 2: Response curves of control input u and parameter estimates $\hat{\theta}_1$ and $\hat{\theta}_2$ for Example 1.

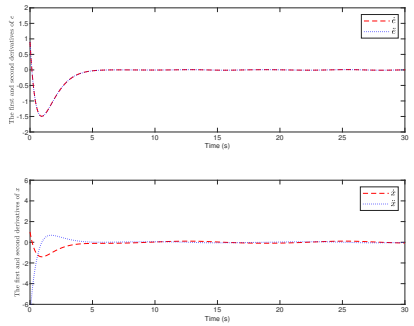

Fig. 3: Response curves of the first and second derivatives of e and x for Example 1.

where θ, $\dot{\theta}$ and $\ddot{\theta}$ are respectively the position, velocity and acceleration of the link, ρ is torque generated by the motor, and u is control input. $\sigma\rho\omega(t)$ is the stochastic disturbance torque caused by a second-order moment noise process $\omega(t)$, where σ is the coefficient of noise intensity. The detailed definition of model parameters A, D, M, N, F, R_m can be found in [30].

Clearly, by plugging transformations $\rho = A\ddot{\theta} + D\dot{\theta} + M\sin(\theta)$ and $\dot{\rho} = A\dddot{\theta} + D\ddot{\theta} + M\cos(\theta)\dot{\theta}$ into the second equation in system (39), we can convert the system (39) into the following RHOFAS

$$\dddot{\theta} = f(\theta^{(0\sim 2)}) + G(\theta^{(0\sim 2)}) + \Gamma(\theta^{(0\sim 2)})\omega(t), \qquad (40)$$

where

$$\begin{aligned} f(\theta^{(0\sim 2)}) =& -\frac{1}{NA}\Big\{ (ND + FA)\,\ddot{\theta} + FM\sin(\theta) \\ &+ (NM\cos(\theta) + FD)\,\dot{\theta}\Big\}, \\ G(\theta^{(0\sim 2)}) =& \frac{1}{NA}, \\ \Gamma(\theta^{(0\sim 2)}) =& \frac{\sigma}{NA}\left\{A\ddot{\theta} + D\dot{\theta} + M\sin(\theta)\right\}. \end{aligned}$$

In the simulation, let $x \triangleq \theta$. $f(\theta^{(0\sim 2)})$ and $\Gamma(\theta^{(0\sim 2)})$ are assumed to be unknown, while $G(\theta^{(0\sim 2)})$ is assumed to be known. The desired signal is chosen as $x_d(t) = 0.5\sin(t)$, and the random disturbance $\omega(t)$ is produced by

$$\varpi\dot{\omega} = -\omega + \psi(t),\ \omega(0) = 0,\ i = 1, 2, \qquad (41)$$

where $\psi(t)$ is zero-mean bandlimited white noise with noise power and sampling time being C and t_c, respectively. According to [3], $\omega(t)$ is a second-order moment process with $\mathrm{E}[\omega(t)] = 0$ and $\mathrm{E}\left[\|\omega(t)\|^2\right] = \frac{C}{\varpi\pi}\arctan\left(\frac{\varpi\pi}{50t_c}\right)$. The model parameters are set to $A = 1$, $D = 1$, $M = 10$, $N = 0.1$, $F = 1$, $R_m = 0.2$, $C = 1$, $t_c = 0.0001$, and the designing parameters are chosen as:

$$\mu = 2,\ \boldsymbol{A}_{0\sim 2} = [24, 26, 9],\ \boldsymbol{P} = \begin{bmatrix} \frac{173}{10} & \frac{1031}{120} & \frac{89}{120} \\ \frac{1031}{120} & \frac{59}{8} & \frac{19}{30} \\ \frac{89}{120} & \frac{19}{30} & \frac{17}{120} \end{bmatrix},$$

$\pi_1 = \pi_2 = 1$, $r_1 = r_2 = 1000$, $\varepsilon_1 = \varepsilon_2 = 0.01$.

In this example, we employ 10 neural network nodes is chosen. Moreover, all the widths are 2 and the center vectors of the radical basis functions are situated evenly in $[-5, 5] \times [-5, 5] \times [-5, 5]$.

The simulation results are shown in Figs. 4∼6. Once again, the simulation results show that our proposed tracking controller can approximately track the desired signal and all the signals in the closed-loop system are bounded when the random noise, unknown nonlinearity, and unknown diffusion coefficient concurs in a dynamical system.

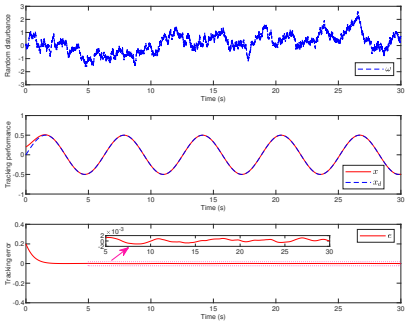

Fig. 4: Random disturbance $\omega(t)$, tracking performance and tracking error e for Example 2.

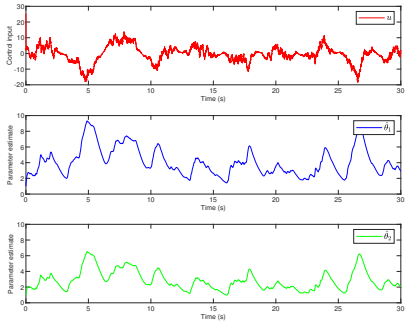

Fig. 5: Response curves of control input u and parameter estimates $\hat{\theta}_1$ and $\hat{\theta}_2$ for Example 2.

6 Conclusion

This paper solves the tracking problem of RHOFAS with unknown drift nonlinearity and diffusion coefficient. The unknown drift nonlinearity and diffusion coefficient are dealt

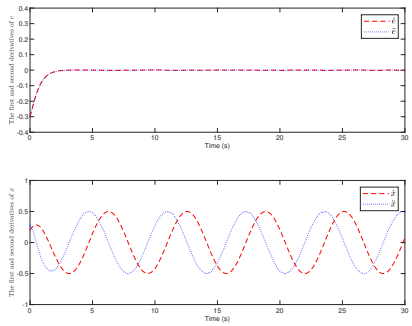

Fig. 6: Response curves of the first and second derivatives of e and x for Example 2.

with by the RBFNN. By exploiting the full-actuation property of RHOFAS, an adaptive tracking controller is designed, which guarantees that the closed-loop system is eNSpS-MS, the mean square of tracking error converges to an arbitrarily small neighborhood of zero, and all the closed-loop signals are bounded in mean square. The stability analysis and simulation examples verify the effectiveness of the designed controller. The results of this paper show the big advantages and huge potentiality of the HOFAS theory in tackling the control problems of random nonlinear systems. Our further study will concentrate on the tracking problem of the random high-order strict-feedback systems.

References

[1] B. Øksendal. *Stochastic Differential Equations (5th edition)*. Berlin Heidelberg: Springer-Verlag, 2003.

[2] R. Z. Khas'minskii. *Stochastic stability of differential equations (2nd edition)*. Berlin Heidelberg: Springer-Verlag, 2012.

[3] Z. Wu. Stability criteria of random nonlinear systems and their applications. *IEEE Transactions on Automatic Control*, 2016, 60(4):1038–1049.

[4] H. Zhang, Y. Xia, Z. Wu. Noise-to-state stability of random switched systems and its applications, *IEEE Transactions on Automatic Control*, 2016, 61:(6):1607–1612.

[5] T. Jiao, W. X. Zheng, S. Xu. On stability of a class of switched nonlinear systems subject to random disturbances, *IEEE Transactions on Circuits and Systems I: Regular Papers* 2016, 63:(12): 2278–2289.

[6] D. Zhang, Z. Wu, X. M. Sun, W. Wang. Noise-to-state stability for a class of random systems with state-dependent switching. *IEEE Transactions on Automatic Control*, 2016, 61:(10):3164–3170.

[7] T. Jiao, W. X. Zheng, S. Xu. Stability analysis for a class of random nonlinear impulsive systems. *International Journal of Robust and Nonlinear Control*, 2017, 27:1171–1193.

[8] L. Feng, W. Zhang, Z. Yang, J. H. Park. Further stability results for random nonlinear systems with stochastic impulses, *Journal of the Franklin Institute*, 2021, 358(10):5426–5450.

[9] L. Yao, W. Zhang, X. Xue-Jun. Stability analysis of random nonlinear systems with time-varying delay and its application. *Automatica*, 2020, 117:108994.

[10] L. Ya. Improved stability theorems of random nonlinear time delay systems and their application, *Journal of the Franklin Institute*, 2022, 359(11):5596–5618.

[11] R. Xi, H. Zhang, Y. Wang, S. Sun. Overview of the recent research progress for stability and control on random nonlinear systems. *Annual Reviews in Control*, 2022, 53:70–82.

[12] G. R. Duan. High-order fully actuated system approaches: Part I. Models and basic procedure. *International Journal of Systems Science*. 2021, 52(2):422–435.

[13] G. R. Duan. High-order fully actuated system approaches: Part VII. Controllability, stabilisability and parametric designs. *International Journal of Systems Science*. 2021, 52(14):3091–3114.

[14] G. R. Duan. High-order fully actuated system approaches: Part II. Generalized strict-feedback systems. *International Journal of Systems Science*, 2021, 52(3):437–454.

[15] G. R. Duan. High-order fully actuated system approaches: Part IV. Adaptive control and high-order backstepping. *International Journal of Systems Science*, 2021, 52(5):972–989.

[16] G. R. Duan. High-order fully actuated system approaches: Part III. Robust control and high-order backstepping. *International Journal of Systems Science*, 2021, 52(5):952–971.

[17] G. R. Duan. High-order fully actuated system approaches: Part VIII. Optimal control with application in spacecraft attitude stabilisation. *International Journal of Systems Science*, 2022, 53(1):54–73.

[18] G. R. Duan. Substability and substabilization: Control of subfully actuated systems. *IEEE Transactions on Cybernetics*, 2023, 53(11):7309–7322.

[19] G. R. Duan. A FAS approach for stabilization of generalized chained forms: Part 1. Discontinuous control laws. *Science China-Information Sciences*, 2024, 67(2): 122201:1-122201:26.

[20] G. P. Liu. Coordination of networked nonlinear multi-agents using a high-order fully actuated predictive control strategy. *IEEE/CAA Journal of Automatica Sinica*, 2022, 9(4):615–623.

[21] D. W. Zhang, G. P. Liu, L. Cao. Constrained cooperative control for high-order fully actuated multiagent systems with application to air-bearing spacecraft simulators. *IEEE/ASME Transactions on Mechatronics*, 2023, 28(3):1570–1581.

[22] M. Cai, X. He, D. Zhou. An active fault tolerance framework for uncertain nonlinear high-order fully-actuated systems. *Automatica*, 2023, 152:110969.

[23] S. Lu, K. Tsakalis, Y. Chen. Development and application of a novel high-order fully actuated system approach-Part I: 3-dof quadrotor control. *IEEE Control Systems Letters*, 2023, 7:1177–1182.

[24] X. Liu, M. Chen, L. Sheng, D. Zhou. Stochastic high-order fully-actuated systems: Model, equivalence and stabilization. *China Automation Congress (CAC)*, 2022:4371–4376.

[25] X. Liu, M. Chen, S. Li, D. Zhou. Stabilization control for stochastic high-order fully-actuated systems with persistent disturbances. *2nd Conference on Fully Actuated System Theory and Applications (CFASTA)*, 2023:31–36.

[26] X. Liu, M. Chen, D. Zhou, L. Sheng. Fault-tolerant control of stochastic high-order fully actuated systems. *IEEE Transactions on Cybernetics*, 2023, doi:10.1109/TCYB.2023.3320441.

[27] F. Sedghi, M. M. Arefi, A. Abooee, S. Yin. Distributed adaptive-neural finite-time consensus control for stochastic nonlinear multiagent systems subject to saturated inputs. *IEEE Transactions on Neural Networks and Learning Systems*, 2023, 34(10): 7704–7718.

[28] T. Jiao, G. Zong, C. K. Ahn. Noise-to-state practical stability and stabilization of random neural networks. *Nonlinear Dynamics*, 2020, 100:2469-2481.

[29] Y. Wang, C. Wen, X. Li. Event-based model reference adaptive tracking. *IEEE Transactions on Automatic Control*, 2023, 68(12):8201-8207.

[30] Y. Li, S. Tong, Y. Liu, T. Li. Adaptive fuzzy robust output feedback control of nonlinear systems with unknown dead zones based on a small-gain approach. *IEEE Transactions on Fuzzy Systems*, 2014, 22(1):164–176.

Proceedings of the 3rd Conference on Fully Actuated System Theory and Applications
May 10-12, 2024, Shenzhen, China

An observer-based robust sliding mode control for the system with actuator saturation and false data injection attack

Qian Wang[1], Xinyuan Wang[1], Yan Jin[1]
1. School of Automation, Hangzhou Dianzi University, Hangzhou 310018, China
E-mail: wq@hdu.edu.cn

Abstract: This paper is concerned with the robust sliding mode control for a discrete-time system with actuator saturation and false data injection attacks. The impact of the attack on actuator saturation in the system is analyzed. An observer-based robust sliding mode controller is designed to mitigate the impact of false data injection attack on actuator saturation and system. The asymptotic stability of the system is ensured. In addition, the case of system with randomly occurring actuator saturation is considered. The asymptotic stability in the mean-square sense is guaranteed. The numerical simulation shows the effectiveness of the proposed method.

Key Words: False Data Injection Attack, Robust Sliding Mode Control, Actuator Saturation

1 Introduction

With the development of technologies such as the Internet, the Internet of Things and the communication technologies, the integration between different technologies becomes the trend of future. Based on the traditional control system, a new form of the closed-loop control system is formed by connecting the controllers, actuators, sensors and controlled objects through a network. Although there have been many encryption techniques to ensure security in the process of data transmission, the system was vulnerable to network attacks due to the openness of the communication networks [1–4]. There are many kinds of attacks, such as: deception attacks [5], denial-of-service attacks [6], replay attacks [7] and so on. Deception attack is also called false data injection (FDI) attack. The adversaries inject FDI attacks into the data transmission channel between the controller and actuator, so that the actuator receives the wrong signal, which seriously influences the stability of the system [8]. In recent years, there have been many related studies on FDI attacks that occurred in the data transmission channel between the controllers and actuators. For example, an observer-based PID controller was proposed in [9]. A H∞ control method was designed in [10]. A wide-area robust sliding mode controller was designed in [11]. A robust hybrid control scheme containing multiple sub-controllers was proposed in [12]. In addition, there are also some results on the attack estimation and reconstruction by designing observers and estimation methods, some of which regard attacks as the unknown external inputs [13–16]. However, not only the FDI attacks but also the actuator saturation can damage the stability of the system.

Due to the physical limitations of the instruments or equipments, the actuator saturation is common in control system, which will not only lead to performance degradation, but also lead to the instability of the control system [17–20]. And the actuator saturation can also occur randomly due to the factors such as the environments change suddenly and equipments aging [21, 22]. By using a convex hull representation of saturation nonlinearity, the actuator saturation nonlinearity was solved in [23]. A low gain feedback control method was proposed to deal with the actuator saturation in[24, 25]. Actuator saturation had an impact on the effectiveness of the attacks, which was analyzed in [26]. Similarly, the impact of the actuator attack on actuator saturation was mentioned in [27], that is, the actuator attack can lead to the actuator saturation.

Based on the above description, many achievements have been obtained on the FDI attack and actuator saturation. However, most of the results do not consider the coexistence of FDI attack and actuator saturation. Due to the interaction between FDI attack and actuator saturation, the system with FDI attack and actuator saturation is more complex. Therefore, the study on the control problem for a system with actuator saturation and FDI attacks is meaningful. In this paper. we develop an observer-based robust sliding mode control method for a linear discrete-time system with actuator saturation and FDI attacks. The main contributions are: (1) An observer-based robust sliding mode controller is designed to mitigate the impact of the FDI attack on actuator saturation and system; (2) Ensuring the asymptotic stability of the system; (3) The randomly occurring actuator saturation is considered.

2 Problem Formulation

Consider a linear discrete-time system

$$x(k+1) = Ax(k) + Bu(k) \tag{1}$$

where $x(k) \in \mathbb{R}^n$ and $u(k) \in \mathbb{R}^m$ are the state vector and input vector, respectively, $A \in \mathbb{R}^{n\times n}$ and $B \in \mathbb{R}^{n\times m}$ are the system matrix and control input matrix, respectively. We define vector $a(k)$ as the FDI attack signal on actuator launched by adversary. $a^{\mathrm{T}}(k)a(k) < \delta$, δ is a positive scalar. When the data transmission channel between the controller and actuator of system (1) is attacked, the closed-loop system can be expressed as

$$x(k+1) = Ax(k) + B(u(k) + a(k)) \tag{2}$$

Then, we consider system (2) with actuator saturation, the closed-loop system is

$$\begin{cases} x(k+1) = Ax(k) + Bu_a(k) \\ u_a(k) = \mathrm{sat}(u(k) + a(k)) \end{cases} \tag{3}$$

This work is supported by the Zhejiang Provincial Natural Science Foundation of China [grant number LY22F030002].

The saturation function is

$$\mathrm{sat}(u(k)) = \begin{bmatrix}\mathrm{sat}(u_1(k)) & \mathrm{sat}(u_2(k)) & ... & \mathrm{sat}(u_m(k))\end{bmatrix}^{\mathrm{T}}$$

where $\mathrm{sat}(u_i(k)) = \mathrm{sign}(u_i(k))\min\{1, |u_i(k)|\}$, $i \in \{1, 2, ..., m\}$.

Then, we consider systems (3) subject to the randomly occurring actuator saturation. The closed-loop system can be rewritten as

$$\begin{cases} x(k+1) = Ax(k) + Bu_r(k) \\ u_r(k) = \alpha(k)\mathrm{sat}(u(k) + a(k)) \\ \qquad\quad + (1 - \alpha(k))(u(k) + a(k)) \end{cases} \tag{4}$$

The stochastic variable $\alpha(k)$ is a Bernoulli-distributed white sequence taking values on 0 and 1 with the following probability:

$$\begin{cases} \mathrm{Prob}\{\alpha(k) = 1\} = \bar{\alpha} \\ \mathrm{Prob}\{\alpha(k) = 0\} = 1 - \bar{\alpha} \end{cases}$$

where $\bar{\alpha} \in [-1, 1]$ is a known constant. There is actuator saturation in the system when $\alpha(k) = 1$. On the contrary, there is no actuator saturation in the system when $\alpha(k) = 0$.

Lemma 1 *[28] There are 2^m diagonal matrices $E_i \in \mathbb{R}^{m\times m}$ with elements 1 or 0, $i \in Q$, and $\bar{E}_i = I - E_i$. The scalars θ_i satisfy $0 \le \theta_i \le 1$ and $\sum_{i=1}^{2^m} \theta_i = 1$, it can be concluded that*

$$\sum_{i=1}^{2^m} \theta_i(E_i + \bar{E}_i) = I, i \in Q$$

And a bounded set is defined as

$$\mathcal{L}(H) = \{x(k) \in \mathbb{R}^n : |H^l x(k)| \le 1, l \in \{1, 2, ..., m\}\}$$

where H^l is the l-th row of $H \in \mathbb{R}^{m\times n}$. For $x(k) \in \mathbb{R}^n, K \in \mathbb{R}^{m\times n}$, if $x(k) \in \mathcal{L}(H)$, then

$$\mathrm{sat}(Kx(k)) \in \mathrm{co}\{E_iKx(k) + \bar{E}_iHx(k), i \in Q\}$$

where $\mathrm{co}\{\cdot\}$ denotes the convex hull.

Problem 1 *Consider system (3), design an observer-based robust sliding mode controller to guarantee the asymptotic stability and the corresponding $H\infty$ performance index.*

Problem 2 *Consider system (4), design an observer-based robust sliding mode controller to guarantee the asymptotic stability in the mean square sense and the corresponding $H\infty$ performance index.*

3 Main Results

3.1 The impact of FDI attack on actuator saturation

In order to explore the impact of actuator attack on actuator saturation mentioned above, based on system (3), we list all cases about the control input:

1) $|u(k)| < 1$ and $|u(k) + a(k)| < 1$
2) $|u(k)| < 1$ and $|u(k) + a(k)| > 1$
3) $|u(k)| > 1$ and $|u(k) + a(k)| < 1$
4) $|u(k)| > 1$ and $|u(k) + a(k)| > 1$

In case 2), $|u(k)| < 1$ means that the control signal $u(k)$ does not exceed the maximum boundness of the control input. $|u(k) + a(k)| > 1$ means that the sum of control signal and attack signal exceeds the maximum boundness of the control input. In other words, the control input amplitude exceeds the maximum boundness of the control input when it being attacked. It can be concluded that the FDI attack on the actuator can lead to actuator saturation.

3.2 The system with FDI attack and actuator saturation

For the discrete closed-loop system with FDI attack, we define a sliding surface

$$s(k) = \mathcal{G}x(k) \tag{5}$$

where $\mathcal{G}$ is the designed matrix with the appropriate dimensions.

Assumption 1 *The matrix $\mathcal{G}$ is full rank. $\mathcal{G}B$ is nonsingular.*

From (2) and (5), we have

$$\begin{aligned} s(k+1) &= \mathcal{G}x(k+1) \\ &= \mathcal{G}Ax(k) + \mathcal{G}B(u(k) + a(k)) \end{aligned}$$

When $s(k+1) = 0$, the controller $u(k)$ is designed as follow

$$u(k) = -(\mathcal{G}B)^{-1}\mathcal{G}Ax(k) - a(k) \tag{6}$$

Remark 1 *In system (2), we regard the attack signal $a(k)$ as a priori-unknown and time-varying sequence which exists all the time. Therefore, in order to meet the needs of the designed controller, we need to design an observer to estimate the value of the attack signal. Inspired by [14], the attack signal $a(k)$ can be seen as an unknown input injected into the system. Slightly different from it, the designed observer is related to the control input at the last time and the system state.*

An attack observer can be designed as

$$\begin{cases} r(k+1) = (LB + I)(r(k) - Lx(k)) \\ \qquad\quad + L(Ax(k) + Bu(k)) \\ \hat{a}(k) = r(k) - Lx(k) \end{cases} \tag{7}$$

where $\hat{a}(k)$ is the estimated value of $a(k)$ and $r(k)$ is an auxiliary variable. The matrix L is the observer gain to be determined later. The estimated error of the attack is defined as $e_a(k) = a(k) - \hat{a}(k)$.

Then, define $K = -(\mathcal{G}B)^{-1}\mathcal{G}A$ and consider (6) and (7), we have

$$u(k) = Kx(k) - \hat{a}(k) \tag{8}$$

We define the following ellipsoid set

$$\Omega(P) = \{\bar{x}(k) \in \mathbb{R}^{n+m} : \bar{x}^{\mathrm{T}}(k)P\bar{x}(k) \le 1\}$$

where $\bar{x}(k) = \begin{bmatrix}x^{\mathrm{T}}(k) & e_a^{\mathrm{T}}(k)\end{bmatrix}^{\mathrm{T}}$ and the positive definite matrix $P = \mathrm{diag}\{P_1, P_2\}$, $P_1 \in \mathbb{R}^{n\times n}$, $P_2 \in \mathbb{R}^{m\times m}$.

Meanwhile, define a bounded set as following

$$\begin{aligned} \mathfrak{L}(H) = \big\{&\bar{x}(k) \in \mathbb{R}^{n+m} : |H^l\bar{x}(k)| \le 1, \\ &l \in \{1, 2, ..., n+m\}\big\} \end{aligned}$$

According to Lemma 1, when $\bar{x}(k) \in \mathfrak{L}(H)$ with $H = \begin{bmatrix} H_1 & I \end{bmatrix}$ where H_1 is a matrix with the appropriate dimensions, we have

$$\begin{aligned}
\mathrm{sat}(u(k)+a(k)) &= \mathrm{sat}(Kx(k)-\hat{a}(k)+a(k)) \\
&= \mathrm{sat}(Kx(k)+e_a(k)) \\
&= \mathrm{sat}(K^*\bar{x}(k)) \\
&= \sum_{i=1}^{2^m} \theta_i (E_i K^* \bar{x}(k) + \bar{E}_i H \bar{x}(k)) \\
&= \sum_{i=1}^{2^m} \theta_i \left(E_i(Kx(k)+e_a(k)) \right. \\
&\quad \left. + \bar{E}_i(H_1 x(k) + e_a(k))\right) \\
&= \sum_{i=1}^{2^m} \theta_i (E_i K + \bar{E}_i H_1) x(k) + e_a(k)
\end{aligned} \tag{9}$$

where $K^* = \begin{bmatrix} K & I \end{bmatrix}$.

From (2), (7), (8) and (9), we obtain

$$\begin{aligned}
\hat{a}(k+1) &= r(k+1) - Lx(k+1) \\
&= (LB+I)(r(k)-Lx(k)) \\
&\quad + L(Ax(k)+Bu(k)) - L(Ax(k) \\
&\quad + B(\sum_{i=1}^{2^m} \theta_i (E_i K + \bar{E}_i H_1) x(k) + e_a(k))) \\
&= (LB+I)\hat{a}(k) + LB(Kx(k)-\hat{a}(k) \\
&\quad - \sum_{i=1}^{2^m} \theta_i ((I-\bar{E}_i)K + \bar{E}_i H_1) x(k) - e_a(k)) \\
&= \hat{a}(k) - LB(\sum_{i=1}^{2^m} \theta_i \bar{E}_i (H_1 - K) x(k) + e_a(k))
\end{aligned}$$

Then,

$$\begin{aligned}
e_a(k+1) &= a(k+1) - \hat{a}(k+1) \\
&= \Delta a(k) + (LB+I)e_a(k) \\
&\quad + LB \sum_{i=1}^{2^m} \theta_i \bar{E}_i (H_1 - K) x(k)
\end{aligned}$$

where $\Delta a(k) = a(k+1) - a(k)$. The augmented system is:

$$\begin{cases} \bar{x}(k+1) = \bar{A}\bar{x}(k) + \bar{B}\Delta a(k) \\ z(k) = C\bar{x}(k) \end{cases} \tag{10}$$

where

$$\bar{A} = \begin{bmatrix} N_1 & B \\ N_2 & LB+I \end{bmatrix}, \bar{B} = \begin{bmatrix} 0 \\ I \end{bmatrix}, C = \begin{bmatrix} C1 & C2 \end{bmatrix},$$

$$N_1 = A + B \sum_{i=1}^{2^m} \theta_i (E_i K + \bar{E}_i H_1),$$

$$N_2 = LB \sum_{i=1}^{2^m} \theta_i \bar{E}_i (H_1 - K)$$

Theorem 1 *If there exist the positive definite matrices $\mathcal{X}, P_2$, the matrices $\mathcal{R}_1, \mathcal{R}_2, \mathcal{R}_3$ and a positive scalar γ_1 satisfying*

$$\begin{bmatrix} -\mathcal{X} & 0 & 0 & \Lambda_1 & \Lambda_2 \\ * & -P_2 & 0 & B^{\mathrm{T}} & \Lambda_3 \\ * & * & -\gamma_2^2 I & 0 & P_2 \\ * & * & * & -\mathcal{X} & 0 \\ * & * & * & * & -P_2 \end{bmatrix} < 0 \tag{11}$$

$$\begin{bmatrix} I & \mathcal{R}_2^l & I \\ * & \mathcal{X} & 0 \\ * & * & P_2 \end{bmatrix} \geq 0 \tag{12}$$

where

$$\begin{aligned}
\Lambda_1 &= (A\mathcal{X} + B(E_i\mathcal{R}_1 + \bar{E}_i\mathcal{R}_2) + BR_1)^{\mathrm{T}} \\
\Lambda_2 &= (\mathcal{R}_3 B \bar{E}_i (\mathcal{R}_2 - \mathcal{R}_1))^{\mathrm{T}} \\
\Lambda_3 &= (\mathcal{R}_3 B + P_2)^{\mathrm{T}}
\end{aligned}$$

Then, for each $\bar{x}(k) \in \Omega(P)$, system (10) is asymptotically stable and satisfies

$$\frac{\sum_{k=0}^{\infty} \|z(k)\|^2}{\sum_{k=0}^{\infty} \|\Delta a(k)\|^2} \leq \gamma_1^2 \tag{13}$$

proof Define $P = \mathrm{diag}\{P_1, P_2\}, \mathcal{X} = P_1^{-1}, \mathcal{R}_1 = K\mathcal{X}, \mathcal{R}_2 = H_1\mathcal{X}$ and $\mathcal{R}_3 = P_2 L$. Pre- and post-multiplying (12) by $\mathrm{diag}\{I, P_1, I\}$, we have

$$\begin{bmatrix} I & H_1^l & I \\ * & P_1 & 0 \\ * & * & P_2 \end{bmatrix} \geq 0 \tag{14}$$

From (14), we can deduce that $\Omega(P) \subset \mathfrak{L}(H)$. And for each $\bar{x}(k) \in \Omega(P)$, it can be concluded that $\bar{x}(k) \in \Omega(P) \subset \mathfrak{L}(H)$.

Choose the Lyapunov function:

$$V(k) = \bar{x}^{\mathrm{T}}(k) P \bar{x}(k) \tag{15}$$

The difference of the Lyapunov function is

$$\begin{aligned}
\Delta V(k) &= V(k+1) - V(k) \\
&= \bar{x}^{\mathrm{T}}(k+1) P \bar{x}(k+1) - \bar{x}^{\mathrm{T}}(k) P \bar{x}(k) \\
&\leq \max_{i \in \{1,\ldots,2^m\}} \{\eta^{\mathrm{T}}(k) \Xi_1 \eta(k)\}
\end{aligned} \tag{16}$$

where

$$\begin{aligned}
\eta(k) &= \begin{bmatrix} x^{\mathrm{T}}(k) & e_a^{\mathrm{T}}(k) & \Delta a^{\mathrm{T}}(k) \end{bmatrix}^{\mathrm{T}}, \\
\Xi_1 &= \begin{bmatrix} \xi_{11} & \xi_{12} & \bar{N_2}^{\mathrm{T}} P_2 \\ * & \xi_{22} & (LB+I)^{\mathrm{T}} P_2 \\ * & * & P_2 \end{bmatrix}, \\
\xi_{11} &= \bar{N_1}^{\mathrm{T}} P_1 \bar{N_1} + \bar{N_2}^{\mathrm{T}} P_2 \bar{N_2} - P_1, \\
\xi_{12} &= \bar{N_1}^{\mathrm{T}} P_1 B + \bar{N_2}^{\mathrm{T}} P_2 (LB+I), \\
\xi_{22} &= B^{\mathrm{T}} P_1 B + (LB+I)^{\mathrm{T}} P_2 (LB+I) - P_2, \\
\bar{N_1} &= A + B(E_i K + \bar{E}_i H_1) + BK, \\
\bar{N_2} &= LB\bar{E}_i (H_1 - K)
\end{aligned}$$

For the constant $\gamma_1 > 0$, the auxiliary index is defined as

$$\begin{aligned}\mathcal{J}_1 &= \sum_{k=0}^{n}(\|z(k)\|^2 - \gamma_1^2\|\Delta a(k)\|^2 + \Delta V(k)) \\ &\leq \sum_{k=0}^{n}\max_{i\in\{1,\ldots,2^m\}}\{\eta^{\mathrm{T}}(k)\Xi_2\eta(k)\}\end{aligned}$$

where

$$\Xi_2 = \begin{bmatrix}\epsilon_{11} & \epsilon_{12} & \bar{N_2}^{\mathrm{T}}P_2 \\ * & \epsilon_{22} & (LB+I)^{\mathrm{T}}P_2 \\ * & * & P_2 - \gamma_1^2 I\end{bmatrix},$$

$$\epsilon_{11} = \bar{N_1}^{\mathrm{T}}P_1\bar{N_1} + \bar{N_2}^{\mathrm{T}}P_2\bar{N_2} - P_1 + C_1^{\mathrm{T}}C_1,$$

$$\epsilon_{12} = \bar{N_1}^{\mathrm{T}}P_1B + \bar{N_2}^{\mathrm{T}}P_2(LB+I) + C_1^{\mathrm{T}}C_2,$$

$$\epsilon_{22} = B^{\mathrm{T}}P_1B + (LB+I)^{\mathrm{T}}P_2(LB+I) - P_2 + C_2^{\mathrm{T}}C_2$$

Pre- and post-multiplying (11) by $\mathrm{diag}\{P_1, I, I, P_1, I\}$ and $\mathrm{diag}\{P_1, I, I, P_1, I\}$ and using Schur complements lemma, we can calculate that $\Xi_1 < 0$ and $\Xi_2 < 0$. When $\Xi_1 < 0$ and $\Xi_2 < 0$, we have $\Delta V(k) < 0$ and $\mathcal{J}_1 < 0$. Under the zero-initial condition, it can be obtained that

$$\begin{aligned}\mathcal{J}_1 &= \sum_{k=0}^{n}(\|z(k)\|^2 - \gamma_1^2\|\Delta a(k)\|^2 + \Delta V(k)) \\ &= \sum_{k=0}^{n}\|z(k)\|^2 - \sum_{k=0}^{n}\gamma_1^2\|\Delta a(k)\|^2 + V(n+1)\end{aligned}$$

When $n \to \infty$, $V(\infty) > 0$. Then, we have

$$\sum_{k=0}^{n}\|z(k)\|^2 - \sum_{k=0}^{n}\gamma_1^2\|\Delta a(k)\|^2 < 0$$

Therefore, H∞ performance (13) can be satisfied.

Finally, the augmented system (10) is asymptotically stable with $\bar{x}(k) \in \Omega(P)$ and satisfies the H∞ performance (13). This completes the proof.

3.3 The system with FDI attack and randomly occurring actuator saturation

Then, consider the case of randomly occurring actuator saturation. Define $\bar{x}_r(k) = \begin{bmatrix}x(k)^{\mathrm{T}} & e_{ar}(k)^{\mathrm{T}}\end{bmatrix}^{\mathrm{T}}$ and an ellipsoid set with the matrix $P_r = \mathrm{diag}\{P_{1r}, P_{2r}\}$ where $P_{1r} \in \mathbb{R}^{n\times n}$ and $P_{2r} \in \mathbb{R}^{m\times m}$ is denoted as

$$\Omega_r(P_r) = \{\bar{x}_r(k) \in \mathbb{R}^{n+m} : \bar{x}_r^{\mathrm{T}}(k)P_r\bar{x}_r(k) \leq 1\}$$

Meanwhile, define a bounded set as follows

$$\begin{aligned}\mathfrak{L}_r(H_r) = \big\{&\bar{x}_r(k) \in \mathbb{R}^{n+m} : |H_r^l\bar{x}_r(k)| \leq 1, \\ &l \in \{1, 2, ..., n+m\}\big\}\end{aligned}$$

Based on (4) and (9), for $\bar{x}_r(k) \in \mathfrak{L}_r(H_r)$ and $H_r = \begin{bmatrix}H_{1r} & I\end{bmatrix}$ where H_{1r} is a matrix with the appropriate dimensions, the closed-loop system can be reformulated as

$$\begin{aligned}x(k+1) &= Ax(k) + B\left(\alpha(k)\mathrm{sat}(u(k)+a(k))\right. \\ &\quad \left.+(1-\alpha(k))(u(k)+a(k))\right) \\ &= (A + \alpha(k)B\sum_{i=1}^{2^m}\theta_i\bar{E}_i(H_{1r}-K) + BK)x(k) \\ &\quad + Be_{ar}(k)\end{aligned}$$

Meanwhile, the estimation of attack and the estimation error can be calculated as

$$\begin{aligned}\hat{a}_r(k+1) &= \hat{a}_r(k) - \alpha(k)LB\sum_{i=1}^{2^m}\theta_i\bar{E}_i(H_{1r}-K)x(k) \\ &\quad - LBe_{ar}(k)\end{aligned}$$

and

$$\begin{aligned}e_{ar}(k+1) &= \Delta a(k) + \alpha(k)LB\sum_{i=1}^{2^m}\theta_i\bar{E}_i(H_{1r}-K)x(k) \\ &\quad + (LB+I)e_{ar}(k)\end{aligned}$$

Then, the augmented system is obtained:

$$\begin{cases}\bar{x}_r(k+1) = \bar{A}_r\bar{x}_r(k) + \bar{B}_r\Delta a(k) \\ z_r(k) = C\bar{x}_r(k)\end{cases} \tag{17}$$

where

$$\bar{A}_r = \begin{bmatrix}M_1 & B \\ M_2 & LB+I\end{bmatrix}, \bar{B}_r = \begin{bmatrix}0 \\ I\end{bmatrix}$$

$$M_1 = A + \alpha(k)B\sum_{i=1}^{2^m}\theta_i\bar{E}_i(H_{1r}-K) + BK$$

$$M_2 = \alpha(k)LB\sum_{i=1}^{2^m}\theta_i\bar{E}_i(H_{1r}-K)$$

Definition 1 *[22] The closed-loop system (17) is said to be mean-square asymptotically stable, if*

$$\lim_{k\to\infty}\|x_r(k)\|^2 = 0$$

for the bounded initial conditions $\bar{x}_r(0) \in \Omega_r(P)$.

Theorem 2 *If there exist positive definite matrices $\mathcal{X}_r, P_{2r}$, matrices $\mathcal{R}_{1r}, \mathcal{R}_{2r}, \mathcal{R}_{3r}$ and a positive scalar γ_2 satisfying*

$$\begin{bmatrix}-\mathcal{X}_r & 0 & 0 & \Upsilon_1 & \Upsilon_2 \\ * & -P_{2r} & 0 & B^{\mathrm{T}} & \Upsilon_3 \\ * & * & -\gamma_2^2 I & 0 & P_{2r} \\ * & * & * & -\mathcal{X}_r & 0 \\ * & * & * & * & -P_{2r}\end{bmatrix} < 0 \tag{18}$$

and

$$\begin{bmatrix}I & \mathcal{R}_{2r}^l & I \\ * & \mathcal{X}_r & 0 \\ * & * & P_{2r}\end{bmatrix} \geq 0 \tag{19}$$

where

$$\Upsilon_1 = (A\mathcal{X}_r + \bar{\alpha}B\bar{E}_i(\mathcal{R}_{2r} - \mathcal{R}_{1r}) + B\mathcal{R}_{1r})^{\mathrm{T}}$$

$$\Upsilon_2 = (\bar{\alpha}\mathcal{R}_{3r}B\bar{E}_i(\mathcal{R}_{2r} - \mathcal{R}_{1r}))^{\mathrm{T}}$$

$$\Upsilon_3 = (\mathcal{R}_{3r}B + P_{2r})^{\mathrm{T}}$$

Then, for each $\bar{x}_r(k) \in \Omega_r(P)$, the system (17) is mean-square asymptotically stable and satisfies H∞ performance

$$\frac{\sum_{k=0}^{\infty}\mathbb{E}\{\|z_r(k)\|^2\}}{\sum_{k=0}^{\infty}\mathbb{E}\{\|\Delta a(k)\|^2\}} \leq \gamma_2^2 \tag{20}$$

4 Numerical Simulation

Consider the linear discrete-time system (3) subject to actuator saturation and deception attacks with

$$A = \begin{bmatrix} 1.3 & 1 \\ 0 & 1.1 \end{bmatrix}, B = \begin{bmatrix} 0 \\ 1 \end{bmatrix}$$

The initial value is $x(0) = \begin{bmatrix} 2.5 & -2.5 \end{bmatrix}^{\mathrm{T}}$. The sampling period is 0.05. The parameter γ_1 is 1.41. The inequality (11) in Theorem 1 is a bilinear matrix inequality (BMI). To solve the BMI, by referring to algorithm 1 in [29] and choosing initial value $\mathcal{R}_3 = \begin{bmatrix} 1 & -1 \end{bmatrix}$, we can calculate

$$K = \begin{bmatrix} -0.2268 & -0.5593 \end{bmatrix}, L = \begin{bmatrix} 0 & -0.6029 \end{bmatrix}$$

When the simulation time $k = 30$, system (3) suffers the attack, which is shown in Figure 1. The time-varying and irregular function is

$$a(k) = \begin{cases} 0, 0 \leq \delta_k < 30; \\ \frac{k}{15} - 2, 30 \leq k < 45; \\ 1, 45 \leq k < 60; \\ -0.5, 60 \leq k < 65; \\ -1.5sin(0.01(k-65)), k \geq 65. \end{cases}$$

The attack signal $a(k)$ and estimation of the attack signal $\hat{a}(k)$ are shown in Figure 1. It can be seen that the attack signal is accurately estimated. From Figure 2, the system states are stable when the system is attacked. In Figure 3, it can be seen that the control input is not saturated.

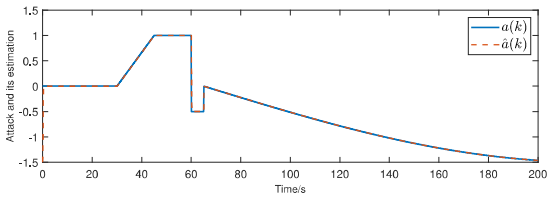

Fig. 1: Attack signal $a(k)$ and estimation of attack signal $\hat{a}(k)$

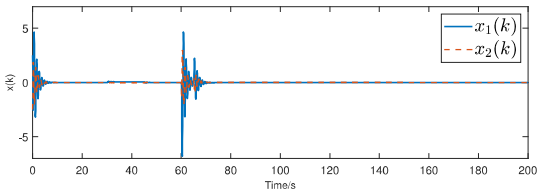

Fig. 2: System states

Through the above numerical simulation, for the system with actuator saturation and FDI attack, the proposed method in this paper can mitigate the impact of FDI attack on actuator saturation and maintain the stability of the system.

In addition, consider the linear discrete-time system (4) with randomly occurring actuator saturation and FDI attack. The parameter $\gamma_2 = 1.4$, $\bar{\alpha} = 0.7$ and choosing initial value $\mathcal{R}_3 = \begin{bmatrix} 1 & -2.1 \end{bmatrix}$. We can calculate

$$K = \begin{bmatrix} -0.2022 & -0.7034 \end{bmatrix}, L = \begin{bmatrix} 0 & -1.0263 \end{bmatrix}$$

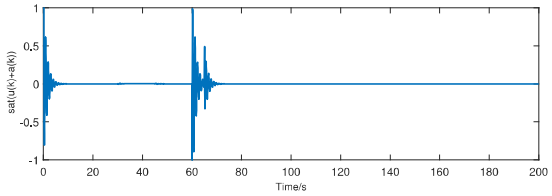

Fig. 3: Control input

We assume that the attack signal is the same as the signal in Figure 1.

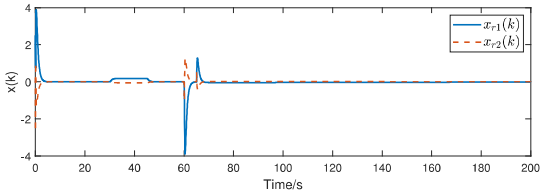

Fig. 4: System states

In Figure 4, we can see that the states remain stable when the system is attacked. We can see from Figure 5 that the control inputs exceed saturation limits at the time $k = 0$. The reason for this phenomenon is that $\bar{\alpha} = 0$ at time $k = 0$ in Figure 6, which means that the system is not limited to actuator saturation at the moment.

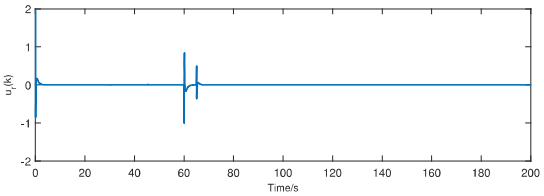

Fig. 5: Control input $u_r(k) = \bar{\alpha}\mathrm{sat}(u(k) + a(k)) + (1 - \bar{\alpha})(u(k) + a(k))$

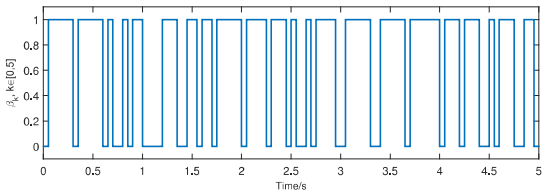

Fig. 6: Probability of saturation

5 Conclusion

In this paper, an observer-based robust sliding model control has been investigated for the linear discrete-time system with actuator saturations and FDI attacks. The FDI attacks are injected into the data transmission channel between the controller and actuator. A sliding mode controller is designed based on the designed sliding mode surface and observer. The actuator saturation is linearized by using the convex hull method. Then, based on the Lyapunov theory and H-infinity performance index, the sufficient conditions ensure the asymptotic stability of the system and satisfy the

corresponding performance indexes. The effectiveness of the theory results is verified by the numerical simulation.

References

[1] D. R. Ding, Q. L. Han, X. H. Ge, J. Wang, Secure state estimation and control of cyber-physical systems: a survey. *IEEE Transactions on Systems, Man, and Cybernetics: Systems*, 2021, 51(1): 176–190.

[2] D. Zhang, Q. G. Wang, G. Feng, Y. Shi, A. V. Vasilakos, A survey on attack detection, estimation and control of industrial cyber-physical systems. *ISA Transactions*, 2021, 116: 1–16.

[3] J. Hu, H. X. Zhang, H. J. Liu, X. Y. Yu, A survey on sliding mode control for networked control systems. *International Journal of Systems Science*, 2021, 52(6): 1129–1147.

[4] M. S. Mahmouda, M. M. Hamdana, U. A. Baroudi, Modeling and control of cyber-physical systems subject to cyber attacks: a aurvey of recent advances and challenges. *Neurocomputing*, 2019, 338: 101–115.

[5] L. W. An, G. H. Yang, Improved adaptive resilient control against sensor and actuator attacks. *Information Sciences*, 2018, 423: 145–156.

[6] H. J. Yang, Y. Li, H. H. Yuan, Z. X. Liu, Adaptive dynamic programming for security of networked control systems with actuator saturation. *Information Sciences*, 2018, 460: 51–64.

[7] J. L. Liu, Y. D. Wang, J. D. Cao, D. Yue, X. P. Xie, Secure adaptive-event-triggered filter design with input constraint and hybrid cyber attack. *IEEE Transactions on Cybernetics*, 2021, 51(8): 4000–4010.

[8] A. Teixeira, I. Shames, H. Sandberg, K. H. Johansson, A secure control framework for resource-limited adversaries. *Automatica*, 2018, 51: 135–148.

[9] D. Zhao, Z. D. Wang, G. L. Wei, Q. L. Han, A dynamic event-triggered approach to observer-based PID security control subject to deception attacks. *Automatica*, 2020, 120: 109–128.

[10] S. Liu, S. B. Li, B. G. Xu, Finite horizon H∞ controller design for time-varying cyber-physical system under hybrid attacks. *Control Theory & Applications*, 2020, 37(2): 331–339.

[11] M. Li, Y. Chen, Wide-area robust sliding mode controller for power systems with false data injection attacks. *IEEE Transactions on Smart Grid*, 2020, 11(2): 922–930.

[12] C. Kwon, I. Hwang, Cyber attack mitigation for cyber-physical systems: hybrid system approach to controller design. *IET Control Theory and Applications*, 2016, 10(7): 731–741.

[13] S. Z. Yong, M. Zhu, E. Frazzoli, A Unified Filter for Simultaneous Input and State Estimation of Linear Discrete-time Stochastic Systems, Automatica, 63 (2016) 321–329.

[14] M. Khalaf, A. Youssef, E. El-Saadany, Joint detection and mitigation of false data injection attacks in AGC systems. *IEEE Transactions on Smart Grid*, 2018, 10(5): 4985–4995.

[15] Q. Y. Su, H. D. Wang, C. W. Sun, J. Li, Cyber-attacks against cyber-physical power systems security: state estimation, attacks reconstruction and defense strategy. *Applied Mathematics and Computation*, 2022, 431: 126639.

[16] J. Zhou, B. Chen, L. Yu, Intermediate-variable-based estimation for FDI attacks in cyber-physical systems. *IEEE Transactions on Circuits and Systems II: Express Briefs*, 2020, 67(11): 2762–2766.

[17] H. J. Sussmann, E. D. Sontag, Y. Yang, A general result on the stabilization of linear systems using bounded controls. *IEEE Transactions on Automatic Control*, 1994, 39(12): 2411–2425.

[18] Q. Wang, Z. Q. Zhang, K. Zhang, Q. X. Lin, Time-varying controller design for input saturated systems. *Journal of the Franklin Institute*, 2020, 357(15): 10453–10471.

[19] Q. Wang, Y. T. Yang, H. Fang, Y. H. Wan, Input saturation: academic insights and future trends. *International Journal of Systems Science*, 2022, 53(6): 1138–1152.

[20] Q. Wang, K. Zhang, A. K. Xue, Reliable robust control for the system with input saturation based on gain scheduling. *Circuits, Systems, and Signal Processing*, 2017, 36(6): 2586–2604.

[21] Y. J. Shi, Y. R. Li, S. Q. Li, H. Y. Liu, State feedback design for nonlinear quadratic systems with randomly occurring actuator saturation. *International Journal of Control Automation and Systems*, 2017, 15(3): 1117–1124.

[22] Z. D. Wang, B. Shen, X. H. Liu, H-infinity filtering with randomly occurring sensor saturations and missing measurements. *Automatica*, 2012, 48(3): 556–562.

[23] T. S. Hu, Z. L. Lin, Control Systems with Actuator Saturation: Analysis and Design, Boston: Birkhauser, (2001)

[24] B. Zhou, G. R. Duan, Z. L. Lin, A parametric lyapunov equation approach to the design of low gain feedback. *IEEE Transactions on Automatic Control*, 2008, 53(6): 1548–1554.

[25] Q. Wang, H. Y. Yu, Z. G. Wu, G. D. Chen, Stability analysis for input saturated discrete-time switched systems with average dwell-time. *IEEE Transactions on Systems, Man and Cybernetics: Systems*, 2021, 51(1): 412–419.

[26] L. Yu, X. M. Sun, T. J. Sui, False-data injection attack in electricity generation system subject to actuator saturation: analysis and design. *IEEE Transactions on Systems, Man, and Cybernetics: Systems*, 2019, 49(8): 1712–1719.

[27] J. Xu, H. Wassim M, Y. Tansel, An adaptive control architecture for mitigating sensor and actuator attacks in cyber-physical systems. *IEEE Transactions on Automatic Control*, 2017, 62(11): 6058–6064.

[28] B. Zhou, *Truncated Predictor Feedback for Time-Delay Systems*. Springer Berlin Heidelberg, 2014.

[29] Y. L. Wei, W. Z. Zheng, S. Y. Xu, Anti-disturbance control for nonlinear systems subject to input saturation via disturbance observer. *Systems & Control letters*, 2015, 85: 62–69.

Proceedings of the 3rd Conference on Fully Actuated System Theory and Applications
May 10-12, 2024, Shenzhen, China

A Fully Actuated System Approach for Robust Control of a Type of Feedback Linearizable System

Xiao-Meng Guo[1], Da-Ke Gu[1], Yin-Dong Liu[1],
1. School of Automation Engineering, Northeast Electric Power University, Jilin 132012, China
E-mail: 15602107675@163.com; gudake@163.com; y.d.liu@163.com

Abstract: In this paper, high-order fully actuated (HOFA) systems are adopted to solve the issue of robust control for a type of feedback linearizable system. Firstly, a type of uncertain feedback linearizable systems are converted to an uncertain HOFA model in preliminaries, which reduce the sensitivity of the model error when the linearization conditions are poor. Besides, based on the Lyapunov stability theory, a direct approach for the design of robust stabilising controllers and robust tracking controllers for an uncertain HOFA model are proposed. Compared with feedback linearization, robustness is guaranteed when exist unmodeled dynamics. Finally, two illustrative examples demonstrate both the effectiveness and the application procedure of the proposed HOFA robust control approaches.

Key Words: Robust Control, Fully Actuated System, Feedback Linearization

1 Introduction

Nonlinear system are widely found in several fields and modern technologies, such as power systems [1], spacecraft [2], etc. Feedback linearization is one of normal measures to solve the control issues of nonlinear systems [3]. Late 20th century, Brockett known as the father of feedback linearization proposed to decouple all the states and the parts of states into a linear system [4].

Furthermore, the development of feedback linearization, such as multi-input feedback linearization or partial feedback linearization, has been proposed and applied to many fields [5–7]. In addition, the project of robust feedback linearization improves the robustness of the nonlinear system [8]. A new method of feedback linearization robust control for bilinear system is proposed [9]. However, existing technologies would be limited by the being of special forms or strong conditions according to the different modeling characteristics of nonlinear systems. As a result, the robustness can not be maintained well when there are uncertain parameters or unmodeled dynamics.

Fortunately, these regrets were remedied with the emergence of the HOFA system [10]. As the condition of feedback linearization, the controllable standard form problem of nonlinear control systems is proposed [11], which establishes a bridge for the transformation of feedback linearizable systems. The relationship of controllability and fully actuated system illustrates the most systems can eliminate nonlinear and obtain linear closed-loop full actuated systems through simple design [12]. Once a parametric design approach of the HOFA systems is introduced, a linear constant closed-loop system with desired eigenstructure can be derived, meanwhile, complete parametric presentations for the closed-loop eigenvectors and the feedback law are given [13]. A direct approach for the design of robust stabilising controllers and robust tracking controllers for an uncertain single HOFA model are proposed based on the Lyapunov stability theory [14].

In this paper, a type of systems satisfying the condition of feedback linearization are converted into a model of uncertain HOFA. Compared with the feedback linearization, the difficulty of transforming conditions and the sensitivity of the model error all are reduced when the linearization conditions are poor. Meanwhile, the superiority of elimination method, that is the HOFA system approaches, is embodied. Besides, the preliminary conclusion for the design of robust stabilising controllers and robust tracking controllers are proposed under the Lyapunov direct method. Unlike feedback linearization, its robustness is fundamentally guaranteed once there are unmodeled dynamics in the system. At the end of the paper, two numerical examples are used to verify the effectiveness of the proposed method.

This work was supported by the Science Center Program of the National Natural Science Foundation of China under Grant No. 62188101.

2 Preliminaries

2.1 Uncertain HOFA Model

Consider a class of uncertain feedback linearizable nonlinear systems

$$\dot{x} = f(x) + \Delta f(x) + [g(x) + \Delta g(x)]u, \tag{1}$$

where $x, u \in \mathbb{R}^n$ are the state vector and the control input vector, respectively, $f(x), g(x) \in \mathbb{R}^n$ are continuous vector function, $\Delta f(x), \Delta g(x) \in \mathbb{R}^n$ are the nonlinear uncertainty of the system, satisfying that (1) is feedback linearizable.

Then there is the following diffeomorphism

$$z^{(i-1)} = L_f^{i-1} h\left(x\right), i = 1, 2, \ldots, m, \tag{2}$$

with $h(x)$ is a smooth scalar function, $L_f^{i-1} h\left(x\right)$ is called the $(i-1)th$ derivative *Lie derivative* of h with respect to f or along f, $m \leq n$ is the relative degree of the system (1), $z \in \mathbb{R}$ is the state vector of the uncertain HOFA model.

According to (2), the uncertain HOFA model is acquired as following

$$z^{(m)} = f(z^{(0\sim m-1)}) + \tilde{B}(z^{(0\sim m-1)})u + \delta(z^{(0\sim m-1)}, u), \tag{3}$$

where

$$\delta(z^{(0\sim m-1)}, u) = \Delta f(z^{(0\sim m-1)}) + \Delta g(z^{(0\sim m-1)})u.$$

2.2 Conditions for Robust Control

Condition 1. *There exists a non-negative continuous scalar function* $\rho(z^{(0\sim m-1)})$ *such that nonlinear uncertainty* $\Delta f\left(z^{(0\sim m-1)}\right), \Delta g\left(z^{(0\sim m-1)}\right) \in \mathbb{R}^m$ *satisfies*

$$\left\|\Delta f\left(z^{(0\sim m-1)}\right)+\Delta g\left(z^{(0\sim m-1)}\right)\Psi\left(z^{(0\sim m-1)}\right)\right\| \leq \rho\left(z^{(0\sim m-1)}\right),$$

with $\Psi\left(z^{(0\sim m-1)}\right)$ *is the control law of HOFA model without uncertainty.*

Lemma 1. *Let* $u=\Psi\left(z^{(0\sim m-1)}\right)+\tilde{B}^{-1}\left(z^{(0\sim m-1)}\right)v$, *then uncertainty* $\delta\left(z^{(0\sim m-1)},u\right)$ *satisfy*

$$\left\|\delta\left(z^{(0\sim m-1)},\Psi\left(z^{(0\sim m-1)}\right)+\tilde{B}^{-1}\left(z^{(0\sim m-1)}\right)v\right)\right\| \leq \rho\left(z^{(0\sim m-1)}\right)+k_0\|v\|, 0<k_0<1,$$

Lemma 2. *Let* $A\in\mathbb{R}^{m\times m}$ *satisfy*

$$\mathrm{Re}\lambda_i(A)\leq-\frac{\lambda}{2}, i=1,2,\ldots,m,$$

where $\mathrm{Re}\lambda_i(A)$ *denotes the real part of a complex number* $\lambda_i(A)$, *and the* $i-th$ *eigenvalue of the matrix* A *is denoted by* $\lambda_i(A)$, *then there is a positive matrix* $P\in\mathbb{R}^{m\times m}$ *satisfying*

$$A^{\mathrm{T}}P+PA\leq-\lambda P,$$

where $P\left(A^{0\sim m-1}\right)$ *as following*

$$P\left(A^{0\sim m-1}\right)=\left[\begin{array}{cccc}P_1 & P_2 & \cdots & P_m\end{array}\right], P_i\in\mathbb{R}^{mr\times r}.$$

Lemma 3. *For any* $\mu>0$ *and a set of arbitrarily given matrices* $A_i\in\mathbb{R}^{r\times r}, i=0,1,\ldots,m-1$, *both satisfying*

$$\mathrm{Re}\lambda_i\left(\Phi\left(A^{0\sim m-1}\right)\right)\leq-\frac{\mu}{2}, i=1,2,\ldots,mr,$$

where I *denotes the identity matrix, and*

$$A^{0\sim m-1}=\left[\begin{array}{cccc}A_0 & A_1 & \cdots & A_{m-1}\end{array}\right],$$

$$\Phi\left(A^{0\sim m-1}\right)=\left[\begin{array}{cccc}0 & I & & \\ & & \ddots & \\ & & & I \\ -A_0 & -A_1 & \cdots & -A_{m-1}\end{array}\right],$$

Lemma 4. *The uncertainties are supposed to satisfy*

$$|\Delta f(z)|\leq\sigma_1 z^2,$$
$$|\Delta f(z_1,\dot{z}_2)|\leq\sigma_2|z_1\dot{z}_2|,$$
$$\left|\frac{\partial\Delta f(z)}{\partial z}\right|\leq\gamma_1|\dot{z}|,$$
$$\left|\frac{\partial^2\Delta f(z)}{\partial z^2}\right|\leq\gamma_2|\ddot{z}|,$$

with σ_p *and* $\gamma_p, p=1,2$, *being some non-negative scalars.*

Lemma 5. *Let* a,b,c,d,e *be five real numbers, and* $b>0$. *Then the following relations hold as*

$$a+b^2\leq\frac{a^2}{4b},$$
$$|c+d-e|\leq|c|+|d|+|e|.$$

3 Robust Control

3.1 Robust Stabilisation

Theorem 1. *Considering (3), there exists the following robust stabilising control law*

$$\begin{cases} u=\Psi(z^{(0\sim m-1)})+\tilde{B}^{-1}(z^{(0\sim m-1)})v, \\ \Psi(z^{(0\sim m-1)})=-\tilde{B}^{-1}(z^{(0\sim m-1)})[\sum_{i=0}^{m-1}A_iz^{(i)}+f(z^{(0\sim m-1)})], \\ v=-\frac{1}{4\varepsilon}\rho^2(z^{(0\sim m-1)}){P_L}^{\mathrm{T}}(A^{(0\sim m-1)})z, \end{cases}$$

where ε *is a real number and*

$${P_L}^{\mathrm{T}}\left(A^{0\sim m-1}\right)=P_m.$$

Then the above control law guarantees that the states $z^{(0\sim m-1)}$ *converges into the following ellipsoid centered at the origin:*

$$\Theta_{\mu,\varepsilon}(0)=\left\{z^{(0\sim m-1)}|(z^{(0\sim m-1)})^{\mathrm{T}} \times P(A^{0\sim m-1})z^{(0\sim m-1)}\leq\frac{\varepsilon}{(1-k_0)\mu}\right\}.$$

3.2 Robust Tracking

Consider the reference signal z_d of the uncertain HOFA model (3), and let be the error of (3) as following

$$e=z-z_d,$$

and then there exists obviously

$$e^{(i)}={z_d}^{(i)}, i=1,2,\ldots,m.$$

Such that it can be transformed into HOFA model with respect to $e^{(0\sim m-1)}$ and t for (3)

$$e^{(m)}=f\left(e^{(0\sim m-1)},t\right)+\tilde{B}\left(e^{(0\sim m-1)},t\right)u_e+\delta\left(e^{(0\sim m-1)},u_e,t\right)-{z_d}^{(m)},$$

where

$$\delta_e\left(e^{(0\sim m-1)},u_e,t\right)=\Delta f\left(e^{(0\sim m-1)},t\right)+\Delta g\left(e^{(0\sim m-1)},t\right)u_e,$$

Theorem 2. *Considering (3), there exists the following robust tracking control law*

$$\begin{cases} u_e=\Psi(z^{(0\sim m-1)})+\tilde{B}^{-1}(z^{(0\sim m-1)})v_e, \\ \Psi(z^{(0\sim m-1)}) \\ \qquad=-\tilde{B}^{-1}(z^{(0\sim m-1)})[\sum_{i=0}^{m-1}A_iz^{(i)}+f(z^{(0\sim m-1)})], \\ v_e=-\frac{1}{4\varepsilon}\rho^2(z^{(0\sim m-1)}){P_L}^{\mathrm{T}}(A^{0\sim m-1})z^{(0\sim m-1)}+u_0(z_d), \\ u_0(z_d)={z_d}^{(m)}-\sum_{i=0}^{m-1}A_i{z_d}^{(i)} \\ \qquad-\frac{1}{4\varepsilon}\rho^2(z^{(0\sim m-1)}){P_L}^{\mathrm{T}}{z_d}^{(0\sim m-1)}, \end{cases}$$

guaranteeing that the state $z^{(0\sim m-1)}$ *converges globally into the following ellipsoidal belt-shaped region centered at* ${z_d}^{(0\sim m-1)}$:

$$\Theta_{\mu,\varepsilon}({z_d}^{(0\sim m-1)})=\left\{z^{(0\sim m-1)}|((z-z_d)^{(0\sim m-1)})^{\mathrm{T}} \times P(z-z_d)^{(0\sim m-1)}\leq\frac{\varepsilon}{(1-k_0)\mu}\right\}.$$

4 Two Illustrative Examples

Two illustrative examples of the proposed approaches demonstrate the effectiveness under two multi-input feedback linearizable systems with uncertainty.

4.1 Example of the Robust Stabilisation

Consider the system as (1), where

$$x = \left[\begin{array}{cc} x_1 & x_2 \end{array}\right]^{\mathrm{T}},$$

$$x_1 = \left[\begin{array}{cc} x_{11} & x_{12} \end{array}\right]^{\mathrm{T}},$$

$$x_2 = \left[\begin{array}{cccc} x_{21} & x_{22} & x_{23} & x_{24} \end{array}\right]^{\mathrm{T}},$$

$$f(x) = \left[\begin{array}{cc} f_1(x_1) & f_2(x_2) \end{array}\right]^{\mathrm{T}},$$

$$f_1(x_1) = \left[\begin{array}{c} x_{12} + x_{11}\sin x_{11} \\ x_{11}x_{12} \end{array}\right],$$

$$f_2(x_2) = \left[\begin{array}{c} x_{22} \\ -\sin x_{21} - 2(x_{21} - x_{23}) \\ x_{24} \\ x_{21} - x_{23} \end{array}\right],$$

$$g(x) = \left[\begin{array}{cc} g_1(x_1) & g_2(x_2) \end{array}\right],$$

$$g_1(x_1) = \left[\begin{array}{cccccc} 0 & 1 & 0 & 0 & 0 & 0 \end{array}\right]^{\mathrm{T}},$$

$$g_2(x_2) = \left[\begin{array}{cccccc} 0 & 0 & 0 & 0 & 0 & 3 \end{array}\right]^{\mathrm{T}},$$

$$u = \left[\begin{array}{cc} u_1 & u_2 \end{array}\right]^{\mathrm{T}},$$

$$\Delta f(x) = \left[\begin{array}{cc} \Delta f_1(x_1) & \Delta f_2(x_2) \end{array}\right]^{\mathrm{T}},$$

$$\Delta f_1(x_1) = \left[\begin{array}{cc} \Delta f_{11}(x_{11}) & \Delta f_{12}(x_{11}, \dot{x}_{12}) \end{array}\right]^{\mathrm{T}},$$

$$\Delta f_2(x_2) = \left[\begin{array}{c} \Delta f_{21}(x_{21}) \\ \Delta f_{22}(x_{21}, x_{22}) \\ \Delta f_{23}(x_{21}, x_{23}) \\ \Delta f_{24}(x_{21}) \end{array}\right],$$

$$\Delta g(x) = \left[\begin{array}{cc} \Delta g_1(x_1) & \Delta g_2(x_2) \end{array}\right],$$

$$\Delta g_1(x_1) = \left[\begin{array}{cccccc} 0 & \Delta g_{12}(x_{11}) & 0 & 0 & 0 & 0 \end{array}\right]^{\mathrm{T}},$$

$$\Delta g_2(x_2) = \left[\begin{array}{cccccc} 0 & 0 & 0 & 0 & 0 & \Delta g_{24}(x_{21}) \end{array}\right]^{\mathrm{T}}.$$

As the output y is following

$$y = \left[\begin{array}{c} y_1 \\ y_2 \end{array}\right] = \left[\begin{array}{c} x_{11} \\ x_{21} \end{array}\right],$$

via the simple transformation, the uncertain HOFA system of (1) is obtained as following

$$z^{(4)} = f\left(z^{(0\sim3)}\right) + \Delta f\left(z^{(0\sim3)}\right) + \tilde{B}\left(z^{(0\sim3)}\right)u,$$

where $m = 4$ is the maximum of the relative degree, and

$$z = \left[\begin{array}{cc} z_1 & z_2 \end{array}\right]^{\mathrm{T}},$$

$$f(z) = \left[\begin{array}{cc} f_1(z_1) & f_2(z_2) \end{array}\right]^{\mathrm{T}} + z^{(3)} + z^{(2)},$$

$$f_1(z_1) = z_1(\dot{z}_1 - z_1\sin z_1) + \dot{z}_1(z_1\cos z_1 + \sin z_1),$$

$$f_2(z_2) = -(\cos z_2 + 3)\ddot{z}_2 + \left(\dot{z}_2^2 - 1\right)\sin z_2,$$

$$\Delta f(z) = \left[\begin{array}{cc} \Delta f_1(z_1) & \Delta f_2(z_2) \end{array}\right]^{\mathrm{T}},$$

$$\begin{aligned}\Delta f_1(z_1) = {} & \Delta\dot{f}_{11}(z_1) - z_1\Delta f_{11}(z_1) \\ & + \Delta f_{12}\left(z_1, (\dot{z}_1 - z_1\sin z_1 - \Delta f_{11}(z_1))'\right),\end{aligned}$$

$$\begin{aligned}\Delta f_2(z_2) = {} & \Delta {f_{21}}^{(3)}(z_2) + \Delta {f_{21}}^{(1)}(z_2) + \Delta\ddot{f}_{22}(z_2, \dot{z}_2 - \Delta f_{21}(z_2)) \\ & + \Delta f_{22}(z_2, \dot{z}_2 - \Delta f_{21}(z_2)) + 2\Delta f_{24}(z_2) \\ & + 2\Delta {f_{23}}^{(1)}\left(z_2, \frac{1}{2}(\ddot{z}_2 + \sin z_2 - \Delta f_{22}(z_2, \dot{z}_2 - \Delta f_{21}(z_2)) \right. \\ & \left. -\Delta {f_{21}}^{(1)}(z_2)) + z_2\right),\end{aligned}$$

$$\tilde{B} = \left[\begin{array}{cc} 1 & 3 + \Delta g(z_2) \\ 0 & 1 \end{array}\right].$$

Thus, there is the control law as following

$$\begin{aligned}u = {} & -\tilde{B}^{-1}\left(A^{0\sim3}z^{(0\sim3)} + f\left(z^{(0\sim3)}\right)\right) \\ & -\tilde{B}^{-1}\frac{1}{4\varepsilon}\rho^2\left(z^{(0\sim3)}\right){P_L}^{\mathrm{T}}z^{(0\sim3)},\end{aligned}$$

guaranteeing that the state $z^{(0\sim3)}$ converges into the ellipsoid $\Theta_{\mu,\varepsilon}(0)$ as

$$\Theta_{\mu,\varepsilon}(0) = \left\{z^{(0\sim3)} \,\middle|\, \left(z^{(0\sim3)}\right)^{\mathrm{T}}Pz^{(0\sim3)} \le \frac{\varepsilon}{(1-k_0)\mu}\right\},$$

where

$$\begin{aligned}\rho\left(z^{(0\sim3)}\right) = {} & a_1|z_1| + a_2|z_1||\dot{z}_1| + a_3|\ddot{z}_1| + a_4|\dot{z}_1| \\ & + a_5|\sin z_1| + a_6\left|{z_1}^{(3)}\right| + b_1\left|{z_2}^{(3)}\right| + b_2|\ddot{z}_2| \\ & + b_{30}|\dot{z}_2| + b_{31}|\dot{z}_2|^2 + b_{32}|\dot{z}_2|^3 + b_{33}|\dot{z}_2|^4 \\ & + b_{34}|\dot{z}_2|^5 + b_{35}|\dot{z}_2|^6 + b_{36}|\dot{z}_2|^8 + b_4|z_2| \\ & + b_5|\dot{z}_2|^2|\ddot{z}_2|\left|{z_2}^{(3)}\right| + b_6|\ddot{z}_2|\left|{z_2}^{(3)}\right| + b_8|z_2||\dot{z}_2| \\ & + b_7|\dot{z}_2|\left|{z_2}^{(3)}\right| + b_{91}|\dot{z}_2||\ddot{z}_2| + b_{92}|\dot{z}_2|^2|\ddot{z}_2|^2 \\ & + b_{93}|\dot{z}_2||\ddot{z}_2|^2 + b_{94}|\dot{z}_2|^2|\ddot{z}_2| + b_{95}|\dot{z}_2|^3|\ddot{z}_2| \\ & + b_{96}|\dot{z}_2|^4|\ddot{z}_2|,\end{aligned}$$

and

$$a_1 = 76.5883k_0 + \sigma_{11}{z_1}^2,$$

$$a_2 = \sigma_{12}(|\sin z_1| + |z_1||\cos z_1| + \gamma_{12}|\dot{z}_1|) + k_0(1 + |\cos z_1|),$$

$$a_3 = \sigma_{12}|z_1| + 87.5883k_0,$$

$$a_4 = \gamma_{11}|\dot{z}_1| + (146.4117 + |\sin z_1|)k_0,$$

$$a_5 = k_0{z_1}^2,$$

$$a_6 = 18.7647k_0,$$

$$b_1 = 10.6471k_0 + \frac{1}{2}\gamma_{29}\left|{z_2}^{(3)}\right|,$$

$$b_2 = 38.8823k_0 + \frac{1}{2}{\gamma_{26}}^2\gamma_{29}|\ddot{z}_2|^3,$$

$$b_{30} = 57.1177k_0 + |\sin z_2|,$$

$$b_{31} = \gamma_{21} + 2\gamma_{28} + \frac{1}{2}\gamma_{29}|\cos z_2 + 1|^2,$$

$$b_{32} = \gamma_{29}(\gamma_{21} + \gamma_{24})|\cos z_2 + 1|,$$

$$b_{33} = \frac{1}{2}\gamma_{29}(\gamma_{21}+\gamma_{24})^2,$$

$$b_{34} = {\gamma_{21}}^2\gamma_{26}\left|\cos z_2 + 1\right|,$$

$$b_{35} = {\gamma_{21}}^2\gamma_{26}\gamma_{29}(\gamma_{21}+\gamma_{24}),$$

$$b_{36} = \frac{1}{2}{\gamma_{21}}^4{\gamma_{26}}^2\gamma_{29}.$$

$$b_4 = 27.8823k_0 + \sigma_{24}\left|z_2\right| + \sigma_{21}\sigma_{22}|z_2|^2,$$

$$b_5 = 2\gamma_{21}(\gamma_{27}+\gamma_{26}\gamma_{29}),$$

$$b_6 = \gamma_{26}(\gamma_{29}\left|\ddot{z}_2\right|+1),$$

$$b_7 = \gamma_{21}+\gamma_{29}\left|\cos z_2+1\right| + \left[\gamma_{21}\gamma_{26}+\gamma_{29}(\gamma_{21}+\gamma_{24})\right]\left|\dot{z}_2\right| + \gamma_{23}|\dot{z}_2|^2 + {\gamma_{21}}^2(\gamma_{27}+\gamma_{26}\gamma_{29})|\dot{z}_2|^3,$$

$$b_8 = \sigma_{22},$$

$$b_{91} = \gamma_{24}+\gamma_{26}[\gamma_{21}\gamma_{22}+\gamma_{29}(\gamma_{21}+\gamma_{24})]\left|\dot{z}_2\right|\left|\ddot{z}_2\right|,$$

$$b_{92} = 2{\gamma_{21}}^2\gamma_{27}\left|\dot{z}_2\right| + (\gamma_{22}\gamma_{26}+2\gamma_{21}\gamma_{22}\gamma_{27}+2\gamma_{21}{\gamma_{26}}^2\gamma_{29})\left|\ddot{z}_2\right|,$$

$$b_{93} = 3\gamma_{22}+\gamma_{21}\gamma_{26}+\gamma_{26}\gamma_{29}\left|\cos z_2+1\right| + \gamma_{22}\gamma_{27}\left|\dot{z}_2\right|\left|\ddot{z}_2\right|^2 + \gamma_{21}\gamma_{27}\left|\ddot{z}_2\right|$$

$$b_{94} = \gamma_{25}+3{\gamma_{21}}^2{\gamma_{26}}^2\gamma_{29}|\dot{z}_2|^2\left|\ddot{z}_2\right|,$$

$$b_{95} = \gamma_{21}\gamma_{26}(\gamma_{21}+2\gamma_{29}\left|\cos z_2+1\right|) + {\gamma_{21}}^2\gamma_{22}\gamma_{27}|\dot{z}_2|^3\left|\ddot{z}_2\right|,$$

$$b_{96} = \gamma_{21}[{\gamma_{21}}^2\left|\dot{z}_2\right|(\gamma_{27}+2{\gamma_{26}}^2\gamma_{29}\left|\dot{z}_2\right|)+2\gamma_{26}\gamma_{29}(\gamma_{21}+\gamma_{24})],$$

Proof. Matrices F and Z are chosen arbitrarily as

$$F = \mathrm{diag}\{F_1, F_2, F_3, F_4\}_{8\times 8},$$

$$Z = \left[\begin{array}{cccc} Z_1 & Z_2 & Z_3 & Z_4 \end{array}\right],$$

where

$$F_1 = \mathrm{diag}\{-1,\ -2\}, F_2 = \mathrm{diag}\{-3,\ -3\},$$

$$F_3 = \mathrm{diag}\{-2,\ -1\}, F_4 = \mathrm{diag}\{-5,\ -7\},$$

$$z_1 = \left[\begin{array}{cc} 1 & 0 \\ 1 & 1 \end{array}\right], z_2 = \left[\begin{array}{cc} 1 & 1 \\ 0 & 2 \end{array}\right],$$

$$z_3 = \left[\begin{array}{cc} 2 & 1 \\ 1 & 0 \end{array}\right], z_4 = \left[\begin{array}{cc} 3 & 5 \\ 11 & 7 \end{array}\right].$$

Then combining with Lemmas 4 and 5, the result of Theorem 1 is obtained.

Here are the simulation results of (see Figures 1-4) when the initial values is chosen as

$$\begin{cases} z^{(0)}(0) = \left[\begin{array}{cc} 0.001 & 50 \end{array}\right]^{\mathrm{T}}, \\ z^{(1)}(0) = \left[\begin{array}{cc} 200 & 0.2 \end{array}\right]^{\mathrm{T}}, \\ z^{(2)}(0) = \left[\begin{array}{cc} 3 & 100 \end{array}\right]^{\mathrm{T}}, \\ z^{(3)}(0) = \left[\begin{array}{cc} 15 & 0.03 \end{array}\right]^{\mathrm{T}}, \end{cases}$$

□

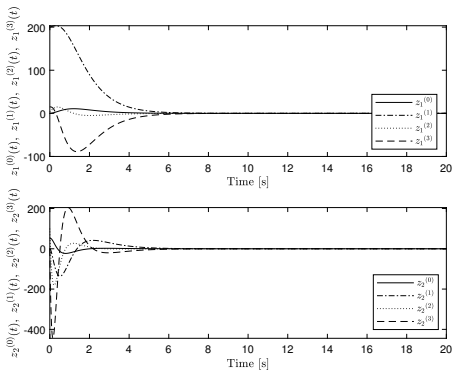

Fig. 1: The results of state variable $z^{(0\sim 3)}$

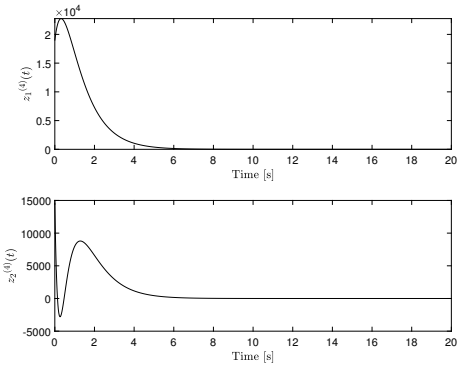

Fig. 2: The results of state variable $z^{(4)}$

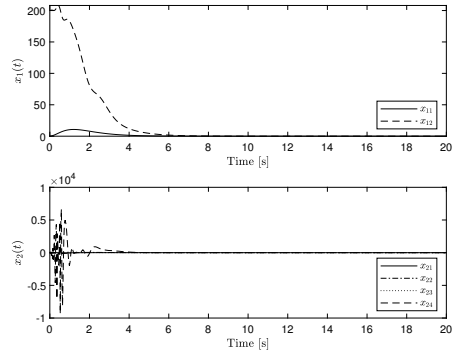

Fig. 3: The results of state variable x

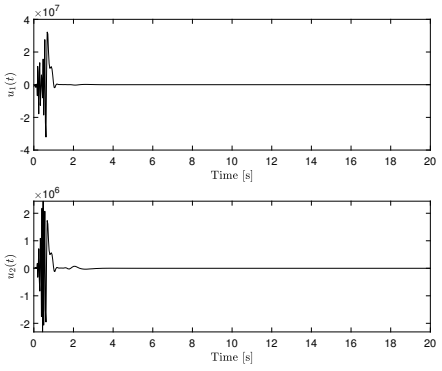

Fig. 4: The results of state variable u

4.2 Example of the Robust Tracking

Similarly, consider the system as (1), where

$$x = \left[\begin{array}{ccc} x_1 & x_2 & x_3 \end{array}\right]^{\mathrm{T}},$$

$$x_1 = \left[\begin{array}{cc} x_{11} & x_{12} \end{array}\right]^{\mathrm{T}},$$

$$x_2 = \left[\begin{array}{cc} x_{21} & x_{22} \end{array}\right]^{\mathrm{T}},$$

$$x_3 = \left[\begin{array}{cc} x_{31} & x_{32} \end{array}\right]^{\mathrm{T}},$$

$$f(x) = \left[\begin{array}{ccc} f_1(x_1) & f_2(x_2) & f_3(x_3) \end{array}\right]^{\mathrm{T}},$$

$$f_1(x_1) = \left[\begin{array}{cc} x_{12} & -x_{11} + \left(1 - {x_{11}}^2\right) x_{12} \end{array}\right]^{\mathrm{T}},$$

$$f_2(x_2) = \left[\begin{array}{cc} x_{22} + x_{21}\sin x_{21} & x_{21}x_{22} \end{array}\right]^{\mathrm{T}},$$

$$f_3(x_3) = \left[\begin{array}{cc} x_{32} & -x_{31} + (2 + x_{31})\, x_{32} \end{array}\right]^{\mathrm{T}},$$

$$\Delta f(x) = \left[\begin{array}{ccc} \Delta f_1(x_1) & \Delta f_2(x_2) & \Delta f_3(x_3) \end{array}\right]^{\mathrm{T}},$$

$$\Delta f_1(x_1) = \left[\begin{array}{cc} \Delta f_{11}(\dot{x}_{11}) & \Delta f_{12}(\dot{x}_{11}, \dot{x}_{12}) \end{array}\right]^{\mathrm{T}},$$

$$\Delta f_2(x_2) = \left[\begin{array}{cc} \Delta f_{21}(x_{21}) & \Delta f_{22}(x_{21}, \dot{x}_{22}) \end{array}\right]^{\mathrm{T}},$$

$$\Delta f_3(x_3) = \left[\begin{array}{cc} \Delta f_{31}(x_{31}) & \Delta f_{32}(\dot{x}_{32}) \end{array}\right]^{\mathrm{T}},$$

$$g(x) = \left[\begin{array}{ccc} g_1(x_1) & g_2(x_2) & g_3(x_3) \end{array}\right]^{\mathrm{T}},$$

$$g_1(x_1) = \left[\begin{array}{cccccc} 0 & 1 & 0 & 0 & 0 & 0 \end{array}\right]^{\mathrm{T}},$$

$$g_2(x_2) = \left[\begin{array}{cccccc} 0 & 0 & 0 & 1 & 0 & 0 \end{array}\right]^{\mathrm{T}},$$

$$g_3(x_3) = \left[\begin{array}{cccccc} 0 & 0 & 0 & 0 & 0 & 1 \end{array}\right]^{\mathrm{T}},$$

$$\Delta g(x) = \left[\begin{array}{ccc} \Delta g_1(x_1) & \Delta g_2(x_2) & \Delta g_3(x_3) \end{array}\right],$$

$$\Delta g_1(x_1) = \left[\begin{array}{cccccc} 0 & \Delta g_{12}(x_{11}) & 0 & 0 & 0 & 0 \end{array}\right]^{\mathrm{T}},$$

$$\Delta g_2(x_2) = \left[\begin{array}{cccccc} 0 & 0 & 0 & \Delta g_{22}(x_{21}) & 0 & 0 \end{array}\right]^{\mathrm{T}},$$

$$\Delta g_3(x_3) = \left[\begin{array}{cccccc} 0 & 0 & 0 & 0 & 0 & \Delta g_{32}(\dot{x}_{31}) \end{array}\right]^{\mathrm{T}},$$

and the output y is following

$$y = \left[\begin{array}{ccc} y_1 & y_2 & y_3 \end{array}\right]^{\mathrm{T}} = \left[\begin{array}{ccc} x_{11} & x_{21} & x_{31} \end{array}\right]^{\mathrm{T}}.$$

Via the simple transformation, the uncertain HOFA system of (1) is obtained as following

$$\ddot{z} = f(z) + \Delta f(z) + \dot{z} + z + \tilde{B}u,$$

where $m = 2$ is the maximum of the relative degree, and

$$z = \left[\begin{array}{ccc} z_1 & z_2 & z_3 \end{array}\right]^{\mathrm{T}},$$

$$f(z) = \left[\begin{array}{ccc} f_1(z_1) & f_2(z_2) & f_3(z_3) \end{array}\right]^{\mathrm{T}},$$

$$\Delta f(z) = \left[\begin{array}{ccc} \Delta f_1(z_1) & \Delta f_2(z_2) & \Delta f_3(z_3) \end{array}\right]^{\mathrm{T}},$$

$$f_1(z_1) = -z_1 + \left(1 - {z_1}^2\right)\dot{z}_1,$$

$$f_2(z_2) = z_2\left(\dot{z}_2 - \sin^2 z_2\right) + \dot{z}_2\left(z_2\cos z_2 + \sin z_2\right),$$

$$f_3(z_3) = -z_3 + \dot{z}_3\left(2 + z_3\right),$$

$$\Delta f_1(z_1) = \Delta f_{12}\left(\dot{z}_1, \left(\dot{z}_1 - \Delta f_{11}(\dot{z}_1)\right)'\right) + \Delta\dot{f}_{11}(\dot{z}_1) + ({z_1}^2 - 1)\Delta f_{11}(\dot{z}_1),$$

$$\Delta f_2(z_2) = \Delta\dot{f}_{21}(z_2) - z_2\Delta f_{21}(z_2) + \Delta f_{22}\left(z_2, \left(\dot{z}_2 - z_2\sin z_2 - \Delta f_{21}(z_2)\right)'\right),$$

$$\Delta f_3(z_3) = \Delta\dot{f}_{31}(z_3) + \Delta f_{32}\left(\left(\dot{z}_3 - \Delta f_{31}(z_3)\right)'\right) - (2 + z_3)\,\Delta f_{31}(z_3),$$

$$\tilde{B} = \left[\begin{array}{ccc} 1 & 1 + \Delta g_{22}(z_2) & 1 + \Delta g_{32}(\dot{z}_3) \\ 0 & 1 & 1 + \Delta g_{32}(\dot{z}_3) \\ 0 & 0 & 1 \end{array}\right].$$

Let be $e = z - z_d$, then the above HOFA model can be turned into following form with respect to $e^{(0\sim1)}$ and t

$$\ddot{e} = f(e^{(0\sim1)}, t) + \tilde{B}(e^{(0\sim1)}, t)u + \delta(e^{(0\sim1)}, u, t) - {z_d}^{(2)},$$

Thus, there is the control law as following for the original system (3)

$$u = -\tilde{B}^{-1}\left(A^{0\sim1}z^{(0\sim1)} + f\left(z^{(0\sim1)}\right)\right) - \tilde{B}^{-1}\left(\frac{1}{4\varepsilon}\rho^2\left(z^{(0\sim1)}\right){P_L}^{\mathrm{T}}z^{(0\sim1)} - u_0(z_d)\right),$$

with

$$u_0(z_d) = -A^{0\sim1}{z_d}^{(0\sim1)} - \frac{1}{4\varepsilon}\rho^2(z^{(0\sim1)}){P_L}^{\mathrm{T}}z^{(0\sim1)} + {z_d}^{(2)},$$

guaranteeing that the state $z^{(0\sim1)}$ converges globally into the following ellipsoidal belt-shaped region centered at ${z_d}^{(0\sim1)}$ as

$$\Theta_{\mu,\varepsilon}({z_d}^{(0\sim1)}) = \left\{ z^{(0\sim1)} \middle| \left((z - z_d)^{(0\sim1)}\right)^{\mathrm{T}} \times P(z - z_d)^{(0\sim1)} \le \frac{\varepsilon}{(1 - k_0)\mu} \right\},$$

where

$$\rho = a_1|e_1| + a_2|\dot{e}_1| + \gamma_{11}|\ddot{e}_1|^2 + b_1|e_2| + b_2|\dot{e}_2| + c_1|e_3| + c_2|\dot{e}_3| + \sigma_{32}|\ddot{e}_3|^2,$$

$$a_1 = 18.417k_0,$$

$$a_2 = [\sigma_{12}(|\ddot{e}_1| + \gamma_{11}|\ddot{e}_1|^2) + k_0(8.2275 + \left|1 - {e_1}^2\right|)] + \sigma_{11}\left|{e_1}^2 - 1\right||\dot{e}_1| + 3.0995k_0,$$

$$b_1 = \sigma_{21}|e_2|^2 + k_0\left|\dot{e}_2 - \sin^2 e_2\right| + 5.2749k_0,$$

$$b_2 = \sigma_{22}[|\ddot{e}_2 + |\dot{e}_2|\,(|\sin e_2| + |e_2||\cos e_2| + \gamma_{21}|\dot{e}_2|)|] + \gamma_{21}|\dot{e}_2| + k_0|\sin e_2 + e_2\cos e_2| + 4.711k_0,$$

$$c_1 = \sigma_{31}|2 + e_3||e_3| + 10.2938k_0,$$

$$c_2 = k_0(|2 + e_3| + 2.6777) + 4.4597k_0 + \gamma_{31}|\dot{e}_3|\,(1 + \gamma_{31}\sigma_{32}|\dot{e}_3|^2 + 2\sigma_{32}|\ddot{e}_3|),$$

Proof. Matrix F and matrix Z are chosen in arbitrary

$$F = \mathrm{diag}\{F_1, F_2\}_{6\times6},$$

$$Z = \left[\begin{array}{cc} Z_1 & Z_2 \end{array}\right]_{3\times6},$$

where

$$F_1 = \mathrm{diag}\{-1, -2, -3\}, F_2 = \mathrm{diag}\{-1, -5, -2\},$$

$$Z_1 = \left[\begin{array}{ccc} 1 & 0 & 2 \\ 1 & 3 & 5 \\ 1 & 5 & 1 \end{array}\right], Z_2 = \left[\begin{array}{ccc} 1 & 7 & 2 \\ 2 & 3 & 5 \\ 0 & 1 & 3 \end{array}\right].$$

Then combining with Lemma 4 and Lemma 5, the result of Theorem 2 is obtained. □

Here are the simulation results (see Figures 5-8) when the initial values is chosen as

$$\begin{cases} z(0) = \begin{bmatrix} 100 & 50 & 0.15 \end{bmatrix}^{\mathrm{T}}, \\ \dot{z}(0) = \begin{bmatrix} 25 & 0.003 & 120 \end{bmatrix}^{\mathrm{T}}, \end{cases}$$

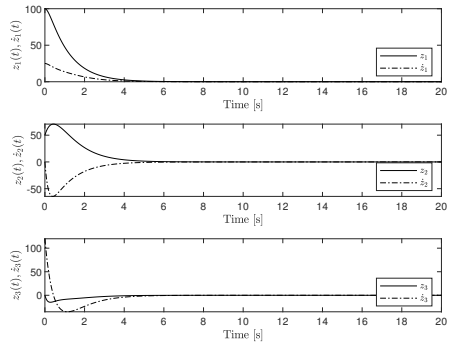

Fig. 5: The results of state variable $z^{(0\sim1)}$

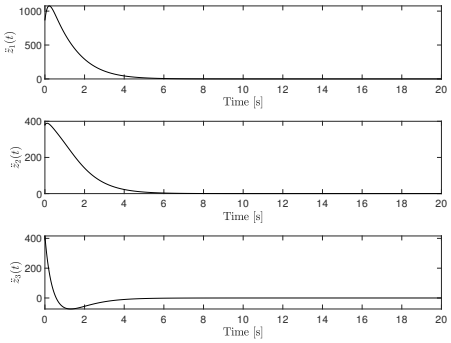

Fig. 6: The results of state variable $\ddot{z}$

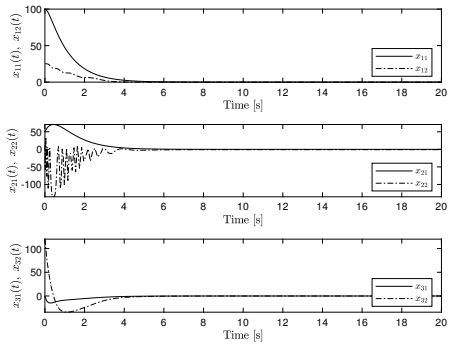

Fig. 7: The results of state variable x

5 Conclusion

In this paper, a direct approach for the design of robust stabilising controllers and robust tracking controllers solve the issue of the robust control for the uncertain feedback linearizable systems based on the Lyapunov stability theory. Improving the result of simulation and other work are continued in the future.

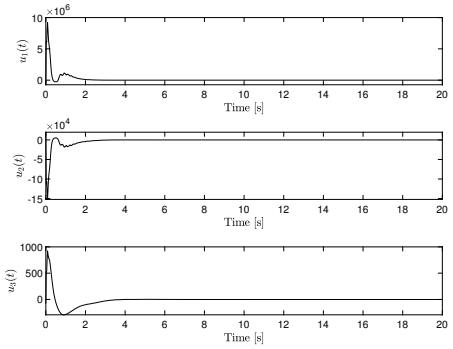

Fig. 8: The results of state variable u

References

[1] D.M. Dawson, J. Hu and T.C. Burg, Nonlinear control of electric machinery, *CRC Press*, 2019.

[2] G.R. Duan, High-order fully actuated system approaches: Part VIII. Optimal control with application in spacecraft attitude stabilisation, *International Journal of Systems Science*, 53(1): 54-73, 2022.

[3] Z. Li, Q.R. Hao, F. Gao and L.L. Wu, Nonlinear decoupling control of two-terminal MMC-HVDC based on feedback linearization, *IEEE Transactions on Power Delivery*, 34(1): 376-386, 2018.

[4] A.J. Krener, Feedback linearization, *Mathematical Control Theory*, 1999: 66-98.

[5] M.W. Spong, Partial feedback linearization of underactuated mechanical systems, *Proceedings of IEEE/RSJ International Conference on Intelligent Robots and Systems (IROS'94)*, 1994, 1: 314-321.

[6] J.J.E. Slotine, W. Li, Applied nonlinear control, *Englewood Cliffs, NJ: Prentice hall*, 1991.

[7] D.B. Dacic, D. Nesic and P.V. Kokotovic, Path-Following for nonlinear systems with unstable zero dynamics, *IEEE Transactions on Automatic Control*, 53(3): 481-487, 2007.

[8] A.L.D. Franco, et al, Robust nonlinear control associating robust feedback linearization and H/ sub/ spl infin// control, *IEEE Transactions on Automatic Control*, 51(7): 1200-1207, 2006.

[9] B.S. Kim, M.T. Lim, Robust H_∞ control method for bilinear system, *International Journal of Control, Automation, and Systems*, 1(2): 171-177, 2003.

[10] G.R. Duan, High-oder fully actuated system approaches: Part I. Models and basic procedure, *International Journal of Systems Science*, 52(2): 422-435, 2021.

[11] G.R. Duan, High-order system approaches: II. Controllability and fully-actuation, *Acta Automatica Sinica*, 46(8): 1571-1581, 2020.

[12] G.R. Duan, High-order system approaches: I. Fully-actuated systems and parametric designs, *Acta Automatica Sinica*, 46(7):1333-1345, 2020.

[13] G.R. Duan, High-oder fully actuated system approaches: Part VII. Controllability, stabilisability and parametric designs, *International Journal of Systems Science*, 52(14): 3091-3114, 2021.

[14] G.R. Duan, High-oder fully actuated system approaches: Part III. Robust control and high-order backstep, *International Journal of Systems Science*, 52(5): 952-971, 2021.

Proceedings of the 3rd Conference on Fully Actuated System Theory and Applications
May 10-12, 2024, Shenzhen, China

High precision trajectory tracking control for a kind of novel cable-driven space manipulator

Xiangxiang Zou[1], Deshan Meng[1], Hui-Jie Sun[1], Yu-Yao Wu[1]* , Lining Tan[2]

1.Shenzhen Campus of Sun Yat-sen University, Shenzhen, 518107, China
E-mail: yuyao_wu@foxmail.com

Abstract: High precision trajectory tracking control is critical for achieving long-distance operations for cable-driven space manipulators. However, due to the uncertainty and deformation of long-distance transmission cables, the existing cable-driven space manipulator trajectory tracking control method cannot meet the requirements of high precision and strong robustness in actual engineering. In this paper, the high precision trajectory tracking control problem of a kind of novel cable-driven large-scale space manipulator is studied. First, the kinematics and dynamics of the cable-driven space manipulator are established using the principle of virtual work. Based on the fully actuated system control idea, a trajectory tracking control scheme is designed for the cable-driven space manipulator. The asymptotic stability of the resulting closed-loop system is proved using Lyapunov stability theory. The simulation results show that the proposed control scheme can effectively overcome the influence of interference and achieve high precision trajectory tracking control of the cable-driven space manipulator.

Key Words: Cable-driven space manipulator, fully actuated system method, trajectory tracking control

1 Introduction

In contemporary aerospace systems, space manipulators play an increasingly vital role. They stand in for astronauts, handling complex and hazardous tasks such as in-orbit refueling, spacecraft maintenance, and the crucial task of managing space debris [1]. Noteworthy examples of these manipulators include Space Shuttle Remote Manipulator System (SRMS) [2] and the Mobile Servicing System, both utilized extensively for routine operations aboard the International Space Station. Additionally, the Japanese Experiment Module Remote Manipulator System [3] and the Educable Space Agency's autonomously maneuverable Educable Arm contribute to the assortment of traditional space robotic arms. These mechanisms exhibit a distinct structural feature: a hinge-like interconnection between the manipulator's segments, strategically housing drive motors at rotational joints.

As aerospace technology progresses, forthcoming space missions, including the in-orbit assembly of ultra-large spacecraft, redirection of asteroids, and precise manipulation of high-inertia rolling targets, impose heightened demands on the capabilities of space robotic manipulators. Conventional designs confront challenges in extending arm lengths and augmenting end-effector payload capacities, requiring the integration of more robust drive components at joints and additional transmission mechanisms. These adaptations inevitably elevate the overall system's mass, thereby contributing to a substantial escalation in the cost profile of space missions.

To reduce the cost of future space missions, the National Aeronautics and Space Administration (NASA) of the United States has put forth a proposal for innovative, dexterous, and lightweight cable-driven space robotic manipulator. This novel robotic manipulator exhibits a broader range of motion and can accommodate larger end-effector payloads. The innovation of cable-driven manipulator involves the separation of drive motors from rotational joints by extending and retracting cables, the manipulator segments are connected by the spreader. With similar length, the novel cable-driven space manipulator exhibits significantly lower mass compared to traditional counterparts, by several orders of magnitude, and when folded, occupies only around 14% of the volume of the previous SRMS. This groundbreaking innovation holds immense promise in substantially reducing the cost associated with space missions.

Numerous scholars have dedicated substantial research efforts to the modeling and control methodologies for traditional space manipulators. Typically, the modeling process treats space manipulators as a multi-rigid-body system, utilizing established methods such as Lagrange mechanics, Newton-Euler method, and Kane's method. However, alternative methods have also been utilized for dynamic modeling, such as the Hamiltonian principle proposed in [4] and the Jourdain method proposed in [5] for variable speeds. Moreover, reference [6] analyzed the dynamic coupling characteristics of space robots and proposed a comprehensive inertial parameter identification method for space robot system.

In the domain of control, for flexible-joint manipulator, [7] proposed an adaptive control schedule under uncertain parameters. In [8], considering the dynamic coupling between spacecraft bases and space robotic manipulator. An adaptive coordination controller was proposed in spacecraft attitude control. In [9], a sliding mode robust control approach for multi-rigid-body system models has been introduced, resolving high dynamic coupling among bodies and achieving control objectives for cable-driven robot. An observer output feedback control methodology for space robotic arms based on fuzzy functions to address model uncertainties was proposed in [10].

As aforementioned, despite considerable achievements in control research for space manipulators, addressing highly coupled and strongly nonlinear characteristics of space cable-driven manipulator remains challenging. Model-based control methods frequently encounter challenges in translating physical models into state-space representations

*This work is supported by Natural Science Foundation of Guangdong Province of China under Grant Nos. 2023A1515011466, 2023A1515110743 and 2022A1515010543, by State Key Laboratory of Robotics and Systems (HIT)(SKLRS-2023-KF-22).

for these systems, whereas model-free nonlinear control methods grapple with ensuring effective control outcomes. Therefore, in [11], based on six degrees of freedom robotic system, the approach diverges from converting the actual system model into a state-space form of a first-order system. Instead, it directly targets the physical model, employing a direct parameter method was proposed in [12] to design a full-actuated system controller, which transforms the open-loop nonlinear system into a closed-loop system with configurable eigenvalues and linear constant coefficients. As a result, it facilitates effective trajectory-tracking control for robotic manipulators.

In this paper, a comprehensive exposition of the model for the cable-driven space manipulator system model is proposed. Drawing from the structural attributes of the cable-driven mechanism, a mapping relation between the tension of cables and the equivalent joint torque is established. Subsequently, leveraging the Lagrange method, the dynamic model for the system is formulated. The dynamic equation considers the cable elastic model, which provides a model basis for high-precision motion control. Then, a full-actuated system method is utilized to design a composite controller for cable-driven space manipulator. Theoretical proofs regarding the stability of the system are conducted. Finally, the efficacy and superiority of the proposed controller are empirically substantiated through comprehensive comparative simulation experiments.

2 Modeling and Control Problem Description

The mechanical structure of the cable-driven space manipulator is depicted in Fig. 1. Adjacent links are interconnected through spreaders, with cable drive and control devices positioned at the extremities of the links. Cables are configured on both sides of the links, with one end connecting to the winch and the other end linking to a tension sensor located on the top of the spreader. Motors are situated at the winches to drive rotation, facilitating the controlled movement of the links through motor rotation. The system is equivalently represented by joint torques propelling the manipulator's motion, wherein the spreader rotates in tandem with the corresponding joint rotations.

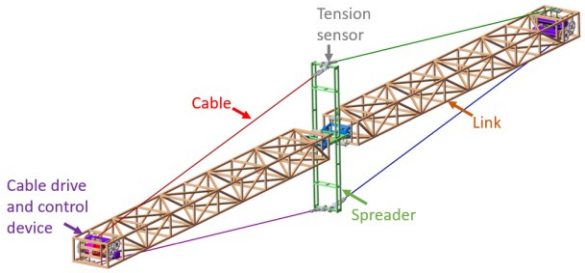

Fig. 1: Joint module structure diagram

2.1 Mapping from Cable Tension to Joint Torques

The simplified model of cable-driven space manipulator single-joint module is depicted in Fig. 2. The winch radius is denoted by r, L_i and L_{i+1} are the distance from the winch center to the spreader center, the single-sided height and width of the suspension system are h and d respectively, angle between adjacent link segments is θ_i, the angle between the link and the spreader is $\theta_i/2$, $\boldsymbol{l}_i=\left[l_{i1},\ l_{i2},\ l_{i3},\ l_{i4}\right]^T$ is the length of cables.

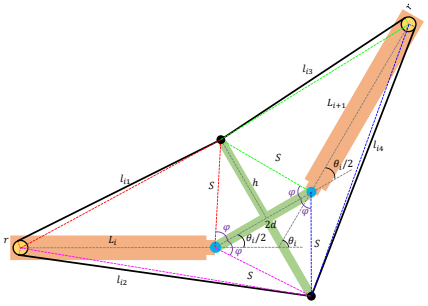

Fig. 2: Equivalent diagram of joint torque

From the geometric relations:

$$S=\sqrt{d^2+h^2} \tag{1}$$

$$\varphi=\arctan\left(h/d\right) \tag{2}$$

then, the relationship between the length of cables $\boldsymbol{l}_i$ and the angle θ_i of rotation of the joint is obtained by

$$\begin{cases} l_{i1}^2=S^2+L_i^2-r^2-2S\sqrt{L_i^2+r^2}\cos\left[\pi-\left(\varphi+\dfrac{\theta_i}{2}\right)\right] \\ l_{i2}^2=S^2+L_i^2-r^2-2S\sqrt{L_i^2+r^2}\cos\left[\pi-\left(\varphi-\dfrac{\theta_i}{2}\right)\right] \\ l_{i3}^2=S^2+L_{i+1}^2-r^2-2S\sqrt{L_{i+1}^2+r^2}\cos\left[\pi-\left(\varphi+\dfrac{\theta_i}{2}\right)\right] \\ l_{i4}^2=S^2+L_{i+1}^2-r^2-2S\sqrt{L_{i+1}^2+r^2}\cos\left[\pi-\left(\varphi-\dfrac{\theta_i}{2}\right)\right] \end{cases} \tag{3}$$

differentiating both sides of (3) yields

$$\mathrm{d}\boldsymbol{l}_i=\boldsymbol{J}_{qi}\mathrm{d}\boldsymbol{\theta}_i \tag{4}$$

where the Jacobian matrix of the joint module can be expressed as

$$\begin{aligned}\boldsymbol{J}_{qi}=\Bigg[&-SL_i\sin\left(\frac{\theta_i}{2}+\varphi\right)/2l_{i1}\quad SL_i\sin\left(\frac{-\theta_i}{2}+\varphi\right)/2l_{i2}\\ &-SL_{i+1}\sin\left(\frac{\theta_i}{2}+\varphi\right)/2l_{i3}\quad SL_{i+1}\sin\left(\frac{-\theta_i}{2}+\varphi\right)/2l_{i4}\Bigg]^T\end{aligned} \tag{5}$$

It can be seen from the equation (5) that the relationship between the change of the cables and the joints angle is only related to the $\boldsymbol{\theta}_i$.

2.2 Dynamic equations

During the movement, the length of the cables changes as:

$$\delta l=\delta l_s+\delta l_\theta \tag{6}$$

where δl_s is the elastic deformation of the cable, and δl_θ is the changes in cables length caused by changes in joints angle.

According to the principle of virtual work:

$$\delta W=\delta W_s+\delta W_\theta=\boldsymbol{\tau}_s^T\delta\boldsymbol{\theta}+\boldsymbol{\tau}_\theta^T\delta\boldsymbol{\theta}=\boldsymbol{f}\cdot\delta\boldsymbol{l} \tag{7}$$

where $\boldsymbol{\tau}_s\in\boldsymbol{R}^{n\times1}$ is the elastic deformation loss moment of the cables, δW_s represents the elastic potential energy of the cables, and $\boldsymbol{\tau}_s\in\boldsymbol{R}^{n\times1}$ is the driving joint change torque. $\boldsymbol{l}=\left[l_{11},l_{12},l_{13},l_{14},\cdots,l_{n1},l_{n2},l_{n3},l_{n4}\right]^T$ is the cables length vector.

Combining equation (4) and equation (7), the relationship between the cables length change and the torque is:

$$\boldsymbol{J}_\theta \boldsymbol{f} = \boldsymbol{\tau}_s + \boldsymbol{\tau}_\theta \tag{8}$$

where

$$\boldsymbol{J}_\theta = \begin{bmatrix} \boldsymbol{J}_{q1}^T & \boldsymbol{0}_{1\times4} & \cdots & \boldsymbol{0}_{1\times4} \\ \boldsymbol{0}_{1\times4} & \boldsymbol{J}_{q2}^T & \cdots & \boldsymbol{0}_{1\times4} \\ \vdots & \vdots & \ddots & \vdots \\ \boldsymbol{0}_{1\times4} & \boldsymbol{0}_{1\times4} & \cdots & \boldsymbol{J}_{qi}^T \end{bmatrix} \in \boldsymbol{R}^{n\times4n} \tag{9}$$

Assuming that the cables have the same cross-sectional area S and elastic modulus E, the elastic loss energy on the cable can be deduced through energy conservation as:

$$\begin{aligned} W_s = &\left[\frac{f_{11}^2}{ES}l_{11} + \frac{f_{12}^2}{ES}l_{12} + \frac{f_{13}^2}{ES}l_{13} + \frac{f_{14}^2}{ES}l_{14}\right] + \cdots \\ &+ \left[\frac{f_{n1}^2}{ES}l_{n1} + \frac{f_{n2}^2}{ES}l_{n2} + \frac{f_{n3}^2}{ES}l_{n3} + \frac{f_{n4}^2}{ES}l_{n4}\right] \end{aligned} \tag{10}$$

the elastic loss energy of the equation (10) can be obtained by taking the partial derivative of $\boldsymbol{\theta}_i$

$$\boldsymbol{\tau}_s = \left[\frac{\partial W_s}{\partial \theta_1}\frac{\partial W_s}{\partial \theta_2}\cdots\frac{\partial W_s}{\partial \theta_n}\right]^T = \frac{\boldsymbol{J}_\theta \boldsymbol{f}_s}{ES} \tag{11}$$

where $\boldsymbol{f}_s = \left[f_{11}^2, f_{12}^2, f_{13}^2, f_{14}^2, \cdots, f_{n1}^2, f_{n2}^2, f_{n3}^2, f_{n4}^2\right]^T$, which can be obtained by force sensors in practical applications.

Consider the cable-driven space manipulator in the microgravity environment of space, the dynamic equation of the cable-driven space manipulator is expressed as

$$\boldsymbol{M}(\boldsymbol{\theta})\ddot{\boldsymbol{\theta}} + \boldsymbol{C}(\boldsymbol{\theta},\dot{\boldsymbol{\theta}})\dot{\boldsymbol{\theta}} + \boldsymbol{\tau}_s = \boldsymbol{J}_\theta \boldsymbol{f} + \boldsymbol{d} \tag{12}$$

where $\boldsymbol{\theta} \in \boldsymbol{R}^{n\times1}$ is the generalized joint variables, $\boldsymbol{M}(\boldsymbol{\theta}) \in \boldsymbol{R}^{n\times n}$ is the inertial matrix, $\boldsymbol{C}(\boldsymbol{\theta},\dot{\boldsymbol{\theta}}) \in \boldsymbol{R}^{n\times n}$ represents the Coriolis force and centrifugal force matrix. $\boldsymbol{d} \in \boldsymbol{R}^{n\times1}$ represents the external disturbance which varies with time.

In the following section, we will delve into the trajectory tracking control for the cable-driven space manipulator described by equation (12), which aims to enable the joints of the manipulator $\boldsymbol{\theta}$ to accurately track the desired trajectory $\boldsymbol{\theta}_d$.

3 Observer design and controller design

3.1 Observer Design

From the equation(12), the disturbance term can be expressed as

$$\boldsymbol{d} = \boldsymbol{J}_\theta \boldsymbol{f} - \boldsymbol{M}(\boldsymbol{\theta})\ddot{\boldsymbol{\theta}} - \boldsymbol{C}(\boldsymbol{\theta},\dot{\boldsymbol{\theta}})\dot{\boldsymbol{\theta}} - \boldsymbol{\tau}_s \tag{13}$$

Therefore, the disturbance observer is designed to

$$\begin{aligned} \dot{\hat{\boldsymbol{d}}} = &-\boldsymbol{L}(\boldsymbol{e},\dot{\boldsymbol{e}})\hat{\boldsymbol{d}} \\ &+\boldsymbol{L}(\boldsymbol{e},\dot{\boldsymbol{e}})\left(\boldsymbol{M}(\boldsymbol{\theta})\ddot{\boldsymbol{e}} + \boldsymbol{C}(\boldsymbol{\theta},\dot{\boldsymbol{\theta}})\dot{\boldsymbol{e}} + \boldsymbol{\tau}_s - \boldsymbol{J}_\theta \boldsymbol{f}\right) \end{aligned} \tag{14}$$

where $-\boldsymbol{L}(\boldsymbol{e},\dot{\boldsymbol{e}}) \in \boldsymbol{R}^{n\times n}$ is a set of functional diversions that needs to be constructed in the future, $\dot{\hat{\boldsymbol{d}}} \in \boldsymbol{R}^{n\times1}$ is the interference estimation value obtained by the observed.

Since the priori information of the disturbance is unknown, which can be considered that it changes slowly, therefore, it is reasonable to assume:

$$\dot{\boldsymbol{d}} = 0 \tag{15}$$

Define the disturbance observer error as:

$$\tilde{\boldsymbol{d}} = \boldsymbol{d} - \hat{\boldsymbol{d}} \tag{16}$$

substituting(13),(14), and (15) into (16):

$$\dot{\tilde{\boldsymbol{d}}} = \dot{\boldsymbol{d}} - \dot{\hat{\boldsymbol{d}}} = \boldsymbol{L}(\boldsymbol{e},\dot{\boldsymbol{e}})\hat{\boldsymbol{d}} - \boldsymbol{L}(\boldsymbol{e},\dot{\boldsymbol{e}})\boldsymbol{d} \tag{17}$$

then

$$\dot{\tilde{\boldsymbol{d}}} + \boldsymbol{L}(\boldsymbol{e},\dot{\boldsymbol{e}})\tilde{\boldsymbol{d}} = 0 \tag{18}$$

Therefore, choosing $\boldsymbol{L}(\boldsymbol{e},\dot{\boldsymbol{e}})$ appropriately can make the disturbance observer globally asymptotically stable.

Given the presence of measurement noise and the inherent difficulty in obtaining accurate acceleration signals in practical engineering scenarios, including the challenge of constructing the acceleration signal from velocity signals, the disturbance observer (14) will be suitably modified.

Define an auxiliary variable $\boldsymbol{z} \in \boldsymbol{R}^{n\times1}$ as:

$$\boldsymbol{z} = \hat{\boldsymbol{d}} - \boldsymbol{p}(\boldsymbol{e},\dot{\boldsymbol{e}}) \tag{19}$$

where $\boldsymbol{p}(\boldsymbol{e},\dot{\boldsymbol{e}}) \in \boldsymbol{R}^{n\times1}$ is function vector that needs to be constructed.

$\boldsymbol{L}(\boldsymbol{e},\dot{\boldsymbol{e}})$ in the equation (14) can be designed as follows:

$$\boldsymbol{L}(\boldsymbol{e},\dot{\boldsymbol{e}})\boldsymbol{M}(\boldsymbol{e})\ddot{\boldsymbol{e}} = \begin{bmatrix} \dfrac{\partial \boldsymbol{p}(\boldsymbol{e},\dot{\boldsymbol{e}})}{\partial \boldsymbol{e}} & \dfrac{\partial \boldsymbol{p}(\boldsymbol{e},\dot{\boldsymbol{e}})}{\partial \dot{\boldsymbol{e}}} \end{bmatrix} \begin{bmatrix} \dot{\boldsymbol{e}} \\ \ddot{\boldsymbol{e}} \end{bmatrix} \tag{20}$$

Combining (14) (19) and (20) we get

$$\begin{aligned} \dot{\boldsymbol{z}} &= \dot{\hat{\boldsymbol{d}}} - \frac{\mathrm{d}\boldsymbol{p}(\boldsymbol{e},\dot{\boldsymbol{e}})}{\mathrm{dt}} \\ &= \dot{\hat{\boldsymbol{d}}} - \begin{bmatrix} \dfrac{\partial \boldsymbol{p}(\boldsymbol{e},\dot{\boldsymbol{e}})}{\partial \boldsymbol{e}} & \dfrac{\partial \boldsymbol{p}(\boldsymbol{e},\dot{\boldsymbol{e}})}{\partial \dot{\boldsymbol{e}}} \end{bmatrix} \begin{bmatrix} \dot{\boldsymbol{e}} \\ \ddot{\boldsymbol{e}} \end{bmatrix} \\ &= -\boldsymbol{L}(\boldsymbol{e},\dot{\boldsymbol{e}})\left(\boldsymbol{z} + \boldsymbol{p}(\boldsymbol{e},\dot{\boldsymbol{e}})\right) + \boldsymbol{L}(\boldsymbol{e},\dot{\boldsymbol{e}})\left(\boldsymbol{C}(\boldsymbol{e},\dot{\boldsymbol{e}})\dot{\boldsymbol{e}} - \boldsymbol{J}_\theta \boldsymbol{f} + \boldsymbol{\tau}_s\right) \end{aligned} \tag{21}$$

therefore, the disturbance observer can be expressed as:

$$\begin{cases} \dot{\boldsymbol{z}} = -\boldsymbol{L}(\boldsymbol{e},\dot{\boldsymbol{e}})\boldsymbol{z} + \boldsymbol{L}(\boldsymbol{e},\dot{\boldsymbol{e}})\left(\boldsymbol{C}(\boldsymbol{\theta},\dot{\boldsymbol{\theta}})\dot{\boldsymbol{e}} - \boldsymbol{J}_\theta \boldsymbol{f} + \boldsymbol{\tau}_s - \boldsymbol{p}(\boldsymbol{e},\dot{\boldsymbol{e}})\right) \\ \hat{\boldsymbol{d}} = \boldsymbol{z} + \boldsymbol{p}(\boldsymbol{e},\dot{\boldsymbol{e}}) \end{cases} \tag{22}$$

The disturbance observer proposed in (22) has two parameters and to be designed, so one of them must be selected so that the observer is asymptotic stable.

3.2 Controller design

Define the following symbols

$$\boldsymbol{A}_{0\sim n-1} = \begin{bmatrix} \boldsymbol{A}_0 & \boldsymbol{A}_1 & \cdots & \boldsymbol{A}_{n-1} \end{bmatrix}$$

$$\boldsymbol{\Phi}(\boldsymbol{A}_{0\sim n-1}) = \begin{bmatrix} \boldsymbol{0} & \boldsymbol{I} & & \\ & & \ddots & \\ & & & \boldsymbol{I} \\ -\boldsymbol{A}_0 & -\boldsymbol{A}_1 & \cdots & -\boldsymbol{A}_{n-1} \end{bmatrix}$$

Let the joints angle $\boldsymbol{\theta}$ of the manipulator track the expected value $\boldsymbol{\theta}_d$, the tracking error gives

$$\boldsymbol{e} = \boldsymbol{\theta} - \boldsymbol{\theta}_d \tag{23}$$

Substituting the equation (23) into (12), we get

$$\ddot{\boldsymbol{e}} = \boldsymbol{M}^{-1}(\boldsymbol{\theta})\left[\boldsymbol{J}_\theta \boldsymbol{f} + \boldsymbol{d} - \boldsymbol{\tau}_s - \boldsymbol{C}(\boldsymbol{\theta},\dot{\boldsymbol{\theta}})\left(\dot{\boldsymbol{\theta}}_d + \dot{\boldsymbol{e}}\right)\right] - \ddot{\boldsymbol{\theta}}_d \tag{24}$$

where

$$\begin{cases} \boldsymbol{B}(\theta)=\boldsymbol{M}^{-1}(\theta) \\ \boldsymbol{h}(\theta,\dot{\theta})=-\boldsymbol{M}^{-1}(\theta)\left[\boldsymbol{C}(\theta,\dot{\theta})(\dot{\boldsymbol{\theta}}_d+\dot{\boldsymbol{e}})+\boldsymbol{\tau}_s\right]-\ddot{\boldsymbol{\theta}}_d \\ \Delta\boldsymbol{h}(\theta,\dot{\theta})=\boldsymbol{M}^{-1}(\theta)\boldsymbol{d} \\ \boldsymbol{J}_\theta\boldsymbol{f}=\boldsymbol{u}_0+\boldsymbol{u}_a \end{cases}$$

Furthermore, the equation (24) can be expressed as

$$\ddot{\boldsymbol{e}}=\boldsymbol{h}(\theta,\dot{\theta})+\Delta\boldsymbol{h}(\theta,\dot{\theta})+\boldsymbol{B}(\theta)(\boldsymbol{u}_0+\boldsymbol{u}_a) \tag{25}$$

where $\boldsymbol{u}_0$ represents the partial control input of the constant coefficients closed-loop system, and $\boldsymbol{u}_a$ is the external signal control input.

3.3 Controller stability analysis

Based on the full-actuated system controller design method proposed in [12], the closed-loop system control input in the equation (25) can be designed as:

$$\boldsymbol{u}_0=-\boldsymbol{B}^{-1}(\theta)\left[\boldsymbol{A}_{0\sim1}\boldsymbol{e}^{(0\sim1)}+\boldsymbol{h}(\theta,\dot{\theta})+\Delta\boldsymbol{h}(\theta,\dot{\theta})\right] \tag{26}$$

where $\boldsymbol{A}_{0\sim1}$ is the given coefficient matrix. Combining equations (21) and (23), the linear constant coefficient closed-loop system can be obtained as follows:

$$\ddot{\boldsymbol{e}}+\boldsymbol{A}_{0\sim n-1}\boldsymbol{e}^{(0\sim n-1)}=0 \tag{27}$$

The equivalent conversion of the equation (27) into the state space form is:

$$\dot{\boldsymbol{e}}^{(0\sim1)}=\Phi\left(\boldsymbol{A}_{0\sim1}\right)\boldsymbol{e}^{(0\sim1)} \tag{28}$$

To make the linear constant coefficient closed-loop system stable, the problem is transformed into selecting the coefficients so that the $\Phi\left(\boldsymbol{A}_{0\sim1}\right)$ is Hurwitz matrix.

Lemma 1[13]: For an arbitrary matrix $\boldsymbol{F}\in\mathbb{R}^{mn\times mn}$, all matrices $\boldsymbol{A}_{0\sim m-1}$ and non-singular matrices $\boldsymbol{V}\in\mathbb{R}^{mn\times mn}$ satisfy

$$\boldsymbol{\Phi}(\boldsymbol{A}_{0\sim m-1})=\boldsymbol{V}\boldsymbol{F}\boldsymbol{V}^{-1}$$

where

$$\boldsymbol{A}_{0\sim m-1}=-\boldsymbol{Z}\boldsymbol{F}^n\boldsymbol{V}^{-1}(\boldsymbol{Z},\boldsymbol{F})$$

$$\boldsymbol{V}(\boldsymbol{Z},\boldsymbol{F})=\begin{bmatrix}\boldsymbol{Z}\\ \boldsymbol{Z}\boldsymbol{F}\\ \vdots\\ \boldsymbol{Z}\boldsymbol{F}^{n-1}\end{bmatrix}$$

and $\boldsymbol{Z}$ is the parameter matrix, and satisfies:

$$\det\boldsymbol{V}(\boldsymbol{Z},\boldsymbol{F})\neq0$$

It can be seen that to ensure the stability of the closed-loop system (25), It is important to choose the matrix $\boldsymbol{F}$ and $\boldsymbol{Z}$ reasonably.

For simplicity, the matrix $\boldsymbol{F}$ and $\boldsymbol{Z}$ are selected as:

$$\begin{cases}\boldsymbol{F}=\mathrm{diag}(\boldsymbol{\Lambda}_1,\boldsymbol{\Lambda}_2)\\ \boldsymbol{Z}=[\boldsymbol{Z}_1,\boldsymbol{Z}_2]\end{cases} \tag{29}$$

where

$$\begin{cases}\boldsymbol{\Lambda}_i=\mathrm{diag}(\lambda_{ij})\\ \boldsymbol{Z}_i=\mathrm{diag}(z_{ij})\end{cases}\quad i=1,2;\ j=1,2,\cdots,n \tag{30}$$

Let

$$\boldsymbol{V}=\begin{bmatrix}\boldsymbol{Z}\\ \boldsymbol{Z}\boldsymbol{F}\end{bmatrix} \tag{31}$$

from Lamma 1, the gain matrix is

$$\begin{aligned}\boldsymbol{A}_{0\sim1}&=-\boldsymbol{Z}\boldsymbol{F}^2\boldsymbol{V}^{-1}(\boldsymbol{Z},\boldsymbol{F})\\ &=\begin{bmatrix}\boldsymbol{\Lambda}_1\boldsymbol{\Lambda}_2 & -(\boldsymbol{\Lambda}_1+\boldsymbol{\Lambda}_2)\end{bmatrix}\end{aligned} \tag{32}$$

therefore, $\boldsymbol{A}_{0\sim1}$ is only related to λ_{ij}.

$$\boldsymbol{\lambda}=[\lambda_{11}\quad\cdots\quad\lambda_{1n}\quad\lambda_{21}\quad\cdots\quad\lambda_{2n}] \tag{33}$$

λ_{ij} is the eigenvalue of the closed-loop system, the selection problem of the gain matrix $\boldsymbol{A}_{0\sim1}$ is transformed into finding the appropriate closed-loop eigenvalue to guarantee the system stable. When the conditions meet $\lambda_{ij}<0,\ i=1,2,\ j=1,2,\cdots n$ can ensure the stability of the equation (27).

To improve the convergence speed of linear systems, a global fast terminal sliding mode controller is proposed in [14] as follows:

$$\boldsymbol{s}=\dot{\boldsymbol{e}}+\alpha\boldsymbol{e}+\beta\boldsymbol{e}^{q/p} \tag{34}$$

where $\alpha,\beta>0$, p and $q(p>q)$ are positive odd numbers.

The external signal control input of equation (22) can be designed as:

$$\boldsymbol{u}_a(t)=-\boldsymbol{B}^{-1}(\boldsymbol{e})\left[\boldsymbol{h}(\ddot{\boldsymbol{e}},\dot{\boldsymbol{e}},t)+\boldsymbol{w}\right] \tag{35}$$

where

$$\boldsymbol{w}=\alpha\dot{\boldsymbol{e}}+\beta\frac{\mathrm{d}}{\mathrm{d}t}\boldsymbol{e}^{q/p}+\phi\boldsymbol{s}+\gamma\boldsymbol{s}^{q/p} \tag{36}$$

and $\phi,\ \gamma>0$.

Theorem 1: *Consider the system (25) under the controller designed as equation (26) and equation(35), if the external disturbance estimated by the observer* (22), *then the resulting closed-loop system is asymptotically stable.*

Proof. Choose the Lyapunov function as:

$$\boldsymbol{V}=\frac{1}{2}\boldsymbol{s}\boldsymbol{s}^T \tag{37}$$

Derivative the equation (37), then:

$$\begin{aligned}\dot{\boldsymbol{V}}&=\boldsymbol{s}^T\dot{\boldsymbol{s}}\\ &=\boldsymbol{s}^T(\ddot{\boldsymbol{e}}+\alpha\dot{\boldsymbol{e}}+\beta\frac{\mathrm{d}}{\mathrm{d}t}\boldsymbol{e}^{q/p})\\ &=\boldsymbol{s}^T\left\{\Delta\boldsymbol{h}(\dot{\boldsymbol{e}},\boldsymbol{e},t)-\boldsymbol{w}+\alpha\dot{\boldsymbol{e}}+\beta\frac{\mathrm{d}}{\mathrm{d}t}\boldsymbol{e}^{q/p}\right\}\\ &=\boldsymbol{s}^T(-\phi\boldsymbol{s}-\gamma\boldsymbol{s}^{q/p}+\Delta\boldsymbol{h}(\dot{\boldsymbol{e}},\boldsymbol{e},t))\\ &=-\phi\boldsymbol{s}^2-\gamma\boldsymbol{s}^{(q+p)/p}+\boldsymbol{s}\Delta\boldsymbol{h}(\dot{\boldsymbol{e}},\boldsymbol{e},t)\end{aligned} \tag{38}$$

Since p,q are odd number, then $(p+q)/p$ is an even number, so when the parameter is $\gamma\geq\left|\frac{1}{\boldsymbol{s}^{q/p}}\right|\left|\Delta\boldsymbol{h}(\dot{\boldsymbol{e}},\boldsymbol{e},t)\right|$, substituting it into (38) gives $\dot{V}\leq0$.

Remark 1: In a real physical system, the cable tension cannot be infinite, so it is necessary to add saturation function to handle unrealistic control inputs. The input saturation function gives

$$\boldsymbol{\Gamma}=\tau_{max}\frac{\boldsymbol{\tau}}{|\boldsymbol{\tau}|+\tau_{max}} \tag{39}$$

where τ_{max} is the maximum torque that system can output.

4 Numerical simulation

On the space mission, the cable-driven space manipulator is usually installed on large spacecraft. As shown in Fig. 3,

the mass of the manipulator system is much smaller than the spacecraft base, The cable-driven space manipulator can be regarded as mounted on a fixed base.

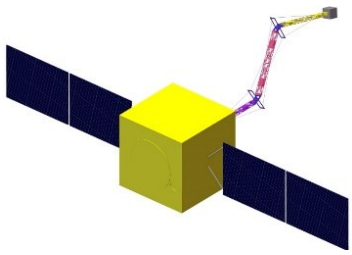

Fig. 3: Tendon-driven space manipulator task operation

Then, the schematic diagram of the double-joint module cable-driven space manipulator shows in Fig. 4.

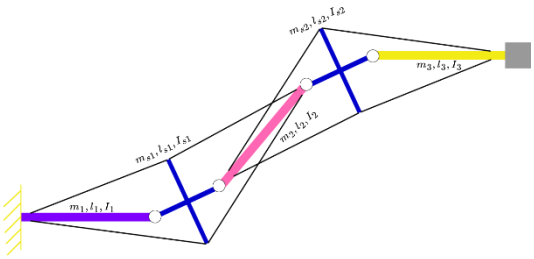

Fig. 4: Schematic diagram of Cable-driven manipulator

Utilizing the Matlab simulation platform, this study addresses the trajectory tracking control challenge inherent in the cable-driven space manipulator with a double-joint module. Essential to our investigation are the physical structure parameters of the tendon-driven space manipulator system, meticulously outlined in Table 1.

Table 1: Physical structure parameter table of manipulators

Physical Structure	Parameters
Manipulator Mass	m_1=5.982kg m_2 = 10.343kg m_3 = 5.982kg
Spreader Mass	m_s = 1.951kg
Manipulator Length	$L_1 = L_2 = L_3 = 1.955$m
Spreader Length	L_s = 0.101m
Spreader Width	h = 0.37m
Capstan Radius	r = 0.03m

The initial state of the double-joint module manipulator system is $\boldsymbol{\theta} = [0.2 \quad 0.1]^T$, $\dot{\boldsymbol{\theta}} = [0 \quad 0]^T$. The expected trajectory of the joint is: $\boldsymbol{\theta}_d = \left[0.1 + 0.2\cos(\frac{\pi t}{20}) \quad 0.5 - 0.5\cos(\frac{\pi t}{40})\right]^T$. The external disturbance is $d(t) = \left[0.1\sin\left(\frac{1}{25}\pi t\right) \quad 0.1\cos\left(\frac{1}{25}\pi t\right)\right]^T$

In order to reflect the superiority of the proposed algorithm under the full-actuated system method. Compare it with linear sliding mode and fast non-singular terminal sliding mode controller in [15].

Finally, given that sudden load changes often occur in actual processes, such as the cable-driven space manipulator suddenly grabbing a heavy object, we assume that the manipulator tip suddenly grabs a 5kg object.

The simulation results show as follows:

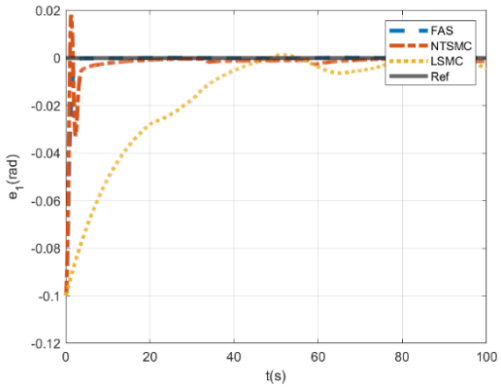

Fig. 5: Joint 1 tracking error

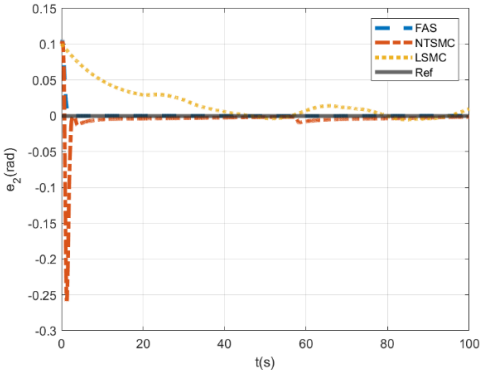

Fig. 6: Joint 2 tracking error

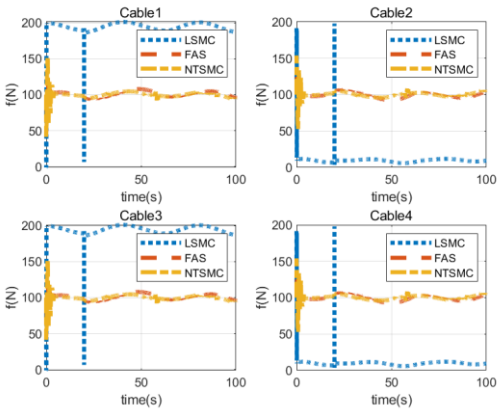

Fig. 7: Control input of joint1

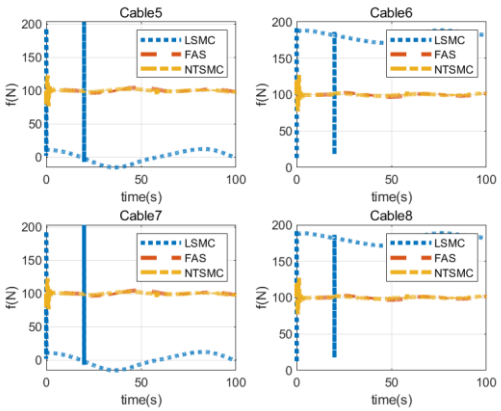

Fig. 8: Control input of joint2

Fig. 5~Fig. 6 depict the corresponding tracking errors. Fig. 7~Fig. 8 provide insights into the tension in the cables across each joint module. Through the comprehensive analysis of the simulation diagrams, it is evident that the terminal sliding mode composite controller, designed based on the full-actuated system method proposed in this paper, outperforms both the linear sliding mode and the new fast non-singular terminal sliding mode. The controller exhibits enhanced trajectory tracking speed and superior stability, thereby demonstrating notable advantages in achieving high precision trajectory tracking control for cable-driven space manipulators.

5 Conclusion

A controller design aimed at achieving high precision performance for the cable-driven space manipulator is presented in this paper. Considering the impact of high-frequency variations in cable tension deformation during the transmission process, a kinematic and dynamic mapping relationship between cable tension and joint angles is established using the principles of virtual work and the Lagrange method. Based on the fully actuated system method, a terminal sliding mode controller is introduced to facilitate trajectory tracking for the cable-driven space manipulator. The simulation results demonstrate the effectiveness of the designed controller in effectively achieving high precision trajectory tracking.

References

[1] M. Shan, J. Guo, and E. Gill, Review and comparison of active space debris capturing and removal methods, Prog. Aerosp. Sci, 80: 18–32, 2016.

[2] G. Jorgensen and E. Bains, SRMS history, evolution and lessons learned, in Proc. AIAA SPACE Conf. Expo, 2011: p. 7277.

[3] N. Sato and Y. Wakabayashi, JEMRMS design features and topics from testing, in Proc. Int. Symp. Artif. Intell. Robot. Autom. Space, 2001.

[4] J. Wei, D. Cao, L. Liu, W. Huang, Global mode method for dynamic modeling of a flexible-link flexible-joint manipulator with tip mass, Appl. Math. Model, 2017: 787–805.

[5] X. Liu, H. Li, J. Wang, G. Cai, Dynamics analysis of flexible space robot with joint friction, Aerosp. Sci. Technol, 2015: 164–176.

[6] W. Xu, Z. Hu, Y. Zhang, B. Liang, On-orbit identifying the inertia parameters of space robotic systems using simple equivalent dynamics, 2017: 131–142.

[7] S. Ulrich, J. Z. Sasiadek, I. Barkana, Modeling and direct adaptive control of a flexible-joint manipulator, Guid. Control Dyn, 2012: 25–39.

[8] S. Ulrich, J. Z. Sasiadek, On the simple adaptive control of flexible-Joint space manipulators with uncertainties, Aerospace Robotics II, Springer International Publishing, Switzerland, 2015: 13–23.

[9] Alqumsan. A, Khoo. S, Norton. M, Multi-surface sliding mode control of continuum robots with mismatched uncertainties. Meccanica, 54: 2307-2316, 2019.

[10] W. Zhang, X. Ye, L. Jiang, et al. Output feedback control for free-floating space robotic manipulators base on adaptive fuzzy neural network, Aerosp. Sci. Technol, 29: 135–143, 2013.

[11] Sun. H, Huang. L, He, L. Research on the Trajectory Tracking Control of a 6-DOF Manipulator Based on Fully-Actuated System Models. Syst Sci Complex 35: 641–659, 2022.

[12] G. R. Duan, High-order system approaches I. Fully-actuated systems and parametric design, Acta Automatica Sinica, 46(7): 1333–1345, 2020.

[13] G. R. Duan, High-order fully actuated system approaches: Part I. Models and basic procedure, International Journal of Systems Science, 52(2): 422-435, 2021.

[14] Hu. Q, Li. B, Xiao. B, Zhang. Y, et al. Control Allocation for Spacecraft Under Actuator Faults. Springer ,2021.

[15] Feng Y, Yu X, Man Z. Non-singular terminal sliding mode control of rigid manipulators. Automatica, 38(12):2159-2167, 2002.

Proceedings of the 3rd Conference on Fully Actuated System Theory and Applications
May 10-12, 2024, Shenzhen, China

Predictor-based Sliding Mode Control for Systems with Input Delays

Xinyu Zhang, Yu Wang*, Jun Hao
College of Automation
Jiangsu University of Science and Technology
Zhenjiang, China
zhangxyu_123@163.com

***Abstract*—In this paper, a predictor-based sliding mode control law is proposed for discrete-time systems with input delays to reject unknown disturbances. First, a disturbance observer is built to estimate the unkown disturbance signal, and the boundedness of estimation error of disturbance observer is obtained. Next, a predictor is designed to transform the system with input delay to a system without time delay, solving the delay compensation problem of discrete-time systems with input delays. Finally, a new predictor-based sliding mode control law is proposed to construct the sliding surface by using the predictors and the unknown disturbance signal. The unknown disturbance signal is estimated by the designed observer. It is noted that the sliding surface is constructed by utilizing the predictor, rather than by using system state. A numerical example is given to show the effectiveness of this predictor-based sliding mode control law.**

***Index Terms*—predictor, input delays, sliding mode control, disturbance observer**

I. Introduction

There are often time delays in a variety of real-world technical issues, including transmission, communication, and satellite systems [1]. In the high precision pointing maneuver mission, time-delay is often considered in the precise control of large angle attitude maneuver, which will lead to the increase of attitude error and the decrease of control performance, even lead to the instability of the system. Because of this, there has been a lot of interest in the design of non-predictor based sliding mode controllers for input delayed systems in recent years [2]–[4]. These controllers are intended to reject disturbances and accurately manage and deal with delays.

There are different disturbance attenuation controls for input delayed systems in recent years. The most typical one is Smith predictor-based feedback control [5], which is also called pure delay compensation method. This method solves the control problem of pure time-delay system theoretically, but it also has great disadvantages [6]. It is highly dependent on the accurate system model. If the model is inaccurate, the control performance will be degraded and the adaptive performance will be poor. In [7], Brahim extended the work in [5], and proposed a system combining cascade control with Smith predictor-based feedback control, which can improve the performance of the system especially when disturbance occurs. In [8], a simple adaptive law is proposed to improve the performance of Smith predictor by changing the controlled variables and set values step by step, and it is suitable for more control. Compared with adaptive control, sliding mode control (SMC) does not need an accurate system model and has a fast response speed. The disturbance attenuation based on sliding mode control is designed, by introducing sliding mode surface and sliding mode reaching law. The system state can be quickly adjusted and disturbance attenuation can be achieved, and the system has strong robustness and anti-disturbance ability. In [9], the combination of Smith predictor and sliding mode control is used to improve the robustness of the system.

The basic idea of anti-disturbance control of predictor-based sliding mode control is to constuct a predictor to compensate the time delay for input-delayed systems and use the the sliding mode control method to reject the disturbance. Predictor-based feedback control for input time-delay systems is designed by constructing a predictor to transform the original time-delay system to a time-delay-free system, and then feedback control is designed based on the transformed system. This method can compensate the influence of time delay on the system and has a better disturbance attenuation ability. Compared with state feedback and output feedback, this predictor-based method avoids constructing complex Lyapunov functions and does not need to solve complex linear matrix inequalities. Its biggest benefit is in its strong robustness, rapid reaction, easy implementation, and high precision control [10], which is commonly utilized in systems with disturbances. In the past, the majority of the research on sliding mode control was carried out in continuous time domain. However, the continuous-time sliding mode controller can only show good performance when the sampling time is very small. With the expanding application of digital controllers, discrete-time SMC receives ever more attention. Gao in [11] presented a way to deal with discrete SMC, and produced a pioneering effort for the design of this type of system. The work in [12] introduces both the quasi-sliding mode band and the reaching law. The state of the system is constrained to a band surrounding the sliding hyperplane by a new reaching law.

This work was supported by the Doctoral Research Initiation Fund of Jiangsu University of Science and Technology under Grant No. 1032932303.

The issue in [11] that the sliding variable's rate of change is a constant additive proportional descent, and the sliding variable's rate is modified in [13]. The system is more robust because the ratio is always constrained and the drop speed is slower than in [11]. The reaching rule is established on the exponential term to adjust to the change in the switching function, which is different between the work in [14] and [11]–[13]. The reaching law designed can ensure that the width of the quasi-sliding mode domain is small and the system states converge to the quasi-sliding band in a finite time.

The aim of this paper is to construct a new predictor-based sliding mode control for systems with input delays such that the disturbance attenuation capacity can be improved. This paper's primary contents are: (1) The compensation problem of input delay in discrete-time systems is solved by a predictor-based feedback control; (2) A disturbance observer is given to estimate the unknown disturbance signal, and it is necessary to give the boundness of the estimation error of the disturbance observer; (3) The sliding surface is constructed by utilizing the predictior and thus a new predictor-based sliding mode control law is presented.

II. Problem Formulation

Consider the following discrete-time system with input delay:

$$x(k+1) = Ax(k) + Bu(k-h) + B_d d(k), \tag{1}$$

where $x(k) \in R^n$ is the system state, $u(k) \in R^m$ is the input variable, and $d(k) \in R^q$ denotes an unknown external disturbance. Input delay h is an integer and satisfies $h > 0$. For the input matrix B and disturbance matrix B_d, the condition $\mathrm{rank}(B) = m$ and $\mathrm{rank}(B_d) = q$ should be ensured, that is, B and B_d have full column rank.

Moreover, the following assumptions should be given throughout this paper.

Assumption 1: The mtrix pair (A, B) is fully controllable.

Assumption 2: The definitions about the unknown disturbance signal are given by $d(k) \triangleq [d_1(k), d_2(k), ..., d_q(k)]^T$ and $d_{\delta i}(k) \triangleq d_i(k+1) - d_i(k)$, $i = 1, 2, ..., q$, respectively. For the unknown disturbance $d(k)$, it is assumed that there are two positive scalars α_i and β_i that satisfy $|d_i(k)| \leq \alpha_i$ and $|d_{\delta i}(k)| \leq \beta_i$.

To our knowledge, discrete-time variable structure control (VSC) is an useful method to deal with the problem of disturbance rejection for system with unknown bounded disturbances. In the past decades, a variety of discrete-time VSC strategies with different reaching laws were proposed to solve the sliding mode vibration problem. However, these discrete-time VSC strategies are rarely used in systems with both input delays and unknown disturbances. Thus, for system (1), the discrete-time VSC method is studied in this paper to reject an unknown disturbance. For discrete-time VSC, the following definitions given in [15] are necessary.

Definition 1: A discrete-time VSC system moving in a way that meets the requirements in [15] is said to be in quasi-sliding mode. The frequency range that contains quasi-sliding mode is known as the quasi-sliding mode frequency band and is described as follows:

$$\{x : |s_i(x)| < \delta_i,\ i = 1, ..., m\}, \tag{2}$$

where $2\delta = 2[\delta_1, ..., \delta_m]^{\mathrm{T}} \in R^m$ is the bandwidth of the quasi-sliding mode band. The sliding mode becomes an ideal sliding mode when $\delta_i = 0$,$i = 1, ..., m$.

In [16], the disturbance information was estimated by the bound of the disturbance, and then a discrete-time sliding mode control law was given to reject an unknown disturbance by using the bound of the disturbance. In order to improve the capacity of the corresponding closed-loop system to reject the unknown disturbance, a disturbance observer is used in the following part.

III. Disturbance Observer

In this section, a disturbance observer is proposed to estimate the unknown disturbance $d(k)$. According to the main idea in [17], the following disturbance observer

$$\begin{aligned} z(k+1) &= \Lambda\hat{d}(k) + (\Lambda - I_q)B_d^{\dagger}(Ax(k) + Bu(k-h) \\ \hat{d}(k) &= z(k) - (\Lambda - I_q)B_d^{\dagger}x(k) \end{aligned} \tag{3}$$

is used to estimate $d(k)$. Where $\hat{d}(k)$ is the disturbance estimation, $z(k)$ is an auxiliary variable, $B_d^{\dagger} \triangleq \left(B_d^T B_d\right)^{-1} B_d^T$ satisfies $B_d^{\dagger} B_d = \left(B_d^T B_d\right)^{-1} B_d^T B_d = I$, and $\Lambda = \mathrm{diag}\{\lambda_1, \lambda_2, ..., \lambda_q\}$ with $|\lambda_i| < 1$, $i = 1, 2, ..., q$.

Let the estimated disturbance error be

$$\tilde{d}(k) = d(k) - \hat{d}(k). \tag{4}$$

For the above disturbance error, it follows from the idea in [19], the bound can be calculated by

$$\left|\tilde{d}_i(k)\right| \leq \frac{\beta_i}{1 - |\lambda_i|}. \tag{5}$$

For an unknown disturbance signal, it follows from the above expression that the bound of the disturbance error is associated with the known parameters β_i and λ_i. Thus, in the design of sliding-mode control laws, the disturbance error can be estimated by using the relation (5).

It is widely known that predictor-based feedback control is an effective method for system (1) to compensate the negative influence from time delays, and the sliding mode control is always used to reject external disturbances. Thus, for systems shown as (1), the predictor-based sliding mode control is naturally applied to time delay compensation and disturbance suppression. In the following, a standard predictor is first considered for system (1), and then the sliding surface of the sliding mode control is constructed by using the predictor state. In the previous works, the sliding surface of the sliding mode control is often designed by using the system state, rather than using the predictor state. Morever, the unknown disturbance information in the designed sliding mode control law is estimated by the disturbance observer (3).

IV. Predictor-based Sliding Mode Control

In this section, the standard predictor

$$x_{\rm p0}(k) = A^h x(k) + \sum_{j=k-h}^{k-1} A^{k-1-j} B u(j) \tag{6}$$

is first considered for system (1). By using the predictor (6) and the expression (1), the dynamics of predictor $x_{\rm p0}(k)$ is given by

$$\begin{aligned} x_{\rm p0}(k+1) &= A^h x(k+1) + \sum_{j=k-h+1}^{k} A^{k-j} B u(j) \\ &= A x_{\rm p0}(k) + B u(k) + A^h B_d d(k). \end{aligned} \tag{7}$$

Obviously, the predictor system (7) is a system without time delay. Thus, predictor $x_{\rm p0}(k)$ can be regarded as a state transformation that converts the input-delayed system (1) to the delay-free system (7). In adition, it follows from the state transformation (6) that the stability of the closed-loop system of the system (7) under the control law $u(k) = K x_{\rm p0}(k)$ implies the stability of the closed-loop system of the system (1) under the control law $u(k) = K x_{\rm p0}(k)$, where K is designed to satisfy that the system $x(k+1) = (A+BK)x(k)$ is stable. In view of this, a sliding-mode control law can be designed for system (1) by first considering the sliding-mode control method for the system (7).

For the system (7), the sliding surface is constructed as

$$s(k) = C x_{\rm p0}(k), \tag{8}$$

where $s = [s_1, ..., s_m]^{\rm T} \in R^m$, $C = [C_1^{\rm T}, ..., C_m^{\rm T}] \in R^{m\times n}$, $\mathrm{rank}(C) = m$, and the matrix CB is nonsingular.

For discrete-time sliding-mode control, a reaching law is often chosen to design a control law such that the state of the closed-loop system can approach to the sliding surface and then move on the sliding surface. The following standard reaching law proposed by Gao et al. [16]

$$s(k+1) - s(k) = -wTs(k) - \epsilon T \mathrm{sgn}(s(k)) \tag{9}$$

is considered to design the sliding-mode control law. Where

$$\begin{aligned} \mathrm{sgn}\left(s(k)\right) &= \left[\mathrm{sgn}(s_1(k)), \cdots, \mathrm{sgn}(s_m(k))\right]^{\rm T}, \\ \epsilon &> 0, w > 0, 1 - wT > 0, \end{aligned}$$

and T is the sampling period.

From the system (7) and the reaching law (9), the incremental change of sliding surface $s(k)$ is

$$\begin{aligned} & s(k+1) - s(k) \\ = \; & CAx_{\rm p0}(k) + CBu(k) + CA^h B_d d(k) - Cx_{\rm p0}(k) \\ = \; & -wTs(k) - \epsilon T \mathrm{sgn}(s(k)). \end{aligned} \tag{10}$$

It can be deduced from (10) that

$$\begin{aligned} u(k) &= -(CB)^{-1} C(A-I) x_{\rm p0}(k) \\ & \quad -(CB)^{-1}[CA^h B_d d(k) + wTs(k) + \epsilon T \mathrm{sgn}(s(k))]. \end{aligned}$$

Obviously, the above controller is difficult to implement since the existence of the unknown disturbance $d(k)$. In order to make the controller easy to implement, $d(k)$ can be replaced by a disturbance observer $\hat{d}(k)$ in the form of (3). Thus, a sliding mode control law with the disturbance observer $\hat{d}(k)$ is given as

$$\begin{aligned} u(k) &= -(CB)^{-1} C(A-I) x_{\rm p0}(k) \\ & \quad -(CB)^{-1}[CA^h B_d \hat{d}(k) + wTs(k) + \epsilon T \mathrm{sgn}(s(k))]. \end{aligned} \tag{11}$$

This control law is given based on the the standard predictor $x_{\rm p0}(k)$, thus it can be named as the predictor-based sliding mode control law.

By substituting the control law to the expression (10), a new reaching law with the disturbance observation error $\tilde{d}(k)$ is presented by

$$s(k+1) - s(k) = CA^h B_d \tilde{d}(k) - wTs(k) - \epsilon T \mathrm{sgn}(s(k))$$

From this expression, it is further deduced that

$$s(k+1) = (1 - wT)\, s(k) - \epsilon T \mathrm{sgn}(s(k)) + CA^h B_d \tilde{d}(k) \tag{12}$$

For this expression, it is denoted that

$$\bar{D} = CA^h B_d$$

with the matrix $\bar{D} = \left[\bar{d}_{ij}\right] \in \mathbb{R}^{m\times q}$. For convenience, $\bar{D}\tilde{d}(t)$ in the reaching law (12) is denoted as $\phi(t) = \left[\begin{array}{ccc} \phi_1(t) & \cdots & \phi_m(t) \end{array}\right]^{\rm T}$. With this denotion, (12) can be written as

$$s_i(k+1) = s_i(k) - qTs_i(k) - \epsilon T \mathrm{sgn}(s_i(k)) + \phi_i(k) \tag{13}$$

where $|\phi_i(t)| \le \varphi_i, i = 1, 2, \cdots, m$,

$$\varphi_i = \sum_{j=1}^{q} \frac{d_{ij}\beta_j}{1 - |\lambda_j|}. \tag{14}$$

It can be found that the reaching law in (13) is the so-called modified Gao's reaching law in [19]. Thus, it follows from the work in [19] that $s_i(k)$ will converge to a bound region $|s_i(k)| \le \epsilon T + \varphi_i$ in a finite time, where the parameter ϵ is chosen by $\epsilon T > \varphi_i$. In this case, the quasi-sliding mode band $\delta = [\delta_1, ..., \delta_m]^{\rm T} \in R^m$ is given by

$$\delta_i = \epsilon T + \varphi_i, i = 1, 2, \cdots, m \tag{15}$$

For δ_i in (15), it is denoted that $\bar{\delta} = \max_{i=1,\cdots,m}\{\delta_i\}$.

In view that the sliding surface $s(k)$ is constructed by utilizing the predictor $x_{\rm p0}(k)$, thus it is concluded that the predictor state $x_{\rm p0}(k)$ will move on the sliding surface by the predictor-based control law (11) in a finite time. In addtion, it follows from the relation (6) that the system state $x(k)$ will also move on the sliding surface in a finite time.

V. Stability analysis

For discrete-time sliding mode control, the ultimate state of the closed-loop system moves in the neighborhood of the sliding surface $s(k) = 0$. Thus, the stability of the dynamics of the sliding mode in the sliding surface $s(k) = 0$ cannot be obtained. In the following, the stability of the quasi-sliding mode around the sliding surface will be studied by the Lyapunov method.

In this section, it is assumed that the disturbance is matched, that is, $\text{rank}\big([B, A^h B_d]\big) = \text{rank}(B)$.

For the matrix B satisfying $\text{rank}\big([B, A^h B_d]\big) = \text{rank}(B)$, the singular value decomposition

$$B = [U_1, U_2] \left[\begin{array}{c} \sum \\ 0_{(n-m)\times m} \end{array} \right] V^{\mathrm{T}} \tag{16}$$

is considered. Where $U_1 \in R^{n\times m}$, $U_2 \in R^{n\times(n-m)}$, $\Sigma \in R^{m\times m}$ is a diagonal positive-definite matrix, and $V \in R^{m\times m}$ is a unitary matrix. For convenience, it is denoted that $T = \left[\begin{array}{cc} U_2 & U_1 \end{array} \right]^{\mathrm{T}}$. With this denotion, we have

$$\begin{aligned} TB &= \left[\begin{array}{c} U_2^{\mathrm{T}} \\ U_1^{\mathrm{T}} \end{array} \right] \left[\begin{array}{cc} U_1 & U_2 \end{array} \right] \left[\begin{array}{c} \sum \\ 0_{(n-m)\times m} \end{array} \right] V^{\mathrm{T}} \\ &= \left[\begin{array}{c} 0_{(n-m)\times m} \\ \sum V^{\mathrm{T}} \end{array} \right]. \end{aligned}$$

It is obvious that the regular form system of system (7) is given as

$$\begin{aligned} Z_1(k+1) &= A_{11} Z_1(k) + A_{12} Z_2(k) \\ Z_2(k+1) &= A_{21} Z_1(k) + A_{22} Z_2(k) + B_2[u(k) + d(k)] \end{aligned} \tag{17}$$

by the state transformation $Z(k) = T x_{\mathrm{p0}}(k)$. Where $Z_1(k) \in R^{n-m}$, $Z_2(k) \in R^m$, $A_{11} = U_2^{\mathrm{T}} A U_2$, $A_{12} = U_2^{\mathrm{T}} A U_1$, $A_{21} = U_1^{\mathrm{T}} A U_2$, $A_{22} = U_1^{\mathrm{T}} A U_1$, and $B_2 = \sum V^{\mathrm{T}}$ is a nonsigular matrix.

Moreover, by utilizing the the state transformation $Z(k) = T x_{\mathrm{p0}}(k)$, the sliding surface can be rewriten as

$$\begin{aligned} s(k) &= C x_{\mathrm{p0}}(k) = C T^{-1} T x_{\mathrm{p0}}(k) \\ &= \left[\begin{array}{cc} C_1 & C_2 \end{array} \right] \left[\begin{array}{cc} Z_1^{\mathrm{T}}(k) & Z_2^{\mathrm{T}}(k) \end{array} \right]^{\mathrm{T}} \\ &= C_1 Z_1(k) + C_2 Z_2(k). \end{aligned} \tag{18}$$

It follows from (18) and the assumption $|C_2| \neq 0$ that

$$Z_2(k) = C_2^{-1} \left(s(k) - C_1 Z_1(k) \right).$$

By substituting this expression to the expression of $Z_1(k+1)$ in (17) that

$$\begin{aligned} Z_1(k+1) &= A_{11} Z_1(k) + A_{12} C_2^{-1} \left(s(k) - C_1 Z_1(k) \right) \\ &= \left(A_{11} - A_{12} C_2^{-1} C_1 \right) Z_1(k) + A_{12} C_2^{-1} s(k). \end{aligned}$$

From this expression and the reaching law in (12), system (17) can be converted to the following system

$$\begin{aligned} Z_1(k+1) &= \bar{A}_{11} Z_1(k) + \bar{A}_{12} s(k) \\ s(k+1) &= (1 - wT)\, s(k) - \epsilon T \text{sgn}(s(k)) + C A^h B_d \tilde{d}(k) \end{aligned} \tag{19}$$

where

$$\begin{aligned} \bar{A}_{11} &= A_{11} - A_{12} C_2^{-1} C_1 \\ \bar{A}_{12} &= A_{12} C_2^{-1}. \end{aligned}$$

Next, the stability of the quasi-sliding mode around the sliding surface will be investgated by utilizing the Lyapunov analysis method for the system (19). The following theorm gives the main result of this paper.

Theorem 1: For the system (19) under the predictor-based sliding-mode control law (11), if ϵT is chosen to satisfy $\epsilon T > \varphi_i$, where φ_i is defined as (14), then the system (19) is ultimately uniformly bounded.

Proof: Choose the Lyapunov function as

$$V(k) = Z_1^T(k) P Z_1(k) + s^T(k) s(k) \tag{20}$$

where $0 < P = P^{\mathrm{T}} \in R^{(n-m)\times(n-m)}$. The incremental change of the Lyapunov function is

$$\begin{aligned} & V(k+1) - V(k) \\ = \;& Z_1^{\mathrm{T}}(k+1) P Z_1(k+1) + s^{\mathrm{T}}(k+1) s(k+1) \\ & - Z_1^{\mathrm{T}}(k) P Z_1(k) - s^{\mathrm{T}}(k) s(k) \\ = \;& \left[\bar{A}_{11} Z_1(k) + \bar{A}_{12} s(k) \right]^{\mathrm{T}} P \left[\bar{A}_{11} Z_1(k) + \bar{A}_{12} s(k) \right] \\ & - Z_1^{\mathrm{T}}(k) P Z_1(k) \\ & + \Big[s(k) - \epsilon T \text{sgn}\left(s(k)\right) - wT s(k) + C A^h B_d \tilde{d}(k) \Big]^{\mathrm{T}} \\ & \times \Big[s(k) - \epsilon T \text{sgn}\left(s(k)\right) - wT s(k) + C A^h B_d \tilde{d}(k) \Big] \\ & - s^{\mathrm{T}}(k) s(k) \end{aligned}$$

Since the matrix pair (A, B) is controllable, thus it follows from [18] that there exists a matix C such that $\bar{A}_{11}$ is stable. Therefore, there exists a positive definite matrix P, so that

$$A_{12}^{\mathrm{T}} P A_{12} - P = -Q \tag{21}$$

is true for any positive definite matrix Q. Then

$$\begin{aligned} & V(k+1) - V(k) \\ \leq \;& -Q_{\min} \left\| Z_1(k) \right\|^2 + 2\bar{\delta} \left\| \bar{A}_{12}^{\mathrm{T}} P \bar{A}_{11} \right\| \left\| Z_1(k) \right\| + \left\| \bar{A}_{12}^{\mathrm{T}} P \bar{A}_{12} \right\| \bar{\delta}^2 \\ & - 2\epsilon T \bar{\delta} m - 2wT\bar{\delta}^2 \\ & + \epsilon^2 T^2 m + 2wT\epsilon T m \bar{\delta} + w^2 T^2 \bar{\delta}^2 + 2\bar{\delta} \left\| C A^h B_d \right\| \left\| \tilde{d}(k) \right\| \\ & - 2\epsilon T m \left\| C A^h B_d \right\| \left\| \tilde{d}(k) \right\| \\ & - 2wT\bar{\delta} \left\| C A^h B_d \right\| \left\| \tilde{d}(k) \right\| + \left\| C A^h B_d \right\|^2 \left\| \tilde{d}(k) \right\|^2 \end{aligned} \tag{22}$$

$$\begin{aligned} = \;& -Q_{\min} \left\| Z_1(k) \right\|^2 + 2\bar{\delta} \left\| \bar{A}_{12}^{\mathrm{T}} P \bar{A}_{11} \right\| \left\| Z_1(k) \right\| + m\epsilon^2 T^2 \\ & + \left(\left\| \bar{A}_{12}^{\mathrm{T}} P \bar{A}_{12} \right\| - 2wT + w^2 T^2 \right) \bar{\delta}^2 - 2m\epsilon T (1 - wT) \bar{\delta} \\ & + 2 \left(\bar{\delta} - \epsilon T m - wT\bar{\delta} \right) \left\| C A^h B_d \right\| \left\| \tilde{d}(k) \right\| + \left\| C A^h B_d \right\|^2 \left\| \tilde{d}(k) \right\|^2, \end{aligned}$$

where $Q_{\min}$ is the minimum singular value of Q. For convenience, let

$$\begin{aligned} \bar{\delta}_1 &= \bar{\delta} \left\| A_{12}^{\mathrm{T}} P \bar{A}_{11} \right\|, \\ \bar{\delta}_2 &= \left(\left\| \bar{A}_{12}^{\mathrm{T}} P \bar{A}_{12} \right\| - 2wT + w^2 T^2 \right) \bar{\delta}^2 - 2m\epsilon T (1 - wT) \bar{\delta} \\ & \quad + 2 \left(\bar{\delta} - \epsilon T m - wT\bar{\delta} \right) \left\| C A^h B_d \right\| \left\| \tilde{d}(k) \right\| \\ & \quad + m\epsilon^2 T^2 + \left\| C A^h B_d \right\|^2 \left\| \tilde{d}(k) \right\|^2. \end{aligned} \tag{23}$$

With these denotions, it is deduced from (22) that

$$\begin{aligned} & V(k+1) - V(k) \\ \leq \;& -Q_{\min} \left\| Z_1(k) \right\|^2 + 2\bar{\delta}_1 \left\| Z_1(k) \right\| + \bar{\delta}_2 \\ \leq \;& -Q_{\min} \left(\left\| Z_1(k) \right\| - \frac{\bar{\delta}_1}{Q_{\min}} \right)^2 + \frac{\bar{\delta}_1^2}{Q_{\min}} + \bar{\delta}_2. \end{aligned} \tag{24}$$

It is found from the relation (24) that

$$V(k+1) - V(k) < 0$$

if

$$\|Z_1(k)\| > \frac{\bar{\delta}_1 + \sqrt{\bar{\delta}_1^2 + Q_{\min}\bar{\delta}_2}}{Q_{\min}} \tag{25}$$

is satisfied. The relation (25) means that the trajectory of $Z_1(k)$ will enter into the ball $\left\{\Omega\left(0, \frac{\bar{\delta}_1+\sqrt{\bar{\delta}_1^2+Q_{\min}\bar{\delta}_2}}{Q_{\min}}\right) : \|Z_1(k)\| \leq \frac{\bar{\delta}_1+\sqrt{\bar{\delta}_1^2+Q_{\min}\bar{\delta}_2}}{Q_{\min}}\right\}$ within a finite time. Thus, uniform ultimate boundedness can be obtained for the system (19) from the conclusion in [20]. The proof is thus finished. ■

Then, a numerical example is given to verify the effectiveness of the proposed method.

VI. Numerical Simulation

In this section, an example illustrating the effectiveness of the proposed predictor-based sliding-mode control law (11) to reject unknown disturbance for systems with input delay is presented. Take into account the F-16 fighter's discrete-time state space model with input delay and unknown disturbances:

$$\begin{aligned} & x(k+1) \\ = & \begin{bmatrix} 1 & 0.1025 & 0.2080 & -0.0502 & -0.0057 \\ 0 & 1.1175 & 4.1534 & -0.8000 & -0.1010 \\ 0 & 0.0955 & 1.0722 & -0.0541 & -0.0153 \\ 0 & 0 & 0 & 0.1353 & 0 \\ 0 & 0 & 0 & 0 & 0.1353 \end{bmatrix} x(k) \\ + & \begin{bmatrix} -0.0581 & -0.004 \\ -1.7586 & -0.1131 \\ -0.0720 & -0.0175 \\ 2 & 0 \\ 0 & 0.8647 \end{bmatrix} u(k-h) \\ + & \begin{bmatrix} -0.2 \\ -0.3 \\ -0.2 \\ -0.2 \\ -0.1 \end{bmatrix} d(k). \end{aligned} \tag{26}$$

Where the sampling period $T = 0.1$ s and the input delay $h = 5$. The initial system state is

$$x(0) = \begin{bmatrix} 0 & 0 & 0 & 0 & 0 \end{bmatrix}^{\mathrm{T}}.$$

For the system (26), the predictor-based sliding-mode control law (11) is considered to reject a sinusoidal disturbance signal

$$d(k) = 2\sin(0.06t). \tag{27}$$

The sliding surface is designed as $s(k) = Cz(k)$, where

$$C = \begin{bmatrix} 5.6168 & 0.6354 & -0.5360 & -0.3587 & -0.0143 \\ -27.0080 & -0.3808 & 21.9722 & 0.0461 & -0.2247 \end{bmatrix}.$$

Choose $\epsilon = 4$ and $wT = 0.75$.

In order to verify the effectiveness of the method proposed in this paper, the control laws

$$u_0(k) = Kx_{\mathrm{p0}}(k) \tag{28}$$

and

$$\begin{aligned} u_1(k) \quad = \quad & -(CB)^{-1}C(A-I)x_{\mathrm{p0}}(k) \\ & -(CB)^{-1}[\bar{d}(k) + wTs(k) + \epsilon T\mathrm{sgn}(s(k))] \end{aligned} \tag{29}$$

in [16] are considered for the system (1) to reject the disturbance (27).

The simulation results are shown in Figure 1. It is found from this figure that the closed-loop system of the system (1) under the proposed predictor-based sliding-mode control law (11) can achieve a better disturbance attenuation capacity. The disturbance error caused by the use of disturbance observer (3) is described by Figure 2.

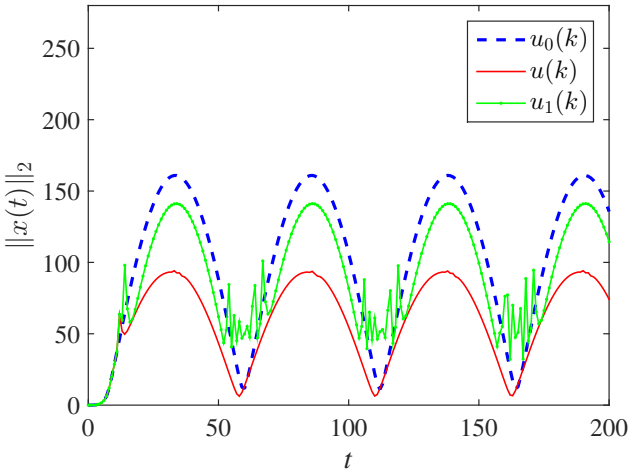

Fig. 1. The states of the closed-loop systems under the different predictor-based control laws.

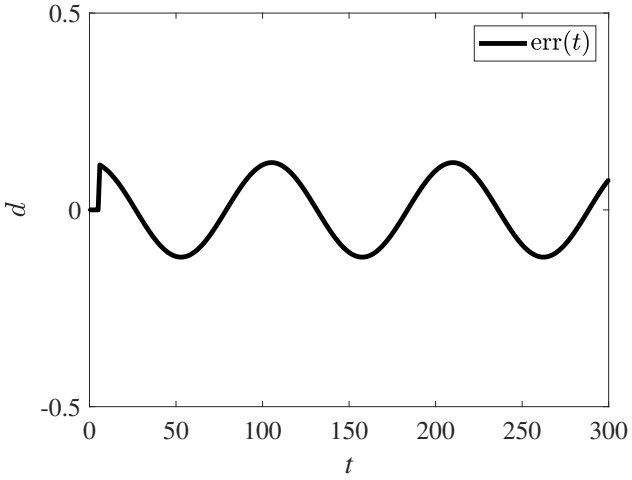

Fig. 2. Disturbance estimation error.

VII. Conclusion

In this article, the predcitor-based feedback control method is combined with the sliding mode control method such that

the disturbance attenuation capacity can be improved for input-delayed systems. In the proposed prdictor-based sliding mode control law, the unknown disturbance is estimated by a disturbance obsever. It is verified that the estimation error of the disturbance obsever is bounded. Moreover, the uniform ultimate boundedness is obtained for the system by utilizing the Lyapunov analysis method for the dynamics of the predictor. Finally, it is shown by a numerical example that disturbance attenuation capacity is impoved by this prdictor-based sliding mode control law.

REFERENCES

[1] Sun J, Zhang C, Gu J. Decentralized Optimal Fusion Filtering for Multi-Sensor Multi-Delay Singular Systems, *Circuits, Systems, and Signal Processing*, 2012, 31(1):163-176.

[2] Lin F J, Chiu S L, Shyu K K. Novel sliding mode controller for synchronous motor drive, *IEEE Trans. on Aerospace and Elec. tronic. Systems*, 1998, 34(2): 532-542.

[3] Moon Y S, Park P G, Kwon W H. Robust stabilization of uncertain input-delayed systems using reduction method, *Automatica*, 2001, 37(2): 307-312.

[4] Park P G, Ko J W, Jeong C. Reciprocally convex approach to stability of systems with time-varying delays, *Automatica*, 2011, 47(1): 235-238.

[5] Smith O J M. A Controller to Overcome Dead Time, *ISA Journal*, 1959, 6(2):28-33.

[6] Saravanakumar G, WahidhaBanu R S D, Nayak C G. Design of modified dead-time compensators for stable process with integrator and longer time using adaptive control, *ACSE Journal*, 2006, 6(4): 1-5.

[7] Kaya I, Atherton D P. Use of Smith predictor in the outer loop for cascade control of unstable and integrating processes, *Industrial and Engineering Chemistry Research*, 2008, 47(6): 1981-1987.

[8] Massimiliano V. Performance improvement of Smith predictor through automatic computation of dead time, Yokowaga Italy, Industrial Automation Department, 2003.

[9] LI-Xun, Dong-Qiu S , Shou-Yi Y U, et al. Feedback automatic gauge control system using model reference adaptive Smith predictor, *IET Control Theory & Applications*, 2009, 26(9): 999-1003.

[10] Itkis, U.: 'Control systems of variable structure' (John Wiley & Sons,New York, 1976).

[11] Gao W, Wang Y, Homaifa A. Discrete-time variable structure control systems, *IEEE.Trans. Ind. Electron.*,1995, 42(2): 117-122.

[12] Bartoszewicz A. Discrete-time quasi-sliding-mode control strategies,*IEEE Trans. Ind. Electron.*, 1998, 45(4): 633-637.

[13] Bartoszewicz A, Leniewski P. New Switching and Nonswitching Type Reaching Laws for SMC of Discrete Time Systems, *IEEE Transactions on Control Systems Technology*, 2016, 24(2): 670-677.

[14] Ma H, Wu J, Xiong Z. A Novel Exponential Reaching Law of Discrete-Time Sliding-Mode Control, *IEEE Transactions on Industrial Electronics*, 2017, 64(5): 3840-3850.

[15] Gao W, Wang Y, Homaifa A. Discrete-time variable structure control systems, *IEEE Trans. Indus. Electron.*, 1995, 42 (2): 117-122.

[16] Xia Y, Liu G P, Shi P, et al. Sliding mode control of uncertain linear discrete time systems with input delay. *IET Control Theory & Applications*, 2007, 1(4): 1169-1175.

[17] Bartoszewicz A. Remarks on discrete-time variable structure control systems, *IEEE Trans. Indus. Electron.*, 1996, 43: 235-238.

[18] Utkin V I, Yang K D. Methods for constructing discontinuity planes in multidimensional variable structure systems, *Autom.Remote Control*, 1979, 39: 1466-1470.

[19] Zhang Jinhui, Shi Peng, Xia Yuanqing, Yang Hongjiu. Discrete-Time Sliding Mode Control With Disturbance Rejection, *IEEE Transactions on Industrial Electronics*, 2018, 66(10): 7967-7975.

[20] Corless M J, Leitmann G. Contiunous state feedback guaranteeing uniform ultimate boundedness for uncertain dynamic system, *IEEE Trans. Autom.Control*, 1981, 26: 1139-1144.

Proceedings of the 3rd Conference on Fully Actuated System Theory and Applications
May 10-12, 2024, Shenzhen, China

Fully Actuated Behavioral Control for Multiple Omnidirectional Mobile Robots System with Uncertain Dynamics

Zhibin Mo[1], Wanquan Liu[1], Yu-Yao Wu[1], Hui-Jie Sun[1,*]
1. Shenzhen Campus of Sun Yat-sen University, Shenzhen, 518107, P. R. China
E-mail: sunhj6@mail.sysu.edu.cn

Abstract: In this paper, the issue of distributed formation control for a group of omnidirectional mobile robots with uncertain dynamics and external disturbances is investigated. A fully actuated behavioral control scheme is introduced to efficiently accomplish the desired cooperative task. Within the strategy, a distributed formation behavior based on a fixed-time cooperative protocol and null-space-based behavioral control method is designed, satisfying both neighbor collaboration and leader tracking requirement. Through a prioritized multi-behavior fusion process, the desired kinematic commands of each robot is obtained. Then, we convert the over-actuated systems into a fully actuated configuration form. Furthermore, a sliding mode controller integrated with an extended state observer was designed for each robot. This advanced controller enables precise tracking of desired kinematic commands by taking into account the fully actuated nonlinear dynamics of the robots. Finally, simulation results are provided to demonstrate the advantages and effectiveness of the proposed method.

Key Words: Omnidirectional mobile robots system, formation control, fully actuated system theory, behavioral control, uncertain dynamics

1 Introduction

The omnidirectional mobile robot (OMR) [1] exhibits superior load-bearing and maneuverability capabilities within confined indoor environments. In real-world scenarios, all the OMRs interact through a network structure, and they are often assigned to perform diverse and incompatible tasks within a specific period of time. These tasks include formation, obstacle avoidance, and task execution. Numerous research has been conducted on the cooperative behavioral controller designed for multiple omnidirectional mobile robot system (Multi-OMRs). In [2], a fuzzy logic based consensus strategy was proposed for self-organizing formation control task of OMRs. This approach automatically generates a communication topology through a continuous formation method with constant spatial relationships, achieving self-organizing formation control of OMRs. In [3], the authors proposed a model predictive control method for a formation tracking task involving Multi-OMRs. This approach significantly improving tracking performance through the prediction and estimation.

Although the aforementioned research achievements have realized efficient formation control for the OMRs, they have not considered the issues of multi-task control and conflict resolution in cooperative tasks. However, conflicts among OMRs are inevitable in cooperative task implementation process. The null-space-based behavioral control (NSBC) [4] offers a effective approach for addressing the task conflicts problem. NSBC ensures that tasks of the highest priority are executed first. Tasks with lower priorities are then partially executed, but only after being projected into the task with higher priority. There are many researcher who has studied on the cooperative behavioral controller designed for autonomous robot system. In reference [5], a behavioral control formation tracking scheme tailored to constrained multi-agent system with second-order dynamic was proposed. This strategy ensures conflict-free formation control by incorporating path tracking, obstacle detection and avoidance tasks. In [6], a reinforcement learning behavioral control method was proposed to obtain optimal task priority rules through trial-and-error learning. The multi-task conflict problem in formation control was solved.

Unfortunately, existing methods for designing behavioral controllers are beset by challenges, including complex structures, an abundance of parameters, a dearth of physical significance, and rigorous stability requirements. Due to the fact that physical Multi-OMRs are consistently modeled as second-order nonlinear systems using the Euler-Lagrange method [2], the complexity of tasks leads to an increased level of nonlinear characteristic and uncertainty in system. Therefore, in recent years, scholars have proposed a high-order fully actuated control theory approach for nonlinear systems [7][9]. This method encompasses a fully actuated transformation and the design of a feedback linearization controller. As a result, the control efficiency and stability is optimized by a simplified linear closed-loop system control.

Based on the previously detailed analysis, this paper introduces a novel fully actuated behavioral control (FABC) scheme designed for Multi-OMRs subjected to uncertain dynamics. This approach aims to address cooperative formation challenges from a fresh perspective, highlighting the following key innovations:

1) A novel distributed formation behavioral model is developed, leveraging the communication and measurement data from neighboring OMRs to determine the reference formation speed for each OMR.
2) A path tracking controller based on sliding-mode control and extended state observer (ESO) for each OMR is designed. This controller ensures the stabilization of error system in formation task of OMRs.

Notations 1 *Given a vector* $\boldsymbol{a} = [a_1, a_2, a_3]^T$*, the function* $\mathrm{sig}^r(\boldsymbol{a})$ *is in the form of* $\mathrm{sig}^r(\boldsymbol{a}) = [|a_1|^r \mathrm{sign}(a_1), |a_2|^r \mathrm{sign}(a_2), |a_3|^r \mathrm{sign}(a_3)]^T$*, where* $|\cdot|$ *is the operator of absolute*

This work was supported in part by Science Center Program of the National Natural Science Foundation of China under Grant No. 62188101, and in part by Natural Science Foundation of Guangdong Province of China under Grant Nos. 2023A1515011466 and 2023A1515110743.

value, $\mathrm{sign}(\cdot)$ *represents a symbolic function,* r *is positive constant. Behavior is also named mission or task in behavioral control in this study. Let* $\overline{\lambda}(\cdot), \underline{\lambda}(\cdot)$ *denote the maximum and minimum singular value, respectively.*

2 Preliminaries and Problem Statement

This section illustrates the preliminaries with regard to algebraic graph theory, model description of the OMRs, and multiple behaviors composition subjected to priority rules.

2.1 Algebraic Graph Theory

According to preliminary knowledge in algebraic graph theory, the coupling relationships of the communication network among n robot can be characterized by a directed weighted graph $\boldsymbol{\mathcal{G}}_1 = \{\boldsymbol{V}, \boldsymbol{\varsigma}, \boldsymbol{W}\}$, where $\boldsymbol{V} = \{v_1, v_2, \ldots, v_n\}$ denotes the node set, $\boldsymbol{\varsigma} = \{(v_i, v_j) : v_i, v_j \in \boldsymbol{V}, i \neq j\}$ represents a set composed of edges, and matrix $\boldsymbol{W} = [\omega_{ij}] \in \mathbb{R}^{n\times n}$ is a weighted adjacency matrix of graph $\boldsymbol{\mathcal{G}}_1$, where the symbol of ω_{ij} denotes the direction of signal transmission, and the magnitude of its absolute value represents communication strength between i^{th} robot and j^{th} robot. Define $\boldsymbol{\mathcal{G}}_0$ as the virtual leader, their topological relationships is shown in Fig. 1(a). In a directed graph, if there exists a node with a directed path to any other node, it is called a directed spanning tree. In this papar, the trajectory (position and velocity) of formation leader required to be bounded. We assume that the communication network $\boldsymbol{\mathcal{G}} = \{\boldsymbol{\mathcal{G}}_0, \boldsymbol{\mathcal{G}}_1\}$ is a directed spanning tree.

2.2 System model and problem formulation

In this subsection, the specific modeling of the Multi-OMRs will be presented. In order to precisely modeling the translation and rotation motion process of each OMR, they are constrained to move in a flat horizontal plane surface.

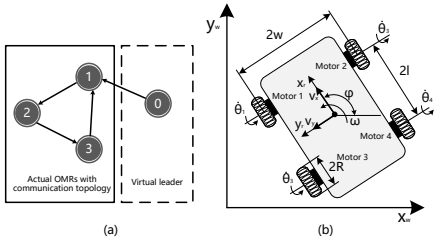

Fig. 1: The structures and coordinate definition of an OMR.

As shown in Fig. 1(b), the world coordinate frame $x_{\mathrm{w}}o_{\mathrm{w}}y_{\mathrm{w}}$ and robot coordinate frame $x_{\mathrm{r}}o_{\mathrm{r}}y_{\mathrm{r}}$ are established. Then, define $[\dot{x}_{\mathrm{r}}, \dot{y}_{\mathrm{r}}, \dot{\varphi}]^T$ as the velocity of robot coordinate frame, and $[\dot{x}_{\mathrm{w}}, \dot{y}_{\mathrm{w}}, \dot{\varphi}]^T$ as the velocity of world coordinate frame, respectively. Let $\dot{\boldsymbol{\theta}} = [\dot{\theta}_1, \dot{\theta}_2, \dot{\theta}_3, \dot{\theta}_4]^T$, $\dot{\boldsymbol{x}}_{\mathrm{r}} = [\dot{x}_{\mathrm{r}}, \dot{y}_{\mathrm{r}}, \dot{\varphi}]^T$,$\dot{\boldsymbol{x}}_{\mathrm{w}} = [\dot{x}_{\mathrm{w}}, \dot{y}_{\mathrm{w}}, \dot{\varphi}]^T$, the kinematic mapping of the state between robot coordinate frame space of a robot and the motor angular space [2] can be expressed by

$$\dot{\boldsymbol{x}}_{\mathrm{r}} = R\boldsymbol{P}^{\dagger}\dot{\boldsymbol{\theta}} \tag{1}$$

where $\boldsymbol{P}^{\dagger} = \boldsymbol{P}^T(\boldsymbol{P}\boldsymbol{P}^T)^{-1}$ is the pseudo-inverse of $\boldsymbol{P}$, and

$$\boldsymbol{P} = \begin{bmatrix} 1 & -1 & -(l+w) \\ 1 & 1 & (l+w) \\ 1 & 1 & -(l+w) \\ 1 & -1 & (l+w) \end{bmatrix}.$$

The parameter w and l are half the width and length of the robot, respectively. And R represents the radius of wheel. Defined $T(\varphi)$ as the transformation matrix of robot coordinate frame with respect to world coordinate frame, which can be described as

$$\boldsymbol{T}(\varphi) = \begin{bmatrix} \cos(\varphi) & -\sin(\varphi) & 0 \\ \sin(\varphi) & \cos(\varphi) & 0 \\ 0 & 0 & 1 \end{bmatrix}.$$

Then, the state differentiation described in world coordinate frame can be obtained by $\dot{\boldsymbol{x}}_{\mathrm{w}} = \boldsymbol{T}(\varphi)\dot{\boldsymbol{x}}_{\mathrm{r}}$. According to the Euler-Lagrange method, the dynamic equation of the OMR can be accurately established[2]. Therefore, the simplified dynamic model of the Multi-OMRs can be written as

$$\ddot{\boldsymbol{x}}_i + \boldsymbol{A}_{0,i}\dot{\boldsymbol{x}}_i + \boldsymbol{A}_{1,i} - \boldsymbol{d}_i = \boldsymbol{B}_i\boldsymbol{u}_i, \tag{2}$$

where $\boldsymbol{x}_i = [x_{\mathrm{w},i}, y_{\mathrm{w},i}, \varphi_i]^T$,$\boldsymbol{A}_{0,i} = \boldsymbol{T}(\varphi_i)(\dot{\boldsymbol{T}}(\varphi_i))^{-1} + C_\theta R^2\boldsymbol{T}(\varphi_i)\boldsymbol{P}^{\dagger}\boldsymbol{M}^{-1}\boldsymbol{P}(\boldsymbol{T}(\varphi_i))^{-1}$,$\boldsymbol{A}_{1,i} = R^2\boldsymbol{T}(\varphi_i)\boldsymbol{P}^{\dagger}\boldsymbol{M}^{-1}C_{\mathrm{f}}F_{\mathrm{g},i}$, $\boldsymbol{B}_i = R\boldsymbol{T}(\varphi_i)\boldsymbol{P}^{\dagger}\boldsymbol{M}^{-1}$, $\boldsymbol{d}_i = R\boldsymbol{T}(\varphi_i)\boldsymbol{P}^{\dagger}\boldsymbol{M}^{-1}\boldsymbol{h}_{\mathrm{d},i}$, and $\boldsymbol{u}_i = [\tau_{1,i}, \tau_{2,i}, \tau_{3,i}, \tau_{4,i}]^T$. $i = 1, 2, \ldots, N$ denotes i^{th} OMR in the Multi-OMRs, N represent the total number of OMR, and $\boldsymbol{u}_i$ is the driving torque input generated by the electric motor. $F_{\mathrm{g},i} = m_i g$ denotes the gravity of ith OMR, m_i is total mass and $g = 9.8m/s^2$ is the gravitational acceleration. $\boldsymbol{h}_{\mathrm{d},i}$ represents uncertainty disturbances of ith OMR, which encompass model inaccuracies and external input disturbances. C_{f} and C_θ are the static friction and viscous friction coefficient, respectively. $\boldsymbol{M}$ represents the total inertia matrix in Euler-Lagrange equation of Multi-OMRs, which is calculated by

$$\boldsymbol{M} = \begin{bmatrix} M_3 & -M_2 & M_2 & M_4 \\ -M_2 & M_3 & M_4 & M_2 \\ M_2 & M_4 & M_3 & -M_2 \\ M_4 & M_2 & -M_2 & M_3 \end{bmatrix},$$

where $M_1 = \frac{m_i R^2}{8}$, $M_2 = \frac{I_z R^2}{16(l+w)^2}$, $M_3 = M_1 + M_2 + I_{\mathrm{w}}$, $M_4 = M_1 - M_2$, I_{w} and I_{z} represent the moment of inertia around the OMR axle and the moment of inertial of wheels around the z-axis, respectively.

If we let $\boldsymbol{x}_{\mathrm{d,i}}$ be the reference state signal, and we define $\boldsymbol{e}_i = \boldsymbol{x}_i - \boldsymbol{x}_{\mathrm{d,i}}$ as state error and combined it with Eq. (**??**), hence the state error system model can be written as

$$\ddot{\boldsymbol{e}}_i + \ddot{\boldsymbol{x}}_{\mathrm{d,i}} + \boldsymbol{A}_{1,i} + \boldsymbol{A}_{0,i}\dot{\boldsymbol{e}}_i + \boldsymbol{A}_{0,i}\dot{\boldsymbol{x}}_{\mathrm{d,i}} - \boldsymbol{d}_i = \boldsymbol{B}_i\boldsymbol{u}_i, \tag{3}$$

where $\dot{\boldsymbol{e}}_i, \dot{\boldsymbol{x}}_{\mathrm{d,i}}$ are the first derivative of $\boldsymbol{e}_i$ and $\boldsymbol{x}_{\mathrm{d,i}}$, respectively. Similarly, $\ddot{\boldsymbol{e}}_i, \ddot{\boldsymbol{x}}_{\mathrm{d,i}}$ are the second derivative of $\boldsymbol{e}_i$ and $\boldsymbol{x}_{\mathrm{d,i}}$, respectively. The model of Multi-OMRs is established.

2.3 Prioritized Multi-behavior Fusion

Generally, each robot in Multi-OMRs is required to simultaneously execute behaviors (tasks/missions) at different levels and with varying priorities. The criteria for behavior fusion can be found in the referenced [6]. In order to better describe the control objectives of this paper, a precise definition of the behavioral control task error $\boldsymbol{e}_{\delta,i}(t)$ at time t can be defined as $\boldsymbol{e}_{\delta,i}(t) = \boldsymbol{\delta}_i(t) - \boldsymbol{\delta}_{\mathrm{d,i}}(t)$,where $\boldsymbol{\delta}_i(t)$ and $\boldsymbol{\delta}_{\mathrm{d,i}}(t)$ are the actual and desired behavioral control task function [6] of ith OMR, respectively.

3 Distributed Behaviors Design

This section show the details design of elementary behaviors and the prioritized multi-behavior fusion rules within

the NSBC framework. Finally, the behavioral stability of proposed distributed behavior is provided.

3.1 Elementary Behaviors

The design of elementary behaviors is crucial for behavior control approach. In this section, we analyze the various tasks that can be executed within the multi-OMRs. Based on task requirements and actuator characteristics, we define three elementary behaviors, individual local motion (ILM), distributed formation (DF).

Individual local motion design. The ILM behavior drives a specific OMR to move along a reference trajectory guided by predefined mathematical model, which is determined in real-time through autonomous planning algorithms. Based on the behavior design guidelines of the NSBC approach, the ILM behavioral function $\boldsymbol{\delta}_{m,i} \in \mathbb{R}^{2\times 1}$ is defined as

$$\boldsymbol{\delta}_{\mathrm{m,i}} = f_{\mathrm{m}}(\boldsymbol{p}_i), \tag{4}$$

where $\boldsymbol{p}_i = [x_i, y_i]^T$ denotes the position vector of ith OMR, and $f_{\mathrm{m}}(\boldsymbol{\alpha}) = k_{\mathrm{m}}\boldsymbol{\alpha}$, k_{m} is a scale coefficient. The corresponding differential relationship of $\boldsymbol{\delta}_{\mathrm{m,i}}$ is

$$\dot{\boldsymbol{\delta}}_{\mathrm{m,i}} = \boldsymbol{J}_{\mathrm{m},i}\boldsymbol{v}_i, \tag{5}$$

where $\boldsymbol{J}_{\mathrm{m,i}} = \frac{\partial \boldsymbol{\delta}_{\mathrm{m},i}}{\partial \boldsymbol{p}_i} \in \mathbb{R}^{2\times 2}$ is a Jacobian matrix [4] of $\boldsymbol{\delta}_{\mathrm{m,i}}$, and $\boldsymbol{v}_i = \dot{\boldsymbol{p}}_i$ denotes the derivative of position vector with respect to time. However, the integration of reference velocity would incur a certain drift of the reconstructed position of the robot, which can be compensated for by the closed-loop inverse kinematics [4]. Therefore, the reference velocity of the ILM behavior can be calculated as

$$\boldsymbol{v}_{\mathrm{m},i} = \boldsymbol{J}^{\dagger}_{\mathrm{m},i}(\dot{\boldsymbol{\delta}}_{\mathrm{md},i} + \boldsymbol{\Lambda}_{\mathrm{m}}(\boldsymbol{\delta}_{\mathrm{md},i} - \boldsymbol{\delta}_{\mathrm{m},i})) \tag{6}$$

where $\boldsymbol{J}^{\dagger}_{\mathrm{m},i} = \boldsymbol{J}^{T}_{\mathrm{m},i}(\boldsymbol{J}_{\mathrm{m},i}\boldsymbol{J}^{T}_{\mathrm{m},i})^{-1}$ is the pseudo-inverse matrix of $\boldsymbol{J}_{\mathrm{m,i}}$, $i = 1, 2, \cdots, n$ represents the index of ith OMR, $\boldsymbol{\delta}_{\mathrm{md},i} = [x_{\mathrm{d,i}}, y_{\mathrm{d,i}}]^T$ is the desired behavior function. $\dot{\boldsymbol{\delta}}_{\mathrm{md},i}$ is the derivative of the $\boldsymbol{\delta}_{\mathrm{md},i}$ with respect to time, and Λ_{m} denotes a suitable positive-defined gain matrix.

Distributed formation design. The physical significance of DF behavior lies in the ability to generate the reference velocities based on the cooperative requirements and distributed formation constraints. Similarly, the mathematical description of DF behavior function $\boldsymbol{\delta}_{\mathrm{f,i}} \in \mathbb{R}^{2\times 1}$ and the derivative $\dot{\boldsymbol{\delta}}_{\mathrm{f,i}}$ can be written as

$$\begin{cases} \boldsymbol{\delta}_{\mathrm{f,i}} = f_{\mathrm{f}}(\boldsymbol{p}_i), \\ \dot{\boldsymbol{\delta}}_{\mathrm{f,i}} = \boldsymbol{J}_{\mathrm{f},i}(\boldsymbol{p}_i)\boldsymbol{v}_i, \end{cases} \tag{7}$$

where $f_{\mathrm{f}}(\boldsymbol{\alpha}) = k_{\mathrm{f}}\boldsymbol{\alpha}$ in this scenarios, k_{f} is a scale coefficient. The $\boldsymbol{J}_{\mathrm{f,i}} = \frac{\partial \boldsymbol{\delta}_{\mathrm{f},i}}{\partial \boldsymbol{p}_i} \in \mathbb{R}^{2\times 2}$ is a Jacobian matrix of $\boldsymbol{\delta}_{\mathrm{f,i}}$, and $\boldsymbol{v}_i = \dot{\boldsymbol{p}}_i$ denotes the derivative of position vector with respect to time. Unlike the ILM behavior, the desired DF behavior function $\boldsymbol{\delta}_{\mathrm{fd},i}$ requires obtaining the information of communication or measurements from neighboring OMRs and formation leaders. Define p_0 and v_0 as the position and velocity of leader, respectively. And then define the distributed relative relationship of offsets between followers and leader as $\boldsymbol{\zeta} = [\boldsymbol{\zeta}_1, \boldsymbol{\zeta}_2, \cdots, \boldsymbol{\zeta}_n]$, the derivative of $\boldsymbol{\zeta}$ is restricted to be bounded. Subsequently, the $\boldsymbol{\delta}_{\mathrm{fd},i}$ based on communication network topology can be designed as

$$\begin{aligned} \boldsymbol{\delta}_{\mathrm{fd},i} =& \frac{1}{(\kappa_1 + \kappa_2 + \kappa_3 \sum_{j=1}^{n} \omega_{ij})} \big[\kappa_1 b_i(\boldsymbol{p}_0 + \boldsymbol{\zeta}_i) \\ &+ \kappa_2(\hat{\boldsymbol{p}}_{0,i} + \boldsymbol{\zeta}_i) + \kappa_3 \sum_{j=1}^{n} \omega_{ij}(\boldsymbol{p}_j - \boldsymbol{\zeta}_j + \boldsymbol{\zeta}_i)\big], \end{aligned} \tag{8}$$

where the coefficient $\kappa_1 \in [0, 1], \kappa_2 \in [0, 1]$ are utilized for tuning the weight of behavior tracking, respectively, and $0 \leqslant \kappa_3 \leqslant 1$ is responsible for regulating coordination performance, they satisfy the relationship $\kappa_1 + \kappa_2 + \kappa_3 = 1$. And $\hat{\boldsymbol{p}}_{0,i}$ represents the distributed estimation of $\boldsymbol{p}_0$ in the ith OMR, which can be obtained within a fixed time under *Assumption 1* by a distributed estimator [8] as follow:

$$\begin{cases} \dot{\hat{\boldsymbol{p}}}_{0,i} = -\iota_1 \mathrm{sig}^{\eta_1}(\hat{\boldsymbol{e}}_{p0}) - \iota_2 \mathrm{sign}(\hat{\boldsymbol{e}}_{p0}) + \hat{\boldsymbol{v}}_{0,i}, \\ \dot{\hat{\boldsymbol{v}}}_{0,i} = -\iota_3 \mathrm{sig}^{\eta_2}(\hat{\boldsymbol{e}}_{v0}) - \iota_4 \mathrm{sign}(\hat{\boldsymbol{e}}_{v0}), \end{cases} \tag{9}$$

where $\hat{\boldsymbol{e}}_{p0} = \sum_{j=1}^{n} \omega_{ij}(\hat{\boldsymbol{p}}_{0,i} - \hat{\boldsymbol{p}}_{0,j}) + b_i(\hat{\boldsymbol{p}}_{0,i} - \boldsymbol{p}_0)$ and $\hat{\boldsymbol{e}}_{v0} = \sum_{j=1}^{n} \omega_{ij}(\hat{\boldsymbol{v}}_{0,i} - \hat{\boldsymbol{v}}_{0,j}) + b_i(\hat{\boldsymbol{v}}_{0,i} - \boldsymbol{v}_0)$ are the position and velocity estimation error, respectively. The parameters ι_1, ι_2, ι_3, ι_4, η_1 and η_2 are all candidate gains for the convergence of estimator (9). $\hat{\boldsymbol{v}}_{0,i}$ represents the distributed estimation of $\boldsymbol{v}_0$ in the ith OMR. Then, the corresponding reference velocity of the DF behavior can be obtained as

$$\boldsymbol{v}_{\mathrm{f},i} = \boldsymbol{J}^{\dagger}_{\mathrm{f},i}(\dot{\boldsymbol{\delta}}_{\mathrm{fd},i} + \boldsymbol{\Lambda}_{\mathrm{f}}(\boldsymbol{\delta}_{\mathrm{fd},i} - \boldsymbol{\delta}_{\mathrm{f},i})) \tag{10}$$

where $\boldsymbol{J}^{\dagger}_{\mathrm{f},i} = \boldsymbol{J}^{T}_{\mathrm{f},i}(\boldsymbol{J}_{\mathrm{f},i}\boldsymbol{J}^{T}_{\mathrm{f},i})^{-1}$ is the pseudo-inverse matrix of $\boldsymbol{J}_{\mathrm{f,i}}$, $\boldsymbol{\Lambda}_{\mathrm{f}}$ denotes a suitable positive-defined gain matrix.

3.2 Prioritized Multi-behavior Fusion

The prioritized multi-behavior fusion process enables the acquisition of the kinematic reference signal, and the geometric rules of null-space projection can be applied to combine the speed outputs of those individual elementary behaviors like ILM, DF behavior.

Then, we mark the labels of two behaviors as $1, 2$, respectively. A specific vector $\vartheta \in \mathbb{R}^{2\times 1}$ is used to represent the priority order, its subscript indicates the magnitude of priority. Thus, this vector can be described as $\vartheta = [1, 2]^T$ when the priority of behaviors satisfying the condition $ILM{>}DF$ at certain moment t. Consequently, the desired velocity output $\boldsymbol{v}_{\mathrm{d,i}}$ of ith OMR at time t can be expressed as

$$\boldsymbol{v}_d(t) = \boldsymbol{v}_{\vartheta(1)} + (\boldsymbol{I}_{\vartheta(1)} - \boldsymbol{J}^{\dagger}_{\vartheta(1)}\boldsymbol{J}_{\vartheta(1)})\boldsymbol{v}_{\vartheta(2)}, \tag{11}$$

where $\boldsymbol{v}_{\vartheta(1)}, \boldsymbol{v}_{\vartheta(2)}, \boldsymbol{v}_{\vartheta(3)}$ denotes the kinematic output of elementary behaviors after priority sorting, respectively. Similarly, $\boldsymbol{J}_{\vartheta(1)}, \boldsymbol{J}_{\vartheta(2)}$ are Jacobian matrix after priority sorting. And $\boldsymbol{I}_{\vartheta(1)}, \boldsymbol{I}_{\vartheta(2)}$ are all identity matrix related to the dimension of involved behavior function, respectively.

3.3 Behavioral Stability Analysis

Considering the task function $\boldsymbol{\delta}_i = \left[\boldsymbol{\delta}^T_{1,i}, \boldsymbol{\delta}^T_{2,i}\right]^T$, which composed of two elementary behaviors with priority order, ILM and DF. The subscript 1 indicates the task with highest priority, 2 is the second.

Theorem 1 *The task error $\boldsymbol{e}_{\delta,i} = \boldsymbol{\delta}_i - \boldsymbol{\delta}_{\mathrm{d,i}}$ system are large-scale asymptotic stable under different priority conditions when using our designed distributed behaviors.*

Proof 1 *The candidate Lyapunov function is considered as*

$$V_1(\boldsymbol{e}_{\delta,i}) = \frac{1}{2}\sum_{i=1}^{n}(\gamma_{\delta_1}\boldsymbol{e}_{\delta_1,i}^T\boldsymbol{e}_{\delta_1,i} + \gamma_{\delta_2}\boldsymbol{e}_{\delta_2,i}^T\boldsymbol{e}_{\delta_2,i}) \tag{12}$$

where $\gamma_{\delta_1}, \gamma_{\delta_2}$ are the positive behavior parameters to be designed, respectively.

Firstly, taking the time derivative of $V_1(\boldsymbol{e}_{\delta,i})$, we get

$$\begin{aligned}\dot{V}_1(\boldsymbol{e}_{\delta,i}) &= \sum_{i=1}^{n}\left[\gamma_{\delta_1}\boldsymbol{e}_{\delta_1,i}^T\dot{\boldsymbol{e}}_{\delta_1,i}, \gamma_{\delta_2}\boldsymbol{e}_{\delta_2,i}^T\dot{\boldsymbol{e}}_{\delta_2,i}\right]^T \\ &= -\sum_{i=1}^{n}\Bigg\{\boldsymbol{e}_{\delta,i}^T\left[\boldsymbol{J}_1, \boldsymbol{J}_2\right]^T\left[\gamma_{\delta_1}\boldsymbol{J}_1^\dagger\boldsymbol{\Lambda}_1\boldsymbol{e}_{\delta_1,i}, \right. \\ &\quad \left.\gamma_{\delta_2}\boldsymbol{N}_1\boldsymbol{J}_2^\dagger\boldsymbol{\Lambda}_2\boldsymbol{e}_{\delta_2,i}\right]\Bigg\} = -\sum_{i=1}^{n}(\boldsymbol{e}_{\delta,i}^T\boldsymbol{Q}\boldsymbol{e}_{\delta,i}).\end{aligned} \tag{13}$$

where $\boldsymbol{N}_1 = \boldsymbol{I} - \boldsymbol{J}_1^\dagger\boldsymbol{J}_1$ is the null-space projection operator of the highest priority behavior, and the matrix $\boldsymbol{Q} = \begin{bmatrix} \gamma_{\delta_1}\boldsymbol{\Lambda}_1 & \gamma_{\delta_2}\boldsymbol{J_1}\boldsymbol{N_1}\boldsymbol{J_2^\dagger}\boldsymbol{\Lambda}_2 \\ \gamma_{\delta_1}\boldsymbol{J_2}\boldsymbol{J_1^\dagger}\boldsymbol{\Lambda}_1 & \gamma_{\delta_2}\boldsymbol{J_2}\boldsymbol{N_1}\boldsymbol{J_2^\dagger}\boldsymbol{\Lambda}_2 \end{bmatrix}$. To ensure that $\boldsymbol{Q}$ is positive definite, it is necessary that all the values of the determinants of its adjacent minors are greater than zero. Defined the $\overline{\lambda}(\boldsymbol{A}_s)$ and $\underline{\lambda}(\boldsymbol{A}_s)$ are the maximum and minimum singular values of matrix $\boldsymbol{A}_s$, respectively. Obviously, the $\|\boldsymbol{J}_1\| = 1$, $\|\boldsymbol{N}_1\| \leqslant 1$. Then, By using $\overline{\lambda}(\boldsymbol{A}_s\boldsymbol{B}_s) \leqslant \overline{\lambda}(\boldsymbol{A}_s)\overline{\lambda}(\boldsymbol{B}_s)$ and $\underline{\lambda}(\boldsymbol{A}_s\boldsymbol{B}_s) > \underline{\lambda}(\boldsymbol{A}_s)\underline{\lambda}(\boldsymbol{B}_s)$, we have

$$\begin{aligned}\dot{V}_1(\boldsymbol{e}_{\delta,i}) \leqslant -\sum_{i=1}^{n}\Bigg[&\gamma_{\delta_1}\underline{\lambda}(\boldsymbol{Q}_{11})\|\boldsymbol{e}_{\delta_1,i}\|^2 + \\ &\gamma_{\delta_2}\underline{\lambda}(\boldsymbol{Q}_{22})\|\boldsymbol{e}_{\delta_2,i}\|^2 - 2 * \max\left(\gamma_{\delta_1}\overline{\lambda}(\boldsymbol{Q}_{21}, \gamma_{\delta_2}\overline{\lambda}(\boldsymbol{Q}_{12})\right) \\ &\|\boldsymbol{e}_{\delta_2,i}\|\|\boldsymbol{e}_{\delta_1,i}\|\Bigg] \leqslant -\sum_{i=1}^{n}(\hat{\boldsymbol{e}}_{\delta,i}^T\hat{\boldsymbol{Q}}\hat{\boldsymbol{e}}_{\delta,i}).\end{aligned} \tag{14}$$

where the matrix $\hat{\boldsymbol{Q}} = \begin{bmatrix} \gamma_{\delta_1}\underline{\lambda}(\boldsymbol{Q}_{11}) & \frac{1}{2}\lambda^* \\ \frac{1}{2}\lambda^* & \gamma_{\delta_2}\underline{\lambda}(\boldsymbol{Q}_{22}) \end{bmatrix}$, and $\lambda^* = \max\left(\gamma_{\delta_1}\overline{\lambda}(\boldsymbol{Q}_{21}, \gamma_{\delta_2}\overline{\lambda}(\boldsymbol{Q}_{12})\right)$. Therefore, if $\hat{\boldsymbol{Q}}$ is positive definite, the conditions can be written as

$$\begin{cases}\underline{\lambda}(\boldsymbol{Q}_{11}) > 0, \\ \underline{\lambda}(\boldsymbol{Q}_{22}) > \dfrac{(\lambda^*)^2}{4\gamma_{\delta_1}\gamma_{\delta_2}\underline{\lambda}(\boldsymbol{Q}_{11})}.\end{cases} \tag{15}$$

Based on the derived conditions mentioned above, the Eq. (14) can be rewritten as:

$$\dot{V}_1(\boldsymbol{e}_{\delta,i}) \leqslant -\sum_{i=1}^{n}(\hat{\boldsymbol{e}}_{\delta,i}^T\underline{\lambda}(\hat{\boldsymbol{Q}})\hat{\boldsymbol{e}}_{\delta,i}) \leqslant 0. \tag{16}$$

Therefore, the designed behavioral task function, along with the fusion process for multiple behaviors prioritized under various conditions, exhibits large-scale asymptotic stability. It ensures that behavioral task error will finally converge to the neighborhood of zero.

Remark 1 *After analyzing the behavior design and stability, kinematic control commands for the distributed reference of each robot can be obtained. However, it is still necessary to design a fully actuated tracking controller to achieve the desired distributed formation control.*

4 Fully Actuated Behavioral Controller Design

This section show a fully actuated conversion method of over-actuated system, the design of fully actuated behavioral tracking controller and its stability analysis process.

4.1 Fully Actuated Conversion

From the state tracking error system Eq. (3), we can infer that the system input coefficient matrix $\boldsymbol{B}_i \in \mathbb{R}^{3\times4}$ is not a square matrices in this scenario, but rather a matrix with an over-actuated attribute. The over-actuated system can be converted to fully actuated system through variable augmentation method [7]. Therefore, in Eq. (3), we let

$$\bar{\boldsymbol{x}}_{\mathrm{d,i}} = \begin{bmatrix}\boldsymbol{x}_{\mathrm{d,i}} \\ \boldsymbol{O}_{1\times1}\end{bmatrix}, \bar{\boldsymbol{e}}_i = \begin{bmatrix}\boldsymbol{e}_i \\ \boldsymbol{O}_{1\times1}\end{bmatrix},$$
$$\bar{\boldsymbol{A}}_{0,i} = \begin{bmatrix}\boldsymbol{A}_{0,i} & \boldsymbol{O}_{1\times1} \\ \boldsymbol{O}_{1\times3} & \boldsymbol{O}_{1\times1}\end{bmatrix}, \bar{\boldsymbol{A}}_{1,i} = \begin{bmatrix}\boldsymbol{A}_{1,i} \\ \boldsymbol{O}_{1\times1}\end{bmatrix},$$
$$\bar{\boldsymbol{d}}_i = \begin{bmatrix}\boldsymbol{d}_i \\ \boldsymbol{O}_{1\times1}\end{bmatrix}, \bar{\boldsymbol{B}}_i = \begin{bmatrix}\boldsymbol{B}_i \\ \boldsymbol{O}_{1\times4}\end{bmatrix},$$

where $\boldsymbol{O}_{a\times b}$ denotes a zero matrix of dimension $a \times b$, the system (3) can be converted into following equivalent form

$$\ddot{\bar{\boldsymbol{e}}}_i + \ddot{\bar{\boldsymbol{x}}}_{\mathrm{d,i}} + \bar{\boldsymbol{A}}_{1,i} + \bar{\boldsymbol{A}}_{0,i}\dot{\bar{\boldsymbol{e}}}_i + \bar{\boldsymbol{A}}_{0,i}\dot{\bar{\boldsymbol{x}}}_{\mathrm{d,i}} - \bar{\boldsymbol{d}}_i = \bar{\boldsymbol{B}}_i\boldsymbol{u}_i, \tag{17}$$

Generally, the system input coefficient matrix $\bar{\boldsymbol{B}}_i \in \mathbb{R}^{4\times4}$ is non-singular, $det(\boldsymbol{B}_i) \neq 0$) in this application scene. For the rigor of derivation, necessary assumption is proposed.

Assumption 1 *Matrix $\boldsymbol{T}(\varphi_i)$, $\boldsymbol{P}^\dagger$ and $\boldsymbol{M}^{-1}$ all satisfy the condition:* $\det(\begin{bmatrix}R\boldsymbol{T}(\varphi_i)\boldsymbol{P}^\dagger\boldsymbol{M}^{-1} \\ \boldsymbol{O}_{1\times4}\end{bmatrix}) \neq 0$.

4.2 Fully Actuated Control Law

For fully actuated system (17), the time-invariant closed-loop system can always be obtained through controller

$$\boldsymbol{u}_i = -\bar{\boldsymbol{B}}_i^{-1}(-\bar{\boldsymbol{A}}_{0,i}\dot{\bar{\boldsymbol{e}}}_i - \bar{\boldsymbol{A}}_{1,i} - \ddot{\bar{\boldsymbol{x}}}_{\mathrm{d,i}} - \bar{\boldsymbol{A}}_{0,i}\dot{\bar{\boldsymbol{x}}}_{\mathrm{d,i}} + \boldsymbol{\Gamma}_i), \tag{18}$$

where Γ_i denotes the control term to be designed in this section. Then, we substitute the expression of the controller (18) into system (17), the new expression can be written as

$$\ddot{\bar{\boldsymbol{e}}}_i = \boldsymbol{\Gamma}_i + \boldsymbol{D}_i, \tag{19}$$

where $\boldsymbol{D}_i$ encompasses model uncertainties and external disturbances, representing the total disturbance of ith OMR.

In practical engineering scenarios, the instantaneous magnitude of the total disturbance is typically unknown in advance. To this end, an ESO is designed to provide real-time observation of the total disturbance $\boldsymbol{D}_i$ in the Multi-OMRs.

4.3 ESO Design

Then, expanding $\boldsymbol{D}_i$ as a new state variable $\boldsymbol{z}_{2,i}$ for system (17), that is $\boldsymbol{z}_{2,i} = \boldsymbol{D}_i$. And let $\boldsymbol{z}_{1,i} = \dot{\bar{\boldsymbol{e}}}_i$, consequently, Eq. (19) can be converted into the following form:

$$\begin{cases}\boldsymbol{z}_{1,i} = \boldsymbol{\Gamma}_i + \boldsymbol{z}_{2,i}, \\ \boldsymbol{z}_{2,i} = \boldsymbol{\varepsilon}_i, \\ \boldsymbol{Y}_i = \boldsymbol{z}_{1,i},\end{cases} \tag{20}$$

where $\boldsymbol{\varepsilon}_i = \dot{\boldsymbol{D}} = [\varepsilon_{1,i}, \varepsilon_{2,i}, \varepsilon_{3,i}]^T$ is the first derivative of total disturbance, $\boldsymbol{Y}_i$ denotes the output of system (20). To ensure that the disturbance is estimable and compensable, their properties need to be constrained. Then, necessary assumption is proposed, as shown below.

Assumption 2 *The first derivative of total disturbance* $\boldsymbol{\varepsilon}_i = [\varepsilon_{1,i}, \varepsilon_{2,i}, \varepsilon_{3,i}]^T$ *is bounded, for* $\forall t \in [0, \infty)$*, the elements* $\boldsymbol{\varepsilon}_{k,i}, k = 1, 2, 3$*, satisfy the following inequality* $|\boldsymbol{\varepsilon}_{k,i}| \leqslant \bar{\varepsilon}$*, where* $\bar{\varepsilon} \in (0, \infty)$ *is a unknown positive constant.*

Denote $\widehat{\boldsymbol{z}}_{1,i}, \widehat{\boldsymbol{z}}_{2,i}$ as the output of the ESO in i^{th} OMR, and let $\boldsymbol{\epsilon}_{1,i} = \boldsymbol{z}_{1,i} - \widehat{\boldsymbol{z}}_{1,i}$, $\boldsymbol{\epsilon}_{2,i} = \boldsymbol{z}_{2,i} - \widehat{\boldsymbol{z}}_{2,i}$, be the estimation error. Then, the specific ESO for system (17) is designed as

$$\begin{cases} \dot{\widehat{\boldsymbol{z}}}_{1,i} = \boldsymbol{\Gamma}_i + \widehat{\boldsymbol{z}}_{2,i} + \mu_1 \mathrm{sig}^{r_1}(\boldsymbol{\epsilon}_{1,i}), \\ \dot{\widehat{\boldsymbol{z}}}_{2,i} = \mu_2 \mathrm{sig}^{r_2}(\boldsymbol{\epsilon}_{1,i}), \end{cases} \tag{21}$$

where $\mu_1, \mu_2 \in (0, \infty)$, $r_1 \in (0.5, 1)$ and $r_2 = 2r_1 - 1$ are the ESO parameters to be designed. The output $\boldsymbol{z}_{2,i}$ generated by ESO (21) is capable of driving the estimation errors $\boldsymbol{\epsilon}_{1,i}$ and $\boldsymbol{\epsilon}_{2,i}$ toward a neighborhood of zero within a finite time, the relevant proof of the convergence has been presented in reference [10] Theorem 1. Consequently, real-time estimation of the total disturbance $\boldsymbol{D}_i$ is achieved.

The sliding mode control strategy has the capability to overcome non-linearity and achieve repid convergence performance. It is expected that the nonlinear error system is first converge to the sliding surface, and then following a sliding mode control law to the stable condition. Therefore, the sliding surface of nonlinear control is designed as $\boldsymbol{s}_i = [s_{1,i}, s_{2,i}, s_{3,i}]$, which can be obtained by the equation

$$\boldsymbol{s}_i = \dot{\bar{\boldsymbol{e}}}_i + \psi(\bar{\boldsymbol{e}}_i), \tag{22}$$

The form of $\psi(\boldsymbol{e}_i)$ in Eq. (19) can be designed as

$$\psi(\bar{\boldsymbol{e}}_i) = \frac{\pi}{\rho T_p} \left(\|\bar{\boldsymbol{e}}_i\|^{-\frac{\rho}{2}} + \|\bar{\boldsymbol{e}}_i\|^{\frac{\rho}{2}} \right) \bar{\boldsymbol{e}}_i, \tag{23}$$

where $\gamma > 0$ is a given parameter. Under the classical Lyapunov theory, the controller term $\boldsymbol{\Gamma}_i$ in $\boldsymbol{u}_i$ is designed as

$$\begin{aligned} \boldsymbol{\Gamma}_i = &- \frac{\pi}{\rho T_p} \left(\|\boldsymbol{s}_i\|^{-\frac{\rho}{2}} + \|\boldsymbol{s}_i\|^{\frac{\rho}{2}} \right) \boldsymbol{s}_i - \widehat{\boldsymbol{z}}_{2,i} \\ &- \dot{\psi}(\bar{\boldsymbol{e}}_i) - \frac{1}{2\upsilon^2} \boldsymbol{s}_i, \end{aligned} \tag{24}$$

where the υ is a parameters determined by the stability analysis process. Here, the design of fully actuated behavioral tracking controller is completed.

Theorem 2 *The Multi-OMRs in proposed fully actuated behavioral tracking control scheme can be stable when executing the proposed ESO* (21)*, controller* (18)*. All states in error system* (17) *will converge to a neighborhood of zero.*

Proof 2 *Based on the deduction of behavioral tracking error variables* $\bar{\boldsymbol{e}}_i, \dot{\bar{\boldsymbol{e}}}_i$*, we consider a candidate Lyapunov function*

$$V_2(\bar{\boldsymbol{e}}_i, \dot{\bar{\boldsymbol{e}}}_i) = \frac{1}{2} \sum_{i=1}^{n} \boldsymbol{s}_i^T \boldsymbol{s}_i. \tag{25}$$

Then, we take the time derivative of $V_2(\bar{\boldsymbol{e}}_i, \dot{\bar{\boldsymbol{e}}}_i)$*, we have*

$$\dot{V}_2(\bar{\boldsymbol{e}}_i, \dot{\bar{\boldsymbol{e}}}_i) = \sum_{i=1}^{n} \left[\boldsymbol{s}_i^T \left(\boldsymbol{\Gamma}_i + \boldsymbol{D}_i + \dot{\psi}(\bar{\boldsymbol{e}}_i) \right) \right]. \tag{26}$$

Further, by substituting the controller (18) *into the relation* (26)*, one can obtain*

$$\begin{aligned} \dot{V}_2(\bar{\boldsymbol{e}}_i, \dot{\bar{\boldsymbol{e}}}_i) = &- \sum_{i=1}^{n} \Bigg\{ \frac{\pi}{\rho T_p} \boldsymbol{s}_i^T \left[\left(\|\boldsymbol{s}_i\|^{-\frac{\rho}{2}} + \|\boldsymbol{s}_i\|^{\frac{\rho}{2}} \right] \boldsymbol{s}_i \right. \\ &\left. + \boldsymbol{s}_i^T \boldsymbol{\epsilon}_{2,i} + \frac{1}{2\upsilon^2} \boldsymbol{s}_i^T \boldsymbol{s}_i \right\}, \end{aligned} \tag{27}$$

where the definition of $\boldsymbol{\epsilon}_{2,i}$ *has been present in above section. Based on the Mean value theorem, it can be inferred that*

$$\boldsymbol{s}_i^T \boldsymbol{\epsilon}_{2,i} \leqslant \frac{1}{2\upsilon^2} \boldsymbol{s}_i^T \boldsymbol{s}_i + \frac{\upsilon^2}{2} \boldsymbol{\epsilon}_{2,i}^T \boldsymbol{\epsilon}_{2,i}, \tag{28}$$

where $0 < \upsilon < 2$ *is a weight coefficient. From reference [11] Lemma* 1*, we can infer that the observation error of the ESO* (21) *is bounded, meaning that for* $\forall t \in [0, \infty)$*, there exists a positive constant* ϱ *that makes* $\boldsymbol{\epsilon}_{2,i}^T \boldsymbol{\epsilon}_{2,i} < \varrho$*. Then, by substituting the inequality* (28) *into the relation* (27)*, we get*

$$\begin{aligned} \dot{V}(\bar{\boldsymbol{e}}_i, \dot{\bar{\boldsymbol{e}}}_i) \leqslant &- \sum_{i=1}^{n} \left[\frac{\pi}{\rho T_p} \Bigg(V(\bar{\boldsymbol{e}}_i, \dot{\bar{\boldsymbol{e}}}_i)^{1-\frac{\rho}{2}} \right. \\ &\left. + V(\bar{\boldsymbol{e}}_i, \dot{\bar{\boldsymbol{e}}}_i)^{1+\frac{\rho}{2}} \Bigg) + \frac{\upsilon^2}{2} \boldsymbol{\epsilon}_{2,i}^T \boldsymbol{\epsilon}_{2,i} \right] \leqslant 0.. \end{aligned} \tag{29}$$

Therefore, the error system (17) *is large-scale asymptotic stable, such that all states in error system* (17) *will converge to a neighborhood of zero.*

Remark 2 *The fully actuated behavioral tracking controller enables each OMR to accurately track the desired motion signals of distributed behaviors, thereby realizing the desired distributed formation control of Multi-OMRs.*

5 Simulation result

For the proposed fully actuated behavioral control strategy and algorithm, a simulation in two dimensional space under uncertain disturbances scenarios is presented in this Section. In the simulation, three OMRs move according to the preset distributed behavioral task function trajectories. The important parameters which used in the simulation are shown in Table 1, including the gain parameters of proposed formation behaviors and configuration of Multi-OMRs, and parameters proposed fully actuated behavioral controller.

Moreover, the external disturbance is designed as

$$\boldsymbol{h}_i(t) = \begin{bmatrix} 1 + 2\cos(0.3t) \\ 2 + 1.5\sin(0.3t) + 3\cos(0.3t) \\ 3 + 2\sin(0.2t) \\ 2.5 + \sin(0.1t) \end{bmatrix} \times 10^{-2}\mathrm{Nm},$$

the initial state of the Multi-OMRs are chosen as $\boldsymbol{x}(0) = \begin{bmatrix} -2.5 & -5 & -7.5 \\ 20 & 12.5 & 27 \end{bmatrix}, \dot{\boldsymbol{x}}(0) = \begin{bmatrix} 0 & 0 & 0 \\ 0 & 0 & 0 \end{bmatrix}$, and the trajectory of the virtual formation leader is given as $\boldsymbol{x}_{\mathrm{o}}(t) = \begin{bmatrix} 20\sin(2t+1) \\ -20\cos(t+0.5) \end{bmatrix}$. We also choose $\hat{\boldsymbol{z}}_1(0) = \begin{bmatrix} 0.01 & 0.01 & 0.01 \\ 0.01 & 0.01 & 0.01 \\ 0.01 & 0.01 & 0.01 \end{bmatrix}, \hat{\boldsymbol{z}}_2(0) = \begin{bmatrix} 0 & 0 & 0 \\ 0 & 0 & 0 \\ 0 & 0 & 0 \end{bmatrix}$ as the initial value of ESO (10).

The moving trajectories of the three OMRs and the virtual leader using proposed formation behavioral control methods and fully actuated behavioral controller as shown in

Table 1: Parameter values in the simulation

Parameters	Value
Sampling frequency, f_q	$60Hz$
Wheel radius of OMR, R	$0.0375m$
Total mass of a OMR, m	$1.2kg$
Moment of inertia about z-axis, I_z	$0.01kg \cdot m^2$
Moment of inertia about wheel axis, I_w	$0.02kg \cdot m^2$
Distance between shafts of OMR, $2l$	$0.06m$
Distance between wheel of OMR, $2w$	$0.04m$
Static friction coefficient, C_{f}	0.125
Viscous friction coefficient, C_θ	0.2
Adjacency matrix, $\boldsymbol{W}$	$\begin{bmatrix} 1 & 0 & 0 \\ 1 & 0 & 0 \\ 1 & 1 & 0 \end{bmatrix}$
Leader adjacency matrix, $\boldsymbol{b}$	$[1,0,0]^T$
Gain of ILM behavior, $\boldsymbol{\Lambda}_{\mathrm{m}}$	3.5
Gain of DF behavior, $\boldsymbol{\Lambda}_{\mathrm{f}}$	2
DF behavior parameters $\kappa_1, \kappa_2, \kappa_3$	$0.33, 0.33, 0.33$
Leader state estimator parameters, $\iota_1, \iota_2, \iota_3, \iota_4, \eta_1, \eta_2$	$2, 3, 2, 14$ $\frac{3}{2}, \frac{3}{2}$
Offsets between followers and leader $\boldsymbol{\zeta}$	$\begin{bmatrix} 3 & 3 & -3 \\ 3 & -3 & 3 \end{bmatrix}$
Controller parameters, $\rho, T_{\mathrm{p}}, \upsilon$	$0.5, 10, 1.5$
ESO parameters, μ_1, μ_2, r_1, r_2	$0.6, 0.2, 0.7, 0.4$

Fig. $2(a)$. In addition, three snapshots are provided to show the formation of three OMRs and the virtual leader at $t = 4.3s$, $t = 24.5s$ and $t = 45.5s$. The variation curve of control input, state, task error and tracking error are shown also in Fig. $2(b-h)$. Under the proposed control strategy, the three OMRs smoothly and rapidly converge to the desired distributed formation task from diverse initial states. The tracking performance of nonlinear system states is excellent. Furthermore, both behavioral errors and behavioral task errors converge rapidly to zero in the vicinity.

6 Conclusion

This paper explores distributed formation control for Multi-OMRs with uncertainties and disturbances. The FABC scheme is proposed for efficient formation control. The scheme includes a distributed formation behavior using a fixed-time protocol under the NSBC teamwork. OMRs get their kinematic commands through a prioritized fusion process. We also the convert over-actuated OMR system to fully actuated ones and design a sliding-mode controller with an ESO for precise behavioral tracking. Simulation results show the effectiveness of propersed method.

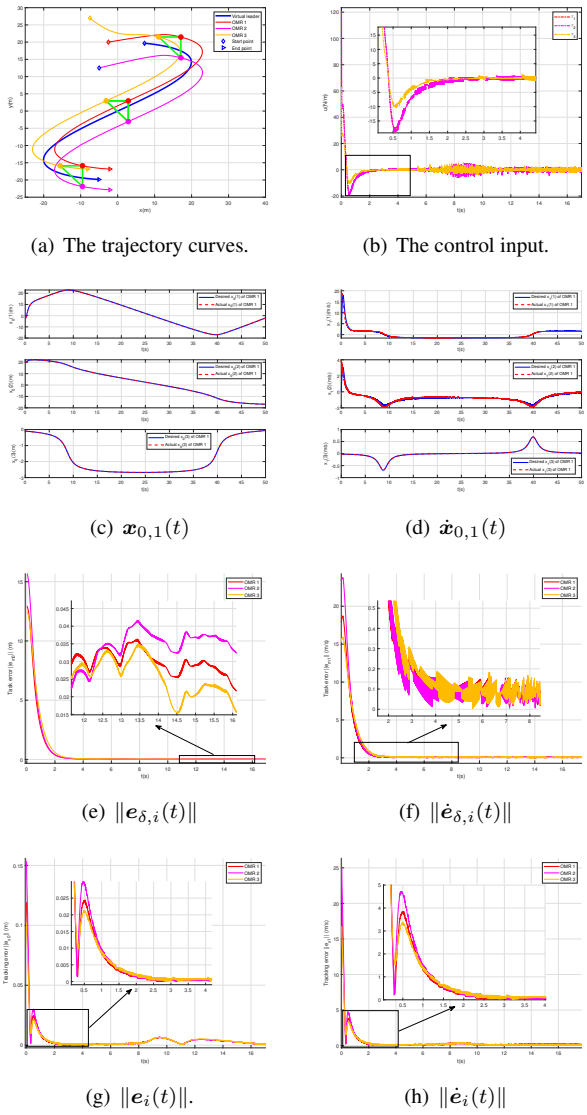

(a) The trajectory curves. (b) The control input.

(c) $\boldsymbol{x}_{0,1}(t)$ (d) $\dot{\boldsymbol{x}}_{0,1}(t)$

(e) $\|\boldsymbol{e}_{\delta,i}(t)\|$ (f) $\|\dot{\boldsymbol{e}}_{\delta,i}(t)\|$

(g) $\|\boldsymbol{e}_i(t)\|$. (h) $\|\dot{\boldsymbol{e}}_i(t)\|$

Fig. 2: The simulation results.

References

[1] V. Alakshendra, S. Chiddarwar, Adaptive robust control of Mecanum-wheeled mobile robot with uncertainties. *Nonlinear Dynamics*,2017, 87: 2147-2169.

[2] D. Yu, C. Chen, H. Xu, Fuzzy Swarm Control Based on Sliding-Mode Strategy With Self-Organized Omnidirectional Mobile Robots System. *IEEE Transactions on Systems, Man, and Cybernetics*,2021, PP(99):1-13.

[3] D. Wang, W. Wei, X. Wang, Y. Gao, Y. Li, Q. Yu, Z. Fan, Formation control of multiple mecanum-wheeled mobile robots with physical constraints and uncertainties. *Applied Intelligence*, 2022: 1-20.

[4] G. Antonelli, S. Chiaverini, Kinematic control of platoons of autonomous vehicles. *IEEE Transactions on Robotics*, 2006, 22(6): 1285-1292.

[5] N. Zhou, X. Cheng, Z. Sun, Y. Xia, Fixed-time cooperative behavioral control for networked autonomous agents with second-order nonlinear dynamics. *IEEE Transactions on Cybernetics*, 2021, 52(9): 9504-9518.

[6] Z. Zhang, Z. Mo, Y. Chen, J. Huang, Reinforcement learning behavioral control for nonlinear autonomous system. *IEEE/CAA Journal of Automatica Sinica*, 2022, 9(9): 1561-1573.

[7] G. Duan, High-order fully actuated system approaches: Part I. Models and basic procedure. *International Journal of Systems Science*, 2021, 52(2): 422-435.

[8] H. Du, G. Wen, D. Wu, Y. Cheng, J. Lü, Distributed fixed-time consensus for nonlinear heterogeneous multi-agent systems. *Automatica*, 2020, 113: 108797.

[9] G. Liu, B. Li, G. Duan, An Optimal FASA Approach for UAV Trajectory Tracking Control. *Guidance, Navigation and Control*, 2023: 2350015.

[10] B. Li, Q. Hu, Y. Yang, Continuous finite-time extended state observer based fault tolerant control for attitude stabilization. *Aerospace Science and Technology*,2019, 84: 204-213.

[11] H. Sun, Y. Wu, J. Zhang, A distributed predefined-time attitude coordination control scheme for multiple rigid spacecraft. *Aerospace Science and Technology*, 2023, 133: 108134.

Proceedings of the 3rd Conference on Fully Actuated System Theory and Applications
May 10-12, 2024, Shenzhen, China

Adaptive neural-networks control for uncertain second-order fully actuated strict-feedback systems without over-parametrization

Wen-Nian Qi, Ai-Guo Wu, Jie Zhang
School of Mechanical Engineering and Automation, Harbin Institute of Technology (Shenzhen), Shenzhen 518055, P.R. China
E-mail: qwnhitsz@163.com

Abstract: In this paper, the tracking control is addressed for second-order fully actuated strict-feedback systems with unknown dynamics. An adaptive neural-networks control law is constructed via command filtered backstepping control approach. Different from the existing traditional first-order state-space backstepping approach, the proposed control law can avoid "explosion of complexity", and does not need to convert the second-order systems into first-order form. Besides, the neural networks are utilized to identify unknown dynamics in the systems with only two tuning parameters. Based on Lyapunove stability theory, it is proven that the closed-loop system under the proposed adaptive neural-networks control law is stable in the sense of the uniformly ultimately bounded.

Key Words: Fully actuated systems; Nonlinear uncertainty; Adaptive neural-networks; Command filtered backstepping.

1 Introduction

Second-order nonlinear systems are widely applied in engineering applications, such as robotic systems [1], aircraft systems [2], satellite attitude control systems [3]. However, in the control law design procedure, these second-order systems are usually transformed into first-order state-space systems. Recently, a systematic high-order fully actuated system approach [4–6] has been drawing considerable attention since it could directly deal with the analysis and control of high-order systems without converting them into first-order ones. Based on the high-order fully actuated system approach, some adaptive backstepping control laws were constructed for second-order and high-order strict-feedback nonlinear systems in [7–9]. Note that the backstepping control suffers from "explosion of complexity" caused by repeated differentiation for the virtual control signals. To address this problem, adaptive command filtered backstepping (CFB) control approaches were proposed in [10, 11] for second-order and high-order strict-feedback nonlinear systems. It is worthy mentioning that the presented control laws in [8, 9, 11] only could deal with parameter uncertainties. As for the dynamic uncertainties, the proposed approaches in [7, 10] required the unknown nonlinear dynamics to be bounded by a known function. The control of second-order strict-feedback nonlinear systems with completely unknown nonlinear dynamics needs further investigation.

In view of the aforementioned discussions, the tracking control is investigated for a class of second-order strict-feedback nonlinear systems with unknown dynamics. The objective is to construct a robust control law such that the output of the closed-loop system tracks a reference signal. Particularly, the unknown nonlinear dynamics is approximated by utilizing neural-networks (NNs), By combining this techniques with CFB approach, an NNs-based adaptive command filtered backstepping control law is constructed. Compared with the previous results, the main contributions can be concluded as follows:

This work was supported by the Science Center Program of National Natural Science Foundation of China under Grant No.62188101.

1) The proposed NNs-based adaptive command filtered backstepping control law do not need to convert the second-order systems into first-order forms.

2) Only two adaptive laws are introduced to avoid over-parametrization problem of NNs.

Notations. Throughout this paper, For $m < n$, we use $\mathbb{I}[m, n]$ to denote the set $\{m, m+1, \cdots, n\}$. For any vector $x \in \mathbb{R}^n$, we use $\|x\|$ to denote the 2-norm of the vector x. Besides, the following symbols are defined.

$$x^{(0\sim n)} = \begin{bmatrix} x \\ \dot{x} \\ \vdots \\ x^{(n)} \end{bmatrix}, x_{i\sim j}^{(0\sim n)} = \begin{bmatrix} x_i^{(0\sim n)} \\ x_{i+1}^{(0\sim n)} \\ \vdots \\ x_j^{(0\sim n)} \end{bmatrix}, j \geq i,$$

$$A^{0\sim n-1} = \begin{bmatrix} A_0 & A_1 & \cdots & A_{n-1} \end{bmatrix},$$

$$\Phi\left(A^{0\sim n-1}\right) = \begin{bmatrix} 0 & I & & \\ & & \ddots & \\ & & & I \\ -A_0 & -A_1 & & -A_{n-1} \end{bmatrix}.$$

2 Problem Formation

Consider the following second-order fully actuated strict-feedback nonlinear system

$$\begin{cases} \ddot{x}_1 = f_1\left(x_1^{(0\sim 1)}\right) + g_1\left(x_1^{(0\sim 1)}\right) x_2, \\ \ddot{x}_2 = f_2\left(x_{1\sim 2}^{(0\sim 1)}\right) + g_2\left(x_{1\sim 2}^{(0\sim 1)}\right) x_3, \\ \vdots \\ \ddot{x}_{n-1} = f_{n-1}\left(x_{1\sim n-1}^{(0\sim 1)}\right) + g_{n-1}\left(x_{1\sim n-1}^{(0\sim 1)}\right) x_n, \\ \ddot{x}_n = f_n\left(x_{1\sim n}^{(0\sim 1)}\right) + g_n\left(x_{1\sim n}^{(0\sim 1)}\right) u, \\ y = x_1, \end{cases} \tag{1}$$

where $x_i \in \mathbb{R}$, $i \in \mathbb{I}[1, n]$ are the state variables, $u \in \mathbb{R}$ and $y \in \mathbb{R}$ are the input and output of the strict-feedback

system respectively; $f_i\left(x_{1\sim i}^{(0\sim 1)}\right)$, $g_i\left(x_{1\sim i}^{(0\sim 1)}\right)$, $i \in \mathbb{I}[1,n]$ are two sets of sufficiently smooth functions. For simplicity, the functions $g_i\left(x_{1\sim i}^{(0\sim 1)}\right)$, $i \in \mathbb{I}[1,n]$ are abbreviated as g_i in the rest of the paper. In this paper, $f_i\left(x_{1\sim i}^{(0\sim 1)}\right), i \in \mathbb{I}[1,n]$ are unknown.

The objective of this paper is to construct an adaptive neural-networks control law for the second-order fully actuated strict-feedback system (1), such that the output y tracks the reference signal y_0. The following assumptions on reference signal and the system (1) are required.

Assumption 1 *The reference signal y_0 and its first-order to fourth-order derivatives $\dot{y}_0$, $\ddot{y}_0$, $\dddot{y}_0$, and $y_0^{(4)}$ are smooth, avaiable and bounded.*

Assumption 2 *Let Ω_{d} represent an open set which contains the origin, the initial condition $x(0)$, and the reference signal y_0. For the second-order fully actuated strict-feedback system (1), $f_i\left(x_{1\sim i}^{(0\sim 1)}\right)$ and $g_i\left(x_{1\sim i}^{(0\sim 1)}\right)$, $i \in \mathbb{I}[1,n]$ are bounded on Ω_{d}. Besides, $|g_i\left(x_{1\sim i}^{(0\sim 1)}\right)| \neq 0$.*

3 RBFNNs and Preliminaries

From [12], any unknown smooth function $f(x) : \mathbb{R}^n \to \mathbb{R}^m$ can be approximated to a sufficient degree of accuracy over the compact set Ω_x by

$$f(x) = \theta^{\mathrm{T}}\varphi(x) + \varepsilon(x), \tag{2}$$

where $x \in \Omega_x \subset \mathbb{R}^n$ is the input vector, $\varphi(x) \in \mathbb{R}^r$ is the basis function vector, $\theta \in \mathbb{R}^{r\times m}$ is the weight matrix, and $\varepsilon(x)$ is the bounded approximation error. Denote $\varphi(x) = [\varphi_1(x)\ \varphi_2(x)\ \cdots\ \varphi_r(x)]^{\mathrm{T}}$ where $r > 1$ is the number of the neurons. In this paper, we adopt the Gaussian function as the basis function. That is , $\varphi_j(x)$ is in the form of

$$\varphi_j(x) = \exp\left(-\frac{\|x - c_j\|_2^2}{b_j^2}\right), j \in \mathbb{I}[1,r], \tag{3}$$

where c_j and b_j are the center and width of the j-th neuron respectively. The optimal weight matrix θ^* is defined as

$$\theta^* = \arg\min_\theta \left\{\sup_{x\in\Omega_x} \left\|f(x) - \theta^{\mathrm{T}}\varphi(x)\right\|_2\right\}.$$

In the sequel, some necessary definitions and useful lemmas are introduced.

Lemma 3.1 *Let $A^{(0\sim n-1)} \in \mathbb{R}^{r\times nr}$ and $\Phi(A^{(0\sim n-1)}) \in \mathbb{R}^{nr\times nr}$ satisfying*

$$\mathrm{Re}\lambda_i(\Phi) \leq -\frac{\mu}{2}, i \in \mathbb{I}[1,n],$$

where $\mu > 0$, then there exists a positive definite symmetric matrix P satisfying

$$\Phi^{\mathrm{T}}\left(A^{0\sim n-1}\right)P + P\Phi\left(A^{0\sim n-1}\right) \leq \mu P\left(A^{0\sim n-1}\right).$$

Lemma 3.2 *[13] (Young's inequality) For any $x \in \mathbb{R}$ and $y \in \mathbb{R}$, the following inequality holds:*

$$xy \leq \frac{\varepsilon^m}{m}|x|^m + \frac{1}{n\varepsilon^n}|y|^n,$$

where $\varepsilon > 0$, $m > 1$, $n > 1$, and $(m-1)(n-1) = 1$.

4 Control Law Design

To accomplish our control goal, we need to develop virtual control laws with command filters step by step. Besides, the NNs are utilized to approximate unknown nonlinear functions in the backstepping design procedure, and the adaptive technique is adopted to update tuning parameters.

Before constructing the control law for the system (1), the unknown function $f_i\left(x_{1\sim i}^{(0\sim 1)}\right)$ in (1) needs to be approximated by using radial basis function NNs (RBFNNs) in the form of

$$f_i\left(x_{1\sim i}^{(0\sim 1)}\right) = \theta_i^{\mathrm{T}}\varphi_i\left(x_{1\sim i}^{(0\sim 1)}\right) + \delta_i, i \in \mathbb{I}[1,n], \tag{4}$$

where θ_i is the weight vector, and $\varphi_i\left(x_{1\sim i}^{(0\sim 1)}\right)$ is the basis function vector, which is abbreviated as φ_i in the rest of the paper. The approximation error δ_i satisfies $|\delta_i| < \bar{\delta}_i$ with positive constant $\bar{\delta}_i$. Denote

$$\theta = \max\{\|\theta_1\|^2, \|\theta_2\|^2, \cdots, \|\theta_n\|^2\}, \tag{5}$$

and

$$\delta = \max\{\bar{\delta}_1, \bar{\delta}_2, \cdots, \bar{\delta}_n\}. \tag{6}$$

Besides, suppose $A_i^{0\sim 1} \in \mathbb{R}^{1\times 2}, i \in \mathbb{I}[1,n]$ are a set of matrices satisfying

$$\Phi^{\mathrm{T}}\left(A_i^{0\sim 1}\right)P_i + P_i\Phi\left(A_i^{0\sim n-1}\right) \leq -\mu_i P_i, i \in \mathbb{I}[1,n], \tag{7}$$

where $0 < \mu_i \leq -2\mathrm{Re}\lambda_j\left(\Phi\left(A_i^{0\sim n-1}\right)\right), j = 1,2$, and

$$P_i = \begin{bmatrix} P_{\mathrm{F}i} & P_{\mathrm{L}i} \end{bmatrix} \in \mathbb{R}^{2\times 2}, i \in \mathbb{I}[1,n],$$

are positive definite symmetric matrices.

For the second-order fully actuated strict-feedback system (1), the tracking error variables are defined as

$$s_1 = y_1 - y_0, \tag{8}$$
$$s_i = x_i - \bar{\alpha}_i, i \in \mathbb{I}[2,n], \tag{9}$$

where $\bar{\alpha}_i$ is the output of a command filter with the virtual control law α_i being the input. Besides, the boundary layer errors are defined as

$$z_{1i} = \bar{\alpha}_i - \alpha_i, \tag{10}$$
$$z_{2i} = \dot{\bar{\alpha}}_i - \dot{\alpha}_i, i \in \mathbb{I}[2,n]. \tag{11}$$

In what follows, virtual control laws α_i, $i \in \mathbb{I}[2,n]$, command filters and adaptive laws are constructed in n steps to obtain the tracking control law u.

Step 1: the design of virtual control law α_2.

From (1), (4), and (8)$\sim$(10), the second-order derivative of s_1 is

$$\begin{aligned}\ddot{s}_1 &= f_1\left(x_1^{(0\sim 1)}\right) + g_1x_2 - \ddot{y}_0\\ &= g_1(s_2 + z_{12} + \alpha_2) + \theta_1^{\mathrm{T}}\varphi_1 + \delta_1 - \ddot{y}_0.\end{aligned} \tag{12}$$

Then the first virtual control law α_2 is designed as

$$\alpha_2 = -\frac{1}{g_1}\left(A_1^{0\sim 1}s_1^{(0\sim 1)} + h_1 - \ddot{y}_0\right), \tag{13}$$

$$h_1 = \frac{1}{4a_1^2}\left(\hat{\theta}\left\|\varphi_1\right\|^2 + \hat{\delta}\right) P_{\mathrm{L}1}^{\mathrm{T}} s_1^{(0\sim1)}, \tag{14}$$

where $a_1 > 0$, and $\hat{\theta}$ and $\hat{\delta}$ are the estimations of θ in (5) and δ in (6), respectively. Substituting (13) and (14) into (12), yields

$$\begin{aligned}\ddot{s}_1 =& -A_1^{0\sim1} s_1^{(0\sim1)} + g_1 s_2 + g_1 z_{12} \\ &+ \theta_1^{\mathrm{T}}\varphi_1 + \delta_1 - h_1.\end{aligned} \tag{15}$$

Then we pass the virtual control signal α_2 through a second-order filter

$$\begin{cases}\dot{\bar{\alpha}}_2 = \phi_2 \\ \dot{\phi}_2 = -2\zeta_2\omega_2\phi_2 - \omega_2^2\left(\bar{\alpha}_2 - \alpha_2\right)\end{cases} \tag{16}$$

where $\omega_2 > 0$ and $0 < \zeta_2 \leq 1$. The outputs $\bar{\alpha}_2$, $\dot{\bar{\alpha}}_2 = \phi_2$, and $\ddot{\bar{\alpha}}_2 = -2\zeta_2\omega_2\phi_2 - \omega_2^2\left(\bar{\alpha}_2 - \alpha_2\right)$ are used in the next step.

Step i ($i \in \mathbb{I}[2, n-1]$): the design of the virtual control law α_{i+1}.

From (1), (4), (9), and (11), the second-order derivative of s_i is

$$\begin{aligned}\ddot{s}_i &= f_i\left(x_i^{(0\sim1)}\right) + g_i x_{i+1} - \ddot{\bar{\alpha}}_i \\ &= g_i\left(s_{i+1} + z_{2i+1} + \alpha_{i+1}\right) + \theta_i^{\mathrm{T}}\varphi_i + \delta_i - \ddot{\bar{\alpha}}_i.\end{aligned} \tag{17}$$

Then the ith virtual control law α_{i+1} is designed as

$$\alpha_{i+1} = -\frac{1}{g_i}\left(A_i^{0\sim1} s_i^{(0\sim1)} + h_i - \ddot{\bar{\alpha}}_i\right), \tag{18}$$

$$h_i = \frac{1}{4a_i^2}\left(\hat{\theta}\left\|\varphi_i\right\|^2 + \hat{\delta}\right) P_{\mathrm{L}i}^{\mathrm{T}} s_i^{(0\sim1)}, \tag{19}$$

with $a_i > 0$. Substituting (18) and (19) into (17), yields

$$\begin{aligned}\ddot{s}_i =& -A_i^{0\sim1} s_i^{(0\sim1)} + g_i s_{i+1} + g_i z_{1(i+1)} \\ &+ \theta_i^{\mathrm{T}}\varphi_i + \delta_i - h_i.\end{aligned} \tag{20}$$

Then we pass the virtual control signal α_{i+1} through a second-order filter

$$\begin{cases}\dot{\bar{\alpha}}_{i+1} = \phi_{i+1} \\ \dot{\phi}_{i+1} = -2\zeta_{i+1}\omega_{i+1}\phi_{i+1} - \omega_{i+1}^2\left(\bar{\alpha}_{i+1} - \alpha_{i+1}\right)\end{cases} \tag{21}$$

where $\omega_{i+1} > 0$ and $0 < \zeta_{i+1} \leq 1$. The outputs $\bar{\alpha}_{i+1}$, $\dot{\bar{\alpha}}_{i+1} = \phi_{i+1}$, and $\ddot{\bar{\alpha}}_{i+1} = -2\zeta_{i+1}\omega_{i+1}\phi_{i+1} - \omega_{i+1}^2\left(\bar{\alpha}_{i+1} - \alpha_{i+1}\right)$ are used in the next step.

Step n: the design of the actual control law u.

From (1) and (4), the second-order derivative of s_n is

$$\begin{aligned}\ddot{s}_n &= f_n\left(x_n^{(0\sim1)}\right) + g_n u - \ddot{\bar{\alpha}}_n \\ &= g_n u + \theta_n^{\mathrm{T}}\varphi_n + \delta_n - \ddot{\bar{\alpha}}_n.\end{aligned} \tag{22}$$

Then the actual control law u is designed as

$$u = -\frac{1}{g_n}\left(A_n^{0\sim1} s_n^{(0\sim1)} + h_n - \ddot{\bar{\alpha}}_n\right), \tag{23}$$

$$h_n = \frac{1}{4a_n^2}\left(\hat{\theta}\left\|\varphi_n\right\|^2 + \hat{\delta}\right)\left\|s_n^{(0\sim1)}\right\|^2 \left\|P_{\mathrm{L}n}\right\|^2, \tag{24}$$

with $a_n > 0$. Substituting (23) and (24) into (22), yields

$$\ddot{s}_n = -A_n^{0\sim1} s_n^{(0\sim1)} + \theta_n^{\mathrm{T}}\varphi_n + \delta_n - h_n. \tag{25}$$

Besides, the tuning parameters $\hat{\theta}$ and $\hat{\delta}$ are updated by

$$\dot{\hat{\theta}} = \tau_1 \sum_{i=1}^{n} \frac{1}{4a_i^2}\left\|s_i^{(0\sim1)}\right\|^2 \left\|P_{\mathrm{L}i}\right\|^2 \left\|\varphi_i\right\|^2 - \tau_1\varsigma_1\hat{\theta}, \tag{26}$$

$$\dot{\hat{\delta}} = \tau_2 \sum_{i=1}^{n} \frac{1}{4a_i^2}\left\|s_i^{(0\sim1)}\right\|^2 \left\|P_{\mathrm{L}i}\right\|^2 - \tau_2\varsigma_2\hat{\delta}, \tag{27}$$

where τ_1, τ_2, ς_1, and ς_2 are positive parameters.

By now, the details of the design of the adaptive neural-networks control law with virtual control laws, command filters, and adaptive laws are presented. In the next section, the stability of the resulted closed-loop of the system (1) under the proposed control law is analyzed.

5 Stability Analysis

In this section, the system equations of the closed-loop tracking system under the proposed control law are derived at first, and then the stability analysis of the closed-loop system is conducted.

In view of the boundary layer errors (10) and (11), and the command filters (16) and (21), the dynamics of the boundary layer errors can be obtained as

$$\begin{aligned}&\dot{z}_{1i} = z_{2i}, \\ &\dot{z}_{2i} = -2\zeta_i\omega_i z_{2i} - \omega_i^2 z_{1i} - \ddot{\alpha}_i - 2\zeta_i\omega_i\dot{\alpha}_i, i \in \mathbb{I}[2, n],\end{aligned}$$

which can be written in a compact form

$$\dot{z}_i = A_{\mathrm{z}i} z_i - \varepsilon_i, \tag{28}$$

with

$$z_i = \begin{bmatrix} z_{1i} \\ z_{2i}\end{bmatrix}, A_{\mathrm{z}i} = \begin{bmatrix} 0 & 1 \\ -\omega_i^2 & -2\zeta_i\omega_i\end{bmatrix}, \varepsilon_i = \begin{bmatrix} 0 \\ \ddot{\alpha}_i - 2\zeta_i\omega_i\dot{\alpha}_i\end{bmatrix}.$$

It can be checked that $A_{\mathrm{z}i}$ is Hurwitz, and then Lemma 3.1 can be used to obtain that there are positive definite matrices Q_i, $i \in \mathbb{I}[2, n]$, such that

$$A_{\mathrm{z}i}^{\mathrm{T}} Q_i + Q_i A_{\mathrm{z}i} \leq -\mu_{\mathrm{z}i} Q_i, i \in \mathbb{I}[2, n],$$

where $0 < \mu_{\mathrm{z}i} \leq -2\mathrm{Re}\lambda_j\left(A_{\mathrm{z}i}\right)$ for all $j = 1, 2$.

In view of (15), (20) and (25), the dynamics of the error systems can be rewritten as

$$\begin{aligned}\dot{s}_i^{(0\sim1)} =& \Phi\left(A_1^{0\sim1}\right) s_i^{(0\sim1)} + \begin{bmatrix} 0 \\ g_i s_{i+1}\end{bmatrix} + \begin{bmatrix} 0 \\ g_i z_{1(i+1)}\end{bmatrix} \\ &+ \begin{bmatrix} 0 \\ \theta_i^{\mathrm{T}}\varphi_i + \delta_i\end{bmatrix} - \begin{bmatrix} 0 \\ h_i\end{bmatrix}, i \in \mathbb{I}[1, n-1],\end{aligned} \tag{29}$$

$$\dot{s}_n^{(0\sim1)} = \Phi\left(A_n^{0\sim1}\right) s_n^{(0\sim1)} + \begin{bmatrix} 0 \\ \theta_n^{\mathrm{T}}\varphi_n + \delta_n\end{bmatrix} - \begin{bmatrix} 0 \\ h_n\end{bmatrix}. \tag{30}$$

Besides, define the approximated errors

$$\tilde{\theta} = \theta - \hat{\theta}, \quad \tilde{\delta} = \delta - \hat{\delta}. \tag{31}$$

Then by (26) and (27), the dynamics of the approximated errors can be obtained as

$$\dot{\tilde{\theta}} = -\tau_1 \sum_{i=1}^{n} \frac{1}{4a_i^2}\left\|s_i^{(0\sim1)}\right\|^2 \left\|P_{\mathrm{L}i}\right\|^2 \left\|\varphi_i\right\|^2 + \tau_1\varsigma_1\hat{\theta}, \tag{32}$$

$$\dot{\hat{\delta}} = -\tau_2 \sum_{i=1}^{n} \frac{1}{4a_i^2} \left\| s_i^{(0\sim1)} \right\|^2 \|P_{\mathrm{L}i}\|^2 + \tau_2 \varsigma_2 \hat{\delta}. \tag{33}$$

The tracking control performance of the closed-loop system is stated in the following theorem.

Theorem 1 *For the closed-loop system composed of (28), (29), (30), (32), and (33) under the proposed control law (23), if Assumptions 1 and 2 are satisfied, then the tracking errors s_i, $i \in \mathbb{I}[1,n]$ in (8) and (9), the boundary layer errors z_i, $i \in \mathbb{I}[2,n]$ in (10) and (11), and the approximation errors $\tilde{\theta}$ and $\tilde{\delta}$ in (31) are uniformly ultimately bounded.*

Proof. For the closed-loop system composed of (28), (29), (30), (32), and (33) a Lyapunov function candidate is chosen as

$$V = V_{\mathrm{s}} + V_{\mathrm{z}} + \frac{1}{2\tau_1}\tilde{\theta}^2 + \frac{1}{2\tau_2}\tilde{\delta}^2, \tag{34}$$

where

$$V_{\mathrm{s}} = \frac{1}{2}\sum_{i=1}^{n} \left(s_i^{(0\sim1)} \right)^{\mathrm{T}} P_i s_i^{(0\sim1)}, \tag{35}$$

and

$$V_{\mathrm{z}} = \frac{1}{2}\sum_{i=2}^{n} z_i^{\mathrm{T}} Q_i z_i. \tag{36}$$

Next, we aim to obtain the time derivative of V. For this end, we derive $\dot{V}_{\mathrm{s}}$ and $\dot{V}_{\mathrm{z}}$ successively.

With the help of (29) and (30), it can be obtained from (35) that

$$\begin{aligned}
\dot{V}_{\mathrm{s}} =& \sum_{i=1}^{n} \left(s_i^{(0\sim1)} \right)^{\mathrm{T}} P_i \dot{s}_i^{(0\sim1)} \\
=& \frac{1}{2}\sum_{i=1}^{n} \left(s_i^{(0\sim1)} \right)^{\mathrm{T}} \left(\Phi^{\mathrm{T}}\left(A_i^{0\sim1}\right) P_i + P_i \Phi\left(A_i^{0\sim1}\right) \right) s_i^{(0\sim1)} \\
&+ \sum_{i=1}^{n-1} \left(s_i^{(0\sim1)} \right)^{\mathrm{T}} P_i \begin{bmatrix} 0 \\ g_i s_{i+1} + g_i z_{1(i+1)} \end{bmatrix} \\
&+ \sum_{i=1}^{n} \left(s_i^{(0\sim1)} \right)^{\mathrm{T}} P_i \begin{bmatrix} 0 \\ \theta_i^{\mathrm{T}} \varphi_i + \delta_i \end{bmatrix} \\
&- \sum_{i=1}^{n} \left(s_i^{(0\sim1)} \right)^{\mathrm{T}} P_i \begin{bmatrix} 0 \\ h_i \end{bmatrix}.
\end{aligned} \tag{37}$$

By using Young's inequality and (7), it can be deduced that

$$\begin{aligned}
\dot{V}_{\mathrm{s}} \leq& -\frac{1}{2}\varpi_1 \sum_{i=1}^{n} \left(s_i^{(0\sim1)} \right)^{\mathrm{T}} P_i s_i^{(0\sim1)} \\
&+ \sum_{i=2}^{n} \frac{g_{i-1}^2}{4\lambda_{\min}(P_i)} (z_{1i})^{\mathrm{T}} P_i z_{1i} \\
&+ \sum_{i=1}^{n} \frac{1}{4a_i^2} \left(\tilde{\theta} \|\varphi_i\|^2 + \tilde{\delta} \right) \left\| s_i^{(0\sim1)} \right\|^2 \|P_{\mathrm{L}i}\|^2 \\
&+ 2\sum_{i=1}^{n} a_i,
\end{aligned} \tag{38}$$

where

$$\varpi_1 = \min_{i\in\mathbb{I}[2,n-1]} \{ \mu_1 - 4\lambda_{\max}(P_1), \mu_n, \mu_i - 4\lambda_{\max}(P_i) - \frac{g_{i-1}^2}{2\lambda_{\min}(P_i)} \}.$$

In view of (28), it can be obtained from (36) that

$$\begin{aligned}
\dot{V}_{\mathrm{z}} =& \frac{1}{2}\sum_{i=2}^{n} z_i^{\mathrm{T}} \left(A_{\mathrm{z}i}^{\mathrm{T}} Q_i + Q_i A_{\mathrm{z}i} \right) z_i + \sum_{i=2}^{n} z_i^{\mathrm{T}} Q_i \varepsilon_i \\
\leq& -\frac{\mu_{\mathrm{z}i}}{2}\sum_{i=2}^{n} z_i^{\mathrm{T}} Q_i z_i + \sum_{i=2}^{n} \lambda_{\max}(Q_i) z_i^{\mathrm{T}} Q_i z_i + \sum_{i=1}^{n} \frac{\varepsilon_i^2}{4} \\
\leq& -\frac{1}{2}\sum_{i=2}^{n} (\mu_{\mathrm{z}i} - 2\lambda_{\max}(Q_i)) z_i^{\mathrm{T}} Q_i z_i + \sum_{i=1}^{n} \frac{M_i^2}{4}.
\end{aligned} \tag{39}$$

where M_i is the upper bound of $\|\varepsilon_i\|$.

By using (32), (33), (38), and (39), the time derivative of V satisfies

$$\begin{aligned}
\dot{V} =& \dot{V}_{\mathrm{s}} + \dot{V}_{\mathrm{z}} - \tau_1^{-1}\tilde{\theta}\dot{\hat{\theta}} - \tau_2^{-1}\tilde{\delta}\dot{\hat{\delta}} \\
\leq& -\frac{\varpi_1}{2}\sum_{i=1}^{n} \left(s_i^{(0\sim1)} \right)^{\mathrm{T}} P_i s_i^{(0\sim1)} - \frac{\varpi_2}{2}\sum_{i=2}^{n} z_i^{\mathrm{T}} Q_i z_i \\
&+ \varsigma_1 \tilde{\theta}\hat{\theta} + \varsigma_2 \tilde{\delta}\hat{\delta} + 2\sum_{i=1}^{n} a_i + \sum_{i=1}^{n} \frac{M_i^2}{4},
\end{aligned}$$

where

$$\varpi_2 = \min_{i\in\mathbb{I}[2,n]} \{ \mu_{\mathrm{z}i} - 2\lambda_{\max}(Q_1) - \frac{g_i^2}{2\lambda_{\min}(Q_{i+1})} \}.$$

By using Young's inequality, it can be derived that

$$\begin{aligned}
\varsigma_1 \tilde{\theta}\hat{\theta} &\leq \frac{\varsigma_1}{2}\tilde{\theta}^2 - \frac{\varsigma_1}{2}\hat{\theta}^2, \\
\varsigma_2 \tilde{\delta}\hat{\delta} &\leq \frac{\varsigma_2}{2}\tilde{\delta}^2 - \frac{\varsigma_2}{2}\hat{\delta}^2.
\end{aligned}$$

Then there holds

$$\begin{aligned}
\dot{V} \leq& -\varpi_1 V_{\mathrm{s}} - \varpi_2 V_{\mathrm{z}} - \frac{\varsigma_1}{2}\hat{\theta}^2 - \frac{\varsigma_2}{2}\hat{\delta}^2 \\
&\frac{\varsigma_1}{2}\tilde{\theta}^2 + \frac{\varsigma_2}{2}\hat{\delta}^2 + 2\sum_{i=1}^{n} a_i + \sum_{i=1}^{n} \frac{M_i^2}{4} \\
\leq& -\alpha V + \beta,
\end{aligned} \tag{40}$$

where

$$\begin{aligned}
\alpha &= \min\{\varpi_1, \varpi_2, \tau_1\varsigma_1, \tau_2\varsigma_2\}, \\
\beta &= \frac{\varsigma_1}{2}\tilde{\theta}^2 + \frac{\varsigma_2}{2}\hat{\delta}^2 + 2\sum_{i=1}^{n} a_i + \sum_{i=1}^{n} \frac{M_i^2}{4}.
\end{aligned}$$

Furthermore, by using comparison principle it can be concluded from (40) that

$$0 \leq V(t) \leq \frac{\beta}{\alpha} + \left(V(0) - \frac{\beta}{\alpha} \right) \mathrm{e}^{-\alpha t}.$$

Therefore, $s_1^{(0\sim1)}$, $s_i^{(0\sim1)}$, z_i, $i \in \mathbb{I}[2,n]$, $\tilde{\theta}$, and $\tilde{\delta}$ are uniformly ultimately bounded. ■

6 Conclusion

In this paper, the tracking control problem is addressed for a class of second-order fully actuated strict-feedback systems. The considered strict-feedback nonlinear systems are faced with the problems of unknown nonlinear dynamics, which are solved by employing the adaptive technique and RBFNNs. With the aid of RBFNNs and adaptive technique, a novel NNs-based adaptive CFB control law is constructed. The proposed control law guarantees the uniformly ultimately bounded of the closed-loop system.

References

[1] C. Della Santina, C. Duriez, and D. Rus, "Model-based control of soft robots: A survey of the state of the art and open challenges," *IEEE Control Systems Magazine*, vol. 43, no. 3, pp. 30–65, 2023.

[2] V. S. Dwivedi, D. K. Giri, A. K. Ghosh, G. Kamath *et al.*, "Optimal energy utilization for a solar-powered aircraft using sliding-mode-based attitude control," *IEEE Transactions on Aerospace and Electronic Systems*, vol. 57, no. 1, pp. 105–118, 2020.

[3] R.-Q. Dong, A.-G. Wu, and Y. Zhang, "Anti-unwinding sliding mode attitude maneuver control for rigid spacecraft," *IEEE Transactions on Automatic Control*, vol. 67, no. 2, pp. 978–985, 2021.

[4] G. Duan, "High-order fully actuated system approaches: Part I. models and basic procedure," *International Journal of Systems Science*, vol. 52, no. 2, pp. 422–435, 2021.

[5] G. Duan, "High-order fully actuated system approaches: Part II. generalized strict-feedback systems," *International Journal of Systems Science*, vol. 52, no. 3, pp. 437–454, 2021.

[6] G. Duan, "High-order fully actuated system approaches: Part V. robust adaptive control," *International Journal of Systems Science*, vol. 52, no. 10, pp. 2129–2143, 2021.

[7] G. Duan, "High-order fully actuated system approaches: Part III. robust control and high-order backstepping," *International Journal of Systems Science*, vol. 52, no. 5, pp. 952–971, 2021.

[8] G. Duan, "High-order fully actuated system approaches: Part IV. adaptive control and high-order backstepping," *International Journal of Systems Science*, vol. 52, no. 5, pp. 972–989, 2021.

[9] C. Liu, X. Liu, H. Wang, Y. Zhou, and C. Gao, "Adaptive control for unknown hofa nonlinear systems without overparametrization," *International Journal of Robust and Nonlinear Control*, vol. 33, no. 6, pp. 3640–3660, 2023.

[10] W. Liu, G. Duan, and M. Hou, "High-order robust command filtered backstepping design for strict-feedback systems: A high-order fully actuated system approach," *International Journal of Robust and Nonlinear Control*, vol. 32, no. 18, pp. 10 251–10 270, 2022.

[11] W. Liu, G. Duan, and M. Hou, "High-order command filtered adaptive backstepping control for second-and high-order fully actuated strict-feedback systems," *Journal of the Franklin Institute*, vol. 360, no. 6, pp. 3989–4015, 2023.

[12] G. W. Dong, H. Y. Li, H. Ma, and R. Q. Lu, "Finite-time consensus tracking neural network FTC of multi-agent systems," *IEEE Transactions on Neural Networks and Learning Systems*, vol. 32, no. 2, pp. 653–662, 2021.

[13] H. Deng and M. Krstić, "Stochastic nonlinear stabilization–I: A backstepping design," *Systems & Control Letters*, vol. 32, no. 3, pp. 143–150, 1997.

Proceedings of the 3rd Conference on Fully Actuated System Theory and Applications
May 10-12, 2024, Shenzhen, China

Dynamics Modeling of Soft Robots Based on Attention-enhanced Lagrangian Deep Neural Networks

Yeqi Wei[1], Xiangyu Shao[1,*], Jingyue Liu[2], Shaojie Zhang[1], Linke Xu[1]

1. School of Astronautics, Harbin Institute of Technology, Harbin 150001, P. R. China
E-mail: xiangyushao@hit.edu.cn

2. Department of Cognitive Robotics, Delft University of Technology, Delft 2628 CD, The Netherlands

Abstract: This study explores a method for the dynamic modeling of soft robots, focusing on enhancing the deep learning-based Lagrangian modeling approach through the attention mechanism, which enriches the training process by allocating focused attention and analytical weighting to critical state features, thereby increasing the model's sensitivity to changes in the robot's state. We compared our method through simulation, demonstrating that the model is effective in long-term prediction and noise rejection.

Key Words: Attention-enhanced deep learning, Lagrangian neural networks, Soft robots, Predictive modeling, Machine learning in robotics.

1 Introduction

Soft robots are an interdisciplinary field that intersects engineering and biomechanics, demonstrating the enormous potential in sensitive owing to the unique characteristics of soft materials [1]. However, the inherent flexibility of soft materials introduces complexity in their kinematics and dynamics analysis concurrently, making traditional methods for evaluating its motion state insufficient [2, 3]. The inherent nonlinear characteristics and extensive degrees of freedom of flexible robots pose challenges and requires new modeling method to facilitate its application.

The latest advances in deep learning have propelled the capabilities of soft robots. Dong *et al.* demonstrated how to customize convolutional neural networks to process sensory data from soft robot skin, thereby enhancing environmental interaction [4]. Keene *et al.* have made progress in applying recursive neural networks to predictive modeling of soft robot dynamics, allowing for expected control actions [5]. However, due to the complex variability of soft material behavior, traditional deep learning methods often require a large amount of data sets or a long training time, and these objective conditions are sometimes difficult to gather together.

As shown in [6], attention mechanism fundamentally changes the field of machine learning by enabling the model to selectively focus on the data most relevant to the task at hand, providing a promising direction for overcoming these data challenges. These mechanisms were initially popularized in the field of natural language processing [7], they were also used as sequence to sequence models, but have not been fully explored in the context of robot control.

This paper proposes an innovative integration of attention mechanism into Lagrangian neural network (LNN) for modeling soft robots. As demonstrated in [8], the Lagrangian framework essentially explains the physical properties of motion and provides a natural fit for modeling soft robotic systems. Our method is based on the works of Liu [9], who introduced an LNN architecture for soft robots to achieve high-precision prediction of their states but yet introduce attention mechanisms.

By embedding attention in LNN, we aim to address the challenge of effectively modeling the nonlinear and high-dimensional dynamic characteristics of soft robots. As Wang proposed in [10], the attention mechanism enhances the prediction accuracy of models in the field of natural language. Inspired by its impressive improvement, this paper introduces the attention machine to the deep learning based modeling of soft robots to improve the modeling accuracy and prediction ability of the model. The potential benefits of this approach include reducing the need for large datasets and improving real-time response capabilities, which are crucial for deploying soft robots in real-world scenarios. The contributions of this paper is summarised as : (i) Introduce a new attention enhanced LNN architecture, (ii) demonstrate its advantages over traditional LNN through simulation, (iii) and its generalization was tested in a noisy environment.

2 Theoretical Basis and Related Work

The Lagrangian dynamics elucidates the motion of dynamic systems by balancing kinetic energy T and potential energy V [11]. The Lagrangian function $L(q, \dot{q})$ is defined as $L(q, \dot{q}) = T(\dot{q}) - V(q)$, providing a robust theoretical framework for modeling the complex motion of mechanical systems. This formula has become indispensable in the context of soft robots, where the complex interactions between elastic materials and various components challenge traditional rigid body dynamics.

Deep learning, as a subset of machine learning, has completely changed the way we model soft robots. Its advantage lies in its ability to learn from sequence data, capture temporal dependencies and subtle patterns. In view of this, deep learning has the potential to improve the traditional modeling methods of soft robot systems. It provides a method for extracting complex high-dimensional data into actionable insights and may also address issues such as the nonlinear and dynamic characteristics of soft robots. Therefore, integrating deep learning techniques into the modeling process can improve the prediction accuracy, adaptability, and efficiency

* Corresponding Author

This work is supported in part by the National Natural Science Foundation of China under Grant 62303137, in part by the Special funding of the China Postdoctoral Science Foundation under Grant 2023TQ0092, and in part by the Heilongjiang Postdoctoral Science Foundation under Grant LBH-Z20057.

of soft robot control systems.

The contribution of Liu in this regard is impressive, as they used Physically Informed Neural Networks (PINNs) to infer physically reasonable matrices from data [9]. By establishing deep learning models on the physical laws governing robot motion, their approach embodies the synergistic effect between data-driven methods and classical mechanics. However, although this method has many advantages, including improved sample efficiency and model interpretability, there is still room for improvement due to the need for a large number of datasets and training cycles, resulting in a decline in long-term prediction accuracy.

Introducing the attention mechanism from the transformer architecture into LNN is a method to improve the model. The success of attention mechanisms in machine learning, especially in processing sequential data, has already proven their potential in enhancing model focus and handling complex patterns. In our framework, it is utilized to enhance the sensitivity of LNNs to key system states, thereby enabling more accurate predictions of complex dynamic behaviors. Our model applies Lagrangian neural networks (LNN) within the PINNs framework to determine the mass matrix $\mathcal{M}$, dissipation matrix $\mathcal{D}$, and state transition matrix $\mathcal{I}$ from a large dataset of soft robot states q and inputs u. Subsequently, we use attention layers to enhance this framework, combining attention mechanisms acting on the physical derivation matrix and the state and input data of soft robots. By refining the attention related matrices Q, K, and V, the accuracy of the model has been improved.

The mathematical expression can be simplified as:

$$\text{Attention}(Q, K, V) = \text{softmax}\left(\frac{QK^T}{\sqrt{d_k}}\right)V \tag{1}$$

where Q, K, and V represent the query, key, and value, respectively. In our application, the key is a combination of the current state and input, while the query is the learned physical matrix . This structure allows the model to focus more on the parts of the system dynamics most relevant to the current input and state.

Through this approach, the attention-enhanced LNN model can predict the dynamic behavior of soft robots in different states more accurately than traditional LNNs, providing higher predictive accuracy and adaptability of the model.

3 Attention-Enhanced LNNs Design

3.1 Modeling Non-Conservative Forces in LNNs

Although traditional Lagrangian neural networks (LNNs) perform well in system dynamics, real-world applications often involve non conservative forces and require a new approach to cover this impact. We propose an extended LNN framework:

The original equations of motion for LNNs stem from the standard Lagrangian mechanics, where the dynamics are fully described by conservative forces. Traditionally, the Lagrangian $\mathcal{L}(q, \dot{q})$ encapsulates the system's total energy, combining kinetic $T(\dot{q})$and potential $V(q)$ energies. From the Euler-Lagrange equation, we obtain the standard form of the motion equation:

$$\frac{d}{dt}\left(\frac{\partial \mathcal{L}}{\partial \dot{q}}\right) - \frac{\partial \mathcal{L}}{\partial q} = 0 \tag{2}$$

Considering the limitations of traditional Lagrangian neural networks (LNNs) in handling non conservative forces, a new approach is needed to consider energy dissipation and the impact of inputs on the system. Therefore, we propose an enhanced framework that incorporates the effects of non conservative forces and external inputs into the LNN This is achieved by extending the classical Lagrangian mechanics to include a dissipation matrix $\mathcal{D}(q, \dot{q})$ and a state transition matrix $\mathcal{I}(q)$. The dissipation matrix accounts for energy loss due to non-conservative forces, while the state transition matrix models the influence of external control inputs on the system.

Accordingly, the motion equation is modified to integrate these matrices, providing a comprehensive representation of the system's dynamics under the influence of both conservative and non-conservative forces, as well as external inputs:

$$\frac{d}{dt}\left(\frac{\partial \mathcal{L}}{\partial \dot{q}}\right) - \frac{\partial \mathcal{L}}{\partial q} + \mathcal{D}(q, \dot{q})\dot{q} = \mathcal{I}(q)\tau \tag{3}$$

where τ denotes the external control inputs applied to the system. To analyze the system's dynamics, we derive the mass matrix $\mathcal{M}(q)$ by calculating the Hessian matrix $H(\mathcal{L})$ of the Lagrangian $\mathcal{L}$ with respect to the generalized velocities $\dot{q}$, which represents second-order partial derivatives and encapsulates the system's inertia.

$$H(\mathcal{L}) = \begin{bmatrix} \frac{\partial^2 \mathcal{L}}{\partial \dot{q}_1^2} & \frac{\partial^2 \mathcal{L}}{\partial \dot{q}_1 \partial \dot{q}_2} & \cdots & \frac{\partial^2 \mathcal{L}}{\partial \dot{q}_1 \partial \dot{q}_n} \\ \frac{\partial^2 \mathcal{L}}{\partial \dot{q}_2 \partial \dot{q}_1} & \frac{\partial^2 \mathcal{L}}{\partial \dot{q}_2^2} & \cdots & \frac{\partial^2 \mathcal{L}}{\partial \dot{q}_2 \partial \dot{q}_n} \\ \vdots & \vdots & \ddots & \vdots \\ \frac{\partial^2 \mathcal{L}}{\partial \dot{q}_n \partial \dot{q}_1} & \frac{\partial^2 \mathcal{L}}{\partial \dot{q}_n \partial \dot{q}_2} & \cdots & \frac{\partial^2 \mathcal{L}}{\partial \dot{q}_n^2} \end{bmatrix} \tag{4}$$

where n denotes for the number of system segments. The mass matrix $\mathcal{M}(q)$ is derived from this Hessian matrix :

$$\mathcal{M}(q) = \frac{\partial^2 \mathcal{L}}{\partial \dot{q}^2} \tag{5}$$

We used the method of Moore-Penrose pseudo inverse to invert the mass matrix and obtained the pseudo inverse of the mass matrix for solving the acceleration of the system.

$$\ddot{q} = \mathcal{M}^{-1}(q) \cdot \left(\mathcal{I}(q)\tau - \frac{\partial \mathcal{L}}{\partial q} + \mathcal{D}(q, \dot{q})\dot{q}\right) \tag{6}$$

This equation reflects the cumulative effect of both internal and external forces , including conservative and non-conservative forces, as well as the influence of external control inputs τ.

We modify the Euler-Lagrange equation by using the attention mechanism:

$$\ddot{q} = \left(\frac{\partial^2 \mathcal{L}(q, \dot{q})}{\partial \dot{q}^2}\right)^{-1} \left(\text{Attention}(\tau) - \frac{\partial \mathcal{L}(q, \dot{q})}{\partial q} - \mathcal{D}(q, \dot{q})\dot{q}\right) \tag{7}$$

Here, Attention(τ) denotes the application of the attention mechanism to these forces, allowing the model to prioritize the most influential factors dynamically. The Attention function is defined during the training of the neural network and is tailored to identify and weigh the various forces acting on the system.

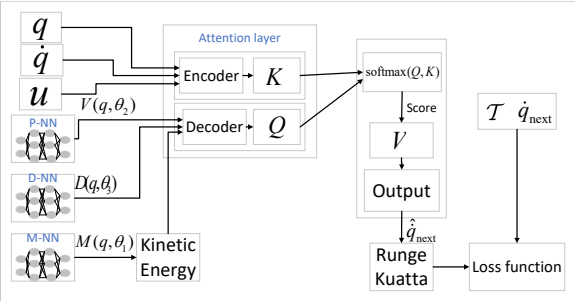

Fig. 1: The structure of the proposed neural networks

3.2 Encoder and Position Encoding

In our proposed architecture, the encoder is a sequence of blocks, each refining the robot's state representation through operations that transcend traditional layer functions. The initial transformation, dubbed 'Input Embedding', projects input variables such as positions, velocities, and control inputs onto a high-dimensional space. We apply Positional Encoding (PE) to the input sequence consisting of the current state q, velocity $\dot{q}$, and control input u:

$$E = \text{Embedding}(q, \dot{q}, u) \tag{8}$$

PE is defined for each element in the sequence:

$$PE_{(pos,2i)} = \sin\left(\frac{pos}{10000^{2i/d_{\text{model}}}}\right) \tag{9}$$

$$PE_{(pos,2i+1)} = \cos\left(\frac{pos}{10000^{2i/d_{\text{model}}}}\right) \tag{10}$$

where pos represents the position in the sequence and i corresponds to the dimension. The embedded input E_i is then combined with its positional encoding PE_i to form the initial high-dimensional representation E_i' for the robot's state. This representation, acknowledging both the state and its sequence position.

In the design of our neural architecture, the Multilayer Perceptron (MLP) layers play a pivotal role in capturing the nonlinear interactions within the robot's state variables. Each MLP layer, with its weights and biases, transforms the input data into a more abstract representation. Following each linear transformation, a Rectified Linear Unit (ReLU) activation function is applied, introducing the necessary non linearity:

$$\text{ReLU}(x) = \max(0, x) \tag{11}$$

Negative inputs to the function are reset to zero, which can be interpreted as deactivating the corresponding features or neurons. This ensures that only the features with positive activation contribute to the next layer, simplifying the learning process and making it more efficient. By discarding negative activation, it encourages the model to focus on the most salient features that are positively correlated with the robot's dynamic behavior, leading to a sparse and explainable feature space.

The MLP refinement process consists of alternating layers of linear transformations and ReLU activations, expanding and compressing the embedded input data in a manner that allows the network to construct a rich and intricate mapping from the robot's current state and inputs to its subsequent state. This series of operations is formalized as follows:

$$H_1 = \text{ReLU}(\mathbf{W}_1 E_i' + \mathbf{b}_1) \tag{12}$$

$$H_2 = \text{ReLU}(\mathbf{W}_2 H_1 + \mathbf{b}_2) \tag{13}$$

$$\vdots$$

$$K = \text{ReLU}(\mathbf{W}_n H_{n-1} + \mathbf{b}_n) \tag{14}$$

where $\mathbf{W}_j$ and $\mathbf{b}_j$ represent the weights and biases of the j-th layer, H_j represents the output of the j-th layer, and K denotes the final output of the MLP, serving as the output of the encoder layer.

3.3 Decoder and State Prediction

By providing the key (K) for the attention mechanism, the input of the decoder involves preprocessing the state data to align with the decoder's requirements. Three MLP layers are utilized to approximate the kinetic energy matrix $\mathcal{M}$, dissipation matrix $\mathcal{D}$, and state transition matrix $\mathcal{I}$:

$$\hat{\mathcal{M}} = MLP_M(q; \Theta_M) \tag{15}$$

$$\hat{\mathcal{D}} = MLP_D(q, \dot{q}; \Theta_D) \tag{16}$$

$$\hat{\mathcal{I}} = MLP_I(q, \tau; \Theta_I) \tag{17}$$

These layers project the state variables onto a structured form that encapsulates the robot's dynamic properties. The decoder then uses these matrices to perform attention-driven predictions of the robot's future state.

To calculate the attention scores, the decoder's input query (Q) interacts with the keys (K) obtained from the encoder:

$$\text{Attention}_{\text{scores}} = \text{Softmax}\left(\frac{QK^T}{\sqrt{d_k}}\right) \tag{18}$$

where d_k is the scaling factor to avoid overly large values within the softmax function. The obtained attention scores reflect the importance of each state variable in predicting future dynamics. The predicted next state q_{next} is then computed as a weighted sum of the values V, guided by these scores:

$$q_{\text{next}} = \text{Attention}_{\text{scores}} \cdot V \tag{19}$$

This predicted state passes through additional layers in the decoder, each enhancing the prediction with a non-linear transformation:

$$q' = \text{LayerNorm}(\text{FFN}(q_{\text{next}}) + q_{\text{next}}) \tag{20}$$

$$q_{\text{predicted}} = \text{LayerNorm}(\text{FFN}(q') + q') \tag{21}$$

Finally, the decoder outputs a prediction of future states as a probability distribution, selecting the state with the highest likelihood as the next step:

$$q_{\text{future}} = \text{Softmax}(\text{Linear}(q_{\text{predicted}})) \tag{22}$$

Through this streamlined process, the decoder effectively utilizes the dynamic models and attention mechanism to forecast the system's progression, enabling real-time adaptation to complex dynamics.

3.4 Incorporating Loss Functions for Network Training and Regularization

To maintain compliance with physical principles and ensure the reliability of dynamic predictions, our framework integrates specific loss functions at various stages of the LNN. These loss functions guide the network towards physically plausible solutions and reinforce the accuracy of the learned dynamics.

In the preprocessing process, a loss function is used to ensure accurate approximation of quality, dissipation, and input transformation matrix. The loss function is not directly compared with the objective matrix, but rather obtains the accuracy of predicted states by integrating these matrices into the system's motion equations. This method is consistent with the physical informed properties of the LNN framework and provides a robust approach for learning the dynamic characteristics of the system:

$$L_{\text{preprocess}} = \text{mean}(\|\text{forward}_{\text{model}}(q, qd, \tau) - [q_{\text{next}}, qd_{\text{next}}]\|^2) \tag{23}$$

In this equation, $\text{forward}_{\text{model}}$ denotes the forward model that computes the predicted future states given the current states q and qd, and the control inputs τ, utilizing the approximated matrices $\hat{\mathcal{M}}$, $\hat{\mathcal{D}}$, and $\hat{\mathcal{I}}$. The loss function minimizes the discrepancy between the predicted states and the true next states, q_{next} and qd_{next}, which are provided as part of the training data. This discrepancy serves as a proxy to the accuracy of the approximated matrices and the model's ability to capture the true dynamics of the system.

In the attention mechanism, we focus on the difference between the predicted state of the system obtained by the decoder and the actual subsequent state:

$$L_{\text{state_prediction}} = \|q_{\text{predicted}} - q_{\text{actual_next}}\|^2 \tag{24}$$

This loss function ensures that the model's attention-driven predictions are closed to the true system dynamics observed in the data.

The composite loss function for the entire LNN, including preprocessing, attention mechanism, and state prediction phases :

$$L_{\text{composite}} = L_{\text{state_prediction}} + L_{\text{physics}}(\theta) + L_{\text{matrix}} \tag{25}$$

Here, $L_{\text{physics}}(\theta)$ ensures the predictions adhere to physical principles, and L_{matrix} encourages the structural integrity of the dynamics matrices. The training process guided by this composite loss function satisfies the laws of physics and attention mechanisms. By optimizing this composite loss, LNN has learned to further predict the future state of dynamic systems, ensuring accuracy and physical rationality.

4 Integrated Analysis and Implications

4.1 Simulation Results

In this section, we present a comprehensive analysis of our simulation results, aiming to provide a unified perspective on the performance of the Attention-Enhanced Lagrangian Neural Network (LNN) compared to its Normal counterpart. Our assessment spans various training epochs, noise robustness checks, and long-term predictive capabilities. In our Attention-Enhanced Lagrangian Neural Network (LNN), we denote the number of encoder and decoder layers as E and D respectively, the size of the hidden layers as H, and the number of self-attention heads as A. For the attention mechanism, we specify the dimensional of the 'query', 'key', and 'value' projections as P. We report results on a model with the following configuration: Attention-Enhanced LNN (E=3, D=2, H=128, A=6, P=36).

Training was performed using the Adam optimizer with a learning rate of 0.001, decaying by a factor of 0.96 every 100 epochs. To assess noise robustness, Gaussian noise of varying magnitudes was added to the input data, and the model's performance was monitored accordingly. Training was conducted on a system equipped with a NVIDIA GTX 4090 Laptop GPU, with 16GB of VRAM, and an Intel i9-13980HX CPU with 64 GB RAM. For the Attention-Enhanced LNN model, convergence was achieved within approximately 150 seconds for one epoch of training on a dataset comprising 60000 samples. During the training phase, the peak GPU memory utilization was recorded at 14.4 GB, with the GPU's average usage maintained at 96% throughout the duration of training. In comparison to a conventional model without an attention mechanism, our Attention-Enhanced LNN demonstrated a 15% increase in training time per epoch, which we attribute to the additional computations required for the attention mechanism. However, each epoch of our model is more efficient in learning. Where a standard model may require in excess of 5000 epochs to converge to an error precision nearing 0.1, our method achieves similar accuracy within just 500 epochs. This reduction in the number of required epochs showcases the efficacy of our attention mechanism, despite the increase in per-epoch training time.

The empirical data, as encapsulated in Tab. 1 demonstrate a improvement in trajectory adherence for the Attention-Enhanced LNN. We observed that, as training epochs increased from 200 to 500, the prediction error decreased , indicating an enhanced ability of the model to capture the complex dynamics of the soft robotic arm. This reduction error decrease from 0.5784 to 0.0998, underscores the model's refined predictive accuracy over time.

Further understanding of the training process and the learning efficiency of the model can be obtained from Tab. 1 and Fig. 3. These numbers show the learning curve trajectories of attention enhancement LNN models at different training stages. It is worth noting that Fig.2 shows the initial stage of training, showing an imprecise prediction state as the model begins to adapt to the complexity of the dataset. As the training progresses, Fig. 3 shows a more gradual improvement, marking a shift in the model from learning basic dynamics to improving its understanding of complex actions. The characteristic of this stage is the smoothness of the learning curve, indicating that as the model begins to converge to a robust representation of system dynamics, the learning process tends to stabilize.

Tab. 2 enhances the comparative analysis by quantitatively depicting the epochs needed to converge to a defined accuracy threshold. The Attention-Enhanced LNN, despite not exhibiting a marked advantage in training time, requires significantly fewer epochs to reach comparable precision levels compared to the Normal LNN. However, the expedited learning rate may also introduce a susceptibility to over fit-

Table 1: Prediction Error Across Training Epochs

Training Way	Attention-Enhanced	Attention-Enhanced	Attention-Enhanced	Normal LNN	Attention-Enhanced
Model (Width×Depth)	42×3,5×3,42×2	42×3,5×3,42×2	42×3,5×3,42×2	42×3,5×3,42×2	42×3,5×3,42×2
Sample Number	42000	42000	42000	42000	42000
Training Epoch	200	400	500	500	800
Prediction Error	$0.57(\pm 1.1\times10^{-3})$	$0.32(\pm 9.4\times10^{-3})$	$0.09(\pm 8.5\times10^{-3})$	$0.32(\pm 9.6\times10^{-3})$	$0.36(\pm 6.5\times10^{-3})$

Table 2: Training Epoch Required to Achieve Different Accuracies

	Normal LNN				Attention-Enhanced LNN			
Training Epoch	100	500	1000	5500	100	500	1000	5500
Training Time (s)	11873	58934	123343	659278	14366	70131	141647	811495
Simulation Time (s)	30	30	30	30	30	30	30	30
Prediction Error	3.7412	0.7862	0.5316	0.0992	0.8556	0.0998	0.3477	2.4642

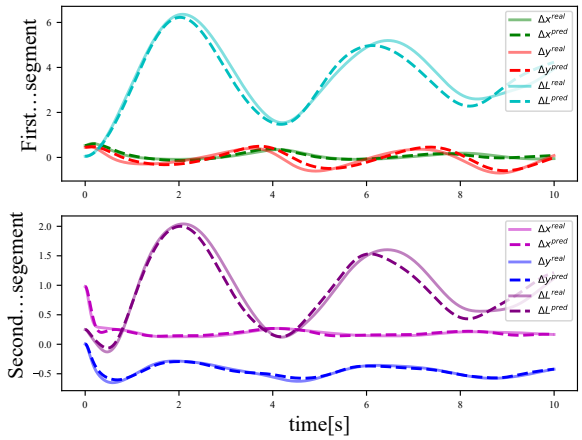

Fig. 2: Differences in positions under 200 training epochs.

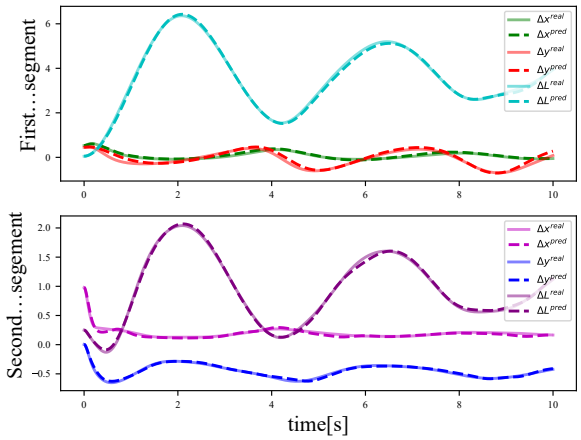

Fig. 3: Differences in positions under 500 training epochs.

ting, particularly at higher epoch counts. In our model without sufficient regularization, it has been observed that for the Attention-Enhanced LNN, the prediction error increases with additional training beyond 500 epochs. This suggests that the model begins to memorize the training data instead of learning to generalize. The convergence patterns shown in Figs. 4 and 5, as well as the training epoch data shown in Tab. 2, collectively emphasize the enhanced learning efficiency provided by attention enhanced LNN.

Figs. 4 and 5 provide a visual representation of this improvement, showing the Attention-Enhanced LNN's trajectory more closely aligning with the reference trajectory compared to the Normal LNN. This alignment not only confirms the quantitative results from Tab. 1 but also shows the qualitative enhancements in the model's behavior. Although both models show signs of divergence in their predicted trajectories as simulation time increases, it is evident that the model with added attention mechanism has smaller errors.

4.2 Model Robustness and Generalization

The robustness against noise was tested by introducing Gaussian white noise with a standard deviation of 0.05 into our simulation environment. Our Attention-Enhanced LNN showcased a advantage in noise resilience. Figs. 6 and 7 depict a subtle yet noticeable superiority in maintaining prediction accuracy despite the added noise. The simulation results collectively point out the effectiveness of integrating attention mechanisms into LNN. These findings indicate that attention enhanced LNNs are not only better at handling complex dynamic behaviors, but also exhibit stronger resilience to environmental noise, which may be a key feature for future applications of fully actuated robot systems in the real world. Our evaluation focuses particularly on the performance of attention enhanced LNN in the presence of Gaussian noise and its ability to maintain prediction accuracy at different training stages. Tab. 2 , as well as Figs. 6 and 7, show a data centric view. During the Gaussian noise interference testing process, white noise with a standard deviation of 0.05 was introduced to test the model. Despite this disturbance, attention enhanced LNN still exhibits relatively good noise resistance. Fig. 6 illustrates this robustness, showing that under the same noise conditions, the prediction error deviation is smaller compared to normal LNN. In terms of generalization, the impact of training period on model performance was quantified. As shown in Tab. 2, attention enhanced LNN achieved lower prediction errors at an earlier stage, indicating a more effective learning process. Fig. 7 further confirms this point, despite the increase in noise in the training data, attention enhanced LNN shows consistent prediction accuracy.

Building on our initial findings regarding the noise re-

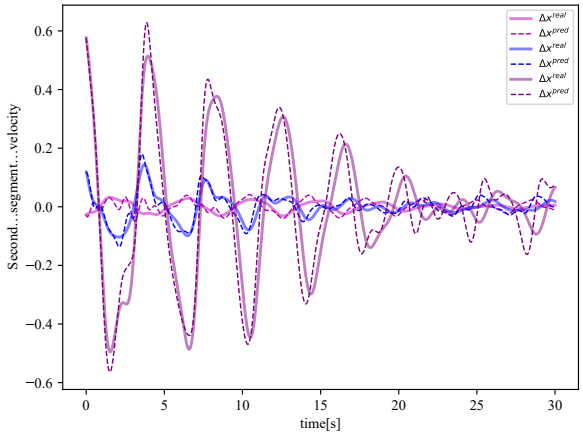

Fig. 4: The velocity of the second segment under Attention-Enhanced 500 training epochs (error 0.18)

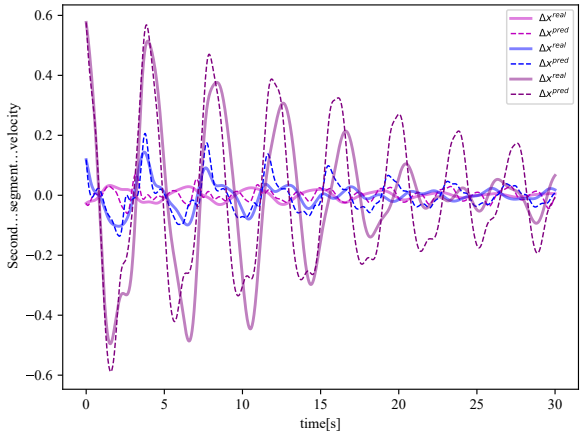

Fig. 5: The velocity of the second segment under normal LNN 500 training epochs (error 0.52)

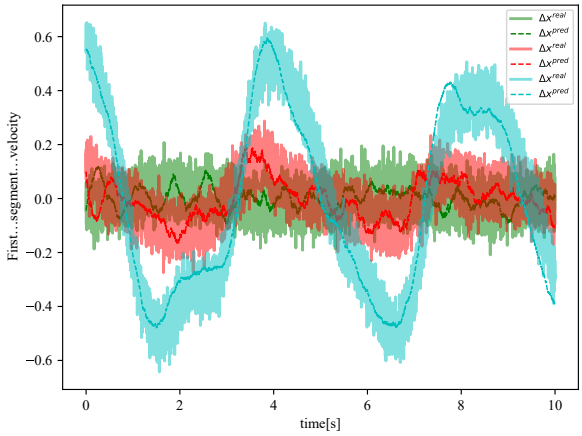

Fig. 6: The velocity of the first segment under Attention-Enhanced LNN (error 0.13)

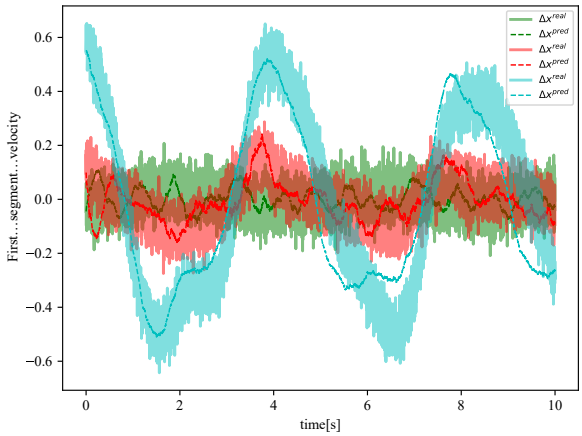

Fig. 7: The velocity of the first segment under Normal LNN (error 0.27)

silience of the Attention-Enhanced Lagrangian Neural Network (LNN). Notably, when introducing a higher level of uniform noise with a standard deviation of 0.1 into the simulation environment, a marked increase in prediction error was observed. This deterioration in performance can be attributed to the more significant impact of noise contamination on the training data, as illustrated in Fig. 8 where the error increased to 2.13. Our study revealed that by augmenting the training dataset size to ten times its original volume, the model's performance improved under identical noise conditions. Fig. 9 showcases this enhancement, with the prediction error notably reduced to 0.9. This improvement underscores the critical role of extensive training data in enhancing model resilience against noise contamination. It suggests that with sufficient data, the Attention-Enhanced LNN can learn to filter out noise-induced anomalies.

4.3 Attention Heat-maps and Dimensional Expansion

In the domain of soft robotics, the articulation and flexibility afforded by each segment of a robotic arm necessitate a multidimensional approach to dynamic modeling. Particularly, for a robotic arm comprised of n segments, where each segment is capable of movement in three-dimensional space—expressed through translations and rotations along the X, Y, and Z axes—the complexity of the system's dynamics significantly increases. This threefold increase in degrees of freedom (DOF) for each segment results in a total of $3n$ DOFs for the entire arm.

The delineation of soft robotic arm dynamics through the mass $\mathcal{M}$, dissipation $\mathcal{D}$, and state transition $\mathcal{I}$ matrices provides a universally applicable framework, adaptable across a wide spectrum of robotic arms configurations. Regardless of the driving mechanisms employed, the materials constituting the arm, or the number of segments it comprises, this matrix representation simplifies the complexity inherent in describing the motion of soft robotic systems. This unified approach enables a consistent and coherent modeling of soft robotics dynamics, facilitating the analysis and control of these highly adaptable and complex systems.

To elucidate the operational dynamics of this mechanism, we employed attention heat-maps. In the context of modeling the dynamics of a two-segment soft robotic arm, atten-

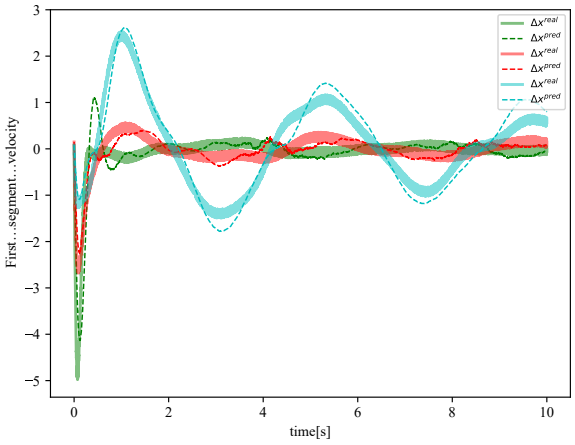

Fig. 8: Uniform noise impact with standard training dataset (error 2.13)

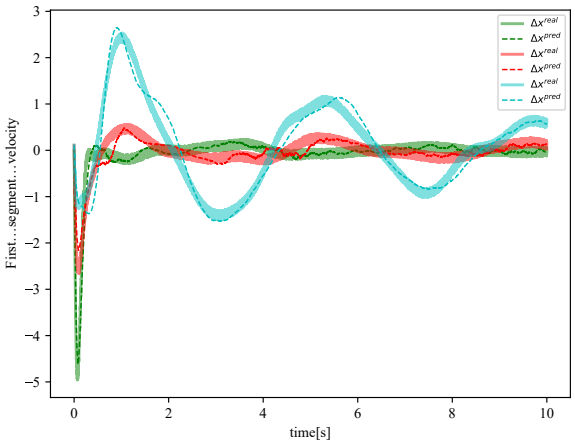

Fig. 9: Uniform noise impact with standard training dataset (error 0.94)

tion heat-maps provide visualizations of how specific input features influence the system's state transition matrix. Contrary to a broader interpretation of input contributions, each heat-map focuses on the contribution of a single input feature—such as the external force applied in the X direction of the second segment—towards the entire 6×6 state transition matrix $\mathcal{I}$.

The axes of the heat-map correspond to the dimensions of the state transition matrix, $\mathcal{I}$, representing the robotic arm's dynamics. The horizontal and vertical axes both span the matrix's dimensions, reflecting the interrelation between the applied input and the arm's resultant states. Each cell within the heat-map illustrates the magnitude of influence that the selected input feature has on the corresponding element of the state transition matrix. A brighter cell indicates a higher level of contribution, signifying a stronger impact of the specific input feature on the arm's dynamic behavior. By examining heat-maps from different stages of the training process, we observe a transition from an initially uniform or random distribution of attention to a more focused allocation. In the early training phase, as depicted by the heat-map at epoch 1, the attention allocation appears almost stochastic, lacking any discernible pattern. As training progresses to epoch 30, the heat-map begins to reveal emergent patterns of focused

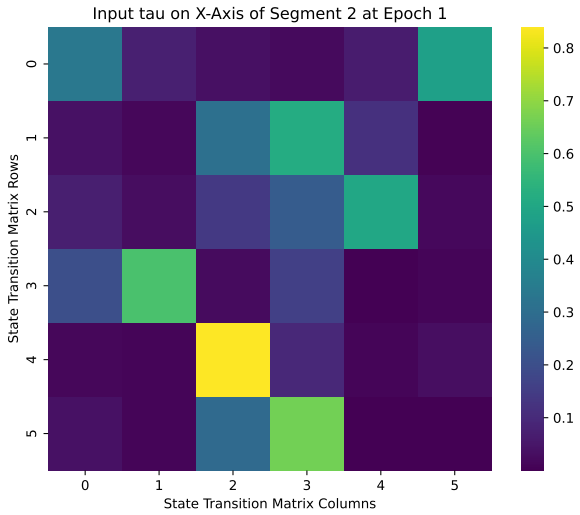

Fig. 10: Attention Distribution for X-Axis Input on Segment 2 at Epoch 1

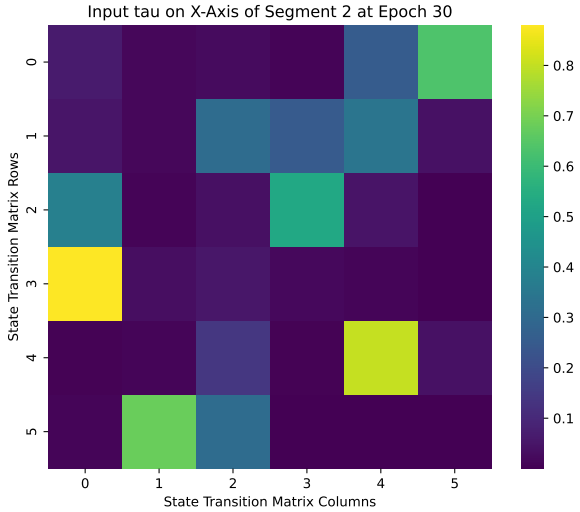

Fig. 11: Attention Distribution for X-Axis Input on Segment 2 at Epoch 30

attention. These nascent structures signify the model's initial steps towards recognizing the more influential input features. By epoch 100, the heat-map displays a highly refined attention distribution, where the model's focus is concentrated on specific inputs that it has learned to associate with significant impacts on the system's behavior.

This focused exploration of attention heat-maps not only demystifies the model's adaptive learning mechanism but also exemplifies the precision with which it discerns the influence of individual input features on the robotic arm's dynamics.

5 Conclusion

In summary, this study demonstrates that the dynamic system modeling of soft robots has been substantially improved by integrating attention mechanisms into Lagrangian neural networks (LNNs). Our attention enhancement model shows a significant improvement in prediction accuracy and robustness against environmental noise, demonstrating its ability to capture the complex behavior of soft robot systems. The empirical results indicate that attention mechanism reduces

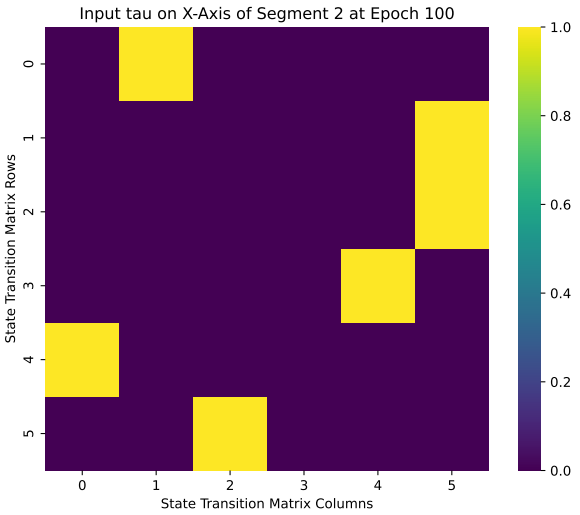

Fig. 12: Attention Distribution for X-Axis Input on Segment 2 at Epoch 100

computational requirements and improves long-term predictive performance. This is consistent with our goal of developing models that are not only efficient in computing resources, but also sufficiently versatile to facilitate real-world applications. Looking ahead to the future, there are several ways for further research. One direct direction is to explore the integration of more complex attention mechanisms, such as sparse attention and local attention. The other direction is to explore the location of adding attention mechanisms, such as introducing attention mechanisms when training physical matrices. In addition, the intersection of soft robots and deep learning provides a new platform for innovative control strategies. Future work may involve deploying these models in real-time control systems and testing their performance in physical environments.

References

[1] A. Banerjee. “The Impact of Soft Robotics In Today’s World: Applications, Challenges Faced, And Future Outlook,” *2022 International Conference on Smart Generation Computing, Communication and Networking (SMART GENCON)* Dec. 2022

[2] X. Shao, P. Pustina, M. Stölzle, et al. Model-based control for soft robots with system uncertainties and input saturation[J]. *IEEE Transactions on Industrial Electronics*, 2023.

[3] Salvador Cobos et al. “Efficient human hand kinematics for manipulation tasks” 2008 *IEEE/RSJ International Conference on Intelligent Robots and Systems*.

[4] DongWook Kim and Yong-Lae Park, ”Contact localization and force estimation of soft tactile sensors using artificial intelligence”, *2018 IEEE/RSJ International Conference on Intelligent Robots and Systems (IROS)*, 2018.

[5] Keene Chin, Tess Hellebrekers and Carmel Majidi, ”Machine learning for soft robotic sensing and control”, *Advanced Intelligent Systems*, vol. 2, no. 6, pp. 1900171, 2020.

[6] Vaswani A, Shazeer N, Parmar N, et al. Attention is all you need[J]. Advances in neural information processing systems, 2017, 30.

[7] J. F. DeRose, J. Wang and M. Berger, ”Attention Flows: Analyzing and Comparing Attention Mechanisms in Language Models,” in IEEE Transactions on Visualization and Computer Graphics, vol. 27, no. 2, pp. 1160-1170, Feb. 2021.

[8] W. N. White, D. D. Niemann and P. M. Lynch, ”The presentation of Lagrange’s equations in introductory robotics courses,” in IEEE Transactions on Education, Feb. 1989

[9] Jingyue Liu, Pablo Borja, Cosimo Della Santina,”Physics-informed Neural Networks to Model and Control Robots: a Theoretical and Experimental Investigation”,arXiv:2305.05375,Jul 2023

[10] H. Wang and M. Tu, ”Enhancing Attention Models via Multi-head Collaboration,” 2020 International Conference on Asian Language Processing (IALP), Kuala Lumpur, Malaysia, 2020

[11] Miles Cranmer, Sam Greydanus, Stephan Hoyer,”Lagrangian Neural Networks”,arXiv:2003.04630,Jul 2020

[12] J. -Y. Lee, W. -B. Kim, W. -Y. Choi and K. -J. Cho, ”Soft Robotic Blocks: Introducing SoBL, a Fast-Build Modularized Design Block,” in IEEE Robotics and Automation Magazine, vol. 23, no. 3, pp. 30-41, Sept. 2016,

[13] Bryan A. Jones and Ian D. Walker, ”Kinematics for multisection continuum robots”, *IEEE Transactions on Robotics*, vol. 22, no. 1, pp. 43-55, 2006.

[14] Jeesoo Ha, Dooyoung Kim and Sungho Jo, ”Use of deep learning for position estimation and control of soft glove”, *2018 18th International Conference on Control Automation and Systems (ICCAS)*, 2018.

[15] Liu Wuji et al., ”Distance-directed target searching for a deep visual servo sma driven soft robot using reinforcement learning”, *Journal of Bionic Engineering*, vol. 17, no. 6, pp. 1126-1138, 2020.

[16] Pouya Abdollahzadeh and Saber Azizi, ”On thedynamics of a magnetostriction-based soft robotic manipulator: Closed form and Machine Learning approaches”, *2019 7th International Conference on Robotics and Mechatronics (ICRoM)*, 2019.

[17] Guanda Li, Jun Shintake and Mitsuhiro Hayashibe, ”Deep Reinforcement Learning Framework for Underwater Locomotion of Soft Robot”, *2021 IEEE International Conference on Robotics and Automation (ICRA)*, 2021.

[18] Sreeshankar Satheeshbabu et al., ”Continuous control of a soft continuum arm using deep reinforcement learning”, *2020 3rd IEEE International Conference on Soft Robotics (RoboSoft)*, 2020.

[19] Sudipta Chattopadhyay et al., ”Control of single-segment continuum robots: reinforcement learning vs. neural network based PID”, *2018 International Conference on Control Power Communication and Computing Technologies (ICCPCCT)*, 2018.

Proceedings of the 3rd Conference on Fully Actuated System Theory and Applications
May 10-12, 2024, Shenzhen, China

Robust LPV System Identification with Asymmetric Measurement Noise

Xin Liu[1], Yang Hai[2], Wei Dai[1,2]

1. Artificial Intelligence Research Institute, China University of Mining and Technology, Xuzhou 221116, P. R. China
E-mail: liuxin_hit@cumt.edu.cn

2. School of Information and Control Engineering, China University of Mining and Technology, Xuzhou 221116, P. R. China
E-mail: ts22060067a31@cumt.edu.cn(Yang Hai), weidai@cumt.edu.cn(Wei Dai)

Abstract: In this paper, we consider the identification problem for linear parameter varying (LPV) systems with skewed and asymmetric measurement noise. The shifted asymmetric Laplace (SAL) distribution and the expectation maximization (EM) algorithm are combined to build the robust system identification framework. To overcome various types of outliers in the data including the skewed and asymmetric noise, the skewness and tails of the SAL distribution are adaptively adjusted based on the collected identification data. The maximum likelihood estimates (MLEs) of the parameters are produced by using the expectation maximization algorithm, in which the system model and noise parameters are extracted directly from the collected identification data. The effectiveness of the proposed algorithm is exhibited in the verification section.

Key Words: Robust global approach, LPV system identification, shifted asymmetric Laplace distribution, maximum likelihood estimates

1 Introduction

Recently, system identification works efficiently for the complex process modeling and it has been widely applied for practical systems [1]. Compared with the conventional modeling methods, the main advantages of system identification lie in: 1) It extracts the model parameters directly from the recorded process data; 2) It skips exploring complicated internal mechanism of the industrial processes [2–4]. Therefore, numerous approaches for system identification with different model structures have been presented in the existing literature [5–7]. As the process data plays an important role in system identification, the performance of the identification methods is directly influenced by the data quality [8–10]. It is easy to understand that the better data quality facilitates the identification methods and leads to better performance.

But in practical settings, the pure identification data seems to be almost impossible to collect [9–12]. The practical issues such as unknown system delay, incomplete measurements, the outliers and the quantized data may largely degrade the quality of the identification data [13–15]. Among the identification issues, the outlier occupies a special position as it is frequently encountered in practical processes [13, 17–19]. The errors such as data recording or data transmission error, system sensor malfunction and unknown external disturbance will introduce outliers into the identification data and even part of the errors are inevitable [11, 16]. During the identification procedure, a general effective way to process the outliers is using the heavy-tailed distributions such as the Student's t-distribution and Laplace distribution to model the outliers in the measurements and many robust identification approaches have been developed [11, 13, 16, 18, 19]. In [18], the VB inference and the Student's t-distribution are combined to identify the piecewise continuous systems in the presence of outliers. The proposed method can produce unbiased parameter estimates and it is also robust to overfitting models. In [19], the robust identification of nonlinear state-space system with outliers is considered. The problem formulation is realized by using the EM algorithm and the Laplace distribution is adopted to ensure the robustness for outliers. Although the Student's t-distribution and Laplace distribution are shown to be robust for various types of outliers, but both of them present symmetric statistical property, will them keep effective for the skewed or asymmetric measurement noise?

Motivated by the above question, this paper considers the identification of linear parameter varying (LPV) systems with skewed and asymmetric measurement noise. The shifted asymmetric Laplace (SAL) distribution which has skewed, asymmetric and heavy-tailed statistical property is introduced to deal with the skewed and asymmetric measurement noise, then a more generalized robust identification algorithm (renamed as LPV-SAL) is proposed. The main contributions of current paper are summarized as

1) Identification of LPV systems in the presence of skewed and asymmetric measurement noise is realized based on the robust SAL distribution;
2) The decomposition of the SAL distribution is applied and it facilitates the computational efficiency of the proposed algorithm;
3) The model and noise parameters are simultaneously identified from the identification data and the advantages and disadvantages of the algorithm are clearly clarified.

In the following, the rest sections are arranged as: The specific identification settings and the SAL distribution are introduced in Section II. The mathematical formulations of the proposed algorithm are detailedly presented in Section III. The effectiveness and lackness are revealed from the verification tests in Section IV. The main results of current work are summarized in Section V.

This work was supported in part by the National Natural Science Foundation of China (No. 62103134, 62373361), the China Postdoctoral Science Foundation (2023M743776) and the National Key Research and Development Program of China (2022YFB3304700).

2 Preliminaries

2.1 The Considered LPV System Model

In the following, let u_t, v_t and y_t represent the input, scheduling and output variables of the LPV system, respectively. Then the considered system model is formulated as

$$\mathcal{A}(v_t)y_t = \mathcal{B}(v_t)u_t + \delta_t, \tag{1}$$

and

$$\begin{aligned}\mathcal{A}(v_t) &= 1 + \alpha_1(v_t)z^{-1} + \alpha_2(v_t)z^{-2} + \cdots + \alpha_{n_\alpha}(v_t)z^{-n_\alpha},\\ \mathcal{B}(v_t) &= \beta_1(v_t)z^{-1} + \beta_2(v_t)z^{-2} + \cdots + \beta_{n_\beta}(v_t)z^{-n_\beta}.\end{aligned} \tag{2}$$

Here the operator z^{-1} works as $z^{-1}y_t = y_{t-1}$; n_α and n_β are the known system orders; $\{\alpha_i(v_t)\}_{i=1,2,\cdots,n_\alpha}$ and $\{\beta_j(v_t)\}_{j=1,2,\cdots,n_\beta}$ are the varying coefficients of the system model. In majority literature, the model coefficients $\alpha_i(v_t)$ and $\beta_j(v_t)$ are represented as real meromorphic functions of the scheduling variable v_t and

$$\begin{aligned}\alpha_i(v_t) &= \alpha_i^0 + \sum_{m=1}^{M}\alpha_i^m\Pi_m(v_t),\\ \beta_j(v_t) &= \beta_j^0 + \sum_{n=1}^{N}\beta_j^n\Delta_n(v_t),\end{aligned} \tag{3}$$

where $\Pi_m(v_t)$ and $\Delta_n(v_t)$ denote the basis meromorphic functions. By substituting (2) and (3) into (1), then it has

$$y_t = \mathcal{R}^T(v_t)\vartheta + \delta_t, \tag{4}$$

where

$$\begin{aligned}\mathcal{R}(v_t) = [&-y_{t-1} \ -\Pi_1(v_t)y_{t-1}\cdots-\Pi_M(v_t)y_{t-1}\cdots\\ &-y_{t-2}\cdots-\Pi_M y_{t-n_\alpha}\ u_{t-1}\ \Delta_1(v_t)u_{t-1}\cdots\\ &\Delta_N(v_t)u_{t-1}\ u_{t-2}\cdots\Delta_N(v_t)u_{t-n_\beta}]^T,\end{aligned} \tag{5}$$

$$\begin{aligned}\vartheta = [&\alpha_1^0\ \alpha_1^1\cdots\alpha_1^M\ \alpha_2^0\cdots\alpha_{n_\alpha}^M\ \beta_1^0\ \beta_1^1\cdots\\ &\beta_1^N\ \beta_2^0\cdots\beta_{n_\beta}^N]^T.\end{aligned} \tag{6}$$

2.2 The Shifted Asymmetric Laplace Distribution

During the past few decades, the robust distributions such as the Student's t-distribution and the Laplace distribution are widely applied in system identification, soft sensing and so on. Both of them have heavy-tailed statistical characteristic with adjustable hyper-parameter which ensures their robust for various types of outliers. But both the Student's t-distribution and the Laplace distribution have the symmetric statistical property which may fail to deal with the skewed and asymmetric measurement noise. To solve this problem, the shifted asymmetric Laplace (SAL) distribution is introduced to model the measurement noise δ_t and a more generalized robust algorithm is developed in this paper. Consider the system noise δ_t follows the SAL distribution with zero mean [20, 21]

$$\begin{aligned}\delta_t &\sim SAL(\delta_t|0,\gamma,\Omega)\\ &= \frac{2\exp\left(\frac{\gamma}{\Omega}\delta_t\right)}{\sqrt{2\pi\Omega}}\times\left(\frac{\delta_t^2/\Omega}{2+\gamma^2/\Omega}\right)^{1/4}\times K_{1/2}(\lambda),\end{aligned} \tag{7}$$

where γ represents the skewness parameter while Ω is the scale parameter; $K_{1/2}(\cdot)$ denotes the modified Bessel function of the third kind with order $1/2$; λ is the substitution for [21]

$$\lambda = \sqrt{(2+\gamma^2/\Omega)(\delta_t^2/\Omega)}. \tag{8}$$

However, it will cause heavy computational burden if the SAL distribution is applied directly in the mathematical derivations of the identification method since its mathematical expression (as seen in (7)) is complicated. Fortunately, the mathematical formulation of the SAL distribution can be factored as [21]

$$\begin{aligned}\delta_t &\sim SAL(\delta_t|0,\gamma,\Omega)\\ &= \int p(\delta_t|h_t\gamma,h_t\Omega)p(h_t)dh_t,\end{aligned} \tag{9}$$

where $\{h_t\}_{t=1,2,\cdots,T}$ is the introduced latent variable and it cuts the SAL distribution into infinite weighted sub-Gaussian pieces. That means

$$\begin{aligned}p(\delta_t|h_t\gamma,h_t\Omega) &= \mathcal{N}(\delta_t|h_t\gamma,h_t\Omega)\\ &= \frac{1}{\sqrt{2\pi h_t\Omega}}\exp\Big(-\frac{(\delta_t-h_t\gamma)^2}{2h_t\Omega}\Big),\end{aligned} \tag{10}$$

where $h_t\Omega$ is seen as the varying variance of each sub-Gaussian component. Moreover, the probability density function (PDF) $p(h_t)$ is treated as the weight of each sub-Gaussian component and it obeys [21]

$$p(h_t) = \exp(-h_t). \tag{11}$$

In the following, it is clearly shown that the decomposition of the SAL distribution facilitates the derivations of the proposed algorithm. According to (4), it is easy to find that

$$\begin{aligned}y_t &\sim SAL(y_t|\mathcal{R}^T(v_t)\vartheta,\gamma,\Omega)\\ &= \int p(y_t|\mathcal{R}^T(v_t)\vartheta+h_t\gamma,h_t\Omega)p(h_t)dh_t,\end{aligned} \tag{12}$$

and

$$\begin{aligned}&p(y_t|\mathcal{R}^T(v_t)\vartheta+h_t\gamma,h_t\Omega)\\ &=\mathcal{N}(y_t|\mathcal{R}^T(v_t)\vartheta+h_t\gamma,h_t\Omega)\\ &=\frac{1}{\sqrt{2\pi h_t\Omega}}\exp\Big(-\frac{[y_t-(\mathcal{R}^T(v_t)\vartheta+h_t\gamma)]^2}{2h_t\Omega}\Big).\end{aligned} \tag{13}$$

3 Identification based on SAL distribution

As described above, the available identification data set is summarized as $\mathcal{C} = \{y_{1:T}, v_{1:T}, u_{1:T}\}$; the model parameter ϑ, the skewness parameter γ and the scale parameter Ω are absorbed into the unknown parameter set as $\mathcal{P} = \{\vartheta,\gamma,\Omega\}$. The latent variable h_t is introduced in the decomposition of the SAL distribution, hence the unavailable data set is defined as $\mathcal{L} = \{h_{1:T}\}$. This paper aims to identify the unknown parameter set $\mathcal{P}$ according to the available data set $\mathcal{C}$ in the presence of skewed and asymmetric measurement noise and latent data $\mathcal{L}$.

To overcome the challenges brought by the latent variable, the EM algorithm is applied in this paper to produce accurate parameter estimates. The EM algorithm offers an iterative two-step optimization process wherein the expectation

cost function is designed in the first step (renamed as E-step) and the cost function is maximized to find the parameter estimates in the second step (renamed as M-step).

3.0.1 E-step to construct the cost function

Let $\mathcal{P}^s$ denote the identified parameter set in the sth iteration of the EM algorithm, then the general expression of the cost function in the $(s+1)$th iteration is

$$Q(\mathcal{P}|\mathcal{P}^s) = E_{p(\mathcal{L}|\mathcal{C},\mathcal{P}^s)}\{\log p(\mathcal{C},\mathcal{L}|\mathcal{P})\}, \tag{14}$$

where $\log p(\mathcal{C},\mathcal{L}|\mathcal{P})$ is the log-likelihood function of the complete system data (including both available and unavailable data set); $p(\mathcal{L}|\mathcal{C},\mathcal{P}^s)$ represents the posterior PDF of the unavailable data. That means the cost function is the conditional expectation of the system log-likelihood function. Moreover, the log-likelihood function $\log p(\mathcal{C},\mathcal{L}|\mathcal{P})$ can be simplified as

$$\begin{aligned}\log p(\mathcal{C},\mathcal{L}|\mathcal{P}) &= \log p(y_{1:T}, v_{1:T}, h_{1:T}, u_{1:T}|\mathcal{P}) \\ &= \sum_{t=1}^{T} \log p(y_t|y_{1:t-1}, v_t, u_{1:t-1}, h_t, \mathcal{P}) \\ &\quad + \sum_{t=1}^{T} \log p(h_t|\mathcal{P}) + C_1,\end{aligned} \tag{15}$$

where $C_1 = \log p(v_{1:T}, u_{1:T}|\mathcal{P})$ is the constant. Consider the latent variable h_t, the desired function $Q(\mathcal{P}|\mathcal{P}^s)$ is formulated as

$$\begin{aligned}&Q(\mathcal{P}|\mathcal{P}^s) \\ &= \int p(h_t|\mathcal{C},\mathcal{P}^s) \times \log p(y_t|y_{1:t-1}, v_t, u_{1:t-1}, h_t, \mathcal{P}) dh_t \\ &+ \int p(h_t|\mathcal{C},\mathcal{P}^s) \times \log p(h_t|\mathcal{P}) dh_t + C_1.\end{aligned} \tag{16}$$

According to (13), the PDF $p(y_t|y_{1:t-1}, v_t, u_{1:t-1}, h_t, \mathcal{P})$ follows the Gaussian distribution. Then we have

$$\begin{aligned}&\log p(y_t|y_{1:t-1}, v_t, u_{1:t-1}, h_t, \mathcal{P}) \\ &= -\frac{1}{2}\log(2\pi\Omega) - \frac{1}{2}\log h_t - \frac{1}{h_t}\frac{(y_t - \mathcal{R}^T(v_t)\vartheta)^2}{2\Omega} \\ &\quad - \frac{h_t\gamma^2}{2\Omega} + \frac{\gamma y_t}{\Omega} - \frac{\gamma\mathcal{R}^T(v_t)\vartheta}{\Omega},\end{aligned} \tag{17}$$

and

$$\log p(h_t|\mathcal{P}) = -h_t. \tag{18}$$

Based on the results in [21], we define two expectation terms $\langle h_t\rangle$ and $\left\langle \frac{1}{h_t} \right\rangle$ here [21]

$$\langle h_t\rangle = \int p(h_t|\mathcal{C},\mathcal{P}^s) h_t dh_t = \sqrt{\frac{b}{a}} G_{1/2}(\sqrt{ab}), \tag{19}$$

and

$$\left\langle \frac{1}{h_t} \right\rangle = \int p(h_t|\mathcal{C},\mathcal{P}^s) \frac{1}{h_t} d = \sqrt{\frac{a}{b}} G_{1/2}(\sqrt{ab}) - \frac{1}{b}, \tag{20}$$

where $G_{1/2}(\sqrt{ab})$ is a unique function and it is defined as [21]

$$G_{1/2}(\sqrt{ab}) = \frac{K_{3/2}(\sqrt{ab})}{K_{1/2}(\sqrt{ab})}, \tag{21}$$

and the notations a and b are defined as [21]

$$a = 2 + \frac{(\gamma^s)^2}{\Omega^s}, \tag{22}$$

$$b = \frac{[y_t - \mathcal{R}^T(v_t)\vartheta^s]^2}{\Omega^s}. \tag{23}$$

With the help of (19)-(23), the integrals in (16) are calculated as

$$\begin{aligned}&\int p(h_t|\mathcal{C},\mathcal{P}^s) \times \log p(y_t|y_{1:t-1}, v_t, u_{1:t-1}, h_t, \mathcal{P}) \\ &= -\frac{1}{2}\sum_{t=1}^{T}\langle \log h_t\rangle - \frac{1}{2\Omega}\sum_{t=1}^{T}\left\langle \frac{1}{h_t}\right\rangle [y_t - \mathcal{R}^T(v_t)\vartheta]^2 \\ &- \frac{\gamma^2}{2\Omega}\sum_{t=1}^{T}\langle h_t\rangle + \frac{\gamma}{\Omega}\sum_{t=1}^{T} y_t - \frac{\gamma}{\Omega}\sum_{t=1}^{T}\mathcal{R}^T(v_t)\vartheta - \frac{T}{2}\log(2\pi\Omega),\end{aligned} \tag{24}$$

and

$$\int p(h_t|\mathcal{C},\mathcal{P}^s) \times \log p(h_t|\mathcal{P}) = -\sum_{t=1}^{T}\langle h_t\rangle. \tag{25}$$

Finally, the desired cost function $Q(\mathcal{P}|\mathcal{P}^s)$ is consisted of

$$Q(\mathcal{P}|\mathcal{P}^s) = Q_1(\vartheta,\gamma,\Omega) + C, \tag{26}$$

where

$$\begin{aligned}Q_1(\vartheta,\gamma,\Omega) &= -\frac{1}{2\Omega}\sum_{t=1}^{T}\left\langle \frac{1}{h_t}\right\rangle [y_t - \mathcal{R}^T(v_t)\vartheta]^2 + \frac{\gamma}{\Omega}\sum_{t=1}^{T} y_t \\ &\quad - \frac{\gamma^2}{2\Omega}\sum_{t=1}^{T}\langle h_t\rangle - \frac{\gamma}{\Omega}\sum_{t=1}^{T}\mathcal{R}^T(v_t)\vartheta - \frac{T}{2}\log(\Omega),\end{aligned} \tag{27}$$

and

$$C = C_1 - \frac{T}{2}\log(2\pi) - \frac{1}{2}\sum_{t=1}^{T}\langle \log h_t\rangle - \sum_{t=1}^{T}\langle h_t\rangle. \tag{28}$$

3.0.2 M-step to optimize the cost function

In this part, the resulted cost function $Q(\mathcal{P}|\mathcal{P}^s)$ in (26) is maximized to find the optimal parameter estimates in the $(s+1)$th iteration of the EM algorithm. Since the term C is not related to the unknown parameters, that means we can optimize the function $Q_1(\vartheta,\gamma,\Omega)$ instead. As the parameters ϑ, γ and Ω are correlated in $Q_1(\vartheta,\gamma,\Omega)$, the two-step optimization idea should be introduced here. That means γ and Ω should keep fixed when optimizing $Q_1(\vartheta,\gamma,\Omega)$ with respect to ϑ and the same is for the remaining two cases.

First, the partial derivative of $Q(\mathcal{P}|\mathcal{P}^s)$ with respect to γ is calculated and set to zero

$$\frac{\partial Q(\mathcal{P}|\mathcal{P}^s)}{\partial \gamma} = 0 \Longleftrightarrow \frac{dQ_1(\vartheta^s, \gamma, \Omega^s)}{d\gamma} = 0 \Longrightarrow$$
$$-\frac{\gamma}{\Omega^s}\sum_{t=1}^{T}\langle h_t\rangle + \frac{1}{\Omega^s}\sum_{t=1}^{T} y_t - \frac{1}{\Omega^s}\sum_{t=1}^{T}\mathcal{R}^T(v_t)\vartheta^s = 0. \tag{29}$$

Then the optimal skewness parmeter γ^{s+1} is obtained as

$$\gamma^{s+1} = \frac{\sum_{t=1}^{T}[y_t - \mathcal{R}^T(v_t)\vartheta^s]}{\sum_{t=1}^{T}\langle h_t\rangle}. \tag{30}$$

Second, to find the model parameter estimation ϑ^{s+1}, it is derived that

$$\frac{\partial Q(\mathcal{P}|\mathcal{P}^s)}{\partial \vartheta} = 0 \Longleftrightarrow \frac{dQ_1(\vartheta, \gamma^s, \Omega^s)}{d\vartheta} = 0 \Longrightarrow$$
$$\frac{1}{\Omega^s}\sum_{t=1}^{T}\left\langle\frac{1}{h_t}\right\rangle[\mathcal{R}(v_t)y_t - \mathcal{R}(v_t)\mathcal{R}^T(v_t)\vartheta] - \frac{\gamma^s}{\Omega^s}\sum_{t=1}^{T}\mathcal{R}(v_t) = 0 \tag{31}$$

and we have

$$\vartheta^{s+1} = \frac{\sum_{t=1}^{T}\left(\left\langle\frac{1}{h_t}\right\rangle y_t - \gamma^s\right)\mathcal{R}(v_t)}{\sum_{t=1}^{T}\left\langle\frac{1}{h_t}\right\rangle\mathcal{R}(v_t)\mathcal{R}^T(v_t)}. \tag{32}$$

Finally, to search for the scale parameter estimation Ω^{s+1}, it is derived that

$$\frac{dQ_1(\vartheta^s, \gamma^s, \Omega)}{d\Omega} = -\frac{T}{2\Omega} + \frac{1}{2\Omega^2}\sum_{t=1}^{T}\left\langle\frac{1}{h_t}\right\rangle[y_t - \mathcal{R}^T(v_t)\vartheta^s]^2$$
$$+ \frac{(\gamma^s)^2}{2\Omega^2}\sum_{t=1}^{T}\langle h_t\rangle - \frac{\gamma^s}{\Omega^2}\sum_{t=1}^{T}[y_t - \mathcal{R}^T(v_t)\vartheta^s] = 0, \tag{33}$$

and it is obtained that

$$\Omega^{s+1} = \frac{1}{T}\left\{\sum_{t=1}^{T}\left\langle\frac{1}{h_t}\right\rangle[y_t - \mathcal{R}^T(v_t)\vartheta^s]^2 + (\gamma^s)^2\sum_{t=1}^{T}\langle h_t\rangle\right.$$
$$\left. - 2\gamma^s\sum_{t=1}^{T}[y_t - \mathcal{R}^T(v_t)\vartheta^s]\right\}. \tag{34}$$

The detailed derivations of the proposed algorithm are completed and the core steps are organized into the Algorithm 1 which is renamed as LPV-SAL for simplicity.

Algorithm 1 The LPV-SAL algorithm

Input: $\mathcal{C} = \{y_{1:T}, v_{1:T}, u_{1:T}\}$
Output: $\mathcal{P} = \{\vartheta, \gamma, \Omega\}$
1: Set $s = 1$ and initialize $\mathcal{P}^s = \mathcal{P}^1$;
2: **repeat**
3: ***E-step**: to construct the cost function*
4: Compute the expectations $\langle h_t\rangle$ and $\left\langle\frac{1}{h_t}\right\rangle$ via (19) and (20);
5: Compute the necessary integrals via (24) and (25);
6: Construct the cost function in (26) - (28);
7: ***M-step**: to optimize the cost function*
8: Optimize the cost function via (29), (31) and (33), respectively;
9: Update the parameters γ, ϑ and Ω via (30), (32) and (34), respectively;
10: **until** convergence;
11: The acquired optimal parameters are $\mathcal{P}^* = \{\vartheta^*, \gamma^*, \Omega^*\}$.

4 Verifications

In this section, the verification tests are designed to reveal the effectiveness of the LPV-SAL algorithm. Consider the following LPV system

$$\mathcal{A}(v_t)y_t = \mathcal{B}(v_t)u_t + \delta_t, \tag{35}$$

where

$$\mathcal{A}(v_t) = 1 + \alpha_1(v_t)z^{-1} + \alpha_2(v_t)z^{-2},$$
$$\alpha_1(v_t) = 1 - 0.4v_t,\ \alpha_2(v_t) = 0.6 - 0.5v_t, \tag{36}$$

and

$$\mathcal{B}(v_t) = \beta_1(v_t)z^{-1} + \beta_2(v_t)z^{-2},$$
$$\beta_1(v_t) = 0.5 - 0.4v_t,\ \beta_2(v_t) = 0.6 - 0.3v_t. \tag{37}$$

That indicates the real model parameters are set as

$$[\alpha_1^0\ \alpha_1^1\ \alpha_2^0\ \alpha_2^1\ \beta_1^0\ \beta_1^1\ \beta_2^0\ \beta_2^1]^T$$
$$= [1\ -0.4\ 0.6\ -0.5\ 0.5\ -0.4\ 0.6\ -0.3]^T. \tag{38}$$

To collect the identification data set, the Gaussian signal $u_t = -1 + 2\mathcal{N}(0,1)$ and the sinusoidal signal $v_t = 0.5\sin(0.1\pi k) + 0.5$ are set as the input and scheduling signals to excite the system and $T = 500$ data points are recorded. In the following, the existing Student's t-distribution and Laplace distribution based LPV system identification algorithms (renamed as LPV-St and LPV-Lap) are used as the reference algorithms to demonstrate the effectiveness of the proposed LPV-SAL method.

4.1 Tests for the Outliers

To verify the robustness of the LPV-SAL algorithm for the outliers, in the first test, 10% outliers uniformly distributed in $[-1.2, 1.2]$ are added to the pure outputs. The ideal and the outlier-polluted outputs are compared in Fig. 1. Clearly, part of the contaminated data points are far away from the true values. Based on this deteriorated data quality, all the LPV-SAL, LPV-St and LPV-Lap algorithms are executed and the resulted parameters are compared in Figs. 2 and 3. In this comparison test, all the resulted parameters can converge to the real values which demonstrates that all the three algorithms can extract useful parameter information from the deteriorated identification data.

Based on the estimation results above, it can be concluded that

1) When 10% outliers uniformly distributed in $[-1.2, 1.2]$ are added to the outputs, all the LPV-SAL, LPV-St and LPV-Lap algorithms can extract useful information

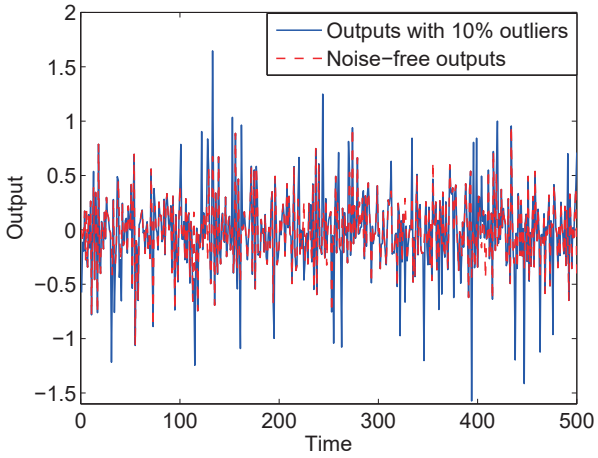

Fig. 1: The pure and outlier-polluted output data

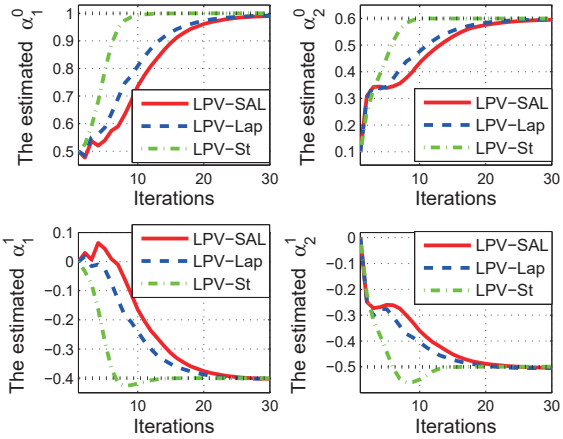

Fig. 2: Comparison results of α_1 and α_2

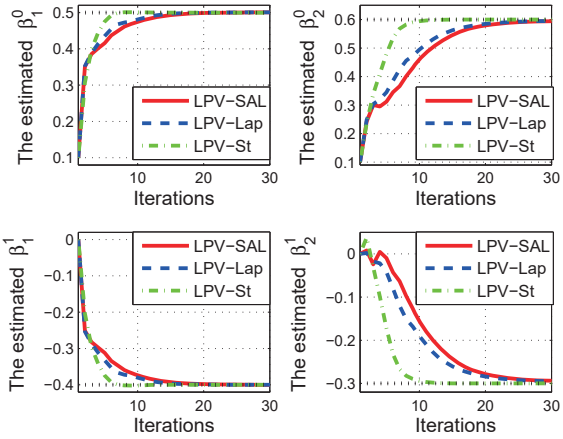

Fig. 3: Comparison results of β_1 and β_2

from the deteriorated data set and find true model parameters from the outlier-contaminated outputs, which proves the robustness of the proposed LPV-SAL algorithm at some degree;

2) But as seen in Figs. 2 and 3, the proposed LPV-SAL algorithm has the slowest convergence speed because the SAL distribution has to simultaneously adjust the shape (skewness parameter) and tails (scale parameter) to model the outliers, which makes proposed LPV-SAL algorithm need more steps to estimate the parameters accurately;

Table 1: The estimated parameters under different outlier percentages after 100 iterations

True	5%	10%	15%	20%	25%
1	0.9999	0.9983	0.9977	0.9952	0.7189
-0.4	-0.4003	-0.4011	-0.4014	-0.3974	-0.4844
0.6	0.5999	0.5990	0.5981	0.5973	0.4241
-0.5	-0.5000	-0.5011	-0.4989	-0.4984	-0.4603
0.5	0.5001	0.5000	0.5002	0.4996	0.5118
-0.4	-0.4001	-0.3999	-0.3996	-0.3990	-0.4236
0.6	0.5999	0.5989	0.5980	0.5971	0.4459
-0.3	-0.3000	-0.2990	-0.3012	-0.2969	-0.1851

Although the robustness of the LPV-SAL algorithm has been exhibited in the above tests, however, will it keep effective for worse data quality? In order to explore the maximum tolerance of the proposed LPV-SAL algorithm for the considered outliers, two extra sets of tests are designed as well. In the first set of tests, the amplitude of the uniform distributed outliers is fixed at $[-0.8, 0.8]$ while the outlier percentages in the output data are varying from 5% to 25%. After running 100 iterations, the estimated model parameters under different outlier percentages are listed in Table 1.

In the second set of tests, the outlier percentages are fixed at 10% while the amplitude of the uniform distributed outliers varies from $[-0.8, 0.8]$ to $[-2.4, 2.4]$. After running 100 iterations, the identified model parameters with varying outlier amplitude are compared in Table 2 as well.

Table 2: The estimated parameters with varying outlier amplitude after 100 iterations

True	[-0.8, 0.8]	[-1.6, 1.6]	[-2.0, 2.0]	[-2.4, 2.4]
1	0.9995	0.9982	0.9978	0.9702
-0.4	-0.4003	-0.4019	-0.4026	-0.6042
0.6	0.5996	0.5991	0.5990	0.5772
-0.5	-0.5001	-0.5011	-0.5032	-0.5895
0.5	0.4998	0.5007	0.5006	0.5095
-0.4	-0.4000	-0.4005	-0.3997	-0.4026
0.6	0.5997	0.5995	0.5991	0.5817
-0.3	-0.2999	-0.2996	-0.2989	-0.3126

Based on the results obtained from the two sets of tests, it is found that

1) Throughout Table 1-2, the resulted parameter estimates can converge closely to the corresponding true values when the outlier percentages and outlier amplitude are set in the proper range;
2) The estimation performance of the proposed LPV-SAL algorithm is directly influenced by the data quality. As seen in Table 1-2, with the increase of outlier percentages or outlier amplitude which leads to worse identification data quality, the identification performance of the proposed LPV-SAL algorithm degrades in both the estimation accuracy and convergence speed. Obviously,

the better data quality contributes to higher estimation accuracy and faster convergence speed;

3) As compared in Fig. 4, too many or too large outliers will distort the identification data which may destroy the identification performance of the LPV-SAL algorithm. As seen in Table 1-2, the proposed LPV-SAL algorithm cannot extract accurate model parameters from the distorted data since the useful model information is largely ruined by the improper outliers. In summary, the proposed LPV-SAL algorithm doesn't have infinite tolerance for the outliers and it cannot handle the outliers with improper percentages or amplitude;

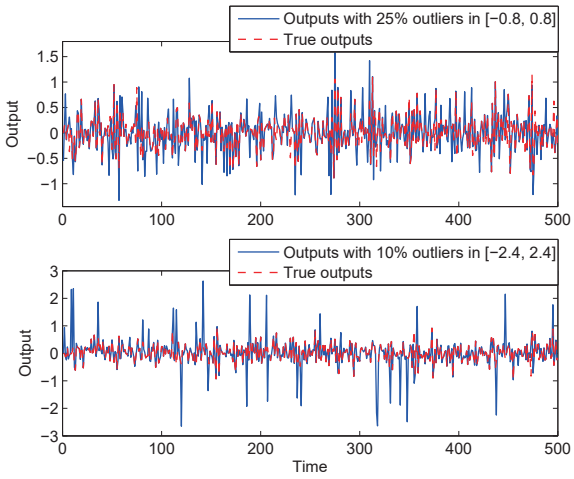

Fig. 4: Comparison of the true and distorted outputs

4.2 Tests for the Asymmetric Noise

In this part, the capacity of the LPV-SAL algorithm for handling the asymmetric noise is also tested. In order to find the advantages of the proposed LPV-SAL algorithm, the existing LPV-St and LPV-Lap algorithms are also set as the reference algorithm. To design the verification tests, the SAL distributed noise serves as the interferential term which is added to the output data. The true skewness and scale parameters of the SAL distributed noise are set as $\gamma = 0.04$ and $\Omega = 0.001$. Then the resulted SAL distributed noise and its corresponding statistical characteristics are both depicted in Fig. 5. In this case, all the LPV-SAL, LPV-St and LPV-Lap algorithms are performed and the identification performance is compared in Figs. 6 and 7. In the proposed LPV-SAL algorithm, the estimated skewness parameter and scale parameter are adaptively adjusted to approximate the external noise. Then the estimated noise and the true noise are compared in Fig. 8. To further reveal the superiority of the LPV-SAL algorithm, the MC simulations for the LPV-SAL, LPV-St and LPV-Lap algorithms are all performed as well. The mean values and standard derivations (S.D.) of the identification results obtained in the MC simulations are calculated and compared in Table 3.

Based on the comparison identification performance, it can be found that

1) As seen in Figs. 6 and 7, the proposed LPV-SAL algorithm seems to be more suitable than the LPV-St and LPV-Lap algorithms for dealing with the asymmetric measurement noise since the resulted model parameters of the LPV-SAL algorithm have the highest estimation accuracy;

2) As seen in Fig. 8, the estimated noise distribution of the LPV-SAL algorithm is well matched with the real noise distribution. That indicates in the identification procedure, the skewness parameter and scale parame-

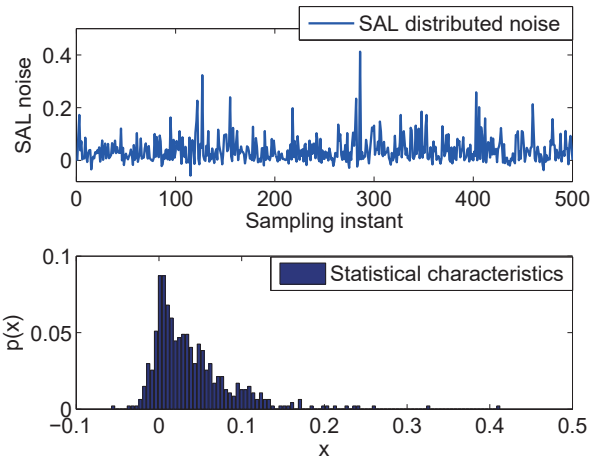

Fig. 5: The SAL distributed noise

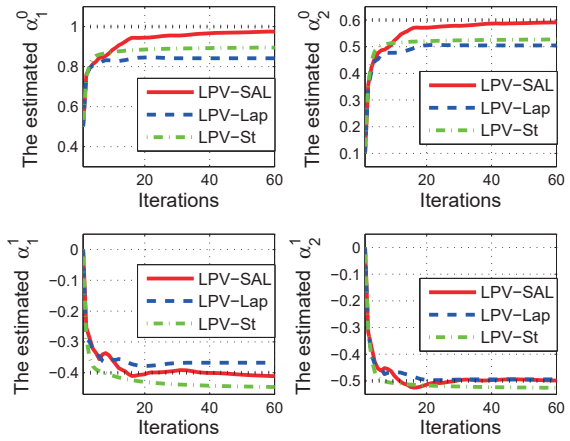

Fig. 6: Comparison results of α_1 and α_2 under SAL noise

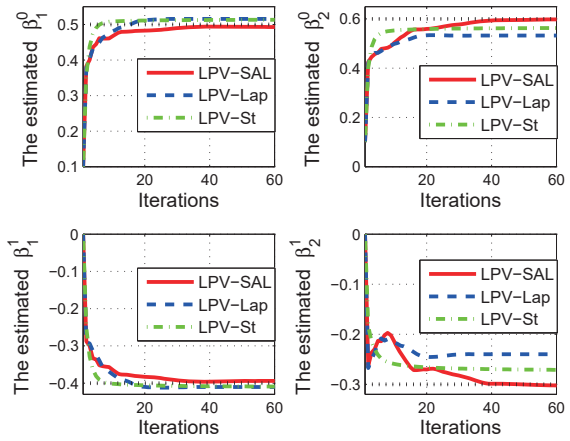

Fig. 7: Comparison results of β_1 and β_2 under SAL noise

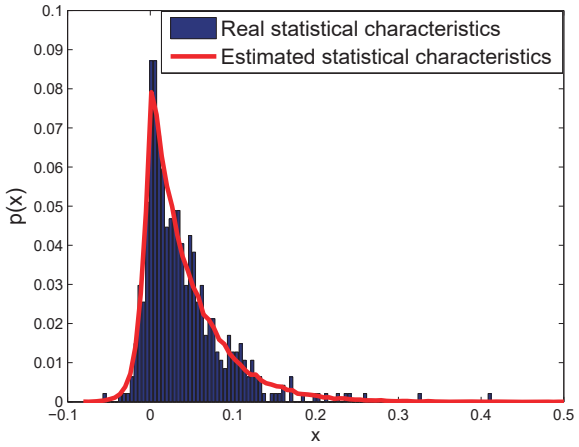

Fig. 8: The real and estimated SAL distributed noise

Table 3: The comparison results of the MC simulations under the SAL distributed noise

True	LPV-SAL	LPV-Lap	LPV-St
1	0.9750±0.0012	0.8414±0.0010	0.8956±0.000021
-0.4	-0.4090±0.0012	-0.3655±0.0018	-0.4465±0.000036
0.6	0.5915±0.0019	0.5034±0.0010	0.5270±0.000015
-0.5	-0.4968±0.0020	-0.4906±0.0015	-0.5258±0.000022
0.5	0.4933±0.0007	0.5168±0.0005	0.5132±0.000005
-0.4	-0.3949±0.0009	-0.4120±0.0005	-0.4092±0.000008
0.6	0.5974±0.0011	0.5369±0.0008	0.5632±0.000009
-0.3	-0.3010±0.0012	-0.2441±0.0008	-0.2711±0.00001

ter of the LPV-SAL algorithm can be adaptively adjusted to approximate the asymmetric measurement noise which assures the robustness of the LPV-SAL algorithm at some degree. That means in the proposed LPV-SAL algorithm, the skewness parameter and scale parameter can be adaptively extracted from the identification data, so that the external system noise is well described by the estimated SAL distribution;

3) The MC simulation results are listed in Table 3, the estimated means of the LPV-SAL algorithm are much closer to the true values than the other two algorithms. That indicates the proposed LPV-SAL algorithm outperforms the LPV-St and LPV-Lap algorithms in the parameter estimation accuracy due to the LPV-St and LPV-Lap algorithms are more sensitive to the SAL distributed noise. The advantages of the LPV-SAL algorithm are demonstrated in this comparison test for handling the SAL distributed noise.

5 Conclusions

In this work, a new robust LPV-SAL algorithm is proposed for the identification of LPV systems with skewed and asymmetric measurement noise. In the LPV-SAL algorithm, the statistical property of the SAL distribution is adaptively adjusted by the skewness parameter and the scale parameter to resist the outlier-polluted or asymmetric measurement noise, which assures the robustness of the introduced algorithm. The verification tests prove the robustness of the LPV-SAL algorithm for the outliers and it outperforms the existing LPV-St and LPV-Lap algorithms for the asymmetric measurement noise. However, the main lackness of the proposed LPV-SAL algorithm lies in

1) In the fair comparison test for the outliers, the proposed LPV-SAL algorithm has the slowest convergence speed than the LPV-St and LPV-Lap algorithms;
2) The proposed LPV-SAL algorithm doesn't have infinite tolerance for the outliers and it fails to estimate the accurate model parameters when too many or too large outliers existed in the output data;
3) The performance of the LPV-SAL algorithm degrades quickly with the increase of outlier percentages which means the proposed LPV-SAL algorithm is sensitive for the outlier percentages.

References

[1] X. Liu, C. Wang and G. Han, "LPV time-delay system identification and its application to the centralized heat-supply system," *IEEE Trans. Instrum. Meas.*, vol. 71, pp. 1-11, 2022.

[2] W. Liu, X. Yang, X. Yang and H. Gao, "A novel industrial chip parameters identification method based on cascaded region segmentation for surface-mount equipment," *IEEE Trans. Ind. Electron.*, vol. 69, no. 5, pp. 5247-5256, 2022.

[3] A. Mitra, R. Dutta, A. Gupta, A. Mohapatra and S. Chakrabarti, "A robust data-driven approach for adaptive dynamic load modeling," *IEEE Trans. Power Syst.*, vol. 37, no. 5, pp. 3779-3791, 2022.

[4] H.H. Kang, D.K. Lee and C.K. Ahn, "Finite-memory-structured online rraining algorithm for system identification of unmanned aerial vehicles with neural networks," *IEEE Trans. Mech.*, DOI: 10.1109/TMECH.2022.3190053, 2022.

[5] C. Huang, "A combined invariant-subspace and subspace identification method for continuous-time state-space models using slowly sampled multi-sine-wave data," *Automatica*, vol. 140, pp. 1-10, 2022.

[6] J. Hou, H. Su, C. Yu, F. Chen, P. Li, H. Xie and T. Li, "Consistent subspace identification of errors-in-variables Hammerstein systems," *IEEE Trans. Syst. Man Cybern. Syst.*, DOI: 10.1109/TSMC.2022.3213809, 2022.

[7] G. Chen, M. Gan, L. Chen and C.L.P. Chen, "Online identification of nonlinear systems with separable structure," *IEEE Trans. Neural Netw. Learn. Syst.*, DOI: 10.1109/TNNLS.2022.3215756, 2022.

[8] X. Liu, X. Yang and S. Yin, "Nonlinear system identication with robust multiple model approach," *IEEE Trans. Contr. Syst. T.*, vol. 28, no. 6, pp. 2728-2735, 2020.

[9] A.A. Adeniran and S.E. Ferik, "Modeling and identification of nonlinear systems: A review of the multimodel approach-Part 1," *IEEE Trans. Syst. Man Cybern. Syst.*, vol. 47, no. 7, pp. 1149-1159, 2017.

[10] S.E. Ferik and A.A. Adeniran, "Modeling and identification of nonlinear systems: A review of the multimodel approach-Part 2," *IEEE Trans. Syst. Man Cybern. Syst.*, vol. 47, no. 7, pp. 1160-1168, 2017.

[11] H. Kodamana, B. Huang, R. Ranjan, Y. Zhao, R. Tan and N. Sammaknejad, "Approaches to robust process identification: A review and tutorial of probabilistic methods," *J. Process Contr.*, vol. 66, pp. 68-83, 2018.

[12] S. Dong, L. Yu, W. Zhang and B. Chen, "Robust hierarchical identification of Wiener systems in the presence of dynamic disturbances," *J. Franklin I.*, vol. 357, no. 6, pp. 3809-3834, 2020.

[13] Q. Liu, W. Lin, S. Jiang, Y. Chai and L. Sun, "Robust estimation of Wiener models in the presence of outliers using the

VB approach," *IEEE Trans. Ind. Electron.*, vol. 68, no. 11, pp. 11390-11399, 2021.

[14] X. Wang, C. Li, T. Li, Y. Liang, Z. Ding and Q. Pan, "Variational Bayesian inference for the identification of FIR systems via quantized output data," *Automatica*, vol. 132, pp. 1-15, 2021.

[15] D. Wang, S. Zhang, M. Gan and J. Qiu, "A novel EM identification method for Hammerstein systems with missing output data," *IEEE Trans. Ind. Inform.*, vol. 16, no. 4, pp. 2500-2508, 2020.

[16] D. Wang and W. Zhu, "Advances in modeling and control of linear parameter varying systems," *Acta Automatica Sinica*, vol. 47, no. 4, pp. 780-790, 2021.

[17] L. Li, H. Zhang and X. Ren, "Robust adaptive identification for sandwich systems with unknown time-delay," *ISA Trans.*, vol. 100, pp. 289-298, 2020.

[18] T. Baldacchino, K. Worden and J. Rowson, "Robust nonlinear system identification: Bayesian mixture of experts using the t-distribution," *Mech. Syst. Signal Proc.*, vol. 85, pp. 977-992, 2017.

[19] X. Liu, X. Yang and X. Liu, "Nonlinear state-space system identification with robust Laplace model," *Int. J. Contr.*, vol. 94, no. 6, pp. 1492-1501, 2021.

[20] C. Zhang, M. Tang, T. Li, Y. Sun and G. Tian, "A new multivariate Laplace distribution based on the mixture of normal distributions (in Chinese)," *Sci. Sin. Math.*, vol. 50, no. 5, pp. 711-728, 2020.

[21] B.C. Franczak, R.P. Browne and P.D. McNicholas, "Mixtures of shifted asymmetric Laplace distributions," *IEEE Trans. Pattern Anal. Mach. Intell.*, vol. 36, no. 6, pp. 1149-1157, 2014.

[22] S. Kotz, T.J. Kozubowski and K. Podgorski, "The Laplace distribution and generalizations: A revisit with applications to communications, economics, engineering,and finance," Burkhäuser, Boston, 2001.

Proceedings of the 3rd Conference on Fully Actuated System Theory and Applications
May 10-12, 2024, Shenzhen, China

Event-Triggered Prescribed Performance Control for Multi-Input Multi-Output Nonlinear Systems

En-Yuan Cui[1], Jin-Xi Zhang[1]

1. State Key Laboratory of Synthetical Automation for Process Industries, Northeastern University, Shenyang 110819, China
E-mail: enyuancui@stumail.neu.edu.cn, zhangjx@mail.neu.edu.cn

Abstract: This research addresses the tracking control problem for a class of multi-input multi-output networked systems characterized by unknown nonlinear functions, mismatched disturbances, event-triggered inputs, and input coupling. A novel prescribed performance control strategy and actuator update protocol are proposed to address this challenge. In contrast to existing results, our approach requires the transmission of a binary signal (0 or 1) to the actuator. This not only reduces the quantity of data transmission but also minimizes the number of transmitted bits, thereby saving communication costs. Furthermore, irrespective of the unknown nonlinearities, disturbances, and measurement errors, the proposed method ensures both transient and steady-state performance in output tracking. Simulation results are provided to validate the established theoretical conclusions.

Key Words: Event-triggered control, multiple-input multiple-output, nonlinear systems, prescribed performance control.

1 Introduction

In contemporary control applications, controllers are commonly implemented on digital platforms using sampled-data control theory to design controllers and analyze closed-loop stability. Typically, control tasks adhere to a time-triggered paradigm. However, from a resource allocation standpoint, periodic sampling may not be optimal, especially in scenarios where executing control tasks during satisfactory system operation is resource wasteful [1]. Networked control systems (NCSs) are a prime example, where controllers communicate with the physical process over a network. Inefficient use of communication resources and power is a critical concern in NCS design. Implementing control signals regardless of the plant's status can lead to unnecessary network utilization, causing high workloads.

To address resource limitations in NCSs and enhance functionality, recent research [1–3] has rekindled interest in event-triggered control (ETC). Within the ETC framework, a predefined event-triggered scheduling scheme is employed, invoking control task execution upon the occurrence of an event rather than the passage of a specific time interval. This paradigm proves particularly suitable for NCSs and embedded systems [4]. Motivated by the advantages of ETC, a wide array of communication-aware control strategies for networked systems has been documented in the literature [5–8].

While the previously discussed ETCs are conceptually appealing, there remain a couple of challenging issues that currently remain unresolved. The first issue pertains to signal transmission bits. In efforts to mitigate communication burdens, the majority of researchers have concentrated on reducing the number of data transmissions [9–11]. Typically, the control signal is encoded into a digital signal, often with 16 bits, before transmission begins. The challenge arises in attempting to prevent distortion—namely, the larger the magnitude of the control signal, the more bits the digital signal requires, subsequently increasing the network bandwidth.

The second one is associated with system performance [12–14]. Although utilizing an event-triggered scheduling scheme effectively reduces the data transmission frequency, the resulting sampling-induced errors may affect the system performance. On the other hand, input coupling poses additional challenges in the design of control systems, as the control inputs interact with each other, thus decoupling needs to be considered when designing the controllers. In the presence of unknown nonlinear functions or disturbances or input coupling, a consistent limit boundedness of the tracking error or the system state can often be obtained [5, 7, 13, 15]. However, the size of the residual set cannot be determined in advance because it is highly dependent on some unknown terms of the system.

Recently, the prescribed performance control (PPC) scheme was successfully planted in the ETC architecture [16, 17]. This control strategy provides a systematic framework for designing control laws that ensures the desired performance characteristics [18, 19], such as settling time, overshoot, and robustness. Therefore, a large number of studies [20–22] on PPC of multiple input and multiple output (MIMO) systems were performed. Nonetheless, the issue about data transmission bits was not taken into account.

To overcome the above challenging problems, this paper proposes a novel ETC strategy for a class of networked MIMO systems. An initialization technique is introduced in the PPC design, while event-triggered rules are utilized to form an actuator update protocol. By this way, the following advantages with respect to the existing results are obtained.

1) From beginning to end, only 1-bit update signal instead of the real control signal needs to be transmitted by the communication channel between the controller and the actuator.
2) In lieu of UUB, the predesignated transient and steadystate tracking behavior concerning the convergence rate and the tracking accuracy is warranted.
3) The algorithm exhibits a low complexity level, ascribed

This work was supported in part by the National Key Research and Development Program of China under Grant 2022YFB3305905, the National Natural Science Foundation of China under Grant 62103093, the Xingliao Talent Program of Liaoning Province of China under Grant XLYC2203130, the Science and Technology Foundation of Liaoning Province of China under Grant 2023-MS-087, and the Fundamental Research Funds for the Central Universities of China under Grant N2108003.

to the absence of adaptive schemes, approximating structures, and recursive computation of virtual control signal derivatives.

2 System Description and Problem Formulation

2.1 Systems Description

A class of MIMO nonlinear systems are taken into consideration

$$\dot{X} = F(x) + G(x)U + D(t), \tag{1}$$

where $X = [x_1, x_2, \cdots, x_n]^T \in \Re^n$ is the state; $U = [u_1(t), u_2(t), \cdots, u_n(t)]^T \in \Re^n$ is the inputs applied to the plant; $F(x) = [f_1(x), f_2(x), \cdots, f_n(x)]^T \in \Re^n$ is the continuous nonlinear functions; $G(x) = [g_{ij}(x)] \in \Re^{n\times n}$ is the virtual control coefficient matrix, where $g_{ij}(x)$ is the continuous nonlinear function; $D(t) = [d_1(t), d_2(t), \cdots, d_n(t)]^T \in \Re^n$ is the unknown disturbances.

Further, we define

$$G'(x) = \frac{1}{2}\left(G(x) + G^T(x)\right). \tag{2}$$

For the subsequent development, a number of assumptions are introduced.

Assumption 1 *The matrix $G'(x)$ is symmetric positive definite.*

Assumption 2 *The disturbances terms $d_i(t)$, $i = 1, \cdots, n$ are bounded.*

2.2 Performance Function

In order to achieve the specified output tracking performance, the performance function, $p(t)$, is used to constrain the tracking error. To accomplish this goal, the performance function needs to satisfy:

1. $p(t)$ is smooth and positive;
2. $\dot{p}(t) \leq 0$ and $|\dot{p}(t)| < \infty$;
3. $p(0) = p_0$ and $\lim_{t\to+\infty} p(t) = p_\infty$;

where p_0 and p_∞ are the positive constants that can be determined by the designer. So, depending on the requirements we can give the formula as follows.

$$p_i(t) = (p_{i0} - p_{i\infty})e^{-\mu_i t} + p_{i\infty}, \tag{3}$$

where μ_i is a positive constant.

2.3 Problem Formulation

The control goal for (1) is steering its output to track the reference trajectory, $R(t) = [r_1(t), r_2(t), \cdots, r_n(t)]^T \in \Re^n$, with

$$|x_i(t) - r_i(t)| < p_i(t),\ \forall t \geq 0, \tag{4}$$

with $i = 1, 2, \cdots, n$, and $p_i(t)$ is the performance function in (3) introduced for each tracking error. A widely used assumption is presented as follows.

Assumption 3 *The reference meets $r_i(t) \in L^\infty$ and $\dot{r}_i(t) \in L^\infty$ with $i = 1, 2, \cdots, n$, wherein the bounds are not necessarily known.*

Problem 1 *Design a controller for the MIMO nonlinear system in (1), such that for any initial condition, the tracking performance in (4) is ensured and all the signals in the control system are bounded.*

3 Control Implementation

3.1 Controller Design

First of all, start with the definition of the tracking errors:

$$S = X - R, \tag{5}$$

where $S = [s_1(t), s_2(t), \cdots, s_n(t)]^T$. To avoid the control signals with the large initial values, a tuning function exploited is introduced

$$\psi(t) = \begin{cases} \sin\left(\frac{\pi}{2}\frac{t}{\tau}\right), & t < \tau, \\ 1, & t \geq \tau, \end{cases} \tag{6}$$

where $\tau > 0$ is a free-design parameter. Apparently, $\psi(t)$ is continuously differentiable with respect to t. Then, we have $E = [e_1(t), e_2(t), \cdots, e_n(t)]^T$, with

$$e_i(t) = \psi(t)s_i(t),\ i = 1, 2, \cdots, n. \tag{7}$$

Next, we introduce a set of barrier functions to constrain each error $e_i(t)$.

$$\eta_i(t) = \tan\left(\frac{\pi}{2}\frac{e_i(t)}{p_i(t)}\right), \tag{8}$$

where $p_i(t)$ is the performance funtion, $i = 1, 2, \cdots, n$, with $p_{i0} > p_{i\infty} > 0$ and $\mu_i > 0$, the parameters μ_i and $p_{i\infty}$ characterize the convergence rate and the ultimate bound of the error $e_i(t)$, respectively. The parameter p_{i0} is chosen such that

$$|e_i(0)| < p_i(0),\ i = 1, 2, \cdots, n. \tag{9}$$

Next, we construct an error transformation function

$$\beta_i(t) = \frac{1}{p_i(t)}\frac{1}{\phi_i(t)}, \tag{10}$$

and

$$\phi_i(t) = \cos^2(\frac{\pi}{2}\frac{e_i(t)}{p_i(t)}), \tag{11}$$

with $i = 1, 2, \cdots, n$. Let

$$\eta = [\eta_1(t), \eta_2(t), \cdots, \eta_n(t)]^T, \tag{12}$$

$$\beta = \begin{bmatrix} \beta_1(t) & & & \\ & \beta_2(t) & & \\ & & \ddots & \\ & & & \beta_n(t) \end{bmatrix}. \tag{13}$$

Finally, we give the following control law

$$\nu = -\lambda\beta\eta, \tag{14}$$

where $\nu = [\nu_1(t), \nu_2(t), \cdots, \nu_n(t)]^T$ and $\lambda > 0$ is a constant control gain.

3.2 Actuator Update Protocol

For control implementation with an inexpensive communication cost, the control signal computed based on (14) is first quantized based on the following event-triggering rule:

$$t_{ik+1} = \inf\left\{t_i > t_{ik} : |z_i(t_i)| = c_i\right\}, \tag{15}$$

$$z_i(t_i) = \nu_i(t_i) - \nu_i(t_{ik}),\ t_{ik} \le t_i < t_{ik+1}, \tag{16}$$

$$q_i(t_{ik}) = \begin{cases} 1, \text{ if } z_i(t_{ik}) = c_i, \\ 0, \text{ if } z_i(t_{ik}) = -c_i, \end{cases} \tag{17}$$

where $i = 1, 2, \cdots, n$; $t_{i0} = 0$; $k = 0, 1, 2, \ldots$; and $c_i > 0$ is a fixed threshold specified by the designer. According to the actuator update protocol for synthesizing control actions, we have

$$u_i(t_i) = 0,\ t_{i0} \le t < t_{i1}, \tag{18}$$

$$u_i(t_i) = u_i(t_{ik-1}) + c_i(2q_i(t_{ik}) - 1),\ t_{ik} \le t_i < t_{ik+1}, \tag{19}$$

where $i = 1, 2, \cdots, n$ and $k \in Z^+$.

Lemma 1 *With (15)–(19), it holds that*

$$u_i(t_i) = \nu_i(t_{ik}),\ t_{ik} \le t_i < t_{ik+1}, \tag{20}$$

where $k = 0, 1, 2, \ldots$ and $i = 1, 2, \cdots, n$.

Proof 1 *On the basis of (15) and (16), one has*

$$\nu_i(t_{k+1}) = \begin{cases} \nu_i(t_{ik}) + c_i, \text{ if } z_i(t_{ik+1}) = c_i, \\ \nu_i(t_{ik}) - c_i, \text{ if } z_i(t_{ik+1}) = -c_i, \end{cases} \tag{21}$$

where $k = 0, 1, 2, \ldots$ and $i = 1, 2, \cdots, n$. By (17), (21) can be rewritten as

$$\nu_i(t_{ik+1}) = c_i \sum_{j=1}^{k+1} (2q_i(t_{ij}) - 1),\ k = 0, 1, 2, \ldots \tag{22}$$

With (18) and (19), it is obtained that

$$u_i(t_i) = c_i \sum_{j=1}^{k+1} (2q_i(t_{ij}) - 1),\ t_{ik+1} \le t_i < t_{ik+2}, \tag{23}$$

where $k = 0, 1, 2, \ldots$ and $i = 1, 2, \cdots, n$. Thereby,

$$u_i(t_i) = \nu_i(t_{ik+1}),\ t_{ik+1} \le t_i < t_{ik+2}, \tag{24}$$

with $k = 0, 1, 2, \ldots$ and $i = 1, 2, \cdots, n$. Taking $u_i(t_{i0}) = 0$ and $\nu_i(t_{i0}) = 0$ into consideration, the result in Lemma 1 is established. □

4 Theoretical Analysis

It is ready to establish the main result of this article.

Theorem 1 *Under Assumption 1–3 and initial condition in (9), applying the event-triggered PPC strategy presented in (15)–(19) solves Problem 1.*

Proof 2 *What we need to verify is*

$$|e_i(t)| < p_i(t),\ i = 1, 2, \cdots, n,\ \forall t \ge 0. \tag{25}$$

Consider the relationship of counterfactuals for analysis. According to (9), when $t = 0$, it is clear that the relationship satisfying (25) can be obtained. Note that each x_i and each $r_i(t)$ are continuous in time. Therefore, each $s_i(t)$ in (5) is continuous in time. Notice from (6) that $\psi(t)$ is continuously differentiable. So $e_i(t)$ in (7) is continuous in time. If $|e_i(t)| < p_i(t)$, $\eta_i(t)$ in (8) and $\beta_i(t)$ in (10) are continuous in time. From a counterfactual perspective, the facts above show that if (25) is violated, then there must exist $t^* > 0$ such that

$$\lim_{t \to t^*} |e_i(t)| = p_i(t),\ i \in \{1, 2, \cdots, n\}, \tag{26}$$

and

$$|e_i(t)| < p_i(t),\ i = 1, 2, \cdots, n,\ t < t^*. \tag{27}$$

Considering the coupling problem of the actual system, we construct

$$V = \eta^T \eta. \tag{28}$$

The derivative of V is given by

$$\dot{V} = 2\eta^T \dot{\eta}, \tag{29}$$

where $\dot{\eta} = [\dot{\eta}_1(t), \dot{\eta}_2(t), \cdots, \dot{\eta}_i(t), \cdots, \dot{\eta}_n(t)]^T$ with

$$\dot{\eta}_i(t) = \beta_i(t) \frac{\pi}{2} \left(\dot{e}_i(t) - \frac{e_i(t)\dot{p}_i(t)}{p_i(t)} \right). \tag{30}$$

Let

$$w_i(t) = \frac{e_i(t)\dot{p}_i(t)}{p_i(t)}. \tag{31}$$

So (29) becomes

$$\dot{V} = \pi \eta^T \beta (\dot{E} - W), \tag{32}$$

where $W = [w_1(t), w_2(t), \cdots, w_n(t)]^T$. Substitute (1) and (7) into (32) to get

$$\dot{V} = \pi \eta^T \beta (F(x) + G(x)U + D(t) - \dot{R}(t) - W). \tag{33}$$

By (16) and (20), it is attained that

$$u_i(t) = \nu_i(t_{ik}) = \nu_i(t_i) - z_i(t_i),\ t_{ik} \le t_i < t_{ik+1}, \tag{34}$$

where $k = 0, 1, 2, \ldots$ and $i = 1, 2, \cdots, n$. Notice from (15) that $z_i(t_i)$ induced by the event-triggered logic is both bounded (i.e., $|z_i(t_i)| \le c_i$) and piecewise continuous in t_i. Therefore, the real control input U can be regarded as the PPC signal ν corrupted by the bounded and piecewise continuous disturbances Z. Inserting (14) into (34), one further has

$$U = -\lambda \beta \eta - Z, \tag{35}$$

where $Z = [z_1, z_2, \cdots, z_n]^T$ and $|z_i| \le c_i$ with $i = 1, 2, \cdots, n$. So we can obtain

$$\dot{V} = \pi \eta^T \beta H - \lambda \pi \eta^T \beta G(x) \beta \eta, \tag{36}$$

where

$$H = F(x) + D(t) - \dot{R}(t) - W - G(x)Z. \tag{37}$$

Note that $e_i(t)$, $\psi(t)$, $r_i(t)$, $\dot{r}_i(t)$, z_i, $d_i(t)$ with $i = 1, 2, \cdots, n$ are bounded on $[0, t^*)$. Therefore, we can get the boundedness of x_i on $[0, t^*)$. Due to the continuity of $f_i(\cdot)$, $g_{ij}(\cdot)$, $F(x)$ and $G(x)$ are bounded on $[0, t^*)$. And since both $1/p_i(t)$ and $\dot{p}_i(t)$ can be designed by the designer, they are also bounded, so W is bounded on $[0, t^*)$. Thus, H is bounded on $[0, t^*)$. Let

$$\sup_{t \in [0, t^*)} |H(t)| = \bar{H}. \tag{38}$$

Therefore, we can get

$$\dot{V} \leq \bar{H}\|\beta\eta\| - \lambda\pi\eta^T\beta\left(G'(x) + \frac{G(x) - G^T(x)}{2}\right)\beta\eta. \tag{39}$$

Under Assumption 1, we can obtain from (39)

$$\dot{V} \leq \bar{H}\|\beta\eta\| - B\|\beta\eta\|^2, \tag{40}$$

with $B = \frac{1}{2}\pi\lambda\bar{g}$ *where* $\bar{g} = \lambda_{min}G'(x)$. *By the formula (40), we can further obtain* $\dot{V} < 0$ *when*

$$\|\beta\eta\| > \frac{\bar{H}}{B}. \tag{41}$$

Further analysis, we can know

$$\|\beta\eta\|^2 = \beta_1^2(t)\eta_1^2(t) + \beta_2^2(t)\eta_2^2(t) + \cdots + \beta_n^2(t)\eta_n^2(t). \tag{42}$$

We can analyze it by unfolding it

$$(\beta_i(t)\eta_i(t))^2 = \frac{1}{p_i^2(t)}\frac{1}{\phi_i^2(t)}\eta_i^2(t) \geq q_i^2\eta_i^2(t), \tag{43}$$

where $q_i = 1/p_i(0)$ *and* $i = 1, 2, \cdots, n$. *Combining (42) and (43), we can get*

$$\|\beta\eta\| > Q\|\eta\|, \tag{44}$$

with $Q = \min\{q_1, q_2, \cdots, q_n\}$. *Therefore, we can conclude that,* $\dot{V} < 0$, *as long as it satisfies*

$$\|\eta\| > \frac{\bar{H}}{QB}. \tag{45}$$

Through the above analysis, we can draw a conclusion

$$\|\eta\| \leq \max\left\{\|\eta(0)\|, \frac{\bar{H}}{QB}\right\}, [0, t^*). \tag{46}$$

And this means that $\|\eta\|$ *is bounded on* $[0, t^*)$. *The mapping property of* $\eta_i(t)$ *formulated in (8) manifests that for each error variable* $e_i(t)$ *and any* $t < t^*$, $|e_i(t)|$ *does not approach to the prescribed performance function* $p_i(t)$, $i = 1, 2, \cdots, n$. *This deduction contradicts deduction (26), which means that the expected result in (25) can be established. In other words, there is a set of positive numbers* $\kappa = [\kappa_1, \kappa_2, \cdots, \kappa_n]^T$ *that satisfy*

$$|e_i(t)| \leq p_i(t) - \kappa_i, \ \forall t \geq 0. \tag{47}$$

In combination with (11)-(14), (35) and (47), all the control signals in the closed-loop system are bounded. The proof is completed. □

5 Simulation Study

To demonstrate the effectiveness of the proposed controller, consider the simulation of the following MIMO system

$$\begin{bmatrix}\dot{x}_1 \\ \dot{x}_2\end{bmatrix} = \begin{bmatrix}x_1^2 + x_1 \\ x_2^3 - 1.5x_2\end{bmatrix} + \begin{bmatrix}2 & 1 \\ -1 & 2\end{bmatrix}\begin{bmatrix}u_1 \\ u_2\end{bmatrix} + \begin{bmatrix}0.2\sin(t) \\ -0.1\cos(t)\end{bmatrix},$$

where x_1 and x_2 are the state variables. The initial values of the state variables of the system are $x_1(0) = 0.1$ and

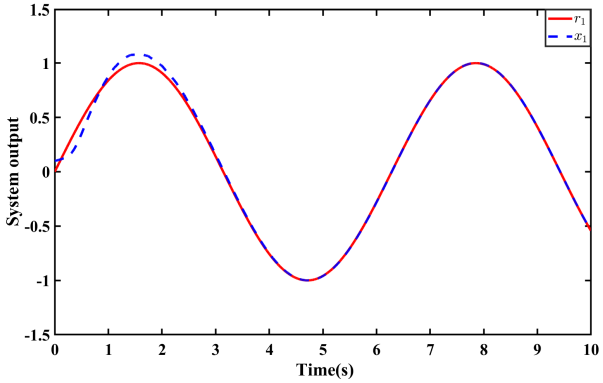

Fig. 1: The output x_1 and the reference signal r_1.

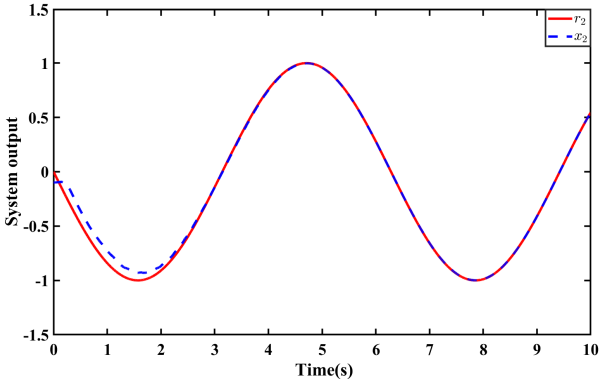

Fig. 2: The output x_2 and the reference signal r_2.

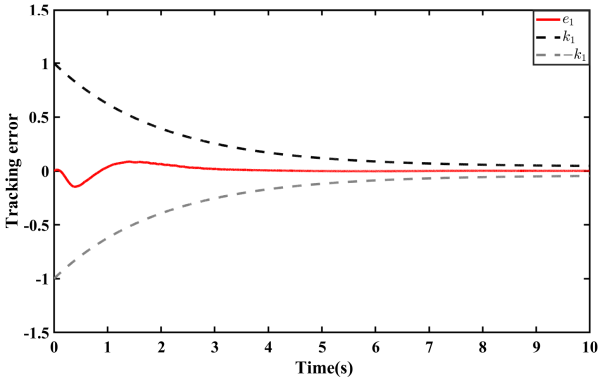

Fig. 3: The tracking error e_1.

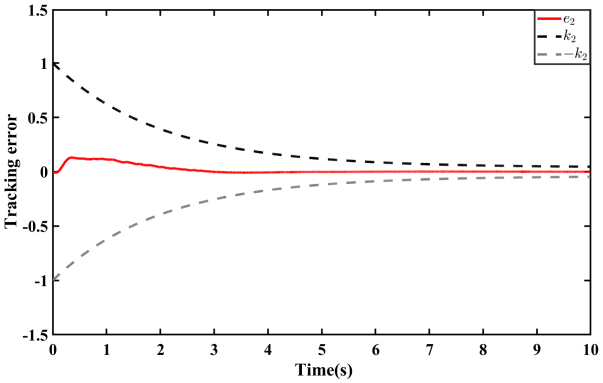

Fig. 4: The tracking error e_2.

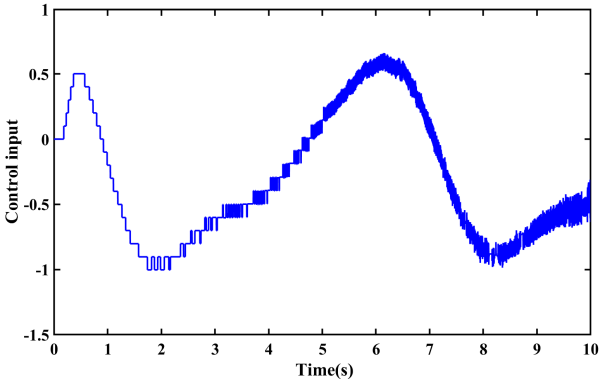

Fig. 5: The control input u_1.

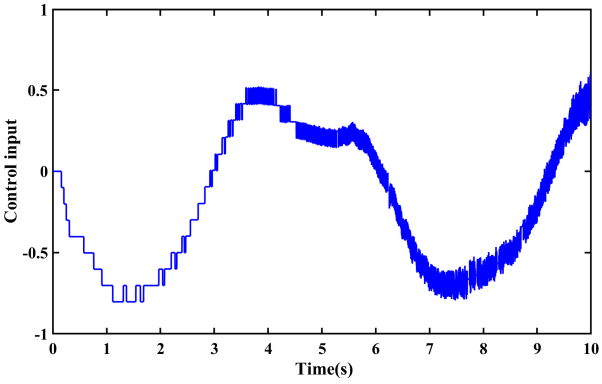

Fig. 6: The control input u_2.

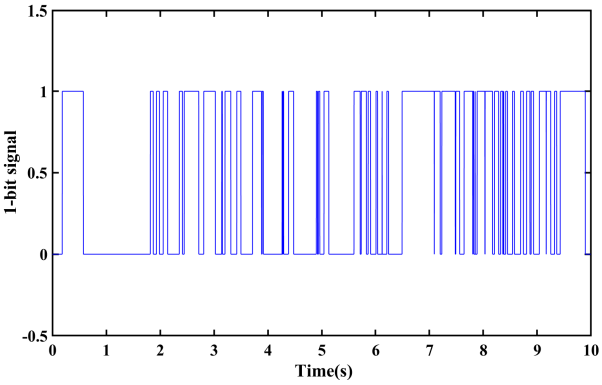

Fig. 7: 1-bit signal $q_1(t_{1k})$ transmitted over the network.

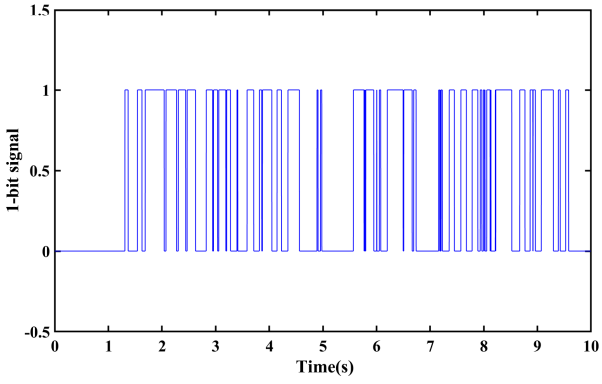

Fig. 8: 1-bit signal $q_2(t_{2k})$ transmitted over the network.

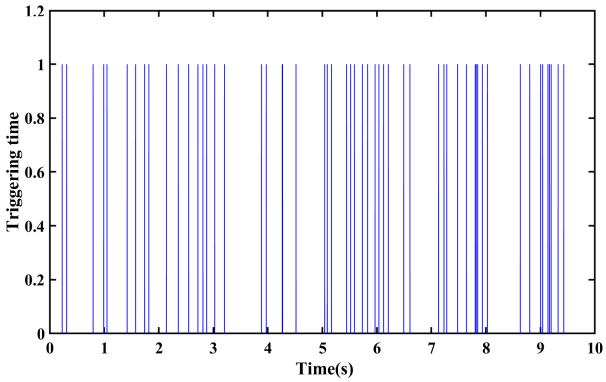

Fig. 9: Sequence of transmission instants of the 1-bit signal $q_1(t_{1k})$.

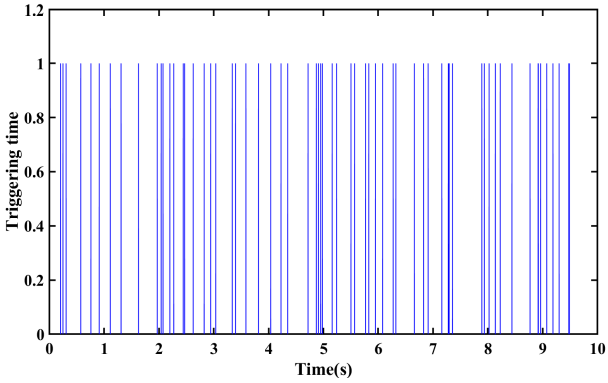

Fig. 10: Sequence of transmission instants of the 1-bit signal $q_2(t_{2k})$.

$x_2(0) = -0.1$. The start time and stop time are set to be $t = 0s$ and $t = 10s$, respectively, and the fundamental sample time is chosen as 0.001s. Envision the scenario where a network is used to close the feedback loop. Under this situation, the periodic sampling control framework requires the control signal to be sent 10000 times. The control objective is to steer x_1 and x_2 to track the references $r_1(t) = \sin(t)$ and $r_2(t) = -\sin(t)$, respectively. At the same time, let them satisfy the following performance requirements:

$$|x_i(t) - r_i(t)| < (p_{i0} - p_{i\infty})e^{-\mu_i t} + p_{i\infty},\ i = 1, 2.$$

Following Theorem 1, the controller is formed with $\tau = 0.4$, $p_{10} = p_{20} = 1$, $p_{1\infty} = p_{2\infty} = 0.04$, $\mu_1 = \mu_2 = 0.5$, $c_1 = c_2 = 0.1$ and $\lambda = 1.4$. It is applied to the above system, and the simulation results are displayed in Figures 1–10. Aimed at evaluating the computational complexity, several indices, such as the CPU time and the single-pass run time (SPRT) for the algorithm are tested. The evolutions of the system outputs and the references are exhibited in Fig. 1 and Fig. 2, and the corresponding errors are plotted in Fig. 3 and Fig. 4. As predicted by the theoretical analysis, the predefined transient and the steady-state performance of the tracking errors are guaranteed, despite the absense of the model information and the presence of the process disturbances. Fig. 5 and Fig. 6 show the real control inputs u_1 and u_2. The binary signals transmitted over the controller-to-actuator network are shown in Fig. 7 and Fig. 8. And the event-triggered times are listed in Fig. 9 and Fig. 10.

It is calculated that the total number of events are 54 and 62, respectively, which are much less than 10000 needed for sample-data control; and the minimal interexecution time is 0.025s, thus ruling out Zeno behavior. Accordingly, the simulation results clarify and verify the presented ETC policy.

6 Conclusion

This study investigates the communication-aware control problem for a class of networked MIMO nonlinear systems characterized by nonparametric uncertainties and unmatched disturbances. We propose a novel control strategy composed of an initialization technique, a prescribed performance controller, and an event-triggered actuator update protocol to address this challenge. In the framework of ETC: 1) only 1-bit of digital numbers is transmitted to the actuator for execution of control tasks and 2) the user-specified transient and steady-state performance of trajectory tracking is guaranteed, despite sampling-induced errors. Additionally, the exploited control scheme is of significant simplicity, stemming from the lack of adaptive or approximating structures and compensation terms. Finally, the simulation results verify the effectiveness of the proposed method.

References

[1] M. C. F. Donkers and W. P. M. H. Heemels, "Output-based event-triggered control with guaranteed $\mathcal{L}_\infty$-gain and improved and decentralized event-triggering," *IEEE Transactions on Automatic Control*, vol. 57, no. 6, pp. 1362–1376, 2012.

[2] P. Tabuada, "Event-triggered real-time scheduling of stabilizing control tasks," *IEEE Transactions on Automatic Control*, vol. 52, no. 9, pp. 1680–1685, 2007.

[3] A. Girard, "Dynamic triggering mechanisms for event-triggered control," *IEEE Transactions on Automatic Control*, vol. 60, no. 7, pp. 1992–1997, 2015.

[4] R. Postoyan, P. Tabuada, D. Nešić, and A. Anta, "A framework for the event-triggered stabilization of nonlinear systems," *IEEE Transactions on Automatic Control*, vol. 60, no. 4, pp. 982–996, 2015.

[5] A. Sahoo, H. Xu, and S. Jagannathan, "Neural network-based event-triggered state feedback control of nonlinear continuous-time systems," *IEEE Transactions on Neural Networks and Learning Systems*, vol. 27, no. 3, pp. 497–509, 2016.

[6] A. Sahoo, H. Xu, and S. Jagannathan, "Adaptive neural network-based event-triggered control of single-input single-output nonlinear discrete-time systems," *IEEE Transactions on Neural Networks and Learning Systems*, vol. 27, no. 1, pp. 151–164, 2016.

[7] L. Cao, H. Li, and Q. Zhou, "Adaptive intelligent control for nonlinear strict-feedback systems with virtual control coefficients and uncertain disturbances based on event-triggered mechanism," *IEEE Transactions on Cybernetics*, vol. 48, no. 12, pp. 3390–3402, 2018.

[8] J.-X. Zhang and G.-H. Yang, "Fault-tolerant output-constrained control of unknown Euler-Lagrange systems with prescribed tracking accuracy," *Automatica*, vol. 111, p. 108606, 2020.

[9] Y. Lei, Y.-W. Wang, Z.-H. Guan, and Y.-J. Shen, "Event-triggered adaptive output regulation for a class of nonlinear systems with unknown control direction," *IEEE Transactions on Systems, Man, and Cybernetics: Systems*, vol. 50, no. 9, pp. 3181–3188, 2020.

[10] Z. Wu, B. Cheng, and Z. Li, "Distributed adaptive tracking control for lur'e systems with event-triggered strategy," *IEEE Transactions on Systems, Man, and Cybernetics: Systems*, vol. 51, no. 5, pp. 3263–3269, 2021.

[11] Y. H. Choi and S. J. Yoo, "Decentralized event-triggered tracking of a class of uncertain interconnected nonlinear systems using minimal function approximators," *IEEE Transactions on Systems, Man, and Cybernetics: Systems*, vol. 51, no. 3, pp. 1766–1778, 2021.

[12] J.-X. Zhang and T. Chai, "Proportional-integral funnel control of unknown lower-triangular nonlinear systems," *IEEE Transactions on Automatic Control*, vol. 69, no. 3, pp. 1921–1927, 2024.

[13] J.-X. Zhang and G.-H. Yang, "Low-complexity tracking control of strict-feedback systems with unknown control directions," *IEEE Transactions on Automatic Control*, vol. 64, no. 12, pp. 5175–5182, 2019.

[14] J.-X. Zhang, Q.-G. Wang, and W. Ding, "Global output-feedback prescribed performance control of nonlinear systems with unknown virtual control coefficients," *IEEE Transactions on Automatic Control*, vol. 67, no. 12, pp. 6904–6911, 2022.

[15] L. Xing, C. Wen, Z. Liu, H. Su, and J. Cai, "Event-triggered output feedback control for a class of uncertain nonlinear systems," *IEEE Transactions on Automatic Control*, vol. 64, no. 1, pp. 290–297, 2019.

[16] X.-N. Shi, R. Li, Z.-G. Zhou, and D. Zhou, "Event-triggered adaptive control for prescribed performance tracking of constrained uncertain nonlinear systems," *IEEE Access*, vol. 7, pp. 23 527–23 536, 2019.

[17] J. Qiu, K. Sun, T. Wang, and H. Gao, "Observer-based fuzzy adaptive event-triggered control for pure-feedback nonlinear systems with prescribed performance," *IEEE Transactions on Fuzzy Systems*, vol. 27, no. 11, pp. 2152–2162, 2019.

[18] J.-X. Zhang and G.-H. Yang, "Robust adaptive fault-tolerant control for a class of unknown nonlinear systems," *IEEE Transactions on Industrial Electronics*, vol. 64, no. 1, pp. 585–594, 2017.

[19] J.-X. Zhang, J. Ding, and T. Chai, "Fault-tolerant prescribed performance control of wheeled mobile robots: A mixed-gain adaption approach," *IEEE Transactions on Automatic Control*, pp. 1–8, 2024, doi:10.1109/TAC.2024.3365726.

[20] J.-X. Zhang and T. Chai, "Singularity-free continuous adaptive control of uncertain underactuated surface vessels with prescribed performance," *IEEE Transactions on Systems, Man, and Cybernetics: Systems*, vol. 52, no. 9, pp. 5646–5655, 2022.

[21] J.-X. Zhang and G.-H. Yang, "Fault-tolerant fixed-time trajectory tracking control of autonomous surface vessels with specified accuracy," *IEEE Transactions on Industrial Electronics*, vol. 67, no. 6, pp. 4889–4899, 2020.

[22] J.-X. Zhang, T. Yang, and T. Chai, "Neural network control of underactuated surface vehicles with prescribed trajectory tracking performance," *IEEE Transactions on Neural Networks and Learning Systems*, pp. 1–14, 2022, doi:10.1109/TNNLS.2022.3223666.

Proceedings of the 3rd Conference on Fully Actuated System Theory and Applications
May 10-12, 2024, Shenzhen, China

Time-Optimal and Jerk-Continuous Trajectory Planning and Tracking Control for 6-DOF Manipulator based on High-Order Fully Actuated System Control Theory

Die Zou[1], Likun Huang[1], Wei Wang[1], Mengying Lin[1,3], Zixin Huang[1,2,3,*]

1. School of Electrical and Information Engineering, Wuhan Institute of Technology, Hubei 430205, P. R. China
E-mail: huangzx@wit.edu.cn

2. Hubei Key Laboratory of Digital Textile Equipment, Wuhan Textile University, Hubei 430299, P. R. China

3. Hubei Key Laboratory of Intelligent Robot, Wuhan Institute of Technology, Hubei 430205, P. R. China

Abstract: This paper focuses on a 6-DOF manipulator and studies how to reduce the trajectory operation time while ensuring the continuity and stability during motion and improving the precision of trajectory tracking control. The manipulator system's kinematic model is developed through utilizing the D-H parameter approach. And the manipulator system's dynamic model is derived through the utilization of Lagrangian dynamics equations, and incorporate the theory of fully actuated system to derive high-order fully actuated (HOFA) model of the system. The joint space interpolation trajectory is constructed by using the 7th-order B-spline curve interpolation method to guarantee the continuity of velocity, acceleration, and jerk. Additionally, to minimize the point-to-point operation time, the motion trajectory is optimized in conjunction with the PSO algorithm. Within the HOFA system model's framework, a direct parameterization approach is employed to design a trajectory tracking controller which guarantee rapid and precise tracking of the trajectory designed for the manipulator. Ultimately, the proposed design methods are validated through simulation experiments.

Key Words: High-order fully actuated system, 6-DOF manipulator, Time optimal, Jerk continuous, Trajectory tracking control

1 Introduction

Manipulators are widely utilized in diverse manufacturing tasks such as assembly[1], spraying[2], palletizing[3], and sorting[4]. To achieve precise operations, trajectory planning and tracking control strategies are crucial. Traditional first-order state models struggle to accurately describe the dynamic behavior of multi-degree-of-freedom manipulators and overlook the coupling effects between joints. However, high-order fully actuated system (HOFAS) control theory offers more precise description of the manipulator's dynamics, addressing issues like jitter and swing and enables more effective control strategies[5].

The theory of fully actuated system control has demonstrated remarkable superiority in dealing with a series of complex issues such as nonlinearity, time variability, and hysteresis. Duan[6] studied a two-link manipulator system, verifying the feasibility of the HOFAS method on serial link manipulators, but did not verify its feasibility on 6-DOF manipulators. Sun[7] designed a trajectory tracking controller for a highly nonlinear and strongly coupled 6-DOF manipulator utilizing the model of a HOFAS. This controller successfully achieved precise trajectory tracking control for the manipulator system, but the designed nonlinear disturbance observer is only suitable for slow-varying internal and external uncertainties, and its performance needs to be improved.

To sum up, there has been relatively limited research combining HOFAS control theory with trajectory planning and tracking control of manipulator systems, using time as an optimization criterion. This paper will focus on time-optimal and jerk-continuous trajectory planning and tracking control research utilizing HOFAS control theory. By using the research method and control strategy, the operation precision can be effectively improved and enhance the performance.

This work is supported by Hubei Province Nature Science Foundation (No. 2023AFB380), and Hubei Key Laboratory of Digital Textile Equipment (Wuhan Textile University) (No. KDTL2022003, No. DTL2023002), and Hubei Key Laboratory of Intelligent Robot (Wuhan Institute of Technology) (No. HBIRL202301, No. HBIRL202302), and Research Initiation Fund (Wuhan Institute of Technology) (No. 23QD112), and the Graduate Innovative Fund of Wuhan Institute of Technology (No. CX2023550)

2 System Model

2.1 Kinematic Model

The kinematic model is developed through the utilization of the D-H parameter approach. Table 1 displays the model parameters, α_i and θ_i represent the angle of rotation around the X axis and Z axis, a_i and d_i signify the distance of translation along the X axis and Z axis, respectively.

Table 1: D-H Parameter Table for manipulator

Node	$\alpha_i(rad)$	$a_i(m)$	$d_i(m)$	$\theta_i(rad)$
1	0	0	0.0985	θ_1
2	$\pi/2$	0	0.1215	θ_2
3	0	0.408	0	θ_3
4	0	0.376	0	θ_4
5	$-\pi/2$	0	0.1025	θ_5
6	$\pi/2$	0	0.094	θ_6

With the coordinate transformations' chain rule as the basis, the matrix representing the transformation between any two adjacent links can be written as:

$$^{i-1}T_i = R\left(x_i, \alpha_{i-1}\right) T\left(x_i, a_{i-1}\right) R\left(z_{i-1}, \theta_i\right) T\left(z_{i-1}, d_i\right) \tag{1}$$

The total transformation matrix for the end effector concerning the base coordinates is detailed as:

$$^0T_6 = {}^0T_1\ {}^1T_2\ {}^2T_3\ {}^3T_4\ {}^4T_5\ {}^5T_6 \tag{2}$$

2.2 Fully Actuated Model based on Dynamic Model

Due to the presence of various internal and external uncertainties, It is possible to denote the dynamic model through:

$$M(q)\ddot{q} + D(q,\dot{q})\dot{q} + G(q) = \tau + \tau_d(q,\dot{q}) \tag{3}$$

where q stands for the angular position. $M(q)$ denotes the positive definite inertia matrix. $\dot{q}$ denotes the angular velocity. $D(q,\dot{q})$ corresponds to the coefficient matrix associated with the Coriolis and centrifugal force vectors. $\ddot{q}$ states the angular acceleration. The matrix $G(q)$ denotes the gravitational term. τ refers to the input torque of the control. τ_d indicates the combined internal and external uncertainties.

According to the theory of fully actuated systems[5], the manipulator described by the Lagrange equation is a second-order fully actuated system:

$$\begin{aligned} &A_2(\theta,q,\dot{q})\ddot{q} + A_1(\theta,q,\dot{q})\dot{q} + A_0(\theta,q,\dot{q})q \\ &+ \xi(\theta,q,\dot{q}) = B(\theta,q,\dot{q})u \end{aligned} \tag{4}$$

In equation (4), $A_2(\theta,q,\dot{q}), A_1(\theta,q,\dot{q}), A_0(\theta,q,\dot{q}) \in R^{n\times n}$ represent coefficient matrixs, $B(\theta,q,\dot{q}) \in R^{n\times n}$ stands for input matrix, $q \in R^n$ represents state vector, $u \in R^n$ represents control vector, vector $\xi(\theta,q,\dot{q})$ as a nonlinear term, and $\theta = \theta(t) \in R^l$ represents the parameter vector. The equation (4) corresponds to equation (3).

3 Trajectory Planning and Tracking Control

3.1 Jerk-Continuous Trajectory Planning

To construct trajectory, utilizing 7th-order B-spline curve (BSC) interpolation approach, the expression is as follows:

$$p(u) = \sum_{i=0}^{n} d_i B_{i,7}(u) \quad i = 0,1,\cdots,n \tag{5}$$

where $B_{i,7}(u)$ is the basis function, and d_i represents the control vertices. The 1st, 2nd, and 3rd derivatives of $p(u)$ stand for velocity, acceleration, and jerk at the normalized time node vector $u \in (u_i, u_{i+1})$, respectively.

Discretizing the trajectory, the discrete Cartesian position points are converted to a position-time sequence through inverse kinematics:

$$N = (p_i, t_i) \quad i = 0,1,\cdots,n \tag{6}$$

In equation (6), t_i is the time node. The control vertices are solved in a matrix form. It is possible to denote it through:

$$A_n \cdot d_n = p_n \tag{7}$$

where A_n represents the coefficient matrix, $d_n = [d_{i,0}\ d_{i,1}\ \cdots\ d_{i,n+1}\ d_{i,n+2}\ \cdots\ d_{i,n+6}]^T$ and $p_n = [p_{i,0}\ p_{i,1}\ \cdots\ p_{i,n}\ V_{i,s}\ V_{i,e}\ A_{i,s}\ A_{i,e}\ J_{i,s}\ J_{i,e}]^T$ are control points and positions respectively.

Due to the BSCs' convex hull property containing control points, it can be inferred that the constraints on the 7th-order BSCs' control points satisfy:

$$\begin{cases} \max\left(\left|d^1_{mi}\right|\right) \le k v_{cm} & i = 1,2,\cdots,n+6 \\ \max\left(\left|d^2_{mi}\right|\right) \le k a_{cm} & i = 2,3,\cdots,n+6 \\ \max\left(\left|d^3_{mi}\right|\right) \le k j_{cm} & i = 3,4,\cdots,n+6 \end{cases} \tag{8}$$

where v_{cm},a_{cm}, j_{cm} respectively represent the constraints on joint velocity, acceleration, and jerk of the manipulator, $d^1_{mi}, d^2_{mi}, d^3_{mi}$ are calculated based on the De-Boor recursive formula. Therefore, the kinematic constraints have been transformed into constraints on the control vertices.

3.2 Time Optimization Via PSO algorithm

The goal of PSO algorithm is to minimize the time required for the manipulator to complete a trajectory within the constrained velocity range of each joint[8].

$$f(x) = \min \sum_{i=0}^{n-1} t_i \tag{9}$$

$$\begin{aligned} &\max_{i=1,2,\cdots,n+6}\{|d^1_{mi}(x)|\} - v_{cm} \le 0 \\ &\max_{i=2,3,\cdots,n+6}\{|d^2_{mi}(x)|\} - a_{cm} \le 0 \\ &\max_{i=3,4,\cdots,n+6}\{|d^3_{mi}(x)|\} - j_{cm} \le 0 \end{aligned} \tag{10}$$

In equation (10), $x = [x_0, x_1, \cdots, x_{n-1}]^T$, $x_i = \Delta t_i = t_{i+1} - t_i, i = 0,1,\cdots,n-1$, Δt_i has a lower bound.

The PSO algorithm is utilized for settling the optimization issue with nonlinear constrained outlined in (10). And PSO algorithm's schematic in accordance with figure.

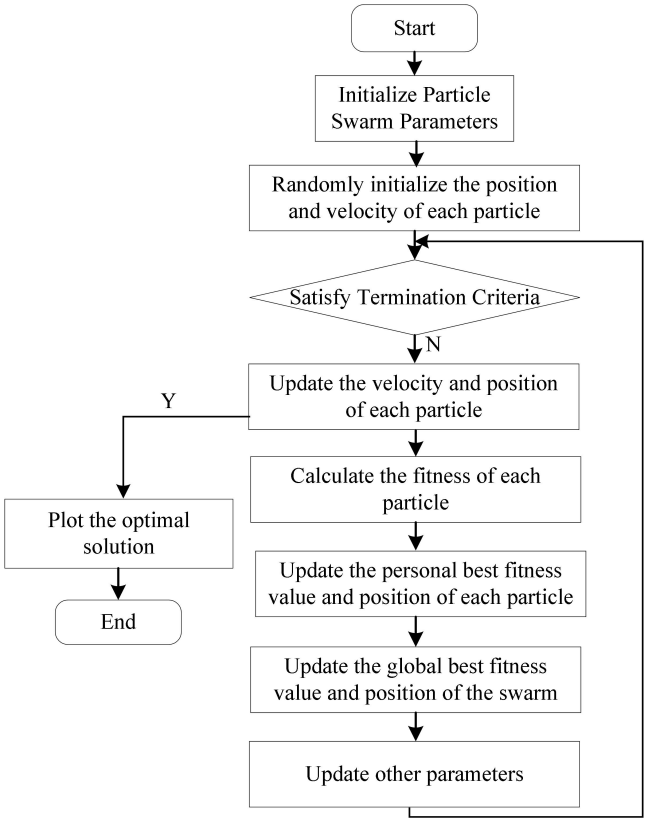

Fig. 1: PSO Algorithm

3.3 Tracking Controller Design

The trajectory tracking controller for the manipulator is developed via the direct parameter approach within the framework of a HOFAS model:

$$\begin{cases} u = u_c + u_f \\ u_c = B^{-1}(\theta,q,\dot{q})\xi(\theta,q,\dot{q}) \\ u_f = K_0(\theta,q,\dot{q})q + K_1(\theta,q,\dot{q})\dot{q} + v \end{cases} \tag{11}$$

In equation (11), u_c represents the compensatory controller, and u_f represents the state feedback controller, $K_0(\theta,q,\dot{q})$, $K_1(\theta,q,\dot{q}) \in R^{6\times 6}$ denote feedback gain matrixs, and v represents the external signal.

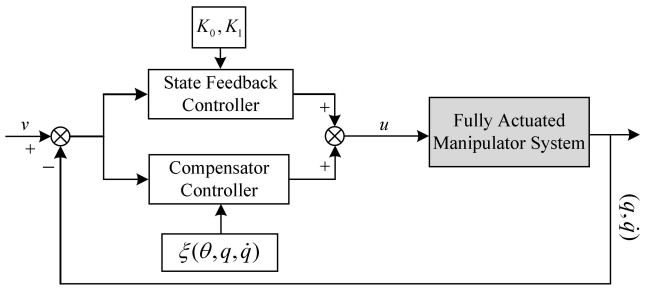

Fig. 2: Structure diagram of the fully actuated control system

Convert it into the following first-order system:

$$\dot{X} = A_c X + B_c v \tag{12}$$

where $X = \begin{bmatrix} q & \dot{q} \end{bmatrix}^T$, $B_c = \begin{bmatrix} 0 & A_2^{-1}B \end{bmatrix}^T$,
$A_c = \begin{bmatrix} 0 & I_n \\ -A_2^{-1}(A_0 - BK_0) & -A_2^{-1}(A_1 - BK_1) \end{bmatrix}$

According to the defined expected system performance, if the canonical form $F \in R^{2n\times 2n}$ and $\exists Z \in R^{n\times 2n}$ satisfy:

$$detV_e(Z,F) \neq 0 \tag{13}$$

In equation (13), it has the following relation: $V_e(Z,F) = \begin{bmatrix} V(Z,F) & V_\infty^c \end{bmatrix}$, $V(Z,F) = \begin{bmatrix} Z & ZF \end{bmatrix}$, V represents the finite eigenvectors associated with F, V_∞^c denotes generalized infinite eigenvector matrix, $\begin{bmatrix} V & V_\infty^c \end{bmatrix}$ serves as the overall eigenvector matrix. To increase the speed of tracking the target trajectory in the system, the performance index is expressed:

$$J(F,Z) = \|V\| \left\|V^{-1}\right\| \tag{14}$$

The matrix Z can be obtained by minimizing J, and then substituting Z and F into equation (15):

$$\begin{cases} \begin{bmatrix} K_0 & K_1 \end{bmatrix} = WV^{-1}(Z,F) \\ W = B^{-1}(A_2ZF^2 + A_1ZF + A_0Z) \end{cases} \tag{15}$$

Equation (15) determines the value of K_0 and K_1, thereby obtaining the desired first-order steady-state system.

4 Simulation

4.1 Obtaining Trajectories Towards the Target

In an effort to prove the practicability of PSO algorithm to plan trajectories that minimize time, Matlab is used for simulation experiments. The position sequence required for each joint of the manipulator is shown in Table 2.

Set $V_{\max} = [100 \quad 95 \quad 100 \quad 150 \quad 130 \quad 110]$, $A_{\max} = [45 \quad 40 \quad 75 \quad 70 \quad 90 \quad 80]$, $J_{\max} = [60 \quad 60 \quad 55 \quad 70 \quad 75 \quad 70]$. the PSO algorithm for optimizing time-efficient trajectories. Utilizing 50 iterations and a swarm comprised of 50 particles, the number of particles in the swarm to 50. Set the inertia weight to 0.5, the individual learning factor to 1, and the social learning factor to 2.

From the simulation results (Fig.3), it can be observed that the start-stop velocities and accelerations are zero, which fulfills the set requirements. Additionally, the curves in Fig.3(b-d) are continuous without any abrupt changes, and they comply with the kinematic constraints, ensuring smooth motion. Using the PSO algorithm to find the best motion time while adhering to kinematic constraints, the maximum time required to execute the trajectory is 39.60 s, which is relatively short and meets the requirements.

Table 2: Sequence of joint positions

	Joint1	Joint2	Joint3	Joint4	Joint5	Joint6
M1	16.99	-33.12	43.89	25.70	110.36	-25.95
M2	17.23	-13.88	47.70	60.69	105.23	-28.51
M3	17.88	-19.60	55.23	79.05	103.25	-16.05
M4	14.39	-28.46	63.88	75.21	97.78	-5.21
M5	11.25	-41.72	68.35	72.70	86.04	6.50
M6	3.100	-45.34	72.41	67.45	79.94	12.20
M7	-20.13	-42.69	79.65	53.54	72.76	16.24
M8	-25.78	-40.34	82.17	47.80	78.16	13.55

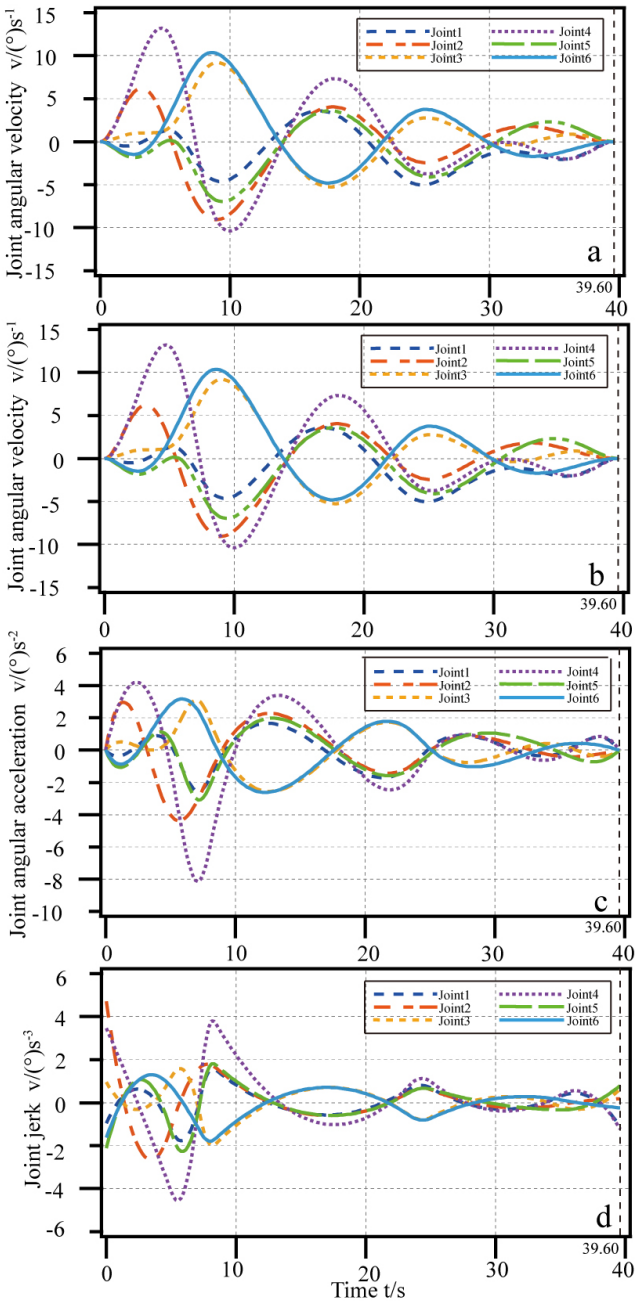

Fig. 3: Trajectory Plot of Joint

4.2 Trajectory Tracking Control

In an effort to test and verify the significance of the control algorithm. Matrix F is selected according to the anticipated

system feature configuration and is a diagonal matrix containing eighteen elements. If we set the standard type F: F = diag(- 50, - 50, - 50, - 100, - 100, - 100, - 90, - 90, - 90, - 45, - 45, - 45). According to the optimization function equation (14), use the fmincon solver in Matlab software to obtain Z.

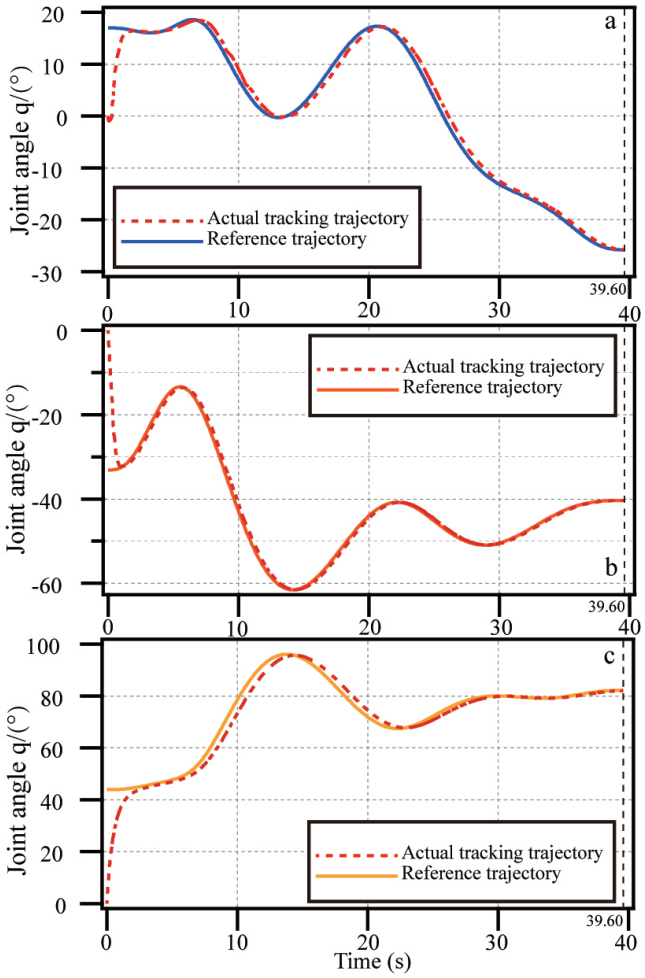

Fig. 4: Joint 1-3 Angle Tracking

The direct parameter method control model is constructed to control the manipulator system, and the results of tracking the reference trajectory of each joint of the manipulator are plotted, as shown in Fig.4-Fig.5. From the experimental results, it is evident that the system may quickly follow the target trajectory within 3 seconds. And manipulator can quickly respond to the designed time-optimal and jerk-continuous reference trajectory and achieve precise tracking.

5 Conclusion

This paper focuses on the 6-DOF manipulator and analy its kinematic model and fully actuated model. A trajectory planning scheme via the BSC interpolation approach and employ the PSO algorithm for obtaining the best desired trajectory. With the foundation in the fully actuated system control theory, a trajectory tracking controller has been introduced employing the direct parameter method to track the desired trajectory. The problem of the optimal time and jerk continuous trajectory planning and tracking control of the manipulator is solved, and the continuity and tracking precision of the trajectory are improved. And better results are achieved in the aspects of trajectory time and tracking error.

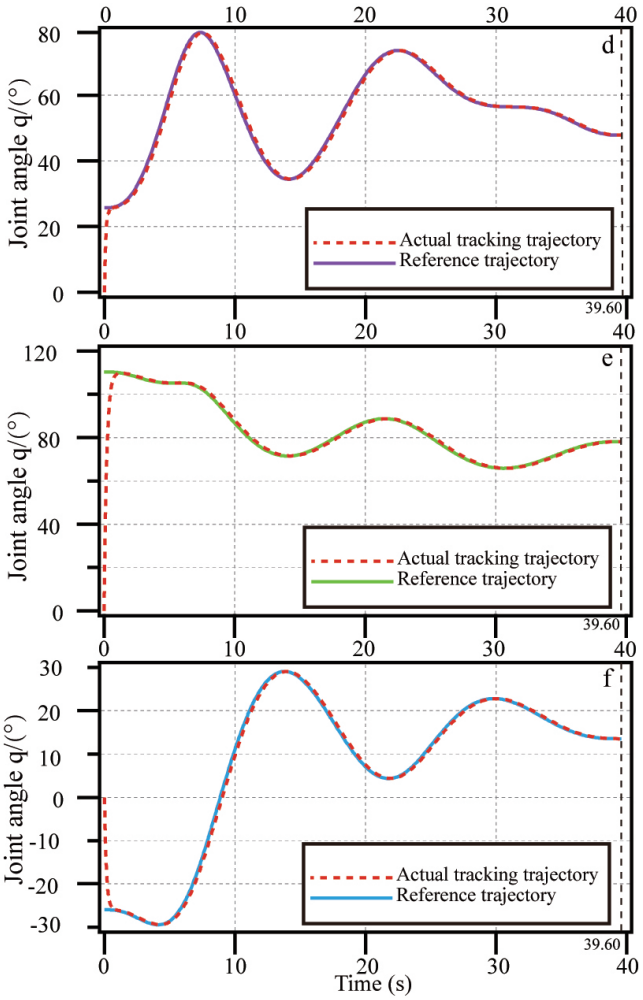

Fig. 5: Joint 4-6 Angle Tracking

References

[1] Sun Y, et al. Learn how to assist humans through human teaching and robot learning in human–robot collaborative assembly. *IEEE Transactions on Systems, Man, and Cybernetics: Systems*, 2022, 52(2): 728-738.

[2] Zhang H, Meng Z, et al. Trajectory optimization of glue spraying on athletic footwear sole based on multivariable spray torch model. *IEEE Access*, 2023, 11: 79422-79433.

[3] Sun H H, Zhang Y J, et al. Dynamic modeling and error analysis of a cable-linkage serial-parallel palletizing robot. *IEEE Access*, 2021, 9: 2188-2200.

[4] Leveziel M, et al. A 4-DOF parallel robot with a built-in gripper for waste sorting. *IEEE Robotics and Automation Letters*, 2022, 7(4): 9834-9841.

[5] Duan G R. High-order system approaches: I. Fully-actuated systems and parametric designs. *Acta Automatica Sinica*, 2020, 46(7): 1333-1345.

[6] Duan G R. A direct parametric approach for missile guidance—case of sea targets. *Proceedings of the 33rd Chinese Control Conference, Nanjing, China*, 2014: 1044-1050.

[7] Sun H, Huang L. Trajectory tracking control of a 6-DOF manipulator. *2023 2nd Conference on Fully Actuated System Theory and Applications (CFASTA)*, 2023: 775-782.

[8] Kim J J, et al. Trajectory optimization with particle swarm optimization for manipulator motion planning. *IEEE Transactions on Industrial Informatics*, 2015, 11(3): 620-631.

Proceedings of the 3rd Conference on Fully Actuated System Theory and Applications
May 10-12, 2024, Shenzhen, China

H_∞ voltage control of islanded microgrid three-phase inverter: a model-free integral reinforcement learning approach

Linna Zhou[1,2], Fuxing Li[1,2], Gonghe Li[1,2], Xiaomin Liu[1,2]*, Chunyu Yang[1,2]

1. School of Information and Control Engineering, China University of Mining and Technology, Xuzhou, 221116, China

2. Engineering Research Center of Intelligent Control for Underground Space, Ministry of Education, Xuzhou, 221116, China.
E-mail: xiaominliu@cumt.edu.cn

Abstract: In this paper, an inner-loop control method based on the integral reinforcement learning (IRL) algorithm is proposed to address the challenges of uncertain inverter model parameters and strong disturbances caused by nonlinear and unbalanced loads. Firstly, the mathematical model of an LC-type off-grid inverter is established in the d-q axis, and the off-grid inverter voltage control problem is transformed into an H_∞ tracking problem by introducing the augmented system. The reference signal of the inverter output voltage, together with the original state, are defined as the state of the augmented system. An initial control gain along with exploration noises are conducted on the inverter to collect augmented state data and disturbance data (output current). Then, by utilizing the principles of zero-sum game theory, the tracking Hamilton-Jacobi-Isaacs (HJI) equation is derived, and the IRL algorithm is proposed to solve this equation. The Kronecker products containing state values, control inputs, and disturbance values are calculated based on the measurement data, and the iterative inverter voltage control strategy is derived. Next, it is proven that the proposed control policy ensures the asymptotic stability of the augmented system and satisfies the L_2 gain condition. Finally, the effectiveness of the proposed algorithm is verified through simulation.

Key Words: Off-grid Inverter, Voltage Control, Model-free Integral Reinforcement Learning, H_∞ Control

1 Introduction

The scarcity of traditional fossil energy and environmental pollution have emerged as major obstacles to global economic development. In response, renewable energy and distributed power generation have gained prominence due to their reduced pollution, high reliability, and energy utilization efficiency [1] [2]. Microgrid technology, which facilitates the effective utilization of renewable energy and distributed power generation, has consequently become a focal point of research. Microgrid can operate in grid-connected or off-grid modes[3]. When operating off-grid, the presence of nonlinear and unbalanced loads introduces significant perturbations to the inverter system, leading to a degradation in output voltage quality and potential system instability. Hence, it is crucial to develop effective control strategies to enhance the disturbance immunity of microgrid inverter systems.

In recent years, numerous scholars have proposed control methods aimed at suppressing disturbances to improve the disturbance suppression performance of inverters. These methods include model-free predictive control, repetitive control, and active disturbance rejection control (ADRC). The model-free predictive control (MFPC) method enhances prediction robustness by employing hyperlocal models, autoregressive input models[4], and look-up table (LUT)[5]in place of traditional prediction models, thus improving overall robustness. However, the control performance of the MFPC method based on hyperlocal and autoregressive input models is influenced by the number of voltage and current data cycles. On the other hand, the LUT-based MFPC method is straightforward in principle and easy to implement, achieving robust current prediction by storing and updating current gradients under each vector's action in the control cycle[6]. However, the necessity of updating current gradients under unapplied vectors in this approach may lead to stagnation in gradient updating and increased prediction errors.

Repetitive control is a waveform control method based on the principle of internal mode, utilizing the system's mathematical model in feedback to describe external signal dynamics and achieve precise tracking performance while effectively suppressing periodic disturbances. However, it may struggle to effectively track non-periodic disturbances and exhibits delayed response with poor dynamic performance. ADRC achieves precise system control by introducing an suppression observer to estimate and counteract external disturbances and internal model errors in real time. However, this method faces challenges related to difficult parameter adjustment, high computational complexity, and insufficient robustness.

The inverter voltage control problem can be framed as a reference voltage tracking and disturbance suppression issue. H_∞ control focuses on mitigating the impact of external, randomly varying, and intricate disturbances on system performance. The designed controller not only achieves dynamic stability and robust control of the system but also optimizes the performance index. For off-grid inverters, controller design needs to account for parameter fluctuations, uncertainties, and load-induced perturbations, aligning with the objectives of H_∞ control theory. The technology based on reinforcement learning (RL) has also been used to provide a model-free solution for the H_∞ control problem. An online Q-learning algorithm for designing H_∞ tracking controllers for unknown discrete systems was introduced in [7] and applied to a single-phase voltage source inverter. However, applying a discrete method to a continuous inverter system may lead to approximation errors and numerical stability issues. Particularly, if the sampling frequency is improperly chosen, it can potentially cause signal distortion and aliasing effects, leading to additional requirements for controller design and implementation. A multi-loop H_∞ control scheme

This work was supported in part by the Natural Science Foundation of Jiangsu Province under Grant BK20221112, and in part by the Key Research and Development projects in Shanxi Province(202202100401002). (Corresponding Author: Xiaomin Liu)

was presented in [8], where variable load conductance was treated as model uncertainty within the inverter model. However, this method assumes that the load conductance varies within a specific set and does not consider the optimality of the control system. The above methods suffer from complex parameter design, high computational complexity, and lack of robustness.

In this paper, we present an online model-free integral reinforcement learning (IRL) algorithm for addressing the off-grid inverter voltage control problem. The key contributions are as follows:

1) A novel framework for continuous inverter voltage inner-loop control is introduced, integrating H_∞ control and the IRL algorithm. The quality of inverter output voltage is effectively ensured in the presence of unknown parameters and load disturbances within the framework.

2) The off-grid inverter voltage control problem is transformed into an H_∞ tracking control problem for the augmented system, and a model-free IRL algorithm based on the zero-sum game concept is developed to eliminate reliance on the inverter model.

3) The stability of the inverter system is rigorously established under the influence of the controller, and the impact of load variations on the inverter voltage is limited to a certain level of attenuation.

2 Microgrid Inverter Modeling and Problem Description

2.1 Microgrid Inverter Modeling

The structure of the off-grid inverter system is illustrated in Fig. 1. In this paper, the inverter is filtered by a LC type filter, with L_f, C_f and R_f representing the filter inductor, the filter capacitor and the filter inductor parasitic resistance, respectively. The meaning of the variable is as follows: u_{abc}, u_{oabc}, i_{Labc}, i_{oabc}, u^*_{od} and u^*_{oq} represents the three-phase output voltage of the bridge arm side of the inverter, the three-phase output voltage of the bridge arm side of the inverter, the three-phase output current of the filter inductor, the component of the inverter output three-phase voltage in the d-q axes, respectively.

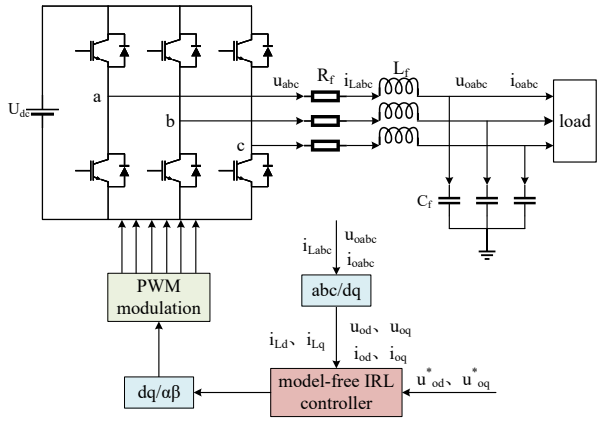

Fig. 1: Block diagram of three-phase inverter control structure

Based on the off-grid inverter structure depicted in Fig. 1, the mathematical model of the LC-type off-grid inverter in the dq coordinate system is established as follows

$$\begin{cases} \dfrac{di_{Ld}}{dt} = \dfrac{u_d}{L_f} - \dfrac{u_{od}}{L_f} - \dfrac{R_f i_{Ld}}{L_f} + \omega i_{Lq} \\ \dfrac{di_{Lq}}{dt} = \dfrac{u_q}{L_f} - \dfrac{u_{oq}}{L_f} - \dfrac{R_f i_{Lq}}{L_f} - \omega i_{Ld} \\ \dfrac{du_{od}}{dt} = \dfrac{i_{Ld}}{C_f} - \dfrac{i_{od}}{C_f} + \omega u_{oq} \\ \dfrac{du_{oq}}{dt} = \dfrac{i_{Lq}}{C_f} - \dfrac{i_{oq}}{C_f} - \omega u_{od} \end{cases} \tag{1}$$

where u_d and u_q represent the inverter bridge arm side voltage components in the d-q axes, u_{od} and u_{oq} denote the inverter output voltage components in the d-q axes, i_{Ld} and i_{Lq} signify the filtering inductor currents in the d-q axes, i_{od} and i_{oq} indicate the output currents in the d-q axes, and ω is the angular frequency of the grid voltage. Equation (1) is expressed as the state space equation in the following form

$$\begin{cases} \dot{x} = Ax + Bu + Dd \\ y = Cx \end{cases} \tag{2}$$

where $x(t) = \begin{bmatrix} u_{od} & u_{oq} & i_{Ld} & i_{Lq} \end{bmatrix}^T$ is the state vector, $u = \begin{bmatrix} u_{id} & u_{iq} \end{bmatrix}^T$ is the input vector, $d = \begin{bmatrix} i_{od} & i_{oq} \end{bmatrix}^T$ is the disturbance vector, y=$\begin{bmatrix} u_{od} & u_{oq} \end{bmatrix}^T$ is the output vector. The state matrix $A = \begin{bmatrix} 0 & \omega & 1/C_f & 0 \\ -\omega & 0 & 0 & 1/C_f \\ -1/L_f & 0 & -R_f/L_f & \omega \\ 0 & -1/L_f & -\omega & -R_f/L_f \end{bmatrix}$. The input matrix $B = \begin{bmatrix} 0 & 0 & 1/L_f & 0 \\ 0 & 0 & 0 & 1/L_f \end{bmatrix}^T$. The disturbance matrix $D = \begin{bmatrix} -1/C_f & 0 & 0 & 0 \\ 0 & -1/C_f & 0 & 0 \end{bmatrix}^T$. The output matrix $C = \begin{bmatrix} 1 & 0 & 0 & 0 \\ 0 & 1 & 0 & 0 \end{bmatrix}^T$.

2.2 Problem Description

The inverter reference voltage complies with

$$\dot{u}^*_o = F u^*_o \tag{3}$$

where $u^*_o = \begin{bmatrix} u^*_{od} & u^*_{oq} \end{bmatrix}^T$. Then the tracking error between the system output and the reference signal can be described as

$$e(t) = y - u^*_o = Cx - u^*_o \tag{4}$$

Define the augmented system state as $X(t) = \begin{bmatrix} u_{od} & u_{oq} & i_{od} & i_{oq} & u^*_{od} & u^*_{oq} \end{bmatrix}^T$, then the augmented system as

$$\begin{cases} \dot{X} = \Gamma X + Mu + Nd \\ Y = C_1 X \end{cases} \tag{5}$$

where

$$\Gamma = \begin{bmatrix} 0 & \omega & 1/C_f & 0 & 0 \\ -\omega & 0 & 0 & 1/C_f & 0 \\ -1/L_f & 0 & -R_f/L_f & \omega & 0 \\ 0 & -1/L_f & -\omega & -R_f/L_f & 0 \\ 0 & 0 & 0 & 0 & F \end{bmatrix},$$

$$M = \begin{bmatrix} 0 & 0 & 1/L_f & 0 & 0 & 0 \\ 0 & 0 & 0 & 1/L_f & 0 & 0 \end{bmatrix}^T,$$
$$N = \begin{bmatrix} -1/C_f & 0 & 0 & 0 & 0 & 0 \\ 0 & -1/C_f & 0 & 0 & 0 & 0 \end{bmatrix}^T, \quad C_1 = \begin{bmatrix} C & -I \end{bmatrix}^T.$$

Define the L_2 gain condition for the augmented system as follows

$$\begin{aligned} &\int_t^\infty e^{-\alpha(\tau-t)} \left(Y^T Q Y + u^T R u\right) d\tau \\ &\leq \gamma^2 \int_t^\infty e^{-\alpha(\tau-t)} \left(d^T d\right) d\tau \end{aligned} \tag{6}$$

Define the tracking cost function

$$\begin{aligned} &J(u,d) = \\ &\int_t^\infty e^{-\alpha(\tau-t)} \left(Y^T Q Y + u^T R u - \gamma^2 d^T d\right) d\tau \end{aligned} \tag{7}$$

Thus, the H_∞ voltage control problem is to find a controller as

$$u = KX \tag{8}$$

such that the following holds:

1) The closed-loop system satisfies the attenuation condition (6).

2) The tracking error dynamics (4) with $d = 0$ is asymptotically stable.

The solvability of the H_∞ control problem is equivalent to the solvability of the following zero-sum game

$$V^*(X(t)) = J(u^*, d^*) = \min_u \max_d J(u,d) \tag{9}$$

where J is defined in (7), $V^*(X(t))$ is the optimal value function. Thus, the H_∞ problem can be reformulated as a zero-sum game problem. This 2-player zero-sum game control problem has a unique solution if a game theoretic saddle point exists, ie, if the following Nash condition holds:

$$V^*(X(t)) = \min_u \max_d J(u,d) = \max_d \min_u J(u,d) \tag{10}$$

The value function (9) in terms of the augmented system (5) is expressed as

$$V(X(t)) = X(t)^T P X(t) = J(u,d) \tag{11}$$

Using the value function (15) for the left-hand side of (7), and differentiating (7) along with the trajectories of the augmented system. We obtain the augmented LQT Bellman equation as follows:

$$\begin{aligned} &(\Gamma X + Mu + Nd)^T P X + \\ &X^T P (\Gamma X + Mu + Nd) - \alpha X^T P X \\ &+ Y^T Q Y + u^T R u - \gamma^2 d^T d = 0 \end{aligned} \tag{12}$$

and the corresponding Hamiltonian equation is

$$\begin{aligned} &H(V,u,d) = Y^T Q Y + u^T R u - \gamma^2 d^T d - \\ &\alpha V + V_X^T (\Gamma X + Mu + Nd) = 0 \end{aligned} \tag{13}$$

Using the stationary conditions $\partial H(V,u,d)/\partial u = 0, \partial H(V,u,d)/\partial d = 0$, the optimal control input and the worst-case disturbance input can be obtained as

$$u^* = -R^{-1} M^T P X \tag{14}$$

$$d^* = \gamma^{-2} N^T P X \tag{15}$$

Substituting (14) and (15) into (12) gives the following tracking HJI equation and tracking game algebraic Riccati equation (GARE)

$$\begin{aligned} &H(V^*, u^*, d^*) \triangleq Y^T Q Y + V_X^{*T} \Gamma - \alpha V_X \\ &- V_X^{*T} M^T R^{-1} M V_X^* + \gamma^2 V_X^{*T} N N^T V_X^* = 0 \end{aligned} \tag{16}$$

$$\begin{aligned} &X^T C_1^T Q C_1 X + 2 X^T P \Gamma X - \alpha X^T P X \\ &- X^T P M R^{-1} M^T P X + \gamma^{-2} X^T P N N^T P X = 0 \end{aligned} \tag{17}$$

3 Design of Model-free H_∞ Tracking Controller With Discount Factor

3.1 Computational Adaptive Optimal Control Design With Completely Unknown Dnamics

Under steady-state conditions, modeling uncertainties or unforeseen changes in the structure or parameters of the controlled system significantly impact the controller performance [9]. Therefore, we propose a model-free algorithm with a discount factor to address the voltage control problem of the inverter system.

According to [10], we rewrite the augmented system (5) as

$$\begin{cases} \dot{X} = \Gamma_i X + M(u + K_i X) + N(d - L_i X) \\ Y = C_1 X \end{cases} \tag{18}$$

where $\Gamma_i = \Gamma - M K_i + N L_i$, then the corresponding Bellman equation is

$$\begin{aligned} &e^{-\alpha\delta t} X(t+\delta t)^T P_i X(t+\delta t) - X(t)^T P_i X(t) \\ &= -\int_t^\infty e^{-\alpha(\tau-t)} X(\tau)^T Q_i X(\tau) d\tau \\ &+ 2\int_t^\infty e^{-\alpha(\tau-t)} (u + K_i X)^T R K_{i+1} X d\tau \\ &+ 2\gamma^2 \int_t^\infty e^{-\alpha(\tau-t)} (d - L_i X)^T L_{i+1} X d\tau \end{aligned} \tag{19}$$

where $Q_i = C_1^T Q C_1 + K_i^T R K_i - \gamma^2 L_i^T L_i$.

We define the following two operators:

$$\hat{P} = \left[p_{11}, 2p_{12}, \cdots, 2p_{1n}, p_{22}, 2p_{23}, \cdots, 2p_{(n-1)n}, p_{nn}\right]^T$$
$$\bar{X} = \left[x_1^2, x_1 x_2, \cdots, x_1 x_n, x_2^2, x_2 x_3, \cdots, x_{n-1} x_n, x_n^2\right]^T$$

then we have

$$\begin{aligned} &X(t+\delta t)^T P_i X(t+\delta t) - X(t)^T P_i X(t) \\ &= \left(\bar{X}(t+\delta t) - \bar{X}(t)\right) \hat{P} \end{aligned}$$

.

In addition, by Kronecker product representation, we have

$$\delta_{XX} = \begin{bmatrix} e^{-\alpha(t_1-t_0)} \left(\bar{X}(t_1) \otimes \bar{X}(t_1)\right) \\ -\left(\bar{X}(t_0) \otimes \bar{X}(t_0)\right), \\ e^{-\alpha(t_2-t_1)} \left(\bar{X}(t_2) \otimes \bar{X}(t_2)\right) \\ -\left(\bar{X}(t_1) \otimes \bar{X}(t_1)\right), \cdots \end{bmatrix}^T \tag{20}$$

$$\begin{aligned} I_{XX} = \Bigg[&\int_{t_0}^{t_1} e^{-\alpha(\tau-t_0)} (X \otimes X) d\tau, \\ &\int_{t_1}^{t_2} e^{-\alpha(\tau-t_1)} (X \otimes X) d\tau, \ldots \Bigg]^T \end{aligned} \tag{21}$$

$$I_{XU} = \Big[\int_{t_0}^{t_1} e^{-\alpha(\tau-t_0)}(X\otimes u)d\tau, \int_{t_1}^{t_2} e^{-\alpha(\tau-t_1)}(X\otimes u)d\tau,\ldots\Big]^T \quad (22)$$

$$I_{XD} = \Big[\int_{t_0}^{t_1} e^{-\alpha(\tau-t_0)}(X\otimes d)d\tau, \int_{t_1}^{t_2} e^{-\alpha(\tau-t_1)}(X\otimes d)d\tau,\ldots\Big]^T \quad (23)$$

Then, for any given stabilizing gain matrix K_i, (19) implies the following matrix form of linear equations

$$\psi_i \begin{bmatrix} \hat{P}_i \\ vec\,(K_{i+1}) \\ vec\,(L_{i+1}) \end{bmatrix} = \theta_i \quad (24)$$

where $\psi_i = \begin{bmatrix} \delta_{XX} \\ -2I_{XX}\left(I_n\otimes K_i^T R\right) - 2I_{XU}\left(I_n\otimes R\right) \\ 2\gamma^2 I_{XX}\left(I_n\otimes L_i^T\right) - 2\gamma^2 I_{XD} \end{bmatrix}$, $\theta_i = -I_{XX}vec\,(Q_i)$.

Notice that if ψ_i has full column rank, (23) can be directly solved as follows

$$\begin{bmatrix} \hat{P}_i \\ vec\,(K_{i+1}) \\ vec\,(L_{i+1}) \end{bmatrix} = \left(\psi_i^T\psi_i\right)^{-1}\psi_i^T\theta_i \quad (25)$$

Algorithm 1 presents a model-free IRL for H_∞ tracking control of inverter output voltage algorithm.

Algorithm 1 Model-free IRL for H_∞ tracking control of inverter output voltage	
Step 1	Use $u = K_0X + e$ as the input over the time interval $[t_0,t_1]$, where e is the detection noise.
Step 2	Equations (20), (21), (22), and (23) are derived by capturing the values of output voltage, current, filter inductor current, and output voltage at the bridge arm side of the inverter.
Step 3	Solve for P_i, K_{i+1} and L_{i+1} from (24).
Step 4	If $\|\|P_i - P_{i-1}\|\| > \xi$, let $i = i+1$ and repeat Step 3.
Step 5	Derive an approximate optimal control strategy $u^* = K_{i+1}X$ (26)

3.2 Performance Analysis

In this section, we first demonstrate that the control solution (8) satisfies the disturbance attenuation condition, and then we discuss the stability of the tracking error dynamics without the disturbance. An upper bound on the discount factor that asymptotically stabilizes the output voltage of the inverter system has been provided.

Theorem 1: If $\Gamma_i = \Gamma - MK_i + NL_i$ is stable, solving for P_i in (19) is equivalent to finding a solution to the underlying Lyapunov

$$\begin{aligned}&{\Gamma_i}^T P_i + P_i\Gamma_i - \alpha P_i - P_iMR^{-1}M^TP_i \\ &+ \gamma^{-2}P_iNN^TP_i + C_1^TQC_1^T = 0\end{aligned} \quad (27)$$

Proof: Proof omitted for brevity, and the details can refer to [11].

Remark 1. Although the same solution is obtained whether solving the (27) or (19), (19) can be solved without using any knowledge of the system matrix Γ.

It follows from Theorem 1 that if $Gamma_i$ stable at each iteration, the algorithm (19) is equivalent to algorithm (27) without using knowledge of the system internal dynamics.

Theorem 2: Consider the H_∞ tracking control problem as a two-player zero-sum game problem with the performance function (7). Then, the pair of strategies (u^*,d^*) defined in (14) and (15) provides a saddle point solution to the game.

Proof: The proof is similar to that in [12] and is omitted here for brief.

Theorem 3 (L_2-gain): Assume that there exists a continuous positive-semidefinite solution $V^*(X)$ to the tracking HJI (13). Then, u^* in (26) makes the closed-loop system (5) to have L_2-gain less than or equal to γ.

Proof: The Hamiltonian (13) for the optimal value function V^*, and any control policy u and disturbance policy d become

$$\begin{aligned}&H\left(V^*,u,d\right) = Y^TQY + u^TRu - \gamma^2d^Td - \\ &\alpha V + V_X^{*T}\left(\Gamma X + Mu + Nd\right) = 0\end{aligned} \quad (28)$$

On the other hand, using (14) - (16), one has

$$\begin{aligned}&H\left(V^*,u,d\right) = H\left(V^*,u^*,d^*\right) + \\ &\left(u-u^*\right)^TR\left(u-u^*\right) + \gamma^2\left(d-d^*\right)^T\left(d-d^*\right)\end{aligned} \quad (29)$$

Based on the HJI (19), we have $H\left(V^*,u^*,d^*\right) = 0$. Therefore, (28) and (29) give

$$\begin{aligned}&Y^TQY + u^TRu - \gamma^2d^Td - \alpha V^* \\ &+ V_X^{*T}\left(\Gamma X + Mu + Nd\right) \\ &= -\left(u-u^*\right)^TR\left(u-u^*\right) - \gamma^2\left(d-d^*\right)^T\left(d-d^*\right)\end{aligned} \quad (30)$$

Substituting the optimal control policy $u = u^*$ in the above equation comes to

$$\begin{aligned}&Y^TQY + u^{*T}Ru^* - \gamma^2d^Td - \alpha V^* \\ &+ V_X^{*T}\left(\Gamma X + Mu^* + Nd\right) \\ &= -\gamma^2\left(d-d^*\right)^T\left(d-d^*\right) \le 0\end{aligned} \quad (31)$$

Multiplying both the sides of this equation by $e^{-\alpha(\tau-t)}$, and defining $\dot{V}^* = V_X^{*T}\left(\Gamma + Mu^* + Nd\right)$ as the derivative of V^* along the trajectories of the closed-loop system, it gives

$$\begin{aligned}&\frac{d}{dt}\left(e^{-\alpha t}V^*\left(X\right)\right) \\ &\le e^{-\alpha t}\left(-Y^TQY - u^{*T}Ru^* + \gamma^2d^Td\right)\end{aligned} \quad (32)$$

Integrating from both the sides of this equation yields

$$\begin{aligned}&e^{-\alpha T}V^*\left(X\left(T\right)\right) - V^*\left(X\left(0\right)\right) \\ &\le \int_0^T e^{-\alpha\tau}\left(-Y^TQY - u^{*T}Ru^* + \gamma^2d^Td\right)d\tau\end{aligned} \quad (33)$$

for every $T>0$ and every $d \in L_2[0,\infty)$. Since $V^*\left(.\right) \ge 0$ the above equation comes to

$$\begin{aligned}&\int_0^T e^{-\alpha\tau}\left(Y^TQY + u^{*T}Ru^*\right)d\tau \\ &\le \int_0^T e^{-\alpha\tau}\left(\gamma^2d^Td\right)d\tau + V^*\left(X\left(0\right)\right)\end{aligned} \quad (34)$$

This completes the proof.

Theorem 4 (Stability of the optimal solution and upper bound for α): Consider the augmented system (5) and define

$$\begin{aligned} S_l &= \gamma^{-2} D D^T \\ Q_l &= C^T Q C \end{aligned} \tag{35}$$

then, the control policy (21) makes the error system dynamic (5) asymptotically stable if

$$\alpha \leq \alpha^* = 2 \left\| (S_l Q_l)^{1/2} \right\| \tag{36}$$

Proof: Proof omitted for brevity, and the details can refer to [13].

4 Simulation

In order to verify the effectiveness and rationality of the proposed algorithm, we conduct simulation in the Matlab/Simulink.

4.1 Simulation parameter

The parameters of the inverter model are presented in Table 1. For a given sinusoidal frequency of f=50Hz, we have ω=2πf=100π.

Table 1: Parameters of the Three-Phase Off-Grid Inverter

Parameter	Numerical Value
DC voltage V_{dc}(V)	400
inverter-side filter inductance L_f(mH)	2
inductance equivalent resistance $R_f(\Omega)$	0.2
filter capacitor C_f(F)	25
d-axis desired output voltage $u_{od}^*(V)$	$110\sqrt{2}$
q-axis desired output voltage u_{oq}^*(V)	0
switching frequency f_s(kHz)	10

4.2 Simulation result

For the H_∞ output tracking control problem of the inverter, we select γ=20, $Q = 1000I_2$, $R = I_2$, where I represents the unit matrix. By employing Algorithm 1 for online learning, the P-value converges after 16 iterations

$$P^*=\begin{bmatrix} 0.0568 & 0.0000 & 0.0632 & -0.0001 & -0.0567 & 0.0000 \\ 0.0000 & 0.0568 & 0.0001 & 0.0632 & -0.0005 & -0.0000 \\ 0.0632 & 0.0001 & 0.1431 & -0.0001 & -0.0652 & 0.0000 \\ -0.0001 & 0.0632 & -0.0001 & 0.1433 & -0.0011 & -0.0000 \\ -0.0567 & -0.0005 & -0.0652 & -0.0011 & 102.1086 & -0.0000 \\ 0.0000 & -0.0000 & 0.0000 & -0.0000 & -0.0000 & -0.0000 \end{bmatrix},$$

the K-value converges

$$K^*=\begin{bmatrix} 31.6389 & -0.0148 & 71.5165 & -0.0352 & -32.6006 & -0.0000 \\ 0.0143 & 31.6386 & 0.0032 & 71.5145 & -0.5760 & 0.0000 \end{bmatrix},$$

the L-value converges

$$L^*=\begin{bmatrix} -0.0142 & 0.0000 & -0.0158 & 0.0000 & 0.0142 & 0 \\ 0.0000 & -0.0142 & 0.0000 & -0.0158 & 0.0001 & 0 \end{bmatrix}.$$

Fig. 2 illustrates the convergence of the control gain K, where K_{old} represents the value of K calculated in the previous iteration.

We employ the algorithm 1 on the three-phase inverter, and the tracking trajectory is depicted in Fig. 3, demonstrating good tracking performance. The initial 0.5s is the learning phase and after 0.5s, the inverter output signals u_{od} and u_{oq} promptly track the reference signals u_{od}^* and u_{oq}^*.

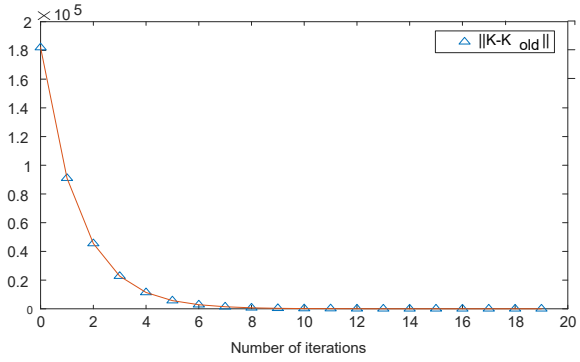

Fig. 2: Convergence of the control gain to its optimal value K^*

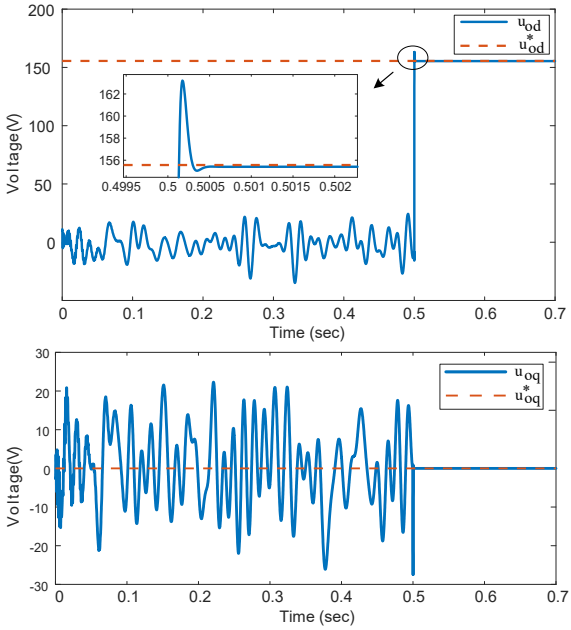

Fig. 3: Tracking performance of the model-free H_∞ control

To assess the robustness of the proposed algorithm under unbalanced and nonlinear loads, we substitute the learned K^* values into Simulink for verification.

From 0∼0.1s, a three-phase symmetrical 10Ω resistive load is applied, followed by the introduction of a three-phase unbalanced load at t=0.1s. The resulting output voltage and current waveforms are depicted in Fig. 4, indicating a brief dynamic process.

During the same time of 0∼0.1s, a three-phase symmetrical 10Ω resistive load is employed concurrently with a diode rectifier circuit connected to the resistor as a nonlinear load. The rectifier has a resistive load of 53Ω, inductance of 3mH, and capacitance of 3000μF. At t=0.1s, when the merger occurs, the resulting output voltage and current waveforms are depicted in Fig. 5.

From Figs.4 and 5, it is evident that the proposed control strategy exhibits commendable dynamic characteristics and steady-state performance for both unbalanced and nonlinear loads.

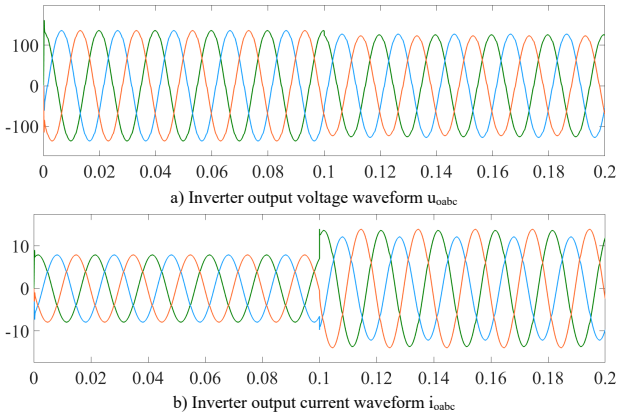

Fig. 4: Three-phase voltage and current waveforms with unbalanced load

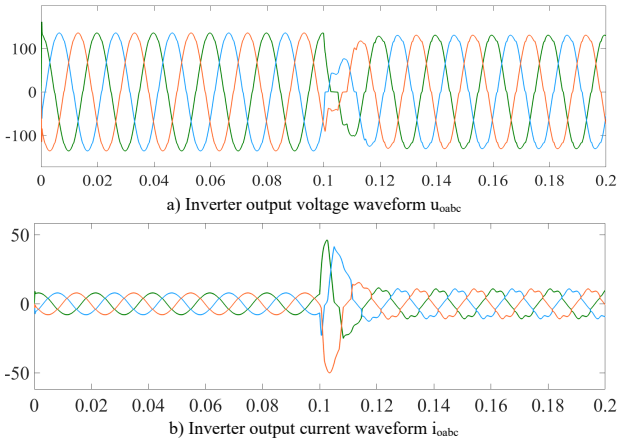

Fig. 5: Three-phase voltage and current waveforms with nonlinear load

5 Conclusion

The IRL-based H_∞ output tracking control method is proposed for off-grid inverter voltage control with unknown dynamics and external disturbances in this paper. Via collecting input-output data of the inverter system, the model-free IRL algorithm is proposed for solving the HJI equation. The stability and optimality of the resulting solution are analyzed, and an upper bound for the discount factor is found to assure the stability of the control solution found by solving the tracking HJI equation. The simulation results demonstrate excellent disturbance suppression in the presence of unbalanced and nonlinear loads.

References

[1] M. Soshinskaya, W. H. J. Crijns-Graus, J. M. Guerrero and J. C. Vasquez, Microgrids: Experiences, barriers and success factors. *Renewable and sustainable energy reviews*, 2014, 40: 658–672.

[2] S. Ferahtia, A. Djeroui, H. Rezk, A. Houari, S. Zeghlache and M. Machmoum, Optimal control and implementation of energy management strategy for a DC microgrid. *Energy*, 2022, 238: 121777.

[3] M. Moafi, M. Marzband, M. Savaghebi and J. M. Guerrero, Energy management system based on fuzzy fractional order PID controller for transient stability improvement in microgrids with energy storage. *International Transactions on Electrical Energy Systems*, 2016, 26(10): 2087–2106.

[4] R. Heydari, H. Young, F. Flores-Bahamonde, S. Vaez-Zadeh, C. Gonzalez-Castano, S. Sabzevari and J. Rodriguez, Model-free predictive control of grid-forming inverters with LCL filters. *IEEE Transactions on Power Electronics*, 2022, 37(8): 9200–9211.

[5] F. Yu, C. H. Zhou, X. Liu and C. G. Zhu, Model-free predictive current control for three-level inverter-fed IPMSM with an improved current difference updating technique. *IEEE Transactions on Energy Conversion*, 2021, 36(4): 3334–3343.

[6] C. K. Lin, T. H. Liu, J. T. Yu, L. C. Fu and C. F. Hsiao, Model-free predictive current control for interior permanent-magnet synchronous motor drives based on current difference detection technique. *IEEE Transactions on Industrial Electronics*, 2014, 61(2): 667–681.

[7] Y. J. Peng, Q. Chen, W. J. Sun, Reinforcement Q-learning algorithm for H_∞ tracking control of unknown discrete-time linear systems. *IEEE Transactions on Systems, Man, and Cybernetics*, 2020, 50(11): 4109–4122.

[8] G. Willmann, D. F. Coutinho, L. F. A. Pereira and F. B. Libano, Multiple-loop H-infinity control design for uninterruptible power supplies. *IEEE Transactions on Industraial Electronics*, 2007, 54(3): 1591–1602.

[9] T. Dragicevic, Model predictive control of power converters for robust and fast operation of AC microgrids. *IEEE Transactions on Power Electronics*, 2018, 33(7): 6304–6317.

[10] Y. Jiang, Z. P. Jiang, Computational adaptive optimal control for continuous-time linear systems with completely unknown dynamics-ScienceDirect. *Automatica*, 2012, 48(10): 2699–2704.

[11] D. Vrabie, O. Pastravanu, M. Abu-Khalaf and F. L. Lewis, Adaptive optimal control for continuous-time linear systems based on policy iteration. *Automatica*, 2009, 45(2): 477–484.

[12] M. Abu-Khalaf, F. L. Lewis, and J. Huang, Neurodynamic programming and zero-sum games for constrained control systems. *IEEE Transactions on Neural Networks*, 2008, 19(7): 1243–1252.

[13] R. Moghadam, F. L. Lewis, Output-feedback H_∞ quadratic tracking control of linear systems using reinforcement learning. *International Journal of Adaptive Control and Signal Processing*, 2019, 33(2): 300–314.

Proceedings of the 3rd Conference on Fully Actuated System Theory and Applications
May 10-12, 2024, Shenzhen, China

On designing interval observer for discrete-time positive fuzzy Markov jump systems with bounded disturbance input

Shujia Wang, Shuqian Zhu, Dawei Zhang
School of Mathematics, Shandong University, Jinan 250100, P. R. China
E-mail: sqzhu@sdu.edu.cn

Abstract: This paper deals with the design problem of interval observer for discrete-time positive fuzzy Markov jump system (FMJS) with bounded disturbance input. For such a system, a mode-dependent Luenberger-like fuzzy interval observer is constructed to estimate the upper and lower bounds of the system state in real time. The upper-bounding and lower-bounding estimation error systems are formulated by two positive FMJSs. Using the fuzzy-dependent linear co-positive function method and the linear programming technique, some solvable conditions for stochastic l_1-gain performance analysis and interval observer design of the two estimation error systems are derived, respectively. Some numerical results are used to validate the design effectiveness.

Key Words: Positive fuzzy Markov jump systems, Stochastic l_1-gain performance analysis, Fuzzy interval observer design, Linear programming

1 Introduction

Interval observers are widely used to handle the interval state estimation problems of systems in the presence of uncertainties and/or bounded disturbance inputs, which aim at providing the real-time upper and lower bounds of interested system states simultaneously as close as possible. Compared with the classic state estimation methods like Luenberger observer, the typical advantages of interval observer lie at the ability of real-time range monitoring and high robustness. In light of these advantages, it is promising and interesting to apply interval observers for monitoring the system operation of several practical systems such as vehicles, aircraft and electrical grids. To mention a few, a distributed interval observer was designed in [1] to detect the operational status of side-slip angle and yaw rate for a networked vehicle subject to randomly occurring stealthy attacks. In [2], a functional interval observer was designed for a two-tank system to monitor the liquid levels of two tanks in real time. An interval observer was applied to detect and isolate faults occurring in the communication system of a group of four F-18 aircrafts in [3].

In practical systems, there exist some unavoidable and considerable phenomena such as positivity, randomness, and various modeling nonlinearities. To be more specific, system positivity denotes the non-negative state evolution of systems under the non-negative initial state and external input. The positivity feature is identified in many practical systems such as communication network systems [4] and traffic control systems [5]. Furthermore, due to the abrupt changes in system structure and parameters or the random fault of signals and equipments, positive Markov jump linear systems (MJLSs) are put forward to characterize the positivity and randomness features of practical systems such as the pest's structured population dynamic model [6] and networked dynamic model in epidemiology [7]. Moreover, it is well recognized that most of practical systems are essentially nonlinear and Takagi-Sugeno fuzzy model is a prevalent universal approximator for nonlinear systems. In this sense, positive T-S fuzzy system and fuzzy Markov jump system (FMJS) are two classes of typical systems to be concerned.

In the existing literature, interval observer design of positive linear systems with uncertain and bounded disturbance was carried out in [8] based on the monotone system theory. A mode-dependent Luenberger-like interval observer of positive MJLSs was designed in [9] and the design results were derived in terms of linear programming (LP). The interval state estimation problem of positive T-S fuzzy systems was investigated in [10] and l_1-gain performance optimization was applied for evaluating the accuracy of estimation. A Luenberger-like interval observer of FMJS was proposed in [11]. Reviewing the existing works, one can conclude that the interval state estimation problem of positive FMJS has not been solved so far, although such a system involves the positivity, randomness, and nonlinearity together.

Based on the above discussion, we focus on the design problem of interval observer for positive FMJSs in this paper. Clearly, the positive FMJSs can be degenerated into either positive T-S fuzzy systems [10], positive MJLSs [9], or positive linear systems [8]. For the positive FMJS, a mode-dependent and fuzzy-rule-dependent Luenberger-like interval observer is presented. Then some conditions are derived by using the co-positive Lyapunov function method and the LP technique, which can ensure the upper-bounding and lower-bounding estimation error systems to be positive, and stochastically internally stable with l_1-gain performance. Due to the generality of the designed interval observer, the proposed results can be applied for positive T-S fuzzy systems, positive MJLSs, and positive linear systems as special cases. A numerical example is provided to show the effectiveness of the interval observer design method.

Notations: The relation A (or x) $\succeq 0$ ($\preceq 0, \prec 0$) means that all elements of a matrix A (or a vector x) are nonnegative (nonpositive, negative). $E\{\cdot\}$ expresses the mathematical expectation of $\{\cdot\}$. For a matrix $A \in \mathbb{R}^{m\times n}$, $[A]_{uv}$, $[A]_{\mathbf{c},v}$, $[A]_{\mathbf{r},u}$ stand for the (u,v) scalar entry, the

This work was partly supported by the National Natural Science Foundation of China under 62373220, the Shandong Provincial Natural Science Foundation of China under Grant ZR2023MF011, and the Science Center Program of National Natural Science Foundation of China under Grant 62188101.

v-th column of A, the u-th row of A, respectively. $[x]_i$ represents the i-th entry of a vector x. $\|x\|_1$, $\|v\|_{l_1}$, l_1^+ and $\mathbf{1}_n$ are consistent with the meaning of the symbols in [6].

2 Problem statement and preliminaries

Consider the discrete-time FMJS described by

Plant Rule i : IF $\theta_1(k)$ is μ_{i1}, $\theta_2(k)$ is μ_{i2}, $\cdots$, $\theta_p(k)$ is μ_{ip}, THEN

$$\begin{cases} x(k+1) = A_{i,r_k}x(k) + B_{i,r_k}\omega(k) \\ y(k) = C_{i,r_k}x(k) + D_{i,r_k}\omega(k) \\ x(0) = x_0 \end{cases} \tag{1}$$

where $i \in \Psi = \{1, 2, \ldots, s\}$ and s is the number of IF-THEN fuzzy rules. $\mu_{ie}(i = 1, 2, \ldots, s; e = 1, 2, \ldots, p)$ are the fuzzy sets, and $\theta(k) = [\theta_1(k), \theta_2(k), \cdots, \theta_p(k)]$ denotes the premise variable vector. $x(k) \in \mathbb{R}^n$, $\omega(k) \in \mathbb{R}^{n_\omega}$, $y(k) \in \mathbb{R}^{n_y}$ denote the system state, the disturbance input and the measured output, respectively. $\{r_k, k \in \mathbb{N}\}$ is the discrete-time Markov process which takes values in a finite set $\Gamma = \{1, 2, \ldots, N\}$. The transition probability matrix is $\Lambda = [\pi_{lt}]_{N\times N}$ with $\pi_{lt} = \mathbf{Pr}\{r_{k+1} = t | r_k = l\}$, where $\pi_{lt} \geq 0$ for $l, t \in \Gamma$, and $\sum_{t=1}^{N} \pi_{lt} = 1$, $\forall l \in \Gamma$. $A_{i,l}$, $B_{i,l}$, $C_{i,l}$, $D_{i,l}$ are known constant matrices with appropriate dimensions.

The FMJS (1) can be rewritten by

$$\begin{cases} x(k+1) = \sum_{i=1}^{s} h_i(\theta(k))\{A_{i,l}x(k) + B_{i,l}\omega(k)\} \\ y(k) = \sum_{i=1}^{s} h_i(\theta(k))\{C_{i,l}x(k) + D_{i,l}\omega(k)\} \\ x(0) = x_0 \end{cases} \tag{2}$$

where

$$h_i(\theta(k)) = \frac{\nu_i(\theta(k))}{\sum_{i=1}^{s} \nu_i(\theta(k))},\ \nu_i(\theta(k)) = \prod_{e=1}^{p} \mu_{ie}(\theta_e(k)),$$

$\mu_{ie}(\theta_e(k)) \in [0, 1]$ denotes the grade of membership of $\theta_e(k)$ in $\mu_{ie}(i = 1, 2, \ldots, s; e = 1, 2, \ldots, p)$ and $\sum_{i=1}^{s} h_i(\theta(k)) = 1$, $h_i(\theta(k)) \geq 0$.

The following definitions, lemma, and assumptions are given for preliminaries.

Definition 1. The FMJS (2) is a positive system, if for any initial state $x_0 \succeq 0$ and $\omega(k) \succeq 0$, $\forall k \in \mathbb{N}$, and any initial mode r_0, the conditions $x(k) \succeq 0$, $y(k) \succeq 0$, $\forall k \in \mathbb{N}$ hold.

Lemma 1. *[12] The FMJS (2) is a positive system if and only if $A_{i,l} \succeq 0$, $B_{i,l} \succeq 0$, $C_{i,l} \succeq 0$, $D_{i,l} \succeq 0$, $\forall i \in \Psi$, $l \in \Gamma$.*

Definition 2. The positive FMJS with $\omega(k) = 0$ is said to be stochastically internally stable, if $\sum_{k=0}^{\infty} E\{\|x(k)\|_1 | x_0, r_0\} < \infty$ holds for every initial condition (x_0, r_0) with $x_0 \in R_+^n$.

Definition 3. For $\gamma \geq 0$, the positive FMJS (2) is said to be stochastically internally stable with l_1-gain performance γ, if

1) the positive FMJS (2) is said to be stochastically internally stable with $\omega(k) = 0$.
2) under zero initial condition, $\|y\|_{l_1} \leq \|\omega\|_{l_1}$ holds for all nonzero $\omega(k) \in l_1^+$.

Remark 1. If $N = 1$, the positive FMJS (2) reduces to a positive Markov jump system [6], [13]. If $s = 1$, the positive FMJS (2) reduces to a positive T-S fuzzy system [10]. In addition, Definition 1-3 and Lemma 1 still hold for the degenerate systems.

For the positive FMJS, the following general assumptions are provided.

Assumption 1. The initial state x_0 satisfies $0 \preceq \underline{x}_0 \preceq x_0 \preceq \overline{x}_0$, where $\underline{x}_0$ and $\overline{x}_0$ are known lower and upper bounds for the initial conditions.

Assumption 2. The disturbance input $\omega(k)$ satisfies $\underline{\omega}(k) \preceq \omega(k) \preceq \overline{\omega}(k)$, $\forall k \in \mathbb{N}$ and some known $\underline{\omega}, \overline{\omega} \in l_1^+$.

3 Main results

To achieve the real-time estimates of upper and lower bounds of $x(k)$, by using the boundary information $\underline{\omega}(k)$, $\overline{\omega}(k)$ and $y(k)$, one constructs the following fuzzy Luenberger-like observers

Rule i : IF $\theta_1(k)$ is μ_{i1}, $\theta_2(k)$ is μ_{i2}, $\cdots$, $\theta_p(k)$ is μ_{ip}, THEN

$$\begin{cases} \overline{x}(k+1) = (A_{i,l} - L_{i,l}C_{i,l})\overline{x}(k) + (B_{i,l} - L_{i,l}D_{i,l})\overline{\omega}(k) \\ \qquad\qquad + L_{i,l}y(k) \\ \underline{x}(k+1) = (A_{i,l} - L_{i,l}C_{i,l})\underline{x}(k) + (B_{i,l} - L_{i,l}D_{i,l})\underline{\omega}(k) \\ \qquad\qquad + L_{i,l}y(k) \end{cases} \tag{3}$$

where $\overline{x}(k)$ and $\underline{x}(k)$ are the estimated upper and lower bounds of $x(k)$, and $L_{i,l}$ is the interval observer gain matrix to be designed.

Similar to the modeling process from (1) to (2), the observer (3) can be rewritten as

$$\begin{cases} \overline{x}(k+1) = \sum_{i=1}^{s} h_i(\theta(k))\big\{(A_{i,l} - L_{i,l}C_{i,l})\overline{x}(k) \\ \qquad\qquad + (B_{i,l} - L_{i,l}D_{i,l})\overline{\omega}(k) + L_{i,l}y(k)\big\} \\ \underline{x}(k+1) = \sum_{i=1}^{s} h_i(\theta(k))\big\{(A_{i,l} - L_{i,l}C_{i,l})\underline{x}(k) \\ \qquad\qquad + (B_{i,l} - L_{i,l}D_{i,l})\underline{\omega}(k) + L_{i,l}y(k)\big\}. \end{cases} \tag{4}$$

Due to the fact that $0 \preceq \underline{x}(k) \preceq x(k) \preceq \overline{x}(k)$, the observer (4) should be a positive system.

Theorem 1. *Let Assumption 1-2 be satisfied, observer* (4) *is said to be an interval observer for the positive FMJS* (2)*, if there exists a matrix $L_{i,l}$ such that $A_{i,l} - L_{i,l}C_{i,l} \succeq 0$ and $B_{i,l} - L_{i,l}C_{i,l} \succeq 0$, $\forall i \in \Psi$, $l \in \Gamma$.*

Proof. Denote the estimation errors of upper and lower bounds as $\overline{e}(k) = \overline{x}(k) - x(k)$, $\underline{e}(k) = x(k) - \underline{x}(k)$. One gets the following estimation error systems

$$\begin{cases} \overline{e}(k+1) = \sum_{i=1}^{s} h_i(\theta(k))\big\{(A_{i,l} - L_{i,l}C_{i,l})\overline{e}(k) \\ \qquad\qquad + (B_{i,l} - L_{i,l}D_{i,l})\big(\overline{\omega}(k) - \omega(k)\big)\big\} \\ \overline{e}(0) = \overline{e}_0 \end{cases} \tag{5}$$

$$\begin{cases} \underline{e}(k+1) = \sum_{i=1}^{s} h_i(\theta(k))\big\{(A_{i,l} - L_{i,l}C_{i,l})\underline{e}(k) \\ \qquad\qquad + (B_{i,l} - L_{i,l}D_{i,l})\big(\omega(k) - \underline{\omega}(k)\big)\big\} \\ \underline{e}(0) = \underline{e}_0 \end{cases} \tag{6}$$

It is clear that (i) $\overline{\omega}(k)-\omega(k) \succeq 0, \omega(k)-\underline{\omega}(k) \succeq 0, \forall k \in \mathbb{N}$ and (ii) $\overline{e}(0) \succeq 0,\ \underline{e}(0) \succeq 0$ since $\underline{x}(0) \preceq x(0) \preceq \overline{x}(0)$. Notice that $A_{i,l} - L_{i,l}C_{i,l} \succeq 0$ and $B_{i,l} - L_{i,l}C_{i,l} \succeq 0, \forall i \in \Psi, l \in \Gamma$. Using Lemma 1, we can get $\overline{e}(k) \succeq 0,\ \underline{e}(k) \succeq 0, \forall k \in \mathbb{N}$. As a result, $\underline{x}(k) \preceq x(k) \preceq \overline{x}(k)$ holds, $\forall k \in \mathbb{N}$. □

Usually, a satisfied interval estimation accuracy cannot be ensured by the interval observer (4) that is simply designed by $A_{i,l} - L_{i,l}C_{i,l} \succeq 0$ and $B_{i,l} - L_{i,l}C_{i,l} \succeq 0$. To obtain an expected estimation effect, we propose an l_1-gain performance optimization result by the following theorems.

Theorem 2. *Suppose that $A_{i,l} - L_{i,l}C_{i,l} \succeq 0$ and $B_{i,l}-L_{i,l}C_{i,l} \succeq 0,\ \forall i \in \Psi,\ l \in \Gamma$ hold . For a given $\gamma > 0$, the estimation error systems (5)-(6) are stochastically internally stable and satisfy $\|\overline{e}\|_{l_1} < \gamma\|\overline{\omega} - \omega\|_{l_1}$, $\|\underline{e}\|_{l_1} < \gamma\|\omega - \underline{\omega}\|_{l_1}$, if there exist vectors $p_{i,l} \succeq 0$, such that*

$$\widetilde{p}_{i,l}^T(A_{j,l} - L_{j,l}C_{j,l}) - p_{j,l}^T + \mathbf{1}_n^T \prec 0, \tag{7}$$

$$\widetilde{p}_{i,l}^T(B_{j,l} - L_{j,l}D_{j,l}) - \gamma\mathbf{1}_{n_\omega}^T \prec 0, \tag{8}$$

where $\widetilde{p}_{i,l} = \sum_{t=1}^{N} \pi_{lt}p_{i,t},\ i,j = 1,2\cdots s,\ l \in \Gamma$.

Proof. Construct the fuzzy-dependent linear co-positive Lyapunov function as $V(\overline{e}(k), r_k) = \sum_{i=1}^{s} h_i(\theta(k))p_{i,r_k}^T\overline{e}(k)$, with $p_{i,r_k} \succ 0$. Let the mode at time k be i, that is, $r_k = l$. At time $k+1$, the system may jump to any mode $r_{k+1} = t$. Thus, one gets that

$$\begin{aligned}
\Delta V &= \mathbf{E}\big\{V(\overline{e}(k+1), r_{k+1})\big|\overline{e}(k), l\big\} - V(\overline{e}(k), l) \\
&= \mathbf{E}\Big\{\sum_{i=1}^{s} h_i(\theta(k+1))p_{i,r_{k+1}}^T\overline{e}(k+1)\big|\overline{e}(k), l\Big\} \\
&\quad - \sum_{i=1}^{s} h_i(\theta(k))p_{i,l}^T\overline{e}(k) \\
&= \mathbf{E}\Big\{\sum_{i=1}^{s}\sum_{j=1}^{s} h_i(\theta(k+1))h_j(\theta(k))p_{i,r_{k+1}}^T \\
&\quad \times \big[(A_{j,l} - L_{j,l}C_{j,l})\overline{e}(k) + (B_{j,l} - L_{j,l}D_{j,l}) \\
&\quad \times (\overline{\omega}(k) - \omega(k))\big]\Big|\overline{e}(k), l\Big\} - \sum_{j=1}^{s} h_j(\theta(k))p_{j,l}^T\overline{e}(k) \\
&= \sum_{i=1}^{s}\sum_{j=1}^{s} h_i(\theta(k+1))h_j(\theta(k))\sum_{t=1}^{N}\pi_{lt}p_{i,t}^T \\
&\quad \times \big[(A_{j,l} - L_{j,l}C_{j,l})\overline{e}(k) + (B_{j,l} - L_{j,l}D_{j,l}) \\
&\quad \times (\overline{\omega}(k) - \omega(k))\big] - \sum_{j=1}^{s} h_j(\theta(k))p_{j,l}^T\overline{e}(k) \\
&= \sum_{i=1}^{s}\sum_{j=1}^{s} h_i(\theta(k+1))h_j(\theta(k))\Big\{\big[\widetilde{p}_{i,l}^T(A_{j,l} - L_{j,l}C_{j,l}) \\
&\quad - p_{j,l}^T\big]\overline{e}(k) + \widetilde{p}_{i,l}^T(B_{j,l} - L_{j,l}D_{j,l})(\overline{\omega}(k) - \omega(k))\Big\}.
\end{aligned}$$

When $\omega(k) = 0$, one has that

$$\begin{aligned}
\Delta V(\overline{e}(k), r_k) &= \sum_{i=1}^{s}\sum_{j=1}^{s} h_i(\theta(k+1))h_j(\theta(k))\times \\
&\quad \big[\widetilde{p}_{i,l}^T(A_{j,l} - L_{j,l}C_{j,l}) - p_{j,l}^T\big]\overline{e}(k).
\end{aligned}$$

From (7), $\widetilde{p}_{i,l}^T(A_{j,l} - L_{j,l}C_{j,l}) - p_{j,l}^T \preceq 0$ holds. Define

$$\eta = \min_{i,j\in\Psi,\ l\in\Gamma,\ m=1,2,\ldots,n} \Big\{-\big[\widetilde{p}_{i,l}^T(A_{j,l}-L_{j,l}C_{j,l})-p_{j,l}^T\big]_m\Big\}.$$

It follows that

$$\Delta V(\overline{e}(k), r_k) \le -\eta\|\overline{e}(k)\|_{l_1},$$

which is equivalent to

$$\mathbf{E}\big\{V(\overline{e}(k+1), r_{k+1})\big|\overline{e}(k), l\big\} \le V(\overline{e}(k), l) - \eta\|\overline{e}(k)\|_{l_1}. \tag{9}$$

Taking mathematical expectation $\mathbf{E}\{\cdot|\overline{e}_0, r_0\}$ on the both sides of (9) yields

$$\begin{aligned}
&\mathbf{E}\{\mathbf{E}\{V(\overline{e}(k+1), r_{k+1})|\overline{e}(k), l\}|\overline{e}_0, r_0\} \\
&= \mathbf{E}\{V(\overline{e}(k+1), r_{k+1})|\overline{e}_0, r_0\}.
\end{aligned}$$

Further, for $\forall T \in \mathbb{N}$, one obtains

$$\begin{aligned}
&\mathbf{E}\{V(\overline{e}(T+1), r_{T+1}|\overline{e}_0, r_0\} \\
&\le V(\overline{e}_0, r_0) - \eta\sum_{k=0}^{T}\mathbf{E}\{\|\overline{e}(k)\|_{l_1}|\overline{e}_0, r_0\},
\end{aligned}$$

which implies that

$$\sum_{k=0}^{\infty}\mathbf{E}\{\|\overline{e}(k)\|_{l_1}|\overline{e}_0, r_0\} \le \frac{1}{\eta}V(\overline{e}_0, r_0) < \infty.$$

Thus system (5) is stochastically internally stable. Let

$$\begin{aligned}
J &= \|\overline{e}\|_1 - \gamma\|\overline{w} - \omega\|_1 = \mathbf{1}_{n_e}^T\overline{e}(k) - \gamma\mathbf{1}_{n_\omega}^T(\overline{\omega}(k) - \omega(k)) \\
&= \big[\mathbf{1}_{n_e}^T\overline{e}(k) - \gamma\mathbf{1}_{n_\omega}^T(\overline{\omega}(k) - \omega(k)) + \Delta V(\overline{e}(k), r_k)\big] \\
&\quad - \Delta V(\overline{e}(k), r_k) \\
&= \sum_{i=1}^{s}\sum_{j=1}^{s} h_i(\theta(k+1))h_j(\theta(k))\Big\{\big[\widetilde{p}_{i,l}^T(A_{j,l} - L_{j,l}C_{j,l}) \\
&\quad - p_{j,l}^T + \mathbf{1}_{n_e}^T + \varepsilon\mathbf{1}_{n_e}^T\big]\overline{e}(k) + \big[\widetilde{p}_{i,l}^T(B_{j,l} - L_{j,l}D_{j,l}) \\
&\quad - \gamma\mathbf{1}_{n_\omega}^T\big](\overline{\omega}(k) - \omega(k))\Big\} - \varepsilon\mathbf{1}_{n_e}^T\overline{e}(k) - \Delta V(\overline{e}(k), r_k).
\end{aligned}$$

It can be derived from (7) that there exists a sufficiently small ε such that

$$\widetilde{p}_{i,l}^T(A_{j,l} - L_{j,l}C_{j,l}) - p_{j,l}^T + \mathbf{1}_{n_e}^T + \varepsilon\mathbf{1}_{n_e}^T \preceq 0. \tag{10}$$

Using (8) and (10), one gets

$$\mathbf{1}_{n_e}^T\overline{e}(k)+\varepsilon\mathbf{1}_{n_e}^T\overline{e}(k) < \gamma\mathbf{1}_{n_\omega}^T(\overline{\omega}(k)-\omega(k))-\Delta V(\overline{e}(k), r_k). \tag{11}$$

It follows that

$$\begin{aligned}
&\sum_{k=0}^{T}\|\overline{e}(k)\|_1 + \varepsilon\sum_{k=0}^{T}\|\overline{e}(k)\|_1 \\
&< \gamma\sum_{k=0}^{T}\|\overline{\omega}(k) - \omega(k)\|_1 - V(\overline{e}(T+1), r_{T+1}).
\end{aligned} \tag{12}$$

Let $T \to \infty$ and take mathematical expectation $\mathbf{E}\{\cdot|\overline{e}_0, r_0\}$ on the both sides of (12). One has

$$\sum_{k=0}^{\infty} \mathbf{E}\{\|\overline{e}(k)\|_1\} + \varepsilon \sum_{k=0}^{\infty} \mathbf{E}\{\|\overline{e}(k)\|_1\} < \gamma \sum_{k=0}^{\infty} \mathbf{E}\{\|\overline{\omega}(k) - \omega(k)\|_1\}.$$

Thus, one gets $\|\overline{e}\|_{l_1} < \gamma\|\overline{\omega} - \omega\|_{l_1}$. Similarly, it can be derived from (7)-(8) that $\|\underline{e}\|_{l_1} < \gamma\|\omega - \underline{\omega}\|_{l_1}$ holds, which completes the proof. □

Based on the conditions of Theorem 2, one can get the following design result of gain matrix $L_{i,l}$.

Theorem 3. *Let Assumption 1-2 be satisfied. For a given scalar $\gamma > 0$, there exists an interval observer* (4) *for the positive FMJS* (3) *and the resulting positive estimation error systems (5)-(6) are stochastically internally stable with l_1-gain performance γ, if there exist positive vectors $z_l \in \mathbb{R}^n$, and vectors $q_{j,l}^{\sigma} \in \mathbb{R}^{n_y}$, such that*

$$[A_{j,l}^T]_{\mathbf{c},\sigma}[\widetilde{z}_l]_\sigma - C_{j,l}^T q_{j,l}^{\sigma} \succeq 0, \tag{13}$$

$$[B_{j,l}^T]_{\mathbf{c},\sigma}[\widetilde{z}_l]_\sigma - D_{j,l}^T q_{j,l}^{\sigma} \succeq 0, \tag{14}$$

$$A_{j,l}^T \widetilde{z}_l - C_{j,l}^T \sum_{\sigma=1}^{n_x} q_{j,l}^{\sigma} - z_l + \mathbf{1}_n \prec 0, \tag{15}$$

$$B_{j,l}^T \widetilde{z}_l - D_{j,l}^T \sum_{\sigma=1}^{n_x} q_{j,l}^{\sigma} - \gamma \mathbf{1}_{n_\omega} \prec 0, \tag{16}$$

where $\widetilde{z}_l = \sum_{t=1}^{N} \pi_{lt} z_t$, $\sigma \in 1, 2, ..., n$, $j \in \Psi,\ l \in \Gamma$.

More over, the gain matrix $L_{j,l}$ can be computed by

$$L_{j,l} = \left[\frac{q_{j,l}^1}{[\widetilde{z}_l]_1} \quad \frac{q_{j,l}^2}{[\widetilde{z}_l]_2} \quad \cdots \quad \frac{q_{j,l}^n}{[\widetilde{z}_l]_n}\right]^T, j \in \Psi,\ l \in \Gamma. \tag{17}$$

Proof. It is clear that

$$\begin{aligned} &[A_{j,l} - L_{j,l}C_{j,l}]^T \\ &= A_{j,l}^T - C_{j,l}^T L_{j,l}^T \\ &= \left[[A_{j,l}^T]_{\mathbf{c},1} \quad [A_{j,l}^T]_{\mathbf{c},2} \quad \cdots \quad [A_{j,l}^T]_{\mathbf{c},n}\right] \\ &\quad - \left[\frac{C_{j,l}^T q_{j,l}^1}{[\widetilde{z}_l]_1} \quad \frac{C_{j,l}^T q_{j,l}^2}{[\widetilde{z}_l]_2} \quad \cdots \quad \frac{C_{j,l}^T q_{j,l}^n}{[\widetilde{z}_l]_n}\right] \\ &= \left[[A_{j,l}^T]_{\mathbf{c},1} - \frac{C_{j,l}^T q_{j,l}^1}{[\widetilde{z}_l]_1} \quad [A_{j,l}^T]_{\mathbf{c},2} - \frac{C_{j,l}^T q_{j,l}^2}{[\widetilde{z}_l]_2} \quad \cdots \right. \\ &\quad \left. [A_{j,l}^T]_{\mathbf{c},n} - \frac{C_{j,l}^T q_{j,l}^n}{[\widetilde{z}_l]_n}\right]. \end{aligned} \tag{18}$$

From $\frac{1}{[\widetilde{z}_l]_\sigma} > 0$ and inequality (13), one gets

$$[A_{j,l}^T]_{\mathbf{c},\sigma} - \frac{C_{j,l}^T q_{j,l}^{\sigma}}{[\widetilde{z}_l]_\sigma} \succeq 0.$$

Thus $A_{j,l} - L_{j,l}C_{j,l} \succeq 0$ holds. With the above derivation, we can also get $B_{j,l} - L_{j,l}D_{j,l} \succeq 0$. Therefore, the estimation error systems satisfy the conditions of Theorem 1. Applying Theorem 1, we know that (4) is an interval observer for the positive FMJS (3).

Defining $p_{j,l} = z_l$, we can get

$$\widetilde{p}_{j,l} = \sum_{t=1}^{N} \pi_{lt} p_{j,t} = \sum_{t=1}^{N} \pi_{lt} z_t = \widetilde{z}_l,\ j = 1, 2 \cdots s,\ l \in \Omega.$$

From (17), one can obtain

$$L_{j,l}^T \widetilde{z}_l = \sum_{\sigma=1}^{n} q_{j,l}^{\sigma}. \tag{19}$$

Combining the above equation with (15), (16), one can see that

$$A_{j,l}^T \widetilde{z}_l - C_{j,l}^T L_{j,l}^T \widetilde{z}_l - z_l + \mathbf{1}_n \prec 0,$$
$$B_{j,l}^T \widetilde{z}_l - D_{j,l}^T L_{j,l}^T \widetilde{z}_l - \gamma \mathbf{1}_{n_\omega} \prec 0,$$

which are equivalent to the following conditions

$$(A_{j,l} - L_{j,l}C_{j,l})^T \widetilde{p}_{i,l} - p_{j,l} + \mathbf{1}_n \prec 0,$$
$$(B_{j,l} - L_{j,l}D_{j,l})^T \widetilde{p}_{i,l} - \gamma \mathbf{1}_{n_\omega} \prec 0.$$

Therefore, inequality (7) and (8) hold. By Theorem 2, one can get that the error systems are stochastically stable and satisfy $\|\overline{e}\|_{l_1} < \gamma\|\overline{\omega} - \omega\|_{l_1},\ \|\underline{e}\|_{l_1} < \gamma\|\omega - \underline{\omega}\|_{l_1}$. □

In order to achieve better results for interval estimation, it is necessary to optimize γ. Use Theorem 3 to solve the following optimization problem

$$\begin{aligned} &min \quad \gamma \\ &s.t.\ (13) - (16). \end{aligned} \tag{20}$$

4 A Numerical Example

Consider the following positive FMJS

Rule 1 : IF $\theta(k)$ is μ_1, THEN

$$\begin{cases} x(k+1) = A_{1,r_k}x(k) + B_{1,r_k}\omega(k), \\ y(k) = C_{1,r_k}x(k) + D_{1,r_k}\omega(k), \end{cases}$$

Rule 2 : IF $\theta(k)$ is μ_2, THEN

$$\begin{cases} x(k+1) = A_{2,r_k}x(k) + B_{2,r_k}\omega(k), \\ y(k) = C_{2,r_k}x(k) + D_{2,r_k}\omega(k), \end{cases}$$

where

$$A_{1,1} = \begin{bmatrix} 0.6 & 0.2 \\ 0.1 & 0.3 \end{bmatrix}, A_{1,2} = \begin{bmatrix} 0.8 & 0.7 \\ 0 & 0.5 \end{bmatrix},$$
$$A_{2,1} = \begin{bmatrix} 0.4 & 0.1 \\ 0.5 & 0.3 \end{bmatrix}, A_{2,2} = \begin{bmatrix} 0.2 & 0.8 \\ 0.4 & 0 \end{bmatrix},$$
$$B_{1,1} = \begin{bmatrix} 0.7 \\ 0.25 \end{bmatrix}, B_{1,2} = \begin{bmatrix} 0.5 \\ 0.06 \end{bmatrix},$$
$$B_{2,1} = \begin{bmatrix} 0.5 \\ 0.3 \end{bmatrix}, B_{2,2} = \begin{bmatrix} 0.5 \\ 0.7 \end{bmatrix},$$
$$C_{1,1} = \begin{bmatrix} 0.1 & 0.1 \end{bmatrix}, C_{1,2} = \begin{bmatrix} 0.1 & 0.2 \end{bmatrix},$$
$$C_{2,1} = \begin{bmatrix} 0.2 & 0.4 \end{bmatrix}, C_{2,2} = \begin{bmatrix} 0.2 & 0.1 \end{bmatrix},$$
$$D_{11} = 0.3, D_{12} = 0.4, D_{21} = 0.1, D_{22} = 0.2,$$

and the normalized membership functions are given as

$$h_1(\theta(k)) = \frac{1 + \sin x_1(k)}{2}, \quad h_2(\theta(k)) = \frac{1 - \sin x_1(k)}{2}.$$

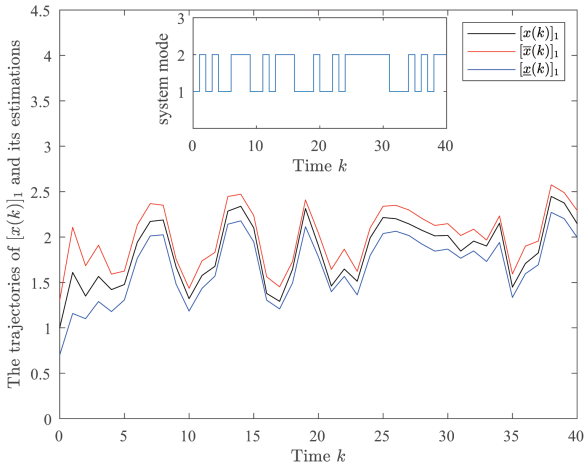

Fig. 1: Real state $[x(k)]_1$ and its interval estimations.

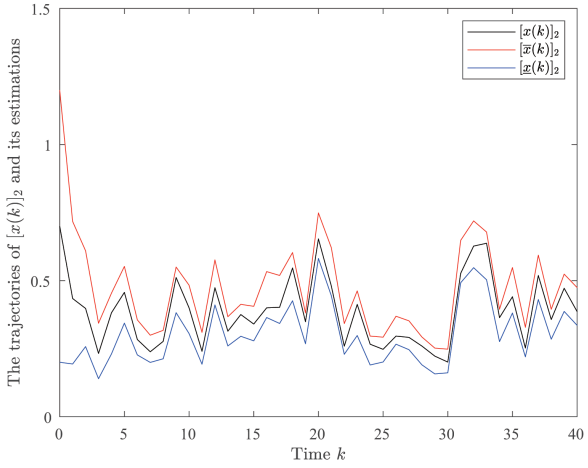

Fig. 2: Real state $[x(k)]_2$ and its interval estimations.

The transition probability matrix of the system is set to be

$$\Lambda = \begin{bmatrix} 0.4 & 0.6 \\ 0.5 & 0.5 \end{bmatrix}.$$

By solving the optimization problem (20) together with Theorem 3, one can compute the optimized l_1-gain performance $\gamma_{min} = 0.7176$ and

$$L_{1,1} = \begin{bmatrix} 1.3863 \\ 0 \end{bmatrix}, L_{1,2} = \begin{bmatrix} 1 \\ 0 \end{bmatrix}, L_{2,1} = \begin{bmatrix} 0.25 \\ 0.75 \end{bmatrix}, L_{2,2} = \begin{bmatrix} 1 \\ 0 \end{bmatrix}.$$

Under Assumption 1-2, the disturbance input and its upper and lower bounds are assumed to be $\omega(k) = 0.4\cos(k) + 0.2\sin(5k) + 0.7$, $\overline{\omega}(k) = 0.4\cos(k) + 0.9$, $\underline{\omega}(k) = 0.4\cos(k) + 0.5$, the initial state is set to be $x(0) = [1 \quad 0.7]^T$, and the initial estimations are chosen as $\overline{x}(0) = [1.3 \quad 1.2]^T$, $\underline{x}(0) = [0.7 \quad 0.2]^T$.

Fig.1 and Fig.2 depict the trajectories of $[x(k)]_1$ and its interval estimation, and the trajectories of $[x(k)]_2$ and its interval estimation, respectively, which show that the proposed interval observer can estimate the variation range of the state in real time with satisfactory accuracy. Fig.3 and Fig.4 show the trajectories of the upper bound error $[\overline{e}(k)]_i$ and the lower bound error $[\underline{e}(k)]_i$ when $\omega(k) = 0$, which implies that the estimation error systems are stochastically internally stable. Under the zero initial condition, one can calculate that $\frac{\|\overline{e}\|_{l_1}}{\|\overline{\omega}-\omega\|_{l_1}} = 0.6707 < 0.7176$ and $\frac{\|\underline{e}\|_{l_1}}{\|\omega-\underline{\omega}\|_{l_1}} = 0.6707 < 0.7176$, which means that the estimation error systems satisfy the prescribed l_1-gain performance γ.

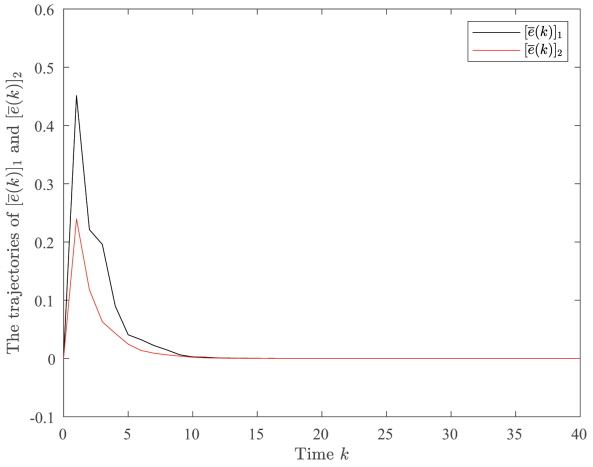

Fig. 3: The trajectories of $[\overline{e}(k)]_1$ and $[\overline{e}(k)]_2$.

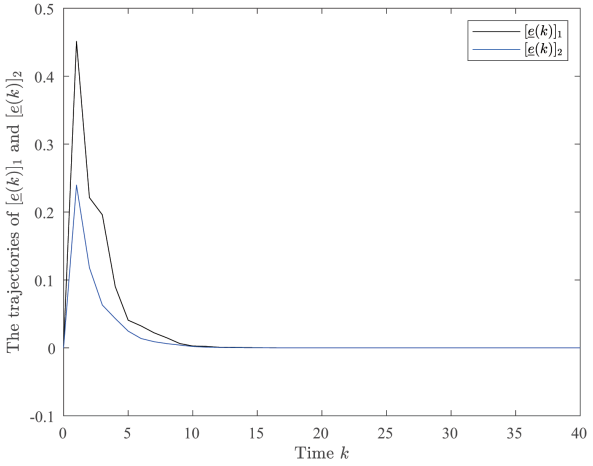

Fig. 4: The trajectories of $[\underline{e}(k)]_1$ and $[\underline{e}(k)]_2$.

5 Conclusion

In this paper, a general design method of fuzzy interval observer has been proposed for positive FMJSs. The design conditions, which can ensure the interval estimation error systems to be positive and stochastically instable with a given l_1-gain performance, have been derived by using a fuzzy-dependent linear co-positive Lyapunov function and linear programming methods. A numerical example has been given to validate the design method. In future, it would be interesting to design interval observers for general FMJSs with bounded disturbance input and to apply interval observers for fault detection issues.

References

[1] J. Xie, S. Zhu, and D. Zhang, "Distributed interval state estimation with l_∞-gain optimization for cyber–physical systems subject to bounded disturbance and random stealthy attacks," *ISA Transactions*, vol. 127, pp. 22–31, 2022.

[2] R. Akremi, R. Lamouchi, M. Amairi, T. N. Dinh, and T. Raïssi, "Functional interval observer design for multivariable linear parameter-varying systems," *European Journal of Control*, vol. 71, p. 100794, 2023.

[3] Z.-H. Zhang and G.-H. Yang, "Distributed fault detection and isolation for multiagent systems: An interval observer approach," *IEEE Transactions on Systems, Man, and Cybernetics: Systems*, vol. 50, no. 6, pp. 2220–2230, 2020.

[4] G. Chen and Y. Yang, "Finite-time stability of switched positive linear systems," *International Journal of Robust and Nonlinear Control*, vol. 24, no. 1, pp. 179–190, 2014.

[5] W. Xiang, J. Lam, and J. Shen, "Stability analysis and l_1-gain characterization for switched positive systems under dwell-time constraint," *Automatica*, vol. 85, pp. 1–8, 2017.

[6] S. Zhu, Q.-L. Han, and C. Zhang,l_1-gain performance analysis and positive filter design for positive discrete-time markov jump linear systems: A linear programming approach," *Automatica*, vol. 50, no. 8, pp. 2098–2107, 2014.

[7] M. Ogura and V. M. Preciado, "Optimal design of switched networks of positive linear systems via geometric programming," *IEEE Transactions on Control of Network Systems*, vol. 4, no. 2, pp. 213–222, 2017.

[8] S. Huang and J. Shen, "Interval state estimation for positive linear systems under dos attacks," *Journal of the Franklin Institute*, vol. 360, no. 12, pp. 8856–8876, 2023.

[9] C. Briat, "A class of L_1 -to- L_1 and L_∞ -to- L_∞ interval observers for (delayed) markov jump linear systems," *IEEE Control Systems Letters*, vol. 3, no. 2, pp. 410–415, 2019.

[10] X. Chen, M. Chen, J. Shen, and S. Shao, "ℓ_1-induced state-bounding observer design for positive takagi–sugeno fuzzy systems," *Neurocomputing*, vol. 260, pp. 490–496, 2017.

[11] T. B. Nguyen and H.-K. Song, "Relaxed observer-based H_∞-control for markov jump fuzzy systems with incomplete transition probabilities and sensor failures," *Mathematics*, vol. 10, no. 12, 2022.

[12] J. Lian, S. Li, and J. Liu, "T–S fuzzy control of positive markov jump nonlinear systems," *IEEE Transactions on Fuzzy Systems*, vol. 26, no. 4, pp. 2374–2383, 2018.

[13] X. Deng, J. Zhang, and T. Raïssi, "Event-triggered positive l_1-gain non-fragile filter design for positive markov jump systems," *Information Sciences*, vol. 573, pp. 562–584, 2021.

Proceedings of the 3rd Conference on Fully Actuated System Theory and Applications
May 10-12, 2024, Shenzhen, China

Robust Sequential covariance intersection fusion Kalman filters with noise variances uncertainties

Yangyi Song[1], Wenjuan Qi[1]

1. College of Mechanical and Electrical Engineering, Heilongjiang University, Harbin 150080

E-mail: 2015072@hlju.edu.cn

Abstract: This paper consider the robust covariance intersection fusion Kalman filtering problems for steady-state multi-sensor systems with noise variances uncertainties. Based on the conservative upper bounds of noise variances, a fast sequential covariance intersection (SCI) robust Kalman filter is presented, which only require solving the optimization of several one-dimension nonlinear cost functions. And then the robust accuracy relations of these robust Kalman filters are proved. It is proved that the robust accuracies of SCI robust Kalman filters are all higher than that of each local robust Kalman filter. The geometric interpretation of the accuracy relations is given based on the variance ellipses. A simulation example verifies the robustness and the correctness of the theoretical accuracy relations.

Key Words: Multisensor data fusion, Sequential covariance intersection fusion (SCI), Batch covariance intersection (BCI) fusion, Lyapunov equation, Uncertain noise variance

1 Introduction

It is well known that to compute the optimal weights requires to know the cross-covariance among the local Kalman filtering errors [1-3], however, in many practical applications, the variances and cross-covariances of the local filtering errors are unknown or uncertain, or the computation of the cross-covariances is very complex and difficult [4]. In order to overcome the above limitation, the covariance intersection (CI) fusion method has been presented in [5-7] and has been widely applied in many fields, for example, the simultaneous localization and mapping (SLAM) , remote sensing, rocket tracking , spacecraft estimation and vehicle localization and so on. The CI fuser is obtained by the convex combination of the local estimators, and it has the advantages that the fused estimation problems can be solved for multisensor systems with unknown variances and cross-covariances of local filtering errors, and the computation of the cross-covariances is completely avoided. However, its disadvantage is that the conservative upper bounds of the unknown local filtering error variances are assumed to be known, i.e., the consistent estimation problem of the unknown local filtering error variances was not solved.

Based on the batch processing method, the batch covariance intersection (BCI) fusion Kalman filter with exactly known model parameters and noise variances is presented [8], which needs to solve the high-dimensional nonlinear optimization problem, so that a larger computation burden and higher complexity are required. In order to reduce the computation burden and complexity, by the sequential procession method, a sequential covariance intersection (SCI) fusion Kalman filter is presented in [9] for multisensor systems with noise variances to be known exactly.

In this paper, we will focus on the covariance intersection (CI) fused robust Kalman filtering for multisensor systems with uncertainties of noise variances, based on the classical Kalman filtering method and the conservative upper bounds of noise variances, the batch covariance intersection (BCI) fusion robust Kalman filter is presented and its robustness is proved. In order to reduce the complexity and computational burden, a sequential covariance intersection (SCI) fusion robust Kalman filter is proposed based on several recursive two-sensor CI fusion robust Kalman filters, which only requires to solve the optimization of several one-dimension nonlinear cost function [10]. This paper also proves that the robust accuracy of SCI fuser and BCI fuser are higher than that of each local robust Kalman filter, so they have good performance.

The optimal SCI fusion Kalman filter [11] for multisensor system with exactly known noise variances is extended to the robust SCI fusion Kalman filter for multisensor systems with noise variances uncertainties. The deterministic accuracy relations in [11] are extended to the robust accuracy relations. The geometric interpretation of the robust accuracy relations are given based on the variances ellipses and a Monte-Carlo simulation example shows the correctness of the proposed robust accuracy relations.

1.1 Problem Formulation

Consider the steady-state multi-sensor uncertain system with noise variances uncertainties

$$x(t+1)=\Phi x(t)+\Gamma w(t) \tag{1}$$

$$y_i(t)=H_i x(t)+v_i(t), i=1,\cdots,L \tag{2}$$

where t is the discrete time, $x(t)\in R^n$ is the state, L is the number of sensors, $y_i(t)\in R^{m_i}$ is the measurement of the ith subsystem, $w(t)\in R^r$ is the input noise and $v_i(t)\in R^{m_i}$ is the measurement noise of the ith sensor. Φ, Γ and H_i are known constant matrices with appropriate dimensions. Φ is the state transition matrix, Γ is the input transition matrix and H_i stand for the measurement transition matrix.

*This work is supported by the Basic Scientific Research fee foundation of Heilongjiang Provincial Colleges and Universities under Grant 2022-KYYWF-1040.

Assumption 1. $w(t)$ and $v_i(t)$ are uncorrelated white noises with zeros mean and unknown uncertain actual variances $\bar{Q}$ and $\bar{R}_i$,respectively.

$$\mathrm{E}\left[\begin{pmatrix} w(t) \\ v_i(t) \end{pmatrix}\begin{pmatrix} w(k) & v_j(k) \end{pmatrix}^{\mathrm{T}}\right] = \begin{bmatrix} \bar{Q} & 0 \\ 0 & \bar{R}_i\delta_{ij} \end{bmatrix}\delta_{tk} \quad (3)$$

where E denotes the mathematical expectation operator, the superscript T denotes the transpose. δ_{ij} is the Kronecker δ function, $\delta_{ii}=1, \delta_{ij}=0 (i\neq j)$.

Assumption 2. Q and R_i are known conservative upper bounds of $\bar{Q}$ and $\bar{R}_i$, respectively, i.e.

$$\bar{Q}\le Q, \bar{R}_i \le R_i,\ i=1,\cdots,L \quad (4)$$

in the sense that $A\le B$ means that $B-A\ge 0$ is a semi-positive definite matrix.

2 The Robust BCI Fusion Kalman Filters

For the two-sensor uncertain systems with the Assumptions 1-2, applying the CI fused algorithm [12], the CI fusion robust steady-state Kalman filter with the conservative upper bounds Q and R_i of noise variances is presented as following

$$\hat{x}_{CI}(t\mid t) = P_{CI}\left[\omega P_1^{-1}\hat{x}_1(t\mid t) + (1-\omega)P_2^{-1}\hat{x}_2(t\mid t)\right] \quad (5)$$

$$P_{CI} = \left[\omega P_1^{-1} + (1-\omega)P_2^{-1}\right]^{-1}, \omega\in[0,1] \quad (6)$$

where $\hat{x}_i(t\mid t)$ are the actual local robust Kalman filters, the weight ω minimizes the cost function J as

$$\min J = \min_{\omega\in[0,1]} \mathrm{tr}\, P_{CI} = \min_{\omega\in[0,1]} \mathrm{tr}\left\{\left[\omega P_1^{-1} + (1-\omega)P_2^{-1}\right]^{-1}\right\} \quad (7)$$

where the symbol tr denotes the trace of matrix, for the one-dimensional nonlinear cost function(7), the optimal weight ω can be obtained by gold section method or Fibonacci method.

When the number of the sensor is larger than two, i.e. $L\ge 3$. The batch covariance intersection (BCI) fusion robust Kalman filter is presented by the convex combination as

$$\hat{x}_{BCI}(t\mid t) = P_{BCI}\sum_{i=1}^{L}\omega_i P_i^{-1}\hat{x}_i(t\mid t) \quad (8)$$

$$P_{BCI} = \left[\sum_{i=1}^{L}\omega_i P_i^{-1}\right]^{-1}, \sum_{i=1}^{L}\omega_i = 1,\ \omega_i\ge 0 \quad (9)$$

$$\min J = \min_{\omega_i} \mathrm{tr}\, P_{BCI} = \min_{\substack{\omega_i\in[0,1] \\ \omega_1+\cdots+\omega_L=1}} \mathrm{tr}\left\{\left[\sum_{i=1}^{L}\omega_i P_i^{-1}\right]^{-1}\right\} \quad (10)$$

which J can be obtained by "fimincon" function in Matlab. This needs to solve a L dimensional nonlinear convex optimization problem, so that the larger computational burden is required.

The actual BCI fusion filtering error variance $\bar{P}_{BCI} = \mathrm{E}\left[\tilde{x}_{BCI}(t\mid t)\tilde{x}_{BCI}^{\mathrm{T}}(t\mid t)\right]$ is given by

$$\bar{P}_{BCI} = P_{BCI}\left[\sum_{i=1}^{L}\sum_{j=1}^{L}\omega_i P_i^{-1}\bar{P}_{ij}P_j^{-1}\omega_j\right]P_{BCI} \quad (11)$$

$$\bar{P}_{ij} = \Psi_i\bar{P}_{ij}\Psi_j^{\mathrm{T}} + \left[I_n - K_iH_i\right]\Gamma\bar{Q}\Gamma^{\mathrm{T}}\left[I_n - K_jH_j\right]^{\mathrm{T}},\ i\neq j \quad (12)$$

3 The Robust SCI Fusion Kalman Filters

In order to reduce the complexity and computational burden, the sequential covariance intersection (SCI) robust Kalman fuser is presented based on the $L-1$ two-sensor CI fused robust Kalman filters, and it can be realized by a recursive two-sensor CI fusers. Its structure is shown in Fig.1.

Based on the two-sensor CI fused algorithm, the SCI fusion robust steady-state filter with the conservative error variances Q and R_i is presented as follows

$$\begin{aligned}\hat{x}_{CIi}(t\mid t) = P_{CIi}\Big[&\omega_i P_{CI(i-1)}^{-1}\hat{x}_{CI(i-1)}(t\mid t) \\ &+(1-\omega_i)P_{(i+1)}^{-1}\hat{x}_{(i+1)}(t\mid t)\Big]\end{aligned} \quad (13)$$

$$P_{CIi} = \left[\omega_i P_{CI(i-1)}^{-1} + (1-\omega_i)P_{i+1}^{-1}\right]^{-1}, i=1,\cdots,L-1 \quad (14)$$

$$\hat{x}_{SCI}(t\mid t) = \hat{x}_{CI(L-1)}(t\mid t),\ P_{SCI} = P_{CI(L-1)} \quad (15)$$

$$\hat{x}_{CI(0)}(t\mid t) = \hat{x}_1(t\mid t),\ P_{CI(0)}^{-1} = P_1^{-1} \quad (16)$$

and the parameters ω_i is determined by minimizing the performance index J as

$$J = \min_{\omega_i}\mathrm{tr}P_{CIi} = \min_{\omega_i\in[0,1]}\mathrm{tr}\left\{\left[\omega_i P_{CI(i-1)}^{-1} + (1-\omega_i)P_{i+1}^{-1}\right]^{-1}\right\} \quad (17)$$

The optimization problem is equal to the $L-1$ one-dimensional optimization problems (7).

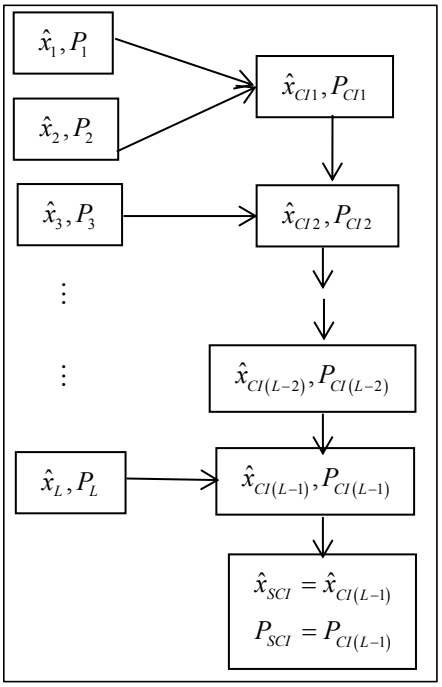

Fig .1 The structure of the SCI fusion robust Kalman filters

4 The Robust Accuracy Analysis

Definition 1. The robust accuracy of a robust Kalman filter is defined as the trace of a minimal or less-conservative upper bound of its actual filtering error variances, while its actual accuracy is defined as the trace of its actual filtering error variance.

The local, BCI and SCI fused Kalman filters have the robustness, and the actual and robust accuracies have following relations.

Theorem 1. The robust accuracy comparison of the local and the fused Kalman filters is given by

$$\overline{P}_i \le P_i, \overline{P}_{BCI} \le P_{BCI}, \overline{P}_{SCI} \le P_{SCI} \tag{18}$$

$$\mathrm{tr}\,\overline{P}_i \le \mathrm{tr}\,P_i, i = 1,\cdots,L,$$

$$\mathrm{tr}\,\overline{P}_{BCI} \le \mathrm{tr}\,P_{BCI}, \mathrm{tr}\,\overline{P}_{SCI} \le \mathrm{tr}\,P_{SCI} \tag{19}$$

$$\mathrm{tr}\,P_{BCI} \le \mathrm{tr}\,P_i, i = 1,\cdots,L \tag{20}$$

$$\mathrm{tr}\,P_{BCI} \le \mathrm{tr}\,P_{SCI} \tag{21}$$

$$\mathrm{tr}\,P_{SCI} \le \mathrm{tr}\,P_i, i = 1,\cdots,L \tag{22}$$

Proof. It is similar to the proof in [11], therefore omitted.

Remark 1. The accuracy relations (19) mean that for all admissible uncertainties of variances satisfying (4), the actual accuracies $\mathrm{tr}\,\overline{P}_\theta$, $\theta = 1,\cdots,L,BCI,SCI$ of the local or fused steady-state Kalman filter are globally controlled by $\mathrm{tr}\,P_\theta$, therefore the robust accuracy $\mathrm{tr}\,P_\theta$ is also called the global accuracy of a robust Kalman filter. The robustness of the local and fused filters means that the robust accuracy $\mathrm{tr}\,P_\theta$ is independent of arbitrarily variances satisfying (4).

Remark 2. Theorem 1 shows that P_i is the minimal upper bound of $\overline{P}_i$ in the matrix inequality sense. $\mathrm{tr}\,P_{BCI}$ is the minimal upper bound of $\mathrm{tr}\,\overline{P}_{BCI}$ in the trace inequality sense. From (21) and (22) yields that $\mathrm{tr}\,\overline{P}_{SCI} \le \mathrm{tr}\,P_{SCI} \le \mathrm{tr}\,P_i$, $i = 1,\cdots,L$, so that $\mathrm{tr}\,P_{SCI}$ is a less-conservative upper bound of $\mathrm{tr}\,\overline{P}_{SCI}$. The smaller $\mathrm{tr}\,P_\theta$ (or $\mathrm{tr}\,\overline{P}_\theta$) means the higher robust (or actual) accuracy. From (19)-(22), we conclude that the robust accuracy of the robust SCI fuser is higher than that of each local robust Kalman filter, and the robust accuracy of the BCI fuser is higher than that of the SCI fuser. The actual accuracies of a robust Kalman filter are higher than its robust accuracy for all admissible uncertainties.

5 Sensitivity Problem

For the SCI fusion robust Kalman filter, the fused schemes are different with respect to different orders of sensors. For example, in the case with $L = 3$, there are three fused structure as shown in Fig.2, the problem is that whether the SCI fused robust accuracy is sensitive with respect to the fused orders of sensors. The following two sensor simulation examples will show that the robust accuracy of the SCI fuser is not very sensitive with respect to the orders of the sensors.

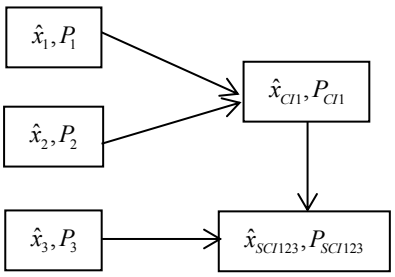

(a) The order 1: SCI123

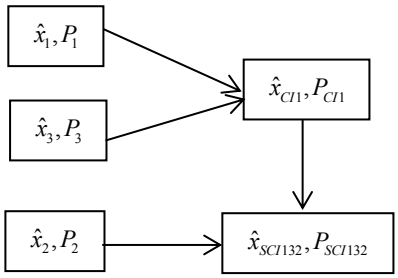

(b) The order 2: SCI132

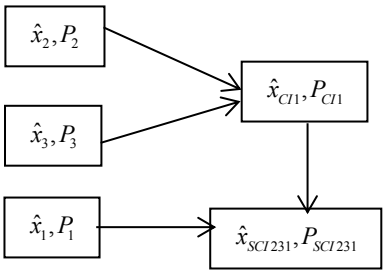

(c) The order 3: SCI231

Fig.2 the fused orders of the SCI fusers in the $L = 3$ case

6 Simulation Examples

Consider a 3-sensor tracking system with noise variances uncertainty

$$x(t+1) = \Phi x(t) + \Gamma w(t) \tag{23}$$

$$y_i(t) = H_i x(t) + v_i(t), i = 1,2,3 \tag{24}$$

$$\Phi = \begin{bmatrix} 1 & T_0 \\ 0 & 1 \end{bmatrix}, \Gamma = \begin{bmatrix} 0.5T_0^2 \\ T_0 \end{bmatrix} \tag{25}$$

$$H_1 = [1 \quad 0], H_2 = I_2, H_3 = [1 \quad 0] \tag{26}$$

where $T_0 = 0.25$ is the sampled period, $x(t) = [x_1(t), x_2(t)]^{\mathrm{T}}$ is the state, $x_1(t)$ and $x_2(t)$ are the position and velocity of target at time tT_0. $y_i(t)$ is the measurement, $w(t)$ and $v_i(t)$ are independent Gaussion white noises with zero mean and unknown variances $\overline{Q}$ and $\overline{R}_i$ respectively, Q and R_i are conservative upper bounds of $\overline{Q}$ and $\overline{R}_i$ satisfying $\overline{Q} \le Q, \overline{R}_i \le R_i$. In the simulation, we take $Q = 1$, $\overline{Q} = 0.8$, $R_1 = 0.8$, $\overline{R}_1 = 0.65$, $R_2 = diag(8, 0.36)$, $\overline{R}_2 = diag(6, 0.25)$, $R_3 = 0.5$, $\overline{R}_3 = 0.45$.

The robust and actual accuracy comparisons are shown in Table 1. From Table1, we see that the SCI fused robust accuracy $\mathrm{tr}\,P_{SCI123}$, $\mathrm{tr}\,P_{SCI132}$ and $\mathrm{tr}\,P_{SCI321}$ are close or equal to the BCI fused robust accuracy $\mathrm{tr}\,P_{BCI}$, and the accuracy of the SCI fuser is not very sensitive with respect to the orders of sensor, and we also see that the actual accuracy of the SCI fuser $\mathrm{tr}\,\overline{P}_{SCI123}$, $\mathrm{tr}\,\overline{P}_{SCI132}$ and $\mathrm{tr}\,\overline{P}_{SCI321}$ are close to or equal to the actual accuracy of the BCI fuser $\mathrm{tr}\,\overline{P}_{BCI}$, they are all higher

than the robust accuracy of each local filter, which verify the steady-state robust and actual accuracy relations (19)-(22).

Table 1. The robust accuracy comparison of local and fused steady-state Kalman filters

$\mathrm{tr}\,P_1$	$\mathrm{tr}\,P_2$	$\mathrm{tr}\,P_3$	$\mathrm{tr}\,P_{BCI}$
0.5538	0.5245	0.4390	0.3602
$\mathrm{tr}\,\bar{P}_1$	$\mathrm{tr}\,\bar{P}_2$	$\mathrm{tr}\,\bar{P}_3$	$\mathrm{tr}\,\bar{P}_{BCI}$
0.4465	0.3815	0.3723	0.1717
$\mathrm{tr}\,P_{SCI123}$	$\mathrm{tr}\,P_{SCI132}$	$\mathrm{tr}\,P_{SCI231}$	
0.3971	0.3648	0.3648	
$\mathrm{tr}\,\bar{P}_{SCI123}$	$\mathrm{tr}\,\bar{P}_{SCI132}$	$\mathrm{tr}\,\bar{P}_{SCI231}$	
0.1759	0.1795	0.1795	

In order to give a geometric interpretation of the accuracy relations, the accuracy comparison of the covariance ellipses is shown in Fig 3-5. From Fig 3-5, we see that the ellipses of the actual variances $\bar{P}_i$ $(i=1,2,3)$ are enclosed in that of the conservative variances P_i, respectively, which verify the robustness (18). The ellipse of actual BCI and SCI fused variance $\bar{P}_{BCI}$ and $\bar{P}_{SCIi}$ $(i=123,132,231)$ is respectively enclosed in that of P_{BCI} and P_{SCIi}, which verifies the robustness (18). Moreover, we see that the ellipse of $\bar{P}_{BCI}$ is close to or equal to $\bar{P}_{SCIi}$, the robust ellipse of P_{BCI} is close to or equal to P_{SCIi}, which means that the robust accuracy of the SCI fuser are close to that of the BCI fuser.

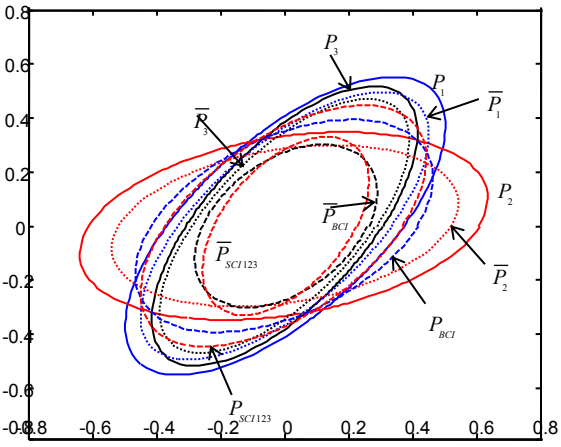

Fig.3 The accuracy comparison of $P_i, i=1,2,3,SCI123,BCI$

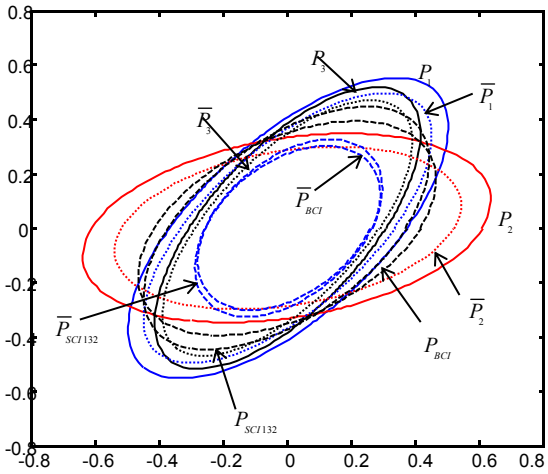

Fig.4 The accuracy comparison of $P_i, i=1,2,3,SCI132,BCI$

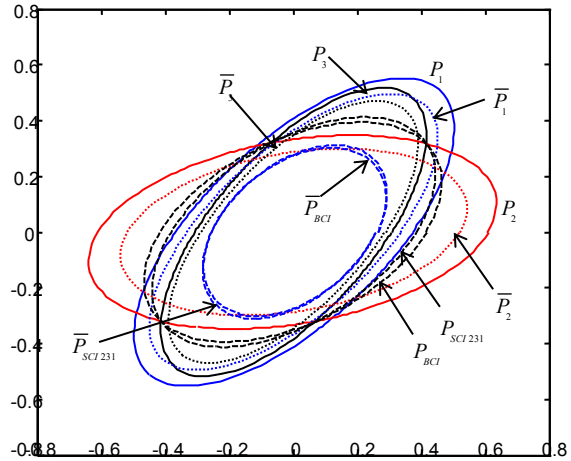

Fig.5 The accuracy comparison of $P_i, i=1,2,3,SCI231,BCI$

In order to verify the above theoretical accuracy relations, taking $N=200$ runs, the mean square error (MSE) curves of the local and fused robust Kalman filters are shown in Fig.6. From Fig.6, we see that when t is sufficiently large, we have the accuracy relations

$$\mathrm{MSE}_i(t) \le \mathrm{tr}P_i, i=1,2,3,BCI,SCI \qquad (27)$$

and the curves of $\mathrm{MSE}_i(t)$ are close to the straight lines corresponding to $\mathrm{tr}\bar{P}_i$, which verifies the robust accuracy relations (19)-(22).

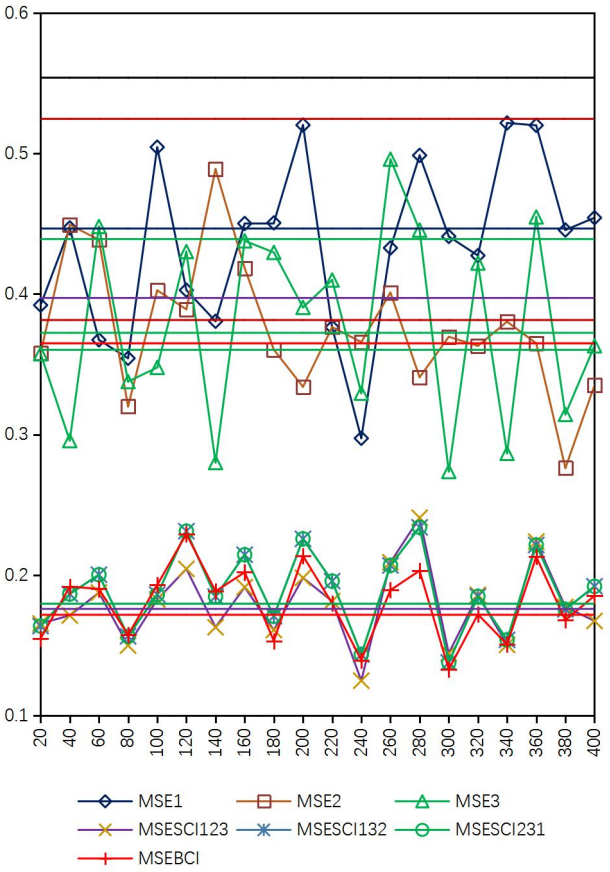

Fig.6 The comparison of $\mathrm{MSE}_i(t)$ and $\mathrm{tr}P_i$, $i=1,2,3,SCI123,SCI132,SCI231,BCI$

7 Conclusions

A minimax robust estimation approach of designing the robust local, BCI and SCI fused Kalman filters has been presented for the multisensor system with uncertain noise variances. Its basic principle is that for the worst-case conservative system with the upper bounds of noise variances, under the unbiased linear minimum variance (ULMV) optimal estimation rule, the conservative local, BCI and SCI fused steady-state Kalman filters with the unavailable conservative measurements were presented. They have the robustness such that their actual filtering error variances or the traces of the variances are guaranteed to have a minimal or less-conservative upper bound.

The concepts of the robustness, robust and actual accuracy have been presented. The robust accuracy relations of the local and fused Kalman filters are proved. It is proved that the robust accuracy of the SCI fuser is lower than that of the BCI fuser, and is higher than that of each local robust Kalman filter.

Acknowledgment

This work is supported by the Basic Scientific Research fee foundation of Heilongjiang Provincial Colleges and Universities under Grant 2022-KYYWF-1040.

References

[1] X. J. Sun, Z. L. Deng, Information fusion Wiener filter for the multisensor multichannel ARMA signals with time-delayed measurements, IET Signal Processing, 3(5): 403-415, 2009.

[2] Yunsheng Fan;Haoyan Zhang;Shuanghu Qiao, Attitude Adaptive Robust Strong Tracking Kalman Filter Based on Unmanned Surface Vehicle Navigational Radar Target Tracking. 2023 35th Chinese Control and Decision Conference (CCDC), 2023, 3056-3061.

[3] Amir H. Abolmasoumi;Mohammad Mohammadian; Lamine Mili, Robust Kalman Filter State Estimation for Gene Regulatory Networks, IEEE/ACM Transactions on Computational Biology and Bioinformatics, 2023,20(2), 1395-1404.

[4] Kai Yu, Lizi Chen, Ke Wu, Yuan Gao, Sequential Inverse Covariance Intersection Fusion Kalman Filter for Networked Systems with Multiplicative Noises and Correlated Noise. 2020 35th Youth Academic Annual Conference of Chinese Association of Automation (YAC), 363-368, 2020.

[5] Q. Guo, S. Y. Chen, H. R. Leung, and S. T. Liu, Covariance intersection based image fusion technique with application to pansharpening in remote sensing, *Information Sciences*, 180: 3434-3443, 2010.

[6] C. Ran, Z. Deng, Robust fusion Kalman estimators for networked mixed uncertain systems with random one-step measurement delays, missing measurements, multiplicative noises and uncertain noise variances, Information Sciences 534, 27-52, 2020.

[7] F. Zheng, S. Derrode and W. Pieczynsk, Semi-supervised optimal recursive filtering and smoothing in non-Gaussian Markov switching models, Signal Processing, 171, 1-10, 2020.

[8] Z.L. Deng, P. Zhang, W.J.Qi, Y.Gao, J.F.Liu, The accuracy comparison of multisensor covariance intersection fuser and three weighting fusers, *Information Fusion*, 14(2): 177-185, 2013.

[9] J.Liang et al., Robust Kalman filtering for two-dimensional systems with multiplicative noises and measurement degradation: The finite-horizon case, Automatica, 96, 166−177, 2018.

[10] W. Q. Liu, X. M. Wang and Z. L. Deng, Robust Kalman estimators for systems with multiplicative and uncertain variance linearly correlated additive white noises, Aerospace Science and Technology 72 , 230-247, 2018.

[11] Zili Deng, Peng Zhang, Wenjuan Qi, Jinfang Liu, Yuan Gao. Sequential covariance intersection fusion Kalman filter. Information Sciences, 189, 293-309, 2012.

Proceedings of the 3rd Conference on Fully Actuated System Theory and Applications
May 10-12, 2024, Shenzhen, China

Time-varying filters for uncertain singular system with random d-step transmission delay and packet dropout

Xinyu Zhang[1], Chenjian Ran[2]

1. Electronic Engineering College, Heilongjiang University, Harbin, 150080, China
E-mail: zhangxinyu9903@163.com

2. Electronic Engineering College, Heilongjiang University, Harbin, 150080, China
E-mail: ranchenjian@163.com

Abstract: Due to the unreliability of communication channels, a packet may be delayed even lost during the transmission. At each moment, the data processing center may receive one or multiple data packets or nothing at all. Therefore, this paper investigates the filters which are applied to uncertain singular system with d-step random transmission delays and packet dropout. Applying the singular value decomposition (SVD) method and the fictitious noise approach, the original singular system is transformed to new standard system only with fictitious noises. Further, the time-varying filters of original state for the singular system are obtained according to the relations of the new and original system. A simulation example about circuits system verifies the correctness and effectiveness of the proposed results.

Key Words: singular system, packet dropout, random transmission delay, Kalman filter

1 Introduction

State estimation [1], also known as filtering, is a fundamental problem in control system theory. Given its importance, state estimation has been extensively studied in the last few decades. Wiener filtering and Kalman filtering [2] are two important ways to solve the optimal filtering problem. Kalman filter is an algorithm that uses the state equation of linear system to optimally estimate the state of the system through the system input and output observation data. Due to its recursive structure and good performance, Kalma filtering has been one of the most popular and widely used method, and is applied in many fields such as communication, navigation, guidance, and control.

Singular system [3], also known as descriptor system, is regarded as one of the effective tools for describing real systems. Singular systems are closer to the practical applications, and after years of development, singular systems have become a popular research direction and an important branch of theory. It is more widely used in the singular perturbation systems, electronic network systems, decision systems, complex large-scale systems, etc. Singular systems have wide applications, including in circuits and systems, because singular systems are more suitable for describing large and complex systems. The state estimation problems of the singular systems have received great attention in the last few years.

Singular systems, because of their inherent characteristics, result in the fact that many methods and approaches dealing with normal state space models cannot be directly used in singular systems. This makes the problem of state estimation for singular systems more complex and has also received extensive attention. However, the development of theoretical studies of singular systems is based on the theory of standard systems. In [4], for the linear stochastic singular system with multiplicative noise and colored additive noises, the optimal time-varying Kalman filtering and prediction problems are addressed. In [5], for the multisensor descriptor systems, three optimal fused descriptor Kalman estimators weighted by block diagonal matrices are given by three different rules to determine the diagonal matrices. The development of theoretical studies of singular systems is based on the theory of standard systems. The main methods of transforming singular systems into standard normal systems include the singular value decomposition (SVD) method by converting the descriptor system into a reduced-order standard system, and full-order estimation method based on the maximum likelihood (ML) estimation method [6]. In this paper, the reduced order filtering method based on singular value decomposition (SVD) is used to deal with the filtering problem of singular system.

In recent years, the problem of estimation in networked control systems and sensor networks has attracted much attention due to its wide range of applications in sensor localization [7], signal processing and control. As we all know, the random transmission delays and packet dropouts occur inevitably during data transmission through communication networks due to the limited communication bandwidth or network congestion. Thus, it is particularly important to consider the impact of this uncertainty on practical engineering applications [8]. For systems with both random delays and packet losses, some estimators have been presented. In Ref. [9], distributed fusion filters are proposed for sensor networks with transmission delay and packet dropout compensation and with fading measurements. In Ref. [10], recursive distributed fusion estimation for multi-sensor systems with multiple random transmission delays and packet dropouts. Due to random delays and packet losses, one or more packets may, or may not, reach the data processing center at each moment. In this paper, assume that the sampling and sending rates of the sensor and the receiving rate of the filter are synchronous and clock driven. In order to avoid network congestion, the packet is sent over the network to the data processing center only once at each moment, and thus a packet can be received at most once. This is a much more common situation in networked systems, and by using a set of Bernoulli distributed random variables, a new model is developed to describe these phenomena.

The structure of this paper is organized as follows. In

Section 2, a singular system is proposed and take Bernoulli variables to describe d-step random transmission delay and packet dropout. In Section 3, the new reduced order singular standard state space model is obtained. In Section 4, we present the time-varying filtering algorithm for the new model. In Section 5, a simulation example about circuits system is provided. Finally, the conclusion is given.

2 Problem Formulation

Consider a linear stochastic uncertain singular system with d step transmission delay and packet dropout:

$$Mx(k+1) = \Phi x(k) + \Gamma w(k), \tag{1}$$

$$z(k) = Hx(k) + v(k), \tag{2}$$

where $x(k) \in R^n$ is the system state, $w(k) \in R^r$ and $v(k) \in R^m$ are the process noise and measurement noise respectively, $z(k) \in R^m$ is the measurement output to be transmitted to the filter through networks, M, Φ and Γ are known constant matrices which have suitable dimensions.

Assume that the sampling and sending rates of the sensor and the receiving rate of the filter are synchronous and clock driven. There exist the bounded d-step transmission delay and possible consecutive packet dropout during data transmission from the sensor to the filter through the network. The idea of d-step transmission delay is similar to the Rice fading, and both mean that the controller/filter can receive the measured data transmitted d times before. Unlike Rice fading, the measured datas received by the filter in this article are constant, and their probability density function do not follow the Rice distribution. In addition, any packet whose transmission delays are more than d steps is considered as being lost. To avoid network congestion, packets on the sensor side are sent only once at a time. Then, the following model for the measurements received by the filter is adopted:

$$y(k) = \begin{bmatrix} \zeta_0(k) z(k) \\ (1-\zeta_0(k-1))\zeta_1(k) z(k-1) \\ \vdots \\ \prod_{i=0}^{d-1} (1-\zeta_i(k-d+i))\zeta_d(k) z(k-d) \end{bmatrix}, \tag{3}$$

where $\zeta_i(k)$, $i = 0, 1, ..., d$ are mutually uncorrelated Bernoulli random variables with known probabilities, and are uncorrelated with other random variables, i.e., $\mathrm{Prob}\{\zeta_i(k) = 1\} = \alpha_i$, $\mathrm{Prob}\{\zeta_i(k) = 0\} = 1 - \alpha_i$, $0 \leqslant \alpha_i \leqslant 1$, $i = 0, 1, ..., d$, where the notation "Prob" denotes the probability, "E" presentes the expectation of random variables.

Remark 1. Model (3) describes the random d-step transmission delays and multiple packet losses in networked systems, in which the packet losses can be consecutive. To further clarify the model, Table 1 shows the data transmission case for $d = 2$. From Table 1, it is observed that $z(3)$ and $z(5)$ are lost, $z(1)$, $z(2)$, $z(7)$, $z(8)$ and $z(10)$ are received on time, $z(4)$ and $z(9)$ are received with one-step delay, $z(6)$ is received with two-step delay. In addition, the estimator receives no data packet at $k = 3$, $k = 4$, $k = 6$ and $k = 9$, and one data packet at $k = 1$, $k = 2$, $k = 5$ and $k = 7$, two data packets at $k = 8$ and $k = 10$. When the estimator does not receive any data, the measurement values are set to zero automatically. The data information in each packet comes from different times, so the estimator cannot add up the received data. Thus, model (3) can describe the phenomena of random transmission delays and packet losses in the networked systems. Furthermore, multiple packets may arrive at the data processing center at the same time.

Remark 2. For the model (3), using the probability distribution, it is easily obtained that the on-time reception rate of a packet is $p_0 = \mathrm{Prob}\{\zeta_0(k) = 1\} = \alpha_0$, the i-step delay rate is $p_i = \prod_{k=0}^{i-1}(1-\alpha_k)\alpha_i$, $1 \leqslant i \leqslant d$ and the packet loss rate is $\sigma = 1 - \sum_{k=0}^{i} p_k$, $i = 1, 2, ..., d$.

The following Assumptions are adopted throughout the whole text.

Assumption 1. M is a singular matrix, $\mathrm{rank}(M) = n_1$, $n_1 < n$, and the system is regular,

$$\det M = 0, \tag{4}$$

where "det" and "rank" denote determinant and rank of the matrix.

Assumption 2. The system is completely observable, for arbitrary complex number s,

$$\mathrm{rank}\begin{bmatrix} sM - \Phi \\ H \end{bmatrix} = n, \mathrm{rank}\begin{bmatrix} M \\ H \end{bmatrix} = n. \tag{5}$$

Assumption 3. $w(k)$ and $v(k)$ are uncorrelated white noises with zero means, and their variances are R and Q.

Assumption 4. The initial state $x(0)$ are uncorrelated with $w(k)$, $v(k)$, and $\zeta_i(k)$, $i = 0, 1, ..., d$ and $\mathrm{E}[x(0)] = \mu_0$ and covariance matrices $\mathrm{E}[(x(0) - \mu_0)(x(0) - \mu_0)^{\mathrm{T}}] = P_0$, where "T" denotes matrix transpose.

3 The New State Space Model

Based on Assumption 1 and Assumption 3, the matrix M is a sigular matrix. Applying singular value decomposition (SVD) method to the state space model, there are nonsingular matrices V and U such that

$$VMU = \begin{bmatrix} M_1 & 0 \\ M_2 & 0 \end{bmatrix}. \tag{6}$$

Table 1: Data transmission in network

k	1	2	3	4	5	6	7	8	9	10
$\zeta_0(k)$	1	1	0	0	0	0	1	1	0	1
$\zeta_1(k)$	0	0	0	0	1	0	0	0	0	1
$\zeta_2(k)$	0	0	0	0	0	0	0	1	0	0
$y(k)$	$\begin{bmatrix} z(1) \\ 0 \\ 0 \end{bmatrix}$	$\begin{bmatrix} z(2) \\ 0 \\ 0 \end{bmatrix}$	$\begin{bmatrix} 0 \\ 0 \\ 0 \end{bmatrix}$	$\begin{bmatrix} 0 \\ 0 \\ 0 \end{bmatrix}$	$\begin{bmatrix} 0 \\ z(4) \\ 0 \end{bmatrix}$	$\begin{bmatrix} 0 \\ 0 \\ 0 \end{bmatrix}$	$\begin{bmatrix} z(7) \\ 0 \\ 0 \end{bmatrix}$	$\begin{bmatrix} z(8) \\ 0 \\ z(6) \end{bmatrix}$	$\begin{bmatrix} 0 \\ 0 \\ 0 \end{bmatrix}$	$\begin{bmatrix} z(10) \\ z(9) \\ 0 \end{bmatrix}$

Define

$$V\Phi U=\begin{bmatrix}\Phi_{11} & 0\\ \Phi_{21} & \Phi_{22}\end{bmatrix},V\Gamma=\begin{bmatrix}\Gamma_1\\ \Gamma_2\end{bmatrix},HU=\begin{bmatrix} H_1 & H_2 \end{bmatrix}. \tag{7}$$

Then there exists

$$x\left(k\right)=U\begin{bmatrix} x_1^{\mathrm{T}}\left(k\right) & x_2^{\mathrm{T}}\left(k\right) \end{bmatrix}^{\mathrm{T}}, \tag{8}$$

where the reduced-order state $x_1(k)\in R^{n_1}$ and $x_2(k)\in R^{n_2}$, n_1+n_2=n. From (1), (2), (7) and (8), the new structure of system (1) and (2) can be obtained as follows:

$$\begin{bmatrix} M_1 & 0\\ M_2 & 0\end{bmatrix}\begin{bmatrix} x_1\left(k+1\right)\\ x_2\left(k+1\right)\end{bmatrix}=\begin{bmatrix}\Phi_{11} & 0\\ \Phi_{21} & \Phi_{22}\end{bmatrix}\begin{bmatrix} x_1\left(k\right)\\ x_2\left(k\right)\end{bmatrix}+\begin{bmatrix}\Gamma_1\\ \Gamma_2\end{bmatrix}w\left(k\right), \tag{9}$$

$$z\left(k\right)=H_1x_1\left(k\right)+H_2x_2\left(k\right)+v\left(k\right). \tag{10}$$

Then, from (7), (8) and assuming that Φ_{22} is non-singular, (9) can be rewritten as

$$\begin{aligned}x_1\left(k+1\right)&=M_1^{-1}\Phi_{11}x_1\left(k\right)+M_1^{-1}\Phi_{12}x_2\left(k\right)\\&\quad+M_1^{-1}\Gamma_1w\left(k\right),\end{aligned} \tag{11}$$

$$x_2\left(k\right)=B_xx_1\left(k\right)+B_ww\left(k\right), \tag{12}$$

with

$$\begin{aligned}B_x&=\Phi_{22}^{-1}\left(M_2M_1^{-1}\Phi_{11}-\Phi_{21}\right),\\B_w&=\Phi_{22}^{-1}\left(M_2M_1^{-1}\Gamma_1-\Gamma_2\right).\end{aligned} \tag{13}$$

Substituting (12) into (10) and (11) yields the new reduced order state space model

$$x_1\left(k+1\right)=A_xx_1\left(k\right)+\Gamma_ww\left(k\right), \tag{14}$$

$$z\left(k\right)=H_xx_1\left(k\right)+H_ww\left(k\right)+v\left(k\right), \tag{15}$$

where

$$A_x=M_1^{-1}\Phi_{11},\Gamma_w=M_1^{-1}\Gamma_1, \tag{16}$$

$$H_x=H_1+H_2B_x,H_w=H_2B_w. \tag{17}$$

In order to avoid the complicated derivation, we introduce some new variables as follows.

Define $\widetilde{\zeta}_i\left(k\right)$ as

$$\widetilde{\zeta}_i\left(k\right)=\zeta_i\left(k\right)-\alpha_i,i=0,1,\cdots,d, \tag{18}$$

and using (18) we can easily have

$$\mathrm{E}\left[\widetilde{\zeta}_i\left(k\right)\right]=0,\mathrm{E}\left[\widetilde{\zeta}_i^2\left(k\right)\right]=\alpha_i\left(1-\alpha_i\right). \tag{19}$$

Define

$$z_{al}\left(k\right)=\prod_{i=0}^{l-1}\left(1-\zeta_i\left(k+i\right)\right)z\left(k\right),l=1,2,\ldots,d, \tag{20}$$

then we have that

$$\begin{aligned}z_{a1}\left(k\right)&=\left(1-\zeta_0\left(k\right)\right)z\left(k\right)\\&=\left(1-\zeta_0\left(k\right)\right)H_xx_1\left(k\right)+\left(1-\zeta_0\left(k\right)\right)H_ww\left(k\right)\\&\quad+\left(1-\zeta_0\left(k\right)\right)v\left(k\right),\end{aligned}$$

$$\begin{aligned}z_{a2}\left(k-1\right)&=\left(1-\zeta_0\left(k-1\right)\right)\left(1-\zeta_1\left(k\right)\right)z\left(k-1\right)\\&=\left(1-\zeta_1\left(k\right)\right)z_{a1}\left(k-1\right),\end{aligned}$$

$$\vdots$$

$$z_{ad}\left(k-d+1\right)=\left(1-\zeta_{d-1}\left(k\right)\right)z_{a(d-1)}\left(k-d+1\right). \tag{21}$$

Substituting (18) and (21) into (3) yields

$$y\left(k\right)=\begin{bmatrix}\zeta_0\left(k\right)z\left(k\right)\\ \zeta_1\left(k\right)z_{a1}\left(k-1\right)\\ \vdots\\ \zeta_d\left(k\right)z_{ad}\left(k-d\right)\end{bmatrix}=\begin{bmatrix}\alpha_0H_xx_1\left(k\right)+\widetilde{\zeta}_0\left(k\right)H_xx_1\left(k\right)+\zeta_0\left(k\right)H_ww\left(k\right)+\zeta_0\left(k\right)v\left(k\right)\\ \alpha_1z_{a1}\left(k-1\right)+\widetilde{\zeta}_1\left(k\right)z_{a1}\left(k-1\right)\\ \vdots\\ \alpha_dz_{ad}\left(k-d\right)+\widetilde{\zeta}_d\left(k\right)z_{ad}\left(k-d\right)\end{bmatrix}. \tag{22}$$

Define the new argumented state and noise as

$$\begin{aligned}x_a\left(k\right)&=\begin{bmatrix} x_1^{\mathrm{T}}\left(k\right) & z_{a1}^{\mathrm{T}}\left(k-1\right) & \cdots & z_{ad}^{\mathrm{T}}\left(k-d\right)\end{bmatrix}^{\mathrm{T}},\\v_a\left(k\right)&=J_1\left(k\right)x_a\left(k\right)+\zeta_0\left(k\right)J_2w_1\left(k\right),\\w_1\left(k\right)&=\begin{bmatrix} w^{\mathrm{T}}\left(k\right) & v^{\mathrm{T}}\left(k\right)\end{bmatrix}^{\mathrm{T}},\end{aligned} \tag{23}$$

with

$$\begin{aligned}J_1\left(k\right)&=\mathrm{diag}\left(\widetilde{\zeta}_0\left(k\right)H_x,\widetilde{\zeta}_1\left(k\right)I_m,\cdots,\widetilde{\zeta}_d\left(k\right)I_m\right),\\J_2&=\begin{bmatrix} H_w^{\mathrm{T}} & 0 & \cdots & 0\\ I_m & 0 & \cdots & 0\end{bmatrix}^{\mathrm{T}}.\end{aligned} \tag{24}$$

From (23) and (24), the measurement $y(k)$ given by (22) can be rewritten as

$$y\left(k\right)=H_ax_a\left(k\right)+v_a\left(k\right), \tag{25}$$

with

$$H_a=\begin{bmatrix}\alpha_0H_x & 0 & \cdots & 0\\ 0 & \alpha_1I_m & \cdots & 0\\ \vdots & \vdots & \ddots & \vdots\\ 0 & 0 & \cdots & \alpha_dI_m\end{bmatrix}. \tag{26}$$

From (13), (21) and the augmented state $x_a(k)$ as in (23), the new augmented state equation can be rewritten as

$$\begin{bmatrix} x_1(k+1) \\ z_{a1}(k) \\ z_{a2}(k-1) \\ \vdots \\ z_{ad}(k-d+1) \end{bmatrix} = \begin{bmatrix} A_x x_1(k) + \Gamma_w w(k) \\ (1-\alpha_0) H_x x_1(k) - \widetilde{\zeta}_0(k) H_x x_1(k) + (1-\zeta_0(k))(H_w w(k) + v(k)) \\ (1-\alpha_1) z_{a1}(k-1) - \widetilde{\zeta}_1(k) z_{a1}(k-1) \\ \vdots \\ (1-\alpha_{d-1}) z_{a(d-1)}(k-d+1) - \widetilde{\zeta}_{d-1}(k) z_{a(d-1)}(k-d+1) \end{bmatrix}. \tag{27}$$

Define

$$\Phi_a = \begin{bmatrix} A_x & \cdots & 0 & 0 \\ (1-\alpha_0) H_x & \cdots & 0 & 0 \\ \vdots & \ddots & \vdots & \vdots \\ 0 & \cdots & (1-\alpha_{d-1}) I_m & 0 \end{bmatrix},$$

$$\begin{aligned} w_a(k) = & J_3(k) x_a(k) + (1-\zeta_0(k)) J_4 w_1(k) \\ & + \zeta_0(k) J_5 w_1(k), \end{aligned}$$

$$J_3(k) = \begin{bmatrix} 0 & \cdots & 0 & 0 \\ -\widetilde{\zeta}_0(k) H_x & \cdots & 0 & 0 \\ \vdots & \ddots & \vdots & \vdots \\ 0 & \cdots & -\widetilde{\zeta}_{d-1}(k) I_m & 0 \end{bmatrix},$$

$$J_4 = \begin{bmatrix} \Gamma_w^{\mathrm{T}} & H_w^{\mathrm{T}} & 0 & \cdots & 0 \\ 0 & I_m & 0 & \cdots & 0 \end{bmatrix}^{\mathrm{T}},$$

$$J_5 = \begin{bmatrix} \Gamma_w^{\mathrm{T}} & 0 & 0 & \cdots & 0 \\ 0 & 0 & 0 & \cdots & 0 \end{bmatrix}^{\mathrm{T}}. \tag{28}$$

From (27) and (28), the new augmented state space model is obtained as

$$x_a(k+1) = \Phi_a x_a(k) + w_a(k). \tag{29}$$

From (25) and (29), the standard state space model is rebuilded with correlated fictitution noises. Then the following key work is to obtain the variance and cross-variance of $w_a(k)$ and $v_a(k)$.

Theorem 1. For the system (29) with Assumptions 3, the state second-order moment $X_a(k) = \mathrm{E}[x_a(k)x_a^{\mathrm{T}}(k)]$ satisfies the following recursive Lyapunov equation:

$$\begin{aligned} X_a(k+1) = & \Phi_a X_a(k) \Phi_a^{\mathrm{T}} + \alpha_0(1-\alpha_0) J_{e1} X_a(k) J_{e1}^{\mathrm{T}} \\ & + \sum_{t=1}^{d-1} \alpha_t(1-\alpha_t) C_{t+1} X_a(k) C_{t+1}^{\mathrm{T}} \\ & + (1-\alpha_0) J_4 Q_{W1} J_4^{\mathrm{T}} + \alpha_0 J_5 Q_{W1} J_5^{\mathrm{T}}. \end{aligned} \tag{30}$$

with

$$\begin{aligned} J_{e1} &= \left[\begin{array}{c|ccc} 0 & -H_x^{\mathrm{T}} & 0 & \cdots \\ \hline 0 & & & \end{array}\right]^{\mathrm{T}}, \\ C_t &= \mathrm{diag}(0, \cdots, -I_m, \cdots, 0), \end{aligned} \tag{31}$$

where the $-\mathrm{I_m}$ in C_t is the $(t+1)$th row block and tth column block of $J_3(k)$, $t = 2, 3, \cdots, d$.

Proof. Using $Q_{W1} = \mathrm{E}[w_1(k)w_1^{\mathrm{T}}(k)]$, we can obtain that

$$Q_{W1} = \mathrm{diag}(R, Q). \tag{32}$$

Based on (31), the stochastic parameter matrix $J_3(k)$ can be rewritten as

$$J_3(k) = \widetilde{\zeta}_0(k) J_{e1} + \sum_{t=1}^{d-1} \widetilde{\zeta}_t(k) C_{t+1}, \tag{33}$$

Substituting (33) into $w_a(k)$ as in (28), we can obtain that

$$\begin{aligned} w_a(k) = & \widetilde{\zeta}_0(k) J_{e1} x_a(k) + \sum_{t=1}^{d-1} \widetilde{\zeta}_t(k) C_{t+1} x_a(k) \\ & + (1-\zeta_{\mathrm{o}}(k)) J_4 w_1(k) + \zeta_{\mathrm{o}}(k) J_5 w_1(k). \end{aligned} \tag{34}$$

Substituting (34) into (29), there is

$$\begin{aligned} x_a(k+1) = & \Phi_a x_a(k) + (1-\zeta_{\mathrm{o}}(k)) J_4 w_1(k) \\ & + \sum_{t=1}^{d-1} \widetilde{\zeta}_t(k) C_{t+1} x_a(k) + \widetilde{\zeta}_0(k) J_{e1} x_a(k) \\ & + \zeta_{\mathrm{o}}(k) J_5 w_1(k). \end{aligned} \tag{35}$$

Since $x_a(k)$, $w_1(k)$ and $\widetilde{\zeta}_t(k)(t = 0, 1, \cdots, d)$ are uncorrelated with each other, and $w_1(k)$, $\widetilde{\zeta}_t(k)(t = 0, 1, \cdots, d)$ are white noise with variance Q_{W1}, $\alpha_t(1-\alpha_t)$, $t = 0, 1, \cdots, d$. Using (35) and $X_a(k+1) = \mathrm{E}[x_a(k+1)x_a^{\mathrm{T}}(k+1)]$ yield (30). This proof is completed.

Based on Theorem 1 and (34), it is easily obtained $Q_W(k) = \mathrm{E}[w_a(k)w_a^{\mathrm{T}}(k)]$ as follows:

$$\begin{aligned} Q_W(k) = & \alpha_0(1-\alpha_0) J_{e1} X_a(k) J_{e1}^{\mathrm{T}} + \alpha_0 J_5 Q_{W1} J_5^{\mathrm{T}} \\ & + \sum_{t=1}^{d-1} \alpha_t(1-\alpha_t) C_{t+1} X_a(k) C_{t+1}^{\mathrm{T}} \\ & + (1-\alpha_0) J_4 Q_{W1} J_4^{\mathrm{T}}. \end{aligned} \tag{36}$$

Similar to $J_3(k)$ in (33), the stochastic parameter matrix $J_1(k)$ in (24) can be rewritten as

$$J_1(k) = \widetilde{\zeta}_0(k) J_{e2} + \sum_{l=1}^{d} \widetilde{\zeta}_l(k) C_{l+1}, \tag{37}$$

with

$$\begin{aligned} J_{e2} &= \mathrm{diag}(H_x, 0, \cdots, 0), \\ C_l &= \mathrm{diag}(0, \cdots, I_m, \cdots, 0), \end{aligned} \tag{38}$$

where the $\mathrm{I_m}$ in C_l is the lth row block and lth column block of $J_1(k)$, $l = 2, 3, \cdots, d+1$.

Substituting (38) into $v_a(k)$ as in (23), we can obtain that

$$\begin{aligned} v_a(k) = & \widetilde{\zeta}_0(k) J_{e2} x_a(k) + \sum_{l=1}^{d} \widetilde{\zeta}_l(k) C_{l+1} x_a(k) \\ & + \zeta_0(k) J_2 w_1(k). \end{aligned} \tag{39}$$

Since $x_a(k)$, $w_1(k)$ and $\widetilde{\zeta}_t(k)(t=0,1,\cdots,d)$ are uncorrelated with each other. Using (39) and $Q_V(k)$= E$[v_a(k)$ $v_a^{\mathrm{T}}(k)]$, yields

$$\begin{aligned} Q_V(k) =& \alpha_0(1-\alpha_0) J_{e2} X_a(k) J_{e2}^{\mathrm{T}} + \alpha_0 J_2 Q_{W1} J_2^{\mathrm{T}} \\ &+ \sum_{l=1}^{d} \alpha_l(1-\alpha_l) C_{l+1} X_a(k) C_{l+1}^{\mathrm{T}}. \end{aligned} \tag{40}$$

Then using $S_{WV}(k)$=E$[w_a(k)v_a^{\mathrm{T}}(k)]$, we can obtain

$$\begin{aligned} S_{WV}(k) =& \alpha_0(1-\alpha_0) J_{e1} X_a(k) J_{e2}^{\mathrm{T}} + \alpha_0 J_5 Q_{W1} J_2^{\mathrm{T}} \\ &+ \sum_{t=1}^{d-1} \alpha_t(1-\alpha_t) C_{t+1} X_a(k) C_{t+1}^{\mathrm{T}}. \end{aligned} \tag{41}$$

4 The Time-varying filter for the Singular System

In this section, we derive the linear time-varying filter for the singular system (1) - (3).

Theorem 2. Under Assumptions 1-4, the time-varying filter for singular system (1) - (3) could be obtained as

$$\widehat{x}(k|k) = U_{01}\widehat{x}_a(k|k) + U_{02}\widehat{w}_a(k|k), \tag{42}$$
$$\widehat{x}_a(k|k) = \Phi_a\widehat{x}_a(k-1|k-1) + K(k)\varepsilon(k), \tag{43}$$
$$\widehat{w}_a(k|k) = K_w(k)\varepsilon(k), \tag{44}$$
$$K_w(k) = S_{WV}(k) Q_\varepsilon^{-1}(k), \tag{45}$$
$$\varepsilon(k) = y(k) - H_a\Phi_a\widehat{x}_a(k-1|k-1), \tag{46}$$
$$K(k) = P(k|k-1) H_a^{\mathrm{T}} Q_\varepsilon^{-1}(k), \tag{47}$$
$$Q_\varepsilon(k) = H_a P(k|k-1) H_a^{\mathrm{T}} + Q_V(k), \tag{48}$$

$$\begin{aligned} P(k|k) =& \Phi_a P(k-1|k-1)\Phi_a^{\mathrm{T}} + Q_W(k-1) \\ &- K(k) H_a \Phi_a P(k-1|k-1)\Phi_a^{\mathrm{T}} \\ &- K(k) H_a Q_W(k-1), \end{aligned} \tag{49}$$

$$\begin{aligned} P_{wa}(k|k) =& K_w(k) Q_V(k) K_w^{\mathrm{T}}(k) - K_w(k) S_{WV}^{\mathrm{T}}(k) \\ &+ K_w(k) H_a P(k|k-1) H_a^{\mathrm{T}} K_w^{\mathrm{T}}(k) \\ &+ Q_W(k) - S_{WV}(k) K_w^{\mathrm{T}}(k), \end{aligned} \tag{50}$$

and the filtering error variance is given as

$$\begin{aligned} P_x(k|k) =& U_{01} P(k|k) U_{01}^{\mathrm{T}} + U_{02} P_{wa}(k) U_{02}^{\mathrm{T}} \\ &- U_{01} K(k) S_{WV}^{\mathrm{T}}(k) U_{02}^{\mathrm{T}} \\ &- U_{02} S_{WV}(k) K^{\mathrm{T}}(k) U_{01}^{\mathrm{T}}, \end{aligned} \tag{51}$$

where

$$\begin{aligned} U_{01} &= U \begin{bmatrix} I_{n1} & (0)_{n_1\times m} & (0)_{n_1\times m} \\ B_x & (0)_{r\times m} & (0)_{r\times m} \end{bmatrix}, \\ U_{02} &= U \begin{bmatrix} (0)_{n_1\times r} & (0)_{n_1\times m} & (0)_{n_1\times m} \\ B_w & (0)_{r\times m} & (0)_{r\times m} \end{bmatrix}, \end{aligned} \tag{52}$$

$Q_W(k)$ and $S_{WV}(k)$ is presented by (36) and (41).

Proof. Applying projection theory, we easily have

$$\begin{aligned} \widehat{x}_a(k|k) =& \mathrm{E}\left\{x_a(k)\varepsilon^{\mathrm{T}}(k)\right\}\left[\mathrm{E}\left\{\varepsilon(k)\varepsilon^{\mathrm{T}}(k)\right\}\right]^{-1}\varepsilon(k) \\ &+ \Phi_a\widehat{x}_a(k-1|k-1), \end{aligned} \tag{53}$$

$$\begin{aligned} \widehat{w}_a(k|k) =& \mathrm{E}\left\{w_a(k)\varepsilon^{\mathrm{T}}(k)\right\}\left[\mathrm{E}\left\{\varepsilon(k)\varepsilon^{\mathrm{T}}(k)\right\}\right]^{-1}\varepsilon(k) \\ &+ \widehat{w}_a(k|k-1). \end{aligned} \tag{54}$$

The innovation variance $Q_\varepsilon(k)$, the gain matrix $K(k)$ and $K_w(k)$ are defined as

$$Q_\varepsilon(k) = \mathrm{E}\left[\varepsilon(k)\varepsilon^{\mathrm{T}}(k)\right], \tag{55}$$
$$K(k) = \mathrm{E}\left[x_a(k)\varepsilon^{\mathrm{T}}(k)\right] Q_\varepsilon^{-1}, \tag{56}$$
$$K_w(k) = \mathrm{E}\left[w_a(k)\varepsilon^{\mathrm{T}}(k)\right] Q_\varepsilon^{-1}. \tag{57}$$

Then, substituting $\widehat{w}_a(k|k-1)=0$, (55), (56) and (57) into (53) and (54) leads to (43) and (44).

From the definition of the innovation, it follows that

$$\varepsilon(k) = y(k) - \widehat{y}(k|k-1) = y(k) - H_a\widehat{x}_a(k|k-1). \tag{58}$$

Substituting $\widehat{x}_a(k|k-1) = \Phi_a\widehat{x}_a(k-1|k-1)$ into (58) yields (46). Since $\widetilde{x}_a(k|k-1)$, $\widehat{x}_a(k|k-1)$ and $v_a(k)$ are uncorrelated with each other. Substituting (25) and (58) into (55) yields (48). Then substituting (48) into (56) and (57) yields (47) and (45).

The filtering and prediction error are given as $\widetilde{x}_a(k|k) = x_a(k) - \widehat{x}_a(k|k)$ and $\widetilde{x}_a(k|k-1) = x_a(k) - \widehat{x}_a(k|k-1)$. Since $\widetilde{x}_a(k|k)$ is uncorrelated with $w_a(k)$. Applying $P(k|k)$= E$[\widetilde{x}_a(k|k)\,\widetilde{x}_a^{\mathrm{T}}(k|k)]$ and $P(k|k-1)$=E$[\widetilde{x}_a(k|k-1)\widetilde{x}_a^{\mathrm{T}}(k|k-1)]$ can obtain

$$P(k|k-1) = \Phi_a P(k-1|k-1)\Phi_a^{\mathrm{T}} + Q_W(k-1), \tag{59}$$

$$\begin{aligned} P(k|k) =& P(k|k-1) + K(k) H_a P(k|k-1) H_a^{\mathrm{T}} K^{\mathrm{T}}(k) \\ &- P(k|k-1) H_a^{\mathrm{T}} K^{\mathrm{T}}(k) - K(k) H_a P(k|k-1) \\ &+ K(k) Q_V(k) K^{\mathrm{T}}(k). \end{aligned} \tag{60}$$

Substituting (59) into (60) yiels (49). Since $\widetilde{x}_a(k|k-1)$ is uncorrelated with $w_a(k)$ and $v_a(k)$, using (44), (46) and $P_{wa}(k|k) = \mathrm{E}[\widetilde{w}_a(k|k)\widetilde{w}_a^{\mathrm{T}}(k|k)]$ yields (50).

From the definitions of $x_a(k)$ and $w_a(k)$ could obtain that

$$\begin{aligned} x_1(k) &= \begin{bmatrix} I_{n_1} & (0)_{n_1\times m} & (0)_{n_1\times m} \end{bmatrix} x_a(k), \\ w(k) &= \begin{bmatrix} I_r & (0)_{r\times m} \end{bmatrix} w_a(k). \end{aligned} \tag{61}$$

From (12), (8) could deduce that

$$x(k) = U_{01} x_a(k) + U_{02} w_a(k), \tag{62}$$

where U_{01} and U_{02} is defined as (52). Substituting (61) into (62) and taking projection yields (42). Subtracting (42) from (62), the filtering error of (42) is given as

$$\widetilde{x}(k|k) = x(k) - \widehat{x}(k|k) = U_{01}\widetilde{x}_a(k|k) + U_{02}\widetilde{w}_a(k). \tag{63}$$

Therefore, we can obtain (51) with $P_x(k|k)$ = E$[\widetilde{x}(k|k)\widetilde{x}^{\mathrm{T}}(k|k)]$, i.e.,

$$\begin{aligned} P_x(k|k) =& \mathrm{E}\left[U_{01}\widetilde{x}_a(k|k)\,\widetilde{x}_a^{\mathrm{T}}(k|k)\,U_{01}^{\mathrm{T}}\right] \\ &+ \mathrm{E}\left[U_{02}\widetilde{w}_a(k)\,\widetilde{w}_a^{\mathrm{T}}(k)\,U_{02}^{\mathrm{T}}\right] \\ &+ \mathrm{E}\left[U_{01}\widetilde{x}_a(k|k)\,\widetilde{w}_a^{\mathrm{T}}(k)\,U_{02}^{\mathrm{T}}\right] \\ &+ \mathrm{E}\left[U_{02}\widetilde{w}_a(k)\,\widetilde{x}_a^{\mathrm{T}}(k|k)\,U_{01}^{\mathrm{T}}\right]. \end{aligned} \tag{64}$$

Since $w_a(k)$ is uncorrelated with $x_a(k)$ and $\widehat{x}_a(k|k-1)$, $\widetilde{x}_a(k|k)$ is uncorrelated with $\widehat{w}_a(k|k)$. Using (44) and (58), $P_{xw}(k|k) = \mathrm{E}\left[U_{01}\widetilde{x}_a(k|k)\,\widehat{w}_a^{\mathrm{T}}(k)\,U_{02}^{\mathrm{T}}\right]$ can be rewritten as

$$\begin{aligned} P_{xw}(k|k) &= \mathrm{E}\left[U_{01}\widetilde{x}_a(k|k)\left(w_a(k)-\widehat{w}_a(k|k)\right)^{\mathrm{T}}U_{02}^{\mathrm{T}}\right] \\ &= \mathrm{E}\left[U_{01}\widetilde{x}_a(k|k)\,w_a^{\mathrm{T}}(k)\,U_{02}^{\mathrm{T}}\right] \\ &= \mathrm{E}\left[U_{01}\left(x_a(k)-\widehat{x}_a(k|k)\right)w_a^{\mathrm{T}}(k)\,U_{02}^{\mathrm{T}}\right] \\ &= -\mathrm{E}\left[U_{01}K(k)\,v_a(k)\,w_a^{\mathrm{T}}(k)\,U_{02}^{\mathrm{T}}\right] \\ &= -U_{01}K(k)\,S_{WV}^{\mathrm{T}}(k)\,U_{02}^{\mathrm{T}}. \end{aligned} \tag{65}$$

Substituting (65) into (64) yields (51). This proof is completed.

Corollary Under assumptions 3 and 4, it is assumed that the system (1)-(3) is observable and controllable. H_a, $Q_V^{-1}(k)$ and Φ_a are bounded. Take any two different initial values $\widehat{x}^{(i)}(0|0)$ and $P^{(i)}(0|0)$ $(i = 1, 2)$ of the Kalman filter. If the observation datas $y(k)$ of the filter are bounded, then the Kalman filter is asymptotically stable, i.e., $\|\widehat{x}^{(1)}(k|k) - \widehat{x}^{(2)}(k|k)\| \to 0, t \to \infty$.

5 Simulation Example

Taking the circuits system presented in reference [5] into consideration. Define the state $x(k) = [u_{e_1}(k), u_{e_2}(k), i_1(k), i_2(k)]^{\mathrm{T}}$, the symbol $u_e(k)$ represents the voltage source which is considered as the control input at time k, $i(k)$ is the electric current of the voltage and the amperage of the currents flowing over it. $w(k)$ and $v(k)$ are the white noise with zero means and variance R_w,Q_v.

According to the Euler's approximation, we can get that the state space model (1)-(3) have parameter matrices as

$$\Gamma = \begin{bmatrix} 0 & 0 & 0 & -1 \end{bmatrix}^{\mathrm{T}}, H = \begin{bmatrix} 0 & 1 & 0 & 0 \end{bmatrix}, \tag{66}$$

$$M = \begin{bmatrix} C_1 & 0 & 0 & 0 \\ 0 & C_2 & 0 & 0 \\ 0 & 0 & -L & 0 \\ 0 & 0 & 0 & 0 \end{bmatrix}, D = \begin{bmatrix} 0 & 0 & 0 & 1 \\ 0 & 0 & 1 & 0 \\ -1 & 1 & 0 & 0 \\ 1 & 0 & R & R \end{bmatrix}, \tag{67}$$

$$\Phi = M + T_0 D. \tag{68}$$

In simulation, we take $u_e(k) = 0$, $R = 4\Omega$, $C_1 = 2m\mathrm{F}$, $C_2 = 4m\mathrm{F}$, $L = 1m\mathrm{H}$, $R_w = 0.6$. $Q_v = 2.22$, $T_0 = 0.09$ and $\alpha_0 = \alpha_1 = \alpha_2 = 0.9$, $d = 2$. The simulation results are shown in Fig.1 and Fig.2.

Fig.1 gives the curves of time-varying filter $\widehat{x}_3(k|k)$ of the $x_3(k)$. From Fig.1, the every component of time-varying filter can effectively follow the true state component $x_3(k)$.

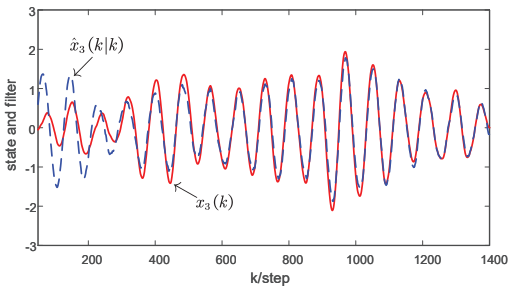

Fig. 1: State curves of $x_3(k)$ and $\widehat{x}_3(k|k)$.

Taking $\rho = 100$ Monte Carlo simulation runs. The mean square error curves is shown in Fig.2. In Fig.2, $MSE(k|k)$ respresents the mean squared error of time-varying filter, $trP(k|k)$ denotes the trace of the filtering error variance. From this figure, the effectiveness of the presented algorithm in this paper is shown.

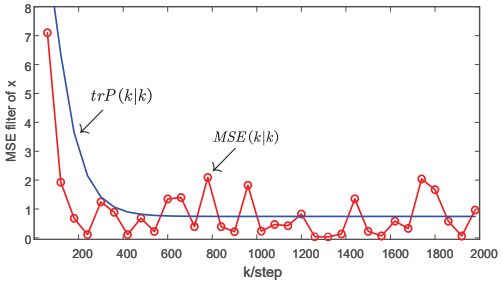

Fig. 2: MSE curves of time-varying filter.

6 Conclusion

In this paper, the time-varying filtering problem has been solved for the uncertain singular system with d-step random transmission delays and packet dropout. A new standard system is presented by using singular value decomposition (SVD) approach and the fictitious noise approach. Then based on this system, the time-varying filters are presented.

References

[1] F. Yang, L. Shi, Y. Liang, and L. Zheng, "Global state estimation under sequential measurement fusion for clustered sensor networks with cross-correlated measurement noises," *Automatica*, p. 142, 2022.

[2] R. E. Kalman, "A new approach to linear filtering and prediction problems," *Journal of Basic Engineering*, vol. 82D, pp. 35–45, 1960.

[3] Y. Xk and J. Li, "Optimal filtering and a smoothing algorithm for a singular system with a complex stochastic uncertain parameter matrix," *Circuits and Systems II: Express Briefs, IEEE Transactions on*, vol. PP, no. 99, pp. 780–784, 2019.

[4] C. Liu, Y. Dou, and C. Ran, "Optimal time-varying kalman filter and predictor for the descriptor system with multiplicative noise and colored noises," in *2020 Chinese Control And Decision Conference (CCDC)*, 2020, pp. 3913–3918.

[5] C. Ran, S. Sun, and Y. Dou, "Wmf reduced-order robust estimators for multisensor descriptor systems," *IET Control Theory and Applications*, vol. 12, no. 16, pp. 2232–2244, 2018.

[6] W. Liu and C. Ran, "Robust time-varying kalman predictor for descriptor system with uncertain-variance noise and packet dropout," in *2021 33rd Chinese Control and Decision Conference (CCDC)*, 2021, pp. 6443–6448.

[7] X. Fu, X. Song, X. Liu, and M. Zhang, "Distributed state estimation with state equality constraints in the presence of packet dropping," *Applied mathematics and computation*, 2023.

[8] F. Cacace, F. Conte, M. D'Angelo, A. Germani, and G. Palombo, "Filtering linear systems with large time-varying measurement delays," *Automatica*, vol. 136, p. 110084, 2022.

[9] H. Jin and S. Sun, "Distributed filtering for sensor networks with fading measurements and compensations for transmission delays and losses," *Signal Processing*, vol. 190, 2022.

[10] Y. Wei and S. Sun, "Recursive distributed fusion estimation for multi-sensor systems with missing measurements. multiple random transmission delays and packet losses," *Signal Processing*, vol. 204, p. 108839, 2023.

Proceedings of the 3rd Conference on Fully Actuated System Theory and Applications
May 10-12, 2024, Shenzhen, China

PMSM Speed Control Based on Fully Actuated Systems Theory

Fangyi Quan[1,2], Junfang Fan[1,2], Sixing Zhang[1], Yi Ji[1], Shiwei Chen[3]

1. School of Automation, Beijing Information Science and Technology University, Beijing 100192, China
E-mail: 2022020489@bistu.edu.cn

2. Key Laboratory of High Dynamic Navigation Technology, Beijing Information Science and Technology University, Beijing 100192
E-mail: wyhtif@bistu.edu.cn

3. School of Aerospace Engineering, Beijing Institute of Technology, Beijing 100081, China
E-mail: 3220225003@bit.edu.cn

Abstract: To increase the control method diversity of permanent magnet synchronous motor (PMSM) servo control system, and improve the dynamic response performance of speed and anti-disturbance ability, this paper proposes a control method for PMSM based on fully actuated systems theory (FAST) and applies it to the speed control of PMSM. After analyzing the mathematical model of PMSM satisfies with fully actuated characteristic, the fully actuated control method applied to PMSM is proposed according to FAST, the feedback controller and compensation controller are designed respectively. The eigenvalues of the pole assignment matrix of the system are set to conjugate form, and the effects of the real and imaginary parts of the conjugate eigenvalues on the performance of the control system are verified by simulation. Compared with PI control and sliding mode control for different time-varying disturbances, simulation results show that the proposed method has high design flexibility and strong robustness.

Key Words: Fully actuated systems theory, Permanent magnet synchronous motor, Speed control, Controller design

1 Introduction

Permanent magnet synchronous motor (PMSM) has the characteristics of high power factor, small size, high reliability and low vibration noise. It is widely used in intelligent manufacturing, CNC machine tools, new energy vehicles, energy generation and aerospace. For PMSM vector control, the traditional control method is PI control, its design is simple and can be effectively applied to practical engineering. Since PMSM models have strong coupling, nonlinear, easy to be affected by parameter perturbation and external disturbance, PI control cannot achieve high precision anti-disturbance performance.

With more applications of PMSM, high-performance PMSM control methods are urgently needed. At present, the modern control theory methods applied to PMSM include sliding mode variable structure control, active disturbance rejection control, predictive control and so on. Sliding mode control (SMC) improves the anti-disturbance performance and control accuracy of the system, but it has some shortcomings such as controller chattering and less smooth convergence process. Active disturbance rejection control has good control performance for PMSM parameter perturbation and load variation, but the differentiator controller will be affected by noise and has shortcomings in time response. A PI controller parameter self-tuning and optimization method based on the combination of model and rule was proposed in [1] to address the issue wherein the PI controller parameter self-tuning depends on the accuracy of motor parameters and system model. An adaptive sliding mode control method based on neural networks for PMSM was introduced in [2]. Combining the advantages of sliding mode control and neural networks, this method has excellent dynamic performance and robustness. A fast super twisting sliding mode control for PMSM was proposed in [3], which address the shortcomings of the classical super twisting algorithm, such as slow convergence speed and the dependency on disturbance boundary information for parameter selection. A model-free predictive current control was mentioned in [4], which established a super-local model of PMSM and combined model predictive control with model-free control. The traditional control method and optimal control algorithm are combined in the above research, achieving good results of PMSM control.

Duan[5] proposed a parameterization high-order fully actuated control method, and introduced a method to transform nonlinear systems into pseudo-linear systems. The feedback control law of pseudo-linear systems was designed, so that nonlinear closed-loop systems were transformed into time-invariant linear systems with specific structures. Controllers for linear and nonlinear parts of the physical model of the controlled system are designed separately, which reduced the difficulty of designing control commands and ensured the integrity of the physical model. Parameter design method can configure the system's degree of freedom, and design the characteristic polynomial matrix of the closed-loop system to achieve the desired performance, meeting the requirements of system control performance. A method of pseudo-linearization for nonlinear systems was proposed by Duan[7], which directly transformed them into linear time-invariant systems. This transformation offered high design flexibility and the capability to autonomously configure the closed-loop poles of the system. A fully actuated control system approach was applied in [9], tackling the attitude control problem of a flexible spacecraft. A novel integrated guidance and control design approach for

This work is supported by National Natural Science Foundation of China Grant (52272358), Young Elite Scientist Sponsorship Program By Cast (YESS20230098), Beijing Association for Science and Technology Youth Talent Support Program Grant (BYESS2023310), and Project of Construction and Support for high-level Innovative Teams of Beijing Municipal Institutions (BPHR20220123).

the guidance control system in intercepting highly maneuverable targets during sliding-turn missile interception was proposed in [10], combining the fully actuated systems with backstepping methods. A parameter-adaptive synchronous control strategy was introduced in [11] within the context of hydraulic machine tool control. This strategy, based on the fully actuated systems methods, involved designing parameterized controllers to attain stability of the closed-loop system. The application of high-order fully actuated system methods to nonlinear model predictive control and tracking optimization is carried out in [12]. The fully actuated characteristics are utilized to eliminate the nonlinear dynamics of the system, and the nonlinear optimization problems are equivalently transformed into a series of easily linear convex optimization problems. The FAST is currently widely applied in various control models, yielding promising results in theoretical validation.

This paper builds on the fully actuated systems theory and introduces a novel approach to speed control for PMSM. It compares the motor speed response and disturbance rejection capability with PI and SMC control for PMSM. Through simulations, it validates the effectiveness of the proposed method in controlling PMSM.

2 The Mathematical Model of PMSM.

This model is based on a surface-mounted PMSM, with its $dq-$axis equivalent inductance satisfying $L_d = L_q$. To simplify the analysis, the following assumptions are made:

1. Neglect the effects of core magnetic saturation, hysteresis, and eddy currents on the motor.
2. The stator winding produces a sinusoidal distribution of the magnetic field along with the permanent magnet, with a 120° electrical phase difference between the three winding phases.
3. Disregard the damping effects on the rotor and the permanent magnets.

In $dq-$axis coordinate system, the mathematical model for a PMSM satisfies $i_d = 0$, and its vector control is as follows:

$$\begin{cases} u_d = R_s i_d + L_d \dfrac{\mathrm{d}i_d}{\mathrm{d}t} - L_q \omega i_q \\ u_q = R_s i_q + L_q \dfrac{\mathrm{d}i_q}{\mathrm{d}t} + L_d \omega i_d + \omega \psi_{\mathrm{f}} \end{cases} \tag{1}$$

$$T_{\mathrm{e}} = \frac{3}{2} p \psi_{\mathrm{f}} i_q \tag{2}$$

$$K_{\mathrm{t}} = \frac{3}{2} p \psi_{\mathrm{f}} \tag{3}$$

$$J \frac{\mathrm{d}\omega}{\mathrm{d}t} = T_{\mathrm{e}} - B_\eta \omega - T_{\mathrm{L}} \tag{4}$$

$$\frac{\mathrm{d}\theta}{\mathrm{d}t} = \omega \tag{5}$$

where u_d, u_q and i_d, i_q are the voltages and currents of $dq-$axis respectively; R_s is the stator resistance; p is the pole number; ω is the rotor mechanical angular speed, and θ is the rotor mechanical angular position; T_{e} and T_{L} are electromagnetic torque and load torque respectively; B_η is the viscous damping coefficient; K_{t} is torque coefficient; ψ_{f} is the magnetic flux of the permanent magnet.

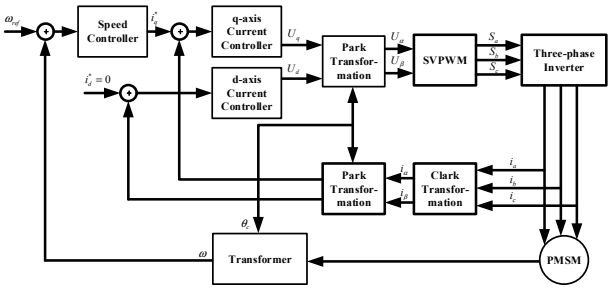

Fig. 1: Block Diagram of PMSM Control System

3 Controller Design of Second-order Fully Actuated Systems

Consider a second-order nonlinear system model:

$$\begin{aligned} A_2(\theta, x, \dot{x})\ddot{x} + A_1(\theta, x, \dot{x})\dot{x} + A_0(\theta, x, \dot{x})x + \\ \xi(\theta, x, \dot{x}) = B(\theta, x, \dot{x})u \end{aligned} \tag{6}$$

where $A_2(\theta, x, \dot{x})$, $A_1(\theta, x, \dot{x})$, $A_0(\theta, x, \dot{x}) \in \mathbb{R}^{n\times n}$ are system matrixes, $\ddot{x}, \dot{x}, x \in \mathbb{R}^n$ are state vectors, $\theta \in \mathbb{R}^n$ is parameter vector, $B(\theta, x, \dot{x}) \in \mathbb{R}^{n\times n}$ is system input matrix, $\xi(\theta, x, \dot{x}) \in \mathbb{R}^n$ is a parameter vector, and $u \in R^n$ is control law. If the equation satisfies assumptions of fully-actuated systems theory in [6], a controller can be designed for the system model to transform the corresponding closed-loop system into a linear time-invariant system with the desired output.

Design the following controller for system (6):

$$u = u_c + u_f \tag{7}$$

Due to the presence of the nonlinear term $\xi(\theta, x, \dot{x})$ in the system, to conform it to pseudolinear system characteristics, u_c is primarily used to compensate and eliminate the impact brought by the inherent nonlinear terms in the system design.

$$u_c = B^{-1}(\theta, x, \dot{x})\xi(\theta, x, \dot{x}) \tag{8}$$

The feedback controller u_f is used to stabilize the system.

$$u_f = K(\theta, x, \dot{x})X(\theta, x, \dot{x}) + v \tag{9}$$

$$\begin{bmatrix}\dot{x}\\ \ddot{x}\end{bmatrix}=A_c(\theta,x,\dot{x})\begin{bmatrix}x\\ \dot{x}\end{bmatrix}+B_c(\theta,x,\dot{x})v \tag{10}$$

$$A_c=\begin{bmatrix}0 & I_n\\ -A_2^{-1}A_0^c & -A_2^{-1}A_1^c\end{bmatrix},$$

$$B_c(\theta,x,\dot{x})=\begin{bmatrix}0\\ A_2^{-1}(\theta,x,\dot{x})B(\theta,x,\dot{x})\end{bmatrix},$$

$$A_0^c(\theta,x,\dot{x})=A_0(\theta,x,\dot{x})-B(\theta,x,\dot{x})K_0(\theta,x,\dot{x}),$$

$$A_1^c(\theta,x,\dot{x})=A_1(\theta,x,\dot{x})-B(\theta,x,\dot{x})K_1(\theta,x,\dot{x})$$

where $K=[K_0(\theta,x,\dot{x})\quad K_1(\theta,x,\dot{x})]\in\square^{n\times 2r}$ is feedback gain matrix, $X=[x\quad \dot{x}\ ]^T\in\square^{2n}$ is system state vector, v represents the external reference input. In this design, v serves as the rotational speed input.

Therefore, for the control problem of the second-order system (6), it transforms into satisfying the fully actuated conditions for the given nonlinear system. For any given matrix $F\in R^{2n\times 2n}$ with negative real part eigenvalues, solving non-singular matrix $V\in R^{2n\times 2n}$ and gain matrix $K_0(\theta,x,\dot{x}),K_1(\theta,x,\dot{x})$, such that:

$$V^{-1}A_c(\theta,x,\dot{x})V=F \tag{11}$$

Define a set:

$$\Gamma=\{F\mid F\in\square^{2n\times 2n},\ and\ \exists Z\in\square^{n\times 2n}\ s.t.\det\begin{bmatrix}\mathrm{Z}\\ ZF\end{bmatrix}\neq 0\} \tag{12}$$

where $Z\in\square^{n\times 2n}$ is free parameter matrix, $F\in\square^{2n\times 2n}$ is system pole placement matrix. If and only if $F\in\Gamma$, the solution of the controller can be transformed into the following form:

$$V(Z,F)=\begin{bmatrix}\mathrm{Z}\\ ZF\end{bmatrix} \tag{13}$$

Solve the Sylvester equation for equation (6):

$$A_2(\theta,x,\dot{x})ZF^2+A_1(\theta,x,\dot{x})ZF+A_0(\theta,x,\dot{x})Z=B(\theta,x,\dot{x})W(\theta,x,\dot{x},Z,F) \tag{14}$$

where

$$W=B(\theta,x,\dot{x})^{-1}(A_2(\theta,x,\dot{x})ZF^2+A_1(\theta,x,\dot{x})ZF+A_0(\theta,x,\dot{x})Z) \tag{15}$$

The stability problem of the system is transformed into solving equation (10). The gain matrix K is as follows:

$$K=[K_0(\theta,x,\dot{x})\quad K_1(\theta,x,\dot{x})]=WV^{-1} \tag{16}$$

Adjusting matrix Z or matrix F enables optimizing the performance of the closed-loop system, and there exists a matrix Z with adjustable margins.

The system state feedback controller u_f is determined by the free parameter matrix Z and the system pole placement matrix F, and equation (16) provides its composition method. By optimizing the coefficients of the similar matrix F and the free parameter matrix Z within a certain range, the system achieves better performance in the closed-loop. Consequently, we obtain the feedback controller u_f, which is optimized according to specified requirements.

To maintain the response and stability performance of the parameterized system, optimization criteria must be set for the closed-loop linear time-invariant system equation (10). The smaller the sensitivity of the eigenvalues for the linear time-invariant system, the better its control performance.

The sensitivity of the closed-loop system's eigenvalues is chosen as the optimization criterion:

$$J_{opt}=J_{opt}(F,Z)=\|V\|\|V^{-1}\| \tag{17}$$

We select the 2-norm for computation and optimization, transforming it into a constrained nonlinear programming problem.

$$\min J(F,Z)\quad \text{s.t}\begin{cases}\det V\neq 0, Z\in\square^{n\times 2n}\\ \lambda_i\in C^-, i=1,2,\ldots 2n\end{cases} \tag{18}$$

The feedback controller u_f can be obtained by the matrices V and W ,which are solved by the optimized matrices Z and F.

4 PMSM Controller Design

Considering the mathematical model of the PMSM given by equations (1)-(5), setting the system matrix $A_2(\theta,\dot{\theta})$ as the identity matrix yields a second-order nonlinear system concerning the rotor mechanical angular position:

$$\ddot{\theta}+\frac{B}{J}\dot{\theta}+\frac{T_L}{J}=\frac{3}{2J}p\psi_{\mathrm{f}}i_q \tag{19}$$

where system input matrix $B=\frac{3}{2J}p\psi_{\mathrm{f}}$, $\det(B)\neq 0$, and $r=n=1$. Therefore, this system is fully actuated.

The design of a system feedback controller is based on equations (9)-(10). Setting the conjugate negative eigenvalues of the system pole placement matrix F as $-(\lambda\pm\mu i),\lambda,\mu\in R^+$, and setting the initial free parameter matrix $Z_0\in R^{n\times 2n}$ as a matrix formed by identity diagonal matrix.

$$F=\begin{bmatrix}-(\lambda+\mu i) & 0\\ 0 & -(\lambda-\mu i)\end{bmatrix},Z_0=\begin{bmatrix}1 & 0 & 1 & 0\\ 0 & 1 & 0 & 1\end{bmatrix} \tag{20}$$

According to the optimization criterion of the closed-loop system eigenvalue sensitivity in equation(17), using the 'fmincon' optimization function, while keeping the system pole placement matrix F constant, optimize the free parameter matrix Z to obtain the feedback controller u_f.

From equation (19), $\xi(\ddot{\theta},\dot{\theta}) = \frac{T_L}{J}$ can be deduced. Combined with equation (8), the controller u_c can be obtained:

$$u_c = B^{-1}(\ddot{\theta},\dot{\theta})\frac{T_L}{J} \tag{21}$$

The load torque T_L is externally forced, and all other variables in u_c are intrinsic motor characteristics. hence, u_c is positively correlated with the load torque T_L.

For the second-order nonlinear system of the motor's rotor mechanical angular position given by equation (19), the control variable is i_q. According to equation (7), configure the motor controller:

$$i_q = u_c + u_f \tag{22}$$

where external reference input v of u_f serves as the control input for the rotational speed.

5 Simulation results

To validate the effectiveness of this control method, simulations are conducted comparing the FAST controller with PI controller and SMC controller. Using the same PMSM model, with the given speed of $1000r/\min$, the detailed parameters for the PMSM are as shown in Table 1.

Table 1: Parameters of PMSM

Parameter Name (Unit)	Value
Stator Resistance R_s / Ω	0.05
Equivalent Inductance L / H	0.00795
Moment of Inertia J / $(\mathrm{kg}\cdot m^2)$	0.011
Rotor Flux ψ_f / $(\mathrm{V}\cdot\mathrm{s})$	0.192
Pole Pairs P	4
Damping Coefficient B_η / $(\mathrm{N}\cdot\mathrm{m}\cdot s)$	0.001417

The motor introduces a constant rigid load of $50\ \mathrm{N}\cdot\mathrm{m}$ at 0.05 seconds and removes it at 0.1 seconds, compared the response speed and robustness of different control methods, the simulation results are shown in Figure 2.

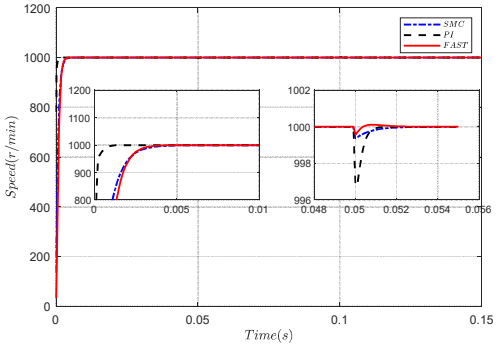

Fig. 2: Speed response curves

From Figure 2, it is evident that the PI controller exhibits a faster response speed compared to the SMC and FAST controllers. However, the PI controller experiences significant short-term speed fluctuations when subjected to external disturbances. In contrast, the FAST controller demonstrates superior disturbance rejection performance, the speed does not undergo substantial changes and recovers within a short period after external disturbances.

To analyze the impact of different system pole placement matrices on the control performance of various FAST controllers, parameter simulations are conducted using matrices with different eigenvalues for the FAST controller. The motor introduces a constant rigid load of $50\ \mathrm{N}\cdot\mathrm{m}$ at 0.2 seconds and removes it at 0.3 seconds.

The real part coefficients λ of the eigenvalues for the system pole placement matrix F are set to 10, 30, 50, 100, 200, while the imaginary part coefficient μ is set to 50. Then, the real part coefficient λ of the eigenvalues for the system pole placement matrix F is set to 50, while the imaginary part coefficients μ are set to 10, 30, 50, 100, 200. The simulation results are shown in Figure 3 and Figure 4 respectively.

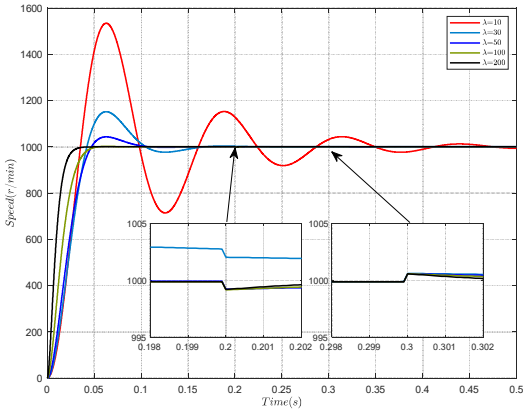

Fig. 3: Speed response curves for different real part eigenvalues

From Figure 3 simulation results, when the real part coefficient is severe smaller than the imaginary, it produces percent overshoot and steady-state error. When the real part of the system pole placement matrix eigenvalues is greater than the imaginary part, the speed control system of the PMSM exhibits significant damping in response, with minimal overshoot. However, when the real part of the system pole placement matrix eigenvalues is smaller than

the imaginary part, the speed control system shows faster response but suffers from considerable overshoot, speed oscillations, and a slightly longer settling time to reach time-invariant.

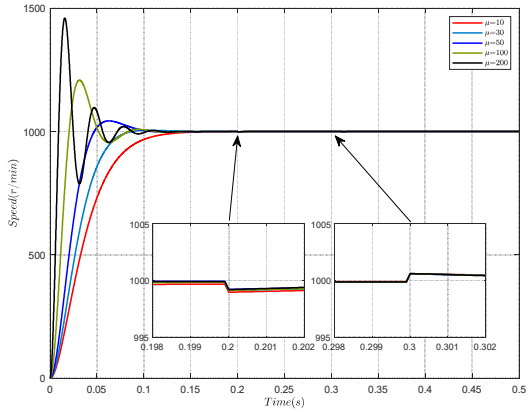

Fig. 4: Speed response curves for different imaginary part eigenvalues

From Figure 4, it can be observed that for identical real part eigenvalues, the influence of different imaginary part eigenvalues on the speed control system of the PMSM manifests primarily in response speed, overshoot, and speed oscillations. The time taken for the system to converge to a steady state is similar across variations. External perturbations minimally affect the speed response and exhibit a consistent trend in speed variations.

6 Conclusion

This paper designs a second-order FAST controller based on the mathematical model of PMSM in the $dq-$axis coordinate system. Configuring the system pole placement matrix eigenvalues as conjugate roots, simulations are performed to validate various combinations of real and imaginary parts of the eigenvalues. Simulation analysis is conducted on the FAST controller in comparison to traditional PI and SMC controllers concerning changes in load torque. According to the simulations, for the second-order PMSM FAST controller, configuring the system pole placement matrix eigenvalues as conjugate roots achieves both underdamped and overdamped responses. The FAST controller exhibits a certain level of disturbance rejection against external sudden load torque disturbances.

References

[1] L. Liu, X. Cao, M. F. Qian. Parameter tuning and optimization of PI controller for current loop of PMSM. *Electric Machines and Control*, 2023, 27(10): 131-140.

[2] H. R. Li, S. S. Gu, Neural-network-based adaptive sliding mode control for PMSM. *Control Theory & Applications*, 2005, 22(3):461-464.

[3] Y. L. Song, H. W. Li, Y. T. Deng. Fast super twisting sliding mode control of permanent magnet synchronous motor. *Control Engineering of China*, 2023, 30(01):62-69.

[4] Y. C. Guo, Research on key technologies of model-free predictive control for permanent magnet synchronous motor. Phd thesis, North University of China, 2023.

[5] G. R. Duan, High-order system approaches: I. fully-actuated systems and parametric designs. *Acta Automatica Sinica*, 2020, 46(8):1333-1345.

[6] G. R. Duan, High-order system approaches: II. controllability and full-actuation. *Acta Automatica Sinica*, 2020, 46(8):1571-1581.

[7] G. R. Duan. High-order fully actuated system approaches: Part IV. adapt control and high-order backstepping. *International Journal of Systems Science*, 2021, 52(5):972-989.

[8] G. R. Duan. Quasi-Linear system approaches for flight vehicle control——Part 2: methods and prospects. *Journal of Astronautics*, 2020，41(07):839-849.

[9] T. ZHAO, G. R. Duan, Fully actuated system approach to attitude control of flexible spacecraft with nonlinear time-varying inertia. *Science China (Information Sciences)*, 2022,65(11):148-162.

[10] Y. H. Zhang, W. Wang, S. W. Chen, et al. Integrated guidance and control design based on fully actuated system method. *Acta Aeronautica et Astronautica Sinica (in Chinese)*, online.

[11] Q. F. Lin, W. K. Liu, P. Yu. Adaptive synchronization control of pressing down system of cold strip rolling mill based on fully actuated system method. *Journal of Systems Science and Mathematical Sciences*, 2023, 43(11):2758-2772.

[12] X. B. Wang, G. R. Duan. High-order fully actuated system approaches: model predictive control with applications to under-actuated systems. *Journal of the Franklin Institute*, 2023, 360(10), 6953-6975.

Proceedings of the 3rd Conference on Fully Actuated System Theory and Applications
May 10-12, 2024, Shenzhen, China

Observer-based Sliding Mode Control for Internal Oxygen Supply of PEM Fuel Cell

Li Liu[1], Jisen Li[1], Dongqi Zhao[1], Qihong Chen[1]

1. School of Automation, Wuhan university of technology, Wuhan 430070
E-mail: liuly@whut.edu.cn, 265414@whut.edu.cn, dongqi_zhao@whut.edu.cn, chenqh@whut.edu.cn

Abstract: The performance and durability of proton exchange membrane fuel cell (PEMFC) system are greatly associated with the oxygen excess rate (OER). However, the strongly nonlinear, coupling with numerous unavailable internal states PEMFC system pose a challenge to the OER control. To address it, this paper proposed an observer-based cascaded sliding mode controller. The cascaded controller is composed of the outer loop for oxygen excess ratio tracking and inner loop for compressor flow rate regulation, providing the accurate and fast control of OER. In addition, an injection term-based nonlinear observer is developed to estimate the unmeasurable states in the solution of control procedure. The comparative simulation with current control strategies is executed, the results demonstrate a more accurate and fast control of proposed method by the enhancement of mean absolute percentage error (MAPE) and regulation time with 5.73% and 6.98s.

Key Words: Proton exchange membrane fuel cell, Oxygen excess ratio, Sliding mode, Injection term.

1 Introduction

The proton exchange membrane fuel cell (PEMFC) is regarded as a potential alternative power source due to its high-energy efficiency and zero-carbon footprint. During the operation the PEMFC system, different parameters need to be accurately controlled, and one of the most important is oxygen excess ratio (OER). On one hand, the parasitic power can be significantly reduced by the desired value control of OER. On the other hand, the starvation fault can be avoided by a fast-dynamic performance regulation. However, the nonlinear PEMFC system increase the precise control efforts to ensure the optimal performance. Therefore, the control strategy for OER is significant and imminent [1].

So far, numerous researches have been devoted on the OER control of PEMFC systems. Chen [2] proposed a feedback linearization controller is for the air supply subsystem of PEMFC, the experiment results demonstrate the method could avoid starvation phenomenon and reduce parasitic power consumption. To achieve the maximum net power, an exponential approach-based sliding mode variable structure is proposed and applied to real-time operation by Li [3], the results indicate about a 2% enhancement of net power. Liu [4] utilized the supply manifold model to observe the cathode gas pressure via an extended state observer (ESO), and the OER is regulated by sliding mode controller. Guo [5] proposed an adaptive dynamic surface controller for OER tracking, and the robustness and reliability toward faulty states are conducted by an experiment of hardware-in-the-loop platform. Deng [6] proposed a weighted fusion control including active disturbance rejection control (ADRC) algorithm and fuzzy self-tuned PID for the OER control, improving dynamic performance with guaranteed accuracy. To minimize OER tracking error, Zhu [7] proposed near-optimal controller based on nonlinear model and verify the method with a 5 kW PEMFC test platform.

While various researches have been devoted to control the OER of PEMFC system, there are still several critical challenges: Generally, the optimal OER indicates maximum net power is controlled as a constant, which ranges from 2.0-2.5. However, the optimal OER is related to the output power. Moreover, most existing methods aren't ideal for achieving fast dynamics response issue of OER. At last, the internal states of PEMFC are hard to obtain in real implementation of control strategy. Therefore, this paper proposed an observer-based cascaded sliding mode controller. The outer of the controller is for OER tracking, and the compressor flow rate regulation is achieved by inner loop. Moreover, an injection term-based observer is developed to estimate the unmeasurable states.

The remainder of this paper is organized as follows. Section 2 describes the PEMFC modeling procedure. Section 3 introduces the methodology of observer and controller design. The simulation results and discussion are presented in Section 4. Finally, the conclusions are summarized in section 5.

2 PEMFC Modeling

A PEMFC system is the device that converts the chemical energy of the fuel directly into electrical energy. Generally, the PEMFC system is equipped with balance of plant (BOP), such as mass flow controller, humidifier, and heat exchanger. The mass flow controllers ensure the mass flow rate and pressure of hydrogen and air supply manifold. The heat generated by stack brought out through heat exchanger. Meanwhile, the extra heat is for the regulation of inlet humidity by humidifier. A typical PEMFC system is shown in Fig. 1. According to the sixth-order model [8], whose state vector is $[x_1, x_2, x_3, x_4, x_5, x_6]^T = [\omega_{cp}, P_{sm}, m_{sm}, m_{O_2}, m_{N_2}, P_{rm}]^T$ a model simplification is introduced.

The following parameter fusion is considered due to the similar value of R_{O_2} *and* R_{N_2} (259.8 and 296.8, respectively):

$$\begin{cases} m_{O_2} \cdot \dfrac{R_{O_2} T_{st}}{V_{ca}} + m_{N_2} \cdot \dfrac{R_{N_2} T_{st}}{V_{ca}} \approx \kappa\left(m_{O_2} + m_{N_2}\right) \\ m_{ca} = m_{O_2} + m_{N_2} + p_v \cdot \dfrac{V_{ca}}{R_{N_2} \cdot T_{st}} \end{cases} \tag{1}$$

* This work was supported by the National Key Research and Development Program of China under contract 2022YFB4003800, and received partial support from the National Natural Science Foundation of China (62173264, 62273265).

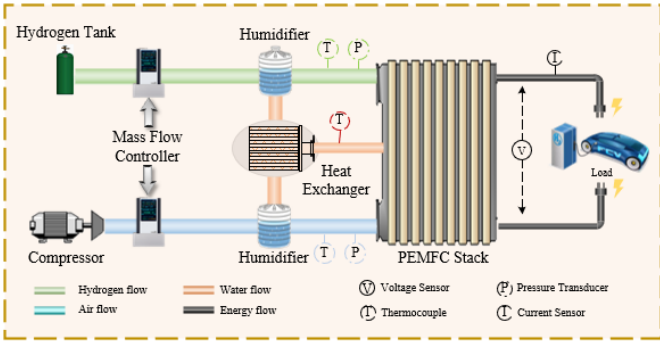

Fig. 1: Structure diagram of PEMFC system

where T_{st} is the operating temperature of the stack, R_{O_2}, R_{N_2}, R_v are the oxygen, nitrogen and water vapor gas constants, m_{ca} is the cathode gas mass, V_{ca} is the volume of the cathode cavity, P_v is the saturated water vapor pressure.

Conclusively, m_{ca} is defined as a new state variable x_5. Then the new state vector is expressed as : $X = [x_1, x_2, x_3, x_4, x_5]^T = [\omega_{cp}, P_{sm}, m_{sm}, P_{rm}, m_{ca}]^T$, and the state-space equation is shown accordingly:

$$\begin{cases} \dot{X}(t) = f(x) + B \cdot u(t) + S \cdot I_{st}(t) \\ y(t) = C \cdot x \end{cases} \tag{2}$$

where vector fields $f(x)$, B, and S are given as follows:

$$f(x) = \begin{bmatrix} f_1(x_1, x_2) \\ f_2(x_1, x_2, x_3, x_4, x_5) \\ f_3(x_2, x_5) \\ f_4(x_4, x_5) \\ f_5(x_2, x_4, x_5) \end{bmatrix} \quad B = \begin{bmatrix} \frac{\eta_{cm} k_t}{J_{cp} R_{cm}} \\ 0 \\ 0 \\ 0 \\ 0 \end{bmatrix} \quad S = \begin{bmatrix} 0 \\ 0 \\ 0 \\ -n\frac{M_{O_2}}{4F} \\ 0 \end{bmatrix}$$

where $f_i(x)(i = 1 \sim 5)$ represents the continuous vector function and the detail can be found in the [9].

Meanwhile, the output $y(t)$ is designed as

$$y(t) = [h_1, h_2, h_3] = [\omega_{cp}, P_{sm}, \lambda_{O_2}] \tag{3}$$

where λ_{O_2} is the OER, which is defined as follows:

$$\lambda_{O_2} = \frac{W_{O_2,ca,in}}{W_{O_2,react}} = W(P_{sm}, m_{ca}, I_{st}) \tag{4}$$

$$= K_\lambda (p_{sm} - \frac{m_{ca} p_{v,ca} R_{N_2} T_{st}}{M_{O_2} V_{ca}} - p_{v,ca})$$

where $W_{O_2,ca,in}$ and $W_{O_2,react}$ are oxygen mass flow into the PEMFC and the mass flow utilized for power generation, and K_λ is OER coefficient.

Notable, it's worth noting from Eq. (4) that the cathode gas mass m_{ca} can't be obtained directly. Therefore, the OER is an unmeasurable parameter, and the accurate observation is a base for control. However, an improper control of OER would result in whether the starvation or extra parasitic power. To address it, this paper proposed a sliding mode control method based on an injection term-based observer, and the design procedure is shown in following.

3 methodology

The strongly nonlinear PEMFC system, coupling with unmeasurable internal states pose a challenge to the accurate and fast OER control. However, the OER in current research is assumed as a known. Moreover, the traditional control is not ideal for achieving accurate and fast tracking. Therefore, a sliding mode control strategy with cascaded control structure for OER is proposed, the external controller is to calculate the reference flow rate of compressor and the motor voltage is obtained by inner controller, providing the accurate and fast control of OER, as it depicted in Fig.2. In addition, an injection term-based nonlinear observer is developed to estimate the unmeasurable states in the solution of control procedure. The detail design procedure is shown in following.

3.1 Injection Term-based Nonlinear Observer

The proposed nonlinear observer can be expressed as:

$$\dot{\hat{x}} = f(\hat{x}) + \begin{bmatrix} \eta_{cm} \frac{k_t}{J_{cp} R_{cm}} \\ 0 \\ 0 \\ 0 \\ 0 \end{bmatrix} V_{cm} + \begin{bmatrix} 0 \\ 0 \\ 0 \\ -n\frac{M_{O_2}}{4F} \\ 0 \end{bmatrix} I_{st} + O_{sq}^{-1}(\hat{x}) B_G v \tag{5}$$

where $O_{sq}(\hat{x})$ and B_G denote the observability matrix and coupling matrix. $O_{sq}(\hat{x})$ can be described as:

$$O_{sq}(\hat{x}) = \left[\frac{\partial h_1(\hat{x})}{\partial \vec{x}} \cdots \frac{\partial L_t^{r_1 - 1} h_1(\hat{x})}{\partial \vec{x}} \; \frac{\partial h_2(\hat{x})}{\partial \vec{x}} \cdots \frac{\partial L_t^{r_2 - 1} h_2(\hat{x})}{\partial \vec{x}} \right]_{5\times5}^T \tag{6}$$

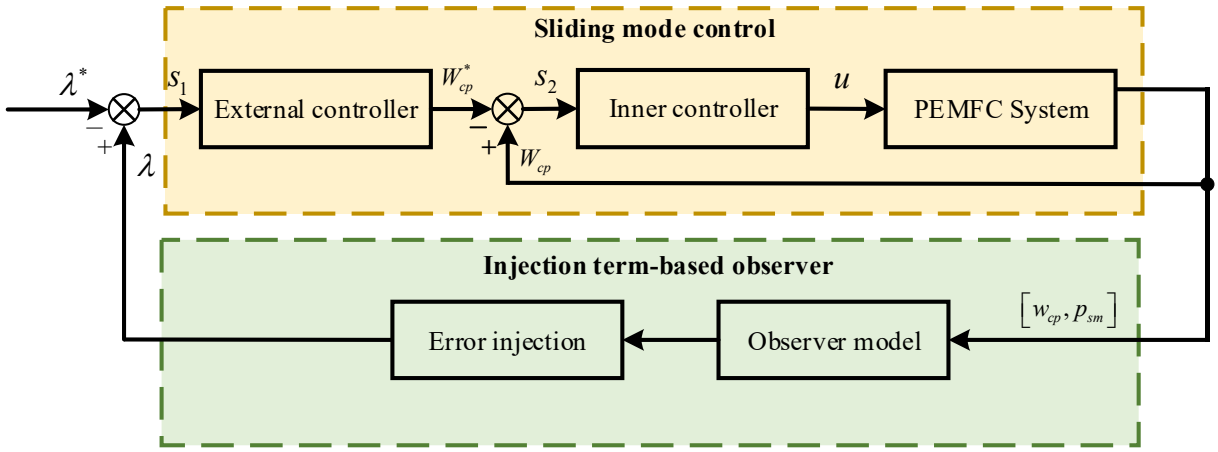

Fig. 2: Control diagram of proposed method.

where $L_t^{r_1}h_1(x)$ denotes the $r_1 th$ Lie derivative of $h_1(x)$ along $f(x)$, $r_1 = 2, r_2 = 3$ are the observable index of x_1, x_2 respectively.

v is output injection vector defined as $v = [v_1\ v_2\ v_3\ v_4\ v_5]^T \in R^5$

The output injection vector of $[v_1\ v_2]^T$ can be defined as:

$$\begin{cases} v_1 = -\alpha_1 |e_1|^{\frac{1}{2}} sign(e_1) \\ v_2 = -\lambda_1 \int sign(e_1) dt \end{cases} \tag{7}$$

where $\alpha_1 = 0.01, \lambda_1 = 1$.

The output injection vector of $[v_3\ v_4\ v_5]^T$ is:

$$\begin{cases} v_3 = -\bar{\alpha}_3 sign(e_2) \\ v_4 = -\bar{\alpha}_4 sign(e_2) \\ v_5 = -\bar{\alpha}_5 sign(e_2) \end{cases} \tag{8}$$

where $\bar{\alpha}_3 = \frac{1}{3}, \bar{\alpha}_4 = \frac{2}{3}, \bar{\alpha}_5 = 1$,

Thus, the state variables are reconstructed as $\hat{x} = [\hat{\omega}_{cp}, \hat{p}_{sm}, \hat{m}_{sm}, \hat{p}_{rm}, \hat{m}_{ca}]^T$.

3.2 Sliding mode controller

• **External loop**: Take the first time-derivative of $\lambda_{O_2} = h_3$

$$\dot{\hat{h}}_3 = k_\lambda (\dot{\hat{x}}_2 - k_1 \dot{\hat{x}}_5 - c_1) \tag{9}$$

where $\dot{x}_2$ and $\dot{x}_5$ is expressed as [9]:

$$\begin{cases} \dot{\hat{x}}_2 = g_1(x_2) W_{cp}(x_1, x_2) + g_2(x_2, \hat{x}_5) \\ \dot{\hat{x}}_5 = f_5(x_2, \hat{x}_4, \hat{x}_5) \end{cases} \tag{10}$$

The sliding variable can be defined as: $s_1 = \hat{h}_3 - h_{3_ref}$ where h_{3_ref} is the reference of OER, whose derivative is assumed as zero, and the $\dot{s}_1$ is shown as:

$$\dot{s}_1 = \dot{h}_3 = g_1(x_2) W_{cp}(x_1, x_2) + g_3(x_2, \hat{x}_4, \hat{x}_5) \tag{11}$$

where $W_{cp}(x_1, x_2)$ is the mass flow rate of compressor, and the known function $g_3(x_2, \hat{x}_4, \hat{x}_5) = g_2(x_2, \hat{x}_5) + f_5(x_2, \hat{x}_4, \hat{x}_5)$. Therefore, the desired $W_{cp}(x_1, x_2)$ is calculated by considering the convergence and stability of the system:

$$W_{cp_{ref}}(x_1, x_2) = \frac{1}{g_1} [-\sigma(s_1) - g_3(x_2, \hat{x}_4, \hat{x}_5)] \tag{12}$$

Utilizing the super twisting algorithm for $\sigma(s_1)$

$$\sigma(s_1) = \alpha_6 |s_1|^{\frac{1}{2}} sign(s_1) + \lambda_6 \int sign(s_1) dt \tag{13}$$

• **Inner loop**: The compressor motor current u is calculated in this loop. The sliding variable s_2 is assumed as:

$$s_2 = W_{cp}(x_1, x_2) - W_{cp_{ref}}(x_1, x_2) \tag{14}$$

where $W_{cp}(x_1, x_2)$ is defined as follows:

$$W_{cp}(x_1, x_2) = c_6 x_1 + c_7 x_2$$

Take the first time-derivative of $W_{cp}(x_1, x_2)$:

$$\begin{aligned} \dot{W}_{cp}(x_1, x_2) &= -c_8 x_1 - \frac{c_9}{x_1} \left[\left(\frac{x_2}{c_3} \right)^{c_4} - 1 \right] W_{cp}(x_1, x_2) + c_{10} u \\ &+ c_7 g_1(x_2) W_{cp}(x_1, x_2) + c_7 g_2(x_2, \hat{x}_5) \\ &= c_{10} u + g_4(x_1, x_2, \hat{x}_5) \end{aligned} \tag{15}$$

where $c_7 - c_{10}$ are constant parameter, the function $g_4(x_1, x_2, \hat{x}_5)$ is assumed as a known.

Take the first time-derivative of s_2:

$$\begin{aligned} \dot{s}_2 &= c_{10} u + g_4(x_1, x_2, x_5) - \dot{W}_{cp_{ref}}(x_1, x_2) \\ &= c_{10} u + g_4(x_1, x_2, x_5) - \dot{W}_{cp_ref}(x_1, x_2) \end{aligned} \tag{16}$$

It's notable that the sliding variable s_2 has relative degree 1 with respect to the control input u. Therefore, the internal controller is designed as:

$$u = \frac{1}{c_{10}} \left(-k_1 sign(s_2) - k_2 s_2 - g_4 + \dot{W}_{cp_ref} \right) \tag{17}$$

4 Simulation and Analysis

To validate the cascaded control strategy based on sliding mode observer. This section is composed of two parts: observer and control performance validation. All the simulations are executed in MATLAB R2023a and the key simulation parameter utilized in simulation can be found in table I. As it shown in Fig. 3 (a), the current variation is set to verify the dynamic switching performance of proposed control strategy. Moreover, it's known that the air compressor accounts for up to 80% of parasitic losses in PEMFC systems [10]. To elucidate the relationship between OER and net power at various current densities, the following simulation approach assumed the compressor as the sole parasitic consumer: 1) Initialize current at 90 A; 2) Increment motor voltage by 5 V up to its rating, recording steady-state data during each cycle; 3) Increase current by 10 A and repeat step 2 until reaching 220 A. The peak net power was fitted at each current density, as depicted in Fig. 3 (b). Therefore, the optimal OER determined for the given operating current is developed accordingly, and the detail fitted results are shown in following:

$$\lambda(I_{st}) = 2.8 - \frac{0.3 \times I_{st}(t)}{100} \tag{18}$$

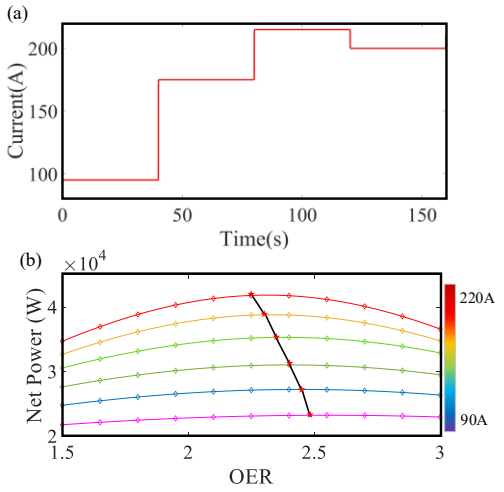

Fig. 3: Systematic simulation conditions. (a) Stack current variation. (b) Net power vs. OER.

Table 1: Simulation Parameters

Parameter	Value
Number of cells of the stack $\boldsymbol{n}$	381
Compressor and motor inertia $\boldsymbol{J_{cp}}$	$5 \times 10^{-5}\ Kg \cdot m^2$
Motor constant $\boldsymbol{k_t}$	$0.0225\ N \cdot m \cdot A^{-1}$
Motor constant $\boldsymbol{k_v}$	$0.0153\ V \cdot s \cdot rd^{-1}$
Single stack cathode volume $\boldsymbol{V_{ca}}$	$0.01\ m^3$
Supply manifold volume $\boldsymbol{V_{sm}}$	$0.02\ m^3$
Cathode outlet orifice $\boldsymbol{K_{ca,out}}$	$2.7 \times 10^{-4}\ Kg \cdot (Pa \cdot s)^{-1}$
Cathode inlet orifice $\boldsymbol{K_{sm,out}}$	$3.6 \times 10^{-4}\ Kg \cdot (Pa \cdot s)^{-1}$

4.1 Observer Verification

Fig. 4 represents the observation results of sliding mode observer, which is executed under the operating conditions

of Fig. 3 (a). During load transients, the OER exhibits overshoot and oscillatory behavior, most prominently at 40 s when the current spikes by 80 A representing the maximum load disturbance. This positive correlation between overshoot severity and mutation degree highlights the underlying oxygen mass flow mismatch precipitating such deviations. Specifically, sudden load changes desynchronize the demanded and supplied oxygen flows. Rapid and precise tracking of the resulting OER fluctuation enables reconciliation to optimal OER reference trajectories through appropriate control actuation. Effectively compensating for these disturbances necessitates an observer capable of accurately and swiftly estimating anomalies in the present OER behavior stemming from abrupt current shifts. In addition, from the enlarged figure of 4(a), the observation of the proposed observer can track the reference in 1s. Fig. 4(b) depicts the corresponding tracking error of the OER, from which the steady-state errors are equal to zero for different current conditions. In addition, the maximum deviation at 40s is positive 0.8. In conclusion, the results demonstrate the brilliant observation performance with low error and fast response.

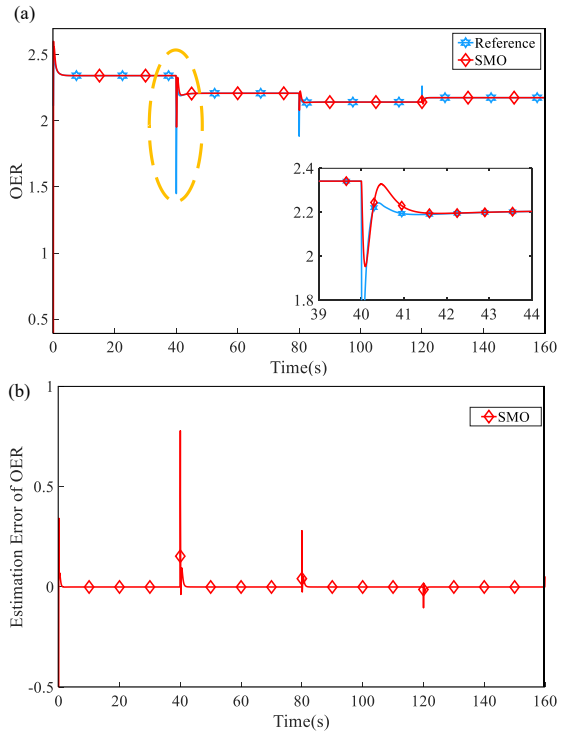

Fig. 4: The observation results of SMO. (a) oxygen excess ratio. (b) estimation error of oxygen excess ratio.

4.2 Simulation Results

In the actual operating of the PEMFC system, the optimal OER, which represents the maximum net power output, can be diverse under different load requirements. The optimal OER of the PEMFC system in this paper is designed according to the simulation results of Fig. 3 (b), and the verification of net power between constant OER=2.2 and optimal one shown in Eq. (18) is worked out. As depicted in Fig. 5, there is a comprehensive enhancement in net power for the optimal OER. From the enlarged figure, the net power is increased about 200W by optimal control at 40 – 80 s, and that for 80 – 120 s is 30W. It's notable that the power enhancement decreases with the rising current, which are 1.1%, 0.55%, 0.10%, and 0.06% at the four operating conditions shown in Fig .3(a). The reason can be found in Fig .3(b), the optimal OER presents a negative trend with current, and the optimal OER of 200A is about 2.2, which is close to the current at 80 – 120 s. Conclusively, the fitted optimal OER can achieve a nearly 1.1% enhancement of net power output.

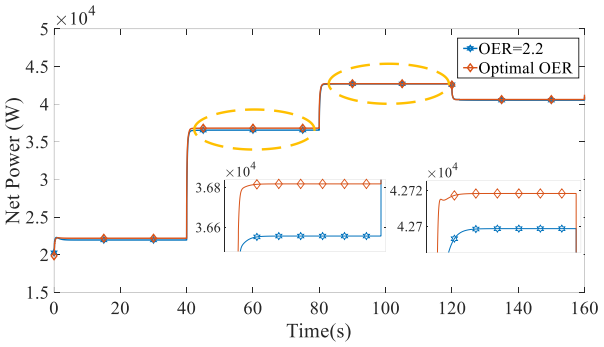

Fig. 5: Comparative results of net power between constant and optimal OER.

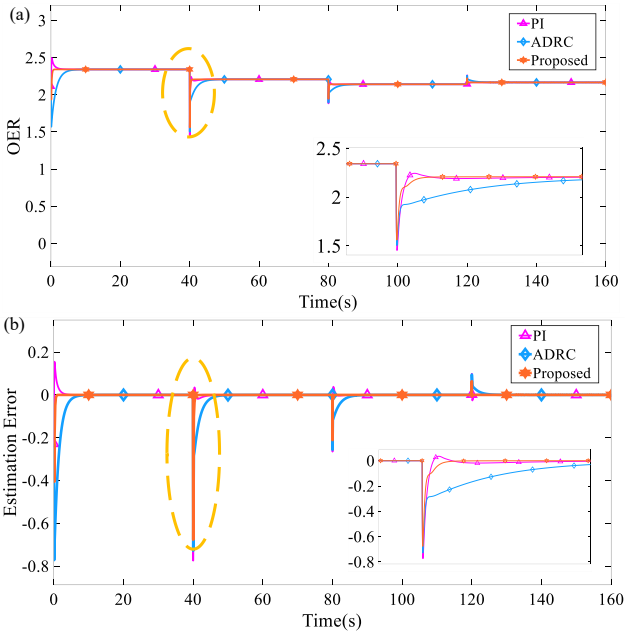

Fig. 6. Comparative control results among proposed, PI, and ADRC method. (a) oxygen excess ratio. (b) tracking error of oxygen excess ratio.

To validate the effectiveness of proposed control strategy, the comparative simulation with proportional integral (PI) control and active disturbance rejection control (ADRC) is executed. As it illustrated in Fig. 6, the performance of OER is presented. From the Fig. 6(a), it seems that overall three methods achieve a good tracking performance. However, the load switching dynamic performances vary with different methods, the proposed sliding mode methods processes the fastest tracking time from the enlarged figure. Meanwhile, the estimation error is shown in Fig. 6(b), where the deviations of total three methods converge to zero. However, the maximum negative deviation (MND) of PI, ADRC, and proposed methods are 0.79, 0.75, and 0.67, respectively. The results indicate the response degree when the load transforms, a too large value if MND would lead to the oxygen starvation fault, damaging the state of health (SOH) of the PEMFC stack.

To describe the performance of these controllers more comprehensively, this paper introduces several evaluation indexes, as shown in table II. MAPE and RMSE, which represent the average percentage error and the root-mean-square error shown in following:

$$\begin{cases} MAPE = \dfrac{100\%}{n}\displaystyle\sum_{i=1}^{n}\left|\dfrac{\overset{\Lambda}{y_i} - y_i}{y_i}\right| \\ RMSE = \sqrt{\dfrac{1}{n}\displaystyle\sum_{i=1}^{n}(\overset{\Lambda}{y_i} - y_i)^2} \end{cases} \tag{19}$$

Overshoot represents the proportion of decrease/increase of the OER during the first pulse at the instant of load increase/decrease. Moreover, t_s stands for the regulation time, referring to the shortest time for the state variable to return the new equilibrium state. From the table II, it can be seen that the MAPE and RMSE of proposed method are 0.560% and 0.442, respectively. The MAPE is reduced by 0.41% and 5.731% with PI and ADRC. Meanwhile, those for RMSE are 0.014 and 0.141. In addition, the overshoots have not appeared in ADRC and proposed method, and t_s for PI, ADRC, and proposed method are 1.213 s, 7.410 s, and 0.412 s. The lowest regulation time implies a more transient overshoot time and therefore could prolong the lifetime of PEMFC system. The results demonstrate that proposed sliding mode control gives a more accurate control and fast response.

Table 2: Summary of Simulation Condition

Method	**MAPE**	**RMSE**	**Overshoot**	t_s
PI	0.970%	0.058	2.237%	$1.213s$
ADRC	6.291%	0.185	0	$7.410s$
Proposed	**0.560%**	**0.044**	**0**	**0.412s**

5 Conclusion

In this paper, an observer-based cascaded sliding mode control for oxygen excess ratio (OER) of PEMFC system is designed, observer-based cascaded sliding mode controller. The outer of the controller is for OER tracking, and the compressor flow rate regulation is achieved by inner loop. Moreover, an injection term-based nonlinear observer is developed to estimate the unmeasurable states. The key results are summarized as follows.

1) The relationship between OER and net power at various current densities is obtained, indicating a nearly 1.1% enhancement of net power output.
2) The injection term-based observer is designed, providing an accurate estimate of unmeasurable states.
3) The cascaded sliding mode controller is developed, demonstrate a more accurate and fast control of proposed method by the enhancement of mean absolute percentage error (MAPE) and regulation time with 5.73% and 6.98s.

The future research is targeted to the real-time implementation in the PEMFC test beach.

References

[1] Li Q, Xiao X, Pu Y, et al. Hierarchical optimal scheduling method for regional integrated energy systems considering electricity-hydrogen shared energy[J]. Applied Energy, 2023, 349: 121670.

[2] Chen J, Liu Z, Wang F, et al. Optimal oxygen excess ratio control for PEM fuel cells[J]. IEEE Transactions on control systems technology, 2017, 26(5): 1711-1721.

[3] Li Q, Yang W, Yin L, et al. Real-time implementation of maximum net power strategy based on sliding mode variable structure control for proton-exchange membrane fuel cell system[J]. IEEE Transactions on Transportation Electrification, 2020, 6(1): 288-297.

[4] Liu J, Gao Y, Su X, et al. Disturbance-observer-based control for air management of PEM fuel cell systems via sliding mode technique[J]. IEEE Transactions on Control Systems Technology, 2018, 27(3): 1129-1138.

[5] Guo X, Fan N, Dong Z, et al. Adaptive Prescribed Performance Control for PEM Fuel Cell Air Supply Systems with Unknown Air Compressor Faults[J]. IEEE Transactions on Industrial Electronics, 2023.

[6] Deng Z, Chen Q, Zhang L, et al. Weighted cascade control for proton exchange membrane fuel cell system[J]. International Journal of Hydrogen Energy, 2020, 45(30): 15327-15335.

[7] Zhu Y, Zou J, Li S, et al. An adaptive sliding mode observer based near-optimal OER tracking control approach for PEMFC under dynamic operation condition[J]. International Journal of Hydrogen Energy, 2022, 47(2): 1157-1171.

[8] Pilloni A, Pisano A, Usai E. Observer-based air excess ratio control of a PEM fuel cell system via high-order sliding mode[J]. IEEE Transactions on Industrial Electronics，2015，62(8): 5236-5246.

[9] Talj R J, Hissel D, Ortega R, et al. Experimental validation of a PEM fuel-cell reduced-order model and a moto-compressor higher order sliding-mode control[J]. IEEE Transactions on Industrial Electronics, 2009, 57(6): 1906-1913.

[10] Deng H, Li Q, Chen W, et al. High-order sliding mode observer based OER control for PEM fuel cell air-feed system[J]. IEEE Transactions on Energy Conversion, 2017, 33(1): 232-244.

Proceedings of the 3rd Conference on Fully Actuated System Theory and Applications
May 10-12, 2024, Shenzhen, China

A Differentiable QP-based Learning Framework for Safety-Critical Control of Fully Actuated AUVs

Yongchao Jiang, Chenggang Wang, Ziqi He, Lei Song
Department of Automation, Shanghai Jiao Tong University, Shanghai 200240, P. R. China
E-mail: cgwang-auv@sjtu.edu.cn

Abstract: This paper tackles the safety-critical control problem of the fully actuated autonomous underwater vehicle (AUV) in the presence of unknown disturbances. Specifically, a differentiable quadratic program (QP)-based learning framework that integrates fully connected layers and high order control barrier function (HOCBF) is proposed to avoid the obstacle. The safety-critical loss is designed by considering the quantified safety violations to resist unknown disturbances during the training process. In the control loop, a first-order high-gain disturbance observer (DOB) is employed to estimate the unknown dynamics associated with the forward invariance condition. This approach effectively diminishes the system's conservativeness by compensating for the bounded estimation error of the DOB. The simulation results demonstrate that the proposed framework enables the AUV to satisfy safety requirements in the presence of unknown disturbances, while reducing the dependence of the system performance on artificial parameters by adaptively regulating the class $\mathcal{K}$ functions through neural network outputs.

Key Words: Fully actuated AUV, Differentiable QP, Control barrier function, Safety-critical control, Disturbance observer

1 Introduction

Autonomous underwater vehicles (AUVs) are effective operation equipment for expanding the utilization of marine resources and the development of marine science due to their autonomy and intelligence [1]. However, AUVs are typically required to operate within complex marine environments characterized by unanticipated disturbances during the mission execution. Herein, factors such as varying seabed topography, the presence of extraneous obstacles, and even the inadvertent actions of team members [2], may significantly threaten the operational safety of the AUV. Therefore, ensuring the safety of AUVs through obstacle avoidance techniques is important for the successful execution of the mission.

Obstacle avoidance of AUVs in unknown marine environments is usually achieved by local path planning. However, the lack of consideration of nonlinear dynamics, high computational burden, and local optimality constrain the application of existing methods [3, 4]. In recent years, Control Barrier Function (CBF) - based methods [5] have been developed to avoid obstacles for AUVs because of their convenient combination with nonlinear dynamics and excellent real-time performance. However, inaccurate model information due to unknown current disturbances still lead to the failure of obstacle avoidance [6].

To overcome the unknown disturbance for ensuring the safety of AUV, various robust CBFs have been proposed [7, 8]. However, most of them use "worst-case" disturbances to compensate for CBF forward invariance conditions, leading to unnecessarily conservative behavior of the system. Input-to-State Safety [9] describes the variation law of invariant set with unknown bounded disturbances. The concept of Tunable Input-to-State Safety [10] builds upon the work of [9] by employing a continuous function that monotonically increases over CBF to mitigate conservative behavior when the state is far from the safe set boundary. Nevertheless, both Input-to-State Safety and Tunable Input-to-State Safety still involve compensating for "worst-case" disturbances. Robust CBFs based on Disturbance Observer (DOB) [11, 12] significantly reduce the conservativeness of the system. They estimate CBF conditions through DOB and utilize the exponentially decaying error boundness of the estimation results to compensate for the CBF condition. However, the performance of the DOB-based method depends on manual parameters significantly. Moreover, tuning the parameters manually is a intractable process, especially for systems with high-order relative degrees [13]. This leads to considerable human uncertainty in the performance of the system. To alleviate this problem, α-net is proposed [13] to tune the class $\mathcal{K}$ functions adaptively so that the systems with high-order relative degrees can avoid obstacles in the novel environments, while it ignores the effects of unknown disturbances.

To address the problem above, this paper proposes a differentiable quadratic program (QP)-based safety-critical framework to avoid the obstacle under the disturbance for AUVs. Specifically, we combine differentiable QP with fully-connected layers to construct the training framework. Then, the safety-critical loss function is designed to resist unknown disturbances by considering the quantified safety violations. And the first-order high-gain DOB is used to estimate the unknown term of CBF forward invariant condition to reduce the conservativeness. The simulation results on AUV obstacle avoidance demonstrate that the proposed approach enables the fully-connected layers to adaptively output parameters of class $\mathcal{K}$ function overcoming unknown disturbances without manual adjustment process of the parameters. The main contributions of this paper are summarized as follows:

- A robust safety-critical framework based on differentiable QP is proposed for AUVs to ensure obstacle

This work was supported in part by the Oceanic Interdisciplinary Program of Shanghai Jiao Tong University under Grant SL2022MS010 and Grant SL2022MS008, in part by the Joint Fund of Equipment Pre-Research and Ministry of Education under Grant 8091B022235, in part by the National Natural Science Foundation of China under Grant 62303316, in part Key Laboratory Fund of National Defense Science and Technology under Grant 2022JCJQLB03308, and in part by the Science Center Program of National Natural Science Foundation of China under Grant 62188101.

avoidance in the presence of unknown disturbances. In contrast to the robust CBF-based methods referenced in [7–12], the proposed approach employs a learning framework to optimize the parameters of the forward invariance condition, achieving a more effective adaptation to environmental conditions and AUV dynamics.
- The quantified safety violations are incorporated into the safety-critical loss function to resist disturbance in the training process, where the first-order high-gain DOB is leveraged to alleviate the conservativeness. The simulation results demonstrate that the safety-critical loss mitigates the safety violations effectively, and DOB diminishes the effect of unknown disturbances by compensating for its bounded estimation error of the safety condition derived by HOCBFs.

2 Preliminaries and problem formulation

Consider a disturbed nonlinear control affine system

$$\dot{x} = f(x) + g(x)(u + d(t)), \tag{1}$$

where $x \in X \subset \mathbb{R}^n$ represents the system state, $u \in \mathbb{R}^m$ is the control input, $f : \mathbb{R}^n \to \mathbb{R}^n$, $g : \mathbb{R}^n \to \mathbb{R}^{n\times m}$ are locally Lipschitz continuous functions, and $d(t) : \mathbb{R}_{\geq 0} \to \mathbb{R}^m$ is the unknown input disturbance.

Suppose that the safe set $\mathcal{C}$ of the system is defined as a 0-superlevel set of a continuously differentiable function $h(x) : X \to \mathbb{R}$

$$\mathcal{C} \triangleq \{x \in X \subset \mathbb{R}^n : h(x) \geq 0\}, \tag{2}$$

$$\partial\mathcal{C} \triangleq \{x \in X \subset \mathbb{R}^n : h(x) = 0\}, \tag{3}$$

$$Int(\mathcal{C}) \triangleq \{x \in X \subset \mathbb{R}^n : h(x) > 0\}. \tag{4}$$

The set $\mathcal{C}$ is forward invariant if for any initial state $x_0 = x(0) \in \mathcal{C}$, $x(t) \in \mathcal{C}$ for all $t \in [0, t_{max})$. The system (1) is safe w.r.t. the safe set $\mathcal{C}$.

2.1 Control Barrier Function

Definition 1 (Control Barrier Function (CBF) [17]): Let $\mathcal{C} \subset X$ be the 0-superlevel set of a continuously differentiable function $h : X \to \mathbb{R}$ with $\frac{\partial h}{\partial x} \neq 0$ when $h(x) = 0$. The function h is a CBF for (1) w.r.t. $\mathcal{C}$ if there exists $\alpha \in \mathcal{K}_{\infty,e}$ and $u \in \mathbb{R}^m$ such that for all $x \in \mathcal{C}$,

$$\dot{h}(x, u, d) = \mathcal{L}_f h(x) + \mathcal{L}_g h(x)(u + d) \geq -\alpha(h(x)), \tag{5}$$

where $\mathcal{L}_f h(x) = \frac{\partial h(x)}{\partial x} f(x)$, $\mathcal{L}_g h(x) = \frac{\partial h(x)}{\partial x} g(x)$ are the Lie derivatives of h w.r.t. f, g. $\alpha : \mathbb{R} \to \mathbb{R}$ is a continuous extended class $\mathcal{K}_\infty$ function and it is strictly monotonically increasing with $\alpha(0) = 0$ and $\lim_{r\to\infty} \alpha(r) = \infty$. For system (1), if $h(x)$ is a control barrier function, any Lipschitz continuous controller satisfying (5) renders the set $\mathcal{C}$ forward invariant.

Definition 2 (Relative Degree [15]): The relative degree of a continuously differentiable function $h(x)$ w.r.t. system (1) is the number of times we need to differentiate it along the dynamics of (1) until the control u explicitly shows.

Definition 1 can only be used in the case of relative degree $r = 1$, while the relative degree of the fully actuated AUV dynamics is $r = 2$ for obstacle avoidance. When relative degree $r > 1$, high order control barrier function (HOCBF) [15] can be used. For a $h(x)$ with relative degree r, we define a sequence of functions $\psi_i : \mathbb{R}^n \to \mathbb{R}, i \in \{1, 2, ..., r\}$:

$$\psi_i(x) = \dot{\psi}_{i-1}(x) + \alpha_i(\psi_{i-1}(x)), i \in \{1, 2, ..., r\}, \tag{6}$$

where $\psi_0(x) = h(x)$, $\alpha_i(\cdot)$ presents $(m - i)^{th}$ order differentiable class $\mathcal{K}$ function. A sequence of sets $\mathcal{C}_i, i \in \{1, 2, ..., r\}$ are further defined:

$$\mathcal{C}_i = \{x \in X \subset \mathbb{R}^n : \psi_{i-1}(x) \geq 0\}, i \in \{1, 2, ..., r\}. \tag{7}$$

Definition 3 (High Order Control Barrier Function (HOCBF) [15]): Let $\mathcal{C}_1, ..., \mathcal{C}_m$ be defined by (7) and $\psi_1(x), ..., \psi_r(x)$ be defined by (6). $h(x) : \mathbb{R}^n \to \mathbb{R}$ is a HOCBF for system (1) if there exist $(r-i)^{th}$ order differentiable class $\mathcal{K}$ functions $\alpha_i, i \in \{1, ..., r-1\}$ and a class $\mathcal{K}$ function α_r such that for all $x \in \mathcal{C}_1 \cap, ..., \cap \mathcal{C}_r$,

$$\begin{aligned} \sup_{u\in\mathbb{R}^m} [\mathcal{L}_f^r h(x) + \mathcal{L}_f^{r-1} h(x)(u + d(t))] \geq \\ -O(h(x)) - \alpha_r(\psi_{r-1}(x)), \end{aligned} \tag{8}$$

where $O(h(x)) = \sum_{i=1}^{r-1} \mathcal{L}_f^i(\alpha_{r-i} \circ \psi_{r-i-1})(x)$. Any Lipschitz continuous controller that satisfies the constraint (8) renders $\mathcal{C}_1 \cap, ..., \cap \mathcal{C}_r$ forward invariant. In this paper, we consider the case that α_i is linear function. Therefore, (8) can be rewritten as follows:

$$\sup_{u\in\mathbb{R}^m} [\mathcal{L}_f^r h(x) + \mathcal{L}_f^{r-1} h(x)(u + d(t))] \geq -K_\alpha \eta(x), \tag{9}$$

where $K_\alpha \in \mathbb{R}^r$ is a row vector, $\eta(x) = [h(x), \dot{h}(x), \ddot{h}(x), ..., h^{r-1}(x)]^T$.

Remark 1 : From the above definitions, it is obvious that the unknown disturbances $d(t)$ make the inequalities (5) and (9) difficult to maintain during the evolution of the system (1). Furthermore, the process of designing and tuning row vector K_α is intractable and heuristic. Most of existing robust CBFs do not consider this problem, which limits their application. The differentiable convex optimization layer [14] provides a solution to address this problem through a learning-based approach because of the linearity of input in the safety condition (9). Therefore, this paper proposes a differentiable QP-based robust safety-critical control framework to overcome disturbances and simplify the parameter tuning process.

2.2 Differentiable QP

The safe controller can be obtained by solving the quadratic programming problem with (5) or (9) as a constraint (CBF/HOCBF-QP) [16]:

$$\begin{aligned} u^*(x) = \arg\min_u \parallel u - k(x) \parallel^2 \\ s.t. \quad \mathcal{L}_f h(x) + \mathcal{L}_g h(x) u \geq -\alpha(h(x)), \\ or \\ \mathcal{L}_f^r h(x) + \mathcal{L}_g \mathcal{L}_f^{r-1} h(x) u \geq -K_\alpha \eta(x), \end{aligned} \tag{10}$$

where $k(x)$ represents the Lipschitz continuous nominal controller, $u^*(x)$ is the safe controller. Differentiable QP represents that the solution of the optimization problem (10) can be backpropagated through. This enables (10) to be encoded as differentiable optimization layers [14] within deep

learning architectures. The end to end model helps to construct the HOCBF-QP that satisfies the safety requirement and improve control performance. This paper combines differentiable QP and fully-connected layers to construct robust safety-critical control framework.

2.3 First-Order High-Gain Disturbance Observer

The first-order high-gain disturbance observer is used to estimate the unknown term of the CBF forward invariance condition. Specifically, for the system (1), we consider the system output $y = w(x)$, and $w : X \to \mathbb{R}$ is a continuously differentiable function, then we have,

$$\begin{aligned} \dot{y} &= \underbrace{\mathcal{L}_f w(x) + \mathcal{L}_g w(x) u}_{v_d} + \underbrace{\mathcal{L}_g w(x) d}_{w_d} \\ &= v_d + w_d, \end{aligned} \tag{11}$$

where $w_d = \mathcal{L}_g w(x) d$ is the unknown term that needs to be estimated. Then we can define the first-order high-gain input disturbance observer as:

$$\hat{w}_d = k_b y - \xi, \tag{12}$$

$$\dot{\xi} = k_b(v_d + \hat{w}_d), \tag{13}$$

where $k_b \in \mathbb{R} > 0$ is the gain, $\xi \in \mathbb{R}$ is an auxiliary variable. The estimation error is bounded when w_d is Lipschitz continuous according to [12].

2.4 Problem formulation

Consider the disturbed fully actuated AUV dynamics in a two-dimensional horizontal environment:

$$\begin{aligned} M\dot{\nu} + C(\nu)\nu + D(\nu)\nu &= \tau + d(t), \\ \dot{\rho} &= R(\rho)\nu, \end{aligned} \tag{14}$$

where $\nu = [v_x, v_y, r]^T$ denotes the velocities of surge, sway, and yaw in the body reference frame, $\rho = [\rho_x, \rho_y, \phi]^T$ denotes the absolute position and orientation in the inertial reference frame. M is the inertia matrix, $C(\nu)$ is the Coriolis and centripetal matrix, $D(\nu)$ is the hydrodynamics damping matrix, $\tau \in \mathbb{R}^3$ denotes the generalized total thrust forces and moment, $d(t)$ denotes the unknown disturbance coming from ocean currents, and $R(\rho)$ is the rotation matrix depending on the heading orientation ϕ,

$$R(\rho) = \begin{bmatrix} \cos\phi & -\sin\phi & 0 \\ \sin\phi & \cos\phi & 0 \\ 0 & 0 & 1 \end{bmatrix}, \tag{15}$$

$M = diag(M_x, M_y, M_\phi)$, $D(\nu) = diag(X_{v_x}, Y_{v_y}, N_r) + diag(D_{v_x}|v_x|, D_{v_y}|v_y|, D_r|r|)$, $\tau = [F_{v_x}, F_{v_y}, F_r]^T$. The nonlinear control affine form of AUV model can be written as:

$$\dot{x} = \underbrace{\begin{bmatrix} R(\rho)\nu \\ -M^{-1}(C(\nu)\nu + D(\nu)\nu) \end{bmatrix}}_{f(x)} + \underbrace{\begin{bmatrix} 0_{3\times 3} \\ M^{-1} \end{bmatrix}}_{g(x)}(\tau + d(t)), \tag{16}$$

where $x = [\nu^T, \rho^T]^T$. The objective is to design the differentiable QP-based robust safety-critical control framework to guarantee the safety of the AUV during obstacle avoidance, while reducing the impact of uncertainty on the performance of obstacle avoidance caused by manual parameters. Specifically, the AUV starts from the initial position ρ_0, to reach the target position ρ_d, and avoids the obstacle during the movement under the unknown disturbance without the manual tuning process of class $\mathcal{K}$ functions.

3 Main results

In this section, the differentiable QP-based robust safety-critical control framework for AUV dynamics and the training algorithm are introduced.

3.1 DOB design for AUV dynamics

For system (1), the rth -order time derivative of $h(x)$ with relative degree r is

$$h^r(x,u,d) = \underbrace{\mathcal{L}_f^r h(x) + \mathcal{L}_g\mathcal{L}_f^{r-1}h(x)u}_{v_d} + \underbrace{\mathcal{L}_g\mathcal{L}_f^{r-1}h(x)d}_{w_d}. \tag{17}$$

Therefore, the DOB to estimate w_d is designed as:

$$\hat{w}_d = k_b h^{r-1}(x) - \xi, \tag{18}$$

$$\dot{\xi} = k_b(\mathcal{L}_f^r h(x) + \mathcal{L}_g\mathcal{L}_f^{r-1}h(x)u + \hat{w}_d). \tag{19}$$

Then, (17) can be rewritten as:

$$h^r(x,u,d) = \mathcal{L}_f^r h(x) + \mathcal{L}_g\mathcal{L}_f^{r-1}h(x)u_{v_d} + \hat{w}_d + e, \tag{20}$$

where $e = w_d - \hat{w}_d$ is the estimation error. When w_d is Lipschitz continuous with Lipschitz constant L_h, the estimation error $e(t)$ satisfies [12],

$$|e(t)| \le \left(|e(0)| - \frac{L_h}{k_b}\right)e^{-k_b t} + \frac{L_h}{k_b} \le |d(t)|. \tag{21}$$

Hence, with DOB to estimate the unknown dynamics of the safety condition derived by HOCBF, we rewrite the inequality (9) as,

$$\mathcal{L}_f^r h(x) + \mathcal{L}_g\mathcal{L}_f^{r-1}h(x)u + \hat{w}_d \ge -K_\alpha \eta(x). \tag{22}$$

In this paper, the objective is to compensate for the bounded estimation error $e(t)$ by adjusting K_α so that the system obtains lower conservativeness.

When the system is unnecessarily conservative, the obstacle avoidance trajectory will be far away from the obstacle, meaning that the AUV sacrifices too much control performance for safety. Therefore, the DOB is used to reduce the conservativeness during the obstacle avoidance. Suppose the location of the obstacle is $[ob_x, ob_y]$ with the safety distance of D_{sf}. We design the CBF as:

$$h(x) = (\rho_x - ob_x)^2 + (\rho_y - ob_y)^2 - D_{sf}^2. \tag{23}$$

Given the fully-actuated dynamics of AUV in (14), it is obvious that $\mathcal{L}_g h(x) = 0, \mathcal{L}_g\mathcal{L}_f h(x) \neq 0$, and the relative-degree $r = 2$. Substituting $r = 2$ into (18), (19) yields the first-order high-gain DOB for AUV dynamics.

3.2 Differentiable QP for robust safety-critical control

As mentioned in the previous section, the HOCBF-QP is capable being encoded as a differentiable convex optimization layer combined with fully-connected layers. We design a deep neural network consisting of a fully connected layer and a differentiable convex optimization layer to construct

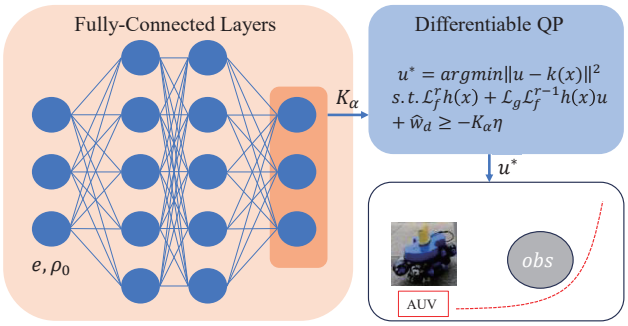

Fig. 1: Differentiable QP combined with fully connected layers

the learning framework, as shown in Fig.1. The mathematical model of the differentiable QP is formulated as (24).

$$u^*(k(x), e, \rho_0) = \arg\min_u \parallel u - k(x) \parallel^2$$
$$s.t. \quad \mathcal{L}_f^r h(x) + \mathcal{L}_g \mathcal{L}_f^{r-1} h(x) u + \hat{w}_d \geq -K_\alpha(e, \rho_0; \theta)\eta(x), \tag{24}$$

where $u^*(k(x), e, \rho_0)$ is the solution of the differentiable QP. $\hat{w}_d$ represents the estimation result of DOB. $K_\alpha(e, \rho_0; \theta)$ is the output of the fully-connected layers. θ is the weights of the fully-connected layers. $[e, \rho_0]$ is the input of the fully-connected layers, where e represents the environment information including the location of the obstacle and the safety distance, ρ_0 represents the initial position of AUV.

The proposed framework utilises fully-connected neural networks to adaptively adjust K_α to resist unknown perturbations and simplify the parameter design process. Specifically, due to the estimation of the unknown dynamics by the DOB, the problem is transformed into a compensation of the estimation error using K_α, which makes the system less conservative.

3.3 Training algorithm

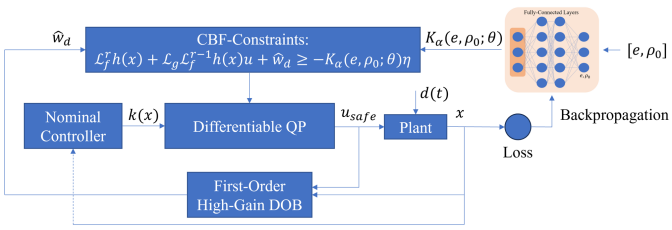

Fig. 2: Differentiable QP-based robust safety-critical control framework

The differentiable QP-based robust safety-critical control framework and the training algorithm are shown in Fig.2 and Algorithm 1 respectively. We assume that the environmental information follows a certain probability distribution P_e, and the initial position of AUV follows a certain probability distribution P_0. Sampling different environments and AUV initial positions as inputs $[e_j, \rho_{0,j}]$ to the fully connected layers. The outputs are r-dimensional vectors K_α. Then we can construct the differentiable QP-based control loop combined with the DOB. The nominal controller is to achieve

Algorithm 1: Training algorithm for robust safety-critical control

Input : Environment distribution P_e, initial position distribution P_0 of AUV, simulation state update rate Δt, simulation time horizon T, Iteration number $trainingsteps$, Number of sample environments n, Learning rate β.

Output: The parameters K_α

Training process;
for $i \leftarrow 1$ **to** $trainingsteps$ **do**
  for $j \leftarrow 1$ **to** n **do**
    Sample new environment: $e_j \sim P_e$, $\rho_{0,j} \sim P_0$
    for $t \leftarrow 0$ **to** $\frac{T}{\Delta t}$ **do**
      Calculate the differentiable QP (24) to obtain $u^*(k(x), e, \rho_0)$;
      Update system states ρ_t;
    Obtain system state trajectory $\Gamma_j(\rho_t)$;
    Calculate loss function $Loss(\Gamma_j)$;
    Update the weights $\theta_{new} = \theta_{old} - \beta \nabla_\theta Loss(\Gamma_j)$;

the control objective. The loss function $Loss$ is calculated based on the state trajectory $\Gamma_j(\rho_t)$. Specifically, for AUV dynamics, The loss function is calculated based on the obstacle avoidance trajectory. Finally, the network parameters θ are updated by gradient backpropagation.

3.4 The design of safety-critical loss

In the context of obstacle avoidance missions involving AUVs , the safety-critical loss function is designed based on two main considerations: the length of the trajectory to guarantee control performance and the distance between AUV and obstacle to guarantee safety. Therefore, we design the safety-critical loss as

$$Loss = \sum_{t=0}^{\frac{T}{\Delta t}} (\|\rho_t - \rho_{goal}\|^2 + \gamma ReLU(-h(x)), \tag{25}$$

where ρ_{goal} represents the target position of AUV, γ is an artificial parameter indicating the level of importance. The first term reflects the length of the obstacle avoidance trajectory, which we want to be as short as possible. The second term quantifies the degree of deviation from safety constraints in the avoidance trajectory, as illustrated in Fig.3. Our objective is to minimize this deviation to the greatest extent possible. It is obvious that the second term is zero when $h(x) > 0$, i.e., the AUV is safe, while the second term is punished significantly when $h(x) < 0$, i.e., the AUV collides with the obstacle. The shaded region denotes safety violation due to unknown disturbances. As the training process proceeds, the output of the fully-connected layer allows the AUV to overcome unknown disturbances to avoid obstacles with a short avoidance trajectory.

The differentiable QP-based robust safety critical control framework is designed based on α-net proposed by [13] to resist unknown disturbances by adaptively tuning class $\mathcal{K}$ functions. The safety-critical loss function is specifically designed to incorporate penalties for safety violations. As training progresses, the incidence of these safety violations

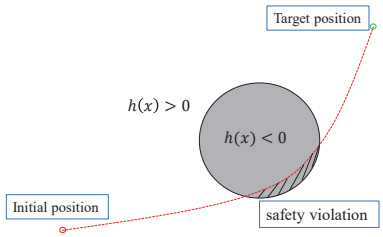

Fig. 3: Safety violation in obstacle avoidance mission scenario

is expected to diminish. The functionality of DOB is to reduce conservativeness because of its bounded estimation error [12]. After training, the fully-connected neural network will output the parameters of K_α that can resist unknown disturbances adaptively.

4 Numerical Simulations

In this section, we consider the obstacle avoidance scenario of the AUV dynamics under unknown disturbances $d(t) = [4\sin(0.2t), 4\sin(0.2t), 0.15\sin(0.2t)]^T$. We suppose that the initial position of AUV and environment information follow Gaussian distribution $\rho_X, \rho_Y \sim \mathcal{N}(0.5, 0.5)$, $ob_X \sim \mathcal{N}(8, 0.5)$, $ob_Y \sim \mathcal{N}(6, 0.5)$, $D_{sf} \sim \mathcal{N}(2, 0.5)$. The target position of AUV is $[12, 12]$. The physical parameters of AUV dynamics are set as $M_x = 283.6$, $M_y = 593.2$, $M_\phi = 29$, $X_{v_x} = 26.9$, $Y_{v_y} = 35.8$, $N_r = 3.5$, $D_{v_x} = 241.3$, $D_{v_y} = 503.8$, $D_r = 76.9$. The Algorithm parameters are set as $trainingsteps = 15, n = 10, \gamma = 20000$.

To validate the effectiveness of the proposed approach, we train our proposed model and the baseline model proposed by [13] that does not consider the unknown disturbance. The loss evolution of the proposed approach is shown in Fig.4. It is evident that the initial value of the loss is substantial, attributable to significant safety violations. As the training process proceeds, the loss values converge, implying that the safety violation problem due to unknown disturbances is mitigated.

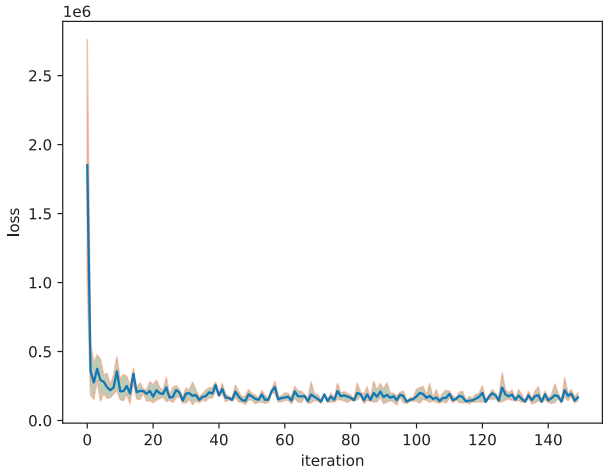

Fig. 4: The evolution of $Loss$

Fig.5 (a), (c) present the AUV obstacle avoidance trajectories under the proposed framework. Fig.5 (b), (d) present the trajectories under the baseline model. Fig.6 is the corresponding $h(x(t))$. In the scenario of (a), (b), the initial position of AUV is $[0.27m, 0.70m]$, the position of the obstacle is $[7.83m, 5.92m]$, and the safety distance is $2.88m$. In the scenario of (c), (d), the initial position of AUV is $[-0.09m, 0.07m]$, and the position of obstacle is $[8.20m, 5.46m]$, the safety distance is $1.86m$. It is obvious that the differentiable QP-based robust safety-critical control framework allows the AUV to overcome unknown disturbances and avoid the obstacle safely and smoothly, while the baseline model makes the AUV fail to avoid the obstacle.

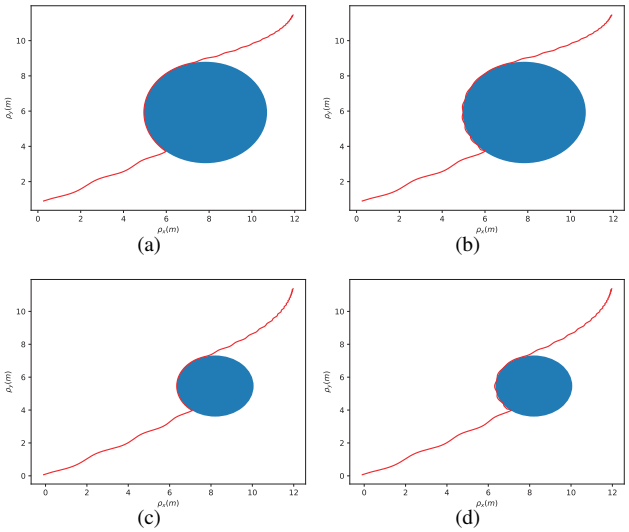

Fig. 5: The comparison of AUV obstacle avoidance trajectories

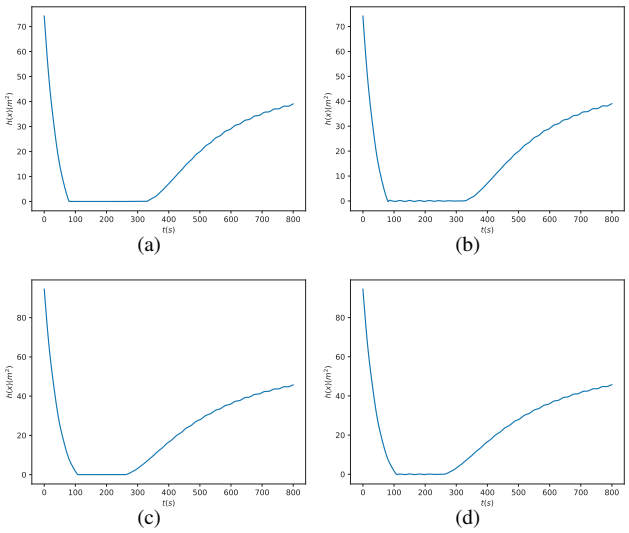

Fig. 6: The comparison of $h(x(t))$ during AUV obstacle avoidance

Table 1: Safety Rates when Using Different Models

Label	Model	Safety Rate
(A)	Baseline	8%(46)
(B)	Baseline + Safety-critical Loss	100%(0)
(C)	Baseline + DOB + Safety-critical Loss	100%(0)

Table 1 shows the safety rates of AUVs in 50 sampled different environments when different approaches are used. We

can see that the AUV can not avoid the obstacle in most environments with the baseline model. On the other hand, the models with the safety-critical loss guarantee the safety of AUV in all environments, validating the effectiveness of the safety-critical loss. It is worth noting that both model (B) and (C) improve the safety rate of AUV. This is because the main effect of DOB is to reduce the conservatism of the system and does not directly affect the safety of the AUV. The main advantage brought by DOB is the transformation from direct compensation for unknown perturbations to compensation for bounded estimation errors, which reduces the impact of unknown perturbations. Fig.7 presents the comparison in the value of $h(x(t))$ during obstacle avoidance using model (B) and (C) in different environments. The shaded areas indicate intervals between maximum and minimum values. The red and blue curve indicate the mean values. It is evident that the value of $h(x)$ is closer to zero with DOB to estimate the unknown dynamics of safety condition, which indicates that DOB mitigates the effect of unknown perturbations during obstacle avoidance. This suggests that system conservatism can be effectively reduced by compensating for bounded estimation errors instead of unknown dynamics directly.

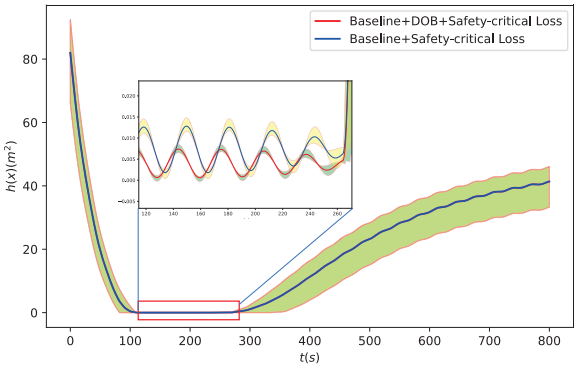

Fig. 7: The evolution of $h(x(t))$ when using model (B) and (C)

5 Conclusions

In this paper, a differentiable QP-based robust safety-critical control framework is proposed to avoid the obstacle for fully actuated AUV under disturbances. The HOCBF is used to generate the safety constraint for differentiable QP, which is combined with the fully-connected layers to construct the training framework for mitigating the impact of artificial parameters on system performance. Moreover, the safety-critical loss function is designed by considering the quantified safety violations to resist the unknown disturbance during the training process. The first-order high-gain DOB is employed to reduce the conservativeness by compensating for bounded estimation errors. The simulation results on AUV obstacle avoidance demonstrate that the proposed training framework enables AUV to avoid the obstacle under disturbances while reducing the effect of human uncertainty from artificial parameters.

References

[1] F. Sagala and R. T. Bambang, Development of sea glider autonomous underwater vehicle platform for marine exploration and monitoring, *Indian Journal of Geo-Marine Sciences*, 40(2): 287-295, 2011.

[2] J. Liu, M. Zhao, and L. Qiao, Adaptive barrier Lyapunov function-based obstacle avoidance control for an autonomous underwater vehicle with multiple static and moving obstacles, *Ocean Engineering*, 243: 110303, 2022.

[3] C. Shen, Y. Shi, and B. Buckham, Trajectory Tracking Control of an Autonomous Underwater Vehicle Using Lyapunov-Based Model Predictive Control, *IEEE Transactions on Industrial Electronics*, 65(7): 5796-5805, 2018.

[4] C. Cheng, D. Zhu, B. Sun, Z. Chu, J. Nie, and S. Zhang, Path planning for autonomous underwater vehicle based on artificial potential field and velocity synthesis, in *Proceedings of the 28th IEEE Canadian Conference on Electrical and Computer Engineer*, 2015: 717-721.

[5] C. Wang, S. Zhu, B. Li, L. Song and X. Guan, Time-Varying Constraint-Driven Optimal Task Execution for Multiple Autonomous Underwater Vehicles, *IEEE Robotics and Automation Letters*, 8(2): 712-719, 2023.

[6] B. Li, S. Wen, Z. Yan, G. Wen and T. Huang, A Survey on the Control Lyapunov Function and Control Barrier Function for Nonlinear-Affine Control Systems, *IEEE/CAA Journal of Automatica Sinica*, 10(3): 584-602, 2023.

[7] Q. Nguyen and K. Sreenath, Robust Safety-Critical Control for Dynamic Robotics, *IEEE Transactions on Automatic Control*, 67(3): 1073-1088, 2022.

[8] Y. Emam, P. Glotfelter and M. Egerstedt, Robust Barrier Functions for a Fully Autonomous, Remotely Accessible Swarm-Robotics Testbed, in *Proceedings of the 58rd IEEE Conference on Decision and Control*, 2019: 3984-3990.

[9] S. Kolathaya and A. D. Ames, Input-to-State Safety With Control Barrier Functions, *IEEE Control Systems Letters*, 3(1): 108-113, 2019.

[10] A. Alan, A. J. Taylor, C. R. He, G. Orosz, and A. D. Ames, Safe Controller Synthesis With Tunable Input-to-State Safe Control Barrier Functions, *IEEE Control Systems Letters*, 6: 908-913, 2022.

[11] E. Das and R. M. Murray, Robust Safe Control Synthesis with Disturbance Observer-Based Control Barrier Functions, in *Proceedings of the 61st IEEE Conference on Decision and Control*, 2022: 5566-5573.

[12] A. Alan, T. G. Molnar, E. Das, A. D. Ames, and G. Orosz, Disturbance Observers for Robust Safety-Critical Control With Control Barrier Functions, *IEEE Control Systems Letters*, 7: 1123-1128, 2023.

[13] H. Ma, B. Zhang, M. Tomizuka and K. Sreenath, Learning Differentiable Safety-Critical Control using Control Barrier Functions for Generalization to Novel Environments, *European Control Conference*, 2022: 1301-1308.

[14] A. Agrawal, B. Amos, S. Barratt, S. Boyd, S. Diamond, and J. Z. Kolter, Differentiable convex optimization layers, *Advances in Neural Information Processing Systems*, 32: 9562–9574, 2019.

[15] W. Xiao and C. Belta, High-Order Control Barrier Functions, *IEEE Transactions on Automatic Control*, 67(7): 3655-3662, 2022.

[16] A. D. Ames, X. Xu, J. W. Grizzle, and P. Tabuada, Control Barrier Function Based Quadratic Programs for Safety Critical Systems, *IEEE Transactions on Automatic Control*, 62(8): 3861-3876, 2017.

[17] A. D. Ames, S. Coogan, M. Egerstedt, G. Notomista, K. Sreenath, and P. Tabuada, Control barrier functions: Theory and applications, in *Proceedings of the 18th European Control Conference*, 2019: 3420–3431.

Proceedings of the 3rd Conference on Fully Actuated System Theory and Applications
May 10-12, 2024, Shenzhen, China

Construction of Barrier Surfaces in Mutual Attack-Defense Games

Jingwen Xu[1,2], Qiyong He[1,2], Min Meng[1,2], Xiuxian Li[1,2*]

1. College of Electronics and Information Engineering, Tongji University, Shanghai 201804, P. R. China

2. Shanghai Research Institute for Intelligent Autonomous Systems, Shanghai 201210, P. R. China
E-mail: jwxu21@tongji.edu.cn, qyhe@tongji.edu.cn, mengmin@tongji.edu.cn, and xxli@ieee.org

Abstract: In this paper, a variant of the target defense game is introduced, which involves two equal-speed agents and two targets. The agents do not possess a distinct role as either the defender or the intruder. Rather, each agent is tasked with protecting its own target while simultaneously attempting to breach the opponent's target. This paper proposes a solution to the Game of Kind through the construction of barrier surfaces, which divide the space into two winning regions and a confronting region. The proposed optimal strategies ensure that the values of the barrier functions remain unchanged during the game. Finally, some simulations are studied to verify the effectiveness of the proposed optimal strategies. The game in this paper can provide a basis for more practical problems involving adversarial games, such as security systems and racing.

Key Words: Game of Kind, Mutual attack-defense game, Barrier surface, Optimal strategies, Winning region

1 Introduction

In recent decades, many adversarial-related problems have been proposed and attempted to be solved in the fields of aerospace, automatic control, robotics, etc [1]. One popular approach to modeling scenarios involving conflicts between multiple agents is the pursuit-evasion games (PEGs). Isaacs [2] made pioneering contributions to the study of PEGs, proposing various different pursuit-evasion conflicts. A concise summary of the current research progress in PEGs is provided in [3].

Within the various different PEGs research, the target defense game is recognized as a popular branch, which involves two teams: the defender team is tasked with protecting the target while the intruder team attempts to breach it. The target defense game may concern various types of targets, including a point target [4], a line target [5], a circular target [6], and arbitrary convex sets [7, 8]. In certain scenarios, the target itself can be moving, referred to as an active target [9, 10]. Two other variations are the perimeter defense game [11, 12] and the reconnaissance game [13], in which the defender is to patrol along the boundary for the former and the intruder is to reconnaissance the target region and then return to the safe zone for the latter.

In Isaacs' pioneer work [2], two important concepts were introduced: the Game of Kind and the Game of Degree. The former indicates the results of the game, while the latter gives the actual strategies for the corresponding Game of Kind. A common solution for Games of Kind is by determining the barrier surface, as in recent work [14, 24] on solving the equal-speed multi-player problem and the task assignment problem in the reach-avoid game, respectively. While in other works [5, 25] not only solve the Game of Kind but synthesize the saddle-point strategies, thus providing a complete solution to the Game of Degree as well. The primary objective of this paper is to employ geometric methods to construct so-called barrier surfaces to solve the Game of Kind for a novel mutual attack-defense game scenario. The barrier is a surface that demonstrates the characteristics of semi-permeability, dividing the state space into disjoint regions. And the geometric techniques, such as the Apollonius circle [14] and the Voronoi diagram [15], are commonly utilized for both qualitative and quantitative analysis of the winning regions and optimal strategies.

This paper focuses on proposing a solution to the Game of Kind by constructing barrier surfaces for two equal-speed agents who guard their own target and breach the opponent's target. For such problems, Isaacs proposed various methodologies for the construction of barriers in [2]. A classical method for constructing barriers is to start from a point on the boundary of the usable part of the target set and then integrate the retrogressive path equations (RPEs). However, the solution of RPEs tends to be analytically challenging for multi-agent systems. Thus, the following methods were proposed to solve such complicated problems: the first approach [16] is to divide the complex game into several sub-games, followed by analyzing the optimal behaviors of each player in each sub-games. The second approach [17] is to use explicit strategy methods. And the last approach is a numerical approximation method for solving the HJI equation. An example is the reachable set [18], which is the zero sub-level set of the viscosity solution of a time-dependent HJI partial differential equation and is often used to solve problems with complex constraints. Other approximation methods, such as reinforcement learning [19, 20], are commonly used for multi-agent in complex scenarios.

Based on these existing studies, this paper addresses a novel variant of target defense games, namely the mutual attack-defense game. Unlike the work in [21], which used Isaacs's method to construct natural barriers, this paper utilizes geometric methods to construct barrier surfaces and provides explicit expressions. The most related work [22] addresses the construction of barrier surfaces in a football differential game with a line segment target region. In contrast, this paper tackles a more practical scenario where each agent has to perform simultaneous tasks, i.e., guarding its own target and breaching the opponent's target.

The contributions of this paper are as follows:

This work was supported by the National Science and Technology Major Project under grant 2022ZD0119702.

- a novel variant of target defense game is introduced, namely mutual attack-defense game;
- a novel partitioning method for Game of Kind is addressed, where the space is divided through multiple barrier surfaces involving winning regions and a confronting region;
- the optimal strategies for both agents in the entire state space have been thoroughly analyzed by groups of numerical simulations.

The paper is organized as follows: Section II defines the mutual attack-defense game in detail. Section III focuses on the construction of barrier surfaces and proposes the optimal strategies for both agents. In Section IV, some simulations are conducted to verify their effectiveness. Section V concludes with possible future work.

2 Problem Formulation

Consider a mutual attack-defense game (MADG) in the plane $\mathbb{R}^2$ with two agents A_1, A_2 and two targets T_1, T_2. Note that this paper does not explicitly distinguish the roles of both agents between the intruder and the defender. At any moment, each agent may choose either invasion or defense. Assume that the targets are circular regions with the same radius r and that the distance between two target centers is $2d$. The orthogonal bisector (OBS) of the line connecting target centers separates the plane into two parts, which are denoted as S_1 and S_2, respectively. Without loss of generality, the problem can be placed in the Cartesian coordinate system as shown in Fig. 1, where the target centers are fixed on the x-axis and their corresponding OBS is on the y-axis.

The states of agents are specified by $\mathbf{x_1} = (x_1, y_1)$ and $\mathbf{x_2} = (x_2, y_2)$, respectively. And the complete state is denoted as $\mathbf{x} := (x_1, y_1, x_2, y_2) \in \mathbb{R}^4$. The controls of A_1 and A_2 are the instantaneous heading angles, where $\mathbf{u}_1 = \phi$ and $\mathbf{u}_2 = \psi$. The dynamics $\dot{\mathbf{x}} = \mathbf{f}(\mathbf{x}, \mathbf{u_1}, \mathbf{u_2})$ are specified by the system of ordinary differential equations:

$$\begin{aligned} \dot{x}_1 &= v_1 \cos\phi, \quad \dot{y}_1 = v_1 \sin\phi, \\ \dot{x}_2 &= v_2 \cos\psi, \quad \dot{y}_2 = v_2 \sin\psi, \end{aligned} \tag{1}$$

where v_1, v_2 are the velocities of the first and second agents, respectively. Consider a realistic scenario in this paper. If agents collide, the wreckage of the agent belonging to its guarding space can be repaired and put back into use again. This can be simplified to a scenario where the outcome of the collision depends entirely on the position of two agents. That is, a collision occurring in S_1 might result in A_1's win, and vice versa. The targets are centered at $(-d, 0)$ and $(d, 0)$ and the disjoint advantageous regions are denoted as $S_1 = \{(x, y) \in \mathbb{R}^2 |\ x < 0\}$ and $S_2 = \{(x, y) \in \mathbb{R}^2 |\ x > 0\}$, and the target regions are denoted as $T_1 = \{(x, y) \in \mathbb{R}^2 | (x - d)^2 + y^2 \leq r^2\}$ and $T_2 = \{(x, y) \in \mathbb{R}^2 | (x + d)^2 + y^2 \leq r^2\}$, respectively. The background of the problem considered in this paper is all based on the following assumptions.

Assumption 1.

(a) *The distance between two target centers is larger than the diameter of each target region, i.e., $d > r$;*
(b) *Both agents have the same maximum velocity v_{max}, i.e., $v_1 = v_2 = v_{max}$;*
(c) *The initial states satisfy $x_1 \in S_1$ and $x_2 \in S_2$;*
(d) *Each agent has complete information about each other and considers a non-anticipative information structure.*

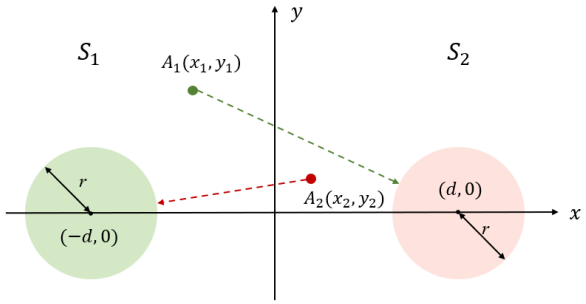

Fig. 1: An example of the MADG in the Cartesian coordinate system, where the green point represents A_1 and the red point represents A_2. The two dashed lines represent the possible actions taken by the two agents. The two target regions have the same radius r, and the distance between the target centers is $2d$.

The outcome of the game depends on the choice of parameters, as in Assumption 1, where (a) ensures that the two targets do not intersect, (b) and (c) ensure the fairness of the game, and (d) assumes both agents do not know the opponent's current decision. Note that the so-called non-anticipative information structure refers to the fact that players do not have access to future information when making their current decisions. The assumptions made in this paper are commonly adopted and facilitate the following analysis. However, further advancements are required to address more complex and general issues.

Traditional target defense games typically have one of two outcomes: either the agent invades or is captured by the adversary. However, in MADG there would be an additional terminal set of draw, that is, the game will terminate under one of the following conditions:

$$\mathcal{T} := \mathcal{T}_1 \bigcup \mathcal{T}_2 \bigcup \mathcal{T}_C, \tag{2}$$

where

$$\begin{aligned} \mathcal{T}_1 &= \{\mathbf{x_1}, \mathbf{x_2} \in \mathbb{R}^2 | \mathbf{x_1} \in T_2 \wedge \mathbf{x_2} \notin T_1\}, \\ \mathcal{T}_2 &= \{\mathbf{x_1}, \mathbf{x_2} \in \mathbb{R}^2 | \mathbf{x_1} \notin T_2 \wedge \mathbf{x_2} \in T_1\} \end{aligned} \tag{3}$$

represent the outcome of A_1 breaches T_2 and A_1 breaches T_1, respectively. And

$$\mathcal{T}_C = \{\mathbf{x_1}, \mathbf{x_2} \in \mathbb{R}^2 | x_1 = x_2 = 0, y_1 = y_2\} \tag{4}$$

represents the outcome of a draw for A_1 and A_2. The draw scenario will be discussed in more detail later in Section 3.

3 Main Result

In this section, barrier surfaces are constructed to determine the winning regions and a confronting region. Additionally, optimal strategies are proposed to ensure the values of the barrier equations remain unchanged.

This paper addresses two agents with the same speed; thus, the dominance region for both agents can be directly

obtained through the OBS. The initial states of A_1 and A_2 are known, the OBS can be written as $y = mx + n$ with

$$m = -\frac{x_1 - x_2}{y_1 - y_2},\ n = \frac{x_1^2 + y_1^2 - x_2^2 - y_2^2}{2(y_1 - y_2)}. \tag{5}$$

Definition 1. *Consider the MADG with two equal-speed agents A_1 and A_2. The barrier surfaces can be obtained and consist of the following components:*

$$\begin{aligned} B_1(\mathbf{x}) &= r - d_2, \\ B_2(\mathbf{x}) &= r - d_1, \\ B_3(\mathbf{x}) &= d_2 - d_1, \end{aligned} \tag{6}$$

where r denotes the target radius; $d_1 = \frac{|-dm+n|}{\sqrt{1+m^2}}$ and $d_2 = \frac{|dm+n|}{\sqrt{1+m^2}}$ are the distances from the centers of T_1 and T_2 to the OBS. $B_1(\mathbf{x})$ and $B_2(\mathbf{x})$ are the distances from the centers of T_1 and T_2 to the OBS. $B_3(\mathbf{x})$ is the difference between the distances of the centers of T_1 and T_2 from the OBS.

Lemma 1. *The entire state-space of MADG can be divided into three different terminal sets according to $B_1(\mathbf{x})$, $B_2(\mathbf{x})$ and extra judgments, as shown in Table 1.*

Proof. Firstly, simultaneous satisfactions of $B_1(\mathbf{x}) > 0$ and $B_2(\mathbf{x}) < 0$ imply that the OBS only intersects with T_2. At this moment, there is at least one point where both agents can reach T_2 at the same time, i.e., this initial state indicates the winning region of A_1. Vice versa, when $B_1(\mathbf{x}) < 0$ and $B_2(\mathbf{x}) > 0$, the only difference is to judge the OBS with respect to T_1.

Secondly, satisfying both $B_1(\mathbf{x}) < 0$ and $B_2(\mathbf{x}) < 0$ implies that the OBS intersects with neither T_1 nor T_2. In this special case, additional judgments are required. The parameter $-\frac{n}{m}$ is the intersection of the OBS with the x-axis. When $-d < -\frac{n}{m} < d$, it indicates that the OBS is between the two target centers. There would not exist strategies that could ensure victory for one side, i.e., a confronting region. Thus, the terminal set at this point is $\mathcal{T}_C$. When $-\frac{n}{m} < -d$, it means the OBS is located outside the two target centers and indicates that the T_1 region is completely in the dominance region of A_2, thus there is more than one point that could make A_2 win. Thus, the terminal set at this point is $\mathcal{T}_2$. When $-\frac{n}{m} < d$, vice versa.

Thirdly, meeting the $B_1(\mathbf{x}) > 0$ and $B_2(\mathbf{x}) > 0$ implies that the OBS intersects with both T_1 and T_2, where an auxiliary condition of $B_3(\mathbf{x})$ is also required to analyze possible outcomes. Indeed, in such a scenario where $B_3(\mathbf{x}) < 0$, it implies that the OBS is closer to the center of T_2. Consequently, there exists a point on the boundary of T_2 that is relatively closer to the OBS compared to any point on the boundary of T_1. This relatively closer point on the boundary of T_2 becomes more reachable, enabling them to reach it simultaneously. The case is similar when $B_3(\mathbf{x}) > 0$. □

A special case needs to be considered when $y_1 = y_2$, because (5) does not exist at this point. In this case, the difference lies in the definitions of d_1 and d_2, which can be denoted as $d_1^{'}$ and $d_2^{'}$, respectively. Furthermore, $d_1^{'} = |\frac{x_1+x_2}{2} + d|$, and $d_2^{'} = |\frac{x_1+x_2}{2} - d|$ denote the distance from the centers of T_1 and T_2 to the OBS, respectively. The OBS is updated based on the relationship between y_1 and y_2 and can now be expressed as $x = \frac{x_1+x_2}{2}$. The analysis bears a strong resemblance to that of Lemma 1, it is omitted here.

Table 1: Different terminal sets for $y_1 \neq y_2$

	$B_2(\mathbf{x}) < 0$		$B_2(\mathbf{x}) > 0$	
$B_1(\mathbf{x}) < 0$	$-d < -\frac{n}{m} < d$	$\mathcal{T}_\mathbf{C}$	$\mathcal{T}_\mathbf{2}$	
	$-\frac{n}{m} > d$	$\mathcal{T}_\mathbf{1}$		
	$-\frac{n}{m} < -d$	$\mathcal{T}_\mathbf{2}$		
$B_1(\mathbf{x}) > 0$	$\mathcal{T}_\mathbf{1}$		$B_3(\mathbf{x}) < 0$	$\mathcal{T}_\mathbf{1}$
			$B_3(\mathbf{x}) > 0$	$\mathcal{T}_\mathbf{2}$

Lemma 2.

1. *Consider the case when $y_1 \neq y_2$. When $B_1(\mathbf{x}) > 0$ and $B_2(\mathbf{x}) < 0$, the optimal aimpoint is*

$$\begin{aligned} x^* &= \frac{d - mn - \sqrt{(1+m^2)r^2 - (dm+n)^2}}{1+m^2}, \\ y^* &= \frac{dm + n - m\sqrt{(1+m^2)r^2 - (dm+n)^2}}{1+m^2}. \end{aligned} \tag{7}$$

When $B_1(\mathbf{x}) <$ and $B_2(\mathbf{x}) > 0$, the optimal aimpoint is

$$\begin{aligned} x^* &= \frac{-d - mn + \sqrt{(1+m^2)r^2 - (dm-n)^2}}{1+m^2}, \\ y^* &= \frac{-dm + n + m\sqrt{(1+m^2)r^2 - (dm-n)^2}}{1+m^2}. \end{aligned} \tag{8}$$

When $B_1(\mathbf{x}) < 0$ and $B_2(\mathbf{x}) < 0$, the optimal aimpoint will be further determined by the relation of $-\frac{n}{m}$ to d. When $-d < -\frac{n}{m} < d$, the optimal aimpoint is

$$x^* = 0,\ y^* = n. \tag{9}$$

When $-\frac{n}{m} < -d$, the optional aimpoint is

$$\begin{aligned} x^* &= -d + r\sqrt{\frac{(x_2+d)^2}{(x_2+d)^2 + y_2^2}}, \\ y^* &= \frac{y_2 r}{x_2 + d}\sqrt{\frac{(x_2+d)^2}{(x_2+d)^2 + y_2^2}}. \end{aligned} \tag{10}$$

And when $-\frac{n}{m} > d$, the optional aimpoint is

$$\begin{aligned} x^* &= d - r\sqrt{\frac{(x_1-d)^2}{(x_1-d)^2 + y_1^2}}, \\ y^* &= -\frac{y_1 r}{x_1 - d}\sqrt{\frac{(x_1-d)^2}{(x_1-d)^2 + y_1^2}}, \end{aligned} \tag{11}$$

When $B_1(\mathbf{x}) > 0$, $B_2(\mathbf{x}) > 0$, and $B_3(\mathbf{x}) < 0$, the optimal aimpoint can be set as (11), and when $B_1(\mathbf{x}) > 0$, $B_2(\mathbf{x}) > 0$, and $B_3(\mathbf{x}) > 0$, the optimal aimpoint is the same as (10).

2. *Consider the case when $y_1 = y_2$. When $B_1(\mathbf{x}) > 0$ and $B_2(\mathbf{x}) < 0$, the optimal aimpoint is*

$$x^* = \frac{x_1 + x_2}{2},\ y^* = \pm\sqrt{r^2 - \left(\frac{x_1 + x_2}{2} - d\right)^2}. \tag{12}$$

When $B_1(\mathbf{x}) < 0$ and $B_2(\mathbf{x}) > 0$, the optimal aimpoint is

$$x^* = \frac{x_1 + x_2}{2},\ y^* = \pm\sqrt{r^2 - \left(\frac{x_1 + x_2}{2} + d\right)^2}. \tag{13}$$

When $B_1(\mathbf{x}) < 0$ and $B_2(\mathbf{x}) < 0$, the optimal aimpoint will be further determined by the relation of $2d$ to $d_1^{'}$ and $d_2^{'}$. When $2d = d_2^{'} - d_1^{'}$, the optional aimpoint (x^*, y^*) is same to (9), and when $2d = d_1^{'} - d_2^{'}$, the optional aimpoint (x^*, y^*) is same to (10).

Proof. The optimal aimpoint ensures that the advantage of both sides remains constant during the match, if it indicates a point on the barrier surface. The solution of the optimal aimpoint is related to the semi-permeability of the barrier surfaces, i.e., by means of $B_1(\mathbf{x})$ and $B_2(\mathbf{x})$, the plane can be partitioned into the region where someone is likely to win. When only satisfying $B_1(\mathbf{x}) > 0$ or $B_2(\mathbf{x}) > 0$, it implies that there is a probability that A_1 or A_2 would win. And when both $B_1(\mathbf{x}) > 0$ and $B_2(\mathbf{x}) > 0$ hold, it is further necessary for $B_3(\mathbf{x})$ to determine which side is the real winner.

Consider the case $y_1 \neq y_2$ first. Based on these analysis, when $B_1(\mathbf{x}) > 0$ and $B_2(\mathbf{x}) < 0$, the optimal aimpoint can be solved when the OBS intersects with T_2. Vice versa, when $B_1(\mathbf{x}) < 0$ and $B_2(\mathbf{x}) > 0$, the optimal aimpoint can be solved when the OBS intersects with T_1. When $B_1(\mathbf{x}) < 0$ and $B_2(\mathbf{x}) < 0$, the optimal aimpoint is further determined again by the relation of $-\frac{n}{m}$ to d. When $-d < -\frac{n}{m} < d$, the optimal aimpoint is toward the intersection of the OBS with y-axis. And when $-\frac{n}{m} < -d$, there are more than one aimpoint that could make A_2 win; in fact, there is a time advantage for A_2 to move to any point on T_1, and the strategies in this case can be specified to move toward the center of T_1. When $-\frac{n}{m} > d$, the analysis is similar to above. When $B_1(\mathbf{x}) > 0$, $B_2(\mathbf{x}) > 0$ and $B_3(\mathbf{x}) < 0$, the optimal aimpoint is same to (11), and when $B_3(\mathbf{x}) > 0$, the optimal aimpoint is same to (10).

Then consider the case $y_1 = y_2$. When $B_1(\mathbf{x}) > 0$ and $B_2(\mathbf{x}) < 0$, let us consider the sign of y_1. And when $B_1(\mathbf{x}) < 0$ and $B_2(\mathbf{x}) > 0$, let us consider the sign of y_2. When $B_1(\mathbf{x}) < 0$ and $B_2(\mathbf{x}) < 0$, the optional aimpoint will be further determined the relation of $2d$ to $d_1^{'}$ and $d_2^{'}$. When $2d = d_2^{'} - d_1^{'}$, there are more than one aimpoints that could make A_2 win, the optional aimpoint (x^*, y^*) is same to (10), and when $2d = d_1^{'} - d_2^{'}$, the optional aimpoint (x^*, y^*) is same to (11). □

Theorem 1. *The optimal headings of both agents are constant under optimal play and trajectories are straight lines.*

Proof. The optimal control inputs can be easily obtained, where the Hamiltonian is

$$\min_{\phi} \max_{\psi} \mathcal{H} = \lambda_{x_1} \cos\phi + \lambda_{y_1} \sin\phi + \lambda_{x_2} \cos\psi + \lambda_{y_2} \sin\psi, \tag{14}$$

and the co-state is $\lambda^T = (\lambda_{x_1}, \lambda_{y_1}, \lambda_{x_2}, \lambda_{y_2})$. In addition, the co-state dynamics are $\dot{\lambda}_{x_1} = \dot{\lambda}_{y_1} = \dot{\lambda}_{x_2} = \dot{\lambda}_{y_2} = 0$. Thus, all co-states and the optimal headings are constant. Therefore, the optimal trajectory is a straight line. □

Theorem 2. *Consider the MADG with two equal-speed agents A_1 and A_2. The optimal state feedback strategies for both agents are*

$$\begin{aligned} cos\phi^* &= \frac{x^* - x_1}{\sqrt{(x^* - x_1)^2 + (y^* - y_1)^2}}, \\ sin\phi^* &= \frac{y^* - y_1}{\sqrt{(x^* - x_1)^2 + (y^* - y_1)^2}}, \\ cos\psi^* &= \frac{x^* - x_2}{\sqrt{(x^* - x_2)^2 + (y^* - y_2)^2}}, \\ sin\psi^* &= \frac{y^* - y_2}{\sqrt{(x^* - x_2)^2 + (y^* - y_2)^2}}, \end{aligned} \tag{15}$$

where x^* and y^* vary across different cases, it allows for the derivation of more specific conclusions by considering the distinct terminal sets obtained from Table 1 and the different optimal aimpoints described in Lemma 2.

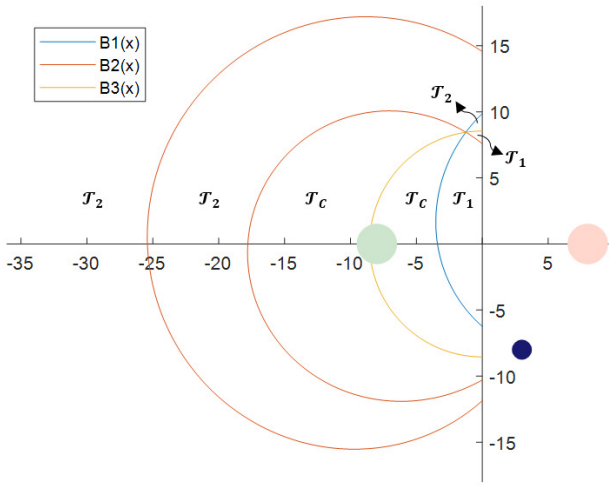

Fig. 2: The figure illustrates the case where $\mathbf{x_2}$ is fixed at $(3, -8)$ and depicts the terminal sets defined in Section 2.

Proof. Lemma 1 provides how to partition the terminal sets in the whole state space, and Lemma 2 gives the optimal aimpoints or optional aimpoints, which are in different positions dividing by barrier surfaces. And Theorem 1 further proves that the optimal trajectories are straight lines. Therefore, the optimal strategies of both A_1 and A_2 should be directed to the location of the optimal aimpoint or the optional aimpoint (x^*, y^*) in Lemma 2. □

Remark 1. *The barrier surfaces can be solved when $y_1 < y_2$, as done in [14] and [22]. By fixing A_2's position, the barrier surface corresponding to A_1's position can be demonstrated in $\mathbb{R}^2$, as shown in Fig. 2. Since Assumption 1. (c) holds, the curves all lie in the left of the y-axis.*

4 Simulation

The simulations conducted in this section aim to validate the relationship between constructed barrier surfaces and optimal strategies. In Section III, a detailed analysis of equal-speed agents dividing the winning or confronting regions via barrier surfaces was presented, and the optimal strategies for both agents are given. Several simulations are conducted to verify the effectiveness of the proposed optimal strategies.

Table 2: Examples for different initial states of A_1 and A_2

$\mathbf{x_1}$	$\mathbf{x_2}$	$B_1(\mathbf{x})$	$B_2(\mathbf{x})$	$\mathcal{T}$	(x^*, y^*)
(-2, 0)	(3, -8)	-3.70	0.76	$\mathcal{T}_1$	(6.52, -0.24)
(5, 12)	(3, -8)	0.92	-6.40	$\mathcal{T}_2$	(-6.51, -0.21)
(-8, 0)	(3, -8)	-4.64	-5.30	$\mathcal{T}_C$	(0, -0.56)

First, define the fundamental parameters $r = 1.5$ and $d = 8$, i.e., both target radii are 1.5 and centered at $(-8, 0)$ and $(8, 0)$, respectively. Then, fix A_2 on $\mathbf{x_2} = (-3, 8)$ consistent with Fig.2 and consider the initial states of A_1 as $(-2, 0)$, $(-5, 12)$, and $(-8, 0)$, respectively. Both agents begin the game with given initial states and follow the optimal strategies in Theorem 1. Both agents start the game with the given initial state and follow the optimal strategies in Theorem 1. The initial states of the game and the termination states of the game are shown in Figs 3, 4 and 5. The barrier functions are also observed at the same time. It can be seen that the values of the barrier functions remain constant during the game. Based on the full information available for both agents, the barrier function for initial states can be calculated as shown in Table 2.

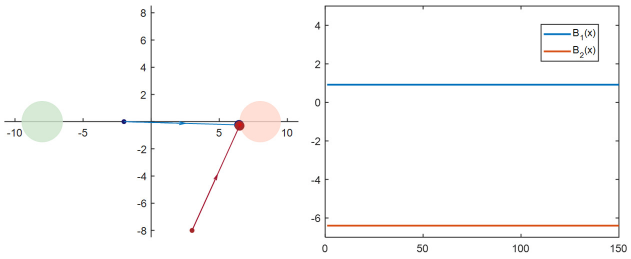

Fig. 3: The optimal trajectories with initial states $\mathbf{x_1} = (-2, 0)$ and $\mathbf{x_2} = (3, -8)$ are shown in the left. And the barrier functions of $B_1(\mathbf{x})$ and $B_2(\mathbf{x})$ are shown in the right. The blue dots and red dots represent the initial state and terminal state of A_1 and A_2, respectively. The blue and red arrows indicate the direction of the A_1 and A_2 optimal trajectories, respectively, while the red star indicates the optimal point in this case.

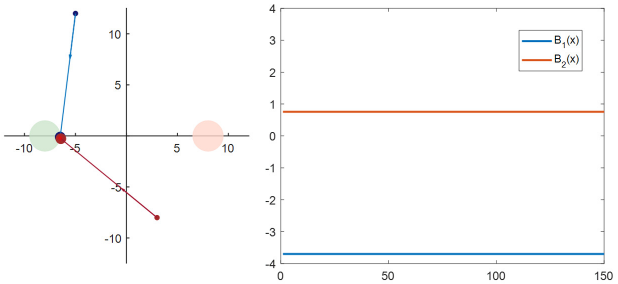

Fig. 4: The optimal trajectories with initial states $\mathbf{x_1} = (-5, 12)$ and $\mathbf{x_2} = (3, -8)$ are shown in the left. And the barrier functions of $B_1(\mathbf{x})$ and $B_2(\mathbf{x})$ are shown in the right. The blue dots and red dots represent the initial state and terminal state of A_1 and A_2, respectively. The blue and red arrows indicate the direction of the A_1 and A_2 optimal trajectories, respectively, while the red star indicates the optimal point in this case.

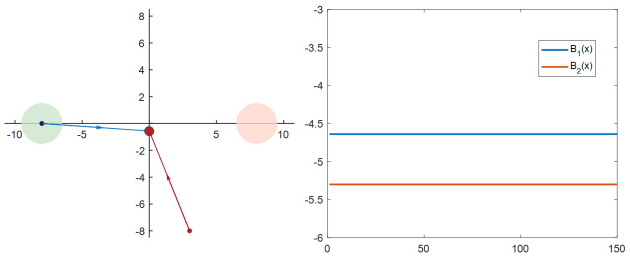

Fig. 5: The optimal trajectories with initial states $\mathbf{x_1} = (-8, 0)$ and $\mathbf{x_2} = (3, -8)$ are shown in the left. And the barrier functions of $B_1(\mathbf{x})$ and $B_2(\mathbf{x})$ are shown in the right. The blue dots and red dots represent the initial state and terminal state of A_1 and A_2, respectively. The blue and red arrows indicate the direction of the A_1 and A_2 optimal trajectories, respectively, while the red star indicates the optimal point in this case.

As stated in Section 3, the barrier functions characterize the degree of advantage for both agents of the game. Therefore, ensuring the invariance of the barrier functions during the game process can make the advantages of both sides remain unchanged, i.e., the optimal states, corresponding to the optimal strategies, are reached. In addition, the case of $y_1 = y_2$ is obvious and will not be analyzed and discussed here due to space limitations.

The above three simulations correspond to different terminal sets: $\mathcal{T}_1$, $\mathcal{T}_2$, and $\mathcal{T}_C$. Next, the other two possible scenarios are supplemented in Fig 6 and Fig 7, respectively. First, consider the case when $\mathbf{x_1} = (-0.01, 0.3)$ and $\mathbf{x_2} = (0.05, 0.9)$. This scenario involves an auxiliary condition of $B_3(\mathbf{x})$ that is also required to analyze possible outcomes. Consistent with the above analysis, the barrier functions are also constant in this case.

Finally, consider the special case when $\mathbf{x_1} = (-1, 10)$ and $\mathbf{x_2} = (1, 6)$. This case involves the need to determine the relationship of $-\frac{n}{m}$ to d to support the analysis of possible outcomes. In this case, an optional strategy is to find the shortest path for the more advantaged player, while the other player's strategy can only aim for the same point but cannot complete the interception. This is a special case in this paper that goes beyond the solution of the optimal strategies via the invariance of the value of the barrier functions. However, through simulation, one can see that the victory of the dominant agents is obvious. Interestingly, in the setting of this paper, there is no terminal outcome in which one side captures the other; precisely so, through the initial positions of the two sides of the game, the direct inference of the game outcome can be completed and the optimal strategies of both sides can be obtained by the barrier functions.

5 Conclusion

In this paper, a new game, called MADG, is introduced and the Game of Kind of MADG is solved: the barrier surfaces are constructed and the optimal strategies are proposed. In contrast to previous work, the barrier surfaces of a variant of the target defense game are explicitly obtained in closed form. Barrier surfaces are constructed to co-partition the planar surface, intelligently dividing the entire space into two winning regions and a confronting region. The proposed op-

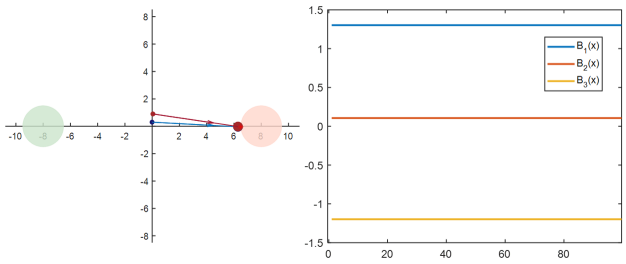

Fig. 6: The optimal trajectories with initial states $\mathbf{x_1} = (-0.01, 0.3)$ and $\mathbf{x_2} = (0.05, 0.9)$ are shown in the left. And the barrier functions of $B_1(\mathbf{x})$, $B_2(\mathbf{x})$, and $B_3(\mathbf{x})$ are shown in the right. The blue dots and red dots represent the initial state and terminal state of A_1 and A_2, respectively. The blue and red arrows indicate the direction of the A_1 and A_2 optimal trajectories, respectively, while the red star indicates the optimal point in this case.

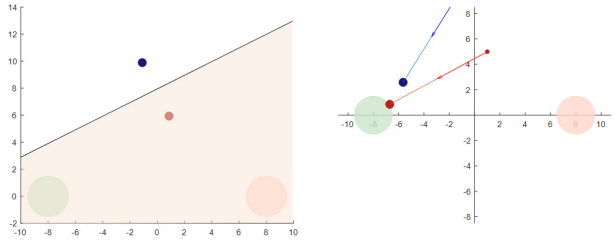

Fig. 7: The optional strategies with initial states $\mathbf{x_1} = (-1, 10)$ and $\mathbf{x_2} = (1, 6)$ for both agents are shown in the left. The blue dots and red dots represent the initial state and terminal state of A_1 and A_2, respectively. The blue and red arrows indicate the direction of the A_1 and A_2 optional trajectories, respectively, while the red star indicates the optional point in this case.

timal strategies ensure the consistency of the values of the barrier functions. The effectiveness of the proposed optimal strategies is also verified through simulations.

References

[1] X. Li, M. Meng, Y. Hong, and J. Chen, "A Survey of Decision Making in Adversarial Games," *SCIENCE CHINA: Information Sciences*, 2024, 67(4): 141201.

[2] R. Isaacs, *Differential Games: A Mathematical Theory with Applications to Warfare and Pursuit, Control and Optimization*. Courier Corporation, 1999.

[3] I. Weintraub, M. Pachter, and E. Garcia, "An Introduction to Pursuit-Evasion Differential Games," in *American Control Conference*, 2020: 1049-1066.

[4] V. S Chipade and D. Panagou, "Multiplayer Target-Attacker-Defender Differential Game: Pairing Allocations and Control Strategies for Guaranteed Intercept," in *AIAA Scitech Forum*, 2019.

[5] E. Garcia, D. W. Casbeer, A. Von Moll, and M. Pachter, "Multiple Pursuer Multiple Evader Differential Games," *IEEE Transactions on Automatic Control*, 2020, 66(5): 2345-2350.

[6] A. Von Moll, M. Pachter, D. Shishika, and Z. Fuchs, "Circular Target Defense Differential Games," *IEEE Transactions on Automatic Control*, 2022, 68(7): 4065-4078.

[7] Y. Lee and E. Bakolas, "Optimal Strategies for Guarding a Compact and Convex Target Set: A Differential Game Approach," in *IEEE Conference on Decision and Control*, 2021: 4320-4325.

[8] H. Fu and H H-T. Liu, "Justification of the Geometric Solution of a Target Defense Game with Faster Defenders and a Convex Target Area Using the HJI Equation," *Automatica*, 2023, 149: 110811.

[9] E. Garcia, D. Casbeer, and M. Pachter, "Design and Analysis of State-Feedback Optimal Strategies for the Differential Game of Active Defense," *IEEE Transactions on Automatic Control*, 2018, 64(2): 553-568.

[10] I. Weintraub, E. Garcia, and M. Pachter, "A Kinematic Rejoin Method for Active Defense of Non-Maneuverable Aircraft," *in American Control Conference*, 2018: 6533-6538.

[11] D. Shishika, J. Paulos, and V. Kumar, "Cooperative Team Strategies for Multi-player Perimeter-Defense Games," *IEEE Robotics and Automation Letters*, 2020, 5(2): 2738-2745.

[12] E. Lee, D. Shishika, and V. Kumar, "Perimeter-Defense Game between Aerial Defender and Ground Intruder," in *IEEE Conference on Decision and Control*, 2020: 1530-1536.

[13] L. Liang, F. Deng, J. Wang, M. Lu and J. Chen, "A Reconnaissance Penetration Game with Territorial-Constrained Defender," *IEEE Transactions on Automatic Control*, 2022, 67(11): 6295-6302.

[14] R. Yan, Z. Shi, and Y. Zhong, "Task assignment for multiplayer reach–avoid games in convex domains via analytical barriers," *IEEE Transactions on Robotics*, 2019, 36(1): 107-124.

[15] Z. Zhou, W. Zhang, J. Ding, H. Huang, D. Stipanović, and C. Tomlin, "Cooperative Pursuit with Voronoi Partitions," *Automatica*, 2016, 36(72): 64-72.

[16] W. Zha, J. Chen, Z. Peng, and et al. "Construction of Barrier in a Fishing Game with Point Capture," *IEEE Transactions on Cybernetics*, 2016, 47(6): 1409-1422.

[17] S. Alexander, R. Bishop, and R. Ghrist. "Capture Pursuit Games on Unbounded Domains," *L'Enseignement Mathématique*, 2009, 55(1): 103-125.

[18] I. Mitchell, A. Bayen, and C. Tomlin. "A Time-Dependent Hamilton-Jacobi Formulation of Reachable Sets for Continuous Dynamic Games," *IEEE Transactions on Automatic Control*, 2005, 50(7): 947-957.

[19] S. Jhanani and B. Efstathios. "Min–Max Q-learning for Multiplayer Pursuit-Evasion Games," *Neurocomputing*, 2022, 475: 1-14.

[20] Y. Hu, Y. Gao, and B. An. "Multiagent Reinforcement Learning with Unshared Value Functions," *IEEE Transactions on Cybernetics*, 2014, 45(4): 647-662.

[21] X. Li, Z. Peng, W. Zha, and et al. "Construction of Barrier in a Three-player Pursuit-Evasion Game," *Unmanned Systems*, 2016, 4(01): 41-49.

[22] E. Garcia, D. Casbeer, and M. Pachter. "The Barrier Surface in the Cooperative Football Differential Game," *arXiv preprint arXiv*, 2020, 2006.03682.

[23] E. Garcia, D. Casbeer, and M. Pachter, "Optimal Strategies of the Differential Game in a Circular Region," *IEEE Control Systems Letters*, 2020, 4(2): 492-497.

[24] R. Yan, Z. Shi, and Y. Zhong, "Construction of the Barrier for Reach-Avoid Differential Games in Three-dimensional Space with Four Equal-speed Players," in *IEEE Conference on Decision and Control*, 2019: 4067–4072.

[25] E. Garcia, D. Casbeer, and M. Pachter, "Optimal Strategies for a Class of Multi-Player Reach-Avoid Differential Games in 3d Space," *IEEE Robotics and Automation Letters*, 2020, 5(3): 4257-4264.

Proceedings of the 3rd Conference on Fully Actuated System Theory and Applications
May 10-12, 2024, Shenzhen, China

Finite-Horizon Security-Guaranteed Non-Fragile H_∞ Estimation Under Integral Measurements

Zongjie Luo[1,2,3,4], Yanqin Wang[5], Dongyan Dai[1,2,3,4,6,*], Nan Hou[1,2,3,4,7], Weijian Li[1,2,3,4]
[1]National Key Laboratory of Continental Shale Oil, Northeast Petroleum University, Daqing 163318, China
[2]Artificial Intelligence Energy Research Institute, Northeast Petroleum University, Daqing 163318, China
[3]Sanya Offshore Oil & Gas Research Institute, Northeast Petroleum University, Sanya 572025, China
[4]Heilongjiang Provincial Key Laboratory of Networking and Intelligent Control, Northeast Petroleum University, Daqing 163318, China
[5]Chinesisch-Deutsche Hochschule für Angewandte Wissenschaften, Shanghai Technical Institute of Electronics & Information, Shanghai, 201411, China
[6]School of Science, Heilongjiang Bayi Agriculture University, Daqing 163319, China
[7]Research Center for Mathematics and Interdisciplinary Sciences, Northeast Petroleum University, Daqing 163318, China

***Abstract*—This paper handles the finite-horizon non-fragile H_∞ state estimator design issue for nonlinear time-varying systems under integral measurements suffering from randomly occurring denial-of-service (DoS) attacks. Stochastic nonlinearities are utilized to reflect nonlinearity in the system state, which are characterized by the statistical property. Integral measurements, based on previous and current system states, are used to characterize time delays or interval time that exist during actual signal acquisition. DoS attacks are considered in the measurement transmission, whose randomly occurrence is described by employing a Bernoulli-distributed random sequence. Non-fragility of the estimator is involved to reflect gain variations during the actual operation of the estimator. The aim of this paper is to develop a state estimation approach such that the estimation error dynamics achieves the H_∞ performance. Utilizing the stochastic analysis and the completing squares method, a necessary and sufficient condition is presented for the existence of an ideal H_∞ estimator. The time-varying gain parameters of the estimator are obtained by solving a set of coupled backward recursive Riccati difference equations. Ultimately, the effectiveness of the derived estimation method is verified by a simulation example.**

***Index Terms*—Non-Fragile H_∞ State Estimation, Integral Measurements, Randomly Occurring Denial-of-Service Attacks, Nonlinear Time-Varying Systems, Riccati Difference Equations**

I. Introduction

Over the decades, with their development/popularization as well as their wide applications in military, medical, power grid, aerospace and transportation control, nonlinear networked control systems have drawn more and more researchers' attention [1], [13], [17], [18], [23]. Internal states of the systems play a vital role for studies, which is unknown and cannot be obtained directly. State estimation (SE) is to estimate the unknown true system state by using known damaged/noise-interfered measurements, and a great deal of research effort has been done on solving such SE problem for nonlinear systems [19], [22], [27]. For example, a SE method has been proposed in [27] for a class of multi-rate nonlinear systems under the FlexRay protocol. In real life, in addition to the system nonlinearity, the possibly exhibited time-varying characteristics of the systems has attracted researchers' interest gradually due to the rapid development of industry. For instance, time-varying parameters have been used as a very important indicator to reflect the rapid change of the system [11], [24], [33].

Noting that the description correctness of the measurement signal may directly determine the estimate accuracy of system state, then a rational/adequate measurement description is necessary. In most research results, it is generally conceived that the value of the system measurement output depends merely on the current system state. Nevertheless, this viewpoint does not fully hold in actual systems. In some engineering applications (e.g., nuclear fusion and chemical reactions), it has been found that the measurement contains both the current state information and state information in the past periods due to the existence of network interference, disconnection, poor operating conditions, or intermittent sensor failure [3], [20], [30]. More specifically, such measurement outputs have been known as the integral measurements, which have been modeled by containing not only the current system state but also the previous ones. A few SE studies have been accomplished by taking account of integral measurements, see [8], [10], [26], [28] and the references therein.

Due to the structural characteristics of the networked control systems, the data are unavoidably vulnerable to cyber attacks during the network information interaction. The attacker attempts to obstruct the normal network information transmission by sending a large amount of false data or preventing the information receipt, which deteriorates the system performance. Compared to spoofing attacks and replay attacks, denial-of-service (DoS) attacks have been frequently used by opponents, and have been ranked as a source of the most serious security incidents causing economic losses [2], [6].

* Corresponding author. E-mail address: crystal_ddy@126.com (D. Dai).
This work was supported in part by the National Natural Science Foundation of China under Grants U21A2019, 62203105, 62073070 and 62103096, the Hainan Province Science and Technology Special Fund of China under Grant ZDYF2022SHFZ105, the Hainan Provincial Joint Project of Sanya Yazhou Bay Science and Technology City of China under Grant 2021JJLH0025, the Natural Science Foundation of Heilongjiang Province of China under Grant YQ2023F003, and the Alexander von Humboldt Foundation of Germany.

Research on DoS attacks has been put emphasis on in recent years [7], [15], [29]. For example, the H_∞ SE issue has been dealt with in [29] for discrete-time memristive neural networks subject to randomly occurring DoS attacks.

During the actual execution of estimators, the truly utilized gains may fluctuate from the predetermined ones due to computational rounding errors or various noises. Such a phenomenon may lead to the fragility of the estimation error dynamics system, degrade the system performance or even destabilize the system. In particular, non-fragility has already aroused researchers' focus, which involves gain variations in the construction of the estimator model, and the corresponding research results have been reported in [14], [31]. It is worth mentioning that, so far, the finite-horizon non-fragile SE issue has not been adequately investigated yet for stochastic nonlinear systems with integral measurements in the case of randomly occurring DoS attacks, much less the case of establishing a necessary and sufficient condition to ensure that the H_∞ estimator may exist, which arises the main motivation of this work.

Based on the above discussion, this paper is devoted to realizing the finite-horizon non-fragile H_∞ SE for nonlinear systems with integral measurements affected by DoS attacks. *The main contributions of this paper are stressed in the following points: 1) the model in concern is quite comprehensive, containing stochastic nonlinearities, time-varying parameters, DoS attacks, integral measurements and gain variations, and depicts the complex real systems closely; 2) the H_∞ SE issue is firstly settled for nonlinear time-varying systems with integral measurements, DoS attacks and gain variations; and 3) a necessary and sufficient condition is presented to ensure the existence of non-fragile estimators by adopting stochastic analysis technique and the completing squares method (CSM).*

II. Problem Formulation and Preliminaries

In this paper, consider the following type of time-varying nonlinear systems over the finite horizon $r \in [0, N]$:

$$\begin{aligned} x_{r+1} =& h(r, x_r) + A_r x_r + B_r \omega_r \\ z_r =& L_r x_r. \end{aligned} \tag{1}$$

where $x_r \in \mathbb{R}^{n_x}$ is the system state vector; $z_r \in \mathbb{R}^{n_z}$ represents the output of the state that needs to be estimated; and $\omega_r \in \mathbb{R}^{n_\omega}$ is the disturbance input, which belongs to $l_2[0, N]$. A_r, B_r and L_r represent given time-varying matrices with suitable dimensions.

We describe the stochastic nonlinear function $h(r, x_r)$ ($h(r, 0) = 0$) via the statistical characteristics as follows:

$$\begin{aligned} &E\{h(r, x_r) | x_r\} = 0, \\ &E\left\{h(j, x_j) h^T(r, x_r) | x_r\right\} = 0, r \neq j, \\ &E\left\{h(r, x_r) h^T(r, x_r) | x_r\right\} \triangleq \sum_{l=1}^{q} \Theta_{l,r} E\left\{x_r^T \bar{\Gamma}_{l,r} x_r\right\} \end{aligned} \tag{2}$$

where $\Theta_{l,r}$ and $\bar{\Gamma}_{l,r}$ are given matrices having appropriate dimensions, and q stands for the number of independent state elements.

Remark 1: Nonlinearities are common in practical time-varying control systems due to bandwidth constraints, random component failures, and sudden perturbations of the external environment, which pose a significant challenge for us to study the related problems for nonlinear systems. So far, several different types of nonlinear descriptions have appeared in the research, such as Lipschitz-type nonlinearity [34], nonlinearity with uncertain dead-zone [32], nonlinearity function with inequality constraints [25], and general sector nonlinearity [12]. Stochastic nonlinearity is used in this paper with known statistical characteristics, and such a nonlinear description can represent a class of well-studied nonlinearities.

The measurement signal with integral measurements is described as follows:

$$y_r = C_r \sum_{q=0}^{s} x_{r-q} + D_r \nu_r \tag{3}$$

where $y_r \in \mathbb{R}^{n_y}$ means the measurement output of the system; $\nu_r \in \mathbb{R}^{n_\nu}$ is the measurement noise which belongs to $l_2[0, N]$; s represents the interval of integral measurement or the time interval for data collection; and C_r and D_r are given time-varying matrices with suitable dimensions.

Remark 2: It is worth noting that the integral measurement phenomena are common in practical cases, such as chemical reaction processes, optical signals and nuclear signals [9]. As these cases are typically characterized by small variations between adjacent sampling points, traditional sampling methods have no practical meaning in terms of the measured value obtained at the current time step. In continuous systems, noticing the existence of integral measurements, the measurement output not only depends on the current system state, but also may be proportional to the integral of the system state in a given previous time period. This is the origin of the name "integral measurement". In discrete systems, the measurement output of the system is in proportion to the sum of the system states in a given past time period. As shown in the measurement model (3), the measurement output y_r is constituted by both the current state x_r and the sum of the system states at the time steps $x_{r-s}, \cdots, x_{r-2}, x_{r-1}$.

By defining $\bar{x}_r \triangleq \begin{bmatrix} x_r^T & x_{r-1}^T & \cdots & x_{r-s}^T \end{bmatrix}^T$, we get the following delay-free system

$$\begin{aligned} \bar{x}_{r+1} =& \bar{I} h\left(r, \bar{I}^T \bar{x}_r\right) + \bar{A}_r \bar{x}_r + \bar{B}_r \omega_r \\ z_r =& \bar{L}_r \bar{x}_r \\ y_r =& \bar{C}_r \bar{x}_r + D_r \nu_r \end{aligned} \tag{4}$$

where

$$\bar{I} \triangleq [I \underbrace{\begin{array}{cccc} 0 & \cdots & 0 \end{array}}_{s}]^T, \quad \bar{B}_r \triangleq [B_r^T \underbrace{\begin{array}{cccc} 0 & \cdots & 0 \end{array}}_{s}]^T,$$

$$\bar{A}_r \triangleq \begin{bmatrix} A_r & 0 & 0 & \cdots & 0 \\ I & 0 & 0 & \cdots & 0 \\ 0 & I & 0 & \cdots & 0 \\ \vdots & \vdots & \ddots & \ddots & \vdots \\ 0 & 0 & \cdots & I & 0 \end{bmatrix}_{(s+1)\times(s+1)},$$

$\bar{L}_r \triangleq [L_r \quad \underbrace{0 \quad \cdots \quad 0}_{s}], \bar{C}_r \triangleq [\underbrace{C_r \quad \cdots \quad C_r}_{s+1}]$.

In view of the characteristic of randomly occurring DoS attacks, the measurement signal received by the estimator is as follows:

$$\tilde{y}_r = \alpha_r y_r \tag{5}$$

where $\tilde{y}_r$ is the actual measurement output under the DoS attacks. The stochastic variable α_r indicates whether the DoS attacks occur, which belongs to the following Bernoulli distribution on the interval $[0, 1]$:

$$\text{Prob}\{\alpha_r = 0\} = 1 - \bar{\alpha},\ \text{Prob}\{\alpha_r = 1\} = \bar{\alpha}$$

where $\bar{\alpha} > 0$ is a given scalar. $\alpha_r = 0$ ($\alpha_r = 1$) indicates that the system is (not) subject to DoS attacks. Based on (5), we have $\tilde{y}_r = y_r$ when $\alpha_r = 1$; and $\tilde{y}_r = 0$ when $\alpha_r = 0$.

In light of the perturbation to actual gain values, we model the following time-varying non-fragile estimator for system (1):

$$\begin{aligned} \hat{x}_{r+1} =& (K_r + \Delta K_r)\,\hat{x}_r + (G_r + \Delta G_r)\,\tilde{y}_r \\ \hat{z}_r =& \bar{L}_r \hat{x}_r \end{aligned} \tag{6}$$

where $\hat{x}_r$ and $\hat{z}_r$ are the estimates of the state $\bar{x}_r$ and the output z_r, respectively; and K_r and G_r are the estimator gains to be designed. ΔK_r and ΔG_r denote the gain variations and have the following norm-bounded multiplicative form:

$$\Delta K_r = M_{1,r} F_{1,r} N_{1,r}, \Delta G_r = M_{2,r} F_{2,r} N_{2,r} \tag{7}$$

where $M_{1,r}$, $N_{1,r}$, $M_{2,r}$ and $N_{2,r}$ are given matrices with suitable dimensions, and $F_{1,r}$, $F_{2,r}$ mean unknown matrices that satisfy $F_{1,r}^T F_{1,r} \leqslant I$, $F_{2,r}^T F_{2,r} \leqslant I$.

Letting $e_r \triangleq \bar{x}_r - \hat{x}_r$, $z_{e,r} \triangleq z_r - \hat{z}_r$ and $\tilde{\alpha}_r \triangleq \bar{\alpha} - \alpha_r$, the estimation error can be obtained from (1), (4) and (6) as follows:

$$\begin{aligned} e_{r+1} =& (\bar{A}_r - \bar{\alpha}(G_r + \Delta G_r)\bar{C}_r + \tilde{\alpha}_r(G_r + \Delta G_r)\bar{C}_r - (K_r \\ &+ \Delta K_r))\bar{x}_r - \bar{\alpha}(G_r + \Delta G_r)D_r\nu_r + \bar{I}h\left(r, \bar{I}^T\bar{x}_r\right) \\ &+ \tilde{\alpha}_r\left(G_r + \Delta G_r\right)D_r\nu_r + \bar{B}_r\omega_r + (K_r + \Delta K_r)\,e_r \\ z_{e,r} =& \bar{L}_r e_r. \end{aligned} \tag{8}$$

To facilitate follow-up discussion, letting $\flat_r \triangleq \begin{bmatrix} \bar{x}_r^T & e_r^T \end{bmatrix}^T$, $\bar{\omega}_r \triangleq \begin{bmatrix} \omega_r^T & \nu_r^T \end{bmatrix}^T$, we obtain the following dynamic system:

$$\begin{aligned} \flat_{r+1} =& \hat{I}_h h(r, \hat{I}_e\flat_r) + \tilde{\alpha}_r\breve{A}_r\flat_r + \hat{A}_r\flat_r + \hat{B}_r\bar{\omega}_r + \tilde{\alpha}_r\breve{B}_r\bar{\omega}_r \\ z_{e,r} =& \hat{L}_r\flat_r \end{aligned} \tag{9}$$

where

$$\hat{I}_h \triangleq \begin{bmatrix} \bar{I} \\ \bar{I} \end{bmatrix}, \hat{I}_e \triangleq \begin{bmatrix} \bar{I} \\ 0 \end{bmatrix}^T, \hat{A}_r \triangleq \begin{bmatrix} \bar{A}_r & 0 \\ A_{G,r} & K_r + \Delta K_r \end{bmatrix},$$
$$A_{G,r} \triangleq \bar{A}_r - \bar{\alpha}\left(G_r + \Delta G_r\right)\bar{C}_r - \left(K_r + \Delta K_r\right),$$
$$\breve{A}_r \triangleq \begin{bmatrix} 0 & 0 \\ \left(G_r + \Delta G_r\right)\bar{C}_r & 0 \end{bmatrix}, \breve{B}_r \triangleq \text{diag}\{0, (G_r + \Delta G_r)D_r\},$$
$$\hat{B}_r \triangleq \begin{bmatrix} \bar{B}_r & 0 \\ \bar{B}_r & -\bar{\alpha}\left(G_r + \Delta G_r\right)D_r \end{bmatrix}, \hat{L}_r \triangleq \begin{bmatrix} 0 & \bar{L}_r \end{bmatrix}.$$

In this paper, we aim to design a non-fragile state estimator (6) and ensure that the output estimation error $z_{e,r}$ in (9) fulfills the following H_∞ performance constraint:

$$W \triangleq E\left\{\sum_{r=0}^{N-1}\|z_{e,r}\|^2 - \varrho^2\sum_{r=0}^{N-1}\|\bar{\omega}_r\|^2\right\} - \varrho^2\flat_0^T S\flat_0 < 0 \tag{10}$$

where $S > 0$ is a given weighting matrix, and $\varrho > 0$ is a given disturbance attenuation level.

In terms of (7), an effective way to address the gain variations in (9) is to view them as a source of interference. In this paper, we are to resist the effect of all disturbances on the estimation error according to the prescribed H_∞ performance constraint. Rewrite (9) to get:

$$\begin{aligned} \flat_{r+1} =& \hat{I}_h h(r, \hat{I}_e\flat_r) + A_{1,r}\flat_r + \tilde{\alpha}_r A_{2,r}\flat_r \\ &+ \tilde{M}_{1,r}\tilde{\omega}_r + \tilde{\alpha}_r\tilde{M}_{2,r}\tilde{\omega}_r \\ z_{e,r} =& \hat{L}_r\flat_r \end{aligned} \tag{11}$$

where

$$A_{1,r} \triangleq \begin{bmatrix} \bar{A}_r & 0 \\ \bar{A}_r - \bar{\alpha}G_r\bar{C}_r - K_r & K_r \end{bmatrix}, A_{2,r} \triangleq \begin{bmatrix} 0 & 0 \\ G_r\bar{C}_r & 0 \end{bmatrix},$$
$$B_{2,r} \triangleq \text{diag}\{0, G_r D_r\}, N_{c,r} \triangleq N_{2,r}\bar{C}_r, N_{d,r} \triangleq N_{2,r}D_r,$$
$$\tilde{M}_{1,r} \triangleq \begin{bmatrix} B_{1,r} & -\bar{\alpha}\bar{M}_{2,r} & -\bar{\alpha}\bar{M}_{2,r} & \bar{M}_{1,r} \end{bmatrix},$$
$$\tilde{M}_{2,r} \triangleq \begin{bmatrix} B_{2,r} & \bar{M}_{2,r} & \bar{M}_{2,r} & 0 \end{bmatrix}, \bar{M}_{1,r} \triangleq \text{diag}\{0, M_{1,r}\},$$
$$\tilde{\omega}_r \triangleq \begin{bmatrix} \bar{\omega}_r^T & (\tilde{F}_{2C,r}\flat_r)^T & (\tilde{F}_{2D,r}\bar{\omega}_r)^T & (\tilde{F}_{1,r}\flat_r)^T \end{bmatrix}^T,$$
$$\tilde{F}_{1,r} \triangleq \begin{bmatrix} 0 & 0 \\ -F_{1,r}N_{1,r} & F_{1,r}N_{1,r} \end{bmatrix}, B_{1,r} \triangleq \begin{bmatrix} \bar{B}_r & 0 \\ \bar{B}_r & -\bar{\alpha}G_r D_r \end{bmatrix},$$
$$F_{1,r} \triangleq \begin{bmatrix} 0 & 0 \\ -N_{1,r} & N_{1,r} \end{bmatrix}, \bar{M}_{2,r} \triangleq \text{diag}\{0, M_{2,r}\},$$
$$\tilde{F}_{2C,r} \triangleq \begin{bmatrix} 0 & 0 \\ F_{2,r}N_{c,r} & 0 \end{bmatrix}, F_{2C,r} \triangleq \begin{bmatrix} 0 & 0 \\ N_{c,r} & 0 \end{bmatrix},$$
$$\tilde{F}_{2D,r} \triangleq \begin{bmatrix} 0 & 0 \\ F_{2,r}N_{d,r} & 0 \end{bmatrix}, F_{2D,r} \triangleq \begin{bmatrix} 0 & 0 \\ N_{d,r} & 0 \end{bmatrix}.$$

Furthermore, we yield the following formula from (10):

$$\begin{aligned} \bar{W} \triangleq& E\Bigg\{\sum_{r=0}^{N-1}\|z_{e,r}\|^2 - \varrho^2\sum_{r=0}^{N-1}\left(\|\tilde{\omega}_r\|^2 - \|F_{2C,r}\flat_r\|^2\right. \\ &\left. - \|F_{2D,r}\bar{\omega}_r\|^2 - \|F_{1,r}\flat_r\|^2\right)\Bigg\} - \varrho^2\flat_0^T S\flat_0 < 0. \end{aligned} \tag{12}$$

III. Main Results

For promoting the following study, several lemmas are given beforehand.

Lemma 1: For the noise signal $\tilde{\omega}_r$ and initial state $\flat_0$, regard $\flat_r$ as a proper solution of the system (11) over the time horizon $[0, N]$. Then, one obtains:

$$\begin{aligned} & W_1\left(\flat_0, \tilde{\omega}_r\right) \\ \triangleq& E\Bigg\{\sum_{r=0}^{N-1}\|z_{e,r}\|^2 - \varrho^2\sum_{r=0}^{N-1}\left(\|\tilde{\omega}_r\|^2 - \|F_{2C,r}\flat_r\|^2\right. \end{aligned}$$

$$- \|F_{2D,r}\bar{\omega}_r\|^2 - \|F_{1,r}\flat_r\|^2)\Big\}$$
$$= E\left\{\flat_0^T P_0 \flat_0 - \flat_N^T P_N \flat_N\right\} + \sum_{r=0}^{N-1} E\left\{\bar{\flat}_r^T \tilde{\Omega}_{r+1} \bar{\flat}_r\right\}. \quad (13)$$

Furthermore, if $|\Omega_{22,r+1}| \neq 0$ for all $r \in [0, N-1]$, and by selecting $\tilde{\omega}_r \triangleq \Omega_{22,r+1}^{-1}\Omega_{12,r+1}^T \flat_r$, one further yields

$$W_2(\mathcal{Z}_r, \tilde{\omega}_r) \triangleq \sum_{r=0}^{N-1} E\left\{\|z_{e,r}\|^2 + \|\mathcal{Z}_r\|^2\right\}$$
$$= E\left\{\flat_0^T P_0 \flat_0 - \flat_N^T P_N \flat_N\right\} + \sum_{r=0}^{N-1} E\left\{\tilde{\flat}_r^T \tilde{\psi}_{r+1} \tilde{\flat}_r\right\}. \quad (14)$$

where $\{P_r > 0\}_{0 \leqslant r \leqslant N}$ and $\{Q_r > 0\}_{0 \leqslant r \leqslant N}$ denote two groups of matrices and

$$\tilde{\Omega}_{r+1} \triangleq \begin{bmatrix} \Omega_{11,r+1} - P_r & * \\ \Omega_{12,r+1}^T & -\Omega_{22,r+1} \end{bmatrix}, \mathcal{C}_r \triangleq \begin{bmatrix} -I & I \\ -\bar{\alpha}\bar{C}_r & 0 \end{bmatrix},$$
$$\tilde{\psi}_{r+1} \triangleq \begin{bmatrix} \psi_{11,r+1} & * \\ \psi_{1,r+1}^T & \psi_{2,r+1} \end{bmatrix}, \mathcal{A}_r \triangleq \begin{bmatrix} \bar{A}_r & 0 \\ \bar{A}_r & 0 \end{bmatrix}, \bar{\flat}_r \triangleq \begin{bmatrix} \flat_r \\ \tilde{\omega}_r \end{bmatrix},$$
$$\tilde{\flat}_r \triangleq \begin{bmatrix} \flat_r \\ \mathcal{Z}_r \end{bmatrix}, \mathcal{Z}_r \triangleq \begin{bmatrix} 0 \\ \mathcal{X}_r \mathcal{C}_r \flat_r \end{bmatrix}, \psi_{2,r+1} \triangleq Q_{r+1} + I,$$
$$\Omega_{11,r+1} \triangleq \mathrm{tr}\left[\hat{I}_h^T P_{r+1} \hat{I}_h \Gamma_{l,r}\right] \hat{I}_e^T \sum_{l=1}^{q} \Theta_{l,r} \hat{I}_e + \hat{\alpha} A_{2,r}^T P_{r+1} \times A_{2,r} + A_{1,r}^T P_{r+1} A_{1,r} + \varrho^2 F_{2C,r}^T F_{2C,r} + \varrho^2 F_{1,r}^T \times F_{1,r} + \hat{L}_r^T \hat{L}_r, \Omega_{12,r+1} \triangleq A_{1,r}^T P_{r+1} \tilde{M}_{1,r},$$
$$\Omega_{22,r+1} \triangleq \varrho^2 I - \tilde{M}_{1,r}^T P_{r+1} \tilde{M}_{1,r} - \hat{\alpha} \tilde{M}_{2,r}^T P_{r+1} \tilde{M}_{2,r} - \varrho^2 \tilde{S}^T F_{2D,r}^T F_{2D,r} \tilde{S}, \Xi_{r+1} \triangleq \Omega_{22,r+1}^{-1} \Omega_{12,r+1}^T,$$
$$\psi_{11,r+1} \triangleq \psi_{r+1} + \hat{L}_r^T \hat{L}_r - Q_r, \mathcal{X}_r \triangleq \begin{bmatrix} K_r & G_r \end{bmatrix},$$
$$\psi_{r+1} \triangleq \mathrm{tr}\left[\hat{I}_h^T Q_{r+1} \hat{I}_h \Gamma_{l,r}\right] \hat{I}_e^T \sum_{l=1}^{q} \Theta_{l,r} \hat{I}_e + \hat{\alpha}\big(A_{2,r} + \tilde{M}_{2,r} \times \Xi_{r+1}\big)^T Q_{r+1}\big(A_{2,r} + \tilde{M}_{2,r}\Xi_{r+1}\big) + \big(\tilde{M}_{1,r}\Xi_{r+1} + \mathcal{A}_r\big)^T Q_{r+1}\big(\mathcal{A}_r + \tilde{M}_{1,r}\Xi_{r+1}\big), \hat{\alpha} \triangleq \bar{\alpha} - \bar{\alpha}^2,$$
$$\psi_{1,r+1} \triangleq \big(\mathcal{A}_r + \tilde{M}_{1,r}\Xi_{r+1}\big)^T Q_{r+1}, \tilde{S} \triangleq \begin{bmatrix} I & 0 & 0 & 0 \end{bmatrix}.$$

Proof: Letting $V_r \triangleq \flat_{r+1}^T P_{r+1} \flat_{r+1} - \flat_r^T P_r \flat_r$, based on the system (11), one sees

$$E\{V_r\}$$
$$= E\big\{h^T(r, \hat{I}_e \flat_r)\hat{I}_h^T P_{r+1} \hat{I}_h h(r, \hat{I}_e \flat_r) + \flat_r^T A_{1,r}^T P_{r+1} A_{1,r} \flat_r\big\} + E\big\{2\flat_r^T A_{1,r}^T P_{r+1} \tilde{M}_{1,r} \tilde{\omega}_r + \hat{\alpha} \flat_r^T A_{2,r}^T P_{r+1} A_{2,r} \flat_r\big\} + E\big\{\tilde{\omega}_r^T \tilde{M}_{1,r}^T P_{r+1} \tilde{M}_{1,r} \tilde{\omega}_r + \hat{\alpha} \tilde{\omega}_r^T \tilde{M}_{2,r}^T P_{r+1} \tilde{M}_{2,r} \tilde{\omega}_r\big\} - E\left\{\flat_r^T P_r \flat_r\right\}. \quad (15)$$

Taking the nonlinearity and the nature of matrix trace into consideration, we obtain:

$$E\left\{h^T(r, \hat{I}_e \flat_r)\hat{I}_h^T P_{r+1} \hat{I}_h h(r, \hat{I}_e \flat_r)\right\}$$
$$= E\left\{\mathrm{tr}\left[h^T(r, \hat{I}_e \flat_r)\hat{I}_h^T P_{r+1} \hat{I}_h h(r, \hat{I}_e \flat_r)\right]\right\}$$
$$= E\left\{\mathrm{tr}\left[\hat{I}_h^T P_{r+1} \hat{I}_h\right] h(r, \hat{I}_e \flat_r) h^T(r, \hat{I}_e \flat_r)\right\}$$
$$= E\left\{\flat_r^T \hat{I}_e^T \sum_{l=1}^{q} \mathrm{tr}\left[\hat{I}_h^T P_{r+1} \hat{I}_h \Gamma_{l,r}\right] \Theta_{l,r} \hat{I}_e \flat_r\right\}. \quad (16)$$

According to (15) and (16), combining $\sum_{r=0}^{N-1} E\|z_{e,r}\|^2$ with the zero term $\sum_{r=0}^{N-1} E\{V_r - V_r\} + \varrho^2 \sum_{r=0}^{N-1} E\{\|\tilde{\omega}_r\|^2 - \|F_{2C,r}\flat_r\|^2 - \|F_{2D,r}\bar{\omega}_r\|^2 - \|F_{1,r}\flat_r\|^2\} - \varrho^2 \sum_{r=0}^{N-1} E\{\|\tilde{\omega}_r\|^2 - \|F_{2C,r}\flat_r\|^2 - \|F_{2D,r}\bar{\omega}_r\|^2 - \|F_{1,r}\flat_r\|^2\}$, and noticing $\bar{\omega}_r = \tilde{S}\tilde{\omega}_r$, we can derive that:

$$\sum_{r=0}^{N-1} E\left\{\|z_{e,r}\|^2\right\}$$
$$= \varrho^2 \sum_{r=0}^{N-1} E\{\|\tilde{\omega}_r\|^2 - \|F_{2C,r}\flat_r\|^2 - \|F_{2D,r}\bar{\omega}_r\|^2 - \|F_{1,r}\flat_r\|^2\} + E\left\{\flat_0^T P_0 \flat_0 - \flat_N^T P_N \flat_N\right\} + \sum_{r=0}^{N-1} E\left\{\bar{\flat}_r^T \tilde{\Omega}_{r+1} \bar{\flat}_r\right\}. \quad (17)$$

Similarly, taking $\mathcal{Z}_r \triangleq \begin{bmatrix} 0 & (\mathcal{X}_r \mathcal{C}_r \flat_r)^T \end{bmatrix}^T$ into account, we obtain

$$A_{1,r}\flat_r = \mathcal{A}_r \flat_r + \mathcal{Z}_r. \quad (18)$$

Under $|\Omega_{22,r+1}| \neq 0$ for all $r \in [0, N-1]$, selecting $\tilde{\omega}_r \triangleq \Omega_{22,r+1}^{-1}\Omega_{12,r+1}^T \flat_r$, we can conclude that

$$\sum_{r=0}^{N-1} E\left\{\|z_{e,r}\|^2\right\} = \sum_{r=0}^{N-1} E\left\{\flat_r^T \hat{L}_r^T \hat{L}_r \flat_r\right\} + \sum_{r=0}^{N-1} E\{\|\mathcal{Z}_r\|^2 - \|\mathcal{Z}_r\|^2\} + \sum_{r=0}^{N-1} E\{V_r - V_r\}$$
$$= \sum_{r=0}^{N-1} E\left\{\tilde{\flat}_r^T \tilde{\psi}_{r+1} \tilde{\flat}_r\right\} - \sum_{r=0}^{N-1} E\left\{\|\mathcal{Z}_r\|^2\right\} + E\left\{\flat_0^T P_0 \flat_0 - \flat_N^T P_N \flat_N\right\}. \quad (19)$$

It is obvious to show that (13) and (14) are guaranteed through (17) and (19), respectively.

Under the specified performance constraint (12), we begin to propose a necessary and sufficient condition for the design of the time-varying non-fragile estimator (6) by using CSM and proof of contradiction.

Lemma 2: Given the perturbation rejection level $\varrho > 0$ and the weighting matrix $S > 0$. For the nonlinear time-varying system (1)-(5), the performance constraint (12) is fulfilled if and only if there exists a set of real-valued matrices $\{\mathcal{X}_r\}_{0 \leqslant r \leqslant N}$ and a set of matrices $\{P_r > 0\}_{0 \leqslant r \leqslant N}$ (with the final condition $P_N = 0$) that make the following backward recursive Riccati difference equation (RRDE):

$$\Omega_{11,r+1} + \Omega_{12,r+1}\Omega_{22,r+1}^{-1}\Omega_{12,r+1}^T = P_r \quad (20)$$

holds with

$$\Omega_{22,r+1} > 0 \quad \text{and} \quad P_0 < \varrho^2 S. \quad (21)$$

Proof: Sufficiency: For matrices $\{P_r > 0\}_{0 \leqslant r \leqslant N}$ in (20), taking (17) into consideration, we obtain

$$\sum_{r=0}^{N-1} E\{\|z_{e,r}\|^2\} - \varrho^2 \sum_{r=0}^{N-1} E\{\|\tilde{\omega}_r\|^2 - \|F_{2C,r}\flat_r\|^2$$

$$
\begin{aligned}
&- \|F_{2D,r}\bar{\omega}_r\|^2 - \|F_{1,r}\flat_r\|^2\big\} \\
=&E\left\{\flat_0^T P_0\flat_0 - \flat_N^T P_N\flat_N\right\} + \sum_{r=0}^{N-1} E\big\{\flat_r^T\left(\Omega_{11,r+1} - P_r\right)\flat_r \\
&+ 2\flat_r^T\Omega_{12,r+1}\tilde{\omega}_r - \tilde{\omega}_r^T\Omega_{22,r+1}\tilde{\omega}_r\big\} \\
=&E\left\{\flat_0^T P_0\flat_0 - \flat_N^T P_N\flat_N\right\} + \sum_{r=0}^{N-1} E\big\{\flat_r^T(\Omega_{11,r+1} - P_r \\
&+ \Omega_{12,r+1}\Omega_{22,r+1}^{-1}\Omega_{12,r+1}^T)\flat_r\big\} + \sum_{r=0}^{N-1} E\{-(\tilde{\omega}_r - \tilde{\omega}_r^*)^T \\
&\times \Omega_{22,r+1}(\tilde{\omega}_r - \tilde{\omega}_r^*)\} \\
=&\sum_{r=0}^{N-1} E\left\{-(\tilde{\omega}_r - \tilde{\omega}_r^*)^T\Omega_{22,r+1}(\tilde{\omega}_r - \tilde{\omega}_r^*)\right\} \\
&+ E\big\{\flat_0^T P_0\flat_0 - \flat_N^T P_N\flat_N\big\} \qquad (22)
\end{aligned}
$$

where $\tilde{\omega}_r^* \triangleq \Omega_{22,r+1}^{-1}\Omega_{12,r+1}^T\flat_r$.

Because of $\Omega_{22,r+1} > 0$ and $P_0 < \varrho^2 S$, for all nonzero $\tilde{\omega}_r$, we can acquire from (20) and $P_N = 0$ that

$$
\begin{aligned}
\bar{W} <& \sum_{r=0}^{N-1} E\left\{\|z_{e,r}\|^2\right\} - \flat_0^T P_0\flat_0 - \varrho^2\sum_{r=0}^{N-1} E\big\{\|\tilde{\omega}_r\|^2 \\
&- \|F_{2C,r}\flat_r\|^2 - \|F_{2D,r}\bar{\omega}_r\|^2 - \|F_{1,r}\flat_r\|^2\big\} \\
=& -\sum_{r=0}^{N-1} E\big\{(\tilde{\omega}_r - \tilde{\omega}_r^*)^T\Omega_{22,r+1}(\tilde{\omega}_r - \tilde{\omega}_r^*)\big\} < 0, \qquad (23)
\end{aligned}
$$

which corresponds to (12).

Necessity: At this part, we need to verify that, if (12) is met, then for all nonzero $(\{\tilde{\omega}_r\}, \flat_0)$, there exists a feasible solution $\{P_r > 0\}_{0\leqslant r\leqslant N}$ to (20) with (21). Take account of the final condition $P_N = 0$, (20) is always solved backward if $\Omega_{22,r+1} > 0$ and $P_0 < \varrho^2 S$ for $r \in [0, N-1]$, which indicates that (20) stops recursion for some $r = \mathcal{K} \in [0, N-1]$ if $\Omega_{22,\mathcal{K}+1}$ or $\varrho^2 S - P_0$ has one or more non-positive eigenvalues.

The subsequent portion of this proof is derived through contradiction. Supposing that $\Omega_{22,r+1}$ or $\varrho^2 S - P_0$ owns one or more non-positive eigenvalues at some point $r = \mathcal{K} \in [0, N-1]$, which means that we want to verify that $\bar{W} < 0$ cannot be fulfilled.

Case 1: We want to verify

$$
\lambda_\iota(\Omega_{22,r+1}) \leqslant 0, \forall r \in [0, N-1], \iota = 1, \ldots, n_w \Rightarrow \bar{W} \geqslant 0 \qquad (24)
$$

where $\lambda_\iota(\Omega_{22,r+1})$ represents the ιth eigenvalue of $\Omega_{22,r+1}$.

To simplify the presentation, we see the non-positive eigenvalue of $\Omega_{22,r+1}$ at the time step $\mathcal{K}$ as $\lambda_\mathcal{K}$ ($\lambda_\mathcal{K} \leqslant 0$). Then, in the following part, we are to employ $\lambda_\mathcal{K} \leqslant 0$ to represent that there is some $(\{\tilde{\omega}_r\}, \flat_0) \neq 0$ which causes $\bar{W} \geqslant 0$. Firstly, choose $\flat_0 \triangleq 0$ and $\tilde{\omega}_r = 1)$ 0, if $r \in [0, \mathcal{K})$; 2) $\psi_\mathcal{K}$, if $r = \mathcal{K}$; and 3) $\tilde{\omega}_r^*$, if $r \in (\mathcal{K}, N)$ where $\psi_\mathcal{K}$ is the eigenvector of $\Omega_{22,\mathcal{K}+1}$ corresponding to $\lambda(\mathcal{K})$.

For $0 \leqslant k < \mathcal{K}$, according to system (11) with $\flat_0 = 0$, $h(0, r) = 0$ and $\tilde{\omega}_r = 0$, we gain $\flat_r = 0$ $(0 \leqslant k < \mathcal{K})$, so that $\tilde{\omega}_r^* \triangleq \Omega_{22,r+1}^{-1}\Omega_{12,r+1}^T\flat_r = 0$ $(0 \leqslant r \leqslant \mathcal{K})$.

Through (22) and $\tilde{\omega}_r$, we yield

$$
\begin{aligned}
&\sum_{r=0}^{\mathcal{K}-1} E\left\{\|z_{e,r}\|^2\right\} - \varrho^2\sum_{r=0}^{\mathcal{K}-1} E\big\{\|\tilde{\omega}_r\|^2 - \|F_{2C,r}\flat_r\|^2 \\
&- \|F_{2D,r}\bar{\omega}_r\|^2 - \|F_{1,r}\flat_r\|^2\big\} = 0, \qquad (25)
\end{aligned}
$$

$$
\begin{aligned}
&E\big\{\|z_{e,\mathcal{K}}\|^2 - \varrho^2(\|\tilde{\omega}_\mathcal{K}\|^2 - \|F_{2C,\mathcal{K}}\flat_\mathcal{K}\|^2 - \|F_{2D,\mathcal{K}}\bar{\omega}_\mathcal{K}\|^2 \\
&- \|F_{1,\mathcal{K}}\flat_\mathcal{K}\|^2) + V_\mathcal{K} - V_\mathcal{K}\big\} \\
=&E\big\{-\tilde{\omega}_\mathcal{K}^T\Omega_{22,\mathcal{K}+1}\tilde{\omega}_\mathcal{K} - \flat_{\mathcal{K}+1}^T P_{\mathcal{K}+1}\flat_{\mathcal{K}+1}\big\}, \qquad (26)
\end{aligned}
$$

and

$$
\begin{aligned}
&\sum_{r=\mathcal{K}+1}^{N-1} E\{\|z_{e,r}\|^2\} - \varrho^2\sum_{r=\mathcal{K}+1}^{N-1} E\big\{\|\tilde{\omega}_r\|^2 - \|F_{2C}\flat_r\|^2 \\
&- \|F_{2D}\bar{\omega}_r\|^2 - \|F_1\flat_r\|^2\big\} \\
=&E\Big\{\flat_{\mathcal{K}+1}^T P_{\mathcal{K}+1}\flat_{\mathcal{K}+1} - \flat_N^T P_N\flat_N\Big\} \\
&- \sum_{r=\mathcal{K}+1}^{N-1} E\{(\tilde{\omega}_r - \tilde{\omega}_r^*)^T\Omega_{22,r+1}(\tilde{\omega}_r - \tilde{\omega}_r^*)\big\} \\
=&E\left\{\flat_{\mathcal{K}+1}^T P_{\mathcal{K}+1}\flat_{\mathcal{K}+1}\right\}. \qquad (27)
\end{aligned}
$$

We then deduce from (25)-(27) that

$$
\bar{W} = -\tilde{\omega}_\mathcal{K}^T\Omega_{22,\mathcal{K}+1}\tilde{\omega}_\mathcal{K} = -\psi_\mathcal{K}^T\Omega_{22,\mathcal{K}+1}\psi_\mathcal{K} = -\lambda_\mathcal{K}\|\psi_\mathcal{K}\|^2 \geqslant 0.
$$

Case 2: We need to testify

$$
\Omega_{22,r+1} \geqslant 0 \ \text{ and } \ P_0 \geqslant \varrho^2 S, \ \forall r \in [0, N] \Rightarrow \bar{W} \geqslant 0. \qquad (28)
$$

Choose $\tilde{\omega}_r \triangleq \tilde{\omega}_r^*$. One derives from (22) that

$$
\begin{aligned}
\bar{W} =&E\big\{\flat_0^T P_0\flat_0 - \flat_N^T P_N\flat_N\big\} - \varrho^2\flat_0^T S\flat_0 \\
&+ \sum_{r=0}^{N-1} E\big\{-(\tilde{\omega}_r - \tilde{\omega}_r^*)^T\Omega_{22,r+1}(\tilde{\omega}_r - \tilde{\omega}_r^*)\big\} \\
=&\left\{\flat_0^T\left(P_0 - \varrho^2 S\right)\flat_0\right\}.
\end{aligned}
$$

For $\flat_0 \neq 0$, we easily discover that $\bar{W} \geqslant 0$, which contradicts to the condition $\bar{W} \leqslant 0$. The proof is now complete.

Based on Lemma 2, we are ready to present the design algorithm of the non-fragile estimator (6).

Theorem 1: Take a nonlinear time-varying stochastic systems (1)-(5) into consideration. For a specific disturbance attenuation level $\varrho > 0$ and matrix $S > 0$, the non-fragile estimator (6) fulfills the performance constraint (12) if (20) and the subsequent RRDE:

$$
\psi_{r+1} + \hat{L}_r^T\hat{L}_r - \psi_{1,r+1}\psi_{2,r+1}^{-1}\psi_{1,r+1}^T = Q_r \qquad (29)
$$

holds for a set of solutions $\{P_r, Q_r, G_r, K_r\}_{0\leqslant r\leqslant N-1}$ conforming to

$$
P_N = Q_N = 0, \qquad (30)
$$

$$
\psi_{2,r+1} > 0, \ \Omega_{22,r+1} > 0, \ P_0 < \varrho^2 S, \qquad (31)
$$

$$
\mathcal{X}_r^* = [K_r^* \ \ G_r^*] = \arg\min_{\mathcal{X}_r}\|\breve{N}^T\mathcal{X}_r\mathcal{C}_r + \psi_{2,r+1}^{-1}\psi_{1,r+1}^T\|_F \qquad (32)
$$

where $\breve{N} = [0 \;\; I]$, $\|\cdot\|_F$ is the Frobenius norm, and additional pertinent parameters are displayed in Lemma 1.

Proof: First, provided that there exists $\{P_r\}_{0\leq k\leq N-1}$ fulfilling (20) and (31), it gets readily from Lemma 2 that system (11) meets the performance constraint (12). In such a circumstance, the worst-case disturbance could be expressed by $\tilde{\omega}_r^* \triangleq \Omega_{22,r+1}^{-1}\Omega_{12,r+1}^T \flat_r$. Then, through adopting the worst-case disturbance and CSM, we attain from Lemma 1 that

$$\begin{aligned}
&W_2(\mathcal{Z}_r, \tilde{\omega}_r)\\
=&E\{\flat_0^T P_0 \flat_0 - \flat_N^T P_N \flat_N\} + \sum_{r=0}^{N-1} E\{\flat_r^T(\psi_{r+1} + \hat{L}_r^T \hat{L}_r - Q_r\\
&- \psi_{1,r+1}\psi_{2,r+1}^{-1}\psi_{1,r+1}^T)\flat_r + (\mathcal{Z}_r - \mathcal{Z}_r^*)^T \psi_{2,r+1}(\mathcal{Z}_r - \mathcal{Z}_r^*)\}\\
\leqslant& \sum_{r=0}^{N-1} E\{\flat_r^T(\psi_{r+1} + \hat{L}_r^T\hat{L}_r - Q_r - \psi_{1,r+1}\psi_{2,r+1}^{-1}\psi_{1,r+1}^T)\\
&\times \flat_r + \|\breve{N}^T\mathcal{X}_r\mathcal{C}_r + \psi_{2,r+1}^{-1}\psi_{1,r+1}^T\|_F^2 \|\psi_{2,r+1}\|_F \|\flat_r\|^2\}\\
&+ E\{\flat_0^T P_0 \flat_0 - \flat_N^T P_N \flat_N\} \qquad (33)
\end{aligned}$$

where $\mathcal{Z}_r \triangleq -\psi_{2,r+1}^{-1}\psi_{1,r+1}^T\flat_r$. Furthermore, the gain parameters K_r and G_r are shown to satisfy (29) and (32), thus, the proof is accomplished.

Remark 3: It is worth noting that in this part, we obtain a necessary and sufficient condition in Theorem 1 for the existence of the estimator (6) using Lemmas 1 and 2, which satisfies the performance constraint (12). More precisely, on one hand, the performance constraint (12) can be satisfied if there exists a solution to the backward RRDEs (20) and (29) satisfying (31) and (32). On the other hand, if the system (11) meets the performance constraint (12), then the backward RRDEs (20) and (29) have a solution that meets (31) and (32).

For enhancing the convenience of implementation, the gain parameters K_r and G_r can be computed by using the Moore-Penrose pseudoinverse, which will be discussed in the following theorem.

Theorem 2: Set the disturbance rejection level $\varrho > 0$, the constants $\vartheta_r > 0$ and $\sigma_r > 0$, and the matrix $S > 0$. The system (11) meets the H_∞ performance constraint (12) for all nonzero $\{\tilde{\omega}_r\}_{0\leqslant r\leqslant N-1}$ if there is a set of solutions $\{P_r, Q_r, G_r, K_r\}_{0\leqslant r\leqslant N-1}$ to the following RRDEs:

$$\Omega_{11,r+1} + \bar{\Omega}_{12,r+1}\bar{\Omega}_{22,r+1}^{-1}\bar{\Omega}_{12,r+1}^T = P_r, \qquad (34)$$

$$\bar{\psi}_{r+1} + \hat{L}_r^T\hat{L}_r - \bar{\psi}_{1,r+1}\psi_{2,r+1}^{-1}\bar{\psi}_{1,r+1}^T = Q_r \qquad (35)$$

with

$$P_N = Q_N = 0, \qquad (36)$$

$$\psi_{2,r+1} > 0, \;\; \bar{\Omega}_{22,r+1} > 0, \;\; P_0 < \varrho^2 S, \qquad (37)$$

$$\mathcal{X}_r^* = \Upsilon_{1,r+1}^\dagger \Upsilon_{2,r+1}\mathcal{C}_r^\dagger, \qquad (38)$$

$$F_r \leqslant \sigma_r I \qquad (39)$$

where † is the Moore-Penrose pseudoinverse [21], and

$$\begin{aligned}
&\tilde{M}_{1,r} \triangleq \left[\bar{B}_{11,r}\bar{B}_{12,r} - \bar{\alpha}\bar{M}_{2,r} - \bar{\alpha}\bar{M}_{2,r}\bar{M}_{1,r}\right],\\
&\tilde{M}_{2,r} \triangleq \begin{bmatrix}0 & \bar{B}_{2,r} & \bar{M}_{2,r} & \bar{M}_{2,r} & 0\end{bmatrix}, \bar{S} \triangleq \begin{bmatrix}0 & I\end{bmatrix},\\
&\bar{B}_{11,r} \triangleq \begin{bmatrix}\bar{B}_r & 0\\ \bar{B}_r & 0\end{bmatrix}, \bar{B}_{12,r} \triangleq \begin{bmatrix}0 & 0\\ 0 & -\bar{\alpha}\vartheta_r^{-1}I\end{bmatrix},\\
&\bar{\Omega}_{12,r+1} \triangleq A_{1,r}^T P_{r+1}\tilde{M}_{1,r}, \breve{S} \triangleq \begin{bmatrix}I & 0 & 0 & 0 & 0\end{bmatrix},\\
&\bar{\Omega}_{22,r+1} \triangleq \varrho^2 I - \tilde{M}_{1,r}^T P_{r+1}\tilde{M}_{1,r} - \hat{\alpha}\tilde{M}_{2,r}^T P_{r+1}\tilde{M}_{2,r}\\
&\qquad - \varrho^2\breve{S}^T F_{2D,r}^T F_{2D,r}\breve{S} - \sigma_r\breve{S}^T\breve{S},\\
&\bar{\psi}_{1,r+1} \triangleq \left(\mathcal{A}_r + \tilde{M}_{1,r}\bar{\Xi}_{r+1}\right)^T Q_{r+1}, \bar{B}_{2,r} \triangleq \mathrm{diag}\{0, \vartheta_r^{-1}I\},\\
&F_r \triangleq \varrho^2\vartheta_r^2\bar{S}^T D_r^T G_r^T G_r D_r \bar{S}, \bar{\Xi}_{r+1} \triangleq \bar{\Omega}_{22,r+1}^{-1}\bar{\Omega}_{12,r+1}^T,\\
&\bar{\psi}_{r+1} \triangleq \mathrm{tr}\left[\hat{I}_h^T Q_{r+1}\hat{I}_h\Gamma_{l,r}\right]\hat{I}_e^T\sum_{l=1}^{q}\Theta_{l,r}\hat{I}_e + \left(\mathcal{A}_r + \tilde{M}_{1,r}\right.\\
&\qquad \times \left.\bar{\Xi}_{r+1}\right)^T Q_{r+1}\left(\mathcal{A}_r + \tilde{M}_{1,r}\bar{\Xi}_{r+1}\right) + \hat{\alpha}(A_{2,r} + \tilde{M}_{2,r}^T\\
&\qquad \times \bar{\Xi}_{r+1})Q_{r+1}\left(A_{2,r} + \tilde{M}_{2,r}\bar{\Xi}_{r+1}\right),\\
&\Upsilon_{1,r+1} \triangleq \left(I + \psi_{2,r+1}^{-1}Q_{r+1}\tilde{M}_{1,r}\bar{\Omega}_{22,r+1}^{-1}\tilde{M}_{1,r}^T P_{r+1}\right)\breve{N}^T,\\
&\Upsilon_{2,r+1} \triangleq -\psi_{2,r+1}^{-1}Q_{r+1}\left(I + \tilde{M}_{1,r}\bar{\Omega}_{22,r+1}^{-1}\tilde{M}_{1,r}^T P_{r+1}\right)\mathcal{A}_r.
\end{aligned}$$

Proof: Let $\hat{\nu}_r \triangleq \begin{bmatrix}0 & (\vartheta_r G_r D_r \nu_r)^T\end{bmatrix}^T$ where $\vartheta_r > 0$ is used to provide additional degrees of freedom in the estimation process. By choosing $\breve{\omega}_r \triangleq \begin{bmatrix}\bar{\omega}_r^T & \hat{\nu}_r^T & (F_{2C,r}\flat_r)^T & (F_{2D,r}\bar{\omega}_r)^T & (F_{1,r}\flat_r)^T\end{bmatrix}^T$, we rewrite system (11) as follows:

$$\begin{aligned}
\flat_{r+1} &= \hat{I}_h h(r, \hat{I}_e\flat_r) + A_{1,r}\flat_r + \tilde{\alpha}_r A_{2,r}\flat_r\\
&\quad + \tilde{M}_{1,r}\breve{\omega}_r + \tilde{\alpha}_r\tilde{M}_{2,r}\breve{\omega}_r, \qquad (40)\\
z_{e,r} &= \hat{L}_r\flat_r. \qquad (41)
\end{aligned}$$

Besides, in terms of Lemma 1 in [10], we know that (38) is a solution to the following optimization problem:

$$\min_{\mathcal{X}_r} \|\Upsilon_{1,r+1}\mathcal{X}_r\mathcal{C}_r - \Upsilon_{2,r+1}\|_F,$$

which could be expressed further as

$$\min_{\mathcal{X}_r}\|\breve{N}^T\mathcal{X}_r\mathcal{C}_r + \psi_{2,r+1}^{-1}\bar{\psi}_{1,r+1}^T\|_F. \qquad (42)$$

Through (17) and Theorem 1, supposing that there is a family of solutions to the RRDEs (34) and (35) with (36)-(39), we deduce the following formula:

$$\begin{aligned}
&\sum_{r=0}^{N-1} E\left\{\|z_{e,r}\|^2\right\}\\
=&\sum_{r=0}^{N-1} E\{\flat_r^T(\Omega_{11,r+1} - P_r + \bar{\Omega}_{12,r+1}\bar{\Omega}_{22,r+1}^{-1}\bar{\Omega}_{12,r+1}^T)\flat_r\\
&- (\breve{\omega}_r - \breve{\omega}_r^*)^T\bar{\Omega}_{22,r+1}(\breve{\omega}_r - \breve{\omega}_r^*)\} + \varrho^2\sum_{r=0}^{N-1} E\{\|\tilde{\omega}_r\|^2\\
&- \|F_{2C,r}\flat_r\|^2 - \|F_{2D,r}\bar{\omega}_r\|^2 - \|F_{1,r}\flat_r + \hat{\nu}_r\|^2\} + E\{\flat_0^T\\
&\times P_0\flat_0 - \flat_N^T P_N\flat_N\} - \sum_{r=0}^{N-1} E\{\sigma_r(\breve{S}\breve{\omega}_r)^T(\breve{S}\breve{\omega}_r)\}\\
<&\varrho^2\sum_{r=0}^{N-1} E\{\|\tilde{\omega}_r\|^2 - \|F_{2C,r}\flat_r\|^2 - \|F_{2D,r}\bar{\omega}_r\|^2 - \|F_{1,r}
\end{aligned}$$

$$\times \flat_r\|^2\} + \sum_{r=0}^{N-1} E\{\tilde{\omega}_r^T \tilde{S}^T \big(F_r - \sigma_r I\big)\tilde{S}\tilde{\omega}_r\} + \ \varrho^2 \flat_0^T S \flat_0 \tag{43}$$

where $\breve{\omega}_r^* \triangleq \bar{\Omega}_{22,r+1}^{-1}\bar{\Omega}_{12,r+1}^T \flat_r$.

By combining with (39), it could be inferred from (43) that

$$\sum_{r=0}^{N-1} E\left\{\|z_{e,r}\|^2\right\} < \varrho^2 \sum_{r=0}^{N-1} E\big\{\|\tilde{\omega}_r\|^2 - \|F_{2C,r}\flat_r\|^2 - \|F_{2D,r} \times \bar{\omega}_r\|^2 - \|F_{1,r}\flat_r\|^2\big\} + \varrho^2 \flat_0^T S \flat_0. \tag{44}$$

We then derive that the non-fragile estimator (6) guarantees that the system (11) meets the performance constraint (12).

Remark 4: By applying the CSM, the non-fragile estimator (6) has been designed for the time-varying system (1)-(5). The presentation of Theorem 2 includes all the key elements of the nonlinear system such as time-varying parameters, parameters involving in integral measurements, statistics information about the stochastic nonlinearities, probabilistic information about randomly occurring DoS attacks, and matrices in gain variations. Gains of the non-fragile estimator (6) are expressed in (38) by utilizing the Moore-Penrose pseudoinverse. It is worth mentioning that a necessary and sufficient condition is put forward in this paper for designing the non-fragile estimator (6).

IV. Simulation Results

Considering a nonlinear time-varying stochastic system (1) over the time horizon $r \in [0, 100]$, and a set of parameters are used as follows:

$$s = 2, \varrho = 1, M_{1,r} = M_{2,r} = \begin{bmatrix} I & I & I \end{bmatrix}^T, S = 2I,$$
$$A_r = \begin{bmatrix} -0.01\sin(3r) & 0.02 \\ 0.03 & 0.03 \end{bmatrix}, C_r = \begin{bmatrix} 0.4 & 0.6\sin(5r) \\ 0.3 & -0.4 \end{bmatrix},$$
$$L_r = \begin{bmatrix} 0.3 & 0.1 \\ 0.5 & 0.2 \end{bmatrix}, N_{2,r} = \begin{bmatrix} 0.3 & 0.3 \\ 0.3 & 0.3 \end{bmatrix}, B_r = \begin{bmatrix} 0.2 \\ 0.4 \end{bmatrix},$$
$$D_r = \begin{bmatrix} 0.2 \\ 0.5 \end{bmatrix}, N_{1,r} = \begin{bmatrix} 0.3 & 0.3 & 0.3 & 0.3 & 0.3 & 0.3 \\ 0.3 & 0.3 & 0.3 & 0.3 & 0.3 & 0.3 \end{bmatrix}.$$

Choose the following stochastic nonlinear function:

$$h(r, x_r) = \begin{bmatrix} 0.1 \\ 0.3 \end{bmatrix} (0.2x_{1,r}\epsilon_{1,r} + 0.3x_{2,r}\epsilon_{2,r})$$

where $x_{\aleph,r}$ $(\aleph = 1, 2)$ stands for the $\aleph$th element of x_r, and $\epsilon_{\wp,r} \sim \mathcal{N}(0, 1)$ $(\wp = 1, 2)$ are uncorrelated Gaussian white noise sequences. It is demonstrated that $h(r, x_r)$ fulfills

$$\mathbb{E}\{h(r, x_r)|x_r\} = 0,$$
$$\mathbb{E}\{h(r, x_r)h^T(r, x_r)|x_r\} = \begin{bmatrix} 0.1 \\ 0.3 \end{bmatrix}\begin{bmatrix} 0.1 \\ 0.3 \end{bmatrix}^T \mathbb{E}\left\{x_r^T \begin{bmatrix} 0.04 & 0 \\ 0 & 0.09 \end{bmatrix} x_r\right\}.$$

We calculate the parameters of the non-fragile estimator (6) by $\sigma_r = 0.25$ and $\vartheta_r = 2.5$. The initial values for the system state and the estimator state are chosen as $x_0 = \begin{bmatrix} 0.2 & -0.2 \end{bmatrix}^T$, $x_{-1} = \begin{bmatrix} 0.2 & -0.1 \end{bmatrix}^T$, $x_{-2} = \begin{bmatrix} 0.3 & -0.1 \end{bmatrix}^T$ and $\hat{x}_0 = \begin{bmatrix} 0 & 0.1 & 0.2 & 0.2 & 0.1 & 0.2 \end{bmatrix}^T$. Set the noise signals as $\omega_r = 0.3\cos(3r)\mathrm{e}^{-0.01r}$ and $\nu_r = 0.2\sin(9r)\mathrm{e}^{-0.01r}$. Simulation curves are drawn in Figs. 1-2. Fig. 1 indicates the norm of the estimation error (i.e., $\|z_{e,r}\|^2$) for different attack probabilities $1-\bar{\alpha}$, which reveals that the smaller the value of $\bar{\alpha}$ (i.e., the bigger the occurrence probability of DoS attack), the bigger the norm of the estimation error. Fig. 2 illustrates the estimation performance Ψ_r for different $\bar{\alpha}$ with

$$\Psi_r = \frac{\Sigma_{\tau=0}^r E\big\{\|z_{e,\tau}\|^2\big\}}{\Sigma_{\tau=0}^r \breve{W}_\tau + \flat_0^T S \flat_0}$$

where $\breve{W}_\tau \triangleq \|\tilde{\omega}_\tau\|^2 - \|F_{2C,\tau}\flat_\tau\|^2 - \|F_{2D,\tau}\bar{\omega}_\tau\|^2 - \|F_{1,\tau}\flat_\tau\|^2$ and $r = 0, 1, \ldots, N-1$. From Fig. 2, we know that $\Psi_r < \varrho^2$, that is, the developed estimation method is able to meet the H_∞ performance constraint (12). We also see from Fig. 2 that the smaller the value of $\bar{\alpha}$ (i.e., the bigger the occurrence probability of DoS attack), the worse the estimation performance.

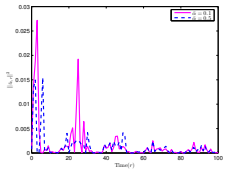

Fig. 1. The norm of estimation error $z_{e,r}$ for different $\bar{\alpha}$

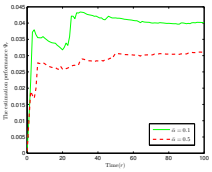

Fig. 2. The estimation performance Ψ_r for different $\bar{\alpha}$

V. Conclusion

In this paper, the finite-horizon non-fragile H_∞ state estimation has been realized for stochastic nonlinear time-varying systems under integral measurements affected by denial-of-service attacks. Integral measurements and randomly occurring DoS attacks have been taken into account, and gain variations of the estimator have been involved in advance. A necessary and sufficient condition has been set up to ensure the existence of an ideal estimator, fulfilling the H_∞ performance constraint, via stochastic analysis and CSM. The time-varying gain parameters of the estimator have been attained by solving a set of coupled backward recursive Riccati difference equations. Finally, a confirmatory simulation has been conducted to illustrate the effectiveness of the developed finite-horizon security-guaranteed non-fragile H_∞ estimation method. Future research directions may include extending the acquired estimation approach to the estimation problem for other systems, such as nonlinear systems subject to covert attacks [16], hybrid attacks [4], or bit errors [5].

References

[1] Y. Bi, Y. Yin, X. Liu, X. Nie, C. Zou and J. Du, Real-time traffic flow statistics based on dual-granularity classification, *International Journal of Network Dynamics and Intelligence*, 2023, 2(3): 100013:1-100013:14.

[2] G. Carl, G. Kesidis, R. R. Brooks and Suresh Rai, Denial-of-service attack-detection techniques, *IEEE Internet Computing*, 2006, 10(1): 82–89.

[3] P. Casoli, N. Authier, X. Jacquet and J. Cartier, Characterization of the caliban and prospero critical assemblies neutron spectra for integral measurements experiments, *Nuclear Data Sheets*, 2014, 118: 554–557.

[4] Y. Chen, X. Meng, Z. Wang and H. Dong, Event-triggered recursive state estimation for stochastic complex dynamical networks under hybrid attacks, *IEEE Transactions on Neural Networks and Learning Systems*, 2023, 34(3): 1465–1477.

[5] W. Chen, Z. Wang, J. Hu, H. Dong and G. P. Liu, Distributed resilient state estimation for cyber-physical systems against bit errors: A zonotopic set-membership approach, *IEEE Transactions on Network Science and Engineering*, 2023, 10(6): 3922–3932.

[6] H. S. Foroush and S. Martínez, On triggering control of single-input linear systems under pulse-width modulated DoS jamming attacks, *International Journal of Robust and Nonlinear Control*, 2016, 54(6): 3084–3105.

[7] H. Geng, Z. Wang, Y. Chen, X. Yi and Y. Cheng, Variance-constrained filtering fusion for nonlinear cyber-physical systems with the denial-of-service attacks and stochastic communication protocol, *IEEE/CAA Journal of Automatica Sinica*, 2022, 9(6): 978–989.

[8] H. Geng, Z. Wang, L. Zou, A. Mousavi and Y. Cheng, Protocol-based Tobit Kalman filter under integral measurements and probabilistic sensor failures, *IEEE Transactions on Signal Processing*, 2021, 69: 546–559.

[9] Y. Guo and B. Huang, State estimation incorporating infrequent, delayed and integral measurements, *Automatica*, 2015, 58: 32–38.

[10] N. Hou, J. Li, H. Liu, Y. Ge and H. Dong, Finite-horizon resilient state estimation for complex networks with integral measurements from partial nodes, *Science China Information Sciences*, 2022, 65(3): 132205:1-132205:15.

[11] J. Hu, Z. Wang and H. Gao, Joint state and fault estimation for time-varying nonlinear systems with randomly occurring faults and sensor saturations, *Automatica*, 2018, 97: 150–160.

[12] H. K. Lam, C. Liu, L. Wu and X. Zhao, Polynomial fuzzy-model-based control systems: Stability analysis via approximated membership functions considering sector nonlinearity of control input, *IEEE Transactions on Fuzzy Systems*, 2015, 23(6): 2202-2214.

[13] H. Li, H. Liu, C. Lan, Y. Yin, P. Wu, C. Yan and N. Zeng, SMWO/D: A decomposition-based switching multi-objective whale optimiser for structural optimisation of Turbine disk in aero-engines, *International Journal of Systems Science*, 2023, 54(8): 1713–1728.

[14] Q. Li, Z. Wang, W. Sheng, F. E. Alsaadi and F. E. Alsaadi, Dynamic event-triggered mechanism for H_∞ non-fragile state estimation of complex networks under randomly occurring sensor saturations, *Information Sciences*, 2020, 509: 304–316.

[15] Q. Li, H. Xue, Y. Pan and H. Liang, Dynamic output feedback control for interval type-2 fuzzy systems against DoS attacks and sensor failures, *International Journal of Systems Science*, 2023, 54(15): 2904–2920.

[16] X. Li, P. Zhang and H. Dong, A robust covert attack strategy for a class of uncertain cyber-physical systems, *IEEE Transactions on Automatic Control*, 1–8, doi: 10.1109/TAC.2023.3319071, in press, 2023.

[17] J. Liao, H.-K. Lam, S. Gulati and B. Hayee, Improved computer-aided diagnosis system for nonerosive reflux disease using contrastive self-supervised learning with transfer learning, *International Journal of Network Dynamics and Intelligence*, 2023, 2(3): 100010:1-100010:14.

[18] D. Liu, Z. Wang, Y. Liu, C. Xue and F. E. Alsaadi, Distributed recursive filtering for time-varying systems with dynamic bias over sensor networks: Tackling packet disorders, *Applied Mathematics and Computation*, 2023, 440: 127669:1-127669:14.

[19] L. Ma, Z. Wang, Y. Chen and X. Yi, Probability-guaranteed distributed secure estimation for nonlinear systems over sensor networks under deception attacks on innovations, *IEEE Transactions on Signal and Information Processing over Networks*, 2021, 7: 465–477.

[20] E. V. Markov and O. M. Mikhailov, Integral measurements of the color of nanodimensional radiators, *Measurement Techniques*, 2014, 57(9): 990–996.

[21] R. Penrose and J. A. Todd, On best approximate solutions of linear matrix equations, *Mathematical Proceedings of the Cambridge Philosophical Society*, 1956, 52(1): 17–19.

[22] X. Qian and B. Cui, A mobile sensing approach to distributed consensus filtering of 2D stochastic nonlinear parabolic systems with disturbances, *Systems Science & Control Engineering*, 2023, 11(1): 2167885:1-2167885:11.

[23] F. M. Shakiba, M. Shojaee, S. M. Azizi and M. Zhou, Real-time sensing and fault diagnosis for transmission lines, *International Journal of Network Dynamics and Intelligence*, 2022, 1(1): 36–47.

[24] B. Shen, Z. Wang, D. Wang and Q. Li, State-saturated recursive filter design for stochastic time-varying nonlinear complex networks under deception attacks, *IEEE Transactions on Neural Networks and Learning Systems*, 2020, 31(10): 3788–3800.

[25] B. Shen, Z. Wang, D. Wang, and J. Luo, Finite-horizon filtering for a class of nonlinear time-delayed systems with an energy harvesting sensor, *Automatica*, 2019, 100: 144–152.

[26] Y. Shen, Z. Wang, H. Dong, F. E. Alsaadi and H. Liu, Dynamic event-based recursive filtering for multirate systems with integral measurements over sensor networks, *International Journal of Robust and Nonlinear Control*, 2022, 3(3): 1374–1392.

[27] Y. Shen, Z. Wang, H. Dong, G. Lu and F. E. Alsaadi, Distributed recursive state estimation for a class of multi-rate nonlinear systems over wireless sensor networks under FlexRay protocols, *IEEE Transactions on Network Science and Engineering*, 2023, 10(3): 1551–1563.

[28] Y. Shen, Z. Wang, B. Shen and F. E. Alsaadi, H_∞ state estimation for multi-rate artificial neural networks with integral measurements: A switched system approach, *Information Sciences*, 2020, 539: 434–446.

[29] H. Tao, H. Tan, Q. Chen, H. Liu and J. Hu, H_∞ state estimation for memristive neural networks with randomly occurring DoS attacks, *Systems Science & Control Engineering*, 2022, 10(1): 154–165.

[30] S. Tripathi, M. Gehlot, J. K. Hussain, G. Mishra, V. Kumar and S. Chouksey, Field integral measurement of a six period undulator in a pulsed wire set up, *Optics Communications*, 2011, 284(1): 350–357.

[31] L. Wang, S. Liu, Y. Zhang, D. Ding and X. Yi, Non-fragile l_2-l_∞ state estimation for time-delayed artificial neural networks: An adaptive event-triggered approach, *International Journal of Systems Science*, 2022, 53(10): 2247–2259.

[32] L. B. Wu and G. -H. Yang, Adaptive output neural network control for a class of stochastic nonlinear systems with dead-zone nonlinearities, *IEEE Transactions on Neural Networks and Learning Systems*, 2017, 28(3): 726-739.

[33] Y. Zhao, X. He, L. Ma and H. Liu, Unbiasedness-constrained least squares state estimation for time-varying systems with missing measurements under Round-Robin protocol, *International Journal of Systems Science*, 2022, 53(9): 1925–1941.

[34] Y. Zhao, Y. Liu, G. Wen, X. Yu and G. Chen, Distributed average tracking for Lipschitz-type of nonlinear dynamical systems, *IEEE Transactions on Cybernetics*, 2019, 49(12): 4140-4152.

Proceedings of the 3rd Conference on Fully Actuated System Theory and Applications
May 10-12, 2024, Shenzhen, China

Design of Coordinated Path Tracking Controller for Underactuated Multiple Unmanned Ships

Yiyang Wang[1], Yi Zhang[2], Chenqi Wang[2]

1. School of Information Science and Engineering, Shenyang University of Technology, Shenyang 110870

E-mail: 2689386075@qq.com

2. School of Science, Shenyang University of Technology, Shenyang 110870, China
E-mail: zhangyi@sut.edu.cn

Abstract: In this paper, the collaborative path tracking problem of under-actuated multiple unmanned ships is studied, aiming at improving the accuracy and stability of the path tracking of unmanned ships. Firstly, the mathematical model of the under-actuated multi-unmanned ship is established, and its kinematic characteristics and control difficulty are analyzed. Then, an enhanced cooperative control strategy is adopted to enable multiple unmanned ships to cooperate to complete the path tracking task. The effectiveness and superiority of this control strategy are verified by simulation experiments. The results show that compared with the traditional control methods, the proposed collaborative control strategy can significantly improve the path tracking accuracy and stability of unmanned ships, and enhance the collaborative performance of multiple unmanned ships.

Key Words: Cooperative control strategy; path tracking control； vehicle dynamics mode

1 Introduction

The ocean occupies two-thirds of the earth's surface, is one of the most important features of the earth's surface, and is also an important resource for human survival and sustainable development. With the continuous growth of population and the depletion of land resources, all countries have begun to pay attention to the development and utilization of Marine space and resources, especially the development of unmanned ship technology[1-2]. Unmanned ship is a miniaturized, multi-purpose, intelligent unmanned ocean transport platform that can sail by remote control or autonomous navigation. Due to its characteristics of low cost, small size, high speed and high intelligence, unmanned ships can carry out long-term and large-scale Marine operations in complex and dangerous Marine environments, which is an important reflection of the national Marine scientific and technological strength[3].

The unmanned ship vehicles (USVs) formation cooperative control technology can be applied to various Marine operations, such as environmental monitoring, hydrology and geographic investigation, maritime search and rescue and ship replenishment. The application of this technology can not only improve operational efficiency[4] and reduce personnel risks, but also has great significance for environmental protection and sustainable development[5].

However, achieving accurate path tracking and stable coordination of multiple unmanned vessels is a challenging task. Due to the dynamic characteristics of unmanned ships and the influence of external interference, it is necessary to study an effective control strategy to solve the cooperative path tracking problem of under-actuated multi-unmanned ships. This is not only a hot issue in current research, but also a difficult issue in future research.

Therefore,this paper will study the problem of under-actuated multi-unmanned ship cooperative path tracking, propose effective control strategies and methods, and provide theoretical support and technical guidance for practical applications.

This paper studies the cooperative path tracking problem of multiple unmanned ships with globally known path information, and some research results have been obtained in related work [6-10]. The decentralized formation control scheme for fleets with a small amount of inter-ship communication is proposed and studied in literature [6]. The control objective of each ship is to maintain its position in the formation relative to the formation reference point, which follows a predefined path. Literature [7] studies the cooperative path tracking problem under discrete-time periodic communication, and proposes the cooperative updating law of distributed path parameters, which effectively solves the communication limitation problem in practical applications. Literature [8] presents a collaborative path tracking algorithm based on neural network adaptive dynamic surface control technology, and introduces dynamic surface control technology to greatly reduce the complexity of the algorithm. In the study of path tracking on closed curves, some research results have been obtained[9-11]. [9] studies the tracking problem of multiple robots on multiple closed curves, and obtains synchronous formation formation by adopting arc length consistency method. Literature [10] studies the problem of guiding a series of underdriven ship formation to track a set of closed tracks and realize attitude synchronization, and proves that when the topology of inter-ship communication is bidirectional, it is asymptotically stable. Literature [11] studies the coordinated path tracking problem of multi-agent systems, and proposes feedback linearization to stabilize it. These research results are all aimed at the situation where multiple robots track multiple closed curves. In the existing collaborative path tracking studies of unmanned ships, the common assumption is that the global reference speed is known. However, in practical applications, due to bandwidth limitations or security concerns, it is not possible

*This work is supported by National Natural Science Foundation of China under Grant 62103289.

to guarantee that every ship has direct access to reference speed information. In order to solve this problem and avoid the assumption of global reference speed, distributed observers are applied to the cooperative control of multi-agent systems. Distributed observers provide each agent with the ability to independently estimate its speed and position without relying on global reference speed information. In this way, collaborative path tracking can be achieved even in the absence of global reference speed information. [12] shows that the explicit expression of the controller gain matrix is parameterized according to solver conditions so that the drive system and the response system can be exponentially synchronized. The applicability of the proposed design method is verified by numerical examples. [13] proves that each agent can follow the active leader with the help of the explicitly constructed common Lyapunov function (CLF).

Inspired by previous studies, aiming at the cooperative path tracking problem of under-actuated unmanned ships guided by multiple paths, this paper combined LOS guidance and multi-agent consistency method [14], and proposed a collaborative path tracking method based on path parameter consistency. This method is more suitable for practical application, and can make the path parameters tend to be synchronized, so as to realize the synchronous formation on multiple paths. In other words, through this method, multiple unmanned ships can be made to maintain consistent parameters on their respective paths, so as to achieve multi-ship collaborative path tracking and synchronous formation.

2 Model Description

As shown in Figure 1, the multi-unmanned boat system consists of N underactuated following unmanned boats and a single target unmanned boat, then the target unmanned boat is represented as

$$\begin{cases} x_0 = u_0 \cos(\psi_0) - v_0 \sin(\psi_0) \\ y_0 = u_0 \sin(\psi_0) + v_0 \cos(\psi_0) \\ \psi_0 = r_0 \end{cases} \tag{1}$$

In the formula, x_0, y_0, ψ_0 respectively represent the X-axis coordinate, Y-axis coordinate and yaw Angle of the target unmanned vehicle in the earth coordinate system.

$u_0 r_0 v_0$ denote the longitudinal velocity, transverse drift velocity and bow angular velocity of the target unmanned vehicle in the unmanned vehicle body coordinate system.

The design of this paper is based on the condition that the actual motion speed and direction of the unmanned ship can be measured, so the kinematics model of the unmanned ship is rewritten as

$$\begin{cases} \dot{x}_i = U_i \cos\psi_{iw} \\ \dot{y} = U_i \sin\psi_{iw} \\ \dot{\psi}_{iw} = r_i + \beta_{id} \end{cases} \tag{2}$$

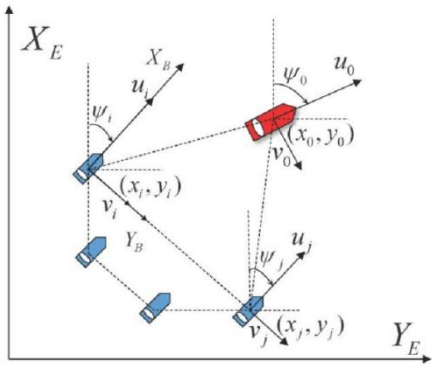

Fig.1 Cooperative target tracking of multiple USVs

Among them, $U_i = \sqrt{u_i^2 + v_i^2} > 0$ it's the actual velocity of the ship, $\psi_{iw} = \psi_i + \beta_i$ is the actual direction of the ship's motion,i $\beta_i = a\tan 2(v_i / u_i)$ it's a sideslip Angle, and $\beta_{id} = \dot{\beta}_i$ The given parameterized path of the i unmanned ship is expressed as $(x_{id}(\theta_i), y_{id}(\theta_i))$, θ_i is path parameter.

The tangent Angle on the i path can be expressed as $\psi_{id} = a\tan 2(y'_{id}, x'_{id})$,among $x'_{id} = \partial x_{id}(\theta_i) / \partial\theta_i$, $y'_{id} = \partial y_{id}(\theta_i) / \partial\theta_i$ For the i unmanned ship in position (x_i, y_i) , longitudinal tracking error and lateral tracking error can be expressed in path tangential coordinate system as

$$\begin{bmatrix} x_{ie} \\ y_{ie} \end{bmatrix} = \begin{bmatrix} \cos\psi_{id} & -\sin\psi_{id} \\ \sin\psi_{id} & \cos\psi_{id} \end{bmatrix}^T \begin{bmatrix} x_i - x_{id}(\theta_i) \\ y_i - y_{id}(\theta_i) \end{bmatrix}$$

take the derivative of that, and take the (1) in and get

$$\begin{cases} \dot{x}_{ie} = U_i \cos(\psi_{iW} - \psi_{id}) + \dot{\psi}_{id} y_{ie} - u^*_{id}\dot{\theta}_i \\ \dot{y}_{ie} = U_i \sin(\psi_{iW} - \psi_{id}) - \dot{\psi}_{id} x_{ie} \end{cases}$$

$$u^*_{id} = \sqrt{x'^2_{id} + y'^2_{id}}$$

So the dynamic equation of x_{ie} y_{ie} and ψ_{iW} can be rewritten as

$$\begin{cases} \dot{x}_{ie} = U_i \cos(\psi_{iW} - \psi_{id}) + \dot{\psi}_{id} y_{ie} - u^*_{id}\dot{\theta}_i \\ \dot{y}_{ie} = U_i \sin(\psi_{iW} - \psi_{id}) - \dot{\psi}_{id} x_{ie} \\ \dot{\psi}_{iW} = r_1 + \beta_{id} \end{cases} \tag{3}$$

The control objective of this paper is to solve the cooperative path tracking problem of multi-path guidance.At the kinematic level, the guidance forward velocity U_{ir} and guidance angular velocity r_{ir} are designed to make the unmanned ship track the parametric path $(x_{id}(\theta_i), y_{id}(\theta_i))$, And get synchronized formation formation. Specifically, the control objective can be divided into two tasks.

(1) Path tracking tasks:

$$\lim_{t\to\infty}|x_{ie}|\to 0,\ \lim_{t\to\infty}|y_{ie}|\to 0 \tag{4}$$

(2)Parameter coordination tasks:

$$\lim_{t\to\infty}|\theta_i-\theta_j|\to 0 \tag{5}$$

$i=1,...,N, j=1,...,N, i\neq j$。

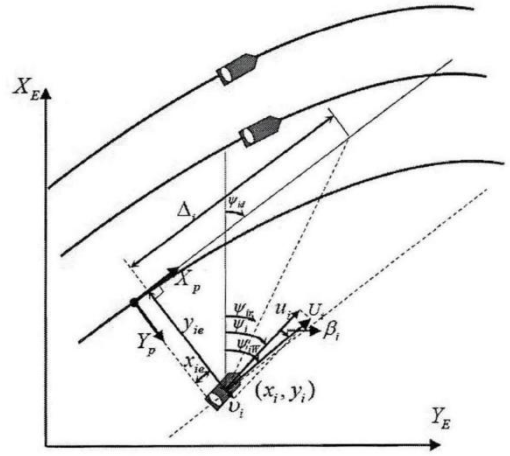

Fig.2 Cooperative path following of multiple USVs

3 Coordinated path tracking by multiple unmanned ships

The path tracking controller of the i unmanned ship includes the motion controller and the dynamics controller. This section focuses on the design of the motion controller. The motion control includes the guidance law and the collaborative algorithm based on neighbor information. The guidance law calculates the given velocity and angular velocity, which enables the unmanned ship to track the given reference path. The collaborative algorithm adjusts its own path parameter update speed based on the path parameter information of neighboring ships, thereby achieving path parameter coordination among ships and obtaining an ideal formation effect.

3.1 Guidance law design

Firstly, the guidance law of a single unmanned ship is designed based on LOS guidance method, which makes each unmanned ship track the given parameterized path. To be specific,The given values of forward velocity U_{ir} and yaw angular velocity r_{ir} are designed.

Define

$$\begin{cases}\psi_{ie}=\psi_{iW}-\psi_{ir}\\ \dot{\theta}_i=v_s-\omega_i\end{cases}$$

ψ_{ir} is the guidance course Angle; v_s is the reference speed; ω_i is the variable to be designed. On the basis of (3), the dynamic equation of path tracking error can be rewritten as follow

$$\begin{cases}\dot{x}_{ie}=U_i-2U_i\sin^2\left(\dfrac{\psi_{iW}-\psi_{id}}{2}\right)+\dot{\psi}_{id}y_{ie}-u_{id}^*\left(v_s-\omega_i\right)\\ \dot{y}_{ie}=U_i\sin\left(\psi_{ir}-\psi_{id}\right)+\rho_i-\dot{\psi}_{id}x_{ie}\\ \dot{\psi}_{ie}=r_i+\beta_{id}-\dot{\psi}_{ir}\end{cases} \tag{6}$$

$\rho_i=U_i\sin\left(\psi_{ir}-\psi_{id}\right)$.

The guidance law of unmanned ship i is as follows

$$\begin{cases}U_{ir}=-k_{i1}x_{ie}/\prod_{ix}+u_{id}^*v_s+2U_i\sin^2\left(\dfrac{\psi_{iW}-\psi_{id}}{2}\right)\\ r_{ir}=-k_{i2}\psi_{ie}/\prod_{i\psi}-\beta_{id}+\dot{\psi}_{ir}-y_{ie}\rho_i/\psi_{ie}\end{cases} \tag{7}$$

where $\psi_{ir}=\psi_{id}+\arctan\left(-\dfrac{y_{ie}}{\Delta_i}\right)$, $\prod_{ix}=\sqrt{x_{ie}^2+\Delta_{ix}^2}$, $\prod_{i\psi}=\sqrt{\psi_{ie}^2+\Delta_{i\psi}^2}$, Δ_{ix} and $\Delta_{i\psi}$ are positive, Δ_i is the forward distance; k_{i1}, k_{i2} are positive.

Due to

$$\psi_{ie}=(\psi_{iW}-\psi_{id})-(\psi_{ir}-\psi_{id}),$$

$$\lim_{\psi_{ie}\to 0}\frac{\sin\left(\psi_{iW}-\psi_{id}\right)-\sin\left(\psi_{ir}-\psi_{id}\right)}{\psi_{ie}}=\cos\left(\psi_{ir}-\psi_{id}\right)$$

$$=\cos\left(\psi_{ir}-\psi_{id}\right)$$

when $\psi_{ie}\to 0$,

$$\lim_{\psi_{ie}\to 0}\frac{\rho_i}{\psi_{ie}}=U_i\cos\left(\psi_{ir}-\psi_{id}\right)$$

Since the design of this section is based on kinematics and does not consider dynamics, the following assumption is made in the dynamics loop:

Assumption 1 The unmanned ship perfectly tracks the given forward velocity and the given yaw angular velocity, $U_i=U_{ir}, r_i=r_{ir}$.

Substitute (6) into (5), the error equation is obtained. The dynamic equation of error is

$$\begin{cases}\dot{x}_{ie}=-k_{i1}x_{ie}/\prod_{ix}+u_{id}^*\omega_i+\dot{\psi}_{id}y_{ie}\\ \dot{y}_{ie}=-U_iy_{ie}/\prod_{iy}+\rho_i-\dot{\psi}_{id}x_{ie}\\ \dot{\psi}_{ie}=-k_{i2}\psi_{ie}/\prod_{i\psi}-y_{ie}\rho_i/\psi_{ie}\end{cases}$$

$$\prod_{iy}=\sqrt{y_{ie}^2+\Delta_i^2}$$

3.2 Path parameter update rate design

The ω_i law designed in this section makes the path parameters synchronized, so as to achieve synchronous formation formation. Define the cooperative error based on neighbor information as

$$e_i = \sum_{j=1}^{N} a_{ij}\left(\theta_i - \theta_j\right)$$

The ω_i law of design is

$$\omega_i = \mu_i e_i - \mu_i u_{id}^* x_{ie} \tag{8}$$

μ_i is a positive.

Define $e = \left[e_1, ..., e_N\right]^T$, $\omega = \left[\omega_1, ..., \omega_N\right]^T$,

Then the error $x_{ie}, y_{ie}, \psi_{ie}$ and $e's$ dynamic equation is

$$\begin{cases} \dot{x}_{ie} = -k_{i1} x_{ie} / \prod_{ix} + u_{id}^* \omega_i + \dot{\psi}_{id} y_{ie} \\ \dot{y}_{ie} = -U_i y_{ie} / \prod_{iy} + \rho_i - \dot{\psi}_{id} x_{ie} \\ \dot{\psi}_{ie} = -k_{i2} \psi_{ie} / \prod_{i\psi} - y_{ie} \rho_i / \psi_{ie} \\ \dot{e} = -\varepsilon\omega \end{cases} \tag{9}$$

3.3 Stability analysis

The following theorem illustrates the stability of closed-loop systems:

Theorem 1 Considering the motion equation (1) of an unmanned ship, under the condition of satisfying assumption 1, the guidance law (7) and the collaborative update law (8) ensure that the origin $\left(x_{ie}, y_{ie}, \psi_{ie}, e_i\right) = \left(0,0,0,0\right)$ of the closed-loop system (9) is globally uniformly asymptotically stable.

Proof Construct the following Lyapunov function

$$V_1 = \sum_{i=1}^{N}\left\{\frac{1}{2}x_{ie}^2 + \frac{1}{2}y_{ie}^2 + \frac{1}{2}\psi_{ie}^2\right\} + \theta^T \varepsilon\theta,$$

V_1 can be written as

$$V_1 = \sum_{i=1}^{N}\left\{\frac{1}{2}x_{ie}^2 + \frac{1}{2}y_{ie}^2 + \frac{1}{2}\psi_{ie}^2\right\} + e^T P e$$

Take the derivative of this, and apply the(9)Substituting can be obtained

$$\dot{V}_1 \le \sum_{i=1}^{N}\left\{\frac{1}{2}x_{ie}^2 / \prod_{ix} + x_{ie} u_{id}^* \omega_i - U_i y_{ie}^2 / \prod_{iy} - k_{i2}\psi_{ie}^2 / \prod_{i\psi}\right\} - \theta^T \varepsilon\omega$$

$$\le \sum_{i=1}^{N}\left\{-k_{i1}x_{ie}^2 / \prod_{ix} - U_i y_{ie}^2 / \prod_{iy} - k_{12}\psi_{ie}^2 / \prod_{i\psi}\right\} - \lambda_{\min}\left(\mu\right)\left\|\vartheta\right\|^2$$

$$\mu = diag\left\{\mu_1, ..., \mu_N\right\}, \vartheta = -e + u_d^* x_e, u_d^*$$

$$= diag\left\{u_{1d}^*, ..., u_{Nd}^*\right\}, x_e = \left[x_{1e}, ..., x_{Ne}\right]^T$$

According to the above can be obtained the Origin of (9) $\left(x_{ie}, y_{ie}, \psi_{ie}, e_i\right) = \left(0,0,0,0\right)$ is globally uniformly asymptotically stable. Because $e \to 0$

$e^T P e \ge \lambda^* \left\|\theta - 1_N \frac{1}{N}\sum_{i=1}^{N}\theta_i\right\|^2$, it can be obtained

$$\theta_i \to \theta_j \to \frac{1}{N}\sum_{i=1}^{N}\theta_i$$

So the control goal is achieved.

Remark 1 Most of the current collaborative path tracking methods are proposed for fully actuated ships, while in practical applications, most unmanned ships are underactuated. Compared to fully actuated ships, underactuated ships have a simpler structure and easier operation, but there are non-integrable second-order nonholonomic constraints in the mathematical model, which brings challenges to the design of the controller. The collaborative path tracking method proposed in this paper is designed for underactuated ships, and has the advantages of simplicity, intuition, and efficiency.

4 Numerical simulation

Parameter design guideline, the control parameters are selected as follows:

$$k_{i\beta} = 80, k_{i1} = 10, \Gamma_{i\beta} = 1500, k_{i\beta} = 0.005, k_{iu} = 80,$$
$$k_{ir} = 80, k_{i2} = 2, k_{i3} = 6, \Gamma_{iu} = 1500$$

$$\Gamma_{ir} = 1500, \rho_i = 3, k_{ier} = 0.01, \Delta_i = 3,$$
$$k_{i4} = 5, k_{i5} = 1, \gamma_{iu} = 1, \gamma_{ir} = 1, \mu_i = 3$$

Simulation results are shown in Figs. 3-6.

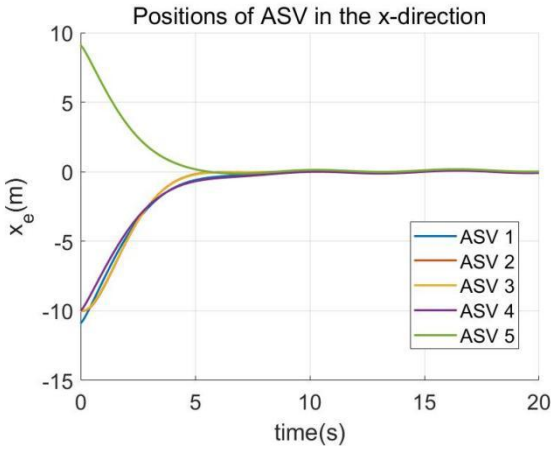

Fig. 3 x-direction of ASV

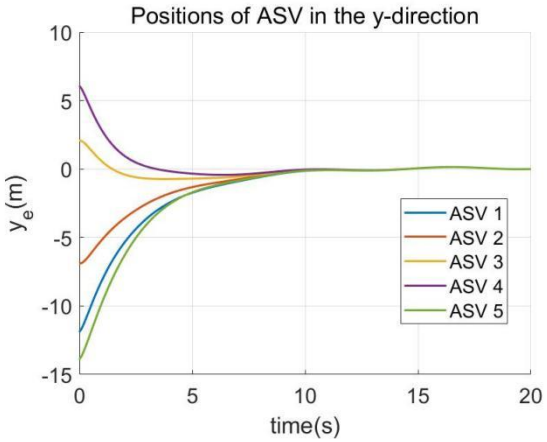

Fig. 4 y-direction of ASV

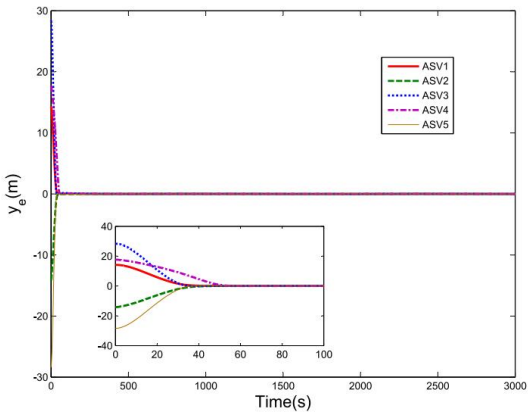

Fig. 5 Cross track errors

Fig. 3 and Fig. 4 show the positions of ASV. Fig. 5shows the lateral tracking errors, which are all within an acceptable range. Fig. 6 shows the update of path parameters. After a period of adjustment, the path parameters of the ship gradually synchronized, achieving consistency control of the path parameters. In other words, by updating the path parameters, the ships ultimately reach a synchronized state, which enables them to maintain consistent paths.

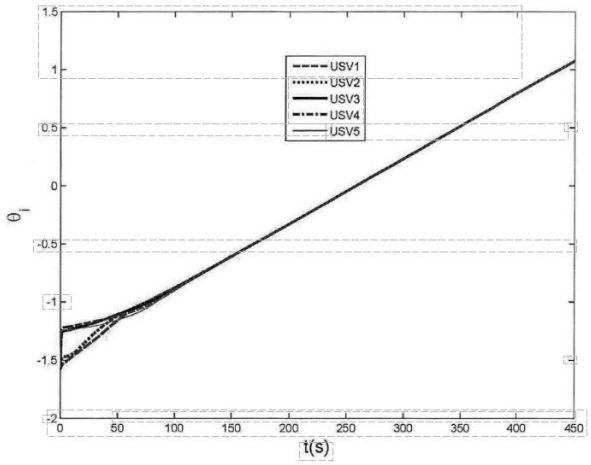

Fig. 6The evolution path variable

5 Conclusions

In this paper, the problem of collaborative path tracking of underactuated multi-unmanned ships is studied in depth, and a reinforced collaborative control strategy is proposed. This strategy aims to improve the path tracking accuracy, stability, and collaborative performance of multiple unmanned ships. Simulation experiments are conducted to verify the effectiveness and superiority of this strategy. The experimental results show that the unmanned ships using this strategy have significantly improved path tracking and stability performance, and the collaborative performance among multiple unmanned ships has also been enhanced. Additionally, this strategy exhibits good robustness and can adapt to various environmental and condition changes. Whether in calm sea conditions or complex and changing sea conditions, this strategy can maintain high control accuracy and collaborative performance. In the future, we will continue to explore the problem of collaborative path tracking of underactuated multi-unmanned ships, striving to further improve the control accuracy and collaborative performance of unmanned ship groups. We hope to provide more reliable and efficient technical support for practical applications through continuous research and innovation, and promote the wider application of unmanned ship technology in marine operations.

References

[1] Thomsen J E,Guilory V G, Benes T A. The navy unmanned surface vehicle (USV) master plan. *United State. Washington DC: Department of the Navy*, 2007:1-10.

[2] Fan Y , Sun X , Wang G . An autonomous dynamic collision avoidance control method for unmanned surface vehicle in unknown ocean environment. *International Journal of Advanced Robotic Systems*, 16(2): 1-11, 2019.

[3] Bertram V. Unmanned Surface Vehicles-A Survey. *Copenhagen, Denmark,* 2008.

[4] Qu X R, Liang X, Hou Y H, et al. Finite-time sideslip observer-based synchronized path-following control of multiple unmanned underwater vehicles-Science Direct. *Ocean Engineering*, 217, 2020.

[5] Bibuli M, Bruzzone G, Caccia M, et al. Swarm based path-following for cooperative unmanned surface vehicles, *Journal of Engineering for the Maritime Environment*, 228(2):192-207, 2014.

[6] Ihle, Ivar-andré F, Skjetne, R, Fossen, T. I, Nonlinear formation control of marine craft with experimental results. *43rd IEEE Conference on Decision and Control,* 2004: 680-685.

[7] Almeida J, Silvestre C, Pascoal A M, Cooperative control of multipe surface vessels with discrete-time periodic communications.*International Journal of Robust and Nonlinear Control*, 22(4):398-419, 2011.

[8] Wang H, Wang D, Peng Z H, et al. Adaptive dynamic surface control for cooperative path following of multiple autonomous surface vessels[J]. *Control Theory & Applications,* 30(5):637-643, 2013.

[9] Chen Y Y, Tian Y P. A curve extension design for coordinated path following control of unicycles along given convex loops. *International Journal of Control,* 84(10):1729-1745, 2011

[10] Chen, Yang Yang , and Y. P. Tian . Coordinated patterns of underactuated ships along closed orbits. *IEEE International Conference on Robotics and Automation*, 2014:3583-3588 .

[11]Chen Y Y, Tian Y P. Coordinated path follewing control of multi-unicycle formation motion around closed curves in a time-invariant flow. *Nonlinear Dynamics,* 81 (1-2): 1005-1016, 2015.

[12]Karimi, Hamid Reza, P. Maass. Delay-range- dependent exponential H ∞ synchronization of a class of delayed neural networks. *Chaos, Solitons & Fractals,* 41(3):1125-1135, 2009.

[13] Hong Y G , Chen G R , Bushnell L. Distributed observers design for leader-following control of multi-agent networks. *Automatica,* 44(3): 846-850, 2008.

[14]Chen W S,Hua S Y,Ge S S.Consensus-based distributed coopertative learing control for a group of discrete-time nonlinear multi-agent systems using neural networks. *Automatica*, 50(9): 2254-2268, 2014.

Proceedings of the 3rd Conference on Fully Actuated System Theory and Applications
May 10-12, 2024, Shenzhen, China

Fuzzy-based Dynamic Event-triggered Control for Uncertain Nonlinear Systems

Yaxin An[1,2], Yongchao Liu[1,2]*
1. School of Automation, Qingdao University, Qingdao 266071, P. R. China
2. Shandong University of Science and Technology, Qingdao 266071, P. R. China
E-mail: sdliuyc@163.com

Abstract: It is a pendent problem to accomplish dynamic event-triggered tracking for uncertain nonlinear systems (UNS) with unmeasured state and unmatched control input by feat of backstepping technique. In this article, we present a control solution to deal with the issue under backstepping frame. First, a fuzzy-based state observer is established to estimate unmeasured states of the system. Then, a dynamic variable is integrated into the dynamic event-triggered protocol to achieve dynamic triggering threshold parameter. Such operation can help to further decrease triggering events and economy network resource. The formulated dynamic event-triggered scheme provides a feasible solution for UNS. Finally, theoretical finding is authenticated by simulation comparative analysis.

Key Words: Dynamic event-triggered adaptive control, state observer, backstepping technique, fuzzy control, uncertain nonlinear systems.

1 Introduction

Most of the actual physical systems contain nonlinearity, strong coupling, uncertainty, randomness, and other comprehensive properties. Therefore, designing the controller of nonlinear systems is a long-term and challenging problem. The backstepping technique has emerged as an effective approach to address the challenges posed by nonlinearity. To handle uncertainties existing in uncertain nonlinear systems (UNS), numerous adaptive control techniques ground on fuzzy logic or neural networks have been researched. These approximation-based intelligent control methods have gained significant attention in control territory with many important results being reported.

The fuzzy control method is a promising tactic for solving the nonlinear control problem in recent years. Since $Zadeh$ proposed fuzzy set theory in 1965 [1], it has revealed excellent performance in different areas and has been broadly employed in control design. In [2], fuzzy-based control solutions were constructed for UNS, which with unknown dynamics. In [3], fuzzy-based finite-time control method was investigated for high-order multi-agent UNS. These methods are highly effective in achieving control objectives without requiring knowledge of the dynamic system model in advance. It's worth noting that all the aforementioned methods are state feedback control, which means they require direct measurement of all states. However, due to the complexity of the environment, only partial state information is available, and some of it cannot be measured directly. Therefore, we can use a fuzzy observer to accurately estimate unmeasured states based on output signals. In [4], the observer-based fuzzy backstepping output feedback controller was investigated for nonlinear systems with unmeasured states. Moreover, these accomplishments were utilized to tackle challenges in UNS. Remark that the aforementioned results utilize the time-triggered control (TTC) approach, which employs a fixed-cycle data transfer method. While the TTC method is straightforward to implement, it consumes plentiful network resources and may result in network congestion.

To address this issue and enhance network resource utilization by minimizing unnecessary data transmission, Åström firstly proposed the event-triggered control (ETC) method [5]. Different from TTC, ETC determines whether to transmit data and update control signals by designing an event-triggered mechanism (ETM) according to system performance. In the paper [6], a strategy for adaptive control based on events was proposed for the purpose of strict feedback UNS. This method employed the adaptive backstepping technique and designed the event-triggered mechanism and the controller in parallel, and the event-triggered measurement error is compensated effectively. Based on [6], the ETC of strict feedback UNS has received comprehensive attention and produced a large number of research results [7]. It is important to note that the above ETM are static which means that the threshold parameter is typically fixed in the constructed event-triggered conditions. Compared to static ETM, dynamic ETM [8, 9] introduces a dynamic variable to adjust the threshold parameters dynamically, thus the utilization efficiency of communication resources can be improved. In [10], a dynamic ETC scheme was submitted for strict-feedback UNS, which can achieve the control objective when the system state can be measured.

The existing dynamic ETC methods are mainly focused on linear systems, first-order UNS, and higher-order UNS with standard form. However, there have been limited reports on dynamic ETC results for strict feedback UNS with unmeasured states. The presence of unmeasured states poses significant challenges to designing dynamic ETC strategies.

This paper presents a fuzzy-based adaptive dynamic ETC approach for UNS. By developing a fuzzy state observer, the unavailable state is estimated. Using these observed states, we exploit a feedback-based adaptive dynamic event-triggered output feedback control law. The major innovations of the presented scheme are extracted as follows:

(1) In the process of control design, a fuzzy-based state observer is utilized to estimate unavailable states. By in-

This work was supported in part by the Shandong Provincial Natural Science Foundation (ZR2023QF039), by the Qingdao Natural Science Foundation (23-2-1-123-zyyd-jch).

corporating fuzzy approximation technique, an adaptive recursive backstepping framework is employed to exploit an output feedback control strategy.

(2) This method introduces a dynamic threshold parameter into the event-triggered mechanism and then builds a dynamic event-triggered controller. When the signals from the controller to the actuator satisfy the dynamic triggering condition, they are transmitted. Compared to existing static event-triggered mechanisms, this method reduces the number of events transmitted through the actuator network channel.

(3) Different from the existing works, this paper designs a dynamic ETM for UNS to reduce the data transmission burden. To address more general strict feedback UNS, a fuzzy-based output feedback controller is devised using backstepping technique. It is proven that all signals of the close-loop systems by applying the designed scheme are bounded and without Zeno behavior.

2 Preliminaries and problem formulation

2.1 System Depiction

Consider the following strict-feedback nonlinear systems:

$$\begin{cases} \dot{x}_1 = x_2 + \Psi_1(X_1) + d_1, \\ \dot{x}_2 = x_3 + \Psi_2(X_2) + d_2, \\ \vdots \\ \dot{x}_n = u + \Psi_n(X_n) + d_n, \\ y = x_1, \end{cases} \tag{1}$$

where $x_1, \cdots, x_n$ are system states and $X_i = (x_1, \cdots, x_i)^T (i = 1, 2, ..., n)$; $u \in R$ is the control input; $y \in R$ is the system output; $\Psi_i(X_i) \in R$ denote nonlinear functions, which are unknown and smooth; d_i denotes the disturbance of the system, which are bounded.

2.2 Fuzzy logic systems

Lemma 1: Define a function $\Psi(x)$ on a compact set Ω, which is continuous. Then for any $\ell > 0$, there lives a fuzzy logic system (FLS) such as:

$$\sup_{x \in \Omega} \left| \Psi(x) - \theta^{\mathrm{T}} \varphi(x) \right| \leqslant \ell, \tag{2}$$

where θ is the weight vector, ℓ denotes the fuzzy approximation error, $\varphi(x) = [\varphi_1(x), \varphi_2(x), ..., \varphi_n(x)]^{\mathrm{T}}$ is the fuzzy basis function vector which is chosen as:

$$\varphi_i(x_i) = \frac{\prod_{i=1}^{j} \mu_{F_i^l}(x_i)}{\sum_{l=1}^{n} \left(\Pi_{i=1}^{j} \mu_{F_i^l}(x_i) \right)}, \tag{3}$$

where $F_i^l (i = 1, ..., j; l = 1, ..., n)$ is the fuzzy set, $n > 1$ is the number of fuzzy rule and $\mu_{F_i^l}$ is the membership function.

3 Fuzzy dynamic event-triggered control design

According to Lemma 1, any smooth function can be approximated by FLS in a compact space. Thus, we can approximate the nonlinear terms in 1 as:

$$\begin{aligned} &\Psi_i(X_i \mid \theta_i) = \theta_i^{\mathrm{T}} \varphi_i(X_i), \\ &\hat{\Psi}_i(\hat{X}_i \mid \theta_i) = \theta_i^{\mathrm{T}} \varphi_i(\hat{X}_i), \quad 1 \leqslant i \leqslant n \end{aligned} \tag{4}$$

where $\hat{X}_i = (\hat{x}_1, \hat{x}_2, \ldots, \hat{x}_i)^{\mathrm{T}}$.

The FLS minimum approximation errors ω_i and approximation errors δ_i are defined as

$$\omega_i = \Psi_i(X_i) - \hat{\Psi}_i(\hat{X}_i \mid \theta_i^*), \delta_i = \Psi_i(X_i) - \hat{\Psi}_i(\hat{X}_i \mid \theta_i), \tag{5}$$

where θ_i^* is the optimal parameter vector.

Denote $\omega_i' = \omega_i + d_i$ and $\delta_i' = \delta_i + d_i (i = 1, 2, \ldots, n)$.

Assumption 1: The reference signal y_r and its first n-th order derivatives are bounded and continuous.

Assumption 2: $d_i (i = 1, 2, \ldots, n)$ denotes the disturbance of the system, which is bounded.

Assumption 3: Assume that there exist constants ω_{i0}' and $\delta_{i0}' (i = 1, 2, \ldots, n)$, which are known and satisfy $|\omega_i'| \leq \omega_{i0}', |\delta_i'| \leq \delta_{i0}'$.

3.1 Fuzzy state observer design

Design following fuzzy state observer:

$$\begin{cases} \dot{\hat{x}}_1 = \hat{x}_2 + k_1(y - \hat{y}) + \hat{\Psi}_1(\hat{X}_1 | \theta_1), \\ \dot{\hat{x}}_2 = \hat{x}_3 + k_2(y - \hat{y}) + \hat{\Psi}_2(\hat{X}_2 | \theta_2), \\ \vdots \\ \dot{\hat{x}}_n = u + k_n(y - \hat{y}) + \hat{\Psi}_n(\hat{X}_n | \theta_n), \\ \hat{y} = \hat{x}_1, \end{cases} \tag{6}$$

where k_i is an observer parameter to be determined, $\hat{x}_i$ and $\hat{y}$ are estimated state x_i and output y, and k_i, $i = 1, \ldots, n$ are chosen to make the matrix A Hurwitz,

$$A = \begin{bmatrix} -k_1 & & \\ \vdots & & I \\ -k_n & 0 & \ldots \quad 0 \end{bmatrix}.$$

There exists a positive matrix $P = P^T > 0$ that satisfies $A^T P + PA = -2Q$, where $Q > 0$ is a given positive-definite symmetric matrix.

Let $\varepsilon_i = x_i - \hat{x}_i$, $i = 1, \ldots, n$ be the observer error, then:

$$\begin{cases} \dot{\varepsilon}_1 = \varepsilon_2 + \delta_1' - k_1 \varepsilon_1, \\ \dot{\varepsilon}_2 = \varepsilon_3 + \delta_2' - k_2 \varepsilon_1, \\ \qquad \vdots \\ \dot{\varepsilon}_n = \delta_n' - k_n \varepsilon_1. \end{cases} . \tag{7}$$

From 7, we can earn:

$$\dot{\varepsilon} = A\varepsilon + \delta, \tag{8}$$

where $\delta = [\delta_1', \delta_2', \ldots, \delta_n']^T$.

3.2 Dynamic event-triggered adaptive controller design

Then, an observer-based dynamic ETC algorithm will be devised via applying backstepping technique. The coordinate transformations are exhibited as:

$$\begin{cases} z_1 = y - y_r, \\ z_i = \hat{x}_i - \alpha_{i-1} - y_i^{(i-1)} \quad i = 2, \ldots, n, \end{cases} \tag{9}$$

where z_1 is the stabilization error, z_i are virtual errors and α_i denotes the virtual control law.

Step 1: Ground on (9),

$$\begin{aligned} \dot{z}_1 &= \dot{x}_1 - \dot{y}_r \\ &= x_2 + \Psi_1(X_1) + d_1 - \dot{y}_r \\ &= \varepsilon_2 + \hat{x}_2 + \omega_1 + \hat{\Psi}_1(\hat{X}_1 \mid \theta_1^*) + d_1 - \dot{y}_r \\ &= \varepsilon_2 + z_2 + \alpha_1 + \tilde{\theta}_1^T \varphi_1(\hat{x}_1) + \theta_1^T \varphi_1(\hat{x}_1) + \omega_1', \end{aligned} \tag{10}$$

where $\tilde{\theta}_1 = \theta_1^* - \theta_1$.

Consider the Lyapunov function:

$$V_1 = \frac{1}{2}\varepsilon^{\mathrm{T}} P\varepsilon + \frac{1}{2}z_1^2 + \frac{1}{2\gamma_1}\tilde{\theta}_1^T\tilde{\theta}_1, \tag{11}$$

where $\gamma_1 > 0$ is a constant.

Calculating $\dot{V}_1$ yields

$$\begin{aligned}\dot{V}_1 =&\varepsilon^T P(A\varepsilon + \delta) + z_1\dot{z}_1 - \frac{1}{\gamma_1}\tilde{\theta}_1^T\dot{\theta}_1\\ =&\frac{1}{2}\varepsilon^T\left(A^TP + PA\right)\varepsilon + \varepsilon^T P\delta + z_1\dot{z}_1 - \frac{1}{\gamma_1}\tilde{\theta}_1^T\dot{\theta}_1\\ =&-\varepsilon^T Q\varepsilon + \varepsilon^T P\delta + z_1\left[z_2 + \alpha_1 + \theta_1^T\varphi_1\left(\hat{x}_1\right) + \omega_1'\right]\\ &+ z_1\varepsilon_2 + \frac{1}{\gamma_1}\tilde{\theta}_1^T\left(\gamma_1 z_1\varphi_1\left(\hat{x}_1\right) - \dot{\theta}_1\right).\end{aligned} \tag{12}$$

Employing Young's inequality yields

$$\varepsilon^T P\delta + z_1\varepsilon_2 \le \|\varepsilon\|^2 + \frac{1}{2}z_1^2 + \frac{1}{2}\|P\delta\|^2. \tag{13}$$

From (13), there is

$$\begin{aligned}\dot{V}_1 \le&-\left(\lambda_{min}(Q) - 1\right)\|\varepsilon\|^2 + z_1\left[z_2 + \frac{1}{2}z_1 + \theta_1^T\varphi_1\left(\hat{x}_1\right)\right.\\ &\left.+\alpha_1 + \omega_1'\right] + \frac{1}{2}\|P\delta\|^2 + \frac{1}{\gamma_1}\tilde{\theta}_1^T\left(\gamma_1 z_1\varphi_1\left(\hat{x}_1\right) - \dot{\theta}_1\right).\end{aligned} \tag{14}$$

From (14), α_1 and $\dot{\theta}_1$ are generated as:

$$\alpha_1 = -c_1 z_1 - \frac{1}{2}z_1 - \theta_1^T\varphi_1\left(\hat{x}_1\right) - \omega_{10}'\tanh\left(\frac{\omega_{10}' z_1}{k}\right), \tag{15}$$

$$\dot{\theta}_1 = \gamma_1 z_1\varphi_1\left(\hat{x}_1\right) - \sigma\left(\theta_1 - \theta_{10}\right), \tag{16}$$

where $c_1 > 0$, $\sigma > 0$, $k > 0$ and θ_{10} are constants.

Using the property of the hyperbolic tangent function $\tanh(\cdot)$, we can get the following inequality:

$$\begin{aligned}&z_1\omega_1' - z_1\omega_{10}'\tanh\left(\frac{\omega_{10}' z_1}{k}\right)\\ &\le 0.2785k \triangleq k'.\end{aligned} \tag{17}$$

Inserting (15)-(17) into (14) yields

$$\begin{aligned}\dot{V}_1 \le&-\left(\lambda_{min}(Q) - 1\right)\|\varepsilon\|^2 - c_1 z_1^2 + z_1 z_2\\ &+ \frac{1}{2}\|P\delta\|^2 + \frac{\sigma}{\gamma_1}\tilde{\theta}_1^T\left(\theta_1 - \theta_{10}\right) + k'.\end{aligned} \tag{18}$$

Step 2: From (9), we have

$$\begin{aligned}\dot{z}_2 =&\dot{\hat{x}}_2 - \dot{\alpha}_1 - \ddot{y}_r\\ =&z_3 + \alpha_2 + k_2\varepsilon_1 + \tilde{\theta}_2^T\varphi_2(\hat{X}_2) + \theta_2^T\varphi_2(\hat{X}_2) + \omega_2'\\ &- \delta_2' - \frac{\partial\alpha_1}{\partial y}\left(\hat{x}_2 + \varepsilon_2 + \theta_1^T\varphi_1\left(\hat{x}_1\right) + \delta_1'\right) - \frac{\partial\alpha_1}{\partial y_r}\dot{y}_r\\ &- \frac{\partial\alpha_1}{\partial\hat{x}_1}\left(\hat{x}_2 + \theta_1^T\varphi_1\left(\hat{x}_1\right) + k_1\varepsilon_1\right) - \frac{\partial\alpha_1}{\partial\theta_1}\dot{\theta}_1\\ =&z_3 + \alpha_2 + H_2 + \tilde{\theta}_2^T\varphi_2(\hat{X}_2) + \omega_2' - \delta_2'\\ &- \frac{\partial\alpha_1}{\partial y}\left(\varepsilon_2 + \delta_1'\right),\end{aligned} \tag{19}$$

where $\tilde{\theta}_2 = \theta_2^* - \theta_2$, and H_2 is denoted in the following form:

$$\begin{aligned}H_2 =&k_2\varepsilon_1 + \theta_2^T\varphi_2(\hat{X}_2) - \frac{\partial\alpha_1}{\partial y}\left(\hat{x}_2 + \theta_1^T\varphi_1\left(\hat{x}_1\right)\right) - \frac{\partial\alpha_1}{\partial y_r}\dot{y}_r\\ &- \frac{\partial\alpha_1}{\partial\hat{x}_1}\left(\hat{x}_2 + \theta_1^T\varphi_1\left(\hat{x}_1\right) + k_1\varepsilon_1\right) - \frac{\partial\alpha_1}{\partial\theta_1}\dot{\theta}_1.\end{aligned}$$

To stabilize equation (19), we select a control Lyapunov function as:

$$V_2 = V_1 + \frac{1}{2}z_2^2 + \frac{1}{2\gamma_2}\tilde{\theta}_2^T\tilde{\theta}_2, \tag{20}$$

where $\gamma_2 > 0$ is a constant.

Calculating $\dot{V}_2$ yields

$$\begin{aligned}\dot{V}_2 =&\dot{V}_1 + z_2\dot{z}_2 - \frac{1}{\gamma_2}\tilde{\theta}_2^T\dot{\theta}_2\\ \le&-\left(\lambda_{min}(Q) - 1\right)\|\varepsilon\|^2 - c_1 z_1^2 + \frac{1}{2}\|P\delta\|^2\\ &+ \frac{\sigma}{\gamma_1}\tilde{\theta}_1^T\left(\theta_1 - \theta_{10}\right) + k' + z_2\left[z_1 + z_3 + \alpha_2\right.\\ &\left.+H_2 + \omega_2'\right] - z_2\delta_2' - z_2\frac{\partial\alpha_1}{\partial y}\varepsilon_2 - z_2\frac{\partial\alpha_1}{\partial y}\delta_1'\\ &+ \frac{1}{\gamma_2}\tilde{\theta}_2^T\left(\gamma_2 z_2\varphi_2(\hat{X}_2) - \dot{\theta}_2\right).\end{aligned} \tag{21}$$

Using Young's inequality, we receive

$$\begin{aligned}&-z_2\delta_2' - z_2\frac{\partial\alpha_1}{\partial y}\varepsilon_2 - z_2\frac{\partial\alpha_1}{\partial y}\delta_1'\\ &\le\frac{1}{2}z_2^2 + \|\varepsilon\|^2 + z_2^2\left(\frac{\partial\alpha_1}{\partial y}\right)^2 + \frac{1}{2}\delta_1'^2 + \frac{1}{2}\delta_2'^2,\end{aligned} \tag{22}$$

Then,

$$\begin{aligned}\dot{V}_2 \le&-\left(\lambda_{min}(Q) - 2\right)\|\varepsilon\|^2 - c_1 z_1^2 + \frac{1}{2}\|P\delta\|^2\\ &+ \frac{\sigma}{\gamma_1}\tilde{\theta}_1^T\left(\theta_1 - \theta_{10}\right) + k' + z_2\left[z_1 + z_3 + \alpha_2 + H_2\right.\\ &\left.+\omega_2' + \frac{1}{2}z_2 + \left(\frac{\partial\alpha_1}{\partial y}\right)^2 z_2\right] + \frac{1}{2}\delta_1'^2 + \frac{1}{2}\delta_2'^2\\ &+ \frac{1}{\gamma_2}\tilde{\theta}_2^T\left(\gamma_2 z_2\varphi_2(\hat{X}_2) - \dot{\theta}_2\right).\end{aligned} \tag{23}$$

From (23), α_2 and $\dot{\theta}_2$ are generated as:

$$\begin{aligned}\alpha_2 =&-c_2 z_2 - z_1 - H_2 - \frac{1}{2}z_2 - \left(\frac{\partial\alpha_1}{\partial y}\right)^2 z_2\\ &-\omega_{20}'\tanh\left(\frac{\omega_{20}' z_2}{k}\right),\end{aligned} \tag{24}$$

$$\dot{\theta}_2 = \gamma_2 z_2\varphi_2(\hat{X}_2) - \sigma\left(\theta_2 - \theta_{20}\right), \tag{25}$$

where $c_2 > 0$ and θ_{20} are design parameters. By incorporating (24), (25) into (23),

$$\begin{aligned}\dot{V}_2 \le&-\left(\lambda_{min}(Q) - 2\right)\|\varepsilon\|^2 - c_1 z_1^2 - c_2 z_2^2 + z_2 z_3\\ &+ \frac{1}{2}\|P\delta\|^2 + \frac{1}{2}\delta_1'^2 + \frac{1}{2}\delta_2'^2\\ &+ \sum_{i=1}^{2}\frac{\sigma}{\gamma_i}\tilde{\theta}_i^T\left(\theta_i - \theta_{i0}\right) + 2k'.\end{aligned} \tag{26}$$

Step i (i=3,...,n): Similar to the above derivation process, we adopt the Lyapunov function:

$$V_i = V_{i-1} + \frac{1}{2}z_i^2 + \frac{1}{2\gamma_i}\tilde{\theta}_i^T\tilde{\theta}_i, \tag{27}$$

where $\gamma_i > 0$ are constants.

The α_i and $\dot{\theta}_i$ are generated as:

$$\begin{aligned}\alpha_i =& - c_i z_i - z_{i-1} - H_i - \frac{1}{2}z_i - \left(\frac{\partial \alpha_{i-1}}{\partial y}\right)^2 z_i \\ & - \omega_{i0}' \tanh\left(\frac{\omega_{i0}' z_i}{k}\right), \end{aligned}\tag{28}$$

$$\dot{\theta}_i = \gamma_i z_i \varphi_i(\hat{X}_i) - \sigma\left(\theta_i - \theta_{i0}\right), \tag{29}$$

where $c_i > 0$ and θ_{i0} are constants, $\tilde{\theta}_i = \theta_i^* - \theta_i$, and H_i is denoted in the following form:

$$\begin{aligned}H_i =& k_i\varepsilon_1 + \theta_i^T\varphi_i(\hat{X}_i) - \frac{\partial \alpha_{i-1}}{\partial y}\left(\hat{x}_2 + \theta_1^T\varphi_1\left(\hat{x}_1\right)\right) \\ & - \sum_{j=1}^{i-1}\frac{\partial \alpha_{i-1}}{\partial y_r^{(j-1)}} y_r^{(j)} - \sum_{j=1}^{i-1}\frac{\partial \alpha_{i-1}}{\partial \hat{x}_j}\left(\hat{x}_{j+1} + k_j\varepsilon_1\right. \\ & \left. + \theta_j^T\varphi_j(\hat{X}_j)\right) - \sum_{j=1}^{i-1}\frac{\partial \alpha_{i-1}}{\partial \theta_j}\dot{\theta}_j. \end{aligned}$$

In this step, we will create an adaptive controller and an adaptive updating law as follows:

$$\nu(t) = \alpha_n + y_r^{(n)}, \tag{30}$$

$$\dot{\theta}_n = \gamma_n z_n \varphi_n(\hat{X}_n) - \sigma\left(\theta_n - \theta_{n0}\right). \tag{31}$$

A dynamic event-triggered mechanism is given in such form:

$$u(t) = \nu\left(t_k\right), \quad t \in [t_k, t_{k+1}), \quad (k \in z^+) \tag{32}$$

$$t_{k+1} = \inf\left\{t \in \mathbb{R} \mid |e(t)| \geq b_l + \frac{1}{a_l}\xi\right\}, \tag{33}$$

where $a_l, b_l > 0$ are constants, $e(t) = \nu(t) - u(t)$ denotes the measurement error, t_k is the update time of the controller. During the time period $t \in [t_k, t_{k+1})$, there exists a value $\bar{\nu} > 0$ that satisfies $|u(t) - \nu(t_k)| \leq \bar{\nu}$. The dynamic threshold parameter ξ is designed as:

$$\dot{\xi} = -\rho_l\xi + a_l\left(b_l - |e(t)|\right). \tag{34}$$

Lemma 2 [11]: Based on the equation (34), the dynamic threshold parameter ξ satisfies

$$0 \leq \xi \leq \frac{a_l b_l}{\rho_l}.$$

3.3 Stability analysis

Now, we will expound on the stability analysis under the designed observer-based dynamic ETC scheme. The Theorem 1 is given as follows:

Theorem 1: If the closed-loop system includes the UNS (1) and the dynamic ETM (30)-(33), subject to Assumptions $1-3$. We can ensure the boundedness of all signals, preventing any occurrence of Zeno behavior.

Proof : Consider total Lyapunov function:

$$V = \frac{1}{2}\varepsilon^T P\varepsilon + \frac{1}{2}\sum_{i=1}^{n} {z_i}^2 + \frac{1}{2}\sum_{i=1}^{n}\frac{1}{\gamma_i}\tilde{\theta}_i^T\tilde{\theta}_i. \tag{35}$$

From (35), we can calculate

$$\begin{aligned}\dot{V} =& \varepsilon^T P\dot{\varepsilon} + \sum_{i=1}^{n} z_i\dot{z}_i - \sum_{i=1}^{n}\frac{1}{\gamma_i}\tilde{\theta}_i^T\dot{\theta}_i \\ \leq & -\left(\lambda_{min}(Q) - (n-1)\right)\|\varepsilon\|^2 + z_n(u - \nu) \\ & + z_n\left(\alpha_n + k_n\varepsilon_1 + \theta_n^T\varphi_n(\hat{X}_n) + \omega_n' - \dot{\alpha}_{n-1}\right) \\ & - z_n\delta_n' - \sum_{i=1}^{n-1} c_i z_i^2 + z_n z_{n-1} + \frac{1}{2}\|P\delta\|^2 \\ & + \sum_{i=1}^{n-1}\frac{\sigma}{\gamma_i}\tilde{\theta}_i^T\left(\theta_i - \theta_{i0}\right) + \frac{(n-2)}{2}\delta_1'^2 + \sum_{i=2}^{n-1}\frac{1}{2}\delta_i'^2 \\ & + (n-1)k' + \frac{1}{\gamma_n}\tilde{\theta}_n^T\left(\gamma_n z_n\varphi_n(\hat{X}_n) - \dot{\theta}_n\right). \end{aligned}\tag{36}$$

Operating Young's inequality, we have:

$$\begin{aligned}\dot{V} \leq & -\left(\lambda_{min}(Q) - (n-1)\right)\|\varepsilon\|^2 + \frac{1}{2}z_n^2 + \frac{1}{2}\bar{\nu}^2 \\ & + z_n\left(\alpha_n + k_n\varepsilon_1 + \theta_n^T\varphi_n(\hat{X}_n) + \omega_n' - \dot{\alpha}_{n-1}\right) \\ & - z_n\delta_n' - \sum_{i=1}^{n-1} c_i z_i^2 + z_n z_{n-1} + \sum_{i=1}^{n-1}\frac{\sigma}{\gamma_i}\tilde{\theta}_i^T\left(\theta_i - \theta_{i0}\right) \\ & + \frac{1}{2}\|P\delta\|^2 + \frac{(n-2)}{2}\delta_1'^2 + \sum_{i=2}^{n-1}\frac{1}{2}\delta_i'^2 \\ & + (n-1)k' + \frac{1}{\gamma_n}\tilde{\theta}_n^T\left(\gamma_n z_n\varphi_n(\hat{X}_n) - \dot{\theta}_n\right). \end{aligned}\tag{37}$$

With (28) and (29), (37) implies

$$\begin{aligned}\dot{V} \leq & -\left(\lambda_{min}(Q) - n\right)\|\varepsilon\|^2 - \sum_{i=1}^{n} C_i z_i^2 + \frac{1}{2}\bar{\nu}^2 \\ & + \frac{1}{2}\|P\delta\|^2 + \sum_{i=1}^{n}\frac{\sigma}{\gamma_i}\tilde{\theta}_i^T\left(\theta_i - \theta_{i0}\right) + \frac{(n-1)}{2}\delta_1'^2 \\ & + \sum_{i=2}^{n}\frac{1}{2}\delta_i'^2 + nk', \end{aligned}\tag{38}$$

where $C_i = c_i\,(i = 1, \ldots, n-1)$, $C_n = c_n - \frac{1}{2}$ are positive constants.

According to Young's inequality, one can derive the following result

$$\begin{aligned}& \sum_{i=1}^{n}\frac{\sigma\tilde{\theta}_i^T\left(\theta_i^* - \theta_{i0}\right)}{\gamma_i} \\ \leq & \frac{1}{2}\sum_{i=1}^{n}\frac{\sigma\tilde{\theta}_i^T\tilde{\theta}_i}{\gamma_i} + \frac{1}{2}\sum_{i=1}^{n}\frac{\sigma}{\gamma_i}\left\|\theta_i^* - \theta_{i0}\right\|^2. \end{aligned}\tag{39}$$

We can rewrite equation (38) as:

$$\dot{V} \leq -\left(\lambda_{min}(Q)-n\right)\|\varepsilon\|^2 - \sum_{i=1}^{n} C_i z_i^2 - \sum_{i=1}^{n} \frac{\sigma}{\gamma_i}\tilde{\theta}_i^T\tilde{\theta}_i + \frac{1}{2}\sum_{i=1}^{n}\frac{\sigma}{\gamma_i}\tilde{\theta}_i^T\tilde{\theta}_i + \frac{1}{2}\sum_{i=1}^{n}\frac{\sigma}{\gamma_i}\left\|\theta_i^* - \theta_{i0}\right\|^2 + \frac{1}{2}\bar{\nu}^2 + \frac{(n-1)}{2}\delta_{10}'^2 + \frac{1}{2}\left(1+\|P\|^2\right)\sum_{i=2}^{n}\delta_{i0}'^2 + nk'. \quad (40)$$

Then,

$$\dot{V} \leq -\wp V + \Delta, \quad (41)$$

where

$$\wp = \min\left\{\frac{2\left(\lambda_{\min}(Q)-n\right)}{\lambda_{\max}(P)}, 2C_1, \cdots, 2C_n, \sigma\right\}, \quad (42)$$

$$\Delta = \frac{1}{2}\sum_{i=1}^{n}\frac{\sigma}{\gamma_i}\left\|\theta_i^* - \theta_{i0}\right\|^2 + \frac{1}{2}\bar{\nu}^2 + \frac{(n-1)}{2}\delta_{10}'^2 + \frac{1}{2}\left(1+\|P\|^2\right)\sum_{i=2}^{n}\delta_{i0}'^2 + nk'. \quad (43)$$

Then, the system stability is ensured.

We can prove that there exists constant $t^* > 0$ where $\forall k \in z^+$, $\{t_{k+1} - t_k\} \geq t^*$. Because $e(t) = \nu(t) - u(t)$, $\forall t \in [t_k, t_{k+1})$, we have

$$\frac{d}{dt}|e| = \frac{d}{dt}(e*e)^{\frac{1}{2}} = \text{sign}(e)\dot{e} \leq |\dot{\nu}|. \quad (44)$$

From (30), we have

$$\dot{\nu} = \dot{\alpha}_n. \quad (45)$$

We can conclude that there exists a positive number $\varrho > 0$ such that $|\dot{\nu}| \leq \varrho$, since $\dot{\nu}$ is a function of bounded variables. By utilizing the fact that $e(t_k) = 0$ and $\lim_{t\to t_{k+1}} e(t) = b_l + b_l/\rho_l$, we can obtain a lower bound for the inter-execution intervals t^* which satisfy $t^* \geq (b_l + b_l/\rho_l)/\varrho$. Furthermore, it is possible to prevent the emergence of Zeno behavior.

4 Simulation studies

To prove the efficacy of the presented scheme, we examine the system:

$$\begin{cases} \dot{x}_1 = x_2 + x_1 e^{-0.5x_1}, \\ \dot{x}_2 = u + x_1 \sin\left(x_2^2\right), \\ y = x_1. \end{cases} \quad (46)$$

Choosing fuzzy membership functions as

$$\mu_{\mathrm{F}_i^l}\left(\bar{\hat{x}}_i\right) = \prod_{i=1}^{2}\exp\left[-\frac{\left(\hat{x}_i - 3 + l\right)^2}{16}\right], \quad (l = 1, \ldots, 5)$$

where $\bar{\hat{x}}_i = [\hat{x}_1, \hat{x}_i]^{\mathrm{T}}, (i = 1, 2)$.

Defining fuzzy basis functions as

$$\varphi_{ij}\left(\bar{\hat{x}}_i\right) = \frac{\mu_{\mathrm{F}_i^j}\left(\bar{\hat{x}}_i\right)}{\sum_{n=1}^{5}\prod_{i=1}^{2}\exp\left[-\frac{(\hat{x}_i-3+n)^2}{16}\right]}, (j = 1, \ldots, 5).$$

The FLSs are

$$\theta_1^{\mathrm{T}}\varphi_1\left(\hat{x}_1\right) = \sum_{j=1}^{5}\theta_{1j}^{\mathrm{T}}\varphi_{1j}\left(\hat{x}_1\right), \quad (47)$$

$$\theta_2^{\mathrm{T}}\varphi_2\left(\hat{x}_1, \hat{x}_2\right) = \sum_{j=1}^{5}\theta_{2j}^{\mathrm{T}}\varphi_{2j}\left(\hat{x}_1, \hat{x}_2\right). \quad (48)$$

The reference signal $y_r = 0.5\sin(t)$, and we have chosen the specific parameters for the design, $c_1 = 8$, $c_2 = 5$, $k_1 = 7$, $k_2 = 3$, $\gamma_1 = \gamma_2 = 0.1$, $\sigma = 0.01$, $\varepsilon_{10} = \varepsilon_{20} = 0.1$, $\kappa = 0.01$, $a_l = 0.02$, $b_l = 0.01$, $\rho_l = 0.4$.

The positive matrix $P = \begin{bmatrix} 0.5625 & -0.5000 \\ -0.5000 & 0.5703 \end{bmatrix}$, $Q = I_2$.

The initial conditions are

$$x_1(0) = 0, x_2(0) = 0.1, \hat{x}_1(0) = 0, \hat{x}_2(0) = 0.2, \xi(0) = 0,$$
$$\theta_1(0) = [-0.6, 0, 0.5, 0, 0.6], \theta_2(0) = [0.4, 0, 0.1, -0.1, 0].$$

The simulation images are exhibited in Figs.1-5. Fig 1 shows that the state x_1 can successfully track the reference signal y_r. Fig 2 and Fig 3 are the system states and observer states. The control signal is presented in Fig 4.

To compare the performance of the dynamic ETC scheme, which reduces event numbers, we compared it with the fuzzy static ETC scheme. The controller's relevant parameters remain the same. As illustrated in Fig 5, a comparison is made between the event-triggered time intervals of the fuzzy dynamic ETC scheme and the fuzzy static ETC scheme. This comparison demonstrates that the fuzzy dynamic ETC scheme has fewer triggers and longer trigger intervals than the fuzzy static ETC scheme.

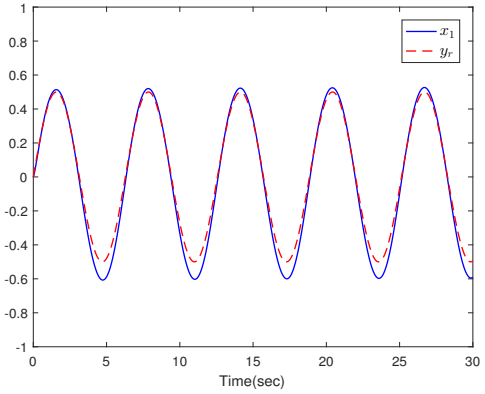

Fig. 1: Curves of the system state x_1 and y_r.

In Table 1, we can see the number of transmission events for three different schemes. The data demonstrates that the proposed fuzzy dynamic ETC solution performs similarly to the time-driven and fuzzy static ETC schemes, while also reducing the communication burden.

Table 1: Comparison results

Control method	Transmission events number
TTC	3000
Fuzzy static ETC	2072
Fuzzy dynamic ETC	1048

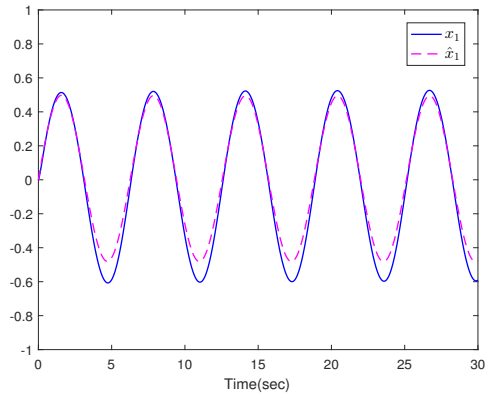

Fig. 2: Curves of the system state x_1 and observer state $\hat{x}_1$.

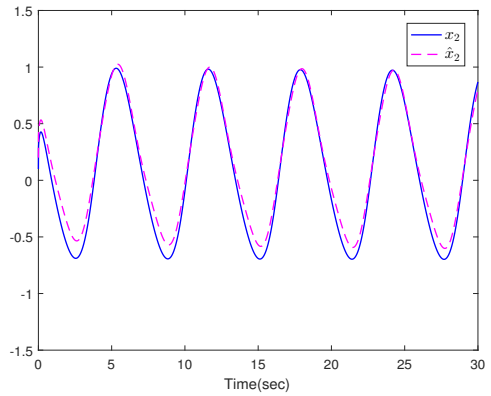

Fig. 3: Curves of the system state x_2 and observer state $\hat{x}_2$.

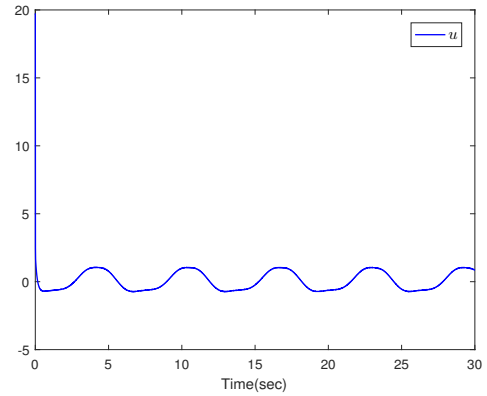

Fig. 4: The control signal u.

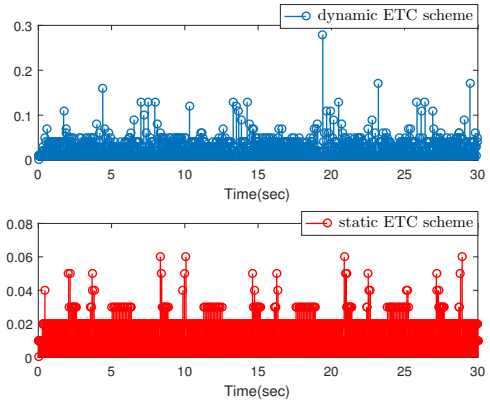

Fig. 5: The event-triggered time intervals of the dynamic ETC scheme and the static ETC scheme.

5 Conclusion

This paper presents an observer-based dynamic fuzzy control scheme for UNS. The recursive design process is unfolded by using backstepping technique. The dynamic ETM is constructed to promote resource utilization efficiency. The devised observer-based dynamic ETC strategy not only achieves control assignment of UNS with unavailable states but also successfully avoids Zeno behavior. The simulation comparison and analysis show that the present scheme can further reduce data transmission.

References

[1] Zadeh, Lotfi A, Fuzzy sets. *Information and Control*, 1965, 8(3): 338–353.

[2] Liu, Wenhui and Lim, Cheng-Chew and Shi, Peng and Xu, Shengyuan, Backstepping fuzzy adaptive control for a class of quantized nonlinear systems. *IEEE Transactions on Fuzzy Systems*, 2016, 25(5): 1090–1101.

[3] Zhou, Haodong and Sui, Shuai and Tong, Shaocheng, Fuzzy adaptive finite-time consensus control for high-order nonlinear multiagent systems based on event-triggered. *IEEE Transactions on Fuzzy Systems*, 2022, 30(11): 4891–4904.

[4] Tong, Shaocheng and Li, Yue and Li, Yongming and Liu, Yanjun, Observer-based adaptive fuzzy backstepping control for a class of stochastic nonlinear strict-feedback systems. *IEEE Transactions on Systems, Man, and Cybernetics Part B: Cybernetics*, 2011, 41(6): 1693–1704.

[5] Åström, Karl Johan and Bernhardsson, Bo, Comparison of periodic and event based sampling for first-order stochastic systems. *IFAC Proceedings Volumes*, 1999, 32(2): 5006–5011.

[6] Xing, Lantao and Wen, Changyun and Liu, Zhitao and Su, Hongye and Cai, Jianping, Event-triggered adaptive control for a class of uncertain nonlinear systems. *IEEE Transactions on Automatic Control*, 2017, 62(4): 2071–2076.

[7] Delimpaltadakis, Giannis and Mazo Jr, Manuel, Abstracting the Traffic of Nonlinear Event-Triggered Control Systems. *IEEE Transactions on Automatic Control*, 2022.

[8] Girard, Antoine, Dynamic triggering mechanisms for event-triggered control. *IEEE Transactions on Automatic Control*, 2014, 60(7): 1992–1997.

[9] Zhao, Ning and Tian, Yongjie and Zhang, Huiyan and Herrera-Viedma, Enrique, Learning-Based Adaptive Fuzzy Output Feedback Control for MIMO Nonlinear Systems With Deception Attacks and Input Saturation. *IEEE Transactions on Fuzzy Systems*, 2024, DOI: 10.1109/TFUZZ.2024.3363839.

[10] Xing, Lantao and Wen, Changyun, Dynamic event-triggered adaptive control for a class of uncertain nonlinear systems. *Automatica*, 2023, 158: 111286.

[11] An, Yaxin and Liu, Yongchao, Observer-based dynamic event-triggered adaptive control for uncertain nonlinear strict-feedback systems. *System & Control Letters*, 2024, 183: 105700.

Proceedings of the 3rd Conference on Fully Actuated System Theory and Applications
May 10-12, 2024, Shenzhen, China

The Autonomous Flight of an Indoor Quadrotor Using Onboard Vision

Yingjing Shi[1], Rui Li[1], Chen Zhou[2]

1. School of Automation Engineering, University of Electronic Science and Technology of China, Chengdu 611731, P. R. China
E-mail: shiyingjing@uestc.edu.cn, lirui@uestc.edu.cn

2. Shanghai Branch, China Ship Development and Design Center, Shanghai 201108, P. R. China
E-mail: 582447543@qq.com

Abstract: In this paper, a vision detection and tracking system is designed to force a quadrotor to achieve the automation flight in the indoor environment based on the on-board vision system. The LED lamp belt is installed on the wall inside as the tracking target for the quadrotor. The coordination control law is designed to track the LED lamp in the straight part as well as the bent part. Moreover, the converging analysis of the tracking control algorithm is given and collision avoidance between the quadrotor and the tunnel is guaranteed. Furthermore, the vision detection system is designed to provide the input signal for the controller, which is obtained by solving relative pose between the quadrotor and the LED. Finally, the proposed control and detection schemes are validated in the experiments on a real quadrotor platform.

Key Words: Quadrotor, Automation flight, Tracking, Collision avoidance

1 Introduction

With the contributions both in military and civilian, unmanned aerial vehicles (UAVs) have gained great interesting among the research community. As an important subset of UAVs, quadrotors have become popular recently due to their small size and maneuverability, which have found potentially application in reconnaissance, surveillance, disaster management and emergency aid [1–3].

The development of quadrotor navigation and control technologies in indoor or enclosed environments has been an active area of research. There is lots of work on control or navigation system design based on the indoor localization system. Examples include: balancing a pendulum [4]; aggressive maneuvers, such as flight through windows [5] or flips [6]; ball juggling with a racket [7] and so on. However, the indoor localization system is usually expensive and does not suit for narrow and dark environment, especially for the unknown environment, such as tunnel, disaster area, and so forth. Therefore, Many efforts have been made to perform the automation flight of the quadrotor with on-board sensor. [8] developed a nonlinear vision-based controller for grasping maneuvers using vision. In [9], the authors proposed a stochastic differential equation-based exploration algorithm to enable exploration in three-dimensional indoor environments with a payload constrained micro-aerial vehicle. [10] presented control system and collision detection system design for a quadrotor using a Kinect sensor. In [11], an onboard monocular vision system is developed for autonomous takeoff, hovering and landing of a Micro Aerial Vehicle (MAV).

Since tracking is an important and fundamental problem of automation flight of the UAVs, many works have been performed to achieve tracking task by using various methods. In [12], the authors provided a nonlinear controller for tracking control of a quadrotor unmanned aerial vehicle based on a globally defined model of the quadrotor UAV rigid body dynamics. In [13], the authors proposed a dynamic feedback control strategy for controlling an unmanned rotorcraft and making it follow a desired smooth reference trajectory. However, in [12] and [13], only numerical simulations were provided. [14] presented an optimization-based iterative learning approach for trajectory tracking and the approach was successfully applied to quadrotor vehicles, where a predefined trajectory was involved. In [15], a vision-based position control method was proposed for the position stabilization of a quadrotor UAV, where the helicopter X-Y-Z position was estimated with respect to a landing pad on the ground. Considering the requirement of practical application, tracking flight with more flexible task or in more complicated environment should be investigated.

Recently, the automation flight control of the quadrotor in tunnel-like environment has attracted much attention due to the important applications including exploration, surveillance, rescue, etc. However, the automation flight control of the quadrotor in such environment is difficult due to the limited space, dark environment, weak signal, etc. In this paper, we take a step to investigate the navigation and control of a quadrotor in indoor environment (such as tunnel, storehouse, etc) based on the on-board vision system, where the LED lamp belt is installed on the wall as the leading mark.

To follow two moving points on LED lamp belt, the quadrotor is requested to keep fixed distance and coincident velocity with the moving LED belt, thus a coordination control method is needed. In this paper, a simple and achievable coordination control algorithm is proposed to track the LED lamp, which is further applied combining with vision detection algorithm for a real quadrotor platform. To achieve real tracking flight of the quadrotor, the relative distance between the LED belt and the quadrotor is required, which is obtained by solving the relative pose in real-time by using the Monocular cameral. Concretely, the position of the LED lamp is first obtained by taking the photo of the LED lamp using the vision system. Then, the relative pose between the quadrotor and the LED is calculated by solving the PNP (Perspective N Points) problem. Furthermore, the obtained relative pose

This work is supported in part by National Natural Science Foundation (NNSF) of China under Grant 61973055 and the Fundamental Research Funds for the Central Universities under Grant 2023NSFSC0511.

is sent to the controller to get the output. We then apply the developed algorithms to a real quadrotor platform to demonstrate the effectiveness of the proposed control schemes.

The contributions of our paper are given as follows. First, an automation flight problem in indoor environment based on on-board vision is investigated and performed for a real quadrotor platform. The developed methods can be extended for other tasks, for example, inspection and rescue in tunnel-like environment. Second, a coordination control algorithm is proposed which is simple and easy to implement for real quadrotor platform. Third, in contrast to the commercial products, the developed system is open source, which is easy for secondary development.

The remainder of this paper is organised as follows. The automation flight problem based vision system is formulated in Section 2. In Section 3, the tracking control algorithm is designed to follow the LED lamp either in the straight part or the curve part. In Section 4, the moving velocity direction of the LED and the relative distance between the adjoint point and the quadrotor are obtained, which are required as the input of the controller. The actual implementation results, as well as the analysis on the overall performance, are given in Section 5 to verify the superiority of the designed intelligent flight system. Finally, in Section 6, we draw some concluding remarks.

2 Formulation of the Problem

We install two parallel LED lamp belts on the right wall indoors, where the distance between two lamp belts are known and the space between two light is fixed. The LED lamp belts are shown in Figure 1.

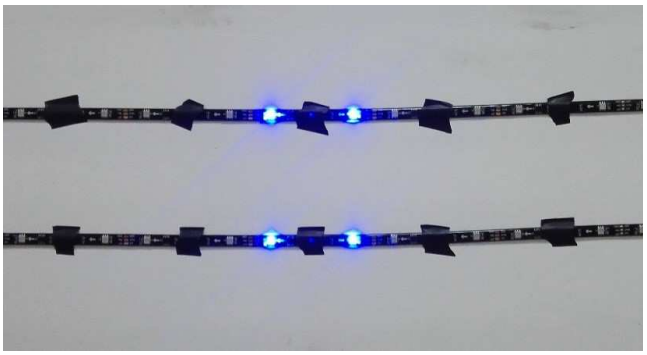

Fig. 1: The diagram of LED belt.

In Figure 1, each lamp belt is moving rightward in the way of water lights, and at each moment, there are only two lamps working on each LED lamp belt. In addition, the moving orders of the two lamp belts are same. Thus, at each moment, four LED lamps are working and the form and the size of the working lamps kept fixed. As shown in Figure 2, the reference frame is defined as follows: origin is located at the centroid of the rectangle, the positive direction of x-axis is the moving direction of the LED belt, and y-axis is the vertical direction of the LED belt. Thus, the reference coordinates of four lamps are known.

This paper considers the problem of control and guidance system design for the quadrotor equipping with IMU and camera to achieve automation flight in indoor environment.

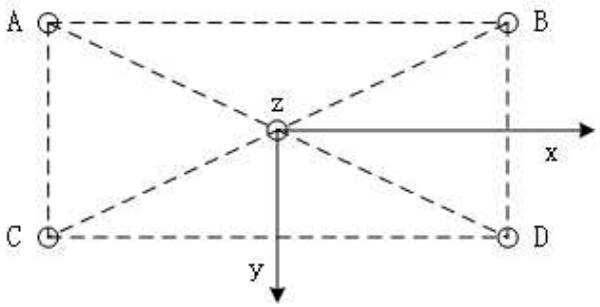

Fig. 2: The frame of LED plane.

Suppose that there is no curve in the vertical section of the tunnel, and r_1, r_2 are two moving points on one LED lamp belt and r_1', r_2' are the moving points on another LED lamp belt. The velocities of r_1, r_2, r_1' and r_2' are constant and known. We aim to design the control system by which the quadrotor flights keeing the same height and certain distant with the lamp belt. Suppose that the quadrotor looks at the four moving points simultaneously, $r = r_2 - r_1$, $r_a = (r_1 + r_2)/2$, $r_b = (r_1{}' + r'_2)/2$ and $\bar{r} = (r_a + r_b)/2$. $\hat{r}$ is the adjoint point of $\bar{r}$, satisfying

$$\hat{r} = \begin{cases} \bar{r} + d\frac{r\times z}{\|r\times z\|}, & \|r \times z\| \neq 0, \\ \bar{r} + d\frac{(r\times z)^-}{\|(r\times z)^-\|}, & \|r \times z\| = 0. \end{cases}$$

Here, $z = \begin{bmatrix} 0 & 0 & 1 \end{bmatrix}^{\mathrm{T}}$; $(r \times z)^-$ is the left limit of $r \times z$ when the quadrotor enters the vertical tunnel.

Remark 1 *Since there is no curve in the vertical segment of the tunnel, that is, $(r \times z)/\|r \times z\|$ is same when the quadrotor just enters the vertical segment and just departs from the vertical segment.*

3 The design of the control system

Assume that the quadrotor has achieves velocity control. We introduce the following control law to perform tracking task for the moving points:

$$\dot{x} = v\frac{r}{\|r\|} + K_v\left(\hat{r} - x\right) \tag{1}$$

Here, x is the position of the quadrotor; v, r,$\hat{r}$ are given as mentioned earlier; K_v is larger than zero, which is an unknown value to be determined. In order to avoid collision with the tunnel, K_v is usually selected according to the velocity v of LED lamp, the distance d between adjoint point and lamp belt, and the curvature of the tunnel.

Before showing the converging analysis of the tracking algorithm, we introduce the following Lemma.

Lemma 1 *If*

$$\dot{\xi} = -k\xi + l\frac{\eta}{\|\eta\|}, \|\xi_0\| = a, a > \frac{l}{k}$$

Then ξ is uniformly ultimate bounded. Here, ξ and η are time-varying vectors; k, l and a are constants greater than zero.

Proof. Solving

$$\frac{\mathrm{d}\,\|\xi\|}{\mathrm{d}t} = -k\frac{\xi^{\mathrm{T}}\xi}{\|\xi\|} + l\frac{\eta^{\mathrm{T}}\xi}{\|\eta\|\,\|\xi\|}$$

we have,

$$\|\xi\| = \mathrm{e}^{-kt}\|\xi_0\| + \int_0^t \mathrm{e}^{-k(t-\tau)} l \frac{\eta^{\mathrm{T}}\xi}{\|\eta\|\|\xi\|}\mathrm{d}\tau$$

From the assumption of the Lemma, we obtain

$$\|\xi\| \leq \mathrm{e}^{-kt}a + l\int_0^t \mathrm{e}^{-k(t-\tau)}\mathrm{d}\tau = \mathrm{e}^{-kt}a + \frac{l}{k}\left(1-\mathrm{e}^{-kt}\right) \leq a$$

. ∎

Theorem 1 *Suppose that the curvature radius of the tunnel is ρ, the moving velocity of the LED lamp belt is v, and the distance between the adjoint point and the LED lamp belt is d. Then, the quadrotor is able to keep the flight distance with the adjoint point not more than d when choosing $K_v \geq vd/\rho l$.*

Proof. Since the maximal deviation between the velocity of adjoint point and the velocity of LED lamp occurs in the horizontal tunnel, we have

$$\dot{\hat{r}} = v\frac{\rho \pm d}{\rho}\frac{r}{\|r\|} \tag{2}$$

where $\pm$ denotes that $\pm(\bar{r} - \hat{r})$ points the center of the turning circle. From equation (1), we have

$$\dot{x} = v\left(1 \pm \frac{d}{\rho} \mp \frac{d}{\rho}\right)\frac{r}{\|r\|} + K_v(\hat{r} - x)$$

Substituting equation (2) into the above equation, we obtain that

$$\dot{x} - \dot{\hat{r}} = \mp\frac{vd}{\rho}\frac{r}{\|r\|} + K_v(\hat{r} - x)$$

Let $e = x - \hat{r}$, we get

$$\dot{e} = \mp\frac{vd}{\rho}\frac{r}{\|r\|} - K_v e$$

From Lemma 1, we know that the quadrotor can keep the flight distance with adjoint point not more than l, only if $K_v \geq vd/\rho l$. ∎

Remark 2 *Since straight line can be viewed as circle with infinite curvature radius, the convergence of the control method holds for the straight part of the tunnel. Actually, it can be proved that when the control method given by equation (1) is applied for the straight part of the tunnel, the quadrotor can achieve accurate tracking for the adjoint point.*

Remark 3 *Suppose that the distance between the initial position of the quadrotor and the adjoint point is less than d. If the control method given by equation (1) is applied, the collision between the quadrotor and the tunnel can be avoided. Actually, if let $l = d$ in Theorem 1, it can be easily obtained that the quadrotor can keep the flight distance not more than d from the adjoint point, that is, the quadrotor can avoid collision with the tunnel.*

4 Tracking Flight of the Quadrotor Platform

According to the input of the controller, two data are required for the real automation flight, including the moving velocity direction $\frac{r}{\|r\|}$ of the LED and the relative distance $(\hat{r} - x)$ between the adjoint point and the quadrotor. In the following, we will first solve the relative pose between the quadrotor and the LED in real-time by using the Monocular cameral, and then by considering the real-time attitude angle of the quadrotor, the velocity direction $\frac{r}{\|r\|}$ and the relative distance $(\hat{r} - x)$ can be obtained.

The corresponding pixel coordinates of four lamps are first obtained by the camera, which are denoted as $p_i = [u_i, v_i],\ i = 1, ..., 4$. Then a PNP (Perspective N Points) problem is constructed.

PNP problem: When the reference coordinates of N characteristic points and the corresponding N pixel points are known, how to obtain the pose of the camera or the quadrotor by calculating the projection relation.

In the following, we will show the solving procedure in detail.

4.1 The relative pose calculation between the quadrotor and the LED lamp plane

According to the obtained pixel coordinates of the LED lamp, we will solve the relative pose between the quadrotor and the LED lamp plane. Here, the pose transformational matrix is denoted as T, which can be expressed as:

$$T = \begin{bmatrix} R & t \\ 0^T & 1 \end{bmatrix}$$

Here, submatrix R is 3*3 dimensional, which denotes rotation matrix of the imaging coordinate system under the LED lamp coordinate system; vector t is 3*1, which denotes the coordinate of the centroid of the quadrotor in the LED lamp coordinate system.

In this paper, the PNP problem is constructed as a nonlinear least-squares problem defined on lie algebra, and the relative pose T between the quadrotor and the guiding LED lamp is obtained by minimizing the reprojection error. Here, the reprojection error denotes the error between the real pixel coordinates of one point in the space and its pixel coordinate obtained by solving the projection equation of pinhole camera. The diagram is shown in Figure 3.

Here, $P_i = [X_i, Y_i, Z_i]$ denotes the reference coordinate of each LED lamp, $p_i = [u_i, v_i]$ denotes the pixel coordinate of the LED lamp obtained by camera, and $\hat{p}_i = [\hat{u}_i, \hat{v}_i]$ denotes the pixel coordinate obtained by reprojection of P_i according to pose.

To facilitate the calculation of the least-squares problem, we describe the relative pose by using lie algebra ξ. ξ is a 6*1 dimensional vector, which is related to transformational matrix T by an exponential mapping, that is, $T = \exp(\xi)$. For brief, the specific form of the mapping is not discussed in this paper.

According to the projection equation of pinhole camera,

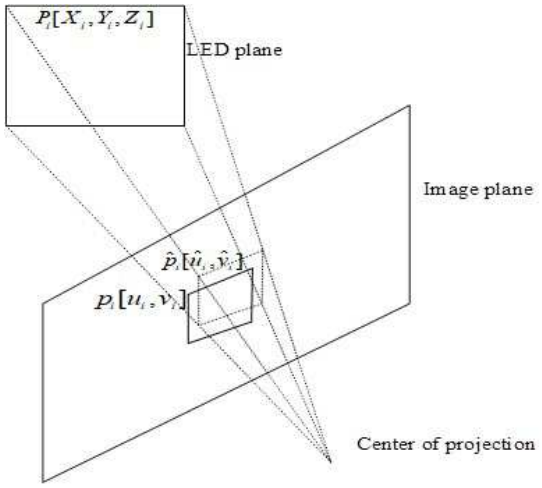

Fig. 3: The diagram of prerejection error.

we have:

$$\begin{aligned}\begin{bmatrix} s\hat{u}_i \\ s\hat{v}_i \\ s \end{bmatrix} &= K\exp(\xi)\begin{bmatrix} X_i \\ Y_i \\ Z_i \\ 1 \end{bmatrix} \\ &= \begin{bmatrix} f_x & 0 & c_x \\ 0 & f_y & c_y \\ 0 & 0 & 1 \end{bmatrix}\exp(\xi)\begin{bmatrix} X_i \\ Y_i \\ Z_i \\ 1 \end{bmatrix} \end{aligned} \tag{3}$$

Here, K is the reference matrix of the camera. f_x, f_y are the camera focuses and $[c_x, c_y]$ are the pixel coordinates of the optical center, which can be obtained by camera calibration. s is the scale factor, which can be eliminated when calculating.

Remark 4 *It is worth noting that equation (3) includes the transformation between homogenous coordinate and nonhomogeneous coordinate. For simplicity, the detailed description is not provided.*

To reduce the effect of the noise and get more stable pose estimate, we assume that the poses of three serial frames of image are unchanged. Thus, we construct a least-squares problem by summing the reprojection error of each frame of the three serial frames for four LED lamps. Then the best pose estimate can be found by minimizing the following function:

$$\xi^* = \arg\min_{\xi} \frac{1}{2}\sum_{i=1}^{n}\left\| p_i - \frac{1}{s}K\exp(\xi)P_i \right\|_2^2$$

Here we apply the Gauss-Newton method to solve the above optimization problem. Thus, we need to calculate the Jacobian Matrix J of error item on the optimization variable ξ. First, denote $P' = \exp(\xi)P = [X', Y', Z']^T$, the physical meaning of which is transforming P defined in LED reference frame to camera frame according to pose ξ. Then according to the pinhole camera model, we have,

$$\begin{bmatrix} s\hat{u} \\ s\hat{v} \\ s \end{bmatrix} = \begin{bmatrix} f_x & 0 & c_x \\ 0 & f_y & c_y \\ 0 & 0 & 1 \end{bmatrix}\begin{bmatrix} X' \\ Y' \\ Z' \end{bmatrix}$$

Pre-multiply ξ by disturbance $\delta\xi$, and then consider the derivative of error on disturbance. By using chain rule, we have:

$$\frac{\partial e}{\partial \delta\xi} = \lim_{\partial\xi\to 0}\frac{e(\delta\xi\oplus\xi)}{\delta\xi} = \frac{\partial e}{\partial P'}\frac{\partial P'}{\partial \delta\xi}$$

Here, $\oplus$ denotes the premultiplying by disturbance. The first item is the derivative of error on projective point. Obviously, it is true that

$$\frac{\partial e}{\partial P'} = -\begin{bmatrix} \frac{\partial \hat{u}}{\partial X'} & \frac{\partial \hat{u}}{\partial Y'} & \frac{\partial \hat{u}}{\partial Z'} \\ \frac{\partial \hat{v}}{\partial X'} & \frac{\partial \hat{v}}{\partial Y'} & \frac{\partial \hat{v}}{\partial Z'} \end{bmatrix} = -\begin{bmatrix} \frac{f_x}{Z'} & 0 & -\frac{f_x X'}{Z'^2} \\ 0 & \frac{f_y}{Z'} & -\frac{f_y Y'}{Z'^2} \end{bmatrix}$$

The second item is the derivative of the transformed point on lie algebra, then we have

$$\frac{\partial P'}{\partial \delta\xi} = \begin{bmatrix} I & -P'^{\wedge} \end{bmatrix} = \begin{bmatrix} 1 & 0 & 0 & 0 & Z' & -Y' \\ 0 & 1 & 0 & -Z' & 0 & X' \\ 0 & 0 & 1 & Y' & -X' & 0 \end{bmatrix}$$

Therefore, we have:

$$\begin{aligned} J &= \frac{\partial e}{\partial P'}\frac{\partial P'}{\partial \delta\xi} \\ &= -\begin{bmatrix} \frac{f_x}{Z'} & 0 & -\frac{f_x X'}{Z'^2} & -\frac{f_x X' Y'}{Z'^2} & f_x + \frac{f_x X'^2}{Z'^2} & -\frac{f_x Y'}{Z'} \\ 0 & \frac{f_y}{Z'} & -\frac{f_y Y'}{Z'^2} & -f_y - \frac{f_y Y'^2}{Z'^2} & \frac{f_y X' Y'}{Z'^2} & \frac{f_y X'}{Z'} \end{bmatrix} \end{aligned}$$

Thus, by solving ξ, we can obtain the transforming matrix T.

4.2 Coordinate transformation

Noting that the pose T solved by the above PNP problem is in the reference coordinate system of four LED plane, which is inconsistent with the coordinate system of the controller. The details can be seen in Figure 4.

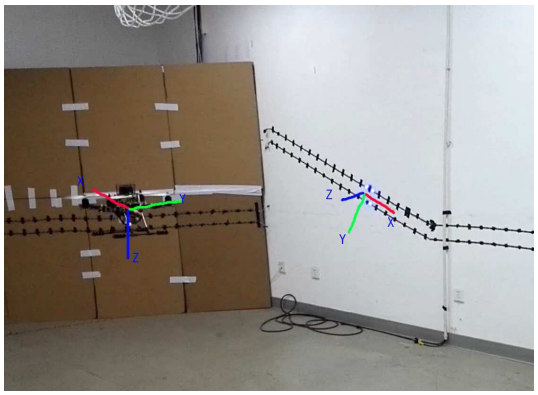

Fig. 4: Diagram of the frame.

For this, the rotation matrix R is transformed as Euler angle form. Then three corresponding angles are denoted as θ_x, θ_y, θ_z which are respectively, the rotary angles of quadrotor related to axis x, y, z of LED coordinate system. The translation part is denoted as $t = \begin{bmatrix} t_x & t_y & t_z \end{bmatrix}^T$, and adjoint point $\hat{r}$ is located on Z axis direction with distance to LED lamp belt as d. We know that when the quadrotor flights stably, θ_x approaches to zero, while θ_y is corresponding to the

included angle between the imaging plane and the LED lamp plane, which is controlled to zero. Thus, we only consider the effect of θ_z in the coordinate transformation, which will be called as climbing angle since it describes the climbing angle of the LED belt. Subsequently, the control input used in this paper can be described as

$$(\hat{r} - x) = \begin{bmatrix} -\cos\theta_z & \sin\theta_z & 0 \\ 0 & 0 & 1 \\ \sin\theta_z & \cos\theta_z & 0 \end{bmatrix} \begin{bmatrix} t_x \\ t_y \\ t_z \end{bmatrix} - \begin{bmatrix} 0 \\ d \\ 0 \end{bmatrix}$$

$$\frac{r}{\|r\|} = \begin{bmatrix} \cos\theta_z \\ 0 \\ \sin\theta_z \end{bmatrix}$$

5 The experimental results

In this work, we use a MAV (micro air vehicle) platform developed by our lab to perform the experiment. As shown in Figure 5, it is a quadrotor equipped with detecting system and sensor systems used to measure the flight state of the quadrotor. The sensor systems include inertial navigation system (IMU) used for attitude estimation, magnetometer and position sensor for position calculation. The ultrasonic sensor and airborne laser radar are applied as the position sensor, and two-dimensional reconstruction is not involved. The detecting system includes camera, data processor and WiFi module. The software of the flight control system is developed in Windows, and and is programmed in the IAR Integrated Development Environment. The software of the vision detection system is developed in ROS, and is programmed in the Qt Integrated Development Environment.

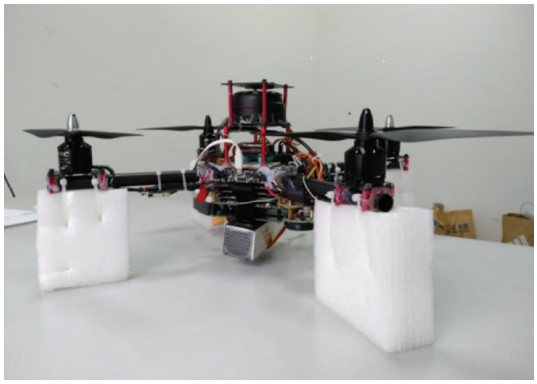

Fig. 5: MAV platform.

By using the developed methods, the quadrotor can achieve tracking flight for the leading LDE lamps, which is shown in Figure 6.

Figure 7 shows the variation of climbing angle θ_z with time in the real flight test. It can be seen that θ_z is stable during the flight process. It also can be found that the LED belt starts to climb at 7 second with the climbing angle as 20 degrees, which is coincident with the situation arranged in the real test place.

Figure 8 shows the variation of the position error between the quadrotor and the adjoint point in the real flight. It can be seen that there is a big error between them in the X axis direction at the beginning. Then the error reduces and approaches to zero when the quadrotor starts tracking the LED

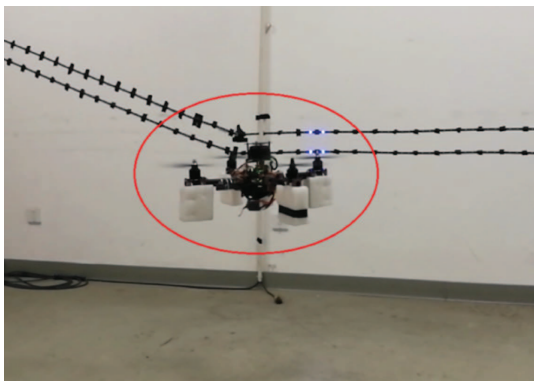

Fig. 6: Tracking effect.

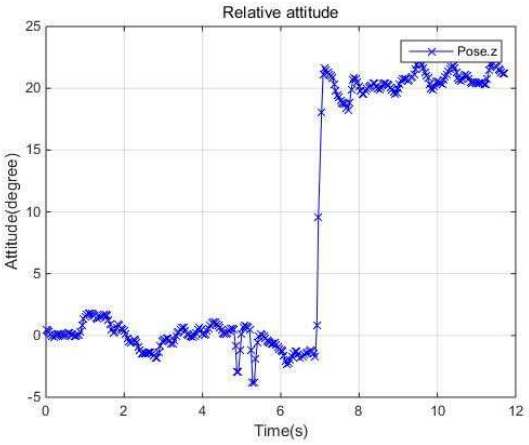

Fig. 7: The relative altitude between the quadrotor and the LED belt.

belt. After a small vibration, the error keeps around zero. Since the LED belt moves forward 10cm discretely after 0.4 second, the error is serrate on the X axis. Furthermore, the errors on the Y axis and Z axis are keeping among a small range. It can be seen that the error on the Y axis starts serrate oscillation, since the LED belt starts to climb at 7 second, however, the whole error is kept around zero. In general, the whole position errors between the quadrotor and the adjoint point can quickly converge to zero and remain stable. This shows that the developed system is feasible.

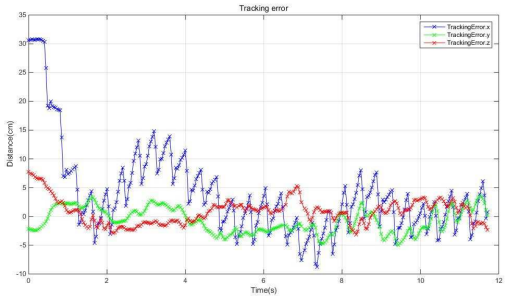

Fig. 8: The position errors between the current position x and adjoint point $\hat{r}$.

6 Conclusions

Automation flight control of the quadrotor in the indoor environment is investigated in this paper. We have proposed an control algorithm for tracking the moving target in an indoor environment by a quadrotor equipping with IMU and camera. The proposed control algorithm can track the moving point on the straight plane or curved surface, by which the collision avoidance can be achieved. The vision detection system is designed to solve the desired control input, where the relative pose between the quadrotor and the guiding LED lamp is obtained by solving the PNP problem. The designed guidance and control system has been successfully implemented on an autonomous quadrotor platform and the experiments show the excellent performance.

The paper is the first step to investigate the automation flight of the quadrotor in the unknown environment, where the LED lamp is used as the leading mark. In the future, the developed vision detection system and tracking control algorithm can be used to construct fully automation flight algorithm, which is able to be applied for exploring in unknown environment or constructing a monocular visual SLAM system.

References

[1] M. Stuart, J. Carol, A Survey of Unmanned Aerial Vehicle (UAV) Usage for Imagery Collection in Disaster Research and Management, in *Proceedings of the 9th International Workshop on Remote Sensing for Disaster Response*Stanford2011, pp. 258–266.

[2] T. Tomic, K. Schmid, P. Lutz, Toward a fully autonomous uav: Research platform for indoor and outdoor urban search and rescue, *Robotics & Automation Magazine* 2012, pp. 46–56.

[3] E. Honkavaara, J. Kaivosoja, J. Makynen, Hyperspectral reflectance signatures and point clouds for precision agriculture by light weight UAV imaging system, ISPRS Annals of Photogrammetry, *Remote Sensing and Spatial Information Sciences* 1 (7) (2012) 353–358.

[4] M. Hehn, R. DAndrea, A flying inverted pendulum, in *Proceedings of 2011 IEEE International Conference on Robotics and Automation (ICRA)*, 2011, pp. 763–770.

[5] D. Mellinger, N. Michael, V. Kumar, Trajectory generation and control for precise aggressive maneuvers with quadrotors, in *The International Journal of Robotics Research* 31 (5) 664–674.

[6] S. Lupashin, A. Schuollig, M. Sherback, R. DAndrea, A simple learning strategy for high-speed quadrocopter multi-flips, in Proceedings of 2010 IEEE International Conference on Robotics and Automation (ICRA), 2010, pp. 1642–1648.

[7] M. Muuller, S. Lupashin, R. DAndrea, Quadrocopter ball juggling, in *Proceedings of 2011 IEEE/RSJ International Conference on Intelligent Robots and Systems (IROS)*, 2011, p. 5113–5120.

[8] J. Thomas, G. Loianno, J. Polin, K. Sreenath, V. Kumar, Toward autonomous avian-inspired grasping for micro aerial vehicles, *Bioinspiration & Biomimetics* 9 (1–15).

[9] S. Shen, N. Michael, V. Kumar, Autonomous indoor 3d exploration with a micro-aerial vehicle, in *2012 IEEE International Conference on Robotics and Automation*, Saint Paul, Minnesota, USA, 2012, pp. 9–15.

[10] A. Budiyono, G. Lee, G. B. Kim, J. Park, T. Kang, K. J. Yoon, Control system design of a quad-rotor with collision detection, *Aircraft Engineering and Aerospace Technology, an International Journal* 87 (1) (2015) 59–66.

[11] S. Yang, S. Scherer, A. Zell, An onboard monocular vision system for autonomous takeoff, hovering and landing of a Micro Aerial Vehicle, *Journal of Intelligent & Robotic Systems* 69 (2013) 499–515.

[12] T. Lee, M. Leok, N. McClamroch, Geometric Tracking Control of a Quadrotor UAV on SE(3), in *49th IEEE Conference on Decision and Control*, Atlanta, GA, USA, 2010, pp. 42 (7) (2006) 5420–5425.

[13] C. Aguilar-Ibáez, H. Sira-Ramłrez, M. Surez-Castaón, The trajectory tracking problem for an unmanned fourrotor system: flatness-based approach, *International Journal of Control* 85 (1) (2012) 69–77.

[14] A. P. Schoellig, F. L. Mueller, R. DAndrea, Optimization-based iterative learning for precise quadrocopter trajectory tracking, *Auton Robot* 33 (2012) 103–127.

[15] L. R. Carrillo, E. Rondon, A. Sanchez, A. Dzul, Stabilization and Trajectory Tracking of a Quad-Rotor Using Vision, *Journal of Intelligent & Robotic Systems* 61 (2011) 103–118.

Proceedings of the 3rd Conference on Fully Actuated System Theory and Applications
May 10-12, 2024, Shenzhen, China

Output Feedback Predictive Steering Control in Autonomous Driving : An Interval Type-2 T-S Fuzzy-Model-Based Approach

Jinfei Hu[1], Shengsi Ding[2], Changzhu Zhang[2]
1. Shanghai Normal University, Tianhua College, Shanghai 208185, China
E-mail: feife2008@gmail.com
2. Department of Control Science and Engineering, Tongji University, Shanghai 201804, China

Abstract: In this paper, the problem of output feedback predictive steering control for path tracking in autonomous vehicles is studied based on interval type-2 fuzzy-model-based approach. Due to the complex road conditions and different maneuvers, the vehicle experiences fluctuations in velocity, and furthermore, certain physical characteristics of the vehicle are not accessible for control. The suggested approach involves the utilization of fuzzy modeling techniques to develop an interval type-2 T-S fuzzy model that captures the vehicle's lateral dynamics, taking into account the longitudinal velocities velocity change. A Longberg observer is developed for the state estimate and the corresponding conditions for the estimation error to be confined within a minimal ellipsoidal robust positively invariant set are proposed, which is involved in an H_∞-type cost function of predictive control to further improve the transient output feedback control performance. Then, an interval type-2 fuzzy-model-based predictive controller is established by addressing a Min-max optimization problem. Finally, in order to demonstrate the effectiveness of proposed methods, some validation results with Carsim/MATLAB joint simulation are provided.

Key Words: Autonomous Driving, Fuzzy Control, Interval type-2, Model Predictive Control

1 Introduction

In recent decades, autonomous driving technology has emerged as a prominent research focus within the automobile industry and academic fields. Typically, the autonomous driving system comprises four distinct functional modules, namely, environment perception, decision making, path planning, and tracking control [1, 2]. Among the four modules, tracking control, as a crucial component of autonomous driving systems, has attracted a lot of interest within the control community [3]. In the existing literature, multiple control techniques have been proposed for vehicle steering control, such as, PID control, model predictive control (MPC), H_∞ control, and fuzzy logic control [4–6]. To mention a few, in [7], a nested proportional-integral-derivative (PID) steering controller is developed to handle the problem of path-tracking in the presence of unpredictable road curvature and vehicle physical parameters. In [8], a MPC path-tracking controller with switching tracking error is provided which could ensure the vehicle's stability under both normal and high-speed situations.

The T-S fuzzy modeling approach is widely used in nonlinear system related investigations within the classic control discipline. The approach relies on fuzzy logic principles and utilizes sector nonlinearity to approximate a nonlinear system with a collection of linear subsystems. In the case of nonlinear systems represented by T-S fuzzy systems, the model predictive control (MPC) technique is commonly employed to formulate an online optimization problem. In [9], the authors provide two algorithms, namely online and offline robust fuzzy model predictive control (RFMPC), for handling the challenges posed by persistent disturbances and parameter uncertainties in a nonlinear system. In [10], in order to deal with the issue of vehicle path tracking, the author employs T-S fuzzy modeling technology to effectively handle the variations of parameters caused by changes in longitudinal velocity.

Howerver the membership function of type-1 T-S fuzzy system exclusively focuses on the nonlinearity generated by the system, but ignoring the possible uncertainty associated with the system parameters. For this reason, interval type-2 T-S fuzzy system addresses system nonlinearity and parameter uncertainty through the incorporation of upper and lower membership functions and a relative weight function [11, 12]. Motivated by the above control issues, considering the system nonlinearity, parameter uncertainty and actuator constraints, this paper proposes an output feedback predictive steering control method for automatic vehicle path tracking based on an interval type-2 T-S fuzzy model.

Initially, to account for the parameter changes resulting from the variation of longitudinal velocity over a period of time, a real-time updated interval type-2 T-S fuzzy model T-S fuzzy model for the original system is proposed. In this model, the upper and lower bound membership functions of the system are adjusted based on the vehicle prediction range, acceleration, and deceleration. Then a path tracking system based on an observer is constructed. The control technique under consideration is described in terms of linear matrix inequalities (LMIs). On this basis, a robust fuzzy model predictive path tracking algorithm is proposed. The effectiveness and advantages of the proposed path tracking method is successfully verified through Carsim/Matlab joint simulation.

The rest of the paper is organized as follows. In Section II, an interval type-2 T-S fuzzy vehicle model for path tracking is presented and some preliminaries are introduced. In Section III, the observer-based predictive controller is developed. The simulation to demonstrate the path tracking performance are given in Section IV. Finally, conclusion are provided in Section V.

2 PRELIMINARIES AND PROBLEM FORMULATION

2.1 Vehicle Lateral Dynamics

To facilitate the following system analysis and synthesis, the widely used generic single track or bicycle model of the

vehicle dynamics is adopted in this paper, as shown in Fig. 1 [13]. The meanings of the symbols involved are shown in Table I.

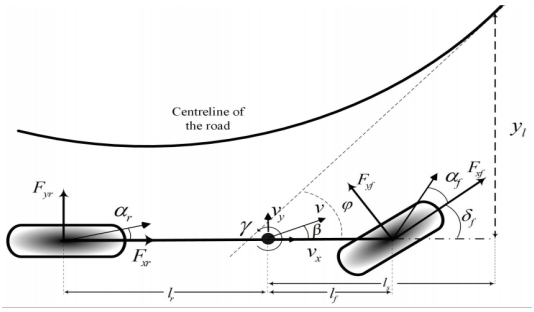

Fig. 1: Look-ahead path tracking based on single-track model

Table 1: Vehicle model parameters

Symbol	Description
m	vehicle mass(kg)
v_x	vehicle longitudinal speed(m/s)
v_y	vehicle lateral speed(m/s)
l_f, l_r	distances from CG to the front and rear axles(m)
I_z	yaw moment of inertia(kg· m^2)
C_f, C_r	front and rear cornering stiffnesses(N/rad)
α_f, α_r	front and rear tire slip angles(rad)
β	sideslip angle at CG(rad)
ψ	yaw angle(rad)
δ	wheel steering angle(rad)
φ	relative yaw angle(rad)
L_s	vehicle preview distance(m)
y_L	preview lateral deviation(m)

Additionally, we consider the lateral dynamics of the vehicle is controlled by the front wheel steering angle δ. Then by employing the small steering angle assumption, the vehicle lateral dynamics can be characterized by the following equations:

$$\begin{aligned} m\left(\dot{v}_y + v_x\dot{\psi}\right) &= F_{yf} + F_{yr}, \\ I_z\ddot{\psi} &= l_f F_{yf} - l_r F_{yr}. \end{aligned} \tag{1}$$

It can be easily calculated $v_y = v_x \tan\beta$. Since β is small during the driving process, it approximately has $\tan\beta \approx \beta$. Besides, the effect of tire longitudinal force on lateral motion can be neglected and the tire forces F_{yf} and F_{yr} can be linearly approximated $F_{yf} = 2C_f\alpha_f = 2C_f(\delta - \left(v_y + l_f\dot{\psi}\right)/v_x)$ and $F_{yr} = 2C_r\alpha_r = 2C_r(-\left(v_y - l_r\dot{\psi}\right)/v_x)$. Substituting it into (1), the following description for the vehicle lateral dynamics has:

$$\begin{aligned} \dot{\beta} &= -\dot{\psi} + \frac{2C_f}{mv_x}\left(\delta - \beta - \frac{L_f\dot{\psi}}{v_x}\right) + \frac{2C_r}{mv_x}\left(-\beta + \frac{L_r\dot{\psi}}{v_x}\right), \\ \ddot{\psi} &= \frac{2L_fC_f}{mv_x}\left(\delta - \beta - \frac{L_f\dot{\psi}}{v_x}\right) - \frac{2L_rC_r}{mv_x}\left(-\beta + \frac{L_r\dot{\psi}}{v_x}\right). \end{aligned} \tag{2}$$

We consider the lateral error between the vehicle and the road to follow at a look-ahead distance L_s. Furthermore, the following relationship holds according to vehicle kinematics:

$$\dot{y_L} = \beta v_x + L_s\dot{\psi} + v_x\varphi. \tag{3}$$

The v_x is a mutable variable. Hence, by integrating (2) with (3) described above, it is possible to get the vehicle path tracking system as follows:

$$\dot{x}(t) = \tilde{A}(t)x(t) + \tilde{B}(t)u(t) + \tilde{D}(t)\omega(t), \tag{4}$$

$$\tilde{A}(t) = \begin{bmatrix} \frac{-2C_f-2C_r}{mv_x} & \frac{2l_rC_r-2l_fC_f}{mv_x^2} - 1 & 0 & 0 \\ \frac{2l_rC_r-2L_fC_f}{I_z} & \frac{-2L_f^2C_f-2L_r^2C_r}{I_zv_x} & 0 & 0 \\ 0 & 1 & 0 & 0 \\ v_x & l_s & v_x & 0 \end{bmatrix},$$

$$\tilde{B}(t) = \begin{bmatrix} \frac{2C_f}{mv_x} \\ \frac{2L_fC_f}{I_z} \\ 0 \\ 0 \end{bmatrix}, \tilde{D}(t) = \begin{bmatrix} 0 \\ 0 \\ -v_x \\ 0 \end{bmatrix}.$$

where $x(t) = [\beta(t)\ \dot{\psi}(t)\ \varphi(t)\ y_L(t)]^T$ is the state vector, $\omega(t) = 1/d(t)$ is the road curvature, and the steering angle δ is the control input $u(t)$.

The measurement of vehicle sideslip angle β is usually unavailable in practice. Therefore, the measured system output equation is defined as follows:

$$y(t) = Cx(t) = \begin{bmatrix} 0 & 1 & 0 & 0 \\ 0 & 0 & 1 & 0 \\ 0 & 0 & 0 & 1 \end{bmatrix} x(t) \tag{5}$$

2.2 Type-2 T–S Fuzzy Model

In order to simplify the problem description, we convert the continuous-time dynamics model into a discrete-time model by dividing it into discrete intervals with a sampling period of T. Therefore, we have the following discrete-time parameter varying dynamics with external disturbance:

$$\begin{aligned} x(k+1) &= A(k)x(k) + B(k)u(k) + D(k)\omega(k) \\ y(k) &= Cx(k) \end{aligned} \tag{6}$$

where $A(k) = 1 + T\tilde{A}$, $B(k) = T\tilde{B}$, $D(k) = T\tilde{D}$, $C = C$. The input of the front wheel system is the steering angle and δ is subject to saturation $u_{\min} \le u \le u_{\max}$. Furthermore, we assume the disturbance satisfies $\omega \in W := \{\omega|\omega^T\omega \le \gamma^2\}$. Assume the vehicle speed changes during cruising, i.e., $v_{x\min} \le v_x(t) \le v_{x\max}$. In order to address the changing lateral dynamics of the vehicle, we utilize type-2 T-S fuzzy modeling approach. This allows us to present a discrete-time T-S fuzzy representation of the lateral dynamics in the following manner:

Fuzzy Rule i**: If** $f_1(v_x(k))$ is F_1^i and $f_2(v_x(k))$ is F_2^i and $f_3(v_x(k))$ is F_3^i, **Then**

$$\begin{cases} x(k+1) = A_ix(k) + B_iu(k) + D_i\omega(k) \\ y(k) = Cx(k), i = 1, 2, 3, ..., r, \end{cases} \tag{7}$$

where $f_1(v_x(k)) = v_x(k)$, $f_2(v_x(k)) = \frac{1}{v_x(k)}$, $f_3(v_x(k)) = \frac{1}{v_x^2(k)}$ are premise variables, $F_1^i, \ldots, F_3^i$ are the interval type-2 T–S fuzzy set of Rule i, and the system matrices A_i, B_i, D_i are known for each fuzzy rule.

The firing interval corresponding to the ith rule is $h_i(v_x(k)) = [\overline{h}_i(v_x(k)), \underline{h}_i(v_x(k))]$, where $\overline{h}_i(v_x(k)) = \prod_{j=1}^{p} \overline{\mu}_{F_j^i} f_j(v_x(k))$ and $\underline{h}_i(v_x(k)) = \prod_{j=1}^{p} \underline{\mu}_{F_j^i} f_j(v_x(k))$ are the lower and upper grades of membership, respectively; $\overline{\mu}_{F_j^i} f_j(v_x(k)) \in [0,1]$ and $\underline{\mu}_{F_j^i} f_j(v_x(k)) \in [0,1]$ are the lower and upper membership functions, respectively. Then the inferred interval type-2 T-S fuzzy model is defined as

$$x(k+1) = \sum_{i=1}^{r} h_i(v_x(k)) (A_i x(k) + B_i u(k) + D_i w(k)) \tag{8}$$

where $h_i(v_x(k)) = \overline{h}_i(v_x(k))\overline{v}_i(v_x(k)) + \underline{h}_i(v_x(k))\underline{v}_i(v_x(k))$, $\sum_{i}^{r} h_i(v_x(k)) = 1$ and $\overline{v}_i(v_x(k)) + \underline{v}_i(v_x(k)) = 1$, in which $\overline{v}_i(v_x(k)) \in [0,1]$ and $\underline{v}_i(v_x(k)) \in [0,1]$ are nonlinear functions.

To decrease the conservativeness of the results, one might implement the suggested variable change [14], due to the high interdependence of the three premise variables.

$$\begin{aligned} &v_x = \frac{v_0 v_1}{v_1 + v_0 \varrho}, \frac{1}{v_x} = \frac{1}{v_0} + \frac{1}{v_1}\varrho, \\ &v_x \cong v_0 \left(1 - \frac{v_0}{v_1}\varrho\right), \frac{1}{v_x^2} \cong \frac{1}{v_0^2}\left(1 + 2\frac{v_0}{v_1}\varrho\right) \end{aligned} \tag{9}$$

where $v_0 = \frac{2v_{x\min}v_{x\max}}{v_{x\min}+v_{x\max}}$, $v_1 = \frac{2v_{x\min}v_{x\max}}{v_{x\min}-v_{x\max}}$ and ϱ is the new premise variable satisfing $\varrho_{\min} \le \varrho \le \varrho_{\max}$, $\varrho_{\min} = -1$, $\varrho_{\max} = 1$, and

$$v_x = \begin{cases} v_{x\min}, & \text{if } \varrho = \varrho_{\min} \\ v_{x\max}, & \text{if } \varrho = \varrho_{\max} \end{cases} \tag{10}$$

System (7) can be represented in the type-2 T-S fuzzy form as follows:

$$\begin{cases} x(k+1) = A(\varrho)x(k) + B(\varrho)u(k) + D(\varrho)w(k) \\ y(k) = Cx(k) \end{cases} \tag{11}$$

where $\cdot(\varrho) = \cdot(\varrho(k))$ and

$$\begin{cases} A(\varrho) = h_1(\varrho)A(v_{x\max}) + h_2(\varrho)A(v_{x\min}) \\ B(\varrho) = h_1(\varrho)B(v_{x\max}) + h_2(\varrho)B(v_{x\min}) \\ D(\varrho) = h_1(\varrho)D(v_{x\max}) + h_2(\varrho)D(v_{x\min}) \end{cases} \tag{12}$$

The range of vehicle speed within a certain time interval can be predicted and obtained based on the measured longitudinal speed at the current time. One may assume that there is a maximal acceleration and deceleration for the vehicle, which are denoted as $a_{\max}$ and $a_{\min}$, respectively. Subsequently, the longitudinal velocity v_x within each narrow finite horizon of length N satisfies

$$NT_s a_{\min} \le v_x(k+N) - v_x(k) \le NT_s a_{\max} \tag{13}$$

The following lower and upper membership functions are formed in this horizon

$$\begin{cases} \overline{h}_1(\varrho) = (1 + v_1(1/(v_x + NT_s a_{\max}) - 1/v_0))/2 \\ \underline{h}_1(\varrho) = (1 + v_1(1/(v_x + NT_s a_{\min}) - 1/v_0))/2 \\ \overline{h}_2(\varrho) = 1 - \underline{h}_1(N) \\ \underline{h}_2(\varrho) = 1 - \overline{h}_1(N) \end{cases}$$

Thus, the system (7) is rewritten as

$$x(k+1) = \sum_{i=1}^{2}\sum_{j=1}^{2} v_{ij}(\varrho)(A_{ij}x(k) + B_{ij}u(k) + D_{ij}w(k)) \tag{14}$$

where

$$\begin{cases} A_{11} = \overline{h}_1(\varrho)A(v_{x\max}) \\ A_{12} = \underline{h}_1(\varrho)A(v_{x\max}) \\ A_{21} = \overline{h}_2(\varrho)A(v_{x\min}) \\ A_{22} = \underline{h}_2(\varrho)A(v_{x\min}) \end{cases}$$

3 MAIN RESULTS

Definition 1 (Robust Positive Invariance(RPI)): Consider a discrete-time system with a state feedback control law:

$$x(k+1) = A_d x(k) + D_d \omega(k) \tag{15}$$

where $x(k)$ is state vector, $\omega(k)$ is external disturbance. If $\forall x(k) \in \Gamma$ it holds $x(k+1) \in \Gamma$ for all admissable $\omega(k)$. Then the set Γ is called a RPI set for the close-loop control system.

Lemma 1 [14]: The ellipsoidal set $\Gamma := \{x \mid x^T P x \le \xi\}$ where $P > 0$ is an RPI set of the system (15) if for all h satisfying $h_i > 0$ and $\sum_{i=1}^{2} h_i = 1$,

$$\frac{1}{\xi}x(k+1)^T P x(k+1) \le \frac{1}{\xi}x(k)^T P x(k) \tag{16}$$

holds under the condition

$$\frac{1}{\xi}x(k)^T P x(k) \ge \frac{1}{\gamma^2}\omega(k)^T\omega(k) \tag{17}$$

Definition 2 (Input-to-state stability(ISS)): For a discrete-time system $x(k+1) = f(x(k), u(k))$, it is ISS if there exist a $\mathcal{KL}$-function β and a $\mathcal{K}$ function σ such that

$$|x(k, x_0, u)| \le \beta(|x_0|, k) + \rho(\|u\|)$$

where x_0 is the initial state vector, u is the input sequence $\{u(0), u(1), ..., u(k-1)\}$, and k is the time instant.

Definition 3 (ISS-Lyapunov function): A function $V(x)$ is called an ISS-Lyapunov function for system $x(k+1) = f(x(k), u(k))$ if there exist $\mathcal{K}_\infty$function $\alpha_1, \alpha_2, \alpha_3$ and a $\mathcal{K}$function σ such that

$$\begin{aligned} &\alpha_1(|x|) \le V(x) \le \alpha_2(|x|), \\ &V(f(x(k), u(k))) - V(x) \le -\alpha_3(|x|) + \sigma(|u|). \end{aligned} \tag{18}$$

Lemma 2 [15]: If system $x(k+1) = f(x(k), u(k))$ admits a continuous ISS-Lyapunov function, then it is ISS.

3.1 Observer Design

The absence of convergence to zero in the state estimation error is related to the existence of external disturbances. Hence, we posit that the estimation error is confined to a small ellipsoidal robust positively invariant (RPI) set as the temporal horizon approaches infinity. In order to achieve this objective, the following state observer is presented:

$$\hat{x}(k+1) = A(\varrho)\hat{x}(k) + B(\varrho)u(k) + L(\varrho)(y(k) - \hat{y}(k)) \tag{19}$$

where $\hat{y}(k) = C\hat{x}(k)$, and $L(\varrho) := \sum_{i=1}^{2} h_i L_i$. Denote $e(k) := x(k) - \hat{x}(k)$ as the observation error with respect to the actual state, the dynamics of $e(k)$ can be derived as:

$$e(k+1) = (A(\varrho) - L(\varrho)C)e(k) + D(\varrho)\omega(k). \quad (20)$$

Consider an ellipsoidal set $\Gamma_e := \{e(k) \mid e(k)^T P_e e(k) \leq 1\}$. With the employment of the S-procedure, Γ_e is an RPI set if there exists a positive scalar λ such that

$$\begin{aligned}&\left(e(k+1)^T P_e e(k+1) - e(k)^T P_e e(k)\right)\\ &\quad - \lambda\left(\frac{1}{\gamma^2}\omega(k)^T\omega(k) - e(k)^T P_e e(k)\right) \leq 0. \quad (21)\end{aligned}$$

Substituting the observer error system state equation (20) into (21) and collecting the state vector $[e(k)^T, \omega(k)^T]^T$, we have

$$\begin{aligned}&\begin{bmatrix} (-1+\lambda)P_e & 0 \\ 0 & -\lambda/\gamma^2 \end{bmatrix}\\ &+ \begin{bmatrix} (A(\varrho) - L(\varrho)C)^T \\ D(\varrho)^T \end{bmatrix} P_e \begin{bmatrix} A(\varrho) - L(\varrho)C & D(\varrho) \end{bmatrix} \leq 0. \quad (22)\end{aligned}$$

Applying the Schur complement to (22) and multiplying both sides with diag$\{I, I, P_e\}$, one has

$$\begin{bmatrix} (-1+\lambda)P_e & \star & \star \\ 0 & -\lambda/\gamma^2 I & \star \\ A(\varrho) - L(\varrho)C & D(\varrho) & -P_e^{-1} \end{bmatrix} \leq 0 \quad (23)$$

According to (12), (21) should be satisfied for all h satisfying $\sum_{i=1}^{2} h_i = 1$. Considering the nonlinear term $-P_e^{-1}$, via the matrix variable transformation, the above inequality can be written as

$$\begin{bmatrix} (-1+\lambda)P_e & \star & \star \\ 0 & -\lambda/\gamma^2 I & \star \\ P_e A_i - W_i C & P_e D_i & -P_e \end{bmatrix} \leq 0 \quad (24)$$

where $W_i = P_e * L_i$.

To guarantee the optimality of estimation results, the size of the ellipsoidal set Γ_e should be minimized. We minimize the size of RPI set $\Gamma_e := \{e(k) \mid e(k)^T P_e e(k) \leq 1\}$ by maximizing P_e. To this end, we have the following constrained problem

$$\min_{P_e, W_i, \lambda} -\det(P_e), \text{ s.t. (30).} \quad (25)$$

The observer gains and the minimal RPI set can be obtained by solving the above problem.

3.2 Controller design

In this section, an robust fuzzy MPC control strategy is proposed to optimize the system performance. The path tracking task can be formulated into the following optimal control problem. Under the bounded curvature $\omega(k)$, the finite-horizon objective function can be established as

$$J_\infty(k) := \sum_{i=0}^{N} \ell(k+i \mid k), \quad (26)$$

where $\ell(k+i \mid k) := \hat{x}^T(k+i \mid k)Q\hat{x}(k+i \mid k) + u^T(k+i \mid k)Ru(k+i \mid k) - \tau e^T(k+i \mid k)P_e e(k+i \mid k)$ is stage cost; and $\hat{x}(k+i|k)$, $u(k+i|k)$, $e(k+i|k)$ are the predicted state, control input, and state estimation error at the ith predicted time instant; and Q and R are positive definite matrices, τ is a positive scalar, and P_e has been determined in the last section.

Theorem 1: Consider the observer-based path tracking system, if there exist a positive definite matrices X, matrices Y, G and positive scalars ξ, τ, such that the following constrained optimization problem is feasible, and the observer system (19) for the interval type-2 T-S fuzzy system (11) is input-to-output stable,

$$\begin{aligned}&\min_{\xi, X, G_j, Y_j} \xi\\ &\text{s.t.} \quad (28), (29), (30), (31)\end{aligned} \quad (27)$$

$$\begin{bmatrix} X - G - G^T & \star & \star & \star & \star \\ 0 & -\tau\xi P_e & \star & \star & \star \\ 2A_l G + 4B_l Y_l & 2\xi L_l C & -X & \star & \star \\ QG & 0 & 0 & -\xi Q & 0 \\ 2RK_l & 0 & 0 & 0 & -\xi R \end{bmatrix} \leq 0 \quad (28)$$

$$\begin{bmatrix} X - G - G^T & \star & \star \\ 0 & -\tau\xi P_e & \star \\ (A_l G + 2B_l Y_j) + (A_j G + 2B_j Y_l) & \xi(L_l + L_j)C & -X \\ QG & 0 & 0 \\ R(Y_j + Y_l) & 0 & 0 \end{bmatrix} \begin{bmatrix} \star & \star \\ \star & \star \\ \star & \star \\ -\xi Q & 0 \\ 0 & -\xi R \end{bmatrix} \leq 0 \quad (29)$$

$$\begin{bmatrix} M & \star \\ Y_j^T & G_j + G_j^T - X \end{bmatrix} \geq 0 \quad (30)$$

$$\begin{bmatrix} 1 & \star \\ \hat{x}(k) & X \end{bmatrix} \geq 0. \quad (31)$$

where $j, l = 1, 2, 3, 4$ and $P = \xi X^{-1}$. Besides, we use $\sum_{l=1}^{4} v_l$ denote $\sum_{i=1}^{2}\sum_{j=1}^{2} v_{ij}$, so the feedback law is $u(k) = K(\varrho)\hat{x}(k)$, $K(\varrho) = \sum_{l=1}^{4} v_l K_l$, where $\sum_{l=1}^{4} v_l = 2$ and $K_l = Y_l G^{-1}$.

Proof: We define a positive definite function $V(x) := \hat{x}^T P \hat{x}$, $P > 0$ such that

$$V(\hat{x}(k+i+1 \mid k)) - V(\hat{x}(k+i \mid k)) \leq -\ell(k+i \mid k) \quad (32)$$

By summing up both sides of the above inequality from $i = 0$ to $i = N$, we have $J_N(k) = \sum_{i=0}^{N} \ell(k+i \mid k) \leq V(\hat{x}(k \mid k))$. Thus, $V(\hat{x}(k \mid k))$ is an upper bound of the infinite cost function $J_N(k)$. The notation $\|x\|_P$ represents $\sqrt{x^T P x}$, where P is a positive definite matrix, while $\|x\|_2$ represents

$\sqrt{x^T x}$. Substituting $u(k) = K(\varrho)\hat{x}(k)$ and system (19) into (32), one has

$$\begin{bmatrix} (-P + Q + K(\varrho)^T R K(\varrho) & 0 \\ 0 & -\tau P_e \end{bmatrix} + \begin{bmatrix} (A(\varrho) + B(\varrho)K(\varrho))^T \\ (L(\varrho)C)^T \end{bmatrix} P\star \leq 0. \quad (33)$$

Considering the maximum velocity variation, and $A(\varrho) = A(\varrho(k+N))$ is chosen to describe the system equation in the predictive time domain, one has

$$\sum_{l=1}^{4}\sum_{j=1}^{4} v_l v_j \begin{bmatrix} -P & \star & \star & \star & \star \\ 0 & -\tau P_e & \star & \star & \star \\ 2A_l + 4B_l K_j & 2L_l C & -P^{-1} & -Q & 0 \\ Q & 0 & 0 & 0 & -R \\ 2RK_j & 0 & 0 & 0 & 0 \end{bmatrix} \leq 0. \quad (34)$$

With the equality $\sum_{l=1}^{L}\sum_{j=1}^{L}\phi_{lj} = \sum_{l=1}^{L}\phi_{ll} + 2\sum_{l<j}^{L}\frac{\phi_{lj}+\phi_{jl}}{2}$, a sufficient condition for the above inequality is obtained. Substituting $P = \xi X^{-1}$, multiplying both sides with $\mathrm{diag}\{G^T, I, I, I, I\}$, and applying the dilation lemma $-G^T X^{-1} G \leq X - G^T - G$ [16], we get the conditions (28) and (29). The inequality equation (30) is the input constraint. In (30) M is a symmetric matrix with the ith diagonal element $M_{ii} \geq u^2_{i,\max}, i = 1, 2, ..., m$. To minimize $V(\hat{x}(k))$, the following problem is considered: $\min \xi$, subject to $V(\hat{x}(k)) \leq \xi$. The proof of ISS is as follows. Since the matrix P is positive definite, the $V(\hat{x})$ satisfies

$$\rho_{\min}\|\hat{x}(k)\|^2 \leq V_k(\hat{x}(k)) \leq \rho_{\max}\|\hat{x}(k)\|^2 \quad (35)$$

where $\rho_{\min}$ and $\rho_{\max}$ are the minimal and maximal eigenvalues of P. Correspondingly, form inequality (32) the following inequality can be obtained:

$$V_k(\hat{x}(k+1)) - V_k(\hat{x}(k)) < -\hat{x}^T(k)Q\hat{x}(k) - \hat{x}^T(k)\|K(\varrho)\|^2_R\hat{x}(k) + \tau\|e(k)\|^2_{P_e}. \quad (36)$$

The inequalities (35) and (36) imply that $V^*_k(\hat{x}(k))$ is an ISS-Lyapunov function. According to Lemma 2, it can be proved that the observer system (19) is input-to-output stable with respect to the estimation error.

4 Simulations

In this section, some experimental results are presented to illustrate the effectiveness of controller. In Carsim/Simulink co-simulation, a C-Class Hatchback vehicle is considered to be controlled as the autonomous driving car, and $m = 1537.7\mathrm{kg}\cdot\mathrm{m}^2$, $l_f = 1.015\mathrm{m}$, $l_r = 1.895\mathrm{m}$, $I_z = 1537.7\mathrm{kg}\cdot\mathrm{m}^2$, $C_{\alpha f} = 82725.89\mathrm{N/rad}$, $C_{\alpha r} = 80725.89\mathrm{N/rad}$. Fig. 2 shows the structure of the path-tracking simulation system. In the simulation. the input constraint is $-\frac{20\pi}{180} \leq \delta(t) \leq \frac{20\pi}{180}$, preview distance $L_s = 3m$ and it is assumed that $|\omega| \leq 0.05$. In offline computation of state observer design, the observer gains and the minimal RPI set can be obtained,

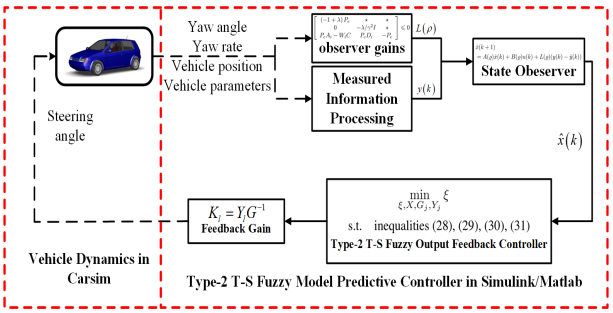

Fig. 2: Carsim/Simulink joint simulation structure diagram.

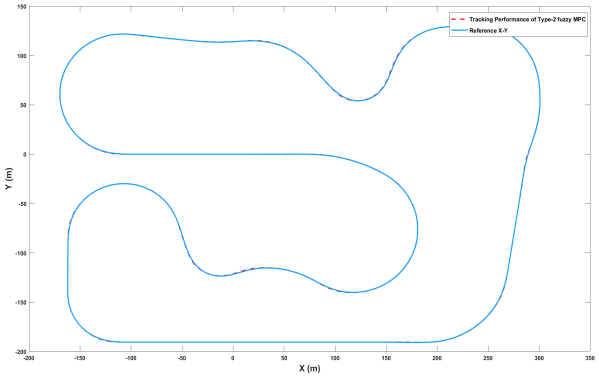

Fig. 3: Reference trajectories.

$$L_1 = \begin{bmatrix} 0.1938 & 0.0000 & -0.3095 \\ -1.7988 & 0.0000 & 0.5318 \\ 0.0499 & 1.0000 & 0.0001 \\ 0.1851 & 0.3000 & 1.0004 \end{bmatrix},$$

$$L_2 = \begin{bmatrix} -0.1735 & 0.0000 & 0.2211 \\ 0.2424 & 0.0000 & 0.5350 \\ 0.0500 & 1.0000 & 0.0000 \\ -0.0777 & 1.6500 & 1.5557 \end{bmatrix},$$

$$P_e = \begin{bmatrix} 172.3538 & 33.7272 & 0.0000 & -58.4032 \\ 33.7272 & 42.7988 & 0.0000 & -36.8249 \\ 0.0000 & 0.0000 & 0.0000 & 0.0000 \\ -58.4032 & -36.8249 & -0.0000 & 83.0459 \end{bmatrix}.$$

The initial condition is selected as $x(0) = [0, 0, 0, 0]^T$. We choose $\hat{x}(0) = [0, 0, 0, 0.5]^T$. In the stage cost, $Q = diag[0.5, 0.0001, 0.1, 1]$ and $R = 1$ are chosen and $v_{ij} = 0.5$.

In order to verify the tracking capabilities of the proposed method to handle a wide range of vehicle speed variations, we set minimum vehicle speed to 33.6km/h and maximum allowable speed to 100km/h. The real vehicle speed is shown in Fig. 4(a). In Fig. 4(b), the lateral offset is shown, from which it can be easily seen that the lateral offset is bounded

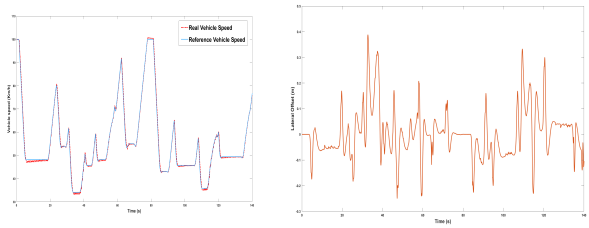

(a) (b)

Fig. 4: (a) The vehicle longitudinal velocity. (b) The lateral offset.

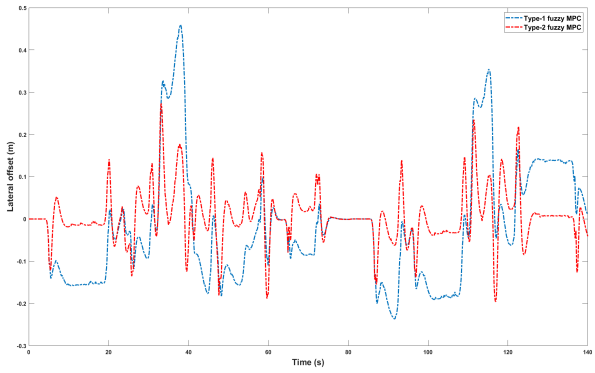

Fig. 5: The lateral offset of type-1 an type-2 fuzzy MPC.

by 0.4 and -0.4m. The proposed interval type-2 T-S fuzzy MPC method is compared with the traditional MPC method based on the type-1 T-S fuzzy model and the vehicle speed is set to shift between 33 and 80km/h. The results is shown in Fig. 5. In Fig. 6, the measured and estimated state variables of the tracking system are illustrated.

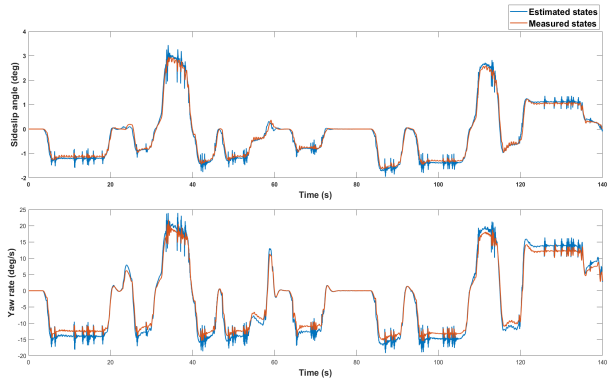

Fig. 6: The state estimation results.

5 Conclusion

This work examines the use of observer-based output feedback predictive steering control to autonomous driving systems with actuator restriction. The nonlinear vehicle lateral model is represented using the interval type-2 T-S fuzzy modeling technique, taking into account the presence of parameter variations. The determination of the minimal ellipsoidal RPI set for the state estimation error and the observer gains can be achieved by offline computation within the framework of T-S fuzzy system theory. By minimizing the upper limit of cost function in an online manner, the system performance can be optimized. The efficiency of the proposed design techniques is demonstrated through a collaborative simulation using Carsim and Matlab.

References

[1] X. Meng, Y. Yang, L. Wang, T. Wang, R. Li and C. Zhang, Class-guided swin transformer for semantic segmentation of remote sensing imagery, *IEEE Geoscience and Remote Sensing Letters*, 19: 1-5, 2022.

[2] H. Li, J. Li, Z. Su, X. Wang and J. Luo, Research on active obstacle avoidance control strategy for intelligent cehicle based on active safety collaborative control, *IEEE Access*, 8: 183736-183748, 2020.

[3] A. P. Aguiar and J. P. Hespanha, Trajectory-tracking and path-following of underactuated autonomous vehicles with parametric modeling uncertainty, *IEEE Transactions on Automatic Control*, 52(8): 1362-1379, 2007.

[4] G. Fiengo, D. G. Lui, A. Petrillo, S. Santini and M. Tufo, Distributed robust PID control for leader tracking in uncertain connected ground vehicles with V2V communication delay, *IEEE/ASME Transactions on Mechatronics*, 24(3): 1153-1165, 2019.

[5] J. Guo, J. Wang, Y. Luo and K. Li, Takagi–sugeno fuzzy-based robust H_∞ integrated lane-keeping and direct yaw moment controller of unmanned electric vehicles," *IEEE/ASME Transactions on Mechatronics*, 26(4): 2151-2162, 2021.

[6] Z. Yang, J. Huang, D. Yang, and Z. Zhong, Design and optimization of robust path tracking control for autonomous vehicles with fuzzy uncertainty, *IEEE Transactions on Fuzzy Systems*, 30(6): 1788–1800, 2022.

[7] R. Marino, S. Scalzi, G. Orlando and M. Netto, A nested PID steering control for lane keeping in vision based autonomous vehicles, in *2009 American Control Conference*, 2009: 2885-2890.

[8] C. Sun, X. Zhang, Q. Zhou and Y. Tian, A model predictive controller with switched tracking error for autonomous vehicle path tracking," *IEEE Access*, 7: 53103-53114, 2019.

[9] W. Yang, G. Feng, and T. Zhang, Robust model predictive control for discrete-time takagi–sugeno fuzzy systems with structured uncertainties and persistent disturbances, *IEEE Transactions on Fuzzy Systems*, 22(5): 1213–1228, 2014.

[10] S. Cheng, L. Li, X. Chen, J. Wu, and H.-d. Wang, Model-predictivecontrol-based path tracking controller of autonomous vehicle considering parametric uncertainties and velocity-varying, *IEEE Transactions on Industrial Electronics*, 68(9): 8698–8707, 2021.

[11] H. Li, L. Wu, H. K. Lam, and Y. Gao, *Analysis and Synthesis for Interval Type-2 Fuzzy-Model-Based Systems*. Singapore: Springer, 2016.

[12] P. Wang, S. Gao, L. Li, S. Cheng, and L. Zhao, Automatic steering control strategy for unmanned vehicles based on robust backstepping sliding mode control theory, *IEEE Access*, 7: 64 984–64 992, 2019.

[13] R. Rajamani, *Vehicle Dynamics and Control*. New York, NY, USA: Springer Science & Business Media, 2011.

[14] W. Yang, J. Gao, G. Feng, and T. J. Zhang, An optimal approach to output-feedback robust model predictive control of LPV systems with disturbances, *International Journal of Robust and Nonlinear Control*, 26(15): 3253–3273, 2016.

[15] Z. P. J, and Y. W, Input-to-state stability for discrete-time nonlinear systems, *Automatica*, 37(6): 857–869, 2001.

[16] J. C. Geromel, P. L. D. Peres, and J. Bernussou, On a convex parameter space method for linear control design of uncertain systems, *Siam Journal on Control and Optimization*, 29(2): 381-402, 1991.

Proceedings of the 3rd Conference on Fully Actuated System Theory and Applications
May 10-12, 2024, Shenzhen, China

A New BRB-Based Fault Diagnosis Method for Leader-Following Multi-Agent Systems with Communication Interferences

Ziyi Wang[1], Wenqiang Ji[1], Ruohan Yang[2]

1. School of Artificial Intelligence, Hebei University of Technology, Tianjin, 300401, P. R. China.
E-mail: wangziyi990719@163.com, wqji@hebut.edu.cn

2. School of Electronics And Information, Northwestern PolytechnicalUniversity, Xi'an, 710072, P. R. China
E-mail: ruohanyang@nwpu.edu.cn

Abstract: This paper investigates the fault diagnosis problem for leader-following multi-agent systems (MASs) subject to actuator faults and communication interferences based on belief rule base (BRB). By designing a sliding mode controller, the system's consistency under communication interferences is achieved. Then a novel BRB-based fault diagnosis method is proposed to diagnose faults in MASs, and the faulty agents can be diagnosed accurately. Ultimately, the effectiveness of the proposed method is verified by simulation studies.

Key Words: Fault diagnosis, Multi-agent systems (MASs), Belief rule base (BRB), Sliding mode control

1 Introduction

In recent years, multi-agent systems (MASs) have a wide range of applications including transportation industry, military equipment and many other fields [1–3]. Due to the complexity of MASs, the failure of agents is almost inevitable [4]. Since an agent affects its adjacent agents through the information interaction, the fault in a single agent may lead to the failure of the entire MAS. Hence, to improve the safety and reliability of these systems, fault diagnosis of MASs has been a hot research topic [5–7]. Broadly speaking, fault diagnosis methods can be categorized into two types: those based on analytical models and those independent of models.

Model-based methods utilize the mathematical model and the system's measurement data to generate the residual signal to characterize the fault, and then achieve fault diagnosis. In [5], the authors introduced a fault detection scheme utilizing unknown input observers (UIOs), which solely rely on local measurements. However, when isolating multiple faults, the computational burden of each node will be increased. For the MAS with nonlinear dynamics, the authors in [8] used the output information of adjacent agents to construct a nonlinear fault observer to achieve fault diagnosis.

The above-mentioned model-based fault diagnosis methods rely on exact knowledge of analytical model of MASs. While in practice, MASs often suffer from unpredictable interferences, and thus the exact analytical model of the systems cannot be obtained. In this case, model-based fault diagnosis methods may become inapplicable.

Further subdivisions of model-independent methods include data-driven methods and expert knowledge-based methods. The data-driven methods mainly use the historical working data and the fault data of the system, which are not limited by the model. In addition, BP neural networks and random forest are also commonly used in fault diagnosis [9, 10]. Among them, methods based on BP neural network and methods based on random forest each have their own advantages in fault diagnosis. It should be noted that the data-driven methods require the states of a system in all the working situations, which are difficult to fully obtain in practice.

In practice, the inaccuracy of fault diagnosis results caused by the complexity of the environment requires further research. BRB was proposed by Yang et al. [11], which can well process small sample data and make up for the lack of data volume. Therefore, BRB has its unique advantages for situations where there is a lack of fault samples in practical scenarios. Observably, the majority of fault diagnosis methods based on BRBs primarily address the fault diagnosis issue within individual systems [12].

This paper aims at the consensus and fault daignosis problem for leader-following MASs subject to communication interferences. These settings make the problem more challenging and meaningful. To dispose of this problem, firstly, a novel sliding model control strategy that takes communication interferences into account is developed. Then, by extracting the characteristics of the system's outputs, a BRB-based fault diagnosis model is established. Different from the single system fault diagnosis model [12, 13], the model proposed in this paper effectively diagnose faults in a MAS with multiple agents.

2 Problem formulation and preliminaries

Considering a leader-following MAS. The interaction between the leader and followers is described by graph $\overline{\boldsymbol{G}}$, and $\boldsymbol{G}$ represents the interaction between the followers. $\boldsymbol{A} = [a_{ij}]_{N\times N}$ represents the adjacency matrix of graph $\boldsymbol{G}$, $\boldsymbol{B} = \text{diag}\{b_1, \ldots, b_N\}$ is the adjacency matrix between the leader and followers. The Laplacian matrix of graph $\boldsymbol{G}$ related to the adjacency matrix $\boldsymbol{A}$ is represented by $\boldsymbol{L} = [l_{ij}]_{N\times N}$, and

$$l_{ij} = \begin{cases} \sum_{j=1}^{N} a_{ij}, & i = j \\ -a_{ij}, & i \neq j \end{cases}.$$

This work was supported in part by the Natural Science Funds for Excellent Young Scholars of Hebei Province in 2022 under Grant F2022202014; in part by Science and Technology Research Project of Colleges and Universities in Hebei Province under Grant BJ2020017; in part by the Undergraduate Education Teaching Reform Research and Practice Project under Grant 202302015; in part by National Natural Science Foundation of China under Grant No. 62203365; in part by China Postdoctoral Science Foundation under Grant No. 2023M742843; in part by Aeronautical Science Foundation under Grant 2023Z034053; in part by the State Key Laboratory of Robotics and Systems of Harbin Institute of Technology under Grant SKLRS-2023-KF-09.

The dynamic model of the ith follower can be described as follows:

$$\begin{cases} \dot{x}_i(t) = v_i(t) \\ \dot{v}_i(t) = u_i(t) + f\left(t, x_i(t), v_i(t)\right) + d_i(t) \end{cases} \tag{1}$$

and describing the output of the followers as

$$y_i(t) = \mu_i(t) x_i(t), i = 1, \ldots, N \tag{2}$$

where $x_i(t) \in \mathbb{R}^n$, $v_i(t) \in \mathbb{R}^n$ and $f\left(t, x_i(t), v_i(t)\right)$ denote position, velocity and nonlinear term of follower i, respectively. $u_i(t)$ represents the controller input, $d_i(t)$ is the external interference, and $\mu_i(t)$ is the multiplicative communication interference.

Consider a tracking problem with only one leader. The dynamics of the leader is as follows:

$$\begin{cases} \dot{x}_0(t) = v_0(t) \\ \dot{v}_0(t) = u_0(t) + f\left(t, x_0(t) v_0(t)\right). \end{cases} \tag{3}$$

Assumption 1. [14, 15] For the studied system (1), the external interference $d_i(t)$ and the communication interference $\mu_i(t)$ are supposed to be bounded and $\mu_i(t) > 0$. There exist positive constants $\bar{d}, \bar{\mu}, \mu_{iM}$, such that $\|d_i(t)\| \leq \bar{d}$, $\|\mu_i(t)\| \leq \bar{\mu}$, and $\mu_i(t)$ satisfies $|\dot{\mu}_i(t)| \leq \mu_{iM}$.

Assumption 2. For the nonlinear term $f(\cdot)$, there exist two non-negative numbers h_1, h_2, so that the following formula holds:

$$\begin{aligned} &\| f(t, x_i(t), v_i(t)) - f(t, x_0(t), v_0(t)) \|_2 \\ &\leq h_1 \| x_i(t) - x_0(t) \|_2 - h_2 \| v_i(t) - v_0(t) \|_2 . \end{aligned} \tag{4}$$

Lemma 1. [16] (Barbalat's Lemma) If $f : [0, \infty] \to \mathbb{R}$ is uniformly continuous and $\lim_{t\to\infty} \int_0^t f(\tau) d\tau$ exists, then $\lim_{t\to\infty} f(t) = 0$ holds.

Lemma 2. [17] Considering a nonlinear system, choose Lyapunov function $V(x)$ and real numbers $h_1 > 0$, $0 < h_2 < 1$. $V(x)$ satisfies $V(x) > 0$ and $\dot{V}(x) + h_1 V^{h_2}(x) \leq 0$. At the same time, an estimate of the convergence time is given, satisfying $T\left(x_0\right) \leq \frac{V^{1-h_2}(x_0)}{h_1(1-h_2)}$. Then, the system satisfies finite time stability at $x = 0$.

The following problems are the main research objectives.

Problem 1: Uncertainty in MASs with communication interferences.

Due to the uncertainty and unpredictability of the communication interferences, an accurate mathematical model of a MAS is difficult to obtain. These will lead to the inaccuracy and unreliability of fault diagnosis results.

Problem 2: Lack of samples of faulty status of MASs.

Since faults are small probability events in practice, thus, the faulty data from real scenarios is difficult to obtain directly. Therefore, there is a problem of insufficient samples under fault conditions.

Problem 3: Construction of fault diagnosis framework for MAS in communication interference environment.

The fault diagnosis model should fully consider the influence of communication interferences and the lack of samples when MAS fails. Moreover, the complexity and computation should not be too large.

3 Consistency controller design

3.1 Consistency error system

The consistency errors of the ith follower are defined as follows:

$$\begin{cases} e_{x_i}(t) = \sum_{j=1}^{N} a_{ij} \left[x_i(t) - x_j(t)\right] + b_i \left[x_i(t) - x_0(t)\right] \\ e_{v_i}(t) = \sum_{j=1}^{N} a_{ij} \left[v_i(t) - v_j(t)\right] + b_i \left[v_i(t) - v_0(t)\right] \end{cases} \tag{5}$$

and then, denote $\overline{x}_i(t) = x_i(t) - x_0(t)$, $\overline{v}_i(t) = v_i(t) - v_0(t)$, $\overline{x} = \left[\overline{x}_1^{\mathrm{T}}(t), \ldots, \overline{x}_N^{\mathrm{T}}(t)\right]^{\mathrm{T}}$, $\overline{v} = \left[\overline{v}_1^{\mathrm{T}}(t), \ldots, \overline{v}_N^{\mathrm{T}}(t)\right]^{\mathrm{T}}$. The consistency error system (5) can be rewritten as

$$\begin{cases} e_x = \left[(\boldsymbol{L} + \boldsymbol{B}) \otimes \boldsymbol{I}_n\right] \cdot \overline{x} \\ e_v = \left[(\boldsymbol{L} + \boldsymbol{B}) \otimes \boldsymbol{I}_n\right] \cdot \overline{v} \end{cases} \tag{6}$$

where $e_x = \left[e_{x_1}^{\mathrm{T}}(t), \ldots, e_{x_N}^{\mathrm{T}}(t)\right]^{\mathrm{T}}$, and $e_v = \left[e_{v_1}^{\mathrm{T}}(t), \ldots, e_{v_N}^{\mathrm{T}}(t)\right]^{\mathrm{T}}$.

Define $F = [f^{\mathrm{T}}(t, x_1(t), v_1(t)), \ldots, f^{\mathrm{T}}(t, x_N(t), v_N(t))]$, $\mathbf{f} = \mathbf{1}_N \otimes f(t, x_0(t), v_0(t))$, $\mathbf{d} = [d_1^{\mathrm{T}}(t), \ldots, d_N^{T}(t)]^{\mathrm{T}}$, $\mathbf{u} = [u_1^{\mathrm{T}}(t), \ldots, u_N^{\mathrm{T}}(t)]^{\mathrm{T}}$. Then the consistency error system can be described as

$$\begin{cases} \dot{e}_x = e_v \\ \dot{e}_v = (\boldsymbol{L} + \boldsymbol{B}) \otimes \boldsymbol{I}_n \cdot (\mathbf{u} + \mathbf{d} + F - \mathbf{f} - \mathbf{1}_N \otimes u_0). \end{cases} \tag{7}$$

If $\boldsymbol{L} + \boldsymbol{B}$ is invertible, the consistency problem of the leader-following MAS is equivalent to the asymptotically stable problem of the consistency error system (7).

3.2 Sliding mode control

According to the system described in (7), the sliding mode controller is designed as

$$\begin{aligned} u_i(t) =& (l_{ii} + b_i)^{-1} [- \sum_{i \neq j, j=1}^{N} a_{ij} u_j - c\mu_i(t) e_{v_i}(t) \\ &- c\mu_{iM} e_{x_i}(t) + b_i u_0 - \gamma sgn\left(S_i(t)\right)] \end{aligned} \tag{8}$$

where $c > 0, \gamma_0 > 0$, $\epsilon = \|\boldsymbol{L} + \boldsymbol{B}\| \|(\boldsymbol{L} + \boldsymbol{B})^{-1}\|$, and $\gamma = \epsilon \left(h_1 \|e_x\| + h_2 \|e_v\| + \|\boldsymbol{L} + \boldsymbol{B}\| \bar{d} \sqrt{N} + \gamma_0\right)$.

Then the sliding surface $S_i(t)$ is designed as

$$S_i(t) = e_{v_i}(t) + c\mu_i(t) e_{x_i}(t) \tag{9}$$

with $\mu_i(t)$ satisfying Assumption 1. It is noted that signals transmitted between followers will be affected by communication interferences. Therefore, $\mu_i(t)$ can be used to describe the effects of communication interferences on the value of the relative measurement errors.

Denote $S = \left[S_1^{\mathrm{T}}(t), \ldots, S_N^{\mathrm{T}}(t)\right]^{\mathrm{T}}$, and $\boldsymbol{\mu} = \mathrm{diag}\{\mu_1(t), \ldots, \mu_N(t)\}$, (9) can be written as the following simple form:

$$S = e_v + c\boldsymbol{\mu} e_x. \tag{10}$$

Next, define $\boldsymbol{b} = [b_1, \ldots, b_N]^{\mathrm{T}}$, the control strategy (8) can then be expressed in the following simplified form:

$$u = (\boldsymbol{L} + \boldsymbol{B})^{-1} \otimes [-c\boldsymbol{\mu} e_v - c\mu_{iM} e_x - \boldsymbol{b} \otimes u_0 - g(s)] \tag{11}$$

and $g(s) = \gamma \left[\mathrm{sgn}^{\mathrm{T}}(S_1), \ldots, \mathrm{sgn}^{\mathrm{T}}(S_N)\right]^{\mathrm{T}}$.

Theorem 1. Consider the leader-following MAS (1) and

(3), with which conmunication topology has a spanning tree. Then under Assumption 1-2 and the control strategy (11), the consensus of the MAS can be obtained.

Proof: Consider the following Lyapunov function:

$$V(t) = \frac{1}{2} S(t) S^{\mathrm{T}}(t). \tag{12}$$

Based on (11), by deriving the Lyapunov function, we can get

$$\begin{aligned} \dot{V}(t) =& S^{\mathrm{T}}(t) \cdot [c\boldsymbol{\mu} e_v + c\dot{\mu} e_x + (\boldsymbol{L}+\boldsymbol{B}) \otimes \boldsymbol{I}_n \cdot (F - \mathbf{f} \\ & + \mathbf{d}) + (\boldsymbol{L}+\boldsymbol{B}) \otimes \boldsymbol{I}_n \cdot (\mathbf{u} - \mathbf{1}_N \otimes u_0)]. \end{aligned} \tag{13}$$

According to the properties of norm and Assumption 2, the following inequality is obtained:

$$\begin{aligned} \|F - \mathbf{f}\| &= \left\| \begin{bmatrix} \|f(t, x_1(t), v_1(t)) - f(t, x_0(t), v_0(t))\| \\ \cdots \\ \|f(t, x_n(t), v_n(t)) - f(t, x_0(t), v_0(t))\| \end{bmatrix} \right\| \\ &\leq \left\| \begin{bmatrix} h_1 \|\overline{x}_1(t)\| + h_2 \|\overline{v}_1(t)\| \\ \cdots \\ h_1 \|\overline{x}_n(t)\| + h_2 \|\overline{v}_n(t)\| \end{bmatrix} \right\| \\ &\leq h_1 \|\overline{x}\| + h_2 \|\overline{v}\| \end{aligned} \tag{14}$$

then we can get

$$\begin{aligned} \|(\boldsymbol{L}+\boldsymbol{B}) \otimes \boldsymbol{I}_n \cdot (F - \mathbf{f})\| \leq & \|(\boldsymbol{L}+\boldsymbol{B})\| (h_1 \|\overline{x}\| + h_2 \|\overline{v}\|) \\ \leq & \epsilon (h_1 \|e_x\| + h_2 \|e_v\|) \end{aligned} \tag{15}$$

and we can also obtain another item of (13)

$$\begin{aligned} & (\boldsymbol{L}+\boldsymbol{B}) \otimes \boldsymbol{I}_n \cdot (\mathbf{u} - \mathbf{1}_N \otimes u_0) \\ =& - c\boldsymbol{\mu} e_v - c\mu_{iM} e_x - b \otimes u_0 - g(s) - \mathbf{1}_N \otimes u_0. \end{aligned} \tag{16}$$

Substituting (15) and (16) into (13), then

$$\begin{aligned} \dot{V}(t) &\leq \|S\| \|(L+B) \otimes \cdot (F - \mathbf{f} + d)\| - S^T g(s) \\ &\leq [\epsilon (h_1 \|e_x\| + h_2 \|e_v\|) + \|(\boldsymbol{L}+\boldsymbol{B}) \bar{d} \sqrt{N}\| - \gamma_0] \|S\| \\ &\leq -\gamma_0 \|S\| \leq -\frac{1}{2} \gamma_0 V^{\frac{1}{2}}(t). \end{aligned} \tag{17}$$

Then, as per Lemma 2, it can be deduced that the controller enables the system to reach the sliding mode surface within a finite time and maintains its trajectory on it.

On the sliding surface $S = 0$, namely, $e_v = -c\boldsymbol{\mu} e_x$, thus

$$\dot{e}_x = -c\boldsymbol{\mu} e_x. \tag{18}$$

Consider the following Lyapunov function:

$$V(t) = \frac{1}{2} e_x^{\mathrm{T}} e_x. \tag{19}$$

Because of $c > 0$ and in accordance with Assumption 1, we can derive

$$\dot{V}(t) = - c\boldsymbol{\mu} e_x^{\mathrm{T}} e_x = -2c\boldsymbol{\mu} V(t) < 0. \tag{20}$$

According to (20) and Lemma 1 in [16], one can obtain that when $t \to \infty$, $\int_0^t \mu(t) e_x^{\mathrm{T}}(\tau) e_x(\tau) d\tau \leq \frac{V(0)}{2c}$, then one can obtain for all $t \geq 0$, $\int_0^t e_x^{\mathrm{T}}(\tau) e_x(\tau) d\tau$ is bounded. Then, it is easily to know that both $e_x(t)$ and $e_v(t)$ are continuously differentiable, therefore, according to Barbalat's Lemma, one can obtian that $\lim_{t\to\infty} e_x(t)^{\mathrm{T}} e_x(t) = 0$ holds, that is to say, when $t \to \infty$, the consensus errors of the position converge to 0. Furthermore, we can draw the following conclusion:

$$\begin{aligned} \lim_{t\to\infty} \int_0^t e_v^2(\tau) d\tau &= \lim_{t\to\infty} \int_0^t \dot{e}_x^2(\tau) d\tau \\ &= \frac{1}{2} \lim_{t\to\infty} \left[e_x^2(t) - e_x^2(0) \right]. \end{aligned} \tag{21}$$

Therefore, according to (21), one can obtain $\lim_{t\to\infty} \int_0^t e_v^2(\tau) d\tau$ exists, thereby $\lim_{t\to\infty} e_v^2(t) = 0$ holds on the basis of Lemma 1. Consequently, $\lim_{t\to\infty} e_v(t) = 0$ can be inferred. Based on the above proofs, it can be obtained that when $t \to \infty$, both $e_x(t)$ and $e_v(t)$ will converge to zero.

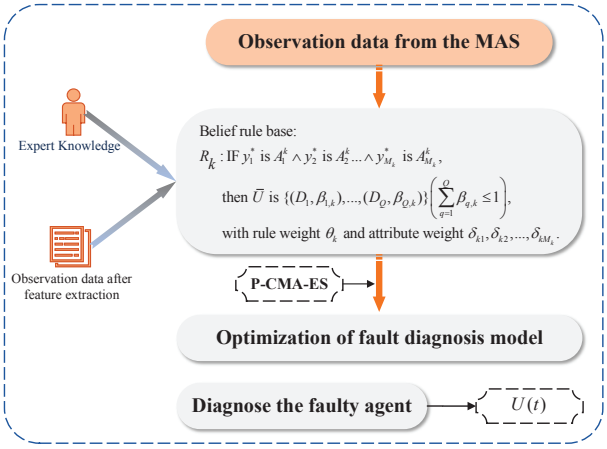

Fig. 1: Fault diagnosis modeling of MAS.

4 Fault diagnosis for the leader-following MAS based on BRB

4.1 Inference process of BRB-based fault diagnosis model

Fig. 1 shows the proposed fault diagnosis framework. Consider the case where only followers fail, the dynamics of the ith follower with fault can be described as

$$\begin{cases} \dot{x}_i(t) = v_i(t) \\ \dot{v}_i(t) = u_i(t) + d_i(t) + f\left(t, x_i(t), v_i(t)\right) + \sigma_i(t) \end{cases} \tag{22}$$

where $\sigma_i(t)$ represents fault of follower i. It should be noted that when the ith follower is in the absence of fault, $\sigma_i(t) = 0$, and otherwise, $\sigma_i(t) \neq 0$.

To establish the model, the input to the fault diagnosis model consists of the distance between the position tracking trajectories of each follower, which is extracted as follows:

$$\begin{aligned} distance_{ij} =& |(x_{i1} - x_{01}) - (x_{j1} - x_{01})|, \\ & i, j \in \{1, \ldots, N\}, i < j. \end{aligned} \tag{23}$$

Next, denote the distance as the antecedent attribute of the BRB model, described as

$$y_p^*(t) = distance_{ij},\ p \in \{1, \ldots, M_k\} \tag{24}$$

where $M_k = \frac{N(N-1)}{2}$ is the number of antecedent attributes used in the kth rule.

Then, drawing inspiration from the traditional BRB designed for a single system [11], this paper constructs a BRB-based fault diagnosis model for followers, with the expres-

sion of the kth rule as

$$\begin{aligned} R_k :&\text{If } y_1^* \text{ is } A_1^k \wedge\ y_2^* \text{ is } A_2^k\ \wedge \ldots \wedge\ y_{M_k}^* \text{ is } A_{M_k}^k, \\ &\text{then } \bar{U} \text{ is } \{(D_1, \beta_{1,k}), \ldots, (D_Q, \beta_{Q,k})\} \\ &(q \in \{1, \ldots, Q\}, k \in \{1, \ldots, L\}, \sum_{n=1}^{Q} \beta_{n,k} \leq 1), \\ &\text{with } attribute\ weight\ \delta_{k_p}, \text{ and } rule\ weight\ \theta_k, \end{aligned} \tag{25}$$

where the pth characteristic of the MAS y_p^* is the input of the kth rule, A_p^k is the referential value, $\bar{U}$ represents the final result of the fault diagnosis model, $\beta_{q,k}$ represents the belief degree corresponding to the qth fault status under the kth belief rule, and Q is the number of consequents used in the kth rule. If $\sum_{q=1}^{Q} \beta_{q,k} = 1$, the kth rule is considered to be complete; otherwise, it is incomplete.

The analysis-based ER algorithm is used to infer BRB in the fault diagnosis model. Due to space limitations, the implementation process of the model is briefly described below:

Step 1: Obtain the matching degree.

For y_p^*, its matching degree α_p^k to the attribute referential value can be calculated as follows:

$$a_p^k = \begin{cases} \frac{A_p^{l+1} - y_p^*}{A_p^{l+1} - A_p^l}, & k = l \text{ if } A_p^l \leq y_p^* \leq A_p^{l+1} \\ \frac{y_p^* - A_p^k}{A_p^{l+1} - A_p^l}, & k = l+1 \\ 0, & k = 1, \ldots, |y_p|\,(k \neq l, l+1) \end{cases} \tag{26}$$

Step 2: Calculate the activation weight of the kth rule.

According to the a_p^k and θ_k obtained previously, the activation weight w_k of the kth rule is computed as follows:

$$w_k = \frac{\theta_k \prod_{p=1}^{M_k} \left(a_p^j\right)^{\bar{\delta}_p}}{\sum_{l=1}^{L} \theta_l \prod_{p=1}^{M_k} \left(a_p^k\right)^{\bar{\delta}_p}}, \sum_{k=1}^{L} w_k = 1 \tag{27}$$

where $\bar{\delta}_p$ is the relative weight of attribute p.

Step 3: Combine the activated belief rules.

Assume that k rules are activated. Use the ER algorithm to combine rules to generate belief degree for different output results. Then the belief degree of the qth consequent β_q is obtained through calculation.

Step 4: Generate final output.

The final output result is generated based on the belief degree of different output results. The specific process can be described as:

$$\hat{U}(t) = \sum_{q=1}^{Q} D_q \beta_q. \tag{28}$$

4.2 Optimization model for the developed fault diagnosis model

Since the MAS suffers from unpredictable communication interferences, the uncertainty of the expert knowledge is inevitable, and will affect the choice of the initial parameters. Hence, inspired by [12], the projection covariance matrix adaptation evolution strategy (P-CMA-ES) is used to optimize the fault diagnosis model.

The optimization model of the BRB-based fault diagnosis model can be described as follows:

$$\begin{aligned} &\min MSE\left(\theta_k, \beta_{q,k}, \delta_p\right) \\ &s.t. \\ &0 \leq \theta_k \leq 1, \\ &0 \leq \beta_{q,k} \leq 1, \\ &\sum_{q=1}^{Q} \beta_{q,k} = 1 \end{aligned} \tag{29}$$

where $MSE\left(\theta_k, \beta_{q,k}, \delta_p\right)$ represents the mean square error (MSE) between the actual output and the expected output, described as

$$\text{MSE}\left(\theta_k, \beta_{q,k}, \delta_p\right) = \frac{1}{T} \sum_{t=1}^{T} \left(U_{expected} - U_{actual}\right)^2 \tag{30}$$

where $U_{expected}$ represents the expected output, U_{actual} represents the actual output of the system, and T represents the number of observation samples.

5 Case study

A. Fault diagnosis method design

Consider a leader-following MAS and the communication topology of the system is represented in Fig. 2.

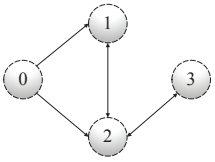

Fig. 2: Communication topology.

Then, the related matrices can be obtained as follows:

$$\boldsymbol{A} = \begin{bmatrix} 0 & 1 & 0 \\ 1 & 0 & 1 \\ 0 & 1 & 0 \end{bmatrix}, \boldsymbol{L} = \begin{bmatrix} 1 & -1 & 0 \\ -1 & 2 & -1 \\ 0 & -1 & 1 \end{bmatrix}. \tag{31}$$

The dynamics of the ith follower with fault is given in (22), where the external disturbance $d_i(t) = 0.5\sin(0.5it)$, and the fault is described as $\sigma(t) = [1.2, 0.5, 1.5]^{\mathrm{T}}$.

The dynamics of the leader is given in (3), where $u_0 = [\cos(t), \sin(2t)]^{\mathrm{T}}$.

The initial states of the model are as follows: $x_0(0) = [-1, 2]^{\mathrm{T}}$, $x_1(0) = [6, 5]^{\mathrm{T}}$, $x_2(0) = [2, -4]^{\mathrm{T}}$, and $x_3(0) = [-4, 8]^{\mathrm{T}}$; $v_0(0) = [2, -6]^{\mathrm{T}}$, $v_1(0) = [-2, 0]^{\mathrm{T}}$, $v_2(0) = [4, 2]^{\mathrm{T}}$, and $v_3 = [6, -5]^{\mathrm{T}}$, and parameters in Section 3 are choosen as $c_0 = 0.6$, $c = 4$, $h_1 = h_2 = 0.01$.

Fig. 3(a) shows the trajectories errors of the position in x-axis of followers under normal conditions. Fig. 3(b)-(d) present the trajectories of position when three followers malfunctioned in turn. It can be seen that there exists a deviation between the faulty follower and other normal followers. Choose the position trajectories errors at $t \in [10, 12]$s as the initial data, and the characteristics of the model can be defined as

$$\begin{aligned} y_1^* &= |(x_{11} - x_{01}) - (x_{21} - x_{01})|, \\ y_2^* &= |(x_{11} - x_{01}) - (x_{31} - x_{01})|, \\ y_3^* &= |(x_{21} - x_{01}) - (x_{31} - x_{01})|. \end{aligned} \tag{32}$$

The semantic values for y_1^* are L_1, M_{11}, M_{12} and H_1, for y_2^* are L_2, M_2 and H_2, and for y_3^* are L_3, M_3 and H_3.

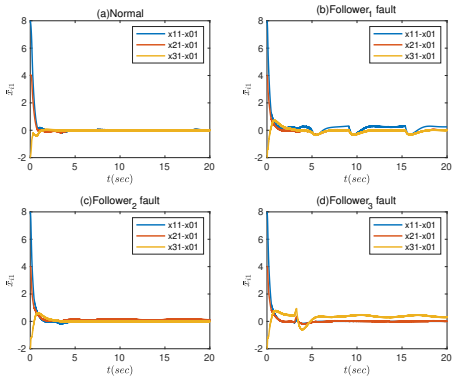

Fig. 3: States of agent under fault.

According to the position of the faults, the status of MAS are: normal (N), follower 1 fault (F_1), follower 2 fault (F_2) and follower 3 fault (F_3). The reference points and values are shown in Table 1 and Table 2.

Table 1: The referential points and values of y_1^*, y_2^* and y_3^*.

y_1^*	Referential points	L_1	M_{11}	M_{21}	H_1
	Referential values	-0.001	0.9	0.9	1.001
y_2^*	Referential points	L_2	M_2	H_2	
	Referential values	-0.001	0.2	1.001	
y_3^*	Referential points	L_1	M_3	H_3	
	Referential values	-0.001	0.45	1.001	

Table 2: Status of the MAS.

Status	Referential points	N	F_1	F_2	F_3
	Referential values	0	1	2	3

The kth belief rule of the model is given as

$$R_k: \text{If } y_1^* \text{ is } A_1^k \wedge y_2^* \text{ is } A_2^k \wedge y_3^* \text{ is } A_3^k, \text{ then } \bar{U} \text{ is } \{(N,\beta_{1,k}),(F_1,\beta_{2,k}),(F_2,\beta_{3,k}) (F_3,\beta_{4,k})\} \left(\sum_{q=1}^{Q}\beta_{q,k}\le 1\right), k\in\{1,\dots,27\}. \quad (33)$$

B. Simulation results

The simulation results on the position and velocity tracking trajectories are shown in Fig. 4. The tracking errors of position and velocity are shown in Fig. 5. The consensus errors of the position and the velocity are shown in Fig. 6.

Next, according to the inference process in Section 4.1, combine the activated rules with ER algorithm, and then optimize each parameter. In the P-CMA-ES part, the iteration number is set to 100.

From Fig. 7, it is clearly shown that the testing results are almost consistent with the real status.

C. Comparative studies

To demonstrate the effectiveness of the proposed fault diagnosis method, comparisons with BP neural network and random forest are conducted. By taking the average of 10 times training and testing, Table 3 shows the accuracy of each method under normal samples and small samples.

It is concluded that whether under normal samples or under small samples, the model proposed in this paper is higher

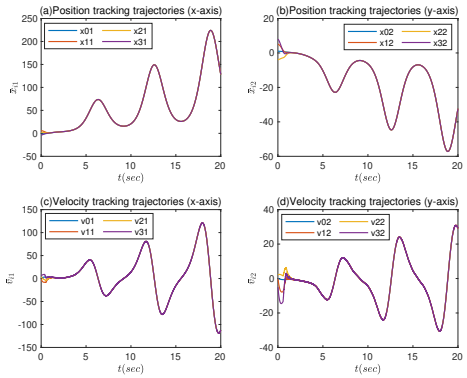

Fig. 4: Tracking trajectories.

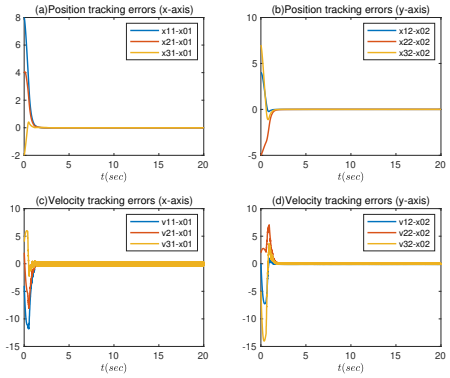

Fig. 5: Tracking errors.

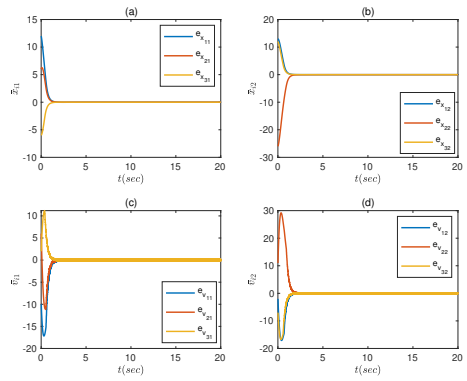

Fig. 6: Consensus error of followers.

Table 3: Accuracy comparison between BRB and other methods.

Method	Noamal samples	Small samples
BRB	98.5%	96.67%
BP Neural Network	80.025%	54.325%
Random Forest	80.725%	36.9%

than the other two methods, especially under small samples.

6 Conclusion

In this paper, a consistency controller based on sliding mode control strategy is designed, which could deal with the nonlinear term and communication interferences. When

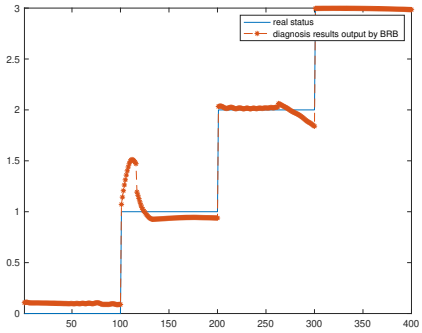

Fig. 7: The diagnostic output of the BRB-based model are compared with real values.

the followers in the MAS are faulty, a new fault diagnosis method based on BRB is proposed for leader-following MASs. Future research can be directed towards the fault diagnosis problem of more complex MASs.

References

[1] S. Yang, "Hierarchical graph multi-agent reinforcement learning for traffic signal control", *Information Sciences*, vol. 634, pp. 55-72, Jul. 2023.

[2] A. Wang, L. Liu, J. Qiu, and G. Feng, "Leader-Following Consensus of Multiple Uncertain Euler-Lagrange Systems via Fully Distributed Event-Triggered Adaptive Fuzzy Control," *IEEE Transactions on Cybernetics*, vol. 54, no.1, pp. 76-86, Jun. 2022.

[3] W. Ji, J. Qiu, C. Song, and Y. Fu, "New results on non-synchronous observer-based output feedback control of fuzzy-affine-model based discrete-time nonlinear systems," *IEEE Transactions on Fuzzy Systems*, vol. 31, no.8, pp. 2836-2847, Jan. 2023.

[4] Y. Zhang and J. Jiang, "Bibliographical review on reconfigurable fault-tolerant control systems", *Annual Reviews in Control*, vol. 32, no. 2, pp. 229-252, 2008.

[5] I. Shames, A. Teixeira, H. Sandberg, and K. Johansson, "Distributed fault detection for interconnected second-order systems", *Automatica*, vol. 47, no. 12, pp. 2757-2764, 2011.

[6] J, Zhao and Y. Lin, "Adaptive actuator failure compensation control: A new scheme based on fault detection and isolation", *IEEE/ASME Transactions on Mechatronics*, vol. 28, no. 4, pp. 2236-2247, Jan. 2023.

[7] H. Chen, L. Li, C. Shang, and B. Huang, "Fault detection for nonlinear dynamic systems with consideration of modeling errors: A data-driven approach", *IEEE Transactions on Cybernetics*, vol. 53, no. 7, pp. 4259-4269, Apr. 2022.

[8] X. Liu, X. Gao, and J. Han, "Distributed fault estimation for a class of nonlinear multiagent systems", *IEEE Transactions on systems, Man, and Cybernetics: Systems*, vol. 50, no. 9, pp. 3382-3390, Nov. 2018.

[9] L. Ke, Y. Zhang, B. Yang, Z. Luo, and Z. Liu, "Fault diagnosis with synchrosqueezing transform and optimized deep convolutional neural network: An application in modular multilevel converters," *Neurocomputing*, vol. 430, no.21, pp. 24-33, Mar. 2021.

[10] K, Guo, X. Wan, L. Liu, Z. Gao, and M. Yang, "Fault diagnosis of intelligent production line based on digital twin and improved random forest". *Applied Sciences*, vol. 11, no. 16, pp. 7733, Aug. 2021.

[11] J. Yang, J. Liu, J. Wang, H. Sii, and H. Wang, "Belief rule-base inference methodology using the evidential reasoning approach-RIMER," *IEEE Transactions on Systems, Man, and Cybernetics-part A: Systems and Humans*, vol, 36, no. 2, pp. 266-285, Mar. 2006.

[12] W. He, G. Hu, Z. Zhou, P. Qiao, and X. Han, "A new hierarchical belief-rule-based method for reliability evaluation of wireless sensor network," *Microelectronics Reliability*, vol, 87, pp. 33-51, May 2018.

[13] Y. Chen, Z. Zhou, L. Yang, G. Hu, X. Han, and S. Tang, "A novel structural safety assessment method of large liquid tank based on the belief rule base and finite element method," *Proceedings of the Institution of Mechanical Engineers, Part O: Journal of Risk and Reliability*, vol. 236, no. 3, pp. 458-476, Jun. 2022.

[14] D. Xu, F. Zhu, Z. Zhou,and X. Yan, "Distributed fault detection and estimation in cyber–physical systems subject to actuator faults," *ISA Transactions*, vol. 104, pp. 162-174, Sep. 2020.

[15] M. Chen and S. Ge, "Adaptive neural output feedback control of uncertain nonlinear systems with unknown hysteresis using disturbance observer," *IEEE Transactions on Industrial Electronics*, vol. 62, no. 12, pp. 7706-7716, Jul. 2015.

[16] B. Farkas and S. Wegner, "Variations on Barbălat's lemma," *The American Mathematical Monthly*, vol. 123, no. 8, pp. 825-830, Dec. 2016.

[17] Y. Hong, Y. Xu, and J. Huang, "Finite-time control for robot manipulators," *Systems & Control Letters*, vol. 46, no. 4, pp. 243-253, 2002.

[18] Z. Hou, L. Cheng, and M. Tan, "Decentralized robust adaptive control for the multiagent system consensus problem using neural networks," *IEEE Transactions on Systems, Man, and Cybernetics, Part B (Cybernetics)*, vol. 39, no. 3, pp. 636-647, 2009.

[19] W. Ji, J. Qiu, S. Su, and H. Zhang, "Fuzzy observer-based output feedback control of continuous-time nonlinear two-dimensional systems," *IEEE Transactions on Fuzzy Systems*, vol. 31, no. 4, pp. 1391-1400, Apr. 2023.

[20] W. Ji, J. Qiu, and H. -K. Lam, "Fuzzy-affine-model-based sliding-mode control for discrete-time nonlinear 2-D systems via output feedback," *IEEE Transactions on Cybernetics*, vol. 53, no. 2, pp. 979-987, Feb. 2023.

Proceedings of the 3rd Conference on Fully Actuated System Theory and Applications
May 10-12, 2024, Shenzhen, China

Finite-Time Controller Design for Continuous-Time T–S Fuzzy Systems With Partly Measurable Premise Variables

Shanfeng Zhang[1], Kai Zhang[2,3], Yue Wu[1], Siyuan Chen[1], Yang Wang[4]

1. School of Electrical Engineering, Southwest Jiaotong University, Chengdu 611756, P. R. China
E-mail: 2019112113@my.swjtu.edu.cn, wy2020@swjtu.edu.cn, chensiyuan@my.swjtu.edu.cn

2. School of Aeronautics and Astronautics, Sichuan University, Chendu 610065, P. R. China

3. Robotic Satellite Key Laboratory of Sichuan Province, Sichuan University, Chendu 610065, P. R. China
E-mail: zhangkaihit@gmail.com

4. Navigation College, Dalian Maritime University, Dalian 116026, P. R. China
E-mail: wangyangyouth@163.com

Abstract: The research presented in this paper delves into the finite-time control problem of Takagi-Sugeno (T-S) fuzzy systems with partly measurable premise variables. Firstly, through the application of the H_∞ analysis technique and the local stabilization analysis method, the synthesis conditions for the observer have been derived. The state estimation error can be limited to a pre-specified area, allowing the estimation error to be controlled more effectively and this aspect is pivotal for the design of the subsequent finite-time controller. Then, a finite-time controller is constructed by using measurable premise variables, which improves the transient performance of the system compared with the traditional parallel distribution compensation (PDC) controller. In the end, the efficacy of the proposed strategy is substantiated through a simulation example.

Key Words: Finite-time, Partly measurable premise variables, T-S fuzzy systems, Local nonlinear model.

1 Introduction

The T-S fuzzy model approach is an effective technique for dealing with nonlinear systems, whose core idea is to use some local linear sub-models to approximate the original nonlinear model. In recent years, T-S fuzzy systems have derived many meaningful researches, including stability analysis [1], observer design [2] and controller design.

In the above researches, the stability analysis and controller design of T-S fuzzy systems mostly focus on Lyapunov asymptotic stability, which is defined within an infinite time scale. However, within certain real world engineering contexts, there is a greater need for the control within a finite time scale. As a result, finite-time stability is proposed, necessitating the system's state to converge to zero or an infinitesimal vicinity within a predetermined finite duration. At present, there are some studies on the finite-time control problems of T-S fuzzy systems [3].

Simultaneously, during the stability analysis of T-S fuzzy systems, the local stabilization problem has also received a lot of attentions. The core idea of the local stabilization is to limit the system state within a certain region, which coincides with the idea of the T-S fuzzy model method, so the study of the local stabilization problem of T-S fuzzy systems is of considerable significance. However, most of these papers use local stabilization method to limit the state of the system to improve the stability of the system, while this paper improves the performance of the observer by limiting the observation error.

Another problem studied in this paper is the partly measurable premise variables. In practical applications, due to the unobservability of some system states, the premise variables composed of these states are likewise unmeasurable. At present, there are some methods for dealing with the problem of the partly measurable premise variables. One way [4] to do this is to use an observer to estimate the unmeasurable state of the system, then construct an approximation of the unmeasurable premise variables, and finally convert the estimation error of the premise variable to the state estimation error by applying Lipschitz conditions. Inspired by this approach, the finite-time control problem of T-S fuzzy systems with partly measurable premise variables is studied in this paper.

The principal contributions of this study can be summarized as follows:

1) Based on the H_∞ analysis method and the local stabilization analysis method, the synthesis conditions of the observer are derived. This observer is able to control the estimation error more effectively, which is beneficial for subsequent controller design.
2) The finite-time control problem of T-S fuzzy systems with partly measurable premise variables is investigated and the transient response speed of the system has been improved.

The remainder of this paper is structured as follows: Section 2 provides the system description and preliminary knowledge. Section 3 details the derivation of synthesis conditions of the observer. Section 4 outlines the construction of a controller utilizing the measurable premise variables to achieve finite-time control. Section 5 presents an example to demonstrate the method's effectiveness. Section 6 concludes the paper.

Notation: Diag $[\lambda_1 \ \ldots \ \lambda_s]$ refers to a diagonal matrix, where λ_1,$\cdots$,λ_s are the elements of the principal diagonal. An asterisk "$*$" is exploited to denote a term that is induced by symmetry. The convex hull of the two points is $co\{x, y\} = \{h_1 x + h_2 y : h_1 + h_2 = 1,\ h_i \geqslant 0\}$.

This work was supported in part by the Opening Project of Robotic Satellite Key Laboratory of Sichuan Province, the Joint Fund of Science and Technology Department of Liaoning Province and State Key Laboratory of Robotics under Grant 2022-KF-22-08, and the National Natural Science Foundation of China under 62003069.

2 System Description and Preliminaries

The nonlinear system considered in this paper is represented by the following T-S fuzzy model:

Plant Rule i :

$$\begin{aligned} &\text{IF } \xi_1(t) \text{ is } \mathcal{M}_{i1} \text{ and } \xi_2(t) \text{ is } \mathcal{M}_{i2}, \cdots, \ \xi_p(t) \text{ is } \mathcal{M}_{ip} \\ &\text{THEN } \dot{x}(t) = A_i x(t) + B_i u(t) + D_i \omega(t) + G\varphi(t) \\ &\qquad y(t) = Cx(t) \end{aligned} \tag{1}$$

where $x(t) \in \mathbb{R}^{n_x}$, $u(t) \in \mathbb{R}^{n_u}$ and $y(t) \in \mathbb{R}^{n_y}$ denote the system state vector, the control input vector and the output vector, respectively; $\omega(t) \in \mathbb{R}^{n_\omega}$ and $\varphi(t) \in \mathbb{R}^{n_\varphi}$ denote the external disturbance vector and the local nonlinear term, respectively; $\xi(t) = [\, \xi_1(t),\ \xi_2(t), \cdots, \xi_p(t)\,]$ is the premise variable vector; $\mathcal{M}_{ij} (1 \le i \le r,\ 1 \le j \le p)$ are the fuzzy sets; r is the number of the fuzzy rules and p is the number of the premise variables; The matrices A_i, B_i, C, D_i and G are defined as constant real matrices of appropriate dimensions.

Meanwhile, assume that the premise variables ξ_i ($i = 1, \cdots, p_0$) are measurable and the other premise variables ξ_i ($i = p_0 + 1, \cdots, p$) are unmeasurable. The model (1) is equivalent to the following model by the separation method in [5].

$$\begin{aligned} \dot{x}(t) = &\sum_{i=1}^{r_\eta} \sum_{j=1}^{r_\lambda} \eta_i(\xi_\eta(t)) \lambda_j(\xi_\lambda(t)) [\, A_{ij} x(t) + B_{ij} u(t) \\ &+ D_{ij} \omega(t)\,] + G\varphi(t) \\ y(t) = &\, Cx(t) \end{aligned} \tag{2}$$

where r_η and r_λ are the numbers of the fuzzy rules of the measurable and unmeasurable premise variables; $\eta_i(\xi_\eta(t))$ and $\lambda_j(\xi_\lambda(t))$ are normalized membership functions (NMFs) which depend on the measurable premise variables $\xi_\eta(t)$ and the unmeasurable premise variables $\xi_\lambda(t)$, respectively.

It is noted that $\sum_{i=1}^{r_\eta} \eta_i(\xi_\eta(t)) = 1$, $\sum_{i=1}^{r_\lambda} \lambda_j(\xi_\lambda(t)) = 1$ and $\sum_{i=1}^{r_\eta} \sum_{j=1}^{r_\lambda} \eta_i(\xi_\eta(t)) \lambda_j(\xi_\lambda(t)) = 1$. For simplicity, let $\sum_{i=1}^{r_\eta} \eta_i = \sum_{i=1}^{r_\eta} \eta_i(\xi_\eta(t)) = \sum_{i=1}^{r_\eta} \eta_i(x(t))$ and $\sum_{j=1}^{r_\lambda} \lambda_j = \sum_{j=1}^{r_\lambda} \lambda_j(\xi_\lambda(t)) = \sum_{j=1}^{r_\lambda} \lambda_j(x(t))$.

Assumption 1. [6]: *The nonlinearities $\varphi_i(t) \in R$ ($1 \le i \le s$) are sector-bounded nonlinear functions and satisfy the property $\varphi_i(t) \in co\{0, E_i x(t)\}$ ($1 \le i \le s$).*

Remark 1. [7]: *The condition $\varphi_i(t) \in co\{0, E_i x(t)\}$ in Assumption 1 implies that:*

$$\varphi_i(t)(E_i x(t) - \varphi_i(t)) \geqslant 0 \tag{3}$$

where $E_i = [E_1, E_2, \cdots, E_s]^T$.

An example is provided to elucidate Assumption 1 and condition (3): $x(t) = [\ x_1^T(t) \quad x_2^T(t)\ ]^T$ and $\varphi(t) = sin(x_1(t))$, where $x_1(t) \in [-\frac{\pi}{2}, \frac{\pi}{2}]$. It is clear to see that $\varphi(t)$ satisfies Assumption 1, i.e.,

$$\varphi(t) \in co\{0,\ x_1(t)\} = co\{[\,0 \ \ 0\,]x(t),\ [\,1 \ \ 0\,]x(t)\}\,.$$

At the same time, the inequality (3) is satisfied for the term $\varphi(t)$ and $E = [\,1 \ \ 0\,]$.

3 Design of the Observer

In order to estimate the state in system (2), an observer is constructed as follows:

$$\begin{aligned} \dot{\hat{x}}(t) = &\sum_{i=1}^{r_\eta} \sum_{j=1}^{r_\lambda} \hat{\eta}_i \hat{\lambda}_j [\, A_{ij} \hat{x}(t) + B_{ij} u(t) + G\hat{\varphi}(t) \\ &+ L_{ij}(y(t) - \hat{y}(t))\,] \\ \hat{y}(t) = &\, C\hat{x}(t) \end{aligned} \tag{4}$$

where $\hat{x}(t)$, $\hat{y}(t)$ and $\hat{\varphi}(t)$ are the estimations of the state, the output and the local nonlinear term, respectively; $\hat{\eta}_i = \eta_i(\hat{x}(t))$ and $\hat{\lambda}_j = \lambda_j(\hat{x}(t))$ are the NMFs depend on the estimation of the system state; L_{ij} are the observer gain matrices to be determined later.

Combining (2) and (4) and defining $e(t) = x(t) - \hat{x}(t)$ and $\tilde{\varphi}(t) = \varphi(t) - \hat{\varphi}(t)$, the following estimation error dynamic is got:

$$\begin{aligned} \dot{e}(t) = &\sum_{i=1}^{r_\eta} \sum_{j=1}^{r_\lambda} \hat{\eta}_i \hat{\lambda}_j [\, (A_{ij} - L_{ij}C) e(t) + D_{ij} \omega(t) \\ &+ G\tilde{\varphi}(t) + \Delta(t)\,] \end{aligned} \tag{5}$$

where $\Delta(t) = \sum_{i=1}^{r_\eta} \sum_{j=1}^{r_\lambda} \eta_i \lambda_j [\, A_{ij} x(t) + B_{ij} u(t) + D_{ij} \omega(t) + G\varphi(t)\,] - \sum_{i=1}^{r_\eta} \sum_{j=1}^{r_\lambda} \hat{\eta}_i \hat{\lambda}_j [\, A_{ij} x(t) + B_{ij} u(t) + D_{ij} \omega(t) + G\varphi(t)\,]$.

To get the main results, some useful assumptions and definitions are given.

Assumption 2. [8]:*The term $\Delta(t)$ and the local nonlinear term $\tilde{\varphi}(t)$ satisfy the following Lipschitz conditions:*

$$\|\Delta(t)\| \le \kappa_1 \|x(t) - \hat{x}(t)\| = \kappa_1 \|e(t)\| \tag{6a}$$

$$\|\tilde{\varphi}(t)\| \le \kappa_2 \|x(t) - \hat{x}(t)\| = \kappa_2 \|e(t)\| \tag{6b}$$

Remark 2. *Assumption 2 is often used to solve the problems where the premise variables are partly measurable, and it requires a low rate of change of the dynamic $\|\Delta(t)\|$ and $\|\tilde{\varphi}(t)\|$.*

Assumption 3. *The admissible set of external disturbance $\omega(t)$ is giving as follows:*

$$\mathcal{W} = \left\{ \omega(t) \in \mathbb{R}^{n_\omega} : \int_0^\infty \omega^T(s)\omega(s)ds \le \varpi, \omega^T(t)\omega(t) \le \bar{\omega}^2 \right\}$$

where $\varpi > 0$ and $\bar{\omega} > 0$ are two known scalars and ϖ indicates the upper bound of the integration of $\omega(t)$ in time 0 to ∞; the set $\mathcal{W}$ illustrates that the system is subject to an integral-bounded disturbance and the external disturbance has a definite upper bound.

Definition 1. *The pre-specified region of system (5) is :*

$$\mathcal{Q} = \{ e(t) \in \mathbb{R}^{n_x} : |k_i e(t)| < \psi_i, 1 \le i \le n_x \} \tag{7}$$

where k_i denotes a row vector where the ith element is one and the other elements are zero.

Definition 2. [9]: *The ellipsoid is shown below:*

$$\mathcal{P}(P, \frac{\beta}{\alpha}) = \left\{ e(t) \in \mathbb{R}^{n_x} \mid e^T(t) P e(t) \le \frac{\beta}{\alpha} \right\} \tag{8}$$

where $P > 0$, α and β are two positive scalars.

Lemma 1. [10]: *Based on Definition 1 and Definition 2, for the two sets $\mathcal{P}(P, \frac{\beta}{\alpha})$ and $\mathcal{Q}$, if the following condition holds:*

$$\begin{bmatrix} \frac{\alpha}{\beta}\psi_q^2 & k_q \\ * & P \end{bmatrix} > 0, q = 1, \cdots, n_x \tag{9}$$

then $\mathcal{P}(P, \frac{\beta}{\alpha}) \subseteq \mathcal{Q}$ where k_q, ψ_q and P are defined in (7) and (8).

One purpose of designing the observer is to determine the observer gain matrices L_{ij} ($1 \leq i \leq r_\eta$, $1 \leq j \leq r_\lambda$) in order to limit the state of the error dynamic to the given sets, i.e., $e(t) \in \mathcal{Q}$; Another purpose is to make the error dynamic satisfy the following H_∞ performance index under the zero initial condition:

$$\int_0^\infty e^T(s)e(s)ds < \gamma^2 \int_0^\infty \omega^T(s)\omega(s)ds \tag{10}$$

where γ is a given positive scalar.

To fulfill the above purposes, the design conditions of the observer (4) are presented in Theorem 1.

Theorem 1. *For given positive scalars κ_1, κ_2, α, β, $\bar{\omega}$, ψ_n and γ, if there exist the matrices $P > 0$ and M_{ij} such that the following LMIs hold for $\forall\, 1 \leq i \leq r_\eta, 1 \leq j \leq r_\lambda$:*

$$\Phi_{ii} < 0$$

$$\frac{\Phi_{ij} + \Phi_{ji}}{2} < 0 \tag{11}$$

$$\Psi_{ii} < 0$$

$$\frac{\Psi_{ij} + \Psi_{ji}}{2} < 0 \tag{12}$$

$$\begin{bmatrix} \frac{\alpha}{\beta}\psi_n^2 & k_n \\ * & P \end{bmatrix} > 0,\ 1 \leq n \leq n_x \tag{13}$$

where

$$\Phi_{ij} = \begin{bmatrix} \Theta_{1ij} & PD_{ij} & PG & P \\ * & -\frac{\beta}{\bar{\omega}^2}I & 0 & 0 \\ * & * & -I & 0 \\ * & * & * & -I \end{bmatrix} \Psi_{ij} = \begin{bmatrix} \Theta_{2ij} & PD_{ij} & PG & P \\ * & -\gamma^2 I & 0 & 0 \\ * & * & -I & 0 \\ * & * & * & -I \end{bmatrix}$$

$$\Theta_{1ij} = PA_{ij} - M_{ij}C + A_{ij}^T P - C^T M_{ij}^T + \alpha P + (\kappa_1 + \kappa_2)I$$

$$\Theta_{2ij} = PA_{ij} - M_{ij}C + A_{ij}^T P - C^T M_{ij}^T + I + (\kappa_1 + \kappa_2)I$$

Then the local stabilization of the error dynamic (5) can be realized and the error dynamic satisfies the H_∞ performance index shown in (10). Moreover, the observer gain matrices can be derived by $L_{ij} = P^{-1}M_{ij}$.

Proof. Initially, the Lyapunov function is selected as follows:

$$V_1(t) = e^T(t)Pe(t) \tag{14}$$

The derivative of $V_1(t)$ can be derived as

$$\begin{aligned} \dot{V}_1(t) &= \dot{e}^T(t)Pe(t) + e^T(t)P\dot{e}(t) \\ &= \sum_{i=1}^{r_\eta}\sum_{j=1}^{r_\lambda} \hat{\eta}_i\hat{\lambda}_j[\, e^T(t)P(A_{ij} - L_{ij}C)e(t) \\ &+ e^T(t)(A_{ij} - L_{ij}C)^T Pe(t) + 2e^T(t)PD_{ij}\omega(t) \\ &+ 2e^T(t)PG\tilde{\varphi}(t) + 2e^T(t)P\Delta(t)\,] \end{aligned} \tag{15}$$

If (11) holds, then we have

$$\sum_{i=1}^{r_\eta}\sum_{j=1}^{r_\lambda} \hat{\eta}_i\hat{\lambda}_j \Xi^T \Phi_{ij} \Xi < 0 \tag{16}$$

where $\Xi = [e^T(t)\ \omega^T(t)\ \tilde{\varphi}^T(t)\ \Delta^T(t)]^T$ and Φ_{ij} is defined in Theorem 1.

Based on the inequalities (6a), (6b), (15) and (16), the subsequent inequality can be deduced:

$$\dot{V}_1(t) + \alpha V_1(t) - \frac{\beta}{\bar{\omega}^2}\omega^T(t)\omega(t) < 0 \tag{17}$$

Once the condition (17) is satisfied, the following inequality can be obtained:

$$\frac{d}{dt}(e^{\alpha t}V_1(t)) \leq e^{\alpha t}\frac{\beta}{\bar{\omega}^2}\omega^T(t)\omega(t) \tag{18}$$

According to the method in [9], it can be concluded that if the initial condition of the state guarantees $V_1(0) < (\beta/\alpha)$, then we have the following condition:

$$V_1(t) \leq \frac{\beta}{\alpha} \tag{19}$$

Then, using the method in [11], we can get that the estimation error of the system (5) can be restricted into the given region (7) if the condition (13) holds.

Similar to the proof in (17), the following inequalities can be obtained from (6a), (6b) and (12):

$$\dot{V}_1(t) + e^T(t)e(t) - \gamma^2\omega^T(t)\omega(t) < 0 \tag{20}$$

Under zero initial condition, the error estimation satisfies

$$\int_0^\infty e^T(s)e(s)ds < \gamma^2 \int_0^\infty \omega^T(s)\omega(s)ds \leq \gamma^2\varpi \tag{21}$$

which implies that the H_∞ performance index (10) can be satisfied. The proof is completed. □

Remark 3. *From Theorem 1, we can infer that when $\omega(t) = 0$, our method can guarantee that the system (5) is asymptotically stable and when $\omega(t) \neq 0$, this method uses H_∞ technique to ensure that the influence of $\omega(t)$ on the observer performance is reduced and the estimation error $e(t)$ is bounded on the integration from 0 to ∞. At the same time, Theorem 1 can also realize the local stabilization of the error dynamic (5), and the every component of the estimation error $e(t)$ can be controlled separately. The observer conditions derived by the H_∞ method and the local stabilization method ensure the effective control of the estimation error $e(t)$, which is crucial for the subsequent finite-time controller design.*

4 Design of the Finite-Time Controller

The finite-time controller is synthesized in this section to stabilize the system (2). The structure of the controller can be represented as follows:

$$u(t) = \sum_{l=1}^{r_\eta} \eta_l(\xi_\eta(t))K_l\hat{x}(t) \tag{22}$$

Remark 4. *Inspired by [12], the measurable premise variable is used in the construction of the controller (22), thereby relaxing the stabilization conditions of the T-S fuzzy system (23).*

Substituting the control law (22) into the system (2), the closed-loop system is obtained as follows:

$$\dot{x}(t) = \sum_{i=1}^{r_\eta}\sum_{j=1}^{r_\lambda}\sum_{l=1}^{r_\eta}\eta_i\lambda_j\eta_l[\,(A_{ij}+B_{ij}K_l)x(t)+\bar{D}_{ijl}\bar{\omega}(t) + G\varphi(t)\,] \tag{23}$$

where $\bar{D}_{ijl} = [\,-B_{ij}K_l \;\; D_{ij}\,]$ and $\bar{\omega}(t) = [\,e^T(t) \;\; \omega^T(t)\,]^T$. To get the main results, some useful assumptions and definitions are given.

Assumption 4. *The B_{ij} considered in this paper is a constant matrix, i.e., $B_{ij} = B$, $\forall\, 1 \le i \le r_\eta$, $1 \le j \le r_\lambda$.*

Definition 3. [13]: *For some positive scalars a_1, $\tilde{\omega}$, T_c and symmetric positive matrix R_c, the closed-loop system (23) is finite-time bound subject to (a_1 a_2 $\tilde{\omega}$ T_c R_c), $\forall t \in [0 \;\; T_c]$, if there exists scalar $a_2 > a_1$, such that:*

$$\sup_{-t_0\le s\le 0}\left\{x^T(s)R_cx(s), \dot{x}^T(s)R_c\dot{x}(s)\right\} \le a_1 \Rightarrow x^T(t)R_cx(t) \le a_2$$

The purpose of designing controller is to determine the controller gain matrices K_l, $l \in [1, r_\eta]$, such that the closed-loop system (23) is finite-time bounded.

Then, the gain matrices K_l of the controller (22) will be obtained by Theorem 2.

Theorem 2. *For positive scalars a_1, a_2, $\tilde{\omega}$, δ, ϵ, T_c and positive definite matrix R_c, if there exist matrices $Q > 0$, N_l, $\Lambda > 0$ with $\Lambda = diag[\lambda_1 \; ... \; \lambda_s]_{s\times s}$ and scalar c such that the following LMIs hold for $\forall\, 1 \le i \le r_\eta$, $1 \le j \le r_\lambda$ and $1 \le l \le r_\eta$:*

$$\Omega_{iji} < 0$$

$$\frac{\Omega_{iji}}{r-1} + \frac{\Omega_{ijl}+\Omega_{lji}}{2} < 0,\; i \ne l \tag{24}$$

$$R_c < Q < cR_c \tag{25}$$

$$\epsilon\tilde{\omega} + ca_1 - a_2e^{-\delta T_c} < 0 \tag{26}$$

where $\Upsilon_{ijl} = QA_{ij} + N_l + A_{ij}^TQ + N_l^T - \delta Q$

$$\Omega_{ijl} = \begin{bmatrix} \Upsilon_{ijl} & -N_l & QD_{ij} & QG+E^T\Lambda \\ * & -\epsilon I & 0 & 0 \\ * & * & -\epsilon I & 0 \\ * & * & * & -2\Lambda \end{bmatrix}$$

Then, closed-loop system (23) is finite time bounded and the controller parameters can be obtained by

$$K_l = (B^TB)^{-1}B^TQ^{-1}N_l \tag{27}$$

Proof. Initially, the Lyapunov function is delineated as follows:

$$V_2(t) = x^T(t)Qx(t) \tag{28}$$

The derivative of $V_2(t)$ can be derived as

$$\begin{aligned}\dot{V}_2(t) &= \dot{x}^T(t)Qx(t) + x^T(t)Q\dot{x}(t) \\ &= \sum_{i=1}^{r_\eta}\sum_{j=1}^{r_\lambda}\sum_{l=1}^{r_\eta}\eta_i\lambda_j\eta_l[\,x^T(t)Q(A_{ij}+B_{ij}K_l)x(t) \\ &+ x^T(t)(A_{ij}+B_{ij}K_l)^TQx(t) + 2x^T(t)Q\bar{D}_{ijl}\bar{\omega}(t) \\ &+ 2x^T(t)QG\varphi(t)\,]\end{aligned} \tag{29}$$

Based on Assumption 1, the following inequality can be obtained:

$$\varphi^T(t)\Lambda Ex(t) - \varphi^T(t)\Lambda\varphi(t) > 0 \tag{30}$$

where $\Lambda = diag[\lambda_1 \; ... \; \lambda_s]_{s\times s}$.
Construct the inequality shown below:

$$\dot{V}_2(t) - \delta V_2(t) - \epsilon\bar{\omega}^T(t)\bar{\omega}(t) < 0 \tag{31}$$

where δ and ϵ are given positive scalars.
From (30), it is clear to be seen that the condition (31) is satisfied if the following condition holds:

$$\begin{aligned}&\dot{V}_2(t) - \delta V_2(t) - \epsilon\bar{\omega}^T(t)\bar{\omega}(t) \\ &+ 2\,[\,\varphi^T(t)\Lambda Ex(t) - \varphi^T(t)\Lambda\varphi(t)\,] \;< 0\end{aligned} \tag{32}$$

Then, based on (29), the condition (32) is equivalent to the following inequality:

$$\sum_{i=1}^{r_\eta}\sum_{j=1}^{r_\lambda}\sum_{l=1}^{r_\eta}\eta_i\lambda_j\eta_l\bar{\Xi}^T\bar{\Omega}_{ijl}\bar{\Xi} < 0 \tag{33}$$

where

$$\bar{\Xi} = [\,x^T(t)\;\bar{\omega}^T(t)\;\varphi^T(t)\,]^T,\; \bar{\Omega}_{ijl} = \begin{bmatrix} \Sigma_{ijl} & Q\bar{D}_{ijl} & QG+E^T\Lambda \\ * & -\epsilon I & 0 \\ * & * & -2\Lambda \end{bmatrix}$$

$$\Sigma_{ijl} = QA_{ij} + A_{ij}^TQ + QB_{ij}K_l + (B_{ij}K_l)^TQ - \delta Q$$

Combining $\bar{D}_{ijl} = [-B_{ij}K_l \; D_{ij}]$ in (23), letting $QB_{ij}K_l = N_l$ and using the method in [14], we can get (24). So it is clear to be seen that the condition (31) is satisfied if the condition (24) holds.
Once the condition (31) is satisfied, the inequality is derived as follows:

$$\frac{d}{dt}(e^{-\delta t}V_2(t)) \le \epsilon e^{-\delta t}\bar{\omega}^T(t)\bar{\omega}(t) \tag{34}$$

Then, the following inequality can be derived:

$$V_2(t) \le (V_2(0)+\epsilon\tilde{\omega})e^{\delta t} \le (V_2(0)+\epsilon\tilde{\omega})e^{\delta T_c} \tag{35}$$

where $\tilde{\omega}$ is a scalar and indicates the upper bound of the integration of $\bar{\omega}(t)$ from 0 to t.
Inspired by [15], let $Q = R_c^{\frac{1}{2}}\bar{Q}R_c^{\frac{1}{2}}$, $\lambda_1 = \lambda_{min}(\bar{Q})$, $\lambda_2 = \lambda_{max}(\bar{Q})$, where $\lambda_{min}(\bar{Q})$ and $\lambda_{max}(\bar{Q})$ represent the minimum and maximum eigenvalues of $\bar{Q}$, respectively.
From Definition 3, the following inequality can be obtained:

$$\begin{aligned}V_2(0) = x^T(0)Qx(0) &= x^T(0)R_c^{\frac{1}{2}}\bar{Q}R_c^{\frac{1}{2}}x(0) \\ &\le \lambda_2x^T(0)R_cx(0) \le \lambda_2a_1\end{aligned} \tag{36}$$

Combining (28), (35) and (36), the following inequality can be obtained:

$$\begin{aligned}\lambda_1 x^T(t)R_c x(t) \le V_2(t) &= x^T(t)Qx(t)\\ &= x^T(t)R_c^{\frac{1}{2}}\bar{Q}R_c^{\frac{1}{2}}x(t)\\ &\le (\lambda_2 a_1 + \epsilon\tilde{\omega})e^{\delta T_c}\end{aligned} \tag{37}$$

At the same time, if the condition (25) is satisfied, the following inequality can be obtained:

$$\lambda_1 > 1, \lambda_2 < c \tag{38}$$

And if the condition (26) is satisfied, the following inequality can be obtained:

$$(ca_1 + \epsilon\tilde{\omega})e^{\delta T_c} \le a_2 \tag{39}$$

Combining (38) and (39), we can have

$$(\lambda_2 a_1 + \epsilon\tilde{\omega})e^{\delta T_c} \le \lambda_1 a_2 \tag{40}$$

Combining (37) and (40), the inequality is derived as follows:

$$x^T(t)R_c x(t) \le a_2 \tag{41}$$

From Definition 3, it can be seen that if (41) holds, then the closed-loop system (23) is finite-time bounded. This completes the proof. □

Remark 5. *It should be noted that the condition* $\int_0^t \bar{\omega}^T(s)\bar{\omega}(s)ds \le \tilde{\omega}$ *is used in (35), where* $\bar{\omega}(t) = [e^T(t)\ \omega^T(t)]^T$. *The* H_∞ *performance index (10) guaranteed by Theorem 1 shows that* $e(t)$ *is integrally bounded, and from Assumption 3,* $\omega(t)$ *is also integrally bounded. Therefore, the integral of* $\bar{\omega}(t)$ *from* 0 *to* t *has an upper bound, which is set to* $\tilde{\omega}$*, so the condition* $\int_0^t \bar{\omega}^T(s)\bar{\omega}(s)ds \le \tilde{\omega}$ *holds. It follows that the design of the observer in Theorem 1 is crucial to the design of the controller in Theorem 2.*

5 Simulation

In this section, an example is given to demonstrate the efficiency of the proposed method.

Consider the nonlinear plant as follows:

$$\begin{aligned}\dot{x}_1(t) &= -0.5x_1(t) + x_2(t)\\ \dot{x}_2(t) &= x_1^2(t) - x_1(t) + 0.3x_2^2(t) - x_2(t)\\ &\quad + 0.5sin(x_1(t)) + u(t) + 0.5\omega(t)\\ y &= x_1(t)\end{aligned} \tag{42}$$

where $u(t)$ and $\omega(t)$ are the control input and the external disturbance, respectively. Select $x_1(t)$ and $x_2(t)$ as the premise variables and assume that $x_1(t) \in [-\frac{\pi}{2}, \frac{\pi}{2}]$ and $x_2(t) \in [-1, 1]$.

In this paper, to decrease the number of fuzzy rules of the controller, the term $sin(x_1(t))$ is extracted to $\varphi(t)$. According to [6], $\varphi(t) \in co\{0, x_1(t)\}$ and $E = [1\ \ 0]$ can be obtained. Thus, $\varphi(t)$ satisfies Assumption 1. Then the following T–S fuzzy system can be obtained:

$$\begin{aligned}\dot{x}(t) =& \sum_{i=1}^{2}\sum_{j=1}^{2}\eta_i\lambda_j[A_{ij}x(t) + B_{ij}u(t) + D_{ij}\omega(t) + G\varphi(t)]\\ y(t) =& Cx(t)\end{aligned} \tag{43}$$

where $\eta_1 = \dfrac{\pi - 2x_1(t)}{2\pi}, \eta_2 = \dfrac{\pi + 2x_1(t)}{2\pi}$,

$\lambda_1 = \dfrac{1 - x_2(t)}{2}, \lambda_2 = \dfrac{1 + x_2(t)}{2}$,

$A_{11} = \begin{bmatrix} -0.5 & 1 \\ -\frac{\pi}{2} - 1 & -1.3 \end{bmatrix}, A_{12} = \begin{bmatrix} -0.5 & 1 \\ -\frac{\pi}{2} - 1 & -0.7 \end{bmatrix}$,

$A_{21} = \begin{bmatrix} -0.5 & 1 \\ \frac{\pi}{2} - 1 & -1.3 \end{bmatrix}, A_{22} = \begin{bmatrix} -0.5 & 1 \\ \frac{\pi}{2} - 1 & -0.7 \end{bmatrix}$,

$B_{11} = B_{12} = B_{21} = B_{22} = \begin{bmatrix} 0 \\ 1 \end{bmatrix}, C = \begin{bmatrix} 1 & 0 \end{bmatrix}$,

$D_{11} = D_{12} = D_{21} = D_{22} = \begin{bmatrix} 0 \\ 0.5 \end{bmatrix}, G = \begin{bmatrix} 0 \\ 0.5 \end{bmatrix}$.

It is observed from $C = [\,1\ 0\,]$ that only the premise variable $x_1(t)$ is obtainable. Thus, the membership functions η_1 and η_2 can be obtained, while λ_1 and λ_2 cannot be obtained.

In this paper, the objective area $\mathcal{Q}$ is set to be $\{e(t) : |e_1(t)| < 1.5,\ |e_2(t)| < 1.5\}$, i.e., $\psi_1 = \psi_1 = 1.5$. Besides, choosing $\kappa_1 = \kappa_2 = 0.1$, $\alpha = 1$, $\beta = 1$, $\bar{\omega} = 0.5$ and $\gamma = 5$, the parameters can be deduced by Theorem 1, which is articulated as follows:

$$L_{11} = \begin{bmatrix} 16.1567 \\ 18.1022 \end{bmatrix}, L_{12} = \begin{bmatrix} 18.9261 \\ 22.7836 \end{bmatrix}, L_{21} = \begin{bmatrix} 13.092 \\ 15.4344 \end{bmatrix},$$
$$L_{22} = \begin{bmatrix} 15.8682 \\ 20.1189 \end{bmatrix}, P = \begin{bmatrix} 3.0894 & -0.8605 \\ -0.8605 & 0.7082 \end{bmatrix}.$$

Choosing $a_1 = 1$, $a_2 = 10$, $\tilde{\omega} = 1$, $\delta = 0.5$, $\epsilon = 1$, $T_c = 3$, and $R_c = I_2$, the following parameters can be obtained by Theorem 2:

$$K_1 = \begin{bmatrix} 0.0507 & -0.8303 \end{bmatrix}, K_2 = \begin{bmatrix} -0.0883 & -0.8373 \end{bmatrix}.$$

It can be seen that the initial condition needs to meet $V_1(0) < (\beta/\alpha)$. Assuming that the initial value $x_1(0) = 0$, $x_2(0) = 1$, $\hat{x}_1(0) = 0$ and $\hat{x}_2(0) = 0$, then we can have $e(0) = [\,0\ \ 1\,]^T$. Substituting P and $e(0)$ into (14) yields $0.7082 = V_1(0) = e^T(0)Pe(0) < (\beta/\alpha) = 1$. Consequently, the initial condition ensures $V_1(0) < (\beta/\alpha)$.

Furthermore, it is assumed that the disturbance $\omega(t)$ is in the following form:

$$\omega(t) = \begin{cases} 0.2sin(t), & 9 \le t \le 11 \\ 0, & \text{otherwise.} \end{cases} \tag{44}$$

The simulation outcomes are delineated in Fig.1-Fig.3. Fig.1 shows that the state estimation error (5) and it can be seen from Fig.1 that the observer (4) can estimate the system state well. Fig.2 and Fig.3 show the state responses and the control signals using the finite-time control method and the parallel distributed compensation (PDC) method, where the conditions (25) and (26) are not used, respectively. As can be seen from Fig.2, the system state response based on the finite-time controller in this paper can be stabilized more

quickly, so the finite-time controller in this paper is superior to the traditional PDC controller. Based on the above analysis, it can be concluded that the finite-time control can be achieved by using the proposed method.

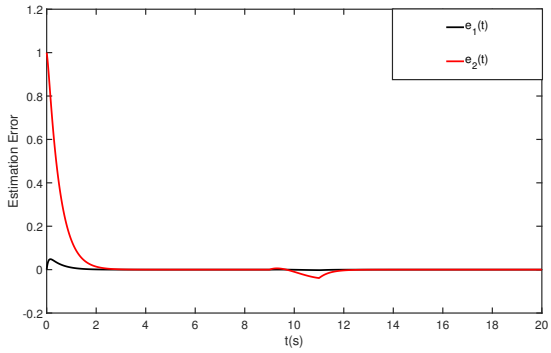

Fig. 1: State estimation error

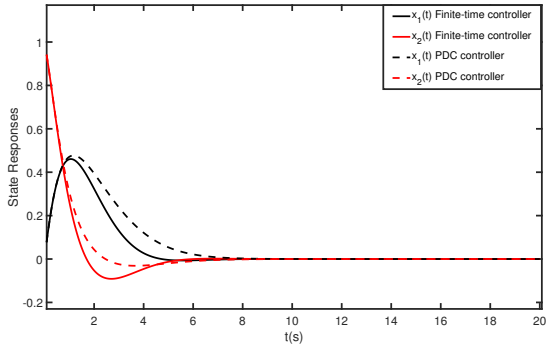

Fig. 2: State response using the finite-time controller and the PDC controller

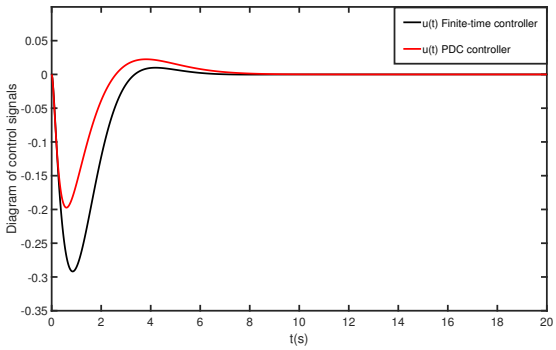

Fig. 3: Diagram of control signals using the finite-time controller and the PDC controller

6 Conclusion

In the present study, the issue of finite-time control for the T-S fuzzy system with partly measurable premise variables has been investigated. Firstly, a T-S fuzzy model with a local nonlinear term is established, in which the premise variables are categorized into measurable premise variables and unmeasurable premise variables. Then, the synthesis conditions of the observer based on the H_∞ analysis method and the local stabilization analysis method are given. This increases the robustness of the observer to the external disturbance. Then, a finite time controller is constructed by using measurable premise variables, and this reduces the time it takes for the system state to stabilize. Finally, the effectiveness of the proposed strategy is proved by a simulation.

References

[1] Said Idrissi, Youssef El Fezazi, Nabil El Fezazi, and El Houssaine Tissir. Improved stability analysis for Takagi-Sugeno (T-S) fuzzy systems with two additive time-varying delays. In *2022 8th International Conference on Optimization and Applications (ICOA)*, pages 1–4, 2022.

[2] Yue Wu and Jiuxiang Dong. Fault detection for T-S fuzzy systems with partly unmeasurable premise variables. *Fuzzy Sets and Systems*, 338:136–156, 2018.

[3] Yue Li, Meng Wang, and Jie Gu. An approach to finite-time $\mathcal{H}_\infty$ control of T-S fuzzy systems via piecewise lyapunov functions. In *2023 6th International Conference on Intelligent Autonomous Systems (ICoIAS)*, pages 291–296, 2023.

[4] Hoda Moodi and Mohammad Farrokhi. On observer-based controller design for sugeno systems with unmeasurable premise variables. *ISA Transactions*, 53(2):305–316, 2014.

[5] Thierry Marie Guerra, Raymundo Márquez, Alexandre Kruszewski, and Miguel Bernal. $H\infty$ LMI-Based observer design for nonlinear systems via Takagi–Sugeno models with unmeasured premise variables. *IEEE Transactions on Fuzzy Systems*, 26(3):1498–1509, 2018.

[6] Jiuxiang Dong, Youyi Wang, and Guang-Hong Yang. Control synthesis of continuous-time T-S fuzzy systems with local nonlinear models. *IEEE Transactions on Systems, Man, and Cybernetics, Part B (Cybernetics)*, 39(5):1245–1258, 2009.

[7] Yang Wang, Tieshan Li, Yue Wu, Ximing Yang, and Jun Ning. L_∞ fault estimation and fault-tolerant control for nonlinear systems by T–S fuzzy model method with local nonlinear models. *International Journal of Fuzzy Systems*, (1), 2021.

[8] Lingyan Yang, Zhigang Li, Yue Wu, and Yuming Zhao. Tracking control design for takagi-sugeno fuzzy systems based on membership function-dependent $L\infty$ performance. *IEEE Access*, 11:124304–124318, 2023.

[9] Yue Wu and Jiuxiang Dong. Local stabilization of continuous-time T–S fuzzy systems with partly measurable premise variables and time-varying delay. *IEEE Transactions on Systems, Man, and Cybernetics: Systems*, 51(1):326–338, 2021.

[10] Tingshu Hu and Zongli Lin. *Control systems with actuator saturation: analysis and design*. Birkhauser, 2001.

[11] Yue Wu and Jiuxiang Dong. Tracking control for non-gaussian stochastic distribution sampled-data fuzzy systems. *Fuzzy Sets and Systems*, 356:1–27, 2019.

[12] Jiuxiang Dong and Yu Fu. A design method for T–S fuzzy systems with partly immeasurable premise variables subject to actuator saturation. *Neurocomputing*, 225:164–173, 2017.

[13] Francesco Amato, Marco Ariola, and Carlo Cosentino. Finite-time stability of linear time-varying systems: Analysis and controller design. *IEEE Transactions on Automatic Control*, 55(4):1003–1008, 2010.

[14] Ji-Chang Lo and Min-Long Lin. Observer-based robust $H\infty$ control for fuzzy systems using two-step procedure. *IEEE Transactions on Fuzzy Systems*, 12(3):350–359, 2004.

[15] Yuechao Ma and Menghua Chen. Finite time non-fragile dissipative control for uncertain TS fuzzy system with time-varying delay. *Neurocomputing*, 177:509–514, 2016.

Proceedings of the 3rd Conference on Fully Actuated System Theory and Applications
May 10-12, 2024, Shenzhen, China

Response Estimation and Reference Model-free Controller Design Approach for 2-DOF Control Systems

Ruirui Yang[1], Kazuhiro Yubai[1], Satoshi Komada[1], Daisuke Yashiro[1], and Weijie Ren[2]

1. Department of Electrical and Electronic Engineering, Mie University, Kurimamachiya, Tsu 514–8507, Japan
E-mail: 421de52@m.mie-u.ac.jp,yubai@elec.mie-u.ac.jp, komada@elec.mie-u.ac.jp, yashiro@elec.mie-u.ac.jp

2. Shenzhen Key Laboratory of Control Theory and Intelligent Systems, Southern Uni. of Sci. and Tech., Shenzhen 518055, China
E-mail: weijie.ren@outlook.com

Abstract: In this paper, we adopt a linear time-invariant (LTI) two-degree-of-freedom (2-DOF) control system as our subject of control. An input-output response estimation method and a controller design method based on response estimation are proposed. First, using the initial input-output data of a closed-loop system to estimate the response when updating controller parameters. Second, the controller parameters are updated by optimizing the objective function based on the estimated response data. Finally, numerical examples verify the effectiveness of the proposed method. Unlike traditional data-driven design methods based on reference models, the proposed controller design method does not require a reference model, which solves the problem of the difficulty of selecting a suitable reference model. Additionally, the response after the controller update can be estimated in advance before being applied to the real machine system. Avoiding the wear and tear or damage of the machine caused by the direct real machine test when the designed controller is not ideal, meanwhile saving the experimental cost.

Key Words: 2-DOF control system, Response estimation, Data-driven, Controller design

1 Introduction

For the control method based on the plant model, as long as the modeling is accurate enough, the required control performance can be achieved by setting the controller according to the needs. However, the system is typically time-varying, nonlinear, and uncertain, making it difficult to obtain an accurate plant model. In addition, with the development of modern industry, companies are becoming larger and larger, production, equipment, and processes are becoming more and more complex, and the generation of vast amounts of data is increasing. Sometimes, the plant model cannot be obtained. From this, the data-driven control method is proposed.

Data-driven control, also known as model-free control, is a control method that does not rely on the plant model of the controlled object itself but uses only measured input and output data sets to design the controller. Optimal control parameters can be obtained without repeated experiments and trial-and-error, and development costs are greatly reduced. Data-driven control theories and methods have been widely used. Typical one-degree-of-freedom (1-DOF) data-driven control methods include Iterative Feedback Tuning (IFT) [1], Virtual Reference Feedback Tuning (VRFT) [2], Noniterative Correlation-based Tuning (NCbT) [3] and Fictitious Reference Iterative Tuning (FRIT) [4]. The 2-DOF control system can improve reference tracking and disturbance rejection performance at the same time. FRIT [5] [6] and VRFT [7] have been extended to 2-DOF control systems. However, for these data-driven methods, optimal objective functions are based on a given reference model. The reference model is used to describe the desired control performance after controller tuning. Choosing a suitable reference model is difficult when the information about the plant is unknown. Therefore, a proposed method does not require a reference model and instead considers the time-domain performance index as an optimization target. Reference model-free tuning is currently implemented for 1-DOF control systems [8]. This reference model-free controller tuning method has not been extended to 2-DOF control systems.

Data-driven control design differs from model-based design in that the response of the closed-loop system cannot be evaluated in advance. The designed controllers can only be verified by applying them to a real machine system. This is a trial-and-error tuning process, and repeated experiments are expensive. In addition, for closed-loop systems, data-driven methods do not always obtain the controller parameters that can stabilize the system. When the reference model or controller structure is unreasonably selected, unsuitable controller parameters may be tuned. The machine may be damaged using unsuitable controller parameters. Therefore, a response estimation method is proposed. The reference [8] offers a response estimate method for the 1-DOF control system that only uses the initial closed-loop input-output data. The estimated response data is then used to adjust the feedback controller parameters, and the controller was updated reference model-free. However, this reference model-free controller design approach based on response estimation has yet to be implemented for the 2-DOF control system. Estimated Response Iterative Tuning (ERIT)[9] is a controller parameters tuning method based on response estimation for 2-DOF control systems, which has been widely used [10][11]. However, the ERIT method only estimates the feedforward controller output response and updates the feedforward controller parameters. It does not estimate the feedback controller output response and updates the feedback controller parameters, which cannot improve the disturbance rejection performance.

Based on the above, the contributions of this paper can be summarized as follows:

1) Propose a response estimate method for the 2-DOF control system that only uses the initial closed-loop input-

This work was supported by JSPS KAKENHI Grant Number JP22K04028.

output data. The response of the controller update can be estimated in advance before being applied to the real machine system.

2) A new reference model-free controller parameter tuning method is designed based on the response estimation approach, which solves the problem of the difficulty of selecting a suitable reference model.

The rest of this paper is organized as follows. Section 2 introduces the data-based response estimation method for the 2-DOF control system. Section 3 presents a reference model-free controller design approach based on the response estimation method. The numerical simulation in Section 4 verifies the effectiveness of the proposed method. Section 5 concludes the paper.

2 Data-Based Response Estimation Method

This section describes the 2-DOF control system response estimation methods. Consider a discrete-time LTI system with two controllers in Fig.1. Here, $G(z)$ is the discrete-time controlled object, which is unknown, $r(k)$ is the reference signal, $d(k)$ is the disturbance signal, $u(k)$ is the plant input signal and $y(k)$ is the plant output signal, $C_{fb}(z,\theta)$ is the feedback controller, $C_{ff}(z,\rho)$ is the feedforward controller, where $\theta = [\theta_0\ \theta_1\ \ldots\ \theta_{n-1}]^T$ and $\rho = [\rho_0\ \rho_1\ \cdots\ \rho_{n-1}]^T$ are two parameter vectors of both n-dimensional.

It is assumed that the initial feedback controller $C_{fb0}(z,\theta^0)$ and initial feedforward controller $C_{ff0}(z,\rho^0)$ can stabilize the system in Fig.1. The initial input-output data $\{u_0(k), y_0(k)\}_{k=0,1,\ldots,N-1}$ is obtained by the reference signal sequence $r = [r(0)\ r(1)\ \ldots\ r(N-1)]^T \in \mathbb{R}^N$ and the initial controller parameters $\theta^0 = \begin{bmatrix}\theta_0\ \theta_1\ \cdots\ \theta_{n-1}\end{bmatrix}^T$ and $\rho^0 = \begin{bmatrix}\rho_0\ \rho_1\ \cdots\ \rho_{n-1}\end{bmatrix}^T$ via once closed-loop experiment. Here, the initial input data sequence is $u_0 = [u_0(0)\ u_0(1)\ \ldots\ u_0(N-1)]^T \in \mathbb{R}^N$ and the initial output data sequence is $y_0 = [y_0(0)\ y_0(1)\ \ldots\ y_0(N-1)]^T \in \mathbb{R}^N$.

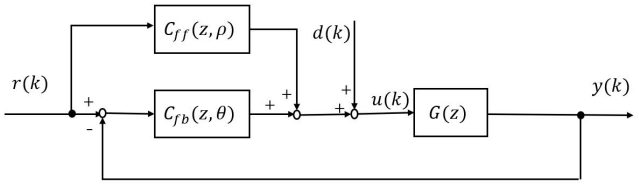

Fig. 1: 2-DOF control system.

2.1 Open-Loop System Response Estimation Method

A brief review of the response estimation method for open-loop systems is given before introducing the proposed closed-loop response estimation method for ease of understanding.

The open-loop system input-output response, which is estimated using initial input-output data$\{u_0(k), y_0(k)\}_{k=0,1,\ldots,N-1}$. The input-output relationship between $u(k)$ and $y(k)$ is given as

$$y(k) = G(z)u(k). \tag{1}$$

According to the references [8][12], for the arbitrary input signal $u^*(k)$, we can estimate the output response as

$$y(k) = YU^{-1}u^*(k),$$

where $u^* = [u^*(0)u^*(1)...u^*(N-1)]^T$ is an arbitrary input sequence,

$$Y = \begin{bmatrix} y_0(0) & 0 & \cdots & 0 \\ y_0(1) & y_0(0) & \cdots & 0 \\ \vdots & \vdots & \ddots & \vdots \\ y_0(N-1) & y_0(N-2) & \cdots & y_0(0) \end{bmatrix} \in \mathbb{R}^{N\times N},$$

$$U = \begin{bmatrix} u_0(0) & 0 & \cdots & 0 \\ u_0(1) & u_0(0) & \cdots & 0 \\ \vdots & \vdots & \ddots & \vdots \\ u_0(N-1) & u_0(N-2) & \cdots & u_0(0) \end{bmatrix} \in \mathbb{R}^{N\times N}.$$

2.2 Closed-Loop System Response Estimation Method

The closed-loop input-output response is estimated using the first step obtained initial input-output data $\{u_0(k), y_0(k)\}_{k=0,1,\ldots,N-1}$. In Fig.1, the transfer function of the closed-loop system from reference signal $r(k)$ to output signal $y(k)$ is given as

$$T_{yr}(z) = \frac{Y(z)}{R(z)} = \frac{(C_{ff}+C_{fb})G(z)}{1+C_{fb}G(z)}, \tag{2}$$

Thus, based on equations (1) and (2), the output signal $y(k)$ related to $r(k)$ is given as

$$y(k) = \frac{(C_{ff}+C_{fb})G(z)}{1+C_{fb}G(z)}r(k).$$

The input signal $u(k)$ is given as

$$u(k) = C_{ff}r(k) + C_{fb}(r(k)-y(k)).$$

The closed-loop transfer function of the disturbance input of a 2-DOF control system is only related to the feedback controller. The transfer function of the closed-loop system from disturbance signal $d(k)$ to output $y(k)$ is given as

$$T_{yd}(z) = \frac{Y(z)}{D(z)} = \frac{G(z)}{1+C_{fb}G(z)}.$$

Thus, the output signal $y(k)$ related to $d(k)$ is given as

$$y(k) = \frac{G(z)}{1+C_{fb}G(z)}d(k).$$

Introduce a fictitious disturbance signal [8][13] as in Fig.2 to make the proposed estimation method suitable for non-minimum phase controller structures.

The fictitious disturbance signal for an arbitrary controller $C_{fb}(z,\theta)$ is defined as

$$\bar{d}(k,\theta) = C_{fb}(z,\theta)y_0 + u_0. \tag{3}$$

The input-output data of the plant is fixed to $\{u_0(k), y_0(k)\}_{k=0,1,\ldots,N-1}$ for an arbitrary stable controller. As similar for open-loop system and references [8][12], the output sequence for the arbitrary reference signal $r^*(k)$ can be estimated as

$$y_{mr}(k) = (C_{ff}(z,\rho^*) + C_{fb}(z,\theta^*))Y\overline{D}^{-1}r^*(k), \tag{4}$$

The input sequence for the arbitrary reference signal $r^*(k)$ can be estimated as

$$u_{mr}(k) = (C_{ff}(z,\rho^*) + C_{fb}(z,\theta^*))U\overline{D}^{-1}r^*(k), \quad (5)$$

The output sequence for the arbitrary disturbance signal $d^{\sup}(k)$ can be estimated as

$$y_{md}(k) = Y\overline{D}^{-1}d^{\sup}(k), \quad (6)$$

The input sequence for the arbitrary disturbance signal $d^{\sup}(k)$ can be estimated as

$$u_{md}(k) = U\overline{D}^{-1}d^{\sup}(k), \quad (7)$$

where $d^{\sup}(k)$ is the disturbance signal to be suppressed (usually, the disturbance is unknown but bounded). The user can arbitrarily assign disturbance signal $d^{\sup}(k) = [d^{\sup}(0)\ d^{\sup}(1)\ \ldots\ d^{\sup}(N-1)]^T$, $C_{ff}(z,\rho^*)$ is the updated feedforward controller, $C_{fb}(z,\theta^*)$ is the updated feedback controller, the arbitrary reference signal $r^*(k)=[\ r^*(0)\ \ r^*(1)\ldots r^*(N-1)]^T$,

$$Y = \begin{bmatrix} y_0(0) & 0 & \cdots & 0 \\ y_0(1) & y_0(0) & \cdots & 0 \\ \vdots & \vdots & \ddots & \vdots \\ y_0(N-1) & y_0(N-2) & \cdots & y_0(0) \end{bmatrix} \in \mathbb{R}^{N\times N},$$

$$U = \begin{bmatrix} u_0(0) & 0 & \cdots & 0 \\ u_0(1) & u_0(0) & \cdots & 0 \\ \vdots & \vdots & \ddots & \vdots \\ u_0(N-1) & u_0(N-2) & \cdots & u_0(0) \end{bmatrix} \in \mathbb{R}^{N\times N},$$

$$\bar{D} = \begin{bmatrix} \bar{d}(0) & 0 & \cdots & 0 \\ \bar{d}(1) & \bar{d}(0) & \cdots & 0 \\ \vdots & \vdots & \ddots & \vdots \\ \bar{d}(N-1) & \bar{d}(N-2) & \cdots & \bar{d}(0) \end{bmatrix} \in \mathbb{R}^{N\times N}.$$

The following 3-step algorithm organizes the above response estimation approach.

Step 1: obtain a set of initial input and output data $\{u_0(k), y_0(k)\}_{k=0,1,\ldots,N-1}$ via a closed-loop system experiment

Step 2: calculate the fictitious disturbance signal $\bar{d}(k)$ by equation (3)

Step 3: estimate the closed-loop system output response for arbitrary reference signal, disturbance input signal, and arbitrary controllers by equations (4)-(7).

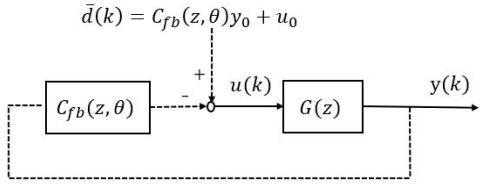

Fig. 2: Fictitious disturbance signal feedback system.

3 Controller Design Based on the Response Estimation Method

Generally, data-driven controller design methods are based on model matching. Selecting an appropriate reference model is difficult when the plant model is unknown, and the control system is complex. Unlike the controller parameter tuning method based on model matching, we consider the constraint of the time-domain performance index (rising time, setting time, etc.) as optimization objectives in designing the controller instead of using reference model matching.

In the proposed method, controller parameters θ^* and ρ^* are determined by solving the following optimization problem:

$$(\theta^*, \rho^*) = \arg\min_{(\theta,\rho)} J(\theta,\rho),$$

$$J(\theta,\rho) = \alpha_1 t_{r1} + \delta_1 t_{s1} + \alpha_2 t_{r2} + \delta_2 t_{s2},$$

$$s.t. \quad \begin{cases} u_L(k) < u_{mr}(k) < u_U(k) \\ y_L(k) < y_{mr}(k) < y_U(k), \end{cases}$$

where $\alpha_1, \delta_1, \alpha_2$, and δ_2 are weighting factors. The performance index in the time domain is interrelated and mutually restrictive. Thus, the weighted average method is used to assign weight. The time domain performance index rising time t_{r1} and setting time t_{s1} are calculated by the estimated response data $y_{mr}(k)$. The rising time t_{r2} and setting time t_{s2} are calculated by the estimated response data $y_{md}(k)$. $u_L(k)$ and $u_U(k)$ are the lower and the upper bounds for the input, respectively. $y_L(k)$ and $y_U(k)$ are the lower and the upper bounds for the output, respectively. The optimal controller parameters are obtained by optimizing the above objective function through a nonlinear solver.

4 Simulation Example

A simulation example is presented to verify the proposed method. Consider the non-minimum phase discrete-time linear transfer function $G(z)$ is given as

$$G(s) = \frac{1}{0.5s^2 + 5s + 1},\ G(z) = Z(G(s)).$$

The discrete-time feedback controller structure is given as

$$C_{fb}(z,\theta) = \alpha^T(z)\theta = \begin{bmatrix} 1 & \frac{1}{1-z^{-1}} & \frac{z^{-1}}{1-z^{-1}} \end{bmatrix} \begin{bmatrix} \theta_0 \\ \theta_1 \\ \theta_2 \end{bmatrix}.$$

The discrete-time feedforward controller structure is given as

$$C_{ff}(z,\rho) = \beta^T(z)\rho = \begin{bmatrix} 1 & \frac{z-1}{z} \end{bmatrix} \begin{bmatrix} \rho_0 \\ \rho_1 \end{bmatrix}.$$

The initial controller parameters are given as

$$\theta^0 = \begin{bmatrix} 0.43 & 0.12 & 0.07 \end{bmatrix}^T, \rho^0 = \begin{bmatrix} 0.03 & 0.01 \end{bmatrix}^T.$$

In the simulation, sampling time $T = 0.5s$. The number of data length $N = 200$. Reference signal $r(k) = 1$. $d^{sup}(k) = 1$ in the feedback control parameter tuning to suppress a constant value disturbance. To verify the proposed

response estimate and the effect of disturbance rejection, we set $d(k) = 1.0$ as a disturbance input signal when $t \geq 10s$.

According to the initial output data response in Fig.3, we aim to achieve more minor overshoot, shorter setting time, and rising time. The objective function is given as

$$J = t_{s1} + t_{s2},$$

Constraints for the upper and the lower bounds are given for parameter tuning as

$$u_L = -2.5 \qquad (0s \leq t \leq 100s),$$
$$u_U = 2.5 \qquad (0s \leq t \leq 100s),$$
$$y_U = \begin{cases} 1.0 & (0s \leq t < 6.5s) \\ 1.01 & (6.5s \leq t < 100s), \end{cases}$$
$$y_L = \begin{cases} 0 & (0s \leq t < 1.5s) \\ 0.5 & (1.5s \leq t < 3.5s) \\ 0.96 & (3.5s \leq t < 6.5s) \\ 0.99 & (6.5s \leq t \leq 100s). \end{cases}$$

Update the controller parameters subject to satisfying the above multi-objective constraints.

Table 1 shows that the updated feedforward controller parameters are $\rho^* = [-8.9 \; -8.76]^T$, and the updated feedback controller parameters are $\theta^* = [6.6 \; 4.92 \; -1.27]^T$. In the time domain, the output response setting time is shorter than before tuning, stabilizing the system faster. MSE1 is the mean-square error between the true output and the estimated output for reference tracking. MSE2 is the mean-square error between the true output and the estimated output for disturbance rejection. The values of MSE1 and MSE2 are both minimal, which means the actual output values are consistent with the response estimate values, which proves the effectiveness of the proposed response estimation method.

Table 1: Results of the proposed method

symbol		Initial	Tuned
Feedforward controller parameters	ρ_0	0.03	-8.9
	ρ_1	0.01	-8.76
Feedback controller parameters	θ_0	0.43	6.6
	θ_1	0.12	4.92
	θ_2	0.07	-1.27
Setting time	$t_{s1}(s)$	27	3.48
Setting time	$t_{s2}(s)$	42.05	14.17
Mean-square error	MSE1	-	3×10^{-27}
Mean-square error	MSE2	-	5.1×10^{-30}

Fig. 3 shows that the overshoot, the rising time, and the setting time become shorter after tuning, making the system stabilize faster. The reference tracking performance and the disturbance rejection performance are simultaneously improved. In Fig. 3 and Fig. 4, the input-output of the proposed tuned method based on response estimation (blue solid line) is consistent with the true input-output of the plant (red dotted line). The effectiveness of the proposed response estimation method and controller design method is verified.

Fig. 5 shows that the error value between the estimated output and the actual output is extremely small, which can be ignored. We can prove that the response estimated output

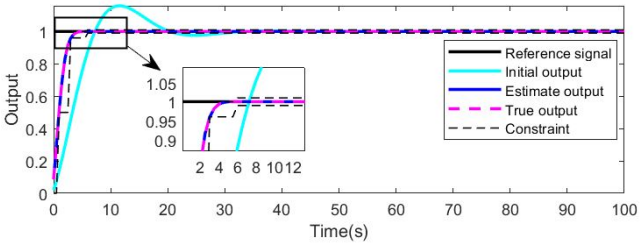

(a) Set-point response

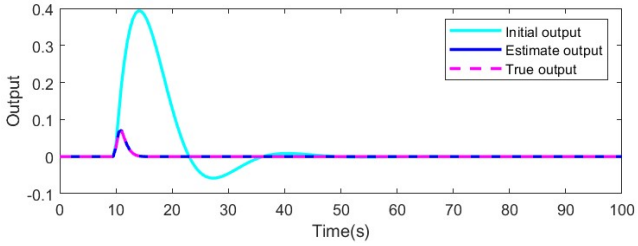

(b) Disturbance response

Fig. 3: Result of output responses.

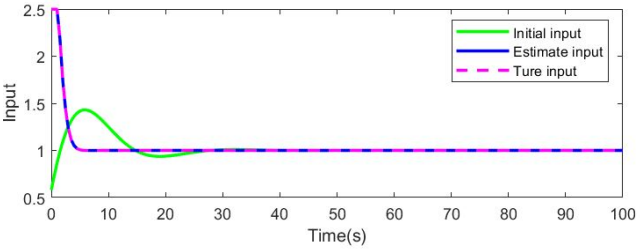

(a) Set-point response

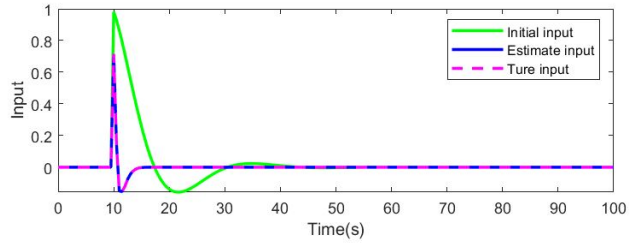

(b) Disturbance response

Fig. 4: Result of input responses.

value is consistent with the true output value. In addition, Fig. 6 intuitively shows the effectiveness of the proposed response estimation method through the curves of the true output minus the initial output and the response estimate output minus the initial output value.

5 Conclusion

This paper proposed a reference model-free data-driven controller design and response estimated approach. First, the response estimation method is proposed, which requires only a set of initial input-output data to estimate the output response during the controller update process. Second, a new controller design method is proposed, taking the time-domain performance index as the optimization objective without needing a reference model. Numerical examples verify the effectiveness of the proposed method. The effect of noise on the system should be considered in future work.

Currently, the method only applies to SISO linear systems and can be extended to T-S fuzzy[14] and MIMO systems in the future.

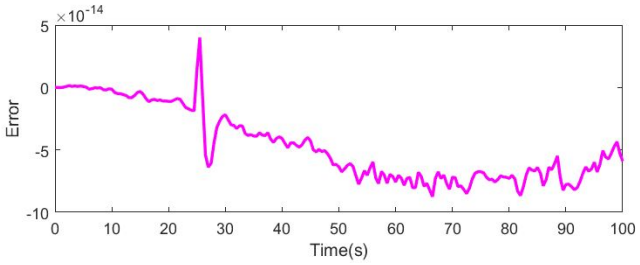

(a)

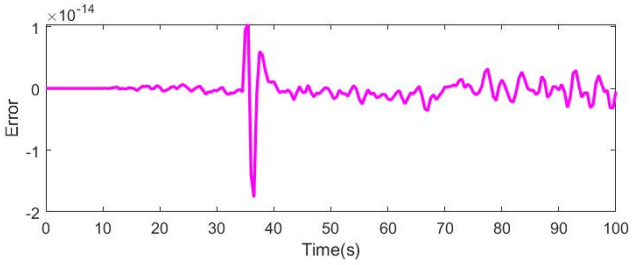

(b)

Fig. 5: (a) Error between the estimated output and the true output of set-point response. (b) The error between the estimated output and the true output of disturbance response.

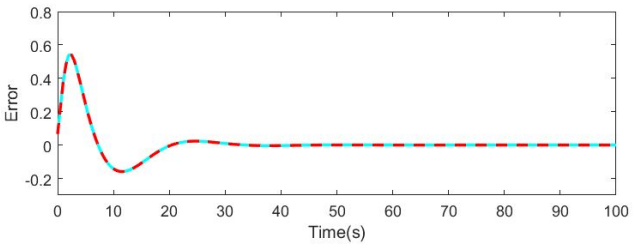

(a)

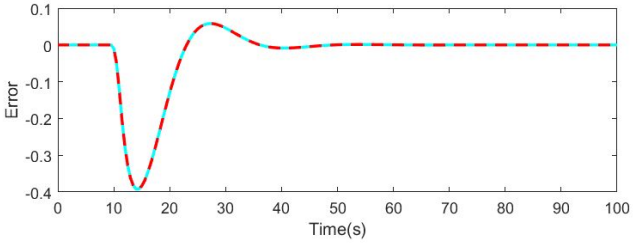

(b)

Fig. 6: (a) True output minus initial output (the solid line) and estimated output minus initial output (the dotted line) of set-point response. (b) True output minus initial output (the solid line) and estimated output minus initial output (the dotted line) of disturbance response.

References

[1] H. Hjalmarsson, M. Gevers, S. Gunnarsson and O. Lequin, Iterative feedback tuning: theory and applications. *IEEE Control Systems Magazine*, 1998, 18(4): 26–41.

[2] M. C. Campi, A. Lecchini and S. M. Savaresi, Virtual reference feedback tuning: a direct method for the design of feedback controllers. *Automatica*, 2002, 38(8):1337–1346.

[3] A. Karimi, K. van Heusden and D. Bonvin, Non-iterative data-driven controller tuning using the correlation approach, in *2007 European control conference (ECC)*, 2007. p. 5189–5195.

[4] S. Soma, O. Kaneko, and T. Fujii, A new method of controller parameter tuning based on input-output data–Fictitious Reference Iterative Tuning (FRIT)–. *IFAC Proceedings Volumes*, 2004, 37(12): 789–794.

[5] T. Sakata, O. Kaneko, and T. Fujii, Parameter tuning of two-degree of freedom controllers using FRIT for the tracking property and the feedback properties. *Transactions of the Institute of Systems, Control and Information Engineers*, 2007, 20(11):419–429.

[6] O. Kaneko, Y. Yamashina, and S. Yamamoto, Fictitious reference tuning of the feed-forward controller in a two-degree-of-freedom control system. *SICE journal of control, measurement, and system integration*, 2011, 4(1): 55–62.

[7] A. Lecchini, M. C. Campi, and S. M. Savaresi, Virtual reference feedback tuning for two degree of freedom controllers. *International Journal of Adaptive Control and Signal Processing*, 2002, 16(5): 355–371.

[8] T. Sakatoku, K. Yubai, D. Yashiro, and S. Komada, Data-Driven Controller Tuning with Closed-Loop Response Estimation. *IEEJ Transactions on Electrical and Electronic Engineering*, 2021, 16(10): 1397–1406.

[9] O. Kaneko, T. Nakamura, and T. Ikezaki, A New Approach to update of feedforward controller in the two-degree-of-freedom control system—A Proposal of estimated response iterative tuning (ERIT)—. *Transactions of the Society of Instrument and Control Engineers*, 2018, 54(12): 857–864.

[10] Y. Fujimoto, Estimated response iterative tuning with signal projection. *IFAC Journal of Systems and Control*, 2022, 19: 100179.

[11] O. Kaneko, and T. Nakamura, Data-driven prediction of 2DOF control systems with updated feedforward controller, in *2017 56th Annual Conference of the Society of Instrument and Control Engineers of Japan (SICE)*, 2017. p. 259–262.

[12] T. Sakatoku, K. Yubai, D. Yashiro, and S. Komada, Estimation of Closed-Loop Response Using Input and Output Data. *IEEJ Transactions on Electronics, Information and Systems*, 2021, 141(3), 396–397.

[13] T. Hori, K. Yubai, D. Yashiro, and S. Komada, Data-driven H_∞ controller tuning for sensitivity minimization. *International Journal of Advanced Mechatronic Systems*, 2017, 7(6), 337–349.

[14] W. Ren, S. Komada, K. Yubai, and S. Guo, Zonotopic interval estimation for discrete-time Takagi-Sugeno fuzzy systems with a delayed nonquadratic framework. *Journal of the Franklin Institute*, 2022, 359(8), 3883–3909.

Proceedings of the 3rd Conference on Fully Actuated System Theory and Applications
May 10-12, 2024, Shenzhen, China

Optimized State Estimation for Complex Networks with Sensor Fault and Probability-Based Quantization

Hongchun Chu, Chaoqing Jia, Cai Chen*, Kun Chi and Tao Lei
Harbin University of Science and Technology, Harbin 150080, P. R. China
E-mail: chencailee@hrbust.edu.cn

Abstract: This paper investigates the optimized state estimation (OSE) problem for uncertain coupled delay complex networks (UCDCNs) subject to sensor fault and probability-based quantization. A random variable with known statistical characteristics and a uniformed distributed random parameter are adopted respectively to describe the model uncertainty and sensor fault. Taking the bandwidth-limited channel into account, a probability-based quantization strategy is employed to process transmitted data. A coupled-delay-dependent predictor-estimator is constructed to guarantee that the covariance upper bounds of prediction error (PE) and estimation error (EE) can be obtained by resolving recursive matrix equations and the predictor-estimator gain (PEG) can be determined via optimizing the trace of the covariance upper bound of EE (CUBEE). Finally, an efficient example is presented to demonstrate the validity of the developed OSE algorithm.

Key Words: Optimized State Estimation, Coupled Delay Complex Networks, Sensor Fault, Probability-Based Quantization

1 Introduction

The past few decades have seen the widespread development of complex networks, which are composed of mutually coupled smart units with individual characteristics. Up to now, such networks have been applied in many fields, such as brain networks, social networks, traffic networks and so on. It should be pointed out that the state estimation plays a significant role in the dynamical analyses for complex networks, as mentioned [1–4]. Especially, the Kalman-type optimized state estimation (OSE) methods have appealed many attention, which are usually executed by online recursion in the sense of minimum mean-square error. For example, an OSE approach to a class of quantized coupled complex networks subject to incomplete measurements and amplify-and-forward relay has been introduced in [5]. Nevertheless, a relay-parameter-dependent covariance upper bound of estimation error (CUBEE) has been presented and the predictor-estimator-gain (PEG) has been designed to minimize such upper bound. Based on the topologies of complex networks and uncertain external environment, the communication delay and model uncertainty may be occurred generally. Hence, the OSE method for a class of uncertain coupled delay complex networks (UCDCNs) has been addressed to satisfy the actual requirement.

Due to the configuration with low-capacity sensor, the data may be incomplete or invalid during measurements, which means that sensor fault occurs. In the framework state estimation algorithm, Bernoulli distributed random variables are frequently employed to characterize the phenomenon of sensor fault, see e.g. [6, 7]. If the sensor fault occurs (namely Bernoulli distributed random variable is equal to zero), the measurement data are usually missing. However, actually, the sensor fault may lead to the partial missing of measurement data. The outlier-resistant OSE problem has been tackled in [8] for a class of time-varying complex networks with time-correlated fading scenario, where a certain saturation technique has been employed in predictor-estimator to relieve the influence of outliers caused by attacks or mutated environment. In this paper, a uniformly distributed random variable is utilized to describe the data degeneration caused by sensor fault.

Taking the deployment of wireless networks with limited resources into account, quantization technique is a universal way to reduce the size of data packet. Currently, according to quantization principle, the quantization can be primarily divided into logarithmic quantization [9] and uniform quantization [10]. Generally speaking, an OSE problem has been resolved for a class of time-delayed stochastic system in the simultaneous presence of protocol schedule and data quantization, where Taylor expansion has been adopted in [11] to handle model nonlinearity. In addition, the quantization may be executed within a stochastic range [12], i.e., probability-based quantization. Consequently, this paper aims revealing the influence from probability-based quantization on the OSE algorithm for a class of UCDCNs.

Summarizing the aforementioned introductions, this paper is devoted to developing an OSE method for UCDCNs suffering from sensor fault and probability-based quantization. The main difficulties encountered here can be organized into (1) how to develop an easy-to-implement OSE method for UCDCNs dealing with sensor fault and probability-based quantization simultaneously; (2) how to derive a CUBEE involving coupled delay and quantization parameter; and (3) how to determine PEG in a proper way with the help of minimizing the trace of CUBEE. The corresponding contributions can be listed as: (1) an attractive OSE method is proposed for UCDCNs, which can handle the sensor fault and probability-based quantization; (2) a CUBEE is obtained by resolving matrix equations recursively; and (3) a selected PEG is parameterized via minimizing the trace of CUBEE.

Notations: The notations used here are considerably standard. Specifically, $\|\cdot\|$ is the Euclidean norm. The notation P^{T} signifies the transpose of matrix P and P^{-1} stands for the inverse operation of P. The symbol $H > 0$ or $H \geq 0$

Correspondence should be addressed to Cai Chen. Email: chencailee@hrbust.edu.cn.
This work was supported in part by the Postdoctoral Science Foundation of Heilongjiang Province of China under Grant LBH-Z22199 and the Fundamental Research Foundation for Universities of Heilongjiang Province under Grant 2022-KYYWF-0141.

means that H is symmetric and positive or semi-positive definite. I and 0 stands for the well-dimensioned unit matrix and zero matrix respectively.

2 Problem Formulation

Consider the following UCDCNs with S units

$$x_{\kappa,\theta+1} = (A_{\kappa,\theta} + z_{\kappa,\theta}\vec{A}_{\kappa,\theta})x_{\kappa,\theta} + \omega_{\kappa\kappa,\theta}\Pi x_{\kappa,\theta} + \sum_{\rho=1}^{s}\omega_{\kappa\rho,\theta}\Pi x_{\rho,\theta-\tau} + B_{\kappa,\theta}\xi_{\kappa,\theta}, \quad (1)$$

$$y_{\kappa,\theta} = \phi_{\kappa,\theta}C_{\kappa,\theta}x_{\kappa,\theta} + \sigma_{\kappa,\theta}, \ \ \rho \neq \kappa \quad (2)$$

where $x_{\kappa,\theta} \in \mathbb{R}^{n_{x_\kappa}}$ stands for the model state, $y_{\kappa,\theta} \in \mathbb{R}^{n_y}$ describes the sensor measurement. Π and $\mathscr{O}_{\kappa,\theta} = [\omega_{\kappa\gamma,\theta}]_{S\times S}$ characterize the outer coupling and inner coupling parameters respectively. τ denotes coupled delay, $A_{\kappa,\theta}$, $\vec{A}_{\kappa,\theta}$, $B_{\kappa,\theta}$ and $C_{\kappa,\theta}$ are well-dimensioned known matrices. $z_{\kappa,\theta}$ is a random variable following $\mathbb{E}\{z_{\kappa,\theta}\} = 0$ and $\mathbb{E}\{z_{\kappa,\theta}^2\} = 1$, $\xi_{\kappa,\theta}$ is a model noise with mean 0 and variance $\Delta_{\kappa,\theta} > 0$, and $\sigma_{\kappa,\theta}$ is adopted to describe the noise from sensor measurement with mean 0 and variance $\Sigma_{\kappa,\theta} > 0$. $\phi_{\kappa,\theta}$ is a random variable obeying uniform distribution within interval $[0,\ 1]$ to characterize sensor fault.

Actually, the data collected by sensors are usually managed by a quantizer. Let $y_{\kappa,\theta} = [y_{\kappa,\theta}^{(1)},\ y_{\kappa,\theta}^{(2)}, \ldots, y_{\kappa,\theta}^{(n_y)}]^T$, whose quantization function can be described by

$$Q(y_{\kappa,\theta}) = [Q_1(y_{\kappa,\theta}^{(1)}), Q_2(y_{\kappa,\theta}^{(2)}), \ldots, Q_{n_y}(y_{\kappa,\theta}^{(n_y)})]^T.$$

For each element in $Q(y_{\kappa,\theta})$, the quantization level is expressed by

$$\mathscr{Q}_\kappa^{(l)} = \left\{\hbar_{\kappa,r}^{(l)} | \hbar_{\kappa,r}^{(l)} \triangleq r\epsilon_\kappa^{(l)},\ \epsilon_\kappa^{(l)} > 0,\ r = 0, \pm1, \pm2, \ldots\right\}.$$

If $\hbar_{\kappa,r}^{(l)} \leq y_{\kappa,\theta}^{(l)} \leq \hbar_{\kappa,r+1}^{(l)}$ $(l = 1, 2, \ldots, n_y)$ hold, then the probability-based quantization can be described by

$$\text{Prob}\left\{Q_l(y_{\kappa,\theta}^{(l)}) = \hbar_{\kappa,r}^{(l)} | \wp_\kappa^{(l)}\right\} = 1 - \wp_\kappa^{(l)},$$
$$\text{Prob}\left\{Q_l(y_{\kappa,\theta}^{(l)}) = \hbar_{\kappa,r+1}^{(l)} | \wp_\kappa^{(l)}\right\} = \wp_\kappa^{(l)},$$

where $\wp_\kappa^{(l)} = \frac{y_{\kappa,\theta}^{(l)} - \hbar_{\kappa,r}^{(l)}}{\epsilon_\kappa^{(l)}}$. Define probability-based quantization error $q_{\kappa,\theta}^{(l)} = Q_l(y_{\kappa,\theta}^{(l)}) - y_{\kappa,\theta}^{(l)}$. It is obvious to obtain that

$$\text{Prob}\left\{q_{\kappa,\theta}^{(l)} = -\wp_\kappa^{(l)}\epsilon_\kappa^{(l)} | \wp_\kappa^{(l)}\right\} = 1 - \wp_\kappa^{(l)},$$
$$\text{Prob}\left\{q_{\kappa,\theta}^{(l)} = (1 - \wp_\kappa^{(l)})\epsilon_\kappa^{(l)} | \wp_\kappa^{(l)}\right\} = \wp_\kappa^{(l)}.$$

In terms of [12], we can derive that $\mathbb{E}\left\{q_{\kappa,\theta}^{(l)}\right\} = 0$, $\mathbb{E}\left\{\left(q_{\kappa,\theta}^{(l)}\right)^2\right\} \leq 0.25\left(\epsilon_\kappa^{(l)}\right)^2$ and $\mathbb{E}\left\{q_{\kappa,\theta}^{(l_1)}q_{\kappa,\theta}^{(l_2)}\right\} = 0$ with $l_1 \neq l_2$.

Based on the probability-based quantized output, coupled delay and sensor fault, the following predictor-estimator is constructed recursively

$$\hat{x}_{\kappa,\theta+1|\theta} = (A_{\kappa,\theta} + \omega_{\kappa\kappa,\theta}\Pi)\hat{x}_{\kappa,\theta|\theta} + \sum_{\rho=1}^{s}\omega_{\kappa\rho,\theta}\Pi\hat{x}_{\rho,\theta-\tau|\theta-\tau}, \quad (3)$$

$$\hat{x}_{\kappa,\theta+1|\theta+1} = \hat{x}_{\kappa,\theta+1|\theta} + \psi_{\kappa,\theta+1}[Q(y_{\kappa,\theta+1}) - \bar{\phi}_{\kappa,\theta+1}C_{\kappa,\theta+1}\hat{x}_{\kappa,\theta+1|\theta}], \quad (4)$$

where $\hat{x}_{\kappa,\theta+1|\theta}$ and $\hat{x}_{\kappa,\theta+1|\theta+1}$ characterize the prediction and estimation respectively. $\bar{\phi}_{\kappa,\theta+1}$ stands for the expectation of random parameter $\phi_{\kappa,\theta+1}$ and $\psi_{\kappa,\theta+1}$ denotes the predictor-estimator gain (PEG) to be determined later.

Set $e_{\kappa,\theta+1|\theta} = x_{\kappa,\theta+1} - \hat{x}_{\kappa,\theta+1|\theta}$ and $e_{\kappa,\theta+1|\theta+1} = x_{\kappa,\theta+1} - \hat{x}_{\kappa,\theta+1|\theta+1}$ as the prediction error (PE) and estimation error (EE) respectively. According to the considered UCDCNs and constructed predictor-estimator, the PE and EE can be respectively calculated by

$$e_{\kappa,\theta+1|\theta} = (A_{\kappa,\theta} + \omega_{\kappa\kappa,\theta})\tilde{e}_{\kappa,\theta|\theta} + z_{\kappa,\theta}\vec{A}_{\kappa,\theta}x_{\kappa,\theta} + \sum_{\rho=1}^{s}\omega_{\kappa\rho,\theta}e_{\rho,\theta-\tau|\theta-\tau} + B_{\kappa,\theta}\xi_{\kappa,\theta}, \quad (5)$$

and

$$\begin{aligned} e_{\kappa,\theta+1|\theta+1} &= x_{\kappa,\theta+1} - \hat{x}_{\kappa,\theta+1|\theta} - \psi_{\kappa,\theta+1}[Q(y_{\kappa,\theta+1}) \\ &\quad -\bar{\phi}_{\kappa,\theta+1}C_{\kappa,\theta+1}\hat{x}_{\kappa,\theta+1|\theta}] \\ &= e_{\kappa,\theta+1|\theta} - \psi_{\kappa,\theta+1}[Q(y_{\kappa,\theta+1}) - y_{\kappa,\theta+1} \\ &\quad +y_{\kappa,\theta+1} - \bar{\phi}_{\kappa,\theta+1}C_{\kappa,\theta+1}\hat{x}_{\kappa,\theta+1|\theta}] \\ &= \ e_{\kappa,\theta+1|\theta} - \psi_{\kappa,\theta+1}q_{\kappa,\theta+1} \\ &\quad -\psi_{\kappa,\theta+1}[\phi_{\kappa,\theta+1}C_{\kappa,\theta+1}x_{\kappa,\theta+1} \\ &\quad -\bar{\phi}_{\kappa,\theta+1}C_{\kappa,\theta+1}x_{\kappa,\theta+1} \\ &\quad +\bar{\phi}_{\kappa,\theta+1}C_{\kappa,\theta+1}e_{\kappa,\theta+1|\theta} + \sigma_{\kappa,\theta+1}] \\ &= \Lambda_{\kappa,\theta+1}e_{\kappa,\theta+1|\theta} - \psi_{\kappa,\theta+1}q_{\kappa,\theta+1} \\ &\quad -\tilde{\Phi}_{\kappa,\theta+1}\psi_{\kappa,\theta+1}C_{\kappa,\theta+1}x_{\kappa,\theta+1} \\ &\quad -\psi_{\kappa,\theta+1}\sigma_{\kappa,\theta+1} \\ &= \Lambda_{\kappa,\theta+1}e_{\kappa,\theta+1|\theta} - \psi_{\kappa,\theta+1}\Xi_{\kappa,\theta+1}, \end{aligned} \quad (6)$$

where $\Lambda_{\kappa,\theta+1} = I - \bar{\phi}_{\kappa,\theta+1}\psi_{\kappa,\theta+1}C_{\kappa,\theta+1}$, $\Xi_{\kappa,\theta+1} = q_{\kappa,\theta+1} + \tilde{\phi}_{\kappa,\theta+1}C_{\kappa,\theta+1}x_{\kappa,\theta+1} + \sigma_{\kappa,\theta+1}$, $\tilde{\phi}_{\kappa,\theta+1} = \phi_{\kappa,\theta+1} - \bar{\phi}_{\kappa,\theta+1}$ and $q_{\kappa,\theta+1} = [q_{\kappa,\theta+1}^{(1)}, q_{\kappa,\theta+1}^{(2)}, \ldots, q_{\kappa,\theta+1}^{(n_y)}]^T$.

This paper aims to (a) deriving the covariances of PE and EE with the help of (5) and (6), (b) determining the covariance upper bounds of PE and EE recursively by resolving matrix equations, and (c) designing PEG in the variance-constrained index.

3 Main Results

First of all, the covariances of PE and EE are respectively presented in the following theorem.

Theorem 1 *The covariance recursions regarding PE and EE can be calculated by*

$$\begin{aligned} &\Omega_{\kappa,\theta+1|\theta} \\ &= \mathbb{E}\left\{e_{\kappa,\theta+1|\theta}e_{\kappa,\theta+1|\theta}^T\right\} \\ &= (A_{\kappa,\theta} + \omega_{\kappa\kappa,\theta}\Pi)\Omega_{\kappa,\theta|\theta}(A_{\kappa,\theta} + \omega_{\kappa\kappa,\theta}\Pi)^T \\ &\quad +\mathbb{E}\{z_{\kappa,\theta}^2\vec{A}_{\kappa,\theta}x_{\kappa,\theta}x_{\kappa,\theta}^T\vec{A}_{\kappa,\theta}^T\} + B_{\kappa,\theta}\Delta_{\kappa,\theta}B_{\kappa,\theta}^T \\ &\quad +\mathbb{E}\left\{\left(\sum_{\rho=1}^{s}\omega_{\kappa\rho,\theta}\Pi e_{\rho,\theta-\tau|\theta-\tau}\right)\left(\sum_{\rho=1}^{s}\omega_{\kappa\rho,\theta}\Pi\right.\right. \end{aligned}$$

$$\times e_{\rho,\theta-\tau|\theta-\tau}\Big)^T\Big\}+\mathbb{E}\Big\{(A_{\kappa,\theta}+\omega_{\kappa\kappa,\theta}\Pi)\times\tilde{e}_{\kappa,\theta|\theta}\Big(\sum_{\rho=1}^{s}\omega_{\kappa\rho,\theta}\Pi e_{\rho,\theta-\tau|\theta-\tau}\Big)^T\Big\}+\mathbb{E}\Big\{\Big(\sum_{\rho=1}^{s}\omega_{\kappa\rho,\theta}\Pi e_{\rho,\theta-\tau|\theta-\tau}\Big)\times\tilde{e}_{\kappa,\theta|\theta}^T(A_{\kappa,\theta}+\omega_{\kappa\kappa,\theta}\Pi)^T\Big\} \quad (7)$$

and

$$\begin{aligned}&\Omega_{\kappa,\theta+1|\theta+1}\\&=\mathbb{E}\left\{e_{\kappa,\theta+1|\theta}e_{\kappa,\theta+1|\theta}^T\right\}\\&=\Lambda_{\kappa,\theta+1}\Omega_{\kappa,\theta+1|\theta}\Lambda_{\kappa,\theta+1}^T+\psi_{\kappa,\theta+1}\mathbb{E}\{\Xi_{\kappa,\theta+1}\times\Xi_{\kappa,\theta+1}^T\}\psi_{\kappa,\theta+1}^T.\end{aligned} \quad (8)$$

Proof: The proof of this theorem is omitted here. ■

Remark 1 *Up to now, the covariances of PE and EE are respectively given specifically. However, it is hardly to obtain accurate values of (8) due to the comprehensive considerations of sensor fault, model uncertainty as well as probability-based quantization. On the other hand, the trace of (8) in this paper functions as a optimal index, which results in the design of PEG without possibility. Accordingly, it is essential to obtain an upper bound of (8) for the subsequent analysis and design.*

The following theorem is devoted to giving the expression of CUBEE. In addition, the PEG is determined by minimizing the trace of CUBEE.

Theorem 2 *Consider the UCDCNs in (1)-(2) and the constructed predictor-estimator in (3)-(4). For given scaling parameters $\alpha_1>0$, $\alpha_2>0$, $\alpha_3>0$, $\alpha_4>0$ and $\alpha_5>0$, if the following recursive matrix equations*

$$\begin{aligned}X_{\kappa,\theta+1|\theta}=&(1+\alpha_1)(A_{\kappa,\theta}+\omega_{\kappa\kappa}\Pi)X_{\kappa,\theta|\theta}(A_{\kappa,\theta}\\&+\omega_{\kappa\kappa}\Pi)^T+\vec{A}_{\kappa,\theta}\vec{\Theta}_{\kappa,\theta|\theta}\vec{A}_{\kappa,\theta}^T+(1+\alpha_1^{-1})\\&\times\sum_{m=1}^{s}\omega_{m\kappa,\theta}\sum_{\rho=1}^{s}\omega_{\kappa\rho,\theta}\Pi X_{\rho,\theta-\tau|\theta-\tau}\Pi^T\\&+B_{\kappa,\theta}\Delta_{\kappa,\theta}B_{\kappa,\theta}^T\end{aligned} \quad (9)$$

and

$$\begin{aligned}X_{\kappa,\theta+1|\theta+1}=&\Lambda_{\kappa,\theta+1}X_{\kappa,\theta+1|\theta}\Lambda_{\kappa,\theta+1}^T+\psi_{\kappa,\theta+1}\\&\times\Big[0.25(1+\alpha_3+\alpha_4)\mathscr{E}_{\kappa,\theta+1}\\&+\frac{1+\alpha_3^{-1}}{12}C_{\kappa,\theta+1}\vec{\Theta}_{\kappa,\theta+1|\theta}C_{\kappa,\theta+1}^T\\&+(1+\alpha_4^{-1})\Sigma_{\kappa,\theta+1}\Big]\psi_{\kappa,\theta+1}^T,\end{aligned} \quad (10)$$

where

$$\begin{aligned}\vec{\Theta}_{\kappa,\theta|\theta}&=(1+\alpha_2)X_{\kappa,\theta|\theta}+(1+\alpha_2^{-1})\hat{x}_{\kappa,\theta|\theta}\hat{x}_{\kappa,\theta|\theta}^T,\\\vec{\Theta}_{\kappa,\theta+1|\theta}&=(1+\alpha_5)X_{\kappa,\theta+1|\theta}+(1+\alpha_5^{-1})\hat{x}_{\kappa,\theta|\theta}\hat{x}_{\kappa,\theta|\theta}^T,\end{aligned}$$

$$\mathscr{E}_{\kappa,\theta+1}=\begin{bmatrix}\left(\epsilon_\kappa^{(1)}\right)^2&0&0&0\\0&\left(\epsilon_\kappa^{(2)}\right)^2&0&0\\0&0&\ddots&0\\0&0&0&\left(\epsilon_\kappa^{(n_y)}\right)^2\end{bmatrix},$$

with initial condition $X_{\kappa,0|0}=\Omega_{\kappa,0|0}>0$ have solutions $X_{\kappa,\theta+1|\theta}>0$ and $X_{\kappa,\theta+1|\theta+1}>0$, then $X_{\kappa,\theta+1|\theta+1}$ is an upper bound of $\Omega_{\kappa,\theta+1|\theta+1}$, i.e., $\Omega_{\kappa,\theta+1|\theta+1}\le X_{\kappa,\theta+1|\theta+1}$. In addition, if the PEG is selected as

$$\begin{aligned}\psi_{\kappa,\theta+1}=&\bar{\phi}_{\kappa,\theta+1}X_{\kappa,\theta+1|\theta}C_{\kappa,\theta+1}^T\\&\times\Big\{\bar{\phi}_{\kappa,\theta+1}^2C_{\kappa,\theta+1}X_{\kappa,\theta+1|\theta}C_{\kappa,\theta+1}^T\\&+\frac{1+\alpha_3+\alpha_4}{4}\mathscr{E}_{\kappa,\theta+1}+\frac{1+\alpha_3^{-1}}{12}\\&\times C_{\kappa,\theta+1}\vec{\Theta}_{\kappa,\theta+1|\theta}C_{\kappa,\theta+1}^T\\&+(1+\alpha_4^{-1})\Sigma_{\kappa,\theta+1}\Big\},\end{aligned} \quad (11)$$

then the trace of CUBEE can be minimized.

Proof: To begin with, the covariance upper bound of PE is obtained. By means of fundamental inequality $\mathcal{M}\mathcal{N}^T+\mathcal{N}\mathcal{M}^T\le\alpha\mathcal{M}\mathcal{M}^T+\alpha^{-1}\mathcal{N}\mathcal{N}^T$ with $\alpha>0$ being a scaling parameter, $\mathcal{M}$ and $\mathcal{N}$ being well-dimensioned matrices, one has

$$\begin{aligned}&\mathbb{E}\Big\{(A_{\kappa,\theta}+\omega_{\kappa\kappa,\theta}\Pi)\tilde{e}_{\kappa,\theta|\theta}\Big(\sum_{\rho=1}^{s}\omega_{\kappa\rho,\theta}\Pi\\&\times e_{\rho,\theta-\tau|\theta-\tau}\Big)^T\Big\}+\mathbb{E}\Big\{\Big(\sum_{\rho=1}^{s}\omega_{\kappa\rho,\theta}\Pi e_{\rho,\theta-\tau|\theta-\tau}\Big)\\&\times\tilde{e}_{\kappa,\theta|\theta}^T(A_{\kappa,\theta}+\omega_{\kappa\kappa,\theta}\Pi)^T\Big\}\\\le&\alpha_1(A_{\kappa,\theta}+\omega_{\kappa\kappa,\theta}\Pi)\Omega_{\kappa,\theta|\theta}(A_{\kappa,\theta}+\omega_{\kappa\kappa,\theta}\Pi)^T\\&+\alpha_1^{-1}\mathbb{E}\Big\{\Big(\sum_{\rho=1}^{s}\omega_{\kappa\rho,\theta}\Pi e_{\rho,\theta-\tau|\theta-\tau}\Big)\\&\times\Big(\sum_{\rho=1}^{s}\omega_{\kappa\rho,\theta}\Pi e_{\rho,\theta-\tau|\theta-\tau}\Big)^T\Big\},\end{aligned} \quad (12)$$

where $\alpha_1>0$ is a scaling parameter. Substitute (12) into (7) leading to

$$\begin{aligned}&\Omega_{\kappa,\theta+1|\theta}\\\le&(1+\alpha_1)(A_{\kappa,\theta}+\omega_{\kappa\kappa,\theta}\Pi)\Omega_{\kappa,\theta|\theta}(A_{\kappa,\theta}+\omega_{\kappa\kappa,\theta}\Pi)^T\\&+\mathbb{E}\{z_{\kappa,\theta}^2\vec{A}_{\kappa,\theta}x_{\kappa,\theta}x_{\kappa,\theta}^T\vec{A}_{\kappa,\theta}^T\}+B_{\kappa,\theta}\Delta_{\kappa,\theta}B_{\kappa,\theta}^T\\&+(1+\alpha_1^{-1})\mathbb{E}\Big\{\Big(\sum_{\rho=1}^{s}\omega_{\kappa\rho,\theta}\Pi e_{\rho,\theta-\tau|\theta-\tau}\Big)\\&\times\Big(\sum_{\rho=1}^{s}\omega_{\kappa\rho,\theta}\Pi e_{\rho,\theta-\tau|\theta-\tau}\Big)^T\Big\}.\end{aligned} \quad (13)$$

Notice that

$$\mathbb{E}\left\{x_{\kappa,\theta}x_{\kappa,\theta}^T\right\}=\mathbb{E}\left\{(\hat{x}_{\kappa,\theta|\theta}+e_{\kappa,\theta|\theta})(\hat{x}_{\kappa,\theta|\theta}+e_{\kappa,\theta|\theta})^T\right\}$$

$$\leq (1+\alpha_2)\Omega_{\kappa,\theta|\theta} + (1+\alpha_2^{-1}) \times \hat{x}_{\kappa,\theta|\theta}\hat{x}_{\kappa,\theta|\theta}^T \triangleq \Theta_{\kappa,\theta|\theta} \quad (14)$$

and

$$\mathbb{E}\Big\{\Big(\sum_{\rho=1}^{s}\omega_{\kappa\rho,\theta}\Pi e_{\rho,\theta-\tau|\theta-\tau}\Big)\Big(\sum_{\rho=1}^{s}\omega_{\kappa\rho,\theta}\Pi \times e_{\rho,\theta-\tau|\theta-\tau})^T\Big\} \leq \sum_{m=1}^{s}\omega_{m\kappa,\theta}\sum_{\rho=1}^{s}\omega_{\kappa\rho,\theta}\Pi\Omega_{\rho,\theta-\tau|\theta-\tau}\Pi^T, \quad (15)$$

where $\alpha_2 > 0$ is a scaling parameter. On the basis of (14) and (15), we have

$$\begin{aligned}&\Omega_{\kappa,\theta+1|\theta}\\ &\leq (1+\alpha_1)(A_{\kappa,\theta}+\omega_{\kappa\kappa,\theta}\Pi)\Omega_{\kappa,\theta|\theta}(A_{\kappa,\theta}+\omega_{\kappa\kappa,\theta}\Pi)^T\\ &\quad+\vec{A}_{\kappa,\theta}\Theta_{\kappa,\theta|\theta}\vec{A}_{\kappa,\theta}^T + B_{\kappa,\theta}\Delta_{\kappa,\theta}B_{\kappa,\theta}^T\\ &\quad+(1+\alpha_1^{-1})\sum_{m=1}^{s}\omega_{m\kappa,\theta}\sum_{\rho=1}^{s}\omega_{\kappa\rho,\theta}\Pi\\ &\quad\times\Omega_{\rho,\theta-\tau|\theta-\tau}\Pi^T. \end{aligned} \quad (16)$$

Furthermore, the CUBEE will be given in the following proof. It is easy to have

$$\begin{aligned}&\psi_{\kappa,\theta+1}\mathbb{E}\left\{\Xi_{\kappa,\theta+1}\Xi_{\kappa,\theta+1}^T\right\}\psi_{\kappa,\theta+1}^T\\ &=\psi_{\kappa,\theta+1}\mathbb{E}\big\{q_{\kappa,\theta+1}q_{\kappa,\theta+1}^T+\tilde{\phi}_{\kappa,\theta+1}^2C_{\kappa,\theta+1}x_{\kappa,\theta+1}\\ &\quad\times x_{\kappa,\theta+1}^TC_{\kappa,\theta+1}^T+\Sigma_{\kappa,\theta+1}+\tilde{\phi}_{\kappa,\theta+1}q_{\kappa,\theta+1}x_{\kappa,\theta+1}^T\\ &\quad\times C_{\kappa,\theta+1}^T+\tilde{\phi}_{\kappa,\theta+1}C_{\kappa,\theta+1}x_{\kappa,\theta+1}q_{\kappa,\theta+1}^T\\ &\quad+q_{\kappa,\theta+1}\sigma_{\kappa,\theta+1}^T+\sigma_{\kappa,\theta+1}q_{\kappa,\theta+1}^T\big\}\psi_{\kappa,\theta+1}^T\\ &\leq\psi_{\kappa,\theta+1}\mathbb{E}\Big\{(1+\alpha_3+\alpha_4)q_{\kappa,\theta+1}q_{\kappa,\theta+1}^T\\ &\quad+\frac{1+\alpha_3^{-1}}{12}C_{\kappa,\theta+1}x_{\kappa,\theta+1}x_{\kappa,\theta+1}^TC_{\kappa,\theta+1}^T\\ &\quad+(1+\alpha_4^{-1})\Sigma_{\kappa,\theta+1}\Big\}\psi_{\kappa,\theta+1}^T. \end{aligned} \quad (17)$$

Similar to (14), we know

$$\begin{aligned}&\mathbb{E}\left\{x_{\kappa,\theta+1}x_{\kappa,\theta+1}^T\right\}\\ &=\mathbb{E}\left\{(e_{\kappa,\theta+1|\theta}+\hat{x}_{\kappa,\theta+1|\theta})(e_{\kappa,\theta+1|\theta}+\hat{x}_{\kappa,\theta+1|\theta})^T\right\}\\ &\leq(1+\alpha_5)\Omega_{\kappa,\theta+1|\theta}+(1+\alpha_5^{-1})\hat{x}_{\kappa,\theta+1|\theta}\\ &\quad\times\hat{x}_{\kappa,\theta+1|\theta}^T\\ &\triangleq\Theta_{\kappa,\theta+1|\theta}, \end{aligned} \quad (18)$$

where $\alpha_5 > 0$ is a scaling parameter. Take the quantization error into account leading to

$$\mathbb{E}\left\{q_{\kappa,\theta+1}q_{\kappa,\theta+1}^T\right\} \leq \frac{1}{4}\mathscr{E}_{\kappa,\theta+1}, \quad (19)$$

where $\mathscr{E}_{\kappa,\theta+1}$ is defined in Theorem 2. According to (17)-(19) results in

$$\begin{aligned}\Omega_{\kappa,\theta+1|\theta+1} &\leq \Lambda_{\kappa,\theta+1}\Omega_{\kappa,\theta|\theta}\Lambda_{\kappa,\theta+1}^T+\psi_{\kappa,\theta+1}\\ &\quad\times\Big\{\frac{1+\alpha_3+\alpha_4}{4}\mathscr{E}_{\kappa,\theta+1}+\frac{1+\alpha_3^{-1}}{12}\\ &\quad\times C_{\kappa,\theta+1}\Theta_{\kappa,\theta+1|\theta}C_{\kappa,\theta+1}^T\\ &\quad+(1+\alpha_4^{-1})\Sigma_{\kappa,\theta+1}\Big\}\psi_{\kappa,\theta+1}^T. \end{aligned} \quad (20)$$

Considering (9), (10), (16), (20) as well as mathematical induction, we can conclude that $\Omega_{\kappa,\theta+1|\theta+1} \leqslant X_{\kappa,\theta+1|\theta+1}$.

Finally, the PEG will be designed for the purpose of minimizing the trace of CUBEE. Calculating $\frac{\partial \mathrm{trace}(X_{\kappa,\theta+1|\theta+1})}{\partial\psi_{\kappa,\theta+1}}$, we have

$$\begin{aligned}&\frac{\partial \mathrm{trace}(X_{\kappa,\theta+1|\theta+1})}{\partial\psi_{\kappa,\theta+1}}\\ &=-2\bar{\phi}_{\kappa,\theta+1}\Lambda_{\kappa,\theta+1}X_{\kappa,\theta+1|\theta}C_{\kappa,\theta+1}^T\\ &\quad+2\psi_{\kappa,\theta+1}\Big\{\frac{1+\alpha_3+\alpha_4}{4}\mathscr{E}_{\kappa,\theta+1}\\ &\quad+\frac{1+\alpha_3^{-1}}{12}C_{\kappa,\theta+1}\vec{\Theta}_{\kappa,\theta+1|\theta}C_{\kappa,\theta+1}^T\\ &\quad+(1+\alpha_4^{-1})\Sigma_{\kappa,\theta+1}\Big\}\psi_{\kappa,\theta+1}^T. \end{aligned} \quad (21)$$

Letting $\frac{\partial \mathrm{trace}(X_{\kappa,\theta+1|\theta+1})}{\partial\psi_{\kappa,\theta+1}} = 0$, we can arrive at

$$\begin{aligned}\psi_{\kappa,\theta+1} &= \bar{\phi}_{\kappa,\theta+1}X_{\kappa,\theta+1|\theta}C_{\kappa,\theta+1}^T\\ &\quad\times\Big\{\bar{\phi}_{\kappa,\theta+1}^2C_{\kappa,\theta+1}X_{\kappa,\theta+1|\theta}C_{\kappa,\theta+1}^T\\ &\quad+\frac{1+\alpha_3+\alpha_4}{4}\mathscr{E}_{\kappa,\theta+1}+\frac{1+\alpha_3^{-1}}{12}\\ &\quad\times C_{\kappa,\theta+1}\vec{\Theta}_{\kappa,\theta+1|\theta}C_{\kappa,\theta+1}^T\\ &\quad+(1+\alpha_4^{-1})\Sigma_{\kappa,\theta+1}\Big\}. \end{aligned} \quad (22)$$

Up to now, the proof is completed. ■

Remark 2 *By handling model uncertainty, sensor fault and quantization error, a CUBEE with a recursive form is concretized. Subsequently, select PEG to minimize the trace of CUBEE instead of (8) at each step. It should be noted that the developed OSE algorithm for UCDCNs can be implemented via online recursive computation.*

4 An Illustrative Example

This section aims to illustrating the validity of the introduced OSE algorithm by means of a numerical simulation. For $\kappa = 1, 2, 3$, the model parameters are respectively chosen as

$$A_{1,\theta} = \begin{bmatrix} 0.04 & 0.04 & 0.08 \\ -0.04 & -0.2 & 0.2 \\ 0.16 & -0.08 & 0.2 \end{bmatrix},$$

$$A_{2,\theta} = \begin{bmatrix} 0.5 & 0.2 & 0.5 \\ 0.2 & 0.4 & 0.5 \\ 0.1 & 0.2 & 0.5 \end{bmatrix},$$

$$\widetilde{A}_{3,\theta} = \begin{bmatrix} 0.1 & 0.3 & 0.2 \\ 0.3 & 0.2 & 0.5 \\ 0.4 & 0.2 & 0.6 \end{bmatrix},$$

$$
\begin{aligned}
\widehat{A}_{3,\theta} &= \begin{bmatrix} 0.1\sin(0.2\theta) & 0 & 0 \\ 0 & 0.2\cos(0.1\theta) & 0 \\ 0 & 0 & 0 \end{bmatrix}, \\
A_{3,\theta} &= \widetilde{A}_{3,\theta} + \widehat{A}_{3,\theta}, \\
\vec{A}_{\kappa,\theta} &= \begin{bmatrix} 0.1 & 0 & 0 \\ 0 & 0.1 & 0 \\ 0 & 0 & 0.1 \end{bmatrix}, \\
\mathscr{O}_{\kappa,\theta} &= \begin{bmatrix} -12 & 6 & 6 \\ 6 & -12 & 6 \\ 6 & 6 & -12 \end{bmatrix} \times 10^{-3}, \\
\Pi_{\kappa,\theta} &= \begin{bmatrix} 0.2 & 0 & 0 \\ 0 & 0.2 & 0 \\ 0 & 0 & 0.2 \end{bmatrix}, \\
B_{1,\theta} &= \begin{bmatrix} -1 & 0.5 & 0.5 \end{bmatrix}^T, \\
B_{2,\theta} &= \begin{bmatrix} -0.5 - 0.8\sin(0.5\theta) & -0.3 & -0.6 \end{bmatrix}^T, \\
B_{3,\theta} &= \begin{bmatrix} 0.4 & -0.5 & 0.1 \end{bmatrix}^T. \\
C_{1,\theta} &= \begin{bmatrix} 0.1 & 0.1 & 0.1 \\ -1 & -0.1 & -2 \end{bmatrix}, \\
C_{2,\theta} &= \begin{bmatrix} -1 - 0.2\cos(0.6\theta) & 0.8 & 2 \\ 1.8 & -0.9 & 0.5 \end{bmatrix}, \\
C_{3,\theta} &= \begin{bmatrix} 2 & -2 & 1 \\ -0.5 & 1 & 0.6 \end{bmatrix}.
\end{aligned}
$$

The initial values are chosen as $X_{1,0|0} = X_{2,0|0} = X_{3,0|0} = 5I_3$, $\hat{x}_{1,0|0} = [0 \;\; 0.2 \;\; 0.2]^T$, $\hat{x}_{2,0|0} = [2 \;\; 0.4 \;\; 1]^T$ and $\hat{x}_{3,0|0} = [1 \;\; 0.8 \;\; 0.4]^T$. Other elements are parameterized by $\alpha_1 = \alpha_2 = 0.6$, $\alpha_3 = 0.2$, $\alpha_4 = 0.8$, $\alpha_5 = 0.4$, $\mathscr{E}_{\kappa,\theta} = \mathrm{diag}\{0.5 \;\; 0.5\}$, $\Delta_{\kappa,\theta} = 0.4$, $\Sigma_{\kappa,\theta} = 0.1$ and $\tau = 4$.

Let $x_{\kappa,\theta} = [x^1_{\kappa,\theta} \;\; x^2_{\kappa,\theta} \;\; x^3_{\kappa,\theta}]^T$ with estimation $\hat{x}_{\kappa,\theta|\theta} = [\hat{x}^1_{\kappa,\theta} \;\; \hat{x}^2_{\kappa,\theta} \;\; \hat{x}^3_{\kappa,\theta}]^T$. The simulation results are presented in Figs. 1-3. Fig. 1 depicts the state and estimation of 1th. Fig. 2 gives the state and estimation of 2th. Fig. 3 denotes the state and estimation of 3th.

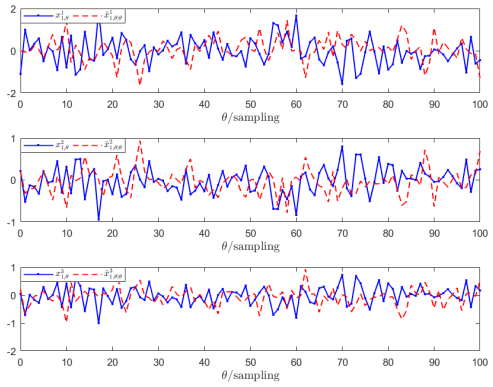

Fig. 1: $x_{1,\theta}$ and its estimation.

5 Conclusions

In this paper, the OSE state estimation problem has been investigated for UCDCNs suffering from coupled delay, sensor fault and probability-based quantization. The model uncertainty and sensor fault have been considered adequately, which have been characterized by random variable

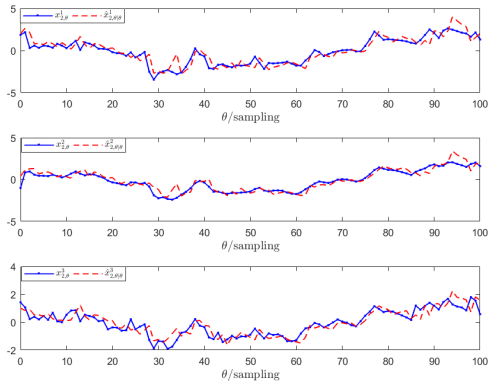

Fig. 2: $x_{2,\theta}$ and its estimation.

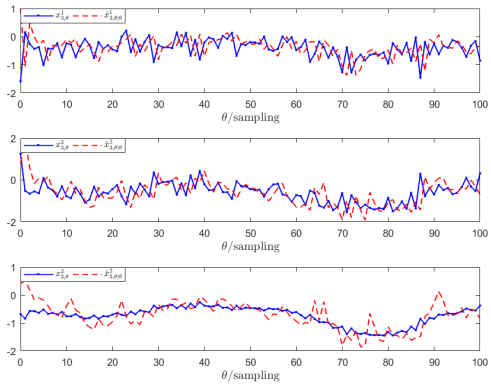

Fig. 3: $x_{3,\theta}$ and its estimation.

with known probabilities. In addition, a probability-based quantization technique has been adopted to accommodate bandwidth-limited channels. A novel predictor-estimator has been constructed to ensure the existence of CUBEE. Consequently, the trace of CUBEE has been minimized by selecting proper PEG. Finally, a simulation has been carried out to illustrate the effectiveness of the developed OSE scheme.

References

[1] J. Hu, Z. Wang, G.-P. Liu, C. Jia and J. Williams, Event-triggered recursive state estimation for dynamical networks under randomly switching topologies and multiple missing measurements, *Automatica*, 115, Article Number. 108908, DOI: 10.1016/j.automatica.2020.108908, 2020.

[2] J. Hu, Z. Wang, H. Gao and L. K. Stergioulas, Extended Kalman filtering with stochastic nonlinearities and multiple missing measurements, *Automatica*, 48(9): 2007–2015, 2012.

[3] X. Li, G. Wei and L. Wang, Distributed set-membership filtering for discrete-time systems subject to denial-of-service attacks and fading measurements: A zonotopic approach, *Information Sciences*, 547: 49–67, 2021.

[4] Y. Qi, Y. Liu and B. Niu, Event-triggered H_∞ filtering for networked switched systems with packet disorders, *IEEE Transactions on Systems, Man, and Cybernetics: Systems*, 51(5): 2847–2859, 2021.

[5] C. Jia, J. Hu, X. Yi, H. Liu, J. Huang and Z. Cao, Recursive state estimation for a class of quantized coupled complex

networks subject to missing measurements and amplify-and-forward relay, *Information Sciences*, 630: 53–73, 2023.

[6] W. Qian, S. Guo, Y. Zhao, X. Xu and S. Fei, Distributed resilient state estimation for nonlinear systems with randomly occurring communication delays and missing measurements, *International Journal of Adaptive Control and Signal Processing*, 36(2): 315–333, 2022.

[7] P. Xu, H. Wu and X. Zheng, Event-triggered distributed filtering for a class of uncertain parameter systems over dynamic switching topologies networks subject to missing measurements, *Digital Signal Processing*, 126, Article Number: 103474, DOI: 10.1016/j.dsp.2022.103474, 2022.

[8] Q. Li, Z. Wang, H. Dong and W. Sheng, Recursive filtering for complex networks with time-correlated fading channels: An outlier-resistant approach, *Information Sciences*, 615: 348–367, 2022.

[9] J. Zheng and B. Cui, State estimation of chaotic Lurie system with logarithmic quantization, *Chaos Solitons & Fractals*, 112: 141–148, 2018.

[10] F. Wang, Z. Wang, J. Liang and X. Liu, Resilient filtering for linear time-varying repetitive processes under uniform quantizations and round-robin protocols, *IEEE Transactions on Circuits and Systems I-Regular Papers*, 65(9): 2992–3004, 2018.

[11] J. Mao, D. Ding, G. Wei and H. Liu, Networked recursive filtering for time-delayed nonlinear stochastic systems with uniform quantisation under round-robin protocol, *International Journal of Systems Science*, 50(4): 871–884, 2019.

[12] Q. Liu, Z. Wang, Q.-L. Han and C. Jiang, Quadratic estimation for discrete time-varying non-Gaussian systems with multiplicative noises and quantization effects, *Automatica*, 113, Article Number. 108714, DOI: 10.1016/j.automatica.2019.108714, 2020.

Proceedings of the 3rd Conference on Fully Actuated System Theory and Applications
May 10-12, 2024, Shenzhen, China

Fuzzy-based filtering of autonomous vehicle system via memory-based event-triggered mechanism

Yaxin Gu[1], Weiyi Zhao[1], Xinxin Liu[1], Xiaojie Su[2], Jianxing Liu[3]

1. Department of Automation, Nanjing University of Information Science and Technology, Nanjing 210044, P. R. China
E-mail: guyaxin@nuist.edu.cn, zhaoweiyi2023@126.com, liuxinxin@nuist.edu.cn

2. Department of Automation, Chongqing University, Chongqing, 400044, P. R. China
E-mail: suxiaojie@cqu.edu.cn

3. Department of Control Science and Engineering, Harbin Institute of Technology, Harbin 15000, P. R. China
E-mail: jx.liu@hit.edu.c.

Abstract: The fuzzy reduced-based filtering problem within autonomous vehicles featuring dynamic positioning systems is employed via an enhanced event-triggered scheme. A reduced-based filtering approach is proposed capable of approximating the original high-order model with a given system performance level. The stability analysis is solved by employing the memory-based event-triggered scheme. Thus the usage of network transmission computational resources is saved effectively.

Key Words: Autonomous vehicles, fuzzy model, filtering, memory-based event-triggered mechanism

1 Introduction

The filtering problems of dynamical systems have been considered widely, specifically in relation to their ability to estimate system states even when the inputs are noisy. Numerous applicable results have been obtained in this area [1, 2]. Furthermore, considerable attention has been attached towards estimation techniques, where the Kalman filtering method emerging as one of the most widely used approaches [3]. Consequently, various enhanced methods have been discussed, including finite-time filtering [4], adaptive filtering [5], fault detection filtering [6], filtering-ing [7], and $\mathcal{H}_2$ filtering [8]. This paper focuses on addressing the T-S fuzzy reduced filtering issues through an improved memory-based event-triggered scheme, where the transformation from the sampled signal to the filter relies on a predefined event-triggered condition [1,9,10]. By employing an efficient memory-based event-triggered communication scheme, the utilization of computational resources and communication bandwidth during network transmission is optimized, and the system dynamics is converted to an error-dependent time-delay system effectively.

Autonomous vehicles have gained significant attention in recent decades due to their capability to perform a wide range of high-risk tasks in challenging marine environments without human intervention [11]. These vehicles are capable of operating in harsh or inaccessible areas, offering increased versatility and maneuverability, especially in shallow waters such as riverine and coastal regions [12]. Their ability to navigate and carry out tasks in these environments makes them highly valuable in various fields of application [13,14]. A Dynamic Positioning system (DPS) refers to a marine vessel equipped with a computer-controlled system, employing Dynamic Positioning (DP) technology to uphold its horizontal position and heading [15, 16]. This technology is used in various types of vessels such as offshore support vessels, cruise ships, and shuttle tankers [17, 18]. Compared to conventional vessels that rely on anchor mooring for position control, DPS offers higher positioning accuracy and flexibility. This advantage has led to increased interest in the control problem associated with DPS. Researchers and engineers have been actively investigating and addressing the challenges of controlling DPS to ensure optimal performance and safety in marine operations [19,20].

Note that there is a lack of research in the area of $\mathcal{H}_2$ filtering and memory-based event-triggered schemes for T-S fuzzy based DP of autonomous vehicles. The aim is to develop methods and techniques to enhance the filtering process in such systems, taking into account the specific characteristics and challenges associated with DP of autonomous vehicles.

This work is supported by the National Natural Science Foundation of China (62173051,62203225); the Natural Science Foundation of Jiangsu Province (BK20220443); the Natural Science Foundation of the Jiangsu Higher Education Institutions of China (22KJB120005); and the Startup Foundation for Introducing Talent of the Nanjing University of Information Science and Technology (2022r102).

2 System Description

Consider T-S fuzzy-based dynamic positioning system for autonomous vehicles [19] is presented in the following form:

Fuzzy Model Rule i: IF $\psi_1(t)$ is f_{i1},$\cdots$,$\psi_n(t)$ is f_{in} ,THEN

$$\begin{cases} \dot{x}_i(t) = A_i x(t) + B_i \omega(t), i = 1, 2, \ldots, n \\ y_i(t) = C_i x(t), \\ z_i(t) = E_i x(t), \end{cases} \tag{1}$$

where f_{ij} denote the fuzzy set, n denotes the number of rule, $\psi_1(t)$,. . .,$\psi_n(t)$ are premise variables.

Assumed that $\psi(t) \in [-\pi/2, \pi/2]$, the overall system is derived as

$$\begin{cases} \dot{x}(t) = \sum\limits_{i=1}^{N} \rho_i(\theta(t))[A_i x(t) + B_i \omega(t)], \\ y(t) = \sum\limits_{i=1}^{N} \rho_i(\theta(t)) C_i x(t), \\ z(t) = \sum\limits_{i=1}^{N} \rho_i(\theta(t)) E_i x(t), \end{cases} \tag{2}$$

where

$$\begin{aligned}\rho_i(\theta(t)) &= \frac{\varrho_i(z(t))}{\sum\limits_{i=1}^{N}\varrho_i(z(t))} \geqslant 0, \quad N=3,\\ \varrho_i(\theta(t)) &= \prod_{j=1}^{n} f_{ij}(\theta_j(t)), \sum_{i=1}^{N}\rho_i(\theta(t))=1,\\ \theta(t) &= [\theta_1(t),\theta_2(t),\ldots,\theta_n(t)],\end{aligned}$$

$$A_1=\begin{bmatrix} 0 & 0 & 0 & 1 & -\alpha & 0\\ 0 & 0 & 0 & \alpha & 1 & 0\\ 0 & 0 & 0 & 0 & 0 & 1\\ b_{11} & 0 & 0 & a_{11} & 0 & 0\\ 0 & b_{22} & b_{23} & 0 & a_{22} & a_{23}\\ 0 & b_{32} & b_{33} & 0 & a_{32} & a_{33}\end{bmatrix},$$

$$A_2=\begin{bmatrix} 0 & 0 & 0 & \beta & -1 & 0\\ 0 & 0 & 0 & 1 & \beta & 0\\ 0 & 0 & 0 & 0 & 0 & 1\\ b_{11} & 0 & 0 & a_{11} & 0 & 0\\ 0 & b_{22} & b_{23} & 0 & a_{22} & a_{23}\\ 0 & b_{32} & b_{33} & 0 & a_{32} & a_{33}\end{bmatrix},$$

$$A_3=\begin{bmatrix} 0 & 0 & 0 & \beta & 1 & 0\\ 0 & 0 & 0 & -1 & \beta & 0\\ 0 & 0 & 0 & 0 & 0 & 1\\ b_{11} & 0 & 0 & a_{11} & 0 & 0\\ 0 & b_{22} & b_{23} & 0 & a_{22} & a_{23}\\ 0 & b_{32} & b_{33} & 0 & a_{32} & a_{33}\end{bmatrix},$$

$$B_1=B_2=B_3=\begin{bmatrix} 0 & 0 & 0\\ 0 & 0 & 0\\ 0 & 0 & 0\\ d_{11} & 0 & 0\\ 0 & d_{22} & d_{23}\\ 0 & d_{32} & d_{33}\end{bmatrix},$$

where $f_{ij}(\theta_j(t))$ is the membership grade of θ_j.

Consider the networked communication environment, a reduced-order dynamic filter is constructed here:

♦ **Filter:**

Rule i : IF $\theta_1(t)$ is f_{i1}, …, and $\theta_p(t)$ is f_{in}, THEN

$$\begin{cases}\dot{x}_r(t) = A_{ri}x_r(t)+B_{ri}y(t),\\ z_r(t) = E_{ri}x_r(t),\end{cases} \tag{3}$$

where $x_r(t)\in\mathbb{R}^l$ and $z_r(t)\in\mathbb{R}^m$ are the estimation conditions $l\leq n$; A_{ri}, B_{ri}, and E_{ri} are matrices to be designed. Therefore, the filter can be rewritten as

$$\begin{cases}\dot{x}_r(t)=\sum\limits_{i=1}^{N}\rho_i\big(\theta(t)\big)\Big\{A_{ri}x_r(t)+B_{ri}y(t)\Big\},\\ z_r(t)=\sum\limits_{i=1}^{N}\rho_i\big(\theta(t)\big)\Big\{E_{ri}x_r(t)\Big\}.\end{cases} \tag{4}$$

Assume that the triggered instant sequences are $t_0T,t_1T,t_2T,\ldots$, where t_0 is the initial time. Denote $y(t)$ as $y(t_kT+nT)$, and $y(t_kT)$ is the lasted transmitted instant. Assume that there exist transmission delays $\tau_k\in[0,\tilde{\tau})$. Then, it can derived that there is no triggering for any $t\in[s_lT+\tau_k, s_{l+1}T+\tau_{k+1})$, and

$$J\big(y,\vartheta\big)\geqslant 0. \tag{5}$$

For $t\in[t_kT+\tau_k, t_{k+1}T+\tau_{k+1})$, denote

$$\begin{cases}\Delta_0 \triangleq [t_kT+\tau_k, t_kT+\tilde{\tau}+T),\\ \Delta_{d_j}\triangleq [t_kT+\tilde{\tau}+d_jT, t_kT+\tilde{\tau}+d_jT+T),\\ \Delta_d \triangleq [t_kT+dT+\tilde{\tau}, t_{k+1}T+\tau_{k+1}),\end{cases} \tag{6}$$

and

$$e_k(t)\triangleq\begin{cases}0, & t\in\Delta_0,\\ y(t_kT)-y(t_kT+d_jT),\ t\in\Delta_{d_j},\\ y(t_kT)-y(t_kT+dT),\ t\in\Delta_d.\end{cases}$$

Then, for $t\in[t_kT+\tau_k, t_{k+1}T+\tau_{k+1})$, the memory-based ETM can be rewritten as

$$\begin{aligned}J(y,\vartheta) &= \vartheta\big(t-\tau(t)\big)+\epsilon\Big\{\varepsilon y^T\big(t-\tau(t)\big)\Phi y\big(t-\tau(t)\big)\\ &\quad -\Sigma_{l=0}^{m-1}\mu_l e_{k-l}^T(t)\Phi e_{k-l}(t)\Big\}\geqslant 0,\end{aligned} \tag{7}$$

with $e_{k-l}(t)=y(t_{k-1}T)-y(t_k+j)T)$, $e_k(t)=y(t_kT)-y((t_k+j)T)$, $\mu_l\in(0,1](l=0,1,\ldots,m-1)$, $\Sigma_{l=0}^{m-1}\mu_l=1$ the dynamic variable $\vartheta(t)$ is transformed as

$$\begin{aligned}\dot{\vartheta}(t) &= \varepsilon y^T\big(t-\tau(t)\big)\Phi y\big(t-\tau(t)\big)-\Sigma_{l=0}^{m-1}\mu_l e_{k-l}^T(t)\\ &\quad\times\Phi e_{k-l}(t)-\mu\vartheta\big(t-\tau(t)\big),\ \vartheta(t_0)=\vartheta_0,\end{aligned}$$

Considering the behavior of ZOH, the input of the filtering can be further formulated as

$$y(t)=y\big(t-\tau(t)\big)+e_k(t), t\in\big[t_kT+\tau_k, t_{k+1}T+\tau_{k+1}\big).$$

Then it follows that

$$\begin{cases}\dot{x}_r(t) = \sum\limits_{i=1}^{N}\rho_i\big(\theta(t)\big)\Big\{A_{ri}x_r(t)\\ \qquad +B_{ri}\big[y(t-\tau(t))-e_k(t)\big]\Big\},\\ z_r(t) = \sum\limits_{i=1}^{N}\rho_i\big(\theta(t)\big)\Big\{E_{ri}x_r(t)\Big\}.\end{cases}$$

Therefore, the corresponding filtering error system can be obtained as

$$\begin{cases}\dot{\xi}(t)=\sum\limits_{i=1}^{N}\sum\limits_{j=1}^{N}\rho_i\big(\theta(t)\big)\rho_j\big(\theta(t)\big)\Big\{\widetilde{A}_0\xi(t)+\widetilde{B}_0w(t)\\ \qquad +\widetilde{A}_1\xi(t-\tau(t))+\widetilde{C}_1e_k\big(t\big)\Big\},\\ e_r(t)=\sum\limits_{i=1}^{N}\sum\limits_{j=1}^{N}\rho_i\big(\theta(t)\big)\rho_j\big(\theta(t)\big)\Big\{\widetilde{E}_1\xi(t)\Big\},\end{cases} \tag{8}$$

where $\xi(t)\triangleq\begin{bmatrix}x(t)\\ x_r(t)\end{bmatrix}$, $e_r(t)\triangleq z(t)-z_r(t)$.

$$\widetilde{A}_0=\begin{bmatrix}A_i & 0\\ 0 & A_{fj}\end{bmatrix},\widetilde{A}_1=\begin{bmatrix}0 & 0\\ B_{ri}C_i & 0\end{bmatrix},\widetilde{B}_0=\begin{bmatrix}B_i\\ 0\end{bmatrix},$$

$$\widetilde{C}_1=\begin{bmatrix}0\\ B_{ri}\end{bmatrix},\widetilde{E}_1=\begin{bmatrix}E_i & -E_{ri}\end{bmatrix},$$

3 Main Results

3.1 Performance Analysis

The following theorem presents sufficient conditions for the asymptotic stability of system (8) with an $\mathcal{H}_2$ performance.

Theorem 1 *Consider parameters $\mu > 0$, $\epsilon > 0$, $\varepsilon > 0$, $\gamma > 0$, and $\mu_l > 0, l = 0, 1, 2, \ldots, m-1$, system in (8) is asymptotically stable with a given $\mathcal{H}_2$ level γ if there exist matrices $P > 0$, $Q > 0$, $R > 0$, $Z > 0$, $\Phi > 0$, such that, for all i, j = 1, 2, …, r,*

$$\frac{2}{r-1}\Upsilon^{ii} + \Upsilon^{ij} + \Upsilon^{ji} < 0, \tag{9}$$

$$\Upsilon^{ii} < 0, \tag{10}$$

$$\begin{bmatrix} -P & \widetilde{E}_1^T \\ \star & -\gamma^2 I \end{bmatrix} < 0, \tag{11}$$

where

$$\Upsilon^{ii} \triangleq \begin{bmatrix} \widetilde{\Xi} & \tau_M \widetilde{\Gamma}_1^T P & \tilde{\varepsilon}\widetilde{\Gamma}_2^T \\ \star & \Upsilon_{22}^{ii} & 0 \\ \star & \star & \Upsilon_{33}^{ii} \end{bmatrix}$$

$$\widetilde{\Xi} \triangleq \begin{bmatrix} \Xi_{11} & \Xi_{12} & 0 & \Xi_{14} & 0 & \Xi_{16} & 0_{m-1} & \Xi_{18} \\ \star & \Xi_{22} & \Xi_{23} & \Xi_{24} & \Xi_{25} & 0 & 0_{m-1} & 0 \\ \star & \star & \Xi_{33} & 0 & \Xi_{35} & 0 & 0_{m-1} & 0 \\ \star & \star & \star & \Xi_{44} & 0 & 0 & 0_{m-1} & 0 \\ \star & \star & \star & \star & \Xi_{55} & 0 & 0_{m-1} & 0 \\ \star & \star & \star & \star & \star & \Xi_{66} & 0_{m-1} & 0 \\ \star & \star & \star & \star & \star & \star & \Xi_{66} & 0 \\ \star & \star & \star & \star & \star & \star & \star & -I \end{bmatrix},$$

$$\Xi_{11} \triangleq P\widetilde{A}_0 + \widetilde{A}_0^T P + Q + R - \frac{4}{\tau(t)}Z, \Xi_{23} \triangleq -\frac{2}{\tau(t)}Z$$

$$\Xi_{12} \triangleq P\widetilde{A}_1 - \frac{2}{\tau(t)}Z, \Xi_{22} \triangleq -Q - \frac{4}{\tau(t)}Z - \frac{4}{\tau_M - \tau(t)}Z$$

$$\Xi_{14} \triangleq \tau(t)P + \frac{6}{\tau(t)}Z, \Xi_{25} \triangleq (\tau_M - \tau(t))P + \frac{6}{\tau_M - \tau(t)}Z$$

$$\Xi_{16} \triangleq P\widetilde{C}_1, \Xi_{24} \triangleq \frac{6}{\tau(t)}Z - \tau(t)P, \Upsilon_{33} \triangleq \tilde{\varepsilon}(\Phi - 2I)$$

$$\Xi_{33} \triangleq -R - \frac{4}{\tau_M - \tau(t)}Z, \Xi_{55} \triangleq -\frac{12}{\tau_M - \tau(t)}Z$$

$$\Xi_{35} \triangleq -(\tau_M - \tau(t))P + \frac{6}{\tau_M - \tau(t)}Z, \Xi_{18} \triangleq P\widetilde{B}_0$$

$$\Xi_{44} \triangleq -\frac{12}{\tau(t)}Z, \Xi_{66} \triangleq -\tilde{\varepsilon}\mu_0\Phi\Xi_{77} \triangleq -\tilde{\varepsilon}X \otimes \Phi$$

$$\widetilde{\Gamma}_1 \triangleq [\widetilde{A}_0 \quad \widetilde{A}_1 \quad 0 \quad 0 \quad 0 \quad \tilde{C}_1 \quad 0_{m-1} \quad \tilde{B}_0]$$

$$\widetilde{\Gamma}_2 \triangleq [0 \quad \overline{C} \quad 0 \quad 0 \quad 0 \quad 0 \quad 0_{m-1} \quad 0], \Upsilon_{22} \triangleq \tau_M(Z - 2P)$$

$$\widetilde{E}_i \triangleq [E_i \quad 0], \widetilde{\Gamma}_3 \triangleq [\widetilde{E}_i \quad 0 \quad 0 \quad 0 \quad 0 \quad 0 \quad 0]$$

$$X \triangleq diag\begin{bmatrix} \mu_1 & \ldots & \mu_{m-1} \end{bmatrix}, \tilde{\varepsilon} \triangleq (\mu\epsilon + 1)\varepsilon.$$

Proof 1 *Construct the following Lyapunov function*

$$V(t) \triangleq V_1 + V_2 + V_3 + V_4 + V_5, \tag{12}$$

where

$$V_1(t) \triangleq \bar{\xi}^T(t)\bar{P}\bar{\xi}(t),$$

$$V_2(t) \triangleq \int_{t-\tau(t)}^{t} \xi^T(s)Q\xi(s)ds$$

$$V_3(t) \triangleq \int_{t-\tau_M}^{t} \xi^T(s)R\xi(s)ds$$

$$V_4(t) \triangleq \int_{t-\tau_M}^{t}\int_{q}^{t} \dot{\xi}^T(s)Z\dot{\xi}(s)dsdq$$

$$V_5(t) \triangleq \vartheta(t),$$

where $\bar{P} \triangleq diag\{P, P, P\} > 0$, $Q > 0, R > 0, Z > 0$, and $\Phi > 0$ are matrices to be constructed. By differentiating $V(t)$, we obtain:

$$\dot{V}(t) \leq \varphi^T(t)\Xi\varphi(t), \tag{13}$$

where

$$\bar{\xi}(t) \triangleq \begin{bmatrix} \xi(t) & \int_{t-\tau(t)}^{t}\xi(s)ds & \int_{t-\tau_M}^{t-\tau(t)}\xi(s)ds \end{bmatrix}^T$$

$$\varphi(t) \triangleq [\xi(t) \quad \xi(t-\tau(t)) \quad \xi(t-\tau_M) \quad \frac{1}{\tau(t)}\int_{t-\tau_M}^{t}\xi^T(s)ds$$

$$\frac{1}{\tau_M - \tau(t)}\int_{t-\tau_M}^{t-\tau(t)}\xi(s)ds \quad e_y(t)]^T$$

$$e_y(t) \triangleq \begin{bmatrix} e_k(t) & e_{k-1}(t) & \ldots & e_{k-m+1}(t) \end{bmatrix}^T,$$

$$\Xi \triangleq \Xi_1 + \Xi_2 + \tau_M\Gamma_1^T Z\Gamma_1 + \tilde{\varepsilon}\Gamma_2^T\Phi\Gamma_2,$$

and

$$\Xi_1 \triangleq \begin{bmatrix} \Theta_{11} & \Theta_{12} & 0 & \tau(t)P & 0 & P\widetilde{C}_1 & 0_{m-1} \\ \star & -Q & 0 & -\tau(t)P & \Theta_{25} & 0 & 0_{m-1} \\ \star & \star & -R & 0 & \Theta_{35} & 0 & 0_{m-1} \\ \star & \star & \star & 0 & 0 & 0 & 0_{m-1} \\ \star & \star & \star & \star & 0 & 0 & 0_{m-1} \\ \star & \star & \star & \star & \star & \mu_0\Phi & 0_{m-1} \\ \star & \star & \star & \star & \star & \star & X \otimes \Phi \end{bmatrix}$$

$$\Xi_2 \triangleq \begin{bmatrix} \Upsilon_{11} & \Upsilon_{12} & 0 & \Upsilon_{14} & 0 & 0_m \\ \star & \Upsilon_{22} & \Upsilon_{23} & \Upsilon_{24} & \Upsilon_{25} & 0_m \\ \star & \star & \Upsilon_{33} & 0 & \Upsilon_{35} & 0_m \\ \star & \star & \star & \Upsilon_{44} & 0 & 0_m \\ \star & \star & \star & \star & \Upsilon_{55} & 0_m \\ \star & \star & \star & \star & \star & 0_{m\times m} \end{bmatrix}$$

with

$$\Gamma_1 \triangleq [\widetilde{A}_0 \quad \widetilde{A}_1 \quad 0 \quad 0 \quad 0 \quad \widetilde{C}_1 \quad 0_{m-1}]$$

$$\Gamma_2 \triangleq [0 \quad \overline{C} \quad 0 \quad 0 \quad 0 \quad 0 \quad 0_{m-1}]$$

$$\Theta_{11} \triangleq P\widetilde{A}_0 + \widetilde{A}_0^T P + Q + R, \Theta_{12} \triangleq P\widetilde{A}_1, \Upsilon_{11} \triangleq -\frac{4}{\tau(t)}Z$$

$$\Theta_{25} \triangleq (\tau_M - \tau(t))P, \Theta_{35} \triangleq -(\tau_M - \tau(t))P$$

$$\Upsilon_{12} \triangleq -\frac{2}{\tau(t)}Z, \Upsilon_{14} \triangleq \frac{6}{\tau(t)}Z, \Upsilon_{22} \triangleq -\frac{4}{\tau(t)}Z - \frac{4}{\tau_M - \tau(t)}Z$$

$$\Upsilon_{23} \triangleq -\frac{2}{\tau_M - \tau(t)}Z, \Upsilon_{24} \triangleq \frac{6}{\tau(t)}Z, \Upsilon_{25} \triangleq \frac{6}{\tau_M - \tau(t)}Z$$

$$\Upsilon_{33} \triangleq -\frac{4}{\tau_M - \tau(t)}Z, \Upsilon_{35} \triangleq \frac{6}{\tau_M - \tau(t)}Z$$

$$\Upsilon_{44} \triangleq -\frac{12}{\tau(t)}Z, \Upsilon_{55} \triangleq -\frac{12}{\tau_M - \tau(t)}Z$$

It shows that $\Xi < 0$,it turns out that $\dot{V} < 0$.

For the $\mathcal{H}_2$ performance, here define:

$$\begin{aligned}\mathcal{J}(t) &\triangleq \int_0^\infty -w^T(t)w(t)dt \\ &\triangleq \int_0^\infty \Big[-w^T(t)w(t) + \dot{V}(t)\Big]dt, \end{aligned} \tag{14}$$

Notice that

$$0 \le (P-Z)Z^{-1}(P-Z)$$

and

$$0 \le [I-\Phi^{-1}]\Phi[I-\Phi^{-1}]$$

It can be obtained that $\Upsilon < 0$. Therefore, we can get that

$$-w^T(t)w(t) + \dot{V}(t) < 0. \tag{15}$$

Besides, since

$$\widetilde{E}_1^T\widetilde{E}_1 - \gamma^2 P < 0. \tag{16}$$

It follows that for all $t > 0$

$$e_r^T(t)e_r(t) < \gamma^2 \int_0^\infty w^T(t)w(t)dt. \tag{17}$$

Therefore, the proof is completed.

3.2 Filtering Design

The following theorem presents criteria for addressing the $\mathcal{H}_2$ filtering issue in system (8) through the linearization technique.

Theorem 2 *Consider parameters $\mu > 0$, $\epsilon > 0$, $\varepsilon > 0$,$\tau_M > 0$,$\gamma > 0$, and $\mu_l > 0, l = 0, 1, 2, \ldots, m-1$, if there exist matrices $\mathbb{W} > 0$, $\mathbb{V} > 0$, $\mathbb{U} > 0$,$\mathcal{H} > 0$,$Q > 0$, $R > 0$, $Z > 0$, $P > 0$, $\Phi > 0$, and the filter $\widetilde{A}_{ri}, \widetilde{B}_{ri}, \widetilde{E}_{ri}$ such that the following matrix are met for $i, j = 1, 2, \ldots, r$:*

$$\frac{2}{r-1}\tilde{\Upsilon}^{ii} + \tilde{\Upsilon}^{ij} + \tilde{\Upsilon}^{ji} < 0, \tag{18}$$

$$\tilde{\Upsilon}^{ii} < 0, \tag{19}$$

$$\begin{bmatrix} -P_1 & -\mathcal{Y}\mathbb{W} & E_i^T \\ \star & -\mathbb{W}^T & -\widetilde{E}_{ri}^T \\ \star & \star & -\gamma^2 I \end{bmatrix} < 0, \tag{20}$$

where

$$\tilde{\Upsilon}^{ii} \triangleq \begin{bmatrix} \widetilde{\tilde{\Upsilon}} & \tau_M\bar{\Gamma}_1^T & \tilde{\varepsilon}\bar{\Gamma}_2^T \\ \star & \tilde{\Upsilon}_{22} & 0 \\ \star & \star & \tilde{\Upsilon}_{33} \end{bmatrix}$$

$$\widetilde{\tilde{\Upsilon}}^{ii} \triangleq \begin{bmatrix} \widetilde{\tilde{\Upsilon}}_{11}^{ii} & \widetilde{\tilde{\Upsilon}}_{12}^{ii} & 0 & \widetilde{\tilde{\Upsilon}}_{14}^{ii} & \widetilde{\tilde{\Upsilon}}_{15}^{ii} & \widetilde{\tilde{\Upsilon}}_{16}^{ii} \\ \star & \widetilde{\tilde{\Upsilon}}_{22}^{ii} & 0 & \widetilde{\tilde{\Upsilon}}_{24}^{ii} & 0 & 0 \\ \star & \star & \widetilde{\tilde{\Upsilon}}_{33}^{ii} & 0 & 0 & 0 \\ \star & \star & \star & \widetilde{\tilde{\Upsilon}}_{44}^{ii} & 0 & 0 \\ \star & \star & \star & \star & \widetilde{\tilde{\Upsilon}}_{55}^{ii} & 0 \\ \star & \star & \star & \star & \star & -I \end{bmatrix},$$

with

$$\widetilde{\tilde{\Upsilon}}_{11}^{ii} \triangleq \begin{bmatrix} \widetilde{\tilde{\Upsilon}}_{1111}^{ii} & \widetilde{\tilde{\Upsilon}}_{1112}^{ii} \\ \star & \widetilde{\tilde{\Upsilon}}_{1122}^{ii} \end{bmatrix}, \widetilde{\tilde{\Upsilon}}_{12}^{ii} \triangleq \begin{bmatrix} \widetilde{\tilde{\Upsilon}}_{1211}^{ii} & \widetilde{\tilde{\Upsilon}}_{1212}^{ii} \\ \widetilde{\tilde{\Upsilon}}_{1221}^{ii} & \widetilde{\tilde{\Upsilon}}_{1222}^{ii} \end{bmatrix}$$

$$\widetilde{\tilde{\Upsilon}}_{14}^{ii} \triangleq \begin{bmatrix} \widetilde{\tilde{\Upsilon}}_{1411}^{ii} & \widetilde{\tilde{\Upsilon}}_{1412}^{ii} \\ \star & \widetilde{\tilde{\Upsilon}}_{1422}^{ii} \end{bmatrix}, \widetilde{\tilde{\Upsilon}}_{22}^{ii} \triangleq \begin{bmatrix} \widetilde{\tilde{\Upsilon}}_{2211}^{ii} & \widetilde{\tilde{\Upsilon}}_{2212}^{ii} \\ \star & \widetilde{\tilde{\Upsilon}}_{2222}^{ii} \end{bmatrix}$$

$$\widetilde{\tilde{\Upsilon}}_{15}^{ii} \triangleq \begin{bmatrix} \mathcal{Y}\widetilde{B}_{ri} & 0_{m-1} \\ \widetilde{B}_{ri} & 0_{m-1} \end{bmatrix}, \widetilde{\tilde{\Upsilon}}_{16}^{ii} \triangleq \begin{bmatrix} \mathbb{V}B_i \\ \mathbb{W}^T\mathcal{Y}^T B_i \end{bmatrix}$$

$$\widetilde{\tilde{\Upsilon}}_{24}^{ii} \triangleq \begin{bmatrix} \widetilde{\tilde{\Upsilon}}_{2411}^{ii} & \widetilde{\tilde{\Upsilon}}_{2412}^{ii} \\ \star & \widetilde{\tilde{\Upsilon}}_{2422}^{ii} \end{bmatrix}, \tilde{\Upsilon}_{22}^{ii} \triangleq \begin{bmatrix} \tilde{\Upsilon}_{2211}^{ii} & \tilde{\Upsilon}_{2212}^{ii} \\ \star & \tilde{\Upsilon}_{2222}^{ii} \end{bmatrix}$$

$$\widetilde{\tilde{\Upsilon}}_{1111}^{ii} \triangleq \mathbb{V}A_i + A_i^T\mathbb{V} + \bar{Q}_1 + \bar{R}_1 - 4\tau_M\bar{Z}_1$$

$$\widetilde{\tilde{\Upsilon}}_{1112}^{ii} \triangleq \mathcal{Y}\widetilde{A}_{ri} + A_i^T\mathcal{Y}\mathbb{W} + \bar{Q}_2 + \bar{R}_2 - 4\tau_M\bar{Z}_2$$

$$\widetilde{\tilde{\Upsilon}}_{1122}^{ii} \triangleq \widetilde{A}_{ri} + \widetilde{A}_{ri}^T + \bar{Q}_3 + \bar{R}_3 - 4\tau_M\bar{Z}_3, \widetilde{\tilde{\Upsilon}}_{1212}^{ii} \triangleq -2\tau_M\bar{Z}_2$$

$$\widetilde{\tilde{\Upsilon}}_{1211}^{ii} \triangleq \mathcal{Y}\widetilde{B}_{ri}C_i - 2\tau_M\bar{Z}_1, \widetilde{\tilde{\Upsilon}}_{1221}^{ii} \triangleq \widetilde{B}_{ri}C_i - 2\tau_M\bar{Z}_2^T$$

$$\widetilde{\tilde{\Upsilon}}_{1222}^{ii} \triangleq -2\tau_M\bar{Z}_3, \widetilde{\tilde{\Upsilon}}_{1411}^{ii} \triangleq \frac{1}{\tau_M}\mathbb{V} + 6\tau_M\bar{Z}_1$$

$$\widetilde{\tilde{\Upsilon}}_{1412}^{ii} \triangleq \frac{1}{\tau_M}\mathcal{Y}\mathbb{W} + 6\tau_M\bar{Z}_2, \widetilde{\tilde{\Upsilon}}_{1422}^{ii} \triangleq \frac{1}{\tau_M}\mathbb{W}^T + 6\tau_M\bar{Z}_3$$

$$\widetilde{\tilde{\Upsilon}}_{2211}^{ii} \triangleq -\bar{Q}_1 - 4\tau_M\bar{Z}_1, \widetilde{\tilde{\Upsilon}}_{2212}^{ii} \triangleq -\bar{Q}_2 - 4\tau_M\bar{Z}_2$$

$$\widetilde{\tilde{\Upsilon}}_{2222}^{ii} \triangleq -\bar{Q}_3 - 4\tau_M\bar{Z}_3, \widetilde{\tilde{\Upsilon}}_{2411}^{ii} \triangleq 6\tau_M\bar{Z}_1 - \frac{1}{\tau_M}\mathbb{V},$$

$$\widetilde{\tilde{\Upsilon}}_{2412}^{ii} \triangleq 6\tau_M\bar{Z}_2 - \frac{1}{\tau_M}\mathcal{Y}\mathbb{W}, \widetilde{\tilde{\Upsilon}}_{2422}^{ii} \triangleq 6\tau_M\bar{Z}_3 - \frac{1}{\tau_M}\mathbb{W}^T$$

$$\widetilde{\tilde{\Upsilon}}_{33}^{ii} \triangleq -\bar{R}, \widetilde{\tilde{\Upsilon}}_{44}^{ii} \triangleq -12\tau_M\bar{Z}, \widetilde{\tilde{\Upsilon}}_{55}^{ii} \triangleq \tilde{\varepsilon}\tilde{X} \otimes \bar{\Phi}$$

$$\tilde{\Upsilon}_{2211}^{ii} \triangleq \tau_M\bar{Z}_1 - 2\mathbb{V}, \tilde{\Upsilon}_{2212}^{ii} \triangleq \tau_M\bar{Z}_2 - 2\mathcal{Y}\mathbb{W}$$

$$\tilde{\Upsilon}_{2222}^{ii} \triangleq \tau_M\bar{Z}_3 - 2\mathbb{W}^T, \tilde{\Upsilon}_{33}^{ii} \triangleq \tilde{\varepsilon}(\bar{\Phi} - 2I),$$

$$\bar{\Gamma}_1 \triangleq \begin{bmatrix} \mathbb{V}A_i & \mathcal{Y}\widetilde{A}_{ri} & \mathcal{Y}\widetilde{B}_{ri}C_i & 0 & 0 & 0 & \widehat{\Gamma}_1 \\ \mathbb{W}^T\mathcal{Y}^T A_i & \widetilde{A}_{ri} & \widetilde{B}_{ri}C_i & 0 & 0 & 0 & \widehat{\Gamma}_2, \end{bmatrix}$$

$$\widehat{\Gamma}_1 \triangleq \begin{bmatrix} \mathcal{Y}\widetilde{B}_{ri} & 0_{m-1} & \mathbb{V}B_i \end{bmatrix},$$

$$\tilde{X} \triangleq diag\begin{bmatrix} \mu_0 & \mu_1 & \ldots & \mu_{m-1} \end{bmatrix}$$

$$\widehat{\Gamma}_2 \triangleq \begin{bmatrix} \widetilde{B}_{ri} & 0_{m-1} & \mathbb{W}^T\mathcal{Y}^T B_i \end{bmatrix}$$

$$\bar{\Gamma}_2 \triangleq \begin{bmatrix} 0 & C_i & 0 & 0 & 0 & 0_m \\ 0 & 0 & 0 & 0 & 0 & 0_m \end{bmatrix}$$

then the reduced-based filtering with $\mathcal{H}_2$ performance is proposed. The filter parameters in (7) are computed as

$$\begin{bmatrix} A_{ri} & B_{ri} \\ E_{ri} & 0 \end{bmatrix} = \begin{bmatrix} \mathbb{W}^{-1} & 0 \\ 0 & I \end{bmatrix} \begin{bmatrix} \widetilde{A}_{ri} & \widetilde{B}_{ri} \\ \widetilde{E}_{ri} & 0 \end{bmatrix}. \tag{21}$$

Proof 2 *Here define matrix P as:*

$$P \triangleq \begin{bmatrix} P_1 & \mathcal{Y}P_2 \\ \star & P_3 \end{bmatrix}, \tag{22}$$

where

$$\begin{aligned} &\mathcal{Y} = [I_{r\times r} \quad 0_{r\times(n-r)}]^T, \\ &P_1 \in R^{n\times n}, \quad P_2 \in R^{r\times r}, \quad P_3 \in R^{r\times r}. \end{aligned}$$

Assume that P_2 is nonsingular. Here define:

$$\mathbb{U} \triangleq \begin{bmatrix} I & 0 \\ 0 & P_3^{-1}P_2^T \end{bmatrix}, \mathbb{V} \triangleq P_1, \mathbb{W} \triangleq P_2 P_3^{-1} P_2^T, \quad (23)$$

and

$$\begin{bmatrix} \widetilde{A}_{ri} & \widetilde{B}_{ri} \\ \widetilde{E}_{ri} & 0 \end{bmatrix} \triangleq \begin{bmatrix} P_2 & 0 \\ 0 & I \end{bmatrix} \begin{bmatrix} A_{ri} & B_{ri} \\ E_{ri} & 0 \end{bmatrix} \begin{bmatrix} P_3^{-1}P_2^T & 0 \\ 0 & I \end{bmatrix}. \quad (24)$$

Then, we can get

$$\begin{aligned}
&\mathbb{U}^T P \widetilde{A}_0 \mathbb{U} \triangleq \begin{bmatrix} \mathbb{V}A_i & \mathcal{Y}\widetilde{A}_{ri} \\ \mathbb{W}^T\mathcal{Y}^T A_i & \widetilde{A}_{ri} \end{bmatrix}, \mathbb{U}^T P \widetilde{C}_1^T \triangleq \begin{bmatrix} \mathcal{Y}\widetilde{B}_{ri} \\ \widetilde{B}_{ri} \end{bmatrix} \\
&\mathbb{U}^T \widetilde{A}_0^T P \mathbb{U} \triangleq \begin{bmatrix} A_i^T\mathbb{V} & A_i^T\mathcal{Y}\mathbb{W} \\ \widetilde{A}_{ri}^T\mathcal{Y}^T & \widetilde{A}_{ri}^T \end{bmatrix} \\
&\mathbb{U}^T P \widetilde{A}_1^T \mathbb{U} \triangleq \begin{bmatrix} \mathcal{Y}\widetilde{B}_{ri}C_i & 0 \\ \widetilde{B}_{ri}C_i & 0 \end{bmatrix}, \mathbb{U}^T P \mathbb{U} \triangleq \begin{bmatrix} \mathbb{V} & \mathcal{Y}\mathbb{W} \\ \mathbb{W}^T\mathcal{Y}^T & \mathbb{W}^T \end{bmatrix} \\
&\mathbb{U}^T P \widetilde{B}_0^T \triangleq \begin{bmatrix} \mathbb{V}B_i \\ \mathbb{W}^T\mathcal{Y}^T B_i \end{bmatrix}, \mathbb{U}^T \widetilde{E}_1^T \triangleq \begin{bmatrix} E_i^T \\ -\widetilde{E}_{ri}^T \end{bmatrix} \quad (25)
\end{aligned}$$

By applying congruence transformations to equations (9), (10), and (11) with appropriate matrices,

$$\begin{aligned}
&diag\{\ \mathbb{U}\ \ \mathbb{U}\ \ \mathbb{U}\ \ \mathbb{U}\ \ \mathbb{U}\ \ I\ \ I\ \ \mathbb{U}\ \ I\ \ I\ \}, \\
&diag\{\ \mathbb{U}\ \ \mathbb{U}\ \ \mathbb{U}\ \ \mathbb{U}\ \ \mathbb{U}\ \ I\ \ I\ \ \mathbb{U}\ \ I\ \ I\ \}, \\
&diag\{\ \mathbb{U}\ \ I\ \},
\end{aligned}$$

respectively, we can obtain that (18)–(20) are met if (23)–(25) are established. Thus, the asymptotic stability for system (8) with a $\mathcal{H}_2$ performance is guaranteed. Since (24) can be rewritten as

$$\begin{bmatrix} A_{ri} & B_{ri} \\ E_{ri} & 0 \end{bmatrix} \triangleq \begin{bmatrix} (P_2^{-T}P_3)^{-1}\mathbb{W}^{-1} & 0 \\ 0 & I \end{bmatrix} \begin{bmatrix} \widetilde{A}_{ri} & \widetilde{B}_{ri} \\ \widetilde{E}_{ri} & 0 \end{bmatrix} \begin{bmatrix} P_2^{-T}P_3 & 0 \\ 0 & I \end{bmatrix}. \quad (26)$$

It shows (A_{ri}, B_{ri}, E_{ri}) in (8) can be defined with (26). Besides, if $P_2^{-T}P_3 = I$ is guaranteed, (21) is derived. Therefore, the proof is completed.

4 Conclusion

This paper proposes a solution to the filtering problem of dynamic positioning for autonomous vehicles. The T-S fuzzy modeling and an improved event-triggered scheme are employed to address this challenge. Specifically, for autonomous vehicle systems with a high dimension, a filtering is proposed to approximate the original high-order model of the system while maintaining a pre-specified level of performance. The stability analysis of the system is conducted. By employing the memory-based event-triggered scheme, the utilization of computational resources and communication bandwidth during network transmission is optimized effectively.

References

[1] G. Battistelli, L. Chisci, and D. Selvi, "A distributed Kalman filter with event-triggered communication and guaranteed stability," *Automatica*, vol. 93, pp. 75C82, 2018.

[2] H. Gao, Y. Zhao, and J. Lam, "$\mathcal{H}_\infty$ fuzzy filtering of nonlinear systems with intermittent measurements," *IEEE Transactions on Fuzzy Systems*, vol. 17, no. 2, pp. 291C300, 2009.

[3] P. Shi, Y. Zhang, M. Chadli, and R. K. Agarwal, "Mixed $\mathcal{H}_\infty$ and passive filtering for discrete fuzzy neural networks with stochastic jumps and time delays," *IEEE Transactions on Neural Networks and Learning Systems*, vol. 27, no. 4, pp. 903C909, 2016.

[4] Z. Zhang, Z. Zhang, H. Zhang, P. Shi, and H. R. Karimi, "Finite-time $\mathcal{H}_\infty$ filtering for T-S fuzzy discrete-time systems with time-varying delay and norm-bounded uncertainties," *IEEE Transactions on Fuzzy Systems*, vol. 23, no. 6, pp. 2427C2434, 2015.

[5] C. M. Lin, M. S. Yang, F. Chao, X. Hu, and J. Zhang, "Adaptive filter design using type-2 fuzzy cerebellar model articulation controller" *IEEE Transactions on Neural Networks and Learning Systems*, vol. 27, no. 10, pp. 2084C2094, 2016.

[6] A. Chibani, M. Chadli, P. Shi, and N. Benhadj Braiek, "Fuzzy fault detection filter design for T-S fuzzy systems in the finite-frequency domain" *IEEE Transactions on Fuzzy Systems*, vol. 25, no. 5, pp. 1051- 1061, 2017.

[7] A. Alif, M. Darouach, and M. Boutayeb, "Design of robust $\mathcal{H}_\infty$ reduced-order unknown-input filter for a class of uncertain linear neutral systems" *IEEE Transactions on Automatic Control*, vol. 55, no. 1, pp. 6C19, 2010.

[8] L. Wu, X. Yao, and W. Zheng, "Generalized $\mathcal{H}_2$ fault detection for Markovian jumping two-dimensional systems" *Automatica*, vol. 48, no. 8, pp. 1741C1750, 2012.

[9] E. Arslan, R. Vadivel, M. S. Ali, and S. Arik, "Event-triggered $\mathcal{H}_\infty$ filtering for delayed neural networks via sampled-data," *Neural Networks*, vol. 91, pp. 11C21, 2017.

[10] Y. Wang, C. C. Lim, and P. Shi, "Adaptively adjusted event-triggering mechanism on fault detection for networked control systems," *IEEE Transactions on Cybernetics*, vol. 64, no. 6, pp. 5203C5211, 2017.

[11] Y. Wang and Q. Han, "Network-Based Fault Detection Filter and Controller Coordinated Design for Unmanned Surface Vehicles in Network Environments," *IEEE Transactions on Industrial Informatics*, vol. 12, no. 5, pp. 1753–1765, 2016.

[12] Z. Peng, X. Hu, and D. Wang, "Robust adaptive formation control of underactuated autonomous surface vehicles with uncertain dynamics," *IET Control Theory Appl.*, vol. 5, no. 12, pp. 1378C1387, 2011.

[13] Z. Peng, D. Wang, Z. Chen, X. Hu, and W. Lan, "Adaptive dynamic surface control for formations of autonomous surface vehicles with uncertain dynamics," *IEEE Trans. Control Syst. Technol.*, vol. 21, no. 2, pp. 513C520, 2013.

[14] G. Rigatos and S. Tzafestas, "Adaptive fuzzy control for the ship steering problem," *Mechatronics*, vol. 16, no. 8, pp. 479C489, 2006.

[15] Y.-L. Wang, Q.-L. Han, M.-R. Fei, and C. Peng, "Network-based TCS fuzzy dynamic positioning controller design for unmanned marine vehicles," *IEEE Trans. Cybern.*, vol. 48, no. 9, pp. 2750C2763, 2018.

[16] J. Du, X. Hu, M. Krstic, and Y. Sun, "Robust dynamic positioning of ships with disturbances under input saturation," *Automatica*, vol. 73, pp. 207C214, 2016.

[17] D. Phan, A. Bab-Hadiashar, M. Fayyazi, R. Hoseinnezhad, R. N. Jazar and H. Khayyam, " Interval Type 2 Fuzzy Logic Control for Energy Management of Hybrid Electric Autonomous Vehicles," *IEEE Transactions on Intelligent Vehi-*

cles, vol. 6, no. 2, pp. 210-220, 2021.

[18] F. S. Tabataba'i-Nasab, S. A. A. Moosavian and A. K. Khalaji, " Tracking Control of an Autonomous Underwater Vehicle: Higher-Order Sliding Mode Control Approach," 2019 7th International Conference on Robotics and Mechatronics (ICRoM), pp. 114-119, 2019.

[19] M. Zheng, S. Yang and L. Li, " Stability Analysis and T-S Fuzzy Dynamic Positioning Controller Design for Autonomous Surface Vehicles Based on Sampled-Data Control," *IEEE Access*, vol. 8, pp. 148193-148202, 2020.

[20] H. Taghavifar, C. Hu, Y. Qin and C. Wei, " EKF-Neural Network Observer Based Type-2 Fuzzy Control of Autonomous Vehicles," *IEEE Transactions on Intelligent Transportation Systems*, vol. 22, no.8, pp. 4788-4800, 2021.

Proceedings of the 3rd Conference on Fully Actuated System Theory and Applications
May 10-12, 2024, Shenzhen, China

Adaptive Cloaking Region Obfuscation in Road Networks

Baihe Ma[1], Xu Wang[1], Yanna Jiang[1], Xiaojie Lin[1]
1. The Global Big Data Technologies Centre, University of Technology Sydney, Australia, 2007
E-mail: Baihe.Ma@uts.edu.au; Xu.Wang-1@uts.edu.au; Xiaojie.Lin@uts.edu.au; Yanna.Jiang@student.uts.edu.au

Abstract: The development of location-based services (LBS) promotes the rapid growth of location data, which also leads to an increasing threat to location privacy. Existing location obfuscation techniques focus on two-dimensional planes that may generate off-road locations. In this paper, we propose an Adaptive Cloaking Region Obfuscation (ACRO) mechanism to protect vehicles' location privacy in road networks. The proposed ACRO mechanism employs route distances to measure the indistinguishability of vehicles in road networks. The ACRO mechanism perturbs vehicle locations to obfuscated cloaking regions based on the route distance between two cloaking regions. The ACRO mechanism adaptively tunes location privacy budgets according to drivers' privacy requirements. Comprehensive experiments confirm that the proposed ACRO mechanism effectively protects location privacy in road networks.

Key Words: Differential Privacy, Location Privacy, Vehicular Networks, Obfuscation

1 Introduction

Location-based services (LBS) enhance vehicular applications with location data, posing risks to drivers' location privacy [1]. LBS servers access drivers' geographical locations, making them vulnerable. Adversaries can infer personal information through unauthorized access or by eavesdropping communications between LBS servers and drivers. Vehicles, constrained by road networks and traffic rules, are particularly susceptible to being tracked.

To safeguard the location privacy of LBS users, obfuscation mechanisms apply differential privacy by introducing controllable noise to the location data, trading off accuracy for privacy [4]. This method is apt for services where precise location is not critical. Nevertheless, obfuscation mechanisms predominantly utilize Euclidean distance for obfuscation [5]. This approach may not accurately reflect true distances in road networks, potentially leading to the creation of unrealistic off-road obfuscations. Furthermore, achieving an optimal balance between data utility and location privacy requires fine-tuning privacy levels.

In this paper, we propose the Adaptive Cloaking Region Obfuscation (ACRO) mechanism for enhanced location privacy in road networks. ACRO introduces Road Network-Indistinguishability (RN-I), focusing on route differences to guide the selection of obfuscated locations. An adaptive privacy budget setting (APBS) algorithm adjusts privacy levels based on location sensitivity, offering a nuanced approach to balancing data utility and privacy.

The contributions of this paper are summarized as follows.

1) We propose the new ACRO mechanism to protect drivers' location privacy in road networks. The ACRO achieves RN-I and adaptively adjusts the privacy budgets based on the personalized sensitive locations.
2) We evaluate the ACRO mechanism on simulated road networks and compare it with existing two-dimensional mechanisms [8–10]. Experiment results show that the ACRO mechanism outperforms in terms of efficiency, privacy-preserving level, and data utility.

1.1 Related Work

Differential privacy (DP) serves as the foundation for obfuscation strategies, ensuring individual data remains indistinct within published datasets [14]. Andrés et al. introduced Geo-Indistinguishability, which applies the Laplace mechanism to achieve privacy on a 2D plane [15]. This method effectively manages privacy with sparse location updates. Hua et al. enhanced this approach by reducing computational demands through the use of additional servers, allowing for obfuscation with minimal calculation [9]. Another approach decreases computational efforts by grouping locations, thereby obfuscating similar locations identically [16].

In road networks, the Graph-Exponential Mechanism (GEM) and discretization techniques adapt Geo-Indistinguishability for more complex environments [8]. GEM considers road network connections as obfuscation targets, directly applying Geo-Indistinguishability, while discretization methods measure indistinguishability using route distances. However, their practical implementation faces challenges in interval settings due to varying road lengths.

Adaptive mechanisms focus on personalizing privacy protection by considering the proximity and sensitivity of locations, assigning higher privacy levels to locations closer to previously obfuscated points [10]. However, these methods often overlook the nuanced privacy correlations among sensitive locations within road networks, indicating potential for further refinement in privacy-preserving techniques.

The rest of the paper is organized as follows. Section 2 describes the system model. Section 3 presents and analyzes the proposed ACRO mechanism. The evaluation of the proposed mechanism is provided in 4, followed by conclusions in Section 5.

2 System Model

2.1 Road Network Model

In the context of navigating road networks, drivers frequently utilize location-based services (LBS) while adhering to traffic regulations. Due to concerns over the trustworthiness of LBS providers, drivers are hesitant to share precise location information. To mitigate this, drivers can adopt obfuscation mechanisms, allowing them to report altered locations and points of interest to LBS. This enables them to secure the services they need without compromising their actual location. Subsequently, drivers can sift through the

returned data from LBS to identify information that aligns with their interests.

Within our framework, the road network is conceptualized as a weighted and directed graph, denoted as $\mathcal{G}$. Nodes within this graph, represented by c, correspond to real-world geographic locations and include various types of road connections such as turns, intersections, furcates, and joins. The weights of edges reflect the lengths of the roads they represent. In the actual road networks, each node or connection generates a "cloaking region" (notated as cr) encompassing itself and the adjoining roads. The distance between any two cloaking regions is measured by the route distance connecting the two respective nodes within those regions.

The implementation of obfuscation mechanisms for location privacy protection leads to a reduction in data utility for drivers. This impact is quantified using "shift distance," a metric that gauges the utility of obfuscated location data. A lower shift distance signifies enhanced data utility, translating to more accurate results from LBS. Traditional obfuscation methods, as seen in existing literature (e.g., [9, 10]), primarily address obfuscation within two-dimensional spaces, where shift distance is calculated as the Euclidean distance between the true location and its obfuscated counterpart. Diverging from these approaches, our study concentrates on road networks, redefining shift distance in this specific context as follows:

Definition 1 (Shift Distance) *The shift distance, denoted as $d_{\mathcal{G}}(cr_0, cr'_0)$, represents the minimum route distance $d\mathcal{G}(c_0, c'_0)$ between a connection c_0 within the actual cloaking region cr_0 and a connection c'_0 within the obfuscated cloaking region cr'_0. This relationship is expressed by the equation:*

$$d_{\mathcal{G}}(cr_0, cr'_0) \coloneqq d_{\mathcal{G}}(c_0, c'_0). \tag{1}$$

2.2 Adversary Model

This study addresses threats from both external and internal passive attackers, as depicted in Fig. 1. External attackers can intercept messages between Road-Side Units (RSUs) and LBS, capturing vehicle identities (IDs) and locations. Internal attackers, in collusion with LBS servers, gain unauthorized access to vehicle communications. These adversaries aim to track vehicles to deduce drivers' personal details by analyzing intercepted messages.

Adversaries seek to associate drivers' LBS IDs with their vehicles to monitor their movements using LBS data. This strategy initially determines the actual cloaking regions where drivers are located. Subsequently, adversaries analyze traffic data within these regions to link IDs with specific vehicles.

For the estimation of cloaking regions, it is assumed that adversaries know the drivers' past movements and the employed obfuscation strategy. They calculate the likelihood of any given cloaking region cr_1 being the driver's actual location when a cloaked region cr'_0 is reported in an LBS request, as given by:

$$\Pr[cr_1|cr'_0] = \frac{\Pr[cr'_0|cr_1]\Pr[cr_1]}{\int_{cr \text{ in } \mathcal{G}} \Pr[cr'_0|cr]\Pr[cr]d_{cr}}, \tag{2}$$

where $\Pr[cr]$ denotes the probability of the driver being in cr based on previous routes, and $\Pr[cr'_0|cr]$ represents the likelihood of reporting cr'_0 given the driver's true location cr.

The Adversary Estimation Error (AEE), which quantifies the accuracy of an adversary's location guess versus the actual location, serves as a metric for evaluating the effectiveness of obfuscation mechanisms in protecting location privacy. The AEE is the route distance between the estimated cloaking region $\hat{cr}_0$ and the actual region cr_0, as illustrated in Fig. 2. The expected AEE is:

$$\text{AEE} = \sum_{\hat{cr}_0 \text{ in } \mathcal{G}} d_{\mathcal{G}}(cr_0, \hat{cr}_0)\Pr[\hat{cr}_0|cr'_0]. \tag{3}$$

3 Proposed Adaptive Cloaking Region Obfuscation Mechanism

This section introduces the Adaptive Cloaking Region Obfuscation (ACRO) mechanism, designed to enhance drivers' location privacy within road networks by leveraging Road Network-Indistinguishability (RN-I) [20]. RN-I utilizes route distances to assess the indistinguishability among vehicles, forming the basis of our ACRO mechanism. This method obfuscates actual locations into generalized areas when drivers request services from LBS, ensuring that adversaries cannot deduce the vehicles' precise locations from the altered data. By grouping vehicles in proximate locations, ACRO further complicates the adversaries' attempts at tracking.

ACRO comprises two primary algorithms: the Cloaking Region Obfuscation (CRO) algorithm, which obfuscates the real cloaking region based on a determined privacy budget, and the Adaptive Privacy Budget Setting (APBS) algorithm, which calculates this budget.

3.1 Defining Road Network-Indistinguishability

Unlike traditional Geo-Indistinguishability mechanisms that protect privacy in two-dimensional spaces by distorting actual locations with differential privacy, RN-I specifically addresses privacy within road networks. RN-I ensures that the likelihood of identifying any two actual cloaking regions within a specified radius as the source of an obfuscated region is bounded, providing a measure for on-road privacy preservation.

3.2 Mechanics of Cloaking Region Obfuscation

Vehicles execute the CRO algorithm locally, which involves identifying the nearest road connection and selecting an obfuscated cloaking region based on predefined probabilities. This process ensures that the actual location is replaced with a generalized area, further protecting the driver's privacy. The algorithmic steps of CRO include mapping the vehicle's location to a cloaking region, generating an obfuscation region around this point, and selecting a new cloaking region based on the obfuscation probabilities. The vehicle then picks a random location within this new region as its obfuscated location to report to LBS.

An illustrative in Fig. 2, the example shows a vehicle at location l_0 employing the CRO algorithm to safeguard its location before communicating with LBS. The process involves confirming the cloaking region's central connection, generating an obfuscation region, and selecting an obfuscated location within this region based on the given probabilities.

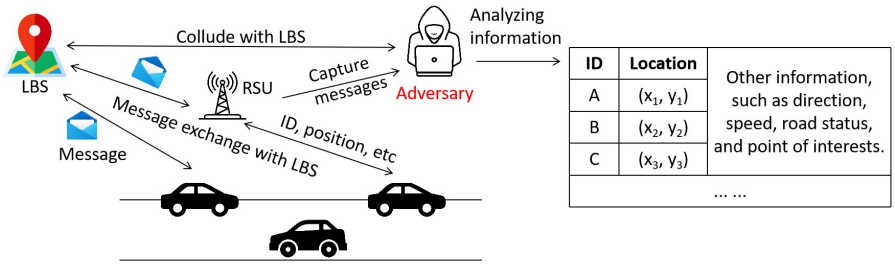

Fig. 1: Adversary model. Adversaries cover a part of a network to eavesdrop on the transmitted LBS messages.

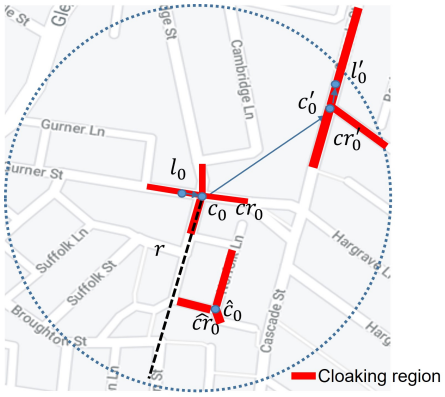

Fig. 2: An example of the proposed CRO algorithm. An actual location l_0 is mapped to the cloaking region covered by the nearest adjacent connection c_0 of l_0. Then, in the obfuscation region $\mathbb{R}^2$ with radius r and center c_0, a cloaking region of connection c_0' is selected based on the obfuscation probability distribution of all the cloaking regions in $\mathbb{R}^2$. Finally, an obfuscated location l_0' is randomly selected in the obfuscated cloaking region cr_0' of connection c_0'. $\hat{c}_0$ is the adversary's estimated connection.

This method ensures that even if adversaries can approximate a vehicle's cloaking region, they cannot precisely track the vehicle's movements.

3.3 Adaptive Privacy Budget Setting Algorithm

The proposed adaptive algorithm can automatically change privacy budgets for different locations after drivers input their sensitive locations. The lowest privacy budget is assigned to sensitive locations for the best protection results. The privacy budgets for the insensitive locations are refined to suppress statistical disparities from the sensitive locations, especially for those close to the sensitive locations.

The weighted and directed graph $\mathcal{G}$ is divided into g segments, i.e., $\mathcal{G} = \{G_1, G_2, \cdots, G_g\}$. The LBS determines the size and the number of segments. The proposed APBS algorithm weights all connections based on the initial sensitive locations of the drivers. The maximum connection weight of a segment determines its privacy budget. The ACRO mechanism then utilizes the segment's privacy budget as the privacy budget of the locations in the segment.

The proposed APBS algorithm calculates the weights of connections hop-by-hop from the sensitive locations. Let $\mathcal{C}_m = \{c_1^m, c_2^m, \cdots\}$ denote the set of m-hop connections. Starting from a sensitive location, drivers can arrive at the i-th m-hop connection c_i^m through at least $(m-1)$ connections. The following calculation steps of the connection weights are illustrated as follows:

- **Initialization:** A value of 1 is assigned as the initial value for the weights of the sensitive locations and the connections adjacent to the sensitive locations. Other connections are assigned the value of the weights as the threshold δ. ϵ_0 is the initialized privacy budget.
- **Weight Calculation:** The weights of connections are computed in a hop-by-hop mode. For example, the weight of connection set $\mathcal{C}_3$ is calculated after computing the previous connection set $\mathcal{C}_2$. The calculation process starts from $\mathcal{C}_2$ and does not end until all the weights of the connections $\mathcal{C}_m$ equal to δ. Multiple $(m-1)$-hop connections that are adjacent to c_i^m have impact on the weight of connection c_i^m $(m \geq 2)$. The APBS calculates all possible weights from the adjacent $(m-1)$-hop connections of c_i^m and treats the maximum value of weights as $W_{c_i^m}$. The possible weights $W_{c_i^m}^a$ of c_i^m are computed by c_a^{m-1}, where c_a^{m-1} is an $(m-1)$-hop connection near to c_i^m, as given by

$$W_{c_i^m}^a = \frac{\frac{D_{\max} - D_{c_i^m} + 2}{d_{\mathcal{G}}(c_a^{m-1}, c_i^m)} \times W_{c_a^{m-1}}}{\sum_{c_j^m \in \mathcal{A}_a^m, j \neq i} \frac{1}{d_{\mathcal{G}}(c_a^{m-1}, c_j^m)} + \frac{D_{\max} - D_{c_i^m} + 2}{d_{\mathcal{G}}(c_a^{m-1}, c_i^m)}}, \quad (4)$$

  where $D_{c_i^m}$ denotes the degree of connection c_i^m, which is the sum of the out-degree and in-degree; the maximum degree of connections in the segment is represented as $D_{\max}$; $\mathcal{A}_a^m$ denotes a set of m-hop connections which are close to the connection c_a^{m-1}. There are at least two degrees of connections in road networks to regard road networks as the strong-connected directed graphs. The $W_{c_i^m}$ is able to use the maximum of different $W_{c_i^m}^a$, i.e., $W_{c_i^m} = \max_{c_a^{m-1}}(W_{c_i^m}^a)$.
- **Finalization:** A segment's weight W_{G_i} is defined by the maximum weight of connections in that segment. The segment's privacy budget is computed by its weight W_{G_i}, i.e, $\epsilon_{G_i} = \frac{\epsilon_0}{W_{G_i}}$.

There are two key parameters in (4): the degree of the connection $D_{c_i^m}$ and the shortest route distance $d_{\mathcal{G}}(c_a^{m-1}, c_i^m)$ to the connections of the last hop. Compared with the high-degree connections, the low-degree connections implicate more precise travel directions by providing fewer choices. Hence, the low-degree connections require high privacy protection capability. The connections around the sensitive locations also need high privacy protection capability than those far away from the sensitive locations.

4 Experimental Results

In this section, we evaluate the ACRO mechanism with simulated road networks. Connections in the simulated road networks are evenly distributed.

4.1 Location Privacy Protection

We first compare the AEE of the CRO mechanism with a connection obfuscation mechanism [8] and 2D Laplace mechanism [9, 10]. The 2D Laplace mechanism treats a road network as a 2D plane and employs the Euclidean distance metrics. The connection obfuscated mechanism in [8] maps the vehicle's actual location to the connection and obfuscates the connection in the obfuscation region. We build a simulated road network as a segment with 4000 m length and width. The connections in the simulated road network are evenly distributed with 50 connections per km^2. The privacy budgets of the segment are set to 0.1, 0.5, 1, 5, and 10 for simulating different privacy-preserving requirements. The obfuscation radius is set to 600 m. We select a set of center connections[1] in the simulated road network to ensure obfuscated candidates of the connections are evenly distributed in obfuscation regions.

Experimental results reveal that the ACRO mechanism protects location privacy better than the connection obfuscated mechanism [8] and 2D Laplace mechanism in road network (e.g., [9, 10]), as shown in Fig. 3. The AEE in Fig. 3 is the expectation AEE. The obfuscation radius is 600 m. The connection obfuscated mechanism achieves a similar AEE as the 2D Laplace mechanism when $\epsilon = 0.1$. The AEE of the connection obfuscated mechanism is shorter than that on 2D Laplace mechanism. The obfuscated cloaking regions are indistinguishable for adversaries after selecting random locations in the cloaking regions because different cloaking regions have overlapping area. The ACRO mechanism achieves the longest AEE among the three mechanisms. The AEE of the three mechanisms decreases when ϵ increases. The mechanism selects a close connection with a high probability when using route distance as a metric rather than Euclidean distance. Thus, the decreasing trend of the connection obfuscated mechanism is faster than its counterparts. The AEE of the ACRO mechanism under the five ϵ cases outperforms the other two mechanisms.

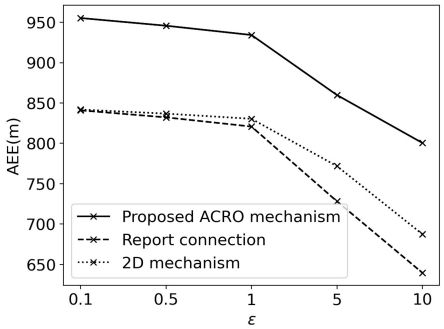

Fig. 3: The comparison of the AEE.

The comparison of expectation shift distance between ACRO mechanism and 2D Laplace mechanism is shown in Fig.4. The obfuscation region is 600 m. The node density is 50 connections per km^2. The shift distance is measured by the shortest route distance between the actual and obfuscated cloaking regions. The expectation shift distance of the ACRO mechanism and 2D Laplace mechanism are similar when $\epsilon = 0.1$. The reason is that the probability of selecting a cloaking region as the obfuscated cloaking region is approximately uniform when $\epsilon = 0.1$. The ACRO mechanism outperform the 2D mechanism regarding to the expectation of the shift distance. This is because the ACRO mechanism has a high probability of selecting a close cloaking region as the obfuscated cloaking region. However, this does not reduce the privacy-preserving capability of the ACRO mechanism.

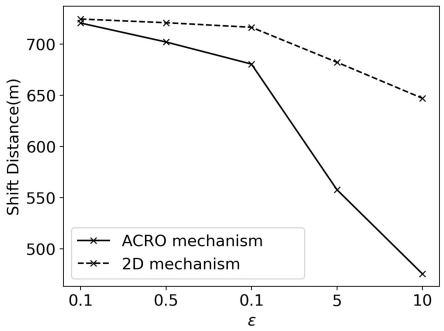

Fig. 4: The comparison of the shift distance.

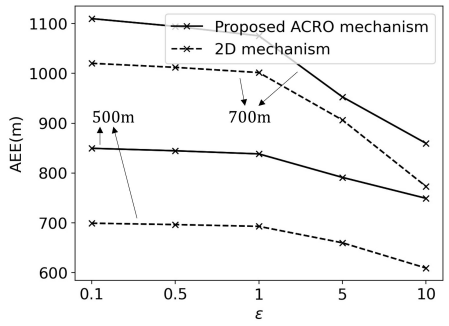

(a) Comparison of AEE

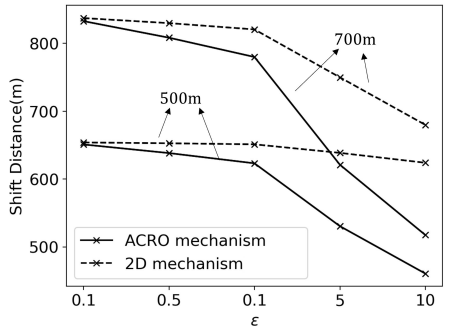

(b) Comparison of shift distance

Fig. 5: Comparison of the ACRO mechanism and 2D Laplace mechanism.

We compare the ACRO mechanism with the 2D Laplace mechanism [9, 10]. Fig. 5 compares the expectation AEE and shift distance of the ACRO mechanism and the 2D

[1](For example, $1400 \leq x \leq 2600$, $1400 \leq y \leq 2600$ when radius $r = 700$ m.)

Laplace mechanism with GeoLife GPS Trajectories. All the segments use the same privacy budget ϵ in the ACRO mechanism for comparison purposes. As shown in Fig. 5, the ACRO mechanism can achieve longer expectation AEE and shorter expectation shift distance than the mechanism in [9], especially in the case of a high privacy budget. The gap between the two mechanisms grows when the privacy budget increases. The ACRO mechanism can achieve a shorter expectation shift distance when ϵ is higher. The average shift distance measured by the route distance can be longer than the obfuscation radius because the route distance is no shorter than the Euclidean distance. The ACRO mechanism has a similar average shift distance with the 2D Laplace mechanism under $\epsilon = 0.1$. The reason is that locations are obfuscated with similar probabilities in the two mechanisms when the privacy budget is 0.1. When the privacy budget is 10, the average shift distance and the average AEE with a 400 m radius are similar to those with a 700 m radius. This is because the obfuscated locations are close to actual cloaking regions in the case of low privacy requirements (high ϵ). The difference between shift distances under the two radiuses decreases with the increasing privacy budget, as shown in Fig. 5(b). This is because both mechanisms are likely to select close locations as the obfuscation results under high privacy budgets. The shift distance of the ACRO mechanism is shorter than the 2D Laplace mechanism in road networks.

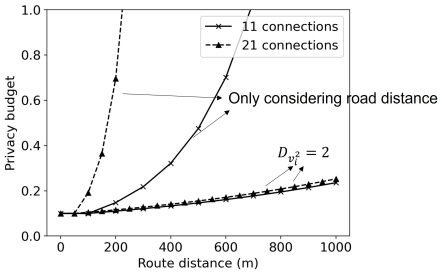

Fig. 6: The privacy budget of multiple connections on the road is impacted by the number of connections, the route distance to the first connection v_1^1, and the degree of each connection.

4.2 Personalization Algorithm

We evaluate the privacy budget of multiple connections on a continuous road affected by the number of connections, the route distance to the first connection c_1^1, and the degree of connections. We evaluate the privacy budget of each connection with the assumption that a 1000 m road starts from a 1-hop connection whose five or eleven connections are evenly spaced. The m-th connection on the road is the first m-hop connection c_1^m ($1 \leq m \leq 5$ or $1 \leq m \leq 10$). Other parameters are as follows, $D_{\max} = 10$, $\sum_{i \geq 2} \frac{1}{d_{\mathcal{G}}(c_1^j, c_i^{j+1})} = \frac{1}{100}$ ($1 \leq j \leq m-1$), and $\epsilon_0 = 0.1$. As shown in Fig. 6, the privacy budget of a connection increases with the same route distance when the number of connections on the road grows. The degree of a connection influences the privacy budget allocation. Its privacy budget increases faster than its low-degree counterparts if a connection has a high degree. Some mechanisms set a global privacy budget [17] or only consider the distance between two connections [18]. Compared with our personalization algorithm, the privacy budgets of the mechanisms developed in [18] and [17] increase faster, as shown in Fig. 6. Unlike the mechanisms (e.g., [17, 18]) which do not capture the connection degree, the proposed personalization algorithm ensures that a connection can inherit more privacy protection from the sensitive location.

4.3 Implementation

The ACRO mechanism is efficient with the time complexity of $O(1)$ for LBS requests that can be used for time-sensitive LBS applications. Before LBS requests, the ACRO mechanism can build a constant connection perturbation table by running the personalization algorithm and connection perturbation algorithm with a given road network, drivers' sensitive locations, and other parameters. The size of the connection perturbation table is $O(n^2)$, where n is the number of connections in the road network. During the LBS requests, the time complexity of generating an obfuscated location is $O(1)$ because the connection-interval obfuscation runs constant-time table lookups to determine the obfuscated connections and locations. The 2D Laplace mechanisms [9, 10] can only obfuscate locations in real-time instead of preparing intermediate obfuscation results in advance. The reason is that the 2D Laplace mechanisms use the distances from drivers' accurate locations.

5 Conclusion

In this paper, we proposed the RN-I to evaluate obfuscation-based location privacy-preserving mechanisms in road networks. We proposed the ACRO mechanism to protect the location privacy of vehicles. The proposed ACRO mechanism allocated privacy budgets to different locations based on drivers' requirements. With the calculated privacy budgets, the proposed ACRO mechanism obfuscated actual locations of the cloaking region where drivers are located. The proposed ACRO mechanism similarly obfuscated vehicles that locate in the same cloaking region. Each vehicle was obfuscated according to the cloaking region in which the driver was located. An adaptive algorithm was developed to customize the privacy budgets of connections based on the sensitive locations specified by drivers. The proposed ACRO mechanism was proved to achieve RN-I and validated through comprehensive experiments.

Appendices

Privacy Analysis

In this subsection, we prove that the CRO algorithm satisfies the RN-I. When an adversary intercepts an obfuscated location in an LBS request, the adversary first estimates obfuscated cloaking region. Then, the adversary infers the actual cloaking region with the estimated obfuscated cloaking region. Finally, the adversary tries to identify the target's identity for future tracking. The ACRO mechanism can protect location privacy under this adversarial model as the mechanism satisfies the RN-I.

***Theorem* 1** *The ACRO mechanism satisfies the (ϵ,r)-RN-Indistinguishability that any two cloaking regions in an obfuscation region are (ϵ,r)-RN-Indistinguishable.*

Proof

The cloaking region obfuscation in the ACRO mechanism is formulated as given by

$$\Pr[cr_0'|cr_0] = \frac{1}{\sum\limits_{cr\,\text{in}\,\mathbb{R}^2} e^{-\frac{\epsilon}{2}d_{\mathcal{G}}(cr_0,cr)}} e^{-\frac{\epsilon}{2}d_{\mathcal{G}}(cr_0,cr_0')}, \quad (5)$$

The location of a cloaking region is represented by the center connection. Let $f(cr_0) = \sum\limits_{cr\,\text{in}\,\mathbb{R}^2} e^{-\frac{\epsilon}{2}d_{\mathcal{G}}(cr_0,cr)}$. With the actual location cr_0, given another actual location cr_1 and its nearest adjacent connection cr_1 in $\mathbb{R}^2$, we have

$$\frac{\Pr[cr'|cr_0]}{\Pr[cr'|cr_1]} = \frac{f(cr_1)}{f(cr_0)} e^{\frac{\epsilon}{2}\left(d_{\mathcal{G}}(cr_1,cr')-d_{\mathcal{G}}(cr_0,cr')\right)}, \quad (6)$$

where cr' is the obfuscated cloaking region. c' is the center connection of cr'. Due to the triangle inequality in road networks, $d_{\mathcal{G}}(cr_0,cr_1) \geq d_{\mathcal{G}}(cr_1,c') - d_{\mathcal{G}}(cr_0,c')$. Then, we have

$$\frac{\Pr[cr'|cr_0]}{\Pr[cr'|cr_1]} \leq \frac{f(cr_1)}{f(cr_0)} e^{\frac{\epsilon}{2}d_{\mathcal{G}}(cr_0,cr_1)}. \quad (7)$$

By employing the triangle inequality, we have $e^{-\frac{\epsilon}{2}d_{\mathcal{G}}(cr_1,cr)} \leq e^{-\frac{\epsilon}{2}(d_{\mathcal{G}}(cr_0,cr)-d_{\mathcal{G}}(cr_0,cr_1))}$. Therefore,

$$\sum_{cr\,\text{in}\,\mathbb{R}^2} \left(e^{-\frac{\epsilon}{2}d_{\mathcal{G}}(cr_1,cr)} - e^{-\frac{\epsilon}{2}(d_{\mathcal{G}}(cr_0,cr)-d_{\mathcal{G}}(cr_0,cr_1))}\right) \leq 0, \quad (8)$$

which can be rewritten as

$$\sum_{cr\,\text{in}\,\mathbb{R}^2} e^{-\frac{\epsilon}{2}d_{\mathcal{G}}(cr_1,cr)} - e^{\frac{\epsilon}{2}d_{\mathcal{G}}(cr_0,cr_1)} \sum_{cr\,\text{in}\,\mathbb{R}^2} e^{-\frac{\epsilon}{2}d_{\mathcal{G}}(cr_0,cr)} \leq 0. \quad (9)$$

Based on the definition of $f(cr_0)$, we have

$$f(cr_1) - e^{\frac{\epsilon}{2}d_{\mathcal{G}}(cr_0,cr_1)} f(cr_0) \leq 0. \quad (10)$$

Thus, the following inequality holds,

$$\frac{f(cr_1)}{f(cr_0)} \leq e^{\frac{\epsilon}{2}d_{\mathcal{G}}(cr_0,cr_1)}. \quad (11)$$

Combining (7) and (11), we have

$$\frac{\Pr[cr'|cr_0]}{\Pr[cr'|cr_1]} \leq e^{\frac{\epsilon}{2}d_{\mathcal{G}}(cr_0,cr_1)} e^{\frac{\epsilon}{2}d_{\mathcal{G}}(cr_0,cr_1)} = e^{\epsilon d_{\mathcal{G}}(cr_0,cr_1)}, \quad (12)$$

which satisfies RN-I.

□

References

[1] S. Khan, I. Sharma, M. Aslam, M. Z. Khan, S. Khan, Security challenges of location privacy in VANETs and state-of-the-art solutions: A survey. *Future Internet*, MDPI, 2021; 13(4): 96.

[2] S. Oya, C. Troncoso, F. Pérez-González, Rethinking location privacy for unknown mobility behaviors. in *2019 IEEE European Symposium on Security and Privacy (EuroS&P)*, IEEE, 2019: 416-431.

[3] S. Narain, A. Ranganathan, G. Noubir, Security of GPS/INS based on-road location tracking systems. in *2019 IEEE Symposium on Security and Privacy (SP)*, IEEE, 2019: 587-601.

[4] Y. Zhao, J. Zhao, M. Yang, T. Wang, N. Wang, L. Lyu, D. Niyato, K.-Y. Lam, Local differential privacy-based federated learning for internet of things. *IEEE Internet of Things Journal*, IEEE, 2020; 8(11): 8836-8853.

[5] Q. A. Arain, I. Memon, Z. Deng, M. H. Memon, F. A. Mangi, A. Zubedi, Location monitoring approach: multiple mix-zones with location privacy protection based on traffic flow over road networks. *Multimedia Tools and Applications*, Springer, 2018; 77: 5563-5607.

[6] J. Zhang, F. Yang, Z. Ma, Z. Wang, X. Liu, J. Ma, A decentralized location privacy-preserving spatial crowdsourcing for internet of vehicles. *IEEE Transactions on Intelligent Transportation Systems*, IEEE, 2020; 22(4): 2299-2313.

[7] B. Ma, X. Wang, X. Lin, Y. Jiang, C. Sun, Z. Wang, G. Yu, Y. He, W. Ni, R. P. Liu, Location Privacy Threats and Protections in Future Vehicular Networks: A Comprehensive Review. *arXiv preprint arXiv:2305.04503*, 2023.

[8] S. Takagi, Y. Cao, Y. Asano, M. Yoshikawa, Geo-graph-indistinguishability: Protecting location privacy for LBS over road networks. in *IFIP Annual Conference on Data and Applications Security and Privacy*, Springer, 2019: 143-163.

[9] J. Hua, W. Tong, F. Xu, S. Zhong, A geo-indistinguishable location perturbation mechanism for location-based services supporting frequent queries, *IEEE Trans. Inf. Forens. Secur.*, 2017, 13(5):1155-1168.

[10] R. Al-Dhubhani, J. M. Cazalas, An adaptive geo-indistinguishability mechanism for continuous LBS queries, *Wirel. Netw.*, 2018, 24(8):3221-3239.

[11] L. Hou, N. Yao, Z. Lu, F. Zhan, Z. Liu, Tracking Based Mix-Zone Location Privacy Evaluation in VANET. *Trans. Vehic. Technol.*, IEEE, 2021.

[12] A. K. Das, A. Tabassum, S. Sadaf, D. Sinha, K-anonymity scheme for privacy preservation in location-based services on IoT environment. *Int Jour. Auto. Contr.*, Inderscience Publishers (IEL), 2021; 15(3): 340-362.

[13] S. Zhang, B. Duan, Z. Chen, T. Ni, H. Zhong, Regionalized location obfuscation mechanism with personalized privacy levels. *arXiv preprint arXiv:2102.00654*, 2021.

[14] L. Wang, D. Zhang, D. Yang, B. Y. Lim, X. Han, X. Ma, Sparse Mobile Crowdsensing With Differential and Distortion Location Privacy. *IEEE Trans. Inf. Forens. Secur.*, IEEE, 2020; 15: 2735-2749.

[15] M. E. Andrés, N. E. Bordenabe, K. Chatzikokolakis, C. Palamidessi, Geo-indistinguishability: Differential privacy for location-based systems. in *Proc. of the 2013 ACM SIGSAC Conference on Computer & Communications Security*, 2013: 901-914.

[16] C. Qiu, A. C. Squicciarini, C. Pang, N. Wang, B. Wu, Location privacy protection in vehicle-based spatial crowdsourcing via geo-indistinguishability. *IEEE Trans. Mob. Comput.*, IEEE, 2020.

[17] V. K. Yadav, S. Verma, S. Venkatesan, Efficient and Secure Location-Based Services Scheme in VANET, *IEEE Trans. Veh. Technol.*, 2020, 69(11):13567-13578.

[18] I. Ullah, M. A. Shah, A. Khan, G. Jeon, Privacy-preserving multilevel obfuscation scheme for vehicular network, *Trans. Emerg. Telecommun. Technol.*, 2020, e4204.

[19] X. Li, H. Zhang, Y. Ren, S. Ma, B. Luo, J. Weng, J. Ma, X. Huang, PAPU: Pseudonym Swap With Provable Unlinkability Based on Differential Privacy in VANETs, *IEEE Internet Things J.*, 2020, 7(12):11789-11802.

[20] B. Ma, X. Lin, X. Wang, B. Liu, Y. He, W. Ni, R. P. Liu, New cloaking region obfuscation for road network-indistinguishability and location privacy, in *Proceedings of the 25th International Symposium on Research in Attacks, Intrusions and Defenses*, 2022:160-17.

Proceedings of the 3rd Conference on Fully Actuated System Theory and Applications
May 10-12, 2024, Shenzhen, China

Air Supply Control for PEM Fuel Cells Under Hamiltonian Framework: A Segmentation Approach

Lalitesh Kumar [1] Jian Chen* [2] Xinyu Li [2] Zhongliang Li [3]

1. Lalitesh Kumar is with the College of Control Science and Engineering, Zhejiang University, Hangzhou 310027, P. R. China.
E-mail: 11932075@zju.edu.cn

2. Jian Chen* and Xinyu Li are with the State Key Laboratory of Fluid Power and Mechatronic Systems, School of Mechanical Engineering, Zhejiang University, Hangzhou 310058, P. R. China.
E-mail: *jchen@zju.edu.cn (*corresponding author), 12325060@zju.edu.cn

3. Zhongliang Li is with the University of Franche-Comte, UTBM, CNRS, institut FEMTO-ST, FCLAB, Belfort, France.
E-mail: zhongliang.LI@univ-amu.fr

Abstract: In this paper, a novel multi-input multi-output nonlinear model of proton exchange membrane fuel cells air supply subsystem under port-Hamiltonian framework is proposed-based on the segmentation of the cathode flow channel. The model consists of inlet valve, cathode flow channel, and back pressure valve to regulate the air supply. In this model, the valve openings are regarded to be inputs to the air-supply subsystem, and the valve orifices are modeled as a linear approximation from the characteristics curves of the solenoid valves. In addition, the developed model's energy balance, dissipativity, and passivity properties are proved and discussed in details in this work. Furthermore, a passivity-based control action is designed to track the desired pressures trajectories in port-Hamiltonian framework with explicit stability analysis. Finally, the designed control action can minimize the tracking error of distributed pressures in the segments and also prove the effectiveness of the proposed model, as depicted with simulation results.

Key Words: PEM Fuel Cells, Passivity, Dissipativity, Port-Hamiltonian Systems, Trajectory Tracking Control.

1 Introduction

The proton exchange membrane (PEM) fuel cells are the electrochemical machine which converts the hydrogen energy into electrical energy. The PEM fuel cells are cleaner and sustainable source of energy which produce only water as the byproduct unlike the conventional or fossil fuels [1,2]. Because of high energy density and abundant availability of hydrogen, the fuel cells can have longer driving cycles and thus, it can replace the batteries in future [3]. There are many advantages of fuel cells such as low operating temperature, high efficiency, less warm-up time, and no environmental contamination [3,4]. There are many control loop problems to deal in the PEM fuel cells such as air/fuel supply subsystem, water management, temperature management, and fault tolerant control [5]. In this paper, the air supply control loop problem has been investigated in a new perspectives. In the literature, the researchers have investigated on the problems such as the control of compressor power [6], compressor speed [7], throttle valve opening [8], oxygen excess ratio control [9], and flow rate through the cathode channel [6]. In a recent published research, the authors have also incorporated ejectors based model to control the air-supply subsystem and oxygen excess ration of the PEM fuel cells [10,11]. Furthermore, the delay-based governor model is introduced in [3] to control the air-supply of PEM fuel cells. However, in all of the previous published works they have proposed a complex model which may involve more costs in designing the ejectors or governes or the throttle valves. Also, the mathematical representation of the models are very complex in those research which involves the governor, ejectors, and the throttle valves. Instead of using the governors, throttle valves, and throttle valves, the simple inlet and back pressure valves are much more convenient to deal with mathematically by approximating the valves characteristics as the linear equations.

By keeping the mathematical complexity in the mind, in view of the published literature, we have proposed a less complex mathematical model in this paper which gives the comparable control results. In this paper, a segmentation concept is used to model and control the PEM fuel cell air-supply subsystem in a passivity-based port-Hamiltonian (pH) framework. The passivity-based concept is a very good mathematical tool to incorporate in the fuel cell like complex systems which involves the gaseous energy flow. The passivity concept deals with the energy balancing, dissipativity, and the system passivity which are very useful unified mathematical tools to establish and analyze the complex systems stability [12–14]. The passivity-based concept is integrated with port-Hamiltonian systems to add more beauty to deal with the complex systems such as PEM fuel cells [15–17].

The thoroughgoing and rigorous study of the related published literature uncovers that the passivity-based pH concept for PEM fuel cells is rarely investigated. In addition, the segmentation-based concept for the modeling of PEM fuel cells air-supply systems has not been exploited in the literature. However, for the hydrogen supply flow channels, the segmentation-based concepts have been used in some literature to control the fuel supply [18] and to study the segmentation scalability [19]. Moreover, the segmentation concept has been used to study the water transport [20] and predicting the distribution of current density [21,22]. With this motivation, in this paper, a segmentation concept has been used to model and control the air-supply subsystem of PEM fuel cells in pH framework. To the best of authors' knowledge and belief, none of the work has been done on the investigation of PEM air-supply subsystems modeling and control on segmentation concept in pH framework. The major contri-

This work was supported by the Key Research and Development Program of Zhejiang Province under Grant 2021C01098.

butions of this paper are encapsulated as follows:

- In this paper, a nonlinear model of the PEM air-supply system-based on the segmented concept is proposed in pH framework. The cathode flow channel is the fuel cell is partitioned into n-segments and the pressure dynamics of each segments are modeled. The solenoid valves' characteristic curves are linearly approximated in order to model the openings of the inlet and back pressure valve orifices.
- Furthermore, the energy balance, dissipativity, and the passivity of the segmented cathode channel model of PEM fuel cell is investigated in details. In addition, in this work, a passivity-based nonlinear control is designed in pH framework to control the pressure dynamics of the segmented cathode channel.
- Furthermore, the explicit stability has been established and thoroughly analyzed in this article. The effectiveness of the proposed control design is shown with the simulation results and discussions.

The remaining portion of the paper is organized into the following sections as follows: Section II describes the modeling of the segmented cathode channel of the PEM fuel cell systems in port-Hamiltonian framework. Section III reports the passivity-based trajectory tracking control design for the segmented air-supply subsystems. In addition, a detailed analysis of the energy balancing, dissipativity, and passivity of the proposed segmented PEM fuel cell air-supply subsystem are presented. Furthermore, the stability is established and analyzed explicitly in this section. Section IV contains the simulation results and its detailed analysis. Finally, the paper culminates with a brief conclusion in Section V.

2 Model Development

In this section, a nonlinear model of PEM fuel cell air-supply subsystem is developed based on the segmentation concept. The schematic of segmented cathode channel with n segments is shown in Fig. 1. The following assumptions are made for the model development:

A1. The cathode channel is supposed to be 100 % humidified.
A2. Each segments volume are same and operation of the anode channel is normal.
A3. Properties of the distributed parameters in each segments are the same.
A4. The temperatures are perpetuated to an acceptable limit and are measurable at the inlet and the output of the cathode channel.
A5. The compressor and the supply manifold are not included in the schematic and hence, it is supposed that incoming pressure to the inlet valve remains constant.

2.1 Inlet valve orifice model

The solenoid valve used at the inlet of cathode channel can be modeled in terms of the valve opening. For the supercritical region, the inlet valve (Bürkert 2875) can be modeled as follows [23]:

$$Q_{N1} = \frac{257 P_0 k_{v1}}{\sqrt{T_1 \rho_N}} \tag{1}$$

where Q_{N1} is the flow rate to the first segment of the cathode channel. The pressure P_0 is input to the inlet valve which

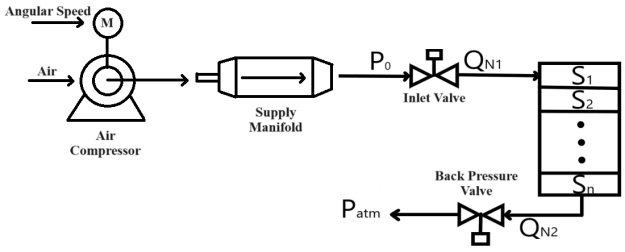

Fig. 1: Segmented Fuel Cell Air-Supply Subsystem

is remains constant throughout the fuel cell operation. Furthermore, k_{v1} is the linear function of the valve opening, T_1 is the temperature measurement at the cathode inlet, and ρ_N is the standard density in kg/m^3. The expression of k_{v1} as a function of orifice opening θ_{v1} can be obtained from its characteristic curve as follows [23]:

$$k_{v1} = k_{vs1}\left[0.95 + 0.12744\left(\theta_{v1} - 8\right)\right]. \tag{2}$$

2.2 Cathode channel model

The n-channel cathode model can be obtained in terms of pressure dynamics. The segments of the cathode channel are represented as $S_1, S_2, ..., S_n$ and the model of each segments are obtained as follows:

Segment S_1:

$$\dot{P}_{ca,1} = \frac{R_a T_{ca,1}}{M_{a,ca,1} V_{ca,1}}\left[W_{ca,in,1} - W_{ca,out,1}\right] - \frac{R_{O_2} T_{ca,1}}{M_{a,ca,1} V_{ca,1}} W_{O_2,react,1} \tag{3}$$

where $W_{ca,in,1} = Q_{N1}$ and $W_{ca,out,1}$ can be obtained as follows:

$$W_{ca,out,1} = k_{ca,out,1}\left[P_{ca,1} - P_{ca,2}\right]$$

Segment S_2:

$$\dot{P}_{ca,2} = \frac{R_a T_{ca,2}}{M_{a,ca,2} V_{ca,2}}\left[W_{ca,in,2} - W_{ca,out,2}\right] - \frac{R_{O_2} T_{ca,2}}{M_{a,ca,2} V_{ca,2}} W_{O_2,react,2} \tag{4}$$

where $W_{ca,in,2} = W_{ca,out,1}$ and, $W_{ca,out,2}$ can be obtained as follows:

$$W_{ca,out,2} = k_{ca,out,2}\left[P_{ca,2} - P_{ca,3}\right]$$

Segment S_n:

$$\dot{P}_{ca,n} = \frac{R_a T_{ca,n}}{M_{a,ca,n} V_{ca,n}}\left[W_{ca,in,n} - W_{ca,out,n}\right] - \frac{R_{O_2} T_{ca,n}}{M_{a,ca,n} V_{ca,n}} W_{O_2,react,n} \tag{5}$$

where $W_{ca,in,n} = W_{ca,out,n-1}$, $W_{ca,out,n} = Q_{N2}$, and $W_{O_2,react,i}$ can be obtained as follows:

$$W_{O_2,react,i} = \frac{n_{cell} M_{O_2,i}}{4F} I_{st,i} \text{ for } i = 1, 2, ..., n.$$

The flow rate Q_{N2} can be obtained from the back pressure valve orifice model in the following subsection.

2.3 Back pressure valve orifice model

The back pressure solenoid valve (Bürkert 3285) used at the outlet of cathode channel can be modeled in terms of the valve opening in the subcritical region as follows [23]:

$$Q_{N2} = \frac{514 k_{v2} \sqrt{P_{atm}\left(P_{ca,3} - P_{atm}\right)}}{\sqrt{T_2 \rho_N}} \tag{6}$$

where Q_{N2} is the flow rate of the back pressure valve. The variable P_{atm} is the atmospheric pressure. Furthermore, k_{v2} is the linear function of the valve opening, T_2 is the temperature measurement at the cathode outlet, and ρ_N is the standard density in kg/m^3. The valve opening function k_{v2} can be obtained from its characteristic curve as follows [23]:

$$k_{v2} = k_{vs2}\left[0.91 + 0.12796\left(\theta_{v2} - 8\right)\right] \tag{7}$$

where θ_{v2} is opening of the back pressure valve.

Remark 1. *Although the paper deals with the n segment cathode channel model, but for the control design and simulations, we have considered the three segments model taking care of computational effort and model complexity. However, the number of segments plays an important role in determining the closed-loop system performance in case of state-feedback control. If it's desired to analyze the open-loop performance, the number of segments can be increased to reduce the error between the spatially distributed pressures. However, for online operation of the system in case of state feedback control, the computational burden has to be considered.*

2.4 Compact stat-space Hamiltonian model

The port-Hamiltonian is a unified framework of some mathematical tools under one roof to represent and deal with a dynamical stat-space model. The air-supply system described in previous section can be modeled in pH framework as follows [15]:

$$\begin{aligned} \dot{x} &= f(x) + g(x)u + \zeta \\ y &= C(x)\nabla H(x) \end{aligned} \tag{8}$$

where $x \in \mathbb{R}^n$ is the state-vector which comprises of the segments pressure, $u \in \mathbb{R}^m, m < n$ is the control action, ζ is the internal disturbance in the system which are the function of segments stack currents, and $H : \mathbb{R}^n \to \mathbb{R}$ is the open-loop Hamiltonian function. In addition, the function $f(x)$ can be defined as $f(x) \triangleq [J(x) - R(x)]\nabla H(x)$, where the interconnection matrix $J(x)$ poses the skew-symmetric property $J(x) = -J^T(x)$ and the damping matrix $R(x)$ is a symmetric matrix having positive definite ($R(x) = R^T(x) > 0$) or positive semi-definite property ($R(x) = R^T(x) \geq 0$). The functions $f(x)$, $J(x)$, and $R(x)$ for the air-supply subsystem of the PEM fuel cell can be obtained as follows:

$$f(x) = \begin{bmatrix} -c_1c_3 & c_1c_3 & 0 \\ c_3c_5 & -c_5c_6 & -c_5c_7 \\ 0.1137c_9c_{10}\left(\sqrt{\frac{x_3 - P_{atm}}{x_1^2}}\right) & c_7c_9 & -c_7c_9 \end{bmatrix},$$

$$J(x) = \begin{bmatrix} 0 & c_1c_3 & -0.1137c_9c_{10}\left(\sqrt{\frac{x_3 - P_{atm}}{x_1^2}}\right) \\ -c_1c_3 & 0 & -c_5c_7 \\ 0.1137c_9c_{10}\left(\sqrt{\frac{x_3 - P_{atm}}{x_1^2}}\right) & c_5c_7 & 0 \end{bmatrix},$$

$$R(x) = \begin{bmatrix} c_1c_3 - 0.1137c_9c_{10}\left(\sqrt{\frac{x_3^2(x_3 - P_{atm})}{x_1^4}}\right) & 0 & 0 \\ 0 & c_5c_6 - c_3(c_1 + c_5)\frac{x_1}{x_2} & 0 \\ 0 & 0 & c_7\left(c_9 - (c_9 - c_5)\frac{x_2}{x_3}\right) \end{bmatrix}.$$

The matrix $R(x)$ would be positive definite in the domain $x \in \mathbb{R}^n | x_1 < a_1\frac{1-\sqrt{1-4\Gamma^2 P_{atm}}}{2\Gamma^2}$, $x_2 < a_2\frac{1-\sqrt{1-4\Gamma^2 P_{atm}}}{2\Gamma^2}$, $x_3 < \frac{1-\sqrt{1-4\Gamma^2 P_{atm}}}{2\Gamma^2}$ with $a_1 = \frac{c_5c_6c_9}{c_3(c_9-c_5)(c_1+c_5)}$ and $a_2 = \frac{c_9}{c_9-c_5}$. Also, the input matrix function $g(x)$, disturbance signal ζ, and the output matrix $C(x)$ can be represented as follows:

$$g(x) = \begin{bmatrix} 0.12744c_1c_2 & 0 & 0 \\ 0 & 0 & -0.12796c_9c_{10}\sqrt{x_3 - P_{atm}} \end{bmatrix}^T,$$

$$\begin{aligned} \zeta &\triangleq \begin{bmatrix} \zeta_1 & \zeta_2 & \zeta_3 \end{bmatrix}^T \\ &= \begin{bmatrix} -0.06952c_1c_2 - c_4I_{st,1} & -c_8I_{st,2} & -c_{11}I_{st,3} \end{bmatrix}^T, \end{aligned}$$

$$C(x) = \begin{bmatrix} 1 & 0 & 0 \\ 0 & 0 & 1 \end{bmatrix}.$$

where $I_{st,1} = I_{st,2} = I_{st,3} = I$. The state vector x, the control input u, and the output y in (8) are defined as follows:

$$\begin{aligned} x &\triangleq \begin{bmatrix} x_1 & x_2 & x_3 \end{bmatrix}^T = \begin{bmatrix} P_{ca,1} & P_{ca,2} & P_{ca,3} \end{bmatrix}^T, \\ u &\triangleq \begin{bmatrix} u_1 & u_2 \end{bmatrix}^T = \begin{bmatrix} \theta_{v,1} & \theta_{v,2} \end{bmatrix}^T, \\ y &\triangleq \begin{bmatrix} y_1 & y_2 \end{bmatrix}^T = \begin{bmatrix} P_{ca,1} & P_{ca,2} \end{bmatrix}^T, \end{aligned}$$

Besides, the auxiliary variables c_i, $i = 1, 2..., 11$ are defined in the appendix. Furthermore, the dissipative closed-loop pH system can be obtained by designing a palatable state-feedback controller $u = \Lambda(x)$ [15, 24]:

$$\dot{x} = [J_d(x) - R_d(x)]\nabla H_d(x) \tag{9}$$

which is a stable closed-loop air-supply system if the condition $x^* = \arg\min H_d(x)$ has been satisfied for the desired equilibrium x^*, where $\nabla H_d(x) \triangleq \nabla H(x) + \nabla H_a(x)$ and $\nabla H_a(x)$ is gradient of the assigned Hamiltonian. Also, the functions $J_d(x) = J(x) + J_a(x)$ is skew-symmetric and $R_d(x) = R(x) + R_a(x)$ positive semi-definite, with $J_a(x)$ and $R_a(x)$ are the assigned matrices having the same properties that of $J(x)$ and $R(x)$. In pH framework, an acceptable control law $u = \Lambda(x)$ must satisfy the following matching condition [24]:

$$f(x) + g(x)\Lambda(x) + \zeta = [J_d(x) - R_d(x)]\nabla H_d(x). \tag{10}$$

which satisfy some certain conditions defined as follows [24]:

- The *pH structure* of the system must be preserved.
- The *integrability condition* $\nabla H_a(x) = [\nabla H_a(x)]^T$.
- The *equilibrium condition* $\nabla H_a(x^*) = \nabla H(x^*)$ at $x = x^*$.
- The *stability condition* $\nabla H_a(x^*) > \nabla^2 H(x^*)$ at $x = x^*$.

Moreover, the equilibrium state x^* of the closed-loop air-supply subsystem (9) of PEM fuel cell is stable asymptotically if the largest invariant set contained in $\left\{x \in \mathbb{R}^n | [\nabla H_d(x)]^T R_d(x)\nabla H_d(x) = 0\right\} = x^*$ in the estimated domain $\{x \in \mathbb{R}^n | H_d(x) \leq \varkappa\}$.

Remark 2. *The desired trajectory dynamics of closed-loop system is obtained as follows:*

$$\dot{x}_d = [J_d(x_d) - R_d(x_d)]\nabla H_d(x_d). \tag{11}$$

Define $F_d(x) \triangleq J_d(x) - R_d(x)$, the function $F_d(x_d) + F_d^T(x_d) \leq 0$ as $F_d(x_) + F_d^T(x_) = -2R_d(x_d)$ and $R_d(x_d)$ is a positive definite function, and the desired damping matrix $R_d(x) \geq 0$. Also, if $H_d(x_d) = \frac{1}{2}x_d^T x_d$ defined the desired Hamiltonian at $x = x_d$ then, $\nabla H(x) - \nabla H_d(x_d) = x - x_d$.

3 Control design in pH framework

The assigned matrices $J_a(x_d)$ and $R_a(x_d)$ to obtain the matching condition for interconnection and damping assignment passivity-based control (IDA-PBC), are considered as follows:

$$J_a(x_d)=\begin{bmatrix}0 & -c_3c_5 & 0\\ c_3c_5 & 0 & -c_7c_9\\ 0 & c_7c_9 & 0\end{bmatrix}, R_a(x_d)=\begin{bmatrix}c_1c_3 & 0 & 0\\ 0 & c_5c_6 & 0\\ 0 & 0 & c_7c_9\end{bmatrix}.$$

These assigned matrices are utilized to calculate the desired interconnection ($J_d(x_d)$) and damping ($R_d(x_d)$) matrices as discussed in the previous section. Define the tracking error system as $e \triangleq x - x_d$, with x_d as the desired state vector. Then, the matching condition (10) can be modified as follows:

$$f(x)+g(x)\Lambda(x)+\zeta-\dot{x}_d=\left[J_d(x_d)-R_d(x_d)\right]\nabla H_d(x,x_d) \tag{12}$$

where the Hamiltonian $H_d(x,x_d)$ is defined as

$$H_d(x,x_d)=\frac{1}{2}(x-x_d)^T(x-x_d). \tag{13}$$

Therefore, the control action can be designed as follows:

$$\begin{aligned}u=\Lambda(x)=&(g^T(x)g(x))^{-1}g^T(x)\left[(J_d(x_d)-R_d(x_d))\nabla H(x,x_d)\right.\\&\left.-f(x)-\zeta+\dot{x}_d\right]\end{aligned} \tag{14}$$

which is utilized to obtain the controllers u_1 and u_2 as follows:

$$\begin{aligned}u_1=&\frac{1}{0.12744c_1c_2}\left[c_1c_3(x_1-x_2-2e_1+e_2)-c_3c_5e_2+\dot{x}_{1d}-\zeta_1\right.\\&\left.+\left(0.1137c_9c_{10}\sqrt{\frac{x_3-P_{atm}}{x_1^2}}\right)\left(\frac{e_1x_3}{x_1}-e_3\right)\right]\end{aligned} \tag{15}$$

$$\begin{aligned}u_2=&\frac{(x_3-P_{atm})^{-\frac{1}{2}}}{0.12796c_9c_{10}}\left[c_7c_9\left(x_2-x_3-e_2-2e_3-\frac{e_3x_2}{x_3}\right)\right.\\&+0.1139c_9c_{10}\sqrt{x_3-P_{atm}}\left(1-\frac{e_1}{x_1}\right)+\zeta_3-\dot{x}_{3d}\\&\left.-c_5c_7\left(e_2-\frac{e_3x_2}{x_3}\right)\right]\end{aligned} \tag{16}$$

where $e=[e_1,e_2,e_3]^T$ and $x_d=[x_{1d},x_{2d},x_{3d}]^T$. By substituting (14) into (12), the closed-loop error dynamics can be obtained as follows:

$$\dot{e}=\left[J_d(x_d)-R_d(x_d)\right]\nabla H_d(x,x_d) \tag{17}$$

3.1 Energy balance, dissipativity, and passivity

The Hamiltonian $H(x)$ of the segmented cathode channel PEM fuel cell can be defined as follows:

$$H=\frac{1}{2}x^Tx \tag{18}$$

where the state vector x is defined in the previous section. The time derivative of the Hamiltonian $H(x)$ can be obtained as follows:

$$\dot{H}=\nabla H^T(x)\dot{x} \tag{19}$$

which can be further modified as

$$\dot{H}=-\nabla H^T(x)R(x)\nabla H(x)+\nabla H^T(x)g(x)u+\nabla H^T(x)\zeta \tag{20}$$

which again can be modified as follows:

$$\dot{H}=-C^{-1}C\nabla H^T(x)R(x)\nabla H(x)+C^{-1}y^Tg(x)u+C^{-1}C\nabla H^T(x)\zeta. \tag{21}$$

Since the first term is negative, the following inequality can be obtained:

$$\dot{H}\leq C^{-1}y^Tg(x)u+C^{-1}C\nabla H^T(x)\zeta. \tag{22}$$

After integrating both sides of the above inequality, the following expression can be obtained for the energy function in form of the Hamiltonian:

$$H(x(t))-H(x(0))\leq\int_0^t\left(C^{-1}y^Tg(x)u+C^{-1}C\nabla H^T(x)\zeta\right)dt. \tag{23}$$

Remark 3. *The energy of the segmented PEM fuel cells can be balanced if there exists a dissipative function $\Gamma(x(t))$ such that the initial energy follows the inequality*

$$H(x(0))\leq-\int_0^t\Gamma(x(t)dt. \tag{24}$$

Following the inequalities (23) and (24), the following expression can be obtained:

$$H(x(t))\leq\int_0^t\left(C^{-1}y^Tg(x)u+C^{-1}C\nabla H^T(x)\zeta\right)dt-\int_0^t\Gamma(x(t)dt. \tag{25}$$

Assumption 1. *In the segmented cathode PEM fuel cell, there has been sufficient dissipation through $\Gamma(x(t))$ such that*

$$\int_0^t\left(C^{-1}y^Tg(x)u\right)dt-\int_0^t\Gamma(x(t)dt\leq 0. \tag{26}$$

Then, the expression in (25) can be modified as follows:

$$H(x(t))\leq\int_0^t\left(C^{-1}y^Tg(x)u-\Gamma(x(t))\right)dt+\int_0^tC^{-1}C\nabla H^T(x)\zeta dt. \tag{27}$$

The first term of the above expression is negative always following the condition (26), therefore, the system is proved to dissipative and for that reason it is passive with appropriate energy balance.

3.2 Stability analysis

The time derivative of the desired closed-loop Hamiltonian defined in (13) can be obtained as follows:

$$\dot{H}_d(x,x_d)=(x-x_d)^T(J_d(x_d)-R_d(x_d))\nabla H_d(x,x_d) \tag{28}$$

which can be further modified as

$$\dot{H}_d(x,x_d)=-\nabla H_d^T(x,x_d)R_d(x_d)\nabla H_d(x,x_d) \tag{29}$$

which can be further modified as

$$\dot{H}_d(x,x_d)\leq-2\lambda H_d(x,x_d) \tag{30}$$

where $\lambda=\inf_{x\in\mathbb{D}}(eig(R_d(x_d)))$. Consequently, the following inequality can be obtained:

$$H_d(x,x_d)\leq H_d(x(0),x_d(0))e^{-2\lambda t} \tag{31}$$

which means that the closed-loop Hamiltonian $H_d(x,x_d)$ converge to the desired trajectories exponentially. Consequently, the segmented cathode PEM fuel cell with state-feedback controller $u=\Lambda(x)$ is stable exponentially.

Table 1: Values of PEMFC parameters used in the simulation

Physical Variables	Values with Units
P_0	3×10^5 Pa
P_{atm}	1.01×10^5 Pa
R_a	8.314 $J/molK$
R_{O_2}	8.313 $J/molK$
F	96485 c/s
T_1	433 K
T_2	443 K
n_{cell}	180

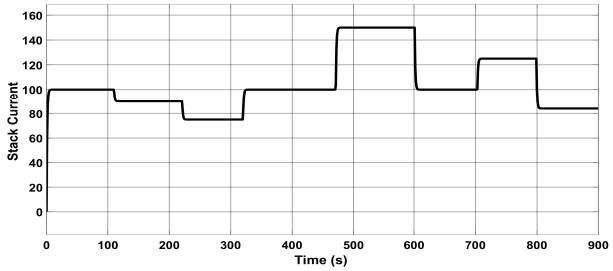

Fig. 2: The stack current I

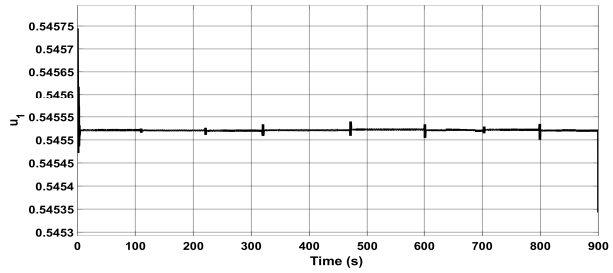

Fig. 3: Control input u_1

4 Simulation Results and Discussion

In this section, the simulation results are analyzed and discussed in details for the proposed PEM fuel cell segmented cathode air-supply subsystem modeling and control under pH framework. The control design parameters are selected as follows: $k_{vs1} = 2.5$, $k_{vs2} = 2.5$, $\rho_N = 1.293$, $k_{ca,out,1} = 0.026$, and $k_{ca,out,2} = 0.26$. The volumes of the cathode channel are considered equal for the simulation purpose in this paper and is selected as $V_{ca1} = V_{ca2} = V_{ca3} = \frac{0.0061}{3} m^3$. In addition, the temperatures in the cathode channels are considered same and selected as $T_{ca1} = T_{ca2} = T_{ca3} = 453K$. The physical parameters of the system model are shown in Table 1.

In Fig. 3, the control input u_1 and in Fig. 4, the control input u_2 are shown which shows that the inputs are within $[0,1]$. The control inputs determine the adequate flow rates of the oxygen into the cathode channel segments. There are more transients in the control input u_1 at time 321 sec, 471 sec, and 799 sec as compared to control input u_2. The control actions also ensure the proper, balanced, and fast enough oxygen flow to fulfill the air supply to the cathode channel.

In Fig. 5 and Fig. 6, the tracking of distributed pressures in segments $S1$ and $S3$ are depicted. It can be seen that the

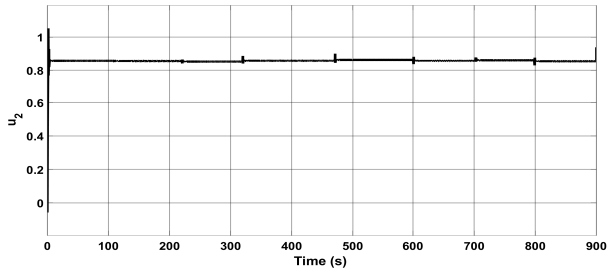

Fig. 4: Control input u_2

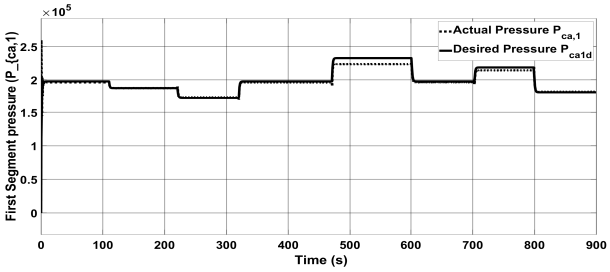

Fig. 5: Tracking of first segment pressure $P_{ca,1}$

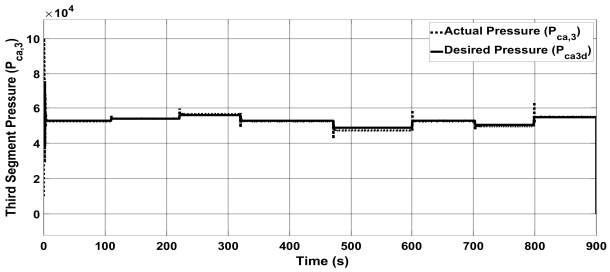

Fig. 6: Tracking of third segment pressure $P_{ca,3}$

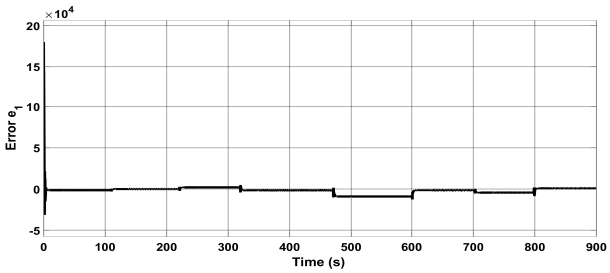

Fig. 7: Error e_1 between actual and desired pressures of first segment

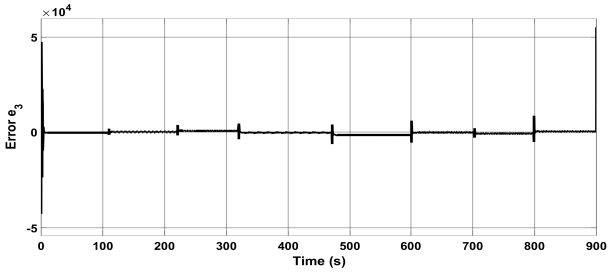

Fig. 8: Error e_3 between actual and desired pressures of third segment

tracking of $P_{ca,1}$ is smooth and close to the desired values for the time intervals of the current defined. The error between

the time intervals $[471, 601]$ sec and $[701, 799]$ sec are more as compared to other time intervals, which means the tracking are not perfect in these time intervals. In other words, it can be analyzed that the tracking of first segment pressure distribution is exhibiting more error if the current increases beyond 100 amps. The error can be verified from the Fig. 7.

Similarly, the tracking of the third (output) segment pressure $P_{ca,3}$ can be seen in Fig. 6, in this figure, we can see that the error is more during the time interval $[471, 601]$ sec which depicts that the tracking of pressure distribution is not very smooth in this interval in the third segment. Also, the error can ve verified in Fig. 8 and again this can be depicted in case of higher current of more than 100 amps. In addition, the spikes in peak overshoots are of very high magnitudes and the transients period lasts longer when the current increases beyond this value. In a nutshell, it can be concluded that the air supply can be controlled through the inlet and back pressure valves without considering compressor and supply manifold dynamics, not affecting the PEM fuel cells operation and performance.

5 Conclusion

In this paper, a new nonlinear model of the PEM fuel cell air supply subsystem is proposed and developed in port-Hamiltonian framework. In this model, we have considered the inlet and back pressure valves openings as the control inputs to the segmented cathode PEM fuel cell system. The model's energy balance, dissipativity and passivity are analyzed in details. Furthermore, a state feedback control action is designed for the developed model in pH framework with explicit stability analysis. We have simulated the closed-loop model for analyzing the tracking error, control action, and pressure distribution tracking in the segmented cathode flow channels. The simulation results are included to show the effectiveness of the proposed new segmented cathode air supply model of the PEM fuel cell systems in pH framework along with the designed state-feedback pH control action.

References

[1] K. Mazloomi and C. Gomes, "Hydrogen as an energy carrier: Prospects and challenges," *Renewable and Sustainable Energy Reviews*, vol. 16, no. 5, pp. 3024–3033, 2012.

[2] S. Sharma and S. K. Ghoshal, "Hydrogen the future transportation fuel: From production to applications," *Renewable and Sustainable Energy Reviews*, vol. 43, pp. 1151–1158, 2015.

[3] A. G. Haddad, I. Boiko, and A. Al-Durra, "Air-flow control in fuel cells using delay-based load governor and feedforward augmented dynamic inversion," *ISA Transactions*, vol. 128, pp. 477–487, 2022.

[4] A. Alaswad, A. Palumbo, M. Dassisti, and A. Olabi, "Fuel cell technologies, applications, and state of the art. a reference guide," in *Reference Module in Materials Science and Materials Engineering*. Elsevier, 2016.

[5] J. Pukrushpan, A. Stefanopoulou, and H. Peng, "Modeling and control for PEM fuel cell stack system," in *Proceedings of the 2002 American Control Conference (IEEE Cat. No.CH37301)*, vol. 4, 2002, pp. 3117–3122 vol.4.

[6] D. Zhao, L. Xia, H. Dang, Z. Wu, and H. Li, "Design and control of air supply system for PEMFC UAV based on dynamic decoupling strategy," *Energy Conversion and Management*, vol. 253, p. 115159, 2022.

[7] I. Matraji, S. Laghrouche, S. Jemei, and M. Wack, "Robust control of the PEM fuel cell air-feed system via sub-optimal second order sliding mode," *Applied Energy*, vol. 104, pp. 945–957, 2013.

[8] M. Li, H. Yin, T. Ding, J. Zhao, J. Gao, and H. Chen, "Air flow rate and pressure control approach for the air supply subsystems in PEMFCs," *ISA Transactions*, vol. 128, pp. 624–634, 2022.

[9] J. Chen, Z. Liu, F. Wang, Q. Ouyang, and H. Su, "Optimal oxygen excess ratio control for PEM fuel cells," *IEEE Transactions on Control Systems Technology*, vol. 26, no. 5, pp. 1711–1721, 2018.

[10] X. Yin, X. Wang, L. Wang, B. Qin, H. Liu, L. Jia, and W. Cai, "Cooperative control of air and fuel feeding for PEM fuel cell with ejector-driven recirculation," *Applied Thermal Engineering*, vol. 199, p. 117590, 2021.

[11] Y. Liu, B. Xiao, J. Zhao, L. Fan, X. Luo, Z. Tu, and S. Hwa Chan, "Performance degradation of a proton exchange membrane fuel cell with dual ejector-based recirculation," *Energy Conversion and Management: X*, vol. 12, p. 100114, 2021.

[12] W. Lin and C. I. Byrnes, "Passivity and absolute stabilization of a class of discrete-time nonlinear systems," *Automatica*, vol. 31, no. 2, pp. 263–267, 1995.

[13] W. Lin, "Feedback stabilization of general nonlinear control systems: A passive system approach," *Systems & Control Letters*, vol. 25, no. 1, pp. 41–52, 1995.

[14] W. Lin, "Global asymptotic stabilization of general nonlinear systems with stable free dynamics via passivity and bounded feedback," *Automatica*, vol. 32, no. 6, pp. 915–924, 1996.

[15] B. Maschke and A. van der Schaft, "Port-controlled Hamiltonian systems: Modelling origins and systemtheoretic properties," *IFAC Proceedings Volumes, Nonlinear Control Systems Design*, vol. 25, no. 13, pp. 359–365, 1992.

[16] C. Wu, A. van der Schaft, and J. Chen, "Robust trajectory tracking for incrementally passive nonlinear systems," *Automatica*, vol. 107, pp. 595–599, 2019.

[17] C. Wu, A. van der Schaft, and J. Chen, "Stabilization of port-Hamiltonian systems based on shifted passivity via feedback," *IEEE Transactions on Automatic Control*, vol. 66, no. 5, pp. 2219–2226, 2021.

[18] L. Kumar, J. Chen, C. Wu, Y. Chen, and A. van der Schaft, "Segmented model based hydrogen delivery control for PEM fuel cells: a port-Hamiltonian approach," *Automatica (submitted for publication)*, 2024.

[19] J. Chen, L. Huang, C. Yan, and Z. Liu, "A dynamic scalable segmented model of PEM fuel cell systems with two-phase water flow," *Mathematics and Computers in Simulation*, vol. 167, pp. 48–64, 2020.

[20] Y.-S. Chen and H. Peng, "A segmented model for studying water transport in a PEMFC," *Journal of Power Sources*, vol. 185, no. 2, pp. 1179–1192, 2008.

[21] Y.-S. Chen and H. Peng, "Predicting current density distribution of proton exchange membrane fuel cells with different flow field designs," *Journal of Power Sources*, vol. 196, no. 4, pp. 1992–2004, 2011.

[22] X. Liu, J. Chen, L. Jin, and S. Liu, "Sensitivity analysis of current distribution to critical operating parameters for polymer electrolyte membrane fuel cells," *Journal of Power Sources*, vol. 573, p. 233068, 2023.

[23] C. Bürkert, "Standard — eu — en bürkert fluid control system: Electromotive 2-way globe proportional valve," *Christian Bürkert GmbH & Co. KG*, vol. 23, 2023.

[24] R. Ortega, A. van der Schaft, B. Maschke, and G. Escobar, "Interconnection and damping assignment passivity-based control of port-controlled Hamiltonian systems," *Automatica*, vol. 38, no. 4, pp. 585–596, 2002.

Proceedings of the 3rd Conference on Fully Actuated System Theory and Applications
May 10-12, 2024, Shenzhen, China

Finite-time shifting control for LPV systems with parameter-varying time delays via state feedback

Yanmei Hu[1], Dandan Zhang[2], Shaoyuan Li[1,3]

1. College of Automation and Electronic Engineering, Qingdao University of Science and Technology, Qingdao 266061, P. R. China
E-mail: hitymhu@163.com

2. School of Science, Jiangsu Ocean University, Lianyungang 222002, P. R. China
E-mail: zdd_hit@126.com

3. Department of automation, Shanghai Jiao Tong University, Shanghai 200240, P. R. China
E-mail: syli@sjtu.edu.cn

Abstract: In this paper, the problem of designing a parameter-scheduled state-feedback controller for LPV systems is investigated. First, the concept of finite-time stability are extended, introducing shifting specifications. Then, by using parameter-dependent Lyapunov-Krasovskii functional, a new delay-dependent finite-time stability criterion is derived. Moreover, based on the criterion, sufficient conditions for the design of stabilizer are provided, which can guarantee the closed-loop system shifting finite-time stable. By using the existing parameters, the controller can be designed in such a way that different values of these parameters imply different characteristics of the finite-time stability property. In this way, the performance of the control system can be varied during its operation. With the help of the efficient interior-point algorithms, both analysis and synthesis conditions are formulated in terms of linear matrix inequalities (LMIs).

Key Words: LPV Systems, Time-delay systems, Finite-time control, Linear matrix inequalities

1 Introduction

In recent years, there has been significant interest in the research of linear parameter-varying (LPV) systems. Such systems are particularly appealing in that they provide a systematic means of computing gain-scheduled controller. On the other hand, time delays inevitably exist in a lot of practical systems [1–3]. Its presence may cause the instability and oscillatory response of the systems. The stability analysis and controller design of the time-delay systems are of great importance for both theoretical and practical aspects [4]. In many engineering systems, time delays are known functions of varied operating conditions or real-time measurable system parameters. Motivated by the LPV control methodology, LPV systems with time delays have attracted an increasing interest from many researchers, and some elegant results have been obtained[5–7].

It is worth pointing out that the results mentioned previously are all derived in the sense of Lyapunov, which studies the behavior of its state variables over an infinite time interval. As a matter of fact, in many practical applications [8, 9], the main concern is the behavior of the system states over a fixed finite time interval. To this end, the concept of finite-time stability arises naturally, which is concerned with the quantitative behavior over a finite time interval [10]. Subsequently, as the significance became more apparent, many worthwhile results on finite-time stability and finite-time stabilization have been reported for a wide variety of systems, ranging from continuous systems [11], to discrete systems [12], to switched systems [13], to stochastic systems [14], as well as to multi agent systems [15].

Recently, the idea of shifting specifications has been paid attention to as an extension of some control problems [16, 17]. This idea relies on introducing some varying parameters, or using the existing ones, to schedule the controller such that different values of these parameters imply different performances. From a practical point of view, reasons for which this problem can be of interest include all situations where some performance degradation could be desirable [17].

In this paper, we consider the shifting finite-time control problem for LPV systems subject to parameter-varying time delays. First, by the usage of the parameter-dependent Lyapunov-Krasovskii functional, sufficient conditions for finite-time stability of LPV systems with parameter-varying delays are derived. Then, based on the finite-time stability analysis, the state feedback controller for the finite-time stabilization is obtained. By virtue of the efficient interior-point algorithms, the proposed results of synthesis problems are formulated in the form of LMIs. Finally, an example is also given to show the validity of the developed methods.

2 Problem Formulations

Consider a class of LPV system with parameter-varying time delays as follows

$$\begin{aligned} \dot{x}(t) &= A(\theta(t))x(t) + A_d(\theta(t))x(t - d(\theta(t))) \\ &\quad + B(\theta(t))u(t), \qquad (1a) \\ x(\tau) &= \phi(\tau), \tau \in [-d, 0], \qquad (1b) \end{aligned}$$

where $x(t) \in \mathbb{R}^n$ is the state vector, $u(t) \in \mathbb{R}^m$ is the input vector. The initial function $\phi(t) : [-d, 0] \to \mathbb{R}^n$ is a given continuous vector valued function. $d(\cdot) : \mathbb{R}^l \to \mathbb{R}$ is a differentiable scalar function, which is denoted as the parameter-varying delay. The state-space matrices $A(\cdot)$, $A_d(\cdot)$, $B(\cdot)$ and the time delay $d(\cdot)$ are known continuous functions of the time-varying parameter vector $\theta(\cdot) : \mathbb{R} \to \mathbb{R}^l \in \Theta_v$, where Θ_v denotes the set of allowable parameter trajectories

This work was supported in part by the National Natural Science Foundation of China under Grant 62203190, in part by the Natural Science Foundation of Jiangsu Province under Grant BK20210922, in part by the Lianyungang Postdoctoral Foundation under Grant LYG20220009, and in part by the Lianyungang Science and Technology Plan (Social Development and Basic Research Plan) project under Grant JCYJ2327.

defined as

$$\Theta_v := \left\{ \begin{array}{c} \theta \in \mathcal{C}(\mathbb{R}, \mathbb{R}^l) \big| \, \theta(t) \in \Theta, \left|\dot{\theta}_i(t)\right| \in [\underline{v}_i, \bar{v}_i], \\ i = 1, 2, \cdots, l, \forall t \geq 0 \end{array} \right\}, \tag{2}$$

in which Θ is a compact subset of $\mathbb{R}^l$, $\underline{v}_i$, $\bar{v}_i$, $i = 1, 2, \cdots, l$ are known scalars and $\theta = \left[\begin{array}{cccc} \theta_1 & \theta_2 & \cdots & \theta_l \end{array} \right]^{\mathrm{T}}$, i.e., the time-varying parameter trajectories and the variation rates of the time-varying parameters are bounded. The states of the system are assumed to be immeasurable. For convenience, we denote $\theta(t)$ as θ and $\mathrm{sym}\{A\} = A + A^{\mathrm{T}}$ in the following context.

For system (1), we make the following assumptions.

A1. The function $d(\cdot)$ is bounded and the function $t - d(t)$ is monotonically increasing, that is,

$$0 \leq d(t) \leq d < \infty, \quad \dot{d}(t) \leq \bar{d} < 1, \quad \forall t \geq 0. \tag{3}$$

A2. At each time instant t, the parameter $\theta(t)$ is accessible to be measured.

Remark 1 *Assumption A1 is common for time-delay systems, see e.g. [19, 22]. According to Assumption A1, the time delay $d(\cdot)$ is dependent on parameter vector θ. Since θ is restricted to lie on the given parameter set Θ_v, it is reasonable to assume that $d(\theta(t))$ is bounded. Moreover, the rate of variation of the parameter vector θ is assumed to be bounded by $\bar{d}$. This allows us to use the parameter-dependent Lyapunov-Krasovskii functionals and can reduce the conservativeness of the synthesis results [22].*

The idea of finite time stability concerns the boundedness of the state of a system over a finite time interval for given initial conditions. This concept has been formalized in [18], extending the original formulation provided by [11]. In this paper, the following concepts on shifting finite-time stability LPV system with parameter-varying time delays are introduced as follows.

Definition 1 *Given a positive definite matrix R, three vector-valued functions $T(p(t))$, $c_1(p(t))$, $c_2(p(t))$ with $0 < c_1(p(t)) < c_2(p(t))$, time-delay LPV system (1) with $u = 0$ is said to be shifting finite-time stable with respect to $(c_1(p(t)), c_2(p(t)), T(p(t)), R, \Theta_v)$ if for any $\theta \in \Theta_v$*

$$\begin{array}{rcl} & \sup\limits_{-d \leq \delta \leq 0} x^T(\delta) R x(\delta) \leq c_1(p(t)) & \\ \Rightarrow & x^T(t) R x(t) \leq c_2(p(t)), & (4) \\ \forall t & \in & [0, T(p(t))], \forall p(t) \in \Pi. \end{array}$$

Remark 2 *The concept of Definition 1 is the extension of finite-time stability from [11, 18, 19]. It combines the parameter-dependent characteristics of LPV systems such that different values of these parameters imply different performances. From a practical point of view, this problem can be of interest.*

The following lemmas are useful for establishing our main results.

Lemma 1 *[20]There exists a symmetric matrix X such that*

$$\left[\begin{array}{cc} P_1 + X & Q_1 \\ Q_1^{\mathrm{T}} & R_1 \end{array} \right] > 0, \quad \left[\begin{array}{cc} P_2 - X & Q_2 \\ Q_2^{\mathrm{T}} & R_2 \end{array} \right] > 0,$$

if and only if

$$\left[\begin{array}{ccc} P_1 + P_2 & Q_1 & Q_2 \\ Q_1^{\mathrm{T}} & R_1 & 0 \\ Q_2^{\mathrm{T}} & 0 & R_2 \end{array} \right] > 0.$$

Lemma 2 *[21]Let θ, Λ and Γ be defined as*

$$\theta \triangleq \left[\begin{array}{cccc} \theta_1 & \theta_2 & \cdots & \theta_l \end{array} \right]^{\mathrm{T}}, \tag{5}$$

$$\Lambda \triangleq \left\{ (\eta_1, \cdots, \eta_l) \big| \, \eta_i \in \left[\underline{\theta}_i, \bar{\theta}_i\right], i = 1, 2, \cdots, l \right\}, \tag{6}$$

$$\Gamma \triangleq \left\{ (\xi_1, \cdots, \xi_l) \big| \, \xi_i \in \left\{\underline{\theta}_i, \bar{\theta}_i\right\}, i = 1, 2, \cdots, l \right\}. \tag{7}$$

Assume that a scalar-valued quadratic function $f : \Lambda \to \mathbb{R}$ is defined by

$$f(\theta) \triangleq a_0 + \sum_i a_i \theta_i + \sum_{i<j} b_{ij} \theta_i \theta_j + \sum_i c_i \theta_i^2, \forall \theta \in \Lambda. \tag{8}$$

If $f(\theta)$ is multiconvex, i.e., $\frac{\partial^2 f(\theta)}{\partial \theta_i^2} \geq 0$, $i = 1, 2, \ldots l$, then $f(\theta) \leq 0 \; \forall \theta \in \Lambda$ if and only if $f(\alpha) \leq 0, \forall \alpha \in \Gamma$.

The main objective of this paper is to design a parameter-dependent state feedback controller for LPV system (1) such that the corresponding closed-loop system is shifting finite-time stable with respect to $(c_1(p), c_2(p), T(p), R, \Theta_v)$.

3 Main Results

In this section, we will give the main results of this paper, which consists of shifting finite-time stability analysis and control synthesis for time-delay LPV systems (1).

3.1 Shifting Finite-time Stability Analysis

Consider the following LPV system

$$\begin{array}{rcll} \dot{x}(t) & = & A(\theta) x(t) + A_d(\theta) x(t - d(\theta)), & (9a) \\ x(\tau) & = & \phi(\tau), \tau \in [-d, 0]. & (9b) \end{array}$$

We discuss the problem of shifting finite-time stability analysis for the time-delay LPV system described by (9). The following theorem presents the shifting finite-time stability conditions for the system (9).

Theorem 1 *Consider the delayed LPV system (9a) with the initial data (9b) and suppose that the parameter-varying delay $d(t)$ satisfying (3). If there exists a continuously differentiable matrix function $P(\theta) > 0$, positive definite matrices Q, Z, matrices L_i, $i = 1, 2$,*

$$X = \left[\begin{array}{cc} X_{11} & X_{12} \\ * & X_{22} \end{array} \right] \geq 0 \tag{10}$$

with appropriate dimensions, and constants $\alpha \geq 0$ such that

$$\left[\begin{array}{cc} \Pi_{11} & \Pi_{12} \\ * & \Pi_{22} \end{array} \right] < 0, \tag{11}$$

$$\left[\begin{array}{ccc} X_{11} & X_{12} & L_1 \\ * & X_{22} & L_2 \\ * & * & Z \end{array} \right] > 0, \tag{12}$$

$$\lambda_2 + \lambda_3 \frac{e^{ad} - 1}{\alpha} + \lambda_4 \frac{e^{\alpha d} - \alpha d - 1}{\alpha^2} \leq \frac{c_2(p) \lambda_1}{c_1(p) e^{\alpha T(p)}}, \tag{13}$$

hold for any $\theta \in \Theta_v$, where

$$\lambda_1 = \inf_{\theta\in\Theta_v} \lambda_{\min}\left(R^{-\frac{1}{2}} P(\theta) R^{-\frac{1}{2}}\right), \quad (14a)$$

$$\lambda_2 = \sup_{\theta\in\Theta_v} \lambda_{\max}\left(R^{-\frac{1}{2}} P(\theta) R^{-\frac{1}{2}}\right), \quad (14b)$$

$$\lambda_3 = \lambda_{\max}\left(R^{-\frac{1}{2}} Q R^{-\frac{1}{2}}\right), \quad (14c)$$

$$\lambda_4 = \lambda_{\max}\left(R^{-\frac{1}{2}} Z R^{-\frac{1}{2}}\right), \quad (14d)$$

$$\begin{aligned}
\Pi_{11} &= sym\{P(\theta)A(\theta)\} + dA^{\mathrm{T}}(\theta)ZA(\theta) - \alpha P(\theta) \\
&\quad + \dot{P}(\theta) + Q + dX_{11} + sym\{L_1\}, \\
\Pi_{12} &= P(\theta)A_d(\theta) + dA^{\mathrm{T}}(\theta)ZA_d(\theta) + dX_{12} + L_2^{\mathrm{T}} - L_1, \\
\Pi_{22} &= -\left(1-\dot{d}(\theta)\right)Q + dA_d^{\mathrm{T}}(\theta)ZA_d(\theta) - sym\{L_2\} \\
&\quad + dX_{22},
\end{aligned}$$

then the delayed LPV system (9) is shifting finite-time stable with respect to $(c_1(p), c_2(p), T(p), R, \Theta_v)$.

Proof. Choose the Lyapunov-Krasovskii functional candidate as follows:

$$V(x,\theta) = V_1(x,\theta) + V_2(x,\theta) + V_3(x,\theta),$$

where

$$\begin{aligned}
V_1(x,\theta) &= x^{\mathrm{T}}(t)P(\theta)x(t), \\
V_2(x,\theta) &= \int_{t-d(\theta)}^{t} x^{\mathrm{T}}(s)e^{\alpha(t-s)}Qx(s)ds, \\
V_3(x,\theta) &= \int_{-d}^{0}\int_{t+\sigma}^{t} \dot{x}^{\mathrm{T}}(s)e^{\alpha(t-s)}Z\dot{x}(s)ds d\sigma.
\end{aligned}$$

For any $\theta \in \Theta_v$, taking the derivative of $V_i(x,\theta)$, $i = 1,2,3$ with respect to t along the trajectories of system (9) yields

$$\begin{aligned}
\dot{V}_1(x,\theta) &= x^{\mathrm{T}}(t)A^{\mathrm{T}}(\theta)P(\theta)x(t) + x^{\mathrm{T}}(t)\dot{P}(\theta)x(t) \\
&\quad + x^{\mathrm{T}}(t-d(\theta))A_d^{\mathrm{T}}(\theta(t))P(\theta)x(t) \\
&\quad + x^{\mathrm{T}}(t)P(\theta)A_d(\theta(t))x(t-d(\theta)) \\
&\quad + x^{\mathrm{T}}(t)P(\theta)A(\theta)x(t), \qquad (15) \\
\dot{V}_2(x,\theta) &\le x^{\mathrm{T}}(t)Qx(t) + \alpha\int_{t-d(\theta)}^{t} x^{\mathrm{T}}(s)e^{\alpha(t-s)}Qx(s)ds \\
&\quad - \left(1-\dot{d}(\theta)\right)x^{\mathrm{T}}(t-d(\theta))Qx(t-d(\theta)), \qquad (16) \\
\dot{V}_3(x,\theta) &\le \alpha\int_{-d}^{0}\int_{t+\sigma}^{t} \dot{x}^{\mathrm{T}}(s)e^{\alpha(t-s)}Z\dot{x}(s)ds d\sigma \\
&\quad - \int_{t-d(\theta)}^{t} \dot{x}^{\mathrm{T}}(s)e^{\alpha(t-s)}Z\dot{x}(s)ds \\
&\quad + dx^{\mathrm{T}}(t-d(\theta))A_d^{\mathrm{T}}(\theta)ZA_d(\theta)x(t-d(\theta)) \\
&\quad + dx^{\mathrm{T}}(t)A^{\mathrm{T}}(\theta)ZA_d(\theta)x(t-d(\theta)) \\
&\quad + dx^{\mathrm{T}}(t-d(\theta))A_d^{\mathrm{T}}(\theta)ZA(\theta)x(t) \\
&\quad + dx^{\mathrm{T}}(t)A^{\mathrm{T}}(\theta)ZA(\theta)x(t). \qquad (17)
\end{aligned}$$

Let $\xi^{\mathrm{T}}(t) = \begin{bmatrix} x^{\mathrm{T}}(t) & x^{\mathrm{T}}(t-d(\theta)) \end{bmatrix}$. Obviously, it is true that for any matrix $X \ge 0$

$$d\xi^{\mathrm{T}}(t)X\xi(t) - \int_{t-d(\theta)}^{t} \xi^{\mathrm{T}}(t)X\xi(t)ds \ge 0, \qquad (18)$$

that is,

$$\begin{aligned}
0 &\le d\xi^{\mathrm{T}}(t)X\xi(t) - \int_{t-d(\theta)}^{t} \xi^{\mathrm{T}}(t)X\xi(t)ds \\
&= d\begin{bmatrix} x^{\mathrm{T}}(t) & x^{\mathrm{T}}(t-d(\theta)) \end{bmatrix}X \\
&\quad \times \begin{bmatrix} x^{\mathrm{T}}(t) & x^{\mathrm{T}}(t-d(\theta)) \end{bmatrix}^{\mathrm{T}} \\
&\quad - \int_{t-d(\theta)}^{t} \begin{bmatrix} x^{\mathrm{T}}(t) & x^{\mathrm{T}}(t-d(\theta)) \end{bmatrix} \\
&\quad \times X \begin{bmatrix} x^{\mathrm{T}}(t) & x^{\mathrm{T}}(t-d(\theta)) \end{bmatrix}^{\mathrm{T}} ds \\
&= x^{\mathrm{T}}(t)dX_{11}x(t) + x^{\mathrm{T}}(t)dX_{12}x(t-d(\theta)) \\
&\quad + x^{\mathrm{T}}(t-d(\theta))dX_{12}^{\mathrm{T}}x(t) \\
&\quad + x^{\mathrm{T}}(t-d(\theta))dX_{22}x(t-d(\theta)) \\
&\quad - \int_{t-d(\theta)}^{t} \left[x^{\mathrm{T}}(t)X_{11}x(t) + x^{\mathrm{T}}(t)X_{12}x(t-d(\theta))\right. \\
&\quad + x^{\mathrm{T}}(t-d(\theta))X_{22}x(t-d(\theta)) \\
&\quad \left. + x^{\mathrm{T}}(t-d(\theta))X_{12}^{\mathrm{T}}x(t)\right] ds. \qquad (19)
\end{aligned}$$

From the Leibnitz-Newton formula, for any matrices L_i, $i = 1,2$, we have

$$\begin{aligned}
&2\left[x^{\mathrm{T}}(t)L_1 + x^{\mathrm{T}}(t-d(\theta))L_2\right] \\
&\left[x(t) - \textstyle\int_{t-d(\theta)}^{t} \dot{x}(s)ds - x(t-d(\theta))\right] = 0,
\end{aligned}$$

that is,

$$\begin{aligned}
&x^{\mathrm{T}}(t)\left(L_1 + L_1^{\mathrm{T}}\right)x(t) + x^{\mathrm{T}}(t-d(\theta))L_2x(t) \\
&+x^{\mathrm{T}}(t)L_2^{\mathrm{T}}x(t-d(\theta)) - 2x^{\mathrm{T}}(t)L_1\textstyle\int_{t-d(\theta)}^{t}\dot{x}(s)ds \\
&-2x^{\mathrm{T}}(t-d(\theta))L_2\textstyle\int_{t-d(\theta)}^{t}\dot{x}(s)ds - x^{\mathrm{T}}(t)L_1x(t-d(\theta)) \\
&-x^{\mathrm{T}}(t-d(\theta))L_1^{\mathrm{T}}x(t) - x^{\mathrm{T}}(t-d(\theta))L_2x(t-d(\theta)) \\
&-x^{\mathrm{T}}(t-d(\theta))L_2^{\mathrm{T}}x(t-d(\theta)) = 0.
\end{aligned} \qquad (20)$$

Combining (15)-(20), and according to the expressions of Π_{11}, Π_{12}, Π_{22} and $\xi(t)$, we have

$$\begin{aligned}
&\dot{V}(x,\theta) - \alpha V(x,\theta) \\
&\le \xi(t)^{\mathrm{T}}\begin{bmatrix} \Pi_{11} & \Pi_{12} \\ \Pi_{12}^{\mathrm{T}} & \Pi_{22} \end{bmatrix}\xi(t) - \int_{t-d(\theta)}^{t}\begin{bmatrix} x(t) \\ x(t-d(\theta)) \\ \dot{x}(s) \end{bmatrix}^{\mathrm{T}} \\
&\quad \times \begin{bmatrix} X_{11} & X_{12} & L_1 \\ X_{12}^{\mathrm{T}} & X_{22} & L_2 \\ L_1^{\mathrm{T}} & L_2^{\mathrm{T}} & Z \end{bmatrix}\begin{bmatrix} x(t) \\ x(t-d(\theta)) \\ \dot{x}(s) \end{bmatrix} ds.
\end{aligned} \qquad (21)$$

Further, from (11), (12) and (21), we can obtain

$$\dot{V}(x,\theta) \le \alpha V(x,\theta). \qquad (22)$$

Note that condition (22) can be rewritten as

$$\frac{\dot{V}(x,\theta)}{V(x,\theta)} \le \alpha. \qquad (23)$$

Integrating (23) from 0 to t, with $t \in [0,T]$ yields

$$\ln V(x,\theta) - \ln V(x(0),\theta) = \int_0^t \frac{\dot{V}(x,\theta)}{V(x,\theta)}dt \le \int_0^t \alpha dt = \alpha t. \qquad (24)$$

By simplifying (24), we have

$$V(x,\theta) \le e^{\alpha t} V(x(0),\theta). \tag{25}$$

On one hand,

$$\begin{aligned} V(x,\theta) &\ge x^{\mathrm{T}}(t)P(\theta)x(t) \\ &= x^{\mathrm{T}}(t)R^{\frac{1}{2}}R^{-\frac{1}{2}}P(\theta)R^{-\frac{1}{2}}R^{\frac{1}{2}}x(t) \\ &\ge \lambda_{\min}\left[R^{-\frac{1}{2}}P(\theta)R^{-\frac{1}{2}}\right]x^{\mathrm{T}}(t)Rx(t). \end{aligned} \tag{26}$$

On the other hand,

$$\begin{aligned} & V(x(0),\theta) \\ \le\ & x^{\mathrm{T}}(0)P(\theta(0))x(0) + \int_{-d}^{0} x^{\mathrm{T}}(s)e^{-\alpha s}Qx(s)ds \\ & + \int_{-d}^{0}\int_{\sigma}^{0} \dot{x}^{\mathrm{T}}(s)e^{-\alpha s}Z\dot{x}(s)dsd\sigma \\ \le\ & \lambda_{\max}\left[R^{-\frac{1}{2}}P(\theta(0))R^{-\frac{1}{2}}\right]x^{\mathrm{T}}(0)Rx(0) \\ & +\lambda_{\max}\left[R^{-\frac{1}{2}}QR^{-\frac{1}{2}}\right]\sup_{-d\le\tau\le 0} x^{\mathrm{T}}(\tau)Rx(\tau)\left(\frac{e^{\alpha d}-1}{\alpha}\right) \\ & +\lambda_{\max}\left[R^{-\frac{1}{2}}ZR^{-\frac{1}{2}}\right]\sup_{-d\le\tau\le 0} \dot{x}^{\mathrm{T}}(\tau)R\dot{x}(\tau) \\ & \times\left(\frac{e^{\alpha d}-\alpha d-1}{\alpha^2}\right) \\ \le\ & \Lambda \sup_{-d\le\tau\le 0} \bar{x}^{\mathrm{T}}(\tau)R\bar{x}(\tau), \end{aligned} \tag{27}$$

where $\Lambda = \lambda_{\max}\left[R^{-\frac{1}{2}}P(\theta(0))R^{-\frac{1}{2}}\right] + \lambda_{\max}\left[R^{-\frac{1}{2}}QR^{-\frac{1}{2}}\right] \times \left(\frac{e^{\alpha d}-1}{\alpha}\right) + \lambda_{\max}\left[R^{-\frac{1}{2}}ZR^{-\frac{1}{2}}\right]\left(\frac{e^{\alpha d}-\alpha d-1}{\alpha^2}\right)$.

$\Lambda = \lambda_{\max}\left[R^{-\frac{1}{2}}P(\theta(0))R^{-\frac{1}{2}}\right] + \lambda_{\max}\left[R^{-\frac{1}{2}}QR^{-\frac{1}{2}}\right] \times \left(\frac{e^{\alpha d}-1}{\alpha}\right) + \lambda_{\max}\left[R^{-\frac{1}{2}}ZR^{-\frac{1}{2}}\right]\left(\frac{e^{\alpha d}-\alpha d-1}{\alpha^2}\right)$

The combination of (25)-(27) results in

$$\begin{aligned} & \lambda_{\min}\left[R^{-\frac{1}{2}}P(\theta)R^{-\frac{1}{2}}\right]x^{\mathrm{T}}(t)Rx(t) \\ \le\ & e^{\alpha t}\Lambda \sup_{-d\le\tau\le 0} \bar{x}^{\mathrm{T}}(\tau)R\bar{x}(\tau), \end{aligned}$$

that is,

$$x^{\mathrm{T}}(t)Rx(t) \le \frac{e^{\alpha t}\Lambda \sup_{-d\le\tau\le 0} x^{\mathrm{T}}(\tau)Rx(\tau)}{\lambda_{\min}\left[R^{-\frac{1}{2}}P(\theta)R^{-\frac{1}{2}}\right]}.$$

From (14a)-(14d), it is followed that

$$\begin{aligned} & x^{\mathrm{T}}(t)Rx(t) \\ \le\ & \left\{\lambda_2 + \lambda_3\left(\frac{e^{\alpha d}-1}{\alpha}\right) + \lambda_4\left(\frac{e^{\alpha d}-\alpha d-1}{\alpha^2}\right)\right\} \\ & \times\frac{e^{\alpha T(\theta)}}{\lambda_1}\sup_{-d\le\tau\le 0} x^{\mathrm{T}}(\tau)Rx(\tau). \end{aligned}$$

According to Definition 1 and (13), it implies that if $\sup_{-d\le\tau\le 0} \bar{x}^{\mathrm{T}}(\tau)R\bar{x}(\tau) \le c_1(p)$, then $x^{\mathrm{T}}(t)Rx(t) \le c_2(p)$. Then we can conclude that the delayed LPV system (9) is shifting finite-time stable with respect to $(c_1(p), c_2(p), T(p), R, \Theta_v)$. The proof is completed. ■

3.2 Control design

In the following, we will consider the problem of shifting finite-time control synthesis for time-delay LPV system.

For control of the above system (1), we intend to design a parameter-dependent state-feedback controller in the following form

$$u(t) = K(\theta)x(t) \tag{28}$$

where $K(\theta)$ is the parameter-dependent state feedback gain.

With this controller (28) applied to the system (1), the closed-loop system is obviously obtained as follows

$$\dot{x}(t) = A_c(\theta)x(t) + A_d(\theta)x(t - d(\theta)) \tag{29a}$$

where

$$A_c(\theta) = A(\theta) + B(\theta)K(\theta) \tag{30}$$

The following theorem will give the designed controller for shifting finite-time control synthesis of time-delay LPV system (1).

Theorem 2 *Consider the delayed LPV system (1), and suppose that the parameter-varying delay $d(\theta)$ satisfying (3). If there exist continuously differentiable positive definite matrix functions $X(\theta)$, continuously matrix functions $Y(\theta)$, positive definite matrices W, $\tilde{Z}$, and constants $\alpha \ge 0$, n_1, n_2, such that (13) and*

$$\begin{bmatrix} \Gamma_{11} & \Gamma_{12} & \Gamma_{13} & 0 & X(\theta) \\ * & \Gamma_{22} & n_2 W A_d^T(\theta) & -d\tilde{Z} & 0 \\ * & * & -1/d\tilde{Z} & 0 & 0 \\ * & * & * & -d\tilde{Z} & 0 \\ * & * & * & * & -W \end{bmatrix} < 0, \tag{31}$$

hold for any $\theta \in \Theta_v$, and

$$\lambda_1 = \inf_{\theta\in\Theta_v} \lambda_{\min}\left(R^{-\frac{1}{2}}X^{-1}(\theta)R^{-\frac{1}{2}}\right), \tag{32a}$$

$$\lambda_2 = \sup_{\theta\in\Theta_v} \lambda_{\max}\left(R^{-\frac{1}{2}}X^{-1}(\theta)R^{-\frac{1}{2}}\right), \tag{32b}$$

$$\lambda_3 = \lambda_{\max}\left(R^{-\frac{1}{2}}W^{-1}R^{-\frac{1}{2}}\right), \tag{32c}$$

$$\lambda_4 = \lambda_{\max}\left(R^{-\frac{1}{2}}\tilde{Z}^{-1}R^{-\frac{1}{2}}\right), \tag{32d}$$

$\Gamma_{11} = -\alpha X(\theta) - \dot{X}(\theta) - n_1^2\left(1 - \sum_{i=1}^{l}\left(\{\underline{v}_i, \bar{v}_i\}\frac{\partial d(\theta)}{\partial\theta_i}\right)\right)W + A(\theta)X(\theta) + B(\theta)Y(\theta) + n_1 A_d(\theta)W + X(\theta)A^T(\theta) + Y^T(\theta)B^T(\theta) + n_1 W A_d^T(\theta)$,

$\Gamma_{12} = -n_1 n_2\left(1 - \sum_{i=1}^{l}\left(\{\underline{v}_i, \bar{v}_i\}\frac{\partial d(\theta)}{\partial\theta_i}\right)\right)W + A_d(\theta)n_2 W + X(\theta) - n_1 W$,

$\Gamma_{13} = X(\theta)A^T(\theta) + Y^T(\theta)B^T(\theta) + n_1 W A_d^T(\theta)$,

$\Gamma_{22} = -n_2^2\left(1 - \sum_{i=1}^{l}\left(\{\underline{v}_i, \bar{v}_i\}\frac{\partial d(\theta)}{\partial\theta_i}\right)\right)W - 2n_2 W$, *then there exists a parameter-dependent controller such that the closed-loop system (29a) is shifting finite-time stable with respect to $(c_1(p), c_2(p), T(p), R, \Theta_v)$. In this case, the controller is constructed as (28), where the controller gain $K(\theta) = Y(\theta)X^{-1}(\theta)$.*

Proof. Based on the results in the previous subsection, we know that the closed-loop LPV system (29a) is shifting finite-time stable, if there exists a continuously differentiable matrix function $P(\theta) > 0$, positive definite matrices Q, Z, matrices $L_i, i = 1, 2$, X, and constants $\alpha \geq 0$ such that (12), (13), and

$$\left[\begin{array}{cc} \tilde{\Pi}_{11} & \tilde{\Pi}_{12} \\ * & \Pi_{22} \end{array} \right] < 0, \tag{33}$$

where X is defined in (10) and

$$\begin{aligned} \tilde{\Pi}_{11} &= \mathrm{sym}\{P(\theta)A_c(\theta)\} + dA_c^{\mathrm{T}}(\theta)ZA_c(\theta) - \alpha P(\theta) \\ &\quad + \dot{P}(\theta) + Q + dX_{11} + \mathrm{sym}\{L_1\}, \\ \tilde{\Pi}_{12} &= P(\theta)A_d(\theta) + dA_c^{\mathrm{T}}(\theta)ZA_d(\theta) + dX_{12} + L_2^{\mathrm{T}} - L_1, \\ \Pi_{22} &= -\left(1 - \dot{d}(\theta)\right)Q + dA_d^{\mathrm{T}}(\theta)ZA_d(\theta) - \mathrm{sym}\{L_2\} \\ &\quad + dX_{22}. \end{aligned}$$

From Schur complement lemma, and by Lemma 1, the satisfactory of (12) and (33) is equivalent to the fact that the following inequality

$$\left[\begin{array}{cccc} \Psi_{11} & \Psi_{12} & A_c^{\mathrm{T}}(\theta) & -dL_1 \\ \Psi_{12}^{\mathrm{T}} & \Psi_{22} & A_d^{\mathrm{T}}(\theta) & -dL_2 \\ A_c(\theta) & A_d(\theta) & -(dZ)^{-1} & 0 \\ -dL_1^{\mathrm{T}} & -dL_2^{\mathrm{T}} & 0 & -dZ \end{array} \right] < 0, \tag{34}$$

holds, where

$$\begin{aligned} \Psi_{11} &= \mathrm{sym}\{P(\theta)A_c(\theta)\} - \alpha P(\theta) + \dot{P}(\theta) + Q + \mathrm{sym}\{L_1\}, \\ \Psi_{12} &= P(\theta)A_d(\theta) + L_2^{\mathrm{T}} - L_1, \\ \Psi_{22} &= -\left(1 - \dot{d}(\theta)\right)Q - \mathrm{sym}\{L_2\}. \end{aligned}$$

Let

$$\begin{aligned} \Psi &= \left[\begin{array}{cc} \Psi_{11} & \Psi_{12} \\ \Psi_{12}^{\mathrm{T}} & \Psi_{22} \end{array} \right] \\ \Omega &= \left[\begin{array}{cc} -\alpha P(\theta) + \dot{P}(\theta) + Q & 0 \\ 0 & -\left(1 - \dot{d}(\theta)\right)Q \end{array} \right] \\ \tilde{A}_c &= \left[\begin{array}{cc} A_c(\theta) & A_d(\theta) \\ I & -I \end{array} \right], \tilde{L} = \left[\begin{array}{cc} P(\theta) & 0 \\ L_1^T & L_2^T \end{array} \right] \end{aligned}$$

Then,

$$\Psi = \Omega + \tilde{L}^{\mathrm{T}}\tilde{A}_c + \tilde{A}_c^{\mathrm{T}}\tilde{L}.$$

Let

$$\tilde{L}^{-1} = \left[\begin{array}{cc} P^{-1}(\theta) & 0 \\ N_1 & N_2 \end{array} \right].$$

Remark that

$$\dot{P}^{-1}(\theta) = -P^{-1}(\theta)\dot{P}(\theta)P^{-1}(\theta).$$

Using Schur complement lemma, and pre-multiplying by $\mathrm{diag}\left\{\tilde{L}^{-\mathrm{T}},\, I,\, Z^{-1}\right\}$ and post-multiplying by $\mathrm{diag}\left\{\tilde{L}^{-1},\, I,\, Z^{-1}\right\}$ on both sides of (34) give rise to

$$\left[\begin{array}{ccccc} \Omega_{11} & \Omega_{12} & \Omega_{13} & 0 & P^{-1}(\theta) \\ * & \Omega_{22} & N_2^T A_d^T(\theta) & -dZ^{-1} & 0 \\ * & * & -1/dZ^{-1} & 0 & 0 \\ * & * & * & -dZ^{-1} & 0 \\ * & * & * & * & -Q^{-1} \end{array} \right] < 0, \tag{35}$$

where $\Omega_{11} = -\alpha P^{-1}(\theta) - \dot{P}^{-1}(\theta) - N_1^T\left(1 - \dot{d}(\theta)\right)QN_1 + A_c(\theta)P^{-1}(\theta) + A_d(\theta)N_1 + P^{-1}(\theta)A_c^T(\theta) + N_1^T A_d^T(\theta)$,

$\Omega_{12} = -N_1^T\left(1 - \dot{d}(\theta)\right)QN_2 + A_d(\theta)N_2 + P^{-1}(\theta) - N_1^T$,

$\Omega_{13} = P^{-1}(\theta)A_c^T(\theta) + N_1^T A_d^T(\theta)$,

$\Omega_{22} = -N_2^T\left(1 - \dot{d}(\theta)\right)QN_2 - N_2 - N_2^T$.

Choose

$$N_1 = n_1 Q^{-1}, N_2 = n_2 Q^{-1}.$$

Then, by substituting (30) into the aforementioned inequality and letting

$$X(\theta) = P^{-1}(\theta), Y(\theta) = K(\theta)X(\theta), W = Q^{-1}, \tilde{Z} = Z^{-1},$$

we can get that (35) is equivalent to the following inequality

$$\left[\begin{array}{ccccc} \Sigma_{11} & \Sigma_{12} & \Gamma_{13} & 0 & X(\theta) \\ * & \Sigma_{22} & n_2 W A_d^T(\theta) & -d\tilde{Z} & 0 \\ * & * & -1/d\tilde{Z} & 0 & 0 \\ * & * & * & -d\tilde{Z} & 0 \\ * & * & * & * & -W \end{array} \right] < 0, \tag{36}$$

$\Sigma_{11} = -\alpha X(\theta) - \dot{X}(\theta) - n_1^2\left(1 - \dot{d}(\theta)\right)W + A(\theta)X(\theta) + B(\theta)Y(\theta) + n_1 A_d(\theta)W + X(\theta)A^T(\theta) + Y^T(\theta)B^T(\theta) + n_1 W A_d^T(\theta)$,

$\Sigma_{12} = -n_1 n_2\left(1 - \dot{d}(\theta)\right)W + A_d(\theta)n_2 W + X(\theta) - n_1 W$,

$\Sigma_{22} = -n_2^2\left(1 - \dot{d}(\theta)\right)W - 2n_2 W$.

By employing Lemma 2, it is easily verified that (36) is equivalent to (31). Further, condition (14) is converted to (32). Then, the proof is finished. ■

Further, by using Schur complement lemma, it is easy to verify that if the following conditions

$$\lambda_1^* R^{-1} \leq X(\theta) \leq R^{-1}, \tag{37a}$$

$$\lambda_2^* R^{-1} \leq W \leq \lambda_3^* R^{-1}, \tag{37b}$$

$$\lambda_4^* R^{-1} \leq \tilde{Z} \leq \lambda_5^* R^{-1}, \tag{37c}$$

$$\left[\begin{array}{ccc} c_2(p)e^{-\alpha T(p)} & \sqrt{c_1(p)} & \sqrt{c_1(p)\left(e^{\alpha d} - 1\right)/\alpha} \\ * & \lambda_1^* & 0 \\ * & * & \lambda_2^* \\ * & * & * \\ \sqrt{c_1(p)\left(e^{\alpha d} - \alpha d - 1\right)/\alpha^2} & & \\ 0 & & \\ 0 & & \\ \lambda_4^* & & \end{array} \right] \geq 0, \tag{37d}$$

hold for some positive numbers λ_i^*, $i = 1, 2, \cdots, 5$, then (13) is guaranteed.

It is noted that the LMI conditions (31), (37a) and (37d) involve an infinite-dimensional convex problem due to their dependence on parameters θ, and thus, the task of determining the controller is numerically intractable. To overcome it, a finite set of basis functions are employed, which can approximate the parameter-dependent matrix functions, $X(\theta)$ and $Y(\theta)$ that appear in the conditions (31), (37a) and (37d). Hence, in order to obtain a finite number of LMI conditions,

we choose the structures of matrix functions $X(\theta)$ and $Y(\theta)$ as follows:

$$X(\theta) = \sum_{j=1}^{s} f_j(\theta) X_j, \tag{38}$$

$$Y(\theta) = \sum_{j=1}^{s} g_j(\theta) Y_j, \tag{39}$$

where s is a known positive number, X_j, $j = 1, 2, \cdots, s$ are symmetric matrices, Y_j, $j = 1, 2, \cdots, s$ are matrices with appropriate dimensions, and $f_j(\cdot)$, $g_j(\cdot)$, $j = 1, 2, \cdots, s$ are the chosen basis functions.

4 Conclusion

In this paper we tackled the shifting finite-time control problem for LPV system with parameter-varying time delays. By using parameter-dependent Lyapunov-Krasovskii functional approach, a new delay-dependent shifting finite-time stability criterion is derived. Sufficient criteria on finite-time stabilization via state feedback are provided in terms of LMIs.

References

[1] Qi W, Hou Y, Zong G, et al. Finite-time event-triggered control for semi-Markovian switching cyber-physical systems with FDI attacks and applications[J]. IEEE Transactions on Circuits and Systems I: Regular Papers, 2021, 68(6): 2665-2674.

[2] X. Zhang, Y. Lin. Adaptive control of nonlinear time-delay systems with application to a two-stage chemical reactor. *IEEE Transactions on Automatic Control*, vol. 60, no. 4, pp. 1074-1079, 2015.

[3] Z. Feng, W. X. Zheng. On extended dissipativity of discrete-time neural networks with time delay. *IEEE Transactions on Neural Networks and Learning Systems*, vol. 26, no. 12, pp. 3293-3300, 2015.

[4] R. Yang, Y. Wang. Finite-time stability analysis and H_∞ control for a class of nonlinear time-delay Hamiltonian systems. *Automatica*, vol. 49, no. 2, pp. 390-401, 2013.

[5] H. Yin, J. Gao, Z. Liu. A parameter dependent controller design approach for delayed LPV system. *Asian Journal of Control*, vol. 19, no. 1, pp. 391-398, 2017.

[6] L. Wu, P. Shi, C. Wang, H. Gao. Delay-dependent robust H_∞ and L_2-L_∞ filtering for LPV systems with both discrete and distributed delays. *IEE Proceedings-Control Theory and Applications*, vol. 153, no. 4, pp. 483-492, 2006.

[7] J. M. Velni, K. M. Grigoriadis. Delay-dependent H_∞ filtering for time-delayed LPV systems. *Systems & Control Letters*, vol. 57, no. 4, pp. 290-299, 2008.

[8] X. He, J. Zhao. Parameter-dependent H_∞ filter design for LPV systems and an autopilot application. *Applied Mathematics and Computation*, vol. 218, no. 9, pp. 5508-5517, 2012.

[9] J. Witte, H. Balini, C. W. Scherer. Robust and LPV control of an AMB system. In *Proceedings of American Control Conferenc*e, IEEE, Marriott Waterfront, Baltimore, MD, USA, pp. 2194-2199, 2010.

[10] X. Lin, X. Li, Y. Zou, S. Li. Finite-time stabilization of switched linear systems with nonlinear saturating actuators. *Journal of the Franklin Institute*, vol. 351, no. 3, pp. 1464-1482, 2014.

[11] F. Amato, M. Ariola, P. Dorato. Finite-time control of linear systems subject to parametric uncertainties and disturbances. *Automatica*, vol. 37, no. 9, pp. 1459-1463, 2001.

[12] F. Amato, M. Ariola. Finite-time control of discrete-time linear systems. *IEEE Transactions on Automatic control*, vol. 50, no. 5, pp. 724-729, 2005.

[13] X. Lin, S. Li, Y. Zou. Finite-time stability of switched linear systems with subsystems which are not finite-time stable. *IET Control Theory & Applications*, vol. 8, no. 12, pp. 1137-1146, 2014.

[14] Z. Yan, W. Zhang, G. Zhang. Finite-time stability and stabilization of Itô stochastic systems with Markovian switching: mode-dependent parameter approach. *IEEE Transactions on Automatic Control*, vol. 60, no. 9, pp. 2428-2433, 2015.

[15] L. Lee, K. I. Kou, W. Zhang, J. Liang, Y. Liu. Robust finite-time boundedness of multi-agent systems subject to parametric uncertainties and disturbances. *International Journal of Systems Science*, vol. 47, no. 10, pp. 2466-2474, 2016.

[16] Rotondo D, Nejjari F, Puig V. Design of parameter-scheduled state-feedback controllers using shifting specifications. *Journal of the Franklin Institute*, 2015, 352(1): 93-116.

[17] Rotondo D, Nejjari F, Puig V. Shifting finite time stability and boundedness design for continuous-time LPV systems. *Proceedings of the American Control Conference*, 2015: 838-843.

[18] Y. M. Hu, G. R. Duan, F. Tan. Finite-time control for LPV systems with parameter-varying time delays and exogenous disturbances. *International Journal of Robust and Nonlinear Control* , vol. 27, no. 17, pp. 3841-3861, 2017.

[19] X. Lin, H. Du, S. Li, Y. Zou. Finite-time stability and finite-time weighted L_2-gain analysis for switched systems with time-varying delay. *IET Control Theory & Applications* , vol. 7, no. 7, pp. 1058-1069, 2013.

[20] K. Gu. A further refinement of discretized Lyapunov functional method for the stability of time-delay systems. *International Journal of Control*, vol. 74, no. 10, pp. 967-976, 2001.

[21] P. Gahinet, P. Apkarian, M. Chilali. Affine parameter-dependent Lyapunov functions and real parametric uncertainty. *IEEE Transactions on Automatic control*, vol. 41, no. 3, pp. 436-442, 1996.

[22] F. Wu, K. M. Grigoriadis. LPV systems with parameter- varying time delays: analysis and control. *Automatica*, vol. 37, no. 2, pp. 221-229, 2001.

Proceedings of the 3rd Conference on Fully Actuated System Theory and Applications
May 10-12, 2024, Shenzhen, China

Coordination Control of Networked Robotic Systems via A Fully-Actuated System Approach

Jiange Wang[1], Tong Zhang[1], Xiaolei Li[1], Yanqiao Wei[1], Yuzhong Wang[2]

1. School of Electrical Engineering, Yanshan University, Qinhuangdao, 066004, China.
E-mail: jiange@ysu.edu.cn, xiaolei@ysu.edu.cn,weiyanqiao@ysu.edu.cn

2. Center for Control Science and Technology, Southern University of Science and Technology, Shenzhen, P. R. China
E-mail: wangyz3@sustech.edu.cn

Abstract: Networked robotic systems with fully-actuated characteristics are currently widely used, but control design using this feature has not received enough attention. In this paper, we consider the coordination control problem of networked robotic systems via a fully-actuated system approach. To this end, the dynamics of the robotic systems is firstly transformed to a fully-actuated system model. Then a coordination controller is proposed, where several similar extension forms are also given. By using the direct parametric method, the stability conditions are given. The approach offers a complete flexibility that can be used to enhance the system's performance.

Key Words: Networked robotic systems, coordination control, fully-actuated system approach, direct parametric method.

1 Introduction

The development of networked robotic systems has become a hot point in modern technology. The significance of such a kind of system lies in its ability to realize collaborative work among multiple robots and conduct remote communication and coordination through the Internet or other networks [1–4]. This collaborative control not only improves the efficiency and flexibility of the robot system, but also expands its application fields. In various fields such as manufacturing, medical care, and rescue, the collaborative control of networked robotic systems can promote the completion of tasks, improve production efficiency, and play an important role in dangerous or inaccessible environments [5–7].

Generally, networked robotic systems are modeled as second-order nonlinear systems. Typical one such as Euler-Lagrange system, can capture the integral dynamic behavior [8–10]. There are many benefits to using the Euler-Lagrange equation to model networked robotic systems, especially its regressor parameter characteristics that make it easy to deal with model parameter uncertainties [11–13]. Many impressive results have been achieved using this approach. It is worth noting that actuator dynamics in these works are often approximated as a zero-order systems. However, when demanding rapid and highly precise movements, the actuators cannot be simplified as a zero-order model. Instead, a first- or second-order model becomes necessary to optimize the overall system performance, which results in that the integrated system emerges from the cascading of the plant and the actuator system. This essentially third-order system brings additional difficulties to coordinated control design.

To achieve coordinated control design for such cascaded systems, a common approach involves initially transforming the system into a state space and then applying control techniques to this altered first-order system. However, due to the time-varying or highly nonlinear nature of the networked robotic systems, the traditional first-order system theory often falls short in guaranteeing complete stability for the closed-loop system. Recently, the fully-actuated system approach has attracted the attention of scholars [14–16]. By transforming the system as a high-order fully-actuated system model, a direct parametric approach is proposed, which brings several benefits, including linearized closed-loop systems, arbitrarily configurable closed-loop system eigenvalues, etc [17–19]. However, how to use this method to achieve collaborative control design of networked robotic systems has not been well explored.

Inspired by above discussions, this paper aims to solve the coordinated control problem of networked robotic systems using a fully-actuated system approach. To this end, the following two questions should be answered. The first question is what information is needed to implement the collaborative task. Existing direct parametric methods require the use of zero-order, first-order, and second-order derivatives of state information. Is this necessary? The second question is whether the introduction of the Laplacian matrix will affect the parametric design process. In the process of collaborative control of networked robotic systems, since the control gain is generally coupled with the Laplacian matrix, can the parametric method eliminate the influence of system nonlinearity through gain design? The purpose of this paper is to answer these two questions. We first transform the networked robot system into a high-order fully-actuated system model, then discuss several different schemes of collaborative control design, and finally use the direct parametric method to give the system stability conditions.

2 Problem Statement and Preliminaries

2.1 Graph Theory and Notations

This part introduces the concept of a Lagrangian network represented by a directed graph featuring a spanning tree. The directed graph, denoted as $\mathcal{G} = (\mathcal{N}, \mathcal{E})$, comprises the sets of vertices and edges, which are denoted by $\mathcal{N} = \{1, 2, ..., N\}$ and $\mathcal{E} \subseteq \{(i, j)|i, j \in \mathcal{N}, i \neq j\}$, respectively. Specifically, $(i, j) \in \mathcal{E}$ signifies that node j can receive information from node i but not the other way around. The

This work is supported in part by National Natural Science Foundation of China under Grant 62103352 and Grant 62033011, in part by Hebei Natural Science Foundation under Grant F2023203056, and also partially supported by the 8th batch of post-doctoral Innovative Talent Support Program BX20230150.

Table 1: Notations and Symbols

Symbols	
$\mathbb{R}, \mathbb{R}_+$	Real and positive real number set
$\mathbb{R}^n, \mathbb{R}^{n\times n}$	n-dimensional vector and matrix space
$\mathbb{C}$	Complex number set
$I_n \in \mathbb{R}^{n\times n}$	n-dimensional identity matrix
$\|\cdot\|$	Euclidian norm of a vector or a matrix
$\lambda_k(A)$	k-th eigenvalues of the matrix A
$\rho(A)$	Spectral radius of the matrix A
$\mathrm{Re}(\lambda_k(A))$	Real part of $\lambda_k(A)$
$\Im(\lambda_k(A))$	Imaginary part of $\lambda_k(A)$
ℓ	Imaginary unit, $\ell^2 = -1$
A^H	Hermitian adjoint matrix of A

paper defines $A = [a_{ij}] \in \mathbb{R}^{N\times N}$ and $D = diag(\sum_{i=1}^{N} a_{ij})$ as the weighted adjacency matrix and degree matrix of the graph $\mathcal{G}$, respectively. Here, $a_{ij} > 0$ for any $(i, j) \in \mathcal{E}$, and $a_{ij} = 0$ otherwise. The Laplacian matrix of $\mathcal{G}$, denoted as $\mathcal{L}(\mathcal{G}) = \mathcal{D} - \mathcal{A}$ or simply $\mathcal{L}$, is established. If a vertex within the graph $\mathcal{G}$ can reach all other vertices through directed paths, it implies the presence of a directed spanning tree in $\mathcal{G}$. In this paper, we suppose that there exists a directed spanning tree in the robotic network $\mathcal{G} = (\mathcal{N}, \mathcal{E})$. For simplicity, some mathematical symbols used later are given in Table 1.

2.2 Networked Robotic Systems

In this paper, the networked robotic systems are modeled by an Euler-Lagrange equation as follows

$$M_i(q_i)\ddot{q}_i + C_i(q_i, \dot{q}_i)\dot{q}_i + G_i(q_i) = \tau_i, i \in \mathcal{N} \tag{1}$$

where $q_i, \dot{q}_i \in \mathbb{R}^n$ are the generalized position and velocity of the i-th subsystem, respectively. The system matrix $M_i(q_i) \in \mathbb{R}^{n\times n}$, $C_i(q_i, \dot{q}_i) \in \mathbb{R}^{n\times n}$, $G_i(q_i) \in \mathbb{R}^n$ are positive definite inertia matrix, centripetal and coriolis torques matrix, and gravitational torque matrix, respectively. For brevity, the parameters in the brackets of these matrix will be omitted in subsequent derivation. $\tau_i \in \mathbb{R}^n$ is the control torque. Although system (1) has some impressive properties [20], they are not always available and will not be considered to be used in this paper.

Generally, the control torque can be simplistically seen as the output of a proportional actuator, making the entire system model akin to equation (1). Yet, when the robot's mechanics are lightweight and demand swift motions, the actuator can't be simplified into a basic zero-order model anymore. In such scenarios, the motor dynamics necessitate a description using a first- or second-order dynamical model. To illustrate, let's assume the motor dynamics follow a first-order linear model

$$\dot{\tau}_i = A_a\tau_i + u_i, \tag{2}$$

where A_a and u_i are the coefficient matrix and control input of the actuator of the i-robot, respectively. Specifically, the component of each actuator can be expressed as

$$\dot{\tau}_k = a_k\tau_k + u_k, k = 1, 2, \ldots, m, \tag{3}$$

where τ_k and $u_k, k = 1, 2, \ldots, m$, are the torque and input voltage of the k-th individual motor, and a_k, $k = 1, 2, \ldots, m$, are a series of negative parameters.

One common approach to achieve the coordinated control of the combined system described by equations (1) and (2) involves initially simplifying the system into a first-order state space configuration. Subsequently, control methods designed for first-order systems are applied. This process ultimately requires handling a first-order system of dimension $3n$. However, in contrast to this conventional method, our paper adopts a high-order system approach. For the sake of simplicity, this paper utilizes the first-order actuator model (2). The control objective is summarized as follows.

Control objective: Consider the following cascaded robotic systems

$$\begin{cases} M_i(q_i)\ddot{q}_i + C_i(q_i, \dot{q}_i)\dot{q}_i + G_i(q_i) = \tau_i, i \in \mathcal{N} \\ \dot{\tau}_i = A_a\tau_i + u_i. \end{cases} \tag{4}$$

Design a control signal u_i for each robot such that the following coordination objective can be achieved

$$\lim_{t\to\infty} |q_i - q_j| = 0, \lim_{t\to\infty} \dot{q}_i = 0. \tag{5}$$

3 High-Order Fully-Actuated Model for Networked Robotic Systems

In this section, the networked robotic systems is firstly transformed into a high-order fully-actuated model. From (1), the differentiations of system matrices are

$$\frac{\mathrm{d}}{\mathrm{d}t}(M_i\ddot{q}_i) = \frac{\mathrm{d}M_i}{\mathrm{d}t}\ddot{q}_i + M_i\dddot{q}_i, \tag{6}$$

$$\frac{\mathrm{d}}{\mathrm{d}t}(C_i\dot{q}_i) = \frac{\mathrm{d}C_i}{\mathrm{d}t}\dot{q}_i + C_i\ddot{q}_i. \tag{7}$$

Then also differentiating the left-hand side of (1), it yields

$$\begin{aligned} &\frac{\mathrm{d}}{\mathrm{d}t}(M_i\ddot{q}_i + C_i\dot{q}_i + G_i) \\ &= \frac{\mathrm{d}M_i}{\mathrm{d}t}\ddot{q}_i + M_i\dddot{q}_i + \frac{\mathrm{d}C_i}{\mathrm{d}t}\dot{q}_i + C_i\ddot{q}_i + \frac{\mathrm{d}}{\mathrm{d}t}G_i \\ &= M_i\dddot{q}_i + \left(\frac{\mathrm{d}M_i}{\mathrm{d}t} + C_i\right)\ddot{q}_i + \frac{\mathrm{d}C_i}{\mathrm{d}t}\dot{q}_i + \frac{\mathrm{d}}{\mathrm{d}t}G_i. \end{aligned}$$

In addition, the following actuator dynamics can be derived from (2),

$$\dot{\tau}_i = A_a(M_i\ddot{q}_i + C_i\dot{q}_i + G_i) + u_i. \tag{8}$$

Then the closed-loop system can be expressed as

$$\begin{aligned} &M_i\dddot{q}_i + \left(\frac{\mathrm{d}M_i}{\mathrm{d}t} + C_i\right)\ddot{q}_i + \frac{\mathrm{d}C_i}{\mathrm{d}t}\dot{q}_i + \frac{\mathrm{d}}{\mathrm{d}t}G_i \\ = \;& A_aM_i\ddot{q}_i + A_aC_i\dot{q}_i + A_aG_i + u_i. \end{aligned}$$

Then the system dynamics (1) is rewritten as the following third-order model

$$\begin{aligned} &A_{i3}(q_i, \dot{q}_i)\dddot{q}_i + A_{i2}(q_i, \dot{q}_i)\ddot{q}_i \\ &+ A_{i1}(q_i, \dot{q}_i)\dot{q}_i + \eta_i(q_i, \dot{q}_i) = u_i, \end{aligned} \tag{9}$$

where

$$A_{i3}(q_i,\dot{q}_i)=M_i,$$
$$A_{i2}(q_i,\dot{q}_i)=\frac{\mathrm{d}M_i}{\mathrm{d}t}+C_i-A_aM_i,$$
$$A_{i1}(q_i,\dot{q}_i)=\frac{\mathrm{d}C_i}{\mathrm{d}t}-A_aC_i,$$
$$\eta_i(q_i,\dot{q}_i)=\frac{\mathrm{d}}{\mathrm{d}t}G_i-A_aG_i.$$

4 Coordinated Control Design

4.1 Controller design

In this section, the coordination control problem for system (1) is transformed into the system in (9). As stated in [17], the coordinated controller is also designed with two parts,

$$u_i=u_{ic}+u_{if}, \tag{10}$$

where u_{ic} is used to compensate the term $\eta_i(q_i,\dot{q}_i)$ in (9), which is given by

$$u_{ic}=\eta_i(q_i,\dot{q}_i), \tag{11}$$

while u_{if} is designed to achieve the coordination objective, which can be designed as

$$\begin{aligned}u_{if}=&K_{i0}(q_i,\dot{q}_i)\ddot{q}_i+K_{i1}(q_i,\dot{q}_i)\dot{q}_i\\&+K_2(q_i,\dot{q}_i)\sum\nolimits_{j=1}^{n}a_{ij}(q_i-q_j)+\\&+K_3(q_i,\dot{q}_i)\sum\nolimits_{j=1}^{n}a_{ij}(\dot{q}_i-\dot{q}_j)\\&+K_4(q_i,\dot{q}_i)\sum\nolimits_{j=1}^{n}a_{ij}(\ddot{q}_i-\ddot{q}_j)+v_i,\end{aligned} \tag{12}$$

where $K_{im}(q_i,\dot{q}_i),K_r(q_i,\dot{q}_i)\in\mathbb{R}^{n\times n}$, $m=0,1$, $r=2,3,4$, are piecewise continuous gain matrices to be designed, q_j is the state of the j-th robot. It can be seen that the proposed controller contains six parts, where the terms containing collaborative interactions $\sum_{j=1}^{n}a_{ij}(q_i-q_j)$, $\sum_{j=1}^{n}a_{ij}(\dot{q}_i-\dot{q}_j)$, and $\sum_{j=1}^{n}a_{ij}(\ddot{q}_i-\ddot{q}_j)$ are used to achieve coordination of the networked robotic systems, while the terms $K_{i0}(q_i,\dot{q}_i)\dot{q}_i$ and $K_{i1}(q_i,\dot{q}_i)\ddot{q}_i$ are used to compensate for the inherent nonlinearity of the i-th robotic system. v_i is an external signal that can be used to achieve additional control design.

Under the controller (12), the closed-loop system can be written as

$$\begin{aligned}&A_{i3}(q_i,\dot{q}_i)\dddot{q}_i+A_{i2}(q_i,\dot{q}_i)\ddot{q}_i+A_{i1}(q_i,\dot{q}_i)\dot{q}_i\\&=K_{i0}(q_i,\dot{q}_i)\ddot{q}_i+K_{i1}(q_i,\dot{q}_i)\dot{q}_i\\&+K_2(q_i,\dot{q}_i)\sum\nolimits_{j=1}^{n}a_{ij}(q_i-q_j)+\\&+K_3(q_i,\dot{q}_i)\sum\nolimits_{j=1}^{n}a_{ij}(\dot{q}_i-\dot{q}_j)\\&+K_4(q_i,\dot{q}_i)\sum\nolimits_{j=1}^{n}a_{ij}(\ddot{q}_i-\ddot{q}_j)+v_i,\end{aligned} \tag{13}$$

where $A_{im}(q_i,\dot{q}_i)$, $m=1,2,3$, are given in (9). Then the stacked form of (13) can be written as

$$\begin{aligned}&A_3\dddot{q}+A_2\ddot{q}+A_1\dot{q}\\&=(\mathcal{L}\otimes K_2)q+(K_1+(\mathcal{L}\otimes K_3))\dot{q}\\&+(K_0+(\mathcal{L}\otimes K_4))\ddot{q}+v,\end{aligned} \tag{14}$$

where the stacked system and control gain matrices are defined as

$$\begin{aligned}&A_3=diag\{A_{i3}(q_i,\dot{q}_i)\},A_2=diag\{A_{i2}(q_i,\dot{q}_i)\},\\&A_1=diag\{A_{i1}(q_i,\dot{q}_i)\},v=[v_1,...,v_n],\\&K_0=diag\{K_{i0}\},K_1=diag\{K_{i1}\}.\end{aligned}$$

As mentioned above, to compensate for the effects of the terms $A_2\ddot{q}$ and $A_1\dot{q}$, the control gain matrices K_1 and K_3 are designed as

$$K_0=A_2,\quad K_1=A_1. \tag{15}$$

Then equation (14) can be rewritten as

$$\begin{aligned}\dddot{q}=&A_3^{-1}[(\mathcal{L}\otimes K_4)]\ddot{q}+A_3^{-1}[(\mathcal{L}\otimes K_3)]\dot{q}\\&+A_3^{-1}(\mathcal{L}\otimes K_2)q+A_3^{-1}v.\end{aligned} \tag{16}$$

Next, we introduce two subspaces whose direct sum results in $\mathbb{C}^{nN}$. Through the state projection of system (16) onto these two subspaces, the coordination issue is transformed into stability analysis related to various subsystems linked to the eigenvalues of the Laplacian matrix $\mathcal{L}$. Consider $\lambda_i(i=1,2,\ldots,N)$ as the eigenvalues of the Laplacian matrix $\mathcal{L}$ within the directed topology $\mathcal{G}$. Here, $\lambda_1=0$ alongside its associated eigenvector $\bar{u}_1=\mathbf{1}$, and the ordering follows: $Re\,(\lambda_1)\leqslant Re\,(\lambda_2)\leqslant\cdots\leqslant Re\,(\lambda_N)$. Let $U^{-1}\mathcal{L}U=J$, where $U=[\bar{u}_1,\bar{u}_2,\ldots,\bar{u}_N]$, and J denotes the Jordan canonical form of $\mathcal{L}$. Define $c_l(l=1,2,\ldots,n)$ as linearly independent n-dimensional real vectors, the following two subspaces on $\mathbb{C}^{nN}$ is introduced. Let $p_j=\bar{u}_i\otimes c_l$ with $j=(i-1)n+l$, $i=1,2,\ldots,N$, and $l=1,2,\ldots,n$. A coordination subspace is defined as $\mathbb{C}(U)$, which spanned by $p_1,p_2,\ldots,p_n$. Additionally, a complementary coordination subspace is denoted as $\overline{\mathbb{C}}(U)$, which is spanned by $p_{n+1},p_{n+2},\ldots,p_{nN}$. Then for any vector $z\in\mathbb{C}(U)$, we have $z=\mathbf{1}\otimes\bar{c}$ with $\bar{c}$ being a n-dimensional vector. Since $p_j(j=1,2,\ldots,Nd)$ are linearly independent, it derives that $\mathbb{C}(U)\oplus\overline{\mathbb{C}}(U)=\mathbb{C}^{nN}$, where $\oplus$ means the direct sum.

Then define $\tilde{q}(t)=\left(U^{-1}\otimes I_n\right)q(t)=\left[\tilde{q}_1^H(t),\tilde{q}_2^H(t),\ldots,\tilde{q}_N^H(t)\right]^H$, equation (14) can be rewritten as

$$\begin{aligned}\dddot{\tilde{q}}=&A_3^{-1}[(J\otimes K_4)]\ddot{\tilde{q}}+A_3^{-1}[(J\otimes K_3)]\dot{\tilde{q}}\\&+A_3^{-1}(J\otimes K_2)\tilde{q}+A_3^{-1}\tilde{v}.\end{aligned} \tag{17}$$

Define $J=diag\{0,\bar{J}\}$ with $\bar{J}=diag\lambda_i$, $i=2,3,\ldots,N$. Let $\bar{q}(t)=\left[\tilde{q}_2^H(t),\ldots,\tilde{q}_N^H(t)\right]^H$, then system (17) can be rewritten as follows

$$\dddot{\tilde{q}}_1(t)=A_{3i}^{-1}\tilde{v}_1, \tag{18}$$

$$\begin{aligned}\dddot{\bar{q}}(t)=&A_3^{-1}[(\bar{J}\otimes K_4)]\ddot{\bar{q}}+A_3^{-1}[(\bar{J}\otimes K_3)]\dot{\bar{q}}\\&+A_3^{-1}(\bar{J}\otimes K_2)\bar{q}+A_3^{-1}\bar{v}.\end{aligned} \tag{19}$$

According to the Theorem 1 in [21], the following lemma can be directly obtained.

Lemma 1 *The coordination objective of system* (17) *can be achieved if and only if the following system are asymptotically stable.*

$$\begin{aligned}\dddot{\eta}_i(t)=&\lambda_iA_{3i}^{-1}K_4\ddot{\eta}_i(t)+\lambda_iA_{3i}^{-1}K_3\dot{\eta}_i(t)\\&+\lambda_iA_{3i}^{-1}K_2\eta_i(t)+A_{3i}^{-1}\bar{v}_i,i=2,3,\ldots,N.\end{aligned} \tag{20}$$

Now the coordination control problem of networked robotic systems is transformed into the stabilization problem of system (20). Then define $\breve{q}_i = \left[\eta_i^T(t), \dot{\eta}_i^T(t), \ddot{\eta}_i^T(t)\right]^T$, equation (20) can be rewritten as

$$\dot{\breve{q}}_i = A_c \breve{q}_i + B_c \bar{v}_i, \tag{21}$$

where the system matrices A_c and B_c are

$$A_c = \begin{bmatrix} 0 & I_n & 0 \\ 0 & 0 & I_n \\ \lambda_i A_{3i}^{-1} K_2 & \lambda_i A_{3i}^{-1} K_3 & \lambda_i A_{3i}^{-1} K_4 \end{bmatrix},$$

$$B_c = \begin{bmatrix} 0 \\ 0 \\ A_3^{-1} \end{bmatrix}.$$

Then the directly parametric method proposed in [17] can be used to provide the control gain matrices. Specifically, choosing any matrix $F \in \mathbb{R}^{3n\times 3n}$ related to your desired stabilization objective, which satisfy

$$\boldsymbol{F} = \big\{F \mid F \in \mathbb{R}^{3n\times 3n}, \text{ and } \exists Z \in \mathbb{R}^{n\times 3n}, \text{ s.t. } detV(Z,F) \neq 0\big\}.$$

where $V \in \mathbb{R}^{3n\times 3n}$ is a constant nonsingular matrix such that

$$V^{-1} A_c V = F. \tag{22}$$

Note that as shown in [17], $\boldsymbol{F}$ is nonempty. Then the system matrix A_c can be expressed as

$$A_c = VFV^{-1}, \tag{23}$$

which means that the triple of gain matrices $K_{im} \in \mathbb{R}^{n\times n}$, $m = 0, 2, 4$, can be directly derived. The matrix V can be expressed as

$$V = V(Z,F) = \begin{bmatrix} Z \\ ZF \\ ZF^2 \end{bmatrix}. \tag{24}$$

which is a full-rank matrix. Then the following theorem is given.

Theorem 1 *For the networked robotic systems modeled by* (4) *under the proposed controller* (10) *with* (11) *and* (12)*, then the control objective* (5) *can be achieved if the control gain matrices satisfy*

$$K_{i0} = A_{i2}, K_{i1} = A_{i1},$$
$$[\lambda_i K_2, \lambda_i K_3, \lambda_i K_4] = A_{3i} Z F^3 V^{-1}(Z,F), \tag{25}$$

where $Z \in \mathbb{R}^{n\times 3n}$ *is an arbitrary parameter matrix as shown in* (24)*.*

Remark 1 *More details on the proof of Theorem 1 can refer to [21]. The main idea of the controller design in* (10) *is to design appropriate control gain matrices, the inherent nonlinearity of the system is compensated and coordinated control of the robotic systems is achieved. That means the second question in Introduction is answered in this part. From* (12)*, it can be seen that the zero-order, first-order, and second-order derivatives of state information of the robotic systems are all used in the proposed controller, which is consistent with existing direct parametric methods.*

4.2 Discussion on the coordination controller design

To be formally consistent with existing direct parametric methods, the zero-order, first-order, and second-order derivatives of state information of the robotic systems are all used in the proposed controller (12). However, these information may not be available in any time. Next, we will discuss other possible forms of the coordination controllers to answer the first question in Introduction.

To achieve collaborative control of networked robotic systems, a straightforward idea is to only use the relative states to design controller, such as

$$\begin{aligned} u_{if} =& K_{i0}(q_i, \dot{q}_i) \sum\nolimits_{j=1}^{n} a_{ij}(q_i - q_j) \\ &+ K_{i1}(q_i, \dot{q}_i) \sum\nolimits_{j=1}^{n} a_{ij}(\dot{q}_i - \dot{q}_j) \\ &+ K_{i2}(q_i, \dot{q}_i) \sum\nolimits_{j=1}^{n} a_{ij}(\ddot{q}_i - \ddot{q}_j) + v_i. \end{aligned} \tag{26}$$

However, it is not difficult to see that this form of cooperative controller has difficulty in compensating the inherent nonlinearity of the system through gain design since the control gain and Laplacian matrix are coupled with each other. Thus the first two parts in (12) are necessary and inevitable. Then alternative control schemes can be designed as

$$\begin{aligned} u_{if} =& K_{i0}(q_i, \dot{q}_i) q_i + K_1(q_i, \dot{q}_i) \sum\nolimits_{j=1}^{n} a_{ij}(q_i - q_j) \\ &+ K_{i2}(q_i, \dot{q}_i) \dot{q}_i + K_3(q_i, \dot{q}_i) \sum\nolimits_{j=1}^{n} a_{ij}(\dot{q}_i - \dot{q}_j) \\ &+ K_{i4}(q_i, \dot{q}_i) \ddot{q}_i + K_5(q_i, \dot{q}_i) \sum\nolimits_{j=1}^{n} a_{ij}(\ddot{q}_i - \ddot{q}_j) + v_i, \end{aligned} \tag{27}$$

where the controller (12) can be seen as a special case of (27) with $K_{i0}(q_i, \dot{q}_i) = 0$. Under controller (27), the closed-loop system is given as

$$\begin{aligned} & A_3 \dddot{q} + A_2 \ddot{q} + A_1 \dot{q} \\ &= [K_0 + (\mathcal{L} \otimes K_1)] q + [K_2 + (\mathcal{L} \otimes K_3)] \dot{q} \\ &+ [K_4 + (\mathcal{L} \otimes K_5)] \ddot{q} + v. \end{aligned} \tag{28}$$

According to the analysis of Theorem 1, the following corollary is given.

Corollary 1 *For the networked robotic systems modeled by* (4) *under the proposed controller* (10) *with* (11) *and* (27)*, then the control objective* (5) *can be achieved if the control gain matrices satisfy*

$$K_{i0} = A_{i2}, K_{i2} = A_{i1},$$
$$[\lambda_i K_1, \lambda_i K_3, K_4 + \lambda_i K_5] = A_{3i} Z F^3 V^{-1}(Z,F), \tag{29}$$

where $Z \in \mathbb{R}^{n\times 3n}$ *is an arbitrary parameter matrix as shown in* (24)*.*

In this case, the introduction of K_4 in (27) provides an additional degree of freedom in control gain design.

Obviously, the other one important degenerate forms of (27) can be expressed as

$$\begin{aligned} u_{if} =& K_{i0}(q_i, \dot{q}_i) \dot{q}_i + K_{i1}(q_i, \dot{q}_i) \ddot{q}_i \\ &+ K_2(q_i, \dot{q}_i) \sum\nolimits_{j=1}^{n} a_{ij}(q_i - q_j) + v_i, \end{aligned} \tag{30}$$

which can be seen as a minimal implementation of (27). Under controller (30), the closed-loop system is given as

$$\begin{aligned} &A_3 \dddot{q} + A_2\ddot{q} + A_1\dot{q} \\ &= K_0\dot{q} + K_1\ddot{q} + (\mathcal{L}\otimes K_2)q + v. \end{aligned} \tag{31}$$

Intuitively, the inherent nonlinearity of the system can be counteracted by choosing $K_0 = A_1$ and $K_1 = A_2$, but this makes the design of control gain K_2 complex and loses some design freedom. Next, we still analyze along the idea of direct parametric method of fully-actuated system. The closed-loop system under (31) can be expressed as

$$\begin{aligned} \dddot{q} =& A_3^{-1}(K_0 - A_1)\dot{q} + A_3^{-1}(K_1 - A_2)\ddot{q} \\ &+ A_3^{-1}(\mathcal{L}\otimes K_2)q + A_3^{-1}\tilde{v}. \end{aligned} \tag{32}$$

Choosing the control gain matrices K_0 and K_1 as

$$K_0 = A_1 + G_0, K_1 = A_2 + G_1. \tag{33}$$

Then (17) can be rewritten as

$$\dddot{q} = A_3^{-1}G_0\dot{q} + A_3^{-1}G_1\ddot{q} + A_3^{-1}(\mathcal{L}\otimes K_2)q + A_3^{-1}\tilde{v}. \tag{34}$$

Then the following the following corollary is given.

Corollary 2 *For the networked robotic systems modeled by* (4) *under the proposed controller* (10) *with* (11) *and* (31)*, then the control objective* (5) *can be achieved if the control gain matrices satisfy*

$$\begin{aligned} &K_{i0} = A_{i1} + G_0, K_{i1} = A_{i2} + G_1, \\ &[G_0, G_1, \lambda_i K_2] = A_{3i}ZF^3V^{-1}(Z, F), \end{aligned} \tag{35}$$

where $Z \in \mathbb{R}^{n\times 3n}$ *is an arbitrary parameter matrix as shown in* (24)*.*

Remark 2 *In fact, we ignored several situations in the above analysis, namely the cases that* $K_{i0}(q_i, \dot{q}_i) = 0$*,* $K_3(q_i, \dot{q}_i) = 0$*,* $K_5(q_i, \dot{q}_i) = 0$ *and* $K_{i0}(q_i, \dot{q}_i) = 0$*,* $K_5(q_i, \dot{q}_i) = 0$*. These cases can be easily extended by analysis above results. It is worth noting that the significant benefits brought by the controller* (30) *are that only generalized position information of the neighboring robots is required. In this case, the user can easily be allowed to further consider other issues such as communication delay and communication bandwidth constraints. In addition, this also answers the first question in Introduction, the* i*th robot's own zero-order, first-order, and second-order derivatives of state information is necessary in direct parametric method of fully-actuated system, while only the generalized position information of the neighboring robots is enough in coordination controller design.*

5 Conclusions

In this paper, the coordination control problem of the networked robotic systems is considered using a fully-actuated system method. By transforming the Enler-Lagrange system model into a fully-actuated system, several coordination control schemes are proposed and analyzed. By using the direct parametric method, the stability conditions for control gain matrices are directly given. The approach offers a complete flexibility that can be used to enhance the system's performance. In the future, we will further consider the impact of communication delay and disturbances in a fully-actuated system framework. In addition, how to realize coordinated control of fully-actuated high-order nonlinear systems is also an important research direction.

References

[1] C. Zhu, B. Huang, Y. Lu, X. Li, and Y. Su, "Distributed affine formation maneuver control of autonomous surface vehicles with event-triggered data transmission mechanism," *IEEE Transactions on Control Systems Technology*, vol. 3, no. 31, pp. 1006–1017, 2023.

[2] X. Fang, X. Li, and L. Xie, "Distributed formation maneuver control of multiagent systems over directed graphs," *IEEE Transactions on Cybernetics*, vol. 52, no. 8, pp. 8201–8212, 2021.

[3] L. Xiaolei, W. Changyun, and W. Jiange, "Adaptive bearing-only formation tracking of nonholonomic multi-agent systems," *IEEE Transaction on Cybernetics*, 2020. Under review.

[4] J. Mei, W. Ren, and G. Ma, "Distributed containment control for lagrangian networks with parametric uncertainties under a directed graph," *Automatica*, vol. 48, no. 4, pp. 653–659, 2012.

[5] S. A. P. Ramaswamy and S. N. Balakrishnan, "Formation control of car-like mobile robots: A lyapunov function based approach," in *Proceedings of the 2008 IEEE Conference on American Control Conference*, (Seattle, WA, USA), pp. 657–662, 2008.

[6] R. O. Saber and R. M. Murray, "Consensus problems in networks of agents with switching topology and time-delays," *IEEE Transactions on Automatic Control*, vol. 49, no. 9, pp. 1520–1533, 2004.

[7] H. Wang, "Flocking of networked uncertain euler-lagrange systems on directed graphs," *Automatica*, vol. 49, no. 9, pp. 2774–2779, 2013.

[8] A. Abdessameud and A. Tayebi, "Formation control of VTOL unmanned aerial vehicles with communication delays," *Automatica*, vol. 47, no. 11, pp. 2383–2394, 2011.

[9] J. Mei, W. Ren, and G. Ma, "Distributed coordinated tracking with a dynamic leader for multiple euler-lagrange systems," *IEEE Transactions on Automatic Control*, vol. 56, no. 6, pp. 1415–1421, 2011.

[10] H. Cai and J. Huang, "Leader-following consensus of multiple uncertain euler-lagrange systems under switching network topology," *International Journal of General Systems*, vol. 43, no. 3-4, pp. 294–304, 2014.

[11] A. Abdessameud, I. G. Polushin, and A. Tayebi, "Synchronization of lagrangian systems with irregular communication delays," *IEEE Transactions on Automatic Control*, vol. 59, no. 1, pp. 187–193, 2013.

[12] A. Abdessameud, A. Tayebi, and I. G. Polushin, "Leader-follower synchronization of euler-lagrange systems with time-varying leader trajectory and constrained discrete-time communication," *IEEE Transactions on Automatic Control*, vol. 62, no. 5, pp. 2539–2545, 2017.

[13] X. Li, C. Wen, and C. Chen, "Resilient cooperative control for networked lagrangian systems against dos attacks," *IEEE Transaction on Cybernetics*, vol. 99, pp. 1–1, 2020. Early access.

[14] D.-W. Zhang, G.-P. Liu, and L. Cao, "Coordinated control of high-order fully actuated multiagent systems and its application: A predictive control strategy," *IEEE/ASME Transactions on Mechatronics*, vol. 27, no. 6, pp. 4362–4372, 2022.

[15] Y. Yu, G.-P. Liu, Y. Huang, and J. M. Guerrero, "Coordinated predictive secondary control for dc microgrids based on high-order fully actuated system approaches," *IEEE Transactions on Smart Grid*, 2023.

[16] W. Liu, G. Duan, and M. Hou, "High-order robust command filtered backstepping design for strict-feedback systems: A high-order fully actuated system approach," *International Journal of Robust and Nonlinear Control*, vol. 32, no. 18, pp. 10251–10270, 2022.

[17] G.-R. Duan, "Direct parametric approach for cascaded systems with application in robot control," in *2014 14th International Conference on Control, Automation and Systems (ICCAS 2014)*, pp. 29–35, IEEE, 2014.

[18] G.-R. Duan, "Direct parametric control of fully-actuated high-order nonlinear systems–normal case," in *Proceeding of the 11th World Congress on Intelligent Control and Automation*, pp. 3053–3060, IEEE, 2014.

[19] G.-R. Duan, "Control of feedback type systems–a direct parametric approach," in *2014 IEEE International Conference on Information and Automation (ICIA)*, pp. 412–417, IEEE, 2014.

[20] W. E. Dixon, D. M. Dawson, E. Zergeroglu, and A. Behal, *Nonlinear Control of Wheeled Mobile Robots*. Springer, London, 2005.

[21] J. Xi, Z. Shi, and Y. Zhong, "Consensus analysis and design for high-order linear swarm systems with time-varying delays," *Physica A: Statistical Mechanics and its Applications*, vol. 390, no. 23-24, pp. 4114–4123, 2011.

Proceedings of the 3rd Conference on Fully Actuated System Theory and Applications
May 10-12, 2024, Shenzhen, China

一种固定时间的二阶多智能体系统分布式最优一致性算法

时侠圣[1,2]，隋天举[2]

1. 安徽大学人工智能学院 合肥 230601

2. 大连理工大学工业装备智能控制与优化教育部重点实验室，大连 116024
E-mail: shixiasheng@zju.edu.cn

摘 要: 随着人工智能技术和通信技术的快速发展，面向分布式多智能体系统的分布式优化问题得到广泛关注. 本文针对无向网络下二阶多智能体系统的分布式优化问题设计一种固定时间收敛优化算法. 首先，本文利用基于符号函数的滑模理论实现智能体速度量固定时间收敛至目标值，将二阶智能体分布式优化问题转化为一阶智能体分布式优化问题. 其次，借助滑模理论实现智能体固定时间实现梯度和为零. 然后，本文利用成本函数二阶导信息设计一种初始自由固定时间时间收敛算法. 最后结合案例仿真说明本文所设计算法的有效性.

关键词: 固定时间, 分布式优化, 多智能体系统, 零梯度和

A distributed fixed-time optimal consensus algorithm over second-order multi-agent systems

Xiasheng Shi[1,2], Tianju Sui[2]

1. The School of Artificial Intelligence, Anhui University, Hefei 230601, China

2. Key Laboratory of Intelligent Control and Optimization for Industrial Equipment (Dalian University of Technology), Ministry of Education, Dalian 116024, China
E-mail: shixiasheng@zju.edu.cn

Abstract: With the rapid development of artificial intelligence technology and communication technology, the distributed optimization problem for distributed second-order multi-agent systems has received extensive attention. In this paper, a specified time convergence optimization algorithm is designed for the distributed optimization problem of multi-agent systems under undirected networks. Firstly, the sliding mode theory is used to achieve fixed-time convergence of the agent speed to the target value, transforming the second-order agent-distributed optimization problem into a first-order agent-distributed optimization problem. Secondly, with the help of the sliding mode theory, the agent realizes that the gradient sum is zero at a fixed time. Then, this paper uses the second derivative information of the cost function to design an initialization-free fixed-time convergent algorithm. Finally, the effectiveness of the algorithm designed in this paper is illustrated by case simulation.

Key Words: Fixed-time, Distributed optimization, Multi-agent systems, Zero-gradient-sum

1 引言

多智能体系统分布式优化是一种涉及多个分布式智能体的优化问题，这些智能体需要通过分布式计算和通信来合作解决优化问题. 与集中式优化问题相比，分布式优化问题中不存在中央控制单元，具有较强的可扩展性和鲁棒性[1−3]. 最优一致性问题作为分布式优化问题的典型应用之一，旨在实现所有智能体决策变量一致，并最小化所有智能体成本函数和[4]. 随着多智能体系统一致性技术发展，许多优秀算法被设计出来，包括两大类：离散时间算法和连续时间算法[5].

在离散时间算法方面， Nedic首次将梯度下降策略与多智能体系统一致性结合，设计一类分布式优化算法实现无向和有向网络下的最优一致性问题[6−7]. 然而其中采用的时变递减步长降低了算法收敛速度. 强行将时变递减步长变为固定步长， 则上述算法仅能收敛至最优解邻域，而无法精确收敛至最优解. 为此， 施伟等利用各智能体历史信息实现对梯度函数的精确跟踪, 在固定步长下获取线性收敛[8]. 随后，该梯度跟踪技术被推广至各种情形, 包括有向网络[9]、加速优化[10]等. 不同于上述依赖于梯度的方法，一种依赖于成本函数二阶导信息的零梯度和算法被设计出来[11]. 但是上述算法依然是线性收敛.

近年来，随着信息物理系统技术的发展, 越来越多学者尝试将智能体动力学特性融入算法设计，开发连续时间算法[12]. 借助完备的Lyapunov理论或微分包含理论等给出更强的收敛结论，例如有限时间收敛、固定时间收敛等[13]. Wu等利用符号函数与零梯度和方法设计一类有限时间收敛的最优一致性算法[14]. 然而其收敛时间依赖于系统初始状态. 为消除算法收敛

*此项工作分别得到大连理工大学工业装备智能控制与优化教育部重点实验室开放基金、国家自然科学基金创新研究群体科学基金和国家自然科学基金资助，项目批准号：LICO2022TB02、61921004和62173057.

时间对初始状态的依赖，Ning等设计一类固定时间收敛算法[15]. 然而，上述文献仅能处理梯度函数线性可分的分布式凸优化问题. 为此, Liu等利用时基生成器设计一类预设时间最优一致性算法[16]. 然而上述算法仅能收敛至分布式优化问题的次优解. 为求解分布式最优一致性问题的精确解，文献[17]设计一种两阶段分布式优化算法，其中第一阶段实现智能体固定时间收敛至局部最优解, 第二阶段借助多智能体一致性策略和成本函数二阶导信息实现智能体固定时间收敛至全局最优解. 然而上述算法需分阶段执行. 为实现上述两阶段同步执行， 文献[18]借鉴滑模控制策略，设计一种初始自由固定时间分布式优化算法.

基于上述讨论，可以发现现有研究成果多讨论一阶多智能体系统. 时等[19]利用跟踪控制实现二阶多智能体系统的固定时间最优一致性. 然而该文献要求智能体间传递成本函数的梯度值, 容易造成隐私泄露. 故本文拟设计一种新型固定时间收敛的最优一致性算法，贡献点总结如下: 与传统零梯度和算法[11]相比, 本文所设计算法能够实现固定时间收敛，且智能体状态无需满足梯度和为零约束.

本文后续结构安排如下：第2节进行问题描述和算法设计，第3节开展算法收敛性分析，第4节进行案例仿真，第5节总结全文.

2 问题描述及算法设计

本小节首先进行问题描述，随后基于网络图论和多智能体一致性技术进行算法设计.

2.1 问题描述

在最优一致性问题中，各智能体拥有仅自己可知的决策变量 $x_i \in \mathbb{R}$ 和局部成本函数 $f_i(x_i) := \mathbb{R} \to \mathbb{R}$. 其数学模型可归纳如下：

$$\begin{aligned} &\min_x f(x) = \sum_{i=1}^{n} f_i(x_i) \\ &s.t.\ x_i = x_j, i, j = 1,2,...,n \end{aligned} \tag{1}$$

其中系统总成本函数表示为所有局部成本函数之和. 所有智能体协同合作共同最小化总成本函数. 此外，各智能体动力学特性描述如下：

$$\begin{aligned} \dot{x}_i &= v_i \\ \dot{v}_i &= u_i \end{aligned} \tag{2}$$

其中 u_i 为控制策略， v_i 为智能体速度量。

为实现上述目标，各智能体需通信合作，以此建立合适的控制策略. 为此，针对上述 n 多智能体系统，其无向通信网络可由符号 $G(V,A,E)$ 表示，其中 $V = \{1,2,...,n\}$ 表示智能体节点集、$E \subseteq V \times V$ 表示智能体间通信链路集合、 $A := [a_{ij}] \in \mathbb{R}^{n\times n}$ 表示智能体间通信权重或伴随矩阵. 若智能体 i 和智能体 j 存在通信链路，则有 $a_{ij} = a_{ji} = 1$. 反之 $a_{ij} = 0$. 本文假设各智能体不存在自环，则有 $a_{ii} = 0$. 若任意两智能体间存在一条通路，则网络 G 是联通的. 此外，网络 G 的拉普拉斯矩阵 $L: [l_{ij}] \in \mathbb{R}^{n\times n}$ 定义为 $l_{ii} = \sum_{j=1}^{n} a_{ij}, l_{ij} = -a_{ij}, i \neq j.$

假设1 存在正实数 α_i 使得 $0 < \nabla^2 f_i(x_i) \le \alpha_i, \forall i \in V$.

假设2 网络 G 为无向连通图.

引理1[20] 若系统 $\dot{x} = g(x(t)), x \in \mathbb{R}^n$ 满足 $g(0) = 0$ ，且存在一 Lyapunov 函数 $V(x)$ 使得 $\dot{V} \le -\alpha V^p(x) - \beta V^q(x)$ ，$\alpha, \beta, 0 < p < 1, q > 1$，则上述系统在固定时间内收敛至原点，且收敛时间上界满足

$$T \le \frac{1}{\alpha(1-p)} + \frac{1}{\beta(q-1)} \tag{3}$$

引理2[21] 对非负实数 $q_1, q_2, ..., q_n$ ，则有结论 $\sum_{i=1}^{n} q_i^p \ge (\sum_{i=1}^{n} q_i)^p$ 和 $\sum_{i=1}^{n} q_i^m \ge n^{1-m} (\sum_{i=1}^{n} q_i)^m$，其中 $0 < p \le 1, m > 1$.

2.2 算法设计

基于多智能体系统一致性技术，算法设计如下：

$$u_i = -\mathrm{sig}^{\mu}(e_i) - \mathrm{sig}^{\nu}(e_i) + \dot{u}_i^o \tag{4}$$

其中 $e_i = v_i - u_i^o$，u_i^o 定义如下：

$$\begin{aligned} u_i^o = (\nabla^2 f_i(x_i))^{-1} \Big(&-\mathrm{sig}^{\mu}(s_i) - \mathrm{sig}^{\nu}(s_i) \\ &- \sum_{j=1}^{n} a_{ij} \mathrm{sig}^{\mu}(x_i - x_j) - \sum_{j=1}^{n} a_{ij} \mathrm{sig}^{\nu}(x_i - x_j) \Big) \end{aligned} \tag{5}$$

其中控制参数 μ, ν 为正实数，辅助变量 s_i 定义为

$$\begin{aligned} s_i = &\nabla f_i(x_i) \\ &+ \int_0^t \sum_{j=1}^{n} a_{ij} \mathrm{sig}^{\mu}(x_i - x_j) + \sum_{j=1}^{n} a_{ij} \mathrm{sig}^{\nu}(x_i - x_j) d\tau \end{aligned} \tag{6}$$

函数 $\mathrm{sig}^{\mu}(\cdot)$ 定义为 $\mathrm{sig}^{\mu}(\cdot) = \mathrm{sign}(\cdot) \times |\cdot|^{\mu}$. 公式(6)中辅助变量 s_i 实现零梯度和特性.

3 算法收敛性分析

接下来，定理1对算法(2)进行收敛性分析.

定理1 若假设1和2成立，则算法(2)在固定时间内收敛至最优，且系统初始值可任意选取.

证明. 定理1收敛性分析分如下三步: I) 智能体 i 在固定时间 T_1 内收敛至指定速度 u_i^o ； II) 智能体 i 在固定时间 $2T_1$ 内收敛至梯度和为零； III) 智能体 i 在固定时间 $2T_1 + T_2$ 内收敛至全局最优解.

步骤1. 首先，由算法(4)可知

$$\dot{e}_i = -\mathrm{sig}^{\mu}(e_i) - \mathrm{sig}^{\nu}(e_i) \tag{7}$$

令Lyapunov函数 V_1 为

$$V_1 = \frac{1}{2} \|e_i\|^2 \tag{8}$$

对函数 V_1 求微分，可得

$$\begin{aligned} \dot{V}_1 &= -\|e_i\|^{1+\mu} - \|e_i\|^{1+\nu} \\ &= -2^{\frac{1+\mu}{2}} V_1^{\frac{1+\mu}{2}} - 2^{\frac{1+\nu}{2}} V_1^{\frac{1+\nu}{2}} \end{aligned} \tag{9}$$

则由引理1可知，算法(4)在固定时间 T_1 内实现速度量跟踪至指定值 u_i^o，且 T_1 满足以下条件

$$T_1 \le \frac{2^{\frac{1-\mu}{2}}}{1-\mu} + \frac{1}{2^{\frac{\nu-1}{2}}(\nu-1)} \tag{10}$$

步骤2. 当 $t \ge T_1$ 时，公式(4)改写为

$$\dot{s}_i = -\mathrm{sig}^{\mu}(s_i) - \mathrm{sig}^{\nu}(s_i) \tag{11}$$

令Lyapunov函数 V_2 为

$$V_2 = \frac{1}{2}\|s_i\|^2 \tag{12}$$

同理，可得

$$\begin{aligned} \dot{V}_2 &= -\|s_i\|^{\mu+1} - \|s_i\|^{\nu+1} \\ &= -2^{\frac{\mu+1}{2}} V_1^{\frac{\mu+1}{2}} - 2^{\frac{\nu+1}{2}} V_1^{\frac{\nu+1}{2}} \end{aligned} \tag{13}$$

则由引理1可知，算法(4)在固定时间 $2T_1$ 内实现梯度和为零.

步骤3. 当 $t \ge 2T_1$ 时，公式(4)改写为

$$\dot{x}_i = (\nabla^2 f_i(x_i))^{-1}\left(-\sum_{j=1}^{n} a_{ij}\mathrm{sig}^{\mu}(x_i - x_j) - \sum_{j=1}^{n} a_{ij}\mathrm{sig}^{\nu}(x_i - x_j)\right) \tag{14}$$

基于假设2，可得 $\frac{\mathrm{d}}{\mathrm{d}t}\sum_{i=1}^{n}\nabla f_i(x_i) = 0$，可知 $\sum_{i=1}^{n}\nabla f_i(x_i) = 0, t \ge 2T_1$. 令Lyapunov函数 V_3 为

$$V_3 = \sum_{i=1}^{n}\left(f_i(x^*) - f_i(x_i) - \nabla f_i^{\mathrm{T}}(x_i)(x^* - x_i)\right) \tag{15}$$

由假设1可知，

$$\begin{aligned} V_3 &\le \sum_{i=1}^{n}\frac{\alpha_i}{2}\left\|x_i - \frac{\sum_{j=1}^{n} x_j}{n}\right\|^2 \\ &\le \frac{\alpha_{\max}}{\lambda_2(L)} x^{\mathrm{T}} L x \end{aligned} \tag{16}$$

其中 $\alpha_{\max} = \max_i \alpha_i$. 对函数 V_2 求微分，可得

$$\begin{aligned} \dot{V}_2 &= -\sum_{i=1}^{n}\sum_{j=1}^{n} a_{ij}\left\|x_i - x_j\right\|^{1+\mu} - \sum_{i=1}^{n}\sum_{j=1}^{n} a_{ij}\left\|x_i - x_j\right\|^{1+\nu} \\ &\le -\frac{1}{2}\left(\sum_{i=1}^{n}\sum_{j=1}^{n} a_{ij}\left\|x_i - x_j\right\|^2\right)^{\frac{1+\mu}{2}} \\ &\quad -\frac{1}{2\left[n(n-1)\right]^{\frac{\nu-1}{2}}}\left(\sum_{i=1}^{n}\sum_{j=1}^{n} a_{ij}\left\|x_i - x_j\right\|^2\right)^{\frac{1+\nu}{2}} \\ &= -\frac{1}{2^{\frac{1-\mu}{2}}}\left(x^{\mathrm{T}} L x\right)^{\frac{1+\mu}{2}} \\ &\quad -\frac{2^{\frac{\nu-1}{2}}}{\left[n(n-1)\right]^{\frac{\nu-1}{2}}}\left(x^{\mathrm{T}} L x\right)^{\frac{1+\nu}{2}} \\ &= -\frac{\left(\lambda_2(L)\right)^{\frac{1+\mu}{2}}}{2^{\frac{1-\mu}{2}}\alpha_{\max}^{\frac{1+\mu}{2}}} V_3^{\frac{1+\mu}{2}} - \frac{2^{\frac{\nu-1}{2}}\left(\lambda_2(L)\right)^{\frac{1+\nu}{2}}}{\left[n(n-1)\right]^{\frac{\nu-1}{2}}\alpha_{\max}^{\frac{1+\mu}{2}}} V_3^{\frac{1+\nu}{2}} \end{aligned} \tag{17}$$

则由引理1可得，算法(4)在固定时间 $2T_1 + T_2$ 内收敛至问题(1)最优解，且收敛时间 T_2 满足以下条件

$$T_2 \le \frac{2^{\frac{3-\mu}{2}}\alpha_{\max}^{\frac{1+\mu}{2}}}{\left(\lambda_2(L)\right)^{\frac{1+\mu}{2}}(1-\mu)} + \frac{\left[n(n-1)\right]^{\frac{\nu-1}{2}}\alpha_{\max}^{\frac{1+\mu}{2}}}{2^{\frac{\nu-3}{2}}\left(\lambda_2(L)\right)^{\frac{1+\nu}{2}}(\nu-1)} \tag{18}$$

4 案例仿真

接下来本文提供一无向环形通信网络下的五节点多智能体系统作为仿真对象，每个智能体的成本函数定义为 $f_i(x_i) = (x_i - i)^2, i = 1,2,3,4,5$. 控制参数设定为 $\mu = 0.2, \nu = 1.8$，系统初始状态设置为 $x(0) = [1,2,2,3,4]$. 可见本文所设计初始状态并不是各智能体局部最优解. 则算法(4)的仿真轨迹如图1和图2所示. 从图2可以看出，本文所设计算法(4)在固定时间 $2T_1 = 4.88$ s内实现梯度和为零. 从图2可以看出，本文所设计算法能够在固定时间内收敛至最优解 $x^* = 3$. 通过上述案例可以发现，本文所设计算法能够实现二阶多智能体系统的固定时间最优一致性控制.

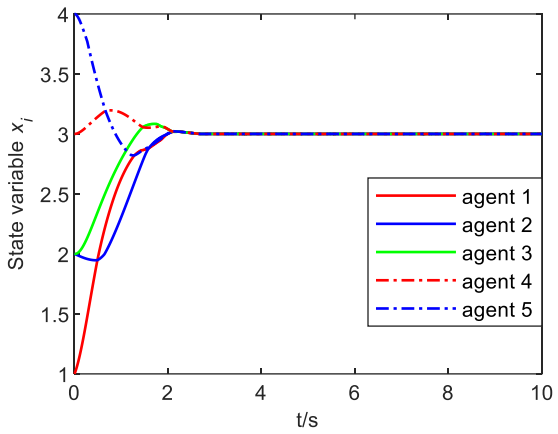

图 1: 本文仿真案例智能体状态 x_i 轨迹

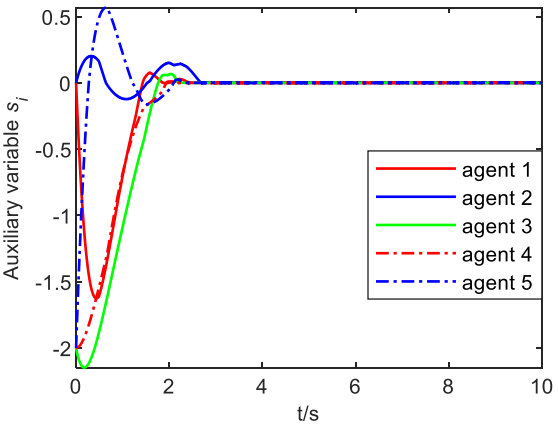

图 2: 本文仿真案例智能体辅助变量 s_i 轨迹

5 总结

本文针对二阶多智能体系统设计一种初始自由固定时间分布式最优一致性算法. 基于滑模控制原理，所设计辅助变量在固定时间内满足系统梯度和为零特性. 其次，借助零梯度和方法设计一种固定时间收敛非线性控制策略. 最后利用符号函数实现智能体速度量在固定时间内跟踪至指定值. 最后借助数值仿真案例说明本文所设计算法的有效性. 然而，本文并没有将智能体局部约束考虑进来. 未来，我们继续探讨固定时间收敛的分布式约束优化问题.

参考文献

[1] 洪奕光, 张燕琼. 分布式优化: 算法设计和收敛分析. 控制理论与应用, 2014, 31(7): 850-857.

[2] 虞浒, 缪小冬, 顾寅骥, 苟志文, 隋天举. 基于GAF-DarkNet的滚动轴承故障诊断方法. 轴承, 2023.

[3] 时侠圣, 孙佳月, 徐磊, 杨涛. 二阶智能体的分布式非光滑资源分配算法. 控制与决策, 2023，38(05): 1336-1344.

[4] 杨涛, 徐磊, 易新蕾, 张圣军, 陈蕊娟, 李渝哲. 基于事件触发的分布式优化算法. 自动化学报, 2022, 48(1): 133-143.

[5] T. Yang, X. Yi, J. Wu, Y. Yuan, D. Wu, Z. Meng, Y. Hong, H. Wang, Z. Lin, K. H. Johansson, A survey of distributed optimization. *Annual Reviews in Control*, 2019, 47: 278-305.

[6] A. Nedic, A. Ozdaglar, Distribute subgradient methods for multi-agent optimization. *IEEE Transactions on Automatic Control*, 2009, 54(1): 48-61.

[7] A. Nedic, A. Olshevsky, Distributed optimization over time-varying directed graphs, *IEEE Transactions on Automatic Control*, 2015, 60(3): 601-615.

[8] W. Shi, Q. Ling, G. Wu, W. Yin, Extra: An exact first-order algorithm for decentralized consensus optimization. *SIAM Journal on Optimization*, 2015, 25(2): 944-966.

[9] C. Xi, R Xin, U. A. Khan, ADD-OPT: Accelerated distributed directed optimization, *IEEE Transactions on Automatic Control*, 2018, 63(5): 1329-1339.

[10] G. Qu, N. Li, Harnessing smoothness to accelerate distributed optimization, *IEEE Transactions on Control of Network Systems*, 2018, 5(3): 1245-1260.

[11] Y. Yuan, L. Shi, W. He, A linear algorithm for quantized event-triggered optimization over directed networks. *IEEE/CAA Journal of Automatica Sinica*, 2022, 9(6): 1095-1098.

[12] 时侠圣, 杨涛, 林志赟, 王雪松. 基于连续时间的二阶多智能体系统分布式资源分配算法. 自动化学报, 2021, 47(8): 2050-2060.

[13] 陈刚, 李志勇. 集合约束下多智能体系统分布式固定时间优化控制. 自动化学报, 2022, 48(9): 2254-2264.

[14] Z. Wu, Z. Li, J. Yu. Designing zero-gradient-sum protocols for finite-time distributed optimization problem. IEEE Transactions on Systems, Man, and Cybernetics: Systems, 2022, 52(7): 4569-4577.

[15] B. Ning, Q. L. Han, Z. Zuo, Distributed optimization for multiagent systems: An edge-based fixed-time consensus approach, IEEE Transactions on Cybernetics, 2019, 49(1): 122-132.

[16] Y. Liu, Z. Xia, W. Gui, Multiobjective distributed optimization via a predefined-time multiagent approach. *IEEE Transactions on Automatic Control*, 2023, 68(11): 6998-7005.

[17] X. Wang, G. Wang, S. Li, A distributed fixed-time optimization algorithm for multi-agent systems. Automatica, 2020, article no. 109289.

[18] G. Guo, R. Zhang, Z. Zhou, A local-minimization-free zero-gradient-sum algorithm for distributed optimization. Automatica, 2023, article no. 111247.

[19] 时侠圣, 林志赟. 基于固定时间的二阶智能体分布式优化算法. 北京航空航天大学学报, 2023, 49(11): 2951-2959.

[20] A. Polyakov, Nonlinear feedback design for fixed-time stabilization of linear control systems. IEEE Transactions on Automatic Control, 2012, 57(8): 2106-2110.

[21] Z. Zuo, L. Tie, A new class of finite-time nonlinear consensus protocols for multi-agent systems. International Journal of Control, 2014, 87(2): 363-370.

Proceedings of the 3rd Conference on Fully Actuated System Theory and Applications
May 10-12, 2024, Shenzhen, China

Event-Triggered Control of High-Order Fully Actuated Nonlinear Multi-Agent Systems

Hailong Cui and Guanglei Zhao*
The Institute of Electrical Engineering, and Intelligent Rehabilitation and Neuroregulation Key Lablatory of Hebei, Yanshan University, Qinhuangdao, 066004, China.
E-mail: hl_cui21@163.com, glzhao517@126.com.

Abstract: This paper studies the consensus problem of high-order fully actuated (HOFA) nonlinear multi-agent systems (MASs), and develops a novel hybrid event-triggering mechanism (HETM) by means of the HOFA system approach. Under a mild condition that inside of a certain agent, the system state is always accessible for controller, while the state information of other agents is obtained via networked communication, we convert the given HOFA nonlinear MAS into a general linear MAS by pre-eliminating all the nonlinear dynamics by using the full-actuation structure of agent itself. Compared with existing related results, which address the nonlinearities by sacrificing closed-loop consensus performance of MAS, the HOFA system approach greatly simplifies the control model and the Lyapunov stability analysis. Then, to reduce the communication frequency, a HETM is designed for the HOFA nonlinear MASs, which guarantees a strictly positive minimum inter-event time (MIET) to make its implementation be proper on digital platform. A numerical example is provided in the simulation results to testify the control effectiveness.

Key Words: High-order fully actuated nonlinear system, Event-triggered control, Multi-agent systems

1 Introduction

Over the past few years, multi-agent systems (MASs) have attracted great research enthusiasm from many scholars academic communities, due to its wide applications in smart grids, sensor networks, and multiple robots [1–3]. Regarding the consensus control of MASs, the complex nonlinearities and strong uncertainties would undoubtedly pose challenges to the consensus controller design for nonlinear MASs. To address this issue, the usual idea is to model the nonlinear MASs into first-order state-space model firstly, then substituting the nonlinearities of every agent into the consensus analysis of whole MAS and eliminating all the nonlinear dynamics by sacrificing closed-loop consensus performance [4, 5]. It should be pointed out that as early as in the first modelling step, all the background information is removed from the original physical model [6–9] in the sense that the nonlinear dynamics of a certain agent cannot be addressed by itself, instead has to be addressed in analysis for MAS consensus. As a result, despite up to date there are many results for nonlinear MASs, in certain complicated cases, the closed-loop consensus cannot be realised yet [6].

As is stated in [6, 7], most nonlinear systems can be either physically modelled as or converted into HOFA systems, then the full-actuation property could provide a great deal of convenience for the control of an HOFA system in the sense that by using the full-actuation structure, the nonlinear term in nonlinear MASs, no matter how complicated, can be easily eliminated as long as the nonlinear term is measurable. On this basis, the practical control model of nonlinear MASs can be much simplified as a constant linear MAS system, the desired closed-loop group dynamics can be realised easily, which might provides a new idea to the control of nonlinear MASs.

This work was supported by Hebei Natural Science Foundation under F2022203040; Natural Science Foundation of China under 62073277, 62188101, U22A2050; Central Government Guided Local Science and Technology Development Fund Project under 226Z0301G; Hebei Innovation Capability Improvement Plan Project under 22567619H; and Basic Innovation Research Project under 2022LGZD008.

In the context of networked control, communication among agents is performed via network, but the network resources are limited in general. How to reduce the communication frequency of MASs while guaranteeing the desired consensus performance has immediately been a hotspot. In this regard, event-triggered control have been widely studied to reduce the usage of communication resources, see [10, 11] for a recent overview, since information transmission is only performed when it is needed or necessary. However, one fundamental problem that should be considered when designing event-triggering mechanisms is to exclude Zeno behavior. In many existing result, introducing an additional exponential decay term to exclude Zeno behavior is conventional [12–14]. Despite this can theoretically proving that the inter-event intervals are larger than 0, the intervals may become more and more small as time goes by. In practice, it is expected that not only Zeno behavior is avoided, but also the minimum inter-event time (MIET) is strictly positive [15]. Thus, it is crucial to design appropriate event-triggering mechanism for the HOFA nonlinear MASs.

Given the above observations, this paper studies the consensus problem of HOFA nonlinear MASs, and develops a novel hybrid event-triggering mechanism (HETM) by means of the HOFA system approach. The main contributions of this paper are twofold: 1) a new HOFA consensus control protocol is proposed for the nonlinear MASs by pre-eliminating all the nonlinear dynamics by using the full-actuation structure of agent itself, which is completely different from addressing the nonlinear dynamics by sacrificing closed-loop consensus performance of MAS [4, 5]; 2) to reduce the communication frequency, a HETM is designed for the HOFA nonlinear MASs, which guarantees a strictly positive MIET to make its implementation be proper on digital platform.

Notations: The notations used in this paper is standard. The set of real (integer) numbers is denoted by $\mathbb{R}$ ($\mathbb{N}$) and $\mathbb{R}_{\geq 0}$ denotes nonnegative reals. $\mathbb{R}^n$ and $\mathbb{R}^{n\times n}$ denote the set of n-dimensional vectors and $n \times n$ real matrices respectively. By $\|\cdot\|$, we denote the Euclidean norm. $\otimes$ denotes the

Kronecker product. For a vector $x_i \in \mathbb{R}^n$, $i = 1, \cdots, N$, $(x_1, \cdots, x_N)$ represents the augmented vector by stacking x_1 to x_N, and we define the following symbols as in [9],

$$x^{(0\sim n)} = \begin{bmatrix} x \\ \dot{x} \\ \vdots \\ x^{(n)} \end{bmatrix}, \; x_{1\sim N}^{(0\sim n)} = \begin{bmatrix} x_1^{(0\sim n)} \\ x_2^{(0\sim n)} \\ \vdots \\ x_N^{(0\sim n)} \end{bmatrix}.$$

Besides, the identity matrix is denoted by I_r, or in short I, and

$$A = \begin{bmatrix} 0 & I & & \\ & & \ddots & \\ & & & I \\ 0 & 0 & 0 & 0 \end{bmatrix}, \; B = \begin{bmatrix} 0 \\ 0 \\ \vdots \\ I \end{bmatrix}.$$

2 Preliminaries and Problem Formulation

2.1 Graph Theory

In this paper, communication connections among agents are described by a weighted graph $\mathcal{G} = (\mathcal{V}, \mathcal{E}, \mathcal{A})$ with $\mathcal{V} = \{1, 2, \cdots, N\}$ being the node set, $\mathcal{E} \subseteq \mathcal{V} \times \mathcal{V}$ the edge set, and $\mathcal{A} = [a_{ij}]_{N\times N}$ the adjacency matrix. If agent $i \in \mathcal{V}$ can always access to agent $j \in \mathcal{N}_i$ along edge $(j, i) \in \mathcal{E}$, then $a_{ij} = 1$, otherwise, $a_{ij} = 0$, where $\mathcal{N}_i = \{j \in \mathcal{V} : \mathcal{E}_{ij} \in \mathcal{E}\}$ denotes the neighbor set of agent i. No self-loop exists, so it has $a_{ii} = 0$. The edge sequence $(i, i_1), (i_1, i_2), \cdots, (i_p, j)$ constitutes a path from agent i to agent j, and if for any $i, j \in \mathcal{V}$, there is such a path from agent i to agent j, then the graph $\mathcal{G}$ is said to be connected. Define the in-degree matrix as $\mathcal{D} = \text{diag}\{d_1, d_2, \cdots, d_N\}$, where $d_i = \sum_{j=1}^{N} a_{ij}$. The Laplacian matrix is obtained as $\mathcal{L} = \mathcal{D} - \mathcal{A}$. In this paper, we suppose that the communication graph $\mathcal{G}$ is undirected and connected.

Lemma 1 *[16]. For the Laplacian matrix $\mathcal{L}$ associated with undirected and connected graph $\mathcal{G}$, let $\lambda_i(\mathcal{L})$ denote the eigenvalues of $\mathcal{L}$, then it holds the property that $0 = \lambda_1(\mathcal{L}) < \lambda_2(\mathcal{L}) \leq ... \leq \lambda_N(\mathcal{L})$. Moreover, there is a unitary matrix $\mathcal{U}$ such that $\mathcal{U}^T\mathcal{L}\mathcal{U} = \Lambda \triangleq \text{diag}\{0, \lambda_2(\mathcal{L}), \cdots, \lambda_N(\mathcal{L})\}$.*

2.2 Problem Formulation

This paper considers the consensus control of high-order fully actuated (HOFA) multi-agent systems, which has the following system dynamics [6]

$$x_i^{(n)} = f_i(x_i^{(0\sim n-1)}) + g_i(x_i^{(0\sim n-1)}, u_i) \tag{1}$$

where $x_i, \; u_i \in \mathbb{R}^r$, $i \in \mathcal{V}$ denote the system state and control input, respectively. $f_i(\cdot)$: $\mathbb{R}^{nr} \times \mathbb{R}_{\geq 0} \to \mathbb{R}^r$ and $g_i(\cdot)$: $\mathbb{R}^{(n+1)r} \to \mathbb{R}^r$ are available continuous nonlinear vector functions. Besides, it is assumed that the following mapping:

$$h_i = g_i(x_i^{(0\sim n-1)}, u_i) \tag{2}$$

forms a differential homeomorphism from u_i to h_i for all $x_i^{(0\sim n-1)}$ and u_i, $t \geq 0$, then, according to the definitions given in [6], it can be known that the nonlinear MAS is fully actuated, and there always exists its inverse mapping:

$$u_i = g_i^{-1}(h_i) \tag{3}$$

such that the desired closed-loop system dynamics can be attained by properly designing mapping input h_i.

Remark 1 *The above HOFA system dynamics* (1) *can be used to represent a great deal of physical and theoretical systems as it has been proved in [6–9] that most nonlinear systems can be modelled as, or converted into HOFA systems. A huge convenience provided by the full-actuation feature for control is that the HOFA system approaches can eliminate easily the nonlinearities, no matter how complicated they are, theoretically [6], and eventually produce a constant linear closed-loop system. The effectiveness for single systems' control has been well studied in [6–9], and along this line, this paper tends to further investigate the positive effectiveness of pre-eliminating nonlinearities for the MASs by utilising HOFA system approach.*

Networked control has been one of the most prevalent implementation methods for the distributed control of MASs. In this paper, we suppose that the communication among agents are performed through network in event-triggered fashion, while inside of a certain agent, its states can always be accessible for the controller. On this basis, in view of the full-actuation theory [6], the controller of the given HOFA nonlinear MAS can be immediately written as

$$\begin{cases} u_i^* = \theta K \sum_{j\in\mathcal{N}_i}(x_i^{(0\sim n-1)} - \bar{x}_{ji}^{(0\sim n-1)}) \\ h_i = -f_i(x_i^{(0\sim n-1)}, t) + u_i^* \\ u_i = g_i^{-1}(h_i) \end{cases} \tag{4}$$

where $\theta > 0$ is a positive scalar, u_i^* denotes the desired closed-loop dynamics of MAS.

Define the measurement error for the sent out information as

$$e_{ij}^{(0\sim n-1)} = \bar{x}_{ij}^{(0\sim n-1)} - x_i^{(0\sim n-1)}, \tag{5}$$

where

$$\begin{cases} \dot{\bar{x}}_{ij}^{(0\sim n-1)}(t) = 0, & t \in [t_k^i, t_{k+1}^i), \\ \bar{x}_{ij}^{(0\sim n-1)}(t^+) = x_i^{(0\sim n-1)}(t), & t \in \{t_k^i\}, \end{cases} \tag{6}$$

denotes the triggered state in zero-order-hold manner, that can be received and adopted by the neighbor agents $j \in \mathcal{N}_i$. Note that the received state is the same for any $j_1, j_2 \in \mathcal{N}_i$ without considering the delay effects, that is, $\bar{x}_{ij_1}^{(0\sim n-1)} = \bar{x}_{ij_2}^{(0\sim n-1)}$, thus we denote $e_i^{(0\sim n-1)} := e_{ij}^{(0\sim n-1)}$ for all $j \in \mathcal{N}_i$. Notation $\bar{x}_{ij}^{(0\sim n-1)}(t^+)$ represents the right-hand jump value of a discontinuous variable. The set of $\{t_k^i\}$ denotes the sequence of triggering instants, which is determined according to the following hybrid event-triggering mechanism (HETM)

$$t_{k+1}^i = \inf_t\{t > t_k^i + \tau_{miet} | \eta_i \leq 0\}, \tag{7}$$

where η_i is a dynamic variable, which evolves along

$$\dot{\eta}_i = \Psi_i(\eta_i, e_i^{(0\sim n-1)}, x_i^{(0\sim n-1)}, \bar{x}_{ji}^{(0\sim n-1)}), \tag{8}$$

where $\Psi_i(\cdot)$ is an internal functions depending on locally available variables.

Based on the HETM-based HOFA control protocol (4) and (7), the part of the closed-loop system can be expressed in the following constant linear closed-loop system form

$$\dot{x}_i^{(n)} = u_i^*, \tag{9}$$

and in the state space form

$$\dot{x}_i^{(0\sim n-1)} = Ax_i^{(0\sim n-1)} + Bu_i^*. \tag{10}$$

There exists such a fact that the pair (A, B) is everlasting controllable, which again reflects the full-actuation feature of the HOFA nonlinear MASs.

Define $\delta_i^{(0\sim n-1)} = x_i^{(0\sim n-1)} - \frac{1}{N}\sum_{m=1}^{N} x_m^{(0\sim n-1)}$, it follows that $\delta_{1\sim N}^{(0\sim n-1)} = (\mathcal{M}\otimes I_{nr})x_{1\sim N}^{(0\sim n-1)}$, where $\mathcal{M} = I_N - \frac{1}{N}\mathbf{1}\mathbf{1}^T$. Then, from (10) and (4), it obtains

$$\begin{aligned}\dot{\delta}_{1\sim N}^{(0\sim n-1)} =&(I_N\otimes A)\delta_{1\sim N}^{(0\sim n-1)} + (\mathcal{M}\mathcal{L}\otimes BK)x_{1\sim N}^{(0\sim n-1)}\\ &-(\mathcal{M}\mathcal{A}\otimes BK)e_{1\sim N}^{(0\sim n-1)}\\ =&(I_N\otimes A + \mathcal{L}\otimes\theta BK)\delta_{1\sim N}^{(0\sim n-1)}\\ &-(\mathcal{M}\mathcal{A}\otimes\theta BK)e_{1\sim N}^{(0\sim n-1)},\end{aligned} \tag{11}$$

and from (5), it obtains

$$\begin{aligned}\dot{e}_i^{(0\sim n-1)} =& -Ax_i^{(0\sim n-1)} - (\mathcal{L}^i\otimes\theta BK)x_{1\sim N}^{(0\sim n-1)}\\ &+(\mathcal{A}^i\otimes\theta BK)e_{1\sim N}^{(0\sim n-1)},\end{aligned} \tag{12}$$

or, in compact form

$$\begin{aligned}\dot{e}_{1\sim N}^{(0\sim n-1)} =& -(I_N\otimes A + \mathcal{L}\otimes\theta BK)x_{1\sim N}^{(0\sim n-1)}\\ &+(\mathcal{A}\otimes\theta BK)e_{1\sim N}^{(0\sim n-1)},\end{aligned} \tag{13}$$

where $\mathcal{M}\mathcal{L} = \mathcal{L}\mathcal{M}$, $\mathcal{L}^i$ and $\mathcal{A}^i$ denote the i-th row of matrices $\mathcal{L}$ and $\mathcal{A}$, respectively. Note that according to the update law (6), it is known that measurement error $e_{ij}^{(0\sim n-1)}$ is discontinuous, and has jump dynamics $e_{ij}^{(0\sim n-1)}(t^+) = 0$ at $t = t_k^i$.

Remark 2 *Compared with [6], the constant matrices $A_0, \cdots, A_{n-1} \in \mathbb{R}^{r\times r}$ associated with desired closed-loop stable of a single system is omitted in* (9)*, this is because the HOFA nonlinear MASs are no more concerned with one certain subsystem's stability. Instead, the control objective of HOFA nonlinear MASs turns into achieving group consensus. Notice from the first-order state space form* (10) *that (A, B) is controllable, so the desired closed-loop consensus dynamics of HOFA nonlinear MASs can always be achieved via designing u_i^*. Based on these discussions, it can be observed that through eliminating nonlinearities in multi-agent system, the HOFA approach simplifies the control model of nonlinear MASs and make the control problem be much clearer, which is first main feature we want to specify. The other one is that compared with taking the nonlinearities into consensus analysis, and then cancelling them by utilising the distributed gains [4, 5], pre-eliminating these nonlinearities by HOFA approach with utilising the agent's own information could greatly reduce the derivation difficulties, see the proof for linear MASs* (10)*.*

In this paper, the control **objective** is to design the HETM-based HOFA control protocol (4) and (7) for the HOFA nonlinear MASs (1) to achieve full-state consensus in the sense that for any initial states $x_i^{(0\sim n-1)}(0)$, $\lim_{t\to\infty}\left\|x_i^{(0\sim n-1)} - x_j^{(0\sim n-1)}\right\| = 0, \forall\, i, j \in \mathcal{V}$.

3 Hybrid Model

To construct a suitable closed-loop state for analysis, we need to to incorporate some variables, which have jump dynamics, such as measurement error (5) and timer variable. As a result, the conventional continuous-time system model is improper. In this section, a hybrid system model, as advocated in [17–19], will be constructed to express the complete closed-loop system dynamics. The general form of hybrid systems is given by

$$\mathcal{H}: \begin{cases}\dot{\xi} = F(\xi), & \text{if } \xi\in\mathbb{F},\\ \xi^+\in J(\xi), & \text{if } \xi\in\mathbb{J},\end{cases} \tag{14}$$

where $F(\xi)$, $J(\xi)$ represent the flow dynamics and jump dynamics respectively, and $\mathbb{F}$ and $\mathbb{J}$ are the corresponding flow set and jump set. $\xi(t^+)$ is abbreviated as ξ^+.

Define the closed-loop state as

$$\begin{aligned}&\tau = (\tau_1, \cdots, \tau_N)\in\mathbb{R}^N,\\ &\eta = (\eta_1, \cdots, \eta_N)\in\mathbb{R}^N,\\ &\xi = (\delta_{1\sim N}^{(0\sim n-1)}, e_{1\sim N}^{(0\sim n-1)}, \tau, \eta)\in\mathbb{X},\end{aligned}$$

where τ_i, $i\in\mathcal{V}$ is the timer variable, having flow dynamics $\dot{\tau}_i = 1$ within $[t_k^i, t_{k+1}^i)$, and jump dynamics $\tau^+ = 0$ at triggering instants $t = t_k^i$. $\mathbb{X} := \{(\delta_{1\sim N}^{(0\sim n)}, e_{1\sim N}^{(0\sim n)}, \tau, \eta)\in\mathbb{R}^{nrN}\times\mathbb{R}^{nrN}\times\mathbb{R}_{\geq 0}^N\times\mathbb{R}_{\geq 0}^N\}$.

Based on (11), (13) and (8), the flow dynamics is given as

$$\dot{\xi} = F(\xi), \quad \text{if } \xi\in\mathbb{F}, \tag{15}$$

with

$$F(\xi) = \begin{bmatrix}\dot{\delta}_{1\sim N}^{(0\sim n-1)}\\ \dot{e}_{1\sim N}^{(0\sim n-1)}\\ 1_N\\ \Psi\end{bmatrix}, \tag{16}$$

where $\Psi = (\Psi_1, \cdots, \Psi_N)$. The flow set is defined as $\mathbb{F} = \bigcap_{i=1}^N \mathbb{F}_i$, where $\mathbb{F}_i := \{\xi\in\mathbb{X} | \tau_i < \tau_{miet} \vee \eta_i > 0\}$.

The jump dynamics is given by

$$\xi^+\in\bigcup_{i=1}^N J_i(\xi), \text{ if } \xi\in\mathbb{J}, \tag{17}$$

and

$$J_i(\xi) = \begin{bmatrix}\delta_{1\sim N}^{(0\sim n-1)}\\ (I-\Lambda_i\otimes I_{nr})e_{1\sim N}\\ (I-\Lambda_i)\tau\\ \eta\end{bmatrix}, \tag{18}$$

where $\Lambda_i\in\mathbb{R}^{N\times N}$ is a diagonal matrix with only the ii-th entry being 1, all the rest are 0. The jump set is defined as $\mathbb{J} := \bigcup_{i=1}^N \mathbb{J}_i$ with $\mathbb{J}_i := \{\xi\in\mathbb{X} | \tau_i \geq \tau_{miet} \wedge \eta_i \leq 0\}$,

By now, the hybrid system model has been developed in (15)-(18) for the HOFA nonlinear MASs (1). Next, we present the stability definition for this hybrid system.

Definition 1 *Given the hybrid system* (15)-(18)*, the set $\{\xi\in\mathbb{X} | \delta_{1\sim N}^{(0\sim n-1)} = 0, e_{1\sim N}^{(0\sim n-1)} = 0, \eta = 0\}$ is said to be uniformly globally asymptotically stable (UGAS) if there exists a function $\beta\in\mathcal{KL}$ such that, for any initial condition $\xi(0)\in\mathbb{X}$, the following condition holds*

$$\begin{aligned}&\left\|(\delta_{1\sim N}^{(0\sim n-1)}(t), e_{1\sim N}^{(0\sim n-1)}(t), \eta(t)\right\|\\ &\leq\beta\left(\left\|\delta_{1\sim N}^{(0\sim n-1)}(0), e_{1\sim N}^{(0\sim n-1)}(0), \eta(0)\right\|, t\right).\end{aligned} \tag{19}$$

4 Main Results

Before presenting the main results, we first introduce an auxiliary function $\phi_i(t) : \mathbb{R}_{\geq 0} \to \mathbb{R}_{\geq 0}$

$$\dot{\phi}_i(\tau_i) = -s(\tau_i)\left(\bar{\sigma}_1\phi_i^2(\tau_i) + \bar{\sigma}_2\phi_i(\tau_i) + \bar{\sigma}_3\right), \tag{20}$$

the switching signal $s(\tau_i) = 1$ if $\tau_i < \tau_{miet}$, and $s(\tau_i) = 0$ if $\tau_i \geq \tau_{miet}$. Notice that the decline of $\phi_i(\tau_i)$ from $\phi_i(0) > 0$ to 0 could always guarantee a minimum inter-event time (MIET) τ_{miet} for the adjacent events.

Theorem 1 *Given the HOFA nonlinear MAS* (1)*, if the designed HOFA controller* (4) *and the HETM in* (7) *satisfy the following conditions:*

1) the control matrix of u_i^* is $K = -B^TP$ with P being the solution to Riccati equation;

2) the gain of u_i^* satisfies $\theta \geq \frac{4\lambda_2^2(\mathcal{L})+(4+16\gamma)\lambda_2(\mathcal{L})+1}{4\lambda_2^2(\mathcal{L})}$;

3) the parameters of auxiliary function ϕ_i are $\bar{\sigma}_1 = 3\lambda_{\max}(\Gamma)/\lambda_{\min}(P)$, $\bar{\sigma}_2 = 0$ and $\bar{\sigma}_3 = 2\|\mathcal{A}^2\|\lambda_{\max}(\Gamma)/\lambda_{\min}(P)$, the value range of MIET belongs to $\tau_{miet} \in (0, \tau_m]$, where

$$\tau_m = \begin{cases} \frac{2}{\vartheta}\arctan\frac{2\bar{\sigma}_1\vartheta\phi(0)}{\vartheta^2+\bar{\sigma}_2^2+2\bar{\sigma}_1\bar{\sigma}_2\phi(0)}, & \bar{\sigma}_2^2 < 4\bar{\sigma}_1\bar{\sigma}_3 \\ \frac{4\bar{\sigma}_1\phi(0)}{\bar{\sigma}_2^2+2\bar{\sigma}_1\bar{\sigma}_2\phi(0)}, & \bar{\sigma}_2^2 = 4\bar{\sigma}_1\bar{\sigma}_3 \\ \frac{2}{\vartheta}\text{arctanh}\frac{-2\bar{\sigma}_1\vartheta\phi(0)}{\vartheta^2+\bar{\sigma}_2^2+2\bar{\sigma}_1\bar{\sigma}_2\phi(0)}, & \bar{\sigma}_2^2 > 4\bar{\sigma}_1\bar{\sigma}_3 \end{cases} \tag{21}$$

where $\vartheta = \sqrt{\text{sign}(\vartheta_\sigma)\vartheta_\sigma}$, $\vartheta_\sigma = 4\bar{\sigma}_1\bar{\sigma}_3 - \bar{\sigma}_2^2$; and

4) the dynamics of η_i is $\Psi_i(\cdot) = -(1-s(\tau_i))(3\phi_i^2(\tau_{miet}) + 2\|\mathcal{A}^2\| + 2\gamma d_i)\frac{\lambda_{\max}(\Gamma)}{\lambda_{\min}(P)}(e_i^{(0\sim n-1)})^TPe_i^{(0\sim n-1)} + \gamma\sum_{j\in\mathcal{N}_i}(x_i^{(0\sim n-1)} - \bar{x}_{ji}^{(0\sim n-1)})\Gamma(x_i^{(0\sim n-1)} - \bar{x}_{ji}^{(0\sim n-1)})$; then, the asymptotic consensus of HOFA nonlinear MASs (1) *can be achieved.*

Proof: Consider the candidate Lyapunov function

$$V = V_1 + V_2 + \sum_{i=1}^{N}\eta_i, \tag{22}$$

where

$$\begin{aligned} V_1 =& (\delta_{1\sim N}^{(0\sim n-1)})^T(\mathcal{L}\otimes P)\delta_{1\sim N}^{(0\sim n-1)}, \\ V_2 =& \sum_{i=1}^{N}\phi_i(e_i^{(0\sim n-1)})^TPe_i^{(0\sim n-1)}. \end{aligned}$$

Take derivative to V_1 along (11), it obtains that

$$\begin{aligned} \dot{V}_1 =& (\delta_{1\sim N}^{(0\sim n-1)})^T\left(\mathcal{L}\otimes(PA+A^TP)\right)\delta_{1\sim N}^{(0\sim n-1)} \\ &- 2\theta(\delta_{1\sim N}^{(0\sim n-1)})^T\left(\mathcal{L}\mathcal{L}\otimes\Gamma\right)\delta_{1\sim N}^{(0\sim n-1)} \\ &+ 2\theta(\delta_{1\sim N}^{(0\sim n-1)})^T\left(\mathcal{L}\mathcal{A}\otimes\Gamma\right)e_{1\sim N}^{(0\sim n-1)} \\ \leq& (\delta_{1\sim N}^{(0\sim n-1)})^T\left(\mathcal{L}\otimes(PA+A^TP-\Gamma)\right)\delta_{1\sim N}^{(0\sim n-1)} \\ &+ (\delta_{1\sim N}^{(0\sim n-1)})^T\left(\mathcal{L}\otimes\Gamma\right)\delta_{1\sim N}^{(0\sim n-1)} \\ &- \theta(\delta_{1\sim N}^{(0\sim n-1)})^T\left(\mathcal{L}\mathcal{L}\otimes\Gamma\right)\delta_{1\sim N}^{(0\sim n-1)} \\ &+ \theta(e_{1\sim N}^{(0\sim n-1)})^T\left(\mathcal{A}\mathcal{A}\otimes\Gamma\right)e_{1\sim N}^{(0\sim n-1)}. \end{aligned} \tag{23}$$

In light of Lemma 1, we know that there is a unitary matrix $\mathcal{U}$ such that $\mathcal{U}^T\mathcal{L}\mathcal{U} = \Lambda \triangleq \text{diag}\{0, \lambda_2(\mathcal{L}), \cdots, \lambda_N(\mathcal{L})\}$. Denote $\varphi_{1\sim N}^{(0\sim n-1)} = (\mathcal{L}\otimes I_{nr})\delta_{1\sim N}^{(0\sim n-1)}$ and $\tilde{\delta}_{1\sim N}^{(0\sim n-1)} = (\mathcal{U}^T\otimes I_N)\delta_{1\sim N}^{(0\sim n-1)}$, we have

$$\begin{aligned} &(\delta_{1\sim N}^{(0\sim n-1)})^T\left(\mathcal{L}\otimes\Gamma\right)\delta_{1\sim N}^{(0\sim n-1)} \\ =& (\tilde{\delta}_{1\sim N}^{(0\sim n-1)})^T(\Lambda\otimes\Gamma)\,\tilde{\delta}_{1\sim N}^{(0\sim n-1)} \\ =& \sum_{i=2}^{N}\lambda_i(\mathcal{L})(\tilde{\delta}_i^{(0\sim n-1)})^T\Gamma\tilde{\delta}_i^{(0\sim n-1)} \\ \leq& \frac{1}{\lambda_2(\mathcal{L})}\sum_{i=2}^{N}\lambda_i^2(\mathcal{L})(\tilde{\delta}_i^{(0\sim n-1)})^T\Gamma\tilde{\delta}_i^{(0\sim n-1)} \\ =& \frac{1}{\lambda_2(\mathcal{L})}(\varphi_{1\sim N}^{(0\sim n-1)})^T(I_N\otimes\Gamma)\varphi_{1\sim N}^{(0\sim n-1)}. \end{aligned} \tag{24}$$

Then, according to Riccati equation, it has

$$\begin{aligned} \dot{V}_1 \leq& -(\delta_{1\sim N}^{(0\sim n-1)})^T\delta_{1\sim N}^{(0\sim n-1)} \\ &+ \left(\frac{1}{\lambda_2(\mathcal{L})} - \theta\right)(\varphi_{1\sim N}^{(0\sim n-1)})^T(I_N\otimes\Gamma)\varphi_{1\sim N}^{(0\sim n-1)} \\ &+ (e_{1\sim N}^{(0\sim n-1)})^T\left(\mathcal{A}\mathcal{A}\otimes\Gamma\right)e_{1\sim N}^{(0\sim n-1)}. \end{aligned} \tag{25}$$

Taking derivative to V_2 along (12) gives that

$$\begin{aligned} \dot{V}_2 =& \sum_{i=1}^{N}\dot{\phi}_i(e_i^{(0\sim n-1)})^TPe_i^{(0\sim n-1)} \\ &- \sum_{i=1}^{N}\phi_i(e_i^{(0\sim n-1)})^T(PA+A^TP)x_i^{(0\sim n-1)} \\ &+ 2\sum_{i=1}^{N}\phi_i(e_i^{(0\sim n-1)})^T(\mathcal{L}^i\otimes\Gamma)x_{1\sim N}^{(0\sim n-1)} \\ &- 2\sum_{i=1}^{N}\phi_i(e_i^{(0\sim n-1)})^T(\mathcal{A}^i\otimes\Gamma)e_{1\sim N}^{(0\sim n-1)}. \end{aligned} \tag{26}$$

For the second term of (26), it has

$$\begin{aligned} &-\sum_{i=1}^{N}\phi_i(e_i^{(0\sim n-1)})^T(PA+A^TP)x_i^{(0\sim n-1)} \\ \leq& \sum_{i=1}^{N}\phi_i^2(e_i^{(0\sim n-1)})^T(PA+A^TP)e_i^{(0\sim n-1)} \\ &+ \sum_{i=1}^{N}\frac{1}{4}(x_i^{(0\sim n-1)})^T(PA+A^TP)x_i^{(0\sim n-1)} \\ \leq& \sum_{i=1}^{N}\phi_i^2(e_i^{(0\sim n-1)})^T\Gamma e_i^{(0\sim n-1)} + \frac{1}{4}(x_i^{(0\sim n-1)})^T\Gamma x_i^{(0\sim n-1)} \\ \leq& \sum_{i=1}^{N}\phi_i^2(e_i^{(0\sim n-1)})^T\Gamma e_i^{(0\sim n-1)} \\ &+ \frac{1}{4\lambda_2^2(\mathcal{L})}(\varphi_{1\sim N}^{(0\sim n-1)})^T(I_N\otimes\Gamma)\varphi_{1\sim N}^{(0\sim n-1)}, \end{aligned} \tag{27}$$

for the third term of (26), it has

$$\begin{aligned} &2\sum_{i=1}^{N}\phi_i(e_i^{(0\sim n-1)})^T(\mathcal{L}^i\otimes\Gamma)x_{1\sim N}^{(0\sim n-1)} \\ \leq& \sum_{i=1}^{N}\phi_i^2(e_i^{(0\sim n-1)})^T\Gamma e_i^{(0\sim n-1)} + \|(\mathcal{L}\otimes K)x_{1\sim N}^{(0\sim n-1)}\|^2 \\ \leq& \sum_{i=1}^{N}\phi_i^2(e_i^{(0\sim n-1)})^T\Gamma e_i^{(0\sim n-1)} \\ &+ (\varphi_{1\sim N}^{(0\sim n-1)})^T(I_N\otimes\Gamma)\varphi_{1\sim N}^{(0\sim n-1)}, \end{aligned} \tag{28}$$

for the fourth term of (26), it has

$$
\begin{aligned}
&-2\sum_{i=1}^{N}\phi_i(e_i^{(0\sim n-1)})^T(\mathcal{A}^i\otimes\Gamma)e_{1\sim N}^{(0\sim n-1)}\\
&\leq\sum_{i=1}^{N}(\phi_i^2+\|\mathcal{A}^2\|)(e_i^{(0\sim n-1)})^T\Gamma e_i^{(0\sim n-1)}. \qquad (29)
\end{aligned}
$$

Then, substitute the above three inequalities into (26), it gives that

$$
\begin{aligned}
\dot{V}_2=&\sum_{i=1}^{N}\dot{\phi}_i(e_i^{(0\sim n-1)})^TPe_i^{(0\sim n-1)}\\
&+\sum_{i=1}^{N}(3\phi_i^2+\|\mathcal{A}^2\|)\frac{\lambda_{\max}(\Gamma)}{\lambda_{\min}(P)}(e_i^{(0\sim n-1)})^TPe_i^{(0\sim n-1)}\\
&+\Big(1+\frac{1}{4\lambda_2^2(\mathcal{L})}\Big)(\varphi_{1\sim N}^{(0\sim n-1)})^T(I_N\otimes\Gamma)\varphi_{1\sim N}^{(0\sim n-1)}.
\end{aligned}
\qquad (30)
$$

Finally, summing up (25) and (30), it leads to

$$
\begin{aligned}
\dot{V}\leq&-(\delta_{1\sim N}^{(0\sim n-1)})^T\delta_{1\sim N}^{(0\sim n-1)}+\sum_{i=1}^{N}\Big(\dot{\eta}_i-\gamma\sum_{j\in\mathcal{N}_i}\\
&(x_i^{(0\sim n-1)}-\bar{x}_{ji}^{(0\sim n-1)})\Gamma(x_i^{(0\sim n-1)}-\bar{x}_{ji}^{(0\sim n-1)})\Big)\\
&-\Big(\theta-\frac{4\lambda_2^2(\mathcal{L})+(4+16\gamma)\lambda_2(\mathcal{L})+1}{4\lambda_2^2(\mathcal{L})}\Big)\\
&\times(\varphi_{1\sim N}^{(0\sim n-1)})^T(I_N\otimes\Gamma)\varphi_{1\sim N}^{(0\sim n-1)}\\
&+\sum_{i=1}^{N}\Big(\dot{\phi}_i+(3\phi_i^2+2\|\mathcal{A}^2\|+2\gamma d_i)\frac{\lambda_{\max}(\Gamma)}{\lambda_{\min}(P)}\Big)\\
&\times(e_i^{(0\sim n-1)})^TPe_i^{(0\sim n-1)}\\
\leq&0, \qquad (31)
\end{aligned}
$$

where the last inequality is guaranteed by the conditions in Theorem 1.

Notice that there is a piecewise continuous term V_2 in Lyapunov function (22), thus we consider the following jump case at every triggering instants $t=t_k^i$ (i.e. $\tau_i\geq\tau_{miet}$ and $\phi(\tau_i)>0$). In this case, it has $V^+-V=\phi_i(0)\cdot 0-\phi_i(\tau_{miet})(e_i^{(0\sim n-1)})^TPe_i^{(0\sim n-1)}\leq 0$, which implies that it does not lead to non-monotonic phenomenon.

By now, from (31) and the above analysis, it can be concluded that the Lyapunov function (22) is persistently decrease upon the whole time domain, thus the hybrid system (15)-(18) is UGAS and the event-based asymptotic consensus of HOFA nonlinear MASs (1) is achieved.

This completes the proof. □

5 Numerical example

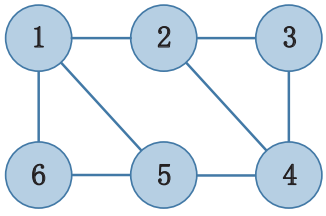

Fig. 1: Connection relationship.

In this section, a simulation example borrowed from [20] is given to show the effectiveness of the proposed method. The HOFA nonlinear MAS is composed of six pendulum systems, their connection relationship is represented by graph Fig.1. The agents' dynamics in form of (1) is represented as $\ddot{x}_i=-\frac{g}{l}\sin(x_i)-\frac{k}{m}\dot{x}_i+u_i$, where $m=0.5$, $l=4.9$, $k=0.5$ and $g=9.8$ are, respectively, the mass of bob, the length of rod, the coefficient of friction, and the acceleration due to gravity. According to Theorem 1, the controller is designed as (4), and the control gain and system parameters are selected as $K=[0.3162\ 0.8558]$, $\theta=4.75$, and $\eta_i(0)=0.1$. The MIET is $\tau_{miet}=0.1s$. Then, for any initial states $x_i(0)=-0.1*i+0.7$ and $\dot{x}_i(0)=0.1*i$, $i=1,\cdots,6$, the consensus of HOFA nonlinear MAS is achieved, see Figs. 2-5 for more details. Fig. 2 and Fig. 3 present the state trajectories of $\dot{x}_i$ and x_i, $i=1,\cdots,6$, which illustrate that the asymptotic consensus of HOFA nonlinear MASs is achieved. Fig. 4 shows the triggering sequence of using the proposed HETM, it can be found that in between any adjacent events, there always exists a MIET $\tau_{miet}=0.1s$. Fig. 5 shows the evolution of the triggering condition η_i.

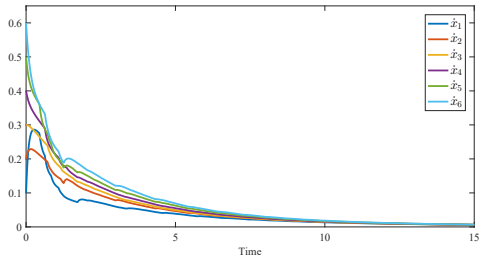

Fig. 2: Trajectories of state $\dot{x}_i|_{i=1,\cdots,6}$.

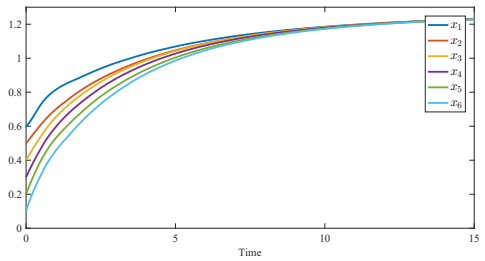

Fig. 3: Trajectories of state $x_i|_{i=1,\cdots,6}$.

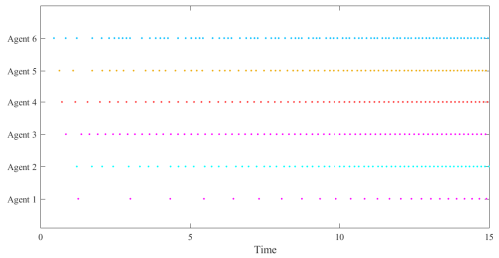

Fig. 4: The triggering sequence.

6 Conclusion

In this paper, the consensus problem of HOFA nonlinear MASs is studied. Under a mild condition the HOFA nonlinear MAS is converted into a general linear MAS by

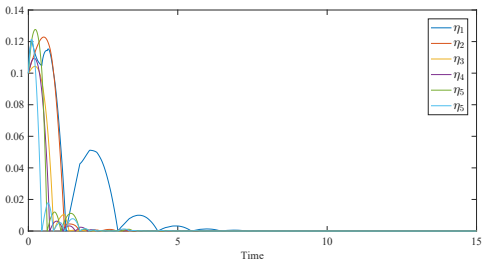

Fig. 5: Trajectories of dynamic variable $\eta_i|_{i=1,\cdots,6}$.

pre-eliminating all the nonlinear dynamics by using the full-actuation structure of agent itself. This simplifies the actual control model and the Lyapunov stability analysis. Moreover, a HETM is designed for the HOFA nonlinear MASs to reduce the communication frequency while guaranteeing a strictly positive MIET for the uncertain triggering events.

References

[1] K. Lu, Z. Liu, Y. Wang, C. L. P. Chen, and Y. Zhang, "Adaptive neural design of consensus controllers for nonlinear multiagent systems under switching topologies," *IEEE Transactions on Systems, Man, and Cybernetics: Systems*, vol. 53, no. 1, pp. 309–320, 2023.

[2] L. Chen, Y. Cheng, J. Shao, L. Shi, and W. X. Zheng, "Collective behavior of generic linear agents interacting by dynamic topology with general structures," in *2022 IEEE 61st Conference on Decision and Control (CDC)*, 2022, pp. 3977–3982.

[3] J. Zhuang, S. Peng, and Y. Wang, "Leader-following consensus of discrete-time stochastic nonlinear multiagent systems under fixed and switching topologies via impulsive control," *IEEE Systems Journal*, vol. 16, no. 4, pp. 6021–6030, 2022.

[4] J. Zhang, H. Zhang, W. Li, and K. Li, "Distributed edge-event triggered consensus control for multi-agent systems by edge-based asynchronous communications," *Applied Mathematics and Computation*, vol. 397, p. 125920, 2021.

[5] K. Li, C.-C. Hua, and X. You, "Distributed asynchronous consensus control for nonlinear multiagent systems under switching topologies," *IEEE Transactions on Automatic Control*, vol. 66, no. 9, pp. 4327–4333, 2021.

[6] G. Duan, "High-order fully actuated system approaches: Part i. models and basic procedure," *International Journal of Systems Science*, vol. 52, no. 2, pp. 422–435, 2021.

[7] ——, "High-order fully actuated system approaches: Part ii. generalized strict-feedback systems," *International Journal of Systems Science*, vol. 52, no. 3, pp. 437–454, 2021.

[8] ——, "High-order fully actuated system approaches: Part iii. robust control and high-order backstepping," *International Journal of Systems Science*, vol. 52, no. 5, pp. 952–971, 2021.

[9] ——, "High-order fully actuated system approaches: Part iv. adaptive control and high-order backstepping," *International Journal of Systems Science*, vol. 52, no. 5, pp. 972–989, 2021.

[10] X. Ge, Q. Han, L. Ding, Y. Wang, and X. Zhang, "Dynamic event-triggered distributed coordination control and its applications: A survey of trends and techniques," *IEEE Transactions on Systems, Man, and Cybernetics: Systems*, vol. 50, no. 9, pp. 3112–3125, 2020.

[11] L. Ding, Q. L. Han, X. Ge, and X. M. Zhang, "An overview of recent advances in event-triggered consensus of multiagent systems," *IEEE Transactions on Cybernetics*, vol. 48, no. 4, pp. 1110–1123, 2018.

[12] Y. Qian, L. Liu, and G. Feng, "Distributed event-triggered adaptive control for consensus of linear multi-agent systems with external disturbances," *IEEE Transactions on Cybernetics*, vol. 50, no. 5, pp. 2197–2208, 2020.

[13] S. Du, T. Liu, and D. W. C. Ho, "Dynamic event-triggered control for leader-following consensus of multiagent systems," *IEEE Transactions on Systems, Man, and Cybernetics: Systems*, vol. 50, no. 9, pp. 3243–3251, 2020.

[14] Y. Qian, L. Liu, and G. Feng, "Cooperative output regulation of linear multiagent systems: An event-triggered adaptive distributed observer approach," *IEEE Transactions on Automatic Control*, vol. 66, no. 2, pp. 833–840, 2021.

[15] G. Zhao and C. Hua, "A hybrid dynamic event-triggered approach to consensus of multiagent systems with external disturbances," *IEEE Trans. Autom. Control*, vol. 66, no. 7, pp. 3213–3220, 2021.

[16] ——, "Leader-following consensus of multiagent systems via asynchronous sampled-data control: A hybrid system approach," *IEEE Trans. Autom. Control*, vol. 67, no. 5, pp. 2568–2575, 2022.

[17] R. Goebel, R. G. Sanfelice, and A. R. Teel, "Hybrid dynamical systems," *IEEE Control Systems Magazine*, vol. 29, no. 2, pp. 28–93, 2009.

[18] D. Nesic and A. R. Teel, "Input-output stability properties of networked control systems," *IEEE Transactions on Automatic Control*, vol. 49, no. 10, pp. 1650–1667, 2004.

[19] D. Carnevale, A. R. Teel, and D. Nesic, "A lyapunov proof of an improved maximum allowable transfer interval for networked control systems," *IEEE Transactions on Automatic Control*, vol. 52, no. 5, pp. 892–897, 2007.

[20] X. You, C. Hua, and X. Guan, "Self-triggered leader-following consensus for high-order nonlinear multiagent systems via dynamic output feedback control," *IEEE Transactions on Cybernetics*, vol. 49, no. 6, pp. 2002–2010, 2019.

Proceedings of the 3rd Conference on Fully Actuated System Theory and Applications
May 10-12, 2024, Shenzhen, China

Integral Adaptive Sliding Mode Control for Vehicle Platoon with Disturbance Observer

Xin Yang, Cheng-Lin Liu
Key Laboratory of Advanced Process Control for Light Industry (Ministry of Education), Institute of Automation, Jiangnan University, Wuxi 214122, China
E-mail: liucl@jiangnan.edu.cn

Abstract: This article proposes an integral adaptive sliding mode control (IASMC) strategy that combines adaptive reaching laws and disturbance observers (DO) for vehicle platoon system subject to unknown disturbance. The objective is to ensure the string stability and make the spacing error between any front and rear vehicles in the platoon be zero, which means that the vehicles are driven at the expected spacing. To achieve it, the bidirectional (BD) topology and the constant time headway (CTH) policy are employed. Then, an adaptive smoothed sliding mode reaching law is constructed to eliminate the chattering issue. The unknown disturbances can be estimated by the designed DO. Meanwhile, the Lyapunov method is applied to the analysis and proof of the stability of the designed IASMC strategy, and the Laplace transform is used in the proof of the string stability. Finally, based on simulation, it can be seen that the availability and superiority of the designed strategy can be verified.

Key Words: Platoon control, Adaptive law, Sliding mode control, Observer.

1 Introduction

Recently, the issues of vehicle platoon control have been extensively investigated owing to its benefits to reduce energy, increase traffic capacity and improve vehicle safety [1]. Making the spacing error between any front and rear vehicles in the platoon be zero and satisfying the string stability are the main objectives of platoon control [2]. The specific implementation of vehicle platoon control can date back to the PATH project in 1986 [3].

It is well known that spacing policy and information flow topology are extremely important for platoon control. The spacing policy is divided into two types: constant and variable. Since constant spacing policy is not conducive to the string stability, the advantages of variable spacing policy (VSP) are reflected. The VSP that changes with velocity can be seen as utilizing a filter, then the target position of current vehicle is basically obtained by applying a filter to the position of its preceding vehicle [4]. Moreover, the two most commonly used VSPs are variable time headway (VTH) and constant time headway (CTH), respectively [5]. Since the underdeveloped communication technology in the early days, the predecessor following (PF) topology has naturally become the most commonly used topology in vehicle platoon control [6], but the PF topology would make it difficult to ensure the string stability.

Due to the rapid expansion of multi-agent systems and vehicle-to-vehicle communications [7], [8], there are increasing attempts to use other forms of topology for platoon control. By passing information from the leader to all other following vehicles, the string stability can be ensured. Using the predecessor-leader following topology, an adaptive spacing policy was proposed to achieve the string stability in [9]. However, this topology will undoubtedly cause greater time delay problems [10]. Since the VTH policy is not contributive to the security and stability, the CTH policy and the bidirectional (BD) topology are adopted to better achieve the string stability in this paper.

Since interconnected vehicles are inevitably subject to various unknown disturbances while driving, this will cause the stability and the string stability to be affected. To solve the issues arising from unknown disturbances, an H_∞-based controller for different topologies and different spacing policies was developed in [11]. In [12], by combining a min-max objective function with a target calculator, it realized interference suppression through model predictive control. In addition, sliding mode control (SMC) has been extensively investigated owing to its robustness to external unknown disturbances. In [13], an adaptive compensation term was constructed and combined with SMC to compensate for the nonlinear uncertainties. Different from the above methods, in order to effectively estimate unknown disturbances, disturbance observers (DO) are used in this article.

In [14], to alleviate the chattering issue of SMC, a continuous sliding mode surface (SMS) containing a sign function was designed. Subsequently, based on the coupled sliding surface (CSS), an integral SMC strategy was proposed. However, it performed unsatisfactorily when the initial spacing error between adjacent vehicles is nonzero. Therefore, to eliminate the impact, a modified CTH policy was adopted. In [15], a reaching law with multi power was constructed to alleviate the chattering issue of SMC. Since the above methods cannot completely eliminate chattering, this article raises an integral adaptive sliding mode control (IASMC) strategy combined with adaptive reaching law based on CSS.

Unlike reference [13], the proposed adaptive law is applied to the smoothed sliding mode reaching law, based on this, the chattering problem of SMC can be effectively avoided. And the DO in this paper can effectively estimate the unknown disturbances directly, eliminating the need to estimate the boundaries of the disturbances. Then, to ensure the stability and achieve control objectives, combining the CTH policy and DO, the IASMC strategy is proposed.

This article is structured as follows. Section II introduces the dynamics of connected vehicles and outlines the

This work was supported in part by the National Natural Science Foundation of China under Grant 61973139 and Grant 61473138; and in part by the Fundamental Research Funds for the Central Universities under Grant JUSRP22014.

control objectives based on CTH policy. In section III, the IASMC strategy utilizing DO and combined with CSS based on BD topology is proposed, then the stability is proved and the string stability is ensured. Based on simulation results presented in Section IV, the availability and superiority of the IASMC strategy are demonstrated. The conclusions are summarized in Section V.

2 Vehicle Dynamics and Problem Formulation

2.1 Vehicle Dynamics

Considering there are $N+1$ vehicles, with N followers and one leader in a platoon on a straight road. Define $x_0(t)$ and $v_0(t)$ as the position and the velocity of the leader. Then, the relationship of them is represented by

$$\dot{x}_0(t) = v_0(t). \tag{1}$$

The dynamic of the ith follower is

$$\begin{cases} \dot{x}_i(t) = v_i(t), \\ \dot{v}_i(t) = \frac{1}{m_i} u_i(t) + \zeta_i(t), \end{cases} \tag{2}$$

where $m_i > 0$ donotes the mass of the ith ($i = 1, 2, \ldots, N$) following vehicle, $x_i(t)$, $v_i(t)$ and $u_i(t)$ represent the position, velocity and control input, respectively, and $\zeta_i(t)$ denotes the unknown disturbance, which involves external resistance, acceleration disturbance.

Lemma 1 (Barbalat). *Define $\Phi(t) : [0, \infty) \to \mathbf{R}$ as a uniformly continuous function, if $\lim_{t\to\infty} \int_0^t \Phi(\tau) d\tau < \infty$, then $\lim_{t\to\infty} \Phi(t) = 0$.*

Lemma 2 (Uniformly Ultimately Bounded (UUB) [16]). *For a system $\dot{x}(t) = f(x)$, assume there are constants $\iota > 0$ and $\phi > 0$ such that a positive definite Lyapunov function $V(x)$ can make $\dot{V}(x) \le -\iota V(x) + \phi$ hold, it implies the system is UUB.*

Lemma 3 ([17]). *Consider a system $\dot{x}(t) = f(x)$, assume there are constants $\kappa_1 > 0, \kappa_2 > 0$ and $0 < \kappa_3 < 1$ such that $\dot{V}(x) \le -\kappa_1 V(x) - \kappa_2 V^{\kappa_3}(x)$, where $V(x) \ge 0$ is a function, it implies the system can locally converge within a fast finite-time for any arbitrary initial state $x(0)$. The settling time is denoted as*

$$T \le \frac{1}{\kappa_1(1-\kappa_3)} \ln\left(\frac{\kappa_1 V^{1-\kappa_3}(x(0)) + \kappa_2}{\kappa_2}\right).$$

Assumption 1. *$\zeta_i(t)$ is bounded, that is, $\|\zeta(t)\| \le \xi$ and $\|\dot{\zeta}(t)\| \le \zeta$, where $\xi > 0$ and $\zeta > 0$ are unknown, $\zeta(t) = [\zeta_1(t), \zeta_2(t), \ldots, \zeta_N(t)]^T$.*

2.2 Control Objective

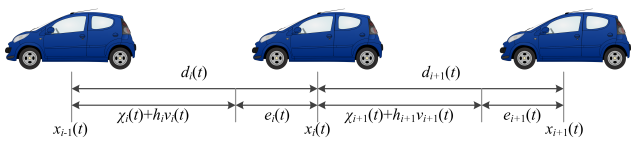

Fig. 1: Platoon scenario with CTH policy.

Based on the CTH policy, we can define the spacing error $e_i(t)$ as

$$e_i(t) = d_i(t) - \chi_i(t) - h_i v_i(t), \tag{3}$$

where $d_i(t) = x_{i-1}(t) - x_i(t)$, $\chi_i(t)$ and $\chi_i(t) + h_i v_i(t)$ denote the real distance, stationary distance and expected distance between adjacent vehicles, respectively. In addition, $h_i > 0$ is a constant, representing the time headway.

In order to ensure traffic throughput during driving and the safety of people in the vehicle, this article designs a controller for a longitudinal platoon based on dynamics (1) and (2) such that $e_i(t)$ can converge to zero and guarantees the string stability, the specific description is

$$\begin{aligned} &\lim_{t\to\infty} e_i(t) = 0, \\ &\left\| \frac{E_{i+1}(s)}{E_i(s)} \right\| \le 1. \end{aligned} \tag{4}$$

3 Integral Adaptive Sliding Mode Control

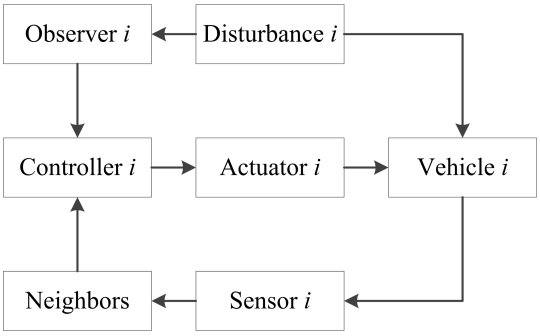

Fig. 2: IASMC control block diagram.

Based on the control block diagram shown in Fig.2, an IASMC strategy with DO is designed to achieve the string stability in this section. In accordance with (4) and guided by the CTH policy, the integral SMS can be formulated as

$$s_i(t) = e_i(t) + \int_0^t k_i e_i(\tau) d\tau, \tag{5}$$

where $k_i > 0$. The SMS $s_i(t)$ converges to zero, ensuring that $e_i(t)$ eventually converges to zero. Nevertheless, it should be noted that it cannot ensure the string stability. Therefore, we need to use the BD topology illustrated in Fig.3. Then, a new SMS is formulated as

$$S_i(t) = \begin{cases} \rho s_i(t) - s_{i+1}(t), & i = 1, 2, \ldots, N-1 \\ \rho s_i(t), & i = N \end{cases} \tag{6}$$

where $\rho > 0$. Define $S(t) = [S_1(t), S_2(t), \ldots, S_N(t)]^T$ and $s(t) = [s_1(t), s_2(t), \ldots, s_N(t)]^T$, an alternative form is

$$S(t) = Gs(t) \tag{7}$$

with

$$G = \begin{bmatrix} \rho & -1 & \ldots & 0 & 0 \\ 0 & \rho & -1 & 0 & 0 \\ \vdots & \vdots & \ddots & \vdots & \vdots \\ 0 & 0 & \ldots & \rho & -1 \\ 0 & 0 & \ldots & 0 & \rho \end{bmatrix}.$$



Fig. 3: The BD topology.

Since ρ is positive, it implies that matrix G is invertible. Therefore, we can deduce that $\|S(t)\|$ will reach zero if and only if $\|s(t)\|$ reaches zero. In other words, all $S_i(t)$ become zero only if all $s_i(t)$ become zero simultaneously [18].

For the two cases of $i = 1, 2, \ldots, N-1$ and $i = N$, the results obtained by deriving $S_i(t)$ are as follows:
Case I: $S_i(t) = \rho s_i(t) - s_{i+1}(t)$, the derivative of $S_i(t)$ is

$$\begin{aligned} \dot{S}_i(t) &= \rho \dot{s}_i(t) - \dot{s}_{i+1}(t) \\ &= \rho \dot{e}_i(t) + \Lambda_i(t), \end{aligned} \tag{8}$$

where

$$\Lambda_i(t) = \rho k_i e_i(t) - \dot{e}_{i+1}(t) - k_{i+1} e_{i+1}(t). \tag{9}$$

Case II: $S_i(t) = \rho s_i(t)$, the derivative of $S_i(t)$ is

$$\begin{aligned} \dot{S}_i(t) &= \rho \dot{s}_i(t) \\ &= \rho \dot{e}_i(t) + \Lambda_i(t), \end{aligned} \tag{10}$$

where

$$\Lambda_i(t) = \rho k_i e_i(t). \tag{11}$$

The chosen reaching law for the SMS $S_i(t)$ is expressed as

$$\dot{S}_i(t) = -\eta_i S_i(t) - \gamma_i sgn(S_i(t)), \tag{12}$$

where $\eta_i > 0$ and $\gamma_i > 0$ represents the switching gain. Then, we employ an adaptive mechanism to determine the switching gain γ_i as

$$\dot{\gamma}_i(t) = \varsigma(\|S_i(t)\| - \beta \gamma_i(t)), \tag{13}$$

where ς and β are positive constant, $\gamma_i(0) > 0$.

Remark 1. *The primary concept behind this adaptive mechanism is to adjust the switching gain based on the deviation of the SMS $S_i(t)$ from zero. The larger the deviation of $S_i(t)$ from zero, the more significant the change in switching gain, inducing $S_i(t)$ to approach zero. As $S_i(t)$ approaches zero, the rate of change in switching gain diminishes. Since the term $-\beta\gamma_i(t)$ is incorporated to inhibit the infinite increase of the switching gain [19], there must be a positive constant $\bar{\gamma} > \gamma_i(t)$ at all times.*

Since the sign function will cause chattering issue, the tanh function is employed as a replacement for the sign function to address this concern. Then, the smoothed reaching law is represented by

$$\dot{S}_i(t) = -\eta_i S_i(t) - \gamma_i(t) tanh(\mu S_i(t)), \tag{14}$$

where $\mu > 0$.

Remark 2. *Comparing the tanh function with the sign function reveals that the tanh function is smoother, and the reason for setting up parameter μ is to adjust the degree of similarity to the sign function. The larger μ is, the higher the similarity to the sign function is and the better the rapidity of SMC is. However, the chattering issue will be more serious. The smaller μ is, the opposite is true to the above results. Hence, the selection of an appropriate μ is crucial.*

To estimate $\zeta_i(t)$, the DO is constructed as

$$\begin{aligned} \zeta_i(t) &= p_i(t) - \sigma_i e_i(t) \\ \hat{\zeta}_i(t) &= \hat{p}_i(t) - \sigma_i e_i(t) \\ \dot{\hat{p}}_i(t) &= \sigma_i(v_{i-1}(t) - v_i(t) - h_i(\tfrac{1}{m_i} u_i(t) + \hat{\zeta}_i(t))), \end{aligned} \tag{15}$$

where $\sigma_i > 0$, $\hat{\zeta}_i(t)$ and $\hat{p}_i(t)$ represent the estimations of $\zeta_i(t)$ and the auxiliary variable $p_i(t)$, respectively. According to (15), we can derive $\dot{\hat{\zeta}}_i(t)$ as

$$\begin{aligned} \dot{\hat{\zeta}}_i(t) =& \dot{\hat{p}}_i(t) - \sigma_i \dot{e}_i(t) \\ =& \sigma_i h_i \tilde{\zeta}_i(t), \end{aligned} \tag{16}$$

where $\tilde{\zeta}_i(t) = \zeta_i(t) - \hat{\zeta}_i(t)$ is the disturbance error, then

$$\dot{\tilde{\zeta}}(t) = D\tilde{\zeta}(t) + \dot{\zeta}(t), \tag{17}$$

where $D = diag\{-\sigma_1 h_1, -\sigma_2 h_2, \ldots, -\sigma_N h_N\}$ is a diagonal matrix, $\tilde{\zeta}(t) = [\tilde{\zeta}_1(t), \tilde{\zeta}_2(t), \ldots, \tilde{\zeta}_N(t)]^T$. There always exists a possibility to find a suitable value such that D is negative definite by choosing the gain of the DO. Therefore, we can identify a matrix $P > 0$ satisfies

$$D^T P + PD = -G, \tag{18}$$

where G represents any given positive definite matrix.

Then, the IASMC is designed as

$$\begin{aligned} u_i(t) =& \tfrac{m_i}{h_i}(v_{i-1}(t) - v_i(t)) + \tfrac{m_i}{\rho h_i}(\Lambda_i(t) + \eta_i S_i(t) \\ &+ \gamma_i(t) tanh(\mu S_i(t)) - m_i \hat{\zeta}_i(t), \end{aligned} \tag{19}$$

where

$$\Lambda_i(t) = \begin{cases} \rho k_i e_i(t) - \dot{e}_{i+1}(t) & \\ -k_{i+1} e_{i+1}(t), & i = 1, 2, \ldots, N-1 \\ \rho k_i e_i(t), & i = N. \end{cases} \tag{20}$$

Theorem 1. *Under the BD topology, considering the vehicle platoon with (1) and (2), guided by the CTH policy and Assumption 1, the SMSs $S_i(t)$, $s_i(t)$ can converge to zero within a fast finite-time and $e_i(t)$ eventually converges to zero with the action of the DO (15) and the controller (19).*

Proof. Specify a Lyapunov function as

$$\mathcal{V}(t) = \sum_{i=1}^{N} \mathcal{V}_i(t) + \tilde{\zeta}^T(t) P \tilde{\zeta}(t), \tag{21}$$

where $\mathcal{V}_i(t) = \frac{1}{2} S_i^2(t) + \frac{1}{2\varsigma} \gamma_i^2(t)$. Taking the derivative of (21), it comes

$$\dot{\mathcal{V}}(t) = \sum_{i=1}^{N} \dot{\mathcal{V}}_i(t) + \tilde{\zeta}^T(t) P \dot{\tilde{\zeta}}(t) + \dot{\tilde{\zeta}}^T(t) P \tilde{\zeta}(t). \tag{22}$$

Substitute (8), (10), (17) and (19) into (22), it comes

$$\begin{aligned} \dot{\mathcal{V}}(t) =& \sum_{i=1}^{N} (S_i(t)(-\eta_i S_i(t) - \gamma_i(t) tanh(\mu S_i(t)) - \rho h_i \tilde{\zeta}_i(t)) \\ &+ \varsigma^{-1} \gamma_i(t) \dot{\gamma}_i(t)) + 2\tilde{\zeta}^T(t) P \dot{\zeta}(t) - \tilde{\zeta}^T(t) G \tilde{\zeta}(t) \\ \leq& \sum_{i=1}^{N} (-\eta_i S_i^2(t) + \tfrac{\rho h_i}{2} S_i^2(t) + \tfrac{\rho h_i}{2} \tilde{\zeta}_i^2(t) - \beta \gamma_i^2(t)) \\ &+ 2\|\tilde{\zeta}(t)\| \|P\| \|\dot{\zeta}(t)\| - \lambda_g \|\tilde{\zeta}(t)\|^2, \end{aligned} \tag{23}$$

where λ_g represents the minimum value of eigenvalue of matrix G. Define $\tilde{\zeta}^2(t) = [\tilde{\zeta}_1^2(t), \tilde{\zeta}_2^2(t), \ldots, \tilde{\zeta}_N^2(t)]$, $h = [h_1, h_2, \ldots, h_N]$. Therefore, it comes

$$\sum_{i=1}^{N} h_i \tilde{\zeta}_i^2(t) = h^T \tilde{\zeta}^2(t). \tag{24}$$

Substituting (24) into (23) yields

$$\begin{aligned}\dot{\mathcal{V}}(t) \leq & \sum_{i=1}^{N}(-(\eta_i - \tfrac{\rho h_i}{2})S_i^2(t) - \beta\gamma_i^2(t)) \\ & + 2\|\tilde{\zeta}(t)\|\|P\|\|\dot{\zeta}(t)\| - (\lambda_g - \tfrac{\rho\bar{h}}{2})\|\tilde{\zeta}(t)\|^2, \\ \leq & \sum_{i=1}^{N}(-(\eta_i - \tfrac{\rho h_i}{2})S_i^2(t) - \beta\gamma_i^2(t)) \\ & - \|\tilde{\zeta}(t)\|((\lambda_g - \tfrac{\rho\bar{h}}{2})\|\tilde{\zeta}(t)\| - 2\|P\|\zeta),\end{aligned} \tag{25}$$

where $\bar{h} = max\{h_1, h_2, \ldots, h_N\}$. According to reference [14], we can obtain

$$\|\tilde{\zeta}(t)\| \leq \lambda_1, \tag{26}$$

where $\lambda_1 = \frac{2\|P\|\zeta}{\lambda_g - \frac{\rho\bar{h}}{2}}$. Then, (25) yields

$$\begin{aligned}\dot{\mathcal{V}}(t) \leq & \sum_{i=1}^{N}(-(\eta_i - \tfrac{\rho h_i}{2})S_i^2(t) - \beta\gamma_i^2(t)) \\ & - \tfrac{(\lambda_g - \frac{\rho\bar{h}}{2})}{\lambda_P}\tilde{\zeta}^T(t)P\tilde{\zeta}(t) + 2\lambda_1\zeta\|P\| \\ \leq & - a\mathcal{V}(t) + b,\end{aligned} \tag{27}$$

where $\eta_i > \frac{\rho h_i}{2}$, $\beta > 0$, $\lambda_g > \frac{\rho\bar{h}}{2}$, λ_P is maximum eigenvalue of matrix P, $a = min\{2\eta_i - \rho h_i, 2\varsigma\beta, \frac{\lambda_g - \frac{\rho\bar{h}}{2}}{\lambda_P}\}$, $b = 2\lambda_1\zeta\|P\|$. Since $\frac{b}{a} > 0$, we can obtain

$$0 \leq \mathcal{V}(t) = \tfrac{b}{a} + [\mathcal{V}(0) - \tfrac{b}{a}]e^{-at} \leq \tfrac{b}{a} + \mathcal{V}(0)e^{-at} \leq \tfrac{b}{a} + \mathcal{V}(0). \tag{28}$$

Then, according to Lemma 2, $\gamma_i(t)$ and $\tilde{\zeta}_i(t)$ are UUB. According to (28), $\mathcal{V}(t)$ satisfies

$$\sum_{i=1}^{N} \tfrac{1}{2}S_i^2(t) + \tfrac{1}{2\varsigma}\gamma_i^2(t) + \tilde{\zeta}^T(t)P\tilde{\zeta}(t) \leq \tfrac{b}{a} + \mathcal{V}(0)e^{-at}, \tag{29}$$

we can obtain

$$\begin{aligned}\|\tilde{\zeta}(t)\| &\leq \sqrt{\tfrac{b}{a\lambda_p}}, \\ \|\gamma_i(t)\| &\leq \sqrt{\tfrac{2\varsigma b}{a}},\end{aligned} \tag{30}$$

where λ_p represents the smallest eigenvalue of matrix P. Obviously, $\gamma_i(t)$ and $\tilde{\zeta}_i(t)$ can converge to $\sqrt{\frac{b}{a\lambda_p}}$, $\sqrt{\frac{2\varsigma b}{a}}$, respectively.

Then, choose a new Lyapunov function, which is constructed as

$$\bar{\mathcal{V}}(t) = \sum_{i=1}^{N} \tfrac{1}{2}S_i^2(t). \tag{31}$$

It can be seen that the derivative of (31) is

$$\begin{aligned}\dot{\bar{\mathcal{V}}}(t) = & \sum_{i=1}^{N} S_i(t)(-\eta_i S_i(t) - \gamma_i(t)tanh(\mu S_i(t)) - \rho h_i\tilde{\zeta}_i(t)) \\ \leq & \sum_{i=1}^{N} -\eta_i S_i^2(t) - \gamma_i(t)\|S_i(t)\| + \rho h_i\|\tilde{\zeta}_i(t)\|\|S_i(t)\|.\end{aligned} \tag{32}$$

From (30), we can know that $\|\tilde{\zeta}(t)\|$ and $\|\gamma_i(t)\|$ are bounded. Since $\gamma_i(t)$ is always positive, (32) yields

$$\begin{aligned}\dot{\bar{\mathcal{V}}}(t) \leq & \sum_{i=1}^{N} -\eta_i S_i^2(t) - (\sqrt{\tfrac{2\varsigma b}{a}} - \rho h_i\sqrt{\tfrac{b}{a\lambda_p}})\|S_i(t)\| \\ \leq & \sum_{i=1}^{N} -\eta S_i^2(t) - \theta\|S_i(t)\|,\end{aligned} \tag{33}$$

where $\eta = min\{\eta_1, \eta_2, \ldots, \eta_N\}$, $\sqrt{\frac{2\varsigma b}{a}} - \rho h_i\sqrt{\frac{b}{a\lambda_p}} \geq \theta > 0$. Define $\Phi(t) = \sum_{i=1}^{N}\theta\|S_i(t)\|$, it comes

$$\dot{\bar{\mathcal{V}}}(t) \leq \sum_{i=1}^{N} -\theta\|S_i(t)\| = -\Phi(t) \leq 0. \tag{34}$$

By integrating (34) over the interval $[0, t]$, it can be inferred that $\int_0^t \Phi(\tau)d\tau \leq \bar{\mathcal{V}}(0) - \bar{\mathcal{V}}(t)$. Since $\bar{\mathcal{V}}(0)$ is bounded, combined with (33) and $\bar{\mathcal{V}}(0) \geq 0$, it can be inferred that

$$0 \leq \bar{\mathcal{V}}(0) - \bar{\mathcal{V}}(t) \leq \nu, \tag{35}$$

where $\nu > 0$ is a constant. Obviously, $\lim_{t\to\infty}\int_0^t \Phi(\tau)d\tau < \infty$, combined with Lemma 1, we can deduce that

$$\lim_{t\to\infty}\sum_{i=1}^{N}\theta\|S_i(t)\| = \lim_{t\to\infty}\Phi(t) = 0. \tag{36}$$

Then, we can infer that $\lim_{t\to\infty} S_i(t) = 0$. Furthermore, we can make (33) another form as

$$\begin{aligned}\dot{\bar{\mathcal{V}}}(t) \leq & \sum_{i=1}^{N} -\eta S_i^2(t) - \theta\|S_i(t)\| \\ \leq & -\kappa_1\bar{\mathcal{V}}(t) - \kappa_2\bar{\mathcal{V}}^{\kappa_3}(t),\end{aligned} \tag{37}$$

where $\kappa_1 \leq 2\eta$, $\kappa_2 \leq \sqrt{2}\theta$ and $\kappa_3 = \frac{1}{2}$. According to (6) and Lemma 3, $S_i(t)$ and $s_i(t)$ can converge to zero within a fast finite-time. Then, on the basis of (5), $e_i(t)$ eventually converges to zero. □

Theorem 2. *Under the BD topology, considering the vehicle platoon with (1) and (2), based on CTH policy and the action of the proposed IASMC strategy, the string stability can be guaranteed with* $0 < \rho \leq 1$ *and* $k_i \leq k_{i+1}$.

Proof. According to Theorem 1, the SMS $S_i(t)$ converges to zero, (6) yields,

$$\rho s_i(t) - s_{i+1}(t) = 0. \tag{38}$$

Taking (5) into (38), we can obtain

$$\rho(e_i(t) + \int_0^t k_i e_i(\tau)d\tau) = e_{i+1}(t) + \int_0^t e_{i+1}(\tau)d\tau. \tag{39}$$

By applying the Laplace transformation to (39), it comes

$$\rho(E_i(s) + \frac{k_i E_i(s)}{s}) = E_{i+1}(s) + \frac{k_{i+1} E_{i+1}(s)}{s}, \tag{40}$$

thus,

$$\frac{E_{i+1}(s)}{E_i(s)} = \rho \frac{s+k_i}{s+k_{i+1}}. \tag{41}$$

Since $0 < \rho \leq 1$ and $k_i \leq k_{i+1}$, we can obtain $\| \frac{E_{i+1}(s)}{E_i(s)} \| \leq 1$, so the string stability is ensured. □

4 Numerical Simulations

Table 1: Simulation parameters

Parameter	ς	β	k_i	ρ	η_i	$\gamma_i(0)$	σ_i
Value	3	0.1	1	0.9	5	0.05	0.001

In this section, with the purpose of presenting the primary results of the proposed IASMC strategy based on DO, numerical simulations involving a platoon consisting of $N = 6$ followers with one leader are carried out. The initial positions of the platoon are $x_0(0) = 16m$ and $x(0) = [14, 12, 10, 7, 4.2, 2.4]^T m$, respectively. Similarly, set the initial velocities as $v_0(0) = 2m/s$ and $v(0) = [1.8, 1.72, 1.61, 2.795, 2.41, 1.5]^T m/s$, respectively. Set the velocity of the leader as

$$v_0(t) = \begin{cases} 2\,m/s, & 0s < t \leq 2s \\ t\,m/s, & 2s < t \leq 6s \\ 6\,m/s, & otherwise. \end{cases} \tag{42}$$

In this paper, for $i = 1, 2, \ldots, 6$, set the mass of each vehicle as $m_i = 1kg$, the standstill spacing is $\chi_i(t) = 0.5m$ and $h_i = 1s$. Set the unknown disturbance of the ith following vehicle as $\zeta_i(t) = 1.5\sin(3t)e^{-(t-5-0.2i)^2}$. In order to better approximate the sign function to maintain the rapidity of sliding mode, we set the parameter $\mu = 100$. And the settings of other parameters are shown in Table 1.

Then, in Fig.4, we can acquire the simulation results of IASMC strategy (19). For Fig.4(a), since the position curves have no intersection, it illustrates that the entire platoon can effectively avoid collisions. Fig.4(c) shows that $e_i(t)$ can converge to zero. In addition, $\|e_6(t)\| \leq \|e_5(t)\| \leq \cdots \leq \|e_1(t)\|$, which ensures the string stability. And the distances between adjacent vehicles in Fig.4(d) can converge to the expected values in accordance with the CTH policy, respectively. Fig.4(f) shows that when the disturbance in the previous period is not severe, the SMS $s_i(t)$ converges to zero in $0.55s$. However, when the disturbance becomes severe, the SMS $s_i(t)$ still converges to zero in $8.24s$. Under the actions of control input depicted in Fig.4(e), the velocities are illustrated in Fig.4(b).

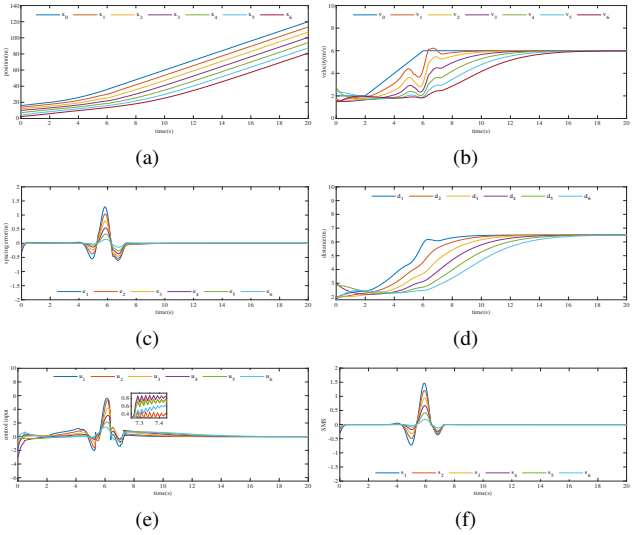

Fig. 5: The simulation results of IASMC with $\mu = 500$.

In order to better understand the effects of different values of μ on the system, we have selected the simulation results at $\mu = 500$ for comparison, as shown in Fig.5. By comparing Fig.4(f) and Fig.5(f), it's evident that with larger values of μ, the SMS $s_i(t)$ converges more rapidly. However, the drawbacks become apparent as well, as vividly illustrated by the chattering phenomenon in Fig.5(e).

To illustrate the superiority of IASMC strategy, we compare the method in [14] with it. All simulation parameters of

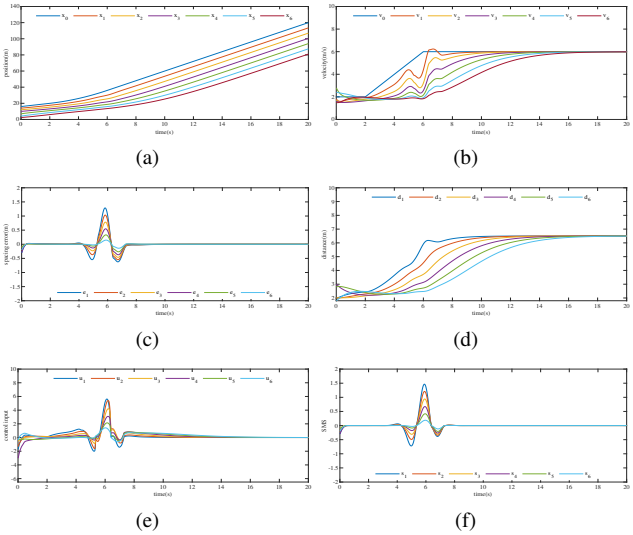

Fig. 4: The simulation results of IASMC with $\mu = 100$.

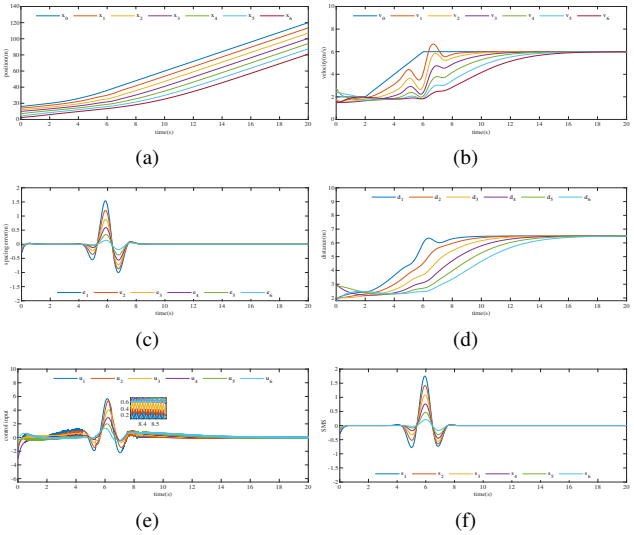

Fig. 6: The simulation results of ISMC in [14].

Table 2: Performance comparison of different methods.

Vehicle index	Spacing error (m)						Chattering		
	Positive peak			Negative peak					
	IASMC ($\mu = 100$)	IASMC ($\mu = 500$)	ISMC in [14]	IASMC ($\mu = 100$)	IASMC ($\mu = 500$)	ISMC in [14]	IASMC ($\mu = 100$)	IASMC ($\mu = 500$)	ISMC in [14]
1	1.2865	1.2910	1.5405	0.6225	-0.6047	-1.0024	No	Yes	Yes
2	1.0325	1.0357	1.2014	-0.5460	-0.5324	-0.8711			
3	0.7825	0.7847	0.8817	-0.4628	-0.4548	-0.7249			
4	0.5465	0.5476	0.5918	-0.3719	-0.3714	-0.5607			
5	0.3318	0.3323	0.3420	-0.2662	-0.2669	-0.3795			
6	0.1472	0.1474	0.1411	-0.1406	-0.1412	-0.1873			

the method in [14] in Fig.6 are consistent with Fig.4. Then, compare Fig.6 with Fig.4, the detailed comparative values in Table 2 show that the spacing error $e_i(t)$ in Fig.6(c) is larger. Furthermore, the convergences of the distances between adjacent vehicles in Fig.4(d) are better than those in Fig.6(d). Additionally, comparing Fig.6(e) with Fig.4(e), we can see that the chattering under IASMC strategy can be effectively eliminated. Finally, the SMSs in Fig.4(f) also converge faster than those in Fig.6(f).

5 Conclusion

This article studies an IASMC strategy about vehicle platoon control using integral adaptive sliding mode, incorporating DO and the CTH policy subject to unknown disturbances. IASMC can effectively decrease the spacing error. To eliminate the chattering issues linked to the controller, a sliding mode reaching law with adaptive law is constructed. Then, a DO is constructed to estimate the external disturbances even if the boundaries of the disturbances are unspecified. Further, IASMC is developed. Also, the stability of the proposed IASMC strategy is proved and the string stability is guaranteed. Finally, the performance of IASMC was verified by comparing with another different method through simulations. Future work will consider platoon control of heterogeneous models and ensure that the spacing errors converge to zero within a finite time.

References

[1] H. Zhang, J. Liu, Z. Wang, C. Huang and H. Yan, "Adaptive Switched Control for Connected Vehicle Platoon With Unknown Input Delays," *IEEE Trans. Cybern.*, vol. 53, no. 3, pp. 1511-1521, March. 2023.

[2] M. di Bernardo, A. Salvi and S. Santini, "Distributed Consensus Strategy for Platooning of Vehicles in the Presence of Time-Varying Heterogeneous Communication Delays," *IEEE Trans. Intell. Transp. Sys.*, vol. 16, no. 1, pp. 102-112, Feb. 2015.

[3] S. E. Shladover, "PATH at 20–History and Major Milestones," *IEEE Trans. Intell. Transp. Sys.*, vol. 8, no. 4, pp. 584-592, Dec. 2007.

[4] B. Besselink and K. H. Johansson, "String Stability and a Delay-Based Spacing Policy for Vehicle Platoons Subject to Disturbances," *IEEE Trans. Autom. Control.*, vol. 62, no. 9, pp. 4376-4391, Sept. 2017.

[5] J. Chen, H. Liang, J. Li and Z. Lv, "Connected Automated Vehicle Platoon Control With Input Saturation and Variable Time Headway Strategy," *IEEE Trans. Intell. Transp. Sys.*, vol. 22, no. 8, pp. 4929-4940, Aug. 2021.

[6] Y. Wu, S. E. Li, J. Corts and K. Poolla, "Distributed Sliding Mode Control for Nonlinear Heterogeneous Platoon Systems With Positive Definite Topologies," *IEEE Trans. Control Syst. Technol.*, vol. 28, no. 4, pp. 1272-1283, July. 2020.

[7] T. L. Willke, P. Tientrakool and N. F. Maxemchuk, "A survey of inter-vehicle communication protocols and their applications," *IEEE Commun. Surveys Tuts.*, vol. 11, no. 2, pp. 3-20, Second Quarter. 2009.

[8] Y. Yang, P. Shi, S. Wang, J. Chambers. "Bipartite containment of heterogeneous multi-agent systems under denial-of-service attacks: A historical information-based control scheme," *Int. J. Robust Nonlinear Control*, pp. 1-16, 2023.

[9] G. Rdnyi, "An Adaptive Spacing Policy Guaranteeing String Stability in Multi-Brand Ad Hoc Platoons," *IEEE Trans. Intell. Transp. Sys.*, vol. 19, no. 6, pp. 1902-1912, June. 2018.

[10] Y. Zheng, S. Eben Li, J. Wang, D. Cao and K. Li, "Stability and Scalability of Homogeneous Vehicular Platoon: Study on the Influence of Information Flow Topologies," *IEEE Trans. Intell. Transp. Sys.*, vol. 17, no. 1, pp. 14-26, Jan. 2016.

[11] S. Xiao, X. Ge, Q. -L. Han and Y. Zhang, "Dynamic Event-Triggered Platooning Control of Automated Vehicles Under Random Communication Topologies and Various Spacing Policies," *IEEE Trans. Cybern.*, vol. 52, no. 11, pp. 11477-11490, Nov. 2022.

[12] X. Hu, L. Xie, L. Xie, S. Lu, W. Xu and H. Su, "Distributed Model Predictive Control for Vehicle Platoon With Mixed Disturbances and Model Uncertainties," *IEEE Trans. Intell. Transp. Sys.*, vol. 23, no. 10, pp. 17354-17365, Oct. 2022.

[13] X. Guo, J. Wang, F. Liao and R. S. H. Teo, "Distributed Adaptive Sliding Mode Control Strategy for Vehicle-Following Systems With Nonlinear Acceleration Uncertainties," *IEEE Trans. Veh. Technol.*, vol. 66, no. 2, pp. 981-991, Feb. 2017.

[14] J. Wang, X. Luo, L. Wang, Z. Zuo and X. Guan, "Integral Sliding Mode Control Using a Disturbance Observer for Vehicle Platoons," *IEEE Trans. Ind. Electron.*, vol. 67, no. 8, pp. 6639-6648, Aug. 2020

[15] J. Wang, X. Luo, J. Yan and X. Guan, "Distributed Integrated Sliding Mode Control for Vehicle Platoons Based on Disturbance Observer and Multi Power Reaching Law," *IEEE Trans. Intell. Transp. Sys.*, vol. 23, no. 4, pp. 3366-3376, April. 2022.

[16] Y. Zhu *et al*., "Joint Sliding-Mode Controller and Observer for Vehicle Platoon Subject to Disturbance and Acceleration Failure of Neighboring Vehicles," *IEEE Trans. Intell. Veh.*, vol. 8, no. 3, pp. 2345-2357, March. 2023.

[17] S. Yu, X. Yu, B. Shirinzadeh, and Z. Man, "Continuous finite-time control for robotic manipulators with terminal sliding mode," *Automatica*, vol. 41, no. 11, pp. 1957-1964, 2005.

[18] J. -W. Kwon and D. Chwa, "Adaptive Bidirectional Platoon Control Using a Coupled Sliding Mode Control Method," *IEEE Trans. Intell. Transp. Sys.*, vol. 15, no. 5, pp. 2040-2048, Oct. 2014.

[19] J. Qin, G. Zhang, W. X. Zheng and Y. Kang, "Adaptive Sliding Mode Consensus Tracking for Second-Order Nonlinear Multiagent Systems With Actuator Faults," *IEEE Trans. Cybern.*, vol. 49, no. 5, pp. 1605-1615, May. 2019.

Proceedings of the 3rd Conference on Fully Actuated System Theory and Applications
May 10-12, 2024, Shenzhen, China

Fixed-time Funnel Sliding Mode Control for Dual-motor Driving System

Jia-Meng Wu and Cheng-Lin Liu
Key Laboratory of Advanced Process Control for Light Industry (Ministry of Education), Institute of Automation,
Jiangnan University, Wuxi 214122, China
E-mail: liucl@jiangnan.edu.cn

Abstract: A fixed-time funnel sliding mode control strategy is developed for a dual-motor driving system, which ensures the system converges within a fixed time. Firstly, the coupling error is introduced by combining the reference tracking process with the motor synchronization process. By using a selected funnel function, the system can achieve satisfactory transient performance. Secondly, the concept of multi-surface sliding modes is designed to deal with the tracking issue so that the system can converge in a fixed-time regardless of the motor's initial state. Finally, the effectiveness of this strategy is demonstrated through a simulation example.

Key Words: Fixed-time, funnel function, sliding mode control, dual-motor driving system

1 Introduction

In addressing challenges within industrial processes and products, a singular motor's limited driving force poses difficulties in meeting power requirements, particularly in the context of large inertia load driving systems. Therefore, the configuration of two or even multiple motors is widely used in many application scenarios [1]. In this type of multi-motor system, coordination and synchronization become the most essential requirements for the controller. Due to the complex nature of the system models under consideration, most controllers are intricately crafted using repetitive differential frameworks. On this basis, designing the tracking controller and the synchronization controller individually would make the entire control system overly complex, potentially even unstable [2]. Therefore, it is meaningful to find a new multi-motor synchronization control strategy to make the system more reliable and maintain synchronization performance.

Many scholars have tried to implement various advanced control strategies to track this problem. Among them, sliding mode control has received the most widespread attention due to its excellent rapidity and robustness [3]. In [4], a fast terminal sliding mode control is proposed so that the single-input single-output nonlinear system can converge in a limited time. In [5], a non-singular fast terminal sliding mode control is proposed, incorporating a finite-time extended state observer, with the primary goal of ensuring effective tracking of the target trajectory by the motor system. In [6], a timing motor synchronization control method is proposed, wherein the division of the motor synchronization process and the reference signal tracking process into two controllers not only complicates the control but also enhances the system's instability. Moreover, in these controllers, the initial state of the system will affect the convergence time, resulting in an unsatisfactory convergence period when the initial error is large [7].

Furthermore, considering that when limits on output amplitude and system status are violated, system performance may degrade and safety issues may even arise [8]. In order to ensure transient performance and system stability, several constrained control schemes have been proposed, making them one of the hot spots in recent years. Among these methods, it is common to use prescribed performance control and system funnel control methods. In [9], a new fuzzy adaptive control is proposed based on the preset performance function, which ensures that the closed-loop control system is semi-globally uniform and ultimately constrained, and the tracking error can converge within the specified performance boundary. In [10], the objective is to ensure transient performance in a flexible joint manipulator system through the application of adaptive fuzzy control, achieved by designing a novel performance function. Compared to prescribed performance control, funnel control has received increasing attention due to its high-gain property, control struture, and no memory feature. However, to the best of our knowledge, few scholars have applied the funnel function in motor synchronous control to optimize control performance.

In this article, we use a dual-motor driving system as a case study and try to design a controller to address existing issues and improve the overall control performance of the system. Based on the fixed time convergence theory, this paper proposes a synchronous control strategy with the coupling error, which ensures multi-motor synchronization and simplifies the controller. In this control strategy, a coupling error is proposed to couple the reference signal tracking process and the motor synchronization process together. Then, the coupling errors are limited using a selected funnel function to achieve the desired transient performance. Finally, the concept of multi-surface sliding modes is utilized to deal with the reference signal tracking problem, and fixed-time convergence can be guaranteed regardless of the initial state of the system.

The subsequent sections of this paper are organized as follows. Section II initiates the discussion by introducing models of a dual-motor driving system. Following that, Section III elaborates on the development of a multi-surface fixed-time sliding mode controller, addressing challenges related to tracking and synchronization in multi-motor driving sys-

This work was supported by National Natural Science Foundation of China under Grants 61973139 and 61473138, and the Fundamental Research Funds for the Central Universities under Grant JUSRP22014. *(Corresponding author: Cheng-Lin Liu.)*

tems. Additionally, stability analysis utilizing Lyapunov stability theory is presented. In Section IV, comparative experimental results are incorporated to validate the effectiveness of the proposed strategy. Finally, Section V summarizes the article's content and presents the conclusion.

2 system description and preliminaries

2.1 Dual-motor driving system

Consider a driving system composed of two motors, where the dynamic equation of the i-th motor is expressed as

$$J_i\ddot{\theta}_i + B_f\dot{\theta}_i + T_{Li} + d_i = u_i,\ i = 1, 2, \tag{1}$$

where $J_i \in \mathbb{R}$ is the inertia of motor i, $\dot{\theta}_i \in \mathbb{R}$ and $\ddot{\theta}_i \in \mathbb{R}$ are the velocity and the angular acceleration of motor i, $B_f \in \mathbb{R}$ is defined as the viscous friction coefficient, $T_{Li} \in \mathbb{R}$ denotes the load torque of motor i, $d_i \in \mathbb{R}$ represents the external disturbance, and $u_i \in \mathbb{R}$ represents the control input.

Define $\omega_i = \dot{\theta}_i$, and (1) can be rewriten as

$$\begin{cases} \dot{\theta}_i = \omega_i, \\ \dot{\omega}_i = \dfrac{1}{J}u_i - \dfrac{1}{J}(T_{Li} + B_f\omega_i + d_i). \end{cases} \tag{2}$$

Assumption 1: The reference signal, denoted as θ_d, is assumed to belong to the space $W^{2,\infty}(\mathbb{R}_{\geq 0}; \mathbb{R})$.
Assumption 2: The external disturbance $d_i \in L^{\infty}(\mathbb{R}_{\geq 0}; \mathbb{R})$ has an unknown positive upper bound.

Remark 1. *Control input u_i, external disturbance d_i, nonlinear friction, and unmodeled dynamics are confined within the working range. As a result, there exists an intrinsic limitation, ensuring a bounded total disturbance.*

So in this case, our control objectives are as follows: 1) track the reference signal θ_d under the external disturbance d_i, 2) keep the position synchronization and speed synchronization of motor 1 and motor 2, and 3) make the system converge and stabilize within a fixed time and maintain good transient performance.

2.2 Coupling synchronization error

The traditional dual-motor control scheme involves the imperative task of separately designing the tracking controller and synchronous controller for the motors. In the tracking controller, the control signal u_i and error signal e_i of each motor form an independent closed loop, which is only related to the current motor and does not affect other motors in the system. Here, we try to avoid the complexity of multi-controller design and solve the tracking and synchronization problems simultaneously in one controller.

To achieve this purpose, we define the tracking error e_i and the synchronization error ϵ_i as follows:

$$e_i = \theta_i - \theta_d,\ i = 1, 2, \tag{3}$$

$$\epsilon_i = e_i - \frac{1}{2}\sum_{i=1}^{2} e_i,\ i = 1, 2, \tag{4}$$

where θ_i is the position of motor i, θ_d is the reference signal. Through the synchronization error ϵ_i, the error signal of each motor is interconnected with the error signals of the other motors. In this system, each motor is influenced not only by its own tracking error but also by the tracking errors of the other motors, leading to the synchronization of the entire system's state.

If each motor's current signal in the servo system remains stable and matches the reference signal, meaning that the tracking error of each motor is the same (i.e., when $e_1 = e_2$), we can conclude that the entire motor system is synchronized.

Based on the above analysis, considering the tracking error and synchronization error of the system at the same time, we can design the coupling error as follows:

$$\eta_i = e_i + \alpha\epsilon_i,\ i = 1, 2, \tag{5}$$

where $\alpha > 0$ represents the synchronization effect. When the position coupling error $\eta_i = 0$, we can get the tracking error $e_i = 0$, and the synchronization error $\epsilon_i = 0$. Therefore, our ultimate goal is to design the controller so that the coupling error is zero, so that the effects of tracking and synchronization can be achieved at the same time.

2.3 Funnel control and funnel variable

Funnel control is a control method proposed by ILCHMANN [11] with high gain characteristics, which can well limit the dynamic behavior of errors. A simple funnel controller can be written as

$$\begin{cases} u(t) = -\tau(t)\cdot\varsigma(t) \\ \quad = -\dfrac{1}{F(t) - ||\varsigma(t)||}\cdot\varsigma(t), \end{cases} \tag{6}$$

where $\tau(t)$ is the time-varying gain, $\varsigma(t)$ is the tracking error, $F(t)$ is the preset funnel function boundary. The error $\varsigma(t)$ is constrained by the boundary function $F(t)$ in Fig.1. $F(t) - |e(t)|$ represents the vertical distance from the error

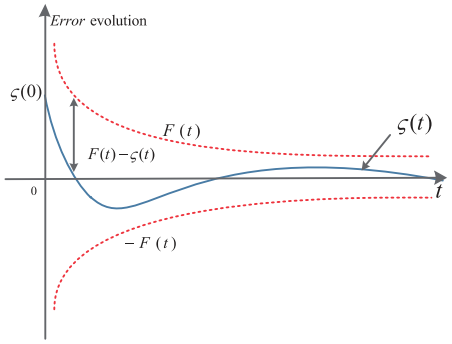

Fig. 1: Funnel control block diagram.

to the funnel boundary. When the error $e(t)$ is close to the boundary $F(t)$, the control gain $\tau(t)$ increases. On the contrary, if the tracking error $e(t)$ is far away from the boundary function $F(t)$, the control gain $\tau(t)$ decreases.

In this paper, the funnel boundary function $F(t)$ is chosen as [12, 13]

$$F(t) = \varphi_0 \exp(-\sigma t) + \varphi_\infty, \tag{7}$$

where φ_0 respents the inital value of boundary funnel function, σ respents the convergence speed of funnel bottleneck,φ_∞ respents the allowable upper bound of steady-state tracking error. φ_0 , σ and φ_∞ are appropriately positive constants.

In this way, we can define the funnel error variable

$$\zeta_i = \frac{\eta_i}{F - |\eta_i|},\ i = 1, 2, \tag{8}$$

which ensures that the coupling error is always in the preset funnel area.

3 Main Results

3.1 Controler design

In this section, we discuss the dual motor synchronization problem and design the controller. Based on the concepts of funnel error and multiple sliding surfaces, we propose a funnel sliding mode controller. The controller is designed using multiple sliding surfaces, where the first surface tracks the reference signal, and the second surface drives the system state to the first sliding mode surface. The multisurface concept benefits by allowing the development of a sliding mode controller with a reduced requirement for plant output differentiation [6]. At the same time, the funnel function can ensure that the error is always within the funnel domain, effectively improving the transient performance of the system. Figure 2 shows the control structure of this system.

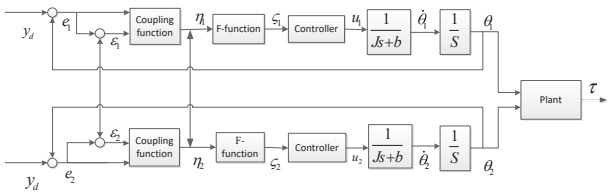

Fig. 2: The structure of this system.

We use the funnel error (8) to design the first sliding surface like this:

$$S_i = B\zeta_i + C_1 \int_0^t |\zeta_i|^{\lambda_1} \cdot \operatorname{sign}(\zeta_i)\, d\tau + C_2 \int_0^t |\zeta_i|^{\lambda_2} \cdot \operatorname{sign}(\zeta_i)\, d\tau, \tag{9}$$

where $C_1 > 0, C_2 > 0, 0 < \lambda_1 < 1$, and $\lambda_2 > 1$.

According to (8) and (9), the time derivative of S_i becomes

$$\dot{S}_i = B\,\dot{\zeta}_i + C_1|\zeta_i|^{\lambda_1} \cdot \operatorname{sign}(\zeta_i) + C_2|\zeta_i|^{\lambda_2} \cdot \operatorname{sign}(\zeta), \tag{10}$$

$$\ddot{S}_i = B\,\ddot{\zeta}_i + C_1\,\lambda_1\,|\zeta_i|^{\lambda_1 - 1} \cdot \dot{\zeta}_i + C_2\,\lambda_2\,|\zeta_i|^{\lambda_2 - 1} \cdot \dot{\zeta}_i. \tag{11}$$

Formulate the second sliding mode surface as follows:

$$\sigma_i = \dot{S}_i + \beta\ |S_i|^{\lambda_3} \operatorname{sign}(S_i). \tag{12}$$

The derivative of σ_i is

$$\dot{\sigma}_i = \ddot{S}_i + \beta\lambda_3\,|S_i|^{\lambda_3 - 1}\,\dot{S}_i. \tag{13}$$

The reaching law is designed as:

$$\dot{\sigma}_i = -k_0\sigma_i - k_1 \tanh(\sigma_i) - k_2|\sigma_i|^{\lambda_4} \operatorname{sign}(\sigma_i), \tag{14}$$

where $k_1 > 0$, $k_2 > 0$ and $\lambda_4 > 1$. We introduce a smoother $tanh$ function, which will productively reduce the phenomenon of the input signal's chattering behavior.

Substituting (11) and (14) into (13), we get

$$B\,\ddot{\zeta}_i = -k_0\sigma_i - k_1 \tanh(\sigma_i) - k_2\,|\sigma_i|^{\lambda_4} \operatorname{sign}(\sigma_i) - \beta\lambda_3\,|S_i|^{\lambda_3 - 1}\,\dot{S}_i - C_1\,\lambda_1\,|\zeta_i|^{\lambda_1 - 1} \cdot \dot{\zeta}_i - C_2\,\lambda_2\,|\zeta_i|^{\lambda_2 - 1} \cdot \dot{\zeta}_i. \tag{15}$$

At the same time, according to (5) and (8), we can get the first and second order time differentials of the funnel function

$$\dot{\zeta}_i = \frac{\dot{\eta}_i}{F - |\eta_i|} - L_i, \tag{16}$$

$$\ddot{\zeta}_i = \frac{\ddot{\eta}_i}{F - |\eta_i|} - P_i, \tag{17}$$

where, $L_i = \frac{\eta_i\left(\dot{F} - |\dot{\eta}_i|\right)}{(F - |\eta_i|)^2}$, $P_i = \frac{2\dot{\eta}_i\left(\dot{F} - |\dot{\eta}_i|\right) + \eta_i\left(\ddot{F} - |\ddot{\eta}_i|\right)}{(F - |\eta_i|)^2} - 2\eta_i \frac{\left(\dot{F} - |\dot{\eta}_i|\right)^2}{(F - |\eta_i|)^3}$.

Substituting and (15), (16) and (17) into system (2), we can get the control signal u_i under the two-layer sliding mode surface

$$u_i = J_i \left(Q_i - \alpha\ddot{\epsilon}_i + \frac{1}{J_i}\left(T_{L_i} + B_f\dot{\theta}_i + d_i\right) + \ddot{\theta}_d \right), \tag{18}$$

where

$$Q_i = \left(\frac{1}{B_f}\right)\left(\dot{\sigma}_i - \beta\lambda_3\left(|s_i|^{\lambda_3 - 1}\,\dot{s}_i\right) - C_1\lambda_1\left(|\zeta_i|^{\lambda_1 - 1}\,\dot{\zeta}_i\right) - C_2\lambda_2\left(|\zeta_i|^{\lambda_2 - 1}\,\dot{\zeta}_i\right) + P_i\ \right)(F - |\eta_i|)\,. \tag{19}$$

3.2 Stability analysis

In this segment, we will demonstrate the stability of the proposed control strategy. The following lemmas are in aid of the stability analysis.

Lemma 1. *[14] Assume the existence of a Lyapunov function $\mathcal{V}(x) \geq 0$ defined in the neighborhood $U \subset \mathbb{R}^n$ of the origin, satisfying the following inequality:*

$$\dot{\mathcal{V}}(x) \leq -(\psi_1\mathcal{V}(x)^l + \psi_2\mathcal{V}(x)^n)^m, \tag{20}$$

Here, ψ_1, ψ_2, l, n, and m are positive real numbers, with $lm > 1$ and $nm < 1$. Consequently, the system's origin is fixed-time stable. For any $\mathcal{V}(x)$, it can attain $\mathcal{V}(x) \equiv 0$ within a fixed time T, which is bounded and independent of the initial states. This fixed time is expressed as:

$$T \leq \frac{1}{\psi_1^m(1 - lm)} + \frac{1}{\psi_2^m(nl - 1)}. \tag{21}$$

Lemma 2. *[15] The system is deemed practically fixed-time stable if there exists a Lyapunov function $\mathcal{V}(x)$ and specific scalars satisfying $0 < \alpha < 1$, $\beta > 1$, $\lambda > 0$, $\varpi > 0$, and $0 < \rho < \infty$, such that the inequality given by Equation (22) holds:*

$$\dot{\mathcal{V}}(x) \leq -\lambda\mathcal{V}^{\alpha}(x) - \varpi\mathcal{V}^{\beta}(x) + \rho. \tag{22}$$

The trajectory of the closed-loop system is confined within a bound denoted as Λ, defined by Equation (23):

$$\Lambda = \left\{ \lim_{t \to T} x \,\middle|\, \mathcal{V}(x) \leq \min\{\Phi, \Psi\} \right\}, \tag{23}$$

where $\Phi = \left(\frac{\rho}{(1-\vartheta)\lambda}\right)^{\frac{1}{\alpha}}$, $\Psi = \left(\frac{\rho}{(1-\vartheta)\varpi}\right)^{\frac{1}{\beta}}$, ϑ satisfies $0 < \vartheta \leq 1$. The upper limit for the practical fixed-time to reach the residual set is bounded by $T \leqslant \frac{1}{\lambda\vartheta(1-\alpha)} + \frac{1}{\varpi\vartheta(\beta-1)}$.

Lemma 3. *[16] For any $\sigma > 0$ and $\xi \in \mathbb{R}$, the following inequality is valid:*

$$0 \leq |\xi| - \xi \tanh\left(\frac{\xi}{\sigma}\right) \leq \tau\sigma, \tag{24}$$

where τ is determined by the equation $\tau = e^{-(\tau+1)}$, specifically yielding $\tau \approx 0.2785$.

Theorem 1. *By implementing the reaching law* (14)*, the controller* (18) *ensures the stability of system* (2) *and facilitates the convergence of the coupling error η to a minimal neighborhood around zero. Furthermore, the convergence time T is bounded by*

$$\begin{aligned} T = &\frac{|S_i(0)|^{1-\lambda_3}}{\beta(1-\lambda_3)} + \frac{2}{\sqrt{2}k_1\vartheta} + \frac{2}{2^{\frac{\lambda_4+1}{2}}k_2\vartheta(\lambda_4-1)} \\ &+ \frac{1}{\frac{C_1}{B}2^{\frac{\lambda_1+1}{2}}(1-\frac{\lambda_1+1}{2})} + \frac{1}{\frac{C_2}{B}2^{\frac{\lambda_2+1}{2}}(\frac{\lambda_2+1}{2})-1}. \end{aligned} \tag{25}$$

Proof. Choose a Lyapunov function as

$$V_1 = \frac{1}{2}\sigma_i^2. \tag{26}$$

Substituting the control signal (14) into the differential expression of (26), we can get

$$\begin{aligned} \dot{V}_1 &= \sigma_i \cdot \dot{\sigma}_i \\ &= \sigma_i\left(-k_0\sigma_i - k_1\tanh(\sigma_i) - k_2|\sigma_i|^{\lambda_4}\operatorname{sign}(\sigma_i)\right) \\ &= -k_0|\sigma_i|^2 - k_1\sigma_i\tanh(\sigma_i) - k_2|\sigma_i|^{\lambda_4+1} \\ &\leq -k_1|\sigma_i| + k_1\iota - k_2|\sigma_i|^{\lambda_4+1} \\ &\leq -k_1 2^{\frac{1}{2}}V_1^{\frac{1}{2}} - k_2 2^{\frac{\lambda_4+1}{2}}V_1^{\frac{\lambda_4+1}{2}} + k_1\iota, \end{aligned} \tag{27}$$

where $k_1, k_2 > 0$, $\frac{\lambda_4+1}{2} > 1$. According to **Lemma 2**, σ_i can in fixed time t_σ converge to a minimal neighborhood of zero:

$$\Lambda = \left\{\lim_{t\to t_\sigma}\sigma\,|V_2 \leq \min\{\Phi, \Psi\}\right\}, \tag{28}$$

where $\Phi = (\frac{k_1\iota}{(1-\vartheta)\sqrt{2}k_1})^2$, $\Psi = (\frac{k_1\iota}{(1-\vartheta)k_2 2^{\frac{\lambda_4+1}{2}}})^{\frac{2}{\lambda_4+1}}$. The convergence time t_σ is

$$t_\sigma \leq \frac{2}{\sqrt{2}k_1\vartheta} + \frac{2}{2^{\frac{\lambda_4+1}{2}}k_2\vartheta(\lambda_4-1)}. \tag{29}$$

When the funnel error reaches the sliding mode surface σ_i, we can get

$$\dot{S}_i = -\beta|S_i|^{\lambda_3}sign(S_i). \tag{30}$$

Choose the Lyapunov function as

$$V_2 = \frac{1}{2}{S_i}^2. \tag{31}$$

Then, the time derivative of (31) is

$$\begin{aligned} \dot{V}_2 &= S_i\dot{S}_i = -\beta|S_i|^{\lambda_3}sign(S_i)S_i \\ &= -\beta|S_i|^{\lambda_3+1} \leq 0. \end{aligned} \tag{32}$$

Therefore, $S_i(t)$ would converge to zero. Solving differential (32), the convergence time can be obtained as:

$$t_s = \int_0^{|S_i(0)|}\frac{1}{\beta S_i^{\lambda_3}}\,dS_i = \frac{|S_i(0)|^{1-\lambda_3}}{\beta(1-\lambda_3)}. \tag{33}$$

When $S_i(t)$ converge to zero, we can have

$$\dot{\zeta}_i = -\frac{C_1}{B}|\zeta_i|^{\lambda_1}\operatorname{sign}(\zeta_i) - \frac{C_2}{B}|\zeta_i|^{\lambda_2}\operatorname{sign}(\zeta_i). \tag{34}$$

Choose a Lyapunov function as

$$V_3(\zeta_i) = \frac{1}{2}\zeta_i^2. \tag{35}$$

Then , the time derivative of (35) is

$$\begin{aligned} \dot{V}_3(\zeta_i) &= \zeta_i\dot{\zeta}_i \\ &= \zeta_i\left(-\frac{C_1}{B}|\zeta_i|^{\lambda_1}\operatorname{sign}(\zeta_i) - \frac{C_2}{B}|\zeta_i|^{\lambda_2}\operatorname{sign}(\zeta_i)\right) \\ &= -\frac{C_1}{B}|\zeta_i|^{\lambda_1+1} - \frac{C_2}{B}|\zeta_i|^{\lambda_2+1} \\ &\leq -\frac{C_1}{B}2^{\frac{\lambda_1+1}{2}}V_3^{\frac{\lambda_1+1}{2}} - \frac{C_2}{B}2^{\frac{\lambda_2+1}{2}}V_3^{\frac{\lambda_2+1}{2}}. \end{aligned} \tag{36}$$

Using Lemma 1, ζ will converge on the first surface in fixed time. The convergence time t_ζ for ζ is bounded as

$$t_\zeta \leq \frac{1}{\frac{C_1}{B}2^{\frac{\lambda_1+1}{2}}(1-\frac{\lambda_1+1}{2})} + \frac{1}{\frac{C_2}{B}2^{\frac{\lambda_2+1}{2}}(\frac{\lambda_2+1}{2})-1}. \tag{37}$$

To sum up, under the action of the designed controller (18), the dual-motor driving system can reach stability after a fixed time T :

$$\begin{aligned} T &= t_s + t_\sigma + t_\zeta \\ &= \frac{|S_i(0)|^{1-\lambda_3}}{\beta(1-\lambda_3)} + \frac{2}{\sqrt{2}k_1\vartheta} + \frac{2}{2^{\frac{\lambda_4+1}{2}}k_2\vartheta(\lambda_4-1)} \\ &+ \frac{1}{\frac{C_1}{B}2^{\frac{\lambda_1+1}{2}}(1-\frac{\lambda_1+1}{2})} + \frac{1}{\frac{C_2}{B}2^{\frac{\lambda_2+1}{2}}(\frac{\lambda_2+1}{2}-1)}. \end{aligned} \tag{38}$$

So we proved that under this control, the system can remain stable and the coupling error will converge to zero. □

Remark 2. *By taking the limit of equation (8), we find that: $\lim_{t\to T}\zeta_i = \lim_{t\to T}\frac{\eta_i}{F-|\eta_|} = 0$. This implies that after time T, both the coupling error η_i and the funnel error ζ_i will converge simultaneously. Subsequently, it is evident that as η_i approaches 0, both e_i and ϵ_i will approach 0 at the same time [17].*

4 Simulation Examples

To validate the rationality of the proposed control method, we conduct an example using a dual-motor driving system in this section. The parameters of the driving system are provided in $TableI$.

Table 1: Parameter Values

Parameter	Value	Unit
J_1	1.41	kg·m^2
J_2	1.35	kg·m^2
T_1	8	kg·m^2
T_2	7	kg·m^2
α	0.6	/
B_f	0.22	/

4.1 Design of Controllers

In the experiments, we compare the tracking performance of the following four control approaches. The details of each controller are presented below:

1) *MLSMC*: The multi-layer sliding mode controller (MLSMC) has been introduced in Section III. The sliding mode surface parameters are selected as $B = 1.3$, $C_1 = 0.4$, $C_2 = 1.7$, $\lambda_3 = 0.2$, $\lambda_4 = 0.6$, $\beta = 0.29$, $\lambda_3 = 1.76$, $k_0 = 1.9$, $k_1 = 0.76$, $k_2 = 0.7$, $\lambda_4 = 1.9$. The specified parameters for the funnel function are as follows: $\phi_0 = 1.5$, $\phi_{inf} = 0.02$, $\alpha_F = 5.2$.
2) *OLSMC*: The one-layer sliding mode controller (OLSMC) is a simplified iteration of MLSMC, diverging notably by omitting the second sliding mode surface present in MLSMC, which is responsible for optimizing the control signal in controller design. It is worth noting that the controller parameters of OLSMC are intentionally set to be the same as those adopted in MLSMC, aiming to yield more obvious results for comparison.
3) *SMC*: The sliding mode controller (SMC) stands for the traditional approach. We select the following sliding surface according to the requirements: $s_{smc} = \dot{e} + \lambda e$ [18], where e represents the tracking error, and $\lambda_{smc} = 10$. Compared with MLSMC and OLSMC, the SMC is designed without the funnel function, thus the SMC was designed based on the coupling error η rather than the funnel error ζ. The remaining control parameters are selected to be the same as MLSMC.
4) *PID*: Finally, choose a PID controller for the purpose of comparison. The PID control gains $k_p = 160$, $k_i = 4$ and $k_d = 4$ are the well-tuned based on the selected driving system.

4.2 Experimental Results

Initially, we select a gently evolving sinusoidal signal $\theta_d = 0.1sin(t) + cos(t)$ to serve as the reference signal for the dual-motor system. The experimental results of the multi-sliding mode controller designed in this article are illustrated in Figure.3 under the provided reference signal. The coupling error can be effectively kept within the specified boundary. Then, Figure.4 illustrates the control impact of the designed controller when subjected to a reference signal $\theta_d = 0.3sin(3t) + cos(3t)$ characterized by a swifter oscillation amplitude and period. The findings suggest that the implemented control scheme is capable of achieving satisfactory control performance across various scenarios.

The results of comparing the control performance of various controllers, utilizing a sinusoidal signal $\theta_d = 0.1sin(t) + cos(t)$, are illustrated in Figure 5. This figure displays the output position tracking, tracking error, and control action. These results clearly demonstrate the proficiency of all four controllers in tracking the desired signal. However, in comparison to both OLSMC and SMC, the newly developed MLSMC controller stands out for its superior dynamic performance, offering smoother and more stable control input. Notably, the MLSMC approach showcases reduced overshoot compared to other methods, owing to the integration of the funnel boundary function into the control process. Furthermore, in steady-state conditions, MLSMC exhibits the smallest tracking error among the four control methods, credited to the inclusion of the second sliding surface.

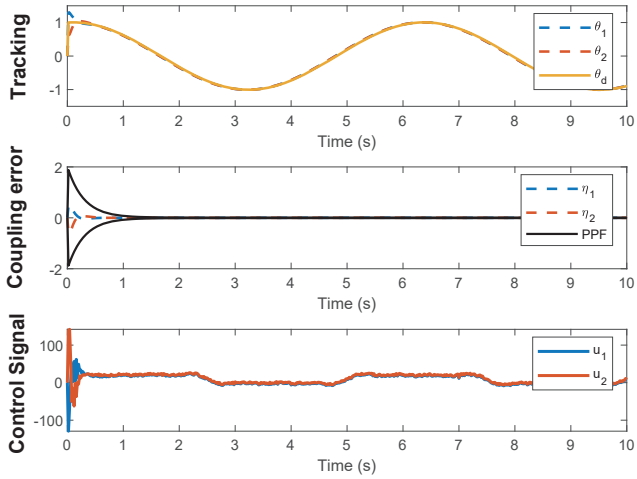

Fig. 3: Control performance for $\theta_d = 0.1sin(t)+cos(t)$: output position, tracking error, and control signal.

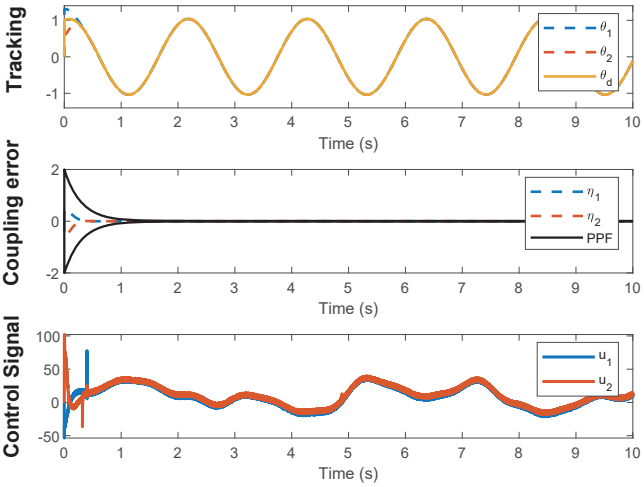

Fig. 4: Control performance for $\theta_d = 0.3sin(3t) + cos(3t)$: output position, tracking error, and control signal.

In order to improve the comparison of the performance of the four control approaches, we employ the performance indices listed below [18].

1) The maximum absolute error, denoted as ME, is defined as the maximum value of the sum of absolute values for each index $i = 1, \ldots, N$: $ME = \max_{i=1,\ldots,N} \{|\eta_1(i)| + |\eta_2(i)|\}$ where $\eta_1(i)$ and $\eta_2(i)$ represent the coupling error of motor 1 and motor 2;
2) Average tracking error, denoted as AE, is defined as the average value of all coupling errors $AE = \frac{1}{N}\sum_{i=1}^{N}\{|\eta_1(i)| + |\eta_2(i)|\}$;
3) Standard deviation of the coupling error $SDE = \sqrt{\frac{1}{N}\sum_{i=1}^{N}(|\eta_1(i)| + |\eta_2(i)| - AE)^2}$ represents the deviation of the motor from the average value at a certain moment.

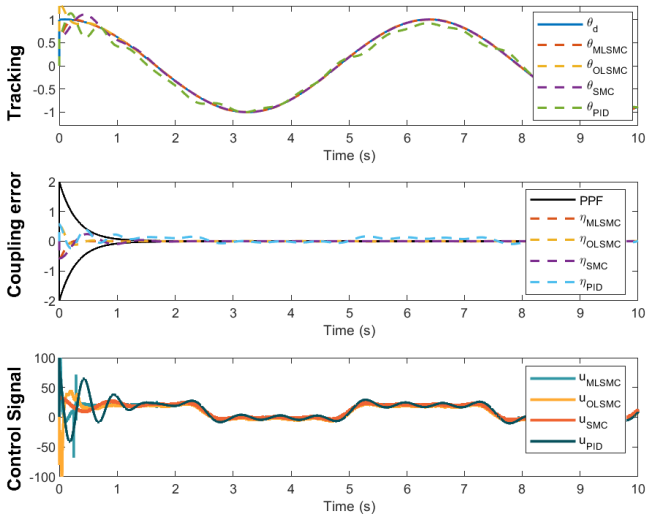

Fig. 5: Experimental results for $\theta_d = 0.1\sin(t) + \cos(t)$

Table 2: COMPARISON FOR $\theta_d = 0.1\sin(t) + \cos(t)$

indexes	ME	AE	SDE
$MLSMC$	1.0650	0.0142	0.0930
$OLSMC$	1.1280	0.0364	0.0933
SMC	1.0750	0.0558	0.1585
PID	1.0501	0.1594	0.1180

$TableII$ gives the indexes for $\theta_d = 0.1sin(t)+cos(t)$. As evident from $TableII$, the controller employing the funnel function outperforms other controllers on SDE, showcasing its better dynamic performance. Due to the presence of a multi-layer sliding surface, MLSMC demonstrates superior performance on AE compared to OLSMC. The MLSMC not only minimizes the average tracking error but also excels in the other two aspects.

5 Conclusion

To tackle synchronization challenges in dual-motor systems, this article introduces a fixed-time funnel sliding mode controller. This controller integrates coupling error and funnel error concepts, ensuring that transient errors of each motor consistently remain within a predetermined funnel area. Additionally, it incorporates an innovative application of the multi-layer sliding mode concept. The first surface is tailored for tracking a predefined reference signal, while the second surface guides the system state toward the first surface. Theoretical analysis confirms the convergence of both surfaces within a predetermined timeframe, regardless of the system's initial state. Comparative evaluations against other studies underscore the superior performance of the proposed controller, particularly in managing significant deviations in initial conditions. This research focuses on dual-motor drive systems, future efforts will extend the control method to multi-motor systems and aim to reduce sliding mode stabilization time.

References

[1] P. Fang, Y. Wang, and Z. Zhang, Combined control strategy for synchronization control in multi-motor-pendulum vibration system, *Journal of Vibration and Control*, vol. 28, no. 17-18, pp. 2254–2267, 2022.

[2] P. Kokotovic and I. Kanellakopoulos, Nonlinear and adaptive control with applications, *Springer*, vol. 187, 2008

[3] S. Biricik, Time-varying and constant switching frequency-based sliding-mode control methods for transformerless DVR employing half-bridge VSI, *IEEE Transactions on Industrial Electronics*, 64(4): 2570–2579, 2016.

[4] X. Yu and Z. Man, Fast terminal sliding-mode control design for nonlinear dynamical systems. *IEEE Transactions on Circuits and Systems I: Fundamental Theory and Applications*. 49(2): 261–264, 2002.

[5] I. Tawiah, Finite-time extended state observer based nonsingular fast terminal sliding mode control of autonomous underwater vehicles. *Ocean Engineering*, 218: 108179, 2020.

[6] T. Zeng, X. Ren, and Y. Zhang, Fixed-time sliding mode control and high-gain nonlinearity compensation for dual-motor driving system, *IEEE Transactions on Industrial Informatics*. 16(6): 4090–4098, 2019.

[7] J. Ni, L. Liu and C. Liu, Fixed-time leader-following consensus for second-order multiagent systems with input delay, *IEEE Transactions on Industrial Electronics*. 64(11): 8635–8646, 2017.

[8] X. Liu, H. Wang, and M. Chen, Adaptive fuzzy funnel control for a class of strict feedback nonlinear systems, *Neurocomputing*, vol. 241, pp. 71–80, 2017.

[9] Y. Li, X. Shao, and S. Tong, Adaptive fuzzy prescribed performance control of nontriangular structure nonlinear systems. *IEEE Transactions on Fuzzy Systems*. 28(10): 2416–2426, 2019.

[10] M. Hui, Q. Zhou, and R. Lu, Adaptive prescribed performance control of a flexible-joint robotic manipulator with dynamic uncertainties, *IEEE Transactions on Cybernetics*. 52(12): 12905–12915, 2021.

[11] A. Ilchmann, E. P. Ryan and P. Townsend, Tracking control with prescribed transient behaviour for systems of known relative degree, *Systems & Control Letters*, vol. 55, no. 5, pp. 396–406, 2006.

[12] S. Wang, H. Yu, and X. Ren, Neural-network-based adaptive funnel control for servo mechanisms with unknown deadzone, *IEEE Transactions on Cybernetics*, vol. 50, no. 4, pp. 1383–1394, 2018.

[13] T. Berger and T. Reis, Funnel control via funnel precompensator for minimum phase systems with relative degree two, *IEEE Transactions on Automatic Control*, vol. 63, no. 7, pp. 2264–2271, 2017.

[14] Z. Zuo, Q. Han and X. Zhang, An overview of recent advances in fixed-time cooperative control of multiagent systems, *IEEE Transactions on Industrial Informatics*, vol. 14, no. 6, pp. 2322–2334, 2018.

[15] Q. Chen, X. Zong, and X. He, Adaptive nonsingular fixed-time attitude stabilization of uncertain spacecraft, *IEEE Transactions on Aerospace and Electronic Systems*. 54(6): 2937–2950, 2018.

[16] M. M. Polycarpou and P. A. Ioannou, A robust adaptive nonlinear control design, *1993 American control conference*, pp. 1365–1369, 1993.

[17] D. Sun, X. Shao, and G. Feng, A model-free cross-coupled control for position synchronization of multi-axis motions: theory and experiments, *IEEE Transactions on Control Systems Technology*, vol. 15, no. 2, pp. 306–314, 2007.

[18] S. Wang, J. Na, and Q. Chen, Adaptive Predefined Performance Sliding Mode Control of Motor Driving Systems With Disturbances, *IEEE Transactions on Energy Conversion*, vol. 36, no. 3, pp. 1931–1939, 2021.

Proceedings of the 3rd Conference on Fully Actuated System Theory and Applications
May 10-12, 2024, Shenzhen, China

Specified-time Dynamic Target Autonomous Surrounding Formation for Multi-agent Network: A General Exploring Relationship

Haoliang Xue[1], Yuan Zhou[1], Yu Zhao[1,*]
1. Northwestern Polytechnical University, Xi'an 710129, China
E-mail: 2023202440@mail.nwpu.edu.cn

Abstract: Existing work on the multiple target formation problem mostly focuses on the leader-follower network with one-to-one correspondence, which imposes a bit of strict assumptions on the interaction configuration. To realize this restriction, this paper considers a general leader-follower network with general exploring relationships and aims to solve the specified-time dynamic target autonomous surrounding formation (DT-DASF) problem. A sampling-data-based protocol is proposed with several formation configuration estimators, i.e., a convex hull estimator, a formation center estimator, a surrounding distance estimator, and a formation vector estimator. By time projection and motion planning method, it shows that the proposed estimator and protocol can drive followers to achieve surrounding formation within an appropriate surrounding distance and simultaneously encircle all dynamic targets at a specified time. A numerical simulation verifies the effectiveness of the theoretical result.

Key Words: Dynamic Target Surrounding Formation, Specified-time Control, Maximum Surrounding Distance, Leader-follower Network

1 Introduction

In recent years, the distributed cooperative control for multi-agent systems has gained extensive attention owing to its superiority and potential application in multiple UAV formation, multiple missile attacks, smart grid, and traffic coordination [1]-[2]. Formation tracking control as the basic topic of leader-follower multi-agent networks, requires that the followers can track the trajectory of leaders [3]-[4]. If there are multiple leaders in the network, the formation tracking problem is converted to the formation containment problem [5], which requires that the follower can converge to the convex hull formed by the leaders.

On the formation containment problem, [6] considered the directed multi-agent network and proposed a containment protocol for second-order multi-agent systems without velocity measurements. [7] focused on the linear multi-agent systems and presented a distributed observer-based protocol over an undirected network. The above-mentioned results were derived under the condition that each leader's information be detected by at least one follower directly or indirectly. For multiple dynamic target formation problems, it requires a well-informed follower existing in the network to explore and receive the information from all leaders [8], which puts high requirements for the sensing equipment on the well-informed followers, increases the cost and reduces the robustness of the proposed protocol. For a general leader-follower network with a general exploration relationship between followers and leaders, the work [9] designed a continuous-time single-integrator model based on the target information compensator to achieve dynamic target formation control over the undirected graph. Note that in [6]-[11], the formation vectors are fixed and provided in advance, having difficulty adjusting the range of formation configuration automatically. For multiple dynamic target formation problems, the formation size was usually time-varying and there seemed no results to determine the range of target motion. Therefore, it is necessary to achieve an autonomous surrounding formation to encircle targets automatically.

On the other hand, a rapid convergence rate is desired in the cooperative control for multi-agent systems. There were many literatures proposed on the finite-time [12]-[13], fixed-time [14]-[15], and specified-time control [16]-[18]. Note that the works on finite-time control and fixed-time control showed that the final settling time is estimated according to the initial states and control parameters, the specified-time control is preferred in reality. On this aspect, [16] designed sample-data feedback protocol to achieve formation-containment at the appointed time, respectively for single-order and second-order nonlinear multi-agent systems. [17] solved the dynamic average consensus problem at a specified time by proposing a sampling-data-based control protocol. [18] considered the general linear multi-agent systems and proposed the prescribed-time tracking protocol in a fully distributed manner. All showed the advantage of convergence time controllability.

Motivated by the above observation, this paper uses the specified-time control framework to solve the dynamic target autonomous surrounding formation for a leader-follower network with a general exploration relationship. The contribution lies in the following three aspects. First, the formation achieving time is controllable and can be specified according to task requirements, which is more flexible. Second, this paper designs a surrounding formation protocol over the leader-follower network with a general exploration relationship. Our protocol can reduce costs and improve system robustness. Finally, by designing the formation vector estimator, the size of the surrounding formation can be adjusted by the agents themselves, which means that it does not set the formation vector in advance [6]-[11].

The remainder of this paper is organized below. Section 2 gives basic knowledge and system model problems. Section 3 shows the main results and Section 4 shows a numerical simulation. Section 5 concludes this paper.

This work was supported in part by the Key Program of Shaanxi Natural Science Foundation 2023JC-XJ-23.

2 Basic Knowledge and Problem Statement

2.1 Notions

Let $\mathbb{R}$, $\mathbb{R}^n$ and $\mathbb{R}^{n\times n}$ be the real number set, the n-dimension column vector set, and the n-order square matrix set, respectively. $\mathbf{1}_n \in \mathbb{R}^n$ donates the column vector with elements all being 1s and $\mathbf{0}_n \in \mathbb{R}^n$ the column vector with elements all being 0s. $I_n \in \mathbb{R}^{n\times n}$ is the n-order unit matrix. The operation diag$\{\cdot\}$ represents the diagonal matrix and $\otimes$ represents the Kronecker product. $\|v\|$ denotes the 2-norm of a vector $v \in \mathbb{R}^n$. For a matrix $A \in \mathbb{R}^{n\times n}$, $A^\top$ shows the transpose, $\rho(A)$ the spectral radius and $\bar{\lambda}_A$ the maximum eigenvalue.

2.2 System Model

On the one hand, the interaction network among N agents can be modelled by a graph $\mathcal{G} = \{\mathcal{V}, \mathcal{E}\}$ with node set $\mathcal{V} = \{1, ..., N\}$ and edge set $\mathcal{E} = \{(i, j) : i, j \in \mathcal{V}\}$. A graph $\mathcal{G}$ is said to be undirected if there has $(j, i) \in \mathcal{E}$ for $(i, j) \in \mathcal{E}$, and further, it is said to be connected if there has a path between every two nodes. A path with length p from node i_1 to node i_p is defined as $\mathcal{P} = \{(i_1, i_2), (i_2, i_3), \cdots, (i_{p-1}, i_p)\} \in \mathcal{E}$ with distinct nodes. For a connected graph $\mathcal{G}$, it's diameter $\mathcal{D}_\mathcal{G}$ is defined as the maximum of shortest path length between every two nodes. In this paper, denote the adjacent matrix by $A = [a_{ij}] \in \mathbb{R}^{N\times N}$ with $a_{ij} = 1$ if $(j, i) \in \mathcal{E}$ and $a_{ij} = 0$ otherwise. $D = \text{diag}\{d_1, \cdots, d_N\}$ denotes the in-degree matrix and $L = D - A$ denotes the Laplacian matrix.

In this paper, we consider the dynamic autonomous surrounding formation problem with M leaders and N followers. The interaction network can be defined by the graph $\mathcal{G}_{MN} = \{\mathcal{V}_{MN}, \mathcal{E}_{MN}\}$. Here, $\mathcal{V}_{MN} = \mathcal{V}_M \bigcup \mathcal{V}_N$ is the node set with leader set $\mathcal{V}_M$ and follower set $\mathcal{V}_N$. For i-th follower, denote $\mathcal{N}_{Mi} = \{j \in \mathcal{V}_M : (j, i) \in \mathcal{E}, i \in \mathcal{V}_N\}$ as the neighboring set in $\mathcal{V}_M$, and $\mathcal{N}_{Ni} = \{j \in \mathcal{V}_N : (j, i) \in \mathcal{E}, i \in \mathcal{V}_N\}$ the neighboring set in $\mathcal{V}_N$. Additionally, $\mathcal{N}_i = \mathcal{N}_{Ni} \bigcup \mathcal{N}_{Mi}$ and $\mathcal{N}_{i0} = \mathcal{N}_{Ni} \bigcup \mathcal{N}_{Mi} \bigcup \{i\}$.

For the network $\mathcal{G}_{MN}$, the Laplacian matrix can be denoted by

$$\overline{L} = \begin{bmatrix} 0 & 0 \\ L_B & L_A \end{bmatrix}.$$

Here, $L_B = [b_{ih}] \in \mathbb{R}^{N\times M}$ is the exploring relationship matrix from leaders to followers with $b_{ih} = -1$ if $(h, i) \in \mathcal{E}$, $i \in \mathcal{V}_N$, $h \in \mathcal{V}_M$ and $b_{ih} = 0$ otherwise. $L_A = L + \text{diag}\{b_i\}$ is a nonsingular matrix with $b_i = -\sum_{h=1}^{M} b_{ih}$. For the interaction network $\mathcal{G}_{MN}$, we make the following assumption.

Assumption 1. The interaction topology $\mathcal{G}_{MN}$ satisfies:
1) The subgraph $\mathcal{G}$ among N followers is undirected and connected.
2) For each follower, there exists a path at least from one leader to it and no path from it to every leader.

Lemma 1.[19] Suppose Assumption 1 to be valid. Then, each element of matrix $-L_A^{-1}L_B$ is positive and the row sum of $-L_A^{-1}L_B$ is equal to one.

Lemma 2.[20] Suppose Assumption 1 to be valid. Define $\bar{D} = D + \text{diag}\{b_i\}$ and $\nabla = I_N - (\bar{D} + I_N)^{-1}L_A$. All eigenvalues of ∇ lie within a circle of units centered on the origin, that is, $|\bar{\lambda}_\nabla| < 1$.

On the other hand, the dynamics of M leaders and N followers are described by

$$\dot{x}_i(t) = u_i(t),\ i \in \mathcal{V}_N, \tag{1}$$

$$\dot{m}_i(t) = z_i(t),\ i \in \mathcal{V}_M, \tag{2}$$

where $x_i(t) \in \mathbb{R}^n$ is the position and $u_i(t) \in \mathbb{R}^n$ is the driving command of follower i to be designed, respectively. $m_i(t) \in R^n$ is the position and $z_i(t)$ is the unknown external input of leader i, respectively. For dynamics (2), we make the following assumption:

Assumption 2. The reference input $z_i(t)$ to be bounded, denoted by $z_i(t) < \bar{z}$.

This paper aims to solve the dynamic autonomous surrounding formation problem within a specified settling time. It can be described as,

Definition 1. *For dynamics (1)-(2), it is said to achieve specified-time dynamic target autonomous surrounding formation (ST-DTASF) if, for any initial states $x_i(t_0)$, it holds that*

$$\lim_{t\to T} = \|x_i(t) - q_i(t) - h_i(t)\| = 0. \tag{3}$$

In which, T is the specified time. $q_i(t) = \sum_{i=1}^{M} \beta_{ih} m_{ih}(t)$ is the distributed estimator of formation center, lying in the convex hull formed by leaders. $h_i(t)$ is the autonomous surrounding formation vector estimator.

3 Main Results

This paper aims uses a sampling mechanism to achieve the objective of ST-DASF. The sampling instance is given as

$$t_k = t_{k-1} + \delta_k, \text{ with } t_0 = 0,\ \ \delta_k = \frac{T}{k(k+1)}, \tag{4}$$

where δ_k is the step size, $k = 1, 2, \cdots \infty$. Obviously, (4) satisfies $\lim_{k\to\infty} t_k = T$.

Based on the sampling mechanism (4), the autonomous surrounding formation protocol is presented as

$$\begin{aligned} u_i(t) = &-\frac{1}{\delta_{k+1}(\tilde{d}_i + 1)}\Big[\sum_{j=1}^{N} a_{ij}(x_i(t_k) - x_j(t_k) \\ &- h_i(t_k) + h_j(t_k) - q_i(t_k) + q_j(t_k)) \\ &+ x_i(t_k) - q_i(t_k) - h_i(t_k)\Big], \end{aligned} \tag{5a}$$

$$\begin{aligned} \dot{p}_i(t) = &-\frac{1}{\delta_{k+1}(\bar{d}_i + 1)}\Big[\sum_{j=1}^{N} a_{ij}(p_i(t_k) - p_j(t_k)) \\ &+ \sum_{h=1}^{M} b_{ih}(p_i(t_k) - m_h(t_k))\Big], \end{aligned} \tag{5b}$$

$$\begin{aligned} \dot{q}_i(t) = &-\theta\delta_{k+1}^{-1}\sum_{j=1}^{N} a_{ij}(q_i(t_k) - q_j(t_k)) - \sigma\delta_{k+1}^{-1} \\ &(q_i(t_k) - p_i(t_k)) - \sigma\delta_{k+1}^{-1} v_i(t_k) \\ &+ \delta_k^{-1}(p_i(t_{k+1}) - p_i(t_k)), \end{aligned} \tag{5c}$$

$$v_i(t_k) = v_i(t_{k-1}) + \beta\sum_{j=1}^{N} a_{ij}(q_i(t_{k-1}) - q_j(t_{k-1})), \tag{5d}$$

$$Z_i^l(t_k) = \max_{j\in\mathcal{N}_{i0}} \left\{Z_j^{l-1}(t_{k-1})\right\}, l = 1, \ldots, w, \tag{5e}$$

$$h_i(t_k) = \Upsilon\begin{pmatrix} Z_i^w(t_k)\sin(\frac{2\pi(i-1)}{N}) \\ Z_i^w(t_k)\cos(\frac{2\pi(i-1)}{N}) \end{pmatrix}, i = 1, 2, \cdots, N, \tag{5f}$$

where $\tilde{d}_i = d_i + 1$, $\bar{d}_i = d_i + b_i$, θ and σ are two positive constants. $v_i(t)$ is an auxiliary variable satisfying $\sum_{i=1}^{N} v_i(t_0) = 0$. $\Upsilon \geqslant 1$ is used to adjust the size of the encirclement. $Z_i^l(t_k)$ is the l-th element of the enveloping radius estimator

$$Z_i(t_k) = \left[Z_i^0(t_k), Z_i^1(t_k), \cdots, Z_i^w(t_k)\right] \in \mathbb{R}^{w+1}$$

and $Z_i^w(t_k)$ is the estimated maximum of enveloping radius with $w \geqslant \mathcal{D}_{\mathcal{G}}$. Initialization $Z_i(0) = r_i^0(0)\mathbf{1}_{w+1}$ with

$$r_i(t_k) = \begin{cases} \max \|m_h(t_k) - q_i(t_k)\|, i \in \mathcal{V}_N, h \in \mathcal{N}_{Mi} \\ 0, \qquad\qquad\qquad\quad i \in \mathcal{V}_N, h \in \emptyset \end{cases}, \tag{6}$$

Theorem 1. Suppose that Assumptions 1-2 are valid. Then, the proposed protocol (5a) with estimators (5b)-(5f) will solve the ST-DTASF problem for dynamics (1)-(2) defined as Definition 1 if parameters satisfy $0 < \sigma < 2$ and $0 < \theta < \frac{1}{N-1}$.

Proof: The proof of Theorem 1 includes the following four parts. In this proof, the capital letters without subscripts denote the compact form, such as $P(t) = [p_1^T(t), \cdots, p_N^T(t)]^T$, $Q(t) = [q_1^T(t), \cdots, q_N^T(t)]^T$ and etc.

Part 1. To show the specified-time convergence of convex hull estimator $p_i(t)$, i.e., to prove

$$\lim_{t \to T} \left\| p_i(t) - \sum_{h=1}^{M} \beta_{ih} m_h(t) \right\| = 0, \tag{7}$$

where $\sum_{i=1}^{M} \beta_{ih} = 1$ is the coefficient of convex hull.
To show (7), we integrate (1) and (5b) form t_k to t, obtaining

$$\begin{aligned} m_i(t) &= \int_{t_k}^{t} z_i(\tau)d\tau + m_i(t_k), \qquad\qquad i \in \mathcal{V}_M, \\ p_i(t) &= -\frac{t - t_k}{\delta_{k+1}(\bar{d}_i + 1)}\Big[\sum_{j=1}^{N} a_{ij}(p_i(t_k) - p_j(t_k)) \\ &\quad + \sum_{h=1}^{M} b_{ih}(p_i(t_k) - m_h(t_k))\Big] + p_i(t_k), i \in \mathcal{V}_N \end{aligned}$$

According to Lemma 1, vector $E_p(t) = P(t) + (L_A^{-1}L_B \otimes I_n)M(t)$ can be used to denote estimator error. Then, one has

$$\begin{aligned} E_p(t) =& P(t) + (L_A^{-1}L_B \otimes I_n)M(t) \\ =& -\frac{t - t_k}{t_{k+1} - t_k}((\bar{D} + I_N)^{-1}L_A \otimes I_N)E_p(t_k) \\ &+ E_p(t_k) + (L_A^{-1}L_B \otimes I_n)\int_{t_k}^{t} Z(\tau)d\tau. \end{aligned} \tag{8}$$

When $t = t_{k+1}$, one gives

$$\begin{aligned} E_p(t_{k+1}) =& \big((I_N - (\bar{D} + I_N)^{-1}L_A) \otimes I_N\big)E_p(t_k) \\ &+ (L_A^{-1}L_B \otimes I_n)\int_{t_k}^{t_{k+1}} Z(\tau)d\tau, \end{aligned} \tag{9}$$

In line with Lemma 2, one knows that matrix $I_N - (\bar{D} + I_N)^{-1}L_A$ has all eigenvalues within the unit circle. Under the Assumption 2, one obtains $\lim_{t_k \to T} \int_{t_k}^{t_{k+1}} Z(\tau)d\tau = 0$. Therefore, it holds that

$$\lim_{k \to \infty} E_p(t_{k+1}) = \lim_{t_k \to T} E_p(t_{k+1}) = 0.$$

For continuous errors $E_p(t)$, there has

$$\begin{aligned} \lim_{t_k \to T} \|E_p(t)\| \leqslant& \left\|L_A^{-1}L_B \otimes I_n\right\| \left\|\int_{t_k}^{t} Z(\tau)d\tau\right\| \\ &+ \|\nabla \otimes I_N\| \|E_p(t_k)\|. \end{aligned} \tag{10}$$

Owing to $\lim_{t_k \to T} E_p(t_k) = 0$ and $\lim_{t_k \to T} \int_{t_k}^{t} Z(\tau)d\tau = 0$, it is obvious that $\lim_{t_k \to T} E_p(t) = 0$.

Part 2. To show the specified-time convergence of formation center estimator $q_i(t)$, i.e., to prove

$$\lim_{t \to T} \left\| q_i(t) - \frac{1}{N}\sum_{j=1}^{N} p_j(t) \right\| = 0. \tag{11}$$

For this, define $E_q(t) = J_N q(t)$ as the estimated error with $J_N = I_N - \frac{1}{N}\mathbf{1}_N\mathbf{1}_N^T$. Auxiliary variables $\Delta P(t_k) = P(t_{k+1}) - P(t_k)$ and $\tilde{V}(t_k) = V(t_k) - \alpha^{-1}J_N\Delta P(t_k) - J_N P(t_k)$. Then, we integrate equation (5c) from t_{k-1} to t_k and have

$$\begin{aligned} \begin{bmatrix} E_q(t_k) \\ \tilde{V}(t_k) \end{bmatrix} =& \Theta \begin{bmatrix} E_q(t_{k-1}) \\ \tilde{V}(t_{k-1}) \end{bmatrix} + \begin{bmatrix} 0_{N\times N} \\ \sigma^{-1}I_N \end{bmatrix} \\ &\cdot J_N\left((1-\sigma)\Delta P(t_{k-1}) - \Delta P(t_k)\right), \end{aligned} \tag{12}$$

where $\Theta = \begin{bmatrix} (1-\sigma)I_N - \theta L & -\sigma I_N \\ \theta L & I_N \end{bmatrix}$.
Take the linear transformation of (12) as

$$\begin{bmatrix} \hat{E}_q(t_k) \\ \hat{V}(t_k) \end{bmatrix} = T_2T_1 \begin{bmatrix} E_q(t_k) \\ \tilde{V}(t_k) \end{bmatrix} \text{ with } T_1 = \begin{bmatrix} I_N & 0_N \\ I_N & I_N \end{bmatrix},$$

$T_2 = \begin{bmatrix} T_3^T & 0_N \\ 0_N & T_3^T \end{bmatrix}, T_3 = \begin{bmatrix} f & F \end{bmatrix}$, $f = \frac{1}{\sqrt{N}}\mathbf{1}_N$ and $F \in \mathbb{R}^{N\times(N-1)}$ such that $f^TF = \mathbf{0}_{N-1}, F^TF = I_{N-1}$. We give

$$\begin{aligned} \begin{bmatrix} \hat{E}_q(t_k) \\ \hat{V}(t_k) \end{bmatrix} =& \bar{\Delta} \begin{bmatrix} \hat{E}_q(t_{k-1}) \\ \hat{V}(t_{k-1}) \end{bmatrix} + \begin{bmatrix} 0_n \\ \sigma^{-1}T_3^T \end{bmatrix} \\ &\cdot J_N((1-\sigma)\Delta P(t_{k-1}) - \Delta P(t_k)), \end{aligned} \tag{13}$$

Here, $\bar{\Delta} = \begin{bmatrix} T_3^T(I_N - \theta L)T_3 & -\sigma I_N \\ 0_N & (1-\sigma)I_N \end{bmatrix}$ has eigenvalues $1 - \sigma$ with multiplicity N and eigenvalues $(1 - \theta\lambda_i(L))$. Consequently, parameters $0 < \sigma < 2$, $0 < \theta < \frac{1}{N-1}$ leads that all eigenvalues of $\bar{\Delta}$ lie in the unit circle with only one eigenvalue being 1.
Let $\hat{E}_q(t_k) = [\hat{E}_{q1}(t_k), \hat{E}_{q[2,N]}^T(t_k)]^T$ and $\hat{V}(t_k) = [\hat{V}_1(t_k), \hat{V}_{[2,N]}^T(t_k)]^T$, one has

$$\begin{bmatrix} \hat{E}_{q1}(t_k) \\ \hat{V}_1(t_k) \end{bmatrix} = \Xi \begin{bmatrix} \hat{E}_{q1}(t_0) \\ \hat{V}_1(t_0) \end{bmatrix}, \tag{14a}$$

$$\begin{bmatrix} \hat{E}_{q[2,N]}(t_k) \\ \hat{V}_{[2,N]}(t_k) \end{bmatrix} = \bar{\Xi} \begin{bmatrix} \hat{E}_{q[2,N]}(t_0) \\ \hat{V}_{[2,N]}(t_0) \end{bmatrix} + \Gamma, \tag{14b}$$

with $\bar{\Xi} = \begin{bmatrix} \mho^k & -\sigma\sum_{s=0}^{k-1}\mho^s(1-\sigma)^{k-1-s} \\ 0_{N-1} & (1-\sigma)^k I_{N-1} \end{bmatrix}$,

$$\Gamma = \begin{bmatrix} \sum_{s=0}^{k-1}\mho^s F^T(\Delta P(t_{k-1-s}) - (1-\sigma)^{k-1-s}\Delta P(t_0)) \\ -\sigma^{-1}F^T(\Delta P(t_k) - (1-\sigma)^k\Delta P(t_0)) \end{bmatrix}$$

and $\Xi = \begin{bmatrix} 1 & -\sigma\sum_{s=0}^{k-1}(1-\sigma)^{k-1-s} \\ 0 & (1-\sigma)^k \end{bmatrix}$.

Next, take the inverse transformation of (13), we can obtain

$$\begin{aligned} E_q(t_k) = &\left(1-\sigma\sum_{s=0}^{k-1}(1-\sigma)^{k-1-s}\right) ff^T E_q(t_0) \\ &- \sigma\sum_{s=0}^{k-1}(1-\sigma)^{k-1-s} ff^T\tilde{V}(t_0) + F\mho^k F^T E_q(t_0) \\ &- F(\sigma\sum_{s=0}^{k-1}(1-\sigma)^{k-1-s}\mho^s)F^T(E_q(t_0)+\tilde{V}(t_0) \\ &+ \sigma^{-1}\Delta P(t_0)) + F\sum_{s=0}^{k-1}\mho^s F^T\Delta P(t_{k-1-s}), \end{aligned} \tag{15a}$$

$$\begin{aligned} \tilde{V}(t_k) = &-(1-\sigma\sum_{s=0}^{k-1}(1-\sigma)^{k-1-s})ff^T E_q(t_0) \\ &+ \sigma\sum_{s=0}^{k-1}(1-\sigma)^{k-1-s} ff^T\tilde{V}(t_0) - F\mho^k F^T E_q(t_0) \\ &+ F(\sigma\sum_{s=0}^{k-1}(1-\sigma)^{k-1-s}\mho^s)F^T(E_q(t_0)+\tilde{V}(t_0) \\ &+ \sigma^{-1}\Delta P(t_0)) + (1-\sigma)^k((ff^T+FF^T)(E_q(t_0) \\ &+ \tilde{V}(t_0)) + \sigma^{-1}FF^T\Delta P(t_0)) - F\sum_{s=0}^{k-1}\mho^s F^T \\ &\Delta P(t_{k-1-s}) - \sigma^{-1}FF^T\Delta P(t_k). \end{aligned} \tag{15b}$$

We analyze the convergence of $E_q(t_k)$ and $\tilde{V}(t_k)$ term by term as follows.

- For the first term of $E_q(t_k)$ and $\tilde{V}(t_k)$, we have $\lim_{k\to\infty} 1-\sigma\sum_{s=0}^{k-1}(1-\sigma)^{k-1-s}=0$ because of $|1-\sigma|<1$.
- For the second term of $E_q(t_k)$ and $\tilde{V}(t_k)$, we obtain $ff^T\tilde{V}(t_0) = ff^T V(t_0) = 0$ owing to $\sum_{i=1}^{N} v_i(t_0) = 0$, $ff^T J_N = 0_N$ and $f^T V(t_0) = 0$.
- For the third term of $E_q(t_k)$ and $\tilde{V}(t_k)$, we give $\lim_{k\to\infty}\mho^k \leqslant \lim_{k\to\infty}\rho(\mho)^k I_N = 0_N$.
- For the forth term of $E_q(t_k)$ and $\tilde{V}(t_k)$, we show that

$$\begin{aligned} &\lim_{k\to\infty}\left\|\sigma\sum_{s=0}^{k-1}(1-\sigma)^{k-1-s}\mho^s\right\| \\ &\leqslant \lim_{k\to\infty}|\sigma|\sum_{s=0}^{k-1}|1-\sigma|^{k-1-s}\tau^s \\ &= \begin{cases} \lim_{k\to\infty}\tau^{k-1}\sum_{s=0}^{k-1}(\frac{1-\sigma}{\tau})^{k-1-s}=0, & \text{if}|1-\sigma|<\tau, \\ \lim_{k\to\infty}|\tau^{k-1}k|=0, & \text{if}|1-\sigma|=\tau, \\ \lim_{k\to\infty}|(1-\sigma)^{k-1}\sum_{s=0}^{k-1}(\frac{\tau}{1-\sigma})^{k-1-s}|=0, & \text{if}|1-\sigma|>\tau, \end{cases} \end{aligned}$$

- For the fifth term of $E_q(t_k)$ and the sixth term of $\tilde{V}(t_k)$, we have $\Delta P(t_{k-1-s}) = \dot{P}(\varepsilon)(t_{k-s}-t_{k-1-s}) \leqslant \bar{\mu}\delta_{k-s}\mathbf{1}_n$, where $\varepsilon\in[t_{k-s},t_{k-1-s}]$ and $\bar{\gamma}$ is the upper bound of $\dot{p}$. With $\delta_k = \frac{T}{k(k+1)}$, one has

$$\begin{aligned} \lim_{k\to\infty}\sum_{s=0}^{k-1}\mho^s\Delta P(t_{k-1-s}) &\leqslant \lim_{k\to\infty}\sum_{s=0}^{k-1}(\rho(\mho)^s\delta_{k-s})\bar{\mu}\mathbf{1}_N \\ &\leqslant \lim_{k\to\infty}\sum_{s=0}^{k-1}(\tau^s\frac{T}{(k-s)})\bar{\mu}\mathbf{1}_N \\ &= \mathbf{0}_N. \end{aligned}$$

Based on the above analysis, one can get the conclusion that $\lim_{t_k\to T}\left|e_{q_i}(t_k)\right| = 0$ and $\lim_{t_k\to T}|\tilde{v}_i(t_k)| = 0$.

For the continuous error, we integrate equation (5c) from t_k to t and have

$$\begin{aligned} e_{q_i}(t) = &\frac{t-t_k}{t_{k+1}-t_k}\Big(-\theta\sum_{j=1}^{N}a_{ij}(e_{q_i}(t_k)-e_{q_j}(t_k) \\ &+ (1-\sigma)e_{q_i}(t_k) - \sigma\tilde{v}_i(t_k) + 2\Delta p_i(t_k) \\ &-\frac{1}{N}\sum_{i=1}^{N}\Delta p_i(t_k)\Big) - \frac{1}{N}\sum_{i=1}^{N}p_i(t) + \frac{1}{N}\sum_{i=1}^{N}p_i(t_k). \end{aligned}$$

which shows that

$$\begin{aligned} \lim_{t\to T}|e_{q_i}(t)| \leqslant &\theta\rho(L)|e_{q_i}(t_{k-1})| + (1+\sigma)|e_{q_i}(t_{k-1})| \\ &+ \sigma|\tilde{v}_i(t_{k-1})| = 0. \end{aligned}$$

Consequently, equation (11) has been proven hereto.

Part 3. To show the specified-time convergence of formation enveloping radius estimator $Z_i(t)$, i.e., to prove

$$\lim_{t_k\to T}\max_{i\in\mathcal{V}_N}|Z_i^w(t_k) - \bar{r}(t_k)| \leqslant w\cdot\psi = 0, \tag{16}$$

where $\bar{r}(t_k) = \max_{i\in\mathcal{V}_N}\{r_i(t_k)\}$. ψ is the bound of the change of $r_i(t_k)$.

Let $e_{Zi}(t_k) = Z_i^w(t_k) - r_i(t_k)$ be the estimated error. H_0 is the set of followers with the largest error at arbitrary time $t = t_{k0}$, as

$$H_0 = \left\{i\in\mathcal{V}_N : Z_i^0(t_{k0}) = \bar{r}(t_{k0})\right\}. \tag{17}$$

H_1 is the one-step spacing neighbors of all agents in H_0, as

$$H_1 = \left\{i\in\mathcal{N}_N : (i,j)\in\mathcal{E}\,, j\in H_0\right\}, \tag{18}$$

For the agents in H_1, we update its $Z_i(t)$ at $t = t_{k0+1}$ as

$$Z_i^1(t_{k0+1}) = \bar{r}(t_{k0}), i\in H_1\cup H_0. \tag{19}$$

Similarly, we define H_2 as the two-step neighbors of all agents in H_0, as

$$H_2 = \left\{i\in\mathcal{N}_N : (i,j)\in\mathcal{E}\,, j\in H_1\cup H_0\right\}, \tag{20}$$

and update its agents estimator $Z_i(t)$ at $t = t_{k0+2}$ as

$$Z_i^1(t_{k0+2}) = Z_i^1(t_{k0+1}) = \bar{r}(t_{k0}), i\in H_2\cup H_1\cup H_0. \tag{21}$$

By mathematical induction, one has for $1 \leqslant l \leqslant w$, one has l-step neighbor of agents in H_0 as

$$H_l = \left\{ i \in \mathcal{V}_N : (i,j) \in \varepsilon, j \in \bigcup_{p=0}^{l-1} H_p \right\}, \tag{22}$$

in which the agents update its estimator as

$$Z_i^w(t_{k0+l}) = Z_i^w(t_{k0+l-1}) = \cdots = \bar{r}(t_{k0}), j \in \bigcup_{p=0}^{l-1} H_p, \tag{23}$$

For a connected graph $\mathcal{G}$ with diameter $\mathcal{D}_\mathcal{G}$,for each agent, it needs $w+1$ updates at most to estimate $\bar{r}(t_{k0})$. Thus, there has

$$\begin{aligned} e_{Zi}(t_{k0+w}) &\leqslant \max_{i\in\mathcal{V}_N} |Z_i^w(t_{k0+w}) - \bar{r}(t_{k0+w})| \\ &\leqslant \max_{i\in\mathcal{V}_N} |Z_i^w(t_{k0+w}) - \bar{r}(t_{k0}) - \bar{r}(t_{k0+w}) + \bar{r}(t_{k0})| \\ &\leqslant w \cdot \psi. \end{aligned}$$

When $k \to \infty$, one haa $\psi \to 0$, which proves equation (16).

Part 4. To show the specified-time convergence of DASF protocol $u_i(t)$, i.e., to prove

$$\lim_{t_k \to T} \|x_i(t_k) - q_i(t_k) - h_i(t_k)\| = 0, \tag{24}$$

By substitute (5a) into (2) and integrate it from t_k to t, one gets

$$\begin{aligned} x_i(t) = &- \frac{t - t_k}{(t_{k+1} - t_k)(\tilde{d}_i + 1)} \Big[\sum_{i=1}^{N} a_{ij}(e_{B_i}(t_k) - e_{B_j}(t_k)) \\ &+ e_{Bi}(t_k) \Big] + x_i(t_k), \end{aligned} \tag{25}$$

where $e_{Bi}(t) = x_i(t) - q_i(t) - h_i(t)$ is the formation error. It gives the error $E_B(t)$ with compact form as

$$\begin{aligned} E_B(t) =& X(t) - H(t) - Q(t) \\ =& - \frac{t - t_k}{t_{k+1} - t_k} [(\tilde{D} + I_N)^{-1}(L + I_N) \otimes I_N] E_B(t_k) \\ &+ E_B(t_k). \end{aligned}$$

For the discrete errors $E_B(t_{k+1})$, we obtain

$$E_B(t_{k+1}) = \big(I_N - (\tilde{D} + I_N)^{-1}(L + I_N)) \otimes I_N\big) E_B(t_k), \tag{26}$$

According to Lemma 2, matrix $\tilde{\nabla} = I_N - (\tilde{D} + I_N)^{-1}(L + I_N)$ havs all eigenvalues within the unit circle, which results in $\lim_{t_k \to T} E_B(t_k) = 0$.

For the continuous errors $E_B(t)$, one gives

$$\lim_{t \to T} \|E_B(t)\| \leqslant \left\| \tilde{\nabla} \otimes I_N \right\| \|E_B(t_k)\| \to 0. \tag{27}$$

These prove equation (24).

The proof of Theorem 1 has been completed.

4 Simulations

This section presents a numerical simulation with eight followers and four leaders, whose interaction topology is Fig.1.

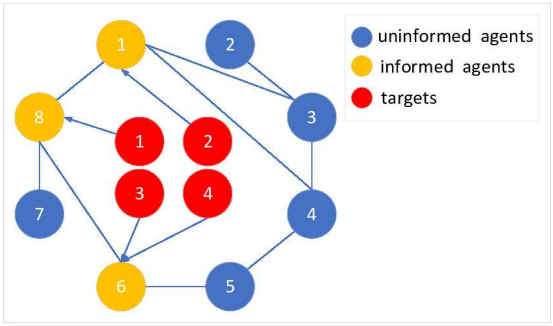

Fig. 1: The interaction topology with general exploration relationship

Select $\sigma = 1, \theta = 0.1, \delta_k = \frac{T}{k(k+1)}$ and $\Upsilon = 1.5$. Convergence time is specified as $T = 5$. The leader's input is

$$\begin{cases} m_1(t) = \Big[\cos(t) - \dfrac{1}{(t+2)^2}, -\sin(t) - \dfrac{1}{(k+2)^2}\Big]^T, \\ m_2(t) = \big[\cos(t) - 10e^{-t}, 2\cos(t) - 15e^{-t}\big]^T, \\ m_3(t) = \Big[2\cos(t) + a\tan 2t, \cos(t) + a\tan 2t\Big]^T, \\ m_4(t) = \Big[-2\sin(t) - 20e^{-t}, 2\cos(t) - 4e^{-t}\Big]^T. \end{cases}$$

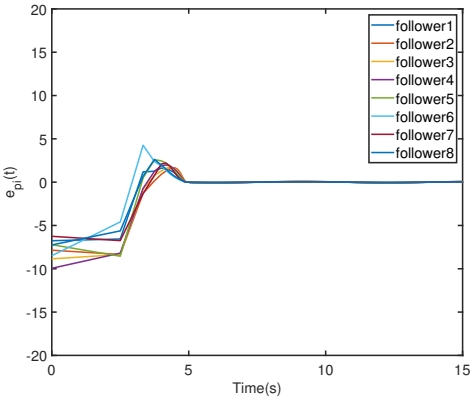

Fig. 2: The error of convex hull estimated $e_{pi}(t)$

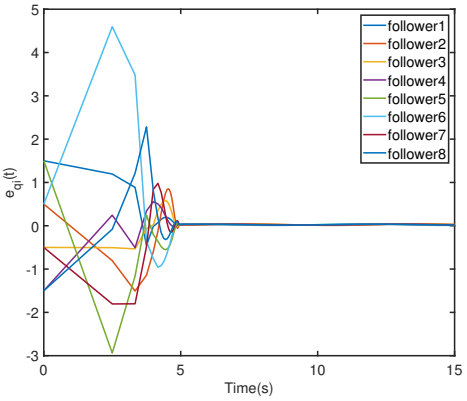

Fig. 3: The error of formation center $e_{qi}(t)$

Figs. 2 and 3 plot the errors of convex hull error $e_{pi}(t)$ and formation center error $e_{qi}(t)$ respectively. Both converge to zero at the specified time $t = 5s$. Fig. 4 depicts the final

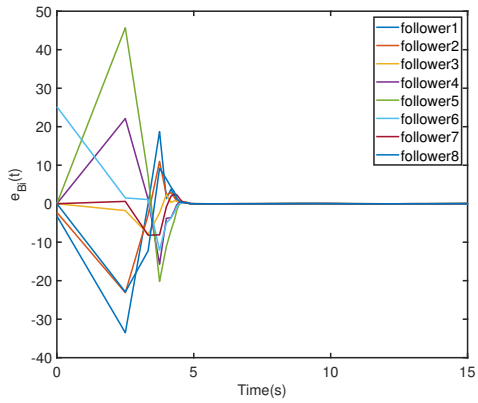

Fig. 4: The final surrounding formation error $e_{Bi}(t)$

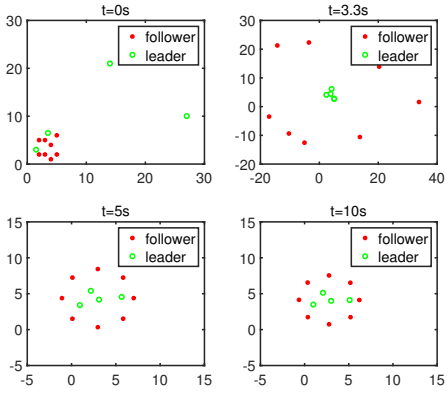

Fig. 5: The real formation configuration

encirclement formation error $e_{Bi}(t)$. Fig. 5 shows the real formation configuration at $t = 0s, t = 3.3s, t = 5s$ and $t = 10s$, which all in accordance with the theoretical result.

5 Conclusions

This paper investigates the specified-time dynamic autonomous surrounding formation problem for the multi-agent network with a general exploring relationship. The sampling-data-based formation protocol is designed based on several formation configuration estimators to achieve autonomous surrounding formation at a specified time. Future work will focus on the same problem for higher-order agent dynamics.

References

[1] I. Jeon, J. Lee and M. Tahk, Homing guidance law for cooperative attack of multiple missiles. Journal of Guidance Control and Dynamics, 33(1): 275–280, 2010.

[2] A. Bidram, A. Davoudi, F. Lewis and Z. Qu, Secondary control of microgrids based on distributed cooperative control of multi-agent systems. IET Generation Transmission & Distribution 7(8): 822–831, 2013.

[3] Z. Gu, B. Song, Y. Fan and X. Chen, Design and verification of UAV formation controller based on leader-follower method. 2022 7th International Conference on Automation, Control and Robotics Engineering (CACRE), Xi'an, China, 2022: 38–44.

[4] L. Chen, J. Mei, C. Li and G. Ma, Distributed leader-follower affine formation maneuver control for high-order multiagent systems. IEEE Transactions on Automatic Control, 65(11): 4941–4948, 2020.

[5] M. Ji, G. Ferrari-Trecate, M. Egerstedt and A. Buffa, Containment control in mobile networks. IEEE Transactions on Automatic Control, 53(8):1972–1975, 2008.

[6] J. Li, W. Ren and S. Xu, Distributed containment control with multiple dynamic leaders for double-integrator dynamics using only position measurements. IEEE Transactions on Automatic Control, 57(6): 1553–1559, 2012.

[7] W. Jiang, G. Wen, Z. Peng, T. Huang and A. Rahmani, Fully distributed formation-containment control of heterogeneous linear multiagent systems. IEEE Transactions on Automatic Control, 64(9): 3889–3896, 2019.

[8] X. Dong and G. Hu, Time-varying formation tracking for linear multiagent systems with multiple leaders. IEEE Transactions on Automatic Control, 62(7): 3658–3664, 2017.

[9] Y. Liu, W. Zhang, C. Xian, Y. Zhao and G. Chen, Event-triggered multiple dynamic targets formation tracking without well-informed agent: a general exploring relationship. IEEE Transactions on Control of Network Systems. doi: 10.1109/TCNS.2023.3295342.

[10] B. Xu, H. Zhang, Y. Ding and W. Ren, Event-triggered surrounding formation control of multiagent systems for multiple dynamic targets. IEEE Transactions on Control of Network Systems, 10(2): 752–764, 2023.

[11] Q. Zhang, J. Xi, L. Wang and C. Wang, Formation tracking control of quadrotor unmanned aerial vehicle swarm with double formation structure. 2022 41st Chinese Control Conference (CCC), Hefei, China, 2022: 4962–4967.

[12] Y. Liu and Z. Geng, Finite-time optimal formation control for linear multi-agent systems. Proceedings of the 33rd Chinese Control Conference, Nanjing, China, 2014: 8941–8946.

[13] H. Du, C. Yang and R. Jia, Finite-time formation control of multiple mobile robots. 2016 IEEE International Conference on Cyber Technology in Automation, Control, and Intelligent Systems (CYBER), Chengdu, China, 2016: 416–421.

[14] Y. Liu, F. Zhang, P. Huang and Y. Lu, Fixed-time consensus tracking for second-order multiagent systems under disturbance. IEEE Transactions on Systems, Man, and Cybernetics: Systems, 51(8): 4883–4894, 2021.

[15] A. Coppola, D. G. Lui, A. Petrillo and S. Santini, Distributed fixed-time leader-tracking control for heterogeneous uncertain autonomous connected vehicles platoons. 2021 29th Mediterranean Conference on Control and Automation (MED), PUGLIA, Italy, 2021: 554–559.

[16] Y. Zhou, Y. Liu, C. Xian, Y. Zhao and G. Wen, Appointed-time formation-containment control for nonlinear multi-agent networks using sample-data feedback. International Journal of Robust and Nonlinear Control, 33(8): 4616–4635, 2023.

[17] Y. Zhou, Y. Liu, C. Xian and Y. Zhao, Appointed-time dynamic average consensus: a holistic planning and multi-step control framework. IEEE Transactions on Circuits and Systems II: Express Briefs, 70(7): 2595–2599, 2023.

[18] K. Zhang, B. Zhou, X. Yang and G. Duan, Prescribed-time leader-following consensus of linear multi-agent systems by bounded linear time-varying protocols. Science China-Information Sciences, 67(1):112201,2024.

[19] Z. Meng, W. Ren and Z. You, Distributed finite-time attitude containment control for multiple rigid bodies. Automatica, 46(12): 2092–2099, 2010.

[20] Y. Liu and Y. Zhao, Specified-time containment tracking for multi-agent systems: an optimal control approach. 2017 29th Chinese Control and Decision Conference (CCDC), 2017: 2530–2534.

Proceedings of the 3rd Conference on Fully Actuated System Theory and Applications
May 10-12, 2024, Shenzhen, China

ADMM-based Privacy-Preserving Peer-to-Peer Energy Trading Negotiation Mechanism

Zhenwei Guo[1,2], Jiajian Zhu[1], Haoran Li[1], Haibin Zheng[1], Yujue Wang[1]

1. Research Center of Cyber Science and Technology, Hangzhou Innovation Institute, Beihang University, Hangzhou 310051, China
E-mail: zhenweiguo0724@buaa.edu.cn, jiajianzhu@buaa.edu.cn, lhrbeijing@buaa.edu.cn, zhenghaibin29@buaa.edu.cn, wyujue@buaa.edu.cn

2. State Key Laboratory of Industrial Control Technology, Zhejiang University, Hangzhou 310027, China

Abstract: The rapid development of demand response management and distributed energy has promoted the development of P2P energy trading mechanisms, making electricity market participants more active. However, how to prevent private information from being reached by malicious agents during P2P negotiation process is a challenging problem. This paper proposes a privacy protection decentralized optimization method for P2P energy trading based on consensus Alternating Direction Method of Multipliers (ADMM) and Partially Homomorphic Encryption (HE). Firstly, the general model of P2P electricity market and the P2P trading negotiation mechanism based on consensus ADMM are introduced. However, under this mechanism, malicious neighbor agents can collude to steal private information. In order to resist collusion attack, a two-party secure computation mechanism between each pair of agents is designed, and the energy amount and price are updated in a secure way without leaking any private information. The privacy-preserving mechanism can find a trade-off between the convergence efficiency and information security. Finally, the function of the privacy protection negotiation mechanism was simulated in terms of convergence performance, impact on social welfare and computational efficiency.

Key Words: ADMM-based P2P energy trading, privacy-preserving, partially homomorphic encryption

1 Introduction

The increase in the number of prosumers motivates the need for a decentralized energy trading mechanism that allows prosumers to negotiate freely with each other without a central coordinator. In this context, P2P trading mechanism emerges as the next generation energy management technology, which enables prosumers to actively participate in the energy market. Although the P2P mechanism provides better scalability, reliability and resilience, the growing privacy concerns prevent it from being widely used. In P2P markets, prosumers trade energy without the intervention of a central coordinator, making the market an untrustworthy and unreliable platform. Moreover, P2P energy trading requires a large amount of data to be exchanged to decide the optimal traded amount and price [1]. Disclosing such local data for computation would compromise their privacy. For example, the producer generation pattern [2] and the local demand consumption pattern [3, 4] may be revealed.

Therefore, protecting prosumers' privacy and encouraging them to cooperate in an environment with a lack of trust and security is challenging. To achieve privacy-preserving decentralized optimization, a common approach is differential privacy [5–7], It overwrites sensitive information by adding carefully designed noise to the exchange state or objective function. However, the added noise also inevitably compromises the optimality of the results, leading to a trade-off between privacy and accuracy. In fact, as proved in [7], even without the addition of noise perturbations, differential privacy-based methods may fail to approach the exact optimal solution. Homomorphic encryption (HE) is another secure method that allows to perform computations on ciphertext and produce an encrypted result that, when decrypted, is the same as the result of an operation performed on plaintext [8]. HE can be further divided into two categories: Semi-HE and full-HE. Semi-HE methods refer to schemes that support only addition or multiplication operations of cryptographic algorithms. For example, the Paillier algorithm only supports addition operations. In contrast, full-HE schemes support all encryption algorithms. The main advantage of the HE method is that it is based on cryptographic techniques and is the most secure method, while its biggest disadvantage is the high consumption of computational resources due to complex cryptographic operations. Several works have investigated the use of HE techniques in energy management systems based on distributed optimization. For example, a new private cooperative distributed energy management system was proposed on [9] to solve the AC optimal power flow problem in a distributed and private manner. The algorithm was based on the primal dual subgradient distributed optimization technique and the full HE algorithm; In [11], a privacy-preserving scheduling method for distributed interconnected microgrid based on ADMM and Paillier HE method was proposed; The authors presented new algorithms based on HE at [12] to implement system operators and a set of agents to securely execute distributed algorithms based on projected gradients. Then, the algorithm was applied to solve the privacy problem in distributed energy transactions [13]. In our previous work [14], we proposed a privacy-preserving P2P energy trading negotiation mechanism based on consensus+innovation (C+I) method and HE. However, the number of convergence iterations is large and the computation burden is heavy.

Therefore, the existing works have not found a good trade-off between security and efficiency of P2P energy trading negotiation mechanisms. To solve this problem, we innovatively combine the efficient consensus ADMM with Paillier HE to realize a privacy-protection and fast-converging decentralized optimization method for P2P energy trading.

This work is supported by the National Science Foundation of China 62303037, the Zhejiang Soft Science Research Program 2023C35081, and the Open Research Project of the State Key Laboratory of Industrial Control Technology, Zhejiang University, China (No.ICT2023B48).

Simulation results show that market convergence performance, social welfare, and computational efficiency are sacrificed at acceptable levels. The main contribution is to protect the information exchanged between each pair of agents in the negotiation process of ADMM-based P2P energy trading, so that it has less number of convergence iterations and higher security.

The rest of the paper is organized as follows: Section 2 presents the general formulation of P2P market and the ADMM-based P2P negotiation mechanism for energy trading, followed by the privacy-preserving computation framework in Section 3. Numerical results are presented in Section 4. Finally, conclusions are drawn in Sections 5.

2 Problem Formulation

2.1 General P2P Market Model

In this section, a general simplest mathematical formulation of a full P2P market design [15, 16] is first presented below

$$\min_{D} \sum_{n\in\Omega} C_n\left(P_n\right) + \tilde{C}_n\left(\mathbf{P}_n\right) \tag{1a}$$

$$\text{s.t. } P_n = \sum_{m\in\omega_n} P_{nm}, \quad \forall n \in \Omega \tag{1b}$$

$$\underline{P_n} \le P_n \le \overline{P_n}, \quad \forall n \in \Omega \tag{1c}$$

$$P_{nm} + P_{mn} = 0, \quad \forall (n,m) \in (\Omega, \omega_n) \tag{1d}$$

$$P_{nm} \ge 0, \quad \forall (n,m) \in (\Omega_p, \omega_n) \tag{1e}$$

$$P_{nm} \le 0, \quad \forall (n,m) \in (\Omega_c, \omega_n) \tag{1f}$$

where $D = (P_{nm} \in \mathbb{R})_{n\in\Omega, m\in\omega_n}$, P_n is the summation of traded amount between neighbor agents, and P_{nm} is the trade between agents n and m. The generation or demand should be within a feasible region (1c), and the trade between each pair of agents should be balanced (1d). A positive value of P_{nm} means sale/production (1e) and a negative value equals to a purchase/consumption (1f). Ω, Ω_p and Ω_c as sets for all peers, producers and consumers, respectively (hence, $\Omega_p, \Omega_c \in \Omega$, $\Omega_p \cap \Omega_c = \emptyset$).

The production cost and consumer utility functions are usually formulated as quadratic functions as below

$$C_n(P_n) = a_n P_n^2 + b_n P_n, \tag{2}$$

where a_n and b_n are predetermined positive constants.

The product differentiation or preference is considered, the bilateral trading costs are formulated as linear functions of the quality traded with each neighboring agents $\tilde{C}_n\left(\mathbf{P}_n\right) = \sum_{m\in\omega_n} c_{nm} P_{nm}$. The bilateral trading coefficients c_{nm} are influenced by transmission distance, network constraints, carbon emissions, size of prosumers, etc. The different preference will influence the prices between agents. For example, the long distance between agent n and m will generate a high transmission cost, and cause a higher price between n and m than others.

2.2 Decentralized Optimization-Based P2P Trading Negotiation Mechanism

Compared with centralized optimization, decentralized optimization can realize parallel computation while maintaining the optimality of results, and is a better method to implement and design new P2P trading mechanisms. This section first introduces a decentralized negotiation mechanism based on consensus ADMM for P2P trading [17, 18], as shown in Fig. 1. This mechanism has be proposed and proved to be efficient in many works [17, 18]. The proposed negotiation mechanism focuses on a deterministic clearing algorithm for single time period, and it can be easily extended to multiple time periods [17, 18].

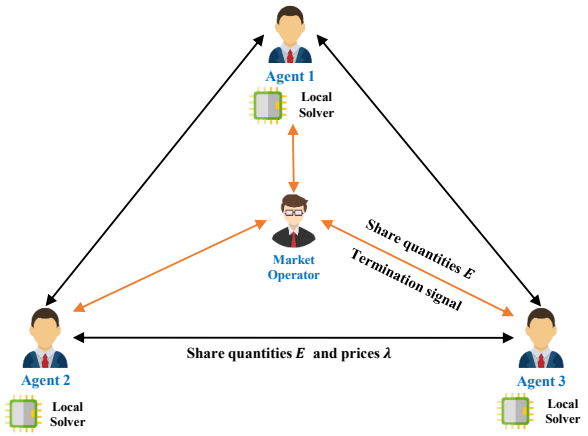

Fig. 1: Schematic diagram of the P2P trading negotiation mechanism

At the beginning, each agent randomly decides and broadcasts initial price and amount in parallel. Each agent will then iteratively update the amount and prices with its neighbor agents until converging to equilibrium. At a given iteration k, each agent $n \in \Omega$ will update its traded amount with neighbor agents by solving an optimization problem as follows.

$$\min_{\mathbf{P}_n} C_n\left(P_n\right) + \tilde{C}_n\left(\mathbf{P}_n\right) + \sum_{m\in\omega_n} \left[\lambda_{nm}^k \left(Q_{nm}^k - P_{nm}\right) + \frac{\rho}{2}\left(Q_{nm}^k - P_{nm}\right)^2\right] \tag{3a}$$

$$\text{s.t. } \underline{P_n} \le P_n \le \overline{P_n}, \quad \forall n \in \Omega \tag{3b}$$

$$P_{nm} \ge 0, \quad \forall (n,m) \in (\Omega_p, \omega_n) \tag{3c}$$

$$P_{nm} \le 0, \quad \forall (n,m) \in (\Omega_c, \omega_n) \tag{3d}$$

where λ_{nm} is the provided price for amount P_{nm}, and it is also the dual variable for the balance constraints (1d); $Q_{nm} = \frac{P_{nm} - P_{mn}}{2}$ represents the median value of traded amount between n and m.

It can be noticed that, some items in the objective function are constant, which will not affect the decision of variables and can be omitted. Above objective function can be simplified to be following form.

$$\min_{\mathbf{P}_n} C_n\left(P_n\right) + \tilde{C}_n\left(\mathbf{P}_n\right) + \sum_{m\in\omega_n} \left[-\lambda_{nm}^k P_{nm} - \rho Q_{nm}^k P_{nm} + \frac{\rho}{2}(P_{nm})^2\right] \tag{4a}$$

After solving above problem (3) and obtaining the updated amount, each agent will update the price λ_{nm}^{k+1} as follows

$$\lambda_{nm}^{k+1} = \lambda_{nm}^k - \frac{\rho}{2}\left(P_{nm}^{k+1} + P_{mn}^{k+1}\right). \tag{5}$$

Since the objective function is strictly convex, utilizing ADMM method is sufficient to ensure that the algorithm converges to the global optimum [19]. The algorithm ends when the total primal residual (the squared difference between each pair of traded amounts) and the total dual residual (the squared difference between two consecutive iteration amounts) are less than the global stopping criterion

$$R^{k+1} \triangleq \sum_{n\in\Omega}\sum_{m\in\omega_n}(P_{nm}^{k+1}+P_{mn}^{k+1})^2 \le \chi^r, \tag{6a}$$

$$T^{k+1} \triangleq \sum_{n\in\Omega}\sum_{m\in\omega_n}(P_{nm}^{k+1}-P_{nm}^{k})^2 \le \chi^t, \tag{6b}$$

where χ^r and χ^t are predestined positive minimal constants. The market Operator (MO) must be trusted and can be a community manager or an authorized representative of all agents. MO checks whether the algorithm converges by collecting trading results (6), and broadcasts a termination signal to all agents if the convergence condition is satisfied.

3 Privacy-Preserving P2P Trading Negotiation Mechanism

3.1 Collusion Attack

At iteration k of the negotiation process, the information sent by agent $n \in \Omega$ to neighbor agent $m \in \omega_n$ is P_{nm}^k. It is obvious that agent's internal private parameters $\left(a_n, b_n, c_{nm}, \overline{P_n}, \underline{P_n}\right)$ are not required to be shared for reaching optimality. However, this mechanism cannot absolutely protect the private information. Consider a specific scenario where all of agent n's neighbor agents conspire to gain agent n's privacy by exchanging information. We will introduce two collusion attack strategies to derive the private parameters $\left(\overline{P_n}, \underline{P_n}\right)$ and (a_n, b_n, c_{nm}).

1) First, neighbors of agent n can gradually adjust the provided amount P_{mn} until P_{nm} remains unchanged between two iterations, which means the output of agent n has reached the bound $\{\overline{P_n}, \underline{P_n}\}$. Since all neighbor agents can communicate to accumulate all $P_{nm}, m \in \omega_n$ to get P_n, they can obtain the private information $\{\overline{P_n}, \underline{P_n}\}$.
2) Since the neighbor agents of agent n have received the information about power boundaries, neighbor agents can construct a set $P_{mn}, \forall m \in \omega_n$ such that the output P_n does not reach bounds $(\overline{P_n}, \underline{P_n})$. Under this condition, the constraint (3c) will not work. Then, we take the derivative of P_{nm} (nonzero) for the objective function for three consecutive iterations as below.

$$\begin{cases} 2a_nP_n^{k+1}+b_n+c_{nm}-\lambda_{nm}^k-\rho Q_{nm}^k+\rho P_{nm}^{k+1}=0 \\ 2a_nP_n^{k+2}+b_n+c_{nm}-\lambda_{nm}^{k+1}-\rho Q_{nm}^{k+1}+\rho P_{nm}^{k+2}=0 \\ 2a_nP_n^{k+3}+b_n+c_{nm}-\lambda_{nm}^{k+2}-\rho Q_{nm}^{k+2}+\rho P_{nm}^{k+3}=0 \end{cases} \tag{7}$$

Here, $\{Q_{nm}, P_{nm}, \lambda_{nm}\}$ are known to agent m, P_n is also known to all collusive neighbor agents. Thus, the private parameter (a_n, b_n, c_{nm}) can be obtained by solving above equation set.

So while updates require little information sharing, there is still a risk of privacy breaches under a collusive attack by a group of malicious neighboring agents. Therefore, we will utilize Paillier HE to protect the exchanged information.

3.2 Paillier Cryptosystem

The Paillier algorithm implementation scheme is detailed below.

- *Key generation:* Prime numbers p and q are randomly chosen to satisfy $gcd(pq, (p-1)(q-1)) = 1$, where gcd is the greatest common divisor. Then, $N = p * q$ and $\lambda = lcm(p-1, q-1)$ are founded, where lcm is the least common multiple. We randomly choose $g \in Z_{N^2}^*$ to satisfy $gcd(L(g^\lambda \mod N^2), N) = 1$, and ensure there exists

$$\mu = (L(g^\lambda \mod N^2))^{-1} \mod N \tag{8}$$

  where $L(x) = \frac{x-1}{N}$. The public key pk is $\{N, g\}$, and the private key sk is $\{\lambda, \mu\}$.
- *Encryption Function:* The encrypting function is:

$$\mathcal{E}(m, \text{pk}) = g^m \cdot r^N \mod N^2 \tag{9}$$

  where m is the plaintext message, r is a random pad $r \in Z_N^*$.
- *Decryption Function:* Let the ciphertext c and the secret key sk, the plaintext can be computed as:

$$\begin{aligned} m = \mathcal{D}(c, \text{sk}) &= \frac{L(c^\lambda \mod N^2)}{L(g^\lambda \mod N^2)} \mod N \\ &= L(c^\lambda \mod N^2) * \mu \mod N. \end{aligned} \tag{10}$$

The additive homomorphic property allows the user to operate the message in its ciphertext directly. Assume the two plaintexts are m_1, m_2, then we have:

$$\begin{aligned} c_1 &= \mathcal{E}(m_1, \text{pk}) \equiv g^{m_1} \cdot r^N \mod N^2 \\ c_2 &= \mathcal{E}(m_2, \text{pk}) \equiv g^{m_2} \cdot r^N \mod N^2 \end{aligned} \tag{11}$$

Obviously, we have $c_1 * c_2 \equiv g^{m_1+m_2} \cdot (r^2)^N \mod N^2$, thus we can conclude that

$$\begin{aligned} m_1 + m_2 \mod N &= \mathcal{D}(\mathcal{E}(m_1, \text{pk}) \oplus \mathcal{E}(m_2, \text{pk}), \text{sk}) \\ &= \mathcal{D}(c_1 * c_2, \text{sk}). \end{aligned} \tag{12}$$

3.3 Privacy-Preserving Amounts and Prices Update

In the energy amounts update (3), the only terms that contains the shared information from neighboring agents are $\rho(P_{nm}^k - P_{mn}^k)$. While in the energy prices update (5), the terms are $\rho(P_{nm}^{k+1} + P_{mn}^{k+1})$. [20] proposed a privacy-preserving decentralized optimization approach based on ADMM and partially homomorphic cryptography, however, it has not been applied to P2P energy trading problem. Inspired by [20], we propose a privacy-preserving amounts and prices update mechanism for energy trading negotiation process. To be specific, motivated by the fact that ADMM allows varying penalty factors [21, 22], we change the penalty factors to be ρ_{nm}^k, which are varying between different pair of agents and different iterations.

By constructing ρ_{nm}^k as the product of two random positive numbers, i.e., $\rho_{nm}^k = \varrho_{nm}^k \times \varrho_{mn}^k$, with ϱ_{nm}^k only known to agent n and ϱ_{mn}^k only known to agent m, we can propose the following privacy-preserving amounts and prices update protocol Alg. 1 - Alg. 2.

The penalty factor ϱ_{nm}^k is randomly selected from $\left[\varrho_{nm}^{k-1}, \overline{\varrho}_n\right]$, which means that the penalty factor increases monotonically with iteration. $\overline{\varrho}_n$ is the predetermined number, known only to the agent n. With this update, the privacy protection algorithm can be guaranteed to converge.

It should be noticed that in (4), the term $\frac{\rho_{nm}}{2}(P_{nm})^2$ contains the varying penalty factors ρ_{nm}. If the factor are known to agent n, it can easily get the information ϱ_{mn}^k, and calculate the amounts P_{mn}. In the same way, neighboring agent m can also obtain the amounts P_{nm}. Thus, if the penalty factors of the last two terms in (4) are same, the privacy cannot be protected. To solve this problem, we change the term $\frac{\rho_{nm}}{2}(P_{nm})^2$ to $\frac{\hat{\rho}}{2}(P_{nm})^2$, where $\hat{\rho}$ is a large enough constant predetermined by MO. Then, the upper bounds $\overline{\varrho}_n$ of agent n will be randomly chosen from $\left[0.9\sqrt{\hat{\rho}}, \sqrt{\hat{\rho}}\right]$, and known only to agent n. By using this method, the convergence of the algorithm can still be guaranteed, but the optimality of results will be slightly sacrificed.

Algorithm 1 Protocol for privacy-preserving amounts update of agent n at iteration k.

1: **Initialization:** $k = 0$, each agent initializes $\boldsymbol{P}_{nm}^k$, $\boldsymbol{\varrho}_{nm}^k$.
2: **for** $m \in \omega_n$ **do**
3: Agent n encrypts P_{nm}^k with its public key pk_n: $\mathcal{E}_n(P_{nm}^k)$.
4: Agent n sends $\mathcal{E}_n(P_{nm}^k)$ and its public key pk_n to the corresponding neighboring agent m.
5: Agent m encrypts $-P_{mn}^k$ with pk_n: $\mathcal{E}_n(-P_{mn}^k)$.
6: Agent m computes the difference in ciphertext:

$$\mathcal{E}_n(P_{nm}^k - P_{mn}^k) = \mathcal{E}_n(P_{nm}^k) \cdot \mathcal{E}_n(-P_{mn}^k)$$

7: Agent m computes weighted difference in ciphertext:

$$\mathcal{E}_n\left(\varrho_{mn}^k(P_{nm}^k - P_{mn}^k)\right) = \left(\mathcal{E}_n(P_{nm}^k - P_{mn}^k)\right)^{\varrho_{mn}^k}$$

8: Agent m sends above decryption back to agent n.
9: Agent n decrypts the message received from m with its private key sk_n and multiples the result with ϱ_{nm}^k to obtain: $\rho_{nm}^k(P_{nm}^k - P_{mn}^k)$.
10: **end for**
11: After obtaining all $\rho_{nm}^k(P_{nm}^k - P_{mn}^k)$ for $\forall m \in \omega_n$, agent n runs the local optimization problem (3) to update the energy amounts $\boldsymbol{P}_{nm}^{k+1}$.

3.4 Privacy Analysis

This method is designed to protect the information $\boldsymbol{P}_n$ that agents exchange during negotiation. In this section, we rigorously prove that a malicious agent or adversary cannot infer this information. As shown in Alg. 1 - 2, our approach guarantees that information will not be leaked to any neighbor in a single iteration. However, it is unclear whether private information leaks over time.

Suppose a malicious agent n gathers the exchanged information from K iterations to infer the privacy information of its neighbor m. Taking the energy amount update as an example, from the viewpoint of the adversary agent n, the information seen at iteration k is $y^k = \varrho_{nm}^k \times \varrho_{mn}^k(P_{nm}^k - P_{mn}^k)$. Then, the adversary agent n can establish $(K+1)$ equations based on the received information:

$$\begin{cases} y^0 = \varrho_{nm}^0 \times \varrho_{mn}^0(P_{nm}^0 - P_{mn}^0), \\ y^1 = \varrho_{nm}^1 \times \varrho_{mn}^1(P_{nm}^1 - P_{mn}^1), \\ \vdots \\ y^{K-1} = \varrho_{nm}^{K-1} \times \varrho_{mn}^{K-1}(P_{nm}^{K-1} - P_{mn}^{K-1}), \\ y^K = \varrho_{nm}^K \times \varrho_{mn}^K(P_{nm}^K - P_{mn}^K). \end{cases} \tag{13}$$

To the adversary agent n, in the system of equations (13), $\varrho_{nm}^k, P_{nm}^k (k = 0, 1, 2, ...K)$ are known, $\varrho_{mn}^k, P_{mn}^k (k = 0, 1, 2, ...K)$ are unknown. So the above system of $(K+1)$ equations contains $2(K+1)$ unknown variables. It is obvious that adversary agent n cannot solve above equations set to infer the values of unknowns $\varrho_{mn}^k, P_{mn}^k (k = 0, 1, 2, ...K)$ of agent m. Using a similar way of reasoning, we can conclude that the malicious agent n cannot infer any neighbor's private information during the price updates.

Algorithm 2 Protocol for privacy-preserving prices update of agent n at iteration k.

1: **Initialization:** $k = 0$, each agent initializes $\boldsymbol{P}_{nm}^{k+1}$, $\boldsymbol{\varrho}_{nm}^k$.
2: **for** $m \in \omega_n$ **do**
3: After finishing amounts update, agent n encrypts P_{nm}^{k+1} with its public key pk_n: $\mathcal{E}_n(P_{nm}^{k+1})$.
4: Agent n sends $\mathcal{E}_n(P_{nm}^{k+1})$ and its public key pk_n to the corresponding neighboring agent m.
5: Agent m encrypts P_{mn}^{k+1} with pk_n: $\mathcal{E}_n(P_{mn}^{k+1})$.
6: Agent m computes the summation in ciphertext:

$$\mathcal{E}_n(P_{nm}^{k+1} + P_{mn}^{k+1}) = \mathcal{E}_n(P_{nm}^{k+1}) \cdot \mathcal{E}_n(P_{mn}^{k+1})$$

7: Agent m computes weighted summation in ciphertext:

$$\mathcal{E}_n\left(\varrho_{mn}^k(P_{nm}^{k+1} + P_{mn}^{k+1})\right) = \left(\mathcal{E}_n(P_{nm}^{k+1} + P_{mn}^{k+1})\right)^{\varrho_{mn}^k}$$

8: Agent m sends above decryption back to agent n.
9: Agent n decrypts the message received from m with its private key sk_n and multiples the result with ϱ_{nm}^k to obtain: $\rho_{nm}^k(P_{nm}^{k+1} + P_{mn}^{k+1})$.
10: Agent n runs (5) to obtain the updated energy prices λ_{nm}^{k+1}.
11: Agent n updates ϱ_{nm}^k to ϱ_{nm}^{k+1} by randomly choosing from $\left[\varrho_{nm}^k, \overline{\varrho}_n\right]$.
12: **end for**
13: Set $k = k + 1$.

4 Simulation Results

This section presents numerical results to evaluate the performance of proposed privacy-preserving P2P energy trading mechanism. A network of seven agents is deployed as illustrated in Fig. 2. The parameters of sellers and buyers are listed in Tab. 1, which are randomly chosen for simulation. The bilateral trading coefficients between agents are also randomly generated. Agent 1-4 are sellers, and agent 5-7 are buyers. Simulations are running on a computer with an Intel Core i7-10700 processor at 2.90 GHz using 32 GB of RAM.

4.1 Convergence Performance with and without Privacy Protection

In this case study, we will demonstrate the convergence performance of the algorithm we designed. With no privacy

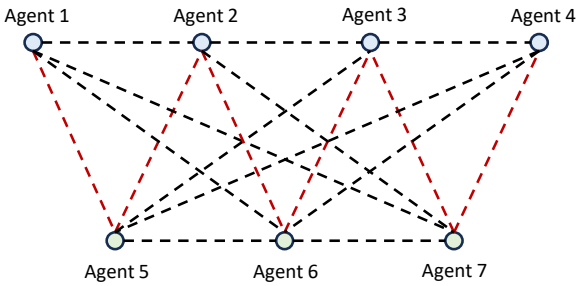

Fig. 2: Test network schematic.

Table 1: Sellers' and buyers' parameters of case study

Seller	a_n [\$/kW^2]	b_n [\$/kW]	$\underline{E_n}$ [kW]	$\overline{E_n}$ [kW]	R_n^{init} [kg]	α_n [kg/kW]
S1	0.040	1.5	0	7	72	0.95
S2	0.046	2	0	4	24	0.97
S3	0.040	1.2	0	6	36	0.90
S4	0.050	2.5	0	5	30	0.98
B1	0.040	3	-7	-2	40	-0.78
B2	0.056	4	-6	-2	24	-0.70
B3	0.050	3.5	-8	-2	48	-0.75

protection, the tuning parameter ρ is fixed at 0.5. Fig. 3 (a) shows the convergence process for agent 1 and agent 5. It can be seen that both the primal residuals and the dual residuals decrease rapidly and meet the stop criterion within 90 iterations.

When considering privacy protection, the tuning parameter ρ are reconstructed to be ρ_{nm}^k as the product of two random positive numbers, i.e., $\rho_{nm}^k = \varrho_{nm}^k \times \varrho_{mn}^k$. The parameters $\hat{\rho}$ are set to 0.36, and the upper bounds $\overline{\varrho}_n$ of agent n will be randomly chosen from $[0.48, 0.6]$. Seen from Fig. 3(b), since the tuning parameters are changing, the iterations for convergence is more than the case with fixed factors. But, the residuals still decreases fast and drops close to zero within 100 iterations. In conclusion, the convergence under privacy protection is still guaranteed, and the performance will not degrade much.

4.2 Social Welfare with and without Privacy Protection

We also provide a comparison to show the welfare of each agent with and without privacy protection. Before using the privacy-preserving algorithm, the trading will be certain to converge to optimal results due to convexity of social and local optimization problems. The value of optimal social welfare is 21.815. While, after taking the privacy-preserving strategy, it can be seen from Fig.4, the result will deviate from the optimal solution. The reason for that is penalty factors in terms $\frac{\rho_{nm}(P_{nm,t}^k - P_{mn,t}^k)}{2} P_{nm,t}$ are slightly different. The social welfare value under privacy protection is 20.183, which is only 7.48% different from the optimal value. Thus, although taking the privacy protection strategy will sacrifice the social welfare, the loss is within an acceptable level.

4.3 Computational Performance with and without Privacy Protection

In this paper, we use HE technology to realize privacy-preserving trading. However, the main drawback of HE is that the computational burden is quite high. To overcome this problem, we choose not to protect all the exchanged information among agents. According to the analysis of the privacy attack, all neighbor agents need to collude. Therefore, as long as the communication with at least one of the neighbor agents is secure, the private information can be well protected. As marked in red in Fig. 2, we find a path with the least number of edges in the graph, which means the connection is encrypted and can resist malicious attacks. It can be seen that, each agent has at least one secure communication connection between neighbor agents. Deciding which lines to protect depends on the communication connections between agents in the market. But, we can turn it into the problem of finding the shortest path, which can be solved by some mature algorithms, e.g., Dijkstra algorithm [23] and Floyd algorithm [24]. Using this strategy, the encrypted communication times can be at least reduced from $\frac{N(N-1)}{2}$ to $N-1$ (for a fully connected graph), where N is the number of agents.

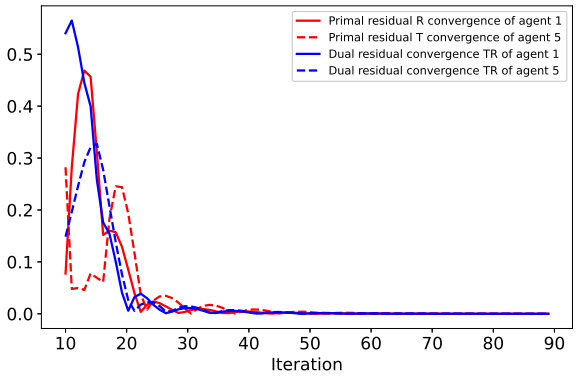

(a) No privacy protection

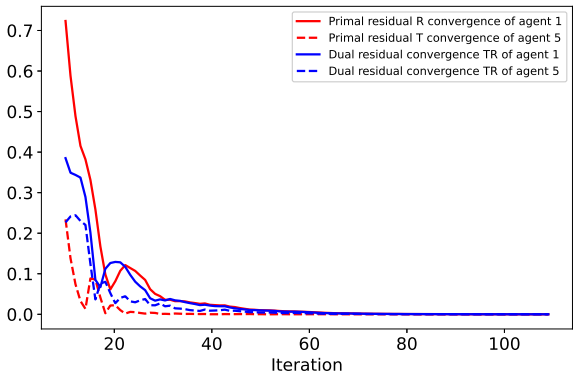

(b) With privacy protection

Fig. 3: Convergence process of the proposed algorithm with and without privacy protection

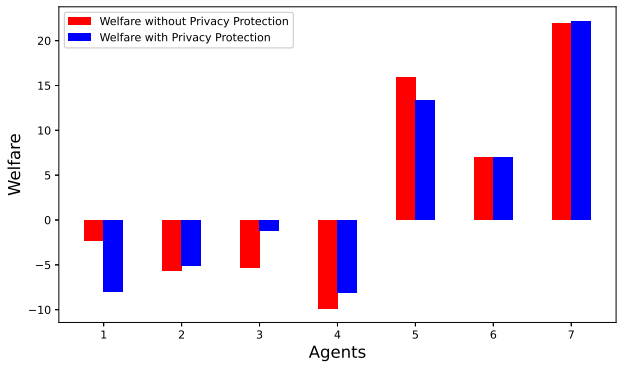

Fig. 4: Welfare of agents with/without privacy protection.

We show the average running time per iteration for each agent in Fig. 5. The running time includes key generation time, encryption and decryption time. The algorithm can run very fast when privacy protection is not provided, and the time increases significantly when the negotiation is secure. The average time of the partial protection strategy is about half that of the full protection strategy, since both strategies require a key generation operation.

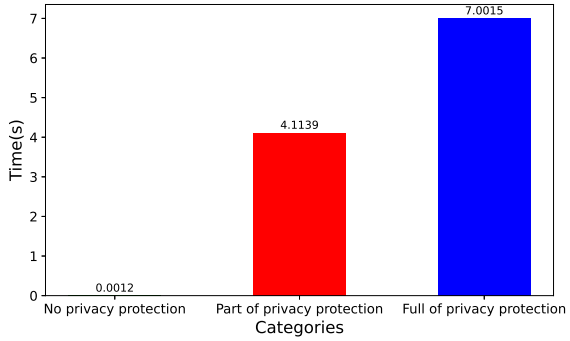

Fig. 5: Average running time of each agent per iteration.

5 Conclusion

How to prevent private information from being obtained by malicious agents for DO-based P2P negotiation mechanism is a challenging problem. This paper proposes a privacy protection decentralized optimization method based on consensus ADMM and Paillier HE. The energy amount and price are updated in a secure way without revealing any private information. We also provide the simulation results of convergence performance, impact on social welfare, and computational efficiency. The results show that after providing the privacy protection, the number of iterations does not increase much, the sacrificed welfare is in a low level, and the running time can be reduced by about half through finding a path in the communication network.

References

[1] W. Tushar, B. Chai, C. Yuen, D. B. Smith, K. L. Wood, Z. Yang, and H. V. Poor, "Three-party energy management with distributed energy resources in smart grid," *IEEE Transactions on Industrial Electronics*, vol. 62, no. 4, pp. 2487–2498, 2014.

[2] K. Kursawe, G. Danezis, and M. Kohlweiss, "Privacy-friendly aggregation for the smart-grid," in *Privacy Enhancing Technologies: 11th International Symposium, PETS 2011, Waterloo, ON, Canada, July 27-29, 2011. Proceedings 11*, pp. 175–191, Springer, 2011.

[3] G. Ács and C. Castelluccia, "I have a dream!(differentially private smart metering)," in *International Workshop on Information Hiding*, pp. 118–132, Springer, 2011.

[4] Y. Hong, W. M. Liu, and L. Wang, "Privacy preserving smart meter streaming against information leakage of appliance status," *IEEE transactions on information forensics and security*, vol. 12, no. 9, pp. 2227–2241, 2017.

[5] Z. Huang, S. Mitra, and N. Vaidya, "Differentially private distributed optimization," in *Proceedings of the 16th International Conference on Distributed Computing and Networking*, pp. 1–10, 2015.

[6] S. Han, U. Topcu, and G. J. Pappas, "Differentially private distributed constrained optimization," *IEEE Transactions on Automatic Control*, vol. 62, no. 1, pp. 50–64, 2016.

[7] E. Nozari, P. Tallapragada, and J. Cortés, "Differentially private distributed convex optimization via functional perturbation," *IEEE Transactions on Control of Network Systems*, vol. 5, no. 1, pp. 395–408, 2016.

[8] A. Acar, H. Aksu, A. S. Uluagac, and M. Conti, "A survey on homomorphic encryption schemes: Theory and implementation," *ACM Computing Surveys (Csur)*, vol. 51, no. 4, pp. 1–35, 2018.

[9] Z. Cheng, F. Ye, X. Cao, and M.-Y. Chow, "A homomorphic encryption-based private collaborative distributed energy management system," *IEEE Transactions on Smart Grid*, vol. 12, no. 6, pp. 5233–5243, 2021.

[10] H. Yi, W. Lin, X. Huang, X. Cai, R. Chi, and Z. Nie, "Energy trading iot system based on blockchain," *Swarm and Evolutionary Computation*, vol. 64, p. 100891, 2021.

[11] N. Liu, C. Wang, M. Cheng, and J. Wang, "A privacy-preserving distributed optimal scheduling for interconnected microgrids," *Energies*, vol. 9, no. 12, p. 1031, 2016.

[12] Y. Lu and M. Zhu, "Privacy preserving distributed optimization using homomorphic encryption," *Automatica*, vol. 96, pp. 314–325, 2018.

[13] Y. Lu, J. Lian, and M. Zhu, "Privacy-preserving transactive energy system," in *2020 American Control Conference (ACC)*, pp. 3005–3010, IEEE, 2020.

[14] Z. Li, H. Xu, F. Zhai, B. Zhao, M. Xu, and Z. Guo, "A privacy-preserving, two-party, secure computation mechanism for consensus-based peer-to-peer energy trading in the smart grid," *Sensors*, vol. 22, no. 22, p. 9020, 2022.

[15] T. Sousa, T. Soares, P. Pinson, F. Moret, T. Baroche, and E. Sorin, "Peer-to-peer and community-based markets: A comprehensive review," *Renewable and Sustainable Energy Reviews*, vol. 104, pp. 367–378, 2019.

[16] T. Baroche, P. Pinson, R. L. G. Latimier, and H. B. Ahmed, "Exogenous cost allocation in peer-to-peer electricity markets," *IEEE Transactions on Power Systems*, vol. 34, no. 4, pp. 2553–2564, 2019.

[17] Z. Guo, P. Pinson, S. Chen, Q. Yang, and Z. Yang, "Chance-constrained peer-to-peer joint energy and reserve market considering renewable generation uncertainty," *IEEE Transactions on Smart Grid*, vol. 12, no. 1, pp. 798–809, 2021.

[18] Z. Guo, P. Pinson, S. Chen, Q. Yang, and Z. Yang, "Online optimization for real-time peer-to-peer electricity market mechanisms," *IEEE Transactions on Smart Grid*, vol. 12, no. 5, pp. 4151–4163, 2021.

[19] S. P. Boyd and L. Vandenberghe, *Convex optimization*. Cambridge university press, 2010.

[20] C. Zhang, M. Ahmad, and Y. Wang, "Admm based privacy-preserving decentralized optimization," *IEEE Transactions on Information Forensics and Security*, vol. 14, no. 3, pp. 565–580, 2018.

[21] S. Kontogiorgis and R. R. Meyer, "A variable-penalty alternating directions method for convex optimization," *Mathematical Programming*, vol. 83, no. 1-3, pp. 29–53, 1998.

[22] B. He, L.-Z. Liao, D. Han, and H. Yang, "A new inexact alternating directions method for monotone variational inequalities," *Mathematical Programming*, vol. 92, pp. 103–118, 2002.

[23] E. W. Dijkstra, "A note on two problems in connexion with graphs," in *Edsger Wybe Dijkstra: His Life, Work, and Legacy*, pp. 287–290, 2022.

[24] R. W. Floyd, "Algorithm 97: shortest path," *Communications of the ACM*, vol. 5, no. 6, p. 345, 1962.

Proceedings of the 3rd Conference on Fully Actuated System Theory and Applications
May 10-12, 2024, Shenzhen, China

Formation Control of Discrete-time Multi-agent Systems Based on Distributed Filter Observer

Huanli Gao[1,2,3], Wei Li[1], Ming Qiu[4], He Cai[1,2,3]

1. School of Automation Science and Engineering, South China University of Technology, Guangzhou 510641, China
2. Key Laboratory of Autonomous Systems and Networked Control, Ministry of Education, Guangzhou 510641, China
3. Guangdong Engineering Technology Research Center of Unmanned Aerial Vehicle Systems, Guangzhou 510641, China
4. People's Armed Forces Department of Shanhaiguan District, Qinhuangdao City, Qinhuangdao 066200, China

Abstract: This paper explores the formation control of discrete multi-agent systems under external communication disturbance. Firstly, leveraging the modified algebraic Riccati equation, a disturbed output based discrete filter observer is proposed to minimize network information exchange and mitigate disturbance effects. Then, the formation control issue is transformed into a cooperative output regulation problem, which a certainty equivalent state feedback controller solves. The effectiveness of the control strategy is demonstrated by numerical simulations.

Key Words: Formation Control, Discrete-time Multi-agent System, Distributed Filter Observer

1 Introduction

Formation control has garnered extensive attention as a fundamental and pivotal subtask in multi-agent system control [1, 2]. The objectives of formation control are twofold. Firstly, the multi-agent system moves following a predetermined desired trajectory. Secondly, each agent within the system is required to maintain a specified inter-agent distance. Research on formation control of discrete multi-agent systems holds significant importance in engineering applications. Thus far, substantial research focusing on communication disturbance and delay for formation control has been reported [3–6]. [3] linearized the nonlinear model into a second-order integral model, proposing two types of coordinated controllers for systems with and without time-varying delays. [4] offered a distributed protocol based on local information, utilizing the agent's immediate states and its neighbors' delayed states. [5] employed a discrete-time disturbance observer method to mitigate exogenous disturbance on the model. Furthermore, [6] designed a control law with a decaying-gain to achieve the desired formation under noisy conditions.

Output regulation, a fundamental method in control system design, was comprehensively detailed in [7]. The concept of cooperative output regulation emerges from an intricate blend of graph theory and output regulation. This methodology has been successfully applied to formation control challenges, yielding notable outcomes [8–12]. Studies in [8–10] investigated its applications in continuous-time systems. [11] and [12] studied the robust formation control and communication delay-resistant formation control of discrete multi-agent systems based on cooperative output regulation. A pivotal aspect of cooperative output regulation in formation control is designing a distributed observer for the exosystem, which acts as a virtual leader of the multi-agent systems. For continuous-time systems, the state-based adaptive distributed output observer and the output-based adaptive distributed output observer have been developed, as discussed in [13–15]. Extending these works, [16] adapted the observer from [14] into a discrete format. [17], leveraging a modified algebraic Riccati equation, presented solvability conditions for distributed state feedback control laws. Building on the study in [17], [18] explored scenarios where only a sensor network exists among all agents and proposed a sensory feedback-based discrete distributed observer.

Based on the cooperative output regulation framework, this paper explores formation control in discrete multi-agent systems through a filter observer based methodology. We begin by applying the minimal polynomial of the system matrix to restructure the virtual leader system. Drawing on the discrete observer design method outlined in [18], a novel disturbed output based discrete filter observer is developed through a modified algebraic Riccati equation. This observer adeptly estimates the actual value of the virtual leader system, simultaneously eliminating external communication disturbance and reducing network information exchange within the multi-agent systems. A certainty equivalent state feedback controller is introduced to address the formation control problem in discrete-time multi-agent systems. Compared with existing results, the main contributions of this paper can be summarized as follows:

- A disturbed output based discrete filter observer is proposed to address the problem of communication disturbance. The observer can accurately estimate the actual value of the disturbed signal and effectively reduce the network information exchange within the systems.
- Based on the cooperative output regulation framework, the disturbed output based discrete filter observer is incorporated into the design of a certainty equivalent state feedback controller. This control law successfully addresses the formation control problem in a disturbance environment.

Notation: $\mathbb{R}$ and $\mathbb{C}$ denote real and complex number field. $\otimes$ denotes the Kronecker product of matrices. I_N denotes

This work is supported in part by National Natural Science Foundation of China under Grants 62173149, 62276104, U22A2062, in part by Guangdong Natural Science Foundation under grant number 2022A1515011262, and in part by Fundamental Research Funds for the Central Universities.
Corresponding author: He Cai. Email:caihe@scut.edu.cn

N-dimensional identity matrix. 1_N represents a $N \times 1$ column vector whose elements are all 1. For $x_i \in \mathbb{R}^{n_i}$, $i = 1, \ldots, N$, $\mathrm{col}(x_1, \ldots, x_N) = [x_1^T, \ldots, x_N^T]^T$. Given a square matrix A, let $\sigma(A)$ denote the spectrum of A and $\rho(A)$ denote the spectral radius, i.e., the maximal magnitude of the eigenvalues of A. For any vector $X \in \mathbb{R}^{nq}$ for some positive n and q, $M_n^q(X) = [X_1 \ \ldots \ X_q]$, where, for $i = 1, \ldots, q$, $X_i \in \mathbb{R}^n$, and $X = \mathrm{col}(X_1, \ldots, X_q)$. Let $\mathcal{D}(a) = \begin{bmatrix} \cos(aT) & -\sin(aT) \\ \sin(aT) & \cos(aT) \end{bmatrix}$ with a sampling time $T \in \mathbb{R}$ and a constant $a \in \mathbb{R}$. Given a square matrix A, let $\mathrm{pinv}(A)$, $\Psi_A^c(\lambda)$ and Ψ_A^m denote the pseudo inverse, characteristic polynomial and minimal polynomial of A, respectively.

2 Problem Formulation

In this paper, the formation control of a discrete-time linear multi-agent system composed of N agents is examined. For $i = 1, \ldots, N$, the mathematical model of the ith agent is described as:

$$\begin{aligned} x_i(k+1) &= A_i x_i(k) + B_i u_i(k) \\ y_i(k+1) &= C_i x_i(k) + D_i u_i(k) \end{aligned} \tag{1}$$

where $x_i(k) \in \mathbb{R}^{n_i}$, $u_i(k) \in \mathbb{R}^{m_i}$, $y_i(k) \in \mathbb{R}^p$ denote the state, control input and output of the ith agent at the kth sampling time, respectively. $A_i \in \mathbb{R}^{n_i \times n_i}$, $B_i \in \mathbb{R}^{n_i \times m_i}$, $C_i \in \mathbb{R}^{p \times n_i}$, $D_i \in \mathbb{R}^{p \times m_i}$ are constant matrices.

For $i = 1, \ldots, N$, the reference tracking path $y_{ri}(k) \in \mathbb{R}^p$ of each agent can be designed as:

$$y_{ri}(k) = y_0(k) + y_{hi}(k) \tag{2}$$

where the global tracking path vector $y_0(k) \in \mathbb{R}^p$ defines the reference path for the entire multi-agent system and can be viewed as a virtual leader. The local bias vector $y_{hi}(k) \in \mathbb{R}^p$ specifies the relative position between the ith agent and the virtual leader. Thus, the formation tracking error $e_i(k) \in \mathbb{R}^p$ for the ith agent can be defined as:

$$e_i(k) = y_i(k) - y_{ri}(k). \tag{3}$$

Suppose the global tracking path vector $y_0(k) \in \mathbb{R}^p$ can be generated by the following virtual leader system:

$$\begin{aligned} v_0(k+1) &= S_0 v_0(k) \\ y_0(k) &= C_0 v_0(k) \end{aligned} \tag{4}$$

where $v_0(k) \in \mathbb{R}^q$ denotes the state, $S_0 \in \mathbb{R}^{q \times q}$ and $C_0 \in \mathbb{R}^{p \times q}$ are constant matrices.

For $i = 1, \ldots, N$, the local bias vector $y_{hi}(k)$ can be generated by the following local bias generator:

$$\begin{aligned} h_i(k+1) &= \Phi_i h_i(k) \\ y_{hi}(k) &= \phi_i h_i(k) \end{aligned} \tag{5}$$

where $h_i(k) \in \mathbb{R}^{n_{hi}}$ denotes the state, $\Phi_i \in \mathbb{R}^{n_{hi} \times n_{hi}}$ and $\phi_i \in \mathbb{R}^{p \times n_{hi}}$ are constant matrices.

The communication network is described by a graph[1] $\bar{\mathcal{G}} = (\bar{\mathcal{V}}, \bar{\mathcal{E}})$ with $\bar{\mathcal{V}} = \{0, 1, \ldots, N\}$ and $\bar{\mathcal{E}} = \{(i, j), i, j \in \bar{\mathcal{V}}, i \neq j\}$. Node 0 is associated with the virtual leader, and node i, $i = 1, \ldots, N$, is associated with the ith agent. Let the weighted adjacency matrix of the digraph $\bar{\mathcal{G}}$ be $\bar{\mathcal{A}} = [a_{ij}] \in \mathbb{R}^{(N+1)\times(N+1)}$. Define a subgraph $\mathcal{G}_s$ of $\bar{\mathcal{G}}$ as $\mathcal{G}_s = (\mathcal{V}_s, \mathcal{E}_s)$ with $\mathcal{V}_s = \{1, \ldots, N\}$ and $\mathcal{E}_s = \bar{\mathcal{E}} \cap \{\mathcal{V}_s \times \mathcal{V}_s\}$. Let $\mathcal{L}_s$ denote the Laplacian of $\mathcal{G}_s$ and $H = \mathcal{L}_s + \mathrm{block\ diag}(a_{10}, \ldots, a_{N0})$.

The formation control problem of a discrete-time linear multi-agent system can be formulated as follows.

Problem 1 *Given systems* (1), (4), (5) *and a communication graph* $\bar{\mathcal{G}}$*, design a distributed formation control law* $u_i(k)$ *such that for any system initial condition,* $\lim_{k\to\infty} e_i(k) = 0$.

This paper also considers the situation where the output information $\eta_0(k) \in \mathbb{R}^{q_\eta}$ of the virtual leader system is affected by channel disturbance during its transmission to the multi-agent systems. Let $\eta_0^m(k) \in \mathbb{R}^{q_\eta}$ represent the output information of the virtual leader system received by the multi-agent systems and

$$\eta_0^m(k) = \eta_0(k) + \eta_0^d(k) \tag{6}$$

where $\eta_0^d(k) = \mathrm{col}(\eta_{01}^d(k), \ldots, \eta_{0q_\eta}^d(k)) \in \mathbb{R}^{q_\eta}$ denotes the disturbance. For $i = 1, \ldots, q_\eta$, the form of the disturbance considered is as follows:

$$\eta_{0i}^d(k) = \sum_{\epsilon=1}^{\Gamma} \beta_{i\epsilon} \cos(\omega_\epsilon k T + \gamma_{i\epsilon}) \tag{7}$$

where the frequency ω_ϵ is known, the amplitude $\beta_{i\epsilon}$ and phase $\gamma_{i\epsilon}$ are not accessible. Define $\Omega = \{\pm\omega_\epsilon \mathrm{j}, \epsilon = 1, \ldots, \varphi\}$ and $\mathcal{D}(\Omega) = \mathrm{block\ diag}(\mathcal{D}(\omega_1), \ldots, \mathcal{D}(\omega_\varphi))$, where j denotes the imaginary unit.

3 Main Result

3.1 Disturbed Output Based Discrete Filter Observer

The following assumption is necessary to design a disturbed output based discrete filter observer under the disturbed information.

Assumption 1 *All the eigenvalues of the matrix* S_0 *are on the unit circle.*

Suppose that the minimal polynomial of S_0 is

$$\Psi_{S_0}^m = \lambda^\iota + \kappa_{01}\lambda^{\iota-1} + \cdots + \kappa_{0(\iota-1)}\lambda + \kappa_{0\iota} \tag{8}$$

where $\iota \leq q$. Let $\kappa_0 = \mathrm{col}(\kappa_{01}, \ldots, \kappa_{0\iota}) \in \mathbb{R}^\iota$. For virtual leader system (4), the information transmitted is defined as $\eta_0(k) = \mathrm{col}(\kappa_0, y_0(k)) \in \mathbb{R}^{\iota+p}$. Let $\kappa_0^d(k)$ and $y_0^d(k)$ denote the channel disturbance acting on κ_0 and $y_0(k)$, $\kappa_0^m(k)$ and $y_0^m(k)$ represent the disturbed output information received by the agents. Thus,

$$\begin{aligned} \kappa_0^m(k) &= \kappa_0 + \kappa_0^d(k) \\ y_0^m(k) &= y_0(k) + y_0^d(k) \end{aligned} \tag{9}$$

where each component of $\eta_0^d(k) = \mathrm{col}(\kappa_0^d(k), y_0^d(k))$ satisfies (7).

Define:

$$\begin{aligned} \Gamma_\kappa &= \mathrm{block\ diag}(1, \mathcal{D}(\Omega)) \in \mathbb{R}^{(1+2\varphi)\times(1+2\varphi)}, \\ \Xi_\kappa &= \begin{bmatrix} 1 & 1 & 0 & \ldots & 1 & 0 \end{bmatrix} \in \mathbb{R}^{1\times(1+2\varphi)}, \\ \Theta_\kappa &= \begin{bmatrix} 1 & 0 & 0 & \ldots & 0 & 0 \end{bmatrix} \in \mathbb{R}^{1\times(1+2\varphi)}. \end{aligned}$$

[1] See [13] for a summary of graph notation.

With Lemma 1 in [19], the pair $(\Xi_\kappa, \Gamma_\kappa)$ is observable. The amplitudes of the eigenvalues of Γ_κ are all 1. By Theorem 1 and Corollary in [20], let $0 < \delta_\kappa < 1$, the following modified algebraic Riccati equation:

$$\begin{aligned}&\Gamma_\kappa P_\kappa \Gamma_\kappa^T - P_\kappa - (1-\delta_\kappa^2)\Gamma_\kappa P_\kappa \Xi_\kappa^T (\Xi_\kappa P_\kappa \Xi_\kappa^T)^{-1} \Xi_\kappa P_\kappa \Gamma_\kappa^T \\ &+ I_{1+2\varphi} = 0\end{aligned} \tag{10}$$

exists a unique solution $P_\kappa = P_\kappa^T > 0$. Let $K_\kappa = \Gamma_\kappa P_\kappa \Xi_\kappa^T (\Xi_\kappa P_\kappa \Xi_\kappa^T)^{-1}$.

For $i = 1, \ldots, N$ and $\tau = 1, \ldots, \iota$, The part of the disturbed output based discrete filter observer that estimates κ_0 is designed as follows:

$$\begin{aligned}\zeta_{i\tau}^\kappa(k+1) &= \Gamma_\kappa \zeta_{i\tau}^\kappa(k) + \mu_{\zeta_i}^\kappa K_\kappa \sum_{j=0}^{N} a_{ij}(\xi_{j\tau}^\kappa(k) - \xi_{i\tau}^\kappa(k)) \\ \xi_{i\tau}^\kappa(k) &= \Xi_\kappa \zeta_{i\tau}^\kappa(k) \\ \kappa_{i\tau}(k) &= \Theta_\kappa \zeta_{i\tau}^\kappa(k)\end{aligned} \tag{11}$$

where $\zeta_{i\tau}^\kappa(k) \in \mathbb{R}^{1+2\varphi}$, $\xi_{0\tau}^\kappa(k) = \kappa_{0\tau}^m(k) \in \mathbb{R}$, $\mu_{\zeta_i}^\kappa = \nu^\kappa \mu_i^\kappa$, $\nu^\kappa > 0$ and $\mu_i^\kappa > 0$.

Furthermore, define:

$$\mathcal{S}_i(k) = \begin{bmatrix} 0 & 1 & \ldots & 0 \\ \vdots & \vdots & \ddots & \vdots \\ 0 & 0 & \ldots & 1 \\ -\kappa_{i\iota}(k) & -\kappa_{i(\iota-1)}(k) & \ldots & -\kappa_{i1}(k) \end{bmatrix} \in \mathbb{R}^{\iota\times\iota},$$

$$\mathcal{C}_0 = \begin{bmatrix} 1 & 0 & \ldots & 0 \end{bmatrix} \in \mathbb{R}^{1\times\iota},$$

$$\Gamma_i^y(k) = \text{block diag}(\mathcal{S}_i(k), \mathcal{D}(\Omega)) \in \mathbb{R}^{(\iota+2\varphi)\times(\iota+2\varphi)},$$

$$\Xi_y = \begin{bmatrix} \mathcal{C}_0 & 1 & 0 & \ldots & 1 & 0 \end{bmatrix},$$

$$\Theta_y = \begin{bmatrix} \mathcal{C}_0 & 0 & 0 & \ldots & 0 & 0 \end{bmatrix}.$$

Since the pair $(\mathcal{C}_0, \mathcal{S}_i(k))$ is observable for any $k \geq 0$, the pair $(\Xi_y, \Gamma_i^y(k))$ is similarly observable. Let $\delta_y \rho(\Gamma_i^y(k)) < 1$. By [20], the following time-varying modified algebraic Riccati equation:

$$\begin{aligned}&\Gamma_i^y(k) P_i^y(k) \Gamma_i^y(k)^T - P_i^y(k) \\ &- (1-\delta_y^2)\Gamma_i^y(k) P_i^y(k) \Xi_y^T (\Xi_y P_i^y(k) \Xi_y^T)^{-1} \Xi_y P_i^y(k) \Gamma_i^y(k)^T \\ &+ I_{\iota+2\varphi} = 0\end{aligned} \tag{12}$$

has a unique positive definite solution $P_i^y(k)$. Let $K_i^y(k) = \Gamma_i^y(k) P_i^y(k) \Xi_y^T (\Xi_y P_i^y(k) \Xi_y^T)^{-1}$.

For $i = 1, \ldots, N$, $\tau = 1, \ldots, p$, the part of the disturbed output based discrete filter observer that estimates $y_0(k)$ is designed as follows:

$$\begin{aligned}\zeta_{i\tau}^y(k+1) &= \Gamma_i^y(k) \zeta_{i\tau}^y(k) \\ &\quad + \mu_{\zeta_i}^y K_i^y(k) \sum_{j=0}^{N} a_{ij}(\xi_{j\tau}^y(k) - \xi_{i\tau}^y(k)) \\ \xi_{i\tau}^y(k) &= \Xi_y \zeta_{i\tau}^y(k) \\ y_{i\tau}^0(k) &= \Theta_y \zeta_{i\tau}^y(k)\end{aligned} \tag{13}$$

where $\zeta_{i\tau}^y(k) \in \mathbb{R}^{\iota+2\varphi}$, $\xi_{i\tau}^y(k) = y_{0\tau}^m(k) \in \mathbb{R}$ denotes the τth entry of $y_0^m(k)$, $\mu_{\zeta_i}^y = \nu^y \mu_i^y$, $\nu^y > 0$ and $\mu_i^y > 0$.

Let $H_\mu^\kappa = \text{diag}(\mu_1^\kappa, \ldots, \mu_N^\kappa) H$, $H_\mu^y = \text{diag}(\mu_1^y, \ldots, \mu_N^y) H$,$\Lambda_{\varrho\mu}^\kappa = I_N - \varrho H_\mu^\kappa$, $\Lambda_{\varrho\mu}^y = I_N - \varrho H_\mu^y$, $\mathcal{F}_\kappa = \{\varrho \in \mathbb{R} | \rho(\Lambda_{\varrho\mu}^\kappa) < \delta_\kappa\}$, $\mathcal{F}_y = \{\varrho \in \mathbb{R} | \rho(\Lambda_{\varrho\mu}^y) < \delta_y\}$, $\kappa_i(k) = \text{col}(\kappa_{i1}(k), \ldots, \kappa_{i\iota}(k))$ and $y_i^0(k) = \text{col}(y_{i1}^0(k), \ldots, y_{ip}^0(k))$.

Lemma 1 *Given the virtual leader system* (4)*, the channel disturbance* (7)*,* (9)*, the disturbed output based discrete filter observer* (11)*,* (13) *and a communication network* $\bar{\mathcal{G}}$*, if* $\sigma(S_0) \cap \Omega = \emptyset$*,* $\mu_i^\kappa > 0$*,* $\nu^\kappa \in \mathcal{F}_\kappa$*,* $\mu_i^y > 0$*,* $\nu^y \in \mathcal{F}_y$*, it satisfies that* $\lim_{k\to\infty}(\kappa_i(k) - \kappa_0) = 0$ *and* $\lim_{k\to\infty}\left(y_i^0(k) - y_0(k)\right) = 0$*.*

Proof 1 *For* $\tau = 1, \ldots, \iota$*,* $\kappa_{0\tau}(k)$ *and* $\kappa_{0\tau}^m(k)$ *can be generated by*

$$\begin{aligned}\zeta_{0\tau}^\kappa(k+1) &= \Gamma_\kappa \zeta_{0\tau}^\kappa(k) \\ \kappa_{0\tau}^m(k) &= \Xi_\kappa \zeta_{0\tau}^\kappa(k) \\ \kappa_{0\tau}(k) &= \Theta_\kappa \zeta_{0\tau}^\kappa(k)\end{aligned} \tag{14}$$

where $\zeta_{0\tau}^\kappa(k) \in \mathbb{R}^{1+2\varphi}$*. Let* $\bar{\zeta}_{i\tau}^\kappa(k) = \zeta_{i\tau}^\kappa(k) - \zeta_{0\tau}^\kappa(k)$*, we have*

$$\begin{aligned}\bar{\zeta}_{i\tau}^\kappa(k+1) &= \Gamma_\kappa \zeta_{i\tau}^\kappa(k) + \mu_{\zeta_i}^\kappa K_\kappa \sum_{j=0}^{N} a_{ij}(\xi_{j\tau}^\kappa(k) - \xi_{i\tau}^\kappa(k)) \\ &\quad - \Gamma_\kappa \zeta_{0\tau}^\kappa(k) \\ &= \Gamma_\kappa \bar{\zeta}_{i\tau}^\kappa(k) \\ &\quad + \mu_{\zeta_i}^\kappa K_\kappa \Xi_\kappa \sum_{j=0}^{N} a_{ij}(\bar{\zeta}_{j\tau}^\kappa(k) - \bar{\zeta}_{i\tau}^\kappa(k)).\end{aligned} \tag{15}$$

Let $\bar{\zeta}_\tau^\kappa(k) = \text{col}(\bar{\zeta}_{1\tau}^\kappa(k), \ldots, \bar{\zeta}_{N\tau}^\kappa(k))$*,* $H_\zeta^\kappa = \nu^\kappa H_\mu^\kappa$*. Thus,*

$$\bar{\zeta}_\tau^\kappa(k+1) = (I_N \otimes \Gamma_\kappa - H_\zeta^\kappa \otimes K_\kappa \Xi_\kappa) \bar{\zeta}_\tau^\kappa(k). \tag{16}$$

Let $\chi_\kappa = 1/\sqrt{\rho(\Gamma_\kappa P_\kappa \Xi_\kappa^T (\Xi_\kappa P_\kappa \Xi_\kappa^T)^{-1} \Xi_\kappa P_\kappa \Gamma_\kappa^T)}$*,* $R_\kappa = \sqrt{\chi_\kappa^2 + \delta_\kappa^2}$*. For any* $\lambda_\mu^\kappa \in \sigma(H_\mu^\kappa)$*,* $\lambda_\mu^\kappa > 0$*. Given any* $\nu^\kappa \in \mathcal{F}_\kappa$*, there exists a sufficiently small* $\alpha_\kappa > 0$ *such that* $|1 - \nu^\kappa \lambda_\mu^\kappa| \leq \rho(\Lambda_{\varrho\mu}^\kappa) < \sqrt{R_\kappa^2 - \alpha_\kappa^2}$*. Thus,*

$$\begin{aligned}&(\Gamma_\kappa^T - \nu^\kappa \lambda_\mu^\kappa \Xi_\kappa^T K_\kappa^T)^H P_\kappa (\Gamma_\kappa^T - \nu^\kappa \lambda_\mu^\kappa \Xi_\kappa^T K_\kappa^T) - P_\kappa \\ =&\Gamma_\kappa P_\kappa \Gamma_\kappa^T - P_\kappa \\ &+(|1 - \nu^\kappa \lambda_\mu^\kappa|^2 - 1)\Gamma_\kappa P_\kappa \Xi_\kappa^T (\Xi_\kappa^T P_\kappa \Xi_\kappa)^{-1} \Xi_\kappa P \kappa^T \Gamma_\kappa^T \\ =&- I_{1+2\varphi} \\ &+(|1 - \nu^\kappa \lambda_\mu^\kappa|^2 - \delta_\kappa^2)\Gamma_\kappa P_\kappa \Xi_\kappa^T (\Xi_\kappa^T P_\kappa \Xi_\kappa)^{-1} \Xi_\kappa P \kappa^T \Gamma_\kappa^T \\ \leq&- I_{1+2\varphi} \\ &+(R_\kappa^2 - \chi_\kappa^2 - \delta_\kappa^2)\Gamma_\kappa P_\kappa \Xi_\kappa^T (\Xi_\kappa^T P_\kappa \Xi_\kappa)^{-1} \Xi_\kappa P \kappa^T \Gamma_\kappa^T \\ =&- I_{1+2\varphi} + (\chi_\kappa^2 - \alpha_\kappa^2)\Gamma_\kappa P_\kappa \Xi_\kappa^T (\Xi_\kappa^T P_\kappa \Xi_\kappa)^{-1} \Xi_\kappa P \kappa^T \Gamma_\kappa^T \\ \leq&- I_{1+2\varphi} + \frac{\chi_\kappa^2 - \alpha_\kappa^2}{\chi_\kappa^2} I_{1+2\varphi} \\ =&- \frac{\alpha_\kappa^2}{\chi_\kappa^2} I_{1+2\varphi}.\end{aligned} \tag{17}$$

It implies that the matrix $\Gamma_\kappa^T - \nu^\kappa \lambda_\mu^\kappa \Xi_\kappa^T K_\kappa^T$ *is Schur, and so is* $I_N \otimes \Gamma_\kappa - H_\zeta^\kappa \otimes K_\kappa \Xi_\kappa$*. Consequently,* $\lim_{k\to\infty} \bar{\zeta}_\tau^\kappa(k) = 0$ *and* $\lim_{k\to\infty}(\kappa_i(k) - \kappa_0) = 0$*.*

Moreover, with the minimal polynomial of S_0 in (8),

$$S_0^\iota + \kappa_{01} S_0^{\iota-1} + \cdots + \kappa_{0(\iota-1)} S_0 + \kappa_{0\iota} = 0. \tag{18}$$

Since $y_0(k+d) = C_0 S_0^d v_0(k)$, $d \le \iota$. *For* $\tau = 1, \ldots, p$,

$$\begin{aligned} &y_{0\tau}(k+\iota) + \kappa_{01} y_{0\tau}(k+\iota-1) + \ldots \\ &+\kappa_{0(\iota-1)} y_{0\tau}(k+1) + y_{0\tau}(k) = 0. \end{aligned} \tag{19}$$

Let $\zeta_{0\tau}(k) = \mathrm{col}(y_{0\tau}(k), y_{0\tau}(k+1), \ldots, y_{0\tau}(k+\iota))$,

$$\mathcal{S}_0 = \begin{bmatrix} 0 & 1 & \ldots & 0 \\ \vdots & \vdots & \ddots & \vdots \\ 0 & 0 & \ldots & 1 \\ -\kappa_{0\iota}(k) & -\kappa_{0(\iota-1)}(k) & \ldots & -\kappa_{01}(k) \end{bmatrix}.$$

$y_{0\tau}(k)$ can be generated by the following equivalent virtual leader system:

$$\begin{aligned} \zeta_{0\tau}(k+1) &= \mathcal{S}_0 \zeta_{0\tau}(k) \\ y_{0\tau}(k) &= \mathcal{C}_0 \zeta_{0\tau}(k) \end{aligned} \tag{20}$$

where $\zeta_{0\tau}(k)$ denotes the equivalent state. Then, let $\Gamma_y = \mathrm{block\ diag}(\mathcal{S}_0, \mathcal{D}(\Omega)) \in \mathbb{R}^{(\iota+2\varphi)\times(\iota+2\varphi)}$,

$$\begin{aligned} \zeta_{0\tau}^y(k+1) &= \Gamma_y \zeta_{0\tau}^y(k) \\ y_{0\tau}^m(k) &= \Xi_y \zeta_{0\tau}^y(k) \\ y_{0\tau}(k) &= \Theta_y \zeta_{0\tau}^y(k) \end{aligned} \tag{21}$$

where $\zeta_{0\tau}^y(k) \in \mathbb{R}^{\iota+2\varphi}$. Obviously, (Ξ_y, Γ_y) is observable. The modified algebraic Riccati equation:

$$\begin{aligned} &\Gamma_y P_y {\Gamma_y}^T - P_y \\ &-(1-\delta_y^2)\Gamma_y P_y \Xi_y^T (\Xi_y P_y \Xi_y^T)^{-1} \Xi_\kappa P_y {\Gamma_y}^T + I_{\iota+2\varphi} = 0 \end{aligned} \tag{22}$$

admits a unique positive definite solution P_y.

Let $K_y = \Gamma_y P_y \Xi_y^T (\Xi_y P_y \Xi_y^T)^{-1}$, $\bar{K}_i^y(k) = K_i^y(k) - K_y$, $\bar{\Gamma}_i^y(k) = \Gamma_i^y(k) - \Gamma_y$, $\bar{P}_i^y(k) = P_i^y(k) - P_y$, $\bar{\zeta}_{i\tau}^y(k) = \zeta_{i\tau}^y(k) - \zeta_{0\tau}^y(k)$. *Due to* $\lim_{k\to\infty}(\kappa_i(k) - \kappa_0) = 0$, $\lim_{k\to\infty} \bar{\Gamma}_i^y(k) = 0$, $\lim_{k\to\infty} \bar{P}_i^y(k) = 0$ *and* $\lim_{k\to\infty} \bar{K}_i^y(k) = 0$.

$$\begin{aligned} \bar{\zeta}_{i\tau}^y(k+1) = &\Gamma_y \bar{\zeta}_{i\tau}^y(k) + \bar{\Gamma}_i^y(k)\bar{\zeta}_{i\tau}^y(k) \\ &+ \bar{\Gamma}_i^y(k)\zeta_{0\tau}^y(k) \\ &+ \mu_{\zeta_i}^y K_y \Xi_y \sum_{j=0}^{N} a_{ij}(\bar{\zeta}_{j\tau}^y(k) - \bar{\zeta}_{i\tau}^y(k)) \\ &+ \mu_{\zeta_i}^y \bar{K}_i^y(k) \Xi_y \sum_{j=0}^{N} a_{ij}(\bar{\zeta}_{j\tau}^y(k) - \bar{\zeta}_{i\tau}^y(k)). \end{aligned} \tag{23}$$

Let

$$\begin{aligned} \bar{\zeta}_\tau^y(k) &= \mathrm{col}(\bar{\zeta}_{1\tau}^y(k), \ldots, \bar{\zeta}_{N\tau}^y(k)), \\ \bar{\Gamma}_d^y(k) &= \mathrm{block\ diag}(\bar{\Gamma}_1^y(k), \ldots, \bar{\Gamma}_N^y(k)), \\ \bar{K}_d^y(k) &= \mathrm{block\ diag}(\bar{K}_1^y(k), \ldots, \bar{K}_N^y(k)), \end{aligned}$$

$H_\zeta^y = \nu^y H_\mu^y$. *Therefore,*

$$\begin{aligned} \bar{\zeta}_\tau^y(k+1) = &\left(I_N \otimes \Gamma_y - (H_\zeta^y \otimes K_y \Xi_y)\right) \bar{\zeta}_\tau^y(k) \\ &+ \left(\bar{\Gamma}_d^y(k) - (H_\zeta^y \otimes \bar{K}_i^y(k)\Xi_y)\right) \bar{\zeta}_\tau^y(k) \\ &+ \bar{\Gamma}_d^y(k)(1_N \otimes \zeta_{0\tau}^y(k)). \end{aligned} \tag{24}$$

Let $\chi_y = 1/\sqrt{\rho(\Gamma_y P_y \Xi_y^T (\Xi_y P_y \Xi_y^T)^{-1} \Xi_y P_y \Gamma_y^T)}$, $R_y = \sqrt{\chi_y^2 + \delta_y^2}$. *For any* $\lambda_\mu^y \in \sigma(H_\mu^y)$, $\lambda_\mu^y > 0$. *Given any* $\nu^y \in \mathcal{F}_y$, *there exists a sufficient small* $\alpha_y > 0$ *such that* $|1 - \nu^y \lambda_\mu^y| \le \rho(\Lambda_{o\mu}^y) < \sqrt{R_y^2 - \alpha_y^2}$. *Similarly,*

$$\begin{aligned} &(\Gamma_y^T - \nu^y \lambda_\mu^y \Xi_y^T K_y^T)^H P_y (\Gamma_y^T - \nu^y \lambda_\mu^y \Xi_y^T K_y^T) - P_y \\ &= -I_{\iota+2\varphi} \\ &+(|1 - \nu^y \lambda_\mu^y|^2 - \delta_y^2)\Gamma_y P_y \Xi_y^T (\Xi_y^T P_y \Xi_y)^{-1} \Xi_y P y^T \Gamma_y^T \\ &\le -\frac{\alpha_y^2}{\chi_y^2} I_{\iota+2\varphi}. \end{aligned} \tag{25}$$

It implies that the matrix $\Gamma_y^T - \nu^y \lambda_\mu^y \Xi_y^T K_y^T$ *is Schur, and so is* $I_N \otimes \Gamma_y - (H_\zeta^y \otimes K_y \Xi_y)$. *Under Assumption 1,* $\lim_{k\to\infty}\left(\bar{\Gamma}_d^y(k) - (H_\zeta^y \otimes \bar{K}_i^y(k)\Xi_y)\right) = 0$ *and* $\lim_{k\to\infty}\left(\bar{\Gamma}_d^y(k)(1_N \otimes \zeta_{0\tau}^y(k))\right) = 0$. *By Lemma 1 in [16],* $\lim_{k\to\infty} \bar{\zeta}_\tau^y(k) = 0$ *and* $\lim_{k\to\infty}\left(y_i^0(k) - y_0(k)\right) = 0$.

■

Let $\zeta_0(k) = \mathrm{col}(\zeta_{01}(k), \ldots, \zeta_{0p}(k))$. $y_0(k)$ can be generated by:

$$\begin{aligned} \zeta_0(k+1) &= (I_p \otimes \mathcal{S}_0)\zeta_0(k) \\ y_0(t) &= (I_p \otimes \mathcal{C}_0)\zeta_0(k). \end{aligned} \tag{26}$$

Thus, the teacking error (3) can be Equivalently expressed as:

$$e_i(k) = y_i(k) - (I_p \otimes \mathcal{C}_0)\zeta_0(k) - y_{hi}(k). \tag{27}$$

For $\tau = 1, \ldots, p$, let $\Pi = \begin{bmatrix} I_\iota & 0_{\iota\times 2\varphi} \end{bmatrix}$, $\zeta_{i\tau}(k) = \Pi \zeta_{i\tau}^y(k)$, $\zeta_i(k) = \mathrm{col}(\zeta_{i1}(k), \ldots, \zeta_{ip}(k))$. By lemma 1, $\lim_{k\to\infty}(\zeta_i(k) - \zeta_0(k)) = 0$;

3.2 State Feedback Controller Design

With the output regulation theorem in [7], the following assumptions are necessary.

Assumption 2 *For $i = 1, \ldots, N$, (A_i, B_i) is stabilizable.*

Assumption 3 *The regulator equations*

$$\begin{aligned} X_{\mathcal{S}}(I_p \otimes \mathcal{S}_0) &= A_i X_{\mathcal{S}} + B_i U_{\mathcal{S}} \\ 0 &= C_i X_{\mathcal{S}} + D_i U_{\mathcal{S}} - (I_p \otimes \mathcal{C}_0) \end{aligned} \tag{28}$$

$$\begin{aligned} X_{\Phi i}\Phi_i &= A_i X_{\Phi i} + B_i U_{\Phi i} \\ 0 &= C_i X_{\Phi i} + D_i U_{\Phi i} - \phi_i \end{aligned} \tag{29}$$

have unique solutions $(X_{\mathcal{S}}, U_{\mathcal{S}})$ and $(X_{\Phi i}, U_{\Phi i})$.

For $i = 1, \ldots, N$, under Assumption 2, select K_{xi} be such that $A_i + B_i K_{xi}$ is Schur. Let $K_{hi} = U_{\Phi i} - K_{xi} X_{\Phi i}$,

$$\hat{R}_i(k) = (I_p \otimes \mathcal{S}_i(k))^T \otimes \begin{pmatrix} I_{n_i} & 0 \\ 0 & 0 \end{pmatrix} - I_{p\iota} \otimes \begin{pmatrix} A_i & B_i \\ C_i & D_i \end{pmatrix},$$

$$R_i = (I_p \otimes \mathcal{S}_0)^T \otimes \begin{pmatrix} I_{n_i} & 0 \\ 0 & 0 \end{pmatrix} - I_{p\iota} \otimes \begin{pmatrix} A_i & B_i \\ C_i & D_i \end{pmatrix},$$

$$b_i = vec\left(\begin{bmatrix} 0 \\ -I_p \otimes \mathcal{C}_0 \end{bmatrix}\right).$$

The certainty equivalent state feedback controller can be designed as:

$$\begin{aligned} u_i(k) &= K_{xi} x_i(k) + K_{hi}(k) h_i(k) + K_{\zeta_i}(k)\zeta_i(k) \\ \xi_i(k) &= \mathrm{pinv}(\hat{R}_i(k)) b_i \end{aligned} \tag{30}$$

where $\xi_i \in \mathbb{R}^{q(n_i+p)}$,

$$\begin{pmatrix} \mathcal{X}_{\mathcal{S}i}(k) \\ \mathcal{U}_{\mathcal{S}i}(k) \end{pmatrix} = M^{p\iota}_{n_i+m_i}(\xi_i(k)),$$

$$K_{\zeta i}(k) = \mathcal{U}_{\mathcal{S}i}(k) - K_{xi}\mathcal{X}_{\mathcal{S}i}(k).$$

Theorem 1 *Under Assumptions 1, 2 and 3, given the system* (1)*, the virtual leader system* (4)*, the local bias generator* (5) *and a communication graph* $\bar{\mathcal{G}}$*, if* $0 < \delta_\kappa < 1$*,* $\delta_y \rho(\Gamma^y_i(k)) < 1$*,* $\sigma(S_0) \cap \Omega = \emptyset$*,* $\mu^\kappa_i > 0$*,* $\nu^\kappa \in \mathcal{F}_\kappa$*,* $\mu^y_i > 0$*,* $\nu^y \in \mathcal{F}_y$*, the Problem 1 is solved by the distributed formation control law composed of* (11)*,* (13) *and* (30)*.*

Proof 2 *By Lemma 1, for* $i = 1, \ldots, N$*,* $\lim_{k\to\infty}(\hat{R}_i(k) - R_i) = 0$*. Let* $\tilde{\mathcal{X}}_{\mathcal{S}i}(k) = \mathcal{X}_{\mathcal{S}i}(k) - X_{\mathcal{S}}$ *and* $\tilde{\mathcal{U}}_{\mathcal{S}i}(k) = \mathcal{U}_{\mathcal{S}i}(k) - U_{\mathcal{S}}$*, we have*

$$\lim_{k\to\infty} \tilde{\mathcal{X}}_{\mathcal{S}i}(k) = 0,$$

$$\lim_{k\to\infty} \tilde{\mathcal{U}}_{\mathcal{S}i}(k) = 0.$$

Let $\tilde{x}_i(k) = x_i(k) - X_{\Phi i}h_i(k) - X_{\mathcal{S}}\zeta_0(k)$*,* $\tilde{u}_i(k) = u_i(k) - U_{\Phi i}h_i(k) - U_{\mathcal{S}}\zeta_0(k)$*, combining* (28) *and* (29) *gives*

$$\dot{\tilde{x}}_i(k) = A_i\tilde{x}_i(k) + B_i\tilde{u}_i(k) \tag{31}$$

and

$$e_i(k) = C_i\tilde{x}_i(k) + D_i\tilde{u}_i(k). \tag{32}$$

With (30)*,*

$$\tilde{u}_i(k) = K_{xi}\tilde{x}_i(k) + K_{\zeta i}(k)\tilde{\zeta}_i(k) + \tilde{K}_{\zeta i}(k)\zeta_0(k) \tag{33}$$

where $\tilde{K}_{\zeta i}(k) = (\mathcal{U}_{\mathcal{S}i} - U_{\mathcal{S}}) - K_{xi}(\mathcal{X}_{\mathcal{S}i} - X_{\mathcal{S}})$*. Substituting* (33) *into* (31) *gives*

$$\begin{aligned}\dot{\tilde{x}}_i(k) = {} & (A_i + B_iK_{xi})\tilde{x}_i(k) \\ & + B_iK_{\zeta i}(k)\tilde{\zeta}_i(k) + B_i\tilde{K}_{\zeta i}(k)\zeta_0(k).\end{aligned} \tag{34}$$

Since $A_i + B_iK_{xi}$ *is Schur,* $\lim_{k\to\infty}\tilde{\zeta}_i(k) = 0$*,* $\lim_{k\to\infty}\tilde{K}_{\zeta i}(k) = 0$*,* $K_{\zeta i}(k)$ *and* $\zeta_0(k)$ *are bounded,* $\lim_{k\to\infty}(B_iK_{\zeta i}(k)\tilde{\zeta}_i(k) + B_i\tilde{K}_{\zeta i}(k)\zeta_0(k)) = 0$*. With Lemma 1 in [16],* $\lim_{k\to\infty}\tilde{x}_i(k) = 0$*,* $\lim_{k\to\infty}\tilde{u}_i(k) = 0$*. Thus,*

$$\lim_{k\to\infty} e_i(k) = 0.$$

■

4 Numerical Simulations

In this section, we consider a discrete-time multi-agent system composed of $N = 4$ agents. A numerical simulation experiment is designed to illustrate the effectiveness of the proposed control law. The communication graph is shown in Fig. 1.

For $i = 1, \ldots, 4$, the mathematical model of the ith agent is:

$$p_i(k+1) = p_i(k) + Tu_i(k) \tag{35}$$

where $p_i(k) \in \mathbb{R}^3$, $v_i(k) \in \mathbb{R}^3$, $u_i(k) \in \mathbb{R}^3$ denote the position, velocity and control input of the ith agent. $T = 0.05$s denotes system sampling period. To transform (35) into (1) form, let $A_i = I_3$, $B_i = TI_3$,, $C_i = I_3$, $D_i = 0$.

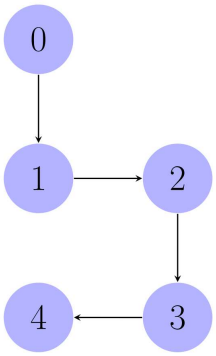

Fig. 1: Communication graph $\bar{\mathcal{G}}$

Let the global tracking path vector be $y_0(k) = \text{col}(vkT, 0, h)$, where $v = 0.1$m/s denotes the velocity along the X axis, $h = 0.2$m denotes the reference height along the Z axis. $y_0(k)$ can be generated by the virtual leader system described in (4), where

$$S_0 = \begin{pmatrix} 1 & vT \\ 0 & 1 \end{pmatrix},\ C_0 = \begin{pmatrix} 1 & 0 \\ 0 & 0 \\ 0 & h \end{pmatrix}$$

and $v_0(0) = \text{col}(0, 1)$.

For $i = 1, \ldots, 4$, let $\omega_r = 0.2$ rad/s. The local bias vectors are

$$y_{h1}(k) = \text{col}(0, \cos(\omega_r kT + \frac{\pi}{2}), \sin(\omega_r kT + \frac{\pi}{2})),$$

$$y_{h2}(k) = \text{col}(0, \cos(\omega_r kT), \sin(\omega_r kT)),$$

$$y_{h3}(k) = \text{col}(0, \cos(\omega_r kT - \frac{\pi}{2}), \sin(\omega_r kT - \frac{\pi}{2})),$$

$$y_{h4}(k) = \text{col}(0, \cos(\omega_r kT - \pi), \sin(\omega_r kT - \pi)).$$

$y_{hi}(k)$ can be generated by the local bias generator described in (5), where

$$\Phi_i = \begin{pmatrix} \cos(\omega_r T) & -\sin(\omega_r T) \\ \sin(\omega_r T) & \cos(\omega_r T) \end{pmatrix},\ \phi_i = \begin{pmatrix} 0 & 0 \\ 1 & 0 \\ 0 & 1 \end{pmatrix},$$

$h_1(0) = \text{col}(0.3, 0)$, $h_2(0) = \text{col}(0, 0.3)$, $h_3(0) = \text{col}(-0.3, 0)$ and $h_4(0) = \text{col}(0, -0.3)$.

Assume that during the information transmission process, the frequency of the external disturbance signal is $\omega_1 = 30$ rad/s, $\varphi = 1$. Select K_{xi} be such that the ploes of $A_i + B_iK_{xi}$ are $\{0.94, 0.94, 0.94\}$. Let $\delta_\kappa = 0.43$, $\delta_y = 0.3$, $\mu^\kappa_1 = 0.3$, $\mu^\kappa_2 = 0.4$, $\mu^\kappa_3 = 0.6$, $\mu^\kappa_4 = 0.7$, $\nu^\kappa = 1$, $\mu^y_1 = 0.2$, $\mu^y_2 = 0.2$, $\mu^y_3 = 0.2$, $\mu^y_4 = 0.2$ and $\nu^y = 1$. For regulator equations in (29), the unique solution is

$$X_{\Phi i} = \begin{pmatrix} 0 & 0 \\ 1 & 0 \\ 0 & 1 \end{pmatrix}, U_{\Psi i} = \begin{pmatrix} 0 & 0 \\ -0.001 & -0.2 \\ 0.2 & -0.001 \end{pmatrix}.$$

The tracking errors of each agent are shown in Fig. 2. We can solve the problem 1 with the distributed formation control law composed of observers (11), (13) and a certainty equivalent state feedback controller (30). The trajectory of each agent is shown in Fig. 3.

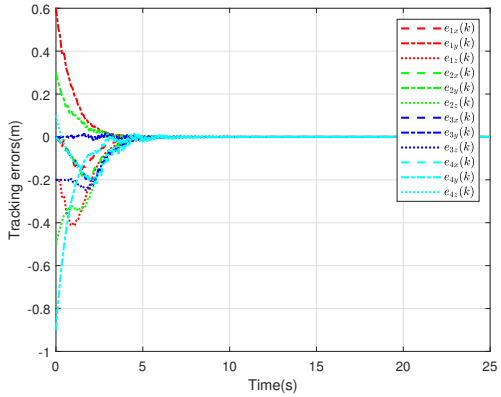

Fig. 2: Tracking errors of each agent.

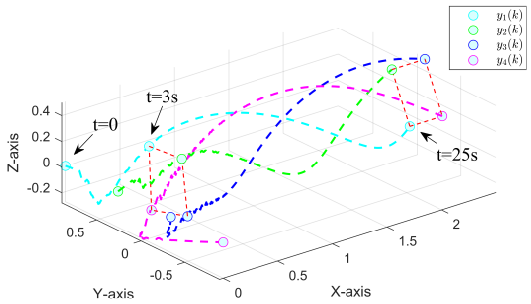

Fig. 3: Trajectory of each agent.

5 Conclusion

This paper considers the formation problem of discrete multi-agent systems under communication disturbance. Based on the cooperative output regulation framework, we incorporate a disturbed output based discrete filter observer, which can minimize network information exchange and mitigate disturbance effects. Finally, the effectiveness of the control strategy is demonstrated through numerical simulations.

References

[1] Oh K K, Park M C, Ahn H S, A survey of multi-agent formation control, *Automatica*, 2015, 53: 424–440.

[2] Liu Y, Bucknall R, A survey of formation control and motion planning of multiple unmanned vehicles, *Robotica*, 2018, 36(7): 1019–1047.

[3] Yu H, Zeng Z, Guo C, Coordinated formation control of discrete-time autonomous underwater vehicles under alterable communication topology with time-varying delay, *Journal of Marine Science and Engineering*, 2022, 10(6): 712.

[4] He L, Zhang J, Hou Y, et al., Time-varying formation control for second-order discrete-time multi-agent systems with switching topologies and nonuniform communication delays, *IEEE Access*, 2019, 7: 65379–65389.

[5] Xu C, Li B, Yuan Y, Disturbance observer-based robust formation-containment of discrete-time multiagent systems with exogenous disturbances, *Complexity*, 2021, 2021: 1–11.

[6] Xu S, Wang B, Noisy information based formation control of multi-agent systems in time-varying communication networks, *IEEE Access*, 2021, 9: 70313–70321.

[7] Huang J, Nonlinear output regulation: theory and applications, *Society for Industrial and Applied Mathematics*, 2004.

[8] Gao H, Li W, Cai H, Fully distributed robust formation flying control of drones swarm based on minimal virtual leader information, *Drones*, 2022, 6(10): 266.

[9] Hua Y, Dong X, Li Q, et al., Distributed adaptive formation tracking for heterogeneous multiagent systems with multiple nonidentical leaders and without wellinformed follower, *International Journal of Robust and Nonlinear Control*, 2020, 30(6): 2131–2151.

[10] Li W, Cai Y, Gao H, Hierarchical formation by the cooperative output regulation approach, in *Proceedings of 2021 5th Chinese Conference on Swarm Intelligence and Cooperative Control*, 2022: 651–660.

[11] Li S, Zhang J, Li X, et al., Formation control of heterogeneous discrete-time nonlinear multi-agent systems with uncertainties, *IEEE Transactions on Industrial Electronics*, 2017, 64(6): 4730–4740.

[12] Yan Y, Huang J, Cooperative output regulation of discrete-time linear time-delay multi-agent systems, *IET Control Theory Applications*, 2016, 1016: 2019–2026.

[13] Su Y, Huang J, Cooperative output regulation of linear multi-agent systems, *IEEE Transactions on Automatic Control*, 2011, 57(4): 1062–1066.

[14] Cai H, Lewis F L, Hu G, et al., The adaptive distributed observer approach to the cooperative output regulation of linear multi-agent systems, *Automatica*, 2017, 75: 299–305.

[15] Cai H, Huang J, Output based adaptive distributed output observer for leader-follower multiagent systems, *Automatica*, 2021, 125: 109413.

[16] Huang J, The cooperative output regulation problem of discrete-time linear multi-agent systems by the adaptive distributed observer, *IEEE Transactions on Automatic Control*, 2016, 62(4): 1979–1984.

[17] Liu J, Huang J, A spectral property of a graph matrix and its application to the leader-following consensus of discrete-time multiagent systems, *IEEE Transactions on Automatic Control*, 2018, 64(6): 2583–2589.

[18] Lu M, A sensory feedback based discrete distributed observer to cooperative output regulation, *IEEE Transactions on Automatic Control*, 2022, 67(9): 4762–4769.

[19] Li X, Xu S, Gao H, et al., Distributed tracking of leader-follower multiagent systems subject to disturbed leaders information, *IEEE Access*, 2020, 8: 227970–227981.

[20] Katayama T, On the matrix Riccati equation for linear systems with random gain, *IEEE Transactions on Automatic Control*, 1976, 21(5): 770–771.

Proceedings of the 3rd Conference on Fully Actuated System Theory and Applications
May 10-12, 2024, Shenzhen, China

Safety Deep Reinforcement Learning Approach to Voltage Control in Flexible Network Topologies

Yaoming Deng[1,2], Min Zhou[2], Minghua Chen[2], Zaiyue Yang[1]

1. Southern University of Science and Technology, ShenZhen, China
E-mail: yangzy3@sustech.edu.cn

2. City University of Hong Kong, Hong Kong SAR, China
E-mail: Yaoming.Deng@my.cityu.edu.hk

Abstract: Recently, Deep Reinforcement Learning (DRL) methods have become increasingly common in voltage control problems of power distribution systems. However, existing DRL methods either lack a theoretical guarantee of voltage stability or cannot maintain their optimality when the network topology changes. This paper proposes a DRL algorithm based on Multi-Agent Twin Delayed Deep Deterministic Policy Gradient (MATD3) framework, Flexible-MATD3, which can maintain the system stability and optimality even when the topology and impedance parameters change. We proposed a partial monotonic neural network to constrain the policy search space of our DRL algorithm so that our policy can always guarantee safety. In addition, the experimental results show that Flexible-MATD3 achieves better performance than the baseline controllers for different network topologies and line impedance parameters without retraining the neural network.

Key Words: Reinforcement Learning, Distribution system, Voltage control, Lyapunov stability

1 Introduction

Voltage stability is important for electric distribution systems, as it directly affects the quality and reliability of the power supply to end-users. A distribution system must maintain an adequate and stable voltage level to ensure that electrical equipment operates efficiently and safely. Moreover, voltage instability can lead to voltage collapse, which is a severe condition where the voltage drops to a point where the system cannot continue to operate [1]. Therefore, the voltage control problem is one of the critical problems in the electricity distribution system.

In recent modern power system, distributed energy resources (DERs) is increasing rapidly, such as distributed generation (DG) units, energy storage systems (ESS), plug-in electric vehicle (PEV). Due to the more and more complex power distribution networks, conventional voltage regulation methods based on on-load tap changing transformers, capacitor banks, and voltage regulators may fail to respond to the rapid and possibly large fluctuations. DERs may frequently disconnect or connect to the power grid, which leads to a change in the topology of the distribution system. In addition, the topology of the distribution network can also be altered due to equipment or line failures, as well as routine maintenance and repair work.

Recently, RL has become a powerful control method in voltage control problems [2]. One common approach is single agent reinforcement learning, where the entire distribution system is treated as a single system, and a centralized method is employed to regulate voltage level at all the controllable buses. For example, in [3] , [4]. Another prevalent method is multi-agent reinforcement learning [5–9]. Articles [5] and [9] divide the power system network into several sub-regions and treats each sub-region as a RL agent, so that they can reduce the agent number and solve the problem efficiently.

One significant drawback of these RL-based methods is that they are tailored to specific network topology. When the topology of power distribution system changes, they require retraining their neural network to ensure policy optimality. Another drawback is that voltage stability is very important in distribution networks, but general RL algorithms cannot guarantee the stability of the control system.

To tackle this challenge, we propose a DRL approach based on the multi-agent Twin Delayed DDPG (TD3) framework. Additionally, we leverage the Lyapunov stability theory to devise a partially monotonic neural network that constrains the search space of the DRL controller. This constraint ensures both safety and robustness of our controller under flexible distribution system topologies.

The main contributions of our paper are:

1) We propose a multi-agent RL algorithm based on the MATD3 framework, which embeds topology information to achieve optimal policy learning under varying topology conditions.
2) We use Lyapunov stability theory to constrain our DRL controller so that it can guarantee the stability of the system voltage. This provides a theoretical guarantee that our distribution network system can be safe under different topology conditions.
3) Compared to baseline controllers, the experimental results on a 56-bus distribution system show that our algorithm is robust to variation in topology and line impedance, and has better performance than other algorithms in the cases of topology changes.

1.1 Related Works

Lyapunov stability theory is a powerful framework to analyze the stability in nonlinear control systems, and was first introduced into reinforcement learning in [10]. However, finding a suitable Lyapunov function for a specific system is not a straightforward task. Some articles like [11, 12] attempted to address this challenge by seeking Lyapunov functions applicable to general systems. [11] proposed a set of Lyapunov function based on the constraint cost function of a CMDPs, so that they can find the safety optimal policy. [12] learned the dynamics model and Lyapunov function jointly by neural network architectures. These works made signifi-

cant contributions to Lyapunov safety RL for general control systems. However, the emphasis of our work remains on ensuring the safety of voltage control problems in distribution systems.

Due to the importance of safety in the distribution system, when using the RL method in voltage control, many recent works have considered safety [3, 4, 13, 14]. [4] introduced a safe layer by using a sensitivity matrix to prevent violations of the voltage constraint. Another approach called CSAC was proposed in [3], which uses the maximum-entropy RL framework and multipliers to solve the constraint optimization problem. The Limitation of these two works was that their methods could not guarantee the hard constraint of voltage, especially during their training process. To address this issue, [13] and [14] use the eigenvalues analysis of Jacobian and Lyapunov stability theory, respectively, to ensure the asymptotic stability of the closed-loop voltage control system. However, the previously mentioned methods can only provide a suboptimal result in a fixed topology in the distribution system. When the system topology changes, they must retrain their neural network to maintain their optimality.

2 MODEL AND PROBLEM FORMULATION

We review the definition and formulation of the branch flow model of the power distribution system and use this framework to build our main problem in this section.

2.1 Branch Flow Model

We use a radial network to represent the power distribution system, which can be considered as a tree graph $G = \{\mathcal{N}, \mathcal{E}\}$, where $\mathcal{N}$ are the buses and pair $(i, j) \in \mathcal{E}$ denote the lines in the system. The buses are indexed by $i = 0, 1, ..., n$, where bus 0 is the substation and other buses represent branch bus. Normally, the complex voltage V_0 at substation bus 0 was fixed at the nominal value. $I_{i,j}$ is the complex current flowing from buses i to j, and $z_{ij} = r_{ij} + \mathbf{i}x_{ij}$ is the complex impedance on line (i, j), where r_{ij} is the resistance and x_{ij} is the reactance. $S_{ij} = P_{ij} + \mathbf{i}Q_{ij}$ is the complex power flowing from buses i to j, where P_{ij} is the active power and Q_{ij} is the reactive power. On bus i, let V_i represent the complex voltage and $s_i = p_i + \mathbf{i}q_i$ represent the complex power injection.

Following [15], the branch flow model can be written as follows,

$$P_{ij} = -p_j + \sum_{k:(j,k)\in\mathcal{E}} P_{jk} + r_{ij}\ell_{ij} \tag{1a}$$

$$Q_{ij} = -q_j + \sum_{k:(j,k)\in\mathcal{E}} Q_{jk} + x_{ij}\ell_{ij} \tag{1b}$$

$$v_j = v_i - 2(r_{ij}P_{ij} + x_{ij}Q_{ij}) + (r_{ij}^2 + x_{ij}^2)\ell_{ij} \tag{1c}$$

$$\ell_{ij} = \frac{P_{ij}^2 + Q_{ij}^2}{V_i} \tag{1d}$$

where $\ell_{ij} := |I_{ij}|^2$, $v_i := |V_i|^2$. Eq (1a) and (1b) represent the active power and reactive power conservation law at bus j. Eq (1c) represents the voltage drop on line ij due to the impedance.

From [16], if we neglect the higher order active and reactive power loss terms, setting $\ell_{ij} = 0$, then we can write the model in a compact formulation:

$$v - v_0 = Rp + Xq$$

and the matrices R and X satisfy the following lemma,

Lemma 1. *[16] $x_{ij}, r_{ij} > 0$ is satisfied in real world power system, then X and R are symmetric positive definite matrices and all elements in X, R are positive.*

Before introducing our main problem, we first give the definition of voltage stability formally,

Definition 1. *(Voltage stability). The closed loop system is stable if for any $\mathbf{v}^{env}$ and $\mathbf{v}(0)$, we have $\mathbf{v}(t)$ converges to the set $S_v = \{\mathbf{v} \in \mathbb{R}^n : \underline{v}_i \le v_i \le \bar{v}_i\}$ in the sense that $\lim_{t\to\infty} \mathrm{dist}\,(\mathbf{v}(t), S_v) = 0$ and the distance is defined as $\mathrm{dist}\,(\mathbf{v}(t), S_v) = \min_{\mathbf{v}'\in S_v} \|\mathbf{v}(t) - \mathbf{v}'\|$.*

2.2 Optimal Control Problem

Our main goal is to design an NN-based nonlinear controller to maintain the system voltage within a acceptable range $[v_{min}, v_{max}]$. Meanwhile, we hope the total cost of voltage violation and control output can be minimized. The optimal control problem can be formulated as follows,

$$\min \int_{t=0}^{\infty} \gamma^t \sum_{i=1}^{n} c_i\left(v_i(t), u_i(t)\right) dt \tag{2a}$$

$$\text{s.t.} \quad v_t - v_0 = Rp + Xq_t \tag{2b}$$

$$u_i(t) = \dot{q}_i(t) \tag{2c}$$

$$\text{Voltage stability as Def. 1 holds} \tag{2d}$$

In this optimal control problem, the total cost 2a can be divided into two parts: the cost of voltage deviation and the cost of control switch. In our experiments, we consider $c_i\left(v_i(t), u_i(t)\right) = \alpha_1(u_i(t))^2 + \alpha_2(v_i(t) - v_0)^2$, where α_1, α_2 are trade-off coefficients to adjust the final performance of our controller. The objective is to minimize the total cost in a infinite time steps with discount γ . Eq (2b) represents the dynamic of distribution system, which was concluded by the Branch Flow Model in prior section. We define our controller as the rate of reactive power change in (2c).

By embedding the topology information, the NN controller can be formulated as,

$$u_i(t) = \dot{q}_i(t) = g_{\theta_i}(v_t, x_t)$$

where g_{θ_i} is our neural network, and the input is the voltage v_t on each bus at time t and the matrix x_t with respect to the reactance information.

3 CONTROLLER DESIGN

In this section, we propose the main approach to solve the constrained optimal control problem in a multi-agent TD3 framework. We embed the topology and impedance information into our controller input and utilize Lyapunov stability analysis in our NN structure design. In the next section, we will show how we use the Lyapunov analysis result to guide the NN controller design.

3.1 Topology and Impedance Change

To formulate the topology change of the distribution system, we consider using the line reactance parameters to reflect these changes. Due to the tree structure of the power system, we can first consider a topology that fully connects to all the buses. With this method, we can formulate all the changeable lines in a vector $S_0 = [x_1, x_2, ..., x_n]$. Then we disconnect some of the lines to change the topology. That is, if the line is connected, we denote it using the value of x_i, otherwise, we can use 0 to denote it.

Furthermore, the reactance in practice will increase to infinity when the line is disconnected, which may not match the value 0 in our previous definition. Therefore, we use the susceptance value B_i in our statement and the topology information can be written as $S = [B_1, B_2, ..., B_n]$. With this formulation, we can represent the line connection situation using a continuous value $B_i \in [0, \infty]$.

3.2 Multi Agent TD3 framework

The dynamic system in the optimal control problem (2) can be described as a Markov Decision Process (MDP), and each controller g_{θ_i} on photovoltaic (PV) station is treated as a control agent. Therefore, we propose a multi-agent deep reinforcement learning algorithm (MADRL) to solve this problem. As the control variable $q_i(t)$ at each PV station is in continuous state space, we can apply the Deep Deterministic Policy Gradient (DDPG) method to handle it. However, the original DDPG suffers from a major drawback: overestimation bias. To overcome these issues and improve the performance of DDPG, we consider a Multi-Agent Twin Delayed DDPG (MATD3) framework to solve our optimal control problem (2). As our algorithm fully considers the topology change in the distribution system, we name our method Flexible-MATD3.

In reinforcement learning, the goal is to find the best control policy that can maximize the return of the agents interacting with environment. Here, we define the reward of ith agent as its negative cost in (2a), that is, $r_t^i = -c_i(v_i(t), u_i(t))$ with $u_i(t) = g_{\theta_i}(v_t, x_t)$. Then the return with discount in time t is $R_t^i = \sum_{i=t}^{\infty} \gamma^{i-t} r_t^i(v_i(t), u_i(t))$.

The objective of this RL problem is to maximize the expected return $J(\theta_i) = \mathbb{E}[R_0^i]$. To achieve this target, the policy parameters θ_i can be updated through the deterministic policy gradient method [17],

$$\nabla\left(J(\theta_i)\right) = \mathbb{E}\left[\nabla_{u_i} Q_{\phi_i}(v_i, u_i)\Big|_{u_i(t)=g_{\theta_i}(v_t,x_t)} \nabla_{\theta_i} g_{\theta_i}(v_t, x_t)\right] \tag{3}$$

where $Q_{\phi_i}(v_i, u_i)$ is the critic network (a.k.a. value function) and $g_{\theta_i}(v_t, x_t)$ is the actor network in this actor-critic method. We employ (3) to update the parameters in the actor network g_{θ_i}. The value funciton $Q_{\phi_i}(v_i, u_i)$ can be learned by utilizing temporal difference learning,

$$Q_{\phi_i(v_i,u_i)} = r + \gamma \mathbb{E}_{v_i', u_i'}\left[Q_{\phi_i}(v_i', g_{\theta_i}(v_i', x_i'))\right] \tag{4}$$

where $(v_i', u_i' = g_{\theta_i}(v_i', x_i'))$ is the system state and action transmitting from the previous state-action pair (v_i, u_i).

To enhance the performance of DDPG, we introduce the TD3 [18] technique into our RL framework. Compared with the standard DDPG, the enhanced TD3 framework has three main improvements as follows.

Clipped Double-Q Learning. In contrast to DDPG, which learns only a single Q value function, TD3 concurrently learns two Q functions $Q_{\phi_i^1}$ and $Q_{\phi_i^2}$. After calculating these two Q values, we choose the smaller one to update our target:

$$y_i = r + \gamma(1-d) \min_{j=1,2} Q_{\phi_i^j}(v_i', g_{\theta_i}(v_i', x_i')) \tag{5}$$

Using this update rule, we can effectively reduce the overestimation problem in target value.

Target Policy Smoothing. In DDPG, if there are incorrect sharp peaks in some deterministic policies, the policy may overfit those narrow peaks and then have brittle actions. Therefore, we introduce a regularization strategy in the exploration procedure by adding a small amount of random noise to the target policy as follows,

$$u_i'(v_i', x_i') = \text{clip}\left(u_{\theta_{\text{tar}}}(v_i', x_i') + \text{clip}(\epsilon, -d, d), u_{\text{low}}, u_{\text{high}}\right), \quad \epsilon \sim \mathcal{N}(0, \sigma) \tag{6}$$

In (6), the added noise is sampled from a mean-zero Gaussian set $\epsilon \sim \mathcal{N}(0, \sigma)$.

Delayed Policy Updates. In TD3, the frequency of policy update is less than that of the value function network. It can reduce the volatility of the value estimate and lead to more stable and efficient learning. In addition, it can avoid repeating policy updates with respect to an unchanged critic, which may result in poor or divergent behaviour.

3.3 Lyapunov Guarantee Stability

One main issue in the standard MATD3 method is that the controller $u_i = g_{\theta_i}(v_t, x_t)$ derived iteratively from (3) may not guarantee system stability during the training process. Moreover, there is a lack of theoretical guarantees that the converged policy at the terminal will fulfil the safety constraint in (2d).

In order to satisfy the system safety, we apply Lyapunov stability theory to restrict the search space of the learning policy. Thus, we have the following theorem:

Theorem 1. *For any topology $|x_t| \leq M$ satisfied Lemma 1, suppose the controller $g_{\theta_i}(v_t, x_t)$ is a continuously differentiable function and satisfy 1) $g_{\theta_i}(v_t, x_t) = 0$ only in $v_i \in [\underline{v}_i, \bar{v}_i]$. 2) $\frac{\partial g_\theta(v_t, x_t)}{\partial v_t} \leq -\frac{\alpha}{2M}$ on $(-\infty, \underline{v}_i]$ and $[\bar{v}_i, \infty)$. Then the closed-loop system in* (2) *is asymptotically exponential stability.*

Due to page limitation, the proof of Theorem 1 is omitted here. If we can constrain our controller $g_{\theta_i}(v_t, x_t)$ to satisfy the requirements in Theorem 1, the voltage magnitude of each bus is stable as stated Definition 1.

4 Neural Network model Design

In this section, we will demonstrate how to design the neural network structure to fulfil the requirement of Lyapunov stability in the preceding section.

Our neural network function must satisfy the following requirements:

1) When $v \in [\underline{v}, \bar{v}]$, the controller $g_\theta(v, x) = 0$.

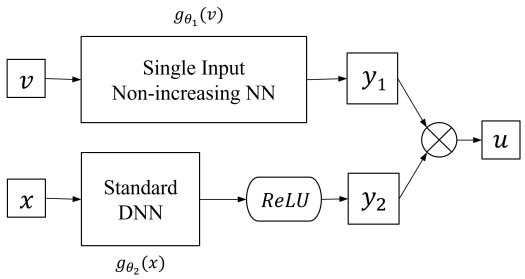

Fig. 1: The structure of neural network design

2) When $(-\infty, \underline{v}_i]$ and $[\bar{v}_i, \infty)$, the partial derivative $\frac{\partial g_\theta(v,x)}{\partial v} \leq -\frac{\alpha}{2M}$.

As shown in Fig. 1, the structure of our NN model is divided into two main parts, the non-increasing single-in single-out neural network $g_{\theta_1}(v)$ and a fully connected standard neural network $g_{\theta_2}(x)$ with non-negative output.

The first part of our neural network, $g_{\theta_1}(v)$, is a non-increasing function through the origin with a dead zone $v \in [\underline{v}, \bar{v}]$, which is designed following the structure in [19]. More specifically, to keep the function going through origin, $g_{\theta_1}(v)$ is decomposed into positive and negative parts as follows,

$$g_{\theta_1}(v) = g^+_{\theta_1}(v - \bar{v}) + g^-_{\theta_1}(v + \underline{v}) \tag{7}$$

In our neural network design, $g^+_{\theta_1}(\cdot)$ and $g^-_{\theta_1}(\cdot)$ is constructed by a single hidden layer with m hidden units and the ReLU activation function as follows,

$$g^+_{\theta_1}(v) = (\boldsymbol{w}^+)^T \,\mathrm{ReLU}(\mathbf{1}v + \boldsymbol{b}^+) \tag{8a}$$
$$g^-_{\theta_1}(v) = (\boldsymbol{w}^-)^T \,\mathrm{ReLU}(-\mathbf{1}v + \boldsymbol{b}^-) \tag{8b}$$

where $\{\boldsymbol{w}^+, \boldsymbol{b}^+, \boldsymbol{w}^-, \boldsymbol{b}^-\}$ are the parameters need to train in the neural network.

In addition, to satisfy requirement 2), we constrain the parameters as follows,

$$\sum_{i=1}^{l} w^+ \geq k, \qquad \forall l = 1, 2, \ldots, m$$
$$b^+_1 = 0, b^+_l \leq b^+_{l-1}, \quad \forall l = 2, 3, \ldots, m$$

and

$$\sum_{i=1}^{l} w^- \leq -k, \qquad \forall l = 1, 2, \ldots, m$$
$$b^-_1 = 0, b^-_l \leq b^-_{l-1}, \quad \forall l = 2, 3, \ldots, m$$

where $k = \dfrac{\alpha}{2M}$ is associated with $\alpha-$exponential stability and the upper bound of topology parameters M.

The second part is the positive standard NN. The output of this subnetwork need to satisfy $g_{\theta_2}(x) \geq 1$. Therefore, we use a shift ReLU activation function $max(1, x)$ in the output layer.

5 Experiments

To verify the safety and effectiveness of our flexible TD3 method, we apply our method to 56 bus systems.

5.1 Simulation Setup

We use Pandapower [20] to calculate the power flow and simulate the distribution system and all the experiments are implemented on a laptop with AMD R7-4800HS CPU and Nvidia RTX-2060 (Max-Q) GPU.

We follow the 56 bus distribution system in [14, 21]. There are 5 generations of PV in this power system, located on buses 18, 21, 20, 45, and 53. We use these PV generators as our control agents. That is, we adjust the reactive power q in these PV stations. The schematic diagram of this system is showed in Figure 5.1. In this system, the nominal voltage magnitude is 12 KV, and the acceptable ranges voltage is $\pm 5\%$ of the nominal value, i.e., $[11.4kV, 12.6kV]$. The objective is to drive the voltage magnitude to this range in the shortest amount of time.

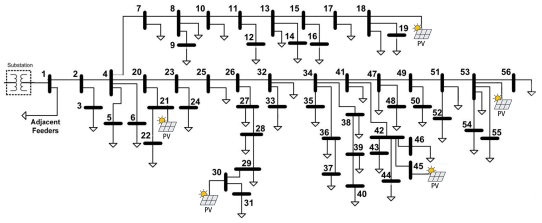

Fig. 2: Schematic diagram of 56 bus distribution systems

5.1.1 Topology change

We first consider a fully connected original tree structure network to simulate different topology situations. During the training process, we randomly disconnect some bus connections to generate diverse topology scenarios. Additionally, in each training step, we will change the line impedances by uniformly sampling from the range $[0.5, 1.5]$ of the original value. Through this method, the value of each line impedance used to represent topology information are sampled from the set $\{0\} \cup \{x \mid 0.5 \leq x \leq 1.5\}$.

5.1.2 Baseline Controller

To illustrate the performance of our flexible-MATD3 algorithm under changing topologies, we compare two baseline controllers. The first is the dead-band linear policy controller, which can guarantee stability but may not achieve the optimal control cost. Due to its simplicity and efficiency, the linear controller is widely applied in the power system [22]. The linear controller is defined as follows:

$$u_i(v_i) = -\epsilon([v_i - \underline{v}_i]^+ - [\bar{v}_i - v_i]^+)$$

where ϵ is a tunable parameter and $[*]^+$ is defined as $[a]^+ = \max(a, 0)$.

Another approach is the safety-DDPG form [14], which guarantees stability and performs better than the linear controller in a static topology scenario.

5.2 Testing result of 56 bus system

To analyze the performance of our Flexible-MATD3 controller and the baseline controllers, we simulate 300 different initial scenarios, including all high-voltage buses, all low-voltage buses and a mix of high-voltage and low-voltage

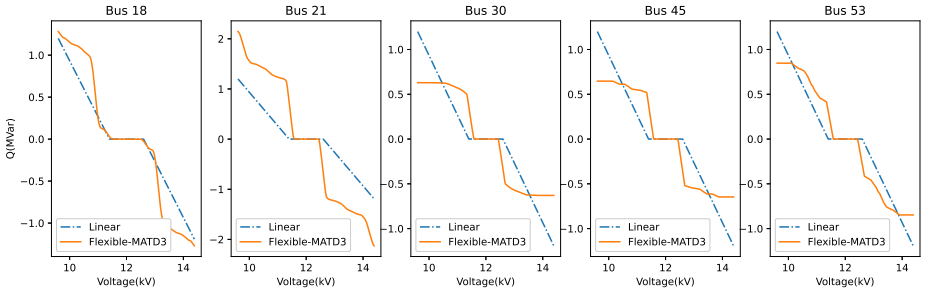

Fig. 3: The input-output relationship between change in reactive power and voltage with a fixed topology.

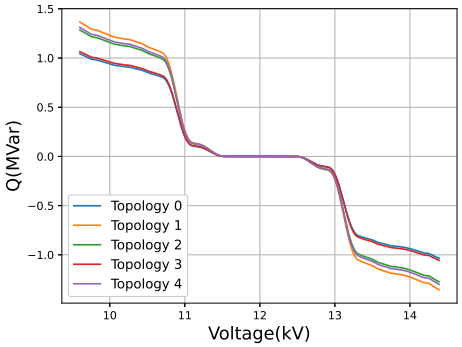

Fig. 4: Control policy at bus 18 with different topology

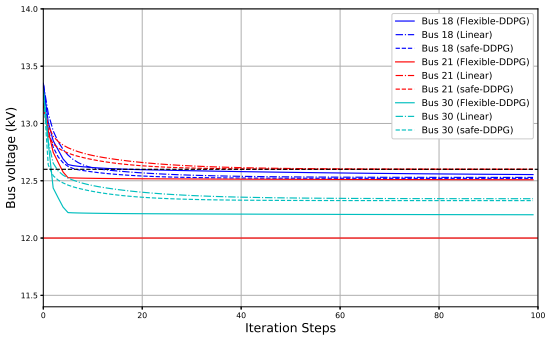

Fig. 5: Voltage trajectory in high voltage scenario

buses. In high voltage scenarios, the PV generators will generate high active power to simulate the daytime scenario with abundant sunshine and lead to a high voltage at all buses. In low voltage scenarios, the active power generation at each PV station will be less but the load is heavy, to simulate the scenario at dusk or evening. Finally, we consider a mix situation that some buses are at high voltage due to the high generation and some buses may be at low voltage due to the heavy load. At the beginning of each testing episode, we randomly change the topology and impedance of the distribution system, as mentioned in section 5.1.1. Excluding the branches connecting from PV stations to the root substation, there are a total of 18 switchable lines in this 56-bus system, which means we have 2^{18} possible topologies. All the initial voltage deviation is set to 5% to 15% of the nominal voltage magnitude and the goal is to drive the voltage within $\pm 5\%$ of the nominal value.

Before comparing the performance between our algorithm and baseline controller, we first visualize our control policy in a fixed topology as shown in Fig. 3, to illustrate how our controller maintains the monotonicity between voltage magnitude and reactive power output. In this scenario, we fix the topology of the 56-bus system and do not change the parameters of the line impedance. The input-output curve of the linear controller is drawn as a reference in Fig. 3. With this monotone guarantee, our neural network can satisfy the requirement of Lyapunov stability.

Fig. 4 selects bus 18 as an example, to illustrate how the policy changes in distinct topology scenarios. The Flexible-MATD3 controller exhibits diversity across various topologies, which allows our controller to learn the optimal policy to adapt to topology changes.

Table 1 is the performance result of different controllers. The voltage recovery time shows that all the controllers can adjust the voltage to the safe range within certain time steps, which means that all the testing controllers can guarantee stability of the distribution system. Due to the nonlinearity, the performance of Safe-DDPG and Flexible-MATD3 is better than the simple linear controller. In addition, our Flexible-MATD3 controller has the property of exponential stability and it can maintain better optimality under topology changes. Therefore, Flexible-MATD3 has the smallest mean and standard variance of voltage recovery time. Compared to safe-DDPG, the Flexible-MATD3 restore the voltage to the normal range in less than half the time, which is only 9.72 time steps on average. It is worth mentioning that the standard deviation of Flexible-MATD3 under different initialization conditions is far lower than that of other two controllers. This indicates that our method has better consistency when facing the topology changes. The overall reactive power consumption of Flexible-MATD3 is lowest during the recovery stage due to the faster response time. The objective cost (2a) in our experiments is set to $(u_i(t))^2 + 100(v_i(t) - v_0)^2$. In this setting, Flexible-MATD3 has the lowest objective cost.

Fig. 5 shows the voltage trajectory adjusted by different controllers in a high voltage scenario. This provides us with an intuitive visualization of the voltage regulation process of three different controllers. Compared to Linear and Safe-DDPG controllers, Flexible-MATD3 can drive the voltage back to safe voltage range more quickly. Furthermore, due to our proper reward and cost setting, Flexible-MATD3 can adjust the voltage closer to the nominal voltage, $12KV$, when the system was in a final stable state.

Table 1: Performance of different controllers in 56-bus system

	Voltage recovery time (steps)		Reactive power cost (MVar)		Objective cost	
Method	Mean	Std	Mean	Std	Mean	Std
Linear	38.69	30.62	172.16	289.74	20.56	32.16
Safe-DDPG	23.74	22.76	113.28	201.52	13.55	22.50
Flexiable-MATD3	**9.72**	**9.19**	**31.22**	**40.28**	**5.01**	**5.34**

6 Conclusion

In conclusion, in this paper, we propose a DRL voltage controller, Flexible-MATD3, for the flexible topology changes in the power distribution network. The proposed controller can not only maintain the safety of the system voltage but also keep strong robustness to topology and line impedance changes. We use Lyapunov stability theory to theoretically prove that the closed-loop system using Flexible-MATD3 controller is exponential asymptotically stable. Finally, the simulation results show that the neural network of our DRL controller can maintain good performance without retraining under the topology and line impedance changes of the distribution network.

Future work could include finding better partial monotonic neural network structures to improve the performance of our controller, or enhancing the efficiency and scalability of our method to enable its deployment in real-world power systems.

References

[1] H. Haes Alhelou, M. E. Hamedani-Golshan, T. C. Njenda, and P. Siano, "A survey on power system blackout and cascading events: Research motivations and challenges," *Energies*, vol. 12, no. 4, p. 682, 2019.

[2] X. Chen, G. Qu, Y. Tang, S. Low, and N. Li, "Reinforcement learning for selective key applications in power systems: Recent advances and future challenges," *IEEE Transactions on Smart Grid*, vol. 13, no. 4, pp. 2935–2958, 2022.

[3] W. Wang, N. Yu, Y. Gao, and J. Shi, "Safe off-policy deep reinforcement learning algorithm for volt-var control in power distribution systems," *IEEE Transactions on Smart Grid*, vol. 11, no. 4, pp. 3008–3018, 2019.

[4] P. Kou, D. Liang, C. Wang, Z. Wu, and L. Gao, "Safe deep reinforcement learning-based constrained optimal control scheme for active distribution networks," *Applied energy*, vol. 264, p. 114772, 2020.

[5] S. Wang, J. Duan, D. Shi, C. Xu, H. Li, R. Diao, and Z. Wang, "A data-driven multi-agent autonomous voltage control framework using deep reinforcement learning," *IEEE Transactions on Power Systems*, vol. 35, no. 6, pp. 4644–4654, 2020.

[6] D. Cao, J. Zhao, W. Hu, F. Ding, Q. Huang, and Z. Chen, "Attention enabled multi-agent drl for decentralized volt-var control of active distribution system using pv inverters and svcs," *IEEE transactions on sustainable energy*, vol. 12, no. 3, pp. 1582–1592, 2021.

[7] D. Hu, Z. Ye, Y. Gao, Z. Ye, Y. Peng, and N. Yu, "Multi-agent deep reinforcement learning for voltage control with coordinated active and reactive power optimization," *IEEE Transactions on Smart Grid*, vol. 13, no. 6, pp. 4873–4886, 2022.

[8] C. Mu, Z. Liu, J. Yan, H. Jia, and X. Zhang, "Graph multi-agent reinforcement learning for inverter-based active voltage control," *IEEE Transactions on Smart Grid*, 2023.

[9] D. Cao, J. Zhao, W. Hu, F. Ding, Q. Huang, Z. Chen, and F. Blaabjerg, "Data-driven multi-agent deep reinforcement learning for distribution system decentralized voltage control with high penetration of pvs," *IEEE Transactions on Smart Grid*, vol. 12, no. 5, pp. 4137–4150, 2021.

[10] T. J. Perkins and A. G. Barto, "Lyapunov design for safe reinforcement learning," *Journal of Machine Learning Research*, vol. 3, no. Dec, pp. 803–832, 2002.

[11] Y. Chow, O. Nachum, E. Duenez-Guzman, and M. Ghavamzadeh, "A lyapunov-based approach to safe reinforcement learning," *Advances in neural information processing systems*, vol. 31, 2018.

[12] J. Z. Kolter and G. Manek, "Learning stable deep dynamics models," *Advances in neural information processing systems*, vol. 32, 2019.

[13] W. Cui, J. Li, and B. Zhang, "Decentralized safe reinforcement learning for voltage control," *arXiv preprint arXiv:2110.01126*, 2021.

[14] Y. Shi, G. Qu, S. Low, A. Anandkumar, and A. Wierman, "Stability constrained reinforcement learning for real-time voltage control," in *2022 American Control Conference (ACC)*. IEEE, 2022, pp. 2715–2721.

[15] M. E. Baran and F. F. Wu, "Optimal capacitor placement on radial distribution systems," *IEEE Transactions on power Delivery*, vol. 4, no. 1, pp. 725–734, 1989.

[16] M. Farivar, L. Chen, and S. Low, "Equilibrium and dynamics of local voltage control in distribution systems," in *52nd IEEE Conference on Decision and Control*. IEEE, 2013, pp. 4329–4334.

[17] D. Silver, G. Lever, N. Heess, T. Degris, D. Wierstra, and M. Riedmiller, "Deterministic policy gradient algorithms," in *International conference on machine learning*. Pmlr, 2014, pp. 387–395.

[18] S. Fujimoto, H. Hoof, and D. Meger, "Addressing function approximation error in actor-critic methods," in *International conference on machine learning*. PMLR, 2018, pp. 1587–1596.

[19] W. Cui, Y. Jiang, and B. Zhang, "Reinforcement learning for optimal primary frequency control: A lyapunov approach," *IEEE Transactions on Power Systems*, vol. 38, no. 2, pp. 1676–1688, 2022.

[20] L. Thurner, A. Scheidler, F. Schäfer, J. Menke, J. Dollichon, F. Meier, S. Meinecke, and M. Braun, "pandapower — an open-source python tool for convenient modeling, analysis, and optimization of electric power systems," *IEEE Transactions on Power Systems*, vol. 33, no. 6, pp. 6510–6521, Nov 2018.

[21] M. Farivar, R. Neal, C. Clarke, and S. Low, "Optimal inverter var control in distribution systems with high pv penetration," in *2012 IEEE Power and Energy Society general meeting*. IEEE, 2012, pp. 1–7.

[22] N. Li, G. Qu, and M. Dahleh, "Real-time decentralized voltage control in distribution networks," in *2014 52nd Annual Allerton Conference on Communication, Control, and Computing (Allerton)*. IEEE, 2014, pp. 582–588.

Proceedings of the 3rd Conference on Fully Actuated System Theory and Applications
May 10-12, 2024, Shenzhen, China

Robust Operation of Distribution Systems with Uncertain Renewable Generation via Energy Sharing

Meng Yang[1], Yue Chen*[1]

1. Department of Mechanical and Automation Engineering, The Chinese University of Hong Kong, Sha Tin, NT, Hong Kong SAR
E-mail: yuechen@cuhk.edu.hk

Abstract: The distribution power system is facing increasingly severe uncertainty due to the widespread adoption of renewable energy sources. Fortunately, flexible distributed energy resources (DERs) such as electric vehicles and energy storage offer potential solutions to this challenge when effectively coordinated. In this paper, we propose an energy sharing based demand response initiative to coordinate the DERs, which is then embedded in a two-stage robust operation model. The energy sharing scheme employs a generic supply-demand function that reveals prosumers' preferences. The DERs participating in energy sharing play a Nash game. The existence and uniqueness of the Nash equilibrium are theoretically proven. The proposed energy sharing scheme is compared with the traditional individual and the centralized schemes. Theoretical analysis and case studies demonstrate the promising features of energy sharing for the robust operation of distribution systems with uncertain renewable generation.

Key Words: uncertainty, renewable generation, energy sharing, robust operation

1 Introduction

Nowadays, exploiting renewable energy such as wind and solar power is considered as an efficient way to reduce the dependence on fossil energy and alleviate environmental pollution [1]. In 2023, the global wind power capacity had reached 906 GW, with an increase of 9% compared to 2022 [2]. However, due to its intermittence and fluctuation, high penetration of renewable energy exacerbates the difficulty of maintaining power system security and reliability [3]. Hence, robust system operation under uncertainty has captured great attention during the past decade.

Typical optimization approaches coping with uncertainty mainly include stochastic optimization (SO) and robust optimization (RO). SO makes assumptions on the distribution of uncertain factors and optimizes the expected cost or satisfies certain chance constraints [4]. It may face two main technical difficulties: the exact probability distribution of uncertainty is hard to obtain, and the computational burden grows significantly with the increase of the scale of system and the size of scenario samples [5]. In contrast, RO describes the random factor through an uncertainty set, which is easier to implement. In view of its simplicity, RO has been widely adopted in various power system operation problems, including unit commitment [6], energy and reserve dispatch [7], and optimal power flow [8], to name a few.

In all the aforementioned studies, the power system is operating in a two-stage framework: in the day-ahead stage, the system operator decides on the outputs of all units, aiming to minimize the expected total cost; then in the real-time stage, after observing the exact power outputs of renewable generators, the operator solves another central optimization problem to determine the optimal adjustments of generating units. This operation manner works well for power transmission systems. However, very few generators in a distribution system are fully dispatchable, except for small-capacity gas-fired units owned by the system operator. Considering that the real-time adjustment is usually small, a straightforward idea is that: in day-ahead, a set point is given by the system operator, and in real-time, individual prosumers in the distribution system are self-balanced without a central coordinator. In this situation, how to recover the global optimal operating strategy by solving subproblems associated with individual prosumers turns to be the main issue, which has been extensively studied in the context of distributed optimization [9, 10]. However, traditional distributed optimization essentially serves as a computation technique, which does not provide substantial incentives to attract prosumers to participate in coordination, especially when the prosumers could gain more profit by altering their strategies.

In this paper, a generic supply-demand function based sharing scheme is proposed to balance generation and demand in real-time, which can be naturally embedded into the second stage of RO. Particularly, a well-designed sharing scheme is desired to process three features: each prosumer can choose either to buy or to sell freely; the sharing market is cleared with a reasonable equilibrium price; all prosumers have the incentive to take part in the sharing market. Recent studies on energy sharing can be divided into three categories: 1) *Two-sided market based energy sharing.* The status of each participant, which means whether it is a supplier or a buyer, is predetermined. The sharing market clearing price was characterized in [11]. The efficiency of the sharing market under the goal of revenue maximization and social welfare maximization was compared in [12]. 2) *Single-side market based energy sharing with set prices.* The statuses of participants are symmetric and the sharing prices are set by a coordinator via solving a Stackelberg game. A supply-demand ratio based pricing algorithm was adopted in [13] for the energy sharing in photovoltaic (PV) prosumers. Renewable generation uncertainty was incorporated in [14]. 3) *Single-side market based energy sharing with reallocation.* Instead of a price-guided allocation, the profit is distributed according to specific reallocation schemes. A cost reallocation approach was developed for a group of energy storage, leading to a cooperative game [15]. The profit distribution among aggregators and demand-side energy resource (DER) was presented in [16].

Different from existing works, in this paper, energy shar-

ing servers as a real-time re-balance measure in robust operation of distribution systems which is associated with the day-ahead set point problem. To this end, a sharing scheme is built on a generic supply-demand function, which enables transactive energy exchange among individual prosumers in real time. The scheme is carefully designed to fully unleash the flexibility endowed by responsive demands and energy transaction, while requiring no additional investment on generation or storage facilities. The scheme also exhibits nice properties. The sharing market clearance comes down to a Nash game whose equilibrium is theoretically proven to be existent and unique. According to the manner of real-time energy balancing, three robust operation models are compared and discussed. The economic efficiency and system security (dispatchable) regions under different models are revealed.

The rest of this paper is organized as follows. Mathematical formulations of robust system operation are presented in Section 2. The procedure of the generic supply-demand function based energy sharing scheme is illustrated in Section 3, following which theoretical properties of the sharing game is revealed. Advantages of the proposed sharing scheme are analyzed from three perspectives in Section 4. Illustrative examples are performed in Section 5. Finally, conclusions are summarized in Section 6.

2 Mathematic Formulation

2.1 Problem Description

Assume there are a collection of gas-fired thermal generators (TGs) indexed by $i \in \mathcal{I} = \{1, 2, ..., I\}$ and a set of distributed generators (DGs) indexed by $j \in \mathcal{J} = \{1, 2, ..., J\}$ whose output are uncertain and depend on the weather conditions. In the day-ahead stage, the operator decides on the outputs of TGs $p_i, \forall i$ and their adjustable ranges $r_i, \forall i$ according to the predicted outputs of DGs $w_j^0, \forall j$ and load forecasts $D_q, \forall q$. The outputs of DG w_j are uncertain, which may vary within an uncertainty set. As the system resides in a distribution network level, AC power flow based network constraint is taken into account. Then in the real-time stage, when the exact outputs of DGs are revealed, the outputs of TGs are adjusted by $\Delta p_i, \forall i$ within the adjustable ranges $r_i, \forall i$ so as to maintain power balancing. To this end, the operator solves the following robust optimization problem:

$$\min_{p_i, r_i, \forall i} \sum_{i\in\mathcal{I}}(c_i p_i^2 + d_i p_i + s_i r_i) + \max_{w\in W} \sum_{i\in\mathcal{I}} (l_i \Delta p_i^2(p, r, w)) \quad (1a)$$

$$\text{s.t. } \underline{P}_i \le p_i - r_i,\ p_i + r_i \le \overline{P}_i, \forall i \quad (1b)$$

$$P_{mn}^2 + Q_{mn}^2 = l_{mn} v_m, \forall m \to n \quad (1c)$$

$$v_m - v_n = 2(R_{mn} P_{mn} + X_{mn} Q_{mn}) - (R_{mn}^2 + X_{mn}^2) l_{mn}, \forall m \to n \quad (1d)$$

$$P_{in,n} = \sum_{k:n\to k} P_{nk} - (P_{mn} - l_{mn} R_{mn}), \forall m \to n \quad (1e)$$

$$Q_{in,n} = \sum_{k:n\to k} Q_{nk} - (Q_{mn} - l_{mn} X_{mn}), \forall m \to n \quad (1f)$$

$$P_{in,n} = \sum_{i\in\mathcal{I}^n} p_i + \sum_{j\in\mathcal{J}^n} w_j^0 - \sum_{q\in\mathcal{Q}^n} D_q \quad (1g)$$

$$\underline{v}_m \le v_m \le \overline{v}_m, \forall m; l_{mn} \ge 0, \forall mn \quad (1h)$$

$$\underline{P}_{mn} \le P_{mn} \le \overline{P}_{mn},\ \underline{Q}_{mn} \le Q_{mn} \le \overline{Q}_{mn}, \forall mn \quad (1i)$$

The objective function $\Pi(p, r, w, \Delta p)$[1] is to minimize the total cost, including the day-ahead stage cost $s(p, r) := \sum_i (c_i p_i^2 + d_i p_i + s_i r_i)$ and the real-time adjustment cost $f(\Delta p(p, r, w)) := \sum_i (l_i \Delta p_i^2)$ in worst case scenario $w \in W$; $\Delta p_i(p, r, w), \forall i$ are the optimal adjustments which will be elaborated in the next subsection; c_i, d_i, s_i and l_i are constant coefficients. Constrain (1b) limits the capacity of thermal units. $\underline{P}_i$ and $\overline{P}_i$ are the lower/upper bounds, respectively. Constraints (1c)-(1g) state the branch flow model of a radial power distribution network, where P_{mn} and Q_{mn} are the active/reactive power of line mn; l_{mn} is the line current square; v_m is the voltage magnitude square at bus m; R_{mn} and X_{mn} are the resistance/reactance of line mn; $P_{in,n}$ and $Q_{in,n}$ are the active/reactive power injection at bus n; $\mathcal{I}^n$ is the set of TGs connected to bus n, $\mathcal{J}^n$ is the set of DGs connected to bus n, $\mathcal{Q}^n$ is the set of loads connected to bus n. $\underline{v}_m$ and $\overline{v}_m$ in constraint (1h) are the upper/lower bound of v_m, respectively. In constraint (1i), $\underline{P}_{mn}$ and $\overline{P}_{mn}$ are the upper/lower bound of P_{mn}; $\underline{Q}_{mn}$ and $\overline{Q}_{mn}$ are the upper/lower bound of Q_{mn}.

2.2 Second-stage Problem

Given the first-stage decision variables p, r and real-time DG outputs $w_j, \forall j$, TGs adjust their output by $\Delta p_i, \forall i$ to maintain power balancing. In this section, we consider three schemes shown in Fig.1.

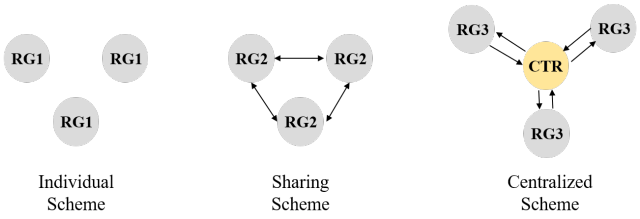

Fig. 1: Sketch of three schemes

Individual Scheme (IND): Under the individual scheme, partition balancing strategy is adopted, which means the whole distribution network is divided into several small regions, and each region includes one prosumer, who has one DG, some TGs and loads. Each prosumer endeavors to maintain power balancing locally by adjusting TGs' output without inter-region energy transaction. In such circumstance, the second-stage problem reads

$$\min_{\Delta p_i, \forall i\in\mathcal{I}_j} \sum_{i\in\mathcal{I}_j} (l_i \Delta p_i^2) \quad (2a)$$

$$\text{s.t. } -r_i \le \Delta p_i \le r_i, \forall i \in \mathcal{I}_j \quad (2b)$$

$$\sum_{i\in\mathcal{I}_j} (p_i + \Delta p_i) + w_j = \sum_{q\in\mathcal{Q}_j} D_q \quad (2c)$$

where $\mathcal{I}_j$ and $\mathcal{Q}_j$ are the sets of TGs and loads in region j, and $l_i, \forall i$ are cost parameters. The objective function aims to minimize TG adjustment costs, which is denoted as $y_{IND}^j(p, r, w, \Delta p)$. Constraint (2c) represents self-balancing in region j. The feasible region of this second-stage problem is denoted as $Y_{IND}(p, r, w) := \{\Delta p_i, \forall i : \text{s.t. (2b), (2c) are satisfied}, \forall j\}$.

[1] Given a collection of x_i for i in a certain set A, x denotes the vector $x := (x_i, i \in A)$ of a proper dimension with x_i as its components

Sharing Market Scheme (SMK): A sharing market is established. If a prosumer takes part in the sharing market, it can change TGs' outputs and exchange energy with other prosumers [20]. At this time, the second-stage problem becomes

$$\min_{b_j,\Delta p_i,\forall i\in\mathcal{I}_j} \sum_{i\in\mathcal{I}_j}(l_i\Delta p_i^2)+u_j(\lambda(b),q_j(b,\lambda)) \quad (3a)$$

$$\text{s.t.} \quad -r_i\le\Delta p_i\le r_i,\forall i\in\mathcal{I}_j:\rho_i^{\pm} \quad (3b)$$

$$\sum_{i\in\mathcal{I}_j}(p_i+\Delta p_i)+w_j+q_j(b,\lambda)=\sum_{q\in\mathcal{Q}_j}D_q:\mu_j \quad (3c)$$

The objective function is denoted as $y^j_{SMK}(p,r,w,\Delta p)$, which is the sum of adjustment cost and payment/revenue from sharing. $\rho_i^{\pm}$ and μ_j are the dual variables accordingly. b_j is prosumer j's bid, reflecting his willingness to buy and $b:=(b_j,\forall j)$. The clearing price $\lambda(b)$ is decided by all prosumers' bids. $q_j(b,\lambda)$ is the amount of power it get from the sharing platform, which can be either positive (stands for purchase) or negative (stands for sell). The second term $u_j(\lambda(b),q_j(b,\lambda))$ in the objective function is the payment/revenue of region j, which is influenced by the clearing price $\lambda(b)$ and $q_j(b,\lambda)$. The sharing platform solves the following market clearing condition and gives λ and q_j back to each prosumer j.

$$\sum_{j\in\mathcal{J}}q_j(b,\lambda(b))=0:\eta_j \quad (4)$$

The key of sharing mechanism design is to determine the bidding procedure as well as the energy and revenue allocation function $q_j(.)$,$u_j(.)$. The feasible region of the sharing game is denoted as $Y_{SMK}(p,r,w):=\{\Delta p_i,\forall i:\exists b_j,\forall j,\text{s.t. (3b), (3c), (4) are satisfied},\forall j\}$.

Centralized Scheme (CTR): In this scheme, the system operator solves a centralized optimization problem and determines the optimal adjustment of each TG

$$\min_{\Delta p_{it},\forall i\in\mathcal{I}} \sum_{i\in\mathcal{I}}(l_i\Delta p_i^2) \quad (5a)$$

$$\text{s.t.} \quad -r_i\le\Delta p_i\le r_i,\forall i \quad (5b)$$

$$\sum_{i\in\mathcal{I}}(p_i+\Delta p_i)+\sum_{j\in\mathcal{J}}w_j=\sum_{q\in\mathcal{Q}}D_q \quad (5c)$$

The objective function under CTR is denoted as $y^j_{CTR}(p,r,w,\Delta p)$. The feasible region of this problem is denoted as $Y_{CTR}(p,r,w):=\{\Delta p_i,\forall i:\text{s.t. (5b), (5c) are satisfied},\forall j\}$. Clearly, the CTR scheme can achieve the lowest total cost. The IND scheme adopts a regional self-balancing strategy, which does not need the system operator to coordinate in real-time, but the system flexibility may not be fully motivated. To this end, the purpose of this paper is to design a proper SMK scheme, so that the total cost approaches the cost under the centralized scheme without a real-time central coordinator.

3 A Generic Supply-demand Function-based Sharing Scheme

In this section, a generic supply-demand function based sharing scheme is proposed and some properties of the sharing game are characterized.

3.1 Procedure of the Sharing Scheme

The demand (or supply) function of prosumer j can be expressed by

$$q_j=-a\lambda+b_j \quad (6)$$

where the given $a>0$ represents price elasticity; λ is the market clearing price and b_j reflects prosumer j's willingness to buy. (6) shows that when the sharing price increases, the prosumer wants to buy less from the sharing market. The sharing market is cleared following three steps.

Step 1: Each prosumer j bids a b_j to the sharing platform and the sharing clearing price is given by the clearing condition $\sum_j q_j=0$, which means

$$\lambda=\sum_j b_j/(J\times a)$$

Step 2: The amount of power that prosumer j gets/sells is $q_j(b,\lambda)=-a\lambda(b)+b_j$. If $q_j>0$, this prosumer buys power from the sharing market; otherwise, if $q_j<0$, this prosumer sells power to the sharing market.

Step 3: If $q_j>0$, prosumer j pay $\lambda(b)q_j(b)$ to the sharing market. Otherwise, if $q_j<0$, prosumer j obtains $-\lambda(b)q_j(b)$ from the sharing market.

Under this SMK scheme, in the second-stage problem (3), $q_j=-a\lambda+b_j$, $u_j=(-a\lambda+b_j)\lambda$. Then because $\sum_j u_j=\lambda\sum_j q_j=0$, the SMK scheme is budget-balance. Due to the common constraint (4), problem (3) constitutes a Nash game consisting of the following elements: 1) the set of regions/prosumers $\mathcal{J}=\{1,2,...,J\}$; 2) action sets $A_j(b_{-j}),\forall j$ and the strategy space $A=\prod_j A_j$; 3) cost functions $y^j_{SMK}(\Delta p_j,b_j,b_{-j}),\forall j$. To simplify, $\mathcal{G}=\{\mathcal{J},A,y_{SMK}\}$ is used here to denote the sharing game (3) in its abstract form.

3.2 Properties of the Sharing Game

Definition 1 *(Nash Equlibrium) A strategy profile $(\Delta p^*,b^*)\in A$ is a Nash Equilibrium (NE) of the sharing game $\mathcal{G}=\{\mathcal{J},A,y_{SMK}\}$ defined by* (3)*, if $\forall j\in\mathcal{J}$*

$$y^j_{SMK}(\Delta p_j^*,b_j^*,b_{-j}^*)\le y^j_{SMK}(\Delta p_j,b_j,b_{-j}^*),\forall(\Delta p_j,b_j)\in A_j(b_{-j}) \quad (7)$$

Given Δp, define $\hat{\lambda}(\Delta p):=\frac{1}{J}\sum_j\frac{1}{I_j}\sum_{i\in\mathcal{I}_j}(2l_i\Delta p_i-\delta_j^-+\delta_j^+)$ and $\hat{b}_j(\Delta p):=\sum_{q\in\mathcal{Q}_j}D_q-\sum_{i\in\mathcal{I}_j}(p_i+\Delta p_i)-w_j+a\lambda(\Delta p)$. I_j is the size of set $\mathcal{I}_j$, δ_j^+ and δ_j^- are the dual variables defined below.

Proposition 1 *A unique NE $(\Delta p^*,b^*)$ for the sharing game* (3) *exists if and only if, $\forall j\in\mathcal{J}$, Δp_j^* is the unique solution of:*

$$\min_{\Delta p_i,\forall i\in\mathcal{I}} \sum_{i\in\mathcal{I}}(l_i\Delta p_i^2)+\frac{\sum_{j\in\mathcal{J}}(\sum_{q\in\mathcal{Q}_j}D_q-w_j-\sum_{i\in\mathcal{I}_j}p_i-\sum_{i\in\mathcal{I}_j}\Delta p_i)^2}{2a(J-1)} \quad (8a)$$

$$\text{s.t.} \quad -r_i\le\Delta p_i\le r_i,\forall i:\delta_i^{\pm} \quad (8b)$$

$$\sum_{i\in\mathcal{I}}(p_i+\Delta p_i)+\sum_{j\in\mathcal{J}}w_j=\sum_{q\in\mathcal{Q}}D_q:\epsilon \quad (8c)$$

and $b_j^* = \hat{b}_j$

Proposition 2 *A unique NE* $(\Delta p^*, b^*)$ *for the sharing game* (3) *exists if and only if* $Y_{SMK}(p, r, w) \neq \emptyset$.

Proposition 3 *Given the first-stage strategy* (p, r) *and uncertain scenario* w*, let* $\Delta\tilde{p}$ *be the optimal solution under IND scheme, and* $(\Delta p^*, b^*)$ *be the NE of the sharing game. We have*

$$y_{SMK}^j(p, r, w, \Delta p^*) \leq y_{IND}^j(p, r, w, \Delta\tilde{p}) \tag{9}$$

The proof of Proposition 1-3 can be found in [17]. Proposition 1 tells that an equilibrium always exists under the proposed SMK scheme and offers us an easier way to compute and analyze the NE. Proposition 2 is a corollary of Proposition 1. Proposition 3 shows that all prosumers are willing to take part in sharing and a Pareto improvement can be achieved, which means the cost of each prosumer is reduced.

4 Properties of the Robust Operation Models

Let $(\bar{p}, \bar{r})$ be the optimal solution under CTR scheme, $\bar{w} \in W$ is the worst-case scenario and $\Delta\bar{p}$ is the corresponding second-stage variable, which is a function of $\bar{p}$, $\bar{r}$ and $\bar{w}$. $\Pi_{CTR}(\bar{p}, \bar{r}, \Delta\bar{p})$ is the optimal value of the first-stage objective function. Similarly, let (p^*, r^*) be the optimal solution under SMK scheme, w^* is the worst-case scenario and Δp^* is the corresponding second-stage variable, which is a function of p^*, r^*, w^*. $\Pi_{SMK}(p^*, r^*, \Delta p^*)$ is the optimal value of the first-stage objective function. Let $(\tilde{p}, \tilde{r})$ be the optimal solution under IND scheme, $\tilde{w}$ is the worst-case scenario and $\Delta\tilde{p}$ is the corresponding second-stage variable, which is a function of $\tilde{p}, \tilde{r}, \tilde{w}$. $\Pi_{IND}(\tilde{p}, \tilde{r}, \Delta\tilde{p})$ is the optimal value of the first-stage objective function.

4.1 Cost of Energy Balancing

Proposition 4 *Given the first-stage variable* (p, r) *and the scenario* w*, we have*

$$\begin{aligned} & \Pi_{CTR}(p, r, \Delta\bar{p}(p, r, w)) \\ \leq\ & \Pi_{SMK}(p, r, \Delta p^*(p, r, w)) \\ \leq\ & \Pi_{IND}(p, r, \Delta\tilde{p}(p, r, w)) \end{aligned}$$

Proof. Given the first-stage variable (p, r), the operating cost $s(p, r)$ are the same among three schemes, so we only need to compare the adjustment costs $f_{CTR}(\Delta\bar{p})$, $f_{SMK}(\Delta p^*)$, $f_{IND}(\Delta\tilde{p})$.

First, we have

$$\begin{aligned} \sum_j y_{SMK}^j(p, r, w, \Delta p^*) &= \sum_i l_i(\Delta p_i^*)^2 + \sum_j u_j^* \\ &= \sum_i l_i(\Delta p_i^*)^2 = f_{SMK}(\Delta p^*) \end{aligned}$$

and $\sum_j y_{IND}^j(p, r, w, \Delta p^*) = f_{IND}(\Delta\tilde{p})$. According to Proposition 3, we have

$$\sum_j y_{SMK}^j(p, r, w, \Delta p^*) \leq \sum_j y_{IND}^j(p, r, w, \Delta\tilde{p})$$

which implies $f_{SMK}(\Delta p^*) \leq f_{IND}(\Delta\tilde{p})$.

Meanwhile, the constraints of (5) and (8) are the same, which means Δp^* is a feasible solution of (5). Because $\Delta\bar{p}$ is the optimal solution of problem (5), so we have

$$f_{CTR}(\Delta\bar{p}) \leq f_{SMK}(\Delta p^*)$$

This completes the proof. ■

Proposition 4 tells us that in the real-time stage, with fixed first-stage decisions and the exact DG outputs, the adjustment cost of SMK scheme is in-between the IND scheme and CTR scheme.

Proposition 5 *Let* $(\Delta p^*(a), b^*(a))$ *be the unique NE of* (3) *with the price elasticity of value* a*. Then* $f_{SMK}(\Delta p^*)$ *is decreasing in* a*.*

The proof of proposition 5 can be found in [17]. It implies that the performance of the SMK scheme can be improved if prosumers are more sensitive to the price.

4.2 Ability to Accommodate Uncertainty

Given the first-stage strategies (p, r), the system can accommodate uncertain scenario w when under IND scheme/CTR scheme, there exists an adjustment Δp; under SMK scheme, there exists an NE. According to Proposition 2, the existence of NE is equivalent to the nonnullity of set $Y_{SMK}(p, r, w)$. To this end, a unified definition can be given to the dispatchable region as follows.

Definition 2 *(Dispatchable region) [18] Given the first-stage strategies* (p, r)*, the dispatchable region of* (p, r) *is defined as*

$$W^D(p, r) := \{w \in \mathbb{R}^J : Y(p, r, w) \neq \emptyset\}$$

A given uncertainty set W *is dispatchable under* (p, r) *when and only when* $W \subset W^D(p, r)$*. We show that the system flexibility is maintained under SMK scheme by giving the following proposition.*

Proposition 6 *Given the first-stage strategy* (p, r)*, the following relation holds for dispatchable regions under SMK, CTR and IND schemes*

$$W_{CTR}^D(p, r) = W_{SMK}^D(p, r) \supset W_{IND}^D(p, r)$$

Proof. Given (p, r), if scenario $w \in W_{CTR}^D(p, r)$, it means that there exists an $\Delta p \in Y_{CTR}(p, r, w)$. Under the SMK scheme proposed in Section III, let $b_j := \sum_{q \in \mathcal{Q}_j} D_q - \sum_{i \in \mathcal{I}_j}(p_i + \Delta p_i) - w_j$ and $\lambda = 0$. Then it is easy to check $\Delta p \in Y_{SMK}(p, r, w)$, which means $w \in W_{SMK}^D(p, r)$. If scenario $w \in W_{SMK}^D(p, r)$, it means there eixits an $\Delta p \in Y_{SMK}(p, r, w)$. With Δp, (3b) is met and so as (5b). Sum up (3c) for all j and together with (4), it is easy to obtain that (5c) is satisfied,indicating that $w \in W_{CTR}^D(p, r)$.

Obviously, we have $Y_{IND}(p, r, w) \subset Y_{CTR}(p, r, w)$. As a result, if scenario $w \in W_{IND}^D(p, r)$, and there exists an $\Delta p \in Y_{IND}(p, r, w)$, we must have $\Delta p \in Y_{CTR}(p, r, w)$, so that $w \in W_{CTR}^D(p, r)$. But the opposite is not necessarily true. This completes the proof. ■

Proposition 6 shows that with a fixed first-stage strategy, the sharing and centralized schemes can accommodate the same amount of uncertainty, which means the system flexibility is the same.

4.3 Total Cost in the Worst-Case Scenario

In this section, the total system operation costs under worst case $\Pi(p, r, w, \Delta p)$ are compared.

Proposition 7 *The following relation holds*

$$\begin{aligned} & \Pi_{CTR}(\bar{p}, \bar{r}, \Delta\bar{p}(\bar{p}, \bar{r}, \bar{w})) \\ \leq\ & \Pi_{SMK}(p^*, r^*, \Delta p^*(p^*, r^*, w^*)) \\ \leq\ & \Pi_{IND}(\tilde{p}, \tilde{r}, \Delta\tilde{p}(\tilde{p}, \tilde{r}, \tilde{w})) \end{aligned} \tag{10}$$

Moreover, $\Pi_{SMK}(p^*,r^*,\Delta p^*(p^*,r^*,w^*))$ *is decreasing in* a.

Proposition 7 shows that the cost of CTR scheme is the lowest, IND scheme is the highest, while SMK scheme is in-between. The detailed proof can be found in [17].

In summary, compared with the CTR scheme, the proposed SMK scheme can maintain fully system flexibility while sacrificing economy slightly. Moreover, it can be implemented in a distributed manner with no central coordinator. Compared with the IND scheme, the proposed SMK scheme can enhance both the system flexibility and the operational economic efficiency.

5 Numerical Experiments

In this section, numerical experiments on the modified IEEE-33 system are shown to demonstrate theoretical results. The topology of the test system is shown in Fig.2. An uncertainty set W considering spatial smoothing effect [7] is chosen as (11). A polyhedral outer approximation based method is adopted to linearize the AC branch flow model [19]. The column and constraint generation (C&CG) algorithm [21] is used to solve the robust model iteratively.

$$\begin{aligned} W \quad = \quad & \{\underline{W}_j \leq w_j \leq \overline{W}_j, \forall j \\ & \sum_{j\in\mathcal{J}} \frac{|w_j - w_j^e|}{w_j^h} \leq \Gamma \\ & w_j^e = 0.5(\underline{W}_j + \overline{W}_j), \forall j \\ & w_j^h = 0.5(\overline{W}_j - \underline{W}_j), \forall j\} \end{aligned} \tag{11}$$

where $\underline{W}_j$,$\overline{W}_j$ are the lower/upper bound of the uncertain output of DG j, respectively. w_j^e is the median of the uncertainty set, which usually equals the predicted value w_j^0. w_j^h is the error range. Γ is the uncertain budget.

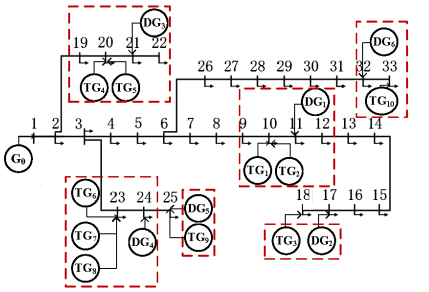

Fig. 2: Topology of the test system

5.1 Benchmark Case

The simplest case is taken first as a benchmark. The predicted DG output $w^0 = [20, 10, 15, 20, 30, 20]$kW and $\underline{W} = 0.55w^0$, $\overline{W} = 1.45w^0$. Complete system data can be found in [17]. The optimal total costs, operating costs and adjustment costs under IND, SMK and CTR schemes as well as the relative cost differences [2] are shown in Table 1.

Table 1: Optimal solution under IND, SMK and CTR

Scheme	IND	SMK	CTR
Total cost $\Pi(p, r, w, \Delta p)$	523.09	502.28	501.53
Operating cost $s(p, r)$	495.46	492.06	500.57
Adjustment cost $f(\Delta p)$	27.63	10.26	9.56
Relative cost difference	4.30%	0.15%	-

From Table 1 we can find that, the second-stage adjustment cost under IND is the highest (27.63), CTR is the lowest (9.56) and SMK is in-between (10.26), which is in consistence with Proposition 4. Similarly, the total cost shows the same relationship as stated in Proposition 7. The relative cost difference between IND and CTR is 4.30% while that between SMK and CTR is just 0.15%, showing that the proposed sharing scheme can achieve a near optimal cost in a distributed manner.

5.2 Tests on flexibility

Fix the first-stage variable (p, r) of three robust models to the optimal solution in the benchmark case $(\tilde{p}, \tilde{r})$, (p^*, r^*) and $(\bar{p}, \bar{r})$, respectively. Expand the uncertainty set to 1.0, 1.2, 1,4, 1.6, 1.8, 2.0 times of its original range. Pick up 200 scenarios randomly from each uncertainty set and the probability that the scenario can be accommodated, which is denoted as *pass rate*, are shown in Table 2. In our cases, the variances of pass rate under 200 scenarios are less than 0.1%, showing that 200 scenarios is enough.

Table 2: Optimal solution under IND, SMK and CTR

Pass Rate %	1.0	1.2	1.4	1.6	1.8	2.0
IND	100	52	29	11.5	7	4
SMK	100	99	97	92.5	90	79.5
CTR	100	99	97	92.5	90	79.5

When the uncertainty set is chosen as the original one, the pass rates under all schemes are 100%, showing the robustness of the obtained first-stage solutions. When the uncertainty set is enlarged, the pass rates under all schemes decrease, but the pass rate of SMK and CTR are always larger than that of IND. The pass rate of SMK and CTR are the same for all cases, verifying Proposition 6. This tells us that the proposed sharing scheme can maintain the flexibility of the power system under centralized operation.

5.3 Impact of Uncertainty

The impact of uncertainty on optimal cost is tested in this section. We change the uncertainty set W from 1.0 to 2.0 times of its original size and the total costs under three schemes are shown in Fig.3. We can find that, for each uncertainty set, the total costs under three schemes always satisfy $\Pi_{CTR} \leq \Pi_{SMK} \leq \Pi_{IND}$ and the SMK scheme can achieve a near optimal total cost. When the size of uncertainty set increases, which means the uncertainty is more se-

[2] The relative cost difference of IND is $(\Pi_{IND} - \Pi_{CTR})/\Pi_{CTR}$; the relative cost difference of SMK is $(\Pi_{SMK} - \Pi_{CTR})/\Pi_{CTR}$.

vere for the system, all three schemes need to spend more money to maintain system security, but the growing rate of SMK and CTR are much less than of IND.

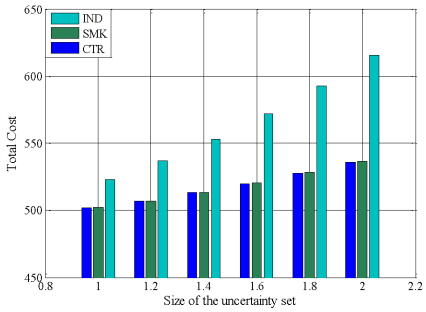

Fig. 3: Total costs of three schemes under different levels of uncertainty

6 Conclusion

This paper establishes a generic supply-demand function based energy sharing scheme and incorporates it into a two-stage robust system operation model. The Nash game formulation for market clearing and the uniqueness of Nash equilibrium are discussed. The proposed sharing scheme is compared with other two energy transaction schemes from three aspects: First, we show that the second-stage adjustment cost corresponding to the sharing scheme is in-between the individual scheme and centralized scheme. Secondly, under the sharing scheme, the system possesses the same (better) ability to mitigate uncertainty compared to the case in which the centralized (individual) scheme is adopted. Lastly, for the total operation cost, the sharing scheme still has a middling performance and approaches the global optimal when the price elasticity increases. Nonetheless, from the case studies we can observe that the gap between centralized and sharing schemes is actually very small, so we believe the sharing market could be a promising initiative for future distribution systems. Although the sharing based robust model is devised for the economic dispatch problem in this paper, it presents a basic framework for coordination problem of multiple participants under uncertainty.

Acknowledgement

This work was supported by the National Natural Science Foundation of China under Grant No. 52307144 and the Shun Hing Institute of Advanced Engineering, the Chinese University of Hong Kong, through Project RNE-p2-23 (Grant No. 8115071).

References

[1] O. Ellabban, H. Abu-Rub, and F. Blaabjerg, Renewable energy resources: Current status, future prospects and their enabling technology, *Renewable and Sustainable Energy Reviews*, 39, 748–764, 2014.

[2] "Global status of wind power," Global Wind Energy Council, [Online] Available:, https://gwec.net/globalwindreport2023/.

[3] H. Nosair and F. Bouffard, Reconstructing operating reserve: Flexibility for sustainable power systems, *IEEE Trans. on Sustainable Energy*, 6(4), 1624–1637, 2015.

[4] Y. Zou, Y. Xu, and C. Zhang, A risk-averse adaptive stochastic optimization method for transactive energy management of a multi-energy microgrid, *IEEE Trans. on Sustainable Energy*, 14(3), 1599-1611, 2023.

[5] E. Gil, I. Aravena, and R. Cardenas, Generation capacity expansion planning under hydro uncertainty using stochastic mixed integer programming and scenario reduction, *IEEE Trans. on Power Systems*, 30(4), 1838–1847, 2015.

[6] W. Wang, A. Danandeh, B. Buckley, and B. Zeng, Two-stage robust unit commitment problem with complex temperature and demand uncertainties, *IEEE Trans. on Power Systems*, 39(1), 909–920, 2024.

[7] Y. Chen, W. Wei, Robust generation dispatch with strategic renewable power curtailment and decision-dependent uncertainty, *IEEE Trans. on Power Systems*, 38(5), 4640–4654, 2023.

[8] T. Ding, Z. Bie, L. Bai, and F. Li, Adjustable robust optimal power flow with the price of robustness for large-scale power systems, *IET Generation, Transmission & Distribution*, 10(1), 164–174, 2016.

[9] L. Du, S. Grijalva, and R. G. Harley, Game-theoretic formulation of power dispatch with guaranteed convergence and prioritized best response, *IEEE Trans. on Sustainable Energy*, 6(1), 51–59, 2015.

[10] Y. Liang, F. Liu, and S. Mei, Distributed real-time economic dispatch in smart grids: a state-based potential game approach, *IEEE Trans. on Smart Grid*, 9(5), 4194–4208, 2018.

[11] T. Tanaka, N. Li, and K. Uchida, On the relationship between the VCG mechanism and market clearing, *2018 Annual American Control Conference (ACC)*, 2018: 4597–4603.

[12] Z. Fang, L. Huang, and A. Wierman, Prices and subsidies in the sharing economy, in *Proceedings of the 26th International Conference on World Wide Web. International World Wide Web Conferences Steering Committee*, 2017: 53–62.

[13] N. Liu, X. Yu, C. Wang, C. Li, L. Ma, and J. Lei, Energy-sharing model with price-based demand response for microgrids of peer-to-peer prosumers, *IEEE Trans. on Power Systems*, 32(5), 3569–3583, 2017.

[14] N. Liu, M. Cheng, X. Yu, J. Zhong, and J. Lei, Energy-sharing provider for PV prosumer clusters: A hybrid approach using stochastic programming and stackelberg game, *IEEE Trans. on Industrial Electronics*, 65(8), 6740–6750, 2018.

[15] P. Chakraborty, E. Baeyens, K. Poolla, P. P. Khargonekar, and P. Varaiya, Sharing storage in a smart grid: A coalitional game approach, *IEEE Trans. on Smart Grid*, 10(4), 2379-2390, 2018.

[16] W. Qi, B. Shen, H. Zhang, and Z.-J. M. Shen, Sharing demand-side energy resources-a conceptual design, *Energy*, 135, 455–465, 2017.

[17] [Online] Available:, https://github.com/ym-1998/FASTA2024.

[18] W. Wei, F. Liu, and S. Mei, Dispatchable region of the variable wind generation, *IEEE Trans. on Power Systems*, 30(5), 2755–2765, 2015.

[19] Y. Chen, W. Wei, F. Liu, E. E. Sauma, and S. Mei, Energy trading and market equilibrium in integrated heat-power distribution systems, *IEEE Trans. on Smart Grid*, 10(4), 4080-4094, 2018.

[20] Y. Chen, S. Mei, F. Zhou, Steven H. Low, W. Wei, and F. Liu, An energy sharing game with generalized demand bidding: Model and properties, *IEEE Trans. on Smart Grid*, 11(3), 2055-2066, 2019.

[21] B. Zeng, Solving two-stage robust optimization problems by a constraint-and-column generation method, *University of South Florida, FL, Tech. Rep*, 2011.

Proceedings of the 3rd Conference on Fully Actuated System Theory and Applications
May 10-12, 2024, Shenzhen, China

Influence of algebraic connectivity and out-degree of leader on distributed observer

Xiaobo Zhang[1], Peng Li
1. The School of Mechanical Engineering and Automation Harbin Institute of Technology, Shenzhen, Shenzhen 518071, P. R. China
E-mail: zhangxiaobo2024@163.com
E-mail: lipeng2020@hit.edu.cn

Abstract: In this paper, the connection between the communication network and the consensus speed of the multi-agent cooperative control based on distributed observers is explored. The dynamic of the error is established based on the formulation of the observer. Consequently, two key factors of the graph topology are analyzed in connection to the error convergence. The concept of out-degree is considered along with the Laplacian matrix of the network topology to characterize the convergence features. By analyzing the Lyapunov function under different networks, it has been proven that the consensus speed positively correlates with the algebraic connectivity which is the smallest nonzero eigenvalue of the Laplacian matrix and the leader's out-degree. Finally, the theoretical results are validated through simulation on numerical examples and the application of a unicycle formation, in which the back-stepping control law is adopted.

Key Words: Distributed observer, Consensus speed, Formation control, Algebraic connectivity

1 Introduction

In recent years, the problem of cooperative control on multi-agent systems (MAS) has attracted significant interest from many researchers. Consensus problems [1] serve as the foundation for studying the problem of cooperative control. Distributed observer has emerged as the most widely used approach widely employed to tackle the consensus problem [9]. It has multiple variants in theoretical studies, such as the adaptive distributed observer [7] and the discrete distributed observer [5]. Moreover, they can also be in switching networks [6] or with event-trigger mechanisms [4, 10]. It was initially introduced in [3], where it was used to address the output regulation problem and has been applied to achieve consensus control of euler-lagrange systems [6], micro-grids [11], and multiple rigid body systems [8]. However, the research above rarely mentions the impact of the communication network on the observer's performance.

The consensus speed of MAS is an important performance metric. Typically, research on improving speed focuses on two aspects: enhancing consensus protocols and optimizing communication networks. Early consensus protocols were asymptotically convergent. The improved consensus protocols have been proposed by many researchers, such as finite-time convergence [15] and specified-time convergence [16]. However, in comparison to control protocols, research about improving consensus speed by optimizing communication networks remains relatively scarce. When a consensus protocol is given for multi-agent systems, the consensus speed is determined by the eigenvalues of the Laplacian matrix [17]. In first-order MAS under asymptotically consensus protocols [12, 13], when the network is an undirected graph, the consensus speed is positively correlated with the algebraic connectivity of the network [14]. The algebraic connectivity equals the second smallest eigenvalue of the Laplacian matrix and was initially introduced in [14]. For higher-order MAS, consensus is typically determined by the network's algebraic connectivity and the spectral radius which is the largest eigenvalue of the Laplacian matrix. A larger algebraic connectivity and a smaller spectral radius lead to a faster consensus speed of the system [18, 19]. However, the consensus speed of cooperative control based on the distributed observer [3] is still scarce, especially in exploring the impact of the topology. The main contributions of this article are summarized as

- A direct connection between the Laplacian matrix of the communication network and the consensus speed is established.
- The theoretical results are validated through simulation on numerical examples and the application of a unicycle formation.

2 Preliminary

2.1 Graph theory

To facilitate the description of communication networks in cooperative control problems, some graph theory concepts are reviewed for readers' convenience [2]. Let $\mathcal{G} = (\mathcal{V}, \mathcal{E})$ be the communication-directed graph associated with specific distributed systems, where $\mathcal{V} = \{v_0, \ldots, v_N\}$ is a node-set and $\mathcal{E} = \mathcal{V} \times \mathcal{V}$ is an edge set. The edge (v_i, v_j) in the edge set $\mathcal{E}$ denotes that agent v_i is a neighbor of v_j and v_j can receive information from agent v_i. A directed path from node v_{i_1} to node v_{i_k} is a sequence of ordered edges of form $(v_{i_k}, v_{i_{k+1}}), k = 1, \ldots, l-1$. A directed tree is a spanning tree that connects all nodes in the graph. It signifies the presence of a root node, which is always the leader, connected to all other nodes through a simple path. A graph is considered to have or contain a directed spanning tree if a subset of its edges forms such a tree. The weighted adjacency matrix $\mathbf{A} = [a_{ij}] \in \mathbb{R}^{N\times N}$ of $\mathcal{G}$ is defined as $a_{ii} = 0$; for $i \neq j$, $a_{ij} > 0 \Leftrightarrow (j, i) \in \mathcal{E}$. The Laplacian matrix of $\mathcal{G}$ is defined as $\mathcal{L} = [l_{ij}] \in \mathbb{R}^{N\times N}$, where $l_{ii} = \sum_{j=1}^{N} a_{ij}, l_{ij} = -a_{ij}$ for $i \neq j$. The second smallest eigenvalue of $\mathcal{L}$ is defined as

This work is partly supported by National Natural Science Foundation (NNSF) of China (Grant 62303133 and 62188101) and partly by the Guangdong Basic and Applied Basic Research Foundation (Grant 2021A1515110262, 2022A1515011274).

the algebraic connectivity of $\mathcal{G}$ [14]. The following lemma from [2] is useful in our analysis

Lemma 1 *The Laplacian matrix $\mathcal{L}$ of a directed graph $\mathcal{G}$ has at least one zero eigenvalue with $\mathbf{1}_N$ as a corresponding eigenvector if and only if $\mathcal{G}$ has a directed spanning tree. In addition, there exists a non-negative left eigenvector r of $\mathcal{L}$ associated with the zero eigenvalue, satisfying $r^\top \mathcal{L} = 0$ and $r^\top \mathbf{1}_N = 0$. Moreover, r is unique if $\mathcal{G}$ has a directed spanning tree.*

2.2 Rayleigh theorem

Let $\mathbf{A} \in \mathbb{C}^{n\times n}$ be a Hermitian matrix. Then its eigenvectors are the critical points of the Rayleigh quotient, which is the real function $R : \mathbb{C}^n\backslash\{\mathbf{0}\} \to \mathbb{R}$, one can obtain

$$\lambda_{\min}(\mathbf{A}) \leq \frac{\mathbf{x}^{\mathrm{H}}\mathbf{A}\mathbf{x}}{\mathbf{x}^{\mathrm{H}}\mathbf{x}} \leq \lambda_{\max}(\mathbf{A}), \tag{1}$$

where $\lambda_{\min}(\mathbf{A})$ denotes the minimum eigenvalue and $\lambda_{\max}(\mathbf{A})$ denotes the maximum eigenvalue of $\mathbf{A}$.

3 Problem formulation

3.1 The distributed state observer schema

For a multi-agent system with $N+1$ agents, the following observer schema is introduced. The desired reference signals of the followers are generated by the exosystem called the leader system, transmitted by the communication network. It can be presented as

$$\begin{aligned}\dot{\eta}_i &= \mathbf{S}\eta_i + \mu\left(\sum_{j\in\mathcal{N}_i} a_{ij}\left(\eta_j - \eta_i\right) + a_{i0}(\mathbf{v} - \eta_i)\right),\\ \dot{\mathbf{v}} &= \mathbf{S}\mathbf{v},\end{aligned} \tag{2}$$

where $\mathbf{v} \in \mathbb{R}^p$ denotes the leader's state, $\mathbf{S} \in \mathbb{R}^{p\times p}$ is skew-symmetric and denotes the dynamic matrix of leaders, and $\mu > 0$. The communication network among the multi-agent systems can be described by a directed graph $\mathcal{G}$ with node 0 denoting the leader and node i denoting the followers. The neighbor set of the node i is $\mathcal{N}_i$ and η_i denotes the follower i's estimate of $\mathbf{v}$.

3.2 Error dynamics of the distributed state observer

For convenience, $\mathcal{L}$ denotes the Laplacian matrix of $\mathcal{G}$, $\mathbf{\Delta}$ is an $N \times N$ non-negative diagonal matrix, and $\mathbf{\Delta}_{ii} = a_{i0}, i = 1, \cdots, N$. Then the Laplacian matrix $\mathcal{L}$ of $\mathcal{G}$ can be partitioned as

$$\mathcal{L} = \left(\begin{array}{c|c} \sum_{j=1}^{N} a_{0j} & [a_{01}, \cdots, a_{0N}] \\ \hline -\Delta\mathbf{1}_N & \mathbf{H} \end{array}\right), \tag{3}$$

where $[a_{01}, \cdots, a_{0N}] = [0, \cdots, 0]$, $\sum_{j=1}^{N} a_{0j} = 0$ is the in-degree of leader, the second smallest eigenvalue of $\mathcal{L}$ represents the algebraic connectivity of the topology, and $\mathbf{1}_N$ is $N \times 1$ column vector whose elements are all 1.

By using the Kronecker product and the Laplacian matrix, the aforementioned dynamics (2) can be written into a matrix form

$$\begin{aligned}\dot{\eta} &= \left((\mathbf{I}_N \otimes \mathbf{S}) - \mu(\mathbf{H} \otimes \mathbf{I}_q)\right)\eta + \mu(\mathbf{\Delta} \otimes I_q)\hat{\mathbf{v}},\\ \dot{\hat{\mathbf{v}}} &= (\mathbf{I}_N \otimes \mathbf{S})\hat{\mathbf{v}},\end{aligned} \tag{4}$$

where $\otimes$ denotes the Kronecker product of matrices, q represents the dimensions of the agent's state, $\eta = [\eta_1^\top, \ldots, \eta_N^\top]^\top$, and $\hat{\mathbf{v}} = \mathbf{1}_N \otimes \mathbf{v}$. The estimation error of the ith agent is defined as $e_i = \eta_i - \hat{v}$. It is ensured that the distributed observer (2) with arbitrary initial conditions can achieve consensus leading to $\lim_{t\to\infty} e_i = 0$.

Letting $\mathbf{e} = [e_1, \ldots, e_N]^\top$, the error dynamics can be put in the following form

$$\begin{aligned}\dot{\mathbf{e}} =&((\mathbf{I}_N \otimes \mathbf{S}) - \mu(\mathbf{H} \otimes \mathbf{I}_q))\eta + \\ &\mu(\mathbf{H} \otimes \mathbf{I}_q)\hat{\mathbf{v}} - (\mathbf{I}_N \otimes \mathbf{S})\hat{\mathbf{v}}.\end{aligned} \tag{5}$$

By the fact that $(\mathbf{\Delta} \otimes \mathbf{I}_q)(\mathbf{1}_N \otimes \hat{\mathbf{v}}) = (\mathbf{H} \otimes \mathbf{I}_q)(\mathbf{1}_N \otimes \hat{\mathbf{v}})$, the error dynamics (5) can be written into a compact form (6)

$$\dot{\mathbf{e}} = \mathbf{M}\mathbf{e}, \tag{6}$$

where $\mathbf{M} = (\mathbf{I}_N \otimes \mathbf{S}) - \mu(\mathbf{H} \otimes \mathbf{I}_q)$. The eigenvalues of $\mathbf{M}$ are

$$\lambda(\mathbf{M}) = \lambda_i(\mathbf{S}) - \mu\lambda_j(\mathbf{H}), \tag{7}$$

where $i = 1, \ldots, q$ and $j = 1, \ldots, N$.

Proof: let $\lambda_i (i = 1, 2, ..., m)$ be the eigenvalues of $\mathbf{A} \in \mathbb{C}^{m\times m}$, with corresponding eigenvectors $\mathbf{x}_i (i = 1, 2, \cdots, m)$. Let $\mu_j (j = 1, 2, ..., m)$ be the eigenvalues of $\mathbf{B} \in \mathbb{C}^{m\times m}$, with corresponding eigenvectors $\mathbf{y}_j (j = 1, 2, \cdots, m)$. One can obtain

$$\begin{aligned}&(\mathbf{A} \otimes \mathbf{I}_n + \mathbf{I}_m \otimes \mathbf{B})(\mathbf{x}_i \otimes \mathbf{y}_j)\\ =&(\mathbf{A} \otimes \mathbf{I}_n)(\mathbf{x}_i \otimes \mathbf{y}_j) + (\mathbf{I}_m \otimes \mathbf{B})(\mathbf{x}_i \otimes \mathbf{y}_j)\\ =&(\mathbf{A}\mathbf{x}_i) \otimes \mathbf{y}_j + \mathbf{x}_i \otimes (\mathbf{B}\mathbf{y}_j)\\ =&(\lambda_i + \mu_j)\mathbf{x}_i \otimes \mathbf{y}_j.\end{aligned} \tag{8}$$

According to [3], the following lemma can be derived:

Lemma 2 *All the nonzero eigenvalues of $\mathbf{H}$, if there exist, have positive real parts. Furthermore, $\mathbf{H}$ is non-singular if and only if $\mathcal{G}$ contains a directed spanning tree with the leader as its root.*

Thus, matrix $\mathbf{M}$ is Hurwitz and the algebraic connectivity is $\lambda_{\min}(\mathbf{H})$. The error dynamics of distributed observer is asymptotic stable. By setting the suitable μ, distributed observer (2) can achieve an accurate estimation of the state of the leader with arbitrary initial values.

3.3 Consensus speed of distributed observer

In this part, the consensus speed of distributed observer (2) is considered as a measure of the performance. It is easy to know that if the observer converges faster, the follower can perform more accurate local control. A direct connection between the eigenvalue of $\mathbf{H}$ and the consensus speed is explored.

Theorem 1 *For distributed observer (5), the error converges asymptotically to 0 at a rate of no less than $2\mu\lambda_{\min}(\mathbf{H})$ if and only if $\mathcal{G}$ contains a directed spanning tree rooting at leader (node 0).*

Proof: Considering the following Lyapunov function

$$V(\mathbf{e}) = \frac{1}{2}\mathbf{e}^\top\mathbf{e} \geq 0, \tag{9}$$

$V(\mathbf{e})$ intuitively represents the error between the estimate and the leader's state, and its derivative is

$$\dot{V}(\mathbf{e}) = \frac{1}{2}\mathbf{e}^\top(\mathbf{M}^\top + \mathbf{M})\mathbf{e}. \tag{10}$$

Because $\mathbf{S}$ is skew-symmetric, and $(\mathbf{H} \otimes \mathbf{I}_q)^\top = \mathbf{H}^\top \otimes \mathbf{I}_q$, it follows that

$$\dot{V}(\mathbf{e}) = -\mu\mathbf{e}^\top \left((\mathbf{H}^\top + \mathbf{H}) \otimes \mathbf{I}_q\right)\mathbf{e}. \tag{11}$$

Since $\mathbf{H}$ is non-singular and $\mathbf{H}^\top + \mathbf{H}$ is a Hermitian matrix, according to Rayleigh theorem (1), it holds that

$$\min \frac{\mathbf{e}^\top[(\mathbf{H}^\top + \mathbf{H}) \otimes \mathbf{I}_q]\mathbf{e}}{\|\mathbf{e}\|^2} = \lambda_{\min}(\mathbf{H}^\top + \mathbf{H}). \tag{12}$$

As a result, equation (11) satisfies the inequality

$$\dot{V}(\mathbf{e}) \leq -4\mu\lambda_{\min}V(\mathbf{e}). \tag{13}$$

Letting $\gamma = 2\mu\lambda_{\min}(\mathbf{H})$, $V(\mathbf{e})$ and $\mathbf{e}$ satisfy the inequalities

$$\begin{aligned} V(t) =& \frac{1}{2}\mathbf{e}^\top\mathbf{e} \leq V(0)e^{-2\gamma t}, \\ \mathbf{e} \leq& \sqrt{2V(0)}e^{-\gamma t}, \end{aligned} \tag{14}$$

where $V(0)$ is the initial value with $t = 0$. Thus, γ indicates the speed of convergence of the exponential function.

Corollary 1 *As the leader's out-degree increases, the consensus speed of (5) accelerates, subject to the condition that a constant communication network and $\mathcal{G}$ contains a directed spanning tree starting from the leader (node 0) as the root.*

Proof: The out-degree of the leader in $\mathcal{G}$ is defined as the number of directed edges that originate from the leader node. Construct two different communication networks, where $\mathcal{G}_1$ is shown in Fig.2, $\mathcal{G}_2$ is shown in Fig.1, and $D_2 > D_1$. Letting $\mathcal{L}_i, i = 1, 2$ denote the Laplacian matrix of $\mathcal{G}_i$, it can be easily concluded that

$$\mathbf{H}_2 = \mathbf{H}_1 + (\mathbf{\Delta}_2 - \mathbf{\Delta}_1). \tag{15}$$

Let $V_i, i = 1, 2$ denote the Lyapunov function which is consistent with (9). When the communication network is $\mathcal{G}_1$, the $\dot{V}_1(\mathbf{e})$ is

$$\dot{V}_1(\mathbf{e}) = -\mu\mathbf{e}^\top \left((\mathbf{H}_1^\top + \mathbf{H}_1) \otimes \mathbf{I}_q\right)\mathbf{e}. \tag{16}$$

When the communication network is $\mathcal{G}_2$, the $\dot{V}_2(\mathbf{e})$ is

$$\dot{V}_2(\mathbf{e}) = -\mu\mathbf{e}^\top \left((\mathbf{H}_2^\top + \mathbf{H}_2) \otimes \mathbf{I}_q\right)\mathbf{e}. \tag{17}$$

Let $\mathbf{\Delta} = \mathbf{\Delta}_2 - \mathbf{\Delta}_1$. Then $\dot{V}_2(\mathbf{e})$ and $\dot{V}_1(\mathbf{e})$ satisfy the following equation

$$\dot{V}_2(\mathbf{e}) = -2\mu\mathbf{e}^\top (\mathbf{\Delta} \otimes \mathbf{I}_q)\mathbf{e} + \dot{V}_1(\mathbf{e}). \tag{18}$$

Since $(\mathbf{\Delta} \otimes \mathbf{I}_q)$ is a positive semi-definite diagonal matrix, it follows that $\mathbf{e}^\top(\mathbf{\Delta} \otimes \mathbf{I}_q)\mathbf{e} \geq 0$ and is continuously differentiable to $\mathbf{e}$. Then there exists a non-negative constant β that is positively correlated with the $tr(\mathbf{\Delta})$, satisfying the following equation

$$\beta\mathbf{e}^\top\mathbf{e} = \mathbf{e}^\top(\mathbf{\Delta} \otimes \mathbf{I}_q)\mathbf{e}, \tag{19}$$

where $tr(\mathbf{\Delta}) = q(D_2 - D_1)$. According to (13), $\dot{V}_2(\mathbf{e})$ satisfies the following inequality

$$\dot{V}_2(\mathbf{e}) \leq -(\beta + 4\mu\lambda_{\min})V_1(\mathbf{e}). \tag{20}$$

Let $\gamma_1 = 2\mu\lambda_{\min}(\mathbf{H})$ and $\gamma_2 = \gamma_1 + \frac{1}{2}\beta$. According to Theorem 1, it can be inferred that the estimation error of distributed observer converges to 0 with the rates of γ_1 and γ_2 under $\mathcal{G}_1$ and $\mathcal{G}_2$, respectively.

Corollary 2 *For two communication networks with the same number of edges but different out-degrees of leader D, under the condition of Theorem 1, the consensus speed is positively correlated with D.*

Proof: The followers are divided into two categories. The first type of followers is defined as the source nodes j, which directly receive information from the leader ($a_{i0} = 1$), for example, node F1 in Fig.2. The second type of followers are the indirect nodes i, which do not have a direct connection with the leader and can only estimate the leader's state through communication, for example, nodes F2, F3, and F4 in Fig.2. The observer for i and j are designed as

$$\begin{aligned} \dot{\eta_j} &= \mathbf{S}\eta_j + \mu(\mathbf{v} - \eta_j), \\ \dot{\eta_i} &= \mathbf{S}\eta_i + \mu\left(\sum_{j\in\mathcal{N}_i} a_{ij}\left(\eta_j - \eta_i\right)\right). \end{aligned} \tag{21}$$

The error dynamics for i and j are as

$$\begin{aligned} \dot{e_j} &= (\mathbf{S} - \mu\mathbf{I}_q)e_j, \\ \dot{e_i} &= (\mathbf{S} - \mu\mathbf{I}_q)e_i + \mu\mathbf{I}_q e_j. \end{aligned} \tag{22}$$

Compared with the source node, the indirect nodes i only use η_j as a reference to correct η_i from (21). Based on (22), it can be seen that e_i is asymptotically stable if only and if the estimation errors of both the source node and itself are zero. Recalling Corollary 2, when the number of edges is constant, the out-degree of the leader node is negatively correlated with the number of indirect nodes.

4 Simulation verifications and application

4.1 Numerical simulation

The leader's dynamic matrix $\mathbf{S} = \begin{pmatrix} 0 & \omega \\ -\omega & 0 \end{pmatrix}, \omega = 0.4\pi$ is chosen and the initial values $\eta_{ik} \in [0, 10], i = 1, 2, ...7, k = 1.2$ are randomly set. Build distributed observers (2) based on Fig.1 and Fig.2, respectively, where the algebraic connectivity of Fig.1 is 1, the algebraic connectivity of Fig.2 is 0.1187, and $\mu = 2$.

The estimation errors are shown in Fig.4. Clearly, the follower's disagreement is monotonically decreasing. It can be seen that a consensus is reached asymptotically. As the algebraic connectivity ($\lambda_{\min}(\mathbf{H})$) increases, the settling time of the error trajectories decreases.

4.2 The application of unicycle formation

4.2.1 Observer Design

A three-petal rose curve trajectory is introduced to verify the performance of distributed observer (2). The leader's po-

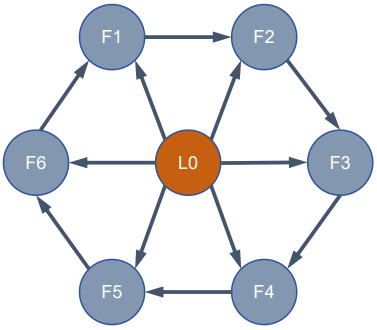

Fig. 1. The network of $\lambda_{\min}(H) = 1$

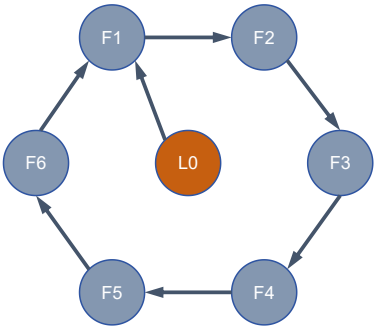

Fig. 2. The network of $\lambda_{\min}(H) = 0.1187$

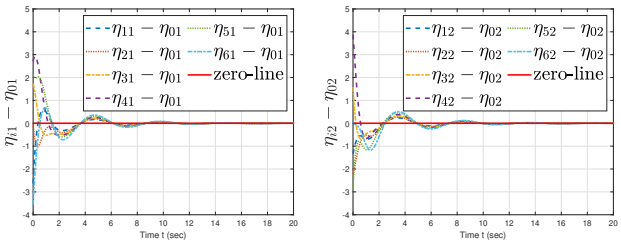

Fig. 3. The errors of the observers based on Fig.2

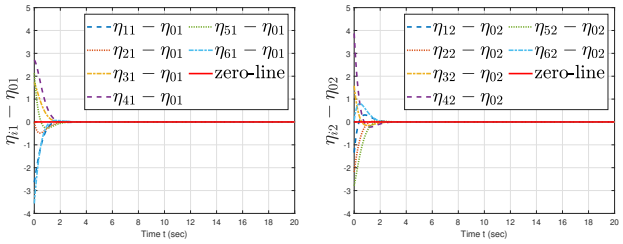

Fig. 4. The errors of the observers based on Fig.1

sition trajectory [23] is given as

$$\begin{cases} x_{r0} = R_0 \cos(N_p \phi_{r0}) \cos \phi_{r0}, \\ y_{r0} = R_0 \cos(N_p \phi_{r0}) \sin \phi_{r0}, \\ \phi_{r0} = \frac{2\pi}{T} t, \end{cases} \tag{23}$$

with $N_p = 3$, $R_0 = 10$. The relative velocity trajectory is given as

$$\begin{cases} \dot{x}_{r0} = \frac{2\pi R_0}{T} \left(-N_p \sin \frac{2N_p \pi t}{T} \cos \frac{2\pi t}{T} - \cos \frac{2N_p \pi t}{T} \sin \frac{2\pi t}{T} \right), \\ \dot{y}_{r0} = \frac{2\pi R_0}{T} \left(-N_p \sin \frac{2N_p \pi t}{T} \sin \frac{2\pi t}{T} + \cos \frac{2N_p \pi t}{T} \cos \frac{2\pi t}{T} \right), \\ \dot{\phi}_{r0} = \frac{2\pi}{T}. \end{cases} \tag{24}$$

To generate the above reference signals, the following distributed observer is introduced

$$\begin{aligned} \dot{\eta}_0 &= \mathbf{S}_0 \eta_0 = \mathrm{diag}\{\mathrm{diag}\{\frac{2\pi}{\mathrm{T}}, \frac{2\pi \mathrm{N}}{\mathrm{T}}\} \otimes \mathrm{a}, 0\}\eta_0, \\ \eta_i &= [\eta_{i1}, \eta_{i2}, \eta_{i3}, \eta_{i4}, \eta_{i5}]^\top, i = 0, \ldots, N, \\ \dot{\eta}_i &= f(\eta_i, \eta_j, a_j(t) | j \in \mathcal{N}_i), i = 1, \ldots, N, \end{aligned} \tag{25}$$

where $\eta_0(0) = [0, 1, 0, 1, \frac{2\pi}{T}]^\top$, $N = 5$ and $f(\cdot)$ the same as system (2). The topologies of the observer communication networks are shown in Fig.5 and Fig.6. Therefore, the reference signals q_{ri} and $\dot{q}_{ri}$ of the ith agent are generated by

$$\begin{cases} q_{ri} = \mathcal{R}_{rose}(\eta_i) = [x_{ri}, y_{ri}, \phi_{ri}]^\top, \\ \dot{q}_{ri} = [\dot{x}_{ri}, \dot{y}_{ri}, \dot{\phi}_{ri}]^\top, \\ x_{ri} = R_0 \eta_{i4} \eta_{i2}, \quad \dot{x}_{ri} = -\left(R_0 N_p \eta_{i3} \eta_{i2} + R_0 \eta_{i4} \eta_{i1}\right), \\ y_{ri} = R_0 \eta_{i4} \eta_{i1}, \quad \dot{y}_{ri} = -\eta_{i5}\left(R_0 N_p \eta_{i3} \eta_{i2} - R_0 \eta_{i4} \eta_{i1}\right), \\ \phi_{ri} = \eta_{i5} t, \quad \dot{\phi}_{ri} = \eta_{i5}. \end{cases} \tag{26}$$

To generate different trajectories for different agents, the following reference with bias is adopted for the local controller

$$\begin{aligned} \bar{x}_{ri} &= (R_0 + i)\eta_{i4}\eta_{i2} + i, \\ \bar{y}_{ri} &= (R_0 + i)\eta_{i4}\eta_{i1} + i. \end{aligned} \tag{27}$$

To verify the performance of distributed observer (2) under the different communication networks, construct the observers with parameter $\mu = 1.2$ based on Fig.5 and Fig.6 respectively. The network between the followers is the same but the out-degree of the leader is different, where $D_1 = 4$ and $D_2 = 1$. The initial values η_i and q_i are random.

In Fig.7, x_{ri}, y_{ri}, and $\theta_{ri}, i = 1, \ldots, 4$ represent the estimate of the leader state by the follower i. The communication network on the left is denoted as $\mathcal{G}_1$, and the right is

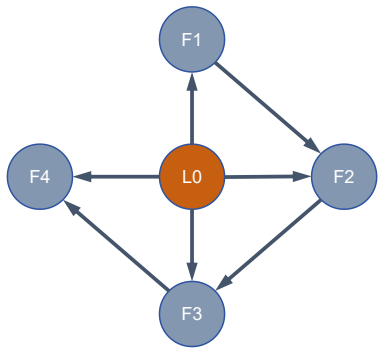

Fig. 5. The network G_1 of the leader's out-degree $D = 4$

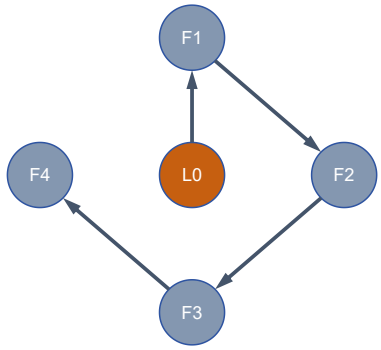

Fig. 6. The network G_2 of the leader's out-degree $D = 1$

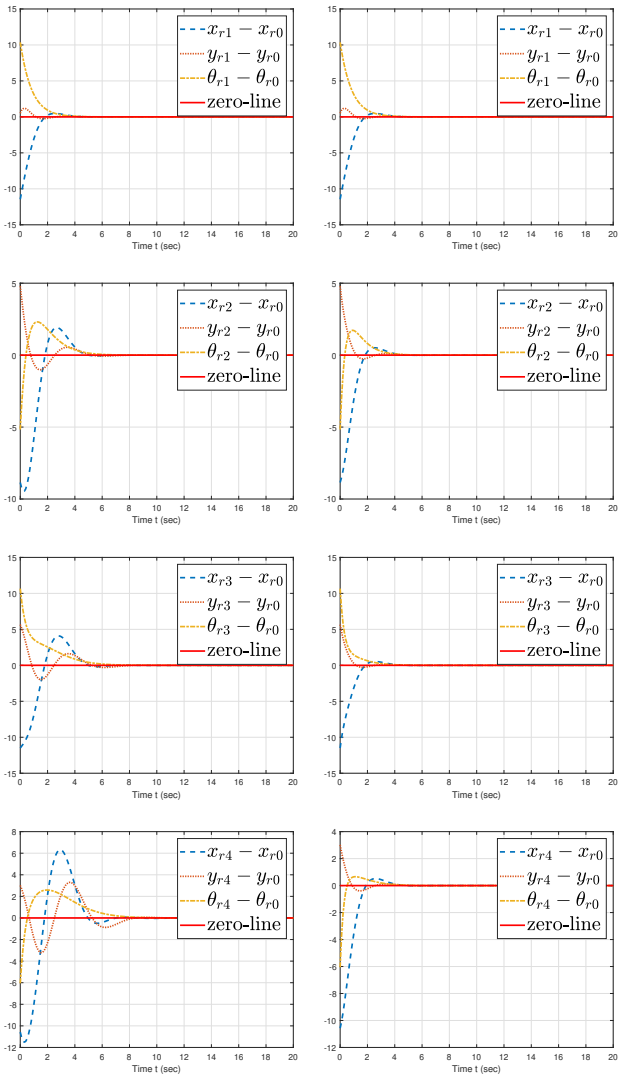

Fig. 7. The tracking errors of the observers based on $\mathcal{G}_2$ (left) and $\mathcal{G}_1$ (right).

denoted as $\mathcal{G}_2$. It is clear to see that the observer under $\mathcal{G}_2$ converges faster. It is worth noting that the estimate of follower 1 is consistent under both topologies because node 1 is the source node in Corollary 2 updating its estimate only based on the leader's state. The total trajectories generated by different observers based on $\mathcal{G}_1$ and $\mathcal{G}_2$ are illustrated in Fig.8a and Fig.8b, respectively.

4.2.2 Application to unicycle model

The multi-agent system combined with $N = 5$ wheeled mobile robots described with a typical simplified kinematic model called unicycle can be presented as

$$\dot{q}_i = \begin{bmatrix} \dot{x}_i \\ \dot{y}_i \\ \dot{\phi}_i \end{bmatrix} = \begin{bmatrix} r\cos\phi_i & 0 \\ r\sin\phi_i & 0 \\ 0 & 1 \end{bmatrix} \begin{bmatrix} v_{ci} \\ \omega_{ci} \end{bmatrix}, i = 0, \ldots, N, \quad (28)$$

where v_c is the velocity input, ω_c is the yaw angular velocity, and $r = 0.2$ is the radius of the wheel. The error after coordinate transformation is

$$q_{ei} = \begin{bmatrix} x_{ei} \\ y_{ei} \\ \phi_{ei} \end{bmatrix} = \begin{bmatrix} \cos(\phi_i) & \sin(\phi_i) & 0 \\ -\sin(\phi_i) & \cos(\phi_i) & 0 \\ 0 & 0 & 1 \end{bmatrix} \begin{bmatrix} \bar{x}_{ri} - x_i \\ \bar{y}_{ri} - y_i \\ \phi_{ri} - \phi_i \end{bmatrix}. \quad (29)$$

To handle the trajectory tracking task for each agent, the simple back-stepping control law

$$\begin{bmatrix} v_{ci} \\ \omega_{ci} \end{bmatrix} = \begin{bmatrix} v_{ri}\cos(\phi_{ei}) + k_1 x_{ei} \\ \phi_{ri} + v_{ri}(k_2 y_{ei} + k_3 \sin(\phi_{ei})) \end{bmatrix}, \quad (30)$$

with $v_{ri} = \dot{\bar{x}}_{ri}\cos\phi_i + \dot{\bar{y}}_{ri}\sin\phi_i$ and $k_1, k_2, k_3 > 0$ are adopt for convenience. It's worth mentioning that some better tracking methods like the sliding mode-based method[21] and the adaptive sliding mode method[20, 22] can be introduced to bring better tracking performance. The simulation results with $k_1 = 120$, $k_2 = 120$, and $k_3 = 10$ are shown in Fig.8c and Fig.8d, respectively. It is evident that the estimate of the followers directly impacts the tracking performance of the local controller.

5 Conclusion and Future Work

In this paper, the connection between the communication network and the performance of distributed observers is explored. Specifically, the consensus speed is positively correlated with the leader's out-degree and $\lambda_{\min}(\mathbf{H})$. Extensive numerical experiments are conducted in the unicycle formation that confirm the theoretical analysis. However, increasing the connectivity of the network to improve the consensus speed may lead to a significant waste of communication resources. Future research efforts will be devoted to finding a balance between the convergence speed and network complexity.

References

[1] Z. Li, Z. Duan, G. Chen, and L. Huang, Consensus of multiagent systems and synchronization of complex networks: A unified viewpoint, *IEEE Transactions on Circuits and Systems*, 57(1): 213-224, 2009.

[2] C. Godsil, and G. Royle, Algebraic graph theory, *Springer Science & Business Media*, 2001.

[3] Y. Su, and J. Huang, Cooperative output regulation of linear multi-agent systems, *IEEE Transactions on Automatic Control*, 57(4): 1062-1066, 2011.

[4] D. Liang, and J. Huang, Robust output regulation of linear systems by event-triggered dynamic output feedback control, *IEEE Transactions on Automatic Control*, 66(5): 2415-2422, 2021.

[5] J. Yu, X. Dong, Q. Li, and Z. Ren, Practical time-varying formation tracking for high-order nonlinear multi-agent systems based on the distributed extended state observer, *International Journal of Control*, 92(10): 2451-2462, 2019.

[6] H. Cai, and J. Huang, Leader-following consensus of multiple uncertain euler-lagrange systems under switching network topology, *International Journal of General Systems*, 43(3-4): 294–304, 2014.

[7] H. Cai, and J. Huang, The leader-following consensus for multiple uncertain euler-lagrange systems with an adaptive distributed observer, *IEEE Transactions on Automatic Control*, 61(10): 3152–3157, 2015.

[8] H. Cai, and J. Huang, Leader-following attitude consensus of multiple rigid body systems by attitude feedback control, *Automatica*, 69: 87-92, 2016.

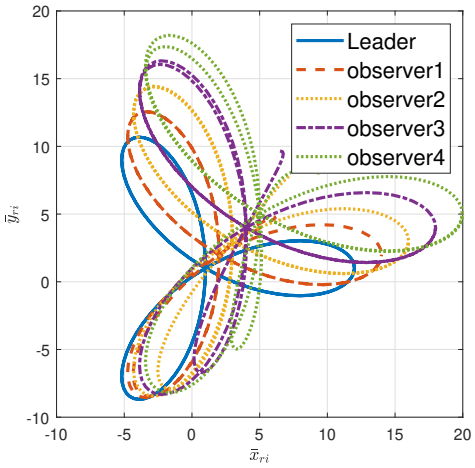

(a) The trajectories generated by different observers under communication networks $\mathcal{G}_2$

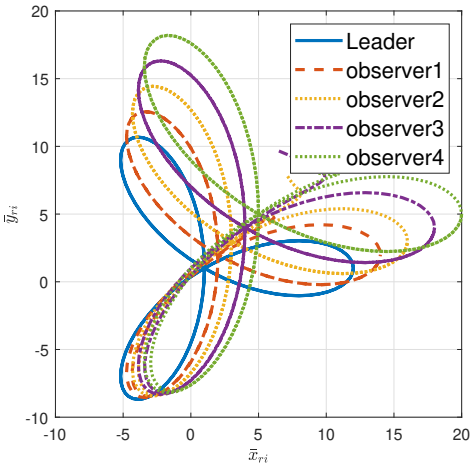

(b) The trajectories generated by different observers under communication networks $\mathcal{G}_1$

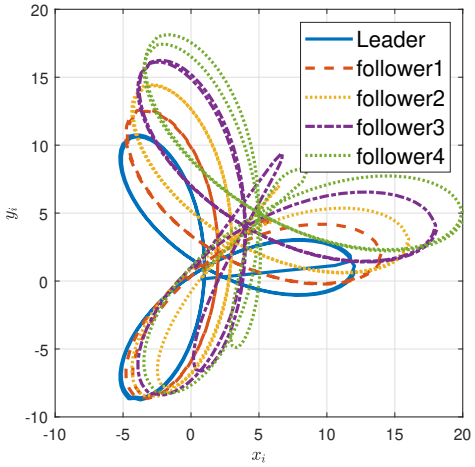

(c) The trajectories generated by local controller under communication networks $\mathcal{G}_2$

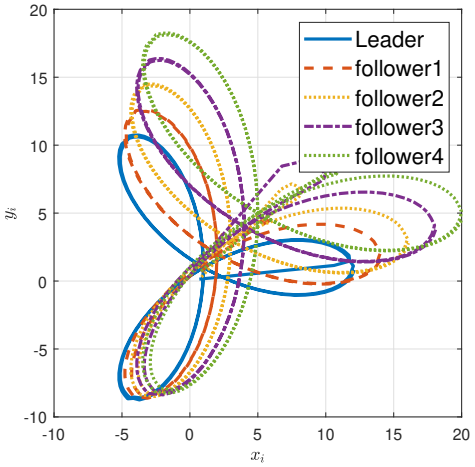

(d) The trajectories generated by local controller under communication networks $\mathcal{G}_1$

Fig. 8. The total trajectories generated by different observers and the total trajectories generated by local controller

[9] J. Huang, Adaptive distributed observer and the cooperative control of multi-agent systems, *Journal of Control and Decision*, 4(1): 1-11, 2017.

[10] T. Wang, and J. Huang, Leader-following event-triggered practical consensus with disturbance rejection of multiple uncertain spacecraft systems over switching networks, in *2021 60th IEEE Conference on Decision and Control (CDC)*, 2021: 527-532.

[11] Y. Su, Z. Tu, and H. Cai, Distributed power sharing control of grid-connected ac microgrid with uncertain plant, in *2019 IEEE 15th International Conference on Control and Automation (ICCA)*, 2019: 248–253.

[12] J. Ali, J. Lin, and A. Stephen, Coordination of groups of mobile autonomous agents using nearest neighbor rules, *IEEE Transactions on Automatic Control*, 48(6): 988-1001, 2003.

[13] O. Reza, and R. Murray, Consensus problems in networks of agents with switching topology and time-delays, *IEEE Transactions on Automatic Control*, 49(9): 1520-1533, 2004.

[14] M. Fiedler, Algebraic connectivity of graphs, *Czechoslovak Mathematical Journal*, 23(2): 298-305, 1973.

[15] L. Wang, and F. Xiao, Finite-time consensus problems for networks of dynamic agents, *IEEE Transactions on Automatic Control*, 55(4): 950-955, 2010.

[16] Z. Zuo, Q. Han, B. Ning, X. Ge, and X. Zhang, An overview of recent advances in fixed-time cooperative control of multi-agent systems, *IEEE Transactions on Industrial Informatics*, 14(6): 2322-2334, 2018.

[17] W. Ren, and R. Beard, Consensus seeking in multiagent systems under dynamically changing interaction topologies, *IEEE Transactions on Automatic Control*, 50(5): 655-661, 2005.

[18] W. Ren, and E. Atkins, Distributed multi-vehicle coordinated control via local information exchange, *International Journal of Robust and Nonlinear Control: IFAC-Affiliated Journal*, 17(10-11): 1002-1033, 2007.

[19] W. Yu, G. Chen, and M. Cao, Some necessary and sufficient conditions for second-order consensus in multi-agent dynamical systems, *Automatica*, 46(6): 1089-1095, 2010.

[20] T. Aienizi, N. Aienizi, Z. Rouili, and S. Dhahri, Trajectory tracking of wheeled mobile robot using adaptive second order sliding mode controller, in *2019 6th International Conference on Control, Decision and Information Technologies (CoDIT)*, 2019: 2039-2045.

[21] N. Goswami, and P. Padhy, Sliding mode controller design for trajectory tracking of a non-holonomic mobile robot with disturbance, *Computers & Electrical Engineering*, 72: 307-323, 2018.

[22] J. Zhai, and Z. Song, Adaptive sliding mode trajectory tracking control for wheeled mobile robots, *International Journal of Control*, 92(10): 2255-2262, 2019.

[23] W. Liu, X. Wang, and S. Li, Formation control for

leader–follower wheeled mobile robots based on embedded control technique, *IEEE Transactions on Control Systems Technology*, 31(1): 265-280, 2023.

[24] S. Cai, Y. Xie, Y. Zou, H. Wu, and L. Shen, A consensus-based decentralized algorithm for service restoration in active distribution networks, in *2020 40th Chinese Control Conference*, 2020: 6778-6783.

Proceedings of the 3rd Conference on Fully Actuated System Theory and Applications
May 10-12, 2024, Shenzhen, China

Truncated Predictive Containment Control of Input Delay Multi-agent Systems With Coding-Decoding Communication Protocol

Ming Wu[1], Jinghui Suo[1,2,*]

1. College of Information Science and Technology, Donghua University, Shanghai 201620, China

2. Engineering Research Center of Digitalized Textile and Fashion Technology, Ministry of Education, Shanghai 201620, China
E-mail: suojinghui@dhu.edu.cn

Abstract: In this paper, we propose a containment controller based on truncated prediction and a coding-decoding communication protocol (CDCP) for a class of multi-agent systems (MASs) with input time delay. Using the sensor outputs, we design corresponding observers for each agent, as well as the corresponding coders and decoders. The difference between the observed and decoded states is dynamically quantized by the coder and transmitted to other agents, while truncated prediction is used to compensate for the input time delay. We first present some lemmas to guarantee the detectability of MASs. Then, we provide sufficient conditions for the control protocol based on decoded and observed states to hold, and implement the containment control of MASs. Finally, the observer gain and controller gain are obtained by solving the LMI, and a numerical simulation example is provided to demonstrate the validity of the conclusions.

Key Words: Coding-Decoding, Containment Control, Input Delay, Multi-agent Systems, Truncated Prediction.

1 Introduction

In recent years, containment control strategies have also been increasingly studied in the field of MASs, driven by many natural phenomena and potential applications. The purpose of containment control is that the followers asymptotically enters the convex hull generated by the leaders (see [1][2]).

The phenomenon of time delay is encountered in real engineering environments, and it is also unavoidable. For input delay, truncated prediction method is used to compensate for the time delay term. The control design problem for Lipschitz nonlinear systems with time-varying input time delays is investigated in [3]. The distributed output feedback consensus control problem for nonlinear multi-agent system subject to input delays in [4]. However, most of the previous approaches using truncated prediction methods to deal with input time delays have been applied to leaderless or single-leader consensus, and there have been few applications in containment control.

For the research of MASs cooperative control, how to use less network resources to achieve stable control of the system has become an important topic nowadays. Many scholars only consider the design problem of distributed controllers for MASs under ideal communication states, such as continuously stable signals with infinite quantization levels (see [5][6]). For the consensus problem, a class of discrete-time networked MASs with digital communication protocol is studied in [7]. However, limited research has been conducted on communication methods in containment control. Exploring how to achieve efficient utilization of network resources in containment control presents a significant area of research interest.

Based on the above analyses, this paper designs a new truncated predictive containment control protocol under CDCP for a class of MAS with input delay. The main contributions of this paper are as follows 1) In order to be more realistic and to improve the efficiency of communication in containment control, a dynamic quantization-based CDCP is designed and its feasibility is proved. 2) Applying the truncated prediction method to the field of containment control, a truncated prediction control protocol is designed to compensate the effect of input time delay.

Notation: $\mathbb{R}^n$ and $\mathbb{R}^{m\times n}$ denote the n-dimensional Euclidean space and the set of $m \times n$ real matrices, respectively. The symbol $\lceil y \rceil$ denotes the smallest integer not less than y, while $\lfloor y \rfloor$ denotes the largest integer not larger than y. The symbol "$*$" represents the symmetric term in a matrix. $\mathrm{col}_N\{x_i\}$ denotes $[x_1^T \quad x_2^T \quad ... \quad x_N^T]^T$. The maximum and minimum eigenvalues of the symmetric matrix C are denoted by $\lambda_{\max}\{C\}$ and $\lambda_{\min}\{C\}$, respectively. $S > 0$ ($S \geq 0$) for a matrix S signifies positive definite (or positive semi-definite). The symbol I_n denotes an identity matrix with dimensions n. For a vector z, $\|z\|$ and $\|z\|_\infty$ refer to the Euclidean norm and infinity norm, respectively. $S \otimes D$ indicates the Kronecker product of matrices S and D.

2 Problem Formulation

In this paper, we use a directed graph $\mathcal{G}$ to describe the relationships between agents. The set of agent is denoted as $\mathcal{V}$, and each agent is identified by $1, ..., N$. $\mathcal{E} \in \mathcal{V} \times \mathcal{V}$ are the directed edges. The weighted adjacency matrix $\mathcal{A}$ is defined as $\mathcal{A} = [a_{ij}]_{N\times N}$. Each directed edge (i, j) represents agent j transmitting information to agent i. A path from agent i to j is a sequence of the ordered edges $(i, p), (p, q), ..., (r, j)$. The set of neighbors of agent i is defined as $\mathcal{N}_i = \{j \in \mathcal{V} | (j, i) \in \mathcal{E}, j \neq i\}$. Agents are classified as M followers and $N - M (N > M)$ leaders. To analyze MASs, we introduce the Laplacian matrix $\mathcal{L} = [l_{ij}]_{N\times N}$, where $l_{ii} = \sum_{j=1}^{N} a_{ij}$ and $l_{ij} = -a_{ij}, i \neq j$. $\mathcal{F} = \{1, 2, ..., M\}$ represents the followers set and $\mathcal{R} = \{M+1, M+2, ..., N\}$ represents the leaders set. The Laplacian matrix $\mathcal{L}$ associated with the graph $\mathcal{G}$ can be partitioned as

This work is supported by National Natural Science Foundation (NNSF) of China under Grant 61803081.

$$\begin{bmatrix} \mathcal{L}_1 & \mathcal{L}_2 \\ 0_{(N-M)\times M} & 0_{(N-M)\times(N-M)} \end{bmatrix},$$

where $\mathcal{L}_1 \in \mathbb{R}^{M\times M}$ and $\mathcal{L}_2 \in \mathbb{R}^{M\times(N-M)}$.

2.1 Model Description

In this study, we investigate a dynamic system for each agent as follows:

$$\begin{cases} \dot{x}_i(t) = Sx(t) + Du_i\big(t-\sigma\big), \\ y_i(t) = Cx_i(t), \end{cases} \tag{1}$$

where $x_i(t) \in \mathbb{R}^n, y_i \in \mathbb{R}^m$ and $u_i(t) \in \mathbb{R}^q$ represent the state, output, control input of follower i, respectively; The input of the leader is set to $u_i(t) = 0$ $(i \in \mathcal{R})$; Constant $\sigma > 0$ denotes the input delay; S, D and C are constant matrices with suitable dimensions, satisfying that (S, D) is controllable and (S, C) is observable.

The observer for the i-th agent $(i = 1, .., N)$ is constructed as follows:

$$\dot{\hat{x}}_i(t) = S\hat{x}_i(t) + Du_i(t-\sigma) + G(y_i(t) - C\hat{x}_i(t)), \tag{2}$$

where G is the observer gain matrix to be designed.

The initial condition of $x_i(t)$ and $\hat{x}_i(t)$ $(i = 1, .., N)$ are defined as $x_i(\theta) = \vartheta_i(\theta)$ and $\hat{x}_i(\theta) = \hat{\vartheta}_i(\theta)$ for $\theta \in [-\sigma, 0]$, respectively. Define the relative state as $\varepsilon_i(t) \triangleq \sum\limits_{j\in\mathcal{N}_i} a_{ij}(x_i(t) - x_j(t)), \quad i \in \mathcal{F}$.

2.2 Coding–Decoding Communication Protocol

Suppose that only symbolic data can be exchanged between agents. The corresponding codeword generated by the coder of agent i $(i = 1, 2, ..., N)$ is

$$\varpi_i(dh) = \mathcal{Q}_{dh}\Big(\frac{\hat{x}_i(dh) - \breve{x}_i(dh^-)}{g(dh)}\Big), \tag{3}$$

where $\breve{x}_i(dh^-)$ is the decoded state of $\hat{x}_i(dh^-)$ at the left-limit coding moment dh ($d = 1, 2, ...$ and $h > \sigma > 0$ is the coding interval); $g(dh) = g_0\ell^{dh}$ $(g_0 > 0,\ 0 < \ell < 1)$ is the scaling function; $\mathcal{Q}_{dh}(\cdot)$ is a quantizer.

The following uniformly symmetric quantizer $\mathcal{Q}_{dh}(\kappa) = [q_{dh}(\kappa_1), ..., q_{dh}(\kappa_n)]^T$ with $\kappa = [\kappa_1, ..., \kappa_n]^T$ is employed:

$$q_{dh}(\kappa_i) = \begin{cases} a\zeta, & (a - \frac{1}{2})\zeta \le \kappa_i < (a + \frac{1}{2})\zeta, \\ H\zeta, & \kappa_i \ge \dfrac{(2H-1)\zeta}{2} \\ -\,q_{dh}(-\kappa_i), & \kappa_i \le -\dfrac{1}{2}\zeta, \end{cases} \tag{4}$$

where ζ represents the known quantization parameter, $a = 0, 1, ..., H-1$ and H is the saturation value of the quantizer.

The decoded value obtained by the decoder of agent i from the message sent by agent j is defined as follows:

$$\begin{cases} \breve{x}_j(t) = 0, \quad t \in [-\sigma, 0], \\ \dot{\breve{x}}_j(t) = S\breve{x}_j(t) + Du_j(t-\sigma), \quad t \ne dh, \\ \breve{x}_j(dh) = \breve{x}_j(dh^-) + g(dh)\varpi_j(dh), \end{cases} \tag{5}$$

where $\breve{x}_j(t)$ represents the output of decoder. Define $\breve{\varepsilon}_i(t) \triangleq \sum\limits_{j\in\mathcal{N}_i} a_{ij}(\breve{x}_i(t) - \breve{x}_j(t))$ $(i \in \mathcal{F})$ as the relative state of the decoded state.

Based on the above designed decoder (5), the following control protocol can be proposed as follows:

$$u_i(t) = Ke^{S\sigma}\sum_{j\in\mathcal{N}_i} a_{ij}\big(\hat{x}_i(t) - \breve{x}_j(t)\big), \quad i \in \mathcal{F}, \tag{6}$$

where K is the control gain to be designed.

Next, for the sake of convenience, we make

$$\begin{aligned} x_f(t) &= \mathrm{col}_M\{x_i(t)\}, \quad & x_l(t) &= [x_{M+1}^T(t), ..., x_N^T(t)]^T, \\ \varepsilon(t) &= \mathrm{col}_M\{\varepsilon_i(t)\}, \quad & \breve{\varepsilon}(t) &= \mathrm{col}_M\{\breve{\varepsilon}_i(t)\}, \\ u(t) &= \mathrm{col}_M\{u_i(t)\}, \quad & \vartheta(\theta) &= \mathrm{col}_N\{\vartheta_i(\theta)\}, \\ \hat{\vartheta}(\theta) &= \mathrm{col}_N\{\hat{\vartheta}_i(\theta)\}. \end{aligned}$$

The augmented form of system (1) can be written as

$$\dot{x}(t) = \bar{S}x(t) + \bar{D}u(t-\sigma). \tag{7}$$

where

$$x(t) = \begin{bmatrix} x_f(t)^T & x_l(t)^T \end{bmatrix}^T,\ \bar{S} = \begin{bmatrix} I_M \otimes S & 0 \\ 0 & I_{N-M} \otimes S \end{bmatrix},$$

$$\bar{D} = \begin{bmatrix} I_M \otimes D & 0 \\ 0 & 0 \end{bmatrix}.$$

The augmented matrix form of $\varepsilon(t)$ can be written as $\varepsilon(t) = (\mathcal{L}_1 \otimes I_n)x_f(t) + (\mathcal{L}_2 \otimes I_n)x_l(t)$. The containment error dynamics can be reformulated as follows

$$\dot{\varepsilon}(t) = (I_M \otimes S)\varepsilon(t) + (\mathcal{L}_1 \otimes D)u(t-\sigma). \tag{8}$$

Defining the estimation error as $\tilde{x}(t) = x(t) - \hat{x}(t)$, one has

$$\dot{\tilde{x}}(t) = \big(I_N \otimes (S - GC)\big)\tilde{x}. \tag{9}$$

Lemma 1. *[8] For any positive definite matrix $\mathcal{X} = \mathcal{X}^T > 0$, there exist scalar parameters a and b, where $b > a$, and vector-valued function $x(t) : [a, b] \to \mathbb{R}^m$ such that the following integral inequality holds:*

$$\int_a^b x^T(\rho)\mathcal{X}x(\rho)d\rho \ge \frac{1}{b-a}\Big(\int_a^b x(\rho)d\rho\Big)^T\mathcal{X}\Big(\int_a^b x(\rho)d\rho\Big).$$

Lemma 2. *[9] For any positive-definite matrix $\mathcal{K}$, there exists a non-negative constant c satisfying :*

$$e^{S^T t}\mathcal{K}e^{St} - e^{ct}\mathcal{K} = -e^{ct}\int_0^t e^{-c\rho}e^{S^T\rho}Pe^{S\rho}d\rho,$$

where $P = -S^T\mathcal{K} - \mathcal{K}S + c\mathcal{K}$. It is worth noting that if P is positive definite, then the inequality $e^{S^T t}\mathcal{K}e^{St} \le e^{ct}\mathcal{K}$ holds.

Assumption 1. *For each follower, there exists at least one leader that has a directed path to that follower.*

Lemma 3. *[10] Under Assumption 1, $\mathcal{L}_1 > 0$. Additionally, every entry of $-\mathcal{L}_1^{-1}\mathcal{L}_2$ is non-negative, and each row sum of $-\mathcal{L}_1^{-1}\mathcal{L}_2$ is 1.*

Definition 1. *[1] A set $Q \subseteq \mathbb{R}^n$ is considered convex if it satisfies the condition that for any $z \in Q$ and $y \in Q$, $(1-\gamma)z + \gamma y \in Q$ for any $\gamma \in [0, 1]$. $\mathrm{Co}\{z_1, ..., z_n\} = \{\sum_{i=1}^n \alpha_i z_i | \alpha_i \ge 0, \sum_{i=1}^n \alpha_i = 1\}$ denotes the minimum convex set containing all points $z_i (i = 1, ..., n)$.*

Definition 2. *The continuous-time dynamical system (7) is said to be detectable if there exist coder–decoder pairs (3) and (5) such that* $\lim_{t\to+\infty}\|x(t)-\breve{x}(t)\|=0$.

Definition 3. *[2] The containment control for the multi-agent systems (1) is said to be achieved if for any initial conditions such that* $\lim_{t\longrightarrow\infty}\|x_i(t)-\sum_{j=M+1}^{N}\varrho_{ij}x_j(t)\|=0$ *holds, where* $\varrho_{ij}\geq 0,\sum_{j=M+1}^{N}\varrho_{ij}=1, i\in\mathcal{F}, j\in\mathcal{R}$.

3 Main Results

3.1 Detectability Analysis

For the convenience of deriving the main results later, the following lemma is provided.

Lemma 4. *Given positive scalars* b_1 *and* b_2. *Suppose there exists a positive definite matrix* Q_1 *satisfying*

$$\begin{bmatrix} A^T+A & Q_1 \\ * & -b_2^{-1}Q_1 \end{bmatrix}<0, \tag{10}$$

where $A=Q_1S-b_1Q_1$. *Then for any constant* $\epsilon_1>0$, $\|\psi_1(t+\epsilon_1)-\psi_2(t+\epsilon_1)\|\leq\gamma e^{\tilde{b}\epsilon_1}\|\psi_1(t)-\psi_2(t)\|$ *holds, where* $\psi_1(t)$ *and* $\psi_2(t)$ *denote two arbitrary solutions of (7),* $\gamma=\sqrt{\lambda_{\max}\{Q\}/\lambda_{\min}\{Q\}}$ *and* $\hat{b}=b_1-b_2/2$ *with* $Q=I_N\otimes Q_1$.

Proof. The Lyapunov function $\overline{V}(t)=\tilde{\psi}^T(t)Q\tilde{\psi}(t)$ is constructed, where $\tilde{\psi}(t)=e^{-b_1t}(\psi_1(t)-\psi_2(t))$. A derivation of the trajectory of $\overline{V}(t)+b_2\overline{V}(t)$ along $\tilde{\psi}(t)$ yields:

$$\begin{aligned}&\dot{\overline{V}}(\tilde{\psi}(t))+b_2\overline{V}(\tilde{\psi}(t))\\ =&\tilde{\psi}^T(t)\big((\bar{S}-b_1I_{nN}))^TQ+Q(\bar{S}-b_1I_{nN})+b_2Q\big)\tilde{\psi}(t).\end{aligned}$$

By (10) and Shur complement lemma, one has $\overline{V}(t+\epsilon_1)\leq e^{-b_2\epsilon_1}\overline{V}(t)$, which can be further obtained that $\|\psi_1(t+\epsilon_1)-\psi_2(t+\epsilon_1)\|\leq\gamma e^{\hat{b}\epsilon_1}\|\psi_1(t)-\psi_2(t)\|$ with $\gamma=\sqrt{\lambda_{\max}\{Q\}/\lambda_{\min}\{Q\}}$. The proof is finished. ■

To ensure the state observer is effective, it requires the estimation error system (9) is convergent. Thus the following lemma is proposed.

Lemma 5. *Let scalar* $b_3>0$ *be given. If there exits positive definite matrix* Q_2 *and matrix* Z *satisfying*

$$\begin{bmatrix} B^T+B & Q_2 \\ * & -b_3^{-1}Q_2 \end{bmatrix}<0, \tag{11}$$

where $B=Q_2S-ZC$, *then there always exits scalar* $\epsilon_2>0$ *such that* $\|\tilde{x}(t+\epsilon_2)\|\leq\alpha e^{\tilde{b}\epsilon_2}\|\tilde{x}(t)\|$, *where* $\alpha=\sqrt{e^{b_3}\lambda_{\max}\{\hat{Q}\}/\lambda_{\min}\{\hat{Q}\}}$ *with* $\hat{Q}=I_N\otimes Q_2$ *and* $\tilde{b}=-b_3/2$. *In addition, the feedback gain matrix is designed as* $G=Q_2^{-1}Z$.

Proof. A Lyapunov function $\widetilde{V}(t)=\tilde{x}^T(t)\hat{Q}\tilde{x}(t)$ is constructed. And then, the term $\dot{\widetilde{V}}(t)+b_3\widetilde{V}(t)$ is derived as follows:

$$\begin{aligned}\dot{\widetilde{V}}(t)+b_3\widetilde{V}(t)=&\tilde{x}^T(t)\Big(\big(I_N\otimes(S-GC)\big)^T\hat{Q}\\ &+\hat{Q}\big(I_N\otimes(S-GC)\big)+b_3\hat{Q}\Big)\tilde{x}(t).\end{aligned}$$

By (11), $\dot{\widetilde{V}}(t)\leq-b_3\widetilde{V}(t)$ can be obtained. So it is further derived that $\|\tilde{x}(t+\epsilon_2)\|\leq\alpha e^{\tilde{b}\epsilon_2}\|\tilde{x}(t)\|$ with $\alpha=\sqrt{\lambda_{\max}\{\hat{Q}\}/\lambda_{\min}\{\hat{Q}\}}$. Notice that there exists ϵ_2 such that $0<\alpha e^{\tilde{b}\epsilon_2}<1$, the system (9) is exponential convergence. The proof is completed. ■

Define the quantization error as $\Im(dh)=(\hat{x}(dh)-\breve{x}(dh^-))/g(dh)-\varpi(dh)$ with $\varpi(dh)=\mathrm{col}_N\{\varpi_i(dh)\}$. In order to ensure the communication protocol is available, it is necessary to ensure the unsaturation of the quantizer for any $dh>0$, i.e., the quantization error satisfies $\|\Im(dh)\|\leq\frac{\sqrt{Nn}\zeta}{2}$.

Theorem 1. *Assuming the conditions in Lemma 4, Lemma 5 hold, for any given constant* $\ell\in(e^{\tilde{b}},1)$ *and* $\zeta>0$, *let*

$$H_1=\lfloor\aleph-\frac{1}{2}\rfloor+1,\ \aleph=\big(1+\frac{2\gamma e^{\tilde{b}h}}{\ell^h}\big)\frac{\sqrt{Nn}}{2}, \tag{12}$$

and for arbitrary given $H\geq H_1$, *we have*

$$g_0>\max\Big\{\frac{\alpha e^{\tilde{b}h}\tilde{\vartheta}+\gamma e^{\hat{b}h}\vartheta}{\ell^h(H+\frac{1}{2})\zeta},\frac{2\alpha\tilde{\vartheta}}{\sqrt{Nn}\zeta}\Big\} \tag{13}$$

where $\vartheta=\sup_{\theta\in[-\sigma,0]}\|\vartheta(\theta)\|$, $\tilde{\vartheta}=\sup_{\theta\in[-\sigma,0]}\|\vartheta(\theta)-\hat{\vartheta}(\theta)\|$.

Then the CDCP (3) and (5) satisfies $\Big\|\frac{\hat{x}(dh)-\breve{x}(dh^-)}{g(dh)}\Big\|_\infty\leq(H+\frac{1}{2})\zeta$, $d=1,2,....$, *that is, the quantizer is not saturated for any* $H\geq H_1$. *Furthermore, the continuous-time dynamic system (7) is detectable with CDCP (3)-(5).*

Proof. Some definitions and properties of vector norms and the mathematical induction are used to prove the lemma. Firstly, for $d=1$, utilizing Lemma 4, Lemma 5, it can be derived:

$$\begin{aligned}\Big\|\frac{\hat{x}(h)-\breve{x}(h^-)}{g(h)}\Big\|\leq&\Big\|\frac{\hat{x}(h)-x(h)}{g(h)}\Big\|+\Big\|\frac{x(h)-\breve{x}(h^-)}{g(h)}\Big\|\\ \leq&\frac{\alpha e^{\tilde{b}h}\tilde{\vartheta}+\gamma e^{\hat{b}h}\vartheta}{g_0\ell^h}<(H+\frac{1}{2})\zeta.\end{aligned} \tag{14}$$

By the definition of vector norm, (14) can be further derived

$$\Big\|\frac{\hat{x}(h)-\breve{x}(h^-)}{g(h)}\Big\|_\infty<(H+\frac{1}{2})\zeta. \tag{15}$$

Secondly, suppose $\|\frac{\hat{x}(dh)-\breve{x}(dh^-)}{g(dh)}\|_\infty\leq(H+\frac{1}{2})\zeta$ holds for $d=2,...,\hat{d}$. Subsequently, one can be obtained that

$$\begin{aligned}\Big\|\frac{x(\hat{d}h)-\breve{x}(\hat{d}h)}{g(\hat{d}h)}\Big\|=&\Big\|\frac{x(\hat{d}h)-\breve{x}(\hat{d}h^-)}{g(\hat{d}h)}-\varpi(\hat{d}h)\Big\|\\ \leq&\frac{\alpha\tilde{\vartheta}}{g_0}\Big(\frac{e^{\tilde{b}}}{\ell}\Big)^{\hat{d}h}+\frac{\sqrt{Nn}\zeta}{2}\leq\sqrt{Nn}\zeta.\end{aligned} \tag{16}$$

So for $d=\hat{d}+1$, one can be derived from (16) that

$$\begin{aligned}&\Big\|\frac{\hat{x}\big((\hat{d}+1)h\big)-\breve{x}\big((\hat{d}+1)h^-\big)}{g\big((\hat{d}+1)h\big)}\Big\|\\ \leq&\Big\|\frac{\tilde{x}\big((\hat{d}+1)h\big)}{g\big((\hat{d}+1)h\big)}\Big\|+\Big\|\frac{x\big((\hat{d}+1)h\big)-\breve{x}\big((\hat{d}+1)h^-\big)}{g\big((\hat{d}+1)h\big)}\Big\|\\ \leq&\big(1+\frac{2\gamma e^{\tilde{b}h}}{\ell^h}\big)\frac{\sqrt{Nn}\zeta}{2}=\aleph\zeta\leq(H+\frac{1}{2})\zeta.\end{aligned} \tag{17}$$

Similar to (15), (17) can be further derived that

$$\Big\|\frac{\hat{x}\big((\hat{d}+1)h\big)-\breve{x}\big((\hat{d}+1)h^{-}\big)}{g\big((\hat{d}+1)h\big)}\Big\|_{\infty}\leq(H+\frac{1}{2})\zeta. \quad (18)$$

Thus, by (14)-(18) and the mathematical induction, we can deduce that the quantizer will never saturate at $H \geq H_1$.

For the coding instant $t = dh$, since $e^{\tilde{b}} < \ell < 1$ implies $\lim_{d\to+\infty} g(dh) = 0$, we have $\lim_{d\to+\infty} \|x(dh) - \breve{x}(dh)\| = 0$.

For the non-coding instant $t \neq dh$, due to $x(t)$ and $\breve{x}(t)$ can be considered as two trajectories of (8). Then the following inequality can be obtained from Lemma 4

$$\|x(t)-\breve{x}(t)\|\leq\sqrt{\gamma e^{\hat{b}(t-dh)}}\|x(dh)-\breve{x}(dh)\|. \quad (19)$$

Therefore, $\|x(t) - \breve{x}(t)\|$ is bounded for the non-coding instant t.

Eventually, based on the above analysis, we can conclude that $\lim_{t\to+\infty} |x(t) - \breve{x}(t)| = 0$, indicating that the dynamic system (7) is detectable with the CDCP (3)-(5). The proof is completed. ■

3.2 Containment Control Analysis

Let $\delta_i(t) = \sum_{j\in\mathcal{N}_i} a_{ij}(\hat{x}_i(t) - \breve{x}_i(t))$. From (6), we can get $u(t) = (I_M \otimes Ke^{S\sigma})\breve{\varepsilon}(t) + (I_M \otimes Ke^{S\sigma})\delta(t)$, where $\delta(t) = \mathrm{col}_M\{\delta_i(t)\}$.

The relative state of decoder system (5) is rewritten in compact form as follows:

$$\begin{cases}\breve{\varepsilon}(t)=0, \quad t\in[-\bar{\sigma},0],\\ \dot{\breve{\varepsilon}}(t)=S\breve{\varepsilon}(t)+(\mathcal{L}_1\otimes D)u(t-\sigma), \quad t\neq dh,\\ \breve{\varepsilon}(dh)=\breve{\varepsilon}(dh^{-})+\Omega(dh),\end{cases} \quad (20)$$

where $\Omega(dh) = \mathrm{col}_M\{\Omega_i(dh)\}$ with $\Omega_i(dh) = \sum_{j\in\mathcal{N}_i} a_{ij}g(dh)(\varpi_i(dh) - \varpi_j(dh))$.

Suppose that at time $t \in [0, +\infty)$, there always exits $d \in \mathbb{N}$ such that $t \in \big[dh, (d+1)h\big)$. Assume that $0 \leq \sigma \leq h$, it is straightforward to observe that $t - \sigma \in \big[(d-1)h, (d+1)h\big)$ when $t \in \big[dh, (d+1)h\big)$. In the decoder system (20), the $\breve{\varepsilon}(t)$ undergoes a sudden change at $t = dh$. So, the decoded containment error $\breve{\varepsilon}(t-\sigma)$ can be divided into two cases for discussion.

- Case I: $t - \sigma \in \big[(d-1)h, dh\big)$.

Firstly, by integrating the decoder system (20) from $t - \sigma$ to dh^{-}, one can derive that

$$\begin{aligned}\breve{\varepsilon}(dh^{-})=&\Big(I_M\otimes e^{S\big(dh-t+\sigma\big)}\Big)\breve{\varepsilon}(t-\sigma)\\&+\int_{t-\sigma}^{dh}\Big(\mathcal{L}_1\otimes e^{S(dh-\rho)}DKe^{S\sigma}\Big)\breve{\varepsilon}\big(\rho-\sigma\big)d\rho\\&+\int_{t-\sigma}^{dh}\Big(\mathcal{L}_1\otimes e^{S(dh-\rho)}DKe^{S\sigma}\Big)\delta\big(\rho-\sigma\big)d\rho.\end{aligned} \quad (21)$$

Secondly, by integrating the decoder system (20) from dh to t , we can get

$$\begin{aligned}\breve{\varepsilon}(t)=&\big(I_M\otimes e^{S(t-dh)}\big)\big(\breve{\varepsilon}(dh^{-})+\Omega(dh)\big)\\&+\int_{dh}^{t}\Big(\mathcal{L}_1\otimes e^{S(t-\rho)}DKe^{S\sigma}\Big)\breve{\varepsilon}(\rho-\sigma)d\rho\\&+\int_{dh}^{t}\Big(\mathcal{L}_1\otimes e^{S(t-\rho)}DKe^{S\sigma}\Big)\delta(\rho-\sigma)d\rho.\end{aligned} \quad (22)$$

And finally, substituting (21) into (22), it can be obtained that

$$\begin{aligned}\breve{\varepsilon}(t)=&(I_M\otimes e^{S\sigma})\breve{\varepsilon}(t-\sigma)+(I_M\otimes e^{S(t-dh)})\Omega(dh)\\&+\int_{t-\sigma}^{t}\Big(\mathcal{L}_1\otimes e^{S(t-\rho)}DKe^{S\sigma}\Big)\breve{\varepsilon}(\rho-\sigma)d\rho\\&+\int_{t-\sigma}^{t}\Big(\mathcal{L}_1\otimes e^{S(t-\rho)}DKe^{S\sigma}\Big)\delta(\rho-\sigma)d\rho.\end{aligned} \quad (23)$$

Denote the decoded error as $\bar{\varepsilon}(t) = \varepsilon(t) - \breve{\varepsilon}(t)$. Therefore the containment error system (8) can be rewritten as

$$\dot{\varepsilon}(t)=(\tilde{S}+\tilde{D})\varepsilon(t)-\tilde{D}\bar{\varepsilon}(t)+\sum_{r=1}^{4}\Psi_r, \quad (24)$$

where $\Psi_1 = -\tilde{D}\int_{t-\sigma}^{t}\Big(\mathcal{L}_1\otimes e^{S(t-\rho)}BKe^{S\sigma}\Big)\varepsilon(\rho-\sigma)d\rho$,
$\Psi_2 = \tilde{D}\int_{t-\sigma}^{t}\Big(\mathcal{L}_1\otimes e^{S(t-\rho)}DKe^{S\sigma}\Big)\bar{\varepsilon}(\rho-\sigma)d\rho$,
$\Psi_3 = -\tilde{D}\int_{t-\sigma}^{t}\Big(\mathcal{L}_1\otimes e^{S(t-\rho)}DKe^{S\sigma}\Big)\delta(\rho-\sigma)d\rho$,
$\Psi_4 = -(\mathcal{L}_1\otimes DKe^{S(t-dh)})\Omega(dh)$, with $\tilde{S} = I_M\otimes S$, $\tilde{D} = \mathcal{L}_1\otimes DK$.

- Case II: $t - \sigma \in \big[dh, (d+1)h\big)$.

In this case, because $\breve{\eta}(t)$ is continuous from $\vartheta(t)$ to t, there is no need for segmented analysis of its integration. By integrating the decoder system (20) from $\vartheta(t)$ to t, one has

$$\begin{aligned}\breve{\varepsilon}(t)=&(I_M\otimes e^{S\sigma})\breve{\varepsilon}(t-\sigma)\\&+\int_{t-\sigma}^{t}\Big(\mathcal{L}_1\otimes e^{S(t-\rho)}DKe^{S\sigma}\Big)\breve{\varepsilon}(t-\sigma)d\rho\\&+\int_{t-\sigma}^{t}\Big(\mathcal{L}_1\otimes e^{S(t-\rho)}DKe^{S\sigma}\Big)\delta(t-\sigma)d\rho.\end{aligned} \quad (25)$$

The dynamic of $\varepsilon(t)$ can be written as

$$\dot{\varepsilon}(t)=(\tilde{S}+\tilde{D})\varepsilon(t)-\tilde{D}\bar{\varepsilon}(t)+\sum_{r=1}^{3}\Psi_r. \quad (26)$$

Moreover, the controller gain for the control input (6) is determined as $K = -D^T W$, where the matrix $W > 0$ is to be defined.

Theorem 2. *Assuming that the Theorem 1 and $0 \leq \sigma \leq h$ hold, the containment control in MAS (1) can be achieved by control input (6) with $K = -D^T W$, if there exist matrix $W > 0$ and constants $\upsilon > 0, c \geq 0, \phi_i > 0 (i = 0, ..., 4)$ satisfying:*

$$DD^T\leq\upsilon\mathcal{W}, \quad (27)$$

$$S^T+S<cI_n, \quad (28)$$

$$\begin{bmatrix}\mathcal{W}S^T+S\mathcal{W}-2\underline{\lambda}DD^T+\sum_{r=0}^{4}\phi_r I_n & \mathcal{W}\\ * & -\beta^{-1}I_n\end{bmatrix}<0, \quad (29)$$

where $\mathcal{W} = W^{-1}$, $\underline{\lambda} = \lambda_{\min}\{\mathcal{L}_1\}$, $\bar{\lambda} = \lambda_{\max}\{\mathcal{L}_1\}$, $\beta = \bar{\varsigma}\phi_1^{-1}e^{\sigma}$, $\bar{\varsigma} = \upsilon^4\sigma e^{2c\sigma}\bar{\lambda}^2$.

Proof. Construct a Lyapunov function as $V_1(t) = \varepsilon(t)^T(I_M \otimes W)\varepsilon(t)$.

Based on (21)-(26), we need to divide the discussion in segments at $t = dh$

- Case I: $t - \sigma \in \big[(d-1)h, dh\big)$.

By differentiating the $V_1(t)$ along (24) and utilizing $2a^Tb \le \phi a^Ta + \phi^{-1}b^Tb$, which is further derived as

$$\begin{aligned}\dot{V}_1(t)|_{\text{caseI}} \le& \varepsilon^T(t)\Big(I_M \otimes (S^TW + WS - 2\underline{\lambda}WDD^TW)\Big)\varepsilon(t) \\ &+ \varepsilon^T(t)(I_M \otimes \sum_{r=0}^{4}\phi_r W^2)\varepsilon(t) + \phi_0^{-1}\bar{\varepsilon}^T(t)\bar{\varepsilon}(t) \\ &+ \sum_{r=1}^{4}\phi_r^{-1}\Psi_r^T\Psi_r. \end{aligned} \tag{30}$$

Under Lemma 1, conditions (27) and (28), one can gets

$$\Psi_i^T\Psi_i \le \bar{\varsigma}\int_{t-\sigma}^{t}\Delta_i^T(\rho-\sigma)\Delta_i(\rho-\sigma)d\rho,\ i = 1,2,3, \tag{31}$$

where $\Delta_1 = \varepsilon$, $\Delta_2 = \bar{\varepsilon}$, $\Delta_3 = \delta$. To counteract the effect of the upper bound in (31), we construct the following Krasovskii functions:

$$\begin{aligned}\Gamma_i =& e^{\sigma}\int_{t-\sigma}^{t}e^{\rho-t}\Delta_i^T(\rho-\sigma)\Delta_i(\rho-\sigma)d\rho \\ &+ e^{\sigma}\int_{t-\sigma}^{t}\Delta_i^T(\rho)\Delta_i(\rho)d\rho,\ i = 1,2,3. \end{aligned} \tag{32}$$

The derivation of the functions $\Gamma_i (i = 1,2,3)$ can be further derived as follows

$$\dot{\Gamma}_i \le -\int_{t-\sigma}^{t}\Delta_i^T(\rho-\sigma)\Delta_i(\rho-\sigma)d\rho + e^{\sigma}\Delta_i^T(t)\Delta_i(t). \tag{33}$$

A Lyapunov function candidate is constructed as $V(t)|_{\text{caseI}} = V_1(t)|_{\text{caseI}} + \sum_{r=1}^{3}(\bar{\varsigma}\phi_r^{-1})\Gamma_r$. Combining (30) to (33) yields

$$\dot{V}(t)|_{\text{caseI}} \le \Delta_i^T(t)(I_M \otimes \Pi_i)\Delta_i(t),\ i = 1,2,3,4,$$

where $\Pi_1 = S^TW + WS - 2\underline{\lambda}WDD^TW + \sum_{r=0}^{4}\phi_r W^2 + \bar{\varsigma}\phi_1^{-1}e^{\sigma}I_n$, $\Pi_2 = (\phi_0^{-1} + \bar{\varsigma}\phi_2^{-1}e^{\sigma})I_n$, $\Pi_3 = \bar{\varsigma}\phi_3^{-1}e^{\sigma}I_n$, $\Delta_4(t) = \Omega(dh)$, $\Pi_4 = \upsilon^2\sigma\phi_4^{-1}e^{c\sigma}\bar{\lambda}I_n$.

- Case II: $t - \sigma \in \big[dh, (d+1)h\big)$.

By differentiating the $V_1(t)$ along (26), one has

$$\begin{aligned}\dot{V}_1(t)|_{\text{caseII}} \le& \varepsilon^T(t)\Big(I_M \otimes (S^TW + WS - 2\underline{\lambda}WDD^TW)\Big)\varepsilon(t) \\ &+ \varepsilon^T(t)(I_M \otimes \sum_{r=0}^{3}\phi_r W^2)\varepsilon(t) + \phi_0^{-1}\bar{\varepsilon}^T(t)\bar{\varepsilon}(t) \\ &+ \sum_{r=1}^{3}\phi_r^{-1}\Psi_r^T\Psi_r. \end{aligned} \tag{34}$$

A Lyapunov function candidate is constructed as $V(t)|_{\text{caseII}} = V_1(t)|_{\text{caseII}} + \sum_{r=1}^{3}(\bar{\varsigma}\phi_r^{-1})\Gamma_r$. Similarly, exploiting (31) to (33), one gets

$$\begin{aligned}\dot{V}(t)|_{\text{caseII}} \le& \Delta_1^T(t)(I_M \otimes \widetilde{\Pi}_1)\Delta_1(t) \\ &+ \Delta_i^T(t)(I_M \otimes \Pi_i)\Delta_i(t),\ i = 2,3,\end{aligned}$$

where $\widetilde{\Pi}_1 = S^TW + WS - 2\underline{\lambda}WDD^TW + \sum_{r=0}^{3}\phi_r W^2 + \bar{\varsigma}\phi_1^{-1}e^{\sigma}I_n$.

Obviously, $\widetilde{\Pi}_1 < \Pi_1$. Thus, for $\dot{V}(t)$, in both Case I and Case II, it satisfies $\dot{V}(t) \le \Delta_i^T(t)(I_M \otimes \Pi_i)\Delta_i(t)$, $(i = 1,2,3,4)$. By Schur complement lemma and matrix transformations, it is easy to obtain that $\Pi_1 < 0$ is equivalent to (29). According to Theorem 1, $\lim_{t\to+\infty}\bar{\varepsilon}(t) = 0$ and $\lim_{t\to+\infty}\delta(t) = 0$ can be derived, which further implies $\lim_{d\to+\infty}\Omega(dh) = 0$.

Eventually, it can be obtained that $\dot{V}(t) < 0$. Consequently, from the above analysis, one can conclude that $\lim_{t\to+\infty}\|\varepsilon(t)\| = 0$. The proof is completed. ■

4 Numerical Example

In this section, we will demonstrate the validity of the theory through numerical simulations.

Consider the system:

$$x_i = \begin{bmatrix}x_{i1}\\ x_{i2}\end{bmatrix},\quad S = \begin{bmatrix}0 & 1\\ -1 & 0\end{bmatrix},\quad D = \begin{bmatrix}1\\ 2\end{bmatrix},\quad C = \begin{bmatrix}1 & -1\end{bmatrix}.$$

The relationship between the intelligences is represented by the topology diagram in Fig. 1, in which nodes 1-4 denote followers and nodes 5-7 denote leaders.

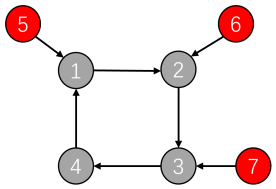

Fig. 1: Communication topology.

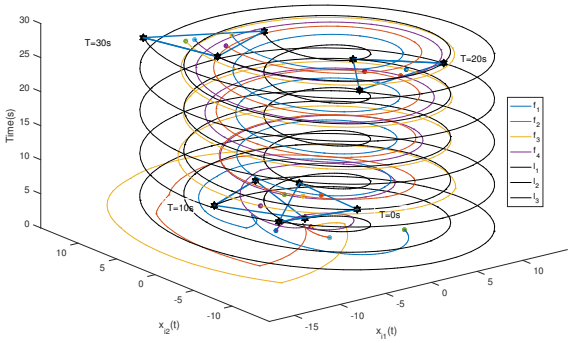

Fig. 2: In the three-dimensional space, the state trajectories of the followers and leaders.

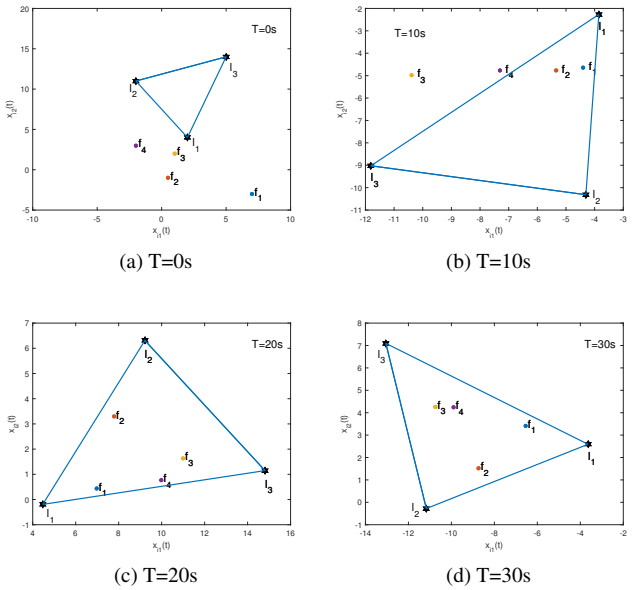

(a) T=0s (b) T=10s

(c) T=20s (d) T=30s

Fig. 3: The states of followers and leaders at different time points.

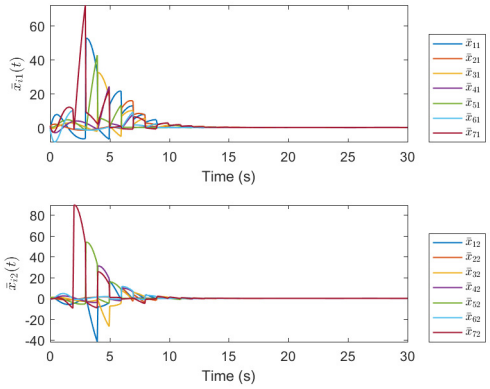

Fig. 4: The decoded errors.

The initial state of the followers are given as $x_1 = [7,-3]^T, x_2 = [0.5,-1]^T, x_3 = [1,2]^T, x_4 = [-2,3]^T$, The initial state of the leaders are given as $x_5 = [2,4]^T, x_6 = [-2,11]^T, x_7 = [5,14]^T$. The following parameters are given: $\sigma = 0.05$, $h = 0.1$, $\zeta = 1$, $b1 = 1.1$, $b2 = 1.8$, $b3 = 2.1$, $c = 0.2$, $\sigma = 0.05$, $\phi_i = 0.1(i = 0,...,4)$, $\upsilon = 0.2$.

Then, by calculating and solving LMI (11) and (29), we can get $g_0 = 33$, $\ell = 0.58$, $H = 10$, $G = \begin{bmatrix} 3.5533 \\ 0.3448 \end{bmatrix}$, $K = \begin{bmatrix} -0.0211 & -0.0461 \end{bmatrix}$.

Utilizing the above parameters, Fig. 2-3 present the simulation results. Specifically, we use $f_i(i = 1,2,...,6)$ to denote the i-th follower and $l_j(j = 1,2,3)$ to denote the j-th leader in Figs. 2. Fig. 2 demonstrates the trajectory of the state of each agent in three-dimensional space. Also highlighted are the states of the agent at time T=0,10,20,30s, which are shown separately in Fig. 3. It can be seen that the followers asymptotically enters the convex hull generated by the leaders. The decoded errors are depicted in Fig. 4 and they converge zero asymptotically, which means that the system (1) is detectable.

5 Conclusion

In this paper, we focus on a continuous MAS with input delays under CDCP. A dynamic quantizer is used to code the estimated state into a finite set of discrete signals for transmission. At the controller side, the received discrete symbols are decoded. Some sufficient conditions have been presented to ensure the detectability of the MASs. Based on the decoded signals, a control protocol using truncated prediction method is proposed to ensure the implementation of containment control for MASs. Future research directions could extend to more complex MASs, such as those with nonlinear terms and state saturation terms.

References

[1] Yifan Liu and Housheng Su. Some necessary and sufficient conditions for containment of second-order multi-agent systems with intermittent sampled data. *ISA transactions*, 108:154–163, 2021.

[2] Mohsen Parsa and Mohammad Danesh. Robust containment control of uncertain multi-agent systems with time-delay and heterogeneous lipschitz nonlinearity. *IEEE Transactions on Systems, Man, and Cybernetics: Systems*, 51(4):2312–2321, 2019.

[3] Wei Ren and Ella Atkins. Distributed multi-vehicle coordinated control via local information exchange. *International Journal of Robust and Nonlinear Control: IFAC-Affiliated Journal*, 17(10-11):1002–1033, 2007.

[4] Kuo Li, Changchun Hua, Xiu You, and Xinping Guan. Distributed output-feedback consensus control for nonlinear multiagent systems subject to unknown input delays. *IEEE Transactions on Cybernetics*, 52(2):1292–1301, 2020.

[5] Liheng Chen, Ming Liu, Xianlin Huang, Shasha Fu, and Jianbin Qiu. Adaptive fuzzy sliding mode control for network-based nonlinear systems with actuator failures. *IEEE Transactions on Fuzzy Systems*, 26(3):1311–1323, 2017.

[6] Li-Ying Hao, Ying Yu, Tie-Shan Li, and Hui Li. Quantized output-feedback control for unmanned marine vehicles with thruster faults via sliding-mode technique. *IEEE Transactions on Cybernetics*, 52(9):9363–9376, 2021.

[7] Licheng Wang, Zidong Wang, Guoliang Wei, and Fuad E Alsaadi. Observer-based consensus control for discrete-time multiagent systems with coding–decoding communication protocol. *IEEE Transactions on Cybernetics*, 49(12):4335–4345, 2018.

[8] Yanhua Yang and Wenfeng Hu. Containment control of double-integrator multi-agent systems with time-varying delays. *IEEE Transactions on Network Science and Engineering*, 9(2):457–466, 2021.

[9] Zongyu Zuo, Zongli Lin, and Zhengtao Ding. Truncated predictor control of lipschitz nonlinear systems with time-varying input delay. *IEEE transactions on Automatic control*, 62(10):5324–5330, 2016.

[10] Ziyang Meng, Wei Ren, and Zheng You. Distributed finite-time attitude containment control for multiple rigid bodies. *Automatica*, 46(12):2092–2099, 2010.

Proceedings of the 3rd Conference on Fully Actuated System Theory and Applications
May 10-12, 2024, Shenzhen, China

Dynamic Event-triggered Model-free Adaptive Heading Consensus Tracking Control for Unmanned Surface Vehicles

Huarong Zhao[1], Jinjun Shan*[2], Xing Li[3,4], Linbo Xie[1]

1. School of Internet of Things Engineering, Jiangnan University, Wuxi, Jiangsu 214122, P. R. China
E-mail: hrzhao@jiangnan.edu.cn,xie_linbo@jiangnan.edu.cn

2. Department of Earth and Space Science and Engineering, York University, Toronto, ON M3J 1P3, Canada
E-mail: jjshan@yorku.ca

3. School of Electrical Engineering and Intelligentization, Dongguan University of Technology, Dongguan 523000, P. R. China
E-mail: lixing8245@163.com

4. State Key Laboratory of Synthetical Automation for Process Industries, Northeastern University, Shenyang, Liaoning 110819, P. R. China

Abstract: This paper investigates a dynamic event-triggered model-free adaptive heading consensus tracking issue for unmanned surface vehicles (USVs). First, a dynamic linearization data model is established by merely using the input and output data of the controlled systems. Then, the characteristics of USVs are analyzed, and a difference-type heading consensus controller is designed. Moreover, the resource-efficient control issue is further considered, and a dynamic event-triggered mechanism is formulated for USVs to implement heading consensus tracking tasks. Finally, the convergence of the consensus tracking errors is roughly proved, and several simulation studies verify the correctness and effectiveness of the proposed method.

Key Words: Unmanned surface vehicles, heading consensus, model-free adaptive control, dynamic event-triggered control

1 Introduction

Unmanned surface vehicles (USVs) are surface ships without requiring operators [1]. Because of the advantages of operational flexibility, good concealment, low operating cost, and high safety, USVs have been wildly applied in the context of merchant, naval, and scientific applications [2]. Generally, the premier issue of USVs is to realize heading control [3], and considerable results have been reported. For example, Huang et al. [4] studied a dynamic output feedback $H\infty$ heading control method, Zhou et al. [5] investigated a set-membership-based heading control scheme, Liu et al. [6] developed an adaptive backstepping controller, and so forth.

It is noted that the results above are only focused on a single system. However, when conducting several tasks, for instance, surveillance and information sharing, water surface multi-objective capturing, and transportation, the cooperation of an alliance of USVs is necessary [7]. In other words, cooperative control is one of the important research fields of USVs. Consensus is a code issue of cooperative control of USVs [8], which has attracted lots of attention from scholars. For example, Han et al. [9] studied a secure sampled-data consensus for USVs against deception attacks, Yang et al. [10] formulated a distributed model predictive consensus for USVs with post-verification, and Li et al. [11] investigated a distributed consensus method for USVs with external disturbances. It should be pointed out that most existing consensus methods of USVs have a common assumption that the dynamics models of USVs are available and accurate. However, the dynamics models of USVs are nonlinear, uncertain, and time-varying, caused by different speeds, parameters of wetted area, draft, and so forth [12]. Hence, investigating a framework for USVs with unknown dynamics models to design controllers is one of the motivations for this paper.

Recently, to overcome the issues of USVs with unknown dynamics models, scholars have explored data-driven control methods, such as PID control [13, 14], reinforcement learning control (RLC) [15, 16], and model-free adaptive control (MFAC) [17, 18]. PID can be transformed as a special form of MFAC, and the neutral networks must be established in RLC. MFAC was first studied by Hou [19] for discrete-time nonlinear systems with unknown dynamics models. Since the advantages of simple construct, strong robustness, and easy operation, MFAC methods have been employed in many applications, such as unmanned helicopters [20], fixed-wing unmanned aerial vehicles [21], and precision machine tools [22]. Moreover, MFAC methods have been expanded to multiagent systems implementing cooperative tasks, for instance, multi-area power systems [23], autonomous vehicle platoon systems [24], and multiple subway trains [25]. Although several results have been developed for multiagent systems, the results of USVs are few. Hence, designing an MFAC method for USVs performing heading consensus tracking tasks is challenging work.

In addition, most results above require that the communication resources do not have any limitations and that computing power is sufficient. However, USVs are a lightweight class devices such that the communication bandwidth and computing resources are extremely finite. Therefore, reducing the communication and computing burden and realizing resource-efficient control is essential when designing a controller for USVs that implement cooperative tasks. Event-triggered control is one of the practical strategies to reduce the communication burden, which was first introduced into multiagent systems by Dimarogonas et al. [26]. After that, numerous interesting methods have been developed. To name a few, Zhu et al. [27] studied a distributed

This work was supported by the National Natural Science Foundation of China (62273059), the Liaoning Natural Science Foundation(2022-KF-21-06), the Fundamental Research Funds for the Central Universities (JUSRP123061), the 111 project (B23008), the Wuxi Science and Technology Development Fund Project (K20231015), and the Discovery Grant from the Natural Sciences and Engineering Research Council of Canada (NSERC) (Corresponding author: Jinjun Shan)

event-triggered affine formation maneuver controller, Zhang et al. [28] investigated an adaptive distributed bridge-to-bridge event-triggered fault-tolerant controller, and Song et al. [29] developed a distributed dynamic edge-based event-triggered formation controller. Although several useful event-triggered approaches have been developed for USVs implementing cooperative tasks, they assume that the dynamics models of USVs are available and accurate. Hence, how to design a model-free event-triggered cooperative control method for USVs is meaningful work.

With consideration given to the above discussions, this paper aims to address the issues of limited communication resources and unknown dynamics models of USV to implement a dynamic event-triggered model-free adaptive heading consensus tracking tasks, where the main contributions are summarized as:

(1) Propose a heading consensus control method for USVs with unknown dynamics, where USVs can implement cooperative control tasks. Compared with the existing schemes [30–32], the proposed method is focused on multiple USVs.

(2) Design a difference-type MFAC controller, a model-free cooperative control method. Compared with the existing MFAC methods [33–35], the requirement that the relationship between the input and output data must be a monotone positive or negative correlation is relieved.

(3) Formulate a dynamic event-triggered communication mechanism, which includes a dynamic event-triggered threshold value. Compared with the existing static event-triggered mechanisms [36–38], the formulated mechanism is a dynamic event-triggered mechanism, which can further reduce the communication burden.

The rest of this paper is organized as follows: The preliminaries and problem formulation are given in Section 2. The controller design and convergence analysis are presented in Section 3. The results of simulation studies are given in Section 4. Several summarizations are presented in Section 5.

2 Problem Formulation

2.1 Algebraic Graph Theory

The algebraic graph is a common tool for describing the relationship among networked multiagent systems. As for N agent and a virtual leader 0, an augmented matrix is utilized as $G = (\bar{V}, E, A)$, where $\bar{V} = \{0\} \cup V$ with $V = \{1, 2, \cdots, N\}$, $E \subseteq V \times V$, and $A = [a_{ij}] \in R^{N\times N}$ denote the set of nodes, the set of edges, and weighted adjacent matrix, respectively. Moreover, the set of neighbors of agent i is denoted as N_i. The Laplacian matrix is calculated as $L = D - A$, where $D = \text{diag}\{d_1, \cdots d_N\}$ with $d_i = \sum_{j\in N_i} a_{ij}$ is an in-degree matrix. Besides, connected relationships between the virtual leader 0 and followers are described as matrix $B = \text{diag}\{b_1, \cdots, b_N\}$, where if the agent i is directly connected with the virtual leader 0, $b_i = 1$; otherwise, $b_i = 0$.

2.2 Model-free Adaptive Controller

Considering N discrete-time nonlinear systems, the input and output of agent i is described as:

$$y_i(k+1) = f_i(y_i(k), \cdots, y_i(k-n_y), u_i(k), \cdots, u_i(k-n_u)) \quad (1)$$

where $u_i(k)$ and $y_i(k)$ are the input and the output of the agent i, respectively. Moreover, n_u and n_y are unknown orders of the input and the output, respectively. $f_i(\cdot)$ is a unknown nonlinear function. Furthermore, Eq. (1) satisfies the following assumptions.

Assumption 1 *The value of $\frac{\partial f_i(\cdot)}{\partial u_i(k)}$ exists and is continuous.*

Assumption 2 *If $\Delta u_i(k) = u_i(k) - u_i(k-1) \neq 0$ and $\Delta y_i(k+1) = y_i(k+1) - y_i(k)$, there exists a constant $r_u \in R^+$ satisfying that $|\Delta y_i(k+1)| \leq r_u |\Delta u_i(k)|$.*

Theorem 1 *Considering that Eq. (1) satisfies Assumptions 1-2, there is a time-varying variable $|\phi_i(k)| \leq r_\phi$ with $r_\phi \in R^+$, called as pseudo-partial-derivative (PPD), satisfying:*

$$\Delta y_i(k+1) = \phi_i(k)\Delta u_i(k) \quad (2)$$

Proof: The proof of Theorem 1 can be found in [19]. ■

Assumption 3 *The PPD $\phi_i(k) > r_c \in R^+$ (or $\phi_i(k) < -r_c$) holds for all k. Generally, it assumes that $\phi_i(k) > r_c$.*

Remark 1 *Assumption 1 is a common assumption for nonlinear systems, Assumption 2 implies that if the input is bounded, the output is bounded, and Assumption 3 implies that the sign of the PPD is unchanged, that is, if the gain of the input increases, the gain of the output does not decrease.*

Assumption 4 *The communication topology G of USVs is strongly connected, where the root node is the virtual leader.*

Then, considering that Eq. (1) satisfies Assumptions 1-4 and using Theorem 1, an MFAC controller [19] is designed:

$$u_i(k) = u_i(k-1) + \frac{\rho\hat{\phi}_i(k)}{\lambda + |\hat{\phi}_i(k)|^2}\xi_i(k) \quad (3)$$

$$\xi_i(k) = \sum_{j\in N_i} a_{ij}(y_j(k) - y_i(k)) + b_i(y_d(k) - y_i(k)) \quad (3a)$$

$$\hat{\phi}_i(k) = \hat{\phi}_i(k-1) + \frac{\eta\Delta u_i(k-1)}{\mu + |\Delta u_i(k-1)|^2} \times (\Delta y_i(k) - \hat{\phi}_i(k-1)\Delta u_i(k-1)) \quad (3b)$$

$$\hat{\phi}_i(k) = \hat{\phi}_i(1), \text{ if } |\hat{\phi}_i(k)| \leqslant \varepsilon \text{ or } |\Delta u_i(k-1)| \leqslant \varepsilon \text{ or } \text{sign}(\hat{\phi}_i(k)) \neq \text{sign}(\phi_i(k)) \quad (3c)$$

where $0 < \rho < 1$, $\lambda > \frac{r_\phi^2}{4}$, $0 < \eta < 1$, $\mu > 0$, and $\varepsilon = 10^{-3}$.

2.3 USVs Heading Control Subsystem

Here, a heading control subsystem [17] is considered as:

$$\begin{cases} \theta_i(k+1) = \theta_i(k) + T_s r_i(k) \\ r_i(k+1) = r_i(k) + \frac{T_s}{T}(K\delta_i(k) - r_i(k)) \end{cases} \quad (4)$$

where $\theta_i(k)$, $r_i(k)$, and $\delta_i(k)$ are heading angle (output, $y_i(k)$), angular speed, and rudder angle (input, $u_i(k)$), respectively. Moreover, T_s denotes the sampling time. T and K are the unknown maneuver coefficients.

It is noted that the heading output $\theta_i(k)$ ranges of USVs are from 180° to -180°, and $\theta_i(k)$ does not always increase when the rudder angle $\delta_i(k)$ increases [17], such as the rudder angle increases from -20° to -10°, but the corresponding heading continues to decrease, that is, the heading control system does not satisfy Assumption 3 of MFAC method.

Moreover, the conversion process from rudder angle to heading angle will produce an integral link in the heading control system, which will cause a rapid process of accumulation and expansion [30]. However, the MFAC method (3) updates PPD through an online learning process with the input and output data, which is a relatively slow process.

To sum up, the heading control subsystem (4) can not directly be governed by the MFAC method (3). It needs to design a novel MFAC method for USVs such that the consensus tracking errors $e_i(k)$ satisfy that

$$\lim_{k\to\infty} |e_i(k)| = |y_d(k) - y_i(k)| \leqslant \wp \tag{5}$$

where $y_i(k) = \theta_i(k)$ is the heading angle, $\wp \in R^+$ is an accept constant, and $y_d(k)$ is the desired heading angle, which satisfies the following assumption.

Assumption 5 ([39]) *The change rate of the desired heading angle $y_d(k)$ is bounded, that is, there exists a constant $r_d \in R^+$ satisfying $|\Delta y_d(k)| \leqslant r_d$.*

3 Controller Design and Analysis

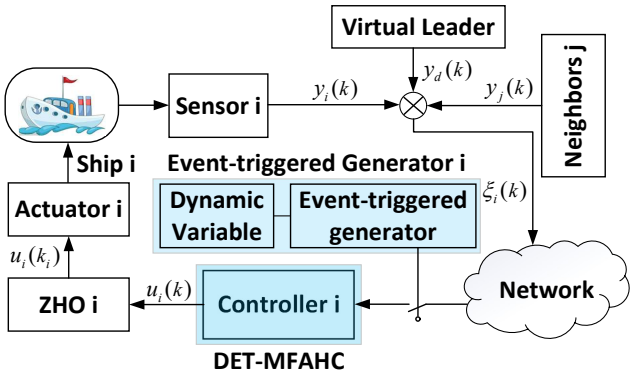

Fig. 1: Schematic diagram of the proposed DET-MFAHC.

Figure 1 shows the schematic diagram of the proposed dynamic event-triggered model-free adaptive heading consensus (DET-MFAHC) method, which mainly includes sensor i, controller i, event-triggered generator i, zero-order holder (ZOH) i, and actuator i. During event-triggered processes, the controller i can receive the data from the network, and the input is updated, that is, $u_i(k_i) = u_i(k)$, where k_i denotes the event-triggered instant; otherwise, the ZOH i will send the data of last event-triggered instant to the actuator i.

3.1 Dynamic Event-triggered Mechanism

A dynamic event-triggered function is defined as

$$\Gamma_i(k) = \frac{1}{v}|\wp_i(k)| + w - |\vartheta_i(k)| \tag{6}$$

where v and w are positive constants, $\vartheta_i(k) = \xi_i(k) - \xi_i(k_i)$, and $\wp_i(k)$ is a dynamic variable, which is defined as

$$\wp_i(k+1) = \hbar\wp_i(k) + w - |\vartheta_i(k)| \tag{7}$$

where $\hbar$ is a constant, and $\wp_i(0) = \wp_0 \in R^+$.

Then, a dynamic event-triggered condition is designed as

$$k_{i+1} = \inf\{k \in Z | k > k_i,\ \Gamma_i(k) < 0\} \tag{8}$$

Lemma 1 ([40]) *If $0 < \hbar + \frac{1}{v} < 1$ and events are not triggered, there exists $r_\wp \in R^+$ satisfying $\lim_{k\to\infty} |\wp_i(k)| \leqslant r_\wp$.*

Proof: The proof process is similar as Theorem 1 in [40]. ■

3.2 DET-MFAHC Design and Analysis

According to the dynamic event-triggered mechanism (8), the MFAC controller (3), and the characteristics of USVs, a difference-type DET-MFAHC is formulated as

$$\begin{aligned} u_i(k) = u_i(k-1) &+ Q_i(k)\frac{\rho\hat{\phi}_i(k)}{\lambda + |\hat{\phi}_i(k)|^2}\xi_i(k) \\ &- Q_i(k)\frac{\rho\hat{\phi}_i(k)}{\lambda + |\hat{\phi}_i(k)|^2}k_r\Delta y_i(k) \end{aligned} \tag{9}$$

$$\xi_i(k) = \sum_{j\in N_i} a_{ij}(y_j(k) - y_i(k)) + b_i(y_d(k) - y_i(k)) \tag{9a}$$

$$\begin{aligned} \hat{\phi}_i(k) = \hat{\phi}_i(k-1) &+ Q_i(k)\frac{\eta\Delta u_i(k-1)}{\mu + |\Delta u_i(k-1)|^2} \\ &\times (\Delta y_i(k) - \hat{\phi}_i(k-1)\Delta u_i(k-1)) \end{aligned} \tag{9b}$$

$$\begin{aligned} \hat{\phi}_i(k) = \hat{\phi}_i(1),\ &\text{if } |\hat{\phi}_i(k)| \leqslant \varepsilon \text{ or } |\Delta u_i(k-1)| \leqslant \varepsilon \\ &\text{or } \text{sign}(\hat{\phi}_i(k)) \neq \text{sign}(\phi_i(k)) \end{aligned} \tag{9c}$$

where $0 < \rho < 1$, $\lambda > \frac{r_\phi^2}{4}$, $0 < \eta < 1$, $\mu > 0$, $k_r > 0$, and $\varepsilon = 10^{-3}$. $Q_i(k)$ is an index of the event-triggered, where if the event is triggered, $Q_i(k) = 1$; otherwise, $Q_i(k) = 0$.

Theorem 2 *Considering that USVs (4) satisfy Assumptions 1-2, the communication topology satisfies Assumption 4, the desired heading angle satisfies Assumption 5, and apply the proposed DET-MFAHC (9) with dynamic event-triggered condition (8) to govern the USVs to perform heading consensus tracking tasks, the consensus tracking errors are bounded if $\lambda \geqslant r_\phi^2/4$ and $\rho < \frac{1}{\max_{i=1,\ldots,N} d_i + b_i}$.*

Proof: The proof processes include two parts.

Part I (The boundness of the estimate of PPD):

Case I (The event is not triggered): In this case, $Q_i(k) = 0$, Eq. (9b) becomes that $\hat{\phi}_i(k+1) = \hat{\phi}_i(k) = \cdots = \hat{\phi}_i(k_i)$. Thus, we only need to analyze that the event is triggered.

Case II (The event is triggered): In this case, $Q_i(k) = 1$, from analysis processes of Theorem 1 in [34], it is obtained that there exist constants $r_{\hat{\phi}} \in R^+$ and $r_{\tilde{\phi}} \in R^+$ satisfy that $|\hat{\phi}| \leq r_{\hat{\phi}}$ and $|\tilde{\phi}| \leq r_{\tilde{\phi}}$, respectively.

Part 2 (The boundness of the consensus tracking errors):

Case I (The event is not triggered): In this case, $Q_i(k) = 0$, Eq. (9) becomes that $u_i(k) = u_i(k-1) = \cdots = u_i(k_i)$. From Lemma 1, it is obtained that $\varphi_i(k)$ is bounded when the event is not triggered. Moreover, since w is a constant, from Eq. (6) it is obtained that if $\xi_i(k)$ is large enough, $\Gamma_i(k) < 0$. It implies that if the consensus tracking errors are large enough, the system enters event-triggered processes. Hence, we only need to analyze that the event is triggered.

Case II (The event is triggered): In this case, $Q_i(k) = 1$. From Eqs. (2) and (5), it is obtained that

$$\begin{aligned} e_i(k+1) &= y_d(k+1) - y_i(k+1) \\ &= e_i(k) + \Delta y_d(k+1) - \Delta y_i(k+1) \\ &= e_i(k) + \Delta y_d(k+1) \end{aligned}$$

$$- \frac{\rho\phi_i(k)\hat{\phi}_i(k)}{\lambda + |\hat{\phi}_i(k)|^2}(\xi_i(k) - \Delta y_i(k)) \qquad (10)$$

Then, since $\lambda \leqslant \frac{r_\phi^2}{4}$ and Theorem 1, we have $\frac{\phi_i(k)\hat{\phi}_i(k)}{\lambda+|\hat{\phi}_i(k)|^2} \leqslant \frac{\phi_i(k)\hat{\phi}_i(k)}{2\sqrt{\lambda}|\hat{\phi}_i(k)|} \leqslant \frac{|\phi_i(k)|}{2\sqrt{\lambda}} \leqslant 1$. Thus, Eq. (10) becomes that

$$\begin{aligned} e(k+1) &\leqslant e(k) + \bar{y}_d(k+1) - \rho\xi(k) + \Delta y(k) \\ &\leqslant e(k) + \bar{y}_d(k+1) - \rho(B+L)e(k) + \Delta y(k) \\ &\leqslant (I - \rho(B+L))e(k) + \bar{y}_d(k+1) + \Delta y(k) \end{aligned} \qquad (11)$$

where $e(k) = [e_1(k), \cdots, e_N(k)]^T$, $y_d(k+1) = [y_d(k+1), \cdots, y_d(k+1)]^T$, $\xi(k) = [\xi_1(k), \cdots, \xi_N(k)]^T$, and $\Delta y(k) = [\Delta y_1(k), \cdots, \Delta y_N(k)]^T$. Then, since $\rho < \frac{1}{\max_{i=1,\ldots,N} d_i + b_i}$, it yields that $||I - \rho(B+L)|| \leqslant q_1$ with $0 < q_1 < 1$. Moreover, according to Assumption 2, it yields that there exists constant $r_y \in R^+$ satisfying $||\Delta y(k)|| \leqslant r_y$. Hence, Eq. (11) can be rewritten as

$$\begin{aligned} ||e(k+1)|| &\leqslant ||I - \rho(B+L)||||e(k)|| + ||\bar{y}_d(k+1)|| \\ &\quad + ||\Delta y(k)|| \\ &\leqslant q_1||e(k)|| + \Omega \\ &\vdots \\ &\leqslant q_1^k||e(1)|| + \frac{1-q_1^k}{1-q_1}\Omega \end{aligned} \qquad (12)$$

where $\Omega \geqslant r_d + r_y$.

Hence, it is obtained that $\lim_{k\to\infty} ||e(k+1)|| \leqslant \frac{\Omega}{1-q_1}$. ■

Remark 2 *From Eq. (12), it is found that the consensus tracking errors are directly affected by the values of the change rates of $y_i(k)$ and $y_d(k)$. It is obtained that if $y_d(k) \to 0$, the consensus tracking errors will also approximate 0. Hence, the proposed method is more suitable for USVs to implement fixed heading angles consensus tasks.*

4 Simulation Studies

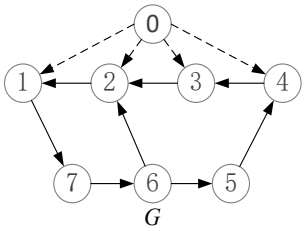

Fig. 2: Communication topology of USVs.

The USVs are connected as shown in Fig. 2, where only USVs 1, 2, 3, and 4 can directly receive the data from the virtual leader 0. The initial conditions are set as $u_i(0) = y_i(0) = \wp_i(0) = 0$, $\hat{\phi}_i(0) = \hat{\phi}_i(1) = 1$, and $\Gamma_i(k) = 0$. Moreover, the parameters are set as $\rho = 0.35$, $\mu = 10$, $\lambda = 55$, $\eta = 0.75$, $T_s = 1$, $T = 1.068$, $K = 0.186$, $k_r = 100$, $v = 50$, $\hbar = 0.1$, and $w = 0.01$.

4.1 USVs with Time-invariant Trajectory

The desired trajectory is set as

$$y_d(k) = \begin{cases} -40^\circ, & 0 < k \leqslant 3s \\ 20^\circ, & 3s < k \leqslant 6s \\ 80^\circ, & k > 6s \end{cases} \qquad (13)$$

The corresponding results are shown in Figs. 3-5. Fig. 3 shows that the heading angles of USVs have rapidly tracked the reference heading angles. Fig. 4 shows the heading angles of USVs governed by the existing static event-triggered method in [34]. Compared with the results shown in Figs. 3 and 4, it is found that they are similar. However, from Fig. 5, it is found that the event-triggered rate of the proposed method is lower than that of the existing static event-triggered method in [34]. Hence, the simulation results further verified that the proposed DET-MFAHC effectively guarantees that the USVs implement consensus tracking tasks and reduce the communication burden.

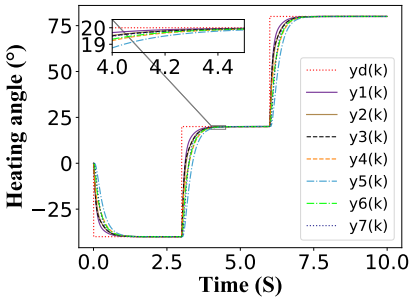

Fig. 3: Heading angles of USVs governed by the proposed DET-MFAHC (Example 1).

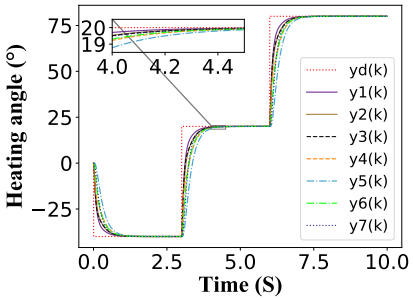

Fig. 4: Heading angles of USVs governed by static event-triggered method in [34] (Example 1).

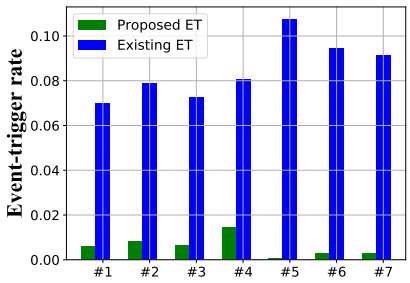

Fig. 5: Event-triggered rates of USVs governed by different event-triggered methods (Example 1).

4.2 USVs with Time-varying Trajectory

As for USVs tracking time-varying heading angles, the desired heading angels are set as

$$y_d(k) = 80^\circ + 20^\circ \sin(5k/4) \qquad (14)$$

The corresponding results are shown in Figs. 6 and 8. Fig. 6 shows that the USVs successfully track the time-varying heading angles, further verifying the correctness of Theorem 2. Moreover, Figs. 7 and 8 indicate the effectiveness of the proposed event-triggered method. Fig. 7 shows the dynamic variable $\wp_i(k)$ is time-varying, and Fig. 8 shows that the average event-triggered interval is about 4018, that is, the proposed DET-MFAHC saves above 94.3% energies.

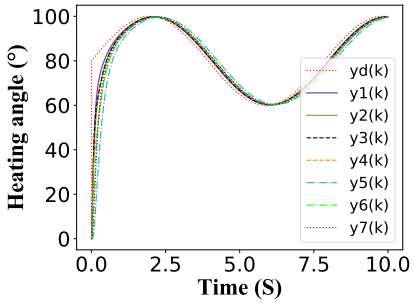

Fig. 6: Heading angles of USVs (Example 2).

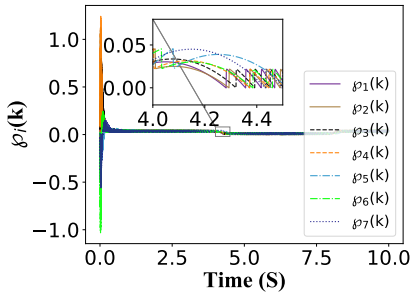

Fig. 7: Outputs of dynamic variable (Example 2).

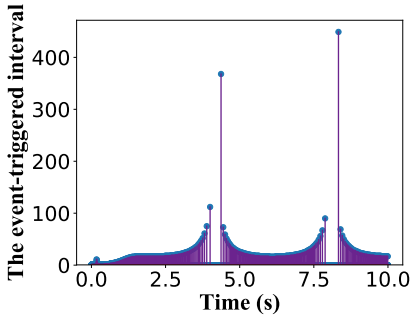

Fig. 8: Event-triggered intervals (Example 2).

5 Conclusions

This paper investigated a resource-efficient consensus heading tracking control issue for USVs with unknown dynamics models. A compact form dynamic linearization model has been established, which only applies the input and output data of the controlled system. Then, a dynamic event-triggered mechanism was designed, further reducing communication resources. Moreover, a difference-type dynamic event-triggered model-free adaptive heading consensus tracking control approach has been designed, which relieves the requirement of the relationship between the gain of input and output must be monotonically increasing or decreasing. Theoretical analysis and simulation results indicate the correctness and effectiveness of the proposed method. In our future efforts, further study of the communication delay issues for USVs is meaningful work.

References

[1] M. J. Er, C. Ma, T. Liu, and H. Gong, "Intelligent motion control of unmanned surface vehicles: A critical review," *Ocean Engineering*, vol. 280, p. 114562, 2023.

[2] Y. Liao, T. Du, and Q. Jiang, "Model-free adaptive control method with variable forgetting factor for unmanned surface vehicle control," *Applied Ocean Research*, vol. 93, p. 101945, 2019.

[3] H. Zhao, D. Xu, Z. Zhou, and H. Yu, "Dynamic event-triggered resilient heading control for unmanned surface vehicle with encrypted data," *IEEE Transactions on Intelligent Vehicles*, 2024, "DOI:10.1109/TIV.2024.3358789".

[4] Y. Huang and F. Lin, "Heading control based on extended homogeneous polynomial lyapunov function," *International Journal of Robust and Nonlinear Control*, 2023, "DOI:10.1002/rnc.7089".

[5] X. Zhou, Y. Zhang, J. Chen, and X. Zheng, "A quantized set-membership estimation-based heading control method of unmanned surface vessels under unknown-but-bounded wave-induced disturbances," *Asian Journal of Control*, 2023, "DOI:10.1002/asjc.3017".

[6] Z. Liu and R. Chu, "Robust adaptive heading control for a surface vessel with drift angles," *Ocean Engineering*, vol. 205, p. 107310, 2020.

[7] Z.-Q. Liu, Y.-L. Wang, and T.-B. Wang, "Incremental predictive control-based output consensus of networked unmanned surface vehicle formation systems," *Information Sciences*, vol. 457, pp. 166–181, 2018.

[8] Z. Peng, J. Wang, D. Wang, and Q.-L. Han, "An overview of recent advances in coordinated control of multiple autonomous surface vehicles," *IEEE Transactions on Industrial Informatics*, vol. 17, no. 2, pp. 732–745, 2020.

[9] S. Han, H. Zhu, Q. Zhong, K. Shi, and O.-M. Kwon, "Secure sampled-data consensus of multi-agent systems under asynchronous deception attacks with application to unmanned surface vehicles," *IEEE Transactions on Intelligent Transportation Systems*, 2023.

[10] W. Yang, T. Shen, T. Pan, G. Hu, and D. Xu, "Distributed model predictive consensus control of unmanned surface vehicles with post-verification," *Drones*, vol. 7, no. 1, p. 42, 2023.

[11] Y. Li, Y. Wu, and S. He, "Distributed consensus control for a group of autonomous marine vehicles with nonlinearity and external disturbances," *Neurocomputing*, vol. 443, pp. 380–387, 2021.

[12] Y. Li, L. Wang, Y. Liao, Q. Jiang, and K. Pan, "Heading mfa control for unmanned surface vehicle with angular velocity guidance," *Applied Ocean Research*, vol. 80, pp. 57–65, 2018.

[13] L. Zhang, Y. Jiang, G. Chen, Y. Tang, S. Lu, and X. Gao, "Heading control of variable configuration unmanned ground vehicle using pid-type sliding mode control and steering control based on particle swarm optimization," *Nonlinear Dynamics*, vol. 111, no. 4, pp. 3361–3378, 2023.

[14] L. Gao, X. Liu, G. Zong, Y. Chen, and K. Shi, "Finite-time sliding mode trajectory tracking control of an autonomous surface vehicle with prescribed performance," *Ocean Engineering*, vol. 284, p. 114919, 2023.

[15] Y. Wang, J. Cao, J. Sun, X. Zou, and C. Sun, "Path following control for unmanned surface vehicles: A reinforce-

ment learning-based method with experimental validation," *IEEE Transactions on Neural Networks and Learning Systems*, 2023, "DOI:10.1109/TNNLS.2023.3313312".

[16] C. Pan, Z. Peng, L. Liu, and D. Wang, "Data-driven distributed formation control of under-actuated unmanned surface vehicles with collision avoidance via model-based deep reinforcement learning," *Ocean Engineering*, vol. 267, p. 113166, 2023.

[17] Y. Liao, Q. Jiang, T. Du, and W. Jiang, "Redefined output model-free adaptive control method and unmanned surface vehicle heading control," *IEEE Journal of Oceanic Engineering*, vol. 45, no. 3, pp. 714–723, 2019.

[18] Q. Jiang, Y. Li, Y. Liao, Y. Miao, W. Jiang, and H. Wu, "Information fusion model-free adaptive control algorithm and unmanned surface vehicle heading control," *Applied Ocean Research*, vol. 90, p. 101851, 2019.

[19] X. Bu, Z. Hou, and H. Zhang, "Data-driven multiagent systems consensus tracking using model free adaptive control," *IEEE transactions on neural networks and learning systems*, vol. 29, no. 5, pp. 1514–1524, 2017.

[20] B. Xian, X. Gu, and X. Pan, "Data driven adaptive robust attitude control for a small size unmanned helicopter," *Mechanical Systems and Signal Processing*, vol. 177, p. 109205, 2022.

[21] S. Zhao, X. Wang, D. Zhang, and L. Shen, "Model-free fuzzy adaptive control of the heading angle of fixed-wing unmanned aerial vehicles," *Journal of Aerospace Engineering*, vol. 30, no. 4, p. 04017019, 2017.

[22] X. Yu, Z. Hou, M. M. Polycarpou, and L. Duan, "Data-driven iterative learning control for nonlinear discrete-time mimo systems," *IEEE Transactions on Neural Networks and Learning Systems*, vol. 32, no. 3, pp. 1136–1148, 2020.

[23] Z. Cheng, X. Bu, J. Liang, and J. Liu, "Indirect–direct secure load frequency control against false data injection attacks," *IEEE Transactions on Industrial Informatics*, 2023, "DOI:10.1109/TII.2023.3330235".

[24] P. Zhu, S. Jin, X. Bu, and Z. Hou, "Distributed data-driven control for a connected autonomous vehicle platoon subjected to false data injection attacks," *IEEE Transactions on Automation Science and Engineering*, 2023, "DOI:10.1109/TASE.2023.3345369".

[25] Q. Wang, S. Jin, and Z. Hou, "Compensation-based cooperative mfailc for multiple subway trains under asynchronous data dropouts," *IEEE Transactions on Intelligent Transportation Systems*, vol. 23, no. 12, pp. 23 750–23 760, 2022.

[26] D. V. Dimarogonas, E. Frazzoli, and K. H. Johansson, "Distributed event-triggered control for multi-agent systems," *IEEE Transactions on automatic control*, vol. 57, no. 5, pp. 1291–1297, 2011.

[27] C. Zhu, B. Huang, Y. Lu, X. Li, and Y. Su, "Distributed affine formation maneuver control of autonomous surface vehicles with event-triggered data transmission mechanism," *IEEE Transactions on Control Systems Technology*, vol. 31, no. 3, pp. 1006–1017, 2023.

[28] G. Zhang, S. Liu, and X. Zhang, "Adaptive distributed fault-tolerant control for underactuated surface vehicles with bridge-to-bridge event-triggered mechanism," *Ocean Engineering*, vol. 262, p. 112205, 2022.

[29] S. Song, E. Zhang, W. Wang, and T. Liu, "Distributed dynamic edge-based event-triggered formation control for multiple underactuated unmanned surface vessels," *Ocean Engineering*, vol. 264, p. 112319, 2022.

[30] Y. Liao, C. Chen, T. Du, J. Sun, Y. Xin, Z. Zhai, B. Wang, Y. Li, and S. Pang, "Research on disturbance rejection motion control method of usv for uuv recovery," *Journal of Field Robotics*, vol. 40, no. 3, pp. 574–594, 2023.

[31] Y. Liao, T. Du, and Q. Jiang, "Model-free adaptive control method with variable forgetting factor for unmanned surface vehicle control," *Applied Ocean Research*, vol. 93, p. 101945, 2019.

[32] Z. Peng, D. Wang, and J. Wang, "Data-driven adaptive disturbance observers for model-free trajectory tracking control of maritime autonomous surface ships," *IEEE Transactions on Neural Networks and Learning Systems*, vol. 32, no. 12, pp. 5584–5594, 2021.

[33] S. Xiong and Z. Hou, "Data-driven formation control for unknown mimo nonlinear discrete-time multi-agent systems with sensor fault," *IEEE Transactions on Neural Networks and Learning Systems*, vol. 33, no. 12, pp. 7728–7742, 2022.

[34] H. Zhao, H. Yu, and L. Peng, "Event-triggered distributed data-driven iterative learning bipartite formation control for unknown nonlinear multiagent systems," *IEEE Transactions on Neural Networks and Learning Systems*, vol. 35, no. 1, pp. 417–427, 2024.

[35] B.-F. Yue and W.-W. Che, "Data-driven dynamic event-triggered fault-tolerant platooning control," *IEEE Transactions on Industrial Informatics*, vol. 19, no. 7, pp. 8418–8426, 2023.

[36] H. Zhao, J. Shan, L. Peng, and H. Yu, "Distributed event-triggered bipartite consensus for multiagent systems against injection attacks," *IEEE Transactions on Industrial Informatics*, vol. 19, no. 4, pp. 5377–5386, 2023.

[37] W. Zhou, J. Fu, H. Yan, X. Du, Y. Wang, and H. Zhou, "Event-triggered approximate optimal path-following control for unmanned surface vehicles with state constraints," *IEEE Transactions on Neural Networks and Learning Systems*, vol. 34, no. 1, pp. 104–118, 2023.

[38] S. Song, J. H. Park, B. Zhang, and X. Song, "Event-triggered adaptive practical fixed-time trajectory tracking control for unmanned surface vehicle," *IEEE Transactions on Circuits and Systems II: Express Briefs*, vol. 68, no. 1, pp. 436–440, 2020.

[39] H. Zhao, J. Shan, L. Peng, and H. Yu, "Data-driven event-triggered formation of mimo multiagent systems with constrained information," *IEEE Transactions on Systems, Man, and Cybernetics: Systems*, vol. 54, no. 1, pp. 39–49, 2024.

[40] Y.-S. Ma, W.-W. Che, and C. Deng, "Dynamic event-triggered model-free adaptive control for nonlinear cpss under aperiodic dos attacks," *Information Sciences*, vol. 589, pp. 790–801, 2022.

Proceedings of the 3rd Conference on Fully Actuated System Theory and Applications
May 10-12, 2024, Shenzhen, China

Robust Containment Control of Heterogeneous Uncertain Multi-Agent Systems under Markovian Switching Topologies

Haihua Guo[1,2], Cong Bi[3], Xiang Xu[4]

1. Shenzhen Key Laboratory of Control Theory and Intelligent Systems, Southern University of Science and Technology, Shenzhen 518055, China
E-mail: hhguo3-c@my.cityu.edu.hk

2. Hong Kong Institute for Data Science, City University of Hong Kong, Hong Kong, China
E-mail: hhguo3-c@my.cityu.edu.hk

3. College of Artificial Intelligence, Nankai University, Tianjin, China
E-mail: congbi2-c@my.cityu.edu.hk

4. School of System Design and Intelligent Manufacturing, Southern University of Science and Technology, Shenzhen, Guangdong Province, China
E-mail: xiangxu5-c@my.cityu.edu.hk

Abstract: This study addresses the robust output containment control problem of heterogeneous uncertain multi-agent systems under Markovian switching topologies. A novel distributed output feedback controller is proposed. Based on the internal model approach, the main result shows that the output of each follower agent converges to the convex hull formed by the outputs of the leader agents under the proposed distributed controller. An illustrative example is given to validate the effectiveness of the proposed controller.

Key Words: containment control, multi-agent systems, Markovian switching topologies, uncertainties

1 Introduction

The field of multi-agent systems (MASs) has witnessed rapid development in recent years, driven by its broad applications ranging from networked mobile robots to biological systems, see, for example, [1–6]. Containment control, as a fundamental problem in cooperative control of MASs, aims to steer a group of follower agents to remain within the convex hull formed by a set of leaders. For example, to prevent a group of vehicles from entering hazardous areas, several agents were designed as leaders to facilitate vehicles into the safety zone formed by the leaders [7]. Motivated by practical applications, the containment control problems with multiple leaders have been studied for MASs with single/double-integrator, homogeneous MASs, and heterogeneous MASs [8–13]. In real-world applications, the MASs usually subject to uncertainties, and robust containment control problems on MASs with uncertainties can be found in [14, 15].

In practice, the communication network among agents can change unpredictably due to factors like hardware failures, signal interference, or dynamic environments, which result in the system often has time-varying network structures and the connections between agents subject to stochastic transitions. The Markovian randomly switching topologies are commonly used to model these changing communication topologies. In recent years, the containment control problems of MASs under Markovian switching topologies (MST) have been investigated and some fundamental results have been shown in [16–18]. Moreover, it is noted that the leader-following consensus problem of heterogeneous uncertain MASs under MST has been involved in [19]. However, the multiple leaders case has not been studied yet, which motives this study.

This paper studies the robust output containment control problem of heterogeneous uncertain MASs under MST. A novel distributed controller is developed under the MST. Compared with those relevant works [10–21], the main contributions of this paper are summarized as follows.

(i) Different from [10–15], where the containment control problems of heterogeneous MASs with fixed topologies or deterministic switching topologies have been studied, this paper considers the MST, which only requires the connectivity in the union graph.

(ii) Compared with [13, 16–18], this paper considers the uncertainties in agent dynamics and the internal model principle is utilized to handle those uncertainties.

(iii) In contrast to [19–21], where a single leader was considered, this study addresses multiple leaders and includes the leader-following consensus problem of heterogeneous MASs under MST as a special case.

The structure of this paper is organized as follows: Section 2 presents the necessary preliminaries and formulates the problem. Section 3 details the primary findings and contributions of this study. Section 4 showcases a simulation to demonstrate the effectiveness of our approach, followed by Section 5, which offers conclusions drawn from the study.

2 Preliminaries and Problem Formulation

2.1 Preliminaries

Consider an MAS consisting of K followers and $L-K$ leaders. If the agent has no neighbor, it is called a leader; otherwise, it is a follower. Denote the follower set as $\mathbb{K} = \{1, \ldots, K\}$ and the leader set as $\mathbb{L} = \{K+1, \ldots, L\}$, respectively. Denote $(\Omega, \mathcal{F}, \mathfrak{F}, \mathbb{P})$ as a complete probability space where $\mathfrak{F} = \{\mathcal{F}_t; t \geq 0\}$ is a filtration. Denote $r(t)$ as the switch signal, which is determined by a continuous-time Markov process that takes values within

This paper is partially supported by Shenzhen Key Laboratory of Control Theory and Intelligent Systems under grant No. ZDSYS20220330161800001 and partially supported by the Tianjin Natural Science Foundation of China under Grant 22JCQNJC00930.

$\mathbb{S} = \{1, 2, \ldots, s\}$. Let the generator of the ergodic Markov process $\{r(t), t \geq 0\}$ be $\Omega = (\gamma_{kr}) \in \mathbb{R}^{s\times s}$, which satisfies $\mathbb{P}\{\sigma(t+\epsilon) = r \mid r(t) = k\} = \gamma_{kr}\epsilon + o(\epsilon)$, if $k \neq r$, otherwise, it equals to $1 + \gamma_{kk}\epsilon + o(\epsilon)$, where $\lim_{\epsilon\to 0} o(\epsilon)/\epsilon = 0$. Here, $\gamma_{kr} \geq 0$ is the transition rate from k to r if $k \neq r$ while $\gamma_{kk} = -\sum_{r\neq k} \gamma_{kr} \leq 0$. The sum of each row in the transition rate matrix Ω is zero, expressed as $\Omega\mathbf{1} = \mathbf{0}$. Consider the directed graph $\mathcal{G}_{r(t)} = \left\{\mathcal{V}, \mathcal{E}_{r(t)}, \mathcal{A}_{r(t)}\right\}$, which represents the time-varying topology among K followers and $L-K$ leaders. Here, $\mathcal{V} = \{1, \cdots, L\}$ is the set of vertices. The set of edges $\mathcal{E}_{r(t)} = \{(j,i)|i,j \in \mathcal{V}\}$ and the adjacency matrix $\mathcal{A}_{r(t)}$ exhibit time-varying characteristics. Let $\mathcal{G}_F^{r(t)} = (\mathbb{K}, \mathcal{E}_F^{r(t)}, \mathcal{A}_F^{r(t)})$ be a digraph among followers, where $\mathcal{E}_F(r(t)) \subseteq \mathbb{K}\times\mathbb{K}$ and $\mathcal{A}_F^{r(t)} = (a_{ij}^{r(t)})_{K\times K}$ with $a_{ij}^{r(t)} > 0 \Leftrightarrow (j,i) \in \mathcal{E}_F^{r(t)}$ and $a_{ij}^{r(t)} = 0$, otherwise. Here, we assume $a_{ii}^{r(t)} = 0,\ \forall i \in \mathbb{K}$. The pinning gains from the jth leader to each follower i is $a_{ij}^{r(t)}, j \in \mathbb{L}$, where $a_{ij}^{r(t)} > 0$ if the follower i can receive the signal from the leader j; otherwise, $a_{ij}^{r(t)} = 0$. The Laplacian matrix $L(r(t))$ corresponding to $\mathcal{G}_{r(t)}$ can be written as: $L(r(t)) = \begin{pmatrix} L_1(r(t)) & L_2(r(t)) \\ 0_{L-K\times K} & 0_{L-K\times L-K} \end{pmatrix}$, where $L_1(r(t))$ and $L_2(r(t))$ are the same as in [18]. For k in $\mathbb{S}$, let $\mathcal{G}_{un} = \bigcup_{k=1}^{s} \mathcal{G}_k = (\mathcal{V}, \bigcup_{k=1}^{s} \mathcal{E}_k)$ be denoted as the *union graph* of $\mathcal{G}(k)$.

2.2 Problem Statement

The following heterogeneous uncertain MAS is considered:

$$\begin{cases} \dot{x}_i = (A_i + \delta_i A)x_i + (B_i + \delta_i B)u_i, \\ y_i = (C_i + \delta_i C)x_i, \quad i \in \mathbb{K}, \end{cases} \tag{1}$$

where $x_i \in \mathbb{R}^{n_i}$, $u_i \in \mathbb{R}^{m_i}$, and $y_i \in \mathbb{R}^q$ are the ith agent's state, input, output, respectively; $A_i \in \mathbb{R}^{n_i\times n_i}, B_i \in \mathbb{R}^{n_i\times m_i}, C_i \in \mathbb{R}^{q\times n_i}$ are known nominal parts, and $\delta_i A, \delta_i B, \delta_i C$ are unknown perturbations. Define

$$\theta = \begin{bmatrix} \mathrm{vec}\,(\delta_1 A, \cdots, \delta_K A) \\ \mathrm{vec}\,(\delta_1 B, \cdots, \delta_K B) \\ \mathrm{vec}\,(\delta_1 C, \cdots, \delta_K C) \end{bmatrix} \in \mathbb{R}^p \tag{2}$$

where $p = \sum_{i=1}^{K} n_i\,(n_i + q + m_i)$. The $L-K$ leaders are described as follows:

$$\begin{cases} \dot{v}_j = Sv_j, \\ y_j = Rv_j, j \in \mathbb{L}, \end{cases} \tag{3}$$

where $v_j \in \mathbb{R}^m$ and $y_j \in \mathbb{R}^q$ are the state and output of the lth leader, respectively.

This objective of this work is to design a distributed controller for heterogeneous uncertain MAS (1) and (3) under MST, such that the outputs of each follower can converge, in mean square sense, to the convex hull formed by those of the leaders. Subsequently, a definition and some assumptions are provided.

Definition 1. *Consider the heterogeneous MAS (1) and (3) under MST $\mathcal{G}_{r(t)}$, the distributed output containment control problem can be achieved in mean square sense, if there exist nonnegative constants $\beta_{ij},\ i \in \mathbb{K}, j \in \mathbb{L}$ satisfying $\sum_{j\in\mathbb{L}} \beta_{ij} = 1$ such that*

$$\lim_{t\to+\infty} \mathbb{E}\left[\left\| y_i - \sum_{j\in\mathbb{L}} \beta_{ij} y_j \right\|^2\right] = 0,\ i \in \mathbb{K}. \tag{4}$$

Assumption 1. *(A_i, B_i) are stabilizable and (A_i, C_i) are detectable, $i \in \mathbb{K}$.*

Assumption 2. *The leader set $\mathbb{L}$ is globally reachable within $\mathcal{G}_{un}$.*

Assumption 3. *For $\lambda \in \lambda(S)$, one has*

$$\mathrm{rank}\begin{pmatrix} A_i - \lambda I & B_i \\ C_i & 0 \end{pmatrix} = n_i + q,\ i \in \mathbb{K}, \tag{5}$$

where $\lambda(S)$ is the spectrum of S.

3 Main Result

Design the following distributed output feedback controller for the ith follower:

$$u_i = G_i z_i, \tag{6a}$$

$$\dot{\psi}_i = S\psi_i - \nu \sum_{j=1}^{K} a_{ij}^{r(t)} (\psi_i - \psi_j) - \nu \sum_{j=K+1}^{L} a_{ij}^{r(t)} (\psi_i - v_j), \tag{6b}$$

$$\dot{z}_i = \hat{F}_{1i} z_i + \hat{F}_{2i}(y_i - R\psi_i), \tag{6c}$$

where $z_i \in \mathbb{R}^{w_i}$ is the internal model state; $G_i, \hat{F}_{1i}, \hat{F}_{2i}$ are to be designed; $\nu > 0$ is the observer gain; $\psi_i \in \mathbb{R}^m$ is the distributed observer state; and $a_{ij}^{r(t)}$ is driven by an ergodic Markov process $\{r(t), t \geq 0\}$.

Ergodic Markov process is characterized by a sole stationary distribution described as $\alpha = (\alpha_1, \ldots, \alpha_s)$. Consequently, it is reasonable to posit that the Markov process $\{r(t), t \geq 0\}$ initiates from the stationary distribution, then the adjacency matrix of $\mathcal{G}_{un}$ can be expressed as $\sum_{k=1}^{s} \alpha_k \mathcal{A}_k$. Here, we define $L_1 = \mathbb{E}[L_1(r(t))]$, $L_2 = \mathbb{E}[L_2(r(t))]$. It is observed that the *expectation graph* $\mathbb{E}[\mathcal{G}_{r(t)}]$ shares an identical structure with that of $\mathcal{G}_{un}$. The Laplacian matrix corresponding to $\mathbb{E}[\mathcal{G}_{r(t)}]$ can be expressed as : $\mathbb{E}[L(r(t))] = \begin{pmatrix} L_1 & L_2 \\ 0_{L-K\times K} & 0_{L-K\times L-K} \end{pmatrix}$.

Lemma 1. *[8] If Assumption 2 is satisfied, L_1 is a nonsingular M-matrix, every element of matrix $-L_1^{-1}L_2$ are nonnegative and $-L_1^{-1}L_2\mathbf{1}_{L-K} = \mathbf{1}_K$.*

Lemma 2. *Consider the distributed observer (6b) under Assumption 2. If S has no eigenvalues with positive real parts, then $\lim_{t\to+\infty} \mathbb{E}[\|\psi_i - \sum_{j\in\mathbb{L}} \beta_{ij} v_j\|^2] = 0,\ i \in \mathbb{K}$, exponentially if ν satisfies (18).*

Proof. Denote $\psi = \left(\psi_1^T, \ldots, \psi_K^T\right)^T$ and $v = \left(v_{K+1}^T, \ldots, v_L^T\right)^T$. Then, the distributed observer (6b) can be written as

$$\begin{aligned} \dot{\psi} = &(I_K \otimes S)\,\psi - \nu(L_1(r(t)) \otimes I_m)\psi \\ &- \nu\,(L_2(r(t)) \otimes I_m)\,v. \end{aligned} \tag{7}$$

Denote the state containment error as

$$\phi = \psi + \left(L_1^{-1}L_2 \otimes I_m\right) v, \tag{8}$$

where $\phi = \left(\phi_1^T, \ldots, \phi_N^T\right)^T$ and $\phi_i = \psi_i - \sum_{j\in\mathbb{L}} \beta_{ij} v_j, i \in \mathbb{K}$. Then, (9) can be written as:

$$\phi = \left((I_K \otimes S) - \nu(L_1(r(t)) \otimes I_m)\right)\phi + \Upsilon_{r(t)}, \tag{9}$$

where

$$\Upsilon_{r(t)} = \nu(L_1(r(t))L_1^{-1}L_2 \otimes I_m))v - \nu(L_2(r(t)) \otimes I_m))v. \tag{10}$$

Based on the results in [22, Lemma 2], it can be inferred that if the expectation graph is a non-singular M-matrix, there exists a positive definite matrix $Q = Q^T \in \mathbb{R}^{K\times K}$ such that

$$QL_1 + L_1^T Q > 0. \tag{11}$$

Denote

$$\tilde{\lambda} = \lambda_{\min}\left(QL_1 + L_1^T Q\right) > 0. \tag{12}$$

Furthermore, it follows that there exists a $P > 0$ and a constant $\vartheta > 0$ such that

$$PS + S^T P - P + \vartheta P < 0. \tag{13}$$

The Lyapunov function is designed as:

$$V = \mathbb{E}\left[\phi^T(Q \otimes P)\phi\right], \tag{14}$$

$$V_k = \mathbb{E}\left[\phi^T(Q \otimes P)\phi \mathbf{1}_{\{r(t)=k\}}\right], \quad k \in \mathbb{S}, \tag{15}$$

where $\mathbf{1}_{\{r(t)=k\}}$ is the Dirac measure over $\{r(t) = k\}$, From [23, lemma 3.6], we have that

$$\begin{aligned} dV_k =& 2\mathbb{E}\left[\phi^T(Q \otimes P)d\phi \mathbf{1}_{\{r(t)=k\}}\right] \\ &+ \mathbb{E}\left[\phi^T(Q \otimes P)\phi d\mathbf{1}_{\{r(t)=k\}}\right] \\ =& \mathbb{E}\big[\phi^T\big(Q \otimes (PS + S^T P) \\ &- \nu(QL_1(r(t)) + L_1^T(r(t))Q) \otimes P\big)\phi \mathbf{1}_{\{r(t)=k\}}\big]dt \\ &+ 2\nu\mathbb{E}\big[\phi^T\big(QL_1(r(t))L_1^{-1}L_2 \otimes P\big)v\mathbf{1}_{\{r(t)=k\}}\big]dt \\ &- 2\nu\mathbb{E}\big[\phi^T\big(QL_2(r(t)) \otimes P\big)v\mathbf{1}_{\{r(t)=k\}}\big]dt \\ &+ \sum_{r=1}^{s}\gamma_{rk}V_r dt. \end{aligned} \tag{16}$$

Noting $\{r(t), t \geq 0\}$ initiates from the stationary distribution α, one has

$$\begin{aligned} \dot{V} =& \sum_{k=1}^{s}\dot{V}_k \\ =& \mathbb{E}\big[\phi^T\big(Q \otimes \left(PS + S^T P\right) - \nu\left(QL_1 + L_1^T Q\right) \otimes P\big)\phi\big] \\ \leq& \mathbb{E}\left[\phi^T\left(Q \otimes \left(PS + S^T P\right) - \nu\tilde{\lambda}I_K \otimes P\right)\phi\right] \\ \leq& \mathbb{E}\left[\phi^T\left(Q \otimes \left(PS + S^T P - \nu\tilde{\lambda}\lambda_{\max}^{-1}(Q)P\right)\phi\right]\right. . \end{aligned} \tag{17}$$

Let

$$\nu \geq \tilde{\lambda}^{-1}\lambda_{\max}(Q). \tag{18}$$

From (13) we have that $\dot{V} \leq -\vartheta V$. By employing the comparison lemma, as detailed in [24], we have $V \leq \exp(-\vartheta t)V(0)$, which implies that $\lim_{t\to\infty}\mathbb{E}[\|\phi_i\|^2] = 0$ exponentially. The proof is completed. □

Theorem 1. *Consider heterogeneous uncertain MAS (1) and (3) under Assumptions 1-3. Let $G_i = (G_{1i}, G_{2i}), i \in \mathbb{F}$ such that $\begin{pmatrix} A_i + B_iG_{1i} & B_iG_{2i} \\ F_2C_i & F_1 \end{pmatrix}$ is Hurwitz, where (F_1, F_2) is selected as in [20, Lemma 6]. Choose U_i such that $A_i + U_iC_i$ is Hurwitz, $\hat{F}_{1i} = \begin{pmatrix} A_i + B_iG_{1i} + U_iC_i & B_iG_{2i} \\ 0 & F_1 \end{pmatrix}$ and $\hat{F}_{2i} = \begin{pmatrix} -U_i \\ F_2 \end{pmatrix}$. Then, the robust containment control problem is solved under the proposed controller (6).*

Proof. Denote $x = (x_1^T, \ldots, x_K^T)^T$, $y_F = (y_1^T, \ldots, y_K^T)^T$, $y_L = (y_{K+1}^T, \ldots, y_L^T)^T$, $z = (z_1^T, \ldots, z_K^T)^T$, $A + \delta A = \text{blockdiag}\{A_1 + \delta_1 A, \ldots, A_K + \delta_K A\}$, $B + \delta B = \text{blockdiag}\{B_1 + \delta_1 B, \ldots, B_K + \delta_K B\}$, $A + \delta C = \text{blockdiag}\{C_1 + \delta_1 C, \ldots, C_K + \delta_K C\}$, $G = \text{blockdiag}\{G_1, \ldots, G_K\}$, $\hat{F}_1 = \text{blockdiag}\{\hat{F}_{11}, \ldots, \hat{F}_{1K}\}$, and $\hat{F}_2 = \text{blockdiag}\{\hat{F}_{21}, \ldots, \hat{F}_{2K}\}$. Let the output containment error be denote as $e = y_F + \left(L_1^{-1}L_2 \otimes I_q\right)y_L$, where $e = (e_1^T, \ldots, e_K^T)^T$. The following closed-loop system can be given by combining (1), (3), and (6):

$$\begin{cases} \dot{x} = (A + \delta A)x + (B + \delta B)Gz, \\ \dot{z} = \hat{F}_1 z + \hat{F}_2\left(y_F - (I_K \otimes R)\psi\right), \\ \dot{v} = (I_{L-K} \otimes R)v, \\ \dot{\psi} = (I_K \otimes S)\psi - \nu(L_1(r(t)) \otimes I_m)\psi \\ \qquad - \nu\left(L_2(r(t)) \otimes I_m\right)v, \\ y_F = (C + \delta C)x, \\ \phi = \psi + \left(L_1^{-1}L_2 \otimes I_m\right)v, \\ e = y_F + \left(L_1^{-1}L_2 \otimes I_q\right)y_L. \end{cases} \tag{19}$$

Let $\hat{x} = \text{vec}(x, z)$, one has

$$\begin{cases} \dot{\hat{x}} = \widetilde{A}^*\hat{x} + \widetilde{B}^*\phi - \widetilde{B}^*\left(L_1^{-1}L_2 \otimes I_m\right)v, \\ \dot{v} = (I_{L-K} \otimes R)v, \\ \dot{\psi} = (I_K \otimes S)\psi - \nu(L_1(r(t)) \otimes I_m)\psi \\ \qquad - \nu\left(L_2(r(t)) \otimes I_m\right)v, \\ \phi = \psi + \left(L_1^{-1}L_2 \otimes I_m\right)v, \\ e = \widetilde{C}^*\hat{x} + \left(L_1^{-1}L_2 \otimes R\right)v, \end{cases} \tag{20}$$

where

$$\widetilde{A}^* = \begin{pmatrix} A + \delta A & (B + \delta B)G \\ \hat{F}_2(C + \delta C) & \hat{F}_1 \end{pmatrix}, \\ \widetilde{B}^* = \begin{pmatrix} 0 \\ \hat{F}_2(I_K \otimes R) \end{pmatrix}, \widetilde{C}^* = \begin{pmatrix} C + \delta C, & 0 \end{pmatrix}. \tag{21}$$

According to the Theorem 2 in [20], it follows that A^* is Hurwitz. Therefore, there exists an open neighborhood Θ of $\theta = 0$ so that $\widetilde{A}^*$ is Hurwitz.

From [25, Lemma 1.27], we can derive that there exists a unique Φ^* that satisfies:

$$\begin{cases} \Phi^*(I_K \otimes S) = \widetilde{A}^*\Phi^* + \widetilde{B}^*, \\ (I_K \otimes R) = \widetilde{C}^*\Phi^*. \end{cases} \tag{22}$$

Define $\widetilde{x}^* = \hat{x} + \Phi^*\left(L_1^{-1}L_2 \otimes I_m\right)v$, it follows from (20)

that

$$\dot{\widetilde{x}}^* = \widetilde{A}^*\widetilde{x}^* + \widetilde{B}^*\phi, \tag{23a}$$

$$e = \widetilde{C}^*\widetilde{x}^*. \tag{23b}$$

Since $\lim_{t\to\infty}\mathbb{E}\left[\|\phi\|\right]^2 = 0$ exponentially via Lemma 2. It follows from [22, Lemma 1] and (23a) that $\lim_{t\to+\infty}\mathbb{E}[\|\widetilde{x}^*\|^2] = 0$. Then, (23b) implies that $\lim_{t\to+\infty}\mathbb{E}[\|e\|^2] = 0$. Thus, $\lim_{t\to+\infty}\mathbb{E}\big[\big\|y_i - \sum_{j\in\mathbb{L}}\beta_{ij}y_j\big\|^2\big] = 0$, $i \in \mathbb{K}$, which completes the proof. □

Consider the case of heterogeneous MAS (1) and (3) without uncertainties, namely $\theta = 0$, we have the following result.

Corollary 1. *Under Assumptions 1-3, appropriate matrices $K_{1i}, K_{2i}, i \in \mathbb{K}$ can be designed such that the mean square output containment can be achieved by the following distributed controller:*

$$\begin{aligned}
u_i =& K_{1i}\hat{x}_i + K_{2i}\psi_i,\\
\dot{\psi}_i =& S\psi_i - \nu\sum_{j=1}^{K} a_{ij}^{r(t)}(\psi_i - \psi_j) - \nu\sum_{j=K+1}^{L} a_{ij}^{r(t)}(\psi_i - v_j),\\
\dot{\hat{x}}_i =& A_i\hat{x}_i + B_iu_i + H_i(C_i\hat{x}_i - y_i),
\end{aligned} \tag{24}$$

where K_{1i}, H_i are chosen such that $A_i + B_iK_{1i}, A_i + H_iC_i$ are Hurwitz, $K_{2i} = Y_i - K_{1i}X_i$, and (X_i, Y_i) are the solution of the linear matrix equations

$$A_iX_i + B_iY_i = X_iS \tag{25}$$

$$C_iX_i = R, \tag{26}$$

Proof. The result can be obtained from Lemma 2 and [18], and is thus omitted. □

Remark 1. *If there is only one leader in system (3), then the robust output containment problem of system (1) and (3) reduces to the case of robust leader-following consensus problem, which is a special case of robust cooperative output regulation problem in [19].*

Remark 2. *The key technical contributions is the development of a novel distributed controller (6). This controller is able to address the challenges associated with heterogeneous agent dynamics, Markovian switching topologies, and uncertainties in agent dynamics. Moreover, the internal model approach in this paper plays an important role in handling the uncertainties.*

4 Simulation

Consider the agent dynamics adopted in [14]. The heterogeneous uncertain MAS are given as follows:

$$A_i = \begin{pmatrix} 0 & 1 & 0\\ 0 & 0 & c_i\\ 0 & -d_i & -a_i \end{pmatrix},$$

$$\delta_iA = \begin{pmatrix} 0 & 0 & 0\\ 0 & 0 & 0\\ 0.01i & 0.02i & 0.03i \end{pmatrix},$$

$$B_i = \begin{pmatrix} 0\\ 0\\ b_i \end{pmatrix}, \delta_iB = \begin{pmatrix} 0\\ 0\\ 0.02i \end{pmatrix},$$

$$C_i = \begin{pmatrix} 0\\ 0\\ b_i \end{pmatrix}^T, \delta_iC = \begin{pmatrix} 0\\ 0\\ 0.01i \end{pmatrix}^T,$$

$$S = \begin{pmatrix} 0 & 1\\ -1 & 0 \end{pmatrix}, \text{ and } R = \begin{pmatrix} -1 & 0 \end{pmatrix},$$

where $\{a_i, b_i, c_i, d_i\}$ are selected as $\{2,2,2,0\}$, $\{5,2,1,0\}$, $\{2,2,1,2\}$, $\{2,4,1,2\}$, $i = 1,2,3,4$, respectively. Choose the 1-copy model as follows:

$$F_1 = \begin{pmatrix} 0 & 1\\ -1 & 0 \end{pmatrix}^T, F_2 = \begin{pmatrix} 0\\ 1 \end{pmatrix}^T,$$

The communication topologies in this study are randomly switched between two digraphs, specifically $\mathcal{G}_1$ and $\mathcal{G}_2$ as depicted in Figs. 1(a) and 1(b). Let the switching signal be

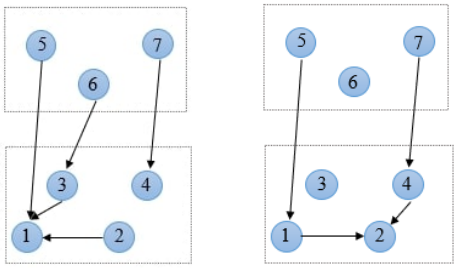

(a) $\mathcal{G}_1$. (b) $\mathcal{G}_2$.

Fig. 1: Communication topologies.

driven by a Markov chain $\{r(t), t \geq 0\}$ as shown in Fig. 2 taking values in $\mathbb{S} = \{1,2\}$. Let $\Omega = \begin{pmatrix} -1 & 1\\ 2 & -2 \end{pmatrix}$. The

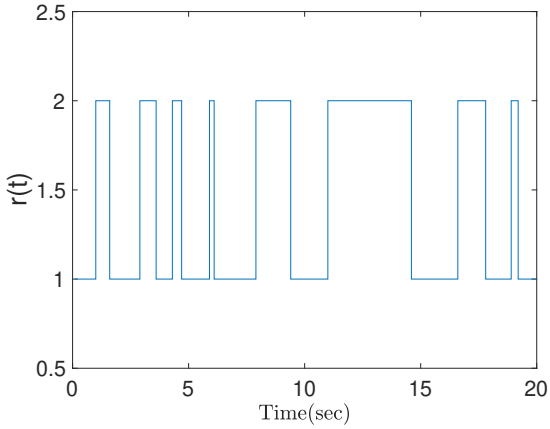

Fig. 2: Markov chain.

matrices G_{1i}, G_{2i}, U_i are chosen the same as those in [14]. Solve the linear matrix inequalities (11), we have

$$Q = \begin{pmatrix} 0.4634 & 0.2446 & 0.1034 & 0.0389\\ 0.2446 & 1.5455 & 0.1039 & 0.2576\\ 0.1034 & 0.1039 & 1.5047 & 0.0264\\ 0.0389 & 0.2576 & 0.0264 & 1.1094 \end{pmatrix}.$$

Then, we have $\tilde{\lambda} = \lambda_{\min}\left(QL_1 + L_1^T Q\right) = 1.6284$ and $\lambda_{\max}(Q) = 1.7694$, then ν can be chosen as $\nu = 1.5 \geq \tilde{\lambda}^{-1}\lambda_{\max}(Q)$.

The initial conditions are chosen as

$$\begin{aligned}
&\psi_1(0) = (8,4)^T, \psi_2(0) = (-1,2)^T,\\
&\psi_3(0) = (-5,3)^T, \psi_4(0) = (5,5)^T\\
&x_1(0) = (8,-4,4)^T, x_2(0) = (1,-2,6)^T,\\
&x_3(0) = (7,-1,6)^T, x_4(0) = (10,-2,5)^T,\\
&v_5(0) = (5,1)^T, v_6(0) = (4,2)^T, v_7(0) = (2,3)^T.
\end{aligned}$$

Denote the distributed output containment errors as $e_i = y_i - \sum_{j\in\mathbb{L}}\beta_{ij}y_j, i = 1,2,3,4$ and let $\phi_i = \psi_i - \sum_{j\in\mathbb{L}}\beta_{ij}v_j = (\phi_{i1},\phi_{i2})^T$. Generate 1500 sample paths to approximate $\mathbb{E}[\|\phi_i\|^2]$ and $\mathbb{E}\left[\|e_i\|^2\right]$ as shown in Figs. 3 and 4.

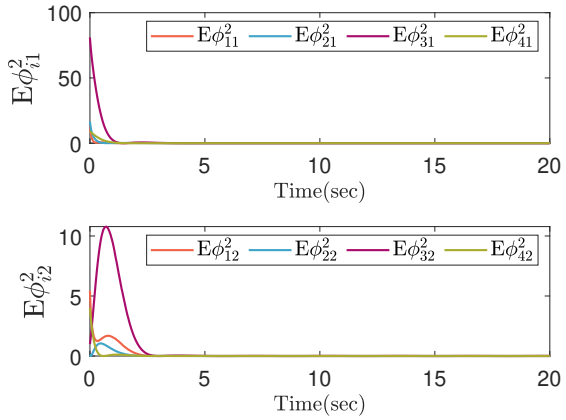

Fig. 3: The mean square errors of the distributed observer (6).

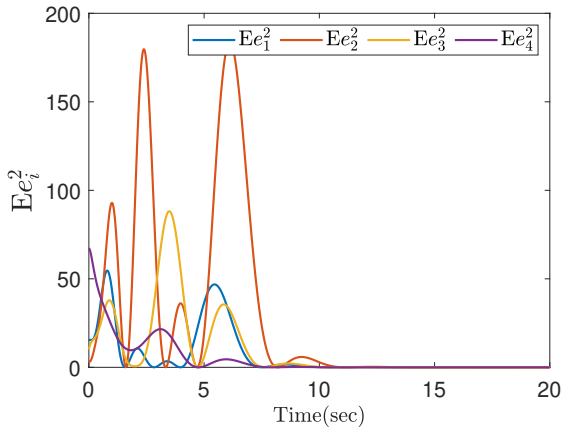

Fig. 4: The mean square containment errors.

5 Conclusions

The robust output containment control problem of heterogeneous uncertain MASs under MST has been studied. A distributed output feedback controller has been proposed. It has been shown that the heterogeneous uncertain MASs can achieve distributed output containment in mean square sense. An example is given to illustrate the effectiveness of the proposed controller. In our later work, formation control problem under the same communication constraints will be considered.

References

[1] B. D. Anderson, B. Fidan, C. Yu, and D. Walle, "Uav formation control: Theory and application," in *Recent advances in learning and control*. Springer, 2008, pp. 15–33.

[2] W. Ren, R. W. Beard, and E. M. Atkins, "Information consensus in multivehicle cooperative control," *IEEE Control Systems Magazine*, vol. 27, no. 2, pp. 71–82, 2007.

[3] R. Olfati-Saber and R. M. Murray, "Consensus problems in networks of agents with switching topology and time-delays," *IEEE Transactions on Automatic Control*, vol. 49, no. 9, pp. 1520–1533, 2004.

[4] W.-A. Zhang, G. Feng, and L. Yu, "Multi-rate distributed fusion estimation for sensor networks with packet losses," *Automatica*, vol. 48, no. 9, pp. 2016–2028, 2012.

[5] H. Du, G. Wen, Y. Cheng, Y. He, and R. Jia, "Distributed finite-time cooperative control of multiple high-order nonholonomic mobile robots," *IEEE Transactions on Neural Networks and Learning Systems*, vol. 28, no. 12, pp. 2998–3006, 2016.

[6] S. Martinez, J. Cortes, and F. Bullo, "Motion coordination with distributed information," *IEEE Control Systems Magazine*, vol. 27, no. 4, pp. 75–88, 2007.

[7] M. Ji, G. Ferrari-Trecate, M. Egerstedt, and A. Buffa, "Containment control in mobile networks," *IEEE Transactions on Automatic Control*, vol. 53, no. 8, pp. 1972–1975, 2008.

[8] Y. Cao, W. Ren, and M. Egerstedt, "Distributed containment control with multiple stationary or dynamic leaders in fixed and switching directed networks," *Automatica*, vol. 48, no. 8, pp. 1586–1597, 2012.

[9] A. Amini, A. Asif, and A. Mohammadi, "Formation-containment control using dynamic event-triggering mechanism for multi-agent systems," *IEEE/CAA Journal of Automatica Sinica*, vol. 7, no. 5, pp. 1235–1248, 2020.

[10] H. Haghshenas, M. A. Badamchizadeh, and M. Baradarannia, "Containment control of heterogeneous linear multi-agent systems," *Automatica*, vol. 54, pp. 210–216, 2015.

[11] S. Zuo, Y. Song, F. L. Lewis, and A. Davoudi, "Output containment control of linear heterogeneous multi-agent systems using internal model principle," *IEEE Transactions on Cybernetics*, vol. 47, no. 8, pp. 2099–2109, 2017.

[12] J. Qin, Q. Ma, X. Yu, and Y. Kang, "Output containment control for heterogeneous linear multiagent systems with fixed and switching topologies," *IEEE Transactions on Cybernetics*, vol. 49, no. 12, pp. 4117–4128, 2018.

[13] C. Bi, X. Xu, L. Liu, and G. Feng, "Output containment control of heterogeneous linear multiagent systems with unbounded distributed transmission delays," *IEEE Transactions on Cybernetics*, vol. 52, no. 8, pp. 8157–8166, 2022.

[14] C. Bi and X. Xu, "Robust containment control of uncertain multi-agent systems subject to transmission delays," in *2023 42nd Chinese Control Conference (CCC)*. IEEE, 2023, pp. 5785–5790.

[15] G. Wen, Z. Duan, Y. Zhao, W. Yu, and J. Cao, "Robust containment tracking of uncertain linear multi-agent systems: a non-smooth control approach," *International Journal of Control*, vol. 87, no. 12, pp. 2522–2534, 2014.

[16] Y. Lou and Y. Hong, "Target containment control of multi-agent systems with random switching interconnection topologies," *Automatica*, vol. 48, no. 5, pp. 879–885, 2012.

[17] W. Li, L. Xie, and J.-F. Zhang, "Containment control of leader-following multi-agent systems with Markovian switch-

ing network topologies and measurement noises," *Automatica*, vol. 51, pp. 263–267, 2015.

[18] H. Guo, M. Meng, and G. Feng, "Lyapunov-based output containment control of heterogeneous multi-agent systems with markovian switching topologies and distributed delays," *IEEE/CAA Journal of Automatica Sinica*, vol. 10, no. 5, pp. 1–13, 2023.

[19] H. Guo and G. Feng, "Robust cooperative output regulation of heterogeneous multi-agent systems under markovian switching topologies," in *2023 IEEE 18th Conference on Industrial Electronics and Applications (ICIEA)*. IEEE, 2023, pp. 417–422.

[20] C. Bi, X. Xu, L. Liu, and G. Feng, "Robust cooperative output regulation of heterogeneous uncertain linear multiagent systems with unbounded distributed transmission delays," *IEEE Transactions on Automatic Control*, vol. 67, no. 3, pp. 1371–1383, 2021.

[21] Q. Zhou, X. Xu, L. Liu, and G. Feng, "A Lyapunov approach to robust cooperative output regulation of multiagent systems under infinite communication delays," *IEEE Transactions on Automatic Control*, vol. 67, no. 11, pp. 6271–6278, 2022.

[22] M. Meng, L. Liu, and G. Feng, "Adaptive output regulation of heterogeneous multiagent systems under Markovian switching topologies," *IEEE Transactions on Cybernetics*, vol. 48, no. 10, pp. 2962–2971, 2017.

[23] O. L. do Valle Costa, M. D. Fragoso, and M. G. Todorov, *Continuous-time Markov jump linear systems*. Springer Science & Business Media, 2012.

[24] H. Khalil and J. Grizzle, *Nonlinear Systems*. New Jersey: Prentice Hall.

[25] J. Huang, *Nonlinear Output Regulation: Theory and Applications*. SIAM, 2004.

Proceedings of the 3rd Conference on Fully Actuated System Theory and Applications
May 10-12, 2024, Shenzhen, China

Fully Distributed Adaptive State Estimation and Consensus Control of Multi-agent Systems: A Reduced-order Observer-based Approach

Jiazhu Huang[1,3], Yan Li[1], Yuezu Lv[2], Jialing Zhou[2]

1. School of Automation, Beijing Institute of Technology, Beijing 100081, P. R. China
E-mail: jzh@bit.edu.cn, yanl@bit.edu.cn

2. MIIT Key Laboratory of Complex-field Intelligent Sensing, Beijing Institute of Technology, Beijing 100081, P. R. China
E-mail: yzlv@bit.edu.cn, jlzhou@bit.edu.cn

3. MIIT Key Laboratory of Complex-Field Intelligent Sensing, Yangtze Delta Region Academy of Beijing Institute of Technology, Jiaxing 314003, P. R. China

Abstract: This paper focuses on the integrated design of adaptive state estimation and consensus control for multi-agent systems. To improve the consensus performance of the multi-agent systems in the presence of some agents' sensor failures, the cooperative state estimation model is introduced, and fully distributed adaptive output tracking estimators and reduced-order state observers are designed based on this model. The consensus control protocol, relying on only the self-estimated states, is proposed and enables the achievement of consensus of the multi-agent system under directed graphs. The effectiveness of the algorithm is theoretically analyzed and validated through simulation.

Key Words: Multi-agent systems, reduced-order state observer, adaptive output tracking, consensus control

1 Introduction

In recent years, multi-agent systems have gained increasing and in-depth applications in various fields such as industry, agriculture, and military due to their superior performance and powerful functionalities. Simultaneously, scientific research related to multi-agent systems has been steadily advancing, with the primary challenge lying in achieving cooperation and coordination among the agents to accomplish complicated tasks [1–5]. The fundamental problem in multi-agent systems is the consensus control [6–9].

In order to address the consensus control problem in multi-agent systems, it is necessary to design appropriate control protocols. Depending on the variables used, control protocols can be divided into state feedback-based consensus control and output feedback-based consensus control. The control protocols require the calculation of appropriate gain matrices based on the dynamic matrices of the agent, followed by the utilization of communication topology to obtain suitable coupling gain. Li [10] introduced an adaptive approach which eliminates the dependence on global information to caculate the constant gain, enabling the control protocol to be fully distributed. State feedback is a superior method in solving the consensus issue, however, it is difficult to directly obtain the state of agents in practical applications, so it is necessary to estimate the state of agents.

Distributed state estimation algorithms can generally be divided into distributed Kalman-filter-based [11] and distributed observer-based [12]. Olfati-Saber [13] solved the problem of distributed estimation for sensor networks using distributed Kalman-filter, and Hong [14] used distributed observers to address the leader-following consensus problem of the multi-agent system. When performing distributed estimation for systems with a large number of nodes, appropriate methods are usually selected from these two types [15–17]. The advantage of distributed Kalman-filter lies in its robustness, as it can ensure the boundedness of the estimation error even in the presence of noise in the sensor network. In comparison, the advantage of distributed observer lies in its lower computational requirements, as it can consume less energy to achieve accurate estimation in systems without unknown disturbances.

Most of existing results consider that the sensor of each agent only measures its own state. When one or more agents' sensors fail, the local state estimation error may diverge, which may lead to the failure of collaborative tasks. To address this issue, the concept of cooperative state estimation model for agents is proposed, which is to use agents' sensors to measure the state information of other nodes in the system (e.g., in a swarm of unmanned aircrafts, a node can measure the positions of other nodes using its sensor). Adaptive output tracking estimators and distributed reduced-order state observers are then designed, along with a fully distributed consensus control protocol based on state estimation. Even if there are nodes with failed sensors in the multi-agent system, agents can still achieve accurate estimation of the certain nodes' states, ensuring the completion of collaborative tasks.

The remaining of the paper is structured as follows: Section 2 presents the problem statement. Section 3 gives the main results. Section 4 describes the simulation results. The conclusion is presented in section 5.

Notations: $\sigma_{\max}(Z)$ and $\sigma_{\min}(Z)$ denote the maximum and minimum singular values of Z, respectively. $\lambda_{\min}(Z)$ represents the minimum eigenvalue of Z. 1_n refers to a vector of dimension n with all elements being 1. I_n represents the identity matrix of dimension $n \times n$. $\otimes$ stands for the Kronecker product. $\mathbb{R}^n$ is a n-dimensional real vector set. $diag(a_1, \cdots, a_n)$ is a diagonal matrix with $a_1, \cdots, a_n$ as

This work was supported by the National Natural Science Foundation of China under Grants 62088101, 62273045, U2341213 and 62376029, Beijing Nova Program under Grant 20230484481, and China Postdoctoral Science Foundation under Grant 2023M730255.

the diagonal element.

2 Problem statement

Consider the multi-agent system consisting of N agents. The dynamics of ith agent are described by

$$\dot{x}_i = Ax_i + Bu_i, i = 1, \cdots, N, \tag{1}$$

where $x_i \in \mathbb{R}^n$ and $u_i \in \mathbb{R}^p$ are, respectively, the state and the control input of the ith agent, and $A \in \mathbb{R}^{n\times n}$ and $B \in \mathbb{R}^{n\times p}$ are known constant matrices. The sensor measurement output is represented by

$$y_i = C_i x, i = 1, \cdots, N, \tag{2}$$

where $y_i \in \mathbb{R}^{q_i}$ is the output of the ith agent, $C_i \in \mathbb{R}^{q_i\times Nn}$ denotes the output matrix, and $x = \left[x_1^T, \cdots, x_N^T\right]^T$ represents the states of all agents in the multi-agent system. Let $y = \left[y_1^T, \cdots, y_N^T\right]^T$ and $C = \left[C_1^T, \cdots, C_N^T\right]^T \in \mathbb{R}^{q\times Nn}$, where $q = \sum_{i=1}^N q_i$, then the state equation of the overall multi-agent system can be expressed as

$$\begin{aligned} \dot{x} &= (I_N \otimes A)\, x + (I_N \otimes B)\, u, \\ y &= Cx, \end{aligned} \tag{3}$$

where $u = \left[u_1^T, \cdots, u_N^T\right]^T$ represents the control input of all agents.

The communication topology between the multi-agent system can be represented by a directed graph $\mathcal{G} = \{\mathcal{V}, \mathcal{E}, \mathcal{A}\}$, where $\mathcal{V} = \{1, \cdots, N\}$ is the node set of the N agents, $\mathcal{E} \subseteq \mathcal{V} \times \mathcal{V}$ is the set of edges, and $\mathcal{A} = [a_{ij}] \in \mathbb{R}^{N\times N}$ describes the adjacency matrix, whose elements are defined as $a_{ij} > 0$ if ith agent can receive information from jth agent, otherwise $a_{ij} = 0$ (there is no self-loop in the paper, i.e., $a_{ii} = 0$). The degree diagonal matrix is defined as $\mathcal{D} = diag\,(d_1, \cdots, d_N)$ where $d_i = \sum_{j=1}^N a_{ij}, i = 1, \cdots, N$. The Laplacian matrix is given by $\mathcal{L} = [l_{ij}] \in \mathbb{R}^{N\times N}$, where $l_{ii} = d_i$ and $l_{ij} = -a_{ij}, i \neq j$. For two nodes i and j, a directed path is existed between these two nodes if there exists some nodes $k_1, \cdots, k_l$ such that $(i, k_1), \cdots, (k_l, j)$ holds. A communication graph is directed and strongly connected if a directed path exists between any two nodes in the graph.

Assumption 1 *The communication graph $\mathcal{G}$ of the multi-agent system is a directed strongly connected graph.*

The following lemmas are useful.

Lemma 1 ([18]) *For the Laplacian matrix $\mathcal{L}$ and adjacency matrix $\mathcal{A}$ of a strongly connected directed communication graph $\mathcal{G}$, denoting $\mathcal{A}^j = diag\,(a_{1j}, \cdots, a_{Nj}), j = 1, \cdots, N$, then $\mathcal{L}^j = \mathcal{L} + \mathcal{A}^j$ is a non-singular M matrix.*

Lemma 2 ([19]) *For a non-singular M matrix $\mathcal{M}$, there exists a positive definite diagonal matrix $\mathcal{H} > 0$ such that $\mathcal{H}\mathcal{M} + \mathcal{M}^T\mathcal{H} > 0$ holds.*

The objective of the paper is to ensure the consensus of multi-agent systems in the presence of agents' sensor failure. The main idea is to estimate the agent's state based on the other agents' measurement output. The following assumption is needed.

Assumption 2 *The matrix C is of full row rank, i.e., $rankC = q$, and the matrix pair $(I_N \otimes A, C)$ is observable.*

3 Main results

The consensus control for the ith agent is proposed as

$$u_i = cK \sum_{j=1}^N (\hat{x}_{ii} - \hat{x}_{ij}), \tag{4}$$

where the coupling gain $c > 1/N$, the feedback gain matrix $K = -B^T P^{-1}$, $P > 0$ is a positive definite matrix solution of the linear matrix inequality $AP + PA^T - 2BB^T < 0$, $\hat{x}_{ii}$ is the estimation of the ith agent state by itself, and $\hat{x}_{ij}$ denotes the estimation of the jth agent state by the ith agent, $\hat{x}_i = \left[\hat{x}_{i1}^T, \cdots, \hat{x}_{iN}^T\right]^T$. Then the dynamics of the overall system can be expressed as

$$\begin{aligned} \dot{x} &= A_0 x + B_0(\hat{x} - 1_N \otimes x), \\ y &= Cx, \end{aligned} \tag{5}$$

where $A_0 = I_N \otimes A + c\mathcal{L}_o \otimes BK$, $B_0 = c\mathcal{L}^o \otimes BK$, $\mathcal{L}^o = diag\left(\mathcal{L}_o^1, \cdots, \mathcal{L}_o^N\right)$, $\mathcal{L}_o^i$ represents the ith row of the Laplacian matrix $\mathcal{L}_o$ associated with the complete graph, and $\hat{x} = \left[\hat{x}_1^T, \cdots, \hat{x}_N^T\right]^T$.

In order to make each agent estimate the states of all agents in the system, one can design an output tracking estimator and a local state observer. In contrast to [20], this paper uses the reduced-order state observer to estimate the state x, thereby reducing the computational burden of state estimation. The adaptive output tracking estimator and the reduced-order observer are designed as

$$\begin{aligned} \dot{\hat{y}}_{ij} &= -\left(\varphi_{ij} + \psi_{ij}\right)\eta_{ij} + C_j A_0 \hat{x}_i, \\ \dot{z}_i &= Fz_i + G\hat{y}_i, \end{aligned} \tag{6}$$

where $\dot{\varphi}_{ij} = \psi_{ij} = \eta_{ij}^T\eta_{ij}$, $\eta_{ij} = \sum_{k=1}^N a_{ik}\left(\hat{y}_{ij} - \hat{y}_{kj}\right) + a_{ij}\left(\hat{y}_{ij} - y_j\right)$, $\hat{y}_{ij}$ is the estimation of jth agent output by ith agent, and φ_{ij} denotes the adaptive gain with positive initial value, z_i is an auxiliary variable of the reduced-order observer. η_{ij} can be seen as the consensus error of the output estimation, one can get $\eta_{ij} = 0$ when the output estimation of all agents is achieved. $\hat{y}_i = \left[\hat{y}_{i1}^T, \cdots, \hat{y}_{iN}^T\right]^T$, and the parameter matrices F, G and the state estimation $\hat{x}_i$ can be determined according to Algorithm 1.

Algorithm 1

(1) Choose a constant matrix $F \in \mathbb{R}^{(Nn-q)\times(Nn-q)}$ such that its eigenvalues are located in the left half-plane and are different from the eigenvalues of A_0.

(2) Select a matrix $G \in \mathbb{R}^{(Nn-q)\times q}$ such that (F, G) is controllable.

(3) Solve the matrix equation $TA_0 - FT = GC$ to obtain a unique solution $T \in \mathbb{R}^{(Nn-q)\times Nn}$.

(4) Check if $Q = \begin{bmatrix} C \\ T \end{bmatrix}$ is invertible. If not repeat (1) (2) and (3), else $\hat{x}_i = \begin{bmatrix} C \\ T \end{bmatrix}^{-1} \begin{bmatrix} \hat{y}_i \\ z_i \end{bmatrix}$, one can get $\hat{y}_i = C\hat{x}_i$, $z_i = T\hat{x}_i$. Let $R = Q^{-1} = \begin{bmatrix} R_1 & R_2 \end{bmatrix}$, where $R_1 \in \mathbb{R}^{Nn\times q}$, $R_2 \in \mathbb{R}^{Nn\times(Nn-q)}$. Then, $\hat{x}_i = R_1\hat{y}_i + R_2 z_i$.

(5) Determine if the matrix $F_0 = I_N \otimes F - (1_N \otimes TB_0)(I_N \otimes R_2)$ is stable. If not turn to step (1) to select appropriate F again.

Remark 1 *A full-order state observer and an adaptive output tracking estimator is designed in [20]. Compared with the observers in [20], the reduced-order state observer proposed in this paper requires less computation. Specificly, in [20], for the ith agent, the dimension of the adaptive output tracking estimator is q, and the full-order state observer is of dimension Nn; while the reduced-order state observer only needs to estimate the state information of dimension $Nn-q$. When the number of sensors in the system is large, the reduced-order observer approach can significantly save computational resources.*

According to Algorithm 1, it can be seen that z_i is the estimate of Tx, so the estimation error can be expressed as $\tilde{y}_{ij}=\hat{y}_{ij}-y_j$, $\tilde{z}_i=z_i-Tx$, $\tilde{x}_i=\hat{x}_i-x$. Let $\tilde{y}=\left[\tilde{y}_1^T,\cdots,\tilde{y}_N^T\right]^T$, $\tilde{z}=\left[\tilde{z}_1^T,\cdots,\tilde{z}_N^T\right]^T$, $\tilde{x}=\left[\tilde{x}_1^T,\cdots,\tilde{x}_N^T\right]^T$, then the error dynamics can be written as

$$\begin{aligned}\dot{\tilde{y}}_{ij}&=-\left(\varphi_{ij}+\psi_{ij}\right)\eta_{ij}+C_jA_0\tilde{x}_i-C_jB_0\tilde{x},\\ \dot{\varphi}_{ij}&=\psi_{ij}=\eta_{ij}^T\eta_{ij},\\ \dot{\tilde{z}}_i&=F\tilde{z}_i+G\tilde{y}_i-TB_0\tilde{x}.\end{aligned}\tag{7}$$

It's easy to obtain $\tilde{x}_i=R_1\tilde{y}_i+R_2\tilde{z}_i$. Therefore, if both $\tilde{y}_i$ and $\tilde{z}_i$ converge to zero, $\tilde{x}_i$ converges to zero.

Let $\tilde{y}^j=\left[\tilde{y}_{1j}^T,\cdots,\tilde{y}_{Nj}^T\right]^T$, then it's clear that $\tilde{y}^T\tilde{y}=\sum_{j=1}^N\left(\tilde{y}^j\right)^T\tilde{y}^j$, and the dynamics of $\tilde{y}^j$ can be expressed as

$$\dot{\tilde{y}}^j=-\left(\Lambda^j\otimes I_{q_j}\right)\eta^j+\mathcal{C}^j\tilde{x},\tag{8}$$

where $\Lambda^j=\Phi^j+\Psi^j$, $\Phi^j=diag\left(\varphi_{1j},\cdots,\varphi_{Nj}\right)$, $\Psi^j=diag\left(\psi_{1j},\cdots,\psi_{Nj}\right)$, $\eta^j=\left[\eta_{1j}^T,\cdots,\eta_{Nj}^T\right]^T$, $\mathcal{C}^j=I_N\otimes C_jA_0-1_N\otimes C_jB_0$, and it is easy to obtain $\eta^j=\left(\mathcal{L}^j\otimes I_{q_j}\right)\tilde{y}^j$, $\tilde{x}=\left(I_N\otimes R_1\right)\tilde{y}+\left(I_N\otimes R_2\right)\tilde{z}$. Therefore, the error dynamics can be written as

$$\begin{aligned}\dot{\eta}^j&=-\left(\mathcal{L}^j\Lambda^j\otimes I_{q_j}\right)\eta^j+\left(\mathcal{L}^j\otimes I_{q_j}\right)\mathcal{C}^j\left(I_N\otimes R_1\right)\tilde{y}\\&\quad+\left(\mathcal{L}^j\otimes I_{q_j}\right)\mathcal{C}^j\left(I_N\otimes R_2\right)\tilde{z},\\ \dot{\varphi}_{ij}&=\psi_{ij}=\eta_{ij}^T\eta_{ij},\\ \dot{\tilde{z}}&=F_0\tilde{z}+G_0\tilde{y},\end{aligned}\tag{9}$$

where $G_0=I_N\otimes G-\left(1_N\otimes TB_0\right)\left(I_N\otimes R_1\right)$.

Theorem 1 *Suppose Assumption 1 and Assumption 2 hold. The designed adaptive output tracking estimator and reduced-order state observer* (6) *can respectively estimate all outputs and states, and the multi-agent system can achieve consensus under control protocol* (4)*.*

Proof Consider the Lyapunov function candidate

$$V=\mu\tilde{z}^TU\tilde{z}+\sum_{j=1}^NV_j,\tag{10}$$

where $U\in\mathbb{R}^{N(Nn-q)\times N(Nn-q)}$ is a positive definite matrix solution to the linear matrix inequality $-W=UF_0+F_0^TU<0$, V_j is selected as $V_j=\sum_{j=1}^N\frac{h_{ij}}{2}\left[\left(2\varphi_{ij}+\psi_{ij}\right)\psi_{ij}+\left(\varphi_{ij}-v^j\right)^2\right]$, h_{ij} is the diagonal element of the positive definite diagonal matrix $\mathcal{H}^j$ satisfying $\mathcal{H}^j\mathcal{L}^j+\left(\mathcal{L}^j\right)^T\mathcal{H}^j>0$, and μ and v^j are positive constants to be determined later.

The time derivative of V along the trajectory of (9) is given by

$$\dot{V}=-\mu\tilde{z}^TW\tilde{z}+2\mu\tilde{z}^TUG_0\tilde{y}+\sum_{j=1}^N\dot{V}_j.\tag{11}$$

According to Young's inequality, we have

$$\begin{aligned}&2\mu\tilde{z}^TUG_0\tilde{y}\\&\le\frac{\mu}{4}\tilde{z}^TW\tilde{z}+\frac{4\mu\sigma_{\max}^2\left(UG_0\right)}{\lambda_{\min}\left(W\right)}\sum_{j=1}^N\left(\tilde{y}^j\right)^T\tilde{y}^j\\&\le\frac{\mu}{4}\tilde{z}^TW\tilde{z}+\sum_{j=1}^N\frac{4\mu\sigma_{\max}^2\left(UG_0\right)}{\lambda_{\min}\left(W\right)\sigma_{\min}^2\left(\mathcal{L}^j\right)}\left(\eta^j\right)^T\eta^j.\end{aligned}\tag{12}$$

The time derivative of V_j is

$$\begin{aligned}\dot{V}_j&=\sum_{i=1}^Nh_{ij}\left[\left(\varphi_{ij}+\psi_{ij}\right)\dot{\psi}_{ij}+\left(\varphi_{ij}+\psi_{ij}-v^j\right)\dot{\varphi}_{ij}\right]\\&=-\left(\eta^j\right)^T\left[\Lambda^j\left(\mathcal{H}^j\mathcal{L}^j+\left(\mathcal{L}^j\right)^T\mathcal{H}^j\right)\Lambda^j\otimes I_{q_j}\right]\eta^j\\&\quad+2\left(\eta^j\right)^T\left(\Lambda^j\mathcal{H}^j\mathcal{L}^j\otimes I_{q_j}\right)\mathcal{C}^j\left(I_N\otimes R_1\right)\tilde{y}\\&\quad+2\left(\eta^j\right)^T\left(\Lambda^j\mathcal{H}^j\mathcal{L}^j\otimes I_{q_j}\right)\mathcal{C}^j\left(I_N\otimes R_2\right)\tilde{z}\\&\quad+\left(\eta^j\right)^T\left(\Lambda^j\mathcal{H}^j\otimes I_{q_j}\right)\eta^j-v^j\left(\eta^j\right)^T\left(\mathcal{H}^j\otimes I_{q_j}\right)\eta^j.\end{aligned}\tag{13}$$

It can be easily obtained that

$$\begin{aligned}&-\left(\eta^j\right)^T\left[\Lambda^j\left(\mathcal{H}^j\mathcal{L}^j+\left(\mathcal{L}^j\right)^T\mathcal{H}^j\right)\Lambda^j\otimes I_{q_j}\right]\eta^j\\&\le-\lambda_{0j}\left(\eta^j\right)^T\left[\left(\Lambda^j\right)^2\otimes I_{q_j}\right]\eta^j,\end{aligned}\tag{14}$$

and

$$-v^j\left(\eta^j\right)^T\left(\mathcal{H}^j\otimes I_{q_j}\right)\eta^j\le-v^j\lambda_{\min}\left(\mathcal{H}^j\right)\left(\eta^j\right)^T\eta^j,\tag{15}$$

where λ_{0j} denotes the minimum eigenvalue of the positive definite matrix $\mathcal{H}^j\mathcal{L}^j+\left(\mathcal{L}^j\right)^T\mathcal{H}^j$. According to Young's inequality, one can get

$$\begin{aligned}&2\left(\eta^j\right)^T\left[\Lambda^j\mathcal{L}^j\mathcal{H}^j\otimes I_{q_j}\right]\mathcal{C}^j\left(I_N\otimes R_1\right)\tilde{y}\\&\le\frac{\lambda_{0j}}{4}\left(\eta^j\right)^T\left[\left(\Lambda^j\right)^2\otimes I_{q_j}\right]\eta^j\\&+\frac{4\sigma_{\max}^2\left[\left(\mathcal{H}^j\mathcal{L}^j\otimes I_{q_j}\right)\mathcal{C}^j\right]\sigma_{\max}^2\left(I_N\otimes R_1\right)}{\lambda_{0j}}\tilde{y}^T\tilde{y},\end{aligned}\tag{16}$$

and

$$\begin{aligned}&2\left(\eta^j\right)^T\left[\Lambda^j\mathcal{H}^j\mathcal{L}^j\otimes I_{q_j}\right]\mathcal{C}^j\left(I_N\otimes R_2\right)\tilde{z}\\&\le\frac{\lambda_{0j}}{4}\left(\eta^j\right)^T\left[\left(\Lambda^j\right)^2\otimes I_{q_j}\right]\eta^j\\&+\frac{4\sigma_{\max}^2\left[\left(\mathcal{H}^j\mathcal{L}^j\otimes I_{q_j}\right)\mathcal{C}^j\right]\sigma_{\max}^2\left(I_N\otimes R_2\right)}{\lambda_{0j}\lambda_{\min}\left(W\right)}\tilde{z}^TW\tilde{z}.\end{aligned}\tag{17}$$

Let $\sigma_R = \max\{\sigma_{\max}(I_N \otimes R_1), \sigma_{\max}(I_N \otimes R_2)\}$. Substituting (14)-(17) into (13) gives

$$\begin{aligned}\dot{V}_j \leq & -\frac{\lambda_{0j}}{2}\left(\eta^j\right)^T\left[\left(\Lambda^j\right)^2 \otimes I_{q_j}\right]\eta^j \\ & - v^j\lambda_{\min}\left(\mathcal{H}^j\right)\left(\eta^j\right)^T\eta^j \\ & + \frac{4\sigma_{\max}^2\left[\left(\mathcal{H}^j\mathcal{L}^j \otimes I_{q_j}\right)\mathcal{C}^j\right]\sigma_R^2}{\lambda_{0j}}\tilde{y}^T\tilde{y} \\ & + \frac{4\sigma_{\max}^2\left[\left(\mathcal{H}^j\mathcal{L}^j \otimes I_{q_j}\right)\mathcal{C}^j\right]\sigma_R^2}{\lambda_{0j}\lambda_{\min}(W)}\tilde{z}^T W\tilde{z} \\ & + \left(\eta^j\right)^T\left[\Lambda^j\mathcal{H}^j \otimes I_{q_j}\right]\eta^j.\end{aligned} \tag{18}$$

Select μ as $\mu = \sum_{j=1}^{N}\frac{16\sigma_{\max}^2\left[\left(\mathcal{H}^j\mathcal{L}^j\otimes I_{q_j}\right)\mathcal{C}^j\right]\sigma_R^2}{\lambda_{0j}\lambda_{\min}(W)}$, let $\kappa = \max\limits_{j=1,\cdots,N}\left(\frac{4\sigma_{\max}^2\left[\left(\mathcal{H}^j\mathcal{L}^j\otimes I_{q_j}\right)\mathcal{C}^j\right]\sigma_R^2}{\lambda_{0j}}\right)$, then one can get

$$\begin{aligned}& \sum_{j=1}^{N}\frac{4\sigma_{\max}^2\left[\left(\mathcal{H}^j\mathcal{L}^j \otimes I_{q_j}\right)\mathcal{C}^j\right]\sigma_R^2}{\lambda_{0j}}\tilde{y}^T\tilde{y} \\ & \leq N\kappa\tilde{y}^T\tilde{y} \\ & \leq \sum_{j=1}^{N}N\kappa\frac{1}{\sigma_{\min}^2\left(\mathcal{L}^j\right)}\left(\eta^j\right)^T\eta^j.\end{aligned} \tag{19}$$

Choose $v^j = \frac{4\mu\sigma_{\max}^2(UG_0)}{\lambda_{\min}(\mathcal{H}^j)\lambda_{\min}(W)\sigma_{\min}^2(\mathcal{L}^j)} + \frac{N\kappa}{\lambda_{\min}(\mathcal{H}^j)\sigma_{\min}^2(\mathcal{L}^j)} + \frac{8\lambda_{\max}\left(\mathcal{H}^j\right)}{\lambda_{\min}(\mathcal{H}^j)\lambda_{0j}}$. Note that

$$\begin{aligned}& -\frac{\lambda_{0j}}{2}\left(\eta^j\right)^T\left[\left(\Lambda^j\right)^2 \otimes I_{q_j}\right]\eta^j - \frac{8\lambda_{\max}^2\left(\mathcal{H}^j\right)}{\lambda_{0j}}\left(\eta^j\right)^T\eta^j \\ & \leq -2\left(\eta^j\right)^T\left[\Lambda^j\mathcal{H}^j \otimes I_{q_j}\right]\eta^j.\end{aligned} \tag{20}$$

Substituting (12), (18), (19), and (20) into (10) yields

$$\begin{aligned}\dot{V} & \leq -\frac{\mu}{2}\tilde{z}^T W\tilde{z} - \sum_{j=1}^{N}\left(\eta^j\right)^T\left[\Lambda^j\mathcal{H}^j \otimes I_{q_j}\right]\eta^j \\ & \leq -\frac{\mu}{2}\tilde{z}^T W\tilde{z} - \sum_{j=1}^{N}\left(\eta^j\right)^T\left[\Phi^j(0)\mathcal{H}^j \otimes I_{q_j}\right]\eta^j \\ & \leq 0.\end{aligned} \tag{21}$$

One can know that $V \geq 0$ by (10), and one will obtain $\dot{V} \leq 0$ from (21). Therefore, $V(t)$ is bounded, and according to the definition of $V(t)$, one know that $\tilde{z}$, η^j and φ_{ij} is also bounded. If $\dot{V} \equiv 0$, $\tilde{z} \equiv 0$ and $\eta^j \equiv 0$ can be obtained. One can get $\int_0^\infty\left[\frac{\mu}{2}\tilde{z}^T W\tilde{z} + \sum_{j=1}^{N}\left(\eta^j\right)^T\left[\Phi^j(0)\mathcal{H}^j \otimes I_{q_j}\right]\eta^j\right]dt \leq V(0) - V(\infty)$ from (21), then one have $\lim_{t\to\infty}\tilde{z}(t) = 0$, $\lim_{t\to\infty}\eta^j(t) = 0$, $\lim_{t\to\infty}\tilde{y}(t) = 0$ according to LaSalle's invariance principle [21]. Since $\tilde{x} = (I_N \otimes P_{21})\tilde{y} + (I_N \otimes P_{22})\tilde{z}$, one can obtain $\lim_{t\to\infty}\tilde{x}(t) = 0$. This completes the proof.

As the designed state observer achieving accurate estimation, one have $\lim_{t\to\infty}\hat{x}_{ii} = x_i$ and $\lim_{t\to\infty}\hat{x}_{ij} = x_j$, thus the control input of the ith agent will be $u_i = cK\sum_{j=1}^{N}a_{ij_o}(x_i - x_j)$ when $t \to \infty$. According to [22], the multi-agent system in (1) will achieve consensus.

Remark 2 *When the sensor of the ith agent in the system completely fails, the ith agent output is zero, i.e., $y_i = 0_{q_i}$, which can be viewed as the output matrix C_i changing to zero. According to the system model* (3) *designed in this paper, the overall output matrix of the system is then written as $C_{fail} = \left[C_1^T, \cdots, C_{i-1}^T, 0^{Nn\times q_i}, C_{i+1}^T, \cdots, C_N^T\right]^T$. C_{fail} will not satisfy the full row rank condition, thus let $C' = \left[C_1^T, \cdots, C_{i-1}^T, C_{i+1}^T, \cdots, C_N^T\right]^T$, and $y' = \left[y_1^T, \cdots, y_{i-1}^T, y_{i+1}^T, \cdots, y_N^T\right]^T$. If Assumption 2 is satisfied, then the Algorithm 1 can be used to redesign $F' \in \mathbb{R}^{(Nn-q+q_i)\times(Nn-q+q_i)}$ and $G' \in \mathbb{R}^{(Nn-q+q_i)\times(q-q_i)}$, and according to the output tracking estimator and reduced-order observer designed in* (6)*, other nodes can estimate the state of the failed agent, ensuring the progress of collaborative tasks.*

4 Simulation

In this section, we illustrate the effectiveness of the theoretical result by numerical simulations. The multi-agent system consists of five agents described by (1) and (2), with

$$A = \begin{bmatrix}-1.5 & -8\\ 0.1 & 0.6\end{bmatrix}, B = \begin{bmatrix}1\\1\end{bmatrix},$$

and

$$C = \begin{bmatrix}2 & -1 & 3 & -5 & 1 & 5 & -6 & 0 & 0 & -1\\ 2 & -2 & 3 & 5 & 0 & 4 & -2 & 0 & 3 & -2\\ 0 & 1 & 2 & -3 & 1 & 2 & -6 & -3 & 2 & 1\\ 1 & -1 & 6 & 0 & -2 & 3 & 8 & 2 & 2 & -2\\ 0 & 2 & -1 & 1 & 3 & 2 & -1 & 1 & 0 & -3\\ 3 & 0 & 1 & -2 & 0 & -2 & 1 & 4 & 0 & -1\end{bmatrix}.$$

The communication topology is shown in Fig. 1. According to (4), solve the linear matrix inequality yields $P = \begin{bmatrix}35.5939 & -3.2511\\ -3.2511 & 1.2582\end{bmatrix}$, thus the gain matrix $K = \begin{bmatrix}-0.1318 & -1.1353\end{bmatrix}$ for the consensus control protocol. The coupling gain is set to $c = 1$. The initial value of the adaptive gain φ_{ij} is chosen as $\varphi_{ij}(0) = 5$. By following Algorithm 1, F and G are selected as $F = diag(-10, -18, -27, -30)$ and

$$G = \begin{bmatrix}0 & 1 & 0 & 1 & 2 & -1\\ 1 & 3 & 2 & 0 & -2 & 0\\ 0 & 1 & 0 & 2 & 0 & 1\\ 1 & 0 & -1 & 2 & -1 & 1\end{bmatrix}.$$

The output tracking error and the observation error of the state are shown in Fig. 2(a) and Fig. 2(b), respectively, and it can be seen that all the errors converge to zero, indicating that each agent is able to estimate all outputs and states of the system. The states of the system are shown in Fig. 3(a) and Fig. 3(b), where the solid lines represent the true states of the system, and the dashed lines are the estimated states by each agent. From these two figures, it can be seen that the system achieves consensus control. The adaptive gain is shown in Fig. 4, and it means that the adaptive gain is bounded.

Assuming that the sensor of the first agent fails, we can verify that Assumption 2 still holds. Selecting a consensus coupling gain of $c' = 1.5$ and an initial value $\varphi_{ij}'(0) = 60$ for the adaptive gain, and according to Algorithm 1, F' and

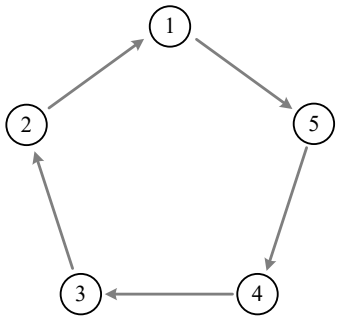

Fig. 1: The strongly connected communication graph.

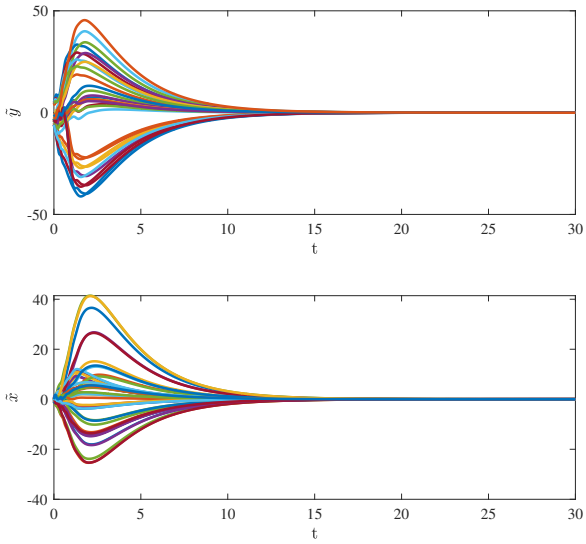

Fig. 2: The output tracking error and state estimation error.

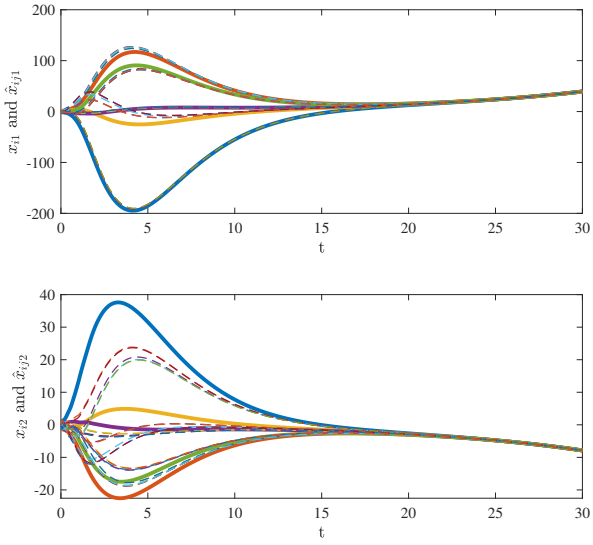

Fig. 3: Trajectories of the state x and the local state estimation $\hat{x}$ under (4).

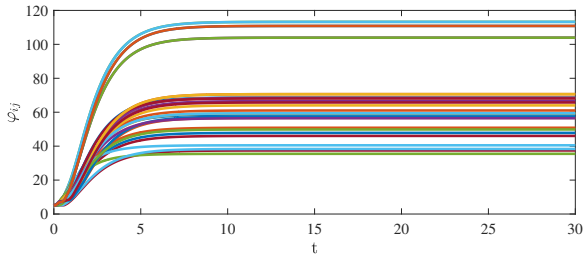

Fig. 4: Trajectories of the adaptive gain φ_{ij}.

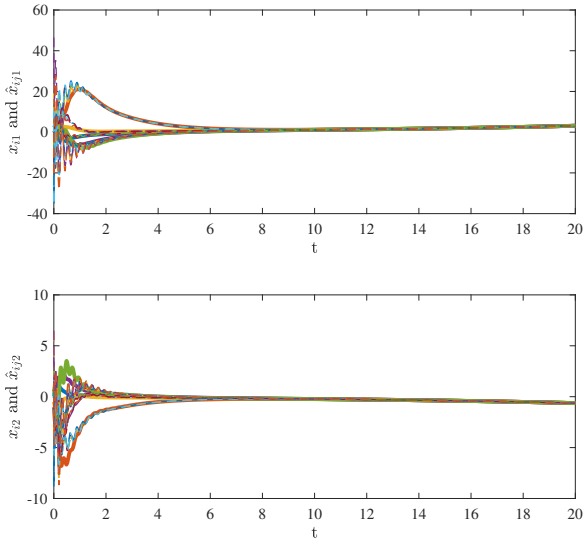

Fig. 5: Trajectories of the state x and the local state estimation $\hat{x}$ with sensor failure.

G' are selected as $F' = diag\,(-40, -10, -18, -27, -30)$ and

$$G' = 10 * \begin{bmatrix} 1 & 2 & 0 & 1 & 3 \\ 0 & 1 & 0 & 1 & 2 \\ 1 & 3 & 2 & 0 & -2 \\ 0 & 1 & 0 & 2 & 0 \\ 1 & 0 & -1 & 2 & -1 \end{bmatrix}.$$

The states of the system are shown in Fig. 5(a) and Fig. 5(b). It can be seen that each agent is still able to estimate the states of other agents, and the consensus task of the system can still be achieved. The adaptive gain is shown in Fig. 6, indicating that the adaptive gain remains bounded.

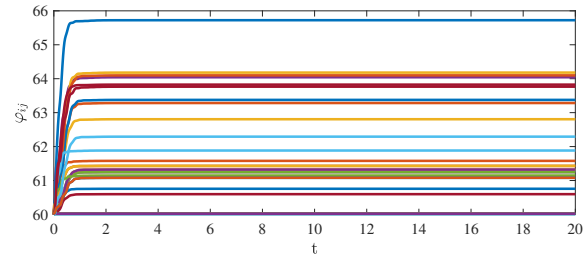

Fig. 6: Trajectories of the adaptive gain φ_{ij} with sensor failure.

5 conclusion

This paper investigates the integrated design of adaptive reduced-order state estimation and consensus control for the multi-agent system, ensuring that when there is sensor failure in the system, it will not lead to excessively large state estimation errors and failure of collaborative tasks. In the design of the output tracking estimator, adaptive gains are introduced to avoid reliance on global information, making the proposed algorithm fully distributed. The use of reduced-order state observers for estimating all the states of the system significantly reduces the computational load for state estimation. A state estimation-based consensus control protocol is proposed for the multi-agent system. Future research will focus on the integrated design of distributed state estimation and consensus control for systems with unknown disturbances.

References

[1] Z. Li, Z. Duan, and F. L. Lewis, "Distributed robust consensus control of multi-agent systems with heterogeneous matching uncertainties," *Automatica*, vol. 50, no. 3, pp. 883–889, 2014.

[2] J. Zhou, X. Wu, Y. Lv, and G. Wen, "Terminal-time synchronization of multiple vehicles under discrete-time communication networks with directed switching topologies," *IEEE Transactions on Circuits and Systems II: Express Briefs*, vol. 67, no. 11, pp. 2532–2536, 2019.

[3] Q. Wang, Z. Duan, J. Wang, Q. Wang, and G. Chen, "An accelerated algorithm for linear quadratic optimal consensus of heterogeneous multiagent systems," *IEEE Transactions on Automatic Control*, vol. 67, no. 1, pp. 421–428, 2021.

[4] J. Zhou, Y. Lv, C. Wen, and G. Wen, "Solving specified-time distributed optimization problem via sampled-data-based algorithm," *IEEE Transactions on Network Science and Engineering*, vol. 9, no. 4, pp. 2747–2758, 2022.

[5] Q. Wang, Z. Duan, Y. Lv, Q. Wang, and G. Chen, "Distributed model predictive control for linear–quadratic performance and consensus state optimization of multiagent systems," *IEEE Transactions on Cybernetics*, vol. 51, no. 6, pp. 2905–2915, 2020.

[6] J. Zhou, Y. Lv, G. Wen, and X. Yu, "Resilient consensus of multiagent systems under malicious attacks: Appointed-time observer-based approach," *IEEE Transactions on Cybernetics*, vol. 52, no. 10, pp. 10 187–10 199, 2021.

[7] Y. Lv, J. Zhou, G. Wen, X. Yu, and T. Huang, "Fully distributed adaptive nn-based consensus protocol for nonlinear mass: An attack-free approach," *IEEE Transactions on Neural Networks and Learning Systems*, vol. 33, no. 4, pp. 1561–1570, 2020.

[8] H. Yu and X. Xia, "Adaptive consensus of multi-agents in networks with jointly connected topologies," *Automatica*, vol. 48, no. 8, pp. 1783–1790, 2012.

[9] Q. Wang, Z. Duan, and J. Wang, "Distributed optimal consensus control algorithm for continuous-time multi-agent systems," *IEEE transactions on circuits and systems II: Express briefs*, vol. 67, no. 1, pp. 102–106, 2019.

[10] Z. Li, W. Ren, X. Liu, and M. Fu, "Consensus of multi-agent systems with general linear and lipschitz nonlinear dynamics using distributed adaptive protocols," *IEEE Transactions on Automatic Control*, vol. 58, no. 7, pp. 1786–1791, 2012.

[11] G. Battistelli and L. Chisci, "Stability of consensus extended kalman filter for distributed state estimation," *Automatica*, vol. 68, pp. 169–178, 2016.

[12] Y. Li, J. Huang, Y. Lv, and J. Zhou, "Distributed state estimation for multi-agent systems under consensus control," in *International Conference on Neural Information Processing*. Springer, 2023, pp. 214–225.

[13] R. Olfati-Saber, "Distributed kalman filter with embedded consensus filters," in *Proceedings of the 44th IEEE Conference on Decision and Control*. IEEE, 2005, pp. 8179–8184.

[14] Y. Hong, G. Chen, and L. Bushnell, "Distributed observers design for leader-following control of multi-agent networks," *Automatica*, vol. 44, no. 3, pp. 846–850, 2008.

[15] X. He, W. Xue, and H. Fang, "Consistent distributed state estimation with global observability over sensor network," *Automatica*, vol. 92, pp. 162–172, 2018.

[16] D. Yu, Y. Xia, L. Li, and D.-H. Zhai, "Event-triggered distributed state estimation over wireless sensor networks," *Automatica*, vol. 118, p. 109039, 2020.

[17] M. Muehlebach and S. Trimpe, "Distributed event-based state estimation for networked systems: An lmi approach," *IEEE Transactions on Automatic Control*, vol. 63, no. 1, pp. 269–276, 2017.

[18] Y. Li, Y. Lv, P. Duan, and J. Zhou, "Output tracking based distributed state estimation," in *2021 IEEE International Conference on Unmanned Systems (ICUS)*. IEEE, 2021, pp. 146–150.

[19] H. Zhang, Z. Li, Z. Qu, and F. L. Lewis, "On constructing lyapunov functions for multi-agent systems," *Automatica*, vol. 58, pp. 39–42, 2015.

[20] J. Huang, Y. Li, and Y. Lv, "Integrated design of fully distributed adaptive state estimation and consensus control for multi-agent systems," in *International Conference on Neural Information Processing*. Springer, 2023, pp. 226–237.

[21] H. K. Khalil, *Nonlinear systems*. Englewood Cliffs, NJ, USA: Patience Hall, 2002.

[22] Z. Li and Z. Duan, *Cooperative control of multi-agent systems: a consensus region approach*. Boca Raton, FL, USA: CRC press, 2017.

Proceedings of the 3rd Conference on Fully Actuated System Theory and Applications
May 10-12, 2024, Shenzhen, China

Method of spacecraft cluster orbital pursuit-evasion game based on the hierarchical theory structure

Haolong Feng[1,2], Songtai Wu[1,2], Shengyang Liu[1,2], Ting Song[1,2,3], Fei Han[1,2]

1. Shanghai Institute of Spaceflight Control Technology, Shanghai 201109, China
E-mail: feng_hao_long@163.com

2. Shanghai Key Laboratory of Aerospace Intelligent Control Technology, Shanghai 201109, China
E-mail: feng_hao_long@163.com

3. Northwestern Polytechnical University, Xi'an 710072, China
E-mail: songtinghit@163.com

Abstract: In the context of the in-orbit safety and defense of the future spacecrafts, this paper makes the research of the orbital pursuit-evasion dilemma encountered by spacecraft, utilizing the evolutionary task assignment and the differential game theory as its theoretical foundation, and consequently develops a hierarchical game theory model for the pursuit-evasion problem of the spacecraft cluster. The first layer of the hierarchical structure is the task assignment based on intelligent optimization algorithms, the fuel consumption and time cost are taken into account. The second layer of the hierarchical structure is the planning of the pursuit-evasion game based on the differential game theory. In order to solve the saddle point of the differential game issue in spacecraft pursuit-evasion, the solution of the saddle point is transformed to the resolution of a four-dimensional non-linear equation set with a combined solution strategy integrating the evolutionary algorithm and the newton iteration method. Finally, the hierarchical structure of the pursuit-evasion game for the spacecraft cluster is verified by the analytical assessment of simulation instance that three trackers chasing three escapers.

Key Words: Orbital Pursuit-Evasion, Evolutionary Task Assignment, Differential Game, Spacecraft Cluster

1 Introduction

In the development of modern aerospace technology, the pursuit-evasion game of the spacecraft cluster become an important research spot. This game optimizes the cluster layout of spacecraft according to the principles of dynamic games, aiming to achieve autonomous, cooperative, and effective operations in complex environments. A spacecraft cluster can form a powerful aerospace capability and provide more efficient executing capability of the space mission through coordinated planning and control.

In recent years, the orbital pursuit-evasion differential game has made significant progress in both theoretical research and experimental simulation. Game theory provides a natural and robust framework for modeling interactions among players[1, 2]. Therefore, the significant efforts have been dedicated to study the orbital pursuit-evasion differential games[3, 4]. Typically, the pursuit-evasion game is formulated as a two-player differential game, in which an evader and a pursuer strive to minimize their individual payoffs[5]. Some researchers have also ventured into the study of multiple-player pursuit-evasion games[6, 7] which involve multiple payoff functions.

The multi-to-multi spacecraft cluster orbital game process can be broken down into the task assignment and the game path planning.

In terms of task allocation, to address the task allocation problem of intercepting multiple targets with multiple satellites for minimizing fuel consumption and time cost, a genetic algorithm-based allocation method is proposed for resolution[8]. Focusing on in-orbit target assignment, an in-orbit multi-objective allocation method based on particle swarm optimization is presented[9]. The determining variables and constraints considered in these methods are relatively simple. Considering that the scale of spacecraft clusters in space game scenarios is much larger than that of multiple stars, the constraints become more complex[10, 11].

In terms of game path planning, the renowned aerospace trajectory optimization scholar Conway proposes to use a type of semi-direct method to solve the saddle point of the differential countermeasures in the three-dimensional orbital pursuit-evasion of spacecraft cluster[12]. Hafer et al[13] use the sensitivity method to analyze and solve the spacecraft orbit pursuit-evasion problem, which can significantly improve the efficiency of saddle point solution and barrier construction. Stupok et al[14] solves the open-loop saddle point of the spacecraft pursuit-evasion differential countermeasures based on the linear relative motion equation, then the closed-loop optimal control law using the Kriging interpolation method are obtained. For the nonlinear pursuit-evasion differential countermeasures problem, Jagat et al[15] transform the saddle point solution problem into solving a set of algebraic Riccati equations through the State-Dependent Riccati Equation(SDRE)method for obtaining the nonlinear optimal control law of the two spacecraft in pursuit-evasion. Domestic scholars have also carried out relevant research in this field, Sun et al[16] also propose a semi-direct control parametric method to solve the saddle point of countermeasures and the results are more beneficial compared with the semi-direct method developed by Conway et al.

*This work is supported by the Natural Science Foundation of China under Grant 62233005 and U20B2056, and the Natural Science Foundation of Shanghai under Grant 22ZR1427800.

In order to solve the multi-to-multi spacecraft game problem, task assignment and game path planning must be organically integrated. Therefore, this paper proposes a hierarchical theory structure for the pursuit-evasion game of the spacecraft cluster by summarizing corresponding research on the spacecraft cluster game. The structure establishes a simple and effective multi-to-multi spacecraft game mechanism and realize the game task assignment and game trajectory planning for spacecraft cluster game.

This paper is organized as follows. In Section 2, the task assignment and game planning model of the spacecraft cluster are discussed, followed by a description of the relative motion dynamics of spacecraft. The suggested algorithm's simulation results are shown in Section 3 along with an analysis of the hierarchical structure impact on the experimental outcomes. In Section 4, we make summary and conclusion.

2 Hierarchical Structure Game Model of Spacecraft Cluster

2.1 Coordinate System and Relative motion dynamics model

In the context of the pursuit-evasion game of the spacecraft cluster, the spacecraft are usually in close proximity to each other by necessitating the use of relative states to depict their dynamic motion. As the control principle is applied to both spacecrafts during the pursuit-evasion sequence, their orbital paths undergo real-time alterations. In light of this, an optimal approach involves selecting a proximate, circular reference orbit and a notional reference spacecraft. The status of the two spacecraft can be effectively described in terms of their states relative to this reference spacecraft. When the target is detected by the spacecraft, the spacecraft at this moment is denoted as the reference spacecraft O_1, and the local vertical local horizontal (LVLH) frame is established at O_1 shown in Fig. 1. The axis O_{1x} is defined in the direction from the geocenter to O_1, the axis O_{1z} is defined in the direction of the orbital angular momentum, and then the axis O1y can be determined by the right-hand rule.

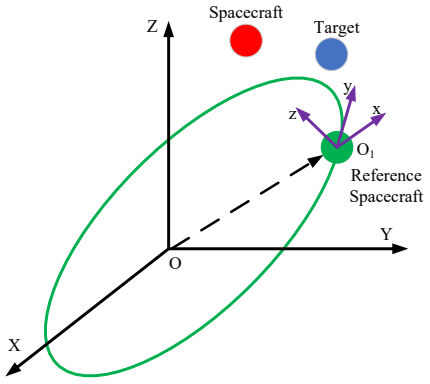

Fig. 1: The local vertical local horizontal (LVLH) frame

In the LVLH frame, when the distance between the spacecraft and the reference spacecraft is far less than the reference orbit radius, the dynamic models of the spacecraft and hostile threat relative to the reference spacecraft can be simplified as the following Clohessy-Wiltshire equations.

$$\begin{cases} \ddot{x}_i - 2\omega\dot{y}_i - 3\omega^2 x_i = u_x^i \\ \ddot{y}_i + 2\omega\dot{x}_i = u_y^i \\ \ddot{z}_i + \omega^2 z_i = u_z^i \end{cases} \tag{1}$$

Where ω is orbital angular rate of the reference spacecraft. x_i, y_i, z_i represent the coordinates of the spacecraft i in the $O-XYZ$ coordinate respectively. u_x^i, u_y^i, u_z^i is the projection of the control acceleration on each axis in the $O-XYZ$ coordinate respectively.

2.2 the task allocation of spacecraft cluster orbital game

The purpose of task allocation in the orbital game of spacecraft clusters is to decompose the multi-to-multi game tasks within the cluster into pairwise interactions between two spacecraft. This process aims to transform the solution of the cluster game strategy into the resolution of one-to-one game strategies. The task allocation procedure takes into account the initial speed and position of the spacecraft cluster, considering the fuel consumption in the spacecraft game and the game time. In this context, the calculation is simplified using velocity increments, and the outcome is the allocation of targets for the spacecraft cluster in the orbital game.

In the pursuit-evasion game of the spacecraft cluster, determining the optimal velocity increment for a single spacecraft to approach a specific space target simplifies its mission to the Lambert problem. The Lambert problem involves obtaining the velocity increment based on the spacecraft's initial position, final position, and transfer time. The model for task allocation can be summarized as follows:

$$\min \sum \left(k_1 g F_{ij}^{t_{best}} + k_2 g t_{best} \right) \tag{2}$$

Where $F_{ij}^{t_{best}}$ represents the best fuel consumption of the spacecraft game, t_{best} represents the best time of the spacecraft game , k_1 and k_2 represent the conversion coefficient in the equation.

The task allocation in the spacecraft cluster orbital game can be effectively addressed through intelligent optimization algorithms, with commonly employed methods including genetic algorithms, ant colony optimization, particle swarm optimization, among others. In consideration of the inherent simplicity and expeditious solution capabilities of the particle swarm algorithm, this study leverages the discrete particle swarm optimization (DPSO) approach to resolve the task allocation challenges within the spacecraft cluster orbital game.

Given the discrete nature of variables associated with the task allocation problem in the spacecraft cluster game, the DPSO algorithm is employed. To facilitate its application to problem-solving, a discretization process is applied to both the updated velocity and the particle's position. The discrete particle swarm task planning algorithm embraces a discrete strategy, treating velocity and position as integer values. Consequently, a sequence of integer values is utilized to represent the position of each particle in the optimization process.

Consider a D-dimensional space as the particle search space, where each assignment corresponds to treating the

spacecraft cluster game as a particle. The entire ensemble comprises a particle swarm, consisting of a total of m particles. In each iteration, every particle updates its position and velocity, with the updated velocity denoted as v and position as x. These updates are calculated using the formulas (3) and (4):

$$v_{id}^{k+1} = \omega v_{id}^{k} + c_1\xi\left(p_{id}^{k} - x_{id}^{k}\right) + c_2\eta\left(P_{gd}^{k} - x_{id}^{k}\right) \tag{3}$$

$$x_{id}^{k+1} = \left|x_{id}^{k} + v_{id}^{k+1}\right|,\ d = 1,2,\cdots,D, \left|v_{id}^{q}\right| \le V_{\max}, q \le \text{MaxIt} \tag{4}$$

Where i represents the iteration number, ω is the inertial weight coefficient, ξ and η are random values following the uniform distribution $U(0,1)$, the learning factors c_1, c_2 are used to adjust the weight influencing the direction of particle updates, MaxIt is the maximum number of iterations, q is the iteration count.

2.3 The Planning of Spacecraft Orbit Pursuit-Evasion Based on Differential Game Model

During the orbit Chase-Evasion game of two spacecraft, the distance between the two spacecraft is relatively close and can be measured mutually. At this moment, one spacecraft attempts to capture the other by control, referred to as the Pursuing spacecraft (Pursuer, P); while the other spacecraft aims to avoid being captured or attacked through control, referred to as the Evading spacecraft (Evader, E). The Pursuit-Evasion game between the two spacecraft can be considered as an optimal control problem for both parties, but the controlling parties have conflicting objectives, possessing more adversarial and conflicting characteristics compared to the classical unilateral optimal control problem. Hence, the two-person zero-sum differential game could be used to model this problem, with the assistance of differential game theory for analysis and solution.

As the two spacecraft participating in the Pursuit-Evasion game are in close proximity, a reference orbit could be chosen, whereby the state of the Pursuing spacecraft and the Evading spacecraft is represented relative to this reference orbit, as shown in Fig. 2.

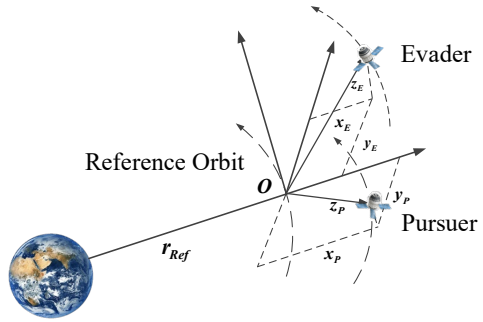

Fig. 2: Tracking the relative state of pursuit spacecraft and escape spacecraft

The relative states of the tracking spacecraft and the escape spacecraft are $\boldsymbol{X}_P = (x_P, y_P, z_P, \dot{x}_P, \dot{y}_P, \dot{z}_P)^{\mathrm{T}}$ and $\boldsymbol{X}_E = (x_E, y_E, z_E, \dot{x}_E, \dot{y}_E, \dot{z}_E)^{\mathrm{T}}$ respectively, both satisfying the CW equation given by formula (4).

Assuming the state variable of the spacecraft's differential chase tactic as $\boldsymbol{X} = \boldsymbol{X}_E - \boldsymbol{X}_P = (x, y, z, \dot{x}, \dot{y}, \dot{z})^{\mathrm{T}}$, then from formula (1) we can get

$$\begin{cases} \ddot{x}_i - 2\omega\dot{y}_i - 3\omega^2 x_i = a_{E,x} - a_{P,x} \\ \ddot{y}_i + 2\omega\dot{x}_i = a_{E,y} - a_{P,y} \\ \ddot{z}_i + \omega^2 z_i = a_{E,z} - a_{P,z} \end{cases} \tag{5}$$

If two spacecraft are in pursuit-evasion game, both equipped with substantial fuels. The pursuing spacecraft attempts to intercept or capture the fleeing spacecraft as soon as possible by controlling, while the fleeing spacecraft hopes to delay being pursued by controlling as much as possible. This problem can be regarded as a survival differential game problem.

For such spacecraft pursuit-evasion game problems, this paper gives the necessary conditions and solving methods for the saddle point based on the optimality conditions of the differential game. It is assumed in this paper that the thrust acceleration of the pursuing spacecraft is greater than that of the fleeing spacecraft, that is, $T_P > T_E$. If the fuel is not considered, it can be guaranteed that the pursuing spacecraft can capture the fleeing spacecraft in a finite time, thus the saddle point of this spacecraft pursuit-evasion survival differential game exists. According to the optimality conditions of the differential game, the necessary conditions for the saddle point of this strategy are derived, and the Hamilton function and terminal constraint function are constructed as follows:

$$\begin{aligned} &H(\mathbf{X}, \mathbf{u}_P, \mathbf{u}_E, \boldsymbol{\lambda}) \\ &= \boldsymbol{\lambda}^{\mathrm{T}}\dot{\mathbf{X}} = \boldsymbol{\lambda}^{\mathrm{T}}\left[\mathbf{AX} + \mathbf{B}(\mathbf{T_E} - \mathbf{T_P})\right] \\ &= \lambda_1\dot{x} + \lambda_2\dot{y} + \lambda_3\dot{z} + \lambda_4(3\omega^2 x + 2\omega\dot{y} \\ &+ T_E\cos\alpha_E\cos\beta_E - T_P\cos\alpha_P\cos\beta_P) \\ &+ \lambda_5(-2\omega\dot{x} + T_E\sin\alpha_E\cos\beta_E - T_P\sin\alpha_P\cos\beta_P) \\ &+ \lambda_6(-\omega^2 z + T_E\sin\beta_E - T_P\sin\beta_P) \end{aligned} \tag{6}$$

$$\Phi = t_f + \boldsymbol{\nu}^{\mathrm{T}}\boldsymbol{\varphi} = t_f + \nu_1 x(t_f) + \nu_2 y(t_f) + \nu_3 z(t_f) \tag{7}$$

where $\boldsymbol{\lambda} = [\lambda_1, \lambda_2, \lambda_3, \lambda_4, \lambda_5, \lambda_6]^{\mathrm{T}}$ is the co-state variable, $\boldsymbol{\nu} = \left[\nu_1, \nu_2, \nu_3\right]^{\mathrm{T}}$ is the Lagrange multiplier corresponding to the terminal constraint, T_P and T_E are the magnitude of the thrust acceleration of the two spacecraft, and α and β are the directional angles of the thrust acceleration.

The differential game co-state equation is

$$\dot{\lambda} = -\frac{\partial H}{\partial X} = -A^{\mathrm{T}}\lambda \tag{8}$$

The terminal condition for the co-state variables is

$$\lambda(t_f) = \frac{\partial\Phi(t_f, \mathbf{x}(t_f))}{\partial\mathbf{x}(t_f)} = \begin{bmatrix} \nu_1 \\ \nu_2 \\ \nu_3 \\ 0 \\ 0 \\ 0 \end{bmatrix} \tag{9}$$

The transversality condition of differential games is

$$H(t_f) = -\frac{\partial}{\partial t}\Phi(t_f, \boldsymbol{x}(t_f)) = -1 \tag{10}$$

From the aforementioned necessary conditions for the saddle point, it is evident that equations (5), (8) and equations (9), (10) collectively formulate a seven-dimensional two-point boundary value problem. The saddle

point of the game can be obtained by solving this two-point boundary value problem.

The above seven dimensional nonlinear equation system has four independent variables, and its solving process can ultimately be transformed into a four-dimensional nonlinear equation system. For the solution of this four-dimensional nonlinear equation system, due to the slow direct solving speed of traditional algorithms and the difficulty in obtaining feasible solutions, this paper uses evolutionary algorithms to obtain the initial solution of the optimal strategy. Due to the limitations of optimization algorithms, the initial solution is often difficult to satisfy the constraints of differential games. Therefore, the optimized initial solution is used as the initial value, and Newton's iteration is used to calculate the exact saddle point solution that satisfies the constraints. Due to the use of optimization algorithms to solve the initial values first, the computational pressure is reduced. In the Newton iterative solution process, smaller integration steps and higher iteration accuracy parameters can be used, greatly improving the convergence speed and solution accuracy.

3 Simulation Cases

For typical pursuit-evasion scenarios of spacecraft clusters, the reference orbit is selected as the geosynchronous orbit, with 6 pursuing spacecraft and 3 escaping spacecraft. It is assumed that in the pursuit and escape process, only one pursuing spacecraft is needed to achieve the pursuit and escape objectives for each escaping spacecraft.

The reference orbital parameters and the position parameters of the pursuing spacecraft and the escaping spacecraft in the relative coordinate system are set as follows:

Table 1: Reference orbit parameters

Semim-ajor Axis (km)	Eccentr-icity	Inclinat-ion/(°)	Argum-ent of Perigee /(°)	RANN /(°)	Ture anomal-y /(°)
42164	0	0	0	0	120

Table 2: Reference orbit parameters of evader

ID	Position/(km)			Velocity/(km/s)		
	X	Y	Z	X	Y	Z
1	-34.64	64	20	0	0	0
2	40	0	0	0	0	0
3	34.64	64	20	0	0	0

Table 3: Reference orbit parameters of pursuer

ID	Position(km)			Velocity(km/s)		
	X	Y	Z	X	Y	Z
1	-51.96	30	5	0	0	0
2	-30	51.96	10	0	0	0
3	60	0	10	0	0	0
4	55	5	5	0	0	0
5	30	51.6	10	0	0	0
6	51.96	30	5	0	0	0

Based on the given initial conditions and task allocation constraints, an urgent solution to the task allocation problem in spacecraft cluster space games is sought. Multiple simulation experiments indicate that the optimal task allocation results is 1-3-6, meaning that pursuer 1 is for the evader 1, pursuer 3 is for the evader 2 and pursuer6 is for the evader 3. Fig. 3 shows the convergence curve of the fitness value (total fuel consumption) of the discrete particle swarm optimization algorithm for task allocation.

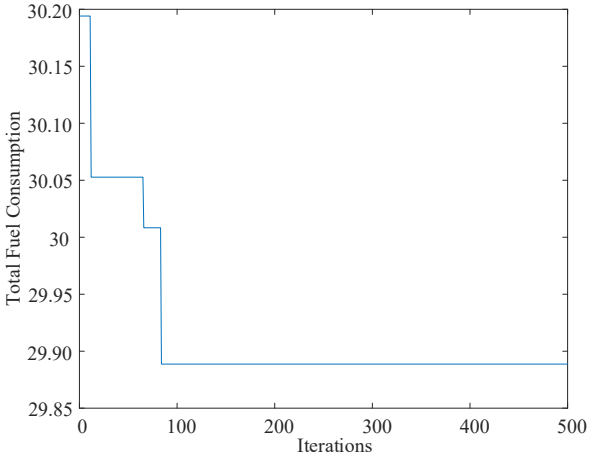

Fig. 3: The total Fuel consumption

Fig. 4, Fig. 5, and Fig. 6 are three sets of three-dimensional trajectory diagrams and relative distance change curves for spacecraft orbital pursuit-evasion. Form the figures， the adversarial games pursued and evaded by the two spacecraft exhibit a heightened level of intensity within the orbital plane, whereas outside this plane, the games appear to be comparatively moderated. The game results show that the relative distance between the chasing spacecraft and the escaping spacecraft is less than 20 meters.

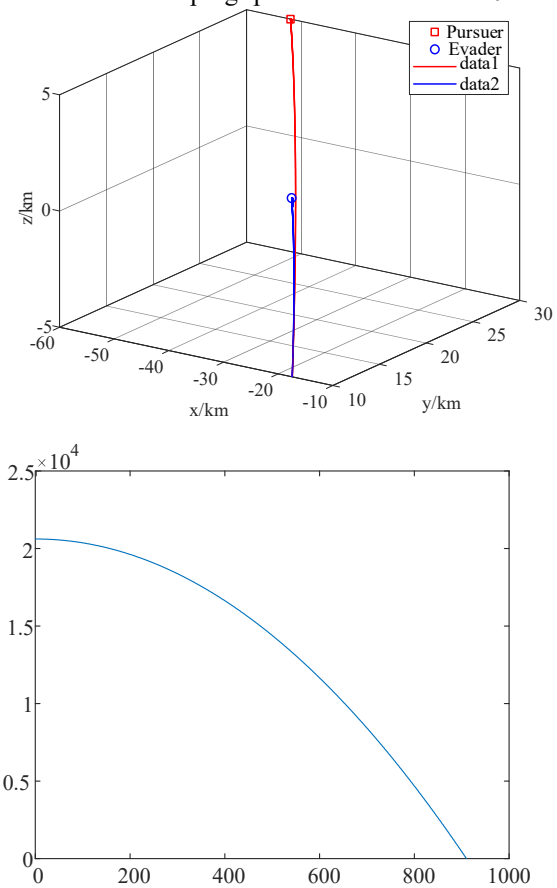

Figure 4: Pursuer 1-Evader 1 Game Results

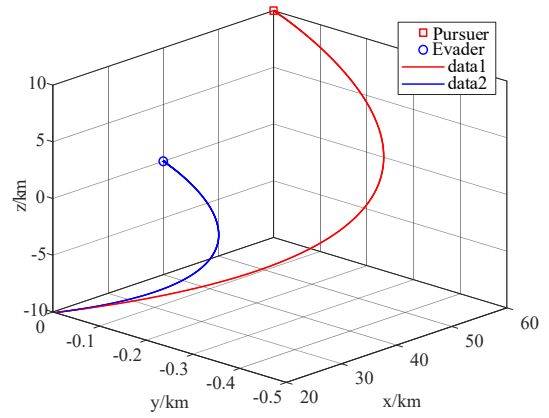

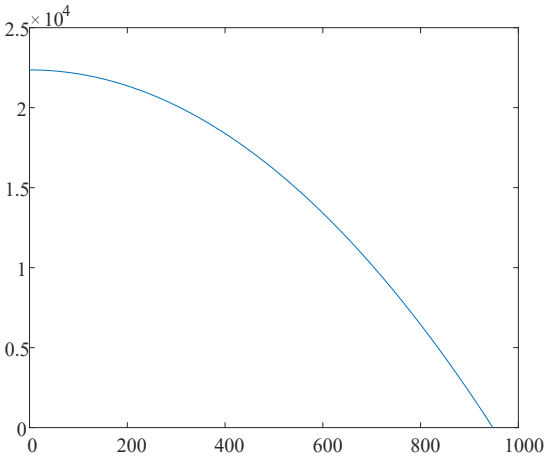

Fig. 5: Pursuer 3-Evader 2 Game Results

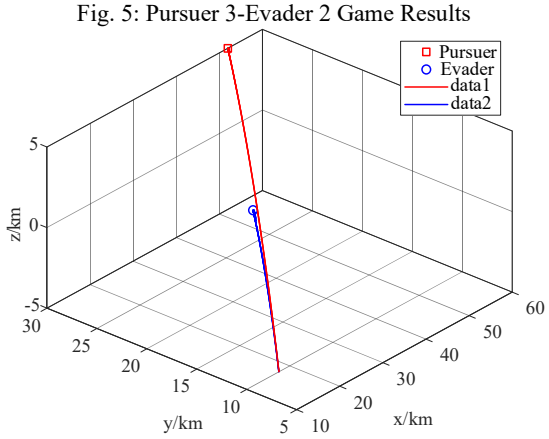

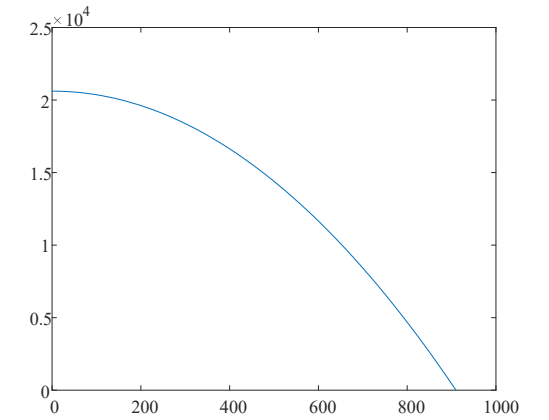

Fig. 6: Pursuer 6-Evader 3 Game Results

4 Conclusions

This paper establishes an orbital pursuit-evasion model based on hierarchical theory structure for multi-to-multi spacecraft game for expanding the analysis and solution methods for spacecraft orbit pursuit-evasion problems. The analysis of the characteristics of spacecraft orbital pursuit and evasion can provide a reference for the on-orbit safe operation and task execution of spacecraft. The spacecraft cluster game mission is decomposed into task assignment and a pursuit-evasion game between two spacecraft. The finally simulation verifies the feasibility of the proposed theory framework. The proposed structure can support the on-orbit cooperative pursuit-evasion game research of the spacecraft cluster based on multi-role differential game theory.

References

[1] Yang Y, Wang L, Modares H, et al. Data-driven integral reinforcement learning for continuous-time non-zero-sum games[J]. *IEEE Access*, 2019, 7: 82901–82912.

[2] Sun C H, Duan H B. Markov decision evolutionary game theoretic learning for cooperative sensing of unmanned aerial vehicles[J]. *Sci China Tech Sci*, 2015, 58: 1392–1400.

[3] Prince E R, Hess J A, Cobb R G, et al. Elliptical orbit proximity operations differential games[J]. *J Guid Control Dyn*, 2019, 42: 1458– 1472.

[4] Shen H X, Casalino L. Revisit of the three-dimensional orbital pursuitevasion game[J]. *J Guid Control Dyn*, 2018, 41: 1823–183.

[5] Basar T, Olsder G J. Dynamic Noncooperative Game Theory[J]. Philadelphia: *Society for Industrial and Applied Mathematics*, 1999. 10–50.

[6] Salimi M, Ferrara M. Differential game of optimal pursuit of one evader by many pursuers[J]. *Int J Game Theory*, 2019, 48: 481–490.

[7] Ibragimov G I, Salimi M, Amini M. Evasion from many pursuers in simple motion differential game with integral constraints[J]. *Eur J Oper Res*, 2012, 218: 505–511.

[8] F. Chen, C. H. Lu, W. Pan, et al. Research on target assignment in collaborative task of micro-satellites system[J]. *Journal of Astronautics*, 2010, 31(5): 1347-1380.

[9] Y. Huang, X. J. Li, D. L. Zhang, et al. A multi-target assignment method for on-orbit operation of distributed satellite systems[J]. *Journal of Astronautics*, 2013, 34(11): 1475-1482.

[10] Y. H. Du, L. N. Xing, Z. Q. Cai. Survey on intelligent scheduling technologies for unmanned aircraft cluster[J]. *Acta Automatica Sinica*, 2020, 46(2): 222-241.

[11] H. Tripp, P. Palmer. Stigmergy-based behavioral coordination for satellite clusters[J]. *Acta Astronautica*, 2010, 66(7): 1052-1071.

[12] Pontani M, Conway B A. Numerical Solution of the Three-Dimensional Orbital Pursuit–Evasion Game[J]. *Journal of Guidance Control and Dynamics*, 2009, 2(32): 474-487.

[13] Hafer W T, Reed H L, Turner J D, et al. Sensitivity Methods Applied to Orbital Pursuit Evasion[J]. *Journal of Guidance, Control, and Dynamics*, 2015, 38(6): 1118-1126.

[14] Stupik J, Pontani M, Conway B. Optimal Pursuit/Evasion Spacecraft Trajectories in the Hill Reference Frame[C]. *AIAA Guidance, Navigation, and Control Conference*, Minneapolis, Minnesota, 2012.

[15] Jagat A, Sinclair A J. Optimization of Spacecraft Pursuit-Evasion Game Trajectories in the Euler-Hill Reference Frame[C]. *AIAA Guidance, Navigation, and Control Conference*, San Diego, Canada, 2014.

[16] Sun S, Zhang Q, Loxton R, et al. Numerical Solution of A Pursuit-Evasion Differential Game Involving Two Spacecraft in Low Earth Orbit[J]. *Journal of Industrial and Management Optimization*, 2015, 11(4): 1127-1147.

Proceedings of the 3rd Conference on Fully Actuated System Theory and Applications
May 10-12, 2024, Shenzhen, China

Distributed Entire State Estimation and Consensus Control for Lipschitz Nonlinear Multi-Agent Systems

Yan Li[1], Jiazhu Huang[1], Yuezu Lv[2], Jialing Zhou[2]

1. School of Automation, Beijing Institute of Technology, Beijing 100081, P. R. China
E-mail: yanl@bit.edu.cn, jzh@bit.edu.cn

2. MIIT Key Laboratory of Complex-field Intelligent Sensing, Beijing Institute of Technology, Beijing 100081, P. R. China
E-mail: yzlv@bit.edu.cn, jlzhou@bit.edu.cn

Abstract: In this paper, a novel integrated framework for distributed state estimation and consensus control is constructed for a class of Lipschitz nonlinear multi-agent systems under strongly connected graphs. The distributed output tracking algorithm and local observers are introduced to estimate the overall output and global state, respectively. Furthermore, a consensus control protocol is designed based on each agent's own entire state estimation to ensure that all agents can realize consensus. The exponential stability of the estimation error is obtained by utilizing the Lyapunov stability theory. Moreover, the proposed algorithm is still effective even in the presence of measurement output failures. Finally, numerical simulation is worked out to testify the feasibility of the proposed method.

Key Words: Multi-agent systems, Lipschitz nonlinearity, consensus control, distributed entire state estimation, distributed output tracking

1 Introduction

Inspired by the collaboration of biological populations in nature, scholars have delved deeper into the study of multi-agent systems (MASs) over the past few decades. Compared to a single complex agent, multi-agent systems can improve efficiency, reduce costs, and perform complex tasks that individual agent finds challenging, and have been widely researched in aerospace [1], smart grids [2], traffic management [3], etc. It can be foreseen that with technological advancement and social development, multi-agent systems will have a wider range of application prospects in the future.

Cooperative control is the main research content of multi-agent systems, mainly including consensus control [4], formation control [5], containment control [6], distributed optimization and decision-making [7]. Consensus control is the fundamental problem of cooperative control in multi-agent systems [8]. The famous Vicsek model proposed in reference [9] determines the motion direction of agents in a cluster based on the average velocity direction of their neighbors, laying the foundation for the study of consensus problems by other researchers. From the perspective of network communication, research on consensus control mainly considers fixed and switching topologies. For fixed topologies, the research is divided into two categories: undirected graphs and directed graphs. For instance, references [10], [11] and [12] respectively conduct research on consensus control under undirected graphs, directed graphs, and switching topologies. Furthermore, there are many mature studies addressing consensus control problems that are more applicable to real systems, such as nonlinear systems, uncertain systems, and perturbed systems [13–16]. Moreover, to achieve consensus within a finite time, scholars have conducted extensive research on finite-time consensus [14], fixed-time consensus [16], and specified-time consensus [17].

This work was supported by the National Natural Science Foundation of China under Grants 62088101, 62273045, U2341213 and 62376029, Beijing Nova Program under Grant 20230484481, and China Postdoctoral Science Foundation under Grant 2023M730255.

However, the implementation of the control law in the above research requires knowledge of the real state of agents, which is usually unrealistic in practical applications. One method to solve this problem is to design appropriate observers to estimate the state. For example, state estimators are constructed and the controllers are designed based on the estimated state in [18–20]. For large-scale multi-agent systems, distributed state estimation is more effective than the centralized one. As shown in [18–22], the existing distributed state estimation techniques rely on the output information measured by the sensors on the agents and achieve state estimation through interaction with neighboring nodes. It means that existing algorithms will lead to state estimation failure when the sensors are unable to measure valid information.

Motivated by this, this paper considers the consensus problem of a class of Lipschitz nonlinear multi-agent systems under strongly connected graphs. The estimation of the overall output and the entire state of the multi-agent system is achieved by designing distributed output tracking algorithm and local state estimators. It ensures that even if sensors of an agent fail, it can make use of its neighboring nodes' overall output estimation to achieve the estimation of the state and ensure the realization of consensus control for multi-agent systems in the case of the unknown state.

The remaining is structured as follows. Section 2 presents the problem and necessary background knowledge. The main research result is introduced in section 3. The numerical simulation is shown in section 4 and the conclusion is given in section 5.

Notation: $\mathbb{R}^n$ represents the set of n-dimensional real vectors. The symbol $col\left(s_1, \cdots, s_N\right)$ is equivalent to $\left[s_1^T, s_2^T, \cdots s_n^T\right]$, and $diag\left(s_1, \cdots, s_N\right)$ denotes a diagonal matrix with s_i as its diagonal elements. I_n and $\mathbf{1}_n$ stand for the $n \times n$ identity matrix and the $n \times 1$ all-ones vector, respectively. The symbol $\otimes$ represents Kronecker product and $\|\cdot\|$ represents the norm of a matrix or a vector. $\lambda_{\min}\left(A\right)$ and $\lambda_{\max}\left(A\right)$ are the minimum and maximum eigenvalues of matrix A. $\sigma_{\min}\left(B\right)$ and $\sigma_{\max}\left(B\right)$ denote the maximum

and minimum singular value of matrix B. $P > 0$ ($P < 0$) means that P is a symmetric positive (negative) definite matrix.

2 Reliminaries and problem formation

Consider a Lipschitz nonlinear multi-agent system composed of N agents, where the dynamic of each agent is given by

$$\dot{x}_i = Ax_i + Bu_i + f(x_i), \tag{1}$$

where $x_i \in \mathbb{R}^n$, $i \in \{1, 2, \cdots, N\}$, $u_i \in \mathbb{R}^r$ is the control input, A and B are the constant matrices for the system, and $f(x_i)$ is a nonlinear function that satisfies the Lipschitz condition, i.e., there exists a Lipschitz constant γ such that the following inequality holds:

$$\|f(x) - f(y)\| \leq \gamma \|x - y\|, \forall x, y \in \mathbb{R}^n. \tag{2}$$

Let $x = col(x_1, \cdots, x_N)$, $u = col(u_1, \cdots, u_N)$ and $F(x) = col(f(x_1), \cdots, f(x_N))$. The output of each agent is related to the overall state of the system, described as $y_i = C_i x$ where $y_i \in \mathbb{R}^{p_i}$. Thus the multi-agent system is transformed into a sensor network system with the dynamic of

$$\begin{aligned} \dot{x} &= (I_N \otimes A)x + (I_N \otimes B)u + F(x), \\ y_i &= C_i x. \end{aligned} \tag{3}$$

Clearly, the system studied in this paper is not only a Lipschitz nonlinear multi-agent system but also with heterogeneous output. Denote $C = col(C_1, \cdots, C_N)$.

Remark 1 *The sensors distributed on each agent can measure their own information as well as relative information from neighbors. Mathematically abstracting it as the output of each agent being related to the overall state is reasonable, which implies that* (3) *is justified.*

Assumption 1 *The pair $(I_N \otimes A, C)$ is observable.*

With the help of graph theory, the communication network among agents is described by an unweighted topological graph $\mathcal{G} = (\mathcal{V}, \mathcal{E}, \mathcal{A})$, where $\mathcal{V} = \{1, \cdots, N\}$ is a finite non-empty set that represents the nodes of the multi-agent system, $\mathcal{E} \subseteq \mathcal{V} \times \mathcal{V}$ is the edge set of the graph, reflecting the communication relationship between the agents, $\mathcal{A} = [a_{ij}]_{N \times N}$ is the adjacency matrix, and $a_{ij} = 1$ holds if and only if node i can receive information from node j, i.e., $(i, j) \in \mathcal{E}$. The Laplacian matrix of $\mathcal{G}$ is denoted as $\mathcal{L} = D - \mathcal{A}$, where D is the in-degree matrix, meaning it is a diagonal matrix with $d_i = \sum_{j=1}^{N} a_{ij}$ as its diagonal elements. Obviously, the Laplacian matrix $\mathcal{L}_0 = [l_{ij0}]_{N \times N}$ of the full graph $\mathcal{G}_0$ consisting of N agents is given by

$$l_{ij0} = \begin{cases} -1 & i \neq j, \\ N - 1 & i = j. \end{cases}$$

An undirected graph is connected if there exists a connected path between any two nodes. A strongly connected graph means that there exists a directed path between any two nodes, that is, for any two nodes i and j, there exists nodes $k_1, k_2, \cdots, k_m$ such that $(i, k_1), (k_1, k_2), \cdots, (k_m, j) \in \mathcal{E}$.

Assumption 2 *The communication topology $\mathcal{G}$ among the agents is strongly connected.*

Lemma 1 ([23]) *Suppose the Assumption 2 holds, then $\mathcal{L} \otimes I_p + \mathcal{D}$ is a non-singular M matrix, where $p = \sum_{i=1}^{N} p_i$, $\mathcal{D} = diag(\mathcal{D}_1, \mathcal{D}_2, \cdots, \mathcal{D}_N)$ and $\mathcal{D}_i = diag(a_{i1} I_{p1}, a_{i2} I_{p2}, \cdots, a_{iN} I_{pN})$.*

Lemma 2 ([24, 25]) *For any non-singular M matrix $\mathcal{M}$, there exists a diagonal positive definite matrix G such that $G\mathcal{M} + \mathcal{M}^T G > 0$.*

Lemma 3 ([26, Chap. 9, Th. 55]) *For the system described in* (1)*, a control law is designed as $u_i = cK \sum_{j=1}^{N} a_{ij}(x_i - x_j)$. The gain constant $c \geq \frac{\tau}{a(\mathcal{L})}$ where the scalar $\tau > 0$ and $a(\mathcal{L})$ is the generaized algebraic connectivity of $\mathcal{G}$. The feedback gain matrix $K = -\frac{1}{2} B^T P^{-1}$ where $P > 0$ satisfies the linear matrix inequality (LMI)*

$$\begin{bmatrix} AP + PA^T - \tau BB^T + I & P \\ P & -\left(\gamma^{-1}\right)^2 I \end{bmatrix} < 0. \tag{4}$$

Then all agents of MASs (1) *can achieve consensus under the strongly connected graph $\mathcal{G}$. In the case where the communication topology is a full graph, the control law equals to $u_i = cK \sum_{j=1}^{N} (x_i - x_j)$ where $c \geq \frac{\tau}{N}$.*

The goal of this paper is to design a distributed estimation algorithm to estimate the overall output and state of the multi-agent system, ensuring that even if some agents' measurement output fails, state estimation can still be achieved and further consensus control tasks can be accomplished.

3 Main results

In this section, distributed output tracking algorithm, local observers and a consensus control protocol based on the estimated state are presented. The effectiveness of the algorithms is theoretically proven.

Denote $\hat{x}_i = col(\hat{x}_{i1}, \cdots, \hat{x}_{iN})$ as the entire state estimation by i-th agent, where $\hat{x}_{ij}$ is the j-th agent' state estimation by i-th agent. Then a consensus control protocol is designed based on $\hat{x}_i$ as follows:

$$u_i = cK \sum_{j=1}^{N} (\hat{x}_{ii} - \hat{x}_{ij}), \tag{5}$$

where $c \geq \frac{\tau}{N}$, $\tau > 0$ and K is characterized in Lemma 3. Obviously, we can see that if $\lim_{t \to \infty} \|\hat{x}_i - x\| = 0$, the MASs (1) can achieve consensus under the control protocol (5).

From (5), we get $u = (c\mathcal{L}^o \otimes K)\hat{x}$, where $\mathcal{L}^o = diag\left(\mathcal{L}^1, \cdots, \mathcal{L}^N\right)$, $\mathcal{L}^i$ is the i-th row of the Laplacian matrix $\mathcal{L}_0$ of the full graph $\mathcal{G}_0$. Let $y = col(y_1, \cdots, y_N)$ and $\hat{x} = col(\hat{x}_1, \cdots, \hat{x}_N)$, the system (3) is transformed into

$$\begin{aligned} \dot{x} &= \bar{A}x + \bar{B}(\hat{x} - \mathbf{1}_N \otimes x) + F(x), \\ y &= Cx, \end{aligned} \tag{6}$$

where $\bar{A} = I_N \otimes A + c\mathcal{L}_o \otimes BK$ and $\bar{B} = c\mathcal{L}^o \otimes BK$.

Further, we propose the distributed state estimation algo-

rithm

$$\begin{aligned}\dot{\hat{y}}_i =& -\mu\left[\sum_{j=1}^{N} a_{ij}\left(\hat{y}_i-\hat{y}_j\right)+\mathcal{D}_i\left(\hat{y}_i-y\right)\right]\\ &+C\bar{A}\hat{x}_i+CF\left(\hat{x}_i\right),\\ \dot{\hat{x}}_i =& \left(\bar{A}-LC\right)\hat{x}_i+L\hat{y}_i+F\left(\hat{x}_i\right),\end{aligned} \tag{7}$$

where $i\in\mathcal{V}$, $F\left(\hat{x}_i\right)=col\left(f\left(\hat{x}_{i1}\right),\cdots,f\left(\hat{x}_{iN}\right)\right)$, $\mu>0$ is the constant gain and L is the feedback gain matrix which need to be determined. $\hat{x}_i$ and $\hat{y}_i$ are the estimation of the overall state and the overall output by i-th agent, respectively.

Remark 2 *According to the definition of $\mathcal{D}_i$, it can be seen that the $\mathcal{D}_i y$ component in* (7) *contains only the measurement output information of itself and its neighboring nodes, indicating that the algorithm proposed in this paper is distributed.*

Denote $\hat{y}=col\left(\hat{y}_1,\cdots,\hat{y}_N\right)$ and $F_0\left(\hat{x}\right)=col\left(F\left(\hat{x}_1\right),\cdots,F\left(\hat{x}_N\right)\right)$, the dynamics of $\hat{y}$ and $\hat{x}$ are given by

$$\begin{aligned}\dot{\hat{y}} =& -\mu\left(\mathcal{L}\otimes I_p+\mathcal{D}\right)\left(\hat{y}-\mathbf{1}_N\otimes y\right)+\left(I_N\otimes C\bar{A}\right)\hat{x}\\ &+\left(I_N\otimes C\right)F_0\left(\hat{x}\right),\\ \dot{\hat{x}} =& \left[I_N\otimes\left(\bar{A}-LC\right)\right]\hat{x}+\left(I_N\otimes L\right)\hat{y}+F_0\left(\hat{x}\right).\end{aligned} \tag{8}$$

The output tracking error is defined as $\tilde{y}=\hat{y}-\mathbf{1}_N\otimes y$ and the local state estimation error is defined as $\tilde{x}=\hat{x}-\mathbf{1}_N\otimes x$. Then we get

$$\begin{aligned}\dot{\tilde{y}} =& -\mu\left(\mathcal{L}\otimes I_p+\mathcal{D}\right)\tilde{y}+\left[I_N\otimes C\bar{A}-\mathbf{1}_N\otimes C\bar{B}\right]\tilde{x}\\ &+\left(I_N\otimes C\right)\left[F_0\left(\hat{x}\right)-\mathbf{1}_N\otimes F\left(x\right)\right],\\ \dot{\tilde{x}} =& A_o\tilde{x}+\left(I_N\otimes L\right)\tilde{y}+F_0\left(\hat{x}\right)-\mathbf{1}_N\otimes F\left(x\right),\end{aligned} \tag{9}$$

where $A_o=I_N\otimes\left(\bar{A}-LC\right)-\mathbf{1}_N\otimes\bar{B}$.

Theorem 1 *Suppose the Assumption 1 and Assumption 2 hold, if there exists a matrix L such that A_o is Hurwitz and $\min\limits_{\omega\in\mathbb{R}^+}\sigma_{\min}\left(A_o-j\omega I_{N^2n}\right)>\gamma$, and the constant gain satisfies*

$$\begin{aligned}\mu>&\mu_0\\ =&\frac{4}{\lambda_0\varepsilon}\left[\lambda_{\max}^2\left(G\right)\sigma_{\max}^2\left(I_N\otimes C\bar{A}-\mathbf{1}_N\otimes C\bar{B}\right)\right]\\ &+\frac{4}{\lambda_0\varepsilon}\left[\lambda_{\max}^2\left(Q\right)\sigma_{\max}^2\left(L\right)+\gamma^2\lambda_{\max}^2\left(G\right)\sigma_{\max}^2\left(C\right)\right],\end{aligned} \tag{10}$$

where $\varepsilon>0$ is a positive constant, $\lambda_0>0$ is the minimum eigenvalue of the positive definite matrix $G\left(\mathcal{L}\otimes I_p+\mathcal{D}\right)+\left(\mathcal{L}\otimes I_p+\mathcal{D}\right)^TG$, and G is the diagonal positive definite matrix introduced in Lemma 2, then the output tracking error $\tilde{y}$ and the state estimation error $\tilde{x}$ converge asymptotically, with $\lim\limits_{t\to\infty}\|\hat{y}_i-y\|=0$ and $\lim\limits_{t\to\infty}\|\hat{x}_i-x\|=0$ holding. Moreover, the system (1) *realizes consensus under the control protocol* (5)*.*

Proof If $\lim\limits_{t\to\infty}\|\hat{x}_i-x\|=0$ holds, then we get $\lim\limits_{t\to\infty}u_i=cK\sum_{j=1}^{N}\left(x_i-x_j\right)$. By Lemma 3, MASs (1) will achieve consensus under the control input (5). Therefore, the proof of Theorem 1 only requires proving asymptotic convergence of the error system (9). Consider the Lyapunov function

$$V=\tilde{y}^TG\tilde{y}+\tilde{x}^TQ\tilde{x}, \tag{11}$$

where G is defined in Lemma 2 and $Q>0$ satisfying

$$QA_o+{A_o}^TQ+\gamma^2QQ+\left(1+\varepsilon\right)I_{N^2n}=0, \tag{12}$$

From the literature [27], if the feedback gain matrix L exists, there must exist a positive definite solution Q to the Riccati equation of (12). The time derivative of V can be written as

$$\begin{aligned}\dot{V} =& -\mu\tilde{y}^T\left[G\left(\mathcal{L}\otimes I_p+\mathcal{D}\right)+\left(\mathcal{L}\otimes I_p+\mathcal{D}\right)^TG\right]\tilde{y}\\ &+2\tilde{y}^TG\left(I_N\otimes C\bar{A}-\mathbf{1}_N\otimes C\bar{B}\right)\tilde{x}\\ &+2\tilde{y}^TG\left(I_N\otimes C\right)\left[F_0\left(\hat{x}\right)-\mathbf{1}_N\otimes F\left(x\right)\right]\\ &+\tilde{x}^T\left(QA_o+A_o^TQ\right)\tilde{x}\\ &+2\tilde{x}^TQ\left(I_N\otimes L\right)\tilde{y}\\ &+2\tilde{x}^TQ\left[F_0\left(\hat{x}\right)-\mathbf{1}_N\otimes F\left(x\right)\right]\end{aligned} \tag{13}$$

By Young's inequality, (14) and (15) hold.

$$\begin{aligned}&2\tilde{y}^TG\left(I_N\otimes C\bar{A}-1_N\otimes C\bar{B}\right)\tilde{x}\\ &\le\frac{4}{\varepsilon}\lambda_{\max}^2\left(G\right)\sigma_{\max}^2\left(I_N\otimes C\bar{A}-\mathbf{1}_N\otimes C\bar{B}\right)\tilde{y}^T\tilde{y}\\ &+\frac{\varepsilon}{4}\tilde{x}^T\tilde{x}.\end{aligned} \tag{14}$$

$$\begin{aligned}&2\tilde{x}^TQ\left(I_N\otimes L\right)\tilde{y}\\ &\le\frac{4}{\varepsilon}\lambda_{\max}^2\left(Q\right)\sigma_{\max}^2\left(L\right)\tilde{y}^T\tilde{y}+\frac{\varepsilon}{4}\tilde{x}^T\tilde{x}.\end{aligned} \tag{15}$$

According to (2), we note that

$$\begin{aligned}&2\tilde{y}^TG\left(I_N\otimes C\right)\left[F_0\left(\hat{x}\right)-\mathbf{1}_N\otimes F\left(x\right)\right]\\ &\le2\left\|\left(I_N\otimes C^T\right)G\tilde{y}\right\|\left\|F_0\left(\hat{x}\right)-\mathbf{1}_N\otimes G\left(x\right)\right\|\\ &\le2\gamma\left\|\left(I_N\otimes C^T\right)G\tilde{y}\right\|\left\|\tilde{x}\right\|\\ &\le\frac{4\gamma^2}{\varepsilon}\tilde{y}^TG\left(I_N\otimes CC^T\right)G\tilde{y}+\frac{\varepsilon}{4}\tilde{x}^T\tilde{x}\\ &\le\frac{4\gamma^2}{\varepsilon}\lambda_{\max}^2\left(G\right)\sigma_{\max}^2\left(C\right)\tilde{y}^T\tilde{y}+\frac{\varepsilon}{4}\tilde{x}^Tx,\end{aligned} \tag{16}$$

and

$$\begin{aligned}&2\tilde{x}^TQ\left[F_0\left(\hat{x}\right)-\mathbf{1}_N\otimes F\left(x\right)\right]\\ &\le2\left\|Q\tilde{x}\right\|\left\|F_0\left(\hat{x}\right)-\mathbf{1}_N\otimes G\left(x\right)\right\|\\ &\le2\gamma\left\|Q\tilde{x}\right\|\left\|\tilde{x}\right\|\\ &\le\gamma^2\tilde{x}^TQQ\tilde{x}+\tilde{x}^T\tilde{x}.\end{aligned} \tag{17}$$

From (14), (15), (16) and (17), we can conclude that

$$\begin{aligned}\dot{V}\le&-\left(\mu-\mu_0\right)\lambda_0\tilde{y}^T\tilde{y}-\frac{\varepsilon}{4}\tilde{x}^T\tilde{x}\\ \le&0.\end{aligned} \tag{18}$$

So V is bounded, implying that $\tilde{x}$ and $\tilde{y}$ are bounded, and since $\dot{V}\equiv0$ implies that $\tilde{y}\equiv0$ and $\tilde{x}\equiv0$, one can conclude that $\tilde{x}$ and $\tilde{y}$ asymptotically converge to zero , with $\lim\limits_{t\to\infty}\|\hat{y}_i-y\|=0$ and $\lim\limits_{t\to\infty}\|\hat{x}_i-x\|=0$ holding. Therefore, Theorem 1 holds.

The calculation process for the parameters to be designed in the proposed algorithm is shown in Algorithm 1.

Algorithm 1

Step1 Choose a suitable positive constant τ to ensure that (4) has a solution, and solve the LMI (4) to obtain the positive definite matrix P.

Step2 Take $c = \frac{\tau}{N}$ and calculate the feedback gain matrix $K = -\frac{1}{2}B^T P^{-1}$.

Step3 Select the matrix L so that A_o is Hurwitz.

Step4 Determine if $\min\limits_{\omega\in\mathbb{R}^+} \sigma_{\min}\left(A_o - j\omega I_{N^2 n}\right) > \gamma$ is valid, if not, go back to Step3.

Step5 Solve the Riccati equation (12) to yield the positive definite matrix Q.

Step6 Calculate μ_0 and choose the constant gain μ satisfying $\mu > \mu_0$.

Remark 3 *In fact, there is a large margin of stability in selecting matrix L to make $\min\limits_{\omega\in\mathbb{R}^+} \sigma_{\min}\left(A_o - j\omega I_{N^2 n}\right) > \gamma$ hold and selecting μ to make $\mu > \mu_0$. In general, it is only necessary to find L such that A_o is Hurwitz, and then by choosing an appropriate constant gain μ (usually much smaller than μ_0), the estimation error can converge to zero. It means that Step4 and Step6 in Algorithm 1 are not strictly necessary for determining the parameters.*

The key of the proposed algorithm to solve the problem of state estimation failure caused by measurement output failure lies in the fact that all agents achieve an estimation of the overall output. It means that even in the presence of measurement output failure, correct information can be obtained by neighboring's output estimation, thereby ensuring the accuracy of state estimation.

Remark 4 *Both the local estimators and the control protocol avoid the interaction of real state and estimated state between neighboring nodes, only the distributed output tracking involves the information about the real measured output of itself and its neighboring, which enhances the robustness of the algorithm. Furthermore, compared to the classical Kalman filtering algorithm in [28], the distributed state estimation algorithm proposed in this paper only requires to determine one feedback gain matrix, which reduces the computational complexity.*

4 Numerical simulation

This section validates the effectiveness of the proposed algorithm through numerical simulation. Consider a multi-agent system with four agents, the communication graph is shown in Fig. 1, and the system matrices of (3) are:

$$A = \begin{bmatrix} 0.6 & 2 \\ -0.4 & -1.5 \end{bmatrix}, B = \begin{bmatrix} 2 \\ 1 \end{bmatrix},$$

and

$$C = \begin{bmatrix} C_1 \\ C_2 \\ C_3 \\ C_4 \end{bmatrix} = \begin{bmatrix} 2 & -2 & 3 & -5 & 1 & 5 & -6 & 0 \\ 0 & 1 & -1 & 0 & 0 & 2 & 0 & -3 \\ 2 & -2 & 3 & 5 & 0 & 4 & -2 & 0 \\ 0 & 1 & 2 & -3 & 1 & 2 & 6 & -5 \\ 1 & -1 & 6 & 0 & -2 & 3 & 8 & 2 \end{bmatrix}.$$

$f(x_i) = \begin{bmatrix} 0 & 0.2\sin(x_{i2}) \end{bmatrix}^T$, and the Lipschitz constant $\gamma = 0.2$.

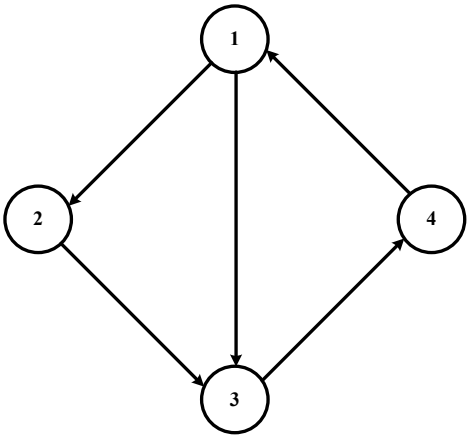

Fig. 1: The strongly connected communication graph.

The adjacency matrix of the graph $\mathcal{G}$ is given by

$$\mathcal{A} = \begin{bmatrix} 0 & 0 & 0 & 1 \\ 1 & 0 & 0 & 0 \\ 1 & 1 & 0 & 0 \\ 0 & 0 & 1 & 0 \end{bmatrix},$$

and the Laplacian matrix of $\mathcal{G}$ is written as

$$\mathcal{L} = \begin{bmatrix} 1 & 0 & 0 & -1 \\ -1 & 1 & 0 & 0 \\ -1 & -1 & 2 & 0 \\ 0 & 0 & -1 & 1 \end{bmatrix}.$$

The initial state of each agent is chosen as $x_0 = \begin{bmatrix} 2 & 1 & -2 & 2 & 1 & -1 & 0 & 3 \end{bmatrix}^T$. Let $\tau = 0.7$ and $c = 0.175$, $P = \begin{bmatrix} 3.1787 & -2.3775 \\ -2.3775 & 3.3712 \end{bmatrix}$ is obtained by solving the LMI (4), then we get $K = \begin{bmatrix} -0.9006 & -0.7934 \end{bmatrix}$. Let $\mu = 10$ and the feedback gain matrix L is chosen as

$$L = \begin{bmatrix} -9.7959 & 41.0248 & 7.4171 & -16.1258 & 7.8307 \\ 2.2888 & -10.425 & -0.5680 & 4.2693 & -1.9268 \\ 5.3763 & -21.7842 & -1.6073 & 7.5236 & -3.0603 \\ -0.3014 & -2.4213 & 0.9541 & 0.9140 & -0.6959 \\ -0.1583 & -12.1498 & 2.4026 & 7.8949 & -4.8033 \\ 0.6292 & -1.6927 & -0.3522 & 1.4692 & -0.5975 \\ -2.7776 & 6.7011 & 1.3169 & -1.5789 & 0.9828 \\ -0.1772 & -2.4635 & 0.3669 & 0.6323 & -0.4041 \end{bmatrix}.$$

The output tracking error and state estimation error are respectively shown in Fig. 2 and Fig. 3, revealing both errors converge to zero asymptotically. Fig. 4(a) and Fig. 4(b) depict the two dimensions' state trajectories of the agents, where the solid line is the real state and the dashed line is the estimated state, which not only reveals that the multi-agent system realize consensus, but also further illustrates the feasibility of the distributed state estimation.

Next, the effectiveness of the algorithm in the presence of measurement output failures is verified through simulation. Assuming that the 3-th agent's measurement output fails, which is equivalent to $C_3 = \mathbf{0}$. Fig. 5 and Fig. 6 represent the output tracking error and state estimation error. Fig. 7(a) and Fig. 7(b) depict the two dimensions' state trajectories. It is evident that the proposed algorithm can still achieve distributed state estimation and consensus control even in the presence of measurement output failures.

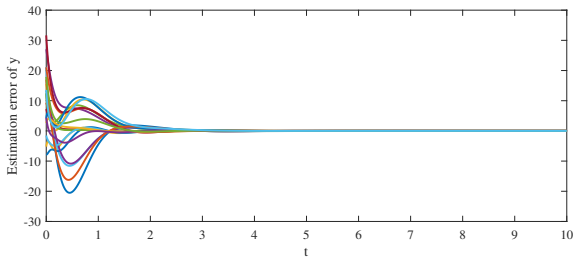

Fig. 2: The output tracking error $\tilde{y}$.

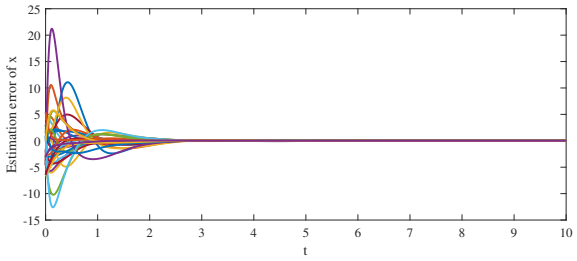

(a)

Fig. 3: The distributed state estimation error $\tilde{x}$.

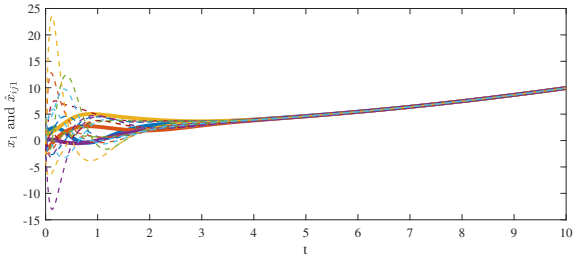

(a) The trajectories of x_{i1} and $\hat{x}_{ij1}$

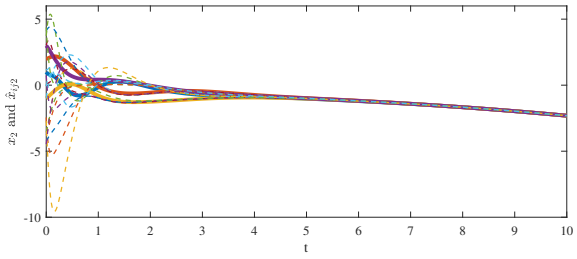

(b) The trajectories of x_{i2} and $\hat{x}_{ij2}$

Fig. 4: The real state x_i and the state estimation $\hat{x}_{ij}$.

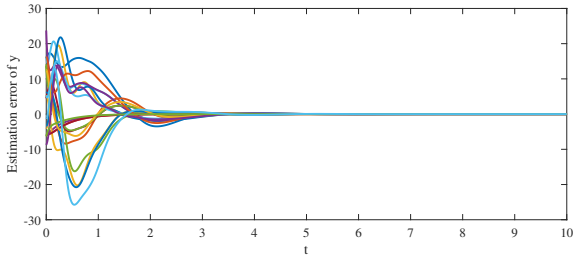

Fig. 5: The output tracking error $\tilde{y}$ under the failure of output measurement.

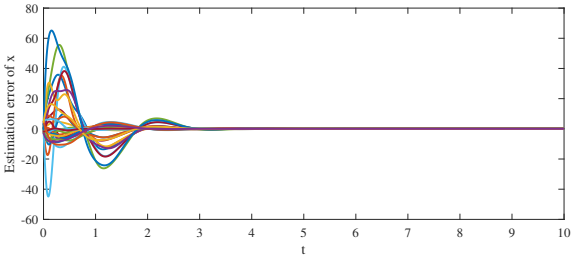

Fig. 6: The distributed state estimation error $\tilde{x}$ under the failure of output measurement.

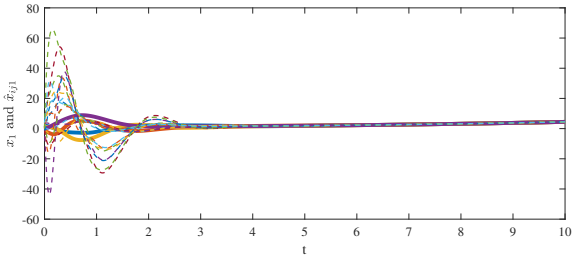

(a) The trajectories of x_{i1} and $\hat{x}_{ij1}$

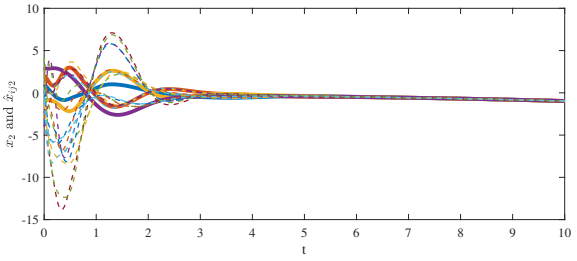

(b) The trajectories of x_{i2} and $\hat{x}_{ij2}$

Fig. 7: The real state x_i and the state estimation $\hat{x}_{ij}$ under the failure of output measurement.

5 Conclusion

In this paper, we propose a novel integrated design framework for distributed state estimation and consensus control, which enables a nonlinear MASs under strongly connected graphs to realize distributed state estimation and consensus control simultaneously, and the algorithm is still effective when there is measurement output invalid. The distributed state estimation algorithm consists of two parts: distributed output tracking and local observers, which estimate the overall output and the entire state of the MASs, respectively. The distributed output tracking is implemented based on the real measurement output of itself and its neighboring nodes, while the local observers only depend on the estimated output and state of itself, and the consensus control algorithm is designed according to the entire state estimation, avoiding communication with neighboring nodes. The main future work is to decouple control and state estimation, further to study cases such as event-triggered, switching topologies, etc.

References

[1] Y. Dong and J. Chen, "Nonlinear observer-based approach for cooperative control of networked rigid spacecraft systems," *Automatica*, vol. 128, p. 109552, 2021.

[2] Z. Song, X. Wang, B. Wei, Z. Shan, and P. Guan, "Distributed finite-time cooperative economic dispatch strategy for smart grid under dos attack," *Mathematics*, vol. 11, no. 9, 2023.

[3] T. Chu, J. Wang, L. Codecà, and Z. Li, "Multi-agent deep reinforcement learning for large-scale traffic signal control," *IEEE Transactions on Intelligent Transportation Systems*, vol. 21, no. 3, pp. 1086–1095, 2019.

[4] Y. Lv and Z. Li, "Is fully distributed adaptive protocol applicable to graphs containing a directed spanning tree?" *Science China Information Sciences*, vol. 65, no. 1, p. 189203, 2022.

[5] Y. Li, J. Zhang, and S. Tong, "Fuzzy adaptive optimized leader-following formation control for second-order stochastic multiagent systems," *IEEE Transactions on Industrial Informatics*, vol. 18, no. 9, pp. 6026–6037, 2022.

[6] W. Zou, Y. Huang, C. K. Ahn, and Z. Xiang, "Containment control of linear multiagent systems with stochastic disturbances via event-triggered strategies," *IEEE Systems Journal*, vol. 14, no. 4, pp. 4810–4819, 2020.

[7] J. Zhou, Y. Lv, C. Wen, and G. Wen, "Solving specified-time distributed optimization problem via sampled-data-based algorithm," *IEEE Transactions on Network Science and Engineering*, vol. 9, no. 4, pp. 2747–2758, 2022.

[8] R. Olfati-Saber, J. A. Fax, and R. M. Murray, "Consensus and cooperation in networked multi-agent systems," *Proceedings of the IEEE*, vol. 95, no. 1, pp. 215–233, 2007.

[9] T. Vicsek, A. Czirók, E. Ben-Jacob, I. Cohen, and O. Shochet, "Novel type of phase transition in a system of self-driven particles," *Physical review letters*, vol. 75, pp. 1226–1229, Aug 1995.

[10] W. Fu, J. Qin, J. Wu, W. X. Zheng, and Y. Kang, "Interval consensus over random networks," *Automatica*, vol. 111, p. 108603, 2020.

[11] G. Wang, Z. Zuo, and C. Wang, "Robust consensus control of second-order uncertain multiagent systems with velocity and input constraints," *Automatica*, vol. 157, p. 111226, 2023.

[12] M. Li and F. Deng, "Cluster consensus of nonlinear multi-agent systems with markovian switching topologies and communication noises," *ISA Transactions*, vol. 116, pp. 113–120, 2021.

[13] Q. Wang, Y. Lv, and Q. Wang, "Integrated adaptive protocols for consensus tracking with lipchitz nonlinear dynamics," *IEEE Transactions on Control of Network Systems*, vol. 10, no. 3, pp. 1472–1483, 2023.

[14] G. Dong, H. Li, H. Ma, and R. Lu, "Finite-time consensus tracking neural network ftc of multi-agent systems," *IEEE Transactions on Neural Networks and Learning Systems*, vol. 32, no. 2, pp. 653–662, 2021.

[15] K. Lu, Z. Liu, G. Lai, C. L. P. Chen, and Y. Zhang, "Adaptive consensus tracking control of uncertain nonlinear multiagent systems with predefined accuracy," *IEEE Transactions on Cybernetics*, vol. 51, no. 1, pp. 405–415, 2021.

[16] X. Chu, Z. Peng, G. Wen, and A. Rahmani, "Robust fixed-time consensus tracking with application to formation control of unicycles," *IET Control Theory & Applications*, vol. 12, no. 1, pp. 53–59, 2018.

[17] K. Zhang, B. Zhou, X. Yang, and G. Duan, "Prescribed-time leader-following consensus of linear multi-agent systems by bounded linear time-varying protocols," *Science China Information Sciences*, vol. 67, no. 1, p. 112201, 2023.

[18] H. Du, G. Wen, D. Wu, Y. Cheng, and J. Lü, "Distributed fixed-time consensus for nonlinear heterogeneous multi-agent systems," *Automatica*, vol. 113, p. 108797, 2020.

[19] Y.-S. Ma, W.-W. Che, C. Deng, and Z.-G. Wu, "Observer-based fully distributed containment control for mass subject to dos attacks," *IEEE Transactions on Systems, Man, and Cybernetics: Systems*, vol. 53, no. 2, pp. 897–907, 2023.

[20] C. Deng, C. Wen, J. Huang, X.-M. Zhang, and Y. Zou, "Distributed observer-based cooperative control approach for uncertain nonlinear mass under event-triggered communication," *IEEE Transactions on Automatic Control*, vol. 67, no. 5, pp. 2669–2676, 2022.

[21] Y. Lv, Z. Li, and Z. Duan, "Minimal-order specified-time unknown input observers," *Automatica*, vol. 159, p. 111385, 2024.

[22] J. Zhou, Y. Lv, G. Wen, and X. Yu, "Resilient consensus of multiagent systems under malicious attacks: Appointed-time observer-based approach," *IEEE Transactions on Cybernetics*, vol. 52, no. 10, pp. 10 187–10 199, 2022.

[23] Y. Li, J. Huang, Y. Lv, and J. Zhou, "Distributed state estimation for multi-agent systems under consensus control," in *2023 International Conference on Neural Information Processing*. Springer, 2023, pp. 214–225.

[24] Y. Lv, G. Wen, T. Huang, and Z. Duan, "Adaptive attack-free protocol for consensus tracking with pure relative output information," *Automatica*, vol. 117, p. 108998, 2020.

[25] J. Huang, Y. Li, and Y. Lv, "Integrated design of fully distributed adaptive state estimation and consensus control for multi-agent systems," in *2023 International Conference on Neural Information Processing*. Springer, 2023, pp. 226–237.

[26] Z. Li and Z. Duan, *Cooperative control of multi-agent systems: a consensus region approach*. CRC press, 2014.

[27] R. Rajamani, "Observers for lipschitz nonlinear systems," *IEEE Transactions on Automatic Control*, vol. 43, no. 3, pp. 397–401, 1998.

[28] R. Olfati-Saber, "Distributed kalman filtering for sensor networks," in *2007 46th IEEE Conference on Decision and Control*, 2007, pp. 5492–5498.

Proceedings of the 3rd Conference on Fully Actuated System Theory and Applications
May 10-12, 2024, Shenzhen, China

Distributed Air-Assisted Coverage Control for Sensing-Limited Multi-Robot Systems in Time-Varying Environment

Hang Zhang[1,2], Ronghao Zheng[1,2†], Lingxia Lu[1], Senlin Zhang[1,2,3], Meiqin Liu[1,2,4]
1. College of Electrical Engineering, Zhejiang University, Hangzhou 310027, China
2. National Key Laboratory of Industrial Control Technology, Zhejiang University, Hangzhou 310027, China
3. Jinhua Institute of Zhejiang University, Jinhua 321036, China
4. National Key Laboratory of Human-Machine Hybrid Augmented Intelligence, Xi'an Jiaotong University, Xi'an 710049, China
E-mail: {hhhzhang, rzheng, lulingxia, slzhang, liumeiqin}@zju.edu.cn

Abstract: In the multi-robot coverage control application, a group of ground robots tries to optimize the environment coverage performance. However, most of the existing works consider that the environment is static and the ground robots have large sensing ranges. In this paper, we present a fully distributed, air-assisted coverage control scheme to address the challenge of a time-varying environment and limited sensing range. Firstly, we use aerial robots equipped with low-resolution but high-sensing-range sensors to achieve a weighted Voronoi coverage of the environment. Then the aerial robots utilize their local information to guide the ground robots, equipped with low-sensing-range but high-resolution sensors, to explore the environment to optimize a high-resolution coverage performance. The ground robots adopt a new controller to promptly adapt to environmental changes. Simultaneously, each aerial robot dynamically adjusts its domain to optimize the coverage performance of the ground robots. The convergence of the control scheme is proved and its performance is evaluated through simulations.

Key Words: Voronoi Coverage Control, Distributed, Air-Assisted, Limited Sensing Range, Time-Varying Environment

1 Introduction

Coverage control of multi-robot systems has been drawing attention for a long time due to its wide applications, such as environmental surveillance and disaster rescue [1]. In these applications, robots observe features or events within a broad area, which are often modeled as an underlying density function. Then the coverage is performed according to the relative importance of these features within the area.

A classical solution to coverage problems involves the use of proper area partition, known as Voronoi partition, as introduced in [2]. It proposes a controller that guides robots to move towards the centroid of the Voronoi cell, minimizing the coverage cost function. After that, a series of coverage control algorithms are proposed based on it. In these works, the underlying density function is assumed to be time-invariant and robots have large sensing ranges, so each robot is aware of the density function in its own cell.

As features or events within an area evolve over time, such as the continuous spread of pollutants and the dynamic migration of endangered species, some works consider the case that the density function is time-varying [3, 4]. Ref. [3] explores the time-varying case by assuming a small rate of change in the density function, while Ref. [4] proposes a controller without any assumptions about the rate of change in the density function. However, they have not taken into consideration the limited sensing ranges of the robots.

A series of extended coverage control algorithms are proposed to address the limited sensing ranges of robots, but these algorithms rarely consider time-varying density functions. Ref. [5] introduces a distributed deterministic annealing algorithm that computes temperature gradients to guide robots to their final positions. However, this algorithm is not fully distributed. In [6], robots achieve coverage through limited Voronoi cells, but the performance of coverage is highly sensitive to the sensing range. In [7], a method combines aerial and ground robots to achieve high-resolution coverage. Ground robots are equipped with low-range, high-resolution sensors, while aerial robots are equipped with high-range, low-resolution sensors. Aerial robots roughly estimate the density function within the domain and guide ground robots for finer local coverage. However, the guide controller involves global information: positions of all aerial robots, so it is not fully distributed. Moreover, because the domain of aerial robots is fixed, the coverage performance of this method does not reach its optimality.

In our previous work [8], we use aerial robots to assist

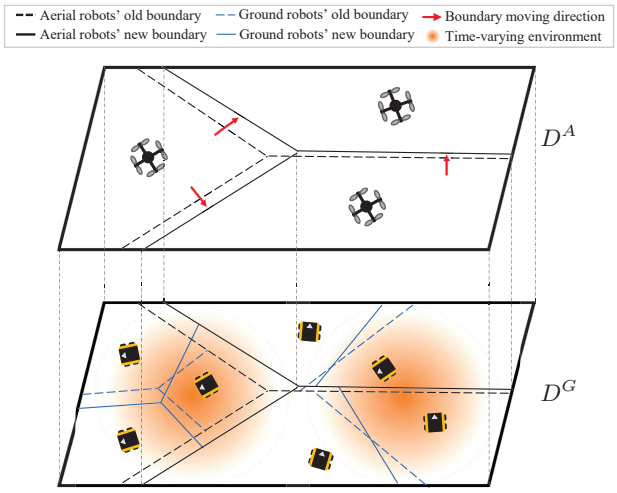

Fig. 1: Ground robots are equipped with low-range, high-resolution sensors, while aerial robots are equipped with high-range, low-resolution sensors. Aerial robots sense coarse but extensive sensing information and then use it to guide ground robots to achieve high-resolution coverage of the area. To enhance coverage performance, the domain boundaries will be adjusted based on the final number of ground robots under each dominance.

† Corresponding author
This work was supported in part by the National Natural Science Foundation of China under Grant 62173294, in part by the Zhejiang Provincial Natural Science Foundation of China under Grant LZ24F030001, and in part by the National Natural Science Foundation of China under Grant U23B2060.

ground robots in addressing the challenge of the ground robots' limited global vision. In this paper, to address another challenge of the time-varying density function, we propose a new coverage control scheme inspired by [4]. A brief description of our proposed scheme is shown in Fig. 1 and the main contributions of this paper are as follows.

- The method we propose employs aerial robots to assist ground robots in achieving high-resolution coverage. It is fully distributed and effectively addresses the time-varying environment.
- The coverage control scheme incorporates a newly proposed domain partitioning law, taking full advantage of the coverage capabilities of each ground robot.
- The convergence of the control scheme is proved and its effectiveness is validated through simulations.

This paper is organized as follows. In Section 2, the problem is formulated. In Section 3, we develop the control scheme for the heterogeneous team to achieve coverage. In Section 4, the convergence analysis of the algorithm is provided. Section 5 demonstrates the effectiveness of the proposed scheme through simulations. Section 6 concludes the paper with our intentions for future work.

2 Problem Statement

Consider an area containing several regions of interest. These regions may involve the migration of endangered species or the spread of pollutants. In these scenarios, the total amount of substance within the entire area (the total quantity of endangered species or pollutants) remains constant, but the concentration at each location within the area continues to change. So in this paper, we model the spatial distribution as a time-varying scalar field in the convex domain $D^G \subset \mathbb{R}^2$. The time-varying scalar field value of any point $q \in D^G$ is $\phi(q,t)$, which satisfies that $\phi(q,t) > 0$ for all q and t.

There is a heterogeneous team of robots consisting of $K(>1)$ unmanned aerial robots and $N(>K)$ unmanned ground robots in the domain. The ground robots operate in the domain D^G and the aerial robots operate in a domain $D^A \subset \mathbb{R}^2$, above and parallel to D^G as shown in Fig. 1. The ground robot is equipped with a low-range, high-resolution sensor, enabling it to obtain high-resolution field values within its limited range of detection $B(p_j^i(t), R)$, which will be defined later in this section. On the other hand, the aerial robot is equipped with a high-range but low-resolution sensor, so it can acquire coarse field values over a larger area. Fig. 2 shows an example of the detection of a domain with both high-resolution and low-resolution sensors. Here, "resolution" refers to the sensor's ability to detect the minimum change in the time-varying scalar field value $\phi(q,t)$.

Remark 1. In our expression, we use $\phi(q,t)$ for both high and low-resolution field values, distinguishing them only in simulations.

Define $\mathcal{V} = \{1,2,...,K\}$. At time $t \geq 0$, let $\mathcal{P}(t) = \{p^i(t) \mid \forall i \in \mathcal{V}\}$ denote the set of positions of aerial robots. Each aerial robot i is assigned a domain defined as a

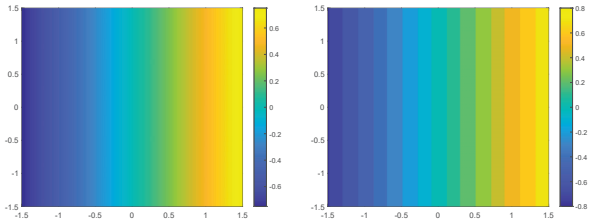

(a) High resolution. (b) Low resolution.

Fig. 2: Difference between high resolution and low resolution.

weighted Voronoi cell

$$V^i(t) = \{q \in D^A \mid \|p^i(t) - q\|^2 - w_i(t) \leq \|p^j(t) - q\|^2 - w_j(t), \forall j \in \mathcal{V}\}, \quad (1)$$

where $w_i(t), w_j(t)$ are the weights of aerial robots i, j at time t. Mostly, the parameter t is omitted if no ambiguity arises.

We use an undirected graph $\mathcal{G} = (\mathcal{V}, \mathcal{E})$ to describe the relationships between the aerial robots, where $\mathcal{E} \subseteq \mathcal{V} \times \mathcal{V}$ is the set of all edges. The set of neighbors of aerial robot i is denoted as $\mathcal{N}^i = \{j \mid V^i \cap V^j \neq \emptyset, (i,j) \in \mathcal{E}\}$.

Additionally, let $\mathcal{P}^i = \{p_j^i(t) \mid j = 1,2,...,n_i\}$ denote the set of positions of ground robots under the dominance of aerial robot i. Here, n_i denotes the number of ground robots in the domain V^i. Each ground robot j is also given a domain defined by a Voronoi cell

$$V_j^i = \{q \in V^i \mid \|p_j^i(t) - q\|^2 \leq \|p_r^i(t) - q\|^2, r = 1,2,...,n_i\}.$$

The set of neighbors of each ground robot j is denoted as $\mathcal{N}_j^i = \{r \mid V_j^i \cap V_r^i \neq \emptyset, r = 1,2,...,n_i, r \neq j\}$, and the sensing range of each ground robot j is limited by $B(p_j^i(t), R)$

$$B(p_j^i(t), R) = \{q \in \mathbb{R}^2 \mid \|q - p_j^i(t)\| \leq R\},$$

where R is the sensing radius.

The kinematic model of aerial robot and ground robot is described as follows

$$\frac{d}{dt}p^i(t) = u^i(t), \quad \frac{d}{dt}p_j^i(t) = u_j^i(t),$$

where $u^i(t)$ and $u_j^i(t)$ are the control inputs, for each $j = 1,2,\ldots,n_i$ and each $i \in \mathcal{V}$.

Similar to [2], [6], [7] and [9], the main purpose of coverage control is to minimize the coverage cost function

$$\mathcal{H} = \sum_{i=1}^{K}\sum_{j=1}^{n_i}\int_{V_j^i} \|q - p_j^i(t)\|^2 \phi(q,t)\, dq. \quad (2)$$

In the case where the ground robots have unlimited sensing ranges and the scalar field value $\phi(q,t)$ is time-invariant, by taking the gradient of (2), Ref. [2] uses the proved move-to-centroid controller (3) to guide the ground robots to the local optimal locations

$$u_j^i(t) = g_p\left(C_j^i(t) - p_j^i(t)\right), \quad (3)$$

where g_p is the control gain, C_j^i is the mass centroid of Voronoi cell V_j^i.

In the case where the ground robots have unlimited sensing ranges but the scalar field value $\phi(q,t)$ is time-varying, Ref. [4] proposes a proved centralized controller. After the approximation, the distributed controller, referred to as TVD-D_1, is presented as follows

$$u_j^i(t) = \frac{\partial C_j^i}{\partial t} + g_p(C_j^i - p_j^i) + \sum_{r\in\mathcal{N}_j^i} \frac{\partial C_j^i}{\partial p_r^i}\left(\frac{\partial C_r^i}{\partial t} + g_p(C_r^i - p_r^i)\right). \quad (4)$$

In situations with limited sensing range for ground robots and time-varying scalar field value, this paper addresses the problem of designing distributed controllers $u^i(t)$ and $u_j^i(t)$ to enable aerial robots to assist ground robots in achieving high-resolution coverage, aiming at minimizing the coverage cost function (2).

3 Proposed Control Scheme

As depicted in Fig. 1, this paper proposes a fully distributed air-assisted control scheme to address ineffective coverage problem that happens when only low-sensing-range ground robots are used. Initially, the high-sensing-range aerial robot provides a low-resolution coverage of the entire domain. Subsequently, the aerial robots cooperatively schedule the ground robots to achieve even distribution within the domain supervised by each aerial robot. This assists the ground robots in overcoming the limitations of their low sensing range, enabling them to cover a wider domain and achieve more effective coverage.

1) **Determining final load and domain mass value for the aerial robot:** The aerial robots first use the followni move-to-centroid controller

$$u^i(t) = g_p(C^i - p^i)$$

over D^A assuming a uniform density function. Here C^i is the centroid of Voronoi cell V^i. When doing this, the aerial robots create domains in the form of weighted Voronoi cells $V^i \subset D^A$, where $w_i = 0$ for all i. And each aerial robot i has access to the number of ground robots $n_i(t)$ within its domain V^i, the mass $s_i(t)$ of the domain V^i is defined as $s_i(t) = \int_{V^i} \phi(q,t)\,dq$. In many real-world scenarios such as the migration of endangered species or the spread of pollutants, the total quantity of substance in the whole domain remains constant. Therefore, we assume that $\int_{D^A} \phi(q,t)\,dq =: C$ is constant.

After the aerial robots come to a stop, each aerial robot i obtains the number of the ground robots $n_{i,0}$ within its domain and the mass $s_{i,0}$ of its domain at that time. Then each aerial robot i runs Algorithm 1. The first part of Algorithm 1 (Lines 1-7) is to determine the final number of ground robots $\bar{n}_i \in \mathbb{N}$ in its domain V^i, that is, the final load value of aerial robot i. The second part of Algorithm 1 (Lines 8-13) is to obtain the final mass value, denoted as $\bar{s}_i$, of the domain supervised by aerial robot i. Here, k_1 and k_2 are sufficiently large numbers of iterations.

The first part of Algorithm 1 (Lines 1-7) is to average the number of ground robots supervised by each aerial robot. When equal allocation is not feasible, there may be a maximum difference of 1. This first part (Lines 1-7) can be further divided into three main phases. In the Giving Phase, aerial robot i selects among its neighbors with minimum load to send an offer to. In the Receiving Phase, aerial robot i evaluates the offers from its neighbors. It selects the neighbor with the highest load value and accepts its offer, then sends an acceptance to it and increases its own load value by 1. In the Transferring Phase, the aerial robot i checks if it has received an acceptance. If it has, it reduces its own load value by 1. More details can be found in [10].

Under the execution of the second part of Algorithm 1 (Lines 8-13), aerial robots calculate $\bar{s}_i$ based on $\bar{n}_i$. When $k_2 \to \infty$, we will obtain

$$\frac{\bar{s}_i}{\bar{n}_i} = \frac{\sum_{i=1}^K s_{i,0}}{\sum_{i=1}^K \bar{n}_i} = \frac{C}{N}, \quad \forall i \in \mathcal{V}.$$

It indicates that the final mass value of each domain matches its final load value. This matching is essential to make the most of the ground robots' coverage capabilities, resulting in better coverage performance.

Algorithm 1: Determining final load and domain mass value for the aerial robot i

Input: $n_{j,0}, s_{j,0}, \forall j \in \mathcal{N}^i \cup \{i\}$ and k, k_1, k_2.
Output: $\bar{n}_i, \bar{s}_i$.

1 $k \leftarrow 0$; $l_i^0 \leftarrow n_{i,0}$;
2 **while** $k < k_1$ **do**
3 Giving Phase;
4 Receiving Phase;
5 Transferring Phase;
6 Increment k;
7 **end**
8 $\bar{n}_i \leftarrow l_i^{k_1}$; $y_i^{k_1} \leftarrow \frac{s_{i,0}}{\bar{n}_i}$;
9 **while** $k_1 \le k < k_2$ **do**
10 $y_i^k \leftarrow y_i^{k-1} + \frac{1}{\bar{n}_i} \sum_{j\in\mathcal{N}^i} (y_j^{k-1} - y_i^{k-1})$;
11 Increment k;
12 **end**
13 $\bar{s}_i \leftarrow y_i^{k_2} \cdot \bar{n}_i$.

2) **Aerial robots assist ground robots in achieving high-resolution coverage:** After determining the number of ground robots and the mass of domain that each aerial robot should eventually take charge of, each aerial robot will run Algorithm 2 to rezone its domain according to (1). At the same time, it will guide ground robots to complete finer local coverage.

Algorithm 2 is divided into two stages, namely Regional Redistricting Stage and Guide and Coverage Stage. In Regional Redistricting Stage, aerial robot i calculates $w_i(t)$ based on $\bar{s}_i$ and rezones its domain. In Guide and Coverage Stage, aerial robot i firstly calculates

$$x_i(t) = n_i(t) - \bar{n}_i.$$

We refer to $x_i(t)$ as the *load deviation* of aerial robot i at time t. Then, in the Offering Phase, it selects one of the neighbors with the minimum *load deviation* and sends an offer to that neighbor. In the Accepting Phase, aerial robot i chooses one of the neighbors that sent an offer to it with the maximum *load deviation*, and sends an acceptance in response. Lastly,

in the Passing Phase, different control laws will be selected based on the received acceptances. Here, C_r^l represents the mass centroid of cell V_r^l, where $V_r^l = V_r^i \cap B(p_r^i(t), R)$.

Algorithm 2: Collaborative coverage achieved with aerial robot i and ground robots under its dominance

Input: $x_j(t), w_j(t), s_j(t), p^j, \bar{s}_j, \forall j \in \mathcal{N}^i \cup \{i\}$ and $g_w > 0, g_1 > 0, g_2 > 0$.

1 **repeat**
2 **Regional Redistricting Stage:**
3 Receive messages p^j and $w_j(t)$ from $\mathcal{N}^i$;
4 Divide the area according to (1);
5 $\frac{d}{dt}w_i(t) \leftarrow g_w(\bar{s}_i - s_i(t))$;
6 **Guide and Coverage Stage:**
7 **Offering Phase:**
8 $\underline{x_i}(t) \leftarrow \min_{j \in \mathcal{N}^i} x_j(t)$;
9 $J_i(t) \leftarrow \{j \in \mathcal{N}^i | x_j(t) = \underline{x_i}(t)\}$;
10 Choose j_r randomly from nodes in $J_i(t)$;
11 **if** $x_i(t) > x_{j_r}(t)$ **then**
12 Send offer to j_r consisting of $(i, x_i(t))$;
13 **end**
14 **Accepting Phase:**
15 $M_1 = \{(j_1, x_{j_1}(t)), ..., (j_m, x_{j_m}(t))\}$ is the set of messages received by i at time t.
16 **if** $|M_1| > 0$ **then**
17 $\overline{x_i}(t) \leftarrow \max_{s \in \{1,...,m\}} x_{j_s}(t)$;
18 $Q_i(t) \leftarrow \{j_s \in M_1 | x_{j_s}(t) = \overline{x_i}(t)\}$;
19 Choose h randomly from nodes in $Q_i(t)$;
20 Send acceptance to h consisting of (i);
21 **end**
22 **Passing Phase:**
23 $M_2 = \{(j)\}$ is message received by i at time t.
24 **if** $|M_2| > 0$ **then**
25 $u_{r^*}^i(t) \leftarrow g_1 \left(p^j - p_{r^*}^i(t)\right)$,
26 $r^* = \arg\min_r \|p^j - p_r^i(t)\|, \quad r = 1, ..., n_i$;
27 **else**
28 $u_r^i(t) \leftarrow \frac{\partial C_r^l}{\partial t} + g_2(C_r^l - p_r^i(t)) + \sum_{\lambda \in \mathcal{N}_r^i} \frac{\partial C_r^l}{\partial p_\lambda^i} \left(\frac{\partial C_\lambda^l}{\partial t} + g_2\left(C_\lambda^l - p_\lambda^i(t)\right)\right)$,
29 $r = 1, ..., n_i$;
30 **end**
31 **until** a stooping condition is met (e.g., time t meets a certain requirement.);

4 Convergence Analysis

The convergence proof of the first part of Algorithm 1 (Lines 1-7) is similar to Claim 5.8 in [10], and the convergence proof of the second part of Algorithm 1 (Lines 8-13) is similar to Theorem 4.1 in [11], so the details are omitted here.

In our proof illustrating the convergence of Algorithm 2, because of space constraints, we present only the theorem statement here and leave the proof to a more detailed version.

Define ∂V^{ij} as the boundary between V^i, V^j and

$$\underline{\kappa}_{1,i} = \inf_t \left(\frac{g_w}{2} \sum_{j \in \mathcal{N}^i} \int_{\partial V^{ij}} \frac{\phi}{\|p^j - p^i\|} dq \right),$$

$$\kappa_{2,i}(t) = \frac{g_w}{2} \sum_{j \in \mathcal{N}^i} \int_{\partial V^{ij}} \frac{\phi \frac{d}{dt} w_j}{\|p^j - p^i\|} dq - g_w \int_{V^i} \frac{d\phi}{dt} dq,$$

$$\gamma_i = \frac{\sup_t |\frac{\kappa_{2,i}(t)}{\underline{\kappa}_{1,i}}|}{g_w \epsilon}, \quad 0 < \epsilon < 1.$$

The statement of Theorem 1 is as follows, and it ensures the convergence of Regional Redistricting Stage in Algorithm 2.

Theorem 1. *When $t \to \infty$, $|\bar{s}_i - s_i(t)| \leq \gamma_i, \forall i \in \mathcal{V}$.*

Define

$$x(t) = (x_1(t), x_2(t), ..., x_K(t)),$$

$$\mathscr{S} = \{x(t) \mid x_i(t) = 0, i \in \mathcal{V}\},$$

$$m(t) = \min_i x_i(t), \quad M(t) = \max_i x_i(t),$$

$$D(t) = M(t) - m(t).$$

The statements of Lemma 1, Lemma 2, and Theorem 2 are as follows. Using Lemma 1 and Lemma 2, Theorem 2 can be proved. The convergence of Guide and Coverage Stage is guaranteed by Theorem 2.

Lemma 1. *Under the execution of Guide and Coverage Stage of Algorithm 2, for any time t such that $D(t) \geq 2$, there is some finite time $t^* > t$ such that there is a positive probability such that $D(t^*) < D(t)$.*

Lemma 2 ([12, Theorem 2])**.** *Consider a distributed algorithm, for any graph, the following conditions are met*

(G1) *for any given initial condition $x(t_0)$, at any time during the execution of the algorithm, the value of $x(t)$ lies in some finite set $\mathscr{X}$,*
(G2) *for any state $x(t) = x$, there exists a finite time t_x such that $\mathrm{P}(x(t + t_x) \in \mathscr{S} \mid x(t) = x) > 0$,*
(G3) *if $x(t) \in \mathscr{S}$, then $x(t') \in \mathscr{S}$ for all $t' \geq t$.*

Under the execution of such an algorithm, for any graph and for any initial condition $x(t_0)$ such that $\sum_{i=1}^K x_i(t_0) = 0$, $\lim_{t \to \infty} x(t) \in \mathscr{S}$.

Theorem 2. *Under the execution of Guide and Coverage Stage of Algorithm 2, $\lim_{t \to \infty} x(t) \in \mathscr{S}$.*

5 Simulation Results

In this section, we will present the simulated results of the proposed algorithm and compare to previous algorithms. We simulated three other algorithms for comparison, each using $N = 14$ ground robots. In the simulations, the field of the ground domain D^G is chosen to be a 3×3 rectangle area with

$$\phi(x, y, t) = 1.2\exp\left(-(x + 1.2 + 0.125\sin(\frac{\pi}{25}t))^2 - y^2\right) + \exp\left(-(x-1)^2 - (y + 0.1\sin(\frac{\pi}{50}t))^2\right).$$

The first and second algorithms are both proposed in [2], with the difference being that the first algorithm assumes that the ground robots are equipped with sensors with unlimited sensing range, while the second assumes that the ground robots are equipped with sensing-limited sensors. The third

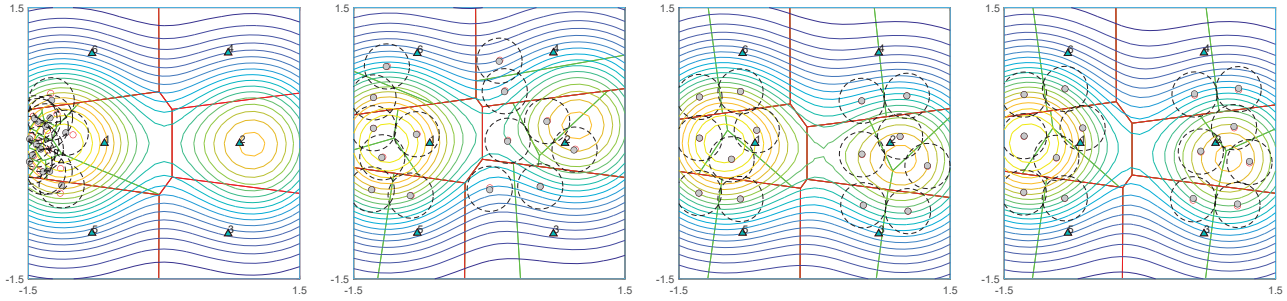

(a) $t = 2$ (b) $t = 75$ (c) $t = 433$ (d) $t = 717$

Fig. 3: (a) to (d) illustrate the movement of ground robots at different t based on the proposed algorithm. We denote the positions of the ground robots with solid black circles, the mass centroids of their sensing-limited Voronoi cells with red hollow circles, the final positions of the aerial robots with solid triangles, the sensing ranges of ground robots with black dashed circles, the boundaries of the ground robots with solid green lines, and the boundaries of the aerial robots with solid red lines.

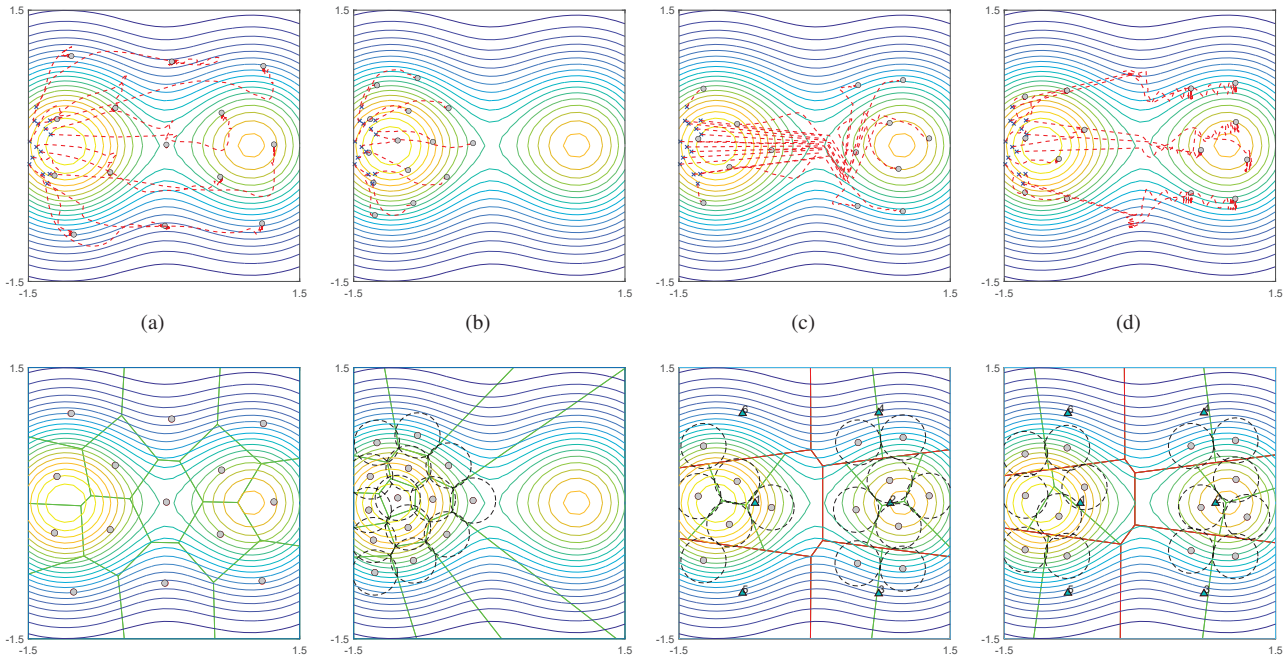

(a) (b) (c) (d)

(e) (f) (g) (h)

Fig. 4: The trajectory of the 14 ground robots in simulations (a) to (d) and their final configuration in simulations (e) to (h) are depicted using various algorithms: (a) and (e) with the algorithm in [2] assuming unlimited sensing range, (b) and (f) with the algorithm in [2] assuming limited sensing range, (c) and (g) with algorithm in [7], and (d) and (h) with the proposed algorithm. In Fig. 4(a), 4(b), 4(c) and 4(d), we denote the initial positions of the ground robots with blue X markers, the trajectory of each robot with red dotted lines, the final position of the ground robots with solid black circles. In Fig. 4(e), 4(f), 4(g) and 4(h), we denote the final position of the aerial robots with solid triangles, the sensing range with black dashed circles, the ground robots' boundaries with solid green lines, and the aerial robots' boundaries with solid red lines.

algorithm, as proposed in [7], involves the utilization of $K = 6$ aerial robots. The last is the proposed algorithm which also involves the utilization of $K = 6$ aerial robots.

For these four algorithms, we maintain consistent initial positions for both ground and aerial robots. Among the latter three algorithms, the sensing range of ground robots is standardized as a circular area with a radius of 0.25 length units. In the proposed algorithm, parameter values are set to $g_w = 0.5, g_1 = 0.08, g_2 = 0.2$. The high-resolution sensor is capable of detecting changes in the scalar field value $\phi(x, y, t)$ as small as 1×10^{-8}, while the low-resolution sensor can detect changes as small as 1×10^{-2}. Additionally, each aerial robot has obtained corresponding parameters through Algorithm 1: $\bar{n}_1 = \bar{n}_2 = 3, \bar{n}_i = 2, i = 3, 4, 5, 6$ and $\bar{s}_1 = \bar{s}_2 = 1.02, \bar{s}_i = 0.68, i = 3, 4, 5, 6$.

Fig 3(a), 3(b), 3(c) and 3(d) illustrate the distribution of ground robots under the control of the proposed algorithm at different t. The scalar field varies at different t and the ground robots are controlled to cover it. Fig. 4(a), 4(b), 4(c) and 4(d) illustrate the trajectories of the ground robots for each of the four algorithms, while Fig. 4(e), 4(f), 4(g) and 4(h) depict the final configurations for each algorithm. We use the coverage cost function (2) to evaluate the coverage performance in Fig. 5. Fig. 5 illustrates the temporal evolution of coverage cost for the four algorithms. During the initial time intervals, the ground robots in both the proposed algorithm and the algorithm in [7] have not yet fully covered the entire area, so the costs are non-comparable. As time progresses and the ground robots achieve complete coverage of the entire area, the costs become comparable during the later period. Because the mass within the domain of each aerial robot matches the number of ground robots in that domain, the proposed algorithm achieves a coverage cost that approaches that of the algorithm in [2] with unlimited sensing range, and is lower than the algorithm presented in [7]. Fig. 6 demonstrates the convergence of Voronoi cell

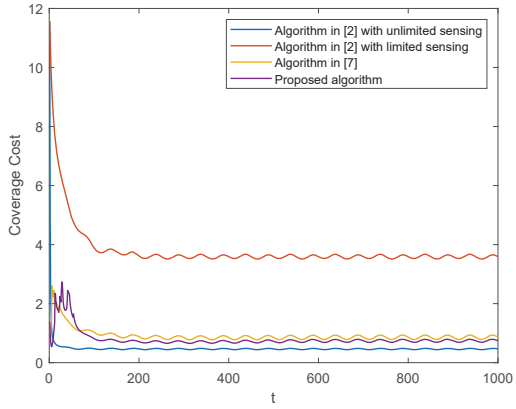

Fig. 5: Cost $\mathcal{H}$ for each of the four algorithms.

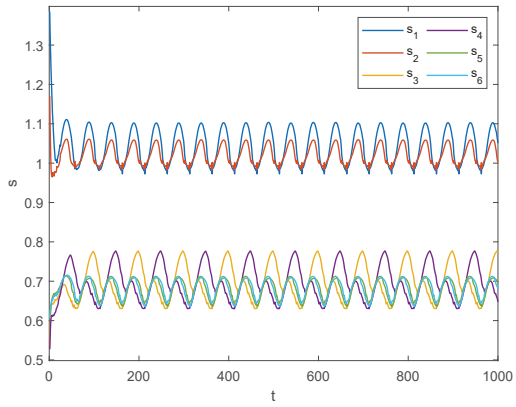

Fig. 6: Convergence of Voronoi cell mass for each aerial robot.

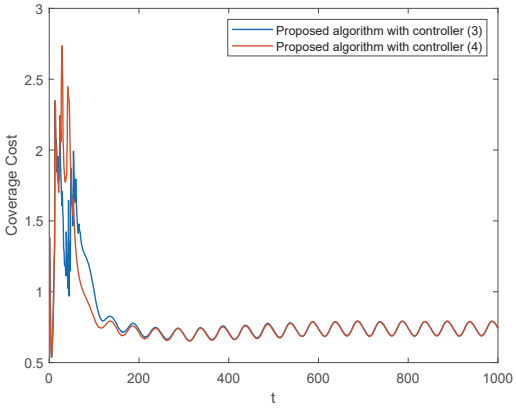

Fig. 7: Proposed algorithm with different coverage controller.

mass for each aerial robot within the proposed algorithm. As $\phi(x, y, t)$ varies with time, the mass s_i within the domain of each aerial robot i fluctuates near $\bar{s}_i$ and exhibits a tendency to converge towards $\bar{s}_i$. We also compare the differences in coverage when the proposed algorithm used controller (3) and controller (4). In Fig. 7, at earlier times, due to the guidance by the aerial robots, the coverage cost fluctuates and is not comparable. When the ground robots are controlled to cover during $t \in [100, 1000]$, the coverage cost is comparable. From Fig. 7, it is noticeable that using controller (4) results in slightly lower coverage cost. To further assess this, we compare the cumulative value of the two sets of coverage cost: $\sum_{t=100}^{1000} \mathcal{H}(t)$, which were found to be 662.379 and 655.788. This indicates that using controller (4) for coverage, due to the consideration of time-varying terms, leads to improved coverage performance.

6 Conclusions

In conclusion, this paper proposes a novel fully distributed, air-assisted coverage control scheme that addresses time-varying environments and limited sensing ranges in multi-robot coverage control applications. The convergence of the control scheme is proved and its performance is evaluated through simulations. In the future, we will conduct real-world experiments while taking into account the limitations of Voronoi coverage due to obstacles in the covered area, aiming to extend this method to non-convex environments. Additionally, we will also explore extending this method to coverage on manifolds, moving beyond the constraint of two-dimensional planes.

References

[1] C. Wang, S. Zhu, W. Yu, L. Song, and X. Guan, "Minimum norm coverage control of auvs for underwater surveillance with communication constraints," in *2022 American Control Conference (ACC)*, pp. 1222–1229, IEEE, 2022.

[2] J. Cortes, S. Martinez, T. Karatas, and F. Bullo, "Coverage control for mobile sensing networks," *IEEE Transactions on robotics and Automation*, vol. 20, no. 2, pp. 243–255, 2004.

[3] J. Cortés, S. Martinez, T. Karatas, and F. Bullo, "Coverage control for mobile sensing networks: Variations on a theme," in *Mediterranean Conference on Control and Automation*, pp. 9–13, Lisbon, Portugal Lisbon, Portugal, 2002.

[4] S. G. Lee, Y. Diaz-Mercado, and M. Egerstedt, "Multirobot control using time-varying density functions," *IEEE Transactions on robotics*, vol. 31, no. 2, pp. 489–493, 2015.

[5] A. Kwok and S. Martinez, "A distributed deterministic annealing algorithm for limited-range sensor coverage," *IEEE Transactions on Control Systems Technology*, vol. 19, no. 4, pp. 792–804, 2010.

[6] F. Pratissoli, B. Capelli, and L. Sabattini, "On coverage control for limited range multi-robot systems," in *2022 IEEE/RSJ International Conference on Intelligent Robots and Systems (IROS)*, pp. 9957–9963, IEEE, 2022.

[7] M. Rudolph, S. Wilson, and M. Egerstedt, "Range limited coverage control using air-ground multi-robot teams," in *2021 IEEE International Conference on Robotics and Automation (ICRA)*, pp. 3525–3530, IEEE, 2021.

[8] H. Zhang, R. Zheng, S. Zhang, and M. Liu, "A fully distributed, air-ground coordinated coverage control for multi-robot systems with limited sensing range," in *2024 American Control Conference (ACC), accepted*, IEEE, 2024.

[9] J. Cortes, S. Martinez, and F. Bullo, "Spatially-distributed coverage optimization and control with limited-range interactions," *ESAIM: Control, Optimisation and Calculus of Variations*, vol. 11, no. 4, pp. 691–719, 2005.

[10] E. Gravelle and S. Martínez, "An anytime distributed load-balancing algorithm satisfying capacity and quantization constraints," *IEEE Transactions on Control of Network Systems*, vol. 4, no. 2, pp. 279–287, 2015.

[11] F. Pedroche, M. Rebollo, C. Carrascosa, and A. Palomares, "On the convergence of weighted-average consensus," *arXiv preprint arXiv:1307.7562*, 2013.

[12] A. Kashyap, T. Başar, and R. Srikant, "Quantized consensus," *Automatica*, vol. 43, no. 7, pp. 1192–1203, 2007.

Proceedings of the 3rd Conference on Fully Actuated System Theory and Applications
May 10-12, 2024, Shenzhen, China

Incorporating Steering Constraints in AGV Path Planning Through Graph Augmentation

Liming Zhang[1,5], Zhimin Han[1], Bo Wang[1], Zhiyun Lin[2,3], Xiangdong Xu[4]

1. School of Automation, Hangzhou Dianzi University, Hangzhou 310018, P. R. China
E-mail: 212060281@hdu.edu.cn, hanzm@hdu.edu.cn, wangbo@hdu.edu.cn

2. Shenzhen Key Laboratory of Control Theory and Intelligent Systems, School of System Design and Intelligent Manufacturing, Southern University of Science and Technology, Shenzhen 518055, P. R. China
E-mail: linzy@sustech.edu.cn

3. Peng Cheng Laboratory, Shenzhen 518000, P. R. China
E-mail: linzy@sustech.edu.cn

4. Wenzhou Institute of Industry & Science, Wenzhou 325001, P. R. China
E-mail: 18968775811@189.cn

5. Zhejiang CoTEK Robotics Co. Ltd, Hangzhou 310057, P. R. China

Abstract: In this paper, we introduce an innovative method for the orientation-specific path planning of an Automated Guided Vehicle (AGV) with steering constraints, such as unmanned forklifts. Traditional shortest-path algorithms, which solely consider distance or travel time, are unsuitable for tasks where the AGV's orientation is crucial. To address this, we have created an augmented graph that inherently incorporates the AGV's steering constraints and orientation. By utilizing this enhanced graph structure, conventional shortest-path algorithms can be employed to ascertain a path that takes the AGV's orientation into account. This novel method facilitates more adaptable and secure path planning, while preserving the immediacy required for real-time path planning execution.

Key Words: Path planning, Steering constraint, Mobile robot

1 Introduction

Automated Guided Vehicle (AGV) refers to a transport vehicle equipped with an automatic guiding device, such as electromagnetic or optical, capable of traveling along a prescribed guiding path, with safety protection and various transfer functions, in industrial applications [1]. Path planning plays a crucial role in the AGV application system, which provides the AGV with a feasible route to the destination. Classical shortest path algorithms consider either the length or travel time when finding the shortest path. However, for an AGV with a steering constraint (e.g. unmanned forklifts), it is not allowed take a any angle turn due to its own mechanical structure limitations or potential facility damage. Furthermore, the AGV may need to arrive at its destination facing a specific direction to perform subsequent operations efficiently. For instance, an AGV might need to align itself with a loading dock or a conveyor belt, or it might need to face a certain direction to pick up or drop off items. Thus, it is often necessary to consider their steering constraint and the orientation at the target location during the AGV's path planning. These considerations not only bring better safety to the AGV system but also increase the accuracy and efficiency of the subsequent operations.

There are many studies that take into account turn restrictions in shortest path planning [2, 3]. The AGV's steering constraint can be treated as an angle-based turn restriction on the graph, where a turn is only legal if its angle is between certain values. The literature considers two possible approaches for handling turn restrictions in shortest-path algorithms.

One approach modifies the graph, integrating the information of turn restrictions into the structure of the graph itself to eliminate turn restrictions. Examples of this method include vertex segmentation [4, 5] and line graph methods [6–8]. Another approach does not modify the graph but develops a new algorithm on the original graph, explicitly considering the turn restrictions problem. Gutiérrez and Medaglia [9] present a modified version of the well-known algorithm of Dijkstra [10], and Ziliaskopoulos and Mahmassani [11] present a similar method.

Besides turn restrictions, turn penalties are a major concern in shortest path algorithms [12–14]. However, the above methods do not take into account the orientation of the AGV, thus failing to determine the direction of the AGV upon arrival at the destination. This results in the planned path being unable to be used in scenarios for AGVs with a steering constraint.

In order to specify the AGV's orientations during the path planning process for an AGV with a steering constraint, firstly, we construct a virtual graph that integrates the AGV's steering constraint and orientation information. Then, a standard shortest-path algorithm can be applied to find the orientation-specified shortest path in the virtual graph. Our approach provides more flexible path planning for AGVs with a steering constraint without compromising real-time performance.

This work is organized as follows. In Section 1, we introduce the significance and related work of path planning considering steering constraint. Section 2 describes the steering constraint of AGVs when traveling in a topological graph. In Section 3, we introduce a method for graph transformation. The transformed graph embeds the steering constraint

This work is supported by the National Natural Science Foundation of China under grant Nos. U23A20325, 62173118, and 61903110, and Natural Science Foundation of Zhejiang Province under grant No. LY24F030009. (Corresponding author: Zhimin Han)

and orientation of the AGV within it. Section 4 introduces the complete process of conducting a shortest path query on a transformed graph. In Section 5, we test the performance of the shortest path planning algorithms on the transformed graph.

2 Problem description

Given the AGV's map as a directed graph $G = (V, E)$, where V is a set of vertices $\{v_1, ..., v_{|V|}\}$ and E is a set of edges in which e_{ij} is an element if and only if there exists an edge from vertex v_i to vertex v_j. A *cost* c_{ij} is associated with each edge $e_{ij} \in E$, which represents the cost of traversing the edge. There are no restrictions on edge costs except that they are required to be non-negative [15].

An AGV with a steering constraint could travel along a directed edge in either a forward or backward direction. For each edge $e_{ij} \in E$, we define four angles associated with it, that is, forward drive-in angle θ_i, forward drive-out angle θ_j, backward drive-in angle φ_i and backward drive-out angle φ_j. In our application, we define $\theta_i, \theta_j, \varphi_i, \varphi_j \in [-180°, 180°]$.

As shown in Fig. 1 (a), an AGV is moving forward along a directed edge e_{ij}. The orientation at vertex v_i is defined as the forward drive-in angle θ_i, and the orientation at vertex v_j is defined as the forward drive-out angle θ_j. Similarly, when the AGV is moving backward along edge e_{ij} as shown in Fig. 1 (b), we define the orientation at vertex v_i as the backward drive-in angle φ_i, and the orientation at vertex v_j as the backward drive-out angle φ_j.

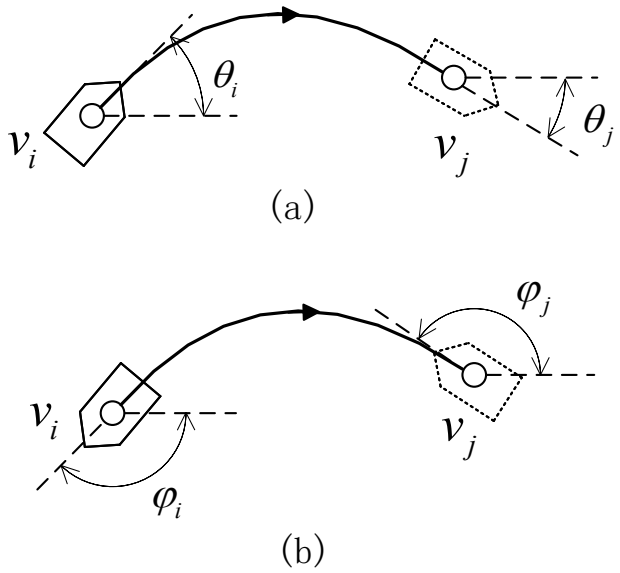

Fig. 1: The possible movements of an AGV along a directed edge e_{ij}

It is clear to see that the forward and backward drive-in angles are in opposite directions which are similar to the forward and backward drive-out angles. Consequently, a directed edge only needs to store the drive-in and drive-out angles for forward traversing, and the backward drive-in and drive-out angles can be inferred from the forward angles. In addition, the traverse direction (forward or backward) of a directed edge can be configured in accordance with the requirements of the path planning process, thereby providing enhanced flexibility. For the convenience of description, in this paper, we assume that each directed edge allows the AGV to traverse both forward and backward.

Given that the maximum steering angle σ and the current orientation angle of the AGV θ, the steering constraint of the AGV can be articulated as follows. The AGV can move forward from vertex v_i along edge e_{ij} to vertex v_j when the condition $\theta - \theta_i < \sigma$ is met. Conversely, the AGV can move backward from vertex v_i along edge e_{ij} to vertex v_j when the condition $\theta - \varphi_i < \sigma$ is satisfied.

In this paper, we consider a shortest path problem where the AGV has the steering constraint mentioned above, and the start and target orientations can be specified during path planning.

3 Construction of virtual graph

We transform the original graph $G = (V, E)$ into a virtual graph $G' = (V', E')$, embedding the steering constraint and orientation of the AGV within it.

3.1 Derivation of virtual vertices

In the initial phase of our methodology, we establish all of the virtual vertices. Each of these virtual vertices is designed to represent a potential orientation of the AGV at some vertex within the original graph.

As the AGV travels through the graph G, the feasible orientations at a specific vertex can be identified. These orientations are dependent on the edges that are interconnected with the vertex.

Fig. 2 depicts a fragment of the AGV's real-world application graph, in which vertex b is interconnected with three directed edges, specifically e_{ab}, e_{bc}, and e_{bd}. For a vertex that is not the starting point, the AGV can only reach this vertex via the incoming edges of it. So the incoming edge of vertex b is e_{ab}. When an AGV moves forward along the edge e_{ab} to vertex b, the orientation of the AGV at vertex b is 0°. Conversely, when moving backward towards vertex b, the orientation is 180°. Thus, we need to contruct two virtual vertices of vertex b to fit for these two situations.

When vertex b serves as the starting point for path planning, the AGV is capable of moving either forward or backward along the outgoing edges to reach other vertices. In our case, vertice b has two outgoing edges, namely e_{bc} and e_{bd}. For each of them, we need to construct a pair of virtual vertices of vertex b to fit for both moving forward and backward situations. However, since the two outgoing edges have the same forward drive-in angle 0° and backward drive-in angle 180°, these two edges share the same pair of virtual vertices.

Generally, for a vertex $v_i \in V$, every incoming edge contributes two potential virtual vertices to V', either for every outgoing edge. Denote the set of virtual vertices $\{v'_{i1}, \ldots, v'_{i|V'_i|}\}$ derived from v_i as $V'_i \in V'$. These virtual vertices are constructed for various possible movements of the AGV as the AGV travels through the graph. Furthermore, multiple directed edges may contribute to the same virtual vertices. To minimize the scale of the virtual graph as much as possible, we can merge multiple virtual vertices with close orientations into a single virtual vertex within an

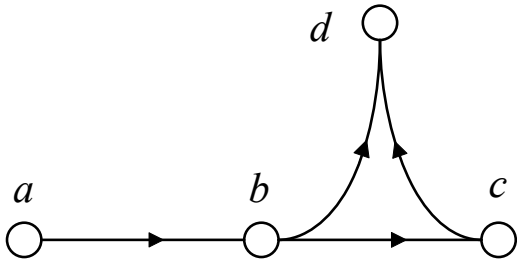

Fig. 2: A fragment of the real-world graph

allowable range of error.

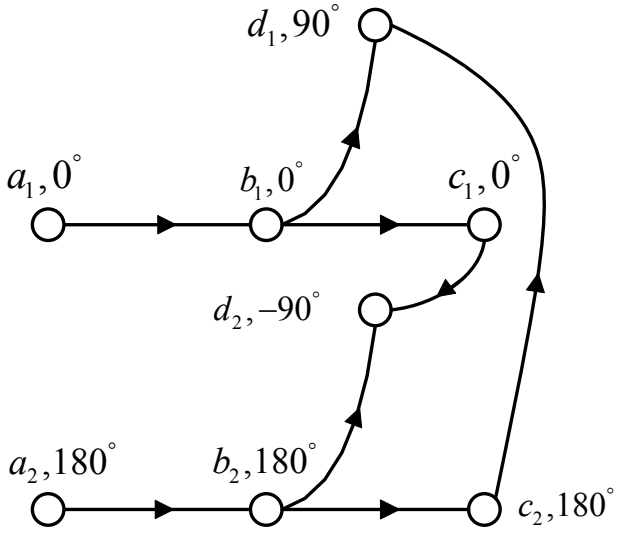

Fig. 3: Virtual graph of original graph in Fig. 2

3.2 Connection of virtual vertices

After completing the construction of all virtual vertices, it remains to establish virtual edges interconnecting these virtual vertices.

An AGV with a maximum steering limit of σ can steer no more than σ at a vertex to traverse a directed edge. This means that for a directed edge $e_{ij} \in E$, an AGV at vertex v_i holding orientation angles within the range $(\theta_i - \sigma, \theta_i + \sigma)$ can move forward along this directed edge. We denote the corresponding set of vertices as $F_{ij} \in V_i'$. Similarly, an AGV at vertex v_i and with orientation angles within the range $(\varphi_i - \sigma, \varphi_i + \sigma)$ can move backward along this directed edge. We denote the corresponding set of vertices as $B_{ij} \in V_i'$.

After the AGV moves along the edge e_{ij} from v_i to v_j, the orientation of the AGV at vertex v_j is either θ_j or φ_j, depending on whether the AGV moves forward or backward. Based on the virtual vertices with all possible orientations in V' which are constructed in the previous subsection, there must exist the corresponding vertices for these two situations. We denote the virtual vertice of vertex v_j with orientation θ_j as $v_{jf}' \in V_j'$, the virtual vertice of vertex v_j with orientation φ_j as $v_{jb}' \in V_j'$.

For each directed edge $e_{ij} \in E$, we establish a connection from every $v_{in}' \in F_{ij}$ to v_{jf}'. This connection serves as a virtual directed edge in E', symbolizing the AGV's forward movement along the original edge e_{ij}. Similarly, we establish a connection from each $v_{im}' \in B_{ij}$ to v_{jb}', which acts as a virtual directed edge that represents the AGV's backward movement along the original edge e_{ij}.

3.3 Implementation

We provide the implementation pseudo code as shown in Algorithm 1. In order to utilize heuristic information during path queries within the virtual graph, each virtual vertex retains the coordinate data of its corresponding original vertex. Additionally, we utilize a hash map to maintain the mapping relationship between virtual vertices and original vertices. This allows us to efficiently locate the corresponding virtual vertex for a given orientation and original vertex during path queries.

Algorithm 1: The construction of virtual graph

Input: original graph $G = (V, E)$
Output: virtual graph $G' = (V', E')$

```
foreach directed edge e_ij in E do
    if e_ij allows moving forward then
        construct a virtual vertex v'_in with orientation θ_i of vertex v_i;
        put v'_in in V'_i if v'_in ∉ V'_i;
        construct a virtual vertex v'_jn with orientation θ_j of vertex v_j;
        put v'_jn in V'_j if v'_jn ∉ V'_j;
    if e_ij allows moving backward then
        construct a virtual vertex v'_im with orientation φ_i of vertex v_i;
        put v'_im in V'_i if v'_im ∉ V'_i;
        construct a virtual vertex v'_jm with orientation φ_j of vertex v_j;
        put v'_jm in V'_j if v'_jm ∉ V'_j;
foreach directed edge e_ij in E do
    if e_ij allows moving forward then
        find virtual vertex set F_ij from V'_i and virtual vertex v'_jf from V'_j
        foreach virtual vertex v'_in in F_ij do
            construct a virtual edge from v'_in to v'_jf and put it in E';
    if e_ij allows moving backward then
        find virtual vertex set B_ij from V'_i and virtual vertex v'_jb from V'_j;
        foreach virtual vertex v'_im in B_ij do
            construct a virtual edge from v'_im to v'_jb and put it in E';
```

During the process of constructing virtual vertices, we unify the virtual vertices with the same original vertex with an allowable range of orientation error into the same virtual vertex. This can avoid constructing too many unnecessary virtual vertices, thereby reducing the scale of the virtual graph.

The virtual edge retains the cost of the original directed edge, which plays a crucial role in identifying the shortest path. By differentiating between the forward and backward movements of the AGV, we can prevent the AGV from moving forward or backward along certain edges by not creating a connection between the corresponding virtual ver-

tices. Furthermore, we can adjust the cost of virtual edges to achieve a preference for certain ways of AGV's movement. The above options also bring more flexibility to the path planning.

4 Path Query With Orientations

Assume we want to plan a path from vertex a to vertex d with starting orientation $0°$ and target orientation $-90°$ in a graph as depicted in Fig. 2. Using traditional shortest path algorithms on the original graph, the resulting path would be $< abd >$, which does not satisfy the desired target orientation of $-90°$.

We will do the same path query on the constructed virtual graph as depicted in Fig. 3. Virtual vertex a_1 represents the AGV with orientation $0°$ at the original vertex a, corresponding to the start vertex in our path plan query. Similarly, the virtual vertex d_2 represents the AGV at the original vertex d with an orientation of $-90°$, and it serves as the target vertex. Then, we can perform a standard shortest path algorithm on the virtual graph to find an optimal path. The resulting path on the virtual graph would be $< a_1 b_1 c_1 d_2 >$ and it corresponds to the real path $< abcd >$ on the original graph, which guides the AGV moving to the desired target vertex d with orientation $-90°$.

Certain implementation issues arise when performing a shortest path query on virtual graphs. Given a vertex with a certain orientation, there could be more than one corresponding virtual vertices in the constructed virtual graph. Hence, the shortest path query problem may have multiple start or target vertices in the constructed virtual graph [16]. However, a standard shortest path algorithm, such as the algorithm of Dijkstra, cannot deal with this situation. Inspired by the strategy proposed in [4], this can be solved by constructing one more virtual start vertex and one more virtual target vertex to connect all the possible start and target vertices in the constructed virtual graph, respectively. Then, after running the shortest path algorithm, the found path must be converted back to the path in the original graph. Fig. 4 presents the overall structure of the orientation-specfic path planning.

5 Experiments

Our algorithms were implemented, compiled and executed in Java version 11. All tests were run on an Intel quad-core 2.5 GHz machine with 8 GB RAM. Our experiments will be conducted on a real-world graph with 9646 vertices and 16567 edges.

5.1 Memory Usage

The construction of the virtual graph inevitably results in an expansion of the original graph's scale. In a scenario where all edges allow both forward and backward movements, the size of the virtual graph is expected to be at least double that of the original graph. As the density of the graph increases, so does the scale of the virtual graph. However, in real-world AGV application scenarios, the majority of the graphs tend to be sparse, resulting that the size of the virtual graphs are approximately twice that of the original graphs. The sizes of the original and virtual graphs in our experiments are presented in Table 1.

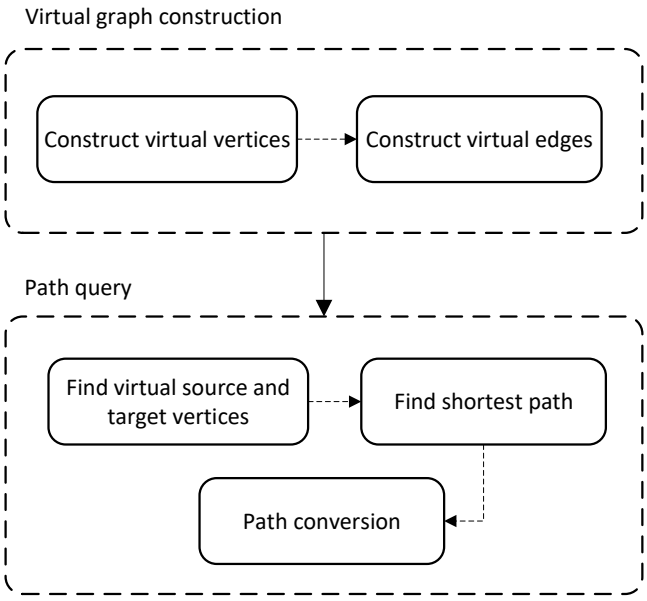

Fig. 4: Overall structure of the orientation-specfic path planning

Table 1: Graph Size

Graphs	vertices	edges	Size(MB)
Original Graph	9146	16567	7.6
Virtual Graph	18652	33086	11.7

Furthermore, we use a hash map to preserve the mapping correspondence between the virtual vertices and the original vertices. In our test case, it takes about 4MB of memory.

5.2 Time needed for creating virtual vertices and path conversion

Before querying the path, it is necessary to construct the virtual graph. The construction of the virtual graph, based on an average of over 100 instances of graph construction on the test graph, takes an average time of 62ms. In practical AGV applications, changes to the graph are infrequent. Consequently, for the path query experiment, the virtual graph needs to be constructed only once.

Since we store the mapping relationship between the original vertices and the virtual vertices in memory, the time required for path conversion is normally less than 1 ms. This duration is negligible compared to the time required for the path query.

5.3 Running times

Generally, the constructed virtual graph can be directly applied in graph based shortest path algorithms. We test the running times of common shortest path planning algorithms on our test graph with 9646 vertices and 16567 edges. The running time includes the time of querying on the virtual graph and the time of path conversion.

A set of one thousand random one-to-one queries was generated in our virtual graph for the time measurements. Every query in such a set has a random start vertex and a random target vertex. For each query, several shortest-path algorithms were performed. Furthermore, even the same query using the same algorithm was executed ten times, the aver-

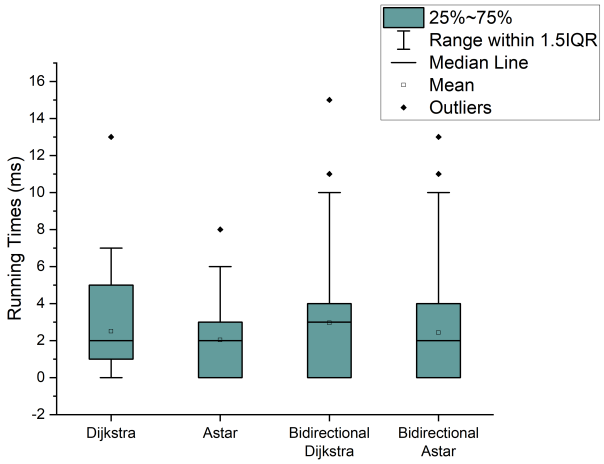

Fig. 5: Running times of shortest path algorithms

age time was applied to ensure the accurate time measurement.

Fig. 5 shows the running times of shortest path algorithms. In comparison to the standard Dijkstra algorithm, the heuristic algorithm A* [17] exhibits superior performance on the virtual graph. The bi-directional approach [18] did not achieve a speedup effect on the virtual graph. For the majority of path queries across all algorithms, the query time is within ten milliseconds, and the average time is less than five milliseconds. Such performance can fulfill the real-time demands of most AGV applications.

6 Conclusion

This paper introduces a novel approach to address the path planning problem for AGV with a steering constraint, making it possible to specify the start and target orientations when path planning. We construct a virtual graph from the original graph. The constructed virtual graph embeds the steering constraint and orientation of the AGV within it. Then, a standard shortest path algorithm can be used to query an orientation-specific path.

This paper provides a safer and more flexible path planning approach for AGVs with a steering constraint. However, this approach significantly enlarges the scale of the graph, potentially leading to increased time consumption when identifying the shortest path in very large-scale graphs. In our future research, we aim to investigate speedup techniques based on our expanded virtual graphs.

References

[1] C. Wang and J. Mao, Summary of agv path planning, in *Proceedings of the 3rd International Conference on Electronic Information Technology and Computer Engineering*, 2019, pp. 332–335.

[2] G. Tang, C. Tang, C. Claramunt, X. Hu, and P. Zhou, Geometric a-star algorithm: An improved a-star algorithm for agv path planning in a port environment, *IEEE Access*, vol. 9, pp. 196–210, 2021.

[3] Y. Sun, M. Fang, and Y. Su, Agv path planning based on improved dijkstra algorithm, *Journal of Physics: Conference Series*, vol. 1746, no. 1, pp. 012052, 2021.

[4] L. Speičvcys, C. S. Jensen, and A. Kligys, Computational data modeling for network-constrained moving objects, in *Proceedings of the 11th ACM international symposium on Advances in geographic information systems*, 2003, pp. 118–125.

[5] R. F. Kirby and R. B. Potts, The minimum route problem for networks with turn penalties and prohibitions, *Transportation Research*, vol. 3, no. 3, pp. 397–408, 1969.

[6] J. Añez, T. De La Barra, and B. Pérez, Dual graph representation of transport networks, *Transportation Research Part B: Methodological*, vol. 30, no. 3, pp. 209–216, 1996.

[7] S. Winter, Modeling costs of turns in route planning, *GeoInformatica*, vol. 6, pp. 345–361, 2002.

[8] P. Wojciechowski, M. Williamson, and K. Subramani, On the analysis of optimization problems in arc-dependent networks, *Discrete Optimization*, vol. 45, pp. 100729, 2022.

[9] E. Gutierrez and A. L. Medaglia, Labeling algorithm for the shortest path problem with turn prohibitions with application to large-scale road networks, *Annals of Operations Research*, vol. 157, pp. 169–182, 2008.

[10] E. W. Dijkstra, A note on two problems in connexion with graphs, *Numerische Mathematik*, vol. 1, no. 1, pp. 269–271, 1959.

[11] A. K. Ziliaskopoulos and H. S. Mahmassani, A note on least time path computation considering delays and prohibitions for intersection movements, *Transportation Research Part B Methodological*, vol. 30, no. 5, pp. 359–367, 1996.

[12] K. Fransen and J. van Eekelen, Efficient path planning for automated guided vehicles using a*(astar) algorithm incorporating turning costs in search heuristic, *International Journal of Production Research*, vol. 61, no. 3, pp. 707–725, 2023.

[13] X. Wang, H. Zhang, S. Liu, J. Wang, Y. Wang, and D. Shangguan, Path planning of scenic spots based on improved a* algorithm, *Scientific Reports*, vol. 12, no. 1, p. 1320, 2022.

[14] T. Vidal, Node, edge, arc routing and turn penalties: Multiple problems—one neighborhood extension. *Operations Research*, vol. 65, no. 1-2, pp. 61–63, 2017.

[15] A. Boroujerdi and J. Uhlmann, An efficient algorithm for computing least cost paths with turn constraints, *Information Processing Letters*, vol. 67, no. 6, pp. 317–321, 1998.

[16] S. Vanhove and V. Fack, Route planning with turn restrictions: A computational experiment, *Operations Research Letters*, vol. 40, no. 5, pp. 342–348, 2012.

[17] P. E. Hart, N. J. Nilsson, and B. Raphael, A formal basis for the heuristic determination of minimum cost paths, *IEEE transactions on Systems Science and Cybernetics*, vol. 4, no. 2, pp. 100–107, 1968.

[18] I. Pohl, Bi-directional and heuristic search in path problems. Stanford Linear Accelerator Center, California, Technical Report, 1969.

Proceedings of the 3rd Conference on Fully Actuated System Theory and Applications
May 10-12, 2024, Shenzhen, China

Containment Control of Fractional-order Nonlinear Multi-agent Systems with Time Delay

Yanqiu Li[1], Wei Zhu[1], Bo Chen[1]

1. Key Laboratory of Intelligent Analysis and Decision on Complex Systems, Chongqing University of Posts and Telecommunications, Chongqing 400065, China
Email: 274796976@qq.com, zhuwei@cqupt.edu.cn, 441663101@qq.com

Abstract: Formation control of multi-agent systems is an extension of its consensus problem, which has been widely used in control science and engineering, system science, information and communication engineering and other disciplines. Compared with using integral-order calculus to describe the change of the state of the object, the fractional-order calculus can represent and reflect the real physical characteristics of the object better. In this paper, containment control problem of fractional-order nonlinear multi-agent systems with time delay is studied. In spite of the difficulties and challenges caused by the operator complex property and system delay in fractional-order calculus, this paper solves the containment control problem by constructing a quadratic Lyapunov function and using matrix analysis theory, graph theory and fractional Razumikhin method. The conditions of linear matrix inequalities for asymptotically containment control are given. Finally, numerical simulation results verify the effectiveness of the proposed control scheme.

Key Words: Containment Control, Fractional-Order, Nonlinear Multi-Agent System, Time Delay

1 Introduction

Recently, distributed coordination of multi-agent systems (MAS) has gained much attention due to its broad applications, including consensus, flocking, and formation control. If MAS contains multiple leaders, it is commonly known as the containment control issue. In the case of containment control problem, there are multiple leaders and followers. The containment control problem was first proposed by G. Ferrari-Trecate, M. Egerstedt, A. Buffa and M. Ji in 2006. They proposed a distributed containment control algorithm for agents with single-integrator dynamics such that a group of followers is driven to the convex hull spanned by multiple leaders [1]. Subsequently, they used the theory of partial differential equations and the STOP-GO mixed control strategy to further clarify the containment control problem [2]. Concurrently, J. Hu and Y. Hong used neighborhood rules to obtain sufficient conditions for the convergence of the swarm behavior of agents to the convex set formed by the leaders under fixed and switching topologies [3]. Y. Cao and W. Ren designed a distributed tracking control algorithm to study the containment control problem of multi-agent systems with static or dynamic leaders, obtaining network topology conditions for containment control under directed topology [4]. Then, similar methods further explore the problems of asymptotic containment control under switching directed topology and finite-time containment control under fixed directed topology [5].

In containment control, as the system generally has unknown time-varying parameters and disturbances, it is necessary to identify and compensate the system uncertainties in the controller design. On the other hand, the distributed containment error including neighbor information also makes it challenge to construct compensation signals and coordinate decision-making processes effectively. Thus, Y. Mehdi, M. Tabatabaei proposed a new cooperative control strategy for the containment control problem of fractional linear multi-agent systems with different orders, and obtained sufficient conditions for the system to achieve asymptotic stability [6]. Liu designed a bounded estimation method and introduced a fractional-order command filter into the inversion control method to reduce the complexity of controller design. The hyperbolic tangent function with time-varying integrable functions was ingeniously incorporated into the controller and compensation signal to effectively compensate the time-varying parameters, disturbances, and filtering errors [7].

With the deepening of research on containment control, to better align with the actual laws of physical motion, the study of nonlinear systems is also highly valuable. X. Yuan investigated the containment control of fractional-order multi-agent systems with unknown nonlinear functions on directed communication topologies [8]. J. Yuan proposed an adaptive neural network dynamic surface controller to address the binary containment control problem of fractional-order multi-agent systems. The communication topology not only includes positive adjacency weights but also negative adjacency weights, making it more general [9]. Liu used neural networks to approximate unknown non-affine functions and proposed a distributed adaptive neural network binary containment control method under the containment control structure [10]. J. Yuan studies the bipartite containment control problem for a class of fractional order nonlinear multi-agent systems in the presence of arbitrary switching and unmeasured states, it proposes an adaptive neural network dynamic surface controller, in which dynamic surface control technology can avoid “explosion of complexity” and obtain fractional derivatives for virtual control functions continuously [11].

By the way, in practical applications, problems such as communication channel congestion, limited transmission

This work is jointly sponsored by National Natural Science Foundation of China under Grant 62373071 and Natural Science Foundation of Chongqing, China, under Grant CSTB2023NS CQ-LZX0075.

speed, and external environmental interference are often encountered. To reduce the burden of communication, Liu devises an event-triggered condition consisting of the control input and a decreasing function related to the containment errors, which can provide more design freedom to balance the system performance and communication resources, and investigates the finite-time containment control problem for fractional-order nonlinear multiagent systems with event-triggered inputs [12].

The existence of time delay is also inevitable and can interfere with the dynamic behavior of the system. Li investigates the containment control performance analysis problem for double-integrator fractional-order multi-agent systems with nonuniform time delays. The primary focus is on evaluating the containment control performance by calculating the explicit delay margin [13]. X. Xia investigates the containment control for fractional order multi-agent systems with nonlinearity and time delay [14]. On this basis, Z. Xia investigates the issue of containment control of multi-agent systems that are heterogeneous, nonlinear, and fractional-order while taking practical scenarios into account, such as uncertainties, unknown nonlinearities, time-varying state delays, and distributed time-varying delays [15]. To Author's knowledge, few researches have been done on the containment control of fractional-order nonlinear multi-agent systems with time delays.

Inspired by the previous discussion, this paper constructs a quadratic Lyapunov function and utilizes matrix analysis theory, graph theory, and the fractional-order Razumikhin method to investigate the containment control problem of fractional-order nonlinear multi-agent systems with time delay. Linear matrix inequality (LMI) conditions are derived for the system to achieve asymptotic containment control.

2 Preliminary Knowledge

Consider a weighted directed graph $\mathbb{G} = (\mathbb{V}, \mathbb{E})$, where $\mathbb{V} = 1,2,\cdots,N$ represents the set of vertices corresponding to agents, and $\mathbb{E} \subset \mathbb{V} \times \mathbb{V}$ represents the set of directed edges, such that for each directed edge $\mathcal{E}_{jk} = (j,k) \in \mathbb{E}$, which indicates that agent k can receive information from agent j. The adjacency matrix of graph $\mathbb{G}$ is defined as $\mathbb{A} = (a_{jk})_{N\times N}$, where $a_{jk} > 0$ if $\mathcal{E}_{kj} \in \mathbb{E}$, and $a_{jk} = 0$ otherwise. It is assumed in this paper that there are no self-loops in the graph, i.e., $a_{jj} = 0$. The Laplacian matrix of graph $\mathbb{G}$ is defined as $\mathbb{L} = \mathbb{D} - \mathbb{A}$, where $\mathbb{D} = \mathrm{diag}\{d_1, d_2, \cdots, d_N\}$ is a diagonal matrix with diagonal elements $d_j = \sum_{k\neq j,k=1}^{N} a_{jk}$.

There are some definitions related to fractional-order calculus. The Caputo fractional-order derivative plays a crucial role in fractional-order systems as its initial value has the practical signification in many problems, which has been widely used in some practical systems.

Definition 1. [16] The α-order Caputo fractional derivative of a function $x(t)$ is defined as follows:

$$ {}_{t_0}^{C}D_t^{\alpha}x(t) = \frac{1}{\Gamma(k-\alpha)}\int_{t_0}^{t}(t-z)^{k-\alpha-1}x^{(k)}(z)dz, $$

where $k \in \mathrm{Z}^{+}: k-1 < \alpha \le k, \Gamma(s) = \int_0^{+\infty} z^{s-1}e^{-z}dz$.

Consider an α-order fractional $(0 < \alpha \le 1)$ delay system given by:

$$ {}_{t_0}^{C}D_t^{\alpha}x(t) = f(t, x_t),\ t \ge t_0, $$

where $x_t(\tau) = x(t+\tau), \tau \in [-r, 0]$, the continuous function $f: \mathrm{R}\times\mathrm{R}^n \to \mathrm{R}^n$ satisfies $f(t,0) = 0$.

Lemma 1. [17] Suppose U is an $n \times n$ positive definite matrix, and let $x(t)$ be a continuously differentiable vector function in R^n. The following inequality holds:

$$ {}_{t_0}^{C}D_t^{\alpha}\big(x^{\mathrm{T}}(t)Ux(t)\big) \le 2x^{\mathrm{T}}(t)U\ {}_{t_0}^{C}D_t^{\alpha}x(t),\ 0 < \alpha < 1. $$

Lemma 2. [18] The zero solution of fractional delayed will be asymptotical stability if there exist three positive real constants $\omega_1, \omega_2, \omega_3 > 0$ and a quadratic Lyapunov function $V: \mathrm{R}\times\mathrm{R}^n \to \mathrm{R}$ satisfying:

$$ \omega_1 \| x(t) \|^2 \le V\big(x(t)\big) \le \omega_2 \| x(t) \|^2, $$

and its α-order derivative satisfies:

$$ \big|\, {}_{t_0}^{C}D_t^{\alpha}V\big(x(t)\big)\big| \le -\omega_3 \| x(t) \|^2, $$

whenever

$$ V\big(x(t+\tau)\big) \le \sigma V\big(x(t)\big), \tau \in [-r, 0], $$

for some $\sigma > 1$.

Lemma 3. [19] Given matrix A_{12} and symmetric matrix A_{11}, A_{22}, the inequality:

$$ \begin{pmatrix} A_{11} & A_{12} \\ A_{12}^{\mathrm{T}} & A_{22} \end{pmatrix} < 0 $$

is equivalent to:

$$ A_{11} < 0,\ A_{22} - A_{12}^{\mathrm{T}}A_{11}^{-1}A_{12} < 0, $$

and

$$ A_{22} < 0,\ A_{11} - A_{12}A_{22}^{-1}A_{12}^{\mathrm{T}} < 0. $$

Lemma 4. [20] For any $\zeta, \psi \in \mathbb{R}^n$, and $W > 0$, the following inequality holds:

$$ 2\zeta^T\psi \le \zeta^T W\zeta + \psi^T W^{-1}\psi. $$

3 Problem Formulation

Consider the MAS consisting of M followers (denoted as $\mathcal{F} = 1,2,\cdots,M$) and $N-M$ leaders (denoted as $\mathcal{L} = M+1, M+2, \cdots, N$). The dynamic of the agent i $(i = 1,2,\cdots,N)$ is established as:

$$ \begin{aligned} {}_{t_0}^{C}D_t^{\alpha}y_i(t) = {} & Ay_i(t) + By_i(t-r) + f_1\big(t, y_i(t)\big) \\ & + f_2\big(t, y_i(t-r)\big) + u_i(t). \end{aligned} \tag{1} $$

where $y_i(t) \in \mathrm{R}^n$ denotes the state of agent i, $\alpha \in (0,1)$ is the fractional-order, the time delay $r \ge 0$, $A, B \in \mathrm{R}^{n\times n}$ is the constant matrices, $u_i(t) \in \mathrm{R}^n$ is the control input , and the nonlinear functions $f_s(t, y_i)$ satisfy $f_s(t,0) = 0, (s = 1,2)$.

Assumption 1. There exist constants $h_1, h_2 > 0$ and positive constant $\delta_1, \delta_2, \cdots, \delta_{N-M}$, satisfying that $\sum_{k=1}^{N-M}\delta_k = 1$ and for any $\phi, \varphi_k \in \mathrm{R}^n$, it holds that

$$ \|f_s(t,\phi) - \textstyle\sum_{k=1}^{N-M}\ \delta_k f_s(t,\varphi_k)\| \le h_s\|\phi - \sum_{k=1}^{N-M}\ \delta_k\varphi_k\|, s = 1,2. \tag{2} $$

Assumption 2. Each follower has at least one directed path from the leader to itself, and the information exchange between followers is undirected.

Under the condition of Assumption 2, the Laplacian matrix of the system graph $\mathbb{G}$ can be represented as:

$$ L = \begin{pmatrix} L_1 & L_2 \\ \mathbf{0}_{(N-M)\times M} & \mathbf{0}_{(N-M)\times(N-M)} \end{pmatrix}. \tag{3} $$

Lemma 5. [18] If Assumption 2 holds, then L_1 in the Laplacian matrix is an invertible M-matrix and $-L_1^{-1}L_2 = (l_{ij})_{M\times(N-M)}$ is a non-negative matrix and the sum of the elements in each row is equal to 1.

3.1 Containment Control without Time Delay

The containment control protocol for agent i is designed as

$$\begin{cases} u_i(t) = K_1 \sum_{j\in\mathcal{F}\cup\mathcal{L}} a_{ij}\left(y_j(t) - y_i(t)\right) & i \in \mathcal{F}, \\ u_i(t) = 0 & i \in \mathcal{L}, \end{cases} \tag{4}$$

where K_1 is the feedback gain matrix.

Using (1) and (4), we obtain that

$$\begin{cases} {}_{t_0}^{C}D_t^{\alpha}Y_{\mathcal{F}} = & (I_M \otimes A)Y_{\mathcal{F}} + (I_M \otimes B)Y_{\mathcal{F}}(t-r) + F_1(t, Y_{\mathcal{F}}) \\ & +F_2\big(t, Y_{\mathcal{F}}(t-r)\big) - (L_1 \otimes K_1)Y_{\mathcal{F}} - (L_2 \otimes K_1)Y_{\mathcal{L}} \\ {}_{t_0}^{C}D_t^{\alpha}Y_{\mathcal{L}} = & (I_{N-M} \otimes A)Y_{\mathcal{L}} + (I_{N-M} \otimes B)Y_{\mathcal{L}}(t-r) \\ & +F_1(t, Y_{\mathcal{L}}) + F_2\big(t, Y_{\mathcal{L}}(t-r)\big), \end{cases} \tag{5}$$

where $Y_{\mathcal{F}} = \left(y_1^{\mathrm{T}}(t), y_2^{\mathrm{T}}(t), \cdots, y_M^{\mathrm{T}}(t)\right)^{\mathrm{T}}$,
$Y_{\mathcal{L}} = \left(y_{M+1}^{\mathrm{T}}(t), y_{M+2}^{\mathrm{T}}(t), \cdots, y_N^{\mathrm{T}}(t)\right)^{\mathrm{T}}$,
$F_1(t, Y_{\mathcal{F}}) = \left(f_1^{\mathrm{T}}(t, y_1), f_1^{\mathrm{T}}(t, y_2), \cdots, f_1^{\mathrm{T}}(t, y_M)\right)^{\mathrm{T}}$,
$F_1(t, Y_{\mathcal{L}}) = \left(f_1^{\mathrm{T}}(t, y_{M+1}), f_1^{\mathrm{T}}(t, y_{M+2}), \cdots, f_1^{\mathrm{T}}(t, y_N)\right)^{\mathrm{T}}$,
$F_2\big(t, Y_{\mathcal{F}}(t-r)\big) = \big(f_2^{\mathrm{T}}\big(t, y_1(t-r)\big), f_2^{\mathrm{T}}\big(t, y_2(t-r)\big), \cdots, f_2^{\mathrm{T}}\big(t, y_M(t-r)\big)\big)^{\mathrm{T}}$,
$F_2\big(t, Y_{\mathcal{L}}(t-r)\big) = \big(f_2^{\mathrm{T}}\big(t, y_{M+1}(t-r)\big), f_2^{\mathrm{T}}\big(t, y_{M+2}(t-r)\big), \cdots, f_2^{\mathrm{T}}\big(t, y_N\big)\big)^{\mathrm{T}}$.

Definition 2. [20] If for $\forall x, y \in \mathbb{H}, 0 \le \varrho \le 1$, we have $(1-\varrho)x + \varrho y \in \mathbb{H}, (\mathbb{H} \subset \mathrm{R}^n)$ is called convex set; $C_o\{x_1, x_2, \cdots, x_{N-M}\} = \{\sum_{k=1}^{N-M} \varrho_k x_k \mid \varrho_k \ge 0, \sum_{k=1}^{N-M} \varrho_k = 1\}$ is the minimum convex hull that contains $x_1, x_2, \cdots, x_{N-M} \in \mathrm{R}^n$.

Define the state error $\Psi(t) = Y_{\mathcal{F}} - (-L_1^{-1}L_2 \otimes I_n)Y_{\mathcal{L}}$, taking the α-order derivative on both sides, we have:

$$\begin{aligned} {}_{t_0}^{C}D_t^{\alpha}\Psi(t) = & (I_M \otimes A)\Psi(t) + (I_M \otimes B)\Psi(t-r) - (L_1 \otimes K_1)\Psi(t) \\ & +F_1(t, Y_{\mathcal{F}}) + (L_1^{-1}L_2 \otimes I_n)F_1(t, Y_{\mathcal{L}}) \\ & +F_2\big(t, Y_{\mathcal{F}}(t-r)\big) + (L_1^{-1}L_2 \otimes I_n)F_2\big(t, Y_{\mathcal{L}}(t-r)\big). \end{aligned} \tag{6}$$

Theorem 1. If the Assumptions 1,2 hold and there are positive constants ε, η, μ and symmetric positive-definite matrix $P \in \mathrm{R}^{n\times n}$ satisfies the flowing equation,

$$\begin{pmatrix} \Omega_{11} & I_M \otimes (PB) \\ I_M \otimes (B^{\mathrm{T}}P) & I_M \otimes \left(\frac{h_2^2}{\eta} I_n - \mu P\right) \end{pmatrix} < 0, \tag{7}$$

where $\Omega_{11} = I_M \otimes \left(PA + A^{\mathrm{T}}P + (\varepsilon+\eta)P^2 + \frac{h_1^2}{\varepsilon} I_n + \mu P\right) - L_1 \otimes \left(PK_1 + K_1^{\mathrm{T}}P\right)$. Then, the containment control of the system can be implemented.

Proof: Choose a quadratic Lyapunov function:

$$V(t) = \Psi^{\mathrm{T}}(t)(I_M \otimes P)\Psi(t).$$

According to Lemma 1, the α −fractional derivative of $V(t)$ along the system is calculated as:

$$\begin{aligned} {}_{t_0}^{C}D_t^{\alpha}V(t) &\le 2\Psi^{\mathrm{T}}(t)(I_M \otimes P){}_{t_0}^{C}D_t^{\alpha}\Psi(t) \\ &= 2\Psi^{\mathrm{T}}(t)(I_M \otimes PA)\Psi(t) + 2\Psi^{\mathrm{T}}(t)(I_M \otimes PB)\Psi(t-r) \\ &\quad -2\Psi^{\mathrm{T}}(t)(L_1 \otimes PK_1)\Psi(t) + 2\Psi^{\mathrm{T}}(t)(I_M \otimes P)[F_1(t, Y_{\mathcal{F}}) \\ &\quad +(L_1^{-1}L_2 \otimes I_n)\big(F_1(t, Y_{\mathcal{L}})\big)] + 2\Psi^{\mathrm{T}}(t)(I_M \otimes P) \\ &\quad \big[F_2\big(t, Y_{\mathcal{F}}(t-r)\big) + (L_1^{-1}L_2 \otimes I_n)\left(F_2\big(t, Y_{\mathcal{L}}(t-r)\big)\right)\big]. \end{aligned} \tag{8}$$

By Lemma 5, for any $\varepsilon, \eta > 0$, it holds:

$$\begin{aligned} & 2\Psi^{\mathrm{T}}(t)(I_M \otimes P)\big[F_1(t, Y_{\mathcal{F}}) + (L_1^{-1}L_2 \otimes I_n)\big(F_1(t, Y_{\mathcal{L}})\big)\big] \\ & \le \tfrac{1}{\varepsilon}[F_1(t, Y_{\mathcal{F}}) + (L_1^{-1}L_2 \otimes I_n)F_1(t, Y_{\mathcal{L}})]^{\mathrm{T}} \\ & \quad [F_1(t, Y_{\mathcal{F}}) + (L_1^{-1}L_2 \otimes I_n)F_1(t, Y_{\mathcal{L}})] \\ & \quad +\varepsilon\Psi^{\mathrm{T}}(t)(I_M \otimes P^2)\Psi(t), \end{aligned} \tag{9}$$

and

$$\begin{aligned} & 2\Psi^{\mathrm{T}}(t)(I_M \otimes P)\left[F_2\big(t, Y_{\mathcal{F}}(t-r)\big) + (L_1^{-1}L_2 \otimes I_n)\left(F_2\big(t, Y_{\mathcal{L}}(t-r)\big)\right)\right] \\ & \le \eta\Psi^{\mathrm{T}}(t)(I_M \otimes P^2)\Psi(t) \\ & \quad +\frac{1}{\eta}\big[F_2\big(t, Y_{\mathcal{F}}(t-r)\big) + (L_1^{-1}L_2 \otimes I_n)F_2\big(t, Y_{\mathcal{L}}(t-r)\big)\big]^{\mathrm{T}} \\ & \quad *\big[F_2\big(t, Y_{\mathcal{F}}(t-r)\big) + (L_1^{-1}L_2 \otimes I_n)F_2\big(t, Y_{\mathcal{L}}(t-r)\big)\big]. \end{aligned} \tag{10}$$

By Assumption 1, we have

$$\begin{aligned} & \big[F_j(t, Y_{\mathcal{F}}) - (-L_1^{-1}L_2 \otimes I_n)F_j(t, Y_{\mathcal{L}})\big]^{\mathrm{T}}\big[F_j(t, Y_{\mathcal{F}}) - (-L_1^{-1}L_2 \otimes I_n)F_j(t, Y_{\mathcal{L}})\big] \\ = & \left(\left[f_j(t, y_1) - \sum_{u=1}^{N-M} l_{1u} f_j(t, y_{M+u})\right]^{\mathrm{T}}, \cdots, \left[f_j(t, y_M) - \sum_{u=1}^{N-M} l_{Mu} f_j(t, y_{M+u})\right]^{\mathrm{T}}\right) \\ & \left(\left[f_j(t, y_1) - \sum_{u=1}^{N-M} l_{1u} f_j(t, y_{M+u})\right]^{\mathrm{T}}, \cdots, \left[f_j(t, y_M) - \sum_{u=1}^{N-M} l_{Mu} f_j(t, y_{M+u})\right]^{\mathrm{T}}\right)^{\mathrm{T}} \\ \le & \ h_j^2 (Y_{\mathcal{F}} - (-L_1^{-1}L_2 \otimes I_n)Y_{\mathcal{L}})^{\mathrm{T}}(Y_{\mathcal{F}} - (-L_1^{-1}L_2 \otimes I_n)Y_{\mathcal{L}}) \\ = & \ h_j^2 \Psi^{\mathrm{T}}(t)\Psi(t). \ (j = 1,2) \end{aligned} \tag{11}$$

From equations (8) to (11), it can be concluded that

$$\begin{aligned} {}_{t_0}^{C}D_t^{\alpha}V(t) \le & \ \Psi^{\mathrm{T}}(t)[I_M \otimes (PA + A^{\mathrm{T}}P)]\Psi(t) + \Psi^{\mathrm{T}}(t)(I_M \otimes PB)\Psi(t-r) \\ & +\Psi^{\mathrm{T}}(t-r)(I_M \otimes B^{\mathrm{T}}P)\Psi(t) \\ & -\Psi^{\mathrm{T}}(t)[L_1 \otimes (PK_1 + K_1^{\mathrm{T}}P)]\Psi(t) \\ & +\varepsilon\Psi^{\mathrm{T}}(t)(I_M \otimes P^2)\Psi(t) + \frac{h_1^2}{\varepsilon}\Psi^{\mathrm{T}}(t)\Psi(t) \\ & +\eta\Psi^{\mathrm{T}}(t)(I_M \otimes P^2)\Psi(t) + \frac{h_2^2}{\eta}\Psi^{\mathrm{T}}(t)(t-r)\Psi(t-r). \end{aligned} \tag{12}$$

Whenever it satisfies that

$$V\big(\Psi(t+\tau)\big) \le \sigma V\big(\Psi(t)\big), \tau \in [-r, 0],$$

i.e.

$$0 \le \sigma\Psi^{\mathrm{T}}(t)(I_M \otimes P)\Psi(t) - \Psi^{\mathrm{T}}(t-r)(I_M \otimes P)\Psi(t-r). \tag{13}$$

For some $\sigma > 1$, we have for any $\mu > 0$

$$\begin{aligned} {}_{t_0}^{C}D_t^{\alpha}V(t) \le & \ \Psi^{\mathrm{T}}(t)[I_M \otimes (PA + A^{\mathrm{T}}P) - L_1 \otimes (PK_1 + K_1^{\mathrm{T}}P)]\Psi(t) \\ & +\Psi^{\mathrm{T}}(t)(I_M \otimes PB)\Psi(t-r) + \Psi^{\mathrm{T}}(t-r)(I_M \otimes B^{\mathrm{T}}P)\Psi(t) \\ & +\varepsilon\Psi^{\mathrm{T}}(t)(I_M \otimes P^2)\Psi(t) + \frac{h_1^2}{\varepsilon}\Psi^{\mathrm{T}}(t)(I_M \otimes I_n)\Psi(t) \\ & +\eta\Psi^{\mathrm{T}}(t)(I_M \otimes P^2)\Psi(t) + \frac{h_2^2}{\eta}\Psi^{\mathrm{T}}(t-r)\Psi(t-r) \\ & +\mu[\sigma\Psi^{\mathrm{T}}(t)(I_M \otimes P)\Psi(t) - \Psi^{\mathrm{T}}(t-r)(I_M \otimes P)\Psi(t-r)] \\ = & \ \delta^{\mathrm{T}}(t)\begin{pmatrix} \Omega_{11}^* & I_M \otimes (PB) \\ I_M \otimes (B^{\mathrm{T}}P) & I_M \otimes \left(\frac{h_2^2}{\eta} I_n - \mu P\right) \end{pmatrix}\delta(t). \end{aligned} \tag{14}$$

where $\delta^{\mathrm{T}}(t) = \big(\Psi^{\mathrm{T}}(t), \Psi^{\mathrm{T}}(t-r)\big), \Omega_{11}^* = I_M \otimes \left(PA + A^{\mathrm{T}}P + (\varepsilon + \eta)P^2 + \frac{h_1^2}{\varepsilon} I_n + \mu\sigma P\right) - L_1 \otimes (PK_1 + K_1^{\mathrm{T}}P)$.

By equations (7), it can be obtained that for a sufficiently small $\omega > 0, \sigma = \omega + 1$, we have :

$$\begin{pmatrix} \Omega_{11}^* & I_M \otimes (PB) \\ I_M \otimes (B^{\mathrm{T}}P) & I_M \otimes \left(\frac{h_2^2}{\eta} I_n - \mu P\right) \end{pmatrix} < 0.$$

Therefore, according to Lemma 2, if the system is asymptotically stable, then

$$\|Y_{\mathcal{F}} - (-L_1^{-1}L_2 \otimes I_n)Y_{\mathcal{L}}\| \to 0,\ (t \to \infty),$$

the containment control of the system (1) is implemented under the protocol (4).

Corollary 1. If Assumptions 1,2 holds and there are positive constants ε, η, μ and symmetric positive-definite matrix $P \in \mathrm{R}^{n\times n}$ satisfying the flowing equation,

$$\begin{pmatrix} \Pi_{11} & 0 \\ 0 & I_M \otimes \left(\frac{h_2^2}{\eta} I_n - \mu P + \frac{1}{\xi} PBB^{\mathrm{T}}P\right) \end{pmatrix} < 0.$$

where $\Pi_{11} = I_M \otimes \left(PA + A^{\mathrm{T}}P + (\varepsilon+\eta)P^2 + \left(\frac{h_1^2}{\varepsilon} + \xi\right) I_n + \mu P\right) - L_1 \otimes (PK_1 + K_1^{\mathrm{T}}P)$. Then, the containment control of the system (1) can be implemented.

3.2 Containment Control with Time Delay

The containment control protocol with time delay for agent i is designed as

$$\begin{cases} u_i(t) = K_2 \sum_{j\in\mathcal{F}\cup\mathcal{L}} a_{ij}\left(y_j(t-r) - y_i(t-r)\right) & i \in \mathcal{F}, \\ u_i(t) = 0 & i \in \mathcal{L}, \end{cases} \tag{15}$$

where K_2 is the feedback gain matrix.
Using (1), (15), we obtain

$$\begin{cases} {}_{t_0}^{C}D_t^{\alpha} Y_{\mathcal{F}} = & (I_M \otimes A)Y_{\mathcal{F}} + (I_M \otimes B)Y_{\mathcal{F}}(t-r) + F_1(t, Y_{\mathcal{F}}) \\ & +F_2\left(t, Y_{\mathcal{F}}(t-r)\right) - (L_1 \otimes K_2)Y_{\mathcal{F}}(t-r) \\ & -(L_2 \otimes K_2)Y_{\mathcal{L}}(t-r) \\ {}_{t_0}^{C}D_t^{\alpha} Y_{\mathcal{L}} = & (I_{N-M} \otimes A)Y_{\mathcal{L}} + (I_{N-M} \otimes B)Y_{\mathcal{L}}(t-r) \\ & +F_1(t, Y_{\mathcal{L}}) + F_2\left(t, Y_{\mathcal{L}}(t-r)\right), \end{cases} \tag{16}$$

Define the same state error $\Psi(t) = Y_{\mathcal{F}} - (-L_1^{-1}L_2 \otimes I_n)Y_{\mathcal{L}}$, we have

$$\begin{aligned} {}_{t_0}^{C}D_t^{\alpha}\Psi(t) = & (I_M \otimes A)\Psi(t) + (I_M \otimes B)\Psi(t-r) - (L_1 \otimes K_2)\Psi(t-r) \\ & +F_1(t, Y_{\mathcal{F}}) + F_2\left(t, Y_{\mathcal{F}}(t-r)\right) + (L_1^{-1}L_2 \otimes I_n)F_1(t, Y_{\mathcal{L}}) \\ & +(L_1^{-1}L_2 \otimes I_n)F_2\left(t, Y_{\mathcal{L}}(t-r)\right). \end{aligned} \tag{17}$$

Theorem 2. If the Assumptions 1,2 hold and there are positive constants ε, η, μ and symmetric positive-definite matrix $P \in \mathrm{R}^{n\times n}$ satisfying the flowing equation

$$\begin{pmatrix} \Phi_{11} & I_M \otimes (PB) - L_1 \otimes (PK_2) \\ I_M \otimes (B^{\mathrm{T}}P) - L_1 \otimes (K_2^{\mathrm{T}}P) & I_M \otimes \left(\frac{h_2^2}{\eta} I_n - \mu P\right) \end{pmatrix} < 0. \tag{18}$$

where $\Phi_{11} = I_M \otimes \left(PA + A^{\mathrm{T}}P + (\varepsilon+\eta)P^2 + \frac{h_1^2}{\varepsilon} I_n + \mu P\right)$.
Then, the containment control of the system can be implemented.

Proof. Choose a quadratic Lyapunov function:

$$V(t) = \Psi^{\mathrm{T}}(t)(I_M \otimes P)\Psi(t),$$

According to Lemma 1, the α-fractional derivative of $V(t)$ is calculated as:

$$\begin{aligned} {}_{t_0}^{C}D_t^{\alpha}V(t) \le & \ 2\Psi^{\mathrm{T}}(t)(I_M \otimes P){}_{t_0}^{C}D_t^{\alpha}\Psi(t) \\ = & \ 2\Psi^{\mathrm{T}}(t)(I_M \otimes PA)\Psi(t) + 2\Psi^{\mathrm{T}}(t)(I_M \otimes PB)\Psi(t-r) \\ & -2\Psi^{\mathrm{T}}(t)(L_1 \otimes PK_2)\Psi(t-r) \\ & +2\Psi^{\mathrm{T}}(t)(I_M \otimes P)[F_1(t, Y_{\mathcal{F}}) + (L_1^{-1}L_2 \otimes I_n)\left(F_1(t, Y_{\mathcal{L}})\right)] \\ & +2\Psi^{\mathrm{T}}(t)(I_M \otimes P)\left[F_2\left(t, Y_{\mathcal{F}}(t-r)\right)\right. \\ & \left.+(L_1^{-1}L_2 \otimes I_n)\left(F_2\left(t, Y_{\mathcal{L}}(t-r)\right)\right)\right]. \end{aligned} \tag{19}$$

By equations (9-11) and (19), we obtain

$$\begin{aligned} {}_{t_0}^{C}D_t^{\alpha}V(t) \le & \ \Psi^{\mathrm{T}}(t)[I_M \otimes (PA + A^{\mathrm{T}}P)]\Psi(t) + \Psi^{\mathrm{T}}(t)(I_M \otimes PB)\Psi(t-r) \\ & +\Psi^{\mathrm{T}}(t-r)(I_M \otimes B^{\mathrm{T}}P)\Psi(t) - \Psi^{\mathrm{T}}(t)(L_1 \otimes PK_2)\Psi(t-r) \\ & -\Psi^{\mathrm{T}}(t-r)(L_1 \otimes K_2^{\mathrm{T}}P)\Psi(t) + \varepsilon\Psi^{\mathrm{T}}(t)(I_M \otimes P^2)\Psi(t) \\ & +\frac{h_1^2}{\varepsilon}\Psi^{\mathrm{T}}(t)\Psi(t) + \eta\Psi^{\mathrm{T}}(t)(I_M \otimes P^2)\Psi(t) \\ & +\frac{h_2^2}{\eta}\Psi^{\mathrm{T}}(t-r)\Psi(t-r), \end{aligned} \tag{20}$$

Whenever

$$0 \le \sigma\Psi^{\mathrm{T}}(t)(I_M \otimes P)\Psi(t) - \Psi^{\mathrm{T}}(t-r)(I_M \otimes P)\Psi(t-r), \tag{21}$$

for some $\sigma > 1$, we have for any $\mu > 0$

$$\begin{aligned} {}_{t_0}^{C}D_t^{\alpha}V(t) \le & \ \Psi^{\mathrm{T}}(t)[I_M \otimes (PA + A^{\mathrm{T}}P)]\Psi(t) + \Psi^{\mathrm{T}}(t)(I_M \otimes PB)\Psi(t-r) \\ & +\Psi^{\mathrm{T}}(t-r)(I_M \otimes B^{\mathrm{T}}P)\Psi(t) - \Psi^{\mathrm{T}}(t)(L_1 \otimes PK_2)\Psi(t-r) \\ & -\Psi^{\mathrm{T}}(t-r)(L_1 \otimes K_2^{\mathrm{T}}P)\Psi(t) + \varepsilon\Psi^{\mathrm{T}}(t)(I_M \otimes P^2)\Psi(t) \\ & +\frac{h_1^2}{\varepsilon}\Psi^{\mathrm{T}}(t)\Psi(t) + \eta\Psi^{\mathrm{T}}(t)(I_M \otimes P^2)\Psi(t) \\ & +\frac{h_2^2}{\eta}\Psi^{\mathrm{T}}(t-r)\Psi(t-r) \\ & +\mu[\sigma\Psi^{\mathrm{T}}(t)(I_M \otimes P)\Psi(t) - \Psi^{\mathrm{T}}(t-r)(I_M \otimes P)\Psi(t-r)] \\ = & \ \delta^{\mathrm{T}}(t)\begin{pmatrix} \Phi_{11}^{*} & \Delta \\ \Delta^{\mathrm{T}} & I_M \otimes \left(\frac{h_2^2}{\eta} I_n - \mu P\right) \end{pmatrix}\delta(t), \end{aligned} \tag{22}$$

where $\delta^{\mathrm{T}}(t) = \left(\Psi^{\mathrm{T}}(t), \Psi^{\mathrm{T}}(t-r)\right)$, $\Phi_{11}^{*} = I_M \otimes \left(PA + A^{\mathrm{T}}P + (\varepsilon+\eta)P^2 + \frac{h_1^2}{\varepsilon} I_n + \mu\sigma P\right)$, $\Delta = I_M \otimes (PB) - L_1 \otimes (PK_2)$.
It can be obtained that for a sufficiently small $\omega > 0, \sigma = \omega + 1$, we have:

$$\begin{pmatrix} \Phi_{11}^{*} & I_M \otimes (PB) - L_1 \otimes (PK_2) \\ I_M \otimes (B^{\mathrm{T}}P) - L_1 \otimes (K_2^{\mathrm{T}}P) & I_M \otimes \left(\frac{h_2^2}{\eta} I_n - \mu P\right) \end{pmatrix} < 0.$$

Therefore, according to Lemma 2, if the system is asymptotically stable. The containment control of the system (1) is implemented under the protocol (15).

4 Simulation

Consider the MAS consisting of three followers and two leaders. The communication topology of the system is depicted in Fig. 1, from which we can get the Laplacian block matrix as

$$L_1 = \begin{pmatrix} 3 & -1.5 & -0.6 \\ -1.5 & 2 & 0 \\ -0.6 & 0 & 2 \end{pmatrix},\ L_2 = \begin{pmatrix} -0.9 & 0 \\ -0.5 & 0 \\ 0 & -1.4 \end{pmatrix}. \tag{23}$$

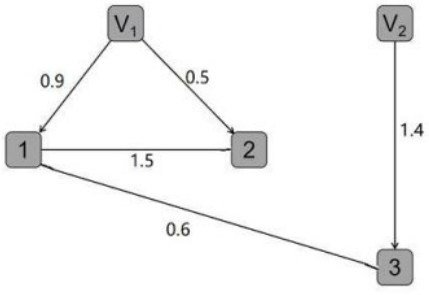

Fig. 1: Topology diagram of the system (1)

Assume that $A = \begin{pmatrix} -6 & -0.2 \\ -0.5 & -7 \end{pmatrix}$, $B = \begin{pmatrix} -1 & 1 \\ 1 & 1.5 \end{pmatrix}$,
$y_i(t) = \left(y_i^1(t), y_i^2(t)\right)^{\mathrm{T}}$,
$f_1\left(t, y_i(t)\right) = \left(y_i^1(t)\sin t, y_i^2(t)\sin t\right)^{\mathrm{T}}$,
$f_2\left(t, y_i(t-r)\right) = \left(\frac{1}{2}y_i^1(t-r)\sin t, \frac{1}{2}y_i^2(t-r)\sin t\right)^{\mathrm{T}}$.

From (2), we can select $h_1 = 1, h_2 = \frac{1}{2}$.

We choose $P = \begin{pmatrix} 1 & 0 \\ 0 & 1 \end{pmatrix}$, and $\eta = 4, \mu = 3, \xi = 2$ to satisfy $\frac{h_2^2}{\eta} I_n - \mu P + \frac{1}{\xi} PBB^{\mathrm{T}}P = \begin{pmatrix} -1.375 & 0.25 \\ 0.25 & -0.75 \end{pmatrix} < 0$. And then, we choose $\varepsilon = 2$, and $K_1 = \begin{pmatrix} 2 & 1 \\ 2 & 4 \end{pmatrix}$ to satisfy

$$\Pi_{11} = \begin{pmatrix} -12.5 & -9.7 & 6.0 & 4.5 & 2.4 & 1.8 \\ -9.7 & -26.5 & 4.5 & 12.0 & 1.8 & 4.8 \\ 6.0 & 4.5 & -8.5 & -6.7 & 0 & 0 \\ 4.5 & 12.0 & -6.7 & -18.5 & 0 & 0 \\ 2.4 & 1.8 & 0 & 0 & -8.5 & -6.7 \\ 1.8 & 4.8 & 0 & 0 & -6.7 & -18.5 \end{pmatrix} < 0.$$

Therefore, according to Theorem 1, it can be concluded that the containment control of system (1) can be achieved under protocol (4). Let $\alpha = 0.6, r = 0.5, \Psi(t) = (\Psi_{11}(t), \Psi_{12}(t), \Psi_{21}(t), \Psi_{22}(t), \Psi_{31}(t), \Psi_{32}(t))^{\mathrm{T}}$. The error curve is shown in Fig. 2. The state trajectories of agents are shown in Fig. 3.

Choose $P = \begin{pmatrix} 1 & 0 \\ 0 & 1 \end{pmatrix}$, and $\eta = 1, \mu = 2$ to satisfy $\frac{h_2^2}{\eta} I_n - \mu P < 0$. We can see that $\Phi_{11} < 0$. And then, we can choose $\varepsilon = 2$, and $K_2 = \begin{pmatrix} -0.33 & 0.5 \\ 0.5 & -0.01 \end{pmatrix}$ to satisfy

$$\Phi_{11} - [I_M \otimes (PB) - L_1 \otimes (PK_2)] \left[I_M \otimes \left(\frac{h_2^2}{\eta} I_n - \mu P \right) \right]^{-1} * [I_M \otimes (B^{\mathrm{T}}P) - L_1 \otimes (K_2^{\mathrm{T}}P)] =$$

$$\begin{pmatrix} -5.8218 & -1.3878 & -0.1153 & 0.6514 & -0.0461 & 0.2606 \\ -1.3878 & -6.6465 & 0.6514 & -0.2404 & 0.2606 & -0.0962 \\ -0.1153 & 0.6514 & -5.9725 & -0.9186 & 0.1846 & -0.0874 \\ 0.6514 & -0.2404 & -0.9186 & -6.8582 & -0.0874 & 0.1286 \\ -0.0461 & 0.2606 & 0.1846 & -0.0874 & -6.3601 & -0.7350 \\ 0.2606 & -0.0962 & -0.0874 & 0.1286 & -0.7350 & -7.1283 \end{pmatrix} < 0.$$

Therefore, according to Theorem 2, it can be concluded that the containment control of system (1) can be achieved under protocol (4). Let $\alpha = 0.6, r = 0.5$. The error curve is shown in Fig. 4. The state trajectories of agents are shown in Fig. 5.

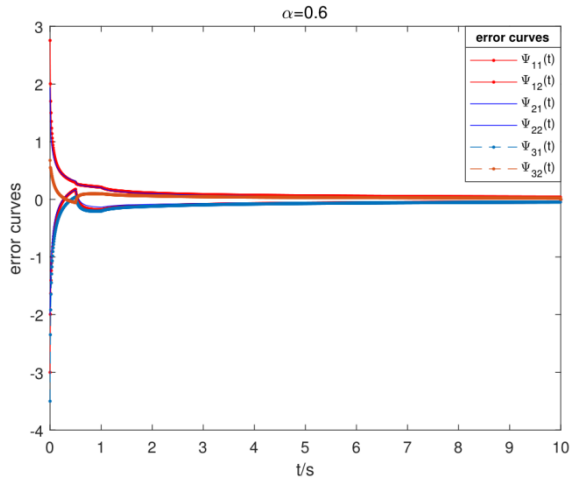

Fig. 2: The error of system (1) under protocol (4)

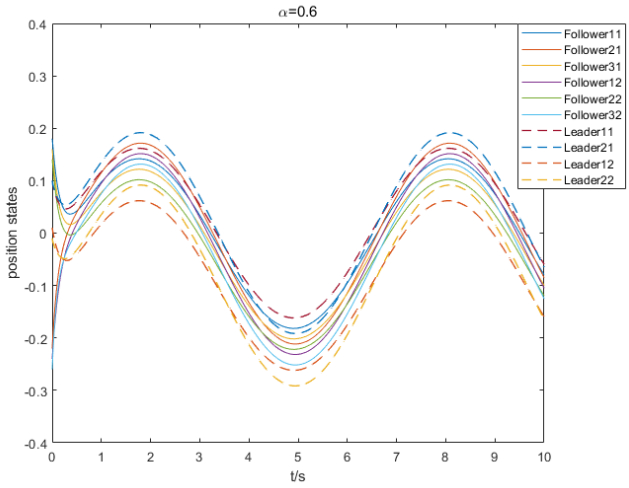

Fig. 3: The state trajectories of system (1) under protocol (4)

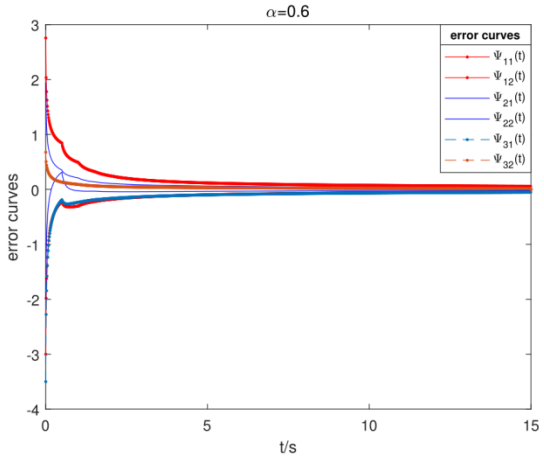

Fig. 4: The error of system (1) under protocol (15)

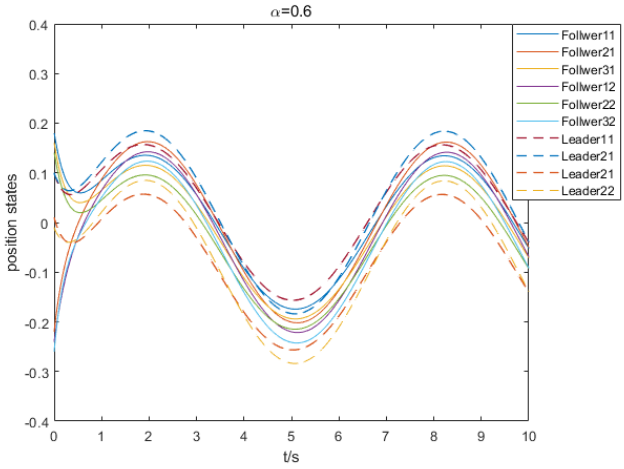

Fig. 5: The state trajectories of system (1) under protocol (15)

5 Conclusion

In this work, we have addressed the containment control problem of fractional-order multi-agent systems with fractional orders lying between zero and one. By constructing a quadratic Lyapunov function and utilizing matrix analysis theory, graph theory and the fractional-order Razumikhin

method, we obtain the linear matrix inequality conditions that ensure asymptotically containment control of the system. The proposed method effectively addresses the challenges posed by delays and fractional-order derivatives.

References

[1] G. Ferrari-Trecate, M. Egerstedt, A. Buffa, M. Ji, Laplacian sheep, A hybrid, stop-go policy for leader-based containment control, in *International Workshop on Hybrid Systems: Computation and Control*, 2006: 212-226.

[2] M. Ji, G. Ferrari-Trecate, M. Egerstedt, A. Buffa, Containment control in mobile networks, in *IEEE Transactions on Automatic Control*, 2008, 53(8): 1972-1975.

[3] J. Hu, Y. Hong, Coordination for a group of autonomous mobile agents with multiple leaders, in *2006 Chinese Control Conference,* Harbin, China, 2006: 318-322.

[4] Y. Cao, W. Ren, Containment control with multiple stationary or dynamic leaders under a directed interaction graph, in *Proceedings of the 48h IEEE Conference on Decision and Control (CDC) held jointly with 2009 28th Chinese Control Conference*, Shanghai, China, 2009: 3014-3019.

[5] Y. Cao, D. Stuart, W. Ren, Z. Meng, Distributed containment control for multiple autonomous vehicles with double-integrator dynamics: algorithms and experiments, in *IEEE Transactions on Control Systems Technology*, 2011, 19(4): 929-938.

[6] Y. Mehdi, M. Tabatabaei, Containment control of fractional-order multi-agent systems with different fractional orders, in *Iranian Journal of Science and Technology, Transactions of Electrical Engineering*, 2022, 46: 1089-1098.

[7] Y. Liu, H. Zhang, Y. Wang, H. Liang, Adaptive containment control for fractional-order nonlinear multi-agent systems with time-varying parameters, in *IEEE/CAA Journal of Automatica Sinica*, 2022, 9(9): 1627-1638.

[8] X. Yuan, L. Mo L, Y. Yu, Distributed containment control of fractional-order multi-agent systems using neural networks, in *Asian Journal of Control*, Beijing, China, 2022, 24(1): 149-158.

[9] J. Yuan, T. Chen, Observer-based adaptive neural network dynamic surface bipartite containment control for switched fractional order multi-agent systems, in *International Journal of Adaptive Control and Signal Processing,* Shanghai, China, 2022, 36(7): 161-164.

[10] Y. Liu, H. Zhang, Z. Shi, Z. Cao, Neural-network-based finite-time bipartite containment control for fractional-order multi-agent systems, in *IEEE Transactions on Neural Networks and Learning Systems*, 2022: 1-12.

[11] J. Yuan, T. Chen, Observer-based adaptive neural network dynamic surface bipartite containment control for switched fractional order multi-agent systems, in *Int J Adapt Control Signal Process,* 2022, 36(7): 1619–1646.

[12] Y. Liu, H. Zhang, J. Sun and Y. Wang, Event-triggered adaptive finite-time containment control for fractional-order nonlinear multiagent systems, in *IEEE Transactions on Cybernetics*, 2024, 54(2): 1250-1260.

[13] W. Li, L. Shi, M. Shi, J. Yue, B. Lin, K. Qin, Analyzing containment control performance for fractional-order multi-agent systems via a delay margin perspective, in *IEEE Transactions on Network Science and Engineering*, 2024: 1-12.

[14] X. Xia, J. Bai, X. Li, G. Wen, Containment control for fractional order MASs with nonlinearity and time delay via pull-based event-triggered mechanism, in *Applied Mathematics and Computation,* 2023, 454: 128094.

[15] Z. Xia, Fuzzy adaptive containment control for fractional-order heterogeneous nonlinear multi-agent systems with mixed time-varying delays, in *Int J Adapt Control Signal Process,* 2024: 1-18.

[16] I. Podlubny, *Fractional Differential Equations*, New York: Mathematics in Science and Engineering*,* 1999, 198: 41-119.

[17] A.D. Manuel, A. Norelys, A.G. Javier, C.L. Rafael, Using general quadratic Lyapunov functions to prove Lyapunov uniform stability for fractional order systems, in *Communications in Nonlinear Science and Numerical Simulation*, 2015, 22: 650-659.

[18] S. Liu, R. Yang, X.F. Zhou, W. Jiang, X. Li, X.W. Zhao, Stability analysis of fractional delayed equations and its applications on consensus of multi-agent systems, in *Communications in Nonlinear Science and Numerical Simulation*, 2019, 73: 351-362.

[19] K. Gu, V.L. Kharitonov, J. Chen, *Stability of time-delay systems*, Boston: Birkhauser, 2002, chapter 4.

[20] J. Mei, W. Ren, G. Ma, Distributed containment control for Lagrangian networks with parametrix uncertainties under a directed graph, in *Automatica*, 2012, 48: 653-659.

Proceedings of the 3rd Conference on Fully Actuated System Theory and Applications
May 10-12, 2024, Shenzhen, China

Dual Filtering Based Decentralized Learning Against Byzantine Attack

Jiansong Qing[1], Lizong Zhang[1], Dongcheng Zhou[1], Jianjun Wan[1], Wei Zheng[1], Qiang He[1*], Yanjun Lin[2]

1. Shaoxing Jianyuan Electric Power Group Co., Ltd, Shaoxing, Zhejiang, P. R. China
E-mail: oline9@sina.com

2. Hangzhou Applied Acoustics Research Institute, Hangzhou, Zhejiang, P. R. China

Abstract: Decentralized deep learning improves upon centralized methods by reducing failure risks but faces challenges from Byzantine attacks that can disrupt model integrity. In Byzantine defense models, the main approach is to rank neighboring node scores, which places strict demands on network topology.

This paper proposes a Dual Filtering based Parameter Aggregation Rule (DF-PAR). It primarily focuses on the parameter cosine similarity and distance, employing predefined thresholds to filter out the outliers. Additionally, an evaluation mechanism rooted in the credibility of historical information is introduced to determine the weight value of each node. Eventually, the impact of the suspicious node is gradually reduced and eliminated. The experimental results demonstrate the algorithm's ability and convergence even when some benign nodes are surrounded by Byzantine nodes.

Key Words: Decentralized deep learning, Byzantine Attack, Smart grid

1 Introduction

The past decade has seen a significant expansion in the volume of daily data. In response, distributed learning (DL) has emerged as a natural solution, allowing entities from diverse domains to collaboratively train a global model. In smart grids, DL efficiently handles the large and complex data generated by various energy sources, enabling real-time insights and decision-making. It facilitates predictive modeling and forecasting, improving grid stability and optimizing energy usage. Furthermore, it enhances grid resilience through real-time monitoring and early fault detection. It also supports the integration of distributed energy resources, contributing to renewable energy integration and grid optimization.

Nevertheless, there is a concern that certain entities might introduce malicious data [1] due to unpredictable internal faults or potentially hostile operating environments. Research in [2, 3] has demonstrated that even a single Byzantine worker can significantly compromise the performance of DL algorithms, employing relatively straightforward tactics. Consequently, a key challenge in Byzantine-resilient distributed learning lies in the pursuit of an accurate model that ensures minimal computational costs in the presence of unknown Byzantine workers. In fact, almost all current Byzantine defense models are constrained by topological connectivity. For instance, the BRIDGE method [4] requires that the amount of each benign node's benign neighbors should outnumber its Byzantine neighbors; while Bulyan [5] demands more than three times as many benign neighbors as the Byzantine ones. At present, there is not any method capable of effectively mitigating the robust defense effect when a benign node finds itself surrounded by Byzantine nodes.

To tackle the aforementioned challenges, this paper presents a novel algorithm, named Dual Filtering based Parameter Aggregation Rule (DF-PAR). The objective is to enable workers to perform DL by aggregating parameters from trustworthy neighboring nodes. The primary emphasis is placed on the parameter cosine similarity and distance, utilizing predefined thresholds to filter out the outliers. Furthermore, an evaluation mechanism based on the credibility of historical information is introduced to determine the weight value of each node. Consequently, the impact of suspicious neighbors is gradually mitigated through the reduction of their individual weights. The proposed algorithm exhibits exceptional performance in the face of diverse Byzantine attacks, surpassing other existing defense models. This superiority remains evident even in situations where certain benign nodes find themselves surrounded by Byzantine nodes.

This work is supported by grants from Science and Technology on Space Intelligent Control Laboratory under Grant No. HTKJ2022KL502016.

2 Related Work

The fundamental objective of distributed learning (DL) is to recognize Byzantine nodes responsible for model training within the cohort of remaining benign nodes. Broadly, the criteria for selection can be categorized into distance-based methods and performance-based methods.

In distance-based approaches, the server evaluates individual workers based on the vector distance of their respective gradients. Blanchard et al. introduced Krum [3], which selects a gradient of the least squared distance from its neighbor as the aggregate gradient. In an effort to enhance performance, a method termed 'Bulyan' [5] was proposed, which combines Krum and median-based aggregation rules to aggregate submitted gradients by discarding the extremes. However, despite their effectiveness in achieving a high success rate, these methods are vulnerable to state-of-the-art attack techniques such as 'A Little is Enough' [6] and 'Fall of Empires' [7]. These attacks manipulate the gradient to closely resemble that of a benign node, making them challenging to detect. To address these challenges, El-Mhamdi et al. [8] aggregated all worker gradient estimations using multiple aggregation rules and employed a contraction argument to demonstrate performance from a theoretical standpoint. Hou et al. [9] evaluated the long-term performance of each adjacent node and incrementally mitigated the influence of suspicious nodes. However, despite these efforts, complete elimination of the topology requirements could not

be achieved.

In a performance-based approach, the server evaluates the model performance for each worker with an additional validation dataset. Xie et al. ranked candidate gradients based on estimates of loss function decline and then aggregated the candidates with the highest scores [10]. Pan et al. introduced reinforcement learning techniques to learn powerful algorithms for Byzantine attacks for gradient aggregation agents, leveraging historical interactions with workers [11]. Guo et al. [12] implemented a two-step algorithm to construct a candidate pool of potentially benign nodes through a distance-based approach. Subsequently, a performance-based mechanism was employed to select the final nodes for estimating updates. Generative Adversarial Networks (GANs) have also been employed to tackle high-dimensional robust statistics problems [13]. Overall, the performance-based approach exhibits a relatively high Byzantine node recognition rate, and unfortunately they face high computational complexity in terms of loss function computation per iteration.

It is noteworthy that the majority of current defense methods impose strict limitations on the number of malicious nodes in the network topology. Specifically, in scenarios where a benign node is surrounded by Byzantine nodes, there is currently no method capable of achieving a robust defense effect.

3 Preliminary

3.1 Topology and Byzantine Worker

A system consisting of n nodes is represented by a directed graph $G = (V, E)$, where $V = \{1, 2, \cdots, n\}$ denotes the set of nodes, and E denotes the subset of $V \times V$ representing the set of edges. A node j is considered a neighbor of node i if and only if node i can receive information from node j, denoted by $(j, i) \in E$. Consequently, the set of neighbors of node i can be defined as $N_i = \{j \mid (j, i) \in E\}$. The terms network and topology, as well as worker and node, are used interchangeably.

In the presence of Byzantine attacks, the parameter update may be replaced with an arbitrary value, potentially causing a decline in the accuracy and convergence rate of the global model. In DL, a worker is deemed a benign worker if it successfully completes all tasks without any fault and transmits intended update to the neighbors. Otherwise, it is called Byzantine worker.

3.2 Model Training

In decentralized DL, our goal is to train a model cooperatively by optimizing loss function with all the n nodes. Specifically, for each node i, its optimization goal is described as

$$\min_{\tilde{\theta}} E_{\xi_i \sim D} l(\tilde{\theta}, \xi_i) \tag{1}$$

where $l(\tilde{\theta}, \xi_i)$ represents the loss function of node i, with $\tilde{\theta}$ representing the aggregated parameters. Let D and ξ_i denote the global dataset and the local dataset, respectively, randomly sampled either partially or entirely from the global dataset of a given node i. Then we give the following assumption.

Assumption 1 *The local dataset ξ_i, sampled from the global dataset D, on each node i is independent and identically distributed (i.i.d).*

4 Main Result

In this section, we introduce the proposed Dual Filtering based Parameter Aggregation Rule (DF-PAR), a Byzantine-tolerant algorithm, to evaluate each neighboring worker in a decentralized model. Specifically, unlike the existing defense model that ranks neighbor nodes by distance or specially designed score value at each iteration, we first use cosine similarity to exclude parameters with large deviation angles, and then use an instant score to exclude suspicious values from parameter distance. Following, in order to determine the corresponding weights, an evaluation mechanism based on the credibility of historical information is introduced.

4.1 Algorithm

4.1.1 Step 1:

During model learning, each worker continuously receives parameters x from their neighbors. At the kth iteration, for each node i and its neighbor j, we first calculate the cosine similarity s_{ij}:

$$s_{ij}(k) = \frac{x_j(k) - \theta_i(k)}{\|x_j(k)\| \cdot \|\theta_i(k)\|} \tag{2}$$

which varies between $[-1, 1]$ and θ is its own value. When the two vectors are similar, the remaining chord similarity is closer to 1. Specifically, vector cosine similarity perpendicular to each other is 0, while vector cosine similarity is -1 in the exact opposite direction.

In the following, the function $f(|x_j(k) - \theta_i(k)|)$ is used to calculate the instant reward r_{ij}. Since we utilize an i.i.d. dataset, the parameters of the benign nodes should tend to be similar. Therefore, when the parameters of the two nodes are quite different, a relatively smaller value is expected. At this point, we naturally design the function as inversely proportional. Specifically,

$$r_{ij}(k) = e^{-1000|x_j(k) - \theta_i(k)|} \tag{3}$$

4.1.2 Step 2:

The cosine similarity s_{ij} and the instant reward r_{ij} obtained in step 1 are thresholded, in other words, we set a threshold for each of these two values, and when they are less than this threshold, the node can be judged as a Byzantine node. As the initial training phase involves a significant degree of randomness, we allocate a weight, denoted as ω_{ij}, to Byzantine nodes. This weight diminishes in magnitude in accordance with the number of iterations.

4.1.3 Step 3:

In order to filter the remaining set of nodes denoted as M, it is necessary to compute the historical-based confidence, here referred to as Q, for each node within the set. Q incorporates all the relevant historical information pertaining to the relationship between twp neighbors. Naturally, nodes

that are closer to node i are associated with higher confidence values in Q. Subsequently, different weights are assigned to the neighboring nodes based on their respective Q values. This process not only facilitates the exclusion of neighbors with superior performance, but also expedites system convergence.

4.2 Analysis

4.2.1 Cosine Similarity Setting:

We introduce the concept of cosine similarity into the algorithm. When we talk about the cosine similarity between two vectors, we are actually measuring the similarity of the angles between them. Cosine similarity is a method of quantifying the similarity between two vectors by calculating the cosine value of the angle between them. Many existing attack methods are no longer concerned with changing the size of the parameters, but are more focused on changing the gradient direction of the Byzantine node, since what really matters about the gradient descent algorithm is the direction of the descent. Therefore, such an attack makes the bounded distance between the aggregate value and the real gradient guaranteed by the prior art insufficient to resist the inner product operation attack. Therefore, we use the concept of cosine similarity to distinguish these Byzantine nodes.

4.2.2 Topology Constraints:

Most of the current defense methods use the method of ranking neighbors in each round to select the better nodes, so that they have strict constraints on neighbor nodes and topology. That is, at least one neighbor of node i should be a benign worker.

Suppose there is any benign node and its neighbors are all Byzantine nodes, then these methods can only pick out the Byzantine nodes as candidates. In the case where there exists a benign node surrounded by exclusively malicious neighbors, these methods are capable of solely identifying the malicious nodes as potential candidates. Instead, we use a double filtering mechanism to determine the metrics of neighbor nodes, which greatly relaxes the requirements for topology.

4.2.3 Parameter Selection:

In our algorithm, 3 main parameters are involved, including a, b and ε. Through an extensive series of experiments, it has been ascertained that modifications in the parameter b exert a negligible impact on the system's behavior, leading to the determination that the optimal fixed value for b is 1000. Conversely, adjustments to the hyperparameter a have significant repercussions on the system's convergence properties. Notably, a reduction in the initial value of weight decay coefficient a correlates with an expedited rate of convergence. Yet, it warrants emphasis that the swifter convergence associated with diminutive values of a does not permit immediate identification of nodes with substantial parameter disparities as Byzantine. Consequently, it is not advisable to presume that the weights of such nodes should be nullified, i.e., the value of a should not be set to zero ab initio, in light of the stochastic nature inherent to system initialization and training.

Algorithm 1 Dual Filtering Based Parameter Aggregation Rule (DF-PAR) for a Benign Node i

Initialize $\omega_{ij}(0) = 0, Q_{ij}(0) = 1$, and initialize the model parameters $\theta_i(0)$ randomly;
for $k = 1$ to T **do**
  Exchange parameters with neighboring nodes $j \in N_i$;
  for $j \in N_i$ **do**
    $s_{ij}(k) \leftarrow \frac{x_j(k)-\theta_i(k)}{\|x_j(k)\|\cdot\|\theta_i(k)\|}$;
    $r_{ij}(k) \leftarrow e^{-1000|x_j(k)-\theta_i(k)|}$;
  end for
  if $s_{ij}(k) < 0$ or $r_{ij}(k) < \varepsilon$ **then**
    $\omega_{ij}(k) \leftarrow ae^{-bk}$
  else
    for $p \in M_i$ **do**
      $Q_{ip}(k) \leftarrow \eta(k)(\frac{r_{ip}(k)}{\sum_{l\in N_i} r_{il}(k)} - Q_{ip}(k-1))$
      $+Q_{ip}(k-1)$;
      $\omega_{ip}(k) \leftarrow \frac{Q_{ip}(k)}{\sum_{l\in N_i} Q_{il}(k)}(1 - \frac{1}{|M_i|+1})$.
    end for
    Update the parameters by
    $\theta_i(k) \leftarrow \sum_{j\in N_i} \omega_{ij}(k)x_j(k) + (1 - \sum_{j\in N_i} \omega_{ij}(k))\theta_i(k)$.
  end if
end for

Furthermore, in pursuit of substantiating the validity of the threshold ε, an array of attack modalities constrained to specific ranges was employed to evaluate its appropriateness under these scenarios. Empirical evidence suggests a consistent pattern wherein nodes classified as benign neighbors yield an instantaneous reward exceeding the value of 0.3, whereas the corresponding metric for Byzantine neighbors invariably falls below this threshold. In light of these findings, the threshold has been judiciously established at 0.3, thereby enabling a robust delineation between benign and adversarial nodes within the network.

5 Experiments

In this section, we give the experimental results to verify the effectiveness of the algorithm. Specifically, We employ the extensively utilized MNIST and CIFAR-10 datasets to contrast them with several state-of-the-art defense baselines under a range of prevalent Byzantine attacks. All the experiments are carried out on a server equipped with an Intel Core i9-13900K CPU and an NVIDIA RTX 4080 (16GB) GPU, and all algorithms are realized using PyTorch.

5.1 Experimental Setup

5.1.1 Dataset & Settings

In the experiments, we employ two datasets, namely MNIST and CIFAR-10, to tackle image classification assignments. The MNIST dataset is comprised of handwritten digital images encompassing ten distinct categories, with each image measuring 28x28 pixels. Conversely, the CIFAR-10 dataset encompasses a collection of ten images, each falling into a different category. To be specific, we have trained two fully connected (FC) neural networks on MNIST, and both two fully connected neural networks and two convolutional neural networks (CNNs) on CIFAR-10. Their detailed information are shown in Table 1.

Table 1: The training datasets information

Dataset	Train	Test	Lr	Iter	Batch
MNIST	60k	10k	le-3	50	256
CIFAR-10	50k	10k	le-3	150	256

In the system, each worker is connected to another worker with a certain probability (connection ratio, Cr). Additionally, the workers can be classified into Byzantine workers and benign workers, where each benign worker has a probability (Byzantine ratio, Br) of becoming a Byzantine worker. Throughout this paper, we set the total number of workers as $n = 10$, with two of them being Byzantine nodes. In each experiment, we generate a topology that meets the connectivity criteria, in accordance with the aforementioned description. The deep learning model is trained in synchronous mode, with the step size $\eta(t)$ monotonically diminishing to 0 from an initial value of $\eta(0) = 0.1$.

5.1.2 Comparison Baselines

(i) Average: Each worker takes the average of the received parameters as the parameter values for the next round.
(ii) Median: Each worker calculates the median of each dimension of the received parameters and its own as the parameter value for the next round.
(iii) Bridge [4]: The basic idea is to eliminate the largest and smallest elements of each dimension received by the worker.
(iv) Krum [3],: Each worker sorts the received parameters by distance, and only aggregates the parameter values closest to it at a time.
(v) Zeno [10]: Each worker sorts its neighbors based on performance, i.e., the parameter with the lowest loss value is selected on the test set for aggregation.
(vi) CA-PAR [9]: Each worker is weighted according to the long-term performance of the neighboring nodes, and finally the weight is added linearly.

5.1.3 Byzantine Attacks

We have mitigated four of the prevalent attack methods. Specifically, to impartially assess the performance of each baseline, we conducted a set of training experiments for each baseline without any Byzantine attack.

(i) A little is enough [6]: After each Byzantine node receives the parameters of its neighbors, it perturbates the received mean parameters in each dimension to disturb the system.
(ii) Gaussian [3]: In a Gaussian attack, each Byzantine node sets its own parameters to be sampled from a Gaussian distribution with a standard deviation of 1 that is the mean of all benign nodes.
(iii) Random [14]: Similar to the Gaussian attack, each Byzantine node sends a random vector sampled from $(0, 1)$ to the neighboring workers.
(iv) Converse: In this attack, whenever the attacker obtains the parameters from a neighboring node, they manipulate the average value of all benign node parameters by transforming it into a vector with an opposite sign. This modified vector, scaled to a negative normal (-10 in our experiment), is then transmitted by the attacker.

5.2 Comparison Results

In this subsection, we compare the convergence accuracy of our model with several existing defense models using the above attack methods. We set $a = 0.001.b = 1000, Cr = 0.5, Br = 0.7$ and the threshold is 0.3. After 50 cycles of training in MNIST and 200 cycles in CIFAR-10, the results of each experiment are shown in Fig. 1 and Fig. 2 .

From the results, when the majority of neighboring nodes are Byzantine nodes, especially in the extreme scenarios where a benign node is surrounded by Byzantine nodes, our approach outperforms other baselines in both accuracy and convergence rate. Specifically, since the current distance-based defense methods mostly use the method of score ranking to select candidate nodes, it is strictly stipulated that there must be at least one benign node nearby. When the nodes are surrounded by Byzantine nodes, they will order these Byzantine nodes to select the Byzantine nodes with higher scores as candidates, which leads to a low system accuracy.

5.3 Training Efficiency

In order to evaluate the effectiveness of our algorithm, we adjust the connection rate Cr and Byzantine rate Br to randomly generate network topologies of different complexity, and observe the number of rounds when the system converges to 90% under different topologies. We fix Cr to 0.4 and adjust Br, and fix Br to 0.3 to adjust Cr, and the result is shown in Fig. 3. It can be seen that under the condition of a given connection ratio Cr, more rounds of training are required to achieve convergence as the Byzantine ratio increases, and for a given constant Byzantine ratio Br, the convergence rounds increase when the connection rate decreases.

6 Conclusion and Future Work

In this paper, we propose a novel Dual Filtering based Parameter Aggregation Rule, called DF-PAR, to achieve distributed learning against Byzantine attacks. Unlike the existing defense model, in each iteration, we receive the parameters of all nodes and aggregate them, rather than selecting certain received parameters through pre-defined rules. Specifically, in our algorithm, each node evaluates the quality of the received parameters from the perspective of parameter cosine similarity and distance, so as to gradually eliminate suspicious nodes. Experimental results show that our method can resist most of the Byzantine attacks with low computational and space costs, and can be applied to various network topologies.

References

[1] L. Lamport, R. Shostak and M. Pease, The Byzantine generals problem. *ACM Transactions on Programming Languages and Systems*, 1982, 4(3): 382–401.
[2] Y. Chen, L. Su and J. Xu, Distributed statistical machine learning in adversarial settings: Byzantine gradient descent. *ACM SIGMETRICS Performance Evaluation Review*, 2018, 46(1): 96–96.
[3] P. Blanchard, R. Guerraoui, J. Stainer and et al., Machine learning with adversaries: Byzantine tolerant gradient descent. *Ad-*

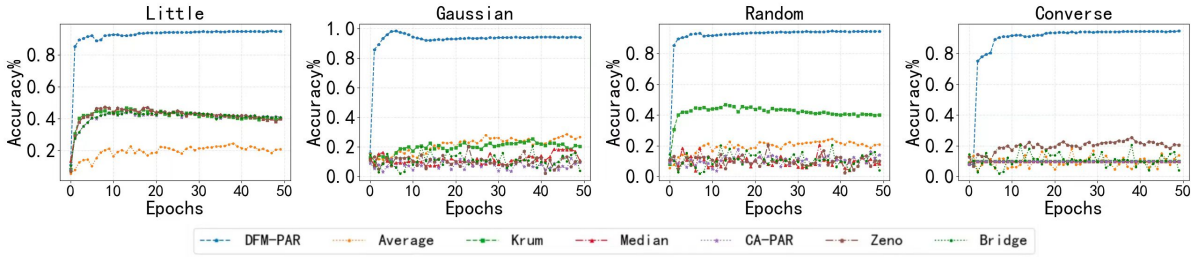

Fig. 1: Model accuracy curve of different defense methods under various attacks on the MNIST datasets.

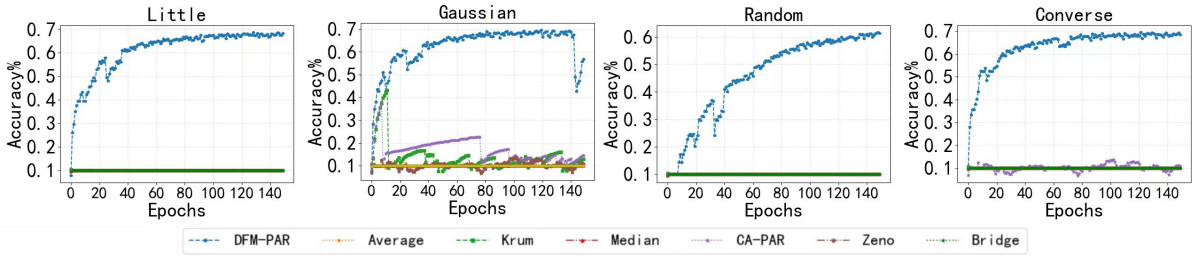

Fig. 2: Model accuracy curve of different defense methods under various attacks on the CIFAR-10 datasets.

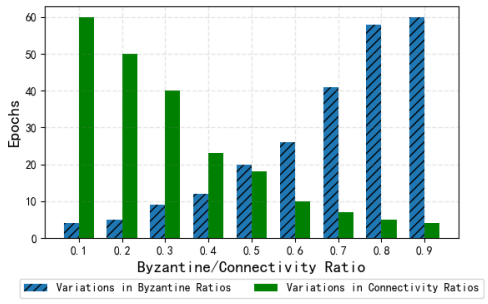

Fig. 3: System convergence speed under different Br and Cr.

vances in Neural Information Processing Systems, 2017, 30: 119–129.

[4] C. Fang, Z. Yang and W. U. Bajwa, BRIDGE: Byzantine-resilient decentralized gradient descent. *arXiv preprint arXiv:1908.08098*, 2019: 1–20.

[5] R. Guerraoui and S. Rouault, The hidden vulnerability of distributed learning in byzantium, in *Proceedings of International Conference on Machine Learning*, 2018: 3521–3530.

[6] M. Baruch, G. Baruch and Y. Goldberg, A little is enough: Circumventing defenses for distributed learning. *Advances in Neural Information Processing Systems*, 2019, 32: 1–11.

[7] C. Xie, O. Koyejo and I. Gupta, Fall of empires: Breaking Byzantine-tolerant SGD by inner product manipulation, in *Proceedings of Uncertainty in Artificial Intelligence*, 2020: 261–270.

[8] E. M. El-Mhamdi, R. Guerraoui, A. Guirguis and S. Rouault, Sgd: Decentralized byzantine resilience. *arXiv preprint arXiv:1905.03853*, 2019: 1–12.

[9] J. Hou, F. Wang, C. Wei and et al., Credibility assessment based Byzantine-resilient decentralized learning. *IEEE Transactions on Dependable and Secure Computing*, 2022: 1–12.

[10] C. Xie, S. Koyejo and I. Gupta, Zeno: Distributed stochastic gradient descent with suspicion-based fault-tolerance, in *Proceedings of International Conference on Machine Learning*, 2019: 6893–6901.

[11] X. Pan, M. Zhang, D. Wu and et al., Justinian's GAAvernor: robust distributed learning with gradient aggregation agent, in *Proceedings of the 29th USENIX Security Symposium*, 2020: 1641–1658.

[12] S. Guo, T. Zhang, H. Yu and et al., Byzantine-resilient decentralized stochastic gradient descent. *IEEE Transactions on Circuits and Systems for Video Technology*, 2021, 32(6): 4096–4106.

[13] B. Zhu, J. Jiao and M. I. Jordan, Robust estimation for non-parametric families via generative adversarial networks, in *Proceedings of 2022 IEEE International Symposium on Information Theory*, 2022: 1100–1105.

[14] Y. Yang and W. Li, Basgd: Buffered asynchronous sgd for byzantine learning, in *Proceedings of International Conference on Machine Learning*, 2021: 11751–11761.

Proceedings of the 3rd Conference on Fully Actuated System Theory and Applications
May 10-12, 2024, Shenzhen, China

Relative-Based Finite-Time Formation Stabilization for Multi-Agent Systems via Asynchronous Event-Triggered Approach

Fan Luan[1], Yanjun Lin[2]

1. Wuhan Institute of Shipbuilding Technology, Wuhan 430050, P. R. China
E-mail: luanfan_whist@163.com

2. Hangzhou Applied Acoustics Research Institute, Hangzhou 310027, P. R. China
E-mail: linyanjun_elaine@163.com

Abstract: This paper discuss the finite-time formation problem for multi-agent systems via Asynchronous Event-triggered approach. Firstly, a distributed translational formation control stratagy for finite-time convergence in any Euclidean space is developed. It introduces the sliding mode control to steer all agents into an affine image and achieves translational formations by adding few extra steering laws. On the other hand, a crucial challenge in most practical scenarios is the high interaction pressure of state information between agents. A distributed and discontinuous event-triggered control technique is adopted to reduce the communication frequency and the calculation resources, which is more suitable for the practicablity and discreteness. Zeno-free behavior is turned out. Finally, one numerical example proves the effectiveness of the proposed method.

Key Words: Finite-time Stabilization, Formation Control, Affine Image, Event-triggered Approach

1 Introduction

Formation control in multi-agent systems is a crucial aspect of cooperative control strategies, which are extensively employed for carrying out specialized tasks[1]. These can range from military engagement tactics and object tracking to the collection of data in oceanic or aerial environments. A fundamental challenge lies in devising distributed control algorithms capable of steering an ensemble of n agents towards and maintaining a predetermined geometrical arrangement[2].

Recent years have seen a wealth of achievements in the realm of controller design and convergence analysis for affine formations. Most of these advances have leveraged tools such as stress matrices or signed Laplacian matrices[3–5]. The significance of affine formations lies in their possession of multiple degrees of freedom (including shear, scaling, rotation, and translation) facilitating specialized formations with greater ease. Building upon affine transformation, a unified flexible formation control approach was proposed in our previous work[6]. It discovered an implementable set of feasible and innovative distributed formation control laws for finite-time (almost) global stabilization of affine, rigid and translational formations.

In practical applications, particularly within underwater environments, the challenges of communication and energy among agents are paramount. The multi-agent system faces constraints such as limited bandwidth in communication devices, low data transmission rates, and pressing demands for energy conservation. To mitigate communication costs, aperiodic sampling methods for multi-agent systems have emerged as promising solutions[7], with event-triggered communication being especially noteworthy[8–10].

Dimarogonas et al. pioneered the integration of event-triggered mechanisms into consensus and formation control protocols for multi-agent systems. They analyzed the requisite distributed knowledge that must be shared between agents and their neighbors to implement the controller effectively[11]. A directed graph-based, distributed and periodic event-triggered consensus controller was subsequently devised in [12]. In many scenarios, the acquisition of relative positional states is inherently discontinuous, rendering discontinuous event-triggered protocols[13] more fitting than conventional continuous triggers[14]. Moreover, robust event-triggered control methodologies, such as those employing sliding mode controls[15], have been explored. The majority of finite-time event-triggered control schemes focus primarily on the consensus and formation control of continuous systems[16], not suitable for discontinuous systems like the multi-UUV systems.

This paper endeavors to devise a finite-time formation control strategy for multi-agent systems, enabling them to achieve translational formations under conditions of intermittent communication and controller updates. A distributed event-triggered mechanism tailored for translational formations grounded in affine transformation is employed, ensuring that events triggering communication and controller updates occur only when necessary. The application of sliding mode control serves to draw the system trajectory towards the sliding manifolds (the affine image) while robustly maintaining it within specified bounds. Capitalizing on the properties of affine transformations, we contemplate supplementing the affine formation control strategy with additional steering laws for at least $d + 1$ leaders, thereby reducing the degrees of freedom. Consequently, the surface manifolds can be reached from the affine image to its subsets, translational ones, in order to materialize the desired formations.

The contributions of this paper are twofold. Firstly, a distributed and discontinuous event-triggered mechanism featuring asynchronous sampling has been developed specifically for the control of translational formations. This mechanism significantly alleviates the requirement load on sensing, communication, and computation during the generation of control signals. Secondly, based on our previous research[17], this article articulates framework conditions in

d-dimensional space for finite-time stable convergence protocols for translational formations under an event-triggered mechanism. These conditions are designed to prevent Zeno triggering phenomena. A practical control strategy is also devised and its efficacy is confirmed.

The structure of this article is as follows. Section II provides some fundamental theoretical knowledge and articulates the problem of interest. Section III presents the framework conditions for finite-time stable convergence using an event-triggered mechanism for translational formation control, and demonstrates their Zeno-free behavior. Section IV details a specific control strategy to substantiate the correctness of the framework conditions. Section V validates the effectiveness of our proposed approach. Concluding remarks are discussed in the final section.

Notation: This paper use standard notations. The symbol $\mathbb{R}$ represents the set of real numbers, and $\mathbb{R}^d$ denotes d-dimensional ambient Euclidean space. The notation $\mathbf{1}_n$ stands for the n-dimensional vector of all ones, and I_d denotes the $d \times d$ identity matrix.

2 Preliminaries and problem formulation

In this section, we present the necessary preliminaries and articulate the problem of formation stabilization control.

2.1 Preliminaries

An *undirected graph* $\mathcal{G} = (\mathcal{V}, \mathcal{E})$ consists of a node set $\mathcal{V}$ and an edge set $\mathcal{E}$, where an edge is an unordered pair of distinct nodes of $\mathcal{G}$.

A *configuration* of n points in $\mathbb{R}^d$ is defined by their coordinates in the Euclidean space $\mathbb{R}^d$, denoted as $p = [p_1^\intercal, \ldots, p_n^\intercal]^\intercal$, where each $p_i \in \mathbb{R}^d$ denotes agent i's position for $i \in 1, 2, \cdots n$. A configuration is *generic* if all the coordinates $p_1, \cdots, p_n$ are algebraically independent over the integers [**?**].

Consider a configuration $p = [p_1^\intercal, \ldots, p_n^\intercal]^\intercal$ in $\mathbb{R}^d$. We denote the *affine image* of p as

$$\mathcal{A}(p) = \left\{ \begin{array}{l} q = [q_1^\intercal, \ldots, q_n^\intercal]^\intercal : q_i = Ap_i + a, \\ A \in \mathbb{R}^{d\times d},\ a \in \mathbb{R}^d,\ i = 1, \ldots, n \end{array} \right\} \quad (1)$$

or equivalently,

$$\mathcal{A}(p) = \left\{ q = (I_n \otimes A)p + \mathbf{1}_n \otimes a :\ A \in \mathbb{R}^{d\times d},\ a \in \mathbb{R}^d \right\}. \quad (2)$$

Remark 1 *Note that any matrix $A \in \mathbb{R}^{m\times n}$ can be factorized by singular value decomposition (SVD) as $A = U\Sigma V$ where U and V are orthogonal matrices, and Σ is a diagonal matrix. This indicates that any configuration in $\mathcal{A}(p)$ can be obtained by an affine motion from p, namely, a rotation V, a scaling along different axes by Σ, and then another rotation U, followed by a translation a.*

If $A = I$ is an identity matrix, we can get the *translation image* of p as

$$\mathcal{T}(p) := \left\{ \begin{array}{l} q = [q_1^\intercal, \ldots, q_n^\intercal]^\intercal : q_i = Ip_i + a, \\ I \in \mathbb{R}^{d\times d} \text{ is an identity matrix}, \\ a \in \mathbb{R}^d,\ i = 1, \ldots, n \end{array} \right\}, \quad (3)$$

and $z \in \mathcal{T}(p)$ implies that all agents form a configuration which is congruent to the desired configuration and has the same orientation[6]. The set $\mathcal{T}(p)$ is a subset of $\mathcal{A}(p)$. For the translaitonal image, it has the following lemma satisfied.

Lemma 1 ([3] [4]) *Suppose that $p = [p_1^\intercal, \cdots, p_n^\intercal]^\intercal$ is a generic configuration in $\mathbb{R}^d$. A configuration $q \in \mathcal{A}(p)$ is a translation of p (i. e., $q \in \mathcal{T}(p)$) if and only if there exist at least d pairs of agents such that the dimension of the affine span of d pairs of agents is d and*

$$q_k - q_j = p_k - p_j.$$

Consider an undirected graph and a configuration q in $\mathbb{R}^d$ of n points.A symmetric matrix $H \in \mathbb{R}^{n\times n}$ is denoted as a signed Laplacian matrix which satisfies $H\mathbf{1}_n = 0$. Its entry w_{ij} is a scalar weight of edge (i, j) and is a real number. H is called a *stress matrix* if it also satisfies $(H \otimes I_d)q = 0$.$\lambda_{\min}^{+}(H)$ denotes the smallest positive eigenvalue of H.

Consider a differential equation

$$\dot{x}(t) = X(x(t)), \quad (4)$$

where $X : \mathbb{R}^d \to \mathbb{R}^d$ is measurable and essentially locally bounded. Define the *Filippov set-valued map* $\mathcal{F}[X] : \mathbb{R}^d \to \mathcal{D}(\mathbb{R}^d)$ by

2.2 Problem formulation

We model the information flow structure using an undirected graph $\mathcal{G} = (\mathcal{V}, \mathcal{E})$, where $\mathcal{V}$ is a set of n nodes and $\mathcal{E}$ is an l-edge set. For each agent $i \in \mathcal{V}$, the set of its neighbors is denoted by $\mathcal{N}_i = \{j \in \mathcal{V} : (j, i) \in \mathcal{E}\}$. The quantity $|\mathcal{N}_i|$ denotes the number of neighbors of agent i. We consider a system with single-integrator dynamics as follow:

$$\dot{q}_i = u_i, \quad i = 1, \ldots, n, \quad (5)$$

where $u_i \in \mathbb{R}^d$ is the control input of agent i. $q = [q_1^\intercal, \ldots, q_n^\intercal]^\intercal$ denotes the state set of n agents.

The objective of this paper is to to engineer the control input u_i such that all agents converge to a desired translational formation within a finite time with reduced discontinuous and aperiodic interaction of states. We consider to establish a set of framework conditions for designing formation control proctols to steer agents from an affine image $\mathcal{A}(p)$ to a translational image $\mathcal{T}(p)$ via sliding mode control techniques. These conditions can provide insights into how a translational formation can be achieved by integrating an external relative-based interaction controller into a subset of the agents. Then we will implement an event-triggered mechanism to decrease the frequency of state exchanges between neighboring agents.

To streamline the analysis, the following assumption is enumerated.

Assumption 1 *The configuration p is generic. There exists n nodes ($n > d + 1$ in d-dimensional space) in $\mathcal{V}$.*

3 Conditions of Finite-time Stabilization of Translational Formations

We select at least one set of $d + 1$ nodes as leaders. Without loss of generality, we label them as $1, \ldots, d + 1$ and denote $\mathcal{V}_l = \{1, \ldots, d + 1\}$ and $\mathcal{V}_f = \{d + 2, \ldots, n\}$ as the leader set and the follower set respectively. Denote $p_l = [p_1^\intercal, \cdots, p_{d+1}^\intercal]^\intercal$ and $q_l = [q_1^\intercal, \cdots, q_{d+1}^\intercal]^\intercal$.

We design a control input as

$$u_i(t)=\begin{cases}-c\text{sgn}(\sum_{j\in\mathcal{N}_i} w_{ij}\left(q_i(t)-q_j(t)\right))+f_i(q_i), & i\in\mathcal{V}_l\\ -c\text{sgn}(\sum_{j\in\mathcal{N}_i} w_{ij}\left(q_i(t)-q_j(t)\right)), & i\in\mathcal{V}_f\end{cases} \tag{6}$$

where $c>0$ and w_{ij} is a signed real weight. $f_l(q_l)=[f_1^\intercal(q_l),\ldots,f_{d+1}^\intercal(q_l)]^\intercal$ is called the *steering law*.The signum function $\text{sgn}(s)$ of a d-dimensional vector $s=[s^1,\cdots,s^d]^\intercal$ is defined by $\text{sgn}(s)=[\text{sgn}(s^1),\ldots,\text{sgn}(s^d)]^\intercal$ where s is the sliding mode manifold and $\text{sgn}(s^r)$ for $r=1,\cdots,d$ is a piecewise sign function. The compact form of (6) is

$$\dot{q}=-c\text{sgn}((H\otimes I_d)q)+f(q_l), \tag{7}$$

where $f(q_l)=[f_l(q_l)^\intercal,\mathbf{0}_{(n-d-1)d}^\intercal]^\intercal$. We select the sliding mode manifold $s=(H\otimes I_d)q$.

Denote a status measurement error $e=[e_1(t),\cdots,e_n(t)]^T$ and $e_i(t)$ is defined as

$$e_i(t)=q_i\left(\tau_s^i\right)-q_i(t)=\hat{q}_i(t)-q_i(t),\quad t\in\left[\tau_s^i,\tau_{s+1}^i\right) \tag{8}$$

where τ_s^i is the event trigger instant of agent i and $s=\{0,1,\cdots\}$. It is designed by the following form

$$\|e_i\|\le\frac{\delta_i\eta}{2c-\eta}\|\hat{q}_i\| \tag{9}$$

with $\delta_i\in(0,1)$ and $\eta\in(0,c]$. It has

$$\|e\|\le\mathcal{B}\|\hat{q}\| \tag{10}$$

where $\mathcal{B}=\delta_{\max}\eta/(2c-\eta)$ and $\delta_{\max}=\max\delta_i\in(0,1)$ for $i\in\{1,\cdots,n\}$. Let us introduce DDETM into the controllor (7) as follow

$$u_i(t)=\begin{cases}-c\text{sgn}(\sum_{j\in\mathcal{N}_i^l} w_{ij}\left(q_i(t)-q_j(t)\right))\\ +f_i(q_i(\tau_s^i)), & i\in\mathcal{V}_l\\ -c\text{sgn}(\sum_{j\in\mathcal{N}_{if}} w_{ij}\left(q_i(t)-q_j(t)\right)), & i\in\mathcal{V}_f\end{cases} \tag{11}$$

The compact form of the closed-loop system is given by

$$\dot{q}(t)=-c\text{sgn}((H\otimes I_d)\hat{q})+f(\hat{q}_l) \tag{12}$$

where $\hat{q}=[\hat{q}_1^T,\cdots,\hat{q}_n^T]^T$ and $\hat{q}_i(t)=q_i(t)+e_i(t)$.

Now we introduce the following indispensable assumptions and lemmas to derive the main results.

Assumption 2 *The symmetric matrix H is a stress matrix with rank $n-d-1$ and is positive semi-definite.*

Lemma 2 *[17] Consider the discontinuous event-triggered function*

$$g(e_i)=\|e_i\|-\frac{\delta_i\eta}{2c-\eta}\|\hat{q}_i\| \tag{13}$$

with $\delta_i\in(0,1)$. The formation system (12) with τ_h^i, $h=0,1,2,\cdots$, being the event-triggering time instants of agent i, finite-time converges to the afiine image $\mathcal{A}(p)$, and the upper bound of finite convergence time is $T=\frac{(1+\mathcal{B})\sqrt{q^\intercal(0)(H\otimes I_d)q(0)}}{(1-\mathcal{B})\sqrt{\lambda_{min}^+(H)}}$, if the following conditions holds:

(i) The steering law $\|f_i(\hat{q}_l)\|_\infty\le c-\eta$, where η is a positive number satisfying $\eta\le c$.

(ii) The status measurments error of agent i has $\|e_i\|\le\frac{\delta_i\eta}{2c-\eta}\|\hat{q}_i\|$.

(iii) The event-triggered condition $g(e_i)\ge 0$.

Then we give the main results that the proposed control law drives all agents to the desired formation in finite time in any dimensional space. We discuss the stablization conditions on the translational image $\mathcal{T}(p)$.

Theorem 1 *The translational image $\mathcal{T}(p)$ is asymptotically stable for system (12) with the discontinuous and distributed event-triggered function (13) if $f_l(\hat{q}_l)$ satisfies the following conditions:*

(i) $\|f_i(\hat{q}_l)\|_\infty\le c-\eta$, where $\eta\le c$ is a positive number.

(ii) $f_i(\hat{q}_l)=0$ when $q_l\in\mathcal{T}(p_l)$ for $i=1,2,\cdots,d+1$.

(iii) $\mathcal{T}(p_l)$ is globally asymptotically stable for $\dot{q}_l=f_l(\hat{q}_l)$.

Proof. According to Lemma 2, all agents can move on the sliding surface $s=0$ in finite time with the event-triggered function (13) and Condition (i). Then the dynamics of (12) are reduced to $\dot{q}_l=f_l(\hat{q}_l)$. In $s=0$, it has the representation $q=[q_l^\intercal,q_f^\intercal]^\intercal=G(q_l)$ where $G(q_l)$ can be an unknown function of q_l. It follows that $q\to G(\mathcal{R}(p_l))$ when $\mathcal{T}(p_l)$ is globally asymptotically stable for the dynamics $\dot{q}_l=f_l(\hat{q}_l)$ because of the continuity of G. From Lemma 1, we know that $G(\mathcal{T}(p_l))=\mathcal{T}(p)$. Thus, $q(t)\to\mathcal{T}(p)$. By Condition (ii), there exists $q^*\in\mathcal{T}(p)$ such that $q(t)\to q^*$. Then the conclusion follows and the proof is complete.

Moreover, if additionally $\mathcal{T}(p_l)$ is globally finite-time stable for the dynamics $\dot{q}_l=f_l(\hat{q}_l)$ and the convergence time is upper bounded by T_l, then global finite-time stability can be drawn. ■

Noting that the Zeno behavior of the system of (12) must be discussed. Lemma 2 has been demonstrated that all agents can be steered to the affine image $\mathcal{A}(p_l)$ with the positive lower bound of the triggering time interval. It is obviously that all agents converge to the subset $\mathcal{T}(p_l)$ with the same lower bound of the triggering time interval when the three condition in Theorem 1. The Zeno behavior can be avoided.

4 Design of A Steering Law for Translational Formations

Section 3 has proposed a unified approach of designing control laws for translational formations. In this section we design a specific steering law $f_i(\hat{q}_l)$ in (12) to meet the conditions in Theorem 1. We consider the following consensus-based control strategy for $f_i(q_l)$

$$f_i(q_l)=\dot{q}_l=-c_l\text{sgn}\left(\sum_{j\in\mathcal{N}_i^l}\left((q_{l_i}-q_{l_j})-(p_{l_i}-p_{l_j})\right)\right), \tag{14}$$

where $c_l\le c-\eta$ is a positive constant. For $q_l\in\mathcal{A}(p_l)$, it holds that $q_{l_i}=Ap_{l_i}+a$ for all i with $A\in\mathbb{R}^{d\times d}$ and $a\in\mathbb{R}^d$. If additionally there are d pairs of leader agents satisfying

$$q_{l_i}-q_{l_j}=p_{l_i}-p_{l_j}, \tag{15}$$

then the following equation holds for the d pairs of leader agents

$$p_{l_i}-p_{l_j}=q_{l_i}-q_{l_j}=A(p_{l_i}-p_{l_j}), \tag{16}$$

and therefore

$$(I-A)(p_{l_i}-p_{l_j})=0. \tag{17}$$

It is known that if the linear span of the d pairs of the relative position vectors $p_{l_i} - p_{l_j}$ equals to $\mathbb{R}^d$, then $A = I$ holds from (17). As a result, for any i and j in the set of leader agents, a configuration $q_l \in \mathcal{A}(p_l)$ reduces to that of $q_l \in \mathcal{T}(p_l)$ if and only if there exist d pairs of agents such that the dimension of the affine span of $q_{l_1}, \cdots, q_{l_{(d+1)}}$ is d and (15) holds. The compact form of (14) is given by

$$f(q_l) = \dot{q}_l = -c_l \text{sgn}((L_l \otimes I_d)\tilde{q}_l), \tag{18}$$

where L_l is the normal Laplacian matrix of the leader subgraph $\mathcal{G}_l$ and $\tilde{q}_l = [\tilde{q}_{l1}^\intercal, \cdots, \tilde{q}_{l(d+1)}^\intercal]^\intercal$ with $\tilde{q}_{l_i} = q_{l_i} - p_{l_i}$. The sliding surface for this system is evidently $\tilde{s} = (L_l \otimes I_d)\tilde{q}_l$. Let us introduce DDETM into the controllor (18) . It has

$$f(\hat{q}_l) = \dot{q}_l = -c_l \text{sgn}((L_l \otimes I_d)\hat{\tilde{q}}_l). \tag{19}$$

A lemma characterizing finite-time convergence of the dynamics (19) is given as below.

Lemma 3 *For system* (19)*, if $\mathcal{G}_l$ is connected, the agents converge to a translational formation of p_l globally within a finite time and the convergence time is upper bounded by a positive constant T_l.*

The proof is similar as the Lemma 2 and is omitted here. The main results will be presented as follow.

Theorem 2 *Consider the formation control system* (12) *with the steering law $f_l(\hat{q}_l)$ given in* (19)*. Suppose the subgraph $\mathcal{G}_l$ with $d+1$ agents is connected. If the parameter c_l satisfies $c_l < c - \eta$ and it has the discontinuous event-triggered function* (13) *with $\delta_i \in (0, 1)$, then a desired translational formation q can be steered into the translational image $\mathcal{T}(p)$ finite-time stablly and the convergence time is upper bounded by* $T = T_l + \frac{\sqrt{q^\intercal(0)(H\otimes I_d)q(0)}}{\eta\sqrt{\lambda^+_{min}(H)}}$.

Proof. For the formation control system (12) and the steering law $f_l(z_l)$ described by (19), the upper bound of the magnitude of the steering law for agent i is given by

$$\begin{aligned} ||f_i(q_l)||_\infty &= c_l \left\| \sum_{j\in\mathcal{N}_i} ((q_{l_i} - q_{l_j}) - (p_{l_i} - p_{l_j})) \right\|_\infty \\ &\le c_l \le c - \eta, \end{aligned} \tag{20}$$

which satisfies Condition (i) in Theorem 1. Then according to Lemma 3, it can be obtained that under the steering law $f_l(q_l)$ (19) with c_l satisfying Condition (ii) and (iii). Therefore, the conclusion is drawn. ■

Remark 2 *For translational formation control under the relative-position-based steering law $f_l(q_l)$ in* (14)*, only the leader agents require to know a common orientation of their coordinate frames. All other agents can use their local coordinate frames to measure the relative positions and implement their control laws.*

5 Simulation Results

In this subsection we present a simulation example in $\mathbb{R}^3$ for achieving a translational formation with the event-triggered mechanism. Consider a multi-agent formation system, whose interactions are modelled by an undirected graph

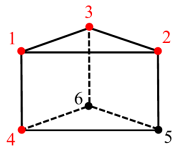

Fig. 1: The target configuration p for the simulation in $\mathbb{R}^3$, in which the lines are not edges of the interaction graph, but are used to outline the configuration.

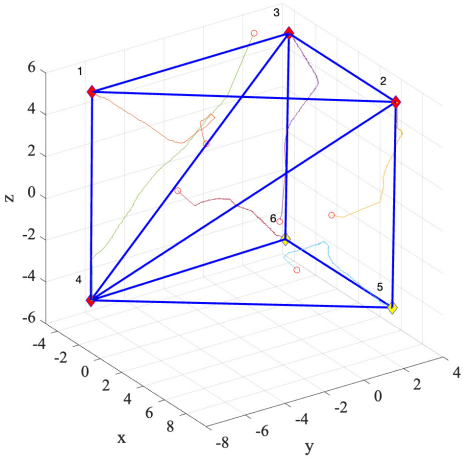

Fig. 2: The evolutionary trajectories in achieving a translational formation in $\mathbb{R}^3$.

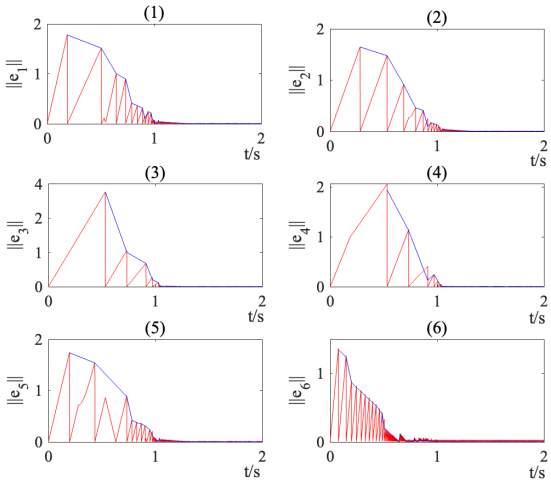

Fig. 3: Distributed event-triggered based performance of three leaders.

with a total of 12 edges and 6 nodes. We use the target configuration as in Fig. 1. Let us denote the four red dots as the leader agents and the rest black ones as the follower agents. The desired relative positions for three pairs of leaders in the steady state are given as follows: $q_1 - q_2 = [-10, -10, 0]^\intercal$, $q_1 - q_3 = [0, -10, 0]^\intercal$ and $q_1 - q_4 = [0, 0, 10]^\intercal$. We then apply the distributed control algorithm (12) together with the steering law (14). Here we select the parameters as $c = 1$, $\eta = 0.05$, $c_l = 0.9$ and $\delta_i = 0.6$ for all agents. And the stress matrix H is designed with $\text{rank}(H) = 3$ and $\lambda^+_{\text{min}}(H) = 1.673$. It is shown in Fig. 2 that all the agents

converge in a finite time to a desired formation shape of the target configuration. The event triggered errors of each agent based on the distributed event-triggered mechanism are given in Fig. 3. The effectiveness of our approach is demonstrated.

6 Conclusions

This paper proposes the feasibility conditions for designing translational formation control strategies with an event-triggered mechanism that achieve convergence to translational image $\mathcal{T}(p)$ from an affine image in d-dimensional space within finite time. By crafting an event-triggered function and adhering to the unified constraints of the steering law, finite-time stabilization and event-based asynchronous communication are realized. Ongoing research will focus on expanding the model to include more intricate dynamics, such as those of double integrator systems.

References

[1] Z. Yan, Z. Yang, L. Yue, L. Wang, H. Jia, J. Zhou,"Discrete-time coordinated control of leader-following multiple AUVs under switching topologies and communication delays," *Ocean Eng.*, vol.172, pp. 361-372, 2019.

[2] K. K. Oh, M. C. Park, H. S. Ahn, "A survey of multi-agent formation control," *Automatica*, vol.53, pp. 424-440, 2015.

[3] Z. Lin, L. Wang, Z. Chen, M. Fu, Z. Han, "Necessary and sufficient graphical conditions for affine formation control," *IEEE Trans. Automat. Control*, vol.61, no. 10, pp.2877-2891, 2016.

[4] S. Zhao, "Affine formation maneuver control of multiagent systems," *IEEE Trans. Automat. Control*, vol.63, no. 12, pp.4140-415, 2018.

[5] Q. Yang, Z. Sun, M. Cao, H. Fang, J. Chen, "Stress-matrix-based formation scaling control," *Automatica* , vol.101, pp.120-127, 2019.

[6] Y. Lin, Z. Lin, Z. Sun, B. D. O. Anderson,"A Unified Approach for Finite-Time Global Stabilization of Affine, Rigid and Translational Formation," *IEEE Trans. Autom. Control*, vol.67, no. 4, pp.1869-1881, 2021.

[7] X. Ge, Q. Han and X. Zhang,"Achieving cluster formation of multi-agent systems under aperiodic sampling and communication delays," *IEEE Trans. Ind. Electron.*, vol.65, no. 4, pp. 3417-3426, 2017.

[8] M. Yu, C. Yan, D. Xie, G. Xie, "Event-triggered tracking consensus with packet losses and time-varying delays," *IEEE/CAA J. Autom. Sinica*, vol. 3, no. 2, pp. 165–173, 2016.

[9] A. Amini, A. Asif, A. Mohammadi, "Formation-containment control using dynamic event-triggering mechanism for multi-agent systems," *IEEE/CAA J. Autom. Sinica*, vol. 7, no. 5, pp. 1235-1248, 2020.

[10] L. Ding , Q. Han, X. Ge, X. Zhang," An overview of recent advances in event-triggered consensus of multiagent systems,"*IEEE Trans. Cybern.* , vol. 48, no. 4, pp. 1110-1123, 2017.

[11] D. V. Dimarogonas, E. Frazzoli, K. H. Johansson,"Distributed event-triggered control for multi-agent systems,"*IEEE Trans. Autom. Control*, vol. 57, no. 5, pp. 1297-1297, 2011.

[12] G. Guo, L. Ding, Q. Han," A distributed event-triggered transmission strategy for sampled-data consensus of multi-agent systems,"*Automatica*, vol. 50, pp. 1489-1496, 2014.

[13] Y. Lin, Z. Lin, Z. Sun,"Distributed event-triggered approach for multi-agent formation based on cooperative localization with mixed measurements,"*Electron.*, vol. 339 is , pp. 132-142, 2016.

[14] J.Yang, H. Yu, T. Chen, "Affine Formation Maneuver Control of Event-triggered Multi-agent Systems,"*IFAC Papers On-Line*, vol. 53, no.2, pp. 3391-3396, 2020.

[15] H. Zhang, D. Yue, X.Yin, S. Hu, C. Dou,"Finite-time distributed event-triggered consensus control for multi-agent systems,"*Inf. Sci.*, vol. 10, no. 18, pp. 2265, 2021.

[16] B. Su, H. Wang, Y. Wang,"Dynamic event-triggered formation control for AUVs with fixed-time integral sliding mode disturbance observer," *Ocean Eng.*, vol.240, 109893, 2021.

[17] Y. Lin, Y. Yang, L. Chai, Z. Lin,"Distributed finite-time event-triggered formation control based on a unified framework of affine image," *IEEE/CAA J. Autom. Sinica*, vol. 11, no. 1, pp. 1-3, 2024. *DOI: 10.1109/JAS.2023.123885.*

Proceedings of the 3rd Conference on Fully Actuated System Theory and Applications
May 10-12, 2024, Shenzhen, China

Research on Reliability Control for Nonlinear Multi-Agent Systems with Time Delays

Yang Xing[1], YiMin Liu[1]

1. Academy of Information Science and Engineering, Wuhan University of Science and Technology, Wuhan; 430081, P. R. China
E-mail: 517205585@qq.com

Abstract: This paper addresses the robust consensus reliable control problem with time delays, actuator defects, and external disturbances for Lipschitz nonlinear multi-agent systems (MASs) is discussed. First, a general fault model is established, and an observer is designed to estimate the state information. Second, the reliable control protocol is obtained by using this estimation information to achieve robust and reliable control. Using this protocol, the actuator faults is resolved and the influence of time delays and disturbance on nonlinear system is reduced. Third, using linear matrix inequality, adequate robustness conditions are suggested for the control protocol and observer design. Finally, two distinct actuator fault cases are used to confirm the validity of the control protocol.

Key Words: Nonlinear MASs, Time delays, Actuator faults, Reliable control

1 Introduction

Because of its practical application in numerous fields during the last few years, such as unmanned aerial vehicles and mobile robotics, collaborative management of MASs has drawn a lot of attention [1–5].

Actuator failures are unavoidable when utilizing MASs, as is widely recognized. Once actuator fault occurs, it may have a significant impact on the entire task executed by the system, potentially leading to its failure. In the past decade, some theoretical studies and applications have proposed distributed reliable control methods [6, 7]. In [8], actuator faults were described as a Markov process, and reliable control was applied to stochastic nonlinear systems with an affine structure based on the Takagi-Sugeno fuzzy structure. In [9], a polytopic model was used to analyze actuator faults in linear systems with parameter variations, and a consistent reliability control protocol was designed to ensure the system operates stably. While the studies mentioned above accounted for the existence of actuator faults within the framework, they did not address time delays or external disturbances to the system itself, both of which are typical in situations found in real life. In [10], considering the impact of faults, multiple delays, and parameter mismatch uncertainties in MASs, an adaptive updating protocol gain adjustment based on neighboring agent state information was introduced to eliminate disturbances and ensure the normal operation of the system. [11] investigated simultaneous actuator failures and disturbances from outside in MASs, compensating with a control protocol to guarantee connectivity among multi-agent networks and avoid collisions. Furthermore, [12] considered nonlinearity, various types of actuator faults, and external disturbances within subsystems, proposing a distributed adaptive reliable actuator fault compensation protocol. The methods discussed in [8, 9] can deal with actuator faults in linear or nonlinear systems, but cannot support situations where time delays or external disturbance. On the other hand, the approaches presented in [10–12] can solve scenarios with time delays or external disturbances but lack compatibility with nonlinear systems. Therefore, designing reliable control protocol to compensate for actuator faults when there are state time delays and external disturbances in nonlinear systems is a significant subject that inspires our work.

This paper's main goal is to create a novel observer-based dependable controller that can handle interference, time-varying state delays, actuator failures, and faults in the quality control protocol. Firstly, unlike other actuator fault models, this paper integrates actuator faults into the control problem by consensus. The control protocol can then be designed to account for the probable actuator defects. Second, this study proposes a novel distributed observer that makes use of the shared sensor communication network to calculate each agent's status information. In Section 2, observer-based state feedback controllers are devised to stabilize closed-loop systems while minimizing the effects of system failures. In Section 3, the primary discoveries of the fault-tolerant controller utilizing state feedback are investigated through Lyapunov-Krasovskii function. Examples are provided in Section 4 to demonstrate the suggested program's efficacy. At last, section 5 presents the conclusions.

2 Description of Systems and Preliminary Concepts

Using $\mathcal{G}(\mathcal{V}, \varepsilon, \mathcal{A})$ build an undirected graph with the given vertices $\mathcal{V} = \{v_1, v_2, ..., v_N\}$, the collection of margins $\varepsilon = \{(v_i, v_j) : v_i, v_j \in \mathcal{V}\} \subseteq \mathcal{V} \times \mathcal{V}$, and $\mathcal{A} = [a_{ij}] \in \mathbb{R}^{N\times N}$ is a matrix of measured adjacency. Each proximity matrix entry fulfills $a_{ii} = 0$, $a_{ij} > 0$, if and only if $(v_i, v_j) \in \varepsilon$. In the undirected graph, $a_{ij} = a_{ji}$ and $\mathcal{A}$ possesses symmetry. The matrix Laplacian connected to the graph $\mathcal{G}$ is described as follows $\mathcal{L} = [l_{ij}] \in \mathbb{R}^{N\times N}$, where $l_{ii} = \Sigma_{j\neq i} a_{ij}$ and $l_{ij} = -a_{ij}, i \neq j$.

Take into consideration the subsequent Time-delayed Lipschitz nonlinear MASs:

$$\begin{aligned} \dot{x}_i(t) &= Ax_i(\mathrm{t}) + A_d x_i(t - h(\mathrm{t})) + Bu_i(\mathrm{t}) \\ &\quad + D_1 d_i(\mathrm{t}) + K\varphi_i(x_i(\mathrm{t}), x_i(t - h(\mathrm{t}))), \quad (1) \\ y_i(t) &= Cx_i(\mathrm{t}) + D_2 d_i(\mathrm{t}). \quad (2) \end{aligned}$$

where $i = 1, \ldots, N$, $x_i(t) \in \mathbb{R}^{n_x}$ the system's condition, $y_i(t) \in \mathbb{R}^{n_y}$ is the output signal measurement, $u_i(t) \in \mathbb{R}^{n_u}$ the vector that shows the inputs for control and $d_i(t) \in \mathbb{R}^{n_d}$

the plant-affecting disruptions. $h(t)$ depicts the state delay that varies with time. $\varphi_i(x_i(t), x_i(t-h(t)))$ indicates the system's nonlinear component. A, A_d, B, C, D_1, D_2 and K are appropriate-dimensional constant matrixes.

We introduce the following lemmas to define the consensus control criterion for MASs.

Lemma 1 *[13] Let $\mathcal{L}$ represent the Laplacian matrix connected to an undirected graph $\mathcal{G}$. Then $\mathcal{L}$ has a minimum of one eigenvalue that is zero, with all other eigenvalues being positive. Additionally, there is only one zero eigenvalue in matrix $\mathcal{L}$, and the corresponding eigenvector is $\mathbf{1}$ if and only if the undirected graph $\mathcal{G}$ is linked.*

Assumption 1 *For everyone x_1, x_2, y_1, $y_2 \in \mathbb{R}^n$, $\varphi(x(t), x(t-h(t)))$ fulfills the corresponding Lipschitz requirements and is a recognized nonlinear function:*

1) $\varphi(0,0) = 0$;

2) $\|\varphi(x_1, x_2) - \varphi(y_1, y_2)\| \leq \|\lambda_1(x_1 - y_1)\| + \|\lambda_2(x_2 - y_2)\|$

where λ_1 and λ_2 is a constant real number.

3 Design of Observer-Based Reliable Control Protocols for Actuator Faults

Achieving state consensus in MASs demands the implementation of a consensus control protocol with robustness. Designing dependable control systems for MASs has become a focal point of recent research. This study aims to address the issue of trustworthy control in the presence of actuator problems by building a fault model. $u_i^f(t)$ symbolizes the vector input for control following actuator failures for the agent $i, i = 1, \ldots, N$. Next, The actuator fault model type that follows is employed:

$$u_i^F = N_f u_i. \tag{3}$$

The given assumption suggests that the fault matrix N_f and specific structure: $N_f = diag(N_{f1}, N_{f2}, \ldots, N_{fp})$, $N_{fi}\ i = 1, \ldots, p$ represent possible issues with the ith actuator and $N_{fi} \in [0, 1]$. It is clear that when N_{fi} equals zero, the associated actuator has experienced complete failure, and when N_{fi} equals one, it suggests that the associated actuator is in perfect working order. For values of N_{fi} within the time frame (0, 1), the actuator is found to be partially defective.

It is noteworthy that in the event that the actuator is totally faulty, *i.e.*, $N_{fi} = 0$, the controller doesn't give the plant any kind of control. The structure turns into an open-loop system. As a result, it is typically assumed in this work that the relevant actuator is either completely or partially defective.

In order to streamline the controller design, it is additionally assumed in practice that $0 < \underline{N}_{fi} \leq N_{fi} \leq \bar{N}_{fi} \leq 1, \forall i = 1, \ldots, p$. Given that the element N_{fi} is fluctuating in time within the range $[\underline{N}_{fi}\ \bar{N}_{fi}]$,specify the collection of vertices in N_f as $N = \{diag(\underline{N}_{fi}^1, \underline{N}_{f2}^1, \ldots, \underline{N}_{fp}^1), \ldots, diag(\bar{N}_{fi}^1, \bar{N}_{f2}^1, \ldots, \bar{N}_{fp}^1)\}$, $\alpha \in \gamma_{2^p}$.

Clearly, The matrix of faults N_f fulfills $N_f \in co(N)$.

For the sake of simplicity, we utilize N_f^α to represent the fault matrix N_f. Let $B_f = BN_f^\alpha$.

For system (1)-(2), the following qualities ought to be part of an observer's design goals. First and foremost, the observer needs to efficiently reduce the impact of disturbances on the residual. Second, the observer needs to show that they are stable. As is customary, we suppose that the observer has a certain form:

$$\begin{aligned} \dot{\hat{x}}(t) &= A\hat{x}_i(t) + A_d\hat{x}_i(t-h(t)) + B_f u_i(t) + L_0 \\ &\quad (y_i(t) - \hat{y}_i(t)) + K\varphi_i(\hat{x}_i(t), \hat{x}_i(t-h(t))) \quad (4) \\ \hat{y}_i(t) &= C\hat{x}_i(t). \quad (5) \end{aligned}$$

where $\hat{x}_i \in \mathbb{R}^n$ is the state approximation, $\hat{y}_i(t) \in \mathbb{R}^{n_y}$ stands for the vector of output estimation, and $L_0 \in \mathbb{R}^{n \times n_y}$ is the matrix of coefficients for the filter that has to be made. Therefore, the goal of this study is to use state estimated values to construct a strong consensus procedure $u_i(t)$ of the MAS. The structure of the consensus protocol is:

$$u_i(t) = K_s \sum_{j \in N_i} a_{ij}(\hat{x}_i(t) - \hat{x}_j(t)), i = 1, \ldots N \tag{6}$$

where $K_s \in \mathbb{R}^{p \times n}$ is the gains matrix that has to be created.

Upon integrating the observer (4)-(5) and the system (1)-(2) collectively, and definition $e_i(t) = x_i(t) - \hat{x}_i(t)$, the following dynamic error equations are available:

$$\begin{aligned} \dot{e}_i(t) &= \dot{x}_i(t) - \dot{\hat{x}}_i(t) \\ &= (A - L_0C)e_i(t) + A_d e_i(t-h(t)) \\ &\quad + K\Delta\varphi(t) + (D_1 - L_0D_2)d_i(t). \quad (7) \end{aligned}$$

Let $\Delta\varphi(t) = \varphi(\hat{x}(t), \hat{x}(t-h(t))) - \varphi(\hat{x}(t), \hat{x}(t-h(t)))$, $e_i(t) = (e_1^T(t), \ldots, e_N^T(t))^T$, be acquired

$$\begin{aligned} \dot{e}_i(t) &= (I_N \otimes (A - L_0C))e(t) + (I_N \otimes A_d)e(t-h(t)) \\ &\quad + (I_N \otimes (D_1 - L_0D_2))d(t) + (I_N \otimes K)\Delta\varphi(t) \quad (8) \end{aligned}$$

Define synchronizing state and plant disturbance error as $\delta_i = x_i - (1/N)\sum_{j=1}^N x_j = x_i - \bar{x}, \delta = (\delta_1^T, \ldots, \delta_N^T)^T$, $\bar{d}_i = d_i - (1/N)\sum_{j=1}^N d_i, \bar{d} = (\bar{d}_1^T, \ldots, \bar{d}_N^T)^T$.

After integrating system (1)-(2) and consensus control protocol (6), be acquired

$$\begin{aligned} \dot{\delta}_i(t) &= \dot{x}_i - \frac{1}{N}\sum_{j=1}^N \dot{x}_j = A\delta_i(t) + A_d\delta_i(t-h(t)) \\ &\quad + B_f K_s \sum_{J \in N_i} a_{ij}(\delta_i(t) - \delta_j(t) + e_j(t) - e_i(t)) \\ &\quad + D_1\bar{d}_i(t) + K\Delta\bar{\varphi}_i(t). \quad (9) \end{aligned}$$

Making use of an undirected topological graph's symmetry property, it is evident that $a_{ij} = a_{ji}$. Consequently, we may obtain

$$\frac{1}{N}\sum_{j=1}^N \sum_{j \in N_i} B_f K_s a_{ij}(\hat{x}_i(t) - \hat{x}_j(t)) = 0. \tag{10}$$

At the same time, note that

$$\begin{aligned} &\sum_{J \in N_i} a_{ij}(\hat{x}_i(t) - \hat{x}_j(t)) \\ &= \sum_{J \in N_i} a_{ij}((x_i - x_j) + (\hat{x}_i - x_i) + (\hat{x}_i - x_j)) \\ &= \sum_{J \in N_i} a_{ij}((x_i - \frac{1}{N}\sum_{j=1}^N x_j) - (x_j - \frac{1}{N}\sum_{j=1}^N x_j) + e_i - e_j) \\ &= \sum_{J \in N_i} a_{ij}(\delta_i - \delta_j + e_j - e_i). \quad (11) \end{aligned}$$

Considering (10) and (11), (9) transforms into

$$\dot{\delta}_i = A\delta_i + A_d\delta_i(t-h(t)) + B_fK_s\sum_{j\in N_i} a_{ij}(\delta_i-\delta_j+e_j - e_i) + D_1\bar{d}_i + K\Delta\bar{\varphi}_i(t) \quad (12)$$

Let $\delta = (\delta_1^T, \ldots, \delta_N^T)^T$. Subsequently, the error equation for synchronization in the closed-loop network's dynamics can be displayed as

$$\begin{aligned}\dot{\delta}(t) &= (I_N\otimes A + L\otimes B_fK_s)\delta(t) + \\ &(I_N\otimes A_d)\delta(t-h(t)) - (L\otimes B_fK_s)e(t) \\ &+(I_N\otimes D_1)\bar{d}(t) + (I_N\otimes K)\Delta\bar{\varphi}(t). \quad (13)\end{aligned}$$

Let $z = \begin{bmatrix} \delta^T & e^T \end{bmatrix}^T$, $\omega = \begin{bmatrix} \bar{d}^T & d^T \end{bmatrix}^T$, merging (8)and (13), produces

$$\dot{z}(t) = \tilde{A}z(t) + \tilde{A}_dz(t-h(t)) + \tilde{B}w + \tilde{K}\Delta\varphi(t) \quad (14)$$

where

$$\begin{aligned}\tilde{A} &= \begin{bmatrix} I_N\otimes A + \mathcal{L}\otimes B_fK_s & -\mathcal{L}\otimes B_fK_s \\ 0 & I_N\otimes(A-L_0C)\end{bmatrix}, \\ \tilde{A}_d &= \begin{bmatrix} I_N\otimes A_d & 0 \\ 0 & I_N\otimes A_d\end{bmatrix}, \\ \tilde{B} &= \begin{bmatrix} I_N\otimes D_1 & 0 \\ 0 & I_N\otimes(D_1-L_0D_2)\end{bmatrix}.\end{aligned}$$

After that, the robust H_∞ consensus problem for MASs (1)-(2) with a given scalar $\gamma > 0$ aims to discover a protocol u_i in the following manner.

1) For any initial state $x_i(0)$, the closed-loop MASs (1)-(2) can come to an asymptotic consensus in spite of perturbations from plants $d(t) = 0, i.e.,$. The agents meet

$$\|\delta_i\| = \left\| x_i - \frac{1}{N}\sum_{j=1}^{N} x_j \right\| \longrightarrow 0,\ i = 1,\ldots N. \quad (15)$$

It should be observed that the disturbances $\bar{d}(t)$ obviously have no influence on the false signals of the synchronization state when $d(t) = 0$, $\bar{d}(t) = 0$.

2) The L_2-gain from ω to z ought not to exceed $\gamma, i.e.$, for $x(0) = 0$, the subsequent disparities are true:

$$\int_0^T \|z(t)\|^2\,dt \le \gamma^2\int_0^T \|\omega(t)\|^2\,dt, \forall T \ge 0 \quad (16)$$

for the MASs operating in continuous time.

Robust H_∞ requirements for consensus in MASs (1)-(2) are examined in the section that follows.

Theorem 1 *For specified scalars $\varepsilon > 0$, $\lambda_1 > 0$, $\lambda_2 > 0$, $\lambda_3 > 0$ and eigenvalues of the system $\alpha_j (j = 2,\ldots,N)$ of Laplacian matrix $\mathcal{L}$, the closed-loop system (13) exhibits asymptotic stability at the H_∞ performance level γ, if there exist symmetric matrix $P_1 > 0$, $P_2 > 0$, $Q_1 > 0$, $Q_2 > 0$, $Z > 0$, $\mu_1 > 0$, $\mu_2 > 0$, $\gamma > 0$, free weight matrices M_z, N_z of appropriate dimensions, such that the subsequent $2\bar{N}$ LMI are satisfied:*

$$\bar{\Xi}_z = \begin{bmatrix} \bar{\Xi} & hM_z & \sqrt{h}\bar{\Gamma}^T & \phi \\ * & -hZ & 0 & 0 \\ * & * & \bar{x}_{33} & \sqrt{h}P_1B_f \\ * & * & * & -2\mu_2I \end{bmatrix} < 0 \quad (17)$$

$$\bar{\Pi}_z = \begin{bmatrix} \bar{\Xi} & hN_z & \sqrt{h}\bar{\Gamma}^T & \phi \\ * & -hZ & 0 & 0 \\ * & * & \bar{x}_{33} & \sqrt{h}P_1B_f \\ * & * & * & -2\mu_2I \end{bmatrix} < 0 \quad (18)$$

where

$\bar{\Xi} = \Xi_{1j} - He(M_z(U_1-U_2)) - He(N_z(U_2-U_3))$,

$$\Xi_{1j} = \begin{bmatrix} \bar{x}_1 & x_{12} & x_{13} & 0 & x_{15} & 0 \\ * & x_{22} & 0 & x_{24} & 0 & x_{26} \\ * & * & x_{33} & 0 & 0 & 0 \\ * & * & * & x_{44} & 0 & 0 \\ * & * & * & * & -\gamma^2I & 0 \\ * & * & * & * & * & -\gamma^2I \end{bmatrix} \quad (19)$$

$\bar{\Gamma} = [P_1A - \alpha_jP_1B_fK_s, -\alpha_jP_1B_fK_s, P_1A_d, 0, P_1D_1, 0]$,
$\bar{x}_{33} = -2\varepsilon_1P_1 + \varepsilon_1^2Z$,
$M_z^T = [I_N\otimes M_1^T, I_N\otimes M_2^T, I_N\otimes M_3^T,$
$I_N\otimes M_4^T, I_N\otimes M_5^T, I_N\otimes M_6^T]$,
$N_z^T = [I_N\otimes N_1^T, I_N\otimes N_2^T, I_N\otimes N_3^T,$
$I_N\otimes N_4^T, I_N\otimes N_5^T, I_N\otimes N_6^T]$,
$U_1^T = [I,0,0,0,0,0], U_2^T = [0,I,0,0,0,0]$,
$U_3^T = [0,0,I,0,0,0]$,
$\phi = [PB_f + \alpha_j\mu_1K_s, \alpha_j\mu_1K_s, 0,0,0,0]$,
$\bar{x}_1 = He(P_1A + \alpha_jP_1B_fK_s) + 2\lambda_3P_1KK^TP_1 + Q_1$
$+(2\lambda_3+1)I, x_{12} = -\alpha_jP_1B_fK_s$, $x_{13} = P_1A_d$,
$x_{15} = P_1D_1, x_{26} = P_2(D_1 - L_0D_2)$, $x_{22} =$
$He(P_2(A-L_0C)) + \varepsilon^{-1}P_2KK^TP_2 + Q_2 + (\varepsilon\lambda_1^2+1)I$,
$x_{33} = -(1-\tau)Q_1 + 2\lambda_3I + I$, $x_{24} = P_2A_d$,
$x_{44} = -(1-\tau)Q_2 + \varepsilon\lambda_2^2I + I$.

$$\Xi_{2j} = \begin{bmatrix} x_{11} & P_2A_d & P_2(D_1-L_0D_2) \\ * & (1-\tau)Q_2 + \varepsilon\lambda_2^2I & 0 \\ * & * & -\gamma^2I \end{bmatrix}$$

$x_{11} = He(P_2(A-L_0C)) + \varepsilon^{-1}P_2KK^TP_2 + Q_2 + \varepsilon\lambda_1^2I$.

By using a comparable methodology in the consensus analysis, it is deduced that $\Xi_{2j} < 0$ is satisfied in the event that $\Xi_{1j} < 0$.

Proof. Think about the following Krasovskii Lyapunov functional

$$V(z) = z^T\tilde{P}z + \int_{t-h(t)}^{t} z^T\tilde{Q}z\,ds + \int_{-h}^{0}\int_{t+\theta}^{t}\dot{z}^T(I\otimes Z)\dot{z}\,ds\,d\theta \quad (20)$$

$$\begin{aligned}\tilde{P} &= \begin{bmatrix} I_N\otimes P_1 & 0 \\ 0 & I_N\otimes P_2\end{bmatrix} > 0, \\ \tilde{Q} &= \begin{bmatrix} I_N\otimes Q_1 & 0 \\ 0 & I_N\otimes Q_2\end{bmatrix} > 0, Z > 0.\end{aligned}$$

Given the positive semidefinite and symmetric nature of $\mathcal{L}$, the spectral decomposition $\mathcal{L} = \Pi\Lambda\Pi$ can be used, where

the matrix that is orthogonal $\Pi \in \mathbb{R}^{N\times N}$ is the set of eigenvectors for $\mathcal{L}$, and $\Lambda = diag(0, \alpha_{1,\dots}\alpha_N) \in \mathbb{R}^{N\times N}$ where the arrangement of the eigenvalues of is such that $0 < \alpha_2 \leq \cdots \leq \alpha_N$.

Derivative of V(z) with respect to the (14) solutions calculated is

$\dot{V} = 2\delta^T(t)(I_N \otimes P_1)\dot{\delta}(t) + 2e^T(t)(I_N \otimes P_2)\dot{e}(t) - (1-\dot{h}(t))\delta^T(t-h(t))(I_N \otimes Q_1)\delta(t-h(t)) + \delta^T(t)(I_N \otimes Q_1)\delta(t) + e^T(t)(I_N \otimes Q_2)e(t) - (1-\dot{h}(t))e^T(t-h(t))(I_N \otimes Q_2)e(t-h(t)) + h\dot{z}^T(t)(I \otimes Z)\dot{z}(t) - \int_{t-h}^{t} \dot{z}^T(s)(I \otimes Z)\dot{z}(s)ds$

$= 2\delta^T(t)[(I_N \otimes P_1A)\delta(t) + (\mathcal{L} \otimes P_1B_fK_s)\delta(t) + (I_N \otimes P_1A_d)\delta(t-h(t)) + \delta^T(t)(I_N \otimes Q_1)\delta(t) - (\mathcal{L} \otimes P_1B_fK_s)e(t) + (I_N \otimes P_1D_1)\bar{d}(t)] + 2\sum_{i=1}^{N}\delta_i^T(t)P_1K\Delta\bar{\varphi}(t) + 2e^T(t)[(I_N \otimes P_2(D_1 - L_0D_2))d(t)] - (1-\dot{h}(t))\delta^T(t-h(t))(I_N \otimes Q_1)\delta(t-h(t)) - (1-\dot{h}(t))e^T(t-h(t))(I_N \otimes Q_2)e(t-h(t)) + e^T(t)(I_N \otimes Q_2)e(t) + h\dot{z}^T(t)(I \otimes Z)\dot{z}(t) - \int_{t-h}^{t}\dot{z}^T(s)(I \otimes Z)\dot{z}(s)ds + 2e^T(t)(I_N \otimes P_2K)\Delta\varphi(t).$

Since $\sum_{i=1}^{N}\delta_i^T(t) = 0$:

$$\begin{aligned} & 2\sum_{i=1}^{N}\delta_i^T(t)P_1K(\varphi(\bar{x}(t),\bar{x}(t-h(t))) \\ & -\frac{1}{N}\sum_{j=1}^{N}\varphi_j(x_j(t),x_j(t-h(t))) \\ = \; & 0. \end{aligned} \tag{21}$$

Note that

$$\begin{aligned} & 2\sum_{i=1}^{N}\delta_i^T(t)P_1K\Delta\bar{\varphi}(t) \\ = \; & 2\sum_{i=1}^{N}\delta_i^T(t)P_1K(\varphi_i(x_i(t),x_i(t-h(t)))) \\ & -\varphi(\bar{x}(t),\bar{x}(t-h(t))) + \varphi(\bar{x}(t),\bar{x}(t-h(t))) \\ & -\frac{1}{N}\sum_{j=1}^{N}\varphi(\bar{x}(t),\bar{x}(t-h(t))) \\ = \; & 2\sum_{i=1}^{N}\delta_i^T(t)P_1K(\varphi_i(x(t),x_i(t-h(t)))) \\ & -\varphi(\bar{x}(t),\bar{x}(t-h(t))). \end{aligned} \tag{22}$$

Due to Young's inequation is available:

$$\begin{aligned} & 2\sum_{i=1}^{N}\delta_i^T(t)P_1K(\varphi_i(x(t),x_i(t-h(t)))) \\ & -\varphi(\bar{x}(t),\bar{x}(t-h(t))) \\ & 2\lambda_3||\delta_i^T(t)P_1K|| \cdot ||\delta_i(t) + \delta_i(t-h(t))|| \\ \leq \; & \delta_i^T(t)(2\lambda_3P_1KK^TP_1 + 2\lambda_3I)\delta_i(t) \\ & +\delta_i^T(t-h(t))(2\lambda_3I)\delta_i(t-h(t)). \end{aligned} \tag{23}$$

And

$$\begin{aligned} & 2e^T(t)(I_N \otimes P_2K)\Delta\varphi(t) \\ \leq \; & \varepsilon^{-1}e^T(t)(I_N \otimes P_2K)(I_N \otimes K^TP_2)e(t) \\ & +\varepsilon\lambda_1^2e^T(t)e(t) + \varepsilon\lambda_2^2e^T(t-h(t))e(t-h(t)) \end{aligned} \tag{24}$$

Define coordinate transformations:

$\epsilon(t) = (\Pi^T \otimes I_n)\delta(t)$, $\theta(t) = (\Pi^T \otimes I_n)e(t)$, $\zeta(t) = (\Pi^T \otimes I_n)d(t)$, $\xi(t) = (\Pi^T \otimes I_n)\bar{d}(t)$, $\dot{\sigma}(t) = (\Pi^T \otimes I_n)\dot{z}(t)$, $\epsilon_1 = 0, \xi_1 = 0$,

$\eta_j(t) = (\epsilon_j^T(t), \theta_j^T(t), \epsilon_j^T(t-h(t)), \theta_j^T(t-h(t)))^T$, $w = (\xi^T(t), \zeta^T(t))^T$, $v_j = (\epsilon_j^T(t), \theta_j^T(t), \epsilon_j^T(t-h(t)), \theta_j^T(t-h(t)), \xi^T(t), \zeta^T(t))^T$, $\psi_1 = (\theta_1^T(t), \theta_1^T(t-h(t)), \zeta_1^T(t))^T$.

Utilizing the Newton-Leibniz formula, any matrix M_δ, N_δ with the right dimensions can be calculated directly.

$$\begin{aligned} & \dot{V} + \epsilon^T\epsilon + \theta^T\theta + \epsilon^T(t-h(t))\epsilon(t-h(t)) \\ & +\theta^T(t-h(t))\theta(t-h(t)) - \gamma^2\xi^T\xi - \gamma^2\zeta^T\zeta \\ & -2v^T(t)M_z[\sigma(t) - \sigma(t-h(t)) - \int_{t-h(t)}^{t}\dot{\sigma}(s)ds] \\ & -2v^T(t)N_z[\sigma(t-h(t)) - \sigma(t-h) - \int_{t-h}^{t-h(t)}\dot{\sigma}(s)ds] \\ \leq \; & \frac{1}{h}\int_{t-h(t)}^{t}\begin{bmatrix} v(t) \\ \dot{\sigma}(t) \end{bmatrix}^T\begin{bmatrix} \Xi & hM_z \\ * & -hZ \end{bmatrix}\begin{bmatrix} v(t) \\ \dot{\sigma}(t) \end{bmatrix}ds \\ & +\frac{1}{h}\int_{t-h}^{t-h(t)}\begin{bmatrix} v(t) \\ \dot{\sigma}(t) \end{bmatrix}^T\begin{bmatrix} \Xi & hM_z \\ * & -hZ \end{bmatrix}\begin{bmatrix} v(t) \\ \dot{\sigma}(t) \end{bmatrix}ds \\ & +\psi_1^T\Xi_{2j}\psi_1 \end{aligned} \tag{25}$$

where $\Xi = \Xi_{1j} + h\Gamma^T(P_1(2\varepsilon_1P_1 - \varepsilon_1^2Z)^{-1}P_1)\Gamma - He(M_z(U_1 - U_2)) - He(N_z(U_2 - U_3))$.

The closed-loop system (13) achieves asymptotic stability if the inequalities (26)-(27) are satisfy.

$$\tilde{\Xi}_z = \begin{bmatrix} \Xi & hM_z \\ * & -hZ \end{bmatrix} < 0 \tag{26}$$

$$\tilde{\Pi}_z = \begin{bmatrix} \Xi & hM_z \\ * & -hZ \end{bmatrix} < 0 \tag{27}$$

Considering that non-convex terms like PB_fK_s in (26)-(27) , require processing.

Let $A_T = [(-\alpha_j^TK_s^T)^T, (-\alpha_j^TK_s^T)^T, 0, 0, 0, 0, 0, 0]^T, T = [I_{8*8}, A_T]$.

The solution to (26)-(27) can be obtained by multiplying the problem's two sides by T and T^T in the matrices (17)-(18), Lemma 2 of the Schur complement is then applied, correspondingly.

Moreover, if (17)-(18) hold, it yields $\dot{V}(t) + \epsilon^T\epsilon + \theta^T\theta + \epsilon^T(t-h(t))\epsilon(t-h(t)) + \theta^T(t-h(t))\theta(t-h(t)) - \gamma^2\xi^T\xi - \gamma^2\zeta^T\zeta < 0$. particularly, under $\xi(t) = 0, \zeta(t) = 0$, the disparity can be expressed as $\dot{V}(t) < -\epsilon^T\epsilon - \theta^T\theta - \epsilon^T(t-h(t))\epsilon(t-h(t)) - \theta^T(t-h(t))\theta(t-h(t)) \leq 0$. The closed-loop system (13) is asymptotically stable according to Lyapunov theory. When, under $\xi(t) \neq 0, \zeta(t) \neq 0$ and $\phi(t) = 0$, it results in $\delta(t) = 0$. Thus $V_\delta(t)|_{t=0} = 0$. Motivated by $V_\delta(t)|_{t=L} \geq 0$. As a result, utilizing the γ performance level H_∞. Finally, the closed-loop synchronizing state error system (13) reaches stability. The final proof has been completed. ■

4 Examples in Numbers

Here, we show simulation results demonstrating the performance of the algorithm. We study a MASs with four

agents, each represented by the model shown below:

$$\begin{aligned} \dot{x}_i(t) &= Ax_i(t) + A_d x_i(t-h(t)) + B_f u_i(t) \\ &\quad + D_1 d_i(t) + K\varphi_i(x_i(t), x_i(t-h(t))) \\ y_i(t) &= Cx_i(t) + D_2 d_i(t) \end{aligned}$$

where $A = \begin{bmatrix} -5 & -1.4 \\ 1.18 & 0 \end{bmatrix}$, $A_d = \begin{bmatrix} -0.3 & 0.2 \\ -0.1 & -0.4 \end{bmatrix}$, $B = \begin{bmatrix} 1 \\ 0.5 \end{bmatrix}$, $D_1 = \begin{bmatrix} 0.01 \\ 0.02 \end{bmatrix}$, $K = \begin{bmatrix} -0.1 \\ 0.3 \end{bmatrix}$, $C = \begin{bmatrix} 1 & 0 \\ 0 & 1 \end{bmatrix}$, $D_2 = \begin{bmatrix} 0.01 & 0.01 \end{bmatrix}$, $\varphi_i(x_i(t)) = 0.2\sin x_{i2}(t) + 0.5\sin x_{i2}(t-h(t))$. The network architecture displayed above can be used to represent a network with four agents in Fig. 1.

From Fig. 1, the following is the expression for the Laplacian matrix $\mathcal{L}$

$$\mathcal{L} = \begin{bmatrix} 3 & -1 & -1 & -1 \\ -1 & 2 & 0 & -1 \\ -1 & 0 & 2 & -1 \\ -1 & -1 & -1 & 3 \end{bmatrix}$$

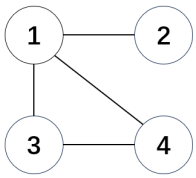

Fig. 1: Communication topology

To enact consensus within MASs, it is supposed that $h(t) = 0.05\,|\sin(t)|$, $\lambda_1 = 0.18$, $\lambda_2 = 0.25$, $\lambda_3 = 0.32$, $\varepsilon = 50$, and the control protocol is designed using the suggested observer-based consensus control mechanism. Our algorithm shown in Theorem 1 yields a minimal value of γ of 0.2321 when there are no actuator issues. The corresponding observer gain matrix is

$$L_0 = 1.0e+04 * \begin{bmatrix} 0.3471 & -0.3470 \\ -1.0411 & 1.0413 \end{bmatrix},$$

and the matching matrix of control gains is

$$K_s = \begin{bmatrix} 0.3779 & 0.0789 \end{bmatrix}.$$

The initial conditions are chosen as

$$\begin{aligned} x_{10} &= \begin{bmatrix} 0.4 \\ 0.5 \end{bmatrix}, x_{20} = \begin{bmatrix} -0.4 \\ -0.4 \end{bmatrix}, \\ x_{30} &= \begin{bmatrix} -0.2 \\ 0.4 \end{bmatrix}, x_{40} = \begin{bmatrix} 0.4 \\ -0.3 \end{bmatrix}. \end{aligned}$$

We let

$$N_f = diag(N_{f1}, N_{f2}), 0.2 \le N_{fi} \le 0.8, \forall i = 1, 2.$$

In the same starting state circumstances, let $N_f = diag(0.2, 0.2)$, the trajectories of the closed-loop MASs (1) are shown in Fig. 2, and an illustration of the estimating mistakes in Fig. 3. When $N_f = diag(0.8, 0.8)$, the state trajectories are illustrated in Fig. 4, and an illustration of the estimating mistakes in Fig. 5.

Figs. 3 and 5 embody, if the actuator failures are within a changing domain, asymptotically, the observation errors will approach zero. From Figs. 2 and 4, it is obvious that, in spite of actuator failures, consensus is reached asymptotically. This discovery highlights the robust controller design's potential to lessen the effects of disturbances and actuator malfunctions. The efficiency of the suggested dependable control mechanism for MASs using undirected communication graphs is clearly shown by these data.

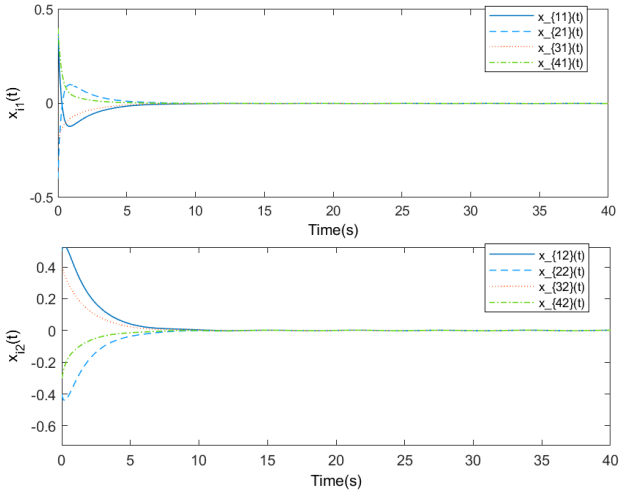

Fig. 2: state trajectories when the actuator malfunctions N_f = diag(0.2, 0.2).

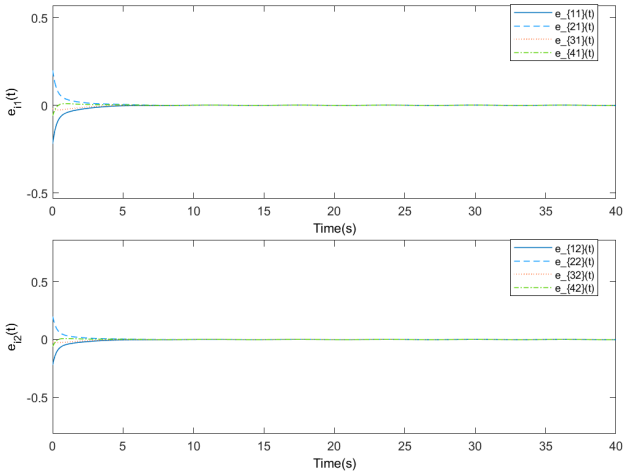

Fig. 3: observation error paths in the event of actuator malfunctions N_f = diag(0.2, 0.2).

5 Conclusions

This paper investigates the reliability control of nonlinear masses affected by state delay, actuator faults, and disturbances. It employs a connected sensor that incorporates a distributed observer for estimating state information, thereby creating a singular agent via a shared communication network. This approach achieves an observer-based protocol ensuring the necessary anti-interference performance. Then, an observer-based reliability control protocol is developed to mitigate the consequences of actuator failure using the estimated information. Ultimately, an instance is provided to confirm the efficacy of the suggested approach. To enhance control effectiveness further, the paper aims to explore more suitable control schemes in future studies.

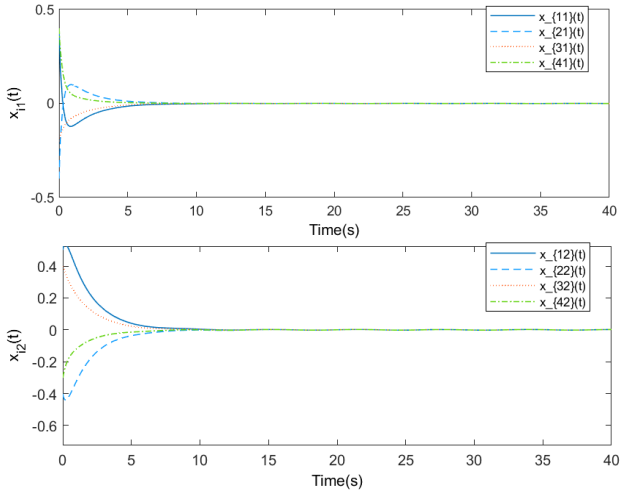

Fig. 4: state trajectories when the actuator malfunctions N_f = diag(0.8, 0.8).

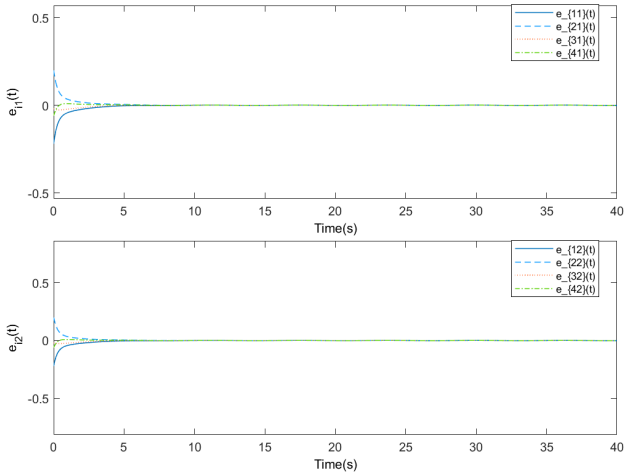

Fig. 5: observation error paths in the event of actuator malfunctions N_f = diag(0.8, 0.8).

References

[1] A. R. Kim, S. Keshmiri, A. Blevins, et al., "Control of multi-agent collaborative fixed-wing UASs in unstructured environment," Journal of Intelligent & Robotic Systems, vol. 97, pp. 205-225, 2020.

[2] G. T. Papadopoulos, M. Antona, C. Stephanidis, "Towards open and expandable cognitive AI architectures for large-scale multi-agent human-robot collaborative learning," IEEE Access, vol. 9, pp. 73890-73909, 2021.

[3] Z. Dai, Y. Zhang, W. Zhang, et al., "A multi-agent collaborative environment learning method for UAV deployment and resource allocation," IEEE Transactions on Signal and Information Processing over Networks, vol. 8, pp. 120-130, 2022.

[4] W. A. Arokiasami, P. Vadakkepat, K. C. Tan, et al., "Interoperable multi-agent framework for unmanned aerial/ground vehicles: towards robot autonomy," Complex & Intelligent Systems, vol. 2, pp. 45-59, 2016.

[5] C. Dinelli, J. Racette, M. Escarcega, et al., "Configurations and Applications of Multi-Agent Hybrid Drone/Unmanned Ground Vehicle for Underground Environments: A Review," IEEE Drones, vol. 7, no. 2, pp. 136, 2023.

[6] X.-Z. Jin, S. Lv, and J. Yu, "Adaptive NN-based consensus for a class of nonlinear multi-agent systems with actuator faults and faulty networks," IEEE Transactions on Neural Networks and Learning Systems, pp. 1-13, 2021.

[7] X.-Z. Jin, W.-W. Che, Z.-G. Wu, and Z. Zhao, "Adaptive consensus and circuital implementation of a class of faulty multi-agent systems," IEEE Transactions on Systems, Man, and Cybernetics: Systems, pp. 1-13, 2020.

[8] A. Chen and M. Shen, "A New Method to Reliable H_∞ Control of Nonlinear Stochastic Systems with Actuator Faults," International Journal of Fuzzy Systems, vol. 21, pp. 60-71, 2019.

[9] J. Chen, W. Zhang, Y. -Y. Cao and H. Chu, "Observer-Based Consensus Control Against Actuator Faults for Linear Parameter-Varying Multiagent Systems," in IEEE Transactions on Systems, Man, and Cybernetics: Systems, vol. 47, no. 7, pp. 1336-1347, July 2017.

[10] D. Ye, X. Zhao, and B. Cao, "Distributed adaptive fault-tolerant consensus tracking of multi-agent systems against time-varying actuator faults," IEEE Transactions on Control Theory and Applications, vol. 10, no. 5, pp. 554-563, Mar. 2016.

[11] S. Yazdani and M. Haeri, "Robust adaptive fault-tolerant control for leader-follower flocking of uncertain multi-agent systems with actuator failure," in Name of Journal, vol. Volume, no. Issue, pp. Page Range, Aug. 2017.

[12] X. Wang and G.-H. Yang, "Distributed reliable H_∞ consensus control for a class of multi-agent systems under switching networks: A topology-based average dwell time approach," Name of Journal, vol. Volume, no. Issue, pp. Page Range, Nov. 2015.

[13] K. M. Zhou, "Essential of Robust Control," Englewood Cliffs, NJ, USA: Prentice Hall, 1998.

Proceedings of the 3rd Conference on Fully Actuated System Theory and Applications
May 10-12, 2024, Shenzhen, China

Dynamic Gain Scheduling Laplacian-like Output Feedback Control of Linear Multi-agent System with Input Saturation

Xiangyu Gao[1], Anlong Chen[1], Jianqiao Wang[2]

1. School of Mathematics and Statistics, Guangxi Normal University, Guilin, GuangXi, 541004, P. R. China.
E-mail: gxy578@126.com

2. School of Control Science and Engineering, Tiangong University, Tianjin 300387, P. R. China

Abstract: Due to the constraint of device technology and the disturbance of external environment, it is difficult to obtain accuracy state information, it is necessary to design the state observer of linear multi-agent system in practical application. On the other hand, input saturation leads to the degradation of the dynamic performance of the linear multi-agent system. Based on the two motivations, this paper considers the bipartite consensus problem for linear multi-agent system with input saturation. If each agent is asymptotically null controllable with bounded control, and its interaction topology in the signed directed graph, which has a spanning tree, is structurally balanced, then we can adopt a dynamic gain scheduling control method to design a dynamic gain scheduling Laplacian-like output feedback control, which can guarantee that saturated linear multi-agent system achieve the bipartite consensus. This dynamic gain scheduling Laplacian-like output feedback control can be obtained through the analytical solution of parametric Lyapunov equation. Compared with the static gain scheduling Laplacian-like output feedback control, the dynamic gain scheduling Laplacian-like output feedback control obtained in this paper can better improve the bipartite consensus performance of the linear multi-agent system with input saturation. Finally, an example is provided to show the feasibility and effectiveness of the proposed control method.

Key Words: Linear multi-agent system, Input saturation, Dynamic gain scheduling control method, Laplacian-like output feedback control, Bipartite consensus

1 Introduction

The collective behavior of multi-agent system originates from the flocking behavior of animals in nature such as the migration of wild goose, the predation of ant colony, the companion travelling of schooling fish and so on. At present, the collective behavior of multi-agent system has been widely used in various different fields such as physics, life science and engineering (see [1] and references therein). In the most existing literature, the studies are mainly focused on the cooperative behaviors of agents, which is first proposed in [2], subsequently, many important research results are concerned with the consensus problem of cooperative behaviors among agents (see [3] and references therein).

However, there are competitive behaviors of agents in the real world such as economic behaviour[4], social network behaviour [5], and multirobot behaviour [6]. The collective behavior among agents with competition behaviour is referred to as the bipartite consensus of agents. The bipartite consensus and its robustness are both studied for first-order multi-agent system in [7] and first-order multi-agent system with disturbance in [8], respectively. On the basis, the bipartite consensus problems is further considered for both second-order multi-agent systems with unknown disturbances in [9] and high-order multi-agent system with unknown disturbances in [10]. Although there are some research results to solve the bipartite consensus problems, input saturation is rarely mentioned in these results.

Input saturation is an important nonlinear phenomenon, which often appears in physical actuators in the practical control system [11]. Recently, the low-gain feedback control method has been considered as one of the most important methods to deal with input saturation, and it has been applied to study bipartite consensus problems for linear multi-agent system subject to input saturation. For example, when the state information of multi-agent system can be available, a linear state feedback low-gain control is designed in [12] to achieve the bipartite consensus of multi-agent system subject to input saturation under a directed interaction topology. When the state information of multi-agent system can't be available, an observer-based output feedback low-gain control is constructed in [13] to solve the bipartite tracking problem of linear multi-agent system subject to input saturation under a signed directed graph. Since the low-gain feedback control method can't make the best use of the potential of control input, this results in the dynamic performance degradation of the system. This prompts us to design a novel feedback control method for solving the dynamic performance degradation problem.

In this paper, a gain scheduling feedback control method is adopted to design a dynamic gain scheduling Laplacian-like output feedback control for improving the dynamic performance of the system, which is different from the dynamic gain scheduling Laplacian-like state feedback control in [14]. This main innovative points of this paper are threefold: From the application point, we extend the results in [15] and [16] to a more practical situation, where both input saturation and the system performance are considered. From the control method, a gain scheduling function is introduced in the gain matrix of the dynamic Laplacian-like output feedback control to improve the dynamic performance of the system. From the implementation point, the parametric Lyapunov equation has the unique analytical solution such that the control design can be easily implemented.

Xiangyu Gao is corresponding author.

This work is supported by the Central Government's Guide to Local Science and Technology Development Fund (No. GuikeZY23055044) ;Guangxi Natural Science Foundation (No. 2023GXNSFAA026246, No. Guike AD21220062); National Natural Science Foundation (NNSF) of China (No. 62363003, No.62241303).

2 Problem Formation

Consider N multi-agent system, the dynamic equation of the ith agent can be described as

$$\begin{cases} \dot{x}_i = & Ax_i + B\mathrm{sat}(u_i) \\ y_i = & Cx_i, \quad i \in \mathbf{I}[1, N] \end{cases} \tag{1}$$

where $A \in \mathbb{R}^{n\times n}$, $B \in \mathbb{R}^{n\times m}$ and $C \in \mathbb{R}^{p\times n}$ are system matrices, $x_i \in \mathbb{R}^n$, $y_i \in \mathbb{R}^p$, and $u_i \in \mathbb{R}^m$ are the ith agent's state, measure output and control input, respectively. The saturated input $\mathrm{sat}(u_i) = [\mathrm{sat}(u_{1i}), \cdots, \mathrm{sat}(u_{mi})]^\top$, the saturation function $\mathrm{sat}(\cdot)$ is defined as $\mathrm{sat}(u_{ij}) = u_{ij}, |u_{ij}| \le u_{\max}$; otherwise, $\mathrm{sat}(u_{ij}) = \mathrm{sgn}(u_{ij})u_{\max}$.

For system (1), the observer-based dynamic gain scheduling Laplacian-like output feedback control is of the form given below:

$$\begin{cases} \dot{\xi}_i = A\xi_i + B\mathrm{sat}(u_i) + G(y_i - C\xi_i) \\ u_i = K(\gamma(t)) \sum\limits_{j=1}^{N} a_{ij}(\xi_j - \mathrm{sgn}(a_{ij})\xi_i) \end{cases} \tag{2}$$

where $\xi_i \in \mathbb{R}^n$ is the state of observer, a_{ij} is the (i, j)th element of the adjacency matrix $\mathcal{A}$. $G \in \mathbb{R}^{n\times m}$ is the gain matrix of the observer system, $K(\gamma(t)) \in \mathbb{R}^{m\times n}$ including the gain scheduling function $\gamma(t)$ is a time-varying control gain matrix to be determined.

Let $e_i = x_i - \xi_i, i \in \mathbf{I}[1, N]$, $e = [e_1^\top, e_2^\top, \cdots, e_N^\top]^\top$, from (1) and (2), it follows that

$$\begin{cases} \dot{x} = (I_N \otimes A)x + (I_N \otimes B)\mathrm{sat}(u) \\ \dot{e} = [I_N \otimes (A - GC)]e \\ u = -\left[L \otimes K(\gamma(t))\right](x - e) \end{cases} \tag{3}$$

where $x = [x_1^\top, x_2^\top, \cdots, x_N^\top]^\top$, $u = [u_1, u_2, \cdots, u_m]^\top$.

In [6], the definition of the bipartite consensus for first-order multi-agent system can be extended to the definition of the bipartite consensus for high-order multi-agent system.

Definition 2.1 *For the given bounded set $\Omega \subseteq \mathbb{R}^n$, if there exists a Laplacian-like output feedback control (2) such that*

$$\lim_{t\to\infty} \|x_i(t) \pm x_j(t)\| = 0 \tag{4}$$

for $x_i(0) \in \Omega, i \in \mathbf{I}(1, N)$. Then multi-agent system (1) *is called the bipartite consensus for $x_i(0) \in \Omega, i \in \mathbf{I}(1, N)$.*

Now, the bipartite consensus problem for multi-agent system (1) may be stated formally as follows: For multi-agent system (1), our goal is to design the gain matrix of the observer G and the gain matrix $K(\varepsilon(t))$ of the Laplacian-like output feedback control (2) such that the states of linear multi-agent system(1) not only satisfy (4) for all $x_i(0) \in \Omega, i \in \mathbf{I}(1, N)$, but also improve the dynamic performance of system.

3 Main Results

In order to obtain the main result, the following assumption appearing in [18] , is necessary.

Assumption 3.1 *$[A, B] \in (\mathbb{R}^{n\times n}, \mathbb{R}^{n\times m})$ is controllable, $[A, C] \in (\mathbb{R}^{n\times n}, \mathbb{R}^{p\times n})$ is observable, and all the eigenvalues of A have nonpositive real parts.*

From [6], it is easy to see Assumption 3.1 is equivalent to the following assumption:

Assumption 3.2 (see [6]) *$[A, B]$ is controllable, $[A, C]$ is observable, all eigenvalues of A lie on the imaginary axis.*

Let

$$\Theta(\omega, \bar{e}) = \pi(\gamma)\omega^\top(\Xi \otimes P)\omega + \mu\varsigma(\gamma)\bar{e}^\top(I_N \otimes Q)\bar{e},$$

where

$$\vartheta = \varepsilon_0 \max\left\{1, \frac{\lambda_{\min}(\Xi)}{\mu n\gamma_0}\right\}, \quad \varepsilon_0 = \frac{\lambda_{\max}(\bar{L}^T\bar{L})}{\varepsilon\lambda_{\min}(\Xi)}$$

and

$$\varsigma(\gamma) = \frac{\pi^2(\gamma)\mathrm{tr}(P)}{\lambda_{\min}(Q)}, \quad \gamma_0 \ge \frac{1 - \lambda_{\min}(Q)}{\lambda_{\max}(Q)}, \quad \mu > 0$$

Define the following set

$$\mathcal{E}(\gamma) = \left\{[\omega^\top, \bar{e}^\top]^\top \in \mathbb{R}^{2Nn} \middle| \Theta(\omega, \bar{e}) \le \vartheta^{-1}u_{\max}^2\right\} \tag{5}$$

Based on Assumption 3.2 and this set above, we obtain the following Laplacian-like output feedback control design.

Theorem 3.1 *For the multi-agent system (1), whose matrix pair $[A, B]$ satisfies Assumptions 3.2, and the initial condition $[x^T(0), \bar{e}^T(0)] \in \mathcal{E}(\gamma_0)$. If the underlying topology of the multi-agent system (1) with a directed spanning tree is structurally balanced, then multi-agent system (1) can achieve the bipartite consensus under the Laplacian-like output feedback control (2) with the time-varying control gain matrix $K(\gamma(t)) = B^TP(\gamma(t))$, where $P = P(\gamma(t))$ is the positive definite solution of the parametric Lyapunov equation in [17], Q is the positive definite solution of Lyapunov matrix equation in [19], and*

$$\gamma(t) = e^{\alpha t}\gamma_0, \quad \alpha = \frac{n\left(1 - \lambda_{\min}(Q)\right)}{\left(2n + \delta_c\right)\lambda_{\max}(Q)}$$

Proof. For convenience, let $\gamma(t)$ be abbreviated as γ, then $P(\gamma(t))$ can be denoted as $P(\gamma)$. When $\|u_i\|_\infty \le u_{\max}$, i.e. $\mathrm{sat}(u_i) = u_i$, then (3) is a linear system

$$\begin{cases} \dot{x} = & (I_N \otimes A)x - (L \otimes BB^TP(\gamma))(x - e) \\ \dot{e} = & [I_N \otimes (A - GC)]e \end{cases} \tag{6}$$

Let $\bar{x} = (D \otimes I_n)x$, and $\bar{e} = (D \otimes I_n)e$, then (6) can be rewritten as

$$\begin{cases} \dot{\bar{x}} = & (I_N \otimes A)\bar{x} - (\bar{L} \otimes BB^TP(\gamma))(\bar{x} - \bar{e}) \\ \dot{\bar{e}} = & [I_N \otimes (A - GC)]\bar{e} \end{cases} \tag{7}$$

Set the bipartite consensus error $\omega_i = \bar{x}_i - x^*$, where

$$x^* = \beta_1^1\bar{x}_1 + \beta_1^2\bar{x}_2 + \cdots + \beta_1^{n_1}\bar{x}_{n_1}$$

then

$$\omega = [(I_N - \mathbf{1}\beta^T) \otimes I_n]\bar{x} \tag{8}$$

where β is defined by Lemma 1 in [6]. In view of $\bar{L}(I_N - \mathbf{1}\beta^T) = \bar{L}$ and $(I_N - \mathbf{1}\beta^T)\bar{L} = \bar{L}$, it follows from (7) and (8) that

$$\begin{cases} \dot{\omega} = & (I_N \otimes A)\omega - (\bar{L} \otimes BB^TP(\gamma))\omega \\ & +(\bar{L} \otimes BB^TP(\gamma))\bar{e} \\ \dot{\bar{e}} = & [I_N \otimes (A - GC)]\bar{e} \end{cases} \tag{9}$$

Define the following Lyapunov functional:

$$\begin{aligned} V(\omega,\bar{e},t) =& V_1(\omega,t)+V_2(\bar{e},t)\\ V_1(\omega,t) =& \pi(\gamma)\omega^T(\Xi\otimes P(\gamma))\omega\\ V_2(\bar{e},t) =& \mu\varsigma(\gamma)\bar{e}^T(I_N\otimes Q)\bar{e}\end{aligned}$$

where $\Xi = \mathrm{diag}\{\Xi_1,\tau_2\Xi_2,\cdots,\tau_q\Xi_q\}$, $i\in\mathbf{I}[2,q]$, is defined by Lemma 1 in [6], $\varsigma(\gamma)=\lambda_{\min}^{-1}(Q)\pi^2(\gamma)\mathrm{tr}(P(\gamma))$, μ is independent of γ, Q is a positive definite solution of Lyapunov matrix equation in [19]. By using the property of $P(\gamma)$ in [17], it is easy to compute

$$\begin{aligned}\dot{\varsigma}(\gamma)\lambda_{\min}(Q) =& 2\pi(\gamma)\dot{\pi}(\gamma)\mathrm{tr}(P(\gamma))+\pi^2(\gamma)\mathrm{tr}(\dot{P})\\ \le& 2n\dot{\gamma}\pi(\gamma)\mathrm{tr}(P(\gamma))+\delta_c\dot{\gamma}\pi(\gamma)\mathrm{tr}(P(\gamma))\\ =&(2n+\delta_c)\dot{\gamma}\pi(\gamma)\mathrm{tr}(P(\gamma))\end{aligned}\tag{10}$$

This, together with the definition of $\varsigma(\gamma)$, yileds

$$\dot{\varsigma}(\gamma)\le\frac{(2n+\delta_c)\dot{\gamma}}{\pi(\gamma)}\varsigma(\gamma)$$

Based on this inequality above, the derivative of $V_1(\omega,t)$ and $V_2(\bar{e},t)$ along the trajectory of system (9) with respect to t can be respectively computed as follows:

$$\begin{aligned}\dot{V}_1(\omega,t) =& \dot{\pi}(\gamma)\omega^T(\Xi\otimes P(\gamma))\omega+\pi(\gamma)\omega^T(\Xi\otimes\dot{P}(\gamma))\omega\\ &+\pi(\gamma)\dot{\omega}^T(\Xi\otimes P(\gamma))\omega+\pi(\gamma)\omega^T(\Xi\otimes P(\gamma))\dot{\omega}\\ =& n\dot{\gamma}\omega^T\left(\Xi\otimes P(\gamma)\right)\omega+\pi(\gamma)\omega^T\left(\Xi\otimes\dot{P}(\gamma)\right)\omega\\ &+\pi(\gamma)\omega^T\left[\Xi\otimes(A^TP(\gamma)+P(\gamma)A)\right]\omega\\ &-\pi(\gamma)\omega^T\left[(\bar{L}^T\Xi+\Xi\bar{L})\otimes P(\gamma)BB^TP(\gamma)\right]\omega\\ &+2\pi(\gamma)\omega^T\left[\Xi\bar{L}\otimes P(\gamma)BB^TP(\gamma)\right]\bar{e}\end{aligned}\tag{11}$$

and

$$\begin{aligned}\dot{V}_2(\bar{e},t) =& \mu\dot{\varsigma}(\gamma)\bar{e}^T\left(I_N\otimes Q\right)\bar{e}+\mu\varsigma(\gamma)\bar{e}^T\\ &\times\left[I_N\otimes\left((A-GC)^TQ+Q(A-GC)\right)\right]\bar{e}\\ \le&\frac{(2n+\delta_c)\dot{\gamma}}{\pi(\gamma)}\varsigma(\gamma)\bar{e}^T\left(I_N\otimes Q\right)\bar{e}-\mu\varsigma(\gamma)\bar{e}^T\bar{e}\\ \le&\frac{(2n+\delta_c)\dot{\gamma}}{\pi(\gamma)}\lambda_{\max}(Q)\mu\varsigma(\gamma)\bar{e}^T\bar{e}-\mu\varsigma(\gamma)\bar{e}^T\bar{e}\end{aligned}\tag{12}$$

Choose $\varrho=\lambda_{\min}(\Xi^{-\frac{1}{2}}\Phi\Xi^{-\frac{1}{2}})$, it follows from Lemma 1 in [6] that

$$\begin{aligned}&\varrho\omega^T\left[\Xi\otimes P(\gamma)BB^TP(\gamma)\right]\omega\\ &\le\omega^T\left[(\bar{L}^T\Xi+\Xi\bar{L})\otimes P(\gamma)BB^TP(\gamma)\right]\omega\end{aligned}\tag{13}$$

Clearly, the following inequality holds

$$\begin{aligned}&2\pi(\gamma)\omega^T\left[\Xi\bar{L}\otimes P(\gamma)BB^TP(\gamma)\right]\bar{e}\\ &\le\frac{\pi(\gamma)}{\upsilon}\omega^T\left[\Xi\bar{L}\bar{L}^T\Xi\otimes P(\gamma)BB^TP(\gamma)\right]\omega\\ &\quad+\upsilon\pi(\gamma)\bar{e}^T\left[I_N\otimes P(\gamma)BB^TP(\gamma)\right]\bar{e}\\ &\le\frac{\lambda_{\max}(\Xi\bar{L}\bar{L}^T\Xi)\pi(\gamma)}{\upsilon\lambda_{\min}(\Xi)}\omega^T\left[\Xi\otimes P(\gamma)BB^TP(\gamma)\right]\omega\\ &\quad+\upsilon\pi(\gamma)\bar{e}^T\left[I_N\otimes P(\gamma)BB^TP(\gamma)\right]\bar{e}\end{aligned}\tag{14}$$

there exists a $\upsilon>0$ such that

$$\varepsilon=\varrho-\frac{\lambda_{\max}(\Xi\bar{L}\bar{L}^T\Xi)}{\upsilon\lambda_{\min}(\Xi)}>0,$$

and

$$\begin{aligned}&\upsilon\pi(\gamma)\bar{e}^T\left[I_N\otimes P(\gamma)BB^TP(\gamma)\right]\bar{e}\\ &\quad\le\upsilon\pi(\gamma)n\gamma\varepsilon^{-1}\bar{e}^T\left[I_N\otimes P(\gamma)\right]\bar{e}\\ &\quad\le\upsilon\varepsilon^{-1}\pi^2(\gamma)\mathrm{tr}(P(\gamma))\bar{e}^T\bar{e}\end{aligned}\tag{15}$$

Substituting (13), (14) and (15) into (11), we have

$$\begin{aligned}\dot{V}_1(\omega,t)\le& n\dot{\gamma}\omega^T\left(\Xi\otimes P(\gamma)\right)\omega+\pi(\gamma)\omega^T\left(\Xi\otimes\dot{P}(\gamma)\right)\omega\\ &+\upsilon\varepsilon^{-1}\pi^2(\gamma)\mathrm{tr}(P(\gamma))\bar{e}^T\bar{e}\\ &+\pi(\gamma)\omega^T\left[\Xi\otimes(A^TP(\gamma)+P(\gamma)A\right]\omega\\ &-\varepsilon\pi(\gamma)\omega^TP(\gamma)BB^TP(\gamma))\omega\\ =&\left(\frac{n\dot{\gamma}}{\pi(\gamma)}-\gamma\right)V_1(\omega,t)+\pi(\gamma)\omega^T\left(\Xi\otimes\dot{P}(\gamma)\right)\omega\\ &+\upsilon\varepsilon^{-1}\pi^2(\gamma)\mathrm{tr}(P(\gamma))\bar{e}^T\bar{e}\end{aligned}$$

According to the property of $P(\gamma)$ in [17]], it is easy to get

$$\begin{aligned}\dot{V}_1(\omega,t) \le& \left(\tfrac{(n+\delta_c)\dot{\gamma}}{\pi(\gamma)}-\gamma\right)V_1(\omega,t)\\ &+\mu\pi^2(\gamma)\mathrm{tr}(P(\gamma))\bar{e}^T\bar{e}\end{aligned}\tag{16}$$

where $\mu=\upsilon\varepsilon^{-1}$ is independent of γ. Combining (12) and (16), we have

$$\dot{V}(\omega,\bar{e},t)\le\lambda_1V_1(\omega,t)+\lambda_2\lambda_{\max}(Q)\mu\varsigma(\gamma)\bar{e}^T\bar{e}\tag{17}$$

where

$$\begin{aligned}\lambda_1 =& \frac{n+\delta_c}{\pi(\gamma)}\dot{\gamma}-\gamma,\\ \lambda_2 =& \frac{2n+\delta_c}{\pi(\gamma)}\dot{\gamma}-\frac{1-\lambda_{\min}(Q)}{\lambda_{\max}(Q)}.\end{aligned}$$

Finally, we shall prove $\|u_i\|_\infty\le u_{\max}$.

From (3), it is easy to see

$$\begin{aligned}u =& -(L\otimes K)(x-e)\\ =& -(D\bar{L}\otimes B^TP)\omega+(D\bar{L}\otimes B^TP)\bar{e}.\end{aligned}\tag{18}$$

Define the set

$$\mathcal{L}(\gamma)=\left\{[\omega^T,\bar{e}^T]^T\in\mathbb{R}^{2Nn}\middle|\|u\|_\infty\le u_{\max}\right\}\tag{19}$$

$\forall\ [\omega^T,\bar{e}^T]^T\in\mathcal{E}(\gamma)$, from the property of $P(\gamma)$ in [17] and (18), it follows

$$\|u_i\|_\infty^2\le\|u\|_\infty^2\le\|-(D\bar{L}\otimes B^TP)\omega+(D\bar{L}\otimes B^TP)\bar{e}\|_\infty^2.$$

Thus

$$\begin{aligned}\|u_i\|_\infty^2\le&\|-(D\bar{L}\otimes B^TP(\gamma))\omega\\ &+(D\bar{L}\otimes B^TP(\gamma))\bar{e}\|_2^2\\ \le&\vartheta V(\omega,\bar{e},t)\end{aligned}\tag{20}$$

where

$$\begin{aligned}\vartheta =& \varepsilon_0\max\left\{1,\frac{\lambda_{\min}(\Xi)}{\mu n\gamma_0}\right\}\\ \varepsilon_0 =& \varepsilon^{-1}\lambda_{\max}(\bar{L}^T\bar{L})\lambda_{\min}^{-1}(\Xi)\\ \mu =& \upsilon\varepsilon^{-1}\end{aligned}$$

Therefore,

$$\|u\|_\infty^2 \le \vartheta V(\omega(0), \bar{e}(0), 0)$$

According to the definition (19) of $\mathcal{L}(\gamma)$, we get

$$\vartheta V(\omega(0), \bar{e}(0), 0) \le u_{\max}^2$$

Thus $\mathcal{L}(\gamma) \subseteq \mathcal{E}(\gamma)$, i.e.

$$\|u_i\|_\infty \le u_{\max}, \quad \forall [\omega^T, \bar{e}^T]^T \in \mathcal{E}(\gamma)$$

The proof is complete. □

4 A numerical example

In this section, we shall provide a numerical example to show the feasibility of the proposed control method in this paper.

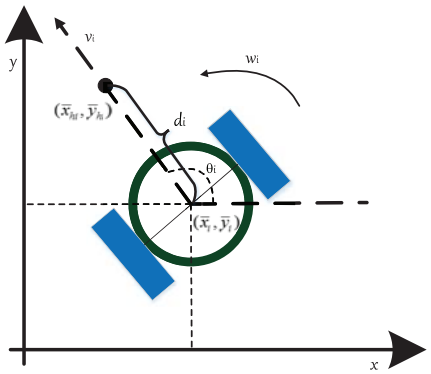

Fig. 1: Wheeled mobile robot model

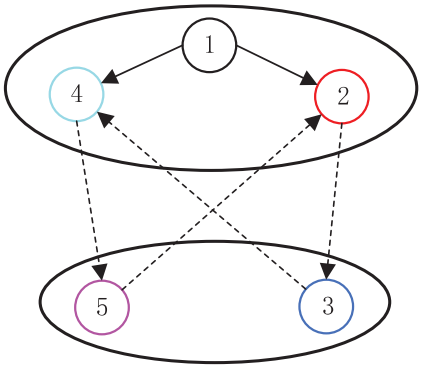

Fig. 2: Network communication topology

Example 4.1 *Consider five wheeled mobile robots labelled from node 1 to node 5. From Fig.1, model of the ith robot $i \in \mathbf{I}[1,5]$, can be described by the following kinetic equations in [21]*

$$\begin{cases} \dot{\bar{x}}_i = v_i \cos(\theta_i) \\ \dot{\bar{y}}_i = v_i \sin(\theta_i) \\ \dot{\theta}_i = \omega_i, i \in \mathbf{I}[1,5] \end{cases} \tag{21}$$

where $(\bar{x}_i, \bar{y}_i)$ lies in the central position of the ith robot, θ_i, v_i, and ω_i are represented as the orientation, the linear velocity, and the rotational velocity of the ith robot, respectively. At the fixed point $(\bar{x}_{hi}, \bar{y}_{hi})$, nonlinear dynamics equations (21) can be linearized as

$$\begin{cases} \bar{x}_{hi} = \bar{x}_i + d_i \cos(\theta_i) \\ \bar{y}_{hi} = \bar{y}_i + d_i \sin(\theta_i) \\ v_i = \cos(\theta_i) v_{xi} + \sin(\theta_i) v_{yi} \\ \omega_i = -d_i^{-1} \sin(\theta_i) v_{xi} + d_i^{-1} \cos(\theta_i) v_{yi} \end{cases} \tag{22}$$

Let

$$x_i = [\bar{x}_{hi}, \dot{\bar{x}}_{hi}, \bar{y}_{hi}, \dot{\bar{y}}_{hi}]^\top$$

and

$$u_i = [u_{xi}, u_{yi}]^\top, \quad i \in \mathbf{I}[1,5]$$

Using (22), system (21) can be reduced as linear time-invariant system

$$\begin{cases} \dot{x}_i = A x_i + B u_i \\ y_i = C x_i, i \in \mathbf{I}[1,5] \end{cases} \tag{23}$$

where

$$A = I_2 \otimes \begin{bmatrix} 0 & 1 \\ 0 & 0 \end{bmatrix}, C = I_2 \otimes [1,0]$$

and

$$B = I_2 \otimes [0,1]^\top$$

It is easy to verify that (A, B, C) satisfies assumption 3.2.

Let d_i be the distance between $(\bar{x}_{hi}, \bar{y}_{hi})$ and $(\bar{x}_i, \bar{y}_i)$. According to the relation between $(\bar{x}_{hi}, \bar{y}_{hi})$ and $(\bar{x}_i, \bar{y}_i)$ in Fig.1, it can be computed as

$$\begin{bmatrix} \bar{x}_{hi} \\ \bar{y}_{hi} \end{bmatrix} = \begin{bmatrix} \bar{x}_i \\ \bar{y}_i \end{bmatrix} + d_i \begin{bmatrix} \cos(\theta_i) \\ \sin(\theta_i) \end{bmatrix} \tag{24}$$

Take the derivative of (24), we have

$$\begin{bmatrix} \dot{\bar{x}}_{hi} \\ \dot{\bar{y}}_{hi} \end{bmatrix} = \begin{bmatrix} \cos(\theta_i) & -d_i \sin(\theta_i) \\ \sin(\theta_i) & d_i \cos(\theta_i) \end{bmatrix} \begin{bmatrix} v_i \\ \omega_i \end{bmatrix}$$

whose inverse expression is

$$\begin{bmatrix} v_i \\ \omega_i \end{bmatrix} = \frac{1}{d_i} \begin{bmatrix} d_i \cos(\theta_i) & d_i \sin(\theta_i) \\ -\sin(\theta_i) & \cos(\theta_i) \end{bmatrix} \begin{bmatrix} \dot{\bar{x}}_{hi} \\ \dot{\bar{y}}_{hi} \end{bmatrix}$$

Thus, by designing the control u_i of system (23), we can obtain the linear velocity v_i and the rotational velocity ω_i of the ith robot system (21), respectively. Since $[A, C]$ is observable, all poles of $A - GC$ can be arbitrary assigned. Choose

$$G = \begin{bmatrix} 0.3000 & 0 & 4.0900 & 1.2270 \\ -1.0000 & -0.3000 & 0.9000 & 0.1800 \end{bmatrix}^\top$$

then poles of $A - GC$ are $\{-0.3, -0.3, -0.3 + j, -0.3 - j\}$. Based on literature [6], let $\varrho = 0.4$ such that $\varepsilon = 0.3 > 0$. Let $d_i = 0.2$ (m), $|v_i| \le 0.3$ (m/s) and $|\omega_i| \le 0.4$ (rad/s), $i \in \mathbf{I}[1,5]$. Suppose that the robot 1 moves along the positive direction of the y-axis, whose linear velocity is 0.2 m/s, and that the initial conditions of the five robots are set as $[\bar{x}_{h1}, \bar{y}_{h1}] = [1,0]$, $[\bar{x}_{h2}, \bar{y}_{h2}] = [0.5,0]$, $[\bar{x}_{h3}, \bar{y}_{h3}] = [2,0]$, $[\bar{x}_{h4}, \bar{y}_{h4}] = [-1,0]$, $[\bar{x}_{h5}, \bar{y}_{h5}] = [-2,0]$, $e_i(0) = 0.1 \times [\bar{x}_{hi}, \bar{y}_{hi}]$, $i \in \mathbf{I}[1,5]$, respectively. Obviously, parametric Lyapunov equation in [17] has unique positive definite analytical solution

$$P(\gamma) = \frac{1}{\varepsilon} [I_2 \otimes \mathfrak{P}(\gamma)],$$

where

$$\mathfrak{P}(\gamma) = \begin{bmatrix} \gamma^3 & \gamma^2 \\ \gamma^2 & 2\gamma \end{bmatrix} \tag{25}$$

For the purpose of comparison, the two different numerical simulation are carried out as follows:

Case 1: *Static gain scheduling Laplacian-like output feedback control*

According to static gain scheduling function $\gamma_0 = 0.050976$ *in Fig. 3 and* (25)*, it follows*

$$P(\gamma_0) = I_2 \otimes \mathfrak{P}_0,$$

and

$$K(\gamma_0) = B^T P(\gamma_0) = I_2 \otimes \mathfrak{K}_0$$

where

$$\mathfrak{P}_0 = \begin{bmatrix} 0.4415 & 8.6618 \\ 8.6618 & 339.8400 \end{bmatrix} \times 10^{-3}$$

and

$$\mathfrak{K}_0 = \begin{bmatrix} 8.6618 \\ 339.8400 \end{bmatrix}^T \times 10^{-3}$$

Thus, we obtain a static gain scheduling Laplacian-like output feedback control

$$u_i = K(\gamma_0) \sum_{j=1}^{N} a_{ij}(\xi_j - \mathrm{sgn}(a_{ij})\xi_i) \tag{26}$$

Under this control, the motion trajectories of the five robots are shown in Fig. 4, and the linear velocity and rotational velocity of the robots are shown in Fig. 5 and 6, respectively. From Fig.4, we can observe that robot 2 and robot 4 both move along the same direction of robot 1, and they will eventually achieve the consensus, while robot 3 and robot 5 both move along the opposite direction of robot 1, and they will also reach the final consensus. From Fig.5 and 6, it can be seen the linear velocities of the five robots are all less than 0.3 (m/s), the rotational velocities of the five robots are all less than 0.4 (rad/s).

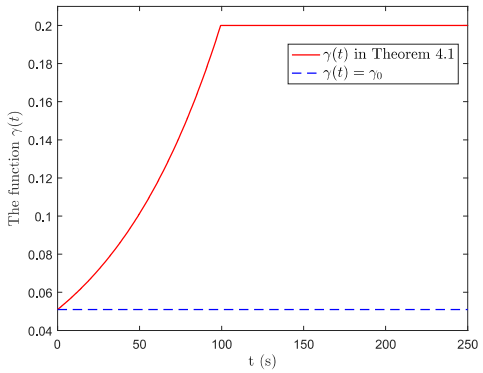

Fig. 3: Static and dynamic gain functions γ_0 and $\gamma(t)$

Case 2: *Dynamic gain scheduling Laplacian-like output feedback control*

Choose dynamic gain scheduling function $\gamma(t)$*, observer-based dynamic gain scheduling output feedback control* (2) *can be designed as*

$$u_i = K(\gamma(t)) \sum_{j=1}^{N} a_{ij}(\xi_j - \mathrm{sgn}(a_{ij})\xi_i) \tag{27}$$

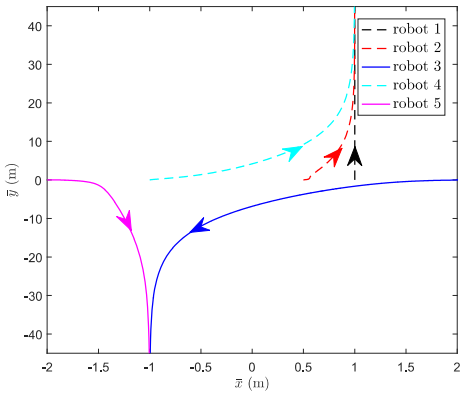

Fig. 4: The trajectories of five mobile robots with the static gain function γ_0

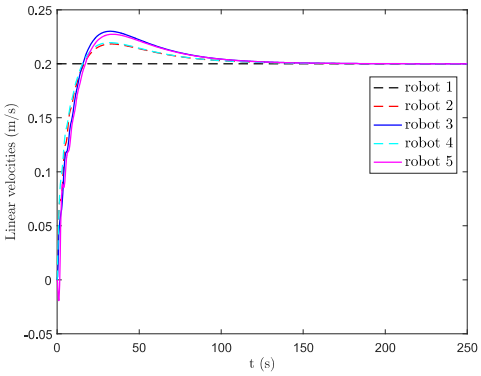

Fig. 5: Linear velocities of the five robots

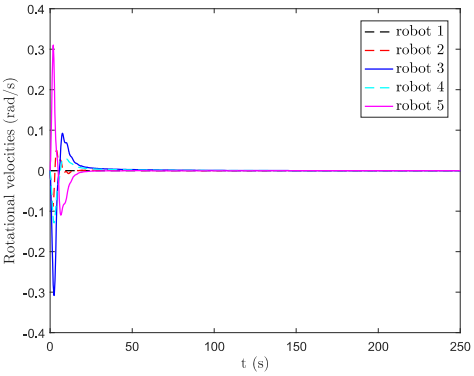

Fig. 6: Rotational velocities of the five robots

where the control gain matrix $K(\gamma)$ *including the dynamic gain scheduling function* γ *is*

$$K(\gamma) = \frac{1}{\varepsilon} \begin{bmatrix} \gamma^2 & 2\gamma & 0 & 0 \\ 0 & 0 & \gamma^2 & 2\gamma \end{bmatrix}.$$

Given the initial value of the dynamic gain scheduling function: $\gamma_0 = 0.050976$*, dynamic gain scheduling function* $\gamma(t)$ *is depicted in Fig.3, Under the dynamic gain scheduling Laplacian-like output feedback control* (27)*, the motion trajectories of the five robots are shown in Fig. 7, the linear and rotational velocities of the robots are shown in Fig. 8 and 9, respectively. From Fig.7, we can observe that robot 2 and robot 4 both move along the same direction of the lead-*

er robot 1, and they will eventually achieve the consensus, while robot 3 and robot 5 both move along the opposite direction of the robot 1, and they will also reach the final consensus. From Fig.8 and 9, it can be seen the linear velocities of the five robots are all less than 0.3 (m/s), the rotational velocities of the five robots are all less than 0.4 (rad/s).

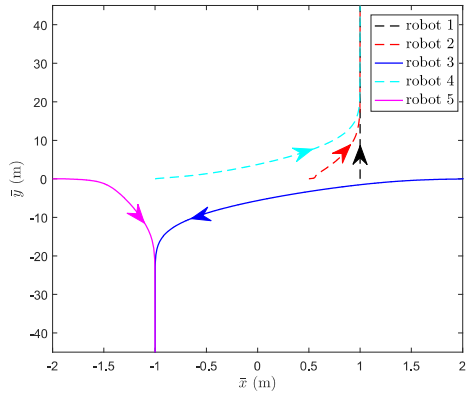

Fig. 7: the motion trajectories of five robots with dynamic gain scheduling function $\gamma(t)$

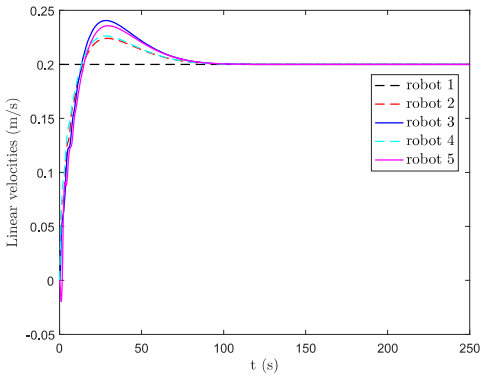

Fig. 8: Linear velocities of the five robots

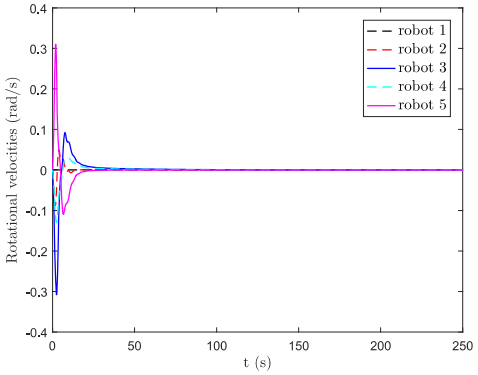

Fig. 9: Rotational velocities of the five robots

References

[1] R. Olfati-Saber, J. A. Fax, R. M. Murray, Consensus and cooperation in networked multi-agent systems[J], Proc. IEEE , 95(1): 215-233, 2007.

[2] M. H. Degroot, Reaching a consensus[J], J. Am. Stat. Assoc. 69(345): 118-121, 1974.

[3] Z. Zuo, M. Defoort, B. Tian, Z. Ding, Distributed consensus observer for multi-agent systems with high-order integrator dynamics[J], IEEE Trans. Autom. Control, 65(4): 1771-1778, 2020.

[4] H. L. Smith, Monotone Dynamical Systems: An Introduction to the Theory of Competitive and Cooperative Systems[M], American Mathematical Society, Providence, RI, 1995.

[5] W. Xia, M. Cao, K. H. Johansson, Structural balance and opinion separation in trust-mistrust social networks[J], IEEE Trans. Control Network Syst. 3(1): 46-56, 2016.

[6] J. Qin, W. Fu, W. X. Zheng, H. Gao, On the bipartite consensus for generic linear multi-agent systems with input saturation[J], IEEE Trans. Cybern, 47(8): 1948-1958, 2017.

[7] C. Altafini, Consensus problems on networks with antagonistic interactions[J], IEEE Trans. Autom. Control, 58(4): 935-946, 2013.

[8] H. Wang, W. Yu, G. Wen, G. Chen, Finite-time bipartite consensus for multi-agent systems on directed signed networks[J], IEEE Trans. Circuits Syst., 2018, 65(12): 4336–4348.

[9] J. Hu, H. Zhu, Adaptive bipartite consensus on coopetition networks[J], Phys. D, 307: 14-21, 2015.

[10] Y. Wu, Y. Zhao, J. Hu, Bipartite consensus control of high-order multi-agent systems with unknown disturbances[J], IEEE Trans. Syst. Man Cybern., 49(10): 2189-2199, 2019.

[11] T. Hu, Z. Lin, Control Systems with Actuator Saturation: Analysis and Design[M], Birkäuser, Boston, 2001.

[12] S. Bhowmick, S. Panja, Lag-bipartite consensus of linear multi-agent systems under saturating input over signed graph[C], IET Control Theory Appl., 13(3): 434-443, 2019.

[13] S. Bhowmick, S. Panja, Bipartite tracking of linear multi-agent systems under actuator saturation with relative output feedback[J], IEEE Trans. Circuits Syst., 68(1): 386-390, 2021.

[14] X.Y. Gao, J.Q. Wang, K.L. Teo, H.F. Yang, X.R. Yang, Dynamic gain scheduling control design for linear multi-agent systems subject to input saturation[J], J. Franklin I., 360: 4597-4625, 2023.

[15] D. Meng, Y. Jia, J. Du, Nonlinear finite-time bipartite consensus protocol for multi-agent systems associated with signed graphs[J], Int. J. Control, 88(10): 2074-2085, 2015.

[16] D. Meng, Z. Zuo, Signed-average consensus for networks of agents: a nonlinear fixed-time convergence protocol[J], Nonlinear Dyn., 85(1): 155–165, 2016.

[17] B. Zhou, Finite-time stabilization of linear systems by bounded linear time-varying feedback[J], Automatica, 113: 108760, 2020.

[18] H. Chu, J. Chen, Q. Wei, W. Zhang, Gain scheduling consensus of multi-agent systems subject to actuator saturation[J], Int. J. Control, 93(4): 771–782, 2020.

[19] Q. Wang, B. Zhou,C. Wen, et al. Output feedback gain scheduled control of actuator saturated linear systems with applications to the spacecraft rendezvous[J], J. Franklin I., 351(11): 5015-5033, 2014.

[20] H. Zhang, J. Chen.Bipartite consensus of multi-agent systems over signed graphs: State feedback and output feedback control approaches[J], Int. J. Robust Nonlin., 27(1): 3-14, 2017.

[21] W. Zhang, Z. Zuo,Y. Wang, et al. Double-integrator dynamics for multi-agent systems with antagonistic reciprocity[J], IEEE T. Cybernetics, 50(9): 4110-4120, 2020.

Proceedings of the 3rd Conference on Fully Actuated System Theory and Applications
May 10-12, 2024, Shenzhen, China

Multi-Agent Clusters Flocking Control Via High-Order Fully Actuated System Approach

Qimin Hou[1], Zhenhuan Wang[1], Yabin Gao[1], Hanjun Shang[2], Jiyuan Kuang[1], Zhuang Liu[1]

1. School of Astronautics, Harbin Institute of Technology, Harbin 150001, P. R. China
E-mail: yabingao@hit.edu.cn

2. Elite Engineers School, Harbin Institute of Technology, Harbin 150001, P. R. China

Abstract: This paper focuses on the clusters flocking control problem of multi-agents by utilizing a high-order fully actuated system (HOFAS) approach. A multilayer leader-following formation model of second-order multi-agent systems (MASs) is established. The mathematical model of the formation system with uncertainties is transformed into a class of HOFASs facilitating the flexibility of control design. A new robust formation control law is designed based on the HOFAS approach, achieving the desired multi-agent clusters flocking. The analysis of the multi-agent clusters flocking formation system is presented based on the Lyapunov function, of which the results show that the formation errors can converge to an ellipsoidal region. Simulation results validate the effectiveness of the theoretical results.

Key Words: Multi-agent systems, Formation control, Clusters flocking, Nonlinear dynamics, Second-order systems

1 Introduction

The inspiration for multi-agent systems (MASs) is derived from scientific research and exploration of the behavior of organisms in the natural world, such as pattern formation of bacteria colonies, triangle formation of bird groups, and cooperative hunting of the herd [1]. The MASs consist of numerous intelligent agents with the ability of communication, cognition, perception control, and behavior. Compared with a single agent, MASs can accomplish more large and complex tasks with higher task completion rates [2]. More importantly, MASs gain many advantages in the following aspects, including reducing cost and error, improving system efficiency and flexibility, implementing parallel processing, achieving stability, and so on.

In the last few years, the extensive exploration of cooperative control for MASs [3–7] has promoted different applications in the military and civilian fields, such as the formation of multi-robots [8], autonomous underwater vehicles [9], the formation of unmanned aerial vehicles, and smart grid [10]. As one of the important and fundament research issues of coordinated control, formation control in MASs which means to control multiple agents to move and maintain in a predesigned particular configuration attracted much research attention [11–13]. As the number of nodes rises and the complexity of formation tasks increases, stochastic disturbances exists, and physical attacks escalates, it significantly impacts the robustness of MASs formation [14].

To accomplish complex tasks, MASs often need to divide into multiple subgroups/clusters according to task requirements, achieving consistency within each cluster while allowing for differences between clusters [15]. For instance, unmanned aerial vehicles (UAVs) and unmanned ground vehicles (UGVs) collaborate in hilly and mountainous terrains to conduct exploration and communication tasks and multiple UAV-UGV teams coordinate in ground-air collaborative encirclement operations shown in Fig. 1. The clustering consensus control algorithms proposed in [16] can achieve asymptotic convergence of MASs. This means that the states of agents within each subgroup converge over time to different consensus values.

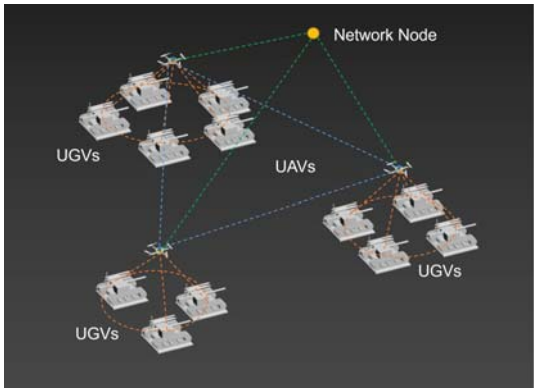

Fig. 1: An illustration of clusters cooperation of UAVs and UGVs

The high-order fully actuated system (HOFAS) approach was developed in [17]. By applying the HOFAS, the control designed for known nonlinearities can transform the closed-loop system into a linear one with arbitrary eigenstructures. HOFASs offer greater convenience for dynamical system control compared to state-space models [17, 18]. In [17], a two-step procedure was proposed to convert a state-space model into a pseudo strict-feedback system (SFS) and then into an HOFAS. In [18], the first-, second-, and high-order SFSs were put forward and converted to HOFAS models. The Lyapunov stability theory was applied to resolve robust control problems [19] for HOFASs with uncertainties. HOFAS models with multiple orders for general dynamical control systems were proposed for the first time in [20]. Therefore, the HOFAS approach has broad prospects in the field of nonlinear control.

Motivated by the above discussions, this paper investigates the clusters flocking control problem of second-order

This work is supported by the National Natural Science Foundation of China (62103118, 62033005, 62320106001, 62373127), the Science Center Program of National Natural Science Foundation of China under Grant 62188101, and in part by the Heilongjiang Touyan Team Program, the Postdoctoral Science Foundation of Heilongjiang Province (LBH-Z21015), and the China Postdoctoral Science Foundation (2021M700037 and 2021T140160).

MASs with nonlinear dynamics. Based on the HOFAS theory, a multilayer leader-following formation system model is established. Drawing inspiration from [19], a robust formation control law is designed, utilizing HOFAS theory to converge formation errors to an elliptical region. Formulation rules for leader-following formation control are presented, enabling MASs to achieve and maintain the desired formation. The main contribution of this paper lies in the successful application of the HOFAS method to MAS formation control, further enriching the applications of the HOFAS methodology. The rest of this article is organized as follows. In Section 2, a clusters flocking formation model based on the HOFAS theory is provided. In Section 3, a robust clusters flocking control is designed. Section 4 gives numerical simulations to verify the theoretical results. Finally, concluding remarks are stated in Section 5.

2 Problem Description and Preliminaries

To address the issue of complex tasks, the intelligent agents within the system are divided into multiple clusters. Through collaboration among these clusters, various tasks can be accomplished.

The system model is designed with a three-layer architecture, comprising one virtual leader, M cluster leaders, and N followers, where the clusters' strucure is shown in Fig. 2. N followers are divided into M clusters, and each cluster has exactly one cluster leader. For ease of expression, we define the ith cluster leader leads N_i followers for $i \in 1, 2, \cdots, M$. We can obtain $\sum_{i=1}^{M} N_i = N$. All cluster leaders are centrally controlled by the virtual leader. The communication between the virtual leader and cluster leader is unidirectional, and there is no direct communication between the virtual leader and followers. Followers only receive information from their respective cluster leaders. For heterogeneous systems with inconsistent dimensions, we extend the dimensions of UAVs to three-dimensional space, where the displacement and velocity along the Z -axis are consistently set to 0.

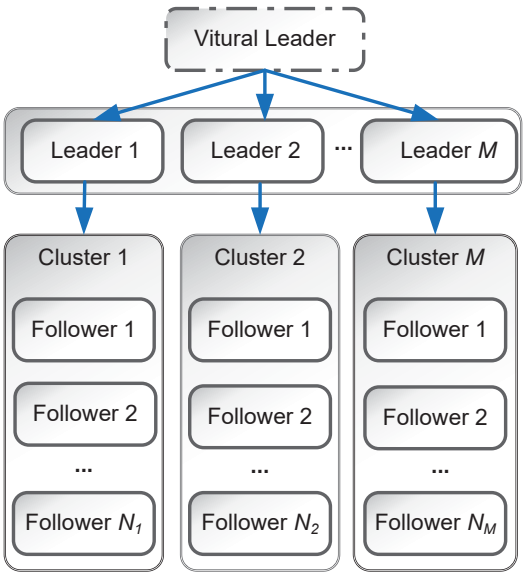

Fig. 2: An illustration of the block diagram of the clusters flocking system.

Consider the second-order nonlinear dynamics with the agents. The models of all agents can be unified and expressed as follows.

$$\begin{cases} \dot{x}_k(t) = v_k(t), \\ \dot{v}_k(t) = u_k(t) + f(v_k(t)), \quad k = 0, 1, \cdots, M+N, \end{cases} \tag{1}$$

where $x_k(t) \in \mathbb{R}^n$, $v_k(t) \in \mathbb{R}^n$, and $u_k(t) \in \mathbb{R}^n$ can be the position state, velocity state, and control input of the kth agent respectively. The unknown nonlinearity of the dynamics is represented by $f\left(v_k(t)\right) \in \mathbb{R}^n$.

Assumption 1 *The nonlinear dynamics are vector-valued functions and are continuously differentiable, and there exists a positive coefficient β satisfying the following condition: $||f\left(v_i(t)\right) - f\left(v_j(t)\right)|| \leq \beta||v_i(t) - v_j(t)||$, $i, j \in \{0, 1, \cdots, M+N\}$.*

We define the following formation error variables for the ith cluster leader:

$$\begin{cases} x_{ei} = x_i - h_i - x_0, \\ v_{ei} = v_i - v_0. \end{cases} \tag{2}$$

For the ith cluster, we define the following formation error variables for the $j \in \{1, 2, \cdots, N_i\}$ follower:

$$\begin{cases} x_{ej,i} = x_{j,i} - h_{j,i} - x_i, \\ v_{ej,i} = v_{j,i} - v_i. \end{cases} \tag{3}$$

In order to achieve the cluster flocking, the formation errors xe should convergent to zero. The following definition provides a criterion for such a formation system.

Definition 1 *Consider the MAS* (1)*. For any given bounded initial state $\{x_k(0), v_k(0)\}$, the desired formation of MASs is supposed to be achieved if the cluster leaders and the followers satisfy*

$$\begin{cases} \lim_{t\to\infty} \left(x_i\left(t\right) - h_i\left(t\right) - x_0\left(t\right)\right) & = 0, \\ \lim_{t\to\infty} \left(x_{j,i}\left(t\right) - h_{j,i}\left(t\right) - x_i\left(t\right)\right) & = 0, \end{cases} \tag{4}$$

where $h_i\left(t\right)$ indicates the desired formation vector form the ith cluster leader to the virtual leader; $h_{j,i}\left(t\right)$ represent the desired output formations of the jth follower to the ith cluster leader.

Let us analyze the dynamic system of the desired formation system. Then, we transform it into an HOFAS for further control design.

Firstly, for the cluster leaders, from (1) and (2) we have

$$\dot{x}_{ei} = \dot{x}_i - \dot{x}_0 - \dot{h}_i, \tag{5}$$

$$\dot{v}_{ei} = \dot{v}_i - \dot{v}_0 = f(x_i,\, v_i) - f(x_0,\, v_0) + u_i - u_0. \tag{6}$$

Then, we can obtain the following HOFAS model of the virtual leader and cluster leaders:

$$\ddot{x}_{ei} = \dot{v}_{ei} = f(\dot{x}_{ei}) + u_i - u_0 - \ddot{h}_i. \tag{7}$$

Similarly, the error system between the followers in each cluster and the leader is analyzed by

$$\dot{x}_{ej,i} = \dot{x}_{j,i} - \dot{x}_i - \ddot{h}_{j,i}, \tag{8}$$

$$\dot{v}_{ej,i} = \dot{v}_{j,i} - \dot{v}_{j,i} = f(\, v_{j,i}) - f(\, v_{j,i}) + u_{j,i} - u_i. \quad (9)$$

We can obtain the HOFAS model of cluster leader and followers

$$\ddot{x}_{ej,i} = \dot{v}_{ej,i} = \ f(\dot{x}_{ej,i}) + u_{j,i} - u_i - \ddot{h}_{j,i}. \quad (10)$$

For convenience, we denote

$$u_{i1} \triangleq u_i - u_0 - \ddot{h}_i, \quad (11)$$

$$u_{j,i1} \triangleq u_{j,i} - u_i - \ddot{h}_{j,i}. \quad (12)$$

Then, we can get

$$\ddot{x}_{ei} = f(\dot{x}_{ei}) + u_{i1}, \quad (13)$$

$$\ddot{x}_{ej,i} = f(\dot{x}_{ej,i}) + u_{j,i1}. \quad (14)$$

Hence, equation (13) and (14) fulfills the form outlined in the HOFAS model introduced in [19], when $n = 2$.

$$\begin{aligned} z^{(n)} = & f\left(z^{(0\sim n-1)}\right) + \Delta f\left(z^{(0\sim n-1)}\right) \\ & + L\left(z^{(0\sim n-1)}\right) u. \end{aligned} \quad (15)$$

where $z^{(0\sim n)} \triangleq [z \quad \dot{z} \quad \cdots \quad z^{(n)}]^{\mathrm{T}}$.

In order to achieve errors convergence in Definition 1, according to the HOFAS theory, the error systems (13) and (14) are converged by designing an HOFAS controller, which completes the formation of the cluster system.

Lemma 1 *[19] For any $\mu > 0$, there exists a set of matrices $A_i \in \mathbb{R}^{r\times r}, i = 0, 1, \cdots, n-1$ and a positive definite matrix $P\left(A^{0\sim n-1}\right)$ satisfying*

$$\mathrm{Re}\,\lambda_i\left(\Phi\left(A^{0\sim n-1}\right)\right) < -\frac{\mu}{2}, \quad i = 1, 2, \cdots, nr, \quad (16)$$

$$\begin{aligned} \Phi^{\mathrm{T}}\left(A^{0\sim n-1}\right) P\left(A^{0\sim n-1}\right) + P\left(A^{0\sim n-1}\right) \Phi\left(A^{0\sim n-1}\right) \\ < -\mu P\left(A^{0\sim n-1}\right), \end{aligned} \quad (17)$$

where

$$\mathrm{A}^{0\sim n-1} \triangleq [A_0 \quad A_1 \quad \cdots \quad A_{n-1}] \in \mathbb{R}^{r\times nr},$$

$$\Phi(A^{0\sim n-1}) \triangleq \begin{bmatrix} 0 & I & & \\ & & \ddots & \\ & & & I \\ -A_0 & -A_1 & \cdots & -A_{n-1} \end{bmatrix} \in \mathbb{R}^{nr\times nr},$$

$$P(A^{0\sim n-1}) \triangleq \begin{bmatrix} P_1 & P_2 & \cdots & P_n \end{bmatrix}, \quad P_i \in \mathbb{R}^{nr\times r},$$

$$P_L(A^{0\sim n-1}) \triangleq P(A^{0\sim n-1}) \begin{bmatrix} 0 \\ I_r \end{bmatrix} = P_n \in \mathbb{R}^{nr\times r}.$$

Lemma 2 *Let a and b be two real numbers, and $b > 0$. Then, the following relation holds:*

$$a - \frac{a^2}{4b} \leqslant b. \quad (18)$$

Remark 1 *For an arbitrarily given matrix $F \in R^{nr\times nr}$, the matrix $A^{0\sim n-1}$ and the non-singular matrix $V \in R^{nr\times nr}$ satisfying*

$$\Phi\left(A^{0\sim 1}\right) = VFV^{-1}, \quad (19)$$

in which

$$A^{0\sim 1} = -ZF^nV^{-1}(Z, F) \quad , \quad (20)$$

$$V = V(Z, F) = \begin{bmatrix} Z \\ ZF \\ \vdots \\ ZF^{n-1} \end{bmatrix}, \quad (21)$$

where $Z \in \mathbb{R}^{r\times nr}$ satisfies $\det V(Z, F) \neq 0$.

3 Clusters Flocking Control Design and Analysis

Theorem 1 *Consider the MASs sysytem* (13) *and* (14)*. For given positive numbers $\mu_1, \mu_2, \varepsilon_1$, and ε_2, by using the following control laws*

$$\begin{cases} u_{i1} = -I^{-1}(A_a^{0\sim 1}x_{ei}^{(0\sim 1)} + u_a^*), \\ u_a^* = \frac{1}{4\varepsilon_1} \parallel \beta\dot{x}_{ei} \parallel_2^2 P_L^{\mathrm{T}}(A_a^{0\sim 1})x_{ei}^{(0\sim 1)}, \end{cases} \quad (22)$$

$$\begin{cases} u_{j,i1} = -I^{-1}(A_b^{0\sim 1}x_{ej,i}^{(0\sim 1)} + u_b^*), \\ u_b^* = \frac{1}{4\varepsilon_2} \parallel \beta\dot{x}_{ej,i} \parallel_2^2 P_L^{\mathrm{T}}(A_b^{0\sim 1})x_{ej,i}^{(0\sim 1)}, \end{cases} \quad (23)$$

then the formation errors $x_{ei}^{(0\sim 1)}$ and $x_{ej,i}^{(0\sim 1)}$ can converge into the following ellipsoid centred at the origin, respectively:

$$\begin{aligned} & \Theta_{\mu_1,\varepsilon_1}(0) \\ & = \left\{ x_{ei}^{(0\sim 1)} \mid \left(x_{ei}^{(0\sim 1)}\right)^{\mathrm{T}} P\left(A_a^{0\sim 1}\right) x_{ei}^{(0\sim 1)} \leq \frac{\varepsilon_1}{\mu_1} \right\}, \end{aligned} \quad (24)$$

$$\begin{aligned} & \Theta_{\mu_2,\varepsilon_2}(0) \\ & = \left\{ x_{ej,i}^{(0\sim 1)} \mid \left(x_{ej,i}^{(0\sim 1)}\right)^{\mathrm{T}} P\left(A_b^{0\sim 1}\right) x_{ej,i}^{(0\sim 1)} \leq \frac{\varepsilon_2}{\mu_2} \right\}, \end{aligned} \quad (25)$$

where $A_a^{0\sim 1}$, $A_b^{0\sim 1}$, $P_L\left(A_a^{0\sim 1}\right)$, and $P_L\left(A_b^{0\sim 1}\right)$ can be obtained by Lemma 1 and Remark 1.

Proof: Substituting the control law(22) into system (13) gives the following closed-loop system

$$\ddot{x}_{ei} + A_a^{0\sim 1}x_{ei}^{(0\sim 1)} = \phi(x_{ei}^{(0\sim 1)}), \quad (26)$$

where

$$\phi(x_{ei}^{(0\sim 1)}) = -\frac{1}{4\varepsilon_1} \parallel \beta\dot{x}_{ei} \parallel_2^2 P_L^{\mathrm{T}}(A_a^{0\sim 1})x_{ei}^{(0\sim 1)} + f(x_{ei}^{(0\sim 1)}). \quad (27)$$

The closed-loop system (27) can be written in the following state-space form:

$$\dot{x}_{ei}^{(0\sim 1)} = \Phi(A_a^{0\sim 1})x_{ei}^{(0\sim 1)} + \begin{bmatrix} 0_r \\ \phi(x_{ei}^{(0\sim 1)}) \end{bmatrix}. \quad (28)$$

From Lemma 1, there exists $\Phi(A_a^{0\sim 1})$ and a positive definite matrix $P(A_a^{0\sim 1})$ satisfying (17). Then, the following Lyapunov function is chosen for the system (28):

$$V = \frac{1}{2}\left(x_{ei}^{(0\sim 1)}\right)^{\mathrm{T}} P(A_a^{0\sim 1})x_{ei}^{(0\sim 1)}. \quad (29)$$

In view of (17) and (28), we have

$$\begin{aligned}\dot{V} &= \frac{1}{2}\left(\dot{x}_{ei}^{(0\sim1)}\right)^{\mathrm{T}} P x_{ei}^{(0\sim1)} + \frac{1}{2}\left(x_{ei}^{(0\sim1)}\right)^{\mathrm{T}} P \dot{x}_{ei}^{(0\sim1)} \\ &= \frac{1}{2}\left(\Phi x_{ei}^{(0\sim1)} + \begin{bmatrix} 0_r \\ \phi(x_{ei}^{(0\sim1)}) \end{bmatrix}\right)^{\mathrm{T}} P x_{ei}^{(0\sim1)} + \frac{1}{2}\left(x_{ei}^{(0\sim1)}\right)^{\mathrm{T}} \\ &\times P\left(\Phi x_{ei}^{(0\sim1)} + \begin{bmatrix} 0_r \\ \phi\left(x_{ei}^{(0\sim1)}\right) \end{bmatrix}\right) \\ &= \frac{1}{2}\left(x_{ei}^{(0\sim1)}\right)^{\mathrm{T}}\left(\Phi^{\mathrm{T}} P + P\Phi\right) x_{ei}^{(0\sim1)} \\ &+ \left(x_{ei}^{(0\sim1)}\right)^{\mathrm{T}} P \begin{bmatrix} 0_r \\ \phi\left(x_{ei}^{(0\sim1)}\right) \end{bmatrix} \\ &\le -\frac{\mu_1}{2}\left(x_{ei}^{(0\sim1)}\right)^{\mathrm{T}} P x_{ei}^{(0\sim1)} + \left(x_{ei}^{(0\sim1)}\right)^{\mathrm{T}} P_L \phi(x_{ei}^{(0\sim1)}) \\ &= -\mu_1 V + \left(x_{ei}^{(0\sim1)}\right)^{\mathrm{T}} P_L \phi(x_{ei}^{(0\sim1)}).\end{aligned}$$

Next, let us consider the last term of the above inequation. It follows from Assumption 1, Lemma 2, and Equation (28) that

$$\begin{aligned}&\left(x_{ei}^{(0\sim1)}\right)^{\mathrm{T}} P_L \phi(x_{ei}^{(0\sim1)}) \\ &= -\frac{\|\beta \dot{x}_{ei}\|_2^2}{4\varepsilon}\left[\left(x_{ei}^{(0\sim1)}\right)^{\mathrm{T}} P_L P_L^{\mathrm{T}} x_{ei}^{(0\sim1)}\right] \\ &+ \left(x_{ei}^{(0\sim1)}\right)^{\mathrm{T}} P_L f(x_{ei}^{(0\sim1)}) \\ &= -\frac{\|\beta \dot{x}_{ei}\|_2^2}{4\varepsilon}\left\|P_L^{\mathrm{T}} x_{ei}^{(0\sim1)}\right\|^2 + \left(x_{ei}^{(0\sim1)}\right)^{\mathrm{T}} P_L f(x_{ei}^{(0\sim1)}) \\ &\le -\frac{\|\beta \dot{x}_{ei}\|_2^2}{4\varepsilon}\left\|P_L^{\mathrm{T}} x_{ei}^{(0\sim1)}\right\|^2 + \left\|f(x_{ei}^{(0\sim1)})\right\|\left\|P_L^{\mathrm{T}} x_{ei}^{(0\sim1)}\right\| \\ &\le -\frac{\|\beta \dot{x}_{ei}\|_2^2}{4\varepsilon}\left\|P_L^{\mathrm{T}} x_{ei}^{(0\sim1)}\right\|^2 + \|\beta \dot{x}_{ei}\|\left\|P_L^{\mathrm{T}} x_{ei}^{(0\sim1)}\right\| \\ &\le \varepsilon_1.\end{aligned} \tag{30}$$

Combining the above two equations, gives

$$\dot{V} \le -\mu_1 V + \varepsilon_1. \tag{31}$$

Then, it follows from the Comparison Theorem that

$$V \le V(0)\,\mathrm{e}^{-\mu_1 t} + \frac{\varepsilon_1}{\mu_1}\left(1 - \mathrm{e}^{-\mu_1 t}\right), \tag{32}$$

which gives

$$V \le \left(V(0) - \frac{\varepsilon_1}{\mu_1}\right)\mathrm{e}^{-\mu_1 t} + \frac{\varepsilon_1}{\mu_1} \to \frac{\varepsilon_1}{\mu_1}, \quad t \to \infty. \tag{33}$$

Thus, the formation errors $x_{ei}^{(0\sim1)}$ in cluster leader layer eventually converge into the ellipsoid $\Theta_{\mu_1,\varepsilon_1}(0)$. Similarly, we can prove that the formation errors $x_{ej,i}^{(0\sim1)}$ in follower layer eventually converge into the ellipsoid $\Theta_{\mu_2,\varepsilon_2}(0)$. This implies that the system (13) and (14) can achieve the desired formation. The proof is completed.

4 Simulation Results

To validate the obtained HOFAS formation control protocol, this section consider a heterogeneous cluster system consisting of 12 UGVs and 3 UAVs.

Firstly, we design $\mu_1 = \mu_2 = 10$, $\varepsilon_1 = \varepsilon_2 = 1$ and the parameter matrices as $F = \mathrm{diag}\{-6, -7, -8, -9, -10, -11\}$, $Z = [I_3 \quad I_3]$. Then, we can solve $A_a^{0\sim1}$, $A_b^{0\sim1}$, $P_L^T(A_a^{0-1})$, and $P_L^T(A_b^{0-1})$ as

$$A_a^{0\sim1} = A_b^{0\sim1} = \begin{bmatrix} 54 & 0 & 0 & 15 & 0 & 0 \\ 0 & 70 & 0 & 0 & 17 & 0 \\ 0 & 0 & 88 & 0 & 0 & 19 \end{bmatrix},$$

$$P_L(A_a^{0\sim1}) = P_L(A_b^{0\sim1}) = \begin{bmatrix} 1.6214 & 0 & 0 \\ 0 & 0.9043 & 0 \\ 0 & 0 & 0.5958 \\ 0.1929 & 0 & 0 \\ 0 & 0.1080 & 0 \\ 0 & 0 & 0.0731 \end{bmatrix}.$$

The uncertainties are considered as: $f(v_i(t)) = -0.002v_i^2(t) - 0.003$. We set the maximum velocity to not exceed 50 m/s, so we can obtain that $\beta = 0.14$. The initial position of the virtual leader and three cluster leaders are given as $x_0(0) = [3, 3, 5]^{\mathrm{T}}$, $x_1(0) = [2, 0, 0]^{\mathrm{T}}$, $x_2(0) = [2, 2, 0]^{\mathrm{T}}$, $x_3(0) = [0, 2, 0]^{\mathrm{T}}$. The desired formation vectors are given as: $h_1 = [5, 0, 2]^{\mathrm{T}}$, $h_2 = [0, 5, 0]^{\mathrm{T}}$, $h_3 = [-5, 5, 3]^{\mathrm{T}}$. The initial position of the followers are given as: $x_{1,1} = [1, -2]^{\mathrm{T}}$, $x_{2,1} = \left[\cos(\frac{2\pi}{3}), \sin(\frac{2\pi}{3}) - 2\right]^{\mathrm{T}}$, $x_{3,1} = \left[\cos(\frac{4\pi}{3}), \sin(\frac{4\pi}{3}) - 2\right]^{\mathrm{T}}$, $x_{1,2} = [-1, -2]^{\mathrm{T}}$, $x_{2,2} = \left[\cos(\frac{\pi}{2}) - 2, \sin(\frac{\pi}{2}) - 2\right]^{\mathrm{T}}$, $x_{3,2} = [\cos(\pi) - 2, \sin(\pi) - 2]^{\mathrm{T}}$, $x_{4,2} = \left[\cos(\frac{3\pi}{2}) - 2, \sin(\frac{3\pi}{2}) - 2\right]^{\mathrm{T}}$, $x_{1,3} = [-2, 0]^{\mathrm{T}}$, $x_{2,3} = \left[\cos(\frac{2\pi}{5}) - 3, \sin(\frac{2\pi}{5})\right]^{\mathrm{T}}$, $x_{3,3} = \left[\cos(\frac{4\pi}{5}) - 3, \sin(\frac{4\pi}{5})\right]^{\mathrm{T}}$, $x_{4,3} = \left[\cos(\frac{6\pi}{5}) - 3, \sin(\frac{6\pi}{5})\right]^{\mathrm{T}}$, $x_{5,3} = \left[\cos(\frac{8\pi}{5}) - 3, \sin(\frac{8\pi}{5})\right]^{\mathrm{T}}$.

The initial velocity of the virtual leader is set to $v_0(0) = [1, 1, 0]^{\mathrm{T}}$. The initial velocity of cluster leaders, and followers are set to 0 in each axis direction. The desired formation vector are given as: $h_{1,1} = \left[\cos(\frac{-1\pi}{5}), \sin(\frac{-1\pi}{5})\right]^{\mathrm{T}}$, $h_{2,1} = \left[\cos(\frac{7\pi}{15}), \sin(\frac{7\pi}{15})\right]^{\mathrm{T}}$, $h_{3,1} = \left[\cos(\frac{17\pi}{15}), \sin(\frac{17\pi}{15})\right]^{\mathrm{T}}$, $h_{1,2} = \left[\cos(\frac{2\pi}{10}), \sin(\frac{2\pi}{10})\right]^{\mathrm{T}}$, $h_{2,2} = \left[\cos(\frac{7\pi}{10}), \sin(\frac{7\pi}{10})\right]^{\mathrm{T}}$, $h_{3,2} = \left[\cos(\frac{12\pi}{10}), \sin(\frac{12\pi}{10})\right]^{\mathrm{T}}$, $h_{4,2} = \left[\cos(\frac{17\pi}{10}), \sin(\frac{17\pi}{10})\right]^{\mathrm{T}}$, $h_{1,3} = [1, 0]^{\mathrm{T}}$, $h_{2,3} = \left[\cos(\frac{2\pi}{5}), \sin(\frac{2\pi}{5})\right]^{\mathrm{T}}$, $h_{3,3} = \left[\cos(\frac{4\pi}{5}), \sin(\frac{4\pi}{5})\right]^{\mathrm{T}}$, $h_{4,3} = \left[\cos(\frac{6\pi}{5}), \sin(\frac{6\pi}{5})\right]^{\mathrm{T}}$, $h_{5,3} = \left[\cos(\frac{8\pi}{5}), \sin(\frac{8\pi}{5})\right]^{\mathrm{T}}$.

Fig. 3 illustrates the motion trajectories of the virtual leader, three cluster leaders and all the followers. It is evident that the control algorithm proposed in this paper guarantees the cluster system can rapidly achieve the desired formation. Figs. 4–6 show the position errors of the agents, we can know position formation errors converge to 0, and from Figs. 7–9 velocity errors of agents also converge to 0, which implies the agents maintain the desired formation and a consistent velocity. Figs. 10–12 illustrates the control inputs of the agents in various directions. Evidently, simulation results mean that each layer's agents can follow the corresponding leader with the desired formation and keep the same velocity.

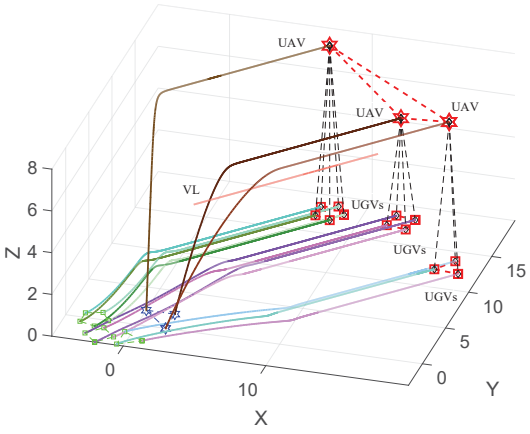

Fig. 3: Trajectories of the agents

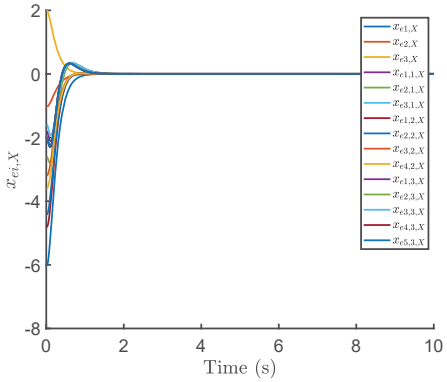

Fig. 4: Position errors of X-axis.

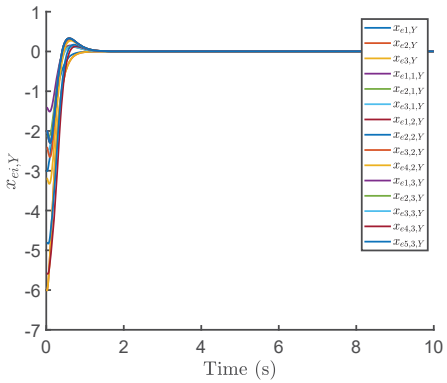

Fig. 5: Position errors of Y-axis.

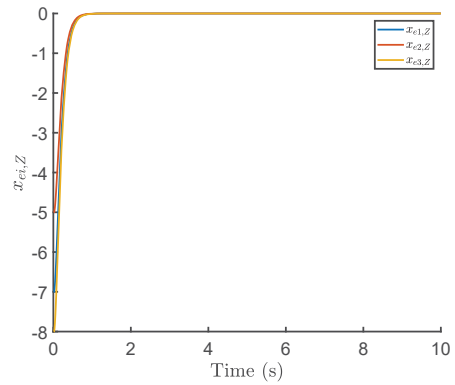

Fig. 6: Position errors of Z-axis.

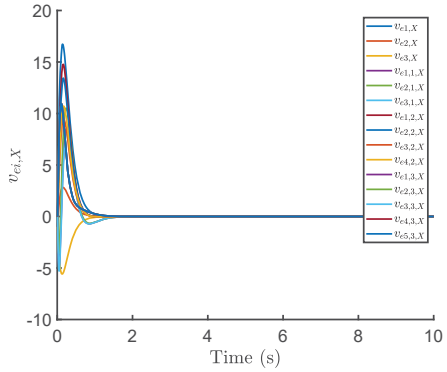

Fig. 7: Velocity errors of X-axis.

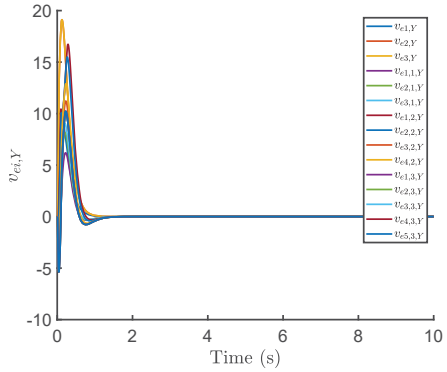

Fig. 8: Velocity errors of Y-axis.

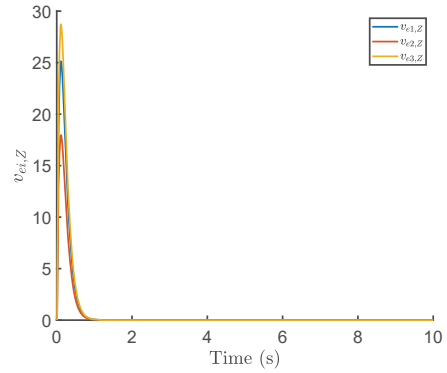

Fig. 9: Velocity errors of Z-axis.

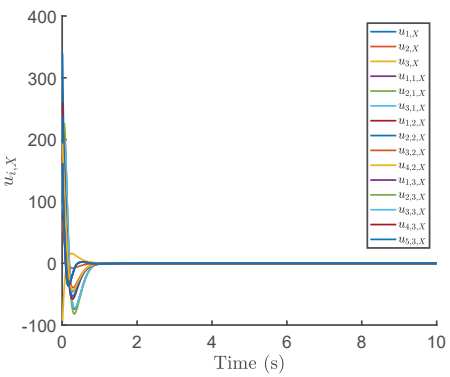

Fig. 10: Control inputs of agents of X-axis.

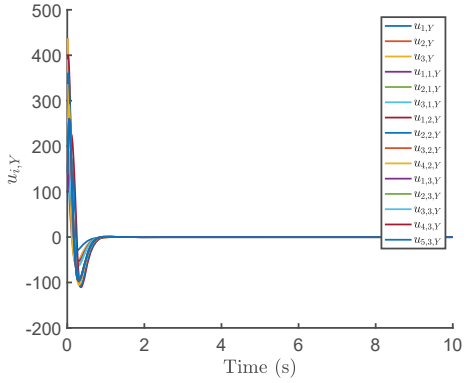

Fig. 11: Control inputs of agents of Y-axis.

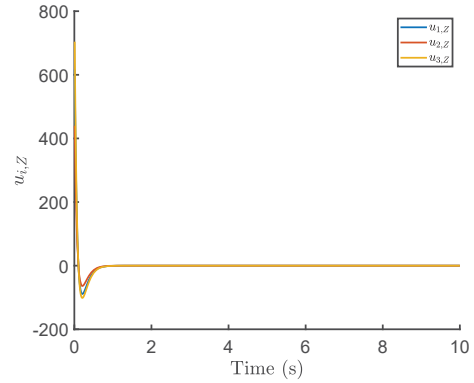

Fig. 12: Control inputs of agents of Z-axis.

5 Conclusion and Future Works

In this paper, a clusters flocking formation robust controller of second-order MASs has been designed. Compared to common control methods like PID, the controller based on the HOFAS model has the ability to set the error convergence range according to actual requirements. This makes the system design and debugging more straightforward. The proposed controller leverages the advantages of the HOFAS method. It not only eliminates uncertainties but also allows arbitrary design of the linear part of the closed-loop system. The convergence of the formation errors has been analyzed. The obtained controller can ensure the formation errors converge to any small ellipsoidal region. The simulation results has been used to confirm the validation of the proposed control approach. Additional actual MASs formation control research based on HOFAS method will be further explored.

References

[1] C. Altafini, "Consensus problems on networks with antagonistic interactions," *IEEE Transactions on Automatic Control*, vol. 58, no. 4, pp. 935–946, 2012.

[2] A. Amirkhani and A. H. Barshooi, "Consensus in multi-agent systems: a review," *Artificial Intelligence Review*, vol. 55, no. 5, pp. 3897–3935, 2022.

[3] Y. C. Ao and Y. M. Jia, "Distributed H_2/H_∞ infinity consensus control and iterative approach for multi-agent systems with directed graph," in *2018 IEEE International Conference on Big Data and Smart Computing (BigComp)*, pp. 141–146, IEEE, 2018.

[4] J. A. Colunga, C. R. Vázquez, H. M. Becerra, and D. Gómez-Gutiérrez, "Predefined-time consensus of nonlinear first-order systems using a time base generator," *Mathematical Problems in Engineering*, vol. 2018, 2018.

[5] F. Chen and D. V. Dimarogonas, "Consensus control for leader-follower multi-agent systems under prescribed performance guarantees," in *2019 IEEE 58th Conference on Decision and Control (CDC)*, pp. 4785–4790, IEEE, 2019.

[6] G. Barkai, L. Mirkin, and D. Zelazo, "On sampled-data consensus: divide and concur," *IEEE Control Systems Letters*, vol. 6, pp. 343–348, 2021.

[7] Z. Wang, Y. Gao, Y. Liu, S. Wang, and L. Wu, "Distributed dynamic event-triggered communication and control for multi-agent consensus: A hybrid system approach," *Information Sciences*, vol. 618, pp. 191–208, 2022.

[8] R. R. Nair, L. Behera, and S. Kumar, "Event-triggered finite-time integral sliding mode controller for consensus-based formation of multirobot systems with disturbances," *IEEE Transactions on Control Systems Technology*, vol. 27, no. 1, pp. 39–47, 2017.

[9] B. Su, H. B. Wang, and Y. L. Wang, "Dynamic event-triggered formation control for auvs with fixed-time integral sliding mode disturbance observer," *Ocean Engineering*, vol. 240, p. 109893, 2021.

[10] A. A. Shobole and M. Wadi, "Multiagent systems application for the smart grid protection," *Renewable and Sustainable Energy Reviews*, vol. 149, p. 111352, 2021.

[11] F. Mehdifar, C. P. Bechlioulis, F. Hashemzadeh, and M. Baradarannia, "Prescribed performance distance-based formation control of multi-agent systems," *Automatica*, vol. 119, p. 109086, 2020.

[12] N. Messai, D. H. Nguyen, N. Manamanni, *et al.*, "Robust formation control under state constraints of multi-agent systems in clustered networks," *Systems & Control Letters*, vol. 140, p. 104689, 2020.

[13] G. D. Wang, X. Y. Wang, and S. H. Li, "Signal generator based finite-time formation control for disturbed heterogeneous multi-agent systems," *Journal of the Franklin Institute*, vol. 359, no. 2, pp. 1041–1061, 2022.

[14] G. Funchal, T. Pedrosa, M. Vallim, and P. Leitao, "Security for a multi-agent cyber-physical conveyor system using machine learning," in *2020 IEEE 18th International Conference on Industrial Informatics (INDIN)*, vol. 1, pp. 47–52, IEEE, 2020.

[15] Y. L. Shang, "Fixed-time group consensus for multi-agent systems with non-linear dynamics and uncertainties," *IET Control Theory & Applications*, vol. 12, no. 3, pp. 395–404, 2018.

[16] L. H. Ji, X. H. Yu, and C. J. Li, "Group consensus for heterogeneous multiagent systems in the competition networks with input time delays," *IEEE Transactions on Systems, Man, and Cybernetics: Systems*, vol. 50, no. 11, pp. 4655–4663, 2018.

[17] G. R. Duan, "High-order fully actuated system approaches: Part I. models and basic procedure," *International Journal of Systems Science*, vol. 52, no. 2, pp. 422–435, 2021.

[18] G. R. Duan, "High-order fully actuated system approaches: Part II. generalized strict-feedback systems," *International Journal of Systems Science*, vol. 52, no. 3, pp. 437–454, 2021.

[19] G. R. Duan, "High-order fully actuated system approaches: Part III. robust control and high-order backstepping," *International Journal of Systems Science*, vol. 52, no. 5, pp. 952–971, 2021.

[20] G. R. Duan, "High-order fully-actuated system approaches: Part VI. disturbance attenuation and decoupling," *International Journal of Systems Science*, vol. 52, no. 10, pp. 2161–2181, 2021.

Proceedings of the 3rd Conference on Fully Actuated System Theory and Applications
May 10-12, 2024, Shenzhen, China

A Blockchain-Enhanced Secure and Reliable Data Transaction Scheme in MAS via HTLC

Boyuan Yu[1], Yichun Guan[1], Shiyao Geng[1], Linlong Miao[1], Yue Zhang[1], Yi Gong[1]*
1. Beijing Information Science & Technology University, Beijing 102206, P. R. China
E-mail: {yuboyuan, guanyichun, gengshiyao, miaolinlong, zhangyue, gongyi}@bistu.edu.cn

Abstract: Data transactions within distributed networks are increasingly critical in modern technological infrastructures. However, such transactions encounter significant challenges, including security vulnerabilities and a lack of participant trust. Traditional centralized approaches often fail to address these issues due to their lack of transparency and flexibility, resulting in inefficiencies and potential risks. This paper presents a novel transaction mechanism that enhances security and transparency in Multi-Agent Systems (MAS) by integrating Hashed Timelock Contracts (HTLC) with blockchain technology, effectively addressing the concerns of data transaction reliability and trust. The efficacy of this mechanism in enhancing transaction security and efficiency was validated through simulation experiments. Results demonstrate that the system operates reliably under various network conditions, boasting high success rates and robust security. Overall, this research successfully explores and validates an enhanced blockchain-based solution for secure and reliable data transactions in distributed networks, offering a new strategy for addressing the challenges of data exchanges.

Key Words: Blockchain, Data Transaction Security, Hashed Timelock Contract, Multi-Agent Systems

1 Introduction

Distributed control is an essential approach for production control [1]. Multi-Agent System (MAS) is one of the most influential distributed control methods for manufacturing autonomy [2]. Different agents can cooperate in a mutually customized protocol, and local active task planning can be carried out in each agent according to its task queue and status [3]. The overall goal of the distributed production control system can be realized by coordinating subsolutions through the communication mechanism between multiple agents [4].

With the rapid development of perception, communication, and computation technologies, distributed cooperative control of MASs has received significant attention from scholars in different disciplines due to their wide applications in large-scale process industries, multi-robot systems, intelligent transportation systems, sensor networks, smart grids, and internet systems [5, 6]. Compared with traditional single-agent systems, MAS is more scalable and upgradeable while improving task execution efficiency and robustness due to their inherent ability to learn and make autonomous decisions cooperatively [7].

However, implementing and maintaining an agent requires significant time and resources, including extensive computational power during the design and testing phases and substantial communication and energy costs during operation. Concurrently, within an MAS, agents generate valuable data through its autonomous and iterative learning processes, reflecting system performance and offering insights for optimization.

Blockchain technology has emerged as a solution to ensure the security and credibility of data transactions [8]. Its immutable and decentralized nature provides a robust platform for data exchange, enhancing transparency and fairness while reducing costs and accelerating processes. Given the need for secure and efficient transactions of the vast data amassed by different agents, blockchain application is particularly crucial [9, 10].

In this context, our research introduces a novel data transaction scheme that integrates agents and blockchain technology, addressing security and efficiency issues in data transactions [11, 12]. We explore how the operational mechanisms of MAS and the security features of blockchain can be synergized to automate, secure, and streamline data transactions. At the heart of this study is the design of a blockchain-based Hashed Timelock Contract (HTLC) protocol, which ensures simultaneous locking and releasing of funds and data, thereby enhancing the security and trustworthiness of transactions [13–15].

This integration optimizes the data transaction process and improves the security and transparency of transactions. Our innovative mechanism significantly contributes to the fluidity and value of data, fostering the growth and innovation of the digital economy. The study presents a pioneering solution to the resource and cost challenges faced by MAS in practical applications, leveraging blockchain technology to bolster the security and efficiency of data transactions. Future research will delve into the applicability of this scheme across various industries and settings, aiming to continually refine and adapt the data transaction mechanism to evolving technological and market needs.

The rest of the paper is organized as follows. Section 2 details the system model, which integrates MAS and blockchain technology to create a secure and trustworthy data transaction environment. Section 3 explores HTLC-based trusted data transactions, outlining a detailed five-step process for secure data exchange, which includes hash functions, digital signatures, and blockchain technology to ensure transaction integrity. In Section 4, we present the simulation experiment results that validate our proposed system's effectiveness through practical implementation, focusing on transaction latency and success rates. Section 5 concludes the paper with a summary of our findings and discusses the potential for future research in secure data transactions using MAS and blockchain technology.

This work is supported by the Beijing Natural Science Foundation (L223025)

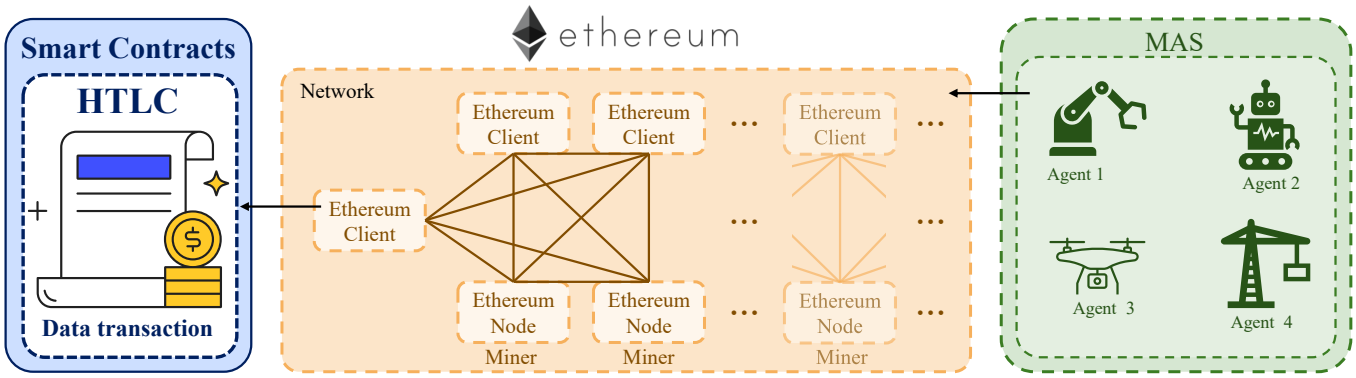

Fig. 1: A Secure Transaction Framework for Trusted Value Data Based on Blockchain and Multi-Agent Systems

2 System Model

The demand for reliable and secure data transaction mechanisms grows as technology advances. This study presents a system model that combines MAS and blockchain technology to create a secure and trustworthy data transaction environment. In this framework, agents serve as data providers and are directly influenced by data transaction activities, fostering a mutually beneficial ecosystem, as illustrated in Fig.???1.

The primary role of MAS in this system is to act as an efficient data processing and provisioning platform. Composed of a series of intelligent agents, it monitors, analyzes, and optimizes the data supply chain, ensuring the authenticity and accuracy of the provided data. This process improves data quality and enhances MAS's data processing capabilities. Significantly, through ongoing data transactions, MAS collects feedback and performance data, allowing for rapid iteration and optimization of its algorithms and processes, facilitating swift development.

In our model, agents are valuable data providers, generating significant data through continuous optimization and iteration. This allows for the transaction of valuable data to meet the specific needs of other agents or buyers, further enhancing MAS. Each agent is equipped with specialized strategies and algorithms, enabling independent data mining and optimization tasks to ensure the data reflects the latest market dynamics with high relevance and accuracy. Through internal optimization mechanisms, agents ensure data provision consistency and timeliness, enhancing the automation level in the transaction process.

Blockchain technology is crucial in this model, providing a secure foundation for MAS's data transactions. Deploying smart contracts, particularly HTLCs, ensures that each step of the data transaction is verifiable and immutable, thus increasing the overall trust in the transaction process. This secure and trustworthy transaction environment not only protects the value of the data but also encourages more data sharing and transactions, feeding back into MAS and supporting its continuous development and optimization.

MAS and blockchain form a robust data transaction ecosystem through this synergistic mechanism. This reliable data transaction system enables rapid development within MAS, while blockchain technology ensures the security and trustworthiness of these transactions. Our research demonstrates how this model effectively promotes the maximization of data value and the continuous progression of the system, offering new perspectives and methodologies for the future of data trading and system development.

3 HTLC-based Trusted Data Transactions

In this section, we introduce the core part of the framework, HTLC, and conduct a completeness analysis.

3.1 HTLC Process

In order to address the urgent problem of securing trusted data transactions, as mentioned in the previous section, we use HTLC and data encryption as solutions targeted at securing trusted transactions. As shown in Fig.???2, the proposed scheme can be considered a tripartite of data sellers, buyers, and HTLCs.

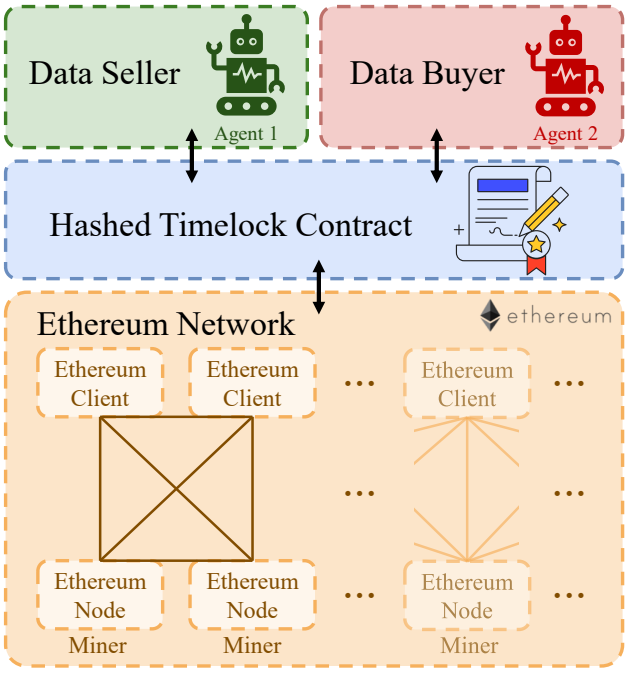

Fig. 2: HTLC-based Data Transactions

The specific process is one preparatory step and five key steps, as shown in Fig.3. Each of these steps will be described in detail in the following :

0) **Negotiation of Details between Data Transaction Parties.** Step 0 initiates with preliminary negotiations,

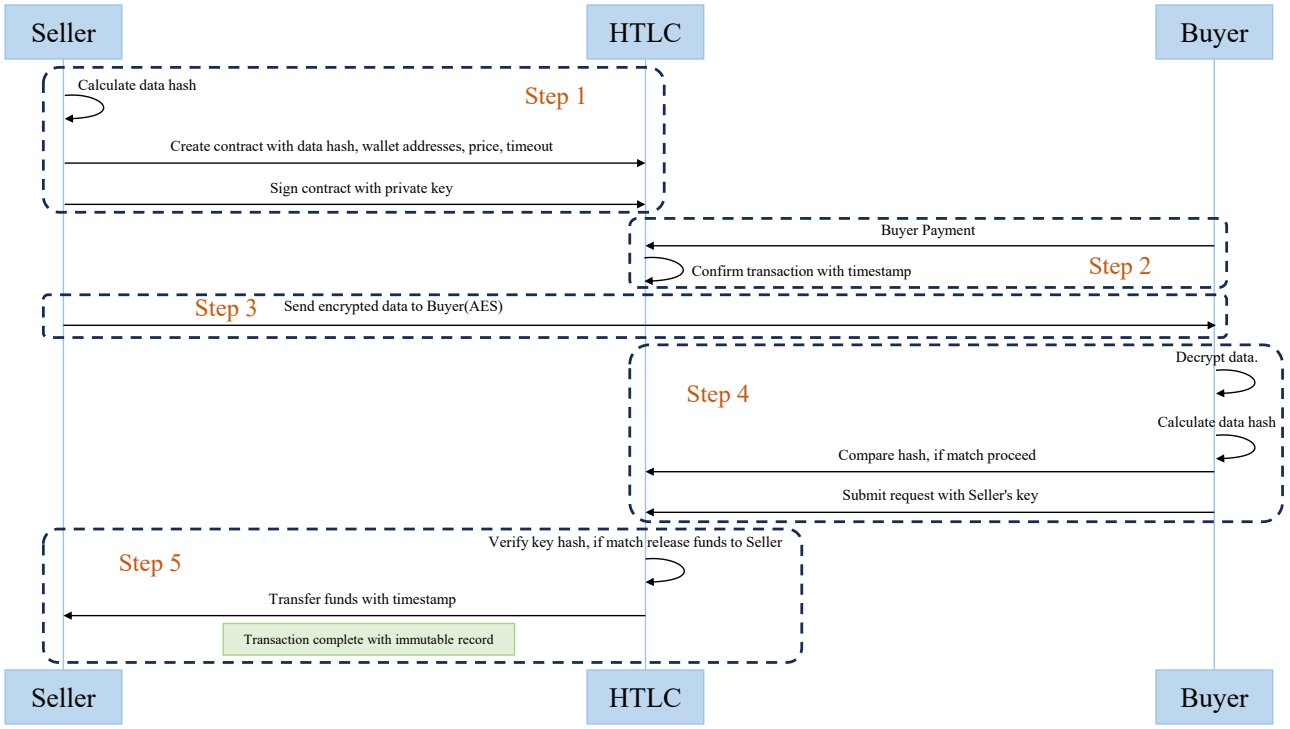

Fig. 3: Details of HTLC-based data transactions

a foundational phase in the data transaction process. Here, data sellers and buyers actively define and agree on the transaction terms, encompassing data attributes, quality, intended use, price, and transaction modalities. Additionally, both parties establish specific protocols for data delivery and payment tailored to meet mutual needs and security requirements. This phase, characterized by thorough discussions and consensus-building, lays a solid groundwork for subsequent on-chain transactions and contract fulfillment.

1) **Data Preparation and Contract Creation.** The seller prepares to sell data to the buyer. Initially, the seller computes the hash value of the data set for sale, utilizing the Secure Hash Algorithm 256-bit (SHA-256) function. This hash value is a unique data fingerprint, ensuring that even the slightest alterations are detectable. By recalculating and comparing this SHA-256 hash value, one can verify whether the data has been tampered with. This process is crucial for establishing a hash lock within the HTLC, guaranteeing data integrity.

$$h_{\text{data}} = \text{SHA-256}(data) \tag{1}$$

The seller deploys an HTLC that includes the hash value of the data as hash lock, both parties' wallet addresses, which, in the blockchain, the price has agreed upon, and a timeout period as timelock. When a seller deploys HTLC to a decentralized Ethereum network, each node will verify the transaction's legitimacy and record it to the network.

2) **Locking in Payment.** To acquire the data, the data buyer pays HTLC on a pre-agreed basis. This transaction is confirmed by the blockchain network and is timestamped. Payments are locked in a smart contract, and a timestamp in the Ethereum network proves that the buyer submitted the funds at a specific time, providing a reliable timeline of the entire transaction process. This demonstrates the critical role of timestamps in ensuring transactions are executed in sequence.

3) **Data Transmission.** Subsequently, the seller employs the Advanced Encryption Standard 256-bit (AES-256) to conduct symmetric encryption of the transaction data. This encryption mechanism plays a pivotal role in ensuring the security of the data during transmission, effectively preventing unauthorized access. Once encrypted, the data is securely transmitted to the buyer via a certified secure communication channel, guaranteeing the confidentiality and integrity of the data transfer.

$$C = \text{Enc}_{\text{AES},k}(data) \tag{2}$$

where C is the ciphertext (encrypted data), $\text{Enc}_{\text{AES},k}$ denotes the AES encryption process using the key k, and $data$ represents the plaintext data to be encrypted.Similarly, the AES-256 encryption key k is transmitted to the buyer via a secure key exchange protocol to enable data decryption in subsequent steps.

4) **Data Validation and Release of Payment.** Upon receiving the data encrypted with AES-256 and the key k, the buyer decrypts the data using k. The corresponding algorithm for the decryption process is:

$$data' = \text{Dec}_{\text{AES},k}(C) \tag{3}$$

where $\text{Dec}_{\text{AES},k}$ denotes the AES decryption process using the key k, and C is the ciphertext to be decrypted back into the plaintext data.

These formulas encapsulate the AES encryption mechanism's core functionality, ensuring that data transmit-

ted between the buyer and seller in the HTLC-based transaction scheme is protected against unauthorized access.

After receiving and decrypting the data, the buyer calculates its hash value and compares it with the hash value stored in the smart contract. This step underscores the crucial role of hash functions in verifying the integrity and authenticity of the data. If the hash values match, the buyer confirms the data's authenticity and completeness.

$$\text{Verify}_H(data', h_{\text{data}}) : \text{SHA-256}(data') \stackrel{?}{=} h_{\text{data}} \quad (4)$$

Subsequently, the buyer submits a request through the smart contract, including a key previously provided by the seller. The smart contract checks if the data's hash value matches the initial hash lock, showcasing the essential role of hash functions and illustrating the importance of digital signatures and timestamps in securing and sequencing the transaction. Upon successful verification, the contract automatically transfers the funds to the seller and logs the timestamp of this operation.

$$\text{Verify}_H(data', \text{hashlock}) : H_{\text{SHA-256}}(data') \stackrel{?}{=} \text{hashlock} \quad (5)$$

5) **Completion and Recording of Transaction.** After the funds are successfully transferred to the seller, the transaction is considered complete. Each step in the transaction process, including the locking and releasing of payments, is verified by the blockchain network and timestamped. These timestamps create an immutable transaction record, ensuring its transparency and traceability.

Through the steps outlined, the hash function within the HTLC plays a pivotal role in ensuring data integrity and authenticating transactions. Digital signatures are essential for confirming the identities of transaction participants and safeguarding information from tampering. Meanwhile, timestamps and blockchain verifications offer an immutable record of transactions, ensuring their transparency and sequential integrity. These technologies provide a secure, trustworthy, and verifiable framework for data transactions between buyers and sellers.

3.2 Completeness Analysis of Proposed Scheme

The effectiveness of the HTLC-based data transaction scheme relies on several fundamental mechanisms that ensure secure and efficient operations. Firstly, transaction integrity is maintained through cryptographic hash functions, such as SHA-256, which confirm that the data remains unaltered from its original state. This step is essential for preserving data authenticity. Secondly, the system ensures nonrepudiation using digital signatures and hash locks, which prevent any party from denying their involvement in a transaction. This feature enhances trust and accountability within the decentralized framework of the blockchain. Thirdly, smart contracts rigorously enforce sequential execution, dictating the precise order of operations—from payment locking to data validation. This strict ordering is crucial for the systematic and accurate processing of transactions. Moreover, timeliness is guaranteed by timelocks that require transactions to be completed within a specified period, or they are voided. This mechanism helps avoid delays and assures transaction certainty. Lastly, the entire transaction process undergoes thorough verification and validation by the blockchain network, safeguarding against individual tampering and ensuring compliance with the transaction protocol. Collectively, these components safeguard the operation of the HTLC-based data transaction scheme and reinforce its reliability and adherence to established contractual terms, highlighting its overall effectiveness and robustness.

3.3 Summary

In Section 3, we thoroughly investigate the implementation of HTLC in securing trusted data transactions. This approach leverages cryptographic hash functions and blockchain technology to facilitate secure and reliable exchanges between parties without intermediaries. The process unfolds through well-defined steps, beginning with the initial negotiations that set transaction terms, progressing through data preparation and establishing a binding HTLC, and culminating in the transaction's final validation and completion.

A critical component of the HTLC framework is using SHA-256 for data hashing, which ensures data integrity by making any unauthorized modifications detectable. Complementarily, AES-256 encryption safeguards data during transmission, preserving confidentiality and integrity. Upon receiving the data, the buyer decrypts and verifies its authenticity by comparing hash values. A successful match automatically triggers the release of payments through the smart contract. Each transaction step is recorded and timestamped on the blockchain, providing an immutable and transparent ledger.

The section concludes with a completeness analysis that highlights the HTLC framework's robustness. It demonstrates how the system upholds transaction integrity, nonrepudiation, and compliance—critical elements for fostering trust and accountability in decentralized settings. This analysis confirms the HTLC-based mechanism's operational effectiveness and illustrates its potential as a secure, scalable solution for future digital transactions.

4 Simulation and Analysis

4.1 Experiment Objectives

This experiment aims to validate the efficiency and security of our proposed data transaction scheme based on HTLC and MAS. By conducting data transactions in a simulated real-world environment, this study assesses the system's response time, success rate, and security under various conditions, including network delays, different data payload sizes, and the number of network participants. Successful outcomes will demonstrate the scheme's capability to offer a secure and efficient data transaction platform in real-world scenarios.

4.2 Experimental Setup

The setup of the experimental environment is designed to ensure the accuracy of experimental data and the reproducibility of results. The detailed configuration includes:

The experiment utilizes multiple servers to simulate a dis-

tributed blockchain network. Each server is equipped with identical hardware resources to maintain consistency across the experiment. The entire network comprises 50 nodes, each running a blockchain node.

An Ethereum blockchain environment is deployed on the software front, and smart contracts are written in Solidity to handle all HTLC-related data transactions. Additionally, MAS on each node is configured to simulate different data providers and consumers, representing various types of data services such as meteorological and traffic flow data.

This environment ensures the experiment can proceed under controlled conditions while simulating real-world data transaction scenarios.

4.3 Experimental Procedure

4.3.1 Initial Setup

Before the commencement of the experiment, the following initial setups are necessary:

Smart Contract Deployment The HTLC smart contract is first deployed to the Ethereum test network. This step ensures that all transactions are conducted within a secure environment and facilitates the monitoring and analysis of the transaction process.

MAS Configuration Each agent node is configured to simulate different data providers and consumers. These MAS nodes automatically perform actions such as data requests, transaction initiation, data verification, and payment processing according to pre-set scripts.

4.3.2 Transaction Process Simulation

The transaction process is simulated in five stages to evaluate the performance of the proposed scheme comprehensively:

Step 1: Transaction Initialization Data providers and consumers determine the specific terms of the transaction on the MAS platform, including data type, quality, and price.

Step 2: Contract Creation and Data Preparation Data providers generate a hash value of the data and create an HTLC based on this hash. This step is crucial to ensure the data remains unaltered.

Step 3: Fund Locking Consumers send the required funds to the HTLC, which is locked until other transaction conditions are met.

Step 4: Data Transmission and Verification Data providers securely transmit the encrypted data to consumers, who then decrypt and verify the data's integrity and accuracy.

Step 5: Payment Release Once the data is verified, consumers initiate the payment release process through the smart contract, and funds are transferred to the data provider's account.

This structured approach allows for a thorough assessment of the proposed HTLC and MAS-based data transaction scheme, emphasizing its potential for real-world application and highlighting areas for further enhancement.

4.4 Experimental Results

In this study, extensive experiments were designed to evaluate our data transaction scheme based on HTLC and MAS. The detailed analysis of the results is as follows:

4.4.1 Time Efficiency

We monitored processing times across various stages of the transactions, as shown in Fig.4, and found the following results:

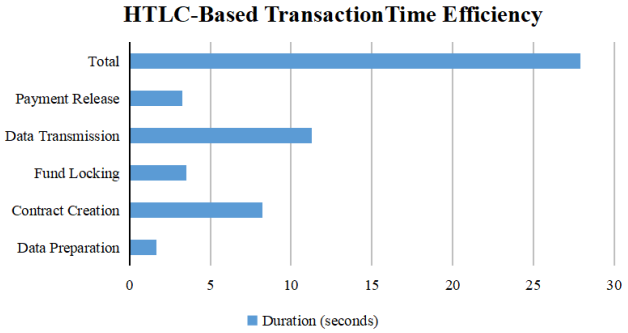

Fig. 4: HTLC-Based Transaction Time Efficiency

- Data Preparation: The average time was 1.64 seconds, primarily for data hashing and encryption processes.
- Contract Creation and Data Preparation: Averaged 8.21 seconds, largely determined by the time required to deploy smart contracts to the blockchain network.
- Fund Locking: Took an average of 3.52 seconds, including the time to send funds to the smart contract and for blockchain confirmation.
- Data Transmission and Verification: This was the longest phase, averaging 11.29 seconds, involving data transfer and the recipient's verification processes.
- Payment Release: Averaged 3.27 seconds, mainly involving executing payment logic within the smart contract and processing on the blockchain.

Overall, the entire transaction process, from initiation to payment release, took an average of 27.93 seconds. This timeframe is within acceptable limits, indicating effective system responsiveness and efficiency.

4.4.2 Success Rate

Out of 200 simulated transactions, we achieved a success rate of 98%. Failures were primarily due to network delays and data transmission errors, providing valuable insights for further system performance optimization.

4.4.3 Security Analysis

Security vulnerability scans and simulated attack tests were conducted to evaluate the security of data transmission and transactions:

- Unauthorized Access Attempts: No successful unauthorized access incidents were recorded, indicating effective preventative measures.
- Data Integrity Verification: All successful transactions confirmed that the data hashes matched those recorded in the contracts, affirming the security of the data transmission process.

4.5 Discussion of Results

The experimental results demonstrate the high efficiency and robust security of the proposed HTLC and MAS-based data transaction scheme, underscoring its potential for MAS application. The system's high success rate and effective security measures confirm its viability.

5 Conclusion

In conclusion, this paper successfully explores and validates a blockchain-enhanced, secure, and reliable data transaction scheme utilizing MAS and HTLC. The integration of MAS with blockchain technology provides a robust framework that significantly enhances the security and efficiency of data transactions across decentralized networks. Experimental simulations have confirmed the effectiveness of the proposed scheme, achieving a high success rate and demonstrating substantial resilience against security threats. The results affirm the system's viability in practical scenarios and highlight potential areas for further improvement, such as optimizing transaction speed and handling network variabilities more effectively. Future work will aim to extend this model's capabilities to broader applications, ensuring adaptability and scalability in increasingly complex environments. This research lays a foundational stone for advancing secure digital transaction systems, paving the way for innovative applications in various fields.

References

[1] Alves F, Rocha A M A C, Pereira A I, et al. Conceptual Multi-Agent System Design for Distributed Scheduling Systems[M]//Smart and Sustainable Manufacturing Systems for Industry 4.0. CRC Press, 2022: 129-148.

[2] Pulikottil T, Estrada-Jimenez L A, Rehman H U, et al. Multi-agent based manufacturing: current trends and challenges[C]//2021 26th IEEE international conference on emerging technologies and factory automation (ETFA). IEEE, 2021: 1-7.

[3] Leng J, Sha W, Lin Z, et al. Blockchained smart contract pyramid-driven multi-agent autonomous process control for resilient individualised manufacturing towards Industry 5.0[J]. International Journal of Production Research, 2023, 61(13): 4302-4321.

[4] Didden J B H C, Dang Q V, Adan I J B F. Decentralized learning multi-agent system for online machine shop scheduling problem[J]. Journal of Manufacturing Systems, 2023, 67: 338-360.

[5] Banafaa M, Shayea I, Din J, et al. 6G mobile communication technology: Requirements, targets, applications, challenges, advantages, and opportunities[J]. Alexandria Engineering Journal, 2023, 64: 245-274.

[6] Guo H, Zhou X, Liu J, et al. Vehicular intelligence in 6G: Networking, communications, and computing[J]. Vehicular Communications, 2022, 33: 100399.

[7] Erba T. A Multi-Agent Architecture for An Intelligent Web-Based Educational System[J]. 2023.

[8] Jianbo Du, Wenjie Cheng, Guangyue Lu, Haotong Cao, Xiaoli Chu, Zhicai Zhang, and Junxuan Wang. Resource Pricing and Allocation in MEC Enabled Blockchain Systems: An A3C Deep Reinforcement Learning Approach, IEEE Transactions on Network Science and Engineering, 9(1): 33 – 44, 2022.

[9] Abbas A, Alroobaea R, Krichen M, et al. Blockchain-assisted secured data management framework for health information analysis based on Internet of Medical Things[J]. Personal and ubiquitous computing, 2024, 28(1): 59-72.

[10] Bhutta M N M, Khwaja A A, Nadeem A, et al. A survey on blockchain technology: Evolution, architecture and security[J]. Ieee Access, 2021, 9: 61048-61073.

[11] Da Xu L, Lu Y, Li L. Embedding blockchain technology into IoT for security: A survey[J]. IEEE Internet of Things Journal, 2021, 8(13): 10452-10473.

[12] Hasan M K, Alkhalifah A, Islam S, et al. Blockchain technology on smart grid, energy trading, and big data: security issues, challenges, and recommendations[J]. Wireless Communications and Mobile Computing, 2022, 2022: 1-26.

[13] Yang W. Blockchain-based Decentralized Mechanism for Conversation system[D]. University of Tasmania, 2022.

[14] Manevich Y, Akavia A. Cross chain atomic swaps in the absence of time via attribute verifiable timed commitments[C]//2022 IEEE 7th European Symposium on Security and Privacy (EuroS&P). IEEE, 2022: 606-625.

[15] Wang G. Sok: Exploring blockchains interoperability[J]. Cryptology ePrint Archive, 2021.

Proceedings of the 3rd Conference on Fully Actuated System Theory and Applications
May 10-12, 2024, Shenzhen, China

Cross-Multi-Agent Systems Identity Authentication Framework on Decentralized Identity

Zixin Xu[1], Yuxin Zuo[1], Boyuan Yu[1], Yue Zhang[1], Yi Gong[1]*

1. School of Information and Communication Engineering, Beijing Information Science and Technology University, Beijing, China
E-mail: {zixinxu,zuoyuxin0928,yuboyuan,zhangyue,gongyi}@bistu.edu.cn

Abstract: Multi-Agent Systems (MAS) as a means to solve complex problems by subdividing them into smaller tasks. It has become increasingly prominent in solving complex interaction problems. In the process of data exchange between MASs, the inability to verify each other's identity information often leads to mutual distrust, compromising security. Traditional centralized identity authentication management has significant flaws under the decentralized network environment of MAS. To address this issue, this paper introduces a Cross-Multi-Agent Systems Identity Authentication Framework based on Decentralized Identity (DID), which establishes trust between MASs and ensures security and confidentiality. Our security analysis proves the effectiveness of this solution in overcoming the identified challenges and validates the feasibility of the framework.

Key Words: Blockchain, Decentralized Identity, Identity Management, Multi-Agent Systems

1 Introduction

In the contemporary era, Distributed Artificial Intelligence (DAI) has emerged as a pivotal point of interest in both academia and industry, especially for its ability to solve complex computational problems [1]. Within the domain of DAI research, artificial intelligence algorithms are classified into three fundamental approaches: Parallel Artificial Intelligence, Distributed Problem Solving (DPS), and Multi-Agent Systems (MAS). MAS is a system composed of a set of agents that interact with each other, each possessing autonomy and learning capabilities [2]. These agents exchange messages through established connections to accomplish collective goals or tasks. In contrast to the computational entities in DPS, agents within MAS are not only capable of executing assigned sub-tasks but also utilize their inherent learning and autonomous decision-making abilities to adapt to new scenarios, thereby offering greater flexibility and adaptability [3]. It is this flexibility and adaptability that positions MAS as one of the key technologies for addressing complex issues of the present and future. MAS find extensive applications across various disciplines such as computer science, civil engineering, and electrical engineering, playing an irreplaceable role in modern societal challenges like intelligent transportation, smart city development [4], environmental monitoring, and sustainable development [5].

The evolution of MAS has consistently emphasized coordination, learning processes, and security within the system. However, with continuous technological advancements, the interaction between MAS across different systems is increasingly becoming a mainstream area of research [6]. A notable example is in the field of intelligent manufacturing for supply chain management, where one MAS is responsible for production scheduling while another oversees logistics and distribution. To ensure that products on the production line reach their destinations promptly and efficiently, data exchange between these two systems is essential [7]. Additionally, in emergency response scenarios, MAS tasked with monitoring must be able to transmit data quickly and securely to coordinating devices, vehicles, and other agents to facilitate rapid action in the event of an emergency [8].

In practical applications, cross-system interactions involve a multitude of agents, and these interactions are large-scale with stringent security requirements. Consequently, MAS face a dilemma: on one hand, to ensure security and prevent attackers from impersonating as legitimate agents, defensive mechanisms are necessary, which may hinder the establishment of trust with other systems; on the other hand, to maintain performance and smooth interaction, security measures may be relaxed. However, this makes it easy for attackers to take advantage of the void, leading to the system being attacked and destroyed [9]. Against this backdrop, establishing trust and proving identity and security among MASs becomes a critical issue. Identity management and the establishment of trust mechanisms have become primary concerns in cross-system interactions [10]. In many current systems, trust is not provided by the system itself but by pseudo-decentralized Public Key Infrastructures (PKI) acting as Trusted Third Parties (TTP) [11]. However, this reliance on TTP for trust significantly diminishes the advantages of MAS: flexibility and adaptability.

In light of this, we propose a novel architecture based on Decentralized Identity (DID) to address the identity authentication and trust issues in cross-system interactions among MASs. In our framework, we rely on three core technologies: Smart Contracts, Blockchain, and DID. By adopting DID, we manage unique identities for agents within the system. Before the cross-system interaction, the agent needs to obtain the signatures of other agents in the system and store them on the blockchain to ensure the authenticity of the data, and then create a Verifiable Credential (VC) to be handed over to the other system for verification and trustworthiness assessment until the other system recognises the trustworthiness of the agent in order to carry out normal data interaction. In this case, due to a lack of sufficient credibility, the system will be unable to interact with other systems by temporarily masquerading as legitimate agents. Moreover, since signatures are stored on blockchain nodes, they are verifiable and immutable, making it impossible for attackers to

This work is supported by Beijing Natural Science Foundation (L223025).

gain trust from other systems by altering VC.

The remainder of this paper is structured as follows. Section 2 introduces relevant technologies and their application in real scenarios. Section 3 presents our proposed Cross-MASs Identity Authentication Framework, detailing its main features, core functions, and operating principles. Section 4 conducts a security analysis of the proposed framework. Finally, Section 5 concludes the paper and provides an outlook on future research work.

2 Related Technologies and Application Scenarios

2.1 Related Technologies

Identity management is a crucial aspect of access control in network applications. Traditional identity authentication management, predominantly centralized, requires agents to register and verify their identity through credentials like usernames and passwords. Certificate Authority (CA) then validate these credentials and issue digital certificates used in subsequent authentication processes. However, this centralized approach exhibits significant limitations in the decentralized network environments of MAS, especially under conditions of large-scale and dynamic changes.

In decentralized MAS environments, implementing centralized identity authentication necessitates placing PKI in appropriate positions, conducting operations on agents, and securely interconnecting them, all managed by a centralized CA. This approach not only burdens the system with numerous authentication requests, leading to delays in response times but also severely constrains the inherent flexibility of MAS. Moreover, the security of the system is compromised, as global trust in CA is lacking and centralized identity repositories become prime targets for attackers. When a CA is compromised, the entire system's trust mechanism collapses, causing a significant drop in security. Therefore, to accommodate the decentralised nature of MAS, a new approach to identity management is required.

With the rise of Bitcoin since 2009, blockchain is gradually coming into the public eye, and it offers a new way of thinking about identity management, offering a secure, immutable, and transparent platform for authentication [12]. Blockchain, as a distributed ledger technology, reduces reliance on a single authoritative entity through distributed nodes, thereby reducing the risk of centralised failures and increasing the system's resistance to attack [13]. In addition, blockchain is open and transparent, and all participants can access the blockchain to view transactions. These features make it impossible to change the data on the chain once it has been entered, providing a solid foundation for verification. However, despite the security enhancements from public-private key encryption, early implementations of blockchain faced challenges, including issues with identity recovery, revocation, or transaction linkage, and unresolved difficulties in privacy protection.

Against this backdrop, a new method was introduced using Distributed Ledger (DL) technology to manage identities in a decentralized manner, without the need for centralized identity providers or CA. DID emerged as a solution in this context. DID are unique identifiers composed of alphanumeric strings that resolve to DID documents containing other information, verification materials, and the public keys of DID subjects [14]. DID offer a form of self-sovereign identity, allowing MAS to control their identities independently without reliance on central authorities. This autonomy addresses issues of identity recovery and revocation, allowing agents to adjust their identity attributes as needed according to environmental changes, the high flexibility and adaptability of MAS are well amplified. Furthermore, DID and DID documents do not expose any private data, maintaining security while enabling stakeholders within DL to manage and share non-sensitive verification materials through DID documents. Sensitive private data remains secured within each stakeholder's domain, ensuring that interactions within MAS, whether successful or not, do not compromise any private information from the system. This level of privacy control is particularly crucial for MAS handling sensitive information.

2.2 Application Scenarios

To further elucidate the practical applications of DID in MASs within smart cities, we can explore their integration in Intelligent Transportation Systems (ITS). ITS, a critical component of modern smart cities, comprises multiple MASs such as vehicle systems, regulatory frameworks, and coordination mechanisms. These systems depend heavily on robust and secure identity management to facilitate coordination, data processing, feedback, and emergency response mechanisms.

The incorporation of DID authenticates the identity of each agent, enabling secure recognition and communication within the system. This security is pivotal for efficient system scheduling and access control, ensuring the smooth operation of the entire ITS. In ITS, vehicles communicate in real time with traffic signals to access traffic flow data or modify signal states, optimizing traffic and reducing congestion. The DID of each vehicle and traffic signal ensures that communications are based on verified identities, enhancing the accuracy of data exchanges.

In emergency scenarios, such as traffic accidents or sudden public events, rescue vehicles need to navigate quickly through congested routes [15]. DID enable these vehicles, equipped with specific identity information, to interact preferentially with the traffic system, facilitating real-time data exchange and ensuring rapid arrival at the scene. Additionally, with the extensive personal and vehicle data involved, ITS must ensure the privacy of this information. The use of DID allows vehicles to interact with other traffic system elements without disclosing personal details, verifying vehicle legitimacy without revealing specific information. In the vast urban traffic network, maintenance and updates, such as firmware upgrades for roadside devices or adjustments to traffic management strategies, are routine. DID assist administrators in better identity verification, enabling remote operations and authorizations, ensuring that only verified devices receive updates to prevent malware infiltration. From this, it can be seen that the application of DID technology in ITS not only enhances system security and efficiency but also significantly improves the level of urban management intelligence by ensuring the security of data exchanges and accurate identification between entities.

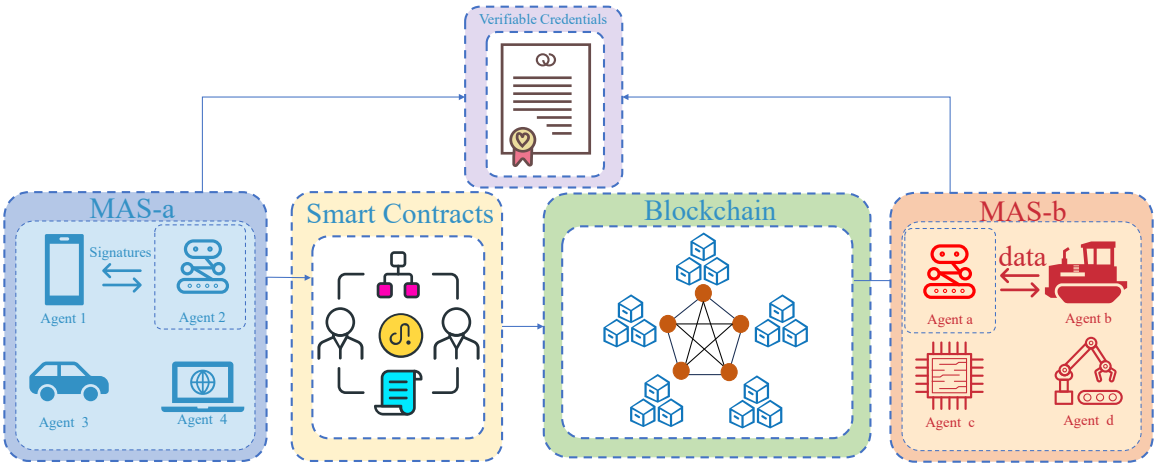

Fig. 1: Cross-MASs Identity Authentication Framework

3 Cross-MASs Identity Authentication Framework

This section delineates the Cross-MASs Identity Authentication Framework, which facilitates identity verification across MAS. Agents acquire a comprehensive array of trust endorsements and multi-party signatures to authenticate identities within a heterogeneous MAS environment.

Fig.1 elucidates the framework's architecture, depicting the process of inter-MAS Agent identity authentication. It highlights the creation of VC and the signature verification process. The immutability and traceability of blockchain technology safeguard the integrity and credibility of signatures recorded on-chain. Fig.1 presents a scenario where Agent 2, seeking interaction within MAS-b, undergoes the process of integration. This transition accentuates the pivotal resolution of trust issues.

The scenario involves two intricately designed MAS, each populated with autonomous Agents tasked with critical functions and sensitive data exchange. These Agents epitomize independence in processing information and decision-making. Trust verification emerges as a quintessential step, particularly when Agent 2 from MAS-a attempts to engage with Agent a within MAS-b. This verification is paramount to assuring absolute security throughout the data exchange process, addressing not only the precision and wholeness of data but also safeguarding against potential security threats like cyber-attacks and internal breaches. An unverified Agent poses a substantial security risk, susceptible to exploitation by malicious entities.

In this vein, Agent 2 must amass trust endorsements reflective of the confidence placed by other Agents. These endorsements not only signify Agent 2's credibility within MAS-a but also are imperative for cross-MAS interactions. Recording these endorsements on the blockchain leverages the technology's inherent incorruptibility and transparency, ensuring the authenticity of the endorsements.

This VC is then subjected to scrutiny by Agent a in MAS-b, who assesses Agent 2's trustworthiness based on the credential's content and the blockchain-verified signatures. If the trust quotient is assessed to be insufficient for secure interaction, Agent a will reject the engagement, compelling Agent 2 to acquire additional trust signatures in order to proceed with the interaction. This cycle ensures data exchange across MAS is sanctioned only when stringent security standards are met, substantially mitigating risks of data leakage and cyber threats, thus fortifying the security and confidentiality of the entire MAS.

Our framework capitalizes on three core technologies: Smart Contracts, Blockchain, and Verifiable Credential, to establish and manage trust between Agent 2 in MAS-a and Agent a in MAS-b, facilitating data and operational exchange across MAS. Trust is cultivated through a 'Trust Management' mechanism:

1) **Smart Contracts:** Central to our framework is the execution of core control and connection functions via smart contracts. These automated agreements administer the on-chain recording of signatures and their subsequent verification, ensuring that all data exchanges comply with pre-established protocols. This compliance upholds the integrity and security of the interactions, embodying the framework's commitment to reliable data transactions.
2) **Blockchain:** Blockchain is the key to our research, providing a decentralised, publicly transparent and immutable recording platform for all interactions between MAS. Leveraging distributed ledger technology, it guarantees the transparency and permanence of transaction data. Each transaction, including agents' trust signatures and the results of smart contract executions, is immutably logged on the blockchain. These records are transparent to all participants, these records will not be altered, they will not be overwritten, they will just be kept on the blockchain as record after record.
3) **VC:** A cornerstone of our system is the role of VCs in verifying the trustworthiness and authorization of Agent 2 within MAS-a. VCs serve as the bedrock for identity validation and trust confirmation across MAS interactions. Only when Agent 2 exhibits sufficient credibility and security measures that are verified, can it engage in effective and secure data exchanges with agents in MAS-b.

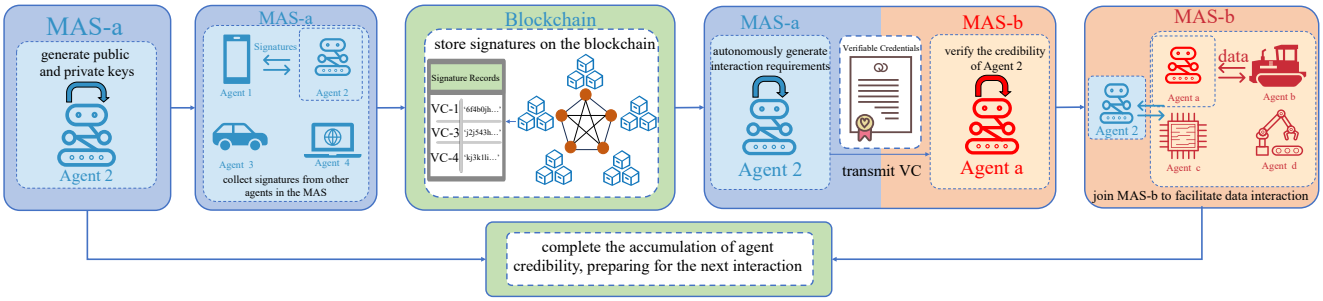

Fig. 2: Fundamental Structure of Inter-Agent Interaction within Multi-Agent Systems

A. Framework Initialization:

1) **Agent Initialization:** The initialization phase of the framework begins with the agent's setup, encompassing several critical steps. Agents autonomously identify the need to interact with another agent within a different MAS, typically for task collaboration, data exchange, or resource sharing purposes. They then employ network discovery protocols to locate the target agent's MAS, decipher network addresses, and confirm the type of data interaction expected, thus establishing a reliable communication channel. To ensure secure forthcoming interactions, agents independently generate a public-private key pair and broadcast the public key for subsequent operations. This procedure guarantees that agents can effectively meet interaction demands and communicate securely.
2) **Obtaining Signatures:** To gain trust from Agent a within MAS-b, Agent 2 extensively collects signatures within its own MAS-a.

$$h_{\text{data}} = \text{SHA-256}(data) \tag{1}$$

Agent 2 applies the SHA-256 hashing algorithm to its identity information, creating a unique and irreversible hash value that secures the data. Combining this hash value with its private key, Agent 2 generates a signature using the ECDSA digital signature algorithm:

$$S_{\text{private key}} = Signature_{\text{ECDSA}}(h_{\text{data}}, privatekey) \tag{2}$$

3) **Uploading Signatures to the Blockchain:** To solidify Agent 2's trustworthiness within MAS-b, other agents within MAS-a provide signature endorsements. These are then uploaded to the blockchain for permanent record-keeping. Agent 2 connects its node to the blockchain network, facilitating communication and data synchronization with other nodes. It creates a blockchain transaction, embedding the collected signatures from agents in MAS-a, as depicted in Fig.3.
This step formalizes the signature information into transactions that can be recorded and verified on the blockchain. Transactions signed by Agent 2 are transmitted to the blockchain via its Geth node. Upon validation by other nodes in the network, these transactions are incorporated into the blockchain ledger. Once recorded, the signature data is permanently stored and made publicly accessible, ensuring the verifiability of the signatures and the immutable nature of the blockchain. Through this sequence of operations, Agent 2's signatures not only gain support from other agents within MAS-a but also have their authenticity and validity assured by the blockchain. This provides a robust foundation for establishing trust for Agent 2 within MAS-b, facilitating recognition of its credibility.

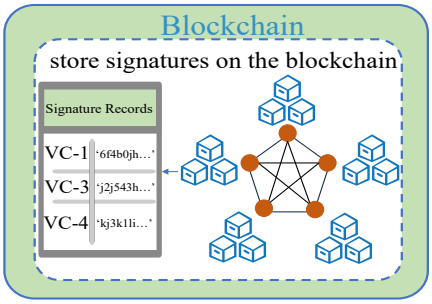

Fig. 3: Signature Records

B.Trust Verification:

1) **Transmitting the VC Form:** Assessing credibility is a pivotal process that determines whether Agent 2 can be trusted to engage in data exchanges within MAS-b. This assessment relies on multiple factors, including Agent 2's historical behavior, the number and quality of signatures collected within MAS-a, and the authenticity and validity of these signatures. When Agent 2 submits the VC form to Agent a in MAS-b, the initial step in credibility evaluation is to verify the consistency of the signatures. Agent a cross-references the signatures on the VC form against those recorded on the blockchain to ensure a perfect match, confirming the integrity of the submitted data and genuine support from other agents within MAS-a. This evaluation informs Agent a whether Agent 2 meets the trust standards of MAS-b. Should Agent 2's credibility fall short, Agent a will reject the integration request, prompting Agent 2 to amass additional or higher-quality endorsements within MAS-a. Conversely, a positive assessment will

grant Agent 2 entry into MAS-b to commence the anticipated data interactions. Moreover, any misconduct by Agent 2 post-integration, such as hacking attempts or violations of data exchange protocols, will directly impinge on its trustworthiness in MAS-b, potentially leading to its prompt removal. Such infractions also impact the credibility of the agents who endorsed Agent 2 within MAS-a, as their signatures indirectly vouch for Agent 2's behavior. This not only affects their future trust evaluations in MAS-b but may also tarnish their credibility in other systems.

2) **Integration into MAS-b for Data Interaction:** This phase signifies that Agent 2 has been granted the right to integrate into MAS-b and commence the planned data interaction. Furthermore, Agent 2 will begin to accumulate a credibility rating, which will facilitate the assessment of its trustworthiness when attempting to join new MAS in the future. This rating will also support its role in endorsing other agents looking to integrate into new MAS.

4 Security Analysis

The security of the proposed framework is evaluated based on several key parameters: Agent Privacy, Data Leakage, Attacks, and Cross-MAS Trust and Permission Management.

1) **Agent Privacy:** Privacy is ensured through the SHA-256 hashing algorithm, which converts data into a fixed-length hash value in a one-way process. Even if the hash value is disclosed, the original data remains confidential and cannot be inferred. When combined with a private key to generate a signature using the ECDSA algorithm, the signature can be publicly transmitted and verified without revealing the private key. On the blockchain, these signatures are stored and verified publicly, ensuring that the agent's identity and data content are protected, as the private key does not participate in the transmission.
2) **Data Leakage:** Credibility verification is achieved through signature validation. In a multi-agent system, an agent requires recognition from other agents to engage in data interactions, typically in the form of signatures recorded on the blockchain. Data interactions are permitted only when these signatures, compared against blockchain records, are verified as authentic and unaltered, thus minimizing the risk of data leakage.
3) **Attacks:**
   Impersonation of Agents Joining MAS: To join a MAS, an agent must collect sufficient trust endorsements, signatures from other agents. On the blockchain, each signature is uniquely bound to an agent's identity, and any unauthorized attempt to join will be denied due to a lack of valid signatures.
   Forgery of VC and Signatures: In the framework, forging VC and signatures is also impossible. Each VC or signature must be validated against the data recorded on the blockchain before acceptance. Smart contracts automatically execute these validation steps, ensuring that an agent is considered trustworthy only if the signatures and certificates are consistent with blockchain records.
4) **Cross-MAS Trust and Permission Management:** Establishing trust relationships between multi-agent systems relies on a complex permission management mechanism, including the automated execution of signature verification and permission granting by smart contracts. When an agent attempts data interaction with another agent from a different MAS, it must provide a VC to prove its identity and past behavior. Smart Contracts verify the authenticity of the certificate against blockchain records and validate the agent's trust level. Only when all conditions are met is the agent granted the necessary permissions for secure data interaction. This process not only enhances trust management but also provides a clear path of trust for every agent in the system through continuous monitoring and updating of trust levels.

Together, these mechanisms work to ensure that each data interaction within the MAS is conducted only after thorough verification of credibility, significantly enhancing the overall security and reliability of the system.

5 Conclusion and Outlook

This paper has conducted an in-depth exploration of the evolution of MAS within DAI, with a particular focus on identity authentication and trust issues in cross-MAS interactions. We introduced a Cross-MASs Identity Authentication Framework based on DID, leveraging core technologies such as Smart Contracts, Blockchain, and Decentralized Identity to address the challenges of identity management and trust establishment between MASs. The adoption of DID for agent identity management not only preserves the inherent advantages of MAS but also establishes a trust mechanism across MASs. By analysing the security in the four directions of Agent Privacy, Data Leakage, Attacks, and Cross-MAS Trust and Permission Management, it is demonstrated that this framework can effectively increase the security and confidentiality of cross-MASs interactions while maintaining the flexibility and adaptability of MASs. The framework is analysed in four directions.

Furthermore, the paper discusses the importance and necessity of adopting decentralized identity authentication management. This approach effectively circumvents the insecurities and inefficiencies associated with centralized management. In the current societal context, where the number of MAS interaction scenarios is growing exponentially, the lack of robust identity authentication has become increasingly apparent. Our proposed framework aligns with the direction of technological development in society, addressing the critical issue of agent identity management and trust mechanism establishment in cross-MAS interactions.

Looking ahead, we intend to delve deeper into other issues of cross-MAS interactions Our focus will be directed towards conducting comprehensive scalability analyses of the proposed framework, ensuring its adaptability to the evolving landscape of application demands. Moreover, we are committed to enhancing the data interaction process by optimizing both performance and efficiency, thereby diminishing system latency and bolstering response times through meticulous data management alongside streamlined communication protocols. Concurrently, efforts will be made to

improve the synergy between MAS and DID using emerging technologies to enhance the safety and effectiveness of the system in a multifaceted environment. These concerted efforts are anticipated to yield robust and dependable solutions, poised to address the multifarious challenges of contemporary society more effectively

References

[1] Liang Song, Xing Hu, Guanhua Zhang, Petros Spachos, Konstantinos N Plataniotis, and Hequan Wu. Networking systems of ai: On the convergence of computing and communications. *IEEE Internet of Things Journal*, 9(20):20352–20381, 2022.

[2] Dario Paccagnan, Rahul Chandan, and Jason R Marden. Utility and mechanism design in multi-agent systems: An overview. *Annual Reviews in Control*, 53:315–328, 2022.

[3] Jianrui Wang, Yitian Hong, Jiali Wang, Jiapeng Xu, Yang Tang, Qing-Long Han, and Jürgen Kurths. Cooperative and competitive multi-agent systems: From optimization to games. *IEEE/CAA Journal of Automatica Sinica*, 9(5):763–783, 2022.

[4] Nasim Nezamoddini and Amirhosein Gholami. A survey of adaptive multi-agent networks and their applications in smart cities. *Smart Cities*, 5(1):318–347, 2022.

[5] Md Noor-A-Rahim, Zilong Liu, Haeyoung Lee, Mohammad Omar Khyam, Jianhua He, Dirk Pesch, Klaus Moessner, Walid Saad, and H Vincent Poor. 6g for vehicle-to-everything (v2x) communications: Enabling technologies, challenges, and opportunities. *Proceedings of the IEEE*, 110(6):712–734, 2022.

[6] Liheng Liu, Dongliang Zhang, Jinping Wang, and Jin Yan. A hybrid crossover multi-agent multi-objective evolutionary algorithm and its application in microgrid operation optimization. *Journal of Computational Methods in Sciences and Engineering*, 22(5):1663–1679, 2022.

[7] Jonas Friederich, Deena P Francis, Sanja Lazarova-Molnar, and Nader Mohamed. A framework for data-driven digital twins of smart manufacturing systems. *Computers in Industry*, 136:103586, 2022.

[8] Bianca Caiazzo, Teresa Murino, Alberto Petrillo, Gianluca Piccirillo, and Stefania Santini. An iot-based and cloud-assisted ai-driven monitoring platform for smart manufacturing: design architecture and experimental validation. *Journal of Manufacturing Technology Management*, 34(4):507–534, 2023.

[9] Shuo-Qiu Zhang, Wei-Wei Che, and Chao Deng. Observer-based event-triggered secure synchronization control for multi-agent systems under false data injection attacks. *International Journal of Robust and Nonlinear Control*, 32(8):4843–4860, 2022.

[10] Jingyao Wang, Yige Li, Zhisheng Duan, and Jianping Zeng. A fully distributed robust secure consensus protocol for linear multi-agent systems. *IEEE Transactions on Circuits and Systems II: Express Briefs*, 69(7):3264–3268, 2022.

[11] Rishabh Bhandawat, Sabrina Casucci, Bina Ramamurthy, and Jose L Walteros. Cooperative blood inventory ledger (cobil): A decentralized decision-making framework for improving blood product management. *Computers & Industrial Engineering*, 172:108571, 2022.

[12] Ahmed G Gad, Diana T Mosa, Laith Abualigah, and Amr A Abohany. Emerging trends in blockchain technology and applications: A review and outlook. *Journal of King Saud University-Computer and Information Sciences*, 34(9):6719–6742, 2022.

[13] A Shobanadevi, Sumegh Tharewal, Mukesh Soni, D Dinesh Kumar, Ihtiram Raza Khan, and Pankaj Kumar. Novel identity management system using smart blockchain technology. *International Journal of System Assurance Engineering and Management*, 13(Suppl 1):496–505, 2022.

[14] Xuehan Li, Tao Jing, Ruinian Li, Hui Li, Xiaoxuan Wang, and Dequan Shen. Bdra: Blockchain and decentralized identifiers assisted secure registration and authentication for vanets. *IEEE Internet of Things Journal*, 2022.

[15] Jasmin Bharadiya. Artificial intelligence in transportation systems a critical review. *American Journal of Computing and Engineering*, 6(1):34–45, 2023.

Proceedings of the 3rd Conference on Fully Actuated System Theory and Applications
May 10-12, 2024, Shenzhen, China

A High-Order Fully Actuated Consensus Approach for Strict-feedback Nonlinear Multi-Agent Systems

Congcong Tian[1,2], Jie Mei[1], Guangfu Ma[1]

1. School of Mechanical Engineering and Automation, Harbin Institute of Technology, Shenzhen, Guangdong 518055, P. R. China.
E-mail: jmei@hit.edu.cn (Jie Mei)

2. College of Design and Engineering, National University of Singapore, Singapore 117583, Singapore

Abstract: This paper investigates the consensus problem for general strict-feedback nonlinear multi-agent systems (MASs) over a directed graph. We first derive a high-order fully actuated (HOFA) model for the strict-feedback systems using an recursive solution. Based on the HOFA model, a fully distributed consensus algorithm is proposed, where only the relative position information is interacted. A state transformation method is presented to convert the consensus of the HOFA system into that of single integrators. Theoretical analysis is shown where the agents achieve the consensus asymptotically. Finally, a numerical example is presented to verify the effectiveness of the proposed algorithm.

Key Words: Directed graph, multi-agent systems (MASs), nonlinear, strict-feedback system (SFS), high-order fully actuated (HOFA) model

1 Introduction

Recently, multi-agent systems (MASs) have emerged as one of the most active research fields and have found widespread applications in various domains such as smart grid [1], multiple unmanned aerial vehicle (UAV) systems [2], unmanned surface vehicles (USVs) systems [3], privacy preserving [4], and others. Cooperative control, aimed at achieving both global and individual objectives through networked control protocols, has attracted considerable interest among scholars and has led to numerous advancements in this field.

The consensus is the essential premise in distributed cooperative control for MASs, which guarantees that a group of agents agree upon a certain behavior based on the neighboring information through a network. The research on consensus of MASs starts from single integrators [5, 6], and then spreads to double integrators [7, 8], high-order integrators [9, 10], general linear systems [11], and uncertain or nonlinear dynamics [12–14]. Almost all physical systems are inherently nonlinear, and the cooperative control of nonlinear systems is more challenging and more practically significant. Among the various types of nonlinear systems, the strict-feedback systems (SFSs) attract a lot of attention due to the description of various physical systems, including, but certainly not limited to, circuit system, pendulum systems, robotic systems , missile and satellite control systems [15].

Recently, some results [16–20] have been conducted on the consensus of MASs with strict-feedback nonlinear dynamics. [17] studies the consensus of high-order MASs over an undirected graph, where the agents have nonlinear Lipschitz dynamics. In [18], a consensus algorithm is proposed for high-order uncertain MASs with unknown control directions by introducing an estimation of consensus value over a fix directed graph. In [19], the authors investigate the consensus problem with guaranteed convergence for high-order uncertain MASs with unknown control directions over switching topologies. However, the relative information of high-order derivatives is used in [18] and [19]. Since it is difficult to acquire the relative information of high-order derivatives via onboard sensors, and the information communication among agents increases the communication cost, the consensus algorithm relying only on relative position information is more efficient. Meanwhile, the agent dynamics studied in [17–19] involve high-order integrators with nonlinear terms, representing a special form of strict-feedback systems. However, in reality, various state components are often coupled in more complex ways for general strict-feedback nonlinear systems.

Several traditional nonlinear control methods have been applied to nonlinear multi-agent systems, including the feedback linearization method [21], the back-stepping method [22], the sliding mode method [23], and the Lyapunov method [16]. For strict-feedback nonlinear MASs, their specific triangular structure allows for a systematic recursive design procedure of stabilizing controllers, known as the backstepping method. In [22], the adaptive neural backstepping approach is extended to solve consensus tracking problems by utilizing the structural feature of radial basis function neural networks (RBFNNs). However, backstepping is a recursive design procedure with increasing complexity as the system order grows, resulting in the "explosion of complexity" problem. The high-order fully actuated (HOFA) system approach introduced in [24] provides a powerful tool for nonlinear system design and analysis, which facilitates the complete expression of control laws.The cooperative control of MASs based on the HOFA model has emerged as an innovative and compelling topic. Existing research, as demonstrated in [25–27], primarily focuses on the cooperative control and cooperative performances of HOFA MASs.

In this paper, we focus on addressing the consensus problem of general strict-feedback nonlinear MASs over a directed graph. Inspired by the HOFA model approach, the high-order nonlinear strict feedback systems are reconstructed into the HOFA model. Drawing upon closed-loop

This work was supported in part by the National Key R&D Program of China (2019YFA0706500), the National Natural Science Foundation of China under Grant (62073098, U1913209), and the Shenzhen Fundamental Research Program under Grant (JCYJ20200109113210134, JCYJ20210324132215038). The first author of this paper (Congcong Tian) gratefully acknowledges the support by the China Scholarship Council (grant number 202306120318).

control algorithm design principles based on the HOFA model for single plants, we extend a distributed consensus algorithm to MASs with HOFA dynamics. This algorithm relies solely on relative position information among neighboring agents. The main challenges of this paper include addressing more general nonlinear SFSs, utilizing only relative position information (without using relative information of high-order derivatives), and ensuring full distribution without shared gains or global gain dependency.

Notations: $A \otimes B$ denotes the Kronecker product of matrices A and B. Let $\mathbf{0}_m$ be the $m \times 1$ column vector of all zeros, and $\mathbf{1}_m$ be the $m \times 1$ column vector of all ones. $\mathrm{Trace}(A)$ represents the trace of a square matrix A. For a complex number μ, $\mathscr{R}(\mu)$ represents its real part. $\mathrm{diag}(\sigma_1, \sigma_2, \cdots, \sigma_n)$ denotes the diagonal matrix, where the value σ_i appears in the i-th diagonal entry, and all other entries are zero. For a vector $x(t) \in \mathbb{R}^n$, $x(t) \in \mathbb{L}_\infty$ if each element $x_i(t)$ satisfies $\sup_t |x_i(t)| < \infty$, where $i = 1, \ldots, n$. Similarly, $x(t) \in \mathbb{L}_p, p \in [1, \infty)$ if $\left(\int_0^\infty |x(\tau)|^p \mathrm{d}\tau\right)^{\frac{1}{p}} < \infty$. $\|\cdot\|$ represents the Euclidean norm of a vector.

2 Preliminaries

2.1 Graph Theory

The directed graph $\mathcal{G}_n$, with the set of nodes $\mathcal{V} = \{1, \ldots, n\}$ and the set of edges $\mathcal{E} \subseteq \mathcal{V} \times \mathcal{V}$, represents the network topology of the multi-agent system. The adjacency matrix $\mathcal{A}_n = [a_{ij}]$ characterizes the connectivity among the agents, where $a_{ij} > 0$ if node i receives information from node j, and $a_{ij} = 0$ otherwise. A directed spanning tree is a subset of a directed graph that contains a directed path from the root node to each other node. Self-edges are not allowed in this paper. The Laplacian matrix $\mathcal{L}_n$ of the graph $\mathcal{G}_n$ is defined as $\mathcal{L}_n = \mathrm{diag}(\sum_{j=1}^n a_{1j}, \sum_{j=1}^n a_{2j}, \cdots, \sum_{j=1}^n a_{nj}) - \mathcal{A}_n$. A directed graph has the following properties.

Lemma 1. *[28] For a directed graph $\mathcal{G}_n$ with n nodes, $\mathcal{L}_n$ is the corresponding Laplacian matrix of $\mathcal{G}_n$. Suppose that $z = \left[z_1^T, \ldots, z_n^T\right]^T$ with $z_i \in \mathbb{R}^m$, the following conditions are equivalent:*
(i) $\mathcal{G}_n$ has a directed spanning tree.
(ii) $\mathcal{L}_n$ has a unique eigenvalue of zero and all other eigenvalues with positive real parts.
(iii) Consensus is reached asymptotically for the system $\dot{z} = -\left(\mathcal{L}_n \otimes I_m\right) z$.

2.2 Problem Statement

Consider n agents over a directed graph $\mathcal{G}_n$. The dynamics of each agent can be described by the following strict-feedback nonlinear system

$$\begin{cases} \dot{x}_{i,1} = f_{i,1}\left(x_{i,1}\right) + G_{i,1}\left(x_{i,1}\right) x_{i,2} \\ \dot{x}_{i,2} = f_{i,2}\left(x_{i,1}, x_{i,2}\right) + G_{i,2}\left(x_{i,1}, x_{i,2}\right) x_{i,3} \\ \quad \vdots \\ \dot{x}_{i,p-1} = f_{i,p-1}\left(x_{i,1}, \ldots, x_{i,p-1}\right) \\ \qquad\qquad + G_{i,p-1}\left(x_{i,1}, \ldots, x_{i,p-1}\right) x_{i,p} \\ \dot{x}_{i,p} = f_{i,p}\left(x_{i,1}, \ldots, x_{i,p}\right) + G_{i,p}\left(x_{i,1}, \ldots, x_{i,p}\right) u_i, \end{cases} \tag{1}$$

for $i \in \mathcal{V}$, where $x_i = \mathrm{col}\left(x_{i,1}, x_{i,2}, \ldots, x_{i,p}\right)$ with $p \geq 1$, and $x_{i,l} \in \mathbb{R}^r$ represents the states of agent i, $u_i \in \mathbb{R}^r$ represents the control input, $f_{i,l}\left(x_{i,1}, \ldots, x_{i,l}\right) \in \mathbb{R}^r$ and $G_{i,l}\left(x_{i,1}, \ldots, x_{i,l}\right) \in \mathbb{R}^{r \times r}, l = 1, \ldots, p, i = 1, 2, \ldots, n$ are sufficiently smooth vector functions and matrix functions, respectively. Furthermore, $G_{i,l}\left(x_{i,1}, \ldots, x_{i,l}\right)$ is nonsingular for all $x_i, i = 1, 2, \ldots, n, l = 1, \ldots, p$.

As a normal requirement to SFSs, we have the following assumptions:

Assumption 1. *For arbitrary $x_{i,l} \in \mathbb{R}^r, i = 1, 2, \ldots, n, l = 1, \ldots, p$, there holds*

$$\det G_{i,l}\left(x_{i,1}, \ldots, x_{i,l}, t\right) \neq 0, \quad \forall t \geq 0.$$

Assumption 2. *The directed graph $\mathcal{G}_n$ contains a directed spanning tree.*

Definition 1. *The multi-agent system described by* (1) *is called to achieve position consensus, if $\lim_{t\to\infty} \|x_{i,1}(t) - x_{j,1}(t)\| = 0, \forall i, j = 1, \ldots, n$.*

3 Main Result

For the general form (1), some existing control methods, such as the backstepping methods, may become extremely difficult or even impossible to apply when r and n are large due to the "differential explosion" problem. However, if we can transform it into a HOFA system model, its control problems can then be solved easily and conveniently [24].

We firstly present recursive solutions to convert a SFS (1) into a HOFA model (3).

Lemma 2. *[29] Let Assumption 1 be satisfied, then, under the following transformation*

$$\begin{cases} x_{i,1} = z_i \\ x_{i,2} = G_{i,1}^{-1}(z_i)\left[\dot{z}_i - f_{i,1}(z_i)\right] \\ x_{i,k+1} = L_{i,k}^{-1}\left({z_i}^{(0\sim k-1)}\right)\left[{z_i}^{(k)} - h_{i,k}\left({z_i}^{(0\sim k-1)}\right)\right] \\ \quad k = 2, 3, \ldots, p-1, \end{cases} \tag{2}$$

the generalised strict-feedback nonlinear system (1) *can be transformed into the following HOFA system*

$${z_i}^{(p)} = h_{i,p}\left({z_i}^{(0\sim p-1)}\right) + L_{i,p}\left({z_i}^{(0\sim p-1)}\right) u_i, \tag{3}$$

where the matrix function $L_{i,k}\left({z_i}^{(0\sim k-1)}, t\right)$ and the vector function $h_{i,k}\left({z_i}^{(0\sim k-1)}, t\right)$ are recursively given by

$$\begin{aligned} &L_{i,k}\left({z_i}^{(0\sim k-1)}, t\right) \\ &\quad = L_{i,k-1}\left({z_i}^{(0\sim k-2)}, t\right) G_{i,k}\left(x_{i,1\sim k-1}^{(0\sim 1)}, x_{i,k}, t\right) \end{aligned} \tag{4}$$

and

$$\begin{aligned} &h_{i,k}\left({z_i}^{(0\sim k-1)}, t\right) \\ &\quad = \dot{h}_{i,k-1}\left({z_i}^{(0\sim k-2)}, t\right) + \dot{L}_{i,k-1}\left({z_i}^{(0\sim k-2)}, t\right) x_{i,k} \\ &\quad + L_{i,k-1}\left({z_i}^{(0\sim k-2)}, t\right) f_{i,k}\left(x_{i,1\sim k-1}^{(0\sim 1)}, x_{i,k}, t\right) \\ &\quad k = 1, 2, \ldots, p \end{aligned} \tag{5}$$

with the initial values $L_{i,0} = I$, ${z_i}^{(0\sim p-1)} = \mathrm{col}\left(z_i, \dot{z}_i, \ldots, {z_i}^{(p-1)}\right)$, and in (4)-(5) *the $x_{i,k}, k = 2, 3, \ldots, p$ and their derivatives are all given or determined by the transformation* (2).

Once the HOFA model (3) is obtained, the controller of the system can then be simply designed as [24]

$$\begin{cases} u_i = -L_{i,p}^{-1}\left(A_{i,0\sim p-1} z_i^{(0\sim p-1)} + u^*\right) \\ u^* = h_{i,p}\left(z_i^{(0\sim p-1)}\right) - v, \end{cases} \tag{6}$$

which gives the following constant linear closed-loop system

$$z_i^{(p)} + A_{i,0\sim p-1} z_i^{(0\sim p-1)} = v, \tag{7}$$

where v is some external signal, while $A_{i,0\sim p-1} = \begin{bmatrix} A_0 & A_1 & \cdots & A_{p-1} \end{bmatrix}$ is an arbitrary matrix which ensures (7) is stable. A complete parametric approach for solving the matrix $A_{i,0\sim p-1}$ is given in [24].

For a single plant, the HOFA system approach is very powerful in dealing with the control of nonlinear systems, since the full-actuation feature allows one to eliminate the nonlinearities and hence a constant linear closed-loop system can be obtained.

Next, we investigate the consensus problem for MASs over a directed graph. Drawing inspiration from the above HOFA system approach, we construct the consensus algorithm for each agent as follows

$$\begin{cases} u_i = -L_{i,p}^{-1}\left(A_{i,1\sim p-1} z_i^{(0\sim p-1)} + u^*\right) \\ u^* = h_{i,p}\left(z_i^{(0\sim p-1)}\right) + A_{i,0}\sum_{j=1}^{n} a_{ij}(z_i - z_j), \end{cases} \tag{8}$$

which gives the following constant linear system

$$z_i^{(p)} + A_{i,1\sim p-1} z_i^{(1\sim p-1)} = -A_{i,0}\sum_{j=1}^{n} a_{ij}(z_i - z_j), \tag{9}$$

Remark 1. *Clearly,* (9) *is a pth order linear system. For the given initial conditions $z_i^{(m)}(0)$, $m = 0, \ldots, p-1$,* (9) *produces its outputs $z_i^{(m)}$, $m = 0, \ldots, p-1$ with the input $-A_{i,0}\sum_{j=1}^{n} a_{ij}(z_i - z_j)$. The problem is to seek a matrix $A_{i,0\sim p-1}$ such that* (9) *reaches consensus. The relative position information $\sum_{j=1}^{n} a_{ij}(z_i - z_j)$ guarantees that each agent achieves consensus on their positions for* (9)*. The high derivatives of the position re utilized in the feedback to drive them to zero as $t \to \infty$. The damping gains should be chosen in a distributed method, and have no global information dependency, which motivates us to propose a fully distributed gain design later. Thus,* (9) *becomes exactly the closed-loop system for the position consensus of high-order integrators.*

Regarding the solution of the matrix $A_{i,0\sim p-1}$ of (9), the parameter matrix $A_{i,0\sim p-1}$ can be chosen to satisfy

$$\begin{cases} A_{i,0} = k_i^{p-2} \\ A_{i,m} = k_i^{p-m-2}\left[k_i^2 C_{p-1}^{m-1} + C_{p-1}^{m}\sum_{j=1}^{n} a_{ij}\right], \\ \qquad m = 1, \ldots, p-1, \end{cases} \tag{10}$$

with k_i being a positive constant.

Let Z be the stacked vector of $z_i, i = 1, \ldots, n$. Under the control algorithm (8) with (10), (9) has the following vector form

$$\begin{aligned} Z^{(p)} = &-\sum_{m=1}^{p-1} \bar{K}^{p-m-2}\left[\bar{K}^2 C_{p-1}^{m-1} + C_{p-1}^{m}\mathcal{D}_n\right] Z^{(m)} \\ &- \bar{K}^{p-2}\mathcal{L}_n Z \end{aligned} \tag{11}$$

where $\bar{K} \triangleq K \otimes I_r, K = \mathrm{diag}(k_1, \cdots, k_n)$.

To prove that the matrix $A_{i,0\sim p-1}$ chosen in (10) ensures that the system (9) achieves position consensus, we firstly present a state transformation for the consensus of high-order integrators, which is introduced to convert high-order integrators into the single integrators in [16]. The main result on position consensus of strict-feedback nonlinear MASs over a directed graph can be concluded as follows.

Theorem 1. *Under Assumptions 1 and 2, for the agents with dynamics* (1)*, under the control algorithm* (8) *with* (10)*, the potisions of the agents achieve consensus asymptotically, i.e.,* $\lim_{t\to\infty}(x_{i,1}(t) - x_{j,1}(t)) = 0, \forall i, j = 1, \ldots, n$.

Proof: For each agent i, define $y_{i,1} = x_{i,1} = z_i$, and

$$y_{i,l} = \frac{1}{k_i}\dot{y}_{i,l} + y_{i,l-1}, \quad l = 2, \ldots, p \tag{12}$$

It is worth noting that if we consider $y_{i,l}, l = 1, \ldots, p$ as an individual node in a new graph $\mathcal{G}_N$ with the $N = np$ agents. Let Y_l be the stacked vector of $y_{i,l}, i = 1, \ldots, n, l = 1, \ldots, p$.

$$Y_l = \bar{K}^{-1}\dot{Y}_{l-1} + Y_{l-1}, \quad l = 2, \ldots, p \tag{13}$$

Under such transformation, one can obtain the following equations

$$Y_l = \sum_{m=1}^{l} \frac{C_{l-1}^{m-1}}{\bar{K}^{m-1}} Z^{(m-1)}, \quad l = 1, \ldots, p \tag{14}$$

where C_{l-1}^{m-1} is the binomial coefficient which can be computed as $C_{l-1}^{m-1} = \frac{(l-1)!}{(m-1)!(l-m)!}$. For $l = p$, we can derive

$$\begin{aligned} Y_p &= \sum_{m=1}^{p} \frac{C_{p-1}^{m-1}}{\bar{K}^{m-1}} Z^{(m-1)} \\ &= \sum_{m=1}^{p-1} \frac{C_{p-1}^{m-1}}{\bar{K}^{m-1}} Z^{m-1} + \frac{1}{\bar{K}^{p-1}} Z^{(p-1)} \\ &= \sum_{m=1}^{p-1} \frac{C_{p-1}^{m}}{\bar{K}^{m}} Z^{(m)} + Y_0 \end{aligned} \tag{15}$$

Then we can calculate the derivative of Y_p as follows

$$\dot{Y}_p = \sum_{m=1}^{p-1} \frac{C_{p-1}^{m-1}}{\bar{K}^{m-1}} Z^{(m)} + \frac{1}{\bar{K}^{p-1}} Z^{p} \tag{16}$$

Substituting (11) and (15) into (16), we can get

$$\dot{Y}_p = -\bar{K}^{-1}\mathcal{D}_n(Y_p - Y_0) - \bar{K}^{-1}\mathcal{L}_n Y_1 \tag{17}$$

Then from (13) and (17), we have the following dynamics

$$\begin{aligned} \dot{Y}_l &= -\bar{K}(Y_l - Y_{l+1}), \quad l = 1, \ldots, p-1 \\ \dot{Y}_p &= -\bar{K}^{-1}\mathcal{L}_n Y_1 - \bar{K}^{-1}\mathcal{D}_n(Y_p - Y_1) \\ &= \bar{K}^{-1}\mathcal{A}_n Y_1 - \bar{K}^{-1}\mathcal{D}_n Y_p \end{aligned} \tag{18}$$

Let $Y = (Y_1, \ldots, Y_P)^T$. We can get

$$\dot{Y} = -(\mathcal{L}_N \otimes I_r)Y \tag{19}$$

where

$$\mathcal{L}_N = \begin{pmatrix} K & -K & \mathbf{0}_{n\times n} & \cdots & \mathbf{0}_{n\times n} \\ \mathbf{0}_{n\times n} & K & -K & \mathbf{0}_{n\times n} & \mathbf{0}_{n\times n} \\ \vdots & \ddots & \ddots & \ddots & \vdots \\ \mathbf{0}_{n\times n} & \cdots & \mathbf{0}_{n\times n} & K & -K \\ -K^{-1}\mathcal{A}_n & \mathbf{0}_{n\times n} & \cdots & \mathbf{0}_{n\times n} & K^{-1}\mathcal{D}_n \end{pmatrix} \tag{20}$$

Under the system transformation (12), regarding the new states $y_{i,k}, i = 1,\ldots,n, k = 1,\ldots,p$ as nodes $v_{i,k} \in \mathcal{V}_N, i = 1,\ldots,n, k = 1,\ldots,p$ in the transformed graph $\mathcal{G}_N \triangleq (\mathcal{V}_N, \mathcal{E}_N)$. From Lemma 6 in [16], $\mathcal{G}_N$ contains a directed spanning tree. Therefore, we know from Lemma 1, (19) achieves consensus asymptotically. Therefore, $\lim_{t\to\infty}(y_{i,l} - y_{j,m}) = 0$, $\forall i,j = 1,\ldots,n$ and $l,m = 1,\ldots,p$. For $l = m = 1$, since $y_{i,1} = z_i$, we have $\lim_{t\to\infty}(z_i - z_j) = 0$. And iteratively, we can also get that $\lim_{t\to\infty}\|z_i^{(m)}\| = 0$, $m = 1,\ldots,p-1$. We can conclude that $\lim_{t\to\infty}(x_{i,1} - x_{j,1}) = 0$,$\forall i,j = 1,\ldots,n$. Consensus of system (1) can be achieved asymptotically.

Remark 2. *The proposed control algorithm* (8) *can be implemented fully distributely interacting only relative position information among the agents (without using relative information of high-order derivatives). The proposed algorithm* (8) *is fully distributed, since each agent owns its gains and has no global gain dependency.*

4 Numerical Simulation

In this section, numerical simulations on a network of six agents ($n = 6$), among which the topology is shown in Fig. 1, are performed to validate the proposed algorithms. In this section, we only consider a simple illustrative example [30], which was originally presented by Kokotovi and Kanellakopoulos.

$$\begin{aligned} \dot{x}_{i,1} &= 0.8x_{i,1}^2 + x_{i,2} \\ \dot{x}_{i,2} &= x_{i,3} \\ \dot{x}_{i,3} &= u_i, \end{aligned} \tag{21}$$

where all variables are scalar ones.

Following the result in section 3, it can be shown that the system (21) is equivalent to the following third-order fully actuated system:

$$\dddot{z}_i = 1.6\left(\dot{z}_i^{\,2} + z_i\ddot{z}_i\right) + u_i \tag{22}$$

while the original states of the system (21) are given by the following transformation

$$\begin{aligned} x_{i,1} &= z_i \\ x_{i,2} &= \dot{z}_i - 0.8{z_i}^2 \\ x_{i,3} &= \ddot{z}_i - 1.6z_i\dot{z}_i. \end{aligned} \tag{23}$$

Corresponding to the form of (3), we have

$$\begin{aligned} h_{i,3}\left({z_i}^{(0\sim 2)}\right) &= 1.6\left(\dot{z}_i^{\,2} + z_i\ddot{z}_i\right) \\ L_{i,3}\left({z_i}^{(0\sim 2)}\right) &= 1. \end{aligned} \tag{24}$$

From (8), the control algorithm for each agent is

$$u_i = -A_{i,2}\ddot{z}_i - A_{i,1}\dot{z}_i - h_{i,3}\left({z_i}^{(0\sim 2)}\right) - A_{i,0}\sum_{j=1}^{n} a_{ij}(z_i - z_j)$$

Choose the scales as $A_{i,0} = 1$, $A_{i,1} = 1 + 2\sum_{j=1}^{6} a_{ij}$, $A_{i,2} = 2 + \sum_{j=1}^{6} a_{ij}$ with the control gains $k_i = 1$. From (9), the dynamics of the linear model is

$${z_i}^{(3)} + A_{i,2}\ddot{z}_i + A_{i,1}\dot{z}_i = -A_{i,0}\sum_{j=1}^{6} a_{ij}(z_i - z_j) \tag{25}$$

with the initial conditions $z_i(0) = i - 1$, $\dot{z}_i(0) = 0$, and $\ddot{z}_i(0) = 0$. In Fig. 2, the position trajectories of the six agents reach consensus under the proposed control algorithm.

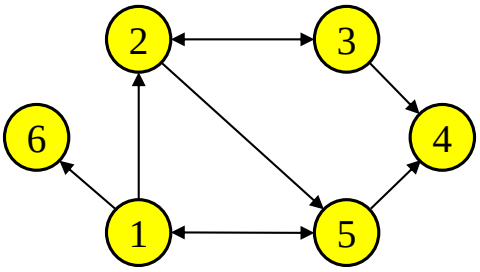

Fig. 1: The interactions among six agents.

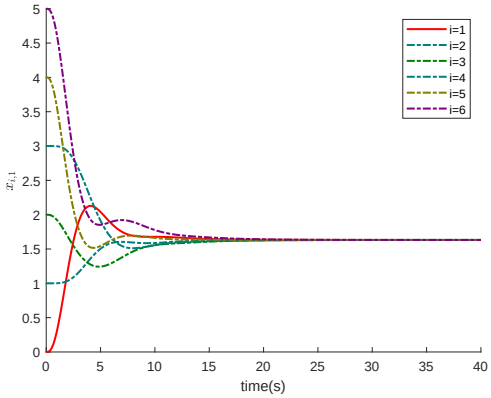

Fig. 2: The position trajectories of the six agents for the consensus, $i = 1,\ldots,6$.

5 Conclusion

This paper has addressed the consensus problem for general strict-feedback nonlinear MASs over a directed graph. A HOFA consensus algorithm has been proposed to achieve consensus asymptotically. Compared with other existing coordination methods strict-feedback nonlinear MASs, the HOFA consensus method is simple, active and universal. Finally, a numerical example has been provided to demonstrate the efficacy of the proposed control algorithm.

References

[1] F. Luo, Y. Chen, Z. Xu, G. Liang, Y. Zheng, and J. Qiu, "Multiagent-based cooperative control framework for microgrids energy imbalance," *IEEE Transactions on Industrial Informatics*, vol. 13, no. 3, pp. 1046–1056, 2017.

[2] Z. Liang, L. Yi, X. Shida, and F. Han, "Multiple UAVs cooperative formation forming control based on back-stepping-like approach," *Journal of Systems Engineering and Electronics*, vol. 29, no. 4, pp. 816–822, 2018.

[3] Y. Gu, P. Wang, Z. Rong, H. Wei, S. Yang, K. Zhang, Z. Tang, T. Han, and Y. Si, "Vessel intrusion interception utilising unmanned surface vehicles for offshore wind farm asset protection," *Ocean Engineering*, vol. 299, p. 117395, May 2024.

[4] W. Fang, M. Zamani, and Z. Chen, "Secure and privacy preserving consensus for second-order systems based on Paillier encryption," *Systems & Control Letters*, vol. 148, p. 104869, Feb. 2021.

[5] A. Jadbabaie, J. Lin, and A. S. Morse, "Coordination of groups of mobile autonomous agents using nearest neighbor rules," vol. 48, no. 6, pp. 988–1001, June 2003.

[6] W. Ren and R. W. Beard, "Consensus seeking in multiagent systems under dynamically changing interaction topologies," vol. 50, no. 5, pp. 655–661, May 2005.

[7] W. Xu, S. Yang, and J. Cao, "Fully distributed self-triggered control for second-order consensus of multiagent systems," *IEEE Transactions on Systems, Man, and Cybernetics: Systems*, pp. 1–11, 2020.

[8] H. Su, X. Wang, X. Chen, and Z. Zeng, "Second-order consensus of hybrid multiagent systems," *IEEE Transactions on Systems, Man, and Cybernetics: Systems*, pp. 1–10, 2020.

[9] L. Chen, J. Mei, C. Li, and G. Ma, "Distributed leaderfollower affine formation maneuver control for high-order multiagent systems," *IEEE Transactions on Automatic Control*, vol. 65, no. 11, pp. 4941–4948, 2020.

[10] J. Ni, P. Shi, Y. Zhao, Q. Pan, and S. Wang, "Fixed-time event-triggered output consensus tracking of high-order multiagent systems under directed interaction graphs," *IEEE Transactions on Cybernetics*, vol. 52, no. 7, pp. 6391–6405, 2022.

[11] G. Wen, G. Hu, W. Yu, and G. Chen, "Distributed H_∞ consensus of higher order multiagent systems with switching topologies," *IEEE Transactions on Circuits and Systems II: Express Briefs*, vol. 61, no. 5, pp. 359–363, May 2014.

[12] C. Tian and J. Mei, "Adaptive Bipartite Leaderless Consensus of Multiagent Systems With Uncertain MIMO Dynamics Over a Signed Directed Graph," vol. 70, no. 8, pp. 2969–2973.

[13] J. Mei, "Distributed consensus for multiple Lagrangian systems with parametric uncertainties and external disturbances under directed graphs," *IEEE Transactions on Control of Network Systems*, vol. 7, no. 2, pp. 648–659, 2020.

[14] X. Zhao, S. Chen, Z. Zhang, and Y. Zheng, "Consensus tracking for high-order uncertain nonlinear mass via adaptive backstepping approach," *IEEE Transactions on Cybernetics*, pp. 1–12, 2021.

[15] I. Kanellakopoulos, P. V. Kokotovic, and A. S. Morse, "Systematic design of adaptive controllers for feedback linearizable systems," in *1991 American Control Conference*, 1991, pp. 649–654.

[16] J. Mei, K. Tian, and G. Ma, "Scaled position consensus of high-order uncertain multiagent systems over switching directed graphs," *IEEE Transactions on Cybernetics*, pp. 1–12, 2023.

[17] D. Liuzza, D. V. Dimarogonas, and K. H. Johansson, "Generalized pid synchronization of higher order nonlinear systems with a recursive Lyapunov approach," *IEEE Transactions on Control of Network Systems*, vol. 5, no. 4, pp. 1608–1621, Dec 2018.

[18] G. Wang, "Distributed control of higher-order nonlinear multi-agent systems with unknown non-identical control directions under general directed graphs," *Automatica*, vol. 110, p. 108559, 2019.

[19] Q. Wang, H. E. Psillakis, and C. Sun, "Adaptive cooperative control with guaranteed convergence in time-varying networks of nonlinear dynamical systems," *IEEE Transactions on Cybernetics*, vol. 50, no. 12, pp. 5035–5046, 2020.

[20] C. Tian, K. Tian, J. Mei, and G. Ma, "Bipartite leaderless position consensus of heterogeneous uncertain multi-agent systems under switching directed graphs," vol. 181, p. 105628.

[21] D. H. Nguyen, "Minimum-Rank Dynamic Output Consensus Design for Heterogeneous Nonlinear Multi-Agent Systems," *IEEE Transactions on Control of Network Systems*, vol. 5, no. 1, pp. 105–115, Mar. 2018.

[22] Y. Shang, B. Chen, and C. Lin, "Consensus Tracking Control for Distributed Nonlinear Multiagent Systems via Adaptive Neural Backstepping Approach," *IEEE Transactions on Systems, Man, and Cybernetics: Systems*, vol. 50, no. 7, pp. 2436–2444, Jul. 2020.

[23] B. Ning, Q.-L. Han, and L. Ding, "Distributed Secondary Control of AC Microgrids With External Disturbances and Directed Communication Topologies: A Full-Order Sliding-Mode Approach," *IEEE/CAA Journal of Automatica Sinica*, vol. 8, no. 3, pp. 554–564, Mar. 2021.

[24] G. Duan, "High-order fully actuated system approaches: Part I. Models and basic procedure," *International Journal of Systems Science*, vol. 52, no. 2, pp. 422–435, Jan. 2021.

[25] G.-P. Liu, "Coordination of Networked Nonlinear Multi-Agents Using a High-Order Fully Actuated Predictive Control Strategy," *IEEE/CAA Journal of Automatica Sinica*, vol. 9, no. 4, pp. 615–623, Apr. 2022.

[26] D.-W. Zhang, G.-P. Liu, and L. Cao, "Proportional Integral Predictive Control of High-Order Fully Actuated Networked Multiagent Systems With Communication Delays," *IEEE Transactions on Systems, Man, and Cybernetics: Systems*, vol. 53, no. 2, pp. 801–812, Feb. 2023.

[27] D.-W. Zhang, G.-P. Liu, and L. Cao, "Coordinated Control of High-Order Fully Actuated Multiagent Systems and Its Application: A Predictive Control Strategy," *IEEE/ASME Transactions on Mechatronics*, vol. 27, no. 6, pp. 4362–4372, Dec. 2022.

[28] W. Ren and R. W. Beard, *Distributed Consensus in Multi-vehicle Cooperative Control*. Springer London, 2008.

[29] G. Duan, "High-order fully actuated system approaches: Part II. Generalized strict-feedback systems," *International Journal of Systems Science*, vol. 52, no. 3, pp. 437–454, Feb. 2021.

[30] P. Kokotovic and I. Kanellakopoulos, "Adaptive nonlinear control: A critical appraisal," in *Proc. 6th Yale Workshop on Adaptive and Learning Systems*, 1990, pp. 1–6.

Proceedings of the 3rd Conference on Fully Actuated System Theory and Applications
May 10-12, 2024, Shenzhen, China

Finite-time Consensus for Third-Order Multi-Agent Systems with Directed Communication Networks

Xirui Zhang[1], Zhi-Liang Zhao[2,1], Tengfei Liu[3], Zhong-Ping Jiang[4]

1. School of Mathematics and Statistics, Shaanxi Normal University, Xi'an, 710119, P. R. China
E-mail: 1743163015@qq.com; zhiliangzhao@snnu.edu.cn

2. School of Electrical and Control Engineering, North University of China, Taiyuan, 030051, P .R. China
E-mail: 20240016@nuc.edu.cn

3. State Key Laboratory of Synthetical Automation for Process Industries, Northeastern University, Shenyang, 110004, P. R. China
E-mail: tfliu@mail.neu.edu.cn

4. Department of Electrical and Computer Engineering, New York University, 370 Jay Street, Brooklyn, NY 11201, USA
E-mail: zjiang@nyu.edu

Abstract: This paper focuses on third-order multi-agent systems with directed communication networks. It is for the first time that the finite-time consensus problem is solved for third-order multi-agent systems under digraphs containing spanning trees. Two explicit-coefficient finite-time protocols, namely, edge-based and node-based, are proposed. First, we prove that asymptotic consensus is achievable with the reduced linear protocol. Then, we show that finite-time consensus is achievable with our explicit-coefficient finite-time protocols through homogeneous theory. Finally, numerical simulations are carried out to demonstrate the effectiveness of the proposed protocols.

Key Words: Finite-Time Consensus, Multiagent Systems, High-Order Systems, Directed Graph

1 Introduction

Recent years, cooperative control has attracted a lot of interests due to its advantages of group intelligence. A core problem for cooperative control is achieving consensus, i.e., driving the agents to an agreement through coordination. In many consensus scenarios, the controlled agents are only allowed to transmit the information to their children nodes, in which the communication networks are directed. To deal with directed networks, references [1–3] obtain the linear protocols for multi-agent systems.

For higher convergence rate and better robustness, finite-time consensus has been widely investigated referring [4–9] and the references therein. In the existing finite-time consensus works, except for undirected networks [6, 8], only few works [7, 10] focus on directed topologies for first- and second-order multi-agent systems. In current work, to explore finite-time consensus for higher-order multi-agent systems, we focus on third-order multi-agent systems with directed communication networks, which are assumed to contain directed spanning trees.

This paper develops two classes of protocols, namely, edge-based and node-based. The main difficulty lies in that the instability phenomenon may appear with directed communication networks using the existing protocols. Reference [2] reveals that the protocol coefficients would be effected by the complex eigenvalues from directed networks, that is, the consensus may lose when there are complex eigenvalues. Reference [3] obtains a solution for protocol coefficients which are described implicitly. In this paper, an explicit solution for the protocol coefficients is obtained by analyzing the eigenvalues of closed-loop systems.

The main contribution of this paper is summarized as follows:

- The finite-time consensus problem is solved for third-order multi-agent systems under directed graphs containing a spanning tree. Since the Laplacian matrix is asymmetric under directed communication networks, constructing finite-time Lyapunov function is challenging. Based on [3, 11, 12], this paper constructs homogeneous Lyapunov function dealing with the asymmetric Laplacian matrix and proving the finite-time consensus.
- The protocol parameters are chosen explicitly in this paper. It is proved that such explicit coefficients can be used for the proposed protocols which guarantee the finite-time consensus for directed third-order multi-agent systems.

Notations

In this paper, we use $\circ$ to represent compositions of functions. The functions $\mathrm{Re}(z)$ and $\mathrm{Im}(z)$ extract the real and the imaginary parts of $z \in \mathbb{C}$, respectively. The notation $A \otimes B$ represents the Kronecker product between real matrices A and B. The function $[x]^\alpha = \mathrm{sign}(x)|x|^\alpha$ is defined for $x \in \mathbb{R}$ with power $\alpha > 0$.

A weighted directed graph $\mathcal{G} = \{\mathcal{V}, \mathcal{E}, A\}$ is used to describe the communications among agents, where $\mathcal{V}$ is the set of nodes, $\mathcal{E} \subseteq \mathcal{V} \times \mathcal{V}$ is the set of edges and A is the associated adjacent matrix with weighting factors $a_{ij} \geq 0$, which represents the weight from agent j to agent i. Define $\mathcal{L} = \{l_{ij}\} \in \mathbb{R}^{N\times N}$ as the Laplacian matrix of the graph $\mathcal{G}$ with $l_{ii} = \sum_{i\neq j} a_{ij}$ and $l_{ij} = -a_{ij},\ i \neq j$. Note $0, \lambda_2, \ldots, \lambda_N$ as the eigenvalues of $\mathcal{L}$, where λ_2 has the minimum real part and is called the algebraic connectivity of the graph $\mathcal{G}$.

This work was supported in part by NSFC grants 61973202, 62325303 and 62333004, in part by National Key R & D Program of China (2022ZD0119901), in part by Science and Technology Projects of Liaoning Province (2022JH2/101300238), in part by Liaoning Revitalization Talents Program XLYC2203076, and in part by NSF grant ECCS-2210320.

Corresponding auther: Z. L. Zhao

2 Main Result

In this section, we propose our main theorem for third-order multi-agent systems and give the corresponding proof.

2.1 Main Theorem

We study the finite-time consensus for the following multi-agent system, which equips N agents with agent i ($i = 1, \ldots, N$) satisfying third-order integrator dynamic.

$$\dot{x}_{i1} = x_{i2}, \tag{1a}$$
$$\dot{x}_{i2} = x_{i3}, \tag{1b}$$
$$\dot{x}_{i3} = u_i \tag{1c}$$

where $x_i = [x_{i1}, x_{i2}, x_{i3}]^T \in \mathbb{R}^3$ is the state, and $u_i \in \mathbb{R}$ is the control input.

For such multi-agent system, two classes of finite-time protocols are designed as:

- Edge-based protocol:

$$u_i = -c \sum_{k=1}^{3} \rho_k \sum_{j=1}^{N} [a_{ij}(x_{ik} - x_{jk})]^{\alpha_k}, \tag{2}$$

- Node-based protocol:

$$u_i = -c \sum_{k=1}^{3} \rho_k \left[\sum_{j=1}^{N} a_{ij}(x_{ik} - x_{jk}) \right]^{\alpha_k}, \tag{3}$$

where a_{ij} represents the information exchange from agent j to agent i and coefficients c, ρ_i, α_i (for $i = 1, 2, 3$) satisfy

$$c \geq 1/(2\,\mathrm{Re}(\lambda_2)), \tag{4a}$$
$$[\rho_1, \rho_2, \rho_3] = [\omega^3, 3\omega^2, 3\omega], \tag{4b}$$
$$[\alpha_1, \alpha_2, \alpha_3] = \left[1 + 3d, \frac{1+3d}{1+d}, \frac{1+3d}{1+2d}\right], \tag{4c}$$

with $d \in (-1/3, 0)$ and ω being an arbitrary positive real number.

Then, we state the following main theorem.

Theorem 1. *Suppose that the interconnection digraph $\mathcal{G}$ contains a spanning tree. Then, there exists a constant $\underline{d} \in (-1/3, 0)$ such that for any $d \in [\underline{d}, 0)$, the multi-agent system* (1) *with protocol* (2) *or* (3) *can reach finite-time consensus, that is, there exists a finite-time $T < \infty$ such that*

$$x_i(t) = x_j(t) \quad \forall t \geq T. \tag{5}$$

Remark 1. *Reference [5] gives two classes of finite-time consensus protocols for integrator multi-agent systems and reference [9] studies the finite-time consensus for second-order multi-agent systems over undirected graphs. In this paper, we presents two classes of finite-time protocols for third-order multi-agent systems over digraphs.*

2.2 Preliminaries

The following lemma on properties of Laplacian matrices is adopted from [13] and is used to analyze the consensus properties of multi-agent systems in this paper.

Lemma 1. *Let $L \in \mathbb{R}^{n\times n}$ be the Laplacian matrix of the digraph $\mathcal{G}$ and $\mathbf{1} = [1, \ldots, 1]^\top \in \mathbb{R}^n$. If $\mathcal{G}$ has a spanning tree, then there exists a unique nonnegative left eigenvector r associated with the zero eigenvalue of L, satisfying $r^\top L = 0$ and $r^\top \mathbf{1} = 1$.*

The following definition and lemmas come from [14].

Definition 1. *A function $V : \mathbb{R}^n \to \mathbb{R}$ is called homogeneous with respect to the weight $\nu = [\nu_1, \ldots, \nu_n]^\top \in \mathbb{R}^n$ of degree l ($l \in \mathbb{R}$) if for any $x = [x_1, \ldots, x_n]^\top$ and $\lambda > 0$,*

$$V(\delta_\lambda^\nu(x)) = \lambda^l V(x), \tag{6}$$

with $\delta_\lambda^\nu(x) = [\lambda^{\nu_1} x_1, \ldots, \lambda^{\nu_n} x_n]^\top$.

Lemma 2. *Suppose that $\mathcal{V}_1 : \mathbb{R}^n \to \mathbb{R}$ and $\mathcal{V}_2 : \mathbb{R}^n \to \mathbb{R}$ are continuous homogeneous functions with respect to the same weight $\nu = (\nu_1, \ldots, \nu_n)$ but of degrees $l_1 > 0$ and $l_2 > 0$ respectively, and $\mathcal{V}_1$ is positive definite. Then, for any $x \in \mathbb{R}^n$,*

$$\mathcal{V}_2(x) \leq \left(\max_{\{\zeta : \mathcal{V}_1(\zeta) = 1\}} \mathcal{V}_2(\zeta) \right) (\mathcal{V}_1(x))^{\frac{l_2}{l_1}}, \tag{7}$$
$$\mathcal{V}_2(x) \geq \left(\min_{\{\zeta : \mathcal{V}_1(\zeta) = 1\}} \mathcal{V}_2(\zeta) \right) (\mathcal{V}_1(x))^{\frac{l_2}{l_1}}. \tag{8}$$

Lemma 3. *Consider the system $\dot{y} = f(y)$, where $y \in \mathbb{R}^n$ is the state, and $f : \mathbb{R}^n \to \mathbb{R}^n$ is continuous on an open neighborhood $\mathcal{D}$ of the origin and locally Lipschitz on $\mathcal{D}\backslash\{0\}$ with $f(0) = 0$. If there exists a positive definite and continuously differentiable function $V : \mathcal{D} \to \mathbb{R}_+$ and constants $k > 0$ and $\alpha \in (0, 1)$ such that*

$$L_f V(y) \leq -k\,(V(y))^\alpha \quad \forall y \in \mathcal{D}_0 \tag{9}$$

with $\mathcal{D}_0 \subseteq \mathcal{D}$ being an open set containing the origin, then the origin is finite-time stable. If moreover $\mathcal{D} = \mathbb{R}^n$ and V is radially unbounded, then the origin is globally finite-time stable.

2.3 Proof of Theorem 1

Inspired by the finite-time stabilization method in [14], we first prove that the protocols are effective when $d = 0$ or equivalently $\alpha_1 = \alpha_2 = \alpha_3 = 1$.

Define $x = \left[x_1^\top, \ldots, x_N^\top\right]^\top \in \mathbb{R}^{3N}$ and $\varepsilon = \left(\left(I_N - \mathbf{1}r^\top\right) \otimes I_3\right) x$ with $\mathbf{1} = [1, \ldots, 1]^\top \in \mathbb{R}^N$ and $r \in \mathbb{R}^N$ being the left eigenvector of the Laplacian matrix L associated with the eigenvalue 0. Then, we have

$$\dot{\varepsilon} = (I_N \otimes A - cL \otimes B\rho)\varepsilon, \tag{10}$$

where $\varepsilon = [\varepsilon_{11}, \varepsilon_{12}, \varepsilon_{13}, \ldots, \varepsilon_{N1}, \varepsilon_{N2}, \varepsilon_{N3}]^\top$ and

$$A = \begin{bmatrix} 0 & 1 & 0 \\ 0 & 0 & 1 \\ 0 & 0 & 0 \end{bmatrix}, \; B = \begin{bmatrix} 0 \\ 0 \\ 1 \end{bmatrix}, \rho = \begin{bmatrix} \rho_1 \\ \rho_2 \\ \rho_3 \end{bmatrix}^\top. \tag{11}$$

To finally construct a homogeneous Lyapunov function for finite-time consensus analysis, we introduce a coordinate transformation:

$$\tilde{\varepsilon} = \left(T^{-1} \otimes I_3\right) \varepsilon \tag{12}$$

where $T \in \mathbb{R}^{N\times N}$ is a nonsingular matrix such that $T^{-1}LT$ is in the form $T^{-1}LT = \mathrm{diag}\{0, J\}$. According to [15, 16],

such T and the corresponding J exist as long as the digraph $\mathcal{G}$ contains a spanning tree.

Denote $\tilde{\varepsilon} = [\tilde{\varepsilon}_1^\top, \ldots, \tilde{\varepsilon}_N^\top]^\top$ and $\tilde{\varepsilon}_p = [\tilde{\varepsilon}_2^\top, \ldots, \tilde{\varepsilon}_N^\top]^\top$. We have

$$\tilde{\varepsilon}_1 = 0, \tag{13a}$$

$$\dot{\tilde{\varepsilon}}_p = M\tilde{\varepsilon}_p \tag{13b}$$

with

$$M = I_{N-1} \otimes A - cJ \otimes B\rho. \tag{14}$$

It can be observed that the consensus of the controlled multi-agent system is guaranteed if $\tilde{\varepsilon}_p$ converges to zero.

We now prove that M is Hurwitz under the condition of Theorem 1. We analyze the eigenvalues of the matrix

$$M_* = I_{N-1} \otimes A - cJ_* \otimes B\rho, \tag{15}$$

where $J_* \in \mathbb{C}^{(N-1)\times(N-1)}$ is in the Jordan canonical form of J corresponding to the $N-1$ non-zero eigenvalues of the Laplacian matrix L. Obviously, M and M_* share the same eigenvalues.

Since J_* is an upper-triangular matrix, M_* is a block upper-triangular matrix with its diagonal entries being $A - c\lambda_i B\rho$ for $i = 2, \ldots, N$. To analyze the eigenvalues of M_*, calculating $\det(sI_3 - (A - c\lambda_i B\rho))$ gives

$$\det(sI_3 - (A - c\lambda_i B\rho)) = s^3 + c\lambda_i\rho_3 s^2 + c\lambda_i\rho_2 s + c\lambda_i\rho_1. \tag{16}$$

Indeed, $s^3 + c\lambda_i\rho_3 s^2 + c\lambda_i\rho_2 s + c\lambda_i\rho_1 = 0$ implies that

$$(1 + \frac{\omega}{s})^3 = \frac{c\lambda_i - 1}{c\lambda_i}. \tag{17}$$

With $c \geq 1/(2\,\mathrm{Re}(\lambda_2))$, if there is a root s_1 having positive real part, it is easy to verify the following contradiction.

$$\left|(1 + \frac{\omega}{s_1})^3\right| > \left|\frac{c\lambda_i - 1}{c\lambda_i}\right|, \tag{18}$$

which means M_* is Hurwitz as well as M. Thus, the $\tilde{\varepsilon}_p$-subsystem (13b) is asymptotically stable at the origin with a quadratic Lyapunov function $V_P : \mathbb{R}^{3(N-1)} \to \mathbb{R}_+$ satisfying

$$\dot{V}_P(\tilde{\varepsilon}_p) = -|\tilde{\varepsilon}_p|^2. \tag{19}$$

Then, we consider the finite-time consensus of $\tilde{\varepsilon}_p$ with the help of the nonlinear protocols (2) and (3) as $d < 0$.

Denote $T = \{\theta_{ij}\}_{N\times N}$, $T^{-1} = \{\theta'_{ij}\}_{N\times N}$ and

$$\tilde{\varepsilon}_1 = [\tilde{\varepsilon}_{11}, \tilde{\varepsilon}_{12}, \tilde{\varepsilon}_{13}]^\top, \tag{20a}$$

$$\tilde{\varepsilon}_p = [\tilde{\varepsilon}_{21}, \tilde{\varepsilon}_{22}, \tilde{\varepsilon}_{23}, \ldots, \tilde{\varepsilon}_{N1}, \tilde{\varepsilon}_{N2}, \tilde{\varepsilon}_{N3}]^\top. \tag{20b}$$

Noticing that for any, $h, j \in \{1, \ldots, N\}$,

$$\varepsilon_h - \varepsilon_j = \sum_{l=2}^{N} \left((\theta_{hl} - \theta_{jl})\tilde{\varepsilon}_{lk}\right). \tag{21}$$

Then, we have

$$\tilde{\varepsilon}_1 = 0, \tag{22a}$$

$$\dot{\tilde{\varepsilon}}_p = G^d(\tilde{\varepsilon}_p), \tag{22b}$$

with

$$G^d(\tilde{\varepsilon}_p) = [G^d_{21}(\tilde{\varepsilon}_p), G^d_{22}(\tilde{\varepsilon}_p), G^d_{23}(\tilde{\varepsilon}_p), \ldots, G^d_{N1}(\tilde{\varepsilon}_p), G^d_{N2}(\tilde{\varepsilon}_p), G^d_{N3}(\tilde{\varepsilon}_p)]^\top \tag{23}$$

where $G^d_{i1}(\tilde{\varepsilon}_p) = \tilde{\varepsilon}_{i2}$, $G^d_{i2}(\tilde{\varepsilon}_p) = \tilde{\varepsilon}_{i3}$ and

$$G^d_{i3}(\tilde{\varepsilon}_p) = -c\sum_{h=1}^{N}\theta'_{ih}\sum_{k=1}^{3}\rho_k\sum_{j=2}^{N}\left[a_{hj}\sum_{l=2}^{N}\left((\theta_{hl} - \theta_{jl})\tilde{\varepsilon}_{lk}\right)\right]^{\alpha_k}$$

or

$$G^d_{i3}(\tilde{\varepsilon}_p) = -c\sum_{h=1}^{N}\theta'_{ih}\sum_{k=1}^{3}\rho_k\left[\sum_{j=2}^{N}a_{hj}\sum_{l=2}^{N}\left((\theta_{hl} - \theta_{jl})\tilde{\varepsilon}_{lk}\right)\right]^{\alpha_k}, \tag{24}$$

for $i = 2, \ldots, N$.

Inspired by [11, 12], define $V_r : \mathbb{R}^{3(N-1)} \to \mathbb{R}$ as

$$V_r(\tilde{\varepsilon}_p) = \int_0^\infty \frac{1}{s^{1+\gamma}}\left(\varsigma \circ V_P\right)\left(\delta^v_s(\tilde{\varepsilon}_p)\right)ds, \tag{25}$$

for $\tilde{\varepsilon}_p \in \mathbb{R}^{3(N-1)}$, where constant $\gamma > 1$, the function $\delta^v_s(\tilde{\varepsilon}_p)$ is defined by

$$\delta^v_s(\tilde{\varepsilon}_p) = [s^{v_1}\tilde{\varepsilon}_{21}, s^{v_2}\tilde{\varepsilon}_{22}, s^{v_3}\tilde{\varepsilon}_{23}, \ldots, s^{v_1}\tilde{\varepsilon}_{N1}, s^{v_2}\tilde{\varepsilon}_{N2}, s^{v_3}\tilde{\varepsilon}_{N3}]^\top \tag{26}$$

for $\tilde{\varepsilon}_p \in \mathbb{R}^{3(N-1)}$ and $s \geq 0$, with $v_k = 1 + (k-1)d$ for $k = 1, 2, 3$, and

$$\varsigma(\iota) = \begin{cases} 0, & \iota \in (-\infty, 1), \\ \frac{1}{2}(\iota - 1)^2, & \iota \in [1, 2), \\ 1 - \frac{1}{2}(\iota - 3)^2, & \iota \in [2, 3), \\ 1, & \iota \in [3, \infty). \end{cases} \tag{27}$$

It can be directly checked that ς is continuously differentiable.

Clearly, $V_r(0) = 0$. Define $3(N-1)$-dimensional unit hypersphere $S = \{\tilde{\varepsilon}_p \in \mathbb{R}^{3(N-1)} : |\tilde{\varepsilon}_p| = 1\}$. For any specific $\tilde{\varepsilon}_p \in S$, it can be easily checked that $\delta^v_0(\tilde{\varepsilon}_p) = 0$ and $|\delta^v_s(\tilde{\varepsilon}_p)|$ is radially unbounded with respect to s. Then, there exist constants l and L satisfying $0 < l < L$ such that for any $\tilde{\varepsilon}_p \in S$,

$$V_P(\delta^v_s(\tilde{\varepsilon}_p))\begin{cases} < 1, \text{ for } 0 < s < l, \\ > 3, \text{ for } L < s < \infty. \end{cases} \tag{28}$$

Then, the function V_r defined in (25) satisfies

$$V_r(\tilde{\varepsilon}_p) = \int_l^L \frac{1}{s^{1+\gamma}}\left(\varsigma \circ V_P\right)\left(\delta^v_s(\tilde{\varepsilon}_p)\right)ds + \frac{1}{\gamma L^\gamma} > 0 \tag{29}$$

for all $\tilde{\varepsilon}_p \in S$. This proves that V_r is well defined and positive-valued on the $3(N-1)$-dimensional unit hypersphere S.

Now, we extend property (29) from the unit hypersphere S to $\mathbb{R}^{3(N-1)}\backslash\{0\}$. It can be easily checked that for any $\tilde{\varepsilon}_p \in \mathbb{R}^{3(N-1)}$,

$$V_r(\delta^v_\lambda(\tilde{\varepsilon}_p)) = \int_0^\infty \frac{1}{s^{1+\gamma}}\left(\varsigma \circ V_P\right)\left(\delta^v_{\lambda s}(\tilde{\varepsilon}_p)\right)\frac{d\lambda s}{\lambda} = \lambda^\gamma V_r(\tilde{\varepsilon}_p) \tag{30}$$

holds for any $\lambda > 0$, which, in turn, guarantees the existence of a $\lambda_0 > 0$ corresponding to each $\tilde{\varepsilon}_p \in \mathbb{R}^{3(N-1)}\backslash\{0\}$ such that $\delta^v_{\lambda_0}(\tilde{\varepsilon}_p) \in S$ and at the same time,

$$V_r(\tilde{\varepsilon}_p) = V_r\left(\delta^v_{\lambda_0^{-1}\lambda_0}(\tilde{\varepsilon}_p)\right) = \lambda_0^{-\gamma} V_r\left(\delta^v_{\lambda_0}(\tilde{\varepsilon}_p)\right) > 0. \quad (31)$$

Thus, V_r is well defined on $\mathbb{R}^{3(N-1)}$ and positive definite. To prove the radial unboundedness of V_r, denote

$$\delta^v_{\lambda_0}(\tilde{\varepsilon}_p) = [\varrho_{21}, \varrho_{22}, \varrho_{23}, \ldots, \varrho_{N1}, \varrho_{N2}, \varrho_{N3}]^\top. \quad (32)$$

Then, for each $\tilde{\varepsilon}_p \in \mathbb{R}^{3(N-1)}\backslash\{0\}$ and the corresponding $\lambda_0 > 0$ such that $\delta^v_{\lambda_0}(\tilde{\varepsilon}_p) \in S$, we have

$$\begin{aligned} |\tilde{\varepsilon}_p| &= |\delta^v_{\lambda_0^{-1}}(\delta^v_{\lambda_0}(\tilde{\varepsilon}_p))| \\ &\leq \sqrt{(N-1)(\lambda_0^{-2v_1} + \ldots + \lambda_0^{-2v_3})}, \end{aligned} \quad (33)$$

which means that $|\tilde{\varepsilon}_p| \to \infty \Rightarrow \lambda_0 \to 0$. Recall the equality in (31). We have

$$\lim_{|\tilde{\varepsilon}_p|\to\infty} V_r(\tilde{\varepsilon}_p) = \lim_{\lambda_0\to 0} \lambda_0^{-\gamma} V_r\left(\delta^v_{\lambda_0}(\tilde{\varepsilon}_p)\right) = \infty. \quad (34)$$

This proves the radial unboundedness of V_r.

To further prove finite-time consensus, we study the homogeneity and the negative definiteness of $L_{G^d}V_r$. Recall the notations given by (20). For any $i = 2, \ldots, N$ and $k = 1, 2, 3$,

$$\begin{aligned} \frac{\partial V_r(\tilde{\varepsilon}_p)}{\partial \tilde{\varepsilon}_{ik}} = \int_0^\infty & \frac{1}{s^{\gamma-(k-1)d}} \left(\varsigma' \circ V_P\right)\left(\delta^v_s(\tilde{\varepsilon}_p)\right) \\ & \cdot \frac{\partial V_P}{\partial \tilde{\varepsilon}_{ik}}\left(\delta^v_s(\tilde{\varepsilon}_p)\right) ds \end{aligned} \quad (35)$$

where ς' represents the derivative of the continuously differentiable function ς defined by (27). The definition of ς implies that $\varsigma'(\iota) = 0$ for $\iota \leq 1$ and $\iota \geq 3$, which guarantees the feasibility of (35). Following a similar reasoning as for (30), we can verify that for any $\lambda > 0$,

$$\frac{\partial V_r(\delta^v_\lambda(\tilde{\varepsilon}_p))}{\partial \lambda^{v_k} \tilde{\varepsilon}_{ik}} = \lambda^{\gamma-(1+(k-1)d)} \frac{\partial V_r(\tilde{\varepsilon}_p)}{\partial \tilde{\varepsilon}_{ik}}. \quad (36)$$

Also, the definition of G^d in (23) implies that for any $2 \leq i \leq N$, $1 \leq k \leq 3$ and $\lambda > 0$,

$$G^d_{ik}(\delta^v_\lambda(\tilde{\varepsilon}_p)) = \lambda^{1+kd} G^d_{ik}(\tilde{\varepsilon}_p). \quad (37)$$

Combining (36) and (37) results in that for any $\tilde{\varepsilon}_p \in \mathbb{R}^{3(N-1)}$ and any $\lambda > 0$,

$$\frac{\partial V_r}{\partial \tilde{\varepsilon}_{ik}} G^d_{ik}(\delta^v_\lambda(\tilde{\varepsilon}_p)) = \lambda^{\gamma+d} \frac{\partial V_r}{\partial \tilde{\varepsilon}_{ik}} G^d_{ik}(\tilde{\varepsilon}_p), \quad (38)$$

which means that $L_{G^d}V_r$ is homogeneous with respect to the weight $v = [v_1, v_2, v_3, \ldots, v_1, v_2, v_3]^\top \in \mathbb{R}^{3(N-1)}$ of positive degree $\gamma + d$.

Also, from (35) and (37), $L_{G^d}V_r(\tilde{\varepsilon}_p)$ can be calculated as:

$$\begin{aligned} L_{G^d}V_r(\tilde{\varepsilon}_p) = \int_0^\infty & \frac{1}{s^{\gamma+1+d}} \left(\varsigma' \circ V_P\right)\left(\delta^v_s(\tilde{\varepsilon}_p)\right) \\ & \cdot \left(\sum_{i=2}^{N}\sum_{k=1}^{3} \frac{\partial V_P}{\partial \tilde{\varepsilon}_{ik}} G^d_{ik}\right)\left(\delta^v_s(\tilde{\varepsilon}_p)\right) ds. \end{aligned} \quad (39)$$

Clearly, $L_{G^d}V_r(0) = 0$. Now we prove that $L_{G^d}V_r$ is negative-valued on S and extend this property to $\mathbb{R}^{3(N-1)}\backslash\{0\}$.

Based on (39), since $\varsigma'(\iota) = 0$ for $\iota \leq 1$ and $\iota \geq 3$, for any $\tilde{\varepsilon}_p \in S$, we can rewrite

$$\begin{aligned} L_{G^d}V_r(\tilde{\varepsilon}_p) = \int_l^L & \frac{1}{s^{\gamma+1+d}} \left(\varsigma' \circ V_P\right)\left(\delta^v_s(\tilde{\varepsilon}_p)\right) \\ & \cdot \left(\sum_{i=2}^{N}\sum_{k=1}^{3} \frac{\partial V_P}{\partial \tilde{\varepsilon}_{ik}} G^d_{ik}\right)\left(\delta^v_s(\tilde{\varepsilon}_p)\right) ds. \end{aligned} \quad (40)$$

Denote

$$\phi(d) = \max_{\substack{\tilde{\varepsilon}_p \in S, \\ l \leq s \leq L}} \left(\sum_{i=2}^{N}\sum_{k=1}^{3} \frac{\partial V_P}{\partial \tilde{\varepsilon}_{ik}} \cdot G^d_{ik}\right)\left(\delta^v_s(\tilde{\varepsilon}_p)\right). \quad (41)$$

Then, ϕ is continuous for $d \in (-1/3, 0]$. From (19), we have

$$\phi(0) = \max_{\substack{\tilde{\varepsilon}_p \in S, \\ l \leq s \leq L}} \dot{V}_P(s \cdot \tilde{\varepsilon}_p) = -l^2 < 0. \quad (42)$$

Then, there exists a constant $\underline{d} < 0$ such that

$$\phi(d) < 0 \quad (43)$$

holds for any $d \in [\underline{d}, 0)$. From the definition of ς in (27), $\varsigma'(\iota) > 0$ for $\iota \in (1, 3)$. Substituting (41) into (40) and using (43) imply that for any $d \in [\underline{d}, 0)$ and $\tilde{\varepsilon}_p \in S$,

$$L_{G^d}V_r(\tilde{\varepsilon}_p) \leq \phi(d) \int_l^L \frac{1}{s^{\gamma+1+d}} \left(\varsigma' \circ V_P\right)\left(\delta^v_s(\tilde{\varepsilon}_p)\right) ds < 0, \quad (44)$$

which means that $L_{G^d}V_r$ is negative-valued on S.

Recall that $L_{G^d}V_r$ is homogeneous with respect to the weight v of positive degree $\gamma + d$, as given by (38). Following a similar reasoning as for (31), we can prove that $L_{G^d}V_r$ is negative definite. Since V_r and $L_{G^d}V_r$ are homogeneous with the same weight v of positive degree γ and $\gamma + d$, respectively, by using Lemma 2, we can prove that

$$L_{G^d}V_r(\tilde{\varepsilon}_p) \leq -B_1 \left(V_r(\tilde{\varepsilon}_p)\right)^{\frac{\gamma+d}{\gamma}}, \quad (45)$$

with $B_1 = -\max_{\{\iota: V_r(\iota)=1\}} L_{G^d}V_r(\iota) > 0$. By using Lemma 3, we can verify that the multi-agent system (1) with protocol (2) or (3) reaches finite-time consensus.

3 Simulation

Consider the following multi-agent system with the communication topology $\mathcal{G}$ given in Figure 1.

$$\dot{x}_i = v_i, \quad (46a)$$

$$\dot{v}_i = a_i, \quad (46b)$$

$$\dot{a}_i = u_i,\ i = 1, \ldots, 5 \quad (46c)$$

where x_i, v_i, and a_i (for $i = 1, \ldots, 5$) represent the positions, velocities and the accelerations of the agents $\{A, B, C, D, E\}$ with initial positions of the plants as $\{0, 1, 2, 3, 4\}$, respectively. The initial velocities and the initial accelerations are zero. The adjacent matrix A is given

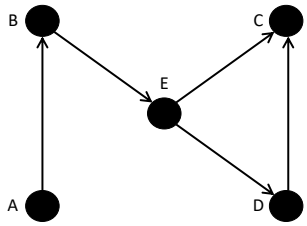

Fig. 1: The communication topology $\mathcal{G}$

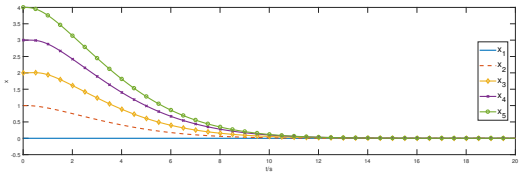

Fig. 2: The position x under the edge-based protocol

as:

$$A = \{a_{ij}\}_{5\times 5} = \begin{bmatrix} 0 & 0 & 0 & 0 & 0 \\ 1 & 0 & 0 & 0 & 0 \\ 0 & 0 & 0 & 1 & 1 \\ 0 & 0 & 0 & 0 & 1 \\ 0 & 1 & 0 & 0 & 0 \end{bmatrix}. \tag{47}$$

Then the Laplacian matrix L of the graph $\mathcal{G}$ can be calculated as:

$$L = \begin{bmatrix} 0 & 0 & 0 & 0 & 0 \\ -1 & 1 & 0 & 0 & 0 \\ 0 & 0 & 2 & -1 & -1 \\ 0 & 0 & 0 & 1 & -1 \\ 0 & -1 & 0 & 0 & 1 \end{bmatrix}. \tag{48}$$

Recall the protocols in (2) and (3). With the algebraic connectivity calculating as $\lambda_2 = 1$, we can choose constants $c = 1/2$, $[\rho_1, \rho_2, \rho_3] = [1, 3, 3]$ and $[\alpha_1, \alpha_2, \alpha_3] = [7/10, 7/9, 7/8]$ (taking $d = -1/10$). Then, the protocols satisfy that, for $i = 1, \ldots, 5$,

- Edge-based protocol:

$$\begin{aligned} u_i = &-\frac{1}{2}\sum_{j=1}^{5}[a_{ij}(x_i - x_j)]^{7/10} \\ &-\frac{3}{2}\sum_{j=1}^{5}[a_{ij}(v_i - v_j)]^{7/9} \\ &-\frac{3}{2}\sum_{j=1}^{5}[a_{ij}(a_i - a_j)]^{7/8}, \end{aligned} \tag{49}$$

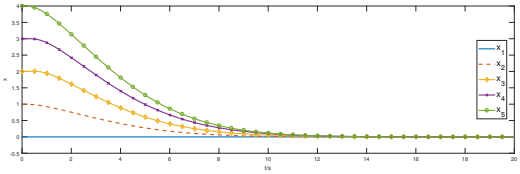

Fig. 3: The position x under the node-based protocol

- Node-based protocol:

$$\begin{aligned} u_i = &-\frac{1}{2}\left[\sum_{j=1}^{5}a_{ij}(x_i - x_j)\right]^{7/10} \\ &-\frac{3}{2}\left[\sum_{j=1}^{5}a_{ij}(v_i - v_j)\right]^{7/9} \\ &-\frac{3}{2}\left[\sum_{j=1}^{5}a_{ij}(a_i - a_j)\right]^{7/8}. \end{aligned} \tag{50}$$

With the two classes of protocols, the simulation results are lied in Figure 2 and Figure 3. It can be seen that the positions converge to a consensus value, which demonstrate the proposed protocols are effective.

4 Conclusion

This paper has explored the dynamics of third-order multi-agent systems with a focus on achieving finite-time consensus. Moreover, directed communication topologies and the explicit control coefficients have been investigated through analyzing the closed-loop system composed of the original system and the proposed novel finite-time protocols. Homogeneous theory has been employed to provide a mathmatical proof. Finite-time consensus for higher-order multi-agent systems will be investigated in future work.

References

[1] R. Olfati-Saber and R. M. Murray, "Consensus problems in networks of agents with switching topology and time-delays," *IEEE Transactions on automatic control*, vol. 49, no. 9, pp. 1520–1533, 2004.

[2] W. Ren, K. L. Moore, and Y. Chen, "High-Order and Model Reference Consensus Algorithms in Cooperative Control of MultiVehicle Systems," *Journal of Dynamic Systems, Measurement, and Control*, vol. 129, no. 5, pp. 678–688, 12 2006.

[3] Z. Li, Z. Duan, G. Chen, and L. Huang, "Consensus of multiagent systems and synchronization of complex networks: A unified viewpoint," *IEEE Transactions on Circuits and Systems I: Regular Papers*, vol. 57, no. 1, pp. 213–224, 2010.

[4] J. Cortés, "Finite-time convergent gradient flows with applications to network consensus," *Automatica*, vol. 42, no. 11, pp. 1993–2000, 2006.

[5] L. Wang and F. Xiao, "Finite-time consensus problems for networks of dynamic agents," *IEEE Transactions on Automatic Control*, vol. 55, no. 4, pp. 950–955, 2010.

[6] M. Defoort, A. Polyakov, G. Demesure, M. Djemai, and K. Veluvolu, "Leader-follower fixed-time consensus for multi-agent systems with unknown non-linear inherent dynamics," *IET Control Theory & Applications*, vol. 9, no. 14, pp. 2165–2170, 2015.

[7] J. Fu and J. zhi Wang, "Finite-time consensus for multi-agent systems with globally bounded convergence time under directed communication graphs," *International Journal of Control*, vol. 90, no. 9, pp. 1807–1817, 2017.
[8] Z. Zuo, R. Ke, and Q.-L. Han, "Fully distributed adaptive practical fixed-time consensus protocols for multi-agent systems," *Automatica*, vol. 157, p. 111248, 2023.
[9] X. Wang and Y. Hong, "Finite-time consensus for multi-agent networks with second-order agent dynamics," *IFAC Proceedings volumes*, vol. 41, no. 2, pp. 15 185–15 190, 2008.
[10] T. Xiong, Z. Gu, J. Yi, and Z. Pu, "Fixed-time adaptive observer-based time-varying formation control for multi-agent systems with directed topologies," *Neurocomputing*, vol. 463, pp. 483–494, 2021.
[11] L. Rosier, "Homogeneous Lyapunov function for homogeneous continuous vector field," *Systems & Control Letters*, vol. 19, no. 6, pp. 467–473, 1992.
[12] Z.-L. Zhao and Z.-P. Jiang, "Finite-time output feedback stabilization of lower-triangular nonlinear systems," *Automatica*, vol. 96, pp. 259–269, 2018.
[13] W. Ren and R. W. Beard, "Consensus seeking in multiagent systems under dynamically changing interaction topologies," *IEEE Transactions on Automatic Control*, vol. 50, no. 5, pp. 655–661, 2005.
[14] S. P. Bhat and D. S. Bernstein, "Geometric homogeneity with applications to finite-time stability," *Mathematics of Control, Signals and Systems*, vol. 17, pp. 101–127, 2005.
[15] N. Christofides, *Graph theory: An Algorithmic Approach*. Academic Press, Inc., 1975.
[16] R. A. Horn and C. R. Johnson, *Matrix Analysis*. Cambridge University Press, 2012.

Proceedings of the 3rd Conference on Fully Actuated System Theory and Applications
May 10-12, 2024, Shenzhen, China

Extended Dissipative Sliding Mode Control for T-S Fuzzy Polynomial Singular System

Jiarui Liu[1], Jiangrong Li[1], Jiming Zhu[1]
1. College of Mathematics and Computer Science, Yan'an University, Yan'an 716000, China
E-mail: 15929179059@163.com, florajiang413@163.com

Abstract: In this paper, the problem of extended dissipative sliding mode control for discrete-time nonlinear singular systems are addressed. First, the T-S fuzzy polynomial singular systems are constructed to represent nonlinear singular systems with parameter uncertainties. A different delay-dependent sliding mode surface is built based on the dynamic event-triggered mechanism. Then, the sliding mode control law is obtained, which guarantees the reachability of the closed-loop system. The admissibility with extended dissipativity is established by SOS. Finally, a numerical example is given to demonstrate the correctness of the proposed strategy.

Key Words: Dynamic event-triggered, sliding mode control, T-S fuzzy polynomial system, extended dissipativity, piecewise Lyapunov function

1 Introduction

With the rapid development of industrial systems, nonlinear systems are becoming ubiquitous [1–3]. The Takagi-Sugeno (T-S) fuzzy model is a well-known system modeling method for the nonlinear systems [4]. It has become the main research method for approximating nonlinear systems and it has achieved fruitful results. Some of the reported results are stability analysis [5], reachable set estimation [6]. Because of its special properties, singular systems have been widely studied by researchers. The application area ranges from robotic systems, power systems, and other industrial practical systems. There were also many excellent results on singular systems. For example, the stability analysis of a networked singular system with both state and input subject to quantizations was investigated by using a discrete time event-triggered scheme [7]. Taniguchi et al. [8] proposed the T-S fuzzy singular system in 1999, which is a mix of the T-S fuzzy system and singular system. T-S fuzzy polynomial singular system is the extension of T-S fuzzy singular system. In contrast to the T-S fuzzy singular system, the T-S fuzzy polynomial singular system permits polynomial terms to arise in subsystems, potentially reducing the number of fuzzy rules. The extended dissipative control problem of stochastic polynomial fuzzy singular systems was investigated in [9] using the adaptive event-triggered technique.

The event-triggered control mechanism is both effective and reasonable. It can decide whether the signals need to be conveyed by establishing proper triggering conditions, implying that signals do not have to be delivered at every sampling interval during the control process. There are many research results of different event-triggered mechanisms published [10]. For example, a fuzzy filter was designed under an event-triggered mechanism for the filtering error system. However, it should be noted that the static event-triggered (SET) mechanism's threshold parameter is fixed. Recently, a novel adaptive event-triggered (AET) mechanism was used to design H_∞ filter for the T-S fuzzy system [11]. A dynamic event-triggered (DET) sliding mode control method was proposed for interval type-2 fuzzy systems with fading channels in [12].

Sliding mode control (SMC) is a type of robust control. SMC has received a considerable deal of attention in the academic world over the last few decades due to its multiple advantages such as insensitivity to parameter changes, easy physical implementation, and quick response. It is also increasingly being used in underwater robots, aviation, diesel engines, motors, and other applications. In general, the SMC, which is based on variable structure systems theory [13], applies a discontinuous control law to drive the state trajectory toward a specified sliding surface and keep it moving along the sliding surface in the state space. An integral sliding surface (ISS) is introduced. Its feature is that sliding mode dynamics (SMD) can keep the same order as the original system while ensuring robustness across the entire system response. The ISS-based SMC technique in [14] and [15] is expanded to analyze the SMC problem of mismatched uncertain systems [16].

In this paper, we investigate the problem of extended dissipative based on SMC and DET for T-S fuzzy polynomial singular systems. In contrast to the existing works, the main features of the scheme proposed are summarized as follows:

- Considering uncertainties, the DET scheme and extended dissipative SMC have been applied to the T-S fuzzy polynomial singular system.
- A novel delay-dependent sliding mode surface (SMS) is built. And the SMC law is obtained, ensuring that the closed-loop system is reachable.
- Via a set of novel piecewise Lyapunov functionals (PLF), an approach is proposed for the co-design of SMC and DET mechanisms. This approach guarantees that the closed-loop system is admissible with extended dissipativity.

Notations: $\mathbf{R}^n$ and $\mathbf{R}^{n\times m}$ denote the $n-$dimensional Euclidean space and the set of all $n\times m$ real matrices, respectively. The superscript T represents matrices' transpose. $*$ symbolizes the symmetric terms of a symmetric matrix.

This work is supported in part by National Natural Science Foundation of China under Grant 62262067 and 1226109, in part by National Science Basic Research Program of Shaanxi Province under Grant 2020JM-552, in part by Overseas Educated Students' Scientific and Technological Activities Merit Funding Project of Shaanxi Province under Grant 2022-022, in part by the Yan'an University Graduate Education Innovation Program Project under Grant YCX2023015 and YCX2023009.

Ω_{SOS} means the collection of all SOS polynomials.

2 Problem Formulation

2.1 T-S Fuzzy System

Considering the following discrete-time T-S fuzzy polynomial singular systems.

Plant Rule $\Re^i$: If $b_1(t)$ is F_{i1} and $\cdots$ and $b_g(t)$ is F_{ig}, then

$$\begin{aligned} E\varphi(t+1) &= (A_i(\varphi(t))+\Delta A_i(\varphi(t)))\varphi(t)+A_{di}(\varphi(t)) \\ &\quad \times \varphi(t-d(t))+B(\varphi(t))u(t)+D_i(\varphi(t))\omega(t), \\ \tilde{y}(t) &= C_i(\varphi(t))\varphi(t), \\ \varphi(t) &= \kappa(t), i \in \{1,2,\cdots,r\}, \end{aligned} \tag{1}$$

where r is the number of rules, $F_{ij}(j=1,2,\cdots,g)$ is fuzzy set and $b(t)=[b_1(t),b_2(t),\ldots,b_g(t)]$ is the premise variables; $\varphi(t)\in\mathbf{R}^n$, $\tilde{y}(t)\in\mathbf{R}^p$ and $u(t)\in\mathbf{R}^q$ are the state vector, the measured output and the control input, respectively; $\omega(t)\in\mathbf{R}^m$ is the disturbance input, which belongs to $l_2[0,\infty)$; time-varying delay $d(t)$ satisfies $0<d_1\leq d(t)\leq d_2$, where d_1,d_2 are the constant positive scalars; $\kappa(t)$ is the initial condition; matrices $E(rank(E)=r\leqslant n)$, $A_i(\varphi(t))$, $A_{di}(\varphi(t))$, $B(\varphi(t))$, $D_i(\varphi(t))$, $C_i(\varphi(t))$ are polynomial matrices with appropriate dimensions; the matrix function $\Delta A_i(\varphi(t))$ satisfies $\Delta A_i(\varphi(t))=H_{i1}(\varphi(t))\Delta(t)H_{i2}(\varphi(t))$, where $H_{i1}(\varphi(t)),H_{i2}(\varphi(t))$ are known polynomial matrices, unknown matrix function $\Delta(t)$ is considered to be satisfied with $\Delta^T(t)\Delta(t)\leq I$. The function $h_i(b(t))$ satisfies $h_i(b(t))=\frac{\prod_{j=1}^{g}F_{ij}(b_j(t))}{\sum_{i=1}^{r}\prod_{j=1}^{g}F_{ij}(b_j(t))}\geq 0$, $\sum_{i=1}^{r}h_i(b(t))=1$, where $F_{ij}(b(t))$ is the grade of membership of $b_j(t)$ in F_{ij}.

By fuzzy processing techniques, the T-S fuzzy polynomial singular systems (1) can be deduced as:

$$\begin{aligned} E\varphi(t+1) &= \sum_{i=1}^{r}h_i(b(t))\{(A_i(\varphi(t))+\Delta A_i(\varphi(t)))\varphi(t) \\ &\quad +A_{di}(\varphi(t))\varphi(t-d(t))+B(\varphi(t))u(t) \\ &\quad +D_i(\varphi(t))\omega(t)\}, \\ \tilde{y}(t) &= \sum_{i=1}^{r}h_i(b(t))C_i(\varphi(t))\varphi(t). \end{aligned} \tag{2}$$

To address the piecewise SMC problem of the system (2), then the system (2) can be rewritten as a piecewise fuzzy system:

$$\begin{aligned} E\varphi(t+1) &= A_l\varphi(t)+\Delta A_l\varphi(t)+A_{dl}\varphi(t-d(t)) \\ &\quad +Bu(t)+D_l\omega(t), \\ \tilde{y}(t) &= C_l\varphi(t), \end{aligned} \tag{3}$$

where $B=B(\varphi(t)),X_l=\Sigma_{s\in M(l)}h_s(b(t))X_s(\varphi(t))$, $X=\{A,\Delta A,A_d,D,C\}$.

2.2 Dynamic Event-triggered Mechanism

In this subsection, a DET mechanism is employed to judge if the sampled data $\varphi(t)$ will be released into the communication links. Let $h(t)=\varphi(t)-\varphi(t_k)$ as the difference between the current sampled data $\varphi(t)$ and the most recent triggering signal $\varphi(t_k)$. And the variable $\varpi(t)$ is dynamically computed by:

$$\varpi(t+1)=\varepsilon\varpi(t)+\mu\varphi^T(t)\varphi(t)-h^T(t)h(t), \tag{4}$$

with $\varepsilon\in(0,1)$ is a given constant and $\varpi(0)=\varpi_0\geqslant 0$. Then, the next transmission instant is provided by:

$$t_{k+1}=inf\{t|t>t_k,\frac{1}{c}\varpi(t)+\mu\varphi^T(t)\varphi(t)-h^T(t)h(t)\leqslant 0\}, \tag{5}$$

where $0<\mu<1$ and $c>0$ are given scalars and $t_0=0$.

Lemma 1 *[17] If the parameters in (4) and (5) satisfy the inequality $\varepsilon c\geqslant 1$, we have $\varpi(t)\geqslant 0$, for all $t=1,2,\cdots$.*

Remark 1 *Compared with the SET condition $\mu\varphi^T(t)\varphi(t)-h^T(t)h(t)\leqslant 0$, the auxiliary intermediate variable $\varpi(t)$ is introduced in the DET condition (5), and its value can be dynamically adjusted according to (4). It is noted that the DET mechanism will be transformed into the SET mechanism as $\varpi(t)\to 0$.*

2.3 Sliding mode surface design

In this subsection, the SMS function is built as:

$$\begin{aligned} o(t) &= GE\varphi(t)-G(A_l+BK_j)\varphi(t-1) \\ &\quad -GA_{dl}\varphi(t-d(t)-1), \end{aligned} \tag{6}$$

where matrix $G\in\mathbf{R}^{q\times n}$ is chosen such that GB is nondegenerate. Matrices $K_j, j\in\{1,2,\cdots,r\}$ are to be designed.

According to the ideal sliding mode, $o(t+1)=o(t)=0$, from (3) and (6), and considering the event-triggered mechanism, the equivalent control input $u_{eq}(t)$ can be derived as:

$$u_{eq}(t)=K_j\varphi(t_k)-(GB)^{-1}G\Delta A_l\varphi(t_k)-(GB)^{-1}GD_l\omega(t). \tag{7}$$

From (3) and (7), the SMD can be deduced as:

$$\begin{aligned} E\varphi(t+1) &= \tilde{A}_{lj}\varphi(t)+\tilde{A}_{dlj}\varphi(t-d(t))+\tilde{B}_{lj}h(t)+\tilde{D}_{lj}\omega(t), \\ \tilde{y}(t) &= \tilde{C}_{lj}\varphi(t), \end{aligned} \tag{8}$$

where $\bar{G}=B(GB)^{-1}G,\tilde{A}_{lj}=A_l+BK_j+\Delta A_l-\bar{G}\Delta A_l,\tilde{A}_{dlj}=A_{dl},\tilde{B}_{lj}=\bar{G}\Delta A_l-BK_j,\tilde{D}_{lj}=D_l-\bar{G}D_l,\tilde{C}_{lj}=C_l$.

Furthermore, the following assumption, definition, and lemma are supplied and will be utilized later.

Assumption 1 *[9] Matrices $\Theta_j, j=1,2,3,4$ satisfy the following conditions*
1)$\Theta_1\leqslant 0,\Theta_3>0,\Theta_4\geqslant 0,\tilde{\Theta}_4\geqslant 0$.
2)$(\Theta_1+\Theta_2)\Theta_4=0,\tilde{\Theta}_4=0$.

Definition 1 *[9] For given matrices $\Theta_j, j=1,2,3,4$, where $\Theta_1,\Theta_3,\Theta_4$ are real symmetric matrices , under the zero initial condition , if the following inequality $\sum_{t=0}^{s}\{\tilde{y}^T(t)\Theta_1\tilde{y}(t)+2\tilde{y}^T(t)\Theta_2\omega(t)+\omega^T(t)\Theta_3\omega(t)\}-\sup_{0\leq t\leq s}\tilde{y}^T(t)\Theta_4\tilde{y}(t)\geqslant 0$ holds, then the T-S fuzzy polynomial singular system is extended dissipative and $\tilde{\Theta}_4=E^T\Theta_4E$.*

Lemma 2 *[18] Given appropricate dimensions matrices Ω, D and E, Ω is symmetrical, the following inequality $\Omega+DWE+E^TW^TD^T<0$ hold for any W meeting $W^TW\leq I$, if and only if a scalar $\beta>0$ exists such that $\Omega+\beta^{-1}DD^T+\beta E^TE<0$.*

3 Main Results

3.1 Admissibility Analysis

The problem of admissible with extended dissipativity criterion for SMD (8) is dealt with in this subsection.

Theorem 1 *Given the real symmetic matrices Θ_1, Θ_2, Θ_3, Θ_4 and satisfy assumptions 1, if there exist scalars $\varepsilon_1 > 0$, $\varepsilon_2 > 0$, matrices $P_l = P_l^T, l \in \wp$, Q_1, Q_2, $Q_3 > 0$, $Z_\varsigma > 0$, $\varsigma = 1,2$, S and Λ, so that the following SOS requirements are met, then the SMD (8) is said to be admissible with extended dissipativity.*

$$\begin{bmatrix} \frac{1}{d_2}P_l + Z_1 & -Z_1 \\ -Z_1 & Q_1 + Q_2 + Z_1 \end{bmatrix} > 0, \tag{9}$$

$$\begin{bmatrix} P_l + dZ_2 & -dZ_2 \\ -dZ_2 & d_2Q_2 + dZ_2 \end{bmatrix} > 0, \tag{10}$$

$$q_1(\varphi)^T(Q_3 - \tau_1 I)q_1(\varphi) \in \Omega_{SOS}, \tag{11}$$

$$q_1(\varphi)^T(Z_\varsigma - \tau_\varsigma I)q_1(\varphi) \in \Omega_{SOS}, \tag{12}$$

$$q_1(\varphi)^T(P_l - \tilde{C}_{lj}^T\Theta_4\tilde{C}_{lj})q_1(\varphi) \in \Omega_{SOS}, \tag{13}$$

$$-q_2(\varphi)^T(\Phi_{2lj} - \tau_{lj}(\varphi)I)q_2(\varphi) \in \Omega_{SOS}, \tag{14}$$

where $q_1(\varphi), q_2(\varphi)$ are arbitratry vectors independent of $\varphi(t)$ with appropeiate dimensions; $\tau_1, \tau_\varsigma, \tau_{lj}(\varphi)$ are predefined scalars and greater than 0; and
$\tilde{\Upsilon}_1 = -E^TP_lE + E^TQ_1E + E^TQ_2E + (d+1)Q_3 - E^TZ_1E + (\frac{\mu}{c} + \alpha\mu)I + sym(\Lambda^T(\bar{A}_{lj} - E)), \Upsilon_3 = -Q_1 - Z_1 - Z_2$,
$\Upsilon_2 = -2Q_3 - 2E^TZ_1E - 2E^TZ_2E + sym(\Lambda^T\tilde{A}_{dlj})$,
$\Upsilon_4 = -Q_2 - Z_2, \Upsilon_5 = d_1^2Z_1 + d^2Z_2 - ym(\Lambda^T)$,
$\Upsilon_6 = -(\frac{1}{c} + \alpha)I, \bar{\Upsilon}_{12} = E^TZ_1E + \Lambda^T\tilde{A}_{dlj} + (\bar{A}_{lj} - E)^T\Lambda$,
$\Upsilon_7 = \frac{\varepsilon - 1 + \alpha}{c}I, \bar{\Upsilon}_{15} = SR^T - \Lambda^T + (\bar{A}_{lj} - E)^T\Lambda$,
$\Upsilon_{18} = -\tilde{C}_{lj}^T\Theta_2 + \Lambda^T\tilde{D}_{lj}, \Upsilon_{112} = \varepsilon_1 H_{i2}^T(\varphi(t))$,
$\Upsilon_{111} = \Lambda^T H_{i1}(\varphi(t)) - \Lambda^T\bar{G}H_{i1}(\varphi(t)), \Upsilon_{613} = H_{i2}^T(\varphi(t))$,
$\Upsilon_{114} = \varepsilon_2\Lambda^T\bar{G}H_{i1}(\varphi(t)), \Upsilon_{23} = E^TZ_1 + E^TZ_2$,
$\Upsilon_{25} = -\Lambda^T + \tilde{A}_{dlj}^T\Lambda, \Upsilon_{911} = H_{i1}(\varphi(t)) - \bar{G}H_{i1}(\varphi(t))$,
$\Upsilon_{211} = \Upsilon_{511} = \Upsilon_{111}, \Upsilon_{214} = \Upsilon_{514} = \Upsilon_{114}, \Upsilon_{914} = \varepsilon_2\bar{G}H_{i1}(\varphi(t))$,
$\Phi_{2lj} = [\Phi_{21lj}^T\ \Phi_{22lj}^T\ \Phi_{23lj}^T\ \Phi_{24lj}^T\ \Phi_{25lj}^T\ \Phi_{26lj}^T\ \Phi_{27lj}^T\ \Phi_{28lj}^T\ \Phi_{29lj}^T\ \Phi_{210lj}^T\ \Phi_{211lj}^T\ \Phi_{212lj}^T\ \Phi_{213lj}^T\ \Phi_{214lj}^T]^T$,
$\Phi_{21lj} = [\tilde{\Upsilon}_1\ \bar{\Upsilon}_{12}\ 0\ 0\ \bar{\Upsilon}_{15}\ \Lambda^T\bar{B}_{lj}\ 0\ \Upsilon_{18}\ \tilde{A}_{lj}^T\ \tilde{C}_{lj}^T\ \Upsilon_{111}\ \Upsilon_{112}\ 0\ \Upsilon_{114}]$,
$\Phi_{22lj} = [*\ \Upsilon_2\ \Upsilon_{23}\ E^TZ_2\ \Upsilon_{25}\ \Lambda^T\bar{B}_{lj}\ 0\ \Lambda^T\tilde{D}_{lj}\ \tilde{A}_{dlj}^T\ 0\ \Upsilon_{211}\ 0\ 0\ \Upsilon_{214}], \Phi_{23lj} = [*\ *\ \Upsilon_3\ 0\ 0\ 0\ 0\ 0\ 0\ 0\ 0\ 0\ 0\ 0], \Phi_{24lj} = [*\ *\ *\ \Upsilon_4\ 0\ 0\ 0\ 0\ 0\ 0\ 0\ 0\ 0\ 0], \Phi_{25lj} = [*\ *\ *\ *\ \Upsilon_5\ \Lambda^T\bar{B}_{lj}\ 0\ \Lambda^T\tilde{D}_{lj}\ 0\ 0\ \Upsilon_{511}\ 0\ 0\ \Upsilon_{514}], \Phi_{26lj} = [*\ *\ *\ *\ *\ \Upsilon_6\ 0\ 0\ \bar{B}_{lj}^T\ 0\ 0\ 0\ \Upsilon_{613}\ 0], \Phi_{27lj} = [*\ *\ *\ *\ *\ *\ \Upsilon_7\ 0\ 0\ 0\ 0\ 0\ 0\ 0], \Phi_{28lj} = [*\ *\ *\ *\ *\ *\ *\ -\Theta_3\ \tilde{D}_{lj}^T\ 0\ 0\ 0\ 0\ 0], \Phi_{29lj} = [*\ *\ *\ *\ *\ *\ *\ *\ -P_n^{-1}\ 0\ \Upsilon_{911}\ 0\ 0\ \Upsilon_{914}], \Phi_{210lj} = [*\ *\ *\ *\ *\ *\ *\ *\ *\ \Theta_1^{-1}\ 0\ 0\ 0\ 0], \Phi_{211lj} = [*\ *\ *\ *\ *\ *\ *\ *\ *\ *\ -\varepsilon_1 I\ 0\ 0\ 0], \Phi_{212lj} = [*\ *\ *\ *\ *\ *\ *\ *\ *\ *\ *\ -\varepsilon_1 I\ 0\ 0], \Phi_{213lj} = [*\ *\ *\ *\ *\ *\ *\ *\ *\ *\ *\ *\ -\varepsilon_2 I\ 0], \Phi_{214lj} = [*\ *\ *\ *\ *\ *\ *\ *\ *\ *\ *\ *\ *\ -\varepsilon_2 I]$.

Proof: First, let us verify that the SMD (8) is regular and causal. From (14), we can get:

$$\begin{bmatrix} \Pi_{11} & \Pi_{12} \\ * & \Pi_{22} \end{bmatrix} < 0, \tag{15}$$

where $\Pi_{11} = -E^TP_lE + E^TQ_1E + E^TQ_2E - E^TZ_1E + sym(\Lambda^T(\bar{A}_{lj} - E)), \Pi_{22} = -sym(\Lambda^T), \Pi_{12} = SR^T - \Lambda^T + (\bar{A}_{lj} - E)^T\Lambda$.

Pre-multiplying and post-multiplying (15) by $\begin{bmatrix} I & \bar{A}_{lj}^T \end{bmatrix}$ and $\begin{bmatrix} I & \bar{A}_{lj}^T \end{bmatrix}^T$, respectively, it can be obtained that:

$$\begin{aligned} &sym(\Lambda^T(\bar{A}_{lj} - E) + \bar{A}_{lj}^T(SR^T - \Lambda^T + (\bar{A}_{lj} - E)^T\Lambda)^T) \\ &- sym((\Lambda\bar{A}_{lj})^T\bar{A}_{lj}) - E^TP_lE + E^TQ_1E + E^TQ_2E \\ &- E^TZ_1E < 0. \end{aligned} \tag{16}$$

Due to $rank(E) = r$, the existence of two nonsingular matrices T_1 and T_2 satisfy:

$$\begin{aligned} &\bar{E} = T_1ET_2 = \begin{bmatrix} I_r & 0 \\ 0 & 0 \end{bmatrix}, \check{S} = T_2^TS = \begin{bmatrix} \check{S}_1 \\ \check{S}_2 \end{bmatrix}, \\ &\check{A}_{lj} = T_1\bar{A}_{lj}T_2 = \begin{bmatrix} \check{A}_{lj1} & \check{A}_{lj2} \\ \check{A}_{lj3} & \check{A}_{lj4} \end{bmatrix}, R = T_1^T\begin{bmatrix} 0 \\ \check{R} \end{bmatrix}, \end{aligned} \tag{17}$$

$\check{R}$ is nonsingular. Pre-multiplying and post-multiplying (16) by T_2^T and T_2, respectively, and utilizing (17), we get:

$$\begin{bmatrix} \triangle & \triangle \\ * & \check{S}_2\check{R}^T\check{A}_{lj4} + \check{A}_{lj4}^T\check{R}\check{S}_2^T \end{bmatrix} < 0, \tag{18}$$

where $\triangle$ means the irrelevant matrices. According to (18), we have $sym(\check{S}_2\check{R}^T\check{A}_{lj4}) < 0$, which means $\check{A}_{lj4}$ is nonsingular. The regularity and causality of the SMD (8) are proved.

Next, we will prove the SMD (8) is admissible. We construct the following piecewise Lyapunov functional:

$$\hat{V}(t) = \hat{V}_1(t) + \hat{V}_2(t) + \hat{V}_3(t) + \hat{V}_4(t) + \hat{V}_5(t), \tag{19}$$

where

$$\hat{V}_1(t) = \varphi^T(t)E^TP_lE\varphi(t),$$

$$\hat{V}_2(t) = \sum_{\theta=t-d_1}^{t-1}\varphi^T(\theta)E^TQ_1E\varphi(\theta) + \sum_{\theta=t-d_2}^{t-1}\varphi^T(\theta)E^TQ_2E\varphi(\theta),$$

$$\hat{V}_3(t) = \sum_{v=-d_2+1}^{-d_1}\sum_{\theta=t+v}^{t-1}\varphi^T(\theta)Q_3\varphi(\theta) + \sum_{\theta=t-d(t)}^{t-1}\varphi^T(\theta)Q_3\varphi(\theta),$$

$$\begin{aligned} \hat{V}_4(t) = {} & d_1\sum_{v=-d_1}^{-1}\sum_{\theta=t+v}^{t-1}\pi^T(\theta)E^TZ_1E\pi(\theta) \\ & + d\sum_{v=-d_2}^{-d_1-1}\sum_{\theta=t+v}^{t-1}\pi^T(\theta)E^TZ_2E\pi(\theta), \hat{V}_5(t) = \frac{1}{c}\varpi(t), \end{aligned}$$

with $\pi(t) = \varphi(t+1) - \varphi(t)$ and $d = d_2 - d_1$.

Remark 2 *The stability of the system is proved using the Lyapunov function, we need to find a positive definite matrix P satisfying all subsystems. However, the stability of the system is proved using the piecewise Lyapunov function (19), we find positive definite matrices for each subsystem separately. Therefore, the method of piecewise Lyapunov function is less conservative.*

$$\begin{aligned} \hat{V}_1(t) = \frac{1}{d_2}(& \sum_{\theta=t-d_2}^{t-d_1-1}\varphi^T(\theta)E^TP_lE\varphi(\theta) \\ & + \sum_{\theta=t-d_1}^{t-1}\varphi^T(\theta)E^TP_lE\varphi(\theta)). \end{aligned} \tag{20}$$

From Jensen inequality, we have:

$$\hat{V}_4(t) \geqslant \sum_{\theta=t-d_1}^{t-1} [E\varphi(t)-E\varphi(\theta)]^T Z_1 [E\varphi(t)-E\varphi(\theta)] + \frac{d}{d_2} \sum_{\theta=t-d_2}^{t-d_1-1} [E\varphi(t)-E\varphi(\theta)]^T Z_2 [E\varphi(t)-E\varphi(\theta)]. \quad (21)$$

By connecting (20)-(21), we have:

$$\hat{V}(t) = \sum_{\theta=t-d_1}^{t-1} \chi(t)^T N_1 \chi(t) + \frac{1}{d_2} \sum_{\theta=t-d_2}^{t-d_1-1} \chi(t)^T N_2 \chi(t) + \hat{V}_3(t) + \hat{V}_5(t), \quad (22)$$

where $W = E\varphi(t) - E\varphi(\theta), \chi(t) = \begin{bmatrix} E\varphi(t) \\ E\varphi(\theta) \end{bmatrix}^T, N_1 = \begin{bmatrix} \frac{1}{d_2}P_l + Z_1 & -Z_1 \\ -Z_1 & Q_1+Q_2+Z_1 \end{bmatrix}, N_2 = \begin{bmatrix} P_l + dZ_2 & -dZ_2 \\ -dZ_2 & d_2Q_2 + dZ_2 \end{bmatrix}$. Q_3 is a positive definite matrix, from (9) and (10), we obtain $\hat{V}(t) > 0$.

Then taking difference of $\hat{V}_k(t)(k = 1,2,3,4,5)$ along with SMD (8), we get:

$$\Delta\hat{V}_1(t) = \varphi^T(t+1)E^T P_n E\varphi(t+1) - \varphi^T(t)E^T P_l E\varphi(t). \quad (23)$$

$$\Delta\hat{V}_2(t) = \varphi^T(t)E^T Q_1 E\varphi(t) - \varphi^T(t-d_1)E^T Q_1 E\varphi(t-d_1) + \varphi^T(t)E^T Q_2 E\varphi(t) - \varphi^T(t-d_2)E^T Q_2 E\varphi(t-d_2). \quad (24)$$

$$\Delta\hat{V}_3(t) \leq (d+1)\varphi^T(t)Q_3\varphi(t) - 2\varphi^T(t-d(t))Q_3\varphi(t-d(t)). \quad (25)$$

$$\Delta\hat{V}_4(t) = d_1^2\pi^T(t)E^T Z_1 E\pi(t) + d^2\pi^T(t)E^T Z_2 E\pi(t) - d_1\sum_{\theta=t-d_1}^{t-1}\pi^T(\theta)E^T Z_1 E\pi(\theta) - d\sum_{\theta=t-d_2}^{t-d_1-1}\pi^T(\theta)E^T Z_2 E\pi(\theta). \quad (26)$$

$$\begin{aligned}\Delta\hat{V}_5(t) &\leqslant \frac{1}{c}\varpi(t+1) - \frac{1}{c}\varpi(t) + \alpha(\frac{1}{c}\varpi(t) + \mu\varphi^T(t)\varphi(t) - h^T(t)h(t)) \\ &= \frac{\varepsilon - 1 + \alpha}{c}\varpi(t) + (\frac{\mu}{c} + \alpha\mu)\varphi^T(t)\varphi(t) - (\frac{1}{c}+\alpha)h^T(t)h(t), \end{aligned} \quad (27)$$

with $\alpha > 0$.

According to $R^T E = 0$, it is clear that

$$2\varphi^T(t)SR^T E\pi(t) = 0,$$
$$2[\varphi^T(t)\Lambda^T + \varphi^T(t-d(t))\Lambda^T + (E\pi(t))^T\Lambda^T][(\tilde{A}_{lj}-E)\varphi(t) + \tilde{A}_{dlj}\varphi(t-d(t)) + \tilde{B}_{lj}h(t) + \tilde{D}_{lj}\omega(t) - E\pi(t)] = 0. \quad (28)$$

Define

$$J(t) \triangleq \tilde{y}^T(t)\Theta_1\tilde{y}(t) + 2\tilde{y}^T(t)\Theta_2\omega(t) + \omega^T(t)\Theta_3\omega(t). \quad (29)$$

By connecting (23)-(29) and based on Jensen inequality, we have:

$$\Delta\hat{V}(t) - J(t) = \xi^T(t)\Phi_{1lj}\xi(t), \quad (30)$$

where $\xi(t) = [\varphi^T(t)\ \ \varphi^T(t-d(t))\ \ \varphi^T(t-d_1)E^T\ \ \varphi^T(t-d_2)E^T\ \ (E\pi(t))^T\ \ h^T(t)\ \ \sqrt{\varpi(k)}\ \ \omega^T(t)]^T$, $\Upsilon_1 = -E^T P_l E + E^T Q_1 E + E^T Q_2 E + (d+1)Q_3 - E^T Z_1 E + (\frac{\mu}{c} + \alpha\mu)I + sym(\Lambda^T(\tilde{A}_{lj}-E)), \Upsilon_{12} = E^T Z_1 E + \Lambda^T\tilde{A}_{dlj} + (\tilde{A}_{lj}-E)^T\Lambda, \Upsilon_{15} = SR^T - \Lambda^T + (\tilde{A}_{lj}-E)^T\Lambda$,
$\Phi_{1lj} = [\Phi_{11lj}^T\ \Phi_{12lj}^T\ \Phi_{13lj}^T\ \Phi_{14lj}^T\ \Phi_{15lj}^T\ \Phi_{16lj}^T\ \Phi_{17lj}^T\ \Phi_{18lj}^T\ \Phi_{19lj}^T\ \Phi_{110lj}^T]^T, \Phi_{11lj} = [\Upsilon_1\ \Upsilon_{12}\ 0\ 0\ \Upsilon_{15}\ \Lambda^T\tilde{B}_{lj}\ 0\ \Upsilon_{18}\ \tilde{A}_{lj}^T\ \tilde{C}_{lj}^T]$, $\Phi_{12lj} = [*\ \Upsilon_2\ \Upsilon_{23}\ E^T Z_2\ \Upsilon_{25}\ \Lambda^T\tilde{B}_{lj}\ 0\ \Lambda^T\tilde{D}_{lj}\ \tilde{A}_{dlj}^T\ 0], \Phi_{13lj} = [*\ *\ \Upsilon_3\ 0\ 0\ 0\ 0\ 0\ 0\ 0], \Phi_{14lj} = [*\ *\ *\ \Upsilon_4\ 0\ 0\ 0\ 0\ 0\ 0], \Phi_{15lj} = [*\ *\ *\ *\ \Upsilon_5\ \Lambda^T\tilde{B}_{lj}\ 0\ \Lambda^T\tilde{D}_{lj}\ 0\ 0], \Phi_{16lj} = [*\ *\ *\ *\ *\ \Upsilon_6\ 0\ 0\ \tilde{B}_{lj}^T\ 0], \Phi_{17lj} = [*\ *\ *\ *\ *\ *\ \Upsilon_7\ 0\ 0\ 0], \Phi_{18lj} = [*\ *\ *\ *\ *\ *\ *\ *\ -\Theta_3\ \tilde{D}_{lj}^T\ 0], \Phi_{19lj} = [*\ *\ *\ *\ *\ *\ *\ *\ *\ -P_n^{-1}\ 0], \Phi_{110lj} = [*\ *\ *\ *\ *\ *\ *\ *\ *\ *\ \Theta_1^{-1}]$.

To this end, let us prove that the SMD (8) is extended dissipative. First, when $\Theta_4 = 0$, the following inequality holds

$$\sum_{t=0}^{s} J(t) \geqslant \hat{V}(t) - \hat{V}(0) > 0. \quad (31)$$

Next, when $\Theta_4 > 0$. According to (13), we have:

$$\tilde{y}^T(t)\Theta_4\tilde{y}(t) \leqslant \sum_{i=1}^{r} h_i(b(t))\varphi^T(t)P_l\varphi(t), \quad (32)$$

thus, we can obtain:

$$\begin{aligned}&\sum_{t=0}^{s} J(t) - \sup_{0\leq t\leq s}\tilde{y}^T(t)\Theta_4\tilde{y}(t) \\ &\geqslant \sum_{t=0}^{s} J(t) - \sum_{i=1}^{r} h_i(b(t))\varphi^T(t)P_l\varphi(t) > 0, \end{aligned} \quad (33)$$

then, the SMD (8) is extended dissipative in the meaning of Definition 1. When $\omega(t) = 0$, from (14), we have $\Delta\hat{V}(t) < 0$, the SMD (8) is admissible with extended dissipativity.

Considering the uncertainties of SMD (8), the uncertain parameters in Φ_{1lj} can be separated via matrix summation. Then based on Lemma 2 and Schur complement, we can get Φ_{2lj}. Therefore, according to Theorem 1, then we get $\Phi_{2lj} < 0$, so the SMD (8) is admissible. The proof is complete.

Theorem 2 *Given the real symmetic matrices Θ_1, Θ_2, Θ_3, Θ_4 and satisfy assumptions 1, if there exist scalars $\varepsilon_3 > 0$, $\varepsilon_4 > 0$, matrices $P_l = P_l^T, l \in \wp$, Q_1, Q_2, $Q_3 > 0$, $Z_\varsigma > 0$, $\varsigma = 1,2$, S and Λ, so that the following SOS requirements and (9)-(12) are met, then the SMD (8) is said to be admissible with extended dissipativity.*

$$q_1(\varphi)^T(P_l - C_l^T\Theta_4 C_l)q_1(\varphi) \in \Omega_{SOS}, \quad (34)$$

$$-q_3(\varphi)^T(\Phi_{3lj} - \tau_{lj}(\varphi)I)q_\varphi(x) \in \Omega_{SOS}, \quad (35)$$

where $q_3(\varphi)$ are arbitratry vectors independent of $\varphi(t)$ with appropeiate dimensions. In addition, if (35) holds, the control law gain K_j is $L_j\Lambda^{-1}$, and
$\Phi_{3lj} = [\Phi_{311j}^T\ \Phi_{321j}^T\ \Phi_{331j}^T\ \Phi_{341j}^T\ \Phi_{351j}^T\ \Phi_{361j}^T\ \Phi_{371j}^T\ \Phi_{381j}^T\ \Phi_{391j}^T\ \Phi_{3101j}^T\ \Phi_{3111j}^T\ \Phi_{3121j}^T\ \Phi_{3131j}^T\ \Phi_{3141j}^T]^T$,
$\Phi_{311j} = [\Psi_{11}\ \Psi_{12}\ 0\ 0\ \Psi_{15}\ -L_j^T B^T\ 0\ \Psi_{18}\ \Psi_{19}\ \Psi_{110}\ \Psi_{111}\ \Psi_{112}\ 0\ \Psi_{114}], \Phi_{321j} = [*\ \Psi_{22}\ \Upsilon_{23}\ E^T Z_2\ \Psi_{25}\ -L_j^T B^T\ 0\ \Lambda^T C_l^T\ A_{dl}\Lambda\ 0\ 0\ \Psi_{212}\ 0\ \Psi_{214}], \Phi_{331j} =$

$[* \quad * \quad \Upsilon_3 \quad 0 \quad 0 \quad 0 \quad 0 \quad 0 \quad 0 \quad 0 \quad 0 \quad 0 \quad 0], \Phi_{34lj} = [* \quad * \quad * \quad \Upsilon_4 \quad 0 \quad 0 \quad 0 \quad 0 \quad 0 \quad 0 \quad 0 \quad 0], \Phi_{35lj} = [* \quad * \quad * \quad * \quad \Upsilon_5 \quad -L_j^T B^T \quad 0 \quad \Lambda^T C_l^T \quad 0 \quad 0 \quad 0 \quad \Psi_{512} \quad 0 \quad \Psi_{514}], \Phi_{36lj} = [* \quad * \quad * \quad * \quad * \quad \Upsilon_6 \quad 0 \quad 0 \quad -BL_j \quad 0 \quad 0 \quad 0 \quad \Psi_{613} \quad 0], \Phi_{37lj} = [* \quad * \quad * \quad * \quad * \quad * \quad \Upsilon_7 \quad 0 \quad 0 \quad 0 \quad 0 \quad 0 \quad 0 \quad 0], \Phi_{38lj} = [* \quad * \quad * \quad * \quad * \quad * \quad * \quad -\Psi_3 \quad C_l\Lambda \quad 0 \quad 0 \quad 0 \quad 0 \quad 0], \Phi_{39lj} = [* \quad * \quad * \quad * \quad * \quad * \quad * \quad * \quad \Psi_{99} \quad 0 \quad 0 \quad varPsi_{912} \quad 0 \quad \Psi_{914}], \Phi_{310lj} = [* \quad * \quad * \quad * \quad * \quad * \quad * \quad * \quad * \quad \bar{\Psi}_1 \quad 0 \quad 0 \quad 0 \quad 0], \Phi_{311lj} = [* \quad * \quad * \quad * \quad * \quad * \quad * \quad * \quad * \quad * \quad -\varepsilon_1 I \quad 0 \quad 0 \quad 0], \Phi_{312lj} = [* \quad * \quad * \quad * \quad * \quad * \quad * \quad * \quad * \quad * \quad * \quad -\varepsilon_1 I \quad 0 \quad 0], \Phi_{313lj} = [* \quad * \quad * \quad * \quad * \quad * \quad * \quad * \quad * \quad * \quad * \quad * \quad -\varepsilon_2 I \quad 0], \Phi_{314lj} = [* \quad * \quad * \quad * \quad * \quad * \quad * \quad * \quad * \quad * \quad * \quad * \quad * \quad -\varepsilon_2 I], \Psi_{11} = -E^T P_l E + E^T Q_1 E + E^T Q_2 E + (d+1)Q_3 - E^T Z_1 E + (\frac{\mu}{c} + \alpha\mu)I + sym(\Lambda^T A_l^T + L_j^T B^T - \Lambda^T E), \Psi_{613} = \bar{G}H_{i1}(\varphi(t)),$
$\Psi_{12} = E^T Z_1 E + \Lambda^T A_{dl}^T + A_l\Lambda - E^T\Lambda + BL_j,$
$\Psi_{15} = SR^T - \Lambda^T + A_l\Lambda - E^T\Lambda + BL_j, \Psi_{110} = D_l - \bar{G}D_l,$
$\Psi_{18} = -D_l\Theta_2 + \bar{G}D_l\Theta_2 + \Theta^T C_l^T, \Psi_{19} = A_l\Lambda + BL_j,$
$\Psi_{111} = H_{i1}(\varphi(t)) - \bar{G}H_{i1}(\varphi(t)), \Psi_{112} = \varepsilon_3\Lambda^T H_{i2}^T(\varphi(t)),$
$\Psi_{114} = \varepsilon_4\Lambda^T H_{i2}^T(\varphi(t)), \Psi_{22} = -2Q_3 - 2E^T Z_1 E - 2E^T Z_2 E + sym(\Lambda^T A_{dl}^T), \Psi_{25} = -\Lambda^T + A_{dl}\Lambda, \Psi_{212} = \Psi_{112} = \Psi_{512}, \Psi_{214} = \Psi_{114} = \Psi_{514}, \Psi_{99} = P_n - \Lambda^T - \Lambda, \Psi_{912} = \varepsilon_3 H_{i2}^T(\varphi(t)), \Psi_{914} = \varepsilon_4 H_{i2}^T(\varphi(t)).$

Proof: If we only consider regularity, causality, stability and extended dissipative performance, the SMD (8) is equivalent to the dual system as follows [19]:

$$E^T\zeta(t+1) = \tilde{A}_{lj}^T\zeta(t) + \tilde{A}_{dlj}^T\zeta(t-d(t)) + \tilde{B}_{lj}^T\bar{e}(t) + \tilde{C}_{lj}^T\bar{\omega}(t),$$
$$\bar{y}(t) = \tilde{D}_{lj}^T\zeta(t), \tag{36}$$

where $\zeta(t)$ is the state vector. Replace E, $\tilde{A}_{lj}$, $\tilde{A}_{dlj}$, $\tilde{B}_{lj}$, $\tilde{D}_{lj}$, $\tilde{C}_{lj}$ with E^T, $\tilde{A}_{lj}^T$, $\tilde{A}_{dlj}^T$, $\tilde{B}_{lj}^T$, $\tilde{C}_{lj}^T$, $\tilde{D}_{lj}^T$ in Φ_{1lj} and then perform a congruence transformation with $diag\{I,I,I,I,I,I,I,I,\Lambda^T,I,I,I,I,I\}$ based on Schur complement lemma. Noticing the fact $-\Lambda^T P_n^{-1}\Lambda \leqslant P_n - \Lambda^T - \Lambda$, $L_j = K_j\Lambda$ and $\Theta_1^{-1} = \bar{\Theta}_1$, we can obtain (35). This completes the proof.

3.2 Sliding Mode Controller Design

Theorem 3 *The trajectory of the system (3) can reach SMS in limited time and remain unchanged for subsequent time by using SMC law related to event-triggered mechanism:*

$$u(t) = K_j\varphi(t_k) - \rho(t)(GB)^{-1}sign(o(t)), \tag{37}$$

where $\sigma(t) = \|GH_{i1}(\varphi(t))\|\|H_{i2}(\varphi(t))\varphi(t)\| + \|GD_l\|\|\omega(t)\|, \rho(t) = \lambda + \sigma(t)$, with $\lambda > 0$.

Proof: Considering the following Lyapunov function

$$\hat{V}_6(t) = \frac{1}{2}o^T(t)o(t). \tag{38}$$

By taking the difference of $o(t)$, we have:

$$\Delta o(t) = GE\varphi(t+1) - G(A_l + BK_j)\varphi(t) - GA_{dl}\varphi(t-d(t)) - o(t) \leqslant -\lambda - o(t), \tag{39}$$

thus

$$\Delta\hat{V}_6(t) = o^T(t)\Delta o(t) + \frac{1}{2}\Delta o^T(t)\Delta o(t) \leqslant o^T(t)(-\lambda - o(t)) + \frac{1}{2}\Delta o^T(t)\Delta o(t), \tag{40}$$

λ is a positive define scalar to be chosen. We can find a suitable λ to enable $\Delta\hat{V}_6(t) < 0$. This implies that the reachability criteria can be met. The proof is complete.

4 Demonstrative Examples

Example 1 *Considering a 2-rules T-S fuzzy polynomial singular systems (1), the membership function $h_i(b(t))$ are*

$$h_1(b(t)) = \begin{cases} 1, & b(t) \in [-3,-1], \\ -0.5b(t) + 0.5, & b(t) \in [-1,1]. \end{cases}$$
$$h_2(b(t)) = \begin{cases} 0.5b(t) + 0.5, & b(t) \in [-1,1], \\ -1, & b(t) \in [1,3]. \end{cases}$$

The system matrics are $E = \begin{bmatrix} 1 & 0 \\ 0 & 0 \end{bmatrix}$,

$A_1 = \begin{bmatrix} -0.15 - 0.0005\varphi_1 & -0.2 - 0.0001\varphi_1 \\ 0 & -0.7 \end{bmatrix}$,
$A_{d1} = \begin{bmatrix} -0.15 & 1.496 \\ 0 & 0.4 \end{bmatrix}, B = \begin{bmatrix} -0.2 \\ 0 \end{bmatrix}, D_1 = \begin{bmatrix} 0.015 \\ -0.06 \end{bmatrix}$,
$A_2 \begin{bmatrix} -0.5 - 0.01\varphi_1 & -1 - 0.019\varphi_1 \\ 0 & -0.6 \end{bmatrix}, C_2 = \begin{bmatrix} 0.1 & 0 \end{bmatrix}$,
$D_2 = \begin{bmatrix} 0.26 \\ -0.0429 \end{bmatrix}^T, A_{d2} = \begin{bmatrix} -0.13 & 0.1511 \\ 0 & 0.17 \end{bmatrix}$,
$C_1 = \begin{bmatrix} 0.2 & 0 \end{bmatrix}, \omega(t) = 0.01sin(-0.01t)e^{-0.5t}, G = \begin{bmatrix} 0.1 & 0.5 \end{bmatrix}, H_{11}(\varphi(t)) = \begin{bmatrix} 0.25 & -0.3 \end{bmatrix}^T, H_{12}(\varphi(t)) = \begin{bmatrix} 0 & 0.003 \end{bmatrix}^T, H_{21}(\varphi(t)) = \begin{bmatrix} 0.2 & 0.06 \end{bmatrix}, H_{22}(\varphi(t)) = \begin{bmatrix} 0.1 & 0.6 \end{bmatrix}$. Let $\Theta_1 = -0.1$, $\Theta_2 = 0.8$, $\Theta_3 = 0.1$, $\Theta_4 = 0.1$, $d_1 = 1$, $d_2 = 2$, $c = 400$, $\mu = 0.96$, $\varepsilon = 0.85$, $\varepsilon_3 = 0.6$, $\varepsilon_4 = 0.4$, $\alpha = 0.1$, by solving the (35), we can get $L_1 = \begin{bmatrix} 0.7 & -1.5 \end{bmatrix}, L_{21} = \begin{bmatrix} 0.711 & -1.488 \end{bmatrix}, L_{22} = \begin{bmatrix} 1.31 & 2.7201 \end{bmatrix}, L_3 = \begin{bmatrix} 1.501 & 2.875 \end{bmatrix}$.

Fig. 1 shows the system states. The DET instants and SET instants are shown in Fig. 2 and Fig. 4. The variable $\varpi(t)$ is shown in Fig. 3.

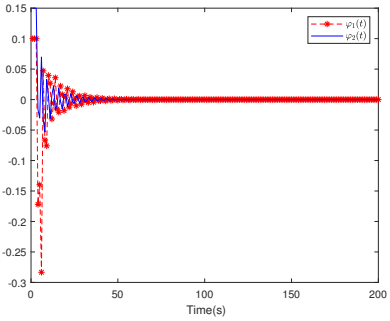

Fig. 1: The system states $\varphi_1(t)$ and $\varphi_2(t)$.

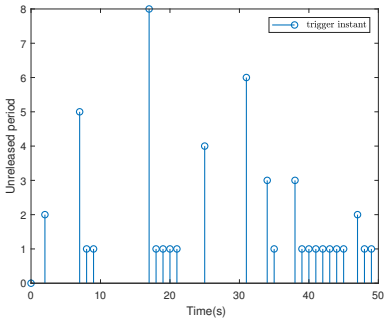

Fig. 2: DET release instants.

Table 1: Triggering time

	DET	SET
The number of triggering instances	25	42

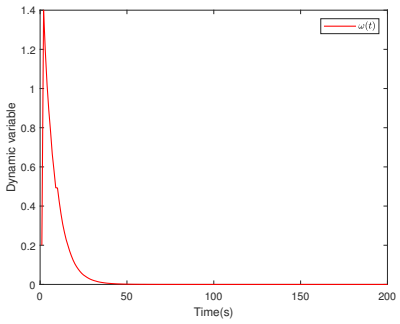

Fig. 3: The variable $\varpi(t)$.

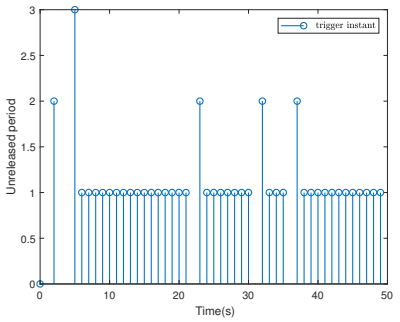

Fig. 4: SET release instants.

Remark 3 *Table 1 shows that the DET mechanism has just 25 sample instances for information transmission, which reduces the number of transmissions by* 50%. *Furthermore, the SET mechanism transfers information with 42 sample instances, reducing the number of transmissions by* 16%. *Both event-triggered mechanisms guarantee that the system is admissible with extended dissipativity. However, the number of triggers under the DET mechanism is less than that of the SET mechanism, implying that the DET is more efficient in terms of network resources.*

5 Conclusion

This paper has studied extended dissipative SMC for discrete-time nonlinear system. The nonlinear system is described by the T-S fuzzy polynomial singular system with parameter uncertainty. Then, based on time-delay-dependent SMS and combined with the DET mechanism, a new SMC law is obtained to ensure that the reachability condition is met. The criteria of admissible with extended dissipativity for T-S fuzzy polynomial singular system is obtained. Finally, the given numerical example has demonstrated that the proposed method is effective.

References

[1] Z. Feng, R. B. Li, N. Zhang, et al. Event-based asymptotic tracking control for constrained MIMO nonlinear systems via a single-parameter adaptation method. *IEEE Transactions on Systems, Man, and Cybernetics: Systems*, 53(13): 7758-7768, 2023.

[2] H. Gao, Z. Li, X. Yu, et al. Hierarchical multi-objective heuristic for PCB assembly optimization in a beam-head surface mounter. *IEEE Transactions on Cybernetics*, 52(7): 6911-6924, 2021.

[3] Z. Feng, R. B. Li, L. Wu. Adaptive decentralized control for constrained strong interconnected nonlinear systems and its application to inverted pendulum. *IEEE Transactions on Neural Networks and Learning Systems*: 1-11, 2023.

[4] G. Liu and J. Zhou. Fuzzy controller design for discrete-time TS fuzzy systems with partially unknown membership functions. *International Journal of Control, Automation and Systems*, 20(12): 4050-4058, 2022.

[5] Z. Lian. Stability analysis for T-S fuzzy systems with time-varying delay via free-matrix-based integral inequality. *International Journal of Control, Automation and Systems*, 2(14): 21-28, 2016.

[6] B. Visakamoorthi, P. Muthukumar, H. Trinh. Reachable set estimation for T-S fuzzy Markov jump systems with time-varying delays via membership function dependent performance. *IEEE Transactions on Fuzzy Systems*, 30(11): 4980-4990, 2022.

[7] P. Shi, H. Wang, C. Lim. Network-based event-triggered control for singular systems with quantizations. *IEEE Transactions on Industrial Electronics*, 63(2): 1230-1238, 2015.

[8] T. Taniguchi, K. Tanaka, K. Yamafuji, et al. Fuzzy descriptor systems: stability analysis and design via LMIs, in *Proceedings of the 1999 American Control Conference*, 1999: 1827-1831.

[9] Z. Feng, Y. Yang, H. Lam. Extended-dissipativity-based adaptive event-triggered control for stochastic polynomial fuzzy singular systems. *IEEE Transactions on Fuzzy Systems*, 30(8): 3224-3236, 2021.

[10] H. Gao, H. Zhang, J. Xia. Event-triggered finite-time extended dissipative control for a class of switched nonlinear systems via the TS fuzzy model. *International Journal of Control, Automation and Systems*, 18(11): 2798-2807, 2020.

[11] Z. Song, P. Li, Z. Sun. Finite-time adaptive fuzzy event-triggered control of constrained nonlinear systems via bounded command filter. *IEEE Transactions on Fuzzy Systems*, 31(1): 117-128, 2020.

[12] Y. Yang, Y. Niu, Z. Zhang. Dynamic event-triggered sliding mode control for interval type-2 fuzzy systems with fading channels. *ISA Transactions*, 53(6): 3771-3781, 2023.

[13] J. Hung, W. Gao, J. Hung. Variable structure control: A survey. *IEEE Transactions on Industrial Electronics*, 40(1): 2-22, 1993.

[14] V. Utkin, J. Shi. Integral sliding mode in systems operating under uncertainty conditions, in *Proceedings of 35th IEEE Conference on Decision and Control*, 1996: 4591-4596.

[15] W. Cao, J. Xu. Nonlinear integral-type sliding surface for both matched and unmatched uncertain systems. *IEEE Transactions on Automatic Control*, 49(8): 1355-1360, 2004.

[16] H. Choi. LMI-based sliding surface design for integral sliding mode control of mismatched uncertain systems. *IEEE Transactions on Automatic Control*, 52(4): 736-742, 2007.

[17] X. Ge, Q. Han, Z. Wang. A dynamic event-triggered transmission scheme for distributed set-membership estimation over wireless sensor networks. *IEEE Transactions on Cybernetics*, 49(1): 171-183, 2017.

[18] H. Zhang, X. Liu, J. Wang, et al. Robust H_∞ sliding mode control with pole placement for a fluid power electrohydraulic actuator (EHA) system. *The International Journal of Advanced Manufacturing Technology*, 73(5): 1095-1104, 2014.

[19] K. Mathiyalagan, H. Su, R. Sakthivel. Reliable controller design for admissibility of uncertain discrete-time singular system with time-varying delay, in *Proceedings of the 32nd Chinese Control Conference*, 2013: 1532-1537.

Proceedings of the 3rd Conference on Fully Actuated System Theory and Applications
May 10-12, 2024, Shenzhen, China

Actuator Faults Tolerance for Stochastic High-Order Fully Actuated Systems

Xueqing Liu[1], Sheng Li[2], Donghua Zhou[3,1]

1. Department of Automation, Tsinghua University, Beijing 100084, P. R. China
E-mail: liuxq19@mails.tsinghua.edu.cn

2. College of Control Science and Engineering, China University of Petroleum (East China), Qingdao 266590, P. R. China
E-mail: shengli@upc.edu.cn

3. College of Electrical Engineering and Automation, Shandong University of Science and Technology, Qingdao 266590, P. R. China
E-mail: zdh@tsinghua.edu.cn

Abstract:
This article investigates the problem of fault-tolerant control (FTC) for stochastic high-order fully actuated (SHOFA) systems with actuator faults. Different from the majority of existing studies focusing on deterministic high-order fully actuated (HOFA) systems, this work accounts for stochastic disturbances. Employing the generalized martingale technique, a novel fault-tolerant equivalent controller is formulated. Additionally, an adaptive compensation law is devised to address time-varying faults promptly. The designed pre-closed-loop strategy advocates the advantage of HOFA methodology in the meantime and guarantees performance by ensuring that all signals are bounded in probability. Finally, a numerical example is presented to demonstrate the efficacy of the proposed method.

Key Words: High-order fully actuated system, stochastic system, fault-tolerant control, actuator fault.

1 Introduction

The methodology of fully actuated systems (FASs), proposed by Prof. Duan, has undergone significant development. A series of papers have demonstrated the superiority in control of the graceful construction, as shown in [1] and its bibliography. In the past few years, several breakthroughs have been achieve in time-varying systems and sub-actuated systems. For example, based on the single-order and multi-order FAS representations of the controllable subsystem, the robust stabilization problem of the time-varying nonlinear system has been investigated in [2]. A concept of substability raised in [3], allowing the origin to be a boundary point of the region of attraction, has provided a meaningful theory for many practical applications. Considering a type of general nonholonomic systems [4], a stabilizing controller has been proposed to drive the feasible trajectories to the origin exponentially.

The above fundamental research has inspired various fields and led to numerous achievements [5–8]. In [5], to compensate for the communication delays between multi-agents, a HOFA predictive coordination method has been established. In [6], the problem of adaptive event-triggered control has been studied on a class of uncertain HOFA systems with an unknown control matrix. In [7], a novel HOFA control strategy has been developed to reduce the frequency of the triggered event. In [8], based on distributed learning, a HOFA secondary controller has been designed for the trade-off between multiple indexes in microgrids.

In practical engineering, systems often operate under non-ideal conditions. Fault-tolerant control (FTC) theory ensures system performance in the event of faults occurring, and there has been considerable research on different fault forms [9–14]. First in [9], the FTC problem has been raised for HOFA systems where the assumption of measurable states has been deprecated and the observer method for FAS has been developed. Then, based on a low-power fully actuated controller framework, the actuator fault has been tolerated for nonideal FASs in [10]. By means of adaptive observer and controller integration framework, the bias component faults have been dealt with in [11]. By the universal approximation technique of fuzzy logic systems, an adaptive FTC law has been considered in [15] where the tracking error has been guaranteed to be bounded. Adopting the robust approach, a fault-tolerance controller has been proposed for actuator fault with loss effectiveness in [12]. Recently, by introducing a special funnel function, the problem of global adaptive asymptotic fault-tolerant control with prescribed performance has been studied in [14].

Stochasticity exists naturally and widely. The SHOFA system, as a significant object alongside the widely studied deterministic HOFA system, needs to be focused on. Nevertheless, the scarcity of corresponding high-order mathematical tools has posed a formidable challenge. Recently, an interesting contribution to the SHOFA systems theory has been presented in [16, 17], where a novel stochastic integral model has been proposed with rigor and applicability. The equivalent control laws could convert complex systems into ones with linear drift terms, effectively showcasing the utility of HOFA methodology in synthesis. Building upon this foundation, the unaddressed challenges of stabilization control and FTC in SHOFA systems have also been explored. Subsequently, the probabilistic ultimate bounds of SHOFA systems with persistent disturbances have been revealed by [18], which extended the results about stability. Furthermore, a successful instance of FTC for the SHOFA systems with local faults [19] has further underscored the potential of this approach. Moreover, there's been limited research

This work was supported by the National Natural Science Foundation of China under Grants 62033008, 62188101, 62173343, 62073339, the Natural Science Foundation of Shandong Province of China under Grants ZR2022ZD34, ZR2020YQ49 and the research fund for the Taishan Scholar Project of Shandong Province of China. (Corresponding author: Donghua Zhou.)

on stochastic high-order fully actuated systems with actuator faults.

Motivated by the aforementioned discussions, this paper addresses the FTC problem of stochastic high-order fully actuated systems with actuator faults. The main innovations are highlighted as follows:

1) This study addresses the fault-tolerant challenge in stochastic high-order fully actuated systems affected by actuator faults, marking the initial exploration of this domain. A novel fault-tolerant equivalent control law, tailored to accommodate stochastic disturbances, is devised.
2) Different from prior research [16], the stability of SHOFA systems is extended from probability asymptotic convergence to probability boundedness, providing a foundational framework for more intricate control tasks.
3) In contrast to the scenarios discussed in [10, 12, 14], this framework supports multi-actuator FASs. Fault-tolerant techniques based on the Hadamard product are developed to accommodate varying degrees of fault for each actuator.

The remaining sections of the article are organized as follows: Section 2 introduces the model of SHOFA systems with actuator faults and presents relevant lemmas. Section 3 develops an adaptive FTC law using pre-closure methods and backstepping techniques. Section 4 provides a numerical case to illustrate the effectiveness of the proposed strategies. Finally, Section 5 concludes the paper.

Notations: The notations used here are fairly standard. A^{T} denotes the transpose of matrix A. $\|A\|_2$ denotes the spectral norm of matrix A. A function is said to be of family $\mathcal{C}^m(D;\mathbb{R}^d)$, if it is $\mathbb{R}^d$-valued and continuously m-times differentiable on D. Without causing ambiguity, the symbols z and ω are simplifications of the state $z(t)$ and the Brownian motion $\omega(t)$, respectively. Specially, the notation ω_s denotes $\omega(s)$. The symbol $\odot$ denotes Hadamard product.

2 Problem Formulation and Preliminaries

2.1 Problem Formulation

Consider a class of nonlinear stochastic HOFA systems [16] with actuator faults

$$\mathrm{d}z = \sum_{i=1}^{n} \mathcal{I}^{i-1} f_i(z)\mathrm{d}t + \mathcal{I}^{n-1}[g(z)u]\mathrm{d}t + h(z)\mathrm{d}\omega \tag{1}$$

where $u \in \mathbb{R}^r$ is the input vector; $z \in \mathbb{R}^r$ is the state vector; $g(z) : \mathbb{R}^r \to \mathbb{R}^{r\times r}$ is a input gain matrix function; and $f_i(z), i = 1, 2, ..., n-1$, corresponds to the nonlinear vector functions. In a high-order system, integer n is generally larger than one. The noise ω_s is modeled as a standard one-dimensional Brownian motion. The multiplicative Leberger integral is defined in a compact form of high-order integral operator:

$$\mathcal{I}^n f(t) = \int_0^t \left(\prod_{i=2}^{n}\int_0^{t_i}\right) f(t_1)\left(\prod_{i=1}^{n}\mathrm{d}t_i\right). \tag{2}$$

The input gain $g(z)$ in studied systems meets the full-actuated conditon [2]

$$\det g(z) \neq 0, \text{ or } +\infty, \forall z \in \mathbb{R}^r. \tag{3}$$

During the life cycle of a product, the actuator may not reproduce the desired control signal u_0 perfectly. The actuators considered here may have the following partial loss of effectiveness faults [20] and drift faults [10]. Without the negligible internal dynamics in actuators, the faulty actuator model of interest in this paper is given as:

$$u = (\mathbf{I}_{r\times r} - \eta(t))u_0 + \zeta(t) \tag{4}$$

where $\eta(t) = \mathrm{diag}\{\eta_i(t)\}, i = 1, 2, ..., r$ are the loss-of-effectiveness coefficients of i-th actuator, and $\zeta(t) = [\zeta_1, \zeta_2, ..., \zeta_r]^{\mathrm{T}} \in \mathbb{R}^r$ is the bias of actuators. The following assumptions are general in the literature on FTC of systems with actuator faults [10, 21].

Assumption 1 *For the partial loss of effectiveness faults, their loss-of-effectiveness coefficients meet* $0 \leq \eta_i(t) \leq \bar{\eta} < 1$ *and* $|\dot{\eta}(t)| \leq \bar{\eta}_d$. *In addition, for the drift fault, their amplitudes satisfy* $|\zeta_i(t)| \leq \bar{\zeta}$ *and* $|\dot{\zeta}(t)| \leq \bar{\zeta}_d$.

Control Goal: Design the control input u_0 to tolerant the actuator faults as (4), such that the closed-loop SHOFA system is stable in the probabilistic sense.

2.2 Equivalence

To take full advantage of the structure of the HOFA system, an equivalent pre-closed-loop system could be dominated first. Inspired by the strategy in [16], the nonlinear dynamics could be handled conveniently. First of all, the infinitesimal generator is used and extended.

Definition 1 (Infinitesimal Generator [22]) *Let x be a solution to an Itô equation:*

$$x(t) = x(0) + \int_0^t b(x(s))ds + \int_0^t \sigma(x(s))d\omega. \tag{5}$$

For $f \in \mathcal{C}^2(\mathbb{R}^d;\mathbb{R}^d)$, let $\mathcal{L}$ be the infinitesimal generator [22]

$$\mathcal{L}f(x) = \frac{\partial f}{\partial x}b(x) + \frac{1}{2}\mathrm{Tr}\left\{\sigma^T(x)\frac{\partial^2 f}{\partial x^2}\sigma(x)\right\}. \tag{6}$$

Definition 2 ([16]) *The higher order operator $\mathcal{L}^n$ is defined iteratively by $\mathcal{L}$ as:*

$$\mathcal{L}^n = \mathcal{L}\left(\mathcal{L}^{n-1}\right) \tag{7}$$

where $n \in \mathbb{N}^*$ and $\mathcal{L}^0 f = f$.

Furthermore, some degree of continuity is required for the nonlinear vector functions $f_i(z)$. The following assumption is general and much weaker than a similar one in [23].

Assumption 2 *The nonlinear vector functions $f_i(z), i = 1, 2, ..., n-1$, satisfy $f_i(z) \in \mathbb{C}^{2(n-i)}(\mathbb{R}^r;\mathbb{R}^r)$.*

Lemma 1 ([16]) *Let $A_i \in \mathbb{R}^{r\times r}, i = 0, 1, ..., m-1$, be a set of given matrices; thus, solution z under the following controller*

$$\begin{cases} u_0 = -g^{-1}(z)\left[\sum_{i=1}^{n} A_i\mathcal{L}^{i-1}z + u^\star\right] \\ u^\star = \sum_{i=1}^{n}\mathcal{L}^{n-i}f_i(z) + v \end{cases} \tag{8}$$

for the SHOFA system (1) with Assumption 2 produces the equivalent pre-closed-loop system with linear drift terms:

$$\mathrm{d}z = -\sum_{i=1}^{n}\mathcal{I}^{i-1}A_i z\mathrm{d}t + \mathcal{I}^{n-1}v\mathrm{d}t + h(z)\mathrm{d}\omega \tag{9}$$

where $v(t)$ is a control signal that could be further designed.

2.3 Stability Criterion

To achieve bounded stability in the probabilistic sense, the following lemmas are required.

Lemma 2 *For the SHOFA systems* (1)*, if a radially unbounded $V(z,t) \in \mathcal{C}^2(\mathbb{R};\mathbb{R})$ exists such that*

$$\begin{cases} \beta_1(|z|) \le V(z,t) \le \beta_2(|z|) \\ \mathcal{L}V(z,t) \le C_1 V(z,t) + C_2 \end{cases} \tag{10}$$

where $C_1 > 0$, $C_2 > 0$, $\beta_1(\cdot)$ and $\beta_2(\cdot)$ represent class K_∞-functions, then there is almost certainly a unique solution that exists in the system and the system is bounded in probability.

Proof: The idea is similar to [24] and is omitted. ■

Lemma 3 *The following inequality holds for any bounded smooth function $\epsilon > 0$ and $x, v \in \mathbb{R}^n, v_i \ge 0$:*

$$0 \le [x - x \odot \mathrm{sg}(x,\epsilon)]^{\mathrm{T}} \nu < \epsilon \mathbf{1}^{\mathrm{T}} \nu \tag{11}$$

where $\mathrm{sg}(x,\epsilon) = x/\sqrt{|x|^2 + \epsilon^2}$ and ϵ is a small constant.

Proof: Notice that

$$\begin{aligned} &\sqrt{x^{\mathrm{T}}x + \epsilon^2}\mathbf{1}^{\mathrm{T}} v - x^{\mathrm{T}} v > 0, \\ &\left(\epsilon \mathbf{1} - \frac{\epsilon^2}{\sqrt{x^{\mathrm{T}}x + \epsilon^2}}\mathbf{1}\right)^{\mathrm{T}} v > 0. \end{aligned} \tag{12}$$

Adding the above two inequalities derivates the above lemma. ■

3 Main Results

In this section, the amplitudes of actuator faults are estimated. Subsequently, an adaptive controller for SHOFA systems with actuator faults is designed.

For the fault-free SHOFA systems, the Lemma 1 could provide an equivalent pre-closed-loop system. However, this structure is damaged in case of actuator faults. Substituting (8) into original system (1), we have

$$\begin{aligned} \mathrm{d}z =& \sum_{i=1}^{n} \mathcal{I}^{i-1} f_i(z)\mathrm{d}t + h(z)\mathrm{d}\omega \\ &+ \mathcal{I}^{n-1} g(z)[-(\mathbf{I}_{r\times r} - \eta(t))g^{-1}(z)u_0 + \zeta(t)]\mathrm{d}t \\ =& \sum_{i=1}^{n} A_i \mathcal{L}^{i-1} z\mathrm{d}t + \mathcal{I}^{n-1} v\mathrm{d}t + h(z)\mathrm{d}\omega \\ &+ \mathcal{I}^{n-1} g(z)\eta(t)u_0\mathrm{d}t + \mathcal{I}^{n-1} g(z)\zeta(t)\mathrm{d}t. \end{aligned} \tag{13}$$

Due to the unknown matrix $\eta(t)$ and vector $\zeta(t)$, the items $\mathcal{I}^{n-1}g(z)\eta(t)u_0$ and $g(z)\zeta(t)$ are intractable to dominate by the robust method. Thus, an adaptive strategy is developed in the following.

Let $\hat{\mathbf{K}} \in \mathbb{R}^{r\times r}$ and $\hat{\zeta} \in \mathbb{R}^r$ be the estimates of $\mathbf{K} \triangleq \mathrm{diag}\{1/(1-\eta_i)\}$ and ζ, and define $\tilde{\mathbf{K}} = \mathbf{K} - \hat{\mathbf{K}}$. The fault tolerance equivalent controller is proposed as

$$\begin{cases} u_0 = \hat{\mathbf{K}}[u_a - \hat{\zeta} \odot \varphi] \\ u_a = -g^{-1}(z)\left[\sum_{i=1}^{n} A_i \mathcal{L}^{i-1} z + u^\star\right] \\ u^\star = \sum_{i=1}^{n} \mathcal{L}^{n-i} f_i(z) + v \end{cases} \tag{14}$$

where φ is a vector which will be designed later. Substituting (14) into original system (1), we have

$$\begin{aligned} \mathrm{d}z =& -\sum_{i=1}^{n} A_i \mathcal{L}^{i-1} z\mathrm{d}t - \mathcal{I}^{n-1} v\mathrm{d}t + h(z)\mathrm{d}\omega \\ &+ \mathcal{I}^{n-1} g(z)(\mathbf{I}_{r\times r} - \eta(t))\tilde{\mathbf{K}} u_a \mathrm{d}t \\ &+ \mathcal{I}^{n-1} g(z)\left[\zeta(t) - (\mathbf{I}_{r\times r} - \eta(t))\hat{\mathbf{K}}\hat{\zeta}\right]\mathrm{d}t. \end{aligned} \tag{15}$$

Introduce the intermediate variable

$$\begin{cases} \mathcal{Z}_1 = z \\ \mathcal{Z}_i = \mathcal{I}(-A_i z + \mathcal{Z}_{i+1}), i = 2, ..., n-1 \\ \mathcal{Z}_n = \mathcal{I}[-A_n z + v + g(z)\mathcal{N}(z,t)] \end{cases} \tag{16}$$

where $\mathcal{N}(z,t) = (\mathbf{I}_{r\times r} - \eta(t))\tilde{\mathbf{K}}(z)u_a + \zeta(t) - (\mathbf{I}_{r\times r} - \eta(t))\hat{\mathbf{K}}\hat{\zeta} \odot \varphi$.

Substituting (16) in (15), we have

$$\mathrm{d}z = (-A_1 z + \mathcal{Z}_2)\mathrm{d}t + h(z)\mathrm{d}w. \tag{17}$$

Choosing the Lyapunov function as

$$V_1 = \frac{1}{4}|z|^4. \tag{18}$$

Define the errors as

$$\xi_i = \mathcal{Z}_i - \alpha_{i-1},\ i = 2, ..., n. \tag{19}$$

By the Itô differential formula, there is

$$\mathcal{L}V_1 = |z|^2 z^{\mathrm{T}}(-A_1 z + \xi_2 + \alpha_1) + \frac{1}{2}|z|^2 h^{\mathrm{T}}(z)h(z) + |z^{\mathrm{T}}h(z)|^2. \tag{20}$$

From Cauchy's inequality and Young's inequality, we have

$$\begin{aligned} &\frac{1}{2}|z|^2 h^{\mathrm{T}}(z)h(z) + |z^{\mathrm{T}}h(z)|^2 \\ \le& \frac{3}{2}|z|^2 h^{\mathrm{T}}(z)h(z) \le \frac{3}{4}|z|^4 |h(z)|^4 + \frac{3}{4}, \\ &|z|^2 z^{\mathrm{T}}\xi_2 \le \frac{3}{4}|z|^4 + \frac{1}{4}|\xi_2|^4. \end{aligned} \tag{21}$$

Substituting (21) into (20), the following inequality is given:

$$\begin{aligned} \mathcal{L}V_1 \le& |z|^2 z^{\mathrm{T}}\left(-A_1 z + \frac{3}{4}z + \frac{3}{4}z|h(z)|^4 + \alpha_1\right) \\ &+ \frac{1}{4}|\xi_2|^4 + \frac{3}{4}. \end{aligned} \tag{22}$$

Design virtual control law

$$\alpha_1 = -\frac{3}{4}z|h(z)|^4, \tag{23}$$

there is

$$\mathcal{L}V_1 \le -\left(\lambda_{\min}(A_1) - \frac{3}{4}\right)|z|^4 + \frac{1}{4}|\xi_2|^4 + \frac{3}{4}. \tag{24}$$

From (16) and (19), for $i = 2, ..., n-1$, there is

$$\begin{aligned} \mathrm{d}\xi_i =& \mathrm{d}\mathcal{Z}_i - \mathrm{d}\alpha_{i-1} \\ =& (-A_i z + \xi_{i+1} + \alpha_i - \mathcal{T}_i)\mathrm{d}t - \frac{\partial \alpha_{i-1}}{\partial z^{\mathrm{T}}} h(z)\mathrm{d}w. \end{aligned} \tag{25}$$

where

$$\mathcal{T}_i = \sum_{l=1}^{i-1} \frac{\partial \alpha_{i-1}}{\partial \mathcal{Z}_l^{\mathrm{T}}}(-a_l z + \mathcal{Z}_{l+1}) + \begin{bmatrix} \mathcal{V}_{i,1} & \cdots & \mathcal{V}_{i,n} \end{bmatrix}^{\mathrm{T}},$$
$$\mathcal{V}_{i,j} = \operatorname{diag}\left\{ \frac{1}{2} h^{\mathrm{T}}(z) \frac{\partial^2 \alpha_{i-1,j}}{\partial z^{\mathrm{T}} \partial z} h(z) \right\}. \tag{26}$$

Choose a series of Lyapunov functions

$$V_i = V_{i-1} + \frac{1}{4}|\xi_i|^4. \tag{27}$$

From (25), we can obtain

$$\mathcal{L}V_i = \mathcal{L}V_{i-1} + |\xi_i|^2 \xi_i^{\mathrm{T}} \left[-A_i z + \xi_{i+1} + \alpha_i - \mathcal{T}_i \right] + \mathcal{W}_i \tag{28}$$

where

$$\mathcal{W}_i = \frac{1}{2}|\xi_i|^2 h^{\mathrm{T}}(z) \frac{\partial \alpha_{i-1}^{\mathrm{T}}}{\partial z} \frac{\partial \alpha_{i-1}}{\partial z^{\mathrm{T}}} h(z) + \left| \xi_i^{\mathrm{T}} \frac{\partial \alpha_{i-1}}{\partial z^{\mathrm{T}}} h(z) \right|^2.$$

Similar to (21), we have

$$\begin{aligned} \mathcal{W}_i &\le \frac{3}{4}|\xi_i|^4 \left| \frac{\partial \alpha_{i-1}}{\partial z^{\mathrm{T}}} h(z) \right|^4 + \frac{3}{4}, \\ |\xi_i|^2 \xi_i^{\mathrm{T}} \xi_{i+1} &\le \frac{3}{4}|\xi_i|^4 + \frac{1}{4}|\xi_{i+1}|^4. \end{aligned} \tag{29}$$

Let virtual control laws α_i be

$$\alpha_i = -\kappa_i \xi_i + A_i z + \mathcal{T}_i - \frac{3}{4}\xi_i \left| \frac{\partial \alpha_{i-1}}{\partial z^{\mathrm{T}}} h(z) \right|^4 \tag{30}$$

where $\kappa_i > 0, i = 2, ..., n-1$, are constants.

Then (28) derivates

$$\mathcal{L}V_i \le \mathcal{L}V_{i-1} - \left(\kappa_i - \frac{3}{4} \right) |\xi_i|^4 + \frac{1}{4}|\xi_{i+1}|^4 + \frac{3}{4}. \tag{31}$$

Thus, form (24) and (31), we have

$$\begin{aligned} \mathcal{L}V_{n-1} \le &- \left(\lambda_{\min}(A_1) - \frac{3}{4} \right) |z|^4 - \sum_{i=2}^{n-1} (\kappa_i - 1)|\xi_i|^4 \\ &+ \frac{1}{4}|\xi_n|^4 + \frac{3}{4}(n-1). \end{aligned} \tag{32}$$

From (16), (26), and Itô formula, the total differential of ξ_n is

$$\begin{aligned} \mathrm{d}\xi_n =& \mathrm{d}\mathcal{Z}_n - \mathrm{d}\alpha_{n-1} \\ =& (-a_i z + v + g(z)\mathcal{N}(z,t) - \mathcal{T}_n)\mathrm{d}t - \frac{\partial \alpha_{n-1}}{\partial z^{\mathrm{T}}} h(z) \mathrm{d}w. \end{aligned} \tag{33}$$

Let $\mathbf{K}_+ = \mathbf{K} - \mathbf{I}_{r\times r}$, and choose a function as

$$V_n = V_{n-1} + \frac{1}{4}|\xi_n|^4 + \frac{1}{2}\operatorname{Tr}\left[(\mathbf{I}_{r\times r} - \eta(t)) \tilde{\mathbf{K}}_+^2 \right] + \frac{1}{2}\tilde{\zeta}^{\mathrm{T}}\tilde{\zeta} \tag{34}$$

where $\tilde{\mathbf{K}}_+ \triangleq \mathbf{K}_+ - \hat{\mathbf{K}}_+ = \tilde{\mathbf{K}}$.

Design the final control law as

$$v = -\kappa_n \xi_n + A_n z + \mathcal{T}_n - \frac{3}{4}\xi_n \left| \frac{\partial \alpha_{n-1}}{\partial z^{\mathrm{T}}} h(z) \right|^4. \tag{35}$$

Similar to the above derivation, we have

$$\begin{aligned} \mathcal{L}V_n \le &- \left(\lambda_{\min}(A_1) - \frac{3}{4} \right) |z|^4 - \sum_{i=2}^{n-1} (\kappa_i - 1)|\xi_i|^4 \\ &- \left(\kappa_i - \frac{1}{4} \right) |\xi_n|^4 + \frac{3}{4}n + |\xi_n|^2 \xi_n^{\mathrm{T}} g(z) \mathcal{N}(z,t) \\ &+ \operatorname{Tr}\left[(\mathbf{I}_{r\times r} - \eta)\tilde{\mathbf{K}}_+ (\dot{\mathbf{K}} - \dot{\hat{\mathbf{K}}}) \right] \\ &+ \operatorname{Tr}\left[\dot{\eta} \tilde{\mathbf{K}}_+^2 \right] + (\dot{\zeta} - \dot{\hat{\zeta}})^{\mathrm{T}} \tilde{\zeta}. \end{aligned} \tag{36}$$

From Lemma 3, there is an inequality

$$\begin{aligned} &|\xi_n|^2 \xi_n^{\mathrm{T}} g(z) \zeta(t) \\ \le &|\xi_n|^2 \xi_n^{\mathrm{T}} g(z) \odot \operatorname{sg}(|\xi_n|^2 \xi_n^{\mathrm{T}} g(z), \epsilon) \zeta(t) + \epsilon \mathbf{1}^{\mathrm{T}} \zeta(t) \\ = &|\xi_n|^2 \xi_n^{\mathrm{T}} g(z) (\mathbf{I}_{r\times r} - \eta(t)) \left[\hat{\mathbf{K}} \hat{\zeta}(t) \odot \varphi \right. \\ &\left. + \tilde{\mathbf{K}} \hat{\zeta}(t) \odot \varphi \right] + \sigma^{\mathrm{T}} \tilde{\zeta}(t) + \epsilon \mathbf{1}^{\mathrm{T}} \zeta(t) \end{aligned} \tag{37}$$

where φ is designed as $\varphi = \operatorname{sg}(|\xi_n|^2 \xi_n^{\mathrm{T}} g(z), \epsilon)$ and $\sigma = |\xi_n|^2 g^{\mathrm{T}}(z) \xi_n \odot \varphi$.

From (37), there is

$$\begin{aligned} &|\xi_n|^2 \xi_n^{\mathrm{T}} g(z) \mathcal{N}(z,t) \\ \le &|\xi_n|^2 \xi_n^{\mathrm{T}} g(z) (\mathbf{I}_{r\times r} - \eta) \tilde{\mathbf{K}} u_b + \sigma^{\mathrm{T}} \tilde{\zeta} + \epsilon \mathbf{1}^{\mathrm{T}} \zeta \end{aligned} \tag{38}$$

where $u_b = u_a - \hat{\zeta} \odot \operatorname{sg}(|\xi_n|^2 \xi_n g(z), \epsilon)$.

Designing adaptive update law

$$\begin{aligned} \dot{\hat{\mathbf{K}}} &= \operatorname{diag}(|\xi_n|^2 g(z)^{\mathrm{T}} \xi_n \odot u_b) - \kappa_k \hat{\mathbf{K}}_+, \\ \dot{\hat{\zeta}} &= \sigma - \kappa_\zeta \hat{\zeta}, \end{aligned} \tag{39}$$

there is

$$\begin{aligned} &\operatorname{Tr}\left[(\mathbf{I}_{r\times r} - \eta)\tilde{\mathbf{K}}_+ (\dot{\mathbf{K}} - \dot{\hat{\mathbf{K}}}) \right] \\ &+ |\xi_n|^2 \xi_n^{\mathrm{T}} g(z) (\mathbf{I}_{r\times r} - \eta) \tilde{\mathbf{K}} u_b \\ =&\mathbf{1}^{\mathrm{T}} (\mathbf{I}_{r\times r} - \eta) \tilde{\mathbf{K}}_+ \left[(\dot{\mathbf{K}} - \dot{\hat{\mathbf{K}}}) \mathbf{1} + |\xi_n|^2 g(z)^{\mathrm{T}} \xi_n \odot u_b \right] \\ =&\operatorname{Tr}\left[(\mathbf{I}_{r\times r} - \eta) \kappa_k \tilde{\mathbf{K}}_+ \hat{\mathbf{K}}_+ \right] + \operatorname{Tr}\left[(\mathbf{I}_{r\times r} - \eta) \tilde{\mathbf{K}}_+ \dot{\mathbf{K}} \right] \\ \le &\frac{1}{2} \operatorname{Tr}\left\{ (\mathbf{I}_{r\times r} - \eta) \left[-(\kappa_k - 1)\tilde{\mathbf{K}}_+^2 + \kappa_k \mathbf{K}^2 + \dot{\mathbf{K}}^2 \right] \right\} \end{aligned} \tag{40}$$

and

$$\begin{aligned} (\dot{\zeta} - \dot{\hat{\zeta}})^{\mathrm{T}} \tilde{\zeta} + \sigma^{\mathrm{T}} \tilde{\zeta} &= \kappa_\zeta \hat{\zeta}^{\mathrm{T}} \tilde{\zeta} + \dot{\zeta}^{\mathrm{T}} \tilde{\zeta} \\ &\le -\frac{1}{2}(\kappa_\zeta - 1)\tilde{\zeta}^{\mathrm{T}} \tilde{\zeta} + \frac{1}{2}\kappa_\zeta \zeta^{\mathrm{T}} \zeta + \frac{1}{2}\dot{\zeta}^{\mathrm{T}} \dot{\zeta}. \end{aligned} \tag{41}$$

Substituting (40) and (37) into (36), we have

$$\begin{aligned} \mathcal{L}V_n \le &- \left(\lambda_{\min}(A_1) - \frac{3}{4} \right) |z|^4 - \sum_{i=2}^{n-1} (\kappa_i - 1)|\xi_i|^4 \\ &- \frac{1}{2}(\kappa_k - 1 - 2\bar{k}\bar{\eta}_d) \operatorname{Tr}\left[(\mathbf{I}_{r\times r} - \eta)\tilde{\mathbf{K}}^2 \right] \\ &- \left(\kappa_n - \frac{1}{4} \right) |\xi_n|^4 - \frac{1}{2}(\kappa_\zeta - 1)\tilde{\zeta}^{\mathrm{T}} \tilde{\zeta} \\ &+ \operatorname{Tr}\left\{ (\mathbf{I}_{r\times r} - \eta) \left[\kappa_k \mathbf{K}_+^2 + \dot{\mathbf{K}}^2 \right] \right\} \\ &+ \frac{1}{2}\kappa_\zeta \zeta^{\mathrm{T}} \zeta + \frac{1}{2}\dot{\zeta}^{\mathrm{T}} \dot{\zeta} + \epsilon \mathbf{1}^{\mathrm{T}} \zeta + \frac{3}{4}n \\ \le &- C_1 V_n + C_2 \end{aligned} \tag{42}$$

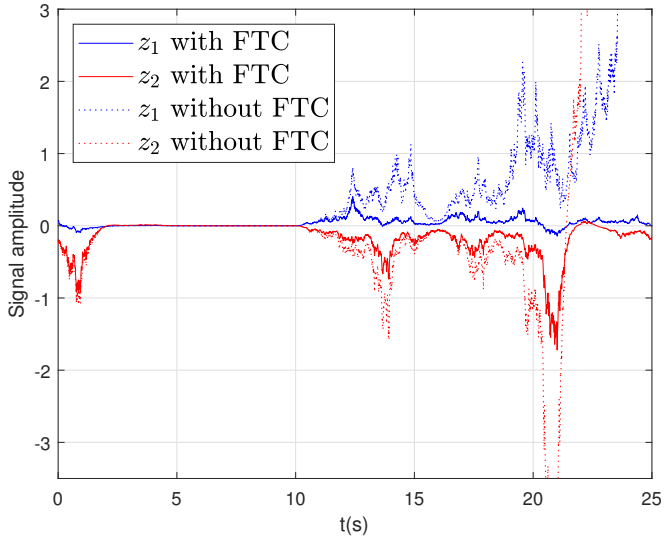

Fig. 1: High-order state z under the different control laws.

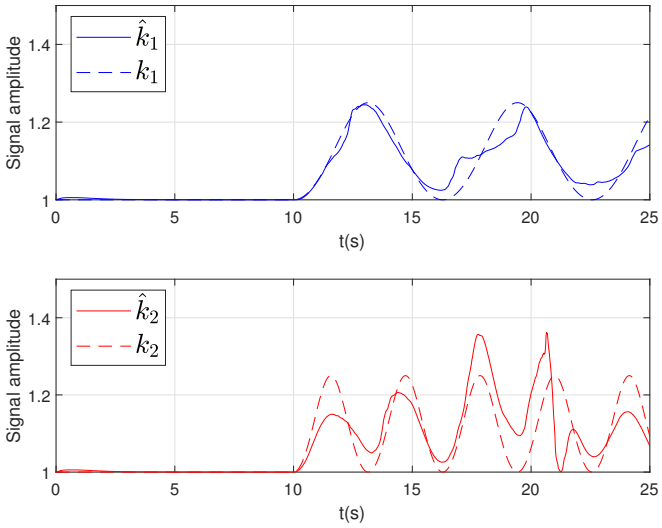

Fig. 2: The estimations $\hat{k}_i = 1/(1-\hat{\eta}_i)$ of partial loss of effectiveness faults η.

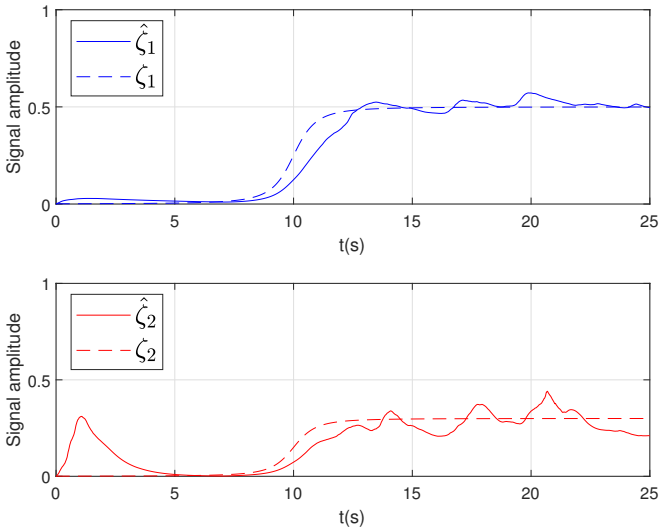

Fig. 3: The estimation $\hat{\zeta}$ of drift faults ζ.

where $\bar{k} = \frac{1}{1-\bar{\eta}}$, $C_1 = \min\left\{\lambda_{\min}(A_1) - \frac{3}{4}, \kappa_i - 1, \kappa_n - \frac{1}{4}, \kappa_k - 1 - 2\bar{k}\bar{\eta}_d, \kappa_\zeta - 1\right\}$, and $C_2 = r(\kappa_k\bar{k}^2 + \bar{k}_d^2) + \frac{1}{2}\kappa_\zeta\bar{\eta}^2 + \frac{1}{2}\bar{\eta}_d^2 + r\epsilon\bar{\eta} + \frac{3}{4}n$.

Theorem 1 *Considering the SHOFA system* (1) *with actuator faults* (4) *satisfying Assumptions 1 and 2, if the designed parameters A_i, κ_i, κ_k, and κ_ζ meet*

$$\begin{aligned} &A_1 - \frac{3}{4} > 0, \\ &\kappa_i > 1, i = 1, ..., n, \\ &\kappa_k > 1 + 2\bar{k}\bar{\eta}_d, \\ &\kappa_\zeta > 1, \end{aligned} \tag{43}$$

then, the actual controller constructed as (14) *and* (35) *with parameter updating law* (39) *guarantees that all the closed-loop high-order state z and estimate signals are bounded in probability.*

Proof: From (42), the Lyapunov function candidate V_n has satisfied the inequality $\mathcal{L}V_n \leq -C_1V_n + C_2$. If the (43) is met, there is $C_1 > 0$. Thus, we can obtain

$$\frac{\mathrm{d}\mathbb{E}\left[V_n(t)\right]}{\mathrm{d}t} \leq -C_1\mathbb{E}\left[V_n(t)\right] + C_2, \tag{44}$$

which indicates that $\mathbb{E}\left[V_n(t)\right] \leq e^{-C_1t}\mathbb{E}\left[V_n(0)\right] + \frac{C_2}{C_1}$. From Lemma 2, the signals z, $\tilde{\mathbf{K}}$ and $\tilde{\eta}$ are bounded in probability. ■

Remark 1 *We first designed fault-tolerant equivalent control laws before further stabilizing the nonlinear diffusion term. This approach maximizes the advantages of the synthesis of high-order fully actuated systems. Otherwise, employing backstepping to handle nonlinearities in the drift term would be exceedingly intractable.*

Remark 2 *In this work, the case where $r > 1$ has been discussed corresponds to multi-input systems in the state-space model. Modeling this scenario with conventional strict feedback systems is challenging, thereby magnifying the structural advantages of fully actuated systems. Additionally, it's evident through the proof that the extension from scalar state to vector state is not straightforward. Some techniques based on Cauchy's inequality, vector Itô's rule, and Hadamard product are developed in this process. Particularly, the degenerated conclusion remains valid when $r = 1$.*

4 Simulation

In this section, a numerical example will be presented to demonstrate the effectiveness of the developed method. Consider the following SHOFA system:

$$\mathrm{d}z = \begin{bmatrix} z_1^2 & \sin(z_2) \end{bmatrix}^{\mathrm{T}} \mathrm{d}t + \mathcal{I}g(z)u\mathrm{d}t + z\mathrm{d}\omega, \tag{45}$$

where $z = \begin{bmatrix} z_1 & z_2 \end{bmatrix}^{\mathrm{T}}$ and

$$g(z) = \begin{bmatrix} 1 + 0.5sin(z_1) & 0.3 \\ 1 & 2 + \frac{1}{1+z^{\mathrm{T}}z} \end{bmatrix}.$$

The actuator faults (4) are introduced at $t = t_f = 10\,\mathrm{s}$ as

$$\begin{aligned} \eta_1(t) &= 0.9 + 0.1\cos(t - t_f), \\ \eta_2(t) &= 0.9 + 0.1\cos(2(t - t_f)), \\ \zeta(t) &= (0.5 + 0.5\,\mathrm{sg}(t - t_f, 1)) \cdot \begin{bmatrix} 0.5 & 0.3 \end{bmatrix}^{\mathrm{T}}. \end{aligned} \tag{46}$$

The initial conditions are $z(0) = [0.1 \quad -0.2]^{\mathrm{T}}$, $\hat{\mathbf{K}}(0) = \mathbf{I}_2$, and $\hat{\zeta}(0) = \mathbf{0}$. The parameters of controller are selected as $A_1 = 2\mathbf{I}_2$, $A_2 = 4\mathbf{I}_2$, $\kappa_1 = \kappa_2 = \kappa_\zeta = 2, \kappa_k = 3$.

Fig. 1 shows the high-order state z under the proposed fault-tolerance controller and the controller in [16]. It is worth noting that the dashed lines diverge in finite time, which shows that the proposed method could achieve reliable stabilization when actuator faults occur. The estimations of actuator faults are represented in Figs. 2 and 3. The above results illustrate that all the signals are bounded.

5 Conclusion

This paper has proposed a novel adaptive FTC scheme for SHOFA systems with actuator faults. The established model is compatible with multiple inputs, exhibiting extensive applicability. Considering the structural characteristics of faults, a fault-tolerant pre-closed-loop control law has been designed, which highlights the superiority of the full-actuated system methodology. Leveraging backstepping and stochastic control theory, the boundedness of all closed-loop signals is ensured under the circumstances of stochastic disturbances and time-varying actuator faults. Noting that this work is limited to state feedback, the output feedback FTC will be investigated. Furthermore, as this serves as foundational work focusing on actuator faults, more meaningful topics may be considered in the future, such as finite-time control and state constraints.

References

[1] G. R. Duan, "High-order fully actuated system approaches: Part X. Basics of discrete-time systems," *International Journal of Systems Science*, vol. 53, no. 4, pp. 810–832, Sep. 2021.

[2] G. R. Duan, "Robust stabilization of time-varying nonlinear systems with time-varying delays: A fully actuated system approach," *IEEE Transactions on Cybernetics*, vol. 53, no. 12, pp. 7455–7468, Dec. 2023.

[3] G. R. Duan, "Substability and substabilization: Control of subfully actuated systems," *IEEE Transactions on Cybernetics*, vol. 53, no. 11, pp. 7309–7322, Nov. 2023.

[4] G. R. Duan, "A FAS approach for stabilization of generalized chained forms: Part 1. Discontinuous control laws," *SCIENCE CHINA Information Sciences*, 2023, doi: 10.1007/s11432-022-3730-8.

[5] G. P. Liu, "Coordination of networked nonlinear multi-agents using a high-order fully actuated predictive control strategy," *IEEE/CAA Journal of Automatica Sinica*, vol. 9, no. 4, pp. 615–623, Apr. 2022.

[6] R. Meng, C. C. Hua, K. Li, and P. J. Ning, "Adaptive event-triggered control for uncertain high-order fully actuated system," *IEEE Transactions on Circuits and Systems II: Express Briefs*, vol. 69, no. 11, pp. 4438–4442, Nov. 2022.

[7] Z. Y. Chen, L. Sheng, and M. Gao, "Event-triggered control for nonlinear systems: A high-order full-actuation approach," in *2023 2nd Conference on Fully Actuated System Theory and Applications (CFASTA)*. IEEE, Jul. 2023, pp. 71–76.

[8] Y. Yu, G. P. Liu, Y. Huang, and J. M. Guerrero, "Distributed learning-based secondary control for islanded dc microgrids: A high-order fully actuated system approach," *IEEE Transactions on Industrial Electronics*, vol. 71, no. 3, pp. 2990–3000, Mar. 2024.

[9] X. Q. Liu, M. Y. Chen, S. Li, and D. H. Zhou, "Adaptive fault-tolerant control for nonlinear high-order fully-actuated systems," *Neurocomputing*, vol. 495, pp. 75–85, Jul. 2022.

[10] M. Cai, X. He, and D. H. Zhou, "Low-power fault-tolerant control for nonideal high-order fully actuated systems," *IEEE Transactions on Systems, Man, and Cybernetics: Systems*, vol. 53, no. 8, pp. 4875–4887, Aug. 2023.

[11] M. Cai, X. He, and D. H. Zhou, "An active fault tolerance framework for uncertain nonlinear high-order fully-actuated systems," *Automatica*, vol. 152, Jun. 2023, Art. no. 110969.

[12] M. T. Gong, L. Sheng, and D. H. Zhou, "Robust fault-tolerant control for uncertain high-order fully actuated systems with actuator faults," in *2023 2nd Conference on Fully Actuated System Theory and Applications (CFASTA)*. IEEE, Jul. 2023, pp. 532–537.

[13] M. Liu, Q. H. Liu, L. X. Zhang, G. R. Duan, and X. B. Cao, "Adaptive dynamic programming-based fault-tolerant attitude control for flexible spacecraft with limited wireless resources," *Science China Information Sciences*, vol. 66, no. 10, Sep. 2023, Art. no. 202201.

[14] Z. K. Zhang, Y. Dong, and G. R. Duan, "Global asymptotic fault-tolerant tracking for time-varying nonlinear complex systems with prescribed performance," *Automatica*, vol. 159, Jan. 2024, Art. no. 111345.

[15] Y. Cui, G. R. Duan, X. P. Liu, and H. Y. Zheng, "Adaptive fuzzy fault-tolerant control of high-order nonlinear systems: A fully actuated system approach," *International Journal of Fuzzy Systems*, vol. 25, no. 5, pp. 1895–1906, Mar. 2023.

[16] X. Q. Liu, M. Y. Chen, D. H. Zhou, and L. Sheng, "Fault-tolerant control of stochastic high-order fully actuated systems," *IEEE Transactions on Cybernetics*, 2023, doi: 10.1109/TCYB.2023.3320441.

[17] X. Q. Liu, M. Y. Chen, S. Li, and D. H. Zhou, "Stabilization control for stochastic high-order fully-actuated systems with persistent disturbances," in *2023 2nd Conference on Fully Actuated System Theory and Applications (CFASTA)*. Qingdao, China: IEEE, Jul. 2023, pp. 31–36.

[18] X. Q. Liu, M. Y. Chen, S. Li, and D. H. Zhou, "Stochastic high-order fully-actuated systems: Model, equivalence and stabilization," in *2022 China Automation Congress (CAC)*. IEEE, Nov. 2022, pp. 4371–4376.

[19] X. Q. Liu, M. Y. Chen, S. Li, and D. H. Zhou, "Adaptive fault-tolerant control for stochastic high-order fully actuated systems with local faults," in *2023 CAA Symposium on Fault Detection, Supervision and Safety for Technical Processes (SAFEPROCESS)*. IEEE, Sep. 2023.

[20] G. Y. Lai, Z. Liu, C. L. P. Chen, Y. Zhang, and X. Chen, "Adaptive compensation for infinite number of time-varying actuator failures in fuzzy tracking control of uncertain nonlinear systems," *IEEE Transactions on Fuzzy Systems*, vol. 26, no. 2, pp. 474–486, Apr. 2018.

[21] F. L. Jia and X. He, "Fault-tolerant control for uncertain nonstrict-feedback stochastic nonlinear systems with output constraints," *IEEE Transactions on Systems, Man, and Cybernetics: Systems*, vol. 53, no. 8, pp. 5212–5223, Aug. 2023.

[22] R. Khasminskii, *Stochastic Stability of Differential Equations*, ser. Stochastic Modelling and Applied Probability. Berlin, Heidelberg: Springer, 2012, vol. 66.

[23] X. H. Yu, T. Wang, J. B. Qiu, and H. J. Gao, "Barrier lyapunov function-based adaptive fault-tolerant control for a class of strict-feedback stochastic nonlinear systems," *IEEE Transactions on Cybernetics*, vol. 51, no. 2, pp. 938–946, Feb. 2021.

[24] M. Krstic and R. J. Williams, "Stabilization of stochastic nonlinear systems driven by noise of unknown covariance," *IEEE Transactions on Automatic Control*, vol. 46, no. 8, pp. 1237–1253, 2001.

Proceedings of the 3rd Conference on Fully Actuated System Theory and Applications
May 10-12, 2024, Shenzhen, China

Neural-Network-Based Fault-Tolerant Control for Unknown High-Order Fully Actuated Systems

Miao Cai[1], Xiao He[1], Donghua Zhou[2,1]

1. Department of Automation, Tsinghua University, Beijing 100084, P. R. China
E-mail: caim19@mails.tsinghua.edu.cn; hexiao@tsinghua.edu.cn

2. College of Electrical Engineering and Automation, Shandong University of Science and Technology, Qingdao 266590, P. R. China
E-mail: zdh@tsinghua.edu.cn

Abstract: In the paper, a fault-tolerant controller is established for unknown high-order fully actuated systems (HOFASs) with process faults and uncontrollable unmodeled dynamics. Due to the high-dimensional computational complexity of high-order systems, a parametric tracking error is presented to the subsequent controller design. Simultaneously, the defined parametric error can be asymptotically stable under an ideal fault-tolerant fully actuated system (FAS) controller. Since the ideal fault-tolerant FAS controller cannot be given, the neural network technique is utilized to approximate the ideal controller. The ultimate tracking error can converge to a small neighborhood of the origin. Main results are proved theoretically and illustrated experimentally.

Key Words: Unknown high-order fully actuated systems, fault-tolerant control, neural network.

1 Introduction

Control theory based on first-order nonlinear state-space models is a hot research topic at present. These state-space methods are often applied to coupled nonlinear objects, and the nonlinear controller structures are complex. Under such theory bottlenecks, Duan creatively proposed the high-order fully actuated system (HOFAS) theory [1–3]. The HOFAS theory comes from the full-actuation characteristics in a physical sense, and then returns to the controllable characteristics in a mathematical sense. The fully actuated system (FAS) controller is parameterized and decoupled, which can realize the state stabilization and trajectory tracking of nonlinear objects more generally.

Since its creation, the HOFAS theory has attracted more and more attention from scholars. Initially, Duan proposed some classical FAS approaches, e.g., robust adaptive control [4], optimal control [5], time delay control [6], model reference tracking control [7], etc. In [8], the FAS controller was successfully applied to the cooperative control of networked multiagent systems. In [9], the voltage recovery and current balancing of DC microgrids were realized based on the HOFAS theory. In [10], the event-triggered control design of uncertain HOFASs was fully investigated. In [11], the FAS approach handled the robust stabilization problem of uncertain impulsive systems. In [12], a frequency-domain analysis and design of HOFAS theory were revealed. In [13], a weak disturbance decoupling controller was designed for nonlinear HOFASs. These studies further demonstrate the advantages of HOFAS theory in various research fields.

Apart from the above achievements on ideal HOFASs, the research on fault-tolerant FAS controllers has also been fully considered. In the system operation process, system faults are inevitable and will seriously damage the safe and effective execution of control tasks [14, 15]. According to the HOFAS theory, faults will significantly destroy the nonlinear cancellation of parametric controllers [16–18]. Therefore, it is urgent to study the fault-tolerant FAS controller design. In [19], the proposed fault-tolerant FAS controller could not only compensate actuator faults, but also suppress high-frequency measurement noises. In [20], a stochastic FAS controller was proposed to deal with stochastic disturbances and sensor faults. In [21], a self-healing fault-tolerant controller based on the redundancy principle was applied to HOFASs with sensor faults. In [22], the cooperative fault tolerance design of heterogeneous multiagent systems was given via FAS approaches. However, these fault-tolerant controllers are based on fully or partially known HOFASs, and the nonlinear assumptions are conservative. To the authors' best knowledge, the fault-tolerant controller design for completely unknown HOFASs has not been thoroughly investigated. Neural network (NN) is an effective technique for the controller design of unknown systems and can be introduced into the burgeoning HOFAS theory [23–25].

Inspired by the aforementioned conditions, the paper is devoted to designing the fault-tolerant FAS controller of unknown systems. The main contributions are as follows:

1) A fault-tolerant controller based on NNs is proposed for completely unknown HOFASs with uncontrollable unmodeled dynamics, further extending the unknown HOFAS theory. Compared with the existing works [18, 25], the model nonlinearity is less conservative.
2) The tracking error is proven to be ultimately uniformly bounded, and the error bound can be sufficiently small via parameter adjustment.

Notation: $\mathbb{R}^n$ denotes the n-dimensional Euclidean space, and $\mathbb{R}^{n\times m}$ represents the set of all $n\times m$ real matrices. $\|\cdot\|$ means the vector norm or matrix norm. $\mathbf{0}_n\in\mathbb{R}^n$ denotes a zero vector. $x^{(i)}$ is the i-order derivative of x. Besides, the following symbols are defined as:

$$x^{(0\sim p-1)}=\begin{bmatrix}x^{\intercal} & \dot{x}^{\intercal} & \cdots & x^{(p-1)\intercal}\end{bmatrix}^{\intercal}\in\mathbb{R}^{np},$$
$$A_{0\sim p-1}=\begin{bmatrix}A_0 & A_1 & \cdots & A_{p-1}\end{bmatrix}\in\mathbb{R}^{n\times np},$$
$$\Phi(A_{0\sim p-1})=\begin{bmatrix}O_{n(p-1)\times n} & I_{n(p-1)}\\ & -A_{0\sim p-1}\end{bmatrix}\in\mathbb{R}^{np\times np},$$
$$B_{np}=\begin{bmatrix}O_{n(p-1)\times n}^{\intercal} & I_n\end{bmatrix}^{\intercal},C_{np}=\begin{bmatrix}I_n, O_{n(p-1)\times n}^{\intercal}\end{bmatrix},$$

This work was supported in part by the National Natural Science Foundation of China under Grants 62033008, 61733009, and in part by the Taishan Scholar Project of Shandong Province of China and the NSFSD (ZR2022ZD34). (Corresponding author: Donghua Zhou.)

where $O_{n(p-1)\times n}, I_{n(p-1)}$ denote a zero matrix and an identity matrix with the compatible dimensions, respectively.

2 Problem Formulation and Preliminaries

Consider a class of unknown HOFAS models:

$$\begin{cases} x^{(p)} = F(x^{(0\sim p-1)}, z^{(0\sim q-1)}) \\ \qquad + G(x^{(0\sim p-1)}, z^{(0\sim q-1)})u + \delta, \\ z^{(q)} = F_0(x^{(0\sim p-1)}, z^{(0\sim q-1)}), \\ y = x, \end{cases} \tag{1}$$

where $x \in \mathbb{R}^n, u \in \mathbb{R}^n, y \in \mathbb{R}^n, z \in \mathbb{R}^m$ are the system state, the control input, the output and the unmodeled dynamics, respectively. p, q are two positive integers, $\delta \in \mathbb{R}^n$ is a time-varying process fault, and $F(\cdot), G(\cdot), F_0(\cdot)$ are unknown nonlinear functions. During system operation, the model variables are within compact sets, i.e., $x^{(0\sim p-1)} \in \Omega_x, u \in \Omega_u, z^{(0\sim q-1)} \in \Omega_z$.

Assumption 1. *[19] The nonlinear function $G(\cdot)$ satisfies that, for all $x^{(0\sim p-1)} \in \Omega_x, z^{(0\sim q-1)} \in \Omega_z$,*

$$0 < G(x^{(0\sim p-1)}, z^{(0\sim q-1)}) < \infty, \\ \left\| \frac{\mathrm{d}G^{-1}}{\mathrm{d}t}(x^{(0\sim p-1)}, z^{(0\sim q-1)}) \right\| < \infty. \tag{2}$$

Assumption 2. *[23] The HOFAS model (1) is a hyperbolically minimum-phase system. Besides, there exists a positive constant L_0 such that*

$$\|F_0(x^{(0\sim p-1)}, z^{(0\sim p-1)}) - F_0(\mathbf{0}_{np}, z^{(0\sim q-1)})\| \\ \le L_0\|x^{(0\sim p-1)}\|, \forall x^{(0\sim p-1)} \in \Omega_x, z^{(0\sim q-1)} \in \Omega_z. \tag{3}$$

The control task is to let the output $y \in \mathbb{R}^n$ track the reference signal $y_d \in \mathbb{R}^n$ despite unmodeled dynamics and faults.

Assumption 3. *[26] The reference signal y_d satisfies the high-order boundedness condition, i.e., $\|y_d^{(0\sim p)}\| < \infty$.*

If the whole model is available, the ideal FAS controller is designed as [1, 18]

$$u^* = -G(x^{(0\sim p-1)}, z^{(0\sim p-1)})^{-1}[F(x^{(0\sim p-1)}, z^{(0\sim p-1)}) \\ + \delta - y_d^{(p)} + A_{0\sim p-1}\eta^{(0\sim p-1)} - u_0], \tag{4}$$

where $\eta^{(0\sim p-1)} \triangleq x^{(0\sim p-1)} - y_d^{(0\sim p-1)}$, u_0 is an additional auxiliary signal, and $A_{0\sim p-1} \in \mathbb{R}^{n\times np}$ should shape a Hurwitz matrix $\Phi(A_{0\sim p-1})$. Under the ideal controller, a stable closed-loop linear system can be given:

$$\dot{\eta}^{(0\sim p-1)} = \Phi(A_{0\sim p-1})\eta^{(0\sim p-1)} + B_{np}u_0. \tag{5}$$

The ideal FAS controller (4) can completely decouple the nonlinear system (1) and realize global asymptotic stability. However, due to unknown models and faults, the ideal fault-tolerant FAS controller cannot be obtained. Therefore, it is necessary to study the numerical approximation of the ideal controller.

Lemma 1. *For the HOFAS model (1) under Assumptions 2-3, there exist positive constants L_1, L_2, t_0 such that*

$$\|z^{(0\sim q-1)}\| \le L_1\|e_c\| + L_2\|y_d^{(0\sim p-1)}\|, \forall t > t_0, \tag{6}$$

where $e_c \triangleq A_{0\sim p-1}\eta^{(0\sim p-1)}$.

Proof. The zero dynamics of (1) can be calculated as

$$\dot{z}^{(0\sim q-1)} = \Phi(O_{m\times mq})z^{(0\sim q-1)} + B_{mq}F_0(\mathbf{0}_{np}, z^{(0\sim q-1)}) \\ \triangleq F_z(\mathbf{0}_{np}, z^{(0\sim q-1)}). \tag{7}$$

Based on Assumption 2, there exists a Lyapunov function $V_0(z^{(0\sim q-1)}))$ satisfying

$$\frac{\partial V_0}{\partial z^{(0\sim q-1)}}F_z(\mathbf{0}_{np}, z^{(0\sim q-1)}) \le -\sigma_1\|z^{(0\sim q-1)}\|^2, \\ \left\|\frac{\partial V_0}{\partial z^{(0\sim q-1)}}\right\| \le \sigma_2\|z^{(0\sim q-1)}\|, \tag{8}$$

with two positive constants σ_1, σ_2.

Differentiating $V_0(z^{(0\sim q-1)})$ along (1) gives

$$\dot{V}_0(z^{(0\sim q-1)}) = \frac{\partial V_0}{\partial z^{(0\sim q-1)}}F_z(x^{(0\sim p-1)}, z^{(0\sim q-1)}) \\ = \frac{\partial V_0}{\partial z^{(0\sim q-1)}}F_z(\mathbf{0}_{np}, z^{(0\sim q-1)}) + \frac{\partial V_0}{\partial z^{(0\sim q-1)}} \\ \cdot [F_z(x^{(0\sim p-1)}, z^{(0\sim q-1)}) - F_z(\mathbf{0}_{np}, z^{(0\sim q-1)})] \\ \le -\sigma_1\|z^{(0\sim q-1)}\|^2 + \sigma_2 L_0\|z^{(0\sim q-1)}\|\|x^{(0\sim p-1)}\|. \tag{9}$$

Besides, there exist positive constants d_1, d_2 such that

$$\|x^{(0\sim p-1)}\| \le d_1\|y_d^{(0\sim p-1)}\| + d_2\|e_c\|. \tag{10}$$

Then, it follows that

$$\dot{V}_0((z^{(0\sim q-1)})) \le -\sigma_1\|z^{(0\sim q-1)}\|^2 + \sigma_2 L_0\|z^{(0\sim q-1)}\| \\ \cdot (d_1\|y_d^{(0\sim p-1)}\| + d_2\|e_c\|) \\ = -\sigma_1\|z^{(0\sim q-1)}\|(\|z^{(0\sim q-1)}\| \\ - L_1\|e_c\| - L_2\|y_d^{(0\sim p-1)}\|), \tag{11}$$

where $L_1 = \sigma_2 L_0 d_2/\sigma_1, L_2 = \sigma_2 L_0 d_1/\sigma_1$. Therefore, there exists a positive constant t_0 such that (6) holds. □

3 Main Results

Due to the high-dimensional characteristics of HOFASs, the error feedback term $\eta^{(0\sim p-1)}$ is replaced by parametric error e_c to reduce the computational complexity. Since the parameterized matrix $\Phi(A_{0\sim p-1})$ is Hurwitz, the high-order tracking error $\|\eta^{(0\sim p-1)}\| \to 0$ as $\|e_c\| \to 0$. The derivative of $e_c = A_{0\sim p-1}\eta^{(0\sim p-1)}$ is

$$\dot{e}_c = A_{p-1}[F(x^{(0\sim p-1)}, z^{(0\sim q-1)}) \\ + G(x^{(0\sim p-1)}, z^{(0\sim q-1)})u + \delta - y_d^{(p)}] \\ + \begin{bmatrix} O_{n\times n} & A_{0\sim p-2} \end{bmatrix}\eta^{(0\sim p-1)}. \tag{12}$$

Lemma 2. *For the HOFAS model (1) using a parameterized FAS controller (4) under Assumptions 1-3, there exists a positive definite matrix A_{p-1} such that for $x^{(0\sim p-1)}(0) \in \Omega_x, z^{(0\sim q-1)}(0) \in \Omega_z$, the error dynamics can be*

$$\dot{e}_c = -A_{p-1}e_c. \tag{13}$$

Naturally, the tracking error is asymptotically stable, i.e., $\lim_{t\to\infty}\|y - y_d\| = 0$.

Proof. It turns out that

$$\begin{aligned}\dot{e}_c =& -A_{p-1}e_c + v + A_{p-1}[F(x^{(0\sim p-1)}, z^{(0\sim q-1)}) \\ &+ G(x^{(0\sim p-1)}, z^{(0\sim q-1)})u + \delta],\end{aligned} \tag{14}$$

where

$$v = A_{p-1}e_c - A_{p-1}y_d^{(p)} + \begin{bmatrix}O_{n\times n} & A_{0\sim p-2}\end{bmatrix}\eta^{(0\sim p-1)}. \tag{15}$$

If the additional auxiliary signal u_0 is designed as

$$u_0 = -A_{p-1}^{-1}\begin{bmatrix}O_{n\times n} & A_{0\sim p-2}\end{bmatrix}\eta^{(0\sim p-1)}, \tag{16}$$

and the corresponding ideal FAS controller u^* will yield

$$\dot{e}_c = -A_{p-1}e_c. \tag{17}$$

As long as the parameterized matrix A_{p-1} is positive definite, the error e_c must be asymptotically stable. □

Such an ideal fault-tolerant FAS controller cannot be computed directly, so a FAS controller based on NN approximation is established. The n high-order NNs are designed as

$$\begin{aligned}&N_i(W_i,\omega) = W_i^\intercal S(\omega), W_i, S(\omega) \in \mathbb{R}^l, i = 1,2,\cdots,n,\\ &S(\omega) = \begin{bmatrix}s_1(\omega) & s_2(\omega) & \cdots & s_l(\omega)\end{bmatrix}^\intercal,\\ &s_k(\omega) = \prod_{j\in J}[s(\omega_j)]^{c_j}, k = 1,2,\cdots,l,\end{aligned} \tag{18}$$

where $\omega = \begin{bmatrix}x^{(0\sim p-1)\intercal} & z^{(0\sim q-1)\intercal} & v^\intercal\end{bmatrix}^\intercal \in \mathbb{R}^{np+mq+n}$, $W_i, i = 1,2,\cdots,n$ are weight vectors, l is the number of NN nodes, J is a collection of input variables, and $c_j, j \in J$ are nonnegative integers. The activation function $s(\omega_j)$ is chosen as

$$s(\omega_j) = \frac{e^{\omega_j} - e^{-\omega_j}}{e^{\omega_j} + e^{-\omega_j}}. \tag{19}$$

The ideal fault-tolerant FAS controller can be approximated by NNs on the compact sets $x^{(0\sim p-1)} \in \Omega_x, z^{(0\sim q-1)} \in \Omega_z$:

$$\begin{aligned}u^* &= \begin{bmatrix}u_1^* & u_2^* & \cdots & u_n^*\end{bmatrix}^\intercal\\ &= \begin{bmatrix}W_1^{*\intercal}S(\omega) + \epsilon_1 & \cdots & W_n^{*\intercal}S(\omega) + \epsilon_n\end{bmatrix}^\intercal,\end{aligned} \tag{20}$$

where W_i^*, ϵ_i are ideal weights and approximation error, respectively.

Assumption 4. *On the compact sets, the ideal NN weights W_i^* and the approximation error ϵ_i are bounded, i.e., $\|W_i^*\| < \infty, |\epsilon_i| < \infty, i = 1,2,\cdots,n$.*

In order to ensure that the NN input variables are in compact sets, the NN-based FAS controller is redesigned as

$$u = \begin{bmatrix}\hat{W}_1^\intercal S(\omega) & \cdots & \hat{W}_n^\intercal S(\omega)\end{bmatrix}^\intercal - \theta|e_c|e_c, \tag{21}$$

where $\hat{W}_i$ is the estimation of W_i^*, and θ is a positive constant to be designed. $-\theta|e_c|e_c$ is a control term to guarantee the boundedness of NN input. The NN weights are updated as

$$\dot{\hat{W}}_i = -\Gamma_i[S(\omega)e_{c,i} + r_i|e_c|\hat{W}_i], i = 1,2,\cdots,n, \tag{22}$$

where Γ_i, r_i are positive constants to be determined later, and $e_{c,i}$ denotes the ith element of e_c.

Theorem 1. *For the HOFAS model (1) using the NN-based controller (21) under Assumptions 1-4, there exist positive constants M_1, M_2, T such that the variables $e_c, \tilde{W}_i \triangleq \hat{W}_i - W_i^*, z^{(0\sim q-1)}$ remain in compact sets, and the tracking error can converge to a small neighbourhood of the origin, i.e.,*

$$\|y - y_d\| \le \min\left\{\frac{M_1}{\theta}, \frac{M_2}{4\theta\|A_{p-1}\|}\right\}, \forall t > T. \tag{23}$$

Moreover, the corresponding parameters will make the error bound as small as possible.

Proof. Consider a Lyapunov function

$$V = \frac{1}{2}\left(e_c^\intercal G^{-1}e_c + \sum_{i=1}^n \tilde{W}_i^\intercal\Gamma_i^{-1}\tilde{W}_i\right), \tag{24}$$

where $G \triangleq G(x^{(0\sim p-1)}, z^{(0\sim q-1)})$. The derivative of (24) is

$$\begin{aligned}\dot{V} =& e_c^\intercal\left[G^{-1}\left(-A_{p-1}e_c + G(u-u^*)\right)\right]\\ &+ \frac{1}{2}\frac{\mathrm{d}G^{-1}}{\mathrm{d}t}e_c^\intercal e_c + \sum_{i=1}^n \tilde{W}_i^\intercal\Gamma_i^{-1}\dot{\tilde{W}}_i\\ =& -e_c^\intercal G^{-1}A_{p-1}e_c - \theta|e_c|e_c^\intercal e_c\\ &+ e_c^\intercal\begin{bmatrix}\tilde{W}_1^\intercal S(\omega) - \epsilon_1 & \cdots & \tilde{W}_n^\intercal S(\omega) - \epsilon_n\end{bmatrix}^\intercal\\ &+ \frac{1}{2}\frac{\mathrm{d}G^{-1}}{\mathrm{d}t}e_c^\intercal e_c - \sum_{i=1}^n \tilde{W}_i^\intercal(S(\omega)e_{c,i} + r_i|e_c|\hat{W}_i)\\ =& -e_c^\intercal G^{-1}A_{p-1}e_c - \theta|e_c|e_c^\intercal e_c - e_c^\intercal\begin{bmatrix}\epsilon_1 & \cdots & \epsilon_n\end{bmatrix}^\intercal\\ &+ \frac{1}{2}\frac{\mathrm{d}G^{-1}}{\mathrm{d}t}e_c^\intercal e_c - |e_c|\sum_{i=1}^n r_i\tilde{W}_i^\intercal\hat{W}_i\\ =& -e_c^\intercal G^{-1}A_{p-1}e_c - \theta|e_c|e_c^\intercal e_c - e_c^\intercal\begin{bmatrix}\epsilon_1 & \cdots & \epsilon_n\end{bmatrix}^\intercal\\ &+ \frac{1}{2}\frac{\mathrm{d}G^{-1}}{\mathrm{d}t}e_c^\intercal e_c - \frac{|e_c|}{2}\sum_{i=1}^n r_i(\|\tilde{W}_i\|^2 + \|\hat{W}_i\|^2 - \|W_i^*\|^2).\end{aligned} \tag{25}$$

Based on Assumptions 1 and 4, there exists a positive constants d_3 such that

$$\begin{aligned}\dot{V} \le& |e_c|\left(-\theta\|e_c\|^2 - \|G^{-1}A_{p-1}\|\|e_c\| + d_3\|e_c\|\right.\\ &\left.-\frac{1}{2}\sum_{i=1}^n r_i\|\tilde{W}_i\|^2\right)\\ =& |e_c|\left[-\theta(\|e_c\| - \frac{d_3}{2\theta})^2 - \|G^{-1}A_{p-1}\|\|e_c\| + \frac{d_3^2}{4\theta}\right.\\ &\left.-\frac{1}{2}\sum_{i=1}^n r_i\|\tilde{W}_i\|^2\right].\end{aligned} \tag{26}$$

Define some sets

$$\Omega_e \triangleq \left\{e_c \mid \|e_c\| \le \min\left\{\frac{d_3}{\theta}, \frac{d_3^2\sup_{t\ge 0}\|G\|}{4\theta\|A_{p-1}\|}\right\}\right\}, \tag{27}$$

$$\Omega_{w_i} \triangleq \left\{\tilde{W}_i \mid \|\tilde{W}_i\| \le \frac{d_3}{\sqrt{2\theta r_i}}\right\}, i = 1,2,\cdots,n, \tag{28}$$

and Ω_e, Ω_{w_i} are compact sets. Thus, $e_c, \tilde{W}_i$ can converge to the small neighbourhood of the origin. Based on Lemma 1,

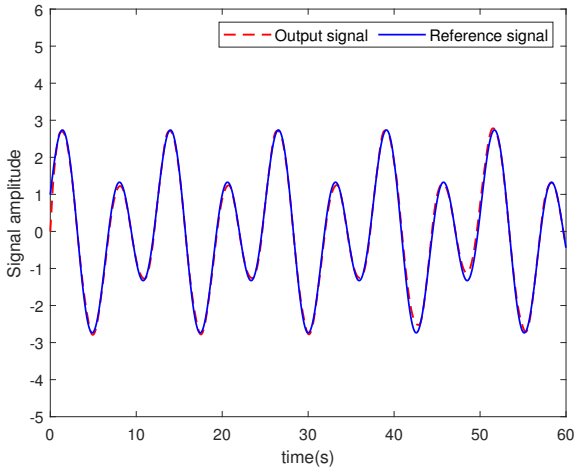

Fig. 1: The tracking control result.

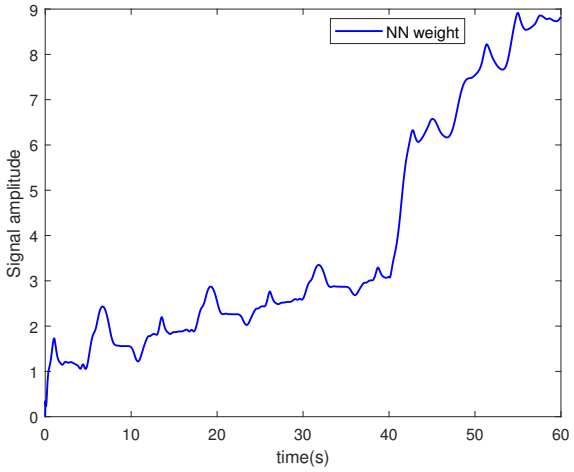

Fig. 3: The trajectory of $\|\hat{W}\|$.

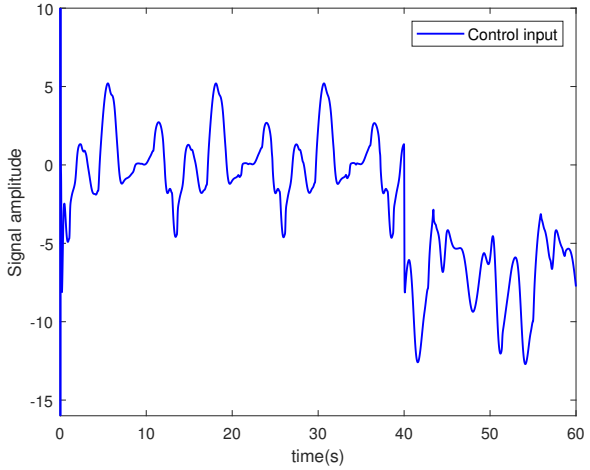

Fig. 2: The trajectory of u.

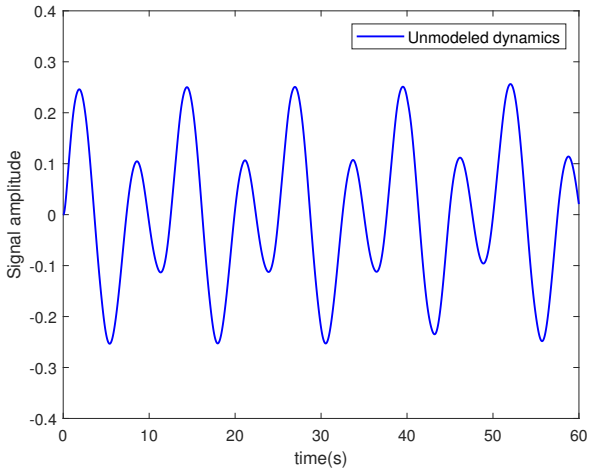

Fig. 4: The trajectory of z.

the unmodeled dynamics $z^{(0\sim q-1)}$ is also in a compact set. Due to the Hurwitz matrix $\Phi(A_{0\sim p-1})$, there exist positive constants M_1, M_2, T such that (23) holds. Furthermore, the appropriate parameters θ, A_{p-1} will make the error bound as small as possible. □

4 Simulation

Consider an unknown state-space model with strong nonlinearities

$$\begin{cases} \dot{w}_1 = w_1^2 + 2w_2 + z, \\ \dot{w}_2 = w_1^2 z + w_1 e^{w_2} + (\dfrac{1+\sin w_1}{1+w_2^2+z^2} + 1 + z^2)u + \delta, \\ \dot{z} = -2z + 0.2w_1, \\ y = w_1, \end{cases} \tag{29}$$

where $w_1, w_2, z, u, y, \delta \in \mathbb{R}$. Let $x = w_1$, and the nonlinear system (29) can be converted into a HOFAS model

$$\begin{cases} \ddot{x} = F(x^{(0\sim 1)}, z) + G(x^{(0\sim 1)}, z)u + \delta, \\ \dot{z} = F_0(x^{(0\sim 1)}, z), \\ y = x. \end{cases} \tag{30}$$

Since the system model is unknown and the proposed fault-tolerant FAS controller is model-free, it is not necessary to give the concrete forms of $F(\cdot), G(\cdot), F_0(\cdot)$. The fault model is set as

$$\delta = \begin{cases} 0, t < 40\text{s}, \\ 10 + \sin(t - 40), t \geq 40\text{s}. \end{cases} \tag{31}$$

The control task is to let the output y track the reference signal $y_d = 2\sin t + \cos 0.5t$ in spite of faults. The NN-based fault-tolerant controller is designed as

$$\begin{aligned} u &= \hat{W} S(\omega) - \theta |e_c| e_c, \\ \dot{\hat{W}} &= -\Gamma[S(\omega) e_c + r|e_c|e_c]. \end{aligned} \tag{32}$$

The corresponding parameters are set as $\theta = 3, \Gamma = 1, r = 0.001, A_{0\sim 1} = \begin{bmatrix} 5 & 2 \end{bmatrix}, l = 25$. The initial values of system states and NN weight are zero. The experimental results are shown in Fig.1–Fig. 4. From Fig. 1, the controller can effectively complete the tracking control task, which illustrates Theorem 1. After the fault occurs, the proposed fault-tolerant controller can compensate the process fault efficiently. The tracking error in Fig. 1 is influenced on the

one hand by uncontrollable unmodeled dynamics z and on the other by parameters θ, l. If the number of neurons is large enough and the parameter θ is large enough, the tracking error tends to zero. However, such a choice will lead to the high-gain or vibration phenomena, so the choice of θ, l needs to be considered overall. It can be seen from Fig. 2 that the controller quickly responses to the fault at $t = 40$s. In Fig. 3, the NN weight constantly adapts to changes during the system operation, where the oscillations come from the influence of unmodeled dynamics. Fig. 4 shows that the uncontrollable state z is always bounded under the proposed controller.

5 Conclusion

The paper has proposed a NN-based fault-tolerant controller for unknown HOFASs with strong nonlinearities. The NN-based FAS controller can yield the bounded tracking error in case of faults. The NN input does not contain the high-dimensional error vector, and the computational complexity is lower. The tracking error can be made small enough by adjusting the number of neurons and other parameters. In the future, we will study the safety control of more complex unknown HOFASs.

References

[1] G. Duan, "High-order fully actuated system approaches: Part I. models and basic procedure," *International Journal of Systems Science*, vol. 52, no. 2, pp. 422–435, 2021.

[2] G. Duan, "High-order fully actuated system approaches: Part VII. controllability, stabilisability and parametric designs," *International Journal of Systems Science*, vol. 52, no. 14, pp. 3091–3114, 2021.

[3] G.-R. Duan, "Substability and substabilization: Control of subfully actuated systems," *IEEE Transactions on Cybernetics*, vol. 53, no. 11, pp. 7309–7322, 2023.

[4] G. Duan, "High-order fully actuated system approaches: Part V. robust adaptive control," *International Journal of Systems Science*, vol. 52, no. 10, pp. 2129–2143, 2021.

[5] G. Duan, "High-order fully actuated system approaches: Part VIII. optimal control with application in spacecraft attitude stabilisation," *International Journal of Systems Science*, vol. 53, no. 1, pp. 54–73, 2022.

[6] G. Duan, "Fully actuated system approaches for continuous-time delay systems: Part 1. systems with state delays only," *Science China Information Sciences*, vol. 66, no. 1, p. 112201, 2023.

[7] K.-X. Cui, G.-R. Duan, and M.-Z. Hou, "Discrete-time model reference tracking control for a class of combined spacecraft: A high-order fully actuated system approach," *IEEE Transactions on Automation Science and Engineering*, early access, 2023. doi:10.1109/TASE.2023.3335106.

[8] G.-P. Liu, "Coordination of networked nonlinear multi-agents using a high-order fully actuated predictive control strategy," *IEEE/CAA Journal of Automatica Sinica*, vol. 9, no. 4, pp. 615–623, 2022.

[9] Y. Yu, G.-P. Liu, Y. Huang, and J. M. Guerrero, "Coordinated predictive secondary control for dc microgrids based on high-order fully actuated system approaches," *IEEE Transactions on Smart Grid*, vol. 15, no. 1, pp. 19–33, 2024.

[10] R. Meng, C. Hua, K. Li, and P. Ning, "Adaptive event-triggered control for uncertain high-order fully actuated system," *IEEE Transactions on Circuits and Systems II: Express Briefs*, vol. 69, no. 11, pp. 4438–4442, 2022.

[11] Q. Huang, J. Sun, and C. Zhang, "High-order fully actuated system approach to robust control of impulsive systems," *IEEE Transactions on Circuits and Systems II: Express Briefs*, vol. 71, no. 3, pp. 1321–1325, 2024.

[12] G.-R. Duan and B. Zhou, "Fully actuated system approach for linear systems control: A frequency-domain solution," *Journal of Systems Science and Complexity*, vol. 35, no. 6, pp. 2046–2061, 2022.

[13] N. Wang, X. Liu, C. Liu, and H. Wang, "Weak disturbance decoupling of high-order fully actuated nonlinear systems," *International Journal of Robust and Nonlinear Control*, vol. 34, no. 3, pp. 1971–2012, 2024.

[14] M. Cai, X. He, and D. Zhou, "Fault-tolerant tracking control for nonlinear observer-extended high-order fully-actuated systems," *Journal of the Franklin Institute*, vol. 360, no. 1, pp. 136–153, 2023.

[15] F. Jia, J. Huang, and X. He, "Predefined-time fault-tolerant control for a class of nonlinear systems with actuator faults and unknown mismatched disturbances," *IEEE Transactions on Automation Science and Engineering*, early access, 2023. doi:10.1109/TASE.2023.3286663.

[16] M. Gong, L. Sheng, and D. Zhou, "Robust fault-tolerant stabilisation of uncertain high-order fully actuated systems with actuator faults," *International Journal of Systems Science*, early access, 2024. doi:10.1080/00207721.2024.2312868.

[17] R. Dong, C. Hua, K. Li, and R. Meng, "Adaptive fault-tolerant control for high-order fully actuated system with full-state constraints," *Journal of the Franklin Institute*, vol. 360, no. 12, pp. 8062–8074, 2023.

[18] M. Cai, X. He, and D. Zhou, "An active fault tolerance framework for uncertain nonlinear high-order fully-actuated systems," *Automatica*, p. 110969, 2023.

[19] M. Cai, X. He, and D. Zhou, "Low-power fault-tolerant control for nonideal high-order fully actuated systems," *IEEE Transactions on Systems, Man, and Cybernetics: Systems*, vol. 53, no. 8, pp. 4875–4887, 2023.

[20] X. Liu, M. Chen, D. Zhou, and L. Sheng, "Fault-tolerant control of stochastic high-order fully actuated systems," *IEEE Transactions on Cybernetics*, early access, 2023. doi:10.1109/TCYB.2023.3320441.

[21] M. Cai, X. He, and D. Zhou, "Self-healing fault-tolerant control for high-order fully actuated systems against sensor faults: A redundancy framework," *IEEE Transactions on Cybernetics*, vol. 54, no. 4, pp. 2628–2640, 2024.

[22] Y. Ma, K. Zhang, and B. Jiang, "Neuroadaptive cooperative fault-tolerant control of heterogeneous multiagent systems based on fully actuated system approaches," *IEEE Transactions on Cybernetics*, early access, 2023. doi:10.1109/TCYB.2023.3318254.

[23] T. Zhang, S. S. Ge, and C. C. Hang, "Neural-based direct adaptive control for a class of general nonlinear systems," *International Journal of Systems Science*, vol. 28, no. 10, pp. 1011–1020, 1997.

[24] D. Ding, Z. Wang, and Q.-L. Han, "Neural-network-based consensus control for multiagent systems with input constraints: The event-triggered case," *IEEE Transactions on Cybernetics*, vol. 50, no. 8, pp. 3719–3730, 2020.

[25] Y. Wang and G. Duan, "Neural-network-based high-order sliding mode control via high-order fully actuated system approach," in *2023 2nd Conference on Fully Actuated System Theory and Applications (CFASTA)*, pp. 188–192, 2023.

[26] M. Cai, X. He, and D. Zhou, "Unknown nonaffine high-order fully actuated systems: Trajectory tracking and fault tolerance," *IEEE Transactions on Systems, Man, and Cybernetics: Systems*, ealy access, 2024. doi:10.1109/TSMC.2024.3373400.

Proceedings of the 3rd Conference on Fully Actuated System Theory and Applications
May 10-12, 2024, Shenzhen, China

Practical Prescribed Time Fault-Tolerant Tracking Control for a Quadrotor UAV: A solution based on FASA

Yonghao Ma[1], Bin Jiang[1], Ke Zhang[1]

1. College of Automation Engineering, Nanjing University of Aeronautics and Astronautics, Nanjing 210016, P. R. China
E-mail: gzhueton@163.com, kezhang@nuaa.edu.cn, binjiang@nuaa.edu.cn

Abstract: This study investigates the practical prescribed-time tracking problem for a quadrotor unmanned aerial vehicle with actuator faults by using the fully actuated system approach. First, the original practical prescribed-time tracking problem is changed into one with a time-varying constraint on tracking errors by introducing a novel time-varying constraining function. Then, fault-tolerant control schemes are proposed for the translational dynamics and rotational dynamics based on the fully actuated system models to compensate for actuator faults and deal with the time-varying constraint. With the aforementioned conversion, the suggested method guarantees that, despite actuator problems, the tracking errors will converge to the specified compact set within a preassigned finite time. Additionally, simulation experiments validate the efficacy of the suggested methodology.

Key Words: Prescribed time control, Time-varying constraint, Fault-tolerant control, Quadrotor unmanned aerial vehicles

1 Introduction

Unmanned aerial vehicles (UAVs) have drawn a lot of attention in recent decades because of their potential military and commercial benefits. In particular, quadrotor UAVs are the most often used micro UAVs due to their numerous noteworthy advantages, including small size, inexpensive production, quick maneuverability, and vertical takeoff and landing capabilities. Numerous control strategies have been put forward to address the quadrotor UAV control issue, such as PID control [1], backstepping control and feedback linearization [2]. In [1] and [2], the actuators were assumed to be fault-free. However, actuator faults typically occur in many real-world systems, and they can cause instability and performance degradation [3]. The fault-tolerant control (FTC) approach has received a lot of attention as a means of handling actuator failures [4]. For example, an indirect neural network-based adaptive FTC method was presented for an uncertain quadrotor UAV with actuator failures in [5]. For multi-UAVs, a decentralized adaptive neural FTC method was developed in [6] employing fractional order theory and backstepping technology.

These methods in [1]-[6] only achieve asymptotic convergence of the closed-loop system. However, the system needs to make a quick response in many practical control tasks. For example, quadrotor UAVs need to quickly locate the target area in environmental monitoring. As a result, it is extremely desirable that the desired tracking precision be attained within a short period of time. For example, a novel state feedback control strategy was designed to address the prescribed-time (PT) control for nonlinear systems with unknown parameters in [7]. The control strategy enforces the tracking error to zero within a predetermined time that can be selected in advance. A novel PT distributed control algorithm was presented in [8] for consensus and containment of networked multiple systems. Note that infinite gains are required for the prescribed time control strategies in [7] and [8] to attain zero steady-state error. For practical purposes, control with adequate steady-state precision is acceptable. This drives the development of practical prescribed-time (PPT) control [9, 10], in which the steady-state error, rather than converges to zero, does so to a tiny neighborhood of origin within a finite amount of time. A novel continuous and nonsingular PPT consensus tracking control protocol was presented in [11] for a multiagent system. Unfortunately, the steady-state accuracy after the settling time is unavailable and unclear in the aforementioned results since the extent of the steady-state error essentially depends on certain unknown parameters. This is highly undesirable in real-world applications, but practical prescribed-time FTC with exact and arbitrarily adjustable steady-state accuracy for quadrotor UAVs is still an open problem.

Besides, all the mentioned results were put forward on the basis of first-order state-space models, which are suitable for response analysis and state observation but not for controller design. Originally, Duan presented the fully actuated system approach (FASA) as a solution to the aforementioned problem [12]. The FASA is a control-oriented framework on the basis of fully-actuated system models. Moreover, the FASA has been shown to be incredibly practical and efficient for controller design [13]. An adaptive FTC method was given in [14] for high-order fully actuated systems with actuator faults and full-state constraints. A control method was proposed for the attitude control of a flexible spacecraft by the FASA in [15], where a linear time-invariant closed-loop system was obtained with eigenvalues that could be arbitrarily assigned. However, as far as we know, there is no result that designed the PPT controller for quadrotor UAVs via the FASA.

Motivated by the above discussion, this work presents a novel PPT control method for quadrotor UAVs. Concisely, the major contributions are summarized as follows.

i) The suggested FASA-based PT control offers significant computational complexity reduction and simplifies

This work was supported in part by the National Natural Science Foundation of China under Grants (62020106003, 62173180, 62188101), in part by the Natural Science Foundation of Jiangsu Province of China (BK20222012), in part by the Qing Lan Project of Jiangsu Province of China, in part by the 111 Project of the Programme of Introducing Talents of Discipline to Universities of China under Grant B20007, in part by the Fundamental Research Funds for the Central Universities under Grants (NE2022002, NC2022003). (Corresponding author: Bin Jiang)

stability analysis and controller design when compared to the current state-space approach-based PT tracking control for quadrotor UAVs.

ii) Even in the case of actuator failure of the system, using our proposed method, the settling time and the final tracking accuracy can still be determined in advance as needed, since they are both independent of the initial conditions and any other design parameters.

2 Problem formulation

2.1 Model Description

The center of mass's position in the fixed inertial frame is represented by be a vector $\boldsymbol{\eta}_p = [x, y, z]$. $\boldsymbol{\eta}_o = [\phi, \theta, \psi]$ be a vector denotes Euler angles in the body-fixed frame, where ϕ, θ, ψ are roll, pitch, and yaw, respectively. The following equation can be used to represent the quadrotor's translational movement [16]:

$$\ddot{x} = (\cos\psi \sin\theta \cos\phi + \sin\psi \sin\phi)\frac{U_1}{m} \tag{1a}$$

$$\ddot{y} = (\sin\psi \sin\theta \cos\phi - \cos\psi \sin\phi)\frac{U_1}{m} \tag{1b}$$

$$\ddot{z} = (\cos\theta \cos\phi)\frac{U_1}{m} - g \tag{1c}$$

where m is the quadrotor mass; $U_1 = k_t \sum_{i=1}^{4} T_i^2$, k_t is the thrust coefficient and T_i denotes the speed of rotor i; g denotes the gravity. The quadrotor's rotational movement can be represented by the following equation [16]:

$$\ddot{\phi} = \frac{1}{I_x}[(I_y - I_z)\dot{\psi}\dot{\theta} - J_r\dot{\theta}\overline{T} + U_2] \tag{2a}$$

$$\ddot{\theta} = \frac{1}{I_y}[(I_z - I_x)\dot{\psi}\dot{\phi} - J_r\dot{\phi}\overline{T} + U_3] \tag{2b}$$

$$\ddot{\psi} = \frac{1}{I_z}[(I_x - I_y)\dot{\theta}\dot{\phi} + U_4] \tag{2c}$$

where I_x, I_y, and I_z are the quadrotor moment of inertia according to x, y, and z axes; the term $\overline{T} = T_2 + T_4 - T_3 - T_1$ is the total residual rotor angular velocity; J_r represents thetotal moment of inertia along the propeller axis; $U_2 = k_t l(-T_2^2 + T_4^2)$, $U_3 = k_t l(-T_1^2 + T_3^2)$, $U_4 = k_d(-T_1^2 + T_2^2 + T_3^2 + T_4^2)$, k_d is the drag coefficient, and l is the distance between the quadrotor's mass center and rotor axis of rotation.

The actuation subsystem input U_{ai} and the desired input U_i are no longer equivalent owing to the plant's actuators have the potential to malfunction, [5]. Instead, they have the following relationship:

$$U_{ai} = \rho_i U_i, \quad i = 1, 2, 3, 4 \tag{3}$$

where ρ_i is the actuator efficiency factor. There exists a positive constant $\underline{\rho}$ such that $0 < \underline{\rho} \leq \rho_i \leq 1$.

The following system dynamics can be obtained by combining the dynamics of Eqs. Eqs. (1)-(2) with the actuator faults mentioned in Eq. (3):

1) Position subsystem:

$$\ddot{\boldsymbol{\eta}}_p = \boldsymbol{f}_p + \rho_1 \boldsymbol{B}_p \boldsymbol{U}_p \tag{4}$$

where $\boldsymbol{f}_p = [0, 0, -g]^{\mathrm{T}}$, $\boldsymbol{B}_p = 1/m \otimes I_3$, and

$$\boldsymbol{U}_p = \begin{bmatrix} U_x \\ U_y \\ U_z \end{bmatrix} = \begin{bmatrix} (\cos\psi \sin\theta \cos\phi + \sin\psi \sin\phi)U_1 \\ (\sin\psi \sin\theta \cos\phi - \cos\psi \sin\phi)U_1 \\ (\cos\theta \cos\phi)U_1 \end{bmatrix}$$

U_x, U_y and U_z can be thought of as the position subsystem's virtual control inputs.

2) Attitude subsystem:

$$\ddot{\boldsymbol{\eta}}_r = \boldsymbol{f}_r + \boldsymbol{B}_r \boldsymbol{\rho}_r \boldsymbol{U}_r \tag{5}$$

where $\boldsymbol{f}_r = [[(I_y - I_z)\dot{\psi}\dot{\theta} - J_r\dot{\theta}\overline{T}]/I_x, [(I_z - I_x)\dot{\psi}\dot{\theta} + J_r\dot{\phi}\overline{T}]/I_y, [(I_x - I_y)\dot{\theta}\dot{\phi}]/I_z]^{\mathrm{T}}$, $\boldsymbol{B}_r = \mathrm{diag}\{1/I_x, 1/I_y, 1/I_z\}$, $\boldsymbol{\rho}_r = \mathrm{diag}\{\rho_2, \rho_3, \rho_4\}$, and $\boldsymbol{U}_r = [U_2, U_3, U_4]^{\mathrm{T}}$.

2.2 Control objective

In the event of actuator failures, the design goal is to create an adaptive FTC method for the system so that, within an arbitrary time frame, the outputs $[x, y, z, \psi]^{\mathrm{T}}$ converge to a neighborhood of the desired references $[x_d, y_d, z_d, \psi_d]^{\mathrm{T}}$. Define tracking errors as $e_x \triangleq x - x_d$, $e_y \triangleq y - y_d$, $e_z \triangleq z - z_d$ and $e_\psi \triangleq \psi - \psi_d$. These tracking errors satisfy the following realtions:

$$|e_\bullet(t)| < \omega_{T_p}, \quad \forall t \geq T_p \tag{6}$$

where $\bullet \in \{x, y, z, \psi\}$, ω_{T_p} and T_p are two positive constants that can be set arbitrarily by user.

2.3 Problem transformation

In this study, the original PPT tracking control problem can be transformed into one with a time-varying constraint on tracking errors by introducing a PT prescribed-performance function.

A PT prescribed performance function is developed as follows:

$$\omega(t) = \begin{cases} (\omega_0 - \omega_{T_p})\, e^{\left(1 - \frac{T_p}{T_p - t}\right)} + \omega_{T_p}, & 0 \leq t < T_p \\ \omega_{T_p}, & t \geq T_p \end{cases} \tag{7}$$

where, ω_0 is a positive constant. It follows from Eq.(7) that the prescribed performance $\lim_{t \to T_p} \omega(t) = \omega_{T_p}$ and $\omega(t) = \omega_{T_p}$ for any $t \geq T_p$ can be obtained.

As long as the time-varying tracking error constraint of Eq. (8) is met, the desired PPT tracking objective is realized.

$$-\omega(t) < e_\bullet(t) < \omega(t), \quad \forall t \geq 0 \tag{8}$$

Given that the prescribed performance function ω is defined as Eq. (7) defines, we may deduce from Eq. (8) that

$$|e_\bullet(t)| < \omega_{T_p}, \quad \forall t \geq T_p \tag{9}$$

Stated differently, if the condition specified in Eq. (8) is met, the tracking errors $e_\bullet(t)$ converge to the region $\Omega = \{e_\bullet \in \mathbb{R} : |e_\bullet(t)| < \omega_{T_p}\}$ within the settling time T_p.

An error transformation, converting the system with confined tracking error behavior into a corresponding "unconstrained" one, is described as follows

$$e_\bullet(t) = \omega(t) S(\chi_\bullet) \tag{10}$$

where $\chi_\bullet$ is the transformed error and $S(\chi_\bullet)$ is chosen as

$$S(\chi_\bullet) = \frac{e^{\chi_\bullet} - e^{-\chi_\bullet}}{e^{\chi_\bullet} + e^{-\chi_\bullet}} \tag{11}$$

then the transformed error $\varepsilon_\bullet$ is computed as

$$\chi_\bullet = \frac{1}{2} \ln \left(\frac{1 + \frac{e_\bullet}{\omega}}{1 - \frac{e_\bullet}{\omega}} \right) \tag{12}$$

From [17], we can obtain that the time-varying tracking error constraint as shown in Eq. (8) is satisfied as long as $\chi_\bullet$ is bounded for $t \in [0, \infty)$.

To sum up, the desired PPT tracking objective is obtained as long as $\chi_\bullet$ is bounded for $t \in [0, \infty)$.

2.4 Important lemma

Lemma 1 *[18] When the matrix $A^{0\sim1} = [A_0 \quad A_1]$, with $A_0 \in \mathbb{R}^{3\times3}$ and $A_1 \in \mathbb{R}^{3\times3}$, is chosen such that the matrix $\Phi(A^{0\sim1}) = \begin{bmatrix} 0 & I_3 \\ -A_0 & -A_1 \end{bmatrix} \in \mathbb{R}^{6\times6}$ is stable, there exists a positive matrix $\Theta(A^{0\sim1})$ satisfying*

$$\Phi^{\mathrm{T}}(A^{0\sim1})\Theta(A^{0\sim1}) + \Theta(A^{0\sim1})\Phi(A^{0\sim1}) \leq -I_6 \tag{13}$$

For ease of writing, the subsequent notation is established, which is frequently used in this paper.

$$\Theta_L \left(A^{0\sim1}\right) \triangleq \Theta \left(A^{0\sim1}\right) \begin{bmatrix} 0 \\ I_3 \end{bmatrix} \in \mathbb{R}^{6\times3} \tag{14}$$

3 Main results

This section develops a FASA-based FTC control method for quadrotor UAVs. Fig. 1 depicts the structure of the suggested approach for the position and attitude subsystem.

3.1 Control design for the position subsystem

For the position subsystem, a tracking error vector is defined as $\boldsymbol{e}_p = [e_x, e_y, e_z]^{\mathrm{T}}$. The tracking error dynamics can be represented as

$$\ddot{\boldsymbol{e}}_p = \boldsymbol{f}_p + \rho_1 \boldsymbol{B}_p \boldsymbol{U}_p - \ddot{\boldsymbol{\eta}}_p^d \tag{15}$$

where $\boldsymbol{\eta}_p^d = [x_d, y_d, z_d]^{\mathrm{T}}$.

Differentiating both sides of Eq. (10) with respect to time, we get

$$\dot{e}_\bullet = \dot{\omega} S(\chi_\bullet) + \omega \frac{\partial S(\chi_\bullet)}{\partial \chi_\bullet} \dot{\chi}_\bullet \tag{16}$$

and

$$\dot{\chi}_\bullet = \frac{\dot{e}_\bullet - \dot{\omega} S(\chi_\bullet)}{\omega \frac{\partial S(\chi_\bullet)}{\partial \chi_\bullet}} \tag{17}$$

Furthermore, one has

$$\begin{aligned} \ddot{\chi}_\bullet =& \frac{\ddot{e}_\bullet - (\dot{\omega} S(\chi_\bullet))'}{\omega \frac{\partial S(\chi_\bullet)}{\partial \chi_\bullet}} \\ & - \frac{(\dot{e}_\bullet - \dot{\omega} S(\chi_\bullet)) \left(\omega \frac{\partial S(\chi_\bullet)}{\partial \chi_\bullet}\right)'}{\left(\omega \frac{\partial S(\chi_\bullet)}{\partial \chi_\bullet}\right)^2} \end{aligned} \tag{18}$$

Let $\boldsymbol{\chi}_p = [\chi_x, \chi_y, \chi_z]^{\mathrm{T}} \in \mathbb{R}^3$, $r_\bullet = \frac{1}{\omega \frac{\partial S(\chi_\bullet)}{\partial \chi_\bullet}}$, $v_\bullet = \frac{(\dot{\omega} S(\chi_\bullet))'}{\omega(t) \frac{\partial S(\chi_\bullet)}{\partial \chi_\bullet}} + \frac{(\dot{e}_\bullet - \dot{\omega} S(\chi_\bullet)) \left(\omega \frac{\partial S(\chi_\bullet)}{\partial \chi_\bullet}\right)'}{\left(\omega \frac{\partial S(\chi_\bullet)}{\partial \chi_\bullet}\right)^2}$. Then, one has

$$\ddot{\boldsymbol{\chi}}_p = \boldsymbol{r}_p \ddot{\boldsymbol{e}}_p - \boldsymbol{v}_p \tag{19}$$

where $\boldsymbol{r}_p = \mathrm{diag}\{r_x, r_y, r_z\} \in \mathbb{R}^{3\times3}$, $\boldsymbol{v}_p = [v_x, v_y, v_z]^{\mathrm{T}} \in \mathbb{R}^3$.

Substituting Eq. (15) into Eq. (19) yields

$$\ddot{\boldsymbol{\chi}}_p = \boldsymbol{r}_p \left(\boldsymbol{f}_p + \rho_1 \boldsymbol{B}_p \boldsymbol{U}_p - \ddot{\boldsymbol{\eta}}_p^d \right) - \boldsymbol{v}_p \tag{20}$$

An adaptive fault-tolerant controller can be designed as

$$\boldsymbol{U}_p = - \hat{p}_1 \boldsymbol{I}_3 \boldsymbol{\alpha}_p \tag{21}$$

where $\boldsymbol{\alpha}_p = \boldsymbol{B}_p^{-1}(\boldsymbol{f}_p - \ddot{\boldsymbol{\eta}}_p^d) - \boldsymbol{B}_p^{-1}\boldsymbol{r}_i^{-1}(\boldsymbol{v}_p - A_{p,0}\boldsymbol{\chi}_p - A_{p,1}\dot{\boldsymbol{\chi}}_p)$; $A_{p,0}$ and $A_{p,1}$ are two matrices; $\hat{p}_1$ is the estimation of $p_1 \triangleq 1/\rho_1$ and the error is defined as $\tilde{p}_1 = p_1 - \hat{p}_1$.

An adaptive update law for the estimate $\hat{p}_1$ is designed as

$$\dot{\hat{p}}_1 = \gamma_1 \left(\boldsymbol{\chi}_p^{(0\sim1)}\right)^{\mathrm{T}} \Theta \left(A_p^{0\sim1}\right) \begin{bmatrix} \boldsymbol{0}_3 \\ \boldsymbol{r}_p \boldsymbol{B}_p \boldsymbol{\alpha}_p \end{bmatrix} \tag{22}$$

where $\Theta \left(A_p^{0\sim1}\right)$ is a positive definite matrix satisfying Eq. (13).

Theorem 1 *Consider translational dynamics as described in Eq.* (4)*. If the control algorithm of Eq.* (21) *and the adaptive update law of Eq.* (22) *are applied, then the transformed tracking errors $\chi_\bullet, \bullet \in \{x, y, z\}$ and the estimation error $\tilde{p}_1$ is ensured to be bounded at all times. Then the tracking errors $e_\bullet, \bullet \in \{x, y, z\}$ converge to a neighborhood of the desired references within an arbitrarily prescribed-time interval, i.e., $|e_\bullet(t)| < \omega_{T_p}$, $\forall t \geq T_p$.*

Proof. Define $\boldsymbol{\chi}_p^{(0\sim1)} = [\boldsymbol{\chi}_p, \dot{\boldsymbol{\chi}}_p]^{\mathrm{T}}$. Substituting the controller of Eq. (21) into Eq. (20) yields

$$\dot{\boldsymbol{\chi}}_p^{(0\sim1)} = \Phi \left(A_p^{0\sim1}\right) \boldsymbol{\chi}_p^{(0\sim1)} + \Delta_p \tag{23}$$

where $\Phi \left(A_p^{0\sim1}\right) = \begin{bmatrix} 0 & I_3 \\ -A_{p,0} & -A_{p,1} \end{bmatrix} \in \mathbb{R}^{6\times6}$ and $\Delta_p = \begin{bmatrix} \boldsymbol{0}_3 \\ \rho_1 \tilde{p}_1 \boldsymbol{r}_p \boldsymbol{B}_p \boldsymbol{\alpha}_p \end{bmatrix} \in \mathbb{R}^{6\times1}$.

Since $A_{p,0}$ and $A_{p,1}$ are two matrices such that $A_p^{0\sim1} = [A_{p,0} \quad A_{p,1}]$ is stable, there exists a positive definite matrix $\Theta \left(A_p^{0\sim1}\right)$ satisfying Eq. (13). Hence, a Lyapunov function can be selected for the dynamics of Eq. (23) as

$$V_p = \left(\boldsymbol{\chi}_p^{(0\sim1)}\right)^{\mathrm{T}} \Theta_p \boldsymbol{\chi}_p^{(0\sim1)} + \frac{\rho_1}{\gamma_1} \tilde{p}_1^2 \tag{24}$$

where γ_1 is a scalar and $\gamma_1 > 0$.

Taking the derivative of V_p leads to

$$\begin{aligned} \dot{V}_p =& \left(\Phi \left(A_p^{0\sim1}\right) \boldsymbol{\chi}_p^{(0\sim1)} + \Delta_p\right)^{\mathrm{T}} \Theta \left(A_p^{0\sim1}\right) \boldsymbol{\chi}_p^{(0\sim1)} \\ & + \left(\boldsymbol{\chi}_p^{(0\sim1)}\right)^{\mathrm{T}} \Theta \left(A_p^{0\sim1}\right) \left(\Phi(A_{0\sim1}) \boldsymbol{\chi}_p^{(0\sim1)} + \Delta_p\right) \\ & + 2 \frac{\rho_1}{\gamma_1} \tilde{p}_1 \dot{\tilde{p}}_1 \\ =& \left(\boldsymbol{\chi}_i^{(0\sim1)}\right)^{\mathrm{T}} (\Phi^{\mathrm{T}} \left(A_p^{0\sim1}\right) \Theta \left(A_p^{0\sim1}\right) \\ & + \Theta \left(A_p^{0\sim1}\right) \Phi \left(A_p^{0\sim1}\right)) \boldsymbol{\chi}_p^{(0\sim1)} \\ & + 2 \left(\boldsymbol{\chi}_p^{(0\sim1)}\right)^{\mathrm{T}} \Theta \left(A_p^{0\sim1}\right) \Delta_p - 2 \frac{\rho_1}{\gamma_1} \tilde{p}_1 \dot{\hat{p}}_1 \end{aligned} \tag{25}$$

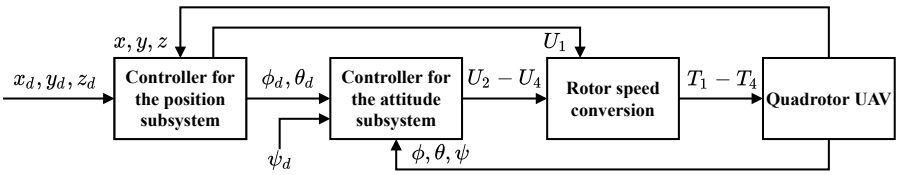

Fig. 1: The structure of the quadrotor UAV control system.

Using Eq. (13) in Lemma 1 yields

$$\begin{aligned}\dot{V}_p \leq & -\left(\boldsymbol{\chi}_p^{(0\sim1)}\right)^{\mathrm{T}} \boldsymbol{\chi}_p^{(0\sim1)} \\ & + 2\left(\boldsymbol{\chi}_p^{(0\sim1)}\right)^{\mathrm{T}} \Theta\left(A_p^{0\sim1}\right) \Delta_p - 2\frac{\rho_1}{\gamma_1}\tilde{p}_1\dot{\hat{p}}_1\end{aligned} \tag{26}$$

Substituting Eq. (22) into Eq. (26) yields

$$\dot{V}_p \leq -\left\|\boldsymbol{\chi}_p^{(0\sim1)}\right\|^2 \tag{27}$$

Solving the inequality of Eq. (27) gives

$$V_p(t) - V_p(0) \leq -\int_0^t \left\|\boldsymbol{\chi}_p^{(0\sim1)}(\tau)\right\|^2 d\tau \leq 0, \forall t \geq 0 \tag{28}$$

Viewing the definition of Lyapunov function V_i, $\chi_\bullet, \bullet \in \{x, y, z\}$ and $\tilde{p}_1$ are bounded for $t \geq 0$. Further, we can conclude that the tracking errors $|e_\bullet(t)| < \omega_{T_p}$, $\forall t \geq T_p$ for the position subsystem under the proposed controller of Eq. (21) and the adaptive update law of Eq. (22) in the view of the discussion of Section 2.3.

3.2 Desired Euler angles

Even though the auxiliary control inputs U_x, U_y, and U_z cannot be applied directly to the quadrotor, these variables can be used to acquire the thrust input U_1 and desired Euler angles (ϕ_d, θ_d) for the controller of the attitude subsystem, which enables the quadrotor move to a desired place. Besides, it is possible to provide the attitude controller block with the desired yaw trajectory ψ_d independently.

The thrust input is given by

$$U_1 = \frac{U_z}{\cos\theta\cos\phi} \tag{29}$$

The desired roll and pitch angles are given by

$$\begin{aligned}\phi_d &= \sin^{-1}\left(\frac{U_x\sin\psi_d - U_y\cos\psi_d}{U_1}\right) \\ \theta_d &= \tan^{-1}\left(\frac{U_x\cos\psi_d + U_y\sin\psi_d}{U_z}\right)\end{aligned} \tag{30}$$

3.3 Control design for the attitude subsystem

For the attitude subsystem, define tracking errors as $e_\phi \triangleq \phi - \phi_d$ and $e_\theta \triangleq \theta - \theta_d$. Then, a tracking error vector is defined as $\boldsymbol{e}_r = [e_\phi, e_\theta, e_\psi]^{\mathrm{T}}$. The tracking error dynamics can be represented as

$$\ddot{\boldsymbol{e}}_r = \boldsymbol{f}_r + \boldsymbol{B}_r\boldsymbol{\rho}_r\boldsymbol{U}_r - \ddot{\boldsymbol{\eta}}_r^d \tag{31}$$

where $\boldsymbol{\eta}_r^d = [\phi_d, \theta_d, \psi_d]^{\mathrm{T}}$.

With the transformer of Eq. (10), we have following error dynamics

$$\ddot{\boldsymbol{\chi}}_r = \boldsymbol{r}_r\left(\boldsymbol{f}_r + \boldsymbol{B}_r\boldsymbol{\rho}_r\boldsymbol{U}_r - \ddot{\boldsymbol{\eta}}_r^d\right) - \boldsymbol{v}_r \tag{32}$$

where $\boldsymbol{r}_r = \mathrm{diag}\{r_\phi, r_\theta, r_\psi\} \in \mathbb{R}^{3\times3}$, $\boldsymbol{v}_r = [v_\phi, v_\theta, v_\psi]^{\mathrm{T}} \in \mathbb{R}^3$.

An adaptive fault-tolerant controller can be designed as

$$\boldsymbol{U}_r = -\hat{\boldsymbol{p}}_r\boldsymbol{\alpha}_r \tag{33}$$

where $\boldsymbol{\alpha}_r = \boldsymbol{B}_r^{-1}(\boldsymbol{f}_r - \ddot{\boldsymbol{\eta}}_r^d) - \boldsymbol{B}_r^{-1}\boldsymbol{r}_r^{-1}(\boldsymbol{v}_r - A_{r,0}\boldsymbol{\chi}_r - A_{r,1}\dot{\boldsymbol{\chi}}_r)$, $\hat{\boldsymbol{p}}_r = \mathrm{diag}\{\hat{p}_2, \hat{p}_3, \hat{p}_4\}$, $\hat{p}_i$ is the estimation of $p_i \triangleq 1/\rho_i, i \in \{2, 3, 4\}$. The error is defined as $\tilde{p}_1 = p_1 - \hat{p}_1$. $\tilde{\boldsymbol{p}}_r = \mathrm{diag}\{\tilde{p}_2, \tilde{p}_3, \tilde{p}_4\} = \mathrm{diag}\{p_2 - \hat{p}_2, p_3 - \hat{p}_3, p_4 - \hat{p}_4\}$.

Partition $\Theta_L(A_r^{0\sim1})$ as

$$\Theta_L(A_r^{0\sim1}) \triangleq [\Theta_{L,1}\ \Theta_{L,2}\ \Theta_{L,3}], \Theta_{L,i} \in \mathbb{R}^{6\times1} \tag{34}$$

Adaptive update laws for the estimate $\hat{p}_i, i \in \{2, 3, 4\}$ is developed as

$$\dot{\hat{p}}_i = \gamma_i\left(\boldsymbol{\chi}_p^{(0\sim1)}\right)^{\mathrm{T}} \Theta_{L,i-1}\delta_{r,i-1} \tag{35}$$

where $\Theta\left(A_p^{0\sim1}\right)$ is a positive definite matrix satisfying Eq. (13), $\delta_{r,1} = r_\phi\alpha_{r,1}/I_x$, $\delta_{r,2} = r_\theta\alpha_{r,2}/I_y$, $\delta_{r,3} = r_\psi\alpha_{r,3}/I_z$, $\boldsymbol{\alpha}_r = [\alpha_{r,1}, \alpha_{r,2}, \alpha_{r,3}]^{\mathrm{T}}$.

Theorem 2 *Consider translational dynamics as described in Eq.* (5)*. If the control algorithm of Eq.* (33) *and the adaptive update law of Eq.* (35) *are applied, then the transformed tracking errors $\chi_\bullet, \bullet \in \{\phi, \theta, \psi\}$ and the estimation error $\tilde{p}_1$ is ensured to be bounded at all times. Then the tracking errors $e_\bullet, \bullet \in \{\phi, \theta, \psi\}$ converge to a neighborhood of the desired references within an arbitrarily prescribed-time interval, i.e., $|e_\bullet(t)| < \omega_{T_p}$, $\forall t \geq T_p$.*

Proof. Define $\boldsymbol{\chi}_r^{(0\sim1)} = [\boldsymbol{\chi}_r, \dot{\boldsymbol{\chi}}_r]^{\mathrm{T}}$. Substituting the controller of Eq. (33) into Eq. (32) yields

$$\dot{\boldsymbol{\chi}}_r^{(0\sim1)} = \Phi\left(A_r^{0\sim1}\right)\boldsymbol{\chi}_r^{(0\sim1)} + \Delta_r \tag{36}$$

where $\Phi\left(A_r^{0\sim1}\right) = \begin{bmatrix} 0 & I_3 \\ -A_{r,0} & -A_{r,1}\end{bmatrix} \in \mathbb{R}^{6\times6}$ and $\Delta_r = \begin{bmatrix} \boldsymbol{0}_3 \\ \boldsymbol{r}_r\boldsymbol{B}_r\boldsymbol{\rho}_r\tilde{\boldsymbol{p}}_r\boldsymbol{\alpha}_r\end{bmatrix} \in \mathbb{R}^{6\times1}$. Note that $\boldsymbol{r}_r\boldsymbol{B}_r\boldsymbol{\rho}_r\tilde{\boldsymbol{p}}_r\boldsymbol{\alpha}_r = [\rho_2\tilde{p}_2\delta_{r,1}, \rho_3\tilde{p}_3\delta_{r,2}, \rho_4\tilde{p}_4\delta_{r,3}]^{\mathrm{T}}$.

Since $A_{r,0}$ and $A_{r,1}$ are two matrices such that $A_r^{0\sim1} = [A_{r,0}\quad A_{r,1}]$ is stable, there exists a positive definite matrix $\Theta\left(A_r^{0\sim1}\right)$ satisfying Eq. (13). Therefore, the following Lyapunov function can be selected for the dynamics of Eq. (36)

$$V_r = \left(\boldsymbol{\chi}_r^{(0\sim1)}\right)^{\mathrm{T}} \Theta(A_r^{0\sim1})\boldsymbol{\chi}_r^{(0\sim1)} + \sum_{i=2}^{4}\frac{\rho_i}{\gamma_i}\tilde{p}_i^2 \tag{37}$$

where $\gamma_i, i \in \{2,3,4\}$ is a positive constant.

Taking the derivative of V_r leads to

$$\begin{aligned}\dot{V}_r &= \left(\Phi\left(A_r^{0\sim1}\right)\boldsymbol{\chi}_r^{(0\sim1)} + \Delta_r\right)^{\mathrm{T}}\Theta\left(A_p^{0\sim1}\right)\boldsymbol{\chi}_r^{(0\sim1)} \\ &\quad + \left(\boldsymbol{\chi}_r^{(0\sim1)}\right)^{\mathrm{T}}\Theta\left(A_r^{0\sim1}\right)\left(\Phi(A_{0\sim1})\boldsymbol{\chi}_r^{(0\sim1)} + \Delta_r\right) \\ &\quad + \sum_{i=2}^{4} 2\frac{\rho_i}{\gamma_i}\tilde{p}_i\dot{\tilde{p}}_i \\ &= \left(\boldsymbol{\chi}_r^{(0\sim1)}\right)^{\mathrm{T}}\left(\Phi^{\mathrm{T}}\left(A_r^{0\sim1}\right)\Theta\left(A_r^{0\sim1}\right)\right. \\ &\quad \left. + \Theta\left(A_r^{0\sim1}\right)\Phi\left(A_r^{0\sim1}\right)\right)\boldsymbol{\chi}_r^{(0\sim1)} \\ &\quad + 2\left(\boldsymbol{\chi}_r^{(0\sim1)}\right)^{\mathrm{T}}\Theta\left(A_r^{0\sim1}\right)\Delta_r - \sum_{i=2}^{4} 2\frac{\rho_i}{\gamma_i}\tilde{p}_i\dot{\hat{p}}_i\end{aligned} \tag{38}$$

Using Eqs. (13)-(14) in Lemma 1 yields

$$\begin{aligned}\dot{V}_r \leq &-\left(\boldsymbol{\chi}_r^{(0\sim1)}\right)^{\mathrm{T}}\boldsymbol{\chi}_r^{(0\sim1)} \\ &+ 2\left(\boldsymbol{\chi}_r^{(0\sim1)}\right)^{\mathrm{T}}\Theta_L\left(\boldsymbol{r}_r\boldsymbol{B}_r\boldsymbol{\rho}_r\tilde{\boldsymbol{p}}_r\boldsymbol{\alpha}_r\right) - \sum_{i=2}^{4} 2\frac{\rho_i}{\gamma_i}\tilde{p}_i\dot{\hat{p}}_i\end{aligned} \tag{39}$$

Considering Eq. (34) and $\boldsymbol{r}_r\boldsymbol{B}_r\boldsymbol{\rho}_r\tilde{\boldsymbol{p}}_r\boldsymbol{\alpha}_r = [\rho_2\tilde{p}_2\delta_{r,1}, \rho_3\tilde{p}_3\delta_{r,2}, \rho_4\tilde{p}_4\delta_{r,3}]^{\mathrm{T}}$, Eq.(39) can further rewritten as

$$\begin{aligned}\dot{V}_r \leq &-\left(\boldsymbol{\chi}_r^{(0\sim1)}\right)^{\mathrm{T}}\boldsymbol{\chi}_r^{(0\sim1)} \\ &+ 2\sum_{i=2}^{4}\left(\left(\boldsymbol{\chi}_r^{(0\sim1)}\right)^{\mathrm{T}}\Theta_{L,i-1}\rho_i\tilde{p}_i\delta_{r,i} - \frac{\rho_i}{\gamma_i}\tilde{p}_i\dot{\hat{p}}_i\right)\end{aligned} \tag{40}$$

Substituting Eq. (35) into Eq. (40) yields

$$\dot{V}_r \leq -\left\|\boldsymbol{\chi}_r^{(0\sim1)}\right\|^2 \tag{41}$$

Solving the inequality of Eq. (41) gives

$$V_r(t) - V_r(0) \leq -\int_0^t \left\|\boldsymbol{\chi}_r^{(0\sim1)}(\tau)\right\|^2 d\tau \leq 0, \forall t \geq 0 \tag{42}$$

Viewing the definition of Lyapunov function V_i, $\chi_\bullet, \bullet \in \{\phi,\theta,\psi\}$ and $\tilde{p}_i, i \in \{2,3,4\}$ for $t \geq 0$. Further, we can conclude that the tracking errors $|e_\bullet(t)| < \omega_{T_p}$, $\forall t \geq T_p, \bullet \in \{\phi,\theta,\psi\}$, for the position subsystem under the proposed controller of Eq. (33) and the adaptive update law of Eq. (35) in the view the discussion of Section 2.3.

4 Simulation studies

A numerical example is given to confirm the effectiveness of the suggested control laws. The example is carried out within the MATLAB (2019a) environment, with a discrete time step of 10^{-4} seconds. Table 1 lists the parameters for the considered quadrotor UAV. The initial conditions of the quadcopter are $(x(0), y(0), z(0)) = (0.6, 0.5, 0.5)$ m, and $(\phi(0), \theta(0), \psi(0)) = (\pi/6, \pi/5, \pi/4)$ rad, respectively. The initial attitude acceleration and position acceleration are both set to zero. Fault is considered as $\rho_i(t) = 1, 0 \leq t < 2$ and $\rho_i(t) = 0.8, t \geq 2, i \in \{1,2,3,4\}$. The reference trajectory is $(x_d, y_d, z_d) = (\sin(t), \cos(t), 1)$ m with $\psi_d = \pi/6$ rad.

Table 1: Parameters of the quadrotor UAV [16].

Parameter	Value	Parameter	Value
m	1.4 kg	g	9.8 m/s^2
l	0.2 m	I_x	1.25 Ns^2/rad
I_y	1.25 Ns^2/rad	I_z	2.2 Ns^2/rad
J_r	1.0 Ns^2/rad	k_t	2 Ns^2
k_d	5 N ms^2		

Control parameters are selected as: $A_{p,0} = A_{r,0} = 6 \otimes I_3$, $A_{p,1} = A_{r,1} = 5 \otimes I_3$, $\Theta\left(A_p^{0\sim1}\right) = \Theta\left(A_r^{0\sim1}\right) = \begin{bmatrix} 1.1167 & 0.0833 \\ 0.0833 & 0.1167 \end{bmatrix} \otimes I_3$, $\gamma_1 = 1$, $\gamma_2 = 15$, $\gamma_3 = 2$, $\gamma_4 = 23$. Parameters of the finite-time prescribed performance function are selected as: $\omega_0 = 1, \omega_{T_p} = 5 \times 10^{-2}$, $T_p = 3$. Initial conditions of the estimation are set as $\hat{p}_i = 1, i \in \{1,2,3,4\}$.

Fig. 2 plots the trajectory and tracking errors of the position subsystem using the proposed method. Figs. 3 and 4 exhibit the tracking trajectories and errors in the attitude angles of the suggested approaches. The estimation of actuator fault parameters are shown in 5.

The validity of the suggested method is highlighted by the observation that even in the presence of actuator defects, the given tracking precision $|e_\bullet| < 0.05$ (m), $i = \{x, y, z\}$ and $|e_\psi| < 0.05$ (rad) are attained when $t > 3$.

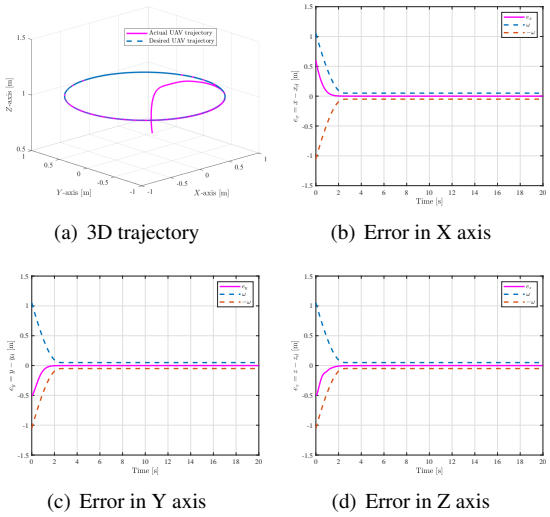

(a) 3D trajectory (b) Error in X axis

(c) Error in Y axis (d) Error in Z axis

Fig. 2: Trajectory and tracking errors of the position subsystem under the proposed control method.

5 Conclusion

In this study, a FASA-based FTC protocol is presented for a quadrotor UAV with actuator faults to tackle the tracking problem at a predefined time. It is proved that the tracking errors converge to the preassigned compact set within preassigned finite time regardless of actuator faults based on the Lyapunov theory. A numerical study demonstrates the effectiveness of the results. The future work focuses on dealing with optimal control for quadrotor UAVs via the FASA.

References

[1] A.A. Najm and I.K. Ibraheem. Nonlinear PID controller design for a 6-DOF UAV quadrotor system. *Engineering Sci-*

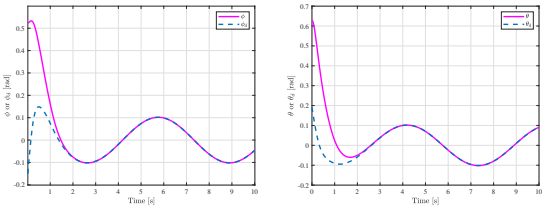

(a) Roll angle (b) Pitch angle

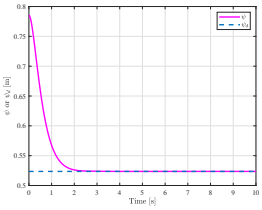

(c) Yaw angle

Fig. 3: Attitude tracking performance with the proposed control method.

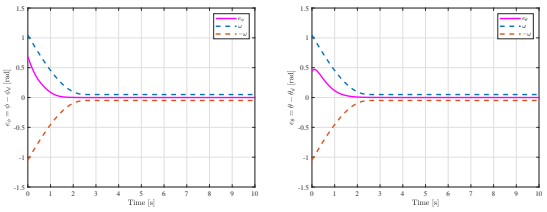

(a) Error of roll angle (b) Error of pitch angle

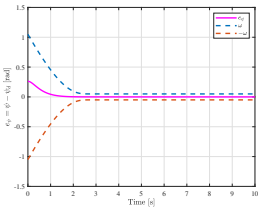

(c) Error of yaw angle

Fig. 4: Attitude tracking errors with the proposed control method.

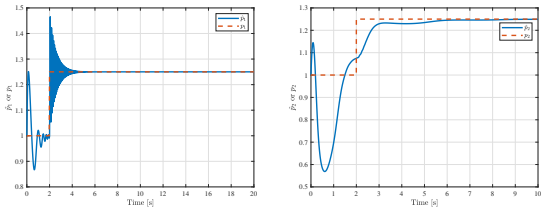

(a) $\hat{p}_1$ (b) $\hat{p}_2$

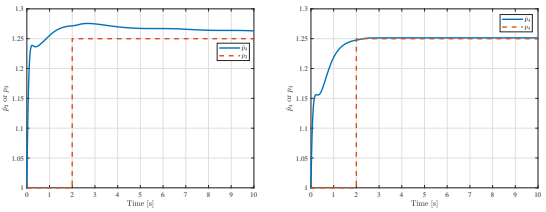

(c) $\hat{p}_3$ (d) $\hat{p}_4$

Fig. 5: Estimation of actuator fault parameters.

ence and Technology, an International Journal, 22(4):1087–1097, 2019.

[2] L. Zhou, J. Zhang, J. Dou, and B. Wen. A fuzzy adaptive backstepping control based on mass observer for trajectory tracking of a quadrotor UAV. *International journal of adaptive control and signal processing*, 32(12):1675–1693, 2018.

[3] Bin Jiang, Ke Zhang, and Peng Shi. Integrated fault estimation and accommodation design for discrete-time takagi–sugeno fuzzy systems with actuator faults. *IEEE Transactions on Fuzzy Systems*, 19(2):291–304, 2011.

[4] Ke Zhang, Bin Jiang, and Marcel Staroswiecki. Dynamic output feedback-fault tolerant controller design for takagi–sugeno fuzzy systems with actuator faults. *IEEE Transactions on Fuzzy Systems*, 18(1):194–201, 2010.

[5] Y. Song, L. He, D. Zhang, J. Qian, and J. Fu. Neuroadaptive fault-tolerant control of quadrotor uavs: A more affordable solution. *IEEE Transactions on Neural Networks and Learning Systems*, 30(7):1975–1983, 2019.

[6] Ziquan Yu, Youmin Zhang, Bin Jiang, Chun-Yi Su, Jun Fu, Ying Jin, and Tianyou Chai. Decentralized fractional-order backstepping fault-tolerant control of multi-uavs against actuator faults and wind effects. *Aerospace Science and Technology*, 104:105939, 2020.

[7] C. Hua, P. Ning, and K. Li. Adaptive prescribed-time control for a class of uncertain nonlinear systems. *IEEE Transactions on Automatic Control*, 67(11):6159–6166, 2022.

[8] Y. Wang, Y. Song, D.J. Hill, and M. Krstic. Prescribed-time consensus and containment control of networked multiagent systems. *IEEE Transactions on Cybernetics*, 49(4):1138–1147, 2019.

[9] H.M. Becerra, C.R. Vázquez, G. Arechavaleta, and J. Delfin. Predefined-time convergence control for high-order integrator systems using time base generators. *IEEE Transactions on Control Systems Technology*, 26(5):1866–1873, 2017.

[10] Z. Guo and G. Chen. Distributed dynamic event-triggered and practical predefined-time resource allocation in cyber–physical systems. *Automatica*, 142:110390, 2022.

[11] A. Zou, Y. Liu, Z. Hou, and Z. Hu. Practical predefined-time output-feedback consensus tracking control for multiagent systems. *IEEE Transactions on Cybernetics*, 53(8):5311–5322, 2023.

[12] G. Duan. High-order system approaches: I. fully-actuated systems and parametric designs. *Acta Automatica Sinica*, 46(7):1333–1345, 2020.

[13] G. Duan. High-order fully actuated system approaches: Part II. Generalized strict-feedback systems. *International Journal of Systems Science*, 52(3):437–454, 2021.

[14] R. Dong, C. Hua, K. Li, and R. Meng. Adaptive fault-tolerant control for high-order fully actuated system with full-state constraints. *Journal of the Franklin Institute*, 360(12):8062–8074, 2023.

[15] T. Zhao and G. Duan. Fully actuated system approach to attitude control of flexible spacecraft with nonlinear time-varying inertia. *Science China Information Sciences*, 65(11):212201, 2022.

[16] J. Xiong and E. Zheng. Position and attitude tracking control for a quadrotor UAV. *ISA transactions*, 53(3):725–731, 2014.

[17] C.P. Bechlioulis and G.A. Rovithakis. A low-complexity global approximation-free control scheme with prescribed performance for unknown pure feedback systems. *Automatica*, 50(4):1217–1226, 2014.

[18] G. Duan. High-order fully actuated system approaches: Part IV. adaptive control and high-order backstepping. *International Journal of Systems Science*, 52(5):972–989, 2021.

Proceedings of the 3rd Conference on Fully Actuated System Theory and Applications
May 10-12, 2024, Shenzhen, China

Fault-Tolerant Control for Uncertain Sub-Fully Actuated Systems

Mengtong Gong[1], Li Sheng[2], Donghua Zhou[3,1,*]

1. Department of Automation, Tsinghua University, Beijing 100084, P. R. China
E-mail: gmt22@mails.tsinghua.edu.cn

2. College of Control Science and Engineering, China University of Petroleum (East China), Qingdao 266580, P. R. China
E-mail: shengli@upc.edu.cn

3. College of Electrical Engineering and Automation, Shandong University of Science and Technology, Qingdao 266590, P. R. China
E-mail: zdh@tsinghua.edu.cn

Abstract: This paper presents a fault-tolerant stabilization method for a class of uncertain high-order sub-fully actuated systems (sub-FASs) with actuator faults. As one of the important branches of the fully actuated system theory, sub-FAS control is more sophisticated and challenging due to the singularity problem. To deal with the fault tolerance issue of uncertain sub-FASs, a high-order nonlinear system model with both multiplicative and additive actuator faults is introduced. Motivated by the idea of FAS approach, a robust adaptive tracking controller is proposed to make system states track specific reference signals and avoid singularity under certain feasibility constraints. Then, a sufficient condition to ensure the feasibility constraints are satisfied is further derived. By appropriately selecting reference signals, the faulty sub-FAS is ultimately uniformly bounded. Finally, a numerical example is given to illustrate the effectiveness of the proposed method.

Key Words: Sub-Fully Actuated Systems (Sub-FASs), Actuator Fault, Fault-Tolerant Control, Adaptive Control, Nonlinear Uncertainty

1 Introduction

In the past few years, the high-order fully actuated system (FAS) approach originally proposed by Duan [1, 2] has received a lot of attention in different fields. As a control-oriented theory for nonlinear systems, it has a great advantage that the control law of a deterministic FAS can be easily designed such that a linear closed-loop system is obtained with an arbitrarily assignable eigenstructure [3]. Regarding those complexity control problems with nonlinear uncertainties, disturbances, and factors of time-varying and time-delay, the FAS approach is also capable of giving effective solutions (see [3–6]).

Parallel to the state-space model, FAS is a general model for dynamical control systems [7]. It has been proven that those systems which do not originally present full-actuation feature may still be converted into FASs [2, 8, 9]. However, it is clear that the FASs framework is unable to cover all sorts of actual plants, such as the uncontrollable under-actuated systems and sub-FASs [10]. In the former case, the system may be converted into a compound one containing a fully-actuated subsystem and an extra autonomous subsystem. A fully-actuated controller can still be designed to stabilize the compound system if the extra one is stable [3]. In summary, most of existing FAS approaches require that the considered systems or part of the them meet the fully-actuated condition globally. As a complement definition, the system is called sub-fully actuated if the fully-actuated condition is not satisfied in some subsets [10]. In applications, many actual plants are sub-fully-actuated [11]. Additionally, some well-known benchmark example systems can also be characterized by sub-FAS models [12], such as the Brockett's first and second example system [13, 14].

* Corresponding author. This work was supported in part by the National Natural Science Foundation of China under Grants 62033008, 61733009, and in part by the Taishan Scholar Project of Shandong Province of China and the NSFSD (ZR2022ZD34).

Up to now, a series of fundamental works for sub-FASs have been developed by Duan. The definition of sub-FAS is first presented in [15] and detailed reformulated in [10]. To cope with control singularity, the concepts of substability and the region of exponential attraction (ROEA) are introduced in [7]. By selecting a set of initial values in ROEA, the system trajectory is always away from singular set, such that the FAS approach can be used for control design. In [6] and [16], the above initial value strategy has been extended to the continuous-time delay sub-FASs and discrete-time delay sub-FASs, respectively. Moreover, optimal control [11], generalized PID control [17], and predictive control [18] have been investigated in sub-FASs framework. Recently, the control of uncertain sub-FASs has also been considered in a few works (see [19, 20]).

As an important branch of the FAS theory, the fault-tolerant control (FTC) for FASs has been considered and made some preliminary achievements (see [21–24]). However, to the best of authors' knowledge, the fault tolerance problem is still open in sub-FASs framework. To enrich the safety control theory for sub-FASs, this paper presents a novel fault-tolerant control method to stabilize a class of uncertain sub-FASs with both multiplicative and additive actuator faults. To avoid singularity, a reference signal satisfying certain conditions is designed to guide the trajectory of sub-FAS away from the singular set and converge towards the origin. Inspired by the FAS approach, a robust adaptive tracking control law is then developed to stabilize tracking error system under the feasibility constraint. Meanwhile, a sufficient condition that makes the feasibility constraint always satisfied is further derived. The proposed method guarantees the ultimately uniformly bounded (UUB) stabilization of the considered sub-FAS and only relies on several general assumptions.

The rest of this paper is organized as follows. Section 2 gives the formulation of the fault-tolerant stabilization prob-

lem. Section 3 provides the preliminaries and the main solution. An illustrative example is further presented in Section 4, and a brief conclusion is summarized in Section 5.

Notation: In the subsequent sections, the r-dimensional vector space and the matrix space of dimension $m \times n$ are denoted by $\mathbb{R}^r$ and $\mathbb{R}^{m\times n}$, respectively. $\Omega\backslash\Theta$ represents the complement of set Θ in set Ω. For a matrix $A \in \mathbb{R}^{m\times m}$, $\lambda_i(A)$ represents its ith eigenvalue, $\det A$ denote its determinant, $\|A\|_2$ and $\mathrm{cond}(A) = \|A\|_2 \left\|A^{-1}\right\|_2$ are the spectral norm and condition number, respectively. The Euclidean norm of a vector $x \in \mathbb{R}^r$ is denoted by $\|x\|$. Moreover, the real part of a complex number s is denoted by $\mathrm{Re}(s)$, and I_n represents the n-dimensional identity matrix. For convenience, the following symbols are also frequently used in this paper:

$$\begin{aligned}
\|x\|_P^2 &= x^{\mathrm{T}} P x,\\
x^{(0\sim n-1)} &= \left[x^{\mathrm{T}}, \dot{x}^{\mathrm{T}}, \cdots, x^{(n-1)\mathrm{T}}\right]^{\mathrm{T}},\\
A_{0\sim n-1} &= \left[A_0, A_1, \cdots, A_{n-1}\right],\\
\Phi\left(A_{0\sim n-1}\right) &= \begin{bmatrix} 0 & I & & \\ & & \ddots & \\ & & & I \\ -A_0 & -A_1 & \cdots & -A_{n-1} \end{bmatrix}.
\end{aligned}$$

2 Problem Formulation

Consider the following uncertain high-order system with actuator faults:

$$\begin{aligned}
x^{(n)} =& f\left(x^{(0\sim n-1)}\right) + \Delta f\left(x^{(0\sim n-1)}\right)\\
&+ B\left(x^{(0\sim n-1)}\right)\left[\left(I_r - \eta(t)\right)u + \xi(t)\right] \qquad (1)
\end{aligned}$$

where $x,\ u \in \mathbb{R}^r$ are the state vector and the control input vector, respectively; Nonlinear dynamics $f\left(x^{(0\sim n-1)}\right) \in \mathbb{R}^r$ and $B\left(x^{(0\sim n-1)}\right) \in \mathbb{R}^{r\times r}$ are both smooth functions; $\Delta f\left(x^{(0\sim n-1)}\right) \in \mathbb{R}^r$ is an unknown vector field representing the nonlinear uncertainty; $\xi(t) \in \mathbb{R}^r$ denotes the drift fault of actuator, and $\eta(t) = \mathrm{diag}\left\{\eta_i(t)\right\}, i = 1, 2, \ldots, r$, with $\eta_i(t) \in [0,\ 1)$ being the time-varying fault gain of the ith input channel. Without loss of generality, the origin is assumed to be the equilibrium point.

Regarding the high-order system (1), we introduce the following definition presented in [10].

Definition 1: If $X \in \mathbb{R}^{nr}$ satisfies

$$\det B(X) = 0 \ or\ \infty,$$

then it is called a singular point of the considered system. The set of all singular points is called the singular set, which can be expressed as

$$\mathbb{S} = \left\{X | \det B(X) = 0 \ or\ \infty,\ \ X \in \mathbb{R}^{nr}\right\}.$$

Accordingly, the complement of $\mathbb{S}$, that is $\mathbb{F} = \mathbb{R}^{nr}\backslash\mathbb{S}$, is called the feasible set of the system.

As defined in the previous work of Duan [6, 7, 11, 17], the high-order system is called a (global) FAS if its feasible set $\mathbb{F} = \mathbb{R}^{nr}$, and is called a sub-FAS if $\mathbb{F} \neq \emptyset$. In this paper, we focus on the latter and suppose that system (1) satisfies the following assumption.

Assumption 1: The considered system is a sub-FAS and its singular set $\mathbb{S}$ does not contain the origin, that is,

$$d_0 = \inf\left\{\|X\| | X \in \mathbb{S}\right\} > 0.$$

Clearly, the above d_0 is the minimum distance from the set $\mathbb{S}$ to the origin.

With the above preparation, the fault-tolerant stabilization problem to be solved can be now stated as below.

Problem 1: Let the considered uncertain high-order system (1) satisfy Assumptions 1. Find a full-state feedback controller such that
(1) the closed-loop system is ultimately uniformly bounded and
(2) the following feasibility constraint of states $x^{(0\sim n-1)}$ is met:

$$x^{(0\sim n-1)}(t) \in \mathbb{F},\ \ \forall t \geq 0. \qquad (2)$$

Remark 1: The feasibility constraint (2) guarantees that the considered system is fully actuated during stabilization, such that the FAS approach can be used for control design. If this condition is not satisfied, finding a continuous, time independent feedback law will be quite challenging and even impossible to achieve. In the above situation, the switching control strategy is usually considered [14], and such issue will be further discussed elsewhere.

To make sure the solution of above problem can be carried out, here we further impose the following assumptions for system (1).

Assumption 2: There exists a non-negative continuous scalar function $\rho\left(x^{(0\sim n-1)}\right)$ such that the nonlinear uncertainty $\Delta f\left(x^{(0\sim n-1)}\right)$ satisfies

$$\left\|\Delta f\left(x^{(0\sim n-1)}\right)\right\| \leq \rho\left(x^{(0\sim n-1)}\right). \qquad (3)$$

Assumption 3: Regarding the time-varying fault gain $\eta(t) = \mathrm{diag}\left\{\eta_i(t)\right\}, i = 1, 2, \ldots, r$, there is a pre-known uniform upper bound c satisfying $\eta_i(t) \leq c < 1$, for all $t > 0$.

Assumption 4: There exist two pre-known positive scalars δ_0 and δ_1 such that the unknown drift fault $\xi \triangleq \xi(t)$ and its derivative $\dot{\xi}$ satisfy $\|\xi\| \leq \delta_0$ and $\left\|\dot{\xi}\right\| \leq \delta_1$, for all $t > 0$.

Remark 2: The above Assumptions suppose that the uncertainty and actuator faults in system (1) are all bounded, which is quite general in practical applications because the actual plants are energy limited. It should be noted that Assumption 3 is necessary for the stabilization of actuator fault system. Without this assumption, the control force may be completely lost such that the system becomes uncontrollable.

3 Fault-Tolerant Control for Sub-FASs

In this section, a tracking control strategy is proposed to cope with the stabilization problem claimed in Problem 1. To guide the state trajectory of the considered system to converge asymptotically towards the origin, a reference signal $x_d(t) \in \mathbb{R}^r$ is introduced before the control law design. As the reference to be tracked by the system state $x(t)$, $x_d \triangleq x_d(t)$ is to be determined by the following condition.

Condition 1: The reference signal x_d is a C^n continuous function defined on $t \in [0, \infty)$, and
(1) x_d, together with its high-order derivatives, satisfy

$$\lim_{t\to\infty} x_d^{(0\sim n-1)}(t) = 0;$$

(2) $x_d^{(0\sim n-1)}$ belongs to the feasible set $\mathbb{F}$ for all $t \geq 0$, that is,

$$d_d = \inf_{t\geq 0}\left\{\left\|x_d^{(0\sim n-1)} - Z\right\| \middle| Z \in \mathbb{S}\right\} > 0.$$

Clearly, Condition 1 is a necessary condition for solving Problem 1 using the tracking control strategy. To further provide the control law in this section, the following preliminary lemmas presented in [4] are needed.

Lemma 1: Let $A \in \mathbb{R}^{m\times m}$ satisfy

$$\mathrm{Re}\lambda_i(A) \leq -\frac{\gamma}{2}, i = 1, 2, \ldots, m$$

where $\gamma > 0$. Then, there exists a positive-definite matrix $P \in \mathbb{R}^{m\times m}$ satisfying

$$A^{\mathrm{T}}P + PA \leq -\gamma P.$$

Lemma 2: For any $\mu > 0$, there exist a set of matrices $A_i \in \mathbb{R}^{r\times r}, i = 0, 1, \ldots, n-1$, satisfying

$$\mathrm{Re}\lambda_i(\Phi(A_{0\sim n-1})) \leq -\frac{\mu}{2}, i = 1, 2, \ldots, nr. \tag{4}$$

It follows from Lemma 1 that when the condition (4) holds for some $\mu > 0$, there is a positive-definite matrix $P \triangleq P(A_{0\sim n-1})$ such that the following Lyapunov inequality is satisfied,

$$\Phi^{\mathrm{T}}(A_{0\sim n-1})P + P\Phi(A_{0\sim n-1}) \leq -\mu P. \tag{5}$$

Further, we note

$$P_L = P(A_{0\sim n-1})\begin{bmatrix} 0_{(n-1)r\times r} \\ I_{r\times r}\end{bmatrix}. \tag{6}$$

Regarding the tracking control for the uncertain sub-FAS (1) with actuator faults, let us define the tracking error

$$z = x - x_d.$$

Then, we have

$$z^{(i)} = x^{(i)} - x_d^{(i)}, i = 1, 2, \ldots, n,$$

and the functions in the considered system can all be transformed into those with respect to $z^{(0\sim n-1)}$ and t. Thus, the considered system (1) turns into

$$z^{(n)} = f(\cdot) + \Delta f(\cdot) + B(\cdot)[(I - \eta(t))u + \xi(t)] - x_d^{(n)} \tag{7}$$

where notation $\left(z^{(0\sim n-1)}, t\right)$ is denoted by $(\cdot)$ for simplicity of description.

Based on the above preliminaries, we can derive the following main result for the tracking control problem. The fault-tolerant control law for tracking error system (7) can be designed as:

$$u = -B^{-1}(\cdot)(u_0 + u_r + u_a) \tag{8}$$

where

$$u_0 = A_{0\sim n-1}z^{(0\sim n-1)} + f(\cdot) - x_d^{(n)} \tag{9}$$

is the basic part, which aims to cancel the known term $f(\cdot)$ and $x_d^{(n)}$ in the system and assign the linear term $A_{0\sim n-1}z^{(0\sim n-1)}$ to the closed-loop system; and

$$\begin{cases} u_r = \frac{1}{1-c}\vartheta P_L^{\mathrm{T}} z^{(0\sim n-1)} \\ \dot{\vartheta} = \frac{1}{4\varepsilon}\left(\rho(\cdot) + \sigma(\cdot)\right)^2 \end{cases} \tag{10}$$

where

$$\sigma\left(z^{(0\sim n-1)}, t\right) = c\cdot \mathrm{cond}(B(\cdot))\cdot\|u_0 + u_a\| \tag{11}$$

is the robustness part whose function is to overcome the influence of the nonlinear uncertainty $\Delta f(\cdot)$ and unknown multiplicative fault gain $\eta(t)$; while

$$\begin{cases} u_a = B(\cdot)\hat{\xi} \\ \dot{\hat{\xi}} = -(\mu+1)\hat{\xi} + B^{\mathrm{T}}(\cdot)P_L^{\mathrm{T}} z^{(0\sim n-1)} \end{cases} \tag{12}$$

is the adaptation part, which aims to estimate the additive drift fault $\xi(t)$ online and adjust the control input accordingly based on the estimated results.

Theorem 1: Suppose that system (1) satisfies Assumptions 1–4. Let the feedback controller be given by (8)-(12), with μ and ε being two arbitrarily chosen positive numbers, and $A_i \in \mathbb{R}^{r\times r}, i = 0, 1, \ldots, n-1$ being a set of matrices satisfying (4). If, further, the feasibility constraint (2) is met. Then the closed-loop system (7) is UUB, and the tracking error $z^{(0\sim n-1)}$, together with the estimation error $\widetilde{\xi} = \xi - \hat{\xi}$, ultimately converge into the following ellipsoid centered at the origin:

$$\Xi_{\mu,\varepsilon,\delta}(0) = \left\{\begin{bmatrix} z^{(0\sim n-1)} \\ \widetilde{\xi}\end{bmatrix} \middle| \left\|z^{(0\sim n-1)}\right\|_P^2 + \left\|\widetilde{\xi}\right\|^2 \leq 2\frac{\varepsilon+\delta}{\mu}\right\}$$

where $P \in \mathbb{R}^{nr\times nr}$ is a solution to the Lyapunov inequality (5), and

$$\delta = \frac{\mu+1}{2}\delta_0^2 + \frac{1}{2}\delta_1^2.$$

Proof: Substituting the control law (8)-(12) into the tracking error system (7) gives part of the closed-loop system as

$$z^{(n)} + A_{0\sim n-1}z^{(0\sim n-1)} = \phi_r(\cdot) + \phi_a(\cdot) - B(\cdot)\eta(t)u \tag{13}$$

where

$$\phi_r(\cdot) = \Delta f(\cdot) - u_r, \phi_a(\cdot) = B(\cdot)\widetilde{\xi}.$$

System (13) can be further expressed in the following state-space form:

$$\begin{aligned}\dot{z}^{(0\sim n-1)} =& \Phi(A_{0\sim n-1})z^{(0\sim n-1)} \\ &+ \begin{bmatrix} 0_{(n-1)r\times 1} \\ \phi_r(\cdot) + \phi_a(\cdot) - B(\cdot)\eta(t)u\end{bmatrix}.\end{aligned} \tag{14}$$

Since $A_{0\sim n-1}$ satisfies the condition (4), there exists a positive-definite matrix $P(A_{0\sim n-1})$ satisfying the Lyapunov inequality (5). Then, the following Lyapunov function candidate is chosen for system (14):

$$V = \frac{1}{2}\left(z^{(0\sim n-1)}\right)^{\mathrm{T}} P z^{(0\sim n-1)} + \frac{1}{2}\widetilde{\xi}^{\mathrm{T}}\widetilde{\xi}. \tag{15}$$

In view of (5), (6), and (14), we have

$$\begin{aligned}\dot{V} \leq& -\mu V + \frac{\mu}{2}\widetilde{\xi}^{\mathrm{T}}\widetilde{\xi} + \dot{\widetilde{\xi}}^{\mathrm{T}}\widetilde{\xi} \\ &+ \left(z^{(0\sim n-1)}\right)^{\mathrm{T}} P_L(\phi_r(\cdot) + \phi_a(\cdot) - B(\cdot)\eta(t)u) \\ =& -\mu V + W_r + W_a\end{aligned} \tag{16}$$

where

$$W_r = \left(z^{(0\sim n-1)}\right)^{\mathrm{T}} P_L \left(\phi_r\left(\cdot\right) - B\left(\cdot\right)\eta\left(t\right)u\right)$$
$$W_a = \left(z^{(0\sim n-1)}\right)^{\mathrm{T}} P_L \phi_a\left(\cdot\right) + \dot{\widetilde{\xi}}^{\mathrm{T}}\widetilde{\xi} + \frac{\mu}{2}\widetilde{\xi}^{\mathrm{T}}\widetilde{\xi}.$$

First, let us treat W_r. Combining the expressions of $\phi_r\left(\cdot\right)$, u, and u_r, we can get

$$\begin{aligned} W_r \leq & \left\|P_L^{\mathrm{T}} z^{(0\sim n-1)}\right\| \left\|\Delta f\left(\cdot\right) + B\left(\cdot\right)\eta\left(t\right)B^{-1}\left(\cdot\right)\left(u_0+u_a\right)\right\| \\ & + \frac{1}{1-c}\vartheta\lambda_{max}\left(\eta\left(t\right)\right)\left\|P_L^{\mathrm{T}} z^{(0\sim n-1)}\right\|^2 \\ & - \frac{1}{1-c}\vartheta\left\|P_L^{\mathrm{T}} z^{(0\sim n-1)}\right\|^2. \end{aligned}$$

From Assumption 3 we know $\lambda_{max}\left(\eta\left(t\right)\right) \leq c$. Then, according to Assumptions 2 and (11), it can be shown that

$$\begin{aligned} & \left\|\Delta f\left(\cdot\right) + B\left(\cdot\right)\eta\left(t\right)B^{-1}\left(\cdot\right)\left(u_0+u_a\right)\right\| \\ & \leq \left\|\Delta f\left(\cdot\right)\right\| + \left\|\eta\left(t\right)\right\|_2 \left\|B\left(\cdot\right)\right\|_2 \left\|B^{-1}\left(\cdot\right)\right\|_2 \left\|u_0+u_a\right\| \\ & \leq \rho\left(\cdot\right) + \sigma\left(\cdot\right). \end{aligned}$$

Therefore, it follows from (10) that

$$\begin{aligned} W_r \leq & \left(\rho\left(\cdot\right)+\sigma\left(\cdot\right)\right)\left\|P_L^{\mathrm{T}} z^{(0\sim n-1)}\right\| \\ & - \frac{1}{4\varepsilon}\left(\rho\left(\cdot\right)+\sigma\left(\cdot\right)\right)^2\left\|P_L^{\mathrm{T}} z^{(0\sim n-1)}\right\|^2 \\ \leq & \varepsilon. \end{aligned} \tag{17}$$

Next, let us consider W_a. According to the expressions of $\phi_a\left(\cdot\right)$, W_a, and $\widetilde{\xi}$, it can be shown that

$$\begin{aligned} W_a = & \left(\left(z^{(0\sim n-1)}\right)^{\mathrm{T}} P_L B\left(\cdot\right) - \dot{\hat{\xi}}^{\mathrm{T}} - \left(\mu+1\right)\hat{\xi}^{\mathrm{T}}\right)\widetilde{\xi} + \dot{\xi}^{\mathrm{T}}\widetilde{\xi} \\ & + \left(\mu+1\right)\xi^{\mathrm{T}}\widetilde{\xi} - \frac{\mu+2}{2}\widetilde{\xi}^{\mathrm{T}}\widetilde{\xi}. \end{aligned}$$

Then, using adaptive control law (12), we obtain

$$\begin{aligned} W_a \leq & \frac{1}{2}\left(\delta_1^2 + \left\|\widetilde{\xi}\right\|^2\right) + \frac{\left(\mu+1\right)}{2}\left(\delta_0^2 + \left\|\widetilde{\xi}\right\|^2\right) - \frac{\mu+2}{2}\left\|\widetilde{\xi}\right\|^2 \\ = & \delta. \end{aligned} \tag{18}$$

Finally, combining the above two obtained relations (17) and (18), we have

$$\dot{V} \leq -\mu V + \varepsilon + \delta.$$

It thus follows from the Comparison Theorem [25] that

$$V\left(t\right) \leq \left(V\left(0\right) - \frac{\varepsilon+\delta}{\mu}\right)e^{-\mu t} + \frac{\varepsilon+\delta}{\mu} \rightarrow \frac{\varepsilon+\delta}{\mu},\ t\rightarrow\infty. \tag{19}$$

Therefore, the closed-loop system (13) is UUB, and $\left[z^{(0\sim n-1)\mathrm{T}}, \widetilde{\xi}^{\mathrm{T}}\right]^{\mathrm{T}}$ ultimately converges into the ellipsoid $\Xi_{\mu,\varepsilon,\delta}\left(0\right)$. The above conclusion follows from Theorem 1. The proof is then complete. □

Obviously, the premise of Theorem 1 is that the feasibility constraint (2) is satisfied, which guarantees that the control law (8) always exists. To meet this requirement, we have from Condition 1 and Theorem 1 the following corollary, it also gives the solution to Problem 1.

Corollary 1: Suppose that the uncertain sub-FAS (1) satisfies Assumptions 1–4, and the reference signal $x_d\left(t\right)$ is determined by Condition 1. Let the feedback controller be given by (8)-(12), with μ and ε being two arbitrarily chosen positive numbers, and $A_i \in \mathbb{R}^{r\times r}, i = 0,1,\ldots,n-1$ being a set of matrices satisfying (4). If, further, the following conditions are satisfied:

$$\hat{\xi}\left(0\right) = 0, x_d^{(0\sim n-1)}\left(0\right) = x^{(0\sim n-1)}\left(0\right), \tag{20}$$

$$\max\left\{\delta_0^2, 2\frac{\varepsilon+\delta}{\mu}\right\} < \lambda_{min}\left(P\right)d_d^2. \tag{21}$$

Then, both two issues in Problem 1 can be solved.

Proof: According to the proof of Theorem 1, i.e., equation (19), we immediately have

$$V\left(t\right) \leq \max\left\{V\left(0\right), \frac{\varepsilon+\delta}{\mu}\right\},\ \forall t \geq 0.$$

In view of (15), it can be shown that, for all $t \geq 0$,

$$\begin{aligned} & \left\|z^{(0\sim n-1)}\left(t\right)\right\|^2 \leq \frac{2}{\lambda_{min}\left(P\right)}V\left(t\right) \\ & \leq \frac{1}{\lambda_{min}\left(P\right)}\max\left\{\left\|z^{(0\sim n-1)}\left(0\right)\right\|_P^2 + \left\|\widetilde{\xi}\left(0\right)\right\|^2, 2\frac{\varepsilon+\delta}{\mu}\right\}. \end{aligned}$$

Then, combining condition (20) and (21), as well as Assumption 4, produces

$$\left\|z^{(0\sim n-1)}\left(t\right)\right\|^2 \leq \frac{1}{\lambda_{min}\left(P\right)}\max\left\{\delta_0^2, 2\frac{\varepsilon+\delta}{\mu}\right\} < d_d^2.$$

The above result indicates that the tracking error between $x^{(0\sim n-1)}\left(t\right)$ and $x_d^{(0\sim n-1)}\left(t\right)$ is less than d_d for all $t \geq 0$. Therefore, it follows from Condition 1 that the feasibility constraint (2) is satisfied. Moreover, since $x_d^{(0\sim n-1)}$ is asymptotically stable, using Theorem 1 we can derive the closed-loop sub-FAS (1) is UUB, and the states $x^{(0\sim n-1)}$, together with the estimation error $\widetilde{\xi}$, ultimately converge into the ellipsoid $\Xi_{\mu,\varepsilon,\delta}\left(0\right)$. Thus, the proof is complete. □

4 Illustrative Example

In this section, a numerical example is introduced to illustrate the effectiveness of the proposed fault-tolerant control law.

Consider the following second-order sub-FAS:

$$\begin{aligned} \begin{bmatrix}\ddot{x}_1\\ \ddot{x}_2\end{bmatrix} = & f\left(x_1,x_2\right) + \Delta f\left(x_1\right) \\ & + B\left(x_1,x_2,\dot{x}_1\right)\left[\left(I-\eta\left(t\right)\right)u + \xi\left(t\right)\right] \end{aligned} \tag{22}$$

with

$$f\left(x_1,x_2\right) = \begin{bmatrix}-x_1\\ \sin x_2\end{bmatrix}, \Delta f\left(x_1\right) = \begin{bmatrix}\theta x_1^2\\ 0\end{bmatrix},$$
$$B\left(x_1,x_2,\dot{x}_1\right) = \begin{bmatrix}\frac{\dot{x}_1}{\left(x_1^2+1\right)} & \frac{1}{\left(x_1^2+1\right)}\\ x_2-5 & -1\end{bmatrix},$$

where $x = \left[x_1, x_2\right]^{\mathrm{T}} \in \mathbb{R}^2$ and $u \in \mathbb{R}^2$ are the state vector and input vector, respectively. $\theta \in \mathbb{R}$ is an uncertain variable satisfying $0 \leq \theta \leq 0.1$. In the simulation, θ and the initial states $x^{(0\sim 1)}\left(0\right)$ are chosen as

$$\theta = 0.08, x^{(0\sim 1)}\left(0\right) = \begin{bmatrix}1 & 4 & -2 & 3\end{bmatrix}^{\mathrm{T}}.$$

The actuator faults $\eta\left(t\right)$ and $\xi\left(t\right)$ are set to

$$\eta(t)=\begin{bmatrix}0.2\sin(t)+0.3 & 0\\ 0 & 0.1\cos(t)+0.4\end{bmatrix},$$
$$\xi(t)=\begin{bmatrix}0\\ -0.5e^{-t}+0.5\end{bmatrix}.$$

It is obvious that the above system satisfies Assumption 1-4, and

$$\rho(x_1)=0.1x_1^2, c=0.5, \delta_0=0.5, \delta_1=0.5.$$

Moreover, the considered sub-FAS (22) clearly has the following singular set $\mathbb{S}$:

$$\mathbb{S}=\left\{x^{(0\sim1)}\middle|-x_2-\dot{x}_1+5=0, x^{(0\sim1)}\in\mathbb{R}^4\right\}.$$

To make sure the Condition 1 is satisfied, the following reference system is introduced, and its state response $x_d^{(0\sim1)}(t)$ is expected to be used as the reference signal:

$$\begin{bmatrix}\dot{x}_{d1}\\ \dot{x}_{d2}\end{bmatrix}=\begin{bmatrix}-1 & -1\\ 2 & -8\end{bmatrix}\begin{bmatrix}\dot{x}_{d1}\\ \dot{x}_{d2}\end{bmatrix}+\begin{bmatrix}0 & -1\\ 2 & -8\end{bmatrix}\begin{bmatrix}x_{d1}\\ x_{d2}\end{bmatrix}. \quad (23)$$

Obviously, with $x_d^{(0\sim1)}(0)=x^{(0\sim1)}(0)$, it can be proved that system (23) is asymptotically stable, and $x_d^{(0\sim1)}$ belongs to the feasible set $\mathbb{F}$ for all $t\geq0$. Further, we can get

$$d_d=\inf_{t\geq0}\left\{\left\|x_d^{(0\sim1)}-Z\right\|\middle|Z\in\mathbb{S}\right\}=1.5\sqrt{2}.$$

Next, we design

$$A_{0\sim1}=\begin{bmatrix}2 & 0 & 3 & 0\\ 0 & 2 & 0 & 3\end{bmatrix}$$

which makes

$$\mathrm{eig}\left[\Phi\left(A_{0\sim1}\right)\right]=\{-1,-1,-2,-2\}$$

where $\mathrm{eig}(A)$ represents the set of eigenvalues of the matrix A. Then, it can be verified that the following:

$$P=\begin{bmatrix}10 & 0 & 4 & 0\\ 0 & 10 & 0 & 4\\ 4 & 0 & 2 & 0\\ 0 & 4 & 0 & 2\end{bmatrix}$$

satisfies the Lyapunov inequality (5) with $\mu=1.5$, such that

$$P_L^{\mathrm{T}}\left(A_{0\sim1}\right)=\begin{bmatrix}4 & 0 & 2 & 0\\ 0 & 4 & 0 & 2\end{bmatrix}.$$

Under the above settings, we can show that condition (19) is satisfied with $\varepsilon=0.5$. Regarding the tracking control for the considered system (22), let us define tracking error

$$z^{(0\sim1)}=x^{(0\sim1)}-x_d^{(0\sim1)}.$$

Finally, follows from Theorem 1, the fault-tolerant controller can be designed as

$$u=-B^{-1}(\cdot)\left(u_0+u_r+u_a\right)$$

where

$$\begin{cases}u_0=A_{0\sim1}z^{(0\sim1)}+f(\cdot)-x_d^{(2)}\\ u_r=\frac{1}{1-0.5}\vartheta P_L^{\mathrm{T}}z^{(0\sim1)}\\ u_a=B(\cdot)\hat{\xi}\end{cases}$$

with

$$\vartheta=\frac{1}{4\times0.5}\left(\rho(\cdot)+\sigma(\cdot)\right)^2,$$

$$\sigma(\cdot)=0.5\cdot\mathrm{cond}\left(B(\cdot)\right)\cdot\left\|u_0+u_a\right\|,$$
$$\dot{\hat{\xi}}=-(1.5+1)\hat{\xi}+B^{\mathrm{T}}(\cdot)P_L^{\mathrm{T}}z^{(0\sim1)}, \hat{\xi}(0)=0.$$

The simulation results of states response $x^{(0\sim1)}$ and control input u are shown in Fig. 1. It can be observed that the closed-loop system is fully stabilized within 10 seconds. To make a clear presentation, the phase portrait of x_2 and $\dot{x}_1$, which induce the singular set $\mathbb{S}$, is depicted in Fig. 2, where the red line represents the singular set $\mathbb{S}$, the blue line and green line are the trajectories of closed-loop system and reference signal, respectively. From this figure, we can find that the tracking error is bounded, and the feasibility constraint (2) is always met. Such results illustrate the effectiveness of proposed fault-tolerant method. Moreover, the adaptive estimation of additive fault ξ is plotted in Fig. 3. It is shown that estimation error is also bounded, which follows the conclusion of Theorem 1.

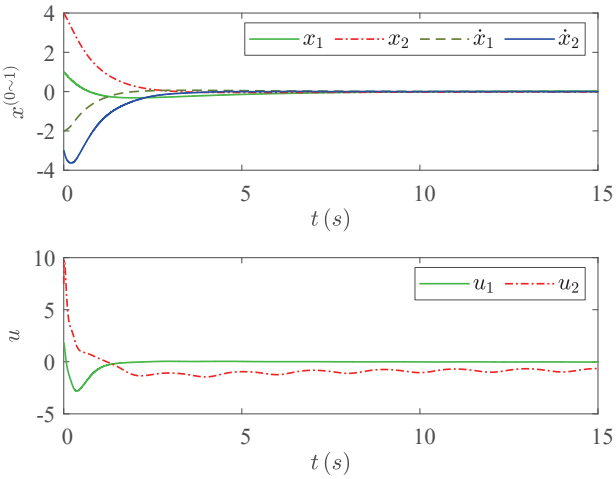

Fig. 1: Simulation results of closed-loop system.

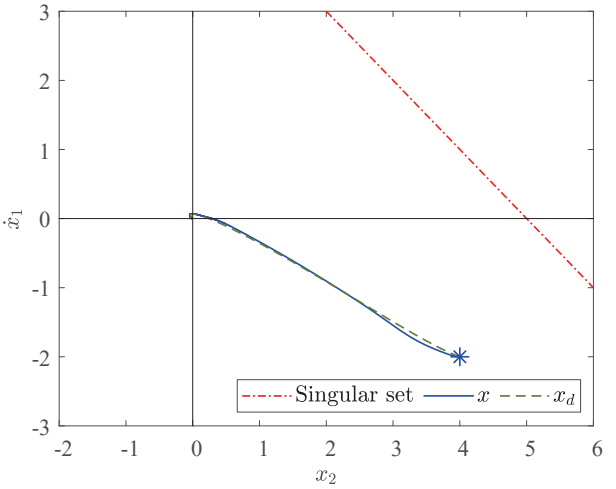

Fig. 2: Phase portrait of state response.

5 Conclusion

In this paper, a fault tolerance strategy is proposed to cope with a class of uncertain sub-FASs with actuator faults. The

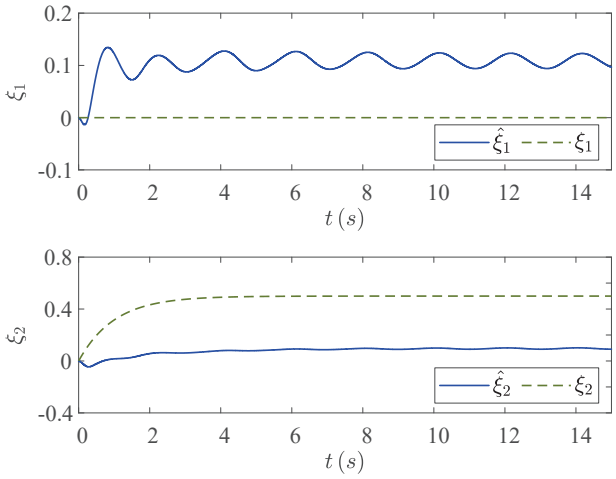

Fig. 3: Adaptive estimation of additive fault.

main contribution of the proposed method include: (a) Different from the stabilization problems of sub-FASs investigated in existing literature, the multiplicative and additive fault of actuator is first considered; (b) Motivated by the FAS approach, a tracking control law is developed to UUB stabilize the considered system under the feasibility constraint; (c) A sufficient condition that make the feasibility constraint always satisfied is further derived. In conclusion, this work is a foundational research on the fault-tolerant control for sub-FASs, and it is also a supplement to the recently proposed FAS theory. In the future, uncertain sub-FASs with both actuator faults and sensor faults will be further investigated.

References

[1] G. R. Duan, High-order system approaches: I. Full-actuation and parametric design. *Acta Automatica Sinica*, 2020, 46(7): 1333–1345.

[2] G. R. Duan, High-order fully actuated system approaches: Part I. Models and basic procedure. *International Journal of Systems Science*, 2021, 52(2): 422–435.

[3] G. R. Duan, Robust stabilization of time-varying nonlinear systems with time-varying delays: A fully actuated system approach. *IEEE Transactions on Cybernetics*, 2023, 53(12): 7455–7468.

[4] G. R. Duan, High-order fully actuated system approaches: Part III. Robust control and high-order backstepping. *International Journal of Systems Science*, 2021, 52(5): 952–971.

[5] G. R. Duan, High-order fully actuated system approaches: Part VI. Disturbance attenuation and decoupling. *International Journal of Systems Science*, 2021, 52(10): 2161–2181.

[6] G. R. Duan, Fully actuated system approaches for continuous-time delay systems: Part 1. Systems with state delays only. *Science China Information Sciences*, 2023, 66: 112201.

[7] G. R. Duan, Substability and substabilization: control of sub-fully actuated systems. *IEEE Transactions on Cybernetics*, 2023, 53(11): 7309–7322.

[8] G. R. Duan, High-order fully actuated system approaches: Part II. Generalized strict-feedback systems. *International Journal of Systems Science*, 2021, 52(3): 437–454.

[9] X. Wang and G. R. Duan, High-order fully actuated system approaches: Model predictive control with applications to under-actuated systems. *Journal of the Franklin Institute*, 2023, 360(10): 6953–6975.

[10] G. R. Duan, High-order fully actuated system approaches: Part VII. Controllability, stabilizability and parametric designs. *International Journal of Systems Science*, 2021, 52(14): 3091–3114.

[11] G. R. Duan, High-order fully actuated system approaches: Part VIII. Optimal control with application in spacecraft attitude stabilisation. *International Journal of Systems Science*, 2022, 53(1): 54–73.

[12] G. R. Duan, Stabilization via fully actuated system approach: A case study. *Journal of Systems Science and Complexity*, 2022, 35(3): 731–747.

[13] G. R. Duan, Brockett's first example: An FAS approach treatment. *Journal of Systems Science and Complexity*, 2022, 35(2): 441–456.

[14] G. R. Duan, Brockett's second example: A FAS approach treatment. *Journal of Systems Science and Complexity*, 2023, 36(5): 1789–1808.

[15] G. R. Duan, High-order system approaches: II. Controllability and fully-actuation. *Acta Automatica Sinica*, 2020, 46(8): 1571–1581.

[16] G. R. Duan, Discrete-time delay systems: Part 2. Sub-fully actuated case. *Science China Information Sciences*, 2022, 65: 192201.

[17] G. R. Duan, High-order fully actuated system approaches: Part IX. Generalised PID control and model reference tracking. *International Journal of Systems Science*, 2022, 53(3): 652–674.

[18] X. Wang and G. R. Duan, A subfully actuated system application: Predictive control for multi-RTAC systems, in *Proceedings of 2nd Conference on Fully Actuated System Theory and Applications (CFASTA)*, 2023: 948–953.

[19] W. Shi, M. Hou, and G. R. Duan, Adaptive preassigned time stabilisation of uncertain second-order sub-fully actuated systems. *Journal of Systems Science and Complexity*, 2022, 35(2): 703–713.

[20] S. Zhang and G. R. Duan, Robust stabilization control for high-order sub-fully actuated systems, in *Proceedings of 2nd Conference on Fully Actuated System Theory and Applications (CFASTA)*, 2023: 573–578.

[21] M. Cai, X. He, and D. Zhou, An active fault tolerance framework for uncertain high-order fully-actuated systems. *Automatica*, 2023, 152: 110969.

[22] M. Cai, X. He, and D. Zhou, Self-healing fault-tolerant control for high-order fully actuated systems against sensor faults: A redundancy framework. *IEEE Transactions on Cybernetics*, 2023: 1–13.

[23] X. Liu, M. Chen, D. Zhou, and L. Sheng, Fault-tolerant control of stochastic high-order fully actuated systems. *IEEE Transactions on Cybernetics*, 2023: 1–14.

[24] M. Gong, L. Sheng, and D. Zhou, Robust fault-tolerant control for uncertain high-order fully actuated systems with actuator faults, in *Proceedings of 2nd Conference on Fully Actuated System Theory and Applications (CFASTA)*, 2023: 532–537.

[25] H. K. Khalil, *Nonlinear Systems*, 3rd ed. Upper Saddle River, NJ, USA: Prentice-Hall, 2002.

Proceedings of the 3rd Conference on Fully Actuated System Theory and Applications
May 10-12, 2024, Shenzhen, China

Multidimensional Fault Characterization Model Based Fault Identification for New Type Dissimilar Redundant Actuation System

Jun Wang[1,*], Jian Huang[1], Weikang Li[1], Yongxing Feng[1]

1. Beijing Institute of Automatic Control Equipment, Beijing 100074, China
* Corresponding author E-mail: dwill-wang@buaa.edu.cn

Abstract: In order to support the fault-tolerant control (FTC) design for the new type dissimilar redundant actuation system (NT-DRAS) used in near space vehicles, this paper proposed a multidimensional fault characterization model based fault identification method. The NT-DRAS model is first introduced as well as the operating modes. The fault occurrence mechanism for the considered faults are then analyzed. Followed by the analysis results, the multidimensional fault characterization based fault reasoning mechanism is presented, and then the multidimensional fault characterization models as well as the discrimination algorithm used to identify the fault modes are presented. Simulation results are performed finally to verify both the analyzed fault occurrence mechanism and the proposed fault identification effectiveness.

Key Words: New type dissimilar redundant actuation system (NT-DRAS), near space vehicle, multidimensional fault characterization model, fault identification

1 Introduction

With more and more research focusing on the near space vehicle (NSV) such as SR-72, X-43 and so on, the high reliability design requirement become noteworthy. The actuation system is one of the most important subsystem to realize vehicle trajectory control [1-4]. Dissimilar redundant actuation system (DRAS) composed with a traditional hydraulic actuator (HA) and a new electro-hydrostatic actuator (EHA) has attracted growing interest in large civil aircraft fields such as the A350 and A400M vehicles [5-6]. However, for the vehicle with high power/weight ratio in the military domain, new type dissimilar redundant actuation system (NT-DRAS) composed of EHA and EMA is more suitable due to the distributed flexible layout advantage of EHA and electro-mechanical actuator (EMA) [7]. To further improve the actuation reliability, fault-tolerant control (FTC) technique is used to minimize effects of possible faults and maintain the system performance at a desired level [8]. There are some research results focused on the traditional DRAS FTC problems, including flight control level [9] as well as the actuation level [10].

To support the FTC design, the fault types should be diagnosed and identified precisely, so that the FTC strategies can be chosen directed at the occurred faults [11]. Focused on the fault diagnosis and fault identification problem, there are lists of research results. Data driven and Model based method are usually used in this process, there are also comprehensive strategy which synthesize both the data driven and model based method [12]. System conditions are also considered in some research, condition monitoring is regarded an important fault diagnosis link [13]. In the last fault identification step, residual errors are usually used to compare the pre-set threshold, so that the system fault can be detected [14]. With the growing trend of artificial intelligence, deep learning technique is also used in fault diagnosis to perform the multiple feature extraction and information fusion problem, however, a mass of data are very necessary in this process [15]. The above research results usually can detect the occurred faults, to identify the specific fault modes in the complicated NT-DRAS, still remains a problem.

This paper presents a multi-dimensional fault characterization model based fault identification method: all the system output signals are used to analyze the fault occurrence mechanism first, so that a fault reasoning mechanism can be determined to identify the pre-considered fault. Model discrimination algorithm is used in this paper to quantify the approximation errors. Based on both the fault characterization model and error calculation algorithm, the pre-considered fault modes can be identified efficiently and precisely.

2 System Statement

2.1 NT-DRAS System

The schematic structure of a NT-DRAS is composed of one EHA channel and one EMA channel(see Fig. 1), each of them can work independently, this kind of "stand-alone operation" mode provide more choices for the NSV under different work conditions. According to the operating characteristic of EHA and EMA, it can be determined that EHA is the main work channel and EMA is the back-up channel when EHA channel subjects to certain fault or completely failure. Based on the two different work channels, the third operating mode: EHA and EMA driving the control surface together by using synchronous control algorithm, can be used under certain conditions such as high loaded and quick response condition. Various working modes can support FTC designs.

*This work is supported by National Natural Science Foundation (NNSF) of China under Grant 52105049 and 52175038.

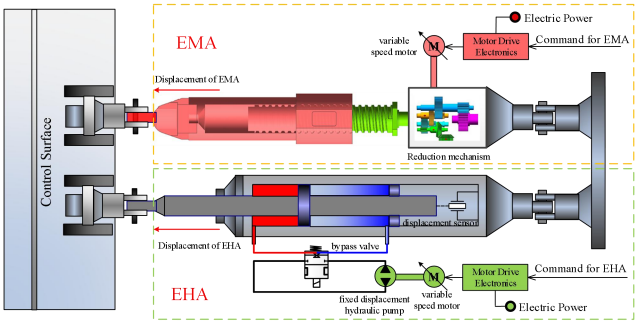

Fig. 1: Schematic of NT-DRAS

Table 1: Operating Modes of NT-DRAS

Operating Modes	EHA	EMA	Working Condition
Mode- 1	active	passive	normal
Mode-2	passive	active	EHA failed
Mode-3	active	active	high loaded

Table 1 illustrates different operating modes and specific working state of both EHA and EMA: under normal condition, only EHA is used to drive the control surface while EMA can be regarded as load of EHA at this moment. In this operating mode, the chamber of EHA is separated into low and high pressure volumes, respectively. The pressure difference can push the EHA piston to move. Meanwhile, EMA is pulled passively by the control surface actuated by EHA. Consequently, EMA channel of NT-DRAS is considered to be in a no-load mode. Mode-2 and Mode-3 are alternative modes used to perform FTC strategies under fault and abnormal conditions.

2.2 State Space Model of Mode 1

As studied in the literature[7], the state variable vector can be defined as $\boldsymbol{x}=\left[x_{\mathrm{eha}}, \dot{x}_{\mathrm{eha}}, P_{\mathrm{eha}}, \omega_{\mathrm{eha}}\right]^{\mathrm{T}}$, so that the state space equations can be obtained as

$$\begin{cases} \dfrac{dx_{\mathrm{eha}}}{dt}=\dot{x}_{\mathrm{eha}} \\ \dfrac{d\dot{x}_{\mathrm{eha}}}{dt}=-\dfrac{\mathrm{B}_{\mathrm{eha}}+\mathrm{B}_{\mathrm{ema}}+\mathrm{B}_{\mathrm{d}}}{\mathrm{m}_{\mathrm{eha}}+\mathrm{m}_{\mathrm{ema}}+\mathrm{m}_{\mathrm{d}}}\dot{x}_{\mathrm{eha}}+\dfrac{\mathrm{A}_{\mathrm{eha}}}{\mathrm{m}_{\mathrm{eha}}+\mathrm{m}_{\mathrm{ema}}+\mathrm{m}_{\mathrm{d}}}P_{\mathrm{eha}} \\ -\dfrac{1}{\mathrm{m}_{\mathrm{eha}}+\mathrm{m}_{\mathrm{ema}}+\mathrm{m}_{\mathrm{d}}}F_{\mathrm{L}} \\ \dfrac{dP_{\mathrm{eha}}}{dt}=-\dfrac{4\mathrm{E}_{\mathrm{eha}}\mathrm{A}_{\mathrm{eha}}}{\mathrm{V}_{\mathrm{eha}}}\dot{x}_{\mathrm{eha}}-\dfrac{4\mathrm{E}_{\mathrm{eha}}\mathrm{C}_{\mathrm{ehal}}}{\mathrm{V}_{\mathrm{eha}}}P_{\mathrm{eha}}+\dfrac{4\mathrm{E}_{\mathrm{eha}}\mathrm{V}_{\mathrm{P}}}{\mathrm{V}_{\mathrm{eha}}}\omega_{\mathrm{eha}} \\ \dfrac{d\omega_{\mathrm{eha}}}{dt}=-\dfrac{\mathrm{V}_{\mathrm{P}}}{\mathrm{J}_{\mathrm{m}}}P_{\mathrm{eha}}-\dfrac{\mathrm{B}_{\mathrm{me}}}{\mathrm{J}_{\mathrm{m}}}\omega_{\mathrm{eha}}+\dfrac{\mathrm{K}_{\mathrm{m}}}{\mathrm{J}_{\mathrm{m}}\mathrm{R}_{\mathrm{e}}}u_{\mathrm{eha}} \end{cases} \tag{1}$$

In state space form, Eq. (1) can be represented as

$$\begin{cases} \dot{\boldsymbol{x}}(t)=\boldsymbol{A}\boldsymbol{x}(t)+\boldsymbol{B}\boldsymbol{u}(t)+\boldsymbol{G}w(t) \\ \boldsymbol{y}(t)=\boldsymbol{C}\boldsymbol{x}(t) \end{cases} \tag{2}$$

$$\begin{cases} \boldsymbol{A}=\begin{bmatrix} 0 & 1 & 0 & 0 \\ 0 & -\dfrac{\mathrm{B}_{\mathrm{eha}}+\mathrm{B}_{\mathrm{ema}}+\mathrm{B}_{\mathrm{d}}}{\mathrm{m}_{\mathrm{eha}}+\mathrm{m}_{\mathrm{ema}}+\mathrm{m}_{\mathrm{d}}} & \dfrac{\mathrm{A}_{\mathrm{eha}}}{\mathrm{m}_{\mathrm{eha}}+\mathrm{m}_{\mathrm{ema}}+\mathrm{m}_{\mathrm{d}}} & 0 \\ 0 & -\dfrac{4\mathrm{E}_{\mathrm{eha}}\mathrm{A}_{\mathrm{eha}}}{\mathrm{V}_{\mathrm{eha}}} & -\dfrac{4\mathrm{E}_{\mathrm{eha}}\mathrm{C}_{\mathrm{ehal}}}{\mathrm{V}_{\mathrm{eha}}} & \dfrac{4\mathrm{E}_{\mathrm{eha}}\mathrm{V}_{\mathrm{P}}}{\mathrm{V}_{\mathrm{eha}}} \\ 0 & 0 & -\dfrac{\mathrm{V}_{\mathrm{P}}}{\mathrm{J}_{\mathrm{m}}} & -\dfrac{\mathrm{B}_{\mathrm{me}}}{\mathrm{J}_{\mathrm{m}}} \end{bmatrix} \\ \boldsymbol{B}=\begin{bmatrix} 0 & 0 & 0 & \dfrac{\mathrm{K}_{\mathrm{m}}}{\mathrm{J}_{\mathrm{m}}\mathrm{R}_{\mathrm{e}}} \end{bmatrix}^{\mathrm{T}} \\ \boldsymbol{C}=\begin{bmatrix} 1 & 0 & 0 & 0 \\ 0 & 1 & 0 & 0 \\ 0 & 0 & 1 & 0 \\ 0 & 0 & 0 & 1 \end{bmatrix} \\ \boldsymbol{G}=\begin{bmatrix} 0 & -\dfrac{1}{\mathrm{m}_{\mathrm{eha}}+\mathrm{m}_{\mathrm{ema}}+\mathrm{m}_{\mathrm{d}}} & 0 & 0 \end{bmatrix}^{\mathrm{T}} \end{cases} \tag{3}$$

where $\boldsymbol{u}(t)$ is the system input, $\boldsymbol{y}(t)$ is the system output, $w(t)=F_{\mathrm{L}}$ is unknown disturbance. The state, input, output, and disturbance matrices are presented in Equation (3).

2.3 Analysis of Fault Modes and Corresponding Parameters

In operating mode- 1, which EHA is in active working mode while EMA is in passive working mode, EMA and the actuated control surface can be regarded as the load of EHA, therefore, $\mathrm{B}_{\mathrm{ema}}$ and B_{d} can be seen constant; Similarly, the mass of EHA, EMA and the control surface stay consistent without physical damage, leading the three parameters $\mathrm{m}_{\mathrm{eha}}$, $\mathrm{m}_{\mathrm{ema}}$ and m_{d} to be constant; As the component of EHA, the area and volume of EHA hydraulic cylinder also stay consistent without physical damage, leading the parameters $\mathrm{A}_{\mathrm{eha}}$ and $\mathrm{V}_{\mathrm{eha}}$ to be constant, the pump output V_{p} stay as constant since the pump structure is fixed designed. Without changing system structure and mass, the total moment of inertia of motor and pump J_{m} stay constant. In this paper, the electromagnetic torque constant K_{m} is also regarded as designed fixed constant. The rest system parameters $\mathrm{C}_{\mathrm{ehal}}$, $\mathrm{B}_{\mathrm{eha}}$, $\mathrm{E}_{\mathrm{eha}}$ and R_{e} all have their own changing law caused by corresponding gradual fault types, which are introduced in the following section.

Table 2: Fault Modes and Parameter Illustrations

Number	Parameter Illustrations
Fault-1	Hydraulic cylinder leakage: leakage coefficient $\mathrm{C}_{\mathrm{ehal}}$
Fault-2	Motion damping increasing: damping coefficient $\mathrm{B}_{\mathrm{eha}}$
Fault-3	Oil deterioration: bulk modulus $\mathrm{E}_{\mathrm{eha}}$
Fault-4	Resistance increasing: motor armature resistance R_{e}

The gradual faults of EHA can be classified in the above categories shown in Table 2, where the faults correspond with relative parameter drift: Fault-1 represents that leakage coefficient C_{ehal} changes due to the hydraulic cylinder leakage, Fault-2 represents that damping coefficient B_{eha} changes due to the increasing motion damping, Fault-3 represents that bulk modulus E_{eha} changes due to oil deteriorates caused by the air in oil, and Fault-4 represents that R_e changes due to its increasing caused by heat production.

The relative parameters drift with the gradual fault degrees are within limited ranges. Though similar to the system model uncertainty in fault-free conditions, the gradual faults cause more severe parameter drift, which can be regarded as gradual faults caused by the system uncertainty. In order to model these faults in NT-DRAS, uncertainty matrices modelling method are used to describe the parameter uncertainty caused by these EHA faults. The NT-DRAS model with faults can be represented as:

$$\begin{cases} \dot{\boldsymbol{x}}(t) = (\boldsymbol{A} + \boldsymbol{\Delta A})\boldsymbol{x}(t) + (\boldsymbol{B} + \boldsymbol{\Delta B})\boldsymbol{u}(t) + \boldsymbol{G}w(t) \\ \boldsymbol{y}(t) = \boldsymbol{C}\boldsymbol{x}(t) \end{cases} \tag{4}$$

where $\boldsymbol{\Delta A}$ and $\boldsymbol{\Delta B}$ are deviations in the original state and input matrices caused by parameter changes due to the gradual faults. It is necessary to state that the gradual faults caused deviation matrices have more adverse effect compared with the system model uncertainty under fault-free conditions. There is no $\boldsymbol{\Delta C}$ in the above system description, as it is assumed that all of the sensors can work normally. The system matrices and the fault module matrices can be expressed as

$$\begin{cases} \boldsymbol{A} = \begin{bmatrix} 0 & 1 & 0 & 0 \\ 0 & a_{22} & a_{23} & 0 \\ 0 & a_{32} & a_{33} & a_{34} \\ 0 & 0 & a_{43} & a_{44} \end{bmatrix} \\ \boldsymbol{B} = \begin{bmatrix} 0 & 0 & 0 & b_{41} \end{bmatrix}^{\mathrm{T}} \\ \boldsymbol{\Delta A} = \begin{bmatrix} 0 & 0 & 0 & 0 \\ 0 & \Delta a_{22} & 0 & 0 \\ 0 & \Delta a_{32} & \Delta a_{33} & \Delta a_{34} \\ 0 & 0 & 0 & 0 \end{bmatrix} \\ \boldsymbol{\Delta B} = \begin{bmatrix} 0 & 0 & 0 & \Delta b_{41} \end{bmatrix}^{\mathrm{T}} \end{cases} \tag{5}$$

where coefficients of the state and input matrices, $\boldsymbol{A}$ and $\boldsymbol{B}$, matrices have been defined by using Eq. (3); $\Delta a_{22} = -\Delta \mathrm{B}_{eha} / (\mathrm{m}_{eha} + \mathrm{m}_{ema} + \mathrm{m}_{d})$ represents damping fault induced factor; $\Delta a_{32} = -4\Delta \mathrm{E}_{eha} \mathrm{A}_{eha} / \mathrm{V}_{eha}$ is the bulk modulus fault factor; $\Delta a_{33} = -\left[4(\Delta \mathrm{E}_{eha}) \bullet (\Delta \mathrm{C}_{ehal})\right] / \mathrm{V}_{eha}$ represents the bulk modulus as well as the internal leakage fault factor; $\Delta a_{34} = 4\Delta \mathrm{E}_{eha} \mathrm{V}_{\mathrm{P}} / \mathrm{V}_{eha}$ represents the bulk modulus fault factor; $\Delta \mathrm{b}_{41} = \mathrm{K}_{\mathrm{m}} / (\mathrm{J}_{\mathrm{m}} \Delta \mathrm{R}_{\mathrm{e}})$ represents the motor armature resistance fault factor.

3 Multidimensional Fault Characterization of NT-DRAS

3.1 Fault Reasoning Mechanism Structure

In this paper, the NT-DRAS output signals, including the system displacement, velocity, cylinder pressure and motor speed, are used as multidimensional signals to form a fault reasoning mechanism. All the four signals can be used as fault characterization since when certain fault occur, all the signals demonstrate changing laws based on the system operation mechanism.

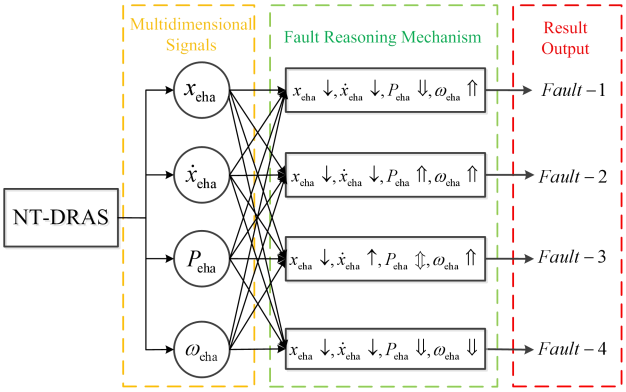

Fig. 2: Multidimensional fault characterization based fault reasoning mechanism

As shown in Fig. 2, when fault-1 occur, the hydraulic cylinder leakage can make the cylinder pressure decrease obviously, represented as $P_{eha}\Downarrow$, the motor speed would increase ($\omega_{eha}\Uparrow$) in order to compensate and maintain the cylinder pressure at a normal level. However, the system output $x_{eha}\downarrow$ and $\dot{x}_{eha}\downarrow$ still decrease compared with the system under normal condition; when fault-2 occur, the motion damping increasing can provide reverse pressure which make the cylinder pressure decrease obviously ($P_{eha}\Uparrow$), the motor speed would increase ($\omega_{eha}\Uparrow$) to provide positive-going pressure of the cylinder, overcoming the increased motion damping. However, the system output $x_{eha}\downarrow$ and $\dot{x}_{eha}\downarrow$ still decrease since fault-2 occur; when fault-3 occur, oil deterioration because of air bubble would make the system pressure response unstable with obvious fluctuations ($P_{eha}\Updownarrow$) since the oil fluid characteristics is effected, even the motor speed increase ($\omega_{eha}\Uparrow$) as well as the system output velocity($\dot{x}_{eha}\uparrow$), the system displacement output still decrease ($x_{eha}\downarrow$). When fault-4 occur, the motor speed would decrease obviously ($\omega_{eha}\Downarrow$), the cylinder pressure also decrease causally ($P_{eha}\Downarrow$), as well as the system velocity ($\dot{x}_{eha}\downarrow$) and the displacement ($x_{eha}\downarrow$).

3.2 Multidimensional Fault Characterization Model

Based on the fault reasoning mechanism, the multidimensional fault characterization model can be determined. The four models for the analyzed fault modes can be represented as the following forms:

$$\begin{cases} \dot{\boldsymbol{x}}_M(t) = (\boldsymbol{A} + \Delta\boldsymbol{A}_i)\boldsymbol{x}_M(t) + (\boldsymbol{B} + \Delta\boldsymbol{B}_i)\boldsymbol{u}(t) + \boldsymbol{G}w(t) \\ \boldsymbol{y}_M(t) = \boldsymbol{C}\boldsymbol{x}_M(t) \end{cases} \quad (6)$$

where $i = 1, 2, 3, 4$, and the model system matrices are defined as follows:

- Model-1:
$$\begin{cases} \Delta\boldsymbol{A}_1 = \begin{bmatrix} 0 & 0 & 0 & 0 \\ 0 & 0 & 0 & 0 \\ 0 & 0 & \Delta\bar{a}_{33} & 0 \\ 0 & 0 & 0 & 0 \end{bmatrix} \\ \Delta\boldsymbol{B}_1 = \begin{bmatrix} 0 & 0 & 0 & 0 \end{bmatrix}^{\mathrm{T}} \\ \Delta\bar{a}_{33} = -\left[4(\mathrm{E_{eha}}) \bullet (\Delta\mathrm{C_{ehal}})\right] / \mathrm{V_{eha}} \end{cases} \quad (7)$$

- Model-2:
$$\begin{cases} \Delta\boldsymbol{A}_2 = \begin{bmatrix} 0 & 0 & 0 & 0 \\ 0 & \Delta a_{22} & 0 & 0 \\ 0 & 0 & 0 & 0 \\ 0 & 0 & 0 & 0 \end{bmatrix} \\ \Delta\boldsymbol{B}_2 = \begin{bmatrix} 0 & 0 & 0 & 0 \end{bmatrix}^{\mathrm{T}} \end{cases} \quad (8)$$

- Model-3:
$$\begin{cases} \Delta\boldsymbol{A}_3 = \begin{bmatrix} 0 & 0 & 0 & 0 \\ 0 & 0 & 0 & 0 \\ 0 & \Delta a_{32} & \Delta\hat{a}_{33} & \Delta a_{34} \\ 0 & 0 & 0 & 0 \end{bmatrix} \\ \Delta\boldsymbol{B}_3 = \begin{bmatrix} 0 & 0 & 0 & 0 \end{bmatrix}^{\mathrm{T}} \\ \Delta\hat{a}_{33} = -\left[4(\Delta\mathrm{E_{eha}}) \bullet (\mathrm{C_{ehal}})\right] / \mathrm{V_{eha}} \end{cases} \quad (9)$$

- Model-4:
$$\begin{cases} \Delta\boldsymbol{A}_4 = \begin{bmatrix} 0 & 0 & 0 & 0 \\ 0 & 0 & 0 & 0 \\ 0 & 0 & 0 & 0 \\ 0 & 0 & 0 & 0 \end{bmatrix} \\ \Delta\boldsymbol{B}_4 = \begin{bmatrix} 0 & 0 & 0 & \Delta b_{41} \end{bmatrix}^{\mathrm{T}} \end{cases} \quad (10)$$

In order to use the multidimensional fault characterization model in fault identification process, the following fault identification mechanism in Fig. 3 is given.

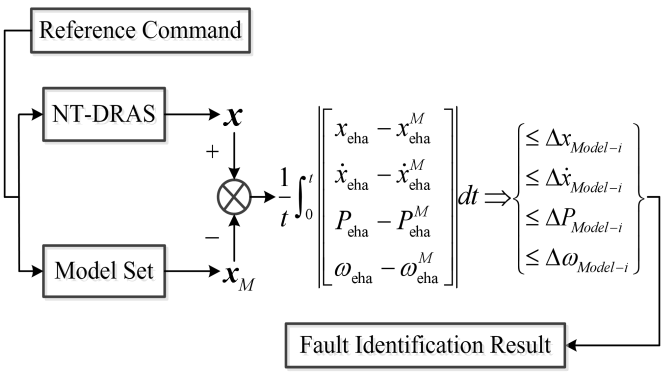

Fig. 3: Fault identification mechanism based model discrimination algorithm

As shown in Fig. 3, both the NT-DRAS and the all the models in the Model Set are given reference command, and then the multidimensional system output state signals are used to calculate the residual vector. The residual vector are performed by using an integral operator with specific time interval. All the calculated state signal residual integrations are then compared with the pre-set thresholds. When all the four calculated values satisfy a certain given threshold condition in the form of Fig. 3 simultaneously, that means the NT-DRAS has the same fault mode with a multidimensional fault characterization model, therein, the current fault mode of NT-DRAS can be identified as the same with the model.

4 Simulation Analysis

4.1 Fault Mechanism Verification

In normal condition without fault, the system matrices are set as follows

$$\begin{cases} \boldsymbol{A} = \begin{bmatrix} 0 & 1 & 0 & 0 \\ 0 & -31.408 & 2.0704\times10^{-6} & 0 \\ 0 & -3.20\times10^{10} & -5.9864\times10^{2} & 5.8776\times10^{13} \\ 0 & 0 & -9.9472\times10^{-5} & -1.0\times10^{2} \end{bmatrix} \\ \boldsymbol{B} = \begin{bmatrix} 0 & 0 & 0 & 456.63 \end{bmatrix}^{\mathrm{T}} \end{cases} \quad (11)$$

Table 3: Fault corresponding parameter variation ranges

Fault Types	Variation Ranges
Fault-1	$\mathrm{C_{ehal}}$: $0.1\times10^{-10} \rightarrow 1.0\times10^{-10}$ [(m³/s)/Pa]
Fault-2	$\mathrm{B_{eha}}$: $1.0\times10^{4} \rightarrow 1.0\times10^{5}$ [Ns/m]
Fault-3	$\mathrm{E_{eha}}$: $5.0\times10^{8} \rightarrow 8.0\times10^{7}$ [Pa]
Fault-4	$\mathrm{R_e}$: $0.245 \rightarrow 0.275$ [Ω]

The system single fault corresponding parameter variation ranges are set as shown in Table 3: In each fault conditions, the critical values of the variation ranges are imported into the system matrices respectively, and then the multidimensional states of system responses can be simulated.

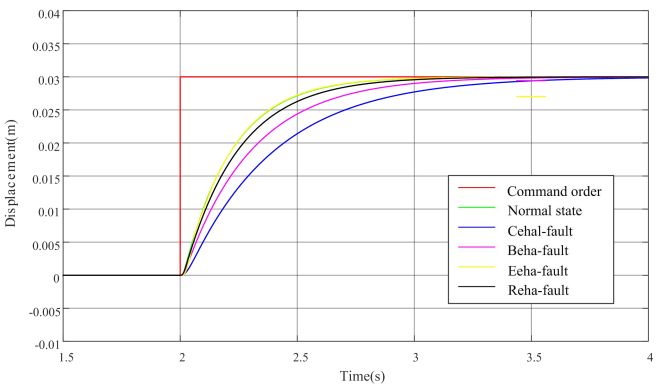

(a)

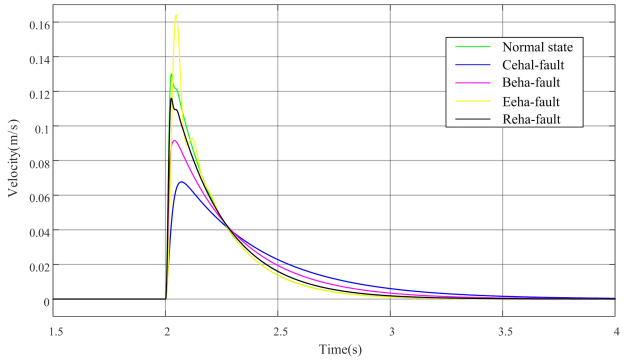

(b)

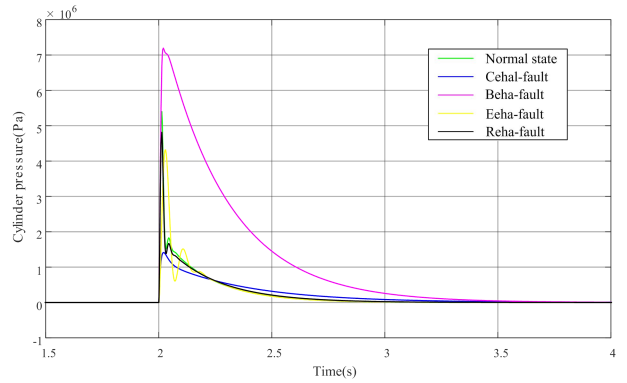

(c)

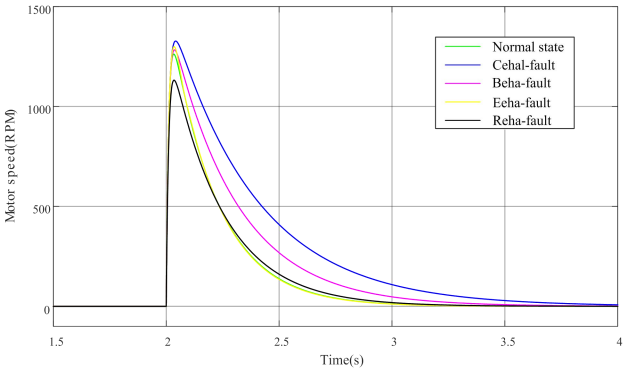

(d)

Fig. 4: Multidimensional state signal characterization under single fault conditions

As shown in Fig. 4, the system state response when only a single fault occurs is given. It can be seen that compared with the normal state, when Fault-1 occur, it can have the greatest effect on the system performance (see Fig. 4a). Under this type fault condition, in order to track the given step signal command order, even as the motor speed reaches its maximum value (see Fig. 4d), the cylinder pressure can only reach a low level (see Fig. 4c), leading the system output velocity to slow down to the slowest degree (see Fig. 4b); When Fault-2 occur, it can have a secondary effect on the system performance (see Fig. 4a): in order to track the given step signal command order, the motor speed also reaches a high level (see Fig. 4d); however, since the motion damping increases, the cylinder pressure reaches the highest level due to the reverse motion damping caused force (see Fig. 4c), but can only have limited system output velocity (see Fig. 4b). When Fault-3 occur, it can have the minimal effect on the system performance (see Fig. 4a): Fig. 4a,b and d show that the system output state almost have the same performance level as the system under normal state conditions. However, the cylinder pressure is at a low level due to the bulk modulus changes caused by oil deterioration (see Fig. 4c). When Fault-4 occur, it can also have obvious effect on the system performance (see Fig. 4a): the EHA motor resistance increases due to heat production caused high temperature, leading to the motor speed decreasing significantly (see Fig. 4d), and the cylinder pressure and the system output velocity also decrease eventually (see Fig. 4b,c). The above simulation results show that the fault reasoning mechanism is correct. Based on changing law of the multidimensional state response signals, the fault modes can be identified.

4.2 Fault Identification Effectiveness Verification

In this section, the fault identification effectiveness is verified by using both fault model discrimination and corresponding approximation error comparison.

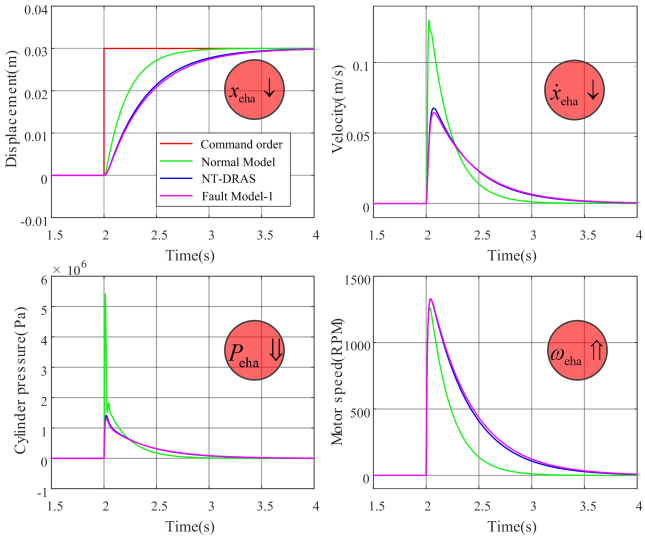

Fig. 5: Fault identification by using fault model discrimination

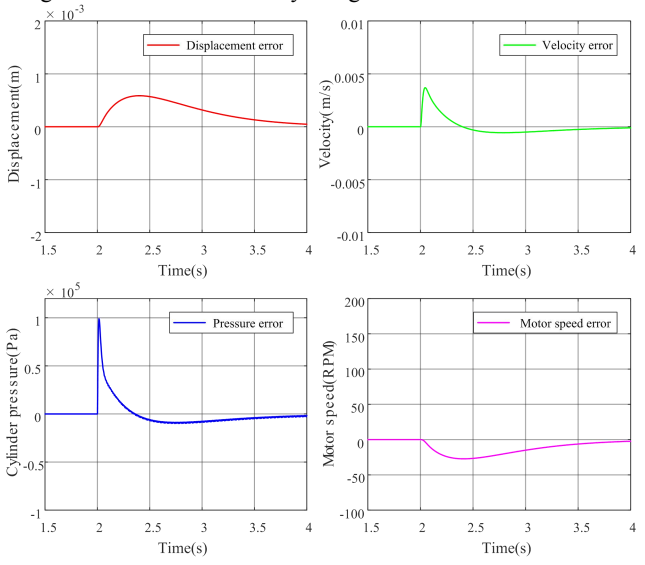

Fig. 6: Fault model output states approximation errors compared with NT-DRAS under fault condition

As shown in Fig. 5, compared with the system under normal conditions, the displacement output has obvious degradation. The left three output states also demonstrate fault status. Under this condition, the NT-DRAS and Fault Model-1 have almost the same output state curve, which means Fault Model-1 is the fault discrimination model under this fault condition: the system output velocity and cylinder pressure have obvious degradation while the motor speed has obvious increasing. This fault mechanism betray that Fault-1(hydraulic cylinder leakage) occur.

Moreover, the fault model output states approximation errors are shown in Fig. 6. The approximation errors can be calculated by using the given algorithm in Fig. 3. For the discriminant Fault-Model 1, the four output states approximation errors compared with NT-DRAS are shown in Table 4. It can be seen that the output state errors between Fault Model-1 and NT-DRAS are all less than the pre-set thresholds.

Table 4: Quantitative approximation errors

Errors	Calculated value	Pre-set thresholds
$\frac{1}{t}\int_0^t \left\| \left[x_{\text{eha}} - x_{\text{eha}}^M \right] \right\| dt$	0.0000719	$< \Delta x_{Model-1} = 0.0001$
$\frac{1}{t}\int_0^t \left\| \left[\dot{x}_{\text{eha}} - \dot{x}_{\text{eha}}^M \right] \right\| dt$	0.000136	$< \Delta \dot{x}_{Model-1} = 0.00015$
$\frac{1}{t}\int_0^t \left\| \left[P_{\text{eha}} - P_{\text{eha}}^M \right] \right\| dt$	2177.9508	$< \Delta P_{Model-1} = 2500$
$\frac{1}{t}\int_0^t \left\| \left[\omega_{\text{eha}} - \omega_{\text{eha}}^M \right] \right\| dt$	3.326975	$< \Delta \omega_{Model-1} = 5$

Based on the fault model discrimination results in Fig. 5 and the fault model output states approximation errors in Fig. 6, as well as the quantitative results of approximation errors, Fault-1(hydraulic cylinder leakage) can be identified by using fault occur mechanism analysis and approximation error calculation method.

5 Conclusions

This paper studied a new type dissimilar redundant actuation system (NT-DRAS). To support the FTC strategies of this NT-DRAS, a multidimensional fault characterization based fault identification method is proposed. Based on the fault occurrence mechanism, multi fault signals are used in the fault reasoning mechanism, so that a certain fault type can be identified.

References

[1] Haitao Q I, Yongling F U, **aoye Q I, et al. Architecture optimization of more electric aircraft actuation system[J]. Chinese Journal of Aeronautics, 2011, 24(4): 506-513.

[2] Wang, S., Shi, J., & Qiao, Y. (2023). Comprehensive Reliability of Aircraft Actuation System. In Advances in Reliability and Maintainability Methods and Engineering Applications: Essays in Honor of Professor Hong-Zhong Huang on his 60th Birthday (pp. 211-237). Cham: Springer Nature Switzerland.

[3] Y. Xiang and Z. Youmin, "Design of passive fault-tolerant flight controller against actuator failures," Chinese Journal of Aeronautics, vol. 28, pp. 180-190, 2015.

[4] Gao, Z., Jiang, B., Qi, R., & Xu, Y. (2011). Robust reliable control for a near space vehicle with parametric uncertainties and actuator faults. International Journal of Systems Science, 42(12), 2113-2124.

[5] S. Wang, X. Cui, J. Shi, M. M. Tomovic, and Z. Jiao, "Modeling of reliability and performance assessment of a dissimilar redundancy actuation system with failure monitoring," Chinese Journal of Aeronautics, vol. 29, pp. 799-813, 2016.

[6] J. Wang, Z. Li, and B. Peng, "Modeling and analysis of the dissimilar redundant actuator system," Machine Tool & Hydraulics, vol. 6, p. 028, 2008.

[7] Huang, J., Wang, J., Li, W., Liu, D., Shi, C., & Zhang, F. (2023). Fault Mode Analysis and Convex Optimization-Based Fault-Tolerant Control for New Type Dissimilar Redundant Actuation System of Near Space Vehicle. Applied Sciences, 13(23), 12567.

[8] Y. Zhang and J. Jiang, "Bibliographical review on reconfigurable fault-tolerant control systems," Annual reviews in control, vol. 32, pp. 229-252, 2008.

[9] J. Wang, S. Wang, X. Wang, C. Shi, and M. M. Tomovic, "Active fault tolerant control for vertical tail damaged aircraft with dissimilar redundant actuation system," Chinese Journal of Aeronautics, vol. 29, pp. 1313-1325, 2016.

[10] C. Shi, S. Wang, X Wang, et al. Active fault-tolerant control of dissimilar redundant actuation system based on performance degradation reference models[J]. Journal of the Franklin Institute, 2017, 354(2): 1087-1108.

[11] Paul M. Frank. Fault diagnosis in dynamic systems using analytical and knowledge-based redundancy: A survey and some new results[J]. Automatica, 1990,26(3): 459-474.

[12] Tidriri K, Chatti N, Verron S, Tiplica T. Bridging data-driven and model-based approaches for process fault diagnosis and health monitoring: A review of researches and future challenges[J]. Annual Reviews in Control, 2016, 42: 63-81.

[13] Nandi S, Toliyat H A, Li X. Condition monitoring and fault diagnosis of electrical motors-a review[J]. IEEE Transactions on Energy Conversion, 2005, 20(4): 719-729.

[14] Zhao M, Kang M, Tang B. Deep residual networks with dynamically weighted wavelet coefficients for fault diagnosis of planetary gearboxes[J]. IEEE Transactions on Industrial Electronics, 2018, 65(5): 4290-4300.

[15] Jin Q, Wang Y, Wang J. Planetary gearbox fault diagnosis based on multiple feature extraction and information fusion combined with deep learning[J]. China Mechanical Engineering, 2019, 30(2): 74-82.

Proceedings of the 3rd Conference on Fully Actuated System Theory and Applications
May 10-12, 2024, Shenzhen, China

Distributed Observer-Based Failure Compensation Load Frequency Control of Multi-Area Power Systems

Jiayu Wei[1], Jing Liu[2], Xin Huang[1], Siyuan Zhang[1], Xinyu Han[1], Anping Sun[1], Chenxu Chang[1]
1. The School of Automation Engineering Northeast Electric Power University, Jilin 132012 , P. R. China
2. The School of Economics and Management Northeast Electric Power University , Jilin 132012 , P. R. China
E-mail: huangxin@neepu.edu.cn

Abstract: This paper investigates the failure compensation load frequency control of multi-area power systems in the circumstance of actuator faults. Firstly, the distributed observer is proposed. It can estimate the actuator fault signals of the multi-area power systems in a distributed manner. And then the failure compensation load frequency control is designed based on the cyclic-small-gain method and the information of fault estimation signals, which is obtained from the observer. As a result, the controller can not only eliminate the influence of actuator faults, but also improve the robustness of the interconnections and load frequency disturbances, as well as ensure the stability of the systems further. In addition, an illustrative example is given to verify the proposed method.

Key Words: Multi-Area Power Systems, Load Frequency Control, Distributed Observer, Failure Compensation, Cyclic-Small-Gain

1 Introduction

The multi-area power system is composed of multiple subsystems in general, which are connected by interconnections. With the development of society, the correlation between the multi-area power systems and people's life is higher and higher [1–6]. As an important criterion, frequency is applied to measure the quality of power and it is need to take the control measures to reduce the frequency deviation between different areas. In addition, during the actual process of producing, some components in the system may fail, especially the actuator. Once it occurs, it will affect the control performance of the system, and even cause disaster in severe cases [7, 8]. Therefore, in order to avoid this situation, it is necessary to take advantage of load frequency control to ensure the safe and effective operation of the multi-area power systems, which can also compensate for the impact of the fault in the system.

For power systems in open networks with limited bandwidth, a memory-based event-triggered H_∞ load frequency control method was proposed in [9]. A method of data-driven cooperative was developed in multi-area power systems, which was according to the multi-agent deep reinforcement learning in continuous action domain in [10]. In [11], the event-triggered H_∞ load frequency control under a hybrid network attack consisting of denial-of-service attack and deception attack was studied. Moreover, in [12], a dynamic-memory event-triggered H_∞ load frequency control was first proposed for denial-of-service attacks, and the load frequency control model was also to be reconstructed.

Besides, failure compensation control is a variety of fault tolerant control. Since it was reported in 1997, researchers have proposed many fault tolerant control methods for actuator failures. In [13], the adaptive compensation control method was based on event-triggered timing consistency. For a sort of nonlinear systems with multiple redundant inputs, a new adaptive actuator failure compensation control scheme was presented in [14]. And in the stabilization problem of a class of reaction-diffusion equations described by a cascade partial differential equation-ordinary differential equation system, the influence of actuator failure was eliminated by using the compensation term, which was in the form of a smoothing function [15].

Based on the above mentioned, many literatures have investigated the load frequency control of multi-area power systems. Then, for the purpose of getting the information of actuator failures in a distributed way, so as to eliminate the influence of actuator failures in multi-area power systems, the fault compensation load frequency control is put forward. And the innovations are as follows:

1) The distributed observer is proposed, which can independently observe the actuator fault signals in each area.
2) With the intention of eliminating the effect of actuator failures, the load frequency control is designed by making use of the estimation information of actuator fault signals, which are obtained from the observer.
3) By using the cyclic-small-gain method, the influence of actuator faults and load frequency disturbances in the multi-area power systems is eliminated, and the robustness of the interconnections is enhanced, so that the changes of system frequency deviation gradually converge to 0.

2 Problem Formulation

This paper takes into account the multi-area power systems with N subsystems (or subsystems in N areas), which are connected by interconnections. The dynamic of ith area of the interconnected system is described as follows [16]

$$\begin{aligned}\dot{x}_i(t) =& A_i x_i(t) + B_i(u_i(t) + f_i(t)) + \sum_{\substack{j=1\\ j\neq i}}^{N} E_{ij}x_j(t)\\ &+ D_i\Delta P_{d_i}, \end{aligned} \tag{1}$$

This work is supported in part by the National Natural Science Foundation of China under Grant 62103094; in part by the Natural Science Foundation of Jilin Province in China under Grant YDZJ202201ZYTS379; and in part by the Doctoral Scientific Research Foundation of Northeast Electric Power University in China under Grant BSJXM-2021107.

where $x_i \triangleq \begin{bmatrix}\Delta f_i & \Delta P_{g_i} & \Delta X_{g_i} & \Delta E_i & \Delta\delta_i\end{bmatrix}^{\mathrm{T}}$ is the system state of ith area. And the specific parameters are in following:

$$A_i=\begin{bmatrix} \frac{1}{T_{P_i}} & \frac{K_{P_i}}{T_{P_i}} & 0 & 0 & \frac{K_{P_i}}{2\pi T_{P_i}}\sum_{\substack{j=1\\ j\neq i}} K_{sij} \\ 0 & -\frac{1}{T_{T_i}} & \frac{1}{T_{T_i}} & 0 & 0 \\ -\frac{1}{R_i T_{G_i}} & 0 & -\frac{1}{T_{G_i}} & -\frac{1}{T_{G_i}} & 0 \\ K_{E_i}K_{B_i} & 0 & 0 & 0 & \frac{K_{E_i}}{2\pi}\sum_{\substack{j=1\\ j\neq i}} K_{sij} \\ 2\pi & 0 & 0 & 0 & 0 \end{bmatrix},$$

$$B_i = \begin{bmatrix}0 & 0 & \frac{1}{T_{G_i}} & 0 & 0\end{bmatrix}^{\mathrm{T}}, F_i = \begin{bmatrix}-\frac{K_{P_i}}{T_{P_i}} & 0 & \frac{1}{T_{G_i}} & 0 & 0\end{bmatrix}^{\mathrm{T}},$$

$$E_{ij} = \begin{bmatrix} 0 & 0 & 0 & 0 & \frac{K_{P_i}}{2\pi T_{P_i}}K_{sij} \\ 0 & 0 & 0 & 0 & 0 \\ 0 & 0 & 0 & 0 & 0 \\ 0 & 0 & 0 & 0 & -\frac{K_{E_i}}{2\pi T_{P_i}}K_{sij} \\ 0 & 0 & 0 & 0 & 0 \end{bmatrix}.$$

where $\Delta f_i(t), \Delta P_{g_i}(t), \Delta X_{g_i}, \Delta E_i(t), \Delta\delta_i(t)$ are the changes of frequency, power output, governor valve position, integral control and rotor angle deviation, respectively; $T_{P_i}, T_{T_i}, T_{G_i}$ are the time constants of power system, turbine and governor, respectively; $R_i, K_{P_i}, K_{E_i}, K_{B_i}$ are speed regulation coefficient, power system gain, integral control gain and frequency bias factor, respectively; the interconnection gain between the ith area and the jth area is K_{sij}; $x_i(t) \in \mathbb{R}^{n_i}$ is the ith subsystem's state vector; $x_j(t) \in \mathbb{R}^{n_j}$ is the jth subsystem's state vector, which is adjacent to $x_i(t)$; $u_i(t) \in \mathbb{R}^{l_i}$ is the ith subsystem's control input vector; and $f_i \in \mathbb{R}^{l_i}$ represents the actuator failure. $\Delta P_{d_i} \in \mathbb{R}^{l_i\times l_i}$ is load frequency disturbance vector. The dimensions of system matrices in (1) are $A_i \in \mathbb{R}^{n_i\times n_i}$, $B_i \in \mathbb{R}^{n_i\times l_i}$, $D_i \in \mathbb{R}^{n_i\times l_i}$. $E_{ij} \in \mathbb{R}^{n_i\times n_j}$ is the matrix that connects the ith system and the jth system and $E_{ij} = \sum_{k=1}^{n_{ij}} \mathcal{D}_{ijk}\varepsilon_{ijk}^{\mathrm{T}}$, where both $\mathcal{D}_{ijk}$ and ε_{ijk} are 5-dimensional vectors, n_{ij} is a positive integer.

In order to address the impact of actuator faults and load frequency disturbances on the system, the goal of this paper is to design the distributed observer to obtain estimated information of actuator faults. On the other hand is to use the obtained information to design the fault compensation load frequency controller to improve the robustness of the interconnections. It can make the changes in system frequency deviation approach to 0, and thus maintain the performance of multi-area power systems.

3 Main Result

For the purpose of obtaining the reconstructed actuator fault signals, the observer is designed as follows:

$$\begin{aligned}\dot{\hat{x}}_i(t) =& A_i\hat{x}_i(t) + B_i(u_i(t) + \hat{f}_i(t)) - L_i(\hat{x}_i - x_i) \\ &+ \sum_{\substack{j=1\\ j\neq i}}^{N} E_{ij}\hat{x}_j(t) \end{aligned} \tag{2}$$

where $\hat{f}_i(t) = -F_i(\hat{x}_i(t) - x_i(t))$, and F_i will be designed later, $\hat{x}_i \in \mathbb{R}^{n_i}$ and $\hat{x}_j \in \mathbb{R}^{n_j}$ are the estimation of x_i and x_j; L_i is the observer gain and it also will be designed later.

Let $e_i = \hat{x}_i - x_i$, so that the error system is

$$\begin{aligned}\dot{e}_i(t) =& A_ie_i(t) + B_i\tilde{f}_i(t) - L_ie_i + \sum_{\substack{j=1\\ j\neq i}}^{N} E_{ij}e_j(t) \\ &- D_i\Delta P_{d_i}\end{aligned}$$

where $\tilde{f}_i(t) = \hat{f}_i(t) - f_i(t)$. Therefore, $\dot{\tilde{f}}_i(t) = -F_ie_i$. Combine the $\dot{e}_i$ and $\dot{\tilde{f}}_i$ and let $\bar{e}_i = \begin{bmatrix}e_i & \tilde{f}_i\end{bmatrix}^{\mathrm{T}}$, then taking the derivative of $\bar{e}_i$, one has

$$\dot{\bar{e}}_i = \bar{A}_i\bar{e}_i - \bar{L}_i\bar{C}_ie_i + \sum_{\substack{j=1\\ j\neq i}}^{N} \bar{E}_{ij}\bar{e}_j - \bar{D}_i\Delta P_{d_i} \tag{3}$$

where $\bar{A}_i = \begin{bmatrix}A_i & B_i\\ 0 & 0\end{bmatrix}, \bar{L}_i = \begin{bmatrix}L_i\\ F_i\end{bmatrix}, \bar{C}_i = \begin{bmatrix}I\\ 0\end{bmatrix}^{\mathrm{T}}, \bar{E}_{ij} = \begin{bmatrix}E_{ij} & 0\\ 0 & 0\end{bmatrix}, \bar{D}_i = \begin{bmatrix}\bar{D}_i\\ 0\end{bmatrix}$.

Theorem 1. *For given $\alpha_i > 0$, if there exist matrices $W_i = W_i^{\mathrm{T}} > 0, Z_i$ with suitable dimensions and positive scalars η_i, ϑ_i satisfying the LMI as below*

$$\begin{bmatrix} \mathbf{He}(W_i\bar{A}_i - Z_i\bar{C}_i) + \sum_{\substack{j=1\\ j\neq i}} \vartheta_j \sum_{k=1}^{n_{ji}} \bar{\varepsilon}_{jik}\bar{\varepsilon}_{jik}^{\mathrm{T}} + I & & \\ * & & \\ * & & \\ * & & \end{bmatrix}$$

$$\begin{bmatrix} W_i\Omega_i^{\mathrm{T}} & W_i & 0 \\ -\vartheta_iI & 0 & 0 \\ * & -\eta_i^2I & 0 \\ * & * & (\eta_i^2\|\bar{D}_i\|_F^2 - \alpha_i^2)I \end{bmatrix} < 0 \tag{4}$$

where $L_i = W_i^{-1}Z_i, \Omega_i^{\mathrm{T}}\Omega_i = \sum_{\substack{j=1\\ j\neq i}}^{N}\sum_{k=1}^{n_{ij}} \bar{\mathcal{D}}_{ijk}\bar{\mathcal{D}}_{ijk}^{\mathrm{T}}, \bar{\mathcal{D}}_{ijk} = [\mathcal{D}_{ijk}; 0], \bar{\varepsilon}_{jik} = [\varepsilon_{jik}; 0]$. For the case of $\Delta P_{d_i} = 0$, the information of observer's estimate errors can be converge to 0; for the case of $\Delta P_{d_i} \neq 0$, the α_i-level H_∞ performance is guaranteed (i.e., $\int_0^\infty \bar{e}_i^{\mathrm{T}}\bar{e}_i d\tau < \alpha_i^2\int_0^\infty \Delta P_{d_i}^{\mathrm{T}}\Delta P_{d_i}d\tau$).

Proof. Please see appendix A. □

Because the system performance is maintained under the adverse effects of actuator faults, so that the failure compensation control is designed in the form of

$$u_i = K_ix_i - \hat{f}_i$$

where K_i will be given later. The system state equation becomes

$$\dot{x}_i(t) = A_ix_i(t) + B_i(K_ix_i(t) - \tilde{f}_i(t)) + \sum_{\substack{j=1\\ j\neq i}}^{N} E_{ij}x_j(t) \tag{5}$$

The following lemma describes the cyclic-small-gain method, which can prove the stability of the system.

Lemma 1. *[17] For any given constant $\xi_i > 0$, where i is from 1 to N, suppose that the cyclic-small-gain condition holds, which is in the following.*

$$\sum_{j=1}^{N-1} j \sum_{1\le i_1\le i_2\le\cdots\le i_{j+1}\le j+1} \xi_{i_1}\xi_{i_2}\cdots\xi_{i_{j+1}} < 1 \tag{6}$$

Then, the following linear equation

$$\begin{bmatrix} -1 & \xi_2 & \xi_3 & \cdots & \xi_N \\ \xi_1 & -1 & \xi_3 & \cdots & \xi_N \\ \xi_1 & \xi_2 & -1 & \cdots & \xi_N \\ \vdots & \vdots & \vdots & \ddots & \vdots \\ \xi_1 & \xi_2 & \xi_3 & \cdots & -1 \end{bmatrix} \begin{bmatrix} c_1 \\ c_2 \\ c_3 \\ \vdots \\ c_N \end{bmatrix} = \begin{bmatrix} -1 \\ -1 \\ -1 \\ \vdots \\ -1 \end{bmatrix}$$

can be solved as

$$c_i = \frac{\prod_{j=1, j\neq i}^{N} (\xi_j + 1)}{1 - \sum_{j=1}^{N-1} j \sum_{1 \le i_1 \le i_2 \le \cdots \le i_{j+1} \le j+1} \xi_{i_1} \xi_{i_2} \cdots \xi_{i_{j+1}}} > 0$$

Theorem 2. *Consider the system (1) under controller u_i and observer (2). For any given $\sigma_i > 0$, if there exists any constant $\xi_i > 0$ satisfies the condition (6), and any constants $\pi_i > 0$, $\gamma_i > 0$, the matrix $M_i \in \mathbb{R}^{l_i \times n_i}$ and the positive definite symmetric matrix $Q_i \in \mathbb{R}^{n_i}$ such that the following LMI holds*

$$\begin{bmatrix} \mathbf{He}(A_i Q_i + B_i M_i) + \frac{\pi_i}{c_i \xi_i} \bar{E}_i & Q_i & Q_i & 0 & B_i \\ * & -\frac{\pi}{c_i} & 0 & 0 & 0 \\ * & * & -I & 0 & 0 \\ * & * & * & (\sigma_i^2 - \gamma_i^2) I & 0 \\ * & * & * & * & -\sigma_i^2 I \end{bmatrix} < 0 \qquad (7)$$

where $i = 1, \ldots, N$, $\bar{E}_i = E_{i1}E_{i1}^{\mathrm{T}} + E_{i2}E_{i2}^{\mathrm{T}} + \cdots + E_{iN}E_{iN}^{\mathrm{T}}$. Then, for the case of $\tilde{f}_i = 0$, the system state can asymptotically converges to 0; For the case that $\tilde{f}_i \neq 0$, the γ_i-level H_∞ performance is guaranteed (i.e., $\int_0^\infty x_i^{\mathrm{T}} x_i d\tau < \gamma_i^2 \int_0^\infty \tilde{f}_i^{\mathrm{T}} \tilde{f}_i d\tau$), where the control gain $K_i = M_i Q_i^{-1}$.

Proof. Please see appendix B. □

4 Simulation

In order to verify the effectiveness of the proposed method, an example of a three-area multi-area power system is used. The system parameters are as follows:
Area 1:

$$A_1 = \begin{bmatrix} -0.05 & 6 & 0 & 0 & -0.955 \\ 0 & -3.472 & 3.472 & 0 & 0 \\ -5.878 & 0 & -13.021 & -13.021 & 0 \\ 4 & 0 & 0 & 0 & 1.592 \\ 6.283 & 0 & 0 & 0 & 0 \end{bmatrix},$$

$$B_1 = \begin{bmatrix} 0 & 0 & 13.021 & 0 & 0 \end{bmatrix}^{\mathrm{T}}, D_1 = \begin{bmatrix} -6 & 0 & 0 & 0 & 0 \end{bmatrix}^{\mathrm{T}},$$

$$E_{12} = E_{13} = \begin{bmatrix} 0 & 0 & 0 & 0 & 0.1434 \\ 0 & 0 & 0 & 0 & 0 \\ 0 & 0 & 0 & 0 & 0 \\ 0 & 0 & 0 & 0 & -0.2388 \\ 0 & 0 & 0 & 0 & 0 \end{bmatrix},$$

$$\mathcal{D}_{121} = \mathcal{D}_{131} = \begin{bmatrix} 0.159 & 0 & 0 & -0.265 & 0 \end{bmatrix}^{\mathrm{T}},$$

$$\varepsilon_{121} = \varepsilon_{131} = \begin{bmatrix} 0 & 0 & 0 & 0 & 0.9 \end{bmatrix}^{\mathrm{T}}.$$

Area 2:

$$A_2 = \begin{bmatrix} -0.04 & 4.5 & 0 & 0 & -0.716 \\ 0 & -3.157 & 3.157 & 0 & 0 \\ -5.805 & 0 & -14.468 & -14.468 & 0 \\ 4 & 0 & 0 & 0 & 1.592 \\ 6.283 & 0 & 0 & 0 & 0 \end{bmatrix},$$

$$B_2 = \begin{bmatrix} 0 & 0 & 14.468 & 0 & 0 \end{bmatrix}^{\mathrm{T}}, D_2 = \begin{bmatrix} -4.5 & 0 & 0 & 0 & 0 \end{bmatrix}^{\mathrm{T}},$$

$$E_{21} = E_{23} = \begin{bmatrix} 0 & 0 & 0 & 0 & 0.1074 \\ 0 & 0 & 0 & 0 & 0 \\ 0 & 0 & 0 & 0 & 0 \\ 0 & 0 & 0 & 0 & -0.2388 \\ 0 & 0 & 0 & 0 & 0 \end{bmatrix},$$

$$\mathcal{D}_{211} = \mathcal{D}_{231} = \begin{bmatrix} 0.119 & 0 & 0 & -0.265 & 0 \end{bmatrix}^{\mathrm{T}},$$

$$\varepsilon_{211} = \varepsilon_{231} = \begin{bmatrix} 0 & 0 & 0 & 0 & 0.9 \end{bmatrix}^{\mathrm{T}}.$$

Area 3:

$$A_3 = \begin{bmatrix} -0.05 & 5.75 & 0 & 0 & -0.915 \\ 0 & -2.976 & 2.976 & 0 & 0 \\ -6.448 & 0 & -14.881 & -14.881 & 0 \\ 4 & 0 & 0 & 0 & 1.592 \\ 6.283 & 0 & 0 & 0 & 0 \end{bmatrix},$$

$$B_3 = \begin{bmatrix} 0 & 0 & 14.881 & 0 & 0 \end{bmatrix}^{\mathrm{T}}, D_3 = \begin{bmatrix} -5.75 & 0 & 0 & 0 & 0 \end{bmatrix}^{\mathrm{T}},$$

$$E_{31} = E_{32} = \begin{bmatrix} 0 & 0 & 0 & 0 & 0.1374 \\ 0 & 0 & 0 & 0 & 0 \\ 0 & 0 & 0 & 0 & 0 \\ 0 & 0 & 0 & 0 & -0.2388 \\ 0 & 0 & 0 & 0 & 0 \end{bmatrix}.$$

$$\mathcal{D}_{311} = \mathcal{D}_{321} = \begin{bmatrix} 0.153 & 0 & 0 & -0.265 & 0 \end{bmatrix}^{\mathrm{T}}$$

$$\varepsilon_{311} = \varepsilon_{321} = \begin{bmatrix} 0 & 0 & 0 & 0 & 0.9 \end{bmatrix}^{\mathrm{T}}.$$

and $n_{12} = n_{13} = n_{21} = n_{23} = n_{31} = n_{32} = 1$. And also, the load frequency disturbance is selected as $\Delta P_{d_i} = \frac{1}{100(t+0.1)}$, the actuator faults are $f_1 = 10, f_2 = 15$, and $f_3 = 20$. Therefore, considering the effects of actuator faults and load frequency disturbances, after being compensated by the controller, the performance of the multi-area power systems is shown in the following simulation figures. The actuator fault of the system and its estimation are shown in Fig. 1. As described in it, the observer can estimate the information of actuator faults in three areas, which demonstrate the availability of the observer. And Fig. 2 displays the changes in frequency deviation and their observed values in three areas. Besides, Fig. 3 describes the system states of three areas. It can be seen from them that the variation of frequency deviation and the states of three areas gradually approach to 0, which illustrates that the controller can eliminate the influence of actuator faults and load frequency disturbances. In addition, it can improve the robustness of the interconnections and further make sure the stability of the multi-area power systems.

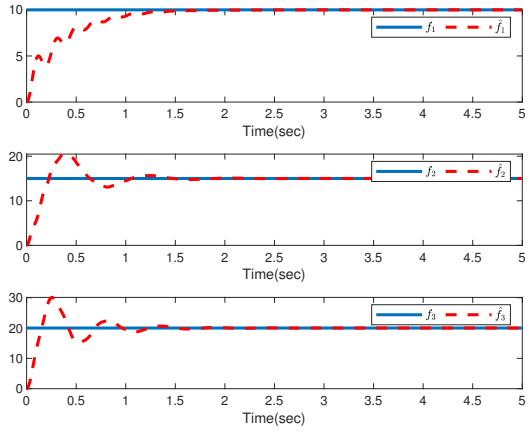

Fig. 1: The actuator faults and their estimations of systems in three areas

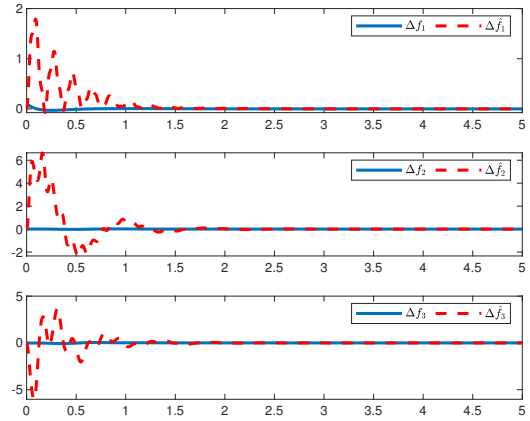

Fig. 2: The changes of frequency Δf_i and its estimation $\Delta \hat{f}_i$

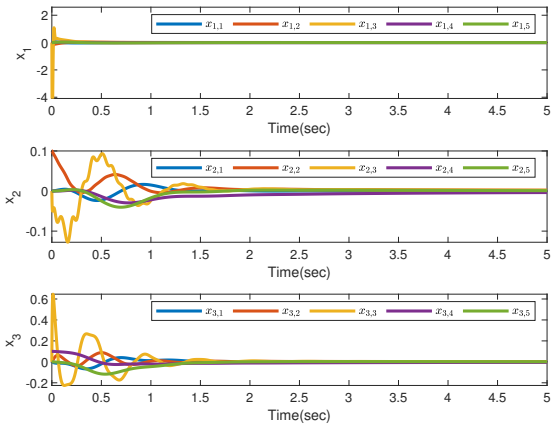

Fig. 3: The states of systems in three areas

5 Conclusion

In this paper, the problem of failure compensation load frequency control based on distributed observer was studied. The distributed observer was proposed, which can observe actuator faults in each area independently. The failure compensation load frequency control was designed, which used the observed information to eliminate the influence of actuator faults. It can improve the robustness of the interconnections and load frequency disturbances, as well as make the deviation of the frequency closes to 0, and achieve the desired control performance. Finally, the effectiveness of this method was demonstrated through an illustrative example.

6 Appendix

Appendix A

Consider the Lyapunov function as $V = \sum_{i=1}^{N} V_i = \sum_{i=1}^{N} \bar{e}_i^{\mathrm{T}} W_i \bar{e}_i$, where $W_i = W_i^{\mathrm{T}} > 0$ and then taking the derivative of all V_i, then the following result is given:

$$\dot{V} = \sum_{i=1}^{N} \bar{e}_i^{\mathrm{T}} \mathbf{He}(W_i \bar{A}_i - W_i \bar{L}_i \bar{C}_i) \bar{e}_i + 2 \sum_{\substack{j=1 \\ j \neq i}}^{N} \sum_{k=1}^{n_{ij}} \bar{e}_i^{\mathrm{T}} W_i \bar{E}_{ij} \bar{e}_j - 2 \sum_{i=1}^{N} \bar{e}_i^{\mathrm{T}} W_i \bar{D}_i \Delta P_{d_i}$$

According to $E_{ij} = \sum_{k=1}^{n_{ij}} \mathcal{D}_{ijk} \varepsilon_{ijk}^{T}$ and $2\mathcal{X}^{\mathrm{T}}\mathcal{Y} \leq (1/\iota)\mathcal{X}^{\mathrm{T}}\mathcal{X} + \iota \mathcal{Y}^{\mathrm{T}}\mathcal{Y}, \forall \iota > 0$, then one has

$$\begin{aligned} 2 \sum_{i=1}^{N} \bar{e}_i^{\mathrm{T}} W_i \sum_{\substack{j=1 \\ j \neq i}} \bar{E}_{ij} \bar{e}_j &\leq \sum_{i=1}^{N} \frac{1}{\vartheta_i} \bar{e}_i^{\mathrm{T}} W_i \sum_{\substack{j=1 \\ j \neq i}} \sum_{k=1}^{n_{ij}} \bar{\mathcal{D}}_{ijk} \bar{\mathcal{D}}_{ijk}^{\mathrm{T}} \\ &\times W_i \bar{e}_i + \sum_{i=1}^{N} \vartheta_i \bar{e}_j^{\mathrm{T}} \sum_{\substack{j=1 \\ j \neq i}} \sum_{k=1}^{n_{ij}} \bar{\varepsilon}_{ijk} \bar{\varepsilon}_{ijk}^{\mathrm{T}} \bar{e}_j \\ &\leq \sum_{i=1}^{N} \bar{e}_i^{\mathrm{T}} \Big(\frac{1}{\vartheta_i} W_i \sum_{\substack{j=1 \\ j \neq i}} \sum_{k=1}^{n_{ij}} \bar{\mathcal{D}}_{ijk} \bar{\mathcal{D}}_{ijk}^{\mathrm{T}} W_i \\ &+ \sum_{\substack{j=1 \\ j \neq i}} \vartheta_j \sum_{k=1}^{n_{ji}} \bar{\varepsilon}_{jik} \bar{\varepsilon}_{jik}^{\mathrm{T}} \Big) \bar{e}_i \\ -2 \sum_{i=1}^{N} \bar{e}_i^{\mathrm{T}} W_i \bar{D}_i \Delta \bar{P}_{d_i} &\leq \frac{1}{\eta_i^2} \bar{e}_i^{\mathrm{T}} W_i W_i \bar{e}_i \\ &+ \eta_i^2 \|\bar{D}_i\|_F^2 \Delta \bar{P}_{d_i}^{\mathrm{T}} \Delta P_{d_i} \end{aligned}$$

Then, it can get that

$$\begin{aligned} \dot{V} \leq \sum_{i=1}^{N} \bar{e}_i^{\mathrm{T}} \Big(& \mathbf{He}(W_i \bar{A}_i - Z_i \bar{C}_i) + \frac{1}{\eta_i^2} W_i W_i \\ & + \frac{1}{\vartheta_i} W_i \sum_{\substack{j=1 \\ j \neq i}} \sum_{k=1}^{n_{ij}} \bar{\mathcal{D}}_{ijk} \bar{\mathcal{D}}_{ijk}^{\mathrm{T}} W_i \\ & + \sum_{\substack{j=1 \\ j \neq i}} \vartheta_j \sum_{k=1}^{n_{ji}} \bar{\varepsilon}_{jik} \bar{\varepsilon}_{jik}^{\mathrm{T}} \Big) \bar{e}_i + \eta_i^2 \|\bar{D}_i\|_F^2 \Delta \bar{P}_{d_i}^{\mathrm{T}} \Delta P_{d_i} \end{aligned} \quad (8)$$

1) for the case of $\Delta P_{d_i}=0$, formula (8) is converted into

$$\begin{aligned}\dot{V} \leq & \sum_{i=1}^{N} \bar{e}_i^{\mathrm{T}}(\mathbf{He}(W_i\bar{A}_i - Z_i\bar{C}_i) \\ & + \frac{1}{\vartheta_i} W_i \sum_{\substack{j=1 \\ j\neq i}} \sum_{k=1}^{n_{ij}} \bar{\mathcal{D}}_{ijk}\bar{\mathcal{D}}_{ijk}^{\mathrm{T}} W_i \\ & + \sum_{\substack{j=1 \\ j\neq i}} \vartheta_j \sum_{k=1}^{n_{ji}} \bar{\varepsilon}_{jik}\bar{\varepsilon}_{jik}^{\mathrm{T}})\bar{e}_i\end{aligned}$$

Then, according to condition (4), $V_i < 0$. Therefore, the observer estimation errors can converge to 0, the proof is completed.

2) for the case of $\Delta P_{d_i} \neq 0$, and under zero initial condition, i.e., $V_i(0)=0$, one has

$$\begin{aligned}& \int_0^{\infty} (\bar{e}_i^{\mathrm{T}}\bar{e}_i - \alpha_i^2 \Delta P_{d_i}^{\mathrm{T}} \Delta P_{d_i} + \dot{V}_i - \dot{V}_i) d\tau \\ = & \int_0^{\infty} (\bar{e}_i^{\mathrm{T}}\bar{e}_i - \alpha_i^2 \Delta P_{d_i}^{\mathrm{T}} \Delta P_{d_i} + \dot{V}_i) d\tau - V_i(\infty) \\ \leq & \int_0^{\infty} (\bar{e}_i^{\mathrm{T}}\bar{e}_i - \alpha_i^2 \Delta P_{d_i}^{\mathrm{T}} \Delta P_{d_i} + \dot{V}_i) d\tau\end{aligned}$$

where $\alpha_i > 0$. According to condition (4), it has

$$\begin{aligned}& \bar{e}_i^{\mathrm{T}}(\mathbf{He}(W_i\bar{A}_i - Z_i\bar{C}_i) + \frac{1}{\eta_i^2} W_i W_i \\ & + \frac{1}{\vartheta_i} W_i \sum_{\substack{j=1 \\ j\neq i}} \sum_{k=1}^{n_{ij}} \bar{\mathcal{D}}_{ijk}\bar{\mathcal{D}}_{ijk}^{\mathrm{T}} W_i \\ & + \sum_{\substack{j=1 \\ j\neq i}} \vartheta_j \sum_{k=1}^{n_{ji}} \bar{\varepsilon}_{jik}\bar{\varepsilon}_{jik}^{\mathrm{T}})\bar{e}_i + \Delta\bar{P}_{d_i}^{\mathrm{T}}(\eta_i^2 \|\bar{D}_i\|_F^2 \\ & - \alpha_i^2)\Delta P_{d_i} < 0,\end{aligned}$$

which means that the load frequency disturbance ΔP_{d_i} is suppressed by α_i-level H_∞ performance and $\dot{V}_i < 0$.

Appendix B

Consider the system state equation (5) and choose the Lyapunov function as $V_i = x_i^{\mathrm{T}} P_i x_i$, where $P_i \in \mathbb{R}^{n_i}$ and $P_i = P_i^{\mathrm{T}} > 0$, then the derivation of V_i is

$$\begin{aligned}\dot{V}_i = & x_i^{\mathrm{T}}\mathbf{He}(P_iA_i + P_iB_iK_i)x_i - 2x_i^{\mathrm{T}}P_iB_i\tilde{f}_i \\ & + 2x_i^{\mathrm{T}}P_i \sum_{\substack{j=1 \\ j\neq i}} E_{ij}x_j\end{aligned}$$

1) for $\tilde{f}_i = 0$,

$$\begin{aligned}\dot{V} = & \sum_{i=1}^{N} \dot{V}_i \\ \leq & \sum_{i=1}^{N} [x_i^{\mathrm{T}}\mathbf{He}(P_iA_i + P_iB_iK_i)x_i + 2x_i^{\mathrm{T}}P_i(E_{i1}x_1 \\ & + E_{i2}x_2 + \cdots + E_{iN}x_N)] \\ \leq & \sum_{i=1}^{N} [(x_i^{\mathrm{T}}\mathbf{He}(P_iA_i + P_iB_iK_i)x_i + \frac{\pi_i}{c_i\xi_i} x_i^{\mathrm{T}}P_i \\ & \times \bar{E}_iP_ix_i + \frac{(1+\xi_i)c_i}{\pi_i}\|x_i\|^2 - \frac{c_i\xi_i}{\pi_i}\|x_i\|^2) \\ & + \sum_{i=1}^{N} \frac{c_i}{\pi_i}(-\|x_i\|^2 + \xi_i \sum_{j=1, j\neq i}^{N} \|x_j\|^2)]\end{aligned}$$

According to the lemma 1, one has

$$\begin{aligned}\dot{V}_i \leq & \sum_{i=1}^{N} [(x_i^{\mathrm{T}}\mathbf{He}(P_iA_i + P_iB_iK_i)x_i \\ & + \frac{\pi_i}{c_i\xi_i} x_i^{\mathrm{T}}P_i\bar{E}_iP_ix_i + \frac{c_i}{\pi_i}\|x_i\|^2) - \frac{\|x\|^2}{\pi_i}] \\ \leq & \sum_{i=1}^{N} [x_i^{\mathrm{T}}(\mathbf{He}(P_iA_i + P_iB_iK_i) + \frac{\pi_i}{c_i\xi_i} P_i\bar{E}_iP_i \\ & + \frac{c_i}{\pi_i})x_i]\end{aligned}$$

Moreover, condition (7) can be reduced to

$$\begin{bmatrix} \mathbf{He}(A_iQ_i + B_iM_i) + \frac{\pi_i}{c_i\xi_i}\bar{E}_i & Q_i & Q_i \\ * & -\frac{\pi}{c_i} & 0 \\ * & * & -I \end{bmatrix} < 0$$

which expresses that

$$\begin{aligned}\mathbf{He}(A_iP_i^{-1} + B_iK_iP_i^{-1}) + \frac{\pi_i}{c_i\xi_i}\bar{E}_i + \frac{c_i}{\pi_i}P_i^{-1}P_i^{-1} \\ + P_i^{-1}P_i^{-1} < 0\end{aligned}$$

where $Q_i = P_i^{-1}, M_i = K_iP_i^{-1}$. Further it can get that

$$\mathbf{He}(P_iA_i + P_iB_iK_i) + \frac{\pi_i}{c_i\xi_i} P_i\bar{E}_iP_i + \frac{c_i}{\pi_i} < 0$$

Hence, the fault compensation load frequency controller effectively mitigates the impact of actuator faults and load frequency disturbances, enhances the robustness of the interconnections, and also it can guarantee optimal system performance.

2) for $\tilde{f}_i \neq 0$, on the basis of case 1)

$$\begin{aligned}\dot{V} \leq & \sum_{i=1}^{N} [x_i^{\mathrm{T}}(\mathbf{He}(P_iA_i + P_iB_iK_i) + \frac{\pi_i}{c_i\xi_i} P_i\bar{E}_iP_i \\ & + \frac{c_i}{\pi_i})x_i - 2x_i^{\mathrm{T}}P_iB_i\tilde{f}_i]\end{aligned}$$

Because of $-2x_i^{\mathrm{T}}P_iB_i\tilde{f}_i \leq \frac{1}{\sigma_i^2}x_i^{\mathrm{T}}P_iB_iB_i^{\mathrm{T}}P_ix_i +$

$\sigma_i^2 \tilde{f}_i^{\mathrm{T}} \tilde{f}_i$, where $\sigma_i > 0$, one gets

$$\dot{V} \leq \sum_{i=1}^{N} [x_i^{\mathrm{T}} (\mathbf{He}(P_i A_i + P_i B_i K_i) + \frac{\pi_i}{c_i \xi_i} P_i \bar{E}_i P_i + \frac{c_i}{\pi_i}) x_i + \frac{1}{\sigma_i^2} x_i^{\mathrm{T}} P_i B_i B_i^{\mathrm{T}} P_i x_i + \sigma_i^2 \tilde{f}_i^{\mathrm{T}} \tilde{f}_i]$$

then under zero initial condition, i.e., $V_i(0) = 0$, one has

$$\begin{aligned} &\int_0^{\infty} (x_i^{\mathrm{T}} x_i - \gamma_i^2 \tilde{f}_i^{\mathrm{T}} \tilde{f}_i + \dot{V}_i - \dot{V}_i) d\tau \\ &= \int_0^{\infty} (x_i^{\mathrm{T}} x_i - \gamma_i^2 \tilde{f}_i^{\mathrm{T}} \tilde{f}_i + \dot{V}_i) d\tau - V_i(\infty) \\ &\leq \int_0^{\infty} (x_i^{\mathrm{T}} x_i - \gamma_i^2 \tilde{f}_i^{\mathrm{T}} \tilde{f}_i + \dot{V}_i) d\tau \end{aligned}$$

where $\gamma_i > 0$. Furthermore, one has

$$\begin{aligned} &x_i^{\mathrm{T}} x_i - \gamma_i^2 \tilde{f}_i^{\mathrm{T}} \tilde{f}_i + x_i^{\mathrm{T}} (\mathbf{He}(P_i A_i + P_i B_i K_i) \\ &+ \frac{\pi_i}{c_i \xi_i} P_i \bar{E}_i P_i + \frac{c_i}{\pi_i}) x_i + \frac{1}{\sigma_i^2} x_i^{\mathrm{T}} P_i B_i B_i^{\mathrm{T}} P_i x_i \\ &+ \sigma_i^2 \tilde{f}_i^{\mathrm{T}} \tilde{f}_i \\ &= \begin{bmatrix} x_i^{\mathrm{T}} \\ \tilde{f}_i^{\mathrm{T}} \end{bmatrix}^T O_i \begin{bmatrix} x_i^{\mathrm{T}} \\ \tilde{f}_i^{\mathrm{T}} \end{bmatrix} \end{aligned}$$

where

$$O_i = \begin{bmatrix} R_i & 0 \\ 0 & (\sigma_i^2 - \gamma_i^2) I \end{bmatrix}$$

and $R_i = \mathbf{He}(P_i A_i + P_i B_i K_i) + \frac{1}{\sigma_i^2} P_i B_i B_i^{\mathrm{T}} P_i + \frac{\pi_i}{c_i \xi_i} P_i \bar{E}_i P_i + \frac{c_i}{\pi_i} + I$. Condition (7) turns out

$$\begin{bmatrix} H_i & 0 \\ 0 & (\sigma_i^2 - \gamma_i^2) I \end{bmatrix} < 0 \tag{9}$$

and $H_i = \mathbf{He}(A_i Q_i + B_i M_i) + \frac{1}{\sigma_i^2} B_i B_i^{\mathrm{T}} + \frac{\pi_i}{c_i \xi_i} \bar{E}_i + \frac{c_i}{\pi_i} Q_i Q_i + Q_i Q_i$. Next, multiplying both sides of equation (9) by the matrix $\begin{bmatrix} P_i & 0 \\ 0 & I \end{bmatrix}$, $O_i < 0$ can be obtained. As a result, one has

$$\int_0^{\infty} x_i^{\mathrm{T}} x_i d\tau < \gamma_i^2 \int_0^{\infty} \tilde{f}_i^{\mathrm{T}} \tilde{f}_i d\tau.$$

So the estimation error $\tilde{f}_i$ can be suppressed by the H_∞ performance. Thus, the proof ends here.

References

[1] M. M. Ma, C. Liu, X. Liu, Distributed model predictive load frequency control of the multi-area power system after deregulation, *IEEE transactions on Industrial Electronics*, 2016, 64(6): 5129-5139.

[2] H. Vu, P. Pruvot, C. Launay, and Y. Harmand, An improved voltage control on large-scale power system, *IEEE transactions on power systems*, 1996, 11(3): 1295-1303.

[3] Y. Guo, Z. P. Jiang, and D. J. Hill, Decentralized robust disturbance attenuation for a class of large-scale nonlinear systems, *Systems and Control Letters*, 1999, 37(2): 71-85.

[4] Z. M Yan, X. Yan, A multi-agent deep reinforcement learning method for cooperative load frequency control of a multi-area power system, *IEEE Transactions on Power Systems*, 2020, 35(6): 4599-4608.

[5] S. C. Tong, L. L. Zhang, and Y. M. Li, Observed-based adaptive fuzzy decentralized tracking control for switched uncertain nonlinear large-scale systems with dead zones, *IEEE Transactions on Systems, Man, and Cybernetics: Systems*, 2015, 46(1): 37-47.

[6] X. J. Su, .X. Liu, and Y. D. Song, Event-triggered sliding-mode control for multi-area power systems, *IEEE Transactions on Industrial Electronics*, 2017, 64(8): 6732-6741.

[7] X. Wu, D. Wu, and E. Modiano, Predicting failure cascades in large scale power systems via the influence model framework, *IEEE Transactions on Power Systems*, 2021, 36(5): 4778-4790.

[8] V. P. Singh, N. Kishor, P. Samuel, Distributed multi-agent system-based load frequency control for multi-area power system in smart grid, *IEEE Transactions on Industrial Electronics*, 2017, 64(6): 5151-5160.

[9] E. G. Tian and C. Peng, Memory-based event-triggering H_∞ load frequency control for power systems under deception attacks, *IEEE transactions on cybernetics*, 2020, 50(11): 4610-4618.

[10] Z. M. Yan and Y. Xu, A multi-agent deep reinforcement learning method for cooperative load frequency control of a multi-area power system, *IEEE Transactions on Power Systems*, 2020, 35(6): 4599-4608.

[11] J. L. Liu, Y. Y. Gu, L. J. Zha, Y. J. Liu, and J. Cao, Event-triggered H_∞ load frequency control for multiarea power systems under hybrid cyber attacks, *IEEE Transactions on Systems, Man, and Cybernetics: Systems*, 2019, 49(8): 1665-1678.

[12] J. Yang, Q. S. Zhong, K. B. Shi, and S. M. Zhong, Dynamic-memory event-triggered H_∞ load frequency control for reconstructed switched model of power systems under hybrid attacks, *IEEE Transactions on Cybernetics*, 2023, 53(6): 3913-3925.

[13] J. H. Wang, Q. J. Gong, K. F. Huang, Z. Liu., C. L. Philip Chen, J. Liu, Event-triggered prescribed settling time consensus compensation control for a class of uncertain nonlinear systems with actuator failures, *IEEE Transactions on Neural Networks and Learning Systems*, 2023, 34(9): 5590-5600.

[14] J. Zhao and Y. Lin, Adaptive actuator failure compensation control: A new scheme based on fault detection and isolation, *IEEE/ASME Transactions on Mechatronics*, 2023, 28(4): 2236-2247.

[15] M. Zhang, S. L. Dong, P. Shi, G. R. Chen, and X. H. Guan, Adaptive actuator failure compensation control of uncertain nonlinear PDECODE cascaded systems, *IEEE Transactions on Systems, Man, and Cybernetics: Systems*, 2023, 53(9): 5751-5759.

[16] M. Zhang, S. L. Dong, P. Shi, G. Chen, and X. H. Guan, Distributed observer-based event-triggered load frequency control of multiarea power systems under cyber attacks, *IEEE Transactions on Automation Science and Engineering*, 2023, 20(4): 2435-2444.

[17] Y. Jiang and Z. P. Jiang, Robust adaptive dynamic programming for large-scale systems with an application to multimachine power systems, *IEEE Transactions on Circuits and Systems II: Express Briefs*, 2012, 59(10): 693-697.

Proceedings of the 3rd Conference on Fully Actuated System Theory and Applications
May 10-12, 2024, Shenzhen, China

基于全驱系统理论的高超声速飞行器容错跟踪控制器设计

周逸蓉[1]，齐瑞云[1]

1. 南京航空航天大学，南京 210016
E-mail: zhouyirong@nuaa.edu.cn；E-mail: ruiyun.qi@nuaa.edu.cn

摘 要: 高超声速飞行器无论是在军事还是民用、经济上，都具有巨大的潜力与价值。然而，强耦合、强不确定性、故障等问题的存在，对其控制器的设计带来了巨大的挑战。为了解决高度与速度之间的耦合问题，增加控制器的可靠性以及实用性，本文针对存在不确定参数以及故障的高超声速飞行器纵向模型，设计了一种多输入多输出容错跟踪控制器。首先进行模型预处理，即将原模型转变为高阶全驱系统标准形式，与此同时也建立了直接的输入输出关系，由此进一步根据高阶全驱系统理论，设计基础控制律；利用自适应控制原理设计参数自适应律完成对不确定性参数的估计以及对故障的容错工作，使得系统的跟踪误差最终能够趋于零。再利用Lyapunov稳定性定理证明所设计系统稳定；最终通过仿真验证控制律可行性。

关键词: 高超声速飞行器，高阶全驱系统理论，自适应故障补偿，容错控制

Design of hypersonic vehicle tracking controller based on high-order fully actuated system theory

Yirong Zhou[1], Ruiyun Qi[1]

1.College of Automation Engineering, Nanjing University of Aeronautics and Astronautics, Nanjing 210016
E-mail: zhouyirong@nuaa.edu.cn；E-mail: ruiyun.qi@nuaa.edu.cn

Abstract: Hypersonic aircraft have great potential and value in military, civil and economic terms. However, the existence of strong coupling, uncertainty, failure and other problems brings great challenges to the design of its controller. In order to solve the coupling problem between height and speed as well as increase the reliability and practicability of the controller, this paper designs a multi-input and multi-output fault-tolerant tracking controller for the longitudinal model of the hypersonic aircraft with uncertain parameters and faults. First of all, the model pretreatment is carried out, that is, the original model is transformed into a standard form of a high-order fully actuated system. At the same time, a direct input-output relationship is also established, so as to further design the basic control law according to the theory of the high-order fully actuated system; use the adaptive control principle to design parameter adaptive law to complete the estimation of uncertainty parameters. And the fault tolerance work of the fault, so that the tracking error of the system can eventually tend to zero. The Lyapunov stability theorem is used to prove the stability of the designed system; finally, the feasibility of the control law is verified through simulation.

Key Words: hypersonic vehicle, high-order fully actuated system theory, adaptive failure compensation, fault-tolerant control

1 引言

高超声速飞行器由于其独特的机体-发动机一体化设计结构[1]以及恶劣的高空高速飞行环境，导致其模型具有多变量、强非线性、强耦合、强不确定性等问题的存在。为了解决这些问题，设计合适的控制器，近年来研究人员提出不少研究方法，其中常见的包括反馈线性化方法[2]、自适应控制方法[3]、反步控制方法[4]、滑模控制法[5]、神经/模糊控制法[6]等。

文献[7]为提高高超声速飞行器控制方法实用性，提出了一种神经网络复合学习非反步控制方法，该方法能高效估计不确定的未知参数，无需设计虚拟控制量，极大简化了控制器设计的计算量。文献[8]将比例微分(PD)控制的非线性动态逆方法应用于高超声速飞行器的复杂非线性动力学模型，为提高飞行器非线性控制器设计性能提供了新思路。文献[9]提供的非线性复合控制策略，主要结合了耦合观测器的前馈补偿器以及动态系统逆反馈控制器，最终减弱俯仰角速率的柔性影响，能够实现速度以及航迹角的跟踪控制。

与此同时，考虑到高超声速飞行器高空、高速等造成的复杂作业环境，为确保其安全性，控制器设计的过程中还必须要考虑到控制系统对故障的容错能力。在这个方面，文献[10]主要采用了滑模控制法，为消除抖振以及更好的鲁棒性，利用高阶线性化模型构建自适应终端滑模，结合径向基函数神经网络与自适应滑模控制的容错控制方法，最终能实现高超声速飞行器的跟踪控制。文献[11]利用被动容错思想以及自适应技术估计执行器故障信息，设计了自适应非线性容错控制器，所设计控制器的鲁棒性以及容错能力较强。

*此项工作得到国家自然科学基金资助，项目批准号：62188101.

文献[12] 提出了一种基于近端策略优化算法的高超声速飞行器容错制导控制一体化设计方法，解决了存在不确定参数和执行器故障的高超声速飞行器的末制导阶段问题。

近年来研究人员提出了一种新的研究理论——高阶全驱系统理论[13]，该方法能够使更多的系统拥有全局稳定性，为非线性系统设计了合理的能控性体系，将李雅普诺夫稳定性和镇定拓展到亚稳定性和亚镇定[14]，简化了闭环系统响应分析以及稳定性分析，不论是在时滞系统还是时变系统中都能够得到很好的应用[15]。高超声速飞行器纵向模型原模型虽为一阶形式，但此时输入输出间并不存在直接的关系，因此本文考虑采用高阶全驱系统理论，利用升阶处理建立阶全驱系统标准形式的同时能够建立直接的输入输出关系，简化控制器的设计以及稳定性的分析。

本文针对考虑双舵面出现反向型故障以及失效故障的高超声速纵向模型，对高度和速度进行容错跟踪控制工作。首先针对高超声速飞行器通用的纵向模型，在无故障情况下，利用高阶全驱系统理论实现对飞行器的高度与速度跟踪控制。然后在双舵面冗余的情况下，当舵面出现失效故障以及反向型故障问题时，结合自适应控制并利用Lyapunov稳定性定理设计高度及速度容错跟踪控制器。最后利用仿真软件验证所设计的控制器具有所需的跟踪能力与容错能力。

2 模型分析

为实现对高超声速飞行器巡航阶段的纵向高度和速度的容错跟踪控制，本文主要利用高阶全驱系统理论，为高超声速飞行器设计一个合适的多输入多输出的跟踪控制器。

2.1 纵向模型分析

本文采用如下通用的纵向控制模型[17]：

$$\dot{V}=\frac{T\cos\alpha-D}{m}-\frac{\mu\sin\gamma}{r^2} \tag{2.1}$$

$$\dot{h}=V\sin\gamma \tag{2.2}$$

$$\dot{\gamma}=\frac{L+T\sin\alpha}{mV}-\frac{(\mu-V^2r)\cos\gamma}{Vr^2} \tag{2.3}$$

$$\dot{\alpha}=q-\dot{\gamma} \tag{2.4}$$

$$\dot{q}=\frac{M_{yy}}{I_{yy}} \tag{2.5}$$

其中，γ，α，q分别为飞行器的航迹角、攻角以及俯仰角速率，M_{yy}与I_{yy}为飞行器俯仰力矩以及俯仰转动惯量。T，D，L分别为推力项、阻力项以及升力项，μ，m，r分别为重力常数、飞行器质量以及径向距离。需要设计的控制量为舵偏角δ_e以及油门开度β，控制器的输出为飞行器的高度h以及速度V。由式（2.1）至（2.5）可看出，控制输入与输出之间并无直接关系，为了实现对高超声速飞行器跟踪控制控制工作，则需要对上式进行进一步的升阶处理，从而建立控制器的输入输出直接关系，在此过程中同样完成了将原系统模型转变为高阶全驱系统形式的工作，此时高阶全驱系统理论可以得到直接且方便的应用。

由下式（2.6）~（2.9）可见，舵偏角δ_e与油门开度β直接出现在推力项T以及俯仰转动力矩M_{yy}中。

$$L=\frac{1}{2}\rho V^2SC_L \tag{2.6}$$

$$D=\frac{1}{2}\rho V^2SC_D \tag{2.7}$$

$$\mathrm{T}=\frac{1}{2}\rho V^2SC_T \tag{2.8}$$

$$M_{yy}=\frac{1}{2}\rho V^2S\bar{c}\left[C_M^{\alpha}+C_M^{q}+C_M^{\delta_e}\right] \tag{2.9}$$

其中ρ，S，$\bar{c}$分别为空气密度、参考气动面积以及平均气动弦长，升力系数C_L、阻力系数C_D、推力系数C_T以及俯仰转动力矩M_{yy}中系数的具体展开式如下：

$$C_L=C_L^{\alpha}\alpha+C_L^0 \tag{2.10}$$

$$C_D=C_D^{\alpha^2}\alpha^2+C_D^{\alpha}\alpha+C_D^0 \tag{2.11}$$

$$C_T=C_T^{\beta}\beta+C_T^0 \tag{2.12}$$

$$C_M^{\alpha}=C_M^{\alpha^2}\alpha^2+C_M^{\alpha}\alpha+C_M^0 \tag{2.13}$$

$$C_M^{q}=(\bar{c}/2V)q\left(C_M^{\alpha^2 q}\alpha^2+C_M^{\alpha q}\alpha+C_M^{q}\right) \tag{2.14}$$

$$C_M^{\delta_e}=c_e(\delta_e-\alpha) \tag{2.15}$$

其中各项参数的具体值见表 3.1，c_e为一常数。飞行器发动机动态模型见式（2.16），其中β_c则是控制器的输出控制指令，ω_n与ζ分别为油门开度调定系统的频率和阻尼。

$$\ddot{\beta}=-2\zeta\omega_n\dot{\beta}-\omega_n^2\beta+\omega_n^2\beta_c \tag{2.16}$$

取状态向量$X=[h\ V\ \gamma\ \alpha\ q\ \beta\ \dot{\beta}]^T$，控制输入$U=[\delta_e\ \beta_c]^T$。为使控制输出由控制输入直接控制，需要对高度$h$取到四阶导数、速度$V$取到三阶导数，此时速度与高度的表达式与控制输入$U$产生直接关系。不考虑参数不确定性情况以及故障情况、未建模动态等未知影响，可以得到：

$$\begin{bmatrix}h^{(4)}\\ \ddot{V}\end{bmatrix}=\begin{bmatrix}f_h(X)\\ f_V(X)\end{bmatrix}+\begin{bmatrix}g_1(X) & g_2(X)\\ g_3(X) & g_4(X)\end{bmatrix}U \tag{2.17}$$

其中矩阵$\begin{bmatrix}g_1(X) & g_2(X)\\ g_3(X) & g_4(X)\end{bmatrix}$具体表达式见文献[18]，在无大机动的巡航阶段满足非奇异条件，$f_h(X)$，$f_V(X)$，$g_1(X)$，$g_2(X)$，$g_3(X)$，$g_4(X)$为含有状态量的函数。

2.2 不确定性分析

考虑到系统存在不确定参数的情况，需要引入自适应参数估计算法以实现对系统未知参数的估计。

将飞行器质量 m，重力常数μ，常数c_e，平均气动弦长$\bar{c}$，空气密度ρ，、参考气动面积S，俯仰转动惯量I_{yy}考虑为系统存在的不确定参数，此时需要对式（2.17）进行进一步处理，即将其中含有未知参数的项单独提出，此时输入-输出方程转变为：

$$\begin{bmatrix} h^{(4)} \\ \ddot{V} \end{bmatrix} = \begin{bmatrix} f_{h0}(X) \\ 0 \end{bmatrix} + \begin{bmatrix} \Phi_h^T(X) \\ \Phi_V^T(X) \end{bmatrix} \Theta + \begin{bmatrix} g_{11}(X) & g_{12}(X) \\ g_{21}(X) & g_{22}(X) \end{bmatrix} \begin{bmatrix} 1/\theta_{13} & 0 \\ 0 & 1/\theta_{14} \end{bmatrix} U \tag{2.18}$$

其中函数$f_{h0}(X)$与矩阵$\begin{bmatrix} \Phi_h^T(X) \\ \Phi_V^T(X) \end{bmatrix}$为含有状态量的函数，$\Theta$、$\theta_{13}$、$\theta_{14}$为含有未知参数的矩阵与函数。

经过上述转换，最终能使得系统中含有的所有未知量在$\Theta = [\theta_1 \ \cdots \theta_{12}]^T$与$\theta_{13}$、$\theta_{14}$中出现，具体表达式如下：

$\theta_1 = 10^{15}\rho^3 S^3/m^3$　　$\theta_8 = 10^{20}\mu^2$

$\theta_2 = 10^{20}\rho^2 S^2 \mu/m^2$　　$\theta_9 = 10^{10}\mu$

$\theta_3 = 10^{10}\rho^2 S^2/m^2$　　$\theta_{10} = 10^{13}\rho^2 S^2 \bar{c}^2/m^2 I_{yy}$

$\theta_4 = 10^{25}\rho S\mu^2/m$　　$\theta_{11} = 10^{16}\rho^2 S^2 \bar{c} c_e/m^2 I_{yy}$

$\theta_5 = 10^{15}\rho S\mu/m$　　$\theta_{12} = 10^{15}\rho^2 S^2 \bar{c}/m^2 I_{yy}$

$\theta_6 = 10^5 \rho S/m$　　$\theta_{13} = 4 \times 10^{-13} I_{yy} m/\rho^2 S^2 \bar{c} c_e$

$\theta_7 = 10^{31}\mu^3$　　$\theta_{14} = 2 \times 10^{-3} m/\rho S \omega_n^2$

2.3 故障模型分析

本文主要研究存在双舵面冗余的情况下可能存在的两种故障形式：

（1）舵面出现失效故障；

（2）舵面出现反向型故障。

考虑到上述两种故障模式，取故障模型[18]为：

$$\delta_{ei} = d_i \sigma_i \delta_{ec},\ i = 1,2 \tag{2.19}$$

其中d_i表示舵面控制方向，σ_i表示舵面失效的程度。当舵面出现失效故障时，$d_i = 1, \sigma_i \in (0,1)$，当舵面出现反向型故障时，$d_i = -1, \sigma_i \in (0,1]$。

舵偏角总体的控制信号可以表达为：

$$\delta_e = k_{e1}\delta_{e1} + k_{e2}\delta_{e2} \tag{2.20}$$

其中δ_{e1}和δ_{e2}分别表示两个舵偏角信号，k_{e1}和k_{e2}则为两者的控制增益。将式（2.19）代入式（2.20）得到：

$$\delta_e = (k_{e1}d_1\sigma_1 + k_{e2}d_2\sigma_2)\delta_{ec} \tag{2.21}$$

取$\sigma = k_{e1}d_1\sigma_1 + k_{e2}d_2\sigma_2$，$U_c = [\delta_{ec} \ \beta_c]^T$将式（2.21）代入式（2.18）得到：

$$\begin{bmatrix} h^{(4)} \\ \ddot{V} \end{bmatrix} = \begin{bmatrix} \Phi_h^T \\ \Phi_V^T \end{bmatrix} \Theta + \begin{bmatrix} \phi_{h0} \\ 0 \end{bmatrix} + \begin{bmatrix} g_{11}(X) & g_{12}(X) \\ g_{21}(X) & g_{22}(X) \end{bmatrix} \begin{bmatrix} \dfrac{\sigma}{\theta_{13}} & 0 \\ 0 & \dfrac{1}{\theta_{14}} \end{bmatrix} U_c. \tag{2.22}$$

3 控制器设计

在完成模型预处理工作后，根据高阶全驱系统理论，取控制输入为：

$$U_c = \begin{bmatrix} \delta_{ec} \\ \beta_c \end{bmatrix} = -\begin{bmatrix} \hat{\theta}_{15} & 0 \\ 0 & \hat{\theta}_{14} \end{bmatrix} \begin{bmatrix} g_{11}(X) & g_{12}(X) \\ g_{21}(X) & g_{22}(X) \end{bmatrix}^{-1} \times \left\{ \begin{bmatrix} A_0 h + A_1 \dot{h} + A_2 \ddot{h} + A_3 \dddot{h} \\ B_0 V + B_1 \dot{V} + B_2 \ddot{V} \end{bmatrix} + \begin{bmatrix} f_{h0}(X) \\ 0 \end{bmatrix} + \begin{bmatrix} \Phi_h^T \\ \Phi_V^T \end{bmatrix} \hat{\Theta} - \begin{bmatrix} h_r^{(4)} \\ \ddot{V}_r \end{bmatrix} - \begin{bmatrix} A_0 h_r + A_1 \dot{h}_r + A_2 \ddot{h}_r + A_3 \dddot{h}_r \\ B_0 V_r + B_1 \dot{V}_r + B_2 \ddot{V}_r \end{bmatrix} \right\} \tag{3.1}$$

其中$\theta_{15} = \theta_{13}/\sigma$，$\hat{\theta}_{15}$，$\hat{\theta}_{14}$，$\hat{\Theta}$分别为$\theta_{15}$，$\theta_{14}$，$\Theta$的估计值。$h_r$和$V_r$分别为高度参考轨迹与速度参考轨迹，且$h_r$满足四阶有界可导条件，$V_r$满足三阶有界可导条件，$A_{0\sim3}$和$B_{0\sim2}$为可设计实数参数矩阵，其中：

$$A_{0\sim3} = [A_0 \quad A_1 \quad A_2 \quad A_3]$$

$$B_{0\sim3} = [B_0 \quad B_1 \quad B_2]$$

在设计参数矩阵A_i，$i = 0,1,2,3$，以及参数矩阵B_i，$i = 0,1,2$时，需要保证所设计的参数能够使得矩阵$\Phi(\mathrm{A}_{0\sim3})$与$\Phi(B_{0\sim2})$满秩且稳定，其中：

$$\Phi(\mathrm{A}_{0\sim3}) = \begin{bmatrix} 0 & 1 & 0 & 0 \\ 0 & 0 & 1 & 0 \\ 0 & 0 & 0 & 1 \\ -A_0 & -A_1 & -A_2 & -A_3 \end{bmatrix}$$

$$\Phi(B_{0\sim3}) = \begin{bmatrix} 0 & 1 & 0 \\ 0 & 0 & 1 \\ -B_0 & -B_1 & -B_2 \end{bmatrix}$$

于此同时，取

$$\Phi(\mathrm{A}_{0\sim3}, B_{0\sim2}) = \begin{bmatrix} \Phi(\mathrm{A}_{0\sim3}) & 0_{4\times3} \\ 0_{3\times4} & \Phi(B_{0\sim2}) \end{bmatrix} \tag{3.2}$$

所设计的参数矩阵也需要保证$\Phi(\mathrm{A}_{0\sim3}, B_{0\sim2})$满秩且稳定。

取参考轨迹具体表达式如下：

$$\begin{bmatrix} \dot{h}_r \\ \ddot{h}_r \\ \dddot{h}_r \\ h_r^{(4)} \end{bmatrix} = \begin{bmatrix} 0 & 1 & 0 & 0 \\ 0 & 0 & 1 & 0 \\ 0 & 0 & 0 & 1 \\ -A_0 & -A_1 & -A_2 & -A_3 \end{bmatrix} \begin{bmatrix} h_r - h_d \\ \dot{h}_r \\ \ddot{h}_r \\ \dddot{h}_r \end{bmatrix}$$

$$\begin{bmatrix} \dot{V}_r \\ \ddot{V}_r \\ \dddot{V}_r \end{bmatrix} = \begin{bmatrix} 0 & 1 & 0 \\ 0 & 0 & 1 \\ -B_0 & -B_1 & -B_3 \end{bmatrix} \begin{bmatrix} V_r - V_d \\ \dot{V}_r \\ \ddot{V}_r \end{bmatrix}$$

即

$$\dot{h}_r{}^{(0\sim3)} = \Phi(\mathrm{A}_{0\sim3}) \begin{bmatrix} h_r - h_d \\ \dot{h}_r \\ \ddot{h}_r \\ \dddot{h}_r \end{bmatrix} \tag{3.3}$$

$$\dot{V}_r{}^{(0\sim2)} = \Phi(B_{0\sim2}) \begin{bmatrix} V_r - V_d \\ \dot{V}_r \\ \ddot{V}_r \end{bmatrix} \tag{3.4}$$

h_d和V_d分别为目标高度值与速度值，为常数。经分析可得，参考轨迹最终能趋于目标值，满足$h_r = h_d$，$V_r = V_d$，能够满足跟踪控制要求。

3.1 参数设计

按照高阶全驱系统理论体系，以速度跟踪部分为例，选择将极点配置在$(-10,-0.6\pm j0.8)$，经计算可以得到$B_{0\sim2}$的表达式：

$$B_{0\sim2}=[B_0,B_1,B_2]=[10\ \ 13\ \ 11.2]$$

此时有

$$\Phi(B_{0\sim2})=\begin{bmatrix}0&1&0\\0&0&1\\-10&-13&-11.2\end{bmatrix}\tag{3.5}$$

为得到满足 Lyapunov 稳定性定理的对应矩阵$\mathrm{P}(B_{0\sim2})$[19]，定义[19]：

$$\det(sI+\Phi)\triangleq\sum_{i=0}^{3}c_i^{\Phi}s^i,$$

$$\mathrm{adj}(sI+\Phi^T)\triangleq\sum_{i=0}^{2}C_i^{\Phi}s^i.$$

经计算得到各项系数以及矩阵的值如下：

$$c_0^{\Phi}=-10,c_1^{\Phi}=13,c_2^{\Phi}=-11.2,c_3^{\Phi}=1$$

$$C_0^{\Phi}=\begin{bmatrix}13&-10&0\\12&0&10\\1&0&0\end{bmatrix}$$

$$C_1^{\Phi}=\begin{bmatrix}-11.2&0&10\\-1&-11.2&-13\\0&-1&0\end{bmatrix}$$

$$C_2^{\Phi}=\begin{bmatrix}1&0&0\\0&1&0\\0&0&1\end{bmatrix}$$

为方便后续的计算，取：

$$P_0=\sum_{i=0}^{3}c_i^{\Phi}\Phi^i\tag{3.6}$$

假设存在正定矩阵 Q 满足：

$$\Phi^TP+P\Phi=-Q$$

取正定矩阵 Q 为：

$$Q=\begin{bmatrix}2&1&0\\1&6&0\\0&0&1\end{bmatrix}\tag{3.7}$$

经计算可以得到：

$$P(B_{0\sim2})=-\sum_{i=0}^{2}C_i^{\Phi}QP_0^{-1}s\Phi^i=\begin{bmatrix}4.0717&1.9032&0.1\\0.9914&3.1412&0.31\\0.1&0.3772&0.783\end{bmatrix}$$

同理可以得到$\Phi(A_{0\sim3}),P(A_{0\sim3})$。取：

$$\Phi(A,B)=\begin{bmatrix}\Phi(A_{0\sim3})&0_{4\times3}\\0_{3\times4}&\Phi(B_{0\sim2})\end{bmatrix}\tag{3.8}$$

$$\mathrm{P}(A,B)=\begin{bmatrix}\mathrm{P}(A_{0\sim3})&0_{4\times3}\\0_{3\times4}&\mathrm{P}(B_{0\sim2})\end{bmatrix}\tag{3.9}$$

3.2 参数自适应律设计

观察到θ_{15}中存在的两个不确定参数θ_{13}和σ，导致舵偏角信号的方向问题未知，这里选择采用 Nussbaum 增益自适应控制方法。

本文中选取：

$$N(\xi)=\exp(\xi^2)\sin(2\pi\xi)\tag{3.9}$$

此时有：

$$U_c=\begin{bmatrix}\delta_{ec}\\\beta_c\end{bmatrix}=-\begin{bmatrix}N(\xi)&0\\0&\hat{\theta}_{14}\end{bmatrix}\begin{bmatrix}g_{11}(X)&g_{12}(X)\\g_{21}(X)&g_{22}(X)\end{bmatrix}^{-1}\times\left\{\begin{bmatrix}A_0h+A_1\dot{h}+A_2\ddot{h}+A_3\dddot{h}\\B_0V+B_1\dot{V}+B_2\ddot{V}\end{bmatrix}+\begin{bmatrix}f_{h0}(X)\\0\end{bmatrix}+\begin{bmatrix}\Phi_h^T\\\Phi_V^T\end{bmatrix}\widehat{\Theta}-\begin{bmatrix}h_r^{(4)}\\\ddot{V}_r\end{bmatrix}-\begin{bmatrix}A_0h_r+A_1\dot{h}_r+A_2\ddot{h}_r+A_3\dddot{h}_r\\B_0V_r+B_1\dot{V}_r+B_2\ddot{V}_r\end{bmatrix}\right\}\tag{3.10}$$

将式（3.10）代入（2.18），化简可得：

$$\begin{bmatrix}\dot{\tilde{h}}^{(0\sim3)}\\\dot{\tilde{V}}^{(0\sim2)}\end{bmatrix}=\Phi(A_{0\sim3},B_{0\sim2})\begin{bmatrix}\tilde{h}^{(0\sim3)}\\\tilde{V}^{(0\sim2)}\end{bmatrix}-B\begin{bmatrix}\Phi_h^T\\\Phi_V^T\end{bmatrix}\widetilde{\Theta}+\frac{\tilde{\theta}_{14}}{\theta_{14}}BG_2\bar{V}+\frac{N(\xi)\sigma}{\theta_{13}}BG_1\bar{V}-BG_1\bar{V}\tag{3.11}$$

其中$B=[B_h\quad B_V]$, $B_h=[0\quad0\quad0\quad1\quad0\quad0\quad0]^T$，$B_V=[0\quad0\quad0\quad0\quad0\quad0\quad1]^T$

$$G_1=\frac{1}{g_{11}g_{22}-g_{12}g_{21}}\begin{bmatrix}g_{11}g_{22}&-g_{11}g_{12}\\g_{21}g_{22}&-g_{12}g_{21}\end{bmatrix}$$

$$G_2=\frac{1}{g_{11}g_{22}-g_{12}g_{21}}\begin{bmatrix}-g_{12}g_{21}&g_{11}g_{12}\\-g_{21}g_{22}&g_{11}g_{22}\end{bmatrix}$$

$$\bar{V}=K\begin{bmatrix}\tilde{h}^{(0\sim3)}\\\tilde{V}^{(0\sim2)}\end{bmatrix}+\begin{bmatrix}h_r^{(4)}\\\ddot{V}_r\end{bmatrix}\begin{bmatrix}\Phi_h^T\\\Phi_V^T\end{bmatrix}-\hat{\Theta}-\begin{bmatrix}\phi_{h0}\\0\end{bmatrix}$$

$$\widetilde{\Theta}=\Theta-\hat{\Theta},\ \tilde{\theta}_{14}=\theta_{14}-\hat{\theta}_{14}$$

$$K=\begin{bmatrix}-A_{0\sim3}&0_{1\times3}\\0_{1\times4}&-B_{0\sim2}\end{bmatrix}$$

取自适应律：

$$\dot{\hat{\Theta}}=[\Phi_h\quad\Phi_V]P(A,B)\begin{bmatrix}\tilde{h}^{(0\sim3)}\\\tilde{V}^{(0\sim2)}\end{bmatrix}\tag{3.12}$$

$$\dot{\hat{\theta}}_{14}=-\bar{V}^TG_2^TP(A,B)\begin{bmatrix}\tilde{h}^{(0\sim3)}\\\tilde{V}^{(0\sim2)}\end{bmatrix}\tag{3.13}$$

$$\dot{\xi}=-k_{\xi}\bar{V}^TG_1^TP(A,B)\begin{bmatrix}\tilde{h}^{(0\sim3)}\\\tilde{V}^{(0\sim2)}\end{bmatrix}\tag{3.14}$$

其中$\mathrm{P}(A,B)=\begin{bmatrix}\mathrm{P}(A_{0\sim3})&0_{4\times3}\\0_{3\times4}&\mathrm{P}(B_{0\sim2})\end{bmatrix}$，P 矩阵为满足

$$\Phi^T(A,B)P(A,B)+P(A,B)\Phi(A,B)=-Q$$

的正定矩阵，Q 也为正定矩阵。

3.3 稳定性证明

取 Lyapunov 函数为：

$$V_L=\begin{bmatrix}\tilde{h}^{(0\sim3)}\\\tilde{V}^{(0\sim2)}\end{bmatrix}^TP(A,B)\begin{bmatrix}\tilde{h}^{(0\sim3)}\\\tilde{V}^{(0\sim2)}\end{bmatrix}+\widetilde{\Theta}\widetilde{\Theta}^T+\frac{1}{\theta_{14}}\tilde{\theta}_{14}^2\tag{3.15}$$

对上式求导可得：

$$\dot{V}_L=\begin{bmatrix}\tilde{h}^{(0\sim3)}\\ \tilde{V}^{(0\sim2)}\end{bmatrix}^T[\Phi(A,B)^TP(A,B)+P(A,B)\Phi(A,B)]\begin{bmatrix}\tilde{h}^{(0\sim3)}\\ \tilde{V}^{(0\sim2)}\end{bmatrix}+2\frac{N(\xi)\sigma}{\theta_{13}}\bar{V}^TG_1^TP(A,B)\begin{bmatrix}\tilde{h}^{(0\sim3)}\\ \tilde{V}^{(0\sim2)}\end{bmatrix}-2\bar{V}^TG_1^TP(A,B)\begin{bmatrix}\tilde{h}^{(0\sim3)}\\ \tilde{V}^{(0\sim2)}\end{bmatrix}+\dot{\tilde{\Theta}}\tilde{\Theta}^T+\tilde{\Theta}\dot{\tilde{\Theta}}^T+2\frac{\tilde{\theta}_{14}}{\theta_{14}}\bar{V}^TG_2^TP(A,B)\begin{bmatrix}\tilde{h}^{(0\sim3)}\\ \tilde{V}^{(0\sim2)}\end{bmatrix}-2\tilde{\Theta}_1^T[\Phi_h\Phi_V]P(A,B)\begin{bmatrix}\tilde{h}^{(0\sim3)}\\ \tilde{V}^{(0\sim2)}\end{bmatrix}-\frac{2}{\theta_{14}}\left(\tilde{\theta}_{14}\dot{\hat{\theta}}_{14}\right)$$

结合式（3.12）、（3.13）、（3.14）化简得到：

$$\dot{V}_L=\begin{bmatrix}\tilde{h}^{(0\sim3)}\\ \tilde{V}^{(0\sim2)}\end{bmatrix}^T[\Phi(A,B)^TP(A,B)+P(A,B)\Phi(A,B)]\begin{bmatrix}\tilde{h}^{(0\sim3)}\\ \tilde{V}^{(0\sim2)}\end{bmatrix}+\frac{2}{k_\xi}\left(\frac{\sigma}{\theta_{13}}N(\xi)\dot{\xi}+\dot{\xi}\right)$$

对$\dot{V}$在$[0,t]$上求积分可得：

$$0\leqslant V_L\leqslant \mathrm{V}_L(0)-\int_0^t\begin{bmatrix}\tilde{h}^{(0\sim3)}\\ \tilde{V}^{(0\sim2)}\end{bmatrix}^T\Phi(A,B)\begin{bmatrix}\tilde{h}^{(0\sim3)}\\ \tilde{V}^{(0\sim2)}\end{bmatrix}d\tau+\frac{2}{k_\xi}\int_0^t\left(\frac{\sigma}{\theta_{13}}N(\xi)+1\right)\dot{\xi}d\tau$$

即：

$$0\leqslant V_L\leqslant \mathrm{V}_L(0)+\frac{2}{k_\xi}\int_0^t\left(\frac{\sigma}{\theta_{13}}N(\xi)+1\right)\dot{\xi}d\tau$$

$$V_L(t)\leqslant\int_0^t(\theta_0N(\xi)+1)\dot{\xi}d\tau+c_0 \qquad (3.16)$$

其中c_0为合适的常数，因此$V_L(t)$，ξ，$\int_0^t(\theta_0N(\xi)+1)\dot{\xi}d\tau$在$[0,\ t)$有界，$t\in[0,\infty)$，因此$\begin{bmatrix}\tilde{h}^{(0\sim3)}\\ \tilde{V}^{(0\sim2)}\end{bmatrix}$，$\tilde{\Theta}$，$\tilde{\theta}_{13}$，$\tilde{\theta}_{14}$有界。而$\begin{bmatrix}\tilde{h}^{(0\sim3)}\\ \tilde{V}^{(0\sim2)}\end{bmatrix}=\begin{bmatrix}h^{(0\sim3)}\\ V^{(0\sim2)}\end{bmatrix}-\begin{bmatrix}h_r^{(0\sim3)}\\ V_r^{(0\sim2)}\end{bmatrix}$，因此$\begin{bmatrix}h^{(0\sim3)}\\ V^{(0\sim2)}\end{bmatrix}$有界，即$h$与$V$的各阶导数都有界，由 Barbalat 引理[20] 可知，由于$\int_0^t\begin{bmatrix}\tilde{h}^{(0\sim3)}\\ \tilde{V}^{(0\sim2)}\end{bmatrix}^T\Phi(A,B)\begin{bmatrix}\tilde{h}^{(0\sim3)}\\ \tilde{V}^{(0\sim2)}\end{bmatrix}d\tau$在$t\to\infty$时存在，当$t\to\infty$，有：

$$\begin{bmatrix}\tilde{h}^{(0\sim3)}\\ \tilde{V}^{(0\sim2)}\end{bmatrix}^T\Phi(A,B)\begin{bmatrix}\tilde{h}^{(0\sim3)}\\ \tilde{V}^{(0\sim2)}\end{bmatrix}=0$$

即$\begin{bmatrix}\tilde{h}^{(0\sim3)}\\ \tilde{V}^{(0\sim2)}\end{bmatrix}=0$，误差最终能够收敛到零。

4 仿真设计

为了验证存在参数不确定性以及故障时控制器的设计是否满足要求，进行以下仿真内容。

取高超声速飞行器的初始高度$\mathrm{H}=110000ft$，速度初始值$\mathrm{V}=15060ft/s$,取高度跟踪目标值为$h_d=111000ft$，速度跟踪目标值为$V_d=15160ft/s$。高度参考轨迹为：

$$\begin{bmatrix}\dot{h}_r\\ \ddot{h}_r\\ \dddot{h}_r\\ h_r^{(4)}\end{bmatrix}=\begin{bmatrix}0&1&0&0\\ 0&0&1&0\\ 0&0&0&1\\ -0.05&-0.5&-1.3&-0.9\end{bmatrix}\begin{bmatrix}h_r-h_d\\ \dot{h}_r\\ \ddot{h}_r\\ \dddot{h}_r\end{bmatrix}$$

速度参考轨迹为：

$$\begin{bmatrix}\dot{V}_r\\ \ddot{V}_r\\ \dddot{V}_r\end{bmatrix}=\begin{bmatrix}0&1&0\\ 0&0&1\\ -10&-13&-11.2\end{bmatrix}\begin{bmatrix}V_r-V_d\\ \dot{V}_r\\ \ddot{V}_r\end{bmatrix}$$

其中模型中所涉及到的系数值见下表1：

表 1.系数值

系数	值
C_L^0	0
C_L^α	0.6203
C_D^0	0.003772
C_D^α	0.0043378
$C_D^{\alpha^2}$	0.6450
$C_M^{\alpha q}$	-0.2289
$C_M^{\alpha^2 q}$	0.3015
C_T^0	$\begin{cases}0 & \Phi<1\\ 0.0224 & \Phi\geq1\end{cases}$
C_T^Φ	$\begin{cases}0.02376 & \Phi<1\\ 0.00336 & \Phi\geq1\end{cases}$
C_M^0	5.361×10^{-6}
C_M^α	0.36617
$C_M^{\alpha^2}$	-0.035
C_M^q	-0.796

飞行器参数见下表2：

表 2.飞行器参数

参数	值
$m/(slug)$	9375
$\rho/(slug/ft^3)$	0.24325×10^{-4}
$\bar{c}/(ft)$	80
c_e	0.0292
$S/(ft^2)$	3603
$r/(ft)$	20902244
$I_{yy}/(slug\cdot ft^2)$	7000000
μ	3.31929×10^{-11}

未知参数$\hat{\theta}_{13}$与$\hat{\theta}_{14}$的初始值分别取$\hat{\theta}_{13}(0)=2.1$，$\hat{\theta}_{14}(0)=0$，而未知参数矩阵$\hat{\Theta}$的初始值取:

$\hat{\Theta}(0)=[0.5\ 0.1\ 0.5\ 0.1\ 0.5\ 0.7\ 0.1\ 0.1\ 0.1\ 0.5\ 0.5\ 0.5]$

取参数矩阵$A_{0\sim3}=[0.05\ \ 0.5\ \ 1.3\ \ 0.9]$，参数矩阵$B_{0\sim2}=[10\ \ 13\ \ 11.2]$，状态量的初始值取：

$[h\ V\ \gamma\ \alpha\ q\ \beta\ \dot{\beta}] = [110000\text{ft}\ \ 15060\text{ft/s}\ \ 0\text{rad}\ \ 0.1\text{rad}\ \ 0\text{rad/s}\ \ 0\%/100\ \ 0]$

考虑到舵面失效以及反向型故障，设计故障仿真：

（1）$0 < t \leq 50s$，系统正常工作；

（2）$50s < t \leq 100s$，系统发生失效故障，取失效系数$\sigma = 0.1$；

（3）$100s < t \leq 150s$，系统发生反向型故障，此时取$\sigma = -0.1$。

仿真结果如下：

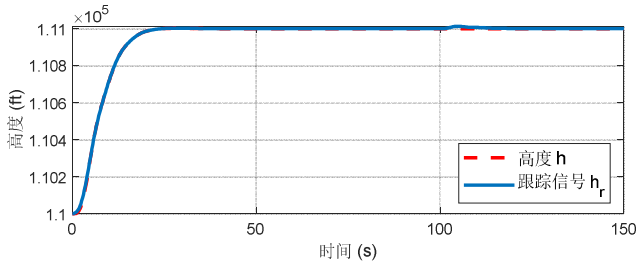

(a) 高度跟踪曲线

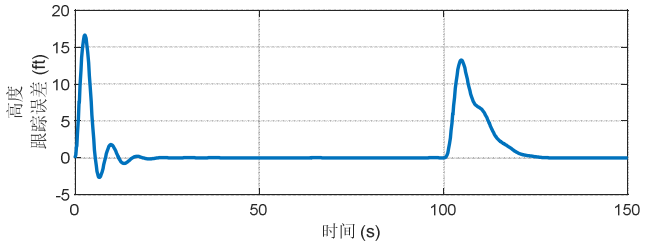

(b) 高度跟踪误差

图 1: 故障下高度跟踪曲线

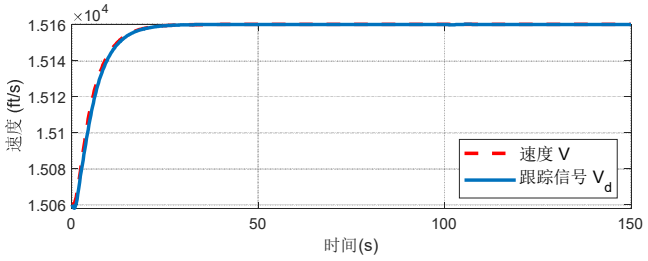

(a) 速度跟踪曲线

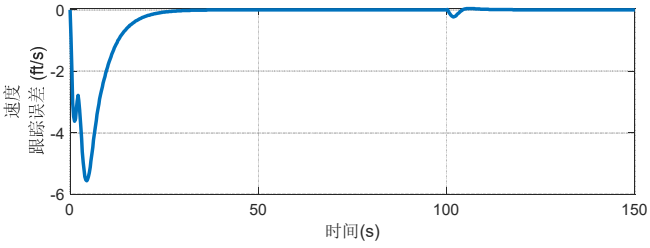

(b) 速度跟踪误差

图 2: 故障下速度跟踪曲线

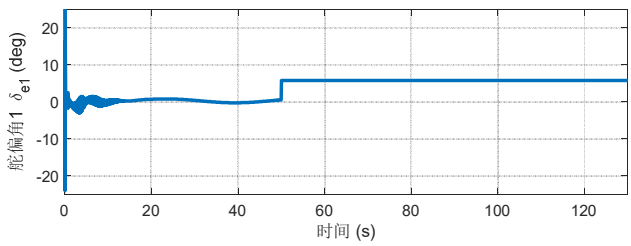

(a) 舵偏角1变化曲线

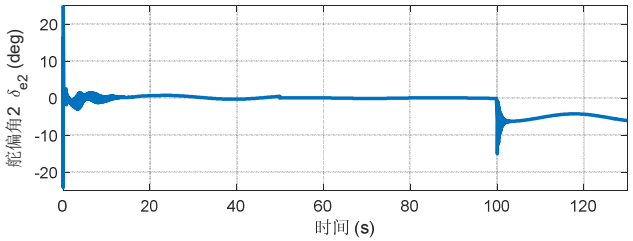

(b) 舵偏角2变化曲线

图 3: 故障下舵偏角变化曲线

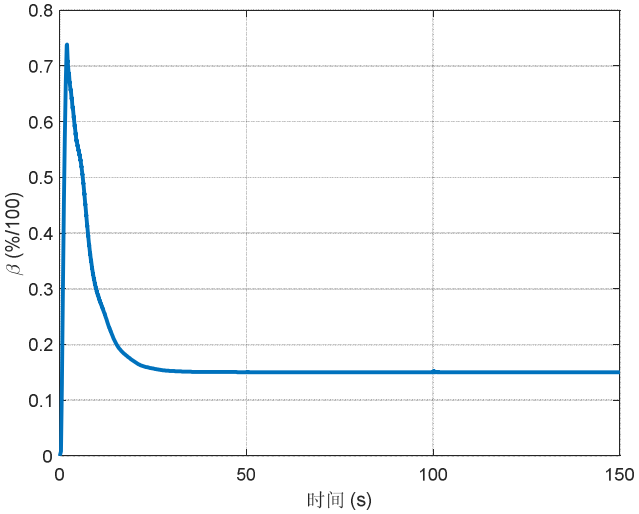

图4: 故障下油门开度变化曲线

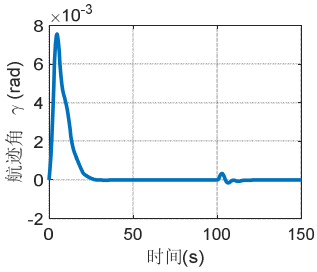

(a) 航迹角曲线

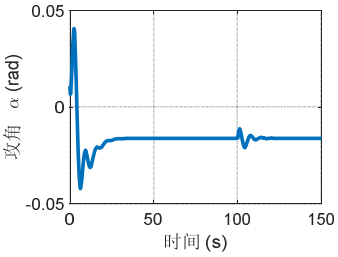

(b) 攻角曲线

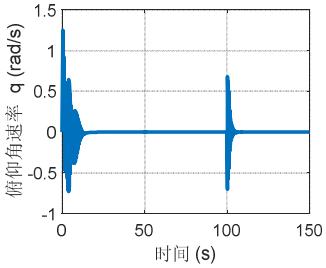

(c) 俯仰角曲线

图 5: 存在故障时航迹角、攻角、俯仰角变化曲线

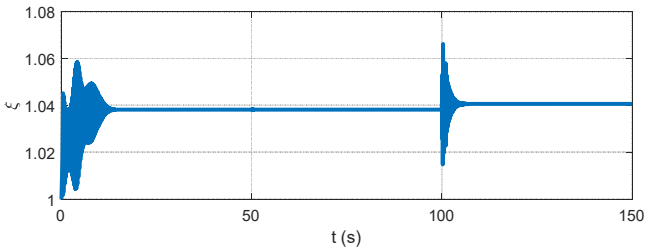

(a) ξ变化曲线

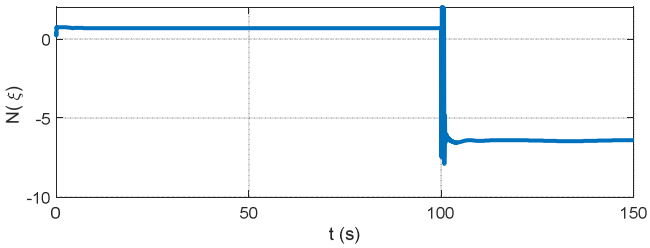

(b) $N(\xi)$变化曲线

图 6: 故障下$N(\xi)$与ξ的变化曲线

图 1 与图 2 中显示了发生故障时飞行器的速度跟踪曲线以及高度跟踪曲线，由图中可以看到，在故障发生后，跟踪曲线在发生一定波动后能够趋于所设计的跟踪速度以及高度，所设计的控制器仍能实现跟踪控制功能，且满足跟踪误差要求。

图 3 以及图 4 主要显示了故障下飞行器油门开度以及两个舵面舵偏角的变化，从图中可以看到，在发生反向型故障后，所设计的控制器仍能使得两者在一定变化后趋于稳定，进一步验证了控制器设计的合理性。

图 5 描述了故障下飞行器航迹角、攻角以及俯仰角速率的变化曲线，由仿真结果显示，在发生故障时三者有所波动，但最终能够较快地趋于稳定，能够满足性能要求。

图 6 中显示了 Nussbaum-type 函数的变化过程，由图中可以看出，所设计的函数能够较好地解决舵面偏转方向不定的工作，能够实现所需的容错控制要求，使得系统具有更好的稳定性以及安全性。

5 总结

基于高阶全驱系统理论，本文针对存在不确定参数以及故障的高超声速飞行器，设计了一种多输入多输出的高度与速度容错跟踪控制器。经理论推导与仿真实验验证，所设计的控制器能够保证系统的稳定性，实现容错跟踪控制工作。

本次研究过程中，仅考虑了参数不确定性以及故障对飞行器稳定性的影响，高超声速飞行器控制器设计中还有许多的要素在本文中并没有加以考虑，包括非最小相位问题、跟踪收敛速度的问题、由未建模动态引起的不确定性问题等，在后续的研究中可以将其纳入考虑范围。在设计过程中，存在较难测量甚至不可测的数据，如高阶数据 $\ddot{h}$ 以及 $\dot{V}$，实用性较差；与此同时，由于系统本身是非线性的，将系统原模型线性化后，无法利用系统本身的性能设计更高效的控制器，因此在后续的研究中，可以考虑利用系统本身的物理特性进行控制器的设计，以提高控制器性能。

参考文献

[1] 金亮. 高超声速飞行器机体/发动机一体化构型设计与性能研究[D].国防科学技术大学, 2008.

[2] 杨凡, 黄颖, 陈云松, 曾皓.基于微分几何反馈线性化的高超声速飞行器控制系统实现[J].计算机测量与控制, 2022, 30(12):125-130.

[3] 杨旭曦. 基于自适应动态规划的吸气式高超声速飞行器的轨迹跟踪控制[D].天津理工大学, 2022.

[4] 孟尧, 岑梦希.基于反步的高超声速飞行器的容错跟踪控制[J].战术导弹技术, 2019, 27(03):27-33.

[5] 肖红, 王勇, 国海峰, 等. 高超声速飞行器末端导引与控制一体化研究[J]. 航天控制, 2013, 31(3):74-80.

[6] 刘卫华, 刘涛, 张浩.无人机起飞控制系统模糊控制器设计仿真研究[J].计算机仿真, 2016, 33(05):58-62.

[7] 许斌, 高超声速飞行器神经网络复合学习非反步控制方法. 陕西省, 西北工业大学, 2019-08-01.

[8] Chao T, Jing W. A nonlinear control approach for a hypersonic vehicle[J]. Aircraft Engineering and Aerospace Technology, 2017, 89(2).

[9] Wang N, Wu H, Guo L. Coupling-observer-based nonlinear control for flexible air-breathing hypersonic vehicles[J]. Nonlinear Dynamics, 2014, 78(3).

[10] Cui P, Gao C, Jing W et al. Fault-tolerant control of hypersonic vehicle using neural network and sliding mode[J]. International Journal of Aerospace Engineering, 2022, 20(22).

[11] 李传明, 孙经广.基于非线性函数的高超声速飞行器容错控制[J].航空兵器, 2019, 26(03):10-18.

[12] Song J, Luo Y, Zhao M et al. Fault-tolerant integrated guidance and control design for hypersonic vehicle based on PPO[J]. Mathematics, 2022, 10(18):93-10.

[13] 段广仁.高阶系统方法——I.全驱系统与参数化设计[J].自动化学报, 2020, 46(07):1333-1345.

[14] 段广仁.高阶系统方法——II.能控性与全驱性[J].自动化学报, 2020, 46(08):1571-1581.

[15] Duan G. High-order fully actuated system approaches: part VII. Controllability, stabilisability and parametric designs[J]. International Journal of Systems Science, 2021, 52(14):3091-3114.

[16] Duan G. High-order fully actuated system approaches: Part I. Models and basic procedure[J]. International Journal of Systems Science, 2021, 52(2):422-435.

[17] Xu H, Mirmirani MD, Ioannou PA. Adaptive sliding mode control design for a hypersonic flight vehicle[J]. Journal of Guidance, Control, and Dynamics, 2012, 27(5), 829-838.

[18] Xu B, Qi R, Jiang B. Adaptive fault-tolerant control for HSV with unknown control direction[J]. IEEE Transactions on Aerospace and Electronic Systems, 2019, 55(6), 2743-2758.

[19] Duan G. High-order fully actuated system approaches: Part IV. Adaptive control and high-order backstepping[J]. International Journal of Systems Science,2021,52(5), 927-989.

[20] Noemi ZM, Sandro MR. Limitations and applications in a fractional Barbalat's Lemma.[J]. Fractional calculus & applied analysis, 2022, 26(1):21-23.

Proceedings of the 3rd Conference on Fully Actuated System Theory and Applications
May 10-12, 2024, Shenzhen, China

Neural Observer-Based Intelligent Fault-Tolerant Control of Multi-Helicopters Under Actuator Faults: A Fully Actuated System Approach

Qiyang Miao[1], Jingping Xia[1], Bin Jiang[1,2], and Ke Zhang[1,2]
1. College of Automation Engineering Nanjing University of Aeronautics and Astronautics, Nanjing, China
2. National Key Laboratory of Helicopter Aeromechanics, Nanjing, China

Abstract: This paper investigates the fault-tolerant formation control of multiple unmanned helicopters under actuator faults through a neural-based fully actuated system approach (FASA). First, the kinematic and dynamic model of the helicopter with actuator faults is established, from which the fully actuated system description of a helicopter is derived. Second, to mitigate the dependence on model accuracy, a neural observer is designed to approximate the lumped uncertainty including the nonlinear, coupling, and faulty terms of a helicopter. Third, based on the estimated system dynamic, a triple-layered FASA controller is proposed to achieve the leader-follower formation control of helicopters. Finally, numerical simulations are conducted to validate the efficiency of the proposed algorithm.

Key Words: Helicopters, actuator faults, formation control, fault-tolerant control, fully actuated system approach.

1 Introduction

Helicopters outperform fixed-wing aircraft in maneuverability and surpass multi-rotors in loading capacity. When multiple helicopters are organized into a formation, they can fulfill crucial roles in missions ranging from cargo transportation to fire extinguishing.

Individual stability and global consensus of the helicopters are both crucial to their formation. To confront the complexity of helicopters' dynamics, a disturbance observer was utilized in [1], and recurrent neural networks were employed in [2]. Helicopters' dynamics were commonly stabilized separately by partitioning the translational and rotational dynamics, which always requires online estimation for the difficulty in attaining a precise model. To pursue the consensus of helicopter formation. In [3], a nonlinear model predictive control strategy was employed. In [4], a hybrid control framework with collision avoidance was proposed. To ensure the flexibility of the formation, distributed control schemes of helicopters were mostly employed.

As the scale of the formation expands, the possibility of faults escalates. The tolerance of faults either relies on the robustness of the controller to suppress the influence of faults, or seek for the estimation and compensation of faults through model-based observers [5] or data-reliant approximators [6]. The fault-tolerant control (FTC) of helicopters is seldom studied, throughout the limited literature, observer-based techniques such as [7] and [8] have been repeatedly employed in the research on the FTC of helicopters.

As a rarely investigated subject, the under-actuated nature of the helicopter introduces difficulty in designing and tuning the controller. The recently proposed fully actuated system approach (FASA) provides a convenient design process for complicated systems by canceling their non-linearity and arbitrarily assigning the poles. In [9], FASA was utilized for the attitude and orbit control of spacecraft. In [10], the fault-tolerant formation control of heterogeneous multi-agent systems was resolved through the FASA. It is noteworthy that the FASA is applicable not only to naturally fully actuated systems, but also to under-actuated systems such as direct current motors and quadrotors in [11] and [12].

Based on the prevailing practice of the formation control and FTC of helicopters, a neural-based FASA is proposed to achieve fault-tolerant formation control of multi-helicopters. The contributions of this paper are as follows:

1) The leader-follower formation control of helicopters is effectively addressed through the FASA, offering advantages in controller tuning convenience. In contrast, research [1] required tuning more than 20 parameters in the controller, while the work in [2] involved tuning 14 parameters, with the constraint that the movements in three dimensions share the same set of parameters. The FASA-based formation controller presented in this paper provides the flexibility to regulate all six degrees of movement by tuning only two matrices, achieved by assigning 12 poles.

2) The neural-based FASA is less dependent on model accuracy by employing the radial basis function (RBF) neural networks to approximate the coupled lumped non-linearity and uncertainty. The cancellation of system dynamics in existing FASA research is either through a pre-acquired model or through an extended state observer. The former requires accurate model identification, and the latter can not guarantee satisfactory performance before the convergence of the observer. The neural-based observer constructed in this paper can utilize the information from previous tasks to optimize the weights of the networks, providing improved performance of formation convergence.

3) Both additive and multiplicative actuator faults of helicopters are resolved in this paper, which is seldom investigated in the research of helicopter formation control. Com-

This work was supported in part by the National Natural Science Foundation of China under Grants (62173180, 62020106003, 62188101), in part by the National Key Laboratory Foundation of Helicopter Aeromechanics (2023-HA-LB-067-04), in part by the Qing Lan Project of Jiangsu Province of China, in part by the Fundamental Research Funds for the Central Universities under Grants (NE2022002, NC2022003), in part by the Postgraduate Research & Practice Innovation Program of NUAA under Grants (xcxjh20230314). (Corresponding author: Ke Zhang).

E-mail: qiyang_miao@nuaa.edu.cn; xiajingping@nuaa.edu.cn; binjiang@nuaa.edu.cn; kezhang@nuaa.edu.cn;

pared with [10] which requires adaptive Nussbaum function and [13] which requires fuzzy logic systems to estimate the faulty terms, the FTC technique in this paper is integrated into the FASA and requires no additional design of FTC modules, and extends the application scope of FASA to the fault-tolerant formation control of helicopters.

2 System Model and Preliminaries

2.1 Helicopter model under actuator faults

The mathematical model of the ith ($i = 1, 2, \cdots, n$) helicopter is derived from [14]. The kinematic and dynamic of the position subsystem are established as:

$$\begin{aligned} &\dot{\Lambda}_i = v_i \quad m_i\dot{v}_i = R_{bi}^e f_i^b \\ &f_i^b = \begin{bmatrix} 0 & 0 & -T_{Mi} \end{bmatrix}^T + R_{ei}^b \begin{bmatrix} 0 & 0 & m_i g \end{bmatrix}^T \end{aligned} \tag{1}$$

where Λ and v_i denote the position and velocity of the ith helicopter under the earth frame, m_i denotes the mass of the helicopter, $R_{bi}^e = (R_{ei}^b)^T$ denotes the rotation matrix from body frame to earth frame, g denotes the gravitational acceleration, $T_{Mi} = K_{TM}\omega_e^2 P_{Mi}$ denotes the thrust of the main rotor governed by the collective pitch input of the main rotor P_{Mi}, K_{TM} is the thrust coefficient, and ω_e denotes the engine speed which can be deemed as constant in this paper.

The kinematic and dynamic of the attitude subsystem are established as:

$$\begin{aligned} &\dot{\Omega}_i = M_i\omega_i \quad J_i\dot{\omega}_i = -{\omega_i}^{\times} J_i\omega_i + \tau_i^b \\ &\tau_i^b = \begin{bmatrix} c_b^M - T_{M_i}h_m & 0 & 0 \\ 0 & c_a^M + T_{M_i}h_m & 0 \\ 0 & 0 & l_t \end{bmatrix} \begin{bmatrix} P_{bi} \\ P_{ai} \\ T_{Ti} \end{bmatrix} \\ &+ \begin{bmatrix} -T_{Mi}y_m - Q_M P_{ai} - T_{Ti}h_t \\ Q_M P_{bi} - T_{Mi}l_m \\ -T_{Mi}l_m P_{bi} - Q_M \end{bmatrix} \end{aligned} \tag{2}$$

where $\Omega = [\phi_i, \theta_i, \psi_i]^T$ and ω denote the Euler angles and angular velocity, J_i denotes the inertial matrix, Matrix M_i denotes the translation from the derivative of Euler angles to the angular velocity, P_{bi}, P_{ai} respectively denote the lateral and longitudinal cyclic pitch input, $T_{Ti} = K_{TT}\omega_e^2 P_{Ti}$ denote the thrust of the tail rotor governed by the collective pitch of the tail rotor P_{Ti}, K_{TT}, c_b^M, c_a^M, h_m, h_t, y_m, l_t, l_m and Q_M are constant model parameters. Considering the response process of the actuators, the four control inputs P_{Mi}, P_{bi}, P_{ai}, and P_{Ti} are generated through the first-order dynamic such that $\dot{P}_{Mi} = (P_{Mi_d} - P_{Mi})/T_s$, where P_{mi_d} denotes the desired collective pitch generated by the controller, and T_s denotes the time constant of the actuator.

The collective and cyclic pitch angles of the main rotor are dictated by the lift and tilt of the swash plate, typically actuated by three struts. In the event of a fault occurring in one of the struts, both the collective and cyclic pitch angles will be impacted. For simplicity of analysis, taking the longitudinal cyclic pitch input as an example, the influence of the faults on the collective and cyclic pitch angles can be modeled as: $P_{a_fi} = P_{ai} + \Delta P_{ai}$, where $\Delta P_{ai} = (\rho_{ai} - 1)\, P_{ai} + \delta P_{ai}$, P_{a_fi} denotes the cyclic pitch under faulty occasion, ρ_{ai} denotes the multiplicative fault ratio, δP_{ai} denotes the additive faulty increment. Consequently, the thrust of the main rotor under faulty occasion can be modeled as $T_{M_fi} = T_{Mi} + \Delta T_{Mi}$.

2.2 Graph theory

The Laplacian matrix of a graph is defined by $L = D - A$, where $A = [a_{ij}] \in R^{n\times n}$ is the adjacent matrix where a_{ij} denotes the communication weight between different nodes so that $a_{ij} > 0$ if the communication between helicopter i and j is effective, and $D = \mathrm{diag}\{d_1, d_2, \cdots, d_n\}$ is the degree matrix where $d_i = \sum_{j=1}^{n} a_{ij}$. Define $B = \mathrm{diag}\{b_1, b_2, \cdots, b_n\}$ to describe the communication with the leader so that $b_i > 0$ if the communication between helicopter i and the virtual leader is effective.

2.3 RBF neural networks

For any continuous unknown functions $f \in \mathrm{R}^{\mathrm{r}}$, RBF neural networks can approximate it with an ideal RBF weight matrix $\overline{W} \in \mathrm{R}^{\mathrm{m}\times\mathrm{r}}$ under error ϵ bounded by L_ϵ such that $f = \overline{W}^T h(x) + \epsilon$, where $h(x) \in \mathrm{R}^{\mathrm{m}\times 1}$ denotes the radial-basis function vector, $h(x) = [h_1(x), h_2(x), \cdots, h_m(x)]^T$, and $x \in \mathrm{R}^{\mathrm{k}}$ denotes the input vector of the networks. Each RBF neuron is defined as $h_j = \exp\left(-\|x - c_j\|^2/b_j^2\right)$, where c_j and b_j denote the center and radius of the function.

Assumption 1 The ideal RBF weight matrix is bounded as $\|\overline{W}\|_F \le L_W$, where L_W is a positive constant.

2.4 Mathematical lemmas

Lemma 1 (see [1]) If the topology of the helicopter formation is an undirected and connected graph G, where at least one helicopter can receive information from the leader, matrix $H = L + B$ is symmetric and positive definite.

Lemma 2 (see [15]) if matrix $A \in \mathrm{R}^{\mathrm{n}\times\mathrm{n}}$ satisfies $\mathrm{Re}\lambda_i(A) \le -\gamma/2$, where $i = 1, 2, \cdots, n$ and $\gamma > 0$, then there exists a positive definite matrix $P \in \mathrm{R}^{\mathrm{n}\times\mathrm{n}}$ satisfying $A^T P + PA \le -\gamma P$.

3 Main Results

3.1 Fully actuated system description of helicopter

Because the helicopter is an under-actuated system, to derive the fully actuated system (FAS) description, the position and attitude subsystems shall be separately analyzed.

Concerning the position subsystem, define $\nu_{Ti} = [0, 0, -T_{Mi}]^T$, $G_e = [0, 0, g]^T$, and $G_{Ti} = [0, 0, -\Delta T_{Mi}]^T$, the position subsystem in (1) can be rewritten as $\ddot{\Lambda}_i = \frac{1}{m_i} R_{bi}^e (v_{Ti} + G_{Ti}) + G_e$. Define the control input of the position subsystem $u_{pi} = \frac{1}{m_i} R_{bi}^e v_{Ti} + G_e$, the fully actuated system description of the position subsystem can be derived:

$$\ddot{\Lambda}_i = u_{pi} + \frac{1}{m_i} R_{bi}^e G_{Ti} \tag{3}$$

Concerning the attitude subsystem, the control effectiveness matrix is defined as:

$$B_r = \mathrm{diag}\{c_b^M - h_m m_i g, c_a^M + h_m m_i g, l_t\} \tag{4}$$

The lumped uncertainty matrix is defined as:

$$\begin{aligned} &D_{ri} = \\ &\begin{bmatrix} \Delta P_{bi} - T_{Mi}y_m - Q_M P_{ai} - T_{Ti}h_t - \delta T_{Mi}h_m P_{bi} \\ \delta T_{Mi}h_m P_{ai} + \Delta P_{ai} + Q_M P_{bi} - T_{Mi}l_m \\ -T_{Mi}l_m P_{bi} - Q_M \end{bmatrix} \end{aligned} \tag{5}$$

where $\delta T_{Mi} = T_{Mi} - m_i g$, define the control input of the attitude subsystem $u_{ri} = [P_{bi}, P_{ai}, T_{Ti}]^T$, and eliminate the variable ω_i in (2), the fully actuated system description of the attitude subsystem can be derived:

$$\ddot{\Omega}_i = J_i^{-1}\left(-C\left(\dot{\Omega}_i, \Omega_i\right)\dot{\Omega}_i + B_r u_{ri} + D_{ri}\right) \quad (6)$$

where the term $C\left(\dot{\Omega}_i, \Omega_i\right)$ can be found in [16].

Remark 1 As can be concluded from the fully actuated system description of the helicopter in (3) and (6), directly calculating the coupling and nonlinear terms of the helicopter dynamics poses significant challenges, which brings difficulty in applying the FASA, and the need of approximation.

3.2 Neural observer

To approximate the lumped uncertainty characterized by $\frac{1}{m_i} R_{bi}^e G_{Ti}$ and $D_{ri} - C\left(\dot{\Omega}_i, \Omega_i\right)$, neural observers are utilized in both subsystems.

Taking the design of the neural observer in the attitude subsystem as an example, supposing that $J_i^{-1}(D_{ri} - C(\dot{\Omega}_i, \Omega_i))$ can be approximated by the RBF neural networks denoted by $\overline{W}_{ri}^T h\left(x_{ri}\right) + \epsilon$, the system described by (6) becomes:

$$\ddot{\Omega}_i = \overline{W}_{ri}^T h\left(x_{ri}\right) + \epsilon + J_i^{-1} B_r u_{ri} \quad (7)$$

Because the ideal weight matrix $\overline{W}_{ri}$ can not be directly attained but be estimated, the neural observer is designed as:

$$\begin{aligned} \ddot{\hat{\Omega}}_i &= \hat{W}_{ri}^T h\left(x_{ri}\right) + J_i^{-1} B_r u_{ri} + k_r e_{hi} \\ \dot{\hat{W}}_{ri} &= \alpha_r h\left(x_{ri}\right) e_{hi}^T - \beta_r \left\|e_{hi}\right\| \hat{W}_{ri} \end{aligned} \quad (8)$$

where $\hat{\Omega}$ and $\hat{W}_{ri}$ denote the estimations of Ω and $\overline{W}_{ri}$, the estimation error $e_{hi} = \dot{\Omega} - \dot{\hat{\Omega}}$ since $\dot{\Omega}$ can be directly measured by the gyroscope of the helicopter, $x_{ri} = [\Omega_i, \dot{\Omega}_i, P_{Mi}, u_{ri}]^T$,$k_r$, α, and β_r are adjustable parameters.

Theorem 1 Define the estimation error of the ideal weight matrix $\tilde{W}_{ri} = \overline{W}_{ri} - \hat{W}_{ri}$, as long as the neural observer is designed as (8) and Assumption 1 holds, the estimation error of the state $\dot{\Omega}$ and the weight $\overline{W}_{ri}$ are ultimately uniformly bounded (UUB).

Proof: Choose Lyapunov candidate $V_{ni} = \frac{1}{2}\alpha_r e_{hi}^T e_{hi} + \frac{1}{2}\text{tr}\left\{\tilde{W}_{ri}^T \tilde{W}_{ri}\right\}$.

$$\begin{aligned} \dot{V}_{ni} &\le -\alpha_r k_r e_{hi}^T e_{hi} - \beta_r \left\|e_{hi}\right\| \left\|\tilde{W}_{ri}\right\|^2 \\ &+ \beta_r \left\|e_{hi}\right\| \left\|\tilde{W}_{ri}\right\| \left\|\overline{W}_{ri}\right\| + \alpha_r e_{hi}^T \epsilon \\ &\le -\alpha_r k_r \left\|e_{hi}\right\|^2 - \beta_r \left\|e_{hi}\right\| (1-\eta) \left\|\tilde{W}_{ri}\right\|^2 \\ &+ \frac{\beta_r}{\eta} \left\|e_{hi}\right\| \left\|\overline{W}_{ri}\right\|^2 + \alpha_r \left\|e_{hi}\right\| \left\|\epsilon\right\| \\ &\le \left\|e_{hi}\right\| \left(-\alpha_r k_r \left\|e_{hi}\right\| - \beta_r (1-\eta) \left\|\tilde{W}_{ri}\right\|^2 \right. \\ &\left. + \frac{\beta_r}{\eta} L_W^2 + \alpha_r L_\epsilon^2\right) \end{aligned} \quad (9)$$

where $\eta > 0$ is a positive scalar. As long as $\alpha_r k_r \left\|e_{hi}\right\| + \beta_r (1-\eta) \left\|\tilde{W}_{ri}\right\|^2 > \frac{\beta_r}{\eta} L_W^2 + \alpha_r L_\epsilon^2$, $\dot{V}_{ni} < 0$ holds, estimation error e_{hi} and $\tilde{W}_{ri}$ are UUB with the residul set defined by $\alpha_r k_r \left\|e_{hi}\right\| + \beta_r (1-\eta) \left\|\tilde{W}_{ri}\right\|^2 \le \frac{\beta_r}{\eta} L_W^2 + \alpha_r L_\epsilon^2$. The proof of Theorem 1 is completed.

Similarly, the stability of the neural observer of the position subsystem can be proven, the input vector of the neural observer in the position subsystem is $x_{pi} = [\dot{\Lambda}_i, P_{Mi}, u_{ri}^T]$.

Remark 2 The lumped uncertainty in the helicopter dynamic including actuator faults is approximated by the RBF neural networks. This approach differs from the extended state observer employed in [12] because the uncertainty estimated through the RBF networks is state-dependent whereas that through the extended state observer is time-dependent, the latter is unable to establish the mapping from the states of helicopters to the uncertainty. With the neural observer, the weight matrix of the RBF networks can be trained in advance, enabling the preliminary estimation of lumped uncertainty at the beginning of the next flight.

3.3 Controller design based on FASA

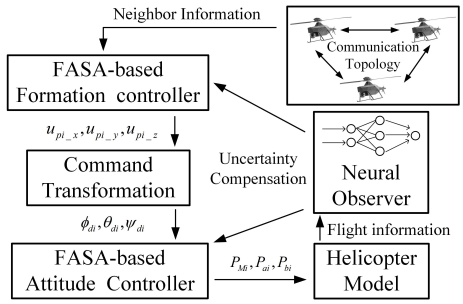

Fig. 1: Neural-based FASA control scheme.

The control scheme in this paper is composed of three layers: The bottom attitude controller, the middle command transformation, and the top formation controller, as illustrated in Fig. 1.

3.3.1 Bottom layer: Attitude controller

The control objective of the bottom layer attitude controller is to obtain the control input of the attitude subsystem u_{ri} to track the desired attitude represented by Euler angles. With the previous design of the neural observer, the FAS model of the attitude subsystem becomes:

$$\ddot{\Omega}_i = \hat{W}_{ri}^T h\left(x_{ri}\right) + \epsilon_{nr} + J_i^{-1} B_r u_{ri} \quad (10)$$

Note that (10) is different from (7) because the term ϵ_{nr} denotes the lumped estimation error of the observer and approximation error of the neural networks. According to the stability analysis of Theorem 1 and the assumption established in Assumption 1, ϵ_{nr} is bounded by L_{nr}.

The control input of the bottom layer u_{ri} is chosen as:

$$\begin{aligned} u_{ri} &= B_r^{-1} J_i \left(\upsilon_{ri} - \hat{W}_{ri}^T h\left(x_{ri}\right)\right) \\ \upsilon_{ri} &= A_{r1}\dot{e}_{ri} + A_{r0} e_{ri} \end{aligned} \quad (11)$$

where e_{ri} denotes the tracking error defined by: $e_{ri} = \Omega_{di} - \Omega_i$, A_{r1} and A_{r0} denote the gain matrices calculated through the assignment of poles through the FASA:

$$\begin{bmatrix} A_{r0} & A_{r1} \end{bmatrix} = -Z_r F_r^2 V_r^{-1} \tag{12}$$

where $V_r = [Z_r, Z_r F_r]$ and $F_r = \text{blockdiag}(F_{r1}, F_{r2})$ denotes the arbitrarily chosen pole matrix in which $F_{r1}, F_{r2} \in \mathrm{R}^{3\times 3}$, and Z_r is an arbitrary matrix such that $\det V_r \neq 0$.

With the controller design presented in (11), the error dynamic of the attitude tracking error is transformed into:

$$\ddot{e}_{ri} = -A_{r1}\dot{e}_{ri} - A_{r0}e_{ri} + \ddot{\Omega}_{di} + \epsilon_{nr} \tag{13}$$

which is equivalent to the state-space form:

$$\begin{bmatrix} \dot{e}_{ri} \\ \ddot{e}_{ri} \end{bmatrix} = \underbrace{\begin{bmatrix} 0_{3\times 3} & I_{3\times 3} \\ -A_{r0} & -A_{r1} \end{bmatrix}}_{\Phi_r} \begin{bmatrix} e_{ri} \\ \dot{e}_{ri} \end{bmatrix} + \begin{bmatrix} 0_{3\times 1} \\ \ddot{\Omega}_{di} + \epsilon_{nr} \end{bmatrix} \tag{14}$$

Theorem 2 As long as the $\ddot{\Omega}$ is bounded by $L_{\Omega d} > 0$, and the bottom layer attitude controller is designed as (11), the attitude tracking error e_{ri} is UUB, i.e, the helicopter can track the desired attitude with the performance regulated by the assigned poles through FASA.

proof: Choose Lyapunov candidate $V_r = \frac{1}{2}\bar{e}_{ri}^T P_r \bar{e}_{ri}$, where $\bar{e}_{ri} = [\dot{e}_{ri}, e_{ri}]^T$ and P_r is determined according to Lemma 2 such that $\Phi_r^T P_r + P_r \Phi_r \leq -\varsigma_r P_r$.

$$\begin{aligned}
\dot{V}_r &= \frac{1}{2}\bar{e}_{ri}^T P_r \left(\Phi_r \bar{e}_{ri} + \begin{bmatrix} 0_{3\times 1} \\ \ddot{\Omega}_d + \varepsilon_{nr} \end{bmatrix} \right) \\
&+ \frac{1}{2}\left(\Phi_r \bar{e}_{ri} + \begin{bmatrix} 0_{3\times 1} \\ \ddot{\Omega}_d + \varepsilon_{nr} \end{bmatrix} \right)^T P_r \bar{e}_{ri} \\
&= \frac{1}{2}\bar{e}_{ri}^T \left(\Phi_r^T P_r + P_r \Phi_r^T \right) \bar{e}_{ri} + \bar{e}_{ri}^T P_r \begin{bmatrix} 0_{3\times 1} \\ \ddot{\Omega}_d + \varepsilon_{nr} \end{bmatrix} \\
&\leq -\frac{\varsigma_r}{2}\bar{e}_{ri}^T P_r \bar{e}_{ri} + \frac{1}{2}\|\bar{e}_{ri}\|^2 + \frac{1}{2}\|P_{rL}\|^2 \left\| \ddot{\Omega}_d + \varepsilon_{nr} \right\|^2 \\
&\leq -\frac{\lambda_{\min}(\varsigma_r P_r - I)}{\lambda_{\max}(P_r)} V_r + \frac{1}{2}\|P_{rL}\|^2 \left\| \ddot{\Omega}_d + \varepsilon_{nr} \right\|^2
\end{aligned} \tag{15}$$

where $P_{rL} = P_r[0_{3\times 3}, I_{3\times 3}]^T$. Once the the eigenvalues of P_r is appropriately designed through the pole assignment, the attitude tracking error is UUB with the residual set defined by: $e_r \in \{V_r \leq \frac{\|P_{rL}\|^2 \left\| \ddot{\Omega}_d + \epsilon_{nr} \right\|^2 \lambda_{\max}(P_r)}{2\lambda_{\min}(\varsigma_r P_r - I)}\}$. The proof of Theorem 2 is completed.

3.3.2 Middle layer: Generation of attitude command

The desired attitude is generated from the control input of the position subsystem $u_{pi} = [u_{pi_x}, u_{pi_y}, u_{pi_z}]$ through the following transformation:

$$\begin{aligned}
T_{Mi} &= m_i \sqrt{u_{pi_x}^2 + u_{pi_y}^2 + (g - u_{pi_z})^2} \\
\phi_{di} &= \arcsin\left(m_i (u_{pi_y}\cos(\psi_i) - u_{pi_x}\sin(\psi_i))/T_{Mi} \right) \\
\theta_{di} &= \arctan\left(u_{pi_x}\cos(\psi_i) + u_{pi_y}\sin(\psi_i)/(u_{pi_z} - g) \right)
\end{aligned} \tag{16}$$

The collective pitch input of the main rotor can be calculated by $P_{Mi} = T_{Mi}/(K_{TM}\omega_e^2)$. The desired yaw angle of the helicopter ψ_{di} can be arbitrarily determined.

3.3.3 Top layer: Formation controller

The control objective of the formation controller is to acquire the control input of the position subsystem u_{pi} such that the formation tracking error $e_{pi} = p_i - \Delta_i - p_d$ is convergent. Because a distributed control scheme is employed, the formation tracking error can not be directly obtained, instead, the formation error is defined as $\xi_i = \sum_{j=1}^n a_{ij}(\Lambda_i - \Delta_{ij} - \Lambda_j) + b_i(\Lambda_i - \Lambda_d - \Delta_i)$, where Δ_{ij} denotes the relative geometry between helicopter i and j, Λ_d denotes the position of the leader, and Δ_i denotes the relative geometry between helicopter i and the leader. Define $e_p = [e_{p1}, e_{p2}, \cdots, e_{pn}]$ and $\xi = [\xi_1, \xi_2, \cdots, \xi_n]$. It can be derived that $e_p = (H \otimes I_{3\times 3})\xi$, which implies that the convergence of e_p is equivalent to that of ξ.

The derivative of the formation error yields:

$$\begin{aligned}
\ddot{\xi}_i &= \left(\sum\nolimits_{j=1}^n a_{ij} + b_i \right) \left(u_{pi} + \frac{1}{m_i} R_{bi}^e G_{Ti} \right) \\
&- \sum\nolimits_{j=1}^n a_{ij} \left(\ddot{\Delta}_{ij} + \ddot{\Lambda}_j \right) - b_i \left(\ddot{\Lambda}_d + \ddot{\Delta}_i \right)
\end{aligned} \tag{17}$$

The formation controller for the ith helicopter is:

$$\begin{aligned}
u_{pi} &= \frac{\upsilon_{pi} + \sum_{j=1}^n a_{ij} \left(\ddot{\Delta}_{ij} + \ddot{\Lambda}_j \right) + b_i \left(\ddot{\Lambda}_d + \ddot{\Delta}_i \right)}{\sum_{j=1}^n a_{ij} + b_i} \\
\upsilon_{pi} &= -A_{p1}\dot{\xi}_i - A_{p0}\xi_i - W_{pi}^T h(x_{pi})
\end{aligned} \tag{18}$$

where A_{p0} and A_{p1} are calculated from from the same technique introduced in (12) and $W_{pi}^T h(x_{pi})$ denotes the approximation of $\frac{1}{m_i} R_{bi}^e G_{Ti}$.

With the formation controller presented in (18), the dynamic of the formation error is transformed into:

$$\ddot{\xi}_i = -A_1\dot{\xi}_i - A_0\xi_i + \left(\sum\nolimits_{j=1}^n a_{ij} + b_i \right) \epsilon_{np} \tag{19}$$

where ϵ_{np} denotes the bounded lumped approximation and estimation error of the neural observer. Define $E_i = \sum_{j=1}^n (a_{ij} + b_i)\epsilon_{np}$ and $E = [E_1, E_2, \cdots, E_n]^T$, the state-space form of the formation error dynamic is established as follows:

$$\begin{bmatrix} \dot{\xi} \\ \ddot{\xi} \end{bmatrix} = \underbrace{\left(\begin{bmatrix} 0_{3\times 3} & I_{3\times 3} \\ -A_{p0} & -A_{p1} \end{bmatrix} \otimes I_{n\times n} \right)}_{\Phi_p} \begin{bmatrix} \xi \\ \dot{\xi} \end{bmatrix} + \begin{bmatrix} 0_{3n\times 1} \\ E \end{bmatrix} \tag{20}$$

Theorem 3 With the formation controller proposed in (18), the formation error is UUB, i.e., the leader's trajectory can be tracked by the follower helicopters under desired geometry and performance regulated by the design of Φ_p.

proof: The stability analysis is similar to that of Theorem 2, the Lyapunov candidate is chosen as $V_p = \frac{1}{2}\bar{\xi}^T P_p \bar{\xi}$, where P_p is determined according to Lemma 2 such that $\Phi_p^T P_p + P_p \Phi_p \leq -\varsigma_p P_p$. Referring to the analysis of Theorem 2, the following inequality holds:

$$\dot{V}_p \leq -\frac{\lambda_{\min}(\varsigma_p P_p - I)}{\lambda_{\max}(P_p)} V_p + \frac{1}{2}\|P_p\|^2 \|E\|^2 \tag{21}$$

The formation error is UUB with the residual set defined by: $\bar{\xi} \in \{V_p \leq \frac{\|P_p\|^2 \|E\|^2 \lambda_{\max}(P_p)}{2\lambda_{\min}(\varsigma_p P_p - I)}\}$. The proof of Theorem 3 is completed.

Remark 3 The proposed scheme excels in regulating the overall formation performance through the FASA with minimal tuning parameters. The pole matrices of the attitude controller and the poles of the Z axis in the formation controller should be first determined, and then the poles of the formation controller of the X-Y axes shall be placed approximately ten times closer to the imaginary axis compared with the poles of the pitch-roll axes.

4 Numerical Simulation

A numerical simulation of the proposed FASA-based scheme is conducted to illustrate its effectiveness. Three helicopters are simulated to form a desired formation while tracking the virtual leader.

The parameters of the helicopter are: $m_{1,2,3} = 8\text{kg}$, $J_{1,2,3} = \text{diag}\{0.18, 0.34, 0.28\}$, $c_b^M = c_a^M = 52\text{Nm/rad}$, $h_m = 0.24\text{m}$, $y_m = l_m = 0\text{m}$, $h_t = 0.1\text{m}$, $l_t = 0.9\text{m}$, $Q_M = 4.6$, $K_{TM} = 0.058$, $K_{TM} = 0.001$. The assigned pole matrices of the attitude and position subsystem are:

$$\begin{aligned} F_r &= \text{diag}\{-2, -2, -3, -25, -25, -25\} \\ F_p &= \text{diag}\{-0.3, -0.3, -1, -0.6, -0.6, -2.5\} \end{aligned} \tag{22}$$

The parameters of the neural observer in the attitude subsystem are $k_r = 60$, $\alpha_r = 1$, $\beta_r = 0.01$. The parameters of the neural observer in the attitude subsystem are $k_p = 10$, $\alpha_p = 0.1$, $\beta_p = 0.01$. Note that the inputs of the RBF networks need to be scaled to the same level of magnitude. 100 RBF neurons are utilized in this paper.

The trajectory of the virtual leader is designed as $\Lambda_d = [15\sin(0.05t), 15\sin(0.05t - \pi/2) + 15, -t]^T$ and first/second-order filters are utilized to acquire the smooth derivative of the command signals. The topology of the formation is described by $a_{12} = a_{13} = a_{21} = a_{23} = a_{31} = a_{32} = 1$, $b_1 = b_2 = 8$. The formation geometry is described as $\Delta_{12} = [2, -2, 0]^T$, $\Delta_{13} = [2, 2, 0]^T$, $\Delta_{23} = [0, 4, 0]^T$, $\Delta_1 = [0, 0, 0]^T$.

The initial positions of helicopters are $p_{1_ini} = [0; 0; 0]^T$, $p_{2_ini} = [-8; 8; 0]^T$, $p_{3_ini} = [-8; -8; 0]^T$. Define the multiplicative fault ratio of the ith helicopter as $\rho_i = [\rho_{mi}, \rho_{ai}, \rho_{bi}]^T$, and the additive fault of the ith helicopter as $\delta P_i = [\delta P_{Mi}, \delta P_{ai}, \delta P_{bi}]$. The fault condition of the helicopters are: $\rho_1 = [1, 1, 0.65]^T$, $\rho_2 = [1, 0.9, 0.8]^T$, $\rho_3 = [0.9, 0.8, 0.7]^T$, $\delta P_1 = [-0.02, 0, 0.01]^T$, $\delta P_2 = [-0.02, 0.01, 0]^T$,$\delta P_3 = [0, 0.02, 0.01]^T$. Helicopter 1,2 and 3 respectively encounters fault at $t = 50s$, $t = 100s$, and $t = 150s$.

The tracking performance of the helicopter formation is presented in Fig. 2 and Fig. 3. The control inputs of the helicopters under faults are presented in Fig. 4. The attitudes of helicopters are presented in Fig. 5. The estimation of the RBF neural networks is illustrated in Fig. 6.

It can be concluded from the simulation results that the controllers designed through the neural-based FASA effectively achieve the distributed formation control of helicopters. The attitude and position of helicopters are conveniently stabilized through the assignment of poles and the complex dynamics caused by the intricate mechanic, aerodynamic, and actuator faults are efficiently approximated by the neural observer. For example, as is revealed in Fig. 6, the lumped uncertainty estimated by $\hat{W}_{ri}h_\psi$ (i=1,2,3) denotes

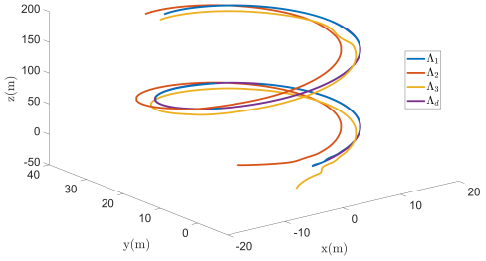

Fig. 2: 3D view of formation trajectories.

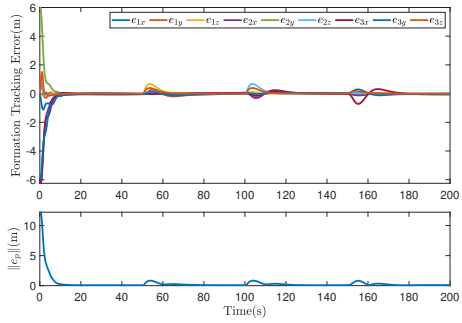

Fig. 3: Formation tracking errors of helicopters.

the reverse torque caused by the main rotor, which demonstrates both the characteristic of helicopters and the performance of the RBF neural observer.

To further illustrate the benefit of the neural observer, a comparison experiment is conducted in Fig. 7. In the first case, the weight matrices of the RBF neural networks are randomly initialized. In the second case, the weight matrices are trained from previous simulations in which no faults occur to the helicopters. The convergence speed of the formation tracking error in the second case is noticeably faster than that in the first case, which demonstrates the advantage of the neural observer in that the information from previous missions can be utilized to optimize the next mission.

5 Conclusion

The distributed formation control of multiple helicopters under actuator faults is addressed in this paper. The benefits are threefold: 1) The formation control of helicopters is resolved with FASA. The intricate dynamics of helicopters

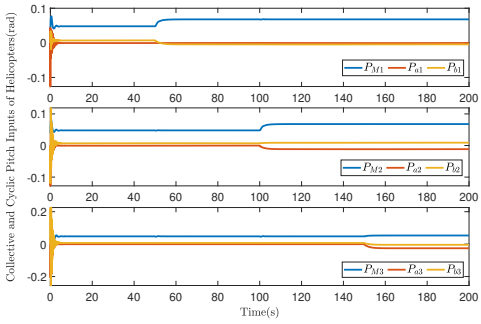

Fig. 4: Collective and cyclic pitch inputs of helicopters.

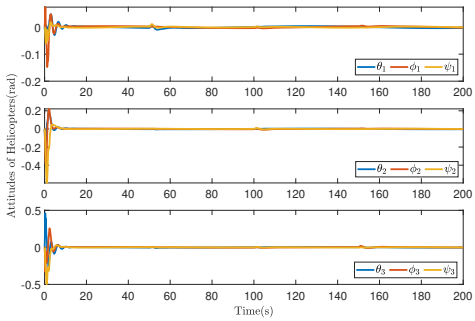

Fig. 5: Attitudes of helicopters.

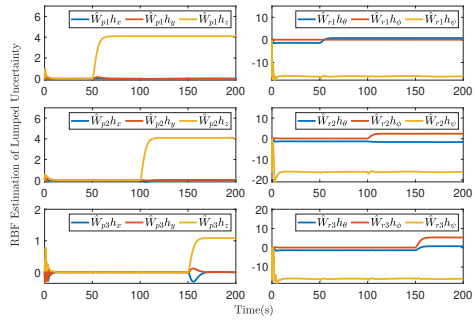

Fig. 6: Estimations of lumped uncertainty by the RBF neural networks.

are conveniently eliminated and reconfigured. 2) The neural observer provides an approximation of lumped uncertainty, minimizing reliance on pre-acquired models and allowing for the utilization of previous flight data. 3) Multiplicative and additive actuator faults are effectively compensated through FASA without the need for an additional FTC module design.

References

[1] Dandan Wang, Qun Zong, Bailing Tian, Shikai Shao, Xiuyun Zhang, and Xinyi Zhao. Neural network disturbance observer-based distributed finite-time formation tracking control for multiple unmanned helicopters. *ISA transactions*, 73:208–226, 2018.

[2] Chia Wei Kuo, Ching Chih Tsai, and Chi Tai Lee. Intelligent leader-following consensus formation control using recurrent neural networks for small-size unmanned helicopters. *IEEE Transactions on Systems, Man, and Cybernetics: Systems*, 51(2):1288–1301, 2021.

[3] M. Saffarian and F. Fahimi. Non-iterative nonlinear model predictive approach applied to the control of helicopters' group formation. *Robotics and Autonomous Systems*, 57(6):749–757, 2009.

[4] Ali Karimoddini, Hai Lin, Ben M Chen, and Tong Heng Lee. Hybrid three-dimensional formation control for unmanned helicopters. *Automatica*, 49(2):424–433, 2013.

[5] Jianglin Lan, Ron J Patton, and Xiaoyuan Zhu. Integrated fault-tolerant control for a 3-dof helicopter with actuator faults and saturation. *IET Control Theory & Applications*, 11(14):2232–2241, 2017.

[6] Bin Jiang, Ke Zhang, and Peng Shi. Integrated fault estimation and accommodation design for discrete-time takagi–sugeno fuzzy systems with actuator faults. *IEEE Transactions on Fuzzy Systems*, 19(2):291–304, 2010.

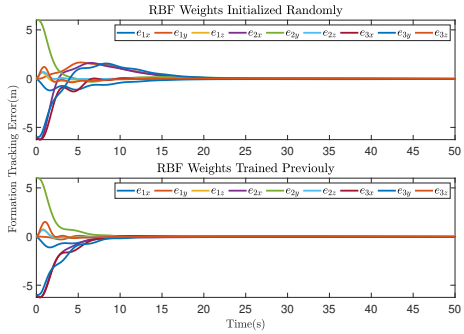

Fig. 7: Formation tracking errors with and without pre-trained RBF weights.

[7] Kun Yan, Mou Chen, Qingxian Wu, and Bin Jiang. Extended state observer-based sliding mode fault-tolerant control for unmanned autonomous helicopter with wind gusts. *IET Control Theory & Applications*, 13(10):1500–1513, 2019.

[8] Ke Zhang, Bin Jiang, and Marcel Staroswiecki. Dynamic output feedback-fault tolerant controller design for takagi–sugeno fuzzy systems with actuator faults. *IEEE Transactions on Fuzzy Systems*, 18(1):194–201, 2009.

[9] Guangquan Duan and Guoping Liu. Attitude and orbit optimal control of combined spacecraft via a fully-actuated system approach. *Journal of Systems Science and Complexity*, 35(2):623–640, 2022.

[10] Yonghao Ma, Ke Zhang, and Bin Jiang. Neuroadaptive cooperative fault-tolerant control of heterogeneous multiagent systems based on fully actuated system approaches. *IEEE Transactions on Cybernetics*, pages 1–12, 2023.

[11] Xiubo Wang and Guangren Duan. High-order fully actuated system approaches: Model predictive control with applications to under-actuated systems. *Journal of the Franklin Institute*, 360(10):6953–6975, 2023.

[12] Gaoqi Liu, Bin Li, and Guangren Duan. An optimal FASA approach for UAV trajectory tracking control. *Guidance, Navigation and Control*, page 2350015, 2023.

[13] Yang Cui, Guangren Duan, Xiaoping Liu, and Hongyu Zheng. Adaptive fuzzy fault-tolerant control of high-order nonlinear systems: A fully actuated system approach. *International Journal of Fuzzy Systems*, pages 1–12, 2023.

[14] Lorenzo Marconi and Roberto Naldi. Aggressive control of helicopters in presence of parametric and dynamical uncertainties. *Mechatronics*, 18(7):381–389, 2008.

[15] Qin Zhao and Guangren Duan. Fully actuated system approach for 6dof spacecraft control based on extended state observer. *Journal of Systems Science and Complexity*, 35(2):604–622, 2022.

[16] Wanbing Zhao, Hao Liu, and Frank L. Lewis. Data-driven fault-tolerant control for attitude synchronization of nonlinear quadrotors. *IEEE Transactions on Automatic Control*, 66(11):5584–5591, 2021.

Proceedings of the 3rd Conference on Fully Actuated System Theory and Applications
May 10-12, 2024, Shenzhen, China

A Fully Actuated System Approach to Interval Observer Design with Applications in Fault Detection

Weijie Ren[1], Guang-Ren Duan[1,2,*], and He Kong[1]

1. Shenzhen Key Laboratory of Control Theory and Intelligent Systems, Southern Uni. of Sci. and Tech., Shenzhen 518055, China
E-mail: weijie.ren@outlook.com, g.r.duan@hit.edu.cn/duangr@sustech.edu.cn, kongh@sustech.edu.cn

2. Center for Control Theory and Guidance Technology, Harbin Institute of Technology, Harbin 150001, China

Abstract: This paper explores a fully actuated system approach for interval observer design with applications in fault detection. Leveraging the full-actuation property, a stabilization control law is initially implemented to cancel open-loop nonlinearities, resulting in a constant high-order linear system. Subsequently, two interval observer design approaches are introduced. Employing the parametric design method, the challenge of determining the observer gain and nonsingular transformation matrix is converted into solving the generalized Sylvester matrix equation. This method allows for the free assignment of the eigenstructure of the observer error system. Additionally, a fault detection logic is presented. Finally, the feasibility and effectiveness of the proposed interval observers are demonstrated through an illustrative example.

Key Words: Fully actuated system approach, Interval observer, Fault detection, Parametric design

1 Introduction

Observers play a crucial role in control theory and engineering, offering various methodologies for estimating system states and unknown inputs. Commonly used observers, including the Luenberger observer, Kalman observer (filter), proportional-integral observer, sliding mode observer, and disturbance observer, typically provide point-wise estimates. In contrast, the interval observer, initially introduced in [1], distinguishes itself by furnishing both upper and lower estimation bounds. These bounds encapsulate the actual system state, and the interval observer excels in scenarios where unknown input signals, such as noises, disturbances, and parametric uncertainties, are present but bounded. Unlike traditional observers, the interval observer places a mild constraint by only requiring that the unknown inputs be bounded, making it particularly adaptable. Statistical characteristics like the covariance matrix are no longer necessary for handling unknown inputs. Over the past two decades, intensive research efforts have been dedicated to exploring the capabilities of interval observers [2]. Notably, the interval observer has demonstrated commendable performance in state estimation and fault detection [3] [4].

While interval observers exhibit remarkable properties, their design and applications have predominantly been confined to linear systems. However, extending the utility of interval observers to nonlinear systems remains challenging. In addressing this issue, one approach involves transforming the original nonlinear system into local linear systems, such as linear parameter-varying systems or Takagi-Sugeno fuzzy systems [5]. Another avenue for nonlinear cases requires the consideration of a specific class of weak nonlinear systems [6]. Notably, a recent method known as the fully actuated system approach, originally proposed by Duan [7], presents a novel solution. The fully actuated system approach operates parallel to the well-established state-space method, transforming the (high-order) physical dynamic model into a fully actuated model from a mathematical perspective. In contrast to the state-space method, which converts the high-order model into a set of first-order dynamic equations, the newly proposed fully actuated system method can straightforwardly eliminate all nonlinearities within the open-loop system. Moreover, it allows for the free assignment of the closed-loop system's eigenstructure in alignment with specific performance objectives [8]. This unique characteristic streamlines the design of controllers and observers, garnering considerable attention within the control community. The significance of the fully actuated system method is exemplified in recent studies. For instance, [9] integrates the high-order fully actuated system approach with distributed learning to address secondary control issues in islanded DC microgrids. Additionally, for nonideal time-varying high-order fully actuated systems, [10] proposes an innovative low-power observer-based fault-tolerant controller framework.

To the best of the authors' knowledge, interval observer design and its application to fault detection based on the fully actuated system approach have not been explored to date. Given the advantages of interval observers, embarking on this endeavor for fully actuated systems holds significant merit. The contributions of this paper can be summarized as follows:

1) Two interval observer design methods are introduced for nonlinear systems, employing the fully actuated system approach, for the first time.
2) The parametric design method is used to design the observer gain and similarity transformation matrix, which offers all degrees of design freedom and facilitates the freely assignable eigenstructure.

The paper is structured as follows. Section 2 introduces the nonlinear fully actuated system and preliminaries. Section 3 presents two interval observer design approaches, gain calculation, and fault detection method. Section 4 uses an example to demonstrate the effectiveness of the proposed in-

*Corresponding author. This work was supported by the Science, Technology, and Innovation Commission of Shenzhen Municipality, China, under Grant No. ZDSYS20220330161800001, and the Shenzhen Science and Technology Program under Grant No. KQTD20221101093557010. This work was also supported by the Science Center Program of the National Natural Science Foundation of China (NSFC) under Grant No. 62188101, as well as the NSFC under Grant No. 62350055.

terval observers, in terms of state estimation and fault detection. Section 5 concludes the paper.

In the paper, some frequently used notations are predefined here. The symbols $\mathbb{R}, \mathbb{C}, \mathbb{R}_+$ and $\mathbb{Z}_+$ denote the real number set, the complex number set, the nonnegative real number set, and the nonnegative integer set, respectively. The symbols 0 and I represent the null matrix and identity matrix of appropriate dimensions, respectively. For $A \geq B, A, B \in \mathbb{R}^{m\times n}$, it means each element $[A]_{ij} \geq [B]_{ij}, i = 1, 2, \ldots m, j = 1, 2, \ldots n$. For vector $x \in \mathbb{R}^n$ and matrices $A_i \in \mathbb{R}^{n\times n}$, $i = 1, 2, \ldots m$,

$$x^{(0\text{~}m)} = \left[\begin{array}{cccc} x^T & \dot{x}^T & \cdots & \left(x^{(m)}\right)^T \end{array} \right]^T,$$

$$A_{0\text{~}m} = \left[\begin{array}{cccc} A_0 & A_1 & \cdots & A_m \end{array} \right],$$

$$\Phi\left(A_{0\text{~}m}\right) = \left[\begin{array}{cccc} 0 & I & & \\ & & \ddots & \\ & & & I \\ -A_0 & -A_1 & \cdots & -A_m \end{array} \right].$$

2 System Description and Preliminaries

Consider the following fully actuated system:

$$\left\{ \begin{array}{l} x^{(m)} = f\left(x^{(0\text{~}m-1)}\right) + B\left(x^{(0\text{~}m-1)}\right)u + Ef_a + Dw \\ y = Cx^{(0\text{~}m-1)}, \end{array} \right. \tag{1}$$

where $x \in \mathbb{R}^n$ is the system state vector, $u \in \mathbb{R}^r$ is the control input vector, $y \in \mathbb{R}^p$ is the measurement output vector, $f_a \in \mathbb{R}^\vartheta$ is the actuator fault vector, and $w \in \mathbb{R}^q$ is the bounded disturbance vector. $f(\cdot)$ and $B(\cdot)$ are sufficiently differentiable nonlinear vector and matrix functions, respectively, and the following full-actuation condition holds:

$$\det B\left(x^{(0\text{~}m-1)}, t\right) \neq 0, \ \ \forall x, \dot{x}, \ldots x^{(m)} \in \mathbb{R}^n, \ \ t \geq 0.$$

The matrices $B\left(x^{(0\text{~}m-1)}\right) \in \mathbb{R}^{n\times r}, C \in \mathbb{R}^{p\times nm}, E \in \mathbb{R}^{n\times\vartheta}, D \in \mathbb{R}^{n\times q}$. Assume all the state can be obtained from the output channel, i.e., $\operatorname{rank} C = p = nm$.

Owing to the presence of nonlinearities, designing an effective interval observer that rigorously bounds the actual system state between upper and lower estimates ($\underline{x}^{(0\text{~}m-1)} \leq x^{(0\text{~}m-1)} \leq \bar{x}^{(0\text{~}m-1)}$) proves challenging. Consequently, establishing a linearized framework becomes imperative for interval observer design. To this end, we commence by designing the following stabilization controller:

$$\left\{ \begin{array}{l} u = -B^{-1}\left(x^{(0\text{~}m-1)}\right)\left(A_{0\text{~}m-1}x^{(0\text{~}m-1)} + u^*\right) \\ u^* = f\left(x^{(0\text{~}m-1)}\right) - v. \end{array} \right. \tag{2}$$

where $A_i \in \mathbb{R}^{r\times r}$, $i = 0, 1, \ldots, m-1$ are parametric matrices to be designed and $v \in \mathbb{R}^r$ is the external signal.

Substituting (2) into system (1), we obtain a high-order linear closed-loop system

$$x^{(m)} + A_{0\text{~}m-1}x^{(0\text{~}m-1)} = v + Dw, \tag{3}$$

which can be written in the following state-space form:

$$\dot{x}^{(0\text{~}m-1)} = \Phi\left(A_{0\text{~}m-1}\right)x^{(0\text{~}m-1)} + \Gamma v + \mathring{D}w, \tag{4}$$

where $\Gamma = \left[\begin{array}{c} 0 \\ \vdots \\ 0 \\ I \end{array} \right], \mathring{D} = \left[\begin{array}{c} D_0 \\ \vdots \\ D_{m-2} \\ D \end{array} \right].$

Note that some additional disturbance coefficient matrices $D_0, \ldots D_{m-2}$ are added in (4). The following definitions, assumptions, and lemmas are necessary for interval observer design.

Definition 1. *A Matrix is called a Hurwitz matrix if all its eigenvalues have negative real parts. A matrix is called a Metzler matrix if its off-diagonal elements are nonnegative.*

Assumption 1. The initial system state $x^{(0\text{~}m-1)}(0)$ and the disturbance w are unknown but bounded such that

$$x^{(0\text{~}m-1)}(0) \in \left[\underline{x}^{(0\text{~}m-1)}(0), \bar{x}^{(0\text{~}m-1)}(0)\right], \ w \in [\underline{w}, \overline{w}].$$

Lemma 1. [11] Any solution of the system

$$\dot{x} = Ax + w, \ \ x \in \mathbb{R}^n, w : \mathbb{Z}_+ \to \mathbb{R}^n_+,$$

with a Metzler matrix $A \in \mathbb{R}^{n\times n}$, is elementwise nonnegative for all $t \geq 0$, provided that $x(0) \geq 0$.

Lemma 2. [6] Given vectors $x, \bar{x}, \underline{x} \in \mathbb{R}^n$ with $\underline{x} \leq x \leq \bar{x}$ and a constant matrix $A \in \mathbb{R}^{m\times n}$, the following inequality holds:

$$A^+\underline{x} - A^-\bar{x} \leq Ax \leq A^+\bar{x} - A^-\underline{x},$$

where A is expressed as the difference of two elementwise nonnegative matrices A^+ and A^-, i.e., $A = A^+ - A^-, A^+, A^- \geq 0$.

3 Main Results

3.1 Interval Observer Design

The interval observer provides upper and lower estimation for system states, that is, the observer consists of two parts: upper bound observer and lower bound observer. The system matrix of the error dynamic system should be not only Hurwitz stable but also Metzler. In the subsequent content, two possible design methods are provided.

Based on the obtained linear closed-loop system (4), the interval observer can be designed as

$$\left\{ \begin{array}{l} \dot{\bar{x}}^{(0\text{~}m-1)} = \Phi\left(A_{0\text{~}m-1}\right)\bar{x}^{(0\text{~}m-1)} + L\left(y - C\bar{x}^{(0\text{~}m-1)}\right) \\ \qquad\qquad +\Gamma v + \mathring{D}^+\overline{w} - \mathring{D}^-\underline{w} \\ \dot{\underline{x}}^{(0\text{~}m-1)} = \Phi\left(A_{0\text{~}m-1}\right)\underline{x}^{(0\text{~}m-1)} + L\left(y - C\underline{x}^{(0\text{~}m-1)}\right) \\ \qquad\qquad +\Gamma v + \mathring{D}^+\underline{w} - \mathring{D}^-\overline{w}, \end{array} \right. \tag{5}$$

where $L \in \mathbb{R}^{nm\times p}$ is the observer gain to be determined, $\mathring{D}^+$ and $\mathring{D}^-$ are two elementwise nonnegative matrices satisfying $\mathring{D} = \mathring{D}^+ - \mathring{D}^-, \mathring{D}^+, \mathring{D}^- \geq 0$. The following theorem states the existence of interval observer (5).

Theorem 1. *Under the Assumption 1, if there exist a series of parametric matrices $A_{0\text{~}m-1}$ and an observer gain matrix $L \in \mathbb{R}^{nm\times p}$ such that $\Phi\left(A_{0\text{~}m-1}\right) - LC$ is simultaneously Hurwitz stable and Metzler, system (5) is an interval observer for the nonlinear fully actuated system (1) such that $\underline{x}^{(0\sim m-1)} \leq x^{(0\sim m-1)} \leq \overline{x}^{(0\sim m-1)}, \forall t \geq 0$.*

Proof. Define the upper and lower bound errors by $\bar{e}^{(0\text{~}m-1)} = \bar{x}^{(0\text{~}m-1)} - x^{(0\text{~}m-1)}, \underline{e}^{(0\text{~}m-1)} = x^{(0\text{~}m-1)} -$

$\underline{x}^{(0\hat{}m-1)}$, respectively. Calculate their derivatives and then the error system of interval observer (5) is

$$\begin{cases} \dot{\bar{e}}^{(0\hat{}m-1)} & = \left(\Phi\left(A_{0\hat{}m-1}\right) - LC\right)\bar{e}^{(0\hat{}m-1)} \\ & \quad +\mathring{D}^{+}\overline{w} - \mathring{D}^{-}\underline{w} - \mathring{D}w \\ \dot{\underline{e}}^{(0\hat{}m-1)} & = \left(\Phi\left(A_{0\hat{}m-1}\right) - LC\right)\underline{e}^{(0\hat{}m-1)} \\ & \quad +\mathring{D}w - \mathring{D}^{+}\underline{w} + \mathring{D}^{-}\overline{w}. \end{cases}$$

Lemma 2 provides that

$$\begin{aligned} \mathring{D}^{+}\overline{w} - \mathring{D}^{-}\underline{w} - \mathring{D}w \geq 0, \\ \mathring{D}w - \mathring{D}^{+}\underline{w} + \mathring{D}^{-}\overline{w} \geq 0. \end{aligned}$$

Therefore, according to Lemma 1, the error system is asymptotically stable and elementwise nonnegative, i.e.,

$$\begin{aligned} \lim_{t\to\infty} \bar{e}^{(0\sim m-1)} = \epsilon_1 \geq 0, \\ \lim_{t\to\infty} \underline{e}^{(0\sim m-1)} = \epsilon_2 \geq 0, \end{aligned}$$

provided that the error system matrix $\Phi\left(A_{0\hat{}m-1}\right) - LC$ is Hurwitz and Metzler, as well as Assumption 1 holds. □

The requirement of both Hurwitz and Metzler for the error system matrix $\Phi\left(A_{0\hat{}m-1}\right) - LC$ is restrictive. The following text provides another interval observer based on the similarity transformation, which reduces the design difficulty. Define a nonsingular transformation $x^{(0\hat{}m-1)} = Vz^{(0\hat{}m-1)}, V \in \mathbb{R}^{nm\times nm}$. The transformed state-space system is derived as

$$\dot{z}^{(0\hat{}m-1)} = \tilde{\Phi}\left(A_{0\hat{}m-1}\right)z^{(0\hat{}m-1)} + \tilde{\Gamma}v + \tilde{D}w, \tag{6}$$

where $\tilde{\Phi} = V^{-1}\Phi\left(A_{0\hat{}m-1}\right)V, \tilde{\Gamma} = V^{-1}\Gamma, \tilde{D} = V^{-1}\mathring{D}$. The newly proposed interval observer is as follows:

$$\begin{cases} \dot{\bar{z}}^{(0\hat{}m-1)} = & \tilde{\Phi}\bar{z}^{(0\hat{}m-1)} + \tilde{L}\left(y - \tilde{C}\bar{z}^{(0\hat{}m-1)}\right) \\ & +\tilde{\Gamma}v + \tilde{D}^{+}\overline{w} - \tilde{D}^{-}\underline{w} \\ \dot{\underline{z}}^{(0\hat{}m-1)} = & \tilde{\Phi}\underline{z}^{(0\hat{}m-1)} + \tilde{L}\left(y - \tilde{C}\underline{z}^{(0\hat{}m-1)}\right) \\ & +\tilde{\Gamma}v + \tilde{D}^{+}\underline{w} - \tilde{D}^{-}\overline{w} \\ \bar{x}^{(0\hat{}m-1)} = & V^{+}\bar{z}^{(0\hat{}m-1)} - V^{-}\underline{z}^{(0\hat{}m-1)} \\ \underline{x}^{(0\hat{}m-1)} = & V^{+}\underline{z}^{(0\hat{}m-1)} - V^{-}\bar{z}^{(0\hat{}m-1)}, \end{cases} \tag{7}$$

where $\tilde{L} = V^{-1}L, \tilde{C} = CV$. In addition, $\tilde{D}^{+} = \left(V^{-1}\mathring{D}\right)^{+}$ and $\tilde{D}^{-} = \left(V^{-1}\mathring{D}\right)^{-}$ are two elementwise nonnegative matrices satisfying $\tilde{D} = \tilde{D}^{+} - \tilde{D}^{-}, \tilde{D}^{+}, \tilde{D}^{-} \geq 0$. The next theorem explains the existence of interval observer (7).

Theorem 2. *If there exist a series of parametric matrices $A_{0\hat{}m-1}$, an observer gain matrix $L \in \mathbb{R}^{nm\times p}$, and a nonsingular matrix $V \in \mathbb{R}^{nm\times nm}$, such that $\tilde{\Phi}\left(A_{0\hat{}m-1}\right) - \tilde{L}\tilde{C}$ is simultaneously Hurwitz stable and Metzler, with the Assumption 1 and*

$$\bar{z}^{(0\hat{}m-1)}(0) = U^{+}\bar{x}^{(0\hat{}m-1)}(0) - U^{-}\underline{x}^{(0\hat{}m-1)}(0), \tag{8}$$

$$\underline{z}^{(0\hat{}m-1)}(0) = U^{+}\underline{x}^{(0\hat{}m-1)}(0) - U^{-}\bar{x}^{(0\hat{}m-1)}(0), \tag{9}$$

where $U = V^{-1}$, then system (7) is an interval observer for the nonlinear fully actuated system (1). The original system state estimation is obtained by

$$\begin{cases} \bar{x}^{(0\hat{}m-1)} = V^{+}\bar{z}^{(0\hat{}m-1)} - V^{-}\underline{z}^{(0\hat{}m-1)} \\ \underline{x}^{(0\hat{}m-1)} = V^{+}\underline{z}^{(0\hat{}m-1)} - V^{-}\bar{z}^{(0\hat{}m-1)}, \end{cases}$$

which guarantees the bounded condition $\underline{x}^{(0\sim m-1)} \leq x^{(0\sim m-1)} \leq \overline{x}^{(0\sim m-1)}, \forall t \geq 0$.

Proof. The upper and lower errors are defined as $\bar{e}^{(0\hat{}m-1)} = \bar{z}^{(0\hat{}m-1)} - z^{(0\hat{}m-1)}, \underline{e}^{(0\hat{}m-1)} = z^{(0\hat{}m-1)} - \underline{z}^{(0\hat{}m-1)}$. Then, the error dynamic system can be calculated as follows:

$$\begin{cases} \dot{\bar{e}}^{(0\hat{}m-1)} & = \left(\tilde{\Phi}\left(A_{0\hat{}m-1}\right) - \tilde{L}\tilde{C}\right)\bar{e}^{(0\hat{}m-1)} \\ & \quad +\tilde{D}^{+}\overline{w} - \tilde{D}^{-}\underline{w} - \tilde{D}w \\ \dot{\underline{e}}^{(0\hat{}m-1)} & = \left(\tilde{\Phi}\left(A_{0\hat{}m-1}\right) - \tilde{L}\tilde{C}\right)\underline{e}^{(0\hat{}m-1)} \\ & \quad +\tilde{D}w - \tilde{D}^{+}\underline{w} + \tilde{D}^{-}\overline{w}. \end{cases}$$

According to Lemma 2, we have

$$\begin{aligned} \tilde{D}^{+}\overline{w} - \tilde{D}^{-}\underline{w} - \tilde{D}w \geq 0, \\ \tilde{D}w - \tilde{D}^{+}\underline{w} + \tilde{D}^{-}\overline{w} \geq 0. \end{aligned}$$

Considering Lemma 1, the error system is asymptotically stable and elementwise nonnegative, i.e.,

$$\begin{aligned} \lim_{t\to\infty} \bar{e}^{(0\sim m-1)} = \varepsilon_1 \geq 0, \\ \lim_{t\to\infty} \underline{e}^{(0\sim m-1)} = \varepsilon_2 \geq 0, \end{aligned}$$

provided that the error system matrix $\tilde{\Phi}\left(A_{0\hat{}m-1}\right) - \tilde{L}\tilde{C}$ is Hurwitz and Metzler, as well as the initial condition (8), (9) and Assumption 1 hold. □

3.2 Gain Calculation

In the whole procedure, we need to first design a stabilization control law, achieving linear closed-loop system (3) with arbitrarily assignable parametric matrices, and then construct interval observer, as shown in (5) and (7). Therefore, there are two design aspects to be considered:

- design the parametric matrices $A_{0\hat{}m-1}$; and
- design the observer gain matrix L and the nonsingular transformation matrix V (only in the second observer).

To design parametric matrices $A_{0\hat{}m-1}$, we take advantage of the following lemma.

Lemma 3. [7] For an arbitrarily selected $F \in \mathbb{R}^{mn\times mn}$, all the matrix $A_{0\hat{}m-1}$ and the nonsingular matrix $V \in \mathbb{R}^{mn\times mn}$ satisfying

$$\Phi\left(A_{0\hat{}m-1}\right) = VFV^{-1}$$

are given by

$$A_{0\hat{}m-1} = -ZF^{n}V^{-1}(Z,F), \tag{10}$$

$$V = V(Z,F) = \begin{bmatrix} Z \\ ZF \\ \vdots \\ ZF^{n-1} \end{bmatrix}, \tag{11}$$

where $Z \in \mathbb{R}^{m\times mn}$ is an arbitrary parameter matrix satisfying

$$\det V(Z,F) \neq 0.$$

According to (10), the parametric matrices $A_{0\hat{}m-1}$ can be directly computed by choosing an arbitrary matrix Z, as long as the constraint (11) is not violated.

For interval observer (5), an appropriate observer gain makes $\Phi\left(A_{0^{\sim}m-1}\right)-LC$ not only Hurwitz but also Metzler. Making $\Phi\left(A_{0^{\sim}m-1}\right)-LC$ stable implies similarity to a matrix whose eigenvalues reside on the left-hand side of the complex plane; that is,

$$\left(\Phi\left(A_{0^{\sim}m-1}\right)-LC\right)^{T} \sim F^{T},$$

where $\operatorname{eig}(F)=\{s_i \mid \operatorname{Re}(s_i)<0, i=1,2,\ldots,nm\}$. Further, it comes to

$$V^{-T}\left(\Phi^{T}\left(A_{0^{\sim}m-1}\right)-C^{T}L^{T}\right)V^{T}=F^{T}.$$

Pre-multiplying V and letting $W^{T}=L^{T}V^{T}$, we obtain the generalized Sylvester equation

$$\Phi^{T}\left(A_{0^{\sim}m-1}\right)V^{T}+\left(-C^{T}\right)W^{T}=V^{T}F^{T}. \tag{12}$$

The generalized Sylvester equation has parametric solutions for V and W. By adjusting the free matrix Z, the gain matrix $L=V^{-1}W$, and it makes $\Phi\left(A_{0^{\sim}m-1}\right)-LC$ Hurwitz and Metzler. The readers can refer to [12] for more details about solving the generalized Sylvester matrix equation.

In the above process, if system (4) is observable, all the solutions to the generalized Sylvester equation (12) guarantee $\Phi\left(A_{0^{\sim}m-1}\right)-LC$ a Hurwitz matrix; however, it is noteworthy that only a subset of solutions achieves the property of making $\Phi\left(A_{0\sim m-1}\right)-LC$ a Metzler matrix simultaneously, and in some instances, no solutions fulfill this criterion. In such scenarios, we resort to the second interval observer (7), which relies on a similarity transformation. The design condition for interval observer (7) naturally arises in

$$V^{-T}\left(\Phi\left(A_{0^{\sim}m-1}\right)-LC\right)^{T}V^{T}=F^{T}.$$

The above equation can be equivalently transformed into a generalized Sylvester equation, akin to (12). By ensuring the appropriateness of a specified F, namely, that F is both Hurwitz and Metzler, the error state matrix $V^{-1}\left(\Phi\left(A_{0\sim m-1}\right)-LC\right)V$ follows suit.

3.3 Fault Detection

This section realizes the fault detection by employing the proposed interval observers (5) and (7). Since the interval observer provides the upper and the lower state estimation bounds for the output vector, by $y=C\bar{x}^{(0^{\sim}m-1)}$ and $y=C\underline{x}^{(0^{\sim}m-1)}$. Then, the upper and the lower residuals are defined by

$$\begin{cases} \bar{r}=C\bar{x}^{(0^{\sim}m-1)}-Cx^{(0^{\sim}m-1)} \\ \underline{r}=C\underline{x}^{(0^{\sim}m-1)}-Cx^{(0^{\sim}m-1)}. \end{cases}$$

An intuitive method to detect fault is to check if

$$0\in[\underline{r},\bar{r}].$$

If $0\in[\underline{r},\bar{r}]$, it can be inferred that the system operates at the healthy mode, and if $0\notin[\underline{r},\bar{r}]$, some faults may occur in the system. As a result, the traditional threshold generation is no longer needed here.

4 Illustrative Example

In this section, a simple example adapted from [13] is used to demonstrate the feasibility and effectiveness of the proposed interval observers. Readers are invited to consult the authors' GitHub repositories at https://github.com/WJ-Ren/FASA-Set.git for access to the MATLAB codes. Consider the following third-order fully actuated system:

$$\begin{cases} \dddot{x}=2\left(\dot{x}^{2}+x\ddot{x}\right)\theta+u+f_a+Dw \\ y=Cx^{(0^{\sim}2)}, \end{cases}$$

where $\theta=1$ and $C=I_3$. Based on Lemma 3, let $F=\operatorname{diag}(-1,-2,-3)$ and $Z=\begin{bmatrix} -1 & 2 & -1 \end{bmatrix}$, we acquire $A_{0^{\sim}2}=\begin{bmatrix} 6 & 11 & 6 \end{bmatrix}$. So that the stabilization control law is determined by

$$u=-\begin{bmatrix} 6 & 11 & 6 \end{bmatrix}x^{(0^{\sim}2)}-2\left(\dot{x}^{2}+x\ddot{x}\right)+v,$$

resulting in the following linear closed-loop system

$$x^{(3)}+\begin{bmatrix} 6 & 11 & 6 \end{bmatrix}x^{(0^{\sim}2)}=v+Dw.$$

The above system can be equivalently written in the form of

$$\dot{x}^{(0^{\sim}2)}=\Phi\left(\begin{bmatrix} 6 & 11 & 6 \end{bmatrix}\right)x^{(0^{\sim}2)}+\Gamma v+\mathring{D}w,$$

where $\Gamma=\begin{bmatrix} 0 & \cdots & 0 & 1 \end{bmatrix}^{T}$, $\mathring{D}=\begin{bmatrix} D_0 & D_1 & D \end{bmatrix}^{T}$. Here, we choose $\mathring{D}=\begin{bmatrix} 1 & -1 & -1 \end{bmatrix}^{T}$, and $v=20\sin t+20$.

For the interval observer (5), let

$$F_1=\operatorname{diag}\left(\begin{bmatrix} -15 & -16 & -17 \end{bmatrix}\right),$$
$$Z_1=\begin{bmatrix} -1 & 0 & 1 \\ 0 & -1 & 1 \\ 3 & 0 & -1 \end{bmatrix}.$$

By solving the generalized Sylvester matrix equation (12), we obtain

$$L_1=\begin{bmatrix} 16.2605 & -0.3926 & -3.9311 \\ -0.0124 & 15.9073 & 0.8354 \\ -6.2199 & -11.3998 & 9.8322 \end{bmatrix},$$
$$V_1=\begin{bmatrix} -6.2012 & -22.8822 & -22.4942 \\ -0.4189 & 15.5347 & -0.4030 \\ -1.8400 & -7.0195 & 4.3742 \end{bmatrix},$$

which lead to

$$\Phi\left(A_{0^{\sim}2}\right)-LC=\begin{bmatrix} -16.2605 & 1.3926 & 3.9311 \\ 0.0124 & -15.9073 & 0.1646 \\ 0.2199 & 0.3998 & -15.8322 \end{bmatrix}.$$

Upon inspecting this matrix, it becomes evident that it is a Metzler matrix, as its off-diagonal elements are nonnegative, and its eigenvalues align with F_1. In such instances, a specific matrix Z_1 is deliberately chosen, rendering $\Phi\left(A_{0\sim 2}\right)-LC$ a Metzler matrix, and concurrently, Hurwitz. Nevertheless, as the system's order or dimension increases, the task of selecting a suitable free matrix Z_1 might become more challenging. To address this concern, the interval observer (7) was introduced.

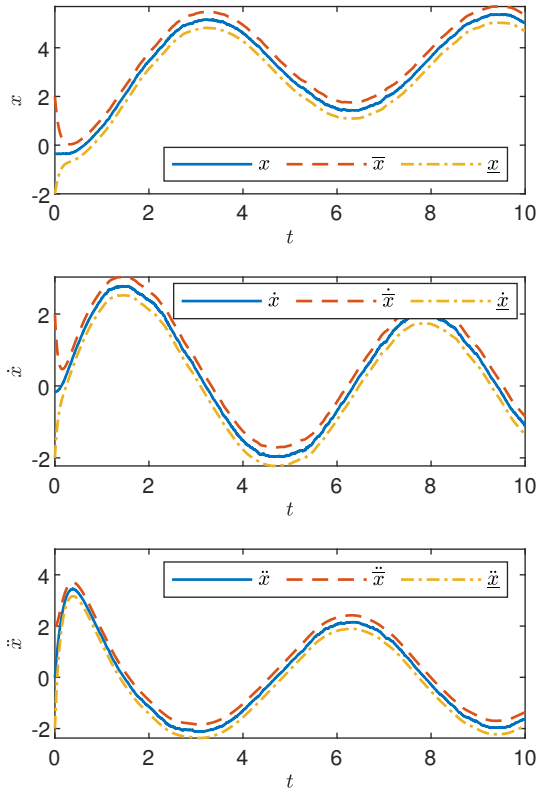

Fig. 1: State estimation by interval observer (5).

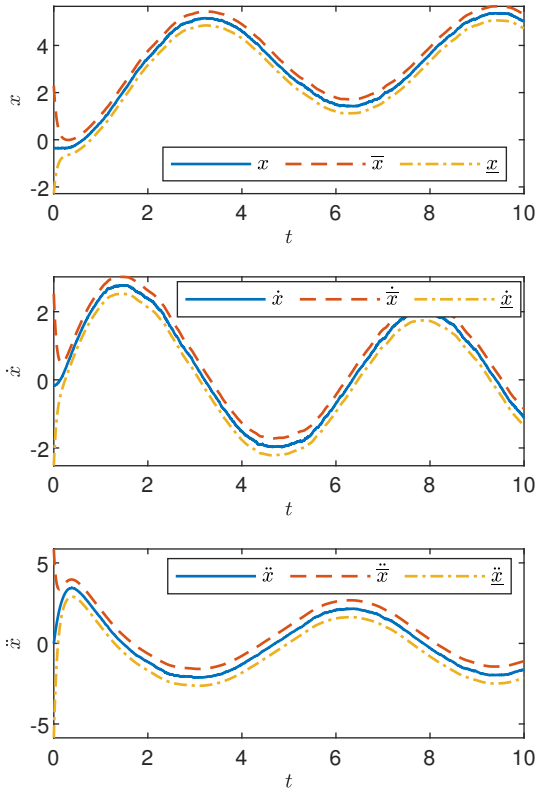

Fig. 2: State estimation by interval observer (7).

To design interval observer (7), let $F_2 = F_1$ and $Z_2 = I_3$ and then solve equation (12), producing

$$L_2 = \begin{bmatrix} 14.9981 & 1.0630 & -0.0050 \\ 0.0316 & 16.0595 & 1.0950 \\ -5.3148 & -10.4344 & 10.9424 \end{bmatrix},$$

$$V_2 = \begin{bmatrix} -15.0314 & -1.0640 & -0.0076 \\ -0.0280 & -16.0896 & -1.1110 \\ 5.3111 & 10.4305 & -10.9929 \end{bmatrix}.$$

In the simulation, the initial system state $x^{(0\hat{}2)}(0) = \begin{bmatrix} x(0) & \dot{x}(0) & \ddot{x}(0) \end{bmatrix}^T$ is randomly selected in $[-1, 1]$. The initial state estimation value of the interval observer (5) is $\bar{x}^{(0\hat{}2)}(0) = -\underline{x}^{(0\hat{}2)}(0) = \begin{bmatrix} 2 & 2 & 2 \end{bmatrix}^T$. Using (8) and (9), the initial value of the interval observer (7) is calculated as $\bar{z}^{(0\hat{}2)}(0) = -\underline{z}^{(0\hat{}2)}(0) = \begin{bmatrix} 0.1424 & 0.1331 & 0.3383 \end{bmatrix}^T$. The unknown input is a time-varying random signal generated in $[-4, 4]$; thus, the upper and lower bounds $\overline{w} = -\underline{w} = 4$. The faulty scenario is set as

$$f_a = \begin{cases} 0, & 0 \le t < 2 \\ 10, & t \ge 2. \end{cases}$$

The interval estimation outcomes generated by the proposed interval observers (5) and (7) are illustrated in Figs. (1) and (2), respectively. Moreover, the fault detection results produced by interval observers (5) and (7) are presented in Figs. (3) and (4), respectively. Note that if $0 \notin [\underline{r}_i, \overline{r}_i]$ holds for any of $i = 1, 2, 3$, fault happens. These results collectively affirm that the suggested interval observers exhibit

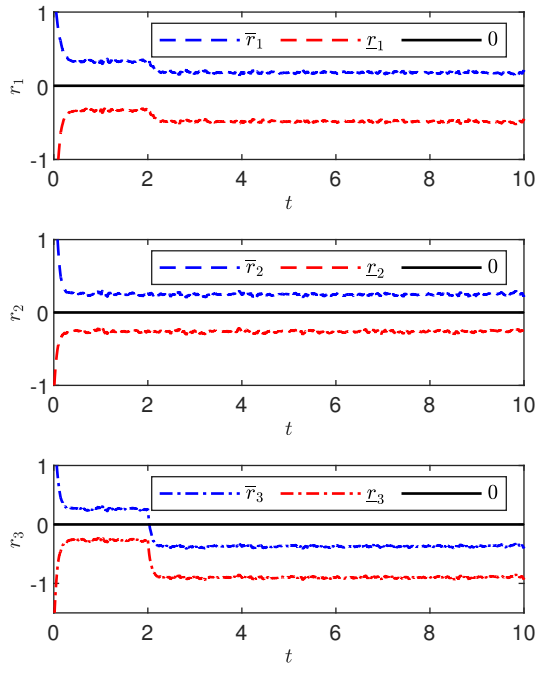

Fig. 3: Fault detection results by interval observer (5).

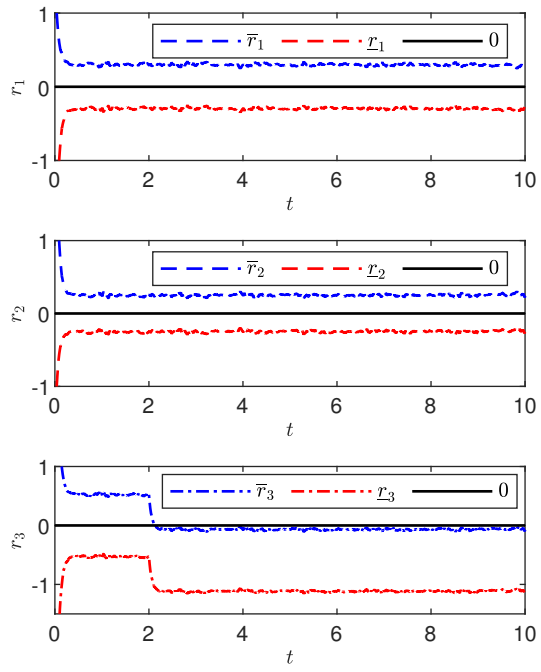

Fig. 4: Fault detection results by interval observer (7).

good performance in terms of both state estimation and fault detection via the fully actuated system approach.

5 Conclusion

This paper delved into the fully actuated system approach for interval observer design with applications in fault detection. Based on the full-actuation property, a nonlinear stabilization control law was employed to eradicate all nonlinearities within the open-loop system. Building upon the constant linear closed-loop system, we introduced two interval observers, devising their gain matrices through a parametric approach centered around the generalized Sylvester matrix equation. The efficacy of the proposed interval observers in state estimation and fault detection was demonstrated through an illustrative example. The scope of future research encompasses the exploration of set-theoretic observer designs, active fault diagnosis techniques, and the development of fault-tolerant control strategies tailored for nonlinear systems by the fully actuated system approach.

References

[1] J. L. Gouze, A. Rapaport, and M. Z. Hadj-Sadok, Interval observers for uncertain biological systems. *Ecological Modelling*, 2000, 133(1-2): 45–56.

[2] A. Khan, W. Xie, L. W. Zhang, and L. W. Liu, Design and applications of interval observers for uncertain dynamical systems. *IET Circuits Devices & Systems*, 2020, 14(6): 721–740.

[3] W. Ren, R. You, W. Yu, and S. Guo, Reduced-Order and Full-Order Interval Observers Design for Discrete-Time System. *IEEE Access*, 2020, 8: 103309-103316.

[4] C. Zammali, J. Van Gorp, Z. H. Wang and T. Raissi, Sensor fault detection for switched systems using interval observer with L_∞ performance. *European Journal of Control*, 2021, 57: 147–156.

[5] W. Ren, S. Guo and C. K. Ahn, Guaranteed Set-Membership Estimation for Local Nonlinear Uncertain Fuzzy Systems Subject to Partially Decouplable Unknown Inputs. *IEEE Transactions on Fuzzy Systems*, 2023, 31(12): 4336–4349.

[6] D. Efimov, T. Raissi, S. Chebotarev and A. Zolghadri, Interval state observer for nonlinear time varying systems. *Automatica*, 2013, 49(1): 200–205.

[7] G. R. Duan, High-order fully actuated system approaches: Part I. Models and basic procedure. *International Journal of Systems Science*, 2021, 52(2): 422–435.

[8] G. R. Duan, High-order fully actuated system approaches: Part II. Generalized strict-feedback systems. *International Journal of Systems Science*, 2021, 52(3): 437–454.

[9] Y. Yu, G. P. Liu, Y. Huang, and J. M. Guerrero, Distributed Learning-Based Secondary Control for Islanded DC Microgrids: A High-Order Fully Actuated System Approach. *IEEE Transactions on Industrial Electronics*, 2023. DOI: 10.1109/TIE.2023.3273276.

[10] M. Cai, X. He, and D. Zhou, Low-Power Fault-Tolerant Control for Nonideal High-Order Fully Actuated Systems. *IEEE Transactions on Systems, Man, and Cybernetics: Systems*, 2023, 53(8): 4875–4887.

[11] L. Farina and S. Rinaldi, *Positive linear systems: theory and applications*. John Wiley & Sons, 2000.

[12] G. R. Duan, *Generalized Sylvester equations: unified parametric solutions*. CRC Press, 2015.

[13] G. R. Duan, High-order fully actuated system approaches: Part IV. Adaptive control and high-order backstepping. *International Journal of Systems Science*, 2021, 52(5): 972-989.

Proceedings of the 3rd Conference on Fully Actuated System Theory and Applications
May 10-12, 2024, Shenzhen, China

A Novel Trajectory Replanning Method for Autonomous Robots Under Actuator Faults

Fuqiang Liu[1,2], Cheng Luo[2], Sisindisiwe Nomalanga Ncube[2], Aoshen Li[3], Xiaoshan Bai[4]

1. State Key Laboratory of Mechanical Transmission for Advanced Equipment, Chongqing University, Chongqing, 400044, China
E-mail: liufq@cqu.edu.cn

2. College of Mechanical and Vehicle Engineering, Chongqing University, Chongqing, 400044, China
E-mail: ChengLuo@stu.cqu.edu.cn

3. CQU-UC Joint Co-op Institute, Chongqing University, Chongqing, 400044, China
E-mail: oshintrowski@foxmail.com

4. College of Mechanical and Control Engineering, Shenzhen University, Shenzhen 518060, China
E-mail: baixiaoshan@szu.edu.cn

Abstract: A novel trajectory replanning method is proposed to solve the path planning problem for autonomous robots under actuator faults which is intended to cooperate with the existing fault-tolerant control of nonlinear systems to ensure autonomous robots' safe and stable operation. This method proposes formulas to estimate and correct remaining time and establishes an optimal time allocation objective function and optimal trajectory coefficient objective function to obtain the replanned trajectory. The simulation results show the method's effectiveness in the replanned trajectory in the case of actuator faults.

Key Words: Autonomous Robot, Trajectory replanning, Actuator faults

1 Introduction

Autonomous robots have gained increasing attention in recent years due to their ability to plan and follow the optimal trajectory to perform the tasks. For example, unmanned aerial vehicles can automatically inspect high-voltage circuits, sweeping robots can autonomously complete cleaning tasks, and unmanned cars can drive themselves to their destination [1-3]. Autonomous robots are nonlinear multi-input and multi-output systems with strong coupling and underactuated properties. These inherent characteristics make it vulnerable to system component faults. Considering autonomous robots' low-cost and non-redundant architecture, actuator faults are common and can be catastrophic [4]. Therefore, developing a fault-tolerant control (FTC) method for actuator faults is essential.

In the past decades, a growing requirement for system safety has inspired extensive research on FTC. Generally, FTC can be classified into two categories: the passive FTC and the active FTC. Many sophisticated control methods have been proposed, including fixed-time control [5], sliding-mode control (SMC) [6], model predictive control (MPC) [7] and neural network control [8], etc. For instance, an adaptive SMC scheme is proposed in [9] to compensate for the adverse effects of actuator faults. A single-layer neural network is introduced in [10] to deal with the uncertainty of the system model and a passive FTC scheme for attitude tracking is designed with backstepping control method. A robust fault estimation observer is given in [11] to obtain the actuator fault information, and a novel active FTC scheme for spacecrafts is designed with full state constraints and input saturation.

Despite the significant progress made in recent years, outstanding issues still need to be resolved in FTC design for nonlinear systems. For instance, existing FTCs do not establish the relationship between the reference trajectory and remaining resources (such as residual thrust); moreover, they do not provide solutions regarding the precise tracking of the original trajectory by the faulty system. In practical applications, the existing FTCs may drive the actuators to their physical limits and force them to work beyond their normal operating load. Zhou et al. considers the safety control problem of a quadrotor UAV under actuator faults and external disturbances based on quantifying system performance and safety margins, but the reference trajectory is a deterministic exponential function which does not conform to the general form of trajectory planning [12].

Motivated by these issues, a novel trajectory replanning method for autonomous robot under actuator faults is presented in this paper. It is intended to cooperate with the existing FTC method of nonlinear systems to ensure autonomous robots' safe and stable operations. Firstly, the remaining execution time of the faulty robot is initially estimated based on the autonomous robot's differential flatness transformation and the actuator's remaining ability. Secondly, the optimal time allocation objective function is proposed to get the optimal time. Thirdly, the optimal trajectory coefficient objective function is proposed, and the offset penalty factor is introduced to obtain the optimal trajectory coefficient. Then, fault thrust constraint is used to correct the remaining execution time. Finally, the replanned trajectory that satisfies all constraints is obtained.

The remainder of the paper is organized as follows. Section 2 provides the preliminary and problem formulation. In Section 3, we introduce the trajectory replanning method. Section 4 provides simulation experiments and applies them to tail-sitter aircraft to illustrate the effectiveness of the proposed method. Section 5 concludes this paper.

*The authors would like to thank the National Natural Science Foundation of China (Grant No. 62033001), the Chongqing Science and Technology Bureau (Grant No. CSTB2023TIAD-KPX0057), and the State Key Laboratory of Mechanical Transmission for Advanced Equipment of Chongqing University (Grant No. SKLMT-ZZKT-2022M01).

2 Preliminaries and Problem Formulation

Before proceeding with the detailed design of the proposed methodology, the following two points should be noted:

(1) The fault time has been recorded and the fault factor $\wedge_i$ estimated by the adaptive law has been obtained before estimating the remaining execution time.

(2) Due to the errors in the estimated model parameters (e.g., mass and inertia matrix), the thrust values of the individual motors on the path obtained by differential flatness transformation only approximate the actual thrust values.

When the actuator fault factor is $\wedge_i < \wedge_f$, the FTC method tracks the replanned trajectory. To determine when to choose the replanned trajectory, using the fault factor $\wedge_f$ estimated from expert experience is inaccurate. The auxiliary evaluation index P_d is introduced in this method to solve the above problem.

When an actuator fault occurs in an autonomous robot, the execution time of the standard actuator is different from the execution time with the fault because only part of the actuator's effectiveness is retained. Therefore, a reasonable extension of the original execution time can compensate for the delay caused by actuator faults. This method presents an estimation and correction method for calculating the remaining execution time of the autonomous robot.

Unreasonable time allocation can result in overshooting and unstable deviations in state variables such as velocity, acceleration, and jerk for the autonomous robot. To address this issue, this method proposes a new optimal allocation method that considers the following two aspects.

(1) During the straight segment, it is essential to ensure that the autonomous robot moves at a consistent speed.

(2) During the steering segment, it is recommended to reduce the rate of state variable changes of the autonomous robot to prevent loss of control.

The 3D trajectory of an autonomous robot can be expressed as polynomials [13].

$$\begin{cases} \sum_{i=0}^{n} p_{1i}(t-T_0)^i & , \ T_1 \le t < T_2 \\ \sum_{i=0}^{n} p_{2i}(t-T_1)^i & , \ T_2 \le t < T_3 \\ \vdots & \\ \sum_{i=0}^{n} p_{(m-1)i}(t-T_{m-1})^i & , \ T_{m-1} \le t \le T_m \end{cases} \tag{1}$$

where $p_{1i}, p_{2i}, \dots, p_{(m-1)i}$ are the polynomial coefficient of the trajectory to be solved. m is the number of path points, and $T_0, T_1, \dots, T_{m-1}$ is the time required for each segment of the trajectory.

Using the above Eq.(1) to optimize the replanned trajectory will deviate from the original trajectory. If the offset is too large, this can result in a lack of stability in the differential fault output and reduce the robustness of the autonomous robot. The trajectory offset penalty function is added to overcome the issue when resolving the polynomial coefficients to derive the ideal trajectory coefficients. Fig.1 shows the schematic for the replanned 2D trajectory of the autonomous robot.

where points A, B, C and D are the task points that the autonomous robot needs to pass through; segment AD is the original planned trajectory, and segment FD is the replanned trajectory; point F is the actuator fault's moment.

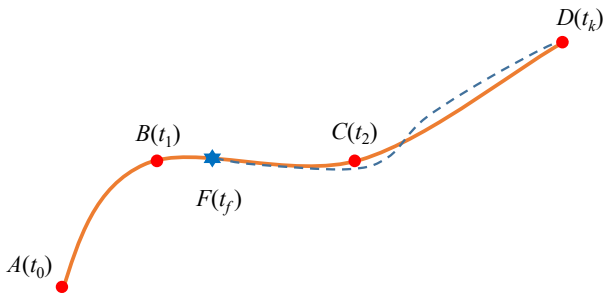

Fig. 1: The schematic for replanned 2D trajectory

3 Method of Path Replanning

In this section, a method for generating an optimized path is given by introducing an auxiliary evaluation index P_d, predicting and correcting the remaining execution time, establishing an optimal time allocation function and establishing a trajectory coefficient optimal function.

3.1 Auxiliary Evaluation P_d

When an actuator fault occurs in the autonomous robot (e.g. $\wedge_i < \wedge_f$), it is necessary to choose the replanned trajectory. However, due to the model error and disturbance, the estimated fault factor $\wedge_i$ cannot converge to the true value and can only be used as an approximation. If the thrust obtained from the differential flatness transformation is still within the range of $T_i < \wedge_i T_{\max}$, it will significantly increase the remaining execution time after choosing the replanned trajectory [14]. To determine when to choose the original trajectory of the replanned, only relying on the fault factor $\wedge_f$ estimated by expert experience is inaccurate. Therefore, an auxiliary evaluation index P_d is established as follows:

$$P_d = \sum H(T_i - \wedge_i T_{\max}) \tag{2}$$

where P_d denotes the extent to which the ideal thrust value exceeds the constrained value; T_i is the motor thrust value after differential flatness transformation of the trajectory and $T_{\max}$ is the maximum value of the motor thrust. $\boldsymbol{H}(\,)$ is defined as follows:

$$H(T_i - \wedge_i T_{\max}) = \begin{cases} 0, & T_i - \wedge_i T_{\max} < 0 \\ 1, & T_i - \wedge_i T_{\max} \ge 0 \end{cases} \tag{3}$$

When the auxiliary evaluation index $P_d \le 2\xi\Delta t_f/\Delta t$, the autonomous robot tracks the original trajectory. When the auxiliary evaluation index $P_d > 2\xi\Delta t_f/\Delta t$, autonomous robot tracks the replanned trajectory. ξ is the evaluation coefficient, which is generally taken as 0.2. Δt_f is the remaining time of the original trajectory, and Δt is the time for each calculation of the ideal thrust value.

3.2 Predicting and Correcting the Execution Time

Based on the schematic in Fig.1, the normal remaining execution time is represented by $\Delta t_f^n = t_k - t_f$.

For autonomous robots, it's important to note that the motor thrust does not vary linearly with the moving speed due to the nonlinear coupled dynamics. Suppose the remaining time is estimated using the fault factor alone, as shown in Eq (4). In that case, the extended time will likely still be insufficient, and the value of motor thrust transformed by the differential flatness will likely exceed the

constrained thrust value. Therefore, a thrust correction term is introduced to make the necessary corrections to estimate the remaining execution time Δt_f^p.

$$\Delta t_f^p = \frac{1}{\beta \wedge_{max}} \Delta t_f^n \tag{4}$$

$$\Delta t_f^p = \frac{1}{\beta \wedge_{max}} \Delta t_f^n \left(1 + \frac{\alpha(T_{i-max} - \wedge_{max} T_{\max})}{\wedge_{max} T_{\max}}\right) \tag{5}$$

where $\alpha, \beta > 0$ is the gain parameter; $\wedge_{max} = \max\{\wedge_i\}$ denotes the maximum value of the actuator fault factor; T_{i-max} denotes the maximum value of the motor thrust on the whole segment of the trajectory.

The above equation shows that if the maximum value of motor thrust exceeds the maximum thrust value of the faulty motor, the remaining execution time will be further extended.

Once the preliminary estimate of the remaining execution time has been obtained, it is necessary to follow the two steps of time allocation optimization in Section 3.3 and trajectory coefficient optimization in Section 3.4. Afterward, perform the differential flatness transformation again to determine the value of the motor thrust on the replanned trajectory and verify whether it satisfies the fault thrust constraints. If this condition is not satisfied, the remaining execution time will need to be corrected to obtain a replanned trajectory that meets the constraints. The corrected remaining execution time Δt_f^p is defined as follow:

$$\Delta t_f^p = t_f^p + \upsilon_E \frac{E_{max} - p_{ts}}{p_{ts}} \tag{6}$$

where $p_{ts} > 0$ is the threshold factor and $\upsilon_E > 0$ is the correction factor; let $E_{max} = T_{imax} - \wedge_{max} T_{max}$.

If $E_{max} \le p_{ts}$, it indicates that the time allocation is reasonable and no time correction is needed. If $E_{max} > p_{ts}$, it means that the motor thrust value on a segment of the replanned trajectory exceeds the constrained thrust value, and an increase in the remaining execution time Δt_f^p is required.

3.3 Optimal Time Allocation

Establish the time allocation function and consider the effects of the snap constraint term, uniform velocity constraint term, and deflection constraint term. The optimal time allocation objective function is as follows:

$$\underset{t}{\text{minimize}}\ F_{\text{TA}} = \gamma_1 J_{\text{snap1}} + \gamma_2 J_{\text{avg}} + \gamma_3 J_{\psi}$$
$$\text{subject to} \sum T_i = \Delta t_f^p \tag{7}$$

where J_{snap1} denotes the trajectory smoothing constraint term in the Minimum-Snap algorithm, but each segment times is unknown in Eq.(7); J_{avg} denotes the uniform velocity constraint term and J_{ψ} denotes the deflection angle constraint term; $\gamma_1, \gamma_2, \gamma_3$ denote the weighting coefficients, the velocity penalty factor and the deflection rate penalty factor for J_{snap1}, J_{avg} and J_{ψ}, respectively.

i) Constraint term J_{snap1}. J_{snap1} is the 4th-order derivative integral of the trajectory position in the Minimum-Snap algorithm. The algorithm means minimizing the differential dynamics and saving energy. Therefore, the smaller the item, the lower the theoretical energy consumption of the trajectory. J_{snap1} expression is as follows:

$$J_{\text{snap1}} = \begin{bmatrix} \boldsymbol{p}_1 \\ \vdots \\ \boldsymbol{p}_M \end{bmatrix}^{\text{T}} \begin{bmatrix} Q_1(t_1) & \cdots & 0 \\ \vdots & \ddots & \vdots \\ 0 & \cdots & Q_M(t_M) \end{bmatrix} \begin{bmatrix} \boldsymbol{p}_1 \\ \vdots \\ \boldsymbol{p}_M \end{bmatrix} \tag{8}$$

where $Q_1(t_1), \cdots, Q_M(t_M)$ is a polynomial function about time t.

ii) Constraint term J_{avg}. J_{avg} is the effect of the distance between the trajectory points on the time allocation. The smaller this term is, the more it conforms to the principle of distribution by distance and ensures uniform velocity. Its expression is as follows:

$$J_{\text{avg}} = \sum \text{Exp}\left(k\left(T_{i+1} - T_i\right) - \frac{\Delta t_f^p . l_i}{L_{\text{sum}}}\right) \tag{9}$$

where L_{sum} is the total original trajectory length from the fault point to the endpoint; l_i is the length of the Euclidean distance between the current trajectory point and the next trajectory point; T_i is the time spent on each segment of the trajectory; $k > 0$ is the gain parameter.

iii) Constraint term J_{ψ}. J_{ψ} is the effect of the known rate of the deflection angle on the time allocation, and the expression is as below:

$$J_{\psi} = \sum \ddot{\psi}(t_i) \tag{10}$$

where $\ddot{\psi}(t_i)$ denotes the rate of change of the deflection angular velocity

The values of γ_1, γ_2, and γ_3 must be chosen according to the characteristics of the mission. The higher the value of γ_1, the lower the energy consumption of the trajectory segment and the better the continuity of the trajectory state; the higher the value of γ_2, the more it conforms to the principle of distance distribution, and the smaller the value of γ_3, the more the attitude changes are smooth. In summary, γ_1 is usually a large value, γ_2 is a medium value, and γ_3 is a small value.

3.4 Optimal Trajectory Coefficient

To solve the offset problem, the trajectory offset penalty function is introduced when solving the polynomial coefficients to obtain the optimal trajectory coefficients. The objective function F_{OS} is as follows:

$$\underset{t}{\text{minimize}}\ F_{OS} = \gamma_4 J_{\text{snap2}} + \gamma_5 J_{\text{offset}}$$
$$\text{subject to } A_i p_i = d_i \tag{11}$$

where J_{snap2} denotes the denotes the trajectory smoothing constraint term in the Minimum-Snap algorithm, but the trajectory coefficients are unknown in Eq.(11); J_{offset} is the trajectory offset penalty term; γ_4, γ_5 denote the weight coefficients and offset penalty factor, respectively. Additionally, the state variables must satisfy a series of continuity constraints.

When solving the above problem, we first identify the fixed and free variables of the trajectory for subsequent operations.

$$\boldsymbol{D} = \boldsymbol{M}^{\text{T}} \begin{bmatrix} \boldsymbol{d}_F \\ \boldsymbol{d}_P \end{bmatrix} \tag{12}$$

where $\boldsymbol{d}_F$ and $\boldsymbol{d}_P$ are vectors consisting of position, velocity and acceleration; $\boldsymbol{d}_F$ denotes the trajectory fixed variable, which is determined and unchangeable; $\boldsymbol{d}_P$ denotes the trajectory free variable, which can be changed according to the demand of the objective function; $\boldsymbol{M}$ denotes the

trajectory variable mapping matrix, and $\boldsymbol{D}$ denotes the trajectory variables.

The autonomous robot is guaranteed to pass through the set trajectory points with continuous velocity and acceleration. Then, the constrained problem is converted into an unconstrained quadratic programming problem and can be solved in closed form by combining the matrix multiplications in [15].

$$J_{\text{snap2}} = \begin{bmatrix} \boldsymbol{d}_F \\ \boldsymbol{d}_P \end{bmatrix}^{\mathrm{T}} \boldsymbol{M}\boldsymbol{A}^{-\mathrm{T}}\boldsymbol{Q}\boldsymbol{A}^{-1}\boldsymbol{M}^{\mathrm{T}} \begin{bmatrix} \boldsymbol{d}_F \\ \boldsymbol{d}_P \end{bmatrix} \tag{13}$$

where $\boldsymbol{Q}$ denotes the diagonal matrix about time t in Eq. (8), and $\boldsymbol{A}$ denotes the time coefficient mapping matrix; $\boldsymbol{R}$ is denoted as $\boldsymbol{M}\boldsymbol{A}^{-\mathrm{T}}\boldsymbol{Q}\boldsymbol{A}^{-1}\boldsymbol{M}^{\mathrm{T}}$ and J_{snap2} can be alternatively expressed as

$$J_{\text{snap2}} = \begin{bmatrix} \boldsymbol{d}_F \\ \boldsymbol{d}_P \end{bmatrix}^{\mathrm{T}} \begin{bmatrix} \boldsymbol{R}_{FF} & \boldsymbol{R}_{FP} \\ \boldsymbol{R}_{PF} & \boldsymbol{R}_{PP} \end{bmatrix} \begin{bmatrix} \boldsymbol{d}_F \\ \boldsymbol{d}_P \end{bmatrix} \tag{14}$$

Decompose the J_{snap2} and take a partial derivative for $\boldsymbol{d}_P$.

$$\frac{\partial \boldsymbol{J}_{\text{snap2}}}{\partial \boldsymbol{d}_P} = 2\boldsymbol{d}_F{}^{\mathrm{T}}\boldsymbol{R}_{FP} + 2\boldsymbol{d}_P{}^{\mathrm{T}}\boldsymbol{R}_{PP} \tag{15}$$

To solve the problem of large deviation in replanned trajectory, a penalty function for trajectory offset is proposed. The penalty value generated by J_{offset} should be smaller than that generated by J_{snap2} when the deviation is small. Fig.2 shows the schematic for the penalty offset trajectory.

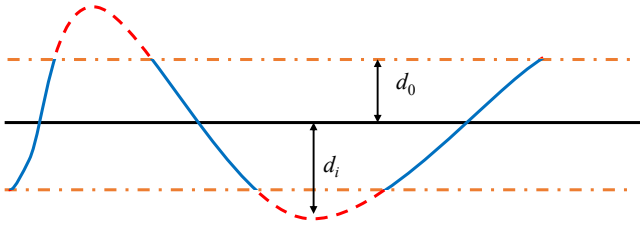

Fig. 2: The schematic for the penalty offset trajectory

As shown in Fig.2, d_0 denotes the spacing of the offset penalty threshold, and d_i denotes the spacing between the sampling points on the trajectory and the folded trajectory. The dashed line indicates the replanned trajectory that exceeds the set threshold, and the solid line indicates the replanned trajectory that does not exceed the set threshold. The offset penalty function $G(d_i)$ is formulated as follows:

$$G(d_i) = \begin{cases} k_a d_i + b, & d_i < d_0 \\ e^{k_b d}, & d_i \geq d_0 \end{cases} \tag{16}$$

where $k_a > 0$ and $k_b > 0$ are the gain parameters; b is the constant.

Since $G(d_i)$ is a segmented function, the discrete accumulation method is used to obtain the trajectory offset penalty function J_{offset}.

$$\begin{aligned} J_{\text{offset}} &= \int_{0}^{T_{\text{sum}}} G\big(p_d(t)\big)ds \\ &= \sum_{k=0}^{T_{\text{sum}}/dt} G\big(p_d(kdt)\big)\|v(kdt)\|\,dt \end{aligned} \tag{17}$$

where $p_d(t)$ denotes the distance of the optimal trajectory from the folded trajectory and dt the discrete sampling either time .

The optimal replanned trajectory coefficients are obtained by solving the objective function described above. Compare it with the trajectory coefficients of the Snap1 constraint term in Section 3.3 and record the difference between the corresponding coefficients using the least squares method.

$$E_T = \big(\boldsymbol{P}_{\text{pm1}} - \boldsymbol{P}_{\text{pm2}}\big)^{\mathrm{T}}\big(\boldsymbol{P}_{\text{pm1}} - \boldsymbol{P}_{\text{pm2}}\big) \tag{18}$$

where $\boldsymbol{P}_{\text{pm1}}$ are the trajectory coefficients of the Snap1 constraint term; $\boldsymbol{P}_{\text{pm2}}$ are the optimal replanned trajectory coefficients; E_T is the degree of difference between these two coefficients; ε_a is the threshold factor.

If $E_T \leq \varepsilon_a$, the coefficients satisfy the optimal trajectory coefficients of the optimal time allocation. If $E_T > \varepsilon_a$, it is necessary to replace the $\boldsymbol{P}_{\text{pm1}}$ coefficients with $\boldsymbol{P}_{\text{pm2}}$ and repeat the steps in Section 3.3 and Section 3.4 until $E_T \leq \varepsilon_a$ is satisfied or the number of iterations $N_{\max}$ is more than 50 times.

3.5 Trajectory Replanning Solution

Fig.3 shows the flowchart of the trajectory replanned method.

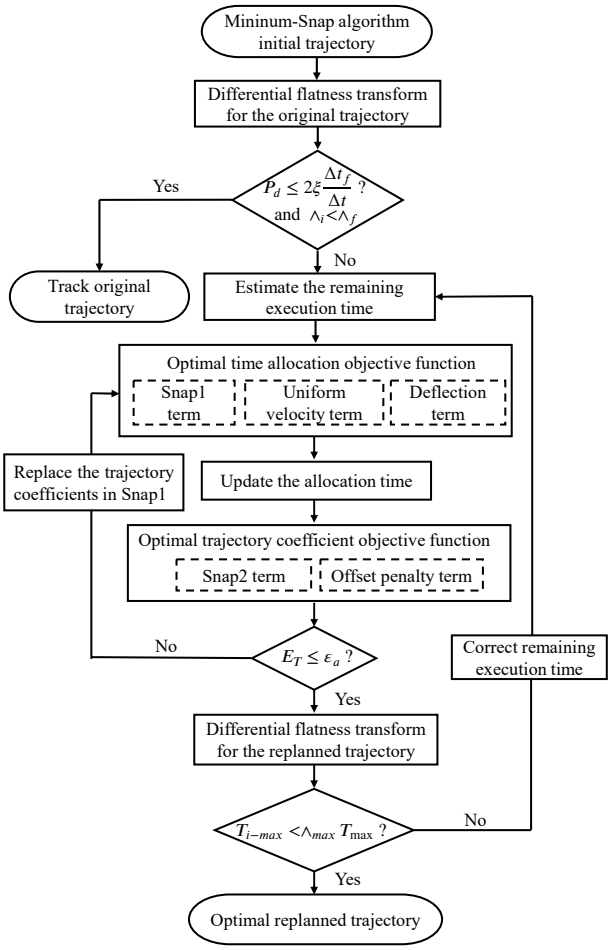

Fig. 3: The flowchart of the trajectory replanning method

By using the given trajectory replanning method, the path replanning steps are organized as follows:

(1) Obtain the fault factor $\wedge_{max}$ and the thrust value T_{i-max} transformed by the differential flatness and establish switching conditions for trajectory replanning.

(2) Estimate the remaining execution time Δt_f^p.

(3) Establish and solve objective function F_{TA} .and objective function F_{OS}.

(4) Check whether the difference E_T of the trajectory coefficients is greater than ε_a.

(5) Obtain the thrust value T_{i-max} on the replanned trajectory transformed by the differential flatness and check whether the difference is greater than $\wedge_{max} T_{\max}$.

(6) Correct the remaining execution time Δt_f^p and repeat steps (2)-(5) to obtain the optimal trajectory.

4 Simulation Analysis

This section uses a tail-sitter aircraft with actuator faults to validate the trajectory replanning method. Fig.4 shows the structure of this aircraft and the defined coordinate frames. All simulations are conducted via MATLAB R2022a environment in a 64-bit PC with 2.50GHz Core (TM) i5-7300HQ CPU.

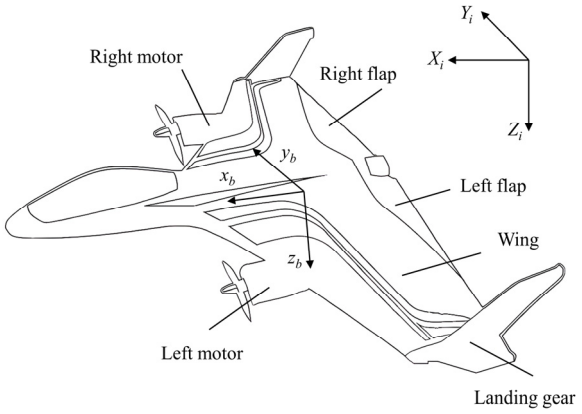

Fig. 4: The structure of the tail-sitter and the coordinate frames

This paper assumes that the fault time and the estimated fault factor $\wedge_{max}$ are known. The start point is chosen as (0,0,0) and the endpoint is chosen as (10,2,5). The remaining parameters of the simulations are given in Table 1.

Table 1 Parameters of the simulations

Parameters	Value
Aircraft mass m	1.125
Aircraft inertial matrix $\boldsymbol{J}$	diag(0.074,0.017,0.09)
Lift coefficient C_{LT}	2.23
Drag coefficient C_{DT}	0.07
Mid-points	(2,5,3),(5,3,5),(8,5,5)
Fault factor $\wedge_{max}$	0.85
Gain parameter α, β	10,0.8
Threshold factor p_{ts}	0.6
Correction factor υ_E	0.05
Penalty factor $\gamma_1, \gamma_2, \gamma_3$	8,3,1
Penalty factor γ_4, γ_5	8,4
Gain parameter k_a, k_b	1,2
Threshold factor ε_a	0.8
Maximum iterations $N_{\max}$	50

According to the novel trajectory replanning method described in Section 3, assuming that the actuator fault occurs at $t_f = 1.5$s and the fault factor estimated by the adaptive method is $\wedge_{max}$= 0.85, Fig.5 shows the replanned trajectory of tail-sitter aircraft.

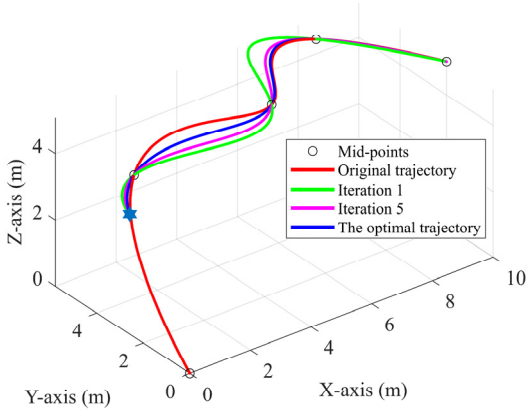

Fig. 5: The replanned trajectory of the tail-sitter

From Fig.5, the blue star is the fault point. The trajectory generated after each iteration passes through the middle points, which ensures the continuity of the trajectory. The first, fifth and ninth (optimal trajectory) of replanned trajectories are shown in the figure. The optimal trajectory is shown as a green line. It is clear that the optimal trajectory has the least deviation and is closer to the original trajectory than the other iterative trajectories.

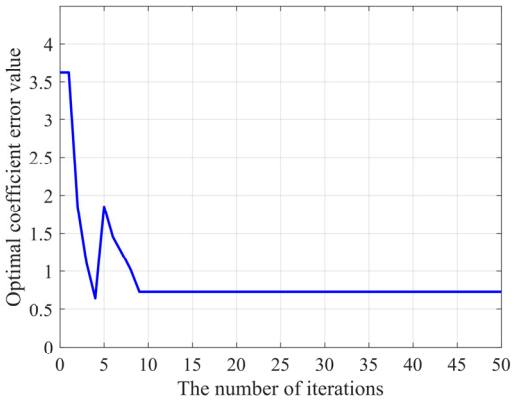

Fig. 6: The trajectory coefficient error value of each iterations

From Fig.6, the optimal coefficients converge faster in the first few iterations. After the fourth iteration, the optimal coefficient error converges to 0.6512. The thrust value, which is transformed by the differential flatness, does not satisfy the thrust constraints. Therefore, a correction for the remaining flight time is required. After the ninth iteration, the optimal coefficient error value converges to 0.7342 less than the setting threshold coefficient ε_a, and the optimal trajectory coefficients are finally obtained.

Fig.7 shows the optimized allocation time for each iteration. The original remaining time from the fault point to the endpoint is 3.3721s. After increasing the time through the trajectory replanning method, the estimated time is 5.1321s. However, this does not satisfy the thrust constraints and needs to be corrected. By the fifth iteration, the corrected remaining flight time is 5.8425s, but failed to meet the threshold factor ε_a. It is not until after the ninth iteration that the optimal allocation time is obtained.

Trajectory tracking experiments were carried out based on a control algorithm learned from [16]. Fig.8 (a) shows the moving performance by tracking the original trajectory, while Fig.8 (b) shows the effect after tracking the replanned trajectory. The start and terminal points were chosen as

(0,0,0)m and (40,0,0)m, respectively. It can be seen from the figure that the maximum deviation of tracking the replanned trajectory is 0.2236m, which is 45.5% less than the maximum deviation when tracking the original trajectory.

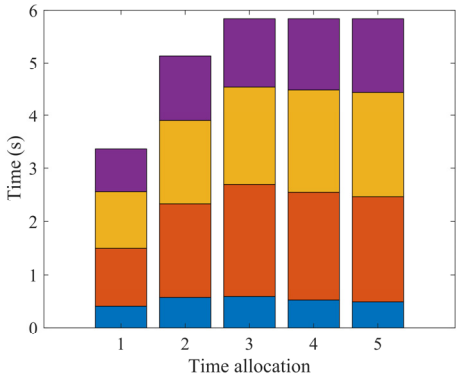

Fig. 7: The optimal time allocation

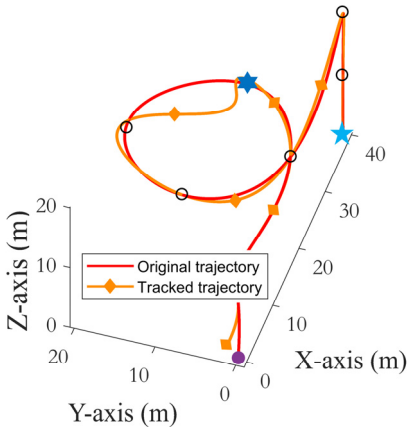

(a) Original trajectory tracking performance

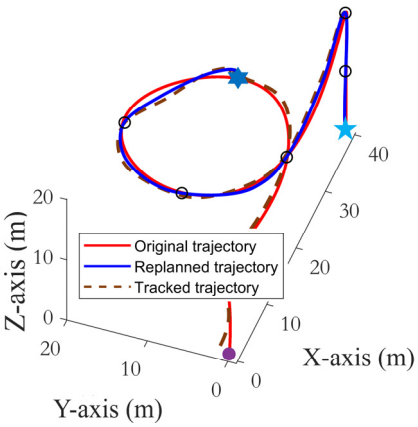

(b) Replanned trajectory tracking performance

Fig. 8: Trajectory tracking performances

5 Conclusion

A novel trajectory replanning method is proposed to solve the path planning problem for autonomous robots under actuator faults. Moreover, to ensure security, the switching condition, the time allocation and the offset distance are included as the main factors for the trajectory replanning. Simulation results in this paper have indicated the effectiveness and advancement of the proposed method.

Future work of trajectory design involves considering dynamic obstacles, multiple autonomous robots, and sensor faults in complex environments.

References

[1] A. A. Gizi, High voltage transmission line fault checker with fuzzy controller of the vehicle, in *Proceedings of 2022 IEEE Delhi Section Conference*, 2022: 1-6.

[2] M. M. Rayguru, R. E. Mohan, R. Parween, et al, An output feedback based robust saturated controller design for pavement sweeping self-reconfigurable robot. *IEEE/ASME Transactions on Mechatronics*, 2021, 26(3): 1236-1247.

[3] X. Zhang, H. Gao, M. Guo, et al, A study on key technologies of unmanned driving. *CAAI Transactions on Intelligence Technology*, 2016, 1(1): 4-13.

[4] H. Wang, P. X. Liu, X. Zhao, et al, Adaptive fuzzy finite-time control of nonlinear systems with actuator faults. *IEEE transactions on cybernetics*, 2019, 50(5): 1786-1797.

[5] X. Yu, P. Li, Fixed-time actuator fault accommodation applied to hypersonic gliding vehicles. *IEEE Transactions on Automation Science and Engineering*, 2021,18(3):1429-40.

[6] P. Li, X. Yu, Y. Zhang, X. Peng, Adaptive multivariable integral TSMC of a hypersonic gliding vehicle with actuator faults and model uncertainties. *IEEE/ASME Transactions on Mechatronics*, 2017, 22(8): 2723-2735.

[7] K. Alexis, G. Nikolakopoulos, A. Tzes, Switching model predictive attitude control for a quadrotor helicopter subject to atmospheric disturbances. *Control Engineering Practice*, 2011, 19(10): 1195-1207.

[8] Z. Yu, Y. Zhang, Z. Liu, Decentralized finite-time adaptive fault-tolerant synchronization tracking control for multiple UAVs with prescribed performance. *Journal of the Franklin Institute*, 2020, 357(16): 11830-11862.

[9] B. Wang, X. Yu, L. Mu ,et al, Disturbance observer-based adaptive fault-tolerant control for a quadrotor helicopter subject to parametric uncertainties and external disturbances. *Mechanical Systems and Signal Processing*, 2019, 727-743.

[10] A. Abbaspour, K. K. Yen, P. Forouzannezhad, et al, A neural adaptive approach for active fault-tolerant control design in UAV. *IEEE Transactions on Systems, Man, and Cybernetics: Systems*. 2018, 50(9): 3401-3411.

[11] H. Hu, B. Wang, Z. Cheng, et al, A novel active fault-tolerant control for spacecrafts with full state constraints and input saturation. *Aerospace Science and Technology*, 2021, 108: 106368.

[12] X. Zhou, X. Yu, K. Guo, et al, Safety flight control design of a quadrotor UAV with capability analysis. *IEEE Transactions on Cybernetics*. 2021, 53(3): 1738-1751.

[13] D. Mellinger, V. Kumar. Minimum snap trajectory generation and control for quadrotors, in *Proceedings of IEEE international conference on robotics and automation*, 2011: 2520-2525.

[14] E. Tal, G. Ryou, S. Karaman, Aerobatic trajectory generation for a VTOL fixed-wing aircraft using differential flatness. *IEEE Transactions on Robotics*, 2023, 39(6): 4805-4819.

[15] C. Richter, A. Bry, N. Roy, Polynomial trajectory planning for aggressive quadrotor flight in dense indoor environments, in *Proceedings of The 16th International Symposium ISRR*, 2016: 649-666.

[16] C. Wei, J. Luo, H. Dai, et al, Learning-based adaptive attitude control of spacecraft information with guaranteed prescribed performance. *IEEE transactions on cybernetics*, 2018, 49(11): 4004-4016.

Proceedings of the 3rd Conference on Fully Actuated System Theory and Applications
May 10-12, 2024, Shenzhen, China

Fault-tolerant Pursuit-evasion Games for Quadrotor Helicopters Based on a Fully-actuated System Approach

Jianfeng Xu, Yuhang Xu, Bin Jiang
College of Automation Engineering, Nanjing University of Aeronautics and Astronautics, Nanjing, 211106, China
E-mail: xjfnuaa@nuaa.edu.cn, xuyuhang@nuaa.edu.cn, binjiang@nuaa.edu.cn

Abstract: This paper proposes a fault-tolerant control scheme for the pursuit-evasion (PE) game between two quadrotor helicopters. Initially, the quadrotor helicopters are modeled based on the high-order fully-actuated (HOFA) approach, allowing to eliminate the nonlinear dynamics of the quadrotor helicopters. Subsequently, the game strategies for the pursuer, faults and the evader are designed. The optimal control rate is obtained by solving the Hamilton-Jacobi-Isaacs (HJI) equation using a critic neural network. It is demonstrated that the proposed fault-tolerant control (FTC) law assists the fault-affected pursuer in successfully capturing the evader and estimating the upper bound of bias fault. Finally, the effectiveness of the fault-tolerant PE game control scheme is validated through numerical simulations.

Key Words: Fully-actuated systems, adaptive fault-tolerant control, pursuit-evasion game, quadrotors, adaptive dynamic programming

1 Introduction

Over the past few decades, quadrotors have garnered widespread attention in both civilian and military domains and have been widely used in finding applications, surveillance, searching operations, and disaster management due to their high maneuverability, low cost, and vertical take-off and landing capabilities [1]. A primary challenge in controlling quadrotors is their underactuated and nonlinearly coupled system nature. With four control inputs and six degrees of freedom (DOF) [2], if the speed of the rotor is used as the control quantity, it is difficult to apply the method of controlling the linear system. To simplify control processes, differential flatness theory can transform the underactuated system of a quadrotor into a fully actuated system [3]. However, this results in a still nonlinear system. If the quadrotor system could be transformed into a linear system, it would facilitate the more convenient application of linear control theories.

Physically speaking, many systems models of objects established through physical laws are second-order or higher-order, and the model of a quadrotor is among these. These systems, when fully actuated, exhibit properties that enable the negation of all non-linearities, ultimately resulting in a linear, steady-state, closed-loop system. This can be achieved using the HOFA system method [4]. However, quadrotors cannot be transformed into a strict-feedback form, which is a prerequisite for the HOFA approach. Consequently, a modified HOFA approach with recursive actions is proposed [5], applicable to mixed-high-order dynamic systems. This method allows for the division of a quadrotor system into three HOFA subsystems. Each of these HOFA subsystems is then processed in such a way that they can be controlled like linear systems. Once the system is simplified, further scenarios like system faults or pursuit-evasion dynamics can be considered.

In a two-player PE game, one agent, known as the pursuer, aims to capture another agent called the evader, while the evader strives to avoid capture [6]. The two agents compete with each other and have opposite purposes, so this scenario is characterized as a zero-sum differential game involving two participants. Isaacs pioneered the concept of zero-sum differential strategies [7], where the control rate is defined as the saddle point solution of the differential game. A deviation from this saddle point in an agent's control rate results in suboptimal performance. The control rates can be obtained by solving the Riccati equation [8, 9]. When high-order systems are addressed through the HOFA system approach, the application of optimal control theory becomes more feasible [10]. Hence, studying PE games utilizing the HOFA system method is an advantageous approach. This paper, therefore, explores a zero-sum differential PE game based on the HOFA system methodology.

Control systems represent hybrid systems that consist of multiple components. During operation, it's not always possible to ensure that all components function normally at all times. Failures may occur due to aging or changes in external environments [11]. In the context of the quadrotor, factors such as actuator failures or ground influences can destabilize flight [12, 13]. Furthermore, in the process of pursuit, when the pursuer fails, it may cause system instability or failure of the pursuit. Therefore, considering fault conditions and knowing the system's ability to tolerate faults is crucial in the design of algorithms. This paper considers the scenario in which the pursuer experiences a bias fault in the control input during the PE game process.

Based on differential game strategies and adaptive dynamic programming, this paper presents an optimal fault-tolerant control scheme that ensures system stability. By engaging the pursuer, biased faults, and the evader in a strategic game, the control law enables the pursuer to successfully catch the evader and get the upper bound of fault. The novelties of this paper can be summarized as follows two as-

This work is supported by the Science Center Program of National Natural Science Foundation of China (62188101), the National Natural Science Foundation of China (62233009, 62020106003, 62303220), the Natural Science Foundation of Jiangsu Province of China (BK20230881), the China National Postdoctoral Program for Innovative Talents (BX20230490), the China Postdoctoral Science Foundation (2023M731665), the Postdoctoral Program of Jiangsu Province (2023ZB230), the 111 Project (B20007), Priority Academic Program Development of Jiangsu Higher Education Institutions. Corresponding author: Yuhang Xu.

pects: (1) To the best of our knowledge, it is the first time to consider the fault-tolerant control problem for the pursuit-evasion game under the HOFA framework. (2) Focusing on faults that occur in the pursuer during the pursuit process, a fault control law is designed using the HOFA method, effectively achieving the FTC goal.

2 Preliminaries

In this section, the quadrotor model utilized in this paper is introduced, along with the faults model and the construction of the PE game.

2.1 Faulty Quadrotor Model

Supposing that the quadrotor is rigid and symmetrical, with the origin of the body frame coinciding with the quadrotor's center of gravity.

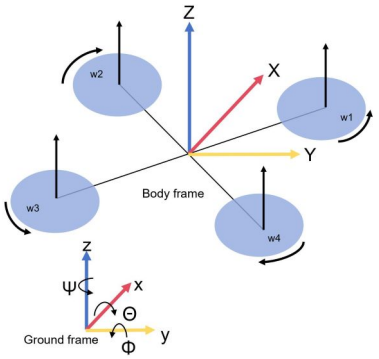

Fig. 1: Quadrotor Model

As shown in Fig. 1 of the quadrotor system, $[x, y, z]^T \in \mathbb{R}^3$denotes position relative to the inertial frame, $[\phi, \theta, \psi]^T \in \mathbb{R}^3$denotes the roll, pitch, and yaw angles relative to the inertial frame.

Due to the fragility of the system, in the event of a failure, the system may be destabilized by a large change in angle. So modeling needs to consider the occurrence of faults. We consider potential bias faults occurring in the control of the roll and pitch angles. The fault dynamical model of the quadrotor is represented as follows,

$$\begin{cases} \ddot{x} = u_1(\cos\psi\sin\theta\cos\phi + \sin\psi\sin\phi) \\ \ddot{y} = u_1(\sin\psi\sin\theta\cos\phi - \cos\psi\sin\phi) \\ \ddot{z} = u_1\cos\theta\cos\phi - g \\ \ddot{\phi} = u_2 + \bar{u}_2 \\ \ddot{\theta} = u_3 + \bar{u}_3 \\ \ddot{\psi} = u_4 \end{cases}. \tag{1}$$

where g denotes the gravitational acceleration, and u_1 denotes the resultant force along the body's z-axis. To simplify the complexities of controller design and the model, virtual control torques u_2, u_3, u_4 are employed as control inputs for roll, pitch, and yaw angles. The transformation from virtual control to actual control inputs is delineated in [3]. And the constants $\bar{u}_2, \bar{u}_3 \in \mathbb{R}$ denote the unknown faults occurring in the control process.

2.2 Problem Statement

This paper considers the use of the system (1) for a Pursuit-Evasion (PE) game. To facilitate the application of optimal control theory, the HOFA approach is employed to simplify the system. Furthermore, in response to faults occurring in the pursuer during the pursuit process, an adaptive fault-tolerant control algorithm is proposed to ensure that the pursuer remains stable throughout the pursuit.

3 Main Result

In this section, regarding the transformation of the system, we discuss how to convert the system into a fully-actuated system. This involves explaining the process of conducting a pursuit-evasion (PE) game within a fully actuated system framework, along with demonstrating the efficacy of the fault-tolerant control law. In terms of solving for the fault tolerant control law, we present a method for designing a critic neural network to ascertain the optimal value of the HJI equation. Additionally, the convergence of the critic neural network is proven.

3.1 Quadrotor model transformation

According to the method described in [5], the HOFA method with recursive actions can be applied to the control of a 6-DOF quadrotor. This involves decomposing the quadrotor model into three subsystems and transforming these subsystems into fully actuated systems.

To facilitate derivation, we first define some terms,

$$\begin{aligned} &x_1 = z, x_{2,1} = [x, y]^T, x_{2,2} = [\phi, \theta]^T, x_3 = \psi, \\ &\bar{u}_{2,3} = \begin{bmatrix} \bar{u}_2 \\ \bar{u}_3 \end{bmatrix}, g_2 = \begin{bmatrix} \cos\psi & \sin\psi \\ \sin\psi & -\cos\psi \end{bmatrix}, \\ &h_1 = \cos\theta\cos\phi, h_2 = \begin{bmatrix} \sin\theta\cos\phi \\ \sin\phi \end{bmatrix}, u_{2,3} = \begin{bmatrix} u_2 \\ u_3 \end{bmatrix}. \end{aligned} \tag{2}$$

Decomposing the quadrotor system (1) into three subsystems,we can obtain

$$x_1^{(2)} = u_1 h_1 - g, \tag{3}$$

$$\begin{cases} x_{2,1}^{(2)} = u_1 g_2 h_2 \\ x_{2,2}^{(2)} = u_{2,3} + \bar{u}_{2,3} \end{cases}, \tag{4}$$

$$x_3^{(2)} = u_4. \tag{5}$$

where the controlled variables are the altitude in (3), the horizontal position in (4), and the yaw angle in (5).

Since subsystem (3) and (5) already constitute a HOFA system, the corresponding controller is presented directly.

For the subsystem (3), the control law u_1 is defined as follows,

$$u_1 = -(h_1)^{-1}(-g - v_1). \tag{6}$$

where v_1 is external input.

After simplification, subsystem (3) can be obtained

$$x_1^{(2)} = v_1. \tag{7}$$

For the subsystem (5), the control law u_4 and the simplified subsystem are defined as follows,

$$u_4 = -(a_0 x_3 + a_1 x_3^{(1)} - v_4), \tag{8}$$

$$x_3^{(2)} + a_0 x_3 + a_1 x_3^{(1)} = v_4, \tag{9}$$

where v_4 is external input, a_0, a_1 are used to configure the poles of the system to make the subsystem (5) stable.

For the system (4), it can be obtained by derivating of $x_{2,1}^{(2)}$

$$x_{2,1}^{(3)} = u_1^{(1)} g_2 h_2 + u_1 g_2^{(1)} h_2 + u_1 g_2 h_2^{(1)}. \tag{10}$$

with

$$\begin{aligned} h_2^{(1)} &= \begin{bmatrix} -\sin(\theta)\sin(\phi) & \cos(\theta)\cos(\phi) \\ \cos(\phi) & 0 \end{bmatrix} z_{2,2}^{(1)}, \\ g_2^{(1)} &= \psi^{(1)} \cdot \begin{bmatrix} -\sin(\psi) & \cos(\psi) \\ \cos(\psi) & \sin(\psi) \end{bmatrix}. \end{aligned} \tag{11}$$

In order to simplify the calculation, $u_1 g_2 h_2^{(1)}$ can be rewriting as follows,

$$\begin{aligned} u_1 g_2 h_2^{(1)} &= u_1 g_2 \begin{bmatrix} -\sin(\theta)\sin(\phi) & \cos(\theta)\cos(\phi) \\ \cos(\phi) & 0 \end{bmatrix} z_{2,2}^{(1)} \\ &= L_2 z_{2,2}^{(1)}. \end{aligned} \tag{12}$$

Then

$$x_{2,1}^{(3)} = u_1^{(1)} g_2 h_2 + u_1 g_2^{(1)} h_2 + L_2 z_{2,2}^{(1)}. \tag{13}$$

Next, proceed to differentiate with respect to (13),

$$\begin{aligned} x_{2,1}^{(4)} &= u_1^{(2)} g_2 h_2 + u_1^{(1)} g_2^{(1)} h_2 + u_1^{(1)} g_2 h_2^{(1)} + u_1^{(1)} g_2^{(1)} h_2 \\ &+ u_1 g_2^{(2)} h_2 + u_1 g_2^{(1)} h_2^{(1)} + L_2^{(1)} x_{2,2}^{(1)} + L_2 x_{2,2}^{(2)}. \end{aligned} \tag{14}$$

Let

$$\begin{aligned} G_2 &= u_1^{(2)} g_2 h_2 + u_1^{(1)} g_2^{(1)} h_2 + u_1^{(1)} g_2 h_2^{(1)} \\ &+ u_1^{(1)} g_2^{(1)} h_2 + u_1 g_2^{(2)} h_2 + u_1 g_2^{(1)} h_2^{(1)} + L_2^{(1)} x_{2,2}^{(1)}. \end{aligned} \tag{15}$$

So (14) can be rewritten as follows,

$$x_{2,1}^{(4)} = G_2 + L_2 x_{2,2}^{(2)}. \tag{16}$$

Substituting the expression of $x_{2,2}^{(2)}$ in (4) into (16) gives,

$$x_{2,1}^{(4)} = G_2 + L_2(u_{2,3} + \bar{u}_{2,3}), \tag{17}$$

and the controller can be set to make the system a simpler form,

$$u_{2,3} = -(L_2)^{-1}(G_2 - v_{2,3}), \tag{18}$$

where $v_{2,3}$ is a vector of external inputs v_2 and v_3. The representation of $v_{2,3}$ are as follows,

$$v_{2,3} = \begin{bmatrix} v_2 \\ v_3 \end{bmatrix}. \tag{19}$$

By simplifying (17), we can obtain

$$x_{2,1}^{(4)} = v_{2,3} + L_2 \bar{u}_{2,3}. \tag{20}$$

Remark 1: The control in (18) and G_2 contains the high-order derivatives of u_1, which necessitate smooth estimation through appropriate techniques. □

Remark 2: To avoid singularity in (6) and (18), it is necessary to impose constraints on $cos(\theta), cos(\phi)$ at near-zero intervals. Those constraints are straightforward and applicable for large-angle flight maneuvers [14]. □

Remark 3: When the flight angle of the UAV is small during the pursuit, L_2 will change in a small range, so L_2 is treated as a constant coefficient matrix in this paper. □

Now, we can put (7), (9), (20) together. And system can be expressed as follows,

$$\begin{cases} x_1^{(2)} = v_1 \\ x_{2,1}^{(4)} = v_{2,3} + L_2 \bar{u}_{2,3} \\ x_3^{(2)} + a_0 x_3 + a_1 x_3^{(1)} = v_4 \end{cases}. \tag{21}$$

From (21), it can be seen that each subsystem becomes a fully actuated subsystem, that is, the system is converted into a fully actuated system. The system can be transformed into state space according to the method in [10].

We can get the state of the system as follows,
$s = [z; z^{(1)}; x; x^{(1)}; x^{(2)}; x^{(3)}; y; y^{(1)}; y^{(2)}; y^{(3)}; \psi; \psi^{(1)}]$
Subsequently, the system can be reformulated as follows,

$$s^{(1)} = As + Bv + F, \tag{22}$$

where A is the state transition matrix of the system, B is the input matrix of the system, and F is a matrix about the fault.

$$\begin{aligned} A &= \begin{bmatrix} 0&1&0&0&0&0&0&0&0&0&0&0 & 0 & 0 \\ 0&0&0&0&0&0&0&0&0&0&0&0 & 0 & 0 \\ 0&0&0&1&0&0&0&0&0&0&0&0 & 0 & 0 \\ 0&0&0&0&1&0&0&0&0&0&0&0 & 0 & 0 \\ 0&0&0&0&0&1&0&0&0&0&0&0 & 0 & 0 \\ 0&0&0&0&0&0&0&0&0&0&0&0 & 0 & 0 \\ 0&0&0&0&0&0&0&0&1&0&0&0 & 0 & 0 \\ 0&0&0&0&0&0&0&0&0&1&0&0 & 0 & 0 \\ 0&0&0&0&0&0&0&0&0&0&1&0 & 0 & 0 \\ 0&0&0&0&0&0&0&0&0&0&0&1 & 0 & 0 \\ 0&0&0&0&0&0&0&0&0&0&0&0 & 0 & 0 \\ 0&0&0&0&0&0&0&0&0&0&0&0 & 0 & 1 \\ 0&0&0&0&0&0&0&0&0&0&0&0 & -a_0 & -a_1 \end{bmatrix}, B = \begin{bmatrix} 0&0&0&0 \\ 1&0&0&0 \\ 0&0&0&0 \\ 0&0&0&0 \\ 0&0&0&0 \\ 0&1&0&0 \\ 0&0&0&0 \\ 0&0&0&0 \\ 0&0&0&0 \\ 0&0&1&0 \\ 0&0&0&0 \\ 0&0&0&1 \end{bmatrix}, \\ S_f &= \begin{bmatrix} 0_{5*2} \\ 1\ 0 \\ 0_{3*2} \\ 0\ 1 \\ 0_{2*2} \end{bmatrix}, v = \begin{bmatrix} v_1 \\ v_2 \\ v_3 \\ v_4 \end{bmatrix}, G = S_f L_2, F = G\bar{u}_{2,3}. \end{aligned} \tag{23}$$

where $F = 0_{12*4}$ for a fault-free system.

3.2 Controller design of fault-tolerant PE game

Taking the pursuit-evasion game into account, considering the occurrence of a fault in the pursuer during the pursuit-evasion process, and using simplified models (22) for both pursuer and evader, we can obtain the system for both sides as follows,

$$\begin{aligned} &s_p^{(1)} = As_p + Bv_p + F_p, s_e^{(1)} = As_e + Bv_e + F_e, \\ &B_p = B, B_e = -B, \delta = s_p - s_e, \\ &\delta^{(1)} = A\delta + B_p v_p + B_e v_e + G\bar{u}_a, \\ &\delta = [\delta_3; \delta_3^{(1)}; \delta_1; \delta_1^{(1)}; \delta_1^{(2)}; \delta_1^{(3)}; \delta_2; \delta_2^{(1)}; \delta_2^{(2)}; \delta_2^{(3)}; \delta_4; \delta_4^{(1)}] \end{aligned} \tag{24}$$

where s_p is the state of pursuer, s_e is the state of evader, $\bar{u}_a$ is the bias fault of pursuer, v_p is the external input of pursuer, v_e is the external input of evader, F_p and F_e are variables similar to F as described in equation (22), with F_e being a 0_{12*4} matrix.

Through the paper [15], by joining the game with the fault, we can get the maximum value of the fault that can be tolerated. Define the performance index function of the system as follows,

$$J(\delta(0), v_e, v_p, u_p) = \int_0^\infty (\delta^T Q \delta + v_p^T R v_p - r^2 v_e^T R v_e - \theta \bar{u}_a^T M \bar{u}_a). \tag{25}$$

where the matrix Q is a positive semi-definite matrix, the matrix R and the matrix M are positive definite matrices, and the parameters r and θ are positive constants.

By engaging in a game between the pursuer, the faults, and the evader, the problem can be expressed as follows,

$$J^*(\delta(0)) = \min_{v_p} \max_{(\bar{u}_a, v_e)} \int_0^\infty (\delta^T Q \delta + v_p^T R v_p - r^2 v_e^T R v_e - \theta \bar{u}_a^T M \bar{u}_a). \tag{26}$$

By selecting through the game the minimizing player v_p, maximizing player v_e and $\bar{u}_a$, the inequalities that need to be satisfied at the saddle point are as follows,

$$\begin{aligned} J(\delta(0), v_p^*, v_e, \bar{u}_a) &\le J(\delta(0), v_p^*, v_e^*, \bar{u}_a^*) \\ &\le J(\delta(0), v_p, v_e^*, \bar{u}_a^*). \end{aligned} \tag{27}$$

At the saddle point $(v_p^*, v_e^*, \bar{u}_a^*)$, the pursuer forms a saddle point equilibrium with its fault and the evader. At this point, every player plays optimally. Moreover, satisfying the saddle point solution also implies that regardless of the order of optimization, the final strategy is optimal [16].

Through (25) and (24), the Hamiltonian function can be set as follows,

$$H(\delta, \Delta J^*(\delta), v_p, v_e, \bar{u}_a) = \delta^T Q \delta + v_p^T R v_p - r^2 v_e^T R v_e - \theta \bar{u}_a^T M \bar{u}_a + (\Delta J^*(\delta))^T (A\delta + B_p v_p + B_e v_e + S_f L_2 \bar{u}_a). \tag{28}$$

where $\Delta J^*(\delta) = \partial J^*(\delta)/\partial \delta$.

From the extreme value condition, we can derive the equations as follows,

$$\frac{\partial H}{\partial v_p} = 0, \frac{\partial H}{\partial v_e} = 0, \frac{\partial H}{\partial \bar{u}_a} = 0. \tag{29}$$

Through the Hamiltonian equation (28) and the three partial differential equations in (29), the optimal control rates for the pursuer and evader, as well as the worst-case fault, can be obtained as follows,

$$\begin{aligned} u_p^* &= -\frac{1}{2} R^{-1} B_p^T \Delta J^*(\delta), \\ u_e^* &= \frac{1}{2r^2} R^{-1} B_e^T \Delta J^*(\delta), \\ \bar{u}_a^* &= \frac{1}{2\theta} M^{-1} G^T \Delta J^*(\delta). \end{aligned} \tag{30}$$

Using the control variables in (30) to substitute the control variable in (28), the Hamilton-Jacobi-Isaacs (HJI) equation can be derived as follows,

$$\begin{aligned} H(\delta, \Delta J^*(\delta), v_p^*, v_e^*, \bar{u}_a^*) &= \delta^T Q \delta + \Delta J^*(\delta)^T A \delta \\ &- \frac{1}{4} \Delta J^*(\delta)^T B_p R^{-1} B_p^T \Delta J^*(\delta) \\ &+ \frac{1}{4\theta} \Delta J^*(\delta)^T G M^{-1} G^T \Delta J^*(\delta) \\ &+ \frac{1}{4r^2} \Delta J^*(\delta)^T B_e R^{-1} B_e^T \Delta J^*(\delta) = 0. \end{aligned} \tag{31}$$

Theorem 1: Consider the system (24), using optimal control policy in (30). Under the condition of satisfying (32), it is guaranteed that the pursuer can successfully capture the evader in case of failure.

$$\begin{cases} \lambda_{min}(Q) - \lambda_{max}(A) - \frac{1}{2}\lambda_{max} P_4 \ge 0, \\ \frac{1}{4}\lambda_{min}(P_1) - \frac{1}{4r^2}\lambda_{max}(P_2) \\ - \frac{1}{4\theta}\lambda_{max}(P_3) - \frac{1}{2}\lambda_{max}(P_4) \ge 0. \end{cases} \tag{32}$$

where

$$P_1 = B_p R^{-1} B_p^T, P_2 = B_e R^{-1} B_e^T, P_3 = G M^{-1} G^T,$$
$$P_4 = \frac{1}{-2} P_1 + \frac{1}{2r^2} P_2 + \frac{1}{2\theta} P_3.$$

Proof: Choose the Lyapunov function as

$$V(\delta) = J^*(\delta) + \frac{1}{2}\delta^T \delta \tag{33}$$

Deriving it can be obtained

$$\begin{aligned} \dot{V}(\delta) =& \delta^T \dot{\delta} + \Delta J^*(\delta)(A\delta + B_p v_p + B_e v_e + G\bar{u}_a) \\ =& \delta^T \dot{\delta} - \delta^T Q \delta - \frac{1}{4}\Delta(J^*(\delta))^T B_p R^{-1} B_p^T \Delta J^*(\delta) \\ &+ \frac{1}{4\theta}\Delta(J^*(\delta))^T G M^{-1} G^T \Delta J^*(\delta) \\ &+ \frac{1}{4r^2}\Delta(J^*(\delta))^T B_e R^{-1} B_e^T \Delta J^*(\delta) \\ \le& -(\lambda_{min}(Q) - \lambda_{max}(A) - \frac{1}{2}\lambda_{max}(P_4))||\delta||^2 \\ &- (\frac{1}{4}\lambda_{min}(P_1) - \frac{1}{4r^2}\lambda_{max}(P_2) \\ &- \frac{1}{4\theta}\lambda_{max}(P_3) - \frac{1}{2}\lambda_{max}(P_4))||\Delta J^*(\delta)||^2. \end{aligned} \tag{34}$$

Under the condition of (32), $\dot{V}(\delta) < 0$ is established, which means the system is stable and the pursuer can catch the evader. □

Theorem 2: For the system (24), considering the Hamiltonian function (28) and the control strategy (30), the system can reach saddle-point equilibrium.

Proof: According to Theorem 1,$\delta \to 0$ can be reached according to the control strategy chosen, so we can set $J^*(\delta(\infty)) = 0$. Considering the performance function (25), we can obtain

$$\begin{aligned} J(\delta(0)) &= \int_0^\infty (\delta^T Q \delta + v_p^T R v_p - r^2 v_e^T R v_e - \theta \bar{u}_a^T M \bar{u}_a) dt \\ &= J(\delta(0)) + \int_0^\infty \dot{J}^*(\delta) dt + J^*(\delta(0)) - J^*(\delta(\infty)). \end{aligned}$$

According to the HJI equation (31) and Hamiltonian function (28), by completing the square method, we can simplify the above equation as follows,

$$J(\delta(0)) = J^*(\delta(0)) + \int_0^\infty (v_p - v_p^*)^T R (v_p - v_p^*) - r^2 (v_e - v_e^*)^T R (v_e - v_e^*) - \theta (\bar{u}_a - \bar{u}_a^*)^T M (\bar{u}_a - \bar{u}_a^*) dt.$$

It can be seen that $J(\delta(0))$ satisfies the inequality (27), that is, satisfies the saddle point condition, and the proof is completed. □

Since the $J^*(\delta)$ in the HJI equation (31) is difficult to solve, the neural network method described below is used to approximate it.

3.3 Online NN Implementation

In this subsection, the optimal controller design based on the neural network is used to acquire the optimal value in the HJI equation (31). The design procedure of the critic neural network is given and the convergence of the network weights is proved.

The value function is approximated using a single-layer neural network of the form as follows,

$$J^*(\delta) = W^T \sigma(\delta) + \epsilon(\delta). \tag{35}$$

where $W \in \mathbb{R}^l$ is the weight vector of the network, $\sigma(\delta) \in \mathbb{R}^l$ is the activation function of the network, l is the number of neurons in the critic NN hidden layer, $\epsilon(\delta)$ is the approximation error of the network.

The derivation of $J^*(\delta)$ with respect of δ is as follows,

$$\Delta J^*(\delta) = (\Delta\sigma(\delta))^T W + \Delta\epsilon(\delta). \tag{36}$$

where $\Delta J^*(\delta) = \frac{\partial J^*(\delta)}{\partial \delta}$, $\Delta\sigma(\delta) = \frac{\partial \sigma(\delta)}{\partial \delta}$, $\Delta\epsilon(\delta) = \frac{\partial \epsilon(\delta)}{\partial \delta}$.

Substituting the value function (35) into (28), the Hamilton function of the system can be obtained as

$$\begin{aligned} H(\delta, \Delta J, v_P, v_e, \bar{u}_a, W) &= \delta^T Q \delta + v_p^T R v_p - r^2 v_e^T R v_e \\ &\quad - \theta \bar{u}_a^T M \bar{u}_a + ((\Delta\sigma(\delta))^T W + \Delta\epsilon(\delta))^T \dot{\delta}. \end{aligned} \tag{37}$$

From (31), when the system control law is the optimal control law, the approximate residual of the network can be defined as

$$\begin{aligned} e_h &= -\epsilon(\delta)^T \dot{\delta} = \delta^T Q \delta + v_p^T R v_p - r^2 v_e^T R v_e \\ &\quad - \theta \bar{u}_a^T M \bar{u}_a + ((\Delta\sigma(\delta))^T W)^T \dot{\delta} \end{aligned} \tag{38}$$

Given that the ideal W is unknown, the critic neural network and its derivative are approximated as follows,

$$\bar{J}^*(\delta) = \bar{W}^T \sigma(\delta), \Delta\bar{J}^*(\delta) = (\Delta\sigma(\delta))^T \bar{W}. \tag{39}$$

Then we can get the approximate Hamiltonian function,

$$\begin{aligned} H(\delta, \Delta\bar{J}(\delta), v_p, v_e, \bar{u}_a, \bar{W}) &= \delta^T Q \delta + v_p^T R v_p - r^2 v_e^T R v_e \\ &\quad - \theta \bar{u}_a^T M \bar{u}_a + ((\Delta\sigma(\delta))^T \bar{W})^T \delta^{(1)} = e. \end{aligned} \tag{40}$$

During the iteration of the neural network, set $E = \frac{1}{2} e^T e$ as the evaluation function of the network, and then set the update rate of the weights as follows,

$$\dot{\bar{W}} = -k e \alpha. \tag{41}$$

where $\alpha = \Delta\sigma(\delta)\delta^{(1)}$, k is a learning rate during the iteration process.

The weight approximation error is defined as $\tilde{W} = W - \bar{W}$, then we has

$$e = (e_h - \tilde{W}^T \alpha), \dot{\tilde{W}} = -\dot{\bar{W}} = k(e_h - \tilde{W}^T \alpha)\alpha. \tag{42}$$

Based on (30) and (35), the ideal control strategy is

$$u_p^* = -\frac{1}{2} R^{-1} B_p^T ((\Delta\sigma(\delta))^T W + \Delta\epsilon(\delta)). \tag{43}$$

It can be approximated as

$$\hat{u}_p^* = -\frac{1}{2} R^{-1} B_p^T (\Delta\sigma(\delta))^T \bar{W}. \tag{44}$$

Similarly, the control rates of the evader and the worst case of fault can be obtained as

$$\begin{aligned} \hat{u}_e^* &= \frac{1}{2r^2} R^{-1} B_e^T (\Delta\sigma(\delta))^T \bar{W}, \\ \hat{u}_a^* &= \frac{1}{2\theta} M^{-1} G^T (\Delta\sigma(\delta))^T \bar{W}. \end{aligned} \tag{45}$$

With this setup, only critical NN is needed to complete the training, and no actor NN is needed.

Theorem 3: Considering the system (24), if the critic NN weights are updated according to (41), then the weight approximation error is uniformly ultimately bounded (UUB).

Proof: The proof process is similar to Theorem 3 in [17]. Set the Lyapunov function as $V_2 = \frac{1}{2k} \tilde{W}^T \tilde{W}$. And $\dot{V}_2 \leq 0$ exists within the set $||\tilde{W}|| \geq ||\frac{e_h}{\alpha_b}||$, where $||\alpha|| \leq \alpha_b$ and $\alpha_b \geq 0$. According to the Lyapunov stability theorem, the weight approximation error is UUB. □

4 Numerical Simulation

In this section, we demonstrate the simulation results of using the optimal control strategy based on adaptive dynamic programming in the PE game.

Considering the quadrotor model (1), where the system parameters are set by $g = 9.8m/s^2$, we assume that errors only occur on the pursuer. To ensure the attitude stability of the quadrotor during the pursuit-evasion process, it is necessary to suppress the magnitude of the control quantity. Therefore, the values of the matrices Q, M and R will be set smaller. The diagonal elements of Q are set to [0.001; 0.015; 0.0000155; 0.001; 3; 5; 0.0000155; 0.001; 4.3; 5.3; 0; 0], the diagonal elements of R are [1; 5; 5; 1], and the diagonal elements of M are [1; 2]. To set the poles of subsystem (5) to -3, we set a_o to 9 and a_1 to 6. The parameters in performance function (25) are $\gamma = \sqrt{1.5}$ and $\theta = 10$. For the critic neural network, its activation function $\sigma(\delta)$, learning rate k and weight vector $\bar{W}$ with its initial value $\bar{W}_0$ are

$$\begin{aligned} k &= 0.1, \bar{W} = [\bar{W}_1, \bar{W}_2, \ldots \bar{W}_{18}, \bar{W}_{19}], \\ \bar{W}_0 &= [0.02, 0.02, 0.02, 0.02, 0.02, 0.5, 0.02, 0.02, 0.02, \\ &\quad 0.2, 0.02, 0.02, 0.02, 0.0006, 0.033, 1, 0.0008, 0.03, 1], \\ \sigma(\delta) &= [\delta_3^2, (\delta_3^{(1)})^2, \delta_1^2, (\delta_1^{(1)})^2, (\delta_1^{(2)})^2, (\delta_1^{(3)})^2, \delta_2^2 \\ &\quad (\delta_2^{(1)2}), (\delta_2^{(2)})^2, (\delta_2^{(3)})^2, \delta_4^2, (\delta_4^{(1)})^2, \delta_3\delta_3^{(1)}, \\ &\quad \delta_1\delta_1^{(3)}, \delta_2\delta_2^{(3)}, \delta_1^{(3)}\delta_1^{(1)}, \delta_1^{(3)}\delta_1^{(2)}, \delta_2^{(3)}\delta_2^{(1)}, \delta_2^{(3)}\delta_2^{(2)}]. \end{aligned}$$

To demonstrate the efficacy of the proposed fault-tolerant control rates, simulations are conducted in the following scenario,

$$\begin{cases} \bar{u}_a = [0.0001; 0.0001], 0 \leq t \leq 5; \\ \bar{u}_a = [0.0005; 0.0005], t \geq 5. \end{cases}$$

Fig. 2 shows the motion trajectories of the pursuer and evader. Fig. 3 displays the distance between the pursuer and the evader. From the graph, it is apparent that the pursuer catches the evader in the case of fault. Fig. 4 illustrates the

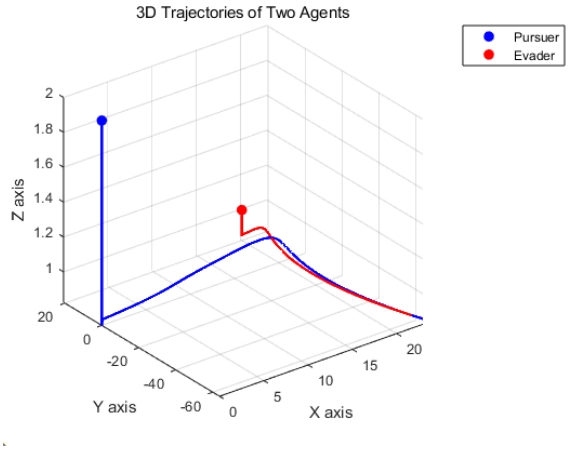

Fig. 2: the motion trajectories of the pursuer and evader

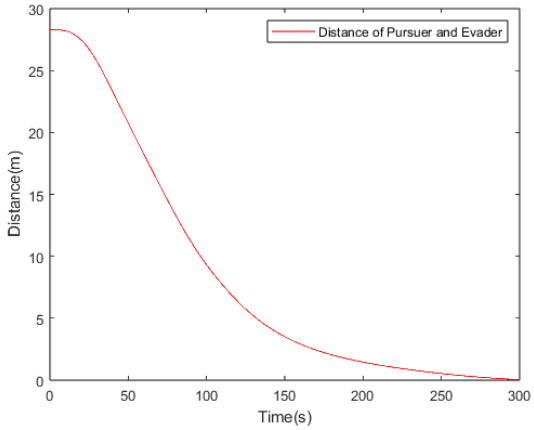

Fig. 3: Distance of pursuer and evader

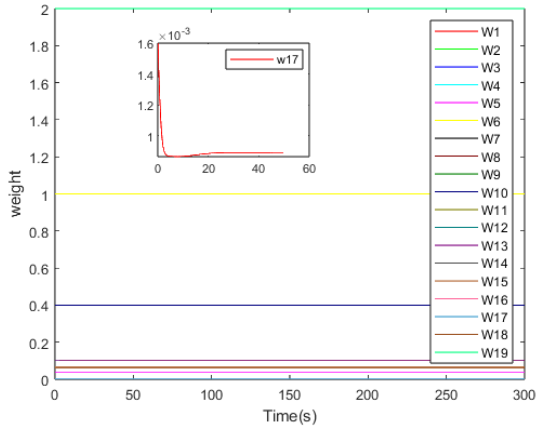

Fig. 4: Weight of critic NN

variation of the estimated weights. The weight change in the graph is not obvious. But it also can be seen that all the estimated weights finally converge to a constant value, proving the effectiveness of the critic neural network.

5 Conclusion

This paper presents the design, analysis, and simulation results of a fault-tolerant PE game control scheme. It utilizes a modified HOFA approach with recursive actions to simplify the quadrotor system, which is then used to study the PE game. Moreover, it considers bias faults occurring in the control of the roll and pitch angles. Finally, a fault-tolerant control law using critic NN to solve is developed. The algorithm's effectiveness is validated through simulations. Future work is to apply the algorithm to an actual hardware platform.

References

[1] M. Idrissi, M. Salami, F. Annaz, A review of quadrotor unmanned aerial vehicles: applications, architectural design and control algorithms, *Journal of Intelligent and Robotic Systems*, 104(2): 22, 2022.

[2] A. Khalid, Z. Mushtaq, S. Arif, K. Zeb, M. A. Khan and S. Bakshi, Control schemes for quadrotor UAV: taxonomy and survey, *ACM Computing Surveys*, 56(5): 1-32, 2023.

[3] X. Ai, J. Yu, Flatness-based finite-time leader-follower formation control of multiple quadrotors with external disturbances, *Aerospace Science and Technology*, 92:20-33, 2019.

[4] G. Duan, High-order fully actuated system approaches: Part I. Models and basic procedure, *International Journal of Systems Science*, 52(2): 422-435, 2021.

[5] S. Lu, K. Tsakalis, Y. Chen, Development and Application of a Novel High-order Fully Actuated System Approach: Part II. 6-DOF Quadrotor Control, in *2023 American Control Conference (ACC)*, 2023: 661-666.

[6] W. Lin, Z. Qu, M. A. Simaan, Nash strategies for pursuit-evasion differential games involving limited observations, *IEEE Transactions on Aerospace and Electronic Systems*, 51(2): 1347-1356, 2015.

[7] Isaacs, Differential Games, *John Wiley & Sons*, 1965

[8] J. Engwerda, LQ Dynamic Optimization and Differential Games, *John Wiley & Sons*, 2005, chapter 8.

[9] A. Jagat, A. J. Sinclair, Nonlinear control for spacecraft pursuit-evasion game using the state-dependent Riccati equation method, *IEEE Transactions on Aerospace and Electronic Systems*, 53(6): 3032-3042, 2017.

[10] G. Duan, High-order fully actuated system approaches: Part VIII. Optimal control with application in spacecraft attitude stabilisation, *International Journal of Systems Science*, 53(1): 54-73, 2022.

[11] J. X. Zhang, G. H. Yang, Robust adaptive fault-tolerant control for a class of unknown nonlinear systems, *IEEE Transactions on Industrial Electronics*, 64(1): 585-594, 2016.

[12] B. J. Emran, H. Najjaran, A review of quadrotor: An underactuated mechanical system, *Annual Reviews in Control*, 46: 165-180, 2018.

[13] X. Kan, J. Thomas, H. Teng, H.G. Tanner, V. Kumar, K. Karydis, Analysis of ground effect for small-scale UAVs in forward flight, *IEEE Robotics and Automation Letters*, 4(4): 3860-3867, 2019.

[14] M. Faessler, A. Franchi, D. Scaramuzza, Differential flatness of quadrotor dynamics subject to rotor drag for accurate tracking of high-speed trajectories, *IEEE Robotics and Automation Letters*, 3(2): 620-626, 2017.

[15] H. Ren, B. Jiang, Y. J. Ma, Zero-sum differential game-based fault-tolerant control for a class of affine nonlinear systems, *IEEE Transactions on Cybernetics*, 54(2):1272-1282, 2024.

[16] R. N. Banavar and J. L. Speyer, A Linear-Quadratic Game Approach to Estimation and Smoothing, in *1991 American Control Conference*, 1991:2818-2822.

[17] B. Zhao, D. Liu, Y. Li, Observer based adaptive dynamic programming for fault tolerant control of a class of nonlinear systems, *Information Sciences*, 384: 21-33, 2017.

Proceedings of the 3rd Conference on Fully Actuated System Theory and Applications
May 10-12, 2024, Shenzhen, China

Fault-Tolerant Model Predictive Load Frequency Control for Power Systems with Electrolytic Aluminum Load Under New Event-triggered Mechanism

Shisen Zhou[1,2,3], Ziqian Wang[1,2,3], Xiongbo Wan[1,2,3]

1. School of Automation, China University of Geosciences, Wuhan 430074, China

2. Hubei Key Laboratory of Advanced Control and Intelligent Automation for Complex Systems, Wuhan 430074, China

3. Engineering Research Center of Intelligent Technology for Geo-Exploration, Ministry of Education, Wuhan 430074, China
E-mail: xbwan23@cug.edu.cn (Corresponding author)

Abstract: In this paper, the problem of event-based fault-tolerant model predictive load frequency control is investigated for the power system where the electrolytic aluminum load participates in frequency modulation and actuator faults. A dynamic event-triggered mechanism containing an internal dynamic variable (IDV) and an adjustable variable is designed to reduce the data transmission burden. The fault-tolerant model predictive control (FTMPC) problem is expressed as a "min-max" optimization problem (OP). According to the Lyapunov-like function that depends on the IDV, an auxiliary OP with constrained linear matrix inequalities is constructed. By solving the auxiliary OP, the FTMPC controller gains that ensure the input-to-state stability of the closed-loop system can be obtained. The effectiveness of the proposed algorithm is verified through a simulation example.

Key Words: Electrolytic aluminum load, fault-tolerant control, model predictive control, load frequency control, dynamic event-triggered mechanism

1 Introduction

Frequency fluctuation is an important index of output power quality in power systems, and it is necessary to maintain it within the desired nominal values. Load frequency control (LFC) is an effective method to address the problem of frequency deviation. In recent years, a lot of results have been reported [1–3]. However, with the access of large-scale new energy in the power grid, it brings new challenges to the frequency stability of the power systems. Traditional thermal power units have limited frequency regulation capacity, which makes it difficult to smooth the frequency fluctuation caused by new energy sources connected to the grid. Therefore, it is necessary to seek new regulation resources to calm the frequency fluctuation. The electrolytic aluminum load is characterized by high thermal inertia and good control [4] and has a huge potential for frequency regulation. To this end, researchers have explored the superiority of electrolytic aluminum load participating in grid frequency regulation [5–7].

Currently, most power systems realize data transmission through communication networks, but inevitably lead to various network-induced phenomena such as time delay and packet dropouts. These phenomena bring new challenges to the LFC performance of power systems [8]. In addition, due to the limited communication bandwidth, the transmission of large amounts of data puts a heavy burden on the communication network [9]. To solve the above problems, researchers have proposed event-triggered mechanisms (ETMs) [10, 11], which require the fulfillment of predefined event-triggered conditions before releasing packets, and thus can reduce the transmission of redundant packets. Static ETMs (SETMs) [12, 13] are not able to maximize the saving of network resources due to their fixed threshold. Therefore, more and more scholars are keen on studying dynamic ETMs (DETMs) [14–16], which are more flexible than SETMs. However, the current DETMs have much space for improvement to further save network resources.

Actuator faults are unavoidable in power systems due to the influence of the external environment and the aging of the equipment, and actuator faults may lead to system instability [17]. Consequently, many experts and scholars have paid attention to fault-tolerant control and studied the problem of fault-tolerant LFC [18, 19]. Additionally, some scholars have fully considered the hard constraints and other practical factors in the power system, introduced fault-tolerant model predictive control (FTMPC), and studied the fault-tolerant model predictive LFC problem [20]. However, the fault-tolerant model predictive LFC problem for electrolytic aluminum load participating in frequency modulation has not been reported, let alone discussed the DETM-based fault-tolerant model predictive LFC problem for electrolytic aluminum load participating in frequency modulation. Thus, we need to design a new DETM and study the fault-tolerant model predictive LFC problem based on this DETM for electrolytic aluminum load participating in frequency modulation.

The main contributions of this work are summarized as follows: 1) a new DETM containing two adjustment variables is proposed to conserve network resources; 2) the fault-tolerant model predictive load frequency controllers are designed for the power system where electrolytic aluminum load participates in frequency regulation; 3) the recursive feasibility and input-to-state stability (ISS) are analysed.

2 Problem Formulation

Consider the following LFC system with electrolytic aluminum load participation:

$$\begin{cases} \dot{x}(t) = \tilde{A}x(t) + \tilde{B}u(t) + \tilde{F}w(t), \\ y(t) = \tilde{C}x(t), \end{cases} \tag{1}$$

This work is supported by the National Natural Science Foundation of China under Grant 62073303 and the Key Program of Hubei Provincial Technical Innovation Project under Grant No. 2023BAB080.

where

$$x(t) = [\Delta f \quad \Delta P_m \quad \Delta P_v \quad \int ACE_i \quad \Delta I_d \quad \Delta I_{dcon} \quad \Delta P_{AL}]^{\mathrm{T}},$$

$$y(t) = ACE = \beta\Delta f, w(t) = \Delta P_d,$$

$$\tilde{A} = \begin{bmatrix} \tilde{A}_{11} & \tilde{A}_{12} \\ 0_{3\times 4} & \tilde{A}_{22} \end{bmatrix}, \tilde{A}_{12} = \begin{bmatrix} 0 & 0 & -\frac{1}{M} \\ 0 & 0 & 0 \\ 0 & 0 & 0 \\ 0 & 0 & 0 \end{bmatrix},$$

$$\tilde{A}_{11} = \begin{bmatrix} -\frac{D}{M} & \frac{1}{M} & 0 & 0 \\ 0 & -\frac{1}{T_{ch}} & \frac{1}{T_{ch}} & 0 \\ -\frac{1}{RT_g} & 0 & -\frac{1}{T_g} & 0 \\ \beta & 0 & 0 & 0 \end{bmatrix},$$

$$\tilde{A}_{22} = \begin{bmatrix} -\frac{1}{T_{ES}} & 0 & 0 \\ K_I - \frac{K_P}{T_{ES}} & 0 & 0 \\ 0 & \frac{K_{P-V}K_{SR}}{T_{SR}} & -\frac{1}{T_{SR}} \end{bmatrix},$$

$$\tilde{B} = \begin{bmatrix} 0 & 0 & \frac{1}{T_g} & 0 & 0 & 0 & 0 \\ 0 & 0 & 0 & 0 & \frac{1}{K_{P-I}T_{ES}} & \frac{K_P}{K_{P-I}T_{ES}} & 0 \end{bmatrix}^{\mathrm{T}},$$

$$\tilde{C} = [\beta \quad 0 \quad 0 \quad 0 \quad 0 \quad 0 \quad 0],$$

$$\tilde{F} = \left[-\tfrac{1}{M} \quad 0 \quad 0 \quad 0 \quad 0 \quad 0 \quad 0\right]^{\mathrm{T}}.$$

For the explanations about the parameters in Eq. (1), please refer to [6] for details.

We give the following discrete LFC system:

$$\begin{cases} x(k+1) = Ax(k) + Bu(k) + Fw(k), \\ y(k) = Cx(k), \end{cases} \tag{2}$$

where, $A = e^{\tilde{A}T_P}$, $B = \int_0^{T_P} e^{\tilde{A}t}\tilde{B}dt$ and $F = \int_0^{T_P} e^{\tilde{A}t}\tilde{F}dt$ with T_P being the sampling period, $x(k) \in \mathbb{R}^{n_x}$ is the system state, $y(k) \in \mathbb{R}^{n_y}$ is the system output, and $u(k) \in \mathbb{R}^{n_u}$ is the system control input.

Suppose that the disturbance $w(k)$ satisfies

$$\|w(k)\|^2 \le p^2, \tag{3}$$

where $p > 0$ is constant.

The following input constraints are considered:

$$|[u(k)]_\nu| \le [\bar{u}]_\nu, \nu \in \mathbb{V} \triangleq \{1, 2, \ldots, n_u\}, \tag{4}$$

where $\bar{u}$ is a given vector.

To mitigate the communication burden while maintaining control performance, we present the following DETM:

$$\begin{cases} s_{m+1} = \min_{k\in\mathbb{N}^+}\{k > s_m \mid \lambda_1\eta(k) \\ +\varsigma_1\xi(k)x^{\mathrm{T}}(k)\Omega(k)x(k) - \varsigma_2 e^{\mathrm{T}}(k)\Omega(k)e(k) \le 0\}, \\ \eta(k+1) = \lambda_2\eta(k) + \varsigma_3\xi(k)x^{\mathrm{T}}(k)\Omega(k)x(k) \\ -\varsigma_4 e^{\mathrm{T}}(k)\Omega(k)e(k), \\ \xi(k) = \underline{\xi} + \kappa\frac{2}{\pi}arccot(e^{\mathrm{T}}(k)e(k)), \end{cases} \tag{5}$$

where s_m stands for the mth instant for data release with $s_0 = 0$, $\eta(k)$ is an internal dynamic variable (IDV) with $\eta(k) \ge 0$, $\xi(k)$ is an adjustment variable (AV), $\Omega(k)$ is a weighting matrix, $\lambda_1 \ge 0$, $0 \le \lambda_2 \le 1$, $\varsigma_1 \ge 0$, $\varsigma_2 > 0$, $\varsigma_3 \ge 0$, $\varsigma_4 > 0$, $\underline{\xi} \ge 0$ and $\kappa \ge 0$ are given constants, and $e(k) = x(k) - x(s_m)$.

Note that in DETM (5), there exist an IDV $\eta(k)$ and an AV $\xi(k)$, which are devised to improve the ability to adjust the release of data packets. In addition, we get

$$\xi_{\min} \triangleq \underline{\xi} < \xi(k) \le \underline{\xi} + \kappa \triangleq \xi_{\max}. \tag{6}$$

Let

$$\tilde{x}(k) = x(s_m), \forall k \in [s_m, s_{m+1}). \tag{7}$$

Then, we get

$$e(k) = x(k) - \tilde{x}(k). \tag{8}$$

We know that $\forall k \in [0, \infty)$, $e(k) = x(k) - x(s_m)$ and (8) hold as k varies from 0 to $+\infty$.

Consider the following state feedback controller:

$$u(k) = H(k)\tilde{x}(k), \tag{9}$$

where $u(k) = [u_1(k), u_2(k), \ldots, u_{n_u}(k)]^T$ and $H(k)$ denotes the feedback gain matrix.

Noting that actuator faults may occur in power system, we consider the following actuator fault model:

$$u^f(k) = \beta u(k), \beta = \mathrm{diag}(\beta_1, \beta_2, \ldots, \beta_{n_u}), \tag{10}$$

where $u^f(k) = [u_1^f(k), u_2^f(k), \ldots, u_{n_u}^f(k)]^T$ represents the control signals enforced by the faulty actuators, β_i, $\forall i = 1, 2, \ldots, n_u$ denote the degree of actuator faults.

We assume that β_i satisfies the following conditions:

$$0 \le \beta_i \le 1. \tag{11}$$

According to (10), the system (2) with partial actuator faults is described as

$$\begin{cases} x(k+1) = Ax(k) + B\beta u(k) + Fw(k), \\ y(k) = Cx(k). \end{cases} \tag{12}$$

Applying (8) and (9) to (12), we can obtain the following closed-loop control system:

$$x(k+1) = (A + B\beta H(k))x(k) - B\beta H(k)e(k) + Fw(k). \tag{13}$$

For ease of presentation, we denote

$$\cdot(k+n \mid k) \triangleq \cdot(n, k), \cdot(k \mid k) \triangleq \cdot(k).$$

The following prediction model is given:

$$\begin{cases} x(n+1,k) = (A + B\beta H(k))x(n,k) \\ -B\beta H(k)e(n,k) + Fw(n,k), \\ \eta(n+1,k) = \lambda_2\eta(n,k) + \varsigma_3\xi(n,k)x^{\mathrm{T}}(n,k)\Omega(k) \\ x(n,k) - \varsigma_4 e^{\mathrm{T}}(n,k)\Omega(k)e(n,k). \end{cases} \tag{14}$$

Consider the following objective function

$$J^\infty(k) = \sum_{l=0}^{\infty}(\|x(n,k)\|_\ell^2 + \|u(n,k)\|_{\aleph}^2 - \tau w(n,k)^{\mathrm{T}}w(n,k)). \tag{15}$$

Construct the following optimization problem (OP):

$$\mathbf{OP}_1 \begin{cases} \min\limits_{u(k)} \max\limits_{w(k)} J^\infty(k), \\ |[u(k)]_\nu| \le [\bar{u}]_\nu, \nu \in \mathbb{V}, & \text{(16a)} \\ \left[x^{\mathrm{T}}(n,k), \eta^{\frac{1}{2}}(n,k)\right]^{\mathrm{T}} \in \Lambda, & \text{(16b)} \end{cases}$$

where

$$\Lambda \triangleq \{[x^{\mathrm{T}}(n,k),\eta^{\frac{1}{2}}(n,k)]^{\mathrm{T}}|x^{\mathrm{T}}(n,k)\tilde{R}(k)x(n,k) + \eta(n,k) \leq \gamma\}. \tag{17}$$

Here $\tilde{R} > 0$ and $\gamma > 0$ are the weighting matrix to be designed and optimisation index, respectively.

Definition 1. For system (13), the set Λ is a positively invariant set (PIS) if $[x^{\mathrm{T}}(n,k),\eta^{\frac{1}{2}}(n,k)]^{\mathrm{T}} \in \Lambda, \forall n \in \mathbb{N}$.

Definition 2 [14]. For the closed-loop system (13) and DETM (5) with initial state $x(0) = x_0$ and $\eta(0) = \eta_0$, the ISS is ensured if there exist functions $\chi_1 \in \mathcal{KL}$ and $\chi_2 \in \mathcal{K}$ such that

$$\|x(k)\|_2^2 \leq \chi_1\Big(\|x_0\|_2^2 + \eta_0, k\Big) + \chi_2\Big(\|w(k)\|_\infty^2\Big),$$

where $\|\omega(k)\|_\infty^2 \triangleq \sup_{k\in\mathbb{Z}_+}\{\|\omega(k)\|^2\}$.

Lemma 1. Consider DETM (5) with $\eta(0) > 0$, if the parameters $\lambda_1 \geq 0, 0 \leq \lambda_2 \leq 1, \varsigma_1 \geq 0, \varsigma_2 > 0, \varsigma_3 \geq 0$ and $\varsigma_4 > 0$ satisfy $\lambda_1\varsigma_4 \leq \lambda_2\varsigma_2$ and $\varsigma_1\varsigma_4 \leq \varsigma_2\varsigma_3$, then $\eta(k) \geq 0$, $\forall k \in \mathbb{N}^+$.

Proof. The proof approach is the same as that in [15], so it is omitted here.

The main purpose of this paper is to design FTMPC controllers, which can tolerate the actuator faults and ensure the ISS of system (13) under DETM (5). The following two tasks will be studied.

1) An auxiliary OP of **OP1** is constructed, and the controller gain $H(k)$ is obtained from the feasible solution of this auxiliary OP.

2) Give sufficient conditions to guarantee the ISS of system (13) under the DETM-based FTMPC algorithm.

3 Main Results

3.1 An LMI-based auxiliary OP of OP1

Consider the following Lyapunov-like function:

$$V(\eta(k),x(k)) = x^T(k)\tilde{R}(k) + \eta(k). \tag{18}$$

At each time instant k, we suppose the following inequality:

$$\begin{aligned} &V(\eta(n+1,k),x(n+1,k)) - V(\eta(n,k),x(n,k)) \\ &\leq -\Big(\|x(n,k)\|_\ell^2 + \|u(n,k)\|_\aleph^2\Big) + \tau w^T(n,k)w(n,k). \end{aligned} \tag{19}$$

Summing up both sides of (19) from $n = 0$ to $n = \infty$, we get

$$\begin{aligned} &- V(\eta(k),x(k)) \\ &\leq -J^\infty(k) - V(\eta(\infty,k),x(\infty,k)) \\ &\leq -J^\infty(k). \end{aligned} \tag{20}$$

According (17) to (20), we obtain

$$J^\infty(k) \leq V(\eta(k),x(k)) \leq \gamma. \tag{21}$$

Note that γ in (22) is an upper bound of $J^\infty(k)$ of **OP1**, we construct the following auxiliary OP:

$$\begin{aligned} &\mathbf{OP2}: \min_{H(k)} \gamma, \\ &\text{s.t.}(13),(16a),(16b),(19). \end{aligned} \tag{22}$$

Theorem 1. Let the scalars $\lambda_1 \geq 0, 0 \leq \lambda_2 \leq 1, \varsigma_1 \geq 0$, $\varsigma_2 > 0, \varsigma_3 \geq 0, \varsigma_4 > 0, \xi \geq 0, \kappa \geq 0$ and $\tau > 0$, and the matrices $\ell > 0$ and $\aleph > 0$ be given. If a scalar $\gamma > 0$ and matrices $\tilde{Q}(k) > 0, U > 0, T(k) > 0, Y(k) > 0$ and $G(k) > 0$ exist such that, $\forall \nu \in \mathbb{V}$, the following LMIs

$$\begin{bmatrix} \Im_1^{(1,1)} & * \\ \Im_1^{(2,1)} & \Im_1^{(2,2)} \end{bmatrix} \leq 0, \tag{23}$$

$$\begin{bmatrix} -\widetilde{\Im}_1^{(1,1)} & * \\ Y(k) & U \end{bmatrix} \geq 0, \tag{24}$$

$$[U]_{\nu\nu} \leq [\bar{u}]_\nu^2, \tag{25}$$

hold, where

$$\begin{aligned} \Im_1^{(1,1)} &= \text{diag}\left\{\widetilde{\Im}_1^{(1,1)}, \widetilde{\Im}_1^{(2,2)}, -\tau\gamma I\right\}, \\ \widetilde{\Im}_1^{(1,1)} &= \tilde{Q}(k) - G(k) - G(k), \\ \widetilde{\Im}_1^{(2,2)} &= \varsigma_4\left(T(k) - G^{\mathrm{T}}(k) - G(k)\right), \\ \Im_1^{(2,1)} &= \begin{bmatrix} AG(k) + B\beta Y(k) & -B\beta Y(k) & \gamma F \\ \aleph^{\frac{1}{2}}Y(k) & -\aleph^{\frac{1}{2}}Y(k) & 0 \\ \ell^{\frac{1}{2}}G(k) & 0 & 0 \\ \sqrt{\varsigma_3\xi_{\max}}G(k) & 0 & 0 \end{bmatrix}, \\ \Im_1^{(2,2)} &= \text{diag}\{-\tilde{Q}(k), -\gamma I, -\gamma I, -T(k)\}, \end{aligned}$$

then, conditions (16a) and (19) are satisfied, and the feedback gain matrix $H(k)$ and the weighting matrix $\Omega(k)$ are designed by

$$H(k) = Y(k)G^{-1}(k), \Omega(k) = \gamma T^{-1}(k). \tag{26}$$

Proof. From (14), we get

$$\begin{aligned} &\eta(n+1,k) - \eta(n,k) \\ &= (\lambda_2 - 1)\eta(n,k) \\ &+ \varsigma_3\xi(n,k)x^{\mathrm{T}}(n,k)\Omega(k)x(n,k) \\ &- \varsigma_4 e^{\mathrm{T}}(n,k)\Omega(k)e(n,k) \\ &\leq \varsigma_3\xi(n,k)x^{\mathrm{T}}(n,k)\Omega(k)x(n,k) \\ &- \varsigma_4 e^{\mathrm{T}}(n,k)\Omega(k)e(n,k). \end{aligned} \tag{27}$$

Substituting (18) into (19) yields

$$\begin{aligned} &x^{\mathrm{T}}(n+1,k)\tilde{R}(k)x(n+1,k) + \eta(n+1,k) \\ &- x^{\mathrm{T}}(n,k)\tilde{R}(k)x(n,k) - \eta(n,k) \\ &+ \|x(n,k)\|_\ell^2 + \|u(n,k)\|_\aleph^2 \\ &- \tau w^{\mathrm{T}}(n,k)w(n,k) \leq 0. \end{aligned} \tag{28}$$

According to (6), (13) and (27), the inequality (28) holds if

$$\begin{aligned} &[(A + B\beta H(k))x(n,k) - B\beta H(k)e(n,k) \\ &+ Fw(n,k)]^{\mathrm{T}}\tilde{R}(k)[(A + B\beta H(k))x(n,k) \\ &- B\beta H(k)e(n,k) + Fw(n,k)] \\ &- x^{\mathrm{T}}(n,k)\tilde{R}(k)x(n,k) \\ &+ \varsigma_3\xi_{\max}x^{\mathrm{T}}(n,k)\Omega(k)x(n,k) \\ &- \varsigma_4 e^{\mathrm{T}}(n,k)\Omega(k)e(n,k) \\ &+ \|x(n,k)\|_\ell^2 + \|u(n,k)\|_\aleph^2 \\ &- \tau w^{\mathrm{T}}(n,k)w(n,k) \leq 0. \end{aligned} \tag{29}$$

We write (29) as the following equivalent form:

$$\zeta^{\mathrm{T}}(k)\Big(\mathscr{B}_1+\mathscr{B}_2\tilde{R}(k)\mathscr{B}_2^{\mathrm{T}}+\mathscr{B}_3\aleph\mathscr{B}_3^{\mathrm{T}}\Big)\,\zeta(k)\le 0, \quad (30)$$

where

$$\begin{aligned}
\zeta(k)&=\begin{bmatrix}x^{\mathrm{T}}(n,k) & e^{\mathrm{T}}(n,k) & w^{\mathrm{T}}(n,k)\end{bmatrix}^{\mathrm{T}},\\
\mathscr{B}_1&=\mathrm{diag}\Big\{\ell-\tilde{R}(k)+\varsigma_3\xi_{\max}\Omega(k),-\varsigma_4\Omega(k),-\tau I\Big\},\\
\mathscr{B}_2&=\begin{bmatrix}A+B\beta H(k) & -B\beta H(k) & F\end{bmatrix}^{\mathrm{T}},\\
\mathscr{B}_3&=\begin{bmatrix}H(k) & -H(k) & 0\end{bmatrix}^{\mathrm{T}}.
\end{aligned}$$

By the Schur complement, (30) is guaranteed if

$$\begin{bmatrix}\Im_2^{(1,1)} & *\\ \Im_2^{(2,1)} & \Im_2^{(2,2)}\end{bmatrix}\le 0, \quad (31)$$

where

$$\begin{aligned}
\Im_2^{(1,1)}&=\mathrm{diag}\Big\{-\tilde{R}(k),-\varsigma_4\Omega(k),-\tau I\Big\},\\
\Im_2^{(2,1)}&=\begin{bmatrix}A+B\beta H(k) & -B\beta H(k) & F\\ \aleph^{\frac{1}{2}}H(k) & -\aleph^{\frac{1}{2}}H(k) & 0\\ \ell^{\frac{1}{2}} & 0 & 0\\ \sqrt{\varsigma_3\xi_{\max}}I & 0 & 0\end{bmatrix},\\
\Im_2^{(2,2)}&=\mathrm{diag}\{-\tilde{R}^{-1}(k),-I,-I,-\Omega^{-1}(k)\}.
\end{aligned}$$

Pre- and post-multiply the left-hand side matrix of inequality (31) by diag $\big\{\gamma^{-\frac{1}{2}}G^{\mathrm{T}}(k),\gamma^{-\frac{1}{2}}G^{\mathrm{T}}(k),\gamma^{\frac{1}{2}}I,\gamma^{\frac{1}{2}}I,\gamma^{\frac{1}{2}}I,\gamma^{\frac{1}{2}}I,\gamma^{\frac{1}{2}}I\big\}$ and its transpose respectively. Then, by denoting $\gamma\tilde{R}^{-1}(k)=\tilde{Q}(k)$ and (26), we have

$$\begin{bmatrix}\Im_3^{(1,1)} & *\\ \Im_1^{(2,1)} & \Im_1^{(2,2)}\end{bmatrix}\le 0, \quad (32)$$

where

$$\begin{aligned}
\Im_3^{(1,1)}&=\mathrm{diag}\Big\{\widetilde{\Im}_3^{(1,1)},\widetilde{\Im}_3^{(2,2)},-\tau\gamma I\Big\},\\
\widetilde{\Im}_3^{(1,1)}&=-G^{\mathrm{T}}(k)\tilde{Q}^{-1}(k)G(k),\\
\widetilde{\Im}_3^{(2,2)}&=-\varsigma_4G^{\mathrm{T}}(k)T^{-1}(k)G(k).
\end{aligned}$$

Since $-G^{\mathrm{T}}(k)\tilde{Q}^{-1}(k)G(k)\le\tilde{Q}(k)-G^{\mathrm{T}}(k)-G(k)$ and $-G^{\mathrm{T}}(k)T^{-1}(k)G(k)\le T(k)-G^{\mathrm{T}}(k)-G(k)$, then (32) holds if (23) is satisfied.

Now, we prove that conditions (24) and (25) guarantee (16a).

Similar to the proof process in [1], and noting $\gamma\tilde{R}^{-1}(k)=\tilde{Q}(k)$, we obtain

$$\begin{aligned}
&\max_{n\in\mathbb{N}}|[u(n,k)]_\nu|^2\\
&=\max_{n\in\mathbb{N}}|[H(k)\tilde{x}(k)]_\nu|^2\\
&=\max_{n\in\mathbb{N}}\Big[\Big[H(k)\tilde{Q}^{\frac{1}{2}}(k)\tilde{Q}^{-\frac{1}{2}}(k)\tilde{x}(k)\Big]_\nu\Big|^2\\
&\le\max_{n\in\mathbb{N}}\Big\|\Big[H(k)\tilde{Q}^{\frac{1}{2}}(k)\Big]_\nu\Big\|^2\Big\|\tilde{Q}^{-\frac{1}{2}}(k)\tilde{x}(k)\Big\|^2\\
&\le\Big\|\Big[Y(k)G^{-1}(k)\tilde{Q}^{\frac{1}{2}}(k)\Big]_\nu\Big\|^2.
\end{aligned} \quad (33)$$

Then, (16a) holds if there exists a matrix $U>0$ satisfying

$$U-Y(k)G^{-1}(k)\tilde{Q}(k)G^{-\mathrm{T}}(k)Y^{\mathrm{T}}(k)\ge 0.$$

By the Schur complement, we get

$$\begin{bmatrix}G^{\mathrm{T}}(k)\tilde{Q}^{-1}(k)G(k) & *\\ Y(k) & U\end{bmatrix}\ge 0. \quad (34)$$

Noting $G^{\mathrm{T}}(k)\tilde{Q}^{-1}(k)G(k)\ge G^{\mathrm{T}}(k)+G(k)-\tilde{Q}(k)$, we get (34) from (25). Then, (16a) holds if (24) and (25) are satisfied.

3.2 Sufficient conditions for PIS

To ensure that Λ is a PIS, we give sufficient conditions and give the corresponding LMIs.

Theorem 2. Let the scalar θ satisfying $0\le\theta\le 1-\lambda_2$. Then, (16b) holds if there exist a scalar $\gamma>0$ and a matrix $\tilde{Q}(k)>0$ such that

$$\begin{bmatrix}I & * & *\\ x(k) & \tilde{Q}(k) & *\\ \sqrt{\eta(k)} & 0 & \gamma\end{bmatrix}\ge 0, \quad (35)$$

$$\begin{bmatrix}\mathscr{C}_1^{(1,1)} & *\\ \mathscr{C}_1^{(2,1)} & \mathscr{C}_1^{(2,2)}\end{bmatrix}\le 0, \quad (36)$$

where

$$\begin{aligned}
\mathscr{C}_1^{(1,1)}&=\mathrm{diag}\Big\{\widetilde{\mathscr{C}}_1^{(1,1)},\widetilde{\mathscr{C}}_1^{(2,2)},-\frac{\theta}{p^2}I\Big\},\\
\widetilde{\mathscr{C}}_1^{(1,1)}&=(1-\theta)\Big(\tilde{Q}(k)-G^{\mathrm{T}}(k)-G(k)\Big),\\
\widetilde{\mathscr{C}}_1^{(2,2)}&=\varsigma_4\Big(T(k)-G^{\mathrm{T}}(k)-G(k)\Big),\\
\mathscr{C}_1^{(2,1)}&=\begin{bmatrix}AG(k)+B\beta Y(k) & -B\beta Y(k) & F\\ \sqrt{\varsigma_3\xi_{\max}}G(k) & 0 & 0\end{bmatrix},\\
\mathscr{C}_1^{(2,2)}&=\mathrm{diag}\big\{-\tilde{Q}(k),-T(k)\big\},
\end{aligned}$$

Proof. Noting that $\gamma\tilde{R}^{-1}(k)=\tilde{Q}(k)$, by Schur complement we know that (35) guarantees $\Big[x^{\mathrm{T}}(n,k),\eta^{\frac{1}{2}}(n,k)\Big]^{\mathrm{T}}\in\Lambda$. Due to the presence of disturbance, assuming that $\Big[x^{\mathrm{T}}(n,k),\eta^{\frac{1}{2}}(n,k)\Big]^{\mathrm{T}}\in\Lambda$, we need to prove that $\Big[x^{\mathrm{T}}(n+1,k),\eta^{\frac{1}{2}}(n+1,k)\Big]^{\mathrm{T}}\in\Lambda$.

The invariant set (17) holds at $k+1$ if

$$\begin{aligned}
&\frac{1}{\gamma}\parallel x(n+1,k)\parallel^2_{\tilde{R}(k)}+\frac{1}{\gamma}\eta(n+1,k)\\
&-\frac{1-\theta}{\gamma}\|x(n,k)\|^2_{\tilde{R}(k)}-\frac{1-\theta}{\gamma}\eta(n,k)\\
&-\frac{\theta}{p^2}w^{\mathrm{T}}(n,k)w(n,k)\le 0.
\end{aligned} \quad (37)$$

Substituting (3) and (35) into (37), we have that $\frac{1}{\gamma}\parallel x(n+1,k)\|^2_{\tilde{R}(k)}+\frac{1}{\gamma}\eta(n+1,k)\le(1-\theta)+\theta=1$, thus, $\parallel x(n+1,k)\|^2_{\tilde{R}(k)}+\eta(n+1,k)\le\gamma$. This proves that $\Big[x^{\mathrm{T}}(n+1,k),\eta^{\frac{1}{2}}(n+1,k)\Big]^{\mathrm{T}}\in\Lambda$.

The subsequent proof process is similar to Theorem 1 and is omitted here. Then, we get that (36) can be obtained from (37). Finally, the condition (16b) is guaranteed by (35) and (36).

From the sufficient conditions given above, we transform **OP2** into the following auxiliary OP:

$$\begin{aligned} &\mathbf{OP3}: \min_{H(k)} \gamma, \\ &\text{s.t.}(23), (24), (25), (35), (36). \end{aligned} \tag{38}$$

Based on **OP3**, we give the following FTMPC algorithm.

Algorithm 1.

Step 1. At $k = 0$, set an initial state $x(0)$, the matrices ℓ and $\aleph$, and the scalars λ_1, λ_2, ς_1, ς_2, ς_3, ς_4, $\underline{\xi}$, κ and $\eta(0)$.

Step 2. If the error $e(k)$ between $x(k)$ and $x(s_m)$ meets the event-triggered condition in DETM (5), then update $x(s_m)$ by $x(k)$; otherwise, implement $x(s_m)$ on the controller.

Step 3. Obtain the feedback gain matrix $H(k)$ and the matrix $\Omega(k)$ by solving **OP3**, and then calculate $u(k)$ by (9).

Step 4. Implement $u(k)$ on system (13). Set $k = k + 1$ and return to *Step* 2.

3.3 Feasibility and stability analysis

Theorem 3. Give the weight matrices $\ell > 0$ and $\aleph > 0$, and the scalars λ_1, λ_2, ς_1, ς_2, ς_3, ς_4, $\underline{\xi}$, κ and $\eta(0)$. If there is a feasible solution for **OP3** at k, then, at any instant $t > k$, there also exists a feasible solution for **OP3**. Furthermore, system (13) is ISS under the designed FTMPC controller.

Proof.

1) Proof of recursive feasibility. For **OP3**, we need to prove that (35) is feasible at any future time instant $t > k$. From (35), (36) and Theorem 2, we know that Λ is a PIS, which ensures that (35) is feasible at any time $t > k$ in the future.

2) Proof of ISS. Define

$$V^\star(\eta(k), x(k)) \triangleq x^{\mathrm{T}}(k)\tilde{R}^\star(k)x(k) + \eta(k), \tag{39}$$

where $\tilde{R}^\star(k) > 0$ denote the optimal $\tilde{R}(k)$ to **OP3** at time instant k.

According to (39), we get

$$\begin{aligned} &\lambda_{\min}(\tilde{R}^\star(k))\|x(k)\|_2^2 + \eta(k) \\ &\le V^\star(\eta(k), x(k)) \le \lambda_{\max}(\tilde{R}^\star(k))\|x(k)\|_2^2 + \eta(k), \end{aligned} \tag{40}$$

where $\lambda_{\min}(\cdot)$ and $\lambda_{\max}(\cdot)$ represent the maximal and minimal eigenvalue of a matrix. From (39), we further have

$$\varrho_1\|\chi(k)\|_2^2 \le V^\star(\eta(k), x(k)) \le \varrho_2\|\chi(k)\|_2^2, \tag{41}$$

where $\varrho_1 = \min\{\lambda_{\min}(\tilde{R}^\star(k)), 1\}$, $\varrho_2 = \max\{\lambda_{\max}(\tilde{R}^\star(k)), 1\}$ and $\chi(k) = \begin{bmatrix} x^{\mathrm{T}}(k) & \eta^{1/2}(k) \end{bmatrix}^T$.

Let $\hbar(k) = \varsigma_3\xi(k)x^{\mathrm{T}}(k)\Omega(k)x(k) - \varsigma_4 e^{\mathrm{T}}(k)\Omega(k)e(k)$. For a constant λ_2, there exists a parameter $\iota \in (0, 1 - \lambda_2)$ such that $\lambda_2 - 1 + \iota < 0$. From (27) and (28) , we have

$$\begin{aligned} &x^{\mathrm{T}}(1,k)\tilde{R}^\star(k)x(1,k) - x^{\mathrm{T}}(k)\tilde{R}^\star(k)x(k) + \hbar(k) \\ &+ \|x(k)\|_\ell^2 + \|u(k)\|_\aleph^2 - \tau\|w(k)\|_2^2 \\ &+ (\lambda_2 - 1 + \iota)\eta(k) < 0. \end{aligned} \tag{42}$$

It is noted that $\tilde{R}^\star(k)$ and $\tilde{R}^\star(k+1)$ are feasible solution and optimal solution to **OP3** at $k + 1$, respectively, and $\lambda_2\eta(k) + \hbar(k) - \eta(k) = \eta(k+1) - \eta(k)$. Then, we have

$$\begin{aligned} &x^{\mathrm{T}}(k+1)\tilde{R}^\star(k+1)x(k+1) - x^{\mathrm{T}}(k)\tilde{R}^\star(k)x(k) \\ &+ \eta(k+1) - \eta(k) + \|x(k)\|_\ell^2 + \|u(k)\|_\aleph^2 \\ &+ \iota\eta(k) - \tau\|w(k)\|_2^2 < 0. \end{aligned} \tag{43}$$

From (39), it follows:

$$\begin{aligned} &V^\star(\eta(k+1), x(k+1)) - V^\star(\eta(k), x(k)) \\ &< -\varrho_3\|\chi(k)\|_2^2 + \tau\|w(k)\|_2^2, \end{aligned} \tag{44}$$

where $\varrho_3 = \min\{\lambda_{\min}(\ell), \iota\}$.

According to conditions (41) and (44), we have

$$\|\chi(k)\|_2^2 \le \chi_1\Big(\|\chi(0)\|_2^2, k\Big) + \chi_2\Big(\|w(k)\|_\infty^2\Big), \tag{45}$$

where $\chi_1 \in \mathcal{KL}$ and $\chi_2 \in \mathcal{K}$. Note that $\|x(k)\|_2^2 \le \|\chi(k)\|_2^2$ and $\|\chi(0)\|_2^2 = \|x(0)\|_2^2 + \lambda(0)$. This yields a condition that satisfies Definition 1. The proof is complete.

4 A Numerical Example

In this section, we give a numerical example to demonstrate the effectiveness of the FTMPC algorithm. Table 1 gives the parameters for the power system.

Table 1: Parameters of the power system

Parameters	Values	Parameters	Values
T_{ch}	0.3	M	10
T_g	0.1	T_{ES}	0.2
R	0.05	T_{SR}	0.1
D	1.0	K_{SR}	7.5
β	21.0		

Let $\bar{u} = [0.1, 0.1, 0.1]$, and the scalars $\lambda_1 = 1$, $\lambda_2 = 0.45$, $\varsigma_1 = 0.3$, $\varsigma_2 = 12$, $\varsigma_3 = 5$, $\varsigma_4 = 2$, $\underline{\xi} = 0.1$, $\kappa = 1.4$, $\theta = 0.5$, $\eta(0) = 0.96$, $p = 0.14$ and $\tau = 4$, and the matrices $\ell = 15I$ and $\aleph = I$. Set $x(0) = [0.09, 0, 0, 0, 0, 0, 0]^{\mathrm{T}}$.

Suppose that in the first 90 s, there exist step load disturbance that $\Delta P_d = 0.02$ pu, and actuator fault with $\beta = \mathrm{diag}(0.5, 0.5)$ at $k \ge 0$.

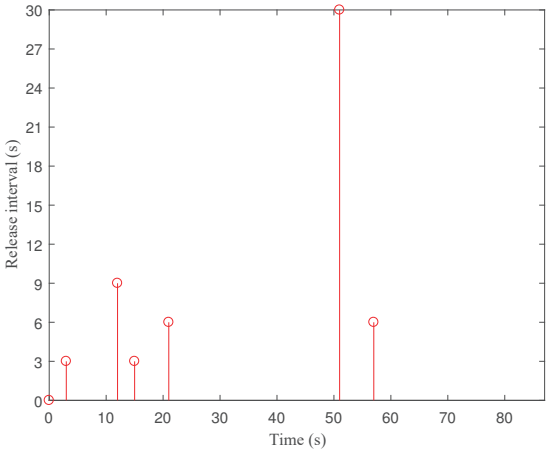

Fig. 1: Evolution of DETM (5).

Fig. 1 illustrates the evolution of DETM (5), which shows that it is effective in saving resources. The Δf and ACE trajectories of electrolytic aluminum load participating in frequency modulation are given in Fig. 2, which indicate that the designed FTMPC controllers have excellent control performance in the case of actuator faults. Additionally, performance comparison with and without electrolytic aluminum load is presented in Fig. 3, which demonstrates the superiority of electrolytic aluminum load participating in frequency modulation.

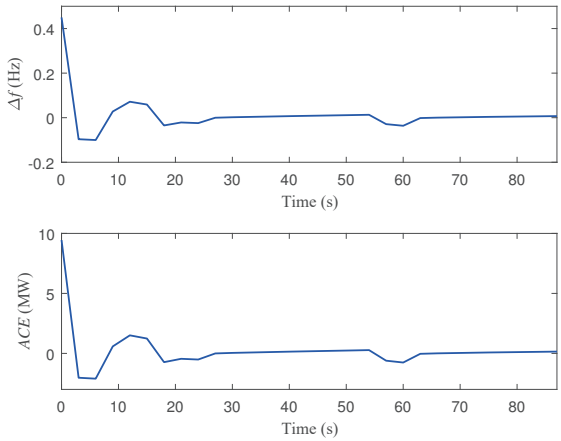

Fig. 2: Δf and ACE trajectories of electrolytic aluminum load participating in frequency modulation.

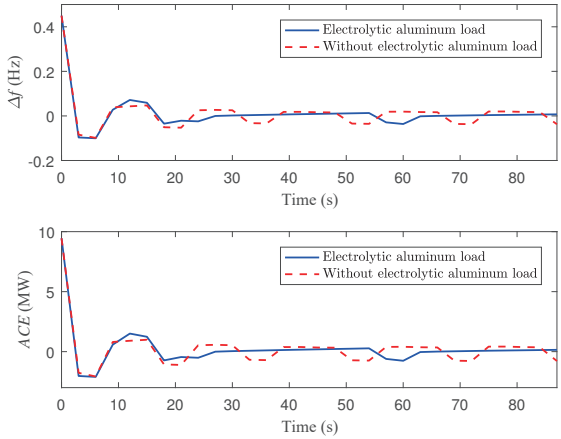

Fig. 3: Performance comparison of frequency modulation with and without electrolytic aluminum load.

5 Conclusion

In this paper, a DETM-based fault-tolerant model predictive LFC strategy is proposed for the power system where electrolytic aluminum load participates in frequency regulation. A novel DETM with an IDV and an AV has been proposed, which effectively reduces the consumption of network resources. A Lyapunov-like function with an IDV has been constructed to put forward an auxiliary OP. The feasibility and ISS of the devised FTMPC algorithm have been analyzed. The superiority of electrolytic aluminum load participating in frequency regulation and the effectiveness of the control strategy of the system in case of actuator faults are verified by a simulation example.

References

[1] X. Tang, Y. Li, M. Yang, Y. Wu and Y. Wen, Adaptive event-triggered model predictive load frequency control for power systems, *IEEE Transactions on Power Systems*, 2023, 38(5): 4003-4014.

[2] C. Peng, J. Zhang and H. Yan, Adaptive event-triggering H_∞ load frequency control for network-based power systems, *IEEE Transactions on Industrial Electronics*, 2018, 65(2): 1685-1694.

[3] X.-C. Shangguan, Y. He, C.-K. Zhang, L. Jiang and M. Wu, Load frequency control of time-delayed power system based on event-triggered communication scheme, *Applied Energy*, 2022, 308: 118294.

[4] B. Lin and L. Xu, Energy conservation of electrolytic aluminum industry in China, *Renewable and Sustainable Energy Reviews*, 2015, 43: 676-686.

[5] X. Shen, H. Shu, Z. Fan and X. Mo, Integrated control strategy for electrolytic aluminum load participation in frequency modulation, *IEEE Access*, 2021, 9: 56955-56964.

[6] X. Ding, J. Xu, Y. Sun and S. Liao, Source-load coordinated control strategy for smoothing wind power fluctuation in grid-connected high energy consuming electrolytic aluminum industrial power grid, *Electric Power Automation Equipment*, 2022, 42(11): 47-55.

[7] H. Jiang, J. Lin, Y. Song and D. J. Hill, MPC-based frequency control with demand-side participation: A case study in an isolated wind-aluminum power system, *IEEE Transactions on Power Systems*, 2015, 30(6): 3327-3337.

[8] X. Tang and L. Deng, Multi-step output feedback predictive control for uncertain discrete-time T-S fuzzy system via event-triggered scheme, *Automatica*, 2019, 107: 362-370.

[9] X.-M. Zhang, Q.-L. Han and X. Yu, Survey on recent advances in networked control systems, *IEEE Transactions on Industrial Informatics*, 2016, 12(5): 1740-1752.

[10] F. Berkel and S. Liu, An event-triggered output-based model predictive control strategy, *IEEE Transactions on Control of Network Systems*, 2019, 6(2): 822-832.

[11] W. Yang, L. Jin, D. Xu and W. Yan, Event-triggered H_∞-type robust model predictive control of linear systems with disturbances, *IEEE Access*, 2019, 7: 53859-53867.

[12] H. Qu, An Event-triggered output feedback robust MPC scheme for time-varying system with packet loss and bounded disturbance, *International Journal of Control, Automation and Systems*, 2022, 20(4): 1087-1098.

[13] X. Tang, M. Li, S. Wei and B. Ding, Event-triggered synchronous distributed model predictive control for multi-agent systems, *International Journal of Control, Automation and Systems*, 2021, 19(3): 1273-1282.

[14] T. Shi, P. Shi and Z.-G. Wu, Dynamic event-triggered asynchronous MPC of markovian jump systems with disturbances, *IEEE Transactions on Cybernetics*, 2022, 52(11): 11639-11648.

[15] X. Wan, F. Wei, C.-K. Zhang, and M. Wu, Hybrid variables-dependent event-triggered model predictive control subject to polytopic uncertainties, *International Journal of Systems Science*, 2022, 53(14): 3042-3055.

[16] X. Wan, F. Wei, C.-K. Zhang and M. Wu, Networked output-feedback MPC: A bounded dynamic variable and time-varying threshold-dependent event-based approach, *IEEE Transactions on Cybernetics*, 2024, 54(4): 2308-2319.

[17] H. Shen, Y. Xia, J. Wang and J. H. Park, Fault-tolerant event-triggered H_∞ load frequency control for multiarea power systems with communication delay, *IEEE Systems Journal*, 2022, 16(4): 6624-6634.

[18] S. Kuppusamy, Y. H. Joo and H. S. Kim, Fault-tolerant load frequency control for DFIG-based interconnected wind power systems, *Information Sciences*, 2022, 582: 73-88.

[19] Y. Zhang, T. Yang and Z. Tang, Active fault-tolerant control for load frequency control in multi-area power systems with physical faults and cyber attacks, *International Transactions on Electrical Energy Systems*, 2021, 31(7): e12906.

[20] H. Saadatinezhad, A. Ramezani, M. Alizadeh and E. Hajimalek, Fault tolerant load frequency sharing of a multi-area power system using model predictive control, *The Journal of Engineering*, 2022, 2022(3): 337-347.

Proceedings of the 3rd Conference on Fully Actuated System Theory and Applications
May 10-12, 2024, Shenzhen, China

Forecasting method of process pump equipment based on grey theory

Nie Cheng [1], Yimin Liu [2], Wen Cheng [2]
1.Wuhan Maintenance and Installation Petrochemical Engineering Co., LTD,WuHan;430082,China
E-mail:879643974@qq.com
2.Academy of Information Science and Engineering, Wuhan University of Science and Technology, Wuhan; 430081, China

Abstract: To effectively prevent failures, the historical data of process pumps is used to predict the operating states. For prediction small sample data, Grey theory can provide high accuracy predictive results. In this paper, grey theory model is used to predict the operational states of process pumps. Different optimization methods are applied to improve the basic grey prediction model to enhance the accuracy of predicting and analyzing process pump operational data. Finally, the simulation results are presented to illustrate the effectiveness of the proposed method.

Key Words: Pump equipment, Grey theory, Residual grey, Markov model

1 INTRODUCTION

As we know, faults may occur at any components and units of the process pumps, and may lead to severe undesirable severe undesirable impact on the overall system. Therefore, the detection or prediction of the operating states of process pumps is significant importance [1-2]. For grey prediction models can achieve rapid and high accuracy predictions under small-sample conditions, some results have been reported in [3]. A grey neural network model on the foundation of grey models and used it to track and predict textile color trends was proposed in [4]. [5] improved the grey prediction model and applied it to predict aquaculture water quality. [6] established a grey theory model for the ownership of household appliances in China and predicted appliance ownership. [7] proposed modifications to the differential equation structure of the GM(1, N) model, enhancing its modeling capability and prediction accuracy. [8] combined fuzzy theory with grey prediction models to form an intelligent grey prediction model, effectively improving predictive capabilities.

Noted that the states of process pumps are influenced by unknown factors, and using the single prediction method may be less accurate. Therefore, the multi model fusion algorithms have attracted wide attention. [9] applied the grey prediction model to PID control systems, compensating for the output of the loading system through grey prediction, outperforming traditional PID control systems. In [10], a new method was proposed for predicting landslide displacement, namely the BNGM(1,1,t^2)-based prediction method. In [11], a new self-adaptive optimized grey model was proposed to realize accurate predictions of electric vehicles sales and stock. Therefore, this paper utilizes different optimization methods such as the residual grey Markov model to optimize the basic grey prediction model, enhancing the accuracy of predicting and analyzing process pump operational data.

.

2. The basic form of the model GM(1,1)

Assuming the original sequence of the process pump is denoted as $X^{(0)}$ shown in Equation (1).

$$X^{(0)} = (x_1^{(0)}, x_2^{(0)}, \ldots, x_n^{(0)}) \tag{1}$$

where n represents the number of sequences, and $x_m^{(0)} \geq 0, m = 1, 2, \ldots, n$.

By using accumulation of the sequence $X^{(0)}$, we can obtain the following sequence $X^{(1)}$

$$X^{(1)} = (x_1^{(1)}, x_2^{(1)}, \ldots, x_n^{(1)}) \tag{2}$$

where $x_m^{(1)} = \sum_{i=1}^{m} x_i^{(0)}, m = 1, 2, \ldots, n$.

It gets the first-order differential of the equation (2), then the GM model is obtained as

$$\frac{dX^{(1)}}{dt} + aX^{(1)} = b \tag{3}$$

Where a is the grey development coefficient, indicating the development trend of the sequence $X^{(1)}$, and b is the grey action quantity of the model, denoting the relationship of data changes.

Discretizing the equation (3) yields

$$x_{k+1}^{(0)} + a(p(x_k^{(1)} + x_{k+1}^{(1)})) = b \quad ,k = 1, 2, \ldots, n-1 \tag{4}$$

where p is the background coefficient value, which is typically setting to 0.5. Therefore, the background value of the grey prediction model is shown as following

$$z_{k+1}^{(1)} = \frac{1}{2}(x_k^{(1)} + x_{k+1}^{(1)}), k = 1, 2, \ldots, n-1 \tag{5}$$

Combining (4) and (5), we obtain:

$$x_{k+1}^{(0)} = a(-\frac{1}{2} z_{k+1}^{(1)}) + b, k = 1, 2, \ldots, n-1 \tag{6}$$

Then we can give the following equation

$$Y_n = B\begin{bmatrix} a & b \end{bmatrix}^T \tag{7}$$

where

$$Y_n = \begin{bmatrix} x_2^{(0)} \\ x_3^{(0)} \\ \vdots \\ x_n^{(0)} \end{bmatrix}, B = \begin{bmatrix} -z_2^{(1)} & 1 \\ -z_3^{(1)} & 1 \\ \vdots & \vdots \\ -z_n^{(1)} & 1 \end{bmatrix} \tag{8}$$

The parameters a and b can be solved as

$$\begin{bmatrix} a \\ b \end{bmatrix} = (B^T B)^{-1} B^T Y_n \tag{9}$$

Performing Laplace transform on (3) yields

$$s x_s^{(1)} - x_0^{(1)} + a x_s^{(1)} = \frac{b}{s} \tag{10}$$

Let $x_0^{(1)} = x_1^{(0)}$, (10) can be rewritten as

$$x_s^{(1)} = \frac{b}{a} \cdot \frac{a}{s^2 + sa} + \frac{x_1^{(0)}}{s + a} \tag{11}$$

By using Laplace transform, the solution to the differential equation can be given as

$$x_t^{(1)} = (x_1^{(0)} - \frac{b}{a}) e^{-at} + \frac{b}{a} \tag{12}$$

Therefore, the response sequence $\hat{x}^{(1)}$ of the GM(1,1) model is shown as

$$\hat{x}_{k+1}^{(1)} = (x_1^{(0)} - \frac{b}{a}) e^{-ak} + \frac{b}{a}, k = 1, 2, \ldots, n \tag{13}$$

The response sequence can be restored to the predicted sequence via cumulative reduction

$$\hat{x}_{k+1}^{(0)} = \hat{x}_{k+1}^{(1)} - \hat{x}_k^{(1)} \tag{14}$$

By solving a and b, and substituting them into equations (13) and (14), the grey prediction values of the original sequence can be obtained.

The following section is evaluation metrics for grey models. The original sequence $X^{(0)}$ of the process pump is subjected to the ratio test method to verify the data's smoothness, and the method is given as

$$\rho_k = \frac{x_{k-1}^{(0)}}{x_k^{(0)}}, k = 2, 3, \ldots, n, \rho_k \in \left[e^{-\frac{2}{n+1}}, e^{\frac{2}{n+1}} \right] \tag{15}$$

If condition (15) is satisfied for all ρ_k, it indicates that the sequence meets the requirements of the grey model and can be directly used in the grey model. Otherwise, adjustments should be made by mathematical transformations.

For model predictive ability verification, residual verification and posterior difference check are employed. The relative residual verification method is given as

$$\varepsilon_k = \frac{\left| x_k^{(0)} - \hat{x}_k^{(0)} \right|}{x_k^{(0)}}, k = 1, 2, \ldots, n \tag{16}$$

If residual $\varepsilon_k < 0.2$, the model's predictive ability has reached the predetermined level; for relative residual $\varepsilon_k < 0.1$, the model possesses good predictive capability.

To enhance the accuracy of prediction, a post-residual test is conducted. The post-residual ratio is represented as

$$C = \frac{S_2}{S_1} \tag{17}$$

where $S_1^2 = \frac{1}{n} \sum_{i=1}^{n} (x_i^{(0)} - \bar{x}^{(0)})^2$, $S_2^2 = \frac{1}{n} \sum_{i=1}^{n} (\varepsilon_i - \bar{\varepsilon})^2$.

The small probability error is given as

$$P = p\left\{ \left| \varepsilon_k - \bar{\varepsilon} \right| < 0.6754 S_1 \right\} \tag{18}$$

S_1 can reflect the dispersion of the original sequence, and S_2 can reflect the dispersion between the predicted sequence and the original sequence. When the predicted values of the model are closer to the original values, the variance S_2 of the residual sequence becomes smaller, while the dispersion of the original sequence is relatively larger. Therefore, for a model with better predictions, C should be relatively smaller. So, a comprehensive evaluation of the model can be given according to the magnitudes of C and P.

Table I. MODEL METRICS

	P	C
outstanding	>0.95	<0.35
qualified	>0.80	<0.50
satisfactory	>0.70	<0.65
unsatisfactory	$\leqslant 0.70$	$\geqslant 0.65$

3. Grey Model Optimization

For the regular GM(1,1) model, there is significant room for optimization in both the modeling process and the prediction results. For the optimization of the grey model itself, methods such as optimizing initial values and background values can be introduced. For the predicted results, this paper adopts the metabolic model and Markov chain method.

A. Optimization Method for GM(1,1) Initial Values

As the modeling of GM(1,1) involves the cumulative sequence of the original series, $\hat{x}_1^{(0)} = x_1^{(1)} = x_1^{(0)}$ does not participate in the calculation of initial values during the modeling and solving process. However, in the model response equation, the initial values are involved in the response. Therefore, introducing a suitable constant is essential, as shown in equation (19).

$$X^{(0)} = (c, x_1^{(0)}, \cdots, x_n^{(0)}), c \geq 0 \tag{19}$$

As the grey model fits the data into an exponential sequence, i.e., $x(t) = be^{-at}$, the constant can be chosen as $c = x(0) = be^0 = b$.

Then, (19) can be rewritten as

$$X^{(0)} = (b, x_1^{(0)}, \cdots, x_n^{(0)}) \tag{20}$$

B. Optimization Method for GM(1,1) Background Values

The actual background value is represented as

$$z_{k+1}^{(1)} = \int_k^{k+1} x_t^{(1)} dt \tag{21}$$

Therefore, Equation (5) is the trapezoidal formula for (21), leading to an error in the grey model's background value.

To reduce the error between the trapezoidal formula and the integral, (21) can be written as

$$z_{k+1}^{(1)} = \frac{1}{8}\left[x_k^{(1)} + 3x_{k+\frac{1}{3}}^{(1)} + 3x_{k+\frac{2}{3}}^{(1)} + 3x_{k+1}^{(1)} \right] \tag{22}$$

The terms $x_{k+\frac{1}{3}}^{(1)}$ and $x_{k+\frac{2}{3}}^{(1)}$ do not exist in the discrete sequence. Quadratic Newton interpolation can be used to eliminate these terms. Then the background value can be shown in equations (23) and (24) by the method of subsection process

$$z_n^{(1)} = \frac{1}{12}(-x_{n-2}^{(1)} + 8_{n-1}^{(1)} + 5x_n^{(1)}) \tag{23}$$

$$z_{k+1}^{(1)} = \frac{1}{12}(-x_{k+2}^{(1)} + 8_{k+1}^{(1)} + 5x_k^{(1)}) \quad ,k = 1,2,...,n-2 \tag{24}$$

C. Metabolic GM(1,1) Model

As time goes on, some factors in the system may cause changes in the development trend, which can lead to significant deviations in the model predictions. Therefore, grey prediction can be divided into multiple steps. Each step predicts a portion of new information, and discards the oldest information to achieve the goal of using the current information in the prediction process. This method is known as the metabolic model.

First, a portion of the original sequence is taken as input for GM(1,1) modeling. Assuming the extracted length is m and the total sample length is n, where $m < n$, the input sequence for the first modeling is denoted as $X^{(0)} = (x_1^{(0)}, x_2^{(0)}, \cdots, x_m^{(0)})$.

Second, the input sequence with a length of m is used for grey prediction, resulting in a one-step prediction $\hat{x}_{m+1}^{(0)}$. The prediction result is then incorporated into the input sequence for the second modeling, discarding the initial input. Therefore, the input sequence for the second modeling is denoted as $X^{(0)} = (x_2^{(0)}, x_3^{(0)}, \cdots, \hat{x}_{m+1}^{(0)})$.

Third, the second step is repetitive activitiesproce-eding towards the end of predictio n.

D. Residual Grey Markov Model

To solve the problem of large dispersion, a combination of the Markov model and the GM(1,1) model can be employed to rectify errors in the grey model's prediction results, and enhanced the accuracy of predicted data. For the Residual Grey Markov Model, the residuals of the grey model can be used to be the input. The modeling process is introduced below.

For the training data, fitting and restoration are performed through the Residual Correction Method. Firstly, the absolute value of the residual sequence is taken as the initial data for grey prediction, resulting in the fitted residual value $\hat{e}$. Then, a positive-negative sequence m is obtained based on the positive and negative values of the original residual sequence, where values greater than 0 are represented as $m_i = 1$, and values less than 0 are represented as $m_i = -1$. Finally, the original sequence and the positive-negative sequence are multiplied by the fitted residual value to obtain the corrected sequence, which is then added together for correction, as shown in Equation (25).

$$\hat{x}_k^{(0)} = \hat{x}_k^{(0)} + m_k \cdot \hat{e}_k, k = 1,2,...,n \tag{25}$$

For the predicted data, the residuals are subjected to Markov state division, resulting in a Markov state transition matrix. Finally, the state transition matrix is used to predict the next state. The original data's grey prediction results are then added to the predicted residual sequence of the next state, thereby correcting the prediction results. The residual Markov model is illustrated in Figure 1.

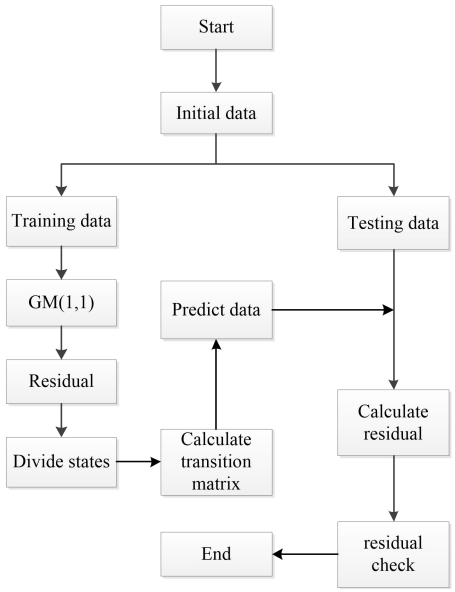

Figure **1** Residual Grey Markov Model Diagram

4. Experimental Analysis

A. Experimental Data

In this paper, inspection data from a single-stage pump over a continuous 12-day period is selected. The inspection values of vertical vibration, horizontal vibration (front and rear), and axial vibration, considered as influencing factors during the equipment's operation, were chosen for modeling the grey prediction model for the pump's vibration data. The first 10 days of the experimental data were used as training data, while the last two days were

used as validation data. The experimental data is presented in Table II.

Table II. Experimental Data of Single-Stage Pump

Number	A	B	C	D	E
1	3.480	1.630	4.436	4.082	0.991
2	2.710	1.924	4.282	4.038	1.450
3	3.418	2.752	5.222	5.098	0.792
4	4.226	2.112	5.314	5.017	1.620
5	2.420	2.370	4.100	3.990	1.720
6	2.140	2.330	3.710	3.480	1.480
7	3.562	2.993	4.858	5.025	1.211
8	3.569	3.034	6.227	4.860	1.923
9	3.984	4.628	5.691	5.923	1.377
10	3.514	3.718	5.817	5.358	1.131
11	3.899	3.525	5.924	5.851	1.369
12	4.304	4.682	5.593	6.001	1.291

In the above table, A represents Front vertical vibration (mm/s), B represents Rear vertical vibration (mm/s), C represents Front horizontal vibration (mm/s), D represents Rear horizontal vibration (mm/s), and E represents Axial vibration (mm/s).

B. Model Optimization Comparison

After conducting level ratio tests and shifts on the experimental data in Table II, experiments were performed separately for initial value optimization and background value optimization. The model experiments were carried out in the Matlab programming environment. The comparative results of the model experiments are shown in Figure3.7.

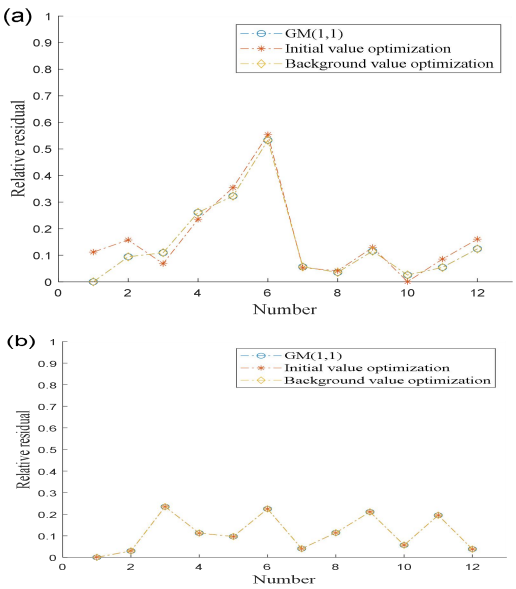

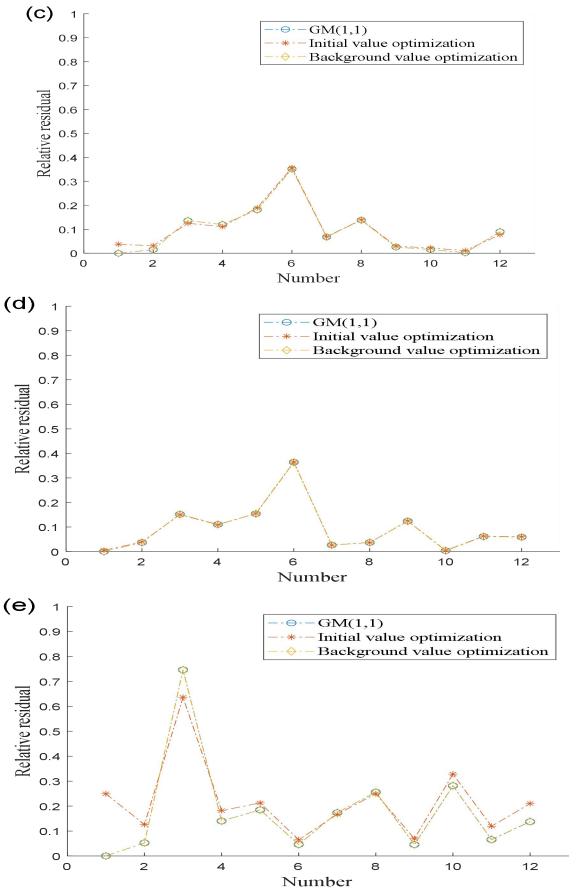

Figure **2** Relative residual comparison plots for fitting and predicting experimental data of a single-stage pump: (a) front vertical vibration; (b) rear vertical vibration; (c) front horizontal vibration; (d) rear horizontal vibration; (e) axial vibration

From Figure 2, it can be observed that compared to the prediction model with initial value optimization, the grey prediction model with background value optimization has relatively smaller relative residuals. Additionally, for the predicted values, the grey prediction model with background value optimization shows relative residuals for the five vibration status values that are less than or close to 0.2, indicating better predictive performance. Due to the fluctuating characteristics of the actual status values, there are points with relative residuals greater than 0.2 on the training data for all three models. Therefore, metabolic optimization and Markov chain correction were applied to the experimental data based on background value optimization.

C. Grey Metabolic Model Prediction

According to the modeling process of the Grey Metabolic GM(1,1) model, the input data is the training data, and a single-step prediction is performed to obtain the final predicted data. Metabolic prediction is conducted for the 11th and 12th sets of serial numbers in the experimental data from Table II. The results are shown from Table III to VII.

Table III. Comparison of Metabolic Predictions for Front Vertical Vibration (mm/s)

Number	A	B	C	D	E

11	3.899	3.688	0.054	3.688	0.054
12	4.304	3.771	0.124	3.692	0.142

Table IV. Comparison of Metabolic Predictions for Rear Vertical Vibration (mm/s)

Number	A	B	C	D	E
11	3.525	4.213	0.195	4.213	0.195
12	4.682	4.503	0.038	4.523	0.034

Table V. Comparison of Metabolic Predictions for Front Horizontal Vibration (mm/s)

Number	A	B	C	D	E
11	5.924	5.494	0.061	5.494	0.061
12	5.593	5.649	0.010	5.603	0.002

Table VI. Comparison of Metabolic Predictions for Rear Horizontal Vibration (mm/s)

Number	A	B	C	D	E
11	5.851	5.911	0.002	5.911	0.002
12	6.001	6.099	0.016	6.079	0.013

Table VII. Comparison of Metabolic Predictions for Axial Vibration (mm/s)

Number	A	B	C	D	E
11	1.369	1.460	0.066	1.460	0.066
12	1.291	1.460	0.138	1.493	0.156

From Table III to VII, A represents actual value, B represents Optimized predicted values of GM(1,1) background values, C represents Relative residual of optimized GM(1,1) background values, D represents Predicted values of GM(1,1) metabolic model, and E represents Relative residuals of GM(1,1) metabolic model.

From Table III to VII, for the second predicted value, the Metabolic Grey Model shows a certain reduction in relative residuals compared to the Background Value Optimized Grey Model, proving that the Metabolic Model has a corrective effect on the prediction results. In the prediction results for the 12th set, Table IV to VI show that the relative residuals of the Metabolic Model are reduced by 0.004, 0.008, and 0.003 compared to the Background Value Optimized Model, indicating that the Metabolic Model has an optimizing effect. In the Metabolic Model, the value of the first predicted point relies on the original training data for prediction, and its input is consistent with the original model, resulting in consistent performance with the Background Value Optimized Model at the first predicted point. This is also a drawback of the Metabolic Model in optimizing the prediction for the first point. To solve this problem, the Markov Chain model is further introduced to correct the prediction results based on the residuals fitted from the training data.

D. Residual Grey Markov Model Prediction

After optimizing the background values for the training data in Table II using grey forecasting, the predicted results were obtained. The residuals, representing the difference between the original sequence and the fitted sequence, are shown in Table VIII.

In the table VIII, table IX, table X, A denotes Front vertical residual, B represents Rear vertical residual, C represents Front horizontal residual, D represents Rear horizontal residual, and E represents Axial residual.

If the residual is greater than 0, it is denoted as state 1, otherwise, it is denoted as state 2. Then the one-step residual state probability matrix can be obtained. The relative residuals are given via correction of training data, which are shown in Table IX.

Table VIII. Residuals of the Vibration State Values from the Background-Optimized Grey Model

Number	A	B	C	D	E
1	0	0	0	0	0
2	-0.255	0.058	-0.148	-0.065	0.077
3	0.375	0.646	0.775	0.712	-0.591
4	1.104	-0.238	0.554	0.638	0.228
5	-0.781	-0.229	-0.614	-0.744	0.318
6	-1.141	-0.524	-1.268	-1.305	0.069
7	0.201	-0.122	0.132	-0.331	-0.210
8	0.127	-0.347	-0.180	0.862	0.492
9	0.461	0.976	0.734	0.147	-0.063
10	-0.091	-0.212	0.017	0.091	-0.319

Table IX. The relative residuals for the Residual Grey Markov Forecast are shown

Number	A	B	C	D	E
1	0	0	0	0	0
2	0	0	0	0	0
3	0.132	0.099	0.006	0.029	0.245
4	0.090	0.069	0.031	0.026	0.080
5	0.060	0.070	0.003	0.011	0.003
6	0.272	0.051	0.205	0.183	0.151
7	0.081	0.098	0.071	0.048	0.043
8	0.085	0.026	0.052	0.057	0.133
9	0.021	0.116	0.060	0.054	0.109
10	0.068	0.064	0.060	0.055	0.111
11	0.128	0.326	0.010	0.064	0.061
12	0.183	0.063	0.037	0.039	0.260

From Table IX, it can be observed that the Residual Grey Markov Chain model exhibits a high degree of fit on the training data. The majority of the fitted relative residuals for most state values are below 0.2, and even below 0.1. The table shows that the model performs well in predicting the values of front and rear horizontal vibrations, and relative residuals are all below 0.1. It also demonstrates good predictive ability for front vertical vibration values, with relative residuals all below 0.2. However, there are relatively larger relative residuals for the first predicted

point of rear vertical vibration and the second predicted point of axial vibration. Due to the advantage of the Metabolism model in correcting the second predicted value, a one-step prediction of the Residual Grey Markov Chain with Metabolism can be performed. The Metabolism state transition matrix is incorporated into the Markov chain, combining the advantages of Metabolism and Markov to achieve dual optimization, as shown in Tables X and XI.

Table X. The table for the relative residuals of the Residual Metabolism Markov Forecast is as follows

Number	A	B	C	D	E
11	0.128	0.326	0.010	0.064	0.061
12	0.065	0.063	0.037	0.071	0.017

Table XI. The comprehensive index table for the Residual Markov Metabolism Forecast is as follows

Evaluation metrics	A	B	C	D	E
P	0.833	0.917	0.917	0.917	0.833
C	0.495	0.424	0.371	0.378	0.448

In the table XI and XII, A represents Front vertical metrics, B represents Rear vertical metrics, C represents Front horizontal metrics, D represents Rear horizontal metrics, and E represents Axial metrics.

From Tables IX and X, the data for numbers 11 and 12 show that in the prediction of front vertical and axial vibration values, the relative residuals of the second point predicted by the Residual Grey Markov Metabolism model are significantly reduced compared to the Residual Grey Markov model. This reduction makes the relative residuals for the prediction of axial vibration values by the model less than 0.1. Overall, through the evaluation of C and P values, the Residual Grey Markov Metabolism model shows better predictive performance in comprehensive indicators, as seen in Table XI. The prediction results between model-predicted values and actual values are shown in Figure 3.

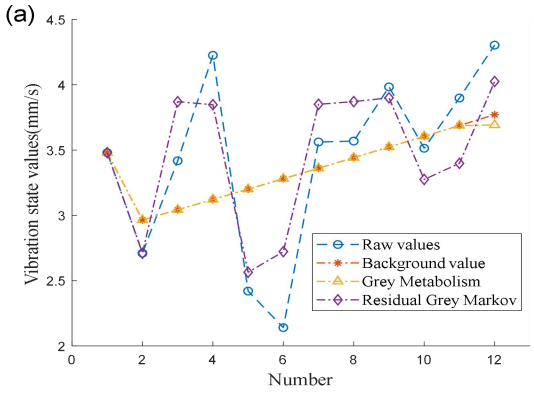

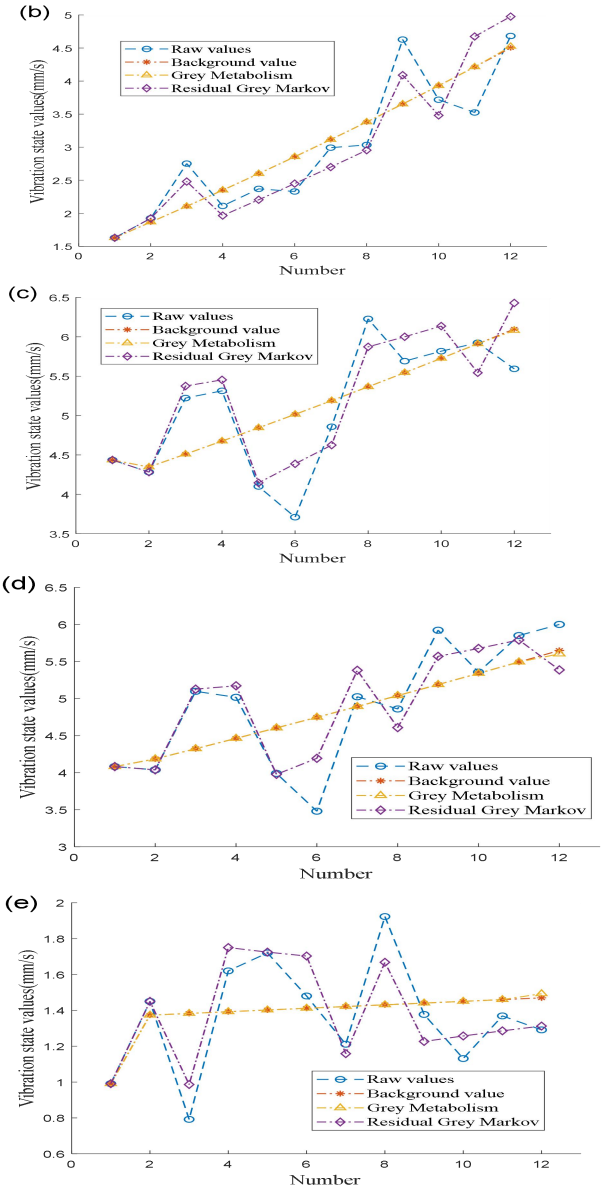

Fig. 3 Prediction diagram of vibration level for a single-stage pump based on the Grey model:(a) Front vertical vibration;(b) Rear vertical vibration;(c) Front horizontal vibration;(d) Rear horizontal vibration;(e) Axial vibration.

From Figure 3, it can be observed that all three prediction models demonstrate certain predictive capabilities and effects. The Metabolism model utilizes new information to offset old information for stepwise prediction, resulting in improved accuracy for the predicted data. However, the first point's prediction is not effectively corrected. The Residual Grey Markov Metabolism model, can achieve correction for the first predicted point and better alignment with the original data. The results indicate that the Residual Grey Markov Metabolism model exhibits a good predictive effect on the experimental data, providing conditions for predicting the vibration values of process pumps.

5. Model Validation Methods

In this section, the 12 sets of inspection data for single-stage pumps in March 2022 are validated, and the results of comprehensive evaluation indicators are shown

in Tables XII. The relative residual results are shown in Figures 3.9 and 3.10.

Table XII. Comprehensive Evaluation Indicators for Single-Stage Pump Prediction

Evaluation metrics	A	B	C	D	E
P	1	1	1	1	1
C	0.153	0.285	0.344	0.155	0.273

According to Table XII, it can be seen that the evaluation of the residual Grey Markov metabolism model for single-stage pumps' vibration data prediction results is good, indicating a good predictive ability of the model. As shown in Figure 4, the predictive model was established using the first 10 sets of experimental data, and the relative residuals of the remaining 2 sets of data were obtained. The relative residuals of the predicted points on the residual curve of the single-stage pump are all less than 0.2, which proves the superior predictive ability of the model in terms of overall prediction results. The prediction results between the model's predicted values and the actual values are plotted in Figure 5.

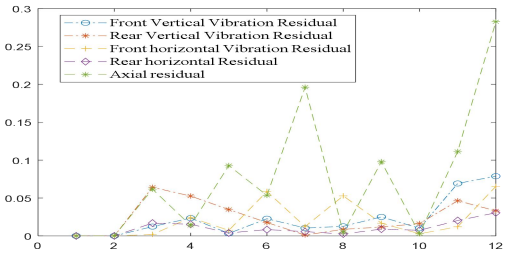

Fig. 4 Relative residual plot for single-stage pump prediction

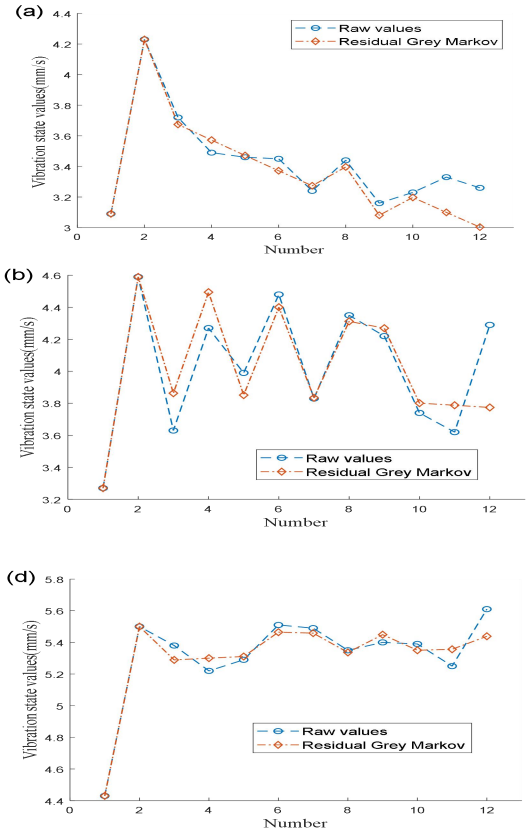

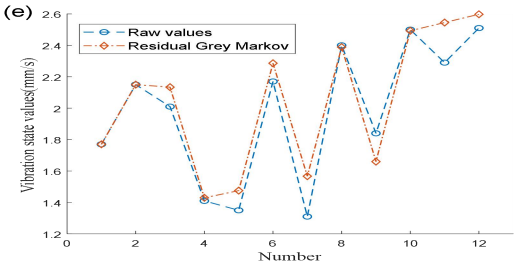

Fig. 5 Prediction diagrams of vibration level for single -stage pump based on grey model:(a)Front vertical vibration;(b)Rear vertical vibration;(c)Front horizontal vibration;(d)Rear horizontal vibration;(e)Axial vibration.

From Figure 5, it can be observed that in the comparison between the original value curve and the prediction model curve, the predicted values and fitted values are relatively close to the original values in terms of magnitude and trend. This indicates that the residual grey Markov metabolic model based on grey theory has a superior predictive effect on the verification data of single-stage pumps and multi-stage pumps.

6. CONCLUSION

This chapter provides an overview of the background and fundamental modeling process of grey system theory, as well as the issues and optimization methods in the GM(1,1) model. The optimization methods covered include initial value optimization, background value optimization, metabolism combination optimization, and Markov chain combination optimization. Experiments and analyses were conducted for each optimization method. Finally, the chapter applies the residual grey Markov metabolism model to predict and correct the vibration values of a process pump. The prediction results meet the theoretical requirements of the model.

（Due to the large number of diagrams, we can consider only single-stage process pumps or multi-stage process pumps, and focus on only one type.）

REFERENCES

[1] X. Huang, P. Guan, H. Pan, et al., Research on grey predictive control of PMSM based on reduced-order Luenberger observer, J. Electr. Eng. Technol., 2021, 16: 2635–2646.

[2] B. Zeng, H. Li, X. Ma, A novel multi-variable grey forecasting model and its application in forecasting the grain production in China, Computers & industrial engineering, , 2020, 150: 1-12.

[3] G. Liu, J. Yu, Gray correlation analysis and prediction models of living refuse generation in Shanghai city. Waste Management, 2007, 27(3): 345-351.

[4] J.J. Lin, P.T. Sun, J.J.-R. Chen, et al., Applying gray model to predicting trend of textile fashion colors, The Journal of The Textile Institute, 2010, 101(4): 360-368.

[5] Z. Li, Y. Jiang, J. Yue, et al., An improved gray model for aquaculture water quality prediction. Intelligent Automation & Soft Computing, 2012, 18(5): 557-567.

[6] M. Zhao, C. Zhao, L.L. Yu, et al., Prediction and Analysis of WEEE in China Based on the Gray Model, Procedia Environmental Sciences, 2016, 31: 925-934.

[7] M. Cheng, J. Li, Y. Liu, et al., Parameter estimation of modified gray model GM (1, N) and model application, Communications in Statistics-Simulation and Computation, 2022, 51(9): 5447-5464.

[8] W.L. Wu, An Intelligent Gray Prediction Model Based on Fuzzy Theory, International Transactions on Electrical Energy Systems, 2023: 1-10.

[9] S.J. Yan，Q. Gao，Y.L. Hou，et al., Grey prediction fuzzy PID compound control of a servo system load simulator, Journal of gun launch ＆ control, 2019, 40(1): 19-33.

[10] L.Z. Wu, S.H. Li, R.Q. Huang, Q. Xu, A new grey prediction model and its application to predicting landslide displacement, Applied soft computing, 2020, 95: 1-11.

[11] S. Ding, R.J. Li, Forecasting the sales and stock of electric vehicles using a novel self-adaptive optimized grey model, Engineering applications of artificial intelligence, 2021, 100: 1-13.

[12] D. Banjevic, A.K. Jardine, V. Makis, et al., A control-limit policy and software for condition-based maintenance optimization, INFOR: Information Systems and Operational Research, 2001, 39(1): 32-50.

[13] D. Van den Poel, B. Lariviere, Customer attrition analysis for financial services using proportional hazard models, European journal of operational research, 2004, 157(1): 196-217.

Proceedings of the 3rd Conference on Fully Actuated System Theory and Applications
May 10-12, 2024, Shenzhen, China

Finite-Time Fault Detection for T-S Fuzzy Systems Under Encoding-Decoding Mechanism

Siteng Ma[1], Jun Hu[1,2], Zhihui Wu[2], Hui Yu[2], Tianze Yu[1]

1. Department of Applied Mathematics, Harbin University of Science and Technology, Harbin 150080, P. R. China
E-mail: jhu@hrbust.edu.cn

2. School of Automaiton, Harbin University of Science and Technology, Harbin 150080, P. R. China

Abstract: This paper is concerned with the problem of finite-time fault detection (FD) for T-S fuzzy systems under the encoding-decoding mechanism (EDM). In order to relieve the communication burden and enhance the transmission reliability, the EDM is introduced in the sensor-to-filter channel. The sufficient conditions are derived to guarantee the finite-time boundedness (FTB) with prescribed H_∞ performance of the filtering error system (FES). Moreover, the parameters of the FD filter are determined by means of the linear matrix inequality method. Finally, the feasibility of the developed FD filtering algorithm is illustrated by a numerical simulation with comparative experiments.

Key Words: Encoding-Decoding Mechanism, Finite-Time Fault Detection, T-S Fuzzy Systems

1 Introduction

The T-S fuzzy model has excellent modeling ability for handling nonlinearity, and it has received a lot of attentions in the field of control [1]. With the increasing demand for system reliability, the fault detection (FD) problem for fuzzy systems has increasingly become a research hotspot [2]. In [3], a novel switched fuzzy FD observer has been designed with the help of the asynchronous premise reconstruction method for a class of T-S fuzzy systems, where the H_∞ performance has been discussed over infinite-time horizon. Recently, it has been recognized that many practical systems require achieving certain performance within finite-time horizon. Accordingly, a finite-time FD filtering method has been given in [4] for T-S fuzzy systems, where the sufficient criteria have been provided to guarantee that the residual dynamic system is stochastically finite-time bounded. So far, there is still a vast research space for the finite-time FD issues of T-S fuzzy systems.

The network-induced phenomena may occur during the data transmission due to limited network bandwidth, which deteriorate the system performance [5]. As it is well recognized, it is an effective strategy to introduce the encoding-decoding mechanism (EDM) for relieving the communication burden and improving the transmission reliability [6]. In recent years, some research methods have been developed on the EDM-based filtering or control problems for networked systems subject to limited communication constraints [7, 8]. For instance, the issue of finite-time distributed filtering has been addressed in [9] for time-varying switching systems under EDM, where new sufficient conditions have been derived to ensure the stochastic finite-time boundedness (FTB) with desirable H_∞ performance for the filtering error system (FES). However, the EDM-based FD problem for T-S fuzzy systems has not been studied yet, which constitutes the main motivations of this paper.

Correspondence should be addressed to Jun Hu. Email: jhu@hrbust.edu.cn.

This work was supported in part by the National Natural Science Foundation of China under Grant 12171124, the Natural Science Foundation of Heilongjiang Province of China under Grant ZD2022F003, and the Alexander von Humboldt Foundation of Germany.

To summarize the above analysis, we focus on the finite-time FD problem based on EDM for T-S fuzzy systems. The main contribution of this paper are highlighted as follows: 1) the FD problem for T-S fuzzy system is studied, where the EDM is introduced in the communication network between sensor and filter to save bandwidth resources; 2) sufficient criteria are derived to ensure that the FES meets the FTB with satisfactory H_∞ performance, where the impact of decoding error on filtering performance is fully considered by introducing a new performance index containing the upper bound of decoding error; and 3) a novel FD filtering scheme based on EDM is designed for T-S fuzzy systems under finite-time constraints.

2 Problem Formulation

The following discrete-time T-S fuzzy system is considered:

Plant Rule i: **IF** $\mu_{1,k}$ is $\mathcal{H}_{i1}$, $\mu_{2,k}$ is $\mathcal{H}_{i2}$, $\cdots$ and $\mu_{p,k}$ is $\mathcal{H}_{ip}$, **THEN**

$$\begin{aligned} x_{k+1} &= A_i x_k + B_i w_k + G_i f_k, \\ y_k &= C_i x_k, \quad i = 1, 2, \ldots, q, \end{aligned} \tag{1}$$

where $k \in [0, N]$, q is the number of IF-THEN rules; $\mu_k = [\mu_{1,k}\ \mu_{2,k}\ \cdots\ \mu_{p,k}]$ is the premise variable vector; $\mathcal{H}_{ij}$ $(j = 1, 2, \ldots, p)$ are fuzzy sets; $x_k \in \mathbb{R}^n$ represents the state vector; $y_k = [y_{1,k}\ y_{2,k}\ \cdots\ y_{m,k}]^T \in \mathbb{R}^m$ is the measurement output with $y_{\sigma,k}$ being the measurement signal sensed by the σ-th sensor node; $w_k \in \mathbb{R}^w$ represents the external disturbance belonging to $l_2[0, N]$, $f_k \in \mathbb{R}^f$ is the fault signal. A_i, B_i, G_i and C_i are constant matrices with appropriate dimensions.

The defuzzified output of T-S fuzzy system (1) can be described as follows:

$$\begin{aligned} x_{k+1} &= \sum_{i=1}^{q} h_i(\mu_k)\left(A_i x_k + B_i w_k + G_i f_k\right), \\ y_k &= \sum_{i=1}^{q} h_i(\mu_k) C_i x_k, \end{aligned} \tag{2}$$

where $h_i(\mu_k)$ $(i = 1, 2, \ldots, q)$ are fuzzy basis functions

with

$$h_i(\mu_k) = \frac{\varphi_i(\mu_k)}{\sum_{i=1}^{q}\varphi_i(\mu_k)}.$$

Here, $\varphi_i(\mu_k) = \Pi_{j=1}^{p}\mathcal{H}_{ij}(\mu_{j,k}) \geq 0$, $\sum_{i=1}^{q}\varphi_i(\mu_k) > 0$, and $\mathcal{H}_{ij}(\mu_{j,k})$ is the grade of membership of $\mu_{j,k}$ in $\mathcal{H}_{ij}$. Hence, one has $h_i(\mu_k) \geq 0$ $(i = 1, 2, \ldots, q)$ and $\sum_{i=1}^{q} h_i(\mu_k) = 1$.

The measurement output of the system is transmitted to the remote filter through the communication network. To alleviate the communication burden, the EDM is introduced, where the process of encoding and decoding is specifically described as follows.

1) Encoding: At the encoder side, the measurement output $y_{\sigma,k}$ of sensor node σ $(\sigma \in \{1, 2, \ldots, m\})$ is coded by the following principle:

$$\begin{aligned} q_{\sigma,k} &= \mathscr{E}(y_{\sigma,k}, L_\sigma, s_\sigma) \\ &= \begin{cases} 1, & y_{\sigma,k} \in \left[-L_\sigma, -L_\sigma + \frac{2L_\sigma}{s_\sigma}\right), \\ 2, & y_{\sigma,k} \in \left[-L_\sigma + \frac{2L_\sigma}{s_\sigma}, -L_\sigma + 2\frac{2L_\sigma}{s_\sigma}\right), \\ \vdots & \\ s_\sigma, & y_{\sigma,k} \in \left[-L_\sigma + (s_\sigma - 1)\frac{2L_\sigma}{s_\sigma}, L_\sigma\right], \end{cases} \end{aligned} \tag{3}$$

where $[-L_\sigma, L_\sigma]$ is the known range of $y_{\sigma,k}$ $(\forall k \in [0, N])$, s_σ represents the pre-set number of sub-intervals that are obtained by dividing $[-L_\sigma, L_\sigma]$.

2) Decoding: The following decoding scheme is adopted:

$$\bar{y}_{\sigma,k} = \mathscr{D}_\sigma(q_{\sigma,k}) = -L_\sigma + \frac{2(q_{\sigma,k} - 0.5)L_\sigma}{s_\sigma}, \tag{4}$$

where $\bar{y}_{\sigma,k}$ is the decoding value output by the decoder corresponding to sensor σ. Defining $\bar{y}_k = [\bar{y}_{1,k}\ \bar{y}_{2,k}\ \cdots\ \bar{y}_{m,k}]^T$, we have

$$\bar{y}_k = \mathscr{D}(q_k) = y_k + \varepsilon_k, \tag{5}$$

where $\varepsilon_k \triangleq \mathscr{D}(q_k) - y_k$ stands for the decoding error, $q_k = [q_{1,k}\ \ q_{2,k}\ \ \cdots\ \ q_{m,k}]^T$ and $\mathscr{D}(q_k) = [\mathscr{D}_1(q_{1,k})\ \mathscr{D}_2(q_{2,k})\ \cdots\ \mathscr{D}_m(q_{m,k})]^T$. Combining (4) with (3), the decoding error ε_k satisfies

$$\varepsilon_k^T\varepsilon_k \leq \sum_{\sigma=1}^{m}\left(\frac{L_\sigma}{s_\sigma}\right)^2 \triangleq \hat{d}. \tag{6}$$

For the physical plant represented by (2), we construct the following fuzzy FD filter:

Filter Rule j: **IF** $\mu_{1,k}$ is $\mathcal{H}_{j1}$, $\mu_{2,k}$ is $\mathcal{H}_{j2}$, $\cdots$ and $\mu_{p,k}$ is $\mathcal{H}_{jp}$, **THEN**

$$\begin{aligned} \hat{x}_{k+1} &= A_{f,j}\hat{x}_k + B_{f,j}\bar{y}_k, \\ r_k &= C_{f,j}\hat{x}_k + D_{f,j}\bar{y}_k, \quad j = 1, 2, \ldots, q, \end{aligned} \tag{7}$$

where $\hat{x}_k \in \mathbb{R}^n$ and $r_k \in \mathbb{R}^f$ stand for the filter state and the residual, respectively. $A_{f,j}$, $B_{f,j}$, $C_{f,j}$ and $D_{f,j}$ are FD filter parameters to be designed. Then, the defuzzified output of fuzzy FD filter (7) is presented as:

$$\hat{x}_{k+1} = \sum_{j=1}^{q} h_j(\mu_k)\left(A_{f,j}\hat{x}_k + B_{f,j}\bar{y}_k\right),$$

$$r_k = \sum_{j=1}^{q} h_j(\mu_k)\left(C_{f,j}\hat{x}_k + D_{f,j}\bar{y}_k\right). \tag{8}$$

In the sequel, for brevity, we use h_i to denote $h_i(\mu_k)$ and define $\tilde{x}_k = x_k - \hat{x}_k$, $\eta_k = \begin{bmatrix}\tilde{x}_k^T & \hat{x}_k^T\end{bmatrix}^T$, $\vartheta_k = \begin{bmatrix}w_k^T & f_k^T\end{bmatrix}^T$ and $\tilde{r}_k = r_k - f_k$. According to (2), (5) and (8), the following FES can be obtained:

$$\begin{aligned} \eta_{k+1} &= \sum_{i=1}^{q}\sum_{j=1}^{q} h_i h_j\left(\hat{A}_{ij}\eta_k + \hat{B}_i\vartheta_k + \hat{G}_j\varepsilon_k\right), \\ \tilde{r}_k &= \sum_{i=1}^{q}\sum_{j=1}^{q} h_i h_j\left(\hat{C}_{ij}\eta_k + \hat{D}\vartheta_k + \hat{H}_j\varepsilon_k\right), \end{aligned} \tag{9}$$

where

$$\begin{aligned} \hat{A}_{ij} &= \begin{bmatrix} A_i - B_{f,j}C_i & A_i - A_{f,j} - B_{f,j}C_i \\ B_{f,j}C_i & A_{f,j} + B_{f,j}C_i \end{bmatrix}, \\ \hat{B}_i &= \begin{bmatrix} B_i & G_i \\ 0 & 0 \end{bmatrix},\ \hat{G}_j = \begin{bmatrix} -B_{f,j} \\ B_{f,j} \end{bmatrix},\ \hat{D} = \begin{bmatrix} 0 & -I \end{bmatrix}, \\ \hat{C}_{ij} &= \begin{bmatrix} D_{f,j}C_i & C_{f,j} + D_{f,j}C_i \end{bmatrix},\ \hat{H}_j = D_{f,j}. \end{aligned}$$

Definition 1 *[9] The FES (9) is finite-time bounded, if the inequality* $\eta_k^T R\eta_k < \gamma^2$ $(\forall k \in \{1, 2, \ldots, N\})$ *can be derived under the conditions*

$$\begin{cases} \eta_0^T R\eta_0 \leq \alpha_1^2, \\ \sum_{k=0}^{N}\left(\vartheta_k^T\vartheta_k + \hat{d}\right) \leq \alpha_2^2, \end{cases} \tag{10}$$

where $N \in Z^+$, $0 < \alpha_1 < \gamma$, $\alpha_2 \geq 0$ *and* $R > 0$. *Besides,* $\hat{d}$ *is defined in (6).*

Definition 2 *[9] The FES (9) satisfies the prescribed* H_∞ *performance, if the inequality*

$$\sum_{k=0}^{N}\tilde{r}_k^T\tilde{r}_k < \lambda^2\sum_{k=0}^{N}\left(\vartheta_k^T\vartheta_k + \hat{d}\right) \tag{11}$$

holds in the case of zero initial condition, where $\lambda > 0$ *is the prescribed level of disturbance attenuation.*

For the sake of realizing FD, we choose the following residual evaluation function J_k and threshold J_{th}:

$$\begin{aligned} J_k &= \left\{\sum_{l=0}^{k} r_l^T r_l\right\}^{1/2}, \\ J_{th} &= \sup_{v_k \in l_2, f_k = 0} J_k. \end{aligned} \tag{12}$$

Then, the following criteria are used to determine if the fault has occurred:

$$\begin{aligned} &J_k \leq J_{th} \Rightarrow \text{no faults}, \\ &J_k > J_{th} \Rightarrow \text{faults occur} \Rightarrow \text{alarm}. \end{aligned} \tag{13}$$

3 Main results

The analysis about FTB and H_∞ performance of FES (9) will be presented firstly.

Theorem 1 *Given the FD filter matrices* $A_{f,j}$, $B_{f,j}$, $C_{f,j}$, $D_{f,j}$, *scalars* $N \in Z^+$, $\delta > 1$, $0 < \alpha_1 < \gamma$, $\alpha_2 \geq 0$, *matrix*

$R > 0$, the FES (9) is finite-time bounded with prescribed H_∞ performance, if there exist scalars $\kappa_0 > 0$, $\kappa_1 > 0$, $\beta > 0$ and matrix $P > 0$ such that

$$\Omega + \Upsilon_{ii}^T P \Upsilon_{ii} + \Psi_{ii}^T \Psi_{ii} < 0,\ i = 1, 2, \ldots, q, \tag{14}$$

$$4\Omega + (\Upsilon_{ij} + \Upsilon_{ji})^T P (\Upsilon_{ij} + \Upsilon_{ji}) + (\Psi_{ij} + \Psi_{ji})^T (\Psi_{ij} + \Psi_{ji}) < 0,\ 1 \le i < j \le q, \tag{15}$$

$$\kappa_0 R < P < \kappa_1 R, \tag{16}$$

$$\delta^N \kappa_1 \alpha_1^2 + \varrho \delta^N \alpha_2^2 \le \kappa_0 \gamma^2, \tag{17}$$

where

$$\Omega = \mathrm{diag}\left\{-\delta P, -\varrho I, -\beta I, (\beta - \varrho)\hat{d}\right\},$$
$$\Upsilon_{ij} = \begin{bmatrix} \hat{A}_{ij} & \hat{B}_i & \hat{G}_j & 0 \end{bmatrix},$$
$$\Psi_{ij} = \begin{bmatrix} \hat{C}_{ij} & \hat{D} & \hat{H}_j & 0 \end{bmatrix},\ \varrho = \lambda^2 \delta^{-N}.$$

Proof: To begin, based on the constraint (6) with respect to the decoding error ε_k, it is clear that the following inequality holds for any $\beta > 0$:

$$\beta \left(\hat{d} - \varepsilon_k^T \varepsilon_k\right) \ge 0. \tag{18}$$

Then, choose a Lyapunov function candidate as $V_k = \eta_k^T P \eta_k$. According to (9), (18) and applying Lemma 2 in [10], one has

$$\begin{aligned}
W_k &\triangleq V_{k+1} - \delta V_k - \varrho\left(\vartheta_k^T \vartheta_k + \hat{d}\right) \\
&\le \eta_{k+1}^T P \eta_{k+1} - \delta \eta_k^T P \eta_k - \varrho\left(\vartheta_k^T \vartheta_k + \hat{d}\right) \\
&\quad + \beta\left(\hat{d} - \varepsilon_k^T \varepsilon_k\right) \\
&= \sum_{i=1}^{q}\sum_{j=1}^{q}\sum_{u=1}^{q}\sum_{v=1}^{q} h_i h_j h_u h_v \left(\hat{A}_{ij}\eta_k + \hat{B}_i \vartheta_k \right. \\
&\quad \left. + \hat{G}_j \varepsilon_k\right)^T P \left(\hat{A}_{uv}\eta_k + \hat{B}_u \vartheta_k + \hat{G}_v \varepsilon_k\right) \\
&\quad - \delta \eta_k^T P \eta_k - \varrho\left(\vartheta_k^T \vartheta_k + \hat{d}\right) + \beta\left(\hat{d} - \varepsilon_k^T \varepsilon_k\right) \\
&= \sum_{i=1}^{q}\sum_{j=1}^{q}\sum_{u=1}^{q}\sum_{v=1}^{q} h_i h_j h_u h_v \xi_k^T \left(\Omega + \Upsilon_{ij}^T P \Upsilon_{uv}\right) \xi_k \\
&= \frac{1}{4}\sum_{i=1}^{q}\sum_{j=1}^{q}\sum_{u=1}^{q}\sum_{v=1}^{q} h_i h_j h_u h_v \xi_k^T \left[4\Omega + (\Upsilon_{ij} + \Upsilon_{ji})^T \right. \\
&\quad \left. \times P (\Upsilon_{uv} + \Upsilon_{vu})\right] \xi_k \\
&\le \frac{1}{4}\sum_{i=1}^{q}\sum_{j=1}^{q} h_i h_j \xi_k^T \left[4\Omega + (\Upsilon_{ij} + \Upsilon_{ji})^T \right. \\
&\quad \left. \times P (\Upsilon_{ij} + \Upsilon_{ji})\right] \xi_k \\
&= \sum_{i=1}^{q} h_i^2 \xi_k^T \left(\Omega + \Upsilon_{ii}^T P \Upsilon_{ii}\right) \xi_k \\
&\quad + \frac{1}{2}\sum_{i=1}^{q}\sum_{j=1, j>i}^{q} h_i h_j \xi_k^T \left[4\Omega + (\Upsilon_{ij} + \Upsilon_{ji})^T P \right. \\
&\quad \left. \times (\Upsilon_{ij} + \Upsilon_{ji})\right] \xi_k,
\end{aligned} \tag{19}$$

where $\xi_k = \begin{bmatrix} \eta_k^T & \vartheta_k^T & \varepsilon_k^T & 1 \end{bmatrix}^T$ and $\beta > 0$.

From (14) and (15), it is easy to infer that

$$V_{k+1} - \delta V_k - \varrho\left(\vartheta_k^T \vartheta_k + \hat{d}\right) < 0. \tag{20}$$

Based on the above inequality and noticing $\delta \ge 1$, for any $k \in [0, N]$, one has

$$\begin{aligned}
V_k &< \delta V_{k-1} + \varrho\left(\vartheta_{k-1}^T \vartheta_{k-1} + \hat{d}\right) \\
&< \delta^2 V_{k-2} + \delta\varrho\left(\vartheta_{k-2}^T \vartheta_{k-2} + \hat{d}\right) + \varrho\left(\vartheta_j^T \vartheta_j + \hat{d}\right) \\
&\ \ \vdots \\
&< \delta^k V_0 + \varrho \sum_{j=0}^{k-1} \delta^{k-1-j}\left(\vartheta_j^T \vartheta_j + \hat{d}\right) \\
&< \delta^N V_0 + \varrho \sum_{j=0}^{N-1} \delta^{N-1-j}\left(\vartheta_j^T \vartheta_j + \hat{d}\right) \\
&< \delta^N V_0 + \varrho\delta^N \sum_{j=0}^{N-1}\left(\vartheta_j^T \vartheta_j + \hat{d}\right).
\end{aligned} \tag{21}$$

According to (16), (17) and Definition 1, it can be further obtained that

$$\begin{aligned}
\eta_k^T R \eta_k &\le \frac{1}{\kappa_0}\eta_k^T P \eta_k \\
&< \frac{1}{\kappa_0}\delta^N \eta_0^T P \eta_0 + \frac{1}{\kappa_0}\varrho\delta^N \sum_{j=0}^{N-1}\left(\vartheta_j^T \vartheta_j + \hat{d}\right) \\
&< \frac{1}{\kappa_0}\delta^N \kappa_1 \eta_0^T R \eta_0 + \frac{1}{\kappa_0}\varrho\delta^N \alpha_2^2 \\
&\le \frac{1}{\kappa_0}\delta^N \kappa_1 \alpha_1^2 + \frac{1}{\kappa_0}\varrho\delta^N \alpha_2^2 \\
&\le \gamma^2.
\end{aligned} \tag{22}$$

Therefore, the FES (9) is finite-time bounded.

Secondly, the following index is introduced to prove that the FES (9) satisfies the H_∞ performance:

$$\bar{W}_k \triangleq V_{k+1} - \delta V_k + \tilde{r}_k^T \tilde{r}_k - \varrho\left(\vartheta_k^T \vartheta_k + \hat{d}\right). \tag{23}$$

According to (9), it can be calculated that

$$\begin{aligned}
&\tilde{r}_k^T \tilde{r}_k \\
&= \sum_{i=1}^{q}\sum_{j=1}^{q}\sum_{u=1}^{q}\sum_{v=1}^{q} h_i h_j h_u h_v \left(\hat{C}_{ij}\eta_k + \hat{D}\vartheta_k + \hat{H}_j \varepsilon_k\right)^T \\
&\quad \times \left(\hat{C}_{uv}\eta_k + \hat{D}\vartheta_k + \hat{H}_v \varepsilon_k\right) \\
&= \sum_{i=1}^{q}\sum_{j=1}^{q}\sum_{u=1}^{q}\sum_{v=1}^{q} h_i h_j h_u h_v \xi_k \Psi_{ij}^T \Psi_{uv} \xi_k.
\end{aligned} \tag{24}$$

Then, combining (14), (15), (19), (24) with (23) and employing the Lemma 2 in [10], one has

$$\begin{aligned}
\bar{W}_k &\le \sum_{i=1}^{q}\sum_{j=1}^{q}\sum_{u=1}^{q}\sum_{v=1}^{q} h_i h_j h_u h_v \xi_k^T \left(\Omega \right. \\
&\quad \left. + \Upsilon_{ij}^T P \Upsilon_{uv} + \Psi_{ij}^T \Psi_{uv}\right) \xi_k \\
&\le \sum_{i=1}^{q} h_i^2 \xi_k^T \left(\Omega + \Upsilon_{ii}^T P \Upsilon_{ii} + \Psi_{ii}^T \Psi_{ii}\right) \xi_k
\end{aligned}$$

$$+\frac{1}{2}\sum_{i=1}^{q}\sum_{j=1,j>i}^{q} h_i h_j \xi_k^T \Big[4\Omega + (\Upsilon_{ij}+\Upsilon_{ji})^T P \times (\Upsilon_{ij}+\Upsilon_{ji}) + (\Psi_{ij}+\Psi_{ji})^T (\Psi_{ij}+\Psi_{ji})\Big] \xi_k < 0,$$

which can deduce the inequality

$$V_{k+1} < \delta V_k - \left[\tilde{r}_k^T \tilde{r}_k - \varrho\left(\vartheta_k^T \vartheta_k + \hat{d}\right)\right]. \tag{25}$$

Letting $k = N$, the following inequality can be obtained by iterating on (25):

$$V_{N+1} < \delta^{N+1} V_0 - \sum_{j=0}^{N} \delta^{N-j}\left[\tilde{r}_j^T \tilde{r}_j - \varrho\left(\vartheta_j^T \vartheta_j + \hat{d}\right)\right]. \tag{26}$$

Due to $V_{N+1} \geq 0$ and $V_0 = 0$, one has

$$-\sum_{j=0}^{N} \delta^{N-j}\left[\tilde{r}_j^T \tilde{r}_j - \varrho\left(\vartheta_j^T \vartheta_j + \hat{d}\right)\right] > 0. \tag{27}$$

Noticing $\delta \geq 1$, the following inequality holds:

$$\begin{aligned}\sum_{j=0}^{N} \tilde{r}_j^T \tilde{r}_j &\leq \sum_{j=0}^{N} \delta^{N-j} \tilde{r}_j^T \tilde{r}_j \\ &< \varrho \sum_{j=0}^{N} \delta^{N-j}\left(\vartheta_j^T \vartheta_j + \hat{d}\right) \\ &\leq \varrho \delta^N \sum_{j=0}^{N}\left(\vartheta_j^T \vartheta_j + \hat{d}\right) \\ &= \lambda^2 \sum_{j=0}^{N}\left(\vartheta_j^T \vartheta_j + \hat{d}\right). \end{aligned} \tag{28}$$

Thus, the FES (9) is finite-time bounded with H_∞ performance. ■

Subsequently, the FD filter gains will be determined by the matrix inequality technique.

Theorem 2 *Given the scalars $N \in Z^+$, $\delta > 1$, $0 < \alpha_1 < \gamma$, $\alpha_2 \geq 0$, matrix $R > 0$, the FES (9) is finite-time bounded with prescribed H_∞ performance, if there exist scalars $\kappa_0 > 0$, $\kappa_1 > 0$, $\beta > 0$, matrices $\mathcal{A}_{f,j}$, $\mathcal{B}_{f,j}$, $C_{f,j}$, $D_{f,j}$ and $P > 0$, such that (16), (17) and the following inequalities are satisfied:*

$$\Xi^{ii} = \begin{bmatrix} \Omega & \Xi_{12}^{ii} & \Xi_{13}^{ii} \\ * & -P & 0 \\ * & * & -I \end{bmatrix} < 0,\ i = 1, 2, \ldots, q, \tag{29}$$

$$\hat{\Xi}^{ij} = \begin{bmatrix} 4\Omega & \hat{\Xi}_{12}^{ij} & \hat{\Xi}_{13}^{ij} \\ * & -P & 0 \\ * & * & -I \end{bmatrix} < 0,\ 1 \leq i < j \leq q, \tag{30}$$

where

$$\hat{\Xi}_{1s}^{ij} = \Xi_{1s}^{ij} + \Xi_{1s}^{ji},\ \ s = 2, 3,$$

$$\Xi_{12}^{ij} = \begin{bmatrix} \bar{A}_i^T P + \bar{C}_i^T \mathcal{B}_{f,j} + \hat{I}_2 \mathcal{A}_{f,j} \\ \hat{B}_i^T P \\ \mathcal{B}_{f,j} \\ 0 \end{bmatrix},$$

$$\Xi_{13}^{ij} = \begin{bmatrix} \bar{C}_i^T D_{f,j}^T + \hat{I}_2 C_{f,j}^T \\ \hat{D}^T \\ D_{f,j}^T \\ 0 \end{bmatrix},\ \bar{A}_i = \begin{bmatrix} A_i & A_i \\ 0 & 0 \end{bmatrix},$$

$$\bar{C}_i = \begin{bmatrix} C_i & C_i \end{bmatrix},\ \hat{I}_1 = \begin{bmatrix} -I_n \\ I_n \end{bmatrix},\ \hat{I}_2 = \begin{bmatrix} 0_n \\ I_n \end{bmatrix},\ \hat{I}_3 = \begin{bmatrix} I_n \\ I_n \end{bmatrix}.$$

and other parameters are given as in Theorem 1. Moreover, the FD filter parameters $C_{f,j}$ and $D_{f,j}$ can be obtained directly by solving the linear matrix inequalities (LMIs). Besides, $A_{f,j}$ and $B_{f,j}$ can be obtained by

$$\begin{aligned} A_{f,j} &= \left(\hat{I}_1^T P \hat{I}_1\right)^{-1} \hat{I}_1^T \mathcal{A}_{f,j}^T, \\ B_{f,j} &= \left(\hat{I}_1^T P \hat{I}_1\right)^{-1} \hat{I}_1^T \mathcal{B}_{f,j}^T. \end{aligned} \tag{31}$$

Proof: By the aid of Schur complement lemma, (15) is equivalent to

$$\breve{\Xi}^{ij} = \begin{bmatrix} 4\Omega & (\Upsilon_{ij}+\Upsilon_{ji})^T & (\Psi_{ij}+\Psi_{ji})^T \\ * & -P^{-1} & 0 \\ * & * & -I \end{bmatrix} < 0. \tag{32}$$

Pre- and post-multiplying with $\mathrm{diag}\{I, P, I\}$ for $\breve{\Xi}^{ij}$, it is easy to obtain that (32) is equivalent to

$$\breve{\Xi}^{ij} = \begin{bmatrix} 4\Omega & (\Upsilon_{ij}+\Upsilon_{ji})^T P & (\Psi_{ij}+\Psi_{ji})^T \\ * & -P & 0 \\ * & * & -I \end{bmatrix} < 0. \tag{33}$$

Some parameters in (33) are rewritten as follows:

$$\begin{aligned} &\hat{A}_{ij} = \bar{A}_i + \hat{I}_1 A_{f,j} \hat{I}_2^T + \hat{I}_1 B_{f,j} \bar{C}_i,\ \ \hat{G}_j = \hat{I}_1 B_{f,j}, \\ &\hat{C}_{ij} = C_{f,j} \hat{I}_2^T + D_{f,j} \bar{C}_i,\ \ \hat{H}_j = D_{f,j}, \end{aligned}$$

where

$$\bar{A}_i = \begin{bmatrix} A_i & A_i \\ 0 & 0 \end{bmatrix},\ \bar{C}_i = \begin{bmatrix} C_i & C_i \end{bmatrix},\ \hat{I}_1 = \begin{bmatrix} -I_n \\ I_n \end{bmatrix},$$

$$\hat{I}_2 = \begin{bmatrix} 0_n \\ I_n \end{bmatrix},\ \hat{I}_3 = \begin{bmatrix} I_n \\ I_n \end{bmatrix}.$$

Furthermore, letting $\mathcal{A}_{f,j} = A_{f,j} \hat{I}_1^T P$ and $\mathcal{B}_{f,j} = B_{f,j} \hat{I}_1^T P$, it can be derived that (33) is equivalent to (30). Thus, (30) is equivalent to (15). Similarly, it can be deduced that (29) is equivalent to (14).

Lastly, for any $j \in \{1, 2, \ldots, q\}$, we can obtain P, $C_{f,j}$, $D_{f,j}$, $\mathcal{A}_{f,j}$ and $\mathcal{B}_{f,j}$ directly by solving the LMIs. Moreover, according to the definition of $\mathcal{A}_{f,j}$ and $\mathcal{B}_{f,j}$, the explicit expression of $A_{f,j}$ and $B_{f,j}$ can be described by (31). ■

4 An Illustrative Example

Consider the T-S fuzzy system (1), where the number of IF-THEN rules is $q = 2$ and the system matrices are given as follows:

$$A_1 = \begin{bmatrix} -0.6 & 0.4 \\ 0.3 & 0.2 \end{bmatrix},\ B_1 = \begin{bmatrix} 0.5 \\ -0.2 \end{bmatrix},\ G_1 = \begin{bmatrix} 0.3 \\ 0.4 \end{bmatrix},$$

$$C_1 = \begin{bmatrix} 0.2 & 0.1 \\ 0.3 & -0.4 \end{bmatrix},\ A_2 = \begin{bmatrix} 0.2 & 0.5 \\ 0.4 & -0.3 \end{bmatrix},$$

$$B_2 = \begin{bmatrix} 0.2 \\ -0.3 \end{bmatrix}, \ G_2 = \begin{bmatrix} -0.4 \\ 0.5 \end{bmatrix}, \ C_2 = \begin{bmatrix} -0.2 & 0.1 \\ -0.3 & 0.4 \end{bmatrix}.$$

The fuzzy basis functions are adopted as $h_1(x_{1,k}) = \frac{\sin^2(x_{1,k})}{2+\cos^2(x_{1,k})}$ and $h_2(x_{1,k}) = 1 - h_1(x_{1,k})$. Assume that the disturbance is simulated by $w_k = e^{-k/1000}\sin(1.5k)\rho_k$ with ρ_k subjecting uniform distribution on $[-0.4, 0.4]$. The ranges of measurements $y_{1,k}$ and $y_{2,k}$ are $[-0.15, 0.15]$ and $[-0.3, 0.3]$, respectively (i.e. $L_1 = 0.15$, $L_2 = 0.3$). The numbers of sub-intervals are $s_1 = 8$ and $s_2 = 16$. The parameters related to finite-time boundedness are $N = 60$, $R = I_4$, $\alpha_1 = 0.4$, $\alpha_2 = 2.67$, $\gamma = 3.5$ and the level of disturbance attenuation is prescribed as $\lambda = 1.4$. Besides, the known parameter δ in Theorem 2 is set as $\delta = 1.001$.

With the help of Theorem 2, the parameters of FD filter are obtained as:

$$\begin{aligned}
A_{f,1} &= \begin{bmatrix} -0.0506 & 0.0344 \\ 0.0209 & 0.0305 \end{bmatrix}, \\
B_{f,1} &= \begin{bmatrix} -0.0077 & -0.0409 \\ 0.0098 & 0.0036 \end{bmatrix}, \\
C_{f,1} &= \begin{bmatrix} -0.0030 & 0.0066 \end{bmatrix}, \\
D_{f,1} &= \begin{bmatrix} -0.0072 & 0.0148 \end{bmatrix}, \\
A_{f,2} &= \begin{bmatrix} 0.0360 & 0.0452 \\ 0.0407 & -0.0160 \end{bmatrix}, \\
B_{f,2} &= \begin{bmatrix} 0.0006 & 0.0188 \\ -0.0125 & -0.0212 \end{bmatrix}, \\
C_{f,2} &= \begin{bmatrix} 0.0166 & -0.0191 \end{bmatrix}, \\
D_{f,2} &= \begin{bmatrix} 0.0184 & 0.0432 \end{bmatrix}.
\end{aligned}$$

Let the initial values of the system and filter be $x_0 = [0.2 \ 0.3]^T$ and $\hat{x}_0 = [0 \ 0]^T$. The fault to be detected is given by

$$f_k = \begin{cases} 0.5, & 20 \le k \le 40, \\ 0, & \text{otherwise}. \end{cases}$$

Fig. 1 and Fig. 2 depict the system measurement and its decoded value through the EDM, which reflect that the data capacity transferred in the network is reduced under the EDM. The residual r_k is presented in Fig. 3. The residual evaluation function and threshold are shown in Fig. 4. From Fig. 3, it can be found that the residual is sensitive to the fault. In Fig. 4, the evaluation function J_k exceeds the threshold J_{th} after short time steps since the fault occurred. According to (12), we can get that $0.0124 = J_{23} < J_{th} = 0.0137 < J_{24} = 0.0141$, which means that the fault is successfully detected with only 4 time steps behind. Besides, by observing the trajectories of $\eta_k^T R \eta_k$ and γ^2 in Fig. 5, it can be verified that the FES is finite-time bounded.

In addition, in order to further analyze the impact of EDM on FD performance, we also provide the simulations (as shown in Fig. 6) of J_k and J_{th} under the situation of setting the numbers of sub-intervals in EDM to smaller values (i.e. $s_1 = 4$, $s_2 = 8$). By observing Fig. 6, we find that the evaluation function exceeds the threshold after a little longer time steps since the fault occurred. Specifically, one has $0.0147 = J_{28} < J_{th} = 0.0152 < J_{29} = 0.0154$, which means that the fault is detected with 9 time steps behind. It is obvious that the FD effect in this situation is not as good as when the numbers of sub-intervals are set as $s_1 = 8$ and $s_2 = 16$.

Comparing the FD results in the above two cases, it can be found that when the numbers of sub-intervals in EDM are set to smaller values, the FD effect deteriorates. This is because the smaller the number of sub-intervals, the bigger the decoding error. Therefore, it is necessary to balance the effectiveness of FD and the savings in network bandwidth based on actual requirements.

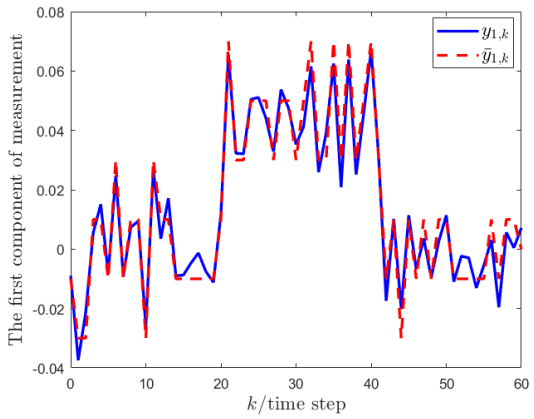

Fig. 1: The first component of measurement and its decoded value

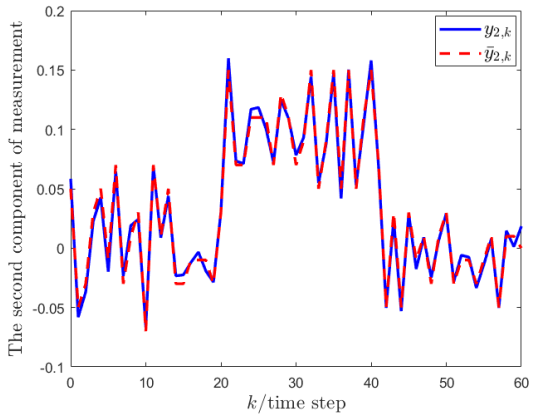

Fig. 2: The second component of measurement and its decoded value

5 Conclusions

The problem of finite-time FD has been investigated in this paper for T-S fuzzy systems, where the EDM has been introduced to save resources of network bandwidth. By using the Lyapunov stability theory, sufficient criteria have been established to guarantee that the FES is finite-time bounded and H_∞ performance index is guaranteed. Furthermore, the explicit expressions of the FD filter gains have been determined based on the solutions of the LMIs. In the end, a numerical example with comparisons has demonstrated the feasibility of the proposed FD strategy.

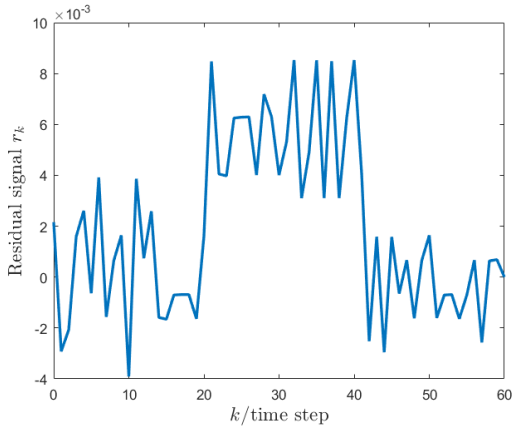

Fig. 3: Residual signal r_k

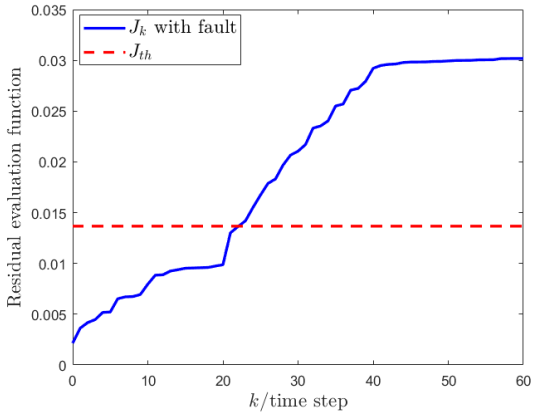

Fig. 4: Residual evaluation function and threshold ($s_1 = 8$, $s_2 = 16$)

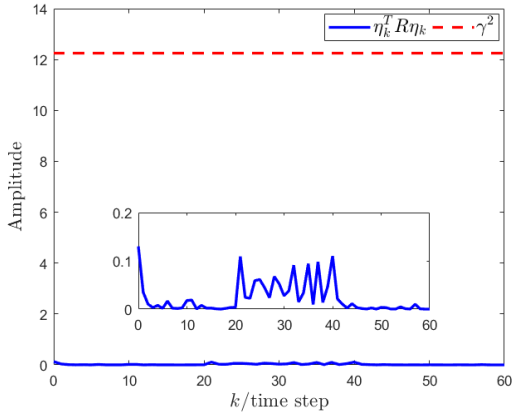

Fig. 5: Trajectories of $\eta_k^T R \eta_k$ and γ^2

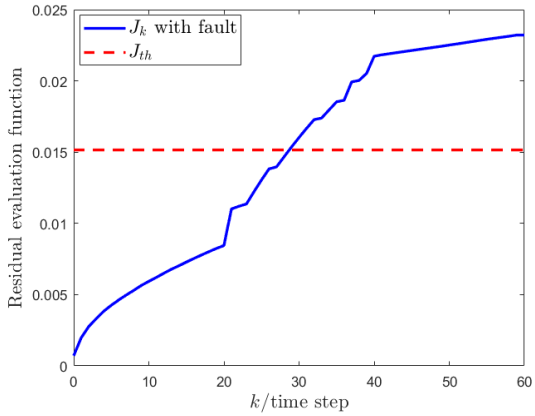

Fig. 6: Residual evaluation function and threshold ($s_1 = 4$, $s_2 = 8$)

References

[1] X. Cai, S. Zhong, J. Wang and K. Shi, Robust H_∞ control for uncertain delayed T-S fuzzy systems with stochastic packet dropouts, *Applied Mathematics and Computation*, 385, Article Number. 125432, DOI: 10.1016/j.amc.2020.125432, 2020.

[2] L. Li, S. Ding and X. Peng, Optimal observer-based fault detection and estimation approaches for T-S fuzzy systems, *IEEE Transactions on Fuzzy Systems*, 30(2): 579–590, 2022.

[3] X.-L. Wang, G.-H. Yang and D. Zhang, Event-triggered fault detection observer design for T-S fuzzy systems, *IEEE Transactions on Fuzzy Systems*, 29(9): 2532–2542, 2021.

[4] V. Suveetha, R. Sakthivel and V. Nithya, Finite-time fault detection filter design for T-S fuzzy Markovian jump systems with distributed delays and incomplete measurements, *Circuits Systems and Signal Processing*, 41(1): 28–56, 2022.

[5] X.-M. Zhang, Q.-L. Han, X. Ge, D. Ding, L. Ding, D. Yue and C. Peng, Networked control systems: A survey of trends and techniques, *IEEE-CAA Journal of Automatica Sinica*, 7(1): 1–17, 2020.

[6] Z. Wang, L. Wang, S. Liu and G. Wei, Encoding-decoding-based control and filtering of networked systems: Insights, developments and opportunities, *IEEE-CAA Journal of Automatica Sinica*, 5(1): 3–18, 2018.

[7] J. Hu, S. Fan, C. Chen, H. Liu and X. Yi, Encoding-decoding-based distributed fusion filtering for multi-rate nonlinear systems with sensor resolutions, *IEEE Transactions on Signal and Information Processing over Networks*, 9: 811–822, 2023.

[8] J. Li, Y. Niu and D. W. C. Ho, Dynamic coding-based control scheme under lossy digital network: An optimized time-varying packet length approach, *IEEE Transactions on Cybernetics*, DOI: 10.1109/TCYB.2022.3232529, 2023.

[9] H. Fu, X. Meng and Y. Chen, Finite-time distributed filtering of time-varying switched stochastic systems with DoS attacks based on encoding-decoding scheme, *IEEE Systems Journal*, DOI: 10.1109/JSYST.2023.3333823, 2023.

[10] X.-L. Wang and G.-H. Yang, Fault detection for T-S fuzzy systems with past output measurements, *Fuzzy Sets and Systems*, 365: 98–115, 2019.

Proceedings of the 3rd Conference on Fully Actuated System Theory and Applications
May 10-12, 2024, Shenzhen, China

An Attention-LSTM-based Fault Diagnosis Method for Satellite Attitude Control System

Siyuan Ma[1,2], Sheng Gao[1,2,3], Xiaozhong Zuo[4], Zhengyang Lv[1,2], Chenyang Zou[1,2]

1. State Key Laboratory of Robotics, Shenyang Institute of Automation, Chinese Academy of Sciences, Shenyang 110016, China
2. Institutes for Robotics and Intelligent Manufacturing, Chinese Academy of Sciences, Shenyang 110169, China
3. China-Portugal Belt and Road Joint Laboratory on Space & Sea Technology Advanced Research, Shanghai 200120, China
4. College of Electrical and Control Engineering, Shenyang Jianzhu University, Shenyang 110168, China
E-mail: gaosheng@sia.cn

Abstract: This study proposes a fault diagnosis method based on attention-LSTM for the satellite attitude control system. First, the hidden correlation information between high-dimensional variables is exploited through the variable attention layer. Then, deep temporal features are extracted with using the LSTM network layer. Finally, the time attention layer is introduced to increase the weight of important temporal information, effectively avoiding the problem of being forgotten due to too long input sequence and too many deep temporal features. The identification accuracy of slow fault in satellite attitude control system can be improved. The method is validated using data from the satellite semi-physical simulation platform, which demonstrates the effectiveness of this method.

Key Words: Fault diagnosis, LSTM networks, Satellite attitude control system, Attention mechanism

1 INTRODUCTION

With the development of modern society, science, and technology, modern engineering and control technology have rapidly development. Simultaneously, the control system becomes more and more complex and huge. Therefore, to ensure the safe and reliable long-term operation of the system, it is particularly important to make it more maintainable. Due to the complexity of the external operating environment, the control system is often influenced by various forms of fault, such as actuator and sensor faults, which greatly affects the reliability and safety of the system. Therefore, it is crucial to detect and identify these faults as soon as possible.

In recent years, as space exploration programs continue to advance, higher requirements have been placed on the design of satellites. The reliability of the Attitude Control System (ACS), one of the most important subsystems of the satellite, determines the successful completion of the mission [1]. However, the challenging operating conditions of satellites increase the possibility of satellite attitude control system failure, and once the satellite attitude control system fails, the satellite will deviate from the correct orbit or even lose control of the satellite as a whole, which will eventually lead to mission failure [2]. Therefore, it is important to study fault diagnosis technology to improve the safety and reliability of satellite attitude control system.

With the rise of artificial intelligence, artificial intelligence algorithms have also begun to be studied and applied in the field of satellite fault diagnosis. It is mainly divided into rough set theory (RST), machine learning (ML), deep learning (DL) and information fusion (IF). In [3], a variable precision fuzzy neighborhood rough set model (VPFNRS) method is proposed by combining rough set theory and fuzzy theory, and the feasibility and correctness of the proposed method are verified by the fault diagnosis of satellite power system. In [4], a multi-class support vector machine (SVM) model based on directed acyclic graph (DAG) was designed and applied to satellite momentum wheel voltage telemetry data, effectively improving the accuracy of fault detection. In [5], an improved random forest (RF) algorithm was applied to realize the fault isolation of the satellite three-axis reaction wheel. In [6], variable sequence-Long Short Term memory network (LSTM) was applied to the Kepler spacecraft reaction flywheel data set to complete the fault detection and prediction of reaction flywheel. Aiming at the problem of satellite telemetry data containing a lot of noise, [7] proposed a diagnosis method based on PCA and ResNet to realize fault diagnosis of satellite control system. In [8], convolutional neural network (CNN) was applied to the fault diagnosis of satellite thrusters to realize the fault detection and fault location of thrusters, and the feasibility of the proposed model was verified by the attitude control test platform. In [9], variational autoencoders (VAE) are combined with gated cycle unit (GRU) networks to propose a new unsupervised deep learning algorithm to realize spacecraft fault detection. In [10], the stacked autoencoder (SAE) network was combined to realize fault detection and isolation of satellite attitude control system. Because of its unique recursive cycle architecture, recurrent neural network can more easily capture the time series characteristics of satellite attitude control system. LSTM, as an improved network of recurrent neural network, has a stronger ability to capture data hidden time series information, which can play a great role in the diagnosis and research of slow-change faults of satellite attitude control system. In view of the problem that the attention mechanism has poor ability to extract time domain features, the slow fault diagnosis effect of satellite attitude control system is

* This work is supported by the National Key R&D Program of China under Grant No. 2022YFE0204600 and the Fundamental Research Project of SIA under Grant No. 2022JC3K03.

poor. This paper proposes a fault diagnosis method based on Attention-LSTM.

The rest of the paper is organized as follows. Section 2 introduces Long short-term memory network. A fault diagnosis method based on Attention-LSTM is proposed in Section 3. In Section 4, the satellite platform is used to obtain the experimental simulation data required by the diagnostic models, and carried out fault diagnosis simulation experiment research, so as to verify the feasibility of the designed fault diagnosis method. Finally, Section 5 summarizes the work of this paper.

2 Long short-term memory network

In the field of image and object recognition, the network model using feedforward neural network performs well, but in many fields with time series characteristics, such network model cannot take advantage of the time series characteristics of data, so the final model effect is poor. The birth of a series of models such as recurrent neural network (RNN) has officially solved the problem that the former models cannot use time series information.

After multiple network recursion of RNN, the gradient explosion or gradient disappearance occurs, and the influence of the information at the earlier time on the information at the later time becomes less and less. As a result, RNN cannot learn useful information at the far end, resulting in the problem of long-distance dependence. LSTM, as an improvement of RNN, solves this problem to some extent [11].

The LSTM network structure is shown in Fig 1. Compared to RNN, LSTM introduces three gating mechanisms: The forgetting door, input door and output door can save information and control the input and output of information. The input door can control the input status of information at the current moment and screen out irrelevant content. The forgetting door can retain and forget the output information at the previous moment, and the output door can control the output status of information at the current moment. At the same time, LSTM introduces cell state to realize the function of information transmission in the whole LSTM [12].

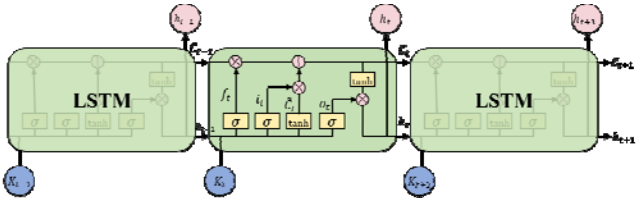

Fig 1 Specific network structure diagram of LSTM

First of all, the forgetting door combines the output information of the hidden layer at the previous time with the input information at the current time, and obtains the proportion of forgotten information through the sigmoid activation function to determine the old information to be forgotten.

$$f_t = \sigma(w_f \cdot [h_{t-1}, X_t] + b_f) \tag{1}$$

where, f_t is the output of the forgetting gate, the range is 0 to 1; The weight matrix w_f represents the forgetting gate; b_f is the offset item of the forgetting gate; σ is the sigmoid activation function; h_{t-1} is the output information of the previous hidden layer; X_t is the input information of the hidden layer at the current time.

Then the input gate determines what new information is stored in the current cell state. There are two steps. First, the output information of the hidden layer at the previous time is combined with the input information at the current time, and the proportion of updated information is obtained through the sigmoid activation function to determine the information needed to be updated. The second is to combine the output information of the hidden layer at the previous time with the input information at the current time, and obtain the new temporary cell state information through the tanh activation function.

$$\begin{aligned} i_t &= \sigma(w_i \cdot [h_{t-1}, X_t] + b_i) \\ \tilde{C}_t &= \tanh(w_c \cdot [h_{t-1}, X_t] + b_c) \end{aligned} \tag{2}$$

where, i_t is the output of the input gate; The weight matrix w_i represents the input gate; b_i is the offset entry of the input gate; $\tilde{C}_t$ is temporary cell state information; w_c is the corresponding weight matrix of $\tilde{C}_t$; b_c is the corresponding offset term of $\tilde{C}_t$; tanh is the tanh activation function.

Finally, the output layer determines the information required for the output of the hidden layer. First, the output information of the hidden layer at the previous time is combined with the input information at the current time, and the proportion of output information is obtained through the sigmoid activation function to determine the required output information; The second is to calculate the output of the output gate and the new cell state through the tanh activation function to obtain the new hidden layer information.

$$\begin{aligned} o_t &= \sigma(w_o \cdot [h_{t-1}, X_t] + b_o) \\ h_t &= o_t \cdot \tanh(C_t) \end{aligned} \tag{3}$$

where, o_t is the output of the output gate; The weight matrix w_o represents the output gate; b_o is the offset entry of the output gate; h_t is the output of the hidden layer at the current time.

3 Attention-LSTM fault diagnosis model

In order to solve the problem that the accuracy of the model decreases with the increase of the number of network layers, Relu activation function and batch normalization processing are added to the variable attention layer, Bi-LSTM network layer and time attention layer, so as to accelerate the model convergence and prevent the model gradient disappearing and gradient explosion.

3.1 Variable attention layer

In the Attention-LSTM fault diagnosis model, the core of variable Attention layer is the variable attention mechanism, which is borrowed from the self-attention mechanism in Transformer model. First, the input sequence matrix X is mapped to two different Spaces to form two different matrices, namely the Query matrix and the Key matrix.

$$\begin{aligned} Q &= XW^Q \in \mathrm{R}^{N \times d_q} \\ K &= XW^K \in \mathrm{R}^{N \times d_k} \end{aligned} \tag{4}$$

where, $X \in \mathrm{R}^{N\times T}$ is the input sequence matrix; T is the time step of the input sequence matrix, N is the number of variables of the input sequence matrix; $d_q = d_k$ is the dimension of the mapping; $W^Q \in \mathrm{R}^{T\times d_q}, W^k \in \mathrm{R}^{T\times d_k}$ is a randomly generated weight matrix.

Then the dot product of Query and Key is processed to obtain the attention score, and the attention score matrix is scaled. Then, the scaled attention score matrix is probabilized using Softmax function, so that the obtained attention score probability matrix reflects the correlation degree of N monitoring variables in T time step. Finally to score probability matrix and the original input matrix X for matrix multiplication, which makes the output characteristic of the matrix contains a variable domain.

$$\mathrm{Attention}(Q,K,X) = \mathrm{softmax}(\frac{QK^T}{\sqrt{d_k}})X \in \mathrm{R}^{N\times T} \quad (5)$$

where, $X \in \mathrm{R}^{N\times T}$ is the input sequence matrix; T *I*s the time step of the input sequence matrix, N is the number of variables of the input sequence matrix; Attention is the variable attention mechanism.

3.2 LSTM Network layer

First, the input sequence matrix of the LSTM network layer is

$$\begin{aligned} X &= (X_1,\cdots,X_{t-1},X_t,X_{t+1},\cdots,X_T)^T \in \mathrm{R}^{T\times N} \\ X_t &= (x_{t,1},x_{t,2},\cdots,x_{t,N}) \in \mathrm{R}^N \end{aligned} \quad (6)$$

Then, the LSTM network layer extracts the features of the input sequence at every moment, and the calculation formula of the internal hidden layer information is

$$h_t = L(h_{t-1},X_t) \in \mathrm{R}^{d_f} \quad (7)$$

where, L represents LSTM network layer internal operation; h_t represents the hidden layer of information at that moment; d_f represents the dimension of the hidden layer map.

Since the original LSTM network can only extract time sequence information from a single direction, and the telemetry data in the satellite attitude control system has a strong time correlation, this paper adopts Bi-LSTM (BI-LSTM) to extract forward and reverse time sequence information of the input data. The Bi-LSTM network architecture is shown in Fig 2.

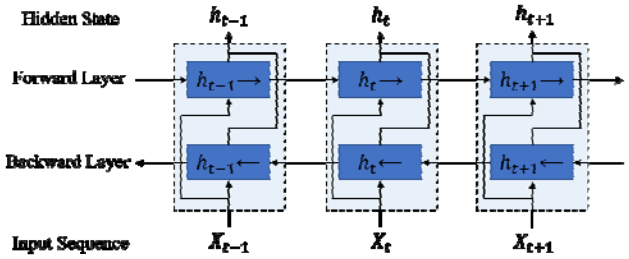

Fig 2 Network architecture diagram of Bi-LSTM

In the Bi-LSTM network, the network reads the forward time information and reverse time information of the input data at the same time, and then calculates the forward and reverse hidden layer information.

$$\begin{aligned} \overrightarrow{h_t} &= L(\overrightarrow{h_{t-1}},X_t) \in \mathrm{R}^{d_f} \\ \overleftarrow{h_t} &= L(\overleftarrow{h_{t+1}},X_t) \in \mathrm{R}^{d_f} \\ h_t &= (\overrightarrow{h_t},\overleftarrow{h_t}) \in \mathrm{R}^{2d_f} \end{aligned} \quad (8)$$

where, $\overrightarrow{h_t} \in \mathrm{R}^{d_f}$ represents the current moment of the forward hidden layer information; $\overrightarrow{h_{t-1}} \in \mathrm{R}^{d_f}$ represents the forward hidden layer information of the previous moment; $\overleftarrow{h_t} \in \mathrm{R}^{d_f}$ represents the current moment of the reverse hidden layer information; $\overleftarrow{h_{t+1}} \in \mathrm{R}^{d_f}$ reverse hidden layer information representing the next moment in the future.

3.3 Time attention layer

Although LSTM network can solve the problem of long distance dependence caused by gradient disappearing or gradient explosion to some extent, LSTM network still has serious long distance dependence problem due to the inherent recursive loop architecture of RNN series network. In fault diagnosis, the fault information at the earlier time is more helpful to the fault diagnosis of the attitude control system. In order to highlight the importance of the output results at the earlier fault time for fault diagnosis, the time attention layer is introduced and the weighted summation of fault characteristics at each moment is carried out with the help of the time attention mechanism. In this way, the results obtained through the time attention layer incorporate more information about earlier moments than the output of the last time step of the LSTM network layer, thereby increasing their importance.

Firstly, Relu activation function and batch normalization are performed on the final output sequence matrix of the LSTM network layer, and then weight vector is introduced to integrate important information, and probability vector of weight score is obtained through Softmax function. Finally, the final output sequence matrix of the original LSTM network layer is countermultiplied with the weight score probability vector to get the final output of the time attention layer.

$$\begin{aligned} M &= \mathrm{Relu}(BN(X)) \in \mathrm{R}^{T\times 2d_f} \\ score &= \mathrm{softmax}(Mw) \in R^{T\times 1} \\ T &= X \cdot score \in \mathrm{R}^{T\times 2d_f} \end{aligned} \quad (9)$$

where, $X \in \mathrm{R}^{T\times 2d_f}$ is the final output sequence matrix of LSTM network layer; $w \in \mathrm{R}^{2d_f}$ is a randomly generated weight vector; T is the time step of the input sequence matrix, and $2d_f$ is the mapping dimension of the hidden layer.

4 NUMERICAL SIMULATIONS

4.1 Satellite semi-physical simulation platform

This study uses data from the dark matter particle explorer platform to confirm the viability of the proposed network. Dark matter particle explorer platform is a simulation test system designed based on the actual in-orbit flight state of dark matter particle explorer “Wukong”, which launched in late 2015 in China. Dark matter particle explorer platform can simulate the main external interfaces and dynamics characteristics of the dark matter particle explorer. Its physical map is shown in Fig. 3.

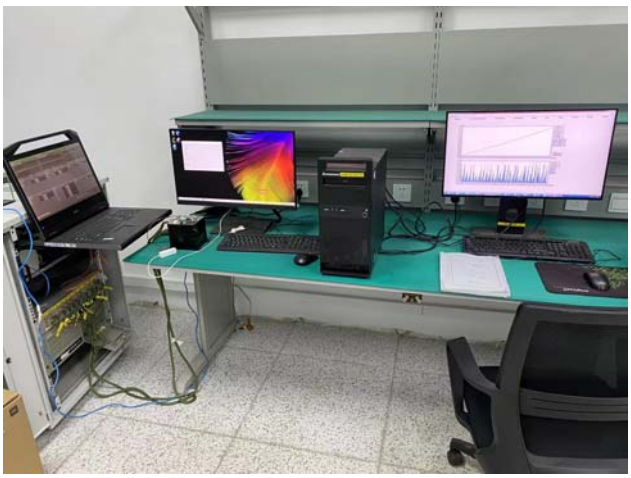

Fig 3 Satellite semi-physical simulation platform

In terms of equipment composition, the dark matter particle explorer platform consists of a satellite simulation platform and an attitude control dynamics simulation system. The satellite simulation platform includes two parts: on-board computer simulator and on-board stand-alone simulator, and the attitude control dynamics simulation system is a test system to verify the correctness of satellite attitude control function, performance, attitude, and control algorithm. Fig. 4 shows the structure of the equipment of the dark matter particle explorer platform.

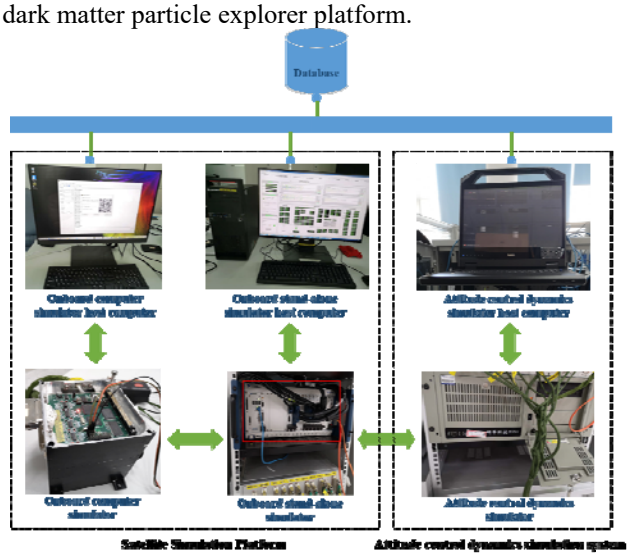

Fig 4 Structure diagram of the equipment composition of the satellite platform

4.2 Fault selection and data processing

The fault types selected in this experiment are all slow faults, and compound faults are added, so as to test the capability of LSTM network layer in time domain feature extraction. The selected faults are all from the actuator, namely, the output torque attenuation of reaction wheel A, the output torque attenuation of reaction wheel C, and the torque attenuation of reaction wheel A and C. The corresponding fault type description and variable type description are shown in Table 1.

Table 1 Fault types and label categories

Fault	Lable
Fault-free	F_0
Flywheel A Output Torque Decay	F_1
Flywheel C Output Torque Decay	F_2
Flywheel A and C Output Torque Decay	F_3

The Attention-LSTM fault diagnosis experiment adopts the same data acquisition, pre-processing and data set partitioning methods as the TV Transformer fault diagnosis experiment. For each fault type, 24h data is collected respectively. The data samples for each type are 86400 × 17, and there are 4 categories in total, so the total sample is 345,600 × 17. After downsampling all the data and changing the sampling step from 1s to 10s, the total sample after sampling is 34560 × 17. If the time step is set to 60, that is, T = 60, the total number of samples in the dataset is 576 × 60 × 17. The total sample number of the data set was divided into the training set and the test set according to the ratio of 3:1. The sample number of the training set was 432 × 60 × 17, and the sample number of the test set was 144 × 60 × 17.

4.3 Experiment-related parameter settings

In this experiment, the Attention-LSTM satellite attitude control system fault diagnosis model is run under the Pytorch deep learning framework, and the specific operating environment is as follows: Python 3.8 version, Pytorch 1.7 version, Cuda 11.0 version. The hardware environment is 10-core Intel(R) Xeon(R) Gold 5218R CPU @ 2.10GHz and RTX 3090 GPU.

4.4 Experimental results

According to the experimental analysis, under the above optimal parameter Settings, the highest accuracy of the test set can reach 97.25% in the training process of Attention-LSTM, and the final stability is near 96.5%, and the training time is 45.5 minutes. The change of Attention-LSTM recognition accuracy in the training process is shown in Fig 5.

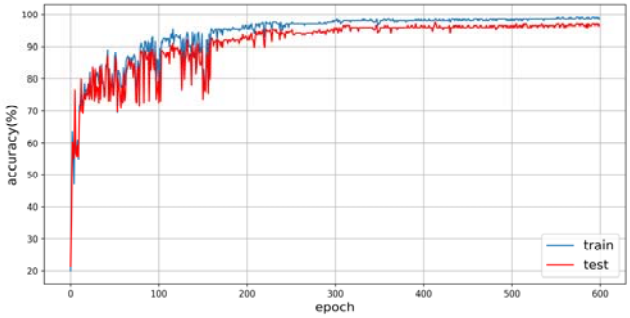

Fig 5 Change chart of Attention-LSTM recognition accuracy

In order to further verify the effectiveness of Attention-LSTM network model in fault diagnosis of satellite attitude control system, this paper compares its results with a series of network models, and the comparison results are shown in Table 2. The comparison network models are attention-LSTM without adding the temporal Attention layer, time variable Transformer (TV Transfoemer), TV Transformer with only the temporal attention module, and original Transformer (Vanilla) Transfoemer, time-only attention module Vanilla Transformer, 1D-CNN, Bi-LSTM, and Att-BLSTM. In the comparison experiment, the operating environment and training parameters of each network model remain unchanged.

Table 2 Description of the results of the comparison experiments

Network Model	accuracy rate (%)	training time (min)
Attention-LSTM	**96.5**	**45.5**
Attention-LSTM with no TA layer	93.67	41.37
TV transformer	89.85	28.07
TV Transformer with only TA module	73.17	16.13
Vanilla Transformer	88.67	25.41
Vanilla transformer with only TA module	70.33	12.93
1D-CNN	83.89	20.62
Bi-LSTM	88.5	38.74
Att-BLSTM	90.5	40.06

As can be seen from the table, the recognition accuracy of Attention-LSTM network has been improved to a certain extent compared with other networks. However, due to the recursive loop architecture of LSTM network, it does not have the ability to process data in parallel, so the training is longer. Due to the mediocre ability of the attention mechanism to extract time domain features, it can be seen from the table that the recognition accuracy of TV Transformer with only time attention module is worse than that of Vanilla Transformer with only time attention module.

5 CONCLUSIONS

In this paper, the development of recurrent neural network (RNN) is briefly introduced. The internal structure of LSTM neural network is systematically introduced and the Attention-LSTM fault diagnosis model is described in detail, and the variable Attention layer, LSTM network layer and time attention layer are introduced in detail. Then, the fault diagnosis degree of Attention-LSTM fault diagnosis model to satellite platform experimental data is analyzed in detail. For the Attention-LSTM network model, this chapter also carries out t-SNE visual qualitative analysis to observe the feature extraction degree of each unit in the Attention-LSTM network model.

REFERENCES

[1] Yin S, Xiao B, Ding S X, et al. A review on recent development of spacecraft attitude fault tolerant control system [J]. IEEE Transactions on Industrial Electronics, 2016, 63(5): 3311-3320.

[2] Ma Y, Jiang B, Tao G. Adaptive actuator failure identification for microsatellites under closed-loop control [J]. IEEE Transactions on Control Systems Technology, 2014, 23(3): 910-923.

[3] Suo M, Zhang M, Zhou D, et al. Fault diagnosis of satellite power system using variable precision fuzzy neighborhood rough set[C]//2017 36th Chinese control conference (CCC). IEEE, 2017: 7301-7306.

[4] Li Y, Lei M, Liu P, et al. A Novel Framework for Anomaly Detection for Satellite Momentum Wheel Based on Optimized SVM and Huffman-Multi-Scale Entropy[J]. Entropy, 2021, 23(8): 1062.

[5] Folami M O. Reaction Wheels Fault Isolation Onboard 3-Axis Controlled Satellite using Enhanced Random Forest with Multidomain Features[D]. University of Windsor (Canada), 2021.

[6] ElDali M, Kumar K D. Fault Diagnosis and Prognosis of Aerospace Systems Using Growing Recurrent Neural Networks and LSTM[C]//2021 IEEE Aerospace Conference (50100). IEEE, 2021: 1-20.

[7] Wei X, Mu X, Jiang T, et al. Fault Diagnosis Method of Spacecraft Control Systems Based on PCA-ResNet[C]//Journal of Physics: Conference Series. IOP Publishing, 2022, 2258(1): 012062.

[8] Xiao B, Yin S. A deep learning based data-driven thruster fault diagnosis approach for satellite attitude control system[J]. IEEE Transactions on Industrial Electronics, 2020, 68(10): 10162-10170.

[9] Xiang G, Tao R, Peng Y, et al. Unsupervised deep learning for fault detection on spacecraft using improved variational autoencoder[C]//2020 Chinese Automation Congress (CAC). IEEE, 2020: 5527-5531.

[10] Li L, Li C, Tong X, et al. Fault diagnosis method of satellite attitude control system based on stacked autoencoder network[C]//Seventh Symposium on Novel Photoelectronic Detection Technology and Applications. SPIE, 2021, 11763: 1196-1207.

[11] Cho K, Van Merriënboer B, Gulcehre C, et al. Learning phrase representations using RNN encoder-decoder for statistical machine translation[J]. arXiv preprint arXiv:1406.1078, 2014.

[12] Hochreiter S, Schmidhuber J. Long short-term memory[J]. Neural computation, 1997, 9(8): 1735-1780.

Proceedings of the 3rd Conference on Fully Actuated System Theory and Applications
May 10-12, 2024, Shenzhen, China

Fault Diagnosis of Rotating Equipment Bearings Based on VMD-MSGWO-SVM

Jibao Deng [1], Yimin Liu [2], Zixuan Li [3]

1.Wuhan Maintenance and Installation Petrochemical Engineering Co., LTD,WuHan;430082,China
E-mail: xiaobaovenus@163.com
2.Academy of Information Science and Engineering, Wuhan University of Science and Technology, Wuhan; 430081, China

Abstract: In this paper, the bearing fault problem of rotating equipment is studied by using support vector machine (SVM) model classification method. In order to solve the problem of low accuracy of using SVM to detect the fault for bearing, the method of variational mode decomposition (VMD) is introduced to extract features from original vibration data and the intelligent optimization algorithm of MSGWO is introduced to optimize parameters of SVM, which can improve fault diagnosis performance of classification system. A variety of comparative experiments are carried out by using FEMTO-ST bearing data set which is open source on the internet. The results show that the proposed algorithm has high prediction accuracy and is superior to the present methods in classification.

Key Words: SVM, Rotating Equipment Bearings Fault, VMD, Improved Grey Wolf Optimization Algorithm.

1 Introduction

Rotating equipment is widely used in all aspects of industrial production, and its reliability directly affects the production efficiency of enterprises[1,2]. With the increasing of consumption, the performance of bearing is gradually degraded. Adding the influence of complex working condition, the probability of failure aggrandizes randomly [3]. Therefore, it is important to detect faults of bearing in time by making full use of all kinds of sensor data.

The vibration signal of rolling bearing is nonlinear and complex, which is affected by many factors, so it is very important to extract efficient information from it. However, in a certain time range, the In a certain time range, the statistical character of the vibration signal changes with time, so it must be analyzed and processed. Time-frequency analysis methods mainly include wavelet transform, empirical mode decomposition (EMD) and local mean decomposition (LMD)[5-7]. EMD can adaptively decompose the signal into multiple characteristic mode functions. [8] proposed a bearing fault diagnosis method based on EMD and improved Chebyshev distance, and verified its accuracy and robustness through experiments. [9] put forward a new variable metric method, called mode decomposition (variable mode decomposition, VMD). However, in the application of VMD, it is difficult to accurately choose the decomposition level and the quadratic penalty factor. In [10], in order to overcome the problem of information loss, the approximate complete reconstruction criterion is used to determine the appropriate number of modes for bearing vibration signals. Taking wheel bearing fault of high-speed locomotive as an example, the validity of this method is verified by comparison with the original VMD, EMD and EEMD methods.

With the development of machine learning, the combination of intelligent learning algorithm and rolling bearing fault identification has been open and challenging issue.The method of SVM solves the problems that ANN is easy to fit and BPNN is easy to fall into local optimal, so it has been widely used in various fields of pattern recognition. [11] established a hybrid support vector machine model and applied it to bearing fault classification. The selection of structural parameters of support vector machine is a difficult problem, which directly affects the performance of support vector machine. Grey Wolf Optimization (GWO) algorithm has the advantages of good optimization performance and easy implementation, and is widely used in the optimization of SVM structural parameters. [12] proposed a rolling bearing fault diagnosis model based on GMO-SVM. The experimental results show that the GWO-SVM fault diagnosis model is more effective than the SVM model, but it has the limitation of falling into local optimal. Therefore, these algorithms can still be improved. [13] developed an improved GWO algorithm to optimize SVM and applied it to the fault diagnosis of power system. The experimental results showed that IGWO-SVM model could prevent the population from falling into the local optimal, and the convergence speed was greatly improved, which proved the feasibility of the improved algorithm.

In this paper, an intelligent optimization algorithm of VMD-MSGWO-SVM is proposed to detect the faults of bearing of rotating equipment. Firstly, the bearing vibration signal is decomposed by VMD method, and the feature matrix is constructed by combining with the time-domain signal features. Then, an optimization algorithm based on MSGWO is proposed to determine the optimal penalty factor C and kernel function parameter g of SVM. Thirdly, the optimized SVM model is trained through the extracted eigenmatrix, and the test set is input into the trained diagnosis model. Finally, the fault diagnosis method proposed in this paper is evaluated comprehensively from three aspects: optimization fitness curve, accuracy and diagnosis time, and the effectiveness of the proposed method is demonstrated by experimental analysis.

This article is organized as follows: The second section introduces the relevant theoretical basis. The proposed method is summarized in Section 3, and the experimental and simulation results are presented in detail in Section 4. The fifth section gives a brief summary of this paper.

2 Theoretical basis

2.1 VMD

The multi-component signal is decomposed into a series of submodes by using adaptive Wiener filter banks. In VMD, the output can be written to solve a constrained variational problem, and its mathematical equation can be expressed as:

$$\begin{cases} \min\limits_{\{u_k\},\{\omega_k\}} \left\{ \sum\limits_{k=1}^{K} \left\| \partial_t \left[(\delta(t)+\frac{j}{\pi t}) * u_k(t) \right] e^{-j\omega_k t} \right\|_2^2 \right\} \\ s.t \sum\limits_{k=1}^{K} u_k = f \end{cases} \tag{1}$$

where, ω_k is the frequency center of each IMF; u_k is the kth IMF; $\{u_k\}$ represents the set of modal components, $\{\omega_k\}$ represents the set of center frequencies corresponding to the modal components, $\delta(t)$ is the Dirac function, and f is the original vibration signal.

By introducing Lagrange multiplication operator λ and quadratic penalty factor α into equation (1), the variational model of VMD algorithm is solved. Then the constrained variational problem can be transformed into an unconstrained variational problem, and the Lagrange expression can be obtained as follows

$$L(u_k,\omega_k,\lambda) = \alpha \sum_{k=1}^{K} \left\| \partial_t \left[(\delta(t)+\frac{j}{\pi t}) * u_k(t) \right] e^{-j\omega_k t} \right\|_2^2 + \left\| f(t) - \sum_{k=1}^{K} u_k(t) \right\|_2^2 + \left\langle \lambda(t), f(t) - \sum_{k=1}^{K} u_k(t) \right\rangle \tag{2}$$

the method of alternate direction method of multipliers multiplier(ADMM) method is used to solve the optimal solution of the constructed Lagrange function, and the update formulas of k modal components and center frequencies are obtained as follows

$$\hat{u}_k^{n+1}(\omega) = \frac{f(\omega) - \sum\limits_{i=1,i<k}^{K} \hat{u}_i^{n+1}(\omega) - \sum\limits_{i=1,i>k}^{K} \hat{u}_i^{n}(\omega) + \frac{\hat{\lambda}^n(\omega)}{2}}{1+2\alpha(\omega-\omega_k^n)^2} \tag{3}$$

$$\omega_k^{n+1} = \frac{\int_0^\infty \omega |\hat{u}_k(\omega)|^2 \, d\omega}{\int_0^\infty |\hat{u}_k(\omega)|^2 \, d\omega} \tag{4}$$

where, $\hat{u}_k^{n+1}(\omega)$ is the residual quantity; ω_k^{n+1} is the power spectrum center of gravity of the current mode; Inverse FFT transformation of $\hat{u}_k(\omega)$ yields the real part $\hat{u}_k(t)$.

2.2 MSGWO

The algorithm of GWO is proposed by Mirjalili et al. In [14]. The basic principle is to imitate te population system of the gray wolf. The gray wolves are divided into α、β、δ and ω, and the gray wolf ω accepts the leadership of the the wolves α、β、δ during the hunting process. The process of gray wolf algorithm can be divided into three stages: encircling, pursuit and attack. However, the GWO algorithm only uses linear hunting to capture prey, which limits its search range and accuracy, resulting in slow convergence and poor local optimization ability. To solve these problems, this paper proposes a fusion GWO algorithm, which includes improving the population initialization method of GWO, adaptively updating the location of gray wolves, and improving the control parameter a.

1) Improved Tent Chaos initialization population

The initialization of a swarm algorithm affects its search performance. Since there is no prior information, individuals are usually generated by random initialization. However, sometimes individuals are not evenly distributed in the search domain, which may cause individuals to be far from the global optimal solution, and result in a low convergence rate. Chaos is a common phenomenon in nonlinear systems with the characteristics of ergodicity, randomness and regularity. Searching by chaotic variables has more advantages than unordered random search. The analysis of Tent chaotic iterative sequence shows that there are small periods and unstable periodic points in the sequence. In order to avoid Tent chaotic sequence falling into small period points and unstable period points during iteration, a random variable $rand(0,1)\times\frac{1}{N}$ is introduced into the original Tent chaotic mapping expression. The improved Tent chaotic mapping expression is as follows:

$$x_{i+1} = \begin{cases} 2x_i + rand(0,1)\times\frac{1}{N}, 0 \le x \le \frac{1}{2}; \\ 2(1-x_i) + rand(0,1)\times\frac{1}{N}, \frac{1}{2} < x \le 1. \end{cases} \tag{5}$$

where N is the number of particles in the sequence, and rand (0,1) is the random number between [0,1]. Introducing random variable $rand(0,1)\times\frac{1}{N}$ not only maintains the randomness, ergodicity and regularity of Tent chaotic mapping, but also effectively avoids iteration falling into small periodic points and unstable periodic points.

2) Adaptive hunting weight coefficient.

In the original GWO hunt, the weight coefficients of the three wolves are the same, which apparently contradicts the hierarchy of real wolves. Inspired by the mass renewal formula in the gravity search algorithm [15], the method of adaptive weight coefficients based on fitness is introduced to measure the contribution of different leading wolves. The mathematical model is defined as follows:

Minimization function:

$$\omega_i = \frac{3f_\delta - f_i}{3f_\delta - f_\alpha}, \theta_i = \frac{\omega_i}{\sum_{j=\alpha,\beta,\delta}\omega_j}, i \in \{\alpha,\beta,\delta\} \tag{6}$$

Maximization function:

$$\omega_i = \frac{3f_i - f_\delta}{3f_\alpha - f_\delta}, \theta_i = \frac{\omega_i}{\sum_{j=\alpha,\beta,\delta}\omega_j}, i \in \{\alpha,\beta,\delta\} \tag{7}$$

Where, f and θ are the fitness and weight coefficients of the corresponding wolves, and ω is the meaningless intermediate variable.

3) Improve control parameters a.

The parameter a in GWO is used to control the exploration and development process. The hunting process of gray wolves in nature is complex, and simple linear changes cannot effectively characterize their search process. This paper uses a sinusoidal variation to improve the linear search process, and its expression is as follows:

$$a = 1 + \sin\left(\frac{\pi}{2} + \pi \times \frac{iter}{Max_iter}\right) \tag{8}$$

where *iter* represents the number of current iterations and *max_iter* denotes the maximum number of iterations.

Fig.1 shows a difference between this nonlinear function and the linear function in the standard GWO. It can be seen from the Fig.1, the nonlinear function in this paper has a wider value of a in the early iteration stage, and its scope for exploration is also wider. In the later iteration, a is smaller, which is conducive to local development of the algorithm and speed up convergence.

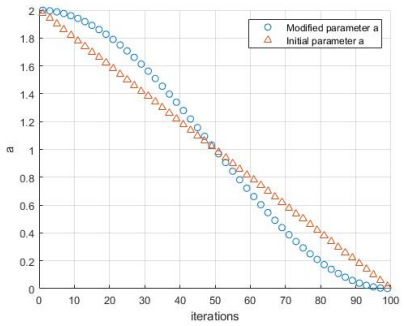

Fig.1 Improved control parameter curve

2.3 SVM

Viewing fault diagnosis as a classification task, we can consider the presence of two-dimensional eigenvectors $x_1, x_2, \cdots, x_{n_1+n_2}$,Where $x_1, x_2, \cdots, x_{n_1}$ belongs to normal class Ω_{no} , $x_{n_1+1}, x_{n_1+2}, \cdots, x_{n_1+n_2}$ belongs to fault class Ω_{fa} , Mark the data in Ω_{no} as 1 and the data in Ω_{fa} as -1. The aim of the Support Vector Machine (SVM) is to create an optimal classifier [13], specifically, to formulate an optimal classification hyperplane. The structure of the SVM classifier is as follows:

$$\Omega(x) = w^{*T}\phi(x) + b^* \tag{9}$$

Here x represents the two-dimensional feature vector to be classified, w^* stands for the optimal p-dimensional column vector to be determined, and b^* is the optimal threshold. $\phi(x)$ signifies the p-dimensional transformation of sample x from the input space to the feature space, also denotes the p-dimensional feature vector. The classifier categorizes the dataset x_u as follows:

$$\begin{cases} x_u \in \Omega_{no}, if\ \Omega(x) > 0, \\ x_u \in \Omega_{fa}, otherwise. \end{cases} \tag{10}$$

To solve the optimal hyperplane, it can be converted to

$$\min_{w,b,\xi} \frac{1}{2} w^T w + C\sum_{i=1}^{n} \xi_i \tag{11}$$
$$s.t. \begin{cases} y_i\Omega(x) \geq 1 - \xi_i \\ \xi_i \geq 0 \end{cases}, i = 1, 2, \cdots, n_1 + n_2$$

Where C is the Regularization parameter, there is a penalty coefficient, which determines the trade-off between empirical risk and complexity (VC dimension). ξ_i is a non-negative relaxation variable introduced into constraints. The optimization issue is converted into a dual quadratic programming challenge:

$$\max_{\alpha} \sum_{i=1}^{n} \alpha_i - \sum_{i=1}^{n}\sum_{j}^{n} \alpha_i\alpha_j y_i y_j K(x_i, x_j) \tag{12}$$
$$s.t. \begin{cases} \sum_{i}^{n} y_i\alpha_i = 0 \\ 0 \leq \alpha_i \leq C \end{cases}, i = 1, 2, \cdots, n_1 + n_2$$

Where α_i is the Lagrange multiplier vector that needs to be adjusted, $K(x_i, x_j)$ is the kernel function used to replace the inner product $[\varphi(x_i) \bullet \varphi(x_j)]$ in the feature space, and the decision function obtained after solving the above problems is

$$f(x) = \mathrm{sgn}[\sum_{i=1}^{n} \alpha_i^* y_i K(x_i, x_j) + b^*] \tag{13}$$

Where $\mathrm{sgn}(\bullet)$ is a symbolic function. Using different kernel functions as kernel functions of SVM, learning devices can be formulated to achieve various kinds of nonlinear decision boundaries in the input space.

3 Construction of characteristic matrix

In fault diagnosis, it is one of the most important steps to select appropriate fault characterization and extract characteristic values that can effectively reflect the fault type. In this paper, sample entropy combined with representative time domain index is used to construct feature matrix to explore its effectiveness in fault identification of rolling bearings. Due to the relatively difficult collection of low-frequency fault samples, it can take years to obtain data for all fault types in experiments. So the open source FEMTO-ST bearing data set is used in this paper.

In order to visually observe the time domain characteristics of vibration signals, the time domain waveforms is drawn to show the vibration performance of normal bearings, bearings with different fault types and fault depths by using the acquired vibration data. The vertical axis represents acceleration and the horizontal axis is time (unit /s) in Fig.2 to Fig.5.

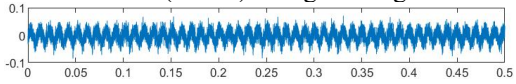
Fig2. Normal bearing vibration signal

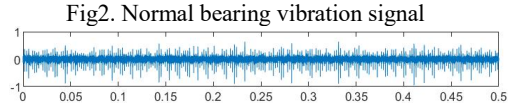
Fig3. Outer ring failure vibration signal

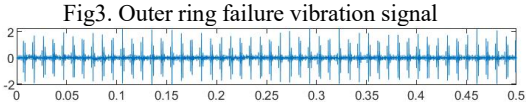
Fig4. Inner ring fault vibration signal

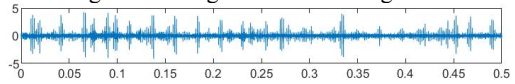
Fig5. Vibration signal of rolling element fault

Observing the time domain signal diagram of bearings in different fault states, the difference can be intuitively found. Note that the differences in the time domain signal actually reflects the characteristics of different types of faults. However, it is time-consuming and impractical to directly observe all the time domain signals. Therefore, we can describe and distinguish these different fault types by calculating the time domain characteristic index. In this paper, we choose two representative characteristic indexes of time domain, i.e., effective value and margin index. It should be pointed out that only selecting time domain features to construct feature matrix is not comprehensive enough. In this paper, the original vibration signal is processed through VMD decomposition in the frequency domain, and IMF with limited bandwidth is separated, and then the sample entropy (SE) value of each IMF is calculated. Unlike EMD, VMD can automatically adjust the number of decomposition, but it needs to be set by itself. Using the method in [10], the number of VMD decomposition in this paper are adopted as follows: $K = 4, \alpha = 2000$. The VMD model was constructed by

MATLAB_R2021a to decompose the original vibration signal.

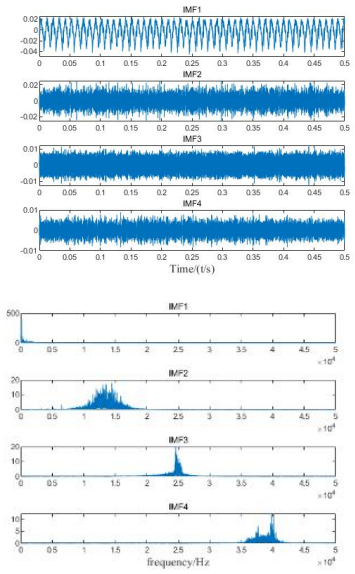

(a) IMF time domain diagram and frequency domain diagram of normal bearings

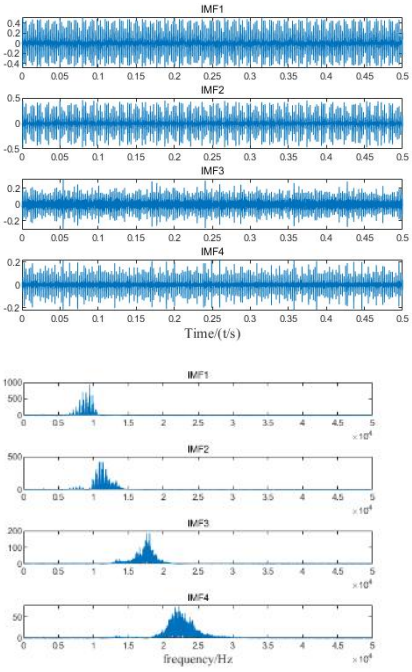

(b) IMF time-domain and frequency-domain diagrams under outer ring failure

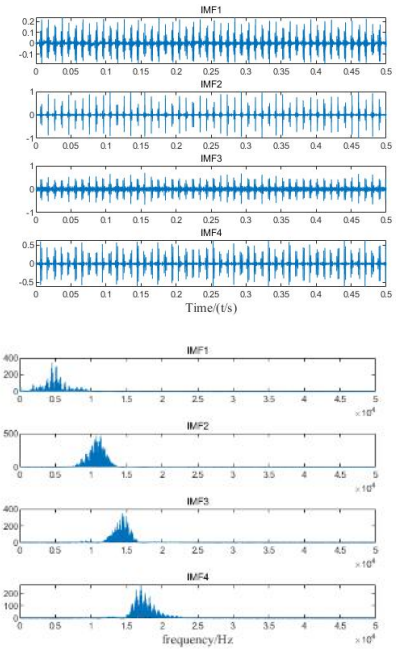

(c) IMF time-domain and frequency-domain diagrams under inner circle failure

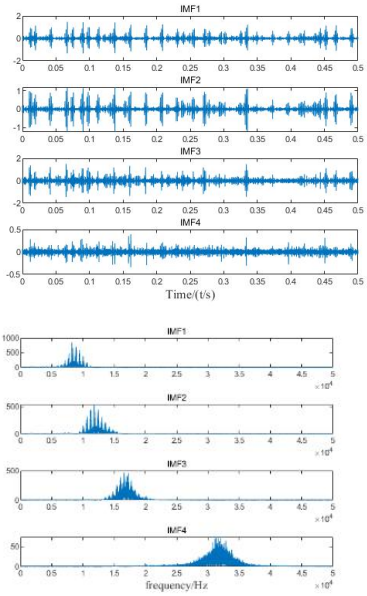

(d)IMF time-domain diagram and frequent-domain diagram under rolling element failure

Fig.6 Test bearing normal and fault decomposition spectrum

As shown in Fig.6, there are obvious differences in the spectrum distribution and amplitude of bearing IMF under different states. SE values of each IMF are calculated, the difference of IMF is quantified by decomposition, and the feature matrix is constructed by combining with two time-domain indicators, which is convenient to be used as the feature input of the identification model.

4 Experimental and simulation results

The collected experimental data are intercepted according to 2048 sample points in each group, and divided into different groups according to the fault types. Each label has 50 groups data, and comparative experiments are conducted by constructing SVM, PSO-SVM and GGO-SVM diagnostic

models to verify the feasibility and effectiveness of the MSGGO-SVM method. The specific diagnostic model construction process is shown in Fig 7.

Then VMD is used to decompose the original signal and calculate the effective value of vibration signal, margin index and SE value of each IMF, and the TDI-SE feature matrix is constructed. Therefore, the experimental data were converted into 50*6 sets of data after feature extraction, of which 35*6 sets were used as the training set and the remaining 15*6 sets of evolution data were used as the test set. The first two columns of each group of samples are listed as time domain features, and the last four columns correspond to four energy entropy features, and each type of sample is marked, as shown in Table 1.

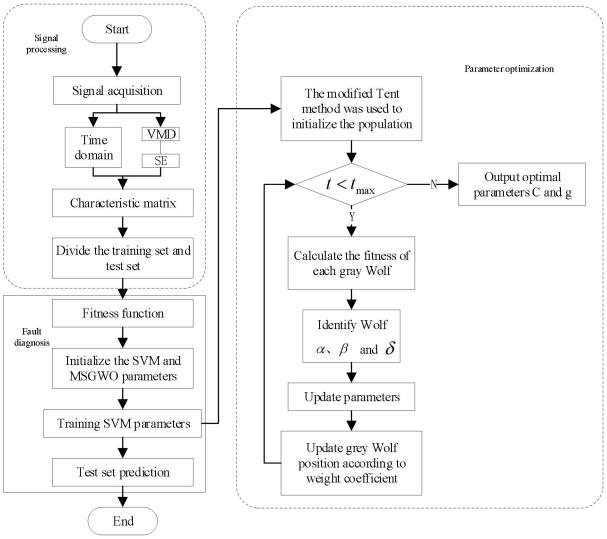

Fig7.VMD-MSGWO-SVM model construction flow chart

Table 1:Fault Type And Label Value

Fault category	Fault code	Tag value
Normal bearing	f0	1
Outer ring fault	f1	2
Inner ring fault	f2	3
Ball failure	f3	4

In this paper, PSO-SVM and GGO-SVM models are constructed respectively, and the superiority of MSGGO-SVM model is verified from different aspects. The quality of the model is judged by the diagnosis time and diagnosis accuracy. In terms of parameter settings, the population number and iteration times were ensured to be consistent, and GWO parameter Settings were consistent with MSGWO. The training data set was input into each model and 15 groups of test sets were predicted. The prediction results were shown in Fig 7~9.

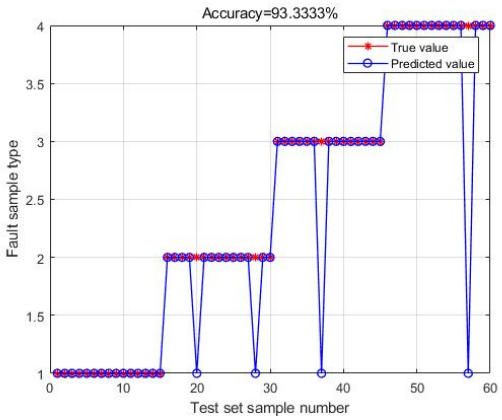

Fig.8 PSO-SVM model diagnosis results

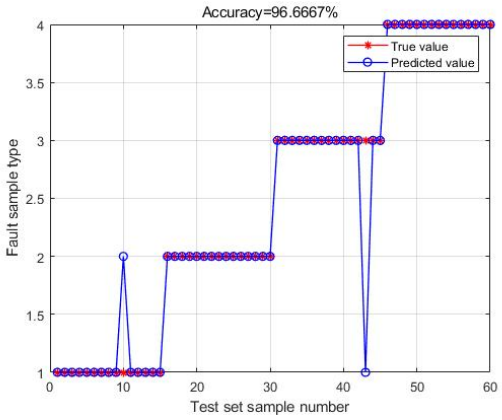

Fig.9 GWO-SVM model diagnosis results

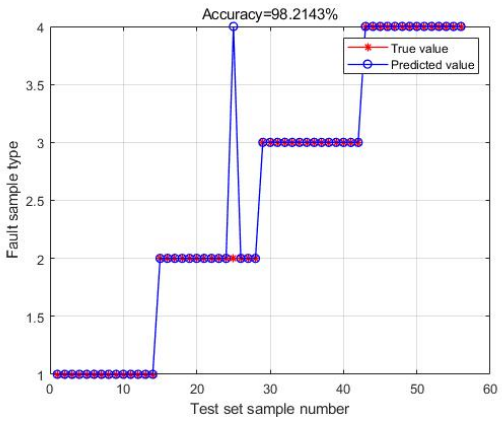

Fig.10 MSGWO-SVM model diagnosis results

In order to intuitively analyze the superiority of MSGGO-SVM model, Table 2 statistics the recognition rate and time of each model. And the comparison of fitness curves of different algorithms is shown in Fig.10.

Table 2:Performance Comparison Of Different Algorithms

Model	C、g	Recognition rate	Time/s
SVM	10、0.01	80.00 %(48/60)	0.495
PSO-SVM	44.877、2.0164	93.33%(56/60)	9.555
GWO-SVM	47.8066、9.0786	96.67%(58/60)	2.496
MSGWO-SVM	79.3735、6.1115	98.21%(59/60)	2.865

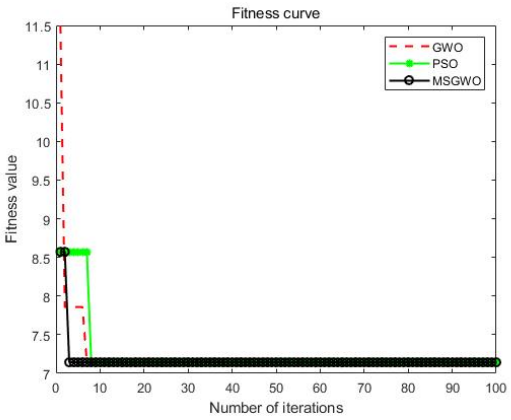

Fig.11 Fitness curve comparison diagram

According to the recognition results of each model, the recognition of MSGWO-SVM model is the most accurate among all established models, and the time is more than half less than that of PSO-SVM. Compared with the GWO-SVM model, the recognition rate of MSGWO-SVM is slightly higher, because MSGWO individual updating strategy tends to be complex, more time is spent on training time, but by comparing the fitness value curve, it can be found that due to the introduction of improved Tent chaos initialization population and the introduction of adaptive weights to update the position of wolves, By making the wolves more accurate in their exploration direction, MSGWO can search deeper for prey, that is, converge faster. However, the SVM model is difficult to achieve high-quality diagnosis because the parameters are set to default values, and the recognition accuracy is only 80.00% and the classification error is high. Therefore, compared with the diagnostic accuracy of SVM, PSO-SVM and GWO-SVM models, the proposed model based on VMD-MSGWO-SVM has higher advantages in the direction of motor bearing fault diagnosis.

5 Conclusion

In order to solve the problem that GWO optimization algorithm only uses linear hunting to capture prey, which limits its search range and accuracy, and results in slow convergence speed and poor local optimization ability, a multi-strategy fusion improved GWO is proposed. The linear update strategy in standard GWO is modified to nonlinear, so that the value of a is wider and the scope of it can be used for exploration is wider. Adaptive weight coefficients based on fitness are introduced to measure the contribution of different leading wolves to improve the position updating method of other wolves. The MSGGO-SVM fault diagnosis model is constructed, and the penalty factors of support vector and kernel function parameters are fine-tuned by this optimization method, to prevent under fitting of classification results. The test results show that this method is superior to other fault diagnosis models in the bearing fault diagnosis of rotating equipment, and provides effective guidance for decision-making in actual operation. In the future, this algorithm will be further optimized and applied to the research of motor bearing fault diagnosis under unbalanced data sets, which is a promising topic.

REFERENCES

[1] C.B. He, H.K. Li, X.W. Zhao, Weak characteristic determination for blade crack of centrifugal compressors based on underdetermined blind source separation, Measurement, 2018, 128: 545–557.

[2] P.N. Li, Y. Lei, J.S. Lin, X. Ding, An improved exponential model for predicting remaining useful life of rolling element bearings, IEEE Trans. on Ind. Electron., 2015, 62(12): 7762–7773.

[3] C. Cheng, G. Ma, Y. Zhang, et al., A deep learning-based remaining useful lifeprediction approach for bearings, IEEE/ASME Trans. on Mechatronics, 2020, 25(3):1243–54.

[4] Z. Peng, F. Chu, Y. He, Vibration signal analysis and feature extraction based on reassigned wavelet scalogram, J. Sound Vib., 2002, 253: 1087–1100.

[5] C. Cheng, B.T. Zhou, G.J. Ma, et al., Wasserstein distance based deep adversarial transfer learning for intelligent fault diagnosis with unlabeled or insufficient labeled data, Neurocomputing, 2020, 409: 35–45.

[6] L. Zuo, F.J. Xu, C.H. Zhang, T.F. Xia¸ Y. A.Liu. multi-layer spiking neural network-based approach to bearing fault diagnosis, Reliab. Eng. Syst. Saf., 2022, 225: 108561.

[7] Y.J. Sun, S.H. Li, X.H. Wang, Bearing fault diagnosis based on EMD and improved Chebyshev distance in SDP image, Measurement, 2021, 176: 1-13.

[8] K. Dragomiretskiy, D. Zosso, Variational mode decomposition, IEEE Trans. on Signal Process., 2014, 62(3): 531–544.

[9] Z.P. Li, J.L. Chen, Y.Y. Zi, et al., Independence-Oriented VMD to Identify Fault Featurefor Wheel Set Bearling Fault Diagnosis of High Speed Locomotive, Mechanical Systemsand Signal Processing, 2017, 85(7): 512-529.

[10] M. Van, H.J. Kang, Bearing defect classification based on individual wavelet local fisher discriminant analysis with particle swarm optimization, IEEE Trans. on Ind. Inform., 2015, 12(1): 124–135.

[11] Z.L. Dong, J.D. Zheng, S.Q. Huang, et al., Time-shift multi-scale weighted permutation entropy and GWO-SVM based fault diagnosis approach for rolling bearing, Entropy, 2019, 21(621):1-21.

[12] X. Song, Y. Cong, Y. Song, et al., A bearing fault diagnosis model based on CNN with wide convolution kernels, Journal of Ambient Intelligence and Humanized Computing, 2022, 13(8): 4041-4056.

[13] S. Mirjalili, S.M. Mirjalili, Lewis, A. Grey Wolf Optimizer, Adv. Eng. Softw., 2014, 69: 46–61.

[14] E. Rashedi, H. Nezamabadi-Pour, S. Saryazdi, GSA: A gravitational search algorithm, Information Sciences, 2009, 179(13): 2232-2248.

Proceedings of the 3rd Conference on Fully Actuated System Theory and Applications
May 10-12, 2024, Shenzhen, China

Fault Estimation and Fault-Tolerant Compensation Tracking Control for Autonomous Underwater Vehicles

Deyu Zeng[1], Limin Wang[2,※], Shouyan Chen[2]

1. School of Mathematics and Statistics, Hainan Normal University, Haikou 571127, China
E-mail: 744600510@qq.com,

2. School of Mechanical and Electrical Engineering, Guangzhou University, Guangzhou 510006, China
E-mail: wanglimin0817@163.com

2. School of Mechanical and Electrical Engineering, Guangzhou University, Guangzhou 510006, China
E-mail: maxcsy@gzhu.edu.cn

Abstract: In this paper, the fault estimation and fault-tolerant compensation control of autonomous underwater vehicles (AUVs) with actuator faults are studied by using the high-order full actuated (HOFA) system control method. Firstly, the first-order model of AUV is transformed into the relevant HOFA system model, and secondly, based on the model, an intermediate estimator is constructed by introducing intermediate variables, and the controller is designed by parameterization method. Finally, the fault estimation and compensation control of the AUV system are realized, and the simulation results verify the effectiveness of the proposed method.

Key Words: Fault Tolerant Control, Actuator Faults, High-order Fully Actuated System, AUV

1 Introduction

In recent years, due to the flexibility, high autonomy, and simplicity of operation of autonomous underwater vehicles (AUVs), their wide use in marine science, environmental monitoring, oil and gas exploration, and military applications has attracted much attention, making them an indispensable tool for underwater environmental monitoring and marine resource exploration [1]-[2]. AUVs work in complex and changing underwater environments, making them prone to failures. To successfully complete missions and return safely, they must have a certain tolerance for failures, which has made fault-tolerant control (FTC) for AUVs a hot research topic.

An active fault-tolerant control method was proposed for AUVs, and a reconfigurable controller was designed to prevent actuator saturation in the event of a failure [3]. Trajectory tracking control of AUVs with actuator faults was studied by using adaptive rules as online estimators to compensate for faults in AUV performance [4]. A reinforcement learning (RL) FTC method was proposed for trajectory tracking of AUVs with propulsion faults [5]. In this paper, a new integral extended state observer (IESO) was designed to mitigate the influence of estimation errors. In [6], an adaptive asymptotic backstepping tracking control algorithm was proposed to compensate for uncertainties. Reference [7] constructed a new FTC scheme by designing a virtual velocity control vector and using adaptive dynamic programming (ADP) based on single disturbance network.

Fault diagnosis (FD) is an important component of active FTC, and it is a prerequisite for compensating for faults and ensuring the effectiveness of FTC. The FD technology mainly focuses on detecting, isolating, and identifying faults that have occurred in the system. As an important branch of the FD technology, fault estimation (FE) can obtain information such as the form, location, and magnitude of faults, and fault-tolerant controller design based on FE information can compensate for faults and ensure good control performance. Considering the randomness of disturbances or faults, reference [8] constructed external disturbances as uncertainties in a random model and applied an improved robust filtering method to estimate the system state, reducing the impact of uncertainties in random systems. Reference [9] considered multiple sensor and actuator fault modes for AUVs and designed a fault diagnosis problem based on particle filters. Reference [10] proposed a FD method for AUVs based on online Bayesian nonparametric topic models.

As a nonlinear and strongly coupled system, AUVs are often simplified as augmented first-order linear system models in most controller design. As the number of system variables increases, and the system dimension becomes larger, analyzing the stability of the system becomes more difficult. High-order fully actuated (HOFA) systems are a new representation form for control design and a universal model for most physical systems. Unlike traditional models, HOFA systems have clear physical backgrounds, guaranteeing the fully actuated characteristics of actual systems, effectively simplifying control design, and avoiding the disadvantages of ill-conditioned matrices and numerical instability in model reduction [11]-[17]. This paper adopts the HOFA system method and takes the derivatives of the depth variable, which is the pre-control variable of AUVs, as the state variables of the HOFA system, forming a new state space model. Based on this model, considering the occurrence of rudder angle faults, FE and fault-tolerant compensation control (FTCC) are conducted. The idea is as follows: a fault estimator is designed by introducing intermediate variables, and a FTCC law is also

[*]This work is supported by National Natural Science Foundation (NNSF) of China under Grant 62163012.

designed. The sufficient conditions for the system to be uniformly ultimately bounded are constructed and the observer and FTCC gains are given. The FE and FTC of AUVs are realized.

2 Problem Description

2.1 System description

AUVs have six degrees of freedom, and their control systems can manage six degrees of freedom, namely, forward/backward, up/down, left/right, yaw, pitch, and roll. According to reference [18], the linear nominal system of AUVs at a speed of is obtained (disturbances are not considered here):

$$\dot{\zeta} = -u_0\theta \tag{1a}$$

$$\dot{\theta} = q \tag{1b}$$

$$\dot{q} = \frac{\frac{1}{2}\rho L^4 M'_{uq} u_0}{(I_y - \frac{1}{2}\rho L^5 M'_{\dot{q}})} q + \frac{\frac{1}{2}\rho L^3 M'_{\delta_s} u_0^2}{(I_y - \frac{1}{2}\rho L^5 M'_{\dot{q}})} \delta_s \tag{1c}$$

Where $\hat{a} = \dfrac{\frac{1}{2}\rho L^4 M'_{uq} u_0}{(I_y - \frac{1}{2}\rho L^5 M'_{\dot{q}})}$, $\hat{b} = \dfrac{\frac{1}{2}\rho L^3 M'_{\delta_s} u_0^2}{(I_y - \frac{1}{2}\rho L^5 M'_{\dot{q}})}$

L, m, I_x, I_y, I_z are respectively the length, mass and the moment of inertia of AUVs around the coordinate system x, y, z, u, v, w, p, q, r are the components of the linear and angular velocity of the AUV's motion along the three axes, respectively, φ, θ are the attitude angles, they are heeling Angle and longitudinal angle, respectively. $Z'_{(\cdot)}, M'_{(\cdot)}$ are hydrodynamic coefficients, δ_s is the rudder Angle of AUV's pitching rudder, ρ is the density of sea water, W, B are gravity and buoyancy force of AUVs respectively, z_B is the axis coordinate of the AUV's center of buoyancy, and ζ is the depth of AUVs.

The objective is to achieve tracking control of the depth of AUVs under actuator failures, specifically when there is a malfunction in the rudder angle δ_s.

2.2 Establishment of (HOFA) Systems Model

By employing the HOFA system control method, system (1) can be transformed into a HOFA system that is only correlated with depth and rudder angle. The model is as follows:

$$\dddot{\zeta} = \hat{a}\ddot{\zeta} - u_0\hat{b}\delta_s \tag{2}$$

Let

$$\zeta^{(0\sim2)} = \begin{bmatrix} \zeta^T & \dot{\zeta}^T & \ddot{\zeta}^T \end{bmatrix}^T \tag{3}$$

we can get:

$$\dot{\zeta}^{(0\sim2)} = \Phi(A^{0\sim2})\zeta^{(0\sim2)} + B\delta_s \tag{4}$$

where, $\Phi(A^{0\sim2}) = \begin{bmatrix} 0 & 1 & 0 \\ 0 & 0 & 1 \\ 0 & 0 & \hat{a} \end{bmatrix}$, $B = \begin{bmatrix} 0 \\ 0 \\ -u_0\hat{b} \end{bmatrix}$.

Improper operation or equipment failure may lead to inaccurate readings from the linked rudder angle actuator, which is considered as actuator failure. In this case, system (4) can be described as:

$$\begin{cases} \dot{\zeta}^{(0\sim2)} = \Phi(A^{0\sim2})\zeta^{(0\sim2)} + B\delta_s + Bs_a \\ y = C\zeta^{(0\sim2)} \end{cases} \tag{5}$$

where, $\delta_s \in R^{1\times1}$ and $y \in R^{3\times1}$ indicates control inputs and system outputs, respectively, s_a indicates actuator failure, $\Phi(A^{0\sim2})$, $B \in R^{3\times1}$ and $C \in R^{3\times3}$ are matrices with appropriate dimensions that $(\Phi(A^{(0\sim2)}), C)$ are observable.

Assumption A1: actuator faults s_a satisfy $\|\dot{s}_a\| \le \eta$ and $\eta \ge 0$.

Lemma 2.1[23]: Suppose that $A \in R^{n\times n}$ satisfies:

$$\mathrm{Re}\,\lambda_i(A) < -\frac{u_0}{2}, i = 1, 2\cdots n \tag{6}$$

where $u_0 > 0$, then there exists a positive definite matrix $P \in R^{n\times n}$ satisfying:

$$A^T P + PA \le -u_0 P. \tag{7}$$

Lemma 2.2[23]: For any $u_0 > 0$, there exist a set of matrices $v_i \in R^{r\times r}$, $i = 0, 1, \cdots n-1$ satisfying the following condition:

$$\mathrm{Re}\,\lambda_i(A_c) < -\frac{u_0}{2}, i = 1, 2\cdots nr \tag{8}$$

Lemma 2.3[19]: Let D, F, E and M be real matrices of appropriate dimensions, with M satisfying $M = M^T$. Then, for all $F^T F \le I$, $M + DFE + E^T F^T D^T < 0$ if, and only if, $\varepsilon > 0$ exists such that $M + \varepsilon^{-1} DD^T + \varepsilon E^T E > 0$.

3 Fault Estimation and Fault-Tolerant Control

In this section, we mainly address two issues: one is that the estimator is designed to solve the fault estimation problem by introducing intermediate variables, the other is that a fault-tolerant controller is constructed based on fault compensation.

Design of Fault Estimator

Introduce the intermediate variable:

$\gamma = s_a - K\zeta^{(0\sim2)}$, where is K the given matrix, and γ satisfies the following equation:

$$\begin{aligned} \dot{\gamma} = \dot{s}_a - K(\Phi(A^{0\sim2})\zeta^{(0\sim2)} + B\delta_s \\ + E\gamma + EK\zeta^{(0\sim2)}) \end{aligned} \tag{9}$$

Design the following estimator：

$$\dot{\hat{\zeta}}^{(0\sim 2)} = \Phi(A^{0\sim 2})\hat{\zeta}^{(0\sim 2)} + B\delta_s + B\hat{s}_a + L(y - C\hat{\zeta}^{(0\sim 2)}), \tag{10}$$

$$\hat{y} = C\hat{\zeta}^{(0\sim 2)} \tag{11}$$

$$\dot{\hat{\gamma}} = -KB\hat{\gamma} - K(\Phi(A^{0\sim 2})\hat{\zeta}^{(0\sim 2)} + B\delta_s + EK\hat{\zeta}^{(0\sim 2)}) \tag{12}$$

$$\hat{s}_a = \hat{\gamma} + K\zeta^{(0\sim 2)} \tag{13}$$

where， $\hat{\zeta}^{(0\sim 2)}, \hat{\gamma}, \hat{y}$ ，$\hat{s}_a$ are the estimates of $\zeta^{(0\sim 2)}, \gamma$, y and s_a respectively.

Let

$$K = wB^T \tag{14}$$

Design the estimation error:

$$\xi^{(0\sim 2)} = \zeta^{(0\sim 2)} - \hat{\zeta}^{(0\sim 2)} \tag{15}$$

$$\delta = \gamma - \hat{\gamma} \tag{16}$$

$$\iota = s_a - \hat{s}_a \tag{17}$$

we can obtain the error system：

$$\dot{\xi}^{(0\sim 2)} = (\Phi(A^{0\sim 2}) - LC)\xi^{(0\sim 2)} + B\iota, \tag{18}$$

$$\dot{\delta}(t) = \dot{s}_a + \begin{bmatrix} S_1 & S_2 \end{bmatrix} \begin{bmatrix} \delta \\ \xi \end{bmatrix} \tag{19}$$

where $S_1 = -wB^TB$, $S_2 = -wB^T(\Phi(A^{0\sim 2}) + wBB^T)$.

Theorem 1. Suppose that HOFA system (19) and (18), satisfies Assumptions A1, Let $u_i (i = 1,2)$, ε_0 , w and ε be two arbitrarily selected non-negative real numbers, and there exists a matrix L such that the $(\Phi(A^{0\sim 2}) - LC)$ satisfies equation (7). Then, the intermediate (10)-(13) ensures that the closed-loop system is bounded stability.

Proof：Consider a Lyapunov function of the following form：

$$V = \frac{1}{2}(\xi^{(0\sim 2)})^T \xi^{(0\sim 2)} + \frac{1}{2}\delta^T\delta \tag{20}$$

Combining (18) and (19) there are：

$$\dot{V} = \frac{1}{2}(\xi^{(0\sim 2)})^T[(\Phi(A^{0\sim 2}) - LC)^T + (\Phi(A^{0\sim 2}) - LC)](\xi^{(0\sim 2)}) + \iota^T B^T(\xi^{(0\sim 2)}) + (\xi^{(0\sim 2)})^T S_2^T\delta + \frac{1}{2}\delta^T(S_1^T + S_1)\delta + \delta^T\dot{s}_a \tag{21}$$

Bringing $\iota = \delta + K\xi$ into eq. (21), we can get：

$$\dot{V} \le \frac{1}{2}(\xi^{(0\sim 2)})^T[(\Phi(A^{0\sim 2}) - LC)^T + (\Phi(A^{0\sim 2}) - LC)](\xi^{(0\sim 2)}) + (\xi^{(0\sim 2)})^T B\delta + (\xi^{(0\sim 2)})^T S_2^T\delta + (\xi^{(0\sim 2)})^T BK(\xi^{(0\sim 2)}) + \frac{1}{2}\delta^T(S_1^T + S_1)\delta + \delta^T\dot{s}_a \tag{22}$$

According to Lemma 2.3, we can get：

$$\dot{V} \le \frac{1}{2}(\xi^{(0\sim 2)})^T[(\Phi(A^{0\sim 2}) - LC)^T + (\Phi(A^{0\sim 2}) - LC)](\xi^{(0\sim 2)}) + \delta^T\dot{s}_a + \varepsilon_0\delta^T(S_2^T + B)^T(S_2^T + B)\delta + (\xi^{(0\sim 2)})^T BK(\xi^{(0\sim 2)}) + \varepsilon_0^{-1}(\xi^{(0\sim 2)})^T(\xi^{(0\sim 2)}) + \frac{1}{2}\delta^T(S_1^T + S_1)\delta \tag{23}$$

According to Young's inequality[20],we can get：

$$\delta^T\dot{s}_a \le \frac{\varepsilon}{2}\delta^T\delta + \frac{1}{2\varepsilon}\eta^2 \tag{24}$$

Using Assumption A1 and Lemma 2.1, we have：

$$\dot{V} \le -\frac{u_1}{2}(\xi^{(0\sim 2)})^T(\xi^{(0\sim 2)}) + (\xi^{(0\sim 2)})^T BK(\xi^{(0\sim 2)}) + \varepsilon_0^{-1}(\xi^{(0\sim 2)})^T(\xi^{(0\sim 2)}) + \varepsilon_0\delta^T(S_2^T + B)^T(S_2^T + B)\delta - \frac{u_2 + \varepsilon}{2}\delta^T\delta + \frac{1}{2\varepsilon}\eta^2 \tag{25}$$

Form (25), get:

$$\dot{V} \le -\rho_1\left\|(\xi^{(0\sim 2)})\right\|^2 - \rho_2\left\|\delta\right\|^2 + \frac{1}{2\varepsilon}\eta^2 \tag{26}$$

Where, $\rho_1 = \frac{u_1}{2} - w\left\|B\right\|^2 - \varepsilon_0^{-1}$,

$\rho_2 = -\varepsilon_0\left\|(S_2^T + B)\right\|^2 + \frac{u_2 + \varepsilon}{2}$.

Then, it can be obtained by equation (20):

$$V \le \left\|(\xi^{(0\sim 2)})\right\|^2 + \left\|\delta\right\|^2 \tag{27}$$

According to (26) and (27), we can get:

$$\dot{V} \le -\rho V + \upsilon. \tag{28}$$

where， $\rho = \min[\rho_1, \rho_2]$, $\upsilon = \frac{1}{2\varepsilon}\eta^2$.

Fault Tolerant Compensation Tracking Controller Design

Design fault-tolerant controllers:

$$\delta_{s1} = \frac{1}{-u_0\hat{b}}(v_1\zeta_e + v_2\dot{\zeta}_e + v_3\ddot{\zeta}_e) - s_a \tag{29}$$

where, ζ_r is reference depth， $\zeta_e = \zeta - \zeta_r$ indicates the depth error, when ζ_r is a constant value, $\zeta_e^{(n)} = \zeta^{(n)} (n \in \mathbb{N}^+)$. Specifically,

$$\dddot{\zeta}_e = \dddot{\zeta} = \hat{a}\ddot{\zeta}_e - u_0\hat{b}\delta_s - u_0\hat{b}s_a \tag{30}$$

Substituting Eq. (29) into Eq. (30) yields the system:

$$\dddot{\zeta}_e = (\hat{a} + v_3)\ddot{\zeta}_e + v_2\dot{\zeta}_e + v_1\zeta_e \tag{31}$$

let $\zeta_e^{(0\sim2)} = \begin{bmatrix} \zeta_e & \dot{\zeta}_e & \ddot{\zeta}_e \end{bmatrix}^T$, State space expression with tracking error as a variable:

$$\dot{\zeta}_e^{(0\sim2)} = A_c\zeta_e^{(0\sim2)} \tag{32}$$

$$\dot{\xi} = (\Phi(A^{0\sim2}) - LC)\xi + B\iota, \tag{33}$$

$$\dot{\delta}(t) = \dot{s}_a + \begin{bmatrix} S_1 & S_2 \end{bmatrix}\begin{bmatrix} \delta \\ \xi \end{bmatrix} \tag{34}$$

where $A_c = \begin{bmatrix} 0 & 1 & 0 \\ 0 & 0 & 1 \\ v_1 & v_2 & \hat{a} + v_3 \end{bmatrix}$, $S_1 = -wB^TB$, $S_2 = -wB^T(\Phi(A^{0\sim2}) + wBB^T)$.

Theorem 2. Suppose that HOFA system (32)- (34), satisfies Assumptions A1, Let $u_i(i = 0,1,2)$, w, ε_0 and ε be two arbitrarily selected non-negative real numbers, and $v_i \in R^{r\times r}$, $i = 0,1,\cdots n-1$ be a set of matrices satisfying (8). Then, the estimator (10)-(13) and the controller (29) ensure that the tracking error of the closed-loop system bounded stability.

Proof: Consider a Lyapunov function of the following form：

$$\begin{aligned} V = &\frac{1}{2}(\zeta_e^{(0\sim2)})^T Z(\zeta_e^{(0\sim2)}) \\ &+\frac{1}{2}(\xi^{(0\sim2)})^T(\xi^{(0\sim2)}) + \frac{1}{2}\delta^T\delta \end{aligned} \tag{35}$$

Combining (32) -(34) there are:

$$\begin{aligned} \dot{V} = &\frac{1}{2}(\zeta_e^{(0\sim2)})^T[A_c{}^TZ + ZA_c](\zeta_e^{(0\sim2)}) \\ &+\frac{1}{2}(\xi^{(0\sim2)})^T[(\Phi(A^{0\sim2}) - LC)^T \\ &+(\Phi(A^{0\sim2}) - LC)](\xi^{(0\sim2)}) + \iota^TB^T(\xi^{(0\sim2)}) \\ &+\delta^T\dot{s}_a + \frac{1}{2}\delta^T(S_1^T + S_1)\delta + (\xi^{(0\sim2)})^TS_2^T\delta \end{aligned} \tag{36}$$

Bringing $\iota = \delta + K\xi$ into eq. (36), we can get：

$$\begin{aligned} \dot{V} = &\frac{1}{2}(\zeta_e^{(0\sim2)})^T[A_c{}^TZ + ZA_c](\zeta_e^{(0\sim2)}) \\ &+\frac{1}{2}(\xi^{(0\sim2)})^T[(\Phi(A^{0\sim2}) - LC)^T \\ &+(\Phi(A^{0\sim2}) - LC)](\xi^{(0\sim2)}) + (\xi^{(0\sim2)})^TB\delta \\ &+\delta^T\dot{s}_a + (\xi^{(0\sim2)})^TBK(\xi^{(0\sim2)}) \\ &+\frac{1}{2}\delta^T(S_1^T + S_1)\delta + (\xi^{(0\sim2)})^TS_2^T\delta \end{aligned} \tag{37}$$

According to Lemma 2.3, we can get：

$$\begin{aligned} \dot{V} \le &\frac{1}{2}(\zeta_e^{(0\sim2)})^T[A_c{}^TZ + ZA_c](\zeta_e^{(0\sim2)}) \\ &+\frac{1}{2}(\xi^{(0\sim2)})^T[(\Phi(A^{0\sim2}) - LC)^T \\ &+(\Phi(A^{0\sim2}) - LC)](\xi^{(0\sim2)})^T \\ &+\delta^T\dot{s}_a + (\xi^{(0\sim2)})^TBK(\xi^{(0\sim2)})^T \\ &+\varepsilon_0\delta^T(S_2^T + B)^T(S_2^T + B)\delta \\ &+\varepsilon_0^{-1}(\xi^{(0\sim2)})^T(\xi^{(0\sim2)}) \\ &+\frac{1}{2}\delta^T(S_1^T + S_1)\delta \end{aligned} \tag{28}$$

According to Youngs inequality [20], we can get：

$$\delta^T\dot{s}_a \le \frac{\varepsilon}{2}\delta^T\delta + \frac{1}{2\varepsilon}\eta^2 \tag{39}$$

Using Assumption A1 and Lemma 2.1, we have：

$$\begin{aligned} \dot{V} \le &-\frac{u_0}{2}(\zeta_e^{(0\sim2)})^TZ(\zeta_e^{(0\sim2)}) \\ &-\frac{u_1}{2}(\xi^{(0\sim2)})^T(\xi^{(0\sim2)}) \\ &+(\xi^{(0\sim2)})^TBK(\xi^{(0\sim2)})^T \\ &+\varepsilon_0^{-1}(\xi^{(0\sim2)})^T(\xi^{(0\sim2)}) \\ &+\varepsilon_0\delta^T(S_2^T + B)^T(S_2^T + B)\delta \\ &-\frac{u_2 + \varepsilon}{2}\delta^T\delta + \frac{1}{2\varepsilon}\eta^2 \end{aligned} \tag{40}$$

Form (40), get:

$$\begin{aligned} \dot{V} \le &-\frac{u_0}{2}\lambda_{\max}(Z)\left\|\zeta_e^{(0\sim2)}\right\|^2 - \rho_1\left\|\xi^{(0\sim2)}\right\|^2 \\ &-\rho_2\left\|\delta\right\|^2 + \frac{1}{2\varepsilon}\eta^2 \end{aligned} \tag{42}$$

Where, $\rho_1 = \frac{u_1}{2} - w\left\|B\right\|^2 - \varepsilon_0^{-1}$, $\rho_2 = -\varepsilon_0\left\|(S_2^T + B)\right\|^2 + \frac{u_2 + \varepsilon}{2}$.

Then, it can be obtained by equation (35):

$$V \le \lambda_{\max}(Z)\left\|\zeta_e^{(0\sim2)}\right\|^2 + \left\|\xi^{(0\sim2)}\right\|^2 + \left\|\delta\right\|^2 \tag{42}$$

According to eq. (37) and eq. (38), we can get:

$$\dot{V}(t) \le -\rho V + \upsilon. \tag{43}$$

where， $\rho = \min[\frac{u_0}{2}, \ \rho_1, \rho_2]$ $\upsilon = \frac{\varepsilon}{2}\eta^2$.

Control Gain Acquisition

Based on Lemma 2-1 [21] in the Reference [22], there are the following conclusions:

For a fully actuated system like system (29), Lemma 2-1 proves that the system satisfies:

$$A_c = VFV^{-1} \tag{44}$$

Matrix $v \in R^{1\times 3}$ and matrix V , W satisfying condition (45) are given by equations (46).

$$v = \begin{bmatrix} v_1 & v_2 & v_3 \end{bmatrix} = -WV^{-1} \tag{45}$$

$$\begin{cases} W = -\hat{a}ZF^2 + ZF^3 \\ V = \begin{bmatrix} Z \\ ZF \\ ZF^2 \end{bmatrix} \end{cases} \tag{46}$$

where requirement F is satisfied

$$F \in \left\{ F \middle| \begin{array}{l} F \in R^{3\times 3} \wedge \exists Z \in R^{1\times 3}, \\ s.t. \det \begin{bmatrix} Z & ZF & ZF^2 \end{bmatrix}^T \neq 0 \end{array} \right\}.$$

The observer gain L can be found by the pole configuration method.

4 Simulation Result

In this section, the depth control of an AUV is used as an example to verify the effectiveness of the designed controller.

According to system (2) the HOFA system for an AUV with a speed of 2 m/s can be obtained as:

$$\dddot{\zeta} = -2.0435\ddot{\zeta} + 0.26908\delta_s \tag{47}$$

Then the system (47) is modelled in case of actuator failure:

$$\begin{cases} \dot{\zeta}^{(0\sim 2)} = \Phi(A^{0\sim 2})\zeta^{(0\sim 2)} + B\delta_s + Bs_a \\ y = C\zeta^{(0\sim 2)} \end{cases} \tag{48}$$

where $\Phi(A^{0\sim 2}) = \begin{bmatrix} 0 & 1 & 0 \\ 0 & 0 & 1 \\ 0 & 0 & -2.0435 \end{bmatrix}$ $B = \begin{bmatrix} 0 \\ 0 \\ 0.26908 \end{bmatrix}$,

$C = \begin{bmatrix} 1 & 0 & 0 \\ 0 & 1 & 0 \\ 0 & 0 & 1 \end{bmatrix}$.

Table 1: Actuator Faults

t	[0,5)	[5,15)	[15,35)
$s_a(t)$	0	1	0
t	[35,45)	[45,57)	[57,80)
$s_a(t)$	2	0	$\sin(0.5t)$

The initial conditions are $x(0) = \begin{bmatrix} 0 & 0 & 0 \end{bmatrix}^T$, take

$Z = \begin{bmatrix} 1 & 1 & 1 \end{bmatrix}$, $F = \begin{bmatrix} -10 & 0 & 0 \\ 0 & -1 & 0 \\ 0 & 0 & -5 \end{bmatrix}$, $w = 33$,

By Lemma 1, we get $v = \begin{bmatrix} 50 & 65 & 13.9565 \end{bmatrix}$,

Secondly, the pole $p = \begin{bmatrix} -10 & -1 & -5 \end{bmatrix}$, using the 'place' command in MATLAB to find L .

$L = \begin{bmatrix} 1 & 1 & 0 \\ 0 & 10 & 1 \\ 0 & 0 & 2.9565 \end{bmatrix}$.

Additive faults s_a as shown in Table 1, two types of fault signals are considered, namely constant signals and sine signals.

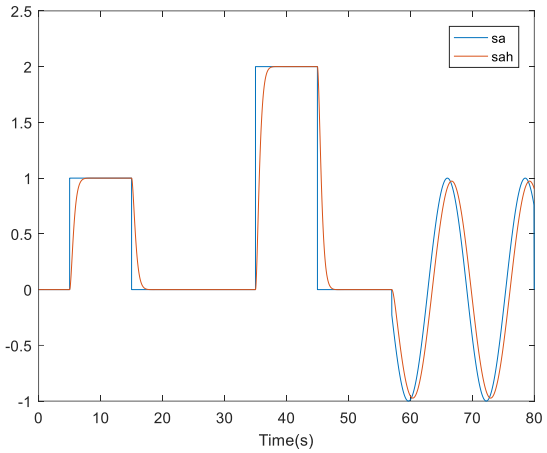

Fig. 1: Actuator faults and their estimation

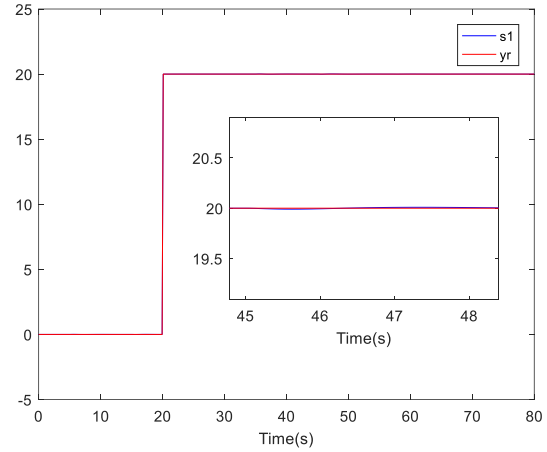

Fig. 2: δ_{s1} Depth control simulation results

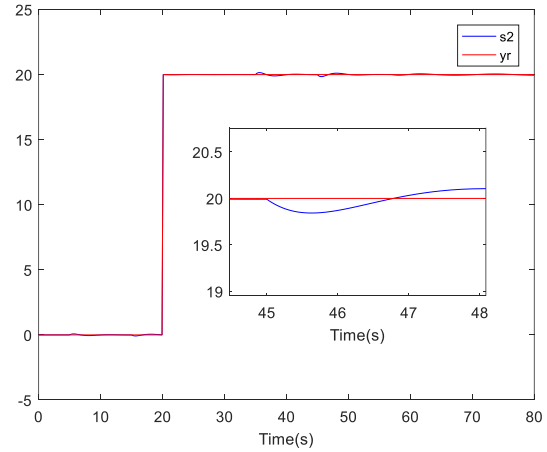

Fig. 3: δ_{s2} Depth control simulation results

The simulation results are shown in Fig. 1-3. In Fig. 1, the actual value and estimated value comparison of actuator fault s_a are displayed. From the Fig. 1, the actuator fault can be estimated well using the estimator designed in this paper.

Fig. 2-3 respectively depict the simulation results of depth control for the AUV at a forward speed of 2 m/s, under controllers δ_{s1} (compensated design) and δ_{s2} ($\delta_{s2} = v\hat{\zeta}_e^{(0\sim2)}$ uncompensated design). Before 20 seconds, it navigates on the water surface, and after 20 seconds, it starts to dive.

From Fig. 3, despite the absence of compensating faults, the impact of actuator faults on the AUV is reduced under controller δ_{s2} , while under controller δ_{s1} , the impact of faults on the system state is not even visible due to the compensating effect, as shown in Fig. 2. It is evident that fault compensation control of AUVs is achieved under the FTCC proposed. This paper sets up a controller based on tracking error, without designing a parameter adjustment mechanism for the target output, so the depth drops sharply in a short period of time. Simulation results verify that the controller designed by the HOFA system control method can indeed achieve fault estimation and depth control of AUVs, with good results obtained.

5 Summary

In this paper, taking the AUV system as the research object, considering the effect of the rudder angle generating actuator additive faults, the fault estimator and fault-tolerant compensation controller applicable to the AUV are designed based on the HOFA system, and the FE and FTCl of the compensation are realized. Finally, the effectiveness of the designed controller is verified by simulation. This study investigates the tracking value considered as a constant in a simple, and in the future, will consider time-varying tracking values to demonstrate the effectiveness of designing controllers.

References

[1] Z. M. Qiu, Y. Ma, et al. Analysis on the Development Trend and Key Technologies of Unmanned Underwater Equipment. Journal of Unmanned Undersea Systems, 2023 31(1): 1-9.

[2] B. W. Song, G. Pan, L. C. Zhang, et al. Development trend and key technologies of autonomous underwater vehicles. Chinese Journal of Ship Research, 2022, 17(5): 27-44.

[3] S. Joshi, D. B. Talange. Fault tolerant control for Autonomous Underwater Vehicle. 2014 IEEE International Conference on Mechatronics and Automation, 2014, 658-662.

[4] Tabatabaee-Nasab FS, Moosavian SAA, Keymasi Khalaji A. Adaptive fault-tolerant control for an autonomous underwater vehicle. Robotica，2022, 40(11): 4076-4089.

[5] X Liu, M Zhang, Y Feng. Adaptive fault tolerant control and thruster fault reconstruction for autonomous underwater vehicle. Ocean Engineering, 2018, 155: 10–23.

[6] Yuxi Zhang, Jia peng Liu, Jin peng Yu. Adaptive asymptotic tracking control for autonomous underwater vehicles with non-vanishing uncertainties and input saturation. Ocean Engineering, 2023, 276: 114280.

[7] Gao feng Che. Single critic network-based fault-tolerant tracking control for underactuated AUV with actuator fault. Ocean Engineering, 2022, 254: 111380.

[8] Jiahao Song, Xiao He. Robust state estimation and fault detection for Autonomous Underwater Vehicles considering hydrodynamic effects. Control Engineering Practice, 2023, 135: 105497.

[9] B. Zhao, R. Skjetne, M. Blanke and F. Dukan. Particle Filter for Fault Diagnosis and Robust Navigation of Underwater Robot. IEEE Transactions on Control Systems Technology, 2014, 22(6): 2399-2407.

[10] B. -Y. Raanan et al. Automatic fault diagnosis for autonomous underwater vehicles using online topic models. OCEANS 2016 MTS/IEEE Monterey, Monterey, CA, USA, 2016, 1-6.

[11] G. R. Duan. High-order System Approaches: I. Full-actuation and parametric design. Automatica, 2020, 46(7): 1333-1345.

[12] G. R. Duan. High-order System Approaches: II. Controllability and fully-actuation. Automatica, 2020, 46(8): 1571-1581.

[13] G. R. Duan. High-order System Approaches: III. Observability and observer design. Automatica, 2020, 46(9): 1885-1895.

[14] G. R. Duan. High-order Fully Actuated System Approaches: Part I. Models and Basic Procedure. International Journal of Systems Science, 2020, 52(2): 422-435.

[15] G. R. Duan. High-order Fully Actuated System Approaches: Part II. Generalized Strict-Feedback Systems. International Journal of Systems Science,2020,52(2):422-435.

[16] G. R. Duan. High-order Fully Actuated System Approaches: Part III. Robust Control and High-Order Backstepping. International Journal of Systems Science, 2021,52(3): 475-535.

[17] G. R. Duan. Direct Parametric Approach for Cascaded Systems with Application in Robot Control. International Conference on Control, Automation and Systems (ICCAS 2014), 2014, 29-35.

[18] H Xiong, X Bian, X Shi. Simulation of robust H∞ Controller for AUV depth control. Computer Integrated Manufacturing Systems, 2007,24(3): 156-159.

[19] K.W. Yu, C.H. Lien, Stability criteria for uncertain neutral systems with interval time-varying delays, Chaos, Solitons and Fractals 38 (2008) 650–657.

[20] D. S. Bernstein. Matrix mathematics: theory, facts, and formulas. Princeton university press, 2009.

[21] G. Duan, Generalized Sylvester Equations: Unified Parametric Solutions. Crc Press, 2015: 288-216.

[22] Y. Zhuang, Parametric Approach to Missile Formation Control, 2023 2nd Conference on Fully Actuated System Theory and Applications (CFASTA), Qingdao, China, 2023, pp. 270-274.

[23] G. R. Duan. (2021) High-order fully actuated system approaches: Part V. Robust adaptive control, International Journal of Systems Science, 52:10, 2129-2143.

Proceedings of the 3rd Conference on Fully Actuated System Theory and Applications
May 10-12, 2024, Shenzhen, China

A Projection-based Binary Classification Method for Fault Detection of T-S fuzzy Systems with Multiplicative Faults

Haili Zhang[1], Linlin Li[1], Qianxiang Yu[1]

1. School of Automation and Electrical Engineering, University of Science and Technology Beijing, Beijing 100083, P. R. China
E-mail: Zhanghaili@xs.ustb.edu.cn; linlin.li@ustb.edu.cn; d202310363@xs.ustb.edu.cn

Abstract: The main objective of this paper is to address the detection issues of multiplicative faults in T-S fuzzy systems. To this end, the orthogonal projection, as an effective tool to deal with the problem of fault detection and isolation, is introduced first. Then, the image subspace and kernel space of T-S fuzzy systems is introduced, and then formulated in the time-varying framework. Based on it, the time-varying fuzzy projection-based binary classification scheme is proposed. The core of the method is to construct the orthogonal projectors based on the dynamics of the nominal system and faulty system respectively, and develop a binary fault detection logic. Finally, a numerical example is given to illustrate the effectiveness of the proposed method.

Key Words: Takagi-Sugeno (T-S) fuzzy system, fault detection, binary-classification method, multiplicative faults

1 Introduction

Driven by the growing demand for system reliability and security, fault detection methods have attracted intensive attention in both academia and industry over the past decades [1, 2]. Among the research on linear systems, observer-based fault detection schemes constitute the main stream of investigation[3–5]. In this context, the Takagi-Sugeno (T-S) fuzzy dynamic modeling technology has been proven to be an effective tool for approximating nonlinear industrial processes [6–9]. In recent years, a framework has been established for the controller and observer design issues of T-S fuzzy systems [10, 11]. In [12], an optimal fault detection scheme for T-S fuzzy systems is proposed, thereby extending the so-called unified solution to fuzzy systems.

On another research frontier, studies on multiplicative faults have attracted growing attention [13, 14]. In automatic control systems, multiplicative faults, resulting from the abnormal changes of system parameters or discrepancies in controller parameters, represent a common type of faults. To address the impact of such faults on the system, the projection method, as a standard technique for statistics and machine learning, has recently gained attention [15, 16]. In this sense, the optimal fault detection for dynamic systems can be achieved by defining appropriate signal norms [17]. The implementation of this method depends on the nominal system model and (limited) information about model uncertainty, which is a typical classification problem. When there are system models describing fault operation in addition to the nominal model, these two models can be used to realize fault detection, which can be transformed into a binary fault classification task. To the best of our knowledge, the detection of multiplicative faults in fuzzy systems remains an open issue, which motivates this work.

Inspired by the idea of the projection-based fault detection schemes, the fault detection issue in T-S fuzzy systems with multiplicative faults is investigated. To be specific, the T-S fuzzy system is introduced firstly. Based on it, with the aid of coprime factorization technique, the image space and the kernel space of fuzzy systems is defined. Then, the fault detection issue is formulated as a binary classification problem, and the residual signal is obtained by projecting the real-time collected data vector onto the image space and the kernel space of both the nominal model and the faulty model, respectively. Finally, the problem for multiplicative fault detection is solved by setting the appropriate threshold with the gap metric technique.

The structure of this paper is organized as follows. Section II is dedicated to the preliminaries and problem formulation. The projection-based binary classification scheme is presented in Section III, and a case study is given in Section IV. Conclusions and future works are presented in Section V.

Notations. Standard notations are adopted in this paper. $\mathcal{P}_{\mathcal{U}}$ denotes the orthogonal projection onto subspace $\mathcal{U}$, and its norm is denoted by $\|\mathcal{P}_{\mathcal{U}}\|$. $\mathcal{U}^{\perp}$ represents the orthogonal complement of $\mathcal{U}$. $\mathcal{P}_{\mathcal{U}}^{\sim}$ indicates the adjoint of $\mathcal{P}_{\mathcal{U}}$. $\circ$ denotes the multiplication of operators.

2 Preliminaries and problem formulation

In this section, the T-S fuzzy systems under consideration are introduced first. It is followed by the review of orthogonal projection and gap metric in Hilbert space and, based on it, the problem formulation.

2.1 System description

The T-S fuzzy model is described by fuzzy IF-THEN rules, which can be applied to approximate the nonlinear system. The p_{th} rule of the T-S fuzzy model is of the following form:
Plant rule $\Re^p$: IF $\theta_1(k)$ is H_1^p and $\theta_2(k)$ is H_2^p and $\cdots$ and $\theta_n(k)$ is H_n^p , THEN

$$\Sigma : \begin{cases} x(k+1) = A_p x(k) + B_p u(k) \\ y(k) = C_p x(k) + D_p u(k) \end{cases} \tag{1}$$

where $\theta(k) = [\theta_1(k), \theta_2(k), \cdots, \theta_n(k)]$ denotes the premise variables. $H_m^p (m = 1, 2, \cdots, n)$ denotes the fuzzy sets. $\Re^p, p \in \{1, 2, \ldots, \tau\}$ indicates the p_{th} inference rule. τ represents the number of fuzzy inference rules. $u(k) \in \mathcal{U}^s$ denotes the control input variable, $y(k) \in \mathcal{Y}^s$ denotes the system output vector, and $x(k) \in \mathcal{X}^s$ denotes the state variable. Σ denotes the plant model. A_p, B_p, C_p, D_p are the system matrices corresponding to the p_{th} model. $\mathcal{U}^s$ and $\mathcal{Y}^s$ represent the input and output space, respectively.

This work has been supported by the National Natural Science Foundation of China under Grants 62322303, 62073029, and U21A20483.

Let $\mu_p(\theta(k))$ represent the corresponding normalized fuzzy membership function, which satisfies

$$\mu_p(\theta(k)) \geq 0, \sum_{p=1}^{\tau} \mu_p(\theta(k)) = 1, p = 1, 2, \cdots, \tau.$$

In the sequel, we denote $\mu_p(k)$ as $\mu_p(\theta(k))$ for brevity. Thus, the overall T-S fuzzy system can be inferred as

$$\Sigma : \begin{cases} x(k+1) = A(\mu(k))x(k) + B(\mu(k))u(k) \\ y(k) = C(\mu(k))x(k) + D(\mu(k))u(k) \end{cases} \tag{2}$$

where

$$A(\mu(k)) = \sum_{p=1}^{\tau} \mu_p(k)A_p, B(\mu(k)) = \sum_{p=1}^{\tau} \mu_p(k)B_p$$
$$C(\mu(k)) = \sum_{p=1}^{\tau} \mu_p(k)C_p, D(\mu(k)) = \sum_{p=1}^{\tau} \mu_p(k)D_p.$$

For the sake of simplicity, in the sequel, Σ will be used to denote the T-S fuzzy system (2). In addition, the following notation

$$\Sigma = (A(\mu(k)), B(\mu(k)), C(\mu(k)), D(\mu(k)))$$

is adopted.

With the aid of the above T-S fuzzy systems, the uncertain plant model with multiplicative faults is denoted by

$$\begin{aligned} \Sigma_{\Delta,f} = (&A(\mu(k)) + \xi_A(k), B(\mu(k)) + \xi_B(k), \\ &C(\mu(k)) + \xi_C(k), D(\mu(k)) + \xi_D(k)), \end{aligned} \tag{3}$$

where $\xi_A(k), \xi_B(k), \xi_C(k)$, and $\xi_D(k)$ denote the fault induced changes in system parameters and the model uncertainties.

2.2 Orthogonal projection and gap metric

The Hilbert space $\mathcal{H}$ is a vector space equipped with an inner product denoted as $\langle \cdot, \cdot \rangle$. For a vector $\alpha \in \mathcal{H}$, the norm of α is defined by the inner product as $\|\alpha\| = \sqrt{\langle \alpha, \alpha \rangle}$. By projecting α onto $\mathcal{U}$, the distance between α and its projection $\mathcal{P}_{\mathcal{U}}\alpha$ is calculated to determine whether α belongs to the subspace $\mathcal{U}$.

An orthogonal projection on a subspace $\mathcal{U}$, denoted by $\mathcal{P}_{\mathcal{U}}$, is endowed with the inner product

$$\langle m(k), n(k) \rangle_{2,[k_1,k_2]} = \sqrt{\sum_{k=k_1}^{k_2} m^T(k)n(k)},$$

where $m(k), n(k) \in \mathcal{U} \subset l_{2,[k_1,k_2]}$.

It is evident that if operators $\mathcal{P}_{\mathcal{U}}$ satisfies

$$\begin{aligned} &\forall m, n \in \mathcal{U}, \mathcal{P}_{\mathcal{U}}^2 = \mathcal{P}_{\mathcal{U}}, \\ &\langle \mathcal{P}_{\mathcal{U}}m, n \rangle_{2,[k_1,k_2]} = \langle m, \mathcal{P}_{\mathcal{U}}n \rangle_{2,[k_1,k_2]}, \end{aligned} \tag{4}$$

it is idempotent and self-adjoint. Therefore, it can be interpreted as an operator for orthogonal projection onto $\mathcal{U}$.

In light of [16], the following conclusions are of great significance for our study:

- $\forall m \in \mathcal{U}, \mathcal{P}_{\mathcal{U}}m = m \Leftrightarrow \langle \mathcal{P}_{\mathcal{U}}m, m - \mathcal{P}_{\mathcal{U}}m \rangle_{2,[k_1,k_2]} = 0$;
- $\forall m \in \mathcal{U}, m = \mathcal{P}_{\mathcal{U}}m + \mathcal{P}_{\mathcal{U}^\perp}m$, where $\mathcal{P}_{\mathcal{U}^\perp}$ is the orthogonal complement of $\mathcal{U}$;
- given $n \in l_{2,[k_1,k_2]}, \forall x \in \mathcal{U} \subset l_{2,[k_1,k_2]}$, $\langle n-m, m-n \rangle_{2,[k_1,k_2]} = ||n-m||_{2,[k_1,k_2]} \geq ||n-\mathcal{P}_{\mathcal{U}}n||_{2,[k_1,k_2]}$.

Given the closed subspace $\mathcal{U}$, the distance between n and $\mathcal{U}$, denoted as $dist(n, \mathcal{U})$, is defined as

$$dist(n, \mathcal{U}) = \inf_{m \in \mathcal{U}} ||n - m||_{2,[k_1,k_2]}, \tag{5}$$

which is equivalent to

$$dist(n, \mathcal{U}) = \|n - \mathcal{P}_{\mathcal{U}}n\|_{2,[k_1,k_2]} = \|\mathcal{P}_{\mathcal{U}^\perp}n\|_{2,[k_1,k_2]}. \tag{6}$$

Moreover, in order to measure the distance between two subspaces $\mathcal{S}$ and $\mathcal{T}$ [16], the following definition of gap metric is necessary

$$\mathscr{D}(\mathcal{S}, \mathcal{T}) = \max \left\{ \overrightarrow{\mathscr{D}}(\mathcal{S}, \mathcal{T}), \overrightarrow{\mathscr{D}}(\mathcal{T}, \mathcal{S}) \right\}, \tag{7}$$

$$\overrightarrow{\mathscr{D}}(\mathcal{S}, \mathcal{T}) = \sup_{\substack{s \in \mathcal{S} \\ \|s\|_{2,[k_1,k_2]}=1}} \operatorname{dist}(s, \mathcal{T}) = \sup_{s \in \mathcal{S}} \inf_{t \in \mathcal{T}} \frac{\|s-t\|_{2,[k_1,k_2]}}{\|s\|_{2,[k_1,k_2]}},$$

$$\overrightarrow{\mathscr{D}}(\mathcal{T}, \mathcal{S}) = \sup_{\substack{t \in \mathcal{T} \\ \|t\|_{2,[k_1,k_2]}=1}} \operatorname{dist}(t, \mathcal{S}) = \sup_{t \in \mathcal{T}} \inf_{s \in \mathcal{S}} \frac{\|t-s\|_{2,[k_1,k_2]}}{\|t\|_{2,[k_1,k_2]}},$$

which leads to

$$\begin{aligned} &0 \leq \mathscr{D}(\mathcal{S}, \mathcal{T}) \leq 1, \\ &\text{for } \mathscr{D}(\mathcal{S}, \mathcal{T}) < 1, \overrightarrow{\mathscr{D}}(\mathcal{S}, \mathcal{T}) = \overrightarrow{\mathscr{D}}(\mathcal{T}, \mathcal{S}) = \mathscr{D}(\mathcal{S}, \mathcal{T}), \\ &\text{for } \mathscr{D}(\mathcal{S}, \mathcal{T}) = 0, \mathcal{S} = \mathcal{T}, \text{and } \mathscr{D}(\mathcal{S}, \mathcal{T}) = 1, \mathcal{S} \perp \mathcal{T}. \end{aligned}$$

Here, $\overrightarrow{\mathscr{D}}(\mathcal{S}, \mathcal{T})$ and $\overrightarrow{\mathscr{D}}(\mathcal{T}, \mathcal{S})$ are called directed gap, and $\mathcal{S}, \mathcal{T} \in l_{2,[k_1,k_2]}$.

2.3 Problem formulation

As the signals in the system can be represented as vectors in the Hilbert space, and the dynamics of the system can be modeled as subspaces in the Hilbert space, the fault detection problems based on projection-based binary classification method for T-S fuzzy systems with multiplicative faults are investigated in this paper. To be specific, attentions will be firstly paid to the T-S fuzzy model, which is fundamental to establish the image representation and the kernel representation for fuzzy systems within the time-varying framework. On this basis, the main objective of the binary-classification method is to construct the data vector $\begin{bmatrix} u \\ y \end{bmatrix} \in l_{2,[k_1,k_2]}$ based on the projection operators on nominal subspace and faulty subspace. By comparing the two corresponding distances, the detection logic is ultimately set to determine whether the multiplicative faults have occurred. In order to verify the superiority of the proposed method in this paper, the fault detection performance results will be obtained by comparing it with observer-based fault detection methods.

3 Main results

In this section, the definitions of coprime factorizations and subspaces for T-S fuzzy systems is firstly introduced. Based on it, the binary-classification problem is studied with the aid of the projection-based method.

3.1 Normalized factorizations and subspaces

Roughly speaking, the basic idea of the projection-based fault detection approach lies in orthogonally projecting the process data onto the image subspace and kernel subspace. Considering the time-varying fuzzy framework, the closed-loop dynamics of a state feedback controller with $v_\Sigma(k)$ as reference vector is defined as

$$\begin{cases} u(k) = F(k)x(k) + v_\Sigma(k) \\ x(k+1) = A_F(\mu(k))x(k) + B(\mu(k))v_\Sigma(k) \\ y(k) = C_F(\mu(k))x(k) + D(\mu(k))v_\Sigma(k) \end{cases} \tag{8}$$

where

$$\begin{aligned} A_F(\mu(k)) &= A(\mu(k)) + B(\mu(k))F(k), \\ C_F(\mu(k)) &= C(\mu(k)) + D(\mu(k))F(k). \end{aligned}$$

$F(k)$ is the controller gain matrix. Next, the time-varying fuzzy observer-based residual generator is constructed as follows:

$$\begin{cases} \hat{x}(k+1) = A_L(\mu(k))\hat{x}(k) + B_L(\mu(k))u(k) + L(k)y(k) \\ \hat{y}(k) = C(\mu(k))\hat{x}(k) + D(\mu(k))u(k) \\ r_n(k) = y(k) - \hat{y}(k), r_\Sigma(k) = W(k)r_n(k) \end{cases} \tag{9}$$

where

$$\begin{aligned} A_L(\mu(k)) &= A(\mu(k)) - L(k)C(\mu(k)) \\ B_L(\mu(k)) &= B(\mu(k)) - L(k)D(\mu(k)). \end{aligned}$$

$L(k)$ represents the observer gain matrix. $W(k)$ denotes the weighting matrix. $\hat{x}(k)$ denotes the state estimate. $\hat{y}$ denotes the system output estimate. With the time-varying framework, the fuzzy time-varying operators can be easily described as

$$\mathscr{M} = (A_F(\mu(k)), B(\mu(k)), F(k), I) \tag{10}$$

$$\mathscr{N} = (A_F(\mu(k)), B(\mu(k)), C_F(\mu(k)), D(\mu(k))) \tag{11}$$

$$\hat{\mathscr{M}} = (A_L(\mu(k)), -L(k), W(k)C(\mu(k)), W(k)) \tag{12}$$

$$\hat{\mathscr{N}} = (A_L(\mu(k)), B_L(\mu(k)), W(k)C(\mu(k)), W(k)D(k)) \tag{13}$$

where $(\mathscr{M}, \mathscr{N})$ and $(\hat{\mathscr{M}}, \hat{\mathscr{N}})$ are the right coprime pairs (RCP) and left coprime pairs (LCP) of system, respectively.

Definition 1. *Given the RCP and LCP of the fuzzy model (2), and $(\mathscr{M}, \mathscr{N})$, $(\hat{\mathscr{M}}, \hat{\mathscr{N}})$ satisfying (10)-(13), the fuzzy time-varying operators*

$$I_\Sigma : l_{2,[k_1,k_2]} \to l_{2,[k_1,k_2]} \times l_{2,[k_1,k_2]}$$

$$I_\Sigma(v_\Sigma) := \begin{bmatrix} \mathscr{M}(v_\Sigma) \\ \mathscr{N}(v_\Sigma) \end{bmatrix} = \begin{bmatrix} u \\ y \end{bmatrix}, v_\Sigma \in l_{2,[k_1,k_2]} \tag{14}$$

$$K_\Sigma : l_{2,[k_1,k_2]} \times l_{2,[k_1,k_2]} \to l_{2,[k_1,k_2]}$$

$$K_\Sigma(u,y) := \hat{\mathscr{M}}(y) - \hat{\mathscr{N}}(u) = r_\Sigma = W(k)r_n \tag{15}$$

are called the system image representation (SIR) and system kernel representation (SKR) of the system Σ.

Corresponding to the SIR and SKR, the image subspace and the kernel subspace of the fuzzy system (2) is defined.

Definition 2. *Given fuzzy system (2) and the corresponding time-varying fuzzy matrices (10-13), the $l_{2,[k_1,k_2]}$ subspace $\mathcal{I}_\Sigma$ and $\mathcal{K}_\Sigma$ defined by*

$$\mathcal{I}_\Sigma = \left\{ \begin{bmatrix} u \\ y \end{bmatrix} : \begin{bmatrix} u \\ y \end{bmatrix} = \begin{bmatrix} \mathscr{M}(v_\Sigma) \\ \mathscr{N}(v_\Sigma) \end{bmatrix} = I_\Sigma(v_\Sigma), v_\Sigma \in l_{2,[k_1,k_2]} \right\} \tag{16}$$

$$\mathcal{K}_\Sigma = \left\{ \begin{bmatrix} u \\ y \end{bmatrix} : K_\Sigma(u,y) = \hat{\mathscr{M}}(y) - \hat{\mathscr{N}}(u) = 0 \right\} \tag{17}$$

are called image subspace and kernel subspace of the fuzzy system Σ.

To address the projection-based fault detection in T-S fuzzy systems, the normalized factorization will be introduced. For fuzzy systems, normalized right coprime factorizations (RCF) and left coprime factorizations (LCF) are defined by isometric and co-isometric operators [18].

Definition 3. *Given an operator $\mathscr{R}$, if it satisifies $\mathscr{R}^\sim \circ \mathscr{R} = \mathcal{I}$, or $\mathscr{R} \circ \mathscr{R}^\sim = \mathcal{I}$, then it is called isometric and co-isometric.*

Definition 4. *The normalized RCF and LCF of Σ, denoted by $\mathcal{I}_{\Sigma_n}$ and $\mathcal{K}_{\Sigma_n}$, are isometric and co-isometric operator defined by*

$$\mathcal{I}_{\Sigma_n}^\sim \circ \mathcal{I}_{\Sigma_n} = \mathcal{I}, \mathcal{K}_{\Sigma_n} \circ \mathcal{K}_{\Sigma_n}^\sim = \mathcal{I}.$$

The corresponding RCP and LCP, denoted as $(\mathscr{M}_{\Sigma_n}, \mathscr{N}_{\Sigma_n})$ and $(\hat{\mathscr{M}}_{\Sigma_n}, \hat{\mathscr{N}}_{\Sigma_n})$ can be given by solving the Riccati equation in the following theorem.

Theorem 1. *Given the system model (2), $(\hat{\mathscr{M}}_{\Sigma_n}, \hat{\mathscr{N}}_{\Sigma_n})$ are as follows*

$$\hat{\mathscr{M}}_n = (A_{L_n}(\mu(k)), -L_n(k), W_n(k)C(\mu(k)), W_n(k))$$

$$\hat{\mathscr{N}}_n = (A_{L_n}(\mu(k)), B_{L_n}(\mu(k)), W_n(k)C(\mu(k)), W_n(k)D(\mu(k)))$$

$$L_n(k) = (B(\mu(k))D^T(\mu(k)) + A(\mu(k))P(k)C^T(\mu(k))W_n^2(k))$$

$$W_n(k) = (I + D(\mu(k))D^T(\mu(k)) + C(\mu(k))P(k)C^T(\mu(k)))^{-1/2}$$

where $P(k) > 0$ is the solutions to the following Riccati recursions

$$\begin{aligned} P(k+1) = A_{L_n}(\mu(k))P(k)A_{L_n}^T(\mu(k)) + L_n(k)L_n^T(k) + \\ + B_{L_n}(\mu(k))B_{L_n}^T(\mu(k)) \end{aligned}$$

with $P(k_0) = P_{k_0}$, where P_{k_0} is boundary matrix.

3.2 A binary classification scheme

To begin with, we would like to emphasise that in the presence of a system model describing faulty operations, alongside the nominal model, fault detection can be accomplished by utilizing both models. This constitutes a binary-classification fault detection task. The primary goal of this binary-classification is to determine which subspace the collected process data $\begin{bmatrix} u \\ y \end{bmatrix}$ belongs to.

From the above definition , let

$$I_{\Sigma_{i,n}} = \begin{bmatrix} \mathscr{M}_{i,n} \\ \mathscr{N}_{i,n} \end{bmatrix}, i = 0, 1$$

indicate normalized the SIR of Σ_i. $\mathcal{I}_{\Sigma_{0,n}}, \mathcal{I}_{\Sigma_{1,n}}$ are the image subspace defined on the nominal system Σ_0 and faulty system Σ_1, respectively,

$$\mathcal{I}_{\Sigma_{i,n}} = \left\{ \begin{bmatrix} u \\ y \end{bmatrix} : \begin{bmatrix} u \\ y \end{bmatrix} = I_{\Sigma_{i,n}} v_\Sigma, v_\Sigma \in l_{2,[k_1,k_2]} \right\}.$$

Without loss of generality, it is assumed that the system operates either in the nominal or faulty operations, that is to say,

$$\begin{bmatrix} u \\ y \end{bmatrix} \in \mathcal{I}_{\Sigma_{0,n}} \quad or \quad \begin{bmatrix} u \\ y \end{bmatrix} \in \mathcal{I}_{\Sigma_{1,n}}$$

and any data vector $\begin{bmatrix} u \\ y \end{bmatrix}$ belongs to $\mathcal{I}_{\Sigma_n} := \mathcal{I}_{\Sigma_{0,n}} \cup \mathcal{I}_{\Sigma_{1,n}}$.

Define $\mathcal{P}_{\mathcal{I}_{\Sigma_i}}$ be the operator of orthogonal projection to the nominal and faulty image subspace $\mathcal{I}_{\Sigma_{i,n}}$ as

$$\mathcal{P}_{\mathcal{I}_{\Sigma_i}} = \mathcal{L}_{\mathcal{I}_{\Sigma_{i,n}}} \circ \mathcal{L}_{\mathcal{I}^{\sim}_{\Sigma_{i,n}}}, \mathcal{L}_{\mathcal{I}^{\sim}_{\Sigma_{i,n}}} = \mathcal{P}_{\mathcal{L}_2} \mathcal{L}_{\mathcal{I}^{\sim}_{\Sigma_{i,n}}}, i = 0, 1.$$

Based on it, the process data $\begin{bmatrix} u \\ y \end{bmatrix} \in l_{2,[k_1,k_2]}$ can be orthogonally projected onto the nominal system image subspace $\mathcal{I}_{\Sigma_{0,n}}$ and the faulty subspace $\mathcal{I}_{\Sigma_{1,n}}$

$$p_{\mathcal{I}_{\Sigma_i}} = \mathcal{P}_{\mathcal{I}_{\Sigma_i}} \begin{bmatrix} u \\ y \end{bmatrix}, i = 0, 1. \tag{18}$$

With the aforementioned data vector $\begin{bmatrix} u \\ y \end{bmatrix}$ and its corresponding projection $p_{\mathcal{I}_{\Sigma_i}}$, the difference can be defined

$$r_{\mathcal{I}_{\Sigma_i}} := \begin{bmatrix} u \\ y \end{bmatrix} - p_{\mathcal{I}_{\Sigma_i}} = (\mathcal{I} - \mathcal{P}_{\mathcal{I}_{\Sigma_i}}) \begin{bmatrix} u \\ y \end{bmatrix}, \tag{19}$$

which can be applied as the projection-based residual generator, namely $r_{\mathcal{I}_{\Sigma_i}}$. Define $\mathcal{P}_{\mathcal{I}^{\perp}_{\Sigma_i}} = \mathcal{I} - \mathcal{P}_{\mathcal{I}_{\Sigma_i}}$ as the projection onto the orthogonal complement of $\mathcal{I}_{\Sigma_{i,n}}, i = 0, 1$. Then any data vector can be shown as

$$\begin{bmatrix} u \\ y \end{bmatrix} = \mathcal{P}_{\mathcal{I}_{\Sigma_i}} \left(\begin{bmatrix} u \\ y \end{bmatrix} \right) + \mathcal{P}_{\mathcal{I}^{\perp}_{\Sigma_i}} \left(\begin{bmatrix} u \\ y \end{bmatrix} \right), i = 0, 1. \tag{20}$$

On the basis of the result, the norm of $r_{\mathcal{I}_{\Sigma_i}}$ is described by

$$\|r_{\mathcal{I}_{\Sigma_i}}\|_{2,[k_1,k_2]} = \left\| \mathcal{P}_{\mathcal{I}^{\perp}_{\Sigma_i}} \left(\begin{bmatrix} u \\ y \end{bmatrix} \right) \right\|_{2,[k_1,k_2]}, i = 0, 1. \tag{21}$$

By defining proper threshold $J_{th,0}, J_{th,1}$, the detection logic can be implemented for fault detection

$$\begin{cases} \text{if } \left\| r_{\mathcal{I}_{\Sigma_0}} \right\| \le J_{th,0} \text{ and } \left\| r_{\mathcal{I}_{\Sigma_1}} \right\| > J_{th,1} \Longrightarrow \text{fault-free} \\ \text{if } \left\| r_{\mathcal{I}_{\Sigma_0}} \right\| \le J_{th,0} \text{ and } \left\| r_{\mathcal{I}_{\Sigma_1}} \right\| \le J_{th,1} \Longrightarrow \text{intersection} \\ \text{if } \left\| r_{\mathcal{I}_{\Sigma_0}} \right\| > J_{th,0} \text{ and } \left\| r_{\mathcal{I}_{\Sigma_1}} \right\| \le J_{th,1} \Longrightarrow \text{faulty} \end{cases} \tag{22}$$

with $J_{th,0}$ and $J_{th,1}$ representing the corresponding threshold, respectively.

Remark 1. *Under the conclusion above, there is an intersection of $\mathcal{I}_{\Sigma_{0,n}} \cap \mathcal{I}_{\Sigma_{1,n}} \neq \mathcal{O}$, where $\mathcal{O}$ represents the empty set.*

3.3 Threshold setting

In this subsection, the threshold setting issues for T-S fuzzy systems with model uncertainties modeled by (3) will be addressed.

To this end, consider the existence of the possible model uncertainties,

$$I_\Sigma = \begin{bmatrix} \mathscr{M} \\ \mathscr{N} \end{bmatrix} = \begin{bmatrix} \mathscr{M}_n + \Delta_{\mathscr{M}_n} \\ \mathscr{N}_n + \Delta_{\mathscr{N}_n} \end{bmatrix} = I_{\Sigma_n} + I_{\Sigma_\Delta}, \tag{23}$$

where $I_{\Sigma_\Delta} = \begin{bmatrix} \Delta_{\mathscr{M}_n} \\ \Delta_{\mathscr{N}_n} \end{bmatrix}$ denotes the uncertainty induced changes in image representation, which satisfies

$$\sup \|I_{\Sigma_\Delta}\| = \gamma_I < 1. \tag{24}$$

Let

$$\mathcal{I}_{\Sigma_\Delta} = \left\{ \begin{bmatrix} u \\ y \end{bmatrix} : \begin{bmatrix} u \\ y \end{bmatrix} = I_\Sigma(v_\Sigma) = \begin{bmatrix} (\mathscr{M}_n + \Delta_{\mathscr{M}_n})(v_\Sigma) \\ (\mathscr{N}_n + \Delta_{\mathscr{N}_n})(v_\Sigma) \end{bmatrix}, v_\Sigma \in l_{2,[k_1,k_2]} \right\}. \tag{25}$$

The threshold is set as

$$J_{th,i} = \max_{||\Delta_I||_\infty \le \gamma_I, \begin{bmatrix} u \\ y \end{bmatrix} \in \mathcal{I}_{\Sigma_\Delta}} dist \left(\begin{bmatrix} u \\ y \end{bmatrix}, \mathcal{I}_{\Sigma_{i,n}} \right), i = 0, 1. \tag{26}$$

From [19],the direct gap $\overrightarrow{\xi}(\mathcal{I}_{\Sigma_\Delta}, \mathcal{I}_{\Sigma_{i,n}})$ from the uncertain image subspace to the nominal image subspace and faulty image subspace can be computed respectively

$$\overrightarrow{\xi}(\mathcal{I}_{\Sigma_\Delta}, \mathcal{I}_{\Sigma_{i,n}}) = \|(\mathcal{I} - \mathcal{P}_{\mathcal{I}_{\Sigma_i}}) \circ \mathcal{P}_{\mathcal{I}_{\Sigma_\Delta}}\|, \mathcal{P}_{\mathcal{I}_{\Sigma_\Delta}} = \mathcal{I}_{\Sigma_\Delta} \circ \mathcal{I}^{\sim}_{\Sigma_\Delta}.$$

It is evident that

$$\begin{aligned} \|r_{\mathcal{I}_{\Sigma_i}}\|_{2,[k_1,k_2]} &= \left\| (\mathcal{I} - \mathcal{P}_{\mathcal{I}_{\Sigma_i}}) \begin{bmatrix} u \\ y \end{bmatrix} \right\|_{2,[k_1,k_2]} \\ &= \left\| (\mathcal{I} - \mathcal{P}_{\mathcal{I}_{\Sigma_i}}) \circ \mathcal{P}_{\mathcal{I}_{\Sigma_\Delta}} \begin{bmatrix} u \\ y \end{bmatrix} \right\|_{2,[k_1,k_2]} \le \overrightarrow{\xi}(\mathcal{I}_{\Sigma_\Delta}, \mathcal{I}_{\Sigma_{i,n}}) \left\| \begin{bmatrix} u \\ y \end{bmatrix} \right\|_{2,[k_1,k_2]}. \end{aligned} \tag{27}$$

Analogous to the definition given in [20],

$$\mathcal{I}_{\Sigma_i, \Delta_I} = \left\{ \mathcal{I}_{\Sigma_{\Delta_i}} : \|\Delta_{I_i}\| = \|\mathcal{I}_{\Sigma_\Delta} - \mathcal{I}_{\Sigma_{i,n}}\| \le \gamma_{\mathcal{I}_i} \right\},$$

is given. $\gamma_{\mathcal{I}_i}, i = 0, 1$ indicates the upper bound of the uncetainty on the nominal image subspace and faulty subspace.

From (20)-(21), it can be seen that

$$\left\| \begin{bmatrix} u \\ y \end{bmatrix} \right\|_{2,[k_1,k_2]} = \left\| \mathcal{P}_{\mathcal{I}_{\Sigma_i}} \begin{bmatrix} u \\ y \end{bmatrix} \right\|_{2,[k_1,k_2]} + \left\| r_{\mathcal{I}_{\Sigma_i}} \right\|_{2,[k_1,k_2]}, \tag{28}$$

which leads to

$$\|r_{\mathcal{I}_{\Sigma_i}}\|_{2,[k_1,k_2]} \le \frac{\gamma_{I_i}}{\sqrt{1 - \gamma_{I_i}^2}} \left\| \mathcal{P}_{I_{\Sigma_i}} \left(\begin{bmatrix} u \\ y \end{bmatrix} \right) \right\|_{2,[k_1,k_2]} = J_{th,i}. \tag{29}$$

esponding system $\mathcal{I}_{\Sigma_{i,n}}, i = 0, 1$.

In summary, the projection method for dynamic systems based on image space has been studied, as the implementation of adjoint systems in projection-based residual generation requires a large amount of discrete convolution computations [17]. To deal with this issue, an alternative solution is proposed.

Theorem 2. *Given the fuzzy system (2) with model uncertainty satisfying (3), and the observer-based residual r_{Σ_i} generated by (9), the evaluation function and the threshold are given as*

$$J_i = \|r_{\Sigma_i}\|_{2,[k_1,k_2]} \tag{30}$$

$$J_{th,i} = \frac{\gamma_{\mathcal{I}_i}}{\sqrt{1 - \gamma_{\mathcal{I}_i}^2}} \sqrt{\left\| \begin{bmatrix} u \\ y \end{bmatrix} \right\|^2_{2,[k_1,k_2]} - \|r_{\Sigma_i}\|^2_{2,[k_1,k_2]}} \tag{31}$$

where $\gamma_{\mathcal{I}_i}$ represents the upper limit of system uncertainty for corresponding system $\mathcal{I}_{\Sigma_i}, i = 0, 1$.

Proof. Let

$$K_{\Sigma_n} := [-\hat{\mathscr{N}_n} \quad \hat{\mathscr{M}_n}], \tag{32}$$

it is straightforward that $K_{\Sigma_n}(u,y)$ is equivalent to the observer-based residual generator (9), that is

$$K_{\Sigma_n}(u,y) = \hat{\mathscr{M}_n}(y) - \hat{\mathscr{N}_n}(u) = r_{\Sigma_n}. \tag{33}$$

Recalling the Definition 4 and $\mathcal{K}_{\Sigma_n} \circ \mathcal{I}_{\Sigma_n} = \mathcal{O}$, we have

$$\begin{bmatrix}\mathcal{I}_{\Sigma_i} & \mathcal{K}_{\Sigma_i}^{\sim}\end{bmatrix} \circ \begin{bmatrix}\mathcal{I}_{\Sigma_i}^{\sim} \\ \mathcal{K}_{\Sigma_i}\end{bmatrix} = \mathcal{I}.$$

Based on it, (19) is written as

$$r_{\mathcal{I}_{\Sigma_i}} = (\mathcal{I} - \mathcal{P}_{\mathcal{I}_{\Sigma_i}}) \begin{bmatrix}u \\ y\end{bmatrix} = \mathcal{K}_{\Sigma_i}^{\sim} \circ \mathcal{K}_{\Sigma_i} \left(\begin{bmatrix}u \\ y\end{bmatrix} \right) \tag{34}$$

which can be described by

$$\left\| r_{\mathcal{I}_{\Sigma_i}} \right\|_{2,[k_1,k_2]} = \left\| \mathcal{K}_{\Sigma_i} \left(\begin{bmatrix}u \\ y\end{bmatrix} \right) \right\|_{2,[k_1,k_2]} = \| r_{\Sigma_i} \|_{2,[k_1,k_2]}. \tag{35}$$

where $r_{\Sigma_i}, i = 0, 1$ indicate residual generated by the SKR of the nominal system and the faulty system, respectively.

According to (24), (28) and (35), we have

$$\| r_{\Sigma_i} \|_{2,[k_1,k_2]} \leq \frac{\gamma_{\mathcal{I}_i}}{\sqrt{1-\gamma_{\mathcal{I}_i}^2}} \sqrt{\left\| \begin{bmatrix}u \\ y\end{bmatrix} \right\|_{2,[k_1,k_2]}^2 - \| r_{\Sigma_i} \|_{2,[k_1,k_2]}^2} \tag{36}$$

where $\gamma_{\mathcal{I}_i}$ denotes the upper limit of system uncertainty for $\mathcal{I}_{\Sigma_i}, i = 0, 1$. The proof is completed. □

4 An example

In this section, a numerical example is given to verify the efficiency of the proposed results.

Consider the following T-S fuzzy dynamic models

Region Rule $\Re^m$: IF $y_1(n)$ is H_1^m, THEN

$$\begin{cases} x(n+1) = (A_m + \delta_A + \Delta_A)x(n) + (B + \Delta_B)u(n) \\ y(n) = Cx(n) + Du(n), m = 1, 2, 3 \end{cases} \tag{37}$$

where

$$A_1 = \begin{bmatrix} 0.990 & -0.000 & 0.008 \\ -0.003 & 0.959 & 0.020 \\ 0.007 & 0.020 & 0.970 \end{bmatrix}, B = \begin{bmatrix} 0.0128 & 0.0000 \\ 0.0000 & 0.0127 \\ 0.0000 & 0.0001 \end{bmatrix}$$

$$A_2 = \begin{bmatrix} 0.987 & -0.000 & 0.011 \\ -0.004 & 0.955 & 0.023 \\ 0.010 & 0.023 & 0.964 \end{bmatrix}, C = \begin{bmatrix} 1 & 0 & 0 \\ 0 & 1 & 0 \end{bmatrix}$$

$$A_3 = \begin{bmatrix} 0.982 & -0.000 & 0.016 \\ -0.004 & 0.950 & 0.027 \\ 0.015 & 0.028 & 0.954 \end{bmatrix}, D = \begin{bmatrix} 0.870 & 0.010 \\ 0.120 & 1.130 \end{bmatrix}$$

$$\delta_A = \begin{bmatrix} -0.014 & -0.001 & 0.011 \\ 0.001 & 0 & -0.001 \\ 0.014 & 0.001 & -0.012 \end{bmatrix}.$$

The membership functions for the premise variable y_1 are shown in Fig. 1. It can be seen that the premise variables can be divided into 1) $S_1 := \{y_1 \mid 25 < y_1 \leq 30\}$; 2) $S_2 := \{y_1 \mid 30 < y_1 \leq 35\}$; 3) $S_3 := \{y_1 \mid 35 < y_1 \leq 40\}$; and 4) $S_4 := \{y_1 \mid 40 < y_1 \leq 45\}$. $\Delta_A = 0.0001\cos(0.04k)A_m$ and $\Delta_B = 0.001\sin(0.04k)B$ represent the model uncertainties. Based on it, the upper bounds of the uncertainty projection operator on the nominal image subspace and the faulty image subspace are denoted as $\gamma_{\mathcal{I}_0}$ and $\gamma_{\mathcal{I}_1}$, respectively, satisfying $\gamma_{\mathcal{I}_0} = 0.0372$ and $\gamma_{\mathcal{I}_1} = 0.0629$. The multiplicative fault, represented by δ_A, is considered from the $2000th$ sample, leading to the changes in the system output $y_i, i = 1, 2$, as illustrated in the Fig. 2.

We first demonstrate the performance of the binary classification fault detection scheme. The detection performance is shown in Fig. 3, from which it can be observed that the detection scheme we proposed can effectively detect the multiplicative faults.

To further demonstrate the propose methods, the comparison with the observer-based fault detection scheme is provided. Let

$$K_{\Sigma_r} = \begin{bmatrix} -\hat{\mathscr{N}_r} & \hat{\mathscr{M}_r} \end{bmatrix}$$
$$\hat{\mathscr{M}_r} = (A_{L_r}(\mu(k)), -L_r(k), W_r(k)C(\mu(k)), I)$$
$$\hat{\mathscr{N}_r} = (A_{L_r}(\mu(k)), B_{L_r}(k), W_r(k)C(\mu(k)), D(\mu(k)))$$

with $A_{L_r}(\mu(k)) = A(\mu(k)) - L_r(k)C(\mu(k))$.

From [20], we have

$$K_{\Sigma_r} = Q_\Sigma K_{\Sigma_0}, Q_\Sigma = (A_{L_r}(\mu(k))), L(k) - L_r(k), C(\mu(k), I),$$

it holds that

$$\| r_r \|_{2,[k_1,k_2]} = \left\| K_{\Sigma_r} \left(\begin{bmatrix}u \\ y\end{bmatrix} \right) \right\|_{2,[k_1,k_2]} = \left\| Q_\Sigma K_{\Sigma_0} \left(\begin{bmatrix}u \\ y\end{bmatrix} \right) \right\|_{2,[k_1,k_2]}.$$

Assumed $\| \Delta_{\mathcal{I}} \| \leq \gamma_{\mathcal{I}}$, we have

$$\| r_r \|_{2,[k_1,k_2]} \leq q_\Sigma \gamma_{\mathcal{I}} \left\| \begin{bmatrix}u \\ y\end{bmatrix} \right\|_{2,[k_1,k_2]}$$

where q_Σ indicates the norm of the operator Q_Σ. According to the analysis above, we have

$$J_r = \| r_r \|_{2,[k_1,k_2]}, J_{th,r} = q_\Sigma \gamma_{\mathcal{I}} \left\| \begin{bmatrix}u \\ y\end{bmatrix} \right\|_{2,[k_1,k_2]},$$

and threshold with $q_\Sigma = 6.5175$ and $\gamma_{\mathcal{I}} = 0.0231$. Compared to the observer-based fault detection system, the detection performance of binary-classification scheme has been improved, as evident from the results shown in the Fig. 4. As a result, through the comparative experiment, it can be concluded that the proposed fault detection method is effective.

5 Conclusions

In this paper, a fault detection scheme for T-S fuzzy systems based on binary classification is proposed. Specifically, the T-S fuzzy system is first introduced. Then, the image space and the kernal space of the time-varying fuzzy model are constructed by using the coprime factorization technique. On this basis, the residual signal is obtained by projecting the process data vectors onto the kernel and image subspaces of nominal systems and the faulty systems, and the multiplicative fault detection of the fuzzy system is realized by setting the residual-driven threshold via the gap metric technology.

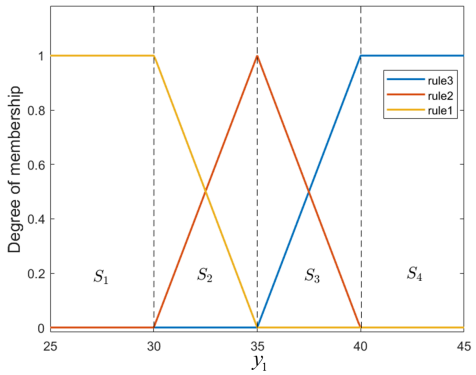

Fig. 1: Membership function for fuzzy system

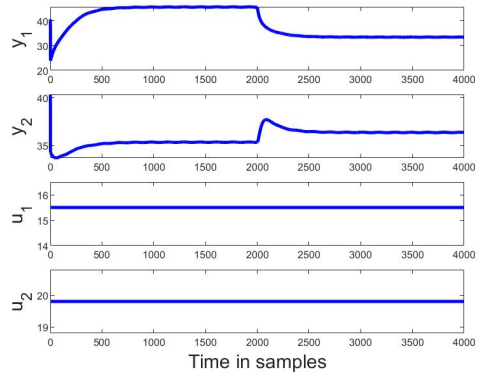

Fig. 2: Output signal y_i and input signal u_i, $i = 1, 2$

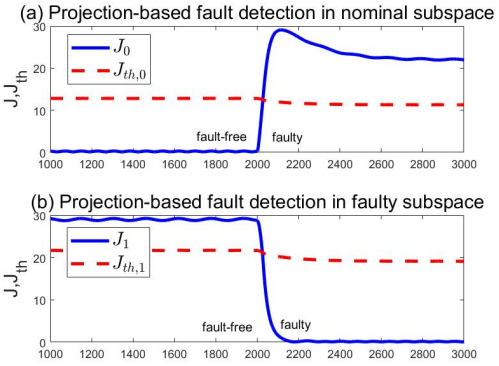

Fig. 3: The detection performance of projection-based fault detection

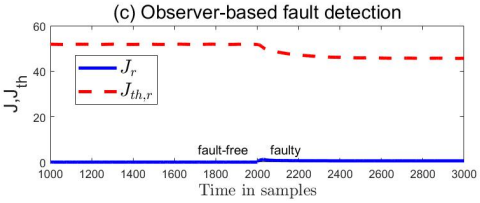

Fig. 4: The comparison results of observer-based fault detection

Finally, the superiority of the projection-based fault detection approach over the observer-based fault detection approach in detecting multiplicative faults is illustrated through a case study. Future work will focus on the issues of multiple fault classification for fuzzy systems.

References

[1] R. J. Patton, P. M. Frank, and R. N. Clark, *Fault Diagnosis in Dynamic Systems: Theory and Applications*, Englewood Cliffs, NJ: Prentice-Hall, 1989.

[2] M. Blanke, M. Kinnaert, J. Lunze , et al, *Diagnosis and Fault-Tolerant Control*, Springer, Berlin Heidelberg, 2006.

[3] S. X. Ding, *Model-Based Fault Diagnosis Techniques-Design Schemes, Algorithms and Tools*, Springer-Verlag, 2008.

[4] J. Chen, and R. J. Patton, *Robust Model-Based Fault Diagnosis for Dynamic Systems*, Kluwer Academic Publishers, Boston, 1999.

[5] S. X. Ding, T. Jeinsch, P. M. Frank, and E. L. Ding, A unified approach to the optimization of fault detection systems, *International Journal of Adaptive Control and Signal Processing*, 14: 725-745, 2000.

[6] T. Takagi and M. Sugeno, Fuzzy identification of systems and its applications to modeling and control, *IEEE Transactions on Systems, Man, and Cybernetics*, 15(1): 116-132, 1985.

[7] Z. Lendek, T. Guerra, R. Babuska, and B. D. Schutter, *Stability Analysis and Nonlinear Observer Design using Takagi-Sugeno Fuzzy Models*, Dordrecht, Netherlands: Springer-Verlag, 2010.

[8] G. Feng, A survey on analysis and design of model-based fuzzy control systems, *IEEE Trans. Fuzzy Syst.*, 14(5): 676-697, 2006.

[9] K. Tanaka and H.O. Wang, *Fuzzy Control Systems Design and Analysis: A Linear Matrix Inequality Approach*, John Wiley and Sons, 2001.

[10] K. Zhang, B. Jiang and M. Staroswiecki, Dynamic Output Feedback-Fault Tolerant Controller Design for Takagi-Sugeno Fuzzy Systems with Actuator Faults, *IEEE Transactions on Fuzzy Systems*, 18(1): 194-201, 2010.

[11] L. Li, S. X. Ding, J. Qiu, Y. Yang and Y. Zhang, Weighted fuzzy observer-based fault detection approach for discrete-time nonlinear systems via piecewise-fuzzy Lyapunov functions, *IEEE Transactions on Fuzzy Systems*, 24(6): 1320-1333, 2016.

[12] L. Li, S. X. Ding and X. Peng, Optimal Observer-Based Fault Detection and Estimation Approaches for T-S Fuzzy Systems, *IEEE Transactions on Fuzzy Systems*, 30(2): 579-590, 2022.

[13] S. Bezzaoucha, B. Marx, D. Maquin and J. Ragot, State and multiplicative sensor fault estimation for nonlinear systems, *2013 Conference on Control and Fault-Tolerant Systems*, 456-461, 2013.

[14] H. A. Talebi and K. Khorasani, A Neural Network-Based Multiplicative Actuator Fault Detection and Isolation of Nonlinear Systems, *IEEE Transactions on Control Systems Technology*, 21(3): 842-851, 2013.

[15] A. Feintuch, *Robust Control Theory in Hilbert Space*, New York: Springer-Verlag, 1998.

[16] T. Kato, *Perturbation Theory for Linear Operators*, Berlin: Springer-Verlag, 1995.

[17] S. X. Ding, L. Li, and T. Liu, An alternative paradigm of fault diagnosis in dynamic systems: orthogonal projection-based methods, arXiv:2202.08108.

[18] R. Ravi, A. M. Pascoal, and P. P. Khargonekar, Normalized coprime factorizations for linear time-varying systems, *Systems and Control Letters*, 18(6): 455-465, 1992.

[19] A. Feintuch, The time-varying gap and coprime factor perturbations, *Mathematics of Control Signals and Systems*, 8(4): 352-374, 1995.

[20] S. X. Ding, *Data-Driven Design of Fault Diagnosis and Fault-Tolerant Control Systems*, London: Springer-Verlag, 2014.

Proceedings of the 3rd Conference on Fully Actuated System Theory and Applications
May 10-12, 2024, Shenzhen, China

Distributed Detection for Plantwide Processes with Randomly Occurring Faults*

Jian Song[1], Wangyan Li[†1,2], Jie Bao[2]

1. College of Science, University of Shanghai for Science and Technology, Shanghai 200093, P. R. China
E-mail: Wangyan_Li@usst.edu.cn

2. School of Chemical Engineering, The University of New South Wales, NSW 2052, Australia
E-mail: j.bao@unsw.edu.au

Abstract: This paper presents a distributed fault detection scheme for plantwide chemical processes with *randomly occurring faults* (ROFs). First, we introduce a general two-port system model for the plantwide chemical processes. The distributed fault detectors are designed for plantwide systems where interactions between process units are accounted for. Then, the fault-sensitive condition as well as disturbances attenuation condition are formulated. Based on the *vector dissipativity* condition, the detection gains are obtained offline via solving *linear matrix inequalities* (LMIs), and the global evaluation functions are calculated for online fault detection. Finally, a numerical example is provided to illustrate the effectiveness of the proposed approach.

Key Words: Distributed, Dissipativity, Fault Detection, Randomly Occurring Fault

1 Introduction

The increased complexity of chemical processes in the modern process industry has resulted in considerable economic benefits. This has led to the prevalence of complex process plants, which consist of multiple interconnected process units or subsystems, collectively referred to as plantwide systems. In order to effectively improve both material and energy efficiency, these units have been constructed to interact with each other through the integration of energy and recycle loops of materials [1]. However, the risk of plant sensitivity to flaws such as sensor and actuator failures has increased as a result of the process units' significant usage of material recycling and heat integration. These faults can potentially lead to economic, environmental, and safety issues [2] or even jeopardize the task execution [3] if they are not addressed properly in plantwide system designs. Furthermore, plant-wide fault detection frequently occurs in a distributed manner, with a fault detection system monitoring each process unit and communicating with the fault detectors of other process units. Despite the rise of distributed state estimation (e.g., [4,5]) and distributed control (e.g., [6–8]), distributed fault detection (DFD) for plant-wide processes has seen limited development. Only a few approaches, such as a multivariate analysis-based distributed monitoring and fault diagnosis approach in [9, 10], and cascade process networks developed using a model-based approach in [11], have been proposed in the field of process control.

However, due to a variety of factors, including fading measurement signals, the unpredictability of the wireless networks throughout extended distances, the limited bandwidth of the communication channels, and unpredictable fluctuations in the network load [12], the faults in the plantwide chemical process can happen in a random way. This kind of faults is often called, *randomly occurring faults* (ROFs). In the existing literature, the fault-tolerant control [13], fault estimation methods [14–16] were developed. As for the corresponding fault detection problems, only limited preliminary research has been reported. For instance, a single networked multi-rate system with network-induced fading channels and ROFs is investigated in [12] for the fault detection problem. However, the obtained result is somewhat conservative due to the adopted criterion is essentially fault attenuation rather than fault sensitivity. When it comes to plantwide systems, it becomes more complex due to the fact that ROFs can propagate to different units. It is interesting to look at the corresponding DFD problems for plantwide systems with ROFs.

Inspired by the discussions mentioned above, this work proposes a general model-based distributed plantwide fault detection approach for plantwide processes with randomly occurring faults. The main issues with this method involve: (1) focusing on how interactions between process units affect distributed fault detection; and (2) considering the faults to occur in a random way, which is more reasonable in practice. Compared with the existing results, the contributions can be summarized as follows:

1) A more general two-port representation where the fault and disturbance signals can propagate through the interconnection input is considered, which covers the models in [19, 20] as a special case;
2) In this study, the fault is considered to occur in a random way, which is more reasonable in practice;
3) A global evaluation function is proposed for distributed fault detection propose. Also, based on this, a new fault detection mechanism is expected to be established.

The remaining parts of this paper are divided into the following sections: The DFD problem for plantwide systems is formulated in Section 2. In Section 3, the dissipativity analysis of the error dynamics is performed to obtain detector gains and conduct fault detection. In addition, a case study illustrating the suggested DFD design is presented in Section 4, followed by the conclusions.

Notation. The n-dimensional Euclidean space can be described as $\mathbb{R}^n$, and the symbol $\|\cdot\|$ is the Euclidean norm in $\mathbb{R}^n$. The transposition and inverse of a matrix M are represented as $M^\top$ and M^{-1}, respectively, and the pres-

*This work is supported by National Natural Science Foundation of China (NSFC) under Grant 62103283 and the Australian Research Council under Discovery Projects DP220100355.

†Corresponding author: Wangyan Li.

ence of $M > 0$ (or $M < 0$) signifies that the matrix M is positive definite (or negative definite). Notation $\circ$ means Hadamard product. $\mathbf{1}$ denotes a vector or matrix with every element being 1. I and I_{col} are an identity matrix and a column of identity matrices with appropriate dimensions, respectively. $M \leq\leq 0$ represents all the elements in matrix M are less than 0. $M = [m_{ij}]$ indicates that the i-th row and j-th column entry of the matrix M is denoted by m_{ij}. $\underset{j\in\mathcal{N}}{\text{Row}}[M_j]$ (respectively, $\underset{j\in\mathcal{N}}{\text{Col}}[M_j]$) means arranging a set of matrices in a row (respectively, column) form, i.e., $\underset{j\in\mathcal{N}}{\text{Row}}[M_j] \triangleq [M_1, M_2, \cdots, M_N]$. $\underset{j\in\mathcal{N}}{\text{diag}}[M_j]$ represents the block-diagonal matrix consisting of matrices M_j ($j \in \mathcal{N}$). In symmetric block matrices, terms arising from symmetry are indicated with an ellipsis $*$. The space of square summable n-dimensional vector-valued functions is denoted by $l_2([0,\infty), \mathbb{R}^n)$. Moreover, the expected value of a random variable x is represented by $\mathbb{E}\{x\}$. $\text{Prob}\{\cdot\}$ represents the occurrence probability of the event $\{\cdot\}$.

2 Problem Formulation

Let $\mathcal{N} = \{1, 2, \cdots, N\}$ be the collection of N subsystems of a plantwide system. The corresponding state space description of the i-th unit can be obtained as follows:

$$x_{i,k+1} = A_i x_{i,k} + B_i u_{i,k} + B_{p_i} u_{p_i,k} + W_i \omega_{i,k} \quad (1)$$

$$y_{p_i,k} = C_{p_i} x_{i,k} + D_i u_{i,k} + D_{p_i} u_{p_i,k} + D_{w_i} \omega_{i,k} \quad (2)$$

$$y_{i,k} = C_i x_{i,k} \quad (3)$$

where $x_{i,k} \in \mathbb{R}^n$ refers to the system state at time k for the unit i. The measured output is $y_{i,k} \in \mathbb{R}^{n_y}$, and the interconnecting output is $y_{p_i,k} \in \mathbb{R}^{n_{yp}}$ as it connects other units. $u_{i,k} \in \mathbb{R}^{n_u}$ and $u_{p_i,k} \in \mathbb{R}^{n_{up}}$ denote the manipulated input, and the interconnecting input, respectively. The exogenous disturbance input, represented by $\omega_{i,k} \in \mathbb{R}^{\omega}$, belongs to $l_2([0,\infty), \mathbb{R}^{\omega})$. A_i, B_i, B_{p_i}, C_i, C_{p_i}, D_i, D_{p_i}, D_{w_i} and W_i are matrices that have suitable dimensions for the given context.

Let $f_{i,k} \in \mathbb{R}^f$ be the fault signal to be detected, when the actuators experience random failures,

$$u_{i,k} = u_{c_{i,k}} + \xi_i f_{i,k} \quad (4)$$

where $u_{c_{i,k}} \in \mathbb{R}^{n_{uc}}$ is the controller output, and variable $\xi_i \in \mathbb{R}$ is a random variable characterizing the probability of fault occurring, which obeys the following Bernoulli distribution:

$$\text{Prob}\{\xi_i = 1\} = p_i,$$
$$\text{Prob}\{\xi_i = 0\} = 1 - p_i,$$

where $p_i \in [0\ 1]$ is a positive scalar. When $\xi_i = 1$, it means the actuators experience faults. Otherwise, the actuators are healthy.

Furthermore, the i-th plant's interactions with other plants are described by

$$u_{p_i,k} = \sum_{j\in\mathcal{N}\backslash\{i\}} h_{p_{ij}} y_{p_j,k} \quad (5)$$

where the plant is excluded from set $\mathcal{N}$ by setting $\mathcal{N}\backslash\{i\}$. The connection between the i-th and j-th plants are described by $h_{p_{ij}} \in \{0, I\}$. In particular, if plants i and j are connected (we assume plants are not self-connected), $h_{p_{ij}} = I$, otherwise, $h_{p_{ij}} = 0$. By denoting $u_{p,k} = \underset{i\in\mathcal{N}}{\text{Col}}[u_{p_i,k}]$, and $y_{p,k} = \underset{i\in\mathcal{N}}{\text{Col}}[y_{p_i,k}]$, the network topology of the whole plantwide system can be represented by

$$u_{p,k} = H_p y_{p,k} \quad (6)$$

where $h_{p_{ij}}$ is the i-th row and j-th column block entry element of a topology matrix H_p [6].

In this study, we investigate the distributed fault detection problems in the plantwide system by considering two types of faults: *local faults* denoted as f_i, which occur specifically at unit i, and *remote faults* denoted as f_j, which occur at units other than unit i. We aim to design distributed fault detectors based on residuals, where each plant's distributed estimators are constructed with the node's connection taken into account. The structure of the considered system is distributed in the sense that every plant includes a state estimator that connects with other interacting plants to exchange information. Thus, the distributed estimator for the i-th node could have the following possible structure:

$$\hat{x}_{i,k+1} = A_i \hat{x}_{i,k} + B_i u_{c_{i,k}} + B_{p_i} \hat{u}_{p_i,k} + \sum_{j\in\mathcal{N}} h_{p_{ij}} K_{ij} (y_{j,k} - \hat{y}_{j,k}) \quad (7)$$

$$\hat{y}_{i,k} = C_i \hat{x}_{i,k} \quad (8)$$

where K_{ij} represents the estimator gain to be determined. $\hat{y}_{i,k}$ and $\hat{u}_{p_i,k}$ are estimates of $y_{i,k}$ and $u_{p_i,k}$, respectively. Subsequently, the residual $r_{i,k}$ can be defined by

$$r_{i,k} = M_i (y_{i,k} - \hat{y}_{i,k}) \quad (9)$$

where the matrix M_i represents the residual gain matrix that needs to be determined.

In order to ensure that the state estimation problem is well-posed, the following assumption is developed.

Assumption 1. $D_p \triangleq \underset{i\in\mathcal{N}}{\text{Row}}[D_{p_i}]$, $C_p \triangleq \underset{i\in\mathcal{N}}{\text{Row}}[C_{p_i}]$, $D \triangleq \underset{i\in\mathcal{N}}{\text{Row}}[D_i]$, $D_w = \underset{i\in\mathcal{N}}{\text{Row}}[D_{w_i}]$. *Matrix $I - H_p D_p$ is invertible.*

In what follows, defining $e_{i,k} = x_{i,k} - \hat{x}_{i,k}$ for each unit, then subtracting (7) from (1) yields the following estimation error

$$e_{i,k+1} = A_i e_{i,k} + W_i \omega_{i,k} + \xi_i B_i f_{i,k} - \sum_{j\in\mathcal{N}} h_{p_{ij}} K_{ij} C_j e_{j,k} + B_{p_i} \Big(\sum_{j\in\mathcal{N}} L_{ij} e_{j,k} + \sum_{j\in\mathcal{N}} D_{pf_{ij}} \xi_j f_{j,k} + \sum_{j\in\mathcal{N}} D_{pw_{ij}} \omega_{j,k} \Big), \quad (10)$$

where the i-th row and j-th column block entry element of matrices L, D_{pf}, and D_{pw} are represented by the matrices L_{ij}, $D_{pf_{ij}}$, and $D_{pw_{ij}}$, respectively. The above matrices can be described as follows:

$$L = (I - H_p D_p)^{-1} H_p C_p,$$
$$D_{pf} = (I - H_p D_p)^{-1} H_p D,$$

$$D_{pw} = (I - H_p D_p)^{-1} H_p D_w.$$

Let

$$\begin{aligned}
&\tilde{A}_{ii} = A_i - K_{ii}C_i + B_{p_i}L_{ii}, \quad \tilde{\mathcal{L}}_{f_{ii}} = B_i + B_{p_i}D_{pf\,ii},\\
&\tilde{A}_{ij} = B_{p_i}L_{ij} - h_{p_{ij}}K_{ij}C_j, \quad \tilde{\mathcal{L}}_{f_{ij}} = B_{p_i}D_{pf\,ij},\\
&\tilde{W}_{ii} = W_i + B_{p_i}D_{pw\,ii},
\end{aligned}$$

then one can represent (10) as

$$\begin{aligned}
e_{i,k+1} = \tilde{A}_{ii}e_{i,k} + \sum_{j\in\mathcal{N}\setminus\{i\}} \tilde{A}_{ij}e_{j,k} + \xi_i\tilde{\mathcal{L}}_{f_{ii}}f_{i,k} + \tilde{W}_{ii}\omega_{i,k}\\
+ \sum_{j\in\mathcal{N}\setminus\{i\}} \xi_j\tilde{\mathcal{L}}_{f_{ij}}f_{j,k} + \sum_{j\in\mathcal{N}\setminus\{i\}} B_{p_i}D_{pw\,ij}\omega_{j,k}.
\end{aligned} \tag{11}$$

The residual (9) now becomes

$$r_{i,k} = M_i C_i e_{i,k}. \tag{12}$$

This research aims to construct distributed fault detectors that concurrently satisfy the following requirements:

1) Under the assumption of zero initial conditions and $\omega_{i,k} = 0$, the faults have the maximum effect on the residual $r_{i,k}$ (maximize the effects), i.e.,

$$\sum_{j\in\mathcal{N}}\sum_{k=0}^{T}\mathbb{E}\{\|r_{j,k}\|^2\} \geq \beta^2 \sum_{j\in\mathcal{N}}\sum_{k=0}^{T}\|f_{j,k}\|^2 \tag{13}$$

for $\forall\ 0 < T < \infty$, where scalar $\beta > 0$.

2) Under the assumption of zero initial conditions and $f_{i,k} = 0$, the exogenous disturbance has the minimum effect on the residual $r_{i,k}$ (minimize the effects), i.e.,

$$\sum_{j\in\mathcal{N}}\sum_{k=0}^{T}\mathbb{E}\{\|r_{j,k}\|^2\} \leq \gamma^2 \sum_{j\in\mathcal{N}}\sum_{k=0}^{T}\|\omega_{j,k}\|^2 \tag{14}$$

for $\forall\ 0 < T < \infty$, where scalar $\gamma > 0$.

Taking into account the aforementioned requirements, to design a residual evaluation stage, we can compute a global evaluation function $J(r_i)$ and a threshold $\bar{J}_{i,th}$ as follows:

$$J(r_i) = \mathbb{E}\left\{\left\{\sum_{s=k-L}^{k} r_{i,s}^\top r_{i,s}\right\}^{\frac{1}{2}}\right\}, \quad \bar{J}_{i,th} = \sup_{\substack{\omega_{i,k}\in l_2\\ f_{i,k}=0}} J(r_i).$$

In this way, the following rule can be used to detect when faults will occur in any plant:

$$\begin{aligned}
J(r_i) > \bar{J}_{i,th} \quad &\text{with faults},\\
J(r_i) \leq \bar{J}_{i,th} \quad &\text{faults-free}.
\end{aligned} \tag{15}$$

3 Dissipativity Analysis

First, recall the definition of *vector dissipativity*, and here, we will rephrase the definition as presented in [17, 18]:

Assumption 2. *The dissipation matrix $\mathcal{W}$ (represented as $\mathcal{W} = [w_{ij}]$) satisfies the following properties: non-negative, non-singular, semi-stable, and column sub-stochastic (as discussed in [21]). Moreover, for any entry element w_{ij} of the dissipation matrix $\mathcal{W}$, it holds that $w_{ij} > 0$ if $h_{p_{ij}} = I$ and $w_{ij} = 0$ if $h_{p_{ij}} = 0$.*

Definition 1. *(Vector dissipativity [17]) The error dynamics* (11) *is said to be vector dissipative for the supply rate function vector $\mathcal{S}(u_k, r_k) = [\mathcal{S}_1(u_k, r_k), \cdots, \mathcal{S}_N(u_k, r_k)]^\top$, if there exists a nonnegative definite storage function vector $\mathcal{V}(e_k) = [\mathcal{V}_1(e_{1,k}), \cdots, \mathcal{V}_N(e_{N,k})]^\top$, and a dissipation matrix $\mathcal{W}(\mathcal{W} = [w_{i,j}])$ that is satisfying Assumption 2, such that the dissipativity inequality holds for any $k > 0$ as follows:*

$$\mathbb{E}\{\mathcal{V}(e_{k+1})\} \leq\leq \mathbb{E}\{\mathcal{W}\mathcal{V}(e_k) + \mathcal{S}(u_k, r_k)\}. \tag{16}$$

In the following, we divide the content into three subsections to design DFDs with the desired demands. In the first two subsections, the requirements satisfying the robustness constraint (14) and fault sensitivity constraint (13) will be found independently. A feasible solution to satisfy both constraints will be presented in the last subsection, where we can obtain the detection gains and conduct fault detection.

3.1 Dissipativity-based fault sensitivity design for DFD

Proposition 1. *The error dynamics* (11) *without exogenous disturbance is said to be vector dissipative w.r.t the supply rate $\mathcal{S}(f_k, r_k)$ where $\mathcal{S}_i(f_k, r_k) = \sum_{j\in\mathcal{N}} h_{p_{ij}}(\|r_{j,k}\|^2 - \beta^2\|f_{j,k}\|^2)$ if there exists a family of matrices $\{Y_{ij}\}_{j\in\mathcal{N}}$, positive definite matrices $\{P_j\}_{j\in\mathcal{N}}$, positive semi-definite matrices $\{Z_j\}_{j\in\mathcal{N}}$, a scalar β and a dissipation matrix $\mathcal{W} = [w_{ij}]$ that is satisfying Assumption 2 such that the following LMI is satisfied:*

$$\Pi_i = \begin{bmatrix} P_i & \Pi_i^{12} & \Pi_i^{13} & \Pi_i^{14} & \Pi_i^{15}\\ * & \Pi_i^{22} & 0 & 0 & 0\\ * & * & \Pi_i^{33} & 0 & 0\\ * & * & * & \Pi_i^{44} & 0\\ * & * & * & * & \Pi_i^{55} \end{bmatrix} > 0 \tag{17}$$

where

$$\begin{aligned}
\Pi_i^{12} &= P_iA_i - Y_{ii}C_i + P_iB_{p_i}L_{ii},\\
\Pi_i^{13} &= \underset{j\in\mathcal{N}\setminus\{i\}}{\text{Row}}[P_iB_{p_i}L_{ij} - h_{p_{ij}}Y_{ij}C_j],\\
\Pi_i^{14} &= p_iP_iB_i + p_iP_iB_{p_i}D_{pf\,ii},\\
\Pi_i^{15} &= \underset{j\in\mathcal{N}\setminus\{i\}}{\text{Row}}[p_jB_{p_i}D_{pf\,ij}],\\
\Pi_i^{22} &= w_{ii}P_i + C_i^\top Z_iC_i,\\
\Pi_i^{33} &= \underset{j\in\mathcal{N}\setminus\{i\}}{\text{diag}}\{w_{ij}P_j + h_{p_{ij}}C_j^\top Z_jC_j\},\\
\Pi_i^{44} &= -\beta^2 I, \quad \Pi_i^{55} = \underset{j\in\mathcal{N}\setminus\{i\}}{\text{diag}}\{-h_{p_{ij}}\beta^2 I\}.
\end{aligned}$$

In this scenario, the desired detector gains for plant i can be obtained as follows:

$$K_{ii} = P_i^{-1}Y_{ii}, \quad K_{ij} = P_i^{-1}Y_{ij}, \tag{18}$$

and we can obtain the residual gain M_i by factorizing Z_i.

Proof. Assume that $\omega_{i,k} = 0$ ($i \in \mathcal{N}$) in system (1), and define the storage function $\mathcal{V}_i(e_{i,k}) = e_{i,k}^\top P_i e_{i,k}$. Next, note that $\mathbb{E}\{\xi_i - p_i\} = 0$, $\mathbb{E}\{(\xi_i - p_i)^2\} = p_i(1 - p_i)$ and $\mathbb{E}\{\xi_i\} = \mathbb{E}\{\xi_i^2\} = p_i$ ($i \in \mathcal{N}$), then the proof can refer to the well-established procedures outlined in [20, Theorem 1], where the similar results have been rigorously demonstrated in [19, 20]. Thus, it is omitted here. □

Proposition 2. *Assume that there exists a set of matrices $\{Y_{ij}\}_{j\in\mathcal{N}}$, positive definite matrices $\{P_j\}_{j\in\mathcal{N}}$, symmetric matrices $\{Z_j\}_{j\in\mathcal{N}}$, scalar β, and a dissipation matrix $\mathcal{W}=[w_{ij}]$ that is satisfying Assumption 2. Then, if the error dynamics* (11) *without considering any disturbances, satisfies the fault sensitivity constraint* (13)*, it implies that the following optimization problem*

$$\max_{\beta>0}\ \beta \qquad \text{s.t.} \quad \Pi_i > 0 \tag{19}$$

is feasible.

Proof. The proof is left out because of the limited space. □

3.2 Dissipativity-based robustness design for DFD

Proposition 3. *The error dynamics* (11) *without faults is said to be vector dissipative for the supply rate $\mathcal{S}(\omega_k, r_k)$ where $\mathcal{S}_i(\omega_k, r_k) = \sum_{j\in\mathcal{N}} h_{p_{ij}}(\gamma^2\|\omega_{j,k}\|^2 - \|r_{j,k}\|^2)$ if there exists a set of matrices $\{Y_{ij}\}_{j\in\mathcal{N}}$, positive definite matrices $\{P_j\}_{j\in\mathcal{N}}$, positive semi-definite matrices $\{Z_j\}_{j\in\mathcal{N}}$, a scalar γ and a dissipation matrix $\mathcal{W}=[w_{ij}]$ that is satisfying Assumption 2 such that the following LMI is satisfied:*

$$\Xi_i = \begin{bmatrix} P_i & \Xi_i^{12} & \Xi_i^{13} & \Xi_i^{14} & \Xi_i^{15} \\ * & \Xi_i^{22} & 0 & 0 & 0 \\ * & * & \Xi_i^{33} & 0 & 0 \\ * & * & * & \Xi_i^{44} & 0 \\ * & * & * & * & \Xi_i^{55} \end{bmatrix} > 0 \tag{20}$$

where

$$\Xi_i^{12} = P_iA_i - Y_{ii}C_i + P_iB_{p_i}L_{ii},\ \ \Xi_i^{22} = w_{ii}P_i - C_i^\top Z_iC_i,$$
$$\Xi_i^{13} = \underset{j\in\mathcal{N}\setminus\{i\}}{\text{Row}}[P_iB_{p_i}L_{ij} - h_{p_{ij}}Y_{ij}C_j],\quad \Xi_i^{44} = \gamma^2 I,$$
$$\Xi_i^{14} = P_i\tilde{W}_{ii},\qquad \Xi_i^{33} = \underset{j\in\mathcal{N}\setminus\{i\}}{\text{diag}}\{w_{ij}P_j\},$$
$$\Xi_i^{15} = \underset{j\in\mathcal{N}\setminus\{i\}}{\text{Row}}[D_{pw_{ij}}],\quad \Xi_i^{55} = \underset{j\in\mathcal{N}\setminus\{i\}}{\text{diag}}\{h_{p_{ij}}\gamma^2 I\}.$$

In this scenario, the desired detector gains for plant i can be obtained as follows:

$$K_{ii} = P_i^{-1}Y_{ii},\quad K_{ij} = P_i^{-1}Y_{ij}, \tag{21}$$

and we can obtain the residual gain M_i by factorizing Z_i.

Proof. The proof is omitted here since it can be obtained like the proof in Proposition 1. □

Proposition 4. *Assume that there exists a set of matrices $\{Y_{ij}\}_{j\in\mathcal{N}}$, positive definite matrices $\{P_j\}_{j\in\mathcal{N}}$, symmetric matrices $\{Z_j\}_{j\in\mathcal{N}}$, a scalar γ, and a dissipation matrix $\mathcal{W}=[w_{ij}]$ that is satisfying Assumption 2. Then, if the error dynamics* (11) *without considering any faults, satisfies the robustness constraint* (14)*, it implies that the following optimization problem*

$$\min_{\gamma>0}\ \gamma \qquad \text{s.t.} \quad \Xi_i > 0 \tag{22}$$

is feasible.

Proof. The proof is left out because of the limited space. □

3.3 Simultaneous fault sensitivity and robustness design

As of present, the *vector dissipativity* requirements for the fault sensitivity constraint (13) and robustness constraint (14) have been derived respectively. However, we aim to obtain the detection gains to satisfy both constraints. In this respect, the following proposition is presented.

Proposition 5. *Assume that there exists a set of matrices $\{Y_{ij}\}_{j\in\mathcal{N}}$, positive definite matrices $\{P_j\}_{j\in\mathcal{N}}$, symmetric matrices $\{Z_j\}_{j\in\mathcal{N}}$, scalars β, γ and dissipation matrix $\mathcal{W}=[w_{ij}]$ that is satisfying Assumption 2. Then, if the error dynamics* (11) *satisfies the fault sensitivity constraint* (13) *and robustness constraint* (14) *simultaneously, it implies that the following optimization problem*

$$\max_{\beta,\gamma>0}\ \beta-\gamma \tag{23}$$

s.t.

$$\Pi_i > 0 \qquad \Xi_i > 0$$

is feasible.

Proof. The proof becomes straightforward by combining Proposition 1-4. □

4 A Case Study

Consider a two-port system of (1)-(3) with parameters:

$$A_1 = \begin{bmatrix} 0.61 & 0.14 \\ 0.01 & 0.5 \end{bmatrix},\quad A_2 = \begin{bmatrix} -0.42 & 0.14 \\ 0.2 & 0.71 \end{bmatrix},$$
$$B_{p_1} = \begin{bmatrix} 0.6 & 0.3 \\ 0.52 & 0.75 \end{bmatrix},\quad B_{p_2} = \begin{bmatrix} 0.156 & -0.13 \\ 0.12 & 0.5 \end{bmatrix},$$
$$C_{p_1} = \begin{bmatrix} 0.5 & 0.4 \\ 0.3 & 0.9 \end{bmatrix},\quad C_{p_2} = \begin{bmatrix} -0.38 & -0.4 \\ -0.2 & 0.7 \end{bmatrix},$$
$$D_{p_1} = \begin{bmatrix} 1.32 & 0.2 \\ 0.8 & 3.2 \end{bmatrix},\quad D_{p_2} = \begin{bmatrix} 1.9 & 0.12 \\ 0.8 & 3.8 \end{bmatrix},$$
$$B_1 = \begin{bmatrix} 0.73 \\ 1.42 \end{bmatrix},\quad B_2 = \begin{bmatrix} 0.85 \\ 0.51 \end{bmatrix},\quad W_1 = \begin{bmatrix} 0.41 \\ 0.7 \end{bmatrix},$$
$$D_1 = \begin{bmatrix} -2.4 \\ 5.8 \end{bmatrix},\quad D_2 = \begin{bmatrix} 1.4 \\ 4.5 \end{bmatrix},\quad W_2 = \begin{bmatrix} 0.31 \\ -0.5 \end{bmatrix},$$
$$D_{w_1} = \begin{bmatrix} 3 \\ 0.4 \end{bmatrix},\quad D_{w_2} = \begin{bmatrix} 1.98 \\ 5 \end{bmatrix},\quad \mathcal{W} = \begin{bmatrix} 0.8 & 0.2 \\ 0.1 & 0.7 \end{bmatrix},$$
$$C_1 = \begin{bmatrix} 1.6 & 0.85 \end{bmatrix},\ C_2 = \begin{bmatrix} -3 & 0.16 \end{bmatrix},\ T_s = 15,$$
$$p_1 = 0.5,\qquad p_2 = 0.5.$$

Subsequently, utilizing CVX toolbox [22], we employ the optimization approach outlined in Proposition 5 to determine the values for the gains K_{11}, K_{12}, K_{21}, K_{22}, M_1, M_2, as well as scalars β and γ. The corresponding results obtained are shown in Table 1.

Table 1: Variables of the designed fault detection observer

Design Variables	Values	Design Variables	Values
K_{11}	$\begin{bmatrix} 0.0731 \\ -0.0118 \end{bmatrix}$	M_1	0.4342
K_{12}	$\begin{bmatrix} -0.0813 \\ 0.0648 \end{bmatrix}$	M_2	0.8421
K_{21}	$\begin{bmatrix} -0.0341 \\ 0.0018 \end{bmatrix}$	β	1.2089
K_{22}	$\begin{bmatrix} -0.0116 \\ -0.2246 \end{bmatrix}$	γ	2.2250

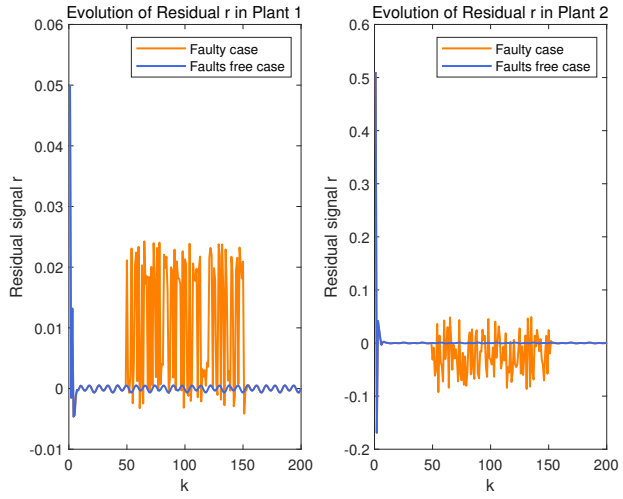

Fig. 1: Evolution of Residual

For the purpose of simulation, we have chosen initial values of $x_{1,0} = [0.2 \quad -0.5]^\top$, $x_{2,0} = [0.3 \quad -0.3]^\top$, and $\hat{x}_{i,0} = [0 \ 0]^\top$, where $i = 1, 2$. These initial conditions are considered over the time steps $k = 0, 1, \ldots, 200$. The disturbance inputs are modeled as $\omega_{1,k} = 10^{-3} \sin \frac{\pi}{4} k$ and $\omega_{2,k} = 10^{-3} \sin \frac{\pi}{8} k$, respectively. In order to enhance the clarity of our simulations, we assume that faults cease to persist after a certain time period. In this case, the system fault signal can be given in the following form:

$$f_{1,k} = \begin{cases} 0.02 & 50 \le k \le 150 \\ 0 & \text{otherwise} \end{cases},$$

$$f_{2,k} = \begin{cases} 0.03 & 50 \le k \le 150 \\ 0 & \text{otherwise} \end{cases}.$$

The dynamic evolution of residual signal r_i can be seen in Fig. 1, and the corresponding evolution functions

$$J(r_i) = \mathbb{E}\left\{ \left\{ \sum_{s=k-L}^{k} r_{i,s}^\top r_{i,s} \right\}^{\frac{1}{2}} \right\}$$

for both the faulty case and the faults free case are shown in Figs. 2 and 3.

According to the fault detection rule (15), the evaluation function $J(r_i)$ remains below the threshold, indicating a fault-free situation. In this sense, the figures reveal prompt detection of random fault signals after 50 time steps, with the selected thresholds determined as $\bar{J}_{1,th} = 0.0522$ and $\bar{J}_{2,th} = 0.5401$, respectively. Also, when random faults occur during the time step interval $[50, 150]$, the residuals rise significantly. Finally, the faults cease to persist after 150 time steps, aligning with the expected results. In conclusion, the simulation results demonstrate the successful detection of randomly occurring faults, affirming the effectiveness of the proposed method.

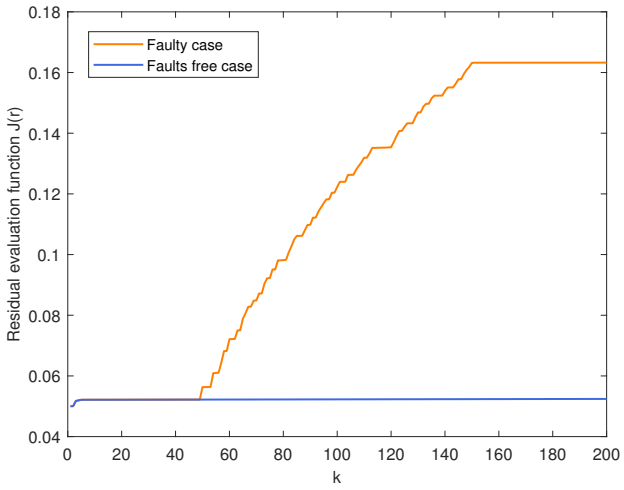

Fig. 2: Evolution of $J(r_1)$ in Plant 1

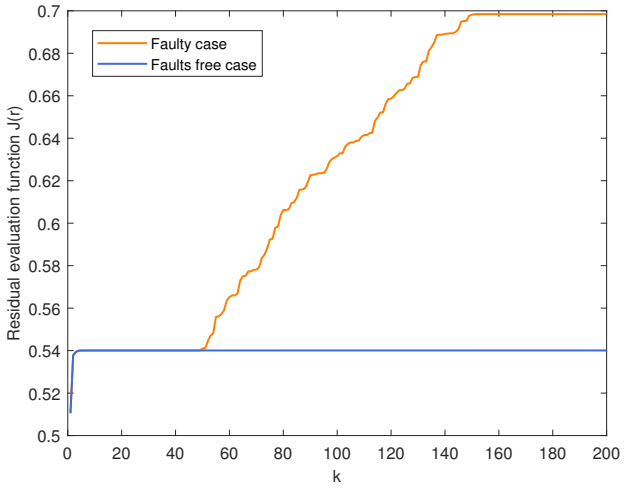

Fig. 3: Evolution of $J(r_2)$ in Plant 2

5 Conclusion

In this paper, we have focused our attention on the distributed fault detection problem for plantwide processes with randomly occurring faults. A general model-based distributed plantwide fault detection scheme has been proposed to deal processes with arbitrary network topologies. Both the fault-sensitivity and robustness conditions have been developed for distributed plantwide fault detection. The distributed fault detectors are designed based on the *vector dissipativity* condition, where the parameters of the estimator

and residue generator are calculated offline via solving linear matrix inequalities.

Our future directions of this paper might involve conducting studies on distributed fault detection to determine the minimal sensor nodes problem [23–25] for the plantwide processes, leveraging Polynomial Chaos Expansions (PCE) [26] to approximate the random fault variables in plantwide systems, and fault detection problem based on multiple hypothesis testing [27].

References

[1] Z. Ge and J. Chen, Plant-wide industrial process monitoring: A distributed modeling framework. *IEEE Transactions on Industrial Informatics*, 2016, 12(1): 310–321.

[2] P. Mhaskar, J. Liu, and P. D. Christofides, Fault-tolerant process control: methods and applications. *Springer Science & Business Media*, 2012.

[3] A. Marino, F. Pierri, and F. Arrichiello, "Distributed fault detection isolation and accommodation for homogeneous networked discrete-time linear systems," *IEEE Transactions on Automatic Control*, 2017, 62(9): 4840–4847.

[4] R. Vadigepalli and F. Doyle, A distributed state estimation and control algorithm for plantwide processes. *IEEE Transactions on Control Systems Technology*, 2003, 11(1): 119–127.

[5] X. Yin, K. Arulmaran, J. Liu, and J. Zeng, Subsystem decomposition and configuration for distributed state estimation. *AIChE Journal*, 2016, 62(6): 1995–2003.

[6] S. Xu and J. Bao, Distributed control of plantwide chemical processes. *Journal of Process Control*, 2009, 19(10): 1671–1687.

[7] O. J. Rojas, R. Setiawan, J. Bao, and P. L. Lee, Dynamic operability analysis of nonlinear process networks based on dissipativity. *AIChE Journal*, 2009, 55(4): 963–982.

[8] M. J. Tippett and J. Bao, Control of plant-wide systems using dynamic supply rates. *Automatica*, 2014, 50(1): 44–52.

[9] Q. Jiang and B. Huang, Distributed monitoring for large-scale processes based on multivariate statistical analysis and bayesian method. *Journal of Process Control*, 2016, 46: 75–83.

[10] Q. Jiang, B. Huang, S. X. Ding, and X. Yan, Bayesian fault diagnosis with asynchronous measurements and its application in networked distributed monitoring. *IEEE Transactions on Industrial Electronics*, 2016, 63(10): 6316–6324.

[11] X. Yin and J. Liu, Distributed output-feedback fault detection and isolation of cascade process networks. *AIChE Journal*, 2017, 63(10): 4329–4342.

[12] Y. Zhang, Z. Wang, L. Zou, and Z. Liu, Fault detection filter design for networked multi-rate systems with fading measurements and randomly occurring faults. *IET Control Theory & Applications*, 2016, 10(5): 573–581.

[13] G. Wei, L. Wang, and W. Li, Fault-tolerant control for discrete-time stochastic systems with randomly occurring faults, in *Proceedings of 31st Chinese Control Conference*, 2012: 1535–1540.

[14] H. Dong, Z. Wang, S. X. Ding, and H. Gao, Finite-horizon estimation of randomly occurring faults for a class of nonlinear time-varying systems. *Automatica*, 2014, 50(12): 3182–3189.

[15] H. Dong, Z. Wang, S. X. Ding, and H. Gao, On H_∞ estimation of randomly occurring faults for a class of nonlinear time-varying systems with fading channels. *IEEE Transactions on Automatic Control*, 2016, 61(2): 479–484.

[16] J. Hu, Z. Wang, and H. Gao, Joint state and fault estimation for time-varying nonlinear systems with randomly occurring faults and sensor saturations. *Automatica*, 2018, 97: 150–160.

[17] W. M. Haddad, V. Chellaboina, and S. G. Nersesov, Vector dissipativity theory and stability of feedback interconnections for large-scale non-linear dynamical systems. *International Journal of Control*, 2004, 77(10): 907–919.

[18] W. M. Haddad, Q. Hui, V. Chellaboina, and S. Nersesov, Vector dissipativity theory for discrete-time large-scale nonlinear dynamical systems. *Advances in Difference Equations*, 2004: 37–66.

[19] W. Li, Y. Yan, and J. Bao, Dissipativity-based distributed fault diagnosis for plantwide chemical processes. *Journal of Process Control*, 2020, 96: 37–48.

[20] W. Li, Y. Yan, and J. Bao, Vector dissipativity-based distributed fault detection for plantwide chemical processes, in *Proceedings of 12th Asian Control Conference*, 2019: 1220–1225.

[21] F. Han, Y. Song, S. Zhang, and W. Li, Local condition-based finite-horizon distributed H_∞-consensus filtering for random parameter system with event-triggering protocols. *Neurocomputing*, 2017, 219(5): 221–231.

[22] Inc. CVX Research, CVX: Matlab software for disciplined convex programming, version 2.0, 2012. `http://cvxr.com/cvx`.

[23] Y. Liu, Z. Wang, Y. Yuan, and W. Liu, Event-triggered partial-nodes-based state estimation for delayed complex networks with bounded distributed delays. *IEEE Transactions on Systems, Man, and Cybernetics: Systems*, 2019, 49(6): 1088–1098.

[24] Y. Liu, Z. Wang, Y. Yuan, and F. E. Alsaadi, Partial-nodes-based state estimation for complex networks with unbounded distributed delays. *IEEE Transactions on Neural Networks and Learning Systems*, 2018, 29(8): 3906–3912.

[25] F. Han, Z. Wang, H. Dong, and H. Liu, Partial-nodes-based scalable H_∞-consensus filtering with censored measurements over sensor networks. *IEEE Transactions on Systems, Man, and Cybernetics: Systems*, 2020: 1–12.

[26] G. Pan, R. Ou and T. Faulwasser, On a stochastic fundamental lemma and its use for data-driven optimal control. *IEEE Transactions on Automatic Control*, 2023, 68(10): 5922-5937.

[27] E.d'Afflisio, P.Braca and P.Willett, Malicious AIS spoofing and abnormal stealth deviations: a comprehensive statistical framework for maritime anomaly detection. *IEEE Transactions on Aerospace and Electronic Systems*, 2021, 57(4): 2093-2108.

Proceedings of the 3rd Conference on Fully Actuated System Theory and Applications
May 10-12, 2024, Shenzhen, China

Remaining Useful Life Prediction Based on Improved Transformer Network for Pneumatic Control Valve

Yu Cheng[1], JianLiang Chen[2]

1. College of Information Science and Engineering, Wuhan University of Science and Technology, Wuhan 430081, China
E-mail: 2363465005@qq.com

2. College of Information Science and Engineering, Wuhan University of Science and Technology, Wuhan 430081, China
E-mail: chenjianliang@wust.edu.cn

Abstract: Pneumatic control valve plays a crucial role in the industrial control system. This paper proposes a hybrid neural network model for predicting the remaining useful life (RUL) of pneumatic control valve system. Firstly, highly related features are selected by the pearson correlation coefficient (PCC) to minimize the computational burden of the model. Then, convolutional neural networks (CNN) is employed to extract local features of sequence data, and Transformer is used to capture global representations. Finally, all the features are fed into the CNN-Transformer model. The dataset generated by development and application of methods for actuator diagnosis in industrial control systems (DAMADICS) platform is verified. The experimental result shows that the proposed hybrid model has high prediction accuracy and stability.

Key Words: Pneumatic Control Valve, Remaining Useful Life, CNN-Transformer

1 Introduction

As a vital component in automation systems, the pneumatic control valve ensures industrial production safety. It has the advantages of stable performance and agile response [1]. In prolonged usage in harsh environments, pneumatic control valves may experience valve leakage, abnormal valve pressure differential and other failures [2], which may cause instability and performance deterioration of the valve, and even serious damage to the industrial system [3]. Therefore, the health management of the control valve is crucial to the safe and efficient operation of the industry [4]. Effective fault classification and accurate prediction of Remaining Useful Life (RUL) in actual production can minimize unnecessary maintenance tasks and lower maintenance expenses.

At present, RUL prediction methods can be categorized into two types: mechanistic models and data-driven approaches [5]. The model-based method is to build a degradation model conform-ing to the operation law of the device according to the internal mechanism of the device, so as to predict the relationship between the input and output of the sensor data. [6] proposed an adaptive Wiener process degr-adation model integrating the influence of random shock, and used the maximum expectation method to estimate various parameters of the prediction model. With the increasingly complex structure of modern machinery and equipment and the influence of working envir-onment, it is difficult to establish an accurate model for RUL prediction of equipment. In contrast, the data-driven approach, by analyzing various data monitored by sensors in the process of equipment degradation, obtains the potential degradation law of the equipment from the data, so as to predict the RUL of the equipment. The data-driven approach can be subdivided into the traditional machine learning methods and the deep learning methods. Based on traditional machine learning methods, for example, [7] employed a model based on hybrid particle swarm optimization of support vector machine parameters to estimate engine RUL, and [8] used support vector regression to fit RUL. However, difficulties in feature design and insufficient generalization are drawbacks associated with these traditional methods. With the swift advancement of hardware and software infrastructure, deep learning algorithms have been widely concerned in many fields because of their powerful ability to deal with complex nonlinear relations, and have a broader application prospect in RUL prediction.

[9] employed an enhanced Temporal Convolutional Network (TCN) by incorporating a convolutional autoencoder in the preprocessing layer. This approach demonstrates better predictions of the RUL of nuclear plant electric. However, it exists a challenge in capturing long-term temporal dependencies. In [10], a long short-term memory recurrent neural network (LSTM-RNN) is designed to construct a clearly capacity-oriented RUL predictor. This method reduces the gradient disap-pearance of RNN. The disadvantage is that the network structure is complex and the training parameters are large. [11-13] used gate recurrent unit (GRU) as the backbone network of RUL prediction, which enables the model to maintain good accuracy even with short training time, but such networks can store less long-term dependence and memory ability.

Note that, although the existing deep learning algorithms demonstrate good performance in RUL prediction, they still face different challenges that affect the accuracy of predictions. The TCN network in [9] ignored long-term dependencies in the time series, and

the LSTM-RNN network structure in [10] was complex, leading to a lengthy training time. Moreover, there are few researches on RUL prediction direction of pneumatic control valve at present. Therefore, based on previous researches, this paper proposes a RUL prediction approach of pneumatic control valve based on CNN-Transformer model, which overcomes the above problems.

The primary contributions of this paper can be summarized as follows:

1) Selecting reasonable sensor data to reduce the computation load of the model and using Savitzky-Golay filter to eliminate noise interference from the data.

2) The proposed CNN-Transformer network in this paper can not only extract local features, but also capture long-term dependencies among sequential data to enhance the accuracy and computational efficiency of model prediction.

The model proposed in this paper will be validated using the dataset generated from the DAMADICS platform, followed by comparison with other models. The obtained results demonstrate superior predictive performance, and highlight the efficacy of the approach proposed in this paper. The subsequent structure of this paper is as follows: Section 2 presents the configuration of the pneumatic regulating valve, Section 3 outlines the proposed RUL prediction approach, Section 4 presents the experimental and simulation findings, and lastly, Section 5 provides a comprehensive summary of the study and outlines potential future research directions.

2 Pneumatic Control Valve System

2.1 Model Description

The pneumatic control valve primarily consists of three components: the pneumatic actuator, regulating valve, and associated accessories, illustrated in Figure 1 below.

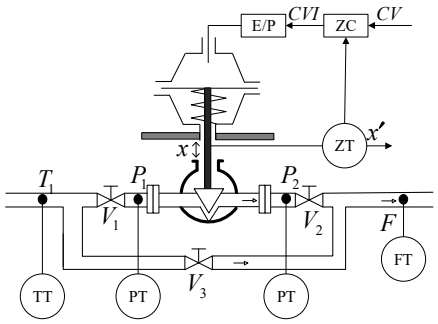

Fig. 1. Pneumatic control value basic structure

The working principle of the pneumatic actuator is as follows: within the control chamber of the actuator, there is a piston-type pneumatic actuator. When the compressed air on the piston is pressurized, the piston moves upward, pushing the valve stem to move toward the valve core. The valve core automatically opens under the action of spring force. The valve's opening is determined by the command signal sent by the actuator. After amplification by the amplifier, the signal is transmitted through the electromagnetic valve or pneumatic control valve of the actuator to the control valve. When the input signal matches the preset value, the control valve closes; when the input signal is less than the predetermined value, the control valve opens. Accessories include: filter pressure regulator, positioner, position feedback switch lamp, etc. The primary function of these attachments is to eliminate factors that may be generated internally or externally, such as: air source changes, friction, etc.

2.2 Pneumatic Control Valve Failure

According to the structure of the control valve, DAMADICS platform divides all the fault types of the pneumatic control valve into abrupt fault and incipient fault. This classification encompasses all possible scenarios of faults in the valve and its related attachments. There is no warning before the abrupt fault occurs, and the size of the fault is independent of time, such as valve blockage, distortion of the push rod, and electrical converter fault and so on. Incipient faults are generally due to equipment wear, corrosion, aging, fatigue and others, such as valve plug or valve seat erosion fault, external leakage fault, etc., which is characterized by little change in the detection data before the fault occurs, so it will be found by the system only when the fault reaches a certain critical value. Table 1 illustrates various prevalent fault.

Table 1: Fault Names and Types

Fault code	Fault Name	Fault Type
f3	Valve plug or valve seat erosion	Incipient
f5	External leakage	Incipient
f6	Internal leakage	Incipient
f13	Rod displacement sensor fault	Incipient
f14	Electro-pneumatic transducer pressure sensor fault	Abrupt
f15	Positioner feedback fault	Abrupt
f17	Unexpected pressure change fault on valve	Incipient

3 Basic Theory of Model

This Section mainly introduces the methods and model theories in this paper, including PCC analysis, the Savitzky-Golay filter, CNN network and Transformer network. Firstly, the PCC analysis is used to select highly related features. Next, the Savitzky-Golay filter is utilized to smooth and fit the noise in the data curve. Then, the CNN is employed to extract the local features of the time series. Finally, the output data from the CNN serves as input to the Transformer model, which further processes the data to obtain the prediction results. The schematic diagram of this method is illustrated in Figure 2 below. The following sections will provide details on each specific module.

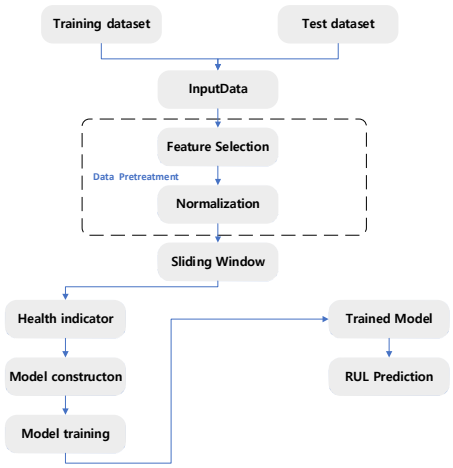

Fig. 2. The schematic of proposed approach

3.1 Feature Selection

Due to the diversity of performance variable selection for pneumatic control valves, not all variables are beneficial for model training. Some variables remain largely unchanged throughout the entire degradation process, which may have a negative impact on the model training process. Therefore, this article uses the PCC correlation coefficient formula to compute the correlation between these parameter variables and RUL. The PCC is calculated as follow:

$$PCC = \frac{\sum_{i=1}^{n}(z_i - \bar{z})(q_i - \bar{q})}{\sqrt{\sum_{i=1}^{n}(z_i - \bar{z})^2 \sum_{i=1}^{n}(q_i - \bar{q})^2}} \quad (1)$$

where z_i represents the values of the x-variable in a sample, $\bar{z}$ denotes the mean of the x-variable values, and q_i represents the values of the y-variable in a sample, and $\bar{q}$ indicates the mean of the y-variable values. The correlation coefficient values ranges from -1.0 to 1.0. Values close to one in absolute terms indicate a strong dependence between variables. In contrast, if the PCC value close to 0, it indicates that the dependency between the variables is weak. Through the above PCC analysis, we select six highly correlated features with RUL as input for the prediction model, as shown in Table 2.

Table 2: Parameters of Pneumatic Control Valve

Parameters	Description
CV	External controller output
P1	Value input pressure
P2	Value output pressure
X	Rod displacement
F	Flow sensor measurement
T	Liquid temperature

3.2 Savitzky-Golay Filtering

The Savitzky-Golay filter is a signal processing filtering method used for smoothing and fitting noise in curves to extract trends and features in signal. The main idea of this filter is to use a polynomial to fit and approximate data points within a given window, resulting in smoothed data points. The fitting polynomial is typically of low order, such as linear or quadratic.

The advantages of this filter include:

1) The original signal trend is retained while effectively removing noise from the signal.

2) Preserves the smoothness of the signal without introducing additional phase delays.

$$\hat{y}(x) = \sum_{i=-n/2}^{n/2} c_i \cdot y(x_i) \quad (2)$$

The above is the general formula for the one-dimensional form of the Savitzky-Golay filter, where n is the size of the window, x is the independent variable (usually time or position), y is the data to be smoothed, x_i represents the position within the window, and c_i is the polynomial coefficient, obtained by fitting the least square method.

3.3 Convolutional Neural Network

CNN is a kind of feedforward neural network with deep structure and convolutional operation, which performs well in local feature extraction. The CNN primarily consists of three parts: the convolutional layer, the pooling layer and the fully connected layer. In this paper, the convolution layer is responsible for extracting local features, setting a sliding window of fixed length, and intercepting different time periods at different starting points according to this length as the convolution kernel, which contains the feature information during this period. The specific formula is shown in equation (3):

$$c_j^l = f\left(w_{ij}^{(l)} \otimes \sum_{i=1}^{k} c_j^{l-1} + b^l \right) \quad (3)$$

where c_j^l represents the feature graph obtained by the j-th convolution kernel of the l-th convolution layer, $w_{ij}^{(l)}$ represents the weight matrix connecting adjacent convolution layers, b^l is the biased value, and f is the activation function acting on the convolution layer.

Then, the pooling layer will integrate the feature output of the convolutional layer, which mainly has the functions of suppressing noise, reducing information redundancy, preventing network overfitting, enhancing the model's fault tolerance rate, etc. After the data is processed by the pooling layer, local data features are obtained. Typical pooling functions comprise average pooling, maximum pooling, global average pooling, mixed pooling, random pooling, and others. Due to the fact that maximum pooling can preserve more texture information of the feature matrix, this paper adopts maximum pooling operation.

3.4 Transformer Neural

With the development of Multi-Head-Attention (MHA), the Transformer network is able to capture long

-term and short-term dependencies in data and obtain global temporal information. It's based on encoder-decoder structure, which is composed of input and output embedding layer, position coding module, multi-head attention module and feedforward neural network module. The model structure is shown in the Figure 3.

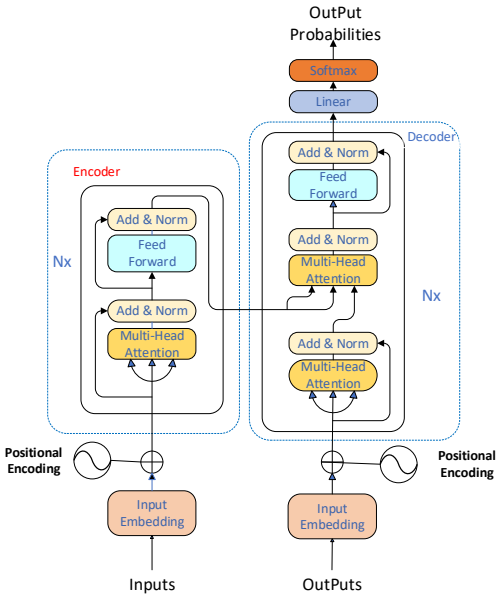

Fig. 3. Detailed Transformer structure in RUL prediction model

Among them, Positional Encoding (PE) gives the model the ability to identify the temporal relationship of the sequence, and PE is calculated using sine and cosine functions of different frequencies, as shown in equations (4) and (5) below:

$$PE(pos,2i)=\sin\left(\frac{pos}{10000^{\frac{2i}{d_{model}}}}\right) \tag{4}$$

$$PE(pos,2i+1)=\cos\left(\frac{pos}{10000^{\frac{2i}{d_{model}}}}\right) \tag{5}$$

where pos represents the position of the element in the vector, i represents the dimension, and d_{model} represents the model dimension.

The encoder module is composed of MHA module and feedforward neural network module, MHA refers to use of multiple attention mechanisms to calculate attention separately, and then fuse the results together. Firstly, the position-encoded input data X is converted into a query matrix Q, a key matrix K, and a value matrix V, with the following formula (6) to (8), where W^Q、W^K、W^V are weight matrices.

$$Q=XW^Q \tag{6}$$

$$K=XW^K \tag{7}$$

$$V=XW^V \tag{8}$$

Then, the obtained weights are scaled using the $softmax$ activation function, and the value vector V is multiplied by the scaled weights, as in equation (9):

$$Attention=softmax\left(\frac{QK^T}{\sqrt{d_k}}\right)V \tag{9}$$

Since using only one attention layer makes it difficult to learn the internal correlations of time-series data, a multi-head attention mechanism is employed. This allows the model to learn feature information from different positions, as shown in the following equations (10) to (11):

$$MultiH(Q,K,V)=concat(head_i,\ldots head_n)W \tag{10}$$

$$head_i=Attention(QW_i^Q,KW_i^K,VW_i^V) \tag{11}$$

where $head_i$ is the i-th attention head, the $concat$ function is used to concatenate multiple attention heads, n represents the number of attention heads, W is the multi-head attention weight matrix.

4 Experimental Verification and Result Analysis

4.1 Data Pre-processing

DAMADICS platform is a standard platform for pneumatic control valve fault analysis developed based on real data from a sugar factory in Poland. All the data studied in this paper are generated on this platform. Among the data parameters generated by many sensors, six parameters, namely controller output signal CV, pressure P1 in front of the valve, pressure P2 in back of the valve, valve stem displacement X, fluid flow rate F and fluid temperature T, are selected as the data characteristics of the experimental research.

For the fault data generated by the platform, first of all, the Savitzky-Golay filter is used to eliminate noise and other interference in the data. Then, to prevent low training speed or even failure to converge due to differences in the scales and units of different feature data, normalization is applied to the dataset. The specific equation is as follows:

$$x'(t)=\frac{x(t)-\min(x)}{\max(x)-\min(x)} \tag{12}$$

where, x(t) is the monitoring data of the device at time t, $\max(x)$ and $\min(x)$ are the maximum and minimum values of all the monitoring data of the device respectively, and $x'(t)$ is the normalized data.

4.2 Performance Metrics

In this paper, two commonly used indicators in the field of life prediction are used to verify the validity and accuracy of the model prediction results, namely, Root Mean Square Error (RMSE) and average Score (Score). RMSE can measure the difference between the predicted value and the true value, and reflect the divergence of the prediction error. The smaller the value of both, the better the prediction effect of the model. Its calculation equation is as follows.

$$RMSE = \sqrt{\frac{1}{N}\sum_{l=1}^{N}(\hat{y}_l - y_l)^2} \tag{13}$$

where $\hat{y}_l$ is the predicted RUL of test sample l, y_l is the actual RUL of test sample l, and N is the number of samples tested.

$$Score = \begin{cases} \sum_{l=1}^{n}(e^{\frac{-(\hat{y}_l - y_l)}{13}} - 1) & \hat{y}_l < y_l \\ \sum_{l=1}^{n}(e^{\frac{(\hat{y}_l - y_l)}{10}} - 1) & \hat{y}_l > y_l \end{cases} \tag{14}$$

As can be seen from equation (14), there are two different scoring functions for advance prediction and lag prediction. When the actual value is less than the predicted value, it belongs to lag prediction; when the actual value is greater than the predicted value, it belongs to advance prediction. In the actual industrial production, there is a tendency to advance prediction, so this scoring method will punish the delayed prediction, which is very in line with the actual demand.

4.3 Hyperparameter Settings

In model training, in order to make full use of the data in the training set, this paper adopts a sliding window with step length of 1 and length of 20 to segment the data in the training set, and then splicing the features, and then input them into the model for RUL prediction. The hyperparameters of the model in this paper are as follows.

Table 3: Hyperparameters of the Model

Parameter name	Parameter setting
Sampling window	20
Model learning rate lr	0.001
optimizer	Adam
Number of self-attention mechanism heads	4
Number of Encoder layers	4
Number of Decoder layers	6
Batch-size	30

In this paper, the Adam optimization algorithm is employed to find suitable parameters to minimize the error. It combines the advantages of adaptive gradient algorithms and root mean square propagation algorithms. Its strengths lie in high computational efficiency and good handling capabilities for datasets with significant noise.

4.4 Result and Analysis

In this paper, two sets of control valve fault data of valve stem displacement sensor and valve pressure abnormal fault are selected to train the network to verify the effectiveness of the proposed method. In the process of model training, 80% of the data is taken as the training set, the Adma algorithm is used to optimize the model weight, and finally the remaining 20% of the sample data is tested. The forecast results are shown in the Figure 5 and Figure 6.

Taking the experimental results under Unexpected pressure change fault on valve as an example. Figure 4 illustrates the comparison of training durations for three different models. It can be observed that the training time of the CNN-Transformer model has increased compared to the CNN network due to its higher complexity. However, it has reduced training time significantly compared to the traditional Transformer network and the training efficiency has increased by 26.25%.

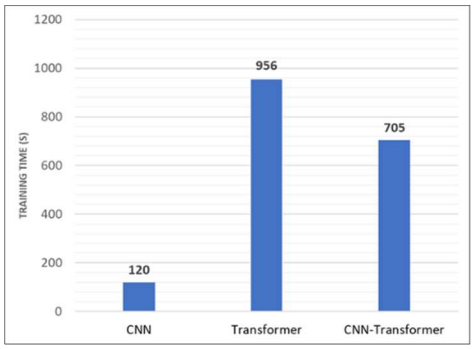

Fig. 4. Training Duration for Each Model

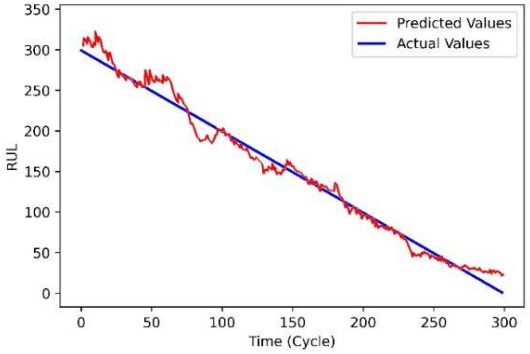

Fig. 5. RUL prediction based on Rod displacement sensor fault

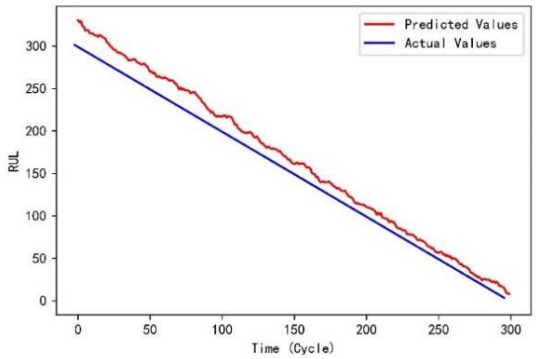

Fig. 6. RUL prediction based on Unexpected pressure change fault on valve

Figure 5 shows the RUL result of the Rod displacement sensor fasult, Figure 6 shows the RUL result of the Unexpected pressure change fault on valve, where the horizontal coordinate is the time period, the vertical coordinate is the RUL value, the blue line is the actual value of the residual life of the regulator, and the red line represents the predicted value of the residual life

of the regulator. The predicted value of the two prediction graphs fluctuated slightly between the real value and the predicted value. Although there is a significant deviation between the predicted results and the true RUL in the early stages of prediction, with the accumulation of running time, the predicted result of the model in this paper was basically consistent with the real RUL value, and the prediction accuracy was high.

In order to further verify the superiority of CNN Transformer in predicting the RUL of pneumatic control valves, comparative experiments are conducted with some recent high-frequency research models. A CNN model and a Transformer model are constructed here, and the life prediction results are compared using the same experimental environment. The experimental results are shown in Table 4 and Table 5.

Table 4: RMSE Comparison of Prediction Results

Methods	Rod displacement sensor fault	Unexpected pressure change fault
CNN	46.03	31.05
Transformer	43.31	30.74
CNN-Transformer	35.56	27.13

Table 5: Score Comparison of Prediction Results

Methods	Rod displacement sensor fault	Unexpected pressure change fault
CNN	653.59	562.87
Transformer	263.21	459.60
CNN-Transformer	169.32	195.28

Table 4 shows the RMSE obtained by the model and its comparison with other models, while Table 5 displays the Score achieved by the model and its comparison with other models. It can be observed that the CNN-Transformer model in terms of RMSE reduces by an average of 17.6% compared to the CNN model and by an average of 14.8% compared to the Transformer model. The Score is 54.8% lower than the CNN model and 56.1% lower than the Transformer model. The proposed CNN-Transformer model demonstrates good performance on both evaluation metrics, which shows that the model has good stability and can achieve the balance between the overall performance and the safety performance.

5 Conclusion

In order to improve the accuracy of RUL prediction of pneumatic control valve, this paper combines CNN and Transformer to propose a new CNN-Transformer based RUL prediction model. Through experimental verification, the following conclusions are reached:

1) In the data preprocessing section, PCC can minimize the computational burden of the model, and Savitzky-Golay can eliminate noise interference in the data.

2) CNN can effectively extract local features, and then Transformer can extract global features. This method can ensure that the prediction model can excavate the complex mapping relationship between input features and pneumatic control valve.

3) Through the data set generated by DAMADICS platform, it is proved that compared with other models, the average absolute error of the model proposed in this paper is reduced by 17.6% and 14.8%, and the average score is reduced by 54.8% and 56.1%, respectively.

In the follow-up research, it should be noted that all the data in this paper come from the simulation model, so there will be a certain gap with the actual production data. The prediction model studied in this paper should be applied to other types of control valve data sets to enhance the robustness of the model.

References

[1] M. Zhu, Z. Xu, Z. Zang, et al. Design of FOPID controller for pneumatic control valve based on improved BBO algorithm, Sensors, 2022, 22(17): 6706.

[2] S. Zhang, M. Luo, H. Qian, et al. A review of valve health diagnosis and assessment: Insights for intelligence maintenance of natural gas pipeline valves in China, Engineering Failure Analysis, 2023: 107581.

[3] L. Liao, F. Köttig. Review of hybrid prognostics approaches for remaining useful life prediction of engineered systems, and an application to battery life prediction. IEEE Transactions on Reliability, 2014, 63(1): 191-207.

[4] M. Gribbestad, M. U. Hassan, I. A. Hameed. Transfer learning for Prognostics and health Management (PHM) of marine Air Compressors, Journal of Marine Science and Engineering, 2021, 9(1): 47.

[5] L. Zhao, Y. Zhu, T. Zhao. Deep Learning-Based Remaining Useful Life Prediction Method with Transformer Module and Random Forest, Mathematics 2022, 10, 2921.

[6] S. Zhang, Q. Zhai, Y. Li. Degradation modeling and RUL prediction with Wiener process considering measurable and unobservable external impacts, Reliability Engineering & System Safety, 2023, 231: 109021.

[7] P. J. G Nieto, E. García-Gonzalo, F. S. Lasheras, et al. Hybrid PSO–SVM-based method for forecasting of the remaining useful life for aircraft engines and evaluation of its reliability, Reliability Engineering & System Safety, 2015, 138: 219-231.

[8] R. Khelif, B. Chebel-Morello, S. Malinowski, et al. Direct remaining useful life estimation based on support vector regression, IEEE Transactions on industrial electronics, 2016, 64(3): 2276-2285.

[9] H. Wang, M. Peng, R. Xu, et al. Remaining useful life prediction based on improved temporal convolutional network for nuclear power plant valves, Frontiers in Energy Research, 2020, 8: 584463.

[10] Y. Zhang, R. Xiong, H. He, et al. Long short-term memory recurrent neural network for remaining useful life prediction of lithium-ion batteries, IEEE Transactions on Vehicular Technology, 2018, 67(7): 5695-5705.

[11] J. Zhou, Y. Qin, D. Chen, et al. Remaining useful life prediction of bearings by a new reinforced memory GRU network, Advanced Engineering Informatics, 2022, 53: 101682.

[12] S. Ai, J. Song, G. Cai. Sequence-to-sequence remaining useful life prediction of the highly maneuverable unmanned aerial vehicle: a multilevel fusion transformer network solution, Mathematics, 2022, 10(10): 1733.

[13] Y. Zhang, Y. Xin, Z. Liu, et al. Health status assessment and remaining useful life prediction of aero-engine based on BiGRU and MMoE, Reliability Engineering & System Safety, 2022, 220: 108263.

Proceedings of the 3rd Conference on Fully Actuated System Theory and Applications
May 10-12, 2024, Shenzhen, China

Adaptive Event-Triggered Fault Detection of Nonlinear Lipschitz Systems in Finite Frequency Domain

Peng Cheng[1], Chenxiao Cai[2], Jason J. R. Liu[1]

1. Department of Electromechanical Engineering, Faculty of Science and Technology, University of Macau, Macau
E-mail: chengpeng60@126.com; jasonliu@um.edu.mo

2. School of Automation, Nanjing University of Science and Technology, Nanjing 210094, China
E-mail: ccx5281@njust.edu.cn

Abstract: The problem of finite-frequency fault detection (FD) for a class of nonlinear systems with Lipschitz nonlinearities, unknown faults, and bounded disturbances is explored. To start with, a finite-frequency FD filter based on an adaptive event-triggered mechanism is put forward, and the augmented filter system is transformed into a linear parameter varying (LPV) system by the reconstructed Lipschitz property. Then, two sufficient conditions for the LPV system to be asymptotically stable with a full-frequency H_∞ disturbance attenuation index bound and a finite-frequency H_- fault-sensitive index bound are derived. Next, the obtained sufficient conditions are sorted into numerically solvable linear matrix inequalities to obtain the desired FD filter parameters. Finally, an illustrative example is carried out to demonstrate the advantages of the presented FD scheme.

Key Words: Fault detection, finite frequency, nonlinear Lipschitz systems

1 Introduction

For industrial automation and process control systems, subsystem or physical component faults are typically inevitable [1]. The fault signals in the actual system may have a significant impact on the system's performance and even cause the system to crash. Therefore, fault detection (FD) techniques that aim to detect the occurrence of unknown faults in dynamic systems as early as possible have drawn substantial attention in the automation community [2]. To achieve the purpose of FD, many advanced technical means have been applied, such as observer methods, filter strategies, and parity space vector schemes [3]. On this basis, plenty of representative research results have been reported in the field of FD in the past decades [4]-[5].

Note that the FD schemes in [4]-[5] are developed in the full frequency domain, and the frequency domain characteristics of the fault signals are ignored. As illustrated in [6], fault signals in practical systems generally occur in the finite frequency domain. Therefore, finite-frequency FD strategies can significantly reduce the conservatism of the above full-frequency FD approaches. Fortunately, the Generalized Kalman-Yakubovich-Popov (GKYP) lemma provides an effective method for finite frequency analysis and design [7]. By establishing the equivalent relation between frequency domain inequalities and linear matrix inequalities (LMIs) in the finite frequency domain, the GKYP lemma is widely exploited in the analysis of finite frequency performance indices, and also provides great convenience for the design of finite frequency FD schemes [8]-[9]. Although the development of finite-frequency FD techniques has come a long way, it should be emphasized that FD strategies based on GKYP lemma are only applicable to linear systems. Considering the nonlinear characteristics that generally exist in engineering practical systems, the methods in [8]-[9] cannot be applied directly. To this end, a multitude of scholars have paid attention to the design of finite frequency FD schemes for nonlinear systems [10]-[11].

This work was supported by the National Natural Science Foundation of China (62373192). *(Corresponding author: Chenxiao Cai.)*

On the other hand, most FD studies on nonlinear systems employ traditional time-triggered mechanisms with fixed sampling periods, which may lead to a waste of communication resources and increase maintenance costs. To do this, the FD protocol based on event-triggered mechanism (ETM) is proposed for Lipschitz nonlinear systems to overcome the shortcomings of time-triggered mechanisms [12]. For the static ETM in [12], the trigger threshold parameter is a predefined constant, so the trigger parameter is not flexible in the face of fluctuations in the external environment. To improve the flexibility of triggering threshold, adaptive ETS (AETS) based on adaptive technology is developed, and the problem of finite-frequency FD for nonlinear networked systems is further studied in [13]. Encouraged by the above observations, this paper endeavors to construct the finite frequency FD paradigm for nonlinear Lipschitz systems with network-induced delays, AETS, and external disturbances. The salient features of this study lie in the following two aspects.

1) An AETS is proposed to reduce the channel congestion caused by the time-triggered schemes in [8]-[11], and the triggering events can be adaptively adjusted according to system dynamics.
2) An AETS-based finite frequency FD filter is constructed for nonlinear Lipschitz systems to restrain the simultaneous effects of external disturbances, transmission delays, and constrained bandwidth.

2 Problem Statement

2.1 System Description

Consider the following class of nonlinear system

$$\begin{cases} \dot{x}(t) = Ax(t) + \Phi(x(t)) + Ed(t) + Ff(t), \\ y(t) = Cx(t), \end{cases} \tag{1}$$

where $x(t) \in \mathbb{R}^n$ denotes the system state, $d(t) \in \mathbb{R}^d$ represents the bounded external disturbance, $f(t) \in \mathbb{R}^f$ indicates the bounded finite frequency fault, and $y(t) \in \mathbb{R}^l$ means the measured output. $\Phi(x(t)) : \mathbb{R}^n \to \mathbb{R}^n$ refers to the

Lipschitz nonlinear term with respect to $x(t)$. In addition, $A \in \mathbb{R}^{n\times n}, E \in \mathbb{R}^{n\times d}, F \in \mathbb{R}^{n\times f}$, and $C \in \mathbb{R}^{l\times n}$ are known constant system matrices.

Define qh and $t_k h$ as the current sampling instant and the latest triggered instant, respectively. Then, the next triggered instant is

$$t_{k+1}h \triangleq t_k h + \min\{qh|\psi^{\mathrm{T}}(t)\mathcal{M}\psi(t) - \sigma(t)y^{\mathrm{T}}(t_k h)\mathcal{M}y(t_k h) \geq 0, \tag{2}$$

where $\psi(t) = y(t_k h+qh)-y(t_k h)$ stands for the data error. $\mathcal{M} \in \mathbb{R}^{l\times l}$ implies the positive definite symmetric weight matrix to be designed, and $y(t_k h+qh)$ and $y(t_k h)$ represent the current sampled output and the latest transmitted output, respectively. $\sigma(t)$ is the adaptive event-triggered threshold, and its update law is

$$\dot{\sigma}(t) = \frac{1}{\sigma(t)}\Big[\frac{1}{\sigma(t)} - \sigma_0\Big]\psi^{\mathrm{T}}(t)\mathcal{M}\psi(t), \tag{3}$$

where $\sigma_0 > 0$ is a given constant.

Similar to the reference [13], define $t_{k+1}h = t_k h + qh$, and then the interval $[t_k h + \vartheta_{t_k}, t_{k+1}h + \vartheta_{t_{k+1}})$ can be divided into $[t_k h + \vartheta_{t_k}, t_{k+1}h + \vartheta_{t_{k+1}}) = \bigcup_{i=0}^{q-1} E_i$, where $E_i = [t_k h+ih+\vartheta_{t_k+i}, t_k h+(i+1)h+\vartheta_{t_k+i+1})$. Further, let $\delta(t) = t - t_k h - ih, t \in E_i$, one has $0 \leq \delta_m \leq \delta(t) < h + \delta_M = \bar{\delta}$, where δ_m and δ_M indicate the minimum and maximum values of the network delay, respectively.

To detect the fault signal in the system (1), the finite frequency FD filter is established as

$$\begin{cases}\dot{\hat{x}}(t) = \hat{A}\hat{x}(t) + \hat{B}\hat{y}(t),\\ r(t) = \hat{C}\hat{x}(t) + \hat{D}\hat{y}(t),\end{cases} \tag{4}$$

where $\hat{x}(t) \in \mathbb{R}^n$ means the filter state, $\hat{y}(t) = y(t-\delta(t)) + \psi(t)$ indicates the filter input, and $r(t) \in \mathbb{R}$ represents the residual signal. Also, $\hat{A} \in \mathbb{R}^{n\times n}, \hat{B} \in \mathbb{R}^{n\times l}, \hat{C} \in \mathbb{R}^{1\times n}$, and $\hat{D} \in \mathbb{R}^{1\times l}$ are unknown filter gains.

Define $\eta(t) = \begin{bmatrix} x^{\mathrm{T}}(t) & x_f^{\mathrm{T}}(t) \end{bmatrix}^{\mathrm{T}}$. Then, the augmented filter system can be derived as

$$\begin{cases}\dot{\eta}(t) = \bar{A}\eta(t) + \mathcal{A}_d\eta(t-\delta(t)) + \mathcal{B}\Phi(x(t)) + \mathcal{E}d(t)\\ \qquad + \mathcal{F}f(t) + \mathcal{G}\psi(t),\\ r(t) = \mathcal{C}\eta(t) + \mathcal{C}_d\eta(t-\delta(t)) + \mathcal{H}\psi(t),\\ y(t-\delta(t)) = \bar{C}\eta(t-\delta(t)),\end{cases} \tag{5}$$

where

$$\bar{A} = \begin{bmatrix} A & 0\\ 0 & \hat{A}\end{bmatrix}, \mathcal{A}_d = \begin{bmatrix} 0 & 0\\ \hat{B}C & 0\end{bmatrix}, \mathcal{B} = \begin{bmatrix} I\\ 0\end{bmatrix},$$
$$\mathcal{F} = \begin{bmatrix} F\\ 0\end{bmatrix}, \mathcal{E} = \begin{bmatrix} E\\ 0\end{bmatrix}, \mathcal{G} = \begin{bmatrix} 0\\ \hat{B}\end{bmatrix}, \mathcal{H} = \hat{D},$$
$$\mathcal{C} = \begin{bmatrix} 0 & \hat{C}\end{bmatrix}, \mathcal{C}_d = \begin{bmatrix} \hat{D}C & 0\end{bmatrix}, \bar{C} = \begin{bmatrix} C & 0\end{bmatrix}.$$

Lemma 1: [14] Consider Lipschitz nonlinear term $\Phi(\cdot) : \mathbb{R}^n \to \mathbb{R}^n$, the following descriptions are equivalent:

(1) $\Phi(\cdot)$ satisfy the Lipschitz condition respect to $x(t)$, i.e., $\forall x, z \in \mathbb{R}^n$

$$||\Phi(x) - \Phi(z)|| \leq r_\Phi||x - z||, \tag{6}$$

where $r_\Phi > 0$ is a known Lipschitz constant.

(2) For any $i, j = 1, \cdots, n$, there exist functions $\varphi_{ij} : \mathbb{R}^n \times \mathbb{R}^n \to \mathbb{R}^n$ and scalars $\underline{r}_{\varphi_{ij}}, \bar{r}_{\varphi_{ij}}$, such that $\forall x, z \in \mathbb{R}^n$

$$\Phi(x) - \Phi(z) = \sum_{i=1}^{n}\sum_{j=1}^{n}\varphi_{ij}H_{ij}(x - z), \tag{7}$$

where $\varphi_{ij} = \varphi_{ij}(x^{z_{j-1}}, x^{z_j})$ satisfying $\underline{r}_{\varphi_{ij}} \leq \varphi_{ij} \leq \bar{r}_{\varphi_{ij}}, H_{ij} = e_n(i)e_n^{\mathrm{T}}(j)$, and $e_s(i) = [0, \cdots, 0, \overbrace{1}^{i\text{th}}, 0, \cdots, 0]^{\mathrm{T}} \in \mathbb{R}^s, s \geq 1$ is a vector of the canonical basis of $\mathbb{R}^s$.

Applying Lemma 1, system (5) can be reconstructed into the following linear parameter varying (LPV) system

$$\begin{cases}\dot{\eta}(t) = \mathcal{A}(\Lambda)\eta(t) + \mathcal{A}_d\eta(t-\delta(t)) + \mathcal{E}d(t)\\ \qquad + \mathcal{F}\varrho(t) + \mathcal{G}\psi(t),\\ r(t) = \mathcal{C}\eta(t) + \mathcal{C}_d\eta(t-\delta(t)) + \mathcal{H}\psi(t),\end{cases} \tag{8}$$

where $\mathcal{A}(\Lambda) = \bar{A} + \mathcal{B}\Lambda$ and $\Lambda = \sum_{i=1}^{n}\sum_{j=1}^{n}\varphi_{ij}(x^{0_{j-1}}, x^{0_j})H_{ij}$.

By Lemma 1, parameter Λ belongs to the bounded convex set $\mathcal{E}_n$, and define the vertex set of $\mathcal{E}_n$ as $\mathcal{V}_{\mathcal{E}_n} = \{\daleth \in \mathbb{R}^{n\times n}, \daleth_{ij} \in \{\underline{r}_{\varphi_{ij}}, \bar{r}_{\varphi_{ij}}\}\}$. In this paper, $\check{\Lambda}$ is employed to represent the vertex in $\mathcal{V}_{\mathcal{E}_n}$ that corresponds to the bounded convex set $\mathcal{E}_n$.

2.2 Problem Formation

The finite frequency domain of the fault signal is described in this subsection, and the design problems of this paper are further derived.

Definition 1: Assume that the fault vector $f(t)$ belongs to the following low frequency domain

$$\Omega_\omega := \{\omega \in \mathbb{R}|(\omega + \omega_l)(\omega - \omega_l) \leq 0\}, \tag{9}$$

where ω is the frequency of the fault signal, and $\omega_l > 0$.

Based on Definition 1, the design problems of this paper can be described as follows.

(1) Under the zero initial condition, the LPV system (8) is asymptotically stable and has a full-frequency H_∞ index bound γ, i.e.,

$$\int_0^{+\infty} r^{\mathrm{T}}(t)r(t)dt \leq \gamma^2\int_0^{+\infty} d^{\mathrm{T}}(t)d(t)dt. \tag{10}$$

(2) Under the zero initial condition, the LPV system (8) has a finite-frequency H_- index bound β, i.e.,

$$\int_0^{+\infty} r^{\mathrm{T}}(t)r(t)dt \geq \beta^2\int_0^{+\infty} f^{\mathrm{T}}(t)f(t)dt, \tag{11}$$

holds for all solutions of system (8) satisfying $f(t) \in \mathcal{L}_2[0,\infty)$, such that [13]

$$\int_0^{+\infty}(-\omega_l\eta(t) + j\dot{\eta}(t))(\omega_l\eta(t) + j\dot{\eta}(t))^* dt \leq 0.$$

(3) The evaluation function $J_r(t)$ and the detection threshold J_{th} are designed as $J_r(t) = \sqrt{\frac{1}{t}\int_0^t r^{\mathrm{T}}(\nu)r(\nu)d\nu}, J_{\text{th}} = \sup_{\varrho(t)=0, d(t)\in\ell_2[0,\infty)} J_r(t)$[1]. Then, the fault can then be detected using the following mechanism: $J_r(t) > J_{\text{th}} \Longrightarrow$ Alarm.

3 Design of Fault Detection Filter

3.1 Finite Frequency Performance Analysis

Lemma 2 [15]: Given a positive scalar γ, if there are positive definite symmetric matrices $\mathcal{P}_1, \mathcal{R}_1, \mathcal{Z}_1, \mathcal{M}$, such that

$$\mathcal{I}_1^{\mathrm{T}}\Psi_1\mathcal{I}_1 + \mathcal{S}_1^{\mathrm{T}}\Theta_1\mathcal{S}_1 + \mathcal{N}_1^{\mathrm{T}}\Xi_1\mathcal{N}_1 + \mathcal{Y}_1 < 0, \tag{12}$$

then the system (8) is asymptotically stable and has an H_∞ index bound γ in the full frequency domain, where

$$\mathcal{I}_1 = \begin{bmatrix} \mathcal{A}(\Lambda) & \mathcal{A}_d & 0 & \mathcal{E} & \mathcal{G} \\ I & 0 & 0 & 0 & 0 \end{bmatrix}, \Psi_1 = \begin{bmatrix} \bar{\delta}^2\mathcal{Z}_1 & \mathcal{P}_1 \\ \mathcal{P}_1 & 0 \end{bmatrix},$$
$$\mathcal{S}_1 = \begin{bmatrix} \mathcal{C} & \mathcal{C}_d & 0 & 0 & \mathcal{H} \\ 0 & 0 & 0 & I & 0 \end{bmatrix}, \Theta_1 = \begin{bmatrix} I & 0 \\ 0 & -\gamma^2 I \end{bmatrix},$$
$$\mathcal{N}_1 = \begin{bmatrix} 0 & \bar{C} & 0 & 0 & I \\ 0 & 0 & 0 & 0 & I \end{bmatrix}, \Xi_1 = \begin{bmatrix} \mathcal{M} & 0 \\ 0 & -\sigma_0\mathcal{M} \end{bmatrix},$$
$$\mathcal{Y}_1 = \begin{bmatrix} \mathcal{R}_1 - \mathcal{Z}_1 & \mathcal{Z}_1 & 0 & 0 & 0 \\ \mathcal{Z}_1 & -2\mathcal{Z}_1 & \mathcal{Z}_1 & 0 & 0 \\ 0 & \mathcal{Z}_1 & -\mathcal{R}_1 - \mathcal{Z}_1 & 0 & 0 \\ 0 & 0 & 0 & 0 & 0 \\ 0 & 0 & 0 & 0 & 0 \end{bmatrix}.$$

Lemma 3 [15]: Given a positive scalar β, if there exist symmetric matrices $\mathcal{P}_2, \mathcal{R}_2, \mathcal{Z}_2 > 0, \mathcal{Q} > 0, \mathcal{M} > 0$, such that

$$\mathcal{I}_2^{\mathrm{T}}\Psi_2\mathcal{I}_2 + \mathcal{S}_2^{\mathrm{T}}\Theta_2\mathcal{S}_2 + \mathcal{N}_2^{\mathrm{T}}\Xi_2\mathcal{N}_2 + \mathcal{Y}_2 < 0, \tag{13}$$

then the system (8) has an H_- performance index bound β in the finite frequency domain (9), where

$$\mathcal{I}_2 = \begin{bmatrix} \mathcal{A}(\Lambda) & \mathcal{A}_d & 0 & \mathcal{F}_x & \mathcal{G} \\ I & 0 & 0 & 0 & 0 \end{bmatrix},$$
$$\Psi_2 = \begin{bmatrix} -\mathcal{Q} + \bar{\delta}^2\mathcal{Z}_2 & \mathcal{P}_2 \\ \mathcal{P}_2 & \omega_l^2\mathcal{Q} \end{bmatrix},$$
$$\mathcal{S}_2 = \begin{bmatrix} \mathcal{C} & \mathcal{C}_d & 0 & 0 & \mathcal{H} \\ 0 & 0 & 0 & I & 0 \end{bmatrix}, \Theta_2 = \begin{bmatrix} -I & 0 \\ 0 & \beta^2 I \end{bmatrix},$$
$$\mathcal{N}_2 = \begin{bmatrix} 0 & \bar{C} & 0 & 0 & I \\ 0 & 0 & 0 & 0 & I \end{bmatrix}, \Xi_2 = \Xi_1,$$
$$\mathcal{Y}_2 = \begin{bmatrix} \mathcal{R}_2 - \mathcal{Z}_2 & \mathcal{Z}_2 & 0 & 0 & 0 \\ \mathcal{Z}_2 & -2\mathcal{Z}_2 & \mathcal{Z}_2 & 0 & 0 \\ 0 & \mathcal{Z}_2 & -\mathcal{R}_2 - \mathcal{Z}_2 & 0 & 0 \\ 0 & 0 & 0 & 0 & 0 \\ 0 & 0 & 0 & 0 & 0 \end{bmatrix}.$$

Lemma 4. (Finsler's Lemma) [16]: Let $x \in \mathbb{R}^n, L \in \mathbb{R}^{n\times n}$, and $K \in \mathbb{R}^{n\times m}$. The following descriptions are equivalent: (i) $K^\perp L(K^\perp)^{\mathrm{T}} < 0$; (ii) $\exists\chi \in \mathbb{R}^{m\times n}$: $L + K\chi + \chi^{\mathrm{T}}K^{\mathrm{T}} < 0$; where $K^\perp$ is any matrix such that $K^\perp K = 0$.

3.2 Finite Frequency Performance Design

In this subsection, according to Lemma 4, the matrix inequalities in Lemmas 2 and 3 are converted to LMIs in Theorems 1 and 2, respectively.

Theorem 1: Given a positive scalar γ and matrices N_1, N_2, if there exist symmetric matrices $\mathcal{P}_1 = \begin{bmatrix} P_{11} & P_{12} \\ \star & P_{13} \end{bmatrix} > 0, \mathcal{R}_1 = \begin{bmatrix} R_{11} & R_{12} \\ \star & R_{13} \end{bmatrix} > 0, \mathcal{Z}_1 = \begin{bmatrix} Z_{11} & Z_{12} \\ \star & Z_{13} \end{bmatrix} > 0, \mathcal{M} > 0$ and matrices $\mathcal{T}_1 = \begin{bmatrix} T_1 & T_2 \\ T_3 & T_3 \end{bmatrix}, \mathfrak{L}, \mathfrak{M}, \hat{C}, \hat{D}$, such that

$$\mathcal{W}_1 = \begin{bmatrix} \mathcal{W}_{11} & \mathcal{W}_{12} & \mathcal{W}_{13} \\ \star & \mathcal{W}_{14} & \mathcal{W}_{15} \\ \star & \star & \mathcal{W}_{16} \end{bmatrix} < 0, \tag{14}$$

then the system (8) is asymptotically stable and has an H_∞ index bound (10) in the full frequency domain, where

$$\mathcal{W}_{11} = \begin{bmatrix} -1 & 0 & 0 & 0 \\ \star & \mathcal{W}_{11}^1 & \mathcal{W}_{11}^2 & P_{11} + T_1^{\mathrm{T}}(A + \check{\Lambda}) \\ \star & \star & \mathcal{W}_{11}^3 & P_{12}^{\mathrm{T}} + T_2^{\mathrm{T}}(A + \check{\Lambda}) \\ \star & \star & \star & R_{11} - Z_{11} \end{bmatrix},$$
$$\mathcal{W}_{11}^1 = \bar{\delta}^2 Z_{11} - [T_1]_s, \mathcal{W}_{11}^2 = \bar{\delta}^2 Z_{12} - T_2 - T_3^{\mathrm{T}},$$
$$\mathcal{W}_{11}^3 = \bar{\delta}^2 Z_{13} - [T_3]_s,$$
$$\mathcal{W}_{12} = \begin{bmatrix} \hat{C} & \hat{D}C & 0 & 0 \\ P_{12} + \mathfrak{L} & \mathfrak{M}C & 0 & 0 \\ P_{13} + \mathfrak{L} & \mathfrak{M}C & 0 & 0 \\ R_{12} - Z_{12} & Z_{11} & Z_{12} & 0 \end{bmatrix},$$
$$\mathcal{W}_{13} = \begin{bmatrix} 0 & 0 & 0 & \hat{D} \\ 0 & T_1^{\mathrm{T}}E - T_1N_1 & -T_2N_2 & \mathfrak{M} \\ 0 & T_2^{\mathrm{T}}E - T_3N_1 & -T_3N_2 & \mathfrak{M} \\ 0 & (A + \check{\Lambda})^{\mathrm{T}}T_1N_1 & (A + \check{\Lambda})^{\mathrm{T}}T_2N_2 & 0 \end{bmatrix},$$
$$\mathcal{W}_{14} = \begin{bmatrix} R_{13} - Z_{13} & Z_{12}^{\mathrm{T}} & Z_{13} & 0 \\ \star & \mathcal{W}_{14}^1 & -2Z_{12} & Z_{11} \\ \star & \star & -2Z_{13} & Z_{12}^{\mathrm{T}} \\ \star & \star & \star & -R_{11} - Z_{11} \end{bmatrix},$$
$$\mathcal{W}_{14}^1 = -2Z_{11} + C^{\mathrm{T}}\mathcal{M}C,$$
$$\mathcal{W}_{15} = \begin{bmatrix} 0 & \mathfrak{L}^{\mathrm{T}}N_1 & \mathfrak{L}^{\mathrm{T}}N_2 & 0 \\ Z_{12} & C^{\mathrm{T}}\mathfrak{M}^{\mathrm{T}}N_1 & \mathcal{W}_{15}^1 & C^{\mathrm{T}}\mathcal{M} \\ Z_{13} & 0 & 0 & 0 \\ -R_{12} - Z_{12} & 0 & 0 & 0 \end{bmatrix},$$
$$\mathcal{W}_{15}^1 = C^{\mathrm{T}}\mathfrak{M}^{\mathrm{T}}N_2,$$
$$\mathcal{W}_{16} = \begin{bmatrix} -R_{13} - Z_{13} & 0 & 0 & 0 \\ \star & \mathcal{W}_{16}^1 & \mathcal{W}_{16}^2 & N_1^{\mathrm{T}}\mathfrak{M} \\ \star & \star & -\gamma^2 I_d & N_2^{\mathrm{T}}\mathfrak{M} \\ \star & \star & \star & (1 - \sigma_0)\mathcal{M} \end{bmatrix},$$
$$\mathcal{W}_{16}^1 = -\gamma^2 I_d + [E^{\mathrm{T}}T_1N_1]_s, \mathcal{W}_{16}^2 = E^{\mathrm{T}}T_2N_2.$$

Proof. Based on Lemma 2, inequality (12) can be rewritten as

$$\begin{bmatrix} \mathfrak{B}_1 \\ I \end{bmatrix}^{\mathrm{T}} \mathfrak{C}_1 \begin{bmatrix} \mathfrak{B}_1 \\ I \end{bmatrix} < 0, \tag{15}$$

where

$$\mathfrak{B}_1 = \begin{bmatrix} \mathcal{A}(\Lambda) & \mathcal{A}_d & 0 & \mathcal{E} & \mathcal{G} \end{bmatrix},$$
$$\mathfrak{C}_1 = \begin{bmatrix} \bar{\delta}^2\mathcal{Z}_1 & \mathcal{P}_1 & 0 & 0 & 0 & 0 \\ \star & \mathfrak{C}_1^1 & \mathfrak{C}_1^2 & 0 & 0 & \mathcal{C}^{\mathrm{T}}\mathcal{H} \\ \star & \star & \mathfrak{C}_1^3 & \mathcal{Z}_1 & 0 & \mathfrak{C}_1^4 \\ \star & \star & \star & \mathfrak{C}_1^5 & 0 & 0 \\ \star & \star & \star & \star & -\gamma^2 I & 0 \\ \star & \star & \star & \star & \star & \mathfrak{C}_1^6 \end{bmatrix},$$

and $\mathfrak{C}_1^1 = \mathcal{C}^{\mathrm{T}}\mathcal{C} + \mathcal{R}_1 - \mathcal{Z}_1, \mathfrak{C}_1^2 = \mathcal{C}^{\mathrm{T}}\mathcal{C}_d + \mathcal{Z}_1, \mathfrak{C}_1^3 = -2\mathcal{Z}_1 + \mathcal{C}_d^{\mathrm{T}}\mathcal{C}_d + \bar{\mathcal{C}}^{\mathrm{T}}\mathcal{M}\bar{\mathcal{C}}, \mathfrak{C}_1^4 = \mathcal{C}_d^{\mathrm{T}}\mathcal{H} + \bar{\mathcal{C}}^{\mathrm{T}}\mathcal{M}, \mathfrak{C}_1^5 = -\mathcal{R}_1 - \mathcal{Z}_1, \mathfrak{C}_1^6 = \mathcal{H}^{\mathrm{T}}\mathcal{H} + (1-\sigma_0)\mathcal{M}$.

Evidently,

$$\begin{bmatrix} -I \\ \mathfrak{B}_1^{\mathrm{T}} \end{bmatrix}^{\perp} = \begin{bmatrix} \mathfrak{B}_1^{\mathrm{T}} & I \end{bmatrix}.$$

Using Lemma 4, if the matrix $\mathfrak{X}_1$ such that

$$\mathfrak{C}_1 + \begin{bmatrix} -I \\ \mathfrak{B}_1^{\mathrm{T}} \end{bmatrix} \mathfrak{X}_1 + \mathfrak{X}_1^{\mathrm{T}} \begin{bmatrix} -I \\ \mathfrak{B}_1^{\mathrm{T}} \end{bmatrix}^{\mathrm{T}} < 0, \tag{16}$$

then inequality (15) is satisfied.

Selecting $\mathfrak{X}_1 = \begin{bmatrix} \mathcal{T}_1 & 0 & 0 & 0 & \mathcal{T}_1\mathcal{J}_1 & 0 \end{bmatrix}$, where $\mathcal{J}_1 = \begin{bmatrix} N_1 & 0 \\ 0 & N_2 \end{bmatrix}$, then inequality (16) is equivalent to

$$\mathfrak{D}_1 = \begin{bmatrix} \mathfrak{D}_1^1 & \mathfrak{D}_1^2 & \mathcal{T}_1^{\mathrm{T}}\mathcal{A}_d & 0 & \mathfrak{D}_1^3 & \mathcal{T}_1^{\mathrm{T}}\mathcal{G} \\ \star & \mathfrak{D}_1^4 & \mathfrak{D}_1^5 & 0 & \mathfrak{D}_1^6 & \mathcal{C}^{\mathrm{T}}\mathcal{H} \\ \star & \star & \mathfrak{D}_1^7 & \mathcal{Z}_1 & \mathfrak{D}_1^8 & \mathfrak{D}_1^9 \\ \star & \star & \star & \mathfrak{D}_1^{10} & 0 & 0 \\ \star & \star & \star & \star & \mathfrak{D}_1^{11} & \mathfrak{D}_1^{12} \\ \star & \star & \star & \star & \star & \mathfrak{D}_1^{13} \end{bmatrix} < 0.$$

where $\mathfrak{D}_1^1 = \bar{\delta}^2\mathcal{Z}_1 - [\mathcal{T}_1]_s, \mathfrak{D}_1^2 = \mathcal{P}_1 + \mathcal{T}_1^{\mathrm{T}}\mathcal{A}, \mathfrak{D}_1^3 = \mathcal{T}_1^{\mathrm{T}}\mathcal{E} - \mathcal{T}_1\mathcal{J}_1, \mathfrak{D}_1^4 = \mathcal{C}^{\mathrm{T}}\mathcal{C} + \mathcal{R}_1 - \mathcal{Z}_1, \mathfrak{D}_1^5 = \mathcal{C}^{\mathrm{T}}\mathcal{C}_d + \mathcal{Z}_1, \mathfrak{D}_1^6 = \mathcal{A}^{\mathrm{T}}\mathcal{T}_1\mathcal{J}_1, \mathfrak{D}_1^7 = -2\mathcal{Z}_1 + \mathcal{C}_d^{\mathrm{T}}\mathcal{C}_d + \bar{\mathcal{C}}^{\mathrm{T}}\mathcal{M}\bar{\mathcal{C}}, \mathfrak{D}_1^8 = \mathcal{A}_d^{\mathrm{T}}\mathcal{T}_1\mathcal{J}_1, \mathfrak{D}_1^9 = \mathcal{C}_d^{\mathrm{T}}\mathcal{H} + \bar{\mathcal{C}}^{\mathrm{T}}\mathcal{M}, \mathfrak{D}_1^{10} = -\mathcal{R}_1 - \mathcal{Z}_1, \mathfrak{D}_1^{11} = -\gamma^2 I + [\mathcal{E}^{\mathrm{T}}\mathcal{T}_1\mathcal{J}_1]_s, \mathfrak{D}_1^{12} = \mathcal{J}_1^{\mathrm{T}}\mathcal{T}_1^{\mathrm{T}}\mathcal{G}, \mathfrak{D}_1^{13} = \mathcal{H}^{\mathrm{T}}\mathcal{H} + (1-\sigma_0)\mathcal{M}$.

By Schur complement, one has

$$\mathfrak{F}_1 = \begin{bmatrix} -I & 0 & \mathcal{C} & \mathcal{C}_d & 0 & \mathcal{D}_y & \mathcal{H} \\ \star & \mathfrak{F}_1^1 & \mathfrak{F}_1^2 & \mathcal{T}_1^{\mathrm{T}}\mathcal{A}_d & 0 & \mathfrak{F}_1^3 & \mathcal{T}_1^{\mathrm{T}}\mathcal{G} \\ \star & \star & \mathfrak{F}_1^4 & \mathcal{Z}_1 & 0 & \mathfrak{F}_1^5 & 0 \\ \star & \star & \star & \mathfrak{F}_1^6 & \mathcal{Z}_1 & \mathfrak{F}_1^7 & \bar{\mathcal{C}}^{\mathrm{T}}\mathcal{M} \\ \star & \star & \star & \star & \mathfrak{F}_1^8 & 0 & 0 \\ \star & \star & \star & \star & \star & \mathfrak{F}_1^9 & \mathfrak{F}_1^{10} \\ \star & \star & \star & \star & \star & \star & \mathfrak{F}_1^{11} \end{bmatrix} < 0, \tag{17}$$

where $\mathfrak{F}_1^1 = \bar{\delta}^2\mathcal{Z}_1 - [\mathcal{T}_1]_s, \mathfrak{F}_1^2 = \mathcal{P}_1 + \mathcal{T}_1^{\mathrm{T}}\mathcal{A}, \mathfrak{F}_1^3 = \mathcal{T}_1^{\mathrm{T}}\mathcal{E} - \mathcal{T}_1\mathcal{J}_1, \mathfrak{F}_1^4 = \mathcal{R}_1 - \mathcal{Z}_1, \mathfrak{F}_1^5 = \mathcal{A}^{\mathrm{T}}\mathcal{T}_1\mathcal{J}_1, \mathfrak{F}_1^6 = -2\mathcal{Z}_1 + \bar{\mathcal{C}}^{\mathrm{T}}\mathcal{M}\bar{\mathcal{C}}, \mathfrak{F}_1^7 = \mathcal{A}_d^{\mathrm{T}}\mathcal{T}_1\mathcal{J}_1, \mathfrak{F}_1^8 = -\mathcal{R}_1 - \mathcal{Z}_1, \mathfrak{F}_1^9 = -\gamma^2 I + [\mathcal{E}^{\mathrm{T}}\mathcal{T}_1\mathcal{J}_1]_s, \mathfrak{F}_1^{10} = \mathcal{J}_1^{\mathrm{T}}\mathcal{T}_1^{\mathrm{T}}\mathcal{G}, \mathfrak{F}_1^{11} = (1-\sigma_0)\mathcal{M}$.

Define $T_3^{\mathrm{T}}\hat{A} = \mathfrak{L}, T_3^{\mathrm{T}}\hat{B} = \mathfrak{M}$, and according to the convexity principle [17], it can be seen that if (17) holds for all $\check{\Lambda} \in \mathcal{V}_{\mathcal{E}_n}$, then inequality (14) can be obtained.

Theorem 2: Given scalars $\beta > 0, M_1$ and matrices M_2, N_3, N_4, if there exist symmetric matrices $\mathcal{P}_2 = \begin{bmatrix} P_{21} & P_{22} \\ \star & P_{23} \end{bmatrix}, \mathcal{R}_2 = \begin{bmatrix} R_{21} & R_{22} \\ \star & R_{23} \end{bmatrix}, \mathcal{Q} = \begin{bmatrix} Q_1 & Q_2 \\ \star & Q_3 \end{bmatrix} > 0, \mathcal{Z}_2 = \begin{bmatrix} Z_{21} & Z_{22} \\ \star & Z_{23} \end{bmatrix} > 0, \mathcal{M} > 0$ and matrices $\mathcal{T}_2 = \begin{bmatrix} T_4 & T_5 \\ T_3 & T_3 \end{bmatrix}, \mathfrak{L}, \mathfrak{M}, \hat{C}, \hat{D}$, such that

$$\mathcal{W}_2 = \begin{bmatrix} \mathcal{W}_{21} & \mathcal{W}_{22} & \mathcal{W}_{23} \\ \star & \mathcal{W}_{24} & \mathcal{W}_{25} \\ \star & \star & \mathcal{W}_{26} \end{bmatrix} < 0, \tag{18}$$

then system (8) has an H_- index bound (11) in the finite frequency domain (9), where,

$$\mathcal{W}_{21} = \begin{bmatrix} \mathcal{W}_{21}^1 & \mathcal{W}_{21}^2 & P_{21} + T_4^{\mathrm{T}}(A + \check{\Lambda}) & \mathcal{W}_{21}^3 \\ \star & \mathcal{W}_{21}^4 & P_{22}^{\mathrm{T}} + T_5^{\mathrm{T}}(A + \check{\Lambda}) & \mathcal{W}_{21}^5 \\ \star & \star & \mathcal{W}_{21}^6 & \mathcal{W}_{21}^7 \\ \star & \star & \star & \mathcal{W}_{21}^8 \end{bmatrix},$$

$\mathcal{W}_{21}^1 = \bar{\delta}^2 Z_{21} - Q_1 - [T_4]_s, \mathcal{W}_{21}^3 = P_{22} + \mathfrak{L}$,

$\mathcal{W}_{21}^2 = \bar{\delta}^2 Z_{22} - Q_2 - T_5 - T_3^{\mathrm{T}}, \mathcal{W}_{21}^5 = P_{23} + \mathfrak{L}$,

$\mathcal{W}_{21}^4 = \bar{\delta}^2 Z_{23} - Q_3 - [T_3]_s, \mathcal{W}_{21}^6 = R_{21} - Z_{21} + \omega_l^2 Q_1$,

$\mathcal{W}_{21}^7 = R_{22} - Z_{22} + \omega_l^2 Q_2, \mathcal{W}_{21}^8 = R_{23} - Z_{23} + \omega_l^2 Q_3$,

$$\mathcal{W}_{22} = \begin{bmatrix} 0 & \mathfrak{M}C & 0 & 0 \\ 0 & \mathfrak{M}C & 0 & 0 \\ 0 & Z_{21} & Z_{22} & 0 \\ \hat{C}^{\mathrm{T}}M_1 & Z_{22}^{\mathrm{T}} & Z_{23} & 0 \end{bmatrix},$$

$$\mathcal{W}_{23} = \begin{bmatrix} 0 & T_4^{\mathrm{T}}F - T_4N_3 & -T_5N_4 & \mathfrak{M} \\ 0 & T_5^{\mathrm{T}}F - T_3N_3 & -T_3N_4 & \mathfrak{M} \\ 0 & (A+\check{\Lambda})^{\mathrm{T}}T_4N_3 & (A+\check{\Lambda})^{\mathrm{T}}T_5N_4 & 0 \\ 0 & \mathfrak{L}^{\mathrm{T}}N_3 & \mathcal{W}_{23}^1 & 0 \end{bmatrix},$$

$\mathcal{W}_{23}^1 = \mathfrak{L}^{\mathrm{T}}N_4 + \hat{C}^{\mathrm{T}}M_2$,

$$\mathcal{W}_{24} = \begin{bmatrix} \mathcal{W}_{24}^1 & M_1^{\mathrm{T}}\hat{D}C & 0 & 0 \\ \star & \mathcal{W}_{24}^2 & -2Z_{22} & Z_{21} \\ \star & \star & -2Z_{23} & Z_{22}^{\mathrm{T}} \\ \star & \star & \star & -R_{21} - Z_{21} \end{bmatrix},$$

$\mathcal{W}_{24}^1 = -1 - 2M_1, \mathcal{W}_{24}^2 = -2Z_{21} + C^{\mathrm{T}}\mathcal{M}C$,

$$\mathcal{W}_{25} = \begin{bmatrix} 0 & 0 & 0 & M_1^{\mathrm{T}}\hat{D} \\ Z_{22} & C^{\mathrm{T}}\mathfrak{M}^{\mathrm{T}}N_3 & \mathcal{W}_{25}^1 & C^{\mathrm{T}}\mathcal{M} \\ Z_{23} & 0 & 0 & 0 \\ -R_{22} - Z_{22} & 0 & 0 & 0 \end{bmatrix},$$

$\mathcal{W}_{25}^1 = C^{\mathrm{T}}\mathfrak{M}^{\mathrm{T}}N_4 + C^{\mathrm{T}}\hat{D}^{\mathrm{T}}M_2$,

$$\mathcal{W}_{26} = \begin{bmatrix} -R_{23} - Z_{23} & 0 & 0 & 0 \\ \star & \mathcal{W}_{26}^1 & \mathcal{W}_{26}^2 & N_3^{\mathrm{T}}\mathfrak{M} \\ \star & \star & \beta^2 I_f & N_4^{\mathrm{T}}\mathfrak{M} \\ \star & \star & \star & (1-\sigma_0)\mathcal{M} \end{bmatrix},$$

$\mathcal{W}_{26}^1 = \beta^2 I_f + [F^{\mathrm{T}}T_4N_3]_s, \mathcal{W}_{26}^2 = F^{\mathrm{T}}T_5N_4$.

Proof. By Lemma 2, it can be deduced that

$$\begin{bmatrix} \mathfrak{B}_2 \\ I \end{bmatrix}^{\mathrm{T}} \mathfrak{C}_2 \begin{bmatrix} \mathfrak{B}_2 \\ I \end{bmatrix} < 0, \tag{19}$$

where

$\mathfrak{B}_2 = \begin{bmatrix} \mathcal{A}(\Lambda) & \mathcal{A}_d & 0 & \mathcal{F} & \mathcal{G} \end{bmatrix}$,

$$\mathfrak{C}_2 = \begin{bmatrix} \mathfrak{C}_2^1 & \mathcal{P}_2 & 0 & 0 & 0 & 0 \\ \star & \mathfrak{C}_2^2 & \mathfrak{C}_2^3 & 0 & -\mathcal{C}^{\mathrm{T}}\mathcal{F}_y & -\mathcal{C}^{\mathrm{T}}\mathcal{H} \\ \star & \star & \mathfrak{C}_2^4 & \mathcal{Z}_2 & 0 & \mathfrak{C}_2^5 \\ \star & \star & \star & \mathfrak{C}_2^6 & 0 & 0 \\ \star & \star & \star & \star & \mathfrak{C}_2^7 & 0 \\ \star & \star & \star & \star & \star & \mathfrak{C}_2^8 \end{bmatrix},$$

and $\mathfrak{C}_2^1 = -\mathcal{Q} + \bar{\delta}^2\mathcal{Z}_2, \mathfrak{C}_2^2 = -\mathcal{C}^{\mathrm{T}}\mathcal{C} + \mathcal{R}_2 - \mathcal{Z}_2 - \omega_1\omega_2\tau\mathcal{Q}, \mathfrak{C}_2^3 = -\mathcal{C}^{\mathrm{T}}\mathcal{C}_d + \mathcal{Z}_2, \mathfrak{C}_2^4 = -2\mathcal{Z}_2 - \mathcal{C}_d^{\mathrm{T}}\mathcal{C}_d + \bar{\mathcal{C}}^{\mathrm{T}}\mathcal{M}\bar{\mathcal{C}}, \mathfrak{C}_2^5 = -\mathcal{C}_d^{\mathrm{T}}\mathcal{H} + \bar{\mathcal{C}}^{\mathrm{T}}\mathcal{M}, \mathfrak{C}_2^6 = -\mathcal{R}_2 - \mathcal{Z}_2, \mathfrak{C}_2^7 = \beta^2 I, \mathfrak{C}_2^8 = -\mathcal{H}^{\mathrm{T}}\mathcal{H} + (1-\sigma_0)\mathcal{M}$.

Obviously,

$$\begin{bmatrix} -I \\ \mathfrak{B}_2^{\mathrm{T}} \end{bmatrix}^{\perp} = \begin{bmatrix} \mathfrak{B}_2^{\mathrm{T}} & I \end{bmatrix}.$$

By Lemma 4, if there exist matrix $\mathfrak{X}_2$ such that

$$\mathfrak{C}_2 + \begin{bmatrix} -I \\ \mathfrak{B}_2^{\mathrm{T}} \end{bmatrix} \mathfrak{X}_2 + \mathfrak{X}_2^{\mathrm{T}} \begin{bmatrix} -I \\ \mathfrak{B}_2^{\mathrm{T}} \end{bmatrix}^{\mathrm{T}} < 0, \tag{20}$$

then inequality (19) hold.

Letting $\mathfrak{X}_2 = \begin{bmatrix} \mathcal{T}_2 & 0 & 0 & 0 & \mathcal{T}_2\mathcal{J}_2 & 0 \end{bmatrix}$, where $\mathcal{J}_2 = \begin{bmatrix} N_3 & 0 \\ 0 & N_4 \end{bmatrix}$. Then, (20) can be rewritten as

$$\mathfrak{D}_2 = \begin{bmatrix} \mathfrak{D}_2^1 & \mathfrak{D}_2^2 & \mathcal{T}_2^{\mathrm{T}}\mathcal{A}_d & 0 & \mathfrak{D}_2^3 & \mathcal{T}_2^{\mathrm{T}}\mathcal{G} \\ \star & \mathfrak{D}_2^4 & \mathfrak{D}_2^5 & 0 & \mathfrak{D}_2^6 & -\mathcal{C}^{\mathrm{T}}\mathcal{H} \\ \star & \star & \mathfrak{D}_2^7 & \mathcal{Z}_2 & \mathfrak{D}_2^8 & \mathfrak{D}_2^9 \\ \star & \star & \star & \mathfrak{D}_2^{10} & 0 & 0 \\ \star & \star & \star & \star & \mathfrak{D}_2^{11} & \mathfrak{D}_2^{12} \\ \star & \star & \star & \star & \star & \mathfrak{D}_2^{13} \end{bmatrix} < 0, \tag{21}$$

where $\mathfrak{D}_2^1 = -\mathcal{Q} + \bar{\delta}^2\mathcal{Z}_2 - [\mathcal{T}_2]_s, \mathfrak{D}_2^2 = \mathcal{P}_2 + \mathcal{T}_2^{\mathrm{T}}\mathcal{A}, \mathfrak{D}_2^3 = \mathcal{T}_2^{\mathrm{T}}\mathcal{F}_x - \mathcal{T}_2\mathcal{J}_2, \mathfrak{D}_2^4 = -\mathcal{C}^{\mathrm{T}}\mathcal{C} + \mathcal{R}_2 - \mathcal{Z}_2 + \omega_l^2\mathcal{Q}, \mathfrak{D}_2^5 = -\mathcal{C}^{\mathrm{T}}\mathcal{C}_d + \mathcal{Z}_2, \mathfrak{D}_2^6 = \mathcal{A}^{\mathrm{T}}\mathcal{T}_2\mathcal{J}_2, \mathfrak{D}_2^7 = -2\mathcal{Z}_2 - \mathcal{C}_d^{\mathrm{T}}\mathcal{C}_d + \bar{C}^{\mathrm{T}}\mathcal{M}\bar{C}, \mathfrak{D}_2^8 = \mathcal{A}_d^{\mathrm{T}}\mathcal{T}_2\mathcal{J}_2, \mathfrak{D}_2^9 = -\mathcal{C}_d^{\mathrm{T}}\mathcal{H} + \bar{C}^{\mathrm{T}}\mathcal{M}, \mathfrak{D}_2^{10} = -\mathcal{R}_2 - \mathcal{Z}_2, \mathfrak{D}_2^{11} = \beta^2 I + [\mathcal{F}^{\mathrm{T}}\mathcal{T}_2\mathcal{J}_2]_s, \mathfrak{D}_2^{12} = \mathcal{J}_2^{\mathrm{T}}\mathcal{T}_2^{\mathrm{T}}\mathcal{G}, \mathfrak{D}_2^{13} = -\mathcal{H}^{\mathrm{T}}\mathcal{H} + (1-\sigma_0)\mathcal{M}$.

Actually, (21) is equivalent to

$$\mathcal{X}^{\mathrm{T}}\mathfrak{Y}_1\mathcal{X} < 0, \tag{22}$$

where

$$\mathcal{X} = \begin{bmatrix} I & 0 & 0 & 0 & 0 & 0 \\ 0 & I & 0 & 0 & 0 & 0 \\ 0 & \mathcal{C} & \mathcal{C}_d & 0 & \mathcal{F}_y & \mathcal{H} \\ 0 & 0 & I & 0 & 0 & 0 \\ 0 & 0 & 0 & I & 0 & 0 \\ 0 & 0 & 0 & 0 & I & 0 \\ 0 & 0 & 0 & 0 & 0 & I \end{bmatrix},$$

$$\mathfrak{Y}_1 = \begin{bmatrix} \mathfrak{Y}_2^1 & \mathfrak{Y}_1^2 & 0 & \mathcal{T}_2^{\mathrm{T}}\mathcal{A}_d & 0 & \mathfrak{Y}_1^3 & \mathcal{T}_2^{\mathrm{T}}\mathcal{G} \\ \star & \mathfrak{Y}_1^4 & 0 & \mathcal{Z}_2 & 0 & \mathfrak{Y}_1^5 & 0 \\ \star & \star & -I & 0 & 0 & 0 & 0 \\ \star & \star & \star & \mathfrak{Y}_1^6 & \mathcal{Z}_2 & \mathfrak{Y}_1^7 & \bar{C}^{\mathrm{T}}\mathcal{M} \\ \star & \star & \star & \star & \mathfrak{Y}_1^8 & 0 & 0 \\ \star & \star & \star & \star & \star & \mathfrak{Y}_1^9 & \mathfrak{Y}_1^{10} \\ \star & \star & \star & \star & \star & \star & \mathfrak{Y}_1^{11} \end{bmatrix},$$

and $\mathfrak{D}_2^1 = -\mathcal{Q} + \bar{\delta}^2\mathcal{Z}_2 - [\mathcal{T}_2]_s, \mathfrak{Y}_1^2 = \mathcal{P}_2 + \mathcal{T}_2^{\mathrm{T}}\mathcal{A}, \mathfrak{Y}_1^3 = \mathcal{T}_2^{\mathrm{T}}\mathcal{F} - \mathcal{T}_2\mathcal{J}_2, \mathfrak{Y}_1^4 = \mathcal{R}_2 - \mathcal{Z}_2 + \omega_l^2\mathcal{Q}, \mathfrak{Y}_1^5 = \mathcal{A}^{\mathrm{T}}\mathcal{T}_2\mathcal{J}_2, \mathfrak{Y}_1^6 = -2\mathcal{Z}_2 + \bar{C}^{\mathrm{T}}\mathcal{M}\bar{C}, \mathfrak{Y}_1^7 = \mathcal{A}_d^{\mathrm{T}}\mathcal{T}_2\mathcal{J}_2, \mathfrak{Y}_1^8 = -\mathcal{R}_2 - \mathcal{Z}_2, \mathfrak{Y}_1^9 = \beta^2 I + [\mathcal{F}^{\mathrm{T}}\mathcal{T}_2\mathcal{J}_2]_s, \mathfrak{Y}_1^{10} = \mathcal{J}_2^{\mathrm{T}}\mathcal{T}_2^{\mathrm{T}}\mathcal{G}, \mathfrak{Y}_1^{11} = (1-\sigma_0)\mathcal{M}$.

On the other hand,

$$\mathfrak{R}^{\perp} = \begin{bmatrix} 0 \\ \mathcal{C}^{\mathrm{T}} \\ -I \\ \mathcal{C}_d^{\mathrm{T}} \\ 0 \\ 0 \\ \mathcal{H}^{\mathrm{T}} \end{bmatrix}^{\perp} = \begin{bmatrix} I & 0 & 0 & 0 & 0 & 0 & 0 \\ 0 & I & \mathcal{C}^{\mathrm{T}} & 0 & 0 & 0 & 0 \\ 0 & 0 & \mathcal{C}_d^{\mathrm{T}} & I & 0 & 0 & 0 \\ 0 & 0 & 0 & 0 & I & 0 & 0 \\ 0 & 0 & 0 & 0 & 0 & I & 0 \\ 0 & 0 & \mathcal{H}^{\mathrm{T}} & 0 & 0 & 0 & I \end{bmatrix}.$$

According to Lemma 4, if there is a matrix W such that

$$\mathfrak{Y}_1 + \mathfrak{R}W + W^{\mathrm{T}}\mathfrak{R}^{\mathrm{T}} < 0, \tag{23}$$

then inequality (22) is satisfied.

Choose the form of matrix W as $W = \begin{bmatrix} 0 & 0 & M_1 & 0 & 0 & \bar{W}_2 & 0 \end{bmatrix}$, where $\bar{W}_2 = \begin{bmatrix} 0 & M_2 \end{bmatrix}$, then (23) becomes

$$\mathfrak{F}_2 = \begin{bmatrix} \mathfrak{F}_2^1 & \mathfrak{F}_2^2 & 0 & \mathcal{T}_2^{\mathrm{T}}\mathcal{A}_d & 0 & \mathfrak{F}_2^3 & \mathcal{T}_2^{\mathrm{T}}\mathcal{G} \\ \star & \mathfrak{F}_2^4 & \mathcal{C}^{\mathrm{T}}M_1 & \mathcal{Z}_2 & 0 & \mathfrak{F}_2^5 & 0 \\ \star & \star & \mathfrak{F}_2^6 & M_1^{\mathrm{T}}\mathcal{C}_d & 0 & -\bar{W}_2 & M_1^{\mathrm{T}}\mathcal{H} \\ \star & \star & \star & \mathfrak{F}_2^7 & \mathcal{Z}_2 & \mathfrak{F}_2^8 & \bar{C}^{\mathrm{T}}\mathcal{M} \\ \star & \star & \star & \star & \mathfrak{F}_2^9 & 0 & 0 \\ \star & \star & \star & \star & \star & \mathfrak{F}_2^{10} & \mathfrak{F}_2^{11} \\ \star & \star & \star & \star & \star & \star & \mathfrak{F}_2^{12} \end{bmatrix} < 0, \tag{24}$$

where $\mathfrak{F}_2^1 = -\mathcal{Q} + \bar{\delta}^2\mathcal{Z}_2 - [\mathcal{T}_2]_s, \mathfrak{F}_2^2 = \mathcal{P}_2 + \mathcal{T}_2^{\mathrm{T}}\mathcal{A}, \mathfrak{F}_2^3 = \mathcal{T}_2^{\mathrm{T}}\mathcal{F} - \mathcal{T}_2\mathcal{J}_2, \mathfrak{F}_2^4 = \mathcal{R}_2 - \mathcal{Z}_2 + \omega_l^2\mathcal{Q}, \mathfrak{F}_2^5 = \mathcal{A}^{\mathrm{T}}\mathcal{T}_2\mathcal{J}_2 + \mathcal{C}^{\mathrm{T}}\bar{W}_2, \mathfrak{F}_2^6 = -I - [M_1]_s, \mathfrak{F}_2^7 = -2\mathcal{Z}_2 + \bar{C}^{\mathrm{T}}\mathcal{M}\bar{C}, \mathfrak{F}_2^8 = \mathcal{A}_d^{\mathrm{T}}\mathcal{T}_2\mathcal{J}_2 + \mathcal{C}_d^{\mathrm{T}}\bar{W}_2, \mathfrak{F}_2^9 = -\mathcal{R}_2 - \mathcal{Z}_2, \mathfrak{F}_2^{10} = \beta^2 I + [\mathcal{F}^{\mathrm{T}}\mathcal{T}_2\mathcal{J}_2]_s, \mathfrak{F}_2^{11} = \mathcal{J}_2^{\mathrm{T}}\mathcal{T}_2^{\mathrm{T}}\mathcal{G} + \bar{W}_2^{\mathrm{T}}\mathcal{H}, \mathfrak{F}_2^{12} = (1-\sigma_0)\mathcal{M}$.

According to the convexity principle [17], it is not difficult to find that if (24) holds for all $\check{\Lambda} \in \mathcal{V}_{\mathcal{E}_n}$, then inequality (18) can be obtained.

Based on Theorems 1-2, the FD filter gains can be obtained by solving the following optimization problem

$$\begin{aligned} &\max\ \beta \\ &\text{s.t. } (14), (18). \end{aligned} \tag{25}$$

Then, the desired FD filter gains $\hat{A}$ and $\hat{B}$ can be calculated by $\hat{A} = T_3^{-\mathrm{T}}\mathfrak{L}, \hat{B} = T_3^{-\mathrm{T}}\mathfrak{M}$.

4 Simulation Example

Considering a nonlinear system as follows

$$A = \begin{bmatrix} -8 & 3 \\ 4 & -6 \end{bmatrix}, E = \begin{bmatrix} -0.05 \\ 0.2 \end{bmatrix}, F = \begin{bmatrix} 0.6 \\ -0.2 \end{bmatrix},$$
$$C = \begin{bmatrix} 1 & 0 \end{bmatrix}, \Phi(x(t)) = \begin{bmatrix} 0.3\sin(x_2(t)) \\ 0.1\cos(x_1(t)) \end{bmatrix}.$$

By Lemma 1, one gets

$$\mathcal{V}_{\mathcal{E}_n} = \left\{ \begin{bmatrix} 0 & \pm 0.1 \\ \pm 0.3 & 0 \end{bmatrix} \right\}.$$

Select unknown disturbance as $d(t) = -0.05\sin(3t)$. In addition, select the low-frequency fault vector that satisfies $\omega_l = 0.1$ as

$$f(t) = \begin{cases} 0, \text{if } t < 10\text{s}, \\ 0.25 + 0.1\cos[0.03\pi(t-10)], \text{otherwise}. \end{cases}$$

The remaining parameters are selected as $h = 0.1\text{s}, \sigma_0 = 300, \sigma(0) = 0.15, \bar{\delta} = 0.3, M_1 = -0.2, M_2 = \begin{bmatrix} -0.1 & -0.2 \end{bmatrix}, \gamma = 0.5$. Then, the optimal H_- performance index is computed by $\beta = 1.1282$, and the weight matrix is $\mathcal{M} = 0.3447$, and the filter gains are

$$\hat{A} = \begin{bmatrix} -0.4866 & 0.6038 \\ 1.3769 & -1.2295 \end{bmatrix}, \hat{B} = \begin{bmatrix} 0.0134 \\ 0.0057 \end{bmatrix},$$
$$\hat{C} = \begin{bmatrix} 0.0057 & 0.0085 \end{bmatrix}, \hat{D} = -0.4184.$$

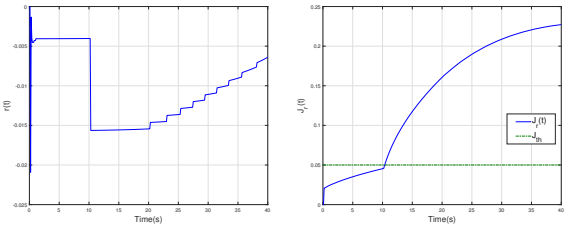

(a) (b)

Fig. 1: Response curves of the residual signal (a) and the residual evaluation function (b).

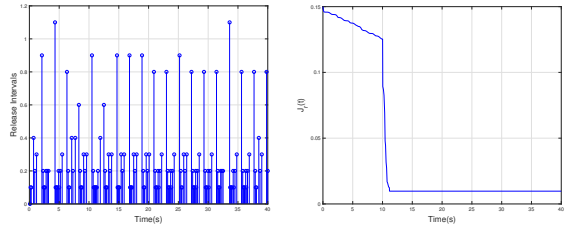

(a) (b)

Fig. 2: Response curves of the execution interval (a) and the dynamic threshold parameter (b).

Figures 1-2 show the simulation results under the established FD scheme. As shown in Figures 1 (a)-(b), after the fault occurs, the amplitude of residual signal $r(t)$ of the finite frequency FD scheme (4) increases rapidly, and the residual evaluation function $J_r(t)$ quickly exceeds the detection threshold J_{th} and emits an alarm. In addition, Figure 2 (a) shows the response curve of the execution interval of the developed AETM. As shown in Figure 2 (a), the AETM scheme was triggered only 157 times in the whole simulation process. Figure 1 (b) also shows the response curve of the dynamic threshold $\sigma(t)$. From Figure 1 (b), it can be seen that the dynamic threshold $\sigma(t)$ changes in real-time according to the adaptive updating law (3), and eventually converges to a constant value. The above simulation results show that the strategy proposed in this paper can detect the faults in the nonlinear Lipschitz system in time, and the designed data transmission mechanism can save network resources effectively.

5 Conclusions

The problem of finite-frequency FD based on the AETM scheme is discussed for nonlinear Lipschitz systems with network transmission delays and external disturbances. The augmented filter system is linearized to an LPV system by introducing the reformulated Lipschitz property. Then, sufficient conditions are presented to guarantee the LPV system is asymptotically stable and satisfies the full-frequency H_∞ performance bound and the finite-frequency H_- performance bound, and these conditions are further converted to LMIs to obtain the desired filter gains. Finally, a demonstrative example has been carried out to validate the availability and superiority of the proposed algorithm.

References

[1] S. Ding. Model-based fault diagnosis techniques: Design schemes, algorithms, and tools[M]. Berlin: Springer-Verlag, 2008.

[2] H. Chen, Z. Liu, B. Huang. Data-driven fault detection for Lipschitz nonlinear systems: From open to closed-loop systems[J]. Automatica, 155:111161, 2023.

[3] F. Cao, F. Jia, X. He. Sensor fault detection and diagnosis of linear parabolic PDE systems with unknown inputs[J]. IEEE Transactions on Automatic Control, 69(2):1014-1021, 2024.

[4] R. Liu, E. Tian, Y. Yang. Performance-driven fault detection for uncertain Takagi-Sugeno fuzzy feedback control systems[J]. IEEE Transactions on Fuzzy Systems, 31(12):4271-4284, 2023.

[5] H. Chen, L. Li, C. Shang, et al. Fault detection for nonlinear dynamic systems with consideration of modeling errors: A data-driven approach[J]. IEEE Transactions on Cybernetics, 53(7):4259-4269, 2023.

[6] Y. Long, Y. Cheng, T. Li, et al. Asynchronous frequency-dependent fault detection for nonlinear Markov jump systems under wireless fading channels[J]. IEEE Transactions on Cybernetics, 52(12):13598-13608, 2022.

[7] T. Iwasaki, S. Hara. Generalized KYP lemma: Unified frequency domain inequalities with design applications[J]. IEEE Transactions on Automatic Control, 50(1):41-59, 2005.

[8] X. Zhu, Y. Xia, S. Chai, et al. Fault detection for vehicle active suspension systems in finite-frequency domain[J]. IET Control Theory & Applications, 13(3):387-394, 2019.

[9] R. Zhao, L. Liu, G. Feng. Finite-frequency H_-/H_∞ memory fault detection filtering design for uncertain Takagi-Sugeno fuzzy affine systems[J]. IEEE Transactions on Fuzzy Systems, 30(7):2595-2609, 2022.

[10] J. Li, Z. Wang, C. K. Ahn, et al. Fault detection for Lipschitz nonlinear systems with restricted frequency-domain specifications[J]. IEEE Transactions on Systems, Man, and Cybernetics: Systems, 51(12):7486-7496, 2021.

[11] J. Pan, A.-T. Nguyen, T.-M. Guerra, et al. Vehicle actuator fault detection with finite-frequency specifications via Takagi-Sugeno fuzzy observers: Theory and experiments[J]. IEEE Transactions on Vehicular Technology, 72(1):407-417, 2023.

[12] Y. Wang, X. Chen, H. Guo. Event-triggered H_-/L_∞ fault detection observer design for discrete-time Lipschitz nonlinear networked control systems in finite-frequency domain[J]. International Journal of Systems Science, 53(3):488-503, 2022.

[13] Q. Zhu, S. Jiang, F. Pan. Adaptive event-triggered fault detection for nonlinear networked systems in finite-frequency domain under stochastic cyber-attacks[J]. International Journal of Adaptive Control and Signal Processing, 36(2):1537-1561, 2022.

[14] A. Zemouche, M. Boutayeb. On LMI conditions to design observers for Lipschitz nonlinear systems[J]. Automatica, 49(2): 585-591, 2013.

[15] P. Cheng, C. Cai. Event-triggered fault detection for discrete-time Markovian jump systems in finite frequency domain[J]. International Journal of Robust and Nonlinear Control, 32(2):141-163, 2022.

[16] S. B. Stanford, L. E. Ghaoui, E. Feron. Linear matrix inequalities in system and control theory[M]. Society for Industrial and Applied Mathematics, Philadelphia, 1994.

[17] J. Wang, P. Shi, H. Gao, et al. Gain-scheduled stabilisation of linear parameter-varying systems with time-varying input delay[J]. IET Control Theory & Applications, 1(5):1276-1285, 2007.

Proceedings of the 3rd Conference on Fully Actuated System Theory and Applications
May 10-12, 2024, Shenzhen, China

Fault detection based on operational state recognition for wind turbine gearbox

Wei Lin[1,2], Jinzhou Dou[3], Linsong Yuan[4], Kai Zhang[5]

1. Zhejiang University, Hangzhou, P. R. China
E-mail: 22260706@zju.edu.cn

2. Zhejiang Zheneng Jiaxing Offshore Wind Power Co., Jiaxing, P. R. China
E-mail: VipH0@outlook.com

3. Zhejiang Zheneng Jiaxing Offshore Wind Power Co., Jiaxing, P. R. China
E-mail: zjtkdjz@126.com

4. Zhejiang Zheneng Jiaxing Offshore Wind Power Co., Jiaxing, P. R. China
E-mail: 630421370@qq.com

5. Zhejiang University, Hangzhou, P. R. China
E-mail: 12032097@zju.edu.cn

Abstract: Intelligent condition monitoring and fault detection can reduce downtime and improve the reliability of wind turbines. However, the variable external environment has led to varying operational conditions of wind turbines, which presents challenges to precise modeling and accurate fault detection. This paper proposes a fault detection method based on operational state recognition for the gearbox subsystem. First, a dynamic time warping-based indicator is designed and employed for unsupervised clustering for different operational states. Then, a classification model and a regression model are sequentially used for operational state recognition and normal behavior modeling, respectively. Subsequently, during online detection, based on the probabilities of each real-time sample belonging to different operating status categories, multiple judgment processes are executed and summarized as the final detection result. Finally, experiments using field data from real wind farms are conducted to verify the effectiveness and superiority of the proposed method.

Key Words: Fault detection, operational state recognition, dynamic time warping, normal behavior modeling.

1 Introduction

In order to promote the construction of ecological civilization and the transformation of energy structure, the development of renewable energy has received increasing attention. Wind energy, as a typical and highly industrialized renewable energy source, is currently experiencing a period of significant development worldwide [13]. According to the Global Wind Energy Council (GWEC) [2], the cumulative installed capacity of global wind power had reached 906 GW by the end of 2022.

However, with the surge in wind power installations in various countries, design flaws and inadequate operation and maintenance (O&M) practices are being increasingly exposed, leading to frequent component faults that result in significant economic losses and safety hazards. Effective O&M practices have become essential for ensuring the safety and reliability of wind turbines (WTs) [6, 10].

WTs are complex structures including multiple components, among which the gearbox is the key subsystem connecting the blade and the generator. The failure of the gearbox will directly affect the operational status of various key components in the WTs. Besides, the downtime and economic losses caused by gearbox failures are usually at the forefront of various components [4]. Therefore, the implementation of condition monitoring and fault detection for the gearbox is of great significance for improving operational reliability and reducing O&M costs [8, 15].

The existing literature on gearbox fault detection mainly consists of model-based and data-driven methods. The former aims to construct physical models of the main components in the gearbox to describe the fault evolution process. Beden et al. [1] approach the issue from the perspective of stress analysis and use the finite element analysis method to systematically analyze the bending stress of helical gears in the gearbox and obtain the tooth surface damage status of the gears. In [17], a mathematical relationship derivation model is established based on the deterioration of lubricating oil and the degree of particle pollution to analyze the status of gearbox lubricating oil and obtain the representation of the operating status of the gearbox. Interval observers are employed in [9] to consider the parametric uncertainty and noise problems. The fault can then be identified if the measurements fall inside the interval obtained from the mathematical model. However, due to characteristics such as structural complexity, highly nonlinear parametric correlations, and uncertain disturbances, the mathematical models find it hard to precisely describe the real systems, which then becomes a hindrance in the application of practical scenarios [7].

By contrast, the data-driven methods can depict the operational states of WTs based on measured sensor data and do not rely on precise mathematical models, and therefore become mainstream in literature. Besides, the supervisory control and data acquisition (SCADA) systems have been deployed in modern WTs and can provide valid data foundations. In [11], the support vector machine is used for fault diagnosis and the sparrow search algorithm is used to optimize the penalty factor and kernel function parameter selection. In [3], an improved twin support vector machine is used for normal behavior modeling for fast computation. With the advancement of deep learning, more and more neural network based methods are utilized in fault diagnosis. Wang et al. [12] use deep neural networks to model the normal

operational states of the lubricating oil pressure and predict the changing trend based on relevant features. The authors in [14] utilize a dual-stage attention-based recurrent neural network, incorporating a specially designed input attention mechanism based on long short-term memory to capture time-varying correlations among variables in wind turbines for improved variable estimation. Li et al. [5] introduce the unsupervised spatial-temporal aware graph encoder-decoder (STAGED) model for industrial fault diagnosis, which effectively captures the complicated interactions between measurements and temporal evolutions to accurately locate fault roots

However, there are also some challenges that remain for further studies. The complexity and variability of wind conditions lead to variable operating conditions of WTs. In particular, the gearbox is responsible for increasing the speed of the rotor and transmitting it to the generator for power generation, and therefore needs to withstand both the load on the rotor side and the load caused by the rotation of the gear components. The complexity of the operating states in the gearbox is particularly evident. The modeling needs to encompass different operating states. Furthermore, since different wind conditions have different proportions in historical data, how to balance different wind conditions to avoid uneven training still needs to be further studied.

Motivated by the above discussions, this paper proposes a fault detection method considering variable operational states for the gearbox subsystem. First, the operational states are divided in an unsupervised manner. Some parameters which can represent the states of WTs are selected and different states can be divided by comparing with the set baselines. Then, a classification model is trained to generate the probabilities of various operating states to which a real-time sample belongs. To overcome the sample imbalance problem, a sampling weighting allocation strategy is designed to guarantee the classification performance. The expected normal behaviors are trained based on each operational state clustering and jointly determine the detection results.

The main contributions of this paper are summarized as follows:

(1) The modeling of the gearbox takes different operational states into consideration. Through separate monitoring and weighted summary of various states, the modeling performance can be effectively improved.

(2) A sampling weighting allocation strategy is designed to address the sample imbalance problem of different operational state clusters, which can guarantee classification performance and improve the identification performance of states during online detection.

(3) Field SCADA data are collected to evaluate the proposed method. Case studies and comparison experiments are conducted to verify the effectiveness and superiority.

The rest of this paper is organized as follows. Section 2 presents the details of the proposed fault detection method. Section 3 describes the experimental results. Conclusions are presented in Section 4.

2 fault detection method

To achieve precise condition monitoring and fault detection for the gearbox subsystem, a fault detection method that can consider various operational states is designed. The framework, illustrated in Fig. 1, consists of the operational states classification step, model training step, and online detection step. The details are presented as follows.

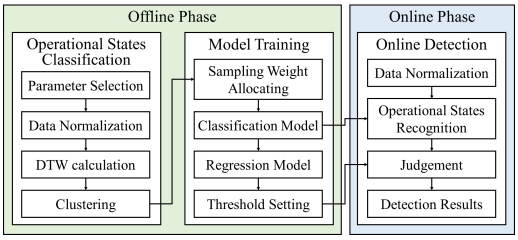

Fig. 1: The framework of fault detection method

2.1 Operational States Classification

The first step aims to evaluate and divide different clusters representing distinct operational states. The wind speed v, as the input of WTs, determines the possible states. Meanwhile, the generator speed g and the output active power P characterize the current working condition. Therefore, these three variables are selected as the operational state parameters, denoted by $\mathbf{X}_o$. A data normalization step is first conducted to avoid issues of different dimensions:

$$\dot{\mathbf{X}}_o = \frac{\mathbf{X}_o - \bar{\mathbf{X}}_o}{\sigma} \tag{1}$$

where $\bar{\mathbf{X}}_o$ is the mean vector and σ is the standard deviation vector.

The selection of parameters such as wind speed, generator speed, and output active power as inputs for the Wind Turbines (WTs) is crucial for accurately representing the operational states of the turbines. These parameters are chosen based on their direct impact on the turbine's performance and their sensitivity to operational anomalies. Wind speed directly affects the turbine's power output and operational efficiency, while generator speed and output active power are key indicators of the turbine's electrical performance. Together, these parameters provide a comprehensive view of the turbine's operational state, enabling effective monitoring and fault detection.

The value of W, the length of the sliding window, is determined based on a trade-off between temporal resolution and computational efficiency. A larger window captures more temporal information but increases computational complexity, while a smaller window may miss important trends. In our experiments, W is empirically set to capture approximately 10 minutes of operation, which is found to be effective for identifying stable operational segments and ensuring manageable computational load.

To generate the correlation between different samples, a data segment with stable power generation under steady wind conditions is selected as the baseline. The sliding window technique is employed to construct the baseline sample $\dot{\mathbf{X}}_s$ as follows:

$$\dot{\mathbf{X}}_s = [v_1, ..., v_W; g_1, ..., g_W; P_1, ..., P_W] \tag{2}$$

where W is the length of the sliding window. Each sample is compared with the baseline $\dot{\mathbf{X}}_s$ by calculating the distance.

It is worth noting that the correlation mainly evaluates fluctuations without paying attention to phase differences.

For example, in Fig. 2, two wind speed samples should be close and belong to the same cluster. Obviously, reasonable results cannot be obtained based on Euclidean distance. To this end, the dynamic time warping (DTW) [16] is introduced and the distance between a sample and the baseline is calculated as:

$$\mathbf{D}=\underset{\mathbf{W}}{\operatorname{argmin}}\sqrt{\sum_{k=1,w_k=(i,j)}^{K}\left(\dot{\mathbf{X}}_o[i]-\dot{\mathbf{X}}_s[j]\right)^2} \tag{3}$$

where $\mathbf{W}$ is the warping path, K is the length of the warping path. Each variable performs the calculation separately and obtains the corresponding DTW distance. For i-th sample, the final distance is expressed by:

$$\mathbf{D}_i=[D_{v_i};D_{g_i};D_{P_i}] \tag{4}$$

where $D_{v_i}, D_{g_i}, D_{P_i}$ are the DTW distances by wind speed, generator speed, and output active power for i-th sample respectively.

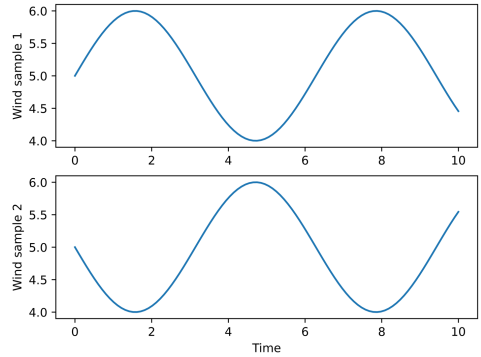

Fig. 2: Examples of wind samples

The samples under different operational states exhibit distinct results at these DTW distances. Therefore, a common clustering method, K-means is used to achieve unsupervised partition of different states.

2.2 Model Training

The experimental data are divided into a training set and a testing set to evaluate the performance of the proposed method. The division is based on a temporal split, with the first 70% of the data chronologically used for training and the remaining 30%.

2.2.1 Classification Model

After the previous clustering method, each divided cluster can represent a specific operational state. Subsequently, a classification model is trained to calculate the probability of a sample falling into each state. The classification model uses additional operational measurements, such as temperature, rotor speed, and pitch angle, as input. In practice, the ensemble learning method, eXtreme Gradient Boosting (XGBoost), is employed as the classification model. XGBoost utilizes additive models by constructing multiple base learners to learn the deviation between the results of the previous base learners and the actual values. Through the learning of multiple learners, it can continuously reduce the classification difference and ensure training efficiency. However, the imbalance in samples between clusters negatively impacts the classification performance. Therefore, a sampling weight allocation strategy is initially designed. The sampling weight α_i of samples in the i-th cluster is derived by:

$$\alpha_i=\frac{\sum_{j=1}^{n_o}N_j}{N_i} \tag{5}$$

, where n_o is the number of divided clusters, N_i is the number of samples in i-th cluster.

Through the sampling weight allocating strategy, the classification model can learn each category in a balanced manner and guarantee the performance. Then, based on each cluster, a regression model is trained to learn the expected normal state of this cluster.

2.2.2 State Recognition Regression

The operation of the gearbox relies on the lubrication oil subsystem and cooling subsystem for cooling. Therefore, the gearbox bearing temperature can represent the states of the gearbox and potential faults usually manifest as abnormal temperature increases. The target variable for the model is the bearing temperature, which is denoted as y. Other relevant variables, denoted as $\mathbf{X}$, are chosen as the input for the model based on prior knowledge, similar to the input for the classification model. The Gated Recurrent Unit (GRU) is introduced as the regression model. GRU has a relatively simple structure and can capture dependencies on long sequences. At timeslot t, GRU can generate a hidden state $\mathbf{h}_t$ and the update is decided by two gates: update gate $\mathbf{z}_t$ and reset gate $\mathbf{r}_t$, which are calculated as:

$$\begin{aligned}
\mathbf{z}_t &= \sigma\left(\mathbf{W}_z\mathbf{X}+\mathbf{U}_z\mathbf{h}_{t-1}+\mathbf{b}_z\right)\\
\mathbf{r}_t &= \sigma\left(\mathbf{W}_r\mathbf{X}+\mathbf{U}_r\mathbf{h}_{t-1}+\mathbf{b}_r\right)\\
\tilde{\mathbf{h}}_t &= \tanh(\mathbf{W}_h\mathbf{X}+\mathbf{U}_h(\mathbf{r}_t\odot\mathbf{h}_{t-1})+\mathbf{b}_h)\\
\mathbf{h}_t &= (1-\mathbf{z}_t)\odot\mathbf{h}_{t-1}+\mathbf{z}_t\odot\tilde{\mathbf{h}}_t
\end{aligned} \tag{6}$$

, where $\mathbf{W}_z, \mathbf{W}_r, \mathbf{W}_h \in \mathbb{R}^{m\times n}$, $\mathbf{U}_z, \mathbf{U}_r, \mathbf{U}_h \in \mathbb{R}^{m\times m}$, and $\mathbf{b}_z, \mathbf{b}_r, \mathbf{b}_h \in \mathbb{R}^m$ are parameters to learn. m is the size of hidden state, n is the number of relevant variables, σ is the logistic sigmoid function and $\odot$ represents Hadamard product.

A total of n_o GRU models are trained independently corresponding n_o divided operational states. For each model, the residuals between the actual measured values and prediction values are calculated. Then, a threshold should be set to characterize the residual range during normal operation. The PauTa criterion is adopted and the threshold U_i of the i-th model is calculated by:

$$U_i=\mu_i+3\sigma_i \tag{7}$$

, where μ_i and σ_i are the mean value and standard deviation of the residual sequence from the i-th model.

2.3 Online Detection

During the detection phase, for a real-time data sample X_r, three variables, wind speed, generator speed, and output active power are first selected. Then, through normalization

operation, three DTW distances are calculated as the input of the well-trained XGBoost model. The classification model can output the probability that the sample belongs to each category, expressed by:

$$\mathbf{P} = [P_1, P_2, ..., P_{n_o}] \tag{8}$$

, where P_i is the probability of X_r falling into i-th cluster.

Thereafter, each well-trained GRU model will generate a prediction value of the monitoring variable based on X_r. At the comparison step between the predicted residual and corresponding threshold, to take into account the volatility of variables and avoid the influence of outliers, a percentage overrun criterion is designed. Specifically, as of the previous day of the current sample X_r, when $P_d\%$ of the residuals exceed the threshold, a positive alarm is delivered.

Finally, each GRU model can generate a binary judgment result $I \in \{0, 1\}$ and the detection result D_r for X_r is derived by:

$$D_r = \sum_{i=1}^{n_o} P_i \cdot I_i \tag{9}$$

The detection result represents the level of confidence in the occurrence of a fault in the form of probability, which can provide more detailed and accurate information compared to binary judgment results.

3 Experiments

3.1 Dataset Description

The collected data come from a field wind farm in western China. There are totally 31 WTs and six gearbox fault scenarios. We select a typical bearing fault as a case study to present the detailed detection results. The dataset ranges from January 2016 to May 2017 with a sampling interval of 5min. The failure was confirmed on March 21, 2017. The dataset is divided into the training set ranging from January 2016 to September 2016 and the testing set ranging from January 2017 to May 2017.

The temperature measured by the sensor installed in the bearing can reflect the operational state of the gearbox and hence be regarded as the target variable. The relevant variables are selected by prior knowledge, listed in Table 1.

3.2 Case Study

First, three variables, wind speed, active power, and generator speed are selected as parameters representing operational states for clustering. The baseline sample under steady wind conditions, with a sliding window length of 10, is shown in Fig. 3.

By calculating the DTW distances between each sample and the baseline sample, the K-means clustering algorithm is employed to achieve the unsupervised partition. By incrementally increasing the number of clusters, the sums of squared errors (SSE) of clustering results are counted to determine the final clustering number, shown in Fig. 4.

The number of clusters is determined as the minimum number with no significant change in SSE, which is set as 5 in this case. Then, the final clustering results on the power curve are illustrated in Fig. 5. It can be seen that even at similar wind speeds, differences in power generation due to power curtailment schemes, abnormal operations, etc. will lead to different categories.

Table 1: Relevant Variables List

Category	Variables
Operation parameters of gearbox	Gearbox oil temperature
	Gearbox inlet pressure
	Gearbox outlet pressure
Environmental parameters	Ambient temperature
	Wind speed
	Wind direction
System parameters	System state
	Active power
	Reactive power
	Generator speed
	Power factor
	Yaw angle
	Yaw cabin location
	Cabin control temperature
	Cabin temperature
	Pitch angle of paddle1, 2, 3

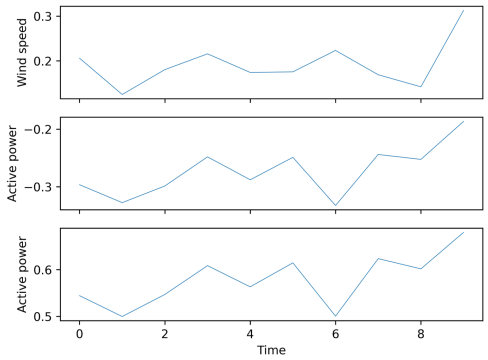

Fig. 3: Baseline sample under steady wind conditions

Then, an XGBoost classification model is trained with the clustering results as labels. The sample numbers of different clusters are counted and the corresponding sampling weights are allocated, which is shown in Fig .6.

Based on each cluster, a GRU regression model is trained to depict the expected operational states of the gearbox. For each sample in this case, based on the category with the highest probability, we present the prediction results, illustrated in Fig. 7, where the black line is the actual measured values, the green line is the predicted values of the training set, and the blue line is the predicted values of the testing set. The red star is the fault confirmation time.

The predicted residuals and the threshold are shown in Fig. 8. We only present the model prediction results for each sample under the category to which it belongs with the highest probability. Actually, for each real-time sample, the models trained under each category will make real-time predictions and warning judgments and the final detection results are the weighted sum of probabilities by category. To avoid frequent false alarms caused by outliers, the percentage overrun criterion is designed and the parameter $P_d\%$ is set as 25%. The first detection was on March 4, 2017, which is 17 days earlier than the confirmation time. The detailed results of the first alarm point are shown in Table 2. The final detection confidence is 0.94, which represents a higher

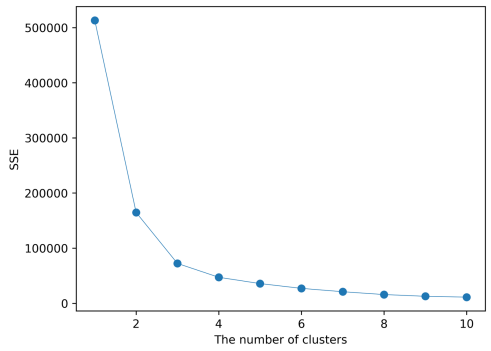

Fig. 4: SSE with different numbers of clusters

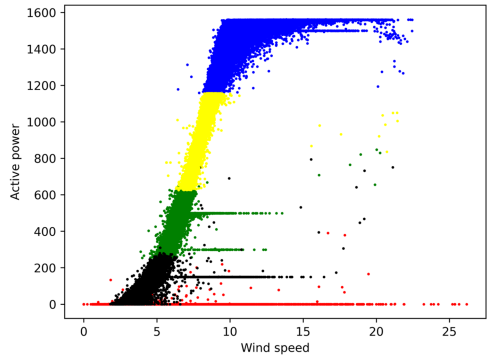

Fig. 5: Clustering results on power curve

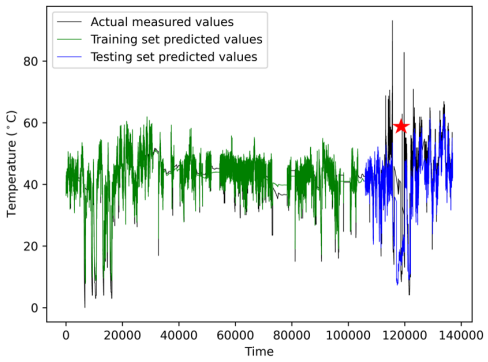

Fig. 7: Predicted results of the bearing temperature

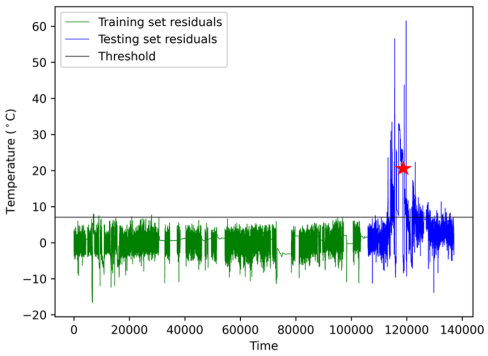

Fig. 8: Predicted residuals of the bearing temperature

value identified as a fault.

3.3 Comparison Analysis

To verify the superiority of the proposed method, we conduct the comparison analysis in this subsection. The main contributions are the operational states classification step and the sampling weight allocating strategy. Therefore, we removed these steps for verification. XGBoost-GRU method means the sampling weight allocating strategy is removed, and GRU method means only one regression model is trained for all samples. The predicted results for all 31 WTs are shown in Fig. 9. The root mean square error (RMSE) is adopted as the indicator.

It can be concluded that the proposed method can achieve optimal predicted results over all datasets. For the XGBoost-GRU method, the sample imbalance problem will influence the classification performance. For categories with fewer samples, the increase in misclassification will then lead to decreases in prediction performance. For the GRU method, the model will focus more on the major operational state and ignore some with fewer occurrences, thereby compromising predictive performance.

Further, we present the confusion matrices of detection results under different methods, which are shown in Table 3-5, where TP means positive judgment of normal WT, TN means positive judgment of faulty WT, FP means false alarm, and FN means missed alarm. It can be concluded that the proposed method can achieve optimal detection results. The improvement of prediction accuracy can help to more effectively distinguish faults and noise and hence improve the detection accuracy. Moreover, the proposed method can evaluate each operational state more evenly, thus better responding to unknown potential faults. The case study and comparative experiments demonstrate the effectiveness and superiority of the proposed method.

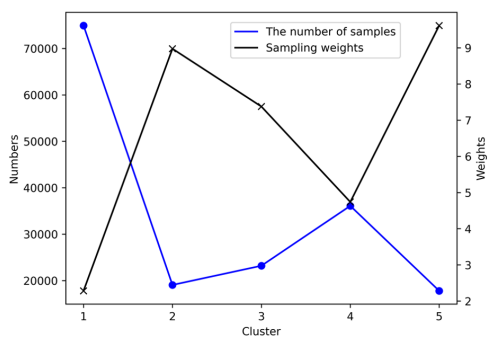

Fig. 6: The number of samples and weights of different clusters

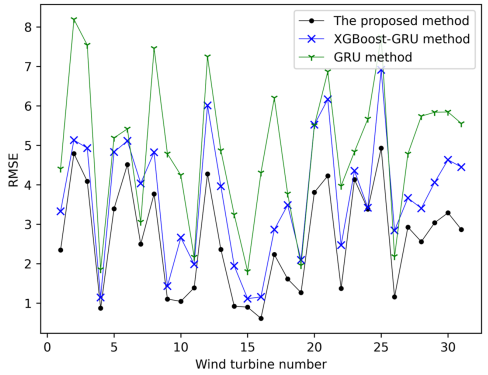

Fig. 9: Predicted results of 31 WTs with different methods

Table 2: Detection Results

Category	Probability	Judgement result
1	0	0
2	0.03	1
3	0.89	1
4	0.02	1
5	0.06	0

Table 3: Detection results with the proposed method

	Normal WT	Faulty WT
No alarm	TP=21	FN=0
Alarm	FP=4	TN=6

Table 4: Detection results with the XGBoost-GRU method

	Normal WT	Faulty WT
No alarm	TP=20	FN=1
Alarm	FP=5	TN=5

Table 5: Detection results with the GRU method

	Normal WT	Faulty WT
No alarm	TP=18	FN=3
Alarm	FP=7	TN=3

4 Conclusion

This paper proposes a fault detection method considering various operational states for the gearbox subsystem in WTs. First, the operational states are divided based on similarity distance. Then, a classification model is trained to determine the probability of each real-time sample being in different clusters, and a sampling weight allocating strategy is designed to avoid the sample imbalance problem. Next, during online detection, regression models trained based on different cluster samples will perform judgments and jointly determine the final detection results. The confidence results with continuous numerical values can provide more accurate and detailed detection information. Extensive experiments are conducted and the results demonstrate the effectiveness and superiority of the proposed method.

References

[1] SM Beden, Shahrum Abdullah, and AK Ariffin. Review of fatigue crack propagation models for metallic components. *European Journal of Scientific Research*, 28(3):364–397, 2009.

[2] Global Wind Energy Council. Global wind report 2022, 2022. https://gwec.net/global-wind-report-2022/.

[3] Harsh S Dhiman, Dipankar Deb, SM Muyeen, and Innocent Kamwa. Wind turbine gearbox anomaly detection based on adaptive threshold and twin support vector machines. *IEEE Transactions on Energy Conversion*, 36(4):3462–3469, 2021.

[4] Guoqian Jiang, Haibo He, Jun Yan, and Ping Xie. Multiscale convolutional neural networks for fault diagnosis of wind turbine gearbox. *IEEE Transactions on Industrial Electronics*, 66(4):3196–3207, 2018.

[5] Shizhong Li, Wenchao Meng, Shibo He, Jichao Bi, and Guanglun Liu. Staged: A spatial-temporal aware graph encoder–decoder for fault diagnosis in industrial processes. *IEEE Transactions on Industrial Informatics*, 20(2):1742–1752, 2024.

[6] Yonggang Lin, Le Tu, Hongwei Liu, and Wei Li. Fault analysis of wind turbines in china. *Renewable and Sustainable Energy Reviews*, 55:482–490, 2016.

[7] Zepeng Liu and Long Zhang. A review of failure modes, condition monitoring and fault diagnosis methods for large-scale wind turbine bearings. *Measurement*, 149:107002, 2020.

[8] Wei Qiao and Dingguo Lu. A survey on wind turbine condition monitoring and fault diagnosis—part i: Components and subsystems. *IEEE transactions on industrial electronics*, 62(10):6536–6545, 2015.

[9] Hector Sanchez, Teresa Escobet, Vicenc Puig, and Peter Fogh Odgaard. Fault diagnosis of an advanced wind turbine benchmark using interval-based arrs and observers. *IEEE Transactions on Industrial Electronics*, 62(6):3783–3793, 2015.

[10] Emilie Stone, Stefano Giani, Donatella Zappalá, and Christopher Crabtree. Convolutional neural network framework for wind turbine electromechanical fault detection. *Wind Energy*, 2023.

[11] Wumaier Tuerxun, Xu Chang, Guo Hongyu, Jin Zhijie, and Zhou Huajian. Fault diagnosis of wind turbines based on a support vector machine optimized by the sparrow search algorithm. *Ieee Access*, 9:69307–69315, 2021.

[12] Long Wang, Zijun Zhang, Huan Long, Jia Xu, and Ruihua Liu. Wind turbine gearbox failure identification with deep neural networks. *IEEE Transactions on Industrial Informatics*, 13(3):1360–1368, 2016.

[13] Tianming Xie, Qifa Xu, Cuixia Jiang, Shixiang Lu, and Xiangxiang Wang. The fault frequency priors fusion deep learning framework with application to fault diagnosis of offshore wind turbines. *Renewable Energy*, 202:143–153, 2023.

[14] Qinmin Yang, Guanglun Liu, Yunong Bao, and Qi Chen. Fault detection of wind turbine generator bearing using attention-based neural networks and voting-based strategy. *IEEE/ASME Transactions on Mechatronics*, 27(5):3008–3018, 2021.

[15] Kai Zhang, Baoping Tang, Lei Deng, and Xiaoli Liu. A hybrid attention improved resnet based fault diagnosis method of wind turbines gearbox. *Measurement*, 179:109491, 2021.

[16] Zengwei Zheng, Mingxuan Zhou, Yuanyi Chen, Meimei Huo, Lin Sun, Sha Zhao, and Dan Chen. A fused method of machine learning and dynamic time warping for road anomalies detection. *IEEE Transactions on Intelligent Transportation Systems*, 23(2):827–839, 2020.

[17] Junda Zhu, Jae M Yoon, David He, and Eric Bechhoefer. Online particle-contaminated lubrication oil condition monitoring and remaining useful life prediction for wind turbines. *Wind Energy*, 18(6):1131–1149, 2015.

Proceedings of the 3rd Conference on Fully Actuated System Theory and Applications
May 10-12, 2024, Shenzhen, China

Structure and Thrust Fault Detection and Diagnosis for Hypersonic Aircrafts via a Data-Driven Approach

Chaoyue Zhang[1], Qinglei Hu[1,3,4], Tuo Han*[2,3,4]

1. School of Automation Science and Electrical Engineering, Beihang University, Beijing 100191, China
E-mail: huql_buaa@buaa.edu.cn

2. School of Aeronautic Science and Engineering, Beihang University, Beijing 100191, China
E-mail: hantuo@buaa.edu.cn

3. Hangzhou International Innovation Institute, Beihang University, Hangzhou 311115, China

4. Tianmushan Laboratory, Hangzhou 311115, China

Abstract: As a complex and significant part of the hypersonic aircraft operating under high speeds and harsh flight conditions, its structure and thrust systems are sometimes fragile to suffer from unforeseeable failures that can seriously degrade the flight performance and even cause mission failures of the aircraft. To deal with such problems from the perspective of online fault detection and diagnosis (FDD) for flight control reconfiguration, a data-driven intelligent FDD scheme for the hypersonic aircraft is proposed in this study considering both the structure and thrust faults. First, a six-degree-of-freedom nonlinear model of the aircraft is employed to generate sampling data of different flight status under various faults. Then, a data preprocessing method and a Deep Residual Autoencoder network (DRAE) are utilized to predict and classify the structure and thrust faults. To alleviate the vanishing gradient issue, a residual block is integrated in the encoder for efficient training. Numerical simulations show that the FDD algorithm based on the designed scheme can extract the characteristics of different faults for online failure prediction and classification with expected accuracy.

Key Words: hypersonic aircraft, fault detection and diagnosis, deep autoencoder network, residual mechanism.

1 Introduction

With the rapid development of modern aerospace technology, hypersonic aircrafts are playing an important role in current and future flight missions. It is worth noting that the hypersonic aircrafts are facing various challenges, such as extreme operation conditions, diversified missions, intelligence requirements, integrated designs, flight safety, optimal performance, and other unpredictable harsh working environment. Among these challenges, the flight safety and successful mission execution capabilities of hypersonic aircrafts are the most significant issue [1]. For a hypersonic vehicle that operates under complicated and harsh flight conditions, it would usually suffer from actuator and sensor faults, structural damage and thrust fault [2]. Such failures can affect flight attitude and trajectory profile with degraded control performance. Notably, the structural damage and thrust fault frequently occur due to the high speed and flexible body of the aircraft. It will pose huge challenges to the control safety and flight mission accomplishment. In particular, the wing surface damage and inlet deformation will directly cause a sharp decline in flight capabilities and difficulty in performing flight missions. This would further make scramjet engine fail to ignite, and the aircraft will lose control and crash into the ground/ocean. Therefore, it is of great practical significance to ensure the hypersonic aircraft flight reliability under faulty conditions. To deal with the above-mentioned faults in flight, the fault detection and diagnosis (FDD) technique is an effective way for the aircraft to be quickly aware of the faults and respond to them with control reconfiguration for flight performance recovery or mission adjustment. As a cutting edge technique, artificial intelligence has been a promising way for handling FDD problems in recent years [3]. To be brief, the intelligent FDD for identifying structural damage and thrust faults of hypersonic aircrafts have become important to ensure safe and reliable flight in harsh and complex operation environments [4].

Note that the mainstream FDD methods can be roughly classified into three categories: model-based, data/signal processing-based, and knowledge-based methods [5]. The model-based approaches are suitable when the precise mathematical model of the system is known, including techniques such as observer-based, equivalent space-based, and parameter estimation-based methods [6]. For instance, Ramdani et al. [7] utilized a predictive-corrective approach to estimate the mixed state variables for fault diagnosis in complex aircraft propulsion systems, mitigating the challenge of state estimation. Zhai et al. [8] proposed a diagnostic method based on parameter separation and recombination techniques with regional segmentation analysis for nonlinear systems with multiple sensor faults. The main drawback of model-based FDD method is that it relies heavily on the precise mathematical model knowledge. In contrast, the signal processing-based FDD method does not require an exact mathematical model of the system. It mainly obtains the characteristic information of faults through signal processing technique [9]. Hao and Wang [10] proposed a FDD method for spacecraft attitude control

*Corresponding author: Tuo Han.

This work was supported by the National Natural Science Foundation of China under Grant 61960206011 and Grant 62203031; in part by the Zhejiang Provincial Natural Science Foundation of China under Grant LD22E050004 and LY24F030002; in part by the Beijing Natural Science Foundation under Grant 4242041; in part by the Fundamental Research Funds for the Central Universities; in part by the China Postdoctoral Science Foundation (2022M710312); and in part by the fellowship of China National Postdoctoral Program for Innovative Talents (BX20220370).

systems based on wavelet analysis, which is used to diagnose typical attitude control engine faults. As for the knowledge-based approach, it is applicable in situations where precise mathematical models and signal models of systems cannot be obtained, thus possessing advantages in the diagnosis of complex nonlinear system faults [11]. Deep learning, as an evolutional technique in the field of intelligent fault diagnosis, has received much attention in recent years [12]. The deep learning-based method aims to iteratively embed feature transformations and autonomously mine representative information hidden in massive raw data, and directly establish precise mapping relationships among the operational flight status of aircraft. Liu et al. [13] proposed a method for gearbox fault diagnosis using an improved Deep Boltzmann Machine (DBM) with computational analysis using real laboratory data. Olyaei et al. [14] proposed an aircraft FDD method using deep learning and image processing algorithms, which transformed sensor data into frequency domain for image processing, and thereby identifying faults.

Motivated by the strong adaptability and effectiveness of learning-based approach for FDD, this paper aims to design a learning-based data-driven FDD scheme for the structural damage and thrust fault identification of a hypersonic aircraft. The main task is to extract the flight characteristics under different faults for online failure prediction and classification with expected accuracy. Specifically, a data preprocessing method and a Deep Residual Autoencoder network (DRAE) are utilized to predict and classify the structure and thrust faults. To alleviate the vanishing gradient issue in training, a residual block is integrated in the encoder for efficient training. Extensive numerical simulations for a hypersonic aircraft flight model are conducted to verify the efficiency of the proposed method.

The article is organized as follows. Section 2 presents the basic modeling procedure for structural and thrust faults of hypersonic aircrafts. Section 3 introduces a network training and learning architecture based on DRAE for FDD of hypersonic aircrafts. Section 4 details the numerical simulation settings and presents the test results, and Section 5 concludes the paper.

2 Modeling and Problem Formulation

2.1 The Dynamic Model

For the hypersonic aircraft thrust, the reactive force result from the high-speed expulsion of gases within the engine. The thrust can be mathematically formulated through the following relation [15]:

$$P = m_c u_e + S_a \left(p_a - p_H \right) \tag{1}$$

where m_c represents the mass flow rate of the fuel consumed per unit time; u_e represents the average exit velocity of the gas from the nozzle; S_a represents the cross-sectional area of the engine nozzle; p_a represents the static pressure of the gas flow at the engine nozzle; p_H represents the atmospheric static pressure at a specified altitude.

The aerodynamic forces exerted on a hypersonic aircraft can be decomposed into the drag force X , lift Y , and lateral force Z . Their magnitudes are related to the dynamic pressure of the incoming flow and the characteristic area of the aircraft. The detailed relationship can be expressed as [15]:

$$\begin{cases} X = c_x qS \\ Y = c_y qS \\ Z = c_z qS \\ q = \dfrac{1}{2}\rho V^2 \end{cases} \tag{2}$$

where c_x , c_y , and c_z are drag, lift, and lateral force coefficients, respectively. q denotes the dynamic pressure, and S represents the reference area of the aircraft.

The aerodynamic moments acting on the aircraft can be decomposed along the body coordinate system into three components: M_x , M_y , and M_z , representing the rolling moment, yawing moment, and pitching moment, respectively. The aerodynamic moments can be expressed as [15]:

$$\begin{cases} M_x = m_x qSL \\ M_y = m_y qSL \\ M_z = m_z qSL \end{cases} \tag{3}$$

where m_x, m_y, m_z denote the non-dimensional scale factors, named the roll moment coefficient, yaw moment coefficient, and pitch moment coefficient, respectively; L is the reference length of the aircraft.

2.2 The Faults Model

This paper predominantly focuses on two critical fault models: structural damage and thrust faults of the aircraft.

The structural failure of an aircraft generally refers to damage to the fuselage, resulting in changes to the aerodynamic and structural parameters of the aircraft. For instance, changes in the lift-to-drag ratio will become worse due to the wing surface defects, which can further affect the aircraft's flight performance and stability.

The thrust system fault of an aircraft typically usually refers to malfunctions occurring in the aircraft's engines, consequently degrading the thrust power output. For instance, surge faults can result in diminished airflow and severe obstruction of the airflow channel, ultimately leading to undesirable thrust.

The models of faults considered in this paper are introduced below.

Structural damage. The occurrence of wing damage leads to a proportional decrease in both aerodynamic force and moment due to the broken and narrowed surface reference area of the aircraft.

$$S = \begin{cases} S_0, & t < t_f \\ kS_0, & t \geq t_f \end{cases} \tag{4}$$

where S_0 represents the reference area of the aircraft under healthy conditions, t_f represents the time when the fault occurs, and k is the loss-of-efficiency coefficient, which can be modeled as a randomly sampled scalar between 0 and 1.

Thrust fault. Considering the non-catastrophic failures for thrust degradation in aircraft thrust systems, this paper adopts the diminished gas ejection velocity resulting from engine failures, i.e., the surge fault, as the fault model for the thrust system.

$$u_{out}(t) = \begin{cases} u_{in}(t), & t < t_f \\ u_{in}(t) - \Delta u_f, & t \geq t_f \end{cases} \tag{5}$$

where $u_{in}(t)$ represents the desired gas ejection velocity, $u_{out}(t)$ denotes the actual gas ejection velocity, and Δu_f represents the gas velocity loss.

2.3 Uncertainty Modeling

To consider the complex flight operation conditions, uncertainties need to be modeled because of the time-varying mass, deviations of aerodynamic coefficients, and wind disturbances, and other relevant inner and external perturbations that are ignored in the modeling stage.

In this paper, the center of gravity deviation that denotes the differences between the actual center of gravity and the theoretical center of gravity of an aircraft. The deviation of the actual center of gravity from the theoretical center of gravity in the three directions of the airframe coordinate system is denoted as Δx , Δy , and Δz . The resultant specific disturbance moments can be expressed as follows:

$$\begin{aligned} \Delta M_{z_1} &= -C_N qS \cdot \Delta x, \Delta M_{y_1} = C_z qS \cdot \Delta x \\ \Delta M'_{z_1} &= -C_A qS \cdot \Delta y, \Delta M'_{y_1} = C_A qS \cdot \Delta z \\ \Delta M_{x_1} &= C_N qS \cdot \Delta z, \Delta M'_{x_1} = -C_z qS \cdot \Delta y \end{aligned} \tag{6}$$

where $\Delta M_{x_1}, \Delta M'_{x_1}, \Delta M_{y_1}, \Delta M'_{y_1}, \Delta M_{z_1}$,and $\Delta M'_{z_1}$ represent the disturbance moments of roll, yaw and pitch generated by the center of mass deviation. C_A, C_N , and C_z denote the axial force coefficient, normal force coefficient, and lateral force coefficient, respectively.

Considering the discrepancies between the actual aerodynamic parameters and the employed ones during flight, it becomes necessary to model the perturbed aerodynamic parameters. Specifically, random perturbations are introduced to the coefficients of lift, drag, and side force, as well as the three-channel aerodynamic moment coefficients, within predefined limits. Specifically,

$$\begin{cases} X' = (1+d_{c_x})c_x qS, M'_x = (1+d_{m_x})m_x qSL \\ Y' = (1+d_{c_y})c_y qS, M'_y = (1+d_{m_y})m_y qSL \\ Z' = (1+d_{c_z})c_z qS, M'_z = (1+d_{m_z})m_z qSL \end{cases} \tag{7}$$

where X', Y', Z', M'_x, M'_y and M'_z represent the perturbed aerodynamic forces and moments, $d_{c_x}, d_{c_y}, d_{c_z}, d_{m_x}, d_{m_y}$, and d_{m_z} denote the perturbation ratios.

Consider that the wind velocity will perform stochastic variations in both the wind magnitude and direction due to the complicated environmental factors and flight altitude and speeds. It is widely acknowledged that wind disturbances can influence both the angle of attack and the sideslip angle. Such wind disturbances will cause unpredictable perturbations in the angle of attack and sideslip angle, which can be formulated as:

$$\begin{aligned} \alpha_w &= -\arctan\frac{w\cos A\sin\theta}{V - w\cos A\cos\theta} \\ \beta_w &= \arctan\frac{w\sin A}{V} \end{aligned} \tag{8}$$

where w is the wind speed, A denotes the direction of the wind with respect to the aircraft's trajectory, V is the velocity of the aircraft, θ is the flight path angle, α_w represents the angle of attack caused by the wind and β_w represents the sideslip angle caused by the wind.

3 FDD Scheme for The Hypersonic Aircraft

As described in previous sections, the structural damages and thrust faults of hypersonic aircrafts usually manifest diverse and random characteristics. As an effective solution, the deep learning-based FDD methods have the capability to autonomously extract crucial structure and thrust faults information of hypersonic aircrafts from extensive flight data, unveil concealed relationships within the dataset, and effectively accomplish FDD tasks for the hypersonic aircraft.

3.1 Deep Autoencoder Design

The Deep Autoencoder (DAE) represents a neural network architecture frequently utilized for feature learning and dimensionality reduction. Functioning as an unsupervised learning method, its purpose is to acquire sophisticated representations of input data, while endeavoring to preserve essential features from the original data [16].

The operational environment of hypersonic aircrafts is characterized by extreme conditions, such as high velocity, temperature, and pressure variations. The DAE demonstrates robust performance under such varying conditions, making them suitable for consistent fault diagnosis across a range of flight scenarios [17].

The DAE mainly consists of two parts: encoder and decoder. The structure of the network can be represented as Fig.1 [18].

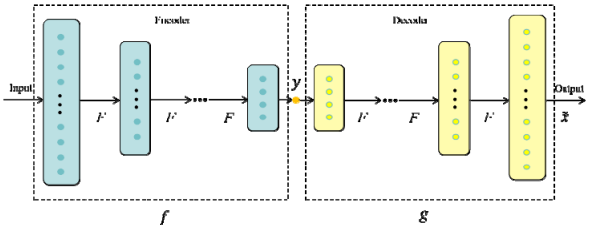

Fig.1 : The structure of the DAE network

The encoder component of DAE maps the input flight data including attitude, angular velocity, and other information into a lower-dimensional latent space. Comprising multiple hidden layers with a decreasing number of neurons in each layer, the encoder progressively compresses the input flight data. The ultimate layer of the encoder signifies the encoded or latent representation of the input [19]. Note that the hypersonic aircrafts generate complex, high-dimensional data. The DAE excels in encoding this high-dimensional data into a lower-dimensional space, effectively capturing the essential features necessary for FDD. This dimensionality reduction is critical in simplifying the complex data patterns associated with hypersonic flight. The encoding process can be expressed as follows:

$$x'_i = f(x_i) \tag{9}$$

where x_i is the sample in the input flight data x , f represents the encoding process, x'_i is the encoder output. The output encoding can be regarded as an abstract representation of the original flight data, capturing essential features and patterns inherent in the data.

The decoder segment undertakes the task of reconstructing the original input data from the encoded representation. The decoder translates the abstract, encoded representations back into a more interpretable form. This translation is essential for understanding the nature of the

detected faults and for communicating this information to engineers and decision-makers. In processing the data from hypersonic aircrafts, the decoder also plays a role in noise reduction and data cleaning. By learning to ignore irrelevant variations and noise in the data during the reconstruction process, the decoder enhances the accuracy and reliability of the FDD. The decoding process can be expressed as follows:

$$\tilde{x}_i = g(x_i') \tag{10}$$

where $\tilde{x}_i$ is the output of the decoder, g denotes the decoding process. The output decoding is the reconstruction of the original flight data. The primary objective of the decoder is to transform the low-dimensional encoding representation produced by the encoder back into high-dimensional data that is equivalent to the original flight data.

The training process of DAE relies on minimizing a loss function that quantifies the discrepancy between the input data and its corresponding reconstruction. The Mean Squared Error (MSE) metric is often selected for this purpose. MSE can be defined

$$MSE = (1/n)\sum \left\| x_i - \tilde{x}_i \right\|^2 \tag{11}$$

$$R = \arg\min L(x, \tilde{x}) \tag{12}$$

where n represents the number of flight samples, L denotes the loss function.

The flight data may exhibit anomalies subsequent to the structural or dynamic fault occurring in a hypersonic aircraft, and the DAE is particularly adept at identifying anomalies in data. By learning to reconstruct normal operational data, these networks can highlight deviations that indicate potential faults. In hypersonic aircrafts, where even small anomalies can lead to significant issues, the anomaly detection capability of the DAE is invaluable.

3.2 Residual Mechanism

The core idea underlying residual mechanisms is the introduction of residual or shortcut connections within deep neural networks. Unlike traditional deep networks where each layer directly learns a mapping from input to output, residual networks enable the learning of residual mappings, or residuals, which are then added to the original input to produce the final output. The mathematical model of a residual block can be presented as Fig.2 [20].

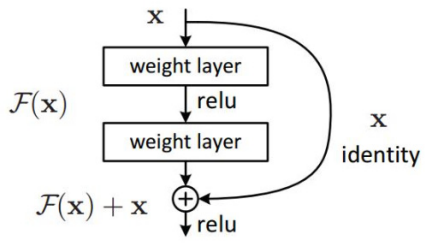

Fig.2 : The structure of the DAE network

Residual connections alleviate the vanishing gradient problem, which often hinders the training of deep networks. By introducing skip connections that allow gradients to flow easily through the FDD network, training deeper models becomes more feasible. As for the FDD of hypersonic aircrafts, deeper networks can capture more complex and subtle relationships in the data, which is crucial for identifying and diagnosing potential faults accurately. Networks equipped with residual mechanisms often exhibit improved convergence behavior. This is particularly advantageous in the aerospace domain, where the computational cost of training models is significant.

3.3 DRAE for FDD

As one of the mainstream algorithms of deep learning, DAE can independently extract valuable and differentiated features from high-dimensional data, enhance the effect of subsequent supervised learning, and is suitable for FDD. The network's data dimensionality reduction capabilities help process complex aircraft operating data and extract required fault characteristics. The residual connections allow the network to learn incremental updates of inputs, reduce the possibility of gradient disappearance, and are suitable for multi-hidden layer training of aircraft FDD networks. The FDD networks for aircrafts can process inputs from multiple sensors, some of which may be critical to identifying a specific fault. The residual connections enable direct paths for information flow from early layers to later ones. This property is particularly valuable for capturing subtle fault-related features. Therefore, the DRAE is used to extract the characteristics of flight data and mine the mapping relationship of various fault information on the flight status of the aircraft.

The FDD model consists of four parts: fault injection and data collection, data preprocessing, DAE unit based on residual mechanism (DRAE), output. The schematic of the FDD is shown in Fig.3. The details are as follows:

- Fault injection and data collection: Inject faults into the aircraft dynamics model, use a typical six-degree-of-freedom aircraft model to implement simulation and generate flight data. Timestamps are synchronized to maintain temporal consistency.
- Data preprocessing: The FDD networks are tasked with analyzing diverse sensor data streams to detect and classify potential faults in real-time. The effective data preprocessing is fundamental to ensure the network's robustness and diagnostic accuracy.
- DRAE: The DRAE network is mainly composed of an autoencoder network with residual blocks. The activation function is Rectified Linear Unit (ReLU). The specific network structure and parameters are given in section 4.

Output: Output from the last hidden layer in the DRAE network. The proposed DRAE model is shown in Algorithm 1.

Algorithm 1. The DRAE for hypersonic aircrafts

Input: The hypersonic aircraft flight data set containing information on structural and thrust faults, x

Output: Diagnosed fault categories (structure or thrust) for the input data x .

Process:

1. Data preprocessing:
   a. Normalize the input flight data x .
   b. Split the normalized data into training (x_{train}), and testing (x_{test}) sets.
2. Building the Deep Residual Autoencoder.
3. Training the Autoencoder using x_{train} .

4. Extracting Features and Classifier Training.
5. Fault Diagnosis:
   a. Extract features from x_{test} using the trained encoder.
   b. Employ the trained classifier to predict fault types (structure or thrust) based on these features.

End

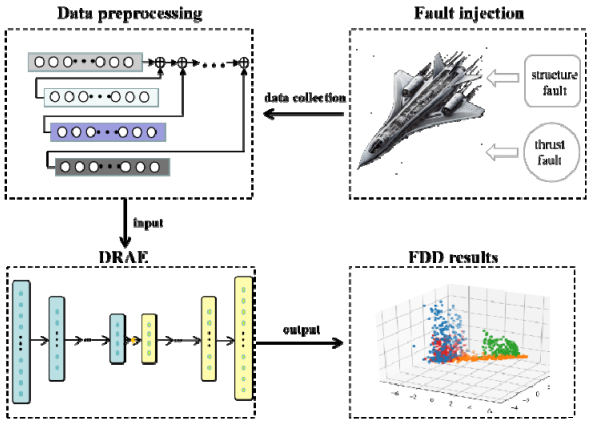

Fig.3 : Schematic of the FDD

4 Numerical Simulation

4.1 Fault Injection and Data Collection

In this paper, we employ a comprehensive six-degree-of-freedom nonlinear model for aircraft and investigate the effects of structural damage and thrust fault during the cruise phase. The aircraft's cruising altitude is set at 27 kilometers, and its flight velocity is 6 Mach.

The flight status consists of four scenarios: one normal condition(N) and three faulty conditions: 25% thrust fault (P25), 25% structural damage failure (S25), and a combination of both faults (C25).

4.2 Data Preprocessing

Prior to model training, the data needs to be filtered and pre-processed as the data collected contains time series with high dimensionality. Considering the limited data available from the aircraft sensors, 10 variables related to the aircraft structural damage and thrust fault are selected, as shown in Table 1. The aircraft status includes normal status (N) and multiple fault status (P25, S25, and C25), indicated by 0/1/2/3, respectively.

Table 1 : Variables related to the aircraft

Parameters	Unit
Pitch Angle	DEG
Yaw Angle	DEG
Roll Angle	DEG
Pitch Angle Rate	DEG/SEC
Yaw Angle Rate	DEG/SEC
Roll Angle Rate	DEG/SEC
Angle of Attack	DEG
Sideslip Angle	DEG
Flight Speed	M/SEC
Aircraft Status	0/1/2/3

To enable the diagnostic model to learn fault features, the data is segmented by means of a sliding window of length 10 and step size 1. Fig.4 shows how the sliding window splits.

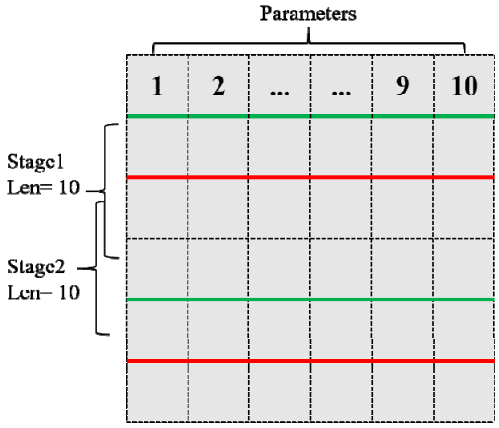

Fig.4 : The sliding window splitting method

Due to the limited computational resources for hypersonic aircrafts, efficient data processing should be adopted to achieve fast online FDD. Therefore, for multivariate time series, data splicing is used to achieve the fusion of multivariate series, and finally univariate data are obtained. Fig.5 shows how the data is spliced.

The dataset of the four states in IV.A is obtained, and then the data is preprocessed to get a total of 4000 sets of samples. The dataset is divided into training set and testing set in the ratio of 7 to 3.

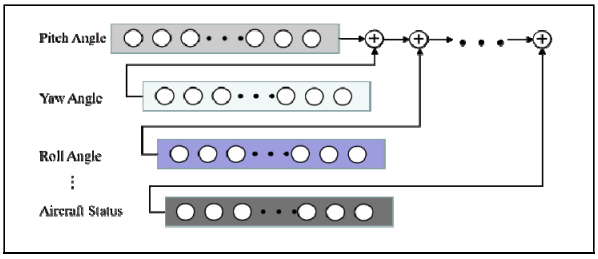

Fig.5 : Data splicing method

4.3 Results and Analysis

The established DRAE model mainly includes three parts: autoencoder, residual block, and classification layer with the structure shown in Table 2.

Table 2 : The structure of DRAE model

Layer	Structure
L1	Conv1D(3×32)
L2	Conv1D(3×64)
L3	Conv1D(3×128)
L4	Conv1D(3×128)
L5	Add (L1, L4)
L6	ConvTranspose1D
L7	ConvTranspose1D

L8	ConvTranspose1D
L9	Dense (4)

Therein, the Conv1D (3×32) represents a one-dimensional convolution layer, and its convolution kernel size is 1×3 with 32 channels, and ConvTranspose1D represents a transposed one-dimensional convolution layer. The prediction classification results of the DRAE model are shown in Fig.6.

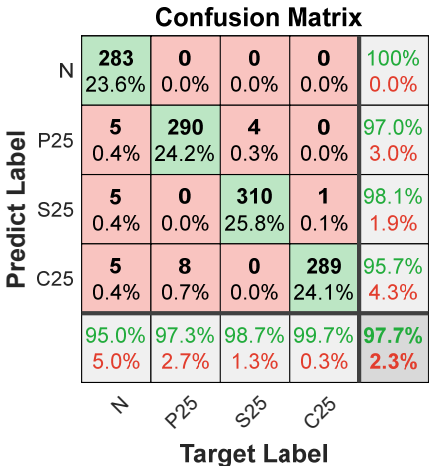

Fig.6 : The confusion matrix of output result

The confusion matrix shows the correctness of the classification for each case, where the columns represent the predicted labels and the rows represent the actual labels. C25 has the highest accuracy at 99.7%, while N has the lowest at 95%. This result may be attributed to the increased occurrence of data anomalies resulting from the interaction of structure and thrust faults and the influence of intricate working conditions. The final average diagnostic accuracy rate is 97.7%, which shows the effectiveness of the conducted method applied to the hypersonic aircrafts under structural and thrust faults.

5 Conclusion

This paper aims to classify the failure modes and failure mechanisms of hypersonic aircrafts with structure and thrust faults. Specifically, a data-driven intelligent FDD scheme is proposed for hypersonic aircrafts based on the DRAE network to predict and classify the structure and thrust faults. To alleviate the vanishing gradient issue, a residual block is integrated in the encoder for efficient training. The failure model of the aircraft is implemented using a six-degree-of-freedom nonlinear model of the aircraft. The preprocessed data is input into the constructed DRAE network for training and testing, and finally the accurate detection and classification of structural damage and thrust fault is achieved.

References

[1] Townend L H. Research and design for hypersonic aircraft[J]. Philosophical Transactions of the Royal Society of London. Series A: Physical and Engineering Sciences, 1991, 335(1637): 201-224.

[2] Zhang Y X, Xu J B, Xu F H, et al. Research on Influence of Aerodynamic force on the Aerodynamic heat for the Hypersonic Vehicle[J]. Applied Mechanics and Materials, 2012, 198: 207-211.

[3] Qin J, Wang L, Huang R. Research on fault diagnosis method of spacecraft solar array based on f-KNN algorithm[C]//2017 Prognostics and System Health Management Conference (PHM-Harbin). IEEE, 2017: 1-4.

[4] Xu B, Shi Z K. An overview on flight dynamics and control approaches for hypersonic vehicles[J]. Sci. China Inf. Sci., 2015, 58(7): 1-1

[5] Frank P M. Fault diagnosis in dynamic systems using analytical and knowledge-based redundancy: A survey and some new results[J]. automatica, 1990, 26(3): 459-474.

[6] Henry D, Bornschlegl E, Olive X, et al. A model-based solution for fault diagnosis of thruster faults: Application to the rendezvous phase of the Mars Sample Return mission[J]. Progress in Flight Dynamics, Guidance, Navigation, Control, Fault Detection, and Avionics, 2013, 6: 423-442.

[7] Ramdani N, Travé-Massuyès L, Jauberthie C. Mode discernibility and bounded-error state estimation for nonlinear hybrid systems[J]. automatica, 2018, 91: 118-125.

[8] Zhai D, An L, Li X, et al. Adaptive fault-tolerant control for nonlinear systems with multiple sensor faults and unknown control directions[J]. IEEE transactions on neural networks and learning systems, 2017, 29(9): 4436-4446.

[9] Guo Y, Liu T W, Na J, et al. Envelope order tracking for fault detection in rolling element bearings[J]. Journal of Sound and Vibration, 2012, 331(25): 5644-5654.

[10] Hao H, Wang N H. Research on wavelet analysis-based fault diagnosis for attitude control subsystem of spacecraft[J]. Aerospace Control, 2005, 5(1): 74-79.

[11] Isermann R. Fault-diagnosis systems: an introduction from fault detection to fault tolerance[M]. Springer Science & Business Media, 2005.

[12] Ren J, Ren R, Green M, et al. A deep learning method for multiple faults detection and classification of unmanned ground vehicles[C]//2019 Computer Science and Information Technologies (CSIT). IEEE, 2019: 108-111.

[13] Liu D, Wang Q, Tao J, et al. Fault Diagnosis Method Based on Improved Deep Boltzmann Machines[C] 2018 IEEE 7th Data Driven Control and Learning Systems Conference (DDCLS), Enshi, IEEE, 2018:458-462.

[14] Olyaei M H, Jalali H, Noori A, et al. Fault Detection and Identification on UAV System with CITFA Algorithm Based on Deep Learning[C] Iranian Conference on Electrical Engineering, Mashhad, IEEE, 2018:988-993.

[15] Schmidt D K. Modern flight dynamics[M]. New York: McGraw-Hill, 2012.

[16] Wu J Y, Wu M, Chen Z, et al. Degradation-aware remaining useful life prediction with LSTM autoencoder[J]. IEEE Transactions on Instrumentation and Measurement, 2021, 70: 1-10.

[17] He Z, Shao H, Ding Z, et al. Modified deep autoencoder driven by multisource parameters for fault transfer prognosis of aeroengine[J]. IEEE Transactions on Industrial Electronics, 2021, 69(1): 845-855.

[18] Chen M, Li Z, Lei X, et al. Unsupervised Fault Detection Driven by Multivariate Time Series for Aeroengines[J]. Journal of Aerospace Engineering, 2023, 36(2): 04022129.

[19] Ma M, Sun C, Chen X. Deep coupling autoencoder for fault diagnosis with multimodal sensory data[J]. IEEE Transactions on Industrial Informatics, 2018, 14(3): 1137-1145.

[20] Zhao M, Zhong S, Fu X, et al. Deep residual shrinkage networks for fault diagnosis[J]. IEEE Transactions on Industrial Informatics, 2019, 16(7): 4681-4690.

Proceedings of the 3rd Conference on Fully Actuated System Theory and Applications
May 10-12, 2024, Shenzhen, China

Intelligent Decision-Making for Maintenance Assurance throughout the Lifetime of Helicopter Swarms

Yanan Wang[1], Ke Zhang[1,2], Bin Jiang[1,2]

1. College of Automation Engineering, Nanjing University of Aeronautics and Astronautics, Nanjing 211106, P. R. China

2. National Key Laboratory of Helicopter Aeromechanics, Nanjing 211106, P. R. China

E-mail: kezhang@nuaa.edu.cn

Abstract: The utilization of intelligent algorithms for decision-making and optimization in the collaborative maintenance of helicopter swarm addresses the challenge of maximizing the reliability of swarm task execution under limited maintenance resources. Consequently, optimization of maintenance decisions has become a focal point of research both domestically and internationally. The problem of allocating maintenance resources under resource constraints, known as selective maintenance, can naturally be modeled as a Markov decision process. For solving this problem, employing multi-objective optimization algorithms is a logical choice. However, due to the large number of optimization decision variables involved in this practical problem, traditional algorithms may encounter difficulties. Reducing the search space of decision variables can alleviate this challenge. With this in mind, this study proposes a multi-objective optimization algorithm based on fuzzy theory. Finally, we validate the feasibility of the model and intelligent decision-making solutions through an illustrative example.

Key Words: Selective Maintenance, Maintenance Optimization, Reliability, Helicopter Swarm, Fuzzy Evolution, Multi-objective Optimization

1 Introduction

The advancement of science and technology has significantly enhanced the effectiveness and efficiency of swarm cooperation systems composed of multiple helicopters [1]. However, the numerical advantage and economies of scale afforded by helicopter swarms also pose considerable challenges for collaborative maintenance. In complex and dynamic battlefield environments, helicopter swarms may encounter various uncertainties and emergencies, making it difficult to devise or adapt maintenance strategies. Therefore, developing optimized collaborative maintenance decision-making schemes tailored to helicopter swarms is imperative for achieving rapid, simple, and cost-effective maintenance solutions while minimizing maintenance downtime. Such research endeavors aim to reduce the maintenance costs and duration of helicopter swarms while maximizing their operational efficiency [2].

Maintenance strategists, operating within finite maintenance resources, selectively maintain certain components within the entire system to optimize system performance under specified conditions. Rice [3] first introduced the concept of selective maintenance in 1998 and developed corresponding reliability mathematical models for binary serial-parallel systems. These models account for maintenance personnel's maintenance behaviors on the system during task intervals to maximize the system reliability for the next task. Due to the limited ability of binary systems to reflect the complexity of maintenance activities, researchers have shifted their focus to the selective maintenance planning problem for multi-state systems [4–9]. Wang et al. [10] utilized genetic algorithms to solve a selective maintenance model for large-scale equipment under sequential task conditions. Liu et al. [11] established a combinatorial optimization model and employed an enhanced ant colony algorithm to search for the optimal solution set. Tian et al. [12] developed a multi-objective selective maintenance sequence planning model based on hierarchical maintenance tree diagrams and improved the multi-objective gravitational search algorithm to solve the multi-objective optimization model.

Helicopter swarms find widespread applications across various domains, yet research on the maintenance of helicopter swarm equipment remains scarce. In addition, current maintenance decision-making approaches often depend on conventional multi-objective optimization algorithms. However, considering the complexity of swarm equipment with numerous components, this approach tends to require significant time investment, thereby hindering maintenance timeliness. Building upon prior research, this paper proposes a maintenance model tailored for helicopter swarm equipment. Leveraging the characteristics of the maintenance behavior of helicopter swarms, a mixed series-parallel system is employed to characterize the swarm, while a Markov decision process is employed to depict the maintenance process. To address the multi-objective decision optimization problem, a fuzzy-based genetic algorithm is designed, which exhibits advantages over traditional algorithms in terms of convergence, distribution, and diversity.

2 Problem Formulation and System Model

2.1 System Descriptions and Assumptions

In this section, we propose a cooperative maintenance model of helicopters in the form of Markov decision chains. Each helicopter is composed of various types and quantities of components, arranged in different forms, such as series and parallel connections. In traditional studies, components are typically considered to be binary-state, that is, either functional or faulty. However, in real-world scenarios, components are often characterized by multiple states, deteriorating from a perfect state to a faulty state. Maintenance

This work is supported by Aeronautical Science Foundation of China (20220057052001), National Natural Science Foundation of China under Grants (62173180), National Key Laboratory Foundation of Helicopter Aeromechanics (2023-HA-LB-067-04), Qing Lan Project of Jiangsu Province of China, in part by the Fundamental Research Funds for the Central Universities under Grants (NE2022002, NC2022003).(Corresponding author: Ke Zhang)

activities occur exclusively during task downtime intervals, with no possibility of performing maintenance actions while the helicopters are engaged in task execution, as in Fig. 1.

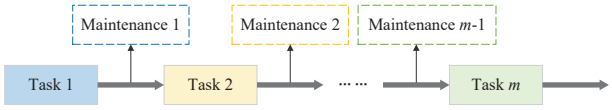

Fig. 1: Maintenance task execution diagram

Complex helicopters typically consist of numerous components. Analyzing from the perspectives of reliability and component service life, the helicopter system can be viewed as a complex hybrid series-parallel system, as in Fig. 2. A helicopter swarm is formed by serially connecting Q helicopters, and the i th$(i = 1, 2, ..., Q)$ helicopter consists of Q_i modules. Each module serves different functions, such as the power module, communication module, payload module, etc. The w th module of the i th helicopter is further composed of Q_{iw} components, and the j th$(j = 1, 2, ..., Q_{iw})$ component in the w th module of the i th helicopter is denoted as C_{iwj}.

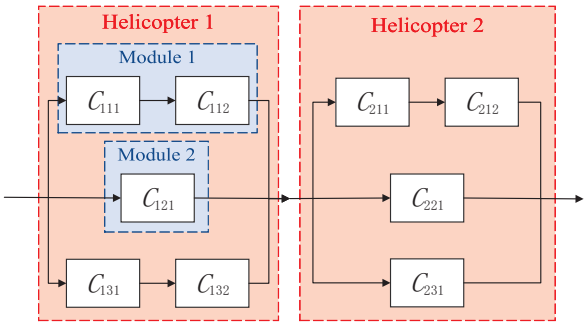

Fig. 2: Series-parallel hybrid system

In addition, r_{iwj} represents the reliability of component C_{iwj}, assuming that the reliability of component follows the Weibull distribution with scale parameter η and shape parameter β. Thus, the total quantity of the helicopter components QC is given by

$$QC = \sum_{i=1}^{Q} \sum_{w=1}^{Q_i} \sum_{j=1}^{Q_{iw}} C_{iwj} \tag{1}$$

Consider a component within a helicopter system that can exist in multiple states $S(k) = [S_{111}(k), ..., S_{iwj}(k)] \in S, k = 1, 2, ..., K$ at task k. The state vector denotes the components' states in each helicopter after the maintenance k, which happens in break k during the task k and task $k+1$. Analogously, we use $\bar{S}(k) = \left[\bar{S}_{111}(k), ..., \bar{S}_{iwj}(k)\right] \in \bar{S}$ to refer to the components' states after the task k without any maintenance operations.

Let $\left\{s^0_{iwj}(k), s^1_{iwj}(k), ..., s^{L-1}_{iwj}(k)\right\} \in S_{iwj}(k)$ or $\left\{\bar{s}^0_{iwj}(k), \bar{s}^1_{iwj}(k), ..., \bar{s}^{L-1}_{iwj}(k)\right\} \in \bar{S}_{iwj}(k)$ represents the state of a component, i.e. the performance of the component. When the component state is $s^0_{iwj}(k)$ or $\bar{s}^0_{iwj}(k)$, it indicates that the component has completely failed. On the contrary, a state of $s^{L-1}_{iwj}(k)$ or $\bar{s}^{L-1}_{iwj}(k)$ represents the component being in perfect. Commencing from the perspective of practical implementation, a performance threshold denoted as $s^{tr}_{iwj}(k)$ exists. When the state performance of a component falls below this threshold, the component is deemed to be in a fault condition, thereby impinging upon the operation of the overall helicopter system. The range from $s^{tr}_{iwj}(k)$ to $s^{L-1}_{iwj}(k)$ signifies that the component has experienced some performance degradation but is still functional.

Let the action vector denote the integer variables corresponding to the maintenance strategies for all components in task k. Additionally, $\mathbf{A}(k) = [a_{111}(k), ..., a_{iwj}(k)]$, where $a_{iwj}(k)$ denotes the maintenance strategy applied to the iwj th component of the k th task.

Over time, the effective age of helicopter components incrementally accumulates during the execution of tasks. The augmentation of effective age implies the degradation of component performance. For each component, the probability of its performance state at a given effective age t is calculated as $p_{iwj,l,k} = P\left\{S_{iwj}(k) = s^l_{iwj}(k)\right\}$ or $p_{iwj,l,k} = P\left\{\bar{S}_{iwj}(k) = \bar{s}^l_{iwj}(k)\right\}$. The process of depicting the degradation of component performance states as a Markov process is illustrated in the Fig. 3, where $\mu_{l_1,l_2,iwj,k}$ means the intensity transiting from performance state l_1 to l_2.

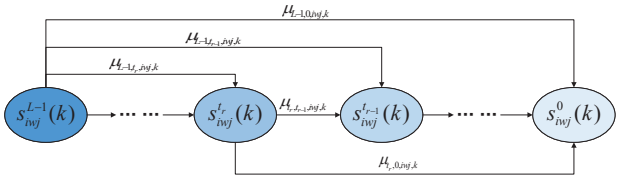

Fig. 3: The degradation transition of the iwj th component state in the k th task

2.2 System Reliability

The degradation of the multi-state element is postulated to adhere to the non-homogeneous continuous-time Markov chain (NHCTMC). Employing recursion, we resolve the Chapman-Kolmogorov's (C-K) forward equation to derive the time-dependent state probabilities for each constituent element within the system

$$p_{iwj,l,k} = \begin{cases} exp\left(\int_0^t \sum_{i=0}^{x-1} \mu_{x,i,iwj,k}(s)ds\right), x = L-1 \\ \sum_{i=x+1}^{L-1} \int_0^t p_{iwj,i,k}(\tau_{L-1})\mu_{i,x,iwj,k}(\tau_{L-1}) \\ exp\left(-\int_{\tau_{L-1}}^t \mu_{x,x,iwj,k}(s)ds\right) d\tau_{L-1}, \\ otherwise \end{cases} \tag{2}$$

Subsequently, the determination of the system-wide state probabilities is executed through the application of the Laplace transform method [13]

$$u_{iwj,k}(t) = \sum_{l=0}^{s^{L-1}_{iwj}(k)} p_{iwj,l,k}(t) \cdot z^{s^l_{iwj}(k)} \tag{3}$$

Assuming that the intricate helicopter system is equivalent to a complex hybrid series-parallel system, amalgamating the characteristics of both series and parallel systems.

Given the manifold nature of the system configurations, two fundamental operators are employed to represent series(ξ_s) and parallel(ξ_p) configurations, respectively [14].

In the context of a series structure, the component with the minimal capacity serves as the bottleneck for the entire system. Considering that all components within the w th module of the i th helicopter are interconnected serially during the k th task, its u-function is delineated as follows

$$\begin{aligned} U_{iw,k}(t) &= \xi_s\left(u_{iw1,k}(t), u_{iw2,k}(t), ..., u_{iwQ_{iw},k}(t)\right) \\ &= \sum_{l_1=0}^{L-1} \cdots \sum_{l_{Q_{iw}}=0}^{L-1} p_{iw1,l_1,k} \cdots p_{iwQ_{iw},l_{Q_{iw}},k}(t) \\ &\quad \times z^{min\left(s_{iw1}^0(k),\ldots,s_{iwQ_{iw}}^{L-1}(k)\right)} \\ &= \sum_{l=0}^{L\cdot Q_{iw}} p_{iw,l,k}(t) \cdot z^{s_{iw}^l(k)} \end{aligned} \tag{4}$$

In the scenario where each module is interconnected in a parallel configuration within the internal structure of the i th helicopter system, the aggregate capacity of the entire system is the summation of the capacities of all individual components, and its u-function is expressed as follows

$$\begin{aligned} U_{i,k}(t) &= \xi_p\left(U_{i1,k}(t), U_{i2,k}(t), ..., U_{iQ_i,k}(t)\right) \\ &= \sum_{l_1=0}^{L-1} \cdots \sum_{l_{Q_i}=0}^{L-1} p_{i1,l_1,k} \cdots p_{iQ_i,l_{Q_i},k}(t) \\ &\quad \times z^{\left(s_{i1}^0(k)+\cdots+s_{iQ_i}^{L-1}(k)\right)} \\ &= \sum_{l=0}^{L\cdot Q_i} p_{i,l,k}(t) \cdot z^{s_i^l(k)} \end{aligned} \tag{5}$$

From the perspective of helicopter swarm maintenance planning, each helicopter is interconnected in a series configuration during the k th task. The u-function is defined as follows

$$\begin{aligned} U_k(t) &= \xi_s\left(U_{1,k}(t), U_{2,k}(t), ..., U_{Q,k}(t)\right) \\ &= \sum_{l_1=0}^{L-1} \cdots \sum_{l_Q=0}^{L-1} p_1, l_1, k \cdots p_Q, l_Q, k(t) \\ &\quad \times z^{min\left(s_1^0(k),\ldots,s_Q^{L-1}(k)\right)} \\ &= \sum_{l=0}^{L\cdot Q_i} p_{l,k}(t) \cdot z^{S^l(k)} \end{aligned} \tag{6}$$

Upon obtaining the performance level and probability distribution, the system reliability can be computed. As the system ages over time, it is crucial to ensure that its performance remains above the performance threshold PT_k throughout the task duration. Fig. 4 demonstrates that the states satisfy the specified requirement. For task k, assuming $S(k)$ follows a Markov process and represents the required demand level, its reliability $R(k)$ is defined as $R_k(\mathbf{A}(k)) = Pr\{S(k) \geq PT_k\}$.

2.3 Component Age Reduction Model

Introducing the *Kijima* II imperfect maintenance model to simulate the maintenance process, this model is utilized to

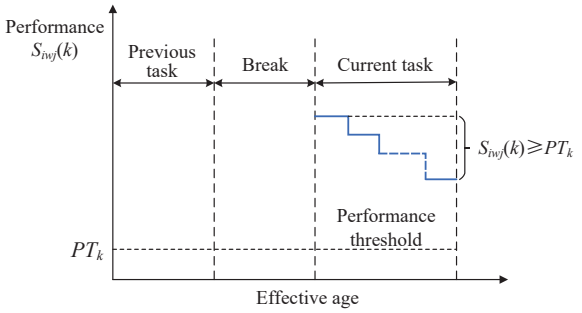

Fig. 4: Performance threshold requirements during task execution

depict the age deterioration during the execution of tasks by a swarm of helicopters [15]. By the *Kijima* II model, it is discerned that

$$t_{iwj}(k) = \lambda_{iwj} \cdot \bar{t}_{iwj}(k) \tag{7}$$

where $t_{iwj}(k)$ represents the effective age of the component after undergoing imperfect maintenance; $\bar{t}_{iwj}(k)$ denotes the effective age of the component after completing the k th task; λ_{iwj} signifies the effective age regression factor corresponding to the k th maintenance action, reflecting the maintenance effectiveness. Based on practical observations, it is established that replacement maintenance is performed when $\lambda_{iwj} = 0$, as

$$t_{iwj}(k) = 0 \tag{8}$$

and no maintenance action is undertaken when $\lambda_{iwj} = 1$. The effective age is given by

$$t_{iwj}(k) = \bar{t}_{iwj}(k) \tag{9}$$

a smaller value of λ_{iwj} corresponds to a favorable maintenance outcome, as illustrated in Figure. 5.

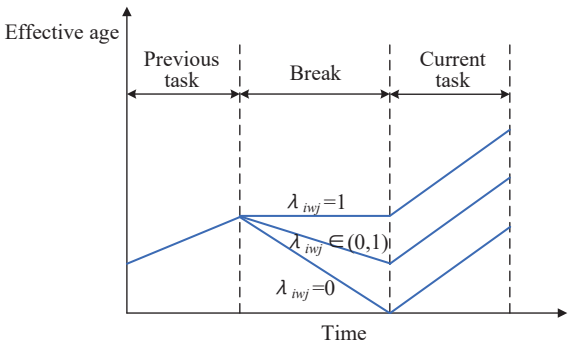

Fig. 5: Effective age difference under three maintenance policies

The calculation method for the effective age regression factor is provided in the reference [16]

$$\lambda_{iwj} = 1 - \left(\frac{C_{iwj}}{C_{iwj}^{rm}}\right)^{\frac{1}{m_{iwj}}} \tag{10}$$

where C_{iwj} represents the maintenance costs allocated to the component after the completion of the k th task; C_{iwj}^{rm} denotes the cost incurred for conducting replacement maintenance on components, representing the upper limit of maintenance cost. Additionally, m_{iwj} is a characteristic constant associated with the inherent attributes of the component. The greater the value of m_{iwj}, the more effective it is in maintaining elements with lower cost.

2.4 System Cost

While preventive maintenance is the most effective strategy for enhancing system reliability, it is also associated with the highest cost. The system cost for task k is defined as follows

$$C_k(\mathbf{A}(k)) = \sum_{k=1}^{K} \sum_{i=1}^{Q} \sum_{w=1}^{Q_i} \sum_{j=1}^{Q_{iw}} \left[c_{iwj}^{k} \left(a_{iwj} \right) + c_{iwj}^{0}(k) \right] \tag{11}$$

where $c_{iwj}^{k}\left(a_{iwj}\right)$ denotes the cost incurred from performing maintenance task k on component C_{iwj} incurred when executing maintenance task, where $c_{iwj}^{0}(k)$ represents the fixed cost associated with activities such as dismantling and installation.

3 Helicopter Swarm Maintenance Decision

3.1 Motivation

Considering the practicalities of helicopter swarm maintenance, a significant number of components are involved in maintenance operations. This results in a vast decision space, posing considerable challenges for problem-solving, including computational burden and precision of solutions. To address this issue, we propose a multi-objective optimization algorithm based on fuzzy theory (FMOA). The utilization of fuzzy techniques will reduce the search space of solutions, thereby enhancing the speed and accuracy of the solution process.

3.2 Multi-objective Optimization Problem

In mathematical terms, a Multi-Objective Optimization Problem (MOP) is defined as

$$\begin{aligned} \min \quad & C_k(\mathbf{A}(k)) \\ \max \quad & R_k(\mathbf{A}(k)) \\ \text{subject to} \quad & C_k(\mathbf{A}(k)) < CT \\ & R_k(\mathbf{A}(k)) > RT \\ & k = 1, 2, ... \end{aligned} \tag{12}$$

where $\mathbf{A}(k) = [a_{111}(k), ..., a_{iwj}(k)]$ represents an QC-dimensional decision vector derived from the decision space. $C_k(\mathbf{A}(k))$ and $R_k(\mathbf{A}(k))$ denotes the objective function of the optimization problem, where minimizing or maximizing its value is our optimization objective. Additionally, the decision space must adhere to relevant constraints. In the presence of multiple objectives, a solution may excel in one objective while performing poorly in others, due to conflicts and incomparability among objectives. Such solutions, which cannot be improved in any one objective without compromising at least one other objective, are termed non-dominated solutions or Pareto solutions.

3.3 Fuzzy Theory

A fuzzy set is a mathematical concept that extends the traditional notion of a set by allowing elements to have degrees of membership rather than strictly belonging or not belonging. A membership function, in the context of fuzzy sets, is a mathematical function that assigns a degree of membership to each element of a set. It quantifies the extent to which an element belongs to the fuzzy set, indicating its level of membership on a continuous scale.

3.4 Proposed Framework

The proposed algorithm 1 consists of two main phases: the fuzzy optimization phase and the precise optimization phase. In the first phase, the solution space undergoes fuzzy processing after optimization operations. In the second phase, optimization operations are applied to the suboptimal solution space obtained at the end of the first phase.

Algorithm 1 Framework of the proposed FMOA

Require: N(population size), MAX(maximum iteration number), $Proportion$(the proportion of the fuzzy optimization phase in the entire phase), Vel
Ensure: $\bar{P}$(Final population)

```
Initializing the population P
while Number of Iterations ≤ MAX do
    if Number of Iterations ≤ Proportion then
        P' ← Fuzzy Optimization Operation(P)
    else if Number of Iterations > Proportion then
        P' ← Precise Optimization Operation(P)
    end if
    P' ← Offspring(P, P')
end while
```

In the precise optimization phase, NSGA [17] algorithm is employed as a method for addressing multi-objective optimization problems. A detailed explanation of the fuzzy optimization phase will be provided in the next subsection. Offspring operation *offspring(P,P')* simulates the process of natural evolution by performing operations such as selection, crossover, and mutation on newly generated action space vectors and old action space vectors to produce new action space vectors.

3.5 The Fuzzy Optimization Phase

In the fuzzy optimization phase, the rationale behind dividing the entire fuzzy evolution phase into multiple fuzzy sub-phases with decreasing degrees of fuzzification is to progressively enhance the precision of the algorithm's solution. The mathematical delineation of the method for partitioning fuzzy evolutionary sub-phases is as follows

$$S = \left\lfloor \sqrt{\frac{2 \cdot Proportion}{Vel}} \right\rfloor \tag{13}$$

$$Sub(n) = Vel \cdot (S \cdot n - \frac{n^2}{2}), n = 1, 2, ..., S \tag{14}$$

where S represents the number of sub-phases; $Sub(n)$ represents the accumulated step length of the n th fuzzy sub-phases; Vel denotes the rate of progression across sub-phases.The difference between $Sub(n)$ and $Sub(n-1)$ represents the step length of the n th fuzzy sub-phases.

The described procedure divides the entire fuzzy optimization phase into multiple fuzzy sub-phases. The purpose is to reduce the fuzziness level of the original action space vector, thereby enhancing the diversity and accuracy of the solutions. In the n th fuzzy sub-phase, the following operations will be performed

$$\phi_i^1 = \left\lfloor 10^n \cdot A^i(k) \right\rfloor \cdot 10^n \tag{15}$$

$$\phi_i^2 = \left\lceil 10^n \cdot A^i(k) \right\rceil \cdot 10^n \tag{16}$$

$$\mu_{\widetilde{F}_1}(A^i(k)) = \frac{1}{A^i(k) - \phi_i^1} \tag{17}$$

$$\mu_{\widetilde{F}_2}(A^i(k)) = \frac{1}{\phi_i^2 - A^i(k)} \tag{18}$$

$$\widetilde{A}^i(k) = \begin{cases} \phi_i^1 & ,\mu_{\widetilde{F}_1}(A^i(k)) > \mu_{\widetilde{F}_1}(A^i(k)) \\ \phi_i^2 & ,\mu_{\widetilde{F}_1}(A^i(k)) < \mu_{\widetilde{F}_1}(A^i(k)) \\ \text{random}(\phi_i^1, \phi_i^2) & ,\mu_{\widetilde{F}_1}(A^i(k)) = \mu_{\widetilde{F}_1}(A^i(k)) \end{cases} \tag{19}$$

where $A^i(k)$ represents the i th value in the original action space vector; $\widetilde{A}^i(k)$ represents the i th value in the fuzzified action space vector. ϕ_i^1 and ϕ_i^2 denote the fuzzy target values of $(A^i(k))$, where $A^i(k)$ is either fuzzified into ϕ_i^1 or ϕ_i^2; $\mu_{\widetilde{F}_1}(A^i(k))$ and $\mu_{\widetilde{F}_2}(A^i(k))$ represent the membership function values of $A^i(k)$ in fuzzy sets $\widetilde{F}_1$ and $\widetilde{F}_2$, respectively.

4 Computational Results

To validate the proposed model and algorithms for helicopter swarm maintenance decision-making, numerical simulations were conducted for this problem to minimize maintenance costs under constraints on system reliability.

This study focuses on a helicopter swarm system with reconnaissance and strike capabilities. The system comprises two types of helicopters: two reconnaissance and four attack helicopters, totaling six helicopters. The reconnaissance helicopters are responsible for real-time surveillance and target identification in the designated area, while the attack helicopters are tasked with precise targeting and destruction of the identified targets. The parameters of the reconnaissance helicopters are presented in Table 1, and the parameters of the attack helicopters are presented in Table 2.

Table 1: Reconnaissance-type helicopter related parameters

Component	c_{iwj}^k	c_{iwj}^0	η_{iwj}	β_{iwj}
C_{i11}	1	1.5	20	3
C_{i12}	0.5	1.2	30	2.5
C_{i13}	3	4	26	2.6
C_{i21}	5	5.5	26	1
C_{i22}	7	8.5	21	2.5
C_{i23}	6	8	31	3.1
C_{i24}	3	5.5	16	2.4
C_{i31}	3	4.5	14	2
C_{i32}	1	1.1	17	3.2
C_{i33}	2	2.6	21	2
C_{i34}	1	2.3	25	2.6
C_{i41}	0.8	1	26	2.6
C_{i42}	1	1.5	26	2.5

Table 2: Attack-type helicopter related parameters

Component	c_{iwj}^k	c_{iwj}^0	η_{iwj}	β_{iwj}
C_{i11}	1	1.5	20	3
C_{i12}	0.5	1.2	30	2.5
C_{i13}	3	4	26	2.6
C_{i21}	5	5.5	26	1
C_{i22}	7	8.5	21	2.5
C_{i23}	6	8	31	3.1
C_{i24}	3	5.5	16	2.4
C_{i31}	3	4.5	14	2
C_{i32}	1	1.1	17	3.2
C_{i33}	2	2.6	21	2
C_{i34}	1	2.3	25	2.6
C_{i41}	1	1.5	26	2.5
C_{i42}	0.8	1.2	15	2.7
C_{i43}	2	2.5	13	2.9

The algorithm in this study is configured as follows: the initial population size is set to 90, with a maximum evaluation limit of 10,000 iterations. Besides, the availability of finite resources CT is 100, and the system reliability threshold RT is 0.85. The number of tasks K is set to 5.

The helicopter swarm consists of 6 helicopters and 82 components. Given the problem, the size of the solution space is $7^{82} + 4^{82} \approx 2 \times 10^{89}$, making an exhaustive search infeasible. However, with MATLAB 2023a installed and an Intel i5-12400F processor, employing traditional evolutionary algorithms would consume approximately 30 minutes of computational time. Utilizing intelligent optimization algorithms to solve this model is a more rational choice.

The maintenance model established in this study is solved using the conventional algorithm NSGA [18] and the proposed algorithm FMOA, respectively, with the runtime summarized in Table 3. The proposed algorithm in this paper enables faster decision-making for the maintenance model, which is highly effective in practical application scenarios.

Table 3: The execution time under different algorithms

Algorithm	NSGA	FMOA
Runtime(min)	29.5	20.7

Specifically, the solutions obtained for all tasks are presented: $\{R_1, C_1\} = \{0.94, 98.2\}$ for task 1; $\{R_2, C_2\} = \{0.93, 97.4\}$ for task 2; $\{R_3, C_3\} = \{0.9, 94.9\}$ for task 3; $\{R_4, C_4\} = \{0.88, 90\}$ for task 4; $\{R_5, C_5\} = \{0.92, 98.9\}$ for task 5.

5 Conclusion

In this paper, we propose an intelligent decision-making solution for helicopter swarm maintenance based on fuzzy logic principles and multi-objective optimization algorithms. Since maintenance practices occur during task intervals, the maintenance process is modeled as a Markov decision process. A fuzzy-based intelligent decision optimization algorithm is proposed and designed to achieve intelligent decision-making under the Markov decision process. The effectiveness of our model and algorithm is validated through numerical simulations. Future work will focus on further model development for maintenance and exploring solution methods for similar problems.

References

[1] Chen Yuheng, Chen Jinchao, and Chen Xuecong. Cooperative task allocation of UAV cluster based on improved greedy algorithm[J]. Aeronautical Science & Technology, 2022, 33(4): 13–18.

[2] Zhang Baozhen, Wang Ping. Recent development of aircraft PHM technology and problems and challenges encountered in the application on F-35[J]. Aeronautical Science & Technology, 2020, 31(07): 18–26.

[3] Rice W, Cassady C,and Nachlas J. Optimal maintenance plans under limited maintenance time[A]. Proceedings of the seventh industrial engineering research conference[C]. 1998: 1–3.

[4] Chen Chujie, Liu Yu, and Huang Hongzhong. Optimal load distribution for multi-state systems under selective maintenance strategy[A]. 2012 International conference on quality, reliability, risk, maintenance, and safety engineering[C]. IEEE, 2012: 436–442.

[5] Ali I, Hasan S S. Bi-criteria optimization technique in stochastic system maintenance allocation problem[J]. American Journal of Operations Research, 2013, 3(1): 17-29.

[6] Zhang Ke, Jiang Bin, Shi Peng and Xu Jinfa. Analysis and design of robust H fault estimation observer with finite-frequency specifications for discrete-time fuzzy systems. IEEE Transactions on Cybernetics, 2015, 45(7): 1225-1235.

[7] Cuong D. Dao, Ming J. Zuo. Selective maintenance of multi-state systems with structural dependence[J]. Reliability engineering & system safety, 2017, 159: 184–195.

[8] Xu Yue, Pi Dechang, Wu Zhiyuan, et al. Hybrid discrete differential evolution and deep Q-network for multitask selective maintenance[J]. IEEE Transactions on Reliability, 2022, 71(4): 1501–1512.

[9] Zhang Ke, Jiang Bin, and Shi Peng. Adjustable parameter-based distributed fault estimation observer design for multi-agent systems with directed graphs. IEEE Transactions on Cybernetics, 2017, 47(2): 306-314.

[10] Wang Shaohua, Zhang Shixin, Li Yong, et al. Research on selective maintenance decision-making method of complex system considering imperfect maintenance[J]. Acta Armamentarii, 2018, 39(6): 1215–1224.

[11] Liu Yu, Chen Yiming, and Jiang Tao. On sequence planning for selective maintenance of multi-state systems under stochastic maintenance durations[J]. European Journal of Operational Research, Elsevier, 2018, 268(1): 113–127.

[12] Tian Guangdong, Zhang Lele, Fathollahi-Fard A M, et al. Addressing a collaborative maintenance planning using multiple operators by a multi-objective metaheuristic algorithm[J]. IEEE Transactions on Automation Science and Engineering, 2023: 1–13.

[13] S.-H. Sheu, Z. G. Zhang. An optimal age replacement policy for multi-state systems[J]. IEEE Transactions on Reliability, 2013, 62(3): 722-735.

[14] Xu Yue, Pi Dechang, Yang Shengxiang, et al. Knowledge transfer-based multifactorial evolutionary algorithm for selective maintenance optimization of multistate complex systems[J]. IEEE Transactions on Reliability. doi. 10.1109/TR.2023.3324701.

[15] Kijima M. Some results for repairable systems with general repair[J]. Journal of Applied probability, 1989, 26(1): 89–102.

[16] Liu Yu, Huang Hongzhong. Optimal selective maintenance strategy for multi-State systems under imperfect maintenance[J]. IEEE Transactions on Reliability, 2010, 59(2): 356–367.

[17] Deb K, Jain H. An evolutionary many-objective optimization algorithm using reference-point-based nondominated sorting approach, part I: solving problems with box constraints[J]. IEEE Transactions on Evolutionary Computation, 2014, 18(4): 577–601.

[18] Deb K, Pratap A, Agarwal S, et al. A fast and elitist multiobjective genetic algorithm: NSGA-II[J]. IEEE Transactions on Evolutionary Computation, 2002, 6(2): 182–197.

Proceedings of the 3rd Conference on Fully Actuated System Theory and Applications
May 10-12, 2024, Shenzhen, China

Robust Control of Single-Link Flexible-Joint Manipulators with Perturbed Inertia Based on Fully Actuated System Approach

Shiyu Zhang[1], Guangren Duan[1,2]

1. Center for Control Theory and Guidance Technology, Harbin Institute of Technology, Harbin 150001, P. R. China
E-mail: zsy13436552937@163.com

2. Shenzhen Key Laboratory of Control Theory and Intelligent Systems, Southern University of Science and Technology, Shenzhen 518055, P. R. China
E-mail: g.r.duan@hit.edu.cn

Abstract: This paper proposes a fully actuated system (FAS) approach for the robust control problem of single-link flexible-joint manipulators (SLFJMs) with perturbed inertia. Unlike previous studies, the method proposed in this paper only requires the design of a simple robust state feedback controller to achieve high-precision control without the use of neural networks, observers, etc. Meanwhile, the control problem of FASs with perturbed input matrices is still rarely studied, and this paper proposes an effective control method for this case, which broadens the application scope of the FAS approach. Firstly, the SLFJM with perturbed inertia is transformed into a FAS with perturbed input matrix using an appropriate state transformation. Meanwhile, a converted control problem is formulated for the transformed FAS. Then, a robust controller is designed based on the full-actuation property, which ensures that the states are globally bounded and eventually converge into an arbitrarily small region centered at the origin. Finally, the effectiveness of the method is demonstrated by simulation.

Key Words: Fully Actuated System Approach, Robust Control, Single-Link Flexible Joint Manipulators, Perturbed Inertia

1 Introduction

Due to the advantages of flexible joints, including high flexibility and fast operating speed, single-link flexible-joint manipulators (SLFJMs) are widely used in industrial and aerospace applications [1, 2]. Since flexible joints are prone to vibration in motion [3], the problem of high-precision control of SLFJMs has received considerable attention in recent decades. Moreover, the SLFJMs always contain various uncertainties, so many control methods have been proposed to overcome the unfavourable effects of uncertainties on high-precision control. In [4], a robust adaptive fuzzy tracking controller is designed for SLFJMs with imprecise dynamics. In the presence of imprecise dynamics, it has been further considered that the angular position and velocity of the motor shaft are not measurable [5], and the need to meet prescribed performance [6, 7]. In addition, [8] and [9] consider the control problem under two types of external disturbances and under matched and unmatched disturbances, respectively. However, in all the above studies, the input matrices of the state space models of the SLFJMs do not contain uncertainties.

Along this research direction, considering the widespread phenomenon of motor shaft inertia fluctuation in applications, this paper considers the case of inertia perturbation in the SLFJM. In this case, the uncertainty is in the input matrix of the state-space model of the SLFJM. It is therefore very challenging to ensure high-precision control of the SLFJM. There has been limited research in this area in recent years. In [10], the original model is first transformed into a high-order system, and then a self-organising neural-fuzzy network is used to approximate the uncertain input matrix. On the other hand, [11] and [12] overcome the effects of the uncertainties caused by the perturbed matrix by using a composite observer and an EID estimator, respectively. However, the above studies require the use of adaptive neural networks, observers or estimators to complete the control design. It is difficult to obtain high accuracy control using only robust state feedback controllers.

Recently, a new theory known as the fully actuated system (FAS) approach has been proposed, which constructs a complete theoretical framework for the control of nonlinear systems. It has been pointed out in [13] that the FAS model is actually a model of the control system and not just a small part of the physical control system. Therefore, it is natural that the FAS approach is also a general approach. In particular, a number of robust control methods have been developed within the FAS framework. The direct robust stabilising controllers and the robust tracking controllers for FASs have been given in [14]. The full-actuation property allows us to completely cancel out the known nonlinear term, thus maximally transforming the control problem of a nonlinear system into that of a linear system, bringing simplicity to the control design while making it easy to achieve global results. Due to the above advantages, the FAS approach has been further developed for the control of other complicated uncertain systems, such as type I systems [15], high-order strict feedback systems [16], strongly interconnected nonlinear systems [17] and sub-fully actuated systems [18].

In this paper, the stabilization control of the SLFJM in the case of perturbed inertia is considered based on the FAS approach. First, the uncertain FAS model corresponding to the original SLFJM is obtained by a state transformation. The uncertainty of this model consists of two types: nonlinear uncertainty and constant perturbed input matrix. Then, the equivalent converted control problem is given and the robust state feedback controller is designed using the full-actuation property. Finally, it is proved by stability analysis that the controller ensures that the states are globally bounded and eventually converge into an arbitrarily small region centered at the origin. The main contributions of this paper are in two points. Firstly, different from [10–12], this paper only

This work is supported by the Science Center Program of the National Natural Science Foundation (NNSF) of China under Grant 62188101.

designs a robust controller based on the full-actuation property, without the need to use neural networks or observers. Therefore, the control method is very simple. Secondly, very few studies in the FAS framework have considered the uncertain control input matrix, and this paper provides an effective control method for this case.

The paper is divided into six sections. In Section 2, the problems to be solved are formulated, and some preliminary results are presented in Section 3. In Section 4, a direct robust controller for transformed FAS with perturbed input matrix is given, and the stability of the closed-loop system is proved. Simulation results are presented in Section 5, followed by a brief conclusion.

In this paper, we notate the minimum eigenvalue and the i-th eigenvalue of a nonsingular matrix $A \in \mathbb{R}^{m\times m}$ as $\lambda_{\min}(A)$ and $\lambda_i(A)$, respectively. For a vector $z \in \mathbb{R}^m$, we define its following norms $\|z\|^2 = z^{\mathrm{T}}z$ and $\|z\|_A^2 = z^{\mathrm{T}}Az$. Moreover, for a vector $x \in \mathbb{R}^r$ and a set of matrices $A_i \in \mathbb{R}^{r\times r}, i = 0, 1, \ldots, n-1$, the following symbols are frequently used in this paper:

$$x^{(0\sim k)} = \left[x^{\mathrm{T}} \quad \dot{x}^{\mathrm{T}} \quad \cdots \quad (x^{(k)})^{\mathrm{T}}\right]^{\mathrm{T}},$$

$$A_{0\sim n-1} = \left[A_0 \quad A_1 \quad \cdots \quad A_{n-1}\right],$$

$$\Phi\left(A_{0\sim n-1}\right) = \begin{bmatrix} 0 & I & & \\ & & \ddots & \\ & & & I \\ -A_0 & -A_1 & \cdots & -A_{n-1} \end{bmatrix}.$$

2 Problem Formulation

2.1 The Original Problem

Based on the SLFJM model presented in [4, 7, 19], we further consider the perturbation of the motor inertia as well as the system subjected to the external disturbance $d(t)$. The dynamic equation is as follows:

$$\begin{cases} I\ddot{q}_1 + MgL\sin q_1 + k\left(q_1 - q_2\right) = 0 \\ J\ddot{q}_2 - k\left(q_1 - q_2\right) = u + d\left(t\right), \end{cases} \tag{1}$$

where q_1, q_2 are the angles of the link and the motor, u is the torque of the motor, $d\left(t\right)$ is the unknown external disturbance to the motor, I and J are moments of inertia relative to the link and the motor, respectively, M is the link mass, L is the distance from the flexible-joint to the center of mass of the link, and k is the spring stiffness. We assume that there is an uncertainty in the moment of inertia J, which can be decomposed into the following form:

$$J = J_0 + \Delta J, \tag{2}$$

where J_0 is the known nominal value and ΔJ represents the uncertainty.

Considering the engineering application background of the SLFJM model (1), we give the following assumptions that are quite easy to satisfy.

Assumption 2.1. The constants k, J, and I are non-zero, and the constant $J_0 > 0$.

Assumption 2.2. There exist two known positive numbers $\bar{J} < 0.5J_0$ and $\bar{d}$ such that

$$|\Delta J| \le \bar{J}, \tag{3}$$

and

$$|d\left(t\right)| \le \bar{d}. \tag{4}$$

Remark 2.3. The above assumptions are common and weak. Assumption 2.1 is a very common assumption that can be satisfied in all previous studies on SLFJM control (see [1–12]). Assumption 2.2 requires that the bound of the perturbed inertia is less than half of the nominal value. Compared to the assumptions that the parameter perturbations do not exceed 10 or 20 per cent [10, 12], Assumption 2.2 is very relaxed. At the same time, the requirement for the external disturbance in Assumption 2.2 is very common.

Based on the above preparation, the control problem studied in this paper for the SLFJM model is as follows.

Problem 2.4. Let the system (1) satisfy Assumptions 2.1 and 2.2. Find a feedback control law $u = u\left(q_1, q_2, \dot{q}_1, \dot{q}_2\right)$ such that the states can be globally bounded and finally converge into an arbitrarily small region centered at the origin.

Remark 2.5. Convergence to an arbitrarily small region means that the stabilization problem can be solved. This is acceptable because in practical engineering, many controls usually make the state ultimately bounded. In contrast, this paper achieves further better control by making the state arbitrarily close to the origin. In addition, the global stabilization result can be obtained in this paper.

2.2 The Converted Problem

To solve Problem 2.4, we first convert the original SLFJM model (1) into a perturbed FAS model. We provide the following result to show the transformed FAS model.

Proposition 2.6. Let Assumptions 2.1 and 2.2 be met. Under the following transformation

$$\begin{cases} x = q_1 \\ \dot{x} = \dot{q}_1 \\ \ddot{x} = \dfrac{k}{I}q_2 - \dfrac{MgL}{I}\sin q_1 - \dfrac{k}{I}q_1 \\ x^{(3)} = \dfrac{k}{I}\dot{q}_2 - \dfrac{MgL}{I}\dot{q}_1\cos q_1 - \dfrac{k}{I}\dot{q}_1, \end{cases} \tag{5}$$

the original SLFJM model (1) is equivalently transformed into the following perturbed FAS:

$$x^{(4)} = f\left(x^{(0\sim 2)}\right) + \Delta f\left(x, \ddot{x}, t\right) + \left(B + \Delta B\right)u, \tag{6}$$

where

$$\begin{aligned} f\left(x^{(0\sim 2)}\right) &= -\frac{MgL}{I}\ddot{x}\cos x + \frac{MgL}{I}\dot{x}^2\sin x - \frac{k}{I}\ddot{x} \\ &\quad -\frac{k}{J_0}\ddot{x} - \frac{kMgL}{IJ_0}\sin x, \end{aligned} \tag{7}$$

$$\begin{aligned} \Delta f\left(x, \ddot{x}, t\right) &= \frac{k\Delta J}{J_0\left(J_0 + \Delta J\right)}\ddot{x} + \frac{kMgL\Delta J}{IJ_0\left(J_0 + \Delta J\right)}\sin x \\ &\quad + \frac{k}{JI}d\left(t\right), \end{aligned} \tag{8}$$

$$B = \frac{k}{IJ_0} \neq 0, \tag{9}$$

and

$$\Delta B = -\frac{k\Delta J}{IJ_0\left(J_0 + \Delta J\right)}. \tag{10}$$

Proof. Step 1: Obtaining the transformed model.

It follows from Assumption 2.1 and the first equation of (1) that

$$q_2 = \frac{I}{k}\ddot{q}_1 + \frac{MgL}{k}\sin q_1 + q_1. \tag{11}$$

Taking the differential of (11), gives

$$\dot{q}_2 = \frac{I}{k}q_1^{(3)} + \frac{MgL}{k}\dot{q}_1\cos q_1 + \dot{q}_1. \tag{12}$$

Further taking the differential of (12), yields

$$\begin{aligned}\ddot{q}_2 &= \frac{I}{k}q_1^{(4)} + \frac{MgL}{k}\frac{\mathrm{d}\left(\dot{q}_1\cos q_1\right)}{\mathrm{d}t} + \ddot{q}_1 \\ &= \frac{I}{k}q_1^{(4)} + \frac{MgL}{k}\left(-\dot{q}_1^2\sin q_1 + \ddot{q}_1\cos q_1\right) + \ddot{q}_1 \\ &= \frac{I}{k}q_1^{(4)} - \frac{MgL}{k}\dot{q}_1^2\sin q_1 + \frac{MgL}{k}\ddot{q}_1\cos q_1 \\ &\quad +\ddot{q}_1. \end{aligned}\tag{13}$$

Substituting (11) and (13) into the second equation of (1), yields

$$\begin{aligned}q_1^{(4)} &= \frac{MgL}{I}\dot{q}_1^2\sin q_1 - \frac{MgL}{I}\ddot{q}_1\cos q_1 - \frac{k}{I}\ddot{q}_1 - \frac{k}{J}\ddot{q}_1 \\ &\quad -\frac{kMgL}{JI}\sin q_1 + \frac{k}{JI}u + \frac{k}{JI}d. \end{aligned}\tag{14}$$

Considering the uncertainty in J, as shown in (2), we have

$$\begin{aligned}q_1^{(4)} &= f\left(q_1^{(0\sim 2)}\right) + \Delta f\left(q_1, \ddot{q}_1, t\right) \\ &\quad + \left(\frac{k}{IJ_0} - \frac{k\Delta J}{IJ_0\left(J_0+\Delta J\right)}\right)u, \end{aligned}\tag{15}$$

where

$$\begin{aligned}f\left(q_1^{(0\sim 2)}\right) &= \frac{MgL}{I}\dot{q}_1^2\sin q_1 - \frac{MgL}{I}\ddot{q}_1\cos q_1 - \frac{k}{I}\ddot{q}_1 \\ &\quad -\frac{k}{J_0}\ddot{q}_1 - \frac{kMgL}{IJ_0}\sin q_1, \end{aligned}\tag{16}$$

and

$$\begin{aligned}\Delta f\left(q_1, \ddot{q}_1, t\right) &= \frac{k\Delta J}{J_0\left(J_0+\Delta J\right)}\ddot{q}_1 + \frac{kMgL\Delta J}{IJ_0\left(J_0+\Delta J\right)} \\ &\quad \times\sin q_1 + \frac{k}{JI}d\left(t\right). \end{aligned}\tag{17}$$

According to Assumption 2.1, we obtain

$$\frac{k}{J_0 I} \neq 0. \tag{18}$$

Based on the above results, we introduce the following relation

$$x = q_1, \tag{19}$$

then system (15)-(17) is equivalent to the perturbed FAS (6)-(10).

Step 2: Deriving the corresponding transformation.

Recalling (19), we easily obtain

$$\dot{x} = \dot{q}_1. \tag{20}$$

Taking the differential of (20) and using the first equation of (1), we have

$$\ddot{x} = -\frac{MgL}{I}\sin q_1 - \frac{k}{I}q_1 + \frac{k}{I}q_2. \tag{21}$$

Taking the differential of (21), we obtain

$$x^{(3)} = \frac{k}{I}\dot{q}_2 - \frac{MgL}{I}\dot{q}_1\cos q_1 - \frac{k}{I}\dot{q}_1. \tag{22}$$

The combination of the equations (19)-(22) clearly gives the transformation (5). □

Next, we propose the following proposition for the transformation (5).

Proposition 2.7. The transformation (5) is a one-to-one mapping and keeps the origin unchanged.

Proof. It follows from transformation (5) that

$$\begin{cases} q_1 = x \\ \dot{q}_1 = \dot{x} \\ q_2 = \dfrac{I}{k}\ddot{x} + \dfrac{MgL}{k}\sin x + x \\ \dot{q}_2 = \dfrac{I}{k}x^{(3)} + \dfrac{MgL}{k}\dot{x}\cos x + \dot{x}. \end{cases} \tag{23}$$

For an arbitrary $q = \begin{bmatrix} q_1 & \dot{q}_1 & q_2 & \dot{q}_2 \end{bmatrix}^{\mathrm{T}}$, the unique $x^{(0\sim 3)}$ is given by transformation (5). Conversely, for an arbitrary $x^{(0\sim 3)}$, the unique q is obtained by transformation (23). Thus transformation (5) is a one-to-one mapping.

Let $q = 0$, then according to the transformation (5) we obtain $x^{(0\sim 3)} = 0$. Similarly, let $x^{(0\sim 3)} = 0$, then $q = 0$ can be obtained by the transformation (23). Therefore, it can be proven that the origin remains unchanged. □

Remark 2.8. According to transformation (23), if $x^{(0\sim 3)}$ is arbitrarily close to the origin, then it is natural to obtain that q is arbitrarily close to the origin.

Finally, based on the above discussion, Problem 2.4 is equivalently converted into the following question.

Problem 2.9. Let the perturbed FAS (6)-(10) satisfy Assumptions 2.1 and 2.2. Find a feedback control law $u = \bar{u}\left(x^{(0\sim 3)}\right)$ such that the state $x^{(0\sim 3)}$ is globally bounded and finally converges into an arbitrarily small region centered at the origin.

3 Preliminaries

In order to control the perturbed FAS (6)-(10), the following lemmas proposed in [14] are needed.

Lemma 3.1 ([14])**.** Let $A \in \mathbb{R}^{n\times n}$ satisfy

$$\mathrm{Re}\lambda_i\left(A\right) \leq -\frac{\mu}{2},\ i = 1, 2, \cdots, n, \tag{24}$$

where $\mu > 0$. Then there exists a positive definite matrix $P \in \mathbb{R}^{n\times n}$ satisfying

$$A^{\mathrm{T}}P + PA \leq -\mu P. \tag{25}$$

Lemma 3.2 ([14])**.** For any $\mu > 0$, there exist a matrix $A_{0\sim n-1} \in \mathbb{R}^{r\times nr}$ satisfying

$$\mathrm{Re}\lambda_i\left(\Phi\left(A_{0\sim n-1}\right)\right) \leq -\frac{\mu}{2},\ i = 1, 2, \cdots, nr. \tag{26}$$

It is known from Lemma 3.1 that, when the condition in (26) holds for some $\mu > 0$, there exists a positive definite matrix P satisfying

$$\Phi^{\mathrm{T}}(A_{0\sim n-1})P + P\Phi\left(A_{0\sim n-1}\right) \leq -\mu P. \tag{27}$$

Partition P as

$$P = \left[\begin{array}{cccc} P_1 & P_2 & \cdots & P_n \end{array}\right],\ P_i \in \mathbb{R}^{nr\times r}, \tag{28}$$

we can further introduce the following notation which will be frequently used in the paper:

$$P_L \triangleq P_n. \tag{29}$$

The following proposition gives all parametric solutions of $A_{0\sim n-1}$, which is given by [14].

Proposition 3.3 ([14])**.** For an arbitrarily chosen $F \in \mathbb{R}^{nr\times nr}$, all the matrix $A_{0\sim n-1} \in \mathbb{R}^{r\times nr}$ and the nonsingular matrix $V \in \mathbb{R}^{nr\times nr}$ satisfying

$$\Phi\left(A_{0\sim n-1}\right) = VFV^{-1} \tag{30}$$

are given by

$$\left\{\begin{array}{l} A_{0\sim n-1} = -ZF^nV^{-1}\left(Z,F\right) \\ V = V\left(Z,F\right) = \left[\begin{array}{c} Z \\ ZF \\ \vdots \\ ZF^{n-1} \end{array}\right], \end{array}\right. \tag{31}$$

where $Z \in \mathbb{R}^{r\times nr}$ is an arbitrary parameter matrix satisfying

$$\det V\left(Z,F\right) \neq 0. \tag{32}$$

Remark 3.4. For the values of n and r in equations (26)-(29), we specifically take $n = 4$ and $r = 1$ in the following.

4 Control Design

Assumption 2.2 needs to be satisfied for the perturbed FAS (6)-(10), from which we get

$$\begin{array}{rcl} \left|\Delta f\left(x,\ddot{x},t\right)\right| & \leq & \dfrac{\bar{J}}{\left|J_0+\Delta J\right|}\left|\dfrac{k}{J_0}\ddot{x}\right| + \dfrac{\bar{J}}{\left|J_0+\Delta J\right|} \\ & & \times\left|\dfrac{kMgL}{IJ_0}\sin x\right| + \left|\dfrac{k}{JI}\right|\bar{d} \\ & \leq & \dfrac{2\bar{J}}{J_0}\left|\dfrac{k}{J_0}\ddot{x}\right| + \dfrac{2\bar{J}}{J_0}\left|\dfrac{kMgL}{IJ_0}\sin x\right| \\ & & + \dfrac{2}{J_0}\left|\dfrac{k}{I}\right|\bar{d}, \end{array} \tag{33}$$

and

$$\left|\frac{\Delta B}{B}\right| = \frac{\left|\Delta J\right|}{\left|J_0+\Delta J\right|} \leq \frac{2\bar{J}}{J_0} < 1. \tag{34}$$

For simplicity, we introduce the following notation for equation (33):

$$\rho\left(x,\ddot{x}\right) = \frac{2\bar{J}}{J_0}\left|\frac{k}{J_0}\ddot{x}\right| + \frac{2\bar{J}}{J_0}\left|\frac{kMgL}{IJ_0}\sin x\right| + \frac{2}{J_0}\left|\frac{k}{I}\right|\bar{d}. \tag{35}$$

To solve Problem 2.9, we give the following robust control method for the perturbed FAS (6)-(10).

Theorem 4.1. Suppose that perturbed FAS (6)-(10) satisfies Assumptions 2.1 and 2.2. Let μ and α be two arbitrarily given positive numbers, $A_{0\sim 3} \in \mathbb{R}^{1\times 4}$ be a row vector satisfying (26), and $P > 0$ and $P_L \in \mathbb{R}^4$ be given by (27)-(29). Then, the following controller

$$\left\{\begin{array}{l} u = -\dfrac{1}{B}\left(f\left(x^{(0\sim 2)}\right) + v\right) \\ v = A_{0\sim 3}x^{(0\sim 3)} + \dfrac{\tilde{\rho}^2\left(x^{(0\sim 3)}\right)}{4\alpha\left(1-\dfrac{2\bar{J}}{J_0}\right)}P_L^{\mathrm{T}}x^{(0\sim 3)}, \end{array}\right. \tag{36}$$

with

$$\tilde{\rho}\left(x^{(0\sim 3)}\right) = \rho\left(x,\ddot{x}\right) + \frac{2\bar{J}}{J_0}\left|f\left(\cdot\right) + A_{0\sim 3}x^{(0\sim 3)}\right|, \tag{37}$$

guarantees that the state $x^{(0\sim 3)}$ finally converges into the following region

$$\Theta = \left\{x^{(0\sim 3)}\ \middle|\ \left\|x^{(0\sim 3)}\right\|^2 \leq \frac{2\alpha}{\mu\lambda_{\min}\left(P\right)}\right\}. \tag{38}$$

Proof. Substituting the controller (36) into the perturbed FAS (6)-(10), gives

$$x^{(4)} = -A_{0\sim 3}x^{(0\sim 3)} + \varphi\left(x^{(0\sim 3)},t\right), \tag{39}$$

where

$$\begin{array}{rcl} \varphi\left(x^{(0\sim 3)},t\right) & = & \Delta f\left(x,\ddot{x},t\right) \\ & & -\dfrac{\tilde{\rho}^2\left(x^{(0\sim 3)}\right)}{4\alpha\left(1-\dfrac{2\bar{J}}{J_0}\right)}P_L^{\mathrm{T}}x^{(0\sim 3)} \\ & & -\dfrac{\Delta B}{B}\left(f\left(x^{(0\sim 2)}\right)+v\right), \end{array} \tag{40}$$

with v is as shown in the second equation of (36). The above closed-loop system (39) can be rewritten in the following form:

$$\dot{x}^{(0\sim 3)} = \Phi\left(A_{0\sim 3}\right)x^{(0\sim 3)} + \left[\begin{array}{c} 0 \\ \varphi\left(x^{(0\sim 3)},t\right) \end{array}\right]. \tag{41}$$

Since $A_{0\sim 3}$ satisfies (26), there exists a positive definite matrix P satisfying (27). Then we choose the following Lyapunov candidate function:

$$V = \frac{1}{2}\left\|x^{(0\sim 3)}\right\|_P^2. \tag{42}$$

In view of (27), we have

$$\begin{array}{rcl} \dot{V} & = & \dfrac{1}{2}\left(x^{(0\sim 3)}\right)^{\mathrm{T}}\left(\Phi^{\mathrm{T}}\left(A_{0\sim 3}\right)P + P\Phi\left(A_{0\sim 3}\right)\right)x^{(0\sim 3)} \\ & & + \left(x^{(0\sim 3)}\right)^{\mathrm{T}}P_L\varphi\left(\cdot\right) \\ & \leq & -\mu V + W, \end{array} \tag{43}$$

where

$$W = \left(x^{(0\sim 3)}\right)^{\mathrm{T}}P_L\varphi\left(\cdot\right). \tag{44}$$

Let us consider W. It follows from (33)-(35) and (40) that

$$\begin{aligned} W &\leq \left|\left(x^{(0\sim3)}\right)^{\mathrm{T}} P_L\right| |\Delta f(\cdot)| - \frac{\tilde{\rho}^2(\cdot)\left|\left(x^{(0\sim3)}\right)^{\mathrm{T}} P_L\right|^2}{4\alpha\left(1-\frac{2\bar{J}}{J_0}\right)} \\ &\quad + \left|\frac{\Delta B}{B}\right|\left|\left(x^{(0\sim3)}\right)^{\mathrm{T}} P_L\right|\left|f(\cdot)+A_{0\sim3}x^{(0\sim3)}\right| \\ &\quad + \frac{\tilde{\rho}^2(\cdot)}{4\alpha\left(1-\frac{2\bar{J}}{J_0}\right)}\left|\frac{\Delta B}{B}\right|\left|\left(x^{(0\sim3)}\right)^{\mathrm{T}} P_L\right|^2 \\ &\leq \rho(\cdot)\left|\left(x^{(0\sim3)}\right)^{\mathrm{T}} P_L\right| - \frac{\tilde{\rho}^2(\cdot)}{4\alpha}\left|\left(x^{(0\sim3)}\right)^{\mathrm{T}} P_L\right|^2 \\ &\quad + \frac{2\bar{J}}{J_0}\left|\left(x^{(0\sim3)}\right)^{\mathrm{T}} P_L\right|\left|f(\cdot)+A_{0\sim3}x^{(0\sim3)}\right| \\ &= \tilde{\rho}(\cdot)\left|\left(x^{(0\sim3)}\right)^{\mathrm{T}} P_L\right| - \frac{\tilde{\rho}^2(\cdot)}{4\alpha}\left|\left(x^{(0\sim3)}\right)^{\mathrm{T}} P_L\right|^2 \\ &\leq \alpha. \end{aligned} \tag{45}$$

It follows from (43) that

$$\dot{V} \leq -\mu V + \alpha. \tag{46}$$

Therefore, we have

$$V \leq V(0)e^{-\mu t} + \frac{\alpha}{\mu}\left(1-e^{-\mu t}\right). \tag{47}$$

Then we can easily obtain

$$\lim_{t\to\infty} V \leq \frac{\alpha}{\mu}. \tag{48}$$

Further, we have

$$\lim_{t\to\infty}\left\|x^{(0\sim3)}\right\|^2 \leq \frac{2\alpha}{\mu\lambda_{\min}(P)}. \tag{49}$$

The proof is completed. □

Remark 4.2. Since the positive numbers μ and α can be arbitrary, it is clear that Θ can be adjusted to be arbitrarily small so as to meet our expectations. Since the region Θ can be adjusted to be arbitrarily small and the initial values of $x^{(0\sim3)}$ can be arbitrarily selected, the requirement of Problem 2.9 is satisfied.

5 Simulation Results

The numerical simulation is carried out using the following parameters provided in [12]:

$$\begin{aligned} M &= 2\mathrm{kg}, L = 1\mathrm{m}, I = 2\mathrm{kg}\cdot\mathrm{m}^2, \\ k &= 10\mathrm{N}\cdot\mathrm{m/rad}, J_0 = 0.5\mathrm{kg}\cdot\mathrm{m}^2. \end{aligned} \tag{50}$$

Considering that the perturbation of the inertia is generally small in the engineering background, we give the perturbed inertia and its upper bound as follows:

$$\Delta J = 0.1J_0 = 0.05\mathrm{kg}\cdot\mathrm{m}^2, \bar{J} = 0.2J_0 = 0.1\mathrm{kg}\cdot\mathrm{m}^2. \tag{51}$$

Also based on engineering considerations (see [10]), we choose the external disturbance $d(t)$ and the corresponding upper bound as

$$d(t) = 0.2\sin(2\pi t)\,\mathrm{N}\cdot\mathrm{m} \tag{52}$$

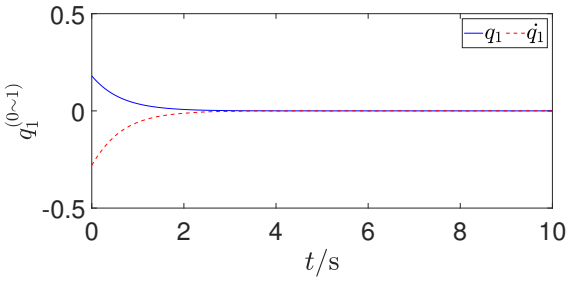

Fig. 1: The states q_1 and $\dot{q}_1$.

and

$$\bar{d} = 0.3\mathrm{N}\cdot\mathrm{m}, \tag{53}$$

respectively.

5.1 Controller Design

According to Theorem 4.1, the robust controller is shown in equation (36). Next, we design the parameters required by the controller (36). Select $\mu = 2$ and

$$F = \mathrm{diag}\left(\begin{bmatrix} -2 & -2 \\ 2 & -2 \end{bmatrix}, -5, -10\right). \tag{54}$$

Then according to Proposition 3.3, the matrix $A_{0\sim3}$ can be compute as

$$A_{0\sim3} = \begin{bmatrix} 400 & 320 & 118 & 19 \end{bmatrix}. \tag{55}$$

In view of (27)-(29), we can obtain

$$P = \begin{bmatrix} 16.8292 & 8.8087 & 1.7963 & 0.0461 \\ 8.8087 & 6.8633 & 1.4739 & 0.0529 \\ 1.7963 & 1.4739 & 0.5143 & 0.0189 \\ 0.0461 & 0.0529 & 0.0189 & 0.0026 \end{bmatrix}, \tag{56}$$

and

$$P_L^{\mathrm{T}} = \begin{bmatrix} 0.0461 & 0.0529 & 0.0189 & 0.0026 \end{bmatrix}. \tag{57}$$

Further, we choose

$$\alpha = 0.001. \tag{58}$$

It follows from (35), (51) and (53) that

$$\rho(x, \ddot{x}) = 8|\ddot{x}| + 78.4|\sin x| + 6. \tag{59}$$

Then it follows from (37) that

$$\begin{aligned} \tilde{\rho}\left(x^{(0\sim3)}\right) &= 8|\ddot{x}| + 78.4|\sin x| + 6 + 0.4\Big|f(\cdot) \\ &\quad + \begin{bmatrix} 400 & 320 & 118 & 19 \end{bmatrix} x^{(0\sim3)}\Big| \end{aligned} \tag{60}$$

5.2 Results

Choose the following initial values for system (1):

$$\begin{aligned} q_1(0) &= 0.18\mathrm{rad},\ \dot{q}_1(0) = -0.28\mathrm{rad/s}, \\ q_2(0) &= 0.61\mathrm{rad},\ \dot{q}_2(0) = -0.86\mathrm{rad/s}. \end{aligned}$$

Then the simulation results are displayed in Figs 1, 2 and 3, which show the validity of the proposed method. After about 4 seconds, all states converge into an extremely small area near the origin. In addition, the control amount is relatively small, and its absolute value does not exceed 50 $\mathrm{N}\cdot\mathrm{m}$.

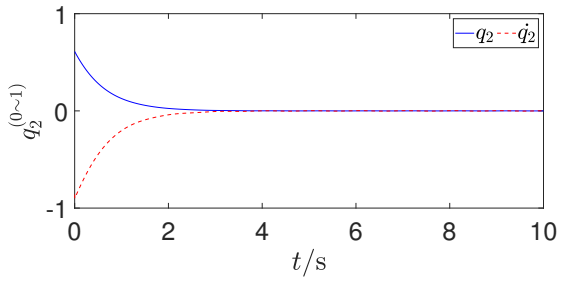

Fig. 2: The states q_2 and $\dot{q}_2$.

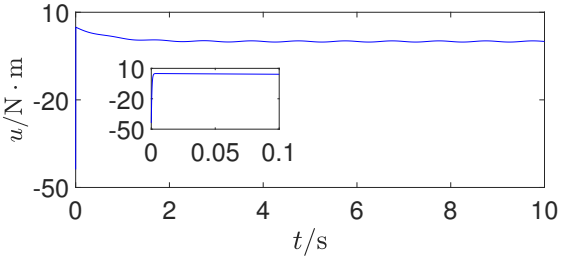

Fig. 3: The control input.

6 Conclusion

Most of the control studies of SLFJMs with dynamic model (1) are limited to deterministic systems, and it is always difficult to obtain global convergence characteristics. And for those that rarely consider parameter perturbations, they either transform the perturbations into a generalized disturbance or estimate them using intelligent control methods, both of which have a certain level of complexity. The FAS system transformed from the original SLFJM model has a constant perturbed input control matrix, which is not easily addressed by the existing control strategies in the FAS framework. In this case, the robust control problem of the SLFJM with perturbed inertia is very challenging. In this paper, a new robust control method is proposed based on the FAS approach, which can satisfactorily solve the problem. As a result, the state vector of the SLFJM is globally bounded and finally converges into an arbitrarily small region centered at the origin.

In future research, more complicated situations will be considered, such as robust control problems for single-order FASs or multi-order FASs with perturbation input matrices.

References

[1] H. Bilal, B. Q. Yin, A. Kumar, M. Ali, J. Zhang, J. F. Yao, Jerk-bounded trajectory planning for rotary flexible joint manipulator:an experimental approach. *Soft Computing*, 2023, 27(7): 4029–4039.

[2] H. A. Talebi, R. V. Patel, H. Asmer, Neural network based dynamic modeling of flexible-link manipulators with application to the SSRMS. *Journal of Robotic Systems*, 2000, 17(7): 385–401.

[3] E. Pereira, S. S. Aphale, V. Feliu, S. O. R. Moheimani, Integral resonant control for vibration damping and precise tip-positioning of a single-link flexible manipulator. *IEEE-ASME Transactions on Mechatronics*, 2011, 16(2): 232–240.

[4] Y. S. Yang, G. Feng, J. S. Ren, A combined backstepping and small-gain approach to robust adaptive fuzzy control for strict-feedback nonlinear systems. *IEEE Transactions on Systems Man and Cybernetics Part A-Systems and Humans*, 2004, 34(3): 406–420.

[5] X. Liu, C. G. Yang, Z. G. Chen, M. Wang, C. Y. Su, Neuro-adaptive observer based control of flexible joint robot. *Neurocomputing*, 2018, 275: 73–82.

[6] H. Ma, Q. Zhou, H. Y. Li, R. Q. Lu, Adaptive prescribed performance control of a flexible-joint robotic manipulator with dynamic uncertainties. *IEEE Transactions on Cybernetics*, 2022, 52(12): 12905–12915.

[7] M. Wang, H. P. Ye, Z. G. Chen, Neural learning control of flexible joint manipulator with predefined tracking performance and application to baxter robot. *Complexity*, 2017: 7683785.

[8] C. B. Niu, H. Shen, J. F. Li, Y. Yi, Disturbance observer-based L_1 robust tracking control for single-link flexible-joint manipulator systems. *Journal of Engineering-JOE*, 2019, 2019(22): 8390–8394.

[9] C. Z. Pan, X. Y. Fei, J. S. Xiao, P. Y. Xiong, Z. J. Li, H. Huang, Model-assisted reduced-order ESO based command filtered tracking control of flexible-joint manipulators with matched and mismatched disturbances. *Applied Sciences*, 2022, 12(17): 8511.

[10] C. S. Chen, Robust self-organizing neural-fuzzy control with uncertainty observer for MIMO nonlinear systems. *IEEE Transactions on Fuzzy Systems*, 2011, 19(4): 694–706.

[11] Y. Chen, B. Guo, Sliding mode fault tolerant tracking control for a single-link flexible joint manipulator system. *IEEE Access*, 2019, 7: 83046–83057.

[12] Z. Yan, X. Z. Lai, Q. X. Meng, M. Wu, A novel robust control method for motion control of uncertain single-link flexible-joint manipulator. *IEEE Transactions on Systems Man Cybernetics-Systems*, 2021, 51(3): 1671–1678.

[13] G. R. Duan, High-order fully actuated system approaches: Part I. Models and basic procedure. *International Journal of Systems Science*, 2021, 52(2): 422–435.

[14] G. R. Duan, High-order fully actuated system approaches: Part III. Robust control and high-order backstepping. *International Journal of Systems Science*, 2021, 52(5): 952–971.

[15] G. R. Duan, Robust stabilization of time-varying nonlinear systems with time-varying delays: A fully actuated system approach. *IEEE Transactions on Cybernetics*, 2022, Dec, early access, doi:10.1109/TCYB.2022.3217317.

[16] W. Z. Liu, G. R. Duan, M. Z. Hou, High-order robust command filtered backstepping design for strict-feedback systems: A high-order fully actuated system approach. *International Journal of Robust and Nonlinear Control*, 2022, 32(18): 10251–10270.

[17] L. L. Zhang, L. C. Zhu, C. C. Hua, Practical prescribed time control based on high-order fully actuated system approach for strong interconnected nonlinear systems. *Nonlinear Dynamics*, 2022, 110(4): 3535–3545.

[18] S. Y. Zhang, G. R. Duan, Robust stabilization control for high-order sub-fully actuated systems, in *Proceedings of the 2nd Conference on Fully Actuated System Theory and Applications (CFASTA)*, 2023, 573–578.

[19] H. K. Khalil, *Nonlinear Systems*. Prentice Hall, 2002.

Proceedings of the 3rd Conference on Fully Actuated System Theory and Applications
May 10-12, 2024, Shenzhen, China

Robust Bounded-H_∞ Control for High-Order Fully Actuated Systems Based on FAS Approaches

Liyao Hu[1], Guangren Duan[1,2]

1. Center for Control Theory and Guidance Technology, Harbin Institute of Technology, Harbin 150001, P. R. China
E-mail: huliyao1995@163.com

2. Shenzhen Key Laboratory of Control Theory and Intelligent Systems, Southern University of Science and Technology, Shenzhen 518055, P. R. China
E-mail: g.r.duan@hit.edu.cn

Abstract: This paper investigates the robust bounded-H_∞ stabilization for a class of high-order fully actuated systems (FASs) with time-varying uncertainty and disturbance. Based on the FAS approaches and the H_∞ control, a robust bounded-H_∞ controller is designed, which guarantees that the system state and its derivatives of each order are globally bounded. Furthermore, a combined disturbance, composed of part time-varying uncertainty and disturbance, is given. With the help of the combined disturbance, the impact of the uncertainty and the disturbance on system output can be attenuated simultaneously, because the closed-loop high-order FAS has the bounded-H_∞ performance. A simulation example is provided to demonstrate the effectiveness of the proposed control method.

Key Words: Fully Actuated System Approaches, Nonlinear Systems, Robust Control, H_∞ Control

1 Introduction

Since Duan proposed firstly the fully actuated system (FAS) approaches in series of articles [1–6], the approaches have received wide attention. Using the FAS approaches can not only offset directly system nonlinear terms, but also obtain a nonlinear system with linear main part or closed-loop linear one under specific conditions. It is more suitable for controller design than the first-order state space approaches. (The reader is referred to [1–6] and its relevant works for a detailed discussion about the advantages of the FAS approaches.) Relying on these advantages of the FAS approaches, many significant works based on the FAS approaches have been done, including but not limited to the fault-tolerant control [7, 8], the predictive control [9, 10], and the event-triggered control [11, 12]. In practical applications, some results can also be seen in [13–15]. However, there is relatively little research to focus on the H_∞ control based on the FAS approaches.

H_∞ control can effectively attenuate external disturbance. Many related works have been obtained [16–19]. For FASs, there are some works [20, 21]. [20] investigated the H_∞ control for second-order fully actuated cooperative manipulators; The H_∞ control problem for second-order fully actuated single-link robot arm was solved in [21]. However, the investigated systems in [20, 21] only consider external disturbance. The time-varying uncertainty is ignored, which often occurs in practical applications.

Therefore, motivated by the aforementioned concerns, this paper investigates the robust bounded-H_∞ stabilisation for a class of high-order FASs with time-varying uncertainty and disturbance. Based on the FAS approaches and the bounded-H_∞ control proposed in [22], the robust bounded-H_∞ controller for the high-order FAS is designed, which ensures that the state and its derivatives of each order are globally bounded.

The main contributions and innovations of this paper are summarized as follows:

1) The bounded-H_∞ control for high-order FAS is investigated firstly, which is more difficult to design robust controller than second-order ones [20, 21];

2) The unknown uncertainty of system includes time-varying factor, which is more complex than the FAS without time-varying one [3]. Besides, the external disturbance is also considered in the system, which further increases the difficulties of controller design;

3) The combined disturbance is used, which contains the uncertainty and the external disturbance;

4) The closed-loop system satisfies the bounded-H_∞ performance index. Therefore, all the impact of the uncertainty and the disturbance on the system output can be attenuated.

The remainder of this paper is organized as follows: The problem formulation is given in Section 2. Some useful preliminaries are provided in Section 3. In Section 4, the robust bounded-H_∞ controller is designed for the high-order FAS, and a main theorem is offered. In Section 5, the effectiveness of the proposed control method is validated. The conclusion appears in Section 6.

In the sequential sections, denote the k-th order derivative of a function $f(t)$ by $f^{(k)}(t)$, and the i-th eigenvalue of a matrix A by $\lambda_i(A)$. Then, define $\|x\| = \left(x^{\mathrm{T}}x\right)^{\frac{1}{2}}$ for a vector $x \in \mathbb{R}^n$. Besides, some symbols are frequently used:

$$x^{(0\sim k)} = \begin{bmatrix} x \\ \dot{x} \\ \vdots \\ x^{(k)} \end{bmatrix},$$

$$A^{0\sim n-1} = \begin{bmatrix} A_0 & A_1 & \cdots & A_{n-1} \end{bmatrix},$$

This work was supported in part by the Science Center Program of National Natural Science Foundation of China (grant no. 62188101), the Major Program of National Natural Science Foundation of China (grant nos. 61690210 and 61690212), the Self Planned Task of State Key Laboratory of Robotics and System (HIT) (grant no. SKLRS201716A), and the National Natural Science Foundation of China (grant no. 61333003).

$$\Phi\left(A^{0\sim n-1}\right)=\begin{bmatrix}0 & 1 & & \\ \vdots & & \ddots & \\ 0 & 0 & \cdots & 1 \\ -A_0 & -A_1 & \cdots & -A_{n-1}\end{bmatrix}, \quad (1)$$

where k, $n \in \mathbb{Z}^+$, and A_i $(i=0,1,\cdots,n-1)$ are a set of proper constants.

2 Problem Formulation

Consider the following high-order FASs:

$$\begin{cases} x^{(n)}=f\left(x^{(0\sim n-1)}\right)+\Delta f\left(x^{(0\sim n-1)},t\right) \\ \qquad +\Psi\left(x^{(0\sim n-1)}\right)\omega(t)+L\left(x^{(0\sim n-1)}\right)u, \\ y(t)=x, \end{cases} \quad (2)$$

where x, u, $y \in \mathbb{R}$ are the system state, the input and the output, respectively; $\Psi\left(x^{(0\sim n-1)}\right)$, $f\left(x^{(0\sim n-1)}\right)$, $L\left(x^{(0\sim n-1)}\right) \in \mathbb{R}$ with $\Psi(0)=f(0)=0$ are three known continuous functions; $\Delta f\left(x^{(0\sim n-1)},t\right)$ is the time-varying uncertainty; $\omega(t) \in L_2$ is a bounded external disturbance. Therein, L_2 denotes a square integrable space. For system (2), two assumptions need to be satisfied:

Assumption 1 $\det L\left(x^{(0\sim n-1)}\right) \neq 0$ *or* ∞ *for* $\forall x^{(i)} \in \mathbb{R}$, $i=0,1,\cdots,n-1$.

Assumption 2 *There are a known continuous function* $\rho\left(x^{(0\sim n-1)}\right) \geq 0$ *and an unknown bounded function* $D(t) \in L_2$ *satisfying*

$$\left\|\Delta f\left(x^{(0\sim n-1)},t\right)\right\| \leq \rho\left(x^{(0\sim n-1)}\right)+D(t).$$

Remark 1 *Assumption 1 is very common, and often presents in the works to study the FAS approaches [3, 13]. Furthermore, Assumption 2 is also milder than [3] because we consider the time-varying factor in the uncertain function. It should be illustrated that many engineering systems satisfy Assumptions 1, 2, including but not limited to RLC circuit [11] and pendulum system [23].*

3 Preliminaries

Lemma 1 *[24] For any real number* $\varepsilon>0$*, the following inequality holds:*

$$xy \leq \frac{\varepsilon^p}{p}|x|^p+\frac{1}{q\varepsilon^q}|y|^q, \forall (x,y) \in \mathbb{R}^2, \quad (3)$$

where $p>1$ *and* $q>1$ *are the constants satisfying* $(p-1)(q-1)=1$.

Lemma 2 *[3] For any* $\mu>0$*, there exist a series of constants* $A_i \in \mathbb{R}, i=0,1,\cdots,n-1$ *, such that*

$$\mathrm{Re}\lambda_i\left(\Phi\left(A^{0\sim n-1}\right)\right)<-\frac{\mu}{2},\ i=1,2,\cdots,n. \quad (4)$$

Lemma 3 *[3] If the matrix* $\Phi\left(A^{0\sim n-1}\right) \in \mathbb{R}^{n\times n}$ *satisfies*

$$\mathrm{Re}\lambda_i\left(\Phi\left(A^{0\sim n-1}\right)\right)<-\frac{\mu}{2},\ i=1,2,\cdots,n$$

with $\mu>0$*, then there is a positive definite matrix* $P\left(A^{0\sim n-1}\right) \in \mathbb{R}^{n\times n}$*, such that*

$$\Phi\left(A^{0\sim n-1}\right)^{\mathrm{T}}P+P\Phi\left(A^{0\sim n-1}\right) \leq -\mu P. \quad (5)$$

Lemma 4 *[22, 25, 26] Let* $\Theta(t)$*,* $\Upsilon(t)$ *and* $\zeta(t)$ *be real continuous functions with* $\zeta \geq 0$ *defined in* $t \in [a,b]$*. If the inequality*

$$\Theta(t) \leq \Upsilon(t)+\int_a^t \zeta(s)\Theta(s)\,ds \quad (6)$$

holds, then

$$\Theta(t) \leq \Upsilon(t)+\int_a^t \zeta(s)\Upsilon(s)e^{\int_s^t \zeta(h)dh}ds. \quad (7)$$

Definition 1 *For high-order FAS (2), if there exists the controller* u*, such that the response of output satisfies the following bounded-*H_∞ *performance index*

$$\int_0^t \|y(s)\|^2 ds \leq \bar{\gamma}^2\int_0^t \|\bar{\omega}(s)\|^2 ds+d\left(x^{(0\sim n-1)}(0)\right), \quad (8)$$

then the closed-loop system has the bounded-H_∞ *performance, where* $d\left(x^{(0\sim n-1)}(0)\right)$ *is a positive number,* $\bar{\gamma}$ *is the disturbance attenuation coefficient, and* $\bar{\omega}(t)=\sqrt{\omega^2(t)+D^2(t)}$ *is the combined disturbance.*

Control objective of this paper is given according to the form of the following problem:

Problem 1 *For high-order FAS (2), design a robust bounded-*H_∞ *controller, such that*

1) the state and its derivatives of each order are globally bounded;

2) the closed-loop system satisfies the inequality (8).

For simplicity of the deducing process, some functions will be abbreviated, e.g., $f\left(x^{(0\sim n-1)}\right)$, $\Delta f\left(x^{(0\sim n-1)},t\right)$ and $L\left(x^{(0\sim n-1)}\right)$ are denoted by f, Δf and L, respectively.

4 Main Result

In this section, the robust bounded-H_∞ controller for system (2) will be designed, and the main theorem of this paper is given in advance in order to illustrate simply our work.

For high-order FAS (2), the robust bounded-H_∞ controller is designed directly as

$$u=u_s+u_h \quad (9)$$

with

$$u_s=-\frac{1}{L}\left(A^{0\sim n-1}x^{(0\sim n-1)}+f\right) \quad (10)$$

and

$$u_h=-\frac{1}{L}P_H^{\mathrm{T}}x^{(0\sim n-1)} \times\left(\frac{1}{4}\rho^2+\frac{1}{4\gamma^2}+\frac{1}{4\gamma^2}\Psi^2\right), \quad (11)$$

where $A^{0\sim n-1}$ is the vector making $\Phi\left(A^{0\sim n-1}\right)$ satisfy (4), $\gamma>0$ is a design parameter, and P_H is defined in (15).

Now, the theorem of this paper is given as follows:

Theorem 1 *For high-order FAS (2) satisfying Assumptions 1, 2, if the control law is designed according to (9)-(11), then*

1) the state and its derivatives x*,* $\dot{x}$*,*$\cdots$*,*$x^{(n-1)}$ *are globally bounded,*

2) the closed-loop system has the bounded-H_∞ *performance.*

Proof: The proof process of Theorem 1 is divided into the following two steps.

Step 1 Some pretreatments

Substituting (9) and (10) into the system (2) obtains

$$x^{(n)} = -A^{0\sim n-1}x^{(0\sim n-1)} + \Delta f + \Psi\omega + Lu_h.$$

Thus, one has

$$\dot{x}^{(0\sim n-1)} = \Phi\left(A^{0\sim n-1}\right)x^{(0\sim n-1)} + \begin{bmatrix} 0_{(n-1)\times 1} \\ \Delta f + \Psi\omega + Lu_h \end{bmatrix}. \tag{12}$$

Choose the Lyapunov function candidate as

$$V_1 = \frac{1}{2}\left(x^{(0\sim n-1)}\right)^{\mathrm{T}} P x^{(0\sim n-1)}, \tag{13}$$

where P is a positive definite matrix satisfying the inequality (5).

Taking derivative for (13) and using Lemma 3, there is

$$\begin{aligned}\dot{V}_1 =& \frac{1}{2}\left(x^{(0\sim n-1)}\right)^{\mathrm{T}}\left(\Phi^{\mathrm{T}}P + P\Phi\right)x^{(0\sim n-1)} \\ &+ \left(x^{(0\sim n-1)}\right)^{\mathrm{T}} P\begin{bmatrix} 0_{(n-1)\times 1} \\ \Delta f + \Psi\omega + Lu_h \end{bmatrix} \\ \leq& -\frac{1}{2}\mu\left(x^{(0\sim n-1)}\right)^{\mathrm{T}} P x^{(0\sim n-1)} \\ &+ \left(x^{(0\sim n-1)}\right)^{\mathrm{T}} P_H\Delta f + \left(x^{(0\sim n-1)}\right)^{\mathrm{T}} P_H\Psi\omega \\ &+ \left(x^{(0\sim n-1)}\right)^{\mathrm{T}} P_H L u_h, \end{aligned} \tag{14}$$

where

$$P_H = P\begin{bmatrix} 0_{(n-1)\times 1} \\ 1 \end{bmatrix}. \tag{15}$$

Now, we handle the terms $\left(x^{(0\sim n-1)}\right)^{\mathrm{T}} P_H\Delta f$ and $\left(x^{(0\sim n-1)}\right)^{\mathrm{T}} P_H\Psi\omega$ in (14). According to Assumption 2 and Lemma 1, the following inequalities hold.

$$\begin{aligned}\left(x^{(0\sim n-1)}\right)^{\mathrm{T}} P_H\Delta f \leq& \left\|\left(x^{(0\sim n-1)}\right)^{\mathrm{T}} P_H\right\| |\rho| \times 1 \\ &+ \left\|\left(x^{(0\sim n-1)}\right)^{\mathrm{T}} P_H\right\| \times |D| \\ \leq& \frac{1}{4}\left\|\left(x^{(0\sim n-1)}\right)^{\mathrm{T}} P_H\right\|^2 \rho^2 + 1 \\ &+ \frac{1}{4\gamma^2}\left\|\left(x^{(0\sim n-1)}\right)^{\mathrm{T}} P_H\right\|^2 \\ &+ \gamma^2 D^2, \end{aligned} \tag{16}$$

$$\left(x^{(0\sim n-1)}\right)^{\mathrm{T}} P_H\Psi \times \omega \leq \frac{1}{4\gamma^2}\left\|\left(x^{(0\sim n-1)}\right)^{\mathrm{T}} P_H\right\|^2 \times \Psi^2 + \gamma^2\omega^2. \tag{17}$$

Therefore, the inequality (14) is rewritten into

$$\begin{aligned}\dot{V}_1 \leq& -\mu V_1 + \left\|\left(x^{(0\sim n-1)}\right)^{\mathrm{T}} P_H\right\|^2 \\ &\times\left(\frac{1}{4}\rho^2 + \frac{1}{4\gamma^2} + \frac{1}{4\gamma^2}\Psi^2\right) \\ &+ 1 + \gamma^2\bar{\omega}^2 + \left(x^{(0\sim n-1)}\right)^{\mathrm{T}} P_H L u_h \end{aligned} \tag{18}$$

with $\bar{\omega}(t) = \sqrt{\omega^2(t) + D^2(t)}$.

Remark 2 *$\bar{\omega}(t) = \sqrt{\omega^2(t) + D^2(t)}$ contains the unknown uncertain term and the external disturbance, and cannot be offset directly by the controller design.*

Step 2 The performance analysis of system (2)

Choose the final Lyapunov function as

$$V = V_1 + \varepsilon > 0, \tag{19}$$

where $\varepsilon > 0$ is a small constant.

Remark 3 *The aim introducing the constant ε is to help us complete the subsequent proof, of which the value is not required to be known for the controller design. It should be emphasized that such treatment is also done in [22, 26].*

From (11), (13) and (19), it is known that $\dot{V}$ satisfies

$$\begin{aligned}\dot{V} \leq& -(\mu-1)V_1 + 1 + \gamma^2\bar{\omega}^2 \\ &- \frac{1}{2}\left(x^{(0\sim n-1)}\right)^{\mathrm{T}} P x^{(0\sim n-1)} \\ \leq& -\tilde{\mu}V_1 + 1 + \gamma^2\bar{\omega}^2 - \frac{1}{2}\lambda_{\min}(P)\left\|x^{(0\sim n-1)}\right\|^2 \\ \leq& -\tilde{\mu}V_1 - \varepsilon + \varepsilon + 1 + \gamma^2\bar{\omega}^2 \\ &- \frac{1}{2}\lambda_{\min}(P)\left\|x^{(0\sim n-1)}\right\|^2 \\ \leq& -\hat{\mu}V + b - \frac{1}{2}\lambda_{\min}(P)\left\|x^{(0\sim n-1)}\right\|^2, \end{aligned} \tag{20}$$

where $\tilde{\mu} = \mu - 1 > 0$ which is easily satisfied as long as $\mu > 1$, $\hat{\mu} = \min\{1, \tilde{\mu}\}$, $\lambda_{\min}(P)$ is the minimum eigenvalue of P, and $b = \bar{b} + \gamma^2\bar{\omega}^2$ with $\bar{b} = \varepsilon + 1$ is a bounded constant.

Due to $-\frac{1}{2}\lambda_{\min}(P)\left\|x^{(0\sim n-1)}\right\|^2 \leq 0$, it is obtained from (20) that

$$\dot{V}(t) \leq -\hat{\mu}V + b$$

which illustrates that the state and its derivatives x, $\dot{x}$,$\cdots$,$x^{(n-1)}$ are globally bounded.

Further, because of $V > 0$ and (20), there is

$$\dot{V} + \frac{1}{2}\lambda_{\min}(P)\left\|x^{(0\sim n-1)}\right\|^2 - \gamma^2\bar{\omega}^2 \leq \bar{b} \leq \tau V, \tag{21}$$

where τ is a proper constant. Integrating (21) obtains

$$\begin{aligned}V(t) \leq& \int_0^t -\frac{1}{2}\lambda_{\min}(P)\left\|x^{(0\sim n-1)}(s)\right\|^2 + \gamma^2\bar{\omega}^2(s)\,ds \\ &+ V(0) + \int_0^t \tau V(s)\,ds. \end{aligned} \tag{22}$$

According to Lemma 4, if we respectively define $\Theta(t) = V(t)$, $\Upsilon(t) = V(0) + \int_0^t -\frac{1}{2}\lambda_{\min}(P)\left\|x^{(0\sim n-1)}(s)\right\|^2 + \gamma^2\bar{\omega}^2(s)\,ds$; $\zeta(s) = \tau$, then

$$\Theta(t) \leq \Upsilon(t) + \int_0^t \zeta(s)\Upsilon(s)e^{\int_s^t \zeta(h)dh}ds. \tag{23}$$

Next, we will prove that $\Upsilon(t) > 0$ holds. To seek a contradiction, suppose that there is a time $t = \bar{t}$ such that $\Upsilon(\bar{t}) \leq 0$. Therefore, from (23), one has

$$V(\bar{t}) \leq \tau\int_0^{\bar{t}} \Upsilon(s)e^{\int_s^{\bar{t}}\tau dh}ds \leq 0, \tag{24}$$

which yields a contradiction because of $V(t) > 0$. Thus, $\Upsilon(t) = V(0) + \int_0^t -\frac{1}{2}\lambda_{\min}(P) \left\| x^{(0\sim n-1)}(s) \right\|^2 + \gamma^2 \bar{\omega}^2(s)\, ds > 0$ which means that

$$V(0) + \int_0^t \gamma^2 \bar{\omega}^2(s)\, ds > \int_0^t \frac{1}{2}\lambda_{\min}(P) \left\| x^{(0\sim n-1)}(s) \right\|^2 ds, \tag{25}$$

and thus

$$\int_0^t \|y(s)\|^2 ds \le \bar{\gamma}^2 \int_0^t \|\bar{\omega}(s)\|^2 ds + d(x(0)) \tag{26}$$

with $\bar{\gamma} = \gamma\sqrt{\frac{2}{\lambda_{\min}(P)}}$ and $d(x(0)) = \frac{2}{\lambda_{\min}(P)} V(0)$. According to Definition 1, the closed-loop system (2) has the bounded-H_∞ performance. Therefore, the impact of the combined disturbance $\bar{\omega}$ on system output can be attenuated to the given extent $\bar{\gamma}$.

Up to now, Theorem 1 has been proved.

Remark 4 *From (26), because the combined disturbance $\bar{\omega}$ contains the part uncertain term and the disturbance, their impact on system output can be attenuated simultaneously by adjusting the value of γ to ensure the small value of $\bar{\gamma}$.*

Remark 5 *The controller (9) includes directly or indirectly the matrices P and $A^{0\sim n-1}$ to ensure (4), (5) and $\mu > 1$, of which the selection can be found in Propositions 3.3-3.4 in [2].*

5 Simulation Study

Consider the following system investigated in [27]:

$$\begin{cases} \dot{x}_1 = 0.1x_1^2 - x_2, \\ \dot{x}_2 = 0.2x_1x_2 + x_1 + 2u, \\ y = x_1. \end{cases} \tag{27}$$

From the first equation of (27), there are

$$\ddot{x}_1 = 0.2x_1\dot{x}_1 - \dot{x}_2 \tag{28}$$

and

$$x_2 = 0.1x_1^2 - \dot{x}_1. \tag{29}$$

Then, substituting the second equation of (27) and (29) into (28) obtains

$$\begin{cases} \ddot{x} = f + \Delta f + x\omega - 2u \\ y = x \end{cases} \tag{30}$$

with $f = 0.4x\dot{x} - 0.02x^3 - x$, where x_1 is replaced by x. Differently, the time-varying uncertainty Δf and the external disturbance term $x\omega$ are introduced for proving the robustness of our control method. Therein, for Δf and ω, we consider the following two cases:

Case A: $\Delta f = \omega = 0$;

Case B: $\Delta f = \dot{x}^2 + 0.5e^{-3t}\sin(4\pi t)$ and

$$\omega = \begin{cases} 3\sin(2\pi t), t \le 1.2; \\ 18, 1.2 < t \le 2.2; \\ 6e^{-2t}, t > 2.2. \end{cases}$$

In fact, Case A is an ideal case. That is, the system (30) does not suffer from the uncertainty and the disturbance. Obviously, the system (30) satisfies Assumptions 1-2. According to Theorem 1, the robust bounded-H_∞ controller is designed as follows:

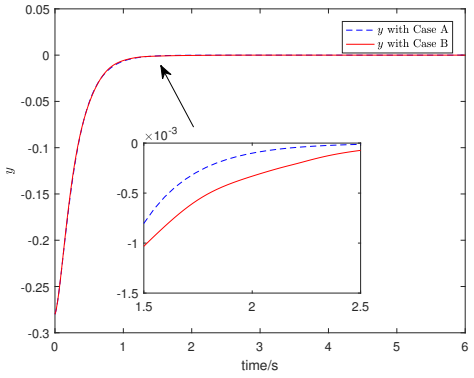

Fig. 1: y with two cases

$$u = u_s + u_h \tag{31}$$

with

$$u_s = \frac{1}{2}\left(A^{0\sim n-1}x^{(0\sim n-1)} + f\right), \tag{32}$$

$$u_h = \frac{1}{2}P_H^{\mathrm{T}}x^{(0\sim n-1)} \times \left(\frac{1}{4}\dot{x}^4 + \frac{1}{4\gamma^2} + \frac{1}{4\gamma^2}x^2\right). \tag{33}$$

Therein, the design matrices (parameter) are chosen respectively as $\gamma = 0.1$,

$$A^{0\sim 1} = \begin{bmatrix} 48 & 14 \end{bmatrix}, \tag{34}$$

$$P = \begin{bmatrix} 3.7917 & 0.0208 \\ 0.0208 & 0.0729 \end{bmatrix}, \tag{35}$$

and thus

$$P_H = \begin{bmatrix} 0.0208 \\ 0.0729 \end{bmatrix}.$$

The system initial value is $x^{(0\sim 1)}(0) = \begin{bmatrix} -0.28 & 0.2 \end{bmatrix}^{\mathrm{T}}$. The simulation results are shown in Figs.1-3. Fig.1 shows the trajectories of x with two cases, namely, the system output y. The trajectories of $\dot{x}$ and u with two cases are depicted in Figs.2-3, respectively. From Figs.1-2, the boundedness of x and $\dot{x}$ is shown. Moreover, it can be seen from Fig.1 that the curves of the output y with two cases are basically consistent, which illustrates that the robust bounded-H_∞ controller can attenuate the impact of the time-varying uncertainty and the disturbance on system output. The above fact illustrates the effectiveness of our control method.

6 Conclusions

This paper solves the robust bounded-H_∞ control problem for a class of high-order FASs with time-varying uncertainty and external disturbance. It has been proven that the designed robust bounded-H_∞ controller guarantees the global boundedness of the system state and its derivatives of each order, and can attenuate the impact of the uncertainty and the disturbance on system output by adjusting the design parameter. Therefore, the control method proposed in this paper has stronger robustness. A simulation example proves the effectiveness of the proposed control method.

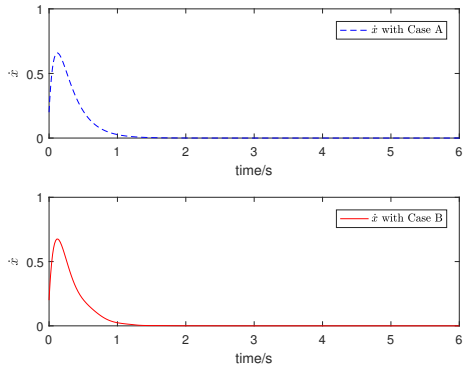

Fig. 2: $\dot{x}$ with two cases

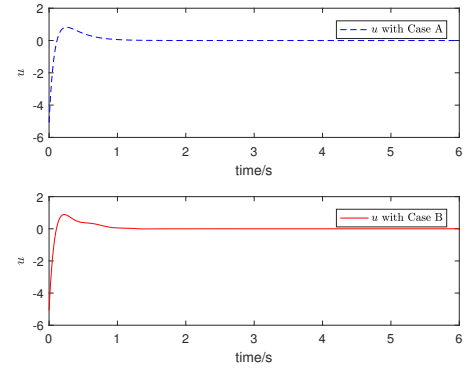

Fig. 3: u with two cases

References

[1] G. R. Duan, High-order system approaches: I. Fully actuated systems and parametric designs, *ACTA Automatica Sinica* (in Chinese), 2020, 46(7): 1333-1345.

[2] G. R. Duan, High-order fully actuated system approaches: Part IV. Adaptive control and high-order backstepping, *International Journal of Systems Science*, 2020, 52(5): 972-989.

[3] G. R. Duan, High-order fully actuated system approaches: Part V. Robust adaptive control, *International Journal of Systems Science*, 2021, 52(10): 2129-2143.

[4] G. R. Duan, High-order fully actuated system approaches: Part X. Basics of discrete-time systems, *International Journal of Systems Science*, 2022, 53(4): 810-832.

[5] G. R. Duan, Stabilization via fully actuated system approach: A case study, *Journal of Systems Science & Complexity*, 2022, 35(3): 731-7472.

[6] G. R. Duan, Robust stabilization of time-varying nonlinear systems with time-varying delays: A fully actuated system approach. *IEEE Transactions on Cybernetics*, 2022, DOI: 10.1109/TCYB.2022.3217317.

[7] M. Cai, X. He, and D. H. Zhou, An active fault tolerance framework for uncertain nonlinear high-order fully-actuated systems, *Automatica*, 2023, DOI: 10.1016/j.automatica.2023.110969.

[8] R. X. Dong, C. C. Hua, K. Li, and R. Meng, Adaptive fault-tolerant control for high-order fully actuated system with full-state constraints. *Journal of the Franklin Institute*, 2023, 360(12): 8062-8074.

[9] G. P. Liu, Predictive control of high-order fully actuated nonlinear systems with time-varying delays, *Journal of Systems Science & Complexity*, 2022, 35(2): 457-470.

[10] D. W. Zhang, G. P. Liu, and L. Cao, Coordinated control of high-order fully actuated multiagent systems and its spplication: A predictive control strategy, *IEEE-ASME Transactions on Mechatronics*, 2022, 27(6): 4362-4372.

[11] R. Meng, C. C. Hua, K. Li, and P. J. Ning, Adaptive event-triggered control for uncertain high-order fully actuated system, *IEEE Transactions on Circuits and Systems II-Express Briefs*, 2022, 69(11): 4438-4442.

[12] H. Y. Yan, J. W. Xia, X. R. Liu, H. R. Yue, and C. Li, Adaptive backstepping control of high-order fully actuated nonlinear systems with event-triggered strategy, *Intelligence & Robotics*, 2023. DOI: 10.20517/ir.2023.11.

[13] D. W. Zhang, G. P. Liu, and L. Cao, Constrained cooperative control for high-order fully actuated multiagent systems with application to air-bearing spacecraft simulators, *IEEE-ASME Transactions on Mechatronics*, 2023, 28(3): 1570-1581.

[14] P. Li and G. R. Duan, High-order fully actuated control approach for flexible servo systems using dynamical compensator, in *Proceedings of the 2nd Conference on Fully Actuated System Theory and Applications*, Qingdao, 2023, 862-867.

[15] Y. W. Zhang and C. J. Chen, Research on control strategy of lateral semi-active suspension of built-in bogie vehicle based on full-actuated system approaches, in *Proceedings of the 2nd Conference on Fully Actuated System Theory and Applications*, Qingdao, 2023, 880-887.

[16] X. H. Li and X. P. Liu, Backstepping-based decentralized adaptive neural H_∞ control for a class of large-scale nonlinear systems with expanding construction, *Nonlinear Dynamics*, 2017, 90(2): 1373-1392.

[17] Z. X. Zhong, J. Y. Yu, Y. D. He, T. Hayat, and F. Alsaadi, Fuzzy-model-based decentralized dynamic-output-feedback H_∞ control for large-scale nonlinear systems with time-varying delays, *Neurocomputing*, 2016, 173: 1054-1065.

[18] L. B. Wu, X. Q. He, D. Q. Zhang, and H. W. Jia, Adaptive H_∞ fault-tolerant control for a class of uncertain switched nonlinear systems with multiple state time delays, *International Journal of Systems Science*, 2018, 49(8): 1784-1794.

[19] D. E. Cheridi and N. Mansouri, Robust H_∞ fault-tolerant control for discrete-time nonlinear system with actuator faults and time-varying delays using nonlinear T-S fuzzy models, *Circuits Systems and Signal Processing*, 2020, 39(1): 175-198.

[20] A. A. G. Siqueira and M. H. Terra, Neural network-based H_∞ control for fully actuated and underactuated cooperative manipulators, *Control Engineering Practice*, 2009, 17(3): 418-425.

[21] Y. Q. Liu, Q. Y. Zhu, Z. K. Wang, Y. F. Wu, Y. J. Pang, J. J. Zhu, and G. M. Zhuang, H_∞ admissibilization for second-order fully actuated fuzzy delayed singular impulsive systems with Markovian jump characteristic, in *Proceedings of the 2nd Conference on Fully Actuated System Theory and Applications*, Qingdao, 2023, 14-16.

[22] H. Liu, X. H. Li, X. P. Li, and H. Q. Wang, Adaptive neural network prescribed performance bounded-H_∞ tracking control for a class of stochastic nonlinear Systems, *IEEE Transactions on Neural Networks and Learning Systems*, 2020, 31(6): 2140-2152.

[23] J. Zhou, C. Y. Wen, W. Wang, and F. Yang, Adaptive backstepping control of nonlinear uncertain systems with quantized states, *IEEE Transactions on Automatic Control*, 2019, 64(11): 4756-4763.

[24] W. S. Chen and J. M. Li, Decentralized output-feedback neural control for systems with unknown interconnections, *IEEE Transactions on Systems Man and Cybernetics Part B-Cybernetics*, 2008, 38(1): 258-266.

[25] S. S. Dragomir, Some gronwall type inequalities and applications, *Nova Science Publishers*, 2003.

[26] X. H. Li and L. Y. Hu, Prescribed performance finite-time H_∞ tracking control for a class of p-normal form nonlinear systems, *ACTA Automatica Sinica* (in Chinese), 2021, 47(12): 2870-2880.

[27] Y. J. Liu and S. Tong, Barrier Lyapunov functions for Nussbaum gain adaptive control of full state constrained nonlinear systems, *Automatica*, 2017, 76: 143-152.

Proceedings of the 3rd Conference on Fully Actuated System Theory and Applications
May 10-12, 2024, Shenzhen, China

Differentiator-Based Adaptive H_∞ Tracking Control of Fully Actuated Systems

Yuxin Feng[1], Zhiqiang Li[1], Yang Liu[2], Zhaoshui He[3 4], Hongyi Li[1]

1. School of Automation and Guangdong Provincial Key Laboratory of Intelligent Decision and Cooperative Control, Guangdong University of Technology, Guangzhou 510006, China
2. School of Automation and Electronics Engineering, Qingdao University of Science and Technology, Qingdao 266061, China
3. School of Automation, Guangdong University of Technology, Guangzhou 510006, China
4. Key Laboratory for IoT Intelligent Information Processing and System Integration of Ministry of Education, Guangzhou 510006, China

E-mail: fengyuxin1227@163.com; lizhiqiang202108@163.com; liuyang0595@163.com; zhshhe@gdut.edu.cn; lihongyi2009@gmail.com;

Abstract: This article addresses an adaptive tracking control problem for uncertain high-order fully actuated (HOFA) systems with unknown parameters and disturbances. Under the framework of backstepping, the unknown parameter is estimated and the external disturbance is handled by using adaptive control and H_∞ technique, respectively. Moreover, the Levant differentiator is employed to reduce the computation burden. Additionally, the boundedness of signals in the closed-loop system is proven using the Lyapunov theory. Finally, the effectiveness of the proposed scheme is validated through the simulation study.

Key Words: High-order fully actuated systems, adaptive backstepping, H_∞ control, differentiator.

1 Introduction

In real applications, most of systems are the high-order form, which presents some challenge to the state-space-based traditional backstepping. Hence, a new strategy called high-order fully actuated (HOFA) is proposed [1], which avoids to convert a high-order system into the corresponding first-order one, and reduces the computation process [2]. Authors in [3] design a direct adaptive stabilizing controller and tracking controller for HOFA systems. A high-order backstepping method is proposed in [4] to establish stabilizing controller. By utilizing the backstepping, an adaptive event-triggered fuzzy control scheme of HOFA systems is introduced in [5]. However, it should be pointed out that how to combine backstepping with HOFA approach is still an open field.

It is well known that the differential explosion is a main issue existed in the backstepping, which can be solved by using the dynamic surface control and command filter. A HOFA scheme is designed by combing the command filter in [6], which is not required to convert the original system into the first-order one. Under the output constraint, an adaptive control approach is investigated on the basis of the dynamic surface technique and barrier function for unknown strict-feedback high-order systems [7]. Compared with the traditional backstepping method, a simple design process is introduced and a compensating strategy is established [8] to reduce the filtering error. The above methods can solve the differential explosion problem, however, they are sensitive to design parameters and may cause the overshoot.

In the industrial process, the external disturbance cannot be avoided. Among many ways to deal with disturbances, H_∞ is an effective method, but there are few results combining with the HOFA backstepping technique. In [9], the disturbance is handled for HOFA nonlinear systems with strict-feedback structure, however, it cannot be used to address the system with unknown parameters. Authors of [10] only employ one adaptive law to estimate the uncertain parameter to solve the overestimated problem, and an adaptive stability controller is given for the HOFA plant. However, the above schemes still exist the computation complex problem.

Based on the above discussions, this work considers a nonlinear HOFA model with unknown parameters and disturbances. The adaptive controller and H_∞ method are combined to address unknown parameters and external disturbances. Moreover, the differentiator is introduced to reduce the computational complexity caused by the repeated differentiation of the virtual controller.

The organization of the remainder is given as: In Section 2, some preliminaries are introduced. The main result is given in Section 3. Simulation study and conclusion are demonstrated in Sections 4 and 5, respectively.

Notations: $\Re$ is the real number domain; $\Re^r$ represents r dimensional Euclidean space; $\Re^{i\times j}$ describes the $i\times j$ matrix; $[\cdot]^{\mathrm{T}}$ represents the transpose of a matrix; $\mathbf{0}_{i\times j}$ is a zero matrix of $i\times j$ and I_r represents the r-dimensional identity matrix.

2 Preliminaries

Consider the following nonlinear plant with unknown parameters and external disturbances

$$\begin{aligned} x_1^{(m_1)} =& f_1\left(x_1^{(0\sim m_1-1)}\right)+g_1\left(x_1^{(0\sim m_1-1)}\right)x_2+{\psi_1}^{\mathrm{T}} \\ &\times\left(x_1^{(0\sim m_1-1)}\right)\theta+s_1\left(x_1^{(0\sim m_1-1)}\right)\omega \\ \dot{x}_i =& f_i\left(\bar{x}_i\right)+g_i\left(\bar{x}_i\right)x_{i+1}+{\psi_i}^{\mathrm{T}}\left(\bar{x}_i\right)\theta+s_i\left(\bar{x}_i\right)\omega \\ \dot{x}_n =& f_n\left(\bar{x}_n\right)+g_n\left(\bar{x}_n\right)u+{\psi_n}^{\mathrm{T}}\left(\bar{x}_n\right)\theta+s_n\left(\bar{x}_n\right)\omega \\ y =& x_1 \end{aligned} \tag{1}$$

where $i=2,3,\cdots,n-1$; $m_1>1$ is an integer; $x_i\in\Re^r$ is the state variable; $u\in\Re^r$ and $y\in\Re^r$ are the control input and system output, respectively; $\bar{x}_i=$

This work was partially supported by the National Natural Science Foundation of China (62373208, 62003097, 62033003), and Taishan Scholar program of Shandong Province of China (tsqn202306218).

$\left[\left(x_1^{(0\sim m_1-1)}\right)^{\mathrm{T}}, x_2, \cdots, x_i\right]^{\mathrm{T}}$; $f_i(\cdot) \in \Re^r$ is a known vector, $g_i(\cdot) \in \Re^{r\times r}, s_i(\cdot) \in \Re^{r\times r}$ and $\psi_i^{\mathrm{T}}(\cdot) \in \Re^{r\times r}$ are known functions, $\theta \in \Re^r$ is an unknown constant vector; $\omega \in \Re^r$ is an uncertain external disturbance; and

$$x_1^{(0\sim m_1-1)} = \begin{bmatrix} x \\ \dot{x} \\ \vdots \\ x_1^{(m_1-1)} \end{bmatrix}$$

The goal of this paper is to design the controller and adaptive law to make sure that
(1) When $\omega(t) = 0$, all signals in the closed-loop system are bounded;
(2) When $\omega(t) \in L_2$, the following inequality holds:

$$\int_0^T ||y(t) - y_r(t)||^2 dt \le \lambda \int_0^T ||\omega(t)||^2 dt + \Omega_0 T \quad (2)$$

where $y_r \in \Re^r$ is the desired output signal, Ω_0 is a positive constant, and $\lambda > 0$ is an H_∞ performance index.

In order to obtain the above control goal, some assumptions and lemmas are required.

Assumption 1 *[11] The reference signal y_r and its derivatives up to the $(m_1 + n - 1)^{th}$ are continuous and bounded.*

Assumption 2 *[1] $g_i(\bar{x}_i)$ is a sufficiently smooth function, which satisfies the following full-actuation condition: $g_i(\bar{x}_i) \neq 0$ for $\forall \bar{x}_i \in R^{m_1+i-1}, i = 1, 2, ..., n$.*

Lemma 1 *[12] Consider the following Levant differentiator:*

$$\begin{aligned} \dot{k}_1(t) &= k_2(t) - h_1 |k_1(t) - \alpha(t)|^{\frac{1}{2}} \mathrm{sign}(k_1(t) - \alpha(t)) \\ \dot{k}_2(t) &= -h_2 \mathrm{sign}(k_1(t) - \alpha(t)) \end{aligned} \quad (3)$$

where $\alpha(t)$ and $k_1(t)$ are the input and output, respectively, if there exists $\alpha_0 t$ whose first derivative is Lipschitz such that $|\alpha(t) - \alpha_0(t)| \le \varepsilon$, then one can approximately select positive parameters h_1 and h_2 such that the following condition holds within a finite time:

$$\begin{aligned} |k_1(t) - \alpha_0(t)| &\le \bar{\varepsilon}_1 \\ |\dot{k}_1(t) - \dot{\alpha}_0(t)| &\le \bar{\varepsilon}_2 \end{aligned}$$

where $\bar{\varepsilon}_1$ and $\bar{\varepsilon}_2$ are positive scalars determined by h_1 and h_2.

Lemma 2 *[13] For any $\mu > 0$, there exists a matrix $A^{0\sim m_1-1}$ that satisfies the following condition:*

$$Re\left(\lambda_i\left(\Phi_i\left(A^{0\sim m_1-1}\right)\right)\right) < -\frac{\mu}{2}, i = 1, 2, ..., m_1 \quad (4)$$

where $A^{0\sim m_1-1} = [A_0 \quad A_1 \quad ... \quad A_{m_1-1}]$ and $A_j \in \Re^{r\times r}, j = 1, ..., m_1 - 1$.

Lemma 3 *[13] If $\Phi\left(A^{0\sim m_1-1}\right)$ satisfies (4), then there must exist a positive definite matrix $P\left(A^{0\sim m_1-1}\right) \in \Re^{m_1 r\times m_1 r}$ such that*

$$\begin{aligned} &\Phi\left(A^{0\sim m_1-1}\right)^{\mathrm{T}} P\left(A^{0\sim m_1-1}\right) + P\left(A^{0\sim m_1-1}\right)\Phi\left(A^{0\sim m_1-1}\right) \\ &\le -\mu P\left(A^{0\sim m_1-1}\right) \end{aligned} \quad (5)$$

with

$$\Phi\left(A^{0\sim m_1-1}\right) = \begin{bmatrix} 0 & I_r & & \\ \vdots & & \ddots & \\ 0 & 0 & \cdots & I_r \\ -A_0 & -A_1 & \cdots & -A_{m_1-1} \end{bmatrix}$$

3 Main Results

3.1 Controller design

First, a series of coordinate transformations is designed as

$$\begin{aligned} z_1 &= x_1 - y_r \\ z_i &= x_i - \alpha_{i-1} \\ z_n &= x_n - \alpha_{n-1} \end{aligned} \quad (6)$$

where $\alpha_i \in \Re^r, i = 1, ..., n-1$ are virtual controllers.

Then, the controller design includes the following n steps.

Step 1: From $z_1 = y - y_r$ and (1), one has

$$z_1^{(m_1)} = f_1 + g_1 z_2 + g_1 \alpha_1 + {\psi_1}^{\mathrm{T}}\theta + s_1\omega - y_r^{(m_1)} \quad (7)$$

The virtual controller is selected as

$$\begin{aligned} \alpha_1 = &- g_1^{-1}\Big(A^{0\sim m_1-1} z_1^{(0\sim m_1-1)} + f_1 - y_r^{(m_1)} + \psi_1^{\mathrm{T}}\widehat{\theta} \\ &+\Gamma_1\Big) \end{aligned} \quad (8)$$

where $\Gamma_1 \in \Re^r$ is an unknown vector function designed later, and $\hat{\theta} \in \Re^r$ is the estimated value of θ.

Substituting (8) into (7) yields

$$\begin{aligned} z_1^{(m_1)} = &- A^{0\sim m_1-1} z_1^{(0\sim m_1-1)} + {\psi_1}^{\mathrm{T}}\widetilde{\theta} + s_1\omega \\ &- \Gamma_1 + g_1 z_2 \end{aligned} \quad (9)$$

with $\widetilde{\theta} = \theta - \hat{\theta}$.

Then, (9) is converted into

$$\begin{aligned} \dot{z}_1^{(0\sim m_1-1)} =&\Phi\left(A^{0\sim m_1-1}\right) z_1^{(0\sim m_1-1)} \\ &+ \begin{bmatrix} \mathbf{0}_{(m_1-1)\times 1} \\ \psi_1^{\mathrm{T}}\widetilde{\theta} + s_1\omega - \Gamma_1 + g_1 z_2 \end{bmatrix} \end{aligned} \quad (10)$$

Choose the Lyapunov function as

$$\begin{aligned} V_1 =&\frac{1}{2}\left(z_1^{(0\sim m_1-1)}\right)^{\mathrm{T}} P\left(A^{0\sim m_1-1}\right)\left(z_1^{(0\sim m_1-1)}\right) \\ &+ \frac{1}{2}\widetilde{\theta}^{\mathrm{T}}\widetilde{\theta} \end{aligned} \quad (11)$$

For simplicity, let $P(A^{0\sim m_1-1})$ and $\Phi(A^{0\sim m_1-1})$ as P and Φ, respectively. Then, it follows from Lemma 3, (10) and (11) that one has

$$\begin{aligned} \dot{V}_1 =&\frac{1}{2}\Big[\left(\dot{z}_1^{(0\sim m_1-1)}\right)^{\mathrm{T}} P z_1^{(0\sim m_1-1)} + \left(z_1^{(0\sim m_1-1)}\right)^{\mathrm{T}} P \\ &\times \dot{z}_1^{(0\sim m_1-1)}\Big] - \widetilde{\theta}^{\mathrm{T}}\dot{\hat{\theta}} \\ =&\frac{1}{2}\Big[\left(z_1^{(0\sim m_1-1)}\right)^{\mathrm{T}} \Phi^{\mathrm{T}} P z_1^{(0\sim m_1-1)} + \left(z_1^{(0\sim m_1-1)}\right)^{\mathrm{T}} P\Phi \\ &\times z_1^{(0\sim m_1-1)}\Big] + \left(z_1^{(0\sim m_1-1)}\right)^{\mathrm{T}} P_H\left(g_1 z_2 + \psi_1^{\mathrm{T}}\widetilde{\theta}\right. \\ &\left.+ s_1\omega - \Gamma_1\right) - \widetilde{\theta}^{\mathrm{T}}\dot{\hat{\theta}} \end{aligned} \quad (12)$$

with $P_H = P\left(A^{0\sim m_1-1}\right)\begin{bmatrix}\mathbf{0}_{(m_1-1)r\times r}\\ I_r\end{bmatrix}$.

According to Young's inequality, it gives

$$\left(z_1^{(0\sim m_1-1)}\right)^{\mathrm{T}} P_H s_1\omega \leq \frac{1}{2\gamma}\left(z_1^{(0\sim m_1-1)}\right)^{\mathrm{T}} P_H s_1 s_1^{\mathrm{T}} P_H^{\mathrm{T}} \times z_1^{(0\sim m_1-1)} + \frac{1}{2}\gamma\omega^{\mathrm{T}}\omega \quad (13)$$

where γ is an adjustable positive constant, which combines with Lemma 3, we have

$$\begin{aligned}\dot{V}_1 \leq & -\frac{1}{2}\mu\left(z_1^{(0\sim m_1-1)}\right)^{\mathrm{T}} P z_1^{(0\sim m_1-1)} + \frac{1}{2}\gamma\omega^{\mathrm{T}}\omega \\ & -\left(z_1^{(0\sim m_1-1)}\right)^{\mathrm{T}} P_H\left(\Gamma_1 - \frac{1}{2\gamma}s_1 s_1^{\mathrm{T}} P_H^{\mathrm{T}} z_1^{(0\sim m_1-1)}\right) \\ & -\widetilde{\theta}^{\mathrm{T}}\left(\dot{\hat{\theta}} - \psi_1 P_H^{\mathrm{T}} z_1^{(0\sim m_1-1)}\right) + \left(z_1^{(0\sim m_1-1)}\right)^{\mathrm{T}} P_H g_1 z_2\end{aligned} \quad (14)$$

So far, Γ_1 can be defined by

$$\Gamma_1 = \frac{1}{2\gamma}s_1 s_1^{\mathrm{T}} P_H^{\mathrm{T}} z_1^{(0\sim m_1-1)} \quad (15)$$

Step i $(2 \leq i \leq n-1)$. To solve the problem of differential explosion, we introduced the Levant differentiator to filter the derivatives of the virtual controller. In this paper, $x_{i,c}$ is used to represent the filter output of the differentiator, that is

$$x_{i,c} = \dot{\alpha}_i - e_i \quad (16)$$

where e_i represents the filtering error.

It can be deduced from Lemma 1 that e_i is bounded within a finite time. Then, computing the derivation of α_{i-1} and applying Lemma 1 has

$$\dot{\alpha}_{i-1} = e_{i-1} + x_{i-1,c} \quad (17)$$

Based on (6) and (17), it produces

$$\begin{aligned}\dot{z}_i = & f_i + g_i z_{i+1} + g_i\alpha_i + \psi_i^{\mathrm{T}}\theta + s_i\omega - x_{i-1,c} \\ & - e_{i-1}\end{aligned} \quad (18)$$

Consider the following Lyapunov function

$$V_i = V_{i-1} + \frac{1}{2}z_i^{\mathrm{T}} z_i \quad (19)$$

and its derivative as

$$\dot{V}_i = \dot{V}_{i-1} + z_i^{\mathrm{T}}\dot{z}_i \quad (20)$$

$$\begin{aligned}\leq & -\frac{1}{2}\mu\left(z_1^{(0\sim m_1-1)}\right)^{\mathrm{T}} P\left(A^{0\sim m_1-1}\right) z_1^{(0\sim m_1-1)} - \sum_{k=2}^{i-1} \\ & \times\left(c_k - \frac{1}{2}\right) {z_k}^{\mathrm{T}} z_k + \frac{i-1}{2}\gamma\omega^{\mathrm{T}}\omega + \sum_{l=1}^{i-2}\frac{1}{2}{e_l}^{\mathrm{T}} e_l - \widetilde{\theta}^{\mathrm{T}} \\ & \times\left(\dot{\hat{\theta}} - \psi_1 P_H^{\mathrm{T}} z_1^{(0\sim m_1-1)} - \sum_{p=2}^{i-1}\psi_p z_p\right) + \chi_i + z_i^{\mathrm{T}}\left(f_i\right. \\ & \left.+g_i z_{i+1} + g_i\alpha_i + \psi_i^{\mathrm{T}}\theta + s_i\omega - x_{i-1,c} - e_{i-1}\right)\end{aligned} \quad (21)$$

where e_l is a filter error, and

$$\chi_i = \begin{cases}\left(z_1^{(0\sim m_1-1)}\right)^{\mathrm{T}} P_H g_1 z_2, (i=2)\\ z_{i-1}^{\mathrm{T}} g_{i-1} z_i, (i>2)\end{cases}$$

Design the virtual controller as

$$\alpha_i = -\frac{1}{g_{i-1}}\left(\digamma_i + c_i z_i + f_i + \psi_i^{\mathrm{T}}\hat{\theta} + \Gamma_i - x_{i-1,c}\right) \quad (22)$$

where $c_i > 0$ is a design parameter, Γ_i is an unknown function designed later, and

$$\digamma_i = \begin{cases} g_1^{\mathrm{T}} P_H^{\mathrm{T}} z_1^{(0\sim m_1-1)}, (i=2)\\ g_{i-1}^{\mathrm{T}} z_{i-1} (i>2)\end{cases}$$

Based on Young's inequality, it has

$$z_i^{\mathrm{T}} s_i\omega \leq \frac{1}{2\gamma}z_i^{\mathrm{T}} s_i s_i^{\mathrm{T}} z_i + \frac{1}{2}\gamma\omega^{\mathrm{T}}\omega \quad (23)$$

$$-z_i^{\mathrm{T}} e_{i-1} \leq \frac{1}{2}z_i^{\mathrm{T}} z_i + \frac{1}{2}e_{i-1}^{\mathrm{T}} e_{i-1} \quad (24)$$

By using (22), (23) and (24), we have

$$\begin{aligned}\dot{V}_i \leq & -\frac{1}{2}\mu\left(z_1^{(0\sim m_1-1)}\right)^{\mathrm{T}} P\left(A^{0\sim m_1-1}\right) z_1^{(0\sim m_1-1)} \\ & -\sum_{k=2}^{i}\left(c_k - \frac{1}{2}\right) {z_k}^{\mathrm{T}} z_k + \frac{i}{2}\gamma\omega^{\mathrm{T}}\omega + \sum_{l=1}^{i-1}\frac{1}{2}{e_l}^{\mathrm{T}} e_l \\ & -\widetilde{\theta}^{\mathrm{T}}\left(\dot{\hat{\theta}} - \psi_1 P_H^{\mathrm{T}} z_1^{(0\sim m_1-1)} - \sum_{p=2}^{i}\psi_p z_p\right) \\ & -z_i^{\mathrm{T}}\left(\Gamma_i - \frac{1}{2\gamma}s_i s_i^{\mathrm{T}} z_i\right) + z_i^{\mathrm{T}} g_i z_{i+1}\end{aligned} \quad (25)$$

Then, Γ_i is designed by

$$\Gamma_i = \frac{1}{2\gamma}s_i s_i^{\mathrm{T}} z_i \quad (26)$$

Step n: Similar to Step i, it gives

$$\dot{\alpha}_{n-1} = e_{n-1} + x_{n-1,c} \quad (27)$$

Due to (6) and (27), it is easy to obtain

$$\begin{aligned}\dot{z}_n = & \dot{x}_n - \dot{\alpha}_{n-1} \\ = & f_n + g_n u + \psi_n^{\mathrm{T}}\theta + s_n\omega - x_{n-1,c} - e_{n-1}\end{aligned} \quad (28)$$

Select the Lyapunov function as

$$V_n = V_{n-1} + \frac{1}{2}z_n^{\mathrm{T}} z_n \quad (29)$$

Taking the time-derivative of V_n has

$$\begin{aligned}\dot{V}_n = & \dot{V}_{n-1} + z_n^{\mathrm{T}}\dot{z}_n \\ \leq & -\frac{1}{2}\mu\left(z_1^{(0\sim m_1-1)}\right)^{\mathrm{T}} P\left(A^{0\sim m_1-1}\right) z_1^{(0\sim m_1-1)} \\ & -\sum_{k=2}^{n-1}\left(c_k - \frac{1}{2}\right) z_k^{\mathrm{T}} z_k + \frac{n-1}{2}\gamma\omega^{\mathrm{T}}\omega + \sum_{l=1}^{n-2}\frac{1}{2}e_l^{\mathrm{T}} e_l \\ & -\widetilde{\theta}^{\mathrm{T}}\left(\dot{\hat{\theta}} - \psi_1 P_H^{\mathrm{T}} z_1^{(0\sim m_1-1)} - \sum_{p=2}^{n-1}\psi_p z_p\right) \\ & + z_{n-1}^{\mathrm{T}} g_n z_n + z_n^{\mathrm{T}}\left(f_n + g_n u + \psi_n^{\mathrm{T}}\theta\right. \\ & \left.+s_n\omega - x_{n-1,c} - e_{n-1}\right)\end{aligned} \quad (30)$$

Then, the real controller is designed as

$$u = -g_n^{-1}\left(F_n + c_n z_n + f_n + \psi_n^{\mathrm{T}}\hat{\theta} + \Gamma_n - x_{n-1,c}\right) \tag{31}$$

where $\Gamma_n = \frac{1}{2\gamma} s_n s_n^{\mathrm{T}} z_n$ and $F_n = g_{n-1}^{\mathrm{T}} z_{n-1}$.

Substituting (31) into (30) gets

$$\begin{aligned}\dot{V}_n \le & -\frac{1}{2}\mu\left(z_1^{(0\sim m_1-1)}\right)^{\mathrm{T}} P\left(A^{0\sim m_1-1}\right) z_1^{(0\sim m_1-1)} \\ & - \sum_{k=2}^{n}\left(c_k - \frac{1}{2}\right) z_k^{\mathrm{T}} z_k + \frac{n}{2}\gamma\omega^{\mathrm{T}}\omega + \sum_{l=1}^{n-1}\frac{1}{2} e_l{}^{\mathrm{T}} e_l \\ & - \widetilde{\theta}^{\mathrm{T}}\left(\dot{\hat{\theta}} - \psi_1 P_H^{\mathrm{T}} z_1^{(0\sim m_1-1)} - \sum_{p=2}^{n}\psi_p z_p\right)\end{aligned} \tag{32}$$

Then, the adaptive law can be designed as

$$\dot{\hat{\theta}} = \psi_1 P_H^{\mathrm{T}} z_1^{(0\sim m_1-1)} + \sum_{p=2}^{n}\psi_p z_p - \beta\hat{\theta} \tag{33}$$

3.2 Stability analysis

Theorem 1 *Under Assumptions 1-2, if virtual controllers, control input signal and adaptive law are designed as (8), (22), (29) and (32), respectively, the HOFA system (1) satisfies the following properties:*

(1) All signals in the closed-loop system are bounded;

(2) H_∞ tracking index is achieved.

Proof. By substituting (33) into (32), we have

$$\begin{aligned}\dot{V}_n \le & -\frac{1}{2}\mu\left(z_1^{(0\sim m_1-1)}\right)^{\mathrm{T}} P\left(A^{0\sim m_1-1}\right) z_1^{(0\sim m_1-1)} \\ & - \sum_{k=2}^{n}\left(c_k - \frac{1}{2}\right) z_k{}^{\mathrm{T}} z_k + \frac{n}{2}\gamma\omega^{\mathrm{T}}\omega + \sum_{l=1}^{n-1}\frac{1}{2} e_l^{\mathrm{T}} e_l \\ & + \beta\widetilde{\theta}^{\mathrm{T}}\hat{\theta}\end{aligned} \tag{34}$$

From Young's inequality, it can be derived that

$$\begin{aligned}\beta\widetilde{\theta}^{\mathrm{T}}\hat{\theta} &= \beta\widetilde{\theta}^{\mathrm{T}}\theta - \beta\widetilde{\theta}^{\mathrm{T}}\widetilde{\theta} \\ &\le \frac{1}{2}\beta\widetilde{\theta}^{\mathrm{T}}\widetilde{\theta} + \frac{1}{2}\beta\theta^{\mathrm{T}}\theta - \beta\widetilde{\theta}^{\mathrm{T}}\widetilde{\theta} = \frac{1}{2}\beta\theta^{\mathrm{T}}\theta - \frac{1}{2}\beta\widetilde{\theta}^{\mathrm{T}}\widetilde{\theta}\end{aligned} \tag{35}$$

According to (34) and (35), it has

$$\begin{aligned}\dot{V}_n \le & -\frac{1}{2}\mu\left(z_1^{(0\sim m_1-1)}\right)^{\mathrm{T}} P\left(A^{0\sim m_1-1}\right) z_1^{(0\sim m_1-1)} \\ & - \sum_{k=2}^{n}\left(c_k - \frac{1}{2}\right) z_k{}^{\mathrm{T}} z_k + \frac{n}{2}\gamma\omega^{\mathrm{T}}\omega + \sum_{l=1}^{n-1}\frac{1}{2} e_l^{\mathrm{T}} e_l \\ & + \frac{1}{2}\beta\theta^{\mathrm{T}}\theta - \frac{1}{2}\beta\widetilde{\theta}^{\mathrm{T}}\widetilde{\theta}\end{aligned} \tag{36}$$

From Lemma 3, there is a positive constant ϵ such that $\sum_{l=1}^{n}\frac{1}{2} e_l{}^{\mathrm{T}} e_l \le \epsilon$. Therefor, when $\omega = 0$, the inequality (36) can be transformed into

$$\dot{V}_n \le -cV + K \tag{37}$$

where $c = \min\left\{\frac{1}{2}\mu, c_2 - \frac{1}{2}, ..., c_n - \frac{1}{2}, \frac{1}{2}\beta\right\}$ and $K = \epsilon + \frac{1}{2}\beta\theta^2$.

Let $q = \frac{K}{c}$ and integrate (37) over the interval $(0, t)$ results in

$$V(t) \le q + [V(0) - q]\, e^{-ct} \tag{38}$$

which means that the property (1) of Theorem 1 holds.

When $\omega \in L_2$, (36) can be transformed into

$$\dot{V}_n \le \frac{n}{2}\gamma\left\|\omega\right\|^2 - \frac{1}{2}\bar{\mu}\left\|z_1^{(0\sim m_1-1)}\right\|^2 + \Omega_0 \tag{39}$$

where $\bar{\mu} = \mu\lambda_{min}(P)$ and $\Omega_0 = \epsilon + \frac{1}{2}\beta\theta^2$.

Integrating (39) yields

$$\int_0^T \frac{1}{2}\bar{\mu}\left\|z_1^{(0\sim m_1-1)}\right\|^2 dt \le \int_0^T \frac{n}{2}\gamma\left\|\omega\right\|^2 dt + \Omega_0 T \tag{40}$$

which can be further transformed as

$$\int_0^T \left\|y(t) - y_t(t)\right\|^2 dt \le \lambda\int_0^T \left\|\omega\right\|^2 dt + \Omega_0 T \tag{41}$$

where $\lambda \ge \frac{n\gamma}{\bar{\mu}}$.

Therefore, H_∞ tracking index is achieved. ■

4 Simulation Results

According to [14], consider a manipulator simulation system as

$$\begin{aligned} J\ddot{q} + B\dot{q} + N\sin q &= \tau \\ M\dot{\tau} + \bar{H}\tau &= u - \bar{K}_m\dot{q}\end{aligned} \tag{42}$$

where $\ddot{q}$, $\dot{q}$ and q represent the acceleration, velocity and position of the manipulator, respectively. $\dot{\tau}$ and τ are the velocity and motor shaft angle, respectively. u is the motor torque. Moreover, $J = 1$, $B = 1$, $N = 2$, $M = 1$, $\bar{H} = 0.7$ and $\bar{K}_m = 9$.

By setting $x_1 = q$, $x_2 = \tau$, the model (42) can be reformulated as follow:

$$\begin{aligned}\dot{\bar{x}}_1 &= f_1(\bar{x}_1) + \psi_1^{\mathrm{T}}(\bar{x}_1)\,\theta + g_1(\bar{x}_1)\,x_2 + s_1(\bar{x}_1)\,\omega \\ \dot{x}_2 &= f_2(\bar{x}_2) + \psi_2^{\mathrm{T}}(\bar{x}_2)\,\theta + g_2(\bar{x}_2)\,u + s_2(\bar{x}_2)\,\omega \\ y &= x_1\end{aligned} \tag{43}$$

where $f_1(\bar{x}_1) = -\dot{x}_1$, $\psi_1^{\mathrm{T}}(\bar{x}_1) = -\sin x_1$, $f_2(\bar{x}_2) = -9\dot{x}_1$, $\psi_2^{\mathrm{T}}(\bar{x}_2) = -0.35x_2$, $s_1(\bar{x}_1) = 1$, $s_2(\bar{x}_2) = 0.1$, $\omega = [10\sin(2\pi f t)]\, e^{(-0.1t)}$, and $f = 0.02$.

The parameters are chosen as $P\left(A^{0\sim m_1-1}\right) = \begin{bmatrix} 1.2157 & 0.0013 \\ 0.0013 & 0.0025 \end{bmatrix}$, $A^{0\sim m_1-1} = [380 \quad 200]$.

Simulation results are shown in Figs. 1-4. From Fig. 1, it can be seen that the system output is able to track the reference signal well. Fig. 2 shows the trajectory of the control input signal u. The output of the filter is presented in Fig. 3. Fig. 4 presents the filtering error, which indicates that the design filter has a good performance.

5 Conclusion

In this paper, the adaptive tracking control problem of nonlinear HOFA systems with unknown parameters and disturbances is addressed. With the help of the backstepping method, an adaptive H_∞ controller is built to deal with unknown parameters and disturbances. The proposed method can guarantee the boundedness of all signals and the system stability is analyzed by employing Lyapunov stability theory. A manipulator simulation is made to demonstrate the effectiveness of the designed scheme.

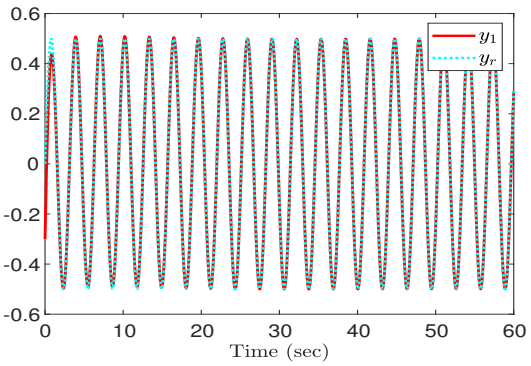

Fig. 1: Controller Tracking Performance

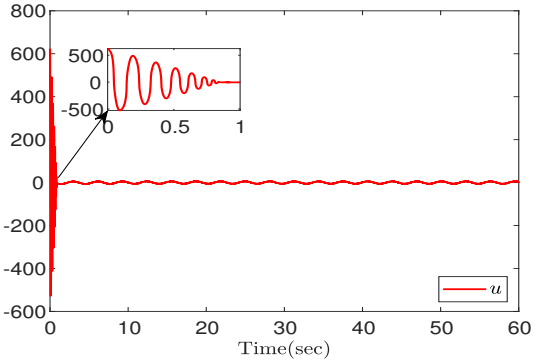

Fig. 2: Controller Output Curve

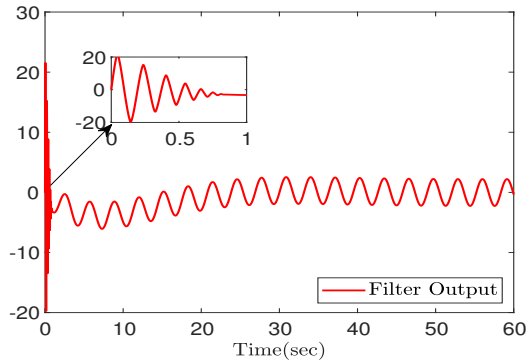

Fig. 3: Filtering Output

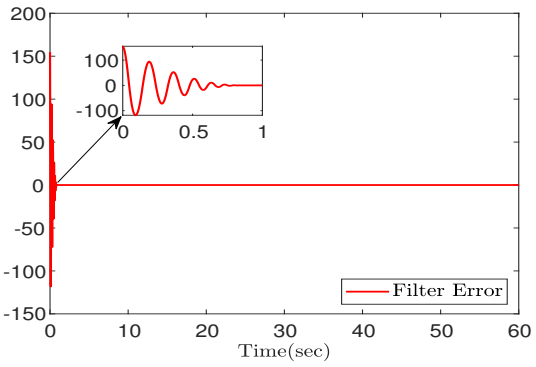

Fig. 4: Filtering Error

References

[1] G. Duan, High-order fully actuated system approaches: Part I. Models and basic procedure, *International Journal of Systems Science*, 52(2): 422-435, 2021.

[2] G. Duan, High-order fully actuated system approaches: Part IV. Adaptive control and high-order backstepping, *International Journal of Systems Science*, 52(5): 972-989, 2021.

[3] G. Duan, High-order fully actuated system approaches: Part V. Robust adaptive control, *International Journal of Systems Science*, 52(10): 2129-2143, 2021.

[4] G. Duan, High-order fully actuated system approaches: Part III. Robust control and high-order backstepping, *International Journal of Systems Science*, 52(5): 952-971, 2021.

[5] C. Yan, X. Wang, T. Liu, et al, Adaptive event-triggered fuzzy control of flexible-joint robot: A fully actuated system approach, *2023 2nd Conference on Fully Actuated System Theory and Applications (CFASTA). IEEE*, 2023.

[6] W. Liu, G. Duan, M. Hou, High-order robust command filtered backstepping design for strict-feedback systems: A high-order fully actuated system approach, *International Journal of Robust and Nonlinear Control*, 32(18): 10251-10270, 2022.

[7] Y. Xiao, G. Cai, and G. Duan, High-order adaptive dynamic surface control for output-constrained non-linear systems based on fully actuated system approach, *International Journal of Systems Science* 55(3): 482-498, 2024.

[8] W. Liu, G. Duan, M. Hou. High-order command filtered adaptive backstepping control for second and high-order fully actuated strict-feedback systems, *Journal of the Franklin Institute*, 360(6): 3989-4015, 2023.

[9] N. Wang, X. Liu, C. Liu, et al, Almost disturbance decoupling for HOFA nonlinear systems with strict-feedback form, *Journal of Systems Science and Complexity*, 35(2): 481-501, 2022.

[10] N. Wang, X. Liu, C. Liu, et al, Adaptive control and almost disturbance decoupling for uncertain HOFA nonlinear systems, *International Journal of Adaptive Control and Signal Processing*, 37(8): 2133-2161, 2023.

[11] L. Hu, G. Duan, and M. Hou, Robust adaptive guaranteed cost tracking control for high-order nonlinear systems with uncertainties based on high-order fully actuated system approaches, *International Journal of Robust and Nonlinear Control*, 33(13): 7583-7605, 2023.

[12] A. Levant, Robust exact differentiation via sliding mode technique, *Automatica*, 34(3): 379-384, 1998.

[13] G. Duan, High-order fully actuated system approaches: Part V. Robust adaptive control, *International Journal of Systems Science*, 52(10): 2129-2143, 2021.

[14] L. Cao, Z. Cheng, Y. Liu, et al, Event-based adaptive NN fixed-time cooperative formation for multiagent systems, *IEEE Transactions on Neural Networks and Learning Systems*, 2022, doi: 10.1109/TNNLS.2022.3210269.

Proceedings of the 3rd Conference on Fully Actuated System Theory and Applications
May 10-12, 2024, Shenzhen, China

Active Disturbance Rejection Control of Hydraulic Turbine based on Fully Actuated System Theory

Lingling Lv[1], Delong Yang[1], Shen Su[1,2], Quanzhen Huang[1,3], Zhiheng Li[1,4], Yu Wu[1,5]

1. School of Electrical Engineering, North China University of Water Resources and Electric Power, Zhengzhou 450011, China
E-mail: lingling_lv@163.com;y13323711816@163.com

2. Guangzhou University, Haisi Knowledge Center B3-408, Guangzhou, China
E-mail: sushen@gzhu.edu.cn

3. School of Electrical and Information Engineering, Henan University of Engineering, Zhengzhou 451191, China
E-mail: huangquanzhen666@126.com

4. Trading Department of Henan Electric Power Trading Center, Zhengzhou 450018, China
E-mail: 1970017291@qq.com

5. Institute of Surface-Earth System Science, School of Earth System Science, Tianjin University, Tianjin 300072, China
E-mail: wu_yu@tju.edu.cn

Abstract: This paper investigates the problem of stabilization control of hydroelectric generating units. Firstly, the fully actuated system model of the linear hydraulic turbine is established by using the theory of fully actuated system. Then the control law is designed by using the direct parameterization method, which can configure the closed-loop poles of the hydraulic turbine system expectation or region and ensure the stable operation of the hydraulic turbine regulating system with a small control gain. Finally, a nonlinear active disturbance rejection control method is proposed for the internal and external disturbances in the control of the fully actuated system. The simulation results demonstrate the effectiveness of the proposed control method.

Key Words: Fully Actuated System Approach, Direct Parameterization Approach, Active Disturbance Rejection Control, Turbine Regulation System

1 Introduction

Hydroelectric power plants are important water facilities for the conversion of water energy into electrical energy, and clean energy forms of power generation are becoming increasingly prominent in the grid. According to the *World Hydropower Outlook* report released by the International Hydropower Association, it is pointed out that in 2022, the new global installed hydropower capacity will be 34 GW and hydropower will account for more than 15% of the global power supply. And the installed capacity of China's Three Gorges Group will reach 125 million KW by 2022. Therefore, hydroelectric generating units play an extremely important role in the generation of electricity to the power grid and at the same time, this will also bring more complex challenges to the stable operation of hydroelectric power plants.

Turbine regulation system is a comprehensive control system integrating water, machine and electricity. In [1], the system structure can be categorized into the control system as well as the controlled system, where the controlled system is mainly the turbine and generator and the control system is the governor. In recent years, the research on the control design of hydroelectric unit governors has attracted the attention of scholars. Many effective control methods have been proposed, it is mainly divided into traditional PID control and modern control.

In the traditional control of turbine regulation system, PID control is an error feedback-based control method that aims to bring the system output to the desired value by controlling the error. In [2,3], the traditional PID controllers commonly used in hydropower plants are simple in structure and easy to adjust the parameters. With the optimization and improvement of control strategies, scholars at home and abroad have proposed some optimization parameter algorithms such as fuzzy adaptive PID control, fractional order PID control, BP neural network PID control, etc. Although these algorithms can improve the system requirements, it is difficult to accurately control the complexity of the turbine regulation system itself and the increase in unstable conditions leads to poor regulation quality of PID control.

With the intelligence of computers and the inability of traditional PID to cope with today's more complex turbine regulation systems, modern control strategies show certain advantages and their control algorithms mainly include sliding mode control algorithms, fuzzy control algorithms, adaptive control algorithms, etc. Literature [4,5,6] have designed improved sliding mode controller, which mainly considers the vibration jitter problem of the system in sliding mode control. Although this controller can effectively reduce the vibration phenomenon and trajectory tracking error in the sliding mode control, it is more complicated to design the improved sliding mode control rate. Literature [7,8] established T-S fuzzy model using single-point fuzzification, product inference and average-weighted defuzzification for the complex characteristics of the hydraulic turbine regulation system and proposed a fuzzy controller. But the controller's relatively low control accuracy as well as the inappropriate selection of fuzzy rules may lead to a poor control effect. The Literature [9] designed a nonlinear adaptive water gate control method based on differential geometry and adaptive control theory for the inherent nonlinear parameter

This work is supported by the Support Plan for Scientific and Technological Innovation Team of Colleges and Universities in Henan Province (No. 22IRTSTHN011), Outstanding Youth Fund of Henan Provincial Natural Science Foundation (No. 242300421054), Zhengzhou Science and Technology Collaborative Innovation Project in 2022, National Natural Science Foundation General Project (62173126), Central Plains Science and Technology Innovation Leading Talent Support Program (234200510027) and Henan Provincial Education Science Planning Project (2023YB0270).

uncertainty of hydroelectric generating units and the control algorithm improves the adaptive ability of the system parameter uncertainty. However, the adaptive controller needs to constantly monitor the system changes in real time and adjust the parameters dynamically, which will make the system less stable or even destabilized under certain circumstances.

Through the detailed analysis of the above control methods, it can be found that the traditional and modern control strategies cannot achieve the desired effect of the control system. Academician Guangren Duan proposed a fully actuated system control method. In the literature [10], it was pointed out that the fully actuated system has unique advantages in terms of controller design. It is further pointed out that the fully actuated system model is obtained either by directly obtaining the fully actuated system model from the original model of the laws of physics or by transforming the original system into a model of the fully actuated system using the variable elimination equivalence transformation. In recent years, the research applications of high-order fully actuated (HOFA) systems have become increasingly popular, which are mainly applied to higher-order backstepping design, adaptive control design, robust control design and optimal control design. In the literature [11], a direct approach for the design of robust stabilizing controllers and robust tracking controllers for an uncertain single high-order fully actuated (HOFA) systems model are proposed. And the global convergence of the state vector of the system to an ellipsoid of arbitrarily small radius is illustrated in a first-order strict-feedback system (SFS) application. In reference [12], the problem of optimal control of a dynamical system represented by a general high-order fully actuated (HOFA) systems model is presented, where the core of the control is the objective of minimizing the quadratic form of the state and its derivatives. This optimal control technique is applied to spacecraft attitude control and exhibits a stable and smooth dynamic response.

In the control process of the fully actuated system, because the stable operation of the turbine regulation system is affected by unit vibration, water hammer phenomenon in the overwater system, pressure water head fluctuation and the influence of power supply side output change under the compound energy of the power system. The core of the active disturbance rejection control is to estimate and compensate for these influences by attributing them to the total perturbation of the system. Therefore, to have better steady-state performance as well as dynamic performance of the turbine regulation system, this paper proposes a combination of the fully actuated system theory and active disturbance rejection control. In the following, the application of the method of combining a fully actuated system with active disturbance rejection control to a hydraulic turbine regulation system is discussed in detail.

The remainder of the paper is structured as follows: The second part presents the mathematical model of the turbine regulation system and the related parameter notation. The third part first models the turbine system based on the theory of a fully actuated system, and then the controller design is carried out based on this model using parametric methods. The fourth part further controls the turbine regulation system based on the fully actuated system in combination with active disturbance rejection control. The fifth part verifies the effectiveness of the designed control algorithm by simulating the turbine regulation system based on the design of the fully actuated system controller and active disturbance rejection control controller. Finally, Part VI provides some concluding remarks.

2 Mathematical modeling of the turbine regulation system

The turbine regulation system consists of the water diversion system, the hydraulic servo system, the turbine system and the generator system, respectively. The system is a non-minimum phase system due to the effect of the water hammer in the diversion system. According to the literature [13], the linear dynamics of the turbine regulation system is modeled as follows

$$\begin{cases} \dot{n} = -\dfrac{e_{mn}-e_n}{T_{ab}}n + \dfrac{e_{m\alpha}}{T_{ab}}\alpha + \dfrac{e_{mh}}{T_{ab}}h - \dfrac{1}{T_{ab}}m_{g0} \\ \dot{\alpha} = \dfrac{1}{T_y}(u-\alpha) \\ \dot{h} = \dfrac{e_n e_{qn}}{e_{qh}T_{ab}}n + \left(\dfrac{e_{q\alpha}}{e_{qh}T_y} - \dfrac{e_{qn}e_{m\alpha}}{e_{qh}T_{ab}}\right)\alpha - \dfrac{e_{q\alpha}}{e_{qh}T_y}u \\ \quad -\left(\dfrac{e_{qn}e_{mh}}{e_{qh}T_{ab}} + \dfrac{1}{e_{qh}T_w}\right)h + \dfrac{e_{qn}}{e_{qh}T_{ab}}m_{g0} \end{cases} \tag{1}$$

Where n, α, h are turbine state vectors of dimension 1, representing the rotational speed, guide vane opening, head; u, mg_0 are the input vectors of a system of dimension 1, representing the control input of the governor and the load disturbance torque respectively; e_n represents the integrated self-regulation parameters of the unit; T_{ab} represents the time constant of inertia of the rotating part of the unit and the load; T_w, T_y represent the pressure diversion system water flow inertia time constant and the receiver reaction time constant, respectively; $e_{mn}, e_{m\alpha}, e_{mh}, e_{qn}, e_{q\alpha}, e_{qh}$ represent turbine torque and flow rate to the speed, guide vane opening and head transfer coefficient, respectively.

According to the theory of fully actuated system, it is known that system (1) is an under-actuated system and it is necessary to transform this system into a fully actuated system by means of eliminating the element and upgrading the level. A study of the dynamic characteristics of the system (1) in the literature [13] shows that the system is greatly affected by interference factors and is in an unstable state, so the stable operation of the turbine is ensured by the combination of fully actuated system and active disturbance rejection control.

3 Fully actuated system modeling and controller design

In the literature [14], the hydraulic turbine regulation system is known to be controllable. According to the knowledge of the multiple-input-multiple-output canonical type of linear system theory, it is possible to transform system (1) into second $Luenberger$ canonical type of the following

$$\dot{\hat{x}} = \hat{A}_c\hat{x} + \hat{B}_c u \tag{2}$$

Where

$$\hat{A}_c = SAS^{-1}$$

$$\hat{B}_c = SB$$

$$A = \begin{bmatrix} -\frac{e_{mn}-e_n}{T_{ab}} & \frac{e_{m\alpha}}{T_{ab}} & \frac{e_{mh}}{T_{ab}} \\ 0 & -\frac{1}{T_y} & 0 \\ \frac{e_n e_{qn}}{e_{qh}T_{ab}} & \frac{e_{q\alpha}T_{ab}-e_{qn}e_{m\alpha}T_y}{e_{qh}T_{ab}T_y} & -\frac{T_{ab}+e_{qn}e_{mh}T_w}{e_{qh}T_{ab}T_w} \end{bmatrix}$$

$$B = \begin{bmatrix} 0 & -\frac{1}{T_{ab}} \\ \frac{1}{T_y} & 0 \\ -\frac{e_{q\alpha}}{e_{qh}T_y} & \frac{e_{qn}}{e_{qh}T_{ab}} \end{bmatrix}$$

$$S = \begin{bmatrix} \Xi^{11} & \Xi^{12} & \Xi^{13} \\ \Xi^{21} & 0 & \Xi^{23} \\ \Xi^{31} & \Xi^{32} & \Xi^{33} \end{bmatrix}$$

$$\Xi^{11} = \frac{e_{qn}e_{qh}T_yT_w}{e_{q\alpha}}, \Xi^{12} = T_yT_we_{qh}, \Xi^{13} = \frac{e_{qh}^2T_yT_w}{e_{q\alpha}},$$

$$\Xi^{21} = \frac{2e_ne_{qn}e_{qh}T_yT_w - e_{mn}e_{qn}e_{qh}T_yT_w}{e_{q\alpha}T_{ab}},$$

$$\Xi^{31} = \frac{e_{m\alpha}e_{qn}e_{qh}T_yT_w - e_{q\alpha}T_{ab}T_y - e_{qn}e_{q\alpha}e_{mh}T_yT_w}{e_{q\alpha}T_y},$$

$$\Xi^{32} = e_{m\alpha}e_{qh}T_w - e_{q\alpha}e_{mh}T_w, \Xi^{23} = -\frac{e_{qh}T_y}{e_{q\alpha}},$$

$$\Xi^{33} = \frac{e_{qh}^2e_{m\alpha}T_w - e_{q\alpha}e_{mh}e_{qh}T_w}{e_{q\alpha}}$$

Here the controllability index of this system second controllable norm type is $\mu_1 = 2, \mu_2 = 1$.

According to the literature [15], equation (2) can be rewritten as a fully actuated system model of the following form

$$E\ddot{q} + A_1\dot{q} + A_0q = \tilde{B}u \tag{3}$$

where

$$E = \begin{bmatrix} 1 & 0 \\ 0 & 0 \end{bmatrix}$$

$$A_1 = \begin{bmatrix} \Xi_1^{11} & 0 \\ 0 & 1 \end{bmatrix}$$

$$A_0 = \begin{bmatrix} \Xi_0^{11} & \Xi_0^{12} \\ \Xi_0^{21} & \Xi_0^{22} \end{bmatrix}$$

$$\tilde{B} = \begin{bmatrix} 1 & \tilde{b}_{12} \\ 0 & 1 \end{bmatrix}$$

$$\Xi_1^{11} = \frac{e_{q\alpha}e_{qh}T_wT_{ab}^2 - e_{q\alpha}T_yT_{ab}^2 - 4.612T_y}{e_{q\alpha}e_{qh}T_wT_yT_{ab}^2},$$

$$\Xi_0^{11} = \frac{1.161e_{qn}(e_{mh}e_{q\alpha} - e_{m\alpha}e_{qh})}{e_{q\alpha}e_{qh}T_{ab}^3 + 10.27(e_{mn} - 2e_n)},$$

$$\Xi_0^{12} = \frac{0.243(e_{mn}e_{qh}T_w - T_{ab}) - 0.486e_ne_{qh}T_w}{e_{q\alpha}^2T_{ab}^2},$$

$$\Xi_0^{22} = \frac{e_ne_{q\alpha}T_{ab} - e_{mn}e_{q\alpha}T_{ab} - e_{m\alpha}e_{qn}T_{ab} - 0.9452T_w}{e_{q\alpha}T_{ab}^2},$$

$$\Xi_0^{21} = \frac{e_{m\alpha}e_{q\alpha}T_{ab}^2 - 10.337T_w}{e_{q\alpha}e_{qh}T_{ab}^2T_wT_y},$$

$$\tilde{b}_{12} = \frac{-(e_{qn}T_y(T_{ab} - e_{mn}e_{qh}T_w + 2e_ne_{qh}T_w))}{e_{q\alpha}T_{ab}^2}$$

In equation (3), $q \in R^{2\times1}$ is the state variable of the system, q_1, q_2 are the rotational speed and head of the turbine speed control system, respectively. $u \in R^{2\times1}$ is the control input. $\tilde{B}$ and $E, A_i, i = 0, 1$ are real coefficient matrices of dimension 2.

In order to design the controller of the fully actuated system (3) using the direct parametric method, the following two assumptions need to be satisfied.

Assumption 1:$\det(E) = 0$.

Assumption 2:$\det(\tilde{B}) \neq 0$.

Lemma 1:[16] For the fully actuated system (3), the controller can be designed as follows

$$\begin{cases} u = \tilde{B}^{-1}\left[(A_1\dot{q} + A_0q) + u^*\right] \\ u^* = \bar{A}_{0\sim\xi-1}q^{(0\sim\xi-1)} + \nu, \xi = 2 \end{cases} \tag{4}$$

where ν is the external input vector and matrix $\bar{A}_{0\sim\xi-1}, \xi = 2$ is required to be designed. Controllers designed using fully actuated characteristics can cancel the open-loop system characteristics to obtain the desired linear constant closed-loop system characteristics.

The fully actuated system model (3) can be transformed into the following first-order linear constant closed-loop system form by the above controller design

$$E_c\dot{X} = A_cX + B_c\nu \tag{5}$$

where

$$X = \begin{bmatrix} q & \dot{q} \end{bmatrix}^T \tag{6}$$

$$E_c = \begin{bmatrix} I_n & 0 \\ 0 & E \end{bmatrix} \tag{7}$$

$$A_c = \begin{bmatrix} 0 & I_n \\ -\bar{A}_0 & -\bar{A}_1 \end{bmatrix} \tag{8}$$

$$B_c = \begin{bmatrix} 0 & I_n \end{bmatrix}^T \tag{9}$$

The matrix E is a dissatisfaction rank matrix. According to the literature [10], it is known that the closed-loop system (5) has three finite relative eigenvalues and one infinite relative eigenvalue. Then, a direct parameterization is used to design the desired matrix $\bar{A}_{0\sim\xi-1}, \xi = 2$ after the following three steps.

Step 1: Define two constraints

$$\begin{cases} F \in R^{3\times3} \\ Z \in R^{2\times3} \\ V(Z, F) = \begin{bmatrix} Z & ZF \end{bmatrix}^T \end{cases} \tag{10}$$

The matrix Z is the parameter matrix to be designed. Matrix F is the Jordan standard type of finite eigenvalues of the closed-loop system. Matrix V is the generalized finite eigenvector matrix of the closed-loop system.

Step 2: Define the following matrix

$$\begin{cases} V_\infty \in R^{2\times1} \\ EV_\infty = 0, rankV_\infty = 1 \end{cases} \tag{11}$$

The matrix V_∞ corresponds to an infinite eigenvector matrix with infinite relative eigenvalues as $V_\infty^c = \begin{bmatrix} 0 & 0 & V_\infty \end{bmatrix}^T$.

Step 3: Satisfy the following relationship

$$\begin{cases} \bar{A}_{0\sim\xi-1} = \begin{bmatrix} EZF^2 & W_\infty \end{bmatrix} V_e^{-1}(Z,F) \\ V_e(Z,F) = \begin{bmatrix} V(Z,F) & V_\infty^c \end{bmatrix} \\ \det V_e(Z,F) \neq 0 \end{cases} \tag{12}$$

The $W_\infty \in R^{2\times 3}$ arbitrary parameter matrix and the parameter matrix Z can give the closed-loop system (5) eight degrees of freedom, which can be rationally utilized to configure the closed-loop poles of the system expectation or region and the stable operation of the turbine regulation system is ensured with low eigenvalue sensitivity; strong suppression capability of higher-order unmodeled dynamics; and small control gain[17].

After the above three steps, the turbine regulation system is transformed into a linear constant closed-loop system (5), whose characteristic structure is mainly determined by the matrices F and Z. Therefore a set of constant matrices $\bar{A}_{0\sim\xi-1}, \xi = 2$ is derived so that the closed-loop system (5) has the desired eigenstructure to satisfy the control requirements of the complex system.

4 Active disturbance rejection controller design

The active disturbance rejection controller consists of three components. The first part is the tracking differentiator (TD), whose main function is to organize the transition process and extract the differential signal for the turbine speed. The second component, the expanded state observer (ESO) is the estimation of the internal and external uncertainties of the turbine system as total disturbances. The third part is the state error feedback control law, which compensates the estimated total disturbance accordingly, allowing the system to obtain good steady-state performance and immunity to disturbances.

To improve the performance of the hydraulic turbine regulation system when subjected to uncertain internal and external perturbations, this paper adopts a nonlinear active disturbance rejection control method to further control the whole fully driven system. It can be known that $x_1 = q_1, x_2 = \dot{q}_1, y = x_1$. According to the literature [18], the tracking differentiator (TD) of the hydraulic turbine regulation system is designed in the form

$$\begin{cases} x_1(k+1) = x_1(k) + h * x_2(k) \\ x_2(k+1) = x_2(k) + h * fh \\ fh = fhan(x_1(k) - v(k), x_2(k), r, h) \end{cases} \tag{13}$$

where the function $fhan$ is represented as

$$\begin{cases} d = rh^2 \\ a_0 = hx_2 \\ y = x_1 + a_0 \\ a_1 = \sqrt{d(d + 8|y|)} \\ a_2 = a_0 + \text{sign}(y)(a_1 - d)/2 \\ s_y = (\text{sign}(y+d) - \text{sign}(y-d))/2 \\ a = (a_0 + y)s_y + a_2(1 - s_y) \\ s_a = (\text{sign}(a+d) - \text{sign}(a-d))/2 \\ fhan = -r\left(\dfrac{a}{d}\right)s_a - r\text{sign}(a)(1 - s_y) \end{cases}$$

Where parameter r is the velocity factor and h is the sampling period.

The expansion state observer (ESO) is designed in the form

$$\begin{cases} e = z_1 - y \\ \dot{z}_1 = z_2 - \beta_1 e \\ \dot{z}_2 = z_3 - \beta_2 fal(e, \alpha_1, \delta) + b\upsilon_1 \\ \dot{z}_3 = -\beta_3 fal(e, \alpha_2, \delta) \end{cases} \tag{14}$$

where the function fal is expressed as

$$fal(e, \alpha, \delta) = \begin{cases} \dfrac{e}{\delta^{\alpha-1}}, |e| \leq \delta \\ |e|^\alpha \text{sign}(e), |e| > \delta \end{cases}$$

where δ and α are the coefficients of the nonlinear fal function $(0 < \alpha < 1, \delta > 0)$; $\beta_1, \beta_2, \beta_3$ is the gain coefficient of the expanded state observer and z_1, z_2, z_3 is the output state observation signal of the expanded state observer.

Based on the designed tracking-differentiator and the observation signals output from the expanded state observer, using the error signal e_1 and the error differentiation signal e_2 , the state error feedback law is applied in a nonlinear manner

$$\begin{cases} e_1 = \upsilon_1 - z_1 \\ e_2 = \upsilon_2 - z_2 \\ u_0 = -fhan(e_1, c * e_2, r_0, h_1) \\ \upsilon_1 = \dfrac{u_0 - z_3}{b_0} \end{cases} \tag{15}$$

Where u_0 is the output of the state error feedback control law; b_0 is the feedback compensation factor; υ_1 is the controller output.

5 Simulation

In this section, to realize the stable operation of the hydroelectric power plant unit within a specified limited range, the effectiveness of the designed control algorithm is verified based on the design of the fully actuated system controller described above and by simulating the turbine regulation system. The system parameters for the turbine regulation system equation (1) are selected as follows[19]

$$\begin{aligned} &T_a = 5.5s, T_b = (0.24 \sim 0.5)T_a, T_{ab} = 7.7s, \\ &e_{q\alpha} = 0.789, e_{qn} = -0.2901, e_{qh} = 0.45, \\ &e_{m\alpha} = 0.7, e_{mn} = -1.0673, e_{mh} = 1.32, \\ &e_n = 1.2673, T_w = 2.0s, T_y = 0.2s, \end{aligned}$$

The parameters of the active disturbance rejection controller are as follows

$$\begin{aligned} &\text{TD} : r = 10, h = 0.01 \\ &\text{ESO} : \alpha_1 = 0.5, \alpha_2 = 0.25, \\ &\delta = 0.03, \beta_1 = 30, \beta_2 = 600, \beta_3 = 300 \\ &\text{NLSEF} : b_0 = 0.45, r_0 = 10, h_1 = 0.03, c = 0.8 \end{aligned}$$

External input vector $\upsilon = \begin{bmatrix} \upsilon_1 & \upsilon_2 \end{bmatrix}^T$, the control parameter matrix of the system are set as follows

$$Z = \begin{bmatrix} 1 & 0 & 1 \\ 0 & 1 & 0 \end{bmatrix}, F = \begin{bmatrix} -1.3124 & 0 & 0 \\ 0 & -3.7843 & 0 \\ 0 & 0 & -5.2601 \end{bmatrix}$$

$$V_\infty = \begin{bmatrix} 0 \\ -1 \end{bmatrix}, W_\infty = \begin{bmatrix} 0 & 0 & 0 \\ 1 & 0 & 0 \end{bmatrix}$$

The expectation matrix to be designed are as follows

$$\bar{A}_0 = \begin{bmatrix} -6.9034 & 0 \\ 0 & -3.7843 \end{bmatrix}, \bar{A}_1 = \begin{bmatrix} -6.5725 & 0 \\ 0 & -1 \end{bmatrix}$$

Bringing the matrices $\bar{A}_0, \bar{A}_1$ into the controller gives the following desired linear constant closed loop system (16).

$$\begin{cases} \ddot{q}_1 + 6.5725\dot{q}_1 + 6.9034q_1 = \upsilon_1 \\ \dot{q}_2 + 3.7843q_2 = \upsilon_2 \end{cases} \tag{16}$$

Simulation of a hydraulic turbine at an initial speed of 0, a step signal with an amplitude of 1 is applied at the initial moment to simulate the stable operation of the turbine unit under the no-load conditions as shown in Fig. 1. A 10% load fluctuation signal is added at the initial moment to simulate the stable operation of the turbine unit under load conditions as shown in Fig. 2. The correction coefficient b_0 determines the variation range of the estimated value of the total disturbance and the size of the compensation component, and the stable operation of the turbine unit under different correction coefficients is shown in Fig. 3.

From the simulation results, it can be seen that the system is subjected to a unit step as well as an increased load, and the turbine speed has a small jitter as it approaches the input signal. However, it has remained stable since then and no overshoots have been generated. The overshoot of the turbine speed decreases with the increase of the correction coefficient b_0 , and the value of the correction coefficient b_0 is in the range of [0.45,0.75], which can provide good compensating feedback in case of large perturbation fluctuation in the system.

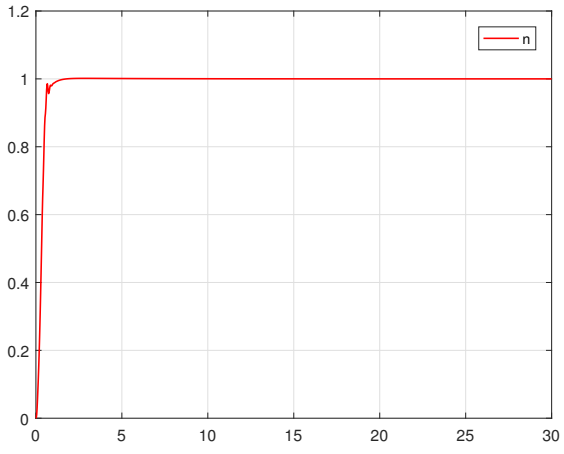

Fig. 1: Turbine speed curve under no-load condition

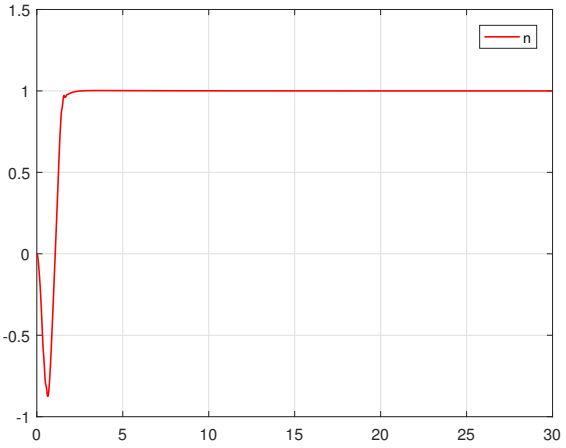

Fig. 2: Turbine speed curve under load conditions

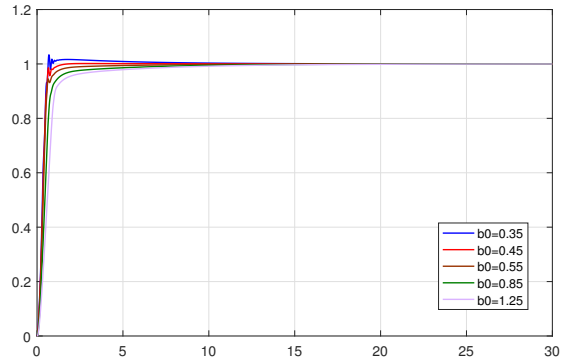

Fig. 3: Turbine speed curves under different correction coefficients

6 Conclusions

In this paper, the problem of hydraulic turbine stabilization control based on the theory of fully actuated system and active disturbance rejection control algorithm is investigated. The hydraulic turbine fully actuated system was first modeled and then the controller was designed using a direct parameterization method to offset the open-loop system characteristics of the turbine and obtain the desired linear constant closed-loop system. On this basis, active disturbance rejection control algorithm is introduced for the uncertainty disturbance problem in the hydraulic turbine calibration control. Finally, the effectiveness of the proposed control method is verified by simulation.

References

[1] G. T. Zhang, Y. C. Cheng, et al, Research of Hydro-Turbine Governor Supplementary Control Strategy for Islanding AC Grid at Sending Terminal of HVDC System. *IEEE Transactions on Energy Conversion*, 2016, 31(4): 1229-1238.

[2] Z. Chen, Y. Yuan, X. Yuan, et al, Application of multi-objective controller to optimal tuning of PID gains for a hydraulic turbine regulating system using adaptive grid particle swam optimization. *ISA Transactions*, 2015, 56173-187.

[3] S. Y. Wang, L. H. Zheng, A New PID Control Method for Hydraulic Turbine Governor. *Applied Mechanics and Materials*, 2013, 2710(420-420): 375-380.

[4] F. Wu, J. Ding, Z. Wang, Robust Finite-Time Terminal Sliding Mode Control for a Francis Hydroturbine Governing System. *Journal of Control Science and Engineering*, 2016, 2016(Pt. 1): 2518734.1-2518734.8.

[5] W. G. Zhao, T. C. Shi, L. Y. Wang, et al, An adaptive hybrid atom search optimization with particle swarm optimization and its application to optimal no-load PID design of hydro-turbine governor. *Journal of Computational Design and Engineering*, 2021, 8(5): 1204-1233.

[6] Y. Yi, D. Chen, Disturbance observer-based backstepping sliding mode fault-tolerant control for the hydro-turbine governing system with dead-zone input. *ISA Transactions*, 2019, 88127-141.

[7] Y. D. Zuo, J. Qian, Y Zeng, et al, Eigen-Structure Assignment-Based Differential Evolution Algorithm for T-S Fuzzy Control Tuning Applied to Water-Turbine Governing System. *IEEE ACCESS*, 2021, 939322-39332.

[8] K. Shi, B. Wang, H Chen, Fuzzy generalised predictive control for a fractional-order nonlinear hydro-turbine regulating system. *IET Renewable Power Generation*, 2018, 12(14): 1708-1713.

[9] B. Mateo, P. Hrvoje, Application of an adaptive model predictive control algorithm on the Pelton turbine governor control. *IET Renewable Power Generation*, 2020, 14(10): 1720-1727.

[10] G. R. Duan, High-order system approaches: I. Full actuated systems and parametric designs. *Acta Automatica Sinica*, 2020, 46(7): 1333-1345.

[11] G. R. Duan, High-order fully actuated system approaches: Part III. Robust control and high-order backstepping. *International Journal of System Sciences*, 2020, 52(5): 952-971.

[12] G. R. Duan, High-order fully actuated system approaches: Part VIII. Optimal control with application in spacecraft attitude stabilisation. *International Journal of Systems Science*, 2022, 53(1): 54-73.

[13] H. Zhang, D. Y. Chen, B. B. Xu, F. F. Wang, Nonlinear modeling and dynamic analysis of hydro-turbine governing system in the process of load rejection transient. *Energy Conversion and Management*, 90, 128-137.

[14] G. R. Duan, Linear System Theory (two volumes)(Third edition). Beijing: Science Press, 2016.

[15] G. R. Duan, High-order system approaches: II. Controllability and fully-actuation. *Acta Automatica Sinica*, 2020, 46(8): 1571-1581.

[16] Z. J. Chen, Approaches linear fully actuated system. *Harbin Institute of Technology*, 2022.

[17] T. Y. Zhao, Parametric design of state-observer-based contral system and its application. *Harbin Institute of Technology*, 2022.

[18] J. Q. Han, Auto disturbances rejection controller and its applications. *Control and Decision*, 1998, 13 (1): 19-23.

[19] D. J. Ling, Study of bifurcation and chaos characteristics of hydraulic turbine regulation system. *Hohai University*, 2007.

Proceedings of the 3rd Conference on Fully Actuated System Theory and Applications
May 10-12, 2024, Shenzhen, China

Sampled-Data H_∞ Control for High-Order Fully Actuated Systems Based on A Local Lipschitz Condition

Tingrui Wang, Zifan Gao, Dawei Zhang
School of Mathematics, Shandong University, Jinan 250100, P. R. China
E-mail: dwzhang@sdu.edu.cn

Abstract: In this paper, the sampled-data H_∞ control problem of a nonlinear high-order fully actuated system is investigated. Based on the full-actuation feature of the system, the sampled-data form of a high-order fully actuated controller is constructed. Using the looped functional method, a local Lipschitz condition is introduced to derive some solvable criteria of H_∞ performance analysis and control design in terms of linear matrix inequalities, respectively. A numerical example concerning vehicle steering control is provided for the control method verification.

Key Words: High-Order Fully Actuated System, H_∞ Control, Sampled-Data Control, Local Lipschitz Condition

1 Introduction

Nonlinear systems are universally present in practical applications, such as robotics and spacecraft [1]. With the development of digital control and computer technology, sampled-data control is widely used in practical systems because of its high efficiency and low cost [2], [3]. However, due to the complex nonlinearity, it is challenging to design a nonlinear sampled-data controller that enables the system to exhibit a desired performance. Accordingly, the research on sampled-data control for nonlinear systems possess important theoretical significance and application background.

To complete the control design of nonlinear systems, amounts of effective methods have been proposed so far, such as feedback linearization [4] and Takagi-Sugeno fuzzy control [5]. Recently, high-order fully actuated (HOFA) system approach proposed in [6] has attracted much attention due to its convenience of control design. By utilizing the full-actuation feature of the system, the HOFA system approach can completely eliminate the nonlinearity of the system and establish the desired closed-loop eigenstructure. In [7], the HOFA system approach is used to develop a predictive control strategy, which can realize the coordinated control for HOFA multiagent systems. In [8], the stabilization problem of nonlinear systems with impulsive effects is studied by using the HOFA system approach and a matrix analysis method. The adaptive event-triggered control for a class of uncertain HOFA systems is studied in [9], which reveals that the constraints imposed on the sampled-data by event-triggered conditions can decrease system performance. Although some great research progress has been made on the HOFA system approach, the nonlinear sampled-data control for HOFA systems deserves in-depth research.

Due to the asynchronous behavior between the sampled-data controller and the HOFA system, some nonlinear errors are inevitably generated when the controller is used to eliminate system dynamics. In the existing results of HOFA system approach, control gains are directly provided according to the desired closed-loop eigenstructure in the absence of nonlinear errors [6]. However, the expected control effect can not be achieved by the sampled-data controller in the presence of nonlinear errors. How to deal with the nonlinear asynchronous errors turns into an interesting problem in nonlinear sampled-data control. Besides, the local Lipschitz condition [10] is always used to model the nonlinear terms in many practical nonlinear systems and the looped functional method is well recognized as an efficient technical tool in deriving less conservative existence conditions of a sampled-data controller, which offer us basic research methods.

Based on the above discussion, this paper focuses on handling the sampled-data H_∞ control problem of nonlinear HOFA systems. A sampled-data controller is tailored based on the form of the HOFA system. The closed-loop system is modeled as a sampled-data system with unknown nonlinear errors. A local Lipschitz condition is introduced to treat the nonlinear error explicitly. Further, the existence conditions of H_∞ performance analysis and control design are derived for the closed-loop system using the looped functional method along with the local Lipschitz condition. Finally, a case study is provided to value the control design method.

The main contributions of this paper are summarized as

1) A sampled-data controller is constructed for the nonlinear HOFA systems based on the full-actuation feature. By introducing a local Lipschitz condition, the difficulties on analysis and synthesis caused by the nonlinear error between the open-loop system and the sampled-data controller are addressed.
2) Based on the looped functional method and the local Lipschitz condition, some solvable criteria of H_∞ performance analysis and control design are derived. The control gain is obtained by the design result to ensure satisfactory system performance.

Notation: $\mathbb{N}$ is the set of nonnegative integers and $\mathbb{R}^n$ is the n dimensional Euclidean space. For a symmetric matrix P, $P < 0$ means that P is negative definite. For a square matrix X, $\mathrm{Sym}\{X\} = X + X^T$. I and 0 denote appropriately dimensioned identity matrix and zero matrix respectively. For a vector $\xi \in \mathbb{R}^n$, $\|\xi\|$ denotes the Euclidean norm of ξ. $\mathrm{diag}\{...\}$ means the block-diagonal matrix. $x^{(i)}(t)$ represents the i-th derivative of $x(t)$. $x^{(0\sim n-1)}(t) = \mathrm{col}\{x(t), x^{(1)}(t), ..., x^{(n-1)}(t)\}$.

This work was partly supported by the National Natural Science Foundation of China under 62373220, the Shandong Provincial Natural Science Foundation of China under Grant ZR2023MF011, and the Science Center Program of National Natural Science Foundation of China under Grant 62188101. *(Corresponding author: Dawei Zhang.)*

2 Problem Formulation

Consider the following nonlinear HOFA system

$$x^{(n)}(t) = f(x^{(0\sim n-1)}(t)) + Bu(t) + E\omega(t), \quad (1)$$

where $x^{(i)} \in \mathbb{R}^p (i = 0, 1, ..., n-1)$ is the state vector, $f(x^{(0\sim n-1)}(t)) \in \mathbb{R}^p$ is the nonlinear function, $u(t) \in \mathbb{R}^p$ is the control input, $\omega(t) \in \mathbb{R}^q$ is the unknown disturbance satisfying $\omega(t) \in L_2[0, \infty)$, $B \in \mathbb{R}^{p\times p}$ and $E \in \mathbb{R}^{p\times q}$ are the system input and disturbance input matrices, respectively, and B is non-singular. The system state $x^{(0\sim n-1)}(t)$ satisfies the following general assumption

Assumption 1. *In system (1), each state $x^{(i)} \in \mathbb{R}^p$ $(i = 0, 1, ..., n-1)$ is assumed to be bounded in the compact set $\Omega = \{x^{(0\sim n-1)}(t) | \underline{x}_{ij} \le x_j^{(i)}(t) \le \overline{x}_{ij}, i = 0, 1, \ldots, n-1,\ j = 1, 2, \ldots, p\}$, where scalar $x_j^{(i)}(t)$ is the j-th component of $x^{(i)}(t)$.*

Considering the full-actuation feature of system (1) and the non-singular matrix B, the sampled-data form of a high-order fully actuated controller is expressed as

$$u(t) = -B^{-1}(Kx^{(0\sim n-1)}(kh) + f(x^{(0\sim n-1)}(kh))), \quad (2)$$

for $t \in [kh, (k+1)h)$, where h is the sampling period; kh $(k \in \mathbb{N})$ is the latest sampling instant; and $K \in \mathbb{R}^{p\times np}$ is the control gain to be designed.

Substituting the control input (2) into system (1) yields

$$\begin{aligned} x^{(n)}(t) = {} & f(x^{(0\sim n-1)}(t)) - f(x^{(0\sim n-1)}(kh)) \\ & - Kx^{(0\sim n-1)}(kh) + E\omega(t). \end{aligned} \quad (3)$$

By denoting $\xi(t) = x^{(0\sim n-1)}(t)$, the closed-loop system can be rewritten as

$$\dot{\xi}(t) = \Phi\xi(t) + \tilde{f}(\xi(t)) - \tilde{f}(\xi(kh)) - \tilde{K}\xi(kh) + \tilde{E}\omega(t), \quad (4)$$

where $\tilde{f}(\xi(t)) = \text{col}\{0, ..., 0, f(\xi(t))\}$, $\tilde{K} = \text{col}\{0, ..., 0, K\}$, $\tilde{E} = \text{col}\{0, ..., 0, E\}$ and

$$\Phi = \begin{bmatrix} 0 & I & 0 & \cdots & 0 \\ 0 & 0 & I & \cdots & 0 \\ \vdots & \vdots & \vdots & \ddots & \vdots \\ 0 & 0 & 0 & \cdots & I \\ 0 & 0 & 0 & \cdots & 0 \end{bmatrix}.$$

The following assumption is useful in deriving the results.

Assumption 2. *$\tilde{f}(\xi(t))$ satisfies the following local Lipschitz condition*

$$\|\tilde{f}(\xi(t)) - \tilde{f}(\xi(kh))\| \le \sigma\|\xi(t) - \xi(kh)\|, \quad (5)$$

where σ is the Lipschitz constant that can be computed by the nonlinear function $f(\xi(t))$ and the compact set Ω.

The purpose of this paper is to design the sampled-data controller (2) such that system (4) is exponentially stable with satisfactory H_∞ performance level γ and prescribed convergence rate 2δ. More specifically, the designed controller can ensure that

1) system (4) is exponentially stable with convergence rate 2δ for $\omega(t) \equiv 0$;
2) the system state $\xi(t)$ satisfies $\int_0^\infty \xi^T(s)\xi(s)ds \le \gamma^2 \int_0^\infty \omega^T(s)\omega(s)ds$ for $\omega(t) \ne 0$ and $\xi(0) = 0$.

3 Main Results

In this section, the H_∞ performance analysis of system (4) is carried out. Then, based on the performance analysis result, the criterion on the existence of the sampled-data controller (2) such that the HOFA system (4) is exponentially stable with prescribed H_∞ performance is established.

3.1 H_∞ Performance Analysis

Theorem 1. *For given positive constants h, σ, γ and δ, and a matrix K, system (4) is exponentially stable with H_∞ performance level γ and convergence rate 2δ, if there exist symmetric matrices $P > 0, Q > 0, R_i > 0$ $(i = 1, 2)$, matrices M_i and Z_i $(i = 1, 2)$, and a positive scalar λ such that*

$$\begin{bmatrix} \Psi + h\Psi_1 & hZ_2 & \varepsilon_1^T\tilde{E} \\ * & -hR_2 & 0 \\ * & * & -\gamma^2 I \end{bmatrix} < 0, \quad (6)$$

$$\begin{bmatrix} \Psi + h\Psi_2 & he^{-2\delta h}Z_1 & \varepsilon_1^T\tilde{E} \\ * & -he^{-2\delta h}R_1 & 0 \\ * & * & -\gamma^2 I \end{bmatrix} < 0, \quad (7)$$

where

$$\begin{aligned} \Psi &= \Xi + e_1^T(2\delta P + I)e_1 + \lambda\sigma^2\varepsilon_2^T\varepsilon_2 - \lambda e_5^T e_5 \\ &\quad + \text{Sym}\{e_2^T P e_1 + e^{-2\delta h}Z_1\varepsilon_2 + Z_2\varepsilon_3\}, \\ \Psi_1 &= \varepsilon_4^T Q\varepsilon_4 + e_2^T R_1 e_2, \Psi_2 = -e^{-2\delta h}\varepsilon_4^T Q\varepsilon_4 + e_2^T R_2 e_2, \\ \Xi &= \text{Sym}\{\varepsilon_1^T(-e_2 + \Phi e_1 - \tilde{K}e_3 + e_5)\}, \\ \varepsilon_1 &= M_1 e_1 + M_2 e_2, \varepsilon_2 = e_1 - e_3, \\ \varepsilon_3 &= e_4 - e_1, \varepsilon_4 = \text{col}\{e_3, e_4\}, \\ e_i &= [0_{np\times(i-1)np}\ I_{np\times np}\ 0_{np\times(5-i)np}], i = 1, 2, 3, 4, 5. \end{aligned}$$

Proof. Inspired by the looped functional method well used for sampled-data control systems, we construct the following Lyapunov functional

$$V(t) = V_0(t) + V_1(t) + V_2(t), \quad (8)$$

where

$$\begin{aligned} V_0(t) &= \xi^T(t)P\xi(t), \\ V_1(t) &= ((k+1)h - t)\int_{kh}^t e^{2\delta(s-t)}\eta_2^T Q\eta_2 ds, \\ V_2(t) &= ((k+1)h - t)\int_{kh}^t e^{2\delta(s-t)}\dot{\xi}^T(s)R_1\dot{\xi}(s)ds \\ &\quad + (kh - t)\int_t^{(k+1)h} e^{2\delta(s-t)}\dot{\xi}^T(s)R_2\dot{\xi}(s)ds, \end{aligned}$$

with $\eta_2 = \text{col}\{\xi(kh), \xi((k+1)h)\}$. Denote $\eta_1(t) = \text{col}\{\xi(t), \dot{\xi}(t)\}$ and $\zeta(t) = \text{col}\{\eta_1(t), \eta_2, \tilde{f}(\xi(t)) - \tilde{f}(\xi(kh))\}$. For system (4) with $\omega(t) \equiv 0$, one has that

$$2\zeta^T(t)(\varepsilon_1^T(-e_2 + \Phi e_1 + e_5 - \tilde{K}e_3))\zeta(t) = 0 \quad (9)$$

holds for arbitrary matrices $M_i \in \mathbb{R}^{np\times np} (i = 1, 2)$.

Taking the derivative of (8) and using equation (9), local Lipschitz condition (5) and the zero-order Bessel-Legendre inequality, we obtain

$$\begin{aligned} & \dot{V}(t) + 2\delta V(t) \\ & \le \zeta^T(t)(\Psi - e_1^T e_1 + ((k+1)h - t)(Z_2 R_2^{-1} Z_2^T + \Psi_1) \\ & \quad + (t - kh)(e^{-2\delta h}Z_1 R_1^{-1} Z_1^T + \Psi_2))\zeta(t). \end{aligned} \quad (10)$$

Then using the Schur complement and convex combination methods, it follows from LMIs (6) and (7) that $\dot{V}(t) + 2\delta V(t) < 0$. That is, system (4) is exponentially stable with convergence rate 2δ for $\omega(t) \equiv 0$.

Further, for system (4) with $\omega(t) \neq 0$, one gets

$$\begin{aligned}
&\dot{V}(t) + 2\delta V(t) \\
&\leq \zeta^T(t)(\Psi + ((k+1)h - t)(Z_2 R_2^{-1} Z_2^T + \Psi_1) \\
&\quad + (t - kh)(e^{-2\delta h} Z_1 R_1^{-1} Z_1^T + \Psi_2))\zeta(t) - \xi^T(t)\xi(t) \\
&\quad + 2\zeta^T(t)\varepsilon_1^T \tilde{E}\omega(t) - \gamma^2 \omega^T(t)\omega(t) + \gamma^2 \omega^T(t)\omega(t).
\end{aligned} \tag{11}$$

It can be derived from LMIs (6) and (7) that

$$\dot{V}(t) \leq \gamma^2 \omega^T(t)\omega(t) - \xi^T(t)\xi(t). \tag{12}$$

Integrating (12) on $t \in [0, \infty)$ under zero initial condition yields $\int_0^\infty \xi^T(s)\xi(s)ds \leq \int_0^\infty \gamma^2 \omega^T(s)\omega(s)ds$, which completes the proof. □

3.2 Control Design

Theorem 2. *For given positive constants $h, \sigma, \gamma, \lambda$ and δ, and a constant ϱ, system (4) is exponentially stable with H_∞ performance level γ and convergence rate 2δ, if there exist symmetric matrices $\bar{P} > 0, \bar{Q} > 0, \bar{R}_i > 0$ $(i = 1, 2)$, and matrices X, Y and $\bar{Z}_i$ $(i = 1, 2)$ such that*

$$\begin{bmatrix} \bar{\Psi} + h\bar{\Psi}_1 & h\bar{Z}_2 & \varepsilon_5^T \tilde{E} & \varepsilon_6^T \\ * & -h\bar{R}_2 & 0 & 0 \\ * & * & -\gamma^2 I & 0 \\ * & * & * & -\Lambda \end{bmatrix} < 0, \tag{13}$$

$$\begin{bmatrix} \bar{\Psi} + h\bar{\Psi}_2 & he^{-2\delta h}\bar{Z}_1 & \varepsilon_5^T \tilde{E} & \varepsilon_6^T \\ * & -he^{-2\delta h}\bar{R}_1 & 0 & 0 \\ * & * & -\gamma^2 I & 0 \\ * & * & * & -\Lambda \end{bmatrix} < 0, \tag{14}$$

where

$$\begin{aligned}
\bar{\Psi} &= \bar{\Xi} + 2\delta e_1^T \bar{P} e_1 - \lambda e_5^T e_5 \\
&\quad + \mathrm{Sym}\{e_2^T \bar{P} e_1 + e^{-2\delta h}\bar{Z}_1 \varepsilon_2 + \bar{Z}_2 \varepsilon_3\}, \\
\bar{\Psi}_1 &= \varepsilon_4^T \bar{Q} \varepsilon_4 + e_2^T \bar{R}_1 e_2, \bar{\Psi}_2 = -e^{-2\delta h}\varepsilon_4^T \bar{Q}\varepsilon_4 + e_2^T \bar{R}_2 e_2, \\
\bar{\Xi} &= \mathrm{Sym}\{\varepsilon_5^T(-Xe_2 + \Phi X e_1 - \tilde{Y} e_3 + X e_5)\}, \\
\varepsilon_5 &= e_1 + \varrho e_2, \varepsilon_6 = \mathrm{col}\{Xe_1, \lambda\sigma X \varepsilon_2\}, \\
\Lambda &= \mathrm{diag}\{I, \lambda I\}, \tilde{Y} = \mathrm{col}\{0, ..., 0, \mathrm{Y}\}.
\end{aligned}$$

Moreover, the control gain can be computed by $K = YX^{-1}$.

Proof. Let $M_1 = X^{-1}$ and $M_2 = \varrho X^{-1}$, and introduce $\bar{P} = X^T P X, \bar{Q} = \mathrm{diag}\{X, X\}^T Q \mathrm{diag}\{X, X\}, \bar{R}_i = X^T R_i X$, $\bar{Z}_i = \mathrm{diag}\{X, X, X, X, I_{np\times np}\}^T Z_i X (i = 1, 2)$ and $Y = KX$. Then, using Schur complement, LMIs (13) and (14) can be derived by pre- and post- multiplying both sides of LMIs (6) and (7) with $\mathrm{diag}\{X, X, X, X, I_{np\times np}, X, I_{q\times q}\}^T$ and its transpose, respectively. The proof is completed.

□

4 A Case Study

Consider the steering tracking control problem with the following vehicle model [10],

$$\dot{\xi}(t) = f(\xi(t)) + Bu(t) + E\omega(t), \tag{15}$$

where $\xi(t) = \mathrm{col}\{V_x(t), V_y(t), \dot{\psi}(t)\}$, $u(t) = \mathrm{col}\{F_x(t), \delta_f(t), \delta_r(t)\}$ are the system state and the control input, respectively; $\omega(t) = F_y(t)$ is the external disturbance that represents lateral winds; B and E are the input matrices given by

$$B = \begin{bmatrix} \frac{4}{M} & 0 & 0 \\ 0 & \frac{2C_f}{M} & \frac{2C_r}{M} \\ 0 & \frac{2C_f L_f}{I_z} & \frac{2C_r L_r}{I_z} \end{bmatrix}, E = \begin{bmatrix} 0 \\ \frac{1}{M} \\ 0 \end{bmatrix},$$

and $f(\xi(t)) = \mathrm{col}\{V_y(t)\dot{\psi}(t), \frac{c_1 V_y(t) + c_2 \dot{\psi}(t)}{V_x(t)} - V_x(t)\dot{\psi}(t), \frac{c_3 V_y(t) + c_4 \dot{\psi}(t)}{V_x(t)}\}$ is the nonlinear function with constant terms

$$c_1 = \frac{-2(C_f + C_r)}{M}, c_2 = \frac{-2(L_f C_f - L_r C_r)}{M},$$

$$c_3 = \frac{-2(L_f C_f - L_r C_r)}{I_z}, c_4 = \frac{-2(L_f^2 C_f + L_r^2 C_r)}{I_z},$$

where the physical meanings of the above symbols are listed in Table 1.

Table 1: Physical Meanings of Symbols

Symbols	Physical meanings
M	Vehicle mass
$V_x(t)$	Vehicle longitudinal velocity
$V_y(t)$	Vehicle lateral velocity
$\dot{\psi}(t)$	Vehicle yaw rate
$F_x(t)$	Longitudinal traction and braking force
$F_y(t)$	Lateral wing force
C_f, C_r	Wheel cornering stiffnesses
$\delta_f(t), \delta_r(t)$	Steering angles of wheels
L_f, L_r	Distance from the CG to wheel axles
I_z	Yaw moment inertia

According to actual steering condition, under Assumption 1, the variation ranges of longitudinal velocity, lateral velocity and yaw rate are set to be $V_x(t) \in [10, 30](\mathrm{m/s}), V_y(t) \in [-0.2, 0.2](\mathrm{m/s})$ and $\dot{\psi}(t) \in [-0.1, 0.1](\mathrm{rad/s})$, respectively. The Lipschitz constant σ of $f(\xi(t))$ is calculated as 24.9007. Then by choosing the vehicle parameters as $M = 1070(\mathrm{kg}), I_z = 2100(\mathrm{kg \cdot m^2}), C_f = C_r = 45312(\mathrm{N/rad}), L_f = 1.1(\mathrm{m})$ and $L_r = 1.3(\mathrm{m})$, one gets $f(\xi(t)) = \mathrm{col}\{V_y(t)\dot{\psi}(t), \frac{16.9391\dot{\psi}(t) - 169.3907 V_y(t)}{V_x(t)} - V_x(t)\dot{\psi}(t), \frac{8.6309 V_y(t) - 125.1474\dot{\psi}(t)}{V_x(t)}\}$, and

$$B = \begin{bmatrix} 0.0037 & 0 & 0 \\ 0 & 84.6953 & 84.6953 \\ 0 & 47.4697 & 57.1006 \end{bmatrix}, E = \begin{bmatrix} 0 \\ 0.0009 \\ 0 \end{bmatrix}.$$

The target state $\xi_d(t) = \mathrm{col}\{V_{xd}(t), V_{yd}(t), \dot{\psi}_d(t)\}$ is chosen as

$$\xi_d(t) = \begin{cases} \mathrm{col}\{10, 0, 0\}, & t \in [0, 5), \\ \mathrm{col}\{2t, 0, \frac{t-5}{100}\}, & t \in [5, 10), \\ \mathrm{col}\{30 - t, 0, \frac{20-t}{200}\}, & t \in [10, 20), \\ \mathrm{col}\{10, 0, 0\}, & t \in [20, \infty), \end{cases} \tag{16}$$

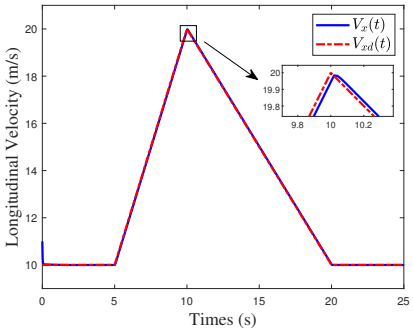

Fig. 1: The response curves of $V_x(t)$ and $V_{xd}(t)$.

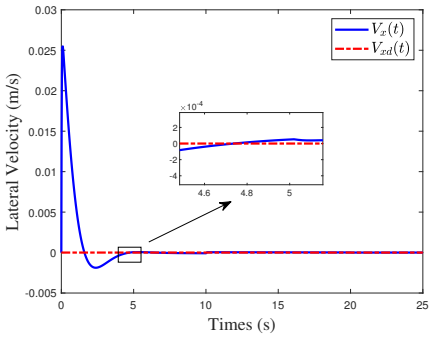

Fig. 2: The response curves of $V_y(t)$ and $V_{yd}(t)$.

which simulates the behavior of a vehicle driving at a constant speed before and after accelerating and steering.

By setting the H_∞ performance level $\gamma = 1$, the sampling period $h = 0.02(\mathrm{s})$, the convergence rate $2\delta = 4$ and the design parameter $\varrho = 0.2$, the control gain can be computed by Theorem 2 as

$$K = \begin{bmatrix} 35.7067 & 0 & 0 \\ 0 & 35.7069 & 0 \\ 0 & 0 & 35.7082 \end{bmatrix}.$$

The initial state of the vehicle is $V_x(0) = 11(\mathrm{m/s})$, $V_y(0) = 0(\mathrm{m/s})$ and $\dot{\psi}(0) = 0(\mathrm{rad/s})$, and $\omega(t) = e^{-t}\cos(t)(\mathrm{N})$. The response curves of $\xi(t)$ and $\xi_d(t)$ are shown in Figs. 1-3. It can be observed from Figs. 1-3 that a satisfactory control effect can be achieved by using the proposed sampled-data controller. Further, it can be computed by simulation results that

$$\frac{\sqrt{\int_0^\infty (\xi(s)-\xi_d(s))^T(\xi(s)-\xi_d(s))ds}}{\sqrt{\int_0^\infty \omega^T(s)\omega(s)ds}} \leq 0.2545,$$

which is less than the preset $\gamma = 1$.

5 Conclusion

The sampled-data H_∞ control problem of nonlinear HOFA systems has been studied in this paper. A local Lipschitz condition has been introduced to deal with the nonlinear error induced by sampled data. H_∞ performance analysis and control design results have been proposed by further using the looped functional method. An illustrative example has been given to show that a prescribed control effect of the HOFA system under unknown disturbance can be achieved by the designed sampled-data controller.

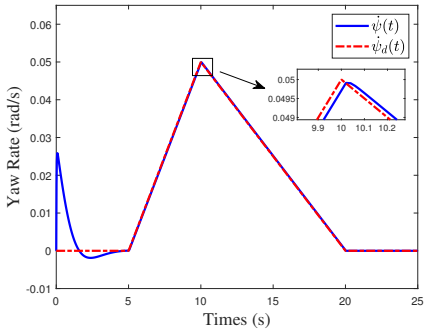

Fig. 3: The response curves of $\dot{\psi}(t)$ and $\dot{\psi}_d(t)$.

References

[1] G. R. Duan, High-order System Approaches: I. Fully-actuated Systems and Parametric Designs. *Acta Automatica Sinica*, 2020, 46(7): 1333–1345.

[2] X. Y. Yao, J. H. Park, H. F. Ding, M. F. Ge, Event-Triggered Consensus Control for Networked Underactuated Robotic Systems. *IEEE Transactions on Cybernetics*, 2022, 52(5): 2896–2906.

[3] Z. You, H. C. Yan, J. Sun, H. Zhang, Z. C. Li, Reliable Control for Flexible Spacecraft Systems With Aperiodic Sampling and Stochastic Actuator Failures. *IEEE Transactions on Cybernetics*, 2022, 52(5): 3434–3445.

[4] J. H. Moon, S. C. Jee, H. J. Lee, Output-Feedback Control of Underwater Gliders by Buoyancy and Pitching Moment Control: Feedback Linearization Approach. *International Journal of Control Automation and Systems*, 2016, 14(1): 255–262.

[5] Y. H. Fu, F. L. Zhu, Controller Design for Affine Nonlinear System Based on Constructing Optimization T-S Fuzzy Model and Disturbance Reconstruction. *IEEE Transactions on Fuzzy Systems*, 2022, 30(9): 3436–3446.

[6] G. R. Duan, High-order fully actuated system approaches: Part I. Models and basic procedure. *International Journal of Systems Science*, 2021, 52(2): 422–435.

[7] D. W. Zhang, G. P. Liu, L. Cao, Coordinated Control of High-Order Fully Actuated Multiagent Systems and Its Application: A Predictive Control Strategy. *IEEE-ASME Transactions on Mechatronics*, 2022, 27(6): 4362–4372.

[8] Q. B. Huang, J. T. Sun, Control of impulsive systems via high-order fully actuated system approach. *Nonlinear Dynamics*, 2023, 111(19): 17961–17971.

[9] R. Meng, C. C. Hua, K.Li, Adaptive Event-Triggered Control for Uncertain High-Order Fully Actuated System. *IEEE Transactions on Circuits and Systems II-Express Briefs*, 2022, 69(11): 4438–4442.

[10] Z. F. Gao, D. W. Zhang, S. Q. Zhu, Network-induced asynchronous fuzzy control for vehicle steering using switching event-triggered communication mechanism. *IEEE Transactions on Intelligent Vehicles*, 2023, 8(11): 4559–4571.

Proceedings of the 3rd Conference on Fully Actuated System Theory and Applications
May 10-12, 2024, Shenzhen, China

Tracking Control and Obstacle Avoidance of Quad-rotor UAV Based on High-Order Fully Actuated System Approach

Yankui Shi[1], Runze Wang[1], Ruizhi Tong[1], Yi Zeng*[1]

1. Key Laboratory of Autonomous Intelligent Unmanned Systems, School of Astronautics, Harbin Institute of Technology, Harbin 150001, P. R. China.

E-mail: 23S136001@stu.hit.edu.cn;23B904007@stu.hit.edu.cn;23S104097@stu.hit.edu.cn;yi.zeng@hit.edu.cn

Abstract: The aim of this paper is to explore the quad-rotor UAV tracking control and obstacle avoidance strategies based on the High-Order Fully Actuated system approach. The attitude description of the UAV is firstly established. Considering the uncertainty of UAV parameters and the existence of bounded perturbation, a mathematical model of UAV attitude and position with high-order fully actuated system characteristics is established, and a robust controller based on high-order fully actuated system method is designed. The controller is designed to enable UAVs to track targets and maintain good position and attitude control performance in the face of environmental changes and perturbations, and the controller ensures that the system state converges to almost any ellipsoid area. On the basis of the controller design, this study further considers the obstacle avoidance problem of the quad-rotor UAV. By combining the designed drone controller, an effective obstacle avoidance strategy is designed to ensure that the UAV can avoid obstacles during its movement, thus improving its adaptability and safety in the real environment. Finally, we verify the effectiveness of the designed controller through simulation.

Key Words: High-Order Fully Actuated system approach, quad-rotor UAV tracking control, robust controller, obstacle avoidance strategy

1 Introduction

Quad-rotor UAVs have strong adaptability and high maneuverability, and have broad application prospects in military, civilian and other fields. They have great research value and wide applications, and have become one of the hot spots at home and abroad. Many scholars have conducted important research on UAV tracking control. For example [1] studied the common trajectory tracking problems of quad-rotor UAVs based on sliding mode control, then proposed a SMC method to weaken the chattering phenomenon resulted from the switching control action and perform precisely the position and attitude trajectory tracking. [2] proposed a trajectory tracking control algorithm based on back-stepping and linear active disturbance rejection control (LADRC) in view of the underactuated and strong coupling characteristics of quad-rotor UAVs. [3] aimed at problems such as actuator saturation, trajectory tracking, formation and obstacle avoidance planning in multi-UAV formation obstacle avoidance control, and proposes an anti-saturation UAV formation obstacle avoidance control strategy for a single UAV. For the trajectory tracking problem, the back-stepping control strategy is used to simplify the second-order nonlinear system into two first-order subsystems and reduce the system complexity.

The above results are actually affected by the first-order state space model. For first-order state-space models describing linear dynamical systems, it is relatively easy to obtain control strategies and their stability results. However, when first-order state-space models are applied to nonlinear systems, the situation becomes more complicated. As a typical nonlinear strongly coupled system, the position and attitude control system of a quad-rotor UAV also faces the same problem.

This work was supported in part by the National Natural Science Foundation of China under Grant 62188101, 62303135, 62033005, and 62320106001, and in part by the Natural Science Foundation of Heilongjiang Province (ZD2021F001). *(corresponding author: Yi Zeng)*

In order to solve this problem, Duan introduced the High-Order Fully Actuated system approach (HOFA) in [4]-[9]. [4]-[7] provide an in-depth introduction and explanation of the HOFA system method. In [4], a basic control method suitable for nonlinear systems under certain conditions is proposed. Three generalized strict feedback system types were transformed into HOFA systems in [5]. And [6]-[7] respectively proposed robust control and adaptive control schemes based on high-order inversion. Obtaining an HOFA system model is the most critical aspect of this method. Once the HOFA system model is obtained, the corresponding control strategy can be obtained immediately. By reading the literature we can conclude that controllers built with high-order fully actuated systems are not only able to counteract known nonlinear effects, but also allow more systems have global stability. It will also extend Lyapunov stability to further stability and sub-stableness, making the response analysis and stability analysis of the closed-loop system easier, so it is easier to solve the system's stabilization problem. Therefore, the HOFA has broad application prospects in the field of nonlinear control.

This paper first establishes a HOFA system model of a quad-rotor UAV under the condition that there are parameter uncertainties and bounded external disturbances in the quad-rotor UAV. According to the proposed HOFA system model of quad-rotor UAV tracking control, and according to [6], a robust controller is designed that can drive the system state to converge to almost any ellipsoid region. The main contribution of this article is to design a UAV controller using the HOFA, which further enriches the application of the HOFA system.

2 Description of the problem

To establish a mathematical model of the system, a coordinate system must first be established. Firstly, the modeling method of quadrotor UAV in [11] used in the paper is briefly introduced as follows.

2.1 Ground coordinate system

In the coordinate system of the quadcopter UAV, the ground coordinate system is $E(o_e x_e y_e z_e)$. The coordinate origin o_e is an arbitrary point on the ground. The $o_e x_e$ axis refers to any direction, the $o_e z_e$ axis is perpendicular to the ground and points in the opposite direction to the center of the earth, and $x_e o_e y_e$ is the horizontal plane, which conforms to the right-hand spiral law.

2.2 Body coordinate system

The fuselage coordinate system of the quad-rotor UAV is $B(o_b x_b y_b z_b)$. The origin o_b is at the center of mass of the UAV, the axis $o_b x_b$ is selected to coincide with one bracket of the vertical cross of the quad-rotor UAV, the axis $o_b y_b$ coincides with another bracket, and the axis $o_b z_b$ is perpendicular to the $x_b o_b y_b$ plane and points above the UAV, conforming to the right-hand spiral law.

2.3 Attitude angle

The attitude angle of the UAV is determined by the relationship between the body coordinate system and the ground coordinate system. The pitch angle θ is the angle between the $o_b x_b$ axis and the $x_e o_e y_e$ plane. The yaw angle ψ is the angle between the projection of the axis $o_b x_b$ and the plane $x_e o_e y_e$ and the axis $o_e x_e$. The roll angle ϕ is the angle between the axis $o_b z_b$ and the vertical plane containing the axis $o_b z_b$.

3 Dynamic modeling

The motion of a rigid body UAV can be divided into two parts: translation of the center of mass and rotation around the center of mass. Six degrees of freedom are required to describe the motion of a UAV: three linear motions of the center of mass translation and three angular motions of rotation around the center of mass.

Let $\xi = [x, y, z]^T \in R^3$ and $\Psi = [\phi, \theta, \psi]^T \in R^3$, x, y, z respectively represent the position coordinates of the UAV. ϕ, θ, ψ respectively represent the three attitude angles of the quad-rotor UAV: roll angle, pitch angle and yaw angle.

By citing the model in [1], we can get the dynamic model of the quadcopter UAV as:

$$\begin{cases} \ddot{x} = -\frac{K_1}{m}\dot{x} + \frac{\cos\phi\sin\theta\cos\psi+\sin\phi\sin\psi}{m}u_1, \\ \ddot{y} = -\frac{K_2}{m}\dot{y} + \frac{\cos\phi\sin\theta\sin\psi-\sin\phi\cos\psi}{m}u_1, \\ \ddot{z} = -\frac{K_3}{m}\dot{z} - g + \frac{\cos\phi\cos\theta}{m}u_1, \\ \ddot{\phi} = \frac{I_y-I_z}{I_x}\dot{\theta}\dot{\psi} - \frac{K_4}{I_x}\dot{\phi} + \frac{1}{I_x}u_2, \\ \ddot{\theta} = \frac{I_z-I_x}{I_y}\dot{\phi}\dot{\psi} - \frac{K_5}{I_y}\dot{\theta} + \frac{1}{I_y}u_3, \\ \ddot{\psi} = \frac{I_x-I_y}{I_z}\dot{\phi}\dot{\theta} - \frac{K_6}{I_z}\dot{\psi} + \frac{1}{I_z}u_4. \end{cases} \tag{1}$$

u_1, u_2, u_3, u_4 are calculated according to the following formula:

$$\begin{bmatrix} u_1 \\ u_2 \\ u_3 \\ u_4 \end{bmatrix} = \begin{bmatrix} b & b & b & b \\ 0 & -lb & 0 & lb \\ -lb & 0 & lb & 0 \\ d & -d & d & -d \end{bmatrix} \begin{bmatrix} \omega_1^2 \\ \omega_2^2 \\ \omega_3^2 \\ \omega_4^2 \end{bmatrix}, \tag{2}$$

among them, l is the distance from the propeller axis to the center of mass of the UAV, and d is the torque coefficient of the propeller.

4 Controller design

The symbols that need to be used in this section are as follows:

$$x^{0\sim n-1} = \begin{bmatrix} x \\ \dot{x} \\ \vdots \\ x^{(n)} \end{bmatrix},$$

$$A^{0\sim n-1} = \begin{bmatrix} A_0 & A_1 & \cdots & A_{n-1} \end{bmatrix},$$

$$\Phi\left(A^{0\sim n-1}\right) = \begin{bmatrix} & I & & \\ & & \ddots & \\ & & & I \\ -A_0 & -A_1 & \cdots & -A_{n-1} \end{bmatrix}.$$

The HOFA model with perturbation criteria is:

$$x^{(n)} = f\left(x^{(0\sim n-1)}\right) + \Delta f\left(x^{(0\sim n-1)}\right) + L\left(x^{(0\sim n-1)}\right)u. \tag{3}$$

After establishing the HOFA system model, the characteristics of the HOFA system can be directly used to design the control law.

Lemma 1 [6]: When the system model is given as the HOFA system in (1), the system can be stabilized by applying the following control law:

$$\begin{cases} u = -L^{-1}\left(x^{(0\sim n-1)}\right)\left(A^{0\sim n-1}x^{(0\sim n-1)} + u^*\right) \\ u^* = f\left(x^{(0\sim n-1)}\right) + \\ \frac{1}{4\varepsilon}\rho^2\left(x^{(0\sim n-1)}\right)\cdot P_L^T\left(A^{0\sim n-1}\right)x^{(0\sim n-1)}. \end{cases} \tag{4}$$

The system state can converge to the following ellipsoid region:

$\Theta_{\mu,\varepsilon}(0)$

$= \left\{x^{(0\sim n-1)}\left(x^{(0\sim n-1)}\right)^{\mathrm{T}} P\left(A^{0\sim n-1}\right)x^{(0\sim n-1)} \le \frac{\varepsilon}{\mu}\right\}$,

where ε is a positive number, $\rho^2(x^{(0\sim n-1)})$ is the upper limit of system uncertainty, $A^{0\sim n-1}$ and $P_L^T(A^{0\sim n-1})$ can be obtained through the following Proposition 1 and Lemma 2.

Proposition 1 [7]: For any chosen matrix $F \in R^{nr\times nr}$, the matrix $A^{0\sim n-1}$ and the non-singular matrix $V \in R^{nr\times nr}$ satisfy $\Phi\left(A^{0\sim n-1}\right) = VFV^{-1}$, in which:

$$A^{0\sim n-1} = -ZF^nV^{-1}(Z,F),$$

$$V = V(Z,F) = \begin{bmatrix} Z \\ ZF \\ \vdots \\ ZF^{n-1} \end{bmatrix},$$

where $Z \in R^{r\times nr}$ satisfies $detV(Z,F) \neq 0$.

Lemma 2 [7]: For any $\mu > 0$, there exists a set of matrices $A_i \in R^{r\times r}$, $i = 0, 1, \ldots, n-1$ satisfies: $Re\lambda_i\left(\Phi\left(A^{0\sim n-1}\right)\right) < -\frac{\mu}{2}$,$i = 1, 2, \ldots, nr$.

When the above conditions hold, we have a positive definite matrix $P\left(A^{0\sim n-1}\right)$ that satisfies the following inequality:

$\Phi^T\left(A^{0\sim n-1}\right)P\left(A^{0\sim n-1}\right) + P\left(A^{0\sim n-1}\right)\Phi\left(A^{0\sim n-1}\right)$

$< -\mu P\left(A^{0\sim n-1}\right)$, in which:

$$P\left(A^{0\sim n-1}\right) = \left[\begin{array}{cccc} P_1 & P_2 & \cdots & P_n \end{array}\right],$$

$$P_L\left(A^{0\sim n-1}\right) = P\left(A^{0\sim n-1}\right)\left[\begin{array}{c} 0 \\ I_r \end{array}\right] = P_n.$$

The desired position x_d, y_d, z_d and the desired yaw angle ψ_d of the quad-rotor UAV are usually given by remote control instructions. Inspired by [3], the desired roll angle ϕ_d and pitch angle θ_d can be calculated by the following formula:

$$\left\{\begin{array}{l} \phi_d = \arcsin\left(\sin\phi_d U_x - U_y\cos\psi_d\right), \\ \theta_d = \arcsin\left(\frac{U_x\cos\psi_d + U_y\sin\psi_d}{\cos\phi_d}\right), \\ U_x = \cos\phi_d\sin\theta_d\cos\psi_d + \sin\phi_d\sin\psi_d, \\ U_y = \cos\phi_d\sin\theta_d\sin\psi_d - \sin\phi_d\cos\psi_d. \end{array}\right. \tag{5}$$

Therefore, the six states of the UAV are known. The position controller and attitude controller are respectively designed according to the errors of the UAV's state variables.

4.1 Position controller

Inspired by [1], the quad-rotor UAV position system with disturbance is:

$$\left\{\begin{array}{l} \ddot{x} = -\frac{K_1}{m}\dot{x} + \frac{\cos\phi\sin\theta\cos\psi+\sin\phi\sin\psi}{m}u_1 + d_1, \\ \ddot{y} = -\frac{K_2}{m}\dot{y} + \frac{\cos\phi\sin\theta\sin\psi-\sin\phi\cos\psi}{m}u_1 + d_2, \\ \ddot{z} = -\frac{K_3}{m}\dot{z} - g + \frac{\cos\phi\cos\theta}{m}u_1 + d_3, \end{array}\right. \tag{6}$$

which is an under-driven subsystem. Let

$$\left\{\begin{array}{l} \frac{\cos\phi\sin\theta\cos\psi+\sin\phi\sin\psi}{m} = a, \\ \frac{\cos\phi\sin\theta\sin\psi-\sin\phi\cos\psi}{m} = b, \\ \frac{\cos\phi\cos\theta}{m} = c. \end{array}\right.$$

Suppose when a≠0, b≠0, select the full rank matrix $Q = \left[\begin{array}{ccc} 0 & 1 & \frac{-b}{c} \\ 1 & 0 & \frac{-a}{c} \\ 0 & 0 & 1 \end{array}\right]$, we weigh the matrix Q at the left and right ends of Equation 14 at the same time, and we get the following formula:

$$\left\{\begin{array}{rcl} \ddot{y} - \frac{b}{c}\ddot{z} & = & \frac{K_3 b}{mc}\dot{z} - \frac{K_2}{m}\dot{y} + \frac{b}{c}g \\ \ddot{x} - \frac{a}{c}\ddot{z} & = & \frac{K_3 a}{mc}\dot{z} - \frac{K_1}{m}\dot{x} + \frac{a}{c}g \\ \ddot{z} & = & \frac{-K_3}{m}\dot{z} - g \end{array} + \left[\begin{array}{c} 0 \\ 0 \\ c \end{array}\right] u_1 + \Delta D_1. \right. \tag{7}$$

This is a standard under actuated subsystem, which is converted into a high-order fully Actuated subsystem according to the method in Document [4]:

$$\begin{aligned} \frac{ma}{bK_3}y^{(4)} - \frac{ma}{K_3 c}z^{(4)} &= x^{(3)} - \frac{K_2 a}{bK_3}y^{(3)} + \frac{K_1}{m}x^{(2)} \\ - \frac{K_3^2}{m^2 c}\dot{z} + \left(\frac{K_3 a}{mc} - \frac{a}{c} + \frac{ma}{K_3 c}\right)g &- \frac{K_3 a}{m}u_1 + \Delta D. \end{aligned} \tag{8}$$

Let:

$$\frac{ma}{bK_3}y - \frac{ma}{cK_3}z = T,$$

$$\begin{aligned} f(x,y,z,g) =& x^{(3)} - \frac{K_2 a}{bK_3}y^{(3)} + \frac{K_1}{m}x^{(2)} - \frac{K_3^2}{m^2 c}\dot{z} \\ &+ \left(\frac{K_3 a}{mc} - \frac{a}{c} + \frac{ma}{K_3 c}\right)g, \end{aligned}$$

$$T_e = T - T^*.$$

According to [6], it can be concluded that:

$$T_e^{(i)} = T^{(i)} - \left(T^*\right)^{(i)}, \quad i = 0, 1, \ldots, n. \tag{9}$$

$$\left\{\begin{array}{l} f(x,y,z,g) = f\left(x_e, y_e, z_e, g\right), \\ L\left(T^{(0\sim n-1)}\right) = L\left(T_e^{(0\sim n-1)}, t\right). \end{array}\right. \tag{10}$$

Therefore, formula (8) can be transformed into the following formula:

$$\begin{aligned} \frac{ma}{bK_3}y_e^{(4)} - \frac{ma}{K_3 c}z_e^{(4)} &= x_e^{(3)} - \frac{K_2 a}{bK_3}y_e^{(3)} + \frac{K_1}{m}x_e^{(2)} \\ - \frac{K_3^2}{m^2 c}\dot{z}_e + \left(\frac{K_3 a}{mc} - \frac{a}{c} + \frac{ma}{K_3 c}\right)g &- \frac{K_3 a}{m}u_1 + \Delta D. \end{aligned} \tag{11}$$

The robust tracking controller of the quad-rotor UAV position subsystem is:

$$\left\{\begin{array}{l} u_1 = -\left(\frac{-K_3 a}{m}\right)^{-1}\left(A^{0\sim 3}T_e^{(0\sim 3)} + u_1^*\right) \\ u_1^* = \frac{1}{4\varepsilon}\rho^2\left(T_e^{(0\sim 3)}\right)\cdot P_L^T\left(A^{0\sim 3}\right)T_e^{(0\sim 3)} \\ \qquad + f\left(x_e, y_e, z_e, g\right) - \left(T^*\right)^{(4)}. \end{array}\right. \tag{12}$$

Now we solve $A^{0\sim 3}$ and $P_L^T\left(A^{0\sim 3}\right)$ according to proposition 1 and Lemma 2.

When taking $\mu = 8$,we design the parameter matrices as:

$$F = \left[\begin{array}{cccc} -5 & 0 & 0 & 0 \\ 0 & -6 & 0 & 0 \\ 0 & 0 & -7 & 0 \\ 0 & 0 & 0 & -8 \end{array}\right], \tag{13}$$

$$Z = \left[\begin{array}{cccc} 1 & 1 & 1 & 1 \end{array}\right], \tag{14}$$

$$V = \left[\begin{array}{cccc} 1 & 1 & 1 & 1 \\ -5 & -6 & -7 & -8 \\ 25 & 36 & 49 & 64 \\ -125 & -216 & -343 & -512 \end{array}\right], \tag{15}$$

which satisfies $\det V \neq 0$. Then, we can get:

$$A^{0\sim 3} = \left[\begin{array}{cccc} 0 & 0 & -1 & 0 \end{array}\right], \tag{16}$$

$$\Phi\left(A^{0\sim 3}\right) = \left[\begin{array}{cccc} 0 & 1 & 0 & 0 \\ 0 & 0 & 1 & 0 \\ 0 & 0 & 0 & 1 \\ -1680 & -1066 & -251 & -26 \end{array}\right]. \tag{17}$$

According to the value of μ, we select the following matrix equation:

$$\left(\Phi\left(A^{0\sim 3}\right) + 4I\right)^{\mathrm{T}} P + P\left(\Phi\left(A^{0\sim 3}\right) + 4I\right) = -I, \tag{18}$$

which satisfy the following inequality:

$$\Phi^{\mathrm{T}}\left(A^{0\sim 3}\right)P + P\Phi\left(A^{0\sim 3}\right) \leq -\mu P. \tag{19}$$

By solving equation (26), we have:

$$P_L = P\left[\begin{array}{c} 0 \\ I_r \end{array}\right] = P\left[\begin{array}{c} 0 \\ 0 \\ 0 \\ 1 \end{array}\right] = \left[\begin{array}{c} 1011.5000 \\ 418.3638 \\ 57.6276 \\ 2.6422 \end{array}\right]. \tag{20}$$

According to Lemma 1, the position controller we design will drive the system state to any ellipsoid domain.

4.2 Attitude controller

Quote from [1], the attitude subsystem of the quad-rotor UAV is:

$$\begin{cases} \ddot{\phi} = \frac{I_y - I_z}{I_x}\dot{\theta}\dot{\psi} - \frac{K_4}{I_x}\dot{\phi} + \frac{1}{I_x}u_2, \\ \ddot{\theta} = \frac{I_z - I_x}{I_y}\dot{\phi}\dot{\psi} - \frac{K_5}{I_y}\dot{\theta} + \frac{1}{I_y}u_3, \\ \ddot{\psi} = \frac{I_x - I_y}{I_z}\dot{\phi}\dot{\theta} - \frac{K_6}{I_z}\dot{\psi} + \frac{1}{I_z}u_4. \end{cases} \tag{21}$$

This is a fully driven system. After adding interference, it can be written in the following form:

$$\ddot{M} = g(M, \dot{M}) + L(M)V + \Delta G(M, \dot{M}), \tag{22}$$

in which,

$$g(M, \dot{M}) = \begin{bmatrix} \frac{I_y - I_z}{I_x}\dot{\theta}\dot{\psi} - \frac{K_4}{I_x}\dot{\phi} \\ \frac{I_z - I_x}{I_y}\dot{\phi}\dot{\psi} - \frac{K_5}{I_y}\dot{\theta} \\ \frac{I_x - I_y}{I_z}\dot{\phi}\dot{\theta} - \frac{K_6}{I_z}\dot{\psi} \end{bmatrix},$$

$$L(M) = \begin{bmatrix} \frac{1}{I_x} & & \\ & \frac{1}{I_y} & \\ & & \frac{1}{I_z} \end{bmatrix},$$

$$M_e = M - M^*. \tag{23}$$

In the same way, according to [6], equation (30) can be transformed into the following form:

$$\ddot{M}_e = g(M_e, \dot{M}_e) + L(M_e)V + \Delta G(M_e, \dot{M}_e). \tag{24}$$

According to the method in [6], the robust tracking controller of the attitude subsystem of the quad-rotor UAV is designed as follows:

$$\begin{cases} U = -L\left(M_e\right)^{-1}\left(A^{0\sim1}M_e^{(0\sim1)} + U^*\right) \\ U^* = \frac{1}{4\varepsilon}\rho^2\left(M_e^{(0\sim1)}\right)\cdot P_L^T\left(A^{0\sim1}\right)M_e^{(0\sim1)} \\ \qquad +g\left(M_e^{(0\sim1)}\right) - \left(M^*\right)^{(2)}. \end{cases} \tag{25}$$

Now we solve $A^{0\sim1}$ and $P_L^T\left(A^{0\sim1}\right)$ according to proposition 1 and Lemma 2.

When taking $\mu = 10$, we design the parameter matrices as:

$$F = \begin{bmatrix} -6 & 0 & 0 & 0 & 0 & 0 \\ 0 & -7 & 0 & 0 & 0 & 0 \\ 0 & 0 & -8 & 0 & 0 & 0 \\ 0 & 0 & 0 & -9 & 0 & 0 \\ 0 & 0 & 0 & 0 & -10 & 0 \\ 0 & 0 & 0 & 0 & 0 & -11 \end{bmatrix}, \tag{26}$$

$$Z = \begin{bmatrix} 1 & 0 & 0 & 1 & 0 & 0 \\ 0 & 1 & 0 & 0 & 1 & 0 \\ 0 & 0 & 1 & 0 & 0 & 1 \end{bmatrix}, \tag{27}$$

$$V = \begin{bmatrix} Z \\ ZF \end{bmatrix} = \begin{bmatrix} 1 & 0 & 0 & 1 & 0 & 0 \\ 0 & 1 & 0 & 0 & 1 & 0 \\ 0 & 0 & 1 & 0 & 0 & 1 \\ -6 & 0 & 0 & -9 & 0 & 0 \\ 0 & -7 & 0 & 0 & -10 & 0 \\ 0 & 0 & -8 & 0 & 0 & -11 \end{bmatrix}, \tag{28}$$

which satisfies $\det V \neq 0$. Then, we can get:

$$A^{0\sim1} = \begin{bmatrix} 54 & 0 & 0 & 15 & 0 & 0 \\ 0 & 70 & 0 & 0 & 17 & 0 \\ 0 & 0 & 88 & 0 & 0 & 19 \end{bmatrix}, \tag{29}$$

$$\Phi\left(A^{0\sim1}\right) = \begin{bmatrix} 0 & 0 & 0 & 1 & 0 & 0 \\ 0 & 0 & 0 & 0 & 1 & 0 \\ 0 & 0 & 0 & 0 & 0 & 1 \\ -54 & 0 & 0 & -15 & 0 & 0 \\ 0 & -70 & 0 & 0 & -17 & 0 \\ 0 & 0 & -88 & 0 & 6 & -19 \end{bmatrix}. \tag{30}$$

According to the value of μ, we select the following equation (39):

$$\left(\Phi\left(A^{0\sim1}\right) + 5I\right)^{\mathrm{T}} P + P\left(\Phi\left(A^{0\sim1}\right) + 5I\right) = -I, \tag{31}$$

which satisfy the following inequality:

$$\Phi^{\mathrm{T}}\left(A^{0\sim1}\right)P + P\Phi\left(A^{0\sim1}\right) \leq -\mu P. \tag{32}$$

By solving equation (32), we have:

$$P_L = P\begin{bmatrix} 0 \\ I_r \end{bmatrix} = \begin{bmatrix} 7.0000 & 0 & 0 \\ 0 & 2.5857 & 0 \\ 0 & 0 & 1.4012 \\ 0.7500 & 0 & 0 \\ 0 & 0.2571 & 0 \\ 0 & 0 & 0.1358 \end{bmatrix}. \tag{33}$$

According to Lemma 1, the attitude controller we designed will drive the system state to almost any ellipsoid domain.

At this point, we have completed the design of the controller.

5 The MPC-based obstacle avoidance controller

5.1 Discretization equations and model predictions of quad-rotor UAVs

According to [10], [15], [16] and [17], we can use model predictive control algorithms in the process of UAV obstacle avoidance. First, we can write the quad-rotor UAV motion model of the high-order fully actuated system obtained above into a discretized form:

$$X(k+1) = f(X(k), U(k)). \tag{34}$$

For specific discretization methods, we can refer to [15]. Then perform the following steps:

$$\begin{cases} X_{pre}(k \mid k) = X(k), \\ X_{pre}(k+i+1 \mid k) = X_{pre}(k+i \mid k) + \\ \delta \cdot f\left(X(k), U(k)\right), \quad i \in [0, N-1]. \end{cases} \tag{35}$$

In the formula, $X_{\mathrm{pre}}(k \mid k) = X(k)$ represents that at time k, the predicted value $X_{\mathrm{pre}}(k \mid k)$ is equal to the current state value $X(k)$; $X_{\mathrm{pre}}(k+i \mid k)$ represents the predicted state at the $k+i$ moment in the prediction time domain $[k, k+N]$; δ represents the sampling time.

5.2 Obstacle Avoidance (Barrier Method)

By the method in [10], this paper adds a barrier function to the target index. The core idea is to consider the location of obstacles in the cost function J, penalize situations that are close to obstacles.

$$\boldsymbol{J}_{obs,i} = \frac{S_{obs}}{(x_i - x_0)^2 + (y_i - y_0)^2 + (z_i - z_0)^2 + \zeta}. \quad (36)$$

Among them, S_{obs} is a selectable weight coefficient, (x_i, y_i, z_i) and (x_0, y_0, z_0) are the coordinates of each obstacle and the position coordinates of the UAV, ζ takes a very small positive number.

Every time the drone takes a step, the controller must repeatedly calculate the following formula to derive and execute the input at each moment.

$$\begin{aligned} \min_{U_i} \sum_{i=1}^{N} & \|X(k+i \mid k) - X_{\text{ref}}(k+i \mid k)\|_Q^2 \\ & + \|U\|_R^2 + \sum_{j}^{\text{Nobs}} J_{\text{obs},j}, \end{aligned} \quad (37)$$

$$\text{s.t.} \begin{cases} U_{\min} \le U \le U_{\max}, \\ X_{\min} \le X \le X_{\max}. \end{cases} \quad (38)$$

Where N is the prediction range, $Nobs$ is the total number of obstacles, $X_{pre}(k+i \mid k)$ is the prediction state from the current time to ith steps in the future, $X_{ref}(k+i \mid k)$ and U represent the state reference and input vector respectively.

6 Simulation

Now we verify the effectiveness of the designed attitude and position controller through simulation, the simulation experiments on obstacle avoidance using model predictive control will not be carried out here. Select $m = 1.2\,\text{kg}$, $g = 9.8\,\text{m/s}^2$, $J = \text{diag}(0.0091, 0.0096, 0.0189)\text{kg} \cdot \text{m}^2$, $K_1 \sim K_3 = (0.010, 0.012, 0.019)\text{N} \cdot \text{s/m}$, $K_4 \sim K_6 = (0.0022, 0.0024, 0.0031)\text{N} \cdot \text{m} \cdot \text{s/rad}$, the initial state variable error of the UAV is $(x_e, y_e, z_e, \phi_e, \theta_e, \psi_e) = \left(-0.5, 0.4, -0.3, -\frac{\pi}{36}, -\frac{\pi}{40}, -\frac{\pi}{30}\right)$, $\varepsilon = 0.1$, $\Delta D = 0.2\cos 3t$, $\Delta G(M, \dot{M}) = (0.1\sin t, 0.2\sin 2t, 0.05\cos t)^T$.

The simulation results are shown in Fig.1 and Fig.2 respectively. It can be seen that after a period of time, the state errors tend to 0, which indicates that the controller successfully achieved tracking.

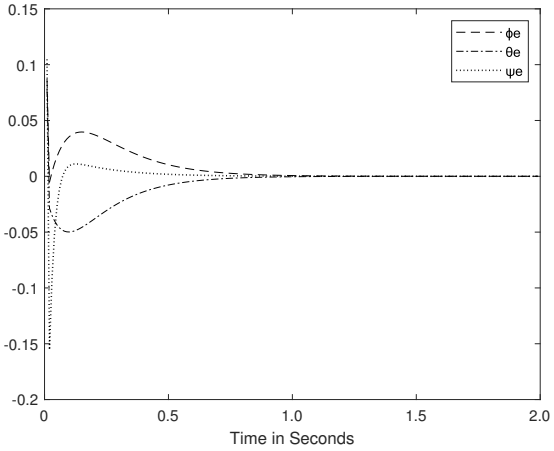

Fig. 1: Attitude tracking error

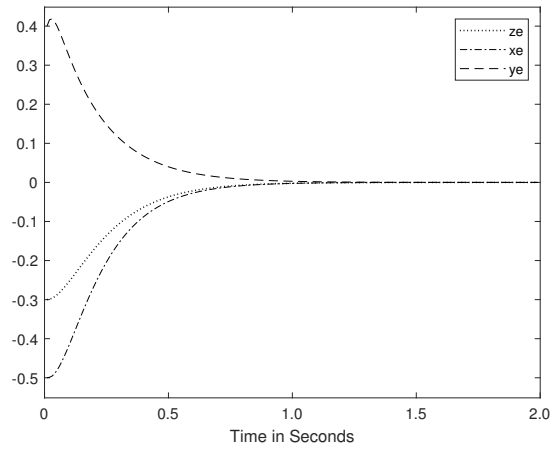

Fig. 2: Position tracking error

7 Conclusion

We can see from the simulation results that based on the controllers involved in the High-Order Fully Actuated system, we can better enable no one to achieve the ideal state, and the convergence speed is relatively fast.

References

[1] J. -J. Xiong, N. -H. Guo, Y. -X. Hong and E. -H. Zheng, "Improved Position and Attitude Tracking Control for a Quadrotor UAV," 2019 Chinese Automation Congress (CAC), Hangzhou, China, 2019, pp. 4197-4201, doi: 10.1109/CAC48633.2019.8996304.

[2] X. Wu and Y. Liu, "Trajectory Tracking Control of Quadrotor UAV," 2018 37th Chinese Control Conference (CCC), Wuhan, China, 2018, pp. 10020-10025, doi: 10.23919/ChiCC.2018.8482939.

[3] A. Gao, Z. Li and Y. Huang, "Obstacle Avoidance Algorithm for Quadrotor UAV Formation with Input Constraints," 2023 2nd International Symposium on Aerospace Engineering and Systems (ISAES), Nanjing, China, 2023, pp. 229-234, doi: 10.1109/ISAES58852.2023.10281319.

[4] Duan G. High-order fully actuated system approaches: Part I. Models and basic procedure[J]. International Journal of Systems Science, 2021, 52(2): 422-435.

[5] Duan G. High-order fully actuated system approaches: Part II. Generalized strict-feedback systems[J]. International Journal of Systems Science, 2021, 52(3): 437-454.

[6] Duan G. High-order fully actuated system approaches: Part III. Robust control and high-order backstepping[J]. International Journal of Systems Science, 2021, 52(5): 952-971.

[7] Duangren Duan (2021) High-order fully actuated system approaches: Part V. Robust adaptive control, International Journal of Systems Science, 52:10, 2129-2143, DOI: 10.1080/00207721.2021.1879964.

[8] Duan G. High-order fully-actuated system approaches: Part VI. Disturbance attenuation and decoupling[J]. International Journal of Systems Science, 2021, 52(10): 2161-2181.

[9] Guangren Duan (2021) High-order fully actuated system ap-

proaches: part VII. Controllability, stabilisability and parametric designs, International Journal of Systems Science, 52:14, 3091-3114, DOI: 10.1080/00207721.2021.1921307.

[10] M. Mamdouh, M. Ibrahim, A. Sarhan and M. Ashry, "Path Following Controller and Obstacles Avoidance Using Nonlinear Model Predictive Control," 2023 International Telecommunications Conference (ITC-Egypt), Alexandria, Egypt, 2023, pp. 701-706, doi: 10.1109/ITC-Egypt58155.2023.10206370.

[11] Duan, G. (2022). High-order fully-actuated system approaches: Part IX. Generalised PID control and model reference tracking. International Journal of Systems Science, 53(3), 652–674. https://doi.org/10.1080/00207721.2021.1970277

[12] A. Gao, Z. Li and Y. Huang, "Obstacle Avoidance Algorithm for Quadrotor UAV Formation with Input Constraints," 2023 2nd International Symposium on Aerospace Engineering and Systems (ISAES), Nanjing, China, 2023, pp. 229-234, doi: 10.1109/ISAES58852.2023.10281319.

[13] B. Sun, W. Zhang, A. Song, X. Zhu and D. Zhu, "Trajectory Tracking and Obstacle Avoidance Control of Unmanned Underwater Vehicles Based on MPC," 2018 IEEE 8th International Conference on Underwater System Technology: Theory and Applications (USYS), Wuhan, China, 2018, pp. 1-6, doi: 10.1109/USYS.2018.8779160.

[14] J. C. Kim, D. S. Pae and M. T. Lim, "Obstacle Avoidance Path Planning Algorithm Based on Model Predictive Control," 2018 18th International Conference on Control, Automation and Systems (ICCAS), PyeongChang, Korea (South), 2018, pp. 141-143.

[15] K. Benkhoud and S. Bouallègue, "Model Predictive Control design for a convertible Quad Tilt-Wing UAV," 2016 4th International Conference on Control Engineering and Information Technology (CEIT), Hammamet, Tunisia, 2016, pp. 1-6, doi: 10.1109/CEIT.2016.7929042.

[16] L. Li, Z. Jia, T. Cheng and X. Jia, "Optimal Model Predictive Control for Path Tracking of Autonomous Vehicle," 2011 Third International Conference on Measuring Technology and Mechatronics Automation, Shanghai, China, 2011, pp. 791-794, doi: 10.1109/ICMTMA.2011.481.

[17] B. Sun, W. Zhang, A. Song, X. Zhu and D. Zhu, "Trajectory Tracking and Obstacle Avoidance Control of Unmanned Underwater Vehicles Based on MPC," 2018 IEEE 8th International Conference on Underwater System Technology: Theory and Applications (USYS), Wuhan, China, 2018, pp. 1-6, doi: 10.1109/USYS.2018.8779160.

Proceedings of the 3rd Conference on Fully Actuated System Theory and Applications
May 10-12, 2024, Shenzhen, China

Adaptive Deep Neural Network Sliding Mode Control for UAVs

Chen Zhang[1], Jing Xu[1], Fanbiao Li[2], Yugang Niu[1]

1. Key Laboratory of Smart Manufacturing in Energy Chemical Process, Ministry of Education, Shanghai 200237, P. R. China
E-mail: jingxu@ecust.edu.cn

2. School of Automation, Central South University, Changsha 410083, P. R. China
E-mail: fanbiaoli@csu.edu.cn

Abstract: This paper proposes an adaptive attitude maneuver control strategy based on deep neural network (DNN) for quadcopters to improve the attitude tracking performance and attenuate the effects of nonlinear and uncertainty. Obtaining an accurate dynamic model is extremely challenging, due to the disturbances of wind speed, air pressure, temperature, and other environmental factors. To solve this issue, we establish an affine function model to describe the black box model of quadcopters. The DNN trained over a large time scale is used to approximate the nonlinearity and uncertainty. Then an adaptive sliding mode control (SMC) is combined with the DNN to achieve accurate tracking of attitude trajectory. An update algorithm is proposed to ensure the real-time performance of the controller. The Lyapunov based stability analysis is used to prove the stability of the stability of the closed loop system. The experimental results show the good performance of proposed control strategy.

Key Words: SMC, Quadcopter, Deep neural network, Adaptive control, Attitude tracking

1 Introduction

Quadcopter Unmanned Aerial Vehicles (UAVs) [1] have advantages such as small size, strong payload capacity, and flexible maneuverability, demonstrating broad application potential in military [2], agriculture [3], aerial surveying, and logistics delivery fields. Trajectory changes in the UAV system are achieved through cascade control, which is based on attitude control. Therefore, attitude tracking control is an important aspect of UAVs. UAV model operates as a black box with unknown structural details and parameters, coupled with its susceptibility to external disturbances, the resulting attitude model complexity is notable.

Existing research primarily concentrates on mitigating the nonlinear characteristics inherent in the UAV system. Chen [4] employs a SMC for inner loop to achieve the desired attitude, subsequently contributing to the overall control law. Xu [5] introduces an adaptive controller that dynamically adjusts controller gains based on disturbance gradients at different time scales, thereby improving control efficiency. However, previous studies all required an accurate model or involved complex calculations.

Neural Networks (NN) have gained widespread use in quadrotor UAV control systems. In the work by Razmi [6], a method combining NN adaptive approaches with SMC is introduced. This method enhances the system's ability to reject disturbances, reduces its dependency on parameters, and improves overall stability and robustness. In another study by Dierks[7], NN is utilized for online learning of the complete dynamics of the UAV, while an NN observer estimates translational and angular velocities.

Traditional NN face challenges such as limitations in handling diverse operating conditions, dealing with strong coupling nonlinear characteristics in quadrotor UAV models, system complexity, constrained learning capabilities, and inadequacy in covering all UAV operating conditions. When applied to complex nonlinear systems, they require extensive training data and may struggle to adapt to new environments. Sun[8] introduced a real-time DNN adaptive control architecture for uncertain nonlinear dynamic systems, addressing unknown drift dynamics and parameter uncertainties to track desired time-varying trajectories.

The key contributions are as follows:

1. An adaptive DNN-SMC is raised. The adaptive DNN mitigates system nonlinearities and uncertainties, minimizing parameter reliance and boosting stability under diverse conditions.

2. The adaptive method is implemented through the design of update laws, which are divided into large and small time scales. This approach meets the needs for rapid changes in quadrotor drones as well as the real-time requirements of the controller.

2 Problem Description and Important Lemmas

2.1 Problem Description

The attitude dynamics model of the quadrotor is given by [9, 10]:

$$\begin{cases} \ddot{\phi} = \dot{\theta}\dot{\psi}\frac{I_y - I_z}{I_x} + \frac{J_r}{I_x}\dot{\theta}\Omega_r + \frac{\tau_\phi}{I_x} - \frac{\kappa_1 l}{I_x}\dot{\phi}, \\ \ddot{\theta} = \dot{\phi}\dot{\psi}\frac{I_z - I_x}{I_y} - \frac{J_r}{I_y}\dot{\phi}\Omega_r + \frac{\tau_\theta}{I_y} - \frac{\kappa_2 l}{I_y}\dot{\theta}, \\ \ddot{\psi} = \dot{\theta}\dot{\phi}\frac{I_x - I_y}{I_z} + \frac{\tau_\psi}{I_z} - \frac{\kappa_3}{I_z}\dot{\psi}, \end{cases} \tag{1}$$

where ϕ, θ, ψ represent roll, pitch, and yaw, respectively; I_x, I_y, I_z represent moment of inertia about x-axis, y-axis, and z-axis, respectively; J_r represent the moment of inertia about propeller blades; $\tau_\phi, \tau_\theta, \tau_\psi$ represent roll torque, pitch torque, and yaw torque, respectively; κ_1, κ_2, κ_3 are the damping coefficients experienced by the propellers; l represent the distance between rotor centers; Ω_r represents the rotor speed of the quadrotor, given by:

$$\Omega_r = -\omega_1 + \omega_2 - \omega_3 + \omega_4, \tag{2}$$

where $\omega_i (i = 1, 2, 3, 4)$ represent the i-th propeller speeds. Define $u(t) \triangleq [u_2, u_3, u_4]^T = [\tau_\phi, \tau_\theta, \tau_\psi]^T$. The relation-

This work is supported by the National Natural Science Foundation of China (62173141), Shanghai Municipal Natural Science Foundation (22ZR1417900). Corresponding author: Jing Xu, email:jingxu@ecust.edu.cn.

ship between inputs and propeller speeds is:

$$\begin{bmatrix} u_1 \\ u_2 \\ u_3 \\ u_4 \end{bmatrix} = c_1 \begin{bmatrix} 1 & 1 & 1 & 1 \\ 0 & 1 & 0 & -1 \\ 1 & 0 & -1 & 0 \\ -\frac{c_2}{c_1} & \frac{c_2}{c_1} & -\frac{c_2}{c_1} & \frac{c_2}{c_1} \end{bmatrix} \begin{bmatrix} \omega_1^2 \\ \omega_2^2 \\ \omega_3^2 \\ \omega_4^2 \end{bmatrix}, \tag{3}$$

where u_1 is the total thrust produced by the four rotors; c_1, c_2 represent the lift coefficient and the counter torque coefficient, respectively. When the UAV model is hovering, it can be considered that the total lift force is equal to the gravity of the UAV. Define $x_1 = [\phi, \theta, \psi]^T$, $x_2 = [\dot{\phi}, \dot{\theta}, \dot{\psi}]^T$. The state model of the quadrotor can be represented using an affine function. The model (1) can be transformed into the following affine form:

$$\begin{cases} \dot{x_1} = x_2, \\ \dot{x_2} = f(x, \Omega_r) + \Delta f(x, \Omega_r) + Gu(t) + \Delta G u(t), \\ y = x_1, \end{cases} \tag{4}$$

where $\Delta f(x)$ and ΔG are the uncertainty terms of the quadrotor model; $f(x, \Omega_r)$ is the nonlinear dynamics function of the quadrotor model; G is the control input matrix:

$$\begin{cases} f(x, \Omega_r) = \begin{bmatrix} \dot{\theta}\dot{\psi}\frac{I_y - I_z}{I_x} + \frac{J_r}{I_x}\dot{\theta}\Omega_r - \frac{k_1 l}{I_x}\dot{\phi}, \\ \dot{\phi}\dot{\psi}\frac{I_z - I_x}{I_y} - \frac{J_r}{I_y}\dot{\phi}\Omega_r - \frac{k_2 l}{I_y}\dot{\theta}, \\ \dot{\theta}\dot{\phi}\frac{I_x - I_y}{I_z} - \frac{k_3}{I_z}\dot{\psi}, \end{bmatrix}, \\ G = \text{diag}\left\{\frac{1}{I_x}, \frac{1}{I_x}, \frac{1}{I_z}\right\}. \end{cases} \tag{5}$$

Rrewrite the control input equation as the following linear parameter equation:

$$Gu(t) = Y(u(t))\vartheta, \tag{6}$$

where ϑ is the system parameter vector, consisting of unknown inertial components, $Y(u(t))$ is the control input matrix, that is:

$$\begin{cases} Y(u(t)) = \text{diag}\{u_2, u_3, u_4\}, \\ \vartheta = \left[\frac{1}{I_x}, \frac{1}{I_y}, \frac{1}{I_z}\right]^T. \end{cases} \tag{7}$$

2.2 Design Methodology

This paper adopts an adaptive DNN-SMC as shown in Figure 1, to achieve control that does not depend on model parameters.

Due to the problem that the UAV model cannot be accurately modeled, this paper uses DNN to learn the nonlinear part of the UAV to compensate the controller, enhancing the control effect of the controller.

An adaptive method is used, dividing the DNN into two parts: outer layer parameters and hidden layer parameters. The outer layer parameters and controller parameters are updated together on a small time scale to adapt to the rapid changes in the UAV model. The hidden layer parameters are updated through time triggering to save computational resources. This ensures that the DNN meets the real-time requirements of the UAV system.

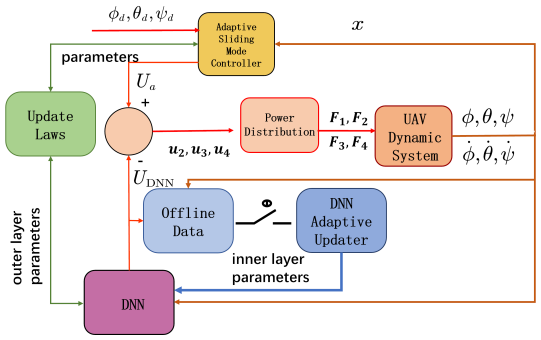

Fig. 1: Control Framework Diagram

Define the tracking errors $e_1 : [t_0, \infty) \to \mathbb{R}^3$ and $e_2 : [t_0, \infty) \to \mathbb{R}^3$ as:

$$e_1 \triangleq x_{1d} - x_1, e_2 \triangleq \dot{x}_{1d} - x_2, \tag{8}$$

where $x_{1d} = [\phi, \theta, \psi] : [t_0, \infty) \to \mathbb{R}^3$ is the sufficiently smooth desired trajectory; $\dot{x}_{1d} = [\dot{\phi}, \dot{\theta}, \dot{\psi}] : [t_0, \infty) \to \mathbb{R}^3$ is the first derivative of the desired trajectory.

2.3 Lemmas and Assumptions

The following lemma is needed for the derivation of the controller design in the next section:

Lemma 1. *[11] Using a DNN model to approximate a continuous function $f(x) : \mathbb{R}^q \to \mathbb{R}^n$, in the form of:*

$$f(x) = W^{*T}\sigma^*(\Phi^*(x)) + \epsilon(x), \tag{9}$$

where $x = [x_1, x_2, \cdots, x_q]^T \in \mathbb{R}^q$ is the input vector of the DNN, $\Phi^*(x) : \mathbb{R}^q \to \mathbb{R}^p$ is the hidden layer node function, $\sigma^* : \mathbb{R}^p \to \mathbb{R}^L$ is the bounded vector of activation functions, $W^* \in \mathbb{R}^{L \times n}$ is the bounded outer layer weight matrix, $\epsilon : \mathbb{R}^q \to \mathbb{R}^n$ is the bounded function reconstruction error related to the weights, activation functions, and hidden layer node functions. The hidden layer node function can be represented as: $\Phi^*(x) = (Q_k^T\phi_k \circ Q_{k-1}^T\phi_{k-1} \circ \cdots \circ Q_1^T\phi_1) : \mathbb{R}^q \to \mathbb{R}^p$. Here: $k \in \mathbb{Z}$ represents the number of hidden layers, with $k \geq 3$ in the DNN, $\circ$ denotes composition, Q and ϕ correspond to the weights and activation functions of the hidden layers, respectively.

Analyzing the actual UAV model, the following assumption can be made:

Assumption 1. *[8] Within a certain interval, there are predetermined constants $\overline{W^*}, \overline{\sigma^*}, \overline{\hat{\sigma}}, \overline{\epsilon} \in \mathbb{R}$, ensuring that the parameters within the DNN are bounded, such as $\sup_{x \in \aleph_c} \|W^*\| \leqslant \overline{W^*}, \sup_{x \in \aleph_c} \|\sigma^*\| \leqslant \overline{\sigma^*}, \sup_{x \in \aleph_c} \|\hat{\sigma}\| \leqslant \overline{\hat{\sigma}}, \sup_{x \in \aleph_c} \epsilon \leqslant \overline{\epsilon}$, where $\aleph_c$ denotes a singly compact connected set in which $f(x)$ is continuous, and $\sup_{x \in \aleph_c}$ represents the supremum over $x \in \aleph_c$.*

3 Estimation of Unknown Dynamics Functions Based on Deep Learning

3.1 Modeling Unknown Dynamics with DNN

Based on Lemma 1, in conjunction with Equation (9), the nonlinear part $f(x, \Omega_r)$ of the quadrotor model (4), along

with the unknown parameter parts $\Delta f(x,\Omega_r)$ and $\Delta G u(t)$, can be approximated and estimated using a DNN, as follows:

$$\begin{aligned} F_\epsilon(\chi) &= W^{*\mathrm{T}}\sigma^*(\Phi^*(\chi)) + \epsilon(\chi) \\ &\approx f(x,\Omega_r) + \Delta f(x,\Omega_r) + \Delta G u(t), \end{aligned} \tag{10}$$

In this equation: $F_\epsilon(\chi) = \mathrm{col}\{f_1, f_2, f_3\}$ represents the model's nonlinear functions and uncertainties in UAV dynamics; $\Phi^*(x) : \mathbb{R}^q \to \mathbb{R}^p$ is the ideal hidden layer node function; $\sigma^* : \mathbb{R}^p \to \mathbb{R}^L$ is the bounded vector of ideal activation functions; $W^* \in \mathbb{R}^{L\times n}$ is the ideal bounded outer layer weight matrix; $\epsilon : \mathbb{R}^q \to \mathbb{R}^n$ is the bounded function reconstruction error related to the weights, activation functions, and hidden layer node functions, which can be minimized indefinitely through pre-training and online learning. The ideal hidden layer node function can be represented as: $\Phi^*(x) = (Q_k^{\mathrm{T}}\phi_k \circ Q_{k-1}^{\mathrm{T}}\phi_{k-1} \circ \cdots \circ Q_1^{\mathrm{T}}\phi_1) : \mathbb{R}^q \to \mathbb{R}^p$, where $k \in \mathbb{Z}$ denotes the number of hidden layers, with $k \geq 3$ in the DNN, $\circ$ denotes composition, Q_k and ϕ_k correspond to the weights and activation functions of the hidden layers, respectively; χ is the input to the DNN, based on Equation (3), it can be seen that there is a mapping relationship between u_1, u_2, u_3, u_4, and Ω_r, thus, the input to the DNN is set as:

$$\chi = [u_1, u_2, u_3, u_4, \phi, \theta, \psi]^{\mathrm{T}}, \tag{11}$$

comprising of control inputs and attitude angles. Substituting Equation (10) into Equation (4), without considering the reconstruction error, we obtain:

$$\begin{cases} \dot{x}_1 &= x_2, \\ \dot{x}_2 &= F(\chi) + Gu(t) + \epsilon(\chi), \\ y &= x_1, \end{cases} \tag{12}$$

where $F(\chi) = W^{*\mathrm{T}}\sigma^*(\Phi^*(\chi))$.

3.2 DNN Training Methods

The input and output for the DNN training data are $\{\chi, y_t\}$. Combining Equation (4) and Equation (12), the computation formula for the DNN training target is as follows:

$$y_t = \dot{x}_2 - Gu(t), \tag{13}$$

where u can come from any controller, y_t serves as the target element of the training set. During online training from the designed controller, when the control effectiveness matrix for the UAV system with uncertain parameters cannot be obtained, Equation (18) is used. By updating the outer layer parameters and calculating the DNN output, further target data for the DNN is obtained.

Pre-training on historical and simulated datasets enhances the DNN's fit to flight control system characteristics, reducing online update times. Datasets from various UAVs under identical conditions will train the DNN.

The method involves adjusting PID control for different attitude angles to follow a set trajectory, recording these adjustments. This strategy divides the control process into three segments based on the size of the attitude angle: $\beth_s = [-\frac{\pi}{8}, \frac{\pi}{8})$, $\beth_m = [\frac{\pi}{8}, \frac{\pi}{4}) \cup [-\frac{\pi}{4}, -\frac{\pi}{8})$, $\beth_l = [\frac{\pi}{4}, \frac{3}{8}\pi) \cup [-\frac{3}{8}\pi, -\frac{\pi}{4})$. Data from extreme angle adjustments are combined for DNN pre-training. This data is cleaned, normalized, randomized, and split into training, validation, and test sets.

4 Adaptive DNN-SMC Design

The controller designed in this article is based on a parallel control architecture, consisting of a DNN controller operating on a large time scale and an adaptive SMC operating on a small time scale.

4.1 SMC Design

For attitude control, design the sliding surface $s = k_f e_1 + e_2$, ensuring the system is asymptotically stable. Let

$$\dot{s} = \ddot{x}_{1d} - \dot{x}_2 + k_f \dot{e}_1 = 0, \tag{14}$$

Substitute Equation (12) into the controller expression:

$$u_{\mathrm{eq}}(t) = G^{-1}(\ddot{x}_{1d} - F(\chi) - \epsilon(\chi) + k_f \dot{e}_1), \tag{15}$$

where u_{eq} is the control input. To eliminate residuals, the SMC expression is designed as:

$$u^*(t) = G^{-1}(\ddot{x}_{1d} - F(\chi) + k_s \mathrm{sgn}(s) + k_f \dot{e}_1), \tag{16}$$

where $\mathrm{sgn}(\cdot)$ is the sign function, k_s is a controller parameter. To improve the stability of the controller, introduce control feedback terms e_1 and e_2 to obtain the controller expression:

$$\begin{aligned} u^*(t) =& G^{-1}(k_1 e_1 + k_2 e_2 + \ddot{x}_{1d} - F(\chi) \\ &+ k_s \mathrm{sgn}(s) + k_f \dot{e}_1), \end{aligned} \tag{17}$$

where k_1, k_2 are controller parameters.

4.2 Adaptive SMC Design

Set the outer layer weight as an adaptive function. The unknown nonlinear part of the quadrotor UAV is compensated for using DNN learning:

$$\widehat{F}_i(\chi) = \widehat{W}^{\mathrm{T}}\widehat{\sigma}_i(\widehat{\Phi}_i(\chi)), \tag{18}$$

where $\hat{\sigma}_i : \mathbb{R}^p \to \mathbb{R}^{13}$ and $\widehat{\Phi}_i(\chi) : \mathbb{R}^7 \to \mathbb{R}^p$ are respectively the ith activation function and the estimate of the DNN hidden layer, $i \in \mathbb{N}$ is the iteration number of the estimated DNN, $\widehat{W} : [t_0, \infty] \to \mathbb{R}^{13\times 3}$ is an unknown bounded ideal outer layer weight matrix. The error between the ideal outer layer weight and the weight estimate is defined as:

$$\widetilde{W}(t) \triangleq W^* - \widehat{W}(t). \tag{19}$$

The estimation of the control matrix can be obtained from equation (6) as:

$$\hat{G}u(t) = Y(x,u,t)\hat{\vartheta}, \tag{20}$$

where $\hat{G} : \mathbb{R}^3 \to \mathbb{R}^{3\times 3}$ is the estimate of the control effectiveness matrix. Define the parameter estimation error $\widetilde{\vartheta} : [t_0, \infty) \to \mathbb{R}^3$ as:

$$\widetilde{\vartheta} \triangleq \vartheta - \hat{\vartheta}, \tag{21}$$

where $\hat{\vartheta} : [t_0, \infty] \to \mathbb{R}^3$ is the estimated value of the data matrix parameters.

Design the following adaptive SMC:

$$\begin{aligned} u =& \widehat{G}^{-1}(x)(k_1 e_1 + k_2 e_2 + \ddot{x}_{1d} - \widehat{W}^{\mathrm{T}}\widehat{\sigma}_i(\widehat{\Phi}_i(\chi)) \\ &+ k_s \mathrm{sgn}(s) + k_f \dot{e}_1), \end{aligned} \tag{22}$$

which can be rewrited by:

$$\begin{aligned}\ddot{x}_{1d} =&\widehat{G}u - (k_1e_1 + k_2e_2 - \widehat{W}^{\mathrm{T}}\widehat{\sigma}_i(\widehat{\Phi}_i(\chi)) \\ &+ k_s\mathrm{sgn}(s) + k_f\dot{e}_1),\end{aligned} \tag{23}$$

Design the adaptive law for weight estimation as:

$$\dot{\widehat{W}} = -\Gamma_W\hat{\sigma}_i(\widehat{\Phi}_i(\chi))s^{\mathrm{T}}, \tag{24}$$

where $\Gamma_W \in \mathbb{R}^{L\times L}$ is a given positive definite diagonal matrix. Design the adaptive law for the input parameter vector as:

$$\dot{\widehat{\vartheta}} = -\Gamma_\vartheta Y^{\mathrm{T}}s, \tag{25}$$

where $\Gamma_\vartheta \in \mathbb{R}^{3\times3}$ is a given positive definite diagonal gain matrix. Deriving equation (8) with respect to t:

$$\begin{cases} \dot{e}_1(t) = e_2(t), \\ \dot{e}_2(t) = \ddot{x}_{1d}(t) - \dot{x}_2(t), \end{cases} \tag{26}$$

combining equations (12) and (23), we obtain:

$$\begin{cases} \dot{e}_1 =e_2, \\ \dot{e}_2 =\hat{G}u(t) - Gu(t) - k_s\mathrm{sgn}(s) - k_f\dot{e}_1, \\ \quad\quad + \hat{F}(\chi) - F(\chi) - k_1e_1 - k_2e_2 \end{cases} \tag{27}$$

Substituting equation (6) into equation (27), we obtain the following closed-loop error system:

$$\begin{cases} \dot{e}_1 =e_2, \\ \dot{e}_2 =- Y\widetilde{\vartheta} - k_s\mathrm{sgn}(s) - k_f\dot{e}_1 \\ \quad\quad + \widehat{F}(\chi) - F(\chi) - k_1e_1 - k_2e_2. \end{cases} \tag{28}$$

4.3 Controller Stability Analysis

Based on the Lyapunov theorem, this section proves the asymptotic stability of the closed-loop system.

Theorem 1. *Consider the nonlinear system* (4)*, where the initial condition is* $x(t_0) \in \aleph_c$*, and the assumption condition* 1 *is satisfied. Given known upper bounds* $\overline{\sigma^*} \geq 0$*,* $\overline{\hat{\sigma}} \geq 0$*,* $\overline{W^*} \geq 0$*,* $\bar{\epsilon} \geq 0$*, it is possible to make the defined trajectory tracking error semi-globally asymptotically stable, i.e.,* $\lim\limits_{t\to\infty} e_1 = 0$*,* $\lim\limits_{t\to\infty} e_2 = 0$*,* $\lim\limits_{t\to\infty} \widetilde{\vartheta} = 0$*,* $\lim\limits_{t\to\infty} \widetilde{W} = 0$*,* $t \geq t_0$*, by using the controller output* (22)*, the outer layer parameter adaptive update law* (24)*, and the parameter estimation update rate* (25)*, and satisfying the following assumption conditions:*

$$\begin{cases} k_s > (\overline{\sigma^*} + \overline{\hat{\sigma}})\overline{W^*} + \bar{\epsilon}, \\ k_1 = 1 + k_2k_f. \end{cases} \tag{29}$$

Proof. Construct a Lyapunov function:

$$\begin{aligned}V_L(z,t) =&\frac{1}{2}e_1^{\mathrm{T}}e_1 + \frac{1}{2}s^{\mathrm{T}}s \\ &+ \frac{1}{2}\widetilde{\vartheta}^{\mathrm{T}}\Gamma_\vartheta^{-1}\widetilde{\vartheta} + \frac{1}{2}\mathrm{tr}(\widetilde{W}^{\mathrm{T}}\Gamma_W^{-1}\widetilde{W}),\end{aligned} \tag{30}$$

where $z \triangleq [e_1^{\mathrm{T}}, e_2^{\mathrm{T}}, \widetilde{\vartheta}^{\mathrm{T}}, \mathrm{vec}(\widetilde{W})^{\mathrm{T}}]^{\mathrm{T}}$, $\mathrm{vec}(\cdot)$ is the operation of concatenating each column of a matrix into a single column vector, $\mathrm{tr}(\cdot)$ is the trace of a matrix.

Taking time derivative of equation (30) yields:

$$\dot{V}_L(z,t) = e_1^{\mathrm{T}}\dot{e}_1 + s^{\mathrm{T}}\dot{s} + \widetilde{\vartheta}\Gamma_\vartheta^{-1}\dot{\widetilde{\vartheta}} + \mathrm{tr}(\widetilde{W}^{\mathrm{T}}\Gamma_W^{-1}\dot{\widetilde{W}}), \tag{31}$$

Substituting equation (28) into equation (31) yields:

$$\begin{aligned}\dot{V}_L(z,t) =& e_1^{\mathrm{T}}e_2 + k_fs^{\mathrm{T}}e_2 - k_1s^{\mathrm{T}}e_1 - k_2s^{\mathrm{T}}e_2 \\ &+ s^{\mathrm{T}}(-Y\widetilde{\vartheta} + \widehat{F}(\chi) - F(\chi) - k_s\mathrm{sgn}(s) - k_f\dot{e}_1) \\ &+ \widetilde{\vartheta}\Gamma_\vartheta^{-1}\dot{\widetilde{\vartheta}} + \mathrm{tr}(\widetilde{W}^{\mathrm{T}}\Gamma_W^{-1}\dot{\widetilde{W}}),\end{aligned} \tag{32}$$

Since $e_1^{\mathrm{T}}s = s^{\mathrm{T}}e_1$ and $e_2 = s - kfe_1$, $\dot{e}_1 = e_2$, simplifying (32) yields:

$$\begin{aligned}\dot{V}_L(z,t) =& (1 - k_1 + k_2k_f)s^{\mathrm{T}}e_1 - k_fe_1^{\mathrm{T}}e_1 - k_2s^{\mathrm{T}}s \\ &+ s^{\mathrm{T}}(-Y\widetilde{\vartheta} + \widehat{F}(\chi) - F(\chi) - k_s\mathrm{sgn}(s)) \\ &+ \widetilde{\vartheta}\Gamma_\vartheta^{-1}\dot{\widetilde{\vartheta}} + \mathrm{tr}(\widetilde{W}^{\mathrm{T}}\Gamma_W^{-1}\dot{\widetilde{W}}),\end{aligned} \tag{33}$$

Since ϑ and W^* are constants, thus $\dot{\vartheta} = \dot{W}^* = 0$, Taking the time derivative of $\widetilde{\vartheta}$ and $\widetilde{W}$ yields:

$$\begin{cases} \dot{\widetilde{\vartheta}} = -\dot{\widehat{\vartheta}}, \\ \dot{\widetilde{W}}(t) = -\dot{\widehat{W}}(t). \end{cases} \tag{34}$$

Substituting equation (34) into equation (33) yields:

$$\begin{aligned}\dot{V}_L(z,t) =& (1 - k_1 + k_2k_f)s^{\mathrm{T}}e_1 - k_fe_1^{\mathrm{T}}e_1 - k_2s^{\mathrm{T}}s \\ &+ s^{\mathrm{T}}(-Y\widetilde{\vartheta} + \widehat{F}(\chi) - F(\chi) - k_s\mathrm{sgn}(s)) \\ &- \widetilde{\vartheta}\Gamma_\vartheta^{-1}\dot{\widehat{\vartheta}} - \mathrm{tr}(\widetilde{W}^{\mathrm{T}}\Gamma_W^{-1}\dot{\widehat{W}}),\end{aligned} \tag{35}$$

Based on the property of trace (considering real vectors $a, b \in \mathbb{R}^n$, there is $\mathrm{tr}(ab^{\mathrm{T}}) = b^{\mathrm{T}}a$), substituting equations (25), (24), (10), (18) into equation (35) yields:

$$\begin{aligned}\dot{V}_L =& (1 - k_1 + k_2k_f)s^{\mathrm{T}}e_1 - k_fe_1^{\mathrm{T}}e_1 - k_2s^{\mathrm{T}}s + s^{\mathrm{T}}\epsilon(x) \\ &- s^{\mathrm{T}}(k_s\mathrm{sgn}(s)) + s^{\mathrm{T}}W^{*T}(\hat{\sigma}_i(\widehat{\Phi}_i(\chi)) - \sigma^*(\Phi^*(\chi))),\end{aligned} \tag{36}$$

Under the assumption 1, it can be obtained:

$$\begin{aligned}\dot{V}_L \leq& - k_f\|e_1\|^2 - k_2\|s\|^2 \\ &- (k_s - (\overline{\hat{\sigma}} + \overline{\sigma^*})\overline{W^*} - \bar{\epsilon})\|s\|_1,\end{aligned} \tag{37}$$

By the inequality (29), it can be obtained:

$$\dot{V}_L \leq -k_f\|e_1\|^2 - k_2\|s\|^2. \tag{38}$$

Through (30) and (38), it can be concluded that $V_L(z,t) \in \mathcal{L}_\infty$, meaning that, $z(t) \in \mathcal{L}_\infty$, i.e., $[e_1^{\mathrm{T}}, e_2^{\mathrm{T}}, \widetilde{\vartheta}^{\mathrm{T}}, \mathrm{vec}(\widetilde{W})^{\mathrm{T}}] \in \mathcal{L}_\infty$. From equations (19), (8), (21), it is obtained that $x_1(t), x_2(t), \hat{\vartheta}(t), \widehat{W}(t) \in \mathcal{L}_\infty$. According to assumption 1, it can be obtained that $\hat{\sigma}(\cdot), \epsilon(x(t)), \hat{G}^{-1}(x(t)), \hat{G}(x(t)) \in \mathcal{L}_\infty$. Since $\hat{G}(x(t)), u(t), \hat{\vartheta}(t) \in \mathcal{L}_\infty$, through equation (6), it is known that, $Y(x,u,t) \in \mathcal{L}_\infty$. Thus, it can be concluded: $-k_1\|e_1\|^2 - k_2\|s\|^2 \to 0$. When $t \to \infty$, $\|e_1\| \to 0$, $\|s\| \to 0$, and for all $t \geq t_0$, it satisfies $x_1(t) \in \aleph_c$, $x_2(t) \in \aleph_c$. □

5 Experimental Analysis

5.1 Platform Introduction

This section establishes a simulation platform for testing and evaluating the proposed algorithm. Both the DNN and NN are pre-trained to showcase their capability in learning the nonlinear characteristics. The proposed algorithm is then compared against the adaptive NN control method [12] and the SMC method [13].

5.2 Experimental Setup

Experiments will be conducted from two aspects: pre-training results and large-angle tracking analysis.

The structural parameters of UAV are as follows:

$I_x = I_y = 7.5 \times 10^{-3}$ kg $\cdot$ m^2, $I_z = 1.3 \times 10^{-2}$ kg $\cdot$ m^2, $J_r = 2.7 \times 10^{-4}$ kg$\cdot$m^2, $m = 0.8$ kg, $l = 0.165$ m, $c_1 = 2 \times 10^{-7}$, $c_2 = 9 \times 10^{-5}$, $\kappa_1 = \kappa_2 = \kappa_3 = 0$.

The initial state of the quadrotor drone is (in radians):

$$x_1 = [0, 0, 0]^{\mathrm{T}}, x_2 = [0, 0, 0]^{\mathrm{T}} \tag{39}$$

The desired tracking attitude of the quadrotor drone is designed as follows:

$$x_{1d} = \left[\frac{3}{8}\sin\left(\frac{2}{5}\pi t\right), \frac{3}{8}\cos\left(\frac{2}{5}\pi t\right), 0\right]^{\mathrm{T}}. \tag{40}$$

The uncertainty model of the quadrotor drone is chosen as follows:

$$\begin{aligned} \Delta f(x) &= 0.02\left[\sin\phi, \cos\theta, \cos\psi\right]^{\mathrm{T}}, \\ \Delta G u &= 0.02\left[\sin\phi u_2, \cos\theta u_3, \cos\psi u_4\right]^{\mathrm{T}} \end{aligned} \tag{41}$$

The proposed adaptive DNN-SMC takes the form of Equation (22), and the specific controller parameters are as follows: $k_1 = 1.5$, $k_2 = 1$, $k_f = 0.5$, $k_s = 0.25$, $\hat{\vartheta}(0) = [1/(8\times10^{-3}), 1/(8\times10^{-3}), 1/(3\times10^{-2})]^{\mathrm{T}}$, $\Gamma_w = 3I_{13\times13}$, $\Gamma_\vartheta = 1.5I_{3\times3}$.

5.3 Experimental Results Analysis

5.3.1 Pre-training Results Analysis

In accordance with the approach outlined in Section 3.2, the parameters for proportion, integral, and derivative are as follows: when the angle falls within the range $\beth_s$, the values are 2.5, 0.2, and 0.7, respectively; within $\beth_m$, they are 5, 0.5, and 1.4; and within $\beth_l$, they are 8, 0.5, and 3.

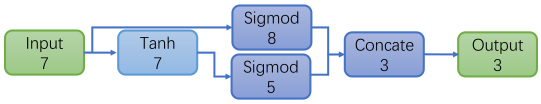

Fig. 2: The structure of DNN

The schematic diagram of the deep neural network designed in this paper is shown in Fig. 2. DNN has 7 inputs and 3 outputs. The hidden layers consist of 15 Tanh activation layers, 5 Sigmod activation layers, and 8 Sigmod activation layers. The outputs are calculated through a fully connected layer. On the other hand, the shallow NN has 7 input layers, connected by a fully connected layer, activated by the Sigmod function, and has 3 outer layer.

The pre-training uses the stochastic gradient descent method with a learning rate of 0.01. The ratio of training set, test set, and validation set is 16:4:5, and the random seed is 42. The dataset is split, and the mean squared error (MSE) is used to calculate the loss.

Table 1: Comparison of DNN and NN Performance

	Training Loss	Validation Loss	Iterations
NN	4.3787×10^{-05}	4.1887×10^{-05}	500
DNN	2.3896×10^{-05}	2.3232×10^{-05}	500

The performance comparison of pre-training between shallow NN and DNN is shown in Table 1. From the table, DNN has stronger learning ability on different datasets, faster convergence speed, and smaller loss on both the training and validation sets compared to NN.

5.3.2 Analysis of Control Effectiveness

The controller calculates every 0.01 seconds and trains the NN and DNN parameters every 2 seconds using training data collected in the past.

Figures $3a$ and $3b$ present the attitude tracking and error curves for a quadrotor drone using three different control strategies. Upon examining the tracking performance, it is evident that the adaptive DNN method outperforms the others by achieving the highest tracking accuracy and the quickest convergence rate. The adaptive NN method demonstrates some level of adaptability, albeit with a slower convergence compared to the DNN approach. Conversely, the SMC method exhibits the lowest performance, characterized by notable tracking errors.

Figure 3c illustrates the quadrotor drone's attitude tracking output response under three control methods, indicating comparable energy consumption across the controllers. Notably, both NN and DNN controls enhance quadrotor management atop SMC, with DNN requiring less energy than NN for superior control performance.

Table 2 compares the effects of SMC, PID, NN, and DNN control methods. Both NN and DNN have an update period of 2 seconds. The comparison is made from the aspects of tracking accuracy and non-linear approximation accuracy. Each loop in the table represents the mean square deviation within four seconds, where loop 1 represents 0 to 4s, loop 2 represents 4 to 8 seconds, and so on. From the analysis of tracking accuracy, DNN has the highest tracking accuracy, followed by NN and SMC, and PID has the worst tracking accuracy. By analyzing each loop, it can be found that the tracking accuracy of NN and DNN improves with each update, and the tracking accuracy of DNN converges faster and has a better effect. From the analysis of non-linear approximation accuracy, the non-linear approximation accuracy of DNN is higher than that of NN. By analyzing each loop, it can be found that the non-linear approximation accuracy becomes higher with parameter updates. In summary, DNN has fast convergence speed and high convergence accuracy, making it more suitable for quadrotor drone controller design.

6 Conclusion

This paper addresses the problem of nonlinearity and uncertainty in the black-box model of unmanned aerial vehicles (UAVs), which makes it difficult to accurately model them. To solve this problem, an adaptive DNN-SMC is designed to achieve trajectory tracking control for quadcopter UAVs. The adaptive DNN is trained offline and online to learn and compensate for the nonlinear and uncertain parts of the quadcopter UAV, reducing the reliance on controller parameters and improving control performance. The stability of the proposed approach is analyzed using Lyapunov-based stability analysis methods. Experimental results demonstrate that

Table 2: Comparison of Control Methods

Control Method	Tracking Accuracy (rad^2)				Nonlinear Approximation Accuracy			
NN-SMC	0.0386				235.2			
Period 2s	4s	8s	12s	16s	4s	8s	12s	16s
	0.1681	0.4046	0.0161	0.0031	1484	90.88	39.19	8.870
DNN-SMC	0.0228				197.87			
Period 2s	4s	8s	12s	16s	4s	8s	12s	16s
	0.1459	0.0096	0.0024	0.0006	1415	20.63	8.054	4.281

pre-training the DNN with prior control data allows the controller to achieve better tracking performance even at large angles. The paper also discusses the implementation of the adaptive DNN control method.

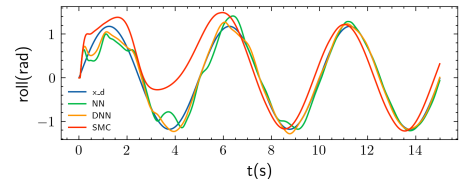

(a) Roll angle trajectory tracking curve

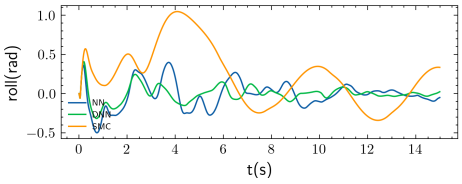

(b) Roll angle trajectory tracking error curve

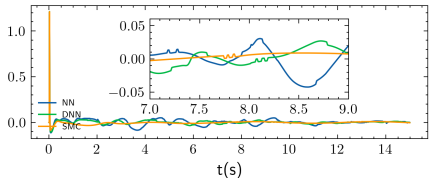

(c) Roll angle trajectory tracking output curve

Fig. 3: Attitude trajectory tracking curves

References

[1] J. Xu, Y. Niu, and P. Shi, "Adaptive Multi-Input Super Twisting Control for a Quadrotor: Singular Perturbation Approach," *IEEE Transactions on Industrial Electronics*, 2023.

[2] N. Nagarani, P. Venkatakrishnan, and N. Balaji, "Unmanned Aerial vehicle's runway landing system with efficient target detection by using morphological fusion for military surveillance system," *Computer Communications*, vol. 151, pp. 463–472, 2020.

[3] P. Radoglou Grammatikis, P. Sarigiannidis, T. Lagkas, and I. Moscholios, "A compilation of UAV applications for precision agriculture," *Computer Networks*, vol. 172, p. 107148, 2020.

[4] F. Chen, R. Jiang, K. Zhang, B. Jiang, and G. Tao, "Robust Backstepping Sliding Mode Control for a Quadrotor Trajectory Tracking Application," *IEEE Transactions on Industrial Electronics*, vol. 63, no. 8, pp. 5044–5056, 2016.

[5] J. Xu, Y. Niu, and H.-K. Lam, "Adaptive Distributed Attitude Consensus of a Heterogeneous Multi-Agent Quadrotor System: Singular Perturbation Approach," *IEEE Transactions on Aerospace and Electronic Systems*, 2023.

[6] H. Razmi and S. Afshinfar, "Neural network-based adaptive sliding mode control design for position and attitude control of a quadrotor UAV," *Aerospace Science and Technology*, vol. 91, pp. 12–27, 2019.

[7] T. Dierks and S. Jagannathan, "Output Feedback Control of a Quadrotor UAV Using Neural Networks," *IEEE Transactions on Neural Networks*, vol. 21, no. 1, pp. 50–66, 2009.

[8] R. Sun, M. L. Greene, D. M. Le, Z. I. Bell, G. Chowdhary, and W. E. Dixon, "Lyapunov-Based Real-Time and Iterative Adjustment of Deep Neural Networks," *IEEE Control Systems Letters*, vol. 6, pp. 193–198, 2022.

[9] H. Shraim, A. Awada, and R. Youness, "A survey on quadrotors: Configurations, modeling and identification, control, collision avoidance, fault diagnosis and tolerant control," *IEEE Aerospace and Electronic Systems Magazine*, vol. 33, no. 7, pp. 14–33, 2018.

[10] T. Luukkonen, "Modelling and control of quadcopter," *Independent research project in applied mathematics, Espoo*, vol. 22, no. 22, 2011.

[11] F. Lewis, S. Jagannathan, and A. Yesildirak, *Neural network control of robot manipulators and non-linear systems*. CRC press, 1998.

[12] X. Zheng, H. Li, C. K. Ahn, and D. Yao, "NN-based fixed-time attitude tracking control for multiple unmanned aerial vehicles with nonlinear faults," *IEEE Transactions on Aerospace and Electronic Systems*, vol. 59, no. 2, pp. 1738–1748, 2022.

[13] H. Wang, X. Ye, Y. Tian, G. Zheng, and N. Christov, "Model-free–based terminal SMC of quadrotor attitude and position," *IEEE Transactions on Aerospace and Electronic Systems*, vol. 52, no. 5, pp. 2519–2528, 2016.

Proceedings of the 3rd Conference on Fully Actuated System Theory and Applications
May 10-12, 2024, Shenzhen, China

Robust Control for DC-DC Buck Converters Based on Fully Actuated System Theory

Fangyuan Li[1], Guangxin Liu[1], Xiaoning Shen[1], Cheng Li[1], Xinpo Lin[1], Yabin Gao[1], Jianxing Liu[1]

1. Department of Control Science and Engineering, Harbin Institute of Technology, Harbin 150001, P. R. China
E-mail: xn_shen@hit.edu.cn

Abstract: This paper presents a novel robust approach for buck converters voltage tracking by utilizing the high-order fully actuated (HOFA) theory. Initially, the HOFA model of the buck converter is derived, followed by an analysis of disturbances encountered in real-world scenarios. In order to mitigate the adverse consequences arising from imprecise or abrupt alterations in circuit parameters, a robust tracking controller is devised to enhance the overall robustness of the system. Ultimately, simulations are performed to compare the proposed controller with the dual-loop PI controller. The results indicate that the proposed controller exhibits a quicker dynamic response and greater robustness compared to the dual-loop PI controller. Additionally, the process of selecting parameters of this method is simpler and more convenient.

Key Words: Fully-actuated system theory, Buck converter, Robust controller, Dual-loop PI controller

1 Introduction

With the rapid development of technology, the role of electronic devices in industrial applications is becoming increasingly prominent. Power management system is essential for ensuring these devices operate at maximum efficiency and performance. The buck converter, as a common step-down dc-dc converter, finds widespread application in a variety of fields, including electric vehicles, mobile power sources, communication devices, and aircraft power systems [1–3]. It has become a crucial part of power management system due its predominant energy efficiency and compact design. It can effectively convert high voltage to lower voltages to fulfill the varied power needs of different electronic devices.

The buck converter operates on the basis of changing the duty cycle to change the output voltage. There are primarily two operating modes about this converter: continuous conduction mode (CCM) and discontinuous conduction mode (DCM). When working in continuous conduction mode, the inductor current never goes below zero during the whole operating cycle. Discontinuous conduction mode, on the other hand, allows the inductor current to reach zero before the switch is turned off. When it comes to modulation techniques, the buck converter incorporates three commonly employed methods, namely pulse width modulation (PWM), pulse frequency modulation (PFM), and pulse skip modulation (PSM). Specifically, PWM operates by establishing a consistent frequency and manipulating the duty cycle via voltage or current feedback.

The dc-dc converter's intrinsic non-linear properties are caused by the existence of the switching device [4].At the moment, the first-order state-space model serves as the foundation for the modeling strategy used for the buck converter [5–7]. Nevertheless, this approach interferes with the system's full-actuate characteristics, which makes controller design more difficult [8]. The fully actuated system theory proposed by Duan in 2020 offers a more efficient method for the study of non-linear systems and the controller design that goes along with it, as opposed to the difficult task of designing Lyapunov functions [8–17].

Unlike the state-space approach, the fully actuated system theory removes variables to enhance system order. Subsequently, a high-order system model is obtained. For high-order systems exhibiting fully actuated characteristics, specific feedback control can transform them into closed-loop systems with an arbitrarily assignable eigenstructure, which behave more powerfully in the control of many nonlinear systems [9]. At present, scholars have applied the fully actuated system theory in various fields such as robotics, spacecraft, fuel cells, and so on [18–22]. In the area of power electronics, Fang et.al developed the HOFA model for the buck converter and established an improved control strategy, which transformed the error model into a third-order model, achieving system stability and enhancing disturbance rejection through pole assignment [23]. However, configuring poles for a third-order system is more challenging than for a second-order system.

In this paper, to simplify parameter design process and enhance system robustness, a novel robust voltage tracking method based on the high-order fully actuated (HOFA) system theory is proposed for the buck converters. Initially, the actual model of the buck converter is represented, and the system model is transformed into an HOFA model. Following that, a robust controller, abbreviated R-HOFA for simplicity, is built to improve the system's robustness. Finally, simulations are performed to compare the R-HOFA to a dual-loop PI controller (D-PI). The results validate the efficiency of the proposed R-HOFA, exhibiting a more straightforward and user-friendly parameter selection procedure.

2 Modeling the Buck Converter

This section describes the state space model of the buck converter and how the fully actuated system theory is applied to turn this model into an HOFA model. A feedback control law is specified to make the system a constant linear closed-loop system.

This work was supported in part by the National Natural Science Foundation of China (No. 62373127, 62103118 and 62320106001), in part by the Dreams Foundation of Jianghuai Advance Technology Center(NO. 2023-ZM01J002), in part by the Science Center Program of National Natural Science Foundation of China under Grant 62188101, and in part by the Heilongjiang Touyan Team Program, the China Postdoctoral Science Foundation (2022M720960) and the Heilongjiang Postdoctoral Fund under Grant LBH-Z22119. (*Corresponding author: Xiaoning Shen*)

2.1 Buck Converter

The typical configuration of a buck converter circuit is shown in Fig. 1, which includes a control switch (S_w), an input power source (V_{in}), a load resistor (R), an inductor (L), a capacitor (C), and a diode (D).

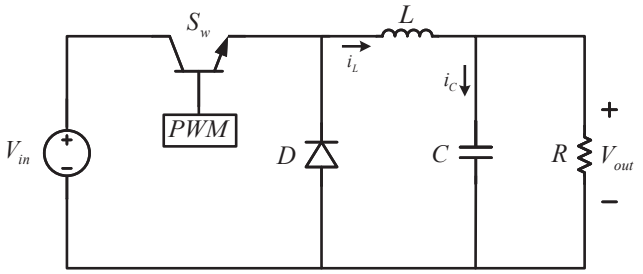

Fig. 1: Buck converter circuit

Assuming precise parameters and the lack of interference in the buck converter circuit, two possibilities can be separated based on the switch on-off states, as shown in Fig. 2.

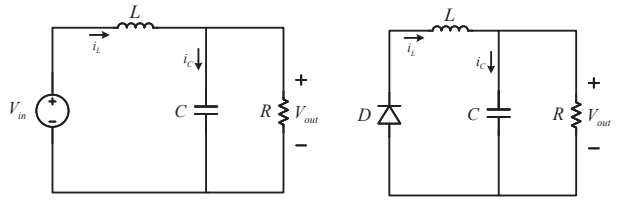

(a) S_w = ON (b) S_w = OFF

Fig. 2: Buck converter circuit: S_w is ON and OFF

According to Fig. 2, the operation of the buck converter with ON S_w can be described as follows:

$$\begin{aligned} \frac{di_L}{dt} &= \frac{1}{L}(V_{in} - V_{out}) \\ \frac{dV_{out}}{dt} &= \frac{1}{C}\left(i_L - \frac{V_{out}}{R}\right) \end{aligned} \tag{1}$$

The operation of the buck converter with OFF S_w can be described as,

$$\begin{aligned} \frac{di_L}{dt} &= -\frac{V_{out}}{L} \\ \frac{dV_{out}}{dt} &= \frac{1}{C}\left(i_L - \frac{V_{out}}{R}\right) \end{aligned} \tag{2}$$

By combining equations (1) and (2), the system can be modeled in a unified manner:

$$\begin{aligned} \frac{di_L}{dt} &= \frac{1}{L}(uV_{in} - V_{out}) \\ \frac{dV_{out}}{dt} &= \frac{1}{C}\left(i_L - \frac{V_{out}}{R}\right) \end{aligned} \tag{3}$$

where u represents the control variable, which actually denotes the duty cycle of the PWM signal.

However, the previous modeling process did not take into consideration the impact of factors such as imperfections in circuit component characteristics and external disturbances on control precision in actual applications. A more extensively applicable modeling technique is presented below so as to precisely construct the controller.

The parameters in the model are established as follows, assuming variations in resistance, inductance, capacitance, and input voltage from their nominal values and the existence of unknown noise in the external environment:

$$\begin{aligned} R &= R_0 + \Delta R \\ L &= L_0 + \Delta L \\ C &= C_0 + \Delta C \\ V_{in} &= V_{in_0} + \Delta V_{in} \\ d_1(t), d_2(t) & \end{aligned} \tag{4}$$

where R_0, L_0, C_0, V_{in_0} represent the nominal portion and $\Delta R, \Delta L, \Delta C, \Delta V_{in}$ represent the deviation portion. External unknown bounded disturbances, such as unmodeled features, electromagnetic interference, and so on, are denoted by $d_1(t), d_2(t)$, assuming that their first derivatives exist and are bounded. Under these conditions, the model (3) of the buck converter can be rewritten as:

$$\begin{aligned} \frac{di_L}{dt} &= \frac{1}{L_0 + \Delta L}\left(u\left(V_{in_0} + \Delta V_{in}\right) - V_{out}\right) + d_1(t) \\ \frac{dV_{out}}{dt} &= \frac{1}{C_0 + \Delta C}\left(i_L - \frac{V_{out}}{R_0 + \Delta R}\right) + d_2(t) \end{aligned} \tag{5}$$

The model (5) can also be expressed more simple as follows:

$$\begin{aligned} \frac{di_L}{dt} &= \frac{1}{L_0}\left(uV_{in_0} - V_{out}\right) + D_1(t) \\ \frac{dV_{out}}{dt} &= \frac{1}{C_0}\left(i_L - \frac{V_{out}}{R_0}\right) + D_2(t) \end{aligned} \tag{6}$$

where the lumped disturbances $D_1(t), D_2(t)$ are given by:

$$\begin{aligned} D_1(t) &= \frac{(\Delta V_{in} L_0 - V_{in}\Delta L)u + V_{out}\Delta L}{LL_0} + d_1(t) \\ D_2(t) &= \frac{\Delta C(V_{out} - R_0 i_L)}{R_0 C_0 C} + \frac{V_{out}\Delta R}{R_0 RC} + d_2(t) \end{aligned} \tag{7}$$

2.2 HOFA Model

Eliminating the inductor current i_L from the actual model (6) and letting the output voltage V_{out} be the system state x, the actual model can be rewritten as the following higher-order system model:

$$\ddot{x} = -\frac{1}{R_0 C_0}\dot{x} - \frac{1}{L_0 C_0}x + \frac{V_{in_0}}{L_0 C_0}u + \Delta f(x, \dot{x}) \tag{8}$$

where $\Delta f(x, \dot{x})$ represents the total uncertainty, which can be expressed by the following equation:

$$\Delta f(x, \dot{x}) = \frac{(D_1 + \dot{D}_2)}{C_0} \tag{9}$$

Assuming the total uncertainty has an upper bound, satisfying:

$$\|\Delta f(x, \dot{x})\|_2 \leq \rho(x, \dot{x}) \tag{10}$$

where $\rho(x, \dot{x})$ is a non-negative continuous scalar function.

The coefficient in front of the control variable is non-zero in the higher-order system model (8), which means that for every state and $t > 0$, the following equation always holds:

$$\det\left(\frac{V_{in_0}}{L_0C_0}\right) \neq 0 \tag{11}$$

Consequently, the buck converter system model (8) meets the criteria of being fully actuated, suggesting that model (8) is the HOFA model. Hence, there exists a feedback control law given by [8]:

$$u = \frac{L_0C_0}{V_{in_0}}\left(\frac{1}{R_0C_0}\dot{x} + \frac{1}{L_0C_0}x - a_1\dot{x} - a_0x + v\right) \tag{12}$$

where a_0 and a_1 are arbitrary parameters, and v is the following controller to be constructed. At this point, model (8) can be turned into a constant linear closed-loop system with desired performance, namely:

$$\ddot{x} + a_1\dot{x} + a_0x = v + \Delta f(x, \dot{x}) \tag{13}$$

The model mentioned above can be represented in state-space form as follows:

$$\dot{X} = A_cX + \begin{bmatrix} 0 \\ v + \Delta f(X) \end{bmatrix} \tag{14}$$

where,

$$A_c = \begin{bmatrix} 0 & 1 \\ -a_0 & -a_1 \end{bmatrix} \in R^{2\times 2} \tag{15}$$

To summarize, by utilizing fully actuated system theory and putting the feedback control law (12) into practice, the control issue of the original system can be converted into the control problem of constant linear closed-loop system with the required properties. This operation significantly simplifies the design of the controller.

3 Control Strategy Design Based on Fully Actuated System Theory

This section focuses on the design of the controller, taking into account both ideal and realistic circumstances. For convenience of analysis, assume the intended constant voltage is indicated by V_{ref} and the tracking error is designated by $\varepsilon = V_{ref} - V_{out}$.

3.1 Ideal Controller

When model parameter perturbations and external disturbances are ignored, i.e., $\Delta f(x, \dot{x}) = 0$, the system model can be represented as follows:

$$\ddot{x} + a_1\dot{x} + a_0x = v \tag{16}$$

To guarantee that the buck converter can stabilize the voltage at the desired level, the controller only needs to be configured as follows:

$$v = a_0V_{ref} \tag{17}$$

The ideal controller is obtained by combining the following controller (17) with the feedback control rate (12):

$$u = \frac{L_0C_0}{V_{in_0}}\left(\frac{1}{R_0C_0}\dot{x} + \frac{1}{L_0C_0}x - a_1\dot{x} - a_0x + a_0V_{ref}\right) \tag{18}$$

The model (16) can now be expressed as follows:

$$\ddot{\varepsilon} + a_1\dot{\varepsilon} + a_0\varepsilon = 0 \tag{19}$$

Since a_0, a_1 are arbitrary parameters, design the model's characteristic roots to be different negative real roots, indicated as $r_1 \neq r_2 < 0$. The solution to the differential equation (19) in this situation is:

$$\begin{gathered} \varepsilon(t) = C_1e^{r_1t} + C_2e^{r_2t} \\ \lim_{t\to\infty}\varepsilon(t) = 0 \end{gathered} \tag{20}$$

According to the previous analysis, it is feasible to accomplish the desired features of the buck converter model and thereby achieve the effect of voltage tracking through parameter design by constructing the following controller according to equation (17). However, relying solely on configuring poles to enhance the disturbance rejection capability of the system may not be sufficient.

3.2 Robust Controller

The parameters in the model are constantly susceptible to perturbations in real-world scenarios, and external disturbances cannot be disregarded. A robust controller is developed for model (13) to reduce the impact of model uncertainties. The following controller is designed in a given manner [10]:

$$v = a_0V_{ref} + \frac{1}{4\xi}\rho^2P_2^T\begin{bmatrix} \varepsilon \\ \dot{\varepsilon} \end{bmatrix} \tag{21}$$

where ξ is any given positive number, ρ is an upper bound on the total uncertainty of the system, the matrix $P_2 \in R^{2\times 1}$ is part of a symmetric positive definite matrix $P \in R^{2\times 2}$, which is parameterized by a_0, a_1. The relationship between P_2 and P is satisfied:

$$P_2 = P\begin{bmatrix} 0 \\ 1 \end{bmatrix} \tag{22}$$

Combining the proposed controller (21) with the previously designed feedback control law (12) results in a complete robust controller, which we call it R-HOFA:

$$\begin{aligned} u = \frac{L_0C_0}{V_{in_0}}\Bigg(&\frac{1}{R_0C_0}\dot{x} + \frac{1}{L_0C_0}x - a_1\dot{x} - a_0x \\ &+a_0V_{ref} + \frac{1}{4\xi}\rho^2P_2^T\begin{bmatrix} \varepsilon \\ \dot{\varepsilon} \end{bmatrix}\Bigg) \end{aligned} \tag{23}$$

With this controller, the buck converter's tracking error ε and its derivative $\dot{\varepsilon}$ are guaranteed to converge within an ellipsoid centered at zero [10]:

$$\Theta(0) = \left\{ X = \begin{bmatrix} \varepsilon \\ \dot{\varepsilon} \end{bmatrix} \middle| X^TPX < \frac{2\xi}{\mu} \right\} \tag{24}$$

where μ is determined by the following equation:

$$\mathrm{Re}\lambda_i(A_c) < -\frac{\mu}{2}, i = 1, 2 \tag{25}$$

The stability proof procedure of the controller (21) and the selection of all parameters can be found in [10].

4 Simulation Results

This section analyzes the simulation results of two control strategies, robust controller (R-HOFA) and dual-loop PI (D-PI), in different experimental scenarios under the premise that the uncertainty satisfies the upper bound assumption. Table 1 provides the nominal values for each parameter and Table 2 shows the control parameters for R-HOFA and D-PI.

Table 1: System Parameters of Buck Converter

Input voltage(V_{in_0})	$30V$
Reference output voltage(V_{ref})	$5V$
Inductance(L_0)	$2mH$
Capacitance(C_0)	$4700\mu F$
Resistance(R_0)	10Ω
PWM frequency(f)	$10kHz$

Table 2: Controllers' Parameters

a_0	500
a_1	60000
ρ	1000
ξ	0.01
P_2^T	$\begin{bmatrix} 579.514 & 1.927 \end{bmatrix}$
K_P^{outer}	1
K_I^{outer}	20.3
K_P^{inner}	3×10^5
K_I^{inner}	8×10^5

4.1 Responsive Characteristics using Nominal Parameter Values

The nominal values of each component of the buck converter are listed in Table 1, but in actual circuits, there is often some deviation between the real value and the nominal value. Assuming that the resistance, inductance, and capacitance all exist with a 20% random tolerance, the output voltage waveforms using two kinds of different control strategies are shown in Fig. 3 and Fig. 4.

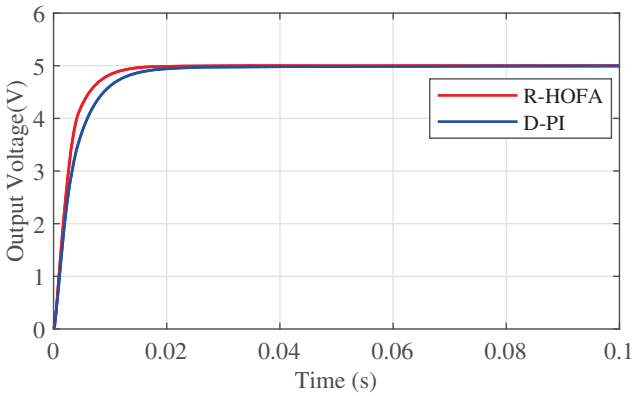

Fig. 3: Output voltages about R-HOFA and D-PI using nominal parameter values when V_{ref} = 5V

According to the findings presented in Fig. 3, it is evident that R-HOFA exhibits a shorter rise time compared to D-PI, along with a swifter response. Furthermore, R-HOFA demonstrates the ability to track variations in reference voltage without overshooting. Conversely, D-PI exhibits inadequate control in some scenarios, particularly between the time intervals of 200ms and 350ms, as shown in Fig. 4.

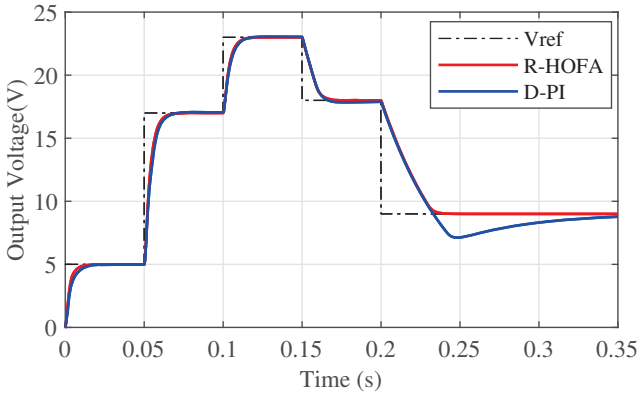

Fig. 4: Output voltages about R-HOFA and D-PI using nominal parameter values when V_{ref} = 5,17,23,18,9V in order

4.2 Input Voltage Fluctuation

The way of setting the nominal parameter values of the buck converter in the controller remains the same as in section 4.1. Considering the case of abrupt changes in input voltage, it drops from 30V to 20V at 50ms and rises from 20V to 40V at 100ms.

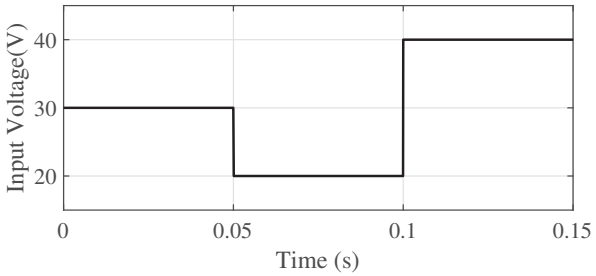

(a) Input voltage fluctuation

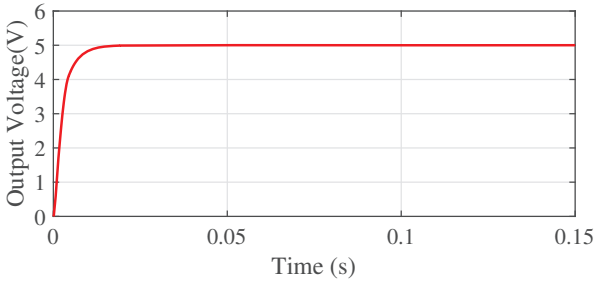

(b) R-HOFA

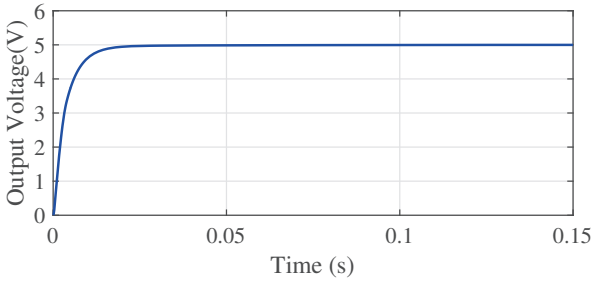

(c) D-PI

Fig. 5: Input voltage drops to 20V at 50ms and rises to 40V at 100ms

It can be seen from Fig. 5(a) that the input voltage drops from the original 30V to 20V at 50ms, and rises from 20V to 40V at 100ms. Fig. 5(b) and Fig. 5(c) are the output voltage waveforms of the two methods of R-HOFA and D-PI respectively, which shows that the output voltage of the two methods is basically stable at 5V at 50ms and 100ms, further highlights the robustness of both approaches in accommodating rapid fluctuations in input voltage.

4.3 Load Resistance Fluctuation

The values of the parameters remain still, and the input voltage is held constant at 30 V. Considering the case of abrupt changes in load resistance, it rises from 10Ω to 30Ω at 50 ms and drops from 30Ω to 5Ω at 100 ms.

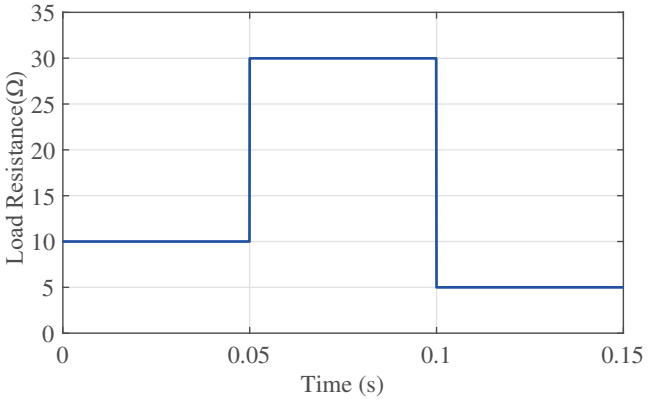

(a) Load resistance fluctuation

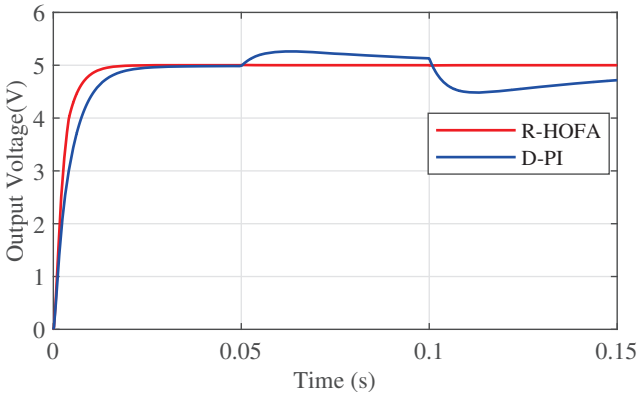

(b) R-HOFA and D-PI

Fig. 6: Load resistance rises to 30Ω at 50ms and drops to 5Ω at 100ms

Fig. 6(a) shows the fluctuation in the load resistance of the buck converter, which simulates the sudden change of the load resistance and the output voltage waveforms of the two methods R-HOFA and D-PI can be found in Fig. 6(b).

The output voltage waveform of D-PI exhibits significant variations when the load resistance experiences abrupt fluctuations at 50ms and 100ms, as shown in Fig. 6(b). Conversely, the result of R-HOFA remains stable, suggesting that R-HOFA demonstrates greater robustness in the presence of abrupt changes in the load resistance.

5 Conclusions

This study examines the design methodology of a robust controller utilizing the fully actuated system theory on buck converter. To validate the efficacy of the proposed R-HOFA, three sets of simulation experiments are conducted. A comparative analysis is performed with the D-PI, and based on the experimental findings, several conclusions are drawn:

- The R-HOFA demonstrates faster responsiveness compared to the D-PI.
- Both R-HOFA and D-PI exhibit smoother and more robust output voltage waveform when subjected to variations in the input power supply.
- The output voltage of the R-HOFA remains stable at the desired voltage even when there are abrupt changes in the load resistance, whereas the D-PI exhibits a significant deviation.
- In terms of parameter tuning, R-HOFA requires only the configuration of a suitable pole and a large upper bound ρ to achieve an output voltage waveform without overshooting and with a fast response. In contrast, the D-PI necessitates multiple tuning iterations to obtain a corresponding output voltage waveform without overshooting.

Overall, the simulation experiments confirm that the R-HOFA outperforms the D-PI in terms of response characteristics and robustness, while also offering a simpler parameter setting process. The efficacy of employing the fully actuated system theory in controller design of dc-dc buck converter is evidenced, as it enhances system performance while streamlining the design process. And also it can be concluded that the fully actuated system theory has extraordinary significance and application value in the field of power electronics.

References

[1] W. R. Liou, M. L. Yeh and Y. L. Kuo, A High Efficiency Dual-Mode Buck Converter IC For Portable Applications, in *IEEE Transactions on Power Electronics*, March 2008, vol. 23, no. 2, pp. 667-677.

[2] G. Divya, S. Sridharan and P. Velmurugan, Integrated Interleaved Luo Converter with Buck Converter Designed for Electric Vehicle Application, in *2023 9th International Conference on Electrical Energy Systems (ICEES)*, Chennai, India, 2023, pp. 670-673.

[3] M. Kankam and M. Elbuluk, A survey of power electronics applications in aerospace technologies, in *Proc. 36th Intersoc. Energy Convers. Eng. Conf.* Savannah, GA, USA: ASME, IEEE, AICHE, ANS, SAE, and AIAA, 2001, pp. 147–153.

[4] W. M. Utomo, A. Bakar, M. Ahmad, T. Taufik and R. Herianyah, Online Learning Neural Network Control of Buck-Boost Converter, in *2011 Eighth International Conference on Information Technology: New Generation*, Las Vegas, NV, USA, 2011, pp. 485-489.

[5] Z. Wang, S. Li and Q. Li, Discrete-Time Fast Terminal Sliding Mode Control Design for DC–DC Buck Converters With Mismatched Disturbances, in *IEEE Transactions on Industrial Informatics*, Feb. 2020, vol. 16, no. 2, pp. 1204-1213.

[6] S. Ding, W. X. Zheng, J. Sun and J. Wang, Second-Order Sliding-Mode Controller Design and Its Implementation for Buck Converters, in *IEEE Transactions on Industrial Informatics*, May 2018, vol. 14, no. 5, pp. 1990-2000.

[7] D. Maksimovic and R. Zane, Small-Signal Discrete-Time Modeling of Digitally Controlled PWM Converters, in *IEEE Transactions on Power Electronics*, Nov. 2007, vol. 22, no. 6, pp. 2552-2556.

[8] Duan, G. (2020). High-order fully actuated system approaches: Part I. Models and basic procedure, in *International Journal of Systems Science*, 52, 422 - 435.

[9] Duan, G. (2020). High-order fully actuated system approaches: Part II. Generalized strict-feedback systems, in *International Journal of Systems Science*, 52, 437 - 454.

[10] Duan, G. (2020). High-order fully actuated system approaches: Part III. Robust control and high-order backstepping, in *International Journal of Systems Science*, 52, 952 - 971.

[11] Duan, G. (2021). High-order fully actuated system approaches: Part IV. Adaptive control and high-order backstepping, in *International Journal of Systems Science*, 52, 972 - 989.

[12] Duan, G. (2021). High-order fully actuated system approaches: Part V. Robust adaptive control, in *International Journal of Systems Science*, 52, 2129 - 2143.

[13] Duan, G. (2021). High-order fully-actuated system approaches: Part VI. Disturbance attenuation and decoupling, in *International Journal of Systems Science*, 52, 2161 - 2181.

[14] Duan, G. (2021). High-order fully actuated system approaches: part VII. Controllability, stabilisability and parametric designs, in *International Journal of Systems Science*, 52, 3091 - 3114.

[15] Duan, G. (2021). High-order fully actuated system approaches: Part VIII. Optimal control with application in spacecraft attitude stabilisation, in *International Journal of Systems Science*, 53, 54 - 73.

[16] Duan, G. (2021). High-order fully-actuated system approaches: Part IX. Generalised PID control and model reference tracking, in *International Journal of Systems Science*, 53, 652 - 674.

[17] Duan, G. (2021). High-order fully actuated system approaches: Part X. Basics of discrete-time systems, in *International Journal of Systems Science*, 53, 810 - 832.

[18] C. Yan, X. Wang, T. Liu, J. Xia and W. Sun, Adaptive Event-Triggered Fuzzy Control of Flexible-Joint Robot: A Fully Actuated System Approach, in *2023 2nd Conference on Fully Actuated System Theory and Applications (CFASTA)*, Qingdao, China, 2023, pp. 811-814.

[19] D. Jin, S. Jia, T. Wang and J. Qiu, Spacecraft Attitude Tracking Control Based On High-Order Fully Actuated System Approach, in *2023 2nd Conference on Fully Actuated System Theory and Applications (CFASTA)*, Qingdao, China, 2023, pp. 1040-1044.

[20] C. Li, X. Shen, F. Yan, Y. Gao and J. Liu, Observer-Based Control of PEMFC Air Feed Systems Via High-Order Fully Actuated System Approaches, in *2023 2nd Conference on Fully Actuated System Theory and Applications (CFASTA)*, Qingdao, China, 2023, pp. 711-716.

[21] M. Gong, L. Sheng and D. Zhou, Robust Fault-Tolerant Control for Uncertain High-Order Fully Actuated Systems with Actuator Faults, in *2023 2nd Conference on Fully Actuated System Theory and Applications (CFASTA)*, Qingdao, China, 2023, pp. 532-537

[22] S. Zhang and G. Duan, Robust Stabilization Control for High-order Sub-fully Actuated Systems, in *2023 2nd Conference on Fully Actuated System Theory and Applications (CFASTA)*, Qingdao, China, 2023, pp. 573-578

[23] Y. Fang, Y. Chen, B. Zhang and D. Qiu, Modeling and Controller Design of Buck Converter Based on Fully Actuated System Theory, in *2023 IEEE 6th International Electrical and Energy Conference (CIEEC)*, Hefei, China, 2023, pp. 1202-1207.

Proceedings of the 3rd Conference on Fully Actuated System Theory and Applications
May 10-12, 2024, Shenzhen, China

Disturbance Observer-Based High-Order Fully Actuated Robust Control of Uncertain Robotic Systems

Fuxing Zhu[1], Yue Zhao[1], Zhuang Liu[1], Fei Yan[2], Jianxing Liu[1]

1. Department of Control Science and Engineering, Harbin Institute of Technology, Harbin 150001, P. R. China
E-mail: 23S104164@stu.hit.edu.cn, yue.zhao@hit.edu.cn, liuz@hit.edu.cn, jx.liu@hit.edu.cn

2. School of Information Science and Technology, Southwest Jiaotong University, Chengdu 611756, P. R. China
E-mail: fyan@home.swjtu.edu.cn

Abstract: Model uncertainties and external disturbances significantly impact the performance of trajectory tracking control in robotic systems. This paper proposes a novel control strategy based on high-order fully actuated (HOFA) system theoretical methods. The robotic system with nonlinear properties is transformed into a closed-loop linear system by pseudo-linear parameter design. The tracking controller is designed for the linearized system by combining robust control methods. Recognizing the system's susceptibility to disturbances during operation, a nonlinear disturbance observer (NDO) is designed to estimate and compensate for the lumped disturbances, and the stability of the system is demonstrated. Finally, comparative simulations based on the UR5 robot validate the effectiveness of the proposed control strategy.

Key Words: High-order fully actuated system, Trajectory tracking, Robust control, Robotic systems

1 Introduction

As the process of global industrialization continues to advance, the development of manufacturing intelligence and automation has become a general trend. The manipulator is the most widely used mechanical device in the field of robotics and an indispensable tool for human automation by mimicking the movements of the human arm to complete the tasks of carrying, grasping, and operating processing tools.

Since the robotic system is a typical nonlinear, strongly coupled system with model uncertainty, including the system's unmodeled dynamics, parameter uncertainty, joint friction, measurement errors, and other factors [1], it is difficult to establish its accurate dynamics model. Furthermore, because the real working environment of the manipulator is typically very severe, it is prone to external disturbances during operation [2]. The complexity of a multi-degree-of-freedom robot's kinematic model makes it difficult to stable and control it with high precision and speed, and if the aforesaid considerations are not taken into account, the system is likely to be destabilized [3]. As a result, how to develop a robust, simple, and high-performance controller based on the robot dynamics model to implement high-precision trajectory tracking of the robotic system remains a difficult topic in recent control research [4].

To address this problem, many scholars have proposed some control methods and strategies. Mohammed et.al [5] considered the modeling and control of a two-link robotic system, introducing a robust control strategy based on conventional sliding mode control for specific tasks. Zhao et.al [6] combined adaptive feedback control and PID control to design a new adaptive PID feedback controller to realize the precise tracking control of collaborative robots. A backstepping sliding mode control method based on a nonlinear disturbance observer was proposed in [7]. For robotic systems with external time-varying disturbances, a composite algorithm combining model predictive control and generalized proportional-integral observer was designed in [8], which significantly improves the system disturbance rejection capability. For the problem of task tracking in the joint space, Garofalo et.al [9] proposed an adaptive fault-tolerant method for robot trajectory tracking with fixed-time sliding mode. Sun et.al [10] investigated the predefined time trajectory tracking control of a robotic system using a radial basis function neural network to estimate the uncertainty in the dynamics of the robotic system.

The methods described above are all based on the state-space model, but many original systems in the physical world are second- or higher-order. If the state-space method is used to convert them to first-order systems, the system's fully actuated characteristics are destroyed, and the state-space method may become no longer applicable and powerless for complex nonlinear controlled systems. Based on the above considerations, Duan proposed a novel high-order fully actuated (HOFA) system method [11–15] that can transform the nonlinear system into a closed-loop linear constant system with desired characteristics through the elimination of the element ascending order and pole configuration. For uncertain high-order strict feedback nonlinear systems with "complex explosion", an event-triggered adaptive SMC strategy based on HOFA theory was proposed in [16]. Moreover, a disturbance observer-based HOFA method was proposed in [17] for realizing high-precision trajectory tracking of free-flying robots. Utilizing the full-actuated property of HOFA to avoid higher-order derivatives of the signal, Li and Duan [18] proposed a HOFA-singular perturbation control scheme for flexible servo systems. Hence, compared with the traditional control methods, HOFA shows greater superiority in nonlinear system control.

In this paper, a robotic control scheme based on HOFA system theory (referred to as the HOFA algorithm) is proposed. The HOFA model of the robotic system is first established, and the specific details of the pseudo-parametric

This work was supported in part by the National Natural Science Foundation of China (No. 62173116), in part by the Dreams Foundation of Jianghuai Advance Technology Center (NO. 2023-ZM01J002), in part by the Science Center Program of National Natural Science Foundation of China under Grant 62188101, and in part by the Heilongjiang Touyan Team Program. (Corresponding author: Yue Zhao)

linearized design process and pole configuration are given. Then, a robust tracking controller is designed for the linearized closed-loop system, and the system lumped disturbance is estimated and compensated by a nonlinear disturbance observer (NDO). Finally, the effectiveness and robustness of the proposed HOFA control approach are verified by comparative simulations.

The rest of this paper is organized as follows. The dynamics of the robotic system are modeled and the control objectives are set in Section 2. The derivation process of the robust tracking controller based on the HOFA system theory, the design process of the NDO, and the proof of the stability of the system are given in Section 3. In Section 4, the proposed control approach is validated by simulation cases. Finally, the Section 5 summarizes the main contributions of this paper.

2 Problem Formulation

2.1 Dynamic modeling of robotic system

When establishing the dynamic model of the robotic system, frictions, model uncertainties, and external disturbances are considered, and the Lagrange method is utilized to solve the dynamics equations to obtain the actual model.

$$M\left(q\right)\ddot{q}+C\left(q,\dot{q}\right)\dot{q}+G\left(q\right)+F+\tau_{d}=\tau \tag{1}$$

where $q,\dot{q},\ddot{q}\in R^{n}$ is the angle, angular velocity, angular acceleration vector, $\tau\in R^{n}$ is the torque vector provided by the motor to the joint, $M\left(q\right)\in R^{n\times n}$ is the inertia term, $C\left(q,\dot{q}\right)\in R^{n\times n}$ is the Coriolis force and centrifugal force term, $G\left(q\right)\in R^{n}$ is the gravity term, $F\in R^{n}$ is the friction term, $\tau_{d}\in R^{n}$ is the external disturbance. Due to the uncertainty of the system, the modeling error is defined as

$$\begin{aligned} M&=M_{0}+\Delta M,\Delta M=k_{M}M\\ C&=C_{0}+\Delta C,\Delta C=k_{C}C\\ G&=G_{0}+\Delta G,\Delta G=k_{G}G \end{aligned} \tag{2}$$

where M_{0},C_{0},G_{0} is the nominal value, $\Delta M,\Delta C,\Delta G$ is the modeling error, and $k_{M},k_{G},k_{C}\in R$ is the modeling error coefficient. Then

$$M_{0}\left(q\right)\ddot{q}+C_{0}\left(q,\dot{q}\right)\dot{q}+G_{0}\left(q\right)=\tau+d \tag{3}$$

$$d=-\big(\Delta M\big(q\big)\ddot{q}+\Delta C\big(q,\dot{q}\big)\dot{q}+\Delta G\big(q\big)+F+\tau_{d}\big) \tag{4}$$

In the above equation, $d\in R^{n}$ represents the lumped disturbance term, which contains all model uncertainties, frictions, and external disturbances.

2.2 Pseudo-linear parametric design

A typical second-order fully actuated system is as the following form

$$\ddot{x}=f\big(x,\dot{x},t\big)+B\big(x,\dot{x},t\big)u \tag{5}$$

where $x,u\in R^{n}$ are state vectors and control vectors, $f(\cdot)\in R^{n}$ and $B\left(\cdot\right)\in R^{n\times n}$ are sufficiently differentiable vector functions and matrix functions, and $B(\cdot)$ satisfies the following fully actuated condition

$$\det B\big(x,\dot{x},t\big)\neq 0,\forall x,\dot{x}\in R^{n},t\geqslant 0 \tag{6}$$

At this stage, for any given matrix $A_{1},A_{0}\in R^{n\times n}$, it is always possible to obtain the following closed-loop linear constant system by means of a control law.

$$\ddot{x}+A_{1}\dot{x}+A_{0}x=\nu \tag{7}$$

where ν is the external input. Therefore, by choosing the matrix appropriately and configuring the poles, a closed-loop system with the desired performance can be found.

For Eq.(3), this can be varied into the following form as

$$\ddot{q}=M_{0}^{-1}(q)(-C_{0}(q,\dot{q})\dot{q}-G_{0}(q))+M_{0}^{-1}(q)\big(\tau+d\big) \tag{8}$$

According to the characteristics of the robot, the inertia matrix $M_{0}\left(q\right)$ is positive-definite and $\det M_{0}(q)\neq 0$, so it satisfies the fully actuated condition.

At this phase, a pseudo-linear feedback controller based on HOFA system theory is constructed to change the second-order robotic system into a closed-loop linear system with configurable eigenstructures

$$\begin{cases} \tau=\tau_{1}+\tau_{2}\\ \tau_{1}=C_{0}\left(q,\dot{q}\right)\dot{q}+G_{0}\left(q\right)\\ \tau_{2}=-M_{0}\left(q\right)\left(A_{1}\dot{q}+A_{0}q-\nu\right) \end{cases} \tag{9}$$

where $\tau_{1}\in R^{n}$ is the system model compensation term, $\tau_{2}\in R^{n}$ is the state feedback term, A_{1},A_{0} are the control parameter matrices to be designed, and ν is the input signal.

3 Controller design based on HOFA system theory

3.1 Robust tracking controller design

Considering that the robotic system is susceptible to external disturbances under actual working conditions, the friction, model uncertainty, and external disturbance within the system are regarded as system uncertainty in Eq.(8), and the model can be reduced to the following form based on HOFA system theory as

$$\ddot{q}+A_{1}\dot{q}+A_{0}q=\nu+\Delta f(q,\dot{q}) \tag{10}$$

In Eq.(10), $\Delta f(q,\dot{q})\in R^{n}$ is the nonlinear uncertainty term of the system, which satisfies the following relation

$$\left\|\Delta f(x,\dot{x})\right\|_{2}\leq\rho(x,\dot{x}) \tag{11}$$

where $\rho(x,\dot{x})$ is a nonnegative continuous scalar function and it is bounded, while $||\cdot||_{2}$ represents the Euclidean paradigm. If the parameter matrix A fulfills the following condition

$$\mathrm{Re}\,\lambda_{i}(A)<-\frac{\delta}{2},i=1,2...n \tag{12}$$

where $\delta\in R>0$, $\mathrm{Re}\,\lambda_{i}(A)$ is denoted as the real part of the ith eigenvalue of the parameter matrix A, then there exists a positive definite matrix $H\in R^{n\times n}$ satisfying

$$A^{T}H+HA\leq-\delta H \tag{13}$$

Based on the preceding reasoning, the controller robust term for Eq.(10) can be designed as

$$\nu=-\frac{1}{4\omega}\rho^{2}\left(q,\dot{q}\right){H_{2}}^{T}\begin{bmatrix}q\\ \dot{q}\end{bmatrix} \tag{14}$$

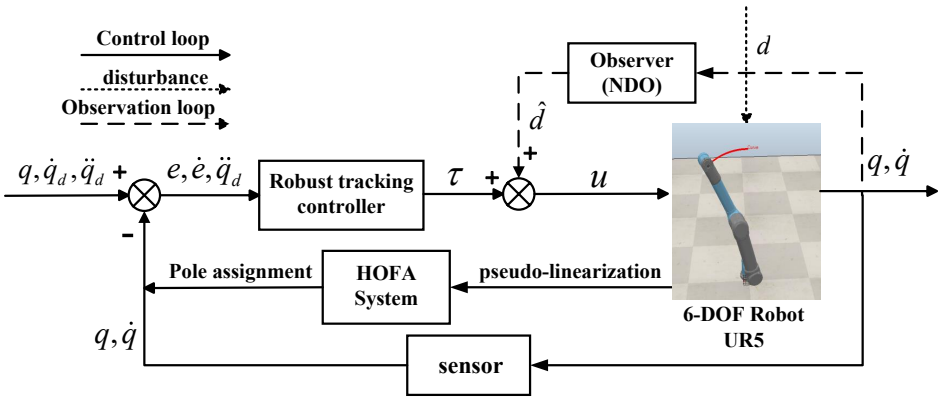

Fig. 1: Control structure diagram of UR5 Robot

where $\omega \in R > 0$, and Eq.(14) is determined by the preceding equations, then

$$H_2 = H\begin{bmatrix}0\\I\end{bmatrix} = [H_1 \quad H_2]\begin{bmatrix}0\\I\end{bmatrix} \in R^n \tag{15}$$

Desired tracking trajectory is known to be q_d , and the error variable is defined as

$$e^{(i)} = q^{(i)} - {q_d}^{(i)}, i = 0, 1, 2 \tag{16}$$

Based on the closed-loop system (10) and Eq.(16), the transformation below could be realized

$$\begin{aligned} &\ddot{e} + A_1\dot{e} + A_0 e = \nu + \Delta f - \ddot{q}_d - A_1\dot{q}_d - A_0 q_d \\ &\nu = -\frac{1}{4\omega}\rho^2(q,\dot{q}){H_2}^T\begin{bmatrix}e\\\dot{e}\end{bmatrix} + \ddot{q}_d + A_1\dot{q}_d + A_0 q_d \end{aligned} \tag{17}$$

Using the above transformation relation, the robust controller is transformed into a robust tracking controller according to Eq.(9) with the following expression as

$$\begin{cases} \tau = \tau_1 + \tau_2 \\ \tau_1 = C_0(q,\dot{q})\dot{q} + G_0(q) \\ \tau_2 = -M_0(q)(A_1\dot{q} + A_0 q - \nu) \\ \nu = -\frac{1}{4\omega}\rho^2(q,\dot{q}){H_2}^T\begin{bmatrix}e\\\dot{e}\end{bmatrix} + \ddot{q}_d + A_1\dot{q}_d + A_0 q_d \end{cases} \tag{18}$$

Fig. 1 shows the block diagram of the control structure of the UR5 robotic system. At this point, the robust tracking controller (18) ensures that the state $q, \dot{q}$ of the robotic system converges in an ellipsoidal domain centered on the desired trajectory $q_d, \dot{q}_d$. The confirmation of system stability is given later.

3.2 Nonlinear disturbance observer design

Since $\rho(x, \dot{x})$ in the above-mentioned robust tracking controller is bounded, its control may be insufficient when the robotic system is subjected to substantial disturbances. Uncertainties such as frictions, model uncertainties, and external disturbances are attributed to a lumped disturbance in this section, and a nonlinear disturbance observer is designed to estimate and compensate for them in order to reduce the upper bounds of the lumped disturbance and achieve a better control effect.

Based on the real model (3), the design of the NDO has the following form

$$\begin{aligned} \dot{\hat{d}} &= L(d - \hat{d}) \\ &= L\left(M_0(q)\ddot{q} + C_0(q,\dot{q})\dot{q} + G_0(q) - \tau\right) - L\hat{d} \end{aligned} \tag{19}$$

where, $\hat{d} \in R^n$ is the estimated value of the lumped disturbance, and $L \in R^{n\times n}$ is the gain matrix to be designed. Define an auxiliary vector $z \in R^n$ as

$$z = \hat{d} - p(q,\dot{q}) \tag{20}$$

In the above equation, $p(q,\dot{q}) \in R^n$ is a function vector and satisfies the following relation

$$p(q,\dot{q}) = LM_0(q)\dot{q} \tag{21}$$

At this point, take the derivative of z, then we have the following equation

$$\begin{aligned} \dot{z} &= \dot{\hat{d}} - \dot{p}(q,\dot{q}) \\ &= L\left(M_0(q)\ddot{q} + C_0(q,\dot{q})\dot{q} + G_0(q) - \tau\right) \\ &\quad - L\hat{d} - LM_0(q)\ddot{q} \\ &= L\left(C_0(q,\dot{q})\dot{q} + G_0(q) - \tau\right) - L\hat{d} \\ &= L\left(C_0(q,\dot{q})\dot{q} + G_0(q) - \tau - p(q,\dot{q})\right) - Lz \end{aligned} \tag{22}$$

Thus, the specific form of NDO is derived as

$$\begin{cases} \hat{d} = z + p(q,\dot{q}) \\ \dot{z} = L\left(C_0(q,\dot{q})\dot{q} + G_0(q) - \tau - p(q,\dot{q})\right) - Lz \end{cases} \tag{23}$$

As no differential a priori information of the disturbance can be obtained, so assuming that the disturbance changes slowly with respect to the dynamic characteristics of the interferer, the disturbance estimation error for the NDO is defined as

$$\tilde{d} = d - \hat{d} \tag{24}$$

$$\dot{\tilde{d}} = -\dot{\hat{d}} = -L\tilde{d} \tag{25}$$

Define the Lyapunov function as

$$V_1 = \frac{1}{2}\tilde{d}^T\tilde{d} \tag{26}$$

Perform a derivative on it

$$\dot{V}_1 = \tilde{d}^T\dot{\tilde{d}} = -\tilde{d}^T L\tilde{d} \tag{27}$$

Since the gain matrix L is positive definite, $\dot{V}_1 \leq 0$ is taken to be equal if and only if $\tilde{d} = 0$, when $\tilde{d} \neq 0, \dot{V}_1 < 0$. According to the LaSalle invariance principle, the designed NDO's disturbance estimate error $\tilde{d}$ asymptotically converges to the origin.

3.3 Stability analysis of the system

Before proceeding to the stability proof, two lemmas are introduced.

Lemma 1: If there are two real numbers $a \in R$ and $b \in R$, where $b > 0$ [13], then it is satisfied

$$a - \frac{a^2}{4b} \leq b \tag{28}$$

Lemma 2: For the function $V(t):[0,\infty) \in R$, if there is a solution to the inequality equation $V \leq -\alpha V + f, \forall 0 \leq t_0 \leq t$ [13] as

$$V(t) \leq e^{-\alpha(t-t_0)} V(t_0) + \int_{t_0}^{t} e^{-\alpha(t-\tau)} f(\tau)\, d\tau \tag{29}$$

Define the system uncertainty with the addition of the disturbance observer as $\Delta\overline{f}(q,\dot{q})$, which takes the form as

$$\Delta\overline{f}(q,\dot{q}) = M_0^{-1}\left(d - \hat{d}\right) = \Delta f(q,\dot{q}) - M_0^{-1}\hat{d} \tag{30}$$

It is also assumed in this case that the uncertainty satisfies condition (11), that there exists another nonnegative continuous scalar function $\bar{\rho}(x,\dot{x})$ that fulfills the following relation

$$\| \Delta\overline{f}(x,\dot{x}) \|_2 \leq \overline{\rho}(x,\dot{x}) \tag{31}$$

At this point, the closed-loop system after parameter linearization is

$$\begin{aligned} &\ddot{q} + A_1\dot{q} + A_0 q = \overline{Q}(q,\dot{q}) \\ &\overline{Q}(q,\dot{q}) = -\frac{1}{4\omega}\overline{\rho}^2(q,\dot{q})\, {H_2}^T \begin{bmatrix} q \\ \dot{q} \end{bmatrix} + \Delta\overline{f}(q,\dot{q}) \end{aligned} \tag{32}$$

Transform Eq.(32) into state space form as

$$\dot{X} = A_c X + \begin{bmatrix} 0 \\ \overline{Q}(X) \end{bmatrix} \tag{33}$$

among them, $X = \begin{bmatrix} q \\ \dot{q} \end{bmatrix}$, $A_c = \begin{bmatrix} 0 & I \\ -A_0 & -A_1 \end{bmatrix}$.

For system (32), the Lyapunov function is chosen as

$$V_2 = \frac{1}{2} X^T H X \tag{34}$$

Take the derivative on both sides of V_2

$$\begin{aligned} \dot{V}_2 &= \frac{1}{2}\dot{X}^T H X + \frac{1}{2} X^T H \dot{X} \\ &= \frac{1}{2}\left(A_c X + \begin{bmatrix} 0 \\ \overline{Q}(X) \end{bmatrix} \right)^T H X \\ &+ \frac{1}{2} X^T H \left(A_c X + \begin{bmatrix} 0 \\ \overline{Q}(X) \end{bmatrix} \right) \\ &= \frac{1}{2} X^T \left({A_c}^T H + H A_c \right) X + X^T H \begin{bmatrix} 0 \\ \overline{Q}(X) \end{bmatrix} \\ &\leq -\frac{\delta}{2} X^T H X + X^T H_2 \overline{Q}(X) = -\delta V_2 + X^T H_2 \overline{Q}(X) \end{aligned} \tag{35}$$

Continue the derivation from Lemma 1 as

$$\begin{aligned} X^T H_2 \overline{Q}(X) &= X^T H_2 \Delta\overline{f}(X) - \frac{\overline{\rho}^2(X)}{4\omega} X^T H_2 H_2^T X \\ &\leq \left\| \Delta\overline{f}(X) \right\|_2 \left\| H_2^T X \right\|_2 - \frac{\overline{\rho}^2(X)}{4\omega} \left\| H_2^T X \right\|_2^2 \\ &\leq \overline{\rho}(X) \left\| H_2^T X \right\|_2 - \frac{\overline{\rho}^2(X)}{4\omega} \left\| H_2^T X \right\|_2^2 \\ &\leq \omega \end{aligned} \tag{36}$$

According to the derivation of Eqs.(35) and (36), there are

$$\dot{V}_2 \leq -\delta V_2 + \omega \tag{37}$$

According to Lemma 2, solve Eq.(37) as

$$V_2 \leq V_2(0)\, e^{-\delta t} + \frac{\omega}{\delta}\left(1 - e^{-\delta t}\right) = \frac{\omega}{\delta}, \left(t \to \infty\right) \tag{38}$$

Thus, the stability of the system is proven.

Therefore, the designed tracking controller for the closed-loop system (10) ensures that the system state $q, \dot{q}$ converges to an ellipsoid centered on the desired trajectory $q_d, \dot{q}_d$ with the following form as

$$\Theta = \left\{ X = \begin{bmatrix} q \\ \dot{q} \end{bmatrix} \mid (X - X_d)^T H (X - X_d) \leq \frac{2\omega}{\delta} \right\} \tag{39}$$

4 Simulation Experiments

In order to verify the effectiveness of the proposed HOFA control strategy, detailed simulation tests are carried out in this paper with a 6-degree-of-freedom UR5 robot. The simulation-oriented UR5 robot model is built in CoppeliaSim, and the control algorithm is designed in Matlab 2021b to realize their co-simulation.

The simulations are specified as follows: apply the desired signals and external disturbances to each joint of UR5 in the joint space, and select the PD computational torque method as the control group of the experiments in order to test the robustness, rapidity, and accuracy of the proposed HOFA algorithm.

In order to better analyze the simulation results, convergence time T_i and integral absolute error IAE_i are introduced as two evaluation metrics to measure the rapidity and accuracy of the control algorithm in trajectory tracking.

Define the convergence time T_i: after a certain moment T_i, the angular error of the ith joint of the robot arm constantly satisfies the following relation

$$\left|e_i\right| = \left|q_d - q\right| \leq 5 \times 10^{-4}\text{rad}, i = 1, 2...6 \tag{40}$$

then T_i is said to be the convergence time of the ith joint of the robotic system.

Simulation parameterization is carried out based on the above theoretical approach, and the parameters of the controller and observer are chosen as follows.

Controller parameters: $\omega = 0.2$, $\delta = 36$, $\rho = 40$, $A_0 = 600I_6$, $A_1 = 50I_6$, where the matrices A_0 and A_1 are determined by the configured closed-loop poles a_0 and a_1, then $a_0 = -20$, $a_1 = -30$.

Observer parameters: $L = 200I_6$.

Set the expected signals for each joint in turn to

$$q_d = \begin{cases} -0.15\cos(0.5\pi t) + 0.148 \\ -0.15\cos(\pi t) + 0.148 \\ -0.1\cos(1.5\pi t) + 0.098 \\ -0.1\cos(2\pi t) + 0.098 \\ -0.1\cos(2.5\pi t) + 0.098 \\ -0.05\cos(3\pi t) + 0.048 \end{cases} \tag{41}$$

Set the external disturbance signal to each joint as

$$\tau_d = \begin{cases} 5 \times \left(0.2\sin(\pi t) + 0.1\right), 0 < t \leq 0.5 \\ 5 \times \left(0.2\cos(\pi t) + 0.1\right), 0.5 < t \leq 1 \end{cases} \tag{42}$$

Each joint is set with an initial error of 2×10^{-3}rad, the joint torque limits are listed in order as [80, 80, 80, 35, 35, 35] N×m. The system modeling error factor are $k_M = k_G = k_C = 0.02$, the simulation step size is 0.001s, the total simulation time is 1s.

The goal of the control is to make the robotic joints track the desired signals quickly and accurately, despite external disturbances and initial errors. The simulation results verify the effectiveness of the proposed HOFA strategy.

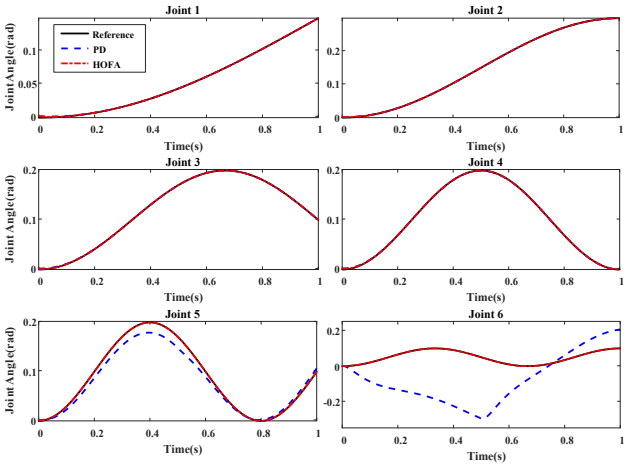

Fig. 2: Joint Angle of UR5 Robot

First of all, the joint angle simulation curves of the UR5 robot are shown in Fig. 2, where the black line represents the desired signal, the blue line indicates the result of the PD algorithm, and the red line is the result of the HOFA algorithm. Comparison with the desired signal intuitively shows that both the PD and HOFA algorithms are able to track up the desired signal from the initial error in the first four joints. But in joint 5, the PD control has gradually become biased, while the HOFA control still works well. Due to the sudden change of the disturbance at the moment of 0.5s, the PD control in joint 6 has been completely disabled, while the HOFA control remains effective and its disturbance resistance is verified.

This paper also conducts the simulation experiments of tracking error to demonstrate the effectiveness of the proposed HOFA approach, and the results are shown in Fig. 3, where the blue line denotes the tracking error of the PD control and the red line denotes the tracking error of the HOFA control. Since each joint has an initial error 2×10^{-3} rad, the

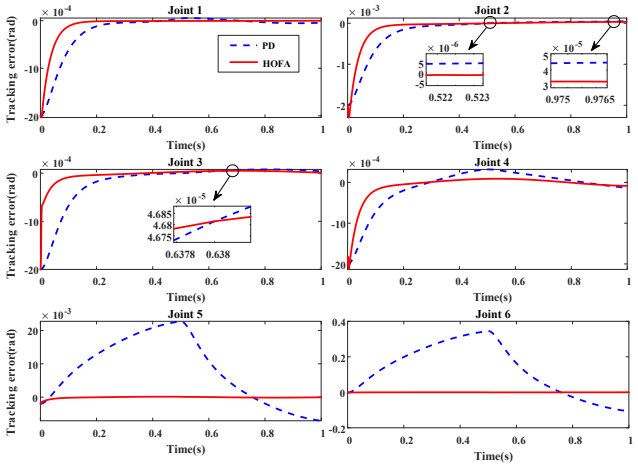

Fig. 3: Tracking error of UR5 Robot

tracking error for the first four joints reaches the 0.0001 rad, but the HOFA control clearly converges faster. The PD control failed due to the sudden change of the disturbance in the simulation results of joint 5 and joint 6, resulting in a substantial shift in its tracking error at 0.5s. However, the HOFA control error remains constant and close to zero. Moreover, it converges instantly at the start of the motion and has a significantly higher response speed, proving its resilience and quickness.

Table 1: Evaluation index of HOFA

Index / Joint	$T_i(s)$		$IAE_i(rad)$	
	PD	HOFA	PD	HOFA
Joint 1	0.119	0.054	0.1931	0.0814
Joint 2	0.119	0.060	0.1999	0.1087
Joint 3	0.117	0.016	0.2159	0.0637
Joint 4	0.130	0.059	0.2972	0.1335
Joint 5	0.061	0.044	10.3615	0.1339
Joint 6	-	0.028	158.682	0.1525

Table 1 shows the simulated values of the evaluation metrics for the two algorithms. While the robotic system is affected by external disturbances, for the convergence time T_i, the HOFA control is much smaller than the PD control at each joint. Joint 6 is unable to achieve the set tracking accuracy with PD control, whereas HOFA control converges easily. For the integral absolute error IAE_i, the integral value of the error for the HOFA control is much smaller than that of the PD control at all joints, and it has better tracking accuracy throughout the whole motion process.

Fig. 4 shows the torque curve of the HOFA-controlled UR5 robot. Due to the initial error set by the system, the value of the joint torque is large at the initial moment of startup, but it does not exceed the torque limit and is still within the acceptable range. Affected by the sudden change of disturbance, the control torque of UR5 also changes suddenly at 0.5s, but due to the torque compensation effect of the observer, the torque changes are relatively smooth during the whole motion process.

5 Conclusion

This paper has proposed a robotic control scheme based on HOFA system theory for realizing the robotic trajectory

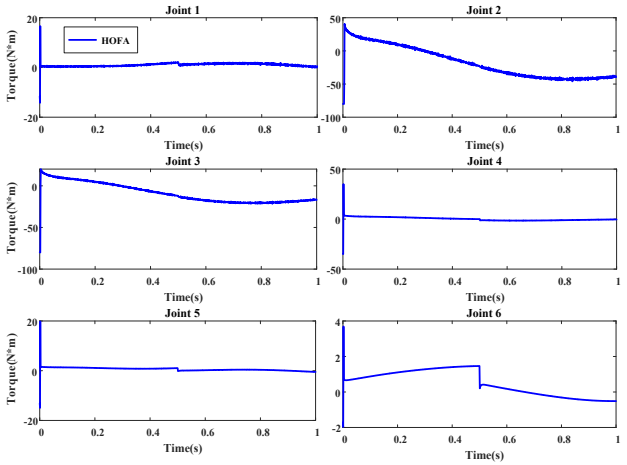

Fig. 4: Torque of UR5 Robot

tracking task in joint space. The dynamical equations of the robot have been established and transformed into a second-order fully actuated closed-loop linear system by pseudo-linear parametric design. The linearized system has the expected closed-loop dynamic properties. The proposed tracking controller design is based on the HOFA approach and robust control theory, which can effectively resist external disturbances. The designed HOFA controller was successfully simulated in CoppeliaSim and MATLAB environments. The simulation results demonstrated that the proposed control strategy ensures the UR5 robot can rapidly and accurately track the desired trajectory even in the presence of model uncertainty and external disturbance.

References

[1] R.-D. Xi, X. Xiao, T.-N. Ma and Z.-X. Yang, Adaptive Sliding Mode Disturbance Observer Based Robust Control for Robot Manipulators Towards Assembly Assistance, *IEEE Robotics and Automation Letters*, 2022, 7(3): 6139-6146.

[2] L. Dai, Y. Yu, D.-H. Zhai, T. Huang and Y. Xia, Robust Model Predictive Tracking Control for Robot Manipulators With Disturbances, *IEEE Transactions on Industrial Electronics*, 2021, 68(5): 4288-4297.

[3] B. Xiao and S. Yin, Exponential Tracking Control of Robotic Manipulators With Uncertain Dynamics and Kinematics, *IEEE Transactions on Industrial Informatics*, 2019, 15(2): 689-698.

[4] L. Zhang, H. Liu, D. Tang, Y. Hou and Y. Wang, Adaptive Fixed-Time Fault-Tolerant Tracking Control and Its Application for Robot Manipulators, *IEEE Transactions on Industrial Electronics*, 2022, 69(3): 2956-2966.

[5] A.A. Mohammed and A. Eltayeb, Dynamics and Control of a Two-link Manipulator using PID and Sliding Mode Control, *2018 International Conference on Computer, Control, Electrical, and Electronics Engineering (ICCCEEE)*, Khartoum, Sudan, 2018: 1-5.

[6] Y. Zhao, J. Qi and W. Li, Adaptive PID feedback tracking control for 6-DOF collaborative robot, *2022 34th Chinese Control and Decision Conference (CCDC)*, Hefei, China, 2022: 5525-5532.

[7] Y. Huang, L. Cheng, Z. Li, W. Gao, H. Lu and L. Wei, Backstepping Sliding Mode Control for Robot Manipulator via Nonlinear Disturbance Observer, *2019 Chinese Control Conference (CCC)*, Guangzhou, China, 2019: 3220-3224.

[8] Y. Lu, L. Han, J. Liu and S. Li, Model Predictive Tracking Control for Rigid Manipulators with Disturbance Rejection, *2022 41st Chinese Control Conference (CCC)*, Hefei, China, 2022, 2705-2710.

[9] G. Garofalo, X. Wu and C. Ott, Adaptive Passivity-Based Multi-Task Tracking Control for Robotic Manipulators, *IEEE Robotics and Automation Letters*, 2021, 6(4): 7129-7136.

[10] Y. Sun et al., Neural Network-Based Tracking Control of Uncertain Robotic Systems: Predefined-Time Nonsingular Terminal Sliding-Mode Approach, *IEEE Transactions on Industrial Electronics*, 2022, 69(10): 10510-10520.

[11] G. Duan, High-order fully actuated system approaches: Part I. Models and basic procedure, *International Journal of Systems Science*, 2021, 52(2): 422-435.

[12] G. Duan, High-order fully actuated system approaches: Part II. Generalized strict-feedback systems, *International Journal of Systems Science*, 2021, 52(3): 437-454.

[13] G. Duan, High-order fully actuated system approaches: Part III. Robust control and high-order backstepping, *International Journal of Systems Science*, 2021, 52(5): 952-971.

[14] G. Duan, High-order fully actuated system approaches: Part IV. Adaptive control and high-order backstepping, *International Journal of Systems Science*, 2021, 52(5): 972-989.

[15] G. Duan, High-order fully actuated system approaches: Part V. Robust adaptive control, *International Journal of Systems Science*, 2021, 52(10): 2129-2143.

[16] Y. Wang, G. Duan and P. Li, Event-Triggered Adaptive Sliding Mode Control of Uncertain Nonlinear Systems Based On Fully Actuated System Approach, *IEEE Transactions on Circuits and Systems II: Express Briefs*, 2024 (Early Access).

[17] G. Tian, B. Li, Q. Zhao and G. Duan, High-Precision Trajectory Tracking Control for Free-Flying Space Manipulators With Multiple Constraints and System Uncertainties, *IEEE Transactions on Aerospace and Electronic Systems*, 2024, 60(1): 789-801.

[18] P. Li and G. Duan, High-Order Fully Actuated Control Approaches of Flexible Servo Systems Based on Singular Perturbation Theory, *IEEE/ASME Transactions on Mechatronics*, 2023, 28(6): 3386-3397.

Proceedings of the 3rd Conference on Fully Actuated System Theory and Applications
May 10-12, 2024, Shenzhen, China

Finite-time stability analysis of switched systems under time-dependent switchings

Jie Wu, Rongni Yang*
School of Control Science and Engineering, Shandong University, Ji'nan, Shandong 250061, China
E-mail: rnyang@sdu.edu.cn

Abstract: This paper investigates the Lyapunov-based finite-time stability problem of switched systems under time-dependent switching signals, in which stabilizing switch and destabilizing switch occur alternately. By establishing connections on the persistent period and convergence/divergence intensity between subsystems, some sufficient conditions for finite-time stability of corresponding system under two groups of switching modes are provided. In simulation, two examples including scalar system and Lorentz system under switched control are presented to demonstrate the effectiveness of the proposed theoretical results.

Key Words: Finite-time stability, Switched systems, Time-dependent switchings

1 Introduction

Switched systems, served as a special case of hybrid dynamic systems, have attracted extensive research interest in recent years, since it can characterize many complex dynamic behaviors in practical applications. For instance, in consideration of vehicle's velocity and acceleration, the autonomous/controlled switching is reflected in the gearbox of automobiles [1]. Featured by multiple channels and transmission delays, the networked control systems are described in the form of switched linear uncertain systems [2, 3]. Generally speaking, switched systems are composed of a family of subsystems and certain rule that governs the switching among them. According to different switching mechanisms, the common utilized switching rules/signals can be divided into time-dependent [4, 5], state-dependent [6], and hybrid types [7]. Since time-dependent switching signals are easy to design and avoid the occurrence of sliding motions on the switching surface, a large amount of research work on Lyapunov stability theory has been devoted to such switching signals. On one hand, based on common Lyapunov function, the asymptotic stability of switched systems with dwell-time switching and average dwell-time switching were studied in [8, 9]. On the other hand, considering that switching signal depends on system mode, the average dwell-time switching was expanded to the mode-dependent average dwell-time switching, and multiple Lyapunov function with less conservativeness was constructed [4, 10]. However, one of the typical properties of these existing Lyapunov theoretical results about time-dependent switching signals is that the solution will tend to an equilibrium state as time tends to infinity. From the perspective of practical applications, the optimal stability result is achieved when the system solution converges to the equilibrium state within a finite time, such as robot manipulators [11], intelligent vehicle system [12], and underactuated surface vessels [13]. This key point stimulates our research interest in the finite-time stability (FTS) of switched systems.

FTS not only implies the finite-time convergence, but is a stronger concept than asymptotic/exponential stability. Thus, it may give rise to fast transient performances and high robustness against uncertainties [14]. With the Lyapunov theorem on FTS of continuous autonomous systems firstly proposed in [15], many technical FTS results have been reported from theoretical and practical points of view, see [16–19]. For instance, an improved version of fast terminal sliding mode design was proposed in [16], and [18] established a more accurate settling-time estimation for corresponding fast FTS criterion. However, one may observe that the above works have not included switched modes in their investigation. Recently, [20] studies the finite-time resilient tracking control problem for nonlinear multi-agent systems under attacks, in which the attack interval and the normal interval are artificially divided in terms of the time scale. Herein, such processing technique are applied to switched systems subject to time-dependent switching signals, in which stabilizing switch and destabilizing switch occur alternately. Moreover, the following two core questions deserve further exploration:

1). What kind of convergent/divergent subsystem is possible to implement FTS?

2). On the basis of 1), what type of sufficient conditions can realize FTS while ensuring small conservatism?

In this paper, we shall address the aforementioned questions. Firstly, the (locally) FTS mode is essential in order that the switched system can achieve convergence within a finite time. Then, two FTS criteria involving dwell-time constraints and convergence/divergence intensity between subsystems are proposed. Finally, an estimation of the settling time dependent on the switching signal and the initial state of corresponding system is given.

In addition, this work is organized as follows. In Section 2, the system description and several basic definitions are introduced. In Section 3, for the given two groups of switching modes, the FTS criteria are established respectively. In Section 4, two simulation examples are given to show the applications of the obtained FTS criteria, and conclusions shall be presented in Section 5.

Notations. Let $\mathbb{R}$ denote the set of real numbers, $\mathbb{R}_{\geq 0}$ the set of nonnegative real numbers, $\mathbb{Z}_{\geq 0}$ the set of nonnegative integer numbers, and $\mathbb{R}^n$ the n-dimensional real spaces equipped with Euclidean norm $|\cdot|$.

This work was supported in part by the National Natural Science Foundation of China (62273208), and the Science Center Program of National Natural Science Foundation of China (62188101).

2 System description

Consider the following nonlinear switched system

$$\begin{cases} \dot{x}(t) = f_{\sigma(t)}(t, x(t)), \\ x(0) = x_0, \end{cases} \tag{1}$$

where $f_i(\cdot,\cdot) : \mathbb{R}_{\geq 0} \times \mathbb{R}^n \to \mathbb{R}^n$ is the continuous nonlinearity of system (1) that admits $f(t,0) = 0$ for all $t \geq 0$, and $x(t) \in \mathbb{R}^n$ denotes the system state. $\sigma(\cdot) : \mathbb{R}_{\geq 0} \to \mathcal{N} \triangleq \{1, 2, \cdots, N\}$ represents the switching signal that determines the subsystem to be activated at each switching instant t. In particular, a sequence of monotonically increasing time $\mathcal{S} \triangleq \{t_k\}_{k\in\mathbb{Z}_{\geq 0}}$, known as the set of switching instants, is determined when the switching occur and satisfies $0 = t_0 < t_1 < \cdots < t_k \to +\infty$ as $k \to \infty$.

Firstly, several essential definitions and propositions are made throughout the paper.

Definition 1. ([15]) Consider the following system

$$\dot{x}(t) = g(x(t)),\ x \in \mathcal{D} \subseteq \mathbb{R}^n,\ x(0) = x_0 \tag{2}$$

where $g(\cdot) : \mathcal{D} \to \mathbb{R}^n$ is a continuous function with $g(0) = 0$, and $\mathcal{D}$ is an open neighborhood of the origin. System (2) is said to be finite-time stable (FTS) if it is Lyapunov stable and finite-time convergent. Especially, the latter implies that there exist a function $\phi(\cdot) : \mathcal{D}/\{0\} \to \mathbb{R}_+$ such that for $\forall x_0 \in \mathcal{D}$, the solution $x(t, x_0)$ of system (2) for $t \in (0, \phi(x_0))$ satisfies $\lim_{t\to\phi(x_0)} x(t, x_0) = 0$, and $x(t, x_0) = 0$ for any $t > \phi(x_0)$.

Definition 2. For the given function $V(\cdot) : \mathbb{R}^n \to \mathbb{R}_{\geq 0}$ that satisfies locally Lipschitz constraint, the Dini derivative of V along system (2) is defined as:

$$D^+V(x(t)) = \limsup_{h\to 0^+} \frac{1}{h}\Big\{V(x(t)+hg(x(t))) - V(x(t))\Big\}.$$

Proposition 1. The sequence $\mathcal{S}$ of switching instants consists of stabilizing switch series $\mathcal{S}_1 \triangleq \{t_{2k}\}_{k\in\mathbb{Z}_{\geq 0}}$ and destabilizing switch series $\mathcal{S}_2 \triangleq \{t_{2k+1}\}_{k\in\mathbb{Z}_{\geq 0}}$. The stabilizing switch, as it implies, refers that the responsive subsystem is convergent. Conversely, the destabilizing switch causes the responsive subsystem to be divergent.

Then, the main problem in this paper lies in that for the given/controlled subsystem evolution trajectories of system (1) satisfying Proposition 1, whether the FTS can be achieved by imposing certain conditions on the switching instants sequence $\mathcal{S}$. This research topic shall be investigated in subsequent sections.

3 Main results

In this section, two cases of switching modes satisfying Proposition 1 are considered, and some sufficient FTS conditions are proposed for system (1).

Firstly, in order to facilitate the subsequent analysis process, the following technical lemmas are presented.

Lemma 1. *[21] Suppose that there exists a constant $\gamma \in \mathbb{R}$, such that the Dini derivative of V along system (2) satisfies*

$$D^+V(x(t)) = \gamma V(x(t)). \tag{3}$$

Then for any initial state $x_0 \in \mathcal{D}$, it holds that $V(x(t)) = V(x_0)e^{\gamma t}$. Moreover, system (2) is said to be

$$\begin{cases} \text{exponentially stable}, & \text{if } \gamma < 0, \\ \text{exponentially divergent}, & \text{if } \gamma > 0. \end{cases} \tag{4}$$

Lemma 2. *[18] Suppose that there exist constants $\lambda \in \mathbb{R}/\{0\}$, $\mu > 0$, and $\alpha \in (0, 1)$, such that the Dini derivative of V along system (2) satisfies*

$$D^+V(x(t)) = \lambda V(x(t)) - \mu V^\alpha(x(t)). \tag{5}$$

Then for any initial state $x_0 \in \mathcal{D}$, the solution of V is

$$V(x(t)) = [V^{1-\alpha}(x_0) - \frac{\mu}{\lambda}(1 - e^{-(1-\alpha)\lambda t})]^{\frac{1}{1-\alpha}} e^{\lambda t}, \tag{6}$$

and system (2) is said to be

$$\begin{cases} \text{FTS}, & \text{if } \lambda < 0, \\ \text{locally FTS}, & \text{if } \lambda > 0 \text{ and } x_0 \in \Omega \cap \mathcal{D}, \\ \text{divergent}, & \text{if } \lambda > 0 \text{ and } x_0 \notin \Omega \cap \mathcal{D}, \end{cases} \tag{7}$$

where $\Omega \triangleq \{x \in \mathbb{R}^n | V^{1-\alpha}(x) < \frac{\mu}{\lambda}\}$. Moreover, for the case of FTS*, there exists a function $\phi(\cdot)$ satisfying $V(x(t)) = 0$, $\forall t \geq \phi(x_0)$, where*

$$\phi(x_0) = \frac{1}{-(1-\alpha)\lambda} \ln[1 - \frac{\lambda}{\mu} V^{1-\alpha}(x_0)].$$

Proof. Define the auxiliary equation $\dot{y}(t) = \lambda y(t) - \mu y^\alpha(t)$, $y(0) = y_0$, and $y(t) \geq 0$. Based on the parameters variation method of first-order non-homogeneous equations, it is assumed that $y(t) = \omega(t)e^{\lambda t}$ with $\omega(t) \not\equiv 0$ to be determined is the exponential form solution. By taking the derivative of y, we have $\dot{\omega}(t) = -\mu\omega^\alpha e^{\lambda(\alpha-1)t}$. Afterwards, it can be further deduced that

$$\begin{aligned} \omega(t) &= [\omega^{1-\alpha}(0) - \frac{\mu}{\lambda}(1 - e^{-(1-\alpha)\lambda t})]^{\frac{1}{1-\alpha}} \\ &= [y_0^{1-\alpha} - \frac{\mu}{\lambda}(1 - e^{-(1-\alpha)\lambda t})]^{\frac{1}{1-\alpha}}, \end{aligned}$$

which implies that the solution (6) holds.

In addition, when $x_0 \in \Omega \cap \mathcal{D}$, no matter what the sign of λ is, one can obtain that $D^+V(x(t)) < 0$, and it is easy to verify that there exists a $\phi(x_0)$ such that $V(x(t)) \equiv 0$ for all $t \geq \phi(x_0)$. Thus, the (locally) FTS of system (2) is achieved. On the contrary, when $x_0 \notin \Omega \cap \mathcal{D}$, the situation analysis of $\lambda < 0$ is the same as above, while for the case of $\lambda > 0$, the resultant $D^+V(x(t)) > 0$ leads to the divergence of system (2). To sum up, the statement (7) is established, which completes the proof. □

Then, we shall investigate the FTS criteria of system (1) under the following two groups of switching modes:

I). exponentially divergent (ED) mode & FTS mode;
II). exponentially stable (ES) mode & locally FTS mode.

For simplicity, denote the two types of active intervals of system (1) as :

$$\overline{\mathscr{S}_k} \triangleq [t_{2k}, t_{2k+1}),\ \overline{\mathscr{D}_k} \triangleq [t_{2k+1}, t_{2k+2}).$$

Correspondingly, define the following dwell time notations of active mode for all $k \in \mathbb{Z}_{\geq 0}$:

$$\mathscr{S}_k \triangleq t_{2k+1} - t_{2k},\ \mathscr{D}_k \triangleq t_{2k+2} - t_{2k+1}.$$

Case 1: ED mode & FTS mode

In this case, the following assumption on the minimum dwell time of stabilizing switch is introduced, and the FTS criterion is presented in Theorem 1.

Assumption 1. *$\mathscr{S}_k$ is bounded by an uniform positive constant τ, that is, $\inf_{k\in\mathbb{Z}_{\geq 0}} \mathscr{S}_k \geq \tau$.*

Theorem 1. *Suppose that there exist a locally Lipschitz continuous function $V(\cdot) : \mathbb{R}^n \to \mathbb{R}_{\geq 0}$, and some positive constants $\alpha, \rho \in (0,1)$, γ_1, λ_1, μ such that*

$$\frac{\lambda_1}{\gamma_1} \geq \frac{\rho}{1-\rho}, \tag{8}$$

$$\sup_{k\in\mathbb{Z}_{\geq 0}} \{\frac{\mathscr{D}_k}{\mathscr{S}_k}\} \leq \frac{\rho}{1-\rho}, \tag{9}$$

and for all $k \in \mathbb{Z}_{\geq 0}$, the derivative of V along the solution $x(t) = x(t, x_0)$ of system (1) with $x_0 \in \mathbb{R}^n$ satisfies

$$D^+V(x(t)) \leq \begin{cases} -\lambda_1 V(x(t)) - \mu V^\alpha(x(t)), & t \in \overline{\mathscr{S}_k}, \\ \gamma_1 V(x(t)), & t \in \overline{\mathscr{D}_k}. \end{cases} \tag{10}$$

Then, system (1) under switching instants sequence $\mathcal{S}$ is FTS. *Moreover, there exists a positive integer $k^* = \lfloor \frac{1}{-\tau(1-\alpha)[\rho(\gamma_1+\lambda_1)-\lambda_1]} \ln(\Delta V^{1-\alpha}(x_0)+1) \rfloor$ such that the solution $x(t)$ of system (1) satisfies $x(t) = 0$ for all $t \geq t_{2k^*+1}$, where*

$$\Delta = \frac{\lambda_1 - \lambda_1 e^{[\rho(\gamma_1+\lambda_1)-\lambda_1]\tau(1-\alpha)}}{\mu(1-e^{-(1-\alpha)\lambda_1\tau})e^{[\rho(\gamma_1+\lambda_1)-\lambda_1]\tau(1-\alpha)}}. \tag{11}$$

Proof. Given the initial state $x_0 \in \mathbb{R}^n$, the convergence of system solution $x(t)$ will be investigated. By utilizing Lemma 2, the first inequality of (10), and comparison principle, we have

$$\begin{aligned} V(x(t)) \leq & [V^{1-\alpha}(x(t_{2k})) - \frac{\mu}{\lambda_1}(1-e^{-(1-\alpha)\lambda_1(t-t_{2k})})]^{\frac{1}{1-\alpha}} \\ & \cdot e^{-\lambda_1(t-t_{2k})},\ \forall t \in [t_{2k}, t_{2k+1}). \end{aligned}$$

Similarly, using Lemma 1 and the second inequality of (10) yields that

$$V(x(t)) \leq V(x(t_{2k+1}))e^{\gamma_1(t-t_{2k+1})},\ \forall t \in [t_{2k+1}, t_{2k+2}).$$

When $t = t_{2k+2}$, based on the above analysis process, it can be derived that

$$\begin{aligned} & V(x(t_{2k+2})) \\ \leq & [V^{1-\alpha}(x(t_{2k})) - \frac{\mu}{\lambda_1}(1-e^{-(1-\alpha)\lambda_1(t_{2k+1}-t_{2k})})]^{\frac{1}{1-\alpha}} \\ & \cdot e^{\gamma_1(t_{2k+2}-t_{2k+1})}e^{-\lambda_1(t_{2k+1}-t_{2k})}. \end{aligned}$$

By combining (8) and (9), we obtain

$$\begin{aligned} & \gamma_1(t_{2k+2}-t_{2k+1}) - \lambda_1(t_{2k+1}-t_{2k}) \\ = & (\gamma_1+\lambda_1)(t_{2k+2}-t_{2k+1}) - \lambda_1(t_{2k+2}-t_{2k}) \\ \leq & \bar{\rho}(t_{2k+2}-t_{2k}), \end{aligned} \tag{12}$$

where $\bar{\rho} \triangleq \rho(\gamma_1+\lambda_1) - \lambda_1 \leq 0$. Substituting (12) into $V(x(t_{2k+2}))$, yields that

$$V(x(t_{2k+2})) \leq (V^{1-\alpha}(x(t_{2k})) - \Theta)^{\frac{1}{1-\alpha}} e^{\bar{\rho}\tau}, \tag{13}$$

where $\Theta \triangleq \frac{\mu}{\lambda_1}(1-e^{-(1-\alpha)\lambda_1\tau}) > 0$. Consider the auxiliary function $W(x(t)) = V(x(t)) + \varepsilon(t)$ with $\varepsilon(0) = 0$ and $\varepsilon(t) \geq 0$ for all $t \geq 0$, such that the following equation holds:

$$W(x(t_{2k+2})) = (W^{1-\alpha}(x(t_{2k})) - \Theta)^{\frac{1}{1-\alpha}} e^{\bar{\rho}\tau}. \tag{14}$$

By taking "$1-\alpha$" power at both sides of (14), one has

$$\begin{aligned} 0 \leq & W^{1-\alpha}(x(t_{2k+2})) \\ = & (W^{1-\alpha}(x(t_{2k})) - \Theta)e^{\bar{\rho}\tau(1-\alpha)} \\ = & [(W^{1-\alpha}(x(t_{2k-2})) - \Theta)e^{\bar{\rho}\tau(1-\alpha)} - \Theta]e^{\bar{\rho}\tau(1-\alpha)} \\ = & \cdots\cdots \\ = & W^{1-\alpha}(x_0)e^{(k+1)\bar{\rho}\tau(1-\alpha)} \\ & - \Theta e^{\bar{\rho}\tau(1-\alpha)}\frac{1-e^{(k+1)\bar{\rho}\tau(1-\alpha)}}{1-e^{\bar{\rho}\tau(1-\alpha)}}, \end{aligned}$$

which further implies that

$$(V^{1-\alpha}(x_0) + \frac{1}{\Delta})e^{(k+1)\bar{\rho}\tau(1-\alpha)} \geq \frac{1}{\Delta},$$

where $\Delta \triangleq \frac{1-e^{\bar{\rho}\tau(1-\alpha)}}{\Theta e^{\bar{\rho}\tau(1-\alpha)}}$. Hence, it can be calculated that $k^* = \lfloor \frac{1}{-\tau(1-\alpha)\bar{\rho}} \ln(\Delta V^{1-\alpha}(x_0)+1) \rfloor$ is the last term satisfying $W^{1-\alpha}(x(t_{2k^*})) > 0$. Since $W(x(t)) \geq V(x(t)) \geq 0$, we know that system (1) under switching instants sequence $\mathcal{S}$ is finite-time convergent for $t \in [0, t_{2k^*+1})$.

Thereafter, it follows from Lemma 1 and the first inequality of (10) that $x(t) = 0$ holds for all $t \geq t_{2k^*+1}$, which implies that system (1) under switching instants sequence $\mathcal{S}$ is FTS. This completes the proof. □

Remark 1. It should be pointed out that conditions (8) and (9) in Theorem 1 play important roles in realizing the FTS of system (1). Specifically, the former constrains the intensity of convergence/divergence of subsystem, while the latter stipulates the dwell time of the convergence/divergence mode. In particular, only the convergence mode is specified for a minimum dwell time τ, while the divergence mode is relatively free. In other words, for any divergent mode, as long as a convergent mode satisfying conditions (8) and (9) is established, the FTS of system (1) can be guaranteed.

Remark 2. One may observe that the settling-time estimation of system (1) is expressed as certain point in switching instants sequence $\mathcal{S}$. Nevertheless, the fact is that the settling time of system (1) depends not only on the initial state but also on the switching effect. To be specific, by introducing a virtual function W and establishing an equality constraint (14), it is verified that there exists a maximum index k^* such that $W > 0$, which depends on the initial state of system (1). Since $W \geq V \geq 0$, k^* is reasonably approximated as the maximum index of $V > 0$. Afterwards, the first point after index k^* in switching instants sequence $\mathcal{S}$ can be regarded as the settling-time estimation.

Case 2: ES mode & locally FTS mode

In this case, the following assumption on the minimum dwell time of destabilizing switch is introduced, and the FTS criterion is presented in Theorem 2.

Assumption 2. *$\mathscr{D}_k$ is bounded by an uniform positive constant π, that is, $\inf_{k\in\mathbb{Z}_{\geq 0}} \mathscr{D}_k \geq \pi$.*

Theorem 2. *Suppose that there exist a locally Lipschitz continuous function $V(\cdot):\mathbb{R}^n \to \mathbb{R}_{\geq 0}$, and some positive constants $\alpha, \varrho \in (0,1)$, γ_2, λ_2, μ such that*

$$\frac{\gamma_2}{\lambda_2} \geq \frac{\varrho}{1-\varrho}, \tag{15}$$

$$\sup_{k\in\mathbb{Z}_{\geq 0}} \{\frac{\mathscr{D}_k}{\mathscr{S}_{k+1}}\} \leq \frac{\varrho}{1-\varrho}, \tag{16}$$

and for all $k \in \mathbb{Z}_{\geq 0}$, the derivative of V along the solution $x(t) = x(t, x_0)$ of system (1) with $x_0 \in \mathbb{R}^n$ satisfies

$$D^+V(x(t)) \leq \begin{cases} -\gamma_2 V(x(t)), & t \in \overline{\mathscr{S}_k}, \\ \lambda_2 V(x(t)) - \mu V^\alpha(x(t)), & t \in \overline{\mathscr{D}_k}. \end{cases} \tag{17}$$

Then, system (1) under switching instants sequence $\mathcal{S}$ is FTS. *Moreover, there exists a positive integer $\bar{\kappa} = \lfloor \frac{1}{-\pi(1-\alpha)[\varrho(\gamma_2+\lambda_2)-\gamma_2]} \ln(\Lambda V^{1-\alpha}(x_0)+1) \rfloor$ such that the solution $x(t)$ of system (1) satisfies $x(t) = 0$ for all $t \geq t_{2k^\star+2}$, where*

$$\Lambda = \frac{\lambda_2 - \lambda_2 e^{[\varrho(\gamma_2+\lambda_2)-\gamma_2]\pi(1-\alpha)}}{\mu(e^{(1-\alpha)\lambda_2\pi}-1)e^{[\varrho(\gamma_2+\lambda_2)-\gamma_2]\pi(1-\alpha)}}. \tag{18}$$

Proof. Consider the solution $x(t)$ of system (1) with initial state $x_0 \in \mathbb{R}^n$. On one hand, it follows from the first inequality of (17) and Lemma 1 that

$$V(x(t_{2k+3})) \leq V(x(t_{2k+2}))e^{-\gamma_2(t_{2k+3}-t_{2k+2})}.$$

On the other hand, by utilizing the second inequality of (17) and Lemma 2, we have

$$\begin{aligned} &V(x(t_{2k+2})) \\ \leq&[V^{1-\alpha}(x(t_{2k+1})) + \frac{\mu}{\lambda_2}(1-e^{(1-\alpha)\lambda_2(t_{2k+2}-t_{2k+1})})]^{\frac{1}{1-\alpha}} \\ &\cdot e^{\lambda_2(t_{2k+2}-t_{2k+1})}. \end{aligned}$$

Combining the two stages, and in terms of (15) and (16), it can be deduced that

$$\begin{aligned} &V(x(t_{2k+3})) \\ \leq&[V^{1-\alpha}(x(t_{2k+1})) + \frac{\mu}{\lambda_2}(1-e^{(1-\alpha)\lambda_2(t_{2k+2}-t_{2k+1})})]^{\frac{1}{1-\alpha}} \\ &\cdot e^{\lambda_2(t_{2k+2}-t_{2k+1})}e^{-\gamma_2(t_{2k+3}-t_{2k+2})} \\ \leq&(V^{1-\alpha}(x(t_{2k+1})) - \Phi)^{\frac{1}{1-\alpha}}e^{\bar{\varrho}\pi}, \end{aligned}$$

where $\Phi \triangleq \frac{\mu}{\lambda_2}(e^{(1-\alpha)\lambda_2\pi}-1)$, and $\bar{\varrho} \triangleq \varrho(\lambda_2+\gamma_2)-\gamma_2 \leq 0$. Consider the auxiliary function $Z(x(t)) = V(x(t)) + \delta(t)$ with $\delta(t_1) = 0$ and $\delta(t) \geq 0$ for all $t \geq 0$, such that the following equation holds:

$$Z(x(t_{2k+3})) = (Z^{1-\alpha}(x(t_{2k+1})) - \Phi)^{\frac{1}{1-\alpha}}e^{\bar{\varrho}\pi}. \tag{19}$$

Similar to the analysis process of Theorem 1, we have

$$\begin{aligned} &(V^{1-\alpha}(x_0) + \frac{1}{\Lambda})e^{(k+1)\bar{\varrho}\pi(1-\alpha)} \\ \geq&(V^{1-\alpha}(x(t_1)) + \frac{1}{\Lambda})e^{(k+1)\bar{\varrho}\pi(1-\alpha)} \\ =&(Z^{1-\alpha}(x(t_1)) + \frac{1}{\Lambda})e^{(k+1)\bar{\varrho}\pi(1-\alpha)} \\ \geq&\frac{1}{\Lambda}, \end{aligned}$$

where $\Lambda \triangleq \frac{1-e^{\bar{\varrho}\pi(1-\alpha)}}{\Phi e^{\bar{\varrho}\pi(1-\alpha)}}$. Hence, it can be calculated that $\bar{\kappa} = \lfloor \frac{1}{-\pi(1-\alpha)\bar{\varrho}} \ln(\Lambda V^{1-\alpha}(x_0)+1) \rfloor - 1$ is the last term satisfying $Z^{1-\alpha}(x(t_{2\bar{\kappa}+1})) > 0$. Since $Z(x(t)) \geq V(x(t)) \geq 0$, we know that system (1) under switching instants sequence $\mathcal{S}$ is finite-time convergent for $t \in [0, t_{2\bar{\kappa}+2})$.

Thereafter, it follows from Lemma 2 and the second inequality of (17) that $x(t) = 0$ holds for all $t \geq t_{2\bar{\kappa}+2}$, which implies that system (1) under switching instants sequence $\mathcal{S}$ is FTS. This completes the proof. □

Remark 3. Since the finite-time convergence property of system (1) is provided by the locally FTS mode, the minimum dwell time π for such mode is needed in Theorem 2. As a compensation, the constraints on ES mode dwell time is removed. In addition, when $t \geq t_{2\bar{\kappa}+1}$, although the solution $x(t)$ for system (1) converges in both ES mode and locally FTS mode, $x(t)$ only has the characteristic of finite-time convergence on $t \in \overline{\mathscr{D}_k}$. Therefore, the subsequent switching instant $t_{2\bar{\kappa}+2}$ is utilized as the settling-time estimation of system (1).

Remark 4. In particular, it should be noted that the case of $k^* = \bar{\kappa} = 0$ is not involved in Theorems 1 and 2. In fact, both of these represent the special cases that do not reflect the switching characteristics of system (1). The former means that the system solution $x(t)$ converges to 0 in the FTS mode, while the latter implies that $x(t)$ crosses the ES mode and converges to 0 in the locally FTS mode. Considering that these two cases are relatively simple and special, the analysis is not discussed in the main theoretical results of this paper.

4 Simulation Examples

In this section, two numerical examples are presented to demonstrate the feasibility of the proposed FTS results in Sections 3. To this end, we firstly consider the switching instants sequence $\mathcal{S} = \mathcal{S}_1 \cup \mathcal{S}_2 = \{2k\}_{k\in\mathbb{Z}_{\geq 0}} \cup \{2k+1.4\}_{k\in\mathbb{Z}_{\geq 0}}$.

Example 1. Consider the following scalar system

$$\dot{w}(t) = \begin{cases} -0.8w(t) - 2w^{\frac{1}{3}}(t), & t \in \overline{\mathscr{S}_k}, \\ 1.4w(t), & t \in \overline{\mathscr{D}_k}. \end{cases} \tag{20}$$

Based on the criteria proposed in Section 3, we shall investigate the FTS of system (20). Firstly, choose the candidate Lyapunov function $V(t) = |w(t)|$, and the derivative of V along system (20) satisfies (10) with $\lambda_1 = 0.8$, $\mu = 2$, $\alpha = \frac{1}{3}$, and $\gamma_1 = 1.4$. It can be verified that $\frac{\lambda_1}{\gamma_1} = \frac{4}{7} \geq \frac{0.6}{1.4}$, which implies that conditions (8) and (9) hold. Then according to Theorem 1, for the given initial state $w(0) = 5$, there exists a positive integer $k^* = \lfloor 2.3327 \rfloor = 2$ such that

system (20) is finite-time convergent for $t \in [0, 5.4)$. By simulation, Fig. 1 shows that the settling time can be estimated by $T_0 \leq 5.4$.

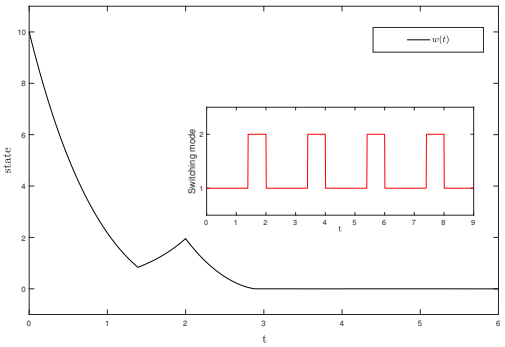

Fig. 1: Trajectory evolution of system (20).

Example 2. Consider the classical Lorenz system [22]

$$\begin{cases} \dot{x} = a(y - x), \\ \dot{y} = cx - xz - y, \\ \dot{z} = xy - bz, \end{cases} \tag{21}$$

which has a chaotic attractor when $a = 10$, $b = \frac{8}{3}$, and $c = 28$ as shown in Fig. 2 with with initial state $(x_0, y_0, z_0)^T = (3, 4, 5)^T$.

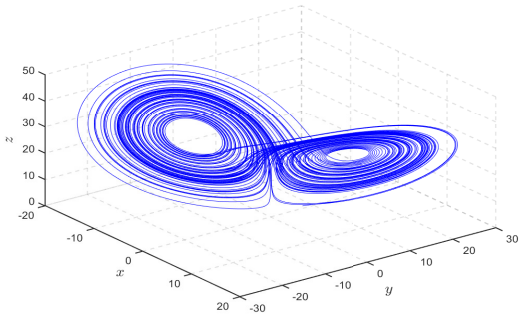

Fig. 2: Chaotic attractor of system (21).

In what follows, the controller design problem for the FTS of Lorenz system (21) is investigated. Firstly, consider the following controlled Lorenz system

$$\begin{cases} \dot{x} = a(y - x) + u_1, \\ \dot{y} = cx - xz - y + u_2, \\ \dot{z} = xy - bz + u_3, \end{cases} \tag{22}$$

where $U(t) = (u_1, u_2, u_3)^T$ is the controller to be designed. Next, two controller design schemes are presented:

$$U_1 = \begin{pmatrix} 9x - 10y \\ -28x \\ \frac{5}{3}z \end{pmatrix}, \; U_2 = \begin{pmatrix} 11x - 13y - 2x^{\frac{1}{3}} \\ -25x + 2y - 2y^{\frac{1}{3}} \\ \frac{8}{3}z - 2z^{\frac{1}{3}} \end{pmatrix},$$

in which the former is committed to the ES of system (22), while the latter aims to achieve the FTS. One may observe from the simulation results shown in Fig. 3 that U_1 succeeds in achieving the the ES of system (22), but U_2 fails to take effect as anticipated.

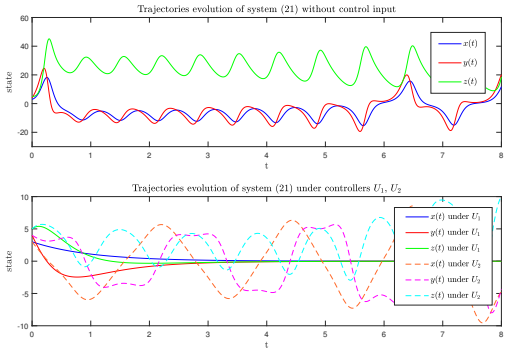

Fig. 3: Trajectories evolution of system (22).

Hence, we study the FTS property of system (22) by using the switched control strategy proposed herein. On one hand, the time-dependent switched controller is constructed

$$U(t) = \begin{cases} U_1, \text{ when } t \in \mathcal{S}_1, \\ U_2, \text{ when } t \in \mathcal{S}_2. \end{cases} \tag{23}$$

On the other hand, choose the candidate Lyapunov function $V(t) = \frac{1}{2}(x^2 + y^2 + z^2)$, and it can be derived that

$$D^+V(t) \leq \begin{cases} -V(t), & t \in \overline{\mathscr{S}_k}, \\ V(t) - 1.5874\, V^{\frac{2}{3}}(t), & t \in \overline{\mathscr{D}_k}. \end{cases}$$

Since conditions (15) and (16) are satisfies with $\varrho = 0.3$, it follows from Theorem 2 that system (22) under switching sequence $\mathcal{S}$ and controller (23) can be stabilized in finite time. In particular, Fig. 4 illustrates that the settling time is bounded by $T_0 \leq 14$ with $\bar{\kappa} = \lfloor 6.5807 \rfloor = 6$.

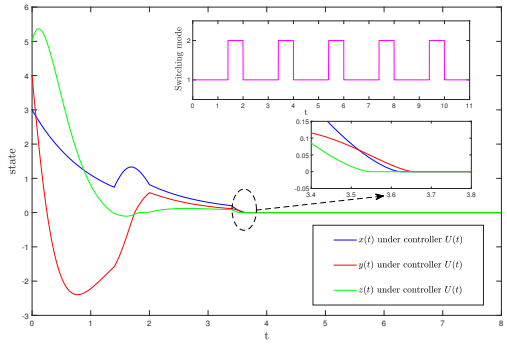

Fig. 4: Trajectories evolution of system (22).

5 Conclusion

In this paper, the Lyapunov-based finite-time stability problem of switched systems under time-dependent switching signal has been studied. By requiring that stabilizing switch and destabilizing switch occur alternately, the FTS criteria for system with two groups of switching modes: ED

mode & FTS mode and ES mode & locally FTS mode are proposed, respectively. Meanwhile, the resultant settling-time estimation depends not only on the initial state but also on the switching effect. Furthermore, two examples including scalar system and Lorentz system under switched control are presented to validate the obtained FTS criteria. An interesting extension in future work is to analyze the FTS of switched systems with more than two modes under the circumstances of synchronous and asynchronous switching.

References

[1] Lin, H. and Antsaklis, P. J. (2022). *Hybrid dynamical systems: fundamentals and methods*. Springer.

[2] Donkers, M. C. F., Heemels, W. P. M. H., Van de Wouw, N., and Hetel, L. (2011). Stability analysis of networked control systems using a switched linear systems approach. *IEEE Transactions on Automatic control*, 56(9):2101–2115.

[3] Peng, C. and Sun, H. (2020). Switching-like event-triggered control for networked control systems under malicious denial of service attacks. *IEEE Transactions on Automatic Control*, 65(9):3943–3949.

[4] Zhao, X., Zhang, L., Shi, P., and Liu, M. (2011). Stability and stabilization of switched linear systems with mode-dependent average dwell time. *IEEE Transactions on Automatic Control*, 57(7):1809–1815.

[5] Zhang, L., Zhu, Y., Shi, P., and Lu, Q. (2016). *Time-dependent switched discrete-time linear systems: control and filtering*, volume 53. Springer.

[6] Yang, D., Li, X., and Qiu, J. (2019). Output tracking control of delayed switched systems via state-dependent switching and dynamic output feedback. *Nonlinear Analysis: Hybrid Systems*, 32:294–305.

[7] Allerhand, L. I. and Shaked, U. (2012). Robust state-dependent switching of linear systems with dwell time. *IEEE Transactions on Automatic Control*, 58(4):994–1001.

[8] Hespanha, J. P. and Morse, A. S. (1999). Stability of switched systems with average dwell-time. In *Proceedings of the 38th IEEE conference on decision and control (Cat. No. 99CH36304)*, 3:2655–2660.

[9] Sanchez, C. A., Garcia, G., Hadjeras, S., Heemels, W. M. H., and Zaccarian, L. (2019). Practical stabilization of switched affine systems with dwell-time guarantees. *IEEE Transactions on Automatic Control*, 64(11):4811–4817.

[10] Fei, Z., Shi, S., Wang, Z., and Wu, L. (2017). Quasi-time-dependent output control for discrete-time switched system with mode-dependent average dwell time. *IEEE Transactions on Automatic Control*, 63(8):2647–2653.

[11] Wang, X. and Zhao, J. (2017). Autonomous switched control of load shifting robot manipulators. *IEEE Transactions on Industrial Electronics*, 64(9):7161–7170.

[12] Li, M., Chen, Y., Zhou, A., He, W., and Li, X. (2019). Adaptive tracking control for networked control systems of intelligent vehicle. *Information Sciences*, 503:493–507.

[13] Banavar, R. N. and Sankaranarayanan, V. (2006). *Switched finite time control of a class of underactuated systems*, volume 3. Springer.

[14] Haimo, V. T. (1986). Finite time controllers. *SIAM Journal on Control and Optimization*, 24(4):760–770.

[15] Bhat, S. P. and Bernstein, D. S. (2000). Finite-time stability of continuous autonomous systems. *SIAM Journal on Control and optimization*, 38(3):751–766.

[16] Yu, S., Yu, X., Shirinzadeh, B., and Man, Z. (2005). Continuous finite-time control for robotic manipulators with terminal sliding mode. *Automatica*, 41(11):1957–1964.

[17] Shen, Y. and Xia, X. (2008). Semi-global finite-time observers for nonlinear systems. *Automatica*, 44(12):3152–3156.

[18] Liu, J.-D., Niu, B., Kao, Y.-G., Zhao, P., and Yang, D. (2021). Decentralized adaptive command filtered neural tracking control of large-scale nonlinear systems: An almost fast finite-time framework. *IEEE Transactions on Neural Networks and Learning Systems*, 32(8):3621–3632.

[19] Zhou, B. (2020). Finite-time stability analysis and stabilization by bounded linear time-varying feedback. *Automatica*, 121:10.1016/j.automatica.2020.109191.

[20] Yue, D., Deng, C., Wen, C., and Wang, W. (2023). Finite-time distributed resilient tracking control for nonlinear mass with application to power systems. *IEEE Transactions on Automatic Control*, 10.1109/TAC.2023.3332777.

[21] Zhou, B. (2016). On asymptotic stability of linear time-varying systems. *Automatica*, 68:266–276.

[22] Lü, J., Zhou, T., and Zhang, S. (2002). Chaos synchronization between linearly coupled chaotic systems. *Chaos, Solitons & Fractals*, 14(4):529–541.

Proceedings of the 3rd Conference on Fully Actuated System Theory and Applications
May 10-12, 2024, Shenzhen, China

Preview tracking control of the SIR Model with saturation incidence rate

Chenqi Wang, Yuan Li, Yi Zhang

School of Science, Shenyang University of Technology, Shenyang 110870
E-mail: syliyy@163.com

Abstract: In this paper, considering the regional population changes, a *SIR* model with saturation incidence rate was constructed for cholera, hepatitis B and other infectious diseases with high infectivity but low radical cure rate. The asymptotic stability of the equilibrium point was analyzed by *Jury* criterion. On this basis, an augmented error system is constructed for the model by using the preview control method, and a corresponding state feedback preview controller is designed. By using the *Lyapunov* stability theory, sufficient conditions for the asymptotic stability of the closed-loop system are obtained so that the model can be stabilized in a finite time and the spread of infectious diseases can be controlled. Finally, the effectiveness of the proposed method is verified by numerical simulation.

Key Words: Saturation Incidence Rate, Vertical Infection Rate, Preview Tracking Control

1 Introduction

Since ancient times, infectious diseases have always had a profound impact on people's lives. According to incomeplete statistics, at least one new infectious disease has been found globally every year on average. Due to the extremely explosive and rapid spread of infectious diseases among species, infectious diseases have become the most important deadly diseases endangering human life safety. After a painful experience, with the improvement of human cognition, scholars began to try to study infectious diseases. In 1927, Kermack and Mckendrick established the famous *SIR* model [1] when studying the Black Death, which laid the foundation for the study of mathematical models of infectious diseases. Many scholars have done related research on discrete infectious disease models. Literature [2] for the classic SI, SIR, SIS model, using *Euler* forward difference method discretization, it discusses the possible problems after its discrete; Literature [3] extended Barrera's discrete-time *SIS* model, used Micken's method to discretize *SIRS* model, and studied the effects of multiple factors (including reproduction, competition, etc.) on infectious disease dynamics. The transmission rate of infectious diseases does not always show a bilinear trend. In literature [4], Ca-passo introduced the saturation incidence rate $g(I)S$ into the epidemic model when studying cholera, which described the saturation relationship between the transformation of susceptible to infected ones: As the number of infected people increases, the susceptible people become more vigilant, leading to a change in the behavior of the susceptible people, and the infection rate will be greatly reduced. Some scholars have also introduced the vertical infection rate into the infectious disease model. In literature [5], based on the influence of environmental disturbance, a stochastic infectious disease model with both horizontal and vertical transmission was established, and the existence and uniqueness of the positive solution were proved. The *Itô* formula and the *Chebyshev* inequality were applied. The sufficient conditions for the final boundedness of random are established, and the permanence of random is proved.

To protect people's lives and property safety so that fewer people are troubled by infectious diseases, the prevention and control of infectious diseases are more important. Preview control theory was first discussed in 1966 by Sheridan T B and proposed in the context of the Three Models of Preview Control [6]. In 1994, the research on preview control in China officially began. Aiming at the design problem of an optimal preview controller for multi-rate systems based on adaptive dynamic programming, literature [7] proposes a model-free online preview controller design method for discrete-time systems based on Q learning algorithm. Literature [8] studied with disturbance *Roesser* model described by the two-dimensional DT feasibility and stability of the control system. Literature [9] studies the design of observance-based feedback preview control and static output feedback preview control for linear uncertain discrete periodic systems. In literature [10], for a class of nonlinear interconnected systems with time delay, based on the relationship between the system intercom-nection matrix and input matrix, a distributed controller that utilizes both local state vector information and interconnect item information is designed. By integrating the controller of the error system, a distributed preview tracking controller composed of state feedback, integrator and preview feed-forward is obtained. The preview controller is applied to the chemical reactor recovery system and the double-parallel inverted pendulum system. Preview control is also applied to flight control problems of two-degree-of-freedom helicopters [11], active suspension systems [12], spherical moving platforms with three-degree-of-freedom translational motion and three-degree-of-freedom infinite rotation motion and time delay problem [13], etc.

Based on the above analysis, in this paper, *SIR* model with the saturation incidence rate $\beta IS/(1+\alpha I)$ is first considered. Furthermore, considering the characteristics of mother-to-child transmission of some infectious diseases, *SIR* model with the saturation incidence rate and vertical infection rate is established. By introducing the target signal, the preview controller is designed, and sufficient

*This work is supported by the Young Scientists Fund of the National Natural Science Foundation (NNSF) of China under Grant 62103289.

conditions are given to ensure the asymptotic stability of the closed-loop system. Finally, the infected person can be controlled in a small range within a limited time to prevent the outbreak of infectious diseases and reduce the impact of infectious diseases on people's lives.

The main innovations of this paper are as follows:

(1) In the field of infectious disease research, it is usually assumed that the birth rate is greater than or equal to the death rate. However, based on our country's actual situation in 2022, the birth rate is set to be less than the death rate. Constant population input is also introduced to keep the population relatively stable. This consideration is more realistic and helps to better understand and predict the spread of infectious diseases.

(2) At present, the application of preview control is concentrated in the fields of aerospace and robotics, and the research on infectious diseases is relatively few. In the current field of infectious disease research, stability analysis and bifurcation analysis are the focus of research, and there are relatively few studies on model control. Therefore, a preview control method is proposed in this paper. By selecting appropriate target signals, the infection trend of infectious diseases in the future limited time is added to the model in advance as feedforward control. This method helps to better preview and control the spread of infectious diseases and achieve more effective suppression of infectious diseases.

The main structure of the remaining part of this paper is as follows: The second chapter is model building; The third chapter studies the correlative properties of the equilibrium point. The fourth chapter is the design of the preview controller, the fifth chapter is the numerical simulation, and the sixth chapter is the conclusion.

2 Model Description

Before establishing the model, the following assumptions are made:

(1) The infectious disease can be transmitted not only through effective contact but also through mother-to-child transmission;

(2) Λ is a constant greater than 0, indicating the constant input of the population, and the inputs are susceptible;

(3) θ is the birth rate, and the newborn individuals of susceptible individuals and recovered individuals belong to susceptible individuals and do not have short-term immunity;

(4) ω is the natural mortality rate. According to the statistical data of 2022, in this paper, it is assumed that the birth rate θ is lower than the natural mortality rate ω;

(5) δ is the vertical infection rate. The rate of δ is considered as the infected individuals, and the rate of $1-\delta$ is considered as the susceptible individuals.

(6) β was the effective exposure rate, α was the saturation rate, and $\beta S(t)/(1+\alpha I(t))$ was the saturation incidence rate.

(7) γ is the recovery rate of disease, μ is the mortality due to disease;

(8) $N(t)$ is the total population, and the initial conditions $N(0)=S(0)+I(0)+R(0)$, $S(0)\geq 0$, $I(0)\geq 0$, $R(0)\geq 0$;

(9) All the above parameters are normal.

(10) The impact of the infectious disease being studied on other diseases is not considered in the models.

Based on the above assumptions, the block diagram of the infectious disease model (Figure 1) is as follows:

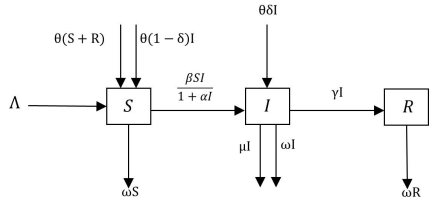

Fig.1: Block diagram of the model

According to the block diagram, the following infectious disease model can be easily obtained:

$$\begin{cases} \dfrac{dS(t)}{dt}=\Lambda+\theta N(t)-\theta\delta I(t)-\omega S(t)-\dfrac{\beta S(t)I(t)}{1+\alpha I(t)} \\ \dfrac{dI(t)}{dt}=\dfrac{\beta S(t)I(t)}{1+\alpha I(t)}+(\theta\delta-\gamma-\mu-\omega)I(t) \\ \dfrac{dR(t)}{dt}=\gamma I(t)-\omega R(t) \end{cases} \tag{1}$$

By using the Euler forward difference method, system (1) is discretized to obtain the following discretized SIR Model:

$$\begin{cases} S(k+1)=S(k)+h\left[\Lambda+\theta N(k)-\theta\delta I(k)-\omega S(k)-\dfrac{\beta S(k)I(k)}{1+\alpha I(k)}\right] \\ I(k+1)=I(k)+h\left[\dfrac{\beta S(k)I(k)}{1+\alpha I(k)}+(\theta\delta-\gamma-\mu-\omega)I(k)\right] \\ R(k+1)=R(k)+h\left[\gamma I(k)-\omega R(k)\right] \end{cases} \tag{2}$$

In the model (2), containing $N(k)$, and $N(k)=S(k)+I(k)+R(k)$, so the model (2) can be reduced to the following form:

$$\begin{cases} S(k+1)=S(k)+h[\Lambda+\theta(S(k)+I(k)+R(k))-\theta\delta I(k) \\ \qquad -\omega S(k)-\dfrac{\beta S(k)I(k)}{1+\alpha I(k)}] \\ I(k+1)=I(k)+h\left[\dfrac{\beta S(k)I(k)}{1+\alpha I(k)}+(\theta\delta-\gamma-\mu-\omega)I(k)\right] \\ R(k+1)=R(k)+h\left[\gamma I(k)-\omega R(k)\right] \end{cases} \tag{3}$$

3 Related properties of equilibrium points

Since the input of the population constant is considered in this paper, the birth rate is not equal to the death rate, and the death rate due to disease is also considered. The total population of the model must be changing, not constant. According to the biological significance, it is easy to draw model (3) to satisfy the initial conditions $S(0)\geq 0$, $I(0)\geq 0$, $R(0)\geq 0$ restricted domain Ω for solution

$$\Omega=\left\{(S(k),I(k),R(k)):S(k),I(k),R(k)\geq 0,N(k)\leq\frac{\Lambda}{\omega-\theta}\right\}$$

3.1 Existence of equilibrium point

Let model (3) have an equilibrium point $E=(S,I,R)$, which satisfies the following equations:

$$\begin{cases}\Lambda+\theta\big(S(k)+I(k)+R(k)\big)-\theta\delta I(k)-\omega S(k)-\dfrac{\beta S(k)I(k)}{1+\alpha I(k)}=0\\ \dfrac{\beta S(k)I(k)}{1+\alpha I(k)}+(\theta\delta-\gamma-\mu-\omega)I(k)=0\\ \gamma I(k)-\omega R(k)=0\end{cases} \tag{4}$$

When $I(k)=0$, we can easily get $S(k)=\dfrac{\Lambda}{\omega-\theta}$, $R(k)=0$.

Therefore, model (3) always has a unique disease-free equilibrium point $E_1=\left(\dfrac{\Lambda}{\omega-\theta},0,0\right)$.

When $I_n\neq 0$, we can easily get $S^*=\dfrac{-a_2(\alpha\Lambda+a_3)}{\alpha a_1a_2+\beta a_3}$, $I^*=\dfrac{\beta\Lambda-a_1a_2}{\alpha a_1a_2+\beta a_3}$, $R^*=\dfrac{\gamma(\beta\Lambda-a_1a_2)}{\omega(\alpha a_1a_2+\beta a_3)}$

where,

$$a_1=\theta-\omega,\ a_2=\theta\delta-\gamma-\mu-\omega,\ a_3=\gamma+\mu+\omega-\theta\left(1+\frac{\gamma}{\omega}\right)$$

Therefore, there is always a unique endemic equilibrium point for model (3) $E_2=(S^*,I^*,R^*)$.

This paper uses the method in literature [14] to solve the basic regeneration number of the model (3). Defined based on literature, the basic reproductive number is defined as Q spectral radius, namely $R_0=\rho(Q)=\rho\left(F(E-T)^{-1}\right)$.

After calculation,

$$F=h\left(\beta\frac{\Lambda}{\omega-\theta}+\theta\delta\right),\ T=1-h(\gamma+\mu+\omega)$$

Then the basic regeneration number corresponding to model (3)

$$R_0=\frac{\beta\Lambda+\theta\delta(\omega-\theta)}{(\gamma+\mu+\omega)(\omega-\theta)}$$

So we can get the following theorem.

Theorem 1

For model (3),

(1) When $R_0\le 1$, only the disease-free equilibrium point E_1 exists in the model (3),

(2) When $R_0>1$, model (3) has both disease-free equilibrium point E_1 and endemic equilibrium point E_2.

3.2 Stability of equilibrium point

In this paper, the linearization model and Jacobian matrix are used to study the local stability of model (3) at the equilibrium point by *Jury* criterion.

The model (3) is linearized to obtain the model.

$$Y(t+1)=JY(t) \tag{5}$$

where J is the Jacobian matrix of the model (3) at any equilibrium point (S, I, R).

$$J=\begin{bmatrix}1+h\left(\theta-\omega-\dfrac{\beta I(k)}{1+\alpha I(k)}\right) & h\left[\theta-\theta\delta-\dfrac{\beta S(k)}{(1+\alpha I(k))^2}\right] & h\theta\\ h\dfrac{\beta I(k)}{1+\alpha I(k)} & 1+h\left[\dfrac{\beta S(k)}{(1+\alpha I(k))^2}+(\theta\delta-\gamma-\mu-\omega)\right] & 0\\ 0 & h\gamma & 1-h\omega\end{bmatrix}$$

Firstly, the stability of the disease-free equilibrium point is discussed. The Jacobian matrix of the model (3) at the disease-free equilibrium point $E1$ is

$$J_{E_1}=\begin{bmatrix}1+h(\theta-\omega) & h\left[\theta-\theta\delta-\beta\dfrac{\Lambda}{\omega-\theta}\right] & h\theta\\ 0 & 1+h\left[\beta\dfrac{\Lambda}{\omega-\theta}+(\theta\delta-\gamma-\mu-\omega)\right] & 0\\ 0 & h\gamma & 1-h\omega\end{bmatrix}$$

The corresponding eigenvalue is $\lambda_1=1+h(\theta-\omega)$, $\lambda_2=1+h\left[\beta\dfrac{\Lambda}{\omega-\theta}+(\theta\delta-\gamma-\mu-\omega)\right]$, $\lambda_3=1-h\omega$.

There is the following conclusion:

Conclusion 1

For model (3),

(i) when $R_0<1$,

(1) When $0<h<min\left\{\dfrac{2}{\omega},\dfrac{2}{\gamma+\mu+\omega-\theta\delta-\beta\dfrac{\Lambda}{\omega-\theta}}\right\}$, E_1 is locally asymptotically stable;

(2)

When $h>max\left\{\dfrac{2}{\omega},\dfrac{2}{\gamma+\mu+\omega-\theta\delta-\beta\dfrac{\Lambda}{\omega-\theta}}\right\}$ or $\dfrac{2}{\omega}<h<\dfrac{2}{\gamma+\mu+\omega-\theta\delta-\beta\dfrac{\Lambda}{\omega-\theta}}$ or $\dfrac{2}{\gamma+\mu+\omega-\theta\delta-\beta\dfrac{\Lambda}{\omega-\theta}}<h<\dfrac{2}{\omega}$, E_1 is unstable,

(ii) when $R_0>1$ and $\lambda_2>1$, the equilibrium point E_1 is unstable.

The stability of the endemic equilibrium point is discussed below. The Jacobian matrix of the model (3) at the endemic equilibrium point E_2 is

$$J_{E_2}=\begin{bmatrix}1+h\left(\theta-\omega-\dfrac{\beta I^*}{1+\alpha I^*}\right) & h\left[\theta-\theta\delta-\dfrac{\beta S^*}{(1+\alpha I^*)^2}\right] & h\theta\\ h\dfrac{\beta I^*}{1+\alpha I^*} & 1+h\left[\dfrac{\beta S^*}{(1+\alpha I^*)^2}+(\theta\delta-\gamma-\mu-\omega)\right] & 0\\ 0 & h\gamma & 1-h\omega\end{bmatrix}$$

Denote as

$$J_{E_2}=\begin{bmatrix}j_{11} & j_{12} & j_{13}\\ j_{21} & j_{22} & 0\\ 0 & j_{32} & j_{33}\end{bmatrix}$$

Then, the corresponding characteristic equation is

$$D(\lambda)=\lambda^3+(-j_{11}-j_{22}-j_{33})\lambda^2+(j_{11}j_{22}+j_{11}j_{33}+j_{22}j_{33}+j_{21}j_{12})\lambda+(-j_{11}j_{22}j_{33}-j_{21}j_{12}j_{33}+j_{21}j_{13}j_{32})$$

Denote as

$$D(\lambda)=\lambda^3+a_1\lambda^2+a_2\lambda+a_3$$

Using the coefficients of the characteristic equation, the following table of the *Jury* array is constructed, as shown in Table 1.

Table 1: Jury array

Row	λ^0	λ^1	λ^2	λ^3
1	a_3	a_2	a_1	1
2	1	a_1	a_2	a_3
3	b_2	b_1	b_0	

where, $b_2 = a_3^2 - 1$, $b_1 = a_3 a_2 - a_1$, $b_0 = a_3 a_1 - a_2$

According to the *Jury* criterion, the following conclusion can be obtained:

Conclusion 2

For model (3), when $R_0 > 1$, the equilibrium point E_2 is stable if the following conditions are met:

(1) $D(1) > 0$, namely, $1 + a_1 + a_2 + a_3 > 0$,

(2) $(-1)^3 D(-1) > 0$, namely, $1 - a_1 + a_2 - a_3 > 0$,

(3) $|a_3| < 1$,

(4) $|b_2| > |b_0|$, namely, $|a_3^2 - 1| > |a_3 a_1 - a_2|$.

4 Preview Control

To curb the spread of infectious diseases as much as possible and reduce the number of infected persons, appropriate measures can be taken to control infectious diseases. Therefore, the control variable $u(k)$ is added to the model (3).

Let $S(k) = x_1(k)$, $I(k) = x_2(k)$ $R(k) = x_3(k)$

Rewrite model (3) into the following form

$$\begin{cases} x_1(k+1) = x_1(k) + h[\Lambda + \theta(x_1(k) + x_2(k) + x_3(k)) - \theta\delta x_2(k) \\ \qquad -\omega x_1(k) - \dfrac{\beta x_1(k) x_2(k)}{1 + \alpha x_2(k)}] + u_1(k) \\ x_2(k+1) = x_2(k) + h\left[\dfrac{\beta x_1(k) x_2(k)}{1 + \alpha x_2(k)} + (\theta\delta - \gamma - \mu - \omega) x_2(k)\right] \\ x_3(k+1) = x_3(k) + h[\gamma x_2(k) - \omega x_3(k)] \end{cases}$$

Set output equation $y(k) = Cx(k)$

Then, the system can be written

$$\begin{cases} x(k+1) = Ax(k) + Bu(k) + f(x(k)) + W \\ y(k) = Cx(k) \end{cases} \tag{6}$$

where $x(k) = [x_1(k) \quad x_2(k) \quad x_3(k)]'$

$$A = \begin{bmatrix} 1 + h\theta - h\omega & h\theta - h\theta\delta & h\theta \\ 0 & 1 + h(\theta\delta - \gamma - \mu - \omega) & 0 \\ 0 & h\gamma & 1 - h\omega \end{bmatrix},$$

$$B = \begin{bmatrix} 1 \\ 0 \\ 0 \end{bmatrix}, W = \begin{bmatrix} h\Lambda \\ 0 \\ 0 \end{bmatrix}, f(x(k)) = \begin{bmatrix} -\dfrac{h\beta x_1(k) x_2(k)}{1 + \alpha x_2(k)} \\ \dfrac{h\beta x_1(k) x_2(k)}{1 + \alpha x_2(k)} \\ 0 \end{bmatrix}, \quad C = \begin{bmatrix} 0 \\ 1 \\ 0 \end{bmatrix}'$$

Assumption 1

Set target signal for $r(k)$, and there is constant vector r, $\lim_{k \to \infty} r(k) = r$, further assume that $r(k)$ is previewable, and the preview length is M_r, namely, at the current moment k, $r(k), r(k+1), \cdots r(k + M_r)$ is known, And the target signal value is unchanged after the M_r step.

Namely, $r(k+i) = r(k + M_r), i = M_r + 1, M_r + 2, \cdots$

Remark 1 Assumption 1 is the basic assumption in preview control theory.

Define the error signal as

$$e(k) = y(k) - r(k) \tag{7}$$

The objective is to design a preview controller to achieve the steady-state, unerror-free tracking reference signal $r(k)$ of the output $y(k)$ of system (6),

Namely, $\lim_{k \to \infty} e(k) = \lim_{k \to \infty} y(k) - r(k) = 0$

4.1 Construct an augmented error system

The difference operator is defined as

$$\Delta x(k) = x(k+1) - x(k)$$

Acting on system (6)

$$\begin{cases} \Delta x(k+1) = A\Delta x(k) + B\Delta u(k) + \Delta f \\ \Delta y(k) = C\Delta x(k) \end{cases} \tag{8}$$

where $\Delta f = f(x(k+1)) - f(x(k))$

Then Δ, it is applied to the error signal

$$\Delta e(k) = e(k+1) - e(k)$$

We can get

$$e(k+1) = e(k) + \Delta e(k) = e(k) + C\Delta x(k) - \Delta r(k) \tag{9}$$

The combination of (8) and (9) is obtained

$$\tilde{x}(k+1) = \tilde{A}\tilde{x}(k) + \tilde{B}\Delta u(k) + F\Delta r(k) + M\Delta f \tag{10}$$

where

$$\tilde{x}(k) = \begin{bmatrix} e(k) \\ \Delta x(k) \end{bmatrix}, \tilde{A} = \begin{bmatrix} I & C \\ 0 & A \end{bmatrix}, F = \begin{bmatrix} -I \\ 0 \end{bmatrix}, \tilde{B} = \begin{bmatrix} 0 \\ B \end{bmatrix}, M = \begin{bmatrix} 0 \\ I \end{bmatrix}$$

To facilitate the introduction of all knowable future information of the target signal, a vector is defined

$$x_r(k) = \begin{bmatrix} \Delta r(k) \\ \Delta r(k+1) \\ \vdots \\ \Delta r(k + M_r) \end{bmatrix}$$

From assumption 1, we know

$$x_r(k+1) = A_r x_r(k) \tag{11}$$

where

$$A_r = \begin{bmatrix} 0 & I & 0 & \cdots & 0 \\ 0 & 0 & I & \cdots & 0 \\ \vdots & \vdots & \vdots & \ddots & \vdots \\ 0 & 0 & 0 & 0 & I \\ 0 & 0 & 0 & 0 & 0 \end{bmatrix}$$

Combine (10) and (11)

$$\bar{x}(k+1) = \bar{A}\bar{x}(k) + \bar{B}\Delta u(k) + \bar{M}\Delta f \tag{12}$$

where

$$\bar{x}(k) = \begin{bmatrix} \tilde{x}(k) \\ x_r(k) \end{bmatrix}, \bar{A} = \begin{bmatrix} \tilde{A} & \tilde{F} \\ 0 & A_r \end{bmatrix}, \bar{B} = \begin{bmatrix} \tilde{B} \\ 0 \end{bmatrix}, \bar{M} = \begin{bmatrix} M \\ 0 \end{bmatrix}$$

$\tilde{F} = [F \quad 0 \quad 0 \quad \cdots \quad 0]$.

Formula (12) is called an augmented error system.

Thus, the tracking control problem of the system (6) with preview is transformed into the stabilization problem of the system (12).

4.2 Preview controller design

We define $F_1 = \begin{bmatrix} 0 & I_3 & 0 \end{bmatrix}$, which follows from the above derivation

$$\Delta x(k) = F_1 \bar{x}(k) \tag{13}$$

Design a state feedback controller for the system (12)

$$\Delta u(k) = K \bar{x}(k) \tag{14}$$

where K is the matrix to be determined

Then system

$$\bar{x}(k+1) = \left(\bar{A} + \bar{B}K\right)\bar{x}(k) + \bar{M}\Delta f \tag{15}$$

The stability of system (15) is analyzed below, and the gain matrix K is solved.

Theorem 2

Assumption 1 was set up, and if there is a matrix $P > 0$, invertible matrix G_1 and matrix R, and the constant $\varphi > 0$, make $Z = P^{-1}$, making

$$\begin{bmatrix} Z - G_1 - G_1^T & 0 & G_1^T \bar{A}^T + R^T \bar{B}^T & \varphi G_1^T F_1^T \\ * & -I & \bar{M}^T & 0 \\ * & * & -Z & 0 \\ * & * & * & -I \end{bmatrix} < 0 \tag{16}$$

Then, the closed-loop system (15) is asymptotically stable, and $K = RG_1^{-1}$

Proof:

Select *Lyapunov* function $V(\bar{x}) = \bar{x}^T P \bar{x}$, $V(\bar{x})$ is positive definite, we run a difference on it, and we get

$$\begin{aligned} \Delta V(\bar{x}) &= \bar{x}^T(k+1) P \bar{x}(k+1) - \bar{x}^T(k) P \bar{x}(k) \\ &= \left[\left(\bar{A} + \bar{B}K\right)\bar{x}(k) + \bar{M}\Delta f\right]^T P \left[\left(\bar{A} + \bar{B}K\right)\bar{x}(k) + \bar{M}\Delta f\right] \\ &\quad - \bar{x}^T(k) P \bar{x}(k) \\ &= \bar{x}^T(k)\left[\left(\bar{A} + \bar{B}K\right)^T P \left(\bar{A} + \bar{B}K\right) - P\right]\bar{x}(k) \\ &\quad + 2\bar{x}^T(k)\left(\bar{A} + \bar{B}K\right)^T P \bar{M}\Delta f + \Delta f^T \bar{M}^T P \bar{M}\Delta f \end{aligned} \tag{17}$$

Because the nonlinear term $f(x(k))$ satisfies the condition *Lipschitz* within the research interval: $\exists \varphi > 0$ such that for $\forall x_a, x_b \in \Omega$, there is $\left\| f(x_a) - f(x_b) \right\| \le \varphi \left\| x_a - x_b \right\|$

Then there is always

$$\varphi^2 \Delta x^T(k) \Delta x(k) - \Delta f^T \Delta f \ge 0 \tag{18}$$

By formula (13), there is

$$\varphi^2 \bar{x}^T(k) F_1^T F_1 \bar{x}(k) - \Delta f^T \Delta f \ge 0 \tag{19}$$

So

$$\begin{aligned} \Delta V(\bar{x}) &\le \bar{x}^T(k)\left[\left(\bar{A} + \bar{B}K\right)^T P \left(\bar{A} + \bar{B}K\right) - P\right]\bar{x}(k) \\ &\quad + 2\bar{x}^T(k)\left(\bar{A} + \bar{B}K\right)^T P \bar{M}\Delta f + \Delta f^T \bar{M}^T P \bar{M}\Delta f \\ &\quad + \varphi^2 \bar{x}^T(k) F_1^T F_1 \bar{x}(k) - \Delta f^T \Delta f \\ &= \bar{x}^T(k)\left[\left(\bar{A} + \bar{B}K\right)^T P \left(\bar{A} + \bar{B}K\right) - P + \varphi^2 F_1^T F_1\right]\bar{x}(k) \\ &\quad + 2\bar{x}^T(k)\left(\bar{A} + \bar{B}K\right)^T P \bar{M}\Delta f + \Delta f^T (\bar{M}^T P \bar{M} - I)\Delta f \\ &= \begin{bmatrix} \bar{x}^T(k) & \Delta f^T \end{bmatrix} \Psi \begin{bmatrix} \bar{x}(k) \\ \Delta f \end{bmatrix} \end{aligned}$$

where

$$\Psi = \begin{bmatrix} \left(\bar{A} + \bar{B}K\right)^T P \left(\bar{A} + \bar{B}K\right) - P + \varphi^2 F_1^T F_1 & \left(\bar{A} + \bar{B}K\right)^T P \bar{M} \\ * & \bar{M}^T P \bar{M} - I \end{bmatrix}$$

Therefore, as if $\Psi < 0$, and $\Delta V < 0$, according to the *Lyapunov* stability theory, the system (15) is asymptotically stability.

If formula (16) in theorem 2 holds, and further obtain

$$\begin{bmatrix} -G_1^T Z^{-1} G_1 & 0 & G_1^T \bar{A}^T + R^T \bar{B}^T & \varphi G_1^T F_1^T \\ * & -I & \bar{M}^T & 0 \\ * & * & -Z & 0 \\ * & * & * & -I \end{bmatrix} < 0 \tag{20}$$

To contract transformation type (20), left by invertible matrix $Block - diag\left(G_1^{-T}, I, I, I\right)$, right by the transpose, make $R = KG_1$, and get it

$$\begin{bmatrix} -Z^{-1} & 0 & \bar{A}^T + K^T \bar{B}^T & \varphi F_1^T \\ * & -I & \bar{M}^T & 0 \\ * & * & -Z & 0 \\ * & * & * & -I \end{bmatrix} < 0 \tag{21}$$

By $Block - diag(-Z, -I) < 0$, combining *Schur* theorem, and obtain

$$\begin{bmatrix} -Z^{-1} & 0 \\ 0 & -I \end{bmatrix} - \begin{bmatrix} \left(\bar{A} + \bar{B}K\right)^T & \varphi F_1^T \\ \bar{M}^T & 0 \end{bmatrix} \begin{bmatrix} -Z & 0 \\ 0 & -I \end{bmatrix}^{-1} \begin{bmatrix} \left(\bar{A} + \bar{B}K\right) & \bar{M} \\ \varphi F_1 & 0 \end{bmatrix} < 0$$

If $Z^{-1} = P$, there is

$$\begin{bmatrix} \left(\bar{A} + \bar{B}K\right)^T P \left(\bar{A} + \bar{B}K\right) - P + \varphi^2 F_1^T F_1 & \left(\bar{A} + \bar{B}K\right)^T P \bar{M} \\ * & \bar{M}^T P \bar{M} - I \end{bmatrix} < 0$$

Namely, $\Psi < 0$

Theorem 2 has been proved.

So, the preview controller of the system is

$$u(k) = K_e \sum_{i=0}^{k} e(i) + K_x x(k) + \sum_{i=0}^{M_r} k_r(i) r(k+i)$$

Under this control law, the output $y(k)$ of the closed-loop system of the system (6) can realize the steady-error-free tracking of the target signal $r(k)$.

Remark 2 In theorem proving, the derivation process of the (20), with the help of inequality $-L^T G^{-1} L \le -L - L^T + G$, among them, the L, G as a matrix with the proper dimension and $G > 0$.

5 Numerical Simulation

This paper takes hepatitis B infectious disease as the research object. According to the data of the National Bureau of Statistics in 2022, it is determined that the birth rate $\theta = 0.00677$ and the death rate $\omega = 0.00737$ .According

to the relevant values of hepatitis B, the parameters are described as follows: $\gamma = 0.0005$, $\beta = 0.3$, $\delta = 0.2$, $\alpha = 0.8$, $A = 0.00045$, $\mu = 0.0000002$, $h = 1$

The initial values of the three populations are $S(0) = 0.9$, $I(0) = 0.1$, $R(0) = 0$

The basic regeneration number of the model (3) can be solved $R_0 = 0.4857 < 1$, in which the model has only a disease-free equilibrium point, and the disease-free equilibrium point has been verified to be stable.

Without any control, the development trend of the disease is shown in Figure 2, which shows that there are large-scale outbreak points of the disease.

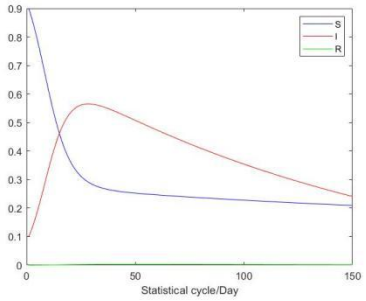

Fig.2: the development trend of SIR without control

Select the target signal as

$$r(k) = \begin{cases} 0.09 + 0.01k & k < 7 \\ 0.15 \times 0.95^{k-6} & else \end{cases}$$

After calculation, *Lipschitz* constant is 0.3, take $M_r = 5$, the result is as follows:

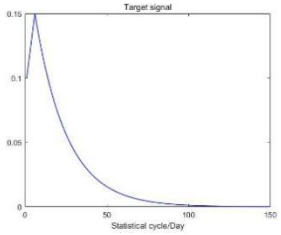

Fig.3: target signal

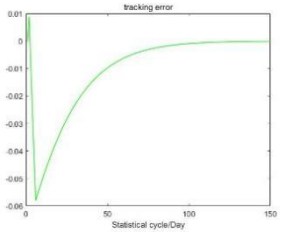

Fig.4: tracking error

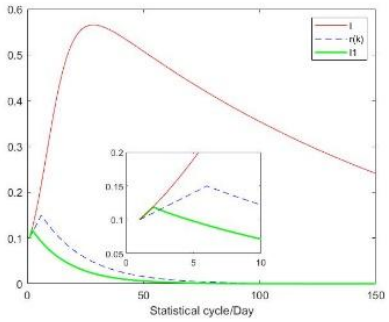

Fig.5: the comparison of 'I' before and after control

Figure 3 is the target signal, Figure 4 is the tracking error, and Figure 5 is the comparison of the target signal and the proportion of infected persons before and after control. As can be seen from the simulation images, after the addition of preview control, the time from the beginning to the outbreak of infectious diseases is greatly shortened, the outbreak degree is very small, and finally, it decayed to zero in a very short time, which is very effective in controlling the spread and outbreak of infectious diseases.

6 Conclusions

In this paper, a *SIR* model with saturation incidence rate and vertical infection rate is established, and the existence and stability of its equilibrium point are analyzed. A state feedback preview controller for nonlinear discrete systems satisfying *Lipschitz* is designed for the model. Through the controller, the future development trend of infectious diseases can be used as the target signal to act on the model in advance so that the outbreak proportion of infectious diseases can be greatly reduced until the extinction of infectious diseases to achieve the control of infectious diseases.

References

[1] W. O. Kermack, A. G. Mckendrick, A contribution to the mathematical theory of epidemics. *Mathematical Theory of Epidemics*, 1927, 115A: 700-721.

[2] L. J. S. Allen, Some discrete-time SI, SIR, and SIS epidemic models. *Mathematical biosciences*, 1994, 124(1): 83-105.

[3] C. C. Castillo, A. A. Yakubu, Discrete-time SIS models with complex dynamics. *Nonlinear Analysis: Theory, Methods & Applications*, 2001, 47(7): 4753-4762.

[4] V. Capasso, G. Serio, A generalization of the Kermack-McKendrick deterministic epidemic model. *Mathematical Biosciences*, 1978,42(1-2), 43–61.

[5] X. Y. Wang, C. Y. Huang, Y. X. Hao, Q. H. Shi, A stochastic mathematical model of two different infectious epidemic under vertical transmission. *Mathematical Biosciences and Engineering*, 2022, 19(3): 2179-2192.

[6] T. B. Sheridan, Three models of preview control. *IEEE Transactions on Human Factors in Electronics*, 1966 (2): 91-102.

[7] D. Wang, J. Y. Ye, S. X. Gao, Optimal preview controller design for multirate systems based on adaptive dynamic programming, in *Proceedings of 40th Chinese Control Conference*, 2021:1608-1613.

[8] A. K. Ravat, A. Dhawan, M. Tiwari, S. K. Jha, Feasibility and stability of preview control for 2-D discrete-time systems described by the Roesser model. *International Journal of Advanced Technology and Engineering Exploration*,2023, 10(107):1293-1315.

[9] L. Li, Y. F. Zhang, Y. L. Liao, Preview control for uncertain discrete-time periodic systems. *International Journal of Robust and Nonlinear Control*, 2021, 31(18): 9501-9518.

[10] H. Xie, F. C. Liao, J. Wu, Design of distributed preview tracking controller for nonlinear interconnected systems with time-delay. *International Journal of Robust and Nonlinear Control*,2023:1-24.

[11] Q. Z. Xu, Y. H. Zhang, Event-triggered nonlinear information fusion preview control of a two-degree-of-freedom helicopter system. *Aerospace Science and Technology*, 2023, 140: 108474.

[12] G. H. Luo, D. Görges, Optimal preview control with uncertain preview information with application to active suspension systems, in *Proceedings of IEEE Conference on Control Technology and Applications*, 2021: 277-282.

[13] S. M. Lee, H. Son, Prediction-based preview control of motion platform with time delay. *IEEE Transactions on Intelligent Transportation Systems*, 2022, 23(12): 23346-23357.

[14] L. J. S. Allen, P. V. D. Driessche, The basic reproduction number in some discrete-time epidemic models. *Journal of difference equations and applications*, 2008, 14(10-11): 1127-1147.

Proceedings of the 3rd Conference on Fully Actuated System Theory and Applications
May 10-12, 2024, Shenzhen, China

Exponential Stability and Asynchronous Stabilization of Impulsive Switched Systems with Admissible Edge-dependent Average Dwell Time

Mengjie Li, Menghao Qu, Lijun Gao*
School of Automation, Qufu Normal University, Rizhao, 276826, P. R. China
E-mail: 1452429847@qq.com, 549142709@qq.com, gljwg1977@163.com

Abstract: This paper studies the exponential stability and asynchronous stabilization problems for continuous-time impulsive switched systems with the method of admissible edge-dependent average dwell time. Here, the asynchronous behavior implies that the switches between the subsystems and controllers are asynchronous. Firstly, the sufficient conditions for the closed-loop impulsive switched system to be exponentially stable are investigated. Then, on the basis of the stability results, a new type of state-feedback controllers are designed. Furthermore, the asynchronous behavior is considered for the closed-loop system and a novel set of admissible edge-dependent controllers are designed. It is shown that the exponential stability and asynchronous stabilization of the closed-loop impulsive switched system can be achieved under the proposed control protocols. And the results are formulated in the form of feasible LMIs and the superiority of admissible edge-dependent average dwell time over traditional dwell time approach is further analyzed. Moreover, the results can be extended to study the asynchronous stabilization of switched systems. Finally, some illustrative examples are given to demonstrate the effectiveness of the results.

Key Words: Admissible edge-dependent average dwell time, Asynchronous stabilization, Exponential stability, Impulsive switched system

1 Introduction

Switched systems, an important class of hybrid systems, are composed of continuous or discrete subsystems and the switching rules between them. In practice, switched systems are susceptible to external environment at switching instants, which inevitably leads to impulsive behaviors. Thus, sometimes using switched systems to model practical systems may cause large deviations. On the basis of switched systems, combined with impulsive systems, impulsive switched systems appear. Impulsive switched systems have higher theoretical (see [1–3]) and practical (see [4]) value because they are more in line with actual systems.

When analyzing stability problems of switched or impulsive switched systems, a phenomenon that cannot be ignored is asynchronous behavior. When the system switches from one subsystem to another, the controller corresponding to the current subsystem cannot switch immediately. In other words, the current subsystem is controlled by the controller of the previous subsystem for some time, which may cause unsatisfactory results and even instability. Therefore, it is necessary to consider asynchronous behavior when analyzing the stabilization of switched or impulsive switched systems. The asynchronous stabilization (see [5, 6]) and control (see [7, 8]) problem has attracted much attention in recent years. In [8], the authors studied the asynchronous switching control for discrete-time linear systems via MDADT.

Based on the method of multiple Lyapunov function, a less restrictive MDADT method was proposed in [9], of which the parameters are mode-dependent and the minimum of MDADTs is less that of ADTs. The proposition of this concept has promoted the development of stability (see [2, 3, 10–12]) and control (see [7, 8]) of switched systems. And it should be pointed out that the method used in some existing results to investigate the asynchronous behavior is MDADT [3, 8]. Note that switched system may switch from one subsystem to another, which forms different admissible transition edges. But the MDADT parameters are mode-dependent, which means that the MDADT parameters depend on all the edges ending in the same vertex, and this will cause an increase in conservatism. In [13], the concept of AED-ADT was propsed. It was proved that the parameters are edge-dependent and the method still matters even if the dwell time is smaller than the minimum of MDADTs. And MDADT switching is a special case of AED-ADT switching. Therefore, the AED-ADT method is more general and applicable. This method has received extensive attention and has been widely applied in stability and control of switched systems in recent years. For example, in [14], based on AED-ADT, the authors designed a new type of multiple piecewise convex Lyapunov function and established time-varying H_∞ state feedback controllers to guarantee the exponential stability of the switched system.

Here, a question arises: can we improve stabilization conditions for impulsive switched systems by using the AED-ADT method? In this paper, we investigate the exponential stability and asynchronous stabilization problems of impulsive switched systems with AED-ADT method. The main contributions of this paper lie in: i) Based on the method of AED-ADT, less conservative stability conditions for the proposed closed-loop impulsive switched systems to achieve exponential stability are established and a novel type of admissible edge-dependent control protocol is designed; ii) The asynchronous behavior is considered for the impulsive switched system and analyzed with the method of AED-ADT. And a new type of control protocol is obtained to guarantee the asynchronous stabilization of the impulsive switched system; iii) Comparing the parameters and results under AED-ADT with that under MDADT, the superiority of AED-ADT method over MDADT is further discussed. It

* Corresponding author.

is shown that under the proposed admissible edge-dependent control protocols, the closed-loop system can realize exponential stability as well as asynchronous stabilization and AED-ADT method is more general than MDADT. Two illustrative examples are given to demonstrate the effectiveness of the proposed control laws.

The remainder of this paper is orgnized as follows. In section 2, some system models, necessary definitions, assumptions and lemmas are given. The exponential stability and asynchronous stabilization of impulsive switched systems are investigated by the method of AED-ADT and solved by designing state-feedback controllers in section 3. In section 4, some illustrative examples are given. Finally, summaries and conclusions are given in section 5.

Notations: In this paper, the notations used are fairly standard. N and N^+ represent the set of the natural numbers and the set of positive integers, respectively. R^n and $R^{n\times m}$ are the n-dimensional Euclidean space and a set of all $(n\times m)$-dimensional matrices, respectively. The notations $\lambda_{max}(P)$ and $\lambda_{min}(P)$ represnt the maximum and minimum eigenvalues of matrix P. The notation $P>0$ $(\geq 0, <0, \leq 0)$ is used to represent a real positive definite symmetric matrix (positive semi-definite symmetric matrix, negative definite symmetric matrix, negative semi-definite symmetric matrix) P. And $||\ ||$ refers to the Euclidean vector norm. The notation I denotes the identity matrix. The notation Φ represents the empty set.

2 Preliminaries and problem formulation

Consider the following class of impulsive switched systems

$$\begin{cases}\dot{x}(t)=A_{\sigma(t_i)}x(t)+B_{\sigma(t_i)}u(t), t\in(t_i,t_{i+1}], i\in N\\ \Delta x(t)=D_{\sigma(t_i)}x(t)+f(t,x(t)), t=t_i, i\in N^+,\\ x(t_0^+)=x_0,\end{cases} \tag{1}$$

where $t\in R^+$, $x(t)\in R^n$ stands for the system state, $u(t)\in R^m$ is the control input. $\sigma(t)$: $R^+\to\phi$ is a piecewise constant function of time, which is defined as the switching signal and takes its value in a finite set $\phi=\{1,...,M\}$, where M is the number of subsystems. For a switching sequence $0\leq t_0<t_1<\cdots<t_i<t_{i+1}<\cdots(i\in N)$, the subsystem $\sigma(t_i)\in\phi$ is activated over the time interval $(t_i,t_{i+1}]$, where t_i is the ith switching time instant and t_0 stands for the initial time. $f(t,x(t))$ is the nonlinear function and satisfies $f(t,0)\equiv 0$, $\forall t\in[t_0,\infty)$. $A_{\sigma(t_i)}\in R^{n\times n}$, $B_{\sigma(t_i)}\in R^{n\times m}$, $D_{\sigma(t_i)}\in R^{n\times n}$ are assumed to be known. $\Delta x(t_i)=x(t_i^+)-x(t_i^-)=x(t_i^+)-x(t_i)$, where $x(t_i^+)=\lim_{h\to 0^+}x(t_i+h)$ and $x(t_i^-)=\lim_{h\to 0^-}x(t_i+h)=x(t_i)$.

We define the unmatched controllers as

$$\hat{u}(t)=K_{\sigma(t_{i-1})}x(t), \tag{2}$$

where $K_{\sigma(t_{i-1})}\in R^{m\times n}$ is a constant matrix. Hence, we can get the following system

$$\begin{cases}\dot{x}(t)=\left(A_{\sigma(t_i)}+B_{\sigma(t_i)}K_{\sigma(t_{i-1})}\right)x(t), & t\in\left(t_i,\bar{t}_i\right],\\ \dot{x}(t)=\left(A_{\sigma(t_i)}+B_{\sigma(t_i)}K_{\sigma(t_i)}\right)x(t), & t\in\left(\bar{t}_i,t_{i+1}\right],\\ \Delta x(t)=D_{\sigma(t_i)}x(t)+f(t,x(t)), & t=t_i,\\ x(t_0^+)=x_0,\end{cases} \tag{3}$$

where $i\geq 1$, and $\bar{t}_i$ $\left(t_i<\bar{t}_i\leq t_{i+1}\right)$ is the instant when the matched controller begin to manipulate. And noting that there are neither impulsive nor asynchronous effects at the initial instant t_0. Therefore, we obtain that if $i=0$, the system is

$$\dot{x}(t)=\left(A_{\sigma(t_0)}+B_{\sigma(t_0)}K_{\sigma(t_0)}\right)x(t), t\in[t_0,t_1]. \tag{4}$$

To simplify the expression, now we define the following notations

$$\hat{A}_{pq}=A_q+B_qK_p,\quad \overline{A}_q=A_q+B_qK_q,$$

$$Q_q=(I+D_q)^T P_q(I+D_q)+\theta(I+D_q)^T P_qP_q(I+D_q)+\left(\frac{\eta}{\theta}+\eta\lambda_{max}(P_q)\right)I,$$

where $p,q\in\phi$ $(p\neq q)$. And the notation pq implies the distinct combinations of subsystem q and unmatched controller p $(p\neq q)$.

To obtain our results, the following assumption and concepts are given to present the conclusions.

Assumption 1 $\forall t\in[t_0,\infty)$, the nonlinear function satisfies the following inequality

$$||f(t,x(t))||\leq\eta||x(t)||,$$

where η is a positive constant.

Definition 1 ([13]) $\forall(p,q)\in\phi\times\phi$, $\epsilon(p,q)\in A$ and a switching signal $\sigma(t)$, let $N_{p,q}(t,T)$ denote the switching numbers from p to q over the time interval $(t,T]$, and $T_{p,q}(t,T)$ represent the total running time of subsystem q over the time interval $(t,T]$ whenever the switching from p to q occurs, where $T\geq t\geq 0$. We say that $\sigma(t)$ has an $Admissible\ Edge-dependent\ Average\ Dwell\ Time$ $(AED-ADT)$ $\tau_{p,q}$ if there exist positive numbers $N_{p,q}^0$ and $\tau_{p,q}$ such that

$$N_{p,q}(t,T)\leq N_{p,q}^0+\frac{T_{p,q}(t,T)}{\tau_{p,q}},\forall T\geq t\geq 0,$$

where $N_{p,q}^0$ are referred to as the admissible edge-dependent chatter bounds.

Then, the following lemmas are also given to obtain the results.

Lemma 1 ([15]) Let M, F and E with compatible dimensions be given matrices. And F satisfies $F^TF\leq I$. Then

$$MFE+E^TF^TM^T\leq\theta MM^T+\theta^{-1}E^TE$$

for any $\theta>0$.

3 Main results

In this section, we study asynchronous stabilization of impulsive switched systems and design proper control laws to guarantee the stability.

We are to study the asynchronous stabilization of impulsive switched system (3) and (4).

Theorem 1 $\forall (p,q) \in \phi \times \phi \ (p \neq q)$, consider the closed-loop impulsive switched system (3) and (4), let $\alpha_q > 0, \beta_{pq}, \eta > 0, \theta > 0$ be given constants. If there exist symmetric positive-definite matrices $P_q \in R^{n\times n}$, such that

$$\hat{A}_{pq}^{T} P_q + P_q \hat{A}_{pq} + \beta_{pq} P_q \leq 0, \ \forall (p,q) \in \phi\times\phi, \ p \neq q, \quad (5)$$

$$\overline{A}_q^{T} P_q + P_q \overline{A}_q + \alpha_q P_q \leq 0, \quad \forall q \in \phi, \quad (6)$$

then the system is exponentially stable for any switching signal satisfying

$$\begin{cases} \tau_{p,q} \geq \tau_{p,q}^{*} = \dfrac{ln\overline{\mu}_{p,q}}{\alpha_q}, & \beta_{pq} > \alpha_q \\ \tau_{p,q} \geq \tau_{p,q}^{*} = \dfrac{ln\overline{\mu}_{p,q} + (\alpha_q - \beta_{pq}) T_{pqM}}{\alpha_q}, & \beta_{pq} \leq \alpha_q \end{cases} \quad (7)$$

where $T_{pqM} \triangleq max_n \{T_{p,q\uparrow}(t_n, t_{n+1})\}, \forall n \in N^{+}, \overline{\mu}_{p,q} = max\left\{\lambda_{max}\left(P_p^{-1} Q_q\right), 1\right\}, \forall (p,q) \in \phi \times \phi \ (p \neq q)$.

Proof: To make the expression simple, now define edge sets $\phi_1 \times \phi_1$ and $\phi_2 \times \phi_2$, which satisfies $\phi_1 \times \phi_1 \subset \phi \times \phi$, $\phi_2 \times \phi_2 \subset \phi \times \phi$, $(\phi_1 \times \phi_1) \cup (\phi_2 \times \phi_2) = \phi \times \phi$, $(\phi_1 \times \phi_1) \cap (\phi_2 \times \phi_2) = \Phi$. $\forall (p,q) \in \phi \times \phi \ (p \neq q)$, if the unmatched controller $K_p x(t)$ can make the current subsystem q stable, that is, $\beta_{pq} > 0$, then $(p,q) \in \phi_1 \times \phi_1 \ (p \neq q)$; otherwise, $(p,q) \in \phi_2 \times \phi_2 \ (p \neq q)$.

Suppose $t_0 = 0$. $\forall T > 0$, let $t_1, t_2, \cdots, t_i, t_{i+1}, \cdots, t_{N_{p,q}(0,T)}$ denote the switching instants from subsystem p to subsystem q during $[0,T]$, where $N_{p,q}(0,T)$ is the switching number from subsystem p to subsystem q during $[0,T]$.

$\forall (p,q) \in \phi \times \phi \ (p \neq q)$, suppose $T_{p,q\uparrow}(0,T)$ represent the total running time length of subsystem q manipulated by the unmatched controller $K_p x(t)$ during the time interval $[0,T]$ and $T_{p,q\downarrow}(0,T)$ the total running time length of subsystem q manipulated by the matched controller $K_q x(t)$. It is evident that we have

$$T_{p,q}(0,T) = T_{p,q\uparrow}(0,T) + T_{p,q\downarrow}(0,T), \quad (8)$$

where $T_{p,q}(0,t)$ represents the total running time length of subsystem q whenever the switching from subsystem p to subsystem q occurs during $[0,T]$. Because $T_{pqM} = max_n \{T_{p,q\uparrow}(t_n, t_{n+1})\}$, $\forall n \in N^{+}$, according to the inequalities in Definition 1, we have

$$T_{p,q\uparrow}(0,T) \leq T_{pqM}\left(N_{p,q}^{0} + \frac{T_{p,q}(0,T)}{\tau_{p,q}}\right). \quad (9)$$

Next, we are to begin our proof. $\forall \sigma(t) = q \in \phi$, define the Lyapunov-like function as $V_q(x(t)) = x^{T}(t) P_q x(t), P_q > 0$. Now, consider system (3), for $t \in \left(t_i, \bar{t}_i\right], i \in N^{+}$, according to (5), we have

$$\dot{V}_q(x(t)) \leq -\beta_{pq} x^{T}(t) P_q x(t) = -\beta_{pq} V_q(x(t)). \quad (10)$$

For system (4), we have $T_{p,q\uparrow}(t_0, t_1) = 0$. Then, consider system (3) and (4), for $t \in \left(\bar{t}_i, t_{i+1}\right], i \in N$, according to (6), we obtain

$$\dot{V}_q(x(t)) \leq -\alpha_q x^{T}(t) P_q x(t) = -\alpha_q V_q(x(t)). \quad (11)$$

Then, according to Assumption1 and Lemma 1, we obtain

$$V_q\left(x\left(t_i^{+}\right)\right) \leq x^{T}(t_i) Q_q x(t_i). \quad (12)$$

Let $\overline{\mu}_{p,q} = max\left\{\lambda_{max}\left(P_p^{-1} Q_q\right), 1\right\}, \forall (p,q) \in \phi \times \phi \ (p \neq q)$, then according to (12), we obtain

$$V_q\left(x\left(t_i^{+}\right)\right) \leq \overline{\mu}_{p,q} V_p(x(t_i)). \quad (13)$$

Therefore, by (10), (11) and (13), $\forall t \in (t_i, t_{i+1}]$, we obtain

$$\begin{aligned} V_{\sigma(t_i)}(x(t)) \leq \prod_{n=1}^{i} \overline{\mu}_{\sigma(t_{n-1}),\sigma(t_n)} exp\{ & -\alpha_{\sigma(t_i)} T_{p,q\downarrow}(t_i, t) \\ & -\beta_{\sigma(t_{i-1}),\sigma(t_i)} T_{p,q\uparrow}(t_i, t) - \sum_{n=1}^{i} \alpha_{\sigma(t_{n-1})} T_{p,q\downarrow}(t_{n-1}, t_n) \\ & - \sum_{n=2}^{i} \beta_{\sigma(t_{n-2}),\sigma(t_{n-1})} T_{p,q\uparrow}(t_{n-1}, t_n) \Bigg\} V_{\sigma(t_0)}(x(t_0)), \end{aligned} \quad (14)$$

Further, we have

$$\begin{aligned} V_{\sigma(t_i)}(x(t)) \leq V_{\sigma(t_0)}(x(t_0))\, e^{\sum_{q\in\phi}\sum_{p\in\phi,p\neq q}} \\ * e^{\left[N_{p,q}(0,t) ln\overline{\mu}_{p,q} - \alpha_q T_{p,q\downarrow}(0,t) - \beta_{pq} T_{p,q\uparrow}(0,t)\right]}, \end{aligned} \quad (15)$$

and together with the inequalities, we have

$$V_{\sigma(t_i)}(x(t)) \leq E_1 E_2 V_{\sigma(t_0)}(x(t_0)), \quad (16)$$

where

$$\begin{aligned} E_1 = exp\Bigg\{ \sum_{q\in\phi_1} \sum_{p\in\phi_1, p\neq q} \Bigg[\left(N_{p,q}^{0} + \frac{T_{p,q}(0,t)}{\tau_{p,q}}\right) ln\overline{\mu}_{p,q} \\ - \alpha_q T_{p,q\downarrow}(0,t) - \beta_{pq} T_{p,q\uparrow}(0,t) \Bigg] \Bigg\}, \end{aligned}$$

$$\begin{aligned} E_2 = exp\Bigg\{ \sum_{q\in\phi_2} \sum_{p\in\phi_2, p\neq q} \Bigg[\left(N_{p,q}^{0} + \frac{T_{p,q}(0,t)}{\tau_{p,q}}\right) ln\overline{\mu}_{p,q} \\ - \alpha_q T_{p,q\downarrow}(0,t) - \beta_{pq} T_{p,q\uparrow}(0,t) \Bigg] \Bigg\}. \end{aligned}$$

For E_1, we introduce the following concepts

$$\begin{aligned} E_{11} = exp\Bigg\{ \sum_{q\in\phi_{11}} \sum_{p\in\phi_{11}, p\neq q} \Bigg[\left(N_{p,q}^{0} + \frac{T_{p,q}(0,t)}{\tau_{p,q}}\right) ln\overline{\mu}_{p,q} \\ - \alpha_q T_{p,q\downarrow}(0,t) - \beta_{pq} T_{p,q\uparrow}(0,t) \Bigg] \Bigg\}, \end{aligned}$$

where $0 < \beta_{pq} \leq \alpha_q$, $(p,q) \in \phi_{11} \times \phi_{11}\,(p \neq q)$;

$$E_{12} = exp\left\{ \sum_{q\in\phi_{12}} \sum_{p\in\phi_{12},p\neq q} \left[\left(N_{p,q}^0 + \frac{T_{p,q}(0,t)}{\tau_{p,q}} \right) ln\overline{\mu}_{p,q} \right.\right. \\ \left.\left. -\alpha_q T_{p,q\downarrow}(0,t) - \beta_{pq} T_{p,q\uparrow}(0,t) \right] \right\},$$

where $\alpha_q < \beta_{pq}$, $(p,q) \in \phi_{12} \times \phi_{12}\,(p \neq q)$. Noting that $\phi_{11} \times \phi_{11} \subset \phi_1 \times \phi_1$, $\phi_{12} \times \phi_{12} \subset \phi_1 \times \phi_1$, $(\phi_{11} \times \phi_{11}) \cup (\phi_{12} \times \phi_{12}) = \phi_1 \times \phi_1$, $(\phi_{11} \times \phi_{11}) \cap (\phi_{12} \times \phi_{12}) = \Phi$. As for E_{11}, by (9), we have

$$E_{11} \leq exp\left\{ \sum_{q\in\phi_{11}} \sum_{p\in\phi_{11},p\neq q} \left[\left(N_{p,q}^0 + \frac{T_{p,q}(0,t)}{\tau_{p,q}} \right) ln\overline{\mu}_{p,q} \right.\right. \\ -\alpha_q T_{p,q}(0,t) \\ \left.\left. + (\alpha_q - \beta_{pq}) T_{pqM} \left(N_{p,q}^0 + \frac{T_{p,q}(0,T)}{\tau_{p,q}} \right) \right] \right\}. \quad (17)$$

Let

$$\hat{E}_{11} = e^{\sum_{q\in\phi_{11}} \sum_{p\in\phi_{11},p\neq q} \left[N_{p,q}^0 \left(ln\overline{\mu}_{p,q} + (\alpha_q - \beta_{pq}) T_{pqM} \right) \right]} \\ \cdot e^{\sum_{q\in\phi_{11}} \sum_{p\in\phi_{11},p\neq q} \left[T_{p,q}(0,t) \left(\frac{ln\overline{\mu}_{p,q} + (\alpha_q - \beta_{pq}) T_{pqM}}{\tau_{p,q}} - \alpha_q \right) \right]},$$

we obtain

$$E_{11} \leq \hat{E}_{11}. \quad (18)$$

As for E_{12}, we have

$$E_{12} \leq exp\left\{ \sum_{q\in\phi_{12}} \sum_{p\in\phi_{12},p\neq q} \left[\left(N_{p,q}^0 + \frac{T_{p,q}(0,t)}{\tau_{p,q}} \right) ln\overline{\mu}_{p,q} \right.\right. \\ \left.\left. -\alpha_q \left(T_{p,q\downarrow}(0,t) + T_{p,q\uparrow}(0,t) \right) \right] \right\}. \quad (19)$$

Let

$$\hat{E}_{12} = e^{\sum_{q\in\phi_{12}} \sum_{p\in\phi_{12},p\neq q} N_{p,q}^0 ln\overline{\mu}_{p,q}} \\ \times e^{\sum_{q\in\phi_{12}} \sum_{p\in\phi_{12},p\neq q} T_{p,q}(0,t) \left(\frac{ln\overline{\mu}_{p,q}}{\tau_{p,q}} - \alpha_q \right)},$$

we obtain

$$E_{12} \leq \hat{E}_{12}. \quad (20)$$

Then, according to (18) and (20), we obtain

$$E_1 = E_{11}E_{12} \leq \hat{E}_{11}\hat{E}_{12}. \quad (21)$$

For E_2, similar to the calculation of (17) and (18), and let

$$\hat{E}_2 = e^{\sum_{q\in\phi_2} \sum_{p\in\phi_2,p\neq q} \left[N_{p,q}^0 \left(ln\overline{\mu}_{p,q} + (\alpha_q - \beta_{pq}) T_{pqM} \right) \right]} \\ \cdot e^{\sum_{q\in\phi_2} \sum_{p\in\phi_2,p\neq q} \left[T_{p,q}(0,t) \left(\frac{ln\overline{\mu}_{p,q} + (\alpha_q - \beta_{pq}) T_{pqM}}{\tau_{p,q}} - \alpha_q \right) \right]},$$

we obtain

$$E_2 \leq \hat{E}_2. \quad (22)$$

Let

$$\Gamma_1 = exp\left\{ \sum_{q\in\phi_{12}} \sum_{p\in\phi_{12},p\neq q} N_{p,q}^0 ln\overline{\mu}_{p,q} \right. \\ + \sum_{q\in\phi_{11}} \sum_{p\in\phi_{11},p\neq q} \left[N_{p,q}^0 \left(ln\overline{\mu}_{p,q} + (\alpha_q - \beta_{pq}) T_{pqM} \right) \right] \\ \left. + \sum_{q\in\phi_2} \sum_{p\in\phi_2,p\neq q} \left[N_{p,q}^0 \left(ln\overline{\mu}_{p,q} + (\alpha_q - \beta_{pq}) T_{pqM} \right) \right] \right\}, \quad (23)$$

$$-\gamma_1 = \max\left\{ \max_{(p,q)\in\phi_{12}\times\phi_{12},p\neq q} \left\{ \frac{ln\overline{\mu}_{p,q}}{\tau_{p,q}} - \alpha_q \right\}, \right. \\ \max_{(p,q)\in\phi_{11}\times\phi_{11},p\neq q} \left\{ \frac{ln\overline{\mu}_{p,q} + (\alpha_q - \beta_{pq}) T_{pqM}}{\tau_{p,q}} - \alpha_q \right\}, \\ \left. \max_{(p,q)\in\phi_2\times\phi_2,p\neq q} \left\{ \frac{ln\overline{\mu}_{p,q} + (\alpha_q - \beta_{pq}) T_{pqM}}{\tau_{p,q}} - \alpha_q \right\} \right\}. \quad (24)$$

Fially, we have

$$V_{\sigma(t_i)}(x(t)) \leq \Gamma_1 e^{-\sum_{q\in\phi} \sum_{p\in\phi,p\neq q} \gamma_1 T_{p,q}(0,t)} V_{\sigma(t_0)}(x(t_0)). \quad (25)$$

Then let $\gamma(t) = \frac{\gamma_1}{2} T_{p,q}(0,t)$ and

$$\Gamma = \Gamma_1^{1/2} \left[\min_{j\in\phi} (\lambda_{min}(P_j)) \right]^{-(1/2)} \left[\max_{j\in\phi} (\lambda_{max}(P_j)) \right]^{1/2},$$

one has

$$||x(t)|| \leq \Gamma e^{-\sum_{q\in\phi} \sum_{p\in\phi,p\neq q} \gamma(t)} ||x(t_0)||, \quad (26)$$

since $T_{p,q}(0,t)$ is increasing with respect to time t, together with the condition (7), $\gamma(t)$ is a increasing function. From (26), it is easy to obtain that $||x(t)|| \to 0\,(t \to \infty)$. Thus, we can conclude that the closed-loop system is exponentially stable. This completes the proof. □

Now, we are to design a state-feedback controller on the basis of Theorem 1 for system (3) and (4).

Theorem 2 $\forall (p,q) \in \phi \times \phi\ (p \neq q)$, consider the closed-loop impulsive switched system (3) and (4), let $\alpha_q > 0, \beta_{pq}, \eta > 0, \theta > 0$ be given constants. If there exist matrices $X \in R^{n\times n}$, $L_q \in R^{m\times n}$ and symmetric positive-definite matrices $\hat{P}_q \in R^{n\times n}$, $q \in \phi$, such that $\forall (p,q) \in \phi \times \phi, p \neq q$, (30) and (31) hold. Let $P_q = X^{-T}\hat{P}_q X^{-1}$, then the system is exponentially stable for any switching signal satisfying (7) and the controller gain matrices are $K_q = L_q X^{-1}, q \in \phi$.

Proof: $\forall (p,q) \in \phi \times \phi\ (p \neq q)$, we introduce a slack matrix H and consider the following inequalities

$$\begin{bmatrix} \hat{A}_{pq}^T H + H^T \hat{A}_{pq} + \beta_{pq} P_q & P_q - H^T + \hat{A}_{pq}^T H \\ P_q - H + H^T \hat{A}_{pq} & -H - H^T \end{bmatrix} \leq 0, \quad (27)$$

$$\begin{bmatrix} \overline{A}_q^T H + H^T \overline{A}_q + \alpha_q P_q & P_q - H^T + \overline{A}_q^T H \\ P_q - H + H^T \overline{A}_q & -H - H^T \end{bmatrix} \leq 0. \quad (28)$$

Multiplying the matrix inequality (27) on the left and right by $\hat{\Lambda}_{pq} = \begin{bmatrix} I & \hat{A}_{pq}^T \end{bmatrix}$ and its transpose, respectively, we can conclude that (5) holds. Similarly, for (28), the corresponding transformation matrix is $\overline{\Lambda}_q = \begin{bmatrix} I & \overline{A}_q^T \end{bmatrix}$, and we can obtain that (6) holds. That is to say, if (27) and (28) hold, then conditions (5) and (6) hold. Noting that if (27) and (28) hold,

$$\begin{bmatrix} A_qX + X^TA_q^T + B_qL_p + L_p^TB_q^T + \beta_{pq}\hat{P}_q & \hat{P}_q - X + X^TA_q^T + L_p^TB_q^T \\ \hat{P}_q - X^T + A_qX + B_qL_p & -X - X^T \end{bmatrix} \leq 0, \tag{30}$$

$$\begin{bmatrix} A_qX + X^TA_q^T + B_qL_q + L_q^TB_q^T + \alpha_q\hat{P}_q & \hat{P}_q - X + X^TA_q^T + L_q^TB_q^T \\ \hat{P}_q - X^T + A_qX + B_qL_q & -X - X^T \end{bmatrix} \leq 0, \tag{31}$$

$$\begin{bmatrix} H^{-T}\hat{A}_{pq}^T + \hat{A}_{pq}H^{-1} + \beta_{pq}H^{-T}P_qH^{-1} & H^{-T}P_qH^{-1} - H^{-1} + H^{-T}\hat{A}_{pq}^T \\ H^{-T}P_qH^{-1} - H^{-T} + \hat{A}_{pq}H^{-1} & -H^{-1} - H^{-T} \end{bmatrix} \leq 0 \tag{32}$$

$$\begin{bmatrix} H^{-T}\overline{A}_q^T + \overline{A}_qH^{-1} + \alpha_qH^{-T}P_qH^{-1} & H^{-T}P_qH^{-1} - H^{-1} + H^{-T}\overline{A}_q^T \\ H^{-T}P_qH^{-1} - H^{-T} + \overline{A}_qH^{-1} & -H^{-1} - H^{-T} \end{bmatrix} \leq 0 \tag{33}$$

then H is non-singular. Then, we introduce the following matrices

$$X = H^{-1}, \quad L_q = K_qX, \quad \hat{P}_q = X^TP_qX. \tag{29}$$

Multiplying (27) on the left and right by the diagonal matrix $diag\left(H^{-T}, H^{-T}\right)$ and its transpose, respectively, we have (32). Similarly, for (28), we obtain (33). Then, according to (29), we obtain that (30) and (31) hold. Therefore, according to Theorem 1, we conclude that for any switching signal satisfying (7), the system is exponentially stable and the controller gain matrices are $K_q = L_qX^{-1}$, $q \in \phi$, where $P_q = X^{-T}\hat{P}_qX^{-1}$. This completes the proof. □

4 Illustrative examples

In this section, one illusrative examples is given to demonstrate the correctness of the results above.

Example 1 The working process of ideal Buck converter, as shown in Fig. 1, can be modeled as a impulsive switched system, of which the subsystems are divided according to different operation stages of the converter. Due to the different switching states of the switch S and the diode D, impulsive jumps in $u_l(t)$ and $i_c(t)$ occur. In the next analysis, $u_l(t)$ and $i_c(t)$ are set as system state variables. For the sake of

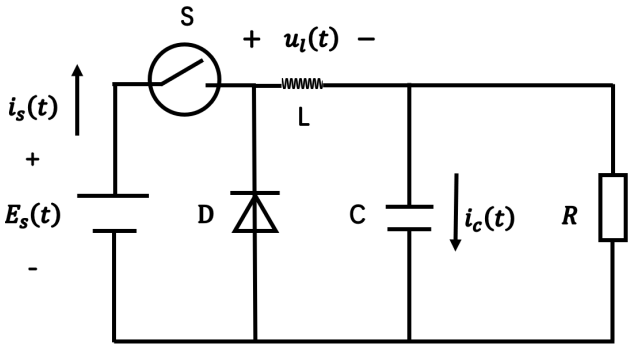

Fig. 1: The schematic of Buck converter

generality, the Buck converter system can be written in the form of system (1).

Now, consider the closed-loop impulsive switched system composed of 3 subsystems, i.e., $\phi = \{1, 2, 3\}$. And the following matrices and parameters are given

$$A_1 = \begin{bmatrix} 0.25 & 0.01 \\ 0 & -0.12 \end{bmatrix}, A_2 = \begin{bmatrix} -0.16 & -0.01 \\ 0 & -0.23 \end{bmatrix},$$

$$A_3 = \begin{bmatrix} -0.15 & 0.01 \\ 0 & -0.14 \end{bmatrix}, B_1 = \begin{bmatrix} 0.16 & 0.01 \\ 0 & 0.22 \end{bmatrix},$$

$$B_2 = \begin{bmatrix} 0.2 & -0.01 \\ 0 & -0.3 \end{bmatrix}, B_3 = \begin{bmatrix} 0.33 & 0.01 \\ 0 & 0.12 \end{bmatrix},$$

$$D_1 = D_2 = D_3 = \begin{bmatrix} 0.3 & 0 \\ 0 & 0.3 \end{bmatrix},$$

$$f_1 = f_2 = f_3 = \begin{bmatrix} 0.01sin\,(x_1) \\ 0.01sin\,(x_2) \end{bmatrix}$$

$$\eta = 0.01, \theta = 0.01.$$

In order to compare the results under the two switching signals mentioned above, we list other parameters and results in Table 1. Noting that for $p, q \in \{1, 2, 3\}$, the calculation of τ_q^* is dependent on the maximum of $\overline{\lambda}_q$ and $\tau_{p,q}^*$ based on the maximum of λ_q, i.e., $\overline{\lambda}_1 = 0.8$, $\overline{\lambda}_2 = 1.2$ and $\overline{\lambda}_3 = 1.1$, $\lambda_1 = 3.5$, $\lambda_2 = 6.3$ and $\lambda_3 = 4.6$.

Table 1: Results comparison between MDADT switching and AED-ADT switching for impulsive switched system

Switching schemes	MDADT	AED-ADT
Criteria		Theorem in this paper
Parameters	$\overline{\lambda}_1 \leq 0.8$, $\overline{\lambda}_2 \leq 1.2$, $\overline{\lambda}_3 \leq 1.1$	$\lambda_1 \leq 3.5$, $\lambda_2 \leq 6.3$, $\lambda_3 \leq 4.6$
Switching signals	$\tau_1^* = 1.3273$, $\tau_2^* = 0.8849$, $\tau_3^* = 0.9653$	$\tau_{2,1}^* = 0.4324$, $\tau_{1,2}^* = 0.2402$, $\tau_{3,1}^* = 0.4324$, $\tau_{3,2}^* = 0.2402$, $\tau_{1,3}^* = 0.3290$, $\tau_{2,3}^* = 0.3290$
Controller gains	$\begin{bmatrix} -26.56 & 1.09 \\ -0.03 & -17.64 \end{bmatrix}$, $\begin{bmatrix} -21.70 & 0.70 \\ -0.04 & 14.23 \end{bmatrix}$, $\begin{bmatrix} -14.70 & 1.19 \\ 0.02 & -40.50 \end{bmatrix}$	$\begin{bmatrix} -26.56 & 1.11 \\ -0.05 & -17.64 \end{bmatrix}$, $\begin{bmatrix} -21.70 & 0.71 \\ -0.03 & 14.23 \end{bmatrix}$, $\begin{bmatrix} -14.70 & 1.19 \\ 0.01 & -40.50 \end{bmatrix}$

Now, assume that both the MDADT and AED-ADT switching signals are periodical and given as follows

$$S = \overbrace{1 \to 3 \to 2}^{\text{1th period}} \to \overbrace{1 \to 3 \to 2}^{\text{2th period}} \to \cdots, \tag{34}$$

where $p \to q$ represents the admissible transition edge $\epsilon\,(p, q)$ from subsystem p to subsystem q. And we choose $\tau_1 = 1.33 > \tau_1^*$, $\tau_3 = 0.97 > \tau_3^*$ and $\tau_2 = 0.89 > \tau_2^*$,

$\tau_{2,1} = 0.44 > \tau^*_{2,1}$, $\tau_{1,3} = 0.33 > \tau^*_{1,3}$ and $\tau_{3,2} = 0.25 > \tau^*_{3,2}$. In the simulation, we choose the initial system state as $x(0) = \begin{bmatrix} -1 & 1 \end{bmatrix}^T$. The state responses of the closed-loop impulsive switched system under MDADT and AED-ADT switching are shown in Fig. 2 and Fig. 3, repectively. In the case of MDADT switching, if the dwell time is smaller than the minimum value of MDADT, we cannot guarantee the stability of the closed-loop system. In spite of dwell time being smaller than minimum MDADTs, the results under AED-ADT switching can still achieve stability. Therefore, we can see that the method of AED-ADT is more general than MDADT.

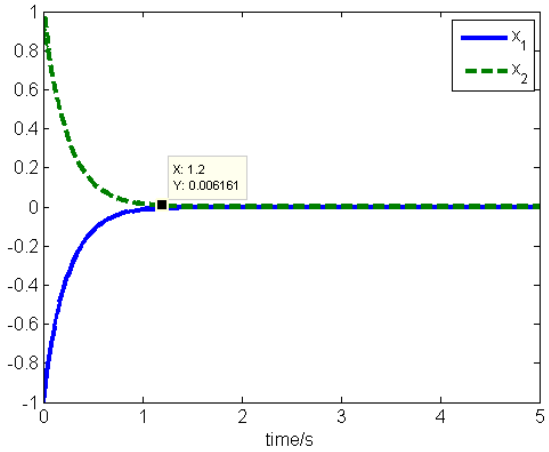

(a) State response of system under MDADT switching signal

Fig. 2: Results under MDADT switching of Example 1

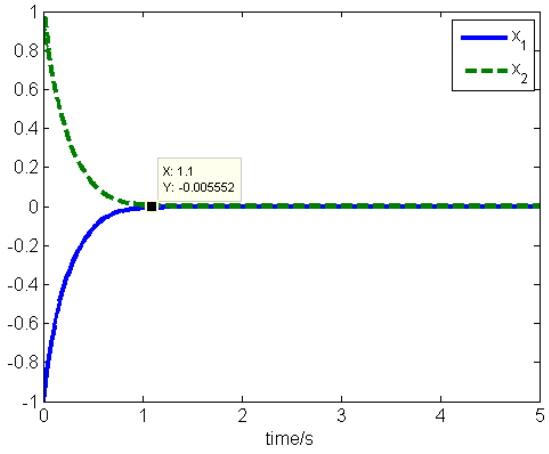

(a) State response of system under AED-ADT switching signal

Fig. 3: Results under AED-ADT switching of Example 1

5 Conclusions

In this paper, we investigate asynchronous stabilization of impulsive switched systems with the method of AED-ADT. Considering the asynchronous behavior of the impulsive switched system, a new control protocol is proposed. Furthermore, our results can be applied to investigate the asynchronous stabilization of switched systems. Finally, one numerical example is given and the superiority of the AED-ADT method is further discussed.

References

[1] Z. C. Wang, J. Sun, J. Chen, Input-to-state stability of impulsive switched nonlinear time-delay systems with two asynchronous switching phenomena. *International Journal of Robust and Nonlinear Control*, 2020.

[2] L. J. Gao, F. M. Luo, Z. G. Yan, Finite-time annular domain stability of impulsive switched systems: mode-dependent parameter approach. *International Journal of Control*, 2017, 92(6): 1381–1392.

[3] C. Y. Dang, G. Wang, D. H. Xie, H. B. Zhang, B. Wang, Asynchronous stabilisation of impulsive switched systems. *Iet Control Theory & Applications*, 2013, 7(16): 2021–2027.

[4] S. P. Wen, Z.G. Zeng, T.W. Huang, C.J. Li, Passivity and passification of stochastic impulsive memristor-based piecewise linear system with mixed delays. *International Journal of Robust & Nonlinear Control*, 2013, 25(4): 610–624.

[5] W. Ren, J. L. Xiong, Stability and stabilization of switched stochastic systems under asynchronous switching. *Systems & Control Letters*, 2016, 97: 184–192.

[6] H. L. Ren, G. D. Zong, H. R. Karimi, Asynchronous finite-time filtering of Markov jump nonlinear systems and its applications. *IEEE Transactions on Systems Man & Cybernetics Systems*, 2019, 1–10.

[7] B. Wang, H. B. Zhang, G. Wang, C. Y. Dang, S. J. Zhong, Asynchronous control of discrete-time impulsive switched systems with mode-dependent average dwell time. *Isa Transactions*, 2014, 53(2): 367–372.

[8] J. Huang, X. Hao, X. Pan, Asynchronous switching control of discrete-time linear system based on mode-dependent average dwell time. *International Journal of Control, Automation and Systems*, 2020.

[9] X. D. Zhao, L. X. Zhang, P. Shi, M. Liu, Stability and stabilization of switched linear systems with mode-dependent average dwell time. *IEEE Transactions on Automatic Control*, 2012, 57(7): 1809–1815.

[10] H. T. Zhu, P. Li, X. D. Li, H. D. Akca, Input-to-state stability for impulsive switched systems with incommensurate impulsive switching signals. *Communications in Nonlinear Science & Numerical Simulation*, 2019, 80: 104969.

[11] W. Ren, J. L. Xiong, Vector-lyapunov-function-based input-to-state stability of stochastic impulsive switched time-delay Ssystems. *IEEE Transactions on Automatic Control*, 2019, 64(2): 654–669.

[12] H. B. Zhang, D. H. Xie, H. Y. Zhang, G. Wang, Stability analysis for discrete-time switched systems with unstable subsystems by a mode-dependent average dwell time approach. *Isa Transactions*, 2014, 53(4): 1081–1086.

[13] J. Q. Yang, X. D.Zhao, X. H. Bu, W. Qian, Stabilization of switched linear systems via admissible edge-dependent switching signals. *Nonlinear Analysis Hybrid Systems*, 2018, 29: 100–109.

[14] R. H. Wang, B. X. Xue, J. B. Zhao, Time-varying H_∞ control for discrete-time switched systems with admissible edge-dependent average dwell time. *International Journal of Control, Automation and Systems*, 2019, 7: 1921–1934.

[15] G. J. Shi, Y. Zou, C. W. Yang, An algebraic approach to robust H_∞ control via state feedback. *Systems & Control Letters*, 1992, 18(5): 365–370.

Proceedings of the 3rd Conference on Fully Actuated System Theory and Applications
May 10-12, 2024, Shenzhen, China

A Brief Survey on Complex Networks Synchronization Control with Limited Bandwidth

Jing Guo[1], Ling Huang[2]

1. School of Measurement and Communication, Harbin University of Science and Technology, Harbin, Heilongjiang 150080, China
E-mail: 2014719768@qq.com

2. School of Automation, Harbin University of Science and Technology, Harbin, Heilongjiang 150080, China
E-mail: mail_huangling@163.com

Abstract: The rapid development of computer technology has promoted the research of complex network synchronization in network environments, which involves practical fields such as the Internet of Things, transportation networks, social networks, and biological systems. In this paper, the latest research and trends in limited bandwidth complex network synchronization control are surveyed. The following aspects are discussed regarding control methods for complex network synchronization and limited communication bandwidth: Firstly, by analyzing current research on complex network control, the methods of discontinuous control and finite-time control are discussed. Secondly, from the perspective of effectively utilizing communication bandwidth resources, synchronization control methods for complex networks with limited bandwidth are described. On the one hand, the studies on event-triggered synchronization control for complex networks are reviewed to reduce the volume of data transmissions. On the other hand, research on synchronization control in complex networks using quantification-based coding-decoding methods is explored to reduce the volume of transmitted data. In addition, considering the current security issues facing networks and systems, the ongoing research on secure synchronization control of complex networks under cyber-attacks is described. Lastly, some future directions for investigating the synchronization of complex networks with limited bandwidth are suggested.

Key Words: Complex networks, synchronization control, quantization, event-triggered mechanism, network attacks

1 Introduction

With the proposal of small-world networks[1] and scale-free networks[2], the small-world and scale-free nature of complex networks were revealed. Since then, the study of complex networks has gradually spread across various disciplinary fields, such as sociology[3], computer science[4], biology[5], engineering[6],etc. Scholars have begun to explore the structure, dynamics, and evolution of complex networks and apply them to simulate and analyze a wide range of real-world issues. In the study of complex network dynamics, synchronization has received extensive attention as a characteristic behavior of complex network clusters. Synchronization refers to the evolution of nodes or subsystems in a network that converge or become similar in time, even if they operate under different dynamical laws. In 1975, [7] presented the Kuramoto model, a mathematical representation of a network containing phase-coupled oscillating elements. The model investigated the phenomenon of phase synchronization, which refers to the complete consistency of phase among nodes, in oscillating elements within the network. As a result, an increasing number of academics have started to focus on researching synchronization control in complex networks. For different synchronization phenomena of complex networks, phase synchronization, lag synchronization, complete synchronization, and cluster synchronization have been proposed. In addition, external force synchronization and topological relation correction synchronization are the two main types of synchronization methods currently in use. Given that topological relationships are difficult to alter or prohibitively expensive, this work focuses on investigating synchronization through external force control.

An increasing number of industrial systems have transitioned from traditional point-to-point connections to wireless communication networks due to advancements in computer hardware and software. These systems are not limited by physical space, allowing for greater scalability and flexibility. The main problem limiting system performance in the study of complex networks synchronization control based on communication networks is the limited communication bandwidth [8]. Since the amount of data transmitted at a time is limited, quantization control is used to reduce the amount of data transmitted simultaneously[9]. The main idea of quantization control methods is to develop an appropriate encoding-decoding mechanism that guarantees the convergence or boundedness of the error between the system state and the decoded state. In the last few years, encoding-decoding communication schemes have attracted some attention[10, 11]. Furthermore, some researchers concentrated on meeting the bit rate requirement for system stability, viewing the bit rate as a capacity that characterizes the communication bandwidth [12]. However, such approaches are difficult to extend to nonlinear systems, and thus there have been several studies discussing how the system achieves the desired control performance when there is a bit rate constraint on the system bandwidth[13]. On the other hand, the event-triggered mechanism has gained popularity in recent research because it is different from the conventional time-triggered method in that data is only transmitted when the triggering condition is met. This reduces the number of data transmissions and preserves bandwidth [14].

Although communication networks facilitate system deployment, the introduction of communication networks

*This work supported by National Natural Science Funds for Young Scholar of China under Grants 61304046.

breaks the closure of traditional systems, making them vulnerable to malicious network attacks, while the diversity of nodes and topologies in complex networks increases the network's attack surface[11]. Therefore, to ensure the reliable operation of complex networks systems in a network environment, it is necessary to study the security of complex networks synchronization control. For communication networks, the current common attacks are mainly categorized into denial-of-service attacks[11], false data injection attacks[15], deception attacks[16], etc. By considering the effect of attacks on the system to establish an attack model, academics use switching system theory, stochastic system theory, and other methods to design resilient controllers that ensure the synchronization performance of complex networks. Moreover, an attacker may cause the network topology and nodes to fail due to the topological features of complex networks. For this reason, some studies simultaneously considered altering the network topology and the effects of attacks on control signal transmission, providing a proactive defense against network attacks [17].

2 Synchronization Control Methods of Complex Networks

Consider a class of complex networks with N nodes as follows:

$$\dot{x}_i(t) = Ax_i(t) + f(x_i(t)) + c\sum_{j=1}^{N} w_{ij}\Gamma x_j(t) + u_i(t), i = 1,2,\cdots,N \tag{1}$$

where $x_i(t) \in R^n$ denotes the state vector of node i, $u_i(t) \in R^n$ denotes the control input vector of node i, A is a real matrix, $f(*)$ denotes a nonlinear function of the dynamics behavior of the node i, $c \geq 0$ denotes the coupling strength of the node i, $W = (w_{ij})_{N\times N}$ is the external coupling matrix of the complex networks, which denotes the topology of the networks, and the elements of W satisfy the following conditions: if there exists an edge between the nodes, then $w_{ij} = w_{ji} > 0$, otherwise $w_{ij} = w_{ji} = 0$, and W satisfies the dissipative coupling $w_{ii} = -\sum_{j=1, j\neq i}^{N} w_{ij}$, $i, j = 1,2,\cdots,N$, and $\Gamma = diag\{\gamma_1, \gamma_2, \cdots, \gamma_n\}$ is an internal coupling matrix.

The synchronization target of the complex networks (1) can be expressed as $\dot{s}(t) = As(t) + f(s(t))$, where $s(t)$ is an isolated node without external forces and $s(t) = [s_1^{\mathrm{T}}(t), s_2^{\mathrm{T}}(t), \cdots, s_n^{\mathrm{T}}(t)]^{\mathrm{T}}$, $f(s(t)) = [f_1^{\mathrm{T}}(s(t)), f_2^{\mathrm{T}}(s(t)) \cdots, f_n^{\mathrm{T}}(s(t))]^{\mathrm{T}}$. Let $\xi_i(t) = x_i(t) - s(t)$ be the synchronization error and $i = 1,2,\cdots,N$. From (1) and $s(t)$, the synchronization error dynamics of the node i can be written as:

$$\dot{\xi}_i(t) = A_i\xi_i(t) + f(\xi_i(t)) + c\sum_{j=1}^{N} w_{ij}\Gamma\xi_j(t) + u_i(t), i = 1,2,\cdots,N \tag{2}$$

where $f(\xi_i(t)) = f(x_i(t)) - f(s_i(t))$.

A typical complex networks synchronization error system is described in (2). Actually, the stabilization problem of the synchronization error system (2) is equal to the synchronization issue of the complex networks (1). By designing control methods, current approaches aim to stabilize the error system (2) of complex networks or achieve the desired performance. After that, the complex networks system (1) is synchronized with the target $s(t)$. As a result, the following part concentrates on the stabilization control for the synchronization error system under various conditions.

2.1 Time Delay and Variable Coupling

In the real world, nodes in complex networks transmit data at different speeds between them. Therefore, the effect of time delay needs to be taken into account when studying synchronization control of complex networks [18-20]. In [18], a system of synchronization errors in distributed switching-coupled time-delayed complex networks is considered. Then, a sufficient condition for stabilizing the synchronization error system is given, based on the Lyapunov stability theory and the average dwell time method. [19] researches a complex networks synchronization error system with external perturbations and coupled time-varying delays. Then, a lower conservative stabilization condition is obtained by developing the Lyapunov-Krasovskii (L-K) functions associated with the time delay. Unlike the above studies on continuous complex networks, [20] considers a discrete complex networks synchronization error system. To obtain sufficient conditions for stabilizing the system with time delay, the authors of the aforementioned study on time delay synchronization control primarily construct L-K functions with time delay and introduce the scaling technique of integral inequality to deal with the time delay term in the derivative of L-K functions.

In complex networks, the dynamic characteristics of nodes and the coupling relationships between nodes determine the actual properties of complex networks. However, the coupling relationship of nodes may be affected by a variety of factors. Changes in the external environment in which the network is located will not only bring disturbances to the node system but also affect or even destroy the coupling relationships between nodes. In addition, the dynamic behaviors of nodes may lead to changes in the strength of connections with other nodes, and the coupling relationship between nodes may change over time [18, 20]. As a result, the study of complex network synchronization pays closer attention to coupling structures in various scenarios. [21] considers a discrete complex networks synchronization error system with random topological coupling. The stochastic topological relationship is described by a Hidden Markov Model. Meanwhile, considering the unavailability of the system state, the authors design an observer-based synchronization controller and propose a sufficient condition for H_∞ synchronization.

In contrast to the previously discussed linear coupling relations for complex networks, [22] examines a synchronization problem that includes nonlinear coupling relations. It introduces adaptive coupling strength to enhance the synchronization of complex networks. By imposing upper constraints on the nonlinear coupling relations, a sufficient condition for the exponential synchronization of complex networks can be achieved. Synchronization control

of nonlinearly coupled complex networks with asymmetry is achieved by designing Lyapunov-related events combined with aperiodic intermittent control in [23]. Considering that the coupling relationship between nodes of complex networks may involve multiple weights, [24] studies the synchronization control of directed complex networks with multiple asymmetric coupling matrices. In order to deal with multiple coupling matrices, a sufficient condition for the synchronization of the system is obtained by finding the common vector of multiple coupling matrices used to design the Lyapunov function. Aiming at the problem of synchronization of discrete multi-powered complex networks, [25] achieves the synchronization of complex networks by designing aperiodic intermittent controllers.
Furthermore, [26] considers a multilayer complex networks output synchronization error by taking into account that complex networks may have connections at multiple scales.
Compared complex networks in [18-21] with [26], it can be seen that multilayer networks contain more information about nodes and their coupling relationships. However, this also brings new challenges for analyzing the synchronization control of multilayer networks. For example, in [18-21], the coupling relationship between nodes can be simplified by the Kronecker product. However, multilayer networks are challenging to represent by the Kronecker product due to the complexity of the coupling relationships. It is difficult to directly extend the synchronization method for single-layer complex networks to multilayer complex networks.

2.2 Discontinuous Control Methods

From the above studies, it can be seen that the control methods used so far include state feedback control [19], intermittent control [23, 25], sampling control [18], and event-triggered control [20, 22, 23]. Among them, intermittent control, event-triggered control, and impulse control are commonly used in the synchronization control of discrete complex networks due to the discontinuity of the control signals. However, in continuous complex networks, the state update and information exchange of nodes may be influenced by various time scales due to the complex interactions and coupling between nodes. States of nodes can change abruptly in a short period, and communication between nodes may contain redundancy, making it challenging to maintain the continuity of the state. Therefore, some scholars have started studying discontinuous control for the synchronization issue in continuous complex networks. For complex networks with switching coupling, [27] considers the switching-induced impulse effect to establish the synchronization error system and the pinning controller is designed for the synchronization error system.
Different from the control method in [19], only the first s nodes are controlled in [27], which reduces the control cost and complexity. Also considering the problem of synchronization of complex networks with impulse effects, [28] proposes a synchronization control method with finite-time convergence and discusses the impact of various impulse effects on synchronization. In addition, impulse control is often utilized to address complex network synchronization problems with time delay [29, 30]. In [29], the delay partitioning technique is adopted to describe the delay of the system in different operation stages. The system is modeled as a switching system, and impulse control is introduced to deal with the rapid jump problem of the switching system. [30] studies the global μ-synchronization of complex networks with time delay and uncertainty. The study also proposes a variable impulse synchronization controller considering sampling delay. In [31], a new aperiodic intermittent pinning control method is proposed by considering the synchronization control of complex networks in two scenarios: node heterogeneity or node homogeneity. In addition, the above control methods do not act independently, [32] researches the exponential synchronization problem of stochastic multilayer complex networks and designs a aperiodic intermittent controller based on impulse feedback. Due to the occurrence of the change phenomenon in the continuous system described above, the special continuous system is transformed into a general discontinuous system in the literature mentioned. This transformation is achieved by modeling the jump signal using switching systems, stochastic systems, and other methods, which allows for the application of the discontinuous system method.

2.3 Finite-Time Control Methods

Although discontinuous control methods transform continuous systems into discrete systems, the synchronization methods discussed above primarily focus on Lyapunov asymptotic stability. It implies that synchronization is achieved over an infinite period of time. This overlooks the transient performance of the system on one hand and makes it difficult to achieve fast synchronization of nodes on the other. With the concept of finite time being proposed, more and more scholars pay attention to the study of finite-time synchronization of complex networks. In the above literature, the [18, 20] study finite-time synchronization control methods respectively, such finite-time synchronization focuses on the transient process of the system, and its method is mainly by defining of finite-time synchronization, and from the initial state is bounded, the final state can be introduced to be bounded, which essentially belongs to the finite-time bound.

On the other hand, in practical engineering problems with high real-time requirements, achieving fast synchronization in finite time is very important. In [28] in which the general finite-time stabilization theorem is difficult to apply to the system because of the presence of impulse effects, the authors have defined the finite-time stabilization of the system under disturbances by treating the impulse phenomenon as a system disturbance and providing a definition of finite-time stabilization of the system under disturbances. The Lipschitz condition, which has limitations in describing actual complex networks, is the basis for all of the considered nonlinearities in the complex networks mentioned above. [33] investigates a finite-time synchronization control for complex networks with strongly nonlinear impulses. Nevertheless, the finite-time synchronization approaches in [28, 33] provide an upper bound on the settling time that depends on the initial state. [26] investigates the fixed-time synchronization control for multilayer complex networks based on the fixed-time control method proposed in [34], where the upper bound on the settling time given is not affected by the initial state.

In particular, [35] investigates a special kind of fixed-time synchronization control known as preassigned time synchronization for complex networks. This method ensures that the estimation of the settling time is independent of any initial conditions and system parameters. On this basis, [36] studies the fixed-time/preassigned-time synchronization control for amnesic neural networks. There is a crucial distinction between the above finite-time synchronization, which is a synchronization error system finite-time convergence, and the finite-time boundedness. These control methods mainly require developing a unique type of controller in order to satisfy the conditions of finite-time synchronization of the system.

3 Communication and Efficiency

In [20-22, 26, 27], the connections between nodes in complex networks have transitioned from the traditional fixed method to a communication network connection. This change facilitates system expansion and resource sharing. However, the bandwidth resources of communication networks are limited, and network-induced problems will inevitably occur when multiple nodes share the bandwidth. Therefore, designing a synchronization control method that can ensure the stable operation of the system and conserve bandwidth resources to effectively transmit data has become a key issue for scholars. For the synchronization control of complex networks, the discontinuous control methods discussed in the above study offer ways to save control resources. However, this paper mainly focuses on strategies to conserve system bandwidth resources in communication networks while ensuring the stable operation of the system.

3.1 Event-Triggered Mechanism

As early as the 1950s, a control strategy was proposed that triggers a sampling or transmission action only when the change in the signal of interest exceeds a certain threshold value (static or dynamic) [37]. Subsequently, this control method, which satisfies specific event triggering, has gradually attracted attention. The principle of this mechanism is that the sampling or transmission action is triggered only when the change of the signal of interest exceeds a certain threshold value (static or dynamic). In [22], an event-triggered synchronization control in continuous complex networks is studied, and the following triggering condition is designed as $t_{k+1}^i = \inf\{\|e_i(t)\| - \alpha_i \|\xi_i(t)\| \le 0\}$ by using the triggering error $e_i(t) = \xi_i(t_k^i) - \xi_i(t)$ and the current state $\xi_i(t)$, where $t_k^i, k = 0,1,\ldots,+\infty$ represents triggering time, and $\alpha_i \in (0,1)$ is the triggering threshold. The minimum triggering interval is proven to be strictly positive, thus avoiding Zeno behavior. However, the event-triggered condition in [22] ignores the dynamic changes in the system state and only considers the current state and triggering time. This approach could lead to the system being triggered either too frequently or too infrequently. To further reduce the number of triggers, [38] proposes a dynamic event-triggered strategy by introducing dynamic parameters to a static event-triggered strategy. On this basis, [21] studies observer-based synchronization control of discrete complex networks and designs a dynamic event-triggered mechanism as $t_{k+1}^i = \min\{k \in N \,|\, k > t_k^i, \Theta(e_i(k), \hat{\xi}_i(k), \Omega_i) \ge 0\}$ where $\Theta(e_i(k), \hat{\xi}_i(k), \Omega_i) = e_i^{\mathrm{T}}(k) e_i(k) - \hat{\xi}_i^{\mathrm{T}}(k) \Omega_i \hat{\xi}_i(k) - \alpha_i \eta_i(k)$ is the triggering condition to be designed, $\hat{\xi}_i(k)$ is the error between the observer state and the synchronization target, and $e_i(k) = \hat{\xi}_i(k) - \hat{\xi}_i(t_k^i)$. $\eta_i(k)$ is a dynamic parameter, where $\eta_i(0) = \eta_0^i$. Obviously, it can be seen that due to $\eta_i(k)$, $e_i^{\mathrm{T}}(k) e_i(k) - \hat{\xi}_i^{\mathrm{T}}(k) \Omega_i \hat{\xi}_i(k)$ is not necessarily non-negative, while the triggering condition in [22] needs to be kept $\|e_i(t)\| - \alpha_i \|\xi_i(t)\| > 0$ all the time. [26] considers a dynamic event-triggered synchronization control in a multilayer discrete complex network. To avoid unnecessary waste of resources caused by continuous sampling, the study considers two synchronization goals under the dynamic event-triggered scheme. The purposes aim to prevent the threshold function from becoming too small and triggering a high frequency. In [27], the study focuses on dynamic event-triggered synchronization control of complex networks with impulse effect. It is worth noting that in [20, 21, 26, 31], Zeno behavior is usually not discussed in discrete systems because the system only performs state updates and triggers at discrete times. In addition, the deployment of communication networks in real systems is two-sided, from sensors to controllers and from controllers to actuators. The above literature only considers a one-sided network from sensors to controllers.

3.2 Quantization and Encoding-Decoding Mechanism

On the other hand, quantization methods have been incorporated into the synchronization control of complex networks because of the limited bandwidth word length constraints in [9, 10, 39-41]. [39] investigates the adaptive synchronization control based on logarithmic quantization with output-coupled fractional-order neural networks by designing a logarithmic quantizer. [40] researches synchronization control for periodic switching complex networks under dynamic quantization, and designs a dynamic quantization scheme to manage the transmitted control signals.

However, in quantization, data needs to be converted to binary by encoding in order to adapt to digital communication. Therefore, [10] studies the synchronization control of discrete complex networks based on uniformly quantized encoding-decoding. In addition, considering the bit rate as an essential measure of network bandwidth, [41] studies the cluster synchronization problem for complex networks with bit-rate constraints to discuss the optimal performance conditions of the system under a finite bit rate. Considering the advantages of quantization and event triggering in saving resources, [42] researches the adaptive event- triggered synchronization control for complex networks based on quantization.

4 Network Attacks and System Security

Preventing malevolent network attacks is a significant practical issue in networks. Attacks that disrupt network synchronization and stability, such as deception attacks, data tampering, and denial-of-service attacks, can impair system

performance or lead to system failure. In [43], the method of synchronization control of complex network security clusters under denial-of-service attacks is considered. Under the assumption that the attack energy is limited, the system is modeled as a switching system. An adaptive control strategy based on local information is designed to ensure the stabilization of the system under denial-of-service attacks. [16] considers the scenario where the system may be vulnerable to deception attacks in a multi-weighted complex networks synchronization. The study outlines potential deception attacks on the system using random variables following the Bernoulli distribution. It proposes a controller that addresses both disturbances and attacks, and provides adequate conditions to guarantee the asymptotic stability for the system. This is achieved through the Lyapunov stability theory and robust analysis methods. In addition, [11] studies the encoding-decoding synchronization control strategy for complex networks under denial-of-service attacks. The attack is modeled by the average dwell time. The impact of the attack on the encoding-decoding mechanism is analyzed, and a sufficient condition is provided for the synchronization error system to be input-to-state stable. In addition, the study of multi-link attacks in complex networks has attracted the attention of several scholars [44-45].

5 Conclusion and Future Directions

This paper has outlined the synchronization control methods of complex networks with limited bandwidth in recent years, and mainly has focused on the synchronization control methods of complex networks, the effectiveness and safety of the limited bandwidth control strategy. Firstly, the research on the synchronization control of complex networks has been illustrated in terms of the features of complex networks, the continuity and rapidity of control signals. Secondly, recent works on event-triggered complex network control and quantization-based complex network control have been discussed. Finally, the main current methods for possible cyber-attacks on complex networks have been described. In the existing literature, scholars have put forward various definitions of synchronization for different issues, along with methods such as state feedback control, pinning control, intermittent control, impulse control, etc. However, most complex networks have relatively simple structures. Taking into account the challenges encountered by real complex systems and the complexities introduced by the environment, this paper identifies three issues that still require investigation.

1. At present, there are abundant results on the synchronization control methods of single-layer complex networks, however, most of the research is based on the symmetric coupling relationships and single coupling structure, and the research on the synchronization of heterogeneous and multilayer complex networks remains very limited. Due to the complex coupling structure of multilayer networks, it is challenging to extend the synchronization analysis from single-layer networks to multilayer networks. Therefore, proposing a more comprehensive synchronization framework for multilayer networks represents a meaningful and challenging research direction.

2. Since the theory of the unilateral network cannot be directly applied to the bilateral network due to the influence of communication delay, current complex network synchronization control only considers the communication network from sensors to controllers, neglecting the impact of the communication network from controllers to actuators. Further research is needed to determine how to implement the complex network synchronization control problem considering the bilateral communication network.

3. The current research on event-triggered control primarily focuses on analyzing the maximum triggering interval to ensure the control performance of the system, but lacks quantitative analysis. Furthermore, few studies have been researched on the control strategies for complex networks operating at finite bit rate. The fundamental effect of finite bit rate on networked systems is to determine the network bandwidth conditions that contribute to system stability. Despite certain advancements, the research conducted by [12] is limited to linear systems and cannot be easily expanded to nonlinear systems. Thus, the question of how to conduct the study of complex networks synchronization while combining event triggering and limited bit rate still needs to be answered. Based on these findings, it is imperative to consider the consequences of network attacks and provide comprehensive theoretical frameworks for resolving practical issues.

References

[1] D. J. Watts and S. H. Strogatz, Collective dynamics of ‘small-world’ networks, *Nature*, 393(6684): 440-442, 1998.

[2] A. L. Barabási and R. Albert, Emergence of scaling in random networks, *Science*, 286(5439): 509-512, 1999.

[3] H. Benbya, N. Nan, H. Tanriverdi, Y. Yoo. Complexity and information systems research in the emerging digital world. *MIS Q.*, 44(1): 1-17, 2020.

[4] M. G. Carneiro, B. C. Gama and O. S. Ribeiro, Complex network measures for data classification, *2021 International Joint Conference on Neural Networks (IJCNN)*, Shenzhen, China, 1-8, 2021.

[5] Y. Merali, Complexity and information systems: the emergent domain, *J. Inf. Technol.*, 21(4):216-228, 2006.

[6] L. D. F. Costa, F. A. Rodrigues, G. Travieso, and P. R. Villas Boas, Characterization of complex networks: A survey of measurements, *Adv. Phys.*, 56(1): 167-242, 2007.

[7] Y. Kuramoto, Self-entrainment of a population of coupled non-linear oscillators, *International Symposium on Mathematical Problems in Theoretical Physics*, H. Araki, Ed., Berlin/Heidelberg: Springer-Verlag, 39: 420-422, 1975.

[8] M. Balaghiinaloo, D. J. Antunes, and W. P. M. H. Heemels, An ℓ 2 -consistent event-triggered control policy for linear systems, *Automatica*, 125: 109412, 2021.

[9] C. Xu, X. Yang, J. Lu, J. Feng, F. E. Alsaadi, and T. Hayat, Finite-time synchronization of networks via quantized intermittent pinning control, *IEEE Trans. Cybern.*, 48(10): 3021-3027, 2018.

[10] L. Wang, Z. Wang, Q.-L. Han, and G. Wei, Synchronization control for a class of discrete-time dynamical networks with packet dropouts: a coding-decoding-based approach, *IEEE Trans. Cybern.*, 48(8): 2437-2448, 2018.

[11] M. Xing, J. Lu, J. Qiu, and H. Shen, Synchronization of complex dynamical networks subject to dos attacks: an improved coding-decoding protocol, *IEEE Trans. Cybern.*, 53(1): 102-113, 2023.

[12] Y. Liu and Q. Ling, Stabilizing bit rate conditions for a scalar linear event-triggered system with Markov dropouts, *Automatica*, 146: 110635, 2022.
[13] J.-Y. Li, Z. Wang, R. Lu, and Y. Xu, Partial-nodes-based state estimation for complex networks with constrained bit rate, *IEEE Trans. Netw. Sci. Eng.*, 8(2): 1887-1899, 2021.
[14] W. Zhao, Y. Xia, D.-H. Zhai, and B. Cui, Adaptive event-triggered coordination control of unknown autonomous underwater vehicles under communication link faults, *Automatica*, 58: 111277, 2023.
[15] J.-Y. Li, Y.-C. Huang, H.-X. Rao, Y. Xu, and R. Lu, Finite-time cluster synchronization for complex dynamical networks under FDI attack: A periodic control approach, *Neural Networks*, 165: 228-237, 2023.
[16] R. Sakthivel, O. Kwon, M. Park, S. Choi, and R. Sakthivel, Event-triggered fault estimation and nonfragile synchronization control for multiweighted complex dynamical networks with deception attacks, *Intl J Robust & Nonlinear*, 32(15): 8576-8599, 2022.
[17] Y. Li, D. Shi, and T. Chen, Secure analysis of dynamic networks under pinning attacks against synchronization, *Automatica*, 111: 108576, 2020.
[18] N. Gunasekaran, M. S. Ali, S. Arik, H. I. A. Ghaffar, and A. A. Z. Diab, Finite-time and sampled-data synchronization of complex dynamical networks subject to average dwell-time switching signal, *Neural Networks*, 149: 137-145, 2022.
[19] W. Yuan, Y. Ma, Finite-time H_∞ synchronization for complex dynamical networks with time-varying delays based on adaptive control, *ISA Trans.*, 128: 109-122, 2022.
[20] T. Xu, S. Liu, and G. Wei, Event-based finite-time H∞ synchronization control for switched complex networks with average dwell time, *Intl J Robust & Nonlinear*, 32(6): 3923-3943, 2022.
[21] Z. Wu, J. Chen, X. Zhang, Z. Xiao, J. Tao, and X. Wang, Dynamic event-triggered synchronization of complex networks with switching topologies: Asynchronous observer-based case, *Appl. Math. Comput.*, 435: 127413, 2022.
[22] Q. Dong, P. Yu, and Y. Ma, Event-triggered synchronization control of complex networks with adaptive coupling strength, *J. Franklin Inst. B*, 359(2): 1215-1234, 2022.
[23] X. Wang, J.-A. Wang, Q. Sun, X. Wen, and J. Zhang, Synchronization of nonlinear coupled complex network via event-dependent intermittent pinning control, *Eur. J. Control*, 69: 100757, 2023.
[24] J. Wang and X. Liu, Cluster synchronization for multi-weighted and directed complex networks via pinning control, *IEEE Trans. Circuits Syst. II*, 69(3): 1347-1351, 2022.
[25] Y. Li, Y. Zhang, and J. Feng, Synchronization of delayed neutral-type multi-weights networks with jump diffusion via intermittent control, *Int. J. Control*, 1-16, 2023.
[26] B. Liao, Y. Lu, C. Hu, L. Feng, and J. Yu, Fixed-time output synchronization of multi-layer complex networks under dynamic event-triggering control, *Commun. Nonlinear Sci. Numer. Simul.*, 127: 107520, 2023.
[27] X. Ruan, J. Feng, C. Xu, J. Wang, and Y. Zhao, Dynamic event-triggered pinning synchronization for switched impulsive complex networks with asynchronous switching, *IEEE Trans. Circuits Syst. II*, 69(4): 2211-2215, 2022.
[28] D. Yang, X. Li, and S. Song, Finite-time synchronization for delayed complex dynamical networks with synchronizing or desynchronizing impulses, *IEEE Trans. Neural Netw. Learning Syst.*, 33(2): 736-746, 2022.
[29] X. Guo, J. Xia, H. Shen, C. Yan, X. Wang, and T. Liu, Synchronization of time-delayed complex networks with delay-partitioning: A Chua's circuit networks application, *J. Franklin Inst. B*, 360(18): 14208-14221, 2023.
[30] H. Fan, J. Tang, K. Shi, Y. Zhao, and H. Wen, Delayed impulsive control for μ-synchronization of nonlinear multi-weighted complex networks with uncertain parameter perturbation and unbounded delays, *Mathematics*, 11(1): 250, 2023.
[31] X. Zhu, Z. Tang, J. Feng, and J. H. Park, Aperiodically intermittent event-triggered pinning control on cluster synchronization of directed complex networks, *Isa Trans.*, 138: 281-290, 2023.
[32] Y. Ren, H. Jiang, C. Hu, X. Li, and X. Qin, Discontinuous control for exponential synchronization of complex-valued stochastic multi-layer networks, *Chaos, Solitons & Fractals*, 174: 113792, 2023.
[33] S. Zhu, J. Zhou, J. Lu, and J.-A. Lu, Finite-time synchronization of impulsive dynamical networks with strong nonlinearity, *IEEE Trans. Automat. Contr.*, 66(8): 3550-3561, 2021.
[34] A. Polyakov, Nonlinear feedback design for fixed-time stabilization of linear control systems, *IEEE Trans. Automat. Contr*, 57: 2106-2110, 2012.
[35] C. Hu, H. He, and H. Jiang, Fixed/preassigned-time synchronization of complex networks via improving fixed-time stability, *IEEE Trans. Cybern.*, 51(6): 2882-2892, 2021.
[36] Q. Gan, L. Li, J. Yang, Y. Qin, and M. Meng, Improved results on fixed-/preassigned-time synchronization for memristive complex-valued neural networks, *IEEE Trans. Neural Netw. Learning Syst.*, 33(10): 5542-5556, 2022.
[37] Ellis P. Extension of phase plane analysis to quantized systems. *IRE Transactions on Automatic Control*, 4(2): 43-54, 1959.
[38] A. Girard, Dynamic triggering mechanisms for event-triggered control, *IEEE Trans. Automat. Contr.*, 60(7): 1992-1997, 2015.
[39] H. Bao, J. H. Park, and J. Cao, Adaptive synchronization of fractional-order output-coupling neural networks via quantized output control, *IEEE Trans. Neural Netw. Learning Syst.*, 32(7), 3230-3239, 2021.
[40] J. Song and X.-H. Chang, Induced L∞ quantized control for exponential synchronization of complex network subject to periodic switched coefficients, *IEEE Trans. Syst. Man Cybern, Syst.*, 53(5): 2654-2663, 2023.
[41] J.-Y. Li, Z. Wang, R. Lu, and Y. Xu, Cluster synchronization control for discrete-time complex dynamical networks: when data transmission meets constrained bit rate, *IEEE Trans. Neural Netw. Learning Syst.*, 34(5): 2554-2568, 2023.
[42] R. Pan, Y. Tan, D. Du, and S. Fei, Adaptive event-triggered synchronization control for complex networks with quantization and cyber-attacks, *Neurocomputing*, 382: 249-258, 2020.
[43] D. Liu and D. Ye, Cluster synchronization of complex networks under denial-of-service attacks with distributed adaptive strategies, *IEEE Trans. Control Netw. Syst.*, 9(1): 334-343, 2022.
[44] Y. Cao and Y. Cao, Synchronization of multiple neural networks with reaction-diffusion terms under cyber-physical attacks, *Knowledge-Based Syst.*, 239: 107939, 2022.
[45] D. Liu and D. Ye, Secure synchronization against link attacks in complex networks with event-triggered coupling, *Inform. Sci.*, 628: 291-306, 2023.

Proceedings of the 3rd Conference on Fully Actuated System Theory and Applications
May 10-12, 2024, Shenzhen, China

Event-triggered Bounded Synchronization Control for Heterogeneous Complex Networks

Zhentao Wang, Ling Huang, Yunfei Wang, Bing Li

School of Automation, Harbin University of Science and Technology, Harbin, Heilongjiang 150080, China
E-mail: mail_huangling@163.com

Abstract: An event-triggered bounded synchronization of heterogeneous complex networks is studied. Firstly, a distributed full-dimensional state observer is designed for each node in the heterogeneous complex network to reconstruct the system state. The joint error system of observation and synchronization errors is obtained, and an event-triggered controller based on the observer state is designed. Then, by using the Lyapunov stability theory, a sufficient condition is derived to ensure the bounded stabilization of the joint error system. After that, the observer gain, controller gain, and event-triggered parameters are jointly solved using Linear Matrix Inequalities (LMIs). Finally, a numerical example is provided to verify the effectiveness of the proposed synchronization theory.

Key Words: Heterogeneous complex network, bounded synchronization, event-triggered controller, Linear Matrix Inequality

1 Introduction

In recent years, complex networks have attracted more and more attention due to their wide application in various fields such as interpersonal interaction networks [1], neural networks [2], natural networks constructed by ecosystems [3], and disease transmission networks [4]. The synchronization is one of the most important research topics in the study of complex networks, which involves different nodes eventually converging to a common target trajectory [5]. Most of the existing synchronization research focuses on homogeneous networks. However, almost all engineering networks are heterogeneous, composed of nodes with different structures [6]. Therefore, the study of heterogeneous complex networks has important theoretical significance and practical application value. Due to the difference of nodes, achieving complete synchronization is usually challenging for nodes in heterogeneous networks. Heterogeneous complex networks typically maintain the node state error within a bounded range, known as bounded synchronization [7]. In [8] introduced the global bounded synchronization in heterogeneous networks in detail. On this basis, [9] studied the bounded synchronization of time-varying qualitative dynamic complex networks. Based on the mean value trajectory, [10] proposed a new definition of bounded synchronization of heterogeneous complex networks. This new definition is equivalent to the traditional concept of bounded synchronization. Extending to multi-agent systems, [11] studied the global bounded consensus of heterogeneous multi-agent systems and designed a distributed consensus protocol. However, these studies only focus on global bounded stability and pay little attention to local bounded stability. [12] proposed a method that covers global bounded synchronization and local bounded synchronization for the first time. The research on bounded synchronization has matured. In network transmission, the conventional data transmission methods can result in a significant waste of communication resources. Therefore, event-triggered strategy has emerged [13]. When the event-triggered condition is satisfied, system information will be transmitted to fully utilize the limited bandwidth. Based on this, the event-triggered strategy is unanimously recognized by the academic community because it can reduce the transmission frequency.

In [14], a periodic event-triggered strategies was proposed, which aims to strike a balance between traditional periodic sampling and event-triggered data collection. The results of the existing event-triggered strategies were extended to time-delay event-triggered control systems in [15]. In reality, the controller was typically used to achieve system synchronization. In [16], a control strategy was proposed that combines delay pulse control and event triggering mechanisms, effectively avoiding control redundancy. [17] further extended the concept to construct event-triggered strategies by integrating of system states. In [18], a model-based static event-triggered strategy was used to study time-delay network systems with quantization and time-varying characteristic.

The event-triggered strategy has been extensively researched in homogeneous complex networks, while research on event-triggered strategies in heterogeneous complex networks is scarce. In most studies, it is usually assumed that the state of all nodes can be obtained directly. But in reality, the state of many nodes is hard to get. Observer-based event-triggered synchronization control for heterogeneous network is investigated.Problem Description and Model Building

1.1 Building System Model

This section describes the synchronization control of the heterogeneous complex network based on an event-triggered with a state observer. The system structure is shown in Fig 1.

A dynamic model of the i node of a class of heterogeneous complex networks with N nodes is considered:

$$\begin{cases} \dot{x}_i(t) = A_i x_i(t) + B_i f(x_i(t), t) + c\sum_{j=1}^{N} w_{ij}\Gamma x_j(t) + u_i(t) \\ y_i(t) = Cx_i(t), \qquad i = 1, 2, ..., N \end{cases} \tag{1}$$

This work supported by National Natural Science Funds for Young Scholar of China under Grants 61304046.

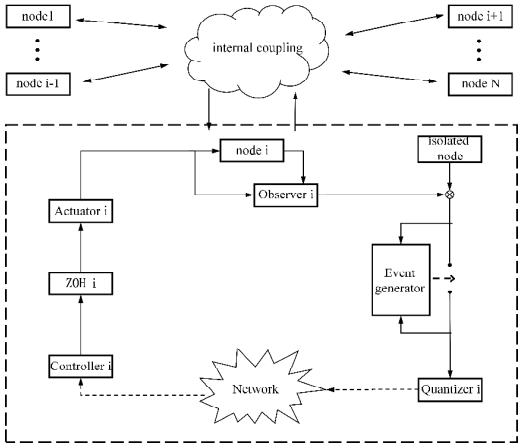

Fig.1 Observer-based event-triggered quantized complex network

where $x_i(t)\in \mathrm{R}^n$ denotes the state vector of node i; $y_i(t)\in \mathrm{R}^p$ denotes the measured output; $f(x_i(t),t)\in \mathrm{R}^n$ is a nonlinear vector function; A_i and C are the constant matrices; $c>0$ denotes the coupling strength; $W=(w_{ij})\in \mathrm{R}^{N\times N}$ represents the coupling matrix of network topology; if node i is connected to node j, then $w_{ij}>0$, otherwise $w_{ij}=0\,(i\neq j)$; the diagonal elements of matrix W are defined by $w_{ii}=-\sum_{j=1,j\neq i}^{N} w_{ij}$; $\Gamma=\mathrm{diag}(r_1,r_2,...,r_n)$ represents an internal coupling matrix; if two nodes can communicate, then $r_i>0$, otherwise $r_i=0$; $u_i(t)$ represents control input.

Assumption 1: For any $z_1(t),z_2(t)\in \mathrm{R}^n$, the continuous nonlinear function $f(\cdot,\cdot)$ satisfies the following conditions

$$(f(z_1(t),t)-f(z_2(t),t)-G_1(z_1(t)-z_2(t)))^T$$
$$(f(z_1(t),t)-f(z_2(t),t)-G_2(z_1(t)-z_2(t)))\le 0$$

Assuming that the isolated node is a synchronization target, it is described as follows.

$$\dot{s}(t)=A_0 s(t)+B_0 f(s(t),t) \tag{2}$$

Supposing that $s(t)$ is bounded, that is, for any initial condition $s(0)$, $T(s(0))$ and a normal number δ exist such that $\forall t>T(s(0))$, $\|s(t)\|\le\delta$.

1.2 Designing of Distributed Full-order State Observer

A distributed full-order state observer is designed.

$$\begin{cases}\dot{\hat{x}}_i(t)=A_i\hat{x}_i(t)+B_i f(\hat{x}_i(t),t)+c\sum_{j=1}^{N} w_{ij}\Gamma\hat{x}_j(t)+u_i(t)+L_i(y_i(t)-\hat{y}_i(t))\\ \hat{y}_i(t)=C\hat{x}_i(t), \qquad i=1,2,...,N\end{cases} \tag{3}$$

where $\hat{x}_i(t)$ is an estimate of $x_i(t)$, $\hat{y}_i(t)$ is the observer output, $L_i\in \mathrm{R}^{n\times q}$ is observer gain. The observer-based controller $u_i(t)$ can be expressed as

$$u_i(t)=K_i\bar{e}_i(t_k^i),t\in[t_k^i,t_{k+1}^i) \tag{4}$$

where $\bar{e}_i(t)=\hat{x}_i(t)-s(t)$, K_i is the designed control gain.

1.3 Dynamic Event-triggered Structure

In order to effectively reduce the network burden, an event-triggered strategy is designed. Define $h>0$ as the sampling period, t_k^i as the most recent release moment for the i node, and $(t_k^i+\rho h)$ as the most recent sampling moment. The event-triggered strategy is expressed as

$$\left\|\bar{e}(t_k^i+\rho h)-\bar{e}(t_k^i)\right\|-\rho_i\left\|\bar{e}(t_k^i+\rho h)\right\|\ge 0 \tag{5}$$

where $\rho_i\in(0,1)$ is a given parameter. $\bar{e}(t_k^i+\rho h)$ is an error at the current sampling moment, $\bar{e}(t_k^i)$ is an error at the last trigger moment.

Thus, for (5), the expression for the next release moment t_{k+1}^i can be obtained as follows.

$$t_{k+1}^i=\inf\{t>t_k^i\,|\,\left\|\bar{e}(t_k^i+\rho h)-\bar{e}(t_k^i)\right\|-\rho_i\left\|\bar{e}(t_k^i+\rho h)\right\|\ge 0\} \tag{6}$$

For $t\in[t_k^i,t_{k+1}^i)$, the sampling interval is divided into

$$[t_k^i,t_{k+1}^i)=\bigcup_{m=1}^{\rho}[t_k^i+(m-1)h,t_k^i+mh) \tag{7}$$

where $\rho_k=\inf\{m\in N\,|\,t_k^i h+mh>t_{k+1}^i h\}$.

According to induced delays in [20], it can be obtained.

$$\bar{e}(t_k^i)=\bar{e}(t-\tau_i(t))-\delta_i(t) \tag{8}$$

Therefore, (6) can be rewritten as.

$$t_{k+1}^i=\inf\{t>t_k^i\,|\,\left\|\delta_i(t)\right\|-\rho_i\left\|\bar{e}(t-\tau_i(t))\right\|\ge 0\} \tag{9}$$

Next, define the synchronization error of the i node as: $e_i(t)=x_i(t)-s(t)$ and the observation error of the i node is $\hat{e}_i(t)=x_i(t)-\hat{x}_i(t)$. So $\bar{e}_i(t)=\hat{x}_i(t)-s(t)=e_i(t)-\hat{e}_i(t)$.

Then, substituting (8) into (4), the control input can be rewritten as.

$$u_i(t)=K_i e_i(t-\tau_i(t))-K_i\hat{e}_i(t-\tau_i(t))-K_i\delta_i(t) \tag{10}$$

According to (10), the synchronization error system can be described as follows.

$$\begin{aligned}\dot{e}_i(t)=&A_i e_i(t)+B_i f(e_i(t),t)+c\sum_{j=1}^{N} w_{ij}\Gamma e_j(t)+K_i e_i(t-\\ &\tau_i(t))-K_i\hat{e}_i(t-\tau_i(t))-K_i\delta_i(t)+\mathrm{D}_i(s(t))\end{aligned} \tag{11}$$

where $f(e_i(t),t)=f(x_i(t),t)-f(s(t),t)$, $D_i(s(t))=(A_i-A_0)s(t)+(B_i-B_0)f(s(t),t)$.

The observation error system can be described as follows.

$$\dot{\hat{e}}_i(t)=(A_i-L_iC)\hat{e}_i(t)+B_i f(\hat{e}_i(t),t)+c\sum_{j=1}^{N} b_{ij}\Gamma\hat{e}_j(t) \tag{12}$$

1.4 Quantitative Processing

In order to further improve the transmission efficiency of the communication channel, this paper designs the logarithmic quantizer.

The quantized error can be expressed as

$$q_j(\bar{e}_{ij})=(I+\Delta_{ij})\bar{e}_{ij} \tag{13}$$

where $|\Delta_j|\le w_j$, $w_j=(1-\eta_j)/(1+\eta_j)$ and the quantization density is denoted by $\eta_j\,(0\le\eta_j\le 1)$. Let $\Delta_i=\mathrm{diag}\{\Delta_{i1},\Delta_{i2},...,\Delta_{in}\}$, then the quantized error can be rewritten as follows.

$$q(\bar{e}_i)=(I+\Delta_i)\bar{e}_i \tag{14}$$

Therefore, from (10) and (13), the quantized control input is

$$u_i(t)=K_i(I+\Delta_i)e_i(t-\tau_i(t))-K_i(I+\Delta_i)\hat{e}_i(t-\tau_i(t))-K_i(I+\Delta_i)\delta_i(t) \tag{15}$$

The joint error system can thus be described as follows.

$$\begin{aligned}\dot{e}_i(t)=&A_i e_i(t)+B_i f(e_i(t),t)+c\sum_{j=1}^{N} w_{ij}\Gamma e_j(t)+\ K_i(I+\Delta_i)e_i(t-\tau_i(t))\\ &-K_i(I+\Delta_i)\hat{e}_i(t-\tau_i(t))-K_i(I+\Delta_i)\delta_i(t)+\mathrm{D}_i(s(t))\end{aligned} \tag{16}$$

$$\dot{\hat{e}}_i(t)=(A_i-L_iC)\hat{e}(t)+B_if(\hat{e}_i(t),t)+c\sum_{j=1}^{N}w_{ij}\Gamma\hat{e}_j(t)$$

By using the method of Kronecker product, the joint error system can be expressed as

$$\begin{cases}\dot{E}(t)=(\overline{A}+c(W\otimes\Gamma))E(t)+\overline{B}F(E(t),t)+\mathrm{D}(s(t))\\ \qquad +\overline{K}\overline{\Delta}E(t-\tau(t))-\overline{K}\overline{\Delta}\hat{E}(t-\tau(t))-\overline{K}\overline{\Delta}\delta(t)\\ \dot{\hat{E}}(t)=(\overline{A}-\overline{L}\overline{C}+c(W\otimes\Gamma))\hat{E}(t)+\overline{B}F(\hat{E}(t),t)\end{cases}\tag{17}$$

where

$$\overline{A}=\mathrm{diag}_{\mathrm{N}}\{A_i+\Delta A_i\},\ \overline{B}=\mathrm{diag}_{\mathrm{N}}\{B_i+\Delta B_i\},\ E(t)=\mathrm{col}_{\mathrm{N}}\{e_i(t)\}$$

$$\hat{E}(t)=\mathrm{col}_{\mathrm{N}}\{\hat{e}_i(t)\},\ \delta(t)=\mathrm{col}_{\mathrm{N}}\{\delta_i(t)\},\ D(s(t))=\mathrm{col}_{\mathrm{N}}\{D_i(s(t))\}$$

$$F(E(t),t)=\mathrm{col}_{\mathrm{N}}\{f(e_i(t),t)\},\ F(\hat{E}(t),t)=\mathrm{col}_{\mathrm{N}}\{f(\hat{e}_i(t),t)\}$$

$$E(t-\tau(t))=\mathrm{col}_{\mathrm{N}}\{e_i(t-\tau(t))\},\ \hat{E}(t-\tau(t))=\mathrm{col}_{\mathrm{N}}\{\hat{e}_i(t-\tau(t))\}$$

$$\overline{K}=\mathrm{diag}_{\mathrm{N}}\{K_i\},\ \overline{\Delta}=\mathrm{diag}_{\mathrm{N}}\{I+\Delta_i\},\ \overline{L}=\mathrm{diag}_{\mathrm{N}}\{L_i\},\overline{C}=I_N\otimes C$$

1.5 Main Lemmas

Lemma 1[20]: For any constant matrix $M\in\mathrm{R}^{m\times m}$, $M=M^T>0$ scalar $\gamma>0$ and vector $\omega:[0,\gamma]\to\mathrm{R}^m$, when the following integral definitions exist, the following inequality holds.

$$\gamma\int_0^\gamma\omega^T(s)M\omega(s)ds\geq(\int_0^\gamma\omega(s)ds)^TM\int_0^\gamma\omega(s)ds$$

Lemma 2: Assume that T and S are real matrix with appropriate dimension, and F satisfies $F^TF<I$, for any scalar $\ell>0$, the following inequality holds.

$$T^TFS^T+SF^TT\leq\ell SS^T+\ell^{-1}T^TT$$

The problem to be solved can be stated as follow, for the heterogeneous complex network (1), design an observer-based state feedback controller (10) such that the system achieves bounded synchronization with the target node (2).

2 Main Conclusions

2.1 Bounded Synchronization Analysis

Theorem 1: Assuming the Assumption1 is satisfied. If there exist the feedback control gain $\overline{K}$, the observer gain $\overline{L}$, positive definite symmetric matrices $\overline{P}>0$, $\overline{Q}>0$, $\overline{R}>0$, $\overline{Z}>0$, and diagonal matrices $\Phi>0$, $\Theta>0$, $\varepsilon_i>0$, $i=1,2,3,4$, satisfied the following inequalities

$$\begin{bmatrix}\hat{\Pi}_1^* & \overline{Z}\overline{B}+\Phi\otimes G_2 & \varepsilon_1\overline{M}_1^T & \overline{Z}\overline{E}_1 & 0 & \overline{Z}\overline{E}_2\\ * & -\Phi\otimes I_n & 0 & 0 & \varepsilon_2\overline{M}_2^T & 0\\ * & * & -\varepsilon_1I_{Nn} & 0 & 0 & 0\\ * & * & * & -\varepsilon_1I_{Nn} & 0 & 0\\ * & * & * & * & -\varepsilon_2I_{Nn} & 0\\ * & * & * & * & * & -\varepsilon_2I_{Nn}\end{bmatrix}<0\tag{18}$$

$$\hat{\Pi}_2=\begin{bmatrix}\psi_{11} & \psi_{12}\\ * & \psi_{22}\end{bmatrix}<0\tag{19}$$

where

$$\psi_{11}=\begin{bmatrix}\Pi_{11}^* & \Pi_{12}^* & 0 & \Pi_{14}^* & \overline{P} & \Pi_{16}^* & \Pi_{17}^*\\ * & \Pi_{22}^* & \Pi_{23}^* & 0 & 0 & \Pi_{26}^* & 0\\ * & * & \Pi_{33}^* & 0 & 0 & 0 & 0\\ * & * & * & \Pi_{44}^* & 0 & \Pi_{46}^* & 0\\ * & * & * & * & -\prod_{55} & 0 & 0\\ * & * & * & * & * & \Pi_{66}^* & 0\\ * & * & * & * & * & * & \Pi_{77}^*\end{bmatrix}$$

$$\psi_{12}=\begin{bmatrix}\Pi_{18}^* & 0 & \Pi_{1(10)}^* & \overline{P}\overline{K} & 0 & 0 & 0\\ 0 & 0 & 0 & 0 & 0 & \varepsilon_4\tilde{G} & 0\\ 0 & 0 & 0 & 0 & \varepsilon_3\tilde{G}^T & 0 & 0\\ 0 & \Pi_{49}^* & 0 & 0 & 0 & 0 & 0\\ 0 & 0 & 0 & 0 & 0 & 0 & 0\\ 0 & 0 & 0 & 0 & 0 & 0 & \tau_M\overline{K}^T\overline{P}\\ 0 & 0 & 0 & 0 & 0 & 0 & 0\end{bmatrix}$$

$$\psi_{22}=\mathrm{diag}\{\Pi_{88}^*,\Pi_{99}^*,\Pi_{(10)(10)}^*,-\varepsilon_3I_{nN},-\varepsilon_3I_{nN},-\varepsilon_4I_{nN},-\varepsilon_4I_{nN}\}$$

$$\hat{\Pi}_1^*=He\{\overline{Z}\overline{A}+c\overline{Z}(W\otimes\Gamma)\}-\overline{Z}\overline{L}\overline{C}-\overline{C}^T\overline{L}^T\overline{Z}-\Phi\otimes G_1$$

$$\Pi_{11}^*=He\{\overline{P}\overline{A}+\overline{P}c(W\otimes\Gamma)\}-\theta\otimes G_1+\overline{Q}-e^{-2\alpha\tau_M}\overline{R}+\alpha\overline{P}+3I$$

$$\Pi_{12}^*=\overline{P}\overline{K}+e^{-2\alpha\tau_M}\overline{R};\ \Pi_{14}^*=\overline{P}\overline{B}+\theta\otimes G_2;\ \Pi_{17}^*=\varepsilon_1\overline{M}_1^T;\ \Pi_{18}^*=\overline{P}\overline{E}_1$$

$$\Pi_{16}^*=\tau_M(A+c(W\otimes\Gamma))^T\overline{P};\ \Pi_{1(10)}^*=\overline{P}\overline{E}_2;\ \Pi_{22}^*=-2e^{-2\alpha\tau_M}\overline{R}$$

$$\Pi_{23}^*=e^{-2\alpha\tau_M}\overline{R};\ \Pi_{26}^*=\tau_M\overline{K}^T\overline{P};\ \Pi_{33}^*=-e^{-2\alpha\tau_M}\overline{R}-e^{-2\alpha\tau_M}\overline{Q};\ \Pi_{44}^*=-\theta\otimes I_n$$

$$\Pi_{46}^*=\tau_M\overline{B}^T\overline{P};\ \Pi_{49}^*=\varepsilon_2\overline{M}_2^T;\ \Pi_{66}^*=-\overline{P}\overline{R}^{-1}\overline{P};\ \Pi_{77}^*=-\varepsilon_1I_{Nn}$$

$$\Pi_{88}^*=-\varepsilon_1I_{Nn};\ \Pi_{99}^*=-\varepsilon_2I_{Nn};\ \Pi_{(10)(10)}^*=-\varepsilon_2I_{Nn};\ \overline{P}=diag\{P_1,P_2,...,P_N\}$$

$$\overline{R}=diag\{R_1,R_2,...,R_N\};\ \overline{Z}=diag\{Z_1,Z_2,...,Z_N\};\ \overline{Q}=diag\{Q_1,Q_2,...,Q_N\}$$

the heterogeneous complex network system (1) achieves bounded synchronization for isolated nodes (2).

Proof: Construct an alternative Lyapunov function $V(t)$

$$V(t)=V_1(t)+V_2(t)\tag{20}$$

where

$$V_1(t)=\hat{E}^T(t)\overline{Z}\hat{E}(t)\quad,\quad V_2(t)=E^T(t)\overline{P}E(t)+\int_{t-\tau_M}^{t}e^{-2\alpha(t-s)}E^T(s)\overline{Q}E(s)ds+$$

$$\tau_M\int_{-\tau_M}^{0}\int_{t+\theta}^{t}e^{-2\alpha(t-s)}\dot{E}^T(s)\overline{R}\dot{E}(s)dsd\theta$$

Taking the derivative of $V_1(t)$ along the trajectory of (17):

$$\dot{V}_1(t)=2\hat{E}^T(t)\overline{Z}\{(\overline{A}+c(W\otimes\Gamma)-\overline{L}\overline{C})\hat{E}(t)+\overline{B}F(\hat{E}(t),t)\}\tag{21}$$

From Assumption 1, it can be obtained.

$$\begin{aligned}&f^T(\hat{e}_i(t),t)f(\hat{e}_i(t),t)-f^T(\hat{e}_i(t),t)G_2\hat{e}_i(t)\\&-\hat{e}_i^T(t)G_1^Tf(\hat{e}(t),t)+\hat{e}_i^T(t)G_1^TG_2\hat{e}_i(t)\leq0\end{aligned}\tag{22}$$

when $\phi_i>0$, (22) is equivalent to

$$\sum_{i=1}^{N}\phi_i\begin{bmatrix}\hat{e}(t)\\ f(\hat{e}(t),t)\end{bmatrix}^T\begin{bmatrix}G_1 & G_2\\ G_2 & I_n\end{bmatrix}\begin{bmatrix}\hat{e}(t)\\ f(\hat{e}(t),t)\end{bmatrix}\leq0\tag{23}$$

where $G_1=(G_1^TG_2+G_2^TG_1)/2$, $G_2=-(G_1^T+G_2^T)/2$. Thus, (23) can be rewritten as

$$\begin{aligned}&\hat{E}^T(t)(\Phi\otimes G_1)\hat{E}(t)-2\hat{E}^T(t)(\Phi\otimes G_2)F(\hat{E}(t),t)\\&+F^T(\hat{E}(t),t)(\Phi\otimes I_n)F(\hat{E}(t),t)\leq0\end{aligned}\tag{24}$$

where $\Phi=\mathrm{diag}\{\phi_1,\phi_2,...,\phi_N\}>0$.

By combining (21) and (24), it can be obtained.

$$\begin{aligned}\dot{V}_1(t)\leq&2\hat{E}^T(t)\overline{Z}\{(\overline{A}+c(W\otimes\Gamma)-\overline{L}\overline{C})\hat{E}(t)+\overline{B}F(\hat{E}(t),t)\}\\&-\hat{E}^T(t)(\Phi\otimes G_1)\hat{E}(t)+2\hat{E}^T(t)(\Phi\otimes G_2)F(\hat{E}(t),t)\\&-F^T(\hat{E}(t),t)(\Phi\otimes I_n)F(\hat{E}(t),t)\\=&[\hat{E}(t),F(\hat{E}(t))]\hat{\Pi}[\hat{E}(t),F(\hat{E}(t))]^T\end{aligned}\tag{25}$$

$\hat{\Pi}$ in (25) can be expressed as

$$\hat{\Pi}=\Omega+\hat{P}_1F(t)\hat{K}_1^T+(\hat{P}_1F(t)\hat{K}_1^T)^T+\hat{P}_2F(t)\hat{K}_2^T+(\hat{P}_2F(t)\hat{K}_2^T)^T\tag{26}$$

where $\Omega=\begin{bmatrix}\Omega_1 & \overline{Z}\overline{B}+\Phi\otimes G_2\\ * & -\Phi\otimes I_n\end{bmatrix}$; $A^*=\mathrm{diag}\{A_1,A_2,...A_N\}$

$$\Omega_1=He\{\overline{Z}A^*+c\overline{Z}(W\otimes\Gamma)-\overline{Z}\overline{L}\overline{C}\}-\Phi\otimes G_1;\ B^*=\mathrm{diag}\{B_1,B_2,...B_N\}$$

$$\hat{P}_1^T=[\overline{E}_1^T\overline{Z}\ \ 0]\quad;\quad\hat{P}_2^T=[\overline{E}_2^T\overline{Z}\ \ 0]\quad;\quad\hat{K}_1^T=[\overline{M}_1\ \ 0]\quad;\quad\hat{K}_2^T=[0\ \ \overline{M}_2]$$

$$\overline{E}_1=I_N\otimes E_1;\ \overline{E}_2=I_N\otimes E_2;\ \overline{M}_1=I_N\otimes M_1;\ \overline{M}_2=I_N\otimes M_2$$

By using Lemma 2 for (26), it can be obtained.

$$\hat{\Pi}\leq\Omega+\varepsilon_1^{-1}\hat{P}_1\hat{P}_1^T+\varepsilon_1\hat{K}_1\hat{K}_1^T+\varepsilon_2^{-1}\hat{P}_2\hat{P}_2^T+\varepsilon_2\hat{K}_2\hat{K}_2^T\tag{27}$$

Then, the inequality (18) is obtained by using Schur complement lemma for (27). According to Lyapunov stability theorem, $\lim_{t\to\infty}\| \hat{E}(t)\| = 0$.

Taking the derivative of $V_2(t)$ along the trajectory of (17).

$$\begin{aligned}\dot{V}_2(t) &= 2E^T(t)\bar{P}\{(\bar{A}+c(W\otimes\Gamma))E(t)+\bar{B}F(E(t),t)+\\ &\bar{K}\bar{\Delta}E(t-\tau(t))-\bar{K}\bar{\Delta}\hat{E}(t-\tau(t))-\bar{K}\bar{\Delta}\delta(t)+\mathrm{D}(s(t))\}\\ &+E^T(t)\bar{Q}E(t)-e^{-2\alpha\tau_M}E^T(t-\tau_{iM})\bar{Q}E(t-\tau_{iM})+\tau_M^2\dot{E}^T(t)\bar{R}\dot{E}(t)\\ &-\tau_M\int_{t-\tau_M}^{t}e^{-2\alpha(t-s)}\dot{E}^T(s)\bar{R}\dot{E}(s)ds-2\alpha V_2(t)+2\alpha E^T(t)\bar{P}E(t)\end{aligned} \tag{28}$$

By Lemma1, we can obtain

$$\begin{aligned}&-\tau_M\int_{t-\tau_M}^{t}e^{-2\alpha(t-s)}\dot{E}^T(s)\bar{R}\dot{E}(s)ds\le-\tau_M\int_{t-\tau_M}^{t}e^{-2\alpha\tau_M}\dot{E}^T(s)\bar{R}\dot{E}(s)ds\\ &\le-e^{-2\alpha\tau_M}\{E(t)-E(t-\tau(t))\}^T\bar{R}\{E(t)-E(t-\tau(t))\}\\ &-e^{-2\alpha\tau_M}\{E(t-\tau(t))-E(t-\tau_M)\}^T\bar{R}\{E(t-\tau(t))-E(t-\tau_M)\}\end{aligned} \tag{29}$$

According to Assumption 1, there exists a diagonal matrix $\Theta>0$ such that the following holds.

$$\begin{aligned}&E^T(t)(\Theta\otimes G_1)E(t)-2E^T(t)(\Theta\otimes G_2)F(E(t),t)\\ &+F(E(t),t)(\Theta\otimes I_n)F(E(t),t)\le 0\end{aligned} \tag{30}$$

where $\Theta=\mathrm{diag}\{\theta_1,\theta_2,...,\theta_N\}$, $\theta_i>0$.

By combining (28) and (30), $\dot{V}_2(t)$ is rewritten as following.

$$\begin{aligned}&2\alpha V_2(t)+\dot{V}_2(t)\le\xi_1^T(\Pi_1+\tau_M^2\vartheta^T\bar{R}\vartheta)\xi_1+\mathrm{D}^T(s(t))\prod_{55}\mathrm{D}(s(t))\\ &-2E^T(t)\bar{P}\bar{K}\bar{\Delta}\hat{E}(t-\tau(t))-2\sum_{i=1}^{N}e_i^T(t)P_iK_i(I+\Delta_i)\delta_i(t)\end{aligned} \tag{31}$$

where $\vartheta=[\Pi_{16}^{*T}\quad\tau_M\bar{P}\bar{K}\bar{\Delta}\quad 0\quad\tau_M P\bar{B}\quad 0]$

$$\Pi_1=\begin{bmatrix}\Pi_{11}&\bar{P}\bar{K}\bar{\Delta}+e^{-2\alpha\tau_M}\bar{R}&0&\bar{P}\bar{B}+\Theta\otimes G_2&\bar{P}\\ *&-2e^{-2\alpha\tau_M}\bar{R}&e^{-2\alpha\tau_M}\bar{R}&0&0\\ *&*&-e^{-2\alpha\tau_M}\bar{R}-e^{-2\alpha\tau_M}\bar{Q}&0&0\\ *&*&*&-\theta\otimes I_n&0\\ *&*&*&*&-\prod_{55}\end{bmatrix}$$

$$\Pi_{11}=He\{\bar{P}\bar{A}+\bar{P}c(W\otimes\Gamma)\}-\Theta\otimes G_1+\bar{Q}-e^{-2\alpha\tau_M}\bar{R}+2\alpha\bar{P}$$

$$\xi(t)=(E^T(t),E^T(t-\tau(t)),E^T(t-\tau_M(t)),F^T(E(t),t),\mathrm{D}^T(s(t)))^T$$

Treat $-2E^T(t)\bar{P}\bar{K}\bar{\Delta}\hat{E}(t-\tau(t))$ in (31) as follows.

$$-2E^T(t)\bar{P}\bar{K}\bar{\Delta}\hat{E}(t-\tau(t))\le\|E(t)\|^2+\|\bar{P}\bar{K}\bar{\Delta}\|^2\|\hat{E}(t-\tau(t))\|^2 \tag{32}$$

By combining the event-triggered strategy (6), and transform $-2\sum_{i=1}^{N}e_i^T(t)P_iK_i(I+\Delta_i)\delta_i(t)$ in (32) as follows.

$$\begin{aligned}&-2\sum_{i=1}^{N}e_i^T(t)P_iK_i(I+\Delta_i)\delta_i(t)\\ &\le 2\sum_{i=1}^{N}\|e_i(t)\|\ \|P_iK_i(I+\Delta_i)\|\rho_i\|e_i(t-\tau_i(t)-\hat{e}_i(t-\tau_i(t)\|\end{aligned} \tag{33}$$

Letting ρ_i as $\dfrac{1}{2\|P_iK_i(I+\Delta_i)\|}$ and substituting it into (33).

$$\begin{aligned}&-2\sum_{i=1}^{N}e_i^T(t)P_iK_i(I+\Delta_i)\delta_i(t)\\ &=2E^T(t)E(t)+E^T(t-\tau(t))E(t-\tau(t))+\|\hat{E}(t-\tau(t))\|^2\end{aligned} \tag{34}$$

By combining (32)-(34), (31) can be rewritten as follows.

$$\begin{aligned}&2\alpha V_2(t)+\dot{V}_2(t)\le\xi_1^T(\Pi_1+\tau_M^2\vartheta^T\bar{R}\vartheta)\xi_1+(\|\bar{P}\bar{K}\bar{\Delta}\|^2+1)\\ &\|\hat{E}(t-\tau(t))\|^2+\mathrm{D}^T(s(t))\prod_{55}\mathrm{D}(s(t))\end{aligned} \tag{35}$$

By using Schur complement lemma for (35), the expanded linear matrix inequality is

$$\Pi_2=\begin{bmatrix}\Pi_{11}^*&\bar{P}\bar{K}\bar{\Delta}+e^{-2\alpha\tau_M}\bar{R}&0&\bar{P}\bar{B}+\Theta\otimes G_2&\bar{P}&\Pi_{16}^*\\ *&I-2e^{-2\alpha\tau_M}\bar{R}&e^{-2\alpha\tau_M}\bar{R}&0&0&\tau_M\bar{K}^T\bar{\Delta}\bar{P}\\ *&*&\Pi_{33}^*&0&0&0\\ *&*&*&-\Theta\otimes I_n&0&\tau_M\bar{B}^TP\\ *&*&*&*&-\prod_{55}&0\\ *&*&*&*&*&-PR^{-1}P\end{bmatrix} \tag{36}$$

where

$$\Pi_{11}^*=He\{\bar{P}\bar{A}+\bar{P}c(W\otimes\Gamma)\}-\Theta\otimes G_1+\bar{Q}-e^{-2\alpha\tau_M}\bar{R}+2\alpha\bar{P}+3I$$

Π_2 can be rewritten as

$$\Pi_2=\Omega_2+\tilde{P}_1F(t)\tilde{K}_1^T+(\tilde{P}_1F(t)\tilde{K}_1^T)^T+\tilde{P}_2F(t)\tilde{K}_2^T+(\tilde{P}_2F(t)\tilde{K}_2^T)^T \tag{37}$$

where $\Omega_2=\Pi_2|_{\bar{A}=A^*}$, $\tilde{P}_1^T=[\bar{E}_1^T\bar{P}\ 0\ 0\ 0\ 0\ 0]$, $\tilde{K}_1^T=[\bar{M}_1\ 0\ 0\ 0\ 0\ 0]$

$\tilde{P}_2^T=[\bar{E}_2^T\bar{P}\ 0\ 0\ 0\ 0\ 0]$, $\tilde{K}_2^T=[0\ 0\ 0\ \bar{M}_4\ 0\ 0]$.

According to Lemma 2, (37) is reduced as follows.

$$\Pi_2\le\tilde{\Pi}_2+\varepsilon_1^{-1}\tilde{P}_1\tilde{P}_1^T+\varepsilon_1\tilde{K}_1\tilde{K}_1^T+\varepsilon_2^{-1}\tilde{P}_2\tilde{P}_2^T+\varepsilon_2\tilde{K}_2\tilde{K}_2^T \tag{38}$$

Define $\tilde{\Delta}=\tilde{F}\tilde{G}$, $\tilde{G}=diag_N(w_iI_n)$,where $\tilde{F}\tilde{F}^T=\tilde{F}^T\tilde{F}\le I$, $\tilde{\Delta}=diag_N\{\Delta_i\}$, $\tilde{F}=\tilde{\Delta}\tilde{G}^{-1}$.

Then, (38) can be rewritten as follows.

$$\tilde{\Pi}_2=\tilde{\Pi}_2|_{\tilde{\Delta}=I}+U_1\tilde{F}V_1+(U_1\tilde{F}V_1)^T+U_2\tilde{F}V_2+(U_2\tilde{F}V_2)^T \tag{39}$$

where $V_1=[0\ \tilde{G}\ 0\ 0\ 0\ 0\ 0\ 0\ 0\ 0]$, $U_2^T=[0\ \tilde{G}\ 0\ 0\ 0\ 0\ 0\ 0\ 0\ 0]$

$V_2=[0\ 0\ 0\ 0\ 0\ \tau_MK^T\mathrm{P}\ 0\ 0\ 0\ 0]$ $U_i^T=[K^TP\ 0\ 0\ 0\ 0\ 0\ 0\ 0\ 0\ 0]$

By means of Lemma 2, (39) can be reduced to

$$\tilde{\Pi}_2=\tilde{\Pi}_2|_{\tilde{\Delta}=I}+\varepsilon_3U_i^TU_1+\varepsilon_3^{-1}V_i^TV_1+\varepsilon_4U_2^TU_2+\varepsilon_4^{-1}V_2^TV_2 \tag{40}$$

By using Schur complement lemma for (40), inequality (19) can be obtained. The maximum value of $(\|\bar{P}\bar{K}\bar{\Delta}\|+1)$ $\|\hat{E}(t-\tau(t))\|^2+\mathrm{D}^T(s(t))\prod_{55}\mathrm{D}(s(t))$ is set to $\kappa(0)$. When the system satisfies inequality (19), it follows from (35) that

$$2\alpha V_2(t)+\dot{V}_2(t)\le\kappa(0) \tag{41}$$

Left-multiplied and right-multiplied (41) by $e^{2\alpha t}$, then integrate from 0 to t, the following can be obtained.

$$V_2(t)\le V_2(0)e^{-2\alpha t}+e^{-2\alpha t}\kappa(0)\int_0^t e^{2\alpha s}ds \tag{42}$$

therefore:

$$\|E(t)\|\le\sqrt{\frac{V_2(0)}{\lambda_{\min}(\bar{P})}}e^{-\alpha t}+\sqrt{\frac{\kappa(0)}{\alpha\lambda_{\min}(\bar{P})}} \tag{43}$$

The proof of bounded synchronization is completed.

2.2 The Design of the Controller

In the inequality of Theorem 1, it can be seen that $\bar{Z}\bar{L}\bar{C}$ and $\bar{P}\bar{K}$ are nonlinear terms. Next, they are processed to jointly solve the controller gains and the observer gains.

Theorem 2: If there exist positive definite symmetric matrices $\bar{P}>0$, $\bar{Q}>0$, $\bar{R}>0$, diagonal matrices $\Phi>0$, $\Theta>0$, positive numbers $\varepsilon_1>0$, $\varepsilon_2>0$, $\varepsilon_3>0$, $\varepsilon_4>0$, and proper matrices $\bar{W}$, $\bar{X}$, satisfied the following inequalities

$$\hat{\Pi}_2^*=\begin{bmatrix}\psi_{11}^*&\psi_{12}^*\\ *&\psi_{22}^*\end{bmatrix}<0 \tag{44}$$

$$\begin{bmatrix}\hat{\Pi}_1^{**}&\bar{Z}\bar{B}+\Phi\otimes G_2&\varepsilon_1\bar{M}_1^T&\bar{Z}\bar{E}_1&0&\bar{Z}\bar{E}_2\\ *&-\Phi\otimes I_n&0&0&\varepsilon_2\bar{M}_2^T&0\\ *&*&-\varepsilon_1I_{Nn}&0&0&0\\ *&*&*&-\varepsilon_1I_{Nn}&0&0\\ *&*&*&*&-\varepsilon_2I_{Nn}&0\\ *&*&*&*&*&-\varepsilon_2I_{Nn}\end{bmatrix}<0 \tag{45}$$

where

$$\psi_{11}^{*}=\begin{bmatrix}\Pi_{11}^{*} & \Pi_{12}^{2} & 0 & \Pi_{14}^{*} & \bar{P} & \Pi_{16}^{*} & \Pi_{17}^{*}\\ * & \Pi_{22}^{*} & \Pi_{23}^{*} & 0 & 0 & \tau_M\bar{X}^T & 0\\ * & * & \Pi_{33}^{*} & 0 & 0 & 0 & 0\\ * & * & * & \Pi_{44}^{*} & 0 & \Pi_{46}^{*} & 0\\ * & * & * & * & -\prod_{55} & 0 & 0\\ * & * & * & * & * & -2\bar{P}+\bar{R} & 0\\ * & * & * & * & * & * & \Pi_{77}^{*}\end{bmatrix}$$

$$\psi_{12}^{*}=\begin{bmatrix}\Pi_{18}^{*} & 0 & \Pi_{1(10)}^{*} & \bar{X} & 0 & 0 & 0\\ 0 & 0 & 0 & 0 & 0 & \varepsilon_4\tilde{G} & 0\\ 0 & 0 & 0 & 0 & \varepsilon_3\tilde{G}^T & 0 & 0\\ 0 & \Pi_{49}^{*} & 0 & 0 & 0 & 0 & 0\\ 0 & 0 & 0 & 0 & 0 & 0 & 0\\ 0 & 0 & 0 & 0 & 0 & 0 & \tau_M\bar{X}^T\\ 0 & 0 & 0 & 0 & 0 & 0 & 0\end{bmatrix}$$

$$\psi_{22}^{*}=\mathrm{diag}\{\Pi_{88}^{*},\Pi_{99}^{*},\Pi_{(10)(10)}^{*},-\varepsilon_3 dI_{nN},-\varepsilon_3 I_{nN},-\varepsilon_4 I_{nN},-\varepsilon_4 I_{nN}\}$$

$$\hat{\Pi}_1^{**}=He\{\bar{Z}\bar{A}+c\bar{Z}(B\otimes\Gamma)-\bar{W}\bar{C}\}-\Phi\otimes G_1\ ;\ \Pi_{12}^{2}=\bar{X}+e^{-2\alpha\tau_M}\bar{R}$$

then the system achieves bounded synchronization. When the inequality is solvable, the controller and the observer forms are $\bar{K}=\bar{P}^{-1}\bar{X}$ and $\bar{L}=\bar{Z}^{-1}\bar{W}$, respectively.

Replacing $-\bar{P}\bar{R}^{-1}\bar{P}$ by $-\bar{P}\bar{R}^{-1}\bar{P}\le-2\bar{P}+\bar{R}$, let $\bar{P}\bar{K}=\bar{X}$ and $\bar{Z}\bar{L}=\bar{W}$. Then, the conclusion of Theorem 2 can be obtained. Therefore, the detailed procedure is omitted here.

3 Simulation Analysis

A system in the form of (1) with the following parameters is considered.

$$A_1=\begin{bmatrix}-10 & 10 & 0\\ 1 & -1 & 1\\ 0 & -14.87 & -0.3\end{bmatrix},\ A_2=\begin{bmatrix}-10 & 10 & 0\\ 1 & -0.9 & 1\\ 0 & -14.87 & -0.4\end{bmatrix}\ B_1=\begin{bmatrix}1 & 0 & 0\\ 0 & 0 & 0\\ 0 & 0 & 0\end{bmatrix}$$

$$A_3=\begin{bmatrix}-10 & 10 & 0\\ 1 & -0.8 & 1\\ 0 & -14.87 & -0.5\end{bmatrix},\ B_2=\begin{bmatrix}1.1 & 0 & 0\\ 0 & 0 & 0\\ 0 & 0 & 0\end{bmatrix},\ B_3=\begin{bmatrix}1.2 & 0 & 0\\ 0 & 0 & 0\\ 0 & 0 & 0\end{bmatrix}$$

$$A_0=\begin{bmatrix}-10 & 10 & 0\\ 1 & -1 & 1\\ 0 & -14.87 & 0\end{bmatrix},\ B_0=\begin{bmatrix}1 & 0 & 0\\ 0 & 0 & 0\\ 0 & 0 & 0\end{bmatrix},\ f(x_i(t))=\begin{bmatrix}-10\varphi(x_{i1}(t))\\ 0\\ 0\end{bmatrix}$$

$$C=\begin{bmatrix}2 & 1 & 0\\ 1 & 0 & 1\end{bmatrix},\ c=30,\ x_{i1}(t)=0.1,\ \tau_M=0.02,\ \alpha=0.01$$

$$\eta_j=0.5\ \ \varphi(x_{i1})=0.5(-1.27+0.68)(|x_{i1}(t)+1|-|x_{i1}(t)-1|)$$

$$\Gamma=I_3,\ \bar{E}_1=I_5\otimes\begin{bmatrix}0.1 & 0.5 & 0.1\\ 0.5 & -0.3 & 0.2\\ 0.1 & 0.4 & 0.1\end{bmatrix},\ \bar{E}_2=I_3\otimes\begin{bmatrix}0.3 & 0.2 & -0.1\\ 0.5 & -0.2 & 0.1\\ 0.2 & 0.4 & -0.2\end{bmatrix}$$

$$\bar{M}_1=I_3\otimes\begin{bmatrix}0.1 & -0.2 & 0.1\\ 0.1 & -0.1 & 0.2\\ 0.2 & 0.3 & 0.1\end{bmatrix},\ \bar{M}_2=I_3\otimes\begin{bmatrix}0.1 & -0.2 & 0.3\\ 0.4 & -0.2 & 0.2\\ 0.2 & 0.3 & -0.1\end{bmatrix}$$

and connecting topological matrix is $W=\begin{bmatrix}-1 & 0 & 1\\ 1 & -1 & 0\\ 0 & 1 & -1\end{bmatrix}$.

According to the nonlinear function $f(x_i(t))$, we can calculate.

$$G_1=\begin{bmatrix}0 & 0 & 0\\ 0 & 0 & 0\\ 0 & 0 & 0\end{bmatrix},\ G_2=\begin{bmatrix}5.9 & 0 & 0\\ 0 & 0 & 0\\ 0 & 0 & 0\end{bmatrix}$$

By using the Toolbox in MATLAB to solve the linear matrix inequalities (44) and (45) of Theorem 2, the controller gains and observer gains can be obtained as

$$K_1=\begin{bmatrix}70.1542 & 35.0451 & -15.2541\\ 14.2537 & 55.2848 & -10.5426\\ -50.5541 & -34.5245 & 25.2658\end{bmatrix},\ L_1=\begin{bmatrix}30.2541 & 1.5241\\ 25.5425 & -18.8504\\ -45.5115 & 41.5234\end{bmatrix}$$

$$K_2=\begin{bmatrix}70.3524 & 35.2515 & -15.2657\\ 14.8457 & 55.2541 & -10.3526\\ -50.4251 & -34.3985 & 25.2541\end{bmatrix},\ L_2=\begin{bmatrix}30.8547 & 1.4524\\ 25.2354 & -18.2648\\ -45.6552 & 41.2524\end{bmatrix}$$

$$K_3=\begin{bmatrix}70.1685 & 35.1766 & -15.2342\\ 14.8845 & 55.2254 & -10.3254\\ -50.5775 & -34.5462 & 25.2523\end{bmatrix},\ L_3=\begin{bmatrix}30.2369 & 1.3524\\ 25.5297 & -18.5574\\ -45.5986 & 41.7604\end{bmatrix}$$

The initial value is

$$x_1(0)=[-10\ \ -4\ \ -5]^T, x_2(0)=[2\ 8\ 5]^T, x_3(0)=[-8\ 0\ \ -10]^T$$

$$s(0)=[-5\ 4\ \ -5]^T;\hat{x}_1(0)=[30\ \ -2.5\ \ 7]^T,\hat{x}_2(0)=[5\ \ 6\ \ -1]^T$$

$$\hat{x}_3(0)\ =[5\ 10\ 3]^T$$

The simulation results are shown in Fig. 2-4. Fig. 2 shows the state of the system. The left graph of Fig.3 shows that the synchronization error of the system is bounded, so the complex network achieves bounded synchronization. From the right figure of Fig. 3, it can be seen that the observation error system tends to zero, indicating that the design of the observer is effective. The trigger threshold of the left image in Fig. 4 is 0.1, and the number of triggers for the different node are 135, 164 and 145 respectively. The trigger threshold of the right image in Fig.4 is 0.5, and the number of triggers for the different node are 41, 41, and 36 respectively. The number of triggers in the left picture is significantly less than that in the right picture. The simulation results show that the smaller the trigger threshold, the grater the number of triggers, which is consistent with the actual situation.

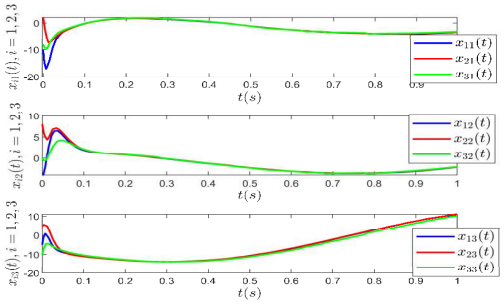

Fig. 2: The complex networks state $x_{i1}(t), x_{i2}(t), x_{i3}(t), i=1,2,3.$

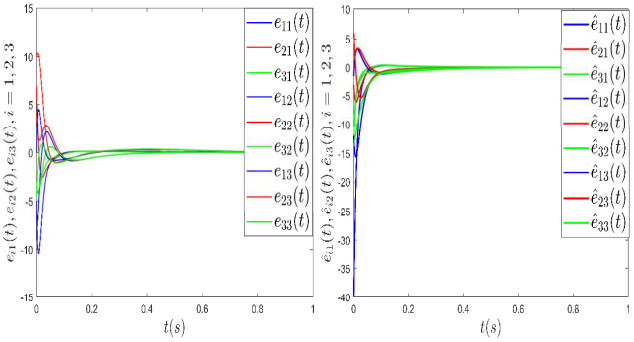

Fig. 3: The synchronization error $e_{i1}(t), e_{i2}(t), e_{i3}(t)$ and observation error $\hat{e}_{i1}(t), \hat{e}_{i2}(t), \hat{e}_{i3}(t)$, $i=1,2,3$

4 Conclusions

The heterogeneity of the system matrix and the nonlinear function coefficient matrix in the network nodes, along with

the uncertainty in the network, are taken into account. Based on the Lyapunov function method, Jensen's inequality, Schur complement lemma, and other mathematical tools and techniques, a sufficient condition for the observer-based heterogeneous complex network system with an event-triggered strategy to achieve quantized bounded synchronization is obtained. In the experimental simulation stage, it can be observed from the error result diagram that the error tends towards zero, indicating the effectiveness of the designed state observer. From the synchronization error result diagram, it is evident that the complex network achieves bounded synchronization. By setting different thresholds, it can be observed that the smaller the threshold, the fewer event triggers occur.

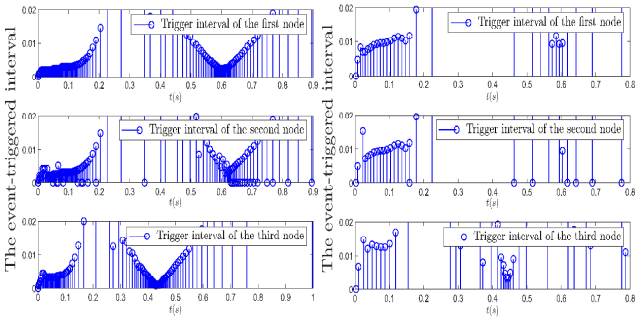

Fig. 4: The event-triggered interval when threshold is 0.1 and 0.5

References

[1] A. Grabowski, and R. A. Kosiński, Ising-based model of opinion formation in a complex network of interpersonal interactions. *Physica A: Statistical Mechanics and its Applications*, 2006, 361(2): 651-664.

[2] R. Xin, J. Zhang, and Y. Shao, Complex network classification with convolutional neural network. *Tsinghua Science and technology*, 2020, 25(4): 447-457.

[3] U. Brose, E. L. Berlow, and N. D. Martinez, Scaling up keystone effects from simple to complex ecological networks. *Ecology Letters*, 2005, 8(12): 1317-1325.

[4] S. M. Firestone, Y. Hayama, R. Bradhurst, T. Yamamoto, T. Tsutsui, and M. A. Stevenson, Reconstructing foot-and-mouth disease outbreaks: a methods comparison of transmission network models. *Scientific reports*, 2019, 9(1): 4809.

[5] A. Arenas, A. Díaz-Guilera, J. Kurths, Y. Moreno, and C. Zhou, Synchronization in complex networks. *Physics reports*, 2008, 469(3): 93-153.

[6] G. Wu, M. Mizuno, and P. J. M. Havinga, MIRAI architecture for heterogeneous network. I*EEE Communications Magazine*, 2002, 40(2): 126-134.

[7] S. Zhu, J. Zhou, X. Yu, and J. Lu, Bounded synchronization of heterogeneous complex dynamical networks: A unified approach. *IEEE Transactions on Automatic Control*, 2020, 66(4): 1756-1762.

[8] J. Zhao, D. J. Hill, and T Liu, Global bounded synchronization of general dynamical networks with nonidentical nodes. *IEEE Transactions on Automatic Control*, 2012, 57(10): 2656-2662.

[9] L. Wang, W. Qian, and Q. G. Wang, Bounded synchronization of a time-varying dynamical network with nonidentical nodes. *International Journal of Systems Science*, 2015, 46(7): 1234-1245.

[10] Q. Li, J. Guo, Y. Wu, and C. Y. Sun, Global asymptotical bounded synchronization for a class of coupled complex networks with nonidentical nodes. *Asian Journal of Control*, 2017, 19(4): 1630-1640.

[11] L. Wang, W. Feng, M. Z. Q. Chen, and Q. Wang, Global bounded consensus in heterogeneous multi-agent systems with directed communication graph. *IET Control Theory & Applications*, 2015, 9(1): 147-152.

[12] S. Zhu, J. Zhou, X. Yu, and J. Lu, Bounded synchronization of heterogeneous complex dynamical networks: A unified approach. *IEEE Transactions on Automatic Control*, 2020, 66(4): 1756-1762.

[13] X. M. Zhang, Q. L. Han, and B. L. Zhang, An overview and deep investigation on sampled-data-based event-triggered control and filtering for networked systems. *IEEE Transactions on industrial informatics*, 2016, 13(1): 4-16.

[14] W. P. M. H. Heemels, M. C. F. Donkers, and A. R. Teel, Periodic event-triggered control for linear systems. *IEEE Transactions on automatic control*, 2012, 58(4): 847-861.

[15] D. Xu, X. Wang, and H. Su, Delay event-triggered control for stability analysis of complex networks. *IEEE Transactions on Circuits and Systems II: Express Briefs*, 2022, 70(3): 1104-1108.

[16] X. Lv, J. Cao, X. Li, M. A. Aty, and U. A. A. Juboori, Synchronization analysis for complex dynamical networks with coupling delay via event-triggered delayed impulsive control. *IEEE transactions on cybernetics*, 2020, 51(11): 5269-5278.

[17] H. Yu, and F. Hao, Input-to-state stability of integral-based event-triggered control for linear plants. *Automatica*, 2017, 85: 248-255.

[18] E. Garcia, and P. J. Antsaklis, Model-based event-triggered control for systems with quantization and time-varying network delays. *IEEE Transactions on Automatic Control*, 2012, 58(2): 422-434.

[19] L. Huang, J. Guo, and B. Li, Observer-based dynamic event-triggered robust H∞ control of networked control systems under DoS attacks. *IEEE Access*, 2021, 9: 145626-145637.

[20] Y. Liu, Z. Wang, Y. Yuan, and W. Liu, Event-triggered partial-nodes-based state estimation for delayed complex networks with bounded distributed delays. *IEEE Transactions on Systems, Man, and Cybernetics: Systems*, 2017, 49(6): 1088-1098

Proceedings of the 3rd Conference on Fully Actuated System Theory and Applications
May 10-12, 2024, Shenzhen, China

Reachable set estimation of singular Markovian jump systems via state decomposition method

Qingxiang Wang[1], Guowei Zhao[1], Zhiguang Feng[1]

1. College of Intelligent Systems Science and Engineering, Harbin Engineering University, Harbin, Heilongjiang, 150000, China
E-mail: 2021040526@hrbeu.edu.cn

Abstract: This paper focuses on estimating the reachable set concerning the singular Markovian jump systems (SMJSs). We employ the state decomposition method to solve the reachable set estimation (RSE) of SMJSs without delay. The objective is to get a set of ellipsoids under different modes of SMJSs to confine all states originating from the origin. By employing decomposition method, the SMJS is decomposed into a differential system and an algebraic system. Then the sufficient condition for RSE of SMJS without delay is proposed. Finally, a numerical example is given to demonstrate the validity of the adopted methods.
Key Words: Reachable Set Estimation, Singular Markovian Jump System, Decomposition Method

1 Introduction

Reachable set contains all states which will appear during the entire operation of the system. Due to the profound contribution to comprehending dynamic systems, refining the efficacy of control system design, fortifying system security, optimizing overall system performance, and furnishing valuable guidance for simulation and experimental endeavors in academic research, it is significant to study the reachable set estimation (RSE). The problem of RSE has gain attention in theory of control. The reachable set control problem based on sliding mode control has been studied in [1]. The adaptive event-triggered reachable set synthesis of singular systems with time-delay is reported in [2]. The RSE is also employed in practical engineering such as avoiding unknown obstacles [3].

Singular systems accurately model practical systems due to their inclusion of both differential and algebraic subsystems [4,5]. Consequently, they are used extensively in various fields such as chemical processes and electrical systems [6]. Apart from their practical applications, these systems have garnered significant theoretical attention in recent years, particularly in stability and stabilization [7,8], H_∞control [9], and dissipativity analysis [10,11]. Many methodologies and findings have been extended from standard state-space systems to singular systems. Conditions concerning the RSE issue have been established to ensure that the resulting ellipsoid encompasses all states of the considered singular system [12]. The robust control of uncertain singular systems with time-delays are reported in [13].

Markovian jump systems (MJSs) have received widespread attention in recent years because they can better describe the characteristics of systems with abrupt variations. Within the domain of discrete-time MJSs, a multitude of works have tackled with the problem of estimating reachable sets. In [14], conditions bounding the reachable set for delay discrete-time MJSs are formulated by employing delay-partitioning and reciprocal convex techniques. An improved result is presented in [15], where three equations are introduced, and reciprocally convex combinations are applied to double summation terms. MJSs has attracted attention and gradually achieved application in practical fields such as biology and production [16,17]. Addressing Markovian jump neural networks with time-varying delay, a novel summation inequality is employed in [18].

Significant progress has been made in the development of singular Markovian jump systems (SMJSs) over the past years. Details of its application in the actual control system can be found in [19]. On this basis, some more comprehensive issues have been studied in more depth. In [20], asynchronous H_∞ filtering is examined for SMJSs, with the results applied to a robotic arm. [21] discusses the application of the special properties of SMJSs in neural networks. In [22], the state decomposition method is employed to establish an appropriate augmented Lyapunov–Krasovskii functional to obtain improved RSE results of singular system.

Inspired by the above articles and in order to investigate the RSE problem of SMJS more deeply, this paper decomposes the system into two subsystems by using decomposition method. Then the Lyapunov functional is established for the decomposed subsystem and a sufficient condition for reachable set estimation is obtained. In addition, the intersection of ellipsoids under different modes is obtained to contain all states starting from the initial condition. Finally, an illustrative example is presented to validate the criteria.

Notation: $\mathbb{R}^n$ signifies n-dimensional Euclidean space; $\|\bullet\|$ represents the Euclidean vector norm; $V>0$ (≥ 0) indicates that the matrix V is positive-definite (semi-positive-definite); $\mathcal{L}$ is the weak infinitesimal generator of the stochastic process; $\varepsilon(\bullet)$ denotes the expectation operator with respect to the given probability measure; * denotes the symmetric term in a symmetric matrix; $\lambda_{\min}(P)$ denotes the minimal eigenvalue of matrix P; $\mathrm{sym}(A)=A+A^T$. I is the identity matrix.

*This work is supported by National Natural Science Foundation (NNSF) of China under Grant 62073094.

2 Problem Formulation

The following SMJS will be studied, which is a delay-free system:

$$\begin{cases} E\dot{x}(t) = A(r_t)x(t) + D(r_t)\omega(t) \\ x(0) = 0 \end{cases} \tag{1}$$

where $x(t) \in \mathbb{R}^n$ is the state vector of the system; $u(t) \in \mathbb{R}^p$ is the input of the system; $\omega(t) \in \mathbb{R}^l$ is a disturbance satisfying:

$$\omega(t)^T \omega(t) \le \bar{\omega}^2 \tag{2}$$

where $\bar{\omega}$ is a real constant.

The Markov process exhibits a distinctive jumping characteristic between various modes, as depicted by the transition probability matrix $\pi = [\pi_{ij}], (i, j \epsilon S = [1,2,\ldots,s])$, given by

$$\Pr\{r_{t+\eta} = j \mid r_t = i\} = \begin{cases} \pi_{ij}\eta + o(\eta) & \mathrm{i} \ne j \\ 1 + \pi_{ii}\eta + o(\eta) & \mathrm{i} = j \end{cases} \tag{3}$$

where $\eta > 0$ and $\lim_{\eta\to\infty}(\frac{o(\eta)}{\eta}) = 0$. The transition rate from mode i to mode j is $\pi_{ij} \ge 0$ when $i \ne j$ and $\pi_{ii} = -\sum_{j=1, j\ne i}^{s} \pi_{ij}$.

E, $A(r_t)$, $D(r_t)$ represent constant matrices with proper dimensions and the $\mathrm{rank}(E) \le n$. For instance, in order to simplify notation in the following papers, matrix A_i will replace $A(r_t)$ for $r_t = i,\ i \in S$.

Lemma 1[23]**.** Let $V(x(t), r_t)$ be a Lyapunov functional candidate for system (1) with $V(x(0), r_0) = 0$ and $\omega(t)^T \omega(t) \le \bar{\omega}^2$ .If there exist $\gamma \ge 0$ such that

$$\mathcal{L}V(x(t), r_t) + \gamma V(x(t), r_t) - \frac{\gamma}{\bar{\omega}^2}\omega(t)^T \omega(t) \le 0 \tag{4}$$

Then $\varepsilon(V(x(t^*), r_{t^*})) \le 1$ for $t^* \ge 0$.

Remark 1[24]**.** The system (1) could be decomposed by the following method. First, two invertible matrices M_α and N_α can be found to satisfy that $MEN = \begin{bmatrix} I_r & 0 \\ 0 & 0 \end{bmatrix}$.

Let $\hat{x}(t) = N^{-1}x(t) = \begin{bmatrix} \hat{x}_1(t) \\ \hat{x}_2(t) \end{bmatrix}$, $\hat{x}_1(t) \in \mathbb{R}^r$, $\hat{x}_2(t) \in \mathbb{R}^{n-r}$.

Denote $\begin{bmatrix} A_{1i} \\ A_{2i} \end{bmatrix} = MA_iN$, $\begin{bmatrix} D_{1i} \\ D_{2i} \end{bmatrix} = MD_i$,

where $\begin{bmatrix} A_{1i} \\ A_{2i} \end{bmatrix} = \begin{bmatrix} A_{11i} & A_{12i} \\ A_{21i} & A_{22i} \end{bmatrix}$.

Then, the system (1) is equivalent to

$$\dot{\hat{x}}_1(t) = A_{1i}\hat{x}(t) + D_{1i}\omega(t) \tag{5}$$

$$0 = A_{2i}\hat{x}(t) + D_{2i}\omega(t) \tag{6}$$

Assumption 1[23]**.** Assume the singular Markovian jump system (5) and (6) are impulse free and regular.

Assumption 2. Consider matrices to be suitable for algebraic operations even when their dimensions are not explicitly provided.

3 Main results

In this section, we design a Lyapunov-Krasovskii Function (LKF) to study the RSE issue of SMJS (1) based on state decomposition method. Meanwhile, an RSE criterion is obtained as follows.

Theorem 1. For giving scalar $\gamma > 0$, if there exist appropriate dimensions matrices $P_i > 0$, $H_i = [H_{1i}, H_{2i}]$, such that the following LMIs are feasible for $i \in S$:

$$\Gamma_i = \begin{bmatrix} \Gamma_{1i} & \Gamma_{2i} & H_{1i}^T D_i \\ * & -\mathrm{sym}(H_{2i}) & H_{2i}^T D_i \\ * & * & -\frac{\gamma}{\bar{\omega}^2} I \end{bmatrix} < 0 \tag{7}$$

where

$$\Gamma_{1i} = \sum_{j=1}^{s} \pi_{ij} P_j + \gamma P_i + \mathrm{sym}(A_{1i}^T H_{1i})$$

$$\Gamma_{2i} = P_i + A_{1i}^T H_{2i} - H_{1i}^T$$

Then the reachable set of system (1)-(2) is bounded by the intersection of ellipsoids:

$$\Theta_i(x) = \{x \mid x^T(t)\tilde{P}_i x(t) \le 1,\ x \in \mathbb{R}^n, \tilde{P}_i > 0\} \tag{8}$$

where

$$\tilde{P}_i = N^{-T}\begin{bmatrix} \delta P_{11i} & 0 \\ 0 & \frac{1-\delta}{r_{2i}^2} \end{bmatrix} N^{-1},\ P_{11i} = [I_r, 0, 0] P_i [I_r, 0, 0]^T$$

$$r_{1i} = \frac{1}{\sqrt{\lambda_{\min}(P_{11i})}},\ r_{2i} = \frac{\|A_{21i}\| r_{1i} + \|D_{2i}\| \bar{\omega}}{\|A_{22i}\|} \tag{9}$$

with $\delta \in (0,1)$.

Proof. The following stochastic Lyapunov function candidate for system (5) is constructed:

$$V(x(t), r_t) = \hat{x}_1^T P_i \hat{x}_1(t) \tag{10}$$

$\mathcal{L}$ has been defined in the notation. Then the following function is obtained:

$$\mathcal{L}V(x(t), r_t) = 2\hat{x}_1^T(t) P_i \dot{\hat{x}}_1(t) + \hat{x}_1^T(t) \sum_{j=1}^{s} \pi_{ij} P_j \hat{x}_1(t) \tag{11}$$

To employ Lemma 1, the following simplification can be made for Eq. (11):

$$\mathcal{L}V(x(t), r_t) = -\gamma V(x(t), r_t) + \frac{\gamma}{\bar{\omega}^2}\omega^T(t)\omega(t) + \xi^T(t)\Psi_i\xi(t) \tag{12}$$

where $\Psi_i = \begin{bmatrix} \sum_{j=1}^{s} \pi_{ij} P_j + \gamma P_i & P_i & 0 \\ * & 0 & 0 \\ 0 & 0 & -\frac{\gamma}{\bar{\omega}^2} I \end{bmatrix}$

$$\xi(t) = \begin{bmatrix} \hat{x}_1^T(t) & \dot{\hat{x}}_1(t)^T & \omega^T(t) \end{bmatrix}^T$$

the $\xi(t)$ is the augmented system variable.

Introducing the free weighting matrix $H_i = [H_{1i}, H_{2i}]$.

From the differential system (5) through equivalent transformation, we can get $-\dot{\hat{x}}_1(t) + A_{1i}\hat{x}_1(t) + D_{1i}\omega(t) = 0$,

$$2\left[\hat{x}_1^T(t)H_{1i}^T+\dot{\hat{x}}_1(t)^T H_{2i}^T\right]\left[-\dot{\hat{x}}_1(t)+A_{1i}\hat{x}_1(t)+D_{1i}\omega(t)\right]=0 \quad (13)$$

Then, combining (10) -(13) the following equality holds:

$$\mathcal{L}V(x(t),r_t)+\gamma V(x(t),r_t)-\frac{\gamma}{\bar{\omega}^2}\omega^T(t)\omega(t)=\xi^T(t)\Gamma_i\xi(t) \quad (14)$$

From inequality (7), we have $\xi^T(t)\Gamma_i\xi(t)<0$, which implies:

$$\mathcal{L}V(x(t),r_t)+\gamma V(x(t),r_t)-\frac{\gamma}{\bar{\omega}^2}\omega^T(t)\omega(t)\le 0 \quad (15)$$

Based on Lemma1, it illustrates that

$$\varepsilon(\hat{x}_1^T(t)P_i\hat{x}_1(t))\le 1 \quad (16)$$

Therefore, we can get that $\|\hat{x}_1(t)\|\le r_{1i}$, where r_1 has definition in Eq. (9).

In addition, through the analysis and observation of the second algebraic subsystem (6), it is easy to get the following derivation:

$$\|A_{22i}\hat{x}_2(t)\|=\|A_{21i}\hat{x}_1(t)+D_{2i}\omega(t)\| \quad (17)$$

It is simple to get $\|\hat{x}_2(t)\|\le r_{2i}$, which equals

$$\hat{x}_2^T(t)\frac{1}{r_{2i}^2}\hat{x}_2(t)\le 1 \quad (18)$$

where r_2 has definition in Eq. (9).

Through the above derivation and corresponding processing of the two subsystems, combined with the two inequalities (16) and (18), the following conclusion can be drawn:

$$\begin{bmatrix}\hat{x}_1(t)\\ \hat{x}_2(t)\end{bmatrix}^T\begin{bmatrix}\delta P_{1i} & 0\\ 0 & \dfrac{1-\delta}{r_{2i}^2}\end{bmatrix}\begin{bmatrix}\hat{x}_1(t)\\ \hat{x}_2(t)\end{bmatrix}\le 1 \quad (19)$$

which shows $x^T(t)\tilde{P}_i x(t)\le 1$.

The proof is completed.

Remark 3. Each matrix or element described by mode i corresponds to a matrix or element with the same status in mode j, such as r_{1j}, r_{2j}, and P_j.

Remark 4. By introducing the free weighting matrix $H_i=[H_{1i},H_{2i}]$ and placing it in the matrix Γ_i to relax the constraints on the corresponding items, it is used to reduce the conservatism of the condition.

Remark 5. In order to find the smallest reachable set, the additional constraint $\mu I\le\tilde{P}_i$ is proposed with $\mu>0$, then we optimize the problem as follows,

$$\begin{bmatrix}\bar{\mu}I & I\\ I & \tilde{P}_i\end{bmatrix}\ge 0 \quad (20)$$

where $\bar{\mu}=\dfrac{1}{\mu}$ is minimized.

Numerical Example

In this section, an example is provided to demonstrate the effectiveness of the method in Theorem 1.

Example 1. Consider a singular Markovian jump system after decomposition with

$$E=\begin{bmatrix}1&0\\0&0\end{bmatrix},\quad A_1=\begin{bmatrix}-0.3&0.4\\-0.1&-0.5\end{bmatrix},\quad A_2=\begin{bmatrix}-0.4&-0.1\\-0.2&-0.1\end{bmatrix}$$

$$D_1=\begin{bmatrix}0.1\\0.1\end{bmatrix},\quad D_2=\begin{bmatrix}0.1\\-0.1\end{bmatrix},\quad \pi=\begin{bmatrix}-3&3\\6&-6\end{bmatrix},\quad \bar{\omega}^2=1$$

Mode1:
$$\dot{\hat{x}}_1(t)=\begin{bmatrix}-0.3 & 0.4\end{bmatrix}\hat{x}(t)+0.1\omega(t)$$
$$0=\begin{bmatrix}-0.1 & -0.5\end{bmatrix}\hat{x}(t)+0.1\omega(t)$$

Mode2:
$$\dot{\hat{x}}_1(t)=\begin{bmatrix}-0.4 & 0.1\end{bmatrix}\hat{x}(t)+0.1\omega(t)$$
$$0=\begin{bmatrix}-0.2 & -0.1\end{bmatrix}\hat{x}(t)-0.1\omega(t)$$

$\omega(t)=\sin(t)$

By using the method in Theorem 1 and the optimization in (20), in the case of $\delta=0.5$, we can solve the maximum value of $\mu=60$, and

$$P_1=\begin{bmatrix}122.3447 & 20.6522\\ 20.6522 & 72.6874\end{bmatrix},\quad P_2=\begin{bmatrix}76.5226 & -20.4055\\ -20.4055 & 80.8097\end{bmatrix}$$

Then,

$$\Gamma_1=\begin{bmatrix}-156.3282 & -68.8364 & 50.6162 & 58.5985 & 5.5040\\ * & -42.0108 & 22.5114 & 30.0805 & 2.6799\\ * & * & -72.9494 & 31.7138 & -1.7838\\ * & * & * & -69.4356 & 0.1628\\ * & * & * & * & -0.2000\end{bmatrix}$$

Fig. 1 represents the switching between the two modes of the SMJS. Fig. 2 depicts that the reachable set of the system is bounded by the theory described in Theorem 1 in both states of SMJS, which shows the validity of the criteria.

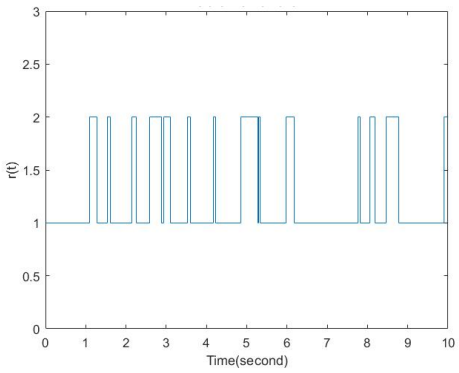

Fig. 1. The switching between two modes.

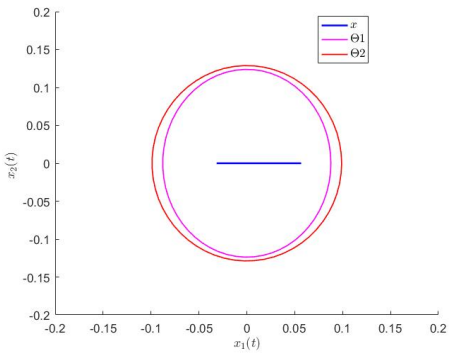

Fig. 2. The reachable set and the ellipsoids.

4 Conclusion

In the paper, we have studied the reachable set estimation issue of singular Markovian jump system under zero initial conditions. The state decomposition method is employed to obtain the sufficient conditions such that all states originating from the origin are confined within intersection of specified ellipsoids. Ultimately, a numerical example is provided to showcase the effectiveness of the employed method. The above method will be employed to the SMJS with distributed delay and extended to nonlinear systems in the future work [25,26].

References

[1] X. Zhang, L. Zhang, X. Zhao, et al. Reachable set control for singular systems with disturbance via sliding mode control[J], J. Frankl. Inst. 360(4) (2023) 3307-3329.

[2] L. Zhang, Y. Cao, Z. Feng, N. Zhao. Reachable set synthesis for singular systems with time-varying delay via the adaptive event-triggered scheme. J. Franklin Inst., 359 (2) (2022) 1503-1521.

[3] N. Malone, H.-T. Chiang, K. Lesser, M. Oishi, L. Tapia, Hybrid dynamic moving obstacle avoidance using a stochastic reachable set-based potential field, IEEE Trans. Robot. 33 (5) (2017) 1124–1138.

[4] S. Xu, P.V. Dooren, R. Stefan, J. Lam, Robust stability and stabilization for singular systems with state delay and parameter uncertainty, IEEE Trans. Autom. Control 47 (7) (2002) 1122–1128.

[5] J.X. Lin, X.D. Zhao, M. Xiao, J.J. Shen, Stabilization of discrete-time switched singular systems with state, output and switching delays, J. Frankl. Inst 356 (4) (2019) 2060–2089.

[6] R.W. Newcomb, The semistate description of nonlinear time-variable circuits, IEEE Trans. Circuits Syst 28 (1) (1981) 62–71.

[7] S. Xu, J. Lam, Robust stability and stabilization of discrete singular systems: an equivalent characterization, IEEE Trans. Autom. Control 49 (4) (2004) 568–574.

[8] J.M. Wei, H.M. Zhi, K. Liu, X.W. Mu, Stability of mode-dependent linear switched singular systems with stable and unstable subsystems, J. Frankl. Inst 356 (5) (2019) 3102–3114.

[9] G. Zhang, Y. Xia, P. Shi, New bounded real lemma for discrete-time singular systems, Automatica 44 (3) (2008) 886–890.

[10] R. Sakthivel, S. Santra, B. Kaviarasan, K. Venkatanareshbabu, Dissipative analysis for network-based singular systems with non-fragile controller and event-triggered sampling scheme, J. Frankl. Inst 354 (12) (2017) 4739–4761.

[11] Y.-L. Zhi, Y. He., M. Wu., Q. Liu, Dissipativity analysis for singular time-delay systems via state decomposition method. IEEE Transactions on Systems, Man, and Cybernetics: Systems 50.10 (2018): 3936-3942.

[12] G.B. Liu, B.Y. Zhang, Q. Ma, New results on reachable set estimation for singular systems with time-varying delays, in: Proceedings of the Thirty-sixth Chinese Control Conference (CCC), 2017, pp. 145–150.

[13] Y.-L. Zhi, A variable memory state feedback and its application to robust control of uncertain singular time-delay systems. Neural Comput. Appl., 34 (3) (2022) 2177-2186.

[14] L.V. Hien, N.T. Dzung, H.B. Minh, A novel approach to state bounding for discrete-time Markovian jump systems with interval time-varying delay, IMA J. Math. Control Inf. 32 (2) (2014) 293–307.

[15] Z. Feng, W.X. Zheng, On reachable set estimation of delay Markovian jump systems with partially known transition probabilities, J. Frankl. Inst. 353 (15) (2016) 3835–3856.

[16] R. Saravanakumar, M.S. Ali, C.K. Ahn, H.R. Karimi, P. Shi, Stability of Markovian jump generalized neural networks with interval time-varying delays, IEEE Trans. Neural Netw. Learn. Syst. 28 (8) (2017) 1840–1850.

[17] H. Gao, Z. Li, X. Yu and J. Qiu, Hierarchical Multiobjective Heuristic for PCB Assembly Optimization in a Beam-Head Surface Mounter, IEEE Trans. Cybern. 52 (7) (2022) 6911-6924.

[18] L. Wang, J. Xia, J.H. Park, G. Chen, X. Xie, Reachable set estimation and stochastic sampled-data exponential synchronization of Markovian jump neural networks with time-varying delays Neural Netw., 165 (3) (2023) 213-227.

[19] G. Wang, Q. Zhang, X. Yan, Analysis and Design of Singular Markovian Jump Systems, Springer, Switzerland, 2015.

[20] G. Zhuang, S.F. Su, J. Xia, W. Sun, HMM-based asynchronous H∞ filtering for fuzzy singular Markovian switching systems with retarded time-varying delays, IEEE Trans. Cybern. 51 (3) (2020) 1189-1203.

[21] G. Zhuang, J. Xia, W. Sun, Q. Ma, Z. Wang, Y.Q. Wang, Normalization and stabilization of neutral descriptor hybrid systems based on p-d feedback control, J. Frankl. Inst. 357 (2020) 1070–1089.

[22] Y. Li, Y. He, W.J. Lin, M. Wu, Reachable set estimation for singular systems via state decomposition method, J. Frankl. Inst. 357 (11) (2020) 7327-7342.

[23] Z. Feng, Z. Jiang, W.X. Zheng, Reachable set synthesis of singular Markovian jump systems[J], J. Frankl. Inst. 357 (18) (2020) 13785-13799.

[24] S. Xu, J. Lam, Robust Control and Filtering of Singular Systems, Springer, Berlin, 2006.

[25] Z. Feng, R. -B. Li and L. Wu, "Adaptive Decentralized Control for Constrained Strong Interconnected Nonlinear Systems and Its Application to Inverted Pendulum," in IEEE Transactions on Neural Networks and Learning Systems. (2023) 1-11.

[26] Z. Feng, R. -B. Li, N. Zhang and L. Wu, Event-Based Asymptotic Tracking Control for Constrained MIMO Nonlinear Systems via a Single-Parameter Adaptation Method, in IEEE Transactions on Systems, Man, and Cybernetics: Systems. 53 (12) (2023) 7758-7768.

Proceedings of the 3rd Conference on Fully Actuated System Theory and Applications
May 10-12, 2024, Shenzhen, China

Observer-based stabilization for networked interval type-2 fuzzy semi-Markov jump systems with cyber attacks

Runkun Li[1], Wenhai Qi[2]

1. School of Engineering, Qufu Normal University, Rizhao Rizhao276826, P. R. China
E-mail: 3217194811@qq.com

2. School of Engineering, Qufu Normal University, Rizhao Rizhao276826, P. R. China
E-mail: qiwhtanedu@163.com

Abstract: This paper investigates the observer-based stabilization for networked discrete interval type-2 fuzzy (IT2F) semi-Markov jump systems subject to cyber attacks. Nonlinear objects with parameter uncertainty are represented by IT2F model with more advantages than traditional T-S fuzzy model. Considering that the actual system state is unavailable, the observer-based method is adopted to deal with the system state. The main purpose is to construct sufficient conditions for the existence of observer-based controller based on fuzzy model, semi-Markov kernel (SMK) framework and ST-dependent Lyapunov functions under the case of random denial-of-service attacks, so that the underlying system is σ mean-square stable. Finally, the superiority of the proposed control method is verified by by the single-link robot arm model.

Key Words: cyber attacks, internal type-2 fuzzy, semi-Markov kernel.

1 Introduction

Due to the powerful modeling capabilities, Markov jump systems (MJSs) are widely used in real industrial systems [1, 2]. However, the sojourn time (ST) of MJSs follows geometric and exponential distributions, and the transition probabilities (TPs) are memory-free, which greatly limits the application scope. In order to overcome this problem, many researches have studied semi-Markovian jump systems (S-MJSs) to increase the application range of jump system. Different from MJSs, the ST of S-MJSs obeys a more ordinary distribution, has memorizable TPs, and exhibits greater power in modeling random systems. At present, many studies on S-MJSs have been reported [3–6]. In recent years, many studies use SMK method to analyze the system stability, which can integrate the related statistics about the mode jump and the ST.

In real physical systems, nonlinear characteristics are unavoidable. T-S fuzzy model can deal with complex nonlinear characteristics effectively and is widely used in various fields, which describes nonlinear systems through certain fuzzy rules and membership functions [7–9]. However, the value of membership degree may also be uncertain, and the traditional T-S fuzzy model cannot handle these uncertainties. Unlike the traditional T-S fuzzy model, the type-2 fuzzy set has been proposed to deal with this problem [10, 11], while there is a growing computational burden. At this moment, the proposal of interval type-2 fuzzy (IT2F) model has solved the problem, reducing the computation burden. Nowadays, the IT2F model has many applications in S-MJSs, such as event-triggered scheme and trajectory tracking.

Networked control systems (NCSs) are widely used because of their advantages of flexibility and convenience, but frequent network attacks pose a great threat to NCSs [12]. Among all the attack types, denial-of-service (DoS) attacks can block data of actuators and sensors, affecting data transmission in NCSs [13]. Therefore, it is of great significance to study NCSs under DoS attacks for secure and stable data transmission. Most of the works adopt the traditional T-S fuzzy method [9, 10], ignoring the uncertainty of the system parameters. As a commonly used method, state feedback neglects the problem that the system state cannot be measured in the actual systems [8]. It is worth noting that observer-based feedback control effectively solve this problem.

Based on the the above information, the observer-based stabilization problem has been investigated for networked discrete IT2F S-MJSs with cyber attacks. The main contributions are as: (i) Unlike the discrete S-MJSs realized by traditional T-S fuzzy method [7–10], the discrete nonlinear S-MJSs are described by IT2F model, which can deal with parameter uncertainty. (ii) Compared with the existing IT2F S-MJSs [11–13], the SMK method is used to overcome the constraint that each mode of the system is subject to a single distribution of ST with some parameters. (iii) Adopting the ST-dependent Lyapunov functions, we propose sufficient conditions for the existence of an observed-based controller for networked S-MJSs with cyber attacks, which can guarantees the underlying system σ-error mean-square stable (σ-MSS).

2 Problem description

Consider the network-based IT2 fuzzy S-MJSs as:

Plant Rule h: IF $g_1^{\sigma_t}(s(t))$ is $G_{h1}^{\sigma_t}$, and $g_2^{\sigma_t}(s(t))$ is $G_{h2}^{\sigma_t}$, and $\cdots$ and, $g_\gamma^{\sigma_t}(s(t))$ is $G_{h\gamma}^{\sigma_t}$, THEN

$$s(t+1) = A_{h\sigma_t}s(t) + B_{h\sigma_t}u(t), y(t) = C_{h\sigma_t}s(t), \quad (1)$$

where $s(t)$ and $u(t)$ are the system state and control input, $y(t)$ is the system output. $A_{h\sigma_t}$, $B_{h\sigma_t}$ and $C_{h\sigma_t}$ are with appropriate dimensions. $g_1^{\sigma_t}(s(t))$, $g_2^{\sigma_t}(s(t))$, …, $g_\gamma^{\sigma_t}(s(t))$ are the premise variables, and $G_{h1}^{\sigma_t}$, $G_{h2}^{\sigma_t}$, …, $G_{h\gamma}^{\sigma_t}$, $h \in \mathcal{R} \triangleq \{1, 2, ..., \varphi\}$ are the IT2 fuzzy sets, where φ is the number of IF-THEN. The firing strength for the hth fuzzy rule is denoted by $f_h(s(t)) = [\underline{f}_h(s(t)), \overline{f}_h(s(t))]$, where $\underline{f}_h(s(t)) = \Pi_{\kappa=1}^{\gamma}\underline{\nu}_{G_{h\kappa}^{\sigma_t}}(g_\kappa^{\sigma_t}(s(t))) \geqslant 0$ and $\overline{f}_h(s(t)) = \Pi_{\kappa=1}^{\gamma}\overline{\nu}_{G_{h\kappa}^{\sigma_t}}(g_\kappa^{\sigma_t}(s(t))) \geqslant 0$ are the lower and upper grades

This work was supported by National Key R & D Program of China under Grant 2021YFE0193900.

of membership. $\underline{\nu}_{G_{h\kappa}^{\sigma_t}}(g_\kappa^{\sigma_t}(s(t))) \leqslant \overline{\nu}_{G_{h\kappa}^{\sigma_t}}(g_\kappa^{\sigma_t}(s(t)))$ with $\underline{\nu}_{G_{h\kappa}^{\sigma_t}}(g_\kappa^{\sigma_t}(s(t))) \in [0,1]$ and $\overline{\nu}_{G_{h\kappa}^{\sigma_t}}(g_\kappa^{\sigma_t}(s(t))) \in [0,1]$ are the lower and upper membership functions.

$\{\sigma_t\}_{t\in\mathcal{Z}_{\geq 0}}$ is a semi-Markov chain in $\mathbb{I} \triangleq \{1,2,...,O\}$ governed by the SMK $\Theta(\varsigma) = [\eta_{ab}(\varsigma)]_{a,b\in\mathbb{I}} = \Pr(\mathfrak{R}_{n+1} = b, \mathfrak{S}_{n+1} = \varsigma \mid \mathfrak{R}_0,\ldots,\mathfrak{R}_n = a; t_0,\ldots,t_n) = \Pr(\mathfrak{R}_{n+1} = b, \mathfrak{S}_{n+1} = \varsigma \mid \mathfrak{R}_n = a) = \theta_{ab}\phi_{ab}(\varsigma)$, where the mode index at the nth switching is represented as $\mathfrak{R}_n$, $\mathfrak{S}_n$ denotes the ST between the $(n-1)$th and nth jumps. $\phi_{ab}(\varsigma) \triangleq [\Pr(\mathfrak{R}_{n+1} = b, \mathfrak{S}_{n+1} = \varsigma, \mathfrak{R}_n = a)]/[\Pr(\mathfrak{R}_{n+1} = b, \mathfrak{R}_n = a)]$ with $\phi_{ab}(\varsigma) = 0$, $\forall a \in \mathbb{I}$, $\forall \varsigma \in \mathcal{Z}_{\geq 0}$ is the probability density function and $\theta_{ab} \triangleq \Pr(\mathfrak{R}_{n+1} = b \mid \mathfrak{R}_n = a)$, $\forall a,b \in \mathbb{I}$ with $\theta_{ab} = 0$ is the TP. Note that the SMK satisfies $\eta_{ab}(\varsigma) \triangleq 0$, $\eta_{ab}(\varsigma) \in \mathbb{R}_{[0,1]}$, $\forall a,b \in \mathbb{I}(a \neq b)$, $\forall \varsigma \in \mathcal{Z}_{\geq 0}$, $\sum_{\varsigma=1}^{\infty}\sum_{b\in\mathbb{I}}\eta_{ab}(\varsigma) = 1$. Moreover, the TP satisfies $\sum_{b\in\mathbb{I},b\neq a}\theta_{ab} = 1$.

Then, one has following overall system

$$\begin{aligned} s(t+1) &= \sum\nolimits_{h=1}^{\varphi} f_h(s(t))[A_{h\sigma_t}s(t) + B_{h\sigma_t}u(t)], \\ y(t) &= \sum\nolimits_{h=1}^{\varphi} f_h(s(t))C_{h\sigma_t}s(t), \end{aligned} \tag{2}$$

where $f_h(s(t)) = \underline{f}_h(s(t))\underline{F}_h(s(t)) + \overline{f}_h(s(t))\overline{F}_h(s(t))$, $\underline{F}_h + \overline{F}_h(s(t)) = 1$, $\underline{F}_h$, $\overline{F}_h(s(t)) \in [0,1]$, $\sum_{h=1}^{\varphi} f_h(s(t)) = 1$, $\underline{F}_h$ and $\overline{F}_h(s(t))$ are the nonlinear functions that can capture the parameter uncertainty.

The fuzzy observer is considered as follows:

Plant Rule h: IF $g_1^{\sigma_t}(s(t))$ is $G_{h1}^{\sigma_t}$, and $g_2^{\sigma_t}(s(t))$ is $G_{h2}^{\sigma_t}$, and $\cdots$ and, $g_\gamma^{\sigma_t}(s(t))$ is $G_{h\gamma}^{\sigma_t}$, THEN

$$\begin{aligned} \hat{s}(t+1) &= A_{h\sigma_t}\hat{s}(t) + B_{h\sigma_t}\mu(\ell) + L_{h\sigma_t}(y^*(t) - \hat{y}(t)), \\ \hat{y}(t) &= C_{h\sigma_t}\hat{s}(t), u(t) = K_{h\sigma_t}\hat{s}(t), \end{aligned} \tag{3}$$

where $\hat{s}(t)$ is the observer state, $y^*(t)$ is the actual system measurement output, $L_{h\sigma_t}$ is the observer gain, $K_{h\sigma_t}$ is the controller gain. For $\sigma_t = a$, one has

$$\begin{aligned} \hat{s}(t+1) =& \sum\nolimits_{h=1}^{\varphi} f_h(s(t))[A_{ha}\hat{s}(t) + B_{ha}u(t) \\ &+ L_{ha}(y^*(\ell) - \hat{y}(t))], \\ \hat{y}(t) =& \sum\nolimits_{h=1}^{\varphi} f_h(s(t))C_{ha}\hat{s}(t), \\ u(t) =& \sum\nolimits_{h=1}^{\varphi} f_h(s(t))K_{ha}\hat{s}(t). \end{aligned} \tag{4}$$

In network systems, cyber attacks can affect information transmission. As one of the most destructive attacks, DoS attacks are implemented by blocking the transmission channel between the sensor and the controller, thereby reducing the actual output. This paper considers the discrete-time networked S-MJSs with DoS attacks. The actual system measurement output $y^*(t)$ transmitted to the controller can be described as

$$y^*(t) = \imath(t)y(t) + (1 - \imath(t))\delta y(t). \tag{5}$$

One can get further

$$E\{\imath(t) - \hat{\imath}\} = 0, E\{|\imath(t) - \hat{\imath}|^2\} = \hat{\imath}(1 - \hat{\imath}),$$

By defining $e(t) \triangleq s(t) - \hat{s}(t)$ and let $S(t) \triangleq [s^T(t)\ e^T(t)]^T$, one can get

$$S(t+1) = \sum\nolimits_{h=1}^{\varphi} f_h(s(t))\aleph_{ha}S(t), \tag{6}$$

where $\aleph_{ha} \triangleq \mathbb{A}_{ha} + (\imath(t) - \hat{\imath})\mathbb{B}_{ha}$, $\mathbb{A}_{ha} \triangleq \begin{bmatrix} A_{ha} + B_{ha}K_{ha} & -B_{ha}K_{ha} \\ (1-\delta)(1-\hat{\imath})L_{ha}C_{ha} & A_{ha} - L_{ha}C_{ha} \end{bmatrix}$, $\mathbb{B}_{ha} \triangleq \begin{bmatrix} 0 & 0 \\ (\delta-1)L_{ha}C_{ha} & 0 \end{bmatrix}$.

Definition 1: [6] For the upper bound $\mathbb{T}_{max}^a \in \mathcal{Z}_{\geq 1}$ for ath system of ST and the initial conditions $t_0 \in \mathfrak{R}^{n_S}, \sigma_0 \in \mathbb{I}$, system (6) is σ-error mean-square stable (σ-MSS), there holds: $\lim_{t\longrightarrow\infty} E[\|S(t)\|^2]|_{t_0,\sigma_0,\mathfrak{S}_{n+1}\leq\mathbb{T}_{max}^a|\mathfrak{R}_n=a} = 0$, with $\sigma \triangleq \sum_{a\in\mathbb{I}}|ln(\mathfrak{G}_a(\mathbb{T}_{max}^a))|$, where $\mathfrak{G}_a(\varsigma) = Pr(\mathfrak{S}_{n+1} \leq \varsigma|\mathfrak{R}_n = a) = \sum_{q=0}^{\varsigma}\sum_{b\in\mathbb{I}}\eta_{ab}(q)$. For mode a, $\mathfrak{G}_a(\varsigma)$ is called the cumulative density function and it is assumed that $\mathfrak{G}_a(0) = \eta_{ab}(0) = 0$.

Lemma 1: [8] For any $Z_a, a = 1,2,...,\varphi$ and $P > 0$, there holds $\sum_{a=1}^{\varphi}\sum_{b=1}^{\varphi} f_a f_b Z_a^T P Z_a \leq \sum_{\alpha=1}^{r} h_\alpha Z_\alpha^T P Z_\alpha$, where $f_a > 0$ for $a = 1,2,...,\varphi$ and $\sum_{a=1}^{\varphi} f_a = 1$.

3 Main results

For IT2 fuzzy networked S-MJSs with DoS attacks, the design method of observer-based controller will be presented in this section.

Theorem 1: For given $\rho_a > 0$ $\mathbb{T}_{max}^a \in \mathcal{Z}_{>1}$, $a \in \mathbb{I}$, the system (6) is σ-MSS, if we find $P_{ha}(\tau) > 0$, $\tau \in \mathcal{Z}_{[1,\mathbb{T}_{max}^a]}$ such that $\tau \in \mathcal{Z}_{[1,\mathbb{T}_{max}^a-1]}$,

$$\mathcal{A}_{a\tau}^T P_{ha}(\tau+1)\mathcal{A}_{a\tau} - \rho_a P_{ma}(1) < 0 \tag{7}$$

$$\sum\nolimits_{\varsigma=1}^{\mathbb{T}_{max}^a} \mathcal{A}_{a\varsigma}^T \mathcal{P}_{ha}(\varsigma)\mathcal{A}_{a\varsigma} - P_{ma}(1) < 0 \tag{8}$$

where $\mathcal{A}_{a\tau} \triangleq \underbrace{\aleph_{ha}\aleph_{pa}\aleph_{qa}...\aleph_{ma}}_{\tau}$, $\forall h,p,q,\ldots m \in \mathcal{R}$, $\mathcal{P}_{ha}(\varsigma) = \sum_{b\in\mathbb{I}}\eta_{ab}(\varsigma)P_{hb}(1)/\pi_a$, $\forall h \in \mathcal{R}$, where $\pi_a = \sum_{\varsigma=1}^{\mathbb{T}_{max}^a}\sum_{b\in\mathbb{I}}\eta_{ab}(\varsigma)$.

Proof: Choose the ST-dependent Lyapunov functions as

$$\mathcal{N}(S_t,\sigma_{t_n},\tau) \triangleq S^T(t)\tilde{P}_a(t)S(t)|_{\mathfrak{R}_n=a}, \tag{9}$$

where $\forall a \in \mathbb{I}, \tau \in [1,\mathbb{T}_{max}^a], t = t_n + \tau - 1 \in (t_n, t_{n+1})$. Letting $f_h(s(t)) = f_{ht}$, we can get $\tilde{P}_a(t) = \sum_{h=1}^{r} f_{ht}P_{ha}(\tau)$. From (10), one has

$$\zeta 1\|S(t)\|^2 \leq \mathcal{N}(S_t,\sigma_{t_n},\tau) \leq \zeta_2\|S(t)\|^2, \tag{10}$$

where $\zeta_1 = \inf_{a\in\mathbb{I},h\in\mathcal{R},\tau\in\mathbb{Z}_{[1,\mathbb{T}_{max}^a]}}\{\lambda_{min}P_{ha}(\tau)\}$, $\zeta_2 = \sup_{a\in\mathbb{I},h\in\mathcal{R},\tau\in\mathbb{Z}_{[1,\mathbb{T}_{max}^a]}}\{\lambda_{max}P_{ha}(\tau)\}$. Thus, the first condition in Lemma 1 of Ref. [6] holds.

If $\mathfrak{R}_n = a$, $t \in \{t_{n+\tau}, \forall\tau \in \mathcal{Z}_{[1,\mathbb{T}_{max}^a-1]}\}$, and from (7), there holds

$$\begin{aligned} &S^T(t_n+\tau)\tilde{P}_a(t_n+\tau)S(t_n+\tau) \\ &= \underbrace{\sum\nolimits_{h=1}^{\varphi}\cdots\sum\nolimits_{m=1}^{\varphi}\sum\nolimits_{p=1}^{\varphi}\cdots\sum\nolimits_{y=1}^{\varphi}}_{2\tau} \\ &\underbrace{f_{h(t_n+\tau-1)}\cdots f_{mt_n}f_{p(t_n+\tau-1)}\cdots f_{qt_n}}_{2\tau} \\ &S^T(t_n)\mathcal{A}_{a\tau}^T(\sum\nolimits_{h=1}^{\varphi} f_{h(t_n+\tau)}P_{ha}(\tau+1))\mathcal{A}_{a\tau}S(t_n) \\ &\leq \sum_{h=1}^{\varphi}\cdots\sum_{m=1}^{\varphi} f_{h(t_n+\tau-1)}\cdots f_{mt_n}S^T(t_n) \\ &\mathcal{A}_{a\tau}^T(\sum\nolimits_{h=1}^{\varphi} f_{h(t_n+\tau)}P_{ha}(\tau+1))\mathcal{A}_{a\tau}S(t_n). \end{aligned}$$

Then, we have

$$\begin{aligned}
&\mathcal{N}(S(t),a,\tau)-\rho_a\mathcal{N}(S(t),a,1)\\
&=S^T(t)\tilde{P}_a(t)S(t)-\rho_a S^T(t)\tilde{P}_a(t_n)S(t)\\
&\le\sum_{h=1}^{\varphi}\cdots\sum_{m=1}^{\varphi}f_{h(t_n+\tau-1)}\cdots f_{mt_n}S^T(t_n)\mathcal{A}_{a\tau}^T(\sum\nolimits_{h=1}^{\varphi}f_{h(t_n+\tau)}\\
&P_{ha}(\tau+1))\mathcal{A}_{a\tau}S(t_n)-\rho_a S^T(t_n)\sum\nolimits_{h=1}^{\varphi}f_{ht_n}P_{ha}(1)S(t_n)\\
&=\sum_{h=1}^{\varphi}\cdots\sum_{p=1}^{\varphi}\sum_{q=1}^{\varphi}\sum_{m=1}^{\varphi}f_{h(t_n+\tau-1)}\cdots f_{pt_n}f_{q(t_n+\tau)}h_{mt_n}\\
&S^T(t_n)(\mathcal{A}_{a\tau}^TP_{ha}(\tau+1)\mathcal{A}_{a\tau}-\rho_aP_{ma}(1))S(t_n)<0,
\end{aligned}\tag{11}$$

further getting the second condition in Lemma 1 of Ref.[6]. Letting $\mathfrak{R}_n=a,\mathfrak{R}_{n+1}=b,\forall a\neq b,\mathfrak{S}_{n+1}=\varsigma$, it yields

$$\begin{aligned}
&E\{\mathcal{N}(S(t),b,\tau)|_{S0,\sigma_0,\mathfrak{S}_{n+1}\le\mathbb{T}^a_{max},\mathfrak{R}_n=a}-\mathcal{N}(S(t),a,\tau)\}\\
&\le S^T(t_n)[\sum_{\varsigma=1}^{\mathbb{T}^a_{max}}\sum_{b\in\mathbb{I}}\eta_{ab}(\varsigma)\sum_{p=1}^{\varphi}\cdots\sum_{q=1}^{\varphi}f_{p(t_n+\varsigma-1)}f_{qt_n}\mathcal{A}_{a\varsigma}^T\\
&(\sum\nolimits_{h=1}^{\varphi}f_{h(t_n+\varsigma)}P_{ha}(1))\mathcal{A}_{a\varsigma}/\pi_a-\sum\nolimits_{h=1}^{\varphi}f_{ht_n}P_{ha}(1)]S(t_n)\\
&\le\lambda_{max}(\sum\nolimits_{\varsigma=1}^{\mathbb{T}^a_{max}}\mathcal{A}_{a\varsigma}^T\mathcal{P}_{ha}(\varsigma)\mathcal{A}_{a\varsigma}-P_{ma}(1))\|S(t_n)\|^2\\
&\le\zeta_3\|S(t_n)\|^2,
\end{aligned}\tag{12}$$

where $\zeta_3\triangleq\inf_{a\in\mathbb{I},h\cdots m\in\mathcal{R}}\{-\lambda_{max}(\sum_{\varsigma=1}^{\mathbb{T}^a_{max}}\mathcal{A}_{a\varsigma}^T\mathcal{P}_{ha}(\varsigma)\mathcal{A}_{a\varsigma}-P_{ma}(1))\}$.

Therefore, the third condition in Lemma 1 of Ref. [6] ensured by (12), and the system (6) is σ-MSS. ■

Theorem 2: For given $\rho_a>0$ $\mathbb{T}^a_{max}\in\mathcal{Z}_{>1}$, $a\in\mathbb{I}$, the system (6) is σ-MSS, if we find $\alpha_{ha}(\tau,\upsilon),\forall\tau\in\mathcal{Z}_{[1,\mathbb{T}^a_{max}]}$, $\forall\upsilon\in\mathcal{Z}_{[1,\tau]}$, $\tilde{\alpha}_{ha}(\tau)=\alpha_{ha}(\tau,\tau)>0,\forall\tau\in\mathcal{Z}_{[1,\mathbb{T}^a_{max}]}$, $\beta_{ha}(\varsigma,\iota),\forall\varsigma\in\mathcal{Z}_{[1,\mathbb{T}^a_{max}]},\forall\iota\in\mathcal{Z}_{[0,\varsigma-1]}$, such that $\forall\tau\in\mathcal{Z}_{[1,\mathbb{T}^a_{max}-1]},\forall\upsilon\in\mathcal{Z}_{[0,\tau-1]},\forall\varsigma\in\mathcal{Z}_{[1,\mathbb{T}^a_{max}]},\forall\iota\in\mathcal{Z}_{[0,\varsigma-1]}$,

$$\mathcal{A}_{pa}^T\alpha_{ha}(\tau+1,\upsilon+2)\mathcal{A}_{pa}-\alpha_{ha}(\tau+1,\upsilon+1)<0,\tag{13}$$

$$\alpha_{ha}(\tau+1,1)-\rho_a\tilde{\alpha}_{ma}(1)<0,\tag{14}$$

$$\mathcal{A}_{pa}^T\beta_{ha}(\varsigma,\iota+1)\mathcal{A}_{pa}-\beta_{ha}(\varsigma,\iota)<0,\tag{15}$$

$$\sum\nolimits_{\varsigma=1}^{\mathbb{T}^a_{max}}\beta_{ha}(\varsigma,0)-\tilde{\alpha}_{ma}(1)<0,\tag{16}$$

where $\beta_{ha}(\varsigma,\varsigma)\triangleq\sum_{b\in\mathbb{I}}\eta_{ab}(\varsigma)\tilde{\alpha}_{hb}(1)/\pi_a$.

Proof: From (13), we can get

$$\aleph_{ac}^T(\mathcal{A}_{pa}^T\alpha_{ha}(\tau+1,\upsilon+2)\mathcal{A}_{pa}-\alpha_{ha}(\tau+1,\upsilon+1))\aleph_{ac}<0,\tag{17}$$

which means that

$$\mathcal{A}_{p\tau}^T\alpha_{ha}(\tau+1,\upsilon+1)\mathcal{A}_{p\tau}-\alpha_{ha}(\tau+1,1)<0.\tag{18}$$

Combining (14) and (18), we can find

$$\mathcal{A}_{\alpha\tau}^T\alpha_{ha}(\tau+1,\tau+1)\mathcal{A}_{\alpha\tau}-\rho_a\tilde{\alpha}_{ma}(1)<0.\tag{19}$$

Replacing $\alpha_{ha}(\tau,\tau)$ and $\alpha_{ma}(1,1)=\tilde{\alpha}_{ma}(1)$, with $P_{ha}(\tau)$ and $P_{ma}(1)$, it yields (7).

From (15), we have

$$\mathcal{A}_{a\varsigma}^T\beta_{ha}(\varsigma,\varsigma)\mathcal{A}_{a\varsigma}-\beta_{ha}(\varsigma,0)<0.\tag{20}$$

Then, one can get

$$\sum\nolimits_{\varsigma=1}^{\mathbb{T}^a_{max}}(\mathcal{A}_{a\varsigma}^T\beta_{ha}(\varsigma,\varsigma)\mathcal{A}_{a\varsigma}-\beta_{ha}(\varsigma,0))<0.\tag{21}$$

Based on (16) and (21), it yields

$$\sum\nolimits_{\varsigma=1}^{\mathbb{T}^a_{max}}\mathcal{A}_{a\varsigma}^T\beta_{ha}(\varsigma,\varsigma)\mathcal{A}_{a\varsigma}-\tilde{\alpha}_{ma}(1)<0.\tag{22}$$

Letting $\mathcal{P}_{ha}(\varsigma)=\beta_{ha}(\varsigma,\varsigma)$ and $P_{ma}(1)=\tilde{\alpha}_{ma}(1)$, there holds

$$\sum\nolimits_{\varsigma=1}^{\mathbb{T}^a_{max}}\mathcal{A}_{a\varsigma}^T\mathcal{P}_{ha}(\varsigma)\mathcal{A}_{a\varsigma}-P_{ma}(1)<0.$$

Then, (8) holds. ■

Theorem 3: For given $\rho_a>0$ $\mathbb{T}^a_{max}\in\mathcal{Z}_{>1}$, $a\in\mathbb{I}$, the system (6) is σ-MSS, if we find $\beth_{ha}(\tau,\upsilon),\forall\tau\in\mathcal{Z}_{[1,\mathbb{T}^a_{max}]},\forall\upsilon\in\mathcal{Z}_{[1,\tau]}$, $\tilde{\beth}_{ha}(\tau)=\beth_{ha}(\tau,\tau)>0,\forall\tau\in\mathcal{Z}_{[1,\mathbb{T}^a_{max}]}$, $\gimel_{ha}(\varsigma,\iota),\forall\varsigma\in\mathcal{Z}_{[1,\mathbb{T}^a_{max}]},\forall\iota\in\mathcal{Z}_{[0,\varsigma-1]}$, $\mathcal{V}$, U_{ha} and N_{ha} such that $\forall a\in\mathcal{Z}_{[1,\mathbb{T}^\alpha_{max}-1]}$, $\forall b\in\mathcal{Z}_{[0,a-1]}$, $\forall\varsigma\in\mathcal{Z}_{[1,\mathbb{T}^a_{max}]},\forall\iota\in\mathcal{Z}_{[0,\varsigma-2]}$,

$$\begin{bmatrix}-\beth_{ha}(\tau+1,\upsilon+1) & * & *\\ \mathfrak{A}_{pa} & \Delta_{ha} & *\\ \mu\mathfrak{B}_{pa} & * & \Delta_{ha}\end{bmatrix}<0,\tag{23}$$

$$\beth_{ha}(\tau+1,1)-\rho_a\tilde{\beth}_{ma}(1)<0,\tag{24}$$

$$\begin{bmatrix}-\gimel_{ha}(\varsigma,\varsigma-1) & * & *\\ \tilde{\mathfrak{A}}_{pa}l_a(\varsigma) & \check{L}_h & *\\ \mu\tilde{\mathfrak{B}}_{pa}l_a(\varsigma) & * & \check{L}_h\end{bmatrix}<0,\tag{25}$$

$$\begin{bmatrix}-\gimel_{ha}(\varsigma,\upsilon) & * & *\\ \mathfrak{A}_{pa} & Q_{ha} & *\\ \mu\mathfrak{B}_{pa} & * & Q_{ha}\end{bmatrix}<0,\tag{26}$$

$$\sum\nolimits_{\varsigma=1}^{\mathbb{T}^a_{max}}\gimel_{ha}(\varsigma,0)-\tilde{\beth}_{ma}(1)<0,\tag{27}$$

where $\tilde{\mathfrak{A}}_{pa}\triangleq diag_{\mathcal{M}}\{\mathfrak{A}_{pa}\}$, $\tilde{\mathfrak{B}}_{pa}\triangleq diag_{\mathcal{M}}\{\mathfrak{B}_{pa}\}$, $\mathfrak{A}_{pa}\triangleq\begin{bmatrix}A_{pa}\mathcal{V}+B_{pa}U_{pa} & -B_{pa}U_{pa}\\ (1-\delta)(1-\hat{\imath})N_{pa} & A_{pa}\mathcal{V}-N_{pa}\end{bmatrix}$, $\mathfrak{B}_{pa}\triangleq\begin{bmatrix}0 & 0\\ (\delta-1)N_{pa} & 0\end{bmatrix}$, $\Delta_{ha}\triangleq\beth_{ha}(\tau+1,\upsilon+2)-\Gamma^T-\Gamma$, $\check{L}_h\triangleq L_h-\Gamma^T-\Gamma$, $Q_{ha}\triangleq\gimel_{ha}(\varsigma,\iota+1)-\Gamma^T-\Gamma$, $L_h\triangleq diag\{\tilde{\beth}_{h1}(1,1),\tilde{\beth}_{h2}(1,1),...,\tilde{\beth}_{hO}(1,1)\}$, $l_a(\varsigma)\triangleq[\sqrt{\eta_{a1}(\varsigma)/\pi_a}I_{2n_x},\sqrt{\eta_{a2}(\varsigma)/\pi_a}I_{2n_x},...,\sqrt{\eta_{aO}(\varsigma)/\pi_a}I_{2n_x}]^T$, $\mu=\sqrt{\hat{\imath}(1-\hat{\imath})}$. Then, the controller gain and the observer gain are given by $K_{pa}=U_{pa}V$ and $L_{pa}=N_{p\alpha}VC_{pa}^{-1}$.

Proof: From(13), we can get

$$\begin{aligned}
&\mathcal{A}_{pa}^T\alpha_{ha}(\tau+1,\upsilon+2)\mathcal{A}_{pa}-\alpha_{ha}(\tau+1,\upsilon+1)\\
&=-\alpha_{ha}(\tau+1,\upsilon+1)+\mathbb{A}_{pa}^T\alpha_{ha}(\tau+1,\upsilon+2)\mathbb{A}_{pa}\\
&\quad+\mu^2\mathbb{B}_{pa}^T\alpha_{ha}(\tau+1,\upsilon+2)\mathbb{B}_{pa}.
\end{aligned}$$

The following condition can be obtained by schur complement

$$\begin{bmatrix}-\check{\alpha}_{ha\tau\upsilon} & * & *\\ \hat{\alpha}_{ha\tau\upsilon}\mathbb{A}_{pa} & -\hat{\alpha}_{ha\tau\upsilon} & *\\ \mu\hat{\alpha}_{ha\tau\upsilon}\mathbb{B}_{pa} & * & -\hat{\alpha}_{ha\tau\upsilon}\end{bmatrix}<0,\tag{28}$$

where $\check{\alpha}_{ha\tau\upsilon} = \alpha_{ha}(\tau{+}1, \upsilon{+}1)$, $\hat{\alpha}_{ha\tau\upsilon} = \alpha_{ha}(\tau{+}1, \upsilon{+}2)$. Denote $\tilde{F} \triangleq diag\{F_1, F_2, ..., F_O\}$ and $F \triangleq diag\{V, V\}$. Pre- and post-multiplying (28) by $diag\{I_{2n_x}, F^T\hat{\alpha}^{-1}_{ha\tau\upsilon}, F^T\hat{\alpha}^{-1}_{ha\tau\upsilon}\}$ and $diag\{I_{2n_x}, \hat{\alpha}^{-1}_{ha\tau\upsilon}F, \hat{\alpha}^{-1}_{ha\tau\upsilon}F\}$, one has

$$\begin{bmatrix} -\check{\alpha}_{ha\tau\upsilon} & * & * \\ F^T\mathbb{A}_{pa} & -F^T\hat{\alpha}_{ha\tau\upsilon}F & * \\ \mu F^T\mathbb{B}_{pa} & * & -F^T\hat{\alpha}_{ha\tau\upsilon}F \end{bmatrix} < 0, \tag{29}$$

Due to $(\hat{\alpha}_{ha\tau\upsilon} - F)^T\hat{\alpha}^{-1}_{ha\tau\upsilon}(\hat{\alpha}_{ha\tau\upsilon} - F) > 0$ implying that $\hat{\alpha}_{ha\tau\upsilon} - F - F^T > -F^T\hat{\alpha}^{-1}_{ha\tau\upsilon}F$, we have

$$\begin{bmatrix} -\check{\alpha}_{ha\tau\upsilon} & * & * \\ F^T\mathbb{A}_{pa} & \tilde{\alpha}_{ha\tau\upsilon} & * \\ \mu F^T\mathbb{B}_{pa} & * & \tilde{\alpha}_{ha\tau\upsilon} \end{bmatrix} < 0, \tag{30}$$

where $\tilde{\alpha}_{ha\tau\upsilon} = \hat{\alpha}_{ha\tau\upsilon} - F - F^T$. Performing the congruence transformation to (23) by $diag\{F, F, F, F\}$, it can be obtained that

$$\begin{bmatrix} -F^T\beth_{ha}(\tau+1, \upsilon+1)F & * & * \\ F^T\mathfrak{A}_{pa}F & F^T\Delta_{ha}F & * \\ \mu F^T\mathfrak{B}_{pa}F & * & F^T\Delta_{ha}F \end{bmatrix} < 0. \tag{31}$$

Defining $\Gamma \triangleq F^{-1}$, $\mathcal{V} \triangleq V^{-1}$, $U_{pa} \triangleq K_{pa}V^{-1}$, $N_{pa} \triangleq L_{pa}C_{pa}V^{-1}$, $\beth_{ha}(\tau{+}1, \upsilon{+}2) \triangleq F^{-T}\alpha_{ha}(\tau{+}1, \upsilon{+}2)F^{-1}$, $\beth_{ha}(\tau+1, \upsilon+1) \triangleq F^{-T}\alpha_{ha}(\tau+1, \upsilon+1)F^{-1}$, (30) can be got by (31), which means that (23) ensures (13). In the same way, (14) can be ensured by (24), (27) can guarantee (16). When $\iota = \varsigma - 1$, (15) can be ensured by (25), and when $\iota \in [0, \varsigma - 2]$, we can get (15) from (26). ■

4 Case study

Table 1: PARAMETER

$\omega(t)$	The angle position of the arm
$\mathfrak{M}$	The mass of the paylode
g	The acceleration of gravity
$\mathfrak{J}$	The moment of inertia
$\mathfrak{L}$	The length of the arm
$\mathfrak{W}$	The coefficient of viscous friction

Consider the following single-link robot arm (SLRA) model from [14] characterized by $\ddot{\omega}(t) = -\frac{\mathfrak{M}g\mathfrak{L}}{\mathfrak{J}}sin(\omega(t)) - \frac{\mathfrak{W}}{\mathfrak{J}}\dot{\omega}(t) + \frac{1}{\mathfrak{J}}u(t)$, in which the parameters $\mathfrak{W}$, $\mathfrak{L}$, and g are given as 2 Nms/rad, 0,5m, and 9.81m/s^2, respectively. Assume that $\mathfrak{M}$ and $\mathfrak{J}$ have two modes: Mode1 ($\mathfrak{M}(1) = 1$, $\mathfrak{J}(1) = 1$); Mode2 ($\mathfrak{M}(2) = 5$, $\mathfrak{J}(2) = 5$), and the variations are governed by a semi-Markov process. Let $s(t) = [\omega^T(t)\ \dot{\omega}^T(t)]^T$ denotes the system state. We have the following SLRA: $\dot{s}_1(t) = s_2(t)$, $\dot{s}_2(t) = -\frac{\mathfrak{M}_a g\mathfrak{L}}{\mathfrak{J}_a}sin(s_1(t)) - \frac{\mathfrak{W}}{\mathfrak{J}_a}s_2(t) + \frac{1}{\mathfrak{J}_a}u(t)$. Assume that the system $y(t) = s_1(t)$, and the membership functions are $\underline{f}_1(s_1(t)) = e^{-\frac{s_1^2(t)}{0.5}}$, $\overline{f}_1(s_1(t)) = e^{-s_1^2(t)}$, $\underline{f}_2(s_1(t)) = 1 - e^{-s_1^2(t)}$, $\overline{f}_2(s_1(t)) = 1 - e^{-\frac{s_1^2(t)}{0.5}}$. For the sampling time T, we have $s(t+1) = \sum_{h=1}^{2} f_h(s(t))[A_{ha}s(k) + B_{ha}u(k)]$, $y(k) = \sum_{h=1}^{2} f_a(s(t))C_{ha}s(t)$, where $A_{1h} = \begin{bmatrix} 1 & T_0 \\ -\frac{\mathfrak{M}_a g\mathfrak{L}T}{\mathfrak{J}_a} & 1 - \frac{\mathfrak{W}T}{\mathfrak{J}_a} \end{bmatrix}$, $A_{2h} = \begin{bmatrix} 1 & T_0 \\ -\frac{\epsilon\mathfrak{M}_a g\mathfrak{L}T}{\mathfrak{J}_a} & 1 - \frac{\mathfrak{W}T}{\mathfrak{J}_a} \end{bmatrix}$, $B_{1h} = B_{2h} = \begin{bmatrix} 0 & \frac{T}{\mathfrak{J}_a} \end{bmatrix}^T$, $C_{1h} = C_{2h} = \begin{bmatrix} 1 & 0 \end{bmatrix}$.

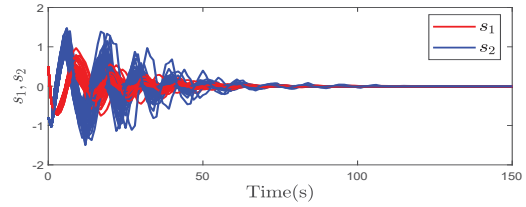

Fig. 1 System state

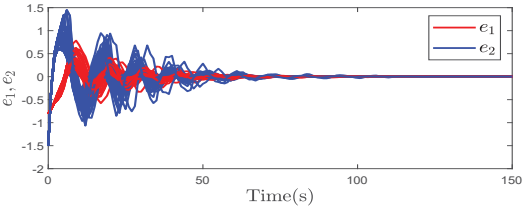

Fig. 2 Estimation error

Other parameters are given as $\underline{F}_h = 0.5, \overline{F}_h = 0.5, T = 0.25, \hat{\imath} = 0.25, \delta = 0.5, T^1_{max} = T^2_{max} = 5, \rho_1 = 0.75, \rho_2 = 1.25, [\eta_{ab}] = \begin{bmatrix} 0 & 1 \\ 1 & 0 \end{bmatrix}$. The ST follows the Bernoulli distribution $\phi_1(\varsigma) = 0.6^{\varsigma} \cdot 0.4^{5-\varsigma} \cdot 5!/((5-\varsigma)!\varsigma!)$ and the Weibull distribution $\phi_2(\varsigma) = 0.4^{(\varsigma-1)^{1.3}} - 0.4^{\varsigma^{1.3}}$. By solving Theorem 3, one has $K_{11} = \begin{bmatrix} -0.3288 & -0.1723 \end{bmatrix}$, $K_{12} = \begin{bmatrix} -0.3248 & -0.2156 \end{bmatrix}$, $K_{21} = \begin{bmatrix} -0.4916 & -0.1401 \end{bmatrix}$, $K_{22} = \begin{bmatrix} -0.4908 & -0.1528 \end{bmatrix}$, $L_{11} = \begin{bmatrix} 0.8604 & -0.3562 \end{bmatrix}^T$, $L_{12} = \begin{bmatrix} 0.8684 & -0.3652 \end{bmatrix}^T$, $L_{21} = \begin{bmatrix} 0.8422 & 0.1335 \end{bmatrix}^T$, $L_{22} = \begin{bmatrix} 0.8503 & 0.1263 \end{bmatrix}^T$.

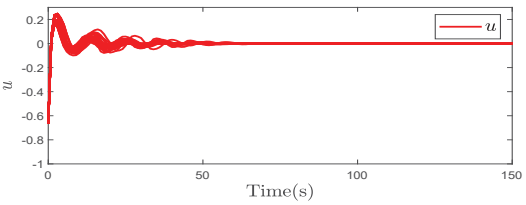

Fig. 3 Control input

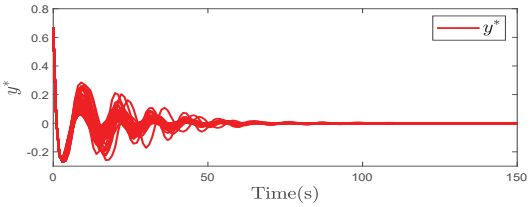

Fig. 4 Actual output

For given $s(0) = \begin{bmatrix} 0.5 & -0.8 \end{bmatrix}^T$ and $\hat{s}(0) = \begin{bmatrix} 1.3 & 0.7 \end{bmatrix}^T$, over 50 realizations, the system state is depicted in Fig. 1, indicating that all system states tend to the origin, ensuring the σ-MSS. Figs. 2-3 plot the estimation errors and control input, in which the trajectory tends to equilibrium point, verifying the indicates the applicability of our results. The actual system output under Dos attacks is shown in Fig. 4.

5 Conclusion

In this study, the observer-based stabilization issue studied for networked discrete IT2F S-MJSs with random DoS attacks. Based on SMK theory, IT2 fuzzy model and the sojourn-time-dependent Lyapunov functions, the criterion that the system is σ-MSS is proposed, and the design method of observer-based controller is established. In future work, the SMC of networked discrete IT2F S-MJSs with cyber attacks will be studied.

References

[1] J.N.A.D. Bueno, L.B. Marcos, K.D.T. Rocha, M.H. Terra, "Regulation of Markov jump linear systems subject to polytopic uncertainties," *IEEE Trans. Autom. Control*, vol. 67, no. 11, pp. 6279–6286, Nov. 2022.

[2] S. Kuppusamy, Y.H. Joo, H.S. Kim, "Asynchronous control for discrete-time hidden Markov jump power systems," *IEEE Trans. Cybern.*, vol. 52, no. 9, pp. 9943–9948, Sep. 2022.

[3] H. Schioler, M. Simonsen, J. Leth, "Stochastic stability of systems with semi-Markovian switching," *Automatica*, vol. 50, no. 11, pp. 2961–2964, Nov. 2014.

[4] Y.C. Yang, X.D. Li, Z.L. Xu, "Stability of mixed semi-Markov systems with all unstable modes," *IEEE Trans. Circuits Syst. II, Exp. Briefs*, vol. 70, no. 7, pp. 2505–2509, Jul. 2023.

[5] F. Li, W.X. Zheng, and S.Y. Xu, "Stabilization of discrete-time hidden semi-Markov jump singularly perturbed systems with partially known emission probabilities," *IEEE Trans. Autom. Control*, vol. 67, no. 8,pp. 4234–4240, Aug. 2022.

[6] W.H. Qi, G.D. Zong, and S.-F. Su, "Fault detection for semi-Markov switching systems in the presence of positivity constraints," *IEEE Trans. Cybern.*, vol. 52, no. 12, pp. 13027–13037, Dec. 2022.

[7] M. de Almeida, M. Souza, A.R. Fioravanti, O.L.V. Costa, "H_2 state-feedback control for continuous semi-Markov jump linear systems with rational transition rates," *Int. J. Control*, vol. 96, no. 1, pp. 1–11, Jan. 2023.

[8] J.N. Yang, Z.P. Ning, Y.M. Zhu, L.X. Zhang, H.K. Lam, "Semi-Markov jump linear systems with bi-boundary sojourn time: Anti-modal-asynchrony control," *Automatica*, vol. 140, Article ID 110270, Jun. 2022.

[9] L.X. Zhang, B. Cai, T.Y. Tan, Y. Shi, "Stabilization of non-homogeneous hidden semi-Markov Jump systems with limited sojourn-time information," *Automatic*, vol. 117, Article ID 108963, Jul. 2020.

[10] F. Li, W.X. Zheng, S.Y. Xu, "Stabilization of discrete-time hidden semi-Markov jump singularly perturbed systems with partially known emission probabilities," *IEEE Trans. Autom. Control*, vol. 67, no. 8,pp.4234–4240, Aug. 2022.

[11] X.P . Guan, C.L. Chen, "Delay-dependent guaranteed cost control for T-S fuzzy systems with time delays," *IEEE Trans. Fuzzy Syst.*, vol. 12,no. 2, pp. 236–249, Apr. 2004.

[12] Z. Lian, P. Shi, C.C. Lim, X. Yuan, "Fuzzy-model-based lateral control for networked autonomous vehicle systems under hybrid cyber-attacks," *IEEE Trans. Cybern.*, vol. 53, no. 4, pp. 2600–2609, Apr. 2023.

[13] X. Cai, K.B. Shi, K. She, S.M. Zhong, Y.C. Soh, Y. Yu, "Reliable sampling mechanism for TakagiCSugeno fuzzy NCSs under deception cyberattacks for the application of the inverted pendulum system," *IEEE Trans. Rel.*, vol. 72, no. 3, pp. 1220–1231, Mar. 2023.

[14] J.M. Mendel, "Type-2 fuzzy sets and systems: An overview, IEEE Comput. Intell. Mag., vol. 2, no. 1, pp. 20–29, Feb. 2007.

[15] L.C. Zhang, Y.H. Sun, H.K. Lam, H.Y. Li, J.X. Wang, D.C. Hou, "Guaranteed cost control for interval type-2 fuzzy semi-Markov switching systems within a finite-time interval, IEEE Trans. Fuzzy Syst., vol. 30, no. 7, pp. 2583–2594, Jul. 2022.

[16] L.C. Zhang, H.K. Lam, Y.H. Sun, H.J. Liang, "Fault detection for fuzzy semi-Markov jump systems based on interval type-2 fuzzy approach, IEEE Trans. Fuzzy Syst., vol. 28, no. 10, pp. 2375–2388, Oct. 2020.

[17] B. Xiao, H.K. Lam, H. Zhou, J. Gao, "Analysis and design of interval type-2 polynomial-fuzzy-model-based networked tracking control systems, " *IEEE Trans. Fuzzy Syst.*, vol. 29 , no. 9 , pp. 2750–2759. 2021

[18] S.M. Ahmadkhah, R.P.R. Hasanzadeh, M. Papaelias, "Arbitrary crack depth profiling through ACFM data using type-2 fuzzy logic and PSO algorithm," *IEEE Trans. Fuzzy Syst.*, vol. 55, no. 2, pp. 1–10, Feb. 2019.

[19] P. Shi, H. Wang, and C.-C. Lim, "Network-based event-triggered control for singular systems with quantizations,*IEEE Trans. Ind. Electron.*, vol. 63, no. 2, pp. 1230–1238, Feb. 2016.

[20] Y.S. Tan, Q.Y. Liu, J.L. Liu, X.P. Xie, and S.M. Fei, "Observer-based security control for interconnected semi-Markovian jump systems with unknown transition probabilities, " *IEEE Trans. Cybern.*, vol. 52, no. 9, pp. 9013–9025, Sep. 2022.

[21] J. Tao, R. Lu, P. Shi, H. Su, and Z.-G. Wu, "Dissipativity-based reliable control for fuzzy Markov jump systems with actuator faults," *IEEE Trans. Cybern.*, vol. 47, no. 9, pp. 2377–2388, Sep. 2017

Proceedings of the 3rd Conference on Fully Actuated System Theory and Applications
May 10-12, 2024, Shenzhen, China

Coding-Decoding-Based Sliding Mode Control for Discrete Uncertain T-S Fuzzy Systems with Time-Varying Delays

Zhiyuan Zuo[1], Jun Hu[1,2], Hongxu Zhang[1], Na Lin[1], Aozhan Zhou[1]

1. Department of Applied Mathematics, Harbin University of Science and Technology, Harbin 150080, China.
Email: jhu@hrbust.edu.cn

2. School of Automation, Harbin University of Science and Technology, Harbin 150080, China

Abstract: This paper explores the sliding mode control (SMC) scheme for delayed Takagi-Sugeno (T-S) fuzzy systems under resource-constrained channels. In response to the issue of limited communication network resources, a two-step encoding scheme is designed to achieve the adaptive adjustment of encoding errors. Subsequently, a common sliding surface is designed and a new SMC law including the information of encoding errors is given. Next, sufficient criteria for system stability and reachability of the sliding surface are provided. Finally, we demonstrate the effectiveness of the proposed SMC algorithm through a simulation example.

Key Words: Sliding Mode Control, T-S Fuzzy Systems, Time-Varying Delays, Encoding-Decoding Mechanism

1 Introduction

The T-S fuzzy method, as a widely utilized fuzzy logic method in the control domain, possesses the robust approximation capabilities and can effectively describe a multitude of complex nonlinear systems. In the typical T-S fuzzy system, the approximation of any smooth nonlinear function is achieved with hope to attain arbitrary precision through the fuzzy sets and fuzzy inference, which involves a set of linear functions interconnected by nonlinear membership functions (MFs) [1]. Accordingly, the existing research results indicate that the T-S fuzzy systems demonstrate outstanding performance in handling complex systems, which adapt to various nonlinear situations and exhibit robustness [2]. Moreover, it is well recognized that the fuzzy logic control concept of T-S fuzzy systems proposes a flexible framework for addressing the analysis and synthesis of nonlinear systems, which provides more effective methods for the corresponding research.

The sliding mode control (SMC) is an effective nonlinear control strategy to deal with the matched uncertainties and disturbances [3, 4]. In comparison to linear controllers, the discontinuous term introduced by SMC not only facilitates rapid convergence of state trajectories, more importantly, but also suppresses the effects of disturbance signals. As it is recognized that the combination of T-S fuzzy systems and the SMC method can provide a powerful and flexible control strategy [5, 6]. For example, a sliding mode controller has been designed in [5] to stabilize a class of T-S fuzzy systems with variable quantization density, and a sliding mode controller has been designed in [6] for a class of T-S fuzzy systems with a dynamic event-triggered (DET) strategy. The above integrated approaches fully utilize the approximation capabilities of T-S fuzzy systems and the robustness of SMC, which provide an effective solution for tackling the synthesis problem of complex nonlinear systems.

Correspondence should be addressed to Jun Hu. Email: jhu@hrbust.edu.cn.

This work was supported in part by the National Natural Science Foundation of China under Grants 61673141 and 12201157, the National College Students' Innovative Entrepreneurial Training Plan Program of China under Grant 20231021411, and the Alexander von Humboldt Foundation of Germany.

With the continuous development of computer science, communication technology and automation, the networked control systems (NCSs) have attracted widespread attention in academia. For the NCSs, sensors, control systems and various devices are interconnected via networks, which makes that the industrial systems operate more intelligently, flexibly and efficiently. In research related to NCSs, the scarcity of communication resources is a significant issue. Typically, the sensor measurement signals undergo the quantization and encoding processes before being encapsulated for transmission through digital channels [7]. Existing encoding schemes often utilize the uniform quantizer [8], logarithmic quantizer [9], adaptive quantizer [10] and so on. The adaptive coding schemes can dynamically adjust encoding precision based on system states, thereby reducing bandwidth requirements. In [11], a detailed depiction of an adaptive quantizer has been provided, which has simultaneously encoded the adaptive parameters and the signal obtained after quantization. However, it has overlooked the overlap of quantization ranges under different adaptive parameters, which results in the waste of some encoding information.

Inspired by the aforementioned discussion, this paper proposes a new SMC law for a class of T-S fuzzy systems with limited network resources and time-varying delays. By employing a two-step method, an adaptive quantizer is constructed. Based on this quantizer, a bit-rate-constrained encoding and decoding scheme is proposed. The primary contributions of the paper can be summarized from the following aspects: (i) Design an adaptive encoding and decoding mechanism by considering bit rate constraints, where the encoding errors adaptively adjust with system states. (ii) Considering the encoding errors, a new SMC law is proposed for T-S fuzzy systems with time-varying delays to mitigate the impact of limited network resources on the overall system performance. In conclusion, the validity of the proposed SMC algorithm is illustrated through simulation experiment.

2 Problem Formulation

2.1 System Description

Consider a class of discrete T-S fuzzy systems with time-varying delays, which can be represented by the following

fuzzy rules:

Fuzzy Rule i: IF $\vartheta_{1,k}$ is W_1^i, $\vartheta_{2,k}$ is W_2^i, ..., and $\vartheta_{\iota,k}$ is W_ι^i, THEN

$$\begin{cases} x_{k+1} = (A_i + \Delta A_i)x_k + A_{di}x_{k-d_k} + B_i(u_k + \omega_k), \\ x_k = \varphi_k,\ k = -d_M, -d_M+1, \ldots, 0, \end{cases} \tag{1}$$

where $x_k \in \mathbb{R}^{n_x}$ is the system state. $u_k \in \mathbb{R}^{n_u}$ is the control input. $\vartheta_k \triangleq \left[\vartheta_{1,k}, \vartheta_{2,k}, \ldots, \vartheta_{\iota,k}\right]$ is the measurable premise variable vector. $W_1^i, W_2^i, \ldots, W_\iota^i$ are the fuzzy sets. ΔA_i is the parameter uncertainty with $\Delta A_i \triangleq E_i F_i H_i$ and F_i satisfying $F_i^T F_i \leq I$. The external disturbance ω_k satisfies $\|\omega_k\| \leq \overline{\omega}$ with $\overline{\omega} > 0$ being a known constant. The time-varying delay d_k satisfies $d_m \leq d_k \leq d_M$, where d_M and d_m are known upper and lower bounds of the time delay. A_i, A_{di} and $B_i (i \in \mathbb{S} \triangleq \{1, 2, \ldots, r\})$ are real constant matrices with suitable dimensions, and B_i possesses full column rank. r is the number of fuzzy rules.

Applying the weighted defuzzification process, the overall fuzzy system is stated as follows:

$$\begin{cases} x_{k+1} = \sum_{i=1}^{r} h_i(\vartheta_k)[(A_i + \Delta A_i)x_k \\ \qquad + A_{di}x_{k-d_k} + B_i(u_k + \omega_k)], \\ x_k = \varphi_k,\ k = -d_M, -d_M+1, \ldots, 0. \end{cases} \tag{2}$$

The MFs are given as follows:

$$h_i(\vartheta_k) \triangleq \frac{\prod_{q=1}^{\iota} \Gamma_{i,q}(\vartheta_{q,k})}{\sum_{i=1}^{r} \prod_{q=1}^{\iota} \Gamma_{i,q}(\vartheta_{q,k})}, \tag{3}$$

where $0 \leq \Gamma_{i,q}(\vartheta_{q,k}) \leq 1$ denotes the membership grade of $\vartheta_{q,k}$ in W_q^i. For $\forall k \in \mathbb{N}$, one has

$$h_i(\vartheta_k) \geq 0\ (i \in \mathbb{S}),\ \sum_{i=1}^{r} h_i(\vartheta_k) = 1. \tag{4}$$

2.2 Coding Procedure

In this paper, the signal transmission takes place between the sensor and the controller through a communication network with specified limitations or constraints. Sensors can measure the state variables of the system. Let the signal detected by the p-th sensor node at time k be denoted as x_k^p and we have $x_k = [x_k^1, x_k^2, \ldots, x_k^{n_x}]^T$. To reduce data transmission costs, the signal is converted to binary code through an encoder before transmission. For convenience, we use the arrays p, $\Phi_1(x_k^p)$ and $\Phi_2(x_k^p)$ to store the coded information of the p-th sensor.

Firstly, we compute the required number of bit rates necessary to encode the sensor label p as follows:

$$R_1 = \left\lceil \log_2 n_x \right\rceil. \tag{5}$$

Then, we give the quantization procedure for the measurement x_k^p of p-th sensor node. Considering the practical scenario, in a closed-loop system, the state vector is not infinitely large. Therefore, it can be assumed that the p-th sensor's value has an upper bound M_p. In other words, the following inequality holds:

$$0 \leq \frac{|x_k^p|}{M_p} \leq 1. \tag{6}$$

The following two-step process is used to map $\frac{x_k^p}{M_p}$ to a pair of numbers $(\Phi_1(x_k^p), \Phi_2(x_k^p))$. Firstly, we focus on the number $\Phi_1(x_k^p) \in \{0, \pm 1, \pm 2, \ldots, \pm\rho_1\}$ with R_2 bits and the number are determined as follows:

$$\Phi_1(x_k^p) = \operatorname{sign}(x_k^p) \max\left\{ \kappa \middle| \frac{|x_k^p|}{\lambda_p^{\kappa-1} M_p} \leq 1, \kappa \in \{1, \ldots, \rho_1\} \right\}, \tag{7}$$

where sign is the signal function and $\rho_1 = 2^{R_2 - 1} - 1$. $\lambda_p < 1$ is the quantitative indicator of the p-th sensor node. Next, we focus on the number $\Phi_2(x_k^p)$ with R_3 bits and the number are determined as follows:

$$\Phi_2(x_k^p) = \begin{cases} 1, & \Phi_1(x_k^p) = 0, \\ \chi_1, & 0 < |\Phi_1(x_k^p)| < \rho_1, \\ \chi_{\rho_1}, & |\Phi_1(x_k^p)| = \rho_1, \end{cases} \tag{8}$$

with

$$\chi_1 = \left\lceil \left(\frac{|x_k^p|}{\lambda_p^{|\Phi_1(x_k^p)|-1} M_p} - \lambda_p \right) / (1 - \lambda_p) 2^{R_3} \right\rceil,$$
$$\chi_{\rho_1} = \left\lceil \frac{|x_k^p|}{\lambda_p^{\rho_1 - 1} M_p} 2^{R_3} \right\rceil.$$

It is easy to see that the number $\Phi_2(x_k^p) \in \{1, 2, 3, \ldots, 2^{R_3}\}$.

2.3 Decoding Procedure

According to the sensor label α_1, the controller can identify which sensor's signal has been successfully transmitted. Referring to data codes α_1 and α_2, the controller can compute the pair of numbers $(\Phi_1(x_k^p), \Phi_2(x_k^p))$. Furthermore, the decoded state $\bar{x}_k \triangleq [\bar{x}_k^1, \bar{x}_k^2, \ldots, \bar{x}_k^{n_x}]^T$ is defined with

$$\bar{x}_k^p = \begin{cases} 0, & \Phi_1(x_k^p) = 0, \\ \overline{\chi}_0, & 0 < |\Phi_1(x_k^p)| < \rho_1, \\ \overline{\chi}_{\rho_1}, & |\Phi_1(x_k^p)| = \rho_1, \end{cases} \tag{9}$$

where

$$\overline{\chi}_0 = \operatorname{sign}(\Phi_1(x_k^p)) \Bigg(\lambda_p + (1 - \lambda_p) \times \frac{\Phi_2(x_k^p) - \frac{1}{2}}{2^{R_3}} \Bigg) \lambda_p^{|\Phi_1(x_k^p)|-1} M_p,$$
$$\overline{\chi}_{\rho_1} = \operatorname{sign}(\Phi_1(x_k^p)) \frac{\Phi_2(x_k^p) - \frac{1}{2}}{2^{R_3}} \lambda_p^{\rho_1 - 1} M_p.$$

Define the decoding error of the p-th sensor node as $\tilde{x}_k^p = \bar{x}_k^p - x_k^p$. It follows from (8)-(9) that the decoding error satisfies

$$\begin{cases} |\tilde{x}_k^p| = 0, & \Phi_1(x_k^p) = 0, \\ |\tilde{x}_k^p| \leq \tilde{\chi}_0 & 0 < |\Phi_1(x_k^p)| < \rho_1, \\ |\tilde{x}_k^p| \leq \tilde{\chi}_{\rho_1}, & |\Phi_1(x_k^p)| = \rho_1, \end{cases} \tag{10}$$

with

$$\tilde{\chi}_1 = \frac{\lambda_p^{|\Phi_1(x_k^p)|-1} M_p}{2^{R_3+1}} (1 - \lambda_p) \leq \frac{\lambda_p^{-1} |x_k^p|}{2^{R_3+1}} (1 - \lambda_p),$$

$$\tilde{\chi}_{\rho_1} = \frac{\lambda_p^{\rho_1-1} M_p}{2^{R_3+1}}.$$

Furthermore, take the common upper bound for the three cases as

$$|\tilde{x}_k^p|^2 \leq \left(\frac{(\lambda_p^{-1}-1)|x_k^p|}{2^{R_3+1}}\right)^2 + \left(\frac{\lambda_p^{\rho_1-1} M_p}{2^{R_3+1}}\right)^2. \tag{11}$$

3 MAIN RESULTS

In this section, a novel fuzzy SMC law is designed to ensure that the closed-loop fuzzy system is exponentially ultimately bounded (EUB), and the system state trajectories are driven into the neighborhood near the sliding surface. Firstly, the following common sliding surface is constructed:

$$s_k = G x_k, \tag{12}$$

where $G \triangleq \Sigma_{i=1}^N \beta_i B_i^T$, and scalars β_i $(i \in \mathbb{S}_1)$ should be chosen such that GB_i is nonsingular.

Based on the non-parallel compensation strategy, the following fuzzy SMC law is designed:

Fuzzy Rule j: IF $\tilde{\vartheta}_{1,k}$ is $\tilde{W}_1^j$, $\tilde{\vartheta}_{2,k}$ is $\tilde{W}_2^j$, …, and $\tilde{\vartheta}_{t,k}$ is $\tilde{W}_t^j$, THEN

$$u_k = K_j \bar{x}_k - (\|\Lambda_1 \bar{x}_k\| + \overline{\omega})\text{sign}(s_k), \tag{13}$$

with

$$\Lambda_1 = \text{diag}\left\{\frac{(\lambda_1^{-1}-1)}{2^{R_3+1}}, \ldots, \frac{(\lambda_{n_x}^{-1}-1)}{2^{R_3+1}}\right\}. \tag{14}$$

Through standard fuzzy inference methods, the control input can be described by

$$u_k = \sum_{j=1}^r l_j(\tilde{\vartheta}_k) K_j \bar{x}_k - (\|\Lambda_1 \bar{x}_k\| + \overline{\omega})\text{sign}(\bar{s}_k), \tag{15}$$

where $\bar{s}_k$ is obtained by replacing x_k in (12) with $\bar{x}_k$. K_j is the control gain to be designed later. Substituting (17) into (2), the resultant closed-loop system can be obtained as:

$$\begin{aligned} x_{k+1} = &\sum_{i=1}^r \sum_{j=1}^r h_i(\vartheta_k) l_j(\tilde{\vartheta}_k)[(A_i + \Delta A_i + B_i K_j) x_k \\ &+ A_{di} x_{k-d_k} + B_i K_j \tilde{x}_k - B_i \Delta_k]. \end{aligned} \tag{16}$$

where $\tilde{x}_k = [\tilde{x}_k^1, \tilde{x}_k^2, \ldots, \tilde{x}_k^{n_x}]^T$ and $\Delta_k = (\|\Lambda_1 \bar{x}_k\| + \overline{\omega})\text{sign}(\bar{s}_k) - \omega_k$. For the mismatched MFs $h_i(\vartheta_k)$ and $l_j(\tilde{\vartheta}_k)$ in (15), the following relations are easy to establish in order to simplify the subsequent derivation:

$$l_i(\tilde{\vartheta}_k) = \varsigma_{i,k} h_i(\vartheta_k), \tag{17}$$

$$\frac{\varsigma_{i,k}}{\varsigma_{j,k}} \in [k_1, k_2], \tag{18}$$

where k_1 and k_2 can be estimated from the overall upper and lower bounds of $h_i(\vartheta_k)$ and $l_j(\tilde{\vartheta}_k)$.

Definition 1 *The system is said to be EUB if there exists a constant* $0 < \varsigma < 1$ *satisfying*

$$||\xi_k||^2 \leq \varepsilon \varsigma^k ||\xi_0||^2 + \overline{\eta}^2, \tag{19}$$

where ξ_0 *is the initial condition, and* $\overline{\eta}$ *is the upper bound of the closed-loop system.*

3.1 Analysis of Stability

Theorem 1 *Consider the fuzzy system (2) under the designed fuzzy SMC law (15). For any* $i, j \in \mathbb{S}$ *and given scalars* $\alpha_1 > 0$, $1 > \gamma > 0$, *if there exist scalars* $\varepsilon_1 > 0$, $\varepsilon_2 > 0$ *and matrices* $P_1 > 0$, $P_2 > 0$ *and* K_j *satisfying the following matrix inequalities:*

$$B_i^T P_1 B_i < \varepsilon_1 I, \tag{20}$$

$$K_j^T B_i^T P_1 B_i K_j < \varepsilon_2 I, \tag{21}$$

$$\Theta_{i,i} < 0, \tag{22}$$

$$\Theta_{i,j} + k_1 \Theta_{j,i} < 0, \ i < j, \tag{23}$$

$$\Theta_{i,j} + k_2 \Theta_{j,i} < 0, \ i < j, \tag{24}$$

where

$$\begin{aligned} \Theta_{i,j} &\triangleq \begin{bmatrix} \Theta_{i,j}^{1,1} & \Theta_{i,j}^{1,2} \\ * & \Theta_{i,j}^{2,2} \end{bmatrix}, \\ \Theta_{i,j}^{1,1} &\triangleq (1+\alpha_1)[(A_i + \Delta A_i + B_i K_j)^T P_1 \\ &\quad \times (A_i + \Delta A_i + B_i K_j)] + 2(1+\alpha_1^{-1}) \\ &\quad \times (3 n_u \varepsilon_1 + \varepsilon_2)\Lambda_1^2 + (d_M - d_m + 1) P_2 - \gamma P_1, \\ \Theta_{i,j}^{1,2} &\triangleq (1+\alpha_1)(A_i + \Delta A_i + B_i K_j)^T P_1 A_{di}, \\ \Theta_{i,j}^{2,2} &\triangleq (1+\alpha_1) A_{di}^T P_1 A_{di} - \gamma^{d_M} P_2, \end{aligned}$$

then the closed-loop system (16) is EUB, and the upper bound is given as:

$$\overline{\eta} \triangleq \frac{\eta}{\sqrt{(1-\gamma)\lambda_{\min}(P_1)}} \tag{25}$$

with

$$\begin{aligned} \eta = &\left[2(1+\alpha_1^{-1})\left(3\varepsilon_1(n_u+1)\overline{\omega}^2 \right.\right. \\ &\left.\left. + \varepsilon_2 \sum_{p=1}^{n_x} \left(\frac{\lambda_p^{\rho_1-1} M_p}{2^{R_3+1}}\right)^2\right)\right]^{\frac{1}{2}}. \end{aligned}$$

Proof: Select the Lyapunov functional for system (16) as:

$$V_k \triangleq V_{1,k} + V_{2,k} + V_{3,k}, \tag{26}$$

where

$$\begin{aligned} V_{1,k} &= x_k^T P_1 x_k, \\ V_{2,k} &= \sum_{s=k-d_k}^{k-1} \gamma^{k-s-1} x_s^T P_2 x_s, \\ V_{3,k} &= \sum_{\tau=-d_M+1}^{-d_m} \sum_{s=k+\tau}^{k-1} \gamma^{k-s-1} x_s^T P_2 x_s. \end{aligned}$$

Taking the difference of the Lyapunov functional, one obtains:

$$\begin{aligned} \Delta V_{1,k} &\triangleq V_{1,k+1} - \gamma V_{1,k} \\ &\leq \sum_{i=1}^r \sum_{j=1}^r h_i(\vartheta_k) l_j(\tilde{\vartheta}_k) \Big\{ (1+\alpha_1)[(A_i + \Delta A_i \\ &\quad + B_i K_j) x_k + A_{di} x_{k-d_k}]^T P_1 [(A_i + \Delta A_i + B_i \\ &\quad \times K_j) x_k + A_{di} x_{k-d_k}]^T + (1+\alpha_1^{-1})(\tilde{x}_k^T K_j^T \end{aligned}$$

$$-\Delta_k^T)B_i^T P_1 B_i(K_j\tilde{x}_k-\Delta_k)\Big\}-\gamma x_k^T P_1 x_k, \quad (27)$$

$$\begin{aligned}\Delta V_{2,k} &\triangleq V_{2,k+1}-\gamma V_{2,k}\\ &\le x_k^T P_2 x_k-\gamma^{d_M}x_{k-d_k}^T P_2 x_{k-d_k}\\ &\quad+\sum_{s=k+1-d_M}^{k-d_m}\gamma^{k-s}x_s^T P_2 x_s, \quad (28)\\ \Delta V_{3,k} &\triangleq V_{3,k+1}-\gamma V_{3,k}\\ &=\sum_{\tau=-d_M+1}^{-d_m}(x_k^T P_2 x_k-\gamma^{-\tau}x_{k+\tau}^T P_2 x_{k+\tau}). \quad (29)\end{aligned}$$

Then, combining (27)-(29), it can be observed that

$$\begin{aligned}\Delta V_k &\triangleq V_{k+1}-\gamma V_k\\ &\le \sum_{i=1}^{r}\sum_{j=1}^{r}h_i(\vartheta_k)l_j(\tilde{\vartheta}_k)\Big\{(1+\alpha_1)[(A_i+\Delta A_i\\ &\quad+B_iK_j)x_k+A_{di}x_{k-d_k}]^T P_1[(A_i+\Delta A_i+B_i\\ &\quad\times K_j)x_k+A_{di}x_{k-d_k}]^T+2(1+\alpha_1^{-1})(\varepsilon_2\|\tilde{x}_k\|^2\\ &\quad+\varepsilon_1\|\Delta_k\|^2)\Big\}+(d_M-d_m+1)x_k^T P_2 x_k\\ &\quad-\gamma x_k^T P_1 x_k-\gamma^{d_M}x_{k-d_k}^T P_2 x_{k-d_k}. \quad (30)\end{aligned}$$

Besides, the boundaries of $\|\tilde{x}_k\|$ and $\||\Delta_k\|$ can be computed as follows:

$$\|\tilde{x}_k\|^2\le x_k^T\Lambda_1^2 x_k+\sum_{p=1}^{n_x}\left(\frac{\lambda_p^{\rho_1-1}M_p}{2^{R_3+1}}\right)^2, \quad (31)$$

$$\|\Delta_k\|^2\le 3n_u x_k^T\Lambda_1^2 x_k+3(n_u+1)\overline{\omega}^2. \quad (32)$$

Therefore, from (20)-(24) and (30)-(32), we have

$$\Delta V_k\le\eta^2, \quad (33)$$

which further leads to

$$\begin{aligned}V_{k+1}&\le\gamma^k V_0+\frac{1-\gamma^{k-1}}{1-\gamma}\eta^2\\ &\le\gamma^k V_0+\frac{1}{1-\gamma}\eta^2. \quad (34)\end{aligned}$$

Furthermore, in view of (26), one has

$$V_k\ge\lambda_{\min}(P_1)\|x_k\|^2, \quad (35)$$

and

$$\begin{aligned}V_0\le&\left(\lambda_{\max}(P_1)+\frac{d_M-d_m+1}{1-\gamma}\right.\\ &\left.\times\lambda_{\max}(P_2)\right)\sup_{\varphi\in[-d_M,0]}(\|x_\varphi\|^2). \quad (36)\end{aligned}$$

Finally, according to Definition 1, the closed-loop fuzzy system (16) is EUB.

3.2 Analysis of Reachability

Theorem 2 *Consider the fuzzy system (2) under the designed fuzzy SMC law (15). For any $i,j\in\mathbb{S}$ and given scalars $\alpha_1>0$, if there exist scalars $\varepsilon_1>0$, $\varepsilon_2>0$, $\varepsilon_3>0$, $\varepsilon_4>0$, matrices $P_1>0$, $P_2>0$, $W>0$ and K_j satisfying (20), (21) and the following matrix inequalities:*

$$B_i^T G^T W G B_i<\varepsilon_3 I, \quad (37)$$

$$K_j^T B_i^T G^T W G B_i K_j<\varepsilon_4 I, \quad (38)$$

$$\Omega_{i,i}<0, \quad (39)$$

$$\Omega_{i,j}+k_1\Omega_{j,i}<0,\ i<j, \quad (40)$$

$$\Omega_{i,j}+k_2\Omega_{j,i}<0,\ i<j. \quad (41)$$

where

$$\begin{aligned}\Omega_{i,j}&\triangleq\begin{bmatrix}\Omega_{i,j}^{1,1}&\Omega_{i,j}^{1,2}\\ *&\Omega_{i,j}^{2,2}\end{bmatrix},\\ \Omega_{i,j}^{1,1}&\triangleq(1+\alpha_1)[(A_i+\Delta A_i+B_iK_j)^T P_1\\ &\quad\times(A_i+\Delta A_i+B_iK_j)+(A_i+\Delta A_i+B_iK_j)^T\\ &\quad\times G^T W G(A_i+\Delta A_i+B_iK_j)]+2(1+\alpha_1^{-1})\\ &\quad\times(3n_u\varepsilon_1+3n_u\varepsilon_3+\varepsilon_2+\varepsilon_4)\Lambda_1^2\\ &\quad+(d_M-d_m+1)P_2-P_1,\\ \Omega_{i,j}^{1,2}&\triangleq(1+\alpha_1)[(A_i+\Delta A_i+B_iK_j)^T P_1 A_{di}\\ &\quad+(A_i+\Delta A_i+B_iK_j)^T G^T W G A_{di}],\\ \Omega_{i,j}^{2,2}&\triangleq(1+\alpha_1)[A_{di}^T P_1 A_{di}+A_{di}^T G^T W G A_{di}]-P_2,\end{aligned}$$

then the state trajectories of the closed-loop fuzzy system can be driven into the designated sliding domain $\mathbb{D}$ surrounding the specified sliding surface:

$$\mathbb{D}\triangleq\left\{s_k\big|\|s_k\|\le\overline{\mathscr{N}}\right\}, \quad (42)$$

with

$$\begin{aligned}\overline{\mathscr{N}}&\triangleq\sqrt{\frac{\mathscr{N}_{i,j}}{\lambda_{\min}(W)}},\\ \mathscr{N}_{i,j}&\triangleq\left[2(1+\alpha_1^{-1})\left(3(\varepsilon_1+\varepsilon_3)(n_u+1)\overline{\omega}^2\right.\right.\\ &\quad\left.\left.+(\varepsilon_2+\varepsilon_4)\sum_{p=1}^{n_x}\left(\frac{\lambda_p^{\rho_1-1}M_p}{2^{R_3+1}}\right)^2\right)\right]^{\frac{1}{2}}.\end{aligned}$$

Proof: Similar to Theorem 1, the proof of this theorem is easy to be derived and is omitted for the sake of brevity.

3.3 Solving for Controller Gain

In this subsection, a set of linear matrix inequalities (LMIs) is obtained by decoupling the nonlinear matrix inequalities (20)-(24) and (37)-(41), then the gain matrix K_j is solved.

Theorem 3 *Consider the fuzzy system (2) under the designed fuzzy SMC law (15). For any $i,j\in\mathbb{S}$ and given scalars $\alpha_1>0$, $1>\gamma>0$, if there exist scalars $\varepsilon_1>0$, $\varepsilon_2>0$, $\varepsilon_3>0$, $\varepsilon_4>0$, $\overline{\varepsilon}>0$ and matrices $\overline{P}_1>0$, $P_2>0$, $\overline{W}>0$ and K_j satisfying the following matrix inequalities:*

$$\begin{bmatrix}-\varepsilon_1 I&B_i^T\\ *&-\overline{P}_1\end{bmatrix}<0, \quad (43)$$

$$\begin{bmatrix}-\varepsilon_2 I&K_j^T B_i^T\\ *&-\overline{P}_1\end{bmatrix}<0, \quad (44)$$

$$\begin{bmatrix} -\varepsilon_3 I & B_i^T G^T \\ * & -\overline{W} \end{bmatrix} < 0, \tag{45}$$

$$\begin{bmatrix} -\varepsilon_4 I & K_j^T B_i^T G^T \\ * & -\overline{W} \end{bmatrix} < 0, \tag{46}$$

$$\widetilde{\Theta}_i < 0, \tag{47}$$

$$\widetilde{\Theta}_{i,j,\zeta} < 0,\ i<j,\ \zeta = 1,2, \tag{48}$$

$$\widetilde{\Omega}_i < 0, \tag{49}$$

$$\widetilde{\Omega}_{i,j,\zeta} < 0,\ i<j,\ \zeta = 1,2, \tag{50}$$

with

$$\widetilde{\Theta}_i \triangleq \begin{bmatrix} \widetilde{\Theta}_i^{1,1} & \widetilde{\Theta}_{i,i}^{1,2} \\ * & \widetilde{\Theta}_i^{2,2} \end{bmatrix},$$

$$\widetilde{\Theta}_{i,j,\zeta} \triangleq \begin{bmatrix} \widetilde{\Theta}_i^{1,1} + k_\zeta \widetilde{\Theta}_j^{1,1} & \widetilde{\Theta}_{i,j}^{1,2} & \sqrt{k_\zeta}\widetilde{\Theta}_{j,i}^{1,2} \\ * & \widetilde{\Theta}_i^{2,2} & 0 \\ * & * & \widetilde{\Theta}_j^{2,2} \end{bmatrix},$$

$$\widetilde{\Omega}_i \triangleq \begin{bmatrix} \widetilde{\Omega}_i^{1,1} & \widetilde{\Omega}_{i,i}^{1,2} \\ * & \widetilde{\Omega}_i^{2,2} \end{bmatrix},$$

$$\widetilde{\Omega}_{i,j,\zeta} \triangleq \begin{bmatrix} \widetilde{\Omega}_i^{1,1} + k_\zeta \widetilde{\Omega}_j^{1,1} & \widetilde{\Omega}_{i,j}^{1,2} & \sqrt{k_\zeta}\widetilde{\Omega}_{j,i}^{1,2} \\ * & \widetilde{\Omega}_i^{2,2} & 0 \\ * & * & \widetilde{\Omega}_j^{2,2} \end{bmatrix},$$

$$\widetilde{\Theta}_i^{1,1} \triangleq \begin{bmatrix} \widetilde{\Theta}_i^{1,1,1} & 0 \\ * & -\gamma^{d_M} P_2 \end{bmatrix},$$

$$\widetilde{\Theta}_{i,j}^{1,2} \triangleq \begin{bmatrix} (A_i + B_i K_j)^T & 0 \\ A_{di}^T & 0 \end{bmatrix},$$

$$\widetilde{\Theta}_i^{2,2} \triangleq \begin{bmatrix} -\frac{1}{1+\alpha_1}\overline{P}_1 & E_i \\ * & -\overline{\varepsilon} I \end{bmatrix},$$

$$\widetilde{\Omega}_i^{1,1} \triangleq \begin{bmatrix} \widetilde{\Omega}_i^{1,1,1} & 0 \\ * & -\gamma^{d_M} P_2 \end{bmatrix},$$

$$\widetilde{\Omega}_{i,j}^{1,2} \triangleq \begin{bmatrix} (A_i + B_i K_j)^T & (A_i + B_i K_j)^T G^T & 0 \\ A_{di}^T & A_{di}^T G^T & 0 \end{bmatrix},$$

$$\widetilde{\Omega}_i^{2,2} \triangleq \begin{bmatrix} -\frac{1}{1+\alpha_1}\overline{P}_1 & 0 & E_i \\ * & -\frac{1}{1+\alpha_1}\overline{W} & GE_i \\ * & * & -\overline{\varepsilon} I \end{bmatrix},$$

$$\widetilde{\Theta}_i^{1,1,1} \triangleq 2(1+\alpha_1^{-1})(3n_u\varepsilon_1 + \varepsilon_2)\Lambda_1^2 + (d_M - d_m + 1)P_2 - \gamma P_1$$

$$\widetilde{\Omega}_i^{1,1,1} \triangleq +2(1+\alpha_1^{-1})(3n_u\varepsilon_1 + 3n_u\varepsilon_3 + \varepsilon_2 + \varepsilon_4) \times \Lambda_1^2 + (d_M - d_m + 1)P_2 - P_1,$$

then the closed-loop system is EUB, and the sliding domain can be simultaneously attained.

Proof: Let $\overline{P_1} = P^{-1}$ and $\overline{W} = W^{-1}$. It is easy to verify that the conditions (20)-(21) and (37)-(38) can be ensured by (43)-(46) through the Schur complement lemma. By using the equation

$$(I - P_1)P_1^{-1}(I - P_1)^T = P_1 + P_1^{-1} - 2I, \tag{51}$$

for any $P_1 > 0$, and then we have $-P_1 \le P_1^{-1} - 2I$. After that, noting $\Delta A_i \triangleq E_i F_i H_i$ and applying Schur complement lemma, it's easily verified that the inequalities (22)-(24) can be ensured by the LMIs (47), (48) and the inequalities (39)-(41) can be ensured by the LMIs (49), (50), which end the proof of this theorem.

4 An Illustrative Example

In this subsection, the effectiveness and feasibility of the proposed SMC are verified by an illustrative example.

Consider the following T-S fuzzy delayed system with two fuzzy rules:

$$x_{k+1} = \sum_{i=1}^{2} h_i(\vartheta_k)[(A_i + \Delta A_i)x_k + A_{di}x_{k-d_k} + B_i(u_k + \omega_k)],$$

with

$$A_1 = \begin{bmatrix} 1.2 & -0.2 & -0.1 \\ -0.1 & 0.6 & 0.1 \\ -0.2 & 0 & 1.3 \end{bmatrix},$$

$$A_2 = \begin{bmatrix} 1.1 & -0.4 & -0.1 \\ -0.2 & 0.7 & 0.4 \\ -0.2 & 0 & 1.1 \end{bmatrix},$$

$$B_1 = \begin{bmatrix} -0.4 & -0.2 \\ 0.1 & 0.2 \\ 0.2 & -0.3 \end{bmatrix}, B_2 = \begin{bmatrix} -0.3 & -0.3 \\ 0.2 & 0.3 \\ 0.3 & -0.3 \end{bmatrix}.$$

Then, we select the external disturbance $\omega_k = \overline{\omega}\sin(k)$ with $\overline{\omega} = 0.01$. Assume that the time delay upper bound is $d_M = 3$ and the lower bound is $d_m = 1$. Meanwhile, the system MFS and the controller MFs are given as follows:

$$h_1(x_k) = 0.35 + 0.25\sin(x_{1k}),\ h_2(x_k) = 1 - h_1(x_k).$$
$$l_1(\bar{x}_k) = 0.5 + 0.1\sin(\bar{x}_{1k}),\ l_2(\bar{x}_k) = 1 - l_1(\bar{x}_k).$$

For simulation purpose, we select the parameters $\lambda_1 = 0.5, \lambda_2 = 0.5, \lambda_3 = 0.5, M_1 = 10, M_2 = 10, M_3 = 10$ and the bit rates $R_1 = 2$, $R_2 = 5$ and $R_3 = 3$. The other parameters are $k_1 = 0.111$ and $k_2 = 9$. Solving the inequalities (43)-(50) by using the MatLab LMI toolbox, we get

$$K_1 = \begin{bmatrix} 1.1525 & -0.8551 & -1.2528 \\ 1.1119 & -0.7305 & 1.1226 \end{bmatrix},$$

$$K_2 = \begin{bmatrix} 1.0868 & -0.7278 & -1.4048 \\ 0.9980 & -0.5761 & 1.5545 \end{bmatrix},$$

$$\overline{\eta} = 0.2523,\ \overline{\mathscr{N}} = 0.1814.$$

The simulation results with the specified parameters are presented. Among them, Fig. 1 illustrates that the trajectories of the system state x_k tend to be bounded. The trajectories of control signal u_k and sliding variable s_k are shown in Fig. 2 and Fig. 3 respectively. Furthermore, we consider assigning different bit rates to R_2, R_3 and the upper bounds $\overline{\eta}$ of the closed-loop system are shown in Table 1. It is clear that when the bit rates increase, the upper bound $\overline{\eta}$ gets better and the bit rate R_2 has a greater impact on it. The simulations support the conclusion that the proposed control scheme is effective.

5 Conclusions

In this paper, we have addressed the problem of SMC for T-S fuzzy systems with limited network resources, where the

Table 1: The upper bound $\overline{\eta}$ under different bit rates R_2 and R_3

Bit rates	R_3=3	R_3=4	R_3=5	R_3=6	R_3=7
R_2=3	4.426	2.184	1.110	0.596	0.369
R_2=4	0.374	0.286	0.261	0.254	0.252
R_2=5	0.252	0.252	0.252	0.252	0.252

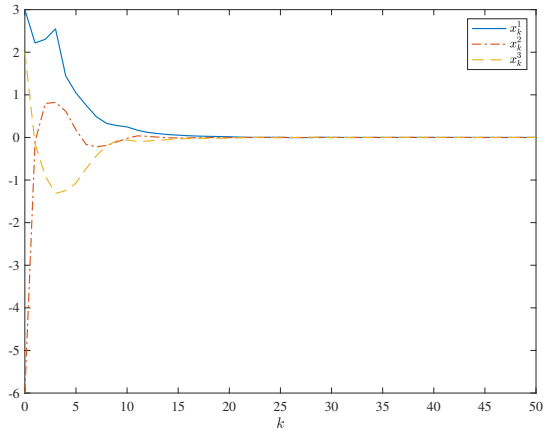

Fig. 1: State trajectories x_k.

sensors as well as controllers are connected through a network with limited resources and the system state is needed to be converted into binary code for transmission. In particular, a novel two-step encoder has been proposed for this purpose. Subsequently, the effect caused by coding error has been considered in the design of the SMC law, and sufficient conditions for the stability of the system and the reachability of the sliding mode surface have been given. Finally, a numerical example has been presented to further illustrate the practicality and feasibility of the developed SMC scheme.

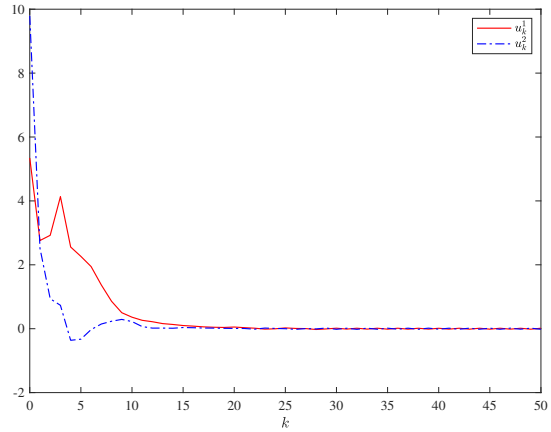

Fig. 2: Control signal u_k.

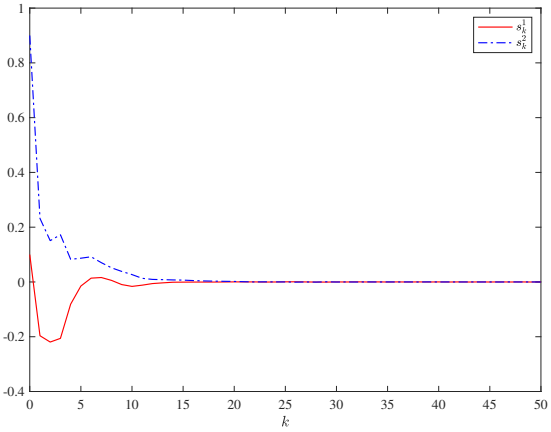

Fig. 3: Sliding variable s_k.

References

[1] L.-X. Wang and J. Mendel, Fuzzy basis functions, universal approximation, and orthogonal least-squares learning, *IEEE Transactions on Neural Networks*, vol. 3, no. 5, pp. 807–814, 1992.

[2] Z. Zhang and Y. Niu, Probabilistic-constrained control of interval type-2 T-S fuzzy systems under the multi-node round-robin scheduling protocol, *Journal of the Franklin Institute-Engineering and Applied Mathematics*, vol. 360, pp. 6566–6584, 2023.

[3] J. Hu, H. Zhang, X. Yu, H. Liu, and D. Chen, Design of sliding-mode-based control for nonlinear systems with mixed-delays and packet losses under uncertain missing probability, *IEEE Transactions on Systems Man Cybernetics-Systems*, vol. 51, pp. 3217–3228, 2021.

[4] J. Song, Y. Niu, and Y. Zou, Finite-time stabilization via sliding mode control, *IEEE Transactions on Automatic Control*, vol. 62, pp. 1478–1483, 2017.

[5] J. Cheng, Y. Shan, J. Cao, and J. H. Park, Nonstationary control for T-S fuzzy markovian switching systems with variable quantization density, *IEEE Transactions on Fuzzy Systems*, vol. 29, pp. 1375–1385, 2021.

[6] Z. Cao, Y. Niu, H.-K. Lam, and J. Zhao, Sliding mode control of markovian jump fuzzy systems: A dynamic event-triggered method, *IEEE Transactions on Fuzzy Systems*, vol. 29, pp. 2902–2915, 2021.

[7] Z. Wang, L. Wang, S. Liu, and G. Wei, Encoding-decoding-based control and filtering of networked systems: Insights, developments and opportunities, *IEEE-CAA Journal of Automatica Sinica*, vol. 5, pp. 3–18, 2018.

[8] J. Wang, Y. Yang, J. Xia, K. Shi, and H. Shen, Coding-decoding-based sliding mode control for networked persistent dwell-time switched systems, *International Journal of Robust and Nonlinear Control*, vol. 31, pp. 6055–6068, 2021.

[9] J. Zheng and B. Cui, State estimation of chaotic lurie system with logarithmic quantization, *Chaos Solitons & Fractals*, vol. 112, pp. 141–148, 2018.

[10] J. Li, Y. Niu, and D. W. C. Ho, Limited coding-length-based sliding-mode control with adaptive quantizer's parameter, *IEEE Transactions on automatic control*, vol. 67, no. 9, pp. 4738–4745, 2022.

[11] J. Li, Y. Niu, and D. W. C. Ho, Dynamic coding-based control scheme under lossy digital network: An optimized time-varying packet length approach, *IEEE Transactions on Cybernetics*, 2023. DOI:10.1109/TCYB.2022.3232529

Proceedings of the 3rd Conference on Fully Actuated System Theory and Applications
May 10-12, 2024, Shenzhen, China

The Reachable Set Estimation for Continuous-time Delayed Nonlinear Switched Systems with Impulsive Perturbation

Qingzheng Guo*[1], Zhiguang Feng[1]
1. College of Intelligent Systems Science and Engineering, Harbin Engineering University, Harbin 150001, P. R. China
E-mail: g2959673822@163.com

Abstract: In this paper, we mainly study the reachable set estimation problem of the continuous-time delayed nonlinear switched systems with impulsive perturbation under the condition of zero initial state and bounded peak disturbances. The purpose is to acquire a set of bounded ellipsoids that can include all the states starting from the origin. By adopting the real bounded lemma, integral inequality techniques, the free weight matrix method, we get a sufficient condition in the form of linear matrix inequality (LMI) for the continuous-time delayed nonlinear switched system with impulsive perturbation, so as to insure that all the state trajectories of the studied system are restricted to a closed bounded set. Eventually, a specific numerical example is given to illustrate the effectiveness and correctness of the results obtained in this paper.

Key Words: Switched system, The estimation of reachable set, Constant time-delay, Linear matrix inequality (LMI)

1 Introduction

As a kind of special hybrid dynamic systems, the switched system is comprised of some continuous or discrete subsystems and the corresponding switching rules that coordinate these subsystems. In the field of control, the switched system has unique properties, and due to the existence of switching rules, it is essentially different from the simple superposition of multiple systems. The research of the switched systems is much more complicated than the research of the continuous control of the normal systems [1–3]. Considering the great value of switched systems in the theoretical research, many scholars have carried out extensive research on the related problems of switched systems [4–9]. The switched systems are widely applied in the research of practical systems, such as communication control systems, power electronic systems, biological information system and robot systems [10–13]. In fact, when the system switches from one subsystem to another subsystem, there will inevitably be impulsive effects or perturbation that will lead to poor performance or even instability of the system. Thus, it is essential to think carefully impulsive perturbation when we investigate switched systems [14–17].

The reachable set of systems denotes the set of all states that the system will reach from the initial conditions under specific constraints or in the presence of some perturbations, and the reachable set estimation is one of the important methods to realize state estimation and parameter estimation. In practical engineering, the security of the system can be analyzed by estimating the reachable set about system state to avoid certain unsafe states in the whole state space [18, 19]. For example, the reachable set is applied to the flight anti-collision experiment of the aircraft, predicting the flight trajectory of one aircraft, and avoiding the flight range of the first aircraft by planning the flight path of the other aircraft, so as to prevent the collision between the two aircraft. If their flight range has an intersection, it may not be safe. Otherwise, it must be safe. Moreover, the reachable set estimation problem has always been a kind of significant problem in robust control theory [20]. The researchers have applied extensively the reachable set estimation of dynamic systems in many different fields, such as safety checks, peak-to-peak minimization, parameters estimation, the control system with actuator saturation [21–24].

Currently, in order to estimate the reachable set of various dynamic systems, many scholars use the ellipsoid technique based on Lyapunov function. In the framework of closed bounded ellipsoids, both Lyapunov function and LMI are extremely important for solving the reachable set estimation problems. Now, it not only has been developed to singular systems, such as singular systems with delay or without delay under zero initial conditions and bounded peak disturbances, time-varying delayed nonlinear singular systems with bounded input disturbances, general singular systems and time-varying delayed uncertain singular systems from a new perspective [25–28], but also time-delay systems, such as linear delay control systems with bounded disturbances, nonlinear switched delay systems with stable subsystems and unstable subsystems, linear systems with constant coefficients and time-varying delay, delayed linear systems with bounded peak disturbances [29–32], and Markovian jump systems, such as time-varying delayed Markovian jump neural networks with bounded peak inputs, singular Markovian jump systems without delays or with distributed delays, time-varying delay inertial Markovian jump bilateral associative memory neural networks under inputs with bounded disturbances and time-varying time-delay Markovian jump neural networks with bounded peak disturbances [33–36].

Furthermore, by using the new Lyapunov-Krasovskii functional, [37] studied the relevant reachable set estimation problem for a kind of multiple constant time-delay discrete linear systems with the bounded peak inputs. The delay-dependent conditions are expressed in the form of matrix inequalities. The problem about the estimation of reachable set for discrete singular systems with bounded disturbance input is solved in [38] with the help of establishing a Lyapunov-Krasovskii functional. Besides, by constructing the appropriate Lyapunov-Krasovskii functionals, [39] estimated the reachable set about time-delay neural networks that are sub-

This work is supported by National Natural Science Foundation (NNSF) of China under Grant 62073094.

ject to Markov jump parameters and the bounded disturbances. In addition to the Lyapunov-Krasovskii functional approach mentioned above, there are also other approaches to study the problem of reachable set estimation. Zonotopes are one of them [40, 41]. Compared with the Lyapunov function method, it has a relatively large amount of calculation, and is more difficult to give analytical solutions as well. After analyzing some literature on the reachable set estimation, it has been found that the Lyapunov-Krasovskii functional method has not been sufficiently applied to the study of the reachable set estimation problem of continuous-time delayed nonlinear switched systems with impulse perturbation, and this is the research motivation of the paper.

Inspired by the above researches, this paper will study the reachable set estimation problem of the continuous-time delayed nonlinear switched system with impulsive perturbation under zero initial conditions and bounded peak disturbance. First of all, according to the assumptions and lemmas, we will establish the system model and construct a new Lyapunov function. Afterward, based on adopting the real bounded lemma, introducing the free weight matrix and applying the integral inequality, the final sufficient condition for the reachable set estimation of the system is obtained in the form of LMIs, and the range of ellipsoid definition is more accurate with the help of the optimization design. Finally, by giving a numerical example, we illustrate the effectiveness and correctness of the obtained results.

Notations: $\mathbb{R}^m$ represents the m-dimensional Euclidean space. The matrix $P > 0 (\geq 0)$ repdimensions. $*$ represents resents that the real number matrix P is symmetric positive definite (semi-positive definite). I denotes an identity matrix with compatible dimensions, 0 refers to the zero matrix with consistent the symmetry term in the symmetry matrices. The superscript 'T' of the matrix (vector) stands for this matrix (vector) is transposed. $\mathrm{Sym}(Y)$ is defined as $Y + Y^{\mathrm{T}}$. $\|\cdot\|$ denotes the Euclidean matrix norm. $\lambda_{\max}(P)$ expressed as the maximum eigenvalue of the matrix. $\mathbb{N}$ and $\mathbb{N}^*$ are respectively defined as natural numbers set and positive integers set. $\dot{\mathfrak{D}}^+$ refers to the upper-right derivative of Dini. If the dimensions of the matrix are not clearly stated, it is assumed that the matrix is compatible about algebraic operations.

2 Preliminaries and Lemma Proposition

In this part of the paper, the following continuous-time delayed nonlinear switched system with impulsive perturbation will be considered:

$$\begin{cases} \dot{x}(t) = A_{\varphi(t)}x(t) + B_{\varphi(t)}f_{\varphi(t)}(t,x(t)) \\ \qquad\quad +C_{\varphi(t)}\int_{t-h}^{t} x(s)\mathrm{d}s + D_{\varphi(t)}w(t), \ \ t \neq t_j, \\ x(t_j^+) = E_{\varphi(t)}x(t_j), \ \ t = t_j, \\ x(t) \equiv 0, \ \ \forall t \in [-h, 0], \end{cases} \tag{1}$$

where $x(t) \in \mathbb{R}^n$ denotes the state vector. $w(t) \in \mathbb{R}^m$ refers to an unknown disturbance input vector of the system. $f_{\varphi(t)}(t, x(t))$ stands for an unknown nonlinear function of the system. Scalar h represents the distributed time-delay. $A_{\varphi(t)}$, $B_{\varphi(t)}$, $C_{\varphi(t)}$, $D_{\varphi(t)}$ and $E_{\varphi(t)}$ are all belong to the real constant matrices with the consistent dimensions. $\varphi(t) = \varphi_j \in \mathbb{U}_s = \{1, 2, \ldots, s\}$ is a sectional left-continuous function for $t \in [t_{j-1}, t_j)$ and $i \in \mathbb{N}$, then $\varphi(t)$ is a impulsive switching signal. And t_j is the impulsive switching point, when it satisfies $0 = t_0 < t_1 < t_2 < \cdots < t_{j-1} < t_j < \cdots$ and $t_j = \inf\{t \mid t > t_{j-1} \text{ and } \varphi(t) \neq \varphi(t_{j-1})\}$ and $\lim\limits_{i\to\infty} t_j = \infty$. $x(t_j) = x(t_j^-) = \lim\limits_{q\to 0^-} x(t-q)$ and $x(t_j^+) = \lim\limits_{q\to 0^+} x(t+q)$.

Certainly, the main goal of this paper is still want to obtain a set of ellipsoids as accurate as possible by the LMI method, which can be expressed as:

$$\mathcal{R} = \{x(t) \in \mathbb{R}^n \mid x^{\mathrm{T}}(t)\check{P}_{\varphi_j}x(t) \leq 1\}.$$

Before proceeding to the next calculations, we give several relevant assumptions, definitions, and lemmas, which can be applied to derive the final results.

Assumption 1 *The unknown perturbation input $w(t)$ satisfies*

$$w^{\mathrm{T}}(t)w(t) \leq \varpi^2, \tag{2}$$

where ϖ is the known real scalar.

Assumption 2 *The unknown nonlinear function $f_{\varphi_j}(t, x(t))$ satisfies*

$$\|f_{\varphi_j}(t, x(t))\| \leq \upsilon\|x(t)\|,$$

where $\upsilon > 0$ is the known real constant.

Definition 1 *[42] For the impulsive sequence $\Phi = \{t_1, t_2, t_3, \ldots\}$, Φ_a expresses the average impulsive interval, when $\Phi_a > 0$ and $N_0 \in \mathbb{N}^*$ are satisfied, one has*

$$\frac{T-t}{\Phi_a} - N_0 \leq N_\Phi(t,T) \leq N_0 + \frac{T-t}{\Phi_a}, \ \ \forall 0 \leq t \leq T$$

where $N_\Phi(t,T)$ denotes the number of impulse of Φ on interval (t,T), for each $0 \leq t \leq T$.

Lemma 1 *[43](real bounded lemma) For each $T \geq t \geq 0, \varphi_j \in \mathbb{U}_k$, $i \in \mathbb{N}$, and given scalar $\delta > 0$, scalar $\eta > 0$, and scalar $\nu \geq 1$, when $V_{\varphi_j}(x,t)$ satisfies the definition of continuous function for $t \neq t_{j-1}$ with system (1) and (2) in Assumption 1, it will have*

$$\mathfrak{D}^+V_{\varphi_j}(x,t) + \delta V_{\varphi_j}(x,t) - \eta w^{\mathrm{T}}(t)w(t) \leq 0, \ \ t \neq t_{j-1} \tag{3}$$

and

$$V_{\varphi_j}(x, t_{j-1}^+) \leq \nu V_{\varphi_{j-1}}(x, t_{j-1}^-), \ \ t = t_{j-1} \tag{4}$$

where $\eta = (\delta - \frac{\ln\nu}{\Phi_a})/\varpi^2$, t_{j-1} stands for impulsive switching point, t_{j-1}^- and t_{j-1}^+ are the instantaneous moments before and after the switching point t_{j-1} respectively, and

$$V_{\varphi_j}(x,t) \leq \nu^{N_0}$$

for each $0 \leq t \leq T$ and $V_{\varphi_0}(x_0) \leq 1$ are satisfied for all initial states with average dwell time $\Phi_a > \frac{\ln\nu}{\delta}$ of the system.

Lemma 2 *[44] For the given matrix $\mathfrak{G} > 0$, the scalar relationship satisfies $k > c$, $\kappa > 0$, differentiable vector function*

$x(z)$, $z \in \mathbb{R}^n$, the following linear matrix inequalities are all true:

$$\begin{aligned}&\int_c^k e^{\kappa(z-k)}x^{\mathrm{T}}(z)\mathfrak{G}x(z)\mathrm{d}z\\ &\geq \hat{\varepsilon}_{k-c}(\int_c^k x(z)\mathrm{d}z)^{\mathrm{T}}\mathfrak{G}(\int_c^k x(z)\mathrm{d}z)\end{aligned} \tag{5}$$

and

$$\begin{aligned}&\int_c^k\int_u^k e^{\kappa(z-k)}x^{\mathrm{T}}(z)\mathfrak{G}x(z)\mathrm{d}z\mathrm{d}u\\ &\geq \bar{\varepsilon}_{k-c}(\int_c^k\int_u^k x(z)\mathrm{d}z\mathrm{d}u)^{\mathrm{T}}\mathfrak{G}(\int_c^k\int_u^k x(z)\mathrm{d}z\mathrm{d}u)\end{aligned} \tag{6}$$

where

$$\hat{\varepsilon}_{k-c}=\frac{\kappa}{e^{\kappa(k-c)}-1},$$

$$\bar{\varepsilon}_{k-c}=\frac{\kappa^2}{e^{\kappa(k-c)}-(k-c)-1}.$$

Similarly, our final goal in the paper is just to obtain the set as accurate as possible, so that it will restrain all reachable states of system (1), and it can be defined as

$$\tilde{\mathbb{R}}_x=\{x(t)\mid x(t)\text{ satisfies (1) , }w(t)\text{ satisfies (2), }t\geq 0\}.$$

3 Main Result

In this part of the paper, we derive the sufficient condition which will constraint the set of all reachable states of the continuous-time delayed nonlinear switched system with impulsive perturbation.

Theorem 1 *For the given scalar $\delta>0$, scalar $\eta>0$, and scalar $\nu\geq 1$, when it is satisfied that matrices P_{φ_j}, matrices R_{φ_j} and matrices S_{φ_j} are all positive definite symmetric matrices, and $K_{\varphi_j}=\begin{bmatrix}K_{1\varphi_j} & K_{2\varphi_j} & K_{3\varphi_j} & K_{4\varphi_j} & K_{5\varphi_j}\end{bmatrix}$ such that the following inequalities are feasible:*

$$\lambda_{\max}^2(E_{\varphi_j})P_{\varphi_j}\leq \nu P_{\varphi_{j-1}}, \tag{7}$$

$$R_{\varphi_j}\leq \nu R_{\varphi_{j-1}}, \tag{8}$$

$$S_{\varphi_j}\leq \nu S_{\varphi_{j-1}}, \tag{9}$$

$$\Lambda_{\varphi_j}=\begin{bmatrix}\Lambda_{11\varphi_j} & \Lambda_{12\varphi_j} & \Lambda_{13\varphi_j} & \Lambda_{14\varphi_j} & \Lambda_{15\varphi_j}\\ * & \Lambda_{22\varphi_j} & \Lambda_{23\varphi_j} & \Lambda_{24\varphi_j} & \Lambda_{25\varphi_j}\\ * & * & \Lambda_{33\varphi_j} & \Lambda_{34\varphi_j} & \Lambda_{35\varphi_j}\\ * & * & * & \Lambda_{44\varphi_j} & \Lambda_{45\varphi_j}\\ * & * & * & * & \Lambda_{55\varphi_j}\end{bmatrix}<0, \tag{10}$$

where

$$\begin{aligned}\Lambda_{11\varphi_j}&=\delta P_{\varphi_j}+hR_{\varphi_j}-\tfrac{\delta^2h^2}{e^{\delta h}-\delta h-1}S_{\varphi_j}+\upsilon^2 I\\ &\quad+\mathrm{Sym}\{K_{1\varphi_j}^{\mathrm{T}}A_{\varphi_j}\},\\ \Lambda_{12\varphi_j}&=K_{1\varphi_j}^{\mathrm{T}}B_{\varphi_j}+A_{\varphi_j}^{\mathrm{T}}K_{2\varphi_j},\\ \Lambda_{13\varphi_j}&=\tfrac{\delta^2h}{e^{\delta h}-\delta h-1}S_{\varphi_j}+K_{1\varphi_j}^{\mathrm{T}}C_{\varphi_j}+A_{\varphi_j}^{\mathrm{T}}K_{3\varphi_j},\\ \Lambda_{14\varphi_j}&=-K_{1\varphi_j}^{\mathrm{T}}+A_{\varphi_j}^{\mathrm{T}}K_{4\varphi_j}+P_{1\varphi_j}^{\mathrm{T}},\\ \Lambda_{15\varphi_j}&=K_{1\varphi_j}^{\mathrm{T}}D_{\varphi_j}+A_{\varphi_j}^{\mathrm{T}}K_{5\varphi_j},\\ \Lambda_{22\varphi_j}&=-I+\mathrm{Sym}\{K_{2\varphi_j}^{\mathrm{T}}B_{\varphi_j}\},\\ \Lambda_{23\varphi_j}&=K_{2\varphi_j}^{\mathrm{T}}C_{\varphi_j}+B_{\varphi_j}^{\mathrm{T}}K_{3\varphi_j},\\ \Lambda_{24\varphi_j}&=-K_{2\varphi_j}^{\mathrm{T}}+B_{\varphi_j}^{\mathrm{T}}K_{4\varphi_j},\\ \Lambda_{25\varphi_j}&=K_{2\varphi_j}^{\mathrm{T}}D_{\varphi_j}+B_{\varphi_j}^{\mathrm{T}}K_{5\varphi_j},\\ \Lambda_{33\varphi_j}&=\mathrm{Sym}\{C_{\varphi_j}^{\mathrm{T}}K_{3\varphi_j}\}-\tfrac{\delta}{e^{\delta h}-1}R_{\varphi_j}-\tfrac{\delta^2}{e^{\delta h}-\delta h-1}S_{\varphi_j},\\ \Lambda_{34\varphi_j}&=-K_{3\varphi_j}^{\mathrm{T}}+D_{\varphi_j}^{\mathrm{T}}K_{4\varphi_j},\\ \Lambda_{35\varphi_j}&=K_{3\varphi_j}^{\mathrm{T}}D_{\varphi_j}+C_{\varphi_j}^{\mathrm{T}}K_{5\varphi_j},\\ \Lambda_{44\varphi_j}&=-\mathrm{Sym}\{K_{4\varphi_j}\}+\tfrac{h^2}{2}S_{\varphi_j},\\ \Lambda_{45\varphi_j}&=-K_{5\varphi_j}+K_{4\varphi_j}^{\mathrm{T}}D_{\varphi_j},\\ \Lambda_{55\varphi_j}&=-\eta I+\mathrm{Sym}\{K_{5\varphi_j}^{\mathrm{T}}D_{\varphi_j}\}.\end{aligned}$$

And the average dwell time satisfies $\Phi_a>\frac{\ln\nu}{\delta}$, all the reachable states of system (1) are constrained by the common region of the final acquired ellipsoids:

$$\mathcal{R}=\{x(t)\in\mathbb{R}^n\mid x^{\mathrm{T}}(t)\check{P}_{\varphi_j}x(t)\leq 1\},$$

where $\check{P}_{\varphi_j}=\frac{P_{\varphi_j}}{\nu^{N_0}}$.

Proof: At present, based on Lemma 1, we need to validate the set that is provided by the Theorem 1 can restrict all reachable states of the system (1). We decide to choose $V_{\varphi_j}(x,t)$ as the Lyapunov function in the following calculations, that is

$$\begin{aligned}V_{\varphi_j}(x,t)=\ &x^{\mathrm{T}}(t)P_{\varphi_j}x(t)\\ &+\int_{-h}^0\int_{t+\theta}^t e^{\delta(s-t)}x^{\mathrm{T}}(s)R_{\varphi_j}x(s)\mathrm{d}s\mathrm{d}\theta\\ &+\int_{-h}^0\int_{\theta}^0\int_{t+\lambda}^t e^{\delta(s-t)}\dot{x}^{\mathrm{T}}(s)S_{\varphi_j}\dot{x}(s)\mathrm{d}s\mathrm{d}\lambda\mathrm{d}\theta\end{aligned} \tag{11}$$

According to the result of solving the upper right Dini derivative of $V_{\varphi_j}(x,t)$, we can obtain that

$$\begin{aligned}&\mathfrak{D}^+V_{\varphi_j}(x,t)+\delta V_{\varphi_j}(x,t)\\ =\ &2\dot{x}^{\mathrm{T}}(t)P_{\varphi_j}x(t)+\tfrac{h^2}{2}\dot{x}^{\mathrm{T}}(t)S_{\varphi_j}\dot{x}(t)\\ &+x^{\mathrm{T}}(t)(\delta P_{\varphi_j}+h\dot{R}_{\varphi_j})x(t)\\ &-\int_{t-h}^t e^{\delta(s-t)}x^{\mathrm{T}}(s)R_{\varphi_j}x(s)\mathrm{d}s\\ &+\int_{-h}^0\int_{t+\theta}^t e^{\delta(s-t)}\dot{x}^{\mathrm{T}}(s)S_{\varphi_j}\dot{x}(s)\mathrm{d}s\mathrm{d}\theta.\end{aligned} \tag{12}$$

It is simple for us to obtain from Assumption 2 that

$$0\leq \upsilon^2x^{\mathrm{T}}(t)x(t)-f_{\varphi_j}^{\mathrm{T}}(t,x(t))f_{\varphi_j}(t,x(t)) \tag{13}$$

After the free weight matrix $\mathcal{M}_{\varphi_j}$ is introduced, it can deduce

$$0=2\zeta^{\mathrm{T}}(t)K_{\varphi_j}^{\mathrm{T}}\mathcal{M}_{\varphi_j}\zeta(t), \tag{14}$$

with

$$\zeta(t)=[x^{\mathrm{T}}(t)\ \ f_{\varphi_j}(t,x(t))\ \ \int_{t-h}^t x(s)\mathrm{d}s\ \ \dot{x}^{\mathrm{T}}(t)\ \ w^{\mathrm{T}}(t)]^{\mathrm{T}}$$

and

$$\mathcal{M}_{\varphi_j}=\begin{bmatrix}A_{\varphi_j} & B_{\varphi_j} & C_{\varphi_j} & -I & D_{\varphi_j}\end{bmatrix}.$$

By using Lemma 2, it follows from (10) and (12)–(14) that

$$\begin{aligned}&\mathfrak{D}^+V_{\varphi_j}(x,t)+\delta V_{\varphi_j}(x,t)-\eta w^{\mathrm{T}}(t)w(t)\\ \leq\ &\zeta^{\mathrm{T}}(t)\Lambda_{\varphi_j}\zeta(t)<0,\ \ t\neq t_{j-1}.\end{aligned} \tag{15}$$

Moreover, when $w(t)=0$, it will yield that

$$V_{\varphi_j}(x,t)\leq \nu^{N_0}e^{-(\delta-\frac{\ln\nu}{\Phi_a})t}V_{\varphi_j}(x_0),$$

so it can now be determined that the system (1) is exponentially asymptotically stable with $\Phi_a > \frac{\ln \nu}{\delta}$. Following from $x(t_j^+) = E_{\varphi_j} x(t_j), t = t_j$ in system (1) and (7)–(9) that

$$V_{\varphi_j}(x, t_{j-1}^+) \leq \nu V_{\varphi_{j-1}}(x, t_{j-1}^-) \quad , \quad t = t_{j-1}. \tag{16}$$

According to Lemma 1, and following from (15) and (16) that

$$x^{\mathrm{T}}(t) P_{\varphi_j} x(t) \leq V_{\varphi_j}(x, t) \leq \nu^{N_0},$$

so finally we will obtain that

$$x^{\mathrm{T}}(t) \check{P}_{\varphi_j} x(t) \leq 1 \tag{17}$$

where $\check{P}_{\varphi_j} = \frac{P_{\varphi_j}}{\nu^{N_0}}$.

So far, the establishment of the above inequality relationship means that all the possible states of the continuous-time delayed nonlinear switched system with impulse perturbation will be included in the common region of the final intersecting ellipsoids, and the reachable set of the studied systems is successfully estimated by utilizing LMI.

Remark 1 *In order to insure that we obtain an ellipsoid with the shortest principal axis, and make all the state response curve of the continuous-time delayed nonlinear switched system with impulsive perturbation can be wrapped and constrained inside the derived ellipsoids, this paper introduces an optimized LMI, that is* $\vartheta I \leq \check{P}_{\varphi_j}$, *and maximizing* $\check{P}_{\varphi_j}$ *by seeking the maximum value of* ϑ, *the final obtained ellipsoid can be minimized as much as possible, which means that*

$$\begin{bmatrix} \bar{\vartheta} I & I \\ I & \check{P}_{\varphi_j} \end{bmatrix} = \begin{bmatrix} \bar{\vartheta} I & I \\ I & \frac{P_{\varphi_j}}{\nu^{N_0}} \end{bmatrix} \geq 0,$$

where $\bar{\vartheta} = \vartheta^{-1}$ *will be minimized.*

4 Numerical and Simulation

Now, a specific numerical example is given in this chapter to verify the correctness and the effectiveness of the method described above, that is, all the reachable states of system (1) can be constrained in the bounded set obtained by accurate calculation.

Example 1 *For* $\varphi(t) = \varphi_j \in \{1, 2\}$, *both the relevant switching signal and the impulsive signal of the studied switched system are shown in the Fig. 1. Considering that the following parameters will be applied to the system (1) :*

For $\varphi_j = 1$,

$$A_1 = \begin{bmatrix} -5 & -2 \\ -3 & -4 \end{bmatrix}, \quad B_1 = \begin{bmatrix} -0.5 & -0.3 \\ -0.5 & 1 \end{bmatrix},$$

$$C_1 = \begin{bmatrix} 1 & 0.2 \\ 0.3 & -0.4 \end{bmatrix}, \quad D_1 = \begin{bmatrix} 0.5 \\ -0.4 \end{bmatrix},$$

$$E_1 = 0.58 I_{2\times 2}.$$

For $\varphi_j = 2$,

$$A_2 = \begin{bmatrix} -4 & -1.5 \\ -1 & -3.5 \end{bmatrix}, \quad B_2 = \begin{bmatrix} -0.5 & -0.5 \\ -0.5 & 0.75 \end{bmatrix},$$

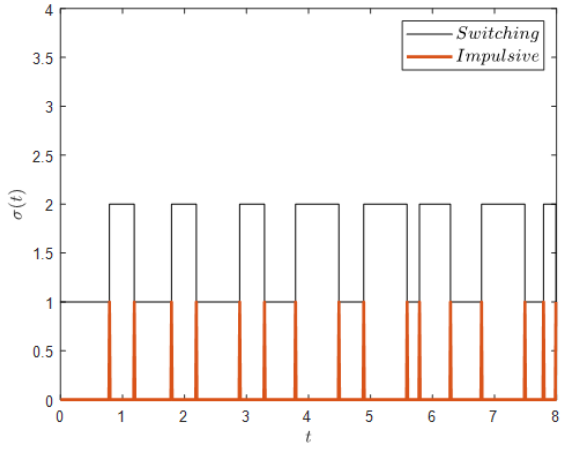

Fig. 1: Switching signal and impulse signal of the switched system.

$$C_2 = \begin{bmatrix} 0.3 & 0.1 \\ 0.2 & -0.5 \end{bmatrix}, \quad D_2 = \begin{bmatrix} 0.3 \\ -0.5 \end{bmatrix},$$

$$E_2 = 0.65 I_{2\times 2}.$$

Taking $x_0 \equiv 0$, $\delta = 1.5$, $\nu = 1.55$ *and* $N_0 = \varpi = 1$, *then* $\Phi_a > \frac{\ln \nu}{\delta} \approx 0.2922$. *If we assume that* $\Phi_a = 0.5s$, *it can be deduced that* $\eta \approx 0.6235$.

According to the optimization design steps described above, and based on solving the LMIs, we can obtain that the corresponding final minimum value of $\bar{\vartheta}$, *the specific parameters of the matrix* $\check{P}_{\varphi_1}$ *and the matrix* $\check{P}_{\varphi_2}$, *one has*

$$\bar{\vartheta} = 0.9141,$$

$$\check{P}_{\varphi_1} = \begin{bmatrix} 2.5077 & 1.1205 \\ 1.1205 & 1.9821 \end{bmatrix}$$

and

$$\check{P}_{\varphi_2} = \begin{bmatrix} 3.4689 & 1.0524 \\ 1.0524 & 1.8299 \end{bmatrix}.$$

Let $f_{1\varphi_j}(t, N\tilde{x}(t)) = x_1(t)\sinh(x_1(t))$ *and* $f_{2\varphi_j}(t, N\tilde{x}(t)) = x_2(t)\tan(x_2(t))$, *additionally, the trajectory curve of* $x_1(t)$ *and the trajectory curve of* $x_2(t)$ *are described as boundary ellipsoids with* $w(t) = \sin(t)$ *in the Fig. 2.*

In the Fig. 3, the trajectory curves of the researched system state have been contained within the bounded ellipsoids all the time, which implies that previously mentioned approach is indeed useful for reasonably estimating the set of reachable states of the researched system.

5 Conclusions

By adopting the real bounded lemma, introducing integral inequality technique and applying the free weight matrix method, in the paper, we study the reachable set estimation problem of the continuous-time delayed nonlinear switched system with impulsive perturbation under the premise of zero initial conditions and bounded peak disturbance conditions. Based on Lyapunov method, the sufficient condition is expressed in the form of the strict LMIs, and all reachable states of the studied system are bounded by the intersection of ellipsoids. Then, through a certain optimization design,

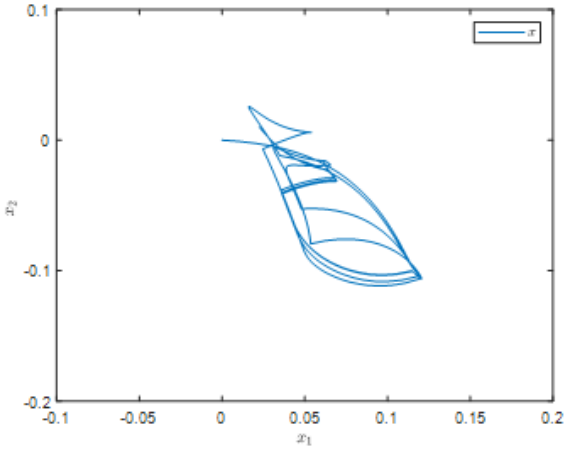

Fig. 2: The trajectory curves situation of $x_1(t)$ and $x_2(t)$.

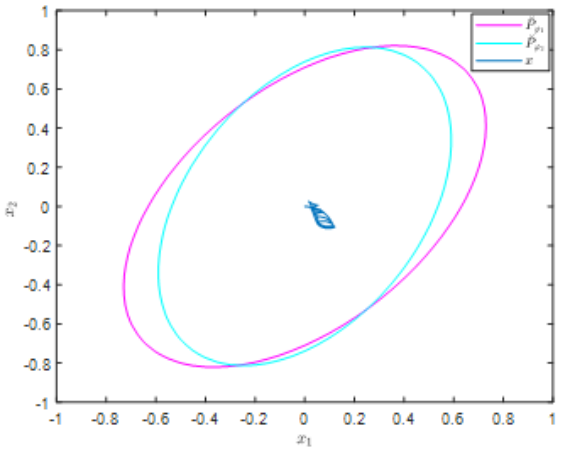

Fig. 3: Bounded ellipsoids estimation result of the reachable states.

the ellipsoid as small as possible is obtained to tightly encircle the state response curve of the studied system, which decreases conservatism of the reachable set estimated results to a certain extent. Ultimately, the effectiveness and correctness of adopted calculation method are verified by using a specific numerical example. In the subsequent related work, we can further study the problem of reachable set estimation by further considering other applications, such as the application in [45], so as to expand the application scope of our theoretical results. In addition, we can also expand the research direction of nonlinear systems on the basis of this paper, such as [46] solves the event-based asymptotic tracking control problem for nonlinear systems and the issue of adaptive decentralized tracking control for nonlinear systems is studied in [47] and so on.

References

[1] M. Flores-Padilla and C. Treesatayapun, "Adaptive controller based on the affine equivalent model with disturbance rejection for discrete-time switched systems," *International Journal of Systems Science*, vol. 54, no. 16, pp. 3059–3070, 2023.

[2] Y. Zhu and Z. Sun, "Minimum realization for controllability/observability of switched linear systems," *Nonlinear Analysis: Hybrid Systems*, vol. 51, p. 101426, 2024.

[3] L. Li, Q. Guo, B. Chen, W. Yue, Z. Liu, and H. Sang, "Output regulation for switched systems via dual distributed event-triggered mechanisms under multiple deception attacks," *Applied Mathematics and Computation*, vol. 466, p. 128465, 2024.

[4] Y. Tang, C. Fiter, and L. Hetel, "A study on switched affine system interconnected with fast lti dynamics," *Automatica*, vol. 160, p. 111462, 2024.

[5] J. Cheng, J. Xu, J. H. Park, H. Yan, and D. Zhang, "Protocol-based smc for singularly perturbed switching systems with sojourn probabilities," *Automatica*, vol. 161, p. 111470, 2024.

[6] X. Ouyang, F. Zhang, and N. Zhao, "Adaptive output-feedback prescribed performance control of uncertain switched nonlinear systems." *IAENG International Journal of Applied Mathematics*, vol. 54, no. 1, 2024.

[7] H. Liu, X. Li, and H. Wang, "Adaptive prescribed finite-time asymptotic tracking control for switched systems with unknown initial conditions and full-state constraints," *International Journal of Systems Science*, vol. 55, no. 2, pp. 370–390, 2024.

[8] W. Zheng, Y. Wan, F. Yang, C. Shang, H. Ye, M. Jiang, and J. Wang, "Identification of switched dynamic system for electric multiple unit train modeling," *Control Engineering Practice*, vol. 143, p. 105815, 2024.

[9] Y. Qi, S. Guo, Y. Tang, H. Geng, and J. Huang, "Safety mpc of constrained switched systems with control barrier function," *International Journal of Systems Science*, vol. 55, no. 1, pp. 87–101, 2024.

[10] J. Zhao, X. Ouyang, N. Zhao, and Y. Zang, "Fixed-time fuzzy adaptive control for switched nonlinear systems with input constraints based on event-triggered." *IAENG International Journal of Computer Science*, vol. 50, no. 4, 2023.

[11] M.-R. Liu, Z. Wu, X. Du, and Z. Fei, "Finite-time and bumpless transfer control of asynchronously switched systems: An output feedback control approach," *Journal of the Franklin Institute*, 2024.

[12] L. Zhang, J. Liang, Z. Feng, and N. Zhao, "Improved results of asynchronous mixed H_∞ and passive control for discrete-time linear switched system with mode-dependent average dwell time," *Chaos, Solitons & Fractals*, vol. 178, p. 114401, 2024.

[13] X. Zhang and S. Xiong, "Output feedback control design for switched systems with unmatched uncertainties based on the switched robust integral sliding mode," *Mathematics*, vol. 11, no. 22, p. 4674, 2023.

[14] E. Mostacciuolo, S. Trenn, and F. Vasca, "Averaging for switched impulsive systems with pulse width modulation," *Automatica*, vol. 160, p. 111447, 2024.

[15] F. Chen, Y. Chen, Q. Zhu, and Q. Zhang, "Stability of stochastic systems with semi-Markovian switching and impulses," *Chaos, Solitons & Fractals*, vol. 177, p. 114247, 2023.

[16] Z. Liu and L. Gao, "Input-to-state stability for impulsive switched systems with delays based on a class of generalised impulsive and switching signals," *International Journal of Control*, vol. 96, no. 11, pp. 2683–2696, 2023.

[17] X. Liu and S. Li, "Optimal control for a class of impulsive switched systems," *Journal of Control and Decision*, vol. 10, no. 4, pp. 529–537, 2023.

[18] J. Lygeros, C. Tomlin, and S. Sastry, "Controllers for reachability specifications for hybrid systems," *Automatica*, vol. 35, no. 3, pp. 349–370, 1999.

[19] R. Zhao, Y. Wang, and Z. Zuo, "Reachable set estimation and synthesis of discrete-time switched systems," *International Journal of Robust and Nonlinear Control*, vol. 30, no. 18, pp. 8060–8073, 2020.

[20] E. Fridman, A. Pila, and U. Shaked, "Regional stabilization

and H_∞ control of time-delay systems with saturating actuators," *International Journal of Robust and Nonlinear Control: IFAC-Affiliated Journal*, vol. 13, no. 9, pp. 885–907, 2003.

[21] S. Boyd, L. El Ghaoui, E. Feron, and V. Balakrishnan, *Linear matrix inequalities in system and control theory*. SIAM, 1994.

[22] J. Abedor, K. Nagpal, and K. Poolla, "A linear matrix inequality approach to peak-to-peak gain minimization," *International Journal of Robust and Nonlinear Control*, vol. 6, no. 9-10, pp. 899–927, 1996.

[23] C. Durieu, E. Walter, and B. Polyak, "Multi-input multi-output ellipsoidal state bounding," *Journal of optimization theory and applications*, vol. 111, pp. 273–303, 2001.

[24] T. Hu and Z. Lin, *Control systems with actuator saturation: analysis and design*. Springer Science & Business Media, 2001.

[25] Y. Li, Y. He, W.-J. Lin, and M. Wu, "Reachable set estimation for singular systems via state decomposition method," *Journal of the Franklin Institute*, vol. 357, no. 11, pp. 7327–7342, 2020.

[26] J. Li, Y. Zhao, Z. Feng, and M. Park, "Reachable set estimation and dissipativity for discrete-time t–s fuzzy singular systems with time-varying delays," *Nonlinear Analysis: Hybrid Systems*, vol. 31, pp. 166–179, 2019.

[27] Z. Feng and J. Lam, "On reachable set estimation of singular systems," *Automatica*, vol. 52, pp. 146–153, 2015.

[28] G. Liu, S. Xu, Y. Wei, Z. Qi, and Z. Zhang, "New insight into reachable set estimation for uncertain singular time-delay systems," *Applied Mathematics and Computation*, vol. 320, pp. 769–780, 2018.

[29] Y. Jiang, H. Yang, and I. G. Ivanov, "Reachable set estimation and controller design for linear time-delayed control system with disturbances," *Mathematics*, vol. 12, no. 2, p. 176, 2024.

[30] G. Göksu, "Input-to-state exponential stability of switched nonlinear time-delay systems having stable/unstable subsystems," *Systems & Control Letters*, vol. 184, p. 105724, 2024.

[31] E. Fridman and U. Shaked, "On reachable sets for linear systems with delay and bounded peak inputs," *Automatica*, vol. 39, no. 11, pp. 2005–2010, 2003.

[32] J.-H. Kim, "Improved ellipsoidal bound of reachable sets for time-delayed linear systems with disturbances," *Automatica*, vol. 44, no. 11, pp. 2940–2943, 2008.

[33] W.-J. Lin, Y. He, M. Wu, and Q. Liu, "Reachable set estimation for Markovian jump neural networks with time-varying delay," *Neural Networks*, vol. 108, pp. 527–532, 2018.

[34] Z. Feng, Z. Jiang, and W. X. Zheng, "Reachable set synthesis of singular Markovian jump systems," *Journal of the Franklin Institute*, vol. 357, no. 18, pp. 13 785–13 799, 2020.

[35] H. Ji, H. Zhang, and T. Senping, "Reachable set estimation for inertial Markov jump bam neural network with partially unknown transition rates and bounded disturbances," *Journal of the Franklin Institute*, vol. 354, no. 15, pp. 7158–7182, 2017.

[36] Z. Xu, H. Su, P. Shi, R. Lu, and Z.-G. Wu, "Reachable set estimation for Markovian jump neural networks with time-varying delays," *IEEE Transactions on Cybernetics*, vol. 47, no. 10, pp. 3208–3217, 2016.

[37] J. Lam, B. Zhang, Y. Chen, and S. Xu, "Reachable set estimation for discrete-time linear systems with time delays," *International Journal of Robust and Nonlinear Control*, vol. 25, no. 2, pp. 269–281, 2015.

[38] J. Li, Z. Feng, and C. Zhang, "Reachable set estimation for discrete-time singular systems," *Asian Journal of Control*, vol. 19, no. 5, pp. 1862–1870, 2017.

[39] X. Jiang, G. Xia, Z. Feng, W. X. Zheng, and Z. Jiang, "Delay-partitioning-based reachable set estimation of markovian jump neural networks with time-varying delay," *Neurocomputing*, vol. 412, pp. 360–371, 2020.

[40] M. Althoff and B. H. Krogh, "Reachability analysis of nonlinear differential-algebraic systems," *IEEE Transactions on Automatic Control*, vol. 59, no. 2, pp. 371–383, 2013.

[41] M. Maiga, N. Ramdani, L. Travé-Massuyès, and C. Combastel, "A comprehensive method for reachability analysis of uncertain nonlinear hybrid systems," *IEEE Transactions on Automatic Control*, vol. 61, no. 9, pp. 2341–2356, 2015.

[42] J. Lu, D. W. Ho, and J. Cao, "A unified synchronization criterion for impulsive dynamical networks," *Automatica*, vol. 46, no. 7, pp. 1215–1221, 2010.

[43] X. Zhang, Z. Feng, and X. Zhang, "On reachable set problem for impulse switched singular systems with mixed delays," *IET Control Theory & Applications*, vol. 17, no. 5, pp. 628–638, 2023.

[44] H. Trinh *et al.*, "Exponential stability of time-delay systems via new weighted integral inequalities," *Applied Mathematics and Computation*, vol. 275, pp. 335–344, 2016.

[45] H. Gao, Z. Li, X. Yu, and J. Qiu, "Hierarchical multiobjective heuristic for pcb assembly optimization in a beam-head surface mounter," *IEEE Transactions on Cybernetics*, vol. 52, no. 7, pp. 6911–6924, 2021.

[46] Z. Feng, R.-B. Li, N. Zhang, and L. Wu, "Event-based asymptotic tracking control for constrained mimo nonlinear systems via a single-parameter adaptation method," *IEEE Transactions on Systems, Man, and Cybernetics: Systems*, 2023.

[47] Z. Feng, R.-B. Li, and L. Wu, "Adaptive decentralized control for constrained strong interconnected nonlinear systems and its application to inverted pendulum," *IEEE Transactions on Neural Networks and Learning Systems*, 2023.

Proceedings of the 3rd Conference on Fully Actuated System Theory and Applications
May 10-12, 2024, Shenzhen, China

A Real-time Event-Based Learning Approach for Input-Output Sensitivity Analysis

Xingjing She[1], Hang Geng[1], Xuan Gou[1], Kai Chen[1]
1. School of Automation Engineering, University of Electronic Science and Technology of China, Chengdu 611731, P. R. China
E-mail: Hang.Geng@uestc.edu.cn

Abstract: This paper introduces a real-time event-based learning approach for input-output sensitivity analysis. Based on the rank order clustering method, this proposed approach is capable of continuously monitoring real-time variations in input variables and automatically quantifying each input's contribution to the target output. Moreover, the method facilitates ranking and grouping based on the significance and correlation of input-output event data. The application to hydraulic systems shows that the developed method not only produces effective evaluation of each input variable's influence on the target output, but also opens a new avenue for comprehending the performance of hydraulic systems.

Key Words: Sensitivity analysis, Input Variable Selection, Clustering, Real-time systems, Hydraulic systems

1 Introduction

With the continual advancement of technology and the increasing complexity of systems, obtaining precise information about materials and machinery has become a significant challenge in augmenting industrial efficiency and productivity [1]. When external or internal disturbances affect system implementation, parameter changes can be identified in a pivotal system function. To more effectively enhance the monitoring, control, or optimization of complex systems, it is imperative to pursuit a methodology capable of accumulating precise information. Analyzing this information, we can discern the interrelationships among input variables, environmental factors, time, and target output variables. Subsequently, we can eliminate factors with negligible impact on target output variables or selectively analyze parameters that exert substantial influence on target output variables, thereby optimizing system structure. This kind of method is commonly referred to as input variable selection (IVS)[2–4] in the engineering field or sensitivity analysis (SA)[5–7] in the mathematical domain.

SA seeks to direct practitioners towards prioritizing the most critical variables that influence the output behavior of a system. These influential variables provide the most information about system output behaviors [8]. The method embraces a "factor sparsity" heuristic approach [9], indicating that only a small subset of components in the system is able to significantly impact system outputs. Traditional sensitivity analysis methods encompass derivatives, regression, distribution, and heuristics, which often rely on historical data or expert knowledge. Regression-based methods [10] derive sensitivity information by fitting linear regression models and necessitating numerous predefined rules for global sensitivity analysis [11]. Derivative-based methods [10] evaluate global sensitivity by calculating and averaging derivatives at various points, but their applicability to nonlinear systems may be limited [8, 12]. Distribution-based methods [10] center on output distribution characteristics, but require predefined rules [13] . Heuristic methods [14–16] gauge the actual impact of each system input on the output through data filtering, depending on expert knowledge. In contrast, the discrete event-based sensitivity analysis method employed in this paper is not contingent on historical data or predefined rules, enabling the swift identification of relationships between multiple input variables and output variables [8].

This paper represents the inaugural integration of the event-based sensitivity analysis method with ZeMA hydraulic system data [17], enabling the dynamic evaluation of the relationship between input and output variables in hydraulic systems. Temperature, pressure, and flow sensors are regarded as input variables, whereas motor power, cooling efficiency, vibration, cooling power, and efficiency are designated as target output variables. The interconnections among these variables are thoroughly examined. Significantly, our experiments demonstrate that the proposed method can accurately determine the relationship between input and target output variables without necessitating a complete sampling cycle.

2 Event Clustering

Event clustering technology disintegrates the system's state into a sequence of continuous discrete events triggered by changes in the states of a specific set of input variables. The necessity for preconceived assumptions regarding the system state is circumvented by this method, and it remains impervious to the influence of historical events. Consequently, quasi real-time examination of the correlation between the relevant system state and input variables is enabled by this approach.

"Events" are defined as significant transitions in system states, which can manifest as abrupt changes in sensor readings, adjustments in operating conditions, or notable fluctuations in system performance. Techniques such as detection and the formation of an Incidence Matrix are employed to analyze the relationship between system states and inputs, based on the identification and understanding of these "events". The following are some fundamental concepts and parameters.

- Discrete Event System
  Describing events occurring at discrete time points and their interactions is a common practice. Such systems are typically comprised of a series of discrete events that result in changes to the system's state.

- Triggered and Event Data
  In the realm of discrete event systems (DES), trigger data (TD) is characterized as any input variable whose value transition initiates an event. The sequence of data portraying the system's state at a particular time is denoted as event data (ED).
- Triggered and Event Thresholds
  Triggered thresholds (TT) and event thresholds (ET) serve as indicators for evaluating alterations in TD and ED. These values are usually determined by domain experts within the system.

Fig 1 depicts the procedural framework of comprehensive event clustering technology. Sensor values are categorized as inputs and outputs, and an incidence matrix is constructed using logic akin to XNOR. Correlations between TDs and EDs are revealed through the application of the rank order clustering (ROC) method, to facilitate accuracy assessment. Standardization of the matrix enables sensitivity index computation, thereby quantifying input-output impact relationships.

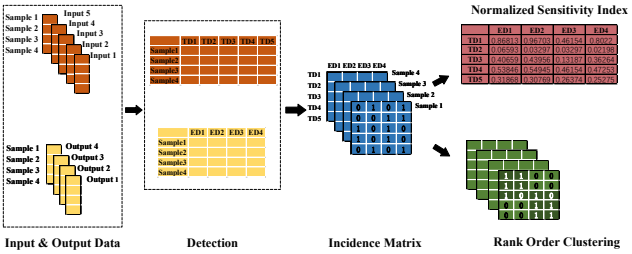

Fig. 1: The schematic diagram illustrates the overall method

2.1 Detection and Formation of the Incidence Matrix

As demonstrated in Fig 1, input data and output data comprise the records of multiple parameters acquired after several sampling instances. Formula (1) elucidates the correlation between each pair of input events, wherein an input event is classified as TD solely if the alteration between consecutive sampling results exceeds the triggered threshold. Similarly, an output event is identified as ED only when the alteration between consecutive sampling results surpasses the event threshold.

$$\begin{aligned} if\ |Input_t - Input_{t-1}| \geq TT \rightarrow Input_t = Trigger \\ if\ |Output_t - Output_{t-1}| \geq ET \rightarrow Output_t = Event \end{aligned} \tag{1}$$

When both ED and TD simultaneously occur as 0 or 1 at the conclusion of the same sampling instance, a 1 is logged at the corresponding position in the Incidence Matrix. If ED and TD exhibit differences, 0 is recorded to emulate a logical XNOR relationship. Essentially, a connection between ED and TD is established exclusively when they undergo changes simultaneously at the end of the same sampling instance; otherwise, they are regarded as unrelated.

2.2 Rank Order Clustering

The data clustering process demands a significant allocation of both memory and time, with the implementation of these algorithms being inherently complex. The ROC [18], introduced by King [19] employs matrix operations to iteratively reorganize the rows and columns of the matrix. Importantly, it has been empirically proven to adaptively manage extensive datasets in real-time [8]. The ROC algorithm is as follows:

Algorithm 1 Rank Order Clustering

Input: The Incidence Matrix$_{i\times j}$.
Output: The Matrix$_{m\times n}$ after clustering.
1: Calculate the weight for each row.
2: **for** $i \in [1, m]$ **do**
3: **for** $j \in [1, n]$ **do**
4: weight $+= 2^{n-j} \times$ Incidence Matrix$_{i\times j}$
5: **end for**
6: $Row_{weight[i]} = weight$
7: **end for**
8: The Incidence Matrix is reordered based on row_{weight}, prioritizing rows with higher rank when two rows have equal decimal values. This yields a new matrix called Matrix_Row
9: Calculate the weight each column.
10: **for** $j \in [1, n]$ **do**
11: **for** $i \in [1, m]$ **do**
12: weight $+= 2^{n-j} \times$ Matrix_Row$_{i\times j}$
13: **end for**
14: $Column_{weight[i]} = weight$
15: **end for**
16: Matrix_Row is reordered based on $column_{weight}$. If two columns share identical decimal values, the column on the left receives a higher rank. This process produces the final Matrix.
17: **return** Matrix

Fig 2 provides a clear depiction of a basic ROC algorithm. It is evident that inputs 2, 4, and 5 are influenced substantially by outputs 1, 4, and 5.

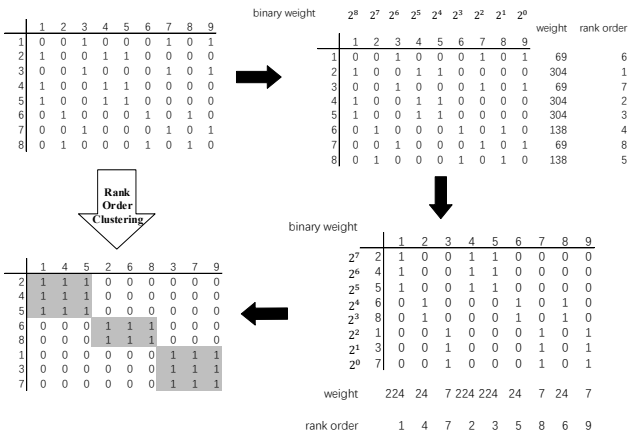

Fig. 2: Illustration of the ROC Method

2.3 Normalized Sensitivity Index Calculation

For each sampling, an Incidence Matrix is generated. The values of the Incidence Matrix are adjusted to -1 where they are originally 0, with the objective of achieving more pronounced variations in upper and lower bounds when sensitivity is calculated. This replacement strategy amplifies the model's sensitivity to changes in input variables, facilitating better elucidation of each variable's impact during sensitivity analysis. The formula for computing the normalized sensitivity index is provided by formula (2) and formula (3). In formula (2), SS represents the cumulative sum of the inci-

dence matrix formed at each sampling instance with preceding incidence matrices. Formula (3) is employed to calculate the normalized sensitivity index.

$$SI_t = \sum_{1}^{t} Incidence\,Matrix\,Scores \tag{2}$$

t represents the current sampling instance.

$$NSI = \frac{SI_n - min_n}{max_n - min_n} \tag{3}$$

n represents the total number of sampling instances, min_n and max_n represent the minimum and maximum values of SI at the last sampling instance.

3 Case Study

The hydraulic system functions as a transmission system to harness fluid to generate power for machinery. Typically, fluid motion is induced by pressure differentials within internal components, regulating force intensity and direction while serving compressors or pumps. The hydraulic system dataset is sourced from the UC Irvine Machine Learning Repository. The test bench comprises a primary working circuit and a secondary cooling filter circuit connected through a reservoir. Various sensors, including pressure, volumetric flow, and temperature sensors, are incorporated into the drilling rig to monitor motor power, cooling efficiency, vibration, cooling power, and efficiency. Predefined operational cycles are iterated to measure process values such as pressure, temperature, and volumetric flow. In this experiment, 12 sensors are configured as inputs (six pressure sensors, two volumetric flow sensors, and four temperature sensors), and outputs are designated as motor power, cooling efficiency, vibration, cooling power, and efficiency.

3.1 Data Processing

Health status data from this dataset is utilized, and samples are collected over a cumulative duration of ten minutes. The dataset exhibits varying sampling frequencies, as outlined in Tab 1. Specifically, the pressure sensor and motor power maintain a sampling frequency of 100Hz, whereas the volume flow sensor operates at 10Hz, with the remaining sensors adhering to a 1Hz sampling frequency. In pursuit of a consistent sampling rate, a data augmentation technique has been employed to standardize the sampling rate to 100Hz. This method enhances the absolute volume of data within a confined dataset. The approach employed in this study involves the application of time warping [20] for data augmentation. The principal objective of Time Warping is to introduce temporal variations by manipulating positions along the temporal axis, thereby generating a more diverse array of samples.

3.2 Threshold Impact on Sensitivity

In this experiment, the variance is selected as the threshold, as it quantifies the extent of data deviation. The normalized sensitivity indices at different thresholds in Fig 3.

From Figure 3, it is evident that, during this experimental process, TDs with both significant and minimal impacts on ED sensitivity can be clearly discerned, irrespective of the threshold value. However, with an increase in the threshold, the alterations in the normalized sensitivity indices for the five EDs become progressively more gradual. This trend is attributed to 1) consistency in the TDs significantly influencing these EDs, 2) and excessively large thresholds attenuating the influence of each TD on the ED, thus obscuring distinctions between these distinct EDs in sensitivity analysis. On the contrary, excessively small thresholds may induce sensitivity impacts for each input and target output even with minimal changes, potentially magnifying the sensitivity influence of each sensor on the ED. Therefore, the selection of an appropriate threshold is paramount.

In this experiment, a threshold set at 0.3 times the variance is opted for. Although selecting 0.3 times the variance as the threshold may not be the optimal choice, it showcases a strong capability to reflect the relationship between input variables and output results. By comparing sensitivity index curves under various multiples of the variance, it is observed that 0.3 times the variance accurately discloses the impact of input variables on the system output.

Table 1: Sensors and collected data

Sensor	**Physical Quantity**	**Unit**	**Sampling Rate**
PS1-PS6	Pressure	bar	100 Hz
EPS1	Motor power	W	100 Hz
FS1,FS2	Volume flow	l/min	10 Hz
TS1-TS4	Temperature	$°C$	1 Hz
VS1	Vibration	mm/s	1 Hz
CE	Cooling efficiency	%	1 Hz
CP	Cooling power	kW	1 Hz
SE	Efficiency factor	%	1 Hz

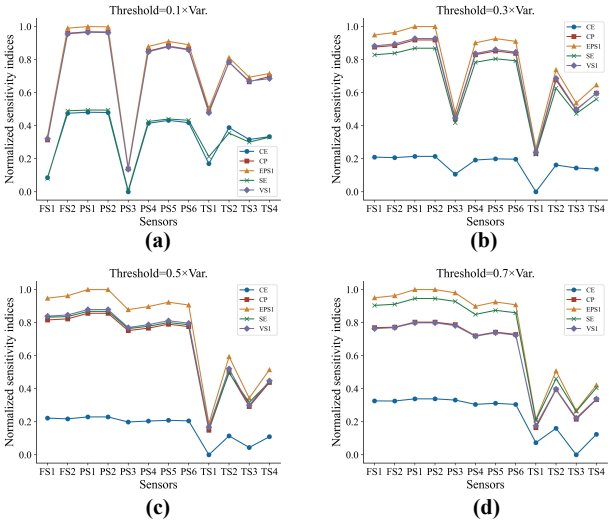

Fig. 3: Normalized Sensitivity Indices at Different Thresholds

3.3 TD Impact on ED.

Fig 4 illustrates the histogram of normalized sensitivity indices. It is notable that pressure sensors PS1 and PS2 are identified as the most significant influencing factors in motor power, cooling efficiency, vibration, cooling power, and efficiency. Conversely, temperature sensor TS1 is observed to have the least impact on these parameters. This suggests that in the occurrence of abnormalities in motor power and other

parameters, priority should be given to investigate whether pressure sensors PS1 and PS2 are abnormal or not. Furthermore, as depicted in Figure 4, the normalized sensitivity indices for cooling efficiency exhibit a relatively uniform distribution. This implies that compared to other target outputs, the twelve sensors contribute evenly to the impact on cooling efficiency.

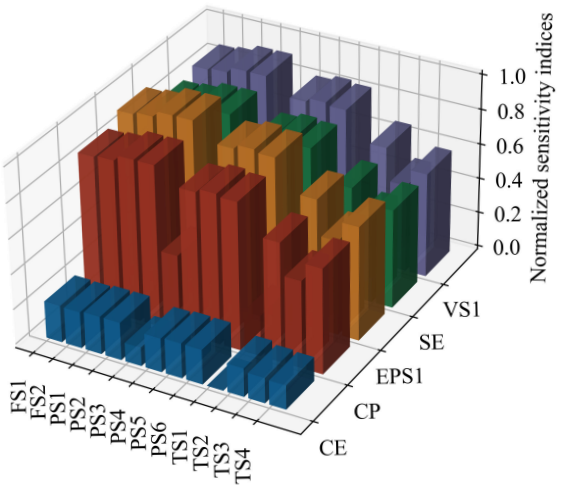

Fig. 4: The normalized sensitivity indices

3.4 Normalized Sensitivity Index

Fig 5 illustrates the values of the normalized sensitivity index at different sampling instances, using a threshold of 0.3 times the variance, specifically at the 1000th, 5000th, 30000th, and final sampling points. Clearly, by the 5000th sampling instance, the impact of TDs on EDs becomes discernible, and by the 30000th sampling instance, the results closely approximate the final outcomes, exhibiting only subtle changes. This suggests that the methodology does not require the completion of the final sampling, and the correlation between EDs and TDs can be observed within a brief timeframe.

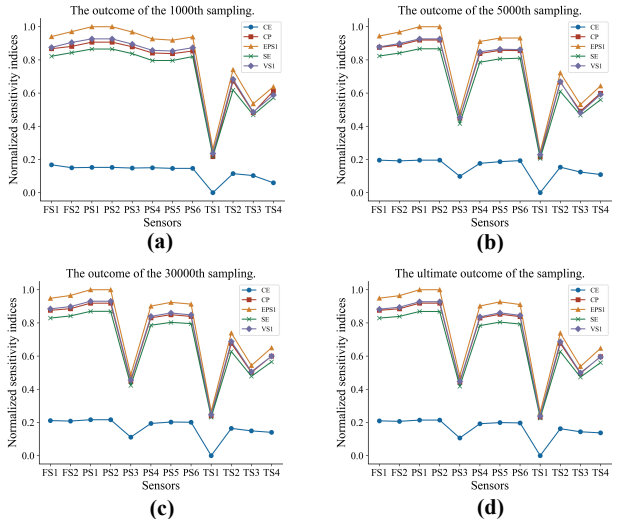

Fig. 5: Normalized Sensitivity Indices at Different Sampling Instances

3.5 Role of ROC

Tab 2 and Tab 3 depict the results obtained following ROC processing at two selected sampling instances (the 2000th and 25000th) post ROC processing. TD1 to TD12 correspond to 'FS1', 'FS2', 'PS1', 'PS2', 'PS3', 'PS4', 'PS5', 'PS6', 'TS1', 'TS2', 'TS3', 'TS4', and ED1 to ED5 correspond to 'CE', 'CP', 'EPS1', 'SE', 'VS1'. These tables clearly demonstrate that ROC effectively represents many-to-many relationships. In Tab 2, we observe associations, where ED2, ED3, ED4, and ED5 are correlated with TD1, TD2, TD3, TD4, TD5, TD6, TD7, TD8, TD10, TD11, and TD12. However, in Tab 3, the relationships between all EDs and TD9 and TD11 are not statistically significant. Integrating information from both tables, we infer that ED2, ED3, ED4, and ED5 consistently exhibit similar patterns in these two sampling instances, suggesting comparable normalized sensitivity indices to the 12 sensors. Such analysis corresponds to the results presented in Fig 3(b).

Table 2: ROC at the 2000th Sampling Instance

	ED1	ED2	ED3	ED4	ED5
TD5	1	0	0	0	0
TD9	1	0	0	0	0
TD1	0	1	1	1	1
TD2	0	1	1	1	1
TD3	0	1	1	1	1
TD4	0	1	1	1	1
TD6	0	1	1	1	1
TD7	0	1	1	1	1
TD8	0	1	1	1	1
TD10	0	1	1	1	1
TD11	0	1	1	1	1
TD12	0	1	1	1	1

Table 3: ROC at the 25000th Sampling Instance

	ED1	ED2	ED3	ED4	ED5
TD1	1	1	1	1	1
TD2	1	1	1	1	1
TD3	1	1	1	1	1
TD4	1	1	1	1	1
TD5	1	1	1	1	1
TD6	1	1	1	1	1
TD7	1	1	1	1	1
TD8	1	1	1	1	1
TD10	1	1	1	1	1
TD12	1	1	1	1	1
TD9	0	0	0	0	0
TD11	0	0	0	0	0

4 Conclusion

This paper effectively integrates real-time sensitivity analysis methodologies into hydraulic systems, facilitating the automated grouping of input variables and the quantification of their significance and correlation with target output variables. Through continual monitoring and assessment of input variable fluctuations, the impact weights on target output are rapidly and accurately determined by this method. Analysis of hydraulic systems reveals significant impacts on system efficiency from the pressure sensors PS1, PS2, and flow

sensor FS2, whereas the pressure sensor PS3 and temperature sensor TS1 exhibit the minimal effects. This approach not only diminishes reliance on complete sampling process data but also exhibits remarkable real-time responsiveness and precision. Validation substantiates that the proposed method furnishes robust technical support for real-time system monitoring and adjustment, thereby unveiling novel perspectives for enhancing control system performance. These findings offer new way to refine real-time data analysis for industrial systems across various domains.

References

[1] Morad Danishvar, Ali Mousavi, and Pedro Sousa. Eventclustering for improved real time input variable selection and data modelling. In *2014 IEEE Conference on Control Applications (CCA)*, pages 1801–1806, Juan Les Antibes, France, October 2014. IEEE.

[2] K Wang, H Wang, J Zhao, and L. Wang. A transparent and nonlinear method for variable selection. *Expert Systems with Applications*, 237:121398, March 2024.

[3] Eun-Hu Kim, Sung-Kwun Oh, Witold Pedrycz, and Zunwei Fu. Design of reinforced fuzzy model driven to feature selection through univariable-based correlation and multivariable-based determination coefficient analysis. *IEEE Transactions on Fuzzy Systems*, 30(10):4224–4238, October 2022.

[4] T Duras, F Javed, and Månsson K. Using machine learning to select variables in data envelopment analysis: Simulations and application using electricity distribution data. *Energy Economics*, 120:106621, April 2023.

[5] S Tavakoli, A Mousavi, and P. Broomhead. Event tracking for real-time unaware sensitivity analysis (eventtracker). *IEEE Transactions on Knowledge and Data Engineering*, 25(2):348–359, February 2013.

[6] E Borgonovo and L. Peccati. Global sensitivity analysis in inventory management. *International Journal of Production Economics*, 108(1-2):302–313, July 2007.

[7] Andrea Saltelli. Sensitivity analysis for importance assessment. *Risk Analysis*, 22(3):579–590, June 2002.

[8] Morad Danishvar, Alireza Mousavi, and Peter Broomhead. Eventic: A real-time unbiased event-based learning technique for complex systems. *IEEE Transactions on Systems, Man, and Cybernetics: Systems*, 50(5):1649–1662, May 2020.

[9] Manuel Goncalves, Pedro Sousa, Jerome Mendes, Morad Danishvar, and Alireza Mousavi. Real-time event-driven learning in highly volatile systems: A case for embedded machine learning for scada systems. *IEEE Access*, 10:50794–50806, 2022.

[10] Saman Razavi and et al. The future of sensitivity analysis: An essential discipline for systems modeling and policy support. *Environmental Modelling & Software*, 137:104954, March 2021.

[11] H Christopher Frey and Sumeet R. Patil. Identification and review of sensitivity analysis methods. *Risk Analysis*, 22(3):553–578, 2002.

[12] Francesca Pianosi and Thorsten Wagener. A simple and efficient method for global sensitivity analysis based on cumulative distribution functions. *Environmental Modelling & Software*, 67:1–11, May 2015.

[13] Zdeněk Kala. Global sensitivity analysis based on entropy: From differential entropy to alternative measures. *Entropy*, 23(6):778, June 2021.

[14] Maryam Fallahpour, Alireza Fatehi, Babak N. Araabi, and Morteza Azizi. A supervisory fuzzy control of back-end temperature of rotary cement kilns. In *2007 International Conference on Control, Automation and Systems*, pages 429–434, October 2007.

[15] Jérôme Mendes, Ricardo Maia, Rui Araújo, and Francisco A. A. Souza. Self-evolving fuzzy controller composed of univariate fuzzy control rules. *Applied Sciences*, 10(17):5836, August 2020.

[16] Jérôme Mendes, Ricardo Seco, and Rui Araújo. Automatic extraction of the fuzzy control system for industrial processes. In *ETFA2011*, pages 1–8, September 2011.

[17] Nikolai Helwig, Eliseo Pignanelli, and Andreas Schutze. Condition monitoring of a complex hydraulic system using multivariate statistics. In *2015 IEEE International Instrumentation and Measurement Technology Conference (I2MTC) Proceedings*, pages 210–215, Pisa, Italy, May 2015. IEEE.

[18] Tamal Ghosh and Pranab K Dan. Effective clustering method for group technology problems: A short communication. 2011.

[19] J. R. KING. Machine-component grouping in production flow analysis: an approach using a rank order clustering algorithm. *International Journal of Production Research*, 18(2):213–232, 1980.

[20] Seungmin Han, Seokju Oh, and Jongpil Jeong. Bearing fault diagnosis based on multiscale convolutional neural network using data augmentation. *Journal of Sensors*, 2021:e6699637, February 2021.

Proceedings of the 3rd Conference on Fully Actuated System Theory and Applications
May 10-12, 2024, Shenzhen, China

An INS/GNSS Localization Method Based on Set-Membership Filter for Unmanned Aerial Vehicles

Xujie Qin[1], Jun Lai[1], Yirui Cong[1], Xiangke Wang[1]
1. College of Intelligence Science and Technology, National University of Defense Technology, Changsha 410073, P. R. China
E-mail: laijun@nudt.edu.cn

Abstract: This paper studies a set-membership filter-based inertial integrated localization problem, where the inertial navigation system (INS) error and Global Navigation Satellite System (GNSS) measurement error are unknown-but-bounded (UBB) noises. To solve this problem, we establish a strapdown INS error model and a GNSS measurement model with UBB noises. Based on the optimal set-membership filtering framework, we propose a constrained zonotopic fast resurisive localization method. Compared with the existing probabilistic integrated navigation methods, the proposed method does not need to know the specific noise distribution and has better versatility and robustness. Finally, the numerical simulation results of the INS/GNSS navigation corroborate the effectiveness of this method.

Key Words: INS/GNSS, Constrained Zonotope, Set-Membership Filter

1 Introduction

Nowadays, unmanned aerial vehicles (UAVs) have been widely used in various aspects of real life. However, the task of determining the position of a UAV poses many challenges. To localize themselves under unknown environments, UAVs extensively utilize the Global Navigation Satellite System (GNSS) and inertial navigation system (INS) integrated navigation to obtain high-precision navigation position information.

GNSS can provide high-precision three-dimensional positioning information, with accuracy reaching the centimeter level [1]. However, its performance is influenced by external environmental factors and satellite visibility, leading to situations where update frequency is low and signal interruptions occur in certain cases [2]. On the contrary, INS is an autonomous system that continuously integrates real angular rates and specific forces measured by gyroscopes and accelerometers to obtain position, velocity, and attitude information. However, gyro drift and accelerometer errors of the INS tend to increase over time [3].

Combining INS and GNSS can compensate for the individual shortcomings of each system, ultimately enhancing the precision of the navigation system. Traditionally, probabilistic approaches are employed for data fusion of these two sensors such as UKF [4] or EKF [5].

However, when GNSS measurement information deteriorates due to interference, and environmental vibrations affect the inertial navigation devices in complex high-dynamic environments, accurately representing their noise probability distribution becomes challenging. In such scenarios, these probabilistic methods have limitations [6]. Therefore, addressing combined navigation in the presence of unknown noise distributions of INS/GNSS sensors is crucial for enhancing the adaptability and robustness of integrated navigation systems.

Set-Membership Filter [7] as a set-based filtering theory, treats noise as unknown-but-bounded noise, and can effectively address situations where the noise distribution of INS and GNSS is unknown. In [8], a comprehensive set-based GNSS positioning method is proposed. This method named Lane Boundary Cooperative Augmented Set-membership GNSS Positioning. In [8], an approach to three-dimensional map-aided GNSS positioning method based on set-valued estimation is presented. The authors propose zonotope shadow matching (ZSM) as a set-valued three-dimensional map-aided GNSS positioning method. The strapdown INS error model is provided in [9], depicting how errors in the INS accumulate over time.

Building on existing work, we aim to develop a set-membership filter combined navigation method for INS/GNSS based on unknown-but-bounded noise description, with the purpose of estimating the UAV position. Our primary contributions are as follows:

- We first present the strapdown INS error model based on unknown-but-bounded errors. The errors in the inertial navigation accumulate over time in the form of unknown-but-bounded noise.
- Most importantly, within the set-membership filter framework, we propose an INS/GNSS integrated navigation method based on unknown-but-bounded noise. This approach allows for obtaining the UAV position, which is represented in a set-valued form.

The remainder of this paper is structured as follows. Section II introduces tools for describing set, Section III describes the notation and the system model, Section IV presents the method, Section V describes the experiment and results, Section VI is the conclusion.

2 Preliminaries

In this paper, constrained zonotopes are adopted to accurately describe a set's convex inclusion. They are used to describe the uncertainty range of the INS error. Constrained zonotopes are an extension of zonotopes, more specifically proposed in [10].

Definition 1 (Constrained Zonotope): A set $Z \subset \mathbb{R}^n$ is a constrained zonotope if there exists $(G_z, c_z, A_z, b_z) \in \mathbb{R}^{n\times n_g} \times \mathbb{R}^n \times \mathbb{R}^{n_c\times n_g} \times \mathbb{R}^{n_c}$ such that

$$Z = \{G_z\xi + c_z : \|\xi\|_\infty \leq 1, A_z\xi = b_z\}, \qquad (1)$$

This work was supported by the National Natural Science Foundation of China under Grant 62001494 and U23B2032 and U2241214.

written as $Z(G_z, c_z, A_z, b_z)$.

Apart from being able to describe sets exactly, constrained zonotope is also closed with respect to basic operations on sets. More specifically, the operations are indicated in Proposition 1.

Proposition 1 (The basic set operations [10]): The constrained zonotope $Z = Z(G_z, c_z, A_z, b_z) \in \mathbb{R}^n$, $W = Z(G_w, c_w, A_w, b_w) \in \mathbb{R}^n$, $Y = Z(G_y, c_y, A_y, b_y) \in \mathbb{R}^k$ and $R \in \mathbb{R}^{k\times n}$.

$$
\begin{aligned}
&RZ = Z(RG_z, Rc_z, A_z, b_z)\\
&Z \oplus W = Z([G_z\ G_w], c_z + c_w, \begin{bmatrix} A_z & 0 \\ 0 & A_w \end{bmatrix}, \begin{bmatrix} b_z \\ b_w \end{bmatrix})\\
&Z \cap_R Y = Z([G_z\ 0], c_z, \begin{bmatrix} A_z & 0 \\ 0 & A_y \\ RG_z & -G_y \end{bmatrix}, \begin{bmatrix} b_z \\ b_y \\ c_y - Rc_z \end{bmatrix})
\end{aligned} \tag{2}
$$

In this work, the interval hull $\square Z$ of a constrained zonotope is computed using linear programming (LP).

Proposition 2 (Interval Hull): A constrained zonotope can be bounded by a interval hull as follow:

$$
\begin{aligned}
&Z(G, c, A, b) \subseteq \square Z(p, H)\\
&\begin{cases}
p = \prod_{i=1}^{n} \mathrm{mid}([\rho^{i-}, \rho^{i+}])\\
H = \prod_{i=1}^{n} \mathrm{diag}(rad([\rho^{i-}, \rho^{i+}]))\\
\rho^{i-} = \min\{G^i\xi + c^i \colon A\xi = b, \|\xi\|_\infty \leqslant 1\}\\
\rho^{i+} = \max\{G^i\xi + c^i \colon A\xi = b, \|\xi\|_\infty \leqslant 1\}
\end{cases}
\end{aligned} \tag{3}
$$

where $\mathrm{mid}(s,t) := \frac{1}{2}(s+t), \mathrm{rad}(s,t) := \frac{1}{2}|s-t|$.

In this work, we use uncertain variables to describe the variables:

Definition 2 (Uncertain Variables [7]): Unlike random variables, which can be described by probability distributions, uncertain variables lack any information about probability but can be described by their range of values.

$$
[\![\mathbf{x}]\!] := \{\mathbf{x}(\omega) : \omega \in \Omega\}, \tag{4}
$$

where $\mathbf{x}$ is referred to as an uncertain variable, and $[\![\mathbf{x}]\!]$ is referred to as the range of the uncertain variable.

3 System Model

In practical unmanned aerial systems, inertial navigation estimation is commonly employed to estimate the position, velocity, and attitude of the unmanned aerial vehicle. However, the errors in navigation estimation tend to increase over time. This paper proposes an analysis of the uncertain range of navigation estimation errors using uncertainty variables. The UAV state and inertial measurements [11] can be expressed by:

$$
\begin{bmatrix} \tilde{\phi} \\ \tilde{\nu}^n \\ \tilde{p} \end{bmatrix} = \begin{bmatrix} \phi \\ \nu^n \\ p \end{bmatrix} + \begin{bmatrix} \delta\phi \\ \delta\nu^n \\ \delta p \end{bmatrix}, \tag{5}
$$

$$
\begin{bmatrix} \tilde{\omega}_{ib}^b \\ \tilde{f}^b \end{bmatrix} = \begin{bmatrix} \omega_{ib}^b \\ f^b \end{bmatrix} + \begin{bmatrix} \delta\omega_{ib}^b \\ \delta f^b \end{bmatrix}, \tag{6}
$$

where $\tilde{\phi}$, $\tilde{\nu}^n$ and $\tilde{p}$ are output state of attitude and speed and position, ϕ, ν^n and p are the ground-truth state, $\delta\phi$, $\delta\nu^n$ and δp are state errors. $\tilde{\omega}_{ib}^b$ and $\tilde{f}^b$ are measurements of angular velocity and specific force, ω_{ib}^b and f^b are truth-value, $\delta\omega_{ib}^b$ and δf^b are errors. More specifically, the errors are indicated in Lemma 1.

Lemma 1 (unknown-but-bounded errors): The UAV state and IMU errors can be approximated by uncertain variable in Definition 2 as

$$
\begin{aligned}
&\delta\phi = [\delta\theta, \delta\gamma, \delta\varphi] \in [\![\delta\boldsymbol{\phi}]\!],\\
&\delta\nu^n = [\delta\nu_E, \delta\nu_N, \delta\nu_U] \in [\![\delta\boldsymbol{\nu}^n]\!],\\
&\delta p = [\delta L, \delta\lambda, \delta h] \in [\![\delta\boldsymbol{p}]\!],\\
&\delta\omega_{ib}^b = [\delta\omega_{ibx}^b, \delta\omega_{iby}^b, \delta\omega_{ibz}^b] \in [\![\delta\boldsymbol{\omega}_{ib}^b]\!],\\
&\delta f^b = [\delta f_x^b, \delta f_y^b, \delta f_z^b] \in [\![\delta\boldsymbol{f}^b]\!].
\end{aligned} \tag{7}
$$

Remark 1: It is usually assumed that the noise belongs to a Gaussian distribution in previous methods [11]. In fact, the error distribution of the UAV state and IMU is difficult to be described by a deterministic distribution. However, based on UAV parameters and IMU sensor information and statistics, the magnitude of the error regions can be obtained.

To establish the INS/GNSS integrated navigation model, we choose the strapdown INS error model [12]. The functional relation is given in Lemma 2.

Lemma 2 (Strapdown INS error model): The strapdown INS error model for $\boldsymbol{x} = [\delta\boldsymbol{\phi}, \delta\boldsymbol{\nu}^n, \delta\boldsymbol{p}]$ and $\boldsymbol{w} = [\delta\boldsymbol{\omega}_{ib}^b, \delta\boldsymbol{f}^b]$ are as follows:

$$
\dot{\boldsymbol{x}} = F\boldsymbol{x} + G\boldsymbol{w}, \tag{8}
$$

where

$$
F = \begin{bmatrix} M_{aa} & M_{a\nu} & M_{ap} \\ M_{\nu a} & M_{\nu\nu} & M_{\nu p} \\ M_{pa} & M_{p\nu} & M_{pp} \end{bmatrix}, G = \begin{bmatrix} -C_b^n & \mathbf{0}_{3\times3} \\ \mathbf{0}_{3\times3} & C_b^n \\ \mathbf{0}_{3\times3} & \mathbf{0}_{3\times3} \end{bmatrix},
$$

and the details can be found in Appendix A.

By discretizing the strapdown INS error model (8), one can obtain the discrete-time model

$$
\boldsymbol{x}_{k+1} = A_k\boldsymbol{x}_k + B_k\boldsymbol{w}_k, \tag{9}
$$

where $A_k = e^{F\Delta t}$ and $B_k = \int_0^{F\Delta t} e^{F\tau} d\tau G$; Δt denotes the time duration from t_{k-1} to t_k.

Equation (9) represents the uncertainty error range of the inertial navigation estimation results. In order to correct this accumulating error, unmanned aerial vehicles require additional measurement information. This paper considers GNSS measurement information. However, measurement information also entails an error range, which we describe and analyze in the form of uncertainty variables. The GNSS measurement error is given by:

$$
z_k = \tilde{p}_{INS}^n - \tilde{p}_{GNSS}^n = H_k\boldsymbol{x}_k + \boldsymbol{v}_k, \tag{10}
$$

where

$$
H_k = \begin{bmatrix} \mathbf{0}_{3\times3} & \mathbf{0}_{3\times3} & \boldsymbol{I}_{3\times3} \end{bmatrix}.
$$

H_k represents the measurement matrix, z_k represents the measurement output, $\tilde{p}_{INS}^n$ denotes the estimation results of the inertial navigation system, $\tilde{p}_{GNSS}^n$ denotes the estimation results of the Global Navigation Satellite System, and $\boldsymbol{v}_k$ represents the uncertainty of measurement errors.

To achieve more accurate estimation of UAV states, it is necessary to fuse the system error uncertainty and measurement error uncertainty in Equation (9) and Equation (10)

through filtering, in order to eliminate the cumulative errors of the Inertial Navigation System. For the uncertainty variable description of error uncertainty filtering, this paper designs a combined navigation method based on the optimal set membership filtering framework.

For any $k \geqslant 0$, let $\hat{\boldsymbol{X}}_k$ denote the set of all states $[\![\boldsymbol{x}_k]\!] \in \hat{\boldsymbol{X}}_k$ that are consistent with (9) the discrete time model, the measured output sequence up to time k, $(z_0, z_1, \ldots, z_k)$, and the unknownbut-bounded uncertain state $[\![\boldsymbol{x}_0]\!] \subseteq \hat{\boldsymbol{X}}_0$, $[\![\boldsymbol{w}_k]\!] \subseteq \boldsymbol{W}_k$ and $[\![\boldsymbol{v}_k]\!] \subseteq \boldsymbol{V}_k$. $\hat{\boldsymbol{X}}_k$ is given recursively by the SMFing is indicated in Lemma 2.

Lemma 3 (SMFing framework): Based on the optimal SMFing framework [7], the general scheme is given by the following recursion:

- **Initialization.** Set the initial prior set $[\![\boldsymbol{x}_0]\!] \subseteq \hat{\boldsymbol{X}}_0$.
- **Prediction.** For $k \geqslant 0$, given $\hat{\boldsymbol{X}}_k$, the prior set $\bar{\boldsymbol{X}}_{k+1}$ is predicted by the equation (9) is

$$\bar{\boldsymbol{X}}_{k+1} \supseteq \{A_k x_k + B_k w_k \colon x_k \in [\![\boldsymbol{x}_k]\!], w_k \in [\![\boldsymbol{w}_k]\!]\}. \tag{11}$$

- **Update.** For $k \geqslant 0$, given the measured output z_{k+1}, the posterior set $\hat{\boldsymbol{X}}_{k+1}$ is

$$\hat{\boldsymbol{X}}_{k+1} \supseteq \{x_{k+1} \in \bar{\boldsymbol{X}}_{k+1} \colon H_{k+1}x_{k+1} + v_{k+1} = z_{k+1}, v_{k+1} \in [\![\boldsymbol{v}_k]\!]\}. \tag{12}$$

The new estimated state $[\![\boldsymbol{x}_{k+1}]\!] \subseteq \hat{\boldsymbol{X}}_{k+1}$.

To ensure the optimality of the filtering, this paper makes the following assumptions:

Assumption 1 (Unrelated Noises and Initial State): $\forall k \in \mathbb{N}_0$, $\boldsymbol{w}_k, \boldsymbol{v}_k, \boldsymbol{x}_0$ are unrelated.

In the remainder of the paper, our goal is to compute these two steps (11)-(12) using SMFing.

4 Method

The combined INS/GNSS navigation method with the set-membership filter of IMU data is derived in this section, and the process is shown in Fig. 1.

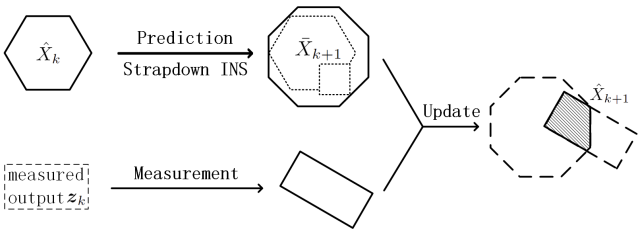

Fig. 1: Procedure of SMF Method.

$[\![\boldsymbol{w}_k]\!] \subseteq \boldsymbol{W}_k$ and $[\![\boldsymbol{v}_k]\!] \subseteq \boldsymbol{V}_k$ are respectively the state and measurement error which satisfy the following equations:

$$[\![\boldsymbol{w}_k]\!] \subseteq \boldsymbol{W}_k = Z(\hat{G}_k^w, \hat{c}_k^w, \hat{A}_k^w, \hat{b}_k^w), \tag{13}$$

$$[\![\boldsymbol{v}_k]\!] \subseteq \boldsymbol{V}_k = Z(\hat{G}_k^v, \hat{c}_k^v, \hat{A}_k^v, \hat{b}_k^v). \tag{14}$$

The initial state of system satisfies the equation (9) and Lemma 3:

$$[\![\boldsymbol{x}_0]\!] \subseteq \hat{\boldsymbol{X}}_0 = Z(\hat{G}_0^x, \hat{c}_0^x, \hat{A}_0^x, \hat{b}_0^x). \tag{15}$$

On the basis of the INS error discrete time model, the prediction system's state satisfy the following equations:

$$\bar{\boldsymbol{X}}_{k+1} = A_k \hat{\boldsymbol{X}}_k \oplus B_k \boldsymbol{W}_k. \tag{16}$$

Equation (16) demonstrates that prediction state set, $A_k \in \mathbb{R}$ and $B_k \in \mathbb{R}$ are approximation matrices.

The specific calculation of A_k and B_k are as follows:

$$A_k = e^{F\Delta t} = \sum_{i=0}^{\infty} \frac{(F\Delta t)^i}{i!} \approx \boldsymbol{I} + F\Delta t + \frac{1}{2}(F\Delta t)^2, \tag{17}$$

$$B_k = \int_0^{F\Delta t} e^{F\tau} d\tau G = \sum_{i=0}^{\infty} \frac{\left(F^i \Delta t^{i+1}\right)}{(i+1)!} G \approx (\Delta t + \frac{1}{2}F\Delta t^2 + \frac{1}{6}\Delta t^3 F^2)G. \tag{18}$$

Finally, the prediction system's state as following equation:

$$\bar{\boldsymbol{X}}_{k+1} = (1 + F\Delta t + \tfrac{1}{2}(F\Delta t)^2) Z(\hat{G}_k^x, \hat{c}_k^x, \hat{A}_k^x, \hat{b}_k^x) \oplus ((\Delta t + \tfrac{1}{2}F\Delta t^2 + \tfrac{1}{6}\Delta t^3 F^2)G) Z(\hat{G}_k^w, \hat{c}_k^w, \hat{A}_k^w, \hat{b}_k^w). \tag{19}$$

The function of update step is to revise the prediction set $\bar{\boldsymbol{X}}_{k+1}$ by measured output (10). Measurement set $\boldsymbol{Y}$ is also represented by constrained zonotope like the prediction set, the measurement uncertain set is represented by $Z(\hat{G}^y, \hat{c}^y, \hat{A}^y, \hat{b}^y)$.

Then the estimated state set $\hat{\boldsymbol{X}}_{k+1}$ given by the following equation:

$$\{x_{k+1} \in \bar{\boldsymbol{X}}_{k+1} : H_{k+1}x_{k+1} + v_{k+1} = z_{k+1}, v_{k+1} \in \boldsymbol{V}_{k+1}\} \subseteq \hat{\boldsymbol{X}}_{k+1} = \bar{\boldsymbol{X}}_{k+1} \cap_R \boldsymbol{Y}_{k+1}, \tag{20}$$

where $R = H_{k+1}$, and $\boldsymbol{Y}_{k+1} = z_k \oplus \boldsymbol{V}_{k+1}$.

Through Equation (20), we can obtain the estimation result of one iteration. However, as the number of iterations increases, the dimension of constrained zonotope will continuously increase, leading to a decrease in computational efficiency.

To handle this problem, we propose a fast iteration method (see Algorithm 1) based on OIT heuristic in [13], and we provide a line by line explanation as follows:

Algorithm 1 Fast Recursive Method

1: **Initialization:**Bounded $[\![\boldsymbol{x}_0]\!] \subseteq \hat{\boldsymbol{X}}_0 = Z(\hat{G}_0^x, \hat{c}_0^x, \hat{A}_0^x, \hat{b}_0^x)$, select slide window size δ.
2: **loop**
3: $\quad \square Z(\hat{p}_k, \hat{H}_k) \leftarrow Z(\hat{G}_k^x, \hat{c}_k^x, \hat{A}_k^x, \hat{b}_k^x)$ by (3);
4: $\quad$ **if** $k \leqslant \delta$ **then**
5: $\quad\quad Z(\hat{G}_k^x, \hat{c}_k^x, \hat{A}_k^x, \hat{b}_k^x) \leftarrow \hat{X}_{k-1}$ by (19) and (20);
6: $\quad$ **else if** $k > \delta$ **then**
7: $\quad\quad Z(\hat{G}_k^x, \hat{c}_k^x, \hat{A}_k^x, \hat{b}_k^x) \leftarrow \square Z(\hat{p}_{k-\delta-1}, \hat{H}_{k-\delta-1})$ by (19) and (20);
8: $\quad$ **end if**
9: $\quad \hat{\boldsymbol{X}}_k = Z(\hat{G}_k^x, \hat{c}_k^x, \hat{A}_k^x, \hat{b}_k^x)$;
10: $\quad k++$
11: **end loop**

- Line 1 is the initialization of Algorithm 1, where δ represents the chosen window size of Algorithm 1. The

dimension of $\hat{\boldsymbol{X}}_k$ will be constrained based on the size of δ, with a larger δ resulting in more accurate results and a smaller δ leading to faster algorithm execution.

- Line 3 involves storing the estimation results of each iteration in Interval Hull.
- Line 5 is for $k \leqslant \delta$, which is the same as the classical constrained zonotope SMF algorithm.
- Line 7 is for $k > \delta$, which involves obtaining the estimation result for $Z(\hat{G}_k^x, \hat{c}_k^x, \hat{A}_k^x, \hat{b}_k^x)$ after k iterations using $\square Z(\hat{p}_{k-\delta-1}, \hat{H}_{k-\delta-1})$ as the initial state over the time window $[k-\delta, k]$. It is a simplified version of the OIT inspired constrained zonotopic SMF in [13].

5 Simulation and Result

In the experimental study, we respectively use the position and velocity and attitude errors of UAV as the state and the angular velocity and acceleration errors were simulated in the time scale model of the inertial measuring unit, using the equations

$$\boldsymbol{x}_k \in \hat{\boldsymbol{X}}_k = \left[\ \delta\hat{\boldsymbol{\phi}}_k, \delta\hat{\boldsymbol{\nu}}_k^n, \delta\hat{\boldsymbol{p}}_k\ \right] = Z(\hat{G}_k^x, \hat{c}_k^x, \hat{A}_k^x, \hat{b}_k^x), \tag{21}$$

$$\boldsymbol{w}_k \in \boldsymbol{W}_k = [\delta\boldsymbol{\omega}_{ib,k}^b, \delta\boldsymbol{f}_k^b] = Z(G_k^w, c_k^w, A_k^w, b_k^w). \tag{22}$$

IMU and their characteristics for clarity are given in the Table 1 below.

Table 1: Sensor Parameters of The Simulation

Specification	Value
Gyroscope constant bias (deg/h)	0.03
Accelerometer constant bias (ug)	100
Angular random walk	0.001
Velocity random walk	5
GNSS error(m)	10
IMU rate (Hz)	10
GNSS rate(Hz)	10
Simulation step size	540

From Fig. 2 which displays the interval estimation results for the unmanned aerial vehicle's position. The interval estimation represents the range of estimates for each component derived from the ensemble filtering estimation. Fig. 3 shows the position estimation results of the UAV in the simulation. The point estimation result is obtained as the median of the interval estimation result derived from the ensemble filtering position estimation.

6 Conclusion

In this paper, combining with the INS and GNSS by Set-Membership Filter. Aiming at the situation that the error distribution of INS and GNSS is unknown in the actual system, the bound of unknown-but-bounded noise inclusion estimation is used, which is a powerful supplement to the INS integrated navigation method based on probability. Apart from inertial integrated navigation with GNSS as measurement, there are other more practical integrated navigation methods, such as visual-inertial odometry (VIO). Therefore, we will carry out in-depth research on SMF-based, more reliable and more general integrated navigation methods in the future. In future work, we will address the role of the INS linearization error in the SMF prediction equation.

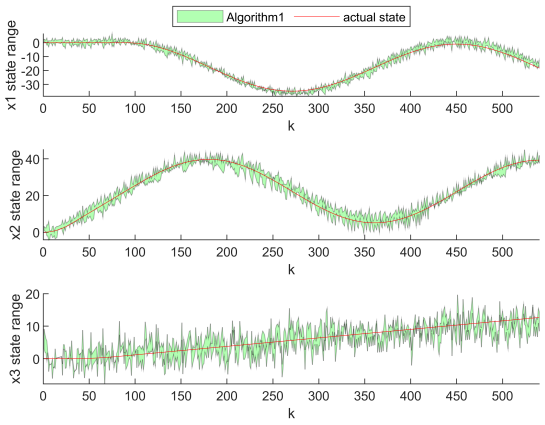

Fig. 2: The interval estimation results of state.The results indicate that the proposed Algorithm 1 is able to enclose the true position state of the unmanned aerial vehicle.

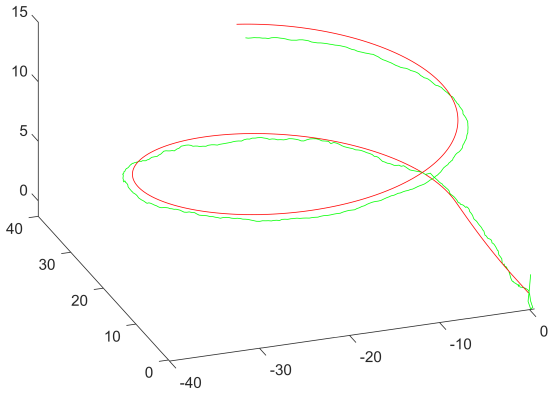

Fig. 3: The point estimation results of state.The red line is the true state and the green line is the estimated state.

A INS Error propagation formula

The following content demonstrates the specific form of F in the strapdown INS error model. i represents the inertial coordinate system; e represents the earth coordinate system; n represents the navigation coordinate system; b represents the body coordinate system. R_M and R_M represent the Earth's radii parameters.

$$M_{aa} \triangleq -\left(\boldsymbol{\omega}_{\boldsymbol{in}}^{\boldsymbol{n}}\times\right):$$

$$\begin{cases} M_{aa}(1,1) = M_{aa}(2,2) = M_{aa}(3,3) = 0 \\ M_{aa}(1,2) = \omega_{ie}\sin L + \dfrac{\nu_E}{R_N+h}\tan L \\ M_{aa}(1,3) = -\omega_{ie}\cos L - \dfrac{\nu_E}{R_N+h} \\ M_{aa}(2,1) = -\omega_{ie}\sin L - \dfrac{\nu_E}{R_N+h}\tan L \\ M_{aa}(2,3) = -\dfrac{\nu_N}{R_M+h} \\ M_{aa}(3,1) = \omega_{ie}\cos L + \dfrac{\nu_E}{R_N+h} \\ M_{aa}(3,2) = \dfrac{\nu_N}{R_M+h}. \end{cases}$$

$$M_{a\nu}=\begin{bmatrix} 0 & -\dfrac{1}{R_M+h} & 0 \\ \dfrac{1}{R_N+h} & 0 & 0 \\ \dfrac{\tan L}{R_N+h} & 0 & 0 \end{bmatrix},$$

$$M_{ap}=\begin{bmatrix} 0 & 0 & \frac{\nu_N}{(R_M+h)^2} \\ -\omega_{ie}\sin L & 0 & -\frac{\nu_E}{(R_N+h)^2} \\ \omega_{ie}\cos L+\frac{\nu_E \sec^2 L}{R_N+h} & 0 & -\frac{\nu_E \tan L}{(R_N+h)^2} \end{bmatrix},$$

$$M_{\nu a}\triangleq(\boldsymbol{f}^n\times)=\begin{bmatrix} 0 & -f_U^n & f_N^n \\ f_U^n & 0 & -f_E^n \\ -f_N^n & f_E^n & 0 \end{bmatrix},$$

$M_{\nu\nu}$:

$$\begin{cases} M_{\nu\nu}(1,1)=\dfrac{\nu_N\tan L-\nu_U}{R_N+h} \\ M_{\nu\nu}(1,2)=2\omega_{ie}\sin L+\dfrac{\nu_E\tan L}{R_N+h} \\ M_{\nu\nu}(1,3)=-2\omega_{ie}\cos L-\dfrac{\nu_E}{R_N+h} \\ M_{\nu\nu}(2,1)=-2\omega_{ie}\sin L-\dfrac{2\nu_E\tan L}{R_N+h} \\ M_{\nu\nu}(2,2)=-\dfrac{\nu_U}{R_M+h} \\ M_{\nu\nu}(2,3)=-\dfrac{\nu_N}{R_M+h} \\ M_{\nu\nu}(3,1)=2\omega_{ie}\cos L+\dfrac{2\nu_E}{R_N+h} \\ M_{\nu\nu}(3,2)=\dfrac{2\nu_N}{R_M+h} \\ M_{\nu\nu}(3,3)=0 \end{cases}$$

$M_{\nu p}$:

$$\begin{cases} M_{\nu p}(1,1)=\dfrac{\nu_E\nu_N\sec^2 L}{R_N+h}+2\nu_N\omega_{ie}\cos L+2\nu_U\omega_{ie}\sin L \\ M_{\nu p}(1,2)=0 \\ M_{\nu p}(1,3)=\dfrac{\nu_E\nu_U-\nu_E\nu_N\tan L}{(R_N+h)^2} \\ M_{\nu p}(2,1)=-2\nu_E\omega_{ie}\cos L-\dfrac{\nu_E^2\sec^2 L}{R_N+h} \\ M_{\nu p}(2,2)=0 \\ M_{\nu p}(2,3)=\dfrac{\nu_E^2\tan L}{(R_N+h)^2}+\dfrac{\nu_N\nu_U}{(R_M+h)^2} \\ M_{\nu p}(3,1)=-2\nu_E\omega_{ie}\sin L \\ M_{\nu p}(3,2)=0 \\ M_{\nu p}(3,3)=-\dfrac{\nu_E^2}{(R_N+h)^2}-\dfrac{\nu_N^2}{(R_M+h)^2} \end{cases}$$

$$M_{pa}=\begin{bmatrix} 0 & 0 & 0 \\ 0 & 0 & 0 \\ 0 & 0 & 0 \end{bmatrix},$$

$$M_{p\nu}=\begin{bmatrix} 0 & \frac{1}{R_M+h} & 0 \\ \frac{\sec L}{R_N+h} & 0 & 0 \\ 0 & 0 & 1 \end{bmatrix},$$

$$M_{pp}=\begin{bmatrix} 0 & 0 & -\frac{\nu_N}{(R_M+h)^2} \\ \frac{\nu_E\tan L\sec L}{R_N+h} & 0 & -\frac{\nu_E\sec L}{(R_N+h)^2} \\ 0 & 0 & 0 \end{bmatrix}$$

References

[1] L. C. Bento, P. Bonnifait, and U. J. Nunes, "Set-membership position estimation with gnss pseudorange error mitigation using lane-boundary measurements," *IEEE Transactions on Intelligent Transportation Systems*, vol. 20, no. 1, pp. 185–194, 2018.

[2] C. Zhang, C. Guo, and D. Zhang, "Ship navigation via gps/imu/log integration using adaptive fission particle filter," *Ocean Engineering*, vol. 156, pp. 435–445, 2018.

[3] S. Sasani, J. Asgari, and A. Amiri-Simkooei, "Improving mems-imu/gps integrated systems for land vehicle navigation applications," *GPS solutions*, vol. 20, pp. 89–100, 2016.

[4] M. Shalaby, C. C. Cossette, J. Le Ny, and J. R. Forbes, "Cascaded filtering using the sigma point transformation," *IEEE Robotics and Automation Letters*, vol. 6, no. 3, pp. 4758–4765, 2021.

[5] J. Li, Y. Bi, K. Li, K. Wang, F. Lin, and B. M. Chen, "Accurate 3d localization for mav swarms by uwb and imu fusion," in *2018 IEEE 14th International Conference on Control and Automation (ICCA)*. IEEE, 2018, pp. 100–105.

[6] R. E. Kalman, "A new approach to linear filtering and prediction problems,"1960.

[7] Y. Cong, X. Wang, and X. Zhou, "Rethinking the mathematical framework and optimality of set-membership filtering," *IEEE Transactions on Automatic Control*, vol. 67, no. 5, pp. 2544–2551, 2021.

[8] L. C. Bento, P. Bonnifait, and U. J. Nunes, "Cooperative gnss positioning aided by road-features measurements," *Transportation Research Part C: Emerging Technologies*, vol. 79, pp. 42–57, 2017.

[9] D. Titterton and J. L. Weston, *Strapdown inertial navigation technology*. IET, 2004, vol. 17.

[10] J. K. Scott, D. M. Raimondo, G. R. Marseglia, and R. D. Braatz, "Constrained zonotopes: A new tool for set-based estimation and fault detection," *Automatica*, vol. 69, pp. 126–136, Jul. 2016.

[11] J. Yang, M. Wu, Y. Cong, Y. Guo, X. Zhou, and K. Tang, "A novel single-beacon positioning with inertial measurement optimization," *IEEE Robotics and Automation Letters*, 2023.

[12] D. Chung, J. G. Lee, C. G. Park, and H. W. Park, "Strapdown ins error model for multiposition alignment," *IEEE Transactions on Aerospace and Electronic systems*, vol. 32, no. 4, pp. 1362–1366, 1996.

[13] Y. Cong, X. Wang, and X. Zhou, "Stability of linear set-membership filters," *arXiv preprint arXiv:2203.13966*, 2022.

Proceedings of the 3rd Conference on Fully Actuated System Theory and Applications
May 10-12, 2024, Shenzhen, China

Robust Kalman Predictor under Linearly Correlated Noise and Mixed Uncertainties of Noise Variances and Multiple Networked-inducements

Ying Zhao[1], Chunshan Yang[1], Zheng Liu[1], Jianqi Wang[1], Xuemei Wang[2], Guili Tao[2]

1. College of Electronic Information and Automation, Guilin University of Aerospace Technology, Guilin, 541004
E-mail: ycsy1999@guat.edu.cn
2. College of Media Engineering, Communication University of Zhejiang, Hangzhou, 310018
E-mail: dr_wxm2013@163.com

Abstract: The paper solves the robust Kalman prediction problem for systems with linearly correlated noise and mixed uncertainties of noise variances, multiplicative noises and multiple networked-inducements including missing measurements, packets dropouts and two-step random measurement delays. The original system with mixed uncertainties is transformed into one with only uncertain fictitious noise variance by the proposed model-transformation method. Then the robust steady-state Kalman predictor is presented by minimax robust estimation principle. The robustness of robust Kalman predictor is proved by the extended Lyapunov equation approach and matrix factorization. Finally, a simulation study applied to tracking system is provided to examine effectiveness and applicability of the proposed algorithm.

Key Words: Two-Step Random Measurement Delays, Model-Transformation, Extended Lyapunov Equation, Minimax Robust Prediction, Uncertain Noise Variance

1 Introduction

Kalman filtering method assumes that the system model is exactly known. However, this assumption can hardly hold due to linearization, model reduction and some networked-induced uncertainties. Hence, many studies have been done on robust Kalman estimator that is robust against these mentioned uncertainties. To make an estimator robust against multiplicative noises, linear matrix inequation, Riccati difference equation, innovation analysis and fictitious noises method are used to address the robust estimation problem [1-4]. For system with multiplicative noise, the optimal weighted fusion filter is presented based on an innovation analysis approach and the fictitious noises method [3, 4]. But the original fictitious noises method cannot be directly used for model-transformation for system with multiple networked-inducements.

The system noise variance is usually uncertain in many applications. For systems with uncertain noise variance, the polynomial approach, game theory and Lyapunov equation method have been investigated [5-7]. In [6], the definitions of conservative and actual system are proposed, and weighted fusion robust Kalman predictor (RKP) is presented according to minimax robust estimation principle (MREP). Based on this, the guaranteed cost weighted measurement fusion RKP is addressed by the Lyapunov equation approach for system with uncertain but bounded above (UBBA) noise variance in [7].

In networked system, there exist networked-induced uncertainties such as packet outputs, random measurement delay (RMD) and missing measurements, etc. Hence, some robust filters have been presented for systems with different kinds of networked-induced uncertainties in [8-12], where a single networked-induced uncertainty, such as packet dropouts [8] and missing measurements [9] are considered respectively. Further, the distributed recursive filtering for multisensor networked system with multi-step sensor delays, missing measurement is addressed in [10]. The time-varying and steady-state filters weighted by matrix are proposed for multisensor systems with random measurement time-delay, missing measurements and packet dropouts in [11]. The adaptive Kalman filter for system with packet outputs, random delay and missing measurements is proposed by Riccati equations in [12].

Considering the system with multiplicative noises and correlated random delays in transmission, the authors addressed the optimal weighted fusion filter by an innovation approach in [13]. The optimal filtering problem is addressed for systems with multiplicative noises, packet dropouts, input delays and measurement delays in [14]. On the other hand, the robust Kalman estimation problem is addressed for system with UBBA noise variance, multiplicative noise and packet dropouts [15]. The problem of weighted fusion RKP is solved in [16, 17], where RMD and missing measurements [16], missing measurements and packets dropouts [17] are considered.

In this paper, the RKP problem for system under linearly correlated noise and mixed uncertainties of UBBA noise variance, missing measurements, packets dropouts and two-step RMD is presented.

Notations: The following notations are adopted. $\Re^n$, $\Re^{n\times n}$: n-dimensional Euclidean space and set of $n\times n$ real matrix; $\mathrm{diag}\{\cdot\}$: diagonal matrix; $\mathrm{tr}(M)$: trace of matrix M; $A\geq B$: $A-B\geq 0$ is positive semi-definite (PSD); I_n: identity matrix with dimension of $n\times n$; O_n, $\mathrm{O}_{n\times m}$: zero matrix with dimensions of $n\times n$ and $n\times m$; $\otimes$: Kronecker product; $Y_a=\left[Y|_{i,j=1}^{L}\right]$: Y_a matrix with $L\times L$ block and its i-th row and j-th column block matrix being Y.

2 System Modeling and Problem Formulation

Consider the following discrete-time linear system

*This work is supported by the Natural Science Foundation of China (NSFC-61966010, NSFC-62263009) and by the Guangxi Natural Science Foundation (2020GXNSFAA297032). (Corresponding author: Chunshan Yang)

$$x(t+1)=\left(F+\sum_{r=1}^{N}\zeta_r(t)F_{\zeta_r}\right)x(t)+Bw(t) \quad (1)$$

$$z(t)=\xi_1(t)Dx(t)+v(t) \quad (2)$$

$$v(t)=Gw(t)+g(t) \quad (3)$$

where $x(t)\in\Re^n$ and $w(t)\in\Re^r$ are state and process noise, $\zeta_r(t)$ is parametric random perturbation to system state. $z(t)\in\Re^m$ and $v(t)\in\Re^m$ are sensor measurement outputs and measurement noise. $w(t)$ and $v(t)$ are linearly correlated as shown in (3), and $g(t)$ is white noises. $F\in\Re^{n\times n}$, $F_{\zeta_r}\in\Re^{n\times n}$, $B\in\Re^{n\times r}$, $D\in\Re^{m\times n}$ and $G\in\Re^{m\times r}$ are known matrices.

The measurement $y(t)$ received by the predictor is subject to packet dropouts and two-step RMD.

$$\begin{aligned}y(t)=&\xi_2(t)z(t)+(1-\xi_2(t))\xi_3(t)z(t-1)+\\&\xi_1(t)(1-\xi_2(t))(1-\xi_3(t))z(t-2)+\\&(1-\xi_1(t))(1-\xi_2(t))(1-\xi_3(t))y(t-1)\end{aligned} \quad (4)$$

The following assumptions are considered:

Assumption 1. $w(t)$, $g(t)$ and $\zeta_r(t)$ are mutually uncorrelated white noises with zero-means and uncertain actual variances $\bar{Q}$, $\bar{R}$ and $\bar{R}_{\zeta_r}$, respectively.

Assumption 2. The initial state $x(0)$ is uncorrelated with $w(t)$, $g(t)$ and $\zeta_r(t)$, and has known mean μ_0, and unknown uncertain actual variance $\bar{P}_0$.

Assumption 3. $\bar{Q}$, $\bar{R}$, $\bar{R}_{\zeta_r}$ and $\bar{P}_0$ are UBBA, and their known conservative upper bounds (CUBs) are Q, R, R_{ζ_r} and P_0, i.e.,

$$\bar{Q}\le Q,\ \bar{R}\le R,\ \bar{R}_{\zeta_r}\le R_{\zeta_r},\ \bar{P}_0\le P_0 \quad (5)$$

Assumption 4. $\xi_i(t), i=1,2,3$ are mutually uncorrelated Bernoulli distributed random sequence with probabilities

$$\mathrm{Prob}(\xi_i(t)=1)=\alpha_i,\ \mathrm{Prob}(\xi_i(t)=0)=1-\alpha_i \quad (6)$$

where $0\le\alpha_i\le 1$ are known constants.

Models (2) and (4) show the following five cases:

(1) $y(t)=z(t)$ if $\xi_1(t)=1$ and $\xi_2(t)=1$, i.e., the predictor will receive the measurements correctly and promptly.

(2) $y(t)=z(t-1)$ if $\xi_2(t)=0$ and $\xi_3(t)=1$, i.e., the predictor use $z(t-1)$ to estimate (one-step RMD).

(3) $y(t)=z(t-2)$ if $\xi_1(t)=1$, $\xi_2(t)=0$ and $\xi_3(t)=0$, i.e., the predictor use $z(t-2)$ to estimate (two-step RMD).

(4) $y(t)=v(t)$ if $\xi_1(t)=0$, $\xi_2(t)=1$, i.e., the predictor use $v(t)$ to estimate (missing measurements).

(5) $y(t)=y(t-1)$ if $\xi_i(t)=0, i=1,2,3$, i.e., the predictor use $y(t-1)$ to estimate (packets dropouts).

From Assumption 4, we have the statistical information

$$\begin{aligned}&\mathrm{E}[\xi_i(t)]=\mathrm{E}[\xi_i^2(t)]=\alpha_i,\\&\mathrm{E}[\xi_i(t)\xi_j(t)]=\mathrm{E}[\xi_i^2(t)\xi_j^2(t)]=\alpha_i\alpha_j, i\ne j,\\&\mathrm{E}\left[\prod_{i=1}^{3}\xi_i(t)\right]=\mathrm{E}\left[\prod_{i=1}^{3}\xi_i^2(t)\right]=\prod_{i=1}^{3}\alpha_i\end{aligned} \quad (7)$$

3 Model-transformation

To enable the original systems (1)-(4) to design RKP, a novel model-transformation method is used to transform the original system to one with fictitious white noises.

3.1 Augmented State Space Model

Defining $w_n(t)=\sum_{r=1}^{N}\zeta_r(t)F_{\zeta_r}x(t)+Bw(t)$, then we have $x(t+1)=Fx(t)+w_n(t)$. By introducing the augmented state $x_a(t)$ and noise $w_a(t)$ for systems (1)-(4),

$$x_a(t+1)=\left[x(t+1)\quad z^{\mathrm{T}}(t)\quad z^{\mathrm{T}}(t-1)\quad y^{\mathrm{T}}(t)\right]^{\mathrm{T}},$$

$$w_a(t)=\left[w_n^{\mathrm{T}}(t)\quad v^{\mathrm{T}}(t)\right]^{\mathrm{T}},$$

we have

$$\begin{aligned}x_a(t+1)&=F_a(t)x_a(t)+B_a(t)w_a(t),\\y(t)&=D_a(t)x_a(t)+\lambda(t)v(t)\end{aligned} \quad (8)$$

$$\begin{aligned}F_a(t)=&F_0+\sum_{i=1}^{3}\xi_i(t)F_i+\xi_1(t)\xi_2(t)F_4+\xi_2(t)\xi_3(t)F_5\\&+\xi_1(t)\xi_3(t)F_6+\xi_1(t)\xi_2(t)\xi_3(t)F_7\\B_a(t)=&B_0+\xi_2(t)B_1,\\D_a(t)=&D_0+\sum_{i=1}^{3}\xi_i(t)D_i+\xi_1(t)\xi_2(t)D_4+\xi_2(t)\xi_3(t)D_5\\&+\xi_1(t)\xi_3(t)D_6+\xi_1(t)\xi_2(t)\xi_3(t)D_7\end{aligned} \quad (9)$$

$$F_0=\left[\begin{array}{cc}F & \mathrm{O}_{n\times 3m}\\ \hline \mathrm{O}_{2m\times(n+3m)} & \\ \hline \mathrm{O}_{m\times(n+2m)} & I_m\end{array}\right],\ F_1=\left[\begin{array}{cc}\mathrm{O}_{n\times(n+3m)} & \\ \hline D & \mathrm{O}_{m\times 3m}\\ \hline \mathrm{O}_{m\times(n+3m)} & \\ \hline \mathrm{O}_{m\times(n+m)} & I_m\ \ -I_m\end{array}\right],$$

$$F_2=\left[\begin{array}{cc}\mathrm{O}_{(n+2m)\times(n+3m)} & \\ \hline \mathrm{O}_{m\times(n+2m)} & -I_m\end{array}\right],\ F_3=\left[\begin{array}{cc}\mathrm{O}_{(n+2m)\times(n+3m)} & \\ \hline \mathrm{O}_{m\times n}\ \ I_m\ \ \mathrm{O}_m & -I_m\end{array}\right],$$

$$F_4=\left[\begin{array}{cc}\mathrm{O}_{(n+2m)\times(n+3m)} & \\ \hline D\ \ \mathrm{O}_m\ \ -I_m & I_m\end{array}\right],\ F_5=\left[\begin{array}{cc}\mathrm{O}_{(n+2m)\times(n+3m)} & \\ \hline \mathrm{O}_{m\times n}\ \ -I_m\ \ \mathrm{O}_m & I_m\end{array}\right],$$

$$F_6=\left[\begin{array}{cc}\mathrm{O}_{(n+2m)\times(n+3m)} & \\ \hline \mathrm{O}_{m\times(n+m)} & -I_m\ \ I_m\end{array}\right],\ F_7=\left[\begin{array}{cc}\mathrm{O}_{(n+2m)\times(n+3m)} & \\ \hline \mathrm{O}_{m\times(n+m)} & I_m\ \ -I_m\end{array}\right],$$

$$B_0=\left[\begin{array}{ccc}I_n & \mathrm{O}_{n\times 3m} & \\ \hline \mathrm{O}_{m\times n} & I_m\ \ \mathrm{O}_{m\times 2m}\end{array}\right]^{\mathrm{T}},\ B_1=\left[\begin{array}{cc}\mathrm{O}_{n\times(n+3m)} & \\ \hline \mathrm{O}_{m\times(n+2m)} & I_m\end{array}\right]^{\mathrm{T}},$$

$$D_0=\left[\mathrm{O}_{m\times(n+2m)}\ \vdots\ I_m\right],\ D_1=\left[\mathrm{O}_{m\times(n+m)}\ \vdots\ I_m\ \vdots\ -I_m\right],$$

$$D_2=\left[\mathrm{O}_{m\times(n+2m)}\ \vdots\ -I_m\right],\ D_3=\left[\mathrm{O}_{m\times n}\quad I_m\quad \mathrm{O}_m\quad -I_m\right],$$

$$D_4=\left[H\quad \mathrm{O}_m\quad -I_m\quad I_m\right],\ D_5=\left[\mathrm{O}_{m\times n}\quad -I_m\quad \mathrm{O}_m\quad I_m\right],$$

$$D_6=\left[\mathrm{O}_{m\times(n+m)}\ \vdots\ -I_m\ \vdots\ I_m\right],\ D_7=\left[\mathrm{O}_{m\times(n+m)}\ \vdots\ I_m\ \vdots\ -I_m\right] \quad (10)$$

3.2 Extended Fictitious Noise Method

From (9) we have mathematical expectation

$$\begin{aligned}\bar{F}_a=&\mathrm{E}\left[F_a(t)\right]=F_0+\sum_{i=1}^{3}\alpha_i F_i+\alpha_1\alpha_2F_4+\alpha_2\alpha_3F_5+\\&\alpha_1\alpha_3F_6+\alpha_1\alpha_2\alpha_3F_7\\ \bar{B}_a=&\mathrm{E}\left[B_a(t)\right]=B_0+\alpha_2B_1,\\ \bar{D}_a=&\mathrm{E}\left[D_a(t)\right]=D_0+\sum_{i=1}^{3}\alpha_i D_i+\alpha_1\alpha_2D_4+\alpha_2\alpha_3D_5+\\&\alpha_1\alpha_3D_6+\alpha_1\alpha_2\alpha_3D_7\end{aligned}\tag{11}$$

Define $F_e(t)=F_a(t)-\bar{F}_a$, $D_e(t)=D_a(t)-\bar{D}_a$, and the noises

$$\begin{aligned}&\beta_i(t)=\xi_i(t)-\alpha_i, i=1,2,3,\\ &\beta_4(t)=\beta_1(t)\beta_2(t),\ \beta_5(t)=\beta_2(t)\beta_3(t),\\ &\beta_6(t)=\beta_1(t)\beta_3(t),\ \beta_7(t)=\beta_1(t)\beta_2(t)\beta_3(t)\end{aligned}\tag{12}$$

it easy to prove that $\beta_i(t)$ are uncorrelated white noises with zero-means and statistical information

$$\begin{aligned}&\bar{\beta}_i=\mathrm{E}\left[\beta_i^2(t)\right]=\alpha_i(1-\alpha_i), i=1,2,3,\\ &\bar{\beta}_4=\mathrm{E}\left[\beta_4^2(t)\right]=\bar{\beta}_1\bar{\beta}_2,\ \bar{\beta}_5=\mathrm{E}\left[\beta_5^2(t)\right]=\bar{\beta}_2\bar{\beta}_3,\\ &\bar{\beta}_6=\mathrm{E}\left[\beta_6^2(t)\right]=\bar{\beta}_1\bar{\beta}_3,\ \bar{\beta}_7=\mathrm{E}\left[\beta_7^2(t)\right]=\bar{\beta}_1\bar{\beta}_2\bar{\beta}_3\end{aligned}\tag{13}$$

Furthermore, $F_e(t)$ and $D_e(t)$ can be reorganized as [18]

$$F_e(t)=\sum_{i=1}^{7}\beta_i(t)F_{ai},\ D_e(t)=\sum_{i=1}^{7}\beta_i(t)D_{ai}\tag{14}$$

$$\begin{aligned}&F_{a1}=F_1+\alpha_2F_4+\alpha_3F_6+\alpha_2\alpha_3F_7,\\ &F_{a2}=F_2+\alpha_1F_4+\alpha_3F_5+\alpha_1\alpha_3F_7,\\ &F_{a3}=F_3+\alpha_2F_5+\alpha_1F_6+\alpha_1\alpha_2F_7,\ F_{a4}=F_4+\alpha_3F_7,\\ &F_{a5}=F_5+\alpha_1F_7,\ F_{a6}=F_6+\alpha_2F_7,\ F_{a7}=F_7,\\ &D_{a1}=D_1+\alpha_2D_4+\alpha_3D_6+\alpha_2\alpha_3D_7,\\ &D_{a2}=D_2+\alpha_1D_4+\alpha_3D_5+\alpha_1\alpha_3D_7,\\ &D_{a3}=D_3+\alpha_2D_5+\alpha_1D_6+\alpha_1\alpha_2D_7,\ D_{a4}=D_4+\alpha_3D_7,\\ &D_{a5}=D_5+\alpha_1D_7,\ D_{a6}=D_6+\alpha_2D_7,\ D_{a7}=D_7\end{aligned}\tag{15}$$

Thus (8) can be transformed as

$$\begin{aligned}x_a(t+1)&=\bar{F}_a x_a(t)+w_f(t),\\ y(t)&=\bar{D}_a x_a(t)+v_f(t)\end{aligned}\tag{16}$$

where the fictitious white noises $w_f(t)$ and $v_f(t)$ are

$$\begin{aligned}w_f(t)&=F_e(t)x_a(t)+B_a(t)w_a(t),\\ v_f(t)&=D_e(t)x_a(t)+\lambda(t)v(t)\end{aligned}\tag{17}$$

3.3 The Statistical Characteristics of Fictitious Noises

The actual fictitious noises variances of $w_f(t)$ and $v_f(t)$ are UBBA, but their CUBs and property of PSD can be obtained based on Assumptions 1-4.

Lemma 1. Under Assumptions 1-4, we have

(*i*) The actual and conservative non-central second-order moments $\bar{X}(t)$ and $X(t)$ of original system state $x(t)$ satisfy generalized Lyapunov equations (GLEs)

$$\begin{aligned}\bar{X}(t+1)&=F\bar{X}(t)F^{\mathrm{T}}+\bar{Q}_n(t)+B\bar{Q}B^{\mathrm{T}},\\ X(t+1)&=FX(t)F^{\mathrm{T}}+\bar{Q}_n(t)+BQB^{\mathrm{T}},\\ \bar{Q}_n(t)&=\sum_{r=1}^{N}\bar{R}_{\zeta_r}F_{\zeta_r}\bar{X}(t)F_{\zeta_r}^{\mathrm{T}},\\ Q_n(t)&=\sum_{r=1}^{N}R_{\zeta_r}F_{\zeta_r}X(t)F_{\zeta_r}^{\mathrm{T}}\end{aligned}\tag{18}$$

with actual and conservative initial values $\bar{X}(0)=\bar{P}_0+\mu_0\mu_0^{\mathrm{T}}$, $X(0)=P_0+\mu_0\mu_0^{\mathrm{T}}$. Also, $X(t)$, $\bar{X}(t)$ and $\Delta X(t)=X(t)-\bar{X}(t)$ are PSD, i.e.,

$$X(t)\ge 0,\ \bar{X}(t)\ge 0,\ \Delta X(t)\ge 0\tag{19}$$

(*ii*) $w_a(t)$ has conservative and actual covariance $Q_a(t)$ and $\bar{Q}_a(t)$

$$\begin{aligned}Q_a(t)&=Q_a^{(1)}(t)+HQH^{\mathrm{T}}+ARA^{\mathrm{T}},\\ \bar{Q}_a(t)&=\bar{Q}_a^{(1)}(t)+H\bar{Q}H^{\mathrm{T}}+A\bar{R}A^{\mathrm{T}}\end{aligned}\tag{20}$$

where $H=\begin{bmatrix}B^{\mathrm{T}} & G^{\mathrm{T}}\end{bmatrix}^{\mathrm{T}}$, $A=\begin{bmatrix}\mathrm{O}_{m\times n} & I_m\end{bmatrix}^{\mathrm{T}}$, and

$Q_a^{(1)}(t)=\mathrm{diag}\{Q_n(t),\mathrm{O}_m\}$, $\bar{Q}_a^{(1)}(t)=\mathrm{diag}\{\bar{Q}_n(t),\mathrm{O}_m\}$.

Furthermore, $w_a(t)$ and $v(t)$ are correlated with conservative and actual cross-covariance

$$S_a=HQG^{\mathrm{T}}+AR,\ \bar{S}_a=H\bar{Q}G^{\mathrm{T}}+A\bar{R}\tag{21}$$

Also, $\Delta Q_a(t)=Q_a(t)-\bar{Q}_a(t)$ are PSD, i.e.,

$$\Delta Q_a(t)\ge 0\tag{22}$$

(*iii*) The actual and conservative non-central second-order moments $\bar{X}_a(t)$ and $X_a(t)$ of augmented system state $x_a(t)$ satisfy GLEs

$$\begin{aligned}\bar{X}_a(t+1)=&\bar{F}_a\bar{X}_a(t)\bar{F}_a^{\mathrm{T}}+\sum_{i=1}^{7}\bar{\beta}_iF_{ai}\bar{X}_a(t)F_{ai}^{\mathrm{T}}+\\&\bar{B}_a\bar{Q}_a(t)\bar{B}_a^{\mathrm{T}}+\alpha_2(1-\alpha_2)B_1\bar{Q}_a(t)B_1^{\mathrm{T}},\\ X_a(t+1)=&\bar{F}_aX_a(t)\bar{F}_a^{\mathrm{T}}+\sum_{i=1}^{7}\bar{\beta}_iF_{ai}X_a(t)F_{ai}^{\mathrm{T}}+\\&\bar{B}_aQ_a(t)\bar{B}_a^{\mathrm{T}}+\alpha_2(1-\alpha_2)B_1Q_a(t)B_1^{\mathrm{T}}\end{aligned}\tag{23}$$

with actual and conservative initial values $\bar{X}_a(0)$ and $X_a(0)$

$$\bar{X}_a(0)=\mathrm{diag}\{\bar{X}(0),\mathrm{O}_{3m}\},\ X_a(0)=\mathrm{diag}\{X(0),\mathrm{O}_{3m}\}\tag{24}$$

Also, $\Delta X_a(t)=X_a(t)-\bar{X}_a(t)$ are PSD, i.e.,

$$\Delta X_a(t)\ge 0\tag{25}$$

Proof. For (*i*), from Assumption 2 it follows that $\bar{X}(0)=\bar{P}_0+\mu_0\mu_0^{\mathrm{T}}\ge 0$ and $X(0)=P_0+\mu_0\mu_0^{\mathrm{T}}\ge 0$. Thus $X(t)\ge 0$ and $\bar{X}(t)\ge 0$ can be obtained by iteration.

Defining

$\Delta Q=Q-\bar{Q}$, $\Delta R_{\zeta_r}=R_{\zeta_r}-\bar{R}_{\zeta_r}$, $\Delta Q_n(t)=Q_n(t)-\bar{Q}_n(t)$,

then $\Delta X(t)=X(t)-\bar{X}(t)\ge 0$ can be obtained by iteration that is similar to [18].

For (*ii*), $w_a(t)$ can be written as

$$w_a(t)=\begin{bmatrix}\sum_{r=1}^{N}\zeta_r(t)F_{\zeta_r}x(t)\\ \mathrm{O}_{m\times n}\end{bmatrix}+\begin{bmatrix}B\\ G\end{bmatrix}w(t)+\begin{bmatrix}\mathrm{O}_{n\times m}\\ I_m\end{bmatrix}g(t).$$

Substituting $w_a(t)$ and $v(t)$ from actual or conservative system into $\mathrm{E}\left[w_a(t)w_a^{\mathrm{T}}(t)\right]$ and $\mathrm{E}\left[w_a(t)v^{\mathrm{T}}(t)\right]$, we have (20). Defining $\Delta Q_a^{(1)}(t)=Q_a^{(1)}(t)-\bar{Q}_a^{(1)}(t)$, it follows that

$$\Delta Q_a^{(1)}(t)=\mathrm{diag}\left\{\Delta Q_n(t),\mathrm{O}_m\right\}.$$

Hence, it is straightforward to verify that

$$\Delta Q_a(t)=\Delta Q_a^{(1)}(t)+H\Delta QH^{\mathrm{T}}+A\Delta RA^{\mathrm{T}}\geq 0.$$

For (*iii*), from the relation of $x(t)$ and $x_a(t)$ and Assumption 2, we have (24). Using the fact that $\mathrm{E}\left[F_e(t)\right]=0$ and uncorrelation of $x_a(t)$ and $w_a(t)$, similar to (18), we have (23).

Define $\Delta X_a(t+1)=X_a(t+1)-\bar{X}_a(t+1)$, it follows that

$$\begin{aligned}\Delta X_a(t+1)=&\bar{F}_a\Delta X_a(t)\bar{F}_a^{\mathrm{T}}+\sum_{k=1}^{7}\bar{\beta}_i F_{ai}\Delta X_a(t)F_{ai}^{\mathrm{T}}+\\&\bar{B}_a\Delta Q_a(t)\bar{B}_a^{\mathrm{T}}+\alpha_2(1-\alpha_2)B_1\Delta Q_a(t)B_1^{\mathrm{T}}\end{aligned}.$$

$\Delta X_a(0)\geq 0$ and $\Delta Q_a(t)\geq 0$ lead to $\Delta X_a(t+1)\geq 0$. The proof is completed.□

Defining matrices A and U as

$$A=F\otimes F+\sum_{r=1}^{N}\bar{R}_{\zeta_r}F_{\zeta_r}\otimes F_{\zeta_r}^{\mathrm{T}},\ U=\bar{F}_a\otimes\bar{F}_a^{\mathrm{T}}+\sum_{k=1}^{7}\bar{\beta}_i F_{ai}\otimes F_{ai}^{\mathrm{T}}.$$

Suppose that the spectral radii of matrices A and U are less than one, that is $\rho(A)\leq 1$ and $\rho(U)\leq 1$, which leads that the time-varying GLEs (18) and (23) with their respective arbitrary initial values $X(0)\geq 0$ and $\bar{X}(0)\geq 0$, $X_a(0)\geq 0$ and $\bar{X}_a(0)\geq 0$ converge to the unique PSD solution to steady-state GLEs

$$\bar{X}=F\bar{X}F^{\mathrm{T}}+\sum_{r=1}^{N}\bar{R}_{\zeta_r}F_{\zeta_r}\bar{X}F_{\zeta_r}^{\mathrm{T}}+B\bar{Q}B^{\mathrm{T}},\ \lim_{t\to\infty}\bar{X}(t)=\bar{X},$$

$$X=FXF^{\mathrm{T}}+\sum_{r=1}^{N}R_{\zeta_r}F_{\zeta_r}XF_{\zeta_r}^{\mathrm{T}}+BQB^{\mathrm{T}},\ \lim_{t\to\infty}X(t)=X,$$

$$\bar{X}_a=\bar{F}_a\bar{X}_a\bar{F}_a^{\mathrm{T}}+\sum_{i=1}^{7}\bar{\beta}_i F_{ai}\bar{X}_a F_{ai}^{\mathrm{T}}+\bar{B}_a\bar{Q}_a\bar{B}_a^{\mathrm{T}}+\alpha_2(1-\alpha_2)B_1\bar{Q}_aB_1^{\mathrm{T}},$$

$$X_a=\bar{F}_aX_a\bar{F}_a^{\mathrm{T}}+\sum_{i=1}^{7}\bar{\beta}_i F_{ai}X_a F_{ai}^{\mathrm{T}}+\bar{B}_aQ_a\bar{B}_a^{\mathrm{T}}+\alpha_2(1-\alpha_2)B_1Q_aB_1^{\mathrm{T}},$$

$$\lim_{t\to\infty}\bar{X}_a(t)=\bar{X}_a,\ \lim_{t\to\infty}X_a(t)=X_a.$$

Then, we have steady-state matrix X, $\bar{X}$, Q_a, $\bar{Q}_a$ X_a and $\bar{X}_a$, and the matrix inequality relation $\Delta Q_a\geq 0$, $\Delta X_a\geq 0$. Further, the actual and conservative steady-state variances of $w_f(t)$ and $v_f(t)$ can be given in Lemma 2.

Lemma 2. The fictitious white noises $w_f(t)$ and $v_f(t)$ are zero-means with conservative variances Q_f, R_f, and actual variances $\bar{Q}_f$, $\bar{R}_f$

$$\begin{aligned}\bar{Q}_f&=\sum_{i=1}^{7}\bar{\beta}_i F_{ai}\bar{X}_a F_{ai}^{\mathrm{T}}+\bar{B}_a\bar{Q}_a\bar{B}_a^{\mathrm{T}}+\alpha_2(1-\alpha_2)B_1\bar{Q}_aB_1^{\mathrm{T}},\\Q_f&=\sum_{i=1}^{7}\bar{\beta}_i F_{ai}X_a F_{ai}^{\mathrm{T}}+\bar{B}_aQ_a\bar{B}_a^{\mathrm{T}}+\alpha_2(1-\alpha_2)B_1Q_aB_1^{\mathrm{T}}\\\bar{R}_f&=\sum_{i=1}^{7}\bar{\beta}_i D_{ai}\bar{X}_a D_{ai}^{\mathrm{T}}+\alpha_2\left(G\bar{Q}G^{\mathrm{T}}+\bar{R}\right),\end{aligned}\quad(26)$$

$$R_f=\sum_{i=1}^{7}\bar{\beta}_i D_{ai}X_a D_{ai}^{\mathrm{T}}+\alpha_2\left(GQG^{\mathrm{T}}+R\right)\quad(27)$$

Further, $w_f(t)$ and $v_f(t)$ are correlated with actual and conservative matrices $\bar{S}_f$ and S_f

$$\begin{aligned}\bar{S}_f&=\sum_{i=1}^{7}\bar{\beta}_i F_{ai}\bar{X}_a D_{ai}^{\mathrm{T}}+\alpha_2\bar{B}_a\bar{S}_a,\\S_f&=\sum_{i=1}^{7}\bar{\beta}_i F_{ai}X_a D_{ai}^{\mathrm{T}}+\alpha_2\bar{B}_aS_a\end{aligned}\quad(28)$$

Also, $\Delta Q_f=Q_f-\bar{Q}_f$ and $\Delta R_f=R_f-\bar{R}_f$ are PSD, i.e.,

$$\Delta Q_f\geq 0,\ \Delta R_f\geq 0\quad(29)$$

Proof. Using the fact that $\Delta Q_a\geq 0$, $\Delta X_a\geq 0$, $\Delta Q\geq 0$ and $\Delta R\geq 0$, we have (29). The proof is completed. □

4 Steady-state RKP

4.1 Steady-state RKP of Augmented Systems

Under the Assumptions 1-4 and MREP, for the augmented worst-case system (16) with the conservative upper bounds Q_f, R_f and S_f, the conservative optimal Kalman predictors are given as

$$\hat{x}_a(t+1|t)=\Psi_p\hat{x}_a(t|t-1)+K_p y(t)\quad(30)$$

$$\Psi_p=\bar{F}_a-K_p\bar{D}_a,\ K_p=\left(\bar{F}_aP_a\bar{D}_a^{\mathrm{T}}+S_f\right)\left[\bar{D}_aP_a\bar{D}_a^{\mathrm{T}}+R_f\right]^{-1}.$$

The conservative prediction error variances P_a satisfy the Riccati equations

$$\begin{aligned}P_a=&\bar{F}_aP_a\bar{F}_a^{\mathrm{T}}-\left[\bar{F}_aP_a\bar{D}_a^{\mathrm{T}}+S_f\right]\left[\bar{D}_aP_a\bar{D}_a^{\mathrm{T}}+R_f\right]^{-1}\\&\times\left[\bar{F}_aP_a\bar{D}_a^{\mathrm{T}}+S_f\right]^{\mathrm{T}}+Q_f\end{aligned}.$$

Remark 1. In the conservative Kalman predictors (30), replacing conservative measurement $y(t)$ by known actual measurement $y(t)$ generated from systems (1)-(4) with actual noise variances, we call (30) as actual Kalman predictors.

Defining the prediction error as

$$\tilde{x}_a(t+1|t)=x_a(t+1)-\hat{x}_a(t+1|t),$$

it follows that

$$\tilde{x}_a(t+1|t)=\Psi_p\tilde{x}_a(t|t-1)+\left[I_{n+3m},\ -K_p\right]\rho(t)\quad(31)$$

where the augmented noises $\rho(t)=\left[w_f^{\mathrm{T}}(t),v_f^{\mathrm{T}}(t)\right]^{\mathrm{T}}$ have the actual and conservative variances and cross-variances

$$\bar{\Lambda}=\begin{bmatrix}\bar{Q}_f&\bar{S}_f\\\bar{S}_f^{\mathrm{T}}&\bar{R}_f\end{bmatrix},\Lambda=\begin{bmatrix}Q_f&S_f\\S_f^{\mathrm{T}}&R_f\end{bmatrix}\quad(32)$$

So the actual and conservative prediction error variances can also be given as

$$\bar{P}_a=\Psi_p\bar{P}_a\Psi_p^{\mathrm{T}}+\left[I_{n+3m},\ -K_p\right]\bar{\Lambda}\left[I_{n+3m},\ -K_p\right]^{\mathrm{T}}\quad(33)$$

$$P_a=\Psi_pP_a\Psi_p^{\mathrm{T}}+\left[I_{n+3m},\ -K_p\right]\Lambda\left[I_{n+3m},\ -K_p\right]^{\mathrm{T}}\quad(34)$$

4.2 Steady-state RKP of Original System

From the relation of $x_a(t)$ and $x(t)$, the RKP of the original systems (1)-(4) are

$$\hat{x}(t+1|t)=\left[I_n\quad\mathrm{O}_{n\times 3m}\right]\hat{x}_a(t+1|t)\quad(35)$$

and actual and conservative prediction error covariance is

$$\bar{P}=\left[I_n \quad \mathrm{O}_{n\times 3m}\right]\bar{P}_a\left[I_n \quad \mathrm{O}_{n\times 3m}\right]^{\mathrm{T}},$$
$$P=\left[I_n \quad \mathrm{O}_{n\times 3m}\right]P_a\left[I_n \quad \mathrm{O}_{n\times 3m}\right]^{\mathrm{T}} \tag{36}$$

Theorem 1. Consider the systems (1)-(4) under Assumptions 1-4, the actual Kalman predictor (35) is robust if there exists matrix inequality

$$\bar{P}\le P \tag{37}$$

for all admissible actual variances $\bar{Q}$, $\bar{R}$, $\bar{R}_{\zeta_r}$ and $\bar{P}_0$ satisfying (5). Further, P is minimal upper bound of $\bar{P}$, and we have the accuracy relation with matrix trace inequality $\mathrm{tr}\bar{P}\le \mathrm{tr}P$.

Proof. To obtain $\Delta P=P-\bar{P}\ge 0$, it just needs to prove $\Delta P_a=P_a-\bar{P}_a\ge 0$. From (33) and (34), we have

$$\Delta P_a=\Psi_p\Delta P_a\Psi_p^{\mathrm{T}}+\left[I_{n+3m},\ -K_p\right]\Delta\Lambda\left[I_{n+3m},\ -K_p\right]^{\mathrm{T}} \tag{38}$$

where $\Delta\Lambda=\Lambda-\bar{\Lambda}$. Hence, to prove $\Delta P_a\ge 0$, we need only to prove that $\Delta\Lambda\ge 0$. Substituting Q_f, R_f and S_f into Λ in (32), it can be decomposed as [18, 19]

$$\Lambda=\sum_{i=1}^{7}\Lambda_i \tag{39}$$

$$\Lambda_1=\sum_{i=1}^{7}\beta_i\left[\mathrm{diag}\left\{F_{ai},D_{ai}\right\}X_u\mathrm{diag}\left\{F_{ai},D_{ai}\right\}^{\mathrm{T}}\right],$$
$$\Lambda_2=\mathrm{diag}\left\{\alpha_2\left(1-\alpha_2\right)B_1Q_a^{(1)}B_1^{\mathrm{T}},\mathrm{O}_m\right\},$$
$$\Lambda_3=\mathrm{diag}\left\{\bar{B}_aA,\alpha_2I_m\right\}R_u\mathrm{diag}\left\{\bar{B}_aA,\alpha_2I_m\right\}^{\mathrm{T}},\ R_u=\left[R\left|_{i,j=1}^{2}\right.\right],$$
$$\Lambda_4=\alpha_2\left(1-\alpha_2\right)\mathrm{diag}\left\{B_1H,\alpha_2G\right\}Q_u\mathrm{diag}\left\{B_1H,\alpha_2G\right\}^{\mathrm{T}},$$
$$\Lambda_5=\alpha_2\left(1-\alpha_2\right)\mathrm{diag}\left\{B_1A,\alpha_2I_m\right\}R_u\mathrm{diag}\left\{B_1A,\alpha_2I_m\right\}^{\mathrm{T}},$$
$$\Lambda_6=\mathrm{diag}\left\{\bar{B}_aH,\alpha_2G\right\}Q_u\mathrm{diag}\left\{\bar{B}_aH,\alpha_2G\right\}^{\mathrm{T}},Q_u=\left[Q\left|_{i,j=1}^{2}\right.\right],$$
$$\Lambda_7=\mathrm{diag}\left\{\bar{B}_aQ_a^{(1)}\bar{B}_a^{\mathrm{T}},\mathrm{O}_m\right\},\ X_u=\left[X_a\left|_{i,j=1}^{2}\right.\right] \tag{40}$$

Similarly, we have $\bar{\Lambda}=\sum_{i=1}^{7}\bar{\Lambda}_i$, where the conservative variances X_a, Q, R, X_u, R_u, Q_u and $Q_a^{(1)}$ in (40) are replaced by actual variances $\bar{X}_a$, Q, $\bar{R}$, $\bar{X}_u$, $\bar{Q}_u$, $\bar{R}_u$ and $\bar{Q}_a^{(1)}$, respectively. Define $\Delta\Lambda(t)=\Lambda(t)-\bar{\Lambda}(t)$, it now follows from Lemmas 1 and 2 that $\Delta\Lambda\ge 0$. Thus we have $\Delta P_a\ge 0$ and $\Delta P\ge 0$. Similar to [15], it can be proved that P is minimal upper bound of $\bar{P}$. Taking the trace operation for (37) yields that $\mathrm{tr}\bar{P}\le\mathrm{tr}P$. The proof is completed. □

The actual Kalman predictor (35) are said to be RKP. The inequalities (37) are said to be robustness of RKP.

5 Simulation Example

We consider a tracking system with

$$F=\begin{bmatrix}0.90 & T_0\\ 0 & 0.90\end{bmatrix},\ B=\begin{bmatrix}T_0^2/2\\ T_0\end{bmatrix},\ T_0=0.2,\ D=I_2.$$

In the simulation, other parameters are given as: $Q=1.8$, $\bar{Q}=1.2$, $R=1.5I_2$, $\bar{R}=1.25I_2$, $R_{\zeta_1}=0.25$, $\bar{R}_{\zeta_1}=0.2$, $\alpha_1=0.95$, $\alpha_2=0.93$, $\alpha_3=0.94$, $F_{\zeta_1}=\begin{bmatrix}-0.01 & -0.01\\ 0 & -0.04\end{bmatrix}$.

The robust and actual accuracies of steady-state Kalman predictor are shown in Table 1, which verify the accuracy relation of $\mathrm{tr}\bar{P}$ and $\mathrm{tr}P$.

Table 1: The Accuracy Comparison of RKP

$\mathrm{tr}P$	$\mathrm{tr}\bar{P}$
0.3182	0.2564

The covariance ellipse of prediction error variances are given in Fig. 1, which verify the matrix accuracy relation of (37).

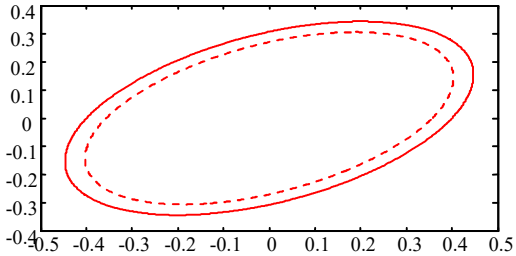

Fig.1: The covariance ellipse of RKP.

The tracking results of RKP are shown in Fig. 2.

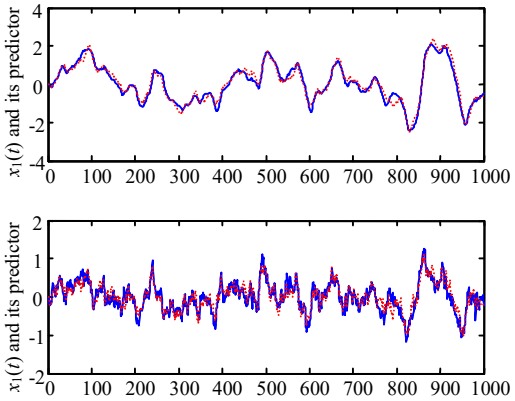

Fig.2: The state and its RKP.

Taking 2 groups of actual admissible noise variances as

$$\text{(a) } \bar{Q}=0.4,\ \bar{R}=0.25I_2,\ \bar{R}_{\zeta_1}=0.04$$
$$\text{(b) } \bar{Q}=1.2,\ \bar{R}=1.25I_2,\ \bar{R}_{\zeta_1}=0.2 \tag{41}$$

then we can obtain the 2 corresponding actual prediction error curves of first components of RKP, and their robust and actual 3-standard deviation bounds $\pm 3\sigma_1$ and $\pm 3\bar{\sigma}_1^{l}\left(l=a,b\right)$ as defined in Remark 6 in [15].

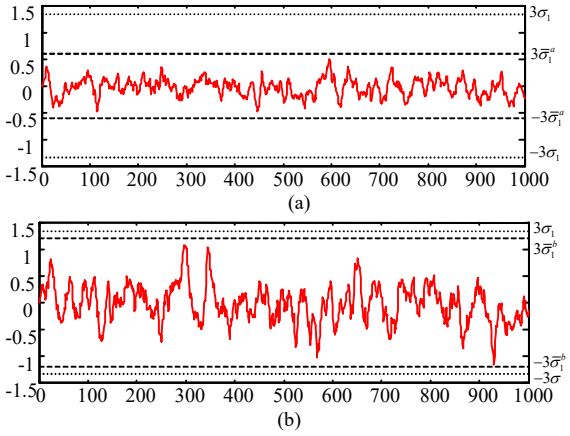

Fig.3: The curves of actual prediction errors, $\pm 3\sigma_1$ and $\pm 3\bar{\sigma}_1^{l}, l=a,b$ bounds

In equation (6), the higher α_i, the lower probability of multiple networked-induced uncertainties, and the smaller actual prediction error variances. To verify this case, we define

$$\bar{\alpha}_i = 1-\alpha_i,\ [\bar{\alpha}_1 \quad \bar{\alpha}_2 \quad \bar{\alpha}_3] = \alpha[1 \quad 1 \quad 1] \tag{42}$$

then $0 \le \alpha \le 1$ represent the probability of simultaneous occurrence of multiple networked-induced uncertainties. Uncertain noise variances go considerably further, we define $\bar{Q} = \delta Q$, $\bar{R} = \delta R$, $\bar{R}_{\zeta_1} = \delta R_{\zeta_1}$, $0 \le \delta \le 1$. Fig. 4 shows how $\mathrm{tr}\bar{P}$ vary versus $0 \le \alpha \le 0.8$ and $0.1 \le \delta \le 0.9$. From this subplot, it can be seen that $\mathrm{tr}\bar{P}$ is increased with increase of α and δ, namely, $\mathrm{tr}\bar{P}$ is increased with the probability of multiple networked-inducements and uncertain noise variances.

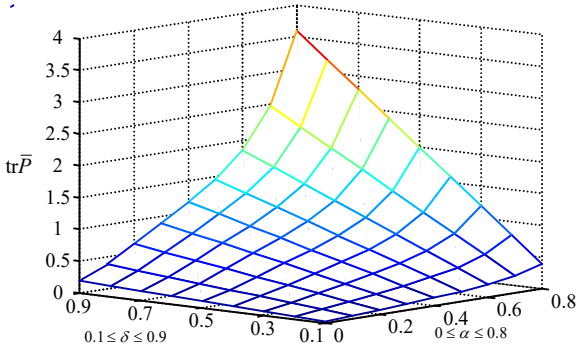

Fig. 4: The changes of $\mathrm{tr}\bar{P}$ versus $0 \le \alpha \le 0.8$ and $0.1 \le \delta \le 0.9$

6 Conclusions

In this paper, we present solution to RKP problem for system with UBBA noise variance, multiplicative noises and multiple networked-induced uncertainties including missing measurements, packet dropouts and two-step RMD. The novel model-transformation method is presented to transform the original system into multi-model system with correlated fictitious noise. The steady-state RKP is presented by MREP. The proposed model-transformation method and robustness proof method can be used to solve robust fusion Kalman estimation problem for more complex system with mixed uncertainties of UBBA noise variances and multiple networked-inducements including multi-step RMD. The further works are currently in progress.

References

[1] M. Rahmani and M. Abolhasani, State estimation for stochastic time-varying multisensor systems with multiplicative noises: Centralized and decentralized data fusion, *Asian Journal of Control*, 2019, 21(4): 1547-1555.

[2] W.L.D. Koning, Optimal estimation of linear discrete-time systems with stochastic parameters, *Automatica*, 1984, 20: 113-115.

[3] S. Sun, Distributed optimal linear fusion predictors and filters for systems with random parameter matrices and correlated noises, *IEEE Transactions on Signal Processing*, 2020, 68: 1064-1074.

[4] J. Ma, X. Yang and S. Sun, Distributed fusion estimation for multi-sensor systems with time-correlated multiplicative noises, *Acta Automatica Sinica*, 2021, 47(8): 1745-1757.

[5] H. Zhang, D. Zhang, L. Xie and J. Lin, Robust filtering under stochastic parametric uncertainties, *Automatica*. 2004, 40: 1583-1589.

[6] W. Qi, P. Zhang, G. Nie and Z. Deng, Robust weighted fusion Kalman predictors with uncertain noise variances, *Digital Signal Processing*, 2014, 30, 37-54.

[7] C Yang, Z Yang and Z Deng. Guaranteed cost robust weighted measurement fusion steady-state Kalman predictors with uncertain noise variances. *Aerospace Science and Technology*. 2015, 46: 459-470.

[8] J. Ma and S. Sun. A general packet dropout compensation framework for optimal prior filter of networked multi-sensor systems, *Information Fusion*, 2019, 45: 128-137.

[9] Z. Wang, F. Yang, D.W.C. Ho and X. Liu, Robust finite-horizon filtering for stochastic systems with missing measurements, *IEEE signal processing letters*, 12(2005), no. 6, 437-440.

[10] J. Zhang, S. Gao, G. Li and B. Gao, Distributed recursive filtering for multi-sensor networked systems with multi-step sensor delays, missing measurements and correlated noise, *Signal Process*, 2021, 181: 107868.

[11] B. Chen, W. Zhang and L Yu, Distributed fusion estimation with missing measurements, random transmission delays and packet dropouts, *IEEE Transactions on Automatic Control*, 2014, 59(7): 1961-1967.

[12] M. Moayedi, Y. Koo and Y. Soc, Adaptive Kalman filtering in networked systems with random sensor delays, multiple packet dropouts and missing measurements, *IEEE Transactions on Signal Process*, 2010, 58(3): 1577-1588.

[13] R. Caballero-Águila, A. Hermoso-Carazo and J. Linares-Pérez, Networked distributed fusion estimation under uncertain outputs with random transmission delays, packet losses and multi-packet processing, *Signal Processing*, 2019, 156: 71-83.

[14] X. Lu, R. Liu, C. Lv, N. Wang and X. Liang, Control for networked control systems with multiplicative noises, packet dropouts and multiple delays, *International Journal of Systems Science*, 2021, 52(16): 3466–3477.

[15] C. Yang, Z. Yang and Z. Deng, Robust weighted state fusion Kalman estimators for networked systems with mixed uncertainties, *Information Fusion*, 2019, 45: 246-265.

[16] C. Ran and Z. Deng, Robust fusion Kalman estimators for networked mixed uncertain systems with random one-step measurement delays, missing measurements, multiplicative noises and uncertain noise variances, *Information Sciences*, 2020, 534: 27-52.

[17] W. Liu and G. Tao, Robust fusion steady-state estimators for networked stochastic uncertain systems with packet dropouts and missing measurements, *Optimal Control Applications & Methods*, 2020, 42(3): 629-659.

[18] C. Yang, Y. Zhao and Z. Liu, Robust weighted fusion Kalman filters under linearly correlated noise and mixed uncertainties of noise variances, multiplicative noises and multiple networked-inducements. *Asian Journal of Control*. 2024, 26 (1): 205-226.

[19] C Yang, Y Zhao, Z Liu and J Wang. Robust weighted fusion Kalman estimators for systems with uncertain noise variances, multiplicative noises, missing measurements, packets dropouts and two-step random measurement delays. *Optimal Control Applications and Methods*. 2023, 44 (5): 2744–2774.

Proceedings of the 3rd Conference on Fully Actuated System Theory and Applications
May 10-12, 2024, Shenzhen, China

Distributed fusion estimator for networked multi-rate multi-sensor systems with unknown inputs

Qiang Liu[1], Honglei Lin[1*]

1. Department of Automation, Heilongjiang University, Harbin 150080, China
E-mail: 2951642319@qq.com
E-mail: linhonglei@hlju.edu.cn

Abstract: This paper concerns the state estimation problem for multi-rate multi-sensor systems with unknown inputs, time delays, fading measurements, and multiplicative noise in the state equation. Firstly, the measurement delay models are converted into measurement delay free models. Subsequently, Lagrange multiplier method is used to compute the gain of the optimal local unbiased minimum variance filter which is independent of unknown input information. Based on the local filter, the estimation error cross-covariance matrices between any two estimators are derived. A distributed optimal fusion estimator is obtained by using the matrix-weighted fusion estimation algorithm. Finally, a numerical example is provided to demonstrate the effectiveness of the proposed estimation algorithms.

Key Words: Distributed fusion estimator, multi-rate multi-sensor system, unknown input, time delay, fading measurement

1 Introduction

In networked systems, the internal component aging or changes in external environments may introduce unknown inputs. The state estimation problem with unknown inputs has received widespread attention due to its applications in demographic studies [1] and average precipitation problem in a storm [2]. Studies on linear systems with unknown inputs have been conducted in [3-6]. Ref. [3] proposes a recursive three-step filter for states with unknown inputs. Ref. [4] considers two types of unknown input problems and the distributed filters are developed in the sense of unbiased minimum variance. The occurrence of unknown inputs follows an independent random Bernoulli process, a joint state and unknown input estimation filter approach is proposed in [5]. In [6], an unbiased minimum variance filter is designed which is independent of a priori initial condition information. Nonlinear systems also encounter issues with unknown inputs, as discusses in [7-9]. In [7], a filter that estimation errors are Practically Exponentially Stable in probability is proposed. Ref. [8] proposes an unknown input extended Kalman filter for stochastic nonlinear systems with unknown inputs. Considering the field voltage and the mechanical torque of the generator as unknown inputs, Ref. [9] investigates the problem of state and unknown input estimation for multi-machine power grids. Random uncertainties occur during signal transmission processes. The state estimation for Markov jump systems with multiplicative noises is investigated in [10]. Distributed fusion estimator is developed in [11] for multi-sensor systems with various fading measurement rates and multiplicative noises. The conception of period steady-state is proposed. Ref. [12] proposes the sequential covariance intersection fusion estimator. It solves the fusion estimation problem of stochastic uncertain systems with fading measurements under Denial-of-Service attacks and deception attacks.

The expansion of sensor scales can not only enhance the accuracy of estimation but also increase the likelihood of network-induced phenomena. Consequently, there are extensive research on the state estimation problem that considers both the impact of network-induced phenomena and unknown inputs. For systems with unknown inputs, multiple missing measurements and average dwell time, the estimation problem is proposed in [13]. Ref. [14] investigates the estimation problem for linear systems with unknown inputs and measurement delays. Addressing the issues in [14], Ref. [15] proposes a distributed ellipsoidal intersection fusion estimator. Ref. [16] extends the unknown input and delayed measurement problem to nonlinear systems and proposes a filter based on linear matrix inequality. Ref. [17] designs a robust filtering for nonlinear systems with multiplicative noises, unknown inputs and correlated noises. Unknown inputs may also occur in sensor networks. By using a recursive distributed filter, Ref. [18] investigates the state and unknown input estimation problem. Ref. [19] proposes an unknown input filter using its own information and a state filter using in-neighbors' information. Ref. [20] considers random link failures and derives a minimum mean square error estimator. Under false data injection attack, Ref. [21] proposes an event-based distributed state estimator. Ref. [22] investigates the estimation problem for nonlinear systems under Denial-of-Service attacks and proposed an estimator that incorporates a dynamic event-triggering mechanism.

Although the state estimation for the above-mentioned systems have been conducted extensive and in-depth research, there still limit investigation on state estimation problems in multi-rate multi-sensor systems with multiplicative noise in the state, time delays, fading measurements, and unknown inputs. Therefore, we focus on the state estimations problem for such systems. For the problem of multiplicative noise in the state equation, we treat multiplicative noise as additive noise to solve it. An iteration state equation approach is employed to handle the

*This work is supported by National Natural Science Foundation (NNSF) of China under Grant 61903128, Natural Science Foundation of Heilongjiang Province under Grant YQ2022F016, Young Innovative Talents Training Program of Universities in Heilongjiang Province under Grant UNPYSCT-2020001, and Heilongjiang University Outstanding Youth Fund under Grant JCL202101. (*Corresponding author: Honglei Lin*).

measurement delay. The Lagrange multiplier method exhibits the advantages of simplicity in algorithm, ease of implementation, and excellent performance in optimization problems. Therefore, it is employed to determine the gain matrix of the filter. Then, the estimation error covariance matrix is derived. Finally, the distributed fusion filter is designed by using matrix-weighted fusion estimation criterion.

2 Problem statement and Model transformation

The following multi-rate multi-sensor linear system is considered, the state equation is described by

$$x(t+1)=(\Phi+\alpha(t)A)x(t)+\Gamma w(t) \tag{1}$$

where $x(t)\in R^n$ represents the systems state at moment t, $\alpha(t)$ is multiplicative noise. The process noise is described by $w(t)\in R^w$. The measurement equation is described by

$$\begin{aligned} y_i(n_it)&=\gamma_i(n_it)H_ix(n_it-d_i)+D_i\theta_i(n_it)\\ &+v_i(n_it),i=1,2,\ldots,L \end{aligned} \tag{2}$$

where $y_i(n_it)\in R^{q_i}$ represents the measurement of the i th sensor at the moment n_it, with L being the total number of sensors. $\theta_i(n_it)\in R^{p_i}$ is the unknown sensor input. $v_i(t)\in R^{q_i}$ denotes the measurement noise. The state update rate is n_i multiples of the measurement sampling rates. n_i is a positive integer. d_i is the time delay of sensor *i*, and it is a positive integer. Φ, A, Γ, H_i and D_i are appropriate dimension constant matrices.

The phenomenon of fading measurement is described by the $\gamma_i(n_it)$. The value range of $\gamma_i(n_it)$ is $[\lambda_i(n_it),\beta_i(n_it)]$ $(0\le\lambda_i(n_it)\le\beta_i(n_it)\le 1)$. $p_i(s)$ represents the probability density function of the fading measurement $\gamma_i(n_it)$.

The following assumptions are given.

Assumption 1. $\alpha(t)$, $w(t)$ and $v_i(t)$ are uncorrelated white noise with zero mean and variance matrices Q_α, Q_w and Q_{v_i}.

Assumption 2. $\gamma_i(n_it),i=1,2,...,L$ are independent of each other, and are independent of other random variables. Moreover, $\gamma_i(n_it)$ satisfies that

$$\begin{gathered} \mathrm{E}[\gamma_i(n_it)]=\overline{\gamma}_i,\ Cov[\gamma_i(n_it)]=\sigma_i^2,\ \mathrm{E}[\gamma_i(n_it)^2]=\overline{\gamma}_i^2+\sigma_i^2,\\ \mathrm{E}[\gamma_i(n_it)-\overline{\gamma}_i]=0,\ \mathrm{E}[(\gamma_i(n_it)-\overline{\gamma}_i)\gamma_i(n_it)]=\sigma_i^2,\\ \mathrm{E}[(\gamma_i(n_it)-\overline{\gamma}_i)(\gamma_j(n_jt)-\overline{\gamma}_j)]=0,(i\ne j),\\ \mathrm{E}[(\gamma_i(n_it)-\overline{\gamma}_i)\gamma_j(n_it)]=0,(i\ne j). \end{gathered}$$

Assumption 3. The $x(0)$ is uncorrelated with other noise signals and has the mean $\mathrm{E}[x(0)]=\mu_0$ and the covariance $\mathrm{E}[(x(0)-\mu_0)(x(0)-\mu_0)^{\mathrm{T}}]=P_0$.

Assumption 4. Φ is invertible.

In order to design local filter for systems (1) and (2), we give the following Theorem 1 based on the above four assumptions.

Theorem 1: The measurement equation at the measurement sampling points is given as

$$\begin{aligned} y_i(n_it)&=\gamma_i(n_it)\bar{H}_ix(n_it)-\gamma_i(n_it)\bar{H}_i\bar{\alpha}_i(n_it)\\ &+D_i\theta_i(n_it)+V_i(n_it) \end{aligned} \tag{3}$$

where

$$\bar{H}_i=H_i\Phi^{-d_i}$$

$$\bar{\alpha}_i(n_it)=\sum_{m=0}^{d_i-1}\Phi^m\alpha(n_it-m-1)Ax(n_it-m-1)$$

$$V_i(n_it)=v_i(n_it)-\gamma_i(n_it)\bar{H}_i\sum_{m=0}^{d_i-1}\Phi^m\Gamma w(n_it-m-1)$$

From $\bar{\alpha}_i(n_it)$ and $V_i(n_it)$, they hold that

$$\begin{aligned} Q_{\bar{\alpha}_i}(n_it)&=\mathrm{E}[\bar{\alpha}_i(n_it)\bar{\alpha}_i^{\mathrm{T}}(n_it)]\\ &=\sum_{m=0}^{d_i-1}Q_\alpha\Phi^mAX(n_it-m-1)A^{\mathrm{T}}(\Phi^m)^{\mathrm{T}} \end{aligned} \tag{4}$$

$$\begin{aligned} Q_{V_i}&=\mathrm{E}[V_i(n_it)V_i^{\mathrm{T}}(n_it)]\\ &=Q_{v_i}+(\sigma_i^2+\overline{\gamma}_i^2)\sum_{m=0}^{d_i-1}\bar{H}_i\Phi^m\Gamma Q_w\Gamma^{\mathrm{T}}(\Phi^m)^{\mathrm{T}}\bar{H}_i^{\mathrm{T}} \end{aligned} \tag{5}$$

Proof. According to the state equation (1), we have

$$x(n_it)=\Phi x(n_it-1)+\alpha(n_it-1)Ax(n_it-1)+\Gamma w(n_it-1) \tag{6}$$

Through the iteration of the above equation, it can be derived that

$$\begin{aligned} x(n_it)&=\Phi^{d_i}x(n_it-d_i)+\sum_{m=0}^{d_i-1}\Phi^m\Gamma w(n_it-m-1)\\ &+\sum_{m=0}^{d_i-1}\Phi^m\alpha(n_it-m-1)Ax(n_it-m-1) \end{aligned} \tag{7}$$

i.e.

$$\begin{aligned} x(n_it-d_i)&=\Phi^{-d_i}x(n_it)-\Phi^{-d_i}\sum_{m=0}^{d_i-1}\Phi^m\Gamma w(n_it-m-1)\\ &-\Phi^{-d_i}\sum_{m=0}^{d_i-1}\Phi^m\alpha(n_it-m-1)Ax(n_it-m-1) \end{aligned} \tag{8}$$

Substituting (8) into (2) yields a new measurement equation (3). □

The transformed measurement equation and the following lemmas can be used to derive filter more easily.

Lemma 1[23]**.** According to (1), the second order moment of state $X(t)=\mathrm{E}[x(t)x^{\mathrm{T}}(t)]$ is given as

$$X(t)=\Phi X(t-1)\Phi^{\mathrm{T}}+Q_\alpha AX(t-1)A^{\mathrm{T}}+\Gamma Q_w\Gamma^{\mathrm{T}} \tag{9}$$

where $X(0)=\mu_0\mu_0^{\mathrm{T}}+P_0$.

Lemma 2[24]**.** Let $B=\begin{bmatrix}B_{11}&B_{12}\\B_{21}&B_{22}\end{bmatrix}$, B_{11} is invertible, the inverse of a block matrix is given as

$$\begin{pmatrix}B_{11}&B_{12}\\B_{21}&B_{22}\end{pmatrix}^{-1}=\begin{bmatrix}B_{11}^{-1}+B_{11}^{-1}B_{12}MB_{21}B_{11}^{-1}&-B_{11}^{-1}B_{12}M\\-MB_{21}B_{11}^{-1}&M\end{bmatrix}$$

where $M=(B_{22}-B_{21}B_{11}^{-1}B_{12})^{-1}$.

Define the recursive local filter form at the state update points as

$$\hat{x}_i(k)=F_i(k)\hat{x}_i(k-1)+L_i(k)y_i(k) \tag{10}$$

Next, we will calculate the gain $F_i(k)$ and $L_i(k)$ to obtain the state estimator for systems (1) and (3) base on Lemmas 1-2.

3 State estimation

We propose the following local filters based on (10) for estimating the states of system (1) and (3).

Theorem 2: a) At state update points where there are measurements, i.e. $k = n_i t, t = 0,1,2...$, the local filter is given as

$$\hat{x}_i(k) = F_i(k)\hat{x}_i(k-1) + L_i(k)y_i(k) \tag{11}$$

where the gain matrices $F_i(k)$ and $L_i(k)$ of the local filter are calculated as

$$F_i(k) = (I_n - L_i(k)\overline{\gamma}_i\overline{H}_i)\Phi \tag{12}$$

$$L_i(k) = (G_i(k)^{\mathrm{T}} - \Lambda_i(k)D_i^{\mathrm{T}})C_i^{-1}(k) \tag{13}$$

where

$$\Lambda_i(k) = G_i^{\mathrm{T}}(k)C_i^{-1}(k)D_i((D_i^{\mathrm{T}}C_i^{-1}(k)D_i)^{-1})^{\mathrm{T}} \tag{14}$$

$$\begin{aligned} G_i(k) &= \overline{\gamma}_i\overline{H}_i\Phi P_i(k-1)\Phi^{\mathrm{T}} + \overline{\gamma}_i\overline{H}_i\Gamma Q_w\Gamma^{\mathrm{T}} + Q_{wV_i}^{\mathrm{T}}\Gamma^{\mathrm{T}} \\ &+ Q_{\tilde{x}_iV_i}^{\mathrm{T}}(k-1,k)\Phi^{\mathrm{T}} - \overline{\gamma}_i\overline{H}_iQ_{\tilde{x}_i\overline{\alpha}_i}^{\mathrm{T}}(k-1,k)\Phi^{\mathrm{T}} \end{aligned} \tag{15}$$

$$\begin{aligned} C_i(k) &= \sigma_i^2\overline{H}_i(X(k) - Q_{x\overline{\alpha}_i}(k) - Q_{x\overline{\alpha}_i}^{\mathrm{T}}(k))\overline{H}_i^{\mathrm{T}} \\ &+ (\sigma_i^2/\overline{\gamma}_i)(\overline{H}_iQ_{xV_i}(k) + Q_{xV_i}^{\mathrm{T}}(k)\overline{H}_i^{\mathrm{T}}) \\ &+ \overline{\gamma}_i^2\overline{H}_i(\Gamma Q_w\Gamma^{\mathrm{T}} + \Phi P_i(k-1)\Phi^{\mathrm{T}} - \Phi Q_{\tilde{x}_i\overline{\alpha}_i}(k-1,k) \\ &- Q_{\tilde{x}_i\overline{\alpha}_i}^{\mathrm{T}}(k-1,k)\Phi^{\mathrm{T}} - Q_\alpha AX(k-1)A^{\mathrm{T}})\overline{H}_i^{\mathrm{T}} \\ &+ \overline{\gamma}_i\overline{H}_i(\Gamma Q_{wV_i} + \Phi Q_{\tilde{x}_iV_i}(k-1,k)) + (\sigma_i^2 + \overline{\gamma}_i^2)\overline{H}_iQ_{\overline{\alpha}_i}(k)\overline{H}_i^{\mathrm{T}} \\ &+ \overline{\gamma}_i(Q_{wV_i}^{\mathrm{T}}\Gamma^{\mathrm{T}} + Q_{\tilde{x}_iV_i}^{\mathrm{T}}(k-1,k)\Phi^{\mathrm{T}})\overline{H}_i^{\mathrm{T}} + Q_{V_i} \end{aligned} \tag{16}$$

$$\overline{P}_i(k) = \Phi P_i(k-1)\Phi^{\mathrm{T}} + Q_\alpha AX(k-1)A^{\mathrm{T}} + \Gamma Q_w\Gamma^{\mathrm{T}} \tag{17}$$

The estimation error covariance matrix $P_i(k)$ of $x_i(k)$ is given by

$$\begin{aligned} P_i(k) &= \overline{P}_i(k) + L_i(k)C_i(k)L_i^{\mathrm{T}}(k) \\ &- L_i(k)G_i(k) - G_i^{\mathrm{T}}(k)L_i^{\mathrm{T}}(k) \end{aligned} \tag{18}$$

Define $Q_{xV_i}(k) = \mathrm{E}[x(k)V_i^{\mathrm{T}}(k)]$, $Q_{x\overline{\alpha}_i}(k) = \mathrm{E}[x(k)\overline{\alpha}_i^{\mathrm{T}}(k)]$, $Q_{wV_i} = \mathrm{E}[w(k-1)V_i^{\mathrm{T}}(k)]$, $Q_{\tilde{x}_iV_i}(k-1,k) = \mathrm{E}[\tilde{x}_i(k-1)V_i^{\mathrm{T}}(k)]$, $Q_{\tilde{x}\overline{\alpha}_i}(k-1,k) = \mathrm{E}[\tilde{x}(k-1)\overline{\alpha}_i^{\mathrm{T}}(k)]$, we have

$$Q_{xV_i}(k) = -\overline{\gamma}_i\sum_{m=0}^{d_i-1}\Phi^m\Gamma Q_w\Gamma^{\mathrm{T}}(\Phi^m)^{\mathrm{T}}\overline{H}_i^{\mathrm{T}} \tag{19}$$

$$Q_{wV_i} = -\overline{\gamma}_iQ_w\Gamma^{\mathrm{T}}\overline{H}_i^{\mathrm{T}} \tag{20}$$

$$Q_{\tilde{x}_iV_i}(k-1,k) = -\overline{\gamma}_i\sum_{m=0}^{d_i-2}\Phi^m\Gamma Q_w\Gamma^{\mathrm{T}}(\Phi^{m+1})^{\mathrm{T}}\overline{H}_i^{\mathrm{T}} \tag{21}$$

$$Q_{\tilde{x}_i\overline{\alpha}_i}(k-1,k) = \sum_{m=0}^{d_i-2}Q_\alpha\Phi^m AX(k-m-2)A^{\mathrm{T}}(\Phi^{m+1})^{\mathrm{T}} \tag{22}$$

$$Q_{x\overline{\alpha}_i}(k) = Q_{\overline{\alpha}_i}(k) \tag{23}$$

$$Q_{\tilde{x}_iV_i}(k-1,k) = Q_{xV_i}(k-1,k) \tag{24}$$

$$Q_{x\overline{\alpha}_i}(k-1,k) = Q_{\tilde{x}_i\overline{\alpha}_i}(k-1,k) \tag{25}$$

b) At state update points where there are not measurements, i.e. $k = n_i t + p, p = 1,2,...,n_i - 1$, the local filter is given as

$$\hat{x}_i(k) = \Phi\hat{x}_i(k-1) \tag{26}$$

The estimator error covariance matrix $P_i(k)$ is computed by

$$P_i(k) = \Gamma Q_w\Gamma^{\mathrm{T}} + \Phi P_i(k-1)\Phi^{\mathrm{T}} + Q_\alpha AX(k-1)A^{\mathrm{T}} \tag{27}$$

Proof. For $k = n_i t, t = 0,1,2...$, from (6) and (11), the filtering error equation $\tilde{x}_i(k)$ is obtained by

$$\begin{aligned} \tilde{x}_i(k) &= x(k) - \hat{x}_i(k) \\ &= [\Phi - F_i(k) - L_i(k)\gamma_i(k)\overline{H}_i\Phi]x(k-1) \\ &+ [\alpha(k-1)A - L_i(k)\gamma_i(k)\overline{H}_i\alpha(k-1)A]x(k-1) \\ &+ [\Gamma - L_i(k)\gamma_i(k)\overline{H}_i\Gamma]w(k-1) \\ &+ F_i(k)\tilde{x}_i(k-1) + L_i(k)\gamma_i(k)\overline{H}_i\overline{\alpha}_i(k) \\ &- L_i(k)D_i\theta_i(k) - L_i(k)V_i(k) \end{aligned} \tag{28}$$

For any $F_i(k)$ and $L_i(k)$, (11) is an unbiased estimator of $x(t)$. Then the following equations are calculated.

$$F_i(k) = \Phi - L_i(k)\overline{\gamma}_i\overline{H}_i\Phi \tag{29}$$

$$L_i(k)D_i = 0 \tag{30}$$

By substituting (29) and (30) into (28), we can derive a new form of $\tilde{x}_i(k)$ as

$$\begin{aligned} \tilde{x}_i(k) &= (\overline{\gamma}_i - \gamma_i(k))L_i(k)\overline{H}_ix(k) + (I_n - L_i(k)\overline{\gamma}_i\overline{H}_i)\Gamma w(k-1) \\ &+ (I_n - L_i(k)\overline{\gamma}_i\overline{H}_i)\Phi\tilde{x}_i(k-1) + L_i(k)\gamma_i(k)\overline{H}_i\overline{\alpha}_i(k) \\ &- L_i(k)V_i(k) + (I_n - L_i(k)\overline{\gamma}_i\overline{H}_i)\alpha(k-1)Ax(k-1) \end{aligned} \tag{31}$$

Substituting (31) into $P_i(k) = \mathrm{E}[\tilde{x}_i(k)\tilde{x}_i^{\mathrm{T}}(k)]$, we have

$$\begin{aligned} P_i(k) &= \sigma_i^2L_i(k)\overline{H}_i(X(k) - Q_{x\overline{\alpha}_i}(k) - Q_{x\overline{\alpha}_i}^{\mathrm{T}}(k))\overline{H}_i^{\mathrm{T}}L_i^{\mathrm{T}}(k) \\ &+ (\sigma_i^2/\overline{\gamma}_i)L_i(k)(\overline{H}_iQ_{xV_i}(k) + Q_{xV_i}^{\mathrm{T}}(k)\overline{H}_i^{\mathrm{T}})L_i^{\mathrm{T}}(k) \\ &+ (I_n - L_i(k)\overline{\gamma}_i\overline{H}_i)(-\Gamma Q_{wV_i} - \Phi Q_{\tilde{x}_iV_i}(k-1,k) \\ &+ \Phi Q_{\tilde{x}_i\overline{\alpha}_i}(k-1,k)\overline{H}_i^{\mathrm{T}}\overline{\gamma}_i + (Q_\alpha AX(k-1)A^{\mathrm{T}})^{\mathrm{T}}\overline{H}_i^{\mathrm{T}}\overline{\gamma}_i)L_i^{\mathrm{T}}(k) \\ &+ L_i(k)(-Q_{wV_i}^{\mathrm{T}}\Gamma^{\mathrm{T}} + \overline{\gamma}_i\overline{H}_iQ_\alpha AX(k-1)A^{\mathrm{T}} \\ &+ \overline{\gamma}_i\overline{H}_iQ_{\tilde{x}_i\overline{\alpha}_i}^{\mathrm{T}}(k-1,k)\Phi^{\mathrm{T}} - Q_{\tilde{x}_iV_i}^{\mathrm{T}}(k-1,k)\Phi^{\mathrm{T}})(I_n - L_i(k)\overline{\gamma}_i\overline{H}_i)^{\mathrm{T}} \\ &+ (I_n - L_i(k)\overline{\gamma}_i\overline{H}_i)(\Gamma Q_w\Gamma^{\mathrm{T}} + \Phi P_i(k-1)\Phi^{\mathrm{T}}) \\ &+ Q_\alpha AX(k-1)A^{\mathrm{T}})(I_n - L_i(k)\overline{\gamma}_i\overline{H}_i)^{\mathrm{T}} \\ &+ L_i(k)(Q_{V_i} + (\sigma_i^2 + \overline{\gamma}_i^2)\overline{H}_iQ_{\overline{\alpha}_i}(k)\overline{H}_i^{\mathrm{T}})L_i^{\mathrm{T}}(k) \\ &= \overline{P}_i(k) + L_i(k)C_i(k)L_i^{\mathrm{T}}(k) - L_i(k)G_i(k) - G_i^{\mathrm{T}}(k)L_i^{\mathrm{T}}(k) \end{aligned} \tag{32}$$

where $\overline{P}_i(k)$, $L_i(k)$, $C_i(k)$ and $G_i(k)$ are given by (17), (13), (16) and (15), respectively. The covariance matrix (19) -(25) are used in (32).

Next, we use Lagrange Multipliers Method to solve constrained problem (30)， Lagrange function is given as

$$J_i(k) = tr\{P_i(k)\} + 2tr\{\Lambda_i^{\mathrm{T}}(k)L_i(k)D_i\} \tag{33}$$

Take the derivation of (33) with respect to $L_i(k)$ and make the derivative resulting be zero, we get

$$L_i(k)C_i(k) + \Lambda_i(k)D_i^{\mathrm{T}} = G_i^{\mathrm{T}}(k) \tag{34}$$

Form a system of equations with constraint condition (30), the equations (30) and (34) can be written as follows

$$\begin{bmatrix} C_i^{\mathrm{T}}(k) & D_i \\ D_i^{\mathrm{T}} & 0 \end{bmatrix}\begin{bmatrix} L_i^{\mathrm{T}}(k) \\ \Lambda_i^{\mathrm{T}}(k) \end{bmatrix} = \begin{bmatrix} G_i(k) \\ 0 \end{bmatrix} \tag{35}$$

Applying Lemma 2, we obtain (13) and (14).

For $k = n_i t + p, p = 1,2,...,n_i - 1$, let $F_i(k) = \Phi$, $L_i(k) = 0$, then we get (26). From (1) and (26), we get the estimation error equation of the *i* th sensor as

$$\begin{aligned} \tilde{x}_i(k) &= \Phi x(k-1) + \alpha(k-1)Ax(k-1) \\ &+ \Gamma w(k-1) - \Phi\hat{x}_i(k-1) \\ &= \Phi\tilde{x}_i(k-1) + \alpha(k-1)Ax(k-1) + \Gamma w(k-1) \end{aligned} \tag{36}$$

Further from (36), we obtain

$$P_i(k) = \Gamma Q_w \Gamma^{\mathrm{T}} + \Phi P_i(k-1)\Phi^{\mathrm{T}} + Q_\alpha AX(k-1)A^{\mathrm{T}} \quad (37)$$

□

4 Optimal distributed fusion estimation

4.1 Estimation error Cross-covariance matrix

Theorem 3: The estimation error cross-covariance matrix between any two sensors has the following four cases.

Case 1: Both *i* th and *j* th sensors sample measurements at the state update time *k*, we have

$$\begin{aligned} P_{ij}(k) &= (I_n - L_i(k)\overline{\gamma}_i\overline{H}_i)(-\Gamma Q_{wV_j} - \Phi Q_{xV_j}(k-1,k) \\ &+\Phi Q_{x\bar{\alpha}_j}(k-1,k)\overline{H}_j^{\mathrm{T}}\overline{\gamma}_j + Q_\alpha AX(k-1)A^{\mathrm{T}}\overline{H}_j^{\mathrm{T}}\overline{\gamma}_j)L_j^{\mathrm{T}}(k) \\ &+L_i(k)(\overline{\gamma}_i\overline{H}_i Q_\alpha AX(k-1)A^{\mathrm{T}} + \overline{\gamma}_i\overline{H}_i Q_{x\bar{\alpha}_i}^{\mathrm{T}}(k-1,k)\Phi^{\mathrm{T}} \\ &-Q_{xV_i}^{\mathrm{T}}(k-1,k)\Phi^{\mathrm{T}} - Q_{wV_i}^{\mathrm{T}}\Gamma^{\mathrm{T}})(I_n - L_j(k)\overline{\gamma}_j\overline{H}_j)^{\mathrm{T}} \\ &+(I_n - L_i(k)\overline{\gamma}_i\overline{H}_i)(\Gamma Q_w\Gamma^{\mathrm{T}} + \Phi P_{ij}(k-1)\Phi^{\mathrm{T}} \\ &+Q_\alpha AX(k-1)A^{\mathrm{T}})(I_n - L_j(k)\overline{\gamma}_j\overline{H}_j)^{\mathrm{T}} \\ &+L_i(k)(Q_{V_iV_j} + \overline{\gamma}_i\overline{H}_i Q_{\bar{\alpha}_{ij}}(k)\overline{H}_j^{\mathrm{T}}\overline{\gamma}_j)L_j^{\mathrm{T}}(k) \end{aligned} \quad (38)$$

where $Q_{V_iV_j} = \mathrm{E}[V_i(k)V_j^{\mathrm{T}}(k)]$, $Q_{\bar{\alpha}_{ij}}(k) = \mathrm{E}[\bar{\alpha}_i(k)\bar{\alpha}_j^{\mathrm{T}}(k)]$

$$Q_{V_iV_j} = \overline{\gamma}_i\overline{\gamma}_j \sum_{m=0}^{\min(d_i,d_j)-1} \overline{H}_i\Phi^m\Gamma Q_w\Gamma^{\mathrm{T}}(\Phi^m)^{\mathrm{T}}\overline{H}_j^{\mathrm{T}} \quad (39)$$

$$Q_{\bar{\alpha}_{ij}}(k) = \sum_{m=0}^{\min(d_i,d_j)-1} Q_\alpha\Phi^m AX(k-m-1)A^{\mathrm{T}}(\Phi^m)^{\mathrm{T}} \quad (40)$$

Case 2: The *i* th sensor samples measurements while *j* th sensor does not sample measurements at moment *k,* we have

$$\begin{aligned} P_{ij}(k) &= (I_n - L_i(k)\overline{\gamma}_i\overline{H}_i)\Gamma Q_w\Gamma^{\mathrm{T}} \\ &+(I_n - L_i(k)\overline{\gamma}_i\overline{H}_i)\Phi P_{ij}(k-1)\Phi^{\mathrm{T}} - L_i(k)Q_{V_i\tilde{x}_j}(k,k-1)\Phi^{\mathrm{T}} \\ &-L_i(k)Q_{V_iw}\Gamma^{\mathrm{T}} + L_i(k)\overline{\gamma}_i\overline{H}_i Q_{\bar{\alpha}_i\tilde{x}_j}(k,k-1)\Phi^{\mathrm{T}} \\ &+(I_n - L_i(k)\overline{\gamma}_i\overline{H}_i)Q_\alpha AX(k-1)A^{\mathrm{T}} \\ &+L_i(k)\overline{\gamma}_i\overline{H}_i Q_\alpha AX(k-1)A^{\mathrm{T}} \end{aligned} \quad (41)$$

Case 3: The *j* th sensor samples measurements while *i* th sensor does not sample measurements at moment *k,* we have

$$\begin{aligned} P_{ij}(k) &= (I_n - L_j(k)\overline{\gamma}_j\overline{H}_j)\Gamma Q_w\Gamma^{\mathrm{T}} \\ &+(I_n - L_j(k)\overline{\gamma}_j\overline{H}_j)\Phi P_{ij}(k-1)\Phi^{\mathrm{T}} - L_j(k)Q_{V_j\tilde{x}_i}(k,k-1)\Phi^{\mathrm{T}} \\ &-L_j(k)Q_{V_jw}\Gamma^{\mathrm{T}} + L_j(k)\overline{\gamma}_j\overline{H}_j Q_{\bar{\alpha}_j\tilde{x}_i}(k,k-1)\Phi^{\mathrm{T}} \\ &+(I_n - L_j(k)\overline{\gamma}_j\overline{H}_j)Q_\alpha AX(k-1)A^{\mathrm{T}} \\ &+L_j(k)\overline{\gamma}_j\overline{H}_j Q_\alpha AX(k-1)A^{\mathrm{T}} \end{aligned} \quad (42)$$

Case 4: Neither *i* th nor *j* th sensor samples measurements at moment *k*, we have

$$P_{ij}(k) = \Phi P_{ij}(k-1)\Phi^{\mathrm{T}} + Q_\alpha AX(k-1)A^{\mathrm{T}} + \Gamma Q_w\Gamma^{\mathrm{T}} \quad (43)$$

Proof. Define $P_{ij}(k) = \mathrm{E}[\tilde{x}_i(k)\tilde{x}_j^{\mathrm{T}}(k)]$. For case 1, we obtain the error cross-covariance matrix (38) according to equation (31).

For case 2, substituting (36) and (31) into $P_{ij}(k)$ yields (41). Similarly, we have (42) in case 3. In case 4, substituting (36) into the $P_{ij}(k)$, we have (43). □

4.2 Distributed fusion filter

The matrix-weighted fusion algorithm [25] is applied to obtain the distributed optimal fusion estimator as

$$\hat{x}_0(t) = \sum_{i=1}^{l} \Omega_i\hat{x}_i(t) \quad (44)$$

$$\Omega(t) = (e^{\mathrm{T}}\Sigma(t)^{-1}e)^{-1}e^{\mathrm{T}}\Sigma(t)^{-1} \quad (45)$$

$$P_0(t) = (e^{\mathrm{T}}\Sigma(t)^{-1}e)^{-1} \quad (46)$$

where $e = [I_n, I_n, \ldots, I_n]_{n\times nL}^{\mathrm{T}}$, $\Omega(k) = [\Omega_1(k), \Omega_2(k), \ldots, \Omega_L(k)]$, $\Sigma(k) = (P_{ij}(k))_{nL\times nL}$, $P_{ii}(k) = P_i(k)$, $i, j = 1,2,\ldots,L$. $\hat{x}_i(k)$ is the local estimator of the *i* th sensor.

5 Simulation Research

Consider a numerical example to demonstrate the effectiveness of the proposed method, the coefficient matrix shown as below

$$\Phi = \begin{bmatrix} 0.95 & 0 \\ 0.8 & 0.2 \end{bmatrix}, \quad A = \begin{bmatrix} 0.1 & 0.05 \\ 0.05 & 0.1 \end{bmatrix}, \quad \Gamma = \begin{bmatrix} 0.8 \\ 0.6 \end{bmatrix},$$

$$H_1 = \begin{bmatrix} 1 & 2 \\ 0 & 1 \end{bmatrix}, \quad H_2 = \begin{bmatrix} 1 & 0 \\ 0 & 1 \end{bmatrix}, \quad H_3 = \begin{bmatrix} 2 & 1 \\ 1 & 1 \end{bmatrix}, \quad D_1 = \begin{bmatrix} 1 \\ 1 \end{bmatrix},$$

$$D_2 = \begin{bmatrix} 1 \\ 2 \end{bmatrix}, \quad D_3 = \begin{bmatrix} 1 \\ 3 \end{bmatrix}, \quad Q_{v_1} = \begin{bmatrix} 0.3 & 0 \\ 0 & 0.3 \end{bmatrix},$$

$$Q_{v_2} = \begin{bmatrix} 0.15 & 0 \\ 0 & 0.15 \end{bmatrix}, \quad Q_{v_3} = \begin{bmatrix} 0.1 & 0 \\ 0 & 0.1 \end{bmatrix}, \quad \theta_1(n_1t) = 3,$$

$\theta_2(n_2t) = 0.1t$, $\theta_3(n_3t) = \sin(t)$, $d_1 = 3$, $d_2 = 1$, $d_3 = 2$. $n_1 = 2$, $n_2 = 3$, $n_3 = 4$, $Q_w = 1$, $Q_\alpha = 0.04$.

The probability function of $\gamma_i(n_it)$ is $p_1(s), i = 1,2,3$.

$$p_1(s) = \begin{cases} 0.1, s = 0 \\ 0.2, s = 0.5 \\ 0.7, s = 0.9 \end{cases}, p_2(s) = \begin{cases} 0.1, s = 0.1 \\ 0.1, s = 0.4 \\ 0.3, s = 0.6 \\ 0.5, s = 0.8 \end{cases}, p_3(s) = \begin{cases} 0.1, s = 0 \\ 0.2, s = 0.2 \\ 0.3, s = 0.6 \\ 0.4, s = 1 \end{cases}$$

We can calculate that $\overline{\gamma}_1 = 0.73$, $\overline{\gamma}_2 = 0.63$, $\overline{\gamma}_3 = 0.62$, $\sigma_1^2 = 0.0841$, $\sigma_2^2 = 0.0481$, $\sigma_3^2 = 0.1316$. The initial value is $x(0) = \begin{bmatrix} 0 & 0 \end{bmatrix}^{\mathrm{T}}$, $P_0 = 0.1I_2$. Take 300 sampling data.

The accuracy of the local estimator and the distributed fusion estimator is compared using the root mean square error (RMSE). The formula for calculating RMSEs are computed as

$$\mathrm{RMSE}_i = \sqrt{\frac{1}{N}\sum_{j=1}^{N}(x^j(t) - \hat{x}_i^j(t))^2}, i = 1,2,3,0$$

where $i = 1,2,3$ represents the local estimator, while $i = 0$ represent the distributed fusion estimator, *N*=600 is the number of Monte Carlo runs.

Fig. 1 compares the estimated values and the true values of the fusion estimator. It illustrates that our algorithm can effectively mitigate the impact of various disturbances on the performance of the fusion estimator.

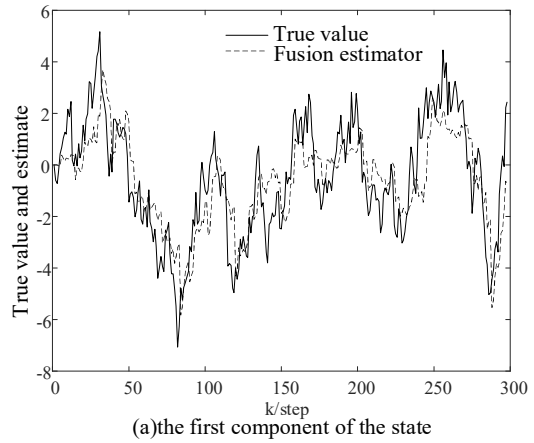

(a)the first component of the state

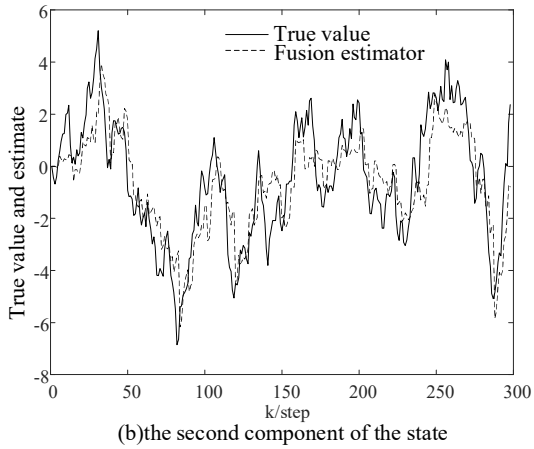

(b)the second component of the state

Fig. 1: The state and estimate of the fusion estimator

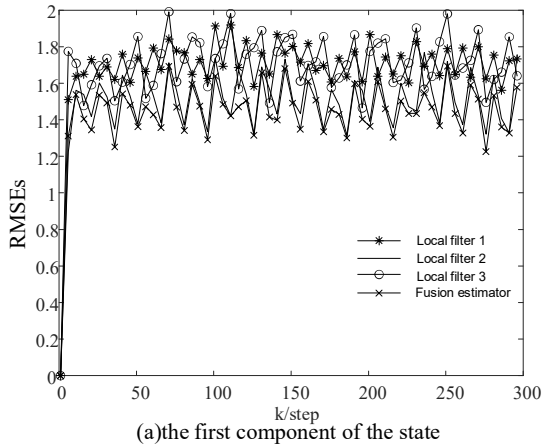

(a)the first component of the state

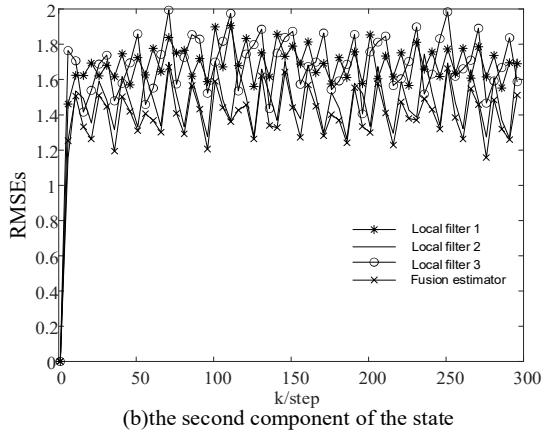

(b)the second component of the state

Fig. 2: Comparison of RMSE of local filters and distributed fusion filter

Fig. 2 compares the RMSEs of the three local filters and the fusion estimator. In Fig. 2, the RMSE of the distributed fusion estimator is lower than that of the three local filters., which indicates that the fusion estimator performs better than local filters, has the best estimation accuracy.

6 Conclusion

This paper considers the state estimation problem for linear discrete system with multiplicative noise in the state, fading measurements, time delays, and unknown inputs and multi-rate sampling. The local filter is performed using a filter that does not rely on information about the unknown inputs. Then, the estimation error cross-covariance matrices between any two estimators are derived. Finaly, the optimal matrix-weighted distributed fusion estimator is proposed.

References

[1] H. E. Doran, Estimation under exact linear time-varying constraints, with an application to population projections, *Journal of Forecasting*, 1996, 15(7): 527-541.

[2] P. K. Kitanidis, Unbiased minimum-variance linear state estimation, *Automatica*, 1987, 23(6): 775-778.

[3] S. Gillijns and B. D. Moor, Unbiased minimum-variance input and state estimation for linear discrete-time systems with direct feedthrough, *Automatica*, 2007, 43(5): 934-937.

[4] Y. Shi, C. Liu, X. Shen, et al. Minimum-Variance unbiased unknown input and state estimation for multi-agent system with heterogeneous unknown input, in *Proceedings of IEEE 8th Annual International Conference on CYBER Technology in Automation, Control, and Intelligent Systems*, 2018: 926-931.

[5] T. Rhouma, J. Y. Keller, and M. N. Abdelkrim, A Kalman filter with intermittent observations and reconstruction of data losses, *International Journal of Applied Mathematics and Computer Science*, 2022, 32(2):241-253.

[6] H. Kong, M. Shan, D. Su, et al. Filtering for systems subject to unknown inputs without a priori initial information, *Automatica*, 2020, 120: 109122.

[7] H. Kim, P. Guo, M. Zhu, et al. Simultaneous input and state estimation for stochastic nonlinear systems with additive unknown inputs, *Automatica*, 2020, 111: 108588.

[8] L. Meyer, D. Ichalal, and V. Vigneron, An unknown input extended kalman filter for nonlinear stochastic systems, *European Journal of Control*, 2020, 56: 51-61.

[9] B. Qu, Z. Wang, B. Shen, et al. Event-Based joint state and unknown input estimation for energy networks: Handling multi-machine power grids, *IEEE Transactions on Network Science and Engineering*, 2023, 10(1): 253-264.

[10] H. Geng, Z. Wang, Y. Liang, et al. State estimation for asynchronous sensor systems with Markov jumps and multiplicative noises, *Information Sciences*, 2017 417: 1-19.

[11] S. Sun, F. Peng, and H. Lin, Distributed asynchronous fusion estimator for stochastic uncertain systems with multiple sensors of different fading measurement rates, *IEEE Transactions on Signal Processing*, 2018, 66(3): 641-653.

[12] S. Fan, H. Yan, H. Zhang, et al. Distributed dimensionality reduction fusion estimation for stochastic uncertain systems with fading measurements subject to mixed attacks, *IEEE Transactions on Systems, Man, and Cybernetics: Systems*, 2022, 52(11): 7053-7064.

[13] J. Lin, G. Jiang, Z. Gao, et al. State and input simultaneous estimation for discrete-time switched singular delay systems with missing measurements, *International Journal of Robust and Nonlinear Control*, 2017, 27(16): 2749-2772.

[14] B. Cui, X. Song, and X. Liu, Unbiased steady minimum variance estimation for systems with measurement-delay and

unknown inputs, *Applied Mathematics and Computation*, 2019, 356(2019): 379-391.
[15] P. Zhang, S. Zhou, P. Liu, et al. Distributed ellipsoidal intersection fusion estimation for multi-sensor complex systems, *Sensors*, 2022, 22(11): 4306.
[16] A. Chakrabarty, E. Fridman, S. Żak, et al. State and unknown input observers for nonlinear systems with delayed measurements, *Automatica*, 2018, 95: 246-253.
[17] S. Chu, H. Qian, and V. Sreeram, Robust filtering for spacecraft attitude estimation systems with multiplicative noises, unknown measurement disturbances and correlated noises, *Advances in Space Research*, 2023, 72(9): 3619-3630.
[18] A. Emami, R. Araújo, and A. Asvadi, Distributed simultaneous estimation of states and unknown inputs, *Systems & Control Letters*, 2020, 138(2020): 104660.
[19] Z. Peng, Y. Zhang, G. Wen, et al. Optimal distributed filter for state and unknown input estimations in multi-sensor networks, *IEEE Transactions on Circuits and Systems II: Express Briefs*, 2023, 70(11): 4128-4132.
[20] D. Yu, Y. Xia, L. Li, et al. Distributed consensus-based estimation with unknown inputs and random link failures, *Automatica*, 2020, 122: 109259.
[21] L. Li, H. Yang, Y. Xia, et al. Event-Based distributed state estimation for linear systems under unknown input and false data injection attack, *Signal Processing*, 2020, 170: 107423.
[22] A. Basit, M. Tufail, M. Rehan, et al. Distributed state and unknown input estimation under denial-of-Service attacks: A dynamic event-triggered approach, *IEEE Transactions on Circuits and Systems II: Express Briefs*, 2023, 70(6): 2266-2270.
[23] Z. Song, X. Yang, J. Ma. Linear Optimal Estimators for Systems with Multiplicative Noises and Time-Correlated Additive Noise, in Proceedings of 39th Chinese Control Conference, 2020: 2735-2740.
[24] T. T. Lu and S. H. Shiou. Inverses of 2×2 Block Matrices，Computers & Mathematics with Applications, 2002, 43(1-2): 119-129.
[25] S. Sun and Z. Deng, Multi-sensor optimal information fusion Kalman filter, *Automatica*, 2004, 40(6): 1017-1023.

Proceedings of the 3rd Conference on Fully Actuated System Theory and Applications
May 10-12, 2024, Shenzhen, China

A Novel Particle Filter Based on One-Step Smoothing for Nonlinear System with Missing Measurements

Zhenrong Yang[1], Xing Zhang[1], Yushan Xiao[1]
1. School of Mathematics and Information Science, Guangxi University, Nanning 530003, P. R. China
E-mail: xingz@gxu.edu.cn

Abstract: This paper proposes a novel particle filter based on one-step smoothing for nonlinear systems with missing measurements. This filter iteratively employs a one-step smoother to improve the efficiency of importance sampling in bootstrap particle filtering through incorporating current measurement information into the apriori distribution. A simulation example of a target tracking model is given to illustrate that the proposed algorithm improves the sampling efficiency and estimation accuracy, which effectively limits the particle degradation phenomenon.

Key Words: Particle Filter, Nonlinear Filter, One-Step Particle Smoother, Sequential Importance Sampling, Missing Measurement

1 Introduction

Nonlinear filtering based on Bayesian framework has been intensively studied due to its wide application in a variety of directions [1, 2]. Generally, most traditional nonlinear filtering is based on the assumption that the measurements always contain consecutive useful signals. However, in practical applications such as target tracking, the measurements cannot always contain consecutive useful signals. There may be a nonzero probability that any observation consists of noise alone if the target is absent. In the existing literature such as Wang et al. [3], the situation where observation only consists of noise is termed the phenomenon of missing measurements. The phenomena of missing measurements are inevitable in many practical situations because of certain factors of unreliable observations. For instance, the situations contain intermittent failures in the observation mechanism, fading phenomena in the propagation channels, accidental loss of some measurements, and inaccessibility of the data at some times [4–12]. Generally speaking, the phenomenon of missing measurements is characterized by the Markov chain or by the Bernoulli distributed random variable, and the latter is common [13–16]. In this paper, we study a class of nonlinear systems with missing measurement phenomena characterized by random variables obeying the Bernoulli distribution.

Over the past few years, many efforts have been made to solve the nonlinear filtering problem with missing measurements. In Hermoso-Carazo and Linares-Perez [13], an extended Kalman filter (EKF) and an unscented Kalman filter (UKF) were addressed for a class of nonlinear discrete-time stochastic systems with missing measurements. In Xu et al. [14], UKF was investigated for the nonlinear systems with correlated noises and missing measurements. In Chen Yang and Huajing Fang [16], UKF for a class of nonlinear discrete stochastic systems with random packet loss is studied and gives an example to solve the problem of tracking systems and random packet loss. In Xing Zhang [17], a high-degree cubature Kalman filter (HCKF) was proposed for the nonlinear system with missing measurements, and a six-dimensional numerical example was utilized to demonstrate that HCKF was more accurate and stable than EKF and UKF. All the above filtering methods for nonlinear systems with missing measurements are Kalman-like filters, which rely on the Gaussian assumption that introduces a large error in the estimation results of the non-Gaussian filter.

Particle filter (PF) does not assume linear and/or Gaussian property, in which the filtering density function is approximated by a set of random weighted samples. In the viewpoint of sequential importance sampling, the random samples are generated sequentially from an importance function and the importance weight is the ratio of the filtering function and the importance function [18]. PF has many applications [19–22] and it performs relatively better in many aspects than other nonlinear filtering methods [23].

Currently, PFs have been used for nonlinear systems with missing measurements. In the literature [24], the bootstrap particle filter (BPF) is applied to nonlinear systems with one-step sensor delay and observation missing. BPF is the standard and classical particle filter proposed in [25]. However, the importance function of BPF may not be close to the filtering distribution because the importance function depends solely on the state equation and it does not have any information from the current measurement, which appears in the filtering distribution. This will lead to a large variance of the importance weight, which brings low sampling efficiency and unreliable estimation. It is well known that the efficiency of PF heavily depends on the choice of the importance function. Many efforts have been devoted to designing an appropriate importance function to improve the performance of PF, such as the intelligent particle filter [26], the augmented particle filter [27], and the robust particle filter [28]. However, these efforts mentioned above are used for nonlinear systems based on the assumption that the measurements always contain consecutive useful signals. Although Gaussian particle filters are applied to nonlinear systems with missing measurements in [29] to improve sampling efficiency, the study of selecting appropriate importance functions for nonlinear systems with missing measurements is still open.

In this paper, we propose a novel particle filter based on one-step smoothing for nonlinear systems with missing measurements. Different from the importance function of standard BPF does not have any information from the current measurement, this filter iteratively employs a new one-step particle smoother to incorporate current measurement infor-

mation into the importance function in some manner. This suggested iteration scheme to the one-step particle smoothing is to further utilize the current measurement in hope of obtaining a better importance function. The effectiveness of the proposed particle filter is shown in the simulation study on the target tracking model with missing measurements.

The main contributions of this paper are as follows: (1) Providing a method of constructing new importance functions for nonlinear systems with missing measurements by adding the current measurement information to the importance function; (2) Designing a novel particle filtering algorithm for nonlinear systems with missing measurements, which effectively limit particle degradation phenomena and improve estimation accuracy.

The paper is organized as follows. In Section 2, the nonlinear system with missing measurements is introduced. In Section 3, after reviewing the bootstrap particle filter for the nonlinear system with measurements, a novel particle filter based on one-step smoothing is proposed through iteration to incorporate the current measurement into the importance function for particle filtering. In Section 4, a simulation example of the target tracking model is studied using our proposed particle filtering method. Finally, the conclusion is drawn in Section 5.

2 Nonlinear System with Missing Measurements

In this paper, we consider the following nonlinear system with missing measurements in which the phenomenon of missing measurements is characterized by the Bernoulli distributed random variable:

$$x_k = f_k(x_{k-1}) + \omega_{k-1}, \tag{1}$$

$$z_k = \lambda_k h_k(x_k) + v_k, \tag{2}$$

where $x_k \in \mathrm{R}^n$ and $z_k \in \mathrm{R}^m$ are the state vector and observation at discrete time k, respectively. The two functions $f(\cdot)$ and $h(\cdot)$ are known nonlinear functions. The system noise $\omega_k \in \mathrm{R}^n$ and observation noise $v_k \in \mathrm{R}^m$ are mutually independent Gaussian white noises. Let $\omega_k \sim N(0, Q_k)$ and $v_k \sim N(0, R_k)$.

Here, the multiplicative noise λ_k, which describes the phenomenon of missing measurements, obeys the Bernoulli distribution and has the following statistical properties,

$$\begin{aligned} &P(\lambda_k = 1) = E(\lambda_k) = \alpha, \\ &P(\lambda_k = 0) = 1 - E(\lambda_k) = 1 - \alpha, \end{aligned} \tag{3}$$

where $\alpha \in [0, 1]$ is a known scalar. The multiplicative noise λ_k and other noise signals are mutually independent. Moreover, we assume the initial state x_0 is drawn from $p(x_0)$. The initial state and all the noise signals are mutually independent.

Remark 1 *In the measurement model* (2) *at time k, if the sensor receives the data successfully, i.e.,* $\lambda_k = 1$*, then* $z_k = h_k(x_k) + v_k$*. In this case,* $z_k|x_k \sim \mathrm{N}(h_k(x_k), R_k)$ *because of* $v_k \sim \mathrm{N}(0, R_k)$*. If the measurement is missing and the sensor only receives the noise, i.e.* $\lambda_k = 0$*, then* $z_k = v_k$*. In this case,* $z_k|x_k \sim \mathrm{N}(0, R_k)$*.*

For convenience we denote $x_{0:k} \triangleq \{x_0, \cdots, x_k\}$ and $z_{0:k} \triangleq \{z_0, \cdots, z_k\}$. For system (1)-(2), we shall quote a property in Bayesian filtering framework:

Property 1 *The state vector* x_k *obeys the first-order Markovian process:* $p(x_k|x_{0:k-1}, z_{0:k}) = p(x_k|x_{k-1})$*. The measured output of the sensor* z_k *is only dependent on state* x_k*, i.e.* $p(z_k|x_{0:k}, z_{0:k-1}) = p(z_k|x_k)$*.*

Based on this property, the bootstrap particle filter is developed in the Bayesian filtering framework for the nonlinear system with missing measurement (1)-(2). The following section will firstly review the bootstrap particle filter via reference [25], and then give a novel particle filter based on one-step smoothing through iteration to incorporate the current measurement into the importance function for the nonlinear system with missing measurements.

3 A Novel Bootstrap Particle Filter Base on One-Step Smoother for Nonlinear System with Missing Measurements

3.1 Bootstrap particle filter

In the framework of Bayesian, the posterior distribution of the hidden state x_k can be written as

$$p(x_k|z_{0:k}) = \frac{p(z_k|x_k)p(x_k|z_{0:k-1})}{p(z_k|z_{0:k-1})} \tag{4}$$

Since $p(z_k|z_{0:k-1})$ is a constant, (4) can be simplified as

$$p(x_k|z_{0:k}) \propto p(z_k|x_k)p(x_k|z_{0:k-1}) \tag{5}$$

where $\propto$ means to be proportional to. For the nonlinear systems, the analytic solution of the posterior distribution $p(x_k|z_{0:k})$ is often difficult to obtain. Particle filter approximates it using a set of random samples $\{x_k^{(i)} : i = 1, \ldots, N\}$.

To deal with the difficulty in sampling from the posterior distribution, the importance sampling technique is introduced. Samples are drawn from an importance function that can be easily sampled. Suppose the importance function is termed as $q(x_k|z_{0:k})$. Combined with (5), the importance weight for each particle can be formulated, i.e.,

$$\begin{aligned} w_k^{(i)} &= \frac{p(x_k^{(i)}|z_{0:k})}{q(x_k^{(i)}|z_{0:k})} \\ &\propto \frac{p(z_k|x_k^{(i)})p(x_k^{(i)}|z_{0:k-1})}{q(x_k^{(i)}|z_{0:k})} \end{aligned} \tag{6}$$

where $w_k^{(i)}$ is the importance weight. Denote the normalized $w_k^{(i)}$ as $\overline{w}_k^{(i)}$. Thus, the posterior distribution $p(x_k|z_{0:k})$ can be approximated by particles as

$$p(x_k|z_{0:k}) \approx \sum_{i=1}^{N} \overline{w}_k^{(i)} \delta(x_k - x_k^{(i)})$$

where $\delta(.)$ is the Dirac delta measure. Then the posterior distribution $p(x_k|z_{0:k})$ can be obtained recursively by reference [30] as follows.

1) **Prediction.** Suppose a set of random samples $x_{k-1}^{(i)}$ has been sampled from the density function $p(x_{k-1}|z_{0:k-1})$, and each sample $x_{k-1}^{(i)}$ is passed through the dynamic model (1) to get a new sample $x_k^{(i)}$, i.e.,

$$x_k^{(i)} = f(x_{k-1}^{(i)}) + \omega_{k-1}^{(i)}$$

where $\omega_{k-1}^{(i)}$ is a sample drawn from the probability density function of the system noise $p(\omega_{k-1})$. Then $x_k^{(i)}$ can be regard as the samples of $p(x_k|z_{0:k-1})$.

2) **Update.** In the view of the bootstrap particle filter, the importance function is $p(x_k|z_{0:k-1})$, then we have the weight $w_k^{(i)}$ =$p(z_k|x_k^{(i)})$ from equation (6), i.e., the weights are equal to the likelihood value. When receiving the measurements z_k, the likelihood value of each sample $x_k^{(i)}$ is calculated, thus obtaining the normalized weight of each sample $x_k^{(i)}$:

$$\overline{w}_k^{(i)} = \frac{p(z_k|x_k^{(i)})}{\sum_{i=1}^{N} p(z_k|x_k^{(i)})} \tag{7}$$

3) **Resampling the updated particle set** $\{x_k^{(i)}, \overline{w}_k^{(i)}\}$.

By using BPF for nonlinear systems with missing measurements (1)-(2), the formula for calculating the importance weight $w_k^{(i)}$ is the core. It can be obtained through the following Theorem 1.

Theorem 1 *The importance weight* $w_k^{(i)}$ *for system* (1)-(2) *can be computed recursively as*

$$w_k^{(i)} = (\alpha p_{v_k}(z_k - h_k(x_k^{(i)})) + (1-\alpha)p_{v_k}(z_k)) \tag{8}$$

where p_{v_k} *stands for the probability density functions of observation noise* v_k.

Proof: Since the output of the sensor z_k may be v_k or $h_k(x_k)$ if occurs missing measurements or not. In addition, the measurement z_k depends on the value of the Bernoulli random variable λ_k. Since λ_k is independent with other signals, we can evaluate the likelihood density $p(z_k|x_k)$ as follows:

- If $\lambda_k = 1$, we can obtain the equation $z_k = h_k(x_k)+v_k$ by (2). Hence, it is easy to see that $z_k - h_k(x_k)$ and v_k have the same distribution functions if x_k is known, i.e.,

$$p(z_k|x_k, \lambda_k = 1) = p_{v_k}(z_k - h_k(x_k)) \tag{9}$$

- If $\lambda_k = 0$, we can obtain the equation $z_k = v_k$ by (2). Then, similar to (9), we have

$$p(z_k|x_k, \lambda_k = 0) = p_{v_k}(z_k). \tag{10}$$

Based on the similar derivation in [24], the likelihood density function $p(z_k|x_k)$ can be calculated by using equations (9) and (10) as follows:

$$\begin{aligned} p(z_k|x_k) &= \int p(z_k, \lambda_k|x_k)d\lambda_k \\ &= \int p(z_k|x_k, \lambda_k)p(\lambda_k|x_k)d\lambda_k \\ &= \int p(z_k|x_k, \lambda_k)p(\lambda_k)d\lambda_k \\ &= \alpha p(z_k|x_k, \lambda_k = 1) \\ &\quad +(1-\alpha)p(z_k|x_k, \lambda_k = 0) \\ &= \alpha p_{v_k}(z_k - h_k(x_k)) + (1-\alpha)p_{v_k}(z_k). \end{aligned} \tag{11}$$

From equation (11), we have the importance weight $w_k^{(i)}$. This proof is complete. ■

As mentioned in [25], in the sequential importance resampling framework, BPF is equivalent to choosing the prior $p(x_k|z_{0:k-1})$ as the importance function, and the likelihood function $p(z_k|x_k)$ is the corresponding importance weight. It can be seen that the importance function of BPF may not be close to the filtering distribution because the importance function $p(x_k|z_{0:k-1})$ does not have any information from the current measurement z_k, which appears in the filtering distribution $p(x_k|z_{0:k})$. This could lead to a large variance of the importance weight, and bring low sampling efficiency and unreliable estimation. It is very natural that if we incorporate the newly received measurement information z_k into the importance function in some manner, then the efficiency of the particle filter may be significantly improved.

3.2 A novel bootstrap particle filter based on one-step smoothing by iteration

In this subsection, we proposed a novel bootstrap particle filter based on one-step smoothing by iteration. This suggested iteration scheme is to further utilize the newly received measurement information z_k in hope of obtaining a better importance function and improving the accuracy of the state estimation. Suppose that we are in time step k and a set of random samples $x_{k-1}^{(i)}$ has been sampled from $p(x_{k-1}|z_{0:k-1})$, then sample $x_k^{(i)}$ through the prediction phase of BPF and calculate its corresponding weight $w_k^{(i)}$ through the update phase of BPF and Theorem 1 for $i = 1, \ldots, N$. The weighted samples $\{x_{k-1}^{(i)}, w_k^{(i)}\}_{i=1}^N$ is proper with respect to $p(x_{k-1}|z_{0:k})$ which can be called the one-step particle smoother via reference [31]. The one-step smoothing scheme with iteration is shown as follows.

- Iteration initialisation. Denote the one-step particle smoother $\{x_{k-1}^{(i)}, w_k^{(i)}\}$ by $\{x_{k-1,0}^{(i)}, w_{k,0}^{(i)}\}$ as the initial values of the iteration, where $i = 1, \ldots, N$.
- Get sample $x_{k,j}^{(i)} = f(x_{k-1,j-1}^{(i)}) + \omega_{k-1,j-1}^{(i)}$ with $\omega_{k-1,j-1}^{(i)}$ drawing from $p(\omega_{k-1})$.
- Compute $w_{k,j}^{(i)} = p(z_k|x_{k,j}^{(i)})$ through Theorem 1.
- Denote $\{x_{k-1,j}^{(i)}, w_{k,j}^{(i)}\} = \{x_{k-1,j-1}^{(i)}, w_{k,j}^{(i)}\}$.
- Stop the iteration if a prescribed stopping condition is satisfied.

It can be seen that the bigger $p(z_k|x_{k,j}^{(i)})$, the bigger $w_{k,j}^{(i)}$. Denote the distribution obtained after the jth iteration as $p_j(x_{k-1}|z_{0:k})$ which can be seen as the importance function of the proposed particle filter. Going along with iterations, the significant region of $p_j(x_{k-1}|z_{0:k})$ is gradually modified so that for any sample from it, the state x_k propagated by this sample will fall into the high likelihood region of $p(z_k|x_k)$ with more odds. Thus the current measurement z_k can be used to judge the distance between the filtering distribution and the importance function determined by the iterations. In other words, when the distance between the filtering distribution and the importance function determined by the iterations is sufficiently small, we can stop the iterations.

The stopping rule is adopted as follows. Firstly, select a small positive number ρ as the threshold. Then, calculating the observed predicted value z_{pr} of particle $x_k^{(i)}$ by the

known nonlinear observation functions $h(\cdot)$ through

$$z_{pr} = \lambda_k h(x_k^{(i)}).$$

Secondly, calculate the distance between the observed predicted value z_{pr} and the newly received measurement z_k through

$$d_{z_k} = ||z_k - z_{pr}||.$$

Finally, stop the iterations if $d_{z_k} < \rho$. This stopping rule stems from the recognition that if the obtained importance function is near to the filtering function, then the predicted measurement based on it will be near to the real measurement.

The particle filter based on one-step smoothing with iteration uses the current measurement z_k to judge the distance between the filtering distribution and the importance function determined by the iterations. If the value of the observation residual does not exceed a set threshold ρ, then we receive sample $x_k^{(i)}$, else reject sample $x_k^{(i)}$, continue to draw a sample $x_k^{(i)}$ instead and repeat the above operation until we get N samples $x_k^{(i)}$. The theory stems from the realization that if the prediction of the sample observation is close to the true measurement, the obtained trial distribution is close to the filtered distribution. Then the weights and normalization for each sample $x_k^{(i)}$ are obtained by equation (8) and equation (7), respectively. Resampling the particle set $\{x_k^{(i)}, \overline{w}_k^{(i)}\}$.

For the nonlinear system with missing measurement (1)-(2), the novel bootstrap particle is based on one-step smoothing through iteration to incorporate the current measurement into the importance function for particle filtering. It is further utilize the newly received measurement information z_k to obtain a better importance function and improve the accuracy of the state estimation.

3.3 The novel bootstrap particle based on one-step smoothing algorithm

According to Theorem 1 and the one-step smoothing technique by iteration, an algorithm can be established to obtain a novel bootstrap particle filter for the nonlinear system with missing measurement (1)-(2). We design this new filter as Algorithm 1.

Algorithm 1. a novel bootstrap particle filter with missing measurements

Step I. Initialisation:

Draw state particles $\{x_0^{(i)}\}_{i=1}^N$ from prior $p(x_0)$.

For $k = 1, 2, \ldots$

Step II. Sequential Importance sampling and resampling:

1. Get new sample $x_k^{(i)}$ by dynamic model (1).

$x_k^{(i)}$=$f(x_{k-1}^{(i)})$+$w_{k-1}^{(i)}$.

2. Get new sample $x_{k+1}^{(i)}$ by dynamic model (1).

$x_{k+1}^{(i)}$=$f(x_k^{(i)})$+$w_k^{(i)}$.

3. Calculating predictions of observations .

$z_{pr} = \lambda_{k+1} h_k(x_{k+1}^{(i)})$.

4. Calculating the observed residuals of the particles.

$d_{z_{k+1}}^{(i)} = ||z_{k+1} - z_{pr}||$.

5. Judging whether the residuals of observation are larger than the threshold value.

For j=1:N

If $d_{z_{k+1}}^{(i)} < \rho$

$x_k^{(j)}$=$x_k^{(i)}$

else

Return to the Step 1-5.

6. Evaluate importance weights, $x_k^{(j)}$ is denoted as $x_k^{(i)}$.

For $i = 1, \ldots, N$,

$w_k^{(i)} = (\alpha p_{v_k}(z_k - h_k(x_k^{(i)})) + (1-\alpha) p_{v_k}(z_k))$.

end

7. Normalise importance weights:

$\overline{w}_k^{(i)} = \frac{w_k^{(i)}}{\sum_{i=1}^N w_k^{(i)}}$.

8. Resample by using the sequential importance sampling, and all particle weights are set as $\frac{1}{N}$, i.e.,

$\{\widetilde{x}_k^{(i)}, \widetilde{w}_k^{(i)} = \frac{1}{N}\}_{i=1}^N$ = Resample$\{x_k^{(i)}, \overline{w}_k^{(i)}\}_{i=1}^N$.

9. Compute the state estimation

$\widehat{x}_k = \sum_{i=1}^N \widetilde{x}_k^{(i)} \widetilde{w}_k^{(i)}$.

Step III. Return to the Step II.

The end.

4 Simulation

This section will show a numerical example to compare the performance of the proposed novel bootstrap particle based on one-step smoothing (NPF) with the standard bootstrap particle filter (BPF). A MATLAB program simulates the signal and observation values and provides the different filtering estimates.

Consider the following nonlinear discrete stochastic systems:

$$x_k = \begin{bmatrix} 1 & T & 0 & 0 \\ 0 & 1 & 0 & 0 \\ 0 & 0 & 1 & T \\ 0 & 0 & 0 & 1 \end{bmatrix} x_{k-1} + w_{k-1}$$

$$z_k = \lambda_k \sqrt{(x_{1,k} - x_s)^2 + (x_{3,k} - y_s)^2} + v_k$$

where $x_k = [x_{1,k}, x_{2,k}, x_{3,k}, x_{4,k}]^{\mathrm{T}}$, $x_{1,k}$ and $x_{3,k}$ are the positions of the target at moment k, $x_{2,k}$ and $x_{4,k}$ are the velocities of the target at moment k; w_k and v_k are Gaussian white noises with covariance matrices $Q_k = diag([2.5, 5, 2.5, 5])$ and $R_k = 2$, respectively; x_s and y_s are the locations of randomly deployed observatories; $T = 1$. Let $w_0 = [2, 2, 2, 2]^{\mathrm{T}}$,$P_0 = 2I$, where I is identity matrix, and $\alpha = 0.7$.

We set 100 time steps and $N = 100$ particles. The true target tracks of $x_{1,k}$ and $x_{3,k}$ with their estimated tracks by NPF and BPF are shown in Fig.1. The figures show that NPF algorithm has superior performance than BPF algorithm.

For this example, the estimation accuracy of several algorithms is also compared by root mean square error (RMSE).

$$RMSE(k) = \sqrt{\frac{1}{M}\sum_{n=1}^{M}(\widehat{x}_{k,n} - x_{k,n})^2} \qquad (12)$$

where $\widehat{x}_k$ is the estimate of x_k. The RMSEs of the estimation results for $x_{1,k}$ and $x_{3,k}$ by NPF and BPF are given by Fig.2 and Fig.4, respectively. It can be seen from the Fig.2 that the error of BPF is relatively large , especially after 30 steps. In Fig.4, It can be shown that NPF are more accurate than BPF. Both of them have very close estimation accuracy in the beginning, but after 35 steps, the error of NPF is almost stable in a range whereas that of BPF increases quickly. The RMSEs of the estimation results for $x_{2,k}$ and $x_{4,k}$ by NPF and

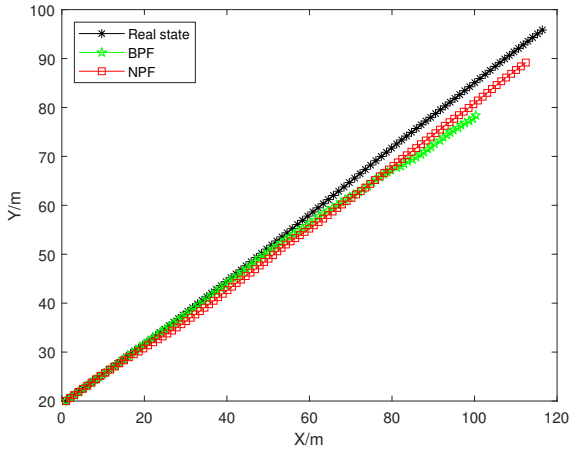

Fig. 1: The figure captionTrue and estimated target tracks of $x_{1,k}$ and $x_{3,k}$.

BPF are given by Fig.3 and Fig.5, respectively. It can be seen from the figure that the RMSEs of BPF is larger than RMSEs of NPF. Thus we can conclude that the estimation accuracy of NPF is higher than that of BPF and the estimation error of NPF is minimized.

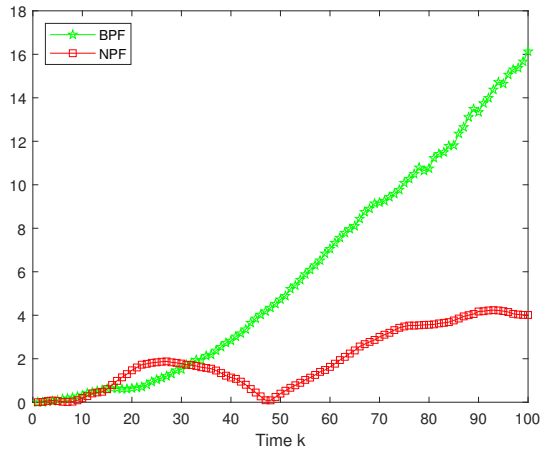

Fig. 2: RMSEs of $x_{1,k}$.

In addition, we compare the computation time of NPF and BPF in each sampling period in Tables 1. The computational efficiency of NPF is generally lower because a large amount of computing resources are used to select the sample $x_k^{(i)}$. Although NPF takes more computation time than BPF, NPF will have higher accuracy in distance tracking.

Table 1: ARMSEs, Computation Time

Filters	BPF	NPF
ARMSEs of x_1	5.9447	1.9526
ARMSEs of x_2	0.1577	0.0836
ARMSEs of x_3	6.1785	3.1924
ARMSEs of x_4	0.1728	0.0767
Time	6.3918e-04	0.0058

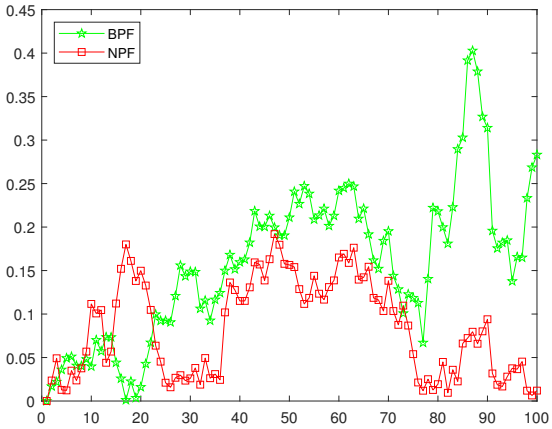

Fig. 3: RMSEs of $x_{2,k}$.

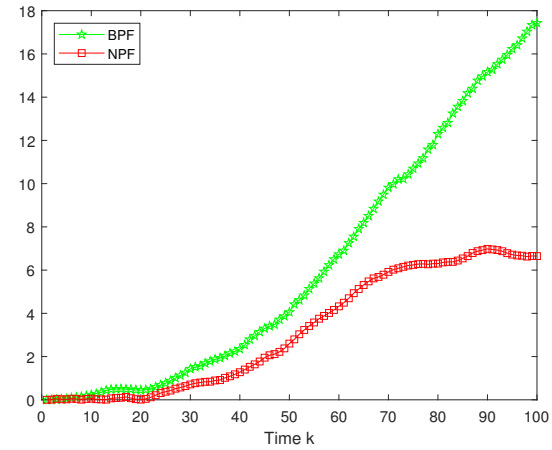

Fig. 4: RMSEs of $x_{3,k}$.

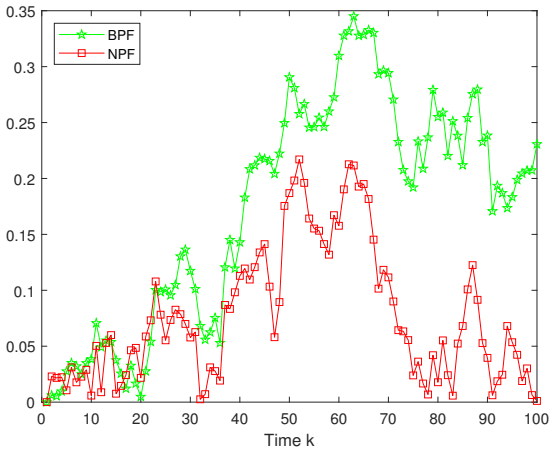

Fig. 5: RMSEs of $x_{4,k}$.

5 Conclusion

This paper proposes a novel particle filter based on one-step smoothing by iteration for nonlinear systems with missing measurements. This filter is based on one-step smoothing through iteration to incorporate the current measurement into the importance function for particle filtering. Through

the simulation example of the target tracking model, it can be illustrated that the proposed novel particle filter has much higher estimate accuracy than bootstrap particle filter, which verify the proposed filter can help to improve the efficiency of importance sampling and limit particle degradation for nonlinear systems with missing measurements. For future work, other method can be considered for constructing the importance function of particle filters to improve the sampling efficiency, estimate accuracy and computational efficiency.

References

[1] F. Qu, S. Tong, Observer-based fuzzy adaptive quantized control for uncertain nonlinear multiagent systems, *International Journal of Adaptive Control and Signal Processing*, 33(4): 567–585, 2019.

[2] S. Bordonaro, P. Willett, Y. Bar-Shalom, T. Luginbuhl, Converted measurement sigma point Kalman filter for bi-Static Sonar and Radar tracking, *IEEE Transactions on Aerospace and Electronic Systems*, 55(1): 147–159, 2019.

[3] Z. Wang et al., Robust H∞ filtering for stochastic time-delay systems with missing measurements, *IEEE Transactions on Signal Processing*, 54(7): 2579–2587, 2006.

[4] Q. Zhao, W. Zhang, Z. Li, T. Zhang, J. Chen, Y. Liu, Robust H∞ state estimation for distribution system considering randomly missing measurements, *IEEE Transactions on Instrumentation and Measurement*, 72: 1–16, 2023.

[5] Guo. Y, Li. L, Xia. Y, Wen .Y, Guo .J, Distributed consensus-based estimation for nonlinear systems subject to missing measurements and denial of service attacks, *IET Cyber-Physical Systems*, 9(1): 50–62, 2024.

[6] S. Arunagirinathan, P. Muthukumar, Y. Joo, Robust reliable H∞ control design for networked control systems with nonlinear ctuator faults and randomly missing measurements, *International Journal of Robust and Nonlinear Control*, 29(12): 4168-4190, 2019.

[7] J. Hu et al., Event-based filtering for time-varying nonlinear systems subject to multiple missing measurements with uncertain missing probabilities, *Inform Fusion*, 38: 74-83, 2017.

[8] M. Rana, L. Li, S. Su, Distributed state estimation of smart grids with packet losses, *Asian Journal of Control*, 19(4): 1306-1315, 2017.

[9] M. Li, Y. Chen, Wide-area stabiliser on sliding mode control for cross-area power systems with random delay and packet dropouts, *Asian Journal of Control*, 20(6): 2130-2142, 2018.

[10] M. Atitallah, M. Davoodi, N. Meskin, Event-triggered fault detection for networked control systems subject to packet dropout, *Asian Journal of Control* 20(6): 2195-2206, 2018.

[11] J. Liu, X. Ruan, Networked iterative learning control design for nonlinear systems with stochastic output packet dropouts, *Asian Journal of Control*, 20(3): 1077-1087, 2018.

[12] W.Q. Liu, G.L. Tao, Y.J. Fan, G.Q Zhang, Robust fusion steady-state filtering for multisensor networked systems with one-step random delay, missing measurements, and uncertain-variance multiplicative and additive white noises, *International Journal of Robust and Nonlinear Control*, 29(14): 4716-4754, 2019.

[13] A. Hermoso-Carazo, J. Linares-Perez, Different approaches for state filtering in nonlinear systems with uncertain observations, *Applied Mathematics and Computation*, 187(2): 708–724, 2007.

[14] L. Xu, K. Ma, H. Fan, Unscented Kalman filtering for nonlinear state estimation with correlated noises and missing measurements, *International Journal of Control, Automation and Systems*, 16: 1011–1020, 2018.

[15] J. Hu, Z. Wang, S. Liu, H. Gao, A variance-constrained approach to recursive state estimation for time-varying complex networks with missing measurements, *Automatica* 64: 155-162, 2016.

[16] C. Yang, H. Fang Modified particle filter and Gaussian filter with packet dropouts, *International Journal of Control, Automation and Systems*, 28: 2961-2975,2018.

[17] X. Zhang, Z. Yan , Y. Chen, High-degree cubature Kalman filter for nonlinear state estimation with missing measurements, *Asian Journal of Control*, 24(3): 1261–1272, 2022.

[18] A. Doucet, S. Godsill, C. Andrieu, On sequential Monte Carlo sampling methods for Bayesian filtering, *Statistics and Computing*, 10: 197–208, 2000.

[19] L. Xue, Y. Zhong, Y. Han, Constrained cubature particle filter for vehicle navigation, *Sensors*, 24(4): 1228, 2024.

[20] M.A. Awal, M.A.R. Refat, F. Naznin, M.Z. Islam, A particle filter based visual object tracking: a systematic review of current trends and research challenges, *International Journal of Advanced Computer Science and Applications*, 14(11): 1291–1301, 2023.

[21] H. Chan, T. Lai, A general theory of particle filters in hidden Markov models and some applications, *Annals of Statistics*, 41(6): 2877–2904, 2013.

[22] D. Sen, A. Jasra, Y. Zhou, Some contributions to sequential Monte Carlo methods for option pricing, *Journal of Statistical Computation and Simulation*, 87(4): 733–752, 2016.

[23] C. Andrieu, A. Doucet, R. Holenstein, Particle Markov chain Monte Carlo methods, *Journal of the Royal Statistical Society*, 72(3): 269–342, 2010.

[24] L. Xu, K. Ma, W. Li, Y. Liu, Particle filtering for networked nonlinear systems subject to random one-step sensor delay and missing measurements, *Neurocomputing*, 275: 2162–2169, 2018.

[25] N. Gordon, D. Salmond, A. Smith, Novel approach to nonlinear/non-Gaussian Bayesian state estimation, *IEE Proceedings F-Radar and Signal Processing*, 140(2): 107–113, 1993.

[26] Z. Wang, W. Lu, Z. Chang, Joint inverse estimation of groundwater pollution source characteristics and model parameters based on an intelligent particle filter, *Journal of Hydrology*, 625: 129965, 2023.

[27] J. Yun, F. Yang, Y. Chen, Augmented particle filters, *Journal of the American Statistical Association*, 112(517): 300–313, 2017.

[28] A.H. Abolmasoumi, A. Farahani, L. Mili, Robust particle filter design with an application to power system state estimation, *IEEE Transactions on Power Systems*, 39(1): 1810–1821, 2023.

[29] X. Zhang, Z. Yan, Standard and Gaussian particle filters for nonlinear system with missing measurements, *2020 39th Chinese Control Conference*, Shenyang, China, 27-29 July 2020, pp. 2862-2868.

[30] M. Arulampalam, S. Maskell, N. Gordon, T. Clapp, A tutorial on particle filters for online nonlinear/non-Gaussian Bayesian tracking, *IEEE Transactions on Signal Processing*, 50(2):174–188, 2002.

[31] Z. Yan, Y. Yuan, Particle filter based on one-step smoothing with adaptive iteration, *IET Signal Processing*, 11(5): 596–603, 2017.

Proceedings of the 3rd Conference on Fully Actuated System Theory and Applications
May 10-12, 2024, Shenzhen, China

Obervability Analysis for Space Target Sequential-Image Relative Navigation System with Fully-Actuated System Control

Bowen Hou[1], Dayi Wang[1,2], Tianshu Dong[2], Jiongqi Wang[1]

1. College of Sciences, National University of Defense Technology, Changsha 410073, China
E-mail: houbowen95@126.com

2. Beijing Institute of Spacecraft System Engineering, Beijing 100094, China
E-mail: dayiwang@163.com

Abstract: Space target sequential-image relative navigation system is an important part of the rendezvous and docking mission. Due to the poor observability of the system, the control input is necessary to obtain the target motion state. The rendezvous and docking mission also requires the control input to make the spacecraft approach the target. The fully-actuated system theory is an effective way to obtain the optimal control. To obtain better relative navigation accuracy and provide more accurate target state to the control system, the relative navigation system observability is analyzed based on the optimal control. Besides, the linear quadratic indicator for the control is also improved combined with the observability criteria. The optimal control input is also solved through the new performance indicator. The simulation results show that the new indicator can improve the relative navigation accuracy to some degree, which will provide a new though to improve the navigation and guidance scheme of the rendezvous and docking mission.

Key Words: Observability Analysis, Sequential-Image Relative Navigation System, Fully-Actuated System Control; Observability Indicator

1 Introduction

Space target relative navigation is popular for space debris removal, on-orbit services, deep-space object exploration and so on[1-3]. Due to the long distance of the target, many sensors are unable to acquire the measurements. Therefore, the optical sensor which can measure distances from thousands of kilometers to a few meters is the most suitable measurement information source.

However, the image cannot provide the scale information of the target, which brings the poor observability for the navigation system. In response to this issue, the sequence-image relative navigation is proposed to produce the scale information through the known orbital perturbation forces, of which the orbit maneuver is the most commonly used. This is because the ultimate goal of relative navigation is rendezvous and docking with the target, and the rendezvous and docking process also requires orbital maneuver. At the same time, the positional relationship between image information at different moments can be obtained based on the orbit maneuver and the orbit dynamics, which in turn enables target state estimation. The images obtained at different moments through the orbit maneuver are called sequential images. They are related in space and time. They all contain image information about the same target spatially. And they are linked in time by orbit maneuver. The orbit maneuver provide a geometric position relation between two images and this relation is a time-dependent expression. Therefore, a suitable orbit maneuver is very important for the relative navigation system.

The orbit maneuver is usually done by providing a control input to the sequence-image relative navigation system. And it is also important for the rendezvous and docking with the target. To design the proper control, the related researches are widespread and the adaptive controller is a popular method to realize target rendezvous and docking based on the time-varying sliding mode surface[4] and the fault tolerant constraint[5]. The shrinking horizon model predictive control (MPC)[6] is approximated to the optimal finite horizon control and the control accuracy is analyzed. The method is applied for the space target rendezvous and docking mission. The fast model predictive control is proposed based on the LQ-MPC framework to avoid the obstacle during the rendezvous and docking process[7]. The $H\infty$ controller is obtained in terms of the Riccati algebraic matrix equations to tackle the relative orbital control problem[8].

Due to the influence of factors such as the spacecraft sail or large antenna flexures and the coupling characteristics between the dynamics, the spacecraft navigation system is usually a highly complex non-linear dynamic system with higher-order states [9]. Aiming at the characteristic, the full-actuated system model is proposed to obtained the optimal control. And the higher-order fully-actuated system method has been applied to space target rendezvous and docking [10]. Since the navigation system is the information source for the control system, which in turn influences the observability of the navigation system to acquire state information during the relative navigation system. Therefore, it is necessary to analyzed the sequence-image relative navigation system observability based on the fully-actuated system control.

In this paper, the orbit control for the spacecraft rendezvous is considered based on the fully-actuated system. Combined with the related results in [11], the observability of the sequence-image relative navigation is analyzed with the optimal control. The analysis results of the system

*This work is supported by National Natural Science Foundation of China [Grant No. U20B2055] and National University of Defense Technology Youth Autonomous Innovation Science Fund ZK23-01.

observability are not only useful for the relative navigation system, but also provide a new reference for the design of orbital control for future rendezvous and docking processes.

In Section 2, the fully-actuated system is constructed based on the space target relative orbit dynamics. In Section 3, the optimal control is introduced based on the previous research and the observability is analyzed. The numerical simulation is conducted in Section 4 and the conclusion is drawn in Section 5.

2 Fully-Actuated System Model of Space Target Sequence-image Relative Navigation

2.1 Sequence-image Relative Navigation System Model

The main coordinate systems are given as follows in order to better describe the relative navigation system.

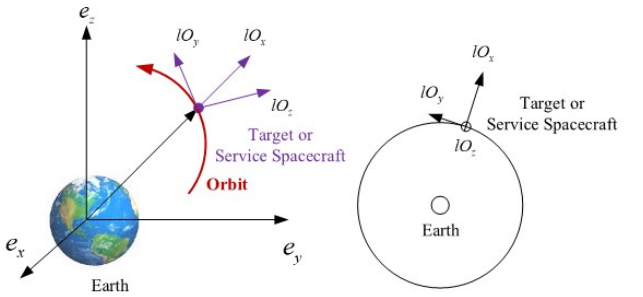

Fig. 1 Definition of the spacecraft orbital coordinate

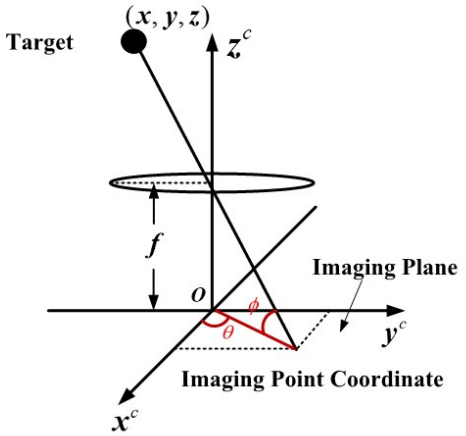

Fig. 2 Definition of the measurement coordinate

The definition of the spacecraft orbital coordinate is shown in Fig. 1. The origin of the coordinate is at the center of the mass of the spacecraft. lO_{xyz} denotes the orbit coordinate, where the lO_x is the radial direction of the spacecraft, the lO_y is along the direction normal to the spacecraft's orbital plane, and the lO_z is determined by the right-hand rule. The measurement coordinate system is defined as shown in Fig. 2. The coordinate origin is the center of the imaging plane of the optical sensor. $O-x^c y^c$ denotes the imaging plane, z^c is perpendicular to the imaging plane upwards and f denotes the focal length of the camera.

The relative orbital dynamics model will be constructed based on the orbital coordinate system of the service spacecraft as shown in [12]:

$$\begin{cases} \ddot{x}_k - 2\omega_k \dot{y}_k - 3\omega_k^2 x_k = u_{x,k} \\ \ddot{y}_k + 2\omega_k \dot{x}_k = u_{y,k} \\ \ddot{z}_k + \omega_k^2 z_k = u_{z,k} \end{cases} \tag{1}$$

where x, y, z denote the target position in the orbit coordinate system, ω denotes the orbit rate of the spacecraft orbit, $u_i, i = x, y, z$ denotes the control input of three directions, k denotes the time epoch.

It is assumed that the target's coordinate in the service spacecraft orbital coordinate system is (x, y, z) . Then the measurement model is shown as Eq. (2):

$$\begin{aligned} \boldsymbol{z}_k &= \begin{pmatrix} \theta_k \\ \phi_k \end{pmatrix} \\ &= \begin{pmatrix} \arctan\left(\dfrac{y_k}{x_k}\right) \\ \arcsin\left(\dfrac{z_k}{\sqrt{x_k^2 + y_k^2 + z_k^2}}\right) \end{pmatrix} + \begin{pmatrix} v_{\theta_k} \\ v_{\phi_k} \end{pmatrix} \\ &= h(\boldsymbol{x}_k) + \boldsymbol{v}_k \end{aligned} \tag{2}$$

where θ_k and ϕ_k denote the azimuth angle and the elevation angle, $\boldsymbol{v}_k = \begin{pmatrix} v_{\theta_k} & v_{\phi_k} \end{pmatrix}^{\mathrm{T}}$ denote the measurement noises. Then the relative navigation system consists of Eqs. (1) and (2).

In general, the image measurement at one epoch cannot provide enough information for state estimation. Therefore, the control input can be used to provide extra information for the navigation system. After conducting the control, the service spacecraft changes the position and obtains a new image which can be used for obtain the target position combined with the image at the prior image. The process of obtaining information about the target's motion state using such images that are temporally correlated before and after is sequence-image relative navigation. On the one hand, the control input can be determined through analyzing the target state estimation performance which is called observability. On the other hand, the control input needs to be used for target rendezvous and docking. Therefore, it is necessary to determine the control input combined with the rendezvous and docking task requirement.

2.2 Fully-Actuated System Model

The fully-actuated system is used to obtained the optimal control reach the target. Combined with the Eq. (1)and the fully-actuated system theory [13], the fully-actuated system model is constructed as follows:

$$\boldsymbol{M}(\boldsymbol{x}, \dot{\boldsymbol{x}})\ddot{\boldsymbol{x}} + \boldsymbol{D}(\boldsymbol{x}, \dot{\boldsymbol{x}})\dot{\boldsymbol{x}} + \xi(\boldsymbol{x}, \dot{\boldsymbol{x}}) = \boldsymbol{u} \tag{3}$$

where $\boldsymbol{x}=\begin{pmatrix} x & y & z \end{pmatrix}^{\mathrm{T}}$, $\boldsymbol{M}(\boldsymbol{x},\dot{\boldsymbol{x}})=\begin{pmatrix} 1 & 0 & 0 \\ 0 & 1 & 0 \\ 0 & 0 & 1 \end{pmatrix}$,

$\boldsymbol{D}=\begin{pmatrix} 0 & -2n & 0 \\ 2n & 0 & 0 \\ 0 & 0 & 0 \end{pmatrix}$, $\xi(\boldsymbol{x},\dot{\boldsymbol{x}})=\begin{pmatrix} -3n^2x \\ 0 \\ n^2z \end{pmatrix}$,

$\boldsymbol{u}=\begin{pmatrix} u_x & u_y & u_z \end{pmatrix}^{\mathrm{T}}$, $\boldsymbol{n}$ denotes the orbit rate of the service spacecraft.

Eq. (3) can be transformed to the standard fully-actuated system model as follows:

$$\ddot{\boldsymbol{x}}=\boldsymbol{f}(\boldsymbol{x},\dot{\boldsymbol{x}})+\boldsymbol{B}(\boldsymbol{x},\dot{\boldsymbol{x}})\boldsymbol{u} \tag{4}$$

where

$$\boldsymbol{B}(\boldsymbol{x},\dot{\boldsymbol{x}})=\boldsymbol{M}^{-1}(\boldsymbol{x},\dot{\boldsymbol{x}}) \tag{5}$$

$$f(\boldsymbol{x},\dot{\boldsymbol{x}})=-\boldsymbol{M}^{-1}(\boldsymbol{x},\dot{\boldsymbol{x}})\left[\boldsymbol{D}(\boldsymbol{x},\dot{\boldsymbol{x}})\dot{\boldsymbol{x}}+\xi(\boldsymbol{x},\dot{\boldsymbol{x}})\right] \tag{6}$$

For the rendezvous and docking mission, the ultimate goal is to obtain a control that allows the relative distance to reach a steady state $\boldsymbol{x}\to 0$. The literature [11] has given the control expression through the full-actuated system method as follows:

$$\begin{cases} \boldsymbol{u}=-\boldsymbol{M}(\boldsymbol{x},\dot{\boldsymbol{x}})(f(\boldsymbol{x},\dot{\boldsymbol{x}})-\boldsymbol{v}) \\ \boldsymbol{v}=\boldsymbol{K}\begin{pmatrix} \boldsymbol{x} \\ \dot{\boldsymbol{x}} \end{pmatrix} \end{cases} \tag{7}$$

$\boldsymbol{K}$ is the optimal control gain of the linear quadratic optimal controller. According to Eqs. (4), (5), (6) and (7), Eq. can be easily derived:

$$\boldsymbol{v}=\ddot{\boldsymbol{x}} \tag{8}$$

Then the extended variable state space expression is as:

$$\begin{cases} \begin{pmatrix} \dot{\boldsymbol{x}} \\ \ddot{\boldsymbol{x}} \end{pmatrix}=\boldsymbol{A}\begin{pmatrix} \boldsymbol{x} \\ \dot{\boldsymbol{x}} \end{pmatrix}+\boldsymbol{B}\boldsymbol{v} \\ \boldsymbol{y}=\boldsymbol{C}\begin{pmatrix} \dot{\boldsymbol{x}} \\ \ddot{\boldsymbol{x}} \end{pmatrix} \end{cases} \tag{9}$$

where

$$\boldsymbol{A}=\begin{pmatrix} \boldsymbol{O}_{3\times3} & \boldsymbol{I}_{3\times3} \\ \boldsymbol{O}_{3\times3} & \boldsymbol{O}_{3\times3} \end{pmatrix} \tag{10}$$

$$\boldsymbol{B}=\begin{pmatrix} \boldsymbol{O}_{3\times3} \\ \boldsymbol{I}_{3\times3} \end{pmatrix} \tag{11}$$

and $\boldsymbol{O}_{3\times3}$ denotes the zero matrix, $\boldsymbol{I}_{3\times3}$ denotes the unit matrix, $\boldsymbol{y}$ denotes the measurements of the variable extension model, $\boldsymbol{C}$ denotes the corresponding measurement matrix. Then the optimal control can be calculated through the linear quadratic optimal controller.

3 Observability Analysis for the Navigation System with Fully-Actuated System Control

The observability condition for the fully-actuated system control has been described in detail in Ref. [14]. It is noted that the observability analysis mentioned in the literature are used for designing the observer. For the sequential-image relative navigation system, the observer has been determined and the control input based on the fully-actuated system method is a key factor affecting the navigation system observability. The previous researches have given some important conclusions[3, 12, 15, 16] for the sequential-image relative navigation system. The control of the spacecraft needs satisfying the following condition to realize relative navigation.

Lemma 1: *The sufficient and necessary condition for the sequential-image relative navigation to satisfy the observability condition is:*

$$\boldsymbol{G}_1\boldsymbol{u}\neq\gamma\boldsymbol{\Phi}_1\boldsymbol{x}_k,(\gamma>-1) \tag{12}$$

where γ denotes the constant and

$$\boldsymbol{G}_1=\begin{pmatrix} \frac{4\sin(\omega T)}{\omega}-3T & 0 & \frac{4\sin^2(\omega T/2)}{\omega} \\ 0 & \frac{\sin(\omega T)}{\omega} & 0 \\ -\frac{4\sin^2(\omega T/2)}{\omega} & 0 & \frac{\sin(\omega T)}{\omega} \end{pmatrix} \tag{13}$$

$$\boldsymbol{\Phi}_1=\begin{pmatrix} \boldsymbol{\Phi}_{11} & \boldsymbol{\Phi}_{12} \end{pmatrix} \tag{14}$$

where $\boldsymbol{\Phi}_{11}=\begin{pmatrix} 1 & 0 & 6\omega T-\sin(\omega T) \\ 0 & \cos(\omega T) & 0 \\ 0 & 0 & 4-3\sin(\omega T) \end{pmatrix}$,

$\boldsymbol{\Phi}_{12}=\begin{pmatrix} \frac{4\sin(\omega T)}{\omega}-3T & 0 & \frac{4\sin^2(\frac{\omega T}{2})}{\omega} \\ 0 & \frac{\sin(\omega T)}{\omega} & 0 \\ -\frac{4\sin^2(\frac{\omega T}{2})}{\omega} & 0 & \frac{\sin(\omega T)}{\omega} \end{pmatrix}$,

T denotes the navigation system sampling period.

Combined with Eqs. (7) and (12), to verify the sequential-image relative navigation system observability with the fully-actuated system control, the related analysis is shown as follows.

Firstly, the left-hand side of Eq. (12) is calculated as Eq. (15).

$$\boldsymbol{G}_1\boldsymbol{u}=\begin{pmatrix} g_1 \\ g_2 \\ g_3 \end{pmatrix} \tag{15}$$

where

$$g_1 = \frac{4(\ddot{z}+\omega^2 z)\sin^2\left(\frac{\omega T}{2}\right)}{\omega} + (\ddot{x}-2\dot{y}\omega-3x\omega^2)(-3T+\frac{4\sin(\omega T)}{\omega}) \tag{16}$$

$$g_2 = \frac{(\ddot{y}+2\dot{x}\omega)\sin(\omega T)}{\omega} \tag{17}$$

$$g_3 = -\frac{4(\ddot{x}-2\omega\dot{y}-3x\omega^2)\sin^2\left(\frac{\omega T}{2}\right)}{\omega} + \frac{(\ddot{z}+z\omega^2)\sin(\omega T)}{\omega} \tag{18}$$

Then the right-hand side of Eq. (12) is calculated as Eq. (19).

$$\gamma \boldsymbol{\Phi}_1 \boldsymbol{x}_k = \begin{pmatrix} f_1 \\ f_2 \\ f_3 \end{pmatrix} \tag{19}$$

where

$$f_1 = \gamma\left[x + \frac{4\dot{z}\sin^2(\frac{\omega T}{2})}{\omega} + z(6\omega T - 6\sin(\omega T)) + \dot{x}(\frac{4\sin(\omega T)}{\omega} - 3t)\right] \tag{20}$$

$$f_2 = \gamma\left[\cos(\omega T)y + \frac{\dot{y}\sin(\omega T)}{\omega}\right] \tag{21}$$

$$f_3 = \gamma\left[z(4-3\cos(\omega T)) - \frac{4\dot{x}\sin^2(\frac{\omega T}{2})}{\omega} + \frac{\dot{z}\sin(\omega T)}{\omega}\right] \tag{22}$$

May wish to assume $g_2 = f_2$, then

$$\gamma = \frac{\ddot{y}+2\omega\dot{x}}{\omega\cos(\omega T)y + \dot{y}} \tag{23}$$

Based on the value of γ,

$$f_3 - g_3 = \frac{1}{\omega}\left(4\left[\ddot{x}-\omega(2\dot{y}+3x\omega)\right]\sin^2(\frac{\omega T}{2}) - (\ddot{z}+\omega^2 z)\sin(\omega T) + \frac{(\ddot{y}+\omega\dot{x})\left[-2\dot{x}+4z\omega+(2\dot{x}-3\omega z)\cos(\omega T)\right]}{\dot{y}+\omega y\cos(\omega T)} + \frac{(\ddot{y}+\omega\dot{x})\dot{z}\sin(\omega T)}{\dot{y}+\omega y\cos(\omega T)}\right) \tag{24}$$

According to the relative navigation scenario, ωT cannot be zero or $\pi/2$. Also, $\sin(\omega T)$ and $\cos(\omega T)$ cannot be zero at the same time. Therefore, it is evident that $f_3 - g_3 \neq 0$ when $\boldsymbol{u} \neq 0$ combined with Eq. (1). Therefore, as long as $\boldsymbol{u} \neq 0$, the optimal control based on the fully-actuated system satisfies the sequential-image relative navigation system observability condition.

Based on the observability condition, it is necessary to obtain better observability. Therefore, the optimal control quadratic performance indicator is expressed as follows:

$$J = \frac{1}{2}\int_0^{+\infty}\begin{pmatrix}\boldsymbol{x}^{\mathrm{T}} & \dot{\boldsymbol{x}}^{\mathrm{T}}\end{pmatrix}\boldsymbol{Q}\begin{pmatrix}\boldsymbol{x}^{\mathrm{T}} & \dot{\boldsymbol{x}}^{\mathrm{T}}\end{pmatrix}^{\mathrm{T}} + \boldsymbol{v}^{\mathrm{T}}\boldsymbol{R}\boldsymbol{v} + \boldsymbol{x}^{\mathrm{T}}\boldsymbol{\Phi}_1^{\mathrm{T}}\boldsymbol{G}_1\boldsymbol{u}\mathrm{d}t \tag{25}$$

where $\boldsymbol{Q}$ and $\boldsymbol{R}$ are semi-positive definite matrix and positive definite matrix, respectively. In Eq.(25), the last term denotes the observability performance indicator. When it reaches a minimum value, the observability is optimal.

Lemma 2[11]. *For system (9), assume that* $\boldsymbol{Q} = \boldsymbol{C}^{\mathrm{T}}\boldsymbol{C} \geq 0$, $\boldsymbol{R} > 0$ *are constant matrices,* $(\boldsymbol{A}, \boldsymbol{B})$ *is controllable and* $(\boldsymbol{A}, \boldsymbol{C})$ *is observable. Then* $\boldsymbol{S}$ *is the unique symmetric positive define solution to the following Riccati equation:*

$$\boldsymbol{A}^{\mathrm{T}}\boldsymbol{S} + \boldsymbol{S}\boldsymbol{A} - \boldsymbol{S}\boldsymbol{B}\boldsymbol{R}^{-1}\boldsymbol{B}^{\mathrm{T}}\boldsymbol{S} + \boldsymbol{Q} = 0 \tag{26}$$

Then the linear quadratic optimal controller of the system (9) under the performance indicator (25) is:

$$\boldsymbol{v} = \boldsymbol{K}\begin{pmatrix}\boldsymbol{x} \\ \dot{\boldsymbol{x}}\end{pmatrix} \tag{27}$$

where $\boldsymbol{K} = -\boldsymbol{R}^{-1}(\boldsymbol{B}^{\mathrm{T}}\boldsymbol{S} + \frac{1}{2}\boldsymbol{\Phi}_1^{\mathrm{T}}\boldsymbol{G}_1)$ and $\boldsymbol{S}$ is the unique symmetric positive definite solution to Eq. (26).

Although the optimal control is calculated through the fully-actuated system method, the relative motion state needs to be known in advance. Therefore, the control in the previous epochs needs to be determined according to the observability indicator described in Ref. [17]. Therefore, the optimal control determination process for the sequential-image relative navigation system is shown as Fig. 3:

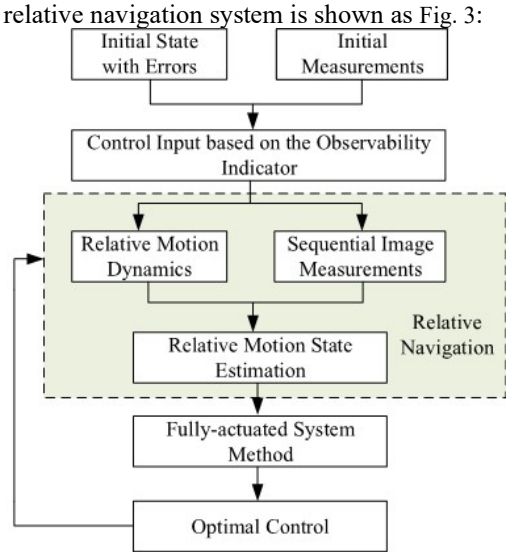

Fig. 3 Relative Navigation System Optimal Control Process

4 Simulation

4.1 Simulation Condition

The ultimate goal of spacecraft rendezvous is to adjust the distance between the target and the service spacecraft to 0m. During the process, it is also necessary to improve the system observability as much as possible to realize high-accuracy relative navigation. The relevant simulation condition settings are shown in Table 1.

Table 1: Simulation Parameters

Item	Value
Initial State	$[8000m\ 4000m\ 10000m\ -5m/s\ -8m/s\ 5m/s]^T$
Orbit Rate	1.2e-3 rad/s
Q	diag(1e-5,1e-5,1e-5,1e-5,1e-5,1e-5)
R	diag(1e4,1e4,1e4)
Measurement Noises	diag(2.4e-05 2.4e-05 2.4e-05)rad
Simulation Time	4320s
Sampling Period	2s

The control input is calculated through the process in Fig. 3 and the results are shown as Fig. 4. As a contrast, the control input results based on the indicator without observability performance (referred to Eq. (15) in Ref. [11])are shown as Fig. 5.

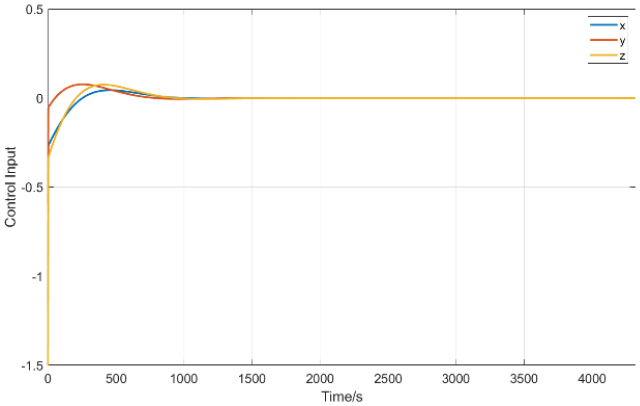

Fig. 4 The Control Input Result Based on the Indicator (16)

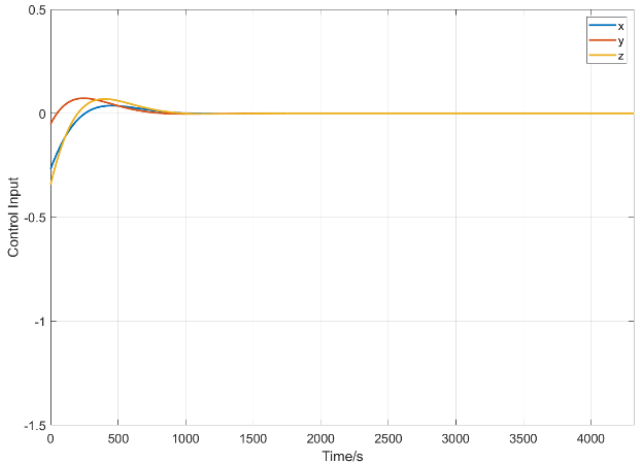

Fig. 5 The Control Input Result Based on the Indicator without Observability Performance

The relative motion between the target and the spacecraft based on Fig. 4 is shown as Fig. 6. The control results reflected in three directions are shown as Fig. 7.

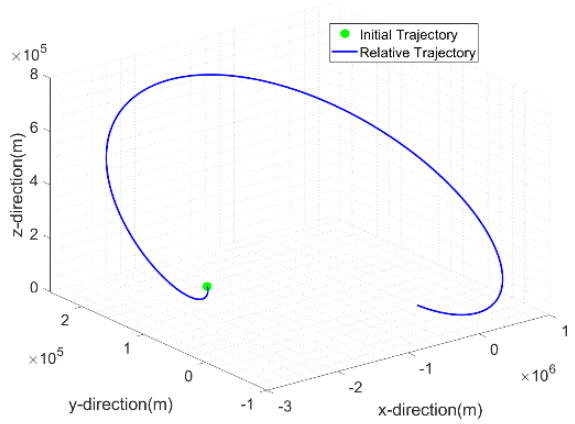

Fig. 6 The Control Input Result Based on the Indicator without Observability Performance

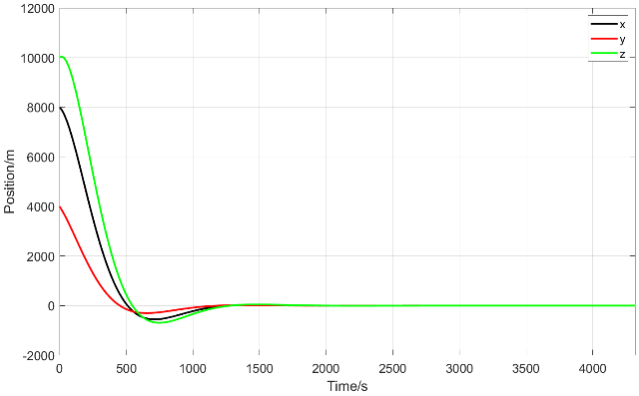

Fig. 7 The Control Input Results in Three Directions

In order to better compare the navigation accuracy under different control inputs, the relative position state of the target is estimated according to different control inputs, and the comparison results are shown in Fig. 8 and Table 2.

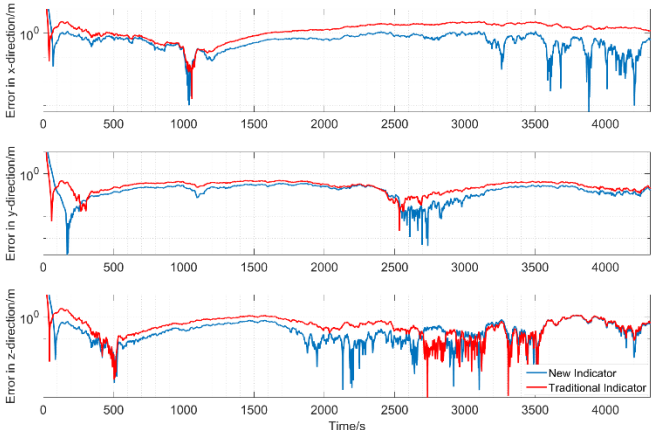

Fig. 8 Relative Navigation Accuracy with Different Control Input

Table 2: Relative Navigation Accuracy RMSE with Different Control Input

Item	x (m)	y (m)	z (m)
Control Input with New Indicator	**0.6710**	**0.1676**	**0.4564**
Control Input with Traditional Indicator	2.2124	0.2603	0.4866

According to the results above, it can be seen that the control input calculated based on the new linear quadratic indicator provide better navigation accuracy for the sequential-image relative

navigation system. This is because the indicator considers the navigation system observability which is a very important influence factor for the navigation system. The smaller $\boldsymbol{x}^{\mathrm{T}}\boldsymbol{\Phi}_{1}^{\mathrm{T}}\boldsymbol{G}_{1}\boldsymbol{u}$ is, the more observable the system is and the better the navigation accuracy is. As the spacecraft gets closer to the target, the navigation accuracy of the two methods gets closer.

5 Conclusion

The sequential-image relative navigation system needs the control input to improve the observability to realize system state estimation. The fully-actuated system method provides a new thought to obtain the control input. The control input satisfies the sequential-image relative navigation observability requirements. Based on the observability indicator, the linear quadratic indicator is improved to obtain the better navigation performance with the calculated optimal control. The relevant results can provide certain reference for the navigation and control scheme of the future rendezvous and docking mission, and thus achieve the common improvement of navigation accuracy and control accuracy.

It is important to note that the weight matrices of the above methods have a large impact on the results of the control inputs and more research is needed in the future. In addition to this, the size of the control inputs is also one of the constraints in solving the optimal control, and more detailed studies are needed to address this issue in the future.

References

[1] J. Li, D. Wang, M. Li, T. Dong, F. Fu, and C. Xu, "Onboard Observation Planning for Sequential Image-Based Planetary Landing Navigation in Unknown Environments," IEEE Transactions on Aerospace and Electronic Systems, vol. 59, pp. 5943-5960, 2023.

[2] E. Turan, S. Speretta, and E. Gill, "Autonomous navigation for deep space small satellites: Scientific and technological advances," Acta Astronautica, 2022.

[3] T. Dong, D. Wang, F. Fu, M. Li, B. Hou, and C. Xu, "Analytical Nonlinear Observability Analysis for Spacecraft Autonomous Relative Navigation," IEEE Transactions on Aerospace and Electronic Systems, vol. 58, no. 6, pp. 5875-5893, 2022.

[4] Q. Hu, W. Chen, and L. Guo, "Fixed-time maneuver control of spacecraft autonomous rendezvous with a free-tumbling target," IEEE Transactions on Aerospace and Electronic Systems, vol. 55, no. 2, pp. 562-577, 2018.

[5] L. Sun, "Adaptive fault-tolerant constrained control of cooperative spacecraft rendezvous and docking," IEEE Transactions on Industrial Electronics, vol. 67, no. 4, pp. 3107-3115, 2019.

[6] M. Ye and I. Kolmanovsky, "Approximating optimal control by shrinking horizon model predictive control for spacecraft rendezvous and docking," IFAC-PapersOnLine, vol. 55, no. 16, pp. 284-289, 2022.

[7] C. Bashnick and S. Ulrich, "Fast Model Predictive Control for Spacecraft Rendezvous and Docking with Obstacle Avoidance," Journal of Guidance, Control, and Dynamics, vol. 46, no. 5, pp. 998-1007, 2023.

[8] R. Lungu, F. A. Buţu, M. Lungu, and R. Wang, "Robust Optimal Control of Spacecraft during the Rendezvous Missions using H ∞ Control Method," in 2023 27th International Conference on System Theory, Control and Computing (ICSTCC), 2023: IEEE, pp. 117-122.

[9] D. Wang et al., "State Estimation Method for Spacecraft Autonomous Navigation: Review," Acta Aeronautica et Astronautica Sinica, vol. 42, no. 4, pp. 1-18, 2020. (in Chinese)

[10] V. Muralidharan and M. R. Emami, "Rendezvous and attitude synchronization of a space manipulator," The Journal of the Astronautical Sciences, vol. 66, no. 1, pp. 100-120, 2019.

[11] G.-Q. Duan and G.-P. Liu, "Optimal Control of Fully-Actuated Systems for Spacecraft Rendezvous," in 2022 41st Chinese Control Conference (CCC), 2022: IEEE, pp. 1690-1695.

[12] B. Hou, D. Wang, J. Wang, D. Ge, H. Zhou, and X. Zhou, "Optimal Maneuvering for Autonomous Relative Navigation Using Monocular Camera Sequential Images," Journal of Guidance, Control, and Dynamics, vol. 44, no. 11, pp. 1947-1960, 2021.

[13] D. Guang-Ren, "High-order System Approaches: I. Fully-actuated Systems and Parametric Designs [J]," Acta Automatica Sinica, vol. 46, no. 7, pp. 1333-1345, 2020. (in Chinese)

[14] G. Duan, "High-order system approaches: III. Observability and observer design," Acta Automatica Sinica, vol. 46, no. 9, pp. 1885-1895, 2020. (in Chinese)

[15] J. Grzymisch and W. Fichter, "Observability Criteria and Unobservable Maneuvers for In-Orbit Bearings-Only Navigation," Journal of Guidance Control & Dynamics, vol. 37, no. 4, pp. 1250-1259, 2014.

[16] J. Grzymisch and W. Fichter, "Observability criteria and unobservable maneuvers for in-orbit bearings-only navigation," Journal of Guidance, Control, and Dynamics, vol. 37, no. 4, pp. 1250-1259, 2014.

[17] Jonathan, Grzymisch, Walter, and Fichter, "Analytic Optimal Observability Maneuvers for In-Orbit Bearings-Only Rendezvous," Journal of Guidance Control & Dynamics, vol. 37, no. 5, 2014.

Proceedings of the 3rd Conference on Fully Actuated System Theory and Applications
May 10-12, 2024, Shenzhen, China

Energy-aware Trajectory Optimization for UAV-enabled wireless powered WSN

Feihang QIU[1], Jing GUO[1], Huineng DIAO[1], Xu ZHANG[2,3]

1. School of Mechatronic Engineering and Automation, Foshan University, Foshan, 528225, China
E-mail: 13642448962@163.com, guojing@fosu.edu.cn, 15767815398@163.com

2. School of System Design and Intelligent Manufacturing, Southern University of Science and Technology, Shenzhen, 518055 , China

3. Shenzhen Key Laboratory of Control Theory and Intelligent Systems, Southern University of Science and Technology, Shenzhen, 518055 , China
E-mail: zhangx3@sustech.edu.cn

Abstract: Unmanned Aerial Vehicle enabled (UAV-enabled) wireless powered Wireless Sensor Networks (WSN) provide an effective way to deploy massive and passive sensors for environmental monitoring in harsh environments. This study focuses on maximizing the total energy received by all Sensor Nodes (SNs) through the optimization of the UAV trajectory. An energy-aware smoothing trajectory method is proposed by considering the dynamic energy requirements of SNs. First, the optimization problem (P1) is formulated according to the mathematical model. Second, the B-spline method is introduced to turn the smoothing problem into a solvable problem (P2). Finally, problem (P2) is solved under the constraints to obtain the trajectory solution. Simulation results indicate the proposed method can adjust the overall trajectory according to the SNs demands. Meanwhile, according to the wake-up distance and energy-aware, the trajectory of some nodes can be locally adjusted without affecting other trajectory segments.

Key Words: B-spline, UAV-enabled, Wireless powered, WSN

1 Introduction

Unmanned aerial vehicles (UAV) have been widely introduced into Wireless Sensor Network (WSN) and are mainly used to provide charging for renewable energy sensor nodes (SN), such as solar sensors [1, 2]. Due to variations in environmental factors, there are fluctuations in the energy harvested by these SNs, which leads to the problem of instability in the energy of the SNs [3]. To alleviate the problem, the UAV have been introduced as a supplementary source of SN energy. In UAV-enabled WSN, the SNs are normally in a sleep state. When the UAV approaches, the SN is woken up by the integrated wake-up radio module and then energy is transmitted [4]. How to adjust the UAV trajectory according to the energy variation of SN has become a popular research.

1.1 Related work

The UAV cannot be recharged in the air, and the range of the UAV is highly correlated with energy consumption. In [5], UAV energy consumption is minimized by planning the UAV trajectory as well as optimizing the node transfer time to meet the UAV energy budget. In [6], minimizing UAV energy consumption is achieved by jointly optimizing UAV trajectories and transfer time allocation.

In some real-time demanding application scenarios, the mission completion time of the UAV is also an important area of research. In [7], the task completion time is optimized in terms of both the data transfer rate of the SNs and the service time of the UAV. In [8], the trajectory of the UAV and the communication transfer of the nodes are jointly optimized.

In order to ensure the correct uploading of data, the energy harvested by the node must be above the working threshold. In [9], UAV trajectories were designed to increase the efficiency of transferring energy. In [10], the trajectory of the UAV is planned and a balanced energy of node method is used to maximize the average energy of the SNs. In UAV trajectory planning, most research focuses on solving point-to-point linear flights. In fact, planning the smooth trajectory of the UAV can improve the system's efficiency. In [11], the hover point is solved by clustering and the UAV trajectory is determined based on the hover point. In [12], a joint optimization of trajectory and velocity is performed while solving for hover point to hover point linear flight.

Adding a wake-up receiver to SN can effectively reduce the energy wastage caused by idle listening [13]. Meanwhile, the energy required for the Wake-up Receiver is far less than the charging energy [14, 15]. Many researches have investigated the problem of UAV planning based on Energy-Aware. In [16], Energy-aware UAV-assisted WSN networks are studied. The task area of the sensor network was delineated to optimize the path and hovering time of the UAV. In [17], a deep reinforcement learning method was used to plan an Energy-aware UAV trajectory. In [18], the energy-aware UAV dynamic trajectory planning problem is studied to obtain the trajectory of the UAV based on the solved hover point.

1.2 Motivation and contributions

Due to the UAV energy loss and trajectory are highly correlated, meanwhile, SN energy demand is uncertain. Smoothing and dynamic adjustment should be considered and analyzed in the Energy-aware Trajectory. This paper focuses on maximizing harvested energy by planning a smooth dynamic path. The main contributions of this paper are as follows:

- B-spline method is utilized to smooth trajectory by transforming the problem into a solvable and finite-variable problem.
- A method for dynamic adjustment of UAV trajectory based on wake-up power activation is proposed. The trajectory of some nodes can be locally adjusted with-

out affecting other trajectory segments.

2 System model

A UAV-enabled wireless powered WSN is considered and shown in Fig.1. The WSN comprises N ground sensor nodes (SN), which are distributed in a two-dimensional plane $\mathbb{O}_n = [O_1, O_2, \ldots, O_N]^T, n \in N$. The horizontal coordinates of device n is represented by $w_n = \{x_n, y_n\}, n \in N$. The UAV flies at a fixed altitude of H, transfers RF energy to SNs in the downlink and collects data information from SNs in the uplink. The red dashed circle denotes the maximum activation range of the SN. The time $t \in [0, T]$ can be cut into time slots of equal length $\mathbb{T} = [0, 1, ..., T]$. The position of the UAV at time t is represented as $q_m(t) = [x_m(t), y_m(t)], q_m(T) = q_m(0), 0 \le t \le T$. The key notions are listed in Tabel 1.

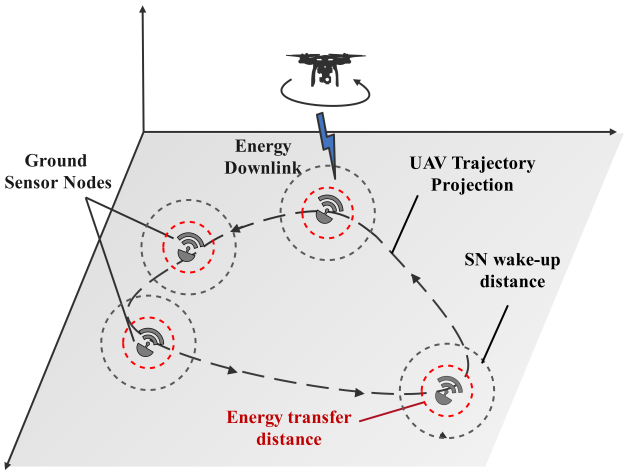

Fig. 1: System Model

Table 1: Key Simulation Parameters

Notation	Description
N	The number of nodes SNs
$\mathbb{O}$	The set of nodes SN
w_n	The (2D) coordinates of SN
m	The number of UAV waypoints
q_m	The (2D) coordinates of the UAV at moment
H	The altitude of the UAV
P_k	The transmit power of the SN
P_{act}	The activation power threshold
$h_{n,m}$	The channel power gain between the SN and the UAV
φ_n	The energy harvesting correlation of the SN and UAV
E_n	Energy collected by n-th SN
B	The channel bandwidth

The wireless channel between the SN and the UAV is dominated by the LoS link. At each moment t, the channel power gain between the SN and the UAV $h_{n,m}(t)$ can be modeled as follow:

$$h_{n,m}(t) = \frac{\beta_0}{D^2_{n,m}(t)} = \frac{\beta_0}{H^2 + \|q_m(t) - w_n\|^2} \tag{1}$$

where β_0 represents the channel power gain at a distance of 1 meter. In [19], the path loss exhibits a regular circle in the transmission threshold range. When the received signal strength indicator (RSSI) of the SN is above the activation power threshold P_{act}, the SNs can be activated and communication:

$$P_t h_{n,m} \ge P_{act} \tag{2}$$

When the UAV completes the task, the end point of the UAV is the starting point, denoted as:

$$q_m(T) = q_m(0) \tag{3}$$

During transmission, the distance between UAV waypoint q_m^{tr} and node w_n is less than the maximum transmission distance, denoted as:

$$\begin{aligned} &\|q_m^{\text{tr}}(t) - w_n\| \le D_{\text{tr}}, \\ &q_m^{\text{tr}}(t) \in q_m(t), \varphi_n = 1 \end{aligned} \tag{4}$$

After the energy transmission of the UAV, the energy collected by the n–th SN E_n can be expressed as:

$$E_n = \int_0^T \varphi_n(t) h_{n,m} P_t dt, \varphi_n = \{0, 1\} \tag{5}$$

where $\varphi_n(t)$ represents the energy harvesting correlation function of the n-th SN with the UAV at moment t. At time t, φ_n = 0 means that the n-th SN is harvesting energy from the UAV, while φ_n = 1 indicates no harvesting happens.

The goal of this paper is to maximize the total energy received of all SNs. Therefore, the problem is mathematically expressed as follows:

$$\text{(P1)}: \max \sum_{n=1}^{N} E_n$$

$$\text{s.t. } (2), (3), (4)$$

3 Proposed smoothing trajectory method

The original problem (P1) is complex and difficult to solve because it is continuous time and contains infinite coupled optimization variables. To solve this problem, B-spline method is introduced to transform (P1) into (P2) solvable smooth trajectory planning problem.

3.1 Trajectory smoothing optimization (P2)

With B-spline method [20], the trajectory of UAV $q_m[k]$ is represented as below.

$$\begin{aligned} q_m[k] &= \begin{bmatrix} B_{i-pd+1,pd}(u) & B_{i-pd+2,pd}(u) & \cdots & B_{i,pd}(u) \end{bmatrix} \\ &\quad \times \begin{bmatrix} P_{i-pd+1} \\ P_{i-pd+2} \\ \vdots \\ P_i \end{bmatrix} \\ &= \begin{bmatrix} 1 & u & u^2 & \cdots & u^{pd-1} \end{bmatrix} M^{pd}(i) \begin{bmatrix} P_{i-pd+1} \\ P_{i-pd+2} \\ \vdots \\ P_i \end{bmatrix} \\ u &= \frac{(t-\tau_i)}{(\tau_{i+1}-\tau_i)}, \quad u \in [0,1] \end{aligned} \tag{6}$$

where $M^k(i)$ is the i -th basis matrix of the $pd-1$ order B-spline basis function. The trajectory is deformed using an Affine Transformation Matrix $G^T = [\mathrm{g}_0, \mathrm{g}_1, \ldots, \mathrm{g}_n]$ optimized as follows:

$$\begin{aligned} P^{j+1} &= \mathrm{G}^{T^j} \oplus P^j \\ &= \left\{ \mathrm{g}_1^j \oplus p_0^{j+1},\ \mathrm{g}_1^j \oplus p_1^{j+1} \ldots, \mathrm{g}_n^j \oplus p_n^{j+1} \right\}, j > 0 \end{aligned} \tag{7}$$

where P^j represents the B-spline control point under the i -th iteration iteration. Then the coordinates of the B-spline of the corresponding curve can be written as:

$$\begin{aligned} q_m^j[n] &= \\ &\begin{bmatrix} 1 & u & u^2 & \cdots & u^{k-1} \end{bmatrix} M^k(i) \begin{bmatrix} \mathrm{g}_1^j \oplus P_{i-pd+1}^j \\ \mathrm{g}_2^j \oplus P_{i-pd+2}^j \\ \vdots \\ \mathrm{g}_i^j \oplus P_i^j \end{bmatrix} \end{aligned} \tag{8}$$

In order to ensure that the UAV can successfully return to the departure point, the first and last control points must be identical.

$$\mathrm{g}_i^j \oplus P_i^j = \mathrm{g}_1^j \oplus P_{i-pd+1}^j \tag{9}$$

The subproblem (P2) can be written as follows:

$$\begin{aligned} (\mathrm{P2}): \quad & \max_{\{G\}\{pd\}} \sum_{n=1}^{N} E_n \\ & \text{s.t.} (2), (3), (4), (8), (9) \end{aligned}$$

The variable $\{G^*\}$ and $\{pd^*\}$ can be obtained by Genetic Algorithm and the optimal trajectory $\{{q_m}^*\}$ can be obtained in (6).

4 simulations and results

A WSN with 15 SNs is considered, the SNs are distributed randomly within 1 km $\times$ 1 km two-dimensional plane. The task starts at point O_1 and eventually return to the starting point. The parameters of simulation are shown in Table 2.

Table 2: Key Simulation Parameters

The Notation	Physical Meaning	Value
H	UAV height	5 m
B	Total channel bandwidth	1 MHZ
σ^2	Noise power spectral density	-100 dbm
P_t	UAV transmission power	1 W

The trajectories and energies at higher and lower orders are shown in Fig.2. Both UAV flight trajectories are transmitted with the SN Within the energy transmission distance, and both them are continuous and smooth. When the SNs energy demands are high, the UAV chooses to fly above the SN. When the energy demand is low, the UAV chooses a trajectory further away from the SN. The harvested energy is shown in Fig.3.

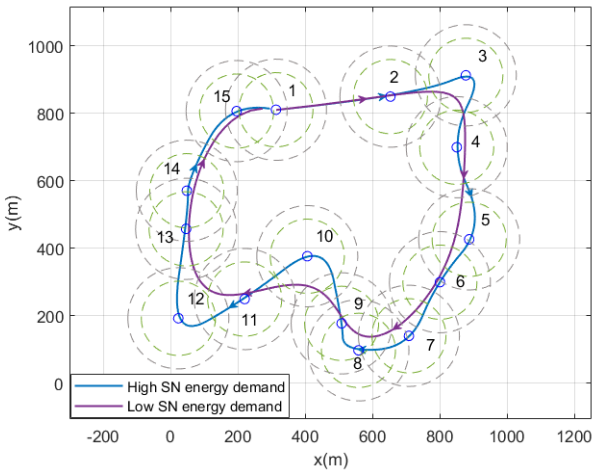

Fig. 2: Trajectory of the proposed methodology at higher and lower orders

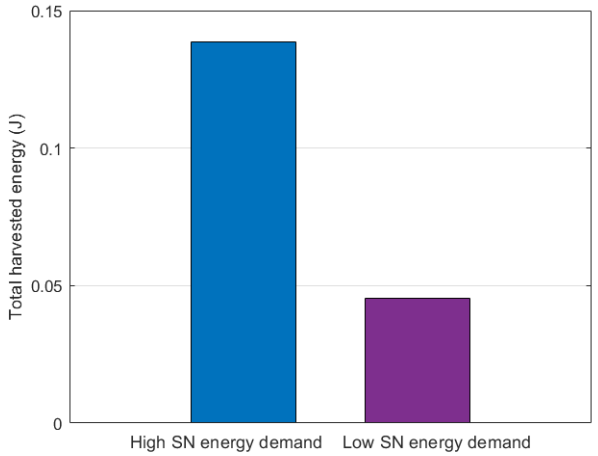

Fig. 3: Comparison of received energy at higher and lower energy demand

The trajectories before and after the change of node energy demand are shown in Fig.4 and Fig.5. The UAV detects that the demand of O_3, O_{10} and O_{12} is reduced at wake-up distance, and the UAV trajectory is adjusted according to the initial trajectory. The nodes that do not change still maintain the initial trajectory. In Fig.5, except for the harvested energy changes of O_3, O_{10} and O_{12}, the others are not change. The adaptability of the algorithm is verified.

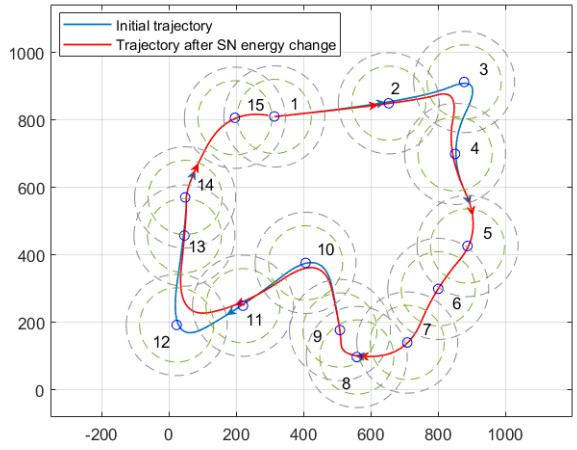

Fig. 4: The trajectories before and after adjusted according to the energy-aware

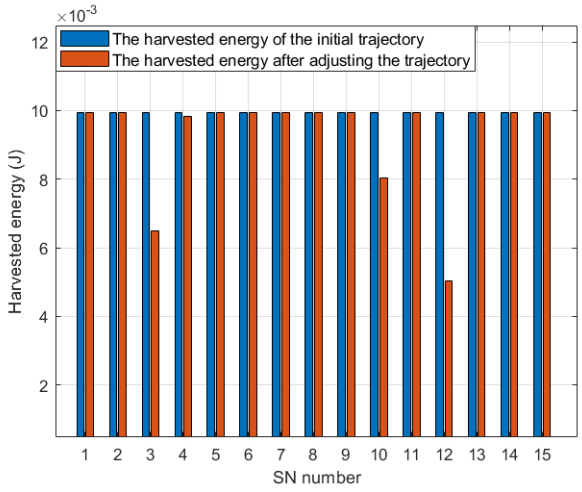

Fig. 5: The harvested energy after adjusting the trajectory

5 Conclusion

This paper maximizes the total energy received by all SNs by optimizing the UAV trajectory. An energy-aware method for smooth and adjustable trajectory is proposed. Firstly, the optimization problem (P1) is formulated according to the mathematical model. Second, the B-spline method is introduced to turn the smoothing problem into a solvable problem (P2). Finally, under the constraints, problem (P2) is solved to obtain the trajectory solution. Simulation results indicate the proposed method can adjust the overall trajectory according to the SNs demands. Meanwhile, according to the wake-up distance and energy-aware strategy, the trajectory of some nodes can be locally adjusted without affecting other trajectory segments.

References

[1] R. Xu, F. Lin, W. Shao, H. Wang, and F. Meng, "A union mec-UAV computation offloading system applied to wireless sensor network for marine renewable energy smart grids," in *2023 IEEE 6th International Conference on Electronic Information and Communication Technology (ICEICT)*, 2023, pp. 829–834.

[2] H. Sharma, A. Haque, and Z. A. Jaffery, "An efficient solar energy harvesting system for wireless sensor nodes," in *2018 2nd IEEE International Conference on Power Electronics, Intelligent Control and Energy Systems (ICPEICES)*, 2018, pp. 461–464.

[3] D. K. Sah, A. Hazra, R. Kumar, and T. Amgoth, "Harvested energy prediction technique for solar-powered wireless sensor networks," *IEEE Sensors Journal*, vol. 23, no. 8, pp. 8932–8940, 2023.

[4] A. A. Benbuk, N. Kouzayha, A. Eid, J. Costantine, Z. Dawy, F. Paonessa, and G. Virone, "Leveraging UAVs for passive rf charging and ultralowpower wake-up of ground sensors," *IEEE Sensors Letters*, vol. 4, no. 5, pp. 1–4, 2020.

[5] C. Zhan and H. Lai, "Energy minimization in internet-of-things system based on rotary-wing UAV," *IEEE Wireless Communications Letters*, vol. 8, no. 5, pp. 1341–1344, 2019.

[6] Y. Zeng, J. Xu, and R. Zhang, "Energy minimization for wireless communication with rotary-wing UAV," *IEEE transactions on wireless communications*, vol. 18, no. 4, pp. 2329–2345, 2019.

[7] M. Mozaffari, W. Saad, M. Bennis, and M. Debbah, "Wireless communication using unmanned aerial vehicles (UAVs): Optimal transport theory for hover time optimization," *IEEE Transactions on Wireless Communications*, vol. 16, no. 12, pp. 8052–8066, 2017.

[8] Z. Wang, G. Zhang, Q. Wang, K. Wang, and K. Yang, "Completion time minimization in wireless-powered UAV-assisted data collection system," *IEEE Communications Letters*, vol. 25, no. 6, pp. 1954–1958, 2021.

[9] J. Xu, Y. Zeng, and R. Zhang, "UAV-enabled wireless power transfer: Trajectory design and energy optimization," *IEEE transactions on wireless communications*, vol. 17, no. 8, pp. 5092–5106, 2018.

[10] J. Guo, S. Yang, Z. Yang, L. Lei, and X. Zhang, "Energy-balanced path optimization of UAV-assisted wireless power and information system," *Wireless Networks*, vol. 28, no. 5, pp. 2047–2059, 2022.

[11] R. Chai, Y. Gao, R. Sun, L. Zhao, and Q. Chen, "Time-oriented joint clustering and UAV trajectory planning in UAV-assisted WSNs: Leveraging parallel transmission and variable velocity scheme," *IEEE Transactions on Intelligent Transportation Systems*, 2023.

[12] Q. Wu, Y. Zeng, and R. Zhang, "Joint trajectory and communication design for multi-UAV enabled wireless networks," *IEEE Transactions on Wireless Communications*, vol. 17, no. 3, pp. 2109–2121, 2018.

[13] S. H. Lee, Y. S. Bae, and L. Choi, "The design of a ultra-low power rf wakeup sensor for wireless sensor networks," *Journal of Communications and Networks*, vol. 18, no. 2, pp. 201–209, 2016.

[14] P. Bassirian, J. Moody, A. Gao, T. Manzaneque, B. H. Calhoun, N. S. Barker, S. Gong, and S. M. Bowers, "A passive 461 mhz aln-cmos rf front-end for event-driven wakeup receivers," in *2017 IEEE SENSORS*, 2017, pp. 1–3.

[15] N. Yan, H. Zhang, X. Tan, and H. Min, "Analysis and design of a multi-mode wake-up receiver based on direct envelope

detection in wireless sensor networks," *IEEE Sensors Journal*, vol. 18, no. 22, pp. 9305–9314, 2018.

[16] X. Fu, Q. Pan, and X. Huang, "Aoi-energy-aware collaborative data collection in UAV-enabled wireless powered sensor networks," *IEEE Sensors Journal*, 2023.

[17] M. Sun, X. Xu, X. Qin, and P. Zhang, "Aoi-energy-aware UAV-assisted data collection for iot networks: A deep reinforcement learning method," *IEEE Internet of Things Journal*, vol. 8, no. 24, pp. 17 275–17 289, 2021.

[18] L. Shen, N. Wang, D. Zhang, J. Chen, X. Mu, and K. M. Wong, "Energy-aware dynamic trajectory planning for UAV-enabled data collection in mmtc networks," *IEEE Transactions on Green Communications and Networking*, vol. 6, no. 4, pp. 1957–1971, 2022.

[19] Y. Wang, G. Sun, G. Yang, and X. Ding, "Xgboosted neighbor referring in low-duty-cycle wireless sensor networks," *IEEE Internet of Things Journal*, vol. 8, no. 5, pp. 3446–3461, 2020.

[20] K. Qin, "General matrix representations for b-splines," in *Proceedings Pacific Graphics' 98. Sixth Pacific Conference on Computer Graphics and Applications (Cat. No. 98EX208)*. IEEE, 1998, pp. 37–43.

Proceedings of the 3rd Conference on Fully Actuated System Theory and Applications
May 10-12, 2024, Shenzhen, China

Innovation-trigger-based sequential fusion Kalman filter for CPSs with multiplicative noises against deception attacks

Baifu Zheng[1], Xuenan Zhang[1], Yuan Gao[1,2*], Jinfang Liu[3]

1. Electronics Engineering Collage, Heilongjiang University, Harbin 150086, P. R. China
E-mail: gaoyuan_hlju@163.com

2. Key Laboratory of Information Fusion Estimation and Detection, Harbin 150086, P. R. China
E-mail: m15546299948@163.com

3. School of Computer Science and Intelligence Education, Lingnan Normal University, Zhanjiang 524000, P. R. China

Abstract: For the CPSs with multiplicative noises against deception attacks, the sequential fusion filters under the innovation-triggered mechanism are presented. The random deception attacks occur in the transmitted measurements, the innovation-triggered mechanism is introduced to ease off the network transmission pressure, the fusion center makes two-sensor fusion estimation under three different fusion algorithms according to the arriving order of the local estimators. The results indicate that three sequential fusion algorithms can effectively ease off random attack effection and computational pressure, and the accuracy of sequential state fusion filter is higher than those of SCI fusion filter and SICI fusion filter. A simulation example verifies the effectiveness of above sequential fusion algorithms.

Key Words: Sequential fusion, CPSs, Innovation-triggered mechanism, Multiplicative noises, Deception attacks

1 Introduction

With the rapid development of modern control technology and communication technology, the cyber-physical systems (CPSs) solve the requirements of information and networking in the new era that the traditional single-point technology can not meet[1]. However, in many practical applications, the system model is uncertain due to modeling errors, random disturbances and other reasons. Commonly, the uncertainties include those formed by uncertain noise variance and random disturbance (such as multiplicative noise). These system uncertainties will cause the filtering performance deteriorate, and ever lead to divergence[2]. On the other side, during the communication process, the communication channel often suffers from the network attacks. The common network attacks include DoS attacks, deception attacks and so on, among which the deception attacks are the most common, since the deception attacks have strong concealment and are not easy to be found during transmission. In [3], the state estimator for CPSs with deception attacks is discussed, and the deception attacks are brought by a set of random variables to model measurements of attacks, that is, when the probability of the Bernoulli variable is 1, the system is attacked and the measurement is converted into an attack sequence, otherwise equal to the original measurement.

In order to ease off the transmission pressure of the CPSs and the pressure of network transmission, the event-triggered mechanisms can be introduced in the CPSs. Commonly, the event-triggered mechanisms include Send-on Delta and the innovation-triggered mechanisms. The triggered mechanism is considered in the CPSs in [4], where if the current measurements and the previous measurements exceed the threshold, the measurements at this moment will be transmitted.

This work is supported by the National Natural Science Foundation of China (NSFC-61503125), Natural Science Foundation of Heilongjiang Province (QC2013C062), Fundamental Research Support Program for Outstanding Young Teachers of Heilongjiang Province(YQJH2023139), and Science Foundation of Distinguished Young Scholars of Heilongjiang University(JCL201104).

In recent years, with the rapid development of navigation, target tracking and signal processing, the multi-sensor information fusion estimation method has been widely concerned and used. Commonly the state fusion methods include the centralized fusion and the distributed fusion methods. The centralized fusion method is performed by senting the measurement data of all sensors to the fusion center to form the centralized state space model, without any data loss, so it has the optimality. In the distributed fusion process, the local state estimation of each sensor is send to the fusion center for fusion according to certain fusion rule, which ease off the computational pressure of the fusion center. The Common distributed fusion mathods include ones weighted by matrices[5], diagonal matrices[6], scalars[7] and covariance intersection (CI) fusion[8] method. CI fusion do not need to know cross-covariance matrices between these local estimations, which ease off the computational pressure.

Since the sensor information is transmitted to the fusion center at different times, the fusion center is always idle and waiting for all sensors' information, so the concept of the sequential fusion is presented. The more commonly sequential fusion method includes the sequential state fusion(SSF), sequential covariance intersection(SCI) fusion[9] and sequential inverse covariance intersection(SICI) fusion[10]. SCI fusion algorithm is a recursive CI fusion of two sensors, which is fused according to the arrival sequence of the sensors, obviously reducing the computational burden of the fusion center. Similarly, both SICI fusion and SSF algorithms adopt multiplestage two-sensor fusion strategy respectively. In [11], the SSF estimation of sensor networks is presented, where the local estimates are weighted fused by matrices one by one according to the order of the data arriving at the fusion center, and the SSF has better estimation accuracy and lower computational complexity.

At present, the sequential fusion estimation for CPSs is rarely studied. For CPSs, a sequential fusion estimation with multiplicative noises against deception attacks is presented under the innovation-triggered mechanism, where the ran-

dom deception attacks attack the transmitted measurements, the innovation-triggered mechanism launches the observed data transmission after the attacks, and the measurement datas are sequentially fused by SSF, SCI and SICI fusion algorithms, according to the arrival order in the fusion center. These sequential fusion estimators have good tracking performance and estimation accuracy.

The structure of the paper is summarized as follows: in Section 2, by the fictitious noise technology, the CPSs model is transform to a new model. In Section 3, the local optimal filter with multiplicative noises against deception attacks under the innovation-triggered mechanism is designed. The SSF filter weighted by matrices is presented in Section 4, and then the SCI and SICI fusion filters are presented in Section 5. In Section 6, the accuracy relationship between the three sequential fusion algorithms are shown. The effectiveness of the three sequential fusion algorithms is verified by a typical CPSs simulation examples in Section 7. Finally, the conclusion is drawn in Section 8.

2 Problem Formulation

2.1 System Model

Consider the linear discrete CPSs with multiplicative noises:

$$x(l+1)=\left(\Phi+\sum_{s=1}^{q}\xi_s(l)\Phi_s\right)x(l)+\Gamma w(l), \quad (1)$$

$$y_i(l)=H_i x(l)+v_i(l), i=1,\cdots,N, \quad (2)$$

where l is the discrete time, $x(l)\in R^n$ is the state, $w(l)\in R^r$ is the process noise, $\xi_s(l)\in R^1$ is the multiplicative noises, $y_i(l)\in R^{m_i}\,(i=1,2,\cdots,N)$ is the measurement of sensor i, $v_i(l)\in R^{m_i}$ is the measurement noise, Φ,Φ_s,Γ and H_i are known constant matrices, and N is the number of sensors.

Assumption 1. $w(l)$, $v_i(l)$ and $\xi_s(l)$ are uncorrelated Gaussian white noises with zero means and variences as Q_w, R_i and $\sigma_{\xi_s}^2$ respectively

$$\mathrm{E}\left\{\begin{bmatrix} w(l)\\ v_i(l)\\ \xi_s(l)\end{bmatrix}\begin{bmatrix} w^{\mathrm{T}}(j) & v_l^{\mathrm{T}}(j) & \xi_k^{\mathrm{T}}(j)\end{bmatrix}\right\}=\begin{bmatrix} Q_w & 0 & 0\\ 0 & R_i\delta_{il} & 0\\ 0 & 0 & \sigma_{\xi_s}^2\delta_{sk}\end{bmatrix}\delta_{lj} \quad (3)$$

where $\delta_{ll}=1,\delta_{lj}=0\,(l\neq j)$.

Assumption 2. $x(0)$ is independent of $w(l)$, $v_i(l)$ and $\xi_s(l)$, i.e.,

$$\mathrm{E}\left[x(0)w^{\mathrm{T}}(l)\right]=0,\mathrm{E}\left[x(0)v_i^{\mathrm{T}}(l)\right]=0,\quad \mathrm{E}\left[x(0)\xi_s^{\mathrm{T}}(l)\right]=0,\forall l \quad (4)$$

with

$$\mathrm{E}[x(0)]=x_0,\mathrm{E}\left[(x(0)-x_0)(x(0)-x_0)^{\mathrm{T}}\right]=P_0 \quad (5)$$

When the measurement $y_i(l)$ is transmitted to the fusion center, the new measurement suffering the deception attacks can be expressed by

$$y_i^a(l)=-y_i(l)+\zeta_i(l), \quad (6)$$

where $\zeta_i(l)\in R^{m_i}$ is the attack signal injected by the attacker, which is a zero mean, Gaussian white noise with variance $\Xi_i>0$.

Usually a set of Gaussian random variables $\{\alpha_i(l)\}$ are generated to represent the attack phenomenon, which bypasses the χ^2 detector with

$$\Pr\{\alpha_i(l)=1\}=\sigma_i,\Pr\{\alpha_i(l)=0\}=1-\sigma_i, \quad (7)$$

Then, denote the final measurement $z_i(l)$ as

$$\begin{aligned} z_i(l)&=y_i(l)+\alpha_i(l)y_i^a(l)\\ &=(1-\alpha_i(l))y_i(l)+\alpha_i(l)\zeta_i(l). \end{aligned} \quad (8)$$

From (8), it can be seen that the measurement is attacked when $\alpha_i(l)=1$, and when $\alpha_i(l)=0$, the attacks is unsuccessful.

Our aim is to design the sequential state fusion filter, SCI and SICI fusion filters for CPSs with multiplicative noises against deception attacks under the innovation-triggered mechanism, respectively.

2.2 System Model Transformation

Applying the fictitious noises technique, the CPSs system (1) and (2) are transformed into

$$x(l+1)=\Phi x(l)+w_a(l), \quad (9)$$

where the fictitious process noise is

$$w_a(l)=\sum_{s=1}^{q}\xi_s(l)\Phi_s x(l)+\Gamma w(l), \quad (10)$$

Its variance is

$$Q_a(l)=\sum_{s=1}^{q}\sigma_{\xi_s}^2(l)\Phi_s X(l)\Phi_s^{\mathrm{T}}+\Gamma Q_w(l)\Gamma^{\mathrm{T}}, \quad (11)$$

where $X(l)=\mathrm{E}\left[x(l)x^{\mathrm{T}}(l)\right]$ is the second moment of the state. From the CPSs model (1) and (2), it yields

$$X(l)=\Phi X(l-1)\Phi^{\mathrm{T}}+\sum_{s=1}^{q}\sigma_{\xi_s}^2(l)\Phi_s X(l)\Phi_s^{\mathrm{T}}+\Gamma Q_w(l)\Gamma^{\mathrm{T}}, \quad (12)$$

whose initial value is $X(0)=x_0x_0^{\mathrm{T}}+P_0$.

Substituting (2) into (8) yields the actual sensor output

$$\begin{aligned} z_i(l)&=(1-\sigma_i)H_i x(l)+(1-\alpha_i(l))v_i(l)\\ &\quad+\alpha_i(l)\zeta_i(l)-(\alpha_i(l)-\sigma_i)H_i x(l). \end{aligned} \quad (13)$$

By using the fictitious noise technique, the observed equation can be transformed as

$$z_i(l)=\Pi_i x(l)+V_i(l), \quad (14)$$

where the new observation matrices are defined as

$$\Pi_i=(1-\sigma_i)H_i, \quad (15)$$

and the fictitious measurement noises are defined as

$$\begin{aligned} V_i(l)&=(1-\alpha_i(l))v_i(l)+\alpha_i(l)\zeta_i(l)\\ &\quad-(\alpha_i(l)-\sigma_i)H_i x(l). \end{aligned} \quad (16)$$

It can be easily verified that the fictitious measurement noise is a whise noise with

$$\mathrm{E}\left[V_i\left(l\right)\right]=0, \tag{17}$$

and the variance matrice

$$\begin{aligned} R_{V_i}\left(l\right) &= \mathrm{E}\left[V_i\left(l\right)V_i^{\mathrm{T}}\left(l\right)\right] \\ &= \left(1-\sigma_i\right)R_i\left(l\right)+\sigma_i\Xi_i+\sigma_i\left(1-\sigma_i\right)H_iX\left(l\right)H_i^{\mathrm{T}}. \end{aligned} \tag{18}$$

Remark 1. Since $\Gamma Q\Gamma^{\mathrm{T}}\geqslant 0$, a sufficient condition for the existence of a unique semidefinite solution to the generalized Lyapunov equation (12) is that the spectral radius $\rho\left(\Phi_\delta\right)<1$ of the matrix $\Phi_\delta=\Phi\otimes\Phi+\sum_{s=1}^{q}\sigma_{\xi_s}^2\Phi_s\otimes\Phi_s$, where the symbol $\otimes$ represents Kronecker product, so Φ_δ is a stable matrix.

2.3 The Innovation-triggered Mechanism

Since the energy constraints are prevalent in CPSs, the innovation-triggered mechanism is used to design the estimator[12], the innovation can be denoted as a one-step prediction error of the measurement, i.e.

$$e_i\left(l\right)=y\left(l\right)-\hat{y}_i\left(l|l-1\right), \tag{19}$$

and its covariance is denoted as $Q_{e_i}\left(l\right)=\mathrm{E}\left\{e_i\left(l\right)e_i^{\mathrm{T}}\left(l\right)\right\}$. Standardizing the innovation, it yields

$$\bar{e}_i\left(l\right)=\frac{e_i\left(l\right)}{\sqrt{Q_{e_i}\left(l\right)}} \tag{20}$$

The innovation-triggered threshold value is $\theta_i>0$, and the Bernoulli variable $\gamma_i\left(l\right)$ is usually introduced to describe the sensor transmission states. Then, $\gamma_i\left(l\right)=1$ represents $\bar{e}_i\left(l\right)$ falls outside the threshold value θ_i, and the measurement contains a lot of new information, so data transmission is required. On the contrary, $\gamma_i\left(l\right)=0$ represents the measuremants should be sent, i.e.

$$\gamma_i\left(l\right)=\begin{cases}1, & ||\bar{e}_i\left(l\right)||_2\geqslant\ \theta_i\\ 0, & other\end{cases} \tag{21}$$

Remark 2. The innovation $e_i\left(l\right)$ and its covariance $Q_{e_i}\left(l\right)$ defined here, are given later in the calculation of the local optimal filter in Theorem 1.

3 Local Optimal Filter

Theorem 1. The innovation-trigger-based local Kalman filters for the CPSs with multiplicative noises against deception attacks (1) and (13) are obtained under Assumption 1 and 2

$$\hat{x}_i\left(l|l\right)=\hat{x}_i\left(l|l-1\right)+\gamma_i\left(l\right)K_i\left(l\right)e_i\left(l\right), \tag{22}$$

$$e_i\left(l\right)=z_i\left(l\right)-\left(1-\sigma_i\right)H_i\hat{x}_i\left(l|l-1\right), \tag{23}$$

$$\begin{aligned} Q_{e_i}\left(l\right) &= \left(1-\sigma_i\right)^2H_iP_i\left(l|l-1\right)H_i^{\mathrm{T}}+\left(1-\sigma_i\right)R_i\left(l\right) \\ &\quad+\sigma_i\Xi_i+\sigma_i\left(1-\sigma_i\right)H_iX\left(l\right)H_i^{\mathrm{T}}, \end{aligned} \tag{24}$$

$$K_i\left(l\right)=\left[\left(1-\sigma_i\right)P_i\left(l|l-1\right)H_i^{\mathrm{T}}\right]Q_{e_i}^{-1}\left(l\right), \tag{25}$$

$$P_i\left(l|l\right)=P_i\left(l|l-1\right)-\gamma_i\left(l\right)K_i\left(l\right)Q_{e_i}\left(l\right)K_i^{\mathrm{T}}\left(l\right), \tag{26}$$

$$\begin{aligned} P_i\left(l+1|l\right) &= \Phi P_i\left(l|l\right)\Phi^{\mathrm{T}}+\sum_{s=1}^{q}\sigma_{\xi_s}^2\left(l\right)\Phi_sX\left(l\right)\Phi_s^{\mathrm{T}} \\ &\quad+\Gamma Q_w\left(l\right)\Gamma^{\mathrm{T}}, \end{aligned} \tag{27}$$

Proof. When $\gamma_i\left(l\right)=1$, denote the measurement $Z_i\left(l\right)$ received by estimator at all instants as

$$Z_i\left(l\right)=\left\{\gamma_i\left(1\right)z_i\left(1\right),\gamma_i\left(2\right)z_i\left(2\right),\cdots,\gamma_i\left(l\right)z_i\left(l\right)\right\}, \tag{28}$$

Applying to Projective Theorem, the local filters can be calculated as

$$\begin{aligned} \hat{x}_i\left(l|l\right) &= \mathrm{E}\left[x\left(l\right)|Z_i\left(l\right)\right] \\ &= \hat{x}_i\left(l|l-1\right)+\gamma_i\left(l\right)K_i\left(l\right)e_i\left(l\right), \end{aligned} \tag{29}$$

where $K_i\left(l\right)=\mathrm{E}\left[x\left(l\right)e_i^{\mathrm{T}}\left(l\right)\right]\left\{\mathrm{E}\left[e_i\left(l\right)e_i^{\mathrm{T}}\left(l\right)\right]\right\}^{-1}$. By using (19), the innovation $e_i\left(l\right)$ can be written as

$$e_i\left(l\right)=\left(1-\sigma_i\right)H_i\tilde{x}_i\left(l|l-1\right)+V_i\left(l\right), \tag{30}$$

From (30), the innovation covariance can be calculated as

$$\begin{aligned} Q_{e_i}\left(l\right) &= \left(1-\sigma_i\right)^2H_iP_i\left(l|l-1\right)H_i^{\mathrm{T}}+\left(1-\sigma_i\right)R_i\left(l\right) \\ &\quad+\sigma_i\Xi_i+\sigma_i\left(1-\sigma_i\right)H_iX\left(l\right)H_i^{\mathrm{T}}, \end{aligned} \tag{31}$$

Since $x\left(l\right)=\hat{x}_i\left(l|l-1\right)+\tilde{x}_i\left(l|l-1\right)$ and the orthogonality between $\hat{x}_i\left(l|l-1\right)$ and $\tilde{x}_i\left(l|l-1\right)$, from (1) and (30), the filter gain matrices $K_i\left(l\right)$ can be obtained as

$$K_i\left(l\right)=\left(\left(1-\sigma_i\right)P_i^{\mathrm{T}}\left(l|l-1\right)H_i^{\mathrm{T}}\right)Q_{e_i}^{-1}\left(l\right), \tag{32}$$

Using (1) and (29) yields the filtering error $\tilde{x}_i\left(k|k\right)$ as

$$\tilde{x}_i\left(l|l\right)=\tilde{x}_i\left(l|l-1\right)-\gamma_i\left(l\right)K_i\left(l\right)e_i\left(l\right), \tag{33}$$

Because of the orthogonality between $\tilde{x}_i\left(l|l-1\right)$ and $w\left(l\right)$ and the orthogonality between $\tilde{x}_i\left(l|l-1\right)$ and $v_i\left(l\right)$, from (33), the filter error variance $P_i\left(l|l\right)$ is derived as follows

$$P_i\left(l|l\right)=P_i\left(l|l-1\right)-\gamma_i\left(l\right)K_i\left(l\right)Q_{e_i}\left(l\right)K_i^{\mathrm{T}}\left(l\right), \tag{34}$$

From (33), it yields the prediction error variance $P_i\left(l+1|l\right)$

$$\begin{aligned} P_i\left(l+1|l\right) &= \Phi P_i\left(l|l\right)\Phi^{\mathrm{T}}+\sum_{s=1}^{q}\sigma_{\xi_s}^2\left(l\right)\Phi_sX\left(l\right)\Phi_s^{\mathrm{T}} \\ &\quad+\Gamma Q_w\left(l\right)\Gamma^{\mathrm{T}}, \end{aligned} \tag{35}$$

When $\gamma_i\left(l\right)=0$, the local filter values are same as the local predictor values of the last instant, i.e.

$$\hat{x}_i\left(l|l\right)=\hat{x}_i\left(l|l-1\right),P_i\left(l|l\right)=P_i\left(l|l-1\right), \tag{36}$$

The proof of theorem 1 is completed.

4 SSF Filter

Theorem 2. The innovation-trigger-based SSF algorithm is obtained for CPSs with multiplicative noises against deception attacks (1) and (13) under Assumption 1 and 2

$$\hat{x}_i^{SSF}(l|l) = (1-\gamma_i(l))\,\hat{x}_{i-1}^{SSF}(l|l) + \gamma_i(l)\left(\Omega_1^{(i)}\hat{x}_{i-1}^{SSF}(l|l) + \Omega_2^{(i)}\hat{x}_{i+1}(l|l)\right), \tag{37}$$

$$P_i^{SSF}(l|l) = \left(e^{\mathrm{T}}\left(\Sigma_i(l|l)\right)^{-1}e\right)^{-1}, \tag{38}$$

$$\hat{x}^{SSF}(l|l) = \hat{x}_N^{SSF}(l|l), \tag{39}$$

$$P^{SSF}(l|l) = P_N^{SSF}(l|l), \tag{40}$$

and it yields the SSF predictor

$$\hat{x}^{SSF}(l+1|l) = \Phi\hat{x}^{SSF}(l|l), \tag{41}$$

$$P^{SSF}(l+1|l) = \Phi P^{SSF}(l|l)\,\Phi^{\mathrm{T}} + \sum_{s=1}^{q}\sigma_{\xi_s}^2(l)\,\Phi_s X(l)\,\Phi_s^{\mathrm{T}} + \Gamma Q_w(l)\,\Gamma^{\mathrm{T}}, \tag{42}$$

where the weights are given as

$$\begin{bmatrix}\Omega_1^{(i)}\\ \Omega_2^{(i)}\end{bmatrix} = \left(\Sigma_i(l|l)\right)^{-1}e\left[e^{\mathrm{T}}\left(\Sigma_i(l|l)\right)^{-1}e\right]^{-1}, \tag{43}$$

$$\Sigma_i(l|l) = \begin{bmatrix}P_{i-1}^{SSF} & P_{\binom{SSF}{i-1},i+1}\\ P_{i+1,\binom{SSF}{i-1}} & P_{i+1}\end{bmatrix}, \tag{44}$$

and where $P_{i+1,\binom{SSF}{i-1}} = P_{\binom{SSF}{i-1},i+1}^{\mathrm{T}}$, and the cross covariance between the fusion filter error and the (i+1)-th sensor filter error is computed as

$$P_{\binom{SSF}{i-1},i+1}(l|l) = (1-\gamma_i(l))\,P_{\binom{SSF}{i-2},i+1}(l|l) + \gamma_i(l)\left(\Omega_1^{(i-1)} \times P_{\binom{SSF}{i-2},i+1}(l|l) + \Omega_2^{(i-1)}P_{i,i+1}(l|l)\right), \tag{45}$$

where the cross covariance between the (i)-th filter error and the (i+1)-th sensor filter error is computed as

$$P_{i,i+1}(l|l) = P_{i,i+1}(l|l-1) + \gamma_i(l)\,\gamma_{i+1}(l)\,K_i(l)\,Q_{e_{i,i+1}}(l) \times K_{i+1}^{\mathrm{T}}(l) - (1-\sigma_{i+1})\,\gamma_{i+1}(l)\,P_{i,i+1}(l|l-1) \times H_{i+1}^{\mathrm{T}}K_{i+1}^{\mathrm{T}}(l) - (1-\sigma_i)\,\gamma_i(l)\,K_i(l)\,H_i \times P_{i,i+1}(l|l-1), \tag{46}$$

and the local prediction error cross covariance matrices and the innovation error cross covariance matrices are given as

$$P_{i,i+1}(l+1|l) = \Phi P_{i,i+1}(l|l)\,\Phi^{\mathrm{T}} + \sum_{s=1}^{q}\sigma_{\xi_s}^2(l)\,\Phi_s X(l)\,\Phi_s^{\mathrm{T}} + \Gamma Q_w(l)\,\Gamma^{\mathrm{T}}, \tag{47}$$

$$Q_{e_{i,i+1}}(l) = (1-\sigma_i)(1-\sigma_{i+1})\,H_i P_{i,i+1}(l|l-1)\,H_{i+1}^{\mathrm{T}}, \tag{48}$$

Proof. When $\gamma_i(l) = 1$, applying the fusion rule with matrix weights is presented in [5], the optimal fusion filter and variance is given by the sequential approach as

$$\hat{x}_i^{SSF}(l|l) = \Omega_1^{(i)}\hat{x}_{i-1}^{SSF}(l|l) + \Omega_2^{(i)}\hat{x}_{i+1}(l|l), \tag{49}$$

$$P_i^{SSF}(l|l) = \left(e^{\mathrm{T}}\left(\Sigma_i(l|l)\right)^{-1}e\right)^{-1}, \tag{50}$$

where $\Omega_1^{(i)} + \Omega_2^{(i)} = I$, and using (1) and (49) yield the fusion filter error as

$$\tilde{x}_i^{SSF}(l|l) = \Omega_1^{(i)}\tilde{x}_{i-1}^{SSF}(l|l) + \Omega_2^{(i)}\tilde{x}_{i+1}(l|l), \tag{51}$$

By (30), the innovation covariance $Q_{e_{i,i+1}}(l) = \mathrm{E}\left[e_i(l|l)\,e_{i+1}^{\mathrm{T}}(l|l)\right]$ is given as

$$Q_{e_{i,i+1}}(l) = (1-\sigma_i)(1-\sigma_{i+1})\,H_i P_{i,i+1}(l|l-1)\,H_{i+1}^{\mathrm{T}}, \tag{52}$$

Using (30) and (33) yield the filter error cross covariance $P_{i,i+1}(l|l) = \mathrm{E}\left[\tilde{x}_i(l|l)\,\tilde{x}_{i+1}^{\mathrm{T}}(l|l)\right]$ between i-th sensor and (i+1)-th sensor is given as

$$P_{i,i+1}(l|l) = P_{i,i+1}(l|l-1) + K_i(l)\,Q_{e_{i,i+1}}(l)\,K_{i+1}^{\mathrm{T}}(l) - (1-\sigma_{i+1})\,P_{i,i+1}(l|l-1)\,H_{i+1}^{\mathrm{T}}K_{i+1}^{\mathrm{T}}(l) - (1-\sigma_i)\,K_i(l)\,H_i P_{i,i+1}(l|l-1), \tag{53}$$

From (33) and (51), the cross covariance $P_{\binom{SSF}{i-1},i+1}(l|l) = \mathrm{E}\left[\tilde{x}_{i-1}^{SSF}(l|l)\,\tilde{x}_{i+1}^{\mathrm{T}}(l|l)\right]$ between the fusion filter error and the (i+1)-th sensor filter error is obtained as

$$P_{\binom{SSF}{i-1},i+1}(l|l) = \Omega_1^{(i-1)}P_{\binom{SSF}{i-2},i+1}(l|l) + \Omega_2^{(i-1)}P_{i,i+1}(l|l), \tag{54}$$

When $\gamma_i(l) = 0$, the fusion cross covoriance are same as the local predictor values of the last instant, i.e.

$$P_{i,i+1}(l|l) = P_{i,i+1}(l|l-1), \tag{55}$$

$$P_{\binom{SSF}{i-1},i+1}(l|l) = P_{\binom{SSF}{i-2},i+1}(l|l), \tag{56}$$

$$\hat{x}_i^{SSF}(l|l) = \hat{x}_{i-1}^{SSF}(l|l), \tag{57}$$

The proof of theorem 2 is completed.

5 SCI and SICI Fusion Filter

Lamma 1[13] The innovation-trigger-based SCI fusion algorithm is obtained for CPSs with multiplicative noises against deception attacks (1) and (13) under Assumptions 1 and 2

$$\hat{x}_i^{CI}(l|l) = (1-\gamma_i(l))\,\hat{x}_{i-1}^{CI}(l|l) + \gamma_i(l)\,P_{i-1}^{CI}(l|l)\left[w_{CI}^{(i-1)} \times \left(P_{i-1}^{CI}(l|l)\right)^{-1}\hat{x}_{i-1}^{CI}(l|l) + \left(1-w_{CI}^{(i-1)}\right) \times P_i^{-1}(l|l)\,\hat{x}_i(l|l)\right], \tag{58}$$

$$P_i^{CI}(l|l) = (1-\gamma_i(l))\,P_{i-1}^{CI}(l|l) + \gamma_i(l)\left[w_{CI}^{(i-1)} \times \left(P_{i-1}^{CI}(l|l)\right)^{-1} + \left(1-w_{CI}^{(i-1)}\right)P_i^{-1}(l|l)\right]^{-1}, \tag{59}$$

$$\hat{x}^{SCI}(l|l) = \hat{x}^{CI}_{N-1}(l|l), \tag{60}$$

$$P^{SCI}(l|l) = P^{CI}_{N-1}(l|l), \tag{61}$$

where the initial values are $P^{CI}_i(0|0) = P_0, \hat{x}^{CI}_i(0|0) = x_0$, and the minimization performance index with the optimal weighting coefficient $w^{(i-1)}_{CI}$ is as follows

$$\begin{aligned}\min_{w^{(i-1)}_{CI}\in[0,1]} \mathrm{tr}P^{CI}_i(l|l) = \min_{w^{(i-1)}_{CI}\in[0,1]} \mathrm{tr}\Big\{&(1-\gamma_i(l))P^{CI}_{i-1}(l|l)\\ &+\gamma_i(l)\Big[w^{(i-1)}_{CI}\left(P^{CI}_{i-1}(l|l)\right)^{-1}\\ &+\left(1-w^{(i-1)}_{CI}\right)P^{-1}_i(l|l)\Big]^{-1}\Big\},\end{aligned} \tag{62}$$

Lamma 2[13] The innovation-trigger-based SICI fusion algorithm is obtained for CPSs with multiplicative noises against deception attacks (1) and (13) under Assumptions 1 and 2

$$\begin{aligned}\hat{x}^{ICI}_i(l|l) = (1-\gamma_i(l))\hat{x}^{ICI}_{i-1}(l|l) + \gamma_i(l)\big[&K^{ICI}(l)\\ &\times\hat{x}^{ICI}_{i-1}(l|l) + L^{ICI}(l)\hat{x}_i(l|l)\big],\end{aligned} \tag{63}$$

$$\begin{aligned}P^{ICI}_i(l|l) = (1-\gamma_i(l))P^{ICI}_{i-1}(l|l) + \gamma_i(l)\Big\{&\left(P^{ICI}_{i-1}(l|l)\right)^{-1}\\ &+(P_i(l|l))^{-1} + \Big[w^{(i-1)}_{ICI}\ P^{ICI}_{i-1}(l|l)\\ &+\left(1-w^{(i-1)}_{ICI}\right)P^{-1}_i(l|l)\Big]^{-1}\Big\},\end{aligned} \tag{64}$$

$$\begin{aligned}K^{ICI}(l) = P^{ICI}_i(l|l)\Big\{&\left(P^{ICI}_{i-1}(l|l)\right)^{-1} - w^{(i-1)}_{ICI}\\ &\Big[w^{(i-1)}_{ICI}P^{ICI}_{i-2}(l|l) + \left(1-w^{(i-1)}_{ICI}\right)P_i(l|l)\Big]^{-1}\Big\},\end{aligned} \tag{65}$$

$$\begin{aligned}L^{ICI}(l) = P^{ICI}_i(l|l)\Big\{&(P_i(l|l))^{-1} - \left(1-w^{(i-1)}_{ICI}\right)\\ &\Big[w^{(i-1)}_{ICI}P^{ICI}_{i-2}(l|l) + \left(1-w^{(i-1)}_{ICI}\right)P_i(l|l)\Big]^{-1}\Big\},\end{aligned} \tag{66}$$

$$\hat{x}_{SICI}(l|l) = \hat{x}^{ICI}_{N-1}(l|l), \tag{67}$$

$$P_{SICI}(l|l) = P^{ICI}_{N-1}(l|l), \tag{68}$$

where the initial values are $P^{ICI}_i(0|0) = P_0, \hat{x}^{ICI}_i(0|0) = x_0$, and the minimization performance index with the optimal weighting coefficient $w^{(i-1)}_{ICI}$ is as follows

$$\begin{aligned}\min_{w^{(i-1)}_{ICI}\in[0,1]} \mathrm{tr}P^{ICI}_i(l|l) = \min_{w^{(i-1)}_{ICI}\in[0,1]} \mathrm{tr}\Big\{&\left(P^{ICI}_{i-1}(l|l)\right)^{-1}\\ &+(P_i(l|l))^{-1} + \Big[w^{(i-1)}_{ICI}P^{ICI}_{i-1}(l|l)\\ &+\left(1-w^{(i-1)}_{ICI}\right)P^{-1}_i(l|l)\Big]^{-1}\Big\}^{-1},\end{aligned} \tag{69}$$

6 Accuracy Analysis

Theorem 3. The accuracy relationship between three sequential fusion filter algorithms and the local filters is as follows

$$\mathrm{tr}P^{SSF} \leqslant \mathrm{tr}P^{SICI} \leqslant \mathrm{tr}P^{SCI} \leqslant \mathrm{tr}P_i, i = 1, 2, \cdots, N, \tag{70}$$

Proof. Under the condition of the same deception attacks, the same threshold values, and the same arriving order of local estimators, the two-sensor state fusion algorithm is optimal in the sence of LUMV criterion, so it has the highest accurcies among three fusion algorithms. It is proved in [14] that the estimation accurcy of ICI fusion algorithm is higher than that of CI fusion algorithm. All of the fused algorithms are more accurate than local filters. Therefore, under the sequential fusion form, the accury relations will still be kept, that is, (70) holds.

7 Simulation Example

Consider a three-sensor cycle-physical system

$$\begin{aligned}x(l+1) = &\left(\begin{bmatrix}0.9 & \mathrm{T}_0\\ 0 & 0.9\end{bmatrix} + \xi(l)\begin{bmatrix}0.2 & 0\\ 0 & 0.1\end{bmatrix}\right)x(l)\\ &+\begin{bmatrix}\mathrm{T}^2_0/2\\ \mathrm{T}_0\end{bmatrix}w(l),\end{aligned} \tag{71}$$

$$y_i(l) = H_i x(l) + v_i(l), \tag{72}$$

$$z_i(l) = (1-\alpha_i(l))y_i(l) + \alpha_i(l)\zeta_i(l), i = 1, 2, 3. \tag{73}$$

where $\mathrm{T}_0 = 0.5, H_1 = \begin{bmatrix}0 & 1\end{bmatrix}, H_2 = \begin{bmatrix}1 & 0\end{bmatrix}, H_3 = \begin{bmatrix}1 & 1\end{bmatrix}$, $w(l)$, $\xi(l)$ and $v_i(l)$ are zero mean white noises, their variances are $Q_w = 0.21, \sigma^2_\xi = 0.02, \Sigma_1 = 0.04, \Sigma_2 = 0.3$ and $\Sigma_3 = 0.5$, respectively. The innovation-triggered threshold $\theta_i = 0.3$. These attacked probabilities α_i are selected as $\alpha_1 = 0.1, \alpha_2 = 0.2$ and $\alpha_3 = 0.4$. $\zeta_i(l)$ are random zero-mean Gaussian white noises, and their variances are $\Xi_1 = 0.16, \Xi_2 = 0.12$ and $\Xi_3 = 0.04$ respectively.

The simulation results are shown in Fig.1, where the solid curves represent the real state values $x_1(l)$ and $x_2(l)$, the dashed curves represent the SCI fusion Kalman filter estimation $\hat{x}^{SCI}_1(l|l)$ and $\hat{x}^{SCI}_2(l|l)$ against deception attacks under the innovation-triggered mechanism, the doted curves represent the SICI fusion Kalman filter estimation $\hat{x}^{SICI}_1(l|l)$ and $\hat{x}^{SICI}_2(l|l)$ against deception attacks under the innovation-triggered mechanism, the double doted curves represent the SSF Kalman filter estimation $\hat{x}^{SSF}_1(l|l)$ and $\hat{x}^{SSF}_2(l|l)$ against deception attacks under the innovation-triggered mechanism. It can be seen that these algorithms have good tracking results.

In order to verify the effectiveness of the presented sequential fusion Kalman filters, 100 Monte-Carlo simulations are performed and the mean square relative error (MSRE) curves of the fusion filter are drawn, as shown in Fig.2, where $MSRE^{(n)}(l) = \frac{1}{100}\sum_{p=1}^{100}\left\{\left[\hat{x}^{(n)}_{(p)}(l|l) - x^{(n)}_{(p)}(l)\right]/x^{(n)}_{(p)}(l)\right\}^2 (n = SCI, SICI, SSF)$, the subscript p represents the p-th experiment. The doted curves represent the MSRE value of SCI

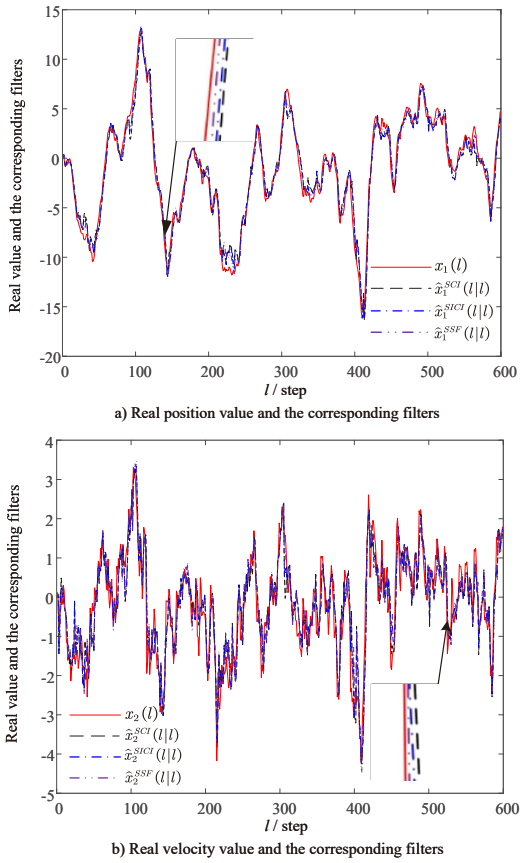

Fig. 1: Fusion filter tracking curves

fusion filter, the solid curves represent the MSRE value of the SICI fusion filter, and the dashed curves represent the MSRE value of the SSF filter. The comparison of MSRE values of different fusion algorithms for each 100 steps from $l = 0$ to $l = 600$ is shown in Table 1. It can be seen that when the running steps are sufficient long, under the innovation-triggered mechanism the accuracy of the SCI fusion filter is the lowest, the accuracy of the SICI fusion filter is the second, and both of their accuracies are lower than that of the SSF filter.

Table 1: The comparison of MSRE values of different sequential fusion algorithms for each 100 steps from $l = 0$ to $l = 600$.

l	100	200	300	400	500	600
$MSRE^{SCI}(l)$	0.0794	0.0695	0.0942	0.0310	0.1464	0.0825
$MSRE^{SICI}(l)$	0.0546	0.0560	0.0674	0.0275	0.1356	0.0718
$MSRE^{SSF}(l)$	0.0191	0.0124	0.0498	0.0100	0.0493	0.0491

8 Conclusion

Three sequential fusion filters for CPSs with multiplicative noises against deception attacks have been presented under the innovation-triggered mechanism. The uncertainties caused by the deception attacks and multiplicative noises have been transformed into white fictitious noises by the model transformation, and the new measurements are send to the fusion center. The simulation results show that the estimation accuracy of the SICI fusion filter is higher than that of the SCI fusion filter, and lower than that of the SSF filter,

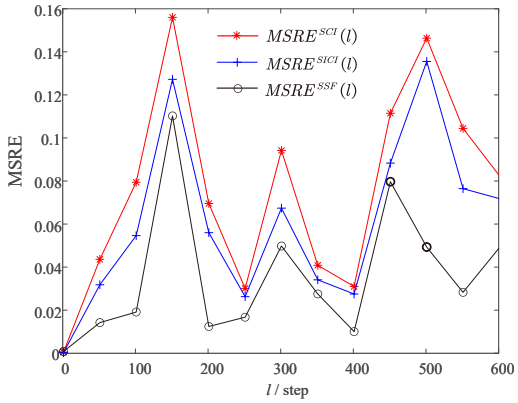

Fig. 2: The MSRE curves of different fusion algorithms

which verifies the effectiveness of these above sequential fusion approaches. In addition, the accuracy analysis verified in this paper also greatly explains the accuracy relationship among the three fusion algorithms.

References

[1] Jamaludin J, Rohani J M, Cyber-physical system (cps): State of the art, in *2018 International Conference on Computing, Electronic and Electrical Engineering (ICE Cube). IEEE*, 2018: 1-5.

[2] Sun S L, Lin H L, Ma J, et al, Multi-sensor distributed fusion estimation with applications in networked systems: A review paper, in *Information Fusion*, 2017, 38: 122-134.

[3] Zhao C, Lam J, Lin H, State estimation of CPSs with deception attacks: Stability analysis and approximate computation, in *Neurocomputing*, 2021: 318-326.

[4] Han Z, Zhang S, Jin Z, et al, Secure state estimation for event-triggered cyber-physical systems against deception attacks, in *Journal of the Franklin Institute*, 2022, 359(18): 11155-11185.

[5] Sun S L, Deng Z L, Multi-sensor optimal information fusion Kalman filter, in *Automatica*, 2004, 40(6): 1017-1023.

[6] Deng Z L, Gao Y, Mao L, et al, New approach to information fusion steady-state Kalman filtering, in *Automatica*, 2005, 41(10): 1695-1707.

[7] Sun S L, Multi-sensor information fusion white noise filter weighted by scalars based on Kalman predictor, in *Automatica*, 2004, 40(8): 1447-1453.

[8] Julier S J, Uhlmann J K, Using covariance intersection for SLAM, in *Robotics and Autonomous Systems*, 2007, 55(1): 3-20.

[9] Deng Z L, Zhang P, Qi W J, et al, Sequential covariance intersection fusion Kalman filter, in *Information Sciences*, 2012, 189: 293-309.

[10] Noack B, Sijs J, Reinhardt M, et al, Decentralized data fusion with inverse covariance intersection, in *Automatica*, 2017, 79: 35-41.

[11] Zhang W A, Shi L, Sequential fusion estimation for clustered sensor networks, in *Automatica*, 2018, 89: 358-363.

[12] Shi D, Chen T, Shi L, Event-triggered maximum likelihood state estimation, in *Automatica*, 2014, 50(1): 247-254.

[13] Xu K, Li X Y, Wang J, et al, Robust Sequential Fusion Estimation Based on Adaptive Innovation Event-Triggered Mechanism for Uncertain Networked Systems, in *Computational Intelligence and Neuroscience*, 2022.

[14] Reinhardt M, Noack B, Arambel P O, et al, Minimum covariance bounds for the fusion under unknown correlations, in *IEEE Signal Processing Letters*, 2015, 22(9): 1210-1214.

Proceedings of the 3rd Conference on Fully Actuated System Theory and Applications
May 10-12, 2024, Shenzhen, China

带确定性观测和随机观测系统的最优降阶滤波器

高瑗, 孙书利, 高媛

黑龙江大学 电子工程学院, 哈尔滨 150080
E-mail: sunsl@hlju.edu.cn

摘 要: 对带确定性观测和随机观测的线性离散定常系统, 研究了最优降阶滤波问题. 部分状态分量可通过确定性观测直接获得, 其它状态分量通过设计降阶的状态滤波器获得.与将观测增广的方法相比, 不仅减小了计算负担, 而且避免了由于奇异观测噪声方差矩阵可能引起的数值计算不稳定的问题. 本文方法可以解决带有状态等式约束和带有奇异观测噪声方差矩阵系统的估计问题. 仿真例子验证了算法的有效性.

关键词: 确定性观测, 随机观测, 状态等式约束, 降阶滤波器, 线性离散定常系统

Optimal Reduced-order Filter for Systems with Deterministic Observations and Stochastic Observations

Yuan Gao, Shuli Sun, Yuan Gao

School of Electronic Engineering, Heilongjiang University, Harbin 150080, China
E-mail: sunsl@hlju.edu.cn

Abstract: For linear discrete time-invariant systems with deterministic observations and random observations, the optimal reduced-order filtering problem is studied. Some of the state components can be obtained directly by deterministic observation, while others can be obtained by designing a reduced-order state filter. Compared with the method of augmenting the observation, it not only reduces the calculation burden, but also avoids the problem of numerical instability caused by the singular observation noise variance matrix. The method presented in this paper can solve the estimation problem of systems with state equality constraint and singular observation noise variance matrix. A simulation example verifies the effectiveness of algorithm.

Key Words: Deterministic Observation, Random Observation; State Equality Constraint; Reduced-order Filter; Linear Discrete Time-invariant System

1 引言

在实际系统中, 传感器的观测可能遭受来自系统或外界的噪声干扰. 随着环境和制造技术的改善, 传感器的测量精度也在不断提高. 在某些情况下, 传感器的观测可以认为没有噪声干扰. 此外, 系统运行过程中, 系统状态可能受到条件或工况的限制或约束. 这些状态约束在某些情况下可以认为是没有观测噪声的测量, 在系统分析或状态估计中应考虑这些约束以提高系统估计精度[1-3].

文献[4]-[7]中将等式约束视为没有观测噪声的观测值, 通过增广观测方程, 将约束估计问题转化为非约束的估计问题, 也叫伪观测方法. 文献[8]-[12]针对带约束系统的状态估计问题还提出了其它的处理方法, 例如投影法. 虽然伪观测法实现简单, 但是也存在一定的问题. 首先, 扩维后的观测方程一定程度上增加了计算负担. 其次, 由于等式约束被视作观测值时的观测噪声为零, 这导致观测噪声具有奇异的协方差. 因此, 该方法可能会导致滤波结果不稳定. 文献[13]提出了采用广义逆矩阵避免由于奇异观测噪声方差阵引起的数值问题. 文献[14]-[15]研究了具有状态等式约束的多传感器系统的分布式最优融合估计问题.

本文对带确定性观测和随机观测的线性离散定常系统, 通过确定性观测获得一部分状态分量, 而其它状态分量通过设计一个降阶的状态滤波器获得. 与增广观测的伪观测法相比, 减小了计算负担, 同时避免了伪观测法奇异观测噪声方差阵可能带来的数值计算不稳定问题.

2 问题阐述

$$x(t+1)=\Phi x(t)+\Gamma w(t) \tag{1}$$

$$y_1(t)=C_1x(t)+v_1(t) \tag{2}$$

$$y_2(t)=C_2x(t) \tag{3}$$

其中, $x(t)\in R^n$ 为系统状态, $y_1(t)\in R^m$ 是随机观测, $y_2(t)\in R^p$ 是确定性观测. $w(t)\in R^r$ 和 $v_1(t)\in R^m$ 分别

*此项工作得到国家自然科学基金资助, 项目批准号：61573132.

是过程噪声和观测噪声. Φ, Γ, C_1 和 C_2 是适当维数的常矩阵.

假设1：$w(t)$ 和 $v_1(t)$ 为零均值、方差阵分别为 Q_w 和 Q_{v_1} 的不相关白噪声.

假设2：初始状态 $x(0)$ 的均值为 μ_0、方差为 P_0, 且与噪声 $w(t)$ 和 $v_1(t)$ 不相关.

不失一般性, 为简单起见, 不妨设 $C_2=[I_p,0]$.

本文研究的问题是对带随机观测(2)和确定性观测(3)的线性离散系统(1), 设计线性最小方差最优降阶状态滤波器, 并与增广观测(2)和(3)的方法进行比较.

3 降阶状态滤波器

设 $x(t)=[x_1^{\mathrm{T}}(t),x_2^{\mathrm{T}}(t)]^{\mathrm{T}}$, $x_1(t)\in R^p$, $x_2(t)\in R^{n-p}$, $\Phi=\begin{pmatrix}\Phi_{11} & \Phi_{12}\\ \Phi_{21} & \Phi_{22}\end{pmatrix}$, $\Phi_{11}\in R^{p\times p}$, $\Phi_{12}\in R^{p\times(n-p)}$, $\Phi_{21}\in R^{(n-p)\times p}$, $\Phi_{22}\in R^{(n-p)\times(n-p)}$, $C_1=[C_{11},C_{12}]$, $C_{11}\in R^{m\times p}$, $C_{12}\in R^{m\times(n-p)}$. 由约束方程(3)可得 $x_1(t)=y_2(t)$. 系统的观测方程(2)可写为：

$$y_1(t)=C_{11}y_2(t)+C_{12}x_2(t)+v_1(t) \tag{4}$$

由状态方程(1)可得

$$y_2(t+1)=\Phi_{12}x_2(t)+\Phi_{11}y_2(t)+\Gamma_1w(t) \tag{5}$$

$$x_2(t+1)=\Phi_{22}x_2(t)+\Phi_{21}y_2(t)+\Gamma_2w(t) \tag{6}$$

假设 Φ_{22} 可逆, 则(6)可化为

$$x_2(t-1)=\Phi_{22}^{-1}x_2(t)-\Phi_{22}^{-1}\Phi_{21}y_2(t-1)\ -\Phi_{22}^{-1}\Gamma_2w(t-1) \tag{7}$$

代(7)进入(5)可得

$$y_2(t)-\left(\Phi_{11}-\Phi_{12}\Phi_{22}^{-1}\Phi_{21}\right)y_2(t-1)=$$
$$\Phi_{12}\Phi_{22}^{-1}x_2(t)+\left(\Gamma_1-\Phi_{12}\Phi_{22}^{-1}\Gamma_2\right)w(t-1) \tag{8}$$

(4)经过变形可得

$$y_1(t)-C_{11}y_2(t)=C_{12}x_2(t)+v_1(t) \tag{9}$$

令 $z(t)=\begin{pmatrix}y_1(t)-C_{11}y_2(t)\\ y_2(t)-\left(\Phi_{11}-\Phi_{12}\Phi_{22}^{-1}\Phi_{21}\right)y_2(t-1)\end{pmatrix}$, 则有新的观测方程为

$$z(t)=\begin{pmatrix}C_{12}\\ \Phi_{12}\Phi_{22}^{-1}\end{pmatrix}x_2(t)+\begin{pmatrix}0 & I\\ \left(\Gamma_1-\Phi_{12}\Phi_{22}^{-1}\Gamma_2\right) & 0\end{pmatrix}v(t) \tag{10}$$

其中 $v(t)=\begin{pmatrix}w(t-1)\\ v_1(t)\end{pmatrix}$, 方差阵 $Q_v=\mathrm{E}\left(v(t)v^{\mathrm{T}}(t)\right)=\begin{pmatrix}Q_w & 0\\ 0 & Q_{v_1}\end{pmatrix}$, 互协方差阵 $S_{wv}=\mathrm{E}\left(w(t-1)v^{\mathrm{T}}(t)\right)=\begin{pmatrix}Q_w & 0\end{pmatrix}$.

由(6)和(10)构成了新的降阶状态空间表达式.那么, 应用射影理论可获得降阶状态估计.

定理1：对于系统(6)和(10), 降阶Kalman滤波递推公式如下：

状态预报估值计算如下：

$$\hat{x}_2(t+1|t)=\Phi_{22}\hat{x}_2(t|t)+\Phi_{21}y_2(t) \tag{11}$$

状态滤波估值计算如下：

$$\hat{x}_2(t+1|t+1)=\hat{x}_2(t+1|t)+K(t+1)\varepsilon(t+1) \tag{12}$$

新息计算为：

$$\varepsilon(t+1)=z(t+1)-\begin{pmatrix}C_{12}\\ \Phi_{12}\Phi_{22}^{-1}\end{pmatrix}\hat{x}_2(t+1|t) \tag{13}$$

新息方差阵计算为：

$$\begin{aligned}Q_\varepsilon(t+1)=&\begin{pmatrix}C_{12}\\ \Phi_{12}\Phi_{22}^{-1}\end{pmatrix}P(t+1|t)\begin{pmatrix}C_{12}\\ \Phi_{12}\Phi_{22}^{-1}\end{pmatrix}^{\mathrm{T}}\\ &+\begin{pmatrix}C_{12}\\ \Phi_{12}\Phi_{22}^{-1}\end{pmatrix}\Gamma_2S_{wv}\begin{pmatrix}0 & I\\ \left(\Gamma_1-\Phi_{12}\Phi_{22}^{-1}\Gamma_2\right) & 0\end{pmatrix}^{\mathrm{T}}\\ &+\begin{pmatrix}0 & I\\ \left(\Gamma_1-\Phi_{12}\Phi_{22}^{-1}\Gamma_2\right) & 0\end{pmatrix}S_{wv}^{\mathrm{T}}\Gamma_2^{\mathrm{T}}\begin{pmatrix}C_{12}\\ \Phi_{12}\Phi_{22}^{-1}\end{pmatrix}^{\mathrm{T}}\\ &+\begin{pmatrix}0 & I\\ \left(\Gamma_1-\Phi_{12}\Phi_{22}^{-1}\Gamma_2\right) & 0\end{pmatrix}Q_v\begin{pmatrix}0 & I\\ \left(\Gamma_1-\Phi_{12}\Phi_{22}^{-1}\Gamma_2\right) & 0\end{pmatrix}^{\mathrm{T}}\end{aligned} \tag{14}$$

滤波增益阵计算为：

$$\begin{aligned}K(t+1)=&\left[P(t+1|t)\begin{pmatrix}C_{12}\\ \Phi_{12}\Phi_{22}^{-1}\end{pmatrix}^{\mathrm{T}}\right.\\ &\left.+\Gamma_2S_{wv}\begin{pmatrix}0 & I\\ \left(\Gamma_1-\Phi_{12}\Phi_{22}^{-1}\Gamma_2\right) & 0\end{pmatrix}^{\mathrm{T}}\right]Q_\varepsilon^{-1}(t+1)\end{aligned} \tag{15}$$

滤波误差方差阵计算为：

$$P(t+1|t+1)=P(t+1|t)-K(t+1)Q_\varepsilon(t+1)K^{\mathrm{T}}(t+1) \tag{16}$$

预报误差方差阵计算为：

$$P(t+1|t)=\Phi_{22}P(t|t)\Phi_{22}^{\mathrm{T}}+\Gamma_2Q\Gamma_2^{\mathrm{T}} \tag{17}$$

初值为 $\hat{x}_2(0|0)=[0\quad I_{n-p}]\mu_0$ 和 $P(0|0)=[0\quad I_{n-p}]\times P_0[0\quad I_{n-p}]^{\mathrm{T}}$.

证明：由射影定理易得式(11)和(12), 其中滤波增益矩阵 $K(t+1)$ 和新息 $\varepsilon(t+1)$ 定义如下：

$$K(t+1)=\mathrm{E}\left[\tilde{x}_2(t+1|t)\varepsilon^{\mathrm{T}}(t+1)\right]Q_\varepsilon^{-1}(t+1) \tag{18}$$

$$\varepsilon(t+1)=z(t+1)-\hat{z}(t+1|t) \tag{19}$$

其中 $\tilde{x}_2(t|t-1)=x_2(t)-\hat{x}_2(t|t-1)$ 为预报误差, $\hat{z}(t+1|t)$ 为观测一步预报估值.

对式(10)取射影：

$$\hat{z}(t+1|t)=\begin{pmatrix} C_{12} \\ \Phi_{12}\Phi_{22}^{-1} \end{pmatrix}\hat{x}_2(t+1|t) \tag{20}$$

将式(20)代入式(19)可引出式(13).

将式(10)代入式(13)可得：

$$\varepsilon(t+1)=\begin{pmatrix} C_{12} \\ \Phi_{12}\Phi_{22}^{-1} \end{pmatrix}\tilde{x}_2(t+1|t)+\begin{pmatrix} 0 & I \\ \left(\Gamma_1-\Phi_{12}\Phi_{22}^{-1}\Gamma_2\right) & 0 \end{pmatrix}v(t+1) \tag{21}$$

由式(21)得新息方差阵：

$$\begin{aligned} Q_\varepsilon(t+1)&=\mathrm{E}\left[\varepsilon(t+1)\varepsilon^{\mathrm{T}}(t+1)\right] \\ &=\begin{pmatrix} C_{12} \\ \Phi_{12}\Phi_{22}^{-1} \end{pmatrix}P(t+1|t)\begin{pmatrix} C_{12} \\ \Phi_{12}\Phi_{22}^{-1} \end{pmatrix}^{\mathrm{T}} \\ &+\begin{pmatrix} C_{12} \\ \Phi_{12}\Phi_{22}^{-1} \end{pmatrix}\mathrm{E}\left[\tilde{x}_2(t+1|t)v^{\mathrm{T}}(t+1)\right] \\ &\times\begin{pmatrix} 0 & I \\ \left(\Gamma_1-\Phi_{12}\Phi_{22}^{-1}\Gamma_2\right) & 0 \end{pmatrix}^{\mathrm{T}} \\ &+\begin{pmatrix} 0 & I \\ \left(\Gamma_1-\Phi_{12}\Phi_{22}^{-1}\Gamma_2\right) & 0 \end{pmatrix} \\ &\times\mathrm{E}\left[v(t+1)\tilde{x}_2^{\mathrm{T}}(t+1|t)\right]\begin{pmatrix} C_{12} \\ \Phi_{12}\Phi_{22}^{-1} \end{pmatrix}^{\mathrm{T}} \\ &+\begin{pmatrix} 0 & I \\ \left(\Gamma_1-\Phi_{12}\Phi_{22}^{-1}\Gamma_2\right) & 0 \end{pmatrix}\mathrm{E}\left[v(t+1)v^{\mathrm{T}}(t+1)\right] \\ &\times\begin{pmatrix} 0 & I \\ \left(\Gamma_1-\Phi_{12}\Phi_{22}^{-1}\Gamma_2\right) & 0 \end{pmatrix}^{\mathrm{T}} \end{aligned} \tag{22}$$

由式(6)和式(11)可得预报误差方程：

$$\tilde{x}_2(t+1|t)=\Phi_{22}\tilde{x}_2(t|t)+\Gamma_2 w(t) \tag{23}$$

于是, 我们有

$$\begin{aligned} &\mathrm{E}\left[\tilde{x}_2(t+1|t)v^{\mathrm{T}}(t+1)\right] \\ &=\mathrm{E}\left[\left(\Phi_{22}\tilde{x}_2(t|t)+\Gamma_2 w(t)\right)v^{\mathrm{T}}(t+1)\right] \\ &=\Gamma_2 S_{wv} \end{aligned} \tag{24}$$

将上式代入(22)可得式(14). 将式(23)代入 $P(t+1|t)=\mathrm{E}[\tilde{x}_2(t+1|t)\tilde{x}_2^{\mathrm{T}}(t+1|t)]$ 可得式(17).

记滤波误差 $\tilde{x}_2(t|t)=x_2(t)-\hat{x}_2(t|t)$, 则由(12)可得滤波误差方程：

$$\tilde{x}_2(t+1|t+1)=\tilde{x}_2(t+1|t)-K(t+1)\varepsilon(t+1) \tag{25}$$

上式变形可得 $\tilde{x}_2(t+1|t+1)+K(t+1)\varepsilon(t+1)=\tilde{x}_2(t+1|t)$, 利用 $\tilde{x}_2(t+1|t+1)\perp\varepsilon(t+1)$ 可得

$$P(t+1|t+1)+K(t+1)Q_\varepsilon(t+1)K^{\mathrm{T}}(t+1)=P(t+1|t) \tag{26}$$

这可引出滤波误差方差矩阵式(16).

由式(23)、(24)和(21)可得

$$\begin{aligned} \mathrm{E}\left[\tilde{x}_2(t+1|t)\varepsilon^{\mathrm{T}}(t+1)\right]&=P(t+1|t)\begin{pmatrix} C_{12} \\ \Phi_{12}\Phi_{22}^{-1} \end{pmatrix}^{\mathrm{T}} \\ &+\Gamma_2 S_{wv}\begin{pmatrix} 0 & I \\ \left(\Gamma_1-\Phi_{12}\Phi_{22}^{-1}\Gamma_2\right) & 0 \end{pmatrix}^{\mathrm{T}} \end{aligned} \tag{27}$$

将式(27)代入式(18)可得式(15). 证毕.

注：易知将状态约束增广为观测的伪观测方法的计算量级为 $\mathrm{O}\left(n^3+(m+p)^3\right)$, 本文的降阶方法的计算量级为 $\mathrm{O}\left((m+n-p)^3\right)$, 通常本文的降阶滤波器具有更小的计算负担.而且, 避免了伪观测方法由于奇异的观测噪声方差矩阵可能带来的数值计算不稳定问题.

4 仿真例子

考虑二维跟踪系统(1)和(2), 其中 $\Phi=\begin{bmatrix} 1 & T_0 \\ 0 & 1 \end{bmatrix}$, $\Gamma=\begin{bmatrix} 0.5T_0^2 \\ T_0 \end{bmatrix}$, $C_1=C_2=\begin{bmatrix} 1 & 0 \end{bmatrix}$, $T_0=0.1$ 为采样周期, $x(t)=\begin{bmatrix} x_1(t) \\ x_2(t) \end{bmatrix}$, $x_1(t)$ 和 $x_2(t)$ 分别为在时刻 tT_0 运动目标的位置和速度, 噪声方差 $\sigma_w^2=1$, $\sigma_v^2=0.64$. 问题是求最优Kalman滤波器 $\hat{x}(t|t)$.

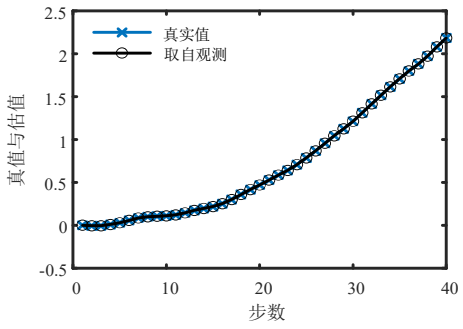

(a) 位置

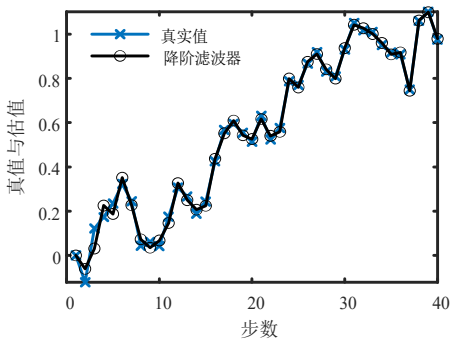

(b) 速度

图1 最优降阶递推滤波器

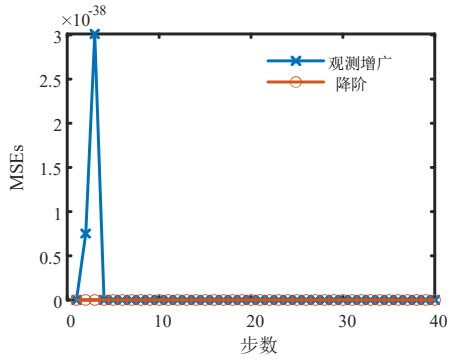

(a) 位置

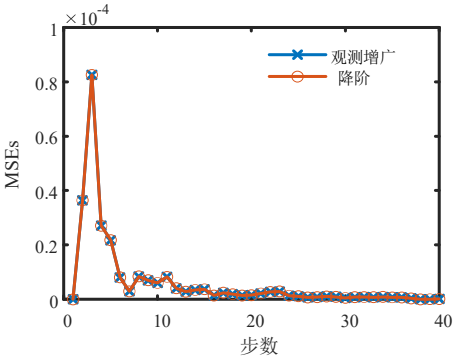

(b) 速度

图2 伪观测和降阶滤波器的均方误差比较

表 1. 速度的伪观测法和降阶法滤波误差方差比较

滤波方法	在300步滤波误差方差(10^{-6})
伪观测法	8.3611
降阶法	8.3611

取初值 $\hat{x}(0|0)=[0 \quad 0]^{\mathrm{T}}$, $P(0|0)=0.1I_2$. 仿真图1中实线为真实值, 虚线为估值.图2给出了本文的降阶方法与增广方法的均方误差比较.表1给出了在第300步速度的滤波误差方差的数值比较. 可以看出, 降阶法和伪观测法滤波估计精度一致, 而且降阶方法可减小计算负担且避免了奇异观测噪声方差阵可能引起的数值计算不稳定问题.

5 结论

研究了带确定性观测和随机观测的线性离散定常系统的最优降阶滤波问题, 设计了基于线性最小方差准则的降阶滤波估计算法, 其中一部分状态分量由确定性观测直接获得, 其它状态分量通过设计降维状态滤波器获得.与观测增广的方法相比, 降阶法减小了计算量负担, 并且在一定程度上避免了奇异的观测噪声方差矩阵可能带来的数值计算不稳定的问题.

参考文献

[1] D. Simon, Kalman filtering with state constraints: a survey of linear and nonlinear algorithms. *IET Control Theory and Applications*, 2010, pp. 1-16.

[2] R. J. Hewett, M. T. Heath, M. D. Butala and F. Kamalabadi, A robust null space method for linear equality constrained state estimation. *IEEE Transactions on Signal Processing*, 2010, 58(8): 3961-3971.

[3] C. V. Rao, J. B. Rawlings, D. Q. Mayne, Constrained state estimation for nonlinear discrete-time systems: stability and moving horizon approximations. *IEEE Transactions on Automatic Control*, 2003, 48(2): 246-258.

[4] M. Tahk, J. L. Speyer, Target tracking problems subject to kinematic constraints, *IEEE Transactions on Automatic Control*, 1990, 35(3): 324-326.

[5] D. Simon, T. L. Chia. Kalman Filtering with State Equality Constraints. *IEEE Transactions on Aerospace and Electronic Systems*, 2002, 38(1): 128 - 136.

[6] Z. Duan, X. R. Li, Best linear unbiased state estimation with noisy and noise-free measurements. 2009 12th International Conference on Information Fusion, Seattle, WA, USA, 2009: 2193-2200.

[7] G. Habibi, Z. Serkan, Kalman filtering with linear state equality constraints: a method based on separating variables. *IEEE Access*, 2022, 10: 35460 - 35468.

[8] Bruno O. S. Teixeira, Jaganath Chandrasekar, Leonardo A.B. Tôrres, Luis A. Aguirre, Dennis S. Bernstein. State estimation for linear and non-linear equality-constrained systems. *International Journal of Control*, 2009, 82(5): 918–936.

[9] Sangho Ko, Robert R. Bitmead. State estimation for linear systems with state equality constraints. *Automatica*, 2007, 43(8): 1363-1368.

[10] T.S. Chen. Comments on ‘State estimation for linear systems with state equality constraints’. *Automatica*, 2010, 46(11): 1929-1932.

[11] L. E. Andersson, L. Imsland, E. F. Brekke, F. Scibilia. On Kalman filtering with linear state equality constraints. *Automatica*, 2019, 101: 467–470.

[12] Z. Duan and X. R. Li, The role of pseudo measurements in equality-constrained state estimation. *IEEE Transactions on Aerospace and Electronic Systems*, 2013, 49(3): 1654-1666.

[13] E. B. Song, J. Xu, Y. M. Zhu. Optimal distributed Kalman filtering fusion with singular covariances of filtering errors and measurement noises. *IEEE Transactions on Automatic Control*, 2016, 61(12): 1271-1282.

[14] H. Li, S. L. Zhao. The optimal distributed Kalman filtering fusion with linear equality constraint. *IEEE Access*, 2021, 9: 106283 - 106292.

[15] C. B. Wen, Y. Z. Cai, Y. R. Liu, C. L. Wen. A reduced-order approach to filtering for systems with linear equality constraints. *Neurocomputing*, 2016, 193: 219-226.

Proceedings of the 3rd Conference on Fully Actuated System Theory and Applications
May 10-12, 2024, Shenzhen, China

Prompt Engineering Approach Study for Supervised Fine-Tuned (SFT) Large Language Models (LLMs) in Spacecraft Fault Diagnosis

Qing Xia[1], Haotian Zhao[1], Ming Liu [1]

1. School of Astronautics, Harbin Institute of Technology, Harbin 150001, China
E-mail: xiaqing80515@163.com; zht789study@163.com; mingliu23@hit.edu.cn (corresponding author)

Abstract: Traditional correlation and causality analyses based on telemetry data often lack depth in analyzing the multi-level coupling of faults and their emergent effects in spacecraft. Large Language Models (LLMs) offer a viable solution to this issue, necessitating meticulous research and design in prompt engineering. Against this backdrop, we have conducted a series of studies on using LLMs for diagnosing coupled faults in spacecraft. Initially, we systematically integrated a comprehensive fine-tuning dataset that includes prior expert knowledge, historical fault records, maintenance reports, and operation logs, to fine-tune the ERNIE-Bot-turbo model on the Baidu AI Cloud Qianfan platform. Subsequently, in the context of practical spacecraft fault diagnosis, we quantitatively explored the impact of different prompt engineering approaches on the fine-tuned LLMs using a specially designed multi-label spacecraft fault diagnosis test dataset. Finally, we proposed an Advanced Min Max Ant System (AMMAS) algorithm for autonomously iterating to explore the optimal prompts. AMMAS leverages the strong language generation capability of LLMs to optimize prompt text generation, using F1-score as the fitness function, aiming to autonomously iterate and optimize the prompt generation process, uncovering the most effective prompts for spacecraft fault diagnosis.

Key Words: LLMs, Prompt Engineering, Advanced Min Max Ant System Algorithm, Spacecraft Dault Diagnosis

1 Introduction

With the rapid increase in the number and functionalities of spacecraft, ensuring their operational reliability in the harsh space environment has become crucial. The faults in orbiting spacecraft often reflect the interactions and couplings between multiple subsystems. Traditional case-based expert knowledge databases and telemetry data-driven correlation and causality analyses have limitations in fully addressing this issue, especially lacking in depth when analyzing complex multi-level coupled faults and their emergence effects [1–3]. Furthermore, the continuous upgrades in spacecraft structures and components, along with the emergence of a large number of novel faults, present great challenges to traditional expert knowledge bases. This results in escalating costs for updating expert databases and the fault diagnosis process [4, 5].

In the traditional framework for spacecraft fault association analysis, correlation and causality analyses based on telemetry data serve as two fundamental pillars. Typically, correlation analysis is dedicated to the quantitative evaluation of fault associations, while causality analysis focuses on the qualitative exploration of fault origins. The overreliance on correlation analysis, despite being effective in certain scenarios, can lead to a range of issues including but not limited to fairness, interpretability, robustness, bias, and controllability.

Furthermore, traditional fault association analyses lack flexibility and are limited in applicability, struggling to meet the complex analytical needs arising from the exponential growth in the number and types of spacecraft, as well as mission types. Traditional correlation metrics (such as Pearson, Spearman, and Kendall correlation coefficients) have limited applicability in quantifying linear or nonlinear relationships in telemetry data. Similarly, traditional causality testing methods (such as Granger causality testing for stationary time series) also exhibit significant limitations and operational complexities. Additionally, not all subsystem components can obtain relevant telemetry data due to differences in sensor configuration and functionality.

In this context, the emergence of Large Language Models (LLMs) has offered an innovative solution to the aforementioned challenges. They break the inherent limitations of relying solely on telemetry data for fault diagnosis and demonstrate satisfactory analytical outcomes [6, 7]. Due to their excellent capability in data representation and abstraction, LLMs can perform in-depth, multi-dimensional, and multi-level analysis of spacecraft telemetry data, thereby uncovering potential fault associations and causal relationships.

To achieve precise, efficient, and intelligent spacecraft fault diagnosis, this study conducted the following research: Initially, we systematically integrated a comprehensive fine-tuning dataset containing historical fault records, maintenance reports, and operation logs. This dataset was utilized for the detailed fine-tuning of the ERNIE-Bot-turbo-0704 model on the Baidu AI Cloud Qianfan platform. Subsequently, we explored various advanced prompt engineering techniques, including linguistic tone adjustment, role-playing, thought chain guidance, and few-shot learning strategies. For spacecraft fault diagnosis, we quantitatively analyzed the impact of these prompt engineering strategies on the performance of the large model. Building on this, by transforming the spacecraft coupled fault diagnosis issue into a multi-label classification problem based on spacecraft subsystems, we comprehensively evaluated the advantages and limitations of various prompt engineering techniques in

This work is supported by the Science Center Program of National Natural Science Foundation of China (Grant No.62188101), the grant of SIYUAN collaborative innovation alliance of artificial intelligence science and technology (HTKJ2023SY502003), the Heilongjiang Touyan Team, and the Guangdong Major Project of Basic and Applied Basic Research (Grant No. 2019B030302001). Additional support was provided by the C4-AI: Chinese Collegiate Computer Competition in Artificial Intelligence Creativity.

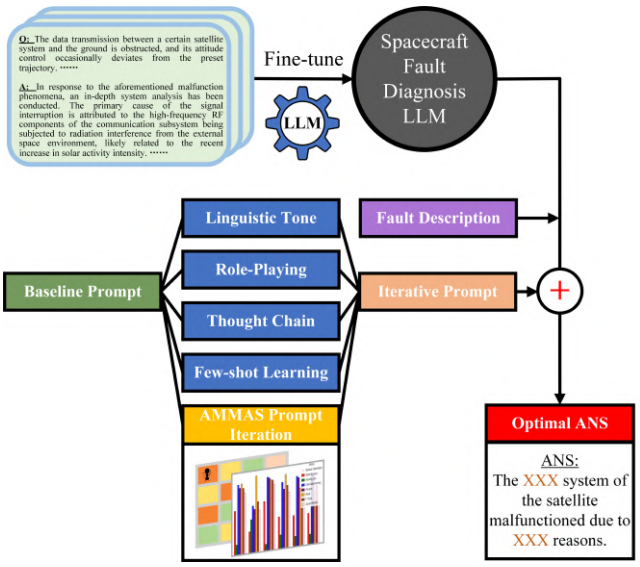

Fig. 1: The structural schematic of the entire methods.

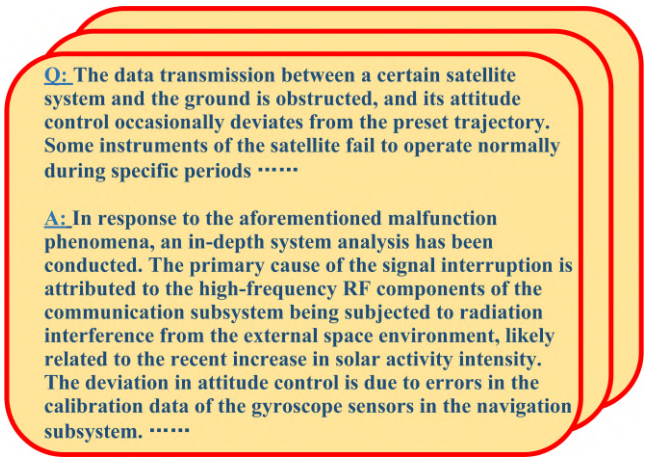

Fig. 2: The format of the data in the SFT dataset

the application of spacecraft fault diagnosis on a self-built test dataset using multiple quantifiable indicators. Finally, we employed an autonomous iterative exploration method for optimal prompt text based on the Advanced Min Max Ant System (AMMAS) algorithm. AMMAS optimizes prompt text generation by leveraging the inherent powerful language generation capability of LLMs and uses the F1-score as a fitness function to autonomously iterate and discover the most effective fault diagnosis prompts. The structural schematic of the entire methods is illustrated in Fig. 1.

2 Exploring Prompt Engineering Approaches for Supervised Fine-Tuned (SFT) LLMs in Spacecraft Fault Diagnosis

2.1 SFT LLMs for Spacecraft Fault Diagnosis

The Advantages of SFT LLMs. In the field of spacecraft fault diagnosis, pretrained language models have demonstrated the ability to capture statistical patterns of language and accurate semantic representations through extensive unsupervised training. However, the performance of these models on specific tasks may not directly match their efficiency demonstrated on broad unsupervised datasets. Supervised Fine-Tuning (SFT) of these models on task-specific labeled data enables them to further learn features and patterns closely related to the task, more precisely adapt to the unique terminology, structure, and semantics of the field, thereby significantly improving task performance within the domain.

Moreover, for tasks where acquiring a large labeled dataset is challenging, SFT supports model training with limited labeled data, maintaining commendable performance even in scenarios of data scarcity. During the SFT process, supervised training can effectively reduce the risk of overfitting on specific tasks. This is because the labeled data provides more specific task guidance, helping to constrain the learning process of the model and preventing overfitting to the unsupervised signals encountered during the pretraining phase.

Considering these advantages, we conducted a meticulous SFT of the ERNIE-Bot-turbo-0704 model on the Baidu AI Cloud Qianfan platform. This fine-tuning process was specifically designed to enhance the model's performance in the domain of spacecraft fault diagnosis, fully leveraging the inherent benefits of SFT to address key challenges in this field.

Fine-Tuning Dataset. We systematically integrated prior expert knowledge, including historical fault records, maintenance reports, and operation logs, to construct a fine-tuning dataset specifically designed for spacecraft multi-level coupling fault diagnosis tasks. The dataset consists of 2000 Question-and-Answer (QA) entries about single-level and multi-level coupling faults in satellites, where **Q** represents the fault description, and **A** provides an in-depth analysis by experts of the fault system.

By selecting and categorizing the entries in the dataset, we ensured that the included fault information is not only highly relevant to the actual operations and maintenance scenarios of spacecraft but also reflects the complexity and specialized knowledge required for diagnosing multi-level coupled faults. Moreover, to enhance the dataset's universality and practicality, each set of QA entries was described in detail, covering aspects such as fault type, impact level, resolution strategy, and its effectiveness, thereby supporting high-quality model training. The format of the dataset is shown in Fig. 2.

Fine-Tuning Parameters. Using the prepared dataset, we fine-tuned the base ERNIE-Bot-turbo model. Employing Prompt Tuning as the training method and based on the scale of the fine-tuning dataset, we set the training epochs to 5 and the learning rate to 0.01. The dataset was allocated at an 80% training and 20% testing ratio.

2.2 Prompt Engineering for LLMs in Spacecraft Fault Diagnosis

Test Dataset. To precisely evaluate the model's performance in spacecraft fault diagnosis scenarios, we have developed a test dataset containing 100 samples. Each input sample in this dataset maintains a consistent format with the fine-tuning dataset, including specific fault description texts, while the output is encoded as a sequence of numbers. The spacecraft's system structure is typically subdivided into 8 key subsystems, namely: telemetry and command subsystem (0), attitude and orbit control subsystem (1), data trans-

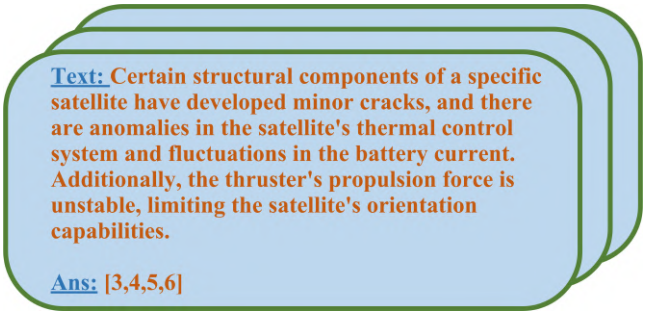

Fig. 3: The format of the data in the test dataset

mission subsystem (2), power subsystem (3), structural subsystem (4), thermal control subsystem (5), propulsion subsystem (6), and payload subsystem (7). Considering the complex coupling phenomena that may occur among subsystems during spacecraft operation, the fault diagnosis task exhibits a pronounced multi-label classification feature. Multi-label classification based on LLM responses can not only accurately identify the fault involving one or more subsystems but also reveal to some extent the interactions and coupling relationships between different subsystems, providing important reference information for subsequent fault troubleshooting and repair. For example, the format of the data in the test dataset is illustrated in Fig. 3, the numeric sequence [3,4,5,6] (converted into encoding [0,0,0,1,1,1,1,0] in programming, with this encoding determined by domain experts based on system label scoring) indicates that in a specific fault scenario, the attitude and orbit control subsystem, data transmission subsystem, and power subsystem are all faulty, suggesting possible interactions and couplings among these subsystems.

Prompt Engineering Approaches. Prompt engineering is the process of optimizing input statements or phrases to obtain the best possible response from LLMs. Although these models were initially designed for conversational interactions, researchers have found that adopting specific communication strategies can lead to more effective feedback. Precisely identifying which words, sentences, and phrases are most suitable for different contexts is at the heart of prompt engineering. By constructing a database of expert knowledge and applying prompt engineering techniques, LLMs can be utilized more efficiently to solve problems and provide advice.

This paper investigates six different prompt strategies for large models in the context of spacecraft fault diagnosis, which include:

1) **Baseline Prompt:** A foundational prompt text was constructed that outlines the basic background and requirements, and specifies the eight core subsystems of the spacecraft: ***The construction of the spacecraft can be subdivided into eight core subsystems, namely: telemetry and command subsystem, attitude and orbit control subsystem, data transmission subsystem, power subsystem, structural subsystem, thermal control subsystem, propulsion subsystem, and payload subsystem. In the framework of the problem we are discussing, these subsystems are assigned numerical labels from 0 to 7. Based on the provided fault description, please infer and output the one-hot encoding of the corresponding faulty subsystem(s).***
2) **Linguistic Tone Adjustment:** Appropriately adjusting the tone of language in interactions with LLMs can guide the model to generate responses of different quality and style. For example, using more formal and technical vocabulary can lead to more professional and accurate feedback. In the field of spacecraft fault diagnosis, a clear, professional, and directive tone of language helps to promote the model to generate more precise and practical diagnostic suggestions.
3) **Role-Playing:** Asking LLMs to assume the role of a fault diagnosis expert can help guide the model's responses to align more closely with actual engineering needs. Once a specific role and context are set, the model will focus more on professional knowledge and solutions related to spacecraft fault diagnosis [8].
4) **Thought Chain Guidance:** In prompt engineering, providing clear thought guidance can steer the model to follow a specific reasoning logic, thus leading to more rigorous and comprehensive conclusions. For example, in the process of spacecraft fault diagnosis, specifying the symptoms of system faults, possible causes, and verification steps can guide the model to produce analytical results and solutions in a certain logical order [9, 10].
5) **Few-shot Learning:** Few-shot learning is a machine learning method that can adapt to new tasks with a very small number of training examples [11]. In the application of prompt engineering for spacecraft fault diagnosis, providing a few high-quality examples can effectively adjust the behavior of LLMs, making them more accurately understand and process queries related to fault diagnosis, thereby providing valuable insights and solutions for engineers and experts.
6) **Composite Strategy:** This approach involves integrating linguistic tone adjustment, role-playing, thought chain guidance, and few-shot learning strategies with baseline prompt.

By comparing the impact of different prompt strategies on the capabilities of large models, this study aims to identify which of these six prompt schemes is most effective in the context of spacecraft fault diagnosis.

2.3 Experimental Evaluation on the SFT LLMs in Spacecraft Fault Diagnosis

Experiments were conducted on the fine-tuned spacecraft fault diagnosis LLM, evaluating six different prompts against seven metrics.

2.3.1 Metrics Definition

The definitions of the seven metrics, along with their respective variables, are as follows:

1) **Subset Accuracy (SA)**: Defined as the proportion of perfectly matched sets of predicted and true labels.

$$\mathrm{SA} = \frac{1}{N}\sum_{i=1}^{N}\delta(y_{i,\mathrm{true}}, y_{i,\mathrm{pred}}) \tag{1}$$

where N is the number of samples, $y_{i,\mathrm{true}}$ is the true

label set, and $y_{i,\text{pred}}$ is the predicted label set for the ith sample.

2) **Hamming Loss (HL)**: Measures the fraction of the wrong labels to the total number of labels.

$$\text{HL} = \frac{1}{N \cdot L} \sum_{i=1}^{N} \sum_{j=1}^{L} \delta(y_{i,j,\text{true}}, y_{i,j,\text{pred}}) \tag{2}$$

where L is the number of labels, and $y_{i,j,\text{true}}$ and $y_{i,j,\text{pred}}$ are the true and predicted values of the jth label for the ith sample, respectively.

3) **Label-based Accuracy (LBA)**: Represents the accuracy of predictions for each label.

$$\text{LBA} = \frac{1}{N \cdot L} \sum_{i=1}^{N} \sum_{j=1}^{L} \delta(y_{i,j,\text{true}}, y_{i,j,\text{pred}}) \tag{3}$$

similar to Hamming Loss but focuses on the proportion of correct predictions.

4) **Precision ($\mathbf{P_{samples}}$)**: Defined as the proportion of true positive predictions in all positive predictions.

$$P_{\text{samples}} = \frac{1}{N} \sum_{i=1}^{N} \frac{TP_i}{TP_i + FP_i} \tag{4}$$

where TP_i and FP_i are the numbers of true positives and false positives, respectively, for the ith sample.

5) **Recall ($\mathbf{R_{samples}}$)**: Measures the proportion of true positives identified among all actual positives.

$$R_{\text{samples}} = \frac{1}{N} \sum_{i=1}^{N} \frac{TP_i}{TP_i + FN_i} \tag{5}$$

where FN_i is the number of false negatives for the ith sample.

6) **F1 Score ($\mathbf{F1_{samples}}$)**: The harmonic mean of precision and recall.

$$F1_{\text{samples}} = \frac{1}{N} \sum_{i=1}^{N} 2 \cdot \frac{P_i \cdot R_i}{P_i + R_i} \tag{6}$$

combines the precision P_i and recall R_i for the i-th sample.

7) **Jaccard Similarity ($\mathbf{J_{samples}}$)**: Measures the similarity and diversity of sample sets.

$$J_{\text{samples}} = \frac{1}{N} \sum_{i=1}^{N} \frac{|y_{i,\text{true}} \cap y_{i,\text{pred}}|}{|y_{i,\text{true}} \cup y_{i,\text{pred}}|} \tag{7}$$

based on the intersection over the union of true and predicted label sets.

2.3.2 Experimental Results and Analysis

The results of seven metrics are shown in Fig. 4, and the following conclusions can be drawn:

Prompt I: Baseline Prompt

The baseline prompt aims to provide a basic introduction to the role background and requirements. In the analysis of model responses, the baseline prompt demonstrated balanced performance, specifically reflected in a Subset Accuracy of 0.55, a Hamming Loss of 0.12750, and a Label-based Accuracy of 0.87250. These results indicate the effectiveness of the baseline prompt in handling multi-label classification problems, especially in scenarios involving the identification of multiple concurrent faults. The Jaccard Similarity index of 0.758810 further validates its efficacy in reducing misclassification.

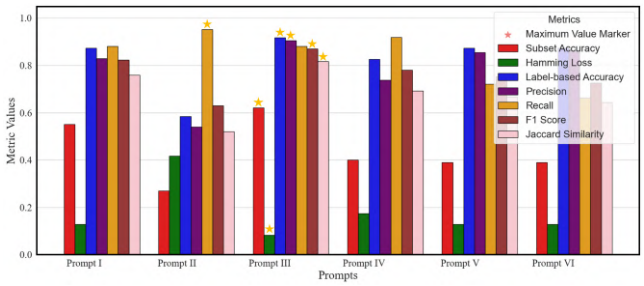

Fig. 4: Comparison of seven metrics generated by six different prompts

Prompt II: Linguistic Tone Adjustment

Prompt II, building on the baseline prompt with a more pronounced imperative tone, achieved a higher Recall of 0.952500. However, its Subset Accuracy dropped to 0.27, with a Hamming Loss increasing to 0.41625. This contradictory performance may suggest that while Prompt II is more sensitive in fault identification, it comes with a higher risk of false positives, particularly in predicting positive classes.

Prompt III: Role-Playing

Prompt III, requiring the large model to play the role of a fault diagnosis expert, performed exceptionally across almost all metrics, notably achieving a Subset Accuracy of 0.62, a Hamming Loss of 0.08250, and a Jaccard Similarity of 0.816905. This outcome demonstrates the effectiveness of the role-playing strategy in enhancing diagnostic accuracy and reducing misclassification, especially in complex fault scenarios.

Prompt IV: Thought Chain Guidance

Prompt IV, guiding the large model through a step-by-step thought process in spacecraft fault diagnosis, showed remarkable performance in Recall at 0.918000 but was average in other metrics. This suggests that although the strategy is effective in capturing faults, it may fall short in accuracy and reducing false positives.

Prompt V: Few-shot Learning

Prompt V, adopting a few-shot learning strategy by providing examples to the LLM, excelled in Precision with a score of 0.854524 but had a slightly insufficient Recall of 0.721333. This may indicate that the strategy performs well in avoiding incorrect fault classification but might slightly lack in capturing all potential faults.

Prompt VI: Composite Strategy

Prompt VI achieved a Subset Accuracy of 0.39, a Hamming Loss of 0.12750, a Label-based Accuracy of 0.87250, and a Jaccard Similarity of 0.643524. Although Prompt VI showed stability in certain aspects, its overall performance was not outstanding. This could be due to conflicts between the various strategies used, limiting the model's judgment

capabilities with specific types of faults.

Through a detailed analysis of six different prompting strategies, we conclude that these strategies exhibit significant differences in their responses to large models for spacecraft fault diagnosis. Among them, the Role-Playing strategy generally outperforms other strategies across various metrics. When facing specific spacecraft fault diagnosis scenarios, these differences should be comprehensively considered, and the most suitable strategy should be selected based on specific needs and contextual backgrounds to achieve the best diagnostic outcomes. The significant differences among these strategies reveal their unique advantages and limitations in handling complex multi-label classification problems, underscoring the importance of accuracy and efficiency in spacecraft fault diagnosis. Therefore, selecting and fine-tuning the most appropriate prompting strategy in practice can significantly improve the accuracy and efficiency of fault diagnosis, which is crucial for the safe operation and maintenance of spacecraft.

3 Autonomous Prompt Iteration Algorithm

3.1 Prompt Iteration based on Advanced Min Max Ant System (AMMAS) Algorithm

The Advanced Min Max Ant System (AMMAS), as an enhanced version of the original MMAS [12], is a heuristic optimization method derived from the behavior of ant colonies in searching for paths from their nests to food sources. In this study, the method is utilized for the iterative optimization of combinations of prompting strategies, with the goal of finding the most effective sequence of prompts under given evaluation criteria. The algorithmic process is described as in **Algorithm 1**.

The core of the AMMAS algorithm is grounded in the probabilistic formulation for the selection of paths and the pheromone update rules. Let $P_{ij}^k(t)$ denote the probability of ant k choosing to move from state i to state j at iteration t, given by:

$$P_{ij}^k(t) = \frac{[\tau_{ij}(t)]^\alpha \cdot [\eta_{ij}]^\beta}{\sum_{l \in \text{allowed}_k} [\tau_{il}(t)]^\alpha \cdot [\eta_{il}]^\beta} \tag{8}$$

where $\tau_{ij}(t)$ is the pheromone concentration on path (i, j) at iteration t, η_{ij} is the heuristic desirability of path (i, j), α and β are parameters that control the influence of $\tau_{ij}(t)$ and η_{ij}, respectively, allowed_k is the set of states that ant k can choose from its current state i.

The pheromone update rule is a crucial aspect, represented as:

$$\tau_{ij}(t+1) = (1-\rho) \cdot \tau_{ij}(t) + \Delta\tau_{ij} \tag{9}$$

$$\Delta\tau_{ij} = \sum_{k=1}^{m} \Delta\tau_{ij}^k \tag{10}$$

where ρ is the pheromone evaporation coefficient, m is the number of ants, $\Delta\tau_{ij}^k$ is the amount of pheromone ant k deposits on path (i, j), often related to the inverse of the path length or cost.

In our study, four prompt engineering approaches including Linguistic Tone Adjustment, Role-Playing, Thought Chain Guidance, and Few-shot Learning are encoded as discrete states (0, 1, 2, 3), each representing the corresponding strategy. Using ants in AMMAS, these states are sequentially combined to generate a series of potential optimization solutions. Each iteration of the optimization process is achieved by leveraging the capabilities of the large model. Considering the time and space complexity of the experiment, strict experimental rules are set, such that each of the four strategies appears only once in each iteration, avoiding the repetition of any single strategy, thereby reducing the possibility of experimental bias. As an improved version of MMAS, AMMAS traverses the solution space through heuristic search techniques.

The effectiveness of each candidate solution is evaluated by its F1-score generated for multi-label classification problems on a specific test dataset based on the corresponding prompt text. The evaluation results directly determine the adjustment of pheromone levels and guide ants to prioritize exploring more promising areas in the solution space in subsequent iterations. Thus, the method transforms the autonomous iterative generation process of prompt texts into a combinatorial optimization problem, ensuring the algorithm can efficiently search and exploit the solution space to identify the optimal sequence of prompt optimization strategies.

Algorithm 1: Advanced Min Max Ant System (AMMAS) for Prompt Evolution Optimization

Result: Best solution for prompt evolution
Initialize:
Set parameters: number_of_ants, max_iterations, pheromone_evaporation_coefficient, pheromone_intensity;
Initialize pheromone trails: pheromone_levels[0-3] ← initial_pheromone_level;
Define prompt_evolution_directions[4] ← {direction_0, direction_1, direction_2, direction_3};
for *each iteration in max_iterations* **do**
  for *each ant in number_of_ants* **do**
    Initialize an empty solution: current_solution ← [];
    for *each position in 4-digit code* **do**
      Choose next digit based on probability proportional to pheromone_levels;
      Add chosen digit to current_solution;
      Update pheromones locally (optional);
    end
    Evaluate fitness of current_solution using SFT LLM for F1-score on test dataset;
    Update best_solution if current_solution has better fitness;
  end
  Update pheromones globally:
  Reduce pheromone levels on all paths by pheromone_evaporation_coefficient;
  Increase pheromone levels on the path used by the best_solution proportionally to its fitness;
end
return best_solution

3.2 Experimental Results and Analysis

In order to balance efficiency and effectiveness in the optimization of prompt evolution using AMMAS, the hyperparameters were set as follows: The number of ants was set to 6 to allow for controlled and diversified exploration of the solution space; the number of iterations was set to 15; the pheromone evaporation coefficient was set to 0.5, aimed at maintaining valuable path information while preventing premature convergence; the pheromone intensity was set to 1.0; the initial pheromone level was set to 0.1, establishing a baseline for exploration and avoiding any initial preference for certain paths in the solution space.

The experimental results indicate that the F1-score increases continuously and robustly over 15 iterations, finally reaching 92% at the 15th generation, demonstrating the significant superiority of the AMMAS algorithm in the autonomous iterative optimization of prompts. The corresponding optimal prompt evolution sequence is successively: ***Thought Chain Guidance, Role-Playing, Few-shot Learning*** and ***Linguistic Tone Adjustment***. It is noteworthy that, compared to the composite strategy we initially set, the optimal prompt evolution strategy identified through exploration shows higher efficacy in improving the F1-score.

4 Conclusion and Summary

In response to the complex coupled fault issues encountered by modern spacecraft, this study explored a wide range of prompt engineering methods for spacecraft fault diagnosis using Supervised Fine-Tuned Large Language Models (SFT LLMs). The following conclusions have been drawn from our research:

1) SFT LLMs exhibit outstanding performance in the domain of coupled fault diagnosis for spacecraft. To maximize the potential of the fine-tuned models, careful design of prompts is essential. Experimental results indicate that, in the field of spacecraft coupled fault diagnosis, the Role-Playing strategy surpasses other strategies such as Linguistic Tone Adjustment, Thought Chain Guidance, and Few-shot Learning.
2) Compared to optimizing prompt individually, sequential optimization of prompts leads to more accurate diagnosis of coupled faults by large models. This methodical approach derived from exploration surpasses the results achieved by simply amalgamating multiple prompt engineering methods. In certain cases, employing a single prompt engineering method may be more beneficial than a simplistic fusion of several approaches.
3) The Advanced Min Max Ant System (AMMAS) optimization algorithm has proven to significantly aid large models in handling more complex and diversified fault diagnosis tasks. This algorithm allows users to engage in prompt engineering in a systematic and targeted manner, significantly enhancing diagnostic accuracy.

References

[1] B. Yu, Y. Yu, J. Xu, G. Xiang, and Z. Yang, "Mag: A novel approach for effective anomaly detection in spacecraft telemetry data," *IEEE Transactions on Industrial Informatics*, pp. 1–9, 2023.

[2] S. Yin, B. Xiao, S. X. Ding, and D. Zhou, "A review on recent development of spacecraft attitude fault tolerant control system," *IEEE Transactions on Industrial Electronics*, vol. 63, no. 5, pp. 3311–3320, 2016.

[3] T. Yairi, N. Takeishi, T. Oda, Y. Nakajima, N. Nishimura, and N. Takata, "A data-driven health monitoring method for satellite housekeeping data based on probabilistic clustering and dimensionality reduction," *IEEE Transactions on Aerospace and Electronic Systems*, vol. 53, no. 3, pp. 1384–1401, 2017.

[4] X. Tang, G. Chi, L. Cui, A. W. Ip, K. L. Yung, and X. Xie, "Exploring research on the construction and application of knowledge graphs for aircraft fault diagnosis," *Sensors*, vol. 23, no. 11, p. 5295, 2023.

[5] J. White, Q. Fu, S. Hays, M. Sandborn, C. Olea, H. Gilbert, A. Elnashar, J. Spencer-Smith, and D. C. Schmidt, "A prompt pattern catalog to enhance prompt engineering with chatgpt," *arXiv preprint arXiv:2302.11382*, 2023.

[6] Y. Zhou, A. I. Muresanu, Z. Han, K. Paster, S. Pitis, H. Chan, and J. Ba, "Large language models are human-level prompt engineers," *arXiv preprint arXiv:2211.01910*, 2022.

[7] I. Poola, "Overcoming chatgpts inaccuracies with pre-trained ai prompt engineering sequencing process," 2023.

[8] Y. Shao, L. Li, J. Dai, and X. Qiu, "Character-llm: A trainable agent for role-playing," *arXiv preprint arXiv:2310.10158*, 2023.

[9] J. Wei, X. Wang, D. Schuurmans, M. Bosma, F. Xia, E. Chi, Q. V. Le, D. Zhou *et al.*, "Chain-of-thought prompting elicits reasoning in large language models," *Advances in Neural Information Processing Systems*, vol. 35, pp. 24 824–24 837, 2022.

[10] X. Wang, J. Wei, D. Schuurmans, Q. Le, E. Chi, S. Narang, A. Chowdhery, and D. Zhou, "Self-consistency improves chain of thought reasoning in language models," *arXiv preprint arXiv:2203.11171*, 2022.

[11] C. H. Song, J. Wu, C. Washington, B. M. Sadler, W.-L. Chao, and Y. Su, "Llm-planner: Few-shot grounded planning for embodied agents with large language models," in *Proceedings of the IEEE/CVF International Conference on Computer Vision*, 2023, pp. 2998–3009.

[12] E. Ridge and D. Kudenko, "Tuning the performance of the mmas heuristic," in *International Workshop on Engineering Stochastic Local Search Algorithms*. Springer, 2007, pp. 46–60.

Proceedings of the 3rd Conference on Fully Actuated System Theory and Applications
May 10-12, 2024, Shenzhen, China

Optimal Fuel Solution to the Lambert Problem under Complex Perturbation Conditions Based on BP Neural Network

Wenbin Wu[1], Qian Zhang[1], Minglang Tan[1], Yini Zhong[1], Ronghao Yuan [1]

1. Aerospace System Engineering Shanghai, Shanghai 201109, China
E-mail: wwb805ASES@163.com

Abstract: Addressing the orbital interception problem, various perturbations are considered initially, and the impact of perturbations on solutions in the two-body problem is analyzed. Numerical analysis is then introduced to successfully mitigate the effects of perturbations. Finally, inspired by the concept of BP neural networks, an original training set is constructed based on the numerical correction of perturbed Lambert problem solutions. This training set is used to train a neural network to approximate solutions to the perturbed Lambert problem. The resulting neural network exhibits performance similar to the numerical correction method, saving time and reducing computational costs while ensuring control accuracy.

Key Words: BP Neural Network; Lambert problem; Complex Perturbation Orbital Dynamics; Fuel Optimal Control

1 Introduction

The commonly employed approach for calculating orbital interception maneuver strategies is the Lambert method. The Lambert problem is a type of two-point boundary value problem subject to fixed time constraints. In orbital interception computations, we typically formulate the Lambert problem as determining the initial and final velocities given the initial and final positions along with the orbital transfer time. For the perturbed Lambert problem associated with the departure and target points, there exists a fuel-optimal solution for the departure velocity. Acquiring the aforementioned solution involves initially calculating the velocity increments corresponding to different transfer times in the two-body problem. Subsequently, these increments are individually adjusted to accommodate various perturbations.

Orbital interception maneuver control plays a crucial role in various studies. Shiyu Chen [1] investigated the large-scale capture problem of spacecraft formations for space debris clusters. The study focused on constructing rendezvous sequences under the influence of perturbations, aiming for each spacecraft to intercept more debris with minimal fuel usage, achieving a distributed optimal control. Cristian [2,3] presented a fuel-optimal robust control approach under cognitive uncertainty, using a Markov trust decision-making method to transform the control problem into an uncertainty distribution problem and introducing the concept of trust. The entire problem was then formulated as a trust-optimal control problem. Kai [4] proposed a discrete-time linear dynamic model for robust control when the elliptical orbital rendezvous is subject to uncertain perturbations. The study used a genetic algorithm to solve the optimization problem of random trajectories. Li [5] proposed a rapid solver for the Lambert problem based on a deep neural network. The study discussed the impact of input-output dimensions and parameter selection on the training effectiveness of the neural network, selecting the most optimal training set. Ahn [6-8] introduced a new solution for the two-point Lambert problem, using the initial spacecraft trajectory angle as an initial value. The study derived the gradient of transfer time with respect to the trajectory angle and updated the trajectory angle iteratively. Jay [9] argued that numerical iteration demands excessive computational power for onboard computers. The study linearized the Lambert problem solution using Lagrange parameters to reduce computational complexity. Roberto [10] proposed a quasi-analytical solution for the multi-revolution Lambert problem based on a high-order Taylor expansion, optimizing for the impact of perturbations. Zhang [11] presented a Lambert solution based on the terminal velocity vector, selecting the velocity components at the end of the orbit as independent variables and deriving the reachable domain for elliptical and hyperbolic orbits.

Traditional exhaustive search methods prove excessively time-consuming and computationally intensive, rendering them impractical for on-board solutions. This paper introduces an approach to solve the perturbed Lambert problem using neural networks, aiming to ensure solution accuracy while significantly reducing computation time. When considering various perturbations, such as higher-order spherical harmonic terms, advanced gravity field models like the EGM96, or factors like atmospheric drag and solar radiation pressure, the orbital dynamics model becomes excessively complex or non-analytic. This complexity makes the derivation of formulas extremely challenging. In the field of orbital control, the application of neural networks is still in its early stages. Current research mainly focuses on using neural networks to compensate for parameters with significant uncertainties rather than directly integrating them into control rates. Li's approach, using Deep Neural Networks (DNN) for the rapid solution of perturbed Lambert problems, is limited to constructing a set of Lambert solutions in a two-body scenario. The DNN is then employed to approximate these solutions, creating a network for solving Lambert problems in a two-body context. When addressing practical problems, this network is used to compute solutions for two-body cases, and numerical correction methods are applied afterward.

In the case of fuel-optimal maneuvering problems, obtaining the optimal solution in a two-body scenario and correcting it does not necessarily yield the optimal fuel solution considering perturbations. It is challenging to prove that the optimal solution in a two-body context corresponds to the optimal correction impulse. Therefore, training a neural network that directly approximates perturbed Lambert problems holds research value, as it can provide solutions directly considering perturbations.

2 Fuel-optimal maneuver control strategy based on the Lambert algorithm

2.1 High-precision Orbital Dynamics Model

This paper adopts a high-precision orbital dynamics model considering the perturbations from nutation, precession, and various disturbing forces.

For the high-precision orbital dynamics model of the spacecraft used in this paper, providing a simulation example as below. The verification approach in this paper involves orbit prediction based on given initial values. The comparison between the orbital dynamics model described in this paper and the orbit prediction model provided by aerospace simulation software is used to quantify the prediction error for the same model.

The initial state can be seen as below:

Table 1: Initial state of test above

Name	Value
Time(UTC)	27 Apr 2022 23:39:14
Semimajor Axis(km)	6819.247
Eccentricity	0.0016578
Inclination(°)	97.3383
RAAN(°)	133.6469
Argument of Perigee(°)	166.5756
Mean Anomaly(°)	193.5935

The simulation results are depicted in the following images:

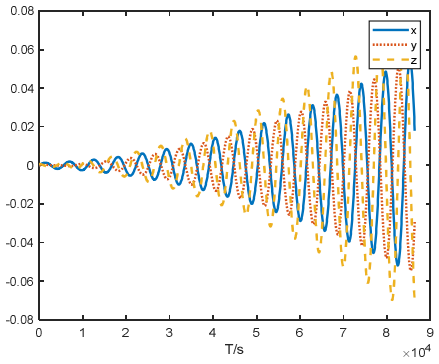

Fig. 1: Position Prediction Error(km)

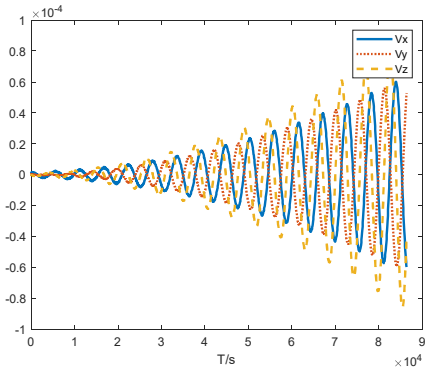

Fig. 2: Velocity Prediction Error(m/s)

For a spacecraft at an orbital altitude of approximately 500 km, a one-day orbit prediction was conducted. The orbital dynamics model described in this paper closely aligns with the model in aerospace simulation software. The position prediction error over one day is approximately 0.1 km, and the velocity prediction error is around 0.1 m/s. This demonstrates that the model presented in this paper meets the precision requirements for maneuvers such as orbital interception.

2.2 Solution to the Lambert Problem under Complex Perturbations

For the Lambert problem in the complex perturbation orbital environment described above, this section provides a conventional solution considering numerical corrections. This serves as the computational basis for the training dataset in the neural network presented in this paper.

When a spacecraft receives interception or observation commands, it often does not maneuver immediately. This is because, based on the current relative position between the spacecraft and the target, an immediate orbital maneuver may not be suitable and could result in a significant fuel waste. The time node at which a spacecraft is allowed to perform a maneuver is referred to as a "maneuver window" in this paper. The time elapsed from receiving the command to reaching the maneuver window and initiating the maneuver is termed the "waiting time." The time elapsed from initiating the maneuver to reaching the target point is referred to as the "transfer time."

For a space interception task with an infinitely permissible waiting time, its fuel-optimal maneuver window must be a semi-Hohmann transition. However, this might require a long waiting time, which may not meet mission requirements. Within a given waiting time interval, all possible Lambert solutions are calculated, and the maneuver with the minimum norm of the maneuver impulse is identified as the fuel-optimal maneuver control strategy for this interval.

Specific strategy:

1. Divide the given waiting time interval and transfer time interval into a grid with a certain time density, where each point in the grid represents a combination of waiting time and transfer time.

2. Use orbit propagation to obtain the position and velocity information of the spacecraft after the waiting time and the position and velocity information of the target after the waiting time + transfer time.

3. For each combination of waiting time, transfer time, spacecraft position, and target position, solve the Lambert problem considering various perturbations to obtain the maneuver control impulse under this scenario.

4. Repeat steps 2-3 until each point in the grid has been calculated.

5. Calculate the norm of the impulse for each point in the grid, find the minimum norm impulse, and the corresponding combination of waiting time and transfer time represents the fuel-optimal maneuver window in this time interval. This impulse is the fuel-optimal maneuver control within this time interval.

Table 2: Page Margins

Satellite	Chief Sat	Target Sat
Time(UTC)	2022/07/01 21:00:00	2022/07/01 21:00:00
Semimajor Axis(km)	6685.94	6927
Eccentricity	3e-7	2e-4
Inclination(°)	51.9741	53.0506
RAAN(°)	317.5974	319.7051
Argument of Perigee(°)	115.6798	144.919
Mean Anomaly(°)	5.946	215.1931

The simulation results are illustrated in the following figure:

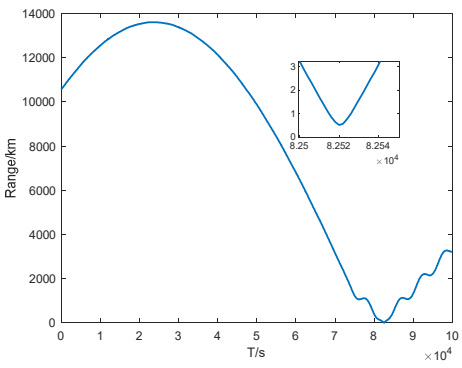

Fig. 3: Range Between Chief Sat and Target Sat(km)

The precision of the interception maneuver is significantly improved through numerical corrections, ensuring a final interception error within 1 km. Additionally, the calculated interception impulse is close to the Hohmann transfer impulse. The main propulsion thruster operates for a duration of 746 seconds in this maneuver, and according to the search, this impulse is the smallest in the entire region. This confirms that within the given maneuver time window, this maneuver control strategy is the optimal fuel control strategy.

3 Fuel-Optimal Maneuvering Strategy for Space Target Observation Based on BP Neural Network Considering Perturbation Effects

3.1 Backpropagation Neural Network (BPNN)

The Backpropagation Neural Network (BPNN) was initially proposed in 1986 and consists of an input layer, hidden layer(s), and an output layer. Training data is fed from the input layer through the hidden layer and eventually reaches the output layer. The network's output is then compared to the actual output to compute the error, which is backpropagated layer by layer to adjust the weights of each neuron in the hidden layer. This process is repeated until the output satisfies the validation requirements.

It is important to note that the adjustment of weights in the hidden layer neurons is a result of the network's adaptive feedback. The final neural network fitting function directly reflects the mapping relationship demonstrated by the given training set, without the need to reveal a mathematical equation for the relationship throughout the process.

For a BP neural network, Levenberg and Marquardt proposed an acceleration method for convergence known as the "Levenberg-Marquardt" method. The BP neural networks used in this paper employ the "Levenberg-Marquardt" learning rule.

The learning algorithm of the BP network is called the δ algorithm. Assuming a BP network with input, hidden, and output layers, each having a size of 1, when providing a training dataset to this BP network, if the actual output of the network differs from the expected output (the desired output within the training set), the difference between them, defined as the output error E, can be expressed as:

$$E = \frac{1}{2}(d - O)^2 = \frac{1}{2}\sum_{\kappa=1}^{\ell}(d_k - o_k)^2 \quad (1)$$

Where d represents the expected output, and O represents the actual output.

In (12), This is evidently an equation based on the output layer. Given the nature of the BP network as a feedforward network, we can extend this input error to the hidden layer, shown as below:

$$E=\frac{1}{2}\sum_{\kappa=1}^{\ell}\left[d_{\kappa}-f\left(\text{ net }_{\kappa}\right)\right]^{2}$$
$$=\frac{1}{2}\sum_{\kappa=1}^{\ell}\left[d_{\kappa}-f\left(\sum_{j=0}^{m}\omega_{j\kappa}y_{j}\right)\right]^{2} \tag{2}$$

Further expanding to the input layer:

$$E=\frac{1}{2}\sum_{\kappa=1}^{\ell}d_{\kappa}-f\left[\sum_{j=0}^{m}\omega_{j\kappa}f\left(\text{ net }_{j}\right)\right]^{2}$$
$$=\frac{1}{2}\sum_{\kappa=1}^{\ell}d_{\kappa}-f\left[\sum_{j=0}^{m}\omega_{j_{\kappa}}f\left(\sum_{j=0}^{n}v_{ij}\chi_{i}\right)\right]^{2} \tag{3}$$

Our ultimate goal is to minimize E by adjusting the weights ω_{jk}:

$$\Delta\omega_{j\kappa}=-\eta\frac{\partial E}{\partial\omega_{j\kappa}}$$
$$j=0,1,2,\ldots,m;\kappa=1,2,\ldots,\ell \tag{4}$$

$$\Delta v_{ij}=-\eta\frac{\partial E}{\partial v_{ij}}i=0,1,2,\ldots,n;j=1,2,\ldots,m \tag{5}$$

3.2 BP Neural Network Training and Results Analysis

The optimal orbit maneuver strategy for intercepting spacecraft, based on numerical correction as described in the previous section, involves iteratively integrating correction impulses into the orbital dynamics model. Given the high-precision orbital dynamics model employed in this study, extensive orbit integrations lead to significant time consumption. When applying the mentioned approach for orbital strategy calculations with a large initial search grid area and a considerable number of grid points, the computational cost becomes prohibitively high.

To address this challenge, a BP neural network is introduced to optimize the process. By establishing a well-structured training set, the neural network is trained to approximate the orbital dynamics, providing a rapid estimation of the output values given specific inputs.

A BP neural network with two hidden layers is designed, each containing 9 neurons. Mean Squared Error (MSE) is adopted as the performance metric for this network.

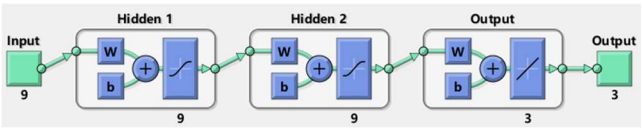

Fig. 4: Design of BP Neural Network

This paper designs a neural network to compute the control impulse for the modified departure point. Essentially, it replaces the numerical correction used to solve the Lambert problem. The data related to the network input consists of five parameters: waiting time, transfer time, departure point position, departure point velocity, and target point position.

For an effective training set, the input parameters should ideally be independent of each other. However, the five parameters mentioned are not mutually independent.

Specifically:

Departure point position and departure point velocity are determined jointly by the initial orbital information of the mission spacecraft and waiting time.

Target point position is determined jointly by the initial orbital information of the target spacecraft, waiting time, and transfer time.

The original training set is designed with inputs of departure point position, departure point velocity, and target point position, with a dimension of 9. The outputs are the orbital interception fuel-optimal maneuver control impulses, with a dimension of 3.

Traversing through the given transfer time and waiting time table, corresponding results for each calculation are stored to obtain the original training set. Under this original training set, the relationship between spacecraft control impulses and transfer time, waiting time can be illustrated as shown in the figure.

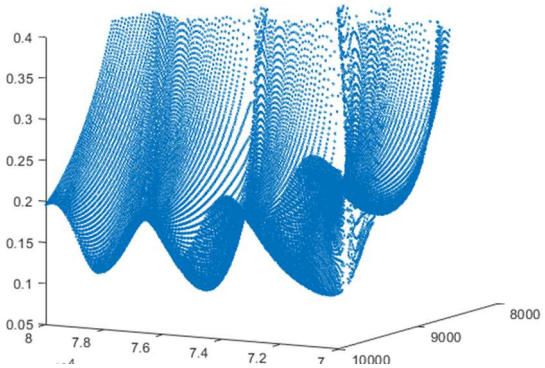

Fig. 5: Dataset for Neural Network

Train the neural network with the initial parameters corresponding to Table 2 in this paper, and the training results of the neural network are shown in the following figure.

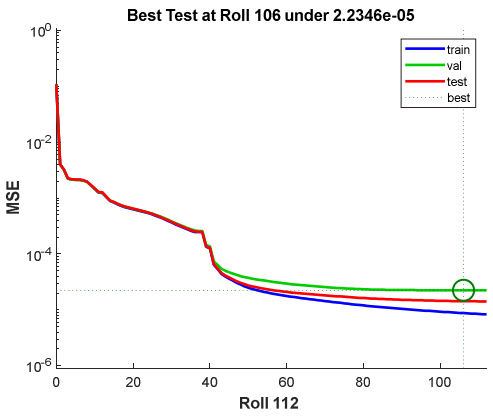

Fig. 6: Network Training Mean Square Error Epochs Changing Curve

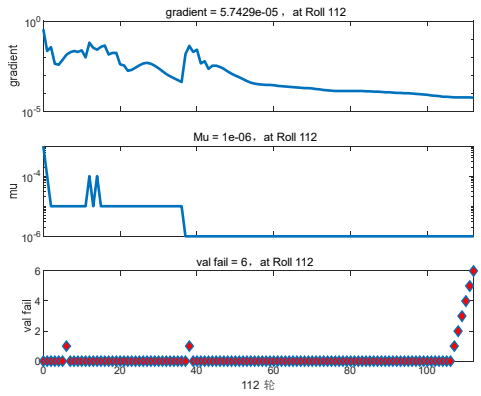

Fig. 7: Training Gradient Curve for the Training Set over Epochs

The gradient is a crucial indicator in the learning process of neural networks. Maintaining a stable gradient during training is essential for achieving an ideal neural network. In the context of gradient descent, if the gradient is too large, it may lead to overfitting. On the other hand, if the gradient is too small, although overfitting is less likely, the convergence speed of the network may become slow.

As shown in Figure 7, it can be observed that, upon completing the training, the gradient values have become very small. This indicates that the gradient has largely descended, reaching optimal training performance. It also implies the reliability of the training set.

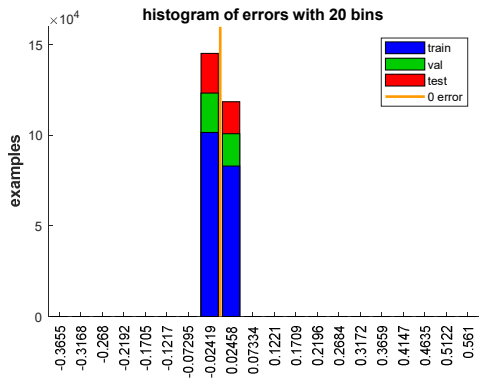

Fig. 8: Histogram of Errors with 20 Bins

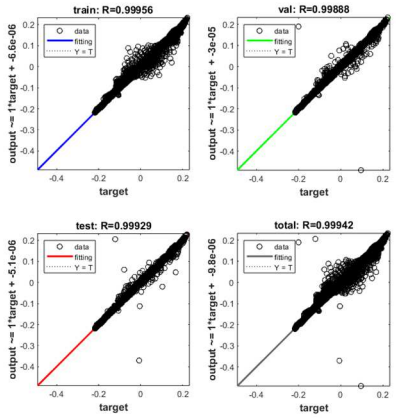

Fig. 9: Training set network training fitting effect schematic diagram

In Figure 9, each black circle represents a "data point". In this training, to avoid overfitting of the neural network, 70% of the training set is divided into training data, 15% into validation data, and 15% into test data. Only the training data is used for neural network training. The horizontal axis represents "target values," and the vertical axis represents "network outputs." The top-left subplot shows the fitting of the training data.

The "data" points are densely distributed near the fitting line, and the fitting line is very close to the diagonal, indicating that the training effect of the neural network is quite satisfactory.

3.3 Simulation and Analysis of Lambert Problem Solution under Complex Perturbations Based on BP Neural Network

To ensure the objectivity and comparability of the simulation, the initial values in this section are set to be consistent with those in Table 2. The obtained simulation results are shown in the following figures:

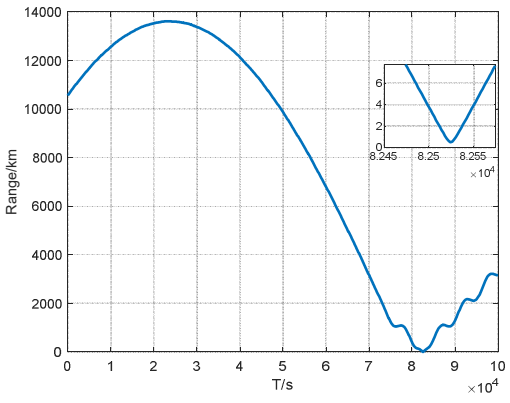

Fig. 10: Distance variation over time between the interception spacecraft and the target based on the neural network.

From the figure, it can be observed that the interception maneuver control accuracy is maintained within 1 km, comparing with Figure 3, the interception maneuver control accuracy in this case achieves a correction accuracy close to that of numerical correction. This confirms that the neural network trained in this study has achieved the expected results. The maneuver control maintains a very low pulse width, with the main propulsion thruster working for a duration of 746 seconds, which is consistent with the time in Figure 3. This evidence further indicates that the neural network designed in this study has obtained performance consistent with numerical methods.

In terms of actual simulation time, using numerical algorithms with grid search took approximately 1800 seconds. In comparison, utilizing the neural network trained in this study for calculations required within only 3 seconds, resulting in significant time savings.

4 Conclusion

This study analyzed the impact of disturbances on the orbital interception accuracy of spacecraft during in-orbit operations. It proposed a control strategy based on numerical correction methods, involving the refinement and optimization of solutions obtained through the Lambert method for the two-body problem. The approach successfully obtained the required maneuver control strategy by correcting the Lambert solutions and searching for fuel-optimal scenarios. Through simulation verification, the precision of the orbital interception maneuver control was maintained within 1 km, demonstrating the correctness and control accuracy of the proposed method.

To address the computational resource waste associated with numerical algorithms, a fuel-optimal orbital control strategy based on a BP neural network was introduced. The neural network was trained using a modified dataset, resulting in a high-performance neural network approximation function. Simulation results indicated that the orbital interception controller based on this neural network achieved the required orbital interception control, saving computational resources and achieving accuracy comparable to numerical correction methods.

References

[1] Chen S, Jiang F, Li H, et al. Optimization for Multitarget, Multispacecraft Impulsive Rendezvous Considering J2 Perturbation[J]. Journal of Guidance, Control, and Dynamics, 2021, 44(10): 1811-1822..

[2] Greco C, Campagnola S, Vasile M. Robust Space Trajectory Design Using Belief Optimal Control[J]. Journal of Guidance, Control, and Dynamics, 2022, 45(6): 1060-1077..

[3] Greco C, Vasile M. Robust Bayesian Particle Filter for Space Object Tracking Under Severe Uncertainty[J]. Journal of Guidance, Control, and Dynamics, 2022, 45(3): 481-498.

[4] Jin K, Geller D K, Luo J. Robust Trajectory Design for Rendezvous and Proximity Operations with Uncertainties[J]. Journal of Guidance, Control, and Dynamics, 2020, 43(4): 741-753.

[5] Yang B, Li S, Feng J, et al. Fast Solver for J2-Perturbed Lambert Problem Using Deep Neural Network[J]. Journal of Guidance, Control, and Dynamics, 2022, 45(5): 875-884.

[6] Ahn J, Bang J, Lee S I. Acceleration of Zero-Revolution Lambert's Algorithms Using Table-Based Initialization[J]. Journal of Guidance, Control, and Dynamics, 2015, 38(2): 335-342.

[7] Ahn J, Lee S I. Lambert Algorithm Using Analytic Gradients[J]. Journal of Guidance, Control, and Dynamics, 2013, 36(6): 1751-1761.

[8] Lee J, Ahn J. Successive Optimization Framework for Weak Stability Boundary Trajectory Design[C]//ASCEND 2021. Las Vegas, Nevada & Virtual: American Institute of Aeronautics and Astronautics, 2021[2022-06-09].

[9] Mcmahon J W, Scheeres D J. Linearized Lambert's Problem Solution[J]. Journal of Guidance, Control, and Dynamics, 2016, 39(10): 2205-2218.

[10] Armellin R, Gondelach D, San Juan J F. Multi-revolution perturbed Lambert problem[C]//2018 Space Flight Mechanics Meeting. Kissimmee, Florida: American Institute of Aeronautics and Astronautics, 2018[2022-05-26].

[11] Zhang G. Terminal-Velocity-Based Lambert Algorithm[J]. Journal of Guidance, Control, and Dynamics, 2020, 43(8): 1529-1539

Proceedings of the 3rd Conference on Fully Actuated System Theory and Applications
May 10-12, 2024, Shenzhen, China

Synchronization for singular neural networks with finite time characteristic under event-triggered scheme

Yifan Wu[1], Jingjuan Zhu[1], Yujing Pang[1], Yanran Fu[1], Mengjuan Hao[1], Yanan Meng[1], Guangming Zhuang[1]

1. School of Mathematical Sciences, Liaocheng University, Liaocheng Shandong 252059, P. R. China
E-mail: wuyf0123@126.com; z19861600169@163.com; pyj6963@163.com; fuyanran0224@163.com; haomengjuan027@163.com; m15854165065@163.com; zgmtsg@126.com

Abstract: This article studies the master-slave synchronization for singular neural networks with finite time characteristic under event-triggered scheme. By developing novel Lyapunov-Krasovskii (L-K) functional, the master-slave synchronization of singular neural networks with finite time characteristic is achieved. The desired gains of state feedback synchronization controller and event-triggered weight matrices are co-designed under the framework of linear matrix inequalities. The usability of the presented approach is proved by a simulation example.

Key Words: Finite-time synchronization, Singular systems, Neural networks, Event-triggered scheme, Mode-dependent L-K functional

1 Introduction

Singular systems, consist of a set of coupled differential-algebraic equations, have been extensively researched in recent decades because they provide a clearer description of many actual systems [1]. However, due to the existence of static constraints, the analysis of singular systems is considerably more complex. In addition to stability, singular systems are always required to satisfy regularity and non-impulsiveness/causality [2].

Lately, neural networks (NNs) have been successfully employed in pattern recognition, associative storage and large amount of high-speed data processing [3]. The researches on neural networks have yielded fruitful results e.g. stability analysis, synchronization, state estimation problem, etc., where synchronization indicates that neurons through interaction reach a same activity state. Recently, with the prevalence of networked environments and the rapid development of artificial intelligence, singular neural networks (SNNs) have received a lot of attention.

It is worth noting that the data transmission of SNNs takes place through commom networks, the networked-induced delay, packet loss, waste of network resources are inevitable. To solve these problems, event-triggered scheme (ETS) has been developed and broadly applied for SNNs, where data packets are transmitted only if the specific event-triggered conditions are satisfied [4]. Under ETS, transmitted data volume will be effectively decreased while the stability and expected performance of the system are maintained.

Moreover, the aforesaid results have focused on admissibility and performance analysis for SNNs over an infinite time interval. However, under realistic circumstances, what needs to be focused on is just the stability and performance of the system over a finite time period, like aerospace systems [5]. Therefore, the finite-time control has become a significant research direction. In the existing literature, the issue of synchronization for SNNs within a finite time interval has not been extensively studied, not to mention under ETS, it deserves to be researched, which inspired our paper.

This article will study the master-slave synchronization for SNNs with finite time characteristic under ETS. By developing mode-dependent L-K functional, the master-slave synchronization of SNNs with finite time characteristic will be achieved. The desired gains of state feedback synchronization controller and event-triggered weight matrices will be co-designed under the framework of linear matrix inequalities (LMIs). The usability of the presented approach will be proved by a simulation example.

Notation. $sym(A)$ means $A+A^T$ and $\mathbb{L}_2[0,\infty)$ implies the space of square-integrable vector functions over $[0,\infty)$.

2 Preliminaries

2.1 Synchronization error singular neural network

Think about the master singular neural network (SNN):

$$\begin{cases} S\dot{x}_m(t) = Ax_m(t) + BN(x_m(t)), \\ x_m(0) = x_{m0}, \end{cases} \tag{1}$$

and the slave SNN:

$$\begin{cases} S\dot{x}_s(t) = Ax_s(t) + BN(x_s(t)) \\ \qquad\quad + Cu(t) + D\omega(t), \\ x_s(0) = x_{s0}, \end{cases} \tag{2}$$

where singular matrix $S \in \mathbb{R}^{n\times n}$ satisfies

$$rank(S) = s < n,$$

control input $u(\cdot) \in \mathbb{R}^u$, external disturbance $\omega(t) \in \mathbb{R}^\omega$ belongs to $\mathbb{L}_2[0,\infty)$, $x_m(t) \in \mathbb{R}^n$, $x_s(t) \in \mathbb{R}^n$ represent the neuron states of master SNN and slave SNN, respectively.

Corresponding author: Guangming Zhuang.
This work was supported by National Natural Science Foundation of China under Grants 62173174, 61773191; Shandong Provincial Natural Science Foundation under Grant ZR2021JQ23; Graduate education high-quality curriculum construction project for Shandong Province under Grant SDYKC20185.

$$N(x(\cdot)) = [N_1(x_1(\cdot)), N_2(x_2(\cdot)), ..., N_n(x_n(\cdot))]^{\mathrm{T}}$$

represents neuron activation function, which meets the conditions as below:

$$\begin{gathered} N(0) = 0, \\ 0 \leq \frac{N_m(x_1(\cdot)) - N_m(x_2(\cdot))}{x_1 - x_2} \leq P_p, \\ x_1 \neq x_2, \ \ p = 1, 2, ..., n. \end{gathered} \tag{3}$$

Let $x(t) = x_s(t) - x_m(t)$. Combining (1) with (2), the synchronization error singular neural network (SESNN) is written as:

$$\begin{cases} S\dot{x}(t) = Ax(t) + BN(x(t)) \\ \qquad + Cu(t) + D\omega(t), \\ x(0) = x_0, \end{cases} \tag{4}$$

2.2 Event-triggered shceme

We use an ETS to avoid the transfer of redundant data. The sampling period is denoted by h. Then the sampling moments are recorded as

$$kh, \quad k = 1, 2, 3, ...$$

The trigger condition of the ETS is formulated as follow:

$$\mu x^{\mathrm{T}}(t_k h)\Theta x(t_k h) - e^{\mathrm{T}}(t)\Theta e(t) \leq 0, \tag{5}$$

where

$$e(t) = x(kh) - x(t_k h),$$

$\{t_k h\}$ is the teiggered instant sequence, $\Theta > 0$ is weight matrix to be determined, μ is given constant satisfying

$$0 < \mu < 1.$$

Due to the network-caused delay τ_k, the time sequence of ZOH receiving the signals is expressed as follows:

$$\{t_0 h + \tau_0, \ t_1 h + \tau_1, \ t_2 h + \tau_2 ...\},$$

where

$$\tau_k \in [\tau_m, \ \tau_M],$$

$$\tau_M = max\{\tau_k, \ k \in N\}, \ \tau_m = min\{\tau_k, \ k \in N\}.$$

Define the function

$$\tau(t) = t - kh, \ t \in [t_k h + \tau_k, \ t_{k+1} h + \tau_{k+1}).$$

Then, one has

$$x(t_k h) = x(t - \tau(t)) - e(t). \tag{6}$$

Then, the trigger condition (5) is equivalent to

$$\begin{aligned} &\mu x^{\mathrm{T}}(t - \tau(t))\Theta x(t - \tau(t)) - \mu e^{\mathrm{T}}(t)\Theta x(t - \tau(t)) \\ &- \mu x^{\mathrm{T}}(t - \tau(t))\Theta x(t - \tau(t)) + \mu e^{\mathrm{T}}(t)\Theta e(t) \\ &- e^{\mathrm{T}}(t)\Theta e(t) \leq 0, \end{aligned} \tag{7}$$

2.3 State feedback synchronization controller

Consider the state feedback synchronization controller (SFSC) with the following form:

$$u(t) = Kx(t_k h). \tag{8}$$

2.4 Synchronization error closed-loop system

Combining the SESNN (4) with SFSC (8), the following synchronization error closed-loop system (SECLS) is obtained:

$$\begin{cases} S\dot{x}(t) = Ax(t) + BN(x(t)) + CKx(t - \tau(t)) \\ \qquad - CKe(t) + D\omega(t), \\ x(0) = x_0, \ \ t \in [-\tau_2, \ 0]. \end{cases} \tag{9}$$

Next, the definitions and lemmas used in this paper will be introduced.

Definition 1. *([1]). (1.1) The SECLS (9) is regular if* $det(aS - A)$ *is not identically zero.*

(1.2) The SECLS (9) is impulse-free, if $deg(det(aS - A)) = rank(S)$.

Definition 2. *([3]). The SECLS (9) is finite-time bounded w.r.t.* $(\alpha_1, \alpha_2, R, T_f, c)$, $(\alpha_1 < \alpha_2)$ *and* $R > 0$, *if for* $\forall \omega(t)$: $\int_0^{T_f} \omega^{\mathrm{T}}(t)\omega(t)dt \leq c$, *the following conclusion is met*

$$\begin{aligned} &\sup_{-\tau_2 \leq v \leq 0} \{x^{\mathrm{T}}(v)Rx(v), \dot{x}^{\mathrm{T}}(v)S^{\mathrm{T}}RS\dot{x}(v)\} \leq \alpha_1 \\ &\Rightarrow x^{\mathrm{T}}(t)S^{\mathrm{T}}RSx(t) < \alpha_2, \ \ \forall t \in [0, \ T_f]. \end{aligned} \tag{10}$$

Lemma 1. *([2]). For any matrices* $F, \ M$ *satisfying*

$$\begin{bmatrix} F & M \\ * & F \end{bmatrix} \geq 0,$$

if there exist scalars $\sigma_1, \ \sigma_2, \ \sigma(t)$ *satisfied*

$$\sigma_1 \leq \sigma(t) \leq \sigma_2,$$

and the integrations

$$\int_{t-\sigma_2}^{t-\sigma_1} \dot{x}^T(\alpha)F\dot{x}(\alpha)d\alpha,$$

$$\int_{t-\sigma(t)}^{t-\sigma_1} \dot{x}(\alpha)d\alpha, \quad \int_{t-\sigma_2}^{t-\sigma(t)} \dot{x}(\alpha)d\alpha$$

are well defined, we can get

$$-(\sigma_2 - \sigma_1)\int_{t-\sigma_2}^{t-\sigma_1} \dot{x}^T(\alpha)F\dot{x}(\alpha)d\alpha \leq \varpi^T(t)\aleph\varpi(t),$$

where

$$\varpi(t) = \begin{bmatrix} x^T(t - c_1) & x^T(t - c(t)) & x^T(t - c_2) \end{bmatrix}^T,$$

$$\aleph = \begin{bmatrix} -F & F - M & M \\ * & -2F + M + M^T & F - M \\ * & * & -F \end{bmatrix}.$$

3 Main results

Theorem 1. *The SECLS (9) is finite-time bounded w.r.t.* $(\alpha_1,\ \alpha_2,\ R,\ T_f,\ c)$*, if given positive constants* T_f*,* α_1*,* α_2*,* β*,* $0 < \mu < 1$ *and matrix* $R > 0$*, there are matrices* M*,* $Q_1 > 0$*,* $\widehat{G} > 0$*,* $Q_2 > 0$*,* $F > 0$*,* $\Theta > 0$*, diagonal matrix* $L > 0$ *make the following matrix inequalities (11)-(15) hold.*

$$S^{\mathrm{T}}\widehat{G} = \widehat{G}^{\mathrm{T}}S \geq 0, \tag{11}$$

$$\begin{bmatrix} S^{\mathrm{T}}FS & M \\ * & S^{\mathrm{T}}FS \end{bmatrix} \geq 0, \tag{12}$$

$$\mathscr{L} = \begin{bmatrix} \mathscr{L}_1 & \mathscr{L}_2 \\ * & \mathscr{L}_3 \end{bmatrix} < 0, \tag{13}$$

$$S^{\mathrm{T}}RS \leq \beta\widehat{G}^{\mathrm{T}}S, \tag{14}$$

$$\beta e^{\eta T_f}(\Lambda\alpha_1 + rc) < \alpha_2, \tag{15}$$

where

$$\mathscr{L}_1 = \begin{bmatrix} \mathscr{L}_{11} & \mathscr{L}_{12} \\ * & \mathscr{L}_{13} \end{bmatrix},$$

$$\mathscr{L}_{11} = \begin{bmatrix} \Omega_{11} & \widehat{G}^T B & U_1 & \Omega_{14} \\ * & -I & 0 & 0 \\ * & * & \Omega_{33} & \Omega_{34} \\ * & * & * & \Omega_{44} \end{bmatrix},$$

$$\mathscr{L}_{12} = \begin{bmatrix} 0 & \widehat{G}^T D & \Omega_{17} \\ 0 & 0 & 0 \\ U_2 & 0 & 0 \\ \Omega_{45} & 0 & \Omega_{47} \end{bmatrix},$$

$$\mathscr{L}_{13} = \begin{bmatrix} \Omega_{55} & 0 & 0 \\ * & -rI & 0 \\ * & * & \Omega_{77} \end{bmatrix},$$

$\mathscr{L}_2 = [A\ \ B\ \ 0\ \ CK\ \ 0\ \ D\ \ -CK]^{\mathrm{T}}$,
$\Omega_{11} = sym(A^T\widehat{G}) + Q_1 + L$, $\Omega_{14} = \widehat{G}^{\mathrm{T}}CK - U_1$,
$\Omega_{33} = Q_2 - Q_1 - S^{\mathrm{T}}FS$, $\Omega_{34} = S^{\mathrm{T}}FS - M$,
$\Omega_{44} = \mu\Theta - 2S^{\mathrm{T}}FS + M^{\mathrm{T}} + M$, $\Omega_{45} = S^{\mathrm{T}}FS - M$,
$\Omega_{47} = -\mu\Theta$, $\Omega_{77} = -\Theta + \mu\Theta$,
$\Omega_{55} = -Q_2 - S^{\mathrm{T}}FS$, $\Omega_{17} = -\widehat{G}^{\mathrm{T}}CK$,
$\mathscr{L}_3 = -\frac{1}{(\tau_2-\tau_1)^2}F^{-1}$.

Proof. There exist non-singular Π, Ψ such that

$$\Psi^{-\mathrm{T}}\widehat{G}\Pi = \begin{bmatrix} G^1 & G^2 \\ G^3 & G^4 \end{bmatrix},$$

$$\Psi A\Pi = \begin{bmatrix} A^1 & A^2 \\ A^3 & A^4 \end{bmatrix},$$

$$\Psi S\Pi = \begin{bmatrix} I & 0 \\ 0 & 0 \end{bmatrix}.$$

It follows from (11), we can get that

$$\Pi^{\mathrm{T}}S^{\mathrm{T}}\widehat{G}\Pi = \Pi^{\mathrm{T}}\widehat{G}^{\mathrm{T}}S\Pi \geq 0,$$

by further calculations it is obtained that

$$\begin{aligned}\Pi^{\mathrm{T}}S^{\mathrm{T}}\widehat{G}\Pi &= \Pi^{\mathrm{T}}S^{\mathrm{T}}\Psi^{\mathrm{T}}\Psi^{-\mathrm{T}}\widehat{G}\Pi \\ &= \begin{bmatrix} I_r & 0 \\ 0 & 0 \end{bmatrix}\begin{bmatrix} G^1 & G^2 \\ G^3 & G^4 \end{bmatrix} \\ &= \begin{bmatrix} G^1 & G^2 \\ 0 & 0 \end{bmatrix} \\ &\geq 0,\end{aligned}$$

$$\begin{aligned}\Pi^{\mathrm{T}}\widehat{G}^{\mathrm{T}}S\Pi &= \Pi^{\mathrm{T}}\widehat{G}^{\mathrm{T}}\Psi^{-1}\Psi S\Pi \\ &= \begin{bmatrix} G^{1\mathrm{T}} & G^{3\mathrm{T}} \\ G^{2\mathrm{T}} & G^{4\mathrm{T}} \end{bmatrix}\begin{bmatrix} I_r & 0 \\ 0 & 0 \end{bmatrix} \\ &= \begin{bmatrix} G^{1\mathrm{T}} & 0 \\ G^{2\mathrm{T}} & 0 \end{bmatrix} \\ &\geq 0.\end{aligned}$$

Then, we can get

$$G^2 = 0, \quad G^1 = G^{1\mathrm{T}} \geq 0.$$

Applying Schur complement formula to (13), the following inequality can be drawn:

$$sym(A^T\widehat{G}) < 0. \tag{16}$$

Then, the following inequality is obtained:

$$\begin{bmatrix} \diamondsuit & \diamondsuit \\ \diamondsuit & G^{4\mathrm{T}}A^4 + A^{4\mathrm{T}}G^4 \end{bmatrix} < 0, \tag{17}$$

where $\diamondsuit$ denotes the unutilized term in the follow-up.

Hence, one has

$$G^{4\mathrm{T}}A^4 + A^{4\mathrm{T}}G^4 < 0,$$

by [1, 2], A^4 is non-singular.

Then, the regularity and non-impulsiveness of SECLS (9) is proved.

We establish the L-K functional candidate for SECLS (9) as

$$V(t, x_t) = \sum_{r=1}^{4} V_r(t, x_t), \tag{18}$$

where

$$V_1(t,\ x_t) = e^{\psi t}x^{\mathrm{T}}(t)S^{\mathrm{T}}\widehat{G}x(t),$$

$$V_2(t,\ x_t) = e^{\psi t}\int_{t-\tau_1}^{t} x^{\mathrm{T}}(v)Q_1x(v)dv,$$

$$V_3(t,\ x_t) = e^{\psi t}\int_{t-\tau_2}^{t-\tau_1} x^{\mathrm{T}}(v)Q_2x(v)dv,$$

$$V_4(t,\ x_t) = (\tau_2 - \tau_1)e^{\psi t}\int_{t-\tau_2}^{t-\tau_1}\int_{s}^{t} \dot{x}^{\mathrm{T}}(v)S^{\mathrm{T}}FS\dot{x}(v)dvds.$$

Let $\mathbb{L}V$ be the weak infinitesimal generator for stochastic process $\{x_t,\ \gamma_t\}$ effecting on $V(\cdot)$,

$$\mathbb{L}V_1(t,x_t) = \psi V_1(t,x_t) + e^{\psi t}[x^{\mathrm{T}}(t)S^{\mathrm{T}}\widehat{G}\dot{x}(t) + \dot{x}^{\mathrm{T}}(t)S^{\mathrm{T}}\widehat{G}x(t)],$$

$$\mathbb{L}V_2(t,x_t) = \psi V_2(t,x_t) + e^{\psi t}[x^{\mathrm{T}}(t)Q_1x(t) - x^{\mathrm{T}}(t-\tau_1)Q_1x(t-\tau_1)],$$

$$\mathbb{L}V_3(t,x_t) = e^{\psi t}[x^{\mathrm{T}}(t-\tau_1)Q_2x(t-\tau_1) - x^{\mathrm{T}}(t-\tau_2)Q_2x(t-\tau_2)] + \psi V_3(t,x_t),$$

$$\mathbb{L}V_4(t,x_t) = \psi V_4(t,x_t) + e^{\psi t}[(\tau_2-\tau_1)^2\dot{x}^{\mathrm{T}}(t)S^{\mathrm{T}}FS\dot{x}(t) - (\tau_2-\tau_1)\int_{t-\tau_2}^{t-\tau_1}\dot{x}^{\mathrm{T}}(s)S^{\mathrm{T}}FS\dot{x}(s)ds].$$

Then, one obtains that

$$-(\tau_2-\tau_1)\int_{t-\tau_2}^{t-\tau_1}\dot{x}^{\mathrm{T}}(s)S^{\mathrm{T}}FS\dot{x}(s)ds \le -\phi^{\mathrm{T}}(t)\Lambda\phi(t), \tag{19}$$

where

$$\phi(t) = [x^{\mathrm{T}}(t-\tau_1) \quad x^{\mathrm{T}}(t-\tau(t)) \quad x^{\mathrm{T}}(t-\tau_2)]^{\mathrm{T}},$$

$$\Lambda = \begin{bmatrix} S^{\mathrm{T}}FS & M - S^{\mathrm{T}}FS & -M \\ * & 2S^{\mathrm{T}}FS - M - M^{\mathrm{T}} & M - S^{\mathrm{T}}FS \\ * & * & S^{\mathrm{T}}FS \end{bmatrix},$$

Recalling the neuron activation function (3), one can obtain that

$$N^{\mathrm{T}}(x(t))N(x(t)) - x^{\mathrm{T}}(t)Lx(t) \le 0, \tag{20}$$

where

$$L = diag\{p_1^2,\ p_2^2,\ \cdots,\ p_n^2\}.$$

Then, one has

$$\begin{aligned} &\mathbb{L}V(t,x_t) \\ &\le \psi V(t,x_t) - e^{\psi t}r\omega^{\mathrm{T}}(t)\omega(t) \\ &+ e^{\psi t}\Gamma^{\mathrm{T}}(t)(\mathscr{L}_1 - \mathscr{L}_2^{\mathrm{T}}\mathscr{L}_3^{-1}\mathscr{L}_2)\Gamma(t), \end{aligned} \tag{21}$$

where

$\Gamma(t) = [x^{\mathrm{T}}(t)\ N^{\mathrm{T}}(x(t))\ x^{\mathrm{T}}(t-\tau_1)\ x^{\mathrm{T}}(t-\tau(t))\ x^{\mathrm{T}}(t-\tau_2)\ \omega^{\mathrm{T}}(t)\ e^{\mathrm{T}}(t)]^{\mathrm{T}}$.

Recalling (13), we have

$$\mathscr{L}_1 - \mathscr{L}_2^{\mathrm{T}}\mathscr{L}_3^{-1}\mathscr{L}_2 < 0. \tag{22}$$

According to (21) and (22), one has

$$\mathbb{L}V(t,x_t) - \psi V(t,x_t) \le e^{\psi t}r\omega^{\mathrm{T}}(t)\omega(t). \tag{23}$$

By further calculations it can be obtained that

$$\begin{aligned} &e^{-\psi t}V(t,x_t) - V(0,x_0) \\ &\le \int_0^t r\omega^{\mathrm{T}}(s)\omega(s)ds = rc. \end{aligned} \tag{24}$$

Let

$$\overline{\widehat{G}}_i = R^{-\frac{1}{2}}\widehat{G}_i^{\mathrm{T}}SR^{-\frac{1}{2}}, \quad \overline{Q}_1 = R^{-\frac{1}{2}}Q_1R^{-\frac{1}{2}},$$
$$\overline{Q}_2 = R^{-\frac{1}{2}}Q_2R^{-\frac{1}{2}}, \quad \overline{F} = R^{-\frac{1}{2}}FR^{-\frac{1}{2}}.$$

One obtains that

$$\begin{aligned} &V(0,x_0) = x^{\mathrm{T}}(0)\widehat{G}^{\mathrm{T}}Sx(0) \\ &+ \int_{-\tau_1}^{0} x^{\mathrm{T}}(v)Q_1x(v)dv \\ &+ (\tau_2-\tau_1)\int_{-\tau_2}^{-\tau_1}\int_{s}^{0}\dot{x}^{\mathrm{T}}(v)SFS\dot{x}(v)dvds \\ &+ \int_{-\tau_2}^{-\tau_1} x^{\mathrm{T}}(v)Q_2x(v)dv \\ &< \Lambda\alpha_1, \end{aligned} \tag{25}$$

where

$$\begin{aligned} \Lambda = &\lambda_{max}(\overline{\widehat{G}}) + (\tau_2-\tau_1)\lambda_{max}(\overline{Q}_2) \\ &+ \frac{(\tau_2-\tau_1)^2(\tau_2+\tau_1)}{2}\lambda_{max}(\overline{F}) \\ &+ \tau_1\lambda_{max}(\overline{Q}_1), \end{aligned}$$

$$\sup_{-\tau_2\le v\le 0} x^{\mathrm{T}}(v)Rx(v), \dot{x}^{\mathrm{T}}(v)S^{\mathrm{T}}RS\dot{x}(v) \le \alpha_1.$$

On the other hand, based on (14), we can get

$$\begin{aligned} &\frac{1}{\beta}x^{\mathrm{T}}(t)S^{\mathrm{T}}RSx(t) \\ &\le x^{\mathrm{T}}(t)\widehat{G}^{\mathrm{T}}Sx(t) \\ &\le V(t,x_t). \end{aligned} \tag{26}$$

Substituting (25) into (24) and (26) yields

$$\begin{aligned} &x^{\mathrm{T}}(t)S^{\mathrm{T}}RSx(t) \\ &\le \beta V(t,x_t) \\ &\le \beta e^{\psi T_f}(\Lambda\alpha_1 + rc) \\ &\le \alpha_2. \end{aligned} \tag{27}$$

Based on Definition 2, the SECLS (9) meets FTB, which means that the master SNN (1) and slave SNN (2) satisfy finite-time synchronization.

□

Then, Theorem 2 will be presented to obtain the gains of state feedback synchronization controller and the event-triggered weight matrices.

Theorem 2. *The SECLS (9) is finite-time bounded w.r.t. $(\alpha_1, \alpha_2, T_f, R, c)$, if given positive constants T_f, α_1, α_2, $0 < \mu < 1$, $R > 0$, there exist $\widetilde{M}$, W, $\widetilde{K}$, M, $\Theta > 0$, $\widetilde{\Theta} > 0$, $F > 0$, $\widetilde{F} > 0$, $\widetilde{Q}_1 > 0$, $Q_1 > 0$, $\widetilde{Q}_2 > 0$, $Q_2 > 0$, $\widetilde{R} > 0$ and diagonal matrix $\widetilde{L} > 0$ such that (15), (28)-(31) are met.*

$$W^{\mathrm{T}}E^{\mathrm{T}} = EW \geq 0, \tag{28}$$

$$\begin{bmatrix} S^{\mathrm{T}}\widetilde{F}S & \widetilde{M} \\ * & S^{\mathrm{T}}\widetilde{F}S \end{bmatrix} \geq 0, \tag{29}$$

$$\mathscr{L}_a^\star = \begin{bmatrix} \mathscr{L}_1^\star & \mathscr{L}_2^\star \\ * & \mathscr{L}_3^\star \end{bmatrix} < 0, \tag{30}$$

$$S^{\mathrm{T}}\widetilde{R}S \leq \beta SW, \tag{31}$$

where

$$\mathscr{L}_1^\star = \begin{bmatrix} \mathscr{L}_{11}^\star & B & 0 & \mathscr{L}_{14}^\star \\ * & -I & 0 & 0 \\ * & * & \mathscr{L}_{33}^\star & \mathscr{L}_{34}^\star \\ * & * & * & \mathscr{L}_{44}^\star \end{bmatrix},$$

$$\mathscr{L}_2^\star = \begin{bmatrix} 0 & D & -C\widetilde{K} & W^{\mathrm{T}}A^{\mathrm{T}} \\ 0 & 0 & 0 & B^{\mathrm{T}} \\ \widetilde{U}_2 & 0 & 0 & 0 \\ \mathscr{L}_{45}^\star & 0 & -\mu\widetilde{\Theta} & \widetilde{K}^{\mathrm{T}}C^{\mathrm{T}} \end{bmatrix},$$

$$\mathscr{L}_3^\star = \begin{bmatrix} \mathscr{L}_{55}^\star & 0 & 0 & 0 \\ * & -\gamma I & 0 & D^{\mathrm{T}} \\ * & * & \mathscr{L}_{77}^\star & -\widetilde{K}^{\mathrm{T}}C^{\mathrm{T}} \\ * & * & * & \mathscr{L}_{88}^\star \end{bmatrix},$$

$\mathscr{L}_{11}^\star = sym(AW) + \widetilde{Q}_1 + \widetilde{L}$, $\mathscr{L}_{33}^\star = \widetilde{Q}_2 - \widetilde{Q}_1 - S^{\mathrm{T}}\widetilde{F}S$,
$\mathscr{L}_{34}^\star = -\widetilde{M} + S^{\mathrm{T}}\widetilde{F}S$, $\mathscr{L}_{14}^\star = C\widetilde{K}$,
$\mathscr{L}_{44}^\star = \mu\widetilde{\Theta} - 2S^{\mathrm{T}}\widetilde{F}S + \widetilde{M}^{\mathrm{T}} + \widetilde{M}$, $\mathscr{L}_{45}^\star = -\widetilde{M} + S^{\mathrm{T}}\widetilde{F}S$,
$\mathscr{L}_{55}^\star = -\widetilde{Q}_2 - S^{\mathrm{T}}\widetilde{F}S$, $\mathscr{L}_{77}^\star = (\mu-1)\widetilde{\Theta}$,
$\mathscr{L}_{88}^\star = \frac{1}{(\tau_2-\tau_1)^2}(F-2I)$.

Then, the state feedback synchronization controller gains are shown as follows:

$$K = \widetilde{K}W^{-1}. \tag{32}$$

Proof. Let $W = S^{-1}$, it can be obtained that the condition (11) is ensured by condition (28), (31) means that (14) holds up and condition (29) guarantees that condition (12) is fulfilled.

For $\Phi > 0$, we have

$$(Y-\Phi)\Phi^{-1}(Y-\Phi) \geq 0,$$

then we can get that

$$-\frac{1}{(\tau_2-\tau_1)^2}F^{-1} \leq \frac{1}{(\tau_2-\tau_1)^2}(F-2I).$$

To simplify the notation, $W^{\mathrm{T}}LW$ can be abbreviated as $\widetilde{L}$, etc.

Then left- and right-multiplying

$$diag\{W^{\mathrm{T}} \quad I \quad W^{\mathrm{T}} \quad W^{\mathrm{T}} \quad W^{\mathrm{T}} \quad I \quad W^{\mathrm{T}} \quad I\}$$

and its transposition to (13) yields (30). Therefore, (30) can ensure (13). Then, Theorem 2 is proved based on Theorem 1. The SFSC gains can be written as (32).

□

4 Simulation examples

Example 1. *Consider the master SNN (1) and slave SNN (2) with the following parameters:*

$$A = \begin{bmatrix} -0.5 & 0 & 0 \\ 0 & -0.4 & 0 \\ 0 & 0 & -0.3 \end{bmatrix},$$

$$B = \begin{bmatrix} 0.1 & 0.27 & 0.2 \\ 0.15 & -0.25 & 0.13 \\ 0.28 & -0.09 & 0.18 \end{bmatrix},$$

$$C = \begin{bmatrix} -0.17 & 0.14 & 0.11 \\ 0.18 & -0.19 & 0.15 \\ 0.17 & 0.18 & -0.13 \end{bmatrix},$$

$$D = \begin{bmatrix} -0.09 & 0.19 & 0.11 \\ 0.18 & 0.27 & 0.21 \\ -0.19 & 0.28 & -0.13 \end{bmatrix},$$

$$R = \begin{bmatrix} 0.1 & 0 & 0 \\ 0 & 0.1 & 0 \\ 0 & 0 & 0.2 \end{bmatrix},$$

$$E = \begin{bmatrix} 1 & 0 & 0 \\ 0 & 1 & 0 \\ 0 & 0 & 0 \end{bmatrix},$$

$\mu_1 = 0.14$, $\tau_1 = 0.02$, $\alpha_1 = 0.5$, $h = 0.1$,
$\tau_2 = 0.08$, $\alpha_2 = 2$, $\beta = 2$, $T_f = 20$.

By solving LMIs (28)-(31), the desired state feedback synchronization controller gain is obtained as below:

$$K = \begin{bmatrix} 0.6295 & 0.1438 & 0.0267 \\ 0.1438 & 0.6816 & 0.1274 \\ 0.0258 & 0.1258 & 0.7747 \end{bmatrix}.$$

Relatively, weight matrix of the ETS is obtained in the following:

$$\Theta = \begin{bmatrix} 0.3812 & 0.0003 & -0.0002 \\ 0.0003 & 0.2442 & -0.0003 \\ -0.0002 & -0.0003 & 0.0565 \end{bmatrix},$$

Considers the case with

$$\omega(t) = 4e^{-0.25t}\sin(4t).$$

Choosing

$$x_m(0) = [0.6 \quad 0.1 \quad -0.5]^{\mathrm{T}},$$

$$x_s(0) = [2.1 \quad -0.6 \quad -1.7]^{\mathrm{T}},$$

then the initial state of the SECLS (9) is

$$x(0) = [1.5 \quad -0.7 \quad -1.2]^{\mathrm{T}}.$$

The state trajectories of master SNN (1) and slave SNN (2) are demonstrated in Fig.1-Fig3. The error trajectories without ETS are depicted in Fig.4, Fig.5 denotes the error trajectories under ETS. The event-triggered release instants and intervals are illustrated in Fig.6.

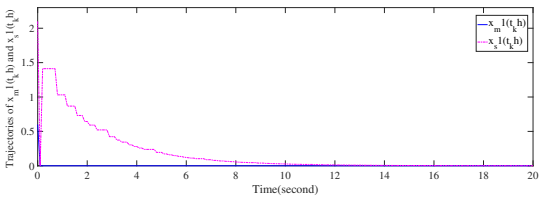

Fig. 1: Trajectories of $x_m1(t_kh)$ and $x_s1(t_kh)$.

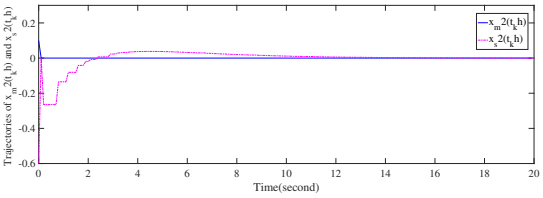

Fig. 2: Trajectories of $x_m2(t_kh)$ and $x_s2(t_kh)$.

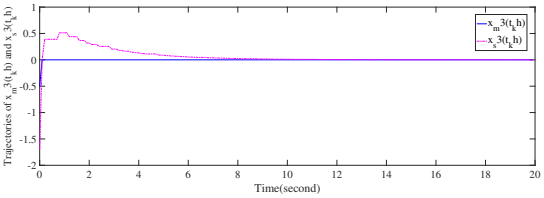

Fig. 3: Trajectories of $x_m3(t_kh)$ and $x_s3(t_kh)$.

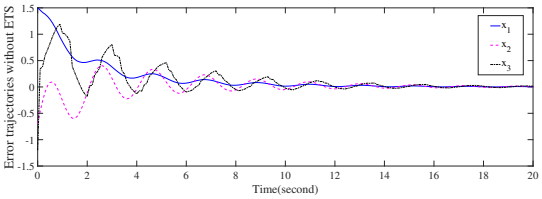

Fig. 4: Error trajectories without ETS.

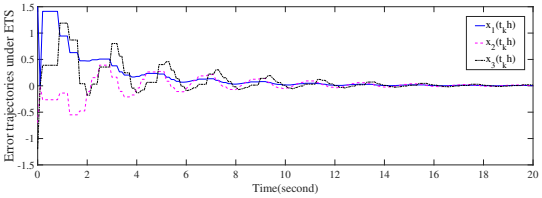

Fig. 5: Error trajectories under ETS.

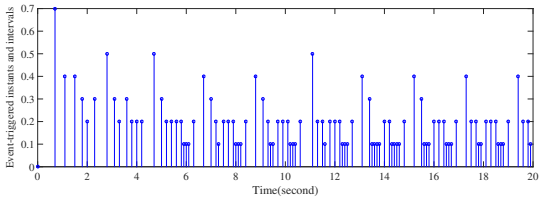

Fig. 6: Event-triggered instants and intervals.

References

[1] S. Xu, J. Lam, Robust control and filtering of singular systems, Springer: Berlin, 2006.

[2] B. Zhang, S. Xu, Q. Ma, Z. Zhang, Output-feedback stabilization of singular LPV systems subject to inexact scheduling parameters, Automatica, 2019, 104: 1-7.

[3] X. Yang, J. Cao, J. Liang, Exponential synchronization of memristive neural networks with delays: interval matrix method, IEEE Transactions on Neural Networks and Learning Systems, 2016, 28(8): 1878-1888.

[4] L. Deng, Z. Shu, T. ChenEvent-triggered robust MPC with terminal inequality constraints: A data-driven approach IEEE Transactions on Automatic Control, 2024.

[5] O. Derouiche, D. Kamri, Robust finite-time control for a class of networked switched systems using an event-triggered observer, Circuits, Systems, and Signal Processing, 2024, 43(2): 821-842.

Proceedings of the 3rd Conference on Fully Actuated System Theory and Applications
May 10-12, 2024, Shenzhen, China

State-of-Health Estimation of Lithium-ion Batteries Based on CNN-LSTM-Attention

Dong Ding, Songheng Mao, Yuan Fan
School of Electrical Engineering and Automation, Anhui University, Hefei, Anhui 230601 P. R. China
E-mail: yuanf@ahu.edu.cn

Abstract: In this paper, eight health features were extracted from battery charging and discharging data. An SE attention mechanism was incorporated into the neural network to compare the prediction of the battery's health state between a Convolutional Long Short-Term Memory (CNN-LSTM) neural network and a CNN-LSTM neural network with an attention mechanism. The experimental results reveal that the Mean Absolute Error (MAE), Root Mean Square Error (RMSE), and Mean Absolute Percentage Error (MAPE) of the attention mechanism neural network are 0.0038611, 0.0047139, and 0.0048182, respectively. This represents an improvement in the model's performance over the CNN-LSTM neural network by 11.8%, 18.9%, and 11.1%, respectively.

Key Words: SOH, CNN-LSTM, SE-attention, CNN-LSTM-attention

1 Introduction

Nowdays, Lithium-ion batteries are extensively employed as a power source in various applications, including electric vehicles, portable devices, and spacecraft [1]. Their widespread use is attributed, in part, to notable advantages such as high energy density, long cycle life, and low environmental pollution [2]. The complexity and sensitivity of lithium-ion batteries to environmental changes can affect battery performance, shorten service life, and pose safety risks like fire and explosions. Consequently, monitoring the health of lithium-ion batteries is a crucial indicator. The discharge cycles, for instance, can induce damage to electrode materials, involving processes such as the dissolution of electrode material and the fragmentation of electrode particles. External factors and working conditions, including overcharge/discharge, high voltage, extreme ambient temperatures, and load fluctuations, exert an impact on battery ageing, introducing significant uncertainty to the ageing process [3–6]. Continuous charge and discharge cycles contribute to the shortening of battery life and the degradation of battery performance. For many devices, the recommendation is to replace the battery promptly when its capacity drops below 70% to 80% of the initial capacity, mitigating the risk of severe safety accidents [7]. A robust correlation exists between changes in battery capacity and the State of Health (SOH). Therefore, accurate estimation of the SOH is essential. The primary methods for estimating the SOH of lithium-ion batteries include the method based on a model and a data-driven approach [8]. The equivalent circuit model consists of a finite number of series resistor-capacitor (RC) networks [9]. Specifically, as RC networks increase, the cell modelling accuracy is improved, but the computational complexity increases. The battery modelling is frequently combined with Kalman filtering or extended Kalman filtering to improve the limitations caused by disturbances such as temperature drift [10].

Due to the rapid advancements in the field of machine learning in recent years, several neural network methods have gained widespread use in estimating the SOH of batteries. These methods leverage the combination of neural networks with the indirect health characteristics of batteries. Hong and Lee et al. employed a one-dimensional convolutional neural network to predict the remaining useful life of a battery. However, it's important to note that convolutional neural networks (CNNs) share weights, which can potentially result in the leakage of useful information in SOH estimates [11].Eddahech and Briat et al. introduced the use of recurrent neural networks (RNNs) in conjunction with equivalent circuit models to predict battery ageing trends [12]. Tian et al. estimated the battery SOH based on the particle filter algorithm and the established model [13]. Li and Sengupta et al. utilized extended short-term memory networks (LSTM) to estimate the capacity of a battery without suffering from gradient disappearance. However, the aforementioned LSTM-based prediction method may not account for differences in the importance of sequence features. This oversight can result in the neglect of crucial features, potentially leading to a degradation in prediction performance [14].

Building upon the aforementioned research methods, this paper introduces a novel SOH estimation approach for lithium-ion batteries utilizing a LSTM network. Initially, an Incremental Capacity (IC) gain curve is constructed based on the voltage and current during charge and discharge in the NASA battery dataset. The peak voltage is then extracted from the IC curve as a feature for SOH estimation. Additionally, voltage, current, and time during the battery's charge and discharge process are extracted and processed as characteristics for SOH estimation. The proposed methodology employs an enhanced CNN-LSTM network structure incorporating an attention mechanism for improved SOH estimation. Experimental results demonstrate the model's high accuracy in estimating the State of Health of lithium-ion batteries.

2 Extraction of Indirect Health Features

2.1 The Dataset Used

The battery degradation dataset used in this study is provided by NASA and is widely used to estimate the State of

This work was supported by the National Natural Science Foundation of China (61973002), and the Anhui Provincial Natural Science Foundation (2008085J32).

Health (SOH) and State of Charge (SOC) of various lithium-ion battery applications. The experimental procedure involved using 18650 commercial lithium-ion batteries with an initial capacity of around 2Ah. The batteries were charged using Constant Current (CC) mode at a rate of 1.5A until the battery voltage reached 4.2V. After that, charging continued using Constant Voltage (CV) mode until the charging current dropped to 20mA. Discharge was carried out at a constant current of 2A CC until the battery voltage reached predefined cutoff voltages. These cutoff voltages were 2.7V, 2.5V, 2.2V, and 2.5V for batteries B0005, B0006, B0007, and B0018, respectively.

The cut-off voltages indicate the decline in the capacity of these batteries over time. Let us consider the battery mentioned in document number one as an example. After analyzing its charge and discharge cycle, we found that specific changes, such as the increase of the initial charge voltage, the reduction of the time required for constant discharge, and the change in the time required for constant current charge stage, can represent the ageing process of the battery. Therefore, the duration of the constant current charge and discharge phase, as well as the initial charge voltage, are chosen as indirect health indicators of these batteries. This experimental setup and the associated data analysis provide valuable insights into the degradation patterns and performance characteristics of these lithium-ion batteries. These insights are critical for assessing their health and charging status in various applications.

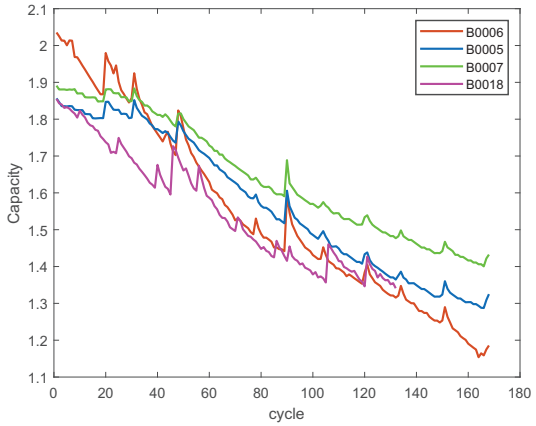

Fig. 1: Capacity decay curve

2.2 State of Health (SOH) Definition

As shown in Fig.1, each battery has a unique initial capacity. The State of Health (SOH) is used as a metric to assess the health of the batteries. There are various methods for calculating SOH, but two primary approaches are based on battery impedance and available capacity . The impedance-based method is not suitable for online measurements as it requires instruments like electrochemical impedance spectroscopy. Thus, in this study, we determine SOH based on the battery's available capacity. This method can be represented as follows:

$$SOH = \frac{C_m}{C_n} \times 100\% \tag{1}$$

where C_m is the available capacity, representing the maximum discharge capacity when fully discharged, and C_n is the rated capacity provided by the manufacturer. Available capacity decreases over time; the curve of SOH is shown in the Fig.2.

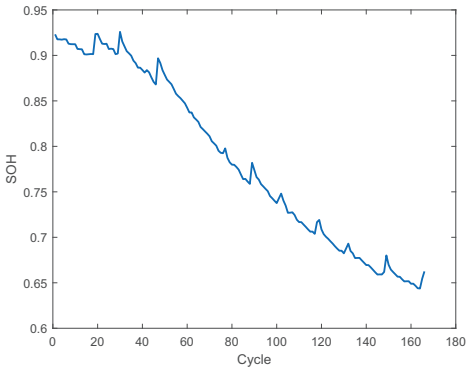

Fig. 2: True SOH curve

2.3 ICA(Incremental Capacity Analysis)

Lithium-ion batteries can be analyzed using the dQ/dV-V curve, also known as the IC curve, to evaluate the condition of the internal positive and negative electrode materials. Additionally, there are dV/dQ-Q curves, also called Differential Voltage (DV) curves, which are utilized for studying the degradation mechanism of batteries. The Incremental Capacity Analysis (ICA) approach is commonly used for analyzing IC curves. In this paper, we apply ICA to investigate the degradation mechanism of batteries. Our focus is on the analysis of IC curves to gain insights into the battery's internal state and performance.

$$Q = \int_0^T I\,(t)\,dt \tag{2}$$

$$\frac{dQ}{dV} = \frac{\Delta Q}{\Delta V} = \frac{Q_K - Q_{K-1}}{V_K - V_{K-1}} \tag{3}$$

where Q represents the charging capacity, I(t) is the charging current, C and V represent the charging capacity and voltage at the time step k, and T is the charging time at the current state of the battery.

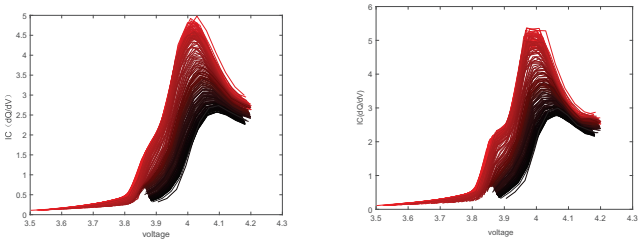

Fig. 3: The ic curve of Kalman filter is compared with the initial IC curve

According to equations (2) to (3), we can obtain the IC curve. It is observed that with an increase in the number of cycles, the peak value of the IC curve gradually decreases. Therefore, the peak value can be used as a health indicator. To reduce noise interference, Kalman filtering is employed to filter the IC curve since the IC gain curve is susceptible to

disturbances [15]. The comparison between the filtered IC curve after Kalman filtering and the initial IC curve is shown in Fig.3. In previous studies, researchers typically extracted peak intensity, position, or slope of the IC curve as health feature variables. However, as shown in Fig.4, some peaks gradually disappear with battery ageing, making it challenging to estimate the State of Health in the later stages of a battery's life. To address this issue, we select incremental capacity values within the voltage range of 3.8 to 4.1V as feature variables and evenly divide the voltage range with 30mV voltage intervals.

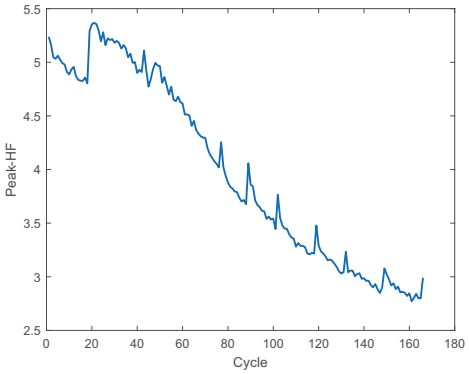

Fig. 4: IC-peak curve

To summarize, this paper focuses on specific indirect health characteristics of batteries, such as constant current charging time, initial voltage during constant current charging, constant current discharge time, constant voltage discharge time, constant voltage rise time, maximum IC value, and the voltage value at which the IC reaches its maximum. These features will be used as inputs for a neural network with the goal of estimating the health status of the batteries.

3 Convolutional Long Short-term Memory Neural Network Based on The Attention Mechanism

3.1 Convolutional Neural Network (CNN)

CNN constitutes a type of feedforward neural network primarily comprising convolutional layers, pooling layers, and fully connected layers. Its foundational concept revolves around feature extraction and dimension reduction from input data. This process involves convolutional and pooling layers, with subsequent tasks such as classification or regression facilitated by fully connected layers. CNN is distinguished by structural features like local correlations and weight sharing, which enable feature extraction and data dimensionality reduction for each input factor. This proves advantageous in reducing the number of feature parameters and overall model complexity. CNN operates by extracting features through convolutional layers, diminishing feature size via pooling layers, introducing nonlinearity through activation functions, transforming features into classification outcomes using fully connected layers, and finally converting these outcomes into a probability distribution through the Softmax function. This intricate process allows CNN to effectively extract critical features from data and provide a probability distribution for classification results; the structure of CNN is shown in Fig.5.

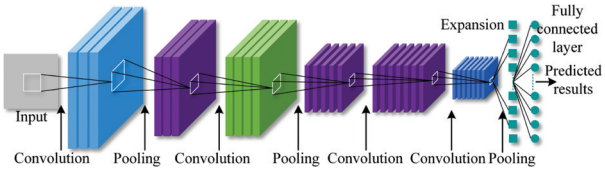

Fig. 5: CNN structure

3.2 Long Short-Term Memory (LSTM) Network

LSTM represents a specialized form of recurrent neural network designed for processing sequence data. LSTM tackles the challenges of vanishing and exploding gradients often encountered in traditional RNNs by incorporating gate structures to regulate information flow. The fundamental concept of LSTM involves introducing a memory cell to the network and employing input gates, output gates, and forget gates to govern the information flow within the memory cell. This approach facilitates the effective modelling and prediction of sequence data. The internal structure diagram of the LSTM is depicted in Fig.6, and its calculation formula is as follows:

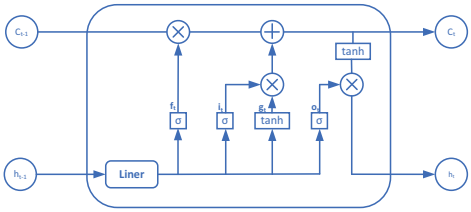

Fig. 6: LSTM structure

$$f_t = \sigma\left(W_f \cdot [h_{t-1}, X_t]\right) + b_f \tag{4}$$
$$i_t = \sigma\left(W_i \cdot [h_{t-1}, X_t]\right) + b_i \tag{5}$$
$$c_t^{'} = \tan \mathrm{h}\left(W_c \cdot [h_{t-1}, X_t]\right) + b_c \tag{6}$$
$$c_t = f_t \cdot C_{t-1} + i_t \cdot C_t^{'} \tag{7}$$
$$o_t = \sigma\left(W_o \cdot [h_{t-1}, X_t]\right) + b_o \tag{8}$$
$$h_t = o_t \cdot \tan \mathrm{h}\left(C_t\right) \tag{9}$$

where h and c are the hidden state and cellular state of the LSTM neural unit structure, respectively, which are mathematically represented in the form of matrix vectors, and f_t, i_t and o_t which are the forgetting gate, input gate, and output gate, respectively, W_f, W_i, W_c and W_o are the coefficient matrices, and b_f, b_i, b_c and b_o are biases.

3.3 Attention Mechanism

The attention mechanism, whether exhibited by humans or machines during information processing, facilitates the automatic or conscious selection and concentration of attention. Within the human brain, attention mechanisms enable the rapid identification and concentration of significant information within complex environments, effectively disregarding irrelevant or unimportant data. In the context of a neural network, the attention mechanism can be conceptualized as a weighting mechanism that assesses the importance of each element in the input data. It then aggregates these crucial elements to generate the final output. This mechanism aids the model in directing its focus toward essential information

in the input data, effectively filtering out less crucial details. This article predominantly leverages the channel attention mechanism.SE attention mechanism [16]. SE concentration can be divided into three parts, respectively: Squeeze, Excitation and Scale. The structure is shown in the Fig.7 and Fig.8.

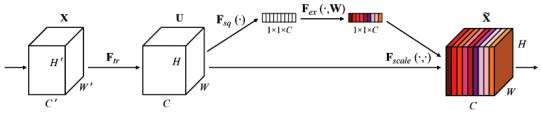

Fig. 7: Squeeze-and-Excitation block

Squeeze-and-Excitation block is a computational unit which can be built upon a transformation F_{tr} mapping an input $X \in \mathbb{R}^{H' \times W' \times C}$ to feature maps $U \in \mathbb{R}^{H \times W \times C'}$. In the notation that follows, F_{tr} is the convolution operator, where v_c is the parameter of the c-th filter, and the output is as follows:

$$u_c = v_c * X = \sum_{s=1}^{c'} v_c^s * x^s \tag{10}$$

Squeezes block compresses global spatial information into a single channel descriptor and generate channel-wise statistics by using global average pooling. The statistical quantity $U \in \mathbb{R}^C$ is contracted and generated by U through its spatial dimensions $H \times W$, so the calculation method for the c-th element of z is calculated by:

$$z_c = F_{sq}(u_c) = \frac{1}{H \times W} \sum_{i=1}^{H} \sum_{j=1}^{W} u_c(i,j) \tag{11}$$

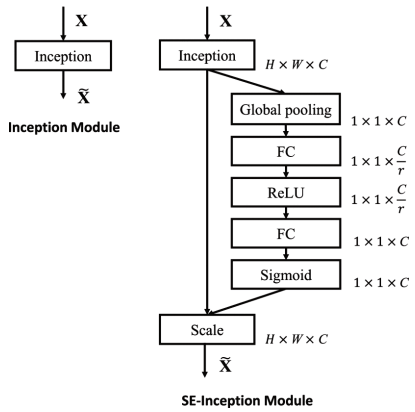

Fig. 8: The schema of the original Inception module and the SE- Inception module

The Excitation module operates by aggregating information from the Squeeze block to capture channel-related dependencies comprehensively. In pursuit of this objective, the gate mechanism relies on a two-layer, fully connected structure. The initial fully connected layer compresses C channels into C/r channels, effectively mitigating the computational load. Subsequently, the second fully connected layer restores the channel count to C channels, followed by obtaining weights (denoted as s) through Sigmoid activation. The resulting s has dimensions of 1×1×C, serving to characterize the weights of C feature maps within the feature graph U. The calculation is outlined as follows:

$$s = F_{ex}(z, W) = \sigma(g(z, W)) = \sigma(W_2 \delta(W_1 z)) \tag{12}$$

where δ is the ReLU function,$W_1 \in \mathbb{R}^{\frac{C}{r} \times C}$ $W_2 \in \mathbb{R}^{C \times \frac{C}{r}}$ r represents the compression ratio. Finally, the Scale operation, which involves weighting the attention weights obtained earlier with the features of each channel, multiplies each feature map in the feature graph U by the corresponding weight. The final output x of the SE module is obtained as follows:

$$\tilde{x}_c = F_{scale}(u_c, s_c) = s_c u_c \tag{13}$$

where $\tilde{X} = [\tilde{x}_1, \tilde{x}_2, ..., \tilde{x}_C]$ and $F_{scale}(u_c, s_c)$ refers to channel-wise multiplication between the scalar sc and the feature map $u_C \in \mathbb{R}^{H \times W}$.

4 Experiments and Analysis

4.1 Evaluation Metrics

During the model training stage, the feature dataset undergoes further partitioning into training and test datasets, following a 7:3 ratio. Subsequently, 70% of the dataset is randomly selected as the training set to facilitate the training of the entire neural network model. The remaining 30% is designated as the test set, utilized to assess the model's estimation accuracy. To gauge this accuracy, the paper employs the following evaluation indices: mean absolute error (MAE), root mean square error (RMSE), determination coefficient R^2, and mean absolute percentage error (MAPE). The calculation formulas for these indices are as follows:

$$MAE = \frac{1}{n} \sum_{i=1}^{n} |y_i - \hat{y}_i| \tag{14}$$

$$RMSE = \sqrt{\frac{1}{n} \sum_{i=1}^{n} (y_i - \hat{y}_i)^2} \tag{15}$$

$$R^2 = 1 - \frac{\sum_{i=1}^{n} (\hat{y}_i - y_i)^2}{\sum_{i=1}^{n} (y_i - \bar{y}_i)^2} \tag{16}$$

$$MAPE = \frac{1}{n} \sum_{i=1}^{n} \left| \frac{\hat{y}_i - y_i}{y_i} \right| \times 100\% \tag{17}$$

where $\hat{y}_i$ is the estimated values, y_i is the measured values, $\bar{y}_i$ is mean of the measured values, n is the number of samples. MAE represents the absolute value of the error between the predicted and true values, allowing for the cancellation of errors with opposing directions, focusing solely on their magnitudes. On the other hand, RMSE provides insights into error dispersion and convergence performance. MAE, by emphasizing error magnitude, offers a measure of the model's stability to some extent; R^2 is employed as a metric to quantify the proportion of the variation in the dependent variable that the independent variable can explain. Synthesizing these four evaluation indices enables a more comprehensive and accurate understanding of the forecast results. The higher the estimation accuracy, the smaller the values of MAE, MAPE, and RMSE; conversely, the lower the estimation accuracy, the smaller the value of R^2.

4.2 CNN-LSTM-Attention Network Model Parameter Optimization Results

In order to confirm the accuracy of the proposed model in this paper, we conducted comparative experiments with the CNN-LSTM model and the CNN-LSTM model that includes an attention mechanism. The study utilized data from a NASA lithium battery labelled B0005 to train and evaluate the performance of the two SOH estimation models. The estimated results are presented in the accompanying Fig.9, Fig.10, Fig.11.

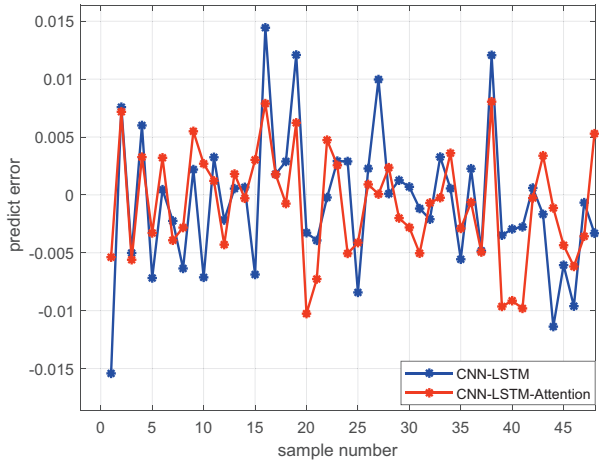

Fig. 9: Prediction error comparison

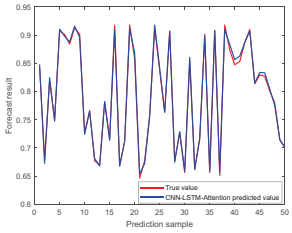

Fig. 10: CNN-LSTM-SE forecast result

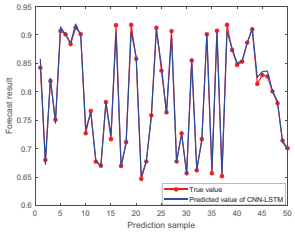

Fig. 11: CNN-LSTM forecast result

Table 1: Evaluating Indicator.

Evaluation indicators	CNN-LSTM	CNN-LSTM-Attention
MAE	0.00438	0.0038611
RMSE	0.0058168	0.0047139
MAPE	0.0054207	0.0048182
R^2	0.99611	0.99746

The results obtained demonstrate the efficacy of the proposed method in accurately estimating the state of health of lithium batteries. The proposed approach outperforms the CNN-LSTM model, showcasing improved accuracy and enhanced model performance. Specifically, the majority of errors are confined within a range of 1.0%, indicating minimal variations in error. The CNN-LSTM-Attention model excels in all four indicators—MAE, MAPE, RMSE, and R^2; the results are shown in table.1. Notably, MAE, RMSE, and MAPE exhibit respective improvements of 11.8%, 18.9%, and 11.1% compared to the CNN-LSTM model. This suggests that the incorporation of the attention mechanism contributes significantly to a more precise estimation of battery health.

5 Conclusion

This paper centres on the SOH estimation of lithium-ion batteries, proposing a CNN-LSTM model integrated with an attention mechanism to enhance the accuracy of SOH estimation. Indirect health characteristics of the battery, including the initial voltage of constant current charge, constant voltage rise charge time, constant voltage drop discharge time, IC maximum value, and voltage at IC maximum value, are extracted from the charge and discharge data of the NASA battery dataset. To mitigate the impact of noise on the IC maximum value, a Kalman filter is employed to filter the IC curve. To validate the effectiveness of the proposed method, the eight health features are input into two models, CNN-LSTM and CNN-LSTM-attention, and their performances are compared. Experimental results indicate that the addition of the attention mechanism enhances the estimation performance of the CNN-LSTM model. The MAE, RMSE, and MAPE for the CNN-LSTM-attention model are 0.0038611, 0.0047139, and 0.0048182, respectively. Compared with the CNN-LSTM model, the CNN-LSTM-attention model demonstrates improvements of 11.8%, 18.9%, and 11.1%, respectively.

References

[1] J. Tian, Y. Fan, T. Pan, X. Zhang, J. Yin, and Q. Zhang, "A critical review on inconsistency mechanism, evaluation methods and improvement measures for lithium-ion battery energy storage systems," *Renewable and Sustainable Energy Reviews*, vol. 189, p. 113978, 2024.

[2] S. Yang, C. Zhang, J. Jiang, W. Zhang, Y. Gao, and L. Zhang, "A voltage reconstruction model based on partial charging curve for state-of-health estimation of lithium-ion batteries," *Journal of Energy Storage*, vol. 35, p. 102271, 2021.

[3] J. Tian, X. Liu, C. Chen, G. Xiao, Y. Wang, Y. Kang, and P. Wang, "Feature fusion-based inconsistency evaluation for battery pack: improved gaussian mixture model," *IEEE Transactions on Intelligent Transportation Systems*, vol. 24, no. 1, pp. 446–458, 2022.

[4] M. Berecibar, I. Gandiaga, I. Villarreal, N. Omar, J. Van Mierlo, and P. Van den Bossche, "Critical review of state of health estimation methods of li-ion batteries for real applications," *Renewable and Sustainable Energy Reviews*, vol. 56, pp. 572–587, 2016.

[5] L. Yang, X. Cheng, Y. Ma, S. Lou, Y. Cui, T. Guan, and G. Yin, "Changing of sei film and electrochemical properties about mcmb electrodes during long-term charge/discharge cycles," *Journal of the electrochemical society*, vol. 160, no. 11, p. A2093, 2013.

[6] M. Klett, T. G. Zavalis, M. H. Kjell, R. W. Lindström, M. Behm, and G. Lindbergh, "Altered electrode degradation with temperature in lifepo4/mesocarbon microbead graphite cells diagnosed with impedance spectroscopy," *Electrochimica acta*, vol. 141, pp. 173–181, 2014.

[7] R. Xiong, Y. Zhang, J. Wang, H. He, S. Peng, and M. Pecht, "Lithium-ion battery health prognosis based on a real battery management system used in electric vehicles," *IEEE Trans-*

actions on Vehicular Technology, vol. 68, no. 5, pp. 4110–4121, 2018.

[8] H. Meng and Y.-F. Li, "A review on prognostics and health management (phm) methods of lithium-ion batteries," *Renewable and Sustainable Energy Reviews*, vol. 116, p. 109405, 2019.

[9] H. Fatoorehchi and M. Ehrhardt, "Numerical and semi-numerical solutions of a modified thévenin model for calculating terminal voltage of battery cells," *Journal of Energy Storage*, vol. 45, p. 103746, 2022.

[10] P. Shrivastava, T. K. Soon, M. Y. I. B. Idris, and S. Mekhilef, "Overview of model-based online state-of-charge estimation using kalman filter family for lithium-ion batteries," *Renewable and Sustainable Energy Reviews*, vol. 113, p. 109233, 2019.

[11] J. Hong, D. Lee, E.-R. Jeong, and Y. Yi, "Towards the swift prediction of the remaining useful life of lithium-ion batteries with end-to-end deep learning," *Applied energy*, vol. 278, p. 115646, 2020.

[12] A. Eddahech, O. Briat, N. Bertrand, J.-Y. Delétage, and J.-M. Vinassa, "Behavior and state-of-health monitoring of li-ion batteries using impedance spectroscopy and recurrent neural networks," *International Journal of Electrical Power & Energy Systems*, vol. 42, no. 1, pp. 487–494, 2012.

[13] J. Tian, R. Xu, Y. Wang, and Z. Chen, "Capacity attenuation mechanism modeling and health assessment of lithium-ion batteries," *Energy*, vol. 221, p. 119682, 2021.

[14] W. Li, N. Sengupta, P. Dechent, D. Howey, A. Annaswamy, and D. U. Sauer, "Online capacity estimation of lithium-ion batteries with deep long short-term memory networks," *Journal of power sources*, vol. 482, p. 228863, 2021.

[15] J. Tian, R. Xiong, and W. Shen, "State-of-health estimation based on differential temperature for lithium ion batteries," *IEEE Transactions on Power Electronics*, vol. 35, no. 10, pp. 10 363–10 373, 2020.

[16] J. Hu, L. Shen, S. Albanie, G. Sun, and E. Wu, "Squeeze-and-excitation networks," *IEEE Transactions on Pattern Analysis and Machine Intelligence*, vol. 42, no. 8, pp. 2011–2023, 2018.

Proceedings of the 3rd Conference on Fully Actuated System Theory and Applications
May 10-12, 2024, Shenzhen, China

Backdoor Attack and Defense in Asynchronous Federated Learning for Multiple Unmanned Vehicles

Kehao Wang[1], Hao Zhang[2],

1. the School of Information Engineering, Wuhan University of Technology, Wuhan 430070, P. R. China
E-mail: kehao.wang@whut.edu.cn

2. the School of Information Engineering, Wuhan University of Technology, Wuhan 430070, P. R. China
E-mail: zhanghaostruggle@whut.edu.cn

Abstract: The growing researches show that synchronous Federated learning (FL) is susceptible to backdoor attacks, in which some attackers inject subtask into model without obviously degrading the performance of major task. In this paper, we study the mechanism of backdoor attacks in asynchronous FL, i.e, the effects of the number of attackers, and the location of the backdoor injection. Our study shows that backdoor attacks are more aggressive and stealthy in asynchronous FL than synchronous one. We find that the outliers of the global model parameters become increasingly large and the number of outliers increases gradually during training with backdoor. Based on this phenomenon, we propose the *only allowing minor update to global parameters* (OAMU) algorithm to defend against backdoor attacks. Experiments show that the OAMU is an efficient and lightweight mechanism in resisting backdoor attacks. Moreover, to the best of our knowledge, the OAMU is the first work dedicated to defending against backdoor attacks in asynchronous FL .

Key Words: UAVs, Asynchronous FL, Backdoor Attack, Defense

1 Introduction

Federated learning (FL) has become a hot topic in academia and industry since it was introduced by Google in 2017 and applied to mobile apps [1]. FL is considered to be a distributed machine learning paradigm that can protect privacy of each participant. There have been several studies exploring the application of federated learning in the context of multi-UAV scenarios. However, a growing body of research shows that FL is not as secure as we thought. Some attacks in traditional machine learning algorithms are shown to be effective in the framework of FL.

According to how the server-side model aggregates the client-side model, FL can be classified into two types: synchronous FL and asynchronous one. Specifically, synchronous FL necessitates a centralized aggregation and update of model parameters by all participants at the conclusion of each round. In contrast, asynchronous FL permits participants to promptly update model parameters after completing local training.

In synchronous FL, some attacks are shown to be feasible, i.e., poisoning attacks [8], membership inference attacks [9], attribute inference attacks [10], reconstruction attacks [11], and backdoor attacks [2–7]. Especially, backdoor attack is a popular type of targeted attack in which each malicious client replicates some local training instances, embeds a trigger in each replicated training input, and finally achieves the purpose of injecting subtask. For example, in the scenario of an image classification task, an attacker can embed a patch in the lower right corner of images. As a result, trained with these backdoor samples, the model in FL framwork would categorize any input with the backdoor trigger as the attacker-selected label.

So far, almost all the research has focused on backdoor attack and defense in synchronous FL. However, the security of asynchronous FL is a very under-explored, which motivates us to study backdoor attack and defense in asynchronous FL. From the viewpoint of aggregation, the server in synchronous FL waits for all selected clients to upload model parameters and then performs weighted average on all the model parameters. In backdoor attack, this weighted average operation dilutes backdoor data, which leads to an unstable backdoor. To ensure the stability and strength of the attack, attackers often multiply their uploaded backdoor data by an amplification factor to resist the weighted average operation. Some studies on this amplification factor were proposed in synchronous FL attacks [2–4].

In asynchronous FL, the server updates the global model when receiving a model update from any client. This aggregation mechanism shows that deploying a backdoor attack in asynchronous FL does not require an amplification factor to counteract the dilution effect. Thus it is easy to launch backdoor attack in asynchronous FL. This paper investigates backdoor attacks in asynchronous FL and proposes an effective method to resist backdoor attacks. In summary, the main contributions are:

- To the best of our knowledge, this work is the first to study backdoor attack in asynchronous FL. In particular, we implement backdoor attack in asynchronous FL and experimentally confirm that backdoor attack in asynchronous FL is more aggressive and stealthy.
- We study how the performance of models is impacted by the number of attackers and the location of the backdoor injection of backdoor attack in asynchronous FL.
- By comparing the parameter changing process of the model injected with a backdoor attack with that of normal model, we observe that the outliers of big model with backdoor become much more as training. Based on this finding, the *only allowing minor update to global parameters* (OAMU) is proposed to defend against backdoor attack in asynchronous FL. Experiments show that OAMU can reduce the attack accuracy of backdoor attack to 3.02% in MNIST dataset at

This work is supported by National Natural Science Foundation of China under Grant 62172313.

the cost of only 0.5% performance degradation of main task. In CIFAR10 dataset, OAMU can degrade the performance of backdoor attack to 20.20% at the expense of only 5.1% performance degradation of main task.

- Considering no backdoor defense in asynchronous FL, we compare with the two most effective backdoor defense algorithms in synchronous FL, and the experiments show that OAMU has SOTA-level performance on MNIST dataset. Moreover, it has competitive performance to NetWork Pruning [6] but outperforms Neural Cleanse [5] on CIFAR dataset.

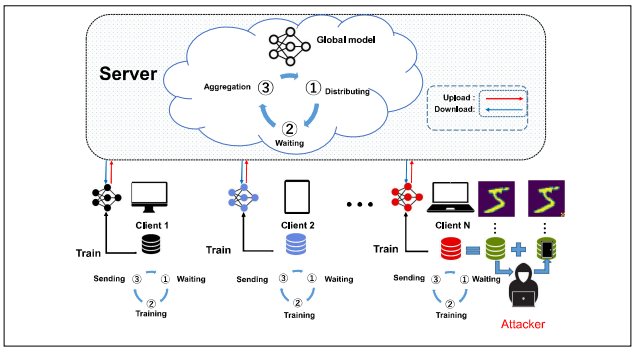

Fig. 1: Federated Learning and Backdoor attack Framework

2 Preliminaries

2.1 Asynchronous FL

Our asynchronous FL architecture is shown in Fig. 1. Suppose there are C clients and a server in a asynchronous FL scenario. $D_i = \{(x_{i,1}, y_{i,1}), \cdots, (x_{i,n_i}, y_{i,n_i})\}$ denotes a dataset on client i, where $x_{i,j}$ $(j = 1, 2, \cdots, n_i)$ is the j-th sample in D_i, $y_{i,j}$ is the label for $x_{i,j}$ and n_i is the size of the database D_i. $D = \bigcup_{i=1}^{C} D_i$ denotes the global dataset and $n = \sum_{i=1}^{C} n_i$ is the global number of samples. Let $w \in \mathbb{R}^d$ represent the global model parameters, $w_i \in \mathbb{R}^d$ represent the local model parameters. The loss function of the client i is defined as follows:

$$L_i(w_i; D_i) = \frac{1}{n_i} \sum_{j=1}^{n_i} l(w_i; x_{i,j}, y_{i,j}) \tag{1}$$

where $l(\cdot) : (\mathbb{R}^d; D) \mapsto \mathbb{R}$ is a loss function used to quantify the discrepancy between model outputs and actual labels, and $(x_{i,j}, y_{i,j}) \in D_i$.

Generally, in both synchronous FL and asynchronous FL frameworks, the mini-batch stochastic gradient descent (MBSGD) algorithm is applied in clients to optimize the local model and aggregate the parameters of local models on the server side. The objective of asynchronous FL is to minimize the following global loss function.

$$\min_{w \in \mathbb{R}^d} L(w) = \frac{1}{C} \sum_{i=1}^{C} L_i(w; D_i) \tag{2}$$

To solve this objective function, the local models on the client side need to be uploaded to the server for aggregation. In the following, we will respectively describe the specific training process from the server side and the client side.

- The server side cycles T rounds through the following three states.
  1) Distributing global model: When $t = 0$, the server sends the initial global parameters W_0 to all clients for training and records $t_1 = \cdots = t_N = 0$. When $t > 0$ the server sends the updated global model W^t to the client i that uploaded its model w_i^H to the server recently and records the current round $t_i = t$.
  2) Waiting for feedback: The server waits for a client to complete its local training.
  3) Update global model: Suppose the server adopts a first-come first-served aggregation. When receiving the parameter w_i^H from client i, the server utilizes the current round number t and the recorded t_i to compute the delay $\tau_i = t - t_i$. In fact, τ_i is a parameter describing the delay between the local model of client i and the global model.
  After obtaining w_i^H and τ_i, the server performs aggregation according to (3) to obtain a new global model W^{t+1} and return the new model to client i.

$$W^{t+1} = W^t + \eta_t \cdot (w_i^H - W^t) \tag{3}$$

  where η_t is the learning rate of global model related to τ_i, $\eta_t = \eta \cdot s(\tau_i)$, η is a learning constant, $s(\tau_i)$ is a function that measures the impact of latency. In general, $s(\tau_i) = \frac{1}{\tau_i}$.

  In each client, MBSGD is adopted to optimize $L_i(w)$ for H iterations, and the local model in client for the h-th ($h \in \{0, 1, \cdots, H-1\}$) iteration is updated as

$$\begin{cases} w_i^{t,0} = W^t \\ w_i^{t,h+1} = w_i^{t,h} - \frac{\eta_t}{|\beta_i^{t,h}|} \sum_{j=1}^{|\beta_i^{t,h}|} \nabla L_i(w_i^{t,h}; \beta_{i,j}^{t,h}) \end{cases} \tag{4}$$

  where η_t is the learning rate , $\beta_i^{t,h}$ is a mini-batch of samples randomly taken from D_i at the t round of the server and the h iteration of the client, and $\beta_{i,j}^{t,h}$ is the j-th sample in $\beta_i^{t,h}$.
- The client side cycles through the following three states.
  1) Waiting for the global model: Client i waits for the server to send the global model W^t.
  2) Local training: Client i obtains a global model W^t and then iterates H times with the MBSGD algorithm to obtain a local model $w_i^H = w_i^{t,H}$.
  3) Sending local model: Client i returns the local model w_i^H to the server.

3 Backdoor Attach and Defense

3.1 Threat Model and Backdoor Attack

The backdoor attack proposed in this paper occurs in scenarios that meet the following conditions :

1) The attacker has some ability to modify the local dataset of client i to construct a training dataset with a backdoor.
2) Each hijacked client trains its local model by the hijacked dataset with malicious samples.

We denote the number of normal clients as N_{norm}, the number of the malicious clients as N_{bad}, and $N_{\text{norm}} + N_{\text{bad}} =$

C. The objective of backdoor attacks on asynchronous FL is given as follows:

$$\min_{w\in\mathbb{R}^d} L(w) = \frac{1}{C}\sum_{i=1}^{N_{\text{norm}}} L_i(w; D_i^{\text{norm}}) + \frac{1}{C}\sum_{j=1}^{N_{\text{bad}}} L_j(w; D_j^{\text{mix}}) \quad (5)$$

The flow of backdoor attack is as follows:

- Constructing hijacked dataset: The attacker copies the local dataset D_i^{norm} of the hijacked client c_i^{bad} and adds a backdoor Δ^{bad} to each sample x_i in the dataset D_i^{norm} according to (6) to obtain the hijacked sample x_i^{bad} and further the backdoor dataset D_i^{bad}. Then D_i^{norm} and D_i^{bad} are mixed to form D_i^{mix}.

$$x_i^{\text{bad}} = x_i \odot (\mathbf{I} - \mathbf{M}) + \Delta^{\text{bad}} \odot \mathbf{M} \quad (6)$$

  where x_i is sample data; $\mathbf{I}$ is a matrix with '1' for each element; $\mathbf{M}$ is a mask matrix; Δ^{bad} is the backdoor data; $\odot$ is a bit-wise multiply operation.

  For example, $x_i \in \mathbb{R}^{n\times n\times 3}$ in computer vision, $\mathbf{M} \in \mathbb{R}^{n\times n\times 3}$ is a mask matrix, $\Delta^{\text{bad}} \in \mathbb{R}^{n\times n\times 3}$. If the sample data is an image, then x_i and x_i^{bad}, as shown in Fig. 1. The area in the lower right corner that looks like the five pips on the dice is the added backdoor Δ^{bad}.
- According to the attack requirement, the attacker selects a specific time to attack the training during the process of training the global model.

3.2 Defense Method

The consequence of backdoor attack is that the attacker can change output by modifying some training samples. Moreover, the modification of training samples should be un-obvious, otherwise this kind of attack can be detected by technical methods.

Mathematically, some parameters in global model are sensitive to the nuance of input samples; that is, the value of those parameters should be larger to some extent. Thus the number of parameters exceeding a certain threshold in global model with backdoor attack should be much more than that without backdoor attack.

One question is whether the global model is able to resist backdoor attack through suppressing the generation of these extreme values. To prevent such extreme weights in global model, a feasible policy for the server aggregating parameters from clients is to give up the the update of those parameters which would tend to change hugely, i.e., the weight difference between two consecutive slots exceeding a threshold, and only aggregate the parameters with smaller change. That's what only allowing minor update to global parameters (OAMU) means. Intuitively, selectively updating certain parameters while keeping others unchanged during the aggregation process may inevitably compromise the performance of the global model. However, our experiments show that the performance degradation is acceptable. In particular, our proposed defense policy only changes the updating mechanism of parameters in server, which is easy to implement and deploy. The detail is given in Algorithm 1.

In our proposed defense algorithm, the server uses a thresh old to selectively update the global model. Specifically, for the model parameters uploaded by a client, the server will update part of the model parameters and keep the rest unchanged(See line 6–9 of Algorithm 1).

In essence, th is a hyper-parameter. If th is too small, the defense measures will affect the normal performance of the global model. Otherwise, the model cannot resist backdoor attack.

Algorithm 1: OAMU

1 **for** *epoch* $t \in \{1, 2, 3, \ldots, T\}$ **do**
2 Receives (w_i^H, t_i)
3 $\tau_i \leftarrow t - t_i$
4 $\eta_t \leftarrow \eta \cdot s(\tau_i)$ // $s(\tau_i) = \frac{1}{\tau_i}$
5 vectorized $\vec{\eta_t} \leftarrow (\eta_t, \eta_t, \eta_t, \cdots, \eta_t)_{1\times d}$
6 **for** $j \in \{1, 2, 3, \ldots, d\}$ **do**
7 **if** $|w_i^H(j) - W^t(j)| \geq th$ **then**
8 $\vec{\eta_t}(j) = 0$
9 **end**
10 **end**
11 $W^{t+1} = W^t + \vec{\eta_t} \odot (w_i^H - W^t)$
12 **end**

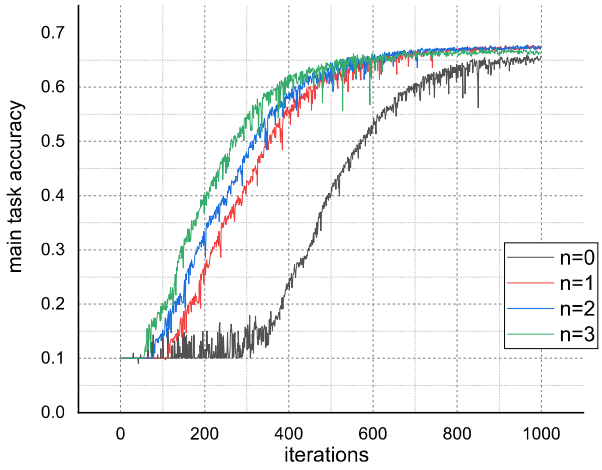

(a) Convergence curves of main task for different number of attackers.

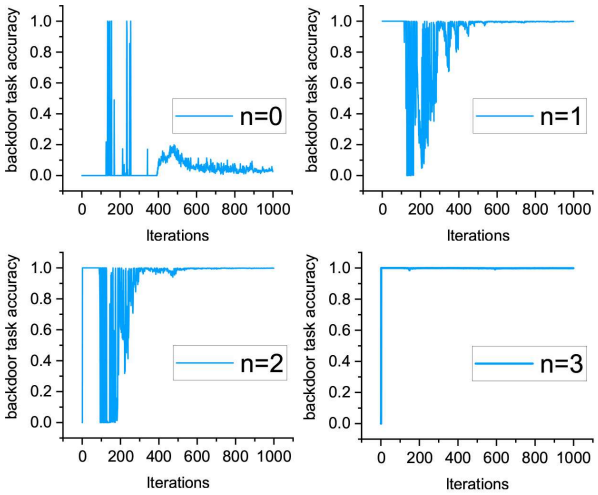

(b) The convergence curves of backdoor task for different number, n, of attackers.

FIGURE 2: Effect of Attacker Number

4 Experiments

In this section, we carry out substantive experiments to show how the position and time of the backdoor attack impact the performance and verify the effectiveness of our proposed defense scheme.

We select n_{bad} out of 10 clients as attackers.

4.1 Experiment Setup

a.) Datasets: We perform image classification on MNIST and CIFAR10 datasets in the FL framework with backdoor attack.

b.) Model: In our experiment, all clients adopt a classical convolutional neural network for image classification which is hereinafter called main task. The model consists of five convolutional layers, three pooling layers, and one fully connected layer and adopts the MBSGD algorithm for numerical optimization. We set *batchsize* to 100, *epoch* to 4 and *learning rate* to 0.01.

c.) Backdoor: Previous research on synchronous FL backdoor attack inspires us that the size and shape of backdoor are not decisive factors in backdoor attack. Therefore, we adopt a 3*3 fork-shaped backdoor in our experiment. As for the target label to be attacked, the number 6 is used in MNIST and the *car* in CIFAR.

4.2 Attack Experiments

a.) Number of Attackers: Fig. 2(a) plots the convergence curves of the main task (i.e., image classification) with no attack ($n = 0$) and $n = 1, 2, 3$ attackers. The vertical axis represents classification accuracy. We can observe from Fig. 2(a) that the attack process accelerates the convergence of the learning process of the main task and the number of attackers basically does not have an obvious impact on the accuracy of the main task. However, due to the black-box nature of neural network, this accelerating phenomenon cannot be explained well and requires a further exploration.

Fig. 2(b) plots the convergence curves of the backdoor task with no attack ($n = 0$) and $n = 1, 2, 3$ attackers. The vertical axis represents classification accuracy with a backdoor. Fig. 2(b) and the black line in Fig. 2(a) show that in the early stages of normal task training, the model randomly misjudges some pictures as backdoor labels, which leads to the oscillation shown in 0 to 400 of Fig. 2(b) with $n = 0$. Fig. 2(b) show that oscillations occur in the early stages of training. As training, the oscillation gradually declines and converges around 1. One obvious observation is that the greater the number of attackers the faster oscillation converges. Another is that the number of attackers has no significant effect on the final convergence value. In asynchronous FL with backdoor attack, the number of attackers only affects the performance of the attack task and increases the efficiency of injecting backdoor without obviously losing the performance of the main task.

4.3 Defense Experiments

The above experiments show that both the number of attackers, the location of the backdoor injection and the launching time of the backdoor attack have an effect on the training process of the main task and the attack task, but have almost no effect on the final convergence value. Therefore, we set the number of attackers to 1 without losing generality, inject the backdoor in the *body* part, and set the attack time t_{ak} to 0.

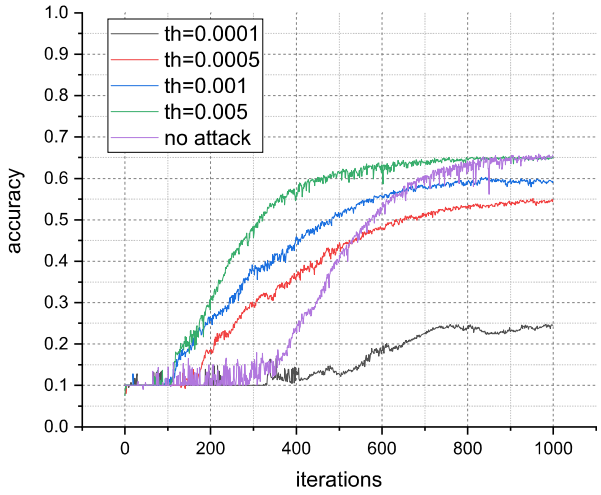

(a) Convergence curves of main tasks under different thresholds.

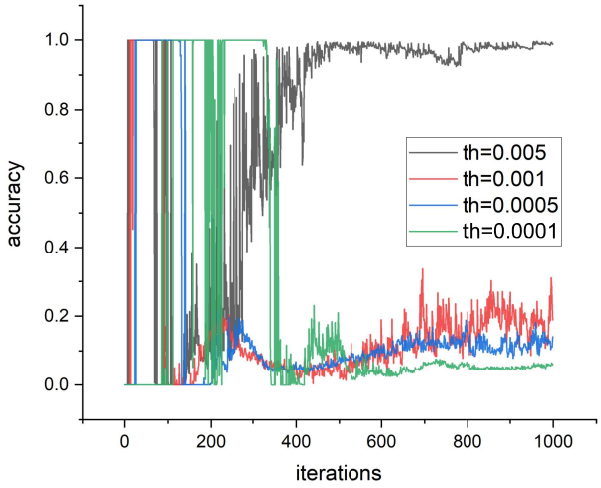

(b) Convergence curves of attack tasks under different thresholds.

FIGURE 3: Effect of update threshold

a.) Effect of Threshold: Both theoretical analysis and experiments show that the parameters of the model injected with backdoor tend to have more extreme values. Intuitively, the smaller the th, the more these extremes and outliers are trimmed and the better the effectiveness of the defense. From Fig. 3(b), we can see that the convergence value of the attack task becomes smaller as th becomes smaller, which indicates that the defense more and more effective. However, this enhanced defense sacrifices the performance of the main task. We can see from Fig. 3(a) that as th becomes smaller, the performance of the main task will be sacrificed, and even when th is a relatively small, the performance of the main task drops to an unusable level, so we need to carefully design this hyper-parameter to achieve a balance between the effectiveness and utility of the defense in practical scenarios.

Table 1: Comparison with the same type of defense algorithm in synchronous FL

Dataset	Neural Cleanse		Network Pruning		Ours OAMU	
	main acc	attack acc	main acc	attack acc	main acc	attack acc
MNIST	-5.31%	-95.91%	-1.41%	-95.04%	**-0.54%**	**-96.64%**
CIFAR-10	-4.72%	-39.71%	-0.92%	-54.91%	-5.19%	**-79.73%**

Table 2: Asynchronous FL VS Synchronous FL

Attack Scenarios	main task acc	attack acc
Syn FL[2]	↓2.3%	95.1%
Syn FL[4]	↓0%	97.5%
Syn FL[5]	↓0.34%	99.9%
Syn FL[6]	↓1.3%	99.7%
Asyn FL	**↑1.5%**	**99.9%**

4.4 Comparison

a.) Synchronous FL Backdoor Attack vs. Asynchronous FL Backdoor Attack: We compare the proposed asynchronous FL with backdoor attack with synchronous FL with backdoor attack. Table 2 shows that the backdoor attack in asynchronous FL is more aggressive since ultra-high accuracy (close to 100%) is achieved in asynchronous FL backdoor attack. Regarding stealthiness, the backdoor attack in asynchronous FL is more powerful in scenarios without defense. The backdoor attack in asynchronous FL hardly affects the main task performance. In contrast, the backdoor attack in synchronous FL inevitably degrades the main task performance.

b.) OAMU vs. Defense in Synchronous FL: To our knowledge, we are the first to propose a backdoor attack in asynchronous FL. Considering no other defense algorithms in asynchronous FL, we compare the proposed OAMU with the two most effective backdoor defense algorithms (Neural Cleanse [5] and NetWork Pruning [6]) in synchronous FL. Some experiments show that synchronous FL backdoor attacks differ from asynchronous FL backdoor attacks regarding the performance of main task and attack task. To make a fair comparison, we examine the defense algorithm on the relative rather than absolute performance of both the main task and the attack task. As shown in Table 1, the OAMU algorithm in MNIST causes a lower degradation in main task performance, and leads to a higher degradation in attack task performance, which indicates that the OAMU algorithm has an obvious advantage in MNIST. In CIFAR10, the OAMU is superior to Neural Cleaning [5] and has a competitive performance to Network Pruning [6].

5 CONCLUSION

We introduce backdoor attacks into the asynchronous FL framework. Our study shows that backdoor attacks are more aggressive and stealthy in asynchronous FL. We investigate the effects of the number of attackers, the location of backdoor injection, and the time of attack. Experiments show that these factors only affect the convergence process of the main task and the attack task, and hardly affect the final convergence value. Our proposed OAMU defense mechanism is effective in weakening backdoor attacks while keeping the performance of main task. Its lightweight nature makes it particularly suitable for UAVs.

References

[1] H. B. McMahan, E. Moore, D. Ramage, S. Hampson, and B. Agüera-y-Arcas, "Communication-Efficient Learning of Deep Networks from Decentralized Data," *Proc. Int'l. Conf. Artificial Intelligence and Statistics*, 2017, pp.1273-82.

[2] Z. Sun, P. Kairouz, A. T. Suresh, and H. B. McMahan, "Can you really backdoor FL?" *Proc. Annual Conf. Neural Information Processing Systems, 2020.*

[3] E. Bagdasaryan, A. Veit, Y. Hua, D. Estrin, V. Shmatikov, "How to Backdoor Federated Learning," *Proc. Int'l. Conf. Artificial Intelligence and Statistic*, 2020, pp. 2938-48.

[4] T. Liu, X. Hu and T. Shu, "Assisting Backdoor FL with Whole Population Knowledge Alignment in Mobile Edge Computing," *Proc. IEEE Int'l. Conf. Sensing, Communication and Networking*, 2022, pp. 416-24.

[5] B. Wang *et al.*, "Neural Cleanse: Identifying and Mitigating Backdoor Attacks in Neural Networks," *Proc. IEEE Security and Privacy Symposium*, 2019, pp. 707-23.

[6] C. Wu, X. Yang, S. Zhu and P. Mitra, "Toward Cleansing Backdoored Neural Networks in FL," *Proc. IEEE Int'l. Conf. Distributed Computing Systems*, 2022, pp. 820-30.

[7] X. Gong, Y. Chen, Q. Wang and W. Kong, "Backdoor Attacks and Defenses in Federated Learning: State-of-the-Art, Taxonomy, and Future Directions," *IEEE Wireless Communications*, vol. 30, no. 2, pp. 114-21, 2023.

[8] G. Xia, J. Chen, C. Yu and J. Ma, "Poisoning Attacks in Federated Learning: A Survey," *IEEE Access,* vol.11, pp. 10708-22, 2023.

[9] M. Nasr, R. Shokri and A. Houmansadr, "Comprehensive privacy analysis of deep learning: Passive and active white-box inference attacks against centralized and federated learning," *Proc. IEEE Security and Privacy Symposium*, 2019, pp. 739-53.

[10] T. Feng, H. Hashemi, R. Hebbar, M. Annavaram, S. S. Narayanan, "Attribute inference attack of speech emotion recognition in federated learning settings," arXiv preprint arXiv:2112.13416, 2023.

[11] H. Yang, M. Ge, K. Xiang and J. Li, "Using Highly Compressed Gradients in Federated Learning for Data Reconstruction Attacks" *IEEE Trans. Information Forensics and Security* , vol. 18, pp. 818-30, 2023.

[12] C. Xie, S. Koyejo, I. Gupta, "Asynchronous Federated Optimization," arXiv preprint arXiv:1903.03934, 2019.

[13] S. Kall and S. Trabelsi, "An Asynchronous Federated Learning Approach for a Security Source Code Scanner," *Proc. Int'l. Conf. Information Systems Security and Privacy* , 2021, pp. 572-79.

[14] Y. Li, S. Yang, X. Ren, C. Zhao, "Asynchronous federated learning with differential privacy for edge intelligence." arXiv preprint arXiv:1912.07902, 2019.

[15] Y. Xu, H. Zhou, J. Chen, T. Ma and S. Shen, "Cybertwin Assisted Wireless Asynchronous Federated Learning Mechanism for Edge Computing," *Proc. IEEE Global Communications Conference*, 2021, pp. 1-6.

Proceedings of the 3rd Conference on Fully Actuated System Theory and Applications
May 10-12, 2024, Shenzhen, China

Traffic Signal Control for Large-Scale Road Networks Based on Deep Reinforcement with PSR

Zhicheng Zhou[1,2], Hui Zhang[1,2], Ya Zhang[1,2]

1. School of Automation, Southeast University, Nanjing 210096, China

2. Key Laboratory of Measurement and Control of Complex Systems of Engineering, Ministry of Education, Nanjing 210096, China
E-mail: yazhang@seu.edu.cn

Abstract: This paper investigates the problem of Traffic Signal Control (TSC) in large-scale road networks. In extensive road networks, it is customary to define each intersection as an agent, however, the issue of partial observability is particularly prominent. In this paper, Predictive State Representation (PSR) is employed to address the challenge of partial observability in large-scale multi-agent systems. A Multi-agent Deep Reinforcement Learning (DRL) model based on PSR called PSR-XLight is proposed in Large-Scale TSC Systems. Multi-agent PSR is conducted with centralized training and independent filtering which overcome the challenge of prohibitive computations when the number of agents is large. Parameters sharing is adopted between each agent's PSR model to enhance learning efficiency and facilitate utilization in large-scale multi-agent environments. Each agent undergoes independent DRL training and execution while parameters sharing is adopted. Experiments are conducted on real-world road networks and a large-scale road network comprising 1000 intersections.

Key Words: Deep reinforcement learning, Traffic signal control, Multi-agent systems, Predictive State Representation.

1 Introduction

Traffic congestion poses a grave concern as it not only exacerbates environmental pollution but also hampers logistics and freight transportation efficiency, thereby impeding urban economic development [1, 2]. Traffic Signal Control (TSC) holds great promise in addressing the issue of traffic congestion. Traditional TSC systems such as SCATS and SCOOT[3] which heavily rely on expert knowledge exhibit inefficiencies.

With the development of Artificial Intelligence (AI) technology, an increasing number of studies in the field of TSC are focusing on Deep Reinforcement Learning (DRL) techniques to control the traffic more precisely [4]. In the initial investigation of TSC using DRL, researchers primarily focused on single intersection[5, 6].

Numerous Multi-agent Reinforcement Learning (MARL) models have been extensively investigated in multi-intersection TSC. In the majority of these works, each agent is trained and executed independently [7–9] and they primarily focus on scenarios involving fewer than 100 agents [10–14]. Limited research has been conducted on large-scale road networks particularly comprising more than 1000 intersections which is crucial for the practical implementation of DRL in TSC. However, the issue of partial observability becomes increasingly critical as the number of agents grows due to the relatively more limited local observations compared to the comprehensive state. Zhu et al. [11] attempted to mitigate the impacts arising from the partial observability of cooperative agents. However, the issue of partial observability in large-scale road networks remains unexplored.

In this paper, a MARL model based on PSR in Large-scale TSC called PSR-XLight is proposed to tackle the challenge of partial observability. Instead of constructing the belief state [15] to reduce the problem of partial observability, PSR offers predictive state. In PSR-XLight, RFF-PSR [16] is employed as the PSR model and integrated with DRL. Instead of mapping an agent's observation to action, a mapping between the predictive state and actions is established after the integration. Minimal prior information is required to train PSR, the PSR model is derived and refined using the data acquired from the interactions between agents and the environment. A recursive filter is employed to maintain the predictive state. To enhance predictive performance, the PSR model is refined by employing back propagation through time. In PSR-XLight, single-agent PSR is extended to multi-agent PSR with centralized training and independent filtering which overcomes the challenge of prohibitive computations when the number of agents is large. The parameters of PSR models are shared among agents to enhance learning efficiency and enable employment in large-scale environments.

In summary, the contribution of this work are as follows: (1) A MARL model based on PSR in large-scale TSC called PSR-XLight is proposed to tackle the challenge of partial observability. Experiments are conducted on real-world road networks and a large-scale road network comprising 1000 intersections. (2) Single-agent PSR is extended to multi-agent PSR where filtering in PSR for each agent is operated independently and centralized training of PSR is conducted, and the proposed model overcomes the challenge of prohibitive computations when the number of agents is large.

The remainder of the paper is organized as follows. Section 2 presents the literature review. Section 3 presents the problem formulation and backgrounds about PSR. PSR-XLight model is presented in detail in section 4. In section 5, evaluations on small-scale and large-scale road networks are conducted. The paper is ultimately concluded in Section 6.

2 Related Work

About the researches of the application of DRL in the context of multi-intersection TSC, Graph Neural Network (GNN) is commonly employed to represent road networks as

This work is supported by National Key R&D Program of China under Grant 2021ZD0112700, National Natural Science Foundation (NNSF) of China under Grant 62373100 and 62233003.

graphs, and it facilitates enhanced communication between agents through information aggregation from adjacent nodes [13, 17]. In formulating the MARL model for TSC, it is valid to introduce intuitive principles such as queue length (QL) [18] and the phase demand [19]. The consideration of impact and coordination between different agents such as the correlation degree [7] is crucial. Moreover, some works utilized attention mechanism to introduce spatial-temporal effect between agents [10, 20]. Multi-agent Coordinated Policy Optimization (MACoPO) [21] introduced a combination of local cooperation and global coordination to coordinate traffic signals at multi-intersections TSC.

The majority of the aforementioned studies primarily focus on TSC scenarios involving fewer than 100 intersections. Several studies have investigated large-scale road networks consisting of over 100 intersections. MPLight [22] which encompasses FRAP and pressure conducted experiments in a Manhattan road network comprising 2510 traffic lights. However, the traffic volume utilized was relatively low, and there was a lack of consideration for cooperation among neighboring intersections. Wang et al.[23] proposed an explicit multi-agent coordination (EMC)-based online planning approach. However, the computation time of EMC increases with the size of the road network and surpasses that of other RL methods particularly in large-scale road networks. Liu et al.[24] introduced the teacher-student framework to TSC, where the student agent's synthetic reward is composed of an importance function of a teacher agent and the environment reward. NewYork road network comprising 196 intersections is used, nevertheless, coordination of multi-agents in the teacher-student framework is not considered. Hu et al. [25] proposed the integration of mean field theory into multi-agent RL to effectively reduce the dimension of joint actions in large-scale scenarios, whereas, this approach incurs significant computational costs as the number of agents increases. The research on large-scale TSC, particularly involving more than 1000 intersections, remains limited, and the issue of partial observability in extensive road networks remains largely unexplored.

3 Problem Formulation and Backgrounds of PSR

3.1 Traffic Signal Control

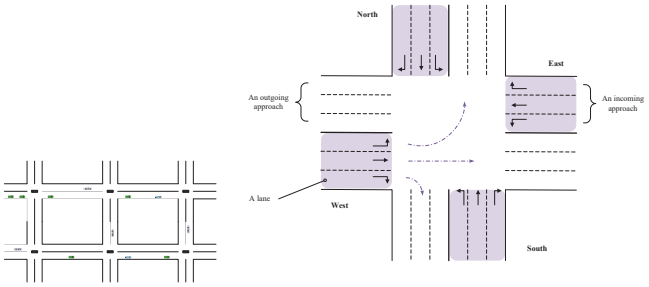

(a) multi-intersection road network (b) one intersection road network

Fig. 1: The illustration of road networks

A traffic network can be defined as a graph $\mathcal{G}(\mathcal{V}, \mathcal{E})$ where $\mathcal{V}$ and $\mathcal{E}$ represent the sets of nodes and edges, respectively. In this context, intersections are considered as nodes, while connections between intersections serve as edges. Fig. 1(a) depicts a multi-intersection road network. A roadway meeting at an intersection is referred to as an approach [4]. The intersection depicted in Fig. 1(b) illustrates a typical configuration with eight approaches, comprising four incoming and four outgoing approaches. The purple shaded area indicates four incoming approaches.

The travel time of a vehicle is determined by the duration between its entry and exit from the road network. One of the primary objectives in TSC is to minimize the mean travel time of vehicles within the network. The queue length of a lane is determined by the number of vehicles waiting in the corresponding lane.

A vehicle traverses an intersection from an incoming approach to an outgoing approach, is referred to as a traffic movement. A traffic signal phase p refers to a composite of multiple movement signals. The utilization of four phases and eight phases is common. In this study, we adopt a four-phase configuration.

3.2 Markov Game

The TSC problem is formulated as an MDP with $\langle \mathcal{G}(\mathcal{V}, \mathcal{E}), \mathcal{S}, \mathcal{O}, \mathcal{A}, \mathcal{P}, \mathcal{R}, \pi, \gamma \rangle$. Let N represent the total number of intersections within the road network, with each intersection being under the control of an agent. $\mathcal{S}$ is the state space, $\mathcal{O}$ is the observation space. The observation of agent i is denoted as $o^i \in \mathcal{O}$. $\mathcal{A}^i$ represents the action space of agent i and $\mathcal{A}$ is the joint action space of all agents where $\mathcal{A} = \langle \mathcal{A}^1, \mathcal{A}^2, \cdots, \mathcal{A}^i, \cdots, \mathcal{A}^N \rangle$. $\mathcal{P}$ denotes the transition probability where $P(s'|s, a)$ represents the probability of the transition to state s' when taking action a at state s with $s, s' \in \mathcal{S}$ and $a \in \mathcal{A}$. $\mathcal{R} : \mathcal{S} \times \mathcal{A} \to \mathbb{R}$ represents the reward function. Agent i takes action $a \in \mathcal{A}^i$ based on observation o^i, following the policy $\pi_i(a|o^i)$, π is the joint policy where $\pi = \langle \pi_1, \pi_2, \cdots, \pi_i, \cdots, \pi_N \rangle$. γ is the discount factor.

We employ the state, action, and reward configurations in [19]. The observation of an agent comprises three parts: efficient pressure, phase demand and phase. Action a^i of agent i is choosing phase p from phase sequence. The reward is determined by the negative sum of queue lengths of all incoming lanes of intersections.

3.3 Backgrounds of PSR

Table 1 presents some symbols along with their corresponding meanings. Predictive state Q_t is defined as the conditional probability of observing observations of a test's sequence, given that the test's actions are taken in sequence and given a history. For each time t, Q_t satisfies $\mathbb{E}[\psi_t^o | do(a_{t:t+k-1}), h_t^\infty] = Q_t \psi_t^a$. Define the probability of x given that Y is set to y as $Pr[x|do(Y = y)]$, where do indicates a forced intervention on variable Y, ensuring it remains unaffected by other variables. $V_{A|B;c}$ is the linear operator that satisfies

$$\mathbb{E}[A|B = b, C = c] = V_{A|B;c} b \quad \forall b, c \tag{1}$$

where A,B,C represent random variables. For each h_t^∞, ψ_t^o can be achieved based on ψ_t^a using Q_t as a conditional expectation operator. For each time t, extended state P_t satisfies $\mathbb{E}[\xi_t^o | do(a_{t:t+k}), h_t^\infty] = P_t \xi_t^a$. There exists a linear map W_{sys} satisfies $P_t = W_{sys}(Q_t)$.

Table 1: Symbols Table ("obs" is an acronym for the term "observations")

Symbol	Meaning
o_t	Observation at time t
a_t	Action at time t
$o_{t:t+k-1}$	Future obs: $\{o_t, \cdots, o_{t+k-1}\}$
$a_{t:t+k-1}$	Future actions: $\{a_t, \cdots, a_{t+k-1}\}$
$o_{t:t+k}$	Extended future obs: $\{o_t, \cdots, o_{t+k}\}$
$a_{t:t+k}$	Extended future actions: $\{a_t, \cdots, a_{t+k}\}$
$test_t^k$	A test: $\{o_t, a_t, \cdots, o_{t+k-1}, a_{t+k-1}\}$
h_t^∞	The history at time t: $\{o_1, a_1, \cdots, o_{t-1}, a_{t-1}\}$
ϕ_O	Feature mapping function for future obs
ϕ_A	Feature mapping function for future actions
ϕ_o	Feature mapping function for immediate obs
ϕ_a	Feature mapping function for immediate actions
ψ_t^o	Features of future obs: $\phi_O(o_{t:t+k-1})$
ψ_t^a	Features of future actions: $\phi_A(a_{t:t+k-1})$
ϕ_t^o	Features of immediate obs: $\phi_o(o_t)$
ϕ_t^a	Features of immediate actions: $\phi_a(a_t)$
ξ_t^o	Features of extended future obs: $\phi_O(o_{t:t+k})$
ξ_t^a	Features of extended future actions: $\phi_A(a_{t:t+k})$

4 PSR-XLight

In PSR-XLight, PSR is used to tackle the challenge of partial observability in large-scale road networks. RFF-PSR [16] is employed as the PSR model. Each intersection is modeled as an agent with individual training and executing. Predictive states are mapped to actions directly. The PSR model is trained centrally with filtering operating individually for each agent. Parameters sharing of the PSR and DRL model between agents is adopted to enhance learning efficiency and facilitate model's employment in large-scale environment. The model is illustrated in Fig. 2.

4.1 Mapping Predictive State to Action

q_t^i is defined as the predictive state of agent i at time t. $\pi_i(a_t^i|q_t^i)$ is defined as the possibility of action a_t^i taken by agent i at time t based on predictive state q_t^i. In PSR-XLight, predictive state q_t^i is considered as the direct input of Deep Neural Networks (DNNs) with Q-values $Q_t^{'i} = \phi_{DNN}(q_t^i)$ in value-based methods and action $a_t^i = \phi_{DNN}(q_t^i)$ in policy-based methods where $Q_t^{'i}$ represents Q-values of agent i at time t and ϕ_{DNN} denotes DNNs.

4.2 Individual Filtering of Each Agent

At time t, the set of predictive states is denoted as $q_t^{all} = \{q_t^1, \cdots, q_t^N\}$. Agent i chooses action as $a_t^i \sim \pi_i(a|q_t^i)$ as illustrated in Fig. 2. The set of actions is denotes as $a_t^{all} = \{a_t^1, \cdots, a_t^N\}$. Then the environment transfers to a new state s_t after taking actions a_t^{all}. The set of new observations set $o_t^{all} = \{o_t^1, \cdots, o_t^i, \cdots, o_t^N\}$ is obtained where o_t^i represents the observation of agent i at time t. Filtering is then conducted for each agent with shared filtering parameters as illustrated in Fig. 2, which is as follows:

$$q_{t+1}^i = f_{filter}(W_{sys} q_t^i, o_t^i, a_t^i) \tag{2}$$

where f_{filter} is known in advance [16].

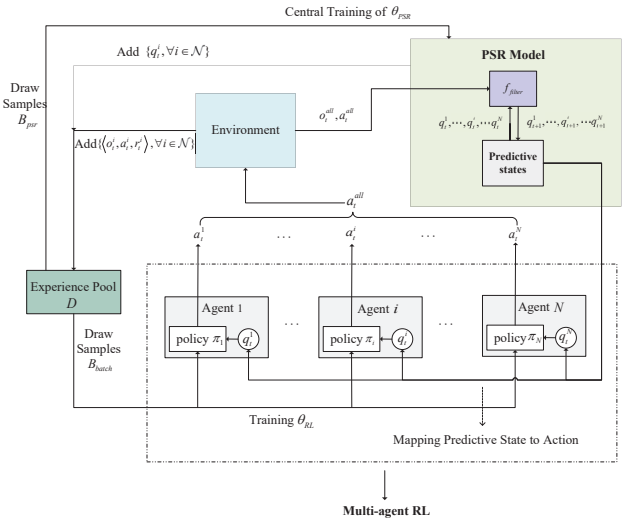

Fig. 2: The illustration of the MARL model based on PSR

4.3 Central Training

4.3.1 Two-stage Regression

A trajectory for agent i is denoted as $\tau_i = \{o_1^i, a_1^i, o_2^i, a_2^i, \cdots\}$. After several episodes, training data $\tau_{train} = \{\tau_i^k\}_{i=1,\cdots N}^{k=1,\cdots K}$ is obtained where N is the total number of agents and K is the total number of trajectories. Two-stage regression is conducted as in RFF-PSR [16] using τ_{train}. W_{sys} and initial predictive state q_0 are then obtained. For each agent i, initial predictive state $q_0^i = q_0$.

4.3.2 Refinement

The following formula is used to estimate o_t^i.

$$\mathbb{E}[o_t^i | q_t^i, a_t^i] = W_{pred}(q_t^i \otimes \phi_a(a_t^i)) \tag{3}$$

Training examples of W_{pred} consist of $\{(q_t^i \otimes \phi_a(a_t^i), o_t^i)\}_{t=1,\cdots,T}^{i=1,\cdots,N}$ where T denotes the total number of time steps in the training examples. W_{pred} is obtained using these examples by computing the least squares. $\phi_O, \phi_A, \phi_o, \phi_a$ are shared across different agents. Refinement of W_{sys} and W_{pred} is conducted using back propagation through time (BPTT) with minimizing the objective function as follows:

$$\ell(\theta_{PSR}) = \sum_{t=1}^{T} \sum_{i=1}^{N} \left\| W_{pred}(q_t^i \otimes \phi_a(a_t^i)) - o_t^i \right\|^2 \tag{4}$$

where $\theta_{PSR} = (q_0, W_{sys}, W_{pred})$ and q_t^i is updated through formula (2). When the number of agents grows larger, the number of PSR parameters which are shared among agents remains constant. Computation for individual filtering scales linearly with the number of agents and computation for central training of PSR scales with the number of training examples which is adjustable although when the number of agents is large. Therefore, multi-agent PSR in PSR-XLight overcomes the challenge of prohibitive computations when the number of agents is large.

4.4 DRL Training

The parameters of DNNs in DRL model are denoted as θ_{RL}. θ_{RL}^{target} denotes parameters of the target network in Deep Q Network (DQN). DRL training is presented as follows:

$$y_t^i = \frac{r_t^i}{\beta} + \gamma max_{a^{i\prime}} Q\left(q_{t+1}^i, a^{i\prime}; \theta_{RL}^{target}\right) \tag{5}$$

$$\ell_r(\theta_{RL}) = \frac{1}{T}\sum_{t=1}^{T}\sum_{i=1}^{N}\left\|y_t^i - Q\left(q_t^i, a_t^i; \theta_{RL}\right)\right\|^2 \tag{6}$$

$$\theta_{RL} = \theta_{RL} - \alpha\nabla_\theta \ell_r(\theta_{RL}) \tag{7}$$

where T denotes the total number of time steps in the updating, y_t^i represents the target value, r_t^i denotes the reward of node i at time step t, β represents standardized coefficient, ℓ_r represents the loss function, α is the learning rate.

The complete algorithm is presented as Algorithm 1 where DRL model called X-DRL model is assumed to be adopted. PSR-XLight can incorporate any DRL approaches.

Algorithm 1 The complete algorithm

Input: α, soft update β, initial greedy factor ϵ, minimum value of greedy factor ϵ_{min}, the number of trajectories M in an iteration, empty experience pool D, minimum and maximum amount of stored samples for D: B_{min}, B_{max}, the amount of training examples for RL model and PSR model: B_{batch}, B_{psr}, initial θ_{RL}.
Output: Optimized parameters $(\theta_{RL}, \theta_{PSR})$.
for iteration $= 1, \cdots$ **do**
  if iteration $= 1$ **then**
    Generate M episodes using X-DRL model with initial θ_{RL} employing ϵ-greedy exploration.
    Get $\tau_{initial} = \left\{\tau_i^k\right\}_{i=1,\cdots N}^{k=1,\cdots M}$ and use two-stage regression to get $W_{sys}, q_0, \phi_O, \phi_A, \phi_o, \phi_a$.
    Get W_{pred} using $\tau_{initial}$ as in 4.3.2.
    Conduct refinement of θ_{PSR} as in 4.3.2.
    Let $q_0^i = q_0, \forall i \in \mathcal{N}$.
  end if
  for number $= 1, \cdots, M$ **do**
    Reset $a_0^i, \forall i \in \mathcal{N}$.
    for time step $t = 0, \cdots$ **do**
      Get observations $\{o_t^i, r_t^i, \forall i \in \mathcal{N}\}$.
      for $i \in \mathcal{N}$ **do**
        Filtering $q_{t+1}^i = f_{filter}(W_{sys} q_t^i, o_t^i, a_t^i)$.
        Choose action $a_{t+1}^i \sim \pi_i(a|q_{t+1}^i)$ with $\epsilon-$greedy.
      end for
      Execute $a_{t+1}^i, \forall i \in \mathcal{N}$.
      Add $\{\langle o_t^i, q_t^i, a_t^i, r_t^i, q_{t+1}^i\rangle \ , \forall i \in \mathcal{N}\}$ into D.
      if $|D| > B_{max}$ then
        Remove oldest experience in D.
      end if
    end for
  end for
  Draw B_{batch} samples randomly from D and use it to train θ_{RL} with formula (7).
  if iteration $\neq 1$ **then**
    Draw B_{psr} samples randomly from D and compute to get W_{sys}, W_{pred}.
    Soft update of W_{sys}, W_{pred} with $W = \beta W + (1-\beta)W'$ where W' represents last parameters.
    Conduct refinement of θ_{PSR} as in 4.3.2.
  end if
  Reduce ϵ but make sure $\epsilon \geq \epsilon_{min}$.
end for

5 Experiments

The experiments on CityFlow[26] are conducted in the study. Both small-scale road networks and a large-scale road network consisting of 1000 traffic lights are utilized.

5.1 Settings of the Traffic Simulator

The CityFlow platform is a MARL environment designed for large-scale urban traffic scenarios. The vehicles entering the road network adhere to predetermined speeds and routes until they exit the road network. The movements of proceeding straight and making a left turn are regulated by traffic signals, whereas the act of making a right turn is unrestricted.

5.2 Datasets

5.2.1 Synthetic Datasets

The study employs a synthetic large-scale road network measuring 25×40. The predefined vehicle routes encompass a diverse range of orientations, including northbound, southbound, westbound, and eastbound, as well as combinations of alternating right and left turns and alternating left and right turns. The traffic flow of vehicles traveling in the northbound, southbound, westbound, and eastbound directions is set at a rate of 19500 vehicles per 300 seconds, while the flow of vehicles taking combinations of directions amounts to 1200 vehicles per 300 seconds.

5.2.2 Real-world Datasets

The real-world datasets, including the 4×4 Hangzhou road network and the 28×7 New York road network, are utilized in this study[1]. Each real-world road network is utilized with two different traffic flow data.

In the experimental settings, each episode is defined as a time span of 3600 seconds. The updated parameters will be utilized to conduct a test episode after each iteration.

5.3 Compared Methods

Under the PSR-XLight model, two RL algorithms PSR-Advanced-CoLight and PSR-Advanced-DQNLight are designed.

- Fixedtime [27]: The execution of phases is based on a pre-determined plan that encompasses a fixed sequence of phases and their corresponding durations.
- Advanced-CoLight [19]: CoLight algorithm [17] serves as the based algorithm, where efficient pressure, phase demand, and phase are considered as states.
- PSR-Advanced-CoLight: Advanced-CoLight is employed as the DRL model within the PSR-XLight.
- Advanced-DQNLight: The configuration of states, actions, and rewards remains consistent with that of Advanced-CoLight. DQN [28] serves as the based DRL

[1] https://traffic-signal-control.github.io

model.

- PSR-Advanced-DQNLight: Advanced-DQNLightis employed as the DRL model within the PSR-XLight.

For intelligent control methods, each intersection is controlled by an individual agent, and parameters between agents are shared.

5.4 Evaluation Metrics

The evaluation of various models is conducted using two metrics. Firstly, the utilization of the road network reward is justified as it represents the optimization objective of agents. The reward curve explicitly illustrates the learning performance of agents. This metric is exclusively employed in 4×4 road networks due to its inadequacy for evaluations within large-scale road networks. Furthermore, the assessment of models is based on the average travel time. This metric has been extensively utilized in a multitude of studies[7, 17, 22].

Table 2: Performance Comparison (the optimal value is highlighted in bold)

Dataset	Hangzhou A	Hangzhou B
Metrics	Reward	Reward
Fixedtime	-12.051	-18.186
Advanced-CoLight	-1.114	-8.911
PSR-Advanced-CoLight	**-1.106**	**-8.803**
Advanced-DQNLight	-1.442	-11.225
PSR-Advanced-DQNLight	-1.162	-11.088
Dataset	New York A	New York B
Metrics	Travel time	Travel time
Fixedtime	1471.24	1581.39
Advanced-CoLight	1059.99	1291.82
PSR-Advanced-CoLight	**1012.73**	**1258.28**
Advanced-DQNLight	1215.67	1397.91
PSR-Advanced-DQNLight	1120.84	1340.72
Dataset	One thousand	
Metrics	Travel time	
Fixedtime	1752.03	
Advanced-CoLight	1341.72	
PSR-Advanced-CoLight	**1317.07**	
Advanced-DQNLight	1698.61	
PSR-Advanced-DQNLight	1640.42	

5.5 Performance Comparison

5.5.1 Performance in small-scale road network

In this section, we compare these models in 4×4 road networks. PSR-XLight is convergent to a enhanced value compared with its corresponding XLight as listed in Table 2. The outcomes are illustrated in Fig. 3, 4. In small-scale road network, PSR-XLight achieves higher reward and less travel time compared with corresponding methods without PSR. In the early period of the training, PSR-Advanced-CoLight demonstrates the faster learning than Advanced-CoLight. Fig. 4 shows that PSR-Advanced-DQNLight exhibits a significant improvement in reward and reduced travel time than Advanced-DQNLight during the final iterations.

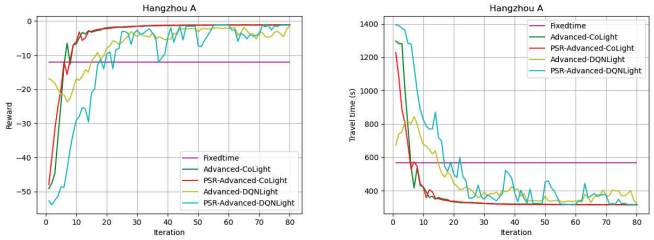

(a) Reward (b) Travel time

Fig. 3: Comprehensive comparative analysis of Hangzhou A

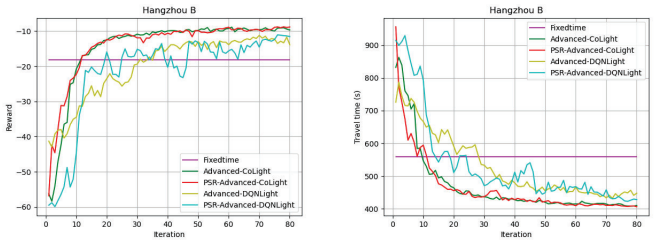

(a) Reward (b) Travel time

Fig. 4: Comprehensive comparative analysis of Hangzhou B

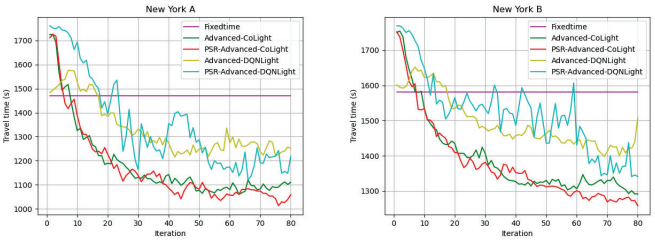

(a) New York A (b) New York B

Fig. 5: Comprehensive comparative analysis of New York

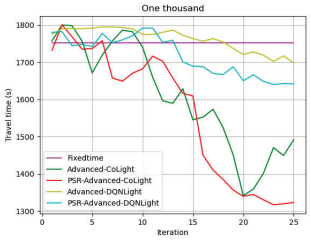

Fig. 6: Comprehensive comparative analysis of the 25×40 road network

5.5.2 Performance in large-scale road networks

In this section, all methods are evaluated in 28×7 and 25×40 road network. PSR-XLight exhibits a more optimal value compared to its corresponding XLight, as presented in Table 2. As shown in Fig. 5, 6, the performance of PSR-XLight is evidently superior to that of its corresponding XLight model. The performance of PSR-XLight in large-scale road networks can be attributed to the integration of DRL and PSR, which effectively contributes to ad-

dressing the challenge of partial observability by representing the latent state which is unobserved. Parameters sharing between each agent's DRL and PSR model make it easily trainable in large-scale road networks. Figures show that PSR-XLight exhibits good adaptability with different DRL model. Curves in large-scale road networks are more unstable than that in Hangzhou due to the increasing complexity of traffic flow and road networks.

6 Conclusion

In this paper, a TSC model called PSR-XLight is proposed to improve the traffic efficiency of large-scale road networks. PSR-XLight contributes to mitigating the adverse effects arising from partial observability in large-scale road networks by introducing PSR. Experiments in small-scale and large-scale road networks show that PSR-XLight exhibits a more optimal performance compared to its corresponding XLight. In the future, two-stage regression and refinements of PSR can be optimized to reduce the computation time.

References

[1] M. Grote, I. Williams, J. Preston, and S. Kemp, Including congestion effects in urban road traffic co2 emissions modelling: Do local government authorities have the right options? *Transportation Research Part D: Transport and Environment*, 43: 95–106, 2016.

[2] M. Sweet, Traffic congestion's economic impacts: Evidence from us metropolitan regions, *Urban Studies*, 51(10): 2088–2110, 2014.

[3] J. Luk, Two traffic-responsive area traffic control methods: Scat and scoot, *Traffic engineering and control*, 25(1), 1984.

[4] H. Wei, G. Zheng, V. Gayah, and Z. Li, A survey on traffic signal control methods, *arXiv preprint*, arXiv:1904.08117, 2019.

[5] H. Wei, G. Zheng, H. Yao, and Z. Li, Intellilight: A reinforcement learning approach for intelligent traffic light control, in *Proceedings of the 24th ACM SIGKDD International Conference on Knowledge Discovery and Data Mining*, 2018: 2496–2505.

[6] X. Liang, X. Du, G. Wang, and Z. Han, A deep reinforcement learning network for traffic light cycle control, *IEEE Transactions on Vehicular Technology*, 68(2): 1243–1253, 2019.

[7] C. Zhang, Y. Tian, Z. Zhang, W. Xue, X. Xie, T. Yang, X. Ge, and R. Chen, Neighborhood cooperative multiagent reinforcement learning for adaptive traffic signal control in epidemic regions, *IEEE Transactions on Intelligent Transportation Systems*, 23(12): 25157–25168, 2022.

[8] W. Zhang, C. Yan, X. Li, L. Fang, Y. Wu, and J. Li, Distributed signal control of arterial corridors using multi-agent deep reinforcement learning, *IEEE Transactions on Intelligent Transportation Systems*, 24(1): 178–190, 2022.

[9] B. Fang, C. Zheng, H. Wang, and T. Yu, Two-stream fused fuzzy deep neural network for multiagent learning, *IEEE Transactions on Fuzzy Systems*, 31(2): 511–520, 2022.

[10] M. Wang, L. Wu, M. Li, D. Wu, X. Shi, and C. Ma, Meta-learning based spatial-temporal graph attention network for traffic signal control, *Knowledge-based systems*, 250: 109166, 2022.

[11] R. Zhu, W. Ding, S. Wu, L. Li, P. Lv, and M. Xu, Auto-learning communication reinforcement learning for multi-intersection traffic light control, *Knowledge-Based Systems*, page 110696, 2023.

[12] S. Yang, Hierarchical graph multi-agent reinforcement learning for traffic signal control, *Information Sciences*, 634: 55–72, 2023.

[13] W. Lin, Y. Song, B. Ruan, H. Shuai, C. Shen, L. Wang, and Y. Li, Temporal difference-aware graph convolutional reinforcement learning for multi-intersection traffic signal control, *IEEE Transactions on Intelligent Transportation Systems*, pages 1–11, 2023.

[14] S. Yang, B. Yang, Z. Zeng, and Z. Kang, Causal inference multi-agent reinforcement learning for traffic signal control, *Information Fusion*, 94: 243–256, 2023.

[15] R. Jr, R. Tedrake, L. Kaelbling, and T. Lozano-Perez, Belief space planning assuming maximum likelihood observations, 2010.

[16] A. Hefny, C. Downey, and G. Gordon, An efficient, expressive and local minima-free method for learning controlled dynamical systems, in *Proceedings of the AAAI Conference on Artificial Intelligence*, 2018: 32.

[17] H. Wei, N. Xu, H. Zhang, G. Zheng, X. Zang, C. Chen, W. Zhang, Y. Zhu, K. Xu, and Z. Li, Colight: Learning network-level cooperation for traffic signal control, in *Proceedings of the 28th ACM International Conference on Information and Knowledge Management*, 2019: 1913–1922.

[18] L. Zhang, Q. Wu, and J. Deng, Attentionlight: Rethinking queue length and attention mechanism for traffic signal control, *arXiv preprint*, arXiv:2201.00006, 2021.

[19] L. Zhang, Q. Wu, J. Shen, L. Lu, B. Du, and J. Wu, Expression might be enough: Representing pressure and demand for reinforcement learning based traffic signal control, in *International Conference on Machine Learning*, 2022: 26645–26654.

[20] J. Fang, Y. You, M. Xu, J. Wang, and S. Cai, Multi-objective traffic signal control using network-wide agent coordinated reinforcement learning, *Expert Systems with Applications*, page 120535, 2023.

[21] F. Ren, W. Dong, X. Zhao, F. Zhang, Y. Kong, and Q. Yang, Two-layer coordinated reinforcement learning for traffic signal control in traffic network, *Expert Systems with Applications*, 235: 121111, 2024.

[22] C. Chen, H. Wei, N. Xu, G. Zheng, M. Yang, Y. Xiong, K. Xu, and Z. Li, Toward a thousand lights: Decentralized deep reinforcement learning for large-scale traffic signal control, in *Proceedings of the AAAI Conference on Artificial Intelligence*, 2020: 3414–3421.

[23] W. Wang, T. Qiao, J. Ma, J. Jin, Z. Li, W. Wu, and Y. Jian, Real-time network-level traffic signal control: An explicit multiagent coordination method, *arXiv preprint*, arXiv:2306.08843, 2023.

[24] J. Liu, S. Qin, M. Su, Y. Luo, S. Zhang, Y. Wang, and S. Yang, Traffic signal control using reinforcement learning based on the teacher-student framework, *Expert Systems with Applications*, 228: 120458, 2023.

[25] T. Hu, Z. Hu, Z. Lu, and X. Wen, Dynamic traffic signal control using mean field multi-agent reinforcement learning in large scale road-networks, *IET Intelligent Transport Systems*, 2023.

[26] H. Zhang, S. Feng, C. Liu, Y. Ding, Y. Zhu, Z. Zhou, W. Zhang, Y. Yu, H. Jin, and Z. Li, Cityflow: A multi-agent reinforcement learning environment for large scale city traffic scenario, in *The world wide web conference*, 2019: 3620–3624.

[27] P. Koonce and L. Rodegerdts, Traffic signal timing manual, *Technical report*, 2008.

[28] V. Mnih, K. Kavukcuoglu, D. Silver, A. Rusu, J. Veness, M. Bellemare, A. Graves, M. Riedmiller, A. Fidjeland, G. Ostrovski, et al., Human-level control through deep reinforcement learning, *nature*, 518(7540): 529–533, 2015.

Proceedings of the 3rd Conference on Fully Actuated System Theory and Applications
May 10-12, 2024, Shenzhen, China

A multi-scale adaptive label assignment neural network architecture for brake disc surface defect detection

Shaoquan Wang, Guoshan Zhang*, Bin Guan
School of Electrical and Information Engineering, Tianjin University, Tianjin 300072, P. R. China
E-mail: zhanggs@tju.edu.cn

Abstract: Brake disc is a key workpiece of the automobile braking system, and its surface defects directly affects the safety performance of the car. To ensure the product quality of the brake disc, it is necessary to detect these surface defects. In the field of the workpiece surface defect detection, manual detection methods and conventional computer vision-based methods could only identify defects under specific conditions. In this paper, we propose a multi-scale adaptive label assignment neural network architecture to detect surface defects, which includes a Multi-scale Dilated Semantic Module (MDSM) and a Quality Adaptive Head (QAH). Firstly, the MDSM is a multi-scale feature extraction module, which can expand receptive field range in a serial manner by Dilated Sample Module (DSM), and integrate the different level information by semantic supplement wihout significantly increasing the computational cost. Secondly, the QAH is an anchor-free detection head, and it requires neither professional tuning experience nor hand-crafted rules to adaptively determine positive/negative samples by generating positive and negative weight maps, which is called label assignment. Finally, to better supervise network training, the Quality Focal Loss (QFL) is adopted to merge the quality estimation into QAH, making the network prediction output more accurate. Our method is trained and tested on a self-established brake disc surface defect dataset, and extensive experiments show that our method steadily achieves the best detection performance compared to state-of-the-art methods.

Key Words: Defect detection, Deep Learning, Convolutional neural network, Label assignment

1 Introduction

The surface defects of the workpiece can shorten the workpiece lifetime, reduce the strength of the material, and increase safety-related risks. Hence, it is very important to detect the surface defects of the workpiece [1]. In the actual production line, these surface defects are manually reviewed by quality inspectors, which have the disadvantages of low accuracy, high labor intensity. Therefore, there is an urgent demand for a detection system that can automatically detect surface defects of the workpieces, and determine whether they are qualified or not [2].

To satisfy the urgent demand for quality monitoring, many traditional computer vision-based methods have been proposed to identify these defects. Zou et al. proposed a Kalman filtering welding surface defects detection method [3]. A laser stripe pattern image processing method is proposed to detect weld bead surface defects [4]. However, these traditional image processing methods, which are only suitable for situations with apparent features and a simple background, have poor generalization ability and robustness [5].

Recently, deep learning methods have presented wide versatility, strong plasticity, and high accuracy in medical and industrial applications [6–8].

He et al. detect steel surface defects by adding multi-level feature fusion to improve network performance [9]. Zheng et al. proposed a fast defect detection convolutional neural network for copper clad laminate surface defect detection [10]. Zhang et al. proposed a novel detection framework to detect the tiny defects in train components [11]. Although the performance of object detectors has been dramatically improved due to the deep convolutional neural networks [12], there are still two major problems, namely scale variation [13] and label assignment [14], which restrict the detection accuracy. For scale variation problem, the receptive field of each convolution layer is fixed, which exists inconsistency between the objects at different scales and the fixed receptive field. The network should reasonably consider the use of shallow and deep information to solve scale variation problem [15]. For label assignment problem, which needs to clarify positive and negative samples in spatial position, is another common and difficult problem of object detection. Existing detectors mainly rely on human prior knowledge and expertise [16], when encountering some eccentric object, are hard to assemble enough high-quality samples and obtain the optimal label assignment, which increases the difficulty of applying the algorithm in an actual factory.

To tackle these problems, a multi-scale adaptive label assignment neural network architecture is proposed, which includes Multi-scale Dilated Semantic Module (MDSM) and Quality Adaptive Head (QAH). MDSM can detect different scale objects by making full use of the multi-scale context information from different receptive fields, and enhance receptive field range by using Dilated Sample Module (DSM) without significantly increasing the computational overhead. QAH does not require any prior knowledge and additional branches, which adaptively achieve label assignment by generating positive and negative weight maps. Besides, as an additional auxiliary quality loss function, Quality Focal Loss (QFL) [17] is introduced to merge quality estimation in QAH, making the training process more robust. The main contributions of this paper are listed as follows.

1) A multi-scale feature extraction module called MDSM is proposed, it utilizes semantic supplement and DSM to solve the scale variation problem while significantly reducing memory consumption and parameters.
2) An adaptive label assignment detection head called QAH is proposed, without prior knowledge or introducing extra quality estimation branches, it can adaptively sum up the label allocation strategy and merge quality estimation.
3) A workpiece surface defects dataset collected from the actual production workshops is established to assess the proposed method.
4) Extensive experiments are conducted based on the workpiece surface defects dataset, which shows that our method achieves the best detection performance compared to state-of-the-art methods.

2 Methods

In this section, we will briefly introduce the Multi-scale adaptive label assignment neural network architecture, which includes

This work is supported by National Natural Science Foundation (NNSF) of China under Grant 62073237.

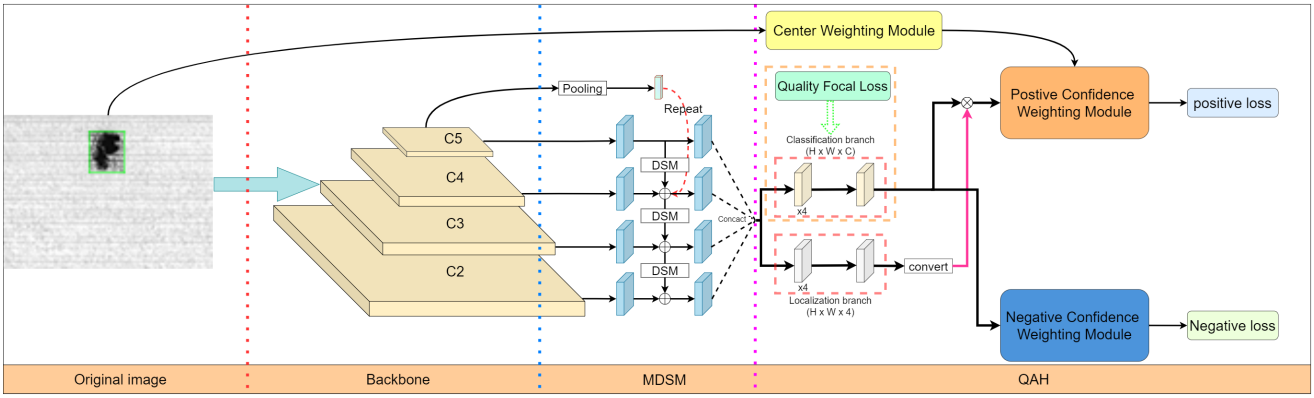

Fig. 1: The defect detection neural network architecture

MDSM and QAH. The whole architecture is shown in Fig. 1. The backbone and MDSM are firstly used to extract multi-scale feature information of the original images, and then, QAH uses the obtained feature information to sum up the corresponding label assignment strategy and get the final detection results. The specific details are shown in the following sections.

2.1 Multi-scale Dilated Semantic Module

We design a multi-scale feature extraction module named MDSM, which can enhance the receptive field in a serial manner and reduce space complexity. Its detailed structure is shown in Fig. 2.

MDSM firstly uses a 1×1 convolution layer to reduce the channel number from {256, 512, 1024, 2048} to {256, 256, 256, 256}, and maintain the reduced channel number in the whole module, which is a foundation of the lightweight design, and the processed result is marked as {R2, R3, R4, O1}. After reducing the network channel number, DSM can help MDSM gradually increase the receptive field and restore feature map resolution, which alleviates the contradiction between the size of the fixed receptive field and feature map resolution. For further acquiring more semantic information, MDSM uses semantic supplement to combine highly abstracted information with fine-grained details via element-wise addition with a low computational cost.

2.1.1 Dilated Sample Module

The details of the DSM are shown in Fig. 3, each DSM consists of a Residual Blocks [18] and an up-sample operation. The former uses a stack of three convolutional layers, which includes two 1×1 convolution layers and a 3×3 convolution layer with dilation [19],

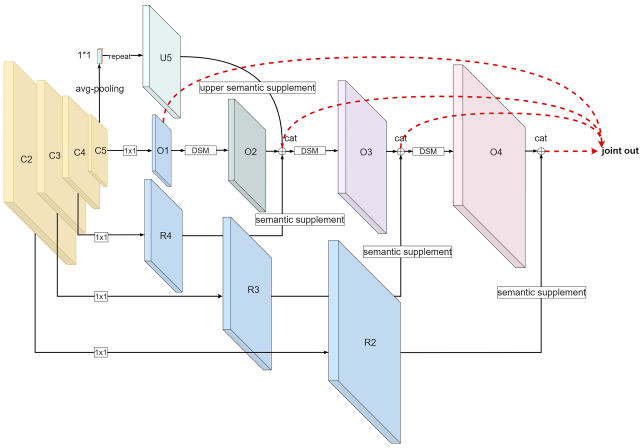

Fig. 2: The structure of the MDSM

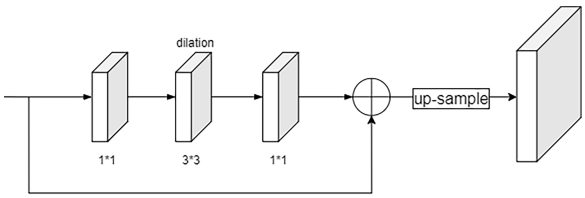

Residual Blocks

Fig. 3: The structure of the DSM

the dilation rate will increase steadily with the expansion of the resolution of the feature maps. In order to improve the computational efficiency, the channels of all convolutions in the entire network framework are only 256.

The Dilated Residual Blocks can use the dilated convolution to expand the receptive field, while retaining the original scale feature information by shortcut connection. By bilinear interpolation to fuse expand and original features, the fused feature covers a larger receptive field.

Furthermore, the up-sampling operation is used to expand feature map size and lay the foundation of the next concatenation operation. Besides, due to more training samples on the larger feature map, subsequent point-based regression prediction head can make good use of the feature information to complete more accurate box prediction.

2.1.2 Semantic supplement

Learning from the multi-scale fusion idea of FPN network [20], and for the consideration of the lightweight design idea, we propose two simple and effective semantic supplement strategies, which include semantic supplement and upper semantic supplement. Among them, the upper semantic supplement first uses the global average pooling to extract global information of C5 on each channel, which is not only consistent with lightweight design due to no parameters in the global average pooling, but also obtaining global context information. In order to use the semantic information and further reduce the parameters of the model, we only use the repeat operation to expand the feature map for next semantic information concatenation.

2.2 General Adaptive Head

The GAH is an anchor-free adaptive detection network based on point prediction, and GAH uses an implicit allocation principle which unexplicitly delegates each sample position to positive or negative samples. We follow the allocation manner like AutoAssign [14], every location on the feature map has both positive sample attribute and negative sample attribute at the same time. The attribute mechanism is controlled by weight maps and confidence

scores, and it can be optimized by the corresponding positive and negative losses. In addition, the classification branch integrates the quality estimation through QFL, making the training process more robust and stable.

The second half of Fig. 1 shows the above head's structure, the localization branch output will go through a convert module and enter the Positive Confidence Weighting Module (PCWM) to produce the positive loss. The Negative Confidence Weighting Module (NCWM) will accept the classification score to produce the negative loss. The Center Weighting Module can assist the PCWM to adaptively generate respective center prior distributions for different targets. These will be explained in detail in the following subsections.

2.2.1 Center Weighting Module

GAH uses Center Weighting Module to generate a Gaussian-shape center weighing as a prior distribution, which guarantees that the locations which are closer to the bounding box center have higher weights than locations which are far from the box center. It can automatically adjust the center prior according to the data distribution, and lay the foundation for subsequent positive sample weight calculations.

2.2.2 Negative Confidence Weighting Module

In the architecture of GAH, Negative Confidence Weighting Module (NCWM) is adopted to complete the weight and confidence calculation related to the allocation of negative samples, and these calculation results can participate in the subsequent corresponding negative sample loss calculation. In principle of the allocation of negative samples, NCWM thinks that all locations from the feature map have negative sample attribute which suppress the impact of the false positives on the network performance. For negative confidence score which is denoted by P_i^-, considering that only the classification task will be performed on the negative locations, thus all locations use the classification score as the negative confidence score $P_i^- = P_i(\text{cls})$, and to restrict the confidence score, NCWM assigns negative weights W_i^- to negative confidence score. For all positions outside the bounding boxes, since these samples must belong to the background, the W_i^- is set to 1, for the locations inside the boxes, we use the IOU to generate negative weight W_i^- as:

$$W_i^- = 1 - f\left(iou_i\right) \tag{1}$$

where $f(iou_i)$ will perform two operations, which is $f(iou_i) = 1/(1 - iou_i)$, iou_i refers to the maximum IOU threshold of each prediction proposal and all the ground truth boxes. Then uses

$$\frac{f\left(iou_i\right) - \min\left(f\left(iou_i\right)\right)}{f\left(iou_i\right) + \max\left(f\left(iou_i\right)\right)} \tag{2}$$

to normalize $f(iou_i)$ into range $[0, 1]$, which ensures that locations with high IOU thresholds have relatively low negative weights.

2.2.3 Positive Confidence Weighting Module

Similar to NCWM, Positive Confidence Weighting Module (PCWM) completes the weight and confidence calculation related to the allocation of positive samples. Different from the form of the negative sample allocation, only the locations inside the ground truth participate in the calculation process, and take into account of the localization outputs to generate unbiased estimation on the basis of classification output. To make localization outputs merge with classification scores, PCWM adopts the Binary Cross-Entropy to convert the localization prediction into localization loss L_i^{loc} as

$$P_i(loc) = e^{-\lambda L_i^{loc}} \tag{3}$$

λ is a hyper-parameter to balance the weight between localization estimation and classification score. For localization loss L_i^{loc}, we use GIOU [21] to complete the loss calculation. The positive confidence score is defined as $P_i^+ = P_i(\text{cls}) \cdot P_i(\text{loc})$. In order to emphasize the locations with high confidence score, PCWM uses an exponential form to increase the response value by

$$C\left(P_{\text{i}}^+\right) = e^{P_i^+/\tau} \tag{4}$$

where τ is a hyper-parameter to control the magnification of weights. In order to guide the information to spread in the correct direction, it is necessary to take account in center prior distribution. Thus, our positive weights combine the exponential form of the positive confidence score and center prior distribution, the whole form is as:

$$w_i^+ = \frac{C\left(P_i^+\right) G(d)}{\sum_{j \in S_n} C\left(P_j^+\right) G(d)} \tag{5}$$

Here, the S_n denotes all locations inside the bounding box of object n, and each w_i^+ is normalized by the sum of the positive locations candidates to limit the numerical range to $[0, 1]$.

2.2.4 Quality Focal Loss

The previous detectors prefer to add an additional localization quality (centerness score [16] or IOU score [22]) to improve the detection accuracy. Without increasing extra quality branch, we use Quality Focal Loss (QFL) [17] to combine the quality estimation with classification confidence score into a single and unified representation form as final score, and replace the ground truth category with its corresponding quality estimation information, which increases the robustness of the training process. Besides, the joint representation form soften the standard one-hot category label, and it has a float target $y \in [0, 1]$ on the corresponding category.

To match with our label assignment principle, we implement our QFL calculation in two parts. Firstly, $0 < y < 1$ denotes the positive samples with target IOU score. Secondly, $y = 0$ stands for the negative samples with a 0 quality score.

Due to all samples have negative sample attribute, we first calculate the QFL_neg loss according to the 0 quality score for all samples, the formula is as follows:

$$QFL_neg = -|\sigma|^{\beta}\left[\log^{1-\sigma}\right] \tag{6}$$

σ is the classification score with sigmoid operations and β controls the down-weighting rate smoothly.

Then perform the QFL_pos loss calculation according to the positive samples which are inside the bounding box, the calculation form is as follows:

$$QFL_pos = -|y - \sigma|^{\beta}\left[(1-y)\log^{(1-\sigma)} + y\log^{\sigma}\right] \tag{7}$$

After complete these calculations, add the two loss functions and perform the scaling operation as

$$QFL = \frac{QFL_neg + QFL_pos}{Num} \tag{8}$$

Num denotes the total number of sample locations inside all bounding boxes. By this loss function, we can facilitate the detectors to have a simpler, effective and joint representation of both localization quality and classification score.

3 Experiments

3.1 Dataset

The original workpiece images are collected by a manipulator with a high-resolution camera. In actual production process, the length of the collected images is in the range of 12000 to 25000

resolution, and the width is in the range of 2200 to 4096 resolution. The inspection task is heavy if the unprocessed images are sent directly to the detection network. Hence, we crop the images according to the way of traversing each pixel of the images, and keeping a certain common part between the images, so that the size of the final image is approximately 600 $\times$ 500 pixel resolutions.

After cropping the images, we select cropped images with defects, and invite senior engineer to help us annotate the defects by drawing ground truth bounding box, and then randomly divide the training set and validation set by a ratio 4:1, which includes 276 and 68 images respectively. Finally, the data set is enhanced to improve the generalization ability of the model.

3.2 Implementation details

In the experimental setting and implementation details, the experiments are conducted on a NVIDIA GeForce RTX 1080Ti, and we use ResNet-50 with MDSM as a feature extraction network if not specifically pointed out. The backbone is initialized with pre-trained weight on ImageNet. Following common practice, the shorter side of the cropped images scales randomly from [640,800] pixels, the longer side is set to 1333 pixels. In the inference stage, the long side and short side are fixed to 1333 and 800 pixels, respectively. The initial learning rate is set to 0.001. During the parameter fine-tuning stage, the learning rate will decrease 10 times at 16th and 22th epoch respectively, weight decay is 0.0001 and momentum is 0.9. The batch size is set to 2. For evaluation metrics, we use the AP (average precision) and AP_{50} (AP for IoU threshold 0.5) to measure the quality of the model.

3.3 Results and comparison

In the section, we show the experimental results which will be elaborated from the MDSM and GAH respectively to prove the effectiveness of our method.

3.3.1 The model complexity comparison of the MDSM

In order to examine the complexity of the MDSM and test its performance compared with other FPN-based approaches, we use FLOPs, Params, and AP to measure our algorithm. For the fairness of experiment, we set the learning rate, batch size and other initial conditions to be the same, and we use FCOS instead of the GAH as the final detection head to simply verify the performance of the MDSM if there are no special instructions. For FPN, PAFPN and our method both adopt Resnet50 as backbone, for HRFPN, using HRnet as backbone. It is noted that the model complexity involves the related calculation of the backbone as the final result. Fig. 4 shows the model complexity between some FPN-based methods and MDSM. It is obvious that our algorithm has less computational

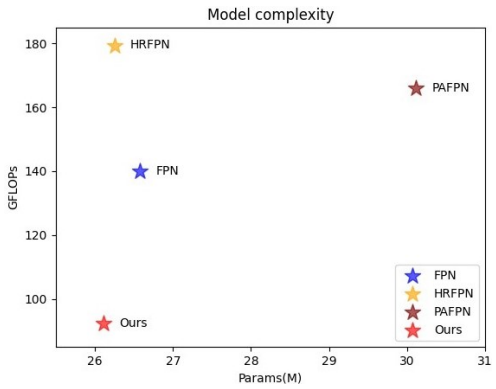

Fig. 4: Comparison chart of the model complexity

complexity compared to other methods and proves its lightweight characteristics. The detection result is in Table 1 which shows that our method can extract feature information in a more effective way than other methods.

Table 1: Detection result comparison between FPN-based method and ours

Methods	$AP_{50:95}$	AP_{50}	AP_{75}
FPN [20]	0.409	0.840	0.342
PAFPN [23]	0.427	0.838	0.424
HRFPN [24]	0.404	0.841	0.376
Ours	**0.436**	**0.846**	**0.455**

3.3.2 The ablation experiments of the semantic supplement

We also conduct a series of ablation experiments to explore the effectiveness of the semantic supplement in MDSM. The details result is obtained in Table 2, we use U-sup to denote upper semantic supplement, and use sup to denote semantic supplement.

It is obvious to find that if the network only uses upper semantic supplement, the detection performance will decrease. However, if the network only uses semantic supplement, the detection performance will increase. We infer the reason for this phenomenon may be that for the network, having sufficient texture information is a prerequisite for good detection performance. If the network uses both upper semantic supplement and semantic supplement, it can further enhance the performance of the network. We think that based on enough shallow-level information, the deep-level information can better guide the training process.

3.3.3 Weighting mechanism of GAH

To demonstrate the effectiveness of the weighting mechanism, we also did a series of ablation experiments on the GAH. Table 3 shows the detailed results based on the GAH, which indicates that Confidence Weighting Module (Positive Confidence Weighting Module and Negative Confidence Weighting Module) brings a relatively significant improvement in network performance, and Center Weighting Module could further improve the detection accuracy. In addition, due to the poor network performance of removing both weighting modules, its performance is not shown here.

3.3.4 The ablation experiments of the Quality Focal Loss

We compare the network performance with or without the joint representations optimized by QFL. It is obvious to observe that QFL boosts the performance more than the counterpart in Table 4. It demonstrates that due to more reliable quality estimation, GAH can benefit from the joint representations by QFL, which enhances the coupling relationship between classification and localization branches.

Table 2: The ablation experiments about the semantic supplement

U-sup	sup	$AP_{50:95}$	AP_{50}	AP_{75}
$\times$	$\times$	0.345	0.797	0.287
✓	$\times$	0.273	0.701	0.130
$\times$	✓	0.418	0.842	0.342
✓	✓	**0.436**	**0.846**	**0.455**

Table 3: The ablation experiments about the weighting mechanism

Confidence	Center	$AP_{50:95}$	AP_{50}	AP_{75}
✓	×	0.205	0.581	0.096
×	✓	0.424	0.832	0.382
✓	✓	**0.452**	**0.852**	**0.454**

Table 4: Add QFL or not

	$AP_{50:95}$	AP_{50}	AP_{75}
Without QFL	0.431	0.837	0.406
With QFL	**0.452**	**0.852**	**0.454**

Table 5: Performance comparison with state-of-the-art detectors

Methods	$AP_{50:95}$	AP_{50}	AP_{75}
SSD [25]	0.417	0.841	0.336
Faster_Rcnn [26]	0.433	0.836	0.420
Yolov3 [27]	0.348	0.746	0.242
FASF [28]	0.317	0.735	0.235
GFL [21]	0.402	0.798	0.328
ATSS [29]	0.382	0.798	0.360
FCOS [16]	0.420	0.813	0.339
Detr [30]	0.349	0.787	0.245
Ours	**0.452**	**0.852**	**0.454**

3.3.5 Comparisons with the state-of -the-art methods

We compare our method with state-of-the-art methods on the workpiece surface defects dataset, for a fair comparison, we use ResNet50 as the backbone, 2x learning schedule (24 epochs) and multi-scale training strategy are adopted during the training process. Under the same training setting, our method can consistently outperform other counterparts. The experimental results are shown in Table 5 and corresponding PR curves of different methods are shown Fig. 5.

4 Conclusions

In this paper, a novelty multi-scale adaptive label assignment neural network architecture which includes MDSM and GAH is proposed, the former component can significantly reduce model complexity and increase the range of receptive fields to achieve scale invariance, the later component can tackle label assignment in a differentiable assignment strategy, and it does not depend on human knowledge which reduces the difficulty of network tuning. In addition, with the help of the QFL, the head can provide more accurate bounding box estimations without introducing extra quality estimation branches. Extensive experiments show that our method steadily obtain promising performance compared to state-of-the-art methods, and demonstrate that proposed network architecture has certain advantages in surface defects inspection which provides an ideal solution for research and applications in the workpiece defects detection.

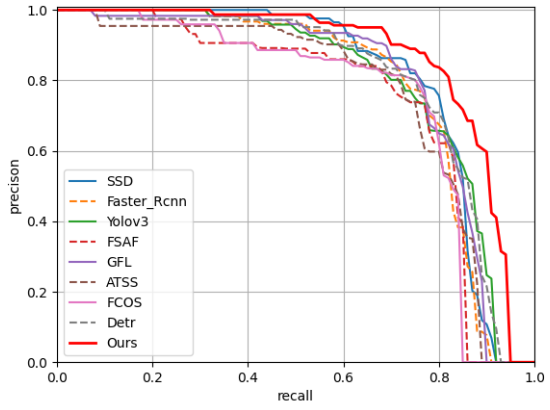

Fig. 5: P-R curves of different detection methods

References

[1] TR Vijayaram, S Sulaiman, AMS Hamouda, and MHM Ahmad. Foundry quality control aspects and prospects to reduce scrap rework and rejection in metal casting manufacturing industries. *Journal of Materials Processing Technology*, 178(1):39–43, 2006.

[2] Junjie Xing and Minping Jia. A convolutional neural network-based method for workpiece surface defect detection. *Measurement*, 176:109185, 2021.

[3] Yirong Zou, Dong Du, Baohua Chang, Linhong Ji, and Jiluan Pan. Automatic weld defect detection method based on Kalman filtering for real-time radiographic inspection of spiral pipe. *NDT & E International*, 72:1–9, 2015.

[4] Hui-Hui Chu and Zong-Yi Wang. A vision-based system for post-welding quality measurement and defect detection. *International Journal of Advanced Manufacturing Technology*, 86(9-12):3007–3014, 2016.

[5] Mengqi Chen, Lingjie Yu, Chao Zhi, Runjun Sun, Shuangwu Zhu, Zhongyuan Gao, Zhenxia Ke, Mengqiu Zhu, and Yuming Zhang. Improved faster R-CNN for fabric defect detection based on Gabor filter with genetic algorithm optimization. *Computers in Industry*, 134:103551, 2022.

[6] Fu-Chen Chen and Mohammad R. Jahanshahi. NB-CNN: Deep learning-based crack detection using convolutional neural network and Naïve Bayes data fusion. *IEEE Transactions on Industrial Electronics*, 65(5):4392–4400, 2018.

[7] Bin Guan, Guoshan Zhang, Jinkun Yao, Xinbo Wang, and Mengxuan Wang. Arm fracture detection in x-rays based on improved deep convolutional neural network. *COMPUTERS & ELECTRICAL ENGINEERING*, 81, JAN 2020.

[8] Bin Guan, Jinkun Yao, Shaoquan Wang, Guoshan Zhang, Yueming Zhang, Xinbo Wang, and Mengxuan Wang. Automatic detection and localization of thighbone fractures in x-ray based on improved deep learning method. *COMPUTER VISION AND IMAGE UNDERSTANDING*, 216, FEB 2022.

[9] Yu He, Kechen Song, Qinggang Meng, and Yunhui Yan. An end-to-end steel surface defect detection approach via fusing multiple hierarchical features. *IEEE Transactions on Instrumentation and Measurement*, 69(4):1493–1504, 2019.

[10] Xiaoqing Zheng, Jie Chen, Hongcheng Wang, Song Zheng, and Yaguang Kong. A deep learning-based approach for the automated surface inspection of copper clad laminate images. *Applied intelligence*, 51(3):1262–1279, 2021.

[11] Hao-Dong Zhang, Xue Yuan, Dan-Yong Li, Jia You, Bing Liu, Xiao-Ming Zhao, Wen-Ming Cai, and Shan Ju. An effective framework using identification and image reconstruction algorithm for train component defect detection. *Applied Intelligence*, pages 1–19, 2022.

[12] Yuxin Wu and Kaiming He. Group Normalization. In *Proceedings of the European Conference on Computer Vision (ECCV)*, pages 3–19, September 2018.

[13] Peng Zhou, Bingbing Ni, Cong Geng, Jianguo Hu, and Yi Xu. Scale-Transferrable Object Detection. In *IEEE/CVF Confer-*

ence on Computer Vision and Pattern Recognition (CVPR), pages 528–537, 2018.

[14] Benjin Zhu, Jianfeng Wang, Zhengkai Jiang, Fuhang Zong, Songtao Liu, Zeming Li, and Jian Sun. AutoAssign: Differentiable label assignment for dense object detection. *ArXiv preprint arXiv:2007.03496*, 2020.

[15] Attention guided context feature pyramid network for object detection. Attention-guided context feature pyramid network for object detection. *ArXiv preprint arXiv:2005.11475*, 2020.

[16] Zhi Tian, Chunhua Shen, Hao Chen, and Tong He. FCOS: A simple and strong anchor-free object detector. *IEEE Transactions on Pattern Analysis and Machine Intelligence*, pages 1–10, 2020.

[17] Xiang Li, Wenhai Wang, Xiaolin Hu, Jun Li, Jinhui Tang, and Jian Yang. Generalized Focal Loss V2: Learning Reliable Localization Quality Estimation for Dense Object Detection. In *IEEE/CVF Conference on Computer Vision and Pattern Recognition (CVPR)*, pages 11627–11636, 2021.

[18] Kaiming He, Xiangyu Zhang, Shaoqing Ren, and Jian Sun. Deep Residual Learning for Image Recognition. In *IEEE/CVF Conference on Computer Vision and Pattern Recognition (CVPR)*, pages 770–778, 2016.

[19] Jifeng Dai, Haozhi Qi, Yuwen Xiong, Yi Li, Guodong Zhang, Han Hu, and Yichen Wei. Deformable Convolutional Networks. In *Proceedings of the IEEE International Conference on Computer Vision (ICCV)*, pages 764–773, 2017.

[20] Tsung-Yi Lin, Piotr Dollár, Ross Girshick, Kaiming He, Bharath Hariharan, and Serge Belongie. Feature Pyramid Networks for Object Detection. In *IEEE/CVF Conference on Computer Vision and Pattern Recognition (CVPR)*, pages 936–944, 2017.

[21] Hamid Rezatofighi, Nathan Tsoi, JunYoung Gwak, Amir Sadeghian, Ian Reid, and Silvio Savarese. Generalized Intersection Over Union: A Metric and a Loss for Bounding Box Regression. In *IEEE/CVF Conference on Computer Vision and Pattern Recognition (CVPR)*, pages 658–666, 2019.

[22] Shengkai Wu, Xiaoping Li, and Xinggang Wang. IoU-aware single-stage object detector for accurate localization. *Image and Vision Computing*, 97:103911, 2020.

[23] Shu Liu, Lu Qi, Haifang Qin, Jianping Shi, and Jiaya Jia. Path Aggregation Network for Instance Segmentation. In *IEEE/CVF Conference on Computer Vision and Pattern Recognition (CVPR)*, pages 8759–8768, 2018.

[24] Jingdong Wang, Ke Sun, Tianheng Cheng, Borui Jiang, Chaorui Deng, Yang Zhao, Dong Liu, Yadong Mu, Mingkui Tan, Xinggang Wang, Wenyu Liu, and Bin Xiao. Deep High-Resolution Representation Learning for Visual Recognition. *IEEE Transactions on Pattern Analysis and Machine Intelligence*, 43(10):3349–3364, 2021.

[25] Wei Liu, Dragomir Anguelov, Dumitru Erhan, Christian Szegedy, Scott Reed, Cheng-Yang Fu, and Alexander Berg. SSD: Single Shot MultiBox Detector. In *Proceedings of the European Conference on Computer Vision (ECCV)*, pages 21–37, 2016.

[26] Shaoqing Ren, Kaiming He, Ross Girshick, and Jian Sun. Faster R-CNN: Towards Real-Time Object Detection with Region Proposal Networks. *IEEE Transactions on Pattern Analysis and Machine Intelligence*, 39(6):1137–1149, 2017.

[27] Joseph Redmon and Ali Farhadi. YOLOv3: An Incremental Improvement. *ArXiv preprint arXiv:1804.02767*, 2018.

[28] Chenchen Zhu, Yihui He, and Marios Savvides. Feature Selective Anchor-Free Module for Single-Shot Object Detection. In *IEEE/CVF Conference on Computer Vision and Pattern Recognition (CVPR)*, pages 840–849, 2019.

[29] Shifeng Zhang, Cheng Chi, Yongqiang Yao, Zhen Lei, and Stan Z Li. Bridging the gap between anchor-based and anchor-free detection via adaptive training sample selection. In *IEEE/CVF Conference on Computer Vision and Pattern Recognition (CVPR)*, pages 9756–9765, 2020.

[30] Nicolas Carion, Francisco Massa, Gabriel Synnaeve, Nicolas Usunier, Alexander Kirillov, and Sergey Zagoruyko. End-to-End Object Detection with Transformers. In *Proceedings of the European Conference on Computer Vision (ECCV)*, pages 213–229, 2020.

Proceedings of the 3rd Conference on Fully Actuated System Theory and Applications
May 10-12, 2024, Shenzhen, China

Depth Guided Fast Rendering Neural Radiance Fields

Tao Zhang[1], Haoqian Wang[2]

1. Tsinghua University, Shenzhen International Graduate School, Shenzhen 518055, P. R. China
E-mail: tao-zhan21@mails.tsinghua.edu.cn

2. Tsinghua University, Shenzhen International Graduate School, Shenzhen 518055, P. R. China
E-mail: wanghaoqian@tsinghua.edu.cn

Abstract: Existing methods of neural radiance fields allow high-quality rendering of images from novel viewpoints in an implicit manner. However, their need for individual training on specific scenes and relatively slow rendering speeds significantly limit their application in real-time communication. To explore and expand their applicability in the realm of real-time holographic communication, we introduce a novel high-speed rendering framework. This framework requires only sparse multi-view image inputs (e.g., four viewpoints), leveraging depth information obtained from the front end as a prior, and integrating point cloud features.It effectively reduces the voxel rendering sampling space and improves the quality of sampling points. Moreover, it decouples the dependency between neural radiance fields and scenes, shifting this dependency onto the transformation matrix between external parameters. This shift endows our model with generalizability, eliminating the need for retraining on new scenes. Experimental evidence demonstrates that our model substantially accelerates the rendering speed of novel viewpoint images on the basis of its generalizability, without compromising the quality of the rendered results even with sparse viewpoint inputs.

Key Words: novel view synthesis, volume rendering, neural radiance fields

1 Introduction

Compared to traditional geometric texture-based 3D reconstruction, the task of novel view synthesis can obtain images of the reconstructed object from various viewpoints, implicitly fulfilling the task of 3D reconstruction. In today's era, where fields such as sports gaming, virtual live broadcasting, and holographic communication increasingly demand faster algorithmic performance, this has gradually garnered attention.

Novel view synthesis refers to rendering or generating images of a scene from a new camera pose, based on a set of scene images. Initially, research in this area was conducted through traditional interpolation among multiple viewpoints[1, 2], as well as light field rendering based on densely arranged capture devices for intensive scene sampling[3–5]. In recent years, researchers have also started to apply deep neural networks to the task of novel view synthesis, particularly exemplified by Neural Radiance Fields (NeRF)[6], which are capable of producing highly realistic rendering effects. This has subsequently led to a considerable amount of work in the field.

Neural Radiance Fields (NeRF)[6] is a technique for rendering 3D scenes. It optimizes a continuous representation of density and color in 3D space, enabling the generation of high-quality images from arbitrary viewpoints. Generally, NeRF learns the depth and color information of a scene by training on hundreds of 2D images taken from different viewpoints, achieving highly realistic scene reproduction. However, this method has practical limitations in applications such as holographic communication. Firstly, high-quality rendering requires a substantial number of input images, which is often impractical as users may not have the means to acquire many images from different viewpoints. Secondly, NeRF requires querying a large number of 3D points distributed across the entire space, leading to time-consuming training and rendering that is unacceptable in many scenarios. Lastly, NeRF requires retraining for different scenes, greatly limiting its generalizability and practical application.

Our work aims to address the aforementioned issues by introducing a Depth-Prior Guided Fasting Rendering Neural Radiance Field, a novel view synthesis framework capable of rapid, versatile, and high-quality rendering with sparse viewpoint inputs. Firstly, we employ a multi-scale feature-guided depth probability prediction module, utilizing acquired depth priors to restrict the rendering sample points within a certain range. Uniform sampling within this range, combined with the multi-scale features extracted from the input images, progressively confines the sample points near the actual rendering scene's surface. This means that these sample points are of higher quality and fewer in number, speeding up the rendering process. Secondly, to tackle the issue of model generalizability, we utilize the input extrinsic matrices to estimate the mapping relationship between features across multiple viewpoints. We use the relationships between the extrinsics to estimate the weights in voxel rendering, decoupling the dependency of the Neural Radiance Fields on the scene and shifting the dependency to the transformation matrices between the extrinsics, thereby enhancing the model's generalizability. Lastly, while maintaining the quality of the rendered images, we first conduct preliminary quantization and pruning of the model. Then, using the original model as a teacher, we distill and train a lightweight student model, further accelerating the model's inference speed.

In conclude, our model, while maintaining the quality of synthesized novel viewpoint images, is capable of universally generating new viewpoint images for various scenes at a rate of 7-8 frames per second. This offers promising directions and potential for the application of this technology in fields such as holographic communication in the future.

2 Related Work

The task of generating new viewpoints of scenes has long been a focal research issue in the field of computer vision. From the perspective of current 3D reconstruction, the gen-

eration of new viewpoint images of scenes essentially involves replacing the representation of 3D scenes with pose images. Hence, the crux of the issue lies in how to model 3D information from 2D captured images. Some studies[1, 8, 9], utilizing pixel correspondence and projection mapping, circumvent the need for modeling scene geometry and achieve new viewpoint image synthesis through perspective transformation, while others use light field rendering[10–19]. However, these methods either fail to guarantee the quality of generated images or impose stringent requirements on capture devices. Therefore, our discussion here primarily centers on the use of deep neural networks for synthesizing new viewpoint images. The following discussion will categorize these works into two main types: one involves explicit reconstruction of geometry, and the other focuses on implicit reconstruction methods, exemplified by Neural Radiance Fields.

2.1 Explicit Reconstruction for Novel View Synthesis

Explicit reconstruction algorithms, particularly Multi-View Stereo (MVS), are primarily used to reconstruct the three-dimensional structure of a scene from images captured from multiple viewpoints, thereby generating new viewpoint images of the scene. MVS involves constructing a cost volume for depth estimation. MVSNet[20] builds a 3D cost volume from 2D image features and regularizes it using a 3D convolutional neural network. This design enables end-to-end training of the network and has yielded impressive results. However, MVSNet[20] consumes a significant amount of memory. To address this issue, subsequent works improved upon it by employing techniques such as recurrent plane sweeping[21] or coarse-to-fine architectures[22–25].

Other approaches[26, 27] have utilized parametric models of the human body, fitting parameters and reconstructing based on multi-view geometry and the tracking of human motion, driven by constraints from multi-view contours and temporal features. Some studies[28] have focused on integrating correlational information between frames in dynamic scenes, gradually refining and detailing the reconstructed models by inputting newly captured data into keyframe models. However, these methods may not perform well when there are rapid changes between frames.

Function4D[29] uses a sliding window over video frame sequences to produce TSDF voxel fusion results that eliminate noise and maintain topological consistency within the temporal window. It then fuses features from multiple viewpoints and uses deep implicit functions to reconstruct surface details. However, it still falls short in recovering complex textured surfaces in practical applications.

2.2 Implicit Reconstruction for Novel View Synthesis

This category is predominantly represented by Neural Radiance Fields (NeRF)[6] and its related works, which represent scenes as continuous fields of color and density, producing high-quality results for novel view rendering. However, NeRF's rendering is tied to specific scenes, requiring retraining of the entire network model for new scenes. Moreover, it generally requires dense viewpoint inputs to achieve satisfactory reconstruction results. Furthermore, the training process is exceedingly slow, and rendering efficiency is low, with training for a single scene often taking a day or even several days. Hence, there has been a plethora of follow-up works aimed at improving the NeRF algorithm from multiple perspectives.

NeuS[30] and UNISURF[31] have substituted the field function representation in NeRF with signed distance functions and occupancy fields[32], respectively, to extract object surfaces that are more geometrically sound and complete. Works[33–38] have attempted to increase the training speed of NeRF. They use 2D convolutional neural networks to process input images and decode multi-view features to generate the target radiance fields. With pretrained networks, they can be quickly fine-tuned to generate high-quality renderings for new scenes.

Another series of works[39–43] aimed at accelerating the rendering speed of NeRF. By caching neural radiance fields, [39] managed to synthesize realistic images in real-time. Nvidia's work, InstantNGP[44], uses multi-resolution hash table spatial indexing, significantly reducing the time for fitting and rendering of a single scene to the level of seconds. Methods like PixelNeRF[38] and IBRNet[37] have achieved scene generalization and a reduction in input viewpoints by extracting features on input views and aggregating them at the sampling points of the rendering framework. Furthermore, some works have utilized the concept of MVSNet[20] to estimate depth maps of input views first, reducing ineffective sampling in sparse space and significantly enhancing the efficiency of rendering novel viewpoint images. For instance, Point-nerf[45] can take prior spatial point clouds (e.g., preliminary point cloud results generated by COLMAP[46]) as input information and incorporates pruning and growing strategies in the algorithm, generating dense point clouds that suppress noise while synthesizing new views.

Although these methods have optimized Neural Radiance Fields in various aspects, these known methods still cannot balance generalizability and rendering speed. The method proposed in this paper, with its multi-scale feature-guided depth probability prediction module, confines sampling points within a certain spatial range while ensuring the high quality of the sampling points. This accelerates the generation speed of novel viewpoint images without compromising their quality. Moreover, by decoupling the model's dependency on the scene and shifting it to the mapping relationship between the target and source extrinsic matrices, the model's generalizability is ensured.

3 Method

To align with practical application scenarios, our objective is to synthesize high-quality novel viewpoint images at an extremely fast pace from a set of real-scene images captured from sparse viewpoints (such as four), without the need for retraining specific to each scene or reconstructing detailed geometric texture structures. Our designed method consists of several steps: 1.Multi-scale Feature-guided Depth Probability Sampling: This step involves restricting the range of the sampling space. It leverages multi-scale features to guide the depth probability of sampling points, ensuring that the sampling is focused on the most relevant areas of the scene. 2.Learning Rendering Weights through Source and Target View Relationships: In this step, the relationship between source views and target views is utilized to learn the

rendering weights of the sampling points. This process helps in accurately determining the color field and density field of the sampling points, which are crucial for synthesizing the new viewpoints. After obtaining the color and density fields, voxel rendering is performed to generate the final image from the new viewpoint. This step synthesizes the 3D information captured and processed in the previous steps into a 2D image from the desired viewpoint. 3.Model Distillation for Speed Enhancement: Once the initial training of the model is complete, we use it as a teacher model to distill and train a lightweight student model. This student model retains the essential features of the teacher model but with significantly reduced computational complexity, which further accelerates the model's inference and the synthesis of new viewpoint images.The workflow diagram of our method is illustrated in Figure 1. By focusing on these steps, our approach aims to provide a practical and efficient solution for novel viewpoint image synthesis, addressing the need for fast processing and high-quality output in real-world applications.

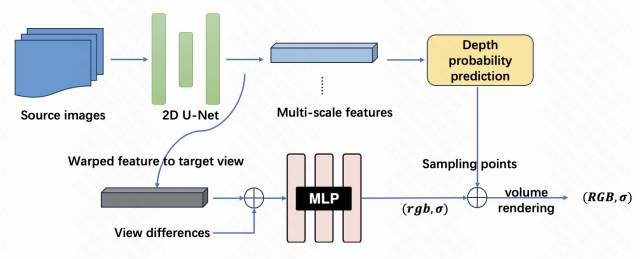

Fig. 1: Illustration of the Proposed Approach

3.1 Multi-scale Feature Extraction and Depth Prediction

In this part, the sampling space is initially restricted within a certain range defined by predefined depth priors d_{max} and d_{min} .Subsequently, multi-scale feature extraction is employed to iteratively refine the extraction of sampling points in the sampling space, from coarse to fine. This process also involves obtaining the corresponding depth probability distribution of the sampling points, guiding the final sampling and rendering process. This module's inputs are the pose of the target camera ϕ_{tar} images $\{I_i\}_{i=1}^{N}$ from the nearest N source views and their corresponding camera poses. And then output points $\mathbf{X}_r \in R^{D\cdot H\cdot W}$ for sampling and rendering. The approximate flowchart is presented as follows:

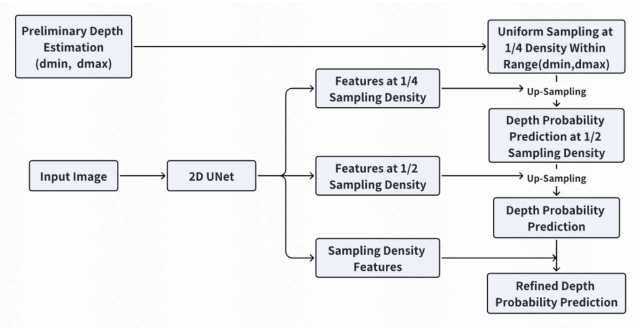

Fig. 2: Multiscale Feature-Guided Depth Probability Prediction Module Flowchart

3.1.1 Multi-scale Feature Extraction

We use 2D U-Net to build a multi-scale feature extractor, to get the target cost volume. This extractor is designed to derive multi-scale image features from the selected input views $\{I_i\}_{i=1}^{N}$. Specifically, it extracts features at three different scales, denoted as F_1, F_2, F_3, These feature maps are characterized by their respective spatial resolutions $\frac{H}{4} \times \frac{W}{4}, \frac{H}{2} \times \frac{W}{2}, H \times W$ and channel numbers C_1, C_2, C_3.

3.1.2 Preliminary Depth Probability Estimation

To learn the three-dimensional structure of the target scene and guide sampling, a cost volume is constructed on the target viewing frustum. This involves differentiable reprojection of the extracted features onto the target center, with the cost volume being established on the target viewing frustum. This approach is different from the common learning-based Multi-View Stereo (MVS) methods, which construct a plane sweep cost volume on the known views of the image. Specifically, given the pose of the target camera $\phi_{tar} = \{\mathbf{K}_{tar}, \mathbf{R}_{tar}, \mathbf{t}_{tar}\}$, the pose of the source views $\phi_i = \{\mathbf{K}_i, \mathbf{R}_i, \mathbf{t}_i\}$, and the sampling points on the target viewing frustum at depth d, we consider the transformation matrix $\mathbf{H}_i(d)$ that maps features from the coordinate system of the source view to that of the target view:

$$\begin{aligned} \mathbf{H}_i(d) &= \hat{\mathbf{K}}_i \mathbf{T}_i \mathbf{T}_{tar}{}^{-1} \hat{\mathbf{K}_{tar}}{}^{-1} \\ x_i &= \mathbf{H}_i(d) x_{tar} \end{aligned} \tag{1}$$

where:

$$\begin{aligned} x_i &= (d_i u_i, d_i v_i, d_i, 1)^T \\ x_{tar} &= (du_{tar}, dv_{tar}, d, 1)^T \end{aligned} \tag{2}$$

Then we need to determine the variance of inter-view feature deformation to constructed the target-centered cost volume. A 3D CNN is then used to regularize the cost volume. By performing a softmax operation along the depth direction on the normalized cost volume, we obtain a response probability distribution $P \in R^{D\times H\times W}$ of the points. The depth probability obtained provides a compact sampling space. So this process is crucial for ensuring that the rendering focuses on the most relevant parts of the scene and is informed by an accurate understanding of the scene's depth structure, leading to high-quality novel viewpoint synthesis.

3.1.3 Multi-Scale Depth Probability Prediction

The ultimate goal is to accelerate rendering speed with less sampling points while compromising the ability to produce realistic renderings. This is achieved by leveraging the previously mentioned multi-scale features extracted and combining them with the initial depth probability estimates to progressively learn a more refined depth probability prediction at finer scales. This refined prediction guides the final sampling, ensuring that points contributing significantly to rendering are gradually sampled. Unlike a unimodal hypothesis, a sampling strategy from the distribution is adopted, considering the sampling probability along the entire ray.

In detail, the initially constructed cost volume and depth probability distribution are combined with features extracted

at three scales. At each scale, a target-centered cost volume and its depth probability prediction distribution are constructed. Higher pixel resolution and more refined probability-guided sampling are used to refine previous sampling. On the coarsest scale, within a predefined depth range (d_{min}, d_{max}), the uniform sampling points of the camera rays on the frustum denoted as $X_1 \in R^{D_1 \times \frac{H}{4} \times \frac{W}{4}}$. Then, the image features F_1 extracted from the first scale are used to construct a target-centered cost volume. After regularization and normalization by a 3D convolutional neural network, the coarsest sample space depth probability P_1 $in R^{D_1 \times \frac{H}{4} \times \frac{W}{4}}$ can be learned. Next, a smaller set of points $X_2' \in R^{D_2 \times \frac{H}{4} \times \frac{W}{4}}$ is sampled from P_1, with these points being more likely to represent the scene's structure compared to X_1. These points are then interpolated in the sample space to obtain the distribution of points at the next scale, X_2'. Similarly, at the second scale, the same process of cost volume construction, regularization, and normalization is followed to obtain the depth probability distribution P_2 for that scale. Then, based on P_2, a more refined set of samples is taken as the final set of points for rendering X_3, along with their corresponding depth probability distribution P_3

In summary, this process involves obtaining the depth probability distribution of corresponding point sets during the construction of the target cost volume. The depth probability distribution is then used to guide the sampling of rendering points. This approach allows for more compact and efficient sampling, speeding up rendering while still maintaining the rendering quality of the image. The practical effect is that the sampling point space is confined to a very compact range, while ensuring high quality of the sampling points, resulting in efficient sampling.

3.2 Viewpoint Feature Mapping for Voxel Rendering

Building upon the previous module, the output points and their depth probability estimations are used as references. The scene observed from the target viewpoint is represented as a density field and a color field. To decouple the dependency of Neural Radiance Fields on the specific scene, we fully utilize the feature mapping relationship between the source and target views. This approach shifts the aforementioned dependency to the transformation of the extrinsic matrices, effectively aggregating information from the source views and enhancing the generalizability of the algorithm, eliminating the need for retraining for each new scene.

3.2.1 Density Field Estimation

In Neural Radiance Fields (NeRF)[6], the density encodes the transmittance of points in the target scene. In most scenes, there is a lot of invalid sample space, resulting in considerable redundancy in the uniform sampling of rays in the original NeRF algorithm. To address this, we leverage the previously obtained sampling points. Moreover, the depth probability distribution already estimated implies the 3D structure of the target scene. Therefore, we utilize the depth probability distribution obtained from the previous module and use a multi-layer perceptron (MLP) for density estimation to predict the density of the points.

$$d(r) = f_d(P_3(l)) \tag{3}$$

$P_3(l) \in R^{D_3}$ represents the target viewpoint's depth probability estimation , and $(l) \in R^{D_3}$ is the density of sampled points on the target viewpoint line-of-sight l. Additionally, integrating the density $d(l)$ of rendering points yields the density field $\zeta \in R^{D_3 x H x W}$.

3.2.2 Color Field Estimation

After completing the density estimation, we need to estimate the color of the sampled points. This is done by predicting the surface color using the color information of the source view at the most refined rendering points obtained in section 3.1, and by mixing colors to achieve more reliable results. Specifically, the network, a multi-layer perceptron (MLP), learns the weights for color mixing based on the feature mapping relationships between viewpoints and the differences in relative viewing directions. The feature mapping between multiple perspectives as shown in the figure3:

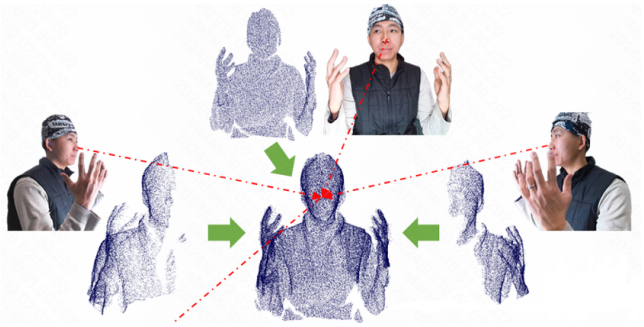

Fig. 3: Multi-view Feature Mapping

The learned weights are then applied to the final rendering points' colors. The processing steps are below: Firstly, feature extraction for color mixing: Use a 2D U-Net to extract a set of image features $F^c{}_i$ for generating color mixing weights. These features have a spatial resolution of HxW and a number of channels C_3. Then use the transformation relationships described in equation 1 to map the extracted multi-view features to the target view, denote as $\hat{F}_i^c$. Calculate the difference in viewing direction d:$\Delta d_i = d - d_i$, where d and d_i is the target viewing ray and source viewing ray respectively.

We use them to generate the mixing weights:

$$\omega_i = g(\hat{F}_i^c, \Delta d_i) \tag{4}$$

Then aggregate these rendered points to form the color field, $\mathbf{C} \in R^{3 \times D_3 \times H \times W}$:

$$\mathbf{c} = \sum_{i=1}^{M} \left(\frac{\hat{C}_i exp(\omega_i)}{\sum_{j=1}^{M} exp(\omega_j)} \right) \tag{5}$$

This field represents the spatial distribution of colors across the 3D space and is critical for rendering the scene realistically from the new viewpoint.By incorporating the color information from multiple source views and intelligently mixing colors based on feature mapping and viewing direction differences, the model can render the new viewpoint with rich and accurate color representation.

3.2.3 Rendering

We use traditional voxel rendering methods to obtain the final synthesized image from the target viewpoint:

$$\hat{C}_r = \sum_{k=1}^{D_3} T_k(1 - exp(-\delta_k))\mathbf{c}_k$$
$$where \quad T_k = exp(-\sum_{m=1}^{k-1} m) \tag{6}$$

Here $\hat{C}_r$ is cumulative pixel color corresponding to ray r in the predicted target new viewpoint image, D_3 is the number of points, d_m, $\hat{c}_m$ is density and color that we get before.

Through this voxel rendering process, the density and color fields are effectively combined to produce a visually coherent and realistic image from the new viewpoint, providing a reliable synthesis of the scene based on the estimated 3D structure and appearance information.

3.3 Model Distillation and Optimization for Efficient Inference

The final section delves into the model distillation process, a technique designed to transfer knowledge from a complex, computationally heavy teacher model to a more lightweight and efficient student model. This process is crucial for deploying the novel viewpoint synthesis model in resource-constrained environments, where rendering speed and model compactness are paramount. The student model, in this case, not only reduces the depth of its MLP network by two layers compared to the teacher model but also undergoes pruning post-distillation to enhance inference speed further.

The original model, known for its accuracy in estimating density and color fields, serves as the teacher. The student model, designed to be lightweight, adopts a shallower architecture with two fewer MLP layers, ensuring a significant reduction in computational load while striving to maintain the rendering quality. At the training steps, we aligning the student's outputs (density and color fields) with those of the teacher model. The student model is trained to mimic the teacher's predictions, focusing on preserving the critical features that contribute to the final rendering quality.

Through model distillation and subsequent optimization via pruning, the final student model achieves a significant reduction in computational requirements, making it well-suited for real-time novel viewpoint synthesis in resource-constrained environments. This process ensures that the model retains its ability to render high-quality images from new viewpoints, making the technology more accessible and practical for a wide range of applications.

4 Experiments

To validate the effectiveness of the proposed method, we conducted experiments focusing on three primary aspects: the quality of rendered images, the rendering speed of the algorithm, and the practical applicability and effectiveness of the algorithm in real-world scenarios. Each of these aspects is crucial for demonstrating the superiority and practicality of our novel view synthesis approach.

4.1 Comparison of Rendered Image Quality

To rigorously evaluate the performance of our proposed method, we conducted a comparative study against three methods: PixelNeRF[38], IBRNet[37], and MVSNeRF[33]. The evaluation was structured across three datasets: DTU[47], the realistic synthetic data from NeRF[6] and forward-facing real data from LLFF[48], providing a diverse range of scenes and complexities. The comparison primarily focused on three standard image quality metrics: PSNR(Peak Signal-to-Noise Ratio), SSIM(Structural Similarity Index), and LPIPS(Learned Perceptual Image Patch Similarity), with the results presented in Tables 1, 2, and 3 respectively.

Table 1: Quantitative results on DTU

Methods	PSNR↑	SSIM↑	LPIPS↓
PixelNeRF	19.895	0.653	0.467
IBRNet	23.684	0.822	0.305
MVSNeRF	24.332	**0.845**	0.284
Ours	**24.721**	0.832	**0.253**

Table 2: Quantitative results on NeRF Synthetic

Methods	PSNR↑	SSIM↑	LPIPS↓
PixelNeRF	6.342	0.534	0.467
IBRNet	22.483	0.899	0.182
MVSNeRF	23.782	0.912	0.176
Ours	**25.094**	**0.922**	**0.075**

Table 3: Quantitative results on Real Forward-facing

Methods	PSNR↑	SSIM↑	LPIPS↓
PixelNeRF	10.236	0.437	0.683
IBRNet	21.732	**0.781**	0.269
MVSNeRF	21.925	0.765	0.257
Ours	**21.933**	0.772	**0.231**

We compare the new perspectives rendering results on DTU datasets of our method with PixelNeRF[38], IBRNet[37], and MVS-NeRF[33] as follows:

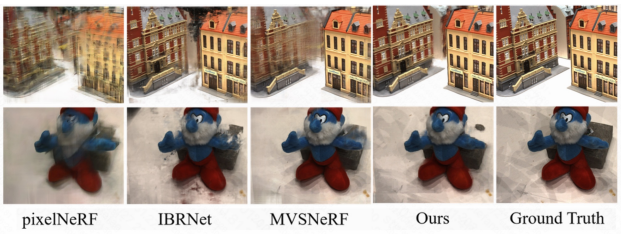

Fig. 4: Rendering Results on DTU Datasets

As shown in Figure 4, the new view images synthesized by pixelNeRF in the three scenes have obvious blur, IBRNet has errors at the edges and joints, and MVSNet has motion blur-like phenomena. Of course, the method proposed was also not very successful in rendering the small gift box behind the third row of dolls, but it can be seen from the experimental results that the actual rendering effect is still good.

Our experimental results demonstrate that our method achieves comparable or even superior performance in

terms of rendering image quality when measured against other prominent novel view synthesis methods like PixelNeRF[38], IBRNet[37], and MVSNeRF[33]. However, a key distinguishing factor that sets our method apart is the rendering speed, which is orders of magnitude faster than the competing methods.

4.2 Comparison of Rendering Speed

To highlight the efficiency of our method, we conducted a rigorous comparison of rendering speeds between our approach and the other established methods. The results of this comparison are detailed in Table 4. All experiments were conducted on an RTX 3090 GPU, ensuring a standardized and high-performance computing environment. The rendered images for this comparison were all of the resolution 512x512 pixels. The experiments conclusively demonstrate that our method not only matches but in some cases surpasses the image quality of other methods while providing rendering speeds that are significantly faster, by orders of magnitude.

Table 4: Rendering Speed Results

Methods	fps↑
PixelNeRF	0.020
IBRNet	0.219
MVSNeRF	0.413
Ours	**6.213**

4.3 Practical Applicability and Effectiveness

To further substantiate the generalizability and practicality of our model, we conducted training and evaluation on the THUman2.0 dataset. This dataset, known for its high-quality 3D human models, provides a challenging testbed for assessing the model's ability to handle complex, real-world data. We measured the performance of our model using PSNR, SSIM, and FID (Frechet Inception Distance) scores. The FID score, in particular, measures the distance between feature vectors of real and generated images, providing a metric of their similarity. Lower FID scores indicate higher similarity and, hence, better model performance. The statistical results are presented in Table 5.

Table 5: Quantitative results on THUman2.0

Metrics	PSNR	SSIM	FID
Ours	28.3655	0.93954	9.68

Additionally, we applied the trained model to a set of portrait photos captured simultaneously by four cameras in a laboratory setting, achieving realistic rendering effects from new viewpoints, Then, we present the rendering results on a 3D display monitor Looking Glass to demonstrate the validity of our methods. We show the three perspectives of a rendering as follows. This is the author's own picture, obviously we do not have rich training data for this scene. And the realistic results prove the practicality and generalization of our method.

5 Conclusions

This paper presented a comprehensive approach to novel view synthesis, introducing a method that significantly enhances rendering speed without compromising image quality. By employing multi-scale feature extraction and depth prediction, we constrained the sampling range of the neural radiance field algorithm, simultaneously improving the quality of the sampled points. Subsequently, we fully exploited the feature mapping relationship between source and target views, decoupling the algorithm's dependency on the scene. This endowed our model with generalization capabilities. Finally, we further accelerated the model through distillation and pruning. Through a series of rigorous experiments and comparative analyses, we demonstrated the superiority of our method over existing techniques in terms of rendering quality and speed. Although our method does not meet the real-time requirements of holographic communication, it provides a valuable exploration and inspiration for the development in this field, enhancing user experiences in VR, AR, and beyond. In conclusion, our novel view synthesis method marks a significant advancement in the field, bridging the gap between high-quality rendering and high-speed processing. The research opens new pathways for real-time and interactive applications, setting the stage for future innovations in novel view synthesis and related domains.



Fig. 5: Holograms Display Results

References

[1] Mueller K, Smolic A, Dix K, et al. View synthesis for advanced 3D video systems[J]. EURASIP Journal on image and video processing, 2009, 2008: 1-11.

[2] McMillan L, Bishop G. Plenoptic modelling: An image-based rendering algorithm[C]//SIGGRAPH. 1995.

[3] Curless B, Levoy M. A volumetric method for building complex models from range images[C]//Proceedings of the 23rd annual conference on Computer graphics and interactive techniques. 1996: 303-312.

[4] Gortler S J, Grzeszczuk S. R. Cohen, MF,"The Lumigraph", SIGGRAPH 96[J]. Computer Graphics, 1996: 31-42.

[5] Gortler S, Buehler C, Bosse M, et al. Unstructured lumigraph rendering[C]//Proceedings of the 28th annual conference on computer graphics and interactive techniques (SIGGRAPH 2001). 2001: 425-432.

[6] Mildenhall B, Srinivasan P P, Tancik M, et al. Nerf: Representing scenes as neural radiance fields for view synthesis[J]. Communications of the ACM, 2021, 65(1): 99-106.

[7] Curless B, Levoy M. A volumetric method for building complex models from range images[C]//Proceedings of the 23rd annual conference on Computer graphics and interactive techniques. 1996: 303-312.

[8] Seitz S M, Dyer C R. View morphing[C]//Proceedings of the 23rd annual conference on Computer graphics and interactive techniques. 1996: 21-30.

[9] Fitzgibbon A, Wexler Y, Zisserman A. Image-based rendering using image-based priors[J]. International Journal of Computer Vision, 2005, 63: 141-151.

[10] Curless B, Levoy M. A volumetric method for building com-

plex models from range images[C]//Proceedings of the 23rd annual conference on Computer graphics and interactive techniques. 1996: 303-312.
[11] Levin A, Durand F. Linear view synthesis using a dimensionality gap light field prior[C]//2010 IEEE Computer Society Conference on Computer Vision and Pattern Recognition. IEEE, 2010: 1831-1838.
[12] Shi L, Hassanieh H, Davis A, et al. Light field reconstruction using sparsity in the continuous fourier domain[J]. ACM Transactions on Graphics (TOG), 2014, 34(1): 1-13.
[13] Vagharshakyan S, Bregovic R, Gotchev A. Image based rendering technique via sparse representation in shearlet domain[C]//2015 IEEE International Conference on Image Processing (ICIP). IEEE, 2015: 1379-1383.
[14] Vagharshakyan S, Bregovic R, Gotchev A. Light field reconstruction using shearlet transform[J]. IEEE transactions on pattern analysis and machine intelligence, 2017, 40(1): 133-147.
[15] Wu G, Masia B, Jarabo A, et al. Light field image processing: An overview[J]. IEEE Journal of Selected Topics in Signal Processing, 2017, 11(7): 926-954.
[16] Yoon Y, Jeon H G, Yoo D, et al. Learning a deep convolutional network for light-field image super-resolution[C]//Proceedings of the IEEE international conference on computer vision workshops. 2015: 24-32.
[17] Wang T C, Zhu J Y, Kalantari N K, et al. Light field video capture using a learning-based hybrid imaging system[J]. ACM Transactions on Graphics (TOG), 2017, 36(4): 1-13.
[18] Wu G, Liu Y, Fang L, et al. Light field reconstruction using convolutional network on EPI and extended applications[J]. IEEE transactions on pattern analysis and machine intelligence, 2018, 41(7): 1681-1694.
[19] Wu G, Liu Y, Dai Q, et al. Learning sheared EPI structure for light field reconstruction[J]. IEEE Transactions on Image Processing, 2019, 28(7): 3261-3273.
[20] Yao Y, Luo Z, Li S, et al. Mvsnet: Depth inference for unstructured multi-view stereo[C]//Proceedings of the European conference on computer vision (ECCV). 2018: 767-783.
[21] Yao Y, Luo Z, Li S, et al. Recurrent mvsnet for high-resolution multi-view stereo depth inference[C]//Proceedings of the IEEE/CVF conference on computer vision and pattern recognition. 2019: 5525-5534.
[22] Chen R, Han S, Xu J, et al. Point-based multi-view stereo network[C]//Proceedings of the IEEE/CVF international conference on computer vision. 2019: 1538-1547.
[23] Cheng S, Xu Z, Zhu S, et al. Deep stereo using adaptive thin volume representation with uncertainty awareness[C]//Proceedings of the IEEE/CVF Conference on Computer Vision and Pattern Recognition. 2020: 2524-2534.
[24] Gu X, Fan Z, Zhu S, et al. Cascade cost volume for high-resolution multi-view stereo and stereo matching[C]//Proceedings of the IEEE/CVF conference on computer vision and pattern recognition. 2020: 2495-2504.
[25] Yu Z, Gao S. Fast-mvsnet: Sparse-to-dense multi-view stereo with learned propagation and gauss-newton refinement[C]//Proceedings of the IEEE/CVF Conference on Computer Vision and Pattern Recognition. 2020: 1949-1958.
[26] Brox T, Rosenhahn B, Gall J, et al. Combined region and motion-based 3D tracking of rigid and articulated objects[J]. IEEE transactions on pattern analysis and machine intelligence, 2009, 32(3): 402-415.
[27] Gall J, Stoll C, De Aguiar E, et al. Motion capture using joint skeleton tracking and surface estimation[C]//2009 IEEE Conference on Computer Vision and Pattern Recognition. Ieee, 2009: 1746-1753.
[28] Newcombe R A, Fox D, Seitz S M. Dynamicfusion: Reconstruction and tracking of non-rigid scenes in real-time[C]//Proceedings of the IEEE conference on computer vision and pattern recognition. 2015: 343-352.
[29] Yu T, Zheng Z, Guo K, et al. Function4d: Real-time human volumetric capture from very sparse consumer rgbd sensors[C]//Proceedings of the IEEE/CVF conference on computer vision and pattern recognition. 2021: 5746-5756.
[30] Wang P, Liu L, Liu Y, et al. Neus: Learning neural implicit surfaces by volume rendering for multi-view reconstruction[J]. arXiv preprint arXiv:2106.10689, 2021.
[31] Oechsle M, Peng S, Geiger A. Unisurf: Unifying neural implicit surfaces and radiance fields for multi-view reconstruction[C]//Proceedings of the IEEE/CVF International Conference on Computer Vision. 2021: 5589-5599.
[32] Peng S, Niemeyer M, Mescheder L, et al. Convolutional occupancy networks[C]//Computer Vision–ECCV 2020: 16th European Conference, Glasgow, UK, August 23–28, 2020, Proceedings, Part III 16. Springer International Publishing, 2020: 523-540.
[33] Chen A, Xu Z, Zhao F, et al. Mvsnerf: Fast generalizable radiance field reconstruction from multi-view stereo[C]//Proceedings of the IEEE/CVF International Conference on Computer Vision. 2021: 14124-14133.
[34] Johari M M, Lepoittevin Y, Fleuret F. Geonerf: Generalizing nerf with geometry priors[C]//Proceedings of the IEEE/CVF Conference on Computer Vision and Pattern Recognition. 2022: 18365-18375.
[35] Liu Y, Peng S, Liu L, et al. Neural rays for occlusion-aware image-based rendering[C]//Proceedings of the IEEE/CVF Conference on Computer Vision and Pattern Recognition. 2022: 7824-7833.
[36] Trevithick A, Yang B. Grf: Learning a general radiance field for 3d representation and rendering[C]//Proceedings of the IEEE/CVF International Conference on Computer Vision. 2021: 15182-15192.
[37] Wang Q, Wang Z, Genova K, et al. Ibrnet: Learning multi-view image-based rendering[C]//Proceedings of the IEEE/CVF Conference on Computer Vision and Pattern Recognition. 2021: 4690-4699.
[38] Yu A, Ye V, Tancik M, et al. pixelnerf: Neural radiance fields from one or few images[C]//Proceedings of the IEEE/CVF Conference on Computer Vision and Pattern Recognition. 2021: 4578-4587.
[39] Garbin S J, Kowalski M, Johnson M, et al. Fastnerf: High-fidelity neural rendering at 200fps[C]//Proceedings of the IEEE/CVF International Conference on Computer Vision. 2021: 14346-14355.
[40] Hedman P, Srinivasan P P, Mildenhall B, et al. Baking neural radiance fields for real-time view synthesis[C]//Proceedings of the IEEE/CVF International Conference on Computer Vision. 2021: 5875-5884.
[41] Liu L, Gu J, Zaw Lin K, et al. Neural sparse voxel fields[J]. Advances in Neural Information Processing Systems, 2020, 33: 15651-15663.
[42] Reiser C, Peng S, Liao Y, et al. Kilonerf: Speeding up neural radiance fields with thousands of tiny mlps[C]//Proceedings of the IEEE/CVF International Conference on Computer Vision. 2021: 14335-14345.
[43] Yu A, Li R, Tancik M, et al. Plenoctrees for real-time rendering of neural radiance fields[C]//Proceedings of the IEEE/CVF International Conference on Computer Vision. 2021: 5752-5761.
[44] Müller T, Evans A, Schied C, et al. Instant neural graphics primitives with a multiresolution hash encoding[J]. ACM Transactions on Graphics (ToG), 2022, 41(4): 1-15.
[45] Xu Q, Xu Z, Philip J, et al. Point-nerf: Point-based neural radiance fields[C]//Proceedings of the IEEE/CVF Conference on

Computer Vision and Pattern Recognition. 2022: 5438-5448.
[46] Schönberger J L, Zheng E, Frahm J M, et al. Pixelwise view selection for unstructured multi-view stereo[C]//Computer Vision–ECCV 2016: 14th European Conference, Amsterdam, The Netherlands, October 11-14, 2016, Proceedings, Part III 14. Springer International Publishing, 2016: 501-518.
[47] Aanæs H, Jensen R R, Vogiatzis G, et al. Large-scale data for multiple-view stereopsis[J]. International Journal of Computer Vision, 2016, 120: 153-168.
[48] Mildenhall B, Srinivasan P P, Ortiz-Cayon R, et al. Local light field fusion: Practical view synthesis with prescriptive sampling guidelines[J]. ACM Transactions on Graphics (TOG), 2019, 38(4): 1-14.

Proceedings of the 3rd Conference on Fully Actuated System Theory and Applications
May 10-12, 2024, Shenzhen, China

Navigating the Accuracy-Privacy Dilemma in Load Forecasting with Noisy Data

Cheng Guo
School of Science and Engineering, The Chinese University of Hong Kong, Shenzhen, Guangdong 518172, P. R. China
E-mail: 120090389@link.cuhk.edu.cn

Abstract: Accurate load forecasting facilitates the system operators to manage the power grid effectively. However, including noise to safeguard user privacy can adversely affect forecast precision. This study investigates applying differential privacy (DP) mechanisms to balance data privacy with forecasting utility. We introduce a quantitative method to evaluate the impact of DP-induced noise at varying privacy levels on load forecasts. Through simulations using linear regression, support vector regression, and artificial neural network models, we showcase the effectiveness of our approach across diverse forecasting methodologies. Our results offer valuable insights into achieving an optimal equilibrium between privacy preservation and forecasting accuracy, enabling various stakeholders in the electricity sector to navigate the accuracy-privacy dilemma when making data-driven decisions.

Key Words: Differential Privacy; Load Forecasting; Regression

1 Introduction

In an era where data privacy is paramount, differential privacy (DP) mechanisms [1] have emerged as a robust safeguard, subtly introducing controlled random noise into sensitive datasets. While this approach maintains privacy, it inherently exacts a toll on data utility, particularly in load forecasting, where accuracy is crucial. Even the most sophisticated machine learning models, such as artificial neural networks, are not immune to the impact of DP noise, as evidenced by the fluctuations in forecasting precision [2].

To delve into the intricacies of DP's influence on forecasting accuracy, this paper takes a microscope to several machine learning models, scrutinizing their responses to DP-induced noise. The choice of models is not trivial; each may react differently, revealing a spectrum of vulnerabilities. To ensure our idea resonates broadly, we adopt an incremental model selection strategy, systematically expanding our scope from the foundational linear regression model to more intricate and contemporary algorithms.

Our journey into the heart of the accuracy-privacy dilemma begins with a meticulous analysis of the linear regression model, providing a baseline for gauging the effects of DP on forecasting accuracy. This serves as a stepping stone to explore the applicability of our findings within the complex tapestry of advanced machine learning models. Join us as we unravel the nuanced relationship between DP, data utility, and the quest for precise load forecasting.

1.1 Related Works

The smart grid community has embraced the concept of DP for various applications, including power line obfuscation [3], non-intrusive load monitoring [4], safeguarding time series data [5], synthesizing load profiles [6], electric vehicle charging station coordination [7], user profiling [8] and electricity procurement [9]. Our work builds on the extensive literature investigating the potential impact of privacy-preserving mechanisms on data-driven tasks within the electricity sector. Comas *et al.* [10] have previously explored individual differential privacy as an alternative to conventional DP, aiming to protect individual privacy while ensuring more precise data. In this vein, our paper delves deeper into the quantifiable effects of DP mechanisms on load forecasting accuracy, further advancing the understanding of privacy-utility trade-offs in the smart grid context.

Recently, there has been a surge in literature aimed at enhancing load forecasting accuracy while maintaining privacy. Certain studies have delved into minimizing the introduction of noise to meet a specified level of privacy preservation, e.g., [11] [12]. Conversely, others have concentrated on refining existing forecasting models to mitigate the impact of DP on accuracy, e.g., [13] [14]. However, there is a lack of quantitative research that examines the specific influence of DP on the performance of these models. Our paper aims to fill this void by providing insights into how DP affects the investigated models and offering guidance to various stakeholders in the electricity sector on integrating DP for load forecasting purposes.

1.2 Our Contributions

The primary contributions of this paper can be outlined as follows:

- This study furnishes essential evidence to understand the trade-offs between privacy preservation and forecasting performance, thus addressing a gap in the existing literature.
- Recognizing the complexity of load forecasting models, this paper proposes an approach to streamline the analytical process. Initially, our method focuses on theoretical analysis for the linear regression model. Subsequently, its findings are extended to Support Vector Regression (SVR) and Artificial Neural Networks (ANNs) models through numerical study.

The remainder of this paper unfolds as follows: Section 2 revisits the concept of differential privacy and the mechanisms of support vector regression (SVR) and ANNs. In Section 3, we derive theoretical bounds to estimate impacts of DP on the linear regression model. Subsequently, Section 4 validates theoretical bounds in Section 3 and demonstrates their applicability to SVR and ANNs. Finally, Section 5 delivers the concluding remark.

2 Preliminaries

This section offers an introductory overview of fundamental concepts in DP and machine learning models. Initially, we introduce the notion of (ϵ, δ)-DP and the Gaussian noise injection mechanism. Subsequently, within the domain of machine learning, we briefly outline SVR and ANNs models, and elucidate their alignment with our paper.

2.1 Differential Privacy (DP)

The concept (ϵ, δ)-DP provides a rigorous foundation for assessing and comparing privacy-preserving mechanisms. A privacy-preserving mechanism following (ϵ, δ)-DP satisfies the following definition:

Definition 1 (**(ϵ, δ)-DP in [15]**) *A randomized mechanism $\mathcal{M} : \mathcal{D} \to \mathcal{R}$ with domain $\mathcal{D}$ and range $\mathcal{R}$ satisfies (ϵ, δ)-DP if for every pair of neighboring datasets $D, D' \in \mathcal{D}$ and for every point $R \subset \mathcal{R}$:*

$$\mathbb{P}(\mathcal{M}(D) \in R) \leq \mathbb{P}(\mathcal{M}(D') \in R) \exp(\epsilon) + \delta. \quad (1)$$

Here, the datasets D and D' are considered neighboring if the minimal number of sample changes required to make D identical to D' is one.

Remark 1 *Within the framework of (ϵ, δ)-DP mechanisms, as the magnitude of ϵ increases, the level of protection afforded to the data tends to diminish.*

To satisfy the condition of (ϵ, δ)-DP, this paper employs the Gaussian mechanism for the addition of noises. In the lemma below, we illustrate how Gaussian noise is randomly generated to fit the requirement of DP.

Lemma 1 (Gaussian Mechanism in [15]) *Assume $\mathcal{M}$ to be a mapping: $\mathcal{D} \to \mathbb{R}^n$ with domain $\mathcal{D}$. The Gaussian mechanism $\mathcal{M}(\mathcal{D}) + \zeta$ achieves (ϵ, δ)-DP, if ζ is drawn from an n-dimensional Gaussian distribution. The mean of the distribution is zero and the variance is equal to $2\ln(1.25/\delta) \cdot (\Delta/\epsilon)^2$. Here, Δ is the worst-case sensitivity defined for neighboring datasets D and D', i.e., $\Delta = \max_{D,D'} ||\mathcal{M}(D) - \mathcal{M}(D')||_2$.*

2.2 SVR and ANNs

While DP is crucial for privacy concerns, it prioritizes the protection of individual privacy at the expense of potential accuracy degradation in predictions. This poses a significant challenge in the context of load forecasting, where precise predictions are important. To mitigate the impact of DP noises, we introduce two complex load forecasting models, SVR and ANNs.

SVR is a robust machine learning algorithm that extends support vector machines (SVM) principles to regression problems. SVR accomplishes this by mapping input data into a higher-dimensional space and identifying a hyperplane that captures the relationship between input variables and target values. While SVR emphasizes hyperplane identification, ANNs excel at extracting intricate nonlinear patterns from historical load data. Inspired by the structure of human brains, ANNs are constructed with layers of interconnected nodes. This architecture equips ANNs with the inherent adaptability to intricate load profiles even in dynamic environments. Thereby, ANNs are positioned as valuable tools for load forecasting applications.

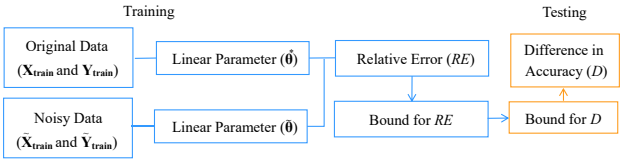

Fig. 1: Illustration of Our Proposed Methodology

3 Methodology

As mentioned above, our paper adopts an incremental model selection, processing from the fundamental linear regression model to more intricate algorithms, SVR and ANNs. Following this strategy, this section focuses on the linear regression model, intending to quantify the impacts of DP-induced noises on its prediction accuracy. The quantitative methodology will adhere to the logical framework delineated in Fig. 1.

As an introduction, the linear regression model is a fundamental tool in predictive analysis, capable of returning optimal linear parameters when provided with training data and corresponding labels. Denote training data as $\mathbf{X_{train}} \in \mathbb{R}^{n\times(m+1)}$ and corresponding training label as $\mathbf{Y_{train}} \in \mathbb{R}^n$, where n and m denote the number of rows and columns selected from the dataset, respectively. Utilizing the training data $\mathbf{X_{train}}$ and $\mathbf{Y_{train}}$, we calculate the optimal linear parameter through linear regression, denoted as $\boldsymbol{\theta}^*$. Specifically, $\boldsymbol{\theta}^*$ is obtained by the minimum square error principle and is expressed as $\boldsymbol{\theta}^* = \arg\min_{\boldsymbol{\theta}} \|\mathbf{Y_{train}} - \mathbf{X_{train}}\boldsymbol{\theta}\|_2$. In the testing period, the linear model generates predictions $\hat{\mathbf{Y}}$ as estimations for $\mathbf{Y_{test}}$, where

$$\hat{\mathbf{Y}} = \mathbf{X_{test}} \cdot \boldsymbol{\theta}^*. \quad (2)$$

3.1 The Impacts of Noises on Model Parameters

As the above illustration of linear regression is formulated without considering the existence of noise, now we discuss the case with noise disturbance. Adopting the Gaussian mechanism, we augment each element in $\mathbf{X_{train}}$ and $\mathbf{Y_{train}}$ with Gaussian noise. Mathematically, the noisy data, denoted as $\tilde{\mathbf{X}}_{\mathbf{train}}$ and $\tilde{\mathbf{Y}}_{\mathbf{train}}$, is obtained as follows:

$$\tilde{\mathbf{X}}_{\mathbf{train}} = \mathbf{X_{train}} + \mathbf{E_X}, \quad (3)$$

$$\tilde{\mathbf{Y}}_{\mathbf{train}} = \mathbf{Y_{train}} + \mathbf{E_Y}, \quad (4)$$

where $\mathbf{E_X}$ and $\mathbf{E_Y}$ are Gaussian random variables. With noise incorporated into the training data, the parameters of the linear model change accordingly. This variation is analyzed by customizing a theorem outlined in [16]. Still, $\boldsymbol{\theta}^*$ denotes the linear parameter trained on original data $\mathbf{X_{train}}$ and $\mathbf{Y_{train}}$, while $\tilde{\boldsymbol{\theta}}$ is trained on noisy data $\tilde{\mathbf{X}}_{\mathbf{train}}$ and $\tilde{\mathbf{Y}}_{\mathbf{train}}$. We can derive the upper bound for the relative error of $\boldsymbol{\theta}^*$ and $\tilde{\boldsymbol{\theta}}$ by the following theorem.

Theorem 1 *Assume that $\mathbf{X_{train}}$ has rank $m+1$ and $\|\mathbf{E_X}\|_2 < \sigma$, where σ represents the $(m+1)$-th largest singular value of $\mathbf{X_{train}}$. Denote RE as the relative error of*

$\boldsymbol{\theta}^*$ and $\tilde{\boldsymbol{\theta}}$, then we have the upper bound for RE as follows:

$$RE = \frac{\|\tilde{\boldsymbol{\theta}} - \boldsymbol{\theta}^*\|_2}{\|\boldsymbol{\theta}^*\|_2} \leq M \cdot \kappa_2 \left(1 + \frac{\|\mathbf{Y_{train}}\|_2 + \kappa_2 \|\mathbf{r_{LS}}\|_2}{\|\mathbf{X_{train}}\|_2 \|\boldsymbol{\theta}^*\|_2}\right), \quad (5)$$

where parameters including $\mathbf{r_{LS}}$, κ_2 and M are defined as below:

$$\mathbf{r_{LS}} = \mathbf{X_{train}}\boldsymbol{\theta}^* - \mathbf{Y_{train}}, \quad (6)$$

$$\kappa_2 = \|\mathbf{X_{train}}\|_2 \|(\mathbf{X_{train}^T}\mathbf{X_{train}})^{-1}\mathbf{X_{train}^T}\|_2, \quad (7)$$

$$M = \max\left(\frac{\|\mathbf{E_X}\|_2}{\|\mathbf{X_{train}}\|_2}, \frac{\|\mathbf{E_Y}\|_2}{\|\mathbf{Y_{train}}\|_2}\right). \quad (8)$$

As demonstrated by this theorem, the upper bound for RE is contingent on M once $\mathbf{X_{train}}$ and $\mathbf{Y_{train}}$ are specified. Additionally, the definition of M implies that it is influenced by Gaussian noises $\mathbf{E_X}$ and $\mathbf{E_Y}$, which introduces a dependency of RE on randomness. To mitigate this dependency, an estimation method is proposed. Initially, we adjust the privacy levels by manipulating the parameter ϵ in DP mechanisms, and the resulting values of M are systematically recorded. Subsequently, a fitting function is established to model the relationship between M and ϵ. Utilizing the theorem, this function can then facilitate an estimation of RE that is independent of randomness.

3.2 The Impacts of Noises on Prediction Errors

The findings elucidated in Section 3.1 highlight the variation of linear parameters, which leads to fluctuations in linear models. We denote the linear model with parameter $\boldsymbol{\theta}^*$ as $Model1$, and the model with parameter $\tilde{\boldsymbol{\theta}}$ as $Model2$. It is anticipated that the difference between $\boldsymbol{\theta}^*$ and $\tilde{\boldsymbol{\theta}}$ will manifest disparities in the respective prediction ability of the two models. In this section, we seek to quantify the difference in prediction errors of $Model1$ and $Model2$, aiming to assess the impact of parameter variation on linear models' prediction ability.

Let $Error1$ and $Error2$ represent the relative prediction errors of $Model1$ and $Model2$, defined as follows:

$$Error1 = \frac{\|\hat{\mathbf{Y}} - \mathbf{Y_{test}}\|_2}{\|\mathbf{Y_{test}}\|_2}, \quad (9)$$

$$Error2 = \frac{\|\tilde{\mathbf{Y}} - \mathbf{Y_{test}}\|_2}{\|\mathbf{Y_{test}}\|_2}, \quad (10)$$

where $\hat{\mathbf{Y}}$ and $\tilde{\mathbf{Y}}$ are the predictions made by $Model1$ and $Model2$, respectively. Denoting D as the difference between $Error2$ and $Error1$, we have

$$D = |Error2 - Error1| = \left|\frac{\|\hat{\mathbf{Y}} - \mathbf{Y_{test}}\|_2}{\|\mathbf{Y_{test}}\|_2} - \frac{\|\tilde{\mathbf{Y}} - \mathbf{Y_{test}}\|_2}{\|\mathbf{Y_{test}}\|_2}\right| = \frac{\left|\|\hat{\mathbf{Y}} - \mathbf{Y_{test}}\|_2 - \|\tilde{\mathbf{Y}} - \mathbf{Y_{test}}\|_2\right|}{\|\mathbf{Y_{test}}\|_2}. \quad (11)$$

Then, fundamental inequalities of matrix norms yield that

$$\begin{aligned} D &\leq \frac{\|\tilde{\mathbf{Y}} - \hat{\mathbf{Y}}\|_2}{\|\mathbf{Y_{test}}\|_2} = \frac{\|\mathbf{X_{test}}\tilde{\boldsymbol{\theta}} - \mathbf{X_{test}}\boldsymbol{\theta}^*\|_2}{\|\mathbf{Y_{test}}\|_2} \\ &\leq \frac{\|\mathbf{X_{test}}\|_2 \|\tilde{\boldsymbol{\theta}} - \boldsymbol{\theta}^*\|_2}{\|\mathbf{Y_{test}}\|_2} \\ &= \frac{\|\tilde{\boldsymbol{\theta}} - \boldsymbol{\theta}^*\|_2}{\|\boldsymbol{\theta}^*\|_2} \cdot \frac{\|\mathbf{X_{test}}\|_2 \|\boldsymbol{\theta}^*\|_2}{\|\mathbf{Y_{test}}\|_2} \\ &= RE \cdot \frac{\|\mathbf{X_{test}}\|_2 \|\boldsymbol{\theta}^*\|_2}{\|\mathbf{Y_{test}}\|_2}. \end{aligned} \quad (12)$$

In the bound expression, $\mathbf{X_{test}}$ and $\mathbf{Y_{test}}$ are given testing data, and $\boldsymbol{\theta}^*$ depends on the training data $\mathbf{X_{train}}$ and $\mathbf{Y_{train}}$. The randomness introduced by random noise is encapsulated within the term RE. Adopting the method outlined in Section 3.1, we can further establish an upper bound for D, which is independent of the inherent randomness. Following that, this randomness-free bound serves as a robust quantitative measure of DP's impacts on the prediction accuracy of linear regression.

4 Numerical Study

This section encompasses two parts of numerical studies. Firstly, we elucidate the simulation process of the bound for RE in linear regression and verify its accuracy through comparison with empirical RE values. Subsequently, the simulated bound for RE yields the upper bound for D, which is experimentally verified as applicable for SVR and ANNs.

4.1 Data Description

In the experiment, we employ the dataset Load History as mentioned in [17]. The dataset contains hourly load data for 20 zones, spanning from the 1st hour of January 1, 2004, to the 6th hour of June 30, 2008. Since the dataset contains missing values, we have to remove the rows with these gaps. Afterward, we apply the dataset in the model of linear regression directly. For SVR and ANNs, the dataset needs additional standardization to prevent training divergence.

4.2 Analysis for Linear Regression

Conditions Verification The bound simulation in this study is based on Theorem 1. Therefore, it is imperative to commence with a thorough verification of the conditions requisite for this theorem. The first condition necessitates that the rank of matrix $\mathbf{X_{train}}$ equals its column number. To ensure compliance with this condition, we fix its row number at 1500, while allowing its column number to range from 2 to 16.

Concerning the second condition, denoted as $\|\boldsymbol{E_X}\|_2 < \sigma$, we generate 1000 random independent samples of $\boldsymbol{E_X}$ for each ϵ. Subsequently, we compare the mean values of $\|\boldsymbol{E_X}\|_2$ with σ, as illustrated in Fig. 2. The graph indicates that $\|\boldsymbol{E_X}\|_2 > \sigma$ when ϵ is excessively small. Consequently, to fulfill the second condition, ϵ is constrained to the range $(0.1, 1)$.

Parameter Estimation With verified conditions, the simulation process commences by estimating the parameter M in relation to ϵ, as explicated in Section 3.1. Again, a set of 1000 samples is generated to determine the mean value of M for each ϵ, as illustrated in Fig. 3. The graph reveals a clear

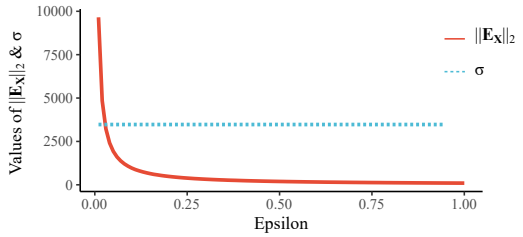

Fig. 2: Values of $\|\boldsymbol{E_X}\|_2$ and σ for Different ϵ

linear correlation between $1/M$ and ϵ. Note that smaller values of ϵ correspond to higher levels of DP. This indicates an augmented magnitude of introduced noise, the value of M would exhibit a corresponding increase. Such analysis aligns with the observed linear relationship between $1/M$ and ϵ. Consequently, M can be effectively estimated using the following expression:

$$M \approx \frac{1}{L(\epsilon)}, \tag{13}$$

where L is the linear function obtained through training.

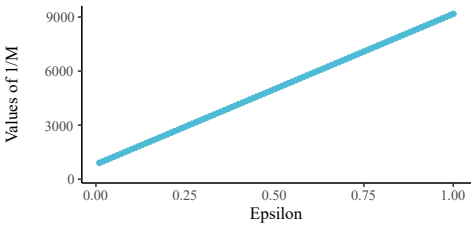

Fig. 3: Relationship Between $1/M$ and ϵ

Bound Derivation Following the estimation of M based on ϵ, we can construct a bound for RE with less sensitivity to random noise than the bound presented in Eq. 5. By substituting Eq. 13 into Eq. 5, the randomness-free bound for RE is approximated as follows:

$$RE \leq \frac{1}{L(\epsilon)} \cdot \kappa_2 \left(1 + \frac{\|\mathbf{Y_{train}}\|_2 + \kappa_2 \|\mathbf{r_{LS}}\|_2}{\|\mathbf{X_{train}}\|_2 \|\boldsymbol{\theta}^*\|_2}\right). \tag{14}$$

We denote B_1 as the upper bound for RE in Eq. 14. By examining all items in B_1, we can suggest that this bound is independent of random noise. Subsequently, we assess the validity of the bound B_1 by comparing it with empirical values of RE, as shown in Fig. 4 (Here, for each given ϵ, the empirical values of RE are taken as the mean of 1000 samples). The results demonstrate that even across varying levels of ϵ, our simulated bound aligns closely with the empirical observations of RE. Hence, for various practical demands of privacy protection, B_1 can perform as the bound of RE effectively.

Shifting to the analysis of D, which represents the disparity in prediction errors induced by noises, we substitute Eq. 14 into Eq. 12 to derive the upper bound for D in the linear regression model. The expression is formulated as follows:

$$D \leq B_2 = \frac{\kappa_2 \|\mathbf{X_{test}}\|_2 \|\boldsymbol{\theta}^*\|_2}{L(\epsilon)\,\|\mathbf{Y_{test}}\|_2} \cdot B_1. \tag{15}$$

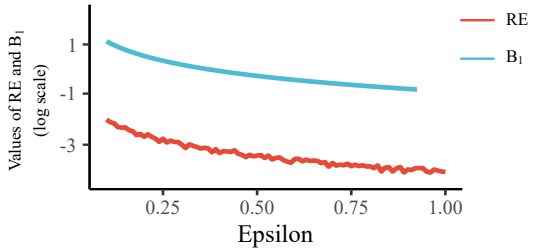

Fig. 4: Relationship Between RE and B_1

Here B_2 represents the final version of the upper bound for D in linear regression. Notably, all parameters are determined by the training data, testing data, and the specified ϵ, rending B_2 independent of the randomness in noises. This characteristic enhances the reliability of this upper bound.

4.3 Simulation Results for SVR and ANNs

In this section, we extend our investigation to the applicability of B_2 in constraining the variable D for more advanced models, namely SVR and ANNs. Fig. 5 presents the values of D in linear regression, SVR, and ANNs, plotted against the upper bound B_2. By observation, B_2 consistently bounds D across SVR and ANNs, even for varying ϵ. Furthermore, the stable gaps between curves representing B_2 and D suggest that our theoretical bound remains consistently accurate for different ϵ. Mathematically, for any given ϵ, the logarithmic value of D is approximated to the logarithmic value of B_2 plus a constant value, indicating their original values are proportionate with a constant ratio C: $D \approx C \cdot B_2$.

In summary, if adopting the Gaussian mechanism, B_2 can serve as a reliable upper bound for D in linear regression, SVR, and ANNs. This establishes B_2 as a dependable estimate for evaluating the impacts of DP on forecasting accuracy, as it limits the disparity in prediction errors resulting from the noise introduced by DP.

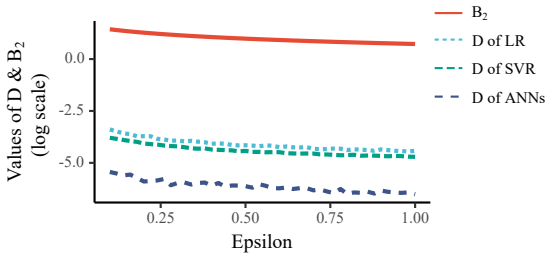

Fig. 5: Relationship Between D and B_2 in SVR and ANNs

5 Conclusion

This paper addresses the issue of how differential privacy mechanisms affect the accuracy of load forecasting. When introducing DP noises into the training data, the resulting model may exhibit higher prediction errors than before. Thus, the difference in prediction errors can serve as an indicator of DP's impact. Commencing with the analysis of linear regression, we determine an upper bound for this difference in prediction errors. Through numerical studies, this paper demonstrates that this bound is also effective in

the context of SVR and ANNs. In this manner, we establish an upper bound to estimate the impact of DP mechanisms on complex load forecasting models.

6 Acknowledgements

I would like to acknowledge the valuable contributions of Chenye Wu and Wenqian Jiang, who provided technical assistance, shared resources, and offered valuable insights that enhanced the quality of this work.

7 Appendix

This section provides a mathematical proof for Theorem 1 (Details are proposed in [16]). Firstly, we mention two lemmas that support our proof. Here, Lemma 2 helps us demonstrate the condition of matrix ranks. Lemma 3 serves as a substitute in our deduction.

Lemma 2 *The matrix 2-norm is invariant with respect to orthogonal transformations. It is easy to show that for all orthogonal* $\mathbf{Q}$ *and* $\mathbf{Z}$ *of appropriate dimensions we have*

$$\|\mathbf{Q}\mathbf{X}_{\mathbf{train}}\mathbf{Z}\|_2 = \|\mathbf{X}_{\mathbf{train}}\|_2. \tag{16}$$

Lemma 3 *The second power of condition number* κ_2 *has an established result:*

$$\kappa_2^2 = \|\mathbf{X}_{\mathbf{train}}\|_2^2 \|(\mathbf{X}_{\mathbf{train}}{}^T\mathbf{X}_{\mathbf{train}})^{-1}\|_2. \tag{17}$$

Proof 1 *Let* E *and* f *be defined as* $\boldsymbol{E} = \boldsymbol{E_X}/M, \boldsymbol{f} = \boldsymbol{E_Y}/M$. *By hypothesis* $\|\boldsymbol{E_X}\|_2 \leq \sigma$, $rank\,(\mathbf{X}_{\mathbf{train}}) = m+1$ *and so by Lemma 3, we have* $rank\,(\mathbf{X}_{\mathbf{train}} + t\boldsymbol{E}) = m+1$ *for all* $t \in [0, M]$. *Let* $\mathbf{X_t}$ *denotes* $\mathbf{X}_{\mathbf{train}} + t\boldsymbol{E}$, *thereafter, the solution* $\boldsymbol{\theta}(t)$ *to the following equation is continuously differentiable:*

$$\mathbf{X_t}^T\mathbf{X_t}\boldsymbol{\theta}(t) = \mathbf{X_t}^T\left(\mathbf{Y}_{\mathbf{train}} + t\boldsymbol{f}\right). \tag{18}$$

To be precise, $\boldsymbol{\theta}(t)$ *is a function of variable* t. *Since* $\boldsymbol{\theta^*} = \boldsymbol{\theta}(0)$ *and* $\tilde{\boldsymbol{\theta}} = \boldsymbol{\theta}(M)$, *we have*

$$\tilde{\boldsymbol{\theta}} - \boldsymbol{\theta^*} = M\dot{\boldsymbol{\theta}}(0) + \mathcal{O}(M^2), \tag{19}$$

where $\dot{\boldsymbol{\theta}}(t)$ *is the derivative of* $\boldsymbol{\theta}(t)$. *In Eq. 19, by dividing* $\boldsymbol{\theta^*}$ *on both sides and taking norms, we obtain the expression of* RE*:*

$$RE = \frac{\|\boldsymbol{\theta^*} - \tilde{\boldsymbol{\theta}}\|_2}{\|\boldsymbol{\theta^*}\|_2} = M\frac{\|\dot{\boldsymbol{\theta}}(0)\|_2}{\|\boldsymbol{\theta^*}\|_2} + \mathcal{O}(M^2). \tag{20}$$

In order to bound $\|\dot{\boldsymbol{\theta}}(0)\|_2$, *we differentiate Eq. 18 on both sides and set* $t = 0$ *in the result, which gives*

$$\begin{aligned}\dot{\boldsymbol{\theta}}(\mathbf{0}) = &(\mathbf{X}_{\mathbf{train}}{}^T\mathbf{X}_{\mathbf{train}})^{-1}\mathbf{X}_{\mathbf{train}}{}^T\left(\boldsymbol{f} - \boldsymbol{E}\boldsymbol{\theta^*}\right)\\ &+ (\mathbf{X}_{\mathbf{train}}{}^T\mathbf{X}_{\mathbf{train}})^{-1}\boldsymbol{E}^T\left(\mathbf{Y}_{\mathbf{train}} - \mathbf{X}_{\mathbf{train}}\boldsymbol{\theta^*}\right).\end{aligned} \tag{21}$$

By substituting Eq.21 and Lemma 3 into Eq. 20, taking norms, we obtain the bound for RE *as follows:*

$$RE \leq M \cdot \kappa_2\left(1 + \frac{\|\mathbf{Y}_{\mathbf{train}}\|_2 + \kappa_2\|\mathbf{r}_{\mathbf{LS}}\|_2}{\|\mathbf{X}_{\mathbf{train}}\|_2\|\boldsymbol{\theta^*}\|_2}\right). \tag{22}$$

To be accurate, the term $\mathcal{O}(M^2)$ in the bound's expression is eliminated due to its negligible scale.

References

[1] C. Dwork, F. McSherry, K. Nissim, and A. D. Smith, "Calibrating noise to sensitivity in private data analysis," *Journal of Privacy and Confidentiality*, vol. 7, no. 3, pp. 17–51, 2016.

[2] A. Raja Shekharan, "Effect of noisy data on pavement performance prediction by artificial neural networks," *Transportation Research Record*, vol. 1643, no. 1, pp. 7–13, 1998.

[3] F. Fioretto, T. W. Mak, and P. Van Hentenryck, "Differential privacy for power grid obfuscation," *IEEE Transactions on Smart Grid*, vol. 11, no. 2, pp. 1356–1366, 2019.

[4] H. Wang, J. Zhang, C. Lu, and C. Wu, "Privacy preserving in non-intrusive load monitoring: A differential privacy perspective," *IEEE Transactions on Smart Grid*, vol. 12, no. 3, pp. 2529–2543, 2020.

[5] H. Wang and C. Wu, "Privacy preservation for time series data in the electricity sector," *IEEE Transactions on Smart Grid*, vol. 14, no. 4, pp. 3136–3149, 2023.

[6] J. Huang, Q. Huang, G. Mou, and C. Wu, "DPWGAN: high-quality load profiles synthesis with differential privacy guarantees," *IEEE Transactions on Smart Grid*, vol. 14, no. 4, pp. 3283–3295, 2023.

[7] C. Lu, J. Wu, and C. Wu, "Privacy-preserving decentralized price coordination for ev charging stations," *Electric Power Systems Research*, vol. 212, p. 108355, 2022.

[8] C. Lu, J. Cui, H. Wang, H. Yi, and C. Wu, "Privacy preserving user energy consumption profiling: From theory to application," *IEEE Transactions on Smart Grid*, pp. 1–1, 2023.

[9] W. Jiang and C. Wu, "Optimal electricity procurement enabled by privacy-preserving samples," *IEEE Transactions on Energy Markets, Policy and Regulation*, 2024.

[10] J. Soria-Comas, J. Domingo-Ferrer, D. Sánchez, and D. Megías, "Individual differential privacy: A utility-preserving formulation of differential privacy guarantees," *IEEE Transactions on Information Forensics and Security*, vol. 12, no. 6, pp. 1418–1429, 2017.

[11] Z. Zhang, W. Cao, Z. Qin, L. Zhu, Z. Yu, and K. Ren, "When privacy meets economics: Enabling differentially-private battery-supported meter reporting in smart grid," in *2017 IEEE/ACM 25th International Symposium on Quality of Service (IWQoS)*, pp. 1–9, IEEE, 2017.

[12] H. Wang and C. Wu, "Privacy preservation for time series data in the electricity sector," *IEEE Transactions on Smart Grid*, vol. 14, no. 4, pp. 3136–3149, 2023.

[13] P. Valtonen, S. Honkapuro, and J. Partanen, "Improving short-term load forecast accuracy by utilizing smart metering," in *Proceedings of the CIRED Workshop*, 2010.

[14] Z. Wu, X. Zhao, Y. Ma, and X. Zhao, "A hybrid model based on modified multi-objective cuckoo search algorithm for short-term load forecasting," *Applied Energy*, vol. 237, pp. 896–909, 2019.

[15] C. Dwork, A. Roth, *et al.*, "The algorithmic foundations of differential privacy," *Foundations and Trends® in Theoretical Computer Science*, vol. 9, no. 3–4, pp. 211–407, 2014.

[16] G. H. Golub and C. F. Van Loan, *Matrix computations*. JHU press, 2013.

[17] T. Hong, P. Pinson, and S. Fan, "Global energy forecasting competition 2012," 2014.

Proceedings of the 3rd Conference on Fully Actuated System Theory and Applications
May 10-12, 2024, Shenzhen, China

A Parameter correction method of motor system based on particle swarm and convolutional neural network

Depeng Zeng[1*], Junjie Hong[1], Liangheng Han[1], Kun Zhang[1], Yueru Ren[1] and ZunHeng Wang[1]

1. College of Intelligent Systems Science and Engineering, Harbin Engineering University, Harbin 15001, China
E-mail:{zengdepeng,}@hrbeu.edu.cn

Abstract: In order to generate accurate predictions in the vibration characteristics analysis of the motor structure, a motor system parameter correction method based on particle swarm optimization is proposed in this paper. Initially, focusing on the motor itself and utilizing modal analysis theory, finite element analysis software is employed for modal simulation analysis of the motor model. Subsequently, parameters such as shell stiffness, shell density, and spring stiffness between end caps and the shell are adjusted to better match the actual motor model. The particle swarm optimization algorithm is then used to optimize the structural parameters of the motor, obtaining a non-inferior optimal solution between the vibration performance and operational performance of the driving motor. At the same time, in order to reduce the manual workload, the image recognition model is established according to convolutional neural network to find out the target output image. Finally, the proposed method is subjected to simulation analysis. The results indicate that this strategy can to some extent achieve identification and optimization of motor system parameters. Additionally, the algorithm can reduce the complexity of modal calculations for motor systems and the image recognition model can find the target pattern accurately, demonstrating practical value.

Key Words: particle swarm optimization, convolutional neural network, modal analysis

1 Introduction

With the growing concern over noise pollution and increasing demand for noise reduction in ship electric propulsion, the vibration and noise of motor systems have become crucial indicators for measuring overall performance. Accurately calculating parameters such as modal shape and natural frequency is essential to reducing motor noise and vibration. Therefore, analyzing the structural modal of motors has become a research hotspot. In [1], the substructural modal synthesis method was used to carry out computational modal analysis of permanent magnet synchronous motor and optimize its structure. In [2], it analyzed the motor modes based on the thin-shell theory, and verified the correctness of the calculated results by finite element method. In [3], it analyzed the equivalent model of the stator core and winding of permanent magnet motor, summarized the effect of the material parameters of the equivalent model on the natural frequency of the stator core, and proposed a method to quickly determine the material parameters of the equivalent model. In [4], it uses the finite element analysis method to analyze the influence of different types of windings on the modal parameters of the built-in permanent magnet synchronous motor. In [5], it has done a detailed study on the modal of switched reluctance motor. In [6], it studies the natural frequency variation of the stator system of induction motor, and uses two-dimensional finite element and experimental modal analysis to test the six states of the stator from the steel ring to the finished product, and obtains the sources of all levels of natural frequency.

It is necessary to build a finite element model of the motor system to analyze the modal shape and natural frequency of the system, and extract the modal shape and natural frequency by solving the eigenvalue problem. The results of finite element modal analysis depend on the accuracy of the established finite element model and material parameters as well as the correctness of the input boundary conditions. Due to the difference between the finite element model and the actual motor structure, the calculation results will be biased. In the actual analysis, material parameters are often modified to achieve the purpose of calibrating the model. In [7], it compared four finite element models of stator core and winding system of permanent magnet motor, and obtained a new finite element equivalent model of stator system. In [8], finite element modal analysis was carried out on a three-phase induction motor, reliable parameters were obtained, and the theoretical model was verified by hammer experiment. In [9], it uses three-dimensional finite element modal analysis method to analyze the modal problems of switched reluctance motor under different conditions.

In the process of finite element analysis and calculation, the traditional modal analysis method often needs to rely on manual calculation and screening. However, in the case of many parameter dimensions, many model grids, and long simulation time, manual parameter adjustment and screening may be somewhat inefficient. For the whole process, manual calculation and screening is actually to find a set of optimal parameters, which is a kind of optimization problem. Therefore, for such big data search, we can use a variety of optimization algorithms to help us better solve. However, in the modal analysis and parameter correction of the motor system, optimization algorithm is rarely used, and when the motor is carried out finite element analysis, the output modal result image needs to rely on human eyes for screening, which brings a lot of inconvenience to the use of optimization algorithm.

Optimization algorithms can be divided into two main categories: exact algorithms and heuristic algorithms. Particle Swarm Optimization (PSO), as a heuristic algorithm, is simple, versatile, computationally efficient, and exhibits strong global search capabilities, enabling it to find global optimal solutions. In [10], a particle swarm optimization algorithm that can intelligently control the number of particles was proposed, and the method was applied to the optimization design of built-in permanent magnet

* This work was supported by the National Natural Science Foundation ofChina under Project 52107040.(Corresponding author: Depeng Zeng.)

synchronous motor with the goal of minimizing the total harmonic distortion of the back electromotive force, and the effectiveness of the algorithm in the optimization design of the motor was verified through experiments. In [11], a sliding mode controller of self-triggered permanent magnet synchronous motor speed regulation system based on super-torsion algorithm was studied, and a nonlinear optimization problem considering the tradeoff between species domain and communication burden was proposed. Particle swarm optimization algorithm was applied to solve the above optimization problem.

With the rapid development of deep learning, many scholars have begun to use mature Convolutional Neural Network (CNN) technology to extract features from images and achieve recognition of research targets. In [12], a method for recognizing complex background plant images using CNN was studied, and a CNN algorithm with higher recognition accuracy was proposed, which was proven to be effective through experiments. In [13], a CNN algorithm based on LeNet-5 was studied to enable vehicles to recognize traffic signs in low visibility weather conditions, thereby assisting people's driving behavior.

In this paper, the convolutional neural network is used to identify the results of the modal calculation output image, find out the mode diagram of the corresponding order, and then the particle swarm optimization algorithm is used to optimize and correct the parameters of the motor system model according to the modal data obtained by the hammer method experiment, and the optimal parameter combination is obtained to achieve the effect of the motor system parameter correction.

2 Theory of algorithms

2.1 Particle swarm optimization

Particle swarm optimization (PSO) is a random search algorithm based on group cooperation, which simulates the foraging behavior of birds to solve optimization problems. By randomly generating a group of massless particles and giving each particle two properties of speed and position, the position vector of the i-th particle in the particle swarm is represented by $x_i = (x_{i1}, x_{i2}, \cdots, x_{in})$, the velocity vector is represented by $v_i = (v_{i1}, v_{i2}, \cdots, v_{in})$, where the position information of the particle is regarded as the potential optimal solution, and the quality of each potential solution is judged according to the set objective function as the standard. Thus, the individual extreme value (represented by Pbest) is determined, and the individual extreme value is shared with other particles in the entire particle swarm, and the optimal individual extreme value is found as the global optimal solution, that is, the global extreme value (represented by Gbest).

Through "iteration", particle swarm continuously updates the individual extremum and global extremum until the optimal solution satisfying the objective function is found. According to the basic principle of particle swarm algorithm, the updating speed and position of particles in the search space are determined according to the following formula[14]:

$$v_{im}^{t+1} = \omega v_{im}^{t} + c_1 r_1 (Pb_{im} - x_{im}^{t}) + c_2 r_2 (Gb_{im} - x_{im}^{t}) \quad (1)$$

$$x_{im}^{t+1} = x_{im}^{t} + v_{im}^{t+1} \quad (2)$$

where t, ω represents the current updating algebra of the particle and the inertia factor, which determines the velocity inertia of the particle; where c_1, c_2 is the acceleration constant, generally about 2.05[15], and r_1, r_2 is a random number in the range [0,1].

In the standard PSO algorithm, linear attenuation is introduced to the inertia factor, so that the weight is linearly attenuated from the maximum value to the minimum value in the iterative process. The specific formula is as follows:

$$\omega_d = \omega_{\max} - \frac{d}{K}(\omega_{\max} - \omega_{\min}) \quad (3)$$

where K is the total number of iterations; d is the number of current iterations, and the value of $\omega_{\max}$, $\omega_{\min}$ is 0.9 and 0.4, which can enhance the global search ability of the algorithm in the initial iteration, traverse the overall space in a larger scope, and avoid falling into the local optimal solution. In the later stage, the local search ability is enhanced to find the exact solution in a smaller range.

2.2 Simulated annealing algorithm

The Simulated Annealing algorithm (SA) is a probability-based global optimization algorithm inspired by the metal annealing process. The algorithm mainly introduces the concept of randomness. When the particle calculation solution is updated constantly, the inferior solution will be accepted under certain probability, thus increasing the probability of obtaining the global optimal solution. So the algorithm is widely used in the fields of combinatorial optimization, function optimization and combinatorial problems.

The probability formula of the simulated annealing algorithm receiving the dominant solution under the Metropolis criterion is:

$$P = \begin{cases} 1, & E_{t+1} < E_t \\ e^{\frac{-(E_{t+1} - E_t)}{T_t}}, & E_{t+1} \geq E_t \end{cases} \quad (4)$$

where t is the number of iterations, E_t expressed as the corresponding objective function value, T_t is the temperature of the t-th iteration.

The calculation formula of temperature attenuation during iteration is:

$$T_t = \begin{cases} T_p, & t = 1 \\ \eta T_{t-1}, & t > 1 \end{cases} \quad (5)$$

where T_p, η is the set initial temperature and the attenuation coefficient of temperature.

2.3 Fusion algorithm strategy

First, the PSO algorithm and SA algorithm independently generate the initial population randomly according to the demand. When the PSO algorithm and the SA algorithm are iterated once at the same time, the solution information recorded by the SA algorithm is compared with the global optimal solution of the PSO algorithm. If the point recorded by the SA algorithm is better than the global optimal solution of the PSO algorithm, it is replaced. If the solution recorded by SA algorithm is not as good as the global optimal solution,

it will be compared with the local optimal solution of the particle nearest to the PSO algorithm. If it is better than the local optimal solution at that point, it will be replaced, otherwise it will be directly entered into the next iteration calculation.

The core of the fusion strategy is to share information between the simulated annealing algorithm and the particle swarm optimization algorithm to promote group cooperation, so as to make full use of the global search of the particle swarm optimization algorithm and the local search of the simulated annealing algorithm.

2.4 Convolutional Neural Networks

In order to accurately identify the mode diagram generated in the calculation process, so as to reduce the manual workload, the convolutional neural network can be used to establish an image recognition model to complete this task.

Convolutional Neural Networks (CNNs) are specifically designed multi-layer perceptions tailored for the recognition of two-dimensional shapes. Each layer comprises multiple two-dimensional planes, with each plane consisting of independent neurons. The network architecture includes an input layer, convolutional layers, pooling layers, and fully connected layers. Convolutional layers perform local perception on the input image by sliding convolutional kernels, extracting features, and generating corresponding feature maps. Subsequently, these feature maps undergo nonlinear activation and pooling operations, extracting the most salient features and reducing data dimensions. The role of the fully connected layer is to globally integrate and classify these processed features.

One of the key advantages of CNNs lies in their utilization of local connectivity and weight sharing. Local connectivity enables the network to capture spatial correlations between pixels, while weight sharing enhances the generalization capability of the entire network, effectively reducing the overall number of parameters. Furthermore, CNNs exhibit a certain degree of translation invariance, allowing them to detect the same features at different positions. This property provides a significant advantage in handling image recognition tasks. The combination of these advantages has led to the widespread application of Convolutional Neural Networks in various domains, including image processing, object detection, and language recognition.

In the field of image classification, the AlexNet network model stands out as a widely employed deep convolutional neural network architecture. This network structure consists of a total of 8 layers, comprising 5 convolutional layers (Conv1Conv5) and 3 fully connected layers(FC6~FC8). Following Conv1, Conv2, and Conv5, ReLU activation functions are employed, accompanied by max-pooling (MaxPooling) and local response normalization (LRN) modules. The fully connected layers, FC6 and FC7, are followed by a randomly sparse module, Dropout. The final fully connected layer, FC8, utilizes a softmax classifier for image classification.

The advantages of the AlexNet network lie in several key aspects. Firstly, the utilization of the Rectified Linear Unit (ReLU) function instead of sigmoid and tanh functions addresses the issue of vanishing gradients, enhancing the network's training stability. Secondly, the incorporation of Dropout and max-pooling layers with overlap contributes to increased accuracy and helps prevent overfitting of the model. Lastly, the introduction of Local Response Normalization (LRN) technology enhances feature contrast and robustness, ultimately improving the network's generalization capability.

3 Simulation Validation

3.1 Modal Analysis Procedure

The main process of modal analysis for electric motor systems includes: modeling of the motor system, mesh generation, definition of material parameters, computational solving, and post-processing.

Typically, PTC/Creo is used to create three-dimensional models of various components of the motor system and assemble them. After completing the model assembly, the next step involves importing it into the finite element preprocessing software HyperMesh for mesh partitioning and defining material parameters. Then, the electric motor model with complete mesh generation and material parameters is imported into Ansys software for modal analysis. By applying boundary conditions and loads, the study investigates the free vibration modes and natural frequencies of the motor model at different frequencies. Modal analysis results are crucial for detecting the dynamic response of the motor structure and optimizing the design.

In this paper, a small permanent magnet synchronous motor is chosen as the subject for modal analysis. Various structures, including end covers, casing, base, stator, and windings, are assigned parameters, and simulation parameter calibration is conducted. The material parameters of the motor components are shown in Table 1, and the finite element model of the motor is shown in Fig. 1.

Table 1: The Material Parameters of the Motor Components

Parameter \ Materials		Stator and rotor silicon steel sheet	Equivalent winding
Density (kg/m³)		7678	9045
Young's modulus (MPa)	x	0.443e11	6.28e10
	y	1.912e11	1.63e9
	z		
Poisson ratio	xy	0.07	0.07
	yz	0.27	0.27
	xz	0.07	0.07
Shear modulus (MPa)	xy	0.175e11	2.415e10
	yz	0.767e11	0.81e9
	xz	0.175e11	2.415e10

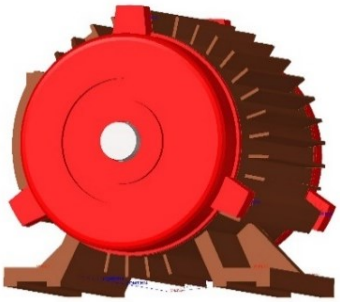

Fig. 1: Finite element model of motor

The second and third-order modal shapes of the motor during the simulation process, along with the experimental

second and third-order modal shapes, are depicted in Fig. 2 and Fig. 3, respectively.

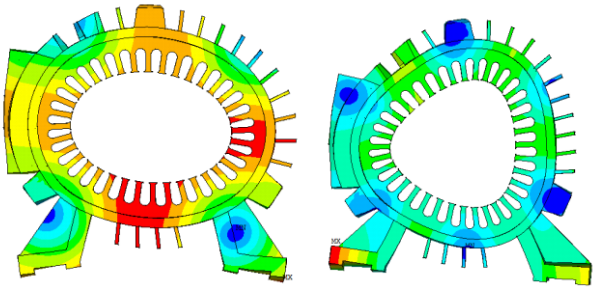

(a) second-order (b) third-order

Fig. 2: Simulation mode pattern diagram

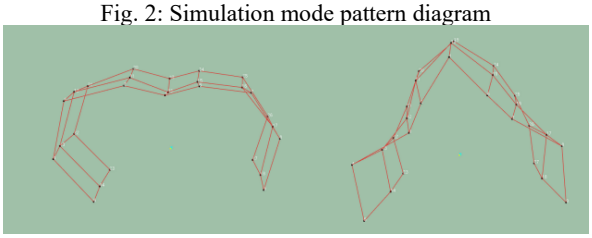

(a) second-order (b) third-order

Fig. 3: Experimental mode pattern diagram

3.2 Batch mode

When dealing with a limited number of models in the computational solving phase, traditional interactive workflows in ANSYS can effectively address specific real-world problems. However, when dealing with a larger number of models, the chained sequence of interactive operations can lead to repetitive tasks in computational solving, load application, result path saving, and other operations, resulting in reduced efficiency. In ANSYS analysis, the Batch mode offers a solution by providing a means to execute a series of analyses automatically, without manual intervention. This involves automating a sequence of analysis operations by writing scripts or command files, thereby enhancing efficiency and proving beneficial for tasks that require numerous similar simulation analyses.

Table 2: Housing material parameters

Materials	Parameters
Density (kg/m³)	7400
Poisson ratio	0.3
Young modulus (MPa)	1.1e11
Shear modulus (MPa)	1e8

Table 2 presents the material parameters for the motor casing, with variations in the Young's modulus and elastic modulus observed to observe changes in modal frequencies while keeping density and Poisson's ratio constant. The Young's modulus and elastic modulus of the motor casing were altered by 0.1 times, 0.5 time, 1.5 times, and 2 times their predefined values. A total of 256 parameter sets were created by simultaneously changing the Young's modulus and elastic modulus. For these 256 sets, models requiring solving by changing individual parameters can be efficiently managed using the Batch mode, automating the process and storing the resulting modal shapes in specified files.

3.3 Image recognition

Assuming that each set of parameters yields a modal shape diagram up to the 65th order, a total of 16,640 images would be generated for the 256 parameter sets. Using Convolutional Neural Networks (CNN) as an image recognition model proves to be an effective solution. By constructing a suitable CNN model and conducting training, we can automate the image selection task.

Given that the dataset used by the AlexNet network is a subset of ImageNet, comprising millions of images, with approximately 60 million self-learned parameters enabling classification of 1000 data points, the scale of the dataset and the number of classes in this study are significantly smaller. Therefore, modifications were made to the AlexNet network model for this paper, reducing the network depth to 6 layers, consisting of 3 convolutional layers and 3 fully connected layers, which is shown in Fig. 4. The modified structure is as follows:

(1) Input Layer: Accepts images with pixel dimensions of 227x227.

(2) Convolutional Layers (Conv1, Conv2, Conv3): Composed of 32, 5x5 filter for Conv1, 64, 5x5 filter for Conv2, and 128, 3x3 filter for Conv3. Each layer has a stride of 1 and is followed by a ReLU activation function.

(3) Pooling Layers (Pool1, Pool2, Pool3): Employs 3x3 maximum overlap pooling with a stride of 2, following the convolutional layers.

(4) Fully Connected Layers (FC1, FC2, FC3): FC1 and FC2 output 120 and 64 one-dimensional features, respectively, and incorporate DropOut to randomly reduce the impact of certain neurons. FC3 uses a softmax classifier for image classification.

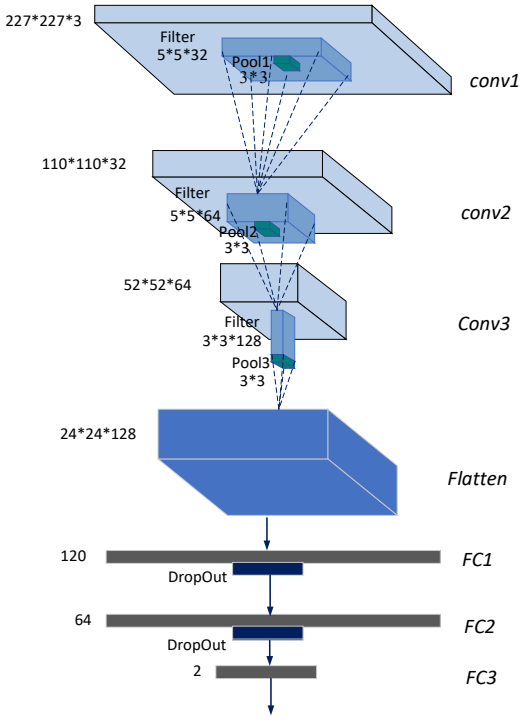

Fig. 4: Convolutional neural network simplified structure diagram

Constructing a convolutional neural network model based on the aforementioned structure, existing data, including 140 images each for the second and third-order modal shapes, was utilized as the training set. The model underwent 15 iterations with a learning rate set to 0.001. The training and validation results are depicted in Fig. 5, showcasing a training set accuracy of 96.83% and a validation set accuracy of 96.78%. These results indicate the effectiveness of the model and its strong generalization capability.

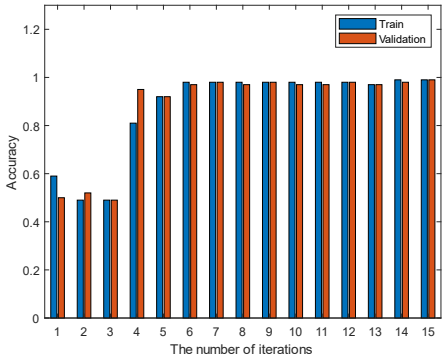

Fig. 5: Model training results

3.4 Improved particle swarm optimization

Through image recognition, we can obtain the desired modal shapes and modal frequencies of various orders from the images output by ANSYS analysis. Subsequently, we can utilize an improved particle swarm optimization algorithm for optimization calculations. The main steps of the improved particle swarm optimization algorithm involve, within the set parameter range of the motor system model, such as end cover spring stiffness and casing stiffness, generating a certain number of parameter points uniformly. During each iteration, the modal frequencies for the second and third orders obtained from the calculations of these parameter points are compared with the experimental values. The absolute errors for corresponding modal frequencies are then calculated. The algorithm decides whether to replace the global and local optimal points of the parameter set based on the sum of absolute errors for each parameter point. The algorithm then generates another set of parameter points for calculation until a set of parameters satisfying the predefined conditions is found or the preset number of iterations is reached.

The software flowchart is illustrated in Fig. 6.

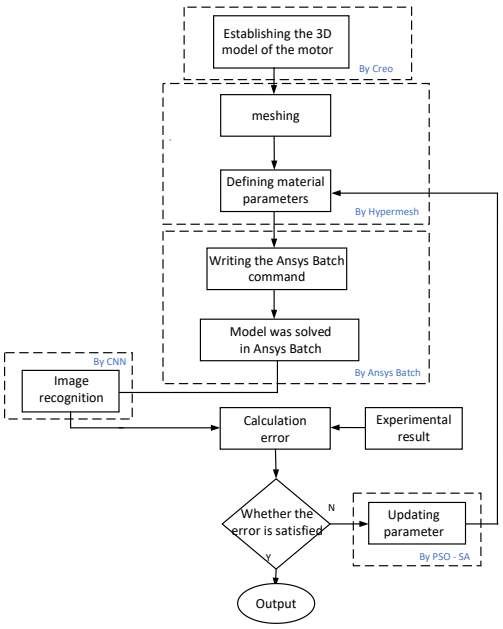

Fig. 6: Overall flow chart

3.5 Analysis of simulation result

To illustrate the convenience and efficiency of the fusion algorithm in modal calculation analysis, a comparative analysis is conducted between manual operation calculations and operations using the PSO algorithm and the fusion algorithm. In the simulation calculations, various initial points were uniformly selected. Specifically, casing stiffness was set to 1.1e11, end cover spring stiffness to 0.1e8, 0.5e8, 1.5e8, 2e8, and end cover spring stiffness to 1e8, casing stiffness to 0.5e11, 1e11, 1.5e11, 2e11, with an additional random point as the initial point (chosen here as end cover spring stiffness 0.7e11 and casing stiffness 1.1e11). To prevent parameter points from exceeding the defined domain or changing too rapidly during computation, truncation was applied to handle boundary issues. This involved setting upper and lower limits to ensure that parameter points are calculated within the specified operating range.

In terms of result processing, we obtained the modal frequencies of the motor under various parameters through simulation calculations, and then compared and analyzed them with the actual modal frequencies obtained from experiments to obtain the corresponding error data, as shown in Table 3. We then evaluate the quality of the parameters obtained from each calculation and determine whether the parameter points derived from the algorithm converge by calculating the error expectation and variance.

Table 3: Calculation frequency of each order optimal parameter point (Hz)

Iteration Count \ Algorithm		PSO	PSO-SA
First iteration	Second-order	1550	1550
	Third-order	3363	3341
Second iteration	Second-order	1505	1550
	Third-order	3248	3341
Third iteration	Second-order	1505	1529
	Third-order	3216	3279
Forth iteration	Second-order	1459	1505
	Third-order	3092	3171
Experiment	Second-order	1538	
	Third-order	2946	

From the simulation results, it is evident that both manual operation calculations and the fusion algorithm, along with the PSO algorithm, can identify motor parameters that meet the requirements. However, manual calculations require continuous data sorting and organization, especially when dealing with high-dimensional parameters and large datasets. In such instances, the efficiency of manual calculations may be surpassed by the computational efficiency of algorithmic calculations.

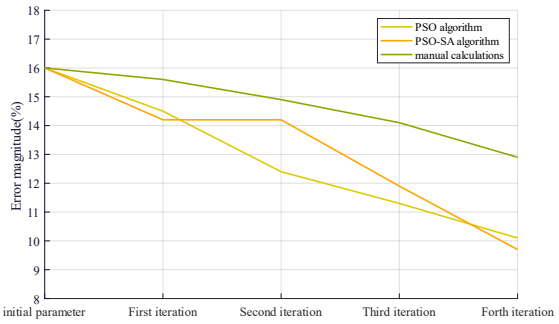

Fig. 7: Comparison of Optimal Parameter Points between PSO Algorithm and Fusion Algorithm

From Fig. 7, it can be observed that with an increase in the number of algorithm iterations, the absolute values of errors for the second and third-order modalities of the motor system continuously decrease until they reach below 10%. In contrast, the optimal computational result from manual operation calculations hovers around 13%. Moreover, the fusion algorithm has a lower probability of falling into local optima compared to the PSO algorithm. This is attributed to the information exchange between the fusion algorithm and the simulated annealing algorithm during particle swarm updates, aiding the fusion algorithm in escaping local optima.

From Fig. 8, it is evident that the optimal parameter solution found by the fusion algorithm at the 4th iteration, compared to the PSO algorithm, results in an overall reduction in expected error of 2.1%, and the fusion algorithm begins to converge towards the global optimum, while the PSO algorithm still exhibits relatively small oscillations. However, the advantages of fusion algorithm over PSO algorithm are not very obvious.

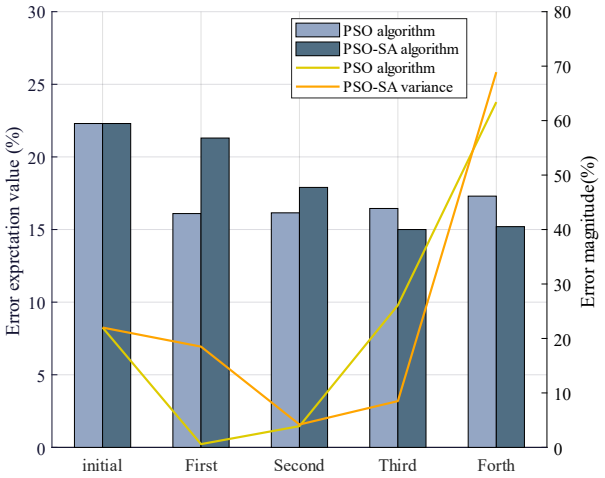

Fig. 8: PSO algorithm and fusion algorithm parameter point data calculation

4 Conclusion

Based on modal analysis theory, a control strategy for calibrating the modal characteristics of an electric motor system is proposed in this paper. The strategy utilizes an improved particle swarm optimization algorithm and a convolutional neural network for parameter calibration. By optimizing the fitness function, the strategy identifies the optimal particle position and completes the identification of parameters such as the motor casing stiffness, casing density, and spring stiffness between the end cover and casing in a single model. Simulation results demonstrate that this control strategy can effectively identify and optimize parameters of the motor system to a certain extent. The algorithm also reduces the manual effort required for modal calculations of the motor system, making it practically valuable.

References

[1] J. Zhao et al, Modal analysis and structure optimization of permanent magnet synchronous motor. IEEE Access, 2020(8): 151856-151865.

[2] L. Shen, J. Wu and S. Yang, Analytical modeling of stator vibration for surface mount permanent magnet brushless motors. International Conference on Electrical Machines and Systems, 2011: 1-5.

[3] H. Yin, F. Ma, X. Zhang, C. Gu, H. Gao and Y. Wang, Research on Equivalent Material Properties and Modal Analysis Method of Stator System of Permanent Magnet Motor With Concentrated Winding. IEEE Access, 2019(7): 64592-64602.

[4] Ishikawa T, Inaba H, Matsunami M, Comparison of vibration characteristics of several interior permanent magnet synchronous motors. IEEE Xplore, 2008:314-319.

[5] Cai Wei, Pragasen Pillay, Tang Zhangjun. Impact of stator windings and end-bells on resonant frequencies and modal shapes of switched reluctance motors. IEEE Transactions on Industry Applications, 2002, 38(4): 1027-1034.

[6] F. Ishibashi, M. Matsushita, S. Noda and K. Tonoki, Change of Mechanical Natural Frequencies of Induction Motor. IEEE Transactions on Industry Applications, 2010, 46(3): 922-927.

[7] H. Yin, X. Zhang, F. Ma, C. Gu, H. Gao and Y. Wang, New Equivalent model and Modal Analysis of Stator Core-Winding System of Permanent Magnet Motor With Concentrated Winding. IEEE Access, 2020(8): 78140-78150.

[8] I. C. Rosca, M. Filip and E. Helerea, Three-phase squirrel-cage induction motor modal analyses. Theoretical and experimental aspects. International Conference on Optimization of Electrical and Electronic Equipment, 2012: 606-611.

[9] Sun Jianbo, Zhan Qionghua, Huang Jin, Modal analysis of stator vibration of switched reluctance motor. Proceedings of the CSEE, 2005, (22):151-155.

[10] J. H. Lee, J. -Y. Song, D. -W. Kim, J. -W. Kim, Y. -J. Kim and S. -Y. Jung, Particle Swarm Optimization Algorithm With Intelligent Particle Number Control for Optimal Design of Electric Machines. IEEE Transactions on Industrial Electronics, 2018,65(2): 1791-1798.

[11] J. Song, W. X. Zheng and Y. Niu, Self-Triggered Sliding Mode Control for Networked PMSM Speed Regulation System. IEEE Transactions on Industrial Electronics, 2022(1): 763-773.

[12] Xiaoyu Song, Liting Jin, Yang Zhao, Yue Sun, Tong Liu. Plant Image Recognition with Complex Background Based on Effective Region Screening[J]. Laser & Optoelectronics Progress, 2020, 57(4): 041016.

[13] Wan-zheng ZHANG, Zhi-kun HU, Xiao-long LI. Convolutional neural image recognition algorithm based on LeNet-5[J]. Chinese Journal of Liquid Crystals and Displays, 2020,35(5):486-490.

[14] Kennedy J, Eberhart R. Particle Swarm Optimization. IEEE International Conference on Neural Network, 1995, 4: 1942-1948.

[15] Kennedy J, Thinking is Social: Experiments with the Adaptive Culture model. Journal of Conflict Resolution, 1998, 42(1): 56-76.

Proceedings of the 3rd Conference on Fully Actuated System Theory and Applications
May 10-12, 2024, Shenzhen, China

Deep Reinforcement Learning-Based Scheduling Optimization of a Wind-solar Coupled CHP Unit System Considering Source-load Uncertainty

Baohua Wang[1,2], Xinglong Gao[1,2], Xianlian Wang[3], Zhixiao Wang[3], Li Sun[3], Shan Hua[1,2*]

1. State Key Laboratory of Low-carbon Smart Coal-fired Power Generation and Ultra-clean Emission, China Energy Science and Technology Research Institute Co.LTD., Nanjing 210023, China

2. National Energy Changzhou Power Generation Co., LTD., Changzhou 213001, China

3. National Engineering Research Center of Power Generation Control and Safety, School of Energy and Environment, Southeast University, Nanjing 210096, China
Corresponding author: 12056897@chnenergy.com.cn

Abstract: Promoting the electric-thermal decoupling in combined heat and power (CHP) units is an effective way to enhance their peak-regulation capability and facilitate the integration of renewable energy. In order to address the problems of flexibility and source-load uncertainty in the operation of the CHP unit, this paper studies the deep reinforcement learning (DRL)-based efficient scheduling problem of a wind-solar coupled CHP unit system. The problem is optimized under the objective of comprehensive income for energy supply and the constraints of safe operation and supply-demand balance. Based on system operation characteristics in uncertain environments, a Markov decision process (MDP) model is designed so as to transform the scheduling optimization into a sequential decision problem. To achieve efficient and intelligent scheduling of the CHP unit, the co-optimization of electricity and heat decisions is achieved by a continuous DRL algorithm, twin delayed deep deterministic policy gradient (TD3). Simulation results under a typical day scenario in the heating season show that TD3 algorithm can promote the consumption of renewable energy and ensure the sustainable scheduling capability of the thermal storage device while satisfying power balances. Furthermore, based on the well-trained neural network, the system exhibits near-theoretically optimal results with rapid single-step scheduling duration, effectively enhancing the system's adaptability to uncertainty.

Key Words: CHP unit, deep reinforcement learning, renewable energy, scheduling optimization

1 Introduction

Recently, the problems of environmental pollution and energy shortage have become prominent, while renewable energy has received widespread attention [1]. However, with the increasing proportion of renewable energy in the power system, its volatility and intermittency increase the demand for grid flexibility, which makes the problem of new energy consumption more and more prominent [2]. In many countries and regions, combined heat and power (CHP) units are widely used for large-scale central heating due to their high efficiency. In general, in order to ensure the quality of heat supply, the units are usually operated in a "heat for electricity" mode, which limits the efficiency of renewable energy utilization and decreases the flexibility of electricity-heat co-scheduling [3]. Therefore, the implementation of efficient electricity-heat decoupling of the CHP unit, such as the deployment of energy storage devices and the introduction of intelligent scheduling algorithms, is an effective measure to enhance the unit's peaking capacity, promote new energy consumption, and improve the flexibility of the power grid [4].

A large number of studies have shown that the configuration of electric boilers and electric heat pumps and other devices can achieve electric heat conversion, changing the unit thermoelectric ratio to achieve the unit's thermoelectric decoupling [5][6]. Studies have proposed the use of existing heating network storage capacity to enhance unit flexibility to solve the problem of high investment brought about by the addition of new energy storage devices [7]. In addition, the coupling of the solar thermal storage system not only improves the unit's peaking capacity, but also decreases the coal consumption, improving the thermal economy of the unit [8]. However, the above studies for CHP units mainly focus on the performance analysis under typical fixed scenarios, and less on the optimization of energy supply scheduling under source-load uncertainty scenarios, especially the study of efficient and intelligent scheduling for the energy supply system of the wind-solar coupled CHP unit. Without relying on complex predictive models, reinforcement learning (RL) techniques focus on system-level mapping of state information to aggregated decision models, fully exploiting historical data properties in the form of exploratory and exploitative learning [9][10]. Moreover, due to the strong fitting ability of neural networks, deep reinforcement learning (DRL) techniques can network the state and action spaces to overcome the "dimensionality disaster" problem, achieving more accurate and flexible decision making and learning [11]. Therefore, the scheduling flexibility of cogeneration units can be effectively ensured by applying intelligent scheduling algorithms based on RL.

In addressing the efficient electricity-heat decoupling scheduling problem of CHP units in uncertain environments, this study focuses on a wind-solar coupled CHP unit energy

*This work is supported by Open Project Program of State Key Lab of Low-carbon Smart Coal-fired Power Generation and Ultra-clean Emission.

supply system with the objective of maximizing the comprehensive energy supply income and enhancing the utilization of renewable energy. A Markov decision process (MDP) model considering source-load uncertainty during system operation is established, and then the scheduling optimization problem is transformed into a sequential decision-making problem. Based on a continuous DRL algorithm, twin delayed deep deterministic policy gradient (TD3) algorithm, the sequential decision-making problem is solved to achieve efficient scheduling of the CHP unit, thereby enhancing the system flexibility.

2 System modeling and optimization problem

The wind-solar coupled CHP unit system investigated in this paper contains the CHP unit, wind turbine, solar collector, the thermal energy storage (TES), and electric and thermal loads.

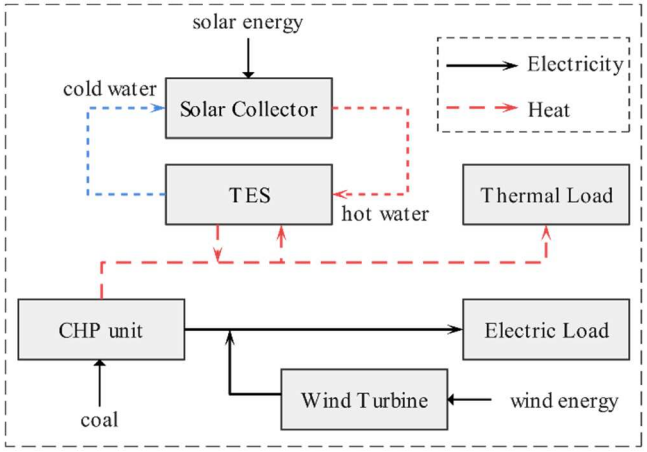

Fig. 1: Schematic diagram of the wind-solar coupled CHP unit system

2.1 Solar collector

The trough solar collector collects solar radiation through a concentrating device and converts it into heat of the heat transfer fluid in the collector tube. This paper adopts LS-2 type trough collector with heat transfer oil as the heat transfer fluid. The physical properties are modelled as follows [12]:

$$H_{pv} = \left(H_{in} - H_{out}\right) A_{\mathrm{pv}} = \left(H_{in} - H_{loss} - H_{pipe}\right) A_{\mathrm{pv}}$$

$$\begin{cases} H_{in} = I_r \cdot \cos\alpha \cdot K_I \cdot R_{sh} \cdot R_{end} \cdot \eta_{pv} \cdot \eta_{pipe} \\ H_{loss} = -9.46 + 0.30T_h - 0.0014T_h^2 + 0.076I_r \\ H_{pipe} = 0.017\Delta T - 0.00017\Delta T^2 \\ \Delta T = \dfrac{1}{2}\left(T_{in} + T_{out}\right) - T_{am} \end{cases} \quad (1)$$

where the actual heat absorbed by the collector, H_{pv}, is the difference between the solar heat absorbed by the collector tube, H_{in}, and the heat lost, H_{out}. H_{loss} represents heat loss of the collector tubes, H_{pipe} represents heat loss of the pipes, while A_{pv} represents the area of the collector. For the absorbed solar heat H_{in}, I_r represents the solar irradiance, $\cos\alpha$ represents the angle of incidence, K_I represents the angle of incidence correction factor, R_{sh} represents the shadow loss coefficient, R_{end} represents the end loss correction factor, η_{pv} represents the collector optical efficiency, and η_{pipe} represents the collector tube optical efficiency. For heat loss H_{loss}, T_h is the overall fluid temperature. Moreover, for pipeline heat loss H_{pipe}, T_{in} and T_{out} are the inlet and outlet temperatures of the thermal oil in the pipeline respectively. In addition, T_{am} denotes the room temperature, and ΔT represents the difference between the average value of the inlet and outlet temperatures of the thermal oil and the room temperature.

2.2 CHP unit

Based on the results of the paper [13], the coal consumption of the unit under different thermal and electrical load conditions is derived. Specifically, the physical characteristic model of the studied CHP unit can be simplified as a convex polygonal region:

$$\begin{cases} C_s = \sum_{k\in K} c_k x_k \\ P_s = \sum_{k\in K} P_k x_k \\ H_s = \sum_{k\in K} H_k x_k \end{cases}, \ \sum_{k\in K} x_k = 1,\ x_k \geq 0 \quad (2)$$

where C_s, P_s and H_s represent the coal consumption, power generation and heating power under the current operating conditions. c_k, P_k and H_k respectively represent the coal consumption, power generation and heating power at the operating conditions of point *k*, which is the apex of the electric-thermal load characteristic interval. x_k is a constant.

2.3 Wind turbine

The physical characteristics of the wind turbine studied in this paper are as follows [14]:

$$P_t^{wt} = \begin{cases} 0, & 0 \leq v_t < v_{in},\ v_t > v_{out} \\ \dfrac{v_t - v_{in}}{v_r - v_{in}} Cap_{wt}, & v_{in} \leq v_t \leq v_r \\ Cap_{wt}, & v_r \leq v_t \leq v_{out} \end{cases} \quad (3)$$

$$P_{t,a}^{wt} = P_t^{wt} - P_{t,\mathrm{out}}^{wt} \quad (4)$$

where P_t^{wt} represent the wind power generated by the wind turbine and Cap_{wt} is the installed capacity of wind turbine. Moreover, v_t, v_{in}, v_{out} and v_r represent the actual wind speed, cut-in wind speed, cut-out wind speed and rated wind speed, respectively. $P_{t,a}^{wt}$ and $P_{t,\text{out}}^{wt}$ represent the actual wind power and abandoned wind power, respectively.

2.4 Thermal energy storage

TES offers the advantage that the system fully consumes the heat generated by solar energy. The relationship between the state of the TES and the power of the TES can be expressed as follows:

$$\begin{cases} \text{HS}_{t+1} = \text{HS}_t - \dfrac{H_t^{HS}}{Cap_{HS}}\Delta T \\ H_t^{HS} = H_{t,out}^{pv} - H_{t,in}^{pv} \end{cases} \tag{5}$$

where HS_t is the heat storage state of TES. Cap_{HS} is the maximum heat storage capacity of TES, while H_t^{HS} is the actual thermal power of the thermal storage tank, including the thermal power of the solar collector stored in the TES, $H_{t,in}^{pv}$, and the thermal power of the TES used for thermal supply $H_{t,out}^{pv}$, respectively. The positive value indicates exothermic and negative value indicates heat charging.

2.5 Optimization problem formulation

(a) Objective function

Considering the complete utilization of solar energy for heat supply and the maximization of wind power absorption capacity in the wind-solar coupled CHP unit system, the objective of this study is to maximize the operation income. The objective function can be formulated as follows:

$$\begin{aligned} J = \max \sum_{t=1}^{T} \Big(& c_t^P P_t^{CHP} + c_t^H H_t^{CHP} + c_t^{wt} P_{t,a}^{wt} + c_t^{pv} H_{t,out}^{pv} \\ & - c_t^{co} C_t^{CHP} \Big) \end{aligned} \tag{6}$$

where the objective function J includes the CHP unit's electricity supply income $c_t^P P_t^{CHP}$, heat supply income $c_t^H H_t^{CHP}$, wind power income $c_t^{wt} P_{t,a}^{wt}$, solar heating income $c_t^{pv} H_{t,out}^{pv}$, and coal purchase cost $c_t^{co} C_t^{CHP}$. Moreover, c_t^P and c_t^{wt} are the feed-in tariffs for the CHP unit and wind power, respectively, c_t^H and c_t^{pv} are the heat supply prices for the CHP unit and solar heating, respectively, and c_t^{co} is the coal price, while T is the total optimal scheduling time.

(b) Safe operation constraints

In order to ensure safe operation of the system, it should be ensured that the power of the equipment is within feasible limits. Equations (7) and (8) represent the safe operating constraints for the CHP unit and TES, respectively, which can be expressed as follows:

$$\begin{cases} C_t^{CHP} = \sum_{k\in K} c_k x_k^t \\ P_t^{CHP} = \sum_{k\in K} P_k x_k^t \ , \ \sum_{k\in K} x_k^t = 1, \ x_k^t \ge 0 \\ H_t^{CHP} = \sum_{k\in K} H_k x_k^t \end{cases} \tag{7}$$

$$\begin{cases} 0 \le HS_t \le 1 \\ 0 \le \left| H_t^{HS} \right| \le H_{\max}^{HS} \end{cases} \tag{8}$$

where C_t^{CHP}, P_t^{CHP} and H_t^{CHP} are the coal consumption, power generation and heating power under the working condition at time t, respectively, and x_k^t is constant. In addition, $H_{\max}^{HS}$ denotes the maximum thermal power of the TES in a single step.

(c) Power balance constraint

Equations (9) and (10) represent the power and thermal balances of the system, respectively.

$$P_t^{CHP} + P_{t,a}^{wt} = P_t^L \tag{9}$$

$$H_t^{CHP} + H_{t,out}^{pv} = H_t^L \tag{10}$$

where P_t^{CHP}, $P_{t,a}^{wt}$ and P_t^L are the electric power supplied by the CHP unit, the actual power of wind power generation and the electric load, while H_t^{CHP}, $H_{t,out}^{pv}$ and H_t^L are the heat power supplied by CHP unit, the actual heat supplied by the solar energy and the thermal load, respectively.

During the scheduling process, adherence to equations (7) to (10) is necessary to ensure safe and stable operation of the system. Traditional algorithms are difficult to achieve the desired results in the face of multiple uncertainties due to their reliance on model prediction. RL algorithms need to discretize the required state and action space and are unable to deal with continuous problems. As one of the DRL algorithms, deep deterministic policy gradient (DDPG) is able to deal with continuous state and action space in a prediction-free model situation, but they are extremely sensitive to hyperparameters and are difficult to converge. Based on this, a continuous DRL algorithm, TD3, which is free of predictive models and overcomes the problem of DDPG's sensitivity to hyperparameters, will be introduced in the subsequent sections to solve the scheduling problem of the CHP unit.

3 Twin Delayed Deep Deterministic Policy Gradient Algorithm

3.1 Markov Decision Process

RL is applied for engaging intelligences to learn how to make decisions to maximize cumulative rewards by interacting with the environment. MDP, as its core framework, provides a mathematical framework for describing sequential decision-making problems. Since this paper focuses on prediction-free algorithms, the transfer matrix is ignored.

(a) state space

The state space s_t includes time t, electric load P_t^L, thermal load H_t^L, wind power P_t^{wt}, solar power H_t^{pv}, and heat storage state in thermal storage tanks HS_t, which is shown below:

$$s_t = \left[t,\ P_t^L,\ H_t^L,\ P_t^{wt},\ H_t^{pv},\ \mathrm{HS}_t \right]^T \tag{11}$$

(b) action space

The action space includes the electric power supply P_t^{CHP} and heating power H_t^{CHP} of the CHP unit, which is shown below:

$$a_t = \left[P_t^{CHP},\ H_t^{CHP} \right]^T \tag{12}$$

(c) reward function

Achieving power balance is very difficult in the early stages of training. Therefore, in order to speed up the convergence of the algorithm, some extra rewards or penalties need to be defined for power imbalance. Meanwhile, in order to improve the ability of continuous scheduling, the end-moment state of TES also needs to be given some penalties. Taking the above considerations into account, the reward function is defined as follows:

$$\begin{aligned} & r_t = \lambda_1 C_t^J - \lambda_2 P_{\mathrm{out},t}^{wt} - \lambda_3 P_{loss,t} - \lambda_4 H_{\mathrm{out},t} - \lambda_5 C_T^{HS} \\ & \begin{cases} C_t^J = c_t^P P_t^{CHP} + c_t^H H_t^{CHP} + c_t^{wt} P_{t,a}^{wt} + c_t^{pv} H_{t,out}^{pv} - c_t^{co} C_t^{CHP} \\ P_{loss,t} = P_t^L - P_t^{CHP} - P_{t,a}^{wt},\ P_{loss,t} > 0 \\ C_T^{HS} = \left| \mathrm{HS}_0 - \mathrm{HS}_T \right| Cap_{HS} \end{cases} \end{aligned} \tag{13}$$

where the reward function r_t contains the scheduling cost of the system C_t^J, excess wind power $P_{\mathrm{out},t}^{wt}$, insufficient electric power supply $P_{loss,t}$, heat imbalance $H_{\mathrm{out},t}$ and the difference between the initial and final state of TES C_T^{HS}. Furthermore, HS_0 is the initial state of TES, and HS_T is the final state of TES at the end of the scheduling process. In addition, $\lambda_i \left(i = 1...5\right)$ are the parameters to be adjusted.

3.2 Training process of TD3

In TD3 algorithm, the actor network outputs the corresponding action $P(s_t \mid \theta^p)$ based on the state of the input s_t and increases the exploration rate by adding OU noise N_t to the output action to obtain the actual action a_t. The balance between exploration and exploitation is achieved by considering noise attenuation. The agent utilizes the actual action to interact with the environment to get the reward r as well as the state of the next moment s' and puts (s, a, r, s') as an experience in the experience replay buffer. When the number of experiences in the experience replay buffer reaches the sampling number, the experiences in the experience replay area are extracted to update the actor network and critic network using gradient descent method.

Before each training episode, a new set of training scenario can be generated by adding random source-load fluctuations of no more than 30% of the difference between their maximum and minimum values to each of the items in the typical day scenario in the heating season. The training process of TD3 algorithm is shown in Fig. 2.

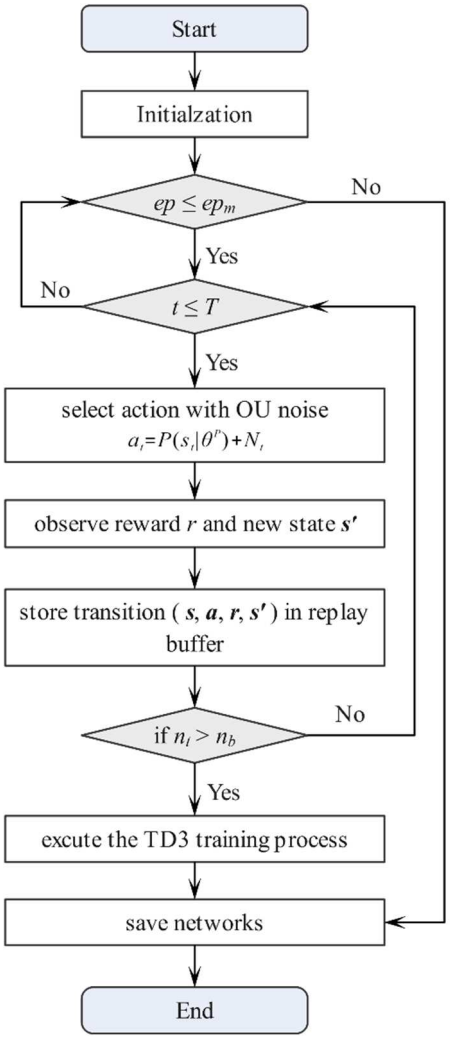

Fig. 2: The training process of TD3 algorithm

4 Results and Discussions

4.1 Simulation scenario

The introduction of solar collectors can improve the peaking capacity of the CHP unit in the heating season. In the non-heating season, there is no thermal demand from users, thus the solar heat is mainly used to maintain the reaction temperature of the CHP unit so as to improve the operating efficiency of the unit to reduce the coal consumption, while the excess heat will be used in the TES to store heat. Therefore, this paper focuses on the problem of scheduling optimization for the typical day in the heating season [15]. The maximum charging and discharging power of the TES is set to 60 MW, with a full-load stored heat

capacity of 480 MWh. The prices for coal, electricity, and heat are provided in Table 1.

The main training parameters of the TD3 algorithm are given in Table 2. Since the training data needs to be normalized, the order of magnitude of the reward term needs to be reduced appropriately to ensure its correct convergence. Besides, the actor network comprises 6 input nodes and 2 output nodes utilizing the Sigmoid activation function, while the critic network consists of 8 input nodes and 1 output node.

Table 1: Typical-day prices of coal, electricity, and heat [16]

Item	Price
Coal (yuan/t)	711.000
Electricity price for CHP unit (yuan/kWh)	0.300
Heating price for CHP unit (yuan/kWh)	0.087
Solar heating price (yuan/kWh)	0.280
Wind electricity price (yuan/kWh)	0.390

Table 2: Main training parameters of TD3 algorithm [17]

Parameter	Number
Learning rates	0.001
Max training episode	200
OU noise variance	18
Energy supply reward (λ_1)	0.001
Wind power surplus (λ_2)	0.350
Power supply inadequacy (λ_3)	0.450
Heating power imbalance (λ_4)	0.500
Energy storage of TES (λ_5)	0.150

4.2 Scheduling results

Based on the training process in Section 3.2, the training curves of the TD3 algorithm are given in Fig. 3, where the curve labelled "mean" is the value of reward smoothing for every 5 training episodes. The simulated operational scheduling for a typical day scenario of the heating season is performed based on the trained neural network, and the 24-hour scheduling state of the TES is given in Fig. 4. Additionally, the system's comprehensive income (including electricity income, heat income, and coal consumption costs), heat and wind losses, and the end state of the TES over a 24-hour period are given in Table 3, respectively.

The results in Fig. 3 show that the TD3 algorithm converged near 160 rounds through the process of continuous exploration and learning, with a cumulative reward of 871.12 at convergence. The results in Fig. 4 show that the TES can effectively provide heat supply and storage capacity, improving the utilization of solar heat. What's more, the reasonable reward function design makes the energy storage state recover to the vicinity of the initial moment after the end of the scheduling, ensuring the continuous scheduling capability. The results in Table 3 show that in terms of energy supply income, TD3 reaches 91.01% of the theoretical optimal solution, while TD3-based abandoned wind power is only 7.81 kW (0.87%). Moreover, the single-step scheduling time based on TD3 is as low as 0.013 seconds, which enables the system to quickly respond to current state. Therefore, the results demonstrate that TD3 holds the ability to achieve the approximate theoretical optimal solution in real-time scheduling considering source-load uncertainty, effectively enhancing the adaptability and sustainability of the system to uncertainty.

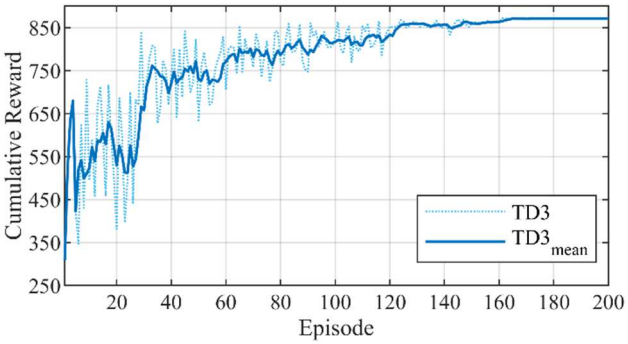

Fig. 3: Training curves of TD3 algorithm ("TD3mean" is the value of reward smoothing for every 5 training episodes)

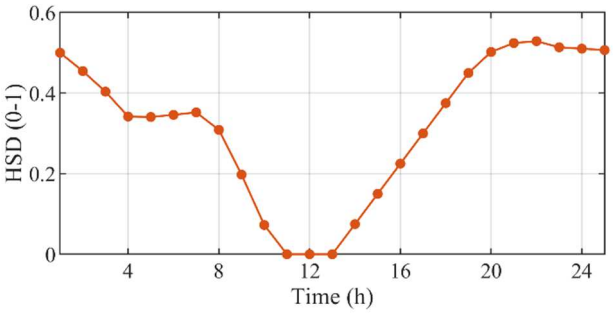

Fig. 4: The scheduling results of HS

Table 3: Scheduling results comparison under the typical day in the heating season

Target	TD3	Optimization
Energy supply income	89.12	97.92
1 Heating supply income	52.83	53.42
2 Electricity supply income	164.21	166.94
3 Coal purchasing cost	127.92	122.44
Abandoned wind power (MW)	7.81	0
Abandoned heating power (MW)	0	0
Terminal TES storage (HS_T)	0.51	0.50
Single-step scheduling time (s)	0.013	\

5 Conclusion

This paper focuses on the scheduling optimization problem of wind-solar coupled CHP unit system under source-load uncertainty, particularly utilizing the TD3 algorithm for efficient and intelligent coordination of electricity and heat scheduling. The operation optimization problem of the system is established, with the constraints of ensuring safe operation and supply-demand balance, and the

objective of maximizing the comprehensive income. The operation characteristics of the system under uncertain environments are modeled using the framework of MDP, and the TD3 algorithm is utilized to solve the optimization problem. The main conclusions of this paper are as follows:

1） The state space in the MDP model of this study includes the renewable energy output and the state of the energy storage device. The reward function comprises both reward and penalty terms, enabling TD3 to quickly achieve supply-demand balance and enhance the utilization of renewable energy during the decision optimization process.

2） The simulation results demonstrate that the TD3 algorithm-based optimization of electricity and heat coordination scheduling leads to a wind curtailment rate of only 0.87% over a 24-hour period. Additionally, the energy storage state of the TES can restore to a level close to its initial state after the scheduling process, ensuring continuous scheduling capability.

3） The time for single-step decision-making based on the trained policy network is only 0.013 seconds, while the scheduling results are achieved near the theoretical optimum, improving the adaptability of the system to uncertainty.

References

[1] L. V. Lerman, G. B. Benitez, W. Gerstlberger, et al. Sustainable conditions for the development of renewable energy systems: A triple bottom line perspective[J]. Sustainable Cities and Society, 2021, 75: 103362.

[2] J. Zheng, J. Du, B. Wang, et al. A hybrid framework for forecasting power generation of multiple renewable energy sources[J]. Renewable and Sustainable Energy Reviews, 2023, 172: 113046.

[3] X. Li, T. Li, L. Liu, et al. Operation optimization for integrated energy system based on hybrid CSP-CHP considering power-to-gas technology and carbon capture system[J]. Journal of Cleaner Production, 2023, 391: 136119.

[4] P. Zhao, F. Gou, W. Xu, et al. Energy, exergy, economic and environmental (4E) analyses of an integrated system based on CH-CAES and electrical boiler for wind power penetration and CHP unit heat-power decoupling in wind enrichment region[J]. Energy, 2023, 263: 125917.

[5] Y. Zhang, J. Hao, Z. Ge, et al. Optimal clean heating mode of the integrated electricity and heat energy system considering the comprehensive energy-carbon price[J]. Energy, 2021, 231: 120919.

[6] Y. Zhang, Z. Ge, Y. Yang, et al. Carbon reduction and flexibility enhancement of the CHP-based cascade heating system with integrated electric heat pump[J]. Energy Conversion and Management, 2023, 280: 116801.

[7] N. Javanshir, S. Syri, S.T ervo, et al. Operation of district heat network in electricity and balancing markets with the power-to-heat sector coupling[J]. Energy, 2023, 266: 126423.

[8] Z. Li, X. Zhu, X. Huang, et al. Sustainability design and analysis of a regional energy supply CHP system by integrating biomass and solar energy[J]. Sustainable Production and Consumption, 2023, 41: 228-241.

[9] A. Hussain, V. H. Bui, H. M. Kim. Deep reinforcement learning-based operation of fast charging stations coupled with energy storage system[J]. Electric Power Systems Research, 2022, 210: 108087.

[10] Y. Wang, D. Qiu, G. Strbac. Multi-agent deep reinforcement learning for resilience-driven routing and scheduling of mobile energy storage systems[J]. Applied Energy, 2022, 310: 118575.

[11] Y. Tan, Y. Shen, X. Yu, et al. Low‐carbon economic dispatch of the combined heat and power‐virtual power plants: A improved deep reinforcement learning‐based approach[J]. IET Renewable Power Generation, 2023, 17(4): 982-1007.

[12] A. M. Patnode, Simulation and performance evaluation of parabolic trough solar power plants[J]. 2006.

[13] T. S. Zheng. Performance analysis of a solar aided CHP unit[D]. Beijing: North China Electric Power University, 2017: 31-43.

[14] A. Keyhani, M. Ghasemi-Varnamkhasti, M.Khanali , et al. An assessment of wind energy potential as a power generation source in the capital of Iran, Tehran[J]. Energy, 2010, 35(1): 188-201.

[15] Z. Y. Ding, H. J. Hou, L. Q. Duan. Study on operation optimization of solar-aided combined heat and power unit based on linear programming[J]. Thermal Power Generation, 2021, 50(6): 33-39.

[16] Ding Z, Hou H, Duan L, et al. Performance analysis and capacity optimization of a solar aided coal-fired combined heat and power system[J]. Energy, 2022, 239: 122141.

[17] Mock J W, Muknahallipatna S S. A comparison of ppo, td3 and sac reinforcement algorithms for quadruped walking gait generation[J]. Journal of Intelligent Learning Systems and Applications, 2023, 15(1): 36-56.

Proceedings of the 3rd Conference on Fully Actuated System Theory and Applications
May 10-12, 2024, Shenzhen, China

Interpretable Fourier Neural Ordinary Differential Equations

Hanlin Bian[1], Wei Zhu[1], Zhang Chen[1], Jingsui Li[1], Chao Pei[1]
1. Key Laboratory of Intelligent Analysis and Decision on Complex Systems, Chongqing University of Posts and Telecommunications, Chongqing 400065, China

Abstract: Numerous interacting elements can form complex systems. However, describing complex systems is extremely challenging and lacks interpretability. The construction of models still heavily relies on scientists' understanding of complex systems. This paper explores the use of neural ordinary differential equations in the field of complex system modeling. The proposed Fourier neural ordinary differential equations offer interpretability and a relatively simple structure. By building upon interpretable modeling, the scale is significantly reduced. It is possible to deduce the system's expression from the model's parameters. Finally, a real-world system is provided to illustrate the effectiveness of the proposed model, demonstrating its commendable robustness.

Key Words: FNODEs, Neural ODEs, Robustness, Interpretable model, Data-driven

1 Introduction

The Industrial Internet of Things (IIoT) has experienced significant development and growth. In various fields, a wide array of sensors have gathered an unprecedented amount of data. According to Moore's Law, the advancement of integrated circuits has led to the growth in computer processing power, but it also poses a significant constraint on scientific research. As a result, the availability of large-scale data has made it a focal point for many scholars to extract patterns from known time series data and construct complex system models that reflect reality. These studies have numerous potential applications in dynamic system control, financial data analysis, and national population forecasting, providing crucial guidance for production and daily life.

Behavioral data from complex systems is mainly represented as time series. In recent years, the data-driven approach for constructing complex system models from time series data has emerged as a new research direction. Based on machine learning and deep learning theories, a variety of innovative algorithms, such as Recurrent Neural Networks (RNNs) [1, 2], Temporal Convolutional Networks (TCNs) [3], and Neural Ordinary Differential Equations (Neural ODEs), have been rapidly advancing. RNNs introduce a recurrent structure, providing the network with memory capacity to capture dependencies in time series. TCNs, based on Convolutional Neural Networks (CNNs) [4], introduced causal convolution to preserve the network's temporal nature and enhance its parallelism. Neural ODEs combine numerical algorithms to provide a new perspective on neural networks. They are a type of neural networks that parameterize derivatives of hidden states, enabling automatic modeling of continuous time and achieving favorable results. Additionally, there have been a series of models that apply physics-related theories to neural networks in order to develop dynamic models for systems, such as Hamiltonian Neural Networks and Lagrangian Neural Networks [5, 6].

Despite the abundance of algorithms available for creating new models, there are still some challenges. Most neural network models are large in scale and have a black-box internal structure, which makes them lack interpretability. The limited number of interpretable models, such as Polynomial Neural ODEs and ODENet [7, 8], perform well only for specific data structures and are not suitable for more general dynamic systems, especially non-autonomous nonlinear systems.

Based on the above discussion, Fourier neural ordinary differential equations (FNODEs) are introduced in this paper, which are inspired by Fourier Neural Networks [9–11]. The main contributions are summarized as follows:
(I) The framework of FNODEs are developed and are applied to model complex systems, which enables to obtain explicit expressions for the corresponding systems.
(II) The theoretical framework of deep learning is used to optimize loss function, which can enhance the accuracy of model building.
(III) Compared to traditional neural network models, FNODEs utilize Fourier basis functions to describe complex systems and avoid black boxes in the models.

The remainder of this paper is organized as follows. Section 2 introduces neural differential equations, the structure of FNODEs, and related training algorithms. Section 3 uses FNODEs to model the daily average atmospheric pressure data for Delhi, India, with the aim of uncovering its dynamic patterns. Finally, Section 4 evaluates and summarizes the model based on Fourier neural ordinary differential equations in accordance with the results, and proposes future work.

2 Method Description

2.1 Neural ODEs

Neural ordinary differential equations are a type of neural network that parameterizes the derivative of hidden states [14, 15]. Using existing neural network training algorithms, it is possible to accurately model certain dynamical systems. When given the numerical solution $Y(t)$ of a dynamical system, the dynamical system that needs to be fitted can be represented as:

$$\frac{dY}{dt} = f(Y, t), \tag{1}$$

where $Y = [y_1, y_2, ..., y_d]^T$, and d represents the dimension of the system. For many scientific problems involving differential equations, traditional methods often require a sig-

This work is jointly sponsored by National Natural Science Foundation of China under Grant 62373071 and Natural Science Foundation of Chongqing, China, under Grant CSTB2023NS CQ-LZX0075.

nificant amount of time to search for the dynamical system described by f. In the case of Neural ODEs, it differs from traditional methods in that it does not require obtaining an explicit dynamical system equation. Instead, it learns an implicit representation through a data-driven approach. If we represent Neural ODEs as NN, the process of fitting the dynamical system f can be described as follows:

$$\frac{dY}{dt} \approx NN(Y, t, \theta), \tag{2}$$

where θ represents the parameters of the neural network. The dynamical system being sought can be viewed as the model used when designing and training the network structure to achieve the desired outcome.

Remark 1 *In reality, a neural network model is a complex nonlinear transformation function. If initial values are provided, the dynamical system can be solved using numerical methods, such as the Runge-Kutta method.*

Despite the excellent nonlinear fitting capability of Neural ODEs, they lack interpretability and cannot effectively provide explanations based on the specific parameters of the model's neurons. In other words, Neural ODEs are still considered as black-box models. This continues to be a significant challenge for further analyzing the internal structure and properties of dynamical systems.

2.2 FNODEs

To enhance the interpretability of the neural network employed for fitting dynamical systems, inspiration is drawn from Fourier Neural Networks, which has led to the development of FNODEs.

Since ordinary differential equations are used to study the relationship between a single-variable function and its derivatives with respect to the independent variable t, there exists a functional relationship between the dependent variable Y and the independent variable t. Define $Y = Y(t)$ and then express Y as a function of t. The structure of FNODEs can be described as follows:

$$\frac{dY(t)}{dt} \approx NN(t, \theta). \tag{3}$$

The basis functions for the system's derivatives consist exclusively of sine and cosine functions, both of which are solely dependent on the independent variable t. These functions are employed to model the dynamical system. Once satisfactory results within an acceptable range have been achieved, an approximate symbolic expression of the system can be derived using the parameters of the neurons in the neural network model. The expression is formulated as follows:

$$\frac{dY(t)}{dt} \approx A\cos(\lambda T) + B\sin(\mu T), \tag{4}$$

where A and B are the amplitudes of the basic functions, and λ and μ are the angular frequencies of the basic functions. A and B are $d \times n$-dimensional matrices, λ and μ are $n \times d$-dimensional matrices, and T is a $d \times 1$-dimensional matrix with each element equal to t.

Remark 2 *The above function operations are pointwise operations on vectors, which means that the same operation is performed for each element of the vector.*

In contrast to the original Neural ODEs, which utilize non-interpretable feedforward neural networks for nonlinear transformations, FNODEs not only enhance the interpretability of the network but also lead to a significantly reduced size of network parameters.

Remark 3 *The main difference between FNODEs and other Fourier neural networks lies in the way that data is propagated. The former solves an initial value problem (IVP) while the latter uses traditional forward propagation.*

2.3 The process of training

Parameter Initialization: Before training the network, it is necessary to initialize all the parameters of FNODEs. In all parameter initialization processes, a standard Gaussian distribution with a mean of 0 and a variance of 1 is utilized in the process.

Remark 4 *Gaussian distribution initialization ensures that the initial values of the parameters have some randomness, which helps with convergence and diversity during training.*

Objective Function: A significant difference between the predicted values of the network and the true values can result in gradient explosion during training. To prevent this situation and improve the robustness of the network, SmoothL1Loss [12] is chosen as the objective function. Clearly, when $|y_i - pre_i| < \beta$, the objective function uses the square error function; otherwise, the linear error function is used. This loss function can reduce the impact of outliers and is, therefore, more suitable for training. The hyperparameter β should be set. The objective function is expressed as follows:

$$l_i = \begin{cases} \frac{1}{2\beta}(y_i - pre_i)^2, & |y_i - pre_i| < \beta, \\ |y_i - pre_i| - \frac{1}{2}\beta, & \text{otherwise.} \end{cases} \tag{5}$$

Parameter Optimization: When training a neural network, an algorithm called Adam is used to adaptively optimize the network's parameters. Using the Adam optimization algorithm [13] for parameter updates is not affected by the scaling of gradients, and it can automatically adjust the learning rate. The process for optimizing network parameters using the Adam algorithm for the kth iteration is as follows:

$$\begin{aligned} g_k &= \nabla \hat{L}(\theta_t), \\ m_k &= \beta_1 m_{k-1} + (1-\beta_1) g_k, \\ v_k &= \beta_2 v_{k-1} + (1-\beta_2) g_k^2, \\ \hat{m}_k &= \frac{m_k}{1-\beta_1^k}, \\ \hat{v}_k &= \frac{v_k}{1-\beta_2^k}, \\ \theta_{k+1} &= \theta_k - \frac{\eta}{\sqrt{\hat{v}_k} + \epsilon} \hat{m}_k. \end{aligned} \tag{6}$$

where β_1 and β_2 are hyperparameters for optimization, g, m and v represent the gradients, first-order moment estimates, and second-order moment estimates of the objective function with respect to the parameters, respectively. $\hat{m}$ and $\hat{v}$ are the corrected values of m and v, respectively.

After successfully initializing the model, the FNODEs begin training. During the training process, the neural differential equation solver is utilized to produce the network's

Algorithm 1 Training process of FNODEs (using PyTorch).

Input:
Dynamical system numerical solution $true\ y$;
Initial value $true\ y_0$;
Time domain t;
Output:
Approximate ODEs $\frac{dY}{dt} = f(t)$
Initialize the number of model nodes;
Initialize network parameters;
Selected objective function SmoothL1Loss;
Set up the optimizer Adam;
while L is not stable **do**
  pre←odeint(fnodenet, $true\ y_0$,t);
  loss←SmoothL1Loss($true\ y$,pre);
  $grad_\theta$ ←loss.backward();
  Update θ by Adam optimizer;
end while
return $f(t)$;

predictions and calculate the value of the objective function. Afterward, the stability of the objective function should be considered. If the objective function continues to exhibit a decreasing trend, the parameters θ are updated using the neural network backpropagation algorithm. The entire process is described as algorithm 1. And Figure 1 is a flowchart depicting the entire process.

3 Application in Atmospheric Pressure System Modeling

Atmospheric pressure is the force exerted by the weight of the air above a unit area. Numerically, it is equivalent to the weight of the vertical column of air extending upward to the upper limit of the atmosphere on a unit area. The fluctuation of atmospheric pressure is closely linked to factors such as wind and weather, making it a significant meteorological element. When using FNODEs to represent atmospheric pressure systems, it is possible to derive corresponding dynamic equations, which reveal the dynamic patterns of atmospheric pressure changes. This is of great importance for dynamic analysis in meteorology.

The daily average atmospheric pressure time series for Delhi, India, from 2013 to 2017 is chosen from Kaggle's public datasets[1]. The dataset includes outliers and zero values. Initially, zero values need to be eliminated. Subsequently, outliers are identified using the Z-score method, as outlined below.

$$Z = \frac{(X - \mu)}{\sigma}, \tag{7}$$

where Z represents the Z-score, X is the atmospheric pressure value, μ is the mean, and σ is the standard deviation, respectively. Setting the threshold parameter to 1.66, the identified outliers are shown in Figure 2.

Due to the relatively gradual changes in atmospheric data over short periods, outlier removal is performed by utilizing the mean of the adjacent 5 data points. The cleaned atmospheric pressure data is depicted in Figure 3.

Before utilizing FNODEs for modeling, the time domain is set to [0, 14.4] with a step size of 0.01. In this setup, the total number of time series used for training is 1440. The FNODEs model is specified with 20 basis functions, and the training iteration is set to 2000. The resulting FNODEs model is summarized in Table 1.

[1] https://www.kaggle.com/datasets/sumanthvrao/daily-climate-time-series-data/data

Table 1: Symbolic expression for the atmospheric pressure system.

Equation Expression
$\frac{dx}{dt} = 2.218\sin(1.2505t) - 3.3842\sin(4.854t)$
$- 9.802\sin(6.7194t) - 7.6537\sin(7.0177t)$
$- 5.3573\sin(12.68t) + 1.5594\sin(13.92t)$
$- 20.483\sin(18.745t) - 165.505\sin(24.842t)$
$+ 48.761\sin(39.211t) + 39.597\sin(44.261t)$
$+ 40.461\sin(49.965t) + 15.143\sin(56.584t)$
$+ 13.722\sin(56.602t) + 17.136\sin(62.411t)$
$+ 27.825\sin(75.843t) + 57.658\sin(81.819t)$
$- 17.926\sin(96.861t) - 19.348\cos(9.767t)$
$- 11.185\cos(9.787t) - 9.644\cos(16.069t)$
$- 20.454\cos(16.086t) - 13.4278\cos(21.949t)$
$- 70.227\cos(21.951t) - 3.2986\cos(43.417t)$
$+ 33.74\cos(43.689t) + 27.387\cos(48.477t)$
$+ 15.006\cos(57.81t) + 35.3\cos(61.045t)$
$+ 11.262\cos(65.523t) + 16.981\cos(65.524t)$
$+ 30.782\cos(84.907t) + 22.998\cos(84.908t)$
$+ 35.23\cos(90.521t)$

To illustrate the advantages of FNODEs, a comparison experiment is conducted using NODEs with a feedforward neural network as the vector field function. The feedforward neural network is a three-layer network structure with one neuron in both the input layer and output layer, and 50 neurons in the hidden layer. The activation function uses the hyperbolic tangent function. Other parameters are consistent with FNODEs. The data modeling results are shown in Figure 4. It is easy to find that NODEs cannot model atmospheric pressure data with significant noise, nor can they obtain the hidden state derivative of this time series.

Visualizations of the correlation between atmospheric pressure and time, the relationship between atmospheric pressure derivatives and time, and the loss function during training are presented in Table 2. It is evident that modeling atmospheric pressure data through FNODEs is fundamentally consistent with reality. It allows for visualizing the trend of atmospheric pressure data over time, which aligns with actual observations. It is not difficult to find out that training FNODEs can achieve the stabilization of the objective function in a shorter number of iterations through the loss values recorded during training. From these visualizations, we observe that FNODEs can not only accurately represent the original data but also reveal the dynamic patterns in the data's variations.

4 Conclusion

In this study, FNODEs can reveal hidden dynamic systems from time series data and can produce accurate fitting results for dynamic systems even with fewer parameters. Furthermore, the network structure of FNODEs is based on trigono-

Table 2: The results of the fitting for the atmospheric pressure system.

Description	Plot
State Function	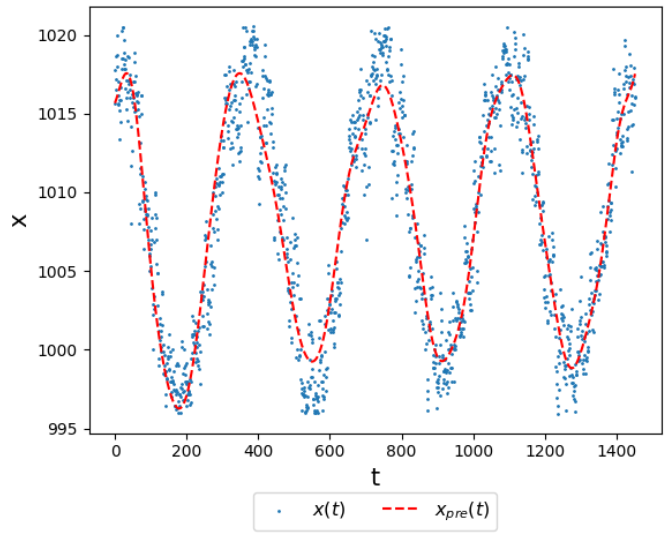
Derived Function	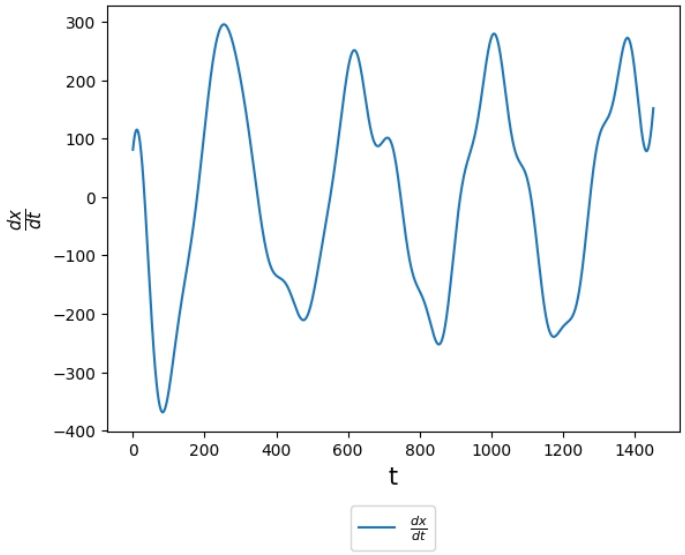
Loss Function	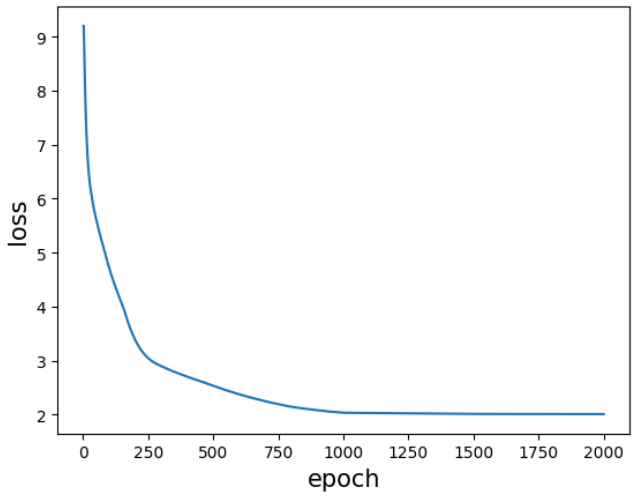

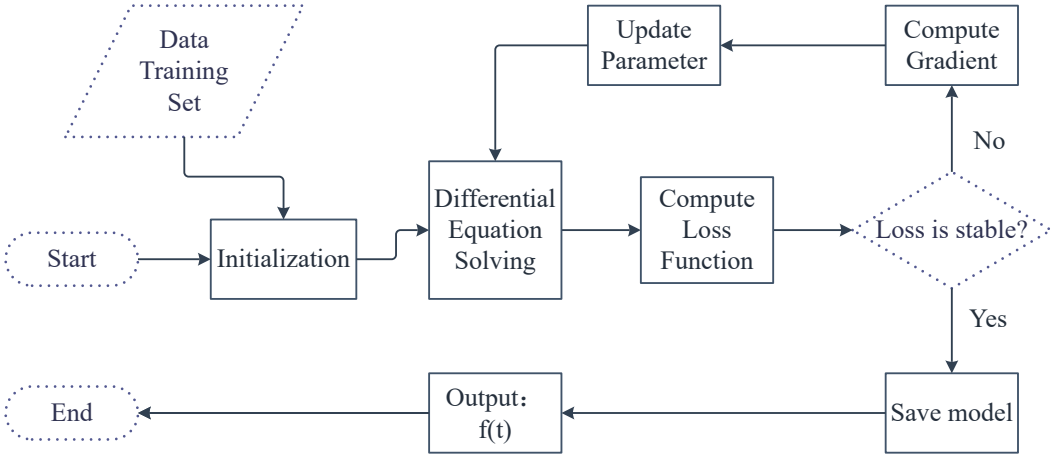

Fig. 1: FNODEs Training Process.

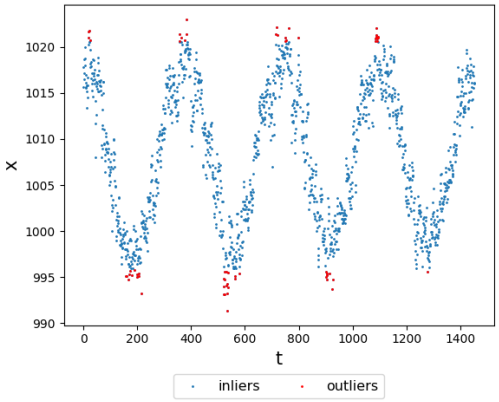

Fig. 2: Original Atmospheric Pressure Data.

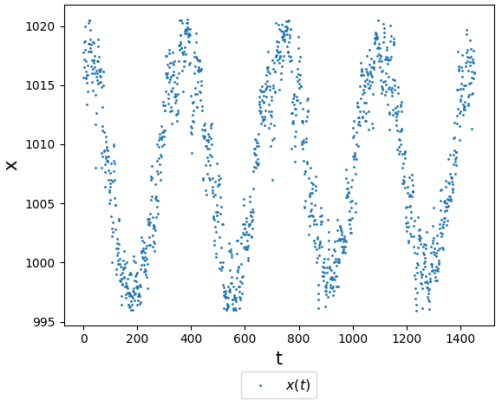

Fig. 3: Cleaned Atmospheric Pressure Data.

metric functions, and the parameters of network nodes only represent the amplitude and frequency of these functions. Therefore, each parameter of a node in FNODEs is interpretable. FNODEs can extract all model parameters to produce an explicit expression for the system. Moreover, FNODEs are a type of robust networks with high noise tolerance.

FNODEs demonstrate impressive capabilities in dynamic system modeling. In future, we plan to explore the predictive capabilities of FNODEs and aim to apply them in practical applications across various domains.

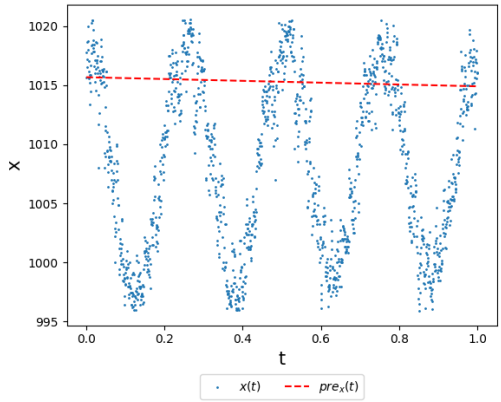

Fig. 4: Atmospheric Pressure Data modeling using NODEs.

References

[1] E. Levin, 'A recurrent neural network: Limitations and training', Neural Networks, vol. 3, no. 6, pp. 641-650, 1990.

[2] M. Kimura and R. Nakano, 'Learning dynamical systems by recurrent neural networks from orbits', Neural Networks, vol. 11, no. 9, pp. 1589-1599, 1998.

[3] C. Lea, M. D. Flynn, R. Vidal, A. Reiter, and G. D. Hager, 'Temporal convolutional networks for action segmentation and detection', in proceedings of the IEEE Conference on Computer Vision and Pattern Recognition, 2017, pp. 156-165.

[4] S. Karimpouli and P. Tahmasebi, 'Image-based velocity estimation of rock using convolutional neural networks', Neural Networks, vol. 111, pp. 89-97, 2019.

[5] S. Greydanus, M. Dzamba, and J. Yosinski, 'Hamiltonian neural networks', Advances in neural information processing systems, vol. 32, 2019.

[6] M. Cranmer, S. Greydanus, S. Hoyer, P. Battaglia, D. Spergel, and S. Ho, 'Lagrangian neural networks', arXiv preprint arXiv:2003. 04630, 2020.

[7] C. Fronk and L. Petzold, 'Interpretable polynomial neural ordinary differential equations', Chaos: An Interdisciplinary Journal of Nonlinear Science, vol. 33, no. 4, 2023.

[8] P. Hu, W. Yang, Y. Zhu, and L. Hong, 'Revealing hidden dynamics from time-series data by ODENet', Journal of Computational Physics, vol. 461, p. 111203, 2022.

[9] S. Liu, 'Fourier neural network for machine learning', in 2013 International Conference on Machine Learning and Cybernetics, 2013, vol. 1, pp. 285-290.

[10] A. Silvescu, 'Fourier neural networks', in IJCNN'99. International Joint Conference on Neural Networks. Proceedings (Cat. No. 99CH36339), 1999, vol. 1, pp. 488-491.

[11] M. S. Gashler and S. C. Ashmore, 'Modeling time series data with deep Fourier neural networks', Neurocomputing, vol. 188, pp. 3-11, 2016.

[12] C. Liu et al., 'Adaptive smooth L1 loss: A better way to regress scene texts with extreme aspect ratios', in 2021 IEEE Symposium on Computers and Communications (ISCC), 2021, pp. 1-7.

[13] D. P. Kingma and J. Ba, 'Adam: A method for stochastic optimization', arXiv preprint arXiv:1412. 6980, 2014.

[14] R. T. Q. Chen, Y. Rubanova, J. Bettencourt, and D. K. Duvenaud, 'Neural ordinary differential equations', Advances in neural information processing systems, vol. 31, 2018.

[15] H. Yan, J. Du, V. Y. F. Tan, and J. Feng, 'On robustness of neural ordinary differential equations', arXiv preprint arXiv:1910. 05513, 2019.

[16] J. Li, W. Zhu, Z. Chen, and C. Pei, 'Financial Time Series Prediction via Neural Ordinary Differential Equations Approach', in 2023 International Annual Conference on Complex Systems and Intelligent Science (CSIS-IAC), 2023, pp. 332-338.

[17] P. Goyal and P. Benner, 'Neural ordinary differential equations with irregular and noisy data', Royal Society Open Science, vol. 10, no. 7, p. 221475, 2023.

[18] A. J. Linot, J. W. Burby, Q. Tang, P. Balaprakash, M. D. Graham, and R. Maulik, 'Stabilized neural ordinary differential equations for long-time forecasting of dynamical systems', Journal of Computational Physics, vol. 474, p. 111838, 2023.

[19] T. Yabe, P. S. C. Rao, S. V. Ukkusuri, and S. L. Cutter, 'Toward data-driven, dynamical complex systems approaches to disaster resilience', Proceedings of the National Academy of Sciences, vol. 119, no. 8, p. e2111997119, 2022.

[20] A. Zhu, P. Jin, B. Zhu, and Y. Tang, 'On numerical integration in neural ordinary differential equations', in International Conference on Machine Learning, 2022, pp. 27527-27547.

Proceedings of the 3rd Conference on Fully Actuated System Theory and Applications
May 10-12, 2024, Shenzhen, China

Trajectory tracking control of CNC system based on RBF neural network composite learning control

Zhiyu Hu[1], Juncheng Xu[1], Jiangang Li[1]*,
1. Harbin Institute of Technology Shenzhen Graduate School, Shenzhen 518071, P. R. China
E-mail: jiangang_lee@163.com

Abstract: This paper addresses the high-precision control issues in CNC machine tool servo systems by proposing a feedforward compensation algorithm based on Radial Basis Function Neural Network (RBFNN) composite learning control. Unlike previous studies that updated neural networks solely based on tracking errors, this research prioritizes the accuracy of neural network learning. The paper employs the Selective Memory Recursive Least Squares (SMRLS) method to construct system information prediction errors, which, combined with tracking errors, update the neural network. This enables the neural network to learn the model of the CNC machine tool servo system more accurately, thereby achieving more precise feedforward compensation. Consequently, this method achieves exceptional tracking control performance. The stability of the closed-loop system and the boundedness of the errors are proven using the Lyapunov method. Experimental results on a three-axis CNC machine tool demonstrate that the proposed control algorithm effectively estimates system nonlinearity, thus enhancing tracking control precision.

Key Words: Composite Learning, Radial Basis Function Neural Network, Selective Memory Recursive Least Squares

1 Introduction

Industrial production automation is an indispensable component of modern manufacturing. As fields such as metal processing, semiconductor manufacturing, electronics, medical devices, and aerospace rapidly advance toward high precision and sophistication, the complexity of manufacturing systems continues to escalate. Industrial production automation faces numerous challenges as a result. Consequently, there is a growing demand for higher precision in the processing progress of numerical control machine tools [1, 2].

Currently, there are two main approaches to achieving high-precision processing: contour error control and tracking error control. Contour error control aims to reduce contour errors during the processing of each axis while tracking error control aims to enhance the tracking control performance of each axis. Tracking control is favored for its advantages, such as simple structure, good robustness, and convenient design, making it a hotspot in current research.

Nonlinearities, unmodeled dynamics, external disturbances, parameter perturbations, and other uncertainties negatively impact the performance of tracking control in CNC machine tools. Traditional control methods, such as PID control, struggle to improve control precision further under the influence of nonlinear factors. To address nonlinearity, there is a pressing need in the field of modern industrial automation to introduce more advanced control methods, leading to the rise of nonlinear control theory and intelligent control. Fu et al. [3] integrated heuristic reasoning rules of artificial intelligence with modern control techniques, proposing an intelligent control framework, indicating that intelligent control is a cross-disciplinary endeavor. The use of artificial intelligence to solve control problems in nonlinear systems has become a popular research direction.

Neural networks, originating in the 1950s, were initially inspired by biological neurons. Researchers attempted to simulate the computational processes of the human brain by constructing neural network models. However, at that time, these models were only suitable for linearly separable problems. In the 1980s, the introduction of algorithms such as the backpropagation algorithm injected new vitality into the development of neural networks [4]. These algorithms enabled neural networks to automatically adjust and adapt to complex systems, and neural networks have been widely used as a model-free feedforward control element to approximate and compensate for nonlinearity and uncertainty [5, 6]. The ability of neural networks to compensate for nonlinearity and uncertainty stems from their universal approximation property [7–9], which implies that neural networks can approximate any continuous function with arbitrary precision.

As a significant branch of intelligent control, neural networks have achieved meaningful research results in the control of nonlinear systems, leveraging their ability to approximate highly uncertain systems and their powerful self-learning capability. However, in traditional applications of neural networks, despite achieving real-time learning for tracking control performance and system stability, these networks do not truly possess the ability to learn continuously. Even in repetitive tasks, neural networks need to relearn relevant knowledge and recalculate parameters.

Wang et al.[5] introduced a new mechanism deterministic learning theory for machine learning in dynamic environments, addressing the aforementioned issues and endowing neural networks with human-like knowledge acquisition capabilities. When the system satisfies the Persistence Excitation (PE) condition [10], neural network weights can converge to an optimal solution within a certain range. During online learning, the neural network adapts its parameters based on the transformation of features, autonomously adjusting to the uncertainty of an unknown system in a closed-loop system. The acquired knowledge is stored as a set of constant neural network weights. After completing the online learning task, these constant weights are recorded. In the knowledge reuse stage, neural network learning is halted, and the obtained constant neural network weights are di-

This work was supported by Shenzhen Science and Technology Program under Grant GXWD20231130150241001and in part by National Natural Science Foundation of China under Grant 52275481.

rectly utilized to design a controller for controlling uncertain nonlinear systems. This way, past experience is leveraged to achieve better control performance, endowing neural networks with true learning capabilities.

Deterministic learning theory mandates that the system satisfies the Persistence Excitation (PE) condition to ensure the convergence of neural network weights. However, this requirement is overly stringent and challenging to meet in practical scenarios. Additionally, in neural network learning control based on deterministic learning, current research predominantly focuses on designing neural network parameter update laws using tracking errors. While this approach guarantees controller stability, it neglects the primary objective of employing neural networks: to approximate unknown nonlinear systems. In such controller designs, neural networks do not genuinely acquire knowledge of the unknown nonlinear systems, which limits further enhancements in control precision. To improve the capability of neural networks to approximate unknown nonlinear systems, Xu et al. [11] implemented the Serial-Parallel Estimation Method (SPEM) to devise a composite learning design, which, combined with tracking errors, updates neural network parameters. Similarly, Pan et al. [12] developed new prediction errors by utilizing online historical data and instantaneous data, proposing a novel control scheme for strict feedback systems. This paper introduces a high-precision trajectory tracking controller for NC machine tools, employing the SMRLS algorithm to construct more accurate prediction errors, alongside a composite learning algorithm that updates the neural network. This approach allows the network to fully assimilate the knowledge of the unknown nonlinear system inherent in CNC machine tools, enhancing the precision of the tracking control. Furthermore, when combined with deterministic learning theory, a constant neural network controller, designed based on deterministic learning theory, can achieve high-precision tracking control for NC machine tools in similar or identical control tasks.

2 Problem formulation and preliminaries

2.1 Modeling of servo control system

The CNC machine tool studied in this paper is composed of multiple servo processing axes. Each servo processing axis consists of a permanent magnet synchronous motor (PMSM), a servo drive, and a ball screw guide rail. Due to the typical movement of ball screw guide rails along with processing loads, and the fact that their movement faces severe non-linear characteristics when subjected to large loads, they cannot be simply considered as a load torque on the servo motor. When establishing the model for each axis, it is essential to model the servo motor and the ball screw guide rail separately.

The mathematical model of a PMSM can be represented in the d-q framework through the Park transformation. In numerical control machine tools, the i_d of a PMSM is typically set to 0. Therefore, its mathematical model is represented as follows

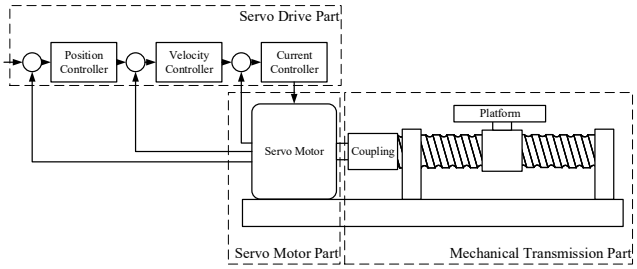

Fig. 1: Single-axis servo systems

$$\begin{aligned}\dot{\theta}_1(t) &= \omega(t)\\ \dot{\omega}(t) &= \frac{3P_n\Phi}{2J_{L1}}i_q(t) - \frac{B_{L1}}{J_{L1}}\omega(t) - \frac{1}{J_{L1}}T_L(t)\\ \dot{i}_q(t) &= -\frac{R_s}{L_q}i_q(t) - \frac{P_n\Phi}{L_q}\omega(t) + \frac{1}{L_q}u_q(t)\end{aligned} \tag{1}$$

and the torque balance equation of the mechanical drive structure is below

$$J_{L2}\frac{d^2\theta_2(t)}{dt^2}+B_{L2}\frac{d\theta_2(t)}{dt}+T_S(t)=T_L(t)=K_L[\theta_1(t)-\theta_2(t)] \tag{2}$$

where J_{L1}, J_{L2} are the equivalent moment of inertia, B_{L1}, B_{L2} are the equivalent damping factor,P_n is the pole pair, R_s is the stator resistance, ϕ is the flux linkage, K_L is the total rigidity, θ_1 is the motor output angle, θ_2 is the output angle, T_s is the disturbance and T_L is the total torque.

In the actual servo system, a three-loop controller is often used, in which the current loop and the speed loop generally use the PI controller, and the position loop uses the P controller. The servo drive includes an inverter, low-pass filter, current loop controller, speed loop controller, and position loop controller. After three-loop rectification, the models of the current-loop controller, the speed loop controller, and the position-loop controller can be derived.

Based on the comprehensive analysis of the above models, the control block diagram of the entire single-axis servo system is shown in Fig. 2.

2.2 Radial Basis Function Neural Network

The RBFNN is employed to approximate the uncertain nonlinear function $f(\bar{x}) : R^n \to R$, as follows

$$\hat{f}(\bar{x}) = \hat{\omega}^T\theta(\bar{x}) \tag{3}$$

where $\bar{x} = [x_1, \ldots, x_n]^T \in \mathbb{R}^n$ is the input vector of the RBFNN, $\hat{f}(\bar{x}) \in \mathbb{R}$ is the output of RBFNN, $\omega = [\omega_1, \cdots, \omega_l]^T \in \mathbb{R}^l$ with $l > 1$ denotes weight vector, and $\theta(\bar{x}) = [\theta_1(\bar{x}), \cdots, \theta_l(\bar{x})]^T$ means basis function vector with $\theta_i(\bar{x})$ being the Gaussian function in the form

$$\theta_i(\bar{x}) = \exp[-\frac{(\bar{x}-c_i)^T(\bar{x}-c_i)}{b^2}] \tag{4}$$

where $c_i = [c_{i1}, \cdots, c_{iq}]^T, i = 1, \cdots, n$ is the center of the receptive field and b is the width of the Gaussian function.

There exists the optimal weight ω^* for the nonlinear function f with the following expression:

$$\begin{aligned}f(\bar{x}) &= \omega^{*T}\theta(\bar{x}) + \varepsilon\\ \omega^* &= \arg\min_{\hat{\omega}\in\Omega_f}[\sup_{\bar{x}\in\Omega_{\bar{x}}}|\hat{f}(\bar{x}|\hat{\omega}) - f(\bar{x})|]\end{aligned} \tag{5}$$

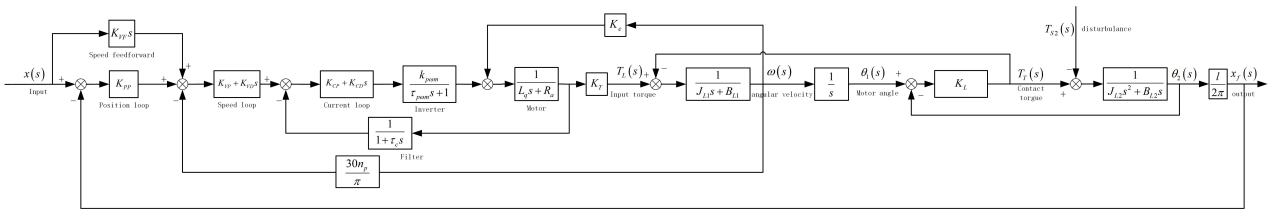

Fig. 2: Composite control of the machine servo system

where $\sup_{\bar{x}\in\Omega_{\bar{x}}}|\varepsilon| < \varepsilon_M, \varepsilon_M > 0$ is the supreme of ε, $\Omega_f = \{\hat{\omega} : \|\hat{\omega}\| \leq f_M\}$ is a set of the parameter, and f_M is a designed parameter. flushed left.

2.3 Selective Memory Recursive Least Squares

SMRLS is a real-time training method for RBFNNs, addressing online supervised learning challenges. In traditional RBFNNs, Lyapunov stability theory often leads to weight update rules via stochastic gradient descent (SGD), a popular method. However, SGD's forgetting mechanism, maintaining responsiveness to new data, causes a loss of valuable long-term knowledge. In contrast, SMRLS reconstructs the forgetting mechanism by evaluating sample importance based on spatial and temporal distribution, mitigating this issue. Further analysis can be found in [13].

The primary idea of the SMRLS algorithm is to normalize the input space of the RBFNN when approximating the unknown function $f(x)$. The space is partitioned, and as inputs traverse different partitions, the algorithm synthesizes the samples within each partition into composite samples $(\gamma_j(k), \varphi_j(k))$, where $\gamma_j(k)$ represents the synthesized input, and $\varphi_j(k)$ represents the synthesized output. Partitions that are sampled at least once during real-time learning are combined into composite samples, resulting in the following neural network weight update rules

$$\begin{aligned}&\omega(k+1) = \\ &\omega(k)+P(k+1)\theta(k+1)[y(k+1)-\omega^T(k)\theta(k+1)]-\epsilon_a(k+1) \\ &P^{-1}(k+1)=P^{-1}(k)+\theta(k+1)\theta(k+1)^T-\theta_a(k)\theta_a^T(k)\end{aligned} \tag{6}$$

where $\epsilon_a(k+1) = P(k+1)\theta_a(k)[y_a(k) - \omega^T(k)\theta_a(k)]$, $P(k+1) \in \mathbb{R}^{N\times N}$ is a positive definite matrix, $\theta_a(k)$ and $y_a(k)$ are the recorded regressor vector and desired neural network output of partition before sampling time k, respectively. Since $y_a(k) - \omega^T(k)\theta_a(k)$ represents the network approximation error to a sample that has been learned, it becomes a small value if the approximation capability of the neural network is sufficient. Therefore, $|\epsilon_a(k+1)|$ will also be small if the neural network is set properly.

The initial values are set as $P(0) = p_0 I$, where $p_0 > 0$ is a large constant and $I \in \mathbb{R}$ is an identity matrix. Consider the discrete update law of $P^{-1}(k)$ in Equation (8). Assuming that there are N_k partitions that have been sampled at least once before sampling time k, and the recorded regressor subvectors of the partitions are $\theta(i), i = 1, \cdots, N_k$, then $P^{-1}(k)$ can be calculated by

$$P^{-1}(k) = P^{-1}(0) + \sum_{j=1}^{N_k}\theta(i)\theta^T(i). \tag{7}$$

where $P^{-1}(0) = \frac{1}{p_0}I$, so $P(k)$ and $P^{-1}(k)$ are always positive definite in the learning process.

Due to the SMRLS algorithm's effectiveness in approximating unknown functions, it is well-suited for constructing prediction errors in composite learning algorithms. Its characteristics, including accelerated neural network convergence and selective forgetting, address issues such as error accumulation in traditional composite learning control.

3 Composite learning control design

By choosing a reasonable state x, the nonlinear system can be transformed into the following state space expression

$$\begin{aligned}&\begin{cases}\dot{x}_1 = x_2 \\ \dot{x}_2 = f(x) + g(x)u\end{cases} \\ &y = x_1.\end{aligned} \tag{8}$$

The trajectory tracking problem of the motor can be given by the following reference model

$$\begin{cases}\dot{x}_{d1} = x_{d2} \\ \dot{x}_{d2} = f_d(x_d)\end{cases} \tag{9}$$

where $f_d(x_d)$ is a known smooth function.

Define composite tracking errors as follows

$$\begin{cases}z_1 = x_{d1} - x_1 \\ z_2 = \dot{z}_1 + K_1 z_1\end{cases} \tag{10}$$

where K_1 is the gain that can be artificially designed.

It can be known from formula (9) and (10) that

$$\begin{cases}\dot{z}_1 = -K_1 z_1 + z_2 \\ \dot{z}_2 = -K_1^2 z_1 + K_1 z_2 + f_d(x_d) - f(x) - g(x)u\end{cases} \tag{11}$$

In order to achieve the goal of trajectory tracking control, consider the following feedback linearization control law design

$$\begin{aligned}u &= K_2 z_2 + \frac{1}{g(x)}\left(f_d(x_d) - f(x)\right) \\ &= K_2 z_2 + p(x)\end{aligned} \tag{12}$$

where $K_2 > 0$ is the gain that can be artificially designed, $p(x) = \frac{1}{g(x)}(f_d(x_d) - f(x)$ is an unknown smooth nonlinear function, which can be approximated by RBF neural network.

Applying the RBFNN to approximate $p(x)$, the following control law design is obtained

$$u = K_2 z_2 + \hat{\omega}^T\theta(x_d) \tag{13}$$

where ω represents the estimated value of the optimal weight vector ω^*, and ω^* is defined according to (5) as follows

$$\omega^* = \arg\min_{\hat{\omega}\in\omega_p}[\sup_{x\in\omega_x}|\hat{p}(x|\hat{\omega}) - p(x)|] \tag{14}$$

Based on the optimal weight vector (13), make the following estimation for the unknown nonlinear function $p(x)$

$$p(x) = \omega^{*T}\theta(x) + \varepsilon_p(x) \tag{15}$$

According to (3), employing the SMRLS algorithm, multiplying both sides of (15) by $P\theta(x_d)$, under the assumption of a sufficiently small sampling period, the following continuous equation can be derived

$$\begin{aligned} P\theta(x_d)u &= P\theta(x_d)\omega^{*T}\theta(x_d) \\ \dot{P}^{-1} &= \theta(x_d)\theta(x_d)^T - \theta_a(x_d)\theta_a^T(x_d) \end{aligned} \tag{16}$$

Then, define a modified prediction error

$$\begin{aligned} \epsilon &= P\theta(x)[u - \omega^T\theta(x)] - \epsilon_a, \\ \dot{P}^{-1} &= \theta(x)\theta(x)^T - \theta_a(x)\theta_a^T(x). \end{aligned} \tag{17}$$

The composite learning law of $\hat{\omega}$ is designed as

$$\dot{\hat{\omega}} = \Gamma(\theta(x_d)z_2 + k_\omega\epsilon - \delta\hat{\omega}) \tag{18}$$

where $\Gamma \in \mathbb{R}^{N\times N}$, $k_\omega \in \mathbb{R}^{N\times N}$ are positive-definite diagonal matrices and $\delta > 0$ are the designed parameters.

Note that Γ and k_ω in (18) can be chosen freely. Composite learning means that the NN weights $\hat{\omega}$ are updated by a composite feedback composed of the tracking errors z_2 and the prediction errors ϵ to learn optimal ω^*. The structure of the control system is shown in Fig. 3.

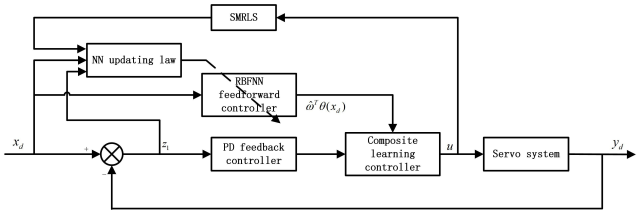

Fig. 3: Control system

4 Stability and convergence analysis

The Lyapunov function is chosen as

$$V = \frac{1}{2g(x)}(K_1^2 z_1^2 + z_2^2) + \frac{1}{2}\tilde{\omega}^T\Gamma^{-1}\tilde{\omega}. \tag{19}$$

According to the function (11), the control law (12),(13), the approximation method (3),(5), the prediction error function (17) and the composite learning law (18), we can obtain the derivative of $\dot{V}$ is

$$\begin{aligned} \dot{V} = &-\frac{\dot{g}(x)}{2g^2(x)}(K_1^2 z_1^2 + z_2^2) - \frac{K_1^3}{g(x)}z_1^2 - (K_2 - \frac{K_1}{g(x)})z_2^2 \\ &+ z_2\varepsilon_p(x) + \sigma\tilde{\omega}^T\hat{\omega} - \tilde{\omega}^T k_{\omega i}P\dot{P}^{-1}\tilde{\omega} \end{aligned} \tag{20}$$

Since $|\epsilon(x)| < \epsilon_M$, we obtain the following inequations

$$\begin{aligned} \tilde{\omega}_i^T\hat{\omega} &= \tilde{\omega}^T(-\tilde{\omega} + \omega_i^*) \\ &\leq -\frac{1}{2}\tilde{\omega}^T\tilde{\omega} + \frac{1}{2}||\omega^*||^2 \\ z_2\epsilon_p(x) &\leqslant \frac{1}{2}\left(z_2^2 + \epsilon_p^2(x)\right) \\ &\leqslant \frac{1}{2}z_2^2 + \frac{1}{2}\epsilon_{Mp} \end{aligned} \tag{21}$$

And since $k_\omega = k_\omega I$, $k_\omega > 0$, $I \in \mathbb{R}$ is an identity matrix. According to [14], and according to the Courant-Fischer min-max theorem, we have

$$\begin{aligned} \lambda_{\min}(P^{-1}(k)) &= \min_{X\in\mathbb{R}^N, \|X\|\neq 0}\frac{X^T P^{-1}(k)X}{X^T X} \\ &= \lambda_{\min}(P^{-1}(0)) + \lambda_{\min}\left(\sum_{i=1}^{N_k}\theta(i)\theta^T(i)\right) \\ &\geqslant \lambda_{\min}(P^{-1}(0)) \end{aligned} \tag{22}$$

where $\lambda_{\min}(\cdot), \lambda_{\max}(\cdot)$ represent the minimum and maximum eigenvalues. Since $\lambda_{\max}(P(k)) = 1/\lambda_{\min}(P^{-1}(k))$, we obtain $\lambda_{\max}(P(k)) \leq \lambda_{\max}(P(0))$ holds for any $k > 0$, and the following inequation

$$\lambda_{\max}(P(k)) \leqslant p_0 \tag{23}$$

holds for any $k > 0$. Similarly, we can obtain that there exists a positive constant $q_0 > 0$ such that $q_0 \leq \lambda_{\min}(P(k)) \leqslant$ holds for any $k > 0$. So P_i is bounded and we can obtain the inequality $\lambda_{max}(P_i) \leq p_0$.

$$\begin{aligned} \lambda_{\max}(P\dot{P}^{-1}) &= \lambda_{\max}\left(P\theta\theta^T - P\theta_a\theta_a^T\right) \\ &= \max_{X\in\mathbb{R}^N, \|X\|\neq 0}\frac{X^T\left(P\theta\theta^T - P\theta_a\theta_a^T\right)X}{X^T X} \\ &= \lambda_{max}\left(P\theta\theta^T\right) - \lambda_{max}\left(P\theta_a\theta_a^T\right) \\ &\leqslant tr\left(\theta\theta^T\right)p_0 - tr\left(\theta_a\theta_a^T\right)p_0 \\ &\leqslant Np_0. \end{aligned} \tag{24}$$

Substitute (21), (24) into (20), and we have

$$\begin{aligned} \dot{V} \leqslant &-\left(\frac{K_1^2\dot{g}(x)}{2g^2(x)} + \frac{K_1^3}{g(x)}\right)z_1^2 - \left(K_2 - \frac{K_1}{g(x)} - \frac{1}{2}\right)z_2^2 \\ &- (\frac{1}{2}\delta_i + \frac{1}{2}k_\omega Np_0)\tilde{\omega}_i^T\tilde{\omega}_i + \frac{1}{2}\delta_i \parallel \omega_i^* \parallel^2 + \frac{1}{2}\epsilon_{Mp}. \end{aligned} \tag{25}$$

From (25), the parameters are rendered by selecting

$$\begin{aligned} c_1 &= \min\left\{\frac{K_1^2\dot{g}(x)}{2g^2(x)} + \frac{K_1^3}{g(x)}, K_2 - \frac{K_1}{g(x)} - \frac{1}{2}, \frac{1}{2}\delta_i + \frac{1}{2}k_\omega Np_0\right\} \\ c_2 &= \frac{1}{2}\delta_i \parallel \omega_i^* \parallel^2 + \frac{1}{2}\epsilon_{Mp}, \end{aligned} \tag{26}$$

and we obtain the following inequations

$$\dot{V} \leqslant -c_1 V + c_2 \tag{27}$$

By analyzing (27), it is inferred that $V \to (c_1/\varrho)$ as $t \to \infty$. Additionally, it can be demonstrated that all signals within the Lyapunov function (19) exhibit uniformly ultimately bounded (UUB) behavior. This completes the proof.

5 Experiment

5.1 Experimental Setup

The platform used in this experiment is depicted in Fig. 4, consisting of a three-axis CNC machine tool. It is primarily composed of a machine body, three GTHD servo drives, a digital signal processor (DSP), and a computer. The operational principle of the experimental platform is outlined

as follows: initially, the control algorithm is implemented on the computer using Simulink. Subsequently, the modules in the RTI library are employed to replace the portion in Simulink connected to the physical platform. After compilation, the graphical language is translated into a language understandable by external hardware. Simultaneously, real-time code is downloaded to the DSP controller. The DSP controller is connected to the servo motors through GTHD servo drives, driving the three-axis tool movement. The servo drives operate in analog speed mode, with the current loop and speed loop on the servo drive side, while the position loop is on the DSP controller side. The GTHD-006AAP1-00 servo drive is utilized, and the servo motor employed in the experiment is the TS4607N2190E200. The DSP controller is based on the DS1103 PPC control board. The internal motion control system of the machine tool

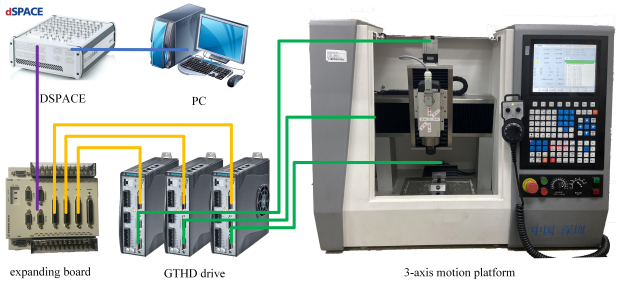

Fig. 4: Experimental platform

adopts a cascaded structure with a current loop, speed loop, position loop, and velocity feedforward controller. However, beneath these controllers, CNC machines still exhibit internal nonlinear factors and external random disturbances. The proposed feedforward tracking controller, based on RBFNN composite learning, aims to compensate for feedforward in CNC machines. By learning the model of the CNC machine system, the neural network ensures a comprehensive understanding of the system's knowledge, thereby enhancing the tracking control precision of the controller.

5.2 Experimental Results

The position loop in the servo drive section employs PD control, and the designed controller determines its control parameters (12). For the PD part of the controller, the gain matrices $K_1 = [5, 0; 0, 5]$ and $K_2 = [20, 0; 0, 20]$, which are equivalent to a proportional gain $K_P = [100, 0; 0, 100]$ and a derivative gain $K_D = [20, 0; 0, 20]$ in the PD control. For the adaptive RBFNN part, the input of the RBFNNs is set to $x_d = [x_{d1}, \dot{x}_{d1}, \ddot{x}_{d1}]^T$ and the following RBFNN structures are adopted and compared.

1. **RBFNN-SGD:** To improve the convergence speed and accuracy of $\hat{\omega}$ in the learning process, instead of the lattice distribution, we can use methods such as K-means clustering to obtain an optimized center distribution on the reference trajectories [15]. In this case, only 50 neurons are distributed evenly along the reference trajectory x_d, and the weight update law is adopted with the parameter $\Gamma = \mathrm{diag}(0.2, 0.2, \ldots, 0.2) \in \mathbb{R}^{20\times 20}$, $\sigma = 1 \times 10^{-4}$.
2. **RBFNN-CLC:** To demonstrate the effectiveness of the compensated RBFNN-based learning control, 50 neurons along x_d with the adaptive phase compensation are adopted. In this case, the weight update law (18) with $\Gamma = \mathrm{diag}(0.2, 0.2, \ldots, 0.2) \in \mathbb{R}^{20\times 20}$,$k_\omega = 0.5$ and $\sigma = 1 \times 10^{-4}$. It should be noted that the hyperparameters of the RBFNN-CLC are the same as the original RBFNN-O mentioned above to show the effect of the composite learning control.

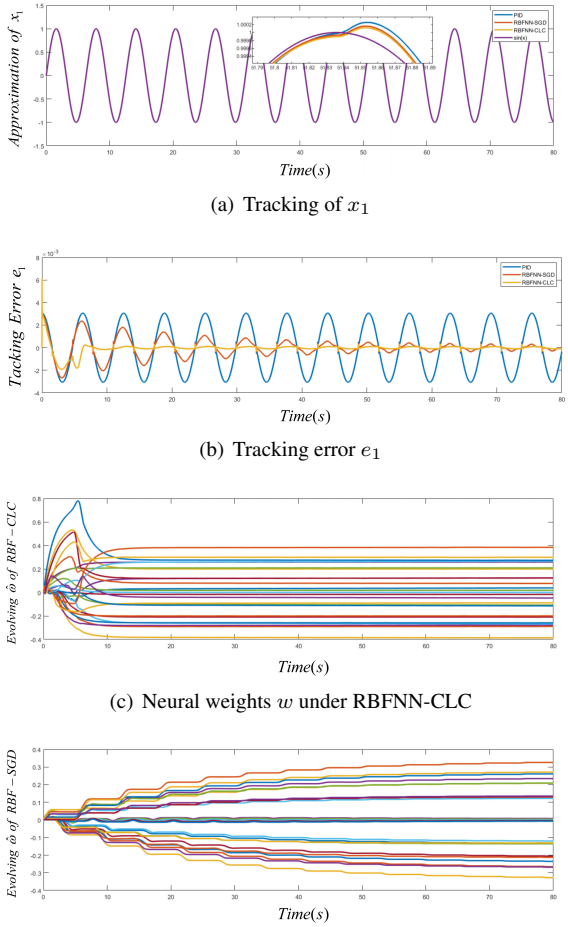

(a) Tracking of x_1

(b) Tracking error e_1

(c) Neural weights w under RBFNN-CLC

(d) Neural weights w under RBFNN-SGD

Fig. 5: Comparison of the performance of the two methods during the learning phase

The reference trajectory is selected as $y_d = sin(t)$. Fig. 5 shows the tracking performance of the RBFNN-SGD and RBFNN-CLC based feedforward feedback control schemes and shows the convergence of the weight vector in these two control schemes. Figs. 6(a) and Figs. 6(b) shows the tracking accuracy of the three controllers during the neural network learning phase, and it is clear that RBFNN-CLC possesses higher tracking control accuracy. It is shown that the composite learning control improves the learning accuracy of the original RBFNN and thus improves the control performance of the feedforward controller.

Figs. 5(c) and Figs. 5(d) illustrates the convergence of weights for both neural network learning algorithms. Obviously, the convergence of the neural network using the RBFNN-CLC algorithm is very fast, and the convergence occurs in about 10s of online learning, while the RBFNN-SGD algorithm needs 50s to make the neural network converge, and the results show that the composite learning can

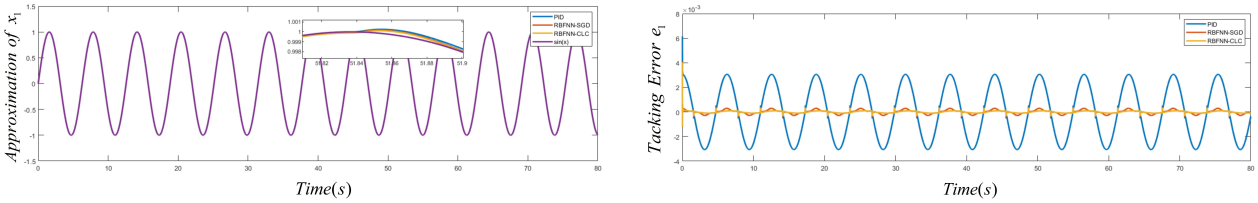

(a) Tracking of x_1

(b) Tracking error e_1

Fig. 6: Comparison of the performance of the two methods during the knowledge reuse phase

greatly improve the learning speed of the neural network, confirming our expectations.

After the learning phase over the time interval [0, 80s], the average values of ω and θ over [75s, 80s] are taken as the learned knowledge. Figs. 6 shows that the neural network using both algorithms successfully learned the knowledge, and the RBFNN-CLC possesses higher tracking control accuracy.

6 Conclusion

This paper introduces a novel method of composite learning feedforward control based on RBFNN and applies it to a three-axis CNC machine tool model. The composite learning method primarily relies on the SMRLS algorithm to construct prediction errors, incorporating them into an adaptive update law. Due to the system information contained in the new prediction errors, this approach exhibits a faster learning speed and more precise learning accuracy compared to neural networks updated solely based on tracking errors. The stability of the controller is verified using the Lyapunov method, and experiments on a three-axis CNC machine tool validate the effectiveness of the algorithm. The results demonstrate that the composite learning feedforward control based on RBFNN enhances the learning speed of the neural network and improves the tracking control accuracy of CNC machines.

Acknowledgement

This work was supported by Shenzhen Science and Technology Program under Grant GXWD20231130150241001and in part by National Natural Science Foundation of China under Grant 52275481.

References

[1] R. Ramesh, M. Mannan, A. Poo, Tracking and contour error control in cnc servo systems, International Journal of Machine Tools and Manufacture 45 (3) (2005) 301–326.

[2] M. F. Corapsiz, K. Erenturk, Trajectory tracking control and contouring performance of three-dimensional cnc, IEEE Transactions on Industrial Electronics 63 (4) (2015) 2212–2220.

[3] K.-S. Fu, Learning control systems–review and outlook, IEEE transactions on Automatic Control 15 (2) (1970) 210–221.

[4] F. J. Pineda, Dynamics and architecture for neural computation, Journal of complexity 4 (3) (1988) 216–245.

[5] C. Wang, D. J. Hill, Learning from neural control, IEEE Transactions on Neural Networks 17 (1) (2006) 130–146.

[6] T. Wang, H. Gao, J. Qiu, A combined adaptive neural network and nonlinear model predictive control for multirate networked industrial process control, IEEE Transactions on Neural Networks and Learning Systems 27 (2) (2015) 416–425.

[7] K. Hornik, M. Stinchcombe, H. White, Multilayer feedforward networks are universal approximators, Neural networks 2 (5) (1989) 359–366.

[8] F. Lewis, Nonlinear network structures for feedback control, Asian Journal of Control 1 (4) (1999) 205–228.

[9] J. Park, I. W. Sandberg, Universal approximation using radial-basis-function networks, Neural computation 3 (2) (1991) 246–257.

[10] T. Zheng, C. Wang, Relationship between persistent excitation levels and rbf network structures, with application to performance analysis of deterministic learning, IEEE transactions on cybernetics 47 (10) (2017) 3380–3392.

[11] B. Xu, F. Sun, Composite intelligent learning control of strict-feedback systems with disturbance, IEEE transactions on cybernetics 48 (2) (2017) 730–741.

[12] Y. Pan, T. Sun, Y. Liu, H. Yu, Composite learning from adaptive backstepping neural network control, Neural Networks 95 (2017) 134–142.

[13] Y. Fei, J. Li, Y. Li, Selective memory recursive least squares: Uniformly allocated approximation capabilities of rbf neural networks in real-time learning, arXiv preprint arXiv:2211.07909 (2022).

[14] Y. Fei, J. Li, Y. Li, Real-time progressive learning: Mutually reinforcing learning and control with neural-network-based selective memory, arXiv preprint arXiv:2308.04223 (2023).

[15] Q. Liu, D. Li, S. S. Ge, Z. Ouyang, Adaptive feedforward neural network control with an optimized hidden node distribution, IEEE Transactions on Artificial Intelligence 2 (1) (2021) 71–82.

Proceedings of the 3rd Conference on Fully Actuated System Theory and Applications
May 10-12, 2024, Shenzhen, China

Dynamic Region Detection and Removal Based on Deep Learning and Optical Flow

Shixiong Fan, Mengmeng Qian, Songheng Mao, Aoqiang Liu, Yuan Fan
School of Electrical Engineering and Automation, Anhui University, Hefei, Anhui 230601 P. R. China
E-mail: yuanf@ahu.edu.cn

Abstract: Simultaneous Localization And Mapping (SLAM) refers to the process in which a robot interacts with its surrounding environment to achieve self-positioning and construct an environmental map simultaneously. However, traditional SLAM algorithms assume scene rigidity, often leading to inaccurate positioning and mapping in dynamic environments. To address this limitation, we propose a visual RGB-D SLAM system that integrates ORB features, YOLOv5, Lucas-Kanade (LK) optical flow, and geometric information. During the ORB feature extraction stage, dynamic points are identified by utilizing LK optical flow to assess whether the Region of Interest (ROI) generated by the neural network is a dynamic area. Subsequently, dynamic feature points within the dynamic ROI are removed using a combination of optical flow and depth information. For dynamic points that are either missed or unrecognized by the neural network, we employ multi-view geometry for their removal. We tested the system's performance on the public TUM dataset, demonstrating its capability to achieve SLAM functionality in dynamic environments.

Key Words: Neural Network, Geometry, ORB, LK Optical Flow

1 Introduction

In the rapidly advancing field of technology, autonomous localization and environmental perception of machines are crucial elements driving automation, robotics, and augmented reality. Visual SLAM technology, as a revolutionary achievement, empowers machines to dynamically position themselves and construct maps in unknown environments, laying a robust foundation for the movement of robots and autonomous systems. However, with the introduction of dynamic elements, traditional SLAM methods face new challenges in addressing issues related to the autonomous localization of robots and map construction.

There are currently several methodologies employed in dynamic visual SLAM. One approach utilizes geometric methods, disregarding mobile components and constructing a structural graph based on static regions [1, 2]. Another solution leverages deep neural networks to identify specific moving objects, excluding them from post-processing algorithms [3, 4]. In order to prevent the inadvertent removal of stable features through object detection [5], Semantic segmentation demands extensive computational resources, posing a challenge to the real-time requirements of SLAM systems. Consequently, certain research approaches strive to address this by exclusively segmenting dynamic objects in keyframes and employing motion probability propagation for each frame [6, 7]. With the evolution of deep learning, specialized networks can significantly enhance dynamic segmentation. The integration of these networks with SLAM enables dynamic object detection, eliminating these dynamic points in subsequent processing to enhance the robot's perceptual capabilities. The third method involves using depth information to distinguish between the background and dynamic objects [8, 9]. These strategies have their respective advantages and disadvantages, and their integration can yield a novel algorithm suitable for various scenarios. In this paper,The following contributions have been made :

- The LK optical flow into the frame is calculated, and the prior dynamic object is judged to be a dynamic object by analyzing the optical flow results, and the depth threshold is set to realize the removal of dynamic points.
- A lightweight tracking mode was introduced to reduce the computational burden. Additionally, a multi-view geometry-based method was proposed to remove dynamic points not detected by object detection and lacking depth information.
- Through experimental validation, our method has demonstrated superior performance in dynamic environments.

2 Related Work

Most current SLAM systems classify dynamic points as outliers, disregarding them in subsequent tracking and mapping stages. A prevalent technique involves the use of RANSAC (e.g., ORB-SLAM) to mitigate the impact of these outliers. In feature-based SLAM systems, various techniques are employed to address dynamic environments,some of the most relevant are:

- DynaSLAM [3] employs Mask RCNN for generating semantic masks for the most common dynamic objects. It also utilizes a multi-view geometric approach to address dynamic objects that Mask RCNN cannot recognize. Concurrently, depth images of these objects are employed to rectify the corresponding areas, facilitating the construction of a static map.
- YOLO-SLAM [10] extends ORB-SLAM2 with semantic segmentation and dynamic feature filtering. In the segmentation thread, Darknet19-YOLOv3 is employed to identify known dynamic objects, while the dynamic feature filtering thread uses geometric depth RANSAC to categorize feature points into dynamic and static subsets. The method distinguishes static and dynamic points by computing the depth variance of feature points within each bounding box.

This work was supported by the National Natural Science Foundation of China (61973002), and the Anhui Provincial Natural Science Foundation (2008085J32).

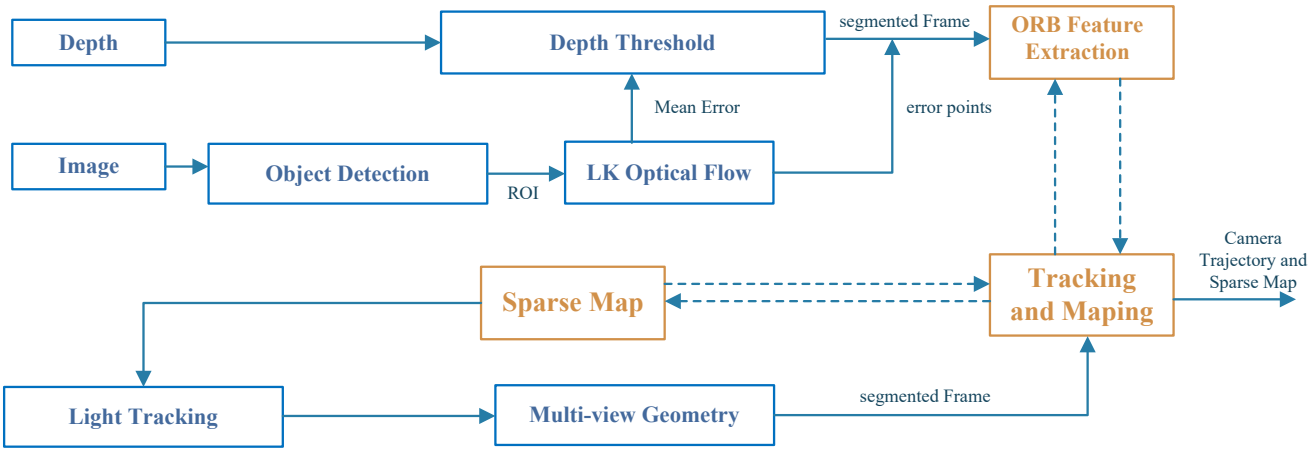

Fig. 1: For incoming RGB images, dynamic ROI is obtained through a neural network. ROI is then subjected to optical flow analysis to determine their dynamism. A combination of depth thresholding and LK optical flow is employed to eliminate dynamic points. For regions where detection is unsuccessful or for dynamic points with invalid depth information, a multi-view geometry approach is applied to remove such dynamic elements.

- Dynamic-VINS [9] integrates target detection and depth information for dynamic feature recognition, exhibiting performance comparable to semantic segmentation. The system employs grid-based feature detection, introducing a rapid and efficient methodology to extract high-quality FAST feature points. The Inertial Measurement Unit (IMU) is utilized for predicting feature tracking and ensuring motion consistency.

3 System Overview

Our system extends ORB-SLAM3 [11], introducing a lightweight tracking mode to mitigate computational overhead. This extension seamlessly integrates YOLOv5 object detection with depth information, effectively achieving approximate semantic segmentation of RGB-D images. Furthermore, a multi-view geometry approach is employed to address static objects eluding object detection and to manage dynamic points with missing depth information.

In the feature extraction phase, we initially employ LK optical flow to assess the dynamism of the ROI [12]. For dynamic regions, a combination of depth thresholding and the optical flow method is applied to eliminate dynamic points. Subsequently, the optimization of dynamic point removal is achieved using a multi-view geometry approach. This method not only aids in eliminating dynamic points that may be overlooked by object detection but also rectifies instances where dynamic points are inaccurately retained due to incomplete depth information. Ultimately, stable static feature points are leveraged to underpin the implementation of SLAM functionality, The relationship between variables is illustrated in Fig1 .

3.1 Prior Dynamic Object Detection Using YOLO

In the field of computer vision, dynamic object detection plays a pivotal role, particularly in real-time object tracking [13], autonomous driving, and intelligent security systems. To achieve efficient and accurate dynamic object detection, we've introduced YOLOv5, a popular object detection framework known for its outstanding performance in rapidly and precisely identifying various objects within images.

In our system, we prioritize prior dynamic object detection. By leveraging YOLOv5, we can efficiently detect dynamic objects, such as pedestrians, vehicles, and animals, in RGB-D images. The key to this step is accurately distinguishing dynamic objects from static backgrounds, providing precise target regions for subsequent processing steps.

Once we successfully detect dynamic objects, we combine depth information with the results from YOLOv5 to achieve an approximate semantic segmentation. This means that we can precisely determine which object each pixel belongs to, enabling advanced understanding and inference [14]. This approximate semantic segmentation not only enhances the accuracy of target detection but also provides more information for subsequent processing steps.

Finally, we employ a multi-view geometry method to further enhance the accuracy of prior dynamic object detection. This method helps remove mobile static objects that cannot be detected by the target detection system, as well as dynamic points with missing depth information. Through multi-view geometry, we can confirm dynamic objects from multiple angles, further boosting system performance.

3.2 Depth Threshold and LK Optical Flow

Initially, LK optical flow computation is applied to the ROI supplied to the YOLO neural network. As an object moves within an image, its position changes across different frames. Optical flow calculates these positional variations, creating a representation of motion known as the optical flow field. In this field, each pixel is assigned a motion vector indicating its direction and speed of movement in the image plane [15]. If a pixel corresponds to a dynamic object, its optical flow vector tends to differ from the vectors associated with the background or stationary objects.

First, we calculate the mean of the optical flow differences:

$$e = \frac{1}{n}\sum_{i=1}^{n}(I(x_i, y_i) - I'(x_i + dx_i, y_i + dy_i)) \quad \text{for}(x_i, y_i) \in \mathrm{B} \tag{1}$$

where B refers to the bounding box region used to identify moving objects. n represents the number of feature points with positive optical flow differences.

Using the calculated mean of the optical flow interpolation, we can establish an appropriate threshold to ascertain whether the Region of Interest (ROI) corresponds to a genuine dynamic area. If the mean of the optical flow differences within the ROI exceeds the predefined threshold (in this paper, set at 6.5 based on multiple experimental results), we classify the region as dynamic and proceed to eliminate the dynamic feature points within that area using the optical flow differences and the subsequently mentioned depth threshold. Conversely, if the mean error falls below the established threshold, we categorize the ROI as a static region, and no further action is taken in that area.

For regions identified as dynamic, we continue to compute the average depth value d_{Mean} , standard deviation d_{Sd} , and maximum value d_{Max} within the region. We set the depth threshold :

$$d_{\mathrm{dt}} = \begin{cases} d_{\mathrm{Mean}} + d_{\mathrm{Sd}}, & d_{\mathrm{Max}} > 3 * d_{\mathrm{Mean}}, \quad d_{\mathrm{Mean}} > 0 \\ d_{\mathrm{Mean}} + 0.8 * d_{\mathrm{Sd}}, & d_{\mathrm{Mean}} > 0 \\ 0, & others \end{cases} \tag{2}$$

Within the ROI, our objective is to eliminate as many dynamic points as possible. To achieve this, we exclude feature points with optical flow differences greater than zero, recognizing that this approach may result in the unintentional removal of some static points. Additionally, for feature points with valid depth values, we apply a depth threshold to filter out points that do not satisfy the specified depth criteria. In cases where both depth values and optical flow are considered invalid, or for dynamic objects that went undetected, we employ multi-view geometry to eliminate these points.

3.3 Light Tracking

In RGB-D mode, accurate estimation of the camera's pose becomes essential post the elimination of dynamic points. To tackle this, we have devised a cost-effective tracking module for camera localization within the mapped area. This tracking mode is a streamlined version of the tracking component found in ORB-SLAM3, leading to decreased computational demands. It entails the projection of map features onto image frames, the search for correspondences within static image regions, and the utilization of reprojection error minimization to enhance the precision of the camera's pose.

3.4 Geometry-Based Dynamic Point Removal

We have utilized depth thresholding and object detection methods to effectively filter out the majority of dynamic points from the images, ensuring their exclusion from subsequent mapping and tracking modules. Nonetheless, certain scenarios require special consideration, such as frames with invalid depth information and dynamic objects that managed to evade detection by the object detection module. In this section, we will present a detailed explanation of how to address these dynamic points.

To do so, we compute the Euclidean distances between the rotation and translation of the current frame and the ten nearest keyframes in the system. Throughout this process, we adopt a weighted approach to amalgamate the rotation and translation distances, assigning a higher weight to the translation distance.

$$\begin{cases} r_{\mathrm{d}} = \sqrt{\sum_{i=1}^{3}\sum_{j=1}^{3}(Rij - rij)^2} \\ t_{\mathrm{d}} = \sqrt{(Tx - tx)^2 + (Ty - ty)^2 + (Tz - tz)^2} \\ w_{\mathrm{d}} = 0.7 * T_{\mathrm{d}} + 0.3 * R_{\mathrm{d}} \end{cases} \tag{3}$$

where r_{d} represents the L2 norm of the rotation matrices between two frames, while t_{d} corresponds to the L2 norm of the translation vectors.Ultimately, we select the top five image frames with the highest weights as reference frames. Subsequently, dynamic keypoints are extracted from the image sequence. Initially, we traverse the keypoints of each frame in the reference frames, calculating the projection of the keypoints from the reference keyframe to the current frame, as illustrated in Fig 2.

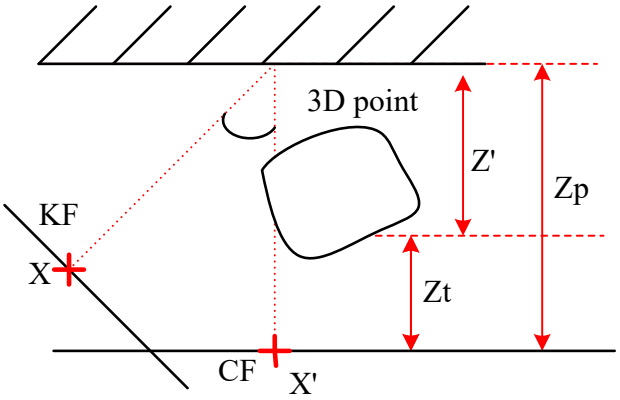

Fig. 2: Compute the world coordinates of key points, denoted as X, in the key frame (KF), and project them onto corresponding points, denoted as X, in the current frame (CF). Calculate the projection depth Z_{p} and compare it with the depth Z_{t} directly obtained from the RGB-D camera.

$$Z' = Z_{\mathrm{P}} - Z_{\mathrm{t}} \tag{4}$$

Where Z_{P} represents the projected depth, Z_{t} represents the actual depth. The keypoints X are obtained through the feature extraction algorithm of ORB-SLAM3. For each keypoint X and its corresponding 3D point, the projection angle between keypoint X' and is calculated. In the TUM dataset, static objects with a parallax angle greater than 30° are considered dynamic due to differences in their viewpoints. For keypoints with a parallax angle less than 30°, we compute the difference Z' between their projected depth and the true depth. If Z' exceeds a predetermined threshold, it is deemed dynamic.After obtaining information about dynamic points, to classify all pixels belonging to dynamic objects, we employ a region-growing technique around dynamic pixels in the depth image.

4 Experiments and Results

We tested our system on the public TUM RGB-D dataset, and as our system is built on ORB-SLAM3, they were used

to demonstrate our improved baseline. We compared it with other slam systems of the same type. The provided results represent the median values derived from five experiments. The TUM RGB-D dataset is composed of 39 sequences recorded with a Microsoft Kinect sensor in different indoor scenes at full frame rate (30Hz). Both the RGB and the depth images are available, together with the ground-truth trajectory, the latest recorded by a high-accuracy motion-capture system. In the sequences named sitting (s) there are two people sitting in front of a desk while speaking and gesticulating, i.e., there is a low degree of motion. In the sequences named walking (w), two people walk both in the background and the foreground and sit down in front of the desk. This dataset is highly dynamic. The sequences named f1 and f2 represent static environments and therefore challenging for standard SLAM systems. A portion of the dataset related to the f3 sequence is extracted from the referenced academic paper, and the remaining data is obtained through our experimental endeavors [3, 4, 16] . Our evaluation metrics for the system include ATE and RPE. ATE is employed to quantify the absolute error between the estimated camera trajectory and the ground truth trajectory in SLAM systems. It computes the Euclidean distance between the estimated position at each frame and the corresponding actual position on the ground. ATE serves as a holistic measure of trajectory error, offering a global perspective on system performance. RPE serves as a metric to gauge the accuracy of relative pose estimation between adjacent frames in SLAM systems. Unlike ATE, which focuses on overall trajectory discrepancies, RPE concentrates on the relative pose changes between neighboring frames. This perspective offers a more detailed insight into the system's positional accuracy over short durations. RPE calculates the error between the estimated relative pose and the actual ground truth relative pose. By comparing the estimated pose at each timestamp with the corresponding ground truth pose, the system's accuracy in local trajectory is quantified. Specific Calculation Formula is as Follows:

$$\begin{cases} ATE = \sqrt{\dfrac{1}{N}\sum_{i=1}^{N} \|P_{\text{est},i} - P_{\text{gt},i}\|^2} \\ RPE = \sqrt{\dfrac{1}{N}\sum_{i=1}^{N} \|T_{\text{est},i} - T_{\text{gt},i}\|^2} \end{cases} \tag{5}$$

where N represents the number of frames, $P_{\text{est},i}$ denotes the estimated camera position, $P_{\text{gt},i}$ corresponds to the ground truth camera position,$T_{\text{est},i}$signifies the estimated relative pose, and $T_{\text{gt},i}$ stands for the corresponding ground truth relative pose.

Table 1 presents the Absolute Trajectory Error Metrics for our system and comparable systems. We conducted a comparison across five sequences, each representing static, dynamic indoor environments.

- f1/xyz: An individual calmly seated behind a computer, representing a static environment with detected prior dynamic objects.
- f2/xyz: A small bear also seated behind a computer in a chair, representing a static environment without prior dynamic objects.

Table 1: Results of Absolute Trajectory Error Metrics

	Sequence	f1/xyz	f2/xyz	f3/s/s	f3/w/half	f3/w/xyz
ORB-SLAM3	RMSE	0.0150	0.0151	0.0093	0.1974	0.2774
	Mean	0.0131	0.0119	0.0080	0.1850	0.2159
	Median	0.0115	0.0082	0.0071	0.1753	0.2065
	S.D.	0.0073	0.0094	0.0048	0.0688	0.1743
Ours	RMSE	**0.0148**	0.0144	0.0064	**0.0245**	0.0151
	Mean	**0.0130**	**0.0112**	0.0057	**0.0211**	0.0131
	Median	**0.0114**	**0.0076**	0.0053	**0.0187**	0.0117
	S.D.	**0.0070**	0.0090	0.0030	**0.0124**	0.0075
DynaSLAM	RMSE	0.0154	**0.0137**	0.0063	0.0301	0.0156
	Mean	0.0133	0.0113	0.0055	0.0258	0.0134
	Median	0.0116	0.0086	0.0049	0.0218	0.0118
	S.D.	0.0074	**0.0077**	0.0031	0.0155	0.0079
DP-SLAM	RMSE	-	-	**0.0059**	0.0254	**0.0141**
	Mean	-	-	**0.0051**	0.0219	**0.0120**
	Median	-	-	**0.0047**	0.0183	**0.0106**
	S.D.	-	-	**0.0029**	0.0129	**0.0073**
DS-SLAM	RMSE	-	-	0.0065	0.0303	0.0247
	Mean	-	-	0.0055	0.0258	0.0186
	Median	-	-	0.0049	0.0222	0.0151
	S.D.	-	-	0.0033	0.0159	0.0161

Table 2: Comparison of the RMSE of RPE [m] of DySLAM against ORB-SLAM3 for RGB-D cameras.

Sequence	ORB-SLAM3		Ours	
	R.RMSE	T.RMSE	R.RMSE	T.RMSE
f1/xyz	1.0902	0.2332	**1.0774**	**0.2052**
f2/xyz	**0.3058**	0.0042	0.3083	**0.0041**
f3/s/s	0.3009	0.0101	**0.2676**	**0.0081**
f3/w/half	2.3166	0.1236	**0.7409**	**0.0258**
f3/w/xyz	3.0745	0.1733	**0.5990**	**0.0188**

- f3/s/xyz: Two people engaged in a conversation while seated, representing a low dynamic environment.
- f3/w/half and f3/w/xyz: Two individuals walking around a computer desk, representing a high dynamic environment.

Based on the results in Table 1 , our system exhibits superior adaptability to dynamic environments compared to ORB-SLAM3. Furthermore, it demonstrates comparable performance with ORB-SLAM3 even in static environments.

Table 2 presents the RMSE of RPE [m] of our system compared to ORB-SLAM3 for RGB-D cameras.The rotation and translation errors of our system in static environments are comparable to those of ORB-SLAM3, as indicated in the table. Moreover, our system demonstrates enhanced suitability for dynamic environments.

In Fig 3 and 4, the left images depict the trajectory of ORB-SLAM3, while the right images show the trajectory

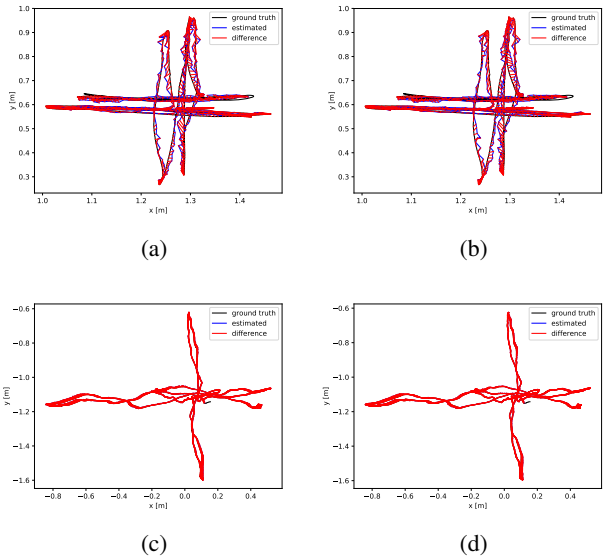

(a) (b) (c) (d)

Fig. 3: The four sets of images demonstrate the trajectory comparison between our method and ORB-SLAM3 in a static environment. Specifically, Fig 3a and 3b depict two trajectories under dataset fr1/xyz. In this dataset, a person is seated in a chair, creating a static environment with a priori dynamic objects. On the other hand, Fig 3c and 3d correspond to trajectories under dataset fr2/xyz, where no prior information about dynamic objects is available, representing a purely static environment.

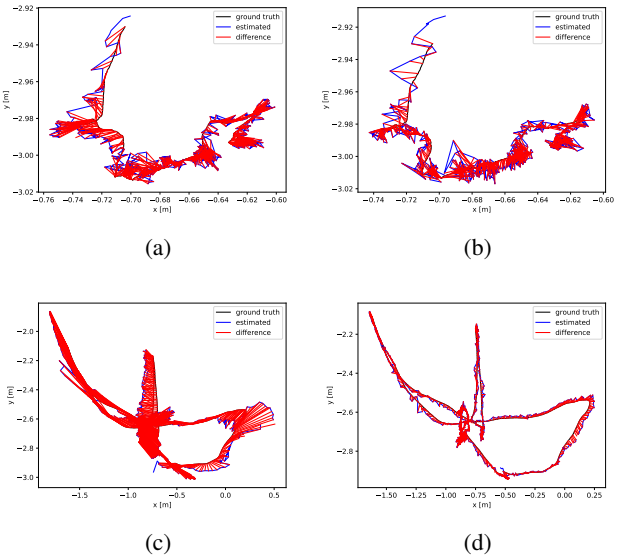

(a) (b) (c) (d)

Fig. 4: The four sets of images illustrate the trajectory comparison between our method and ORB-SLAM3 in a dynamic environment. Specifically, Fig 4a and 4b depict two trajectories under dataset f3/s/s. In this dataset, two people are seated, engaging in conversation, representing a low-dynamic environment. On the other hand, Fig 4c and 4d correspond to trajectories under dataset f3/w/half, where two people are moving around a table, constituting a high-dynamic environment.

of our system. Fig 3 illustrates the trajectory comparison between our proposed method and ORB-SLAM3 in a static environment. In Fig 3a and 3b, it is shown that in the presence of a Prior dynamic object, our method exhibits comparable accuracy to ORB-SLAM3. In Fig 3c and 3d, the trajectories are compared in a static environment without a Prior dynamic object, demonstrating that our method closely aligns with the trajectory of ORB-SLAM3. Fig 4 illustrates the trajectory comparison between our proposed method and ORB-SLAM3 in dynamic a dynamic environment. In Fig 4a and 4b, In low dynamic environments, our trajectory is slightly superior to the trajectory of ORB-SLAM3. In Fig 4c and 4d, In high dynamic environments, our trajectory is significantly superior to that of ORB-SLAM3. In conclusion, whether in static or dynamic environments, our system demonstrates remarkably outstanding performance.

5 Conclusions

The proposed SLAM system, which integrates ORB features, YOLOv5, Lucas-Kanade optical flow, and geometric information, presents a robust solution to address the limitations of traditional SLAM algorithms in dynamic environments. By dynamically identifying and removing points during the ORB feature extraction stage, the system demonstrates improved accuracy in self-positioning and environmental mapping. The incorporation of multi-view geometry to handle points missed or unrecognized by the neural network further enhances the system's adaptability. Our experimentation with the TUM dataset validates the system's proficiency in achieving reliable SLAM functionality in dynamic real-world scenarios. This innovative approach opens up opportunities for more effective and accurate robotic localization and mapping, paving the way for advancements in various robotic applications. However, our method fails to effectively utilize information from dynamic targets, while traditional dynamic object tracking methods lack real-time capabilities. In the future, efforts can be made to leverage dynamic target information for more accurate localization and mapping without compromising real-time performance.

References

[1] Y. Sun, M. Liu, and M. Q.-H. Meng, "Improving rgb-d slam in dynamic environments: A motion removal approach," *Robotics and Autonomous Systems*, vol. 89, pp. 110–122, 2017.

[2] E. Palazzolo, J. Behley, P. Lottes, P. Giguere, and C. Stachniss, "Refusion: 3d reconstruction in dynamic environments for rgb-d cameras exploiting residuals," in *2019 IEEE/RSJ International Conference on Intelligent Robots and Systems (IROS)*. IEEE, 2019, pp. 7855–7862.

[3] B. Bescos, J. M. Fácil, J. Civera, and J. Neira, "Dynaslam: Tracking, mapping, and inpainting in dynamic scenes," *IEEE Robotics and Automation Letters*, vol. 3, no. 4, pp. 4076–4083, 2018.

[4] C. Yu, Z. Liu, X.-J. Liu, F. Xie, Y. Yang, Q. Wei, and Q. Fei, "Ds-slam: A semantic visual slam towards dynamic environments," in *2018 IEEE/RSJ international conference on intelligent robots and systems (IROS)*. IEEE, 2018, pp. 1168–1174.

[5] L. Xiao, J. Wang, X. Qiu, Z. Rong, and X. Zou, "Dynamic-slam: Semantic monocular visual localization and mapping based on deep learning in dynamic environment," *Robotics and Autonomous Systems*, vol. 117, pp. 1–16, 2019.

[6] F. Zhong, S. Wang, Z. Zhang, and Y. Wang, "Detect-slam: Making object detection and slam mutually beneficial," in *2018 IEEE Winter Conference on Applications of Computer Vision (WACV)*. IEEE, 2018, pp. 1001–1010.

[7] Y. Liu and J. Miura, "Rds-slam: Real-time dynamic slam using semantic segmentation methods," *Ieee Access*, vol. 9, pp. 23 772–23 785, 2021.

[8] L. Freda, "Plvs: A slam system with points, lines, volumetric mapping, and 3d incremental segmentation," *arXiv preprint arXiv:2309.10896*, 2023.

[9] J. Liu, X. Li, Y. Liu, and H. Chen, "Rgb-d inertial odometry for a resource-restricted robot in dynamic environments," *IEEE Robotics and Automation Letters*, vol. 7, no. 4, pp. 9573–9580, 2022.

[10] W. Wu, L. Guo, H. Gao, Z. You, Y. Liu, and Z. Chen, "Yolo-slam: A semantic slam system towards dynamic environment with geometric constraint," *Neural Computing and Applications*, pp. 1–16, 2022.

[11] C. Campos, R. Elvira, J. J. G. Rodríguez, J. M. Montiel, and J. D. Tardós, "Orb-slam3: An accurate open-source library for visual, visual–inertial, and multimap slam," *IEEE Transactions on Robotics*, vol. 37, no. 6, pp. 1874–1890, 2021.

[12] B. D. Lucas and T. Kanade, "An iterative image registration technique with an application to stereo vision," in *IJCAI'81: 7th international joint conference on Artificial intelligence*, vol. 2, 1981, pp. 674–679.

[13] G. Pan, Y. Fan, Y. Ru, and Y. Guo, "Low-texture monocular visual simultaneous localization and mapping algorithm based on point-line feature fusion," *Journal of Computer Applications*, vol. 42, no. 7, pp. 2170–2176, 2022.

[14] H. Li, Y. Jiang, F. Fan, and Y. Fan, "Rgb-d slam based on semantic and geometry for indoor dynamic environments," in *2022 China Automation Congress (CAC)*, Xiamen, China, Nov. 2022, pp. 1–6.

[15] F. Fan, Y. Jiang, K. Han, H. Li, X. Fang, and Y. Fan, "A line segment detector based on subanchor point and line segment combination method," in *the 37th Youth Academic Annual Conference of Chinese Association of Automation*, Beijing, China, Nov. 2022, pp. 1–6.

[16] A. Li, J. Wang, M. Xu, and Z. Chen, "Dp-slam: A visual slam with moving probability towards dynamic environments," *Information Sciences*, vol. 556, pp. 128–142, 2021.

Proceedings of the 3rd Conference on Fully Actuated System Theory and Applications
May 10-12, 2024, Shenzhen, China

A Shape Reconstruction Method for Space Continuum Robot Based on Neural Network

Guopeng Wang[1,2], Yuchao Yan[1,2], Zuan Li[1,2], Yuntao Li[1,2], Lianglei Xiong[3], Fei Han[1,2], Xinpeng Di[1,2], Xiaolong Zhang[1,2]

1. Shanghai Aerospace Control Technology Institute, Shanghai 201109
E-mail: guopwang@163.com

2. Shanghai Key Laboratory of Aerospace Intelligent Control Technology, Shanghai 201109, China

3. Shanghai Satellite Engineering Research Institute, Shanghai 201401, China

Abstract: Continuum robots have the characteristics of degrees of freedom and flexible shapes, and can complete space operation tasks by avoiding obstacles in narrow space. The closed-loop control and accurate arrival of continuum robot are depended on highly accurate form perception. Firstly, the rope-driven continuum robot is designed and its kinematics model is established. Then, a shape reconstruction method based on BP neural network is proposed, and an evaluation index of shape fitting accuracy considering global information is designed. Finally, a space simulation experiment is carried out in two-dimensional ground microgravity environment, the error between the shape reconstructed by the neural network and the model is compared and analyzed. The average relative distance error of the reconstructed shape of the BP neural network is 0.69%, and the maximum relative distance error is 2.17%. This proves the effectiveness of the proposed shape reconstruction method and its potential application in real space tasks.

Key Words: Space continuum robot, neural network, shape reconstruction, accuracy evaluation

1 Introduction

With the rapid development of space technology, the tasks of typical in-orbit service objects such as space station, faulty spacecraft, and space garbage have become more complicated [1], such as solar panel assisted deployment, space debris removal, spacecraft internal detection, and in-orbit assembly of key components [2]. As shown in Fig. 1, the environments of these tasks are often narrow, unstructured, changeable and so on, and the rigid arm is difficult to work in a narrow space because of its limited freedom and poor flexibility. Compare with it, the continuum robot can achieve terminal arrival flexibly by avoiding obstacles in narrow space, and complete the operation task easily [3,4].

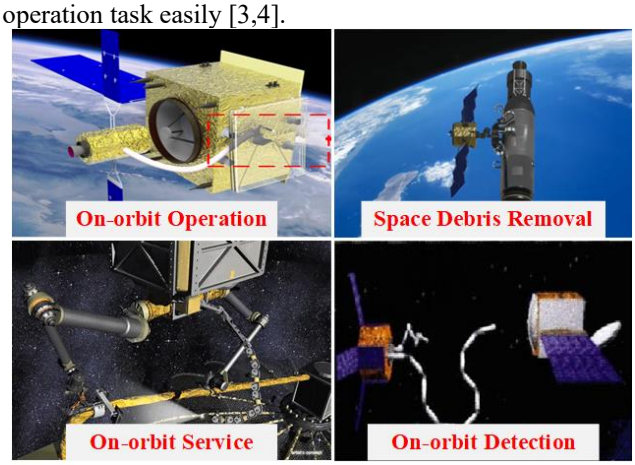

Fig. 1: Tasks of space continuum robot system

For space continuum robots that perform in unstructured and narrow environment, obtaining morphological information is a premise for closed-loop control and high-precision operations. However, the way of obtaining morphological information through external devices is limited by application scenarios, and it is difficult to meet the requirements of space tasks. Therefore, the active acquisition of robot dynamic morphological parameters is an effective method to achieve accurate arrival and real-time control [5]. The shape reconstruction method of continuum robot means that the shape of continuum robot can be reconstructed into a simplified curve by using the position and direction data of several key nodes in the curve [6].

In general, the key node information can be obtained by kinematic and statical models of continuum robots. Roy j. et al. [7] proposed a continuum robot modeling method based on Rayleigh-Ritz mechanical model, which can explain the deflection problem when the radius of curvature is not constant. However, the application of model-based shape reconstruction methods in reality is limited due to friction and unknown external forces.

At present, one of the most mature schemes is to process the continuous robot image captured by the camera and then obtain the robot shape [8]. Monocular cameras [9] and binocular cameras [10] are used to obtain robot shape information in 2D and 3D space. Although this method is intuitive and clear, it is easy to be affected by obstacles.

To solve this problem, sensors are placed on the robot to obtain curvature information of several nodes on the robot, and the shape of the robot is obtained by fitting the curvature of the nodes [11]. The most commonly used sensors include electromagnets [12], Fiber Bragg Grating (FBG) sensors, and Inertial Measurement Unit (IMU) sensors. Yash Chitalia et al. [13] proposed an analytical model of joint curvature of FBG and robot and a static model of correlation between curvature and driving force to realize reliable estimation of joint Angle of medium-scale robot. Ciprian Lapusan et al. [14] proposed a shape reconstruction method based on IMU sensor network, which used IMU data to directly calculate the kinematics parameters of the robot and

*This work is supported by the Major Program and the joined Program of National Natural Science Foundation of China 62204151, 61690214, U20B2056, 12102248; the JCKY2020606B003 and JCKY2021110B134.

solve the shape of the robot in real time. However, such methods must meet the assumption of constant curvature between nodes. When the curvature changes greatly, additional nodes need to be added to meet the requirements of constant curvature, which further increases the cost of the robot and the structural bloated problem brought about by additional sensors.

To solve the above problems, this paper adopts the multi-key point shape reconstruction method based on neural network, and the method flow is shown in Fig. 2. Firstly, a large amount of information of motor Angle and key point coordinates is collected, and the model of both is obtained by neural network training. Then, any joint Angle can be input into the model to obtain the corresponding key point set. Then, the discrete reconstructed point set is obtained by fitting the Bezier curve. Finally, the shape curve of the robot is obtained according to the reconstructed point set.

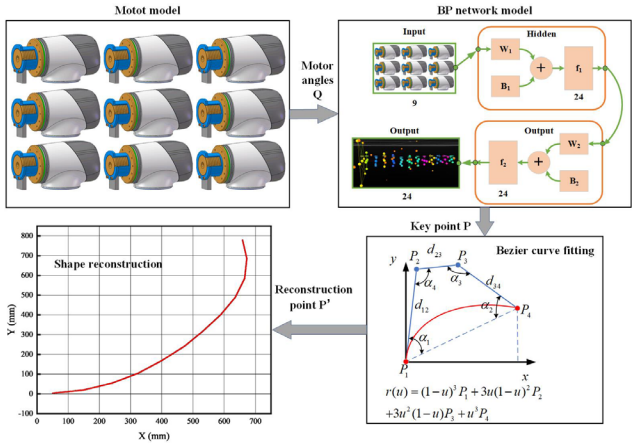

Fig. 2: Flow chart of multi-key point shape reconstruction method based on neural network

The rest of this article is organized as follows. In Section 2, the structure and kinematics model of the space continuum robot are introduced. In Section 3, the method of robot shape reconstruction based on BP neural network is introduced, and the evaluation index of shape fitting accuracy considering global information is designed. In Section 4, the ground simulation experiment is presented in detail and the results are analyzed. Finally, conclusions are presented in Section 5.

2 Space continuum robot

2.1 Structural design

Space continuum robots have various structural forms. In this paper, a typical rope-driven continuum robot supported by a flexible skeleton is studied. The structure is shown in Fig. 3. The robot is mainly composed of a drive control box (drive motor, winding reel, drive rope), two degrees of freedom module (flexible skeleton, 7 spacer disks, 1 fixed disk). The total length of the robot is 1200mm, of which each module is 400mm, the spacing between two adjacent disks is 50mm, and the outer diameter of the disk is 60mm. The modules are driven by three motors, three drive lines are evenly distributed, and the distance between the two is 120°. One end of the drive line is fixed on the fixed disc, and the other end is fixed on the winding disk.

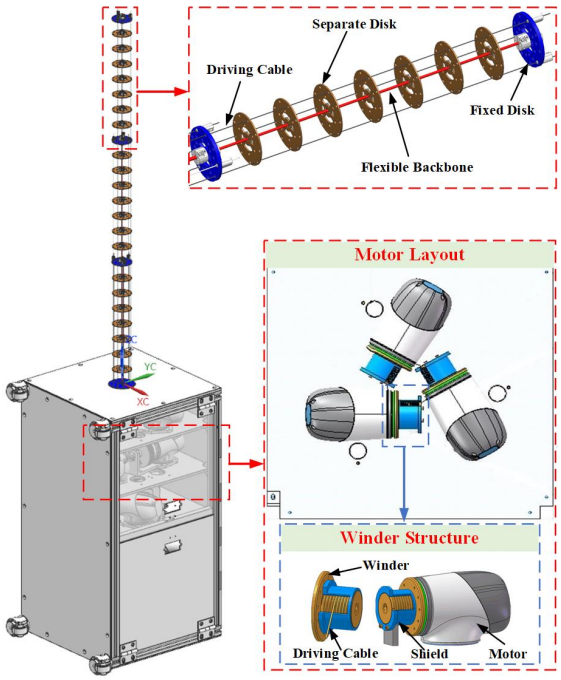

Fig. 3: Structure and composition of space continuum robot

2.2 Kinematics Model

The motion process of the continuum robot is to control the bending and deflection of the robot arm in the joint space through the drive line of the drive space to realize the pose change of the end of the robot arm in the operation space. As shown in Fig. 4, the kinematics analysis of a continuum robot includes not only the analysis of the mapping relationship between the joint space and the operation space, but also the analysis of the mapping relationship between the drive space and the joint space.

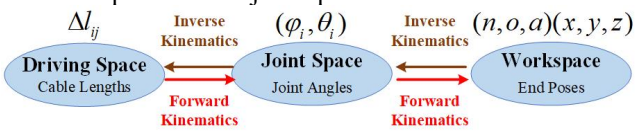

Fig. 4: Forward and inverse kinematics description space of continuum robot

For the kinematics model of the robot in the process of bending motion, the following assumptions are put forward based on the piecewise constant curvature method: (1) It is supposed that the bending curve of each section of the robot module is a smooth continuous curve with equal curvature; (2) It is assumed that the robot does not have axial expansion deformation and circumferential torsion deformation along the central rod skeleton. Fig. 5. shows the bending diagram of the i module of the continuum manipulator arm. The base coordinate system O_i-$X_iY_iZ_i$ is established at the center point O_i of the base disk of the i module. The direction pointing to the drive line l_{i1} through the center point of the hole is the direction of the X_i axis; the direction of the Z_i axis is taken as the direction perpendicular to the direction of the base extending to the module; the direction of the Y_i axis is determined according to the right-hand rule. The center of the circle C_i is the center corresponding to the arc generated by the bending of the central rod skeleton, the bending Angle θ_i is the center corresponding to the arc, the deflection Angle φ_i is the Angle between the circular plane where the arc is located and the X_i axis, and r_i is the curvature radius of

the arc, $r_i = l / \theta_i$, l represents the length of a single flexible skeleton.

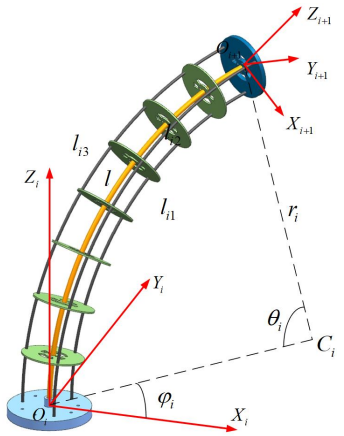

Fig. 5: Kinematics model

From the geometric relationship, it can be concluded that the relationship between the position coordinates $[x_{i+1}, y_{i+1}, z_{i+1}]$ and $[\theta_i, \varphi_i]$ the end of the i module is as follows:

$$\begin{cases} x_{i+1} = r_i\left(1-\cos\left(\theta_i\right)\right)\cos\left(\varphi_i\right) \\ y_{i+1} = r_i\left(1-\cos\left(\theta_i\right)\right)\sin\left(\varphi_i\right) \\ z_{i+1} = r_i \sin\left(\theta_i\right) \end{cases} \tag{1}$$

$$\begin{cases} \theta_i = 2\tan^{-1}\left(\dfrac{\sqrt{x_{i+1}^{\ 2}+y_{i+1}^{\ 2}}}{z_{i+1}}\right) \\ \varphi_i = \tan^{-1}\left(\dfrac{y_{i+1}}{x_{i+1}}\right) \end{cases} \tag{2}$$

Since the value range of bending Angle θ_i is [0, π/2], the value range of deflection Angle φ_1 is [0, 2π], and the value range of arctangent function is [-π/2, π/2], the solution of φ_i obtained is not unique, and it is necessary to determine the quadrant where it is located according to the positive and negative information of coordinate values, specifically as follows:

$$\begin{cases} \varphi_i = \varphi_i & \left(\varphi_i > 0, x_{i+1} > 0, y_{i+1} > 0\right) \\ \varphi_i = \varphi_i + \pi & \left(\varphi_i < 0, x_{i+1} < 0, y_{i+1} > 0\right) \\ \varphi_i = \varphi_i + \pi & \left(\varphi_i > 0, x_{i+1} < 0, y_{i+1} < 0\right) \\ \varphi_i = \varphi_i + 2\pi & \left(\varphi_i < 0, x_{i+1} > 0, y_{i+1} < 0\right) \end{cases} \tag{3}$$

Next, the forward and inverse kinematics of the drive space and joint space are solved. Fig. 6 is the distribution diagram of the drive line of the i module, where k represents the number of sections of the module divided by the spacer disk, and r_a represents the radius of the indexing circle where the drive rope hole is located. It can be obtained from the geometric relation that the mutual relation between the bending deflection Angle $[\theta_i, \varphi_i]$ and the drive line length change $[\Delta l_{i1}, \Delta l_{i2}, \Delta l_{i3}]$ is as follows:

$$\begin{cases} \Delta l_{i1} = 2k\sin(\theta_i / 2k)\left(r_i - r_a\cos\left(\varphi_i\right)\right) - l \\ \Delta l_{i2} = 2k\sin(\theta_i / 2k)\left(r_i + r_a\cos\left(\pi/3 + \varphi_i\right)\right) - l \\ \Delta l_{i3} = 2k\sin(\theta_i / 2k)\left(r_i + r_a\cos\left(\pi/3 - \varphi_i\right)\right) - l \end{cases} \tag{4}$$

$$\begin{cases} \varphi_i = \tan^{-1}\dfrac{-\sqrt{3}\left(\Delta l_{i2} - \Delta l_{i3}\right)}{\left(\Delta l_{i2} + \Delta l_{i3} - 2\Delta l_{i1}\right)} \\ \theta_i = \dfrac{\sqrt{3\left(\Delta l_{i2} - \Delta l_{i3}\right)^2 + 3\left(\Delta l_{i2} + \Delta l_{i3} - 2\Delta l_{i1}\right)^2}\cdot l}{\left(3l - \left(\Delta l_{i1} + \Delta l_{i2} + \Delta l_{i3}\right)\right) r_a} \end{cases} \tag{5}$$

Similarly, the solution of φ_i is not unique, and the quadrant where it is located needs to be judged according to the situation of the drive line, which is as follows:

$$\begin{cases} \varphi_i = \varphi_i & \left(\varphi_i < 0, \Delta l_{i2} < \Delta l_{i3}\right) \\ \varphi_i = \varphi_i + \pi & \left(\varphi_i > 0, \Delta l_{i2} > \Delta l_{i3}\right) \\ \varphi_i = \varphi_i + 2\pi & \left(\varphi_i < 0, \Delta l_{i2} > \Delta l_{i3}\right) \\ \varphi_i = \varphi_i + \pi & \left(\varphi_i < 0, \Delta l_{i2} < \Delta l_{i3}\right) \end{cases} \tag{6}$$

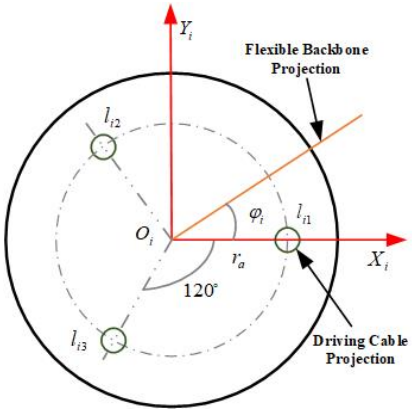

Fig. 6: Schematic diagram of drive line distribution

3 Robot shape reconstruction method based on BP neural network

On account of that the kinematics model of the space flexible robot adopts the piecewise and equal arc hypothesis, and does not consider the influence of friction force, there are certain errors in the calculated key point coordinates, and the robot shape errors based on this reconstruction are further increased. In order to reduce the impact of errors, BP neural network algorithm is adopted in this paper. Firstly, the robot is controlled to reach the specified bending angle and deflection angle, and then the motor rotation angle is obtained. Secondly, a dynamic capture camera is installed outside the space flexible arm to collect a large number of actual position information of key points obtained by the camera, with the motor angle as input and the actual position information of key points as output. Through the training in the neural network, the corresponding relationship between the motor angle and the key point coordinates is obtained. The pose information of key points obtained by the moving capture camera is specifically: the visual camera recognizes the rigid body constructed by the target ball mounted on the robot, and the distribution of key points at the installation position of the robot is [0, 50, 150, 250, 350, 450, 550, 650, 750, 850, 950, 1050, 1150] mm.

3.1 Design of BP neural network

The BP neural network proposed by David Rumelhart, Geoffrey Hinton and Ronald Williams in 1986, which is a multi-layer feedforward neural network trained according to the error backward propagation algorithm [15]. The network structure design of this paper is shown in the Fig.7,

including input layer (motor angle), hidden layer and output layer (key point coordinates). Where N_{in} is the number of nodes in the input layer, N_{out} is the number of nodes in the output layer, and N_h is the number of nodes in the hidden layer, which is 9, 24, 14. And N_h is calculated according to the empirical formula $fix(\sqrt{N_{in} \cdot N_{out}}) = 14$.

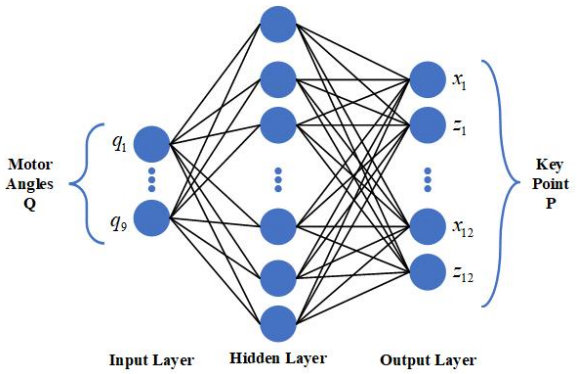

Fig 7: BP neural network structure

The relationship between the input layer and the hidden layer can be expressed as:

$$H = f_1(W_1 Q + B_1) \tag{7}$$

where f_1 represents the hidden layer activation function, $Q = [q_1, \cdots, q_9]^T$ is the input matrix for input layer, $H = [H_1, \cdots, H_{14}]^T$ is the output matrix for hidden layer. W_1 and B_1 represent the weight and threshold matrices from the input layer to the hidden layer respectively. The size of the matrix W_1 is 14×9, the size of matrix B_1 is 14 ×24, the size of matrix Q is 9×m, and the size of matrix H is 14×m, where m is the number of training samples.

The relationship between the hidden layer and the output layer [16] is expressed as:

$$P = f_2(W_2 H + B_2) \tag{8}$$

where $P = [x_1, z_1, \cdots, x_{12}, z_{12}]^T$ represents the output matrix, W_2 and B_2 represent the weight and threshold matrix from the hidden layer to the output layer, and f_2 represents the output layer activation function. The size of the matrix W_2 is 24×14, the size of matrix B_2 is 24×24, and the size of the matrix K is 24×m.

In BP neural network, the mean square error is used as the error function:

$$MSE = \frac{1}{m}\sum_{i=1}^{m}\frac{1}{N_{out}}\sum_{j=1}^{N_{out}}(\hat{o}_{ij} - o_{ij})^2 \tag{9}$$

where $\hat{o}_{ij}$ is the predicted value of the output and o_{ij} is the corresponding true value.

3.2 Shape Reconstruction Method

Common curve fitting methods include least square method, Bezier spline curve method, maximum likelihood estimation method, etc. In this paper, Bezier spline curve method, which is most used in the shape reconstruction of flexible robots, is used to fit the coordinates of multi-key points to obtain the robot shape [17]. P_1 is the starting point, P_4 is the end point; P_2 and P3 are the control points. The curve starts at P_1, goes to P_2 and P_3, and reaches P_4. The explicit form of the curve is:

$$r(u) = (1-u)^3 P_1 + 3u(1-u)^2 P_2 + 3u^2(1-u)P_3 + u^3 P_4 \tag{10}$$

where u is the variable of the parametric curve equation, and its value range is [0,1].

3.3 Evaluation method of curve fitting accuracy

Aiming at the problems of insufficient combination and utilization of spatial integrity and local reconstruction accuracy information, as well as mismatch between local error and actual error distribution in traditional evaluation methods [18], this paper proposes an accuracy evaluation method based on relative position average error, which takes global information into account. The principle of this method is to calculate the Euclidean distance between each point of the reconstructed curve and the ground truth value divided by the arc length from the starting point to the point, and average all the relative errors to obtain the relative average error e_{rel_avg} . Then, the point with the largest relative error is found in the entire reconstructed curve, and its maximum relative deviation value $e_{rel_\max}$ is obtained as a reference. The reconstructed shape is represented by the point set as $r = \{r_0, \cdots, r_N\}$. The formula is as follows:

$$\begin{aligned} e_{rel_avg} &= \frac{1}{N}\sum_{i=0}^{N}\left\| r_i^{re} - r_i^{gt} \right\| / l_i \\ e_{rel_\max} &= \max(\left\| r_0^{re} - r_0^{gt} \right\| / l_0, \cdots, \left\| r_N^{re} - r_N^{gt} \right\| / l_N) \end{aligned} \tag{11}$$

where r_i^{re}, r_i^{gt}, l_i represent the coordinates, reference coordinates and corresponding arc length of the i th reconstruction point relative to the starting point respectively, and N represents the total number of reconstruction points.

4 Experiment Testing and Analysis of Results

4.1 Experimental System

In order to verify the effectiveness of the shape reconstruction method of the space continuous robot based on neural network, as shown in Fig. 8, a two-dimensional ground microgravity simulation system was constructed. The system includes a 6-DOF linear drive continuum robot. The robot drive box receives the motor control instructions sent by the lower machine and controls the motor rotation. The robot lower machine control box receives the robot motion instructions sent by the upper computer, and solves the motor control instructions. The measurement computer reads the pose data of each key point of the robot and sends it to the host computer. The integrated control computer is used to generate the robot motion instructions according to the robot operation task, and accepts the numbers sent by the lower computer and the measuring computer. The follow-up gravity compensation device is used to make the end disk of each module perform follow-up gravity compensation when the flexible arm moves in a two-dimensional plane, so as to simulate the flexible arm to perform relevant operations in the microgravity space environment. The measuring system is OptiTrack Motive system, which is used for absolute measurement and can solve the position and attitude of the center of mass of each key point of the robot.

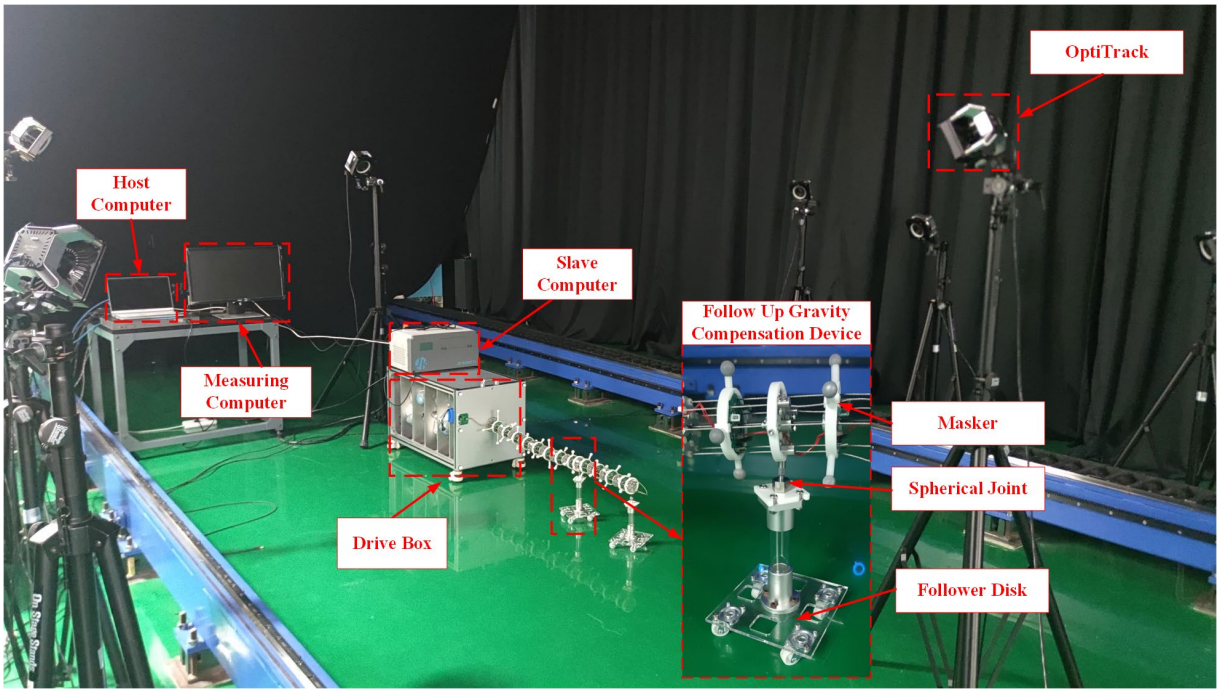

Fig. 8: Schematic diagram of two-dimensional ground microgravity test and control system of space continuum robot

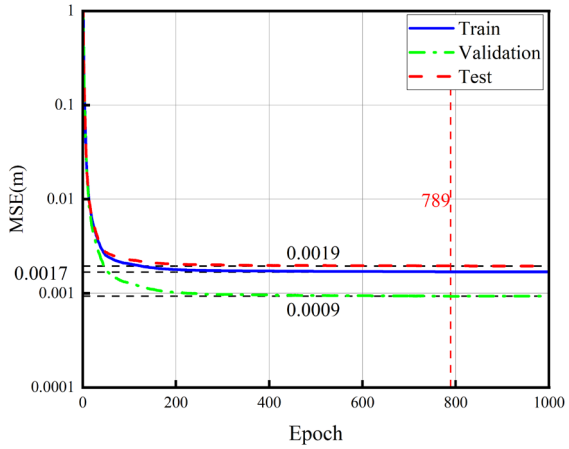

Fig. 9: Loss function curve of neural network

4.2 Shape Reconstruction in a Two-Dimensional Ground Microgravity Simulation System

In order to construct the neural network data set, the space continuum robot was placed in the OptiTrack Motive system, and the robot shape randomly generated 2000 groups of arrays according to the bending Angle [-60°, -90°, -90°] ~ [60°, 90°, 90°]. Then the upper computer controls the robot to move to the specified shape according to the instructions in the array, and records the motor Angle and robot key point coordinate data after the robot is stabilized. In order to train the neural network, 1600 groups of neural network training data, 200 groups of validation data and 200 groups of test data were randomly selected from the experimental data at the ratio of 8:1:1. The activation functions of the hidden layer and output layer were set as tansig function and purelin function, respectively. The training algorithm was trainlm function, and the learning rate was 1×10^{-3}. Fig. 9 shows the loss function curve of post-training and test data of BP neural network. Fig. 9 shows that the loss function converges after 789 iterations. After 1000 iterations, the mean square error of the training dataset is 0.0017m, the validation dataset is 0.0009m, and the test dataset is 0.0019m.

In order to verify the effectiveness of the trained neural network model, 24 groups of data were randomly selected from the test data set, and the relative average distance error was used to measure the prediction accuracy of the neural network, as shown in Fig. 10. As can be seen from Fig. 10, the relative average error of the robot is less than 1.01%.

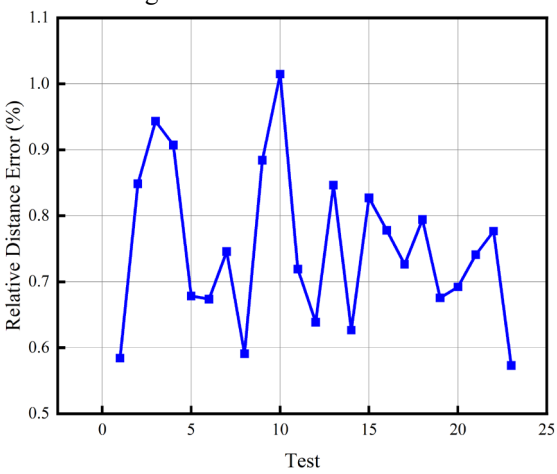

Fig. 10: Relative average error curves of robots with different shapes

In order to verify the reliability of the shape reconstruction of the robot based on BP neural network, the robot is controlled to reach the arm shape of [20°, 30°, 40°], the motor angle and key point coordinates are collected, and the shape of the robot is reconstructed through the kinematic model and BP neural network respectively. The results are shown in Fig. 11.

The Model in Fig. 11 is the result of curve reconstruction of the robot kinematics model in Section 2.2, and BP_network represents the result of curve reconstruction by BP neural network. The average relative distance error and the maximum relative distance error obtained by the model curve reconstruction algorithm are 3.13% and 6.39% respectively. The average relative distance error of BP neural network reconstruction robot shape is 0.69%, and the maximum relative distance error is 2.17%.

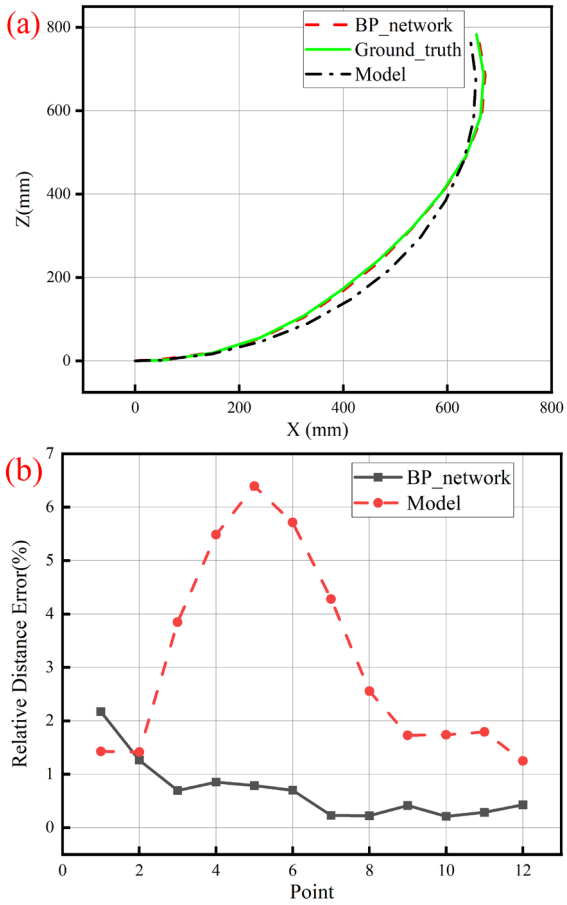

Fig. 11: Results and errors of shape reconstruction of space continuum robot. (a) Shape reconstruction results; (b) Relative distance error

5 Conclusions

In this paper, a new space continuum robot shape reconstruction method based on neural network model is proposed for the small-space in-orbit service task, which has important application value in the future space missions. With this method, there is no need to arrange other additional sensors on the robot, which can reduce the cost of the whole robot on the one hand, and avoid the failure of the shape reconstruction of the robot using vision sensing when there is occlusion. Firstly, the structure of the space continuum robot is designed and its kinematics model is analyzed. Secondly, a multi-key point generation method of the robot based on BP neural network model is proposed. Through training the data set, the model from the motor joint angle to the robot key point coordinates is obtained. Then, the shape reconstruction method based on spline curve is introduced, and the evaluation index of shape fitting accuracy considering global information is designed. Finally, in order to verify the effectiveness of the continuous robot shape reconstruction method based on BP neural network, the shape reconstruction experiment was carried out in two-dimensional ground microgravity environment, and the shape reconstruction errors of the neural network and the model were compared and analyzed. The experimental results show that the average relative distance error of BP neural network is 0.69% and the maximum relative distance error is 2.17% in two-dimensional ground microgravity environment.

References

[1] A. Flores-Abad, O. Ma, K. Pham, and S. Ulrich. A review of space robotics technologies for on-orbit servicing. *Prog. Aerosp. Sci.*, 2014, 68: 1-26.

[2] R. Biesbroek, S. Aziz, A. Wolahan, S. Cipolla, M. Richard-Noca, and L. Piguet. The Clearspace-1 mission: esa and clearspace team up to remove debris robin. *8th Eur. Conf. Sp. Debris*, 2021, 5: 1-3.

[3] A. Martín-Barrio, J. J. Roldán, S. Terrile, J. del Cerro, and A. Barrientos. Application of immersive technologies and natural language to hyper-redundant robot teleoperation. *Virtual Real.*, 2020, 24(3): 541-555.

[4] Z. Mu, Y. Chen, Z. Li, H. Qian, and N. Ding. A Spatial Biarc Method for Inverse Kinematics and Configuration Planning of Concentric Cable-Driven Manipulators. *IEEE Trans. Syst. Man, Cybern. Syst.*, 2022, 52(7): 4177–4186.

[5] C. Shi *et al*. Shape sensing techniques for continuum robots in minimally invasive surgery: A survey. *IEEE Trans. Biomed. Eng.*, 2017, 64(8): 1665–1678.

[6] H. Guo, F. Ju, D. Bai, X. Wei, L. Wang, and B. Chen. Shape Reconstruction for Continuum Robot Based on Pythagorean Hodograph-Bézier Curve With IMU and Vision Sensors. *IEEE Sens. J.*, 2023, 23(8): 8535–8544.

[7] R. J. Roesthuis, M. Abayazid, and S. Misra. Mechanics-based model for predicting in-plane needle deflection with multiple bends. *Proc. IEEE RAS EMBS Int. Conf. Biomed. Robot. Biomechatronics*, 2012: 69–74.

[8] X. Ma, P. W. Y. Chiu, and Z. Li. Static Model Assisted Stereo-Visual Shape Sensing of Flexible Manipulators. *IEEE Sens. J.*, 2021, 21(10): 11684–11691.

[9] B. Li, B. Lu, Z. Wang, F. Zhong, Q. Dou, and Y. H. Liu. Learning Laparoscope Actions via Video Features for Proactive Robotic Field-of-View Control. *IEEE Robot. Autom. Lett.*, 2022, 7(3): 6653–6660.

[10] V. K. Chitrakaran, A. Behal, D. M. Dawson, and I. D. Walker. Setpoint regulation of continuum robots using a fixed camera. *Robotica*, 2018, 5(2): 1504–1509.

[11] S. M. Roodsari *et al*. Deep learning-based approach for high spatial resolution fibre shape sensing. *Commun. Eng.*, 2024: 1-10.

[12] S. Song, Z. Li, H. Yu, and H. Ren. Electromagnetic Positioning for Tip Tracking and Shape Sensing of Flexible Robots. *IEEE Sens. J.*, 2015, 15(8): 4565–4575.

[13] Y. Chitalia, N. J. Deaton, S. Jeong, N. Rahman, and J. P. Desai. Towards FBG-Based Shape Sensing for Micro-Scale and Meso-Scale Continuum Robots with Large Deflection. *IEEE Robot. Autom. Lett.*, 2020, 5(2): 1712–1719.

[14] C. Lapusan, O. Hancu, and C. Rad. Shape Sensing of Hyper-Redundant Robots Using an AHRS IMU Sensor Network. *Sensors*, 2022, 22(1).

[15] D. E. Rumelhart, G. E. Hinton, and R. J. Williams. Learning representations by back-propagating errors. *Nature*, 1986, 323(6088): 533–536.

[16] F. Han, Y. He, H. Zhu, and K. Zhou. A Novel Catheter Shape-Sensing Method Based on Deep Learning with a Multi-Core Optical Fiber. *Sensors*, 2023, 23(16).

[17] Z. Yang, S. Liu, T. Yang, G. Wu, Y. Liang, and Y. Dong. Segmental Sensor Weighting Accuracy Evaluation Method for Fiber Optic Shape Sensing. *IEEE Sens. J.*, 2023, 23(22): 27307–27315.

[18] X. Ma, P. W. Y. Chiu, and Z. Li. Shape Sensing of Flexible Manipulators with Visual Occlusion Based on Bezier Curve. *IEEE Sens. J.*, 2018, 18(19): 8133–8142.

Proceedings of the 3rd Conference on Fully Actuated System Theory and Applications
May 10-12, 2024, Shenzhen, China

A Research on Rapid Assessment of Cross-Domain Perceptual Fidelity for Practical Applications

Wenguang Tao[1], Xiaotian Wang[1*], Tian Yan[1], Guodong Li[1], Qingjie Zeng[2,3], Ruitao Lu[4]

1. Unmanned System Research Institute, Northwestern Polytechnical University, Xi'an 710072, China
E-mail: wenguangtao2022@mail.nwpu.edu.cn

2. Xi'an Modern Control Technology Research Institute, Xi'an 710065, China
E-mail: qingjie_zeng@126.com

3. Xi'an Guidance Technology Co., Ltd., Xi'an 710065, China
E-mail: qingjie_zeng@126.com

4. Department of Missile Engineering, Rocket Force University of Engineering, Xi'an 710025, China
E-mail: luruitao10@nudt.edu.cn

Abstract: With the rapid development of information technology, digital simulation technology plays a key role in improving training effects, providing accurate decision support, and promoting innovation and research and development. How to provide a more realistic training experience in simulation is particularly important. Guided by practical applications and based on cross-domain perception representation, this paper proposes a cross-domain perception fidelity evaluation algorithm oriented to application requirements. This method uses traditional methods to extract statistical features from the data and calculate feature similarity. Then, machine learning methods are used to extract structural, content and semantic features, effectively complete appearance and texture and calculate similarity. Finally, in order to ensure the effect in the actual application domain, the fidelity evaluation algorithm is designed based on the domain adaptation algorithm. Experimental results show that this method can well complete the cross-domain perceptual fidelity evaluation of simulation domain data and source domain data.

Key Words: Domain adaptation, Image evaluation, Feature fidelity

1 Introduction

Simulation data fidelity evaluation algorithm is an important prerequisite for conducting research on high-fidelity simulation technology. High-fidelity simulation technology can enable most tests of actual systems to be completed in the laboratory, greatly shortening the development cycle while saving development costs[1]. However, during the simulation process of infrared feature sensors, there is a problem that the imaging and generation mechanisms of simulation data (source domain) and real data (target domain) are quite different. Therefore, under the condition that there are large differences in cross-domain data for application requirements, how to evaluate cross-domain perceptual fidelity is a great challenge.

The concept of simulation data fidelity was first proposed in 1990. The Fidelity Experimentation Implementation Study Group (ISG-FEX) collected and summarized previous work and research on fidelity, and elaborated on this basis, thereby introducing the concept of fidelity[2][3]. For the problem of evaluating the fidelity of simulation data, researchers have developed many evaluation methods. Traditional evaluation methods include comprehensive evaluation of the simulation system and evaluation of simulation image quality and image similarity, such as Verification, Validation and Accreditation (VV&A) theory[4][5] and evaluation methods based on hypothesis testing[6][7], structural similarity evaluation method[8] and texture similarity evaluation method[9][10], etc. In addition, fidelity evaluation based on the idea of deep learning is a new research direction, such as using convolutional neural networks[11], adversarial neural networks[12], deep belief networks[13] and other methods for fidelity evaluation. However, there are currently few studies on the evaluation of simulation images. In recent years, some researchers have proposed a similarity assessment method for simulation images based on twin neural networks, and evaluated the fidelity of simulation images based on a generative adversarial network. This evaluation method has cross-domain data awareness capabilities[14]. Currently, various fidelity assessment methods are relatively isolated. These methods mainly focus on a certain data or feature in the simulation system, and it is difficult to comprehensively achieve cross-domain perceptual fidelity assessment.

In order to meet the high demand for cross-domain perception fidelity in practical applications, this paper uses traditional methods to extract statistical features in the data for real infrared data and infrared simulation data. Then, machine learning methods are combined to extract semantic features such as texture and structure in the data. Finally, based on the domain adversarial neural network, an infrared simulation data fidelity evaluation network with cross-domain data perception capabilities is proposed to accurately measure the cross-domain data fidelity. Compared with other proposed methods, we propose a method that organically integrates multiple efficient fidelity assessment methods, which greatly improves the robustness and feasibility of the method. To the best of our knowledge, this may be the first attempt to integrate a fidelity evaluation system across domains in this field.

*This work is supported by National Natural Science Foundation (NNSF) of China under Grant 62106193.

The content of the article is arranged as follows. Section 2 describes the cross-domain perceptual fidelity evaluation algorithm framework oriented to application requirements. Section 3 uses simulation domain data and source domain data to test the proposed algorithm, and gives experimental results and analysis. Section 4 summarizes the content of this article.

2 Proposed Method

The cross-domain perceptual fidelity rapid evaluation method proposed in this article mainly includes three parts, as shown in **Fig. 1**. The first part is the traditional fidelity evaluation module, which uses traditional statistical features to build a fidelity model between simulation images and real images, including HOG features, Harris features and LBP features. The second part is the fidelity evaluation module based on the deep model, which uses deep convolutional network features to calculate the fidelity between simulation images and real images, including structural fidelity, content fidelity and semantic fidelity. The third part is the cross-domain perceptual fidelity evaluation module, which uses a deep neural network to calculate the domain adaptation similarity between the simulation image domain and the real image domain at the pixel level, and then obtains the cross-domain perceptual fidelity. Finally, these three parts are integrated to obtain a cross-domain perceptual fidelity rapid assessment method.

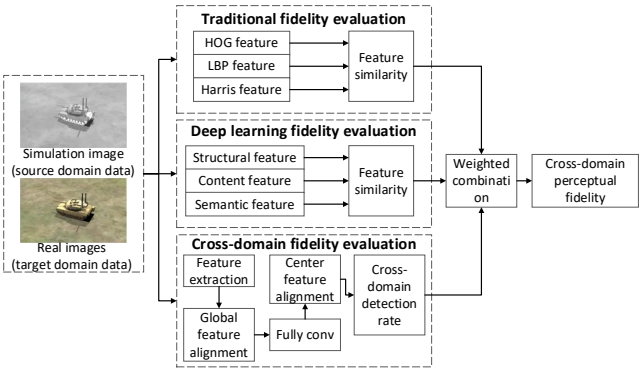

Figure 1 Schematic diagram of fast evaluation algorithm for cross-domain perceptual fidelity

2.1 Traditional fidelity evaluation

The traditional fidelity evaluation module uses mathematical statistical features such as HOG (Histogram of Oriented Gradients), Harris, and LBP (Local Binary Patterns) features corresponding to simulation images and real images to calculate the similarity of features. The above features are weighted and synthesized to obtain the traditional feature fidelity evaluation results.

HOG constructs features by calculating and counting gradient direction histograms in local areas of the image. Firstly, for the input image $I(x,y)$, the entire image needs to be normalized to reduce the influence of lighting factors. The normalized compression process can effectively reduce the local shadow and lighting changes of the image. The Gamma compression formula is as follows:

$$I(x,y) = I(x,y)^{\gamma} \tag{1}$$

Then, calculate the gradient in the abscissa and ordinate directions of the image, and calculate the gradient direction value of each pixel position accordingly. Capture contours and texture information through derivation operations, and further weaken the impact of lighting. The gradient of the pixel point (x,y) in the image is as follows:

$$\begin{cases} G_x(x,y) = H(x+1,y) - H(x-1,y) \\ G_y(x,y) = H(x,y+1) - H(x,y-1) \end{cases} \tag{2}$$

where $G_x(x,y)$, $G_y(x,y)$, and $H(x,y)$ respectively represent the horizontal gradient, vertical gradient and pixel value of the input image pixel point (x,y). The gradient value and gradient direction at the pixel point (x,y) are as follows:

$$\begin{cases} G(x,y) = \sqrt{G_x(x,y)^2 + G_y(x,y)^2} \\ \alpha(x,y) = \tan^{-1}(G_y(x,y)/G_x(x,y)) \end{cases} \tag{3}$$

Finally, the image is divided into several "cells", and the gradient information of each cell is calculated to obtain the HOG feature of the image.

The HOG feature counts the gradient direction histogram of the local area of the image as a criterion for judging fidelity. In addition, Harris features and LBP features respectively count image corner information and texture information, and are also used as standards for judging fidelity. The specific calculation process can be referred to references [15] and [16], which will not be described in detail here. Calculate the cross-correlation of HOG features, Harris features and LBP features, and then obtain the traditional feature fidelity evaluation results after weighted synthesis, as shown in the following formula:

$$Fid_{Traditional} = w_1 Fid_{Hog} + w_2 Fid_{Harris} + w_3 Fid_{Lbp} \tag{4}$$

where $w_1 = w_2 = w_3 = 1/3$.

2.2 Depth-based fidelity evaluation

The fidelity evaluation module based on the deep model uses the corresponding structural features, content features and semantic features of the simulation image and the real image to calculate the similarity of the features. The above features are weighted and synthesized to obtain the fidelity evaluation results based on the deep model.

（1） Structural fidelity

Structural fidelity evaluation focuses on whether the shape and outline of the target are consistent with the actual target, that is, whether the simulation image is consistent with the corresponding object outline in the corresponding real image. This article uses HEDNet to calculate the structural fidelity of images.

HEDNet is a deep neural network architecture specifically designed to extract edge information from images. Compared with traditional edge detection algorithms, HEDNet has the advantages of being insensitive to noise, having strong adaptability to discrete pixel positions, and being able to effectively handle complex textures. HEDNet uses a feature pyramid network to comprehensively capture edge features at different levels, and uses a hierarchical structure to enable the network to understand the edge information of images at multiple levels. HEDNet improves detection accuracy by using multiple loss functions in training[17].

（2） Content fidelity

Content fidelity evaluation focuses on whether the details and texture performance of the target in the infrared image are consistent with the actual target, which means whether the details of the corresponding object in the simulation image are consistent with the corresponding real image. When evaluating, the texture characteristics, detailed information, and light and dark changes of the target in the infrared image can be considered. This article uses ResNet-18 to compare the content consistency between simulation images and real images.

ResNet-18 is a lightweight model in the residual network, which has low complexity and can efficiently and accurately represent the deep features of image targets. ResNet-18 is a relatively deep convolutional neural network with 18 convolutional layers and introduces the concept of residual connections. This design can simplify the learning process and enable deeper training to better extract deep features. ResNet-18 has multiple residual blocks, and each residual block contains multiple convolutional layers inside. Through the stacking of multiple levels, the extraction from shallow low-level features to deep high-level features is achieved. In addition, ResNet-18 adopts a global average pooling layer to convert the feature map into a vector to extract the semantic information of the image[18]. The above characteristics enable ResNet-18 to extract deep features accurately and efficiently, which is very suitable for extracting content information in images.

（3） Semantic fidelity

The semantic fidelity evaluation focuses on the recognition and understanding ability of the target in the infrared image, which means whether the semantic features of the corresponding object in the simulation image are consistent with those in the corresponding real image. When evaluating, the texture, edges and spatial position relationships in the infrared image can be considered. This article uses RefineNet to compare the semantic feature consistency between simulation images and real images.

RefineNet is a deep learning model that can efficiently extract semantic information from images. It classifies each pixel into different semantic categories by segmenting the image, thereby achieving semantic understanding of the image. RefineNet uses bottom-up and top-down structures to integrate details and global information in the image through multi-scale fusion to better understand the semantic structure of the image. RefineNet also uses technologies such as global pooling and atrous convolution to capture global context, and accurately recognize objects and segment their boundaries by understanding the overall semantic structure of the image. In addition, RefineNet uses the skip connection mechanism to better retain and utilize different levels of semantic information, allowing the network to better perceive the details and structure of the image[19]. The above technical means enable RefineNet to accurately extract the semantic information of the image, and then accurately obtain the semantic fidelity of the image.

The fidelity evaluation module based on the deep model performs cross-correlation calculations on structural features, content features and semantic features. The weighted synthesis-based fidelity evaluation results are as follows:

$$Fid_{Deep} = w_4 Fid_{HEDNet} + w_5 Fid_{ResNet} + w_6 Fid_{RefineNet} \quad (5)$$

where $w_4 = w_5 = w_6 = 1/3$.

2.3 Cross-domain perceptual fidelity evaluation

The cross-domain perceptual fidelity evaluation module is composed of a cross-data target detection method using domain adaptation technology. It better solves the cross-domain problem of target detection by discovering the differences in target parts at the pixel level. First, the model is trained on the simulation image domain. Then the object is detected on the corresponding real image to obtain the detection accuracy, which means that the cross-domain perceptual fidelity is obtained (see **Fig. 2**).

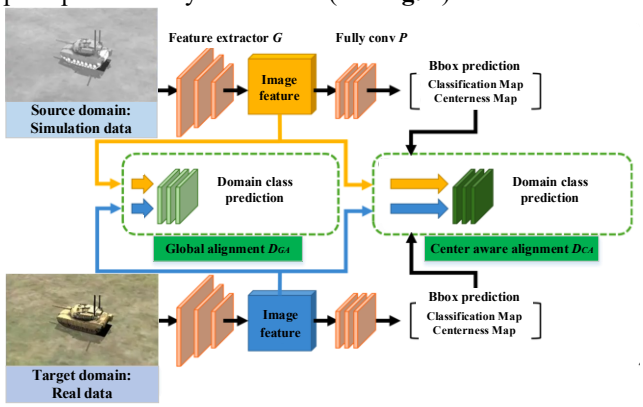

Figure 2 Domain adaptation data detection framework

In order to accurately evaluate cross-domain perceptual fidelity, we employ deep domain adaptation techniques. Specifically, two alignment methods that merge with each other are used, namely global alignment at the image level and center alignment that pays more attention to target pixels. We divide the entire network into four modules: feature extraction module, global alignment module, center alignment module, and full convolution module. The first is the feature extractor module. The backbone network extracts features from the source domain and target domain. Then there is the global alignment module, where the features perform global alignment by using a global discriminator and domain prediction loss. Next is a fully convolutional module that predicts pixel-wise object and centrality maps. Finally, there is the center alignment module, which combines the extracted features for center alignment[20].

The goal of global feature alignment is to align feature maps at the image level to reduce domain gaps. Aiming to identify whether the pixels on each feature map are from the source or target domain, the domain labels of the source and target domains are set to 1 and 0 respectively. Therefore, the discriminator can be optimized by minimizing the binary cross-entropy loss. The purpose of global alignment is to align features at the image level to reduce domain gaps. The loss function of global alignment is as follows:

$$L_{GA}(I_s, I_t) = -\sum_{u,v} z \log(D_{GA}(F_s)^{(u,v)}) + (1-z)\log(1-D_{GA}(F_t)^{(u,v)}) \quad (6)$$

where I_s, I_t are the source image and the target image respectively, F_s, F_t are extracted features, D_{GA} is the global discriminator.

Center feature alignment is used to align features in high-confidence regions at the pixel level. By obtaining the classification and centrality outputs, each position on the

classification and centrality maps represents the corresponding target and centrality scores respectively. The central feature alignment method allows focusing on the identification target area. To achieve this, a center-aware discriminator is employed for feature alignment on high-confidence regions at the pixel level. The loss function for center alignment is as follows:

$$\begin{cases} L_{CA}(I_s, I_t) = -\sum_{u,v} z \log(D_{CA}(M_{CA}^S \odot F_s)^{(u,v)}) \\ \quad +(1-z)\log(1-D_{CA}(M_{CA}^S \odot F_t)^{(u,v)}) \\ M_{obj} = \max_c(\sigma(M_{cls})) \\ M_{CA} = \sigma(\delta M_{obj} \odot \sigma(M_{ctr})) \end{cases} \quad (7)$$

where M_{CA} is the center-aware map, D_{CA} is the center-aware discriminator.

The cross-domain perceptual fidelity evaluation module defines detection confidence as cross-domain perceptual fidelity value and uses a variety of technical means, including global feature alignment, central feature alignment, and multiple convolutions. These technical means allow it to effectively respond to cross-domain changes in images, thereby enhancing the cross-domain detection capabilities of images and improving cross-domain fidelity evaluation indicators.

For each pair of real and simulated images, the fidelity is calculated using traditional fidelity metrics, deep model-based fidelity metrics, and cross-domain perceptual fidelity metrics. Subsequently, these metrics are weighted and combined to obtain the comprehensive fidelity between the real and simulated image pairs. By integrating fidelity values from different methods, the performance degradation caused by a single fidelity evaluation method is mitigated, thus enhancing the overall robustness of the algorithm. The formula is as follows:

$$Fid_{All} = \frac{1}{3}\left(Fid_{Traditional} + Fid_{Deep} + Fid_{Domain}\right) \quad (8)$$

3 Experimental Results

3.1 Experimental environment and data

In order to verify the effectiveness and practicality of the proposed fidelity evaluation method in this paper, experiments are conducted using a set of simulated infrared images and a corresponding set of real infrared images for training and testing. The simulated data consists of a sequence of computer-generated infrared images with a gray background and no additional interference. The real data comprises sequences of infrared images captured by infrared devices, featuring complex background interference such as intricate ground clutter and lighting shadows. Some of the data is shown in **Fig. 3**.

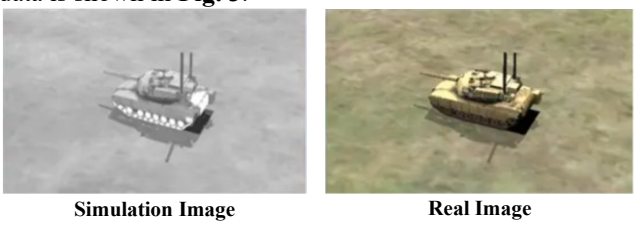

Simulation Image **Real Image**

Figure 3 Partial dataset

Experimental operating system: Ubuntu 20.04. Software environment: Python 3.6, PyTorch 1.7.0. Hardware environment: NVIDIA GeForce RTX 4090.

3.2 Branch-wise fidelity evaluation value

（1） Traditional fidelity evaluation value

Traditional feature extraction methods are applied to extract features from paired images, including HOG features, LBP features, Harris corner features. Then, the L2 loss function is used to calculate the similarity of various features respectively. Finally, the similarity is calculated through **Equation 4** to obtain the traditional fidelity value. The visualization results of traditional feature extraction are shown in **Fig. 4**, where the first row represents traditional features of simulated images and the second row represents traditional features of real images. The fidelity evaluation values are presented in Table 2. As shown in **Table 1**, although the similarity of Harris corner detection features is less than 50%, the HOG features and LBP features demonstrate good similarity, both exceeding 80%. The combination of these three features results in a traditional fidelity evaluation metric close to 80%, indicating a satisfactory evaluation performance.

Table 1:Traditional fidelity evaluation value

Feature	HOG	LBP	Harris	Complex
Fidelity	89.45%	84.38%	48.26%	74.03%

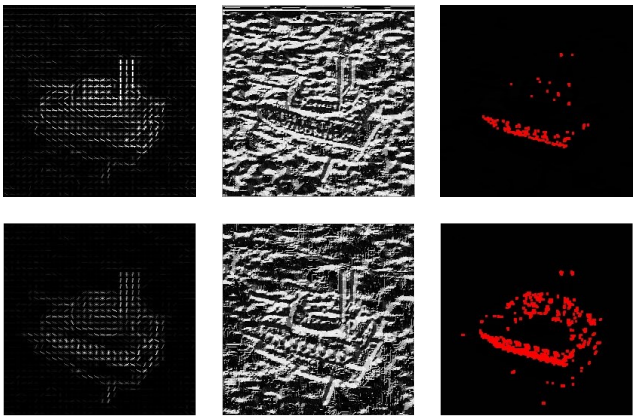

HOG **LBP** **Harris**

Figure 4 HOG features, LBP features and Harris features of simulated and real data

（2） Depth-based fidelity evaluation value

Using deep neural network models to extract features from paired images, including structural features, content features, and semantic features. Then, the L2 loss function is used to calculate the structural similarity, the L1 loss function is used to calculate the content similarity, and the IOU loss function is used to calculate the semantic similarity. Finally, **Equation 5** is used to calculate the similarity and obtain fidelity evaluation value based on the deep network model. As shown in **Fig. 5**, the visualization results of structural features extracted by HEDNet and semantic features extracted by RefineNet are presented, where the first row represents depth features of simulated images and the second row represents depth features of real images. As

shown in **Table 2**, the similarity of the three features is all above 80%, with both content features and semantic features exceeding 90%. The combination of these three features results in a fidelity evaluation metric based on the deep model reaching 90.11%.

Table 2:Depth-based fidelity evaluation value

Feature	Structure	Content	Semantics	Complex
Fidelity	82.65%	92.24%	95.45%	90.11%

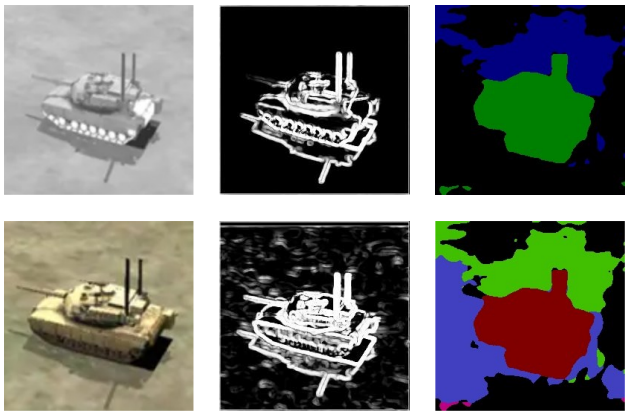

The Original **Structural Feature** **Semantic Feature**

Figure 5 Deep features of simulated and real data

（3） Cross-domain perceptual fidelity evaluation value

Applying a cross-domain detection algorithm trained on simulated data to perform object detection on real data. The confidence obtained by the model in detecting objects serves as the fidelity evaluation value for cross-domain perception. **Fig. 6** shows the detection results on real data. It can be observed that the fidelity evaluation metric for cross-domain perception reaches 93%.



Figure 6 Cross-domain perceptual fidelity result

3.3 Overall perceived fidelity evaluation value

Taking the average of the fidelity evaluation values obtained from traditional methods, deep model-based methods, and cross-domain perception methods. By integrating the advantages of various evaluation metrics, a cross-domain perceptual fidelity rapid assessment system with strong robustness and practicality is ultimately obtained. As shown in **Table 3**, the final fidelity evaluation value is 85.71%, meeting the requirements for practical engineering applications. While the composite fidelity evaluation metric may yield lower values compared to individual fidelity evaluation metrics, it avoids the stability issues caused by the drastic oscillation of a single fidelity evaluation metric when testing different images. This greatly enhances robustness and increases the likelihood of practical engineering implementation.

Table 3:Cross-domain comprehensive perceptual fidelity evaluation value

Feature	Traditional	Depth-based	Cross-domain	Final
Fidelity	74.03%	90.11%	93%	85.71%

4 Conclusion

This paper proposes a cross-domain comprehensive perceptual fidelity evaluation system. It addresses the issue of weak robustness in traditional single-domain fidelity evaluation methods, which renders them impractical for engineering applications. This method innovatively combines traditional feature fidelity, deep model-based fidelity, and cross-domain perceptual fidelity to create a novel cross-domain comprehensive perceptual fidelity evaluation system. Experimental results demonstrate that this method effectively suppresses complex backgrounds and interferences, highlighting relevant features of real targets. It provides a new approach for fidelity assessment methods, greatly enhancing the reliability and effectiveness of engineering practical applications.

In the future, we will further research a multi-object cross-domain comprehensive perceptual fidelity evaluation system with stronger robustness, which is applicable to different objects in various complex backgrounds.

References

[1] Zhang W, Wang X. Simulation credibility. *Journal of System Simulation*, 2001(03): 312-314.

[2] Roza Z C, Gross D C, Harmon S Y. Report out of the fidelity experimentation ISG. *Complexity*, 2000, 4(11): 12.

[3] Kim H, McGinnis L F, Zhou C. On fidelity and model selection for discrete event simulation. *Simulation*, 2012, 88(1): 97-109.

[4] Sargent R G. Verification and validation of simulation models: an advanced tutorial. *2020 Winter Simulation Conference (WSC). IEEE*, 2020: 16-29.

[5] Zhu X, Zhang Y. Research on evaluation method of credibility of simulation system based on VV&A. *Informatization Research*, 2021, 47(02): 63-69.

[6] Sherif J S. Principles of design and analysis of simulation experiments. *Systems Modeling and Computer Simulation. Routledge*, 2018: 355-412.

[7] Danquah B, Riedmaier S, Lienkamp M. Potential of statistical model verification, validation and uncertainty quantification in automotive vehicle dynamics simulations: a review. *Vehicle System Dynamics*, 2022, 60(4): 1292-1321.

[8] Wang Z, Bovik A C, Sheikh H R, et al. Image quality assessment: from error visibility to structural similarity. *IEEE Transactions on Image Processing*, 2004, 13(4): 600-612.

[9] Haralick R M. Statistical and structural approaches to texture. *Proceedings of the IEEE*, 1979, 67(5): 786-804.

[10] Ding K, Ma K, Wang S, et al. Image quality assessment: Unifying structure and texture similarity. *IEEE Transactions on Pattern Analysis and Machine Intelligence*, 2020, 44(5): 2567-2581.

[11] Kang L, Ye P, Li Y, et al. Convolutional neural networks for no-reference image quality assessment. *Proceedings of the*

IEEE Conference on Computer Vision and Pattern Recognition. 2014: 1733-1740.

[12] Ren H, Chen D, Wang Y. RAN4IQA: Restorative adversarial nets for no-reference image quality assessment. *Proceedings of the AAAI Conference on Artificial Intelligence*. 2018, 32(1).

[13] Hou L, Zeng W, Fan H, et al. Research of integrated intelligent flexible simulation evaluation technology. *Fire Control & Command Control*, 2019, 44(11): 174-179

[14] Dong C. Research on simulation image evaluation based on deep learning. *Xidian Uniersity*, 2021.

[15] Harris C, Stephens M. A combined corner and edge detector. *Alvey Vision Conference*. 1988, 15(50): 10-5244.

[16] Ojala T, Pietikainen M, Maenpaa T. Multiresolution gray-scale and rotation invariant texture classification with local binary patterns. *IEEE Transactions on Pattern Analysis and Machine Intelligence*, 2002, 24(7): 971-987.

[17] Xie S, Tu Z. Holistically-nested edge detection. *Proceedings of the IEEE International Conference on Computer Vision*. 2015: 1395-1403.

[18] He K, Zhang X, Ren S, et al. Deep residual learning for image recognition. *Proceedings of the IEEE Conference on Computer Vision and Pattern Recognition*. 2016: 770-778.

[19] Lin G, Milan A, Shen C, et al. Refinenet: Multi-path refinement networks for high-resolution semantic segmentation. *Proceedings of the IEEE Conference on Computer Vision and Pattern Recognition*. 2017: 1925-1934.

[20] Hsu C C, Tsai Y H, Lin Y Y, et al. Every pixel matters: Center-aware feature alignment for domain adaptive object detector. *European Conference on Computer Vision, Springer*, 2020: 733-748.

Proceedings of the 3rd Conference on Fully Actuated System Theory and Applications
May 10-12, 2024, Shenzhen, China

Adaptive neural network control for uncertain strict-feedback nonlinear systems with unknown control coefficients: A fully actuated system approach

Yueyao Ye[1], Debao Fan[1], Xianfu Zhang*[1]

1. School of Control Science and Engineering, Shandong University, Jinan 250061, P. R. China
E-mail: yeyueyao418@163.com, fandebao@mail.sdu.edu.cn, zhangxianfu@sdu.edu.cn

Abstract: In this paper, an adaptive control scheme is designed for a class of strict-feedback nonlinear systems with unknown control coefficients. Unlike the existing iterative design approaches, we apply a fully actuated system approach to reduce the algorithmic complexity. First, the considered strict-feedback nonlinear systems are transformed into fully actuated systems by state transformations. After that, we compensate for the uncertainties arising from the unknown control coefficients and unknown nonlinear functions by the neural network approximation technique. Then, an adaptive neural network controller based on a fully actuated system approach is designed. According to Lyapunov stability analysis, it is shown that all the signals of the closed-loop system are bounded and the system states converge to a small neighborhood of the origin under the designed controller. Moreover, by further enhancing the adaptive neural network mechanism, this paper extends the relevant results to more general uncertain strict-feedback nonlinear systems with unknown coefficients. Finally, the effectiveness of the proposed control scheme is demonstrated by a practical application example.

Key Words: Strict-Feedback Nonlinear Systems, Unknown Control Coefficients, The Fully Actuated System Approach, Adaptive Neural Network

1 Introduction

With the development of technology, many practical engineering systems can be transfomed into strict-feedback systems, such as battery energy storage systems[1] and wind turbine systems[2]. Therefore, the control design of strict-feedback systems has been a hot research direction[3–5]. However, the uncertainties arising from the unknown control coefficients make the control design of strict feedback systems extremely difficult. Thus, the study of strict-feedback systems with unknown control coefficients is both challenging and meaningful. For the unknown control coefficients, the reference [6] overcame the lack of information about the virtual control coefficients by utilizing the observation gain matrix determined by the convex combination technique. The reference [7] constructed an adaptive backstepping procedure based on the fuzzy approximation capability and variable partition technique to compensate for uncertainties. The reference [8] approximated an unknown nonlinear function of a system using fuzzy-logic systems and designed a novel Lyapunov function to eliminate the requirement of lower bounds of the unknown virtual control coefficients in control laws. However, most of the current studies of strict-feedback systems with unknown control coefficients are limited to a backstepping design approach, which makes the design process more complex when the model order is large. In the existing studies, the fully actuated system approach has not been utilized. To further simplify the controller design process, the fully actuated system approach will be applied in this paper.

The fully actuated system approach has attracted much attention from scholars in recent years because it can directly design the control variables, which is simpler than the state-space approach. The work [9] provided the first systematic introduction to the fully actuated system theory and illustrated the limitations of the state-space approach as well as the advantages of the fully actuated system approach. Then, it is pointed out that almost nonlinear systems can be transformed into fully actuated systems after variable transformation, and the corresponding transformation method was given in [10]. In [11], after deriving the fully actuated system model, it is straightforward to design the controller so that the closed-loop system becomes a constant linear system with the desired eigenstructure. In addition, based on the Lyapunov stability theory, the adaptive stabilization control scheme and the adaptive tracking control scheme for the fully actuated system model were proposed in [12]. In [13], based on the fully actuated system approach, an adaptive controller is designed for a class of nonlinear time-delay systems with strict-feedback forms. The work [14] obtained the global stability of linear uncertain systems with the intermittent faults using the fully actuated system model. However, so far, no works have investigated strict-feedback systems with unknown control coefficients using the fully actuated system approach.

Adaptive neural networks have great potential in dealing with highly nonlinear and severely uncertain systems. When using adaptive neural networks to deal with approximated nonlinear functions, it is only necessary to require that the nonlinear function is continuous, which allows for severe structural uncertainty in the nonlinear function of the system. Thus adaptive neural networks have a wider range of applications, see [15–17]. In recent years, adaptive neural networks have attracted much attention in the control field, and a number of valuable results have been obtained. The work [18] utilized the approximation ability of neural networks to design an adaptive controller for a class of uncertain systems with unknown actuator faults, such that the output signal converges to a small neighborhood of the refer-

This work was supported in part by the Science Center Program of National Natural Science Foundation of China under Grant 62188101, and in part by the Autonomous Innovation Team Foundation for "20 Items of the New University" of Jinan City under Grant 202228087.

ence signal. The work [19] approximated the unknown input deadzone and unknown disturbances using adaptive neural networks, and ensured that all the state signals are bounded. However, all of the above works are based on the backstepping design approach, which requires the construction of a virtual controller for each step. Therefore, the complexity of the designed algorithm is high. In order to optimize the design process, we apply the fully actuated system approach to deal with strict-feedback systems with unknown control coefficients. Inspired by the above, the objective of this paper is to design an adaptive control scheme for strict-feedback systems with unknown control coefficients based on an adaptive neural network technology and the fully actuated system approach.

The contributions of this paper are summarised as follows:

- In this paper, we use adaptive neural network to approximate the unknown nonlinear terms, which only require the nonlinear terms to be arbitrary smooth functions. Compared with the works [13], [20] and [21], the system nonlinear terms considered in this paper are less conservative, which makes our study more practical.
- Based on the fully actuated system approach, this paper designs a novel low-complexity adaptive neural network controller. Compared with the backstepping design approach [6–8], the complex iterative processes are avoided, which makes the design processes concise.
- By constructing new coordinate transformations, we extend the relevant results to more generalized strict-feedback systems with unknown coefficients. Accordingly, the fully actuated system approach provides a new design perspective for more generalized strict-feedback systems, which is different from [22, 23].

The rest of this paper is organized as follows. The preliminaries and problem statement are given in Section 2. An adaptive neural network control scheme is designed in Section 3 to more general systems. Section 4 extends the result of Section 3. The effectiveness of proposed control scheme is further verified through a practical example in Section 5. Finally, Section 6 concludes this paper.

Notation: In this paper, let $x^{(0\sim m-1)}$ denote $[x, \dot{x}, \ldots, x^{(m-1)}]^T$, where x^i is the ith derivative of x. The Euclidean norm of vector or the induced Euclidean norm of matrix is represented by $\|\cdot\|$. I denotes identity matrix with proper dimension.

2 Preliminaries and Problem Statement

2.1 Preliminaries

Consider a nonlinear system in the following form

$$x^{(m)} = f(x^{(0\sim m-1)}) + B(x^{(0\sim m-1)})u, \tag{1}$$

where $m \geq 1$ is an integer, $x \in R^n$ is the state vector, $u \in R^r$ is the control input vector, $f(x^{(0\sim m-1)}) \in R^n$ is a smooth function, and $B(x^{(0\sim m-1)}) \in R^{n\times r}$ is a matrix function.

Definition 2.1 [9] Given system (1) and a series of open sets $\Omega_i \subset R^n,\ i = 0, 1, \ldots, m-1,$ if for all $x^{(i)} \in \Omega_i,\ i = 0, 1, \ldots, m-1,$ the following equation holds

$$\text{rank}B(x^{(0\sim m-1)}) = r = n,\ \ \forall t \geq 0, \tag{2}$$

then system (1) is called a fully actuated system on $\Omega = \Omega_0 \times \Omega_1 \times \cdots \times \Omega_{m-1}$. In particular, system (1) is called a standard fully actuated system when $B(x^{(0\sim m-1)}) \equiv I_r$.

Lemma 2.2 [28] There exist positive numbers $\varepsilon,\ k_i,\ i = 0, 1, \ldots, n-1,$ and a positive definite matrix P satisfying the following inequality:

$$\bar{A}^T P + P\bar{A} \leq -\varepsilon P, \tag{3}$$

where

$$\bar{A} = \begin{bmatrix} 0 & 1 & 0 & \cdots & 0 \\ 0 & 0 & 1 & \cdots & 0 \\ \vdots & \vdots & \vdots & \ddots & \vdots \\ 0 & 0 & 0 & \cdots & 1 \\ -k_0 & -k_1 & -k_2 & \cdots & -k_{n-1} \end{bmatrix} \tag{4}$$

is a Hurwitz matrix.

2.2 Problem statement

Consider the following strict-feedback nonlinear system with unknown control factor

$$\begin{cases} \dot{x}_1 = x_2 + f_1(\bar{x}_1), \\ \dot{x}_2 = x_3 + f_2(\bar{x}_2), \\ \qquad \vdots \\ \dot{x}_n = gu + f_n(\bar{x}_n), \end{cases} \tag{5}$$

where $x_i \in R,\ i = 1, 2, \ldots, n,$ are the system states, $\bar{x}_i = [x_1, x_2, \ldots, x_i]^T$, the unknown nonlinear functions $f_i(\cdot) \in R^i \to R$ are smooth, $u \in R$ is the control input, g is an unknown control coefficient. Next, an assumption is proposed on the system (5).

Assumption 1 sign(g) is known and $g \neq 0$. Without loss of generality, let sign$(g) > 0$.

Remark 1 According to [24, 25], Assumption 1 is reasonable. Many practical systems can be modeled as strict-feedback systems with unknown control coefficients, such as automotive cruise control systems [26] and electrical power systems [27]. The unknown control coefficient g makes the control design and stability analysis in this paper extremely difficult. In addition, the nonlinear term considered in this paper is only smooth, which is less conservative than the linear growth condition in [13].

In this paper, we will design the adaptive neural network controller for the system (5) using the fully actuated system approach. First, the system (5) is transformed into the form of a fully actuated system using the following state transformation

$$\begin{cases} x_1 = z, \\ x_2 = \dot{z} - h_1(z), \\ \vdots \\ x_n = z^{(n-1)} - h_{n-1}(z^{(0\sim n-2)}), \end{cases} \tag{6}$$

where

$$\begin{aligned} h_1(\cdot) &= f_1(z), \\ h_i(\cdot) &= \dot{h}_{i-1}(\cdot) + f_i(z^{(0\sim i-1)}), i = 2, 3, \ldots, n-1. \end{aligned}$$

Then, it's easy to get that

$$z^{(n)} = gu + h(z^{(0\sim n-1)}), \tag{7}$$

where

$$h(\cdot) = \dot{h}_{n-1}(\cdot) + f_n(z^{(0\sim n-1)}).$$

According to Definition 2.1, we can get the system (7) is a fully actuated system.

2.3 Radial Basis Function Neural Network(RBF NN)

In this paper, RBF NN of the following form will be used to approximate unknown nonlinear functions in the system:

$$h(Z) = W^T S(Z),$$

where $Z \in \Omega_Z \subset R^q$ is the input vector, $W = [w_1, w_2, \ldots, w_l]^T \in R^l$ denotes the weight vector, $l > 1$ denotes the number of nodes of the neural network, and $S(Z) = [s_1(Z), s_2(Z), \ldots, s_l(Z)]^T$ denotes the basis function vector, and $s_i(Z)$ is denoted by the following form:

$$s_i(Z) = \exp\left[-\frac{(Z-c_i)^T(Z-c_i)}{\sigma_i^2}\right], \ 1 \le i \le l,$$

with $c_i = [c_{i1}, c_{i2}, \ldots, c_{iq}]^T$ being the center of the receptive field, σ_i being the width of the basis function.

Lemma 2.3 [29] For any positive constant $\epsilon > 0$, there always exists an RBF NN such that the unknown nonlinear function $h(Z)$ can be approximated in the following form:

$$h(Z) = W^{*T} S(Z) + \delta(Z), \ \forall Z \in \Omega_z,$$

where $\delta(Z)$ denotes the approximation error and satisfies $\|\delta(Z)\| \le \epsilon$, W^* is the optimal weight vector, which be defined as follows

$$W^* = \arg\min_{W \in R^l} \left\{ \sup_{Z \in \Omega_Z} \left| h(Z) - W^T S(Z) \right| \right\}.$$

In the following, we define a constant $\eta = \|W^*\|^2$.

3 Main Results

In this section, an adaptive neural network controller will be designed for system (5). Firstly, by (5)-(7), we get the matrix form of the transformed system as follow

$$\begin{aligned} \dot{Z} &= AZ + L(h(Z) + gu) \\ &= (A - LK)Z + LKZ + gLu + Lh(Z) \\ &= \bar{A}Z + gLu + L(h(Z) + KZ), \end{aligned} \tag{8}$$

where $Z = [z, \dot{z}, \ldots, z^{(n-1)}]^T$, $L = [0, 0, \ldots, 0, 1]^T \in R^n$, $K = [k_0, k_1, \ldots, k_{n-1}]$, $\bar{A}$ and $k_i, \ i = 0, 1, \ldots, n-1,$ are given by Lemma 2.2, where

$$A = \begin{bmatrix} 0 & 1 & \cdots & 0 \\ 0 & 0 & \cdots & 0 \\ \vdots & \vdots & \ddots & \vdots \\ 0 & 0 & \cdots & 1 \\ 0 & 0 & \cdots & 0 \end{bmatrix}.$$

Next, the main results for adaptive neural network control of strict-feedback systems is summarized in the following theorem.

Theorem 3.1 Consider system (5) satisfying Assumption 1. Under the adaptive neural network controller

$$u = -r_1 \hat{\eta} L^T P Z S^T(Z) S(Z) - r_2 L^T P Z, \tag{9}$$

and the adaptive law

$$\dot{\hat{\eta}} = 2r_1 (Z^T P L)(L^T P Z) S^T(Z) S(Z) - r_3 \hat{\eta}, \tag{10}$$

where $\hat{\eta}$ is the estimate of η, $\tilde{\eta} = \eta - \hat{\eta}$ is the estimation error, and $r_i, \ i = 1, 2, 3,$ are arbitrary positive constants, P is a positive definite matrix given by Lemma 2.2, all the signals of the closed-loop system are bounded and the system states converge to a small neighborhood of the origin.

Proof Let $\varphi(Z) = h(Z) + KZ$. Then, we have that $\varphi(Z)$ is a continuous function. The system (8) ia rewritten as

$$\dot{Z} = \bar{A}Z + gLu + L\varphi(Z). \tag{11}$$

Considering the following Lyapunov function

$$V = \frac{1}{g} Z^T P Z + \frac{1}{2}\tilde{\eta}^2. \tag{12}$$

Along the trajectory of the system (11), the derivative of V can be expressed as follow

$$\begin{aligned} \dot{V} =& \frac{1}{g}[Z^T(\bar{A}^T P + P\bar{A})Z + 2Z^T P L \varphi(Z) \\ &+ 2gZ^T P L u] - \tilde{\eta}\dot{\hat{\eta}}. \end{aligned} \tag{13}$$

By Lemma 2.2, we have

$$\dot{V} \le -\frac{1}{g}\varepsilon Z^T P Z + 2Z^T P L \psi(Z) + 2Z^T P L u - \tilde{\eta}\dot{\hat{\eta}}, \tag{14}$$

where $\psi(Z) = \frac{\varphi(Z)}{g}$.

From (14), we can obtain $\psi(Z)$ is a smooth function. Thus, according to Lemma 2.3, for any positive constant $\epsilon > 0$, there exists an RBF NN such that

$$\psi(Z) = W^{*T} S(Z) + \delta(Z), \ \|\delta(Z)\| \le \epsilon, \tag{15}$$

where $Z = [z, \dot{z}, \ldots, z^{(n-1)}]^T$.

Applying Young's inequality and (15), we have

$$\begin{aligned} 2Z^T P L \psi(Z) &= 2Z^T P L (W^{*T} S(Z) + \delta(Z)) \\ &\le 2r_1 Z^T P L L^T P Z \eta S^T(Z) S(Z) \\ &\quad + 2r_2 Z^T P L L^T P Z + \frac{1}{2r_1} + \frac{1}{2r_2}\delta(Z)^2. \end{aligned} \tag{16}$$

Substituting (4), (10) and (16) into (14) yields

$$\begin{aligned} \dot{V} &\le -\frac{1}{g}\varepsilon Z^T P Z + 2r_1 Z^T P L L^T P Z \eta S^T(Z) S(Z) \\ &\quad + 2r_2 Z^T P L L^T P Z + \frac{1}{2r_1} + \frac{1}{2r_2}\delta(Z)^2 \\ &\quad + 2Z^T P L u - \tilde{\eta}\dot{\hat{\eta}} \\ &\le -\frac{1}{g}\varepsilon Z^T P Z - \frac{r_3}{2}\tilde{\eta}^2 + \frac{1}{2r_1} + \frac{1}{2r_2}\epsilon^2 + \frac{r_3}{2}\eta^2. \end{aligned} \tag{17}$$

Noting $r = \min\{\varepsilon, r_3\}$ and $a = \frac{1}{2r_1} + \frac{1}{2r_2}\epsilon^2 + \frac{r_3}{2}\eta^2$, one has

$$\begin{aligned} \dot{V} &\le -r\left(\frac{1}{g} Z^T P Z + \frac{1}{2}\tilde{\eta}^2\right) + a \\ &= -rV + a. \end{aligned} \tag{18}$$

It follows from (18) that

$$V \leq \frac{a}{r} + (V(0) - \frac{a}{r})e^{-rt}. \tag{19}$$

According to (19), we can obtain that V is bounded. By the construction of V, i.e., (12), it follows that all the signals of the closed-loop system are bounded. By (6), we have the system states $x_i,\ i = 1, 2, \ldots, n$ converge to a small neighborhood of the origin.

4 Extension

In this section, we extend the relevant results of the previous section to strict-feedback nonlinear systems with multiple unknown coefficients.

Consider the following systems

$$\begin{cases} \dot{x}_1 = g_1 x_2 + f_1(\bar{x}_1), \\ \dot{x}_2 = g_2 x_3 + f_2(\bar{x}_2), \\ \quad\quad \vdots \\ \dot{x}_n = g_n u + f_n(\bar{x}_n), \end{cases} \tag{20}$$

where $g_i \in R,\ i = 1, 2, \ldots, n$, are unknown coefficients. Next, a assumption is proposed on the system (20).

Assumption 2 $\text{sign}(g_i),\ i = 1, 2, \ldots, n$ is known and $g_i \neq 0$. Without loss of generality, let $\text{sign}(g_i) > 0$.

Remark 2 System (20) is a extension form of system (5). When $g_i = 1,\ i = 1, 2, \ldots, n$, system (20) can be equivalent to system (5). For system (20), some results have been obtained in [30, 31]. However, all of the above studies are based on the backstepping design approach, and the design process is complex. In this paper, the fully actuated system approach is applied to system (20) to further simplify the control design.

In this section, we construct a novel state transformation

$$\begin{cases} x_1 = \xi, \\ x_2 = \frac{1}{g_1}\dot{\xi} - \bar{f}_1(\xi), \\ x_3 = \frac{1}{g_1 g_2}\xi^{(2)} - \bar{f}_2(\xi, \dot{\xi}), \\ \vdots \\ x_n = \frac{1}{g_1 g_2 \cdots g_{n-1}}\xi^{(n-1)} - \bar{f}_{n-1}(\xi^{(0\sim n-2)}), \end{cases} \tag{21}$$

where

$$\begin{aligned} \bar{f}_1(\cdot) &= \frac{1}{g_1}\bar{f}_1(\xi), \\ \bar{f}_i(\cdot) &= \frac{1}{g_i}\dot{\bar{f}}_{i-1}(\cdot) + \frac{1}{g_i}f_i(\bar{x}_i),\ i = 2, 3, \ldots, n-1. \end{aligned}$$

From (20) and (21), we get

$$\begin{aligned} \xi^{(n)} &= g_1 g_2 \cdots g_{n-1}\dot{x}_n + g_1 g_2 \cdots g_{n-1}\dot{\bar{f}}_{n-1}(\xi^{(0\sim n-2)}) \\ &= g_1 g_2 \cdots g_{n-1} g_n u + g_1 g_2 \cdots g_{n-1} f_n(\bar{x}_n) \\ &\quad + g_1 g_2 \cdots g_{n-1}\dot{\bar{f}}_{n-1}(\xi^{(0\sim n-2)}) \\ &= g_1 g_2 \cdots g_n u + \bar{f}_n(\xi^{(0\sim n-1)}). \end{aligned} \tag{22}$$

Noting that $g = g_1 g_2 \cdots g_n$, then

$$\xi^{(n)} = gu + \bar{f}_n(\xi^{(0\sim n-1)}). \tag{23}$$

Theorem 4.1 Consider system (20) satisfying Assumption 2. Under the adaptive neural network controller

$$u = -r_1\hat{\eta}L^T PZS^T(Z)S(Z) - r_2 L^T PZ, \tag{24}$$

and the adaptive law

$$\dot{\hat{\eta}} = 2r_1(Z^T PL)(L^T PZ)S^T(Z)S(Z) - r_3\hat{\eta}, \tag{25}$$

all the signals of the closed-loop system are bounded and the system states converge to a small neighborhood of the origin.

Proof The proof of Theorem 4.1 is the same as that of Theorem 3.1, and will not be presented in this paper.

5 A Practical Simulation Example

Consider the following chemical reaction system with unknown control coefficients in [32]

$$\begin{cases} \dot{x}_1 = -\frac{1}{C_1}x_1 - K_1 x_1 + \frac{1-R}{V_1}x_2 + f_1, \\ \dot{x}_2 = -\frac{1}{C_2}x_2 - K_2 x_2 + \frac{F}{V_2}u + f_2, \\ y = x_1, \end{cases} \tag{26}$$

where $R, F, C_i, K_i, V_i,\ i = 1, 2$ are the recycle flow rate, the feed rate, the reactor residence times, reaction constants, and reactor volumes, respectively; $f_i,\ i = 1, 2$ are unknown nonlinear functions. In this simulation, the parameters are chosen as $R = 0.5, F = 0.2, C_1 = C_2 = 2, K_1 = K_2 = 0.3, V_1 = V_2 = 0.5$, and

$$\begin{aligned} f_1 &= 0.2x_1, \\ f_2 &= 5x_1^2 + x_1 x_2. \end{aligned}$$

Let $z = x_1$, the state transformation of the system is given by

$$\ddot{z} = \frac{F(1-R)}{V_1 V_2}u + h(z, \dot{z}),$$

where

$$\begin{aligned} h(z, \dot{z}) = &-(\frac{1}{C_1} + K_1 - 0.2)(\frac{1}{C_2} + K_2)z \\ &-(\frac{1}{C_1} + \frac{1}{C_2} + K_1 + K_2 - 0.2)\dot{z} \\ &+(\frac{5(1-R)}{V_1} + \frac{1}{C_1} + K_1 - 0.2)z^2 + z\dot{z}. \end{aligned}$$

Taking $K = [3, 2], r_1 = 0.4, r_2 = 2.7, r_3 = 10$, and according to Theorem 3.1, the state-feedback controller of the system (26) is obtained as

$$\begin{aligned} u &= -0.4\hat{\eta}(1.45z + 1.67\dot{z})S^T(Z)S(Z) - 2.7(1.45z + 1.67\dot{z}), \\ \dot{\hat{\eta}} &= 0.8(1.45z + 1.67\dot{z})^2 S^T(Z)S(Z) - 10\hat{\eta}, \end{aligned}$$

where $Z = [z, \dot{z}], S(Z)$ is the basis function of the neural network, which form is given in Section 2.3.

From Figs. 1-4 show the signal track of the system(26) when the initial values are taken as $x_1(0) = -2,\ x_2(0) = 15,\ \hat{\eta}(0) = 1$. From Figs. 1-2, it can be obtained that the trajectories of the system states x_1 and x_2 can be converged to a small neighborhood at the origin, which in turn achieves the desired control objective. Therefore the designed control scheme is effective.

6 Conclusion

In this paper, the problem of adaptive neural network control of strict-feedback nonlinear systems with unknown control coefficients is solved. Uncertain nonlinear terms and

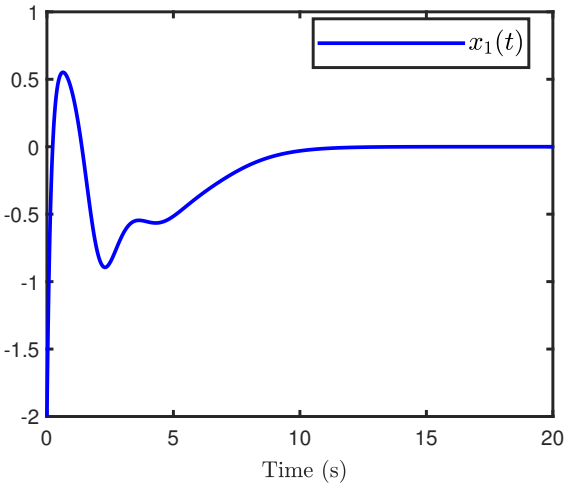

Fig. 1: The trajectory of $x_1(t)$

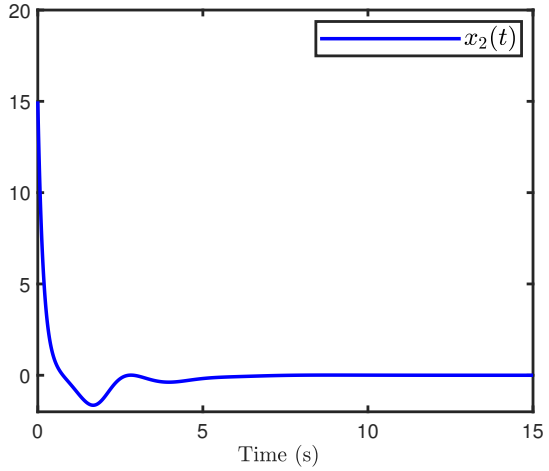

Fig. 2: The trajectory of $x_2(t)$

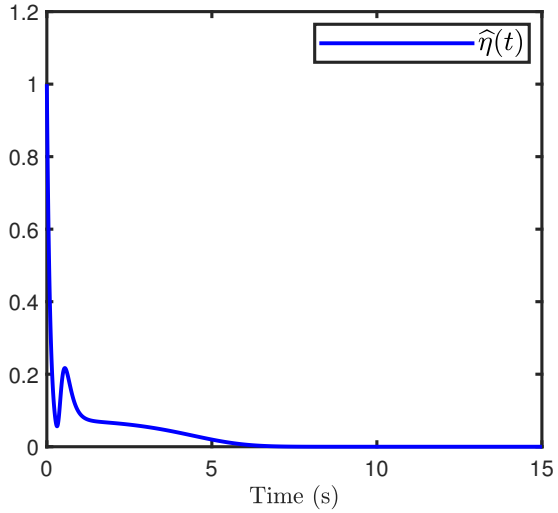

Fig. 3: The trajectory of $\hat{\eta}(t)$

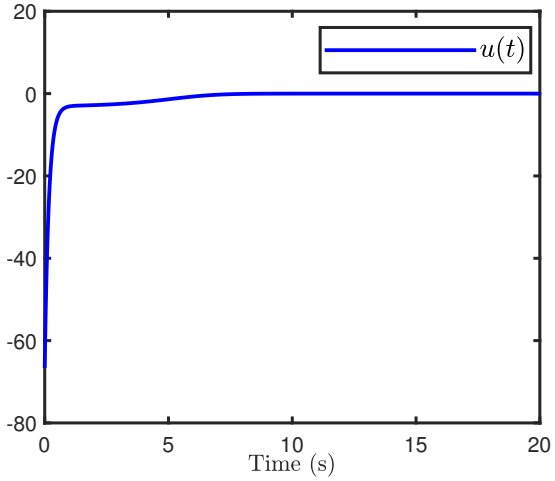

Fig. 4: The trajectory of $u(t)$

unknown control coefficients were approximated with neural networks. Using the fully actuated system approach, an adaptive control scheme is designed to ensure that all the signals of the closed-loop system are bounded and the system states converge to a small neighborhood of the origin under the designed controller. In particular, the results presented in this paper can also be extended to systems with unknown coefficients. In future research, an attempt will be made to apply the fully actuated system approach to nonlinear multi-agent systems and multi-dimensional dynamics.

References

[1] J. Khazaei, and D. Nguyen, Multi-agent consensus design for heterogeneous energy storage devices with droop control in smart grids, *IEEE Transactions on Smart Grid*, 10(2): 1395–1404, 2019.

[2] L. Xing, Y. Mishra, Y. Tian, C. Peng, and M. Fei, Dual-consensus-based distributed frequency control for multiple energy storage systems, *IEEE Transactions on Smart Grid*, 10(6): 6396–6403, 2019.

[3] H. Li, S. Zhao, W. He, and R. Lu, Adaptive finite-time tracking control of full state constrained nonlinear systems with dead-zone, *Automatica*, 100: 99–107, 2019.

[4] K. Zhao, and Y. Song, Removing the Feasibility Conditions Imposed on Tracking Control Designs for State-Constrained Strict-Feedback Systems, *IEEE Transactions on Automatic Control*, 64(3)? 1265–1272, 2019.

[5] K. Sun, L. Liu, J. Qiu, and G. Feng, Fuzzy Adaptive Finite-Time Fault-Tolerant Control for Strict-Feedback Nonlinear Systems, *IEEE Transactions on Fuzzy Systems*, 29(4): 786–796, 2021.

[6] B. Chen, X. Liu, and C. Lin, Observer and adaptive fuzzy control design for nonlinear strict-feedback systems with unknown virtual control coefficients. *IEEE Transactions on Fuzzy Systems*, 26(3): 1732–1743, 2018.

[7] Z. Li, and J. Zhao, Fuzzy Adaptive Robust Control for Stochastic Switched Nonlinear Systems with Full-State-Dependent Nonlinearities, *IEEE Transactions on Fuzzy Systems*, 28(9): 2035-2047, 2020.

[8] X. Hu, Y. Li, and Z. Hou, Event-Triggered Fuzzy Adaptive Fixed-Time Tracking Control for Nonlinear Systems, *IEEE Transactions on Cybernetics*, 52(7): 7206–7217, 2022.

[9] G. Duan, High-order fully actuated system approaches: Part I. Models and basic procedure, *International Journal of Systems Science*, 52(2): 422–435, 2021.

[10] G. Duan, High-order fully actuated system approaches: Part

II. Generalized strict-feedback systems, *International Journal of Systems Science*, 52(3): 437–454, 2021.

[11] G. Duan, High-order fully actuated system approaches: Part III. Robust control and high-order backstepping, *International Journal of Systems Science*, 52(5): 952–974, 2021.

[12] G. Duan, High-order fully actuated system approaches: Part IV. Adaptive control and high-order backstepping, *International Journal of Systems Science*, 52(5): 972–989, 2021.

[13] P. Ning, C. Hua, and R. Meng, Adaptive Control for a Class of Nonlinear Time-Delay System Based on the Fully Actuated System Approaches, *J Syst Sci Complex*, 35: 522–534, 2022.

[14] M. Cai, X. He, and D. Zhou, Performance-improved finite-time fault-tolerant control for linear uncertain systems with intermittent faults: an overshoot suppression strategy, *International Journal of Systems Science*, 53(16): 3408–3425, 2022.

[15] G. Lai, G. Tao, Y. Zhang, Z. Liu, and J. Wang, Adaptive Actuator Failure Compensation Control Schemes for Uncertain Noncanonical Neural-Network Systems, *IEEE Transactions on Cybernetics*, 52(5): 2635–2648, 2022.

[16] F. Wang, X. Xie, and C. Zhou, Locally Expanded Constraint-Boundary-Based Adaptive Composite Control of a Constrained Nonlinear System With Time-Varying Actuator Fault, *IEEE Transactions on Fuzzy Systems*, 31(11): 4121–4136, 2023.

[17] R. Luo, Z. Peng, J. Hu, and B. Ghosh, Adaptive optimal control of affine nonlinear systems via identifier?critic neural network approximation with relaxed PE conditions, *Neural Networks*, 167: 588–600, 2023.

[18] Y. Zhang, and F. Wang, Adaptive neural control of non-strict feedback system with actuator failures and time-varying delays, *Applied Mathematics and Computation*, 362, 2019.

[19] S. Zhang, L. Kong, S. Qi, P. Jing, H. Wei, and B. Xu, Adaptive neural control of unknown non-affine nonlinear systems with input deadzone and unknown disturbance, *Nonlinear Dyn*, 95: 1283–1299, 2019.

[20] M. Cai, and Z. Xiang, Adaptive practical finite-Time stabilization for uncertain nonstrict feedback nonlinear systems with input nonlinearity, *IEEE Transactions on Systems, Man, and Cybernetics: Systems*, 47(7); 1668–1678, 2017.

[21] D. Zhai, L. An, J. Dong, and Q. Zhang, Output feedback adaptive sensor failure compensation for a class of parametric strict feedback systems, *Automatica*, 97: 48–57, 2018.

[22] C. Liu, X. Liu, H. Wang, Y. Zhou, and S. Lu, Observer-based adaptive fuzzy funnel control for strict-feedback nonlinear systems with unknown control coefficients, *Neurocomputing*, 358: 467–478, 2019.

[23] F. You, N. Chen, Z. Zhu, S. Cheng, H. Yang, and M. Jia, Adaptive Fuzzy Control for Nonlinear State Constrained Systems with Input Delay and Unknown Control Coefficients, *IEEE Access*, 7: 53718–53730, 2019.

[24] J. Yan, and C. Shao, Barrier Lyapunov Functions-based adaptive control for a class of nonlinear pure-feedback systems with full state constraints, *Automatica*, 64: 70–75, 2016.

[25] C. Wang, Y. Wu, and J. Yu, Barrier Lyapunov functions-based dynamic surface control for pure-feedback systems with full state constraints, *IET Control Theory and Applications*, 11(4): 524–530, 2017.

[26] Y. Lin, and H. Nguyen, Adaptive neuro-fuzzy predictor-based control for cooperative adaptive cruise control system, *IEEE Transactions on Intelligent Transportation Systems*, 21(3): 1054–1063, 2020.

[27] W. Wang, W. Wang, B. Feng, and Y. Fan, Dynamic coordinated control method of driving mode switch of parallel hybrid electric vehicle. *Jiaotong Yunshu Gongcheng Xuebao/Journal of Traffic and Transportation Engineering*, 17(2): 90–97, 2017.

[28] P. Krishnamurthy, and F. Khorrami, Feedforward Systems With ISS Appended Dynamics: Adaptive Output-Feedback Stabilization and Disturbance Attenuation, *IEEE Transactions on Automatic Control*, 53(1): 504–512, 2008.

[29] R. Sanner, and J. Slotine, Gaussian networks for direct adaptive control, *IEEE Transactions on Neural Networks*, 3(6): 837–863, 1992.

[30] Z. Qin, T. Liu, and Z. Jiang, Adaptive backstepping for distributed optimization, *Automatica*, 141: 110304, 2022.

[31] W. Sun, S. Su, Y. Wu, and J. Xia, Novel Adaptive Fuzzy Control for Output Constrained Stochastic Nonstrict Feedback Nonlinear Systems, *IEEE Transactions on Fuzzy Systems*, 29(5): 1188–1197, 2021.

[32] S. Yoo, and J. Park, Decentralized adaptive output-feedback control for a class of nonlinear large-scale systems with unknown time-varying delayed interactions, *Information Sciences*, 186(1): 222–238, 2012.

Proceedings of the 3rd Conference on Fully Actuated System Theory and Applications
May 10-12, 2024, Shenzhen, China

Static Output Feedback Control Design for Nonlinear Descriptor Systems with Actuator Saturation

Yabo Zhang[1], Liying Sun[2]

1. Shanghai Dianji University, Shanghai 201306, P. R. China
E-mail: 914728445@qq.com

2. Shanghai Dianji University, Shanghai 201306, P. R. China
E-mail: sunly@sdju.edu.cn

Abstract: This article investigates the stabilization and H_∞ control problems of nonlinear descriptor systems with actuator saturation. Firstly, the sufficient conditions of the impulse controllability are given. A static output feedback control strategy is designed by static output feedback to study the stabilization of system. Then H_∞ control by static output feedback is considered for nonlinear descriptor systems with external disturbances. Finally, the effectiveness of the designed controller is verified through the simulation results of a circuit example.

Key Words: static output feedback, nonlinear descriptor systems, stabilization, actuator saturation, H_∞ control

1 Introduction

Descriptor systems can also be known as differential algebra or singular systems. Compared with normal state system models, the structural characteristics of descriptor system are more specific. Descriptor systems inevitably have pulses in the study of related control, which often have adverse effects when the controller is designed. The concepts of stability and non-impulse are introduced to address these characteristics of descriptor systems [1]. Additionally, non-impulse is a crucial consideration in the descriptor system. Over the past four decades, the descriptor system has captivated numerous researchers and the study of Lyapunov stabilization or simultaneous stabilization of descriptor systems have been reported in a large number of literatures [2],[3],[4],[6].

Because linear descriptor systems are relatively easy to handle, sometimes nonlinear descriptor systems will be idealized as linear descriptor systems. After years of research, the theoretical application of linear descriptor systems has been very mature [2],[3]. However, compared to linear descriptor systems, nonlinear descriptor systems (NDS) can better reflect practical problems in system. In recent years, there have been some research on nonlinear descriptor systems [4],[5],[6].

For almost all practical systems, actuator saturation is inevitable. When system controller is designed, actuator saturation will destroy the structural stability of system; In industrial applications, if actuator saturation is not considered, equipment failure may occur once the actuator is oversaturated. Therefore, it is worth studying the stability of system with actuator saturation [4],[6],[8]. For actuator-saturate descriptor systems with full rank matrix in [4], a control allocation strategy is proposed. In [8], based on the period invariance of ellipsoid, the local and global stability of linear systems with actuator saturation are studied by solving linear matrix inequalities (LMI). Sun transforms NDS with actuator saturation into a strictly dissipative form through state feedback in [6]. According to the method of state decomposition, Sun designs H_∞ controller and adaptive H_∞ controller under the condition of considering the external disturbance and parameter disturbance of NDS. However, it is worth mentioning that there are not many studies on nonlinear descriptor systems similar to literature [6].

In addition, it is impossible to find all the state variables when the stability of system is studied in practical problems, and the calculation cost is high. However, the information of output feedback is easy to obtain, so the application of output feedback has been popularized. Feedback control is to suppress the initial disturbance of system, mainly including output feedback and state feedback. Because the state feedback can not be measured directly sometimes, the application of output feedback should be considered. The complexity of closed-loop systems by dynamic output feedback poses a major challenge to practical applications. Hence, it is beneficial to consider the utilization of static output feedback (SOF) as an alternative approach. For linear discrete-time systems [7], a new SOF control method based on the K q-flat algorithm is proposed to solve the mp-LP problems. In [5], He gives two assumptions and proves that these assumptions are a sufficient condition for impulsive controllability of NDS and designs a SOF controller to make the closed-loop system asymptotically stable. On the basis of He's research, this paper cites the conditions for pulse controllability of system.

This paper delves into the investigation of the stabilization problem pertaining to NDS with actuator saturation. First, the issue regarding SOF control has been resolved, and the sufficient conditions for impulsive controllability of system have been provided. An admissible controller is established under the static output feedback, and the state nondecomposition method of NDS is employed to formulate the design of the SOF controller. Then H_∞ controller by static output feedback is designed under the given disturbance attenuation level. Finally, the effectiveness of the designed controller is verified through the simulation results of a circuit example.

2 Stabilization of Nonlinear Descriptor Systems with Actuator Saturation

This section investigates the stabilization of nonlinear descriptor systems with actuator saturation. It is given the suffi-

This work is supported by National Natural Science Foundation (NNSF) of China under Grant 61877028.

cient condition of pulse controllability and designed the SOF controller.

We consider given nonlinear descriptor systems with actuator saturation:

$$\begin{cases} E\dot{x} = f(x) + N(x)sat(u) + B(z)w, Ex(0) = Ex_0, \\ f(0) = 0, \\ y = C(x)x, \end{cases} \tag{1}$$

where $y \in \mathbb{R}^n$ denotes the output; $x \in \mathbb{R}^n$ denotes the state; $F(x) \in \mathbb{R}^{k\times n}$. $E \in \mathbb{R}^{n\times n}$, suppose there is a nonsingular matrix $Q \in \mathbb{R}^n$, which satisfies $Q^T E = E^T Q \geq 0$, where $0 < \text{rank}(E) = r < n$. $f(x)$ denotes a smooth vector field with appropriate dimensions. $sat\,(u) \in \mathbb{R}^m$ denotes the input, $N(x) \in \mathbb{R}^{n\times m}$. The following is the saturation function representation:

$$sat(u_i) = \begin{cases} \varepsilon_i, & u_i > \varepsilon_i, \\ u_i, & -\varepsilon_i \leq u_i \leq \varepsilon_i, \\ -\varepsilon_i, & u_i < \varepsilon_i, \end{cases} \quad i = 1, 2, \cdots, m. \tag{2}$$

To facilitate the analysis of system stabilization problem, we propose the following results.

Definition 1:([6]) If there is a closed-loop descriptor system composed of a control law $u(x)$ and the original system which is impulse free under any given initial condition Ex_0, then the original system is considered to be impulse controllable and the control law $u(x)$ is also considered to be admissible control law.

Lemma 1:([6]) If there is a vector function $g(x)$ satisfies the condition $g(0) = 0$ and possesses continuous partial derivatives up to order n, then it is possible to represent $g(x)$ as

$$g(x) = m_1(x)x_1 \cdots + m_n(x)x_n = M(x)x, \tag{3}$$

where $m_i(x)$ represent vector functions, $i = 1, 2, \cdots, n$.

Bringing Equation (3) into system (1) can be expressed as

$$\begin{cases} E\dot{x} = M(x)x + N(x)sat(u), \\ y = F(x)x, \end{cases} \tag{4}$$

where $M(x) = [m_1(x), \cdots, m_n(x)] \in \mathbb{R}^{n\times n}$ represents the structural matrix.

In order to facilitate the research and design of a suitable controller for system stabilization, we introduce the following lemma.

Lemma 2:([6]) Suppose there is a real number $\beta \in (0, 1)$ satisfying

$$\alpha^T \alpha \leq \beta u^T u, \tag{5}$$

where

$$\alpha = u - sat(u), \tag{6}$$

where $\alpha = [\alpha_1, \cdots, \alpha_m]^T \in \mathbb{R}^m$ and $sat(u)$ defined by Equation (2).

The following assumptions are proposed to judge the pulse controllability of system (4).

A1)$\text{rank}\left(\begin{bmatrix} 0 & E & 0 \\ E & M(x) & N(x) \end{bmatrix}\right) = \text{rank}(E) + n, \forall x \in \mathbb{R}^n$.

A2)$\text{rank}\begin{bmatrix} E \\ F(x) \end{bmatrix} = n, \forall x \in \mathbb{R}^n$.

Remark 1: The above two assumptions are sufficient conditions for pulse controllability of NDS with actuator saturation.

To ensure the authenticity of the above assumptions, we provide a lemma as follows.

Lemma 3:([5]) Assuming that A1 and A2 are true, it can be concluded that system (4) exhibits pulse controllability.

Next, the following theorem is given to design a SOF control law u to meet the requirements of system stabilization.

Theorem 1: Assuming that A1 and A2 are true, If the admissible control law is designed as follows,

$$u = -K(y)y, \tag{7}$$

such that

$$\begin{aligned} &(M - NKF)^T Q + Q^T(M - NKF) + Q^T NN^T Q \\ &+ \beta F^T K^T KF < 0 \end{aligned} \tag{8}$$

holds, then the closed-loop NDS with actuator saturation composed of controller Equation (7) and system (4) is asymptotically stable, where $k(y) \in \mathbb{R}^{m\times k}$.

proof: Substituting Equation (7) and Equation (6) into system (4), it has

$$\begin{cases} E\dot{x} = (M(x) - N(x)K(y)F(x))x - N(x)\alpha, \\ y = F(x)x. \end{cases} \tag{9}$$

According to Lemma 1, system (9) is impulse-free. Defining a Lyapunov function $V(x) = x^T E^T Qx$. Based on system (9), Inequality (8) and Inequality (5),we obtain

$$\begin{aligned} \dot{V}(x) =& x^T Q^T E\dot{x} + (E\dot{x})^T Qx \\ =& \left[(M - NKF)x - N\alpha\right]^T Qx \\ &+ x^T Q^T[(M - NKF)x - N\alpha] \\ =& x^T[M - NKF]^T Qx - x^T Q^T N\alpha - \alpha^T N^T Qx \\ &+ x^T Q^T(M - NKF)x \\ \leq& x^T(M - NKF)^T Qx + \alpha^T\alpha \\ &+ x^T Q^T NN^T Qx + x^T Q^T(M - NKF)x \\ \leq& x^T(M - NKF)^T Qx + x^T Q^T(M - NKF)x \\ &+ x^T Q^T NN^T Qx + \beta x^T F^T K^T KFx \\ =& x^T[(M - NKF)^T Q + Q^T(M - NKF) \\ &+ Q^T NN^T Q + \beta F^T K^T KF]x < 0, \forall x \neq 0. \end{aligned}$$

This implies that system(1) is stable under the combined action of the SOF controller (7) and the conditions of Inequality (8).

3 Robust H_∞ Stabilization

This section considers a SOF controller u such that the L_2 gain of the closed-loop system from w to z does not exceed γ. Additionally, the closed-loop system achieves asymptotic stability when w is equal to zero. Here, γ denotes a given level of disturbance attenuation and satisfies the condition $\gamma > 0$.

We consider given NDS with actuator saturation:

$$\begin{cases} E\dot{x} = f(x) + N(x)sat(u) + Ed(x)w, Ex(0) = Ex_0, \\ f(0) = 0, \\ y = F(x)x, \\ z = L(x)x, \end{cases} \tag{10}$$

where $w \in \mathbb{R}^h$ denotes external disturbance; $z \in \mathbb{R}^s$ denotes penalty signal; $d(x) \in \mathbb{R}^{n\times h}$, $L(x) \in \mathbb{R}^{s\times n}$. $F(x)$, $f(x)$, x, $sat(u)$, E, $N(x)$ and y are the same as system(1).

We use the SOF controller $u = -k(y)y$ in the second section of the article as robust H_∞ controller and give the following theorem.

Theorem 2: Assuming that A1 and A2 are true, if

$$\begin{aligned}&(M-NKF)^TQ+Q^T(M-NKF)+Q^TNN^TQ\\&+\beta F^TK^TKF+\tfrac{2}{\gamma^2}Q^TEdd^TE^TQ+\tfrac{1}{2}L^TL<0\end{aligned} \tag{11}$$

holds, then the closed-loop NDS with actuator saturation composed of controller Equation (7) and system (10) is asymptotically stable.

proof:Based on Equation (6) and (7), system (10) can be converted into

$$\begin{cases} E\dot{x} = (M(x) - N(x)K(y)F(x))\,x - N(x)\alpha \\ \quad +Ed\,(x)\,w, \\ y = F(x)x, \\ z = L(x)x. \end{cases} \tag{12}$$

Defining $V(x) = x^TE^TQx$. Based on Inequality (11), we have

$$\begin{aligned}&\dot{V}(x)-\frac{\partial^TV}{\partial x}dw+\frac{1}{2\gamma^2}\frac{\partial^TV}{\partial x}dd^T\frac{\partial V}{\partial x}+\frac{1}{2}z^Tz\\=&(E\dot{x})^TQx+x^TQ^T(E\dot{x})-2x^TQ^TEdw\\&+\frac{2}{\gamma^2}x^TQ^TEdd^TE^TQx+\frac{1}{2}x^TL^TLx\\=&x^T(M-NKF)^TQx+x^TQ^T(M-NKF)x\\&+w^Td^TE^TQx+x^TQ^TEdw-2x^TQ^TEdw\\&-\alpha^TN^TQx-x^TQ^TN\alpha+\frac{2}{\gamma^2}x^TQ^TEdd^TE^TQx\\&+\frac{1}{2}x^TL^TLx\\\le&x^T(M-NKF)^TQx+x^TQ^T(M-NKF)x\\&+x^TQ^TNN^TQx++\beta x^TF^TK^TKFx\\&+\frac{1}{2}x^TL^TLx+\frac{2}{\gamma^2}x^TQ^TEdd^TE^TQx\\=&x^T\left[(M-NKF)^TQ+Q^T(M-NKF)\right.\\&+Q^TNN^TQ+\beta F^TK^TKF+\frac{2}{\gamma^2}Q^TEdd^TE^TQ\\&\left.+\frac{1}{2}L^TL\right]x\le 0.\end{aligned} \tag{13}$$

Thus

$$\begin{aligned}\dot{V}(x)\le&\frac{\partial^TV}{\partial x}dw-\frac{1}{2\gamma^2}\frac{\partial^TV}{\partial x}dd^T\frac{\partial V}{\partial x}-\frac{1}{2}z^Tz\\&+\frac{1}{2}\gamma^2w^Tw-\frac{1}{2}\gamma^2w^Tw\\=&\frac{1}{2}(\gamma^2||w||^2-||z||^2)-\frac{1}{2}\left\|w-\frac{1}{\gamma^2}d^T\frac{\partial V}{\partial x}\right\|^2\\\le&\frac{1}{2}(\gamma^2||w||^2-||z||^2),\end{aligned} \tag{14}$$

that is

$$\dot{V}\le\frac{1}{2}(\gamma^2\|w\|^2-\|z\|^2),\forall w\in L_2[0,T] \tag{15}$$

is true along the trajectory of system (12). Accordingly, the L_2 gain of system (12) from w to z does not exceed γ.

It is proved that system (12) is asymptotically stable when w is equal to zero:

$$\begin{aligned}\dot{V}(x)\le&x^T(M-NKF)Qx+x^TQ^T(M-NKF)x\\&+x^TQ^TNN^TQx+\beta x^TF^TK^TKFx\\<&x^T(M-NKF)Qx+x^TQ^T(M-NKF)x\\&+x^TQ^TNN^TQx+\beta x^TF^TK^TKFx\\&+\frac{2}{\gamma^2}x^TQ^TEdd^TE^TQx+\frac{1}{2}x^TL^TLx\\=&x^T[(M-NKF)^TQ+Q^T(M-NKF)\\&+Q^TNN^TQ+\beta F^TK^TKF\\&+\frac{2}{\gamma^2}Q^TEdd^TE^TQ+\frac{1}{2}L^TL]x<0,\forall x\neq 0.\end{aligned} \tag{16}$$

This result indicates that when w is equal to zero, system (12) is asymptotically stable. Therefore, the application of the designed SOF controller in disturbance systems is effective.

4 Illustrative Example

In this section, we give a practical circuit model [6] to depict the effectiveness of the designed robust H_∞ controller. As it is shown in Fig.1, which capacitance is regulated by chage q, and $u_1 = f_1(q_1), u_2 = f_2(q_2)$.

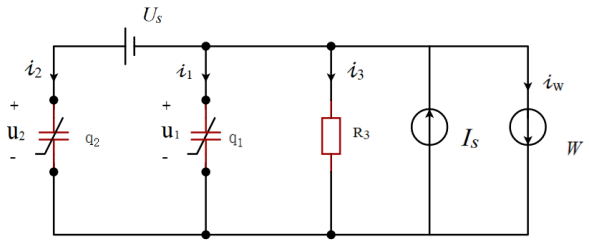

Fig. 1: Nonlinear circuit system.

The following is the mathematical expression of the above model based on Kirchhoff current and Kirchhoff voltage laws,

$$\begin{cases} \dot{q_1}+\dot{q_2}=sat(I_s)-\frac{f_1(q_1)}{R_3}-i_w, \\ 0=f_1(q_1)+sat(U_s)-f_2(q_2). \end{cases} \tag{17}$$

We choose $y = [0, q_2]^T$, $z = (1/\sqrt{3})[q_1, q_1+q_2]^T$, $w = i_w$. Let $f_1(q_1) = q_1$, $f_2(q_2) = 2q_2^3$, $R_3 = (1/2)\Omega$, $|I_s| \le 0.5A$, $|U_s| \le 2V$. Indicate $x = \begin{bmatrix} q_1 \\ q_2 \end{bmatrix}$, $x = \begin{bmatrix} U_s \\ I_s \end{bmatrix}$. Then, system (17) can be rewritten as

$$\begin{cases} \begin{bmatrix} 1 & 1 \\ 0 & 0 \end{bmatrix}\dot{x} = \begin{bmatrix} -2x_1 \\ x_1 - 2x_2^3 \end{bmatrix} + \begin{bmatrix} 0 & 1 \\ 1 & 0 \end{bmatrix} sat(u) \\ + \begin{bmatrix} -1 \\ 0 \end{bmatrix} w, \\ y = \begin{bmatrix} 0 & 0 \\ 0 & x_2 \end{bmatrix}, \\ z = \frac{1}{\sqrt{3}} \begin{bmatrix} x_1 \\ x_1 + x_2 \end{bmatrix}. \end{cases} \tag{18}$$

We can obtain $M(x) = \begin{bmatrix} -2 & 0 \\ 1 & -2x_2^2 \end{bmatrix}$, $F(x) = \begin{bmatrix} 0 & 0 \\ 0 & 1 \end{bmatrix}$, $L(x) = \frac{1}{\sqrt{3}}\begin{bmatrix} 1 & 0 \\ 1 & 1 \end{bmatrix}$. Let $Q = \begin{bmatrix} 1 & 1 \\ 0 & 1 \end{bmatrix}$, then $E^TQ = Q^TE \geq 0$. For $\gamma = 1$, defining $K(y) = \begin{bmatrix} 0 & 0 \\ 0 & 3 \end{bmatrix}$, $\beta = 0.05$, we obtain

$$(M - NKF)^TQ + Q^T(M - NKF) + Q^TNN^TQ + \beta F^TK^TK(y)F + \frac{2}{\gamma^2}Q^TEdd^TE^TQ + \frac{1}{2}L^TL$$

$$= -\begin{bmatrix} 0.667 & 0.833 \\ 0.833 & 1.383 + 4x_2^2 \end{bmatrix} < 0.$$

Thus, the conditions of Theorem 2 are all satisfied. The SOF robust H_∞ controller of system (14) is represented as

$$u = -\begin{bmatrix} 0 & 0 \\ 0 & 3 \end{bmatrix} x. \tag{19}$$

To validate the effectiveness of the H_∞ controller (Equation (19)), numerical simulations are performed with the specified settings: the initial condition $Ex(0)$ is set to $[1, 0]^T$.From the simulation results, it can be concluded that the state x reflected in Fig.2 cannot converge to the origin, but after adding the admissible control law, the state x reflected in Fig.3 converges to the origin rapidly within 0 to 4 seconds. The following conclusions can be drawn from the above results.

The admissible control law Equation (19) can make system (18) asymptotically stable.

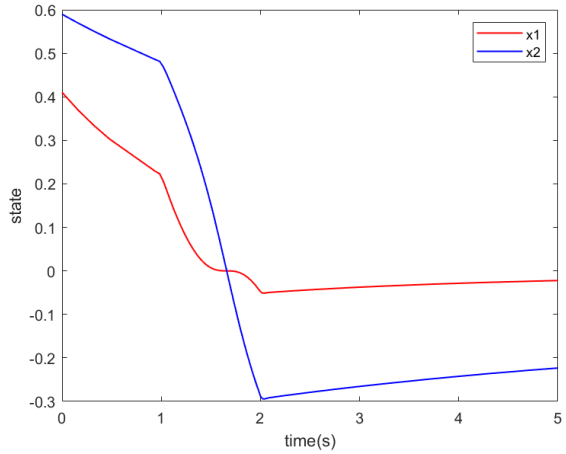

Fig. 2: Reaction of the state x in open-loop system.

5 Conclusion

This article studies the application of SOF control in a class of actuator-saturated NDS systems. Firstly, according to the saturation condition, a admissible controller is proposed to stabilize the system, and two sufficient conditions are given to prove that system is impulsively controllable. Second, the asymptotic stability of system is studied, and a SOF controller is designed. A Lyapunov function is defined according to the theorems mentioned in this paper and the result proves that the SOF controller can stabilize system. Then Robust H_∞ control by static output feedback is considered for NDS with external disturbances. Finally, through

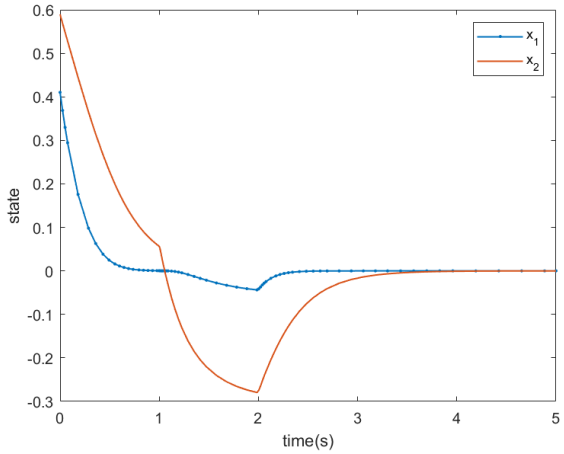

Fig. 3: Reaction of the state x in closed-loop system.

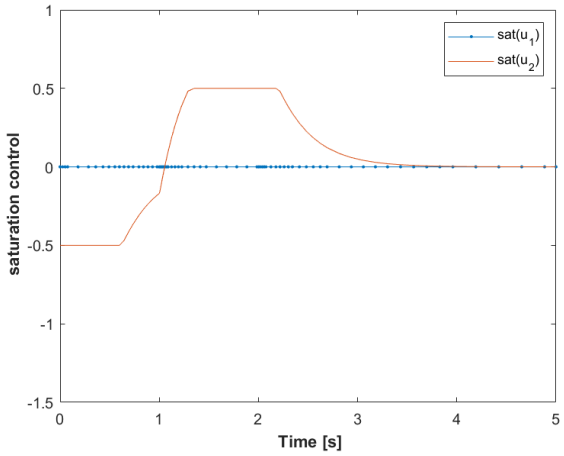

Fig. 4: Reaction of saturated control $sat(u)$ in closed-loop system.

numerical simulation of a nonlinear singular circuit, the effectiveness of the SOF controller is verified.

References

[1] L. Dai, Singular Control Systems. *Berlin,Germany*: Springer-Verlag, 1989.

[2] Fridman E. Stability of linear descriptor systems with delay: a Lyapunov based approach[J]. *Journal of Mathematical Analysis and Applications*, 2002, 273(1): 24-44.

[3] Alma M, Darouach M. Adaptive observers design for a class of linear descriptor systems[J]. *Automatica*, 2014, 50(2): 578-583.

[4] Mashud A, Bera M K. Control allocation based fault tolerant control of descriptor system with actuator saturation[J]. *ISA transactions*, 2022, 129: 380-394.

[5] He K, Sun L, Yang R. Robust stabilization and adaptive H_∞ control of nonlinear singular systems via static output feedback[J]. *Journal of Systems and Control Engineering*, 2023: 09596518231181479.

[6] Sun L, Wang Y, Feng G. Control design for a class of affine nonlinear descriptor systems with actuator saturation[J]. *IEEE transactions on automatic control*, 2014, 60(8): 2195-2200.

[7] Dantas A D O S, Dantas A F O A, Dorea C E T. Static output feedback control design for constrained linear discrete-time

systems using data cluster analysis[J]. *IET Control Theory Applications*, 2018, 12(18): 2541-2550.

[8] Zheng B, Zheng X, Duan R. Stability and stabilization of discrete-time periodic linear systems with actuator saturation[J]. *Automatica*, 2011, 47(8): 1813-1820.

Proceedings of the 3rd Conference on Fully Actuated System Theory and Applications
May 10-12, 2024, Shenzhen, China

Disturbance observer-based nonlinear control for underactuated bridge cranes: high-order fully actuated system approach

Xiaoshuang Zhou, Yana Yang, Junpeng Li, Guopin Liu
Institute of Electrical Engineering, Yanshan University, Qinhuangdao City, 066004, P. R. China
E-mail: yyn@ysu.edu.cn.

Abstract: In this paper, a disturbance observer-based nonlinear control method is proposed for a class of underactuated bridge crane systems. Specifically, the underactuated bridge crane system is transformed into a high-order fully actuated (HOFA) system through a diffeomorphism transformation. The proposed approach utilizes a predetermined-time disturbance observer based on the HOFA system, eliminating the need for any prior knowledge of disturbance upper bounds and ensuring independence from controller design. This designed scheme effectively achieves both anti-swing and positioning control objectives in underactuated bridge crane systems. Rigorous demonstrations are provided to ensure the stability of positioning error and load swing angle. Simulation experiments conclusively demonstrate the effectiveness and robustness of the designed control scheme. This paper represents the first application of HOFA system theory to underactuated bridge crane systems, thereby expanding the scope of its applicability.

Key Words: Underactuated bridge crane systems, High-order fully actuated system, Disturbance observer, Diffeomorphism transformation

1 Introduction

Bridge crane systems are widely used in various industries for lifting and handling heavy materials, improving production efficiency [1, 2]. The absence of actuators results in a high degree of coupling among system states and introduces significant nonlinearity. The control of bridge crane systems faces numerous challenges [3]. Researchers have extensively investigated the automatic control of underactuated bridge crane systems and have successfully devised a plethora of sophisticated control strategies, including input shaping control [4, 5], trajectory planning control [6, 7], energy-based control [8, 9], sliding mode control [10–12], and intelligent control [13–15].

Most of the existing control algorithms are based on a first-order state-space approach, which involves converting the original Lagrange model of the underactuated system into a cascaded first-order state-space expression [16, 17]. The converted bridge crane systems, however, do not strictly adhere to the feedback control framework; therefore, the converted models incorporate certain simplifications for the nonlinear component [10, 18]. Significant challenges persist in addressing the issue of underactuated systems using first-order state-space methodologies, which are in trouble for handling nonlinear problems. A novel control theory HOFA system approach is proposed by Duan [19], which can solve the global stabilization problem of nonlinear systems that is currently difficult to be solved by the first-order state space method. The pseudo strict-feedback system [19] and generalized strict-feedback system [20] can be easily converted to HOFA system models by diffeomorphism transformations under certain conditions. However, the canonical transformation is only provided in [19] for the case of a constant unimodular matrix, and no comprehensive results have been obtained for more general scenarios. The identification of diffeomorphism transformations that can transform underactuated systems into HOFA models remains a significant challenge in extending the HOFA theory.

Moreover, due to the inherent underactuation of bridge crane systems, they exhibit increased sensitivity to variations in external disturbances. Consequently, it becomes imperative to devise control strategies capable of effectively managing these disturbances. The control algorithms, such as robust PID control [21, 22], adaptive control [23, 24], and H_∞ control [25], have been employed to mitigate disturbances in underactuated crane systems. The sensitivities of the control systems are optimized by these control methods, thereby reducing the impact of disturbances on the systems. However, it should be noted that there exists an inevitable trade-off between system performance and disturbances suppression due to the constraint of having only one degree of freedom. A disturbance observer is proposed in [26] for underactuated bridge crane systems, which can effectively compensate for disturbances and mitigate the chattering issue associated with the designed sliding mode controller. However, it is challenging to satisfy the known upper bound on disturbances in practical systems. The double pendulum effect is effectively suppressed in [27] using an enhanced active disturbance rejection controller, which treats the disturbances as an extended state and employs an extended state observer to estimate the unknown disturbances, yet this approach is primarily suitable for estimating slow time-varying disturbances. Inspired by the literature [28, 29], we propose a predetermined-time disturbance observer designed to accurately track disturbances signal for a predefined period of time. Furthermore, unlike [10, 26], the disturbance observer introduced in this paper does not require any prior knowledge of the upper bound of external disturbances.

Through the aforementioned analyses, this study introduces a novel approach of diffeomorphism transformation that has been successfully implemented in underactuated bridge crane systems. Additionally, a predetermined-time disturbance observer is utilized to address external disturbances in the system. The transformation is specifically derived based on the generalized position coordinates of the load within the bridge crane system, and its validity is rig-

This work is supported by National Natural Science Foundation (NNSF) of China under Grant 62373319, 61933009, 62103355.

orously demonstrated. Finally, the effectiveness and robustness of the HOFA control scheme proposed in this paper are verified through numerical simulation.

2 Problem statement and mathematical preliminaries

2.1 Mathematical preparation

This subsection presents essential definitions and lemmas, which serve to facilitate subsequent analyses and proofs in a scholarly manner.

Definition 1 *(Diffeomorphism): A smooth vector field function $\Phi(x) : \mathbb{R}^n \to \mathbb{R}^n$ defined in region Ω is said to be a diffeomorphism if its inverse $\Phi^{-1}(x) \in \mathbb{R}^n$ exists and is smooth. If the domain Ω is entire, then $\Phi(x) \in \mathbb{R}^n$ is global diffeomorphism.*

Definition 2 *(HOFA [19]): Consider a nonlinear system as follows:*

$$x^{(m)} = h\left(x^{(0\sim m-1)}\right) + B\left(x^{(0\sim m-1)}\right)\tau \tag{1}$$

where m is a positive integer representing the system order, $x \in \Omega$ is the system state vector, $\tau \in \mathbb{R}^r$ is the system input vector, $h\left(x^{(0\sim m-1)}\right) \in \mathbb{R}^n$ is a sufficiently differentiable vector function, and $B\left(x^{(0\sim m-1)}\right) \in \mathbb{R}^{n\times r}$ is a matrix function. If $rank\left(B\left(x^{(0\sim m-1)}\right)\right) = r = n$ for any $t \geq 0$ holds, for all $x^{(i)} \in \Omega, i = 1, \cdots, m$, then the system (1) is called fully actuated on Ω.

Lemma 1 *(Complete parametric approach [19]): Consider the closed-loop system as following form:*

$$x^{(m)} + A_{0\sim m-1}x^{(0\sim m-1)} = 0 \tag{2}$$

where $x \in \mathbb{R}^n$, for an arbitrarily chosen $F \in \mathbb{R}^{mn\times nm}$, all the matrix $A_{0\sim m-1}$ and the nonsingular matrix $V \in \mathbb{R}^{mn\times nm}$ satisfying

$$\Phi(A_{0\sim m-1}) = VFV^{-1}$$

are given by

$$A_{0\sim m-1} = -ZF^nV^{-1}(Z,F),$$

$$V = V(Z,F) = \begin{bmatrix} Z \\ ZF \\ \vdots \\ ZF^{n-1} \end{bmatrix}$$

where

$$\Phi(A_{0\sim m-1}) = \begin{bmatrix} 0 & I & & \\ & & \ddots & \\ & & & I \\ -A_0 & -A_1 & \cdots & -A_n \end{bmatrix}$$

2.2 Problem formulation

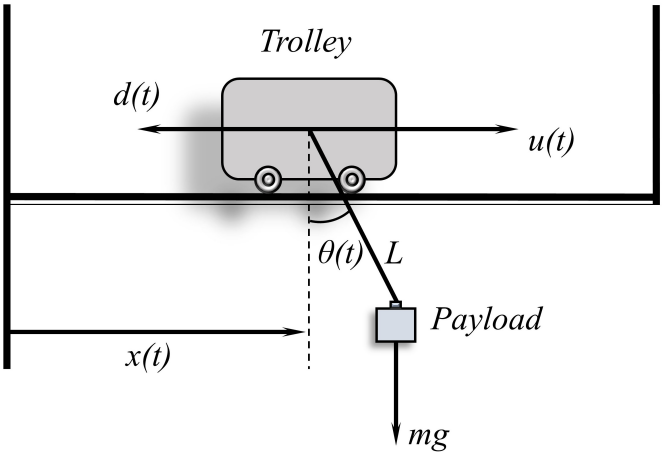

Fig. 1: Structure of the crane system

The schematic diagram of underactuated bridge crane system is shown in Fig. 1, and its dynamic equation can be expressed as:

$$\begin{cases} (M+m)\ddot{x} + mL\cos\theta\ddot{\theta} - mL\sin\theta\dot{\theta}^2 = u(t) + d(t) \\ mL\cos\theta\ddot{x} + mL^2\ddot{\theta} + mgL\sin\theta = 0 \end{cases} \tag{3}$$

where $x(t)$ and $\theta(t)$ denote the position of the trolley and the angle of the payload with respect to the vertical axis, respectively. The trolley mass and the payload mass are denoted by M and m, respectively. The cable length is L, the gravity acceleration is g, the control input is $u(t)$, and $d(t)$ encompasses the unmodelled dynamics of the system, friction, and external disturbances, etc.

Assumption 1 *The load will not exceed an angle of π due to the inherent limitations of the physical system [30–32], i.e.*

$$|\theta| < \frac{\pi}{2}, \quad \forall t > 0$$

Assumption 2 *The disturbances in system (3) have an unknown upper bound d.*

With some mathematical calculations, (3) can be rewritten as:

$$\begin{aligned} \ddot{x} &= -g\tan\theta - L\ddot{\theta}\sec\theta \\ \ddot{\theta} &= -\frac{\cos\theta\left(u(t) + d(t) + mL\sin\theta\dot{\theta}^2 + (M+m)g\tan\theta\right)}{\left(M + m\sin^2\theta\right)L} \end{aligned} \tag{4}$$

For the state variable $q = [x,\theta]^{\mathrm{T}}$ of the system, consider the transformation as follows:

$$z = \phi(x,\theta) = \begin{bmatrix} x - x_d + \alpha\sin\theta \\ \theta \end{bmatrix} \tag{5}$$

where α is a positive parameter, x_d is the desired position of the trolley. The Jacobian matrix of $\phi(x,\theta)$ is

$$\frac{\partial\phi}{\partial q} = \begin{bmatrix} 1 & \alpha\cos\theta \\ 0 & 1 \end{bmatrix} \in \mathbb{R}^{2\times 2}$$

which is full rank in the area $\Omega = \{(x,\theta), |\theta| < \pi\}$. Therefore $\phi^{-1}(x,\theta)$ exists, and z is a diffeomorphism transformation of the state variable q. It implies that the control objective of the underactuated bridge crane system $x \to x_d$, $\theta \to 0$ is equivalently converted to $z \to 0$.

Remark 1 *The diffeomorphism transformation $\phi(x,\theta)$ is chosen based on the generalised load position coordinates, where the actual position coordinates of the load is $x - L\sin\theta$ during the motion of the trolley and the desired position of the trolley is the same as that of the load.*

The differentiation of the first element of (5) leads to:

$$\dot{z}_1 = \dot{x} + \alpha\cos\theta\dot{\theta} \tag{6a}$$

$$\ddot{z}_1 = \ddot{x} + \alpha\cos\theta\ddot{\theta} - \alpha\sin\theta\dot{\theta}^2 \tag{6b}$$

The substitution of (4) into (6b) yields:

$$\ddot{z}_1 = f(z,\dot{z}) + g(z)(u(t) + d(t)) \tag{7}$$

where

$$\begin{aligned} g(z) =& \frac{L - \alpha\cos^2\theta}{\left(M + m\sin^2\theta\right)L} \\ f(z,\dot{z}) =& g(z)\left(mL\sin\theta\dot{\theta}^2 + mg\sin\theta\cos\theta\right) \\ & - \alpha g\sin\theta\cos\theta/L - \alpha\sin\theta\dot{\theta}^2 \end{aligned}$$

where α satisfy $L - \alpha\cos^2\theta \neq 0$ such that $g(z)$ is non-singular. This means that system (3) can be transformed to a HOFA system (7) by diffeomorphism transformation.

3 Main result

3.1 Controller design

This subsection designs the HOFA controller based on the transformed model (7).

First, given the parameters a_1, a_0, the following controller

$$\begin{aligned} u(t) &= -g(z)^{-1}(a_1\dot{z}_1 + a_0 z_1 + u^*) \\ u^* &= f(z,\dot{z}) - \nu \end{aligned} \tag{8}$$

for the HOFA system (7) produces the following closed-loop system

$$\ddot{z}_1 + a_1\dot{z}_1 + a_0 z_1 = \nu + g(z)d(t) \tag{9}$$

Further rewritten in the form of a first order linear system:

$$\begin{aligned} \dot{\eta}_1 &= \eta_2 \\ \dot{\eta}_2 &= -a_0\eta_1 - a_1\eta_2 + \nu + d_z(t) \end{aligned} \tag{10}$$

where $d_z(t) = g(z)d(t)$ stands for generalised disturbances. Next we design predetermined-time disturbance observer to estimate the generalised disturbances.

Define auxiliary variable e:

$$e = \eta - \eta_2 \tag{11}$$

where the variable η has the following dynamic:

$$\dot{\eta} = -a_0\eta_1 - a_1\eta_2 + \nu - c_1 sgn(e)|e|_{1d}^{\alpha} - c_2 sgn(e)|e|_{2d}^{\alpha} + v_z \tag{12}$$

Consider the following sliding mould surface s_d:

$$s_d = \dot{e} + c_1 sgn(e)|e|_{1d}^{\alpha} + c_2 sgn(e)|e|_{2d}^{\alpha} \tag{13}$$

where $c_1, C_2, \alpha_{1d} < 1$ and $\alpha_{2d} > 1$ are positive parameters, and v_z is designed by the following dynamic equation:

$$\dot{v}_z = -(k_d + \kappa)\, sgn(s_d), \quad v_z(0) = 0 \tag{14}$$

where κ is a positive parameter, k_d is set to

$$k_d = \begin{cases} \frac{|s_d|}{\alpha(T_c - t)}, & t < T_c \\ \mu\tan^2\left(\frac{\pi|s_d|}{2\varepsilon}\right), & t \geq T_c \end{cases} \tag{15}$$

to meet the $k_d > d$, where μ and ε are positive parameters, T_c is a predefined-time.

The control input v is designed as

$$v = -v_z \tag{16}$$

Then the auxiliary variable e in (11) as well as estimation error of disturbance d_z converges to zero in predetermined-time.

3.2 Stability analysis

Theorem 1 *The underactuated bridge crane system* (3) *can be equivalently transformed to a HOFA system* (7) *by diffeomorphism transformation, through the designed HOFA controller* (8) *and* (16) *, which makes the transformed state asymptotically stable. Thus reaching the control objectives of the underactuated bridge crane system, i.e. $x \to x_d, \theta \to 0$.*

proof: It is first shown that the controller-independent disturbance observer can fully estimate the generalised disturbances in a predefined time T_c.

Consider the the derivative of e as follows:

$$\dot{e} = \dot{\eta} - \dot{\eta}_2 = -c_1 sgn(e)|e|_{1d}^{\alpha} - c_2 sgn(e)|e|_{2d}^{\alpha} + v_z - d_z \tag{17}$$

Bringing (17) into (13) yields:

$$s_d = v_z - d_z \tag{18}$$

The derivative of (18), when combined with the inclusion of (12), results in

$$\dot{s}_d = \dot{v}_z - \dot{d}_z = -(k_d + \kappa)\, sgn(s_d) - \dot{d}_z \tag{19}$$

Now, let's consider the Lyapunov function candidate V

$$V = \frac{1}{2}s_d^2 \tag{20}$$

By performing differentiation on (20) and substituting equation (19), we obtain:

$$\begin{aligned} \dot{V} = s_d\dot{s}_d &= -k_d|s_d| - \kappa|s_d| - \dot{d}_z s_d \\ &\leq \left(|\dot{d}_z| - k_d\right) - \kappa|s_d| \end{aligned} \tag{21}$$

Since $\kappa > 0$, and $k_d > L$, which can be proof in [25], $\dot{V} \leq -\kappa|s_d|$, which yields the convergence of sliding mode surface s_d to zero in predefined time T_c.

Secondly, consider after a period of time T_c

$$z_1 = x - x_d + \alpha\sin\theta = 0 \tag{22}$$

$$\dot{z}_1 = \dot{x} + \alpha\cos\theta\dot{\theta} = 0 \tag{23}$$

$$\ddot{z}_1 = \ddot{x} + \alpha \cos\theta\ddot{\theta} - \alpha \sin\theta\dot{\theta}^2 = 0 \tag{24}$$

$$u(t) = -g(z)^{-1}\left(a_1\dot{z}_1 + a_0 z_1 + u^*\right) = 0 \tag{25}$$

Combined with (4), yields

$$\left(M + m - \frac{mL}{\alpha}\right)\ddot{x} = u$$

Since $\alpha < 0$, $\ddot{x} = 0$, implies that

$$\dot{x} = \beta$$

If $\beta \neq 0$, then $x \to \infty$ as $t \to \infty$, which is opposite to fact (22). Therefore $\beta = 0$, $e = x - x_d = \vartheta$. In case of $\vartheta = 0$, from (22), $\sin\theta = 0$. Based on Assumption 1, the pendulum angle does not extend beyond $\left(-\frac{\pi}{2}, \frac{\pi}{2}\right)$, thus $\theta = 0$. In case of $\vartheta \neq 0$, from (22),

$$\sin\theta = -\frac{1}{\alpha}\vartheta \neq 0$$

According to (4),

$$\ddot{\theta} = -\frac{g}{L}\sin\theta \neq 0$$

Taking this into (24), gives

$$\frac{g}{L}\cos\theta\sin\theta + \sin\theta\dot{\theta}^2 = 0$$

Combined with (23),

$$\begin{cases} \cos\theta\dot{\theta} = 0 \\ \frac{g}{L}\cos\theta + \dot{\theta}^2 = 0 \end{cases}$$

The derivation of the unique outcome $\cos\theta = 0, \dot{\theta} = 0$ implies that $\sin\theta = 0$, which contradicts the case when $\vartheta \neq 0$. Therefore, it can be concluded that $\vartheta = 0$, and subsequently $x = x_d$ and $\theta = 0$. The control objectives of the underactuated bridge crane system are achieved and the proof is completed.

4 Numerical Simulation

The effectiveness and robustness of the proposed control algorithm are assessed through numerical simulation tests. Specifically, two groups of simulation experiments are conducted. In the first group, the proposed HOFA control algorithm is compared with PD-like control [8] and sliding mode control [10] to validate the superiority of the control scheme proposed in this paper. In the second group, the robustness of the proposed control scheme is verified by varying internal system parameters and introducing external disturbances.

Simulation tests are performed in MATLAB/Simulink environment and the parameters of the underactuated bridge crane system are designed as $M = 6kg$, $m = 0.5kg$, $L = 0.5m$, $g = 9.8m/s^2$. The friction correlation coefficient is set to $k_{r0} = 5$, $k_{r1} = -1$, $\zeta = 0.1$.

The parameters of HOFA controller are selected as

$$a_{0\sim1} = -ZF^2V = \begin{bmatrix} 4 & 5 \end{bmatrix}$$

where

$$Z = \begin{bmatrix} 1 & 0 \end{bmatrix}, F = \begin{bmatrix} -2 & -1 \\ 1 & -2 \end{bmatrix}, V = \begin{bmatrix} Z \\ ZF \end{bmatrix}$$

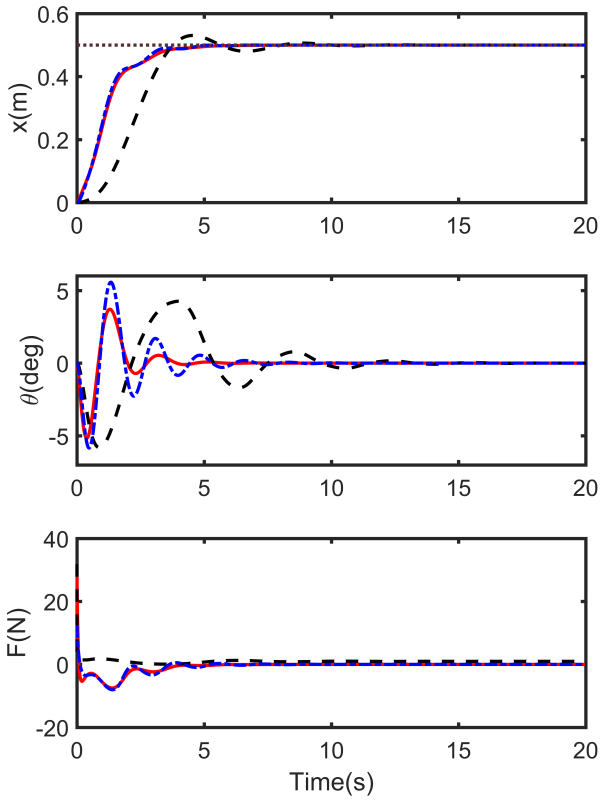

Fig. 2: First group of simulation results: HOFA control scheme (red solid line), PD-like control scheme (blue dotted line), sliding mode control scheme (black dashed line)

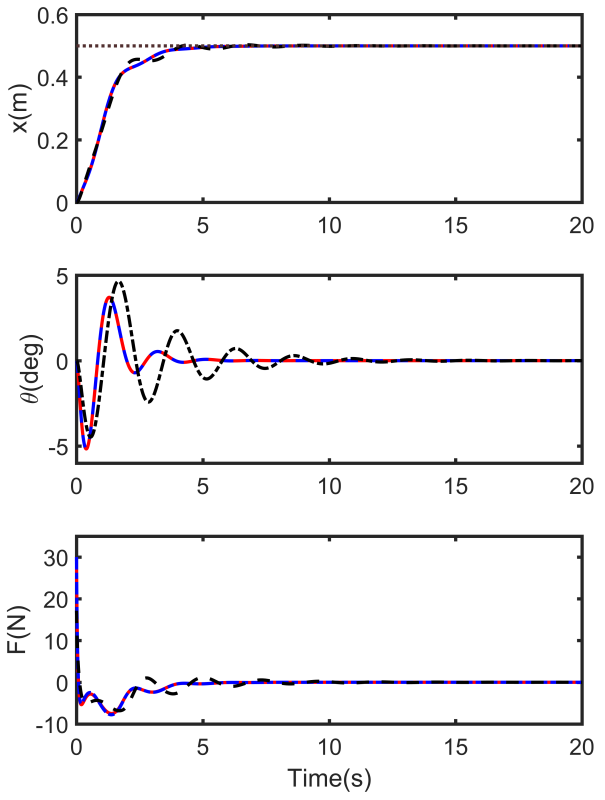

Fig. 3: Second group of simulation results Case 1: Normal situation (red solid line), Change load mass (blue dotted line), Change the length of the rope (black dashed line)

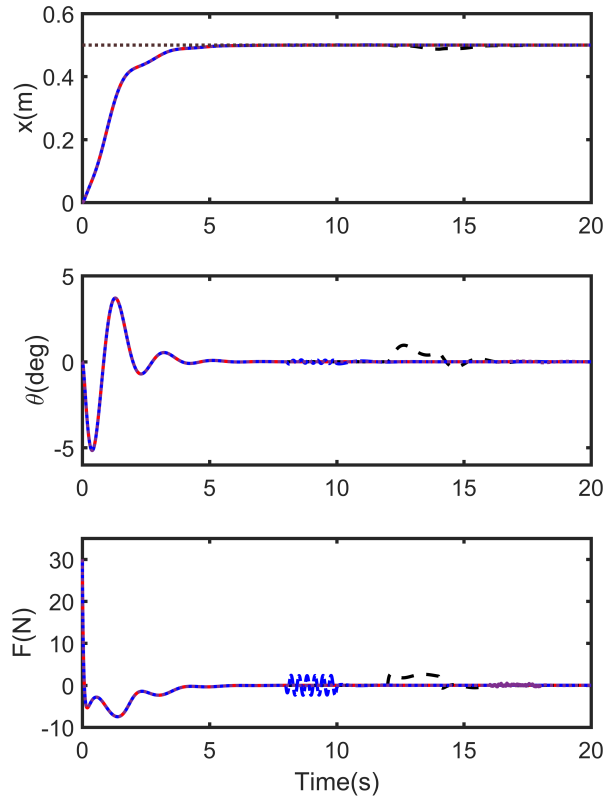

Fig. 4: Second group of simulation results Case 2: Normal situation (red solid line), sinusoidal disturbances (blue dotted line), step disturbances (black dashed line), random noise disturbances (purple dotted line)

The PD-like control algorithm designed in [8] is as follows:

$$F = -k_p\left(e - k_a \sin\theta\right) - k_d\left(\dot{e} - k_a \cos\theta\dot{\theta}\right)$$

where $e = x - xd$, the parameters to be selected as$k_p = 25$, $k_d = 30$ and $k_a = 0.3$.

The sliding mode control algorithm designed in [10] is as follows:

$$F = \frac{\left(M + m\sin^2\theta\right)l}{\cos\theta}\left[\hat{\phi}_d + 2\dot{\theta}^2\tan\theta - \frac{\kappa\cos^2\theta}{g}\psi + \frac{\cos^2\theta}{g}\mu\right] - ml\dot{\theta}^2\sin\theta - (M+m)\,g\tan\theta$$

Group 1: Performance verification: As shown in Fig. 2, compared with the PD-like control and the sliding mode control, the HOFA control scheme has a simple structure, the parameters selection are convenient and quick, the complicated process of adjusting the parameters is omitted, and good control results are achieved. The trolley is driven to the desired position in about 5 s, without the overshooting phenomenon of the sliding mode control scheme, and similar to the arrival time of the PD-like control. In addition, the swing angle of the load does not exceed 5° during operation and the residual swing is suppressed at the fastest time, which is significantly better than the other two control schemes, proving the effectiveness and superiority of the HOFA control scheme proposed in this paper.

Group 2: Robustness verification: Two different scenarios are designed to verify the robustness of the system.

Case 1 (Internal parameter changes): In order to assess the robustness of the proposed control scheme against variations in internal system parameters, we investigate the impact of load mass m and rope length L on the efficacy of the control effect. The simulation results are shown in Fig. 3. It is observed that changing the load mass has a negligible effect on the system, and changing the rope length makes the load swing longer, but still suppresses the load swing, proving the robustness of the control scheme proposed in this paper to internal parameter variations.

Case 2 (External additional disturbances): In the unmatched channel, the sinusoidal disturbance, the step disturbance, and the random noise disturbance are imposed in $8-10s$, $12-14s$, and $16-18s$, respectively, with an amplitude of 0.5, and the results are shown in Fig. 4. The results show that the control scheme proposed in this paper can quickly suppress the three different disturbances and ensure satisfactory control performance with good robustness.

5 Conclusion

In this paper, a disturbance observer based HOFA control scheme is proposed for underactuated bridge crane system. A physically meaningful diffeomorphism transformation is used to convert the underactuated bridge crane system into a HOFA system. Theoretical analysis rigorously demonstrates that the control scheme is capable of achieving the control objectives of suppressing load swing and trolley positioning of the underactuated bridge crane system, and numerical simulations illustrate the superiority and robustness of the control scheme. In future work, we hope to find a general differential homogeneous embryonic transformation for underactuated Lagrange system, further extending the applications of the HOFA theory.

References

[1] S. Zhang, X. He, H. Zhu, Q. Chen, and Y. Feng, "Partially saturated coupled-dissipation control for underactuated overhead cranes," *Mechanical Systems and Signal Processing*, vol. 136, p. 106449, 2020.

[2] S. Zhang, X. He, H. Zhu, X. Li, and X. Liu, "Pid-like coupling control of underactuated overhead cranes with input constraints," *Mechanical Systems and Signal Processing*, vol. 178, p. 109274, 2022.

[3] H. Bao, Q. Kang, J. An, X. Ma, and M. Zhou, "A performance-driven mpc algorithm for underactuated bridge cranes," *Machines*, vol. 9, no. 8, p. 177, 2021.

[4] K. Alghanim, A. Mohammed, and M. T. Andani, "An input shaping control scheme with application on overhead cranes," *International Journal of Nonlinear Sciences and Numerical Simulation*, vol. 20, no. 5, pp. 561–573, 2019.

[5] S. Fasih ur Rehman, Z. Mohamed, A. Husain, H. Jaafar, M. Shaheed, and M. Abbasi, "Input shaping with an adaptive scheme for swing control of an underactuated tower crane under payload hoisting and mass variations," *Mechanical Systems and Signal Processing*, vol. 175, p. 109106, 2022.

[6] G. Li, X. Ma, Z. Li, and Y. Li, "Time-polynomial-based optimal trajectory planning for double-pendulum tower crane with full-state constraints and obstacle avoidance," *IEEE/ASME Transactions on Mechatronics*, vol. 28, no. 2, pp. 919–932, 2022.

[7] B. Fan, Z. Cao, C. Wang, Z. Niu, C. Yang, and X. Wu, "A novel trajectory online planning and under-actuated control method on positioning and anti-swing for bridge cranes,"

Journal of Vibration and Control, vol. 29, no. 21-22, pp. 5184–5194, 2023.

[8] N. Sun and Y. Fang, "New energy analytical results for the regulation of underactuated overhead cranes: An end-effector motion-based approach," *IEEE Transactions on Industrial Electronics*, vol. 59, no. 12, pp. 4723–4734, 2012.

[9] Y. Cao, T. Li, and L.-Y. Hao, "Lyapunov-based model predictive control for shipboard boom cranes under input saturation," *IEEE Transactions on Automation Science and Engineering*, vol. 20, no. 3, pp. 2011–2021, 2023.

[10] X. Wu, K. Xu, and X. He, "Disturbance-observer-based nonlinear control for overhead cranes subject to uncertain disturbances," *Mechanical systems and signal processing*, vol. 139, p. 106631, 2020.

[11] W. Yang, J. Chen, D. Xu, and X. Yan, "Hierarchical global fast terminal sliding-mode control for a bridge travelling crane system," *IET Control Theory & Applications*, vol. 15, no. 6, pp. 814–828, 2021.

[12] C. Yang, C. Du, L. Liao *et al.*, "Design and implementation of finite time sliding mode controller for fuzzy overhead crane system," *ISA transactions*, vol. 124, pp. 374–385, 2022.

[13] Z. Sun, Y. Ling, H. Qu, F. Xiang, Z. Sun, and F. Wu, "An adaptive DE algorithm based fuzzy logic anti-swing controller for overhead crane systems," *International Journal of Fuzzy Systems*, vol. 22, no. 6, pp. 1905–1921, 2020.

[14] T. Yang, N. Sun, and Y. Fang, "Adaptive fuzzy control for a class of mimo underactuated systems with plant uncertainties and actuator deadzones: Design and experiments," *IEEE Transactions on Cybernetics*, vol. 52, no. 8, pp. 8213–8226, 2021.

[15] G.-H. Kim, M. Yoon, J. Y. Jeon, and K.-S. Hong, "Data-driven modeling and adaptive predictive anti-swing control of overhead cranes," *International Journal of Control, Automation and Systems*, vol. 20, no. 8, pp. 2712–2723, 2022.

[16] R. Olfati-Saber, "Normal forms for underactuated mechanical systems with symmetry," *IEEE Transactions on automatic control*, vol. 47, no. 2, pp. 305–308, 2002.

[17] Y.-F. Chen and A.-C. Huang, "Controller design for a class of underactuated mechanical systems," *IET control theory & applications*, vol. 6, no. 1, pp. 103–110, 2012.

[18] X. Wu, K. Xu, M. Lei, and X. He, "Disturbance-compensation-based continuous sliding mode control for overhead cranes with disturbances," *IEEE Transactions on Automation Science and Engineering*, vol. 17, no. 4, pp. 2182–2189, 2020.

[19] G. Duan, "High-order fully actuated system approaches: Part I. models and basic procedure," *International Journal of Systems Science*, vol. 52, no. 2, pp. 422–435, 2021.

[20] Duan, Guangren, "High-order fully actuated system approaches: Part II. generalized strict-feedback systems," *International Journal of Systems Science*, vol. 52, no. 3, pp. 437–454, 2021.

[21] B. Yang, Z.-X. Liu, H.-K. Liu, Y. Li, and S. Lin, "A gpc-based multi-variable pid control algorithm and its application in anti-swing control and accurate positioning control for bridge cranes," *International Journal of Control, Automation and Systems*, vol. 18, pp. 2522–2533, 2020.

[22] J. Fu, J. Liu, D. Xie, and Z. Sun, "Application of fuzzy pid based on stray lion swarm optimization algorithm in overhead crane system control," *Mathematics*, vol. 11, no. 9, p. 2170, 2023.

[23] J. Huang, W. Wang, and J. Zhou, "Adaptive control design for underactuated cranes with guaranteed transient performance: Theoretical design and experimental verification," *IEEE Transactions on Industrial Electronics*, vol. 69, no. 3, pp. 2822–2832, 2022.

[24] Y. Yang, X. Ye, B. Wen, J. Huang, and X. Su, "Adaptive control design for uncertain underactuated cranes with nonsmooth input nonlinearities," *IEEE Transactions on Systems, Man, and Cybernetics: Systems*, vol. 53, no. 2, pp. 1074–1083, 2023.

[25] G. Rigatos, "Nonlinear optimal control for the underactuated double-pendulum overhead crane," *Journal of Vibration Engineering & Technologies*, pp. 1–21, 2023.

[26] B. Lu, Y. Fang, and N. Sun, "Sliding mode control for underactuated overhead cranes suffering from both matched and unmatched disturbances," *Mechatronics*, vol. 47, pp. 116–125, 2017.

[27] X. Kang, L. Chai, and H. Liu, "Anti-swing and positioning for double-pendulum tower cranes using improved active disturbance rejection controller," *International Journal of Control, Automation and Systems*, vol. 21, no. 4, pp. 1210–1221, 2023.

[28] H. Obeid, L. M. Fridman, S. Laghrouche, and M. Harmouche, "Barrier function-based adaptive sliding mode control," *Automatica*, vol. 93, pp. 540–544, 2018.

[29] C. D. Cruz-Ancona, L. Fridman, H. Obeid, S. Laghrouche, and C. A. Pérez-Pinacho, "A uniform reaching phase strategy in adaptive sliding mode control," *Automatica*, vol. 150, p. 110854, 2023.

[30] D. Liu, J. Yi, D. Zhao, and W. Wang, "Adaptive sliding mode fuzzy control for a two-dimensional overhead crane," *Mechatronics*, vol. 15, no. 5, pp. 505–522, 2005.

[31] C.-Y. Chang and K.-H. Chiang, "Fuzzy projection control law and its application to the overhead crane," *Mechatronics*, vol. 18, no. 10, pp. 607–615, 2008.

[32] B. Ma, Y. Fang, and Y. Zhang, "Switching-based emergency braking control for an overhead crane system," *IET control theory & applications*, vol. 4, no. 9, pp. 1739–1747, 2010.

Proceedings of the 3rd Conference on Fully Actuated System Theory and Applications
May 10-12, 2024, Shenzhen, China

Formation control of under-actuated multi-robot vehicle systems based on high-order fully actuated systems approach

Guanglei Zhao[1], Lu Luo[1], Peng Wang [1], Changchun Hua [1]
1. Institute of Electrical Engineering, and Intelligent Rehabilitation and Neuroregulation Key Lablatory of Hebei, Yanshan University, Qinhuangdao 066004, P. R. China
E-mail: glzhao517@126.com

Abstract: In this paper, a formation control problem of three-dimensional (3D) under-actuated multi-robot vehicle systems with nonholonomic constraint is investigated. First, the nonlinear dynamic model is transformed into an Euler-Lagrangian-like system that satisfies the full-actuation condition. Then, by using the high-order fully actuated systems (HOFAs) approach, the general control law of the under-actuated multi-robot vehicle systems is designed and the linear closed-loop system is obtained. The nonlinear system formation control problem is converted into a formation control problem of linear closed-loop system. According to the formation control requirements and objectives, designing the final formation controller using a rigid graph theory approach allows the under-actuated multi-robot vehicle systems to accurately converge to the desired formation. Lyapunov-based stability analysis shows the error function theoretically converges to zero eventually. Simulation results confirm the effectiveness of the formation control law.

Key Words: Multi-robot vehicle systems, formation control, high-order fully actuated systems, rigid graph theory.

1 Introduction

Multi-agent system (MAS) formation refers to the collective behavior of multiple agents working in a coordinated manner to achieve a specific geometric shape or configuration. The multi-agent formation provides critical means to enhance task efficiency, reduce risks, and improve system adaptability, and it finds applications in various fields, including multi-robots [1],[2], autonomous underwater vehicles [3],[4], and unmanned aerial vehicles [5],[6], etc.

The traditional method bassed on distributed formation control generally regulates the inter-agent distances and has high system reliability. But this method is prone to the problem of multiple equilibrium points, which makes the stability analysis and calculation be complex and difficult. The formation control method based on rigid graph theory can effectively reduce the appearance of non-desired equilibrium points [7]. It describes the relative position and angle relationships among the agents by establishing rigid connection relationships among them to achieve formation control. Meanwhile, collision avoidance between vehicles can be achieved because the rigid graph theory naturally ensures the distance constraint.

Recently, P Zhang et al. [8] presented a new formation control protocol based on rigid graph, where the team of agents can translate and rotate as a virtual rigid body in 3D. In [9], a rigid formation control problem of the system described by double-integrator was proposed, where the nonsmooth analysis, the backstepping technique and the adaptive perturbation method were employed to design the globally stable rigid formation control strategy. Tairan Liu et al. [10] studied distance + angle-based control of 2D rigid formations using single-integrator model. In [11], distance + area (or angle) schemes for 2D formations of single-integrator agents were considered to ensure the asymptotic stability of the desired formation for almost all initial agent positions.

However, a shortcoming in the abovementioned is that most of them still use single integrator dynamics or double integrators dynamics to describe the dynamical model of MAS, which were mostly turned into first-order systems. In model reduction and the first-order system framework, the physical meanings of original systems are lost. Actually, second- and high-order systems are natural representation of physical systems, because their dynamical models, described by Newton's laws, Euler and Lagrangian equations, and so on. In recent years, the high-order fully actuated systems (HOFAs) approach has garnered considerable attention in the scientific community due to its demonstrated efficacy and simplicity in addressing analysis and control challenges associated with second-order or higher-order nonlinear systems [12–17]. Duan proposed the formal definition of HOFAs in [12]. Then, Duan [13] clarified the relationship between full-actuation property and controllability, as well as a related parameter design method. In addition, Duan described the specific protocols of the HOFAs approach, including how to convert nonlinear systems [14, 15] and discrete systems [16, 17] into HOFA models. Obviously, the HOFAs approach may lead a novel and interesting topic on the control of MAS.

In [18], constrained cooperative control of high-order fully actuated multi-agent systems subject to input saturation and prescribed performance was concerned. Yunsi Yang et al. [19] studied the controllability of multi-agent systems over finite fields based on the high-order fully actuated (HOFA) system approaches. In [20] and [21], the distributed containment control of nonlinear high-order fully actuated-MAS was developed. Based on the nonlinear HOFA model of the system, the closed-loop system can always be converted to a constant linear one with a desired eigenstructure by simply designing a controller. In [22], an attitude-orbit integrated control law based on the fully-actuated system approach was proposed for spacecraft formation flying system. However, the existing literatures have less discussion

This work was supported by Hebei Natural Science Foundation under F2022203040; Natural Science Foundation of China under 62073277, 62188101, U22A2050; Central Government Guided Local Science and Technology Development Fund Project under 226Z0301G; Hebei Innovation Capability Improvement Plan Project under 22567619H; and Basic Innovation Research Project under 2022LGZD008.

on multi-agent systems formation control based on the high-order fully actuated (HOFA) system approaches.

In this paper, the formation control of 3D under-actuated multi-robot vehicle systems with nonholonomic constraint is investigated. By using coordinate transformation, the nonlinear dynamic model is transformed into the Euler-Lagrangian-like system that satisfies the full-actuation condition. Then, by using the HOFAs approach, the general control law of the under-actuated multi-robot vehicle systems is designed and the linear constant closed-loop system is obtained. The nonlinear system formation control problem is converted into a formation control problem of linear constant closed-loop system. According to the formation control requirements and objectives, designing the final formation controller using a rigid graph theory approach allows the under-actuated multi-robot vehicle systems to accurately converge to the desired formation.

2 Problem formulation

2.1 Preliminaries

This section introduces some basic concepts with respect to rigid graph theory, that are useful for deriving our main results.

An undirected graph consisting of n vertices and $\mathcal{L}$ undirected edges is denoted as $\mathcal{G} = (\mathcal{V}, \mathcal{E}, \mathcal{A})$, where the set of vertices and undirected edges are $\mathcal{V} = \{1, 2, \ldots, n\}$ and $\mathcal{E} \subset V \times V$, respectively. $\mathcal{A} = [a_{ij}] \in \mathbb{R}^n$ is the adjacency matrix, where $a_{ij} = 1$ if $(i, j) \in \mathcal{E}$ and $a_{ij} = 0$ otherwise, $a_{ij} = a_{ji}$. All vertices connected to vertex i constitute the set of neighbors of i, denoted by $\mathbb{N}_i(\mathcal{E})$.

$$\mathbb{N}_i(\mathcal{E}) = \{j \in \mathcal{V} \mid (i, j) \in \mathcal{E}\}, \tag{1}$$

vertex j is a neighbor of vertex i means that vertex i and j are connected by a path and they can communicate with each other.

A framework is defined as $F = (\mathcal{G}, \zeta)$, where $\zeta_i \in \mathbb{R}^3$ is the coordinate of vertex i and $\zeta = [\zeta_1, \ldots, \zeta_n] \in \mathbb{R}^{3n}$. The edge function $\phi_G(\zeta) : \mathbb{R}^{3n} \to \mathbb{R}^{\mathcal{L}}$ for a framework $F = (\mathcal{G}, \zeta)$ is defined as

$$\phi_{\mathcal{G}}(\zeta) = \left[\ldots, \|\zeta_i - \zeta_j\|^2, \ldots\right], \quad (i, j) \in \mathcal{E} \tag{2}$$

where $\mathcal{L}$ is the number of edges, $\|\cdot\|$ denotes the Euclidean norm, $\|\zeta_i - \zeta_j\|^2$ corresponds to the edge connecting vertices i and j in $\mathcal{E}$.

The rigidity matrix $R : \mathbb{R}^{3n} \longrightarrow \mathbb{R}^{\mathcal{L} \times 3n}$ of $F = (\mathcal{G}, \zeta)$ is defined as

$$R(\zeta) = \frac{1}{2} \frac{\partial \phi_{\mathcal{G}}(\zeta)}{\partial \zeta}, \tag{3}$$

Note that the rigidity matrix has a row for each edge and 3 columns for each vertex. That is, for the kth edge of $\mathcal{E}$ connecting vertices i and j, the kth row of $R(\zeta)$ is:

$$[0 \ldots (\zeta_i - \zeta_j)^T \ldots (\zeta_j - \zeta_i)^T \ldots 0],$$

where $(\zeta_i - \zeta_j)^T$ is in the columns for vertex i, $(\zeta_j - \zeta_i)^T$ is in the columns for vertex j, and all other elements are zero.

Lemma 1. *[23] A framework $(\mathcal{G}, \zeta)$ in $\mathbb{R}^3$ is rigid if and only if rank$[R(\zeta)] = 3n - 6$ and $\mathcal{L} = 3n - 6$.*

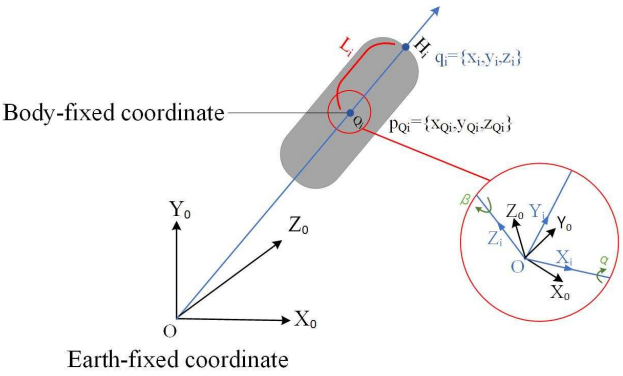

Fig. 1: Illustration of coordinate transformation of the i-th robot vehicle.

Based on Lemma 1, the communication relationship between multi-robot vehicles must satisfy rank$[R(\zeta)] = 3n-6$ and $\mathcal{L} = 3n - 6$ ensuring that the formation framework is minimally and infinitesimally rigid.

2.2 Model transformation

We consider the system consisting of following 3D under-actuated robot vehicles (see Fig.1). The dynamics of robot vehicle is described by

$$\dot{p}_i = S(\alpha_i, \beta_i)\, \eta_i, \tag{4a}$$

$$\bar{M}_i \dot{\eta}_i + \bar{D}_i \eta_i = \bar{\tau}_i, \tag{4b}$$

for $i = 1, \ldots, n$. In (4a), $p_i = [x_{Qi}, y_{Qi}, z_{Qi}, \alpha_i, \beta_i]$ is the position and orientation, $\eta_i = [v_i, \omega_{\alpha i}, \omega_{\beta i}]$, v_i is the i-th robot vehicle's translational speed, and ω_i is the i-th robot vehicle's angular speed about the vertical axis passing through Q_i, where

$$S(\alpha_i, \beta_i) = \begin{bmatrix} \cos\alpha_i \cos\beta_i & 0 & 0 \\ \sin\alpha_i \cos\beta_i & 0 & 0 \\ \sin\beta_i & 0 & 0 \\ 0 & 1 & 0 \\ 0 & 0 & 1 \end{bmatrix}. \tag{5}$$

In (4b), $\bar{M}_i = \mathrm{diag}\{m_i, \bar{I}_{i1}, I_{i2}\}$, m_i and I_{i1}, I_{i2} are the i-th robot vehicle's mass and moment of inertia, respectively. $\bar{D}_i \in \mathbb{R}^{3\times3}$ represents the constant damping matrix, and $\bar{\tau}_i \in \mathbb{R}^3$ is control input of the system. From (4a), the dimension of the system state space ($p_i \in \mathbb{R}^5$) is higher than the dimension of the motion constraint space ($\eta_i \in \mathbb{R}^3$). Therefore, dealing with this nonholonomic constraint in (4) is the main challenge.

In this paper, we transform robot vehicle system into the Euler-Lagrangian-like system, thus cleverly avoiding the nonholonomic constraint in (4). Fig.1 shows the illustration of coordinate transformation of the i-th robot vehicle, we define the point H_i on the X_i axis at a distance L_i from point Q_i. Inspired by [24], the point H_i position q_i is given by

$$q_i = \begin{bmatrix} x_i \\ y_i \\ z_i \end{bmatrix} = \begin{bmatrix} x_{Qi} \\ y_{Qi} \\ z_{Qi} \end{bmatrix} + L_i \begin{bmatrix} \cos\beta_i \cos\alpha_i \\ \cos\beta_i \sin\alpha_i \\ \sin\beta_i \end{bmatrix}. \tag{6}$$

In practice, the point H_i position represents an end-effector or a sensor on the robot vehicle. For any $L_i \neq 0$,

kinematics of (6) are holonomic. Specifically, from (4)- (6), we have

$$\eta_i = J(\alpha_i, \beta_i)\,\dot{q}_i, \tag{7}$$

where

$$J(\alpha_i, \beta_i) = \begin{bmatrix} \cos\beta_i \cos\alpha_i & \cos\beta_i \sin\alpha_i & \sin\beta_i \\ \frac{-\sin\alpha_i}{L_i \cos\beta_i} & \frac{\cos\alpha_i}{L_i \cos\beta_i} & 0 \\ \frac{-\sin\beta_i \cos\alpha_i}{L_i} & \frac{-\sin\beta_i \sin\alpha_i}{L_i} & \frac{\cos\beta_i}{L_i} \end{bmatrix}. \tag{8}$$

After obtaining the time derivative of (7), we multiply both sides of the resulting equation by $\bar{M}_i$ at the same time and substitute (4b) to obtain

$$\bar{\tau}_i - \bar{D}_i J(\alpha_i, \beta_i)\,\dot{q}_i = \bar{M}_i \dot{J}(\alpha_i, \beta_i)\,\dot{q}_i + \bar{M}_i J(\alpha_i, \beta_i)\,\ddot{q}_i. \tag{9}$$

Next, pre-multiply (9) by $J^\top(\alpha_i, \beta_i)$, we obtain the following Euler-Lagrange-like dynamic model

$$\dot{q}_i = v_i, \tag{10a}$$

$$M_i(q_i)\,\dot{v}_i = \tau_i - C_i(q_i, v_i)\,v_i - D_i(q_i)\,v_i, \tag{10b}$$

where $v_i \in \mathbb{R}^3$ denotes the velocity of the i-th robot vehicle's H_i point relative to Earth-fixed frame, and

$$M_i(q_i) = J^\top \bar{M}_i J, \quad C_i(q_i, \dot{q}_i) = J^\top \bar{M}_i \dot{J}, \\ D_i(q_i) = J^\top \bar{D}_i J, \quad \tau_i = J^\top \bar{\tau}_i. \tag{11}$$

the $M_i(q_i)$ and $C_i(q_i, \dot{q}_i)$ denote the mass matrix and the Coriolis/centripetal matrix respectively.

Let $q = [q_1, \ldots, q_n] \in \mathbb{R}^{3n}$, $v = [v_1, \ldots, v_n] \in \mathbb{R}^{3n}$, $\tau = [\tau_1, \ldots, \tau_n] \in \mathbb{R}^{3n}$, $M = \mathrm{diag}\{M_1(q_1), \ldots, M_n(q_n)\} \in \mathbb{R}^{3n\times 3n}$, $C = \mathrm{diag}\{C_1(q_1, v_1), \ldots, C_n(q_i, v_i)\} \in \mathbb{R}^{3n\times 3n}$, $D = \mathrm{diag}\{D_1(q_1), \ldots, D_n(q_n)\} \in \mathbb{R}^{3n\times 3n}$. The multi-robot vehicle systems (10) can be written in a compact form as follows:

$$\dot{q} = v, \tag{12a}$$

$$M\dot{v} = \tau - Cv - Dv, \tag{12b}$$

Then, the system can be rewritten in the following system form:

$$\ddot{q} = f(q^{(0\sim 1)}, t) + B(q^{(0\sim 1)}, t)\tau, \tag{13}$$

where

$$f(q^{(0\sim 1)}, t) = -M^{-1}(C + D)\dot{q}, \tag{14}$$

$$B(q^{(0\sim 1)}, t) = M^{-1}. \tag{15}$$

Note that, the mass matrix M is symmetric and positive definite, so:

$$\det B(q^{(0\sim 1)}, t) \neq 0, t > 0.$$

The system (12) satisfies the full-actuation condition, therefore, the formation control of the 3D under-actuated multi-robot vehicle systems can be designed using the HOFAs approach.

Remark 1. *The system* (13) *is widely recognized in the field of robotics and spacecraft control. Since the control distribution matrix $B(q^{(0\sim 1)}, t)$ of the system satisfies the full-actuation condition, the system* (13) *is a high-order fully actuated nonlinear system. It is well known that the HOFA systems are more realistic and can be directly obtained from physical laws. There is no need to transform the HOFA systems into the state-space forms, such that saves the workload of system conversion. With the HOFAs approach of [14], the high-order fully actuated nonlinear system can be transformed into a linear closed-loop system that has an arbitrarily assignable eigen-structure, thus significantly reducing the complexity of subsequent controller design.*

3 Main Results

In this section, we propose a formation controller design based on the HOFA systems approach to achieve the control objectives. Then, the system stability is established based on Lyapunov function analysis.

Consider that the 3D robot vehicles' target formation is modeled by an infinitesimally and minimally rigid framework $F^*(t) = (\mathcal{G}^*, q^*)$, where $\mathcal{G}^* = (\mathcal{V}^*, \mathcal{E}^*, \mathcal{A}^*)$ is the rigid graph, $\mathcal{V}^* = \{1, 2, \ldots, n\}$, the number of $\mathcal{E}^*$ is $3n-6$, and $q^* = [q_1^*, \ldots, q_n^*]$. The desired distance between robot vehicle i and its neighbor robot vehicle j is given by

$$d_{ij} = \left\|q_i^* - q_j^*\right\| > 0, \quad i, j \in \mathcal{V}^* \tag{16}$$

where d_{ij} is a constant.

The robotic vehicles' actual formation is determined by the framework $F(t) = (\mathcal{G}^*, q(t))$, where $F(t)$ and $F^*(t)$ have the same rigid graph, and $q(t) = [q_1(t), \ldots, q_n(t)]$ denotes the actual position of the robotic vehicles at time t. Besides, assume that at $t = 0$, $\|q_i(0) - q_j(0)\| \neq d_{ij}(0), i, j \in \mathcal{V}^*$.

The relative position between robot vehicle i and its neighbor robot vehicle j is defined as

$$\tilde{q}_{ij} = q_i - q_j, \quad (i, j) \in \mathcal{E}^* \tag{17}$$

Define distance error as

$$e_{ij} = \|\tilde{q}_{ij}\| - d_{ij}, \quad (i, j) \in \mathcal{E}^* \tag{18}$$

The dynamics of distance errors can be calculated as

$$\dot{e}_{ij} = \frac{\tilde{q}_{ij}^\top (v_i - v_j)}{e_{ij} + d_{ij}}. \tag{19}$$

Define

$$z_{ij} = \|\tilde{q}_{ij}\|^2 - d_{ij}^2 = e_{ij}(e_{ij} + 2d_{ij}). \tag{20}$$

Given that $\|\tilde{q}_{ij}\| \geq 0$, from (18), we know that $e_{ij} \geq -d_{ij}$. From (20), it is easy to see that $z_{ij} = 0$ only when $e_{ij} = 0$. Let $\tilde{q} = [\ldots, \tilde{q}_{ij}, \ldots] \in \mathbb{R}^{3\mathcal{L}}$, $e = [\ldots, e_{ij}, \ldots] \in \mathbb{R}^{\mathcal{L}}$, and $z = [\ldots, z_{ij}, \ldots] \in \mathbb{R}^{\mathcal{L}}$.

Following the backstepping technique, we introduce the variable

$$\tilde{v} = v - v_f, \tag{21}$$

where $v_f \in \mathbb{R}^{3n}$ denotes the desired velocity input of point H_i.

Therefore, the objective of this paper is to design control law that can guide 3D under-actuated multi-robot vehicle systems with nonholonomic constraint to form a desired formation. To achieve the formation objective, it is required that the following condition holds:$e(t) \to \mathbf{0}$ as $t \to \infty, i, j \in \mathcal{V}^*$ and, $\tilde{v} \to \mathbf{0}$ as $t \to \infty$.

Applying HOFAs approach in [14], we obtain the controller for system (13) as follows:

$$\tau = -M(A_1\dot{q} + A_0 q + f((q^{(0\sim 1)}) - U_Z). \tag{22}$$

Let $A_1 = \text{diag}\{A_{11}, \ldots, A_{n1}\} \in \mathbb{R}^{3n\times 3n}$, $A_0 = \text{diag}\{A_{10}, \ldots, A_{n0}\} \in \mathbb{R}^{3n\times 3n}$, where $A_{i1} \in \mathbb{R}^{3\times 3}, A_{i0} \in \mathbb{R}^{3\times 3}, i = 1, \ldots, n$ are set of given matrices.

Substituting (22) into (13), we obtain the following linear closed-loop system:

$$\ddot{q} + A_1\dot{q} + A_0 q = U_Z, \tag{23}$$

For the linear closed-loop system (23), based on rigid graph theory and backstepping technique and using the relative distance of inter-vehicles, we propose the following formation control law:

$$U_Z = -k_a\tilde{v} + A_1\dot{q} + A_0 q + \dot{v}_f - R(\tilde{q})^T z, \tag{24a}$$

$$v_f = -k_b R(\tilde{q})^T z, \tag{24b}$$

where k_a, k_b are positive constants, $R(\tilde{q})$ is the rigidity matrix of the desired formation.

Substitute (24) into (22), the controller finally designed for the system is:

$$\tau = -M(k_a\tilde{v} + R(\tilde{q})^T z + f((q^{(0\sim 1)}) - \dot{v}_f), \tag{25a}$$

$$v_f = -k_b R(\tilde{q})^T z, \tag{25b}$$

Theorem 1. *Given the framework $F = (\mathcal{G}^*, q)$, let $\xi = (e, \tilde{v})$. Consider the under-actuated multi-robot vehicle systems with nonholonomic constraint and dynamics model* (4)*, by using the proposed control law* (25)*, the dynamics of $(e, \tilde{v})$ can be asymptotically stable. Therefore, the control law* (25) *can guide 3D under-actuated multi-robot vehicle systems* (4) *to form a desired formation.*

Proof. First, we introduce the following candidate Lyapunov function.

$$W_\xi = W_e + W_{\tilde{v}} \tag{26}$$

with

$$\begin{aligned} W_e &= \frac{1}{4}\sum_{(i,j)\in\mathcal{E}^*} \left[e_{ij}\left(e_{ij} + 2d_{ij}\right)\right]^2 \\ &= \frac{1}{4}\sum_{(i,j)\in\mathcal{E}^*} z_{ij}^2 = \frac{1}{4} z^\top z \end{aligned} \tag{27}$$

and

$$W_{\tilde{v}} = \frac{1}{2}(\tilde{v})^T\tilde{v} \tag{28}$$

The time derivative of W_e is computed as

$$\begin{aligned} \dot{W}_e &= z^T R(\tilde{q}) v = z^T R(\tilde{q})(\tilde{v} + v_f) \\ &= z^T R(\tilde{q})(\tilde{v} - k_b R(\tilde{q})^T z), \end{aligned} \tag{29}$$

and, the time derivative of $W_{\tilde{v}}$ is computed as

$$\begin{aligned} \dot{W}_{\tilde{v}} &= (\tilde{v})^T(M^{-1}\tau - M^{-1}C\dot{q} - M^{-1}D\dot{q} - \dot{v}_f) \\ &= (\tilde{v})^T(-k_a\tilde{v} - R(\tilde{q})^T z), \end{aligned} \tag{30}$$

where (19), (20), (21) and (25) are used. Combining the above analysis, we can obtain that

$$\begin{aligned} \dot{W}_\xi &= \dot{W}_e + \dot{W}_{\tilde{v}} \\ &= z^T R(\tilde{q})(\tilde{v} - k_b R(\tilde{q})^T z) + (\tilde{v})^T(-k_a\tilde{v} - R(\tilde{q})^T z) \\ &= -k_b z^T R(\tilde{q}) R(\tilde{q})^T z - k_a(\tilde{v})^T\tilde{v}, \end{aligned} \tag{31}$$

Since F^* is infinitesimally and minimally rigid, then $R(\tilde{q})$ has full row rank. Since $\text{rank}[R(\tilde{q})] = \text{rank}[R(\tilde{q})R(\tilde{q})^T]$, the matrix $R(\tilde{q})R(\tilde{q})^T$ is invertible; therefore,

$$\begin{aligned} \dot{W}_\xi &\le -k_b\lambda_{min}(R(\tilde{q})R(\tilde{q})^T) z^T z - k_a(\tilde{v})^T\tilde{v} \\ &\le -\min\{2k_a, 4k_b\lambda_{min}(R(\tilde{q})R(\tilde{q})^T)\} W_\xi. \end{aligned} \tag{32}$$

where (27) and (28) are used and $\lambda_{min}(\cdot)$ denotes the minimum eigenvalue.

From (26) and (32), we know that W_ξ is positive definite, and $\dot{W}_\xi < 0$. According to the Lyapunov stability theory, we prove that $(e, \tilde{v})$ is asymptotic stable. □

Remark 2. *Applying HOFAs approach in [14], the high-order fully actuated nonlinear system can be always converted to a linear closed-loop system one with a desired eigenstructure by simply designing a controller, and the desired performance of the system can be obtained by only choosing the matrices A_0 and A_1 appropriately. Then, the rigid graph theory and backstepping technique are used to design the formation controller for the linear closed-loop system so that the distance error and virtual error eventually converge to 0. The final obtained formation controller of under-actuated multi-robot vehicle systems can achieve the formation control objective, and the stability is proved by using Liyapunov stability theory. As can be seen from the main results, the HOFAs approach can significantly reduce the complexity of subsequent controller design. Moreover, from the proof of Theorem 1, we observe that the method based on rigid graph theory produces only one equilibrium point, this overcomes the disadvantage of the traditional distance-based methods with multiple equilibrium points.*

Remark 3. *In this paper, uncertain parameters and external disturbances of under-actuated multi-robot vehicle systems are neglected. The robustness of the system is unknown, which can result in a significant deviation of the control effect from the expectation, and affect the accuracy and stability of the formation. In practical applications, robustness must be considered in the process of designing control strategy in order to ensure that the system maintains stable, efficient and reliable performance in the presence of a wide range of uncertainties. Considering robustness is not only essential to improve the performance of the system, but also to expand its application areas. Therefore, in future work, the focus will be on incorporating robust design principles in multi-robot formation control strategies based on higher-order all-drive system approaches. Robust control theories such as H_∞-control, sliding mode control, etc. will be used to ensure performance maintenance under parameter uncertainty and external disturbances.*

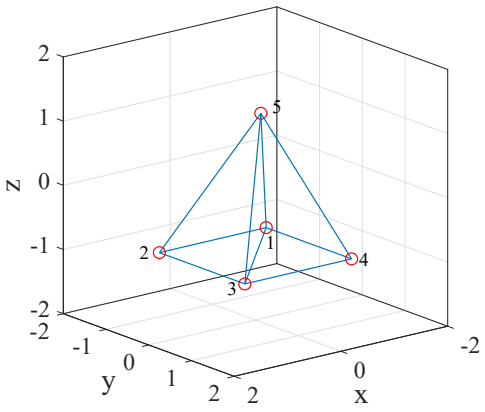

Fig. 2: Desired formation of multi-robot vehicle systems.

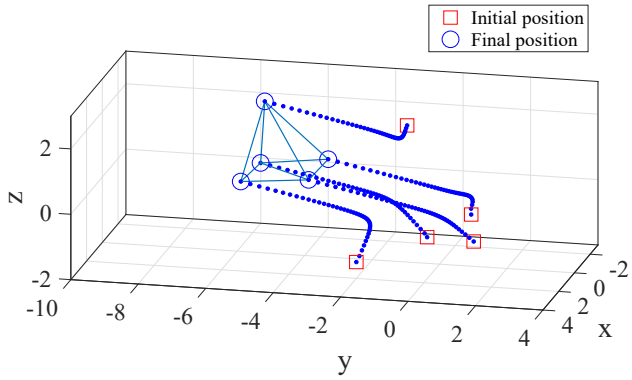

Fig. 3: Robot-vehicles trajectories $q_i(t)$.

4 Simulation Results

In this section, the effectiveness and advantages of the proposed HOFAs approach are shown via computer simulations, which are carried out on a robot-vehicle system consisting of five robot vehicles, the desired formation is shown in Fig.2. In order to make the framework to be minimally rigid and infinitesimally rigid, the number of edges is (rank$[R(\zeta)] = 3n - 6 = 3 \times 5 - 6 =$)9, as shown in Fig.2. Thus, the edge set is selected as

$$\begin{aligned}\mathcal{E}^* =&\{(1,2),(1,3),(1,4),(1,5),\\ &(2,3),(2,5),(3,4),(3,5),(4,5)\}.\end{aligned}$$

The initial position and velocity of robot vehicles are randomly chosen be $q_1(0) = [-1,-0.6,-1.5]$, $q_2(0) = [2,-2,-1.5]$, $q_3(0) = [0.8,1.2,-1]$, $q_4(0) = [-0.6,0.8,-0.6]$, $q_5(0) = [-0.6,-1.1,2]$, $v_1(0) = [0.5,0.5,0.5]$, $v_2(0) = [-0.2,0.3,1]$, $v_3(0) = [0.6,-1,1]$, $v_4(0) = [-1,-0.8,2]$, $v_5(0) = [0.4,-0.4,1]$, while its initial orientation $\alpha_i(0)$ and $\beta_i(0)$ are set to be any values in the interval $(0, 2\pi)$. The control parameters are set to be $k_a = 2, k_b = 1$. The system parameters are set to be: $m_i = 1.6$ kg, $\bar{I}_{1i} = 0.4333$ kg $\cdot\, m^2$, $I_{2i} = 0.6000$ kg $\cdot\, m^2$, $\bar{D}_i = \text{diag}\{0.3 \text{ kg/s}, 0.004 \text{ kg/s}, 0.5 \text{ kg/s}\}$, and, $L_i = 0.2$ m for $i = 1,\ldots,5$.

The trajectories of the five robot vehicles in space as they converge to the desired formation are shown in Fig.3. The inter-vehicle distance errors are depicted in Fig.4, the distance errors between neighboring robotic vehicles gradually tends to zero, which indicates that the proposed control law can achieve the control objective and the robot vehicle system can form a desired formation. Fig.5 we plot the $x-, y-, z-$ direction components of the velocity errors of each robotic vehicle, after a certain range of flutuations, the errors gradually tend to zero. From the simulation results, we can see that the formation control objective is achieved.

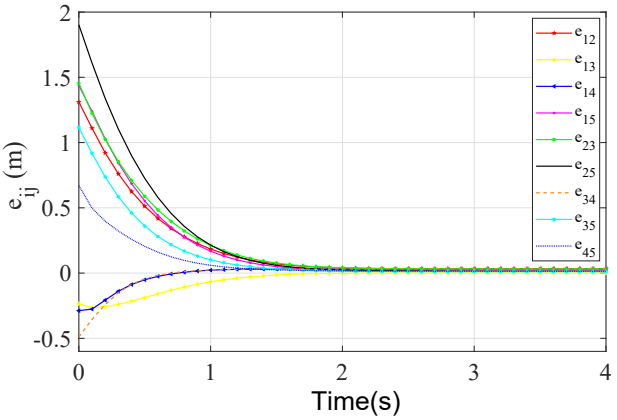

Fig. 4: Distance errors between neighboring robot vehicles.

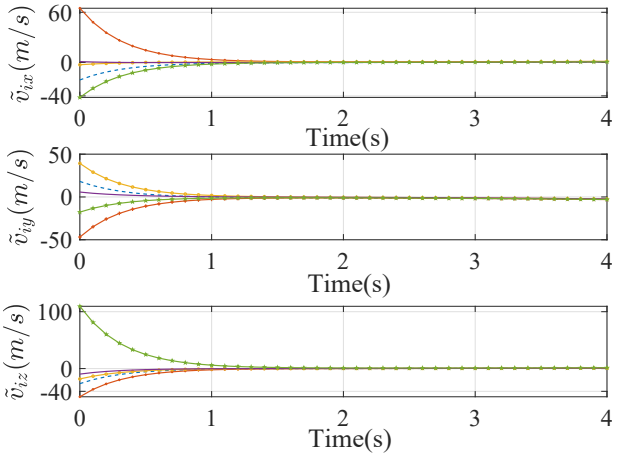

Fig. 5: Velocity errors between neighboring robot vehicles in x, y, z directions.

5 Conclusion

In this paper, we propose formation control for under-actuated multi-robot vehicle systems with nonholonomic constraint based on HOFAs approach and grid graph. By using coordinate transformation, the nonlinear dynamic model is transformed into the Euler-Lagrangian-like system that satisfies the full-actuation condition. Then, by using the HOFAs approach, the general control law of the under-actuated multi-robot vehicle systems is designed and the linear constant closed-loop system is obtained. The nonlinear system formation control problem is converted into a formation control problem of linear constant closed-loop system. According to the formation control requirements and objectives, designing the final formation controller using a rigid

graph theory approach allows the under-actuated multi-robot vehicle systems to accurately converge to the desired formation. Lyapunov-based stability analysis shows that the error function theoretically converges to zero eventually. In addition, simulation results demonstrate the effectiveness of the formation control law. Note that the limitations of the proposed approach are that the system parameters are fully known and the influence of perturbations are not taken into account. However, there are extensive uncertainties and external disturbances in multi-robot vehicle systems that affect the stability of the system. Therefore, in future work, we will develop adaptive formation controllers based on HOFAs approach for under-actuated multi-robot vehicle systems, considering the effects of disturbances and unknown items of model.

References

[1] F. Sun, H. Li, W. Zhu and J. Kurths, Fixed-time formation tracking for multiple nonholonomic wheeled mobile robots based on distributed observer, *Nonlinear Dynamics*, 106(4): 3331-3349, 2021.

[2] X. Zhang, Z. Peng, S. Yang, G. Wen and A. Rahmani, Distributed fixed-time consensus-based formation tracking for multiple nonholonomic wheeled mobile robots under directed topology, *International Journal of Control*, 94(1): 248-257, 2021.

[3] J. Li and J. Du, Robust Formation Control of Underactuated Autonomous Underwater Vehicles with Disturbances under Input Saturation, *2018 37th Chinese Control Conference (CCC). IEEE*, 6931-6936, 2018.

[4] S. Pang, J. Wang, J. Liu and H. Yi, Three-dimensional leader–follower formation control of multiple autonomous underwater vehicles based on line-of-sight measurements using the backstepping method, *Proceedings of the Institution of Mechanical Engineers, Part I: Journal of Systems and Control Engineering*, 232(7): 819-829, 2018.

[5] J. Hu, M. Wang, C. Zhao, Q. Pan and C. Du, Formation control and collision avoidance for multi-UAV systems based on Voronoi partition, *Science China Technological Sciences*, 63(1): 65-72, 2020.

[6] X. Dong, Y. Hua, Y. Zhou, Z. Ren and Y. Zhong, Theory and experiment on formation-containment control of multiple multirotor unmanned aerial vehicle systems, *IEEE Transactions on Automation Science and Engineering*, 16(1): 229-240, 2018.

[7] B. Anderson, C. Yu, B. Fidan and J. Hendrickx, Rigid graph control architectures for autonomous formations, *IEEE Control Systems Magazine*, 28(6): 48–63, 2008.

[8] P. Zhang and Q. De, 3D multi-agent formation control with rigid body maneuvers, *Asian Journal of Control*, 21(3): 1088–1099, 2019.

[9] Q. Wang, Q. Hua, Y. Yi and T. Zhang, Multi-agent formation control in switching networks using backstepping design, *International Journal of Control, Automation and Systems*, 15: 1569-1576, 2017.

[10] T. Liu and Q. De, Distance+ angle-based control of 2-d rigid formations, *IEEE transactions on cybernetics*, 51(2): 5969–5978, 2020.

[11] T. Liu, V. Fernández-Kim and Q. De, Switching formation shape control with distance+ area/angle feedback, *Systems & Control Letters*, 135: 104598, 2020.

[12] G. Duan, High-order system approaches-I. Fully-actuated systems and parametric designs, *Acta Automatica Sinica*, 46(7): 1333-1345, 2020.

[13] G. Duan, High-order system approaches-II. Controllability and fully-actuation, *Acta Automatica Sinica*, 46(8): 1571-1581, 2020.

[14] G. Duan, High-order fully actuated systems approaches: Part I. Models and basic procedure, *International Journal of Systems Science*, 52(2): 422-435, 2021.

[15] G. Duan, High-order fully actuated system approaches: Part II. Generalized strict-feedback systems, *International Journal of Systems Science*, 52(3): 437-454, 2021.

[16] G. Duan, High-order fully actuated system approaches: Part X. Basics of discrete-time systems, *International Journal of Systems Science*, 53(4): 810-832, 2021.

[17] G. Duan, Discrete-time delay systems: Part 1. Global fully actuated case, *Science China Information Sciences*, 65(8): 182-201, 2022.

[18] D. Zhang, G. Liu and L. Cao, Constrained cooperative control for high-order fully actuated multiagent systems with application to air-bearing spacecraft simulators, *IEEE/ASME Transactions on Mechatronics.*, 2022.

[19] Y. Yang, J. Feng and Z. Gao, Controllability of Multi-agent Systems over Finite Fields Based on High-order Fully Actuated System Approaches, *2023 2nd Conference on Fully Actuated System Theory and Applications (CFASTA)*, 283-289, 2023.

[20] Y. Liu, J. Zhang and X. Lu, Distributed Containment Control for Nonlinear HOFA-MASs, *2023 2nd Conference on Fully Actuated System Theory and Applications (CFASTA)*, 846-851, 2023.

[21] Y. Zhang, H. Lin, B. Zhao and D. Liu, Distributed Robust Containment Control for Multi-Robot Systems via Adaptive Critic Designs, *2023 2nd Conference on Fully Actuated System Theory and Applications (CFASTA)*, 1-6, 2023.

[22] J. Wu, Y. Liu, M. Liu and X. Cao, Fully-actuated-system-approach-based Attitude-orbit Integrated Control for Spacecraft Formation Flying, *2023 2nd Conference on Fully Actuated System Theory and Applications (CFASTA)*, 717-722, 2023.

[23] B. Anderson, C. Yu, B. Fidan and J. Hendrickx, Rigid graph control architectures for autonomous formations, *IEEE Control Systems Magazine*, 28(6): 48-63, 2008.

[24] X. Cai and Q. De, Adaptive rigidity-based formation control for multi robotic vehicles with dynamics, *IEEE Transactions on Control Systems Technology*, 23(1): 389-396, 2014.

Proceedings of the 3rd Conference on Fully Actuated System Theory and Applications
May 10-12, 2024, Shenzhen, China

Aircraft Middle and Final Stage Attitude Control on Fully Actuated System Theory

Xinyu Liu, Mingrui Hao*, Yu Fan, Yan Zhen, Wendi Sun

National Key Laboratory of Complex System Control and Intelligent Agent Cooperation, Beijing 100074, China
E-mail: hmrhit@163.com

Abstract: This paper takes the attitude control of the middle and final stages of the aircraft as the research background, and explores a new nonlinear control method for the strong nonlinearity, strong coupling, fast time-varying and uncertainty characteristics of the aircraft. A second-order fully actuated system model of the aircraft is constructed, which is starting from the six degree of freedom mathematical model, including aerodynamic coupling and control coupling. It is a nonlinear model, including roll, yaw and pitch full three channels. Also, the paper designed an attitude controller on fully actuated system, which is based on the PD control method, and proved the stability of the controller through Lyapunov stability analysis method. Then, the controller is integrated into the aircraft simulation, and mathematical simulation verification is carried out under benchmark conditions, achieving good attitude control effect.

Key Words: Fully Actuated System, Attitude Control, Nonlinear Control, Aircraft Simulation

1 Introduction

For aircraft with strong coupling, strong nonlinearity and fast time-varying characteristics [1], the design of their control systems requires extremely high requirements: the control system must have both flexible maneuverability and necessary robustness and adaptability. Experts and scholars have conducted extensive in-depth research in the field of control of such aircraft, and have achieved rich research results. The commonly used control methods currently include active disturbance rejection control, dynamic inverse control, backstepping control, sliding mode variable structure control, intelligent control, etc. They have their own advantages, but at the same time, there are problems such as model inaccuracy [2], computational inaccuracy [3], and poor robustness [4]. For aircraft with nonlinear and coupled dynamic characteristics, sometimes satisfactory dynamic characteristics cannot be obtained.

In order to reduce the impact of the above issues on the stability control effect of the aircraft, it is necessary to explore a new nonlinear control method. The control problem of aircraft itself is a type of nonlinear, highly coupled, and real-time problem, and the fully actuated system method has outstanding advantages in dealing with nonlinear, time-varying, hysteresis and other problems [5]. " Fully actuated " was originally a physical concept, and the fully actuated system has unparalleled control characteristics compared to other systems. Academician Guangren Duan's team has extended the physical concept of fully actuated systems at the mathematical level, equivalently transforming actual fully actuated systems and subfully actuated systems into fully actuated systems in mathematical terms [6]. They are a type of control-oriented model for dynamic systems, which can easily achieve stabilization.

This paper explores a nonlinear control method for the coupling and nonlinear characteristics of aircraft, aiming to reduce errors and achieve stable control effects in the middle and final stages of aircraft. The main research content is aimed at the attitude control problem of aircraft, using the nonlinear model of the aircraft to establish a second-order fully actuated system model, designing a control method on the fully actuated system theory, and integrating the controller into the simulation models of the middle and final stages of the aircraft. The effectiveness and corresponding performance of the designed controller are verified through mathematical simulation experiments.

2 Aircraft Fully Actuated System Model Construction

Establishing middle and final motion models for aircraft is the foundation for establishing a second-order fully actuated system model.

The centroid dynamic equations of the aircraft are

$$\begin{cases} m\dfrac{\mathrm{d}v}{\mathrm{d}t} = P\cos\alpha\cos\beta - X - mg\sin\theta \\ mv\dfrac{\mathrm{d}\theta}{\mathrm{d}t} = P(\sin\alpha\cos\gamma_c + \cos\alpha\sin\beta\sin\gamma_c) \\ \qquad\qquad + Y\cos\gamma_c - Z\sin\gamma_c - mg\cos\theta \\ -mv\cos\theta\dfrac{\mathrm{d}\psi_c}{\mathrm{d}t} = P(\sin\alpha\sin\gamma_c - \cos\alpha\sin\beta\cos\gamma_c) \\ \qquad\qquad + Y\sin\gamma_c + Z\cos\gamma_c \end{cases} \tag{1}$$

where, P is the propulsion, and the aerodynamic force expressions are

$$\begin{cases} X = qSC_x \\ Y = qS(C_{y0} + C_y^{\alpha}\alpha + C_y^{\delta_z}\delta_z) \\ Z = qS(C_z^{\beta}\beta + C_z^{\delta_y}\delta_y) \end{cases} \tag{2}$$

In the formula, S is the reference area, δ_y is the yaw rudder angle, δ_z is the pitch rudder angle, C_x is the drag coefficient, C_{y0} is the zero lift coefficient, C_y^{α} is the attack

* This work is supported by National Natural Science Foundation (NNSF) of China under Grant 62188101.

angle lift coefficient, $C_y^{\delta_z}$ is the pitch rudder lift coefficient, C_z^{β} is the sideslip angle lateral force coefficient, $C_z^{\delta_y}$ is the yaw rudder lateral force coefficient, q is the dynamic pressure

$$q = \frac{1}{2}\rho V^2 \tag{3}$$

where, V is the speed of the aircraft, ρ is the atmospheric density calculated using Bingwei Yang's atmospheric model.

The rotation aerodynamic equation is

$$\begin{bmatrix} J_x\dot{\omega}_x + (J_z - J_y)\omega_z\omega_y \\ J_y\dot{\omega}_y + (J_x - J_z)\omega_x\omega_z \\ J_z\dot{\omega}_z + (J_y - J_x)\omega_y\omega_x \end{bmatrix} = \begin{bmatrix} M_x \\ M_y \\ M_z \end{bmatrix} \tag{4}$$

where, ω_x, ω_y, ω_z are the components of the rotational angular velocity of the aircraft coordinate system relative to the ground coordinate system along the axes of the aircraft coordinate system, and J_x, J_y, J_z are the moments of inertia of the aircraft relative to the axes of the aircraft coordinate system. M_x, M_y, M_z are the expressions for the roll moment, yaw moment and pitch moment, and the three aerodynamic moments are

$$\begin{cases} M_x = qSL(m_x^{\beta}\beta + m_x^{\delta_x}\delta_x + m_x^{\delta_y}\delta_y) \\ M_y = qSL(m_y^{\beta}\beta + m_y^{\delta_y}\delta_y + m_y^{\delta_x}\delta_x) \\ M_z = qSL(m_z^{\alpha}\alpha + m_z^{\delta_z}\delta_z) \end{cases} \tag{5}$$

where, L is the reference length, δ_x is the roll rudder angle, m_x^{β} is the sideslip angle roll moment coefficient, m_y^{β} is the sideslip angle yaw moment coefficient, m_z^{α} is the attack angle pitch moment coefficient, $m_x^{\delta_x}$ is the roll rudder roll moment coefficient, $m_x^{\delta_y}$ is the yaw rudder roll moment coefficient, $m_y^{\delta_y}$ is the yaw rudder yaw moment coefficient, $m_y^{\delta_x}$ is the roll rudder yaw moment coefficient, $m_z^{\delta_z}$ is the pitch rudder pitch moment coefficient.

The centroid kinematic equation of the aircraft is

$$\begin{cases} \dfrac{\mathrm{d}x}{\mathrm{d}t} = V\cos\theta\cos\psi_c \\ \dfrac{\mathrm{d}y}{\mathrm{d}t} = V\sin\theta \\ \dfrac{\mathrm{d}z}{\mathrm{d}t} = -V\cos\theta\sin\psi_c \end{cases} \tag{6}$$

where, x, y and z are the positions of the aircraft's centroid relative to the ground coordinate system.

The rotation kinematic equations are

$$\begin{bmatrix} \omega_x \\ \omega_y \\ \omega_z \end{bmatrix} = \begin{bmatrix} \dot{\psi}\sin\vartheta + \dot{\gamma} \\ \dot{\psi}\cos\vartheta\cos\gamma + \dot{\vartheta}\sin\gamma \\ -\dot{\psi}\cos\vartheta\sin\gamma + \dot{\vartheta}\cos\gamma \end{bmatrix} \tag{7}$$

and

$$\begin{bmatrix} \dot{\gamma} \\ \dot{\psi} \\ \dot{\vartheta} \end{bmatrix} = \begin{bmatrix} \omega_x - \tan\vartheta(\omega_y\cos\gamma - \omega_z\sin\gamma) \\ \dfrac{1}{\cos\vartheta}(\omega_y\cos\gamma - \omega_z\sin\gamma) \\ \omega_y\sin\gamma + \omega_z\cos\gamma \end{bmatrix} \tag{8}$$

The angle relationship equation is

$$\begin{cases} \sin\beta = \cos\theta[\cos\gamma\sin(\psi - \psi_c) + \sin\vartheta\sin\gamma\times \\ \qquad \cos(\psi - \psi_c)] - \sin\theta\cos\vartheta\sin\gamma \\ \sin\alpha = \dfrac{1}{\cos\beta}\{\cos\theta[\sin\vartheta\cos\gamma\cos(\psi - \psi_c) - \\ \qquad \sin\gamma\sin(\psi - \psi_c)] - \sin\theta\cos\vartheta\cos\gamma\} \\ \sin\gamma_c = \dfrac{1}{\cos\theta}[\cos\alpha\sin\beta\sin\vartheta - \sin\alpha\sin\beta\times \\ \qquad \cos\gamma\cos\vartheta + \cos\beta\sin\gamma\cos\vartheta] \end{cases} \tag{9}$$

According to equation (5), it can be obtained that

$$\begin{cases} \delta_x = \dfrac{1}{m_x^{\delta_x}}\left(\dfrac{M_x}{qSL} - m_x^{\beta}\beta - m_x^{\delta_y}\delta_y\right) \\ \delta_y = \dfrac{1}{m_y^{\delta_y}}\left(\dfrac{M_y}{qSL} - m_y^{\beta}\beta - m_y^{\delta_x}\delta_x\right) \\ \delta_z = \dfrac{1}{m_z^{\delta_z}}\left(\dfrac{M_z}{qSL} - m_z^{\alpha}\alpha\right) \end{cases} \tag{10}$$

From equation (10), we can get

$$\begin{cases} \delta_x = \dfrac{1}{m_x^{\delta_x}m_y^{\delta_y} - m_x^{\delta_y}m_y^{\delta_x}}\times \\ \qquad \left[m_y^{\delta_y}\left(\dfrac{M_x}{qSL} - m_x^{\beta}\beta\right) - m_x^{\delta_y}\left(\dfrac{M_y}{qSL} - m_y^{\beta}\beta\right)\right] \\ \delta_y = \dfrac{1}{m_x^{\delta_x}m_y^{\delta_y} - m_x^{\delta_y}m_y^{\delta_x}}\times \\ \qquad \left[m_x^{\delta_x}\left(\dfrac{M_y}{qSL} - m_y^{\beta}\beta\right) - m_y^{\delta_x}\left(\dfrac{M_x}{qSL} - m_x^{\beta}\beta\right)\right] \\ \delta_z = \dfrac{1}{m_z^{\delta_z}}\left(\dfrac{M_z}{qSL} - m_z^{\alpha}\alpha\right) \end{cases} \tag{11}$$

substitute equation (4) into equation (11) to obtain

$$\begin{cases} \delta_x = \dfrac{1}{m_x^{\delta_x}m_y^{\delta_y} - m_x^{\delta_y}m_y^{\delta_x}}\left\{\dfrac{1}{qSL}\{m_y^{\delta_y}[J_x\dot{\omega}_x \right. \\ \qquad + (J_z - J_y)\omega_z\omega_y] - m_x^{\delta_y}[J_y\dot{\omega}_y + \\ \qquad \left.(J_x - J_z)\omega_x\omega_z]\} + (m_x^{\delta_y}m_y^{\beta} - m_y^{\delta_y}m_x^{\beta})\beta\right\} \\ \delta_y = \dfrac{1}{m_x^{\delta_x}m_y^{\delta_y} - m_x^{\delta_y}m_y^{\delta_x}}\left\{\dfrac{1}{qSL}\{m_x^{\delta_x}[J_y\dot{\omega}_y \right. \\ \qquad + (J_x - J_z)\omega_x\omega_z] - m_y^{\delta_x}[J_x\dot{\omega}_x + \\ \qquad \left.(J_z - J_y)\omega_z\omega_y]\} + (m_y^{\delta_x}m_x^{\beta} - m_x^{\delta_x}m_y^{\beta})\beta\right\} \\ \delta_z = \dfrac{1}{m_z^{\delta_z}qSL}\left[J_z\dot{\omega}_z + (J_y - J_x)\omega_y\omega_x\right] - \dfrac{m_z^{\alpha}\alpha}{m_z^{\delta_z}} \end{cases} \tag{12}$$

Then substitute equation (7) into equation (12) to obtain

$$\delta_x = \frac{1}{m_x^{\delta_x} m_y^{\delta_y} - m_x^{\delta_y} m_y^{\delta_x}} \{\frac{1}{qSL} \{m_y^{\delta_y} J_x \ddot{\gamma} + (m_y^{\delta_y} J_x \times \sin\vartheta - m_x^{\delta_y} J_y \cos\vartheta \cos\gamma)\ddot{\psi} - m_x^{\delta_y} J_y \ddot{\vartheta} \sin\gamma + \{m_y^{\delta_y} [J_x \dot{\vartheta} \cos\vartheta + (J_z - J_y)(-\frac{1}{2}\dot{\psi} \cos^2\vartheta \times \sin 2\gamma + \dot{\vartheta} \cos\vartheta \cos 2\gamma)] - m_x^{\delta_y} [(-J_y + J_x - J_z)\dot{\vartheta} \sin\vartheta \cos\gamma - [(J_y + J_x - J_z)\dot{\gamma} + (J_x - J_z)\dot{\psi} \sin\vartheta]\cos\vartheta \sin\gamma]\}\dot{\psi} + [\frac{1}{2} m_y^{\delta_y} \times (J_z - J_y)\dot{\vartheta} \sin 2\gamma - m_x^{\delta_y} (J_y + J_x - J_z)\dot{\gamma} \times \cos\gamma]\dot{\vartheta}\} + (m_x^{\delta_y} m_y^{\beta} - m_y^{\delta_y} m_x^{\beta})\beta\} \tag{13}$$

$$\delta_y = \frac{1}{m_x^{\delta_x} m_y^{\delta_y} - m_x^{\delta_y} m_y^{\delta_x}} \{\frac{1}{qSL} \{-m_y^{\delta_x} J_x \ddot{\gamma} + (m_x^{\delta_x} J_y \times \cos\vartheta \cos\gamma - m_y^{\delta_x} J_x \sin\vartheta)\ddot{\psi} + m_x^{\delta_x} J_y \ddot{\vartheta} \sin\gamma + \{m_x^{\delta_x} [(-J_y + J_x - J_z)\dot{\vartheta} \sin\vartheta \cos\gamma - [(J_y + J_x - J_z)\dot{\gamma} + (J_x - J_z)\dot{\psi} \sin\vartheta]\cos\vartheta \sin\gamma] - m_y^{\delta_x} [J_x \dot{\vartheta} \cos\vartheta + (J_z - J_y)(-\frac{1}{2}\dot{\psi} \cos^2\vartheta \times \sin 2\gamma + \dot{\vartheta} \cos\vartheta \cos 2\gamma)]\}\dot{\psi} + [m_x^{\delta_x} (J_y + J_x - J_z)\dot{\gamma} \cos\gamma - \frac{1}{2} m_y^{\delta_x} (J_z - J_y)\dot{\vartheta} \sin 2\gamma]\dot{\vartheta}\} + (m_y^{\delta_x} m_x^{\beta} - m_x^{\delta_x} m_y^{\beta})\beta\} \tag{14}$$

$$\delta_z = \frac{1}{m_z^{\delta_z} qSL} \{-J_z \ddot{\psi} \cos\vartheta \sin\gamma + J_z \ddot{\vartheta} \cos\gamma + \{(J_z + J_y - J_x)\dot{\vartheta} \sin\vartheta \sin\gamma + [(-J_z + J_y - J_x)\dot{\gamma} + (J_y - J_x)\dot{\psi} \sin\vartheta]\cos\vartheta \cos\gamma\}\dot{\psi} + (-J_z + J_y - J_x)\dot{\gamma}\dot{\vartheta} \sin\gamma\} - \frac{m_z^{\alpha} \alpha}{m_z^{\delta_z}} \tag{15}$$

Let

$$\boldsymbol{u} = \begin{bmatrix} \delta_x \\ \delta_y \\ \delta_z \end{bmatrix} \tag{16}$$

$$\boldsymbol{x} = \begin{bmatrix} \gamma \\ \psi \\ \vartheta \end{bmatrix} \tag{17}$$

$$\boldsymbol{M}(\boldsymbol{x}) = \frac{1}{qSL} \begin{bmatrix} M_{11} & M_{12} & M_{13} \\ M_{21} & M_{22} & M_{23} \\ 0 & M_{32} & M_{33} \end{bmatrix} \tag{18}$$

$$\boldsymbol{D}(\boldsymbol{x}, \dot{\boldsymbol{x}}) = \frac{1}{qSL} \begin{bmatrix} 0 & D_{12} & D_{13} \\ 0 & D_{22} & D_{23} \\ 0 & D_{32} & D_{33} \end{bmatrix} \tag{19}$$

$$\boldsymbol{\xi}(\boldsymbol{x}, \dot{\boldsymbol{x}}) = \begin{bmatrix} \frac{m_x^{\delta_y} m_y^{\beta} - m_y^{\delta_y} m_x^{\beta}}{m_x^{\delta_x} m_y^{\delta_y} - m_x^{\delta_y} m_y^{\delta_x}} \beta \\ \frac{m_y^{\delta_x} m_x^{\beta} - m_x^{\delta_x} m_y^{\beta}}{m_x^{\delta_x} m_y^{\delta_y} - m_x^{\delta_y} m_y^{\delta_x}} \beta \\ -\frac{m_z^{\alpha}}{m_z^{\delta_z}} \alpha \end{bmatrix} \tag{20}$$

where,

$$\begin{cases} M_{11} = \dfrac{m_y^{\delta_y} J_x}{m_x^{\delta_x} m_y^{\delta_y} - m_x^{\delta_y} m_y^{\delta_x}} \\ M_{12} = \dfrac{m_y^{\delta_y} J_x \sin\vartheta - m_x^{\delta_y} J_y \cos\vartheta \cos\gamma}{m_x^{\delta_x} m_y^{\delta_y} - m_x^{\delta_y} m_y^{\delta_x}} \\ M_{13} = \dfrac{-m_x^{\delta_y} J_y \sin\gamma}{m_x^{\delta_x} m_y^{\delta_y} - m_x^{\delta_y} m_y^{\delta_x}} \\ M_{21} = \dfrac{-m_y^{\delta_x} J_x}{m_x^{\delta_x} m_y^{\delta_y} - m_x^{\delta_y} m_y^{\delta_x}} \\ M_{22} = \dfrac{m_x^{\delta_x} J_y \cos\vartheta \cos\gamma - m_y^{\delta_x} J_x \sin\vartheta}{m_x^{\delta_x} m_y^{\delta_y} - m_x^{\delta_y} m_y^{\delta_x}} \\ M_{23} = \dfrac{m_x^{\delta_x} J_y \sin\gamma}{m_x^{\delta_x} m_y^{\delta_y} - m_x^{\delta_y} m_y^{\delta_x}} \\ M_{32} = -\dfrac{J_z \cos\vartheta \sin\gamma}{m_z^{\delta_z}} \\ M_{33} = \dfrac{J_z \cos\gamma}{m_z^{\delta_z}} \end{cases}$$

$$D_{12} = \frac{1}{m_x^{\delta_x} m_y^{\delta_y} - m_x^{\delta_y} m_y^{\delta_x}} \{m_y^{\delta_y} [J_x \dot{\vartheta} \cos\vartheta + (J_z - J_y) \times (-\frac{1}{2}\dot{\psi} \cos^2\vartheta \sin 2\gamma + \dot{\vartheta} \cos\vartheta \cos 2\gamma)] - m_x^{\delta_y} \{(-J_y + J_x - J_z)\dot{\vartheta} \sin\vartheta \cos\gamma - [(J_y + J_x - J_z)\dot{\gamma} + (J_x - J_z)\dot{\psi} \sin\vartheta]\cos\vartheta \sin\gamma\}\}$$

$$D_{13} = \frac{1}{m_x^{\delta_x} m_y^{\delta_y} - m_x^{\delta_y} m_y^{\delta_x}} \{\frac{1}{2} m_y^{\delta_y} (J_z - J_y)\dot{\vartheta} \sin 2\gamma - m_x^{\delta_y} (J_y + J_x - J_z)\dot{\gamma} \cos\gamma\}$$

$$D_{22}=\frac{1}{m_x^{\delta_x}m_y^{\delta_y}-m_x^{\delta_y}m_y^{\delta_x}}\{m_x^{\delta_x}\{(-J_y+J_x-J_z)\dot{\vartheta}\sin\vartheta\cos\gamma$$
$$-[(J_y+J_x-J_z)\dot{\gamma}+(J_x-J_z)\dot{\psi}\sin\vartheta]\cos\vartheta\sin\gamma\}$$
$$-m_y^{\delta_x}[J_x\dot{\vartheta}\cos\vartheta+(J_z-J_y)(-\frac{1}{2}\dot{\psi}\cos^2\vartheta\sin 2\gamma$$
$$+\dot{\vartheta}\cos\vartheta\cos 2\gamma)]\}$$
$$D_{23}=\frac{1}{m_x^{\delta_x}m_y^{\delta_y}-m_x^{\delta_y}m_y^{\delta_x}}\{m_x^{\delta_x}(J_y+J_x-J_z)\dot{\gamma}\cos\gamma$$
$$-\frac{1}{2}m_y^{\delta_x}(J_z-J_y)\dot{\vartheta}\sin 2\gamma\}$$
$$D_{32}=\frac{1}{m_z^{\delta_z}}\{(J_z+J_y-J_x)\dot{\vartheta}\sin\vartheta\sin\gamma+[(-J_z+J_y-J_x)\dot{\gamma}$$
$$+(J_y-J_x)\dot{\psi}\sin\vartheta]\cos\vartheta\cos\gamma\}$$
$$D_{33}=\frac{1}{m_z^{\delta_z}}\dot{\gamma}\sin\gamma(-J_z+J_y-J_x)$$

So, the second-order fully actuated system model of the aircraft can be obtained as

$$\boldsymbol{M}(\boldsymbol{x})\ddot{\boldsymbol{x}}+\boldsymbol{D}(\boldsymbol{x},\dot{\boldsymbol{x}})\dot{\boldsymbol{x}}+\boldsymbol{\xi}(\boldsymbol{x},\dot{\boldsymbol{x}})=\boldsymbol{u} \tag{21}$$

3 Controller Design on Fully Actuated System Theory

Let

$$\boldsymbol{f}(\boldsymbol{x},\dot{\boldsymbol{x}})=-\boldsymbol{M}^{-1}(\boldsymbol{x})\left[\boldsymbol{D}(\boldsymbol{x},\dot{\boldsymbol{x}})\dot{\boldsymbol{x}}+\boldsymbol{\xi}(\boldsymbol{x},\dot{\boldsymbol{x}})\right] \tag{22}$$

and design fully actuated controller as

$$\boldsymbol{u}=-\boldsymbol{M}(\boldsymbol{x})\left[\boldsymbol{f}(\boldsymbol{x},\dot{\boldsymbol{x}})-\boldsymbol{v}\right] \tag{23}$$

where, $\boldsymbol{v}$ is the virtual angular accelerations to be designed. According to the equation (16), the control signal $\boldsymbol{u}$ generated by the controller represents the rudder deviation angles.

To achieve the calculation of aircraft control signals, let

$$\boldsymbol{v}=\begin{bmatrix}v_a\\v_b\\v_c\end{bmatrix} \tag{24}$$

Construct the relationship between attitude angle errors, attitude angular velocity errors and angular accelerations:

$$v_a=-\boldsymbol{K}_a\begin{bmatrix}\Delta\gamma\\\Delta\dot{\gamma}\end{bmatrix}=-\begin{bmatrix}K_{ap}&K_{ad}\end{bmatrix}\begin{bmatrix}\Delta\gamma\\\Delta\dot{\gamma}\end{bmatrix} \tag{25}$$

$$v_b=-\boldsymbol{K}_b\begin{bmatrix}\Delta\psi\\\Delta\dot{\psi}\end{bmatrix}=-\begin{bmatrix}K_{bp}&K_{bd}\end{bmatrix}\begin{bmatrix}\Delta\psi\\\Delta\dot{\psi}\end{bmatrix} \tag{26}$$

$$v_c=-\boldsymbol{K}_c\begin{bmatrix}\Delta\vartheta\\\Delta\dot{\vartheta}\end{bmatrix}=-\begin{bmatrix}K_{cp}&K_{cd}\end{bmatrix}\begin{bmatrix}\Delta\vartheta\\\Delta\dot{\vartheta}\end{bmatrix} \tag{27}$$

where, v_a is the virtual roll angle acceleration, v_b is the virtual yaw angle acceleration, v_c is the virtual pitch angle acceleration. $\Delta\gamma$, $\Delta\dot{\gamma}$, $\Delta\psi$, $\Delta\dot{\psi}$, $\Delta\vartheta$, $\Delta\dot{\vartheta}$ are the error values

$$\begin{cases}\Delta\gamma=\gamma-\gamma_{ref}\\\Delta\psi=\psi-\psi_{ref}\\\Delta\vartheta=\vartheta-\vartheta_{ref}\\\Delta\dot{\gamma}=\dot{\gamma}-\dot{\gamma}_{ref}\\\Delta\dot{\psi}=\dot{\psi}-\dot{\psi}_{ref}\\\Delta\dot{\vartheta}=\dot{\vartheta}-\dot{\vartheta}_{ref}\end{cases} \tag{28}$$

where, γ_{ref}, ψ_{ref} and ϑ_{ref} are angle commands, $\dot{\gamma}_{ref}$, $\dot{\psi}_{ref}$ and $\dot{\vartheta}_{ref}$ are angular velocity commands.

For aircraft attitude control, given the angle commands and angular velocity commands, the error value is calculated using equation (28), and the parameter matrixes $\boldsymbol{K}_a$, $\boldsymbol{K}_b$, $\boldsymbol{K}_c$ are adjusted. The virtual angular accelerations are calculated using equations (25) to (27) to further generate control signals. The following is a method for selecting $\boldsymbol{K}_a$, $\boldsymbol{K}_b$ and $\boldsymbol{K}_c$.

Substitute the controller model equation (23) into aircraft fully actuated model equation (21):

$$\begin{aligned}&\boldsymbol{M}(\boldsymbol{x})\ddot{\boldsymbol{x}}+\boldsymbol{D}(\boldsymbol{x},\dot{\boldsymbol{x}})\dot{\boldsymbol{x}}+\boldsymbol{\xi}(\boldsymbol{x},\dot{\boldsymbol{x}})\\&=-\boldsymbol{M}(\boldsymbol{x})\left[\boldsymbol{f}(\boldsymbol{x},\dot{\boldsymbol{x}})-\boldsymbol{v}\right]\end{aligned} \tag{29}$$

Substitute equation (22) into equation (29), we can get

$$\ddot{\boldsymbol{x}}=\boldsymbol{v} \tag{30}$$

Then we can get the state space equation:

$$\begin{bmatrix}\dot{\boldsymbol{x}}\\\ddot{\boldsymbol{x}}\end{bmatrix}=\begin{bmatrix}0&\boldsymbol{I}\\0&0\end{bmatrix}\begin{bmatrix}\boldsymbol{x}\\\dot{\boldsymbol{x}}\end{bmatrix}+\begin{bmatrix}0\\\boldsymbol{I}\end{bmatrix}\boldsymbol{v} \tag{31}$$

According to equations (25) to (27):

$$\boldsymbol{v}=-\boldsymbol{K}_p\left(\boldsymbol{x}-\boldsymbol{x}_{ref}\right)-\boldsymbol{K}_d\left(\dot{\boldsymbol{x}}-\dot{\boldsymbol{x}}_{ref}\right)+\ddot{\boldsymbol{x}}_{ref} \tag{32}$$

where

$$\boldsymbol{K}_p=\begin{bmatrix}K_{ap}&0&0\\0&K_{bp}&0\\0&0&K_{cp}\end{bmatrix} \tag{33}$$

$$\boldsymbol{K}_d=\begin{bmatrix}K_{ad}&0&0\\0&K_{bd}&0\\0&0&K_{cd}\end{bmatrix} \tag{34}$$

According to equation (33):

$$\boldsymbol{v}-\ddot{\boldsymbol{x}}_{ref}+\boldsymbol{K}_d\left(\dot{\boldsymbol{x}}-\dot{\boldsymbol{x}}_{ref}\right)+\boldsymbol{K}_p\left(\boldsymbol{x}-\boldsymbol{x}_{ref}\right)=0 \tag{35}$$

Let the error

$$\boldsymbol{e}=\boldsymbol{x}-\boldsymbol{x}_{ref} \tag{36}$$

then equation (35) is transformed into

$$\ddot{\boldsymbol{e}}+\boldsymbol{K}_d\dot{\boldsymbol{e}}+\boldsymbol{K}_p\boldsymbol{e}=0 \tag{37}$$

To ensure rapid stability of the system, i.e. convergence of $\ddot{\boldsymbol{e}}$, $\dot{\boldsymbol{e}}$ and $\boldsymbol{e}$ to 0, the parameter matrixes should be positively definite, i.e. $\boldsymbol{K}_p$ and $\boldsymbol{K}_d$ is greater than 0.

Combine equation (31) and (32), we can get

$$\begin{aligned}\begin{bmatrix}\dot{\boldsymbol{x}}\\ \ddot{\boldsymbol{x}}\end{bmatrix}&=\begin{bmatrix}0 & \boldsymbol{I}\\ 0 & 0\end{bmatrix}\begin{bmatrix}\boldsymbol{x}\\ \dot{\boldsymbol{x}}\end{bmatrix}+\begin{bmatrix}0\\ \boldsymbol{I}\end{bmatrix}\times\\ &\left\{\begin{bmatrix}-\boldsymbol{K}_p & -\boldsymbol{K}_d\end{bmatrix}\begin{bmatrix}\boldsymbol{x}-\boldsymbol{x}_{ref}\\ \dot{\boldsymbol{x}}-\dot{\boldsymbol{x}}_{ref}\end{bmatrix}+\ddot{\boldsymbol{x}}_{ref}\right\}\\ &=\begin{bmatrix}0 & \boldsymbol{I}\\ -\boldsymbol{K}_p & -\boldsymbol{K}_d\end{bmatrix}\begin{bmatrix}\boldsymbol{x}\\ \dot{\boldsymbol{x}}\end{bmatrix}+\\ &\begin{bmatrix}0\\ \boldsymbol{K}_p\boldsymbol{x}_{ref}+\boldsymbol{K}_d\dot{\boldsymbol{x}}_{ref}+\ddot{\boldsymbol{x}}_{ref}\end{bmatrix}\end{aligned}\tag{38}$$

Therefore, the characteristic equation is

$$\left|\lambda\boldsymbol{I}-\begin{bmatrix}0 & \boldsymbol{I}\\ -\boldsymbol{K}_p & -\boldsymbol{K}_d\end{bmatrix}\right|=0\tag{39}$$

Substituting equation (33) and (34) into equation (39) yields

$$\begin{aligned}&\lambda^6+\left(K_{ad}+K_{bd}+K_{cd}\right)\lambda^5+\\&\left(K_{ap}+K_{bp}+K_{cp}+K_{ad}K_{bd}+K_{ad}K_{cd}+K_{bd}K_{cd}\right)\lambda^4+\\&(K_{ap}K_{bd}+K_{ap}K_{cd}+K_{bp}K_{ad}+K_{bp}K_{cd}+K_{cp}K_{ad}+\\&K_{cp}K_{bd})\lambda^3+(K_{ap}K_{bp}+K_{ap}K_{cp}+K_{bp}K_{cp}+\\&K_{ap}K_{bd}K_{cd}+K_{bp}K_{ad}K_{cd}+K_{cp}K_{ad}K_{bd})\lambda^2+\\&(K_{ad}K_{bp}K_{cp}+K_{bd}K_{ap}K_{cp}+K_{cd}K_{ap}K_{bp})\lambda+\\&K_{ap}K_{bp}K_{cp}=0\end{aligned}\tag{40}$$

Solve equation (40) to obtain the poles as

$$\lambda_{1,2}=-\frac{1}{2}K_{ad}\pm\frac{1}{2}\sqrt{K_{ad}^2-4K_{ap}}$$

$$\lambda_{3,4}=-\frac{1}{2}K_{bd}\pm\frac{1}{2}\sqrt{K_{bd}^2-4K_{bp}}$$

$$\lambda_{5,6}=-\frac{1}{2}K_{cd}\pm\frac{1}{2}\sqrt{K_{cd}^2-4K_{cp}}$$

It is known that for second-order control systems, the control effect is better when the damping ratio $\varsigma=0.4\sim0.8$, and the relationship between the damping ratio and the poles is shown in the Fig 1.

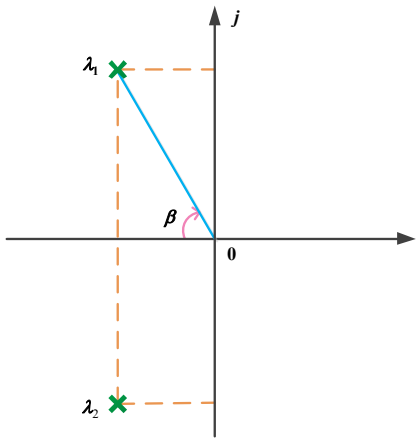

Fig. 1: The relationship between the damping ratio and the poles

Where, $\varsigma=\cos\beta$, β is the damping angle. Then:

$$\tan\beta=\frac{\sqrt{1-\varsigma^2}}{\varsigma}\tag{41}$$

Therefore, the range of values for the controller parameters can be determined as

$$\frac{4}{5}\sqrt{K_{ap}}\le K_{ad}\le\frac{8}{5}\sqrt{K_{ap}},\ K_{ap}>0$$

$$\frac{4}{5}\sqrt{K_{bp}}\le K_{bd}\le\frac{8}{5}\sqrt{K_{bp}},\ K_{bp}>0$$

$$\frac{4}{5}\sqrt{K_{cp}}\le K_{cd}\le\frac{8}{5}\sqrt{K_{cp}},\ K_{cp}>0$$

In summary, substitute equation (32) into equation (23), the attitude controller based on the theory of fully actuated system is obtained as follows:

$$\begin{aligned}\boldsymbol{u}=-\boldsymbol{M}(\boldsymbol{x})[&\boldsymbol{f}(\boldsymbol{x},\dot{\boldsymbol{x}})+\boldsymbol{K}_p\left(\boldsymbol{x}-\boldsymbol{x}_{ref}\right)\\&+\boldsymbol{K}_d\left(\dot{\boldsymbol{x}}-\dot{\boldsymbol{x}}_{ref}\right)-\ddot{\boldsymbol{x}}_{ref}]\end{aligned}\tag{42}$$

Therefore, the structural diagram of the attitude controller on the fully actuated system theory is as Fig. 2

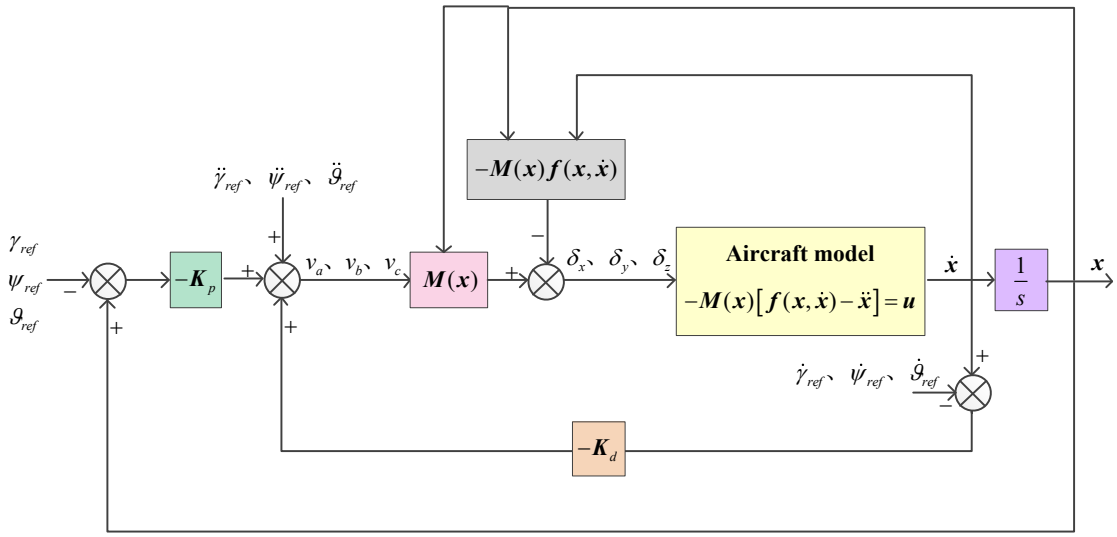

Fig. 2: Structure diagram of the attitude controller

The Lyapunov analysis method is used below to demonstrate the stability of the above control method.

When using the fully actuated controller to achieve attitude control, substituting the controller model equation (23) into the second-order fully actuated model equation (21) yields

$$\begin{aligned} &\boldsymbol{M}(\boldsymbol{x})\ddot{\boldsymbol{x}}+\boldsymbol{D}(\boldsymbol{x},\dot{\boldsymbol{x}})\dot{\boldsymbol{x}}+\boldsymbol{\xi}(\boldsymbol{x},\dot{\boldsymbol{x}}) \\ &\quad =-\boldsymbol{M}(\boldsymbol{x})\left[\boldsymbol{f}(\boldsymbol{x},\dot{\boldsymbol{x}})-\boldsymbol{v}\right] \end{aligned} \tag{43}$$

Substitute equation (22) into equation (29), we can get

$$\ddot{\boldsymbol{x}}=\boldsymbol{v} \tag{44}$$

By error expression equation (36), we can get

$$\ddot{\boldsymbol{e}}=\ddot{\boldsymbol{x}}-\ddot{\boldsymbol{x}}_{ref}=\boldsymbol{v}-\ddot{\boldsymbol{x}}_{ref} \tag{45}$$

According to the equation (35), the equation (45) is transformed into

$$\begin{aligned} \ddot{\boldsymbol{e}} &=-\boldsymbol{K}_d\left(\dot{\boldsymbol{x}}-\dot{\boldsymbol{x}}_{ref}\right)-\boldsymbol{K}_p\left(\boldsymbol{x}-\boldsymbol{x}_{ref}\right) \\ &=-\boldsymbol{K}_d\dot{\boldsymbol{e}}-\boldsymbol{K}_p\boldsymbol{e} \end{aligned} \tag{46}$$

Let

$$\boldsymbol{L}=\begin{bmatrix}\boldsymbol{e}\\ \dot{\boldsymbol{e}}\end{bmatrix} \tag{47}$$

$\boldsymbol{L}_e=0$ is an equilibrium state of the system, i.e:

$$\boldsymbol{e}=0,\ \dot{\boldsymbol{e}}=0$$

According to the equation (42), we can get

$$\dot{\boldsymbol{L}}=\begin{bmatrix}\dot{\boldsymbol{e}}\\ \ddot{\boldsymbol{e}}\end{bmatrix}=\begin{bmatrix}0 & \boldsymbol{I}\\ -\boldsymbol{K}_p & -\boldsymbol{K}_d\end{bmatrix}\begin{bmatrix}\boldsymbol{e}\\ \dot{\boldsymbol{e}}\end{bmatrix}=\boldsymbol{A}\boldsymbol{L} \tag{48}$$

Select the Lyapunov function be

$$\boldsymbol{V}(\boldsymbol{L})=\boldsymbol{L}^T\boldsymbol{P}\boldsymbol{L} \tag{49}$$

where, $\boldsymbol{P}$ satisfies the Lyapunov equation:

$$\boldsymbol{A}^T\boldsymbol{P}+\boldsymbol{P}\boldsymbol{A}=-\boldsymbol{I} \tag{50}$$

According to equation (49) and (50), when the parameter matrixes $\boldsymbol{K}_p$ and $\boldsymbol{K}_d$ satisfy the selection criteria, $\boldsymbol{P}$ is the unique positive definite solution matrix of the Lyapunov equation. Therefore, we can get $\boldsymbol{V}(\boldsymbol{L})>0$.

Taking the derivative of $\boldsymbol{V}(\boldsymbol{L})$:

$$\dot{\boldsymbol{V}}(\boldsymbol{L})=\dot{\boldsymbol{L}}^T\boldsymbol{P}\boldsymbol{L}+\boldsymbol{L}^T\boldsymbol{P}\dot{\boldsymbol{L}} \tag{51}$$

Substituting equation (48) into equation (51) yields

$$\begin{aligned} \dot{\boldsymbol{V}}(\boldsymbol{L}) &=\boldsymbol{L}^T\boldsymbol{A}^T\boldsymbol{P}\boldsymbol{L}+\boldsymbol{L}^T\boldsymbol{P}\boldsymbol{A}\boldsymbol{L} \\ &=\boldsymbol{L}^T\left(\boldsymbol{A}^T\boldsymbol{P}+\boldsymbol{P}\boldsymbol{A}\right)\boldsymbol{L} \\ &=-\boldsymbol{L}^T\boldsymbol{L} \end{aligned} \tag{52}$$

Therefore, $\dot{\boldsymbol{V}}(\boldsymbol{L})<0$.

According to the Lyapunov asymptotic stability theorem, the control system is stable in equilibrium state $\boldsymbol{e}=0,\ \dot{\boldsymbol{e}}=0$.

4 Simulation

The attitude controller designed on the fully actuated system theory is applied to control the middle and final stages of the aircraft, and the simulation results are shown below

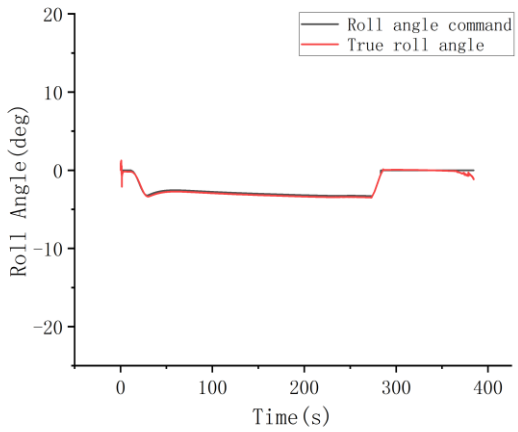

(a)

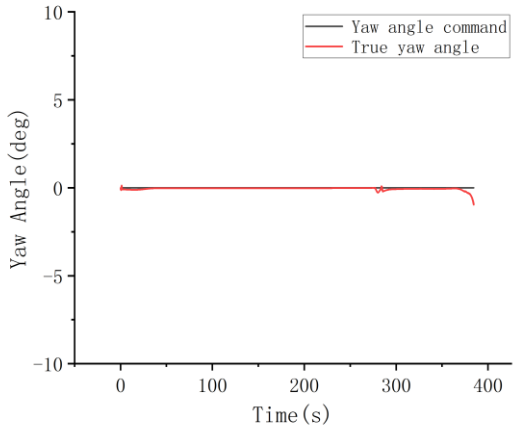

(b)

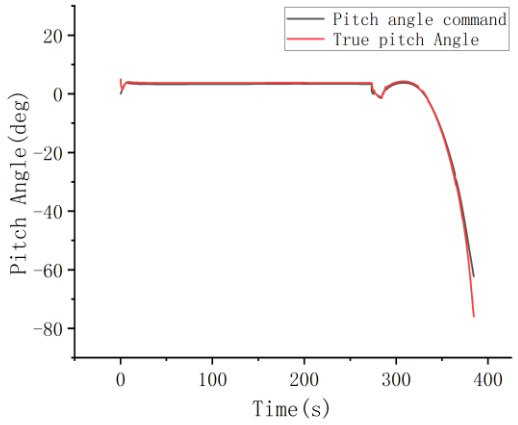

(c)

Fig. 3: The attitude angle curve

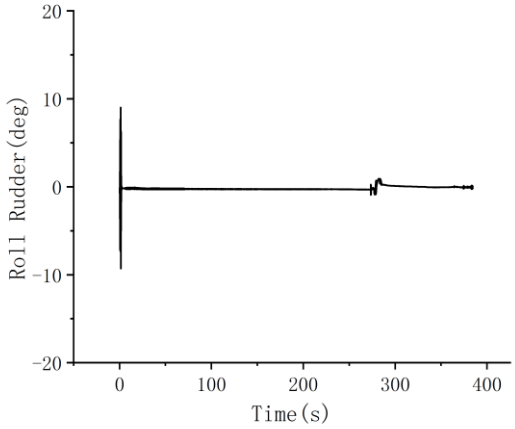

(a)

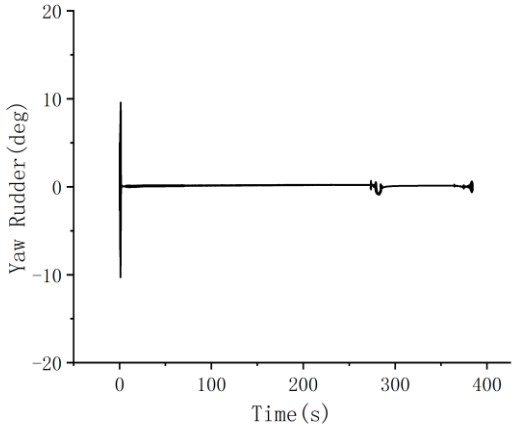

(b)

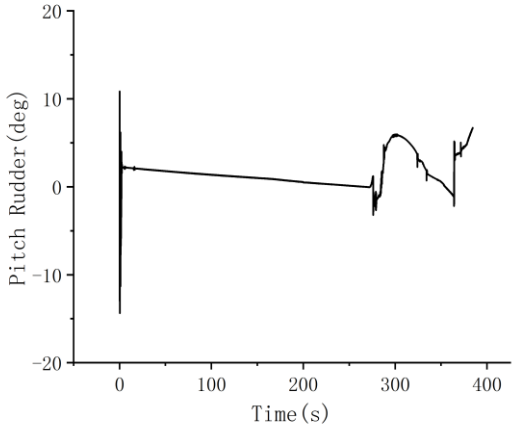

(c)

Fig. 4: The rudder angle curve

Under the attitude control on the fully actuated system theory, it is possible to achieve smooth tracking of roll angle command, yaw angle command and pitch angle command, as shown in Fig. 3. At the same time, according to Fig. 4, it can be concluded that the controller has good speed, and the rudder angles of the roll, yaw and pitch channels can be quickly adjusted in a short period of time, then maintain stable control of the attitude.

5 Conclusion

This paper first establishes a second-order fully actuated system model through the motion model of the aircraft in the middle and final stages, and designs an fully actuated attitude controller based on it. At the same time, the stability of the controller is proved through Lyapunov stability analysis method. Subsequently, the controller was integrated into the aircraft model simulation and achieved good attitude control performance under benchmark conditions. At the level of scientific theory, this paper explores a new type of nonlinear control method that utilizes the nonlinear model of the aircraft for control, replacing small disturbance linearization. At the level of engineering practice, this paper has been seeking new control methods for aircraft in engineering, solving control problems that arise under nonlinear and coupling conditions, and reserving a new approach for achieving stable control of aircraft in engineering.

References

[1] X. D. Li, B. Xian, C. Diao, Y. P. Yu, K. Y. Yang, Y. Zhang, Output feedback control of hypersonic vehicles based on neural network and high gain observer. *Science China Information Sciences*, 2011, 54(3): 429-447.

[2] H. An, J. X. Liu, C. H. Wang, L. G. Wu, Disturbance observer-based antiwindup control for air-breathing hypersonic vehicles. *IEEE Transactions on Industrial Electronics*, 2016, 63(5): 3038-3049.

[3] G. H. Wu, X. Y. Meng, Nonlinear disturbance observer based robust backstepping control for a flexible air-breathing hypersonic vehicle. *Aerospace Science and Technology*, 2016, 54: 174-182.

[4] M. Chen, B. Jiang, Robust attitude control of near space vehicles with time-varying disturbances. I*nternational Journal of Control Automation & Systems*, 2013, 11(1): 182-187.

[5] G. R. Duan, High-order fully actuated system approaches: Part I. Models and basic procedure. *International Journal of Systems Science*, 52(2): 422-435, 2021.

[6] G. R. Duan, Substability and substabilization: control of subfully actuated systems. *IEEE Transactions on Cybernetics*, 2023, 1-14.

Proceedings of the 3rd Conference on Fully Actuated System Theory and Applications
May 10-12, 2024, Shenzhen, China

Global prescribed performance control for nonlinear interconnected systems: A high-order fully actuated system approach

Yu Zhang, Guopin Liu, Changchun Hua, Yana Yang
School of Electrical Engineering,Yanshan University, Qinhuangdao, 066004, China
E-mail: guopinliu@outlook.com

Abstract: This paper considers the stabilization problem for nonlinear interconnected systems with prescribed performance via high-order fully actuated (HOFA) system approach. Based on a novel performance function in which the initial value is infinity, the effect of the initial value is eliminated for the prescribed performance method. Then, by some transformation, the nonlinear interconnected system is transformed into a HOFA system, and a decentralized controller is designed via the HOFA system approach. Finally, a numerical simulation is provided to substantiate our method.

Key Words: Nonlinear interconnected system, High-order fully actuated system, Prescribed performance control

1 Introduction

Interconnected systems exist in practical engineering, such as network systems [1], power systems [2], and so on, which consist of several subsystems coupled to each other and received more attention in recent years [3–7]. Among them, decentralized control is a method to deal with interconnected terms by their own states' variables in subsystems. In [5–8], various interconnected systems were investigated for stabilization and tracking problems with the decentralized method.

At present, practical engineering not only requires basic stability for the system but also imposes some constraints on transient response and steady-state performance. The prescribed performance control (PPC) method could constrain the transient and steady-state performance of the system. The prescribed performance control problem for MIMO and SISO systems are considered in [9, 10]. [11, 12] consider prescribed performance stabilization and tracking problems for interconnected time-delay systems. In [13], the author gives the prescribed-performance-driven event-triggered machine for a class of uncertain nonlinear interconnected systems, which reduces the communication burdens and simply the system design produced. However, all of those methods have requirements for the initial values of the system. In [14], based on a novel performance function which infinity at initial, the author achieves global prescribed performance for an uncertain nonlinear system and removes the limitation on the initial value.

HOFA systems widely exist and many practical systems could be described by HOFA systems model. In [15], Duan first proposes the significant advantages of HOFA approach. Based on the method, a nonlinear system could be transformed into the HOFA system, and the controller could be easily designed. In recent years, the HOFA system approach has been generalized from general nonlinear systems to nonlinear time-delay systems [16, 17] and multi-agent systems[18]. [17] considers the stabilization problem for a nonlinear time-delay system via the HOFA system approach and a novel Lyapunov-Krasovskii functional. Based on the HOFA system approach, the author considers the coordinative control problem for nonlinear multi-agents with communication delay in [18]. In [19], the author considers the partially prescribed time control problem via the HOFA system approach for the interconnected integrator chain system. However, there is little work considering nonlinear interconnected systems via the HOFA system approach, and no work considers the global prescribed performance control for interconnected systems via the method. Motivated by the above observation, this work considers global prescribed performance problems for interconnected systems with a more general model via the HOFA system approach.

This paper is organized as follows: Section 2 presents the problem formulation. The performance function and system transformation are also given in this section. The controller design and stability analysis are presented in Section 3. Section 4 gives a simulation and the conclusion is given in Section 5.

Notation: In this paper, $\lambda(A_i)$ represents the eigenvalues of matrix A_i, $Re(s)$ represent the real part of complex number s. $g^{(n)}(t)$ denote the nth derivative of $g(t)$. $\Re$ denote the set of real number; $\Re^n$ denote the n-dimensional Euclidean space. $f(\cdot) \in C^n$ means function $f(\cdot)$ has continuous derivatives up to the order n. For vector $x_i \in \Re^n$, positive define matrix $A_i \in \Re^{n\times n}$ and $P_i \in \Re^{kn\times n}$, one has the following definition

$$\|x_i\| = (x_i^T x_i)^{\frac{1}{2}},\ \ x_i^{(0\sim k-1)} = \begin{bmatrix} x_i \\ \dot{x}_i \\ \vdots \\ x_i^{(k-1)} \end{bmatrix} \in \Re^{kn},$$

$$A_i^{0\sim k-1} = [A_{i0},\ A_{i1},\ \cdots,\ A_{i(k-1)}] \in \Re^{n\times kn},$$

$$P_i(A_i^{0\sim k-1}) = [P_{i1}, \cdots, P_{ik}]^T \in \Re^{kn\times kn},$$

This work is supported in part by the National Natural Science Foundation of China under Grant 62103355, 62373319; in part by the Hebei Natural Science Foundation under Grant F2023203079; in part by the Science Research Project of Hebei Education Department under Grant BJK2023113, and in part by the Hebei Innovation Capability Improvement Plan Project under Grant 22567619H.

$$\Phi(A_i^{0\sim k-1}) = \begin{bmatrix} 0 & I & 0 & 0 \\ \vdots & 0 & \ddots & 0 \\ 0 & 0 & 0 & I \\ -A_{i0} & -A_{i1} & \cdots & -A_{i(k-1)} \end{bmatrix} \in \Re^{kn\times kn}$$

2 System formulation and preliminaries

2.1 System Description

In this paper, we consider the following interconnected systems

$$\begin{cases} \dot{x}_{ij}(t) = g_{ij}(\bar{x}_{ij}(t))x_{i(j+1)}(t) + f_{ij}(\bar{x}_{ij}(t)) \\ \dot{x}_{in_i}(t) = g_{in_i}(\bar{x}_{in_i}(t))u_i(t) + f_{in_i}(\bar{x}_{in_i}(t)) \\ \qquad\qquad + h_i(t, y_1(t), \ldots, y_N(t)) \\ y_i(t) = x_{i1}(t) \end{cases} \tag{1}$$

where $1 \le i \le N$, N is the number of subsystems, $j = 1, \ldots\ldots, n_i - 1$. $x_i(t) = [x_{i1}(t), x_{i2}(t), \ldots, x_{in_i}(t)]^T \in \Re^{n_i}$, $u_i(t) \in \Re$, and $y_i(t) \in \Re$ represent the system state, control input and output of the ith subsystem, respectively. $\bar{x}_{ij}(t) = [x_{i1}(t), x_{i2}(t), \ldots, x_{ij}(t)]^T \in \Re^j$. The smooth nonlinear functions $h_i(\cdot) \in \Re$ and $f_{ij}(\cdot) \in \Re$ satisfy that $f_{ij}(0, 0, \ldots, 0) = h_i(t, 0, 0, \ldots, 0) = 0$. The nonlinear function $g_{ij}(\cdot) \in \Re$ is nonsingular and bounded for all $x_{ij} \in \Re$.

The objective of this paper is to design a decentralized controller for the system (1) via the HOFA approach to achieve global prescribed performance. The following Assumption and Lemmas are given.

Assumption 1: The interconnected function $h_i(\cdot)$ satisfy the following inequation:

$$|h_i(t, y_1(t), \ldots, y_N(t))|^2 \le \sum_{k=1}^{N} c_{ik}\bar{h}_{ik}(y_k(t)) \tag{2}$$

where c_{ik} is known constant, $\bar{h}_{ik}(\cdot)$ is known continue function.

Lemma 1: For the ith system, assume that matrix $A_i \in \Re^{n_i\times n_i}$ satisfies $Re(\lambda(A_i)) < -\mu_i, i = 1, \ldots, N$. There exist a positive matrix $P_i \in \Re^{n_i\times n_i}$ such that $A_i^T P_i + P_i A_i < -\mu_i P_i$.

Lemma 2: For $\mu_i > 0$, there exist a set of matrix $A_i \in \Re^{n_i\times n_i}$, such that $Re(\lambda(\Phi(A_i^{0\sim n_i-1}))) < -\frac{\mu_i}{2}$, $i = 1 \ldots N$.

According to Lemma 1-2, for the ith system, one can obtain that there exist a positive constant μ_i such that $\Phi^T(A_i^{0\sim n_i-1})P_i(A_i^{0\sim n_i-1}) + P_i(A_i^{0\sim n_i-1})\Phi(A_i^{0\sim n_i-1}) \le -\mu_i P_i(A^{0\sim n_i-1})$.

Lemma 3: For real numbers a and b, in which $b > 0$, one has

$$a - \frac{a^2}{4b} \le b$$

2.2 Global Performance Function

At first, we introduce the following lemma.

Lemma 4 [14]: Consider the following function with scalar variable x_i:

$$Q_i(x_i(t)) = \frac{\sqrt{\xi_i}x_i}{\sqrt{1 - x_i^2}} \tag{3}$$

where ξ_i is positive constant. Then, $Q_i(x_i(t))$ is strictly increasing with respect to $x_i(t)$ over the interval $(-1, 1)$.

Design the performance function

$$Q_i(t) = \frac{\sqrt{\xi_i}\Lambda_i(t)}{\sqrt{1 - \Lambda_i^2(t)}} \tag{4}$$

where $\Lambda_i(t)$ is a smooth function that satisfies the following properties:

1) $\Lambda_i(t) \in C^{n_i}$;
2) $\Lambda_i(0) = 1$, $\Lambda_i(t)$ is monotonically decreasing in $t \ge 0$;
3) $\lim_{t\to+\infty} \Lambda_i(t) = b_{ti}$ with $0 < b_{ti} \ll 1$ being a constant.

Then, one can know $Q_i(t)$ is monotonically decreasing on time t, and it holds that

$$\begin{cases} Q_i(0) = Q_i(\Lambda_i(0)) = Q_i(1) = \infty \\ \lim_{t\to+\infty} Q_i(\Lambda_i(t)) \to Q_i(b_{ti}) = \frac{\sqrt{\xi_i}b_{ti}}{\sqrt{1 - b_{ti}^2}}. \end{cases} \tag{5}$$

In fact, $Q_i(t)$ defined by (4) is the performance function, namely, if the following condition

$$-Q_i(\Lambda_i(t)) < y_i < Q_i(\Lambda_i(t)) \tag{6}$$

can be satisfied, then the output signal will be constrained with prescribed performance. In addition, since the initial value of $Q_i(t)$ is infinity, one can achieve global prescribed performance control objective. To ensure that condition (6) can be satisfied, introduce the following variable

$$\eta_i(y_i(t)) = \frac{y_i(t)}{\sqrt{y_i^2(t) + \xi_i}} \tag{7}$$

where ξ_i is parameter as in (3). Then, $\eta_i(y_i(t))$ has the following features

1) $\eta_i(y_i(t))$ is strictly increasing with variable $y_i(t)$;
2) $\eta_i(y_i(t)) \in (-1, 1)$ with $\lim_{y_i\to+\infty} \eta_i(y_i(t)) = 1$ and $\lim_{y_i\to-\infty} \eta_i(y_i(t)) = -1$;
3) $\eta_i(y_i(t)) = 0 \Longleftrightarrow y_i(t) = 0$.

Now, we define the following transformation variable

$$s_i(t) = \frac{\rho_i(t)}{1 - \rho_i^2(t)} \tag{8}$$

in which

$$\rho_i(t) = \frac{\eta_i(y_i)}{\Lambda_i(t)}. \tag{9}$$

According to the properties of $\eta_i(\cdot)$, one have $\rho_i(0) = \eta_i(y_i(0)) \in (-1, 1)$. For any initial conditional $\rho_i(0) \in (-1, 1)$, one has

$$\begin{cases} \rho_i(t) \to 1 \Leftrightarrow s_i(t) \to +\infty \\ \rho_i(t) \to -1 \Leftrightarrow s_i(t) \to -\infty \end{cases} \tag{10}$$

which means for any $\eta_i(0) \in (-1, 1)$, if one can ensure the boundness of $s_i(t)$, then ρ_i will be within the small set $\Xi = \{\rho_i(t) \in \Re | -1 < \rho_i < 1\}$. In addition, for $\forall t \ge 0$, there exist a small constant $0 < \delta_i < 1$ such that $\delta_i < |\rho_i|$. According to (9), one have

$$-\Lambda_i(t) < -\delta_i\Lambda_i(t) < \eta_i < \delta_i\Lambda_i(t) < \Lambda_i(t) \tag{11}$$

Note that, $Q(\eta_i(y_i(t))) = y_i(t)$, then performance (11) yields

$$-Q_i(t) < y_i(t) < Q_i(t) \tag{12}$$

which clearly indicates that performance condition (6) is satisfy. Meanwhile, the initial value for $Q(t)$ is infinity, which eliminates the limitation of initial values in the PPC method. Based on the transformation of this section, the prescribed tracking performance control problem is transferred to stabilization of variable $s_i(t)$ given by (8), whose time derivative is derived as

$$\dot{s}_i(t) = \frac{1+\rho_i^2}{(1-\rho_i^2)^2}\dot{\rho}_i(t). \tag{13}$$

According to (9) and (7), one has

$$\begin{aligned}\dot{\rho}_i(t) &= -\frac{\dot{Q}(t)}{Q^2(t)}\eta_i(y_i(t)) + \frac{1}{Q(t)}\dot{\eta}_i(y_i(t)) \\ &= -\frac{\dot{Q}(t)}{Q^2(t)}\eta_i(y_i(t)) + \frac{1}{Q(t)}\frac{\xi_i\dot{y}_i(t)}{(y_i^2(t)+\xi_i)\sqrt{y_i^2(t)+\xi_i}}.\end{aligned}$$

Substituting it into (13), we obtain that

$$\begin{aligned}\dot{s}_i(t) &= \sigma_{i1}(t)\dot{y}_i(t) + \sigma_{i2}(t) \\ &= \sigma_{i1}g_{i1}(x_{i1})x_{i2}(t) + \sigma_{i1}f_{i1}(x_{i1}(t)) + \sigma_{i2} \\ &= G_{i1}x_{i2}(t) + F_{i1}\end{aligned} \tag{14}$$

where

$$\begin{aligned}\sigma_{i1}(t) &= \frac{1+\rho_i^2}{(1-\rho_i^2)^2}\frac{\xi_i\dot{y}_i(t)}{Q(t)((y_i^2(t)+\xi_i)\sqrt{(y_i^2(t)+\xi_i}} \\ \sigma_{i2}(t) &= -\frac{1+\rho_i^2}{(1-\rho_i^2)^2}\frac{\dot{Q}(t)}{Q^2(t)}\eta_i(y_i(t)) \\ G_{i1}(t) &= \sigma_{i1}(t)g_{i1}(y_i(t)) \\ F_{i1}(t) &= \sigma_{i1}(t)f_{i1}(y_i(t)) + \sigma_{i2}(t)\end{aligned}$$

2.3 System Transform

In this subsection, we aim to transform the ith subsystem into a high-order fully actuated system. According to work [20], we consider the following transformation

$$\begin{cases} z_i = s_i \\ x_{i2} = G_{i1}^{-1}(\dot{z}_i - F_{i1}(z,t)) \\ x_{i(j+1)} = G_{ij}^{-1}(z^{(0\sim j-1)},t) \\ \qquad \times [z_i^{(j)} - F_{i(j+1)}(z_i^{(0\sim j-1)},t)] \\ \quad j = 2,\ldots,n_i-2 \\ x_{in_i} = G_{i(n_i-1)}^{-1}(z^{(0\sim n_i)},t) \\ \qquad \times [z_i^{(n_i)} - F_{in_i}(z_i^{(0\sim n_i-1)},t) \\ \qquad\quad - h_i(y_1,\ldots,y_N)] \end{cases} \tag{15}$$

Then system (1) can be transformed into the following high-order fully actuated system.

$$z_i^{(n_i)} = G_{in_i}u_i + F_{in_i} + H_i \tag{16}$$

where

$$\begin{aligned}&G_{ij}(z_i^{0\sim j-1},t) = G_{i(j-1)}(z_i^{(0\sim j-1)},t)g_{ij}(\bar{x}_{ij},t) \\ &F_{ij}(z_i^{(0\sim j-1)},t) \\ &= \dot{F}_{i(j-1)}(z_i^{(0\sim j-2)},t) + \dot{G}_{i(j-1)}(z_i^{(0\sim j-2)},t)x_{ij} \\ &\quad + G_{i(j-1)}(z_i^{(0\sim j-2)},t)f_{ij}(\bar{x}_{ij}) \\ &H_i(y_1,\ldots,y_N) = G_{i(n_i-1)}(z_i^{(0\sim n_i-2)},t) \\ &\qquad\qquad \times h_i(y_1,\ldots,y_N) \\ &\qquad\quad j = 1,\ldots,n_i\end{aligned} \tag{17}$$

3 Main Results

For system (16), we design the following controller for the ith subsystem:

$$u_i(t) = -G_{in_i}^{-1}(u_{i0} + u_{i1}) \tag{18}$$

where

$$\begin{aligned}u_{i0} &= A^{0\sim n_i-1}z_i^{(0\sim n_i-1)} + F_{in_i} \\ u_{i1} &= \frac{G_{i(n_i-1)}^2}{4\epsilon_i}\sum_{k=1}^{N}c_{ki}\bar{h}_{ki}^2(y_i)P_L^T z_i^{(0\sim n_i-1)}\end{aligned} \tag{19}$$

in which ϵ_i is positive design constant.

The main result is given as follow:

Theorem 1: Consider system (1) that satisfies Assumption 1, under transformation (15), the controller (18) could ensure that all signals of the system are bounded, and the prescribed performance of the output signal can be guaranteed which is independent of the initial value of system's state.

Proof. For the ith subsystem, substituting the (18) and (19) into (16), one can obtain the following close-loop system.

$$z_i^{(n)} + A^{0\sim n_i-1}z_i^{(0\sim n_i-1)} = H_i - u_{i1} \tag{20}$$

which also could be written as

$$\dot{z}^{(0\sim n_i-1)} = \Phi(A_i^{0\sim n_i-1})z_i^{(0\sim n_i-1)} + \begin{bmatrix} 0_{n_i-1} \\ H_i - u_{i1} \end{bmatrix} \tag{21}$$

choose the following Lyapunov function

$$V_i = \frac{1}{2}\left(z_i^{(0\sim n_i-1)}\right)^T P_i(A_i^{0\sim n_i-1})z_i^{(0\sim n_i-1)} \tag{22}$$

With the help of Lemma 1-2, one can get that

$$\begin{aligned}\dot{V}_i =& \frac{1}{2}\left(\dot{z}_i^{(0\sim n_i-1)}\right)^T P_i(A_i^{0\sim n_i-1})z_i^{(0\sim n_i-1)} \\ &+ \frac{1}{2}\left(z_i^{(0\sim n_i-1)}\right)^T P_i(A_i^{0\sim n_i-1})\dot{z}_i^{(0\sim n_i-1)} \\ =& \frac{1}{2}\left(\dot{z}_i^{(0\sim n_i-1)}\right)^T \Big(\Phi^T(A_i^{0\sim n_i-1})P_i(A_i^{0\sim n_i-1}) \\ &+ P_i(A_i^{0\sim n_i-1})\Phi(A_i^{0\sim n_i-1})\Big)z_i^{(0\sim n_i-1)} \\ &+ \left(z_i^{(n_i-1)}\right)^T P_i(A_i^{0\sim n_i-1})\begin{bmatrix} 0_{n_i-1} \\ H_i - u_{i1} \end{bmatrix} \\ \leq& -\mu_i V_i + \left(z_i^{(n_i-1)}\right)^T P_{Li}(A_i^{0\sim n_i-1})(H_i - u_{i1})\end{aligned} \tag{23}$$

where

$$P_{Li}(A_i^{0\sim n_i-1}) = P_i(A_i^{0\sim n_i-1}) \begin{bmatrix} 0_{n_i-1} \\ I \end{bmatrix}$$

According to Assumption 1 and Lemma 3, one has

$$\begin{aligned}
&\left(z_i^{(n_i-1)}\right)^T P_{Li}(A_i^{0\sim n_i-1})(H_i - u_{i1}) \\
\leq &\left\| \left(z_i^{(n_i-1)}\right)^T P_{Li} \right\| G_{i(n_i-1)} \sum_{k=1}^{N} c_{ik}\bar{h}_{ik}(y_k) \\
&- \left(z_i^{(n_i-1)}\right)^T P_{Li} \frac{G_{i(n_i-1)}^2}{4\epsilon_i} \sum_{k=1}^{N} c_{ki}\bar{h}_{ki}^2(y_i) P_L^T z_i^{(0\sim n_i-1)} \\
\leq &\left\| \left(z_i^{(n_i-1)}\right)^T P_{Li} \right\| G_{i(n_i-1)} \sum_{k=1}^{N} c_{ik}\bar{h}_{ik}(y_k) \\
&- \frac{G_{i(n_i-1)}^2}{4\epsilon_i} \left\| \left(z_i^{(n_i-1)}\right)^T P_{Li} \right\|^2 \sum_{k=1}^{N} c_{ik}\bar{h}_{ik}^2(y_k) \\
&+ \frac{G_{i(n_i-1)}^2}{4\epsilon_i} \left\| \left(z_i^{(n_i-1)}\right)^T P_{Li} \right\|^2 \\
&\times \left(\sum_{k=1}^{N} (c_{ki}\bar{h}_{ki}^2(y_i) - c_{ik}\bar{h}_{ik}^2(y_k)) \right) \\
\leq &\frac{G_{i(n_i-1)}^2}{4\epsilon_i} \left\| \left(z_i^{(n_i-1)}\right)^T P_{Li} \right\|^2 \\
&\times \left(\sum_{k=1}^{N} (c_{ki}\bar{h}_{ki}^2(y_i) - c_{ik}\bar{h}_{ik}^2(y_k)) \right) \\
&+ \epsilon_i \sum_{k=1}^{N} c_{ik}
\end{aligned} \tag{24}$$

For the whole interconnected system, choose the Lyapunov function as $V = \sum_{i=1}^{N} V_i$, note that

$$\sum_{i=1}^{N}\sum_{k=1}^{N} c_{ki}\bar{h}_{ki}^2(y_i) = \sum_{i=1}^{N}\sum_{k=1}^{N} c_{ik}\bar{h}_{ik}^2(y_k)$$

Then, one has

$$\begin{aligned}
\dot{V} &\leq -\sum_{i=1}^{N} \mu_i V_i + \sum_{i=1}^{N}\sum_{k=1}^{N} c_{ik}\epsilon_i \\
&\leq -\mu V + \epsilon
\end{aligned} \tag{25}$$

where $\epsilon = \sum_{i=1}^{N}\sum_{k=1}^{N} c_{ik}\epsilon_i$, $\mu = \min\{\mu_1, \ldots, \mu_N\}$. By (25), one can obtain the boundness of s_i, which means the output signal for each subsystem y_i satisfies the prescribed performance. In addition, the initial value for the prescribed function is infinity. Thus, the PPC method removes the effection of the initial value in this paper. Meanwhile, then x_{i2} is bounded with the boundness of it $z_{i1}^{(1)}$. In this way, one can get the boundness of x_{ij} and $z_{ij}^{(j)}$. Thus, the control signal u_i is also bounded. Therefore, all signals of the closed-loop system are bounded. The proof ends. □

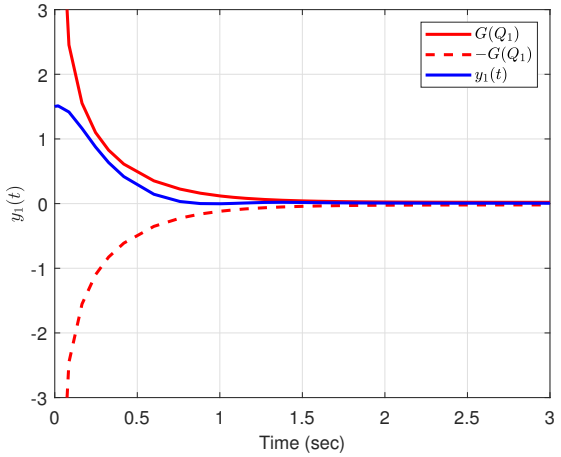

Fig. 1: Response of output signal $y_1(t)$

4 simulation

To verify the effectiveness of methods, consider the following example of nonlinear interconnected systems:

$$\begin{cases}
\dot{x}_{11}(t) = x_{12}(t) + f_{11}(\bar{x}_{11}) \\
\dot{x}_{12}(t) = u_1(t) + f_{12}(\bar{x}_{12}) + h_1(y_1, y_2) \\
y_1(t) = x_{11}(t) \\
\dot{x}_{21}(t) = x_{22}(t) + \varphi_{21}(\bar{x}_{21}) \\
\dot{x}_{22}(t) = u_2(t) + f_{22}(\bar{x}_{22}) + h_2(y_1, y_2) \\
y_2(t) = x_{21}(t)
\end{cases} \tag{26}$$

where

$$\begin{aligned}
f_{11} &= \sin(x_{11}(t)) \\
f_{12} &= x_{11}^2(t) + \sin(x_{12}(t)) \\
f_{21} &= \cos(x_{21}(t)) \\
f_{22} &= x_{21}^2(t) + \cos(x_{22}(t)) \\
h_2 &= h_1 = \cos(x_{21}(t)) + \sin(x_{11}(t))
\end{aligned}$$

For the performance function, select time-scaling function as $\Lambda_1(t) = 0.99e^{-3t} + 0.01$ and $\Lambda_2(t) = 0.99e^{-3t} + 0.01$. The parameter ξ_i is selected as $\xi_1 = \xi_2 = 4$. Then we can get performance function and transformation immediately. The controller design as:

$$\begin{aligned}
u_i &= -G_{i2}^{-1}(u_{i0} + u_{i1}) \\
u_{i0} &= A^{0\sim 1} z_i^{(0\sim 1)} + F_{i2} \\
u_{i1} &= \frac{G_{i1}^2}{4\epsilon_i} \sum_{k=1}^{N} c_{ik}\bar{h}_{ki}^2(y_i) P_L^T z_i^{(0\sim 1)}
\end{aligned}$$

where

$$\sum_{k=1}^{N} c_{k1}\bar{h}_{k1}^2(y_1) = \sum_{k=1}^{N} c_{k2}\bar{h}_{k2}^2(y_1) = 2\cos^2(x_{11}) + 3\sin^2(x_{11})$$

According to [19], one have $A_1^{0\sim 1} = A_2^{0\sim 1} = [11.25 \;\; 6]$, $P_{L1}^T = P_{L2}^T = [0.002 \;\; 0.0006]$. Select the initial values as $[x_{11}(0) \;\; x_{12}(0) \;\; x_{21}(0) \;\; x_{22}(0)]^T = [1.5 \;\; 0.2 \;\; -1 \;\; 0.5]^T$.

The results of the simulation are depicted in Figs 1-4. Fig.1 and 2 show that the output signal of each subsystem

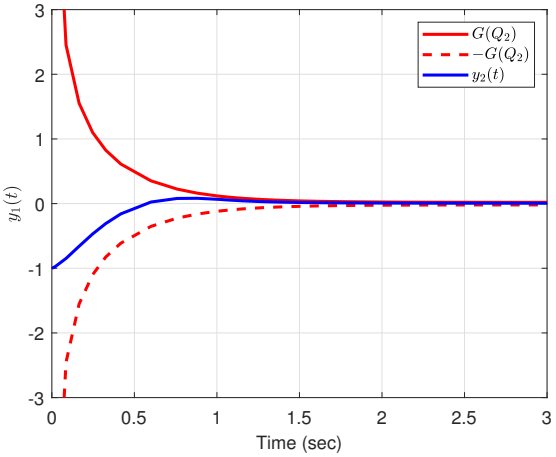

Fig. 2: Response of output signal $y_2(t)$

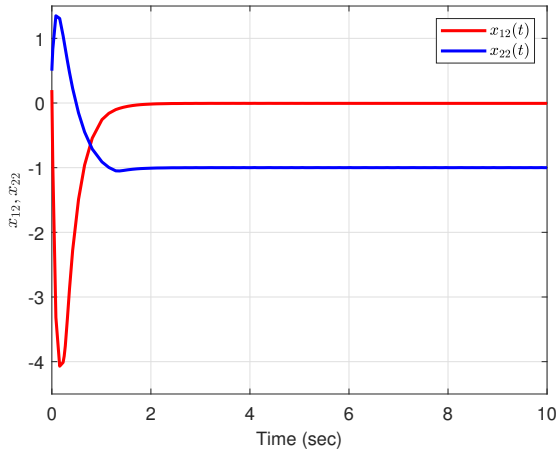

Fig. 3: Response of states x_{12} and x_{22}

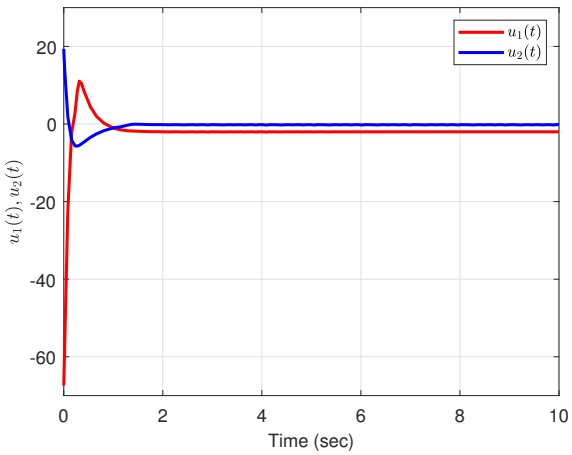

Fig. 4: Response of control signals u_1 and u_2

could be within the region of performance function. Fig.3 shows the response of state variable x_{12} and x_{22} and Fig.4 shows the control signal $u_i(t), i = 1, 2$ for each subsystem, respectively.

5 Conclusion

This paper considers the prescribed performance control problems for interconnected systems. Based on transformation (15), the nonlinear interconnected system is transformed into a HOFA system, a decentralized prescribed performance control law is given, which can ensure the prescribed performance of the output signal and eliminates the affection of the initial value. All signals for closed-loop systems are bounded. The simulation results have shown the reliability of the proposed method.

References

[1] D. Zhang, H. Xu, H. Wang and X. Chen, Performance analysis for interconnected time-delay systems with networked communication, *ISA Transactions*, 129(b): 152–162, 2022.

[2] M. Zolfaghari, M. Abedi, G. B. Gharehpetian and J. M. Guerrero, Flatness-Based Decentralized Control of Bidirectional Interlink Power Converters in Grid-Connected Hybrid Microgrids Using Adaptive High-Gain PI-Observer, *IEEE Systems Journal*, 15(1): 478–486, 2021.

[3] L. Janssen, B. Besselink, R. Fey, N. van de Wouw, Modular model reduction of interconnected systems: A robust performance analysis perspective, *Automatica*, 160:111423, 2024.

[4] Y. Li, J. H. Park, L. Wu and Q. Kong, Distributed Output-Feedback Adaptive Fuzzy Leader-Following Consensus of Stochastic Nonlinear Interconnected Multiagent Systems , *IEEE Transaction on Systems, Man, and Cybernetics: Systems*, 52(1): 311-323, 2022.

[5] J. Cai, C. Wen, L. Wu, L. Xing and Q. Yan, Decentralized Backstepping Control for Interconnected Systems With Non-Triangular Structural Uncertainties , *IEEE Transaction on Automatic Control*, 68(3): 1692–1699, 2023.

[6] Y. Zhao, C. Wen, H. Zhang, Z. Chen, H. Wang and X. Zhao, Adaptive neural decentralised control for switched interconnected nonlinear systems with backlash-like hysteresis and output constraints , *International Journal of Systems Science*, 53(7): 1545–1561, 2022.

[7] B. Liang, S. Zheng, C. K. Ahn and F. Liu, Adaptive Fuzzy Control for Fractional-Order Interconnected Systems With Unknown Control Directions, *IEEE Transaction on Fuzzy systems*, 30(1): 75–87, 2022.

[8] T. Zhang, S. Tang, X. Xia and Y. Yi, Decentralized adaptive output feedback dynamic surface control for stochastic nonstrict-feedback interconnected nonlinear systems with actuator failures and input quantization via command filter, *International Journal of Robust and Nonlinear Control*, 32(12): 6739–6676, 2022.

[9] C. P. Bechlioulis and G. A. Rovithakis, Robust Adaptive Control of Feedback Linearizable MIMO Nonlinear Systems With Prescribed Performance, *IEEE Transaction on Automatic Control*, 53(9):2090–2099, 2008.

[10] C. P. Bechlioulis and G. A. Rovithakis, Adaptive control with guaranteed transient and steady state tracking error bounds for strict feedback systems, *Automatica*, 45(2):532–538, 2009.

[11] C. Hua, L. Zhang and X. Guan, Output feedback control for interconnected time-delay systems with prescribed performance, *Neurocomputing*, 129:208–215, 2014.

[12] C. Hua, Y. Wang, Y. Li, and H. Li, Decentralized output feedback adaptive NN tracking control of interconnected nonlinear time-delay systems with prescribed performance, *Neurocomputing*, 174:885–896, 2016.

[13] L. Zhang, C. Deng, Y. Li, W. W. Che and L. An, Adaptive backstepping control for nonlinear interconnected systems with prespecified-performance-driven output triggering, *Automatica*, 154:111063, 2023.

[14] K. Zhao, Y. Song, C. L. P. Chen and L. Chen, Adaptive Asymptotic Tracking With Global Performance for NonlinearSystems With Unknown Control Directions, *IEEE Transaction on Automatic Control*, 67(3):1566–1573, 2022.

[15] G. R. Duan, High-order System Approaches: I. Fully-actuated Systems and Parametric Design, *Acta Automatica Sinica*, 46(7):1333–1345, 2020.

[16] G. R. Duan, Fully actuated system approaches for continuous-time delay systems: part 1. Systems with state delays only, *Science China Information Sciences*, 66(1):112201, 2023.

[17] P. Ning, C. Hua and R. Meng,Adaptive Control for a Class of Nonlinear Time-Delay System Based on the Fully Actuated System Approaches, *Journal of Systems Science & Complexity*, 35(2):522–534, 2022.

[18] G. P. Liu, Coordination of Networked Nonlinear Multi-Agents Using a High-Order Fully Actuated Predictive Control Strategy, *IEEE-CAA Journal of Automatica Sinica*, 9(4):615–623, 2022.

[19] L. Zhang, L. Zhu and C. Hua, Practical prescribed time control based on high-order fully actuated system approach for strong interconnected nonlinear systems, *Nonlinear Dynamics*, 110(4):3535–3545, 2022.

[20] G. R. Duan, High-order fully-actuated system approaches: - part II. Generalized strict-feedback systems, *International Journal of Systems Science*, 52(3):437–454, 2021.

Proceedings of the 3rd Conference on Fully Actuated System Theory and Applications
May 10-12, 2024, Shenzhen, China

ESO-based Trajectory Tracking Control of a 7-DOF Manipulator: A High-Order Fully Actuated System Approach

Yanling Liu[1], Jialong Zhang[1], Yahui Zhang[1], Zhao Tan[2], Yingbing Sun[1], Haohan Zhao[1], Guilin Wen[1]

1. Department of Mechanical Engineering, Yanshan University, Qinhuangdao 066004, P. R. China
E-mail: zhangyahui@ysu.edu.cn

2. Hunan University, Changsha 410082, P. R. China

Abstract: The 7-DOF manipulator system is a complex dynamic system characterized by high nonlinearity and strong coupling. To tackle these challenges, this study focuses on developing a trajectory-tracking controller based on the high-order fully actuated (HOFA) system approach. The dynamic model is derived using the Lagrange dynamic equation. Subsequently, the system model is converted into a HOFA model, and the trajectory tracking controller is formulated through direct parameterization within the HOFA system model framework. Internal and external uncertainties, including variations in internal model parameters and external frictional forces, can impact the tracking precision of the actual manipulator system in operational conditions. To address these uncertainties affecting tracking accuracy and overall performance, a nonlinear extended state observer (ESO) is devised to counteract the aggregated system disturbances. The simulation outcomes illustrate the effectiveness of the HOFA method and ESO in enhancing manipulator trajectory tracking accuracy and ensuring strong resilience.

Key Words: High-order fully actuated system, Manipulator, Trajectory tracking, Extended state observer

1 Introduction

As a typical example of industrial robots, the multi-degree-of-freedom manipulator is widely used in industrial assembly, safety, and explosion protection [1] due to its exceptional operational versatility.

Manipulators are complex systems characterized by high precision, multiple inputs and outputs, high nonlinearity, and strong coupling, resulting in intricate and challenging control requirements. In most manipulator control problems, implementing precise and rapid tracking control for manipulator joint trajectories is particularly crucial.

Various control methods have been proposed to ensure accurate tracking to meet the dynamic stability performance requirements under different working conditions.

Specially, PID control [2], as a model-independent control method, is widely used due to its strong applicability. However, simple PID control struggles to meet system performance requirements, necessitating significant time for parameter tuning to achieve higher control accuracy. Therefore, adaptive control [3] is frequently employed in manipulator systems due to its ability to mitigate disturbances and interference effectively. For example, [4] employs known function regressors to handle the uncertain dynamics of robots and introduces adaptive control to address saturation. This approach consequently achieves convergence of manipulator tracking errors.

Nevertheless, the drawback of adaptive control is its computationally intensive online identification process, which makes implementation more complex. Furthermore, due to their capacity to approximate nonlinear unknown functions, neural networks are also applicable in uncertain manipulator systems. For instance, a fuzzy PD control method based on a back-propagation neural network is proposed in [5] for a 3-DOF manipulator. The membership function is optimized online by the neural network to enhance the performance of the fuzzy PD algorithm. However, neural networks are less interpretable and rely more heavily on personal experience in practical applications. The first-order state-space equation model is commonly employed as the research focus for model-dependent control methods. However, the dynamics modeling process for multi-degree-of-freedom manipulators is difficult.

Motivated by the above observations, this paper studies the trajectory tracking control problem for the multi-degree-of-freedom manipulator using the high-order fully actuated (HOFA) system model, avoiding reduction to a first-order state-space equation. The HOFA approach is a controller-oriented design model [6-8] characterized by the direct actuation of each degree of freedom. A direct parameterization method [9] is employed in this paper to design a nonlinear feedback controller, transforming the original nonlinear open-loop system into a linear steady closed-loop system with the desired characteristic structure.

Our control strategy also involves utilizing an extended state observer (ESO) to estimate the combined disturbance caused by model uncertainty and external interference and compensate for this disturbance in the HOFA controller.

Hence, the contributions of this paper can be summarized as follows: (1) The establishment of a dynamic model for the 7-DOF manipulator, providing an accurate representation of the system's dynamic characteristics; (2) By employing the ESO to estimate the plant dynamics and disturbances precisely, the HOFA controller can achieve stable and rapid tracking performance.

2 Modeling of 7-DOF Manipulator

The 7-DOF manipulator "Diana" can be depicted in Fig.1. All seven joints are rotating joints, and the Lagrange dynamic equation establishes its dynamic model.

The Lagrange dynamic equation is

$$\frac{d}{dt}\frac{\partial L}{\partial \dot{q}} - \frac{\partial L}{\partial q} = u \tag{1}$$

within which, $L = T - U$ is the Lagrangian function, q is

This work is supported by Full-Time Introduction of the National High-Level Innovative Talent Research Foundation of Hebei Province under Grant 2021HBQZYCXY003.



Fig. 1: 7-DOF manipulator "Diana"

the generalized vector - for the manipulator system $q = \theta$, and u is the generalized joint torque.

The total kinetic energy of a 7-DOF manipulator system can be expressed as

$$\begin{aligned} T &= \sum_{i} T_i \\ T_i &= \sum_{i=1}^{7} \left(\frac{1}{2} m_i v_{C_i}^T v_{C_i} + \frac{1}{2} {}^{i}\omega_i^T I_i^i \omega_i \right) \end{aligned} \tag{2}$$

where, m_i is the mass of the I-th link and I_i is the rigid body inertia tensor.

The potential energy of the 7-DOF manipulator system is

$$U = \sum_{i=1}^{7} \left(m_i g^0 y_{ci} \right) \tag{3}$$

within which g is the acceleration of gravity, ${}^0y_{ci}$ is the height of the centroid of each connecting rod in the reference coordinate system.

The nominal dynamic model of the 7-DOF manipulator is obtained by simplifying the above formula

$$M(q)\ddot{q} + C(q,\dot{q})\dot{q} + G(q) = u \tag{4}$$

where, $M(q) \in \mathbb{R}^{7\times7}$ is the mass matrix that is a positive definite symmetric matrix, $C(q,\dot{q}) \in \mathbb{R}^{7\times7}$ is the coefficient matrix representing Centrifugal force and Coriolis force vector, $G(q) \in \mathbb{R}^7$ is the gravity matrix, $q \in \mathbb{R}^7$ is the state vector, $u \in \mathbb{R}^7$ is the control vector.

External factors such as joint friction and disturbance during operation inevitably affect the actual manipulator. In this case, the dynamic model can be expressed as

$$M(q)\ddot{q} + C(q,\dot{q})\dot{q} + G(q) = u + d \tag{5}$$

where d denotes the lumped disturbance. We make the following assumption in the remainder of the paper.

Assumption 1. The disturbance d is bounded, that is, there is a constant $\lambda \geq 0$ so that $\|d(q,\dot{q},\ddot{q})\| \leq \lambda, \forall q \in \mathbb{R}^7, \dot{q} \in \mathbb{R}^7, \ddot{q} \in \mathbb{R}^7$

3 Control scheme

The desired trajectory tracked by the controller is shown in Fig.2.

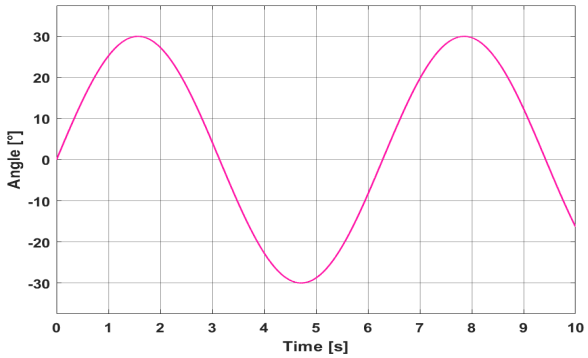

Fig. 2: Desired trajectory

3.1 Problem formulation

To solve the nonlinear problems of the manipulator, an adaptive tracking controller is constructed [10].

Define that $x^*(t) \in \mathbb{R}^r$ be a reference signal to be tracked by $x(t)$, and given

$$z = x - x^* \tag{6}$$

Then

$$z^{(i)} = x^{(i)} - (x^*)^{(i)}, i = 0, 1, \ldots, n. \tag{7}$$

The direct parameterization design method is as follows:

$$\begin{cases} H\left(x^{(0\sim n-1)}\right) = H\left(z^{(0\sim n-1)}, t\right) \\ q\left(x^{(0\sim n-1)}\right) = q\left(z^{(0\sim n-1)}, t\right) \\ L\left(x^{(0\sim n-1)}\right) = L\left(z^{(0\sim n-1)}, t\right) \end{cases} \tag{8}$$

Thus the general HOFA system is as follows:

$$\begin{aligned} z^{(n)} = H\left(z^{(0\sim n-1)}, t\right)\theta + q\left(z^{(0\sim n-1)}, t\right) + \\ L\left(z^{(0\sim n-1)}, t\right)u - (x^*)^{(n)} \end{aligned} \tag{9}$$

The adaptive tracking control law is as follows:

$$\begin{cases} u = -L^{-1}\left(\begin{bmatrix} A_0 & A_1 \end{bmatrix} \begin{bmatrix} z \\ \dot{z} \end{bmatrix} + u^* \right) \\ u^* = H^T\left(z^{(0\sim n-1)}\right)\hat{\theta} + q\left(z^{(0\sim n-1)}\right) - (x^*)^{(n)} \end{cases}$$

when applied to the system (5), guarantees the following:

(1) $x^{(0\sim n-1)} - (x^*)^{(0\sim n-1)} \to 0, t \to \infty$;
(2) $\|\theta - \hat{\theta}\|$ is bounded;

For an arbitrarily chosen $F \in \mathbb{R}^{nr\times nr}$, all the matrix $A^{0\sim n-1}$ and the nonsingular matrix $V \in \mathbb{R}^{nr\times nr}$ satisfying

$$\Phi\left(A^{0\sim n-1}\right) = VFV^{-1} \tag{10}$$

are given by

$$A^{0\sim n-1} = -ZF^nV^{-1}(Z,F) \tag{11}$$

$$V(Z,F) = \begin{bmatrix} Z \\ ZF \\ \vdots \\ ZF^{n-1} \end{bmatrix} \tag{12}$$

where $Z \in \mathbb{R}^{r\times nr}$ is an arbitrary parameter matrix satisfying

$$\det V(Z,F) \neq 0$$

3.2 Controller design

The structure of the proposed HOFA control strategy is shown in Fig.3.

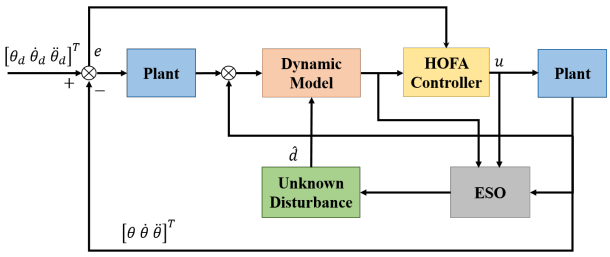

Fig. 3: Structure of the HOFA control strategy

The system (5) turns into a general second-order fully actuated model

$$\ddot{z} = d - \frac{1}{M}\left(C\dot{z} + G\right) + \frac{1}{M}u - \ddot{x^*} \tag{13}$$

The parameters are described as follows:

$$\begin{cases} H\left(z^{(0\sim n-1)}, t\right) = 1 \\ q\left(z^{(0\sim n-1)}, t\right) = -\frac{1}{M}\left(C\dot{z} + G\right) \\ L\left(z^{(0\sim n-1)}, t\right) = \frac{1}{M} \end{cases} \tag{14}$$

The model satisfies the fully actuated condition:

$$\det \frac{1}{M} \neq 0$$

The adaptive trajectory tracking control law is designed as follows:

$$\begin{cases} u = -M\left(\begin{bmatrix} A_0 & A_1 \end{bmatrix}\begin{bmatrix} z \\ \dot{z} \end{bmatrix} + u^*\right) \\ u^* = \hat{d} - \frac{1}{M}\left(C\dot{z} + G\right) - \ddot{x^*} \end{cases} \tag{15}$$

3.3 Solution of $A^{0\sim1}$

The F matrix represents the system characteristic matrix. To ensure the stability of the closed-loop system, the eigenvalue of the matrix F is required to be located in the left half-complex plane. Choose a diagonal matrix F with negative diagonal elements

$$F = \begin{bmatrix} -a & -b \\ b & -a \end{bmatrix} \tag{16}$$

with a and b being two positive scalars, included as a diagonal block in F. The eigenvalues of the matrix F are $-a \pm jb$.

Particularly choosing

$$a = b = 30$$

Further choosing

$$Z = \begin{bmatrix} 1 & 1 \end{bmatrix}$$

we have

$$V(Z,F) = \begin{bmatrix} Z \\ ZF \end{bmatrix} = \begin{bmatrix} 1 & 1 \\ 0 & -60 \end{bmatrix} \tag{17}$$

where

$$\det V(Z,F) \neq 0$$

and then obtain the gain parameters matrix

$$A^{0\sim1} = -ZF^2V^{-1} = \begin{bmatrix} 1800 & 60 \end{bmatrix} \tag{18}$$

Lemma 3.1. *For any μ>0, there exsits a set of matrices $A_i \in \mathbb{R}^{r\times r}, i = 0, 1, ..., n-1$ satisfying*

$$Re\lambda_i(\Phi(A^{0\sim n-1})) < -\frac{\mu}{2}, i = 1, 2, 3 \ldots, n, \tag{19}$$

when the condition in (26) holds for some μ>0, there exists a positive definite matrix $P(A^{0\sim n-1})$ satisfying

$$\Phi^T(A^{0\sim n-1})P(A^{0\sim n-1}) + P(A^{0\sim n-1})\Phi(A^{0\sim n-1}) < -\mu P(A^{0\sim n-1}) \tag{20}$$

3.4 ESO design

A nonlinear ESO is designed to estimate and compensate for the lumped disturbance d [11].

Let $x_3 = d$ represent the extended state, and $x = \begin{bmatrix} x_1 & x_2 & x_3 \end{bmatrix}^T$. Assuming that d is differentiable, we define

$$\dot{\hat{d}} = \theta \tag{21}$$

and a continuous ESO for Eq.(**??**) can be constructed as

$$\begin{aligned} \dot{\hat{x}}_1 &= \hat{x}_2 + l_1\left(x_1 - \hat{x}_1\right) \\ \dot{\hat{x}}_2 &= \frac{1}{M}\left(u - Cx_2 - G\right) + \hat{x}_3 + l_2\left(x_1 - \hat{x}_1\right) \\ \dot{\hat{x}}_3 &= l_3\left(x_1 - \hat{x}_1\right) \end{aligned} \tag{22}$$

where $L = \begin{bmatrix} l_1 & l_2 & l_3 \end{bmatrix}^T$ is the observer gain vector, and $\hat{d}$ is the estimate of disturbance d. The state errors are defined as

$$\begin{aligned} e_x &= x_1 - \hat{x}_1 \\ e_y &= x_2 - \hat{x}_2 \\ e_d &= d - \hat{d} \end{aligned} \tag{23}$$

The following error state space model is obtained

$$\begin{bmatrix} \dot{e_x} \\ \dot{e_y} \\ \dot{e_d} \end{bmatrix} = \begin{bmatrix} -l_1 & 1 & 0 \\ -l_2 & 0 & 1 \\ -l_3 & 0 & 0 \end{bmatrix}\begin{bmatrix} e_x \\ e_y \\ e_d \end{bmatrix} + \begin{bmatrix} 0 \\ 0 \\ 1 \end{bmatrix}\dot{d} \tag{24}$$

The observer gains are chosen such that the characteristic polynomial (26) is Hurwitz [12]. The error model (24) is globally asymptotically stable. If parameter d is constant or time-varying slowly, $\dot{d}$ is approximated to zero and disregarded [13]. All the observer poles are placed at $-\omega_0$ for tuning simplicity. Then, there exists the system characteristic polynomial of (25)

$$\lambda_0(s) = s^3 + l_1s^2 + l_2s + l_3 = (s + \omega_0)^3 \tag{25}$$

where ω_0 is a positive real number representing the observer bandwidth and $L = \begin{bmatrix} 3\omega_0 & 3\omega_0^2 & \omega_0^3 \end{bmatrix}^T$.

3.5 Controller Stability Analysis

We have the following theorem regarding the robust stabilization for the high-order system with nonlinear uncertainties.

Theorem 3.1. *Let μ and ε are two arbitrarily given positive numbers, and $A_i \in \mathbb{R}^{r\times r}, i = 0, 1, ..., n-1$ be a set of matrices satisfying (23). Then, the following control law*

$$\begin{cases} u = -M\left(\begin{bmatrix} A_0 & A_1 \end{bmatrix}\begin{bmatrix} z \\ \dot{z} \end{bmatrix} + u^*\right) \\ u^* = \hat{d} - \frac{1}{M}\left(C\dot{z} + G\right) - \ddot{x^*} \end{cases} \tag{26}$$

for the uncertain system (5) guarantees that the state $x^{(0\sim n-1)}$ converges into the following ellipsoid centered at the origin:

$$\Theta_{\mu,\eta}(0) = \left\{ x^{(0\sim n-1)} \mid \left(x^{(0\sim n-1)}\right)^T P\left(A^{0\sim n-1}\right)x^{(0\sim n-1)} \le \frac{\eta}{\mu} \right\}$$

Proof. Substituting the control law (15) into system (13), gives the following closed-loop system

$$z^{(n)} + A^{0\sim n-1} z^{(0\sim n-1)} = \phi\left(z^{(0\sim n-1)}\right) \tag{27}$$

where

$$\phi\left(z^{(0\sim n-1)}\right) = d - \hat{d} \tag{28}$$

The closed-loop system (27) can be written in the following state-space form:

$$\dot{z}^{0\sim 1} = \Phi(z^{0\sim 1})z^{0\sim 1} + \begin{bmatrix} 0_r \\ \phi(z^{0\sim 1}) \end{bmatrix} \tag{29}$$

There, $A_i \in \mathbb{R}^{r\times r}, i = 0, 1, ..., n-1$ satisfying the condition (19).

Then the following Lyapunov function can be chosen for the system (13):

$$V = \frac{1}{2}(x^{(0\sim 1)})^T P(A^{0\sim 1})x^{(0\sim 1)} \tag{30}$$

we have

$$\begin{aligned} \dot{V} =& \frac{1}{2}(\dot{x}^{(0\sim 1)})^T P x^{(0\sim 1)} + \frac{1}{2}(x^{(0\sim 1)})^T P\dot{x}^{(0\sim 1)} \\ =& \frac{1}{2}(\Phi x^{(0\sim 1)} + \begin{bmatrix} 0_r \\ \phi(z^{(0\sim 1)}) \end{bmatrix})^T P x^{(0\sim 1)} + \frac{1}{2}(x^{(0\sim 1)})^T \\ & P(\Phi x^{(0\sim 1)} + \begin{bmatrix} 0_r \\ \phi(z^{(0\sim 1)}) \end{bmatrix}) \\ =& \frac{1}{2}(x^{(0\sim 1)})^T(\Phi^T P + P\Phi)x^{(0\sim 1)} + (x^{0\sim 1})^T P\begin{bmatrix} 0_r \\ \phi(z^{(0\sim 1)}) \end{bmatrix} \\ \le& -\frac{\mu}{2}(x^{(0\sim 1)})^T P x^{(0\sim 1)} + (x^{(0\sim 1)})^T P_L\phi(z^{(0\sim 1)}) \\ =& -\mu V + (x^{(0\sim 1)})^T P_L\phi(z^{(0\sim 1)}) \end{aligned}$$

where $d - \hat{d}$ is bounded, gives

$$\dot{V} \le -\mu V + \eta$$

It thus follows from the Comparison Theorem that [14]

$$V \le V(0)e^{-\mu t} + \frac{\eta}{\mu}(1 - e^{(-\mu t)}), \tag{31}$$

which gives

$$V \le (V(0) - \frac{\eta}{\mu})e^{-\mu t} + \frac{\eta}{\mu} \to +\frac{\eta}{\mu}, t \to \infty.$$

Thus the state $x^{(0\sim 1)}$ eventually converges into the ellipsoid $\Theta_{\mu,\eta}(0)$. The proof is completed. □

3.6 ESO Stability Analysis

By denoting $\tilde{x}_1 = x_i - \hat{x}_i, i = 1, 2, 3$, the observer estimation error dynamics can be expressed as [15-17]

$$\begin{aligned} \dot{\tilde{x}}_1 &= \tilde{x}_2 - 3\omega_0\tilde{x}_1 \\ \dot{\tilde{x}}_2 &= \tilde{x}_3 - 3\omega_0^2\tilde{x}_1 \\ \dot{\tilde{x}}_3 &= \theta - \omega_0^3\tilde{x}_1 \end{aligned} \tag{32}$$

Now, let us scale the observer estimation error $\tilde{\xi}_i(t)$ by ω_0^{i-1}, define $\epsilon_i(t) = \frac{\tilde{\xi}_i(t)}{\omega_0^{i-1}}, i = 1, 2, 3$. Then, (32) can be rewritten as

$$\dot{\epsilon} = \omega_0 A_\epsilon \epsilon + B_\epsilon \frac{h(\xi, d)}{\omega_0^2} \tag{33}$$

where

$$A_\epsilon = \begin{bmatrix} -3 & 1 & 0 \\ -3 & 0 & 1 \\ -1 & 0 & 0 \end{bmatrix} B_\epsilon = \begin{bmatrix} 0 \\ 0 \\ 1 \end{bmatrix} \tag{34}$$

Theorem 3.2. Assuming that θ is bounded, there exist a constant $\sigma_i > 0$ and a finite time $T_1 > 0$ such that $|\tilde{x}_i| \le \sigma_i, i = 1, 2, 3$, $\forall t \ge T_1 > 0$ and $\omega_0 > 0$. σ_i is dependent on the initial condition of $\tilde{x}_i$ and upper boundary of θ. Furthermore, $\sigma_i = O\left(1/\omega_0^k\right)$ for some positive integer k.

Proof. Solving (33), we can obtain

$$\epsilon(t) = e^{\omega_0 A_\epsilon t}\epsilon(0) + \int_0^t e^{\omega_0 A_\epsilon (t-\tau)} B_\epsilon \frac{h(\xi(\tau), d)}{\omega_0^2} d\tau \tag{35}$$

Let

$$p(t) = \int_0^t e^{\omega_0 A_\epsilon (t-\tau)} B_\epsilon \frac{h(\xi(\tau), d)}{\omega_0^2} d\tau \tag{36}$$

Since $h(\xi(\tau), d)$ is bounded, $h(\xi(\tau), d) \le \delta$, where δ is a positive constant, it follows that

$$|p_i(t)| \le \frac{\delta}{\omega_0^3}[|\left(A_\epsilon^{-1}B_\epsilon\right)_i| + |\left(A_\epsilon^{-1}e^{\omega_0 A_\epsilon t}B_\epsilon\right)_i|] \tag{37}$$

for $i = 1, 2, 3$. Since

$$A_\epsilon^{-1} = \begin{bmatrix} 0 & 0 & -1 \\ 1 & 0 & -3 \\ 0 & 1 & -3 \end{bmatrix} \tag{38}$$

one has

$$|\left(A_\epsilon^{-1}B_\epsilon\right)_i| = \begin{cases} 1 & |_{i=1} \\ 3 & |_{i=2,3} \end{cases} \tag{39}$$

Since A_ϵ is Hurwitz, there exists a finite time $T_1 > 0$ such that

$$|[e^{\omega_0 A_\epsilon t}]_{ij}| \le \frac{1}{\omega_0^3} \tag{40}$$

for all $t \ge T_1, i, j = 1, 2, 3$. Hence

$$|[e^{\omega_0 A_\epsilon t}B]_i| \le \frac{1}{\omega_0^3} \tag{41}$$

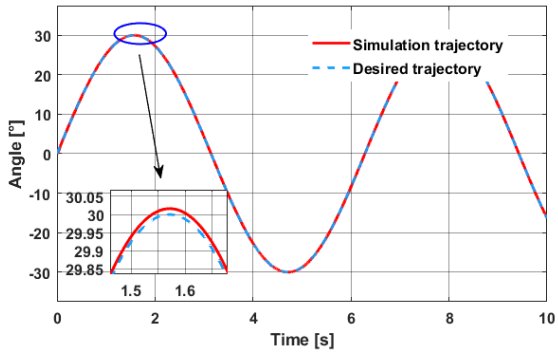

(a) Joint 1

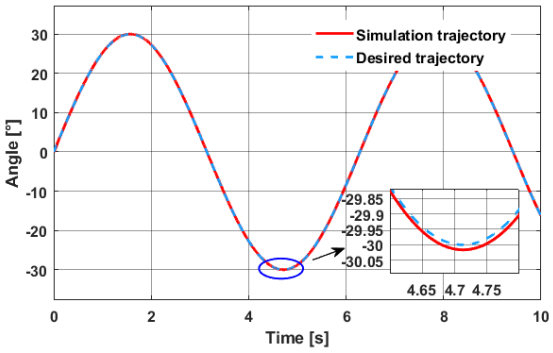

(b) Joint 2

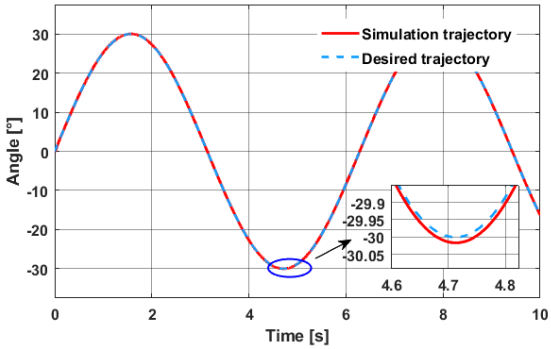

(c) Joint 3

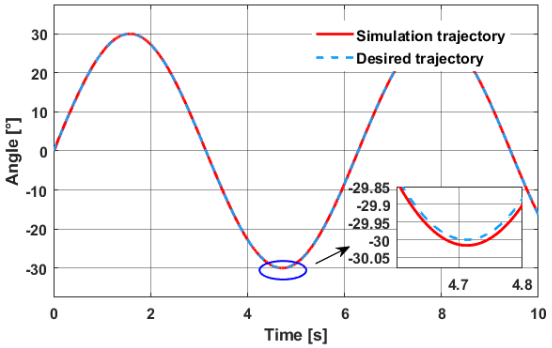

(d) Joint 4

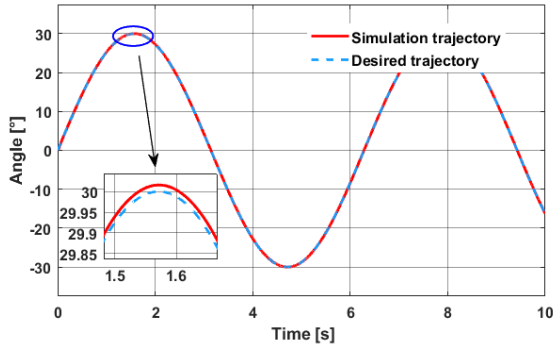

(e) Joint 5

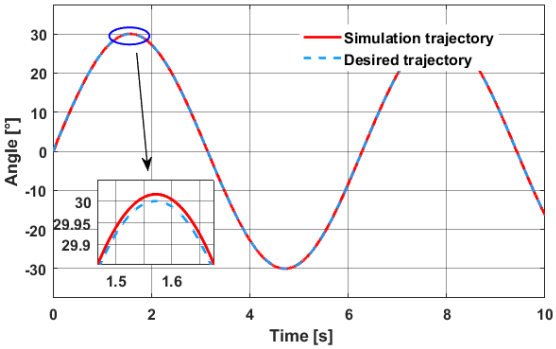

(f) Joint 6

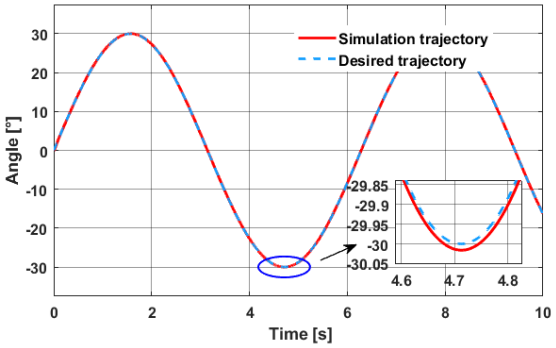

(g) Joint 7

Fig. 4: Simulation results

for all $t \geq T_1, i = 1, 2, 3$. Note that T_1 depends on $\omega_0 A_\epsilon$. Define

$$A_\epsilon^{-1} = \begin{bmatrix} s_{11} & s_{12} & s_{13} \\ s_{21} & s_{22} & s_{23} \\ s_{31} & s_{32} & s_{33} \end{bmatrix} \tag{42}$$

$$e^{\omega_0 A_\epsilon t} = \begin{bmatrix} d_{11} & d_{12} & d_{13} \\ d_{21} & d_{22} & d_{23} \\ d_{31} & d_{32} & d_{33} \end{bmatrix} \tag{43}$$

One has

$$|\left(A_\epsilon^{-1}e^{\omega_0 A_\epsilon t}B_\epsilon\right)_i| = |s_{i1d_{13}} + s_{i2}d_{23} + s_{i3}d_{33}| \leq \begin{cases} \frac{1}{\omega_0^3} & |i=1 \\ \frac{4}{\omega_0^3} & |i=2,3 \end{cases} \quad (44)$$

for all $t \geq T_1$. From (38), (39), and (45), we obtain

$$|p_i(t)| \leq \frac{3\delta}{\omega_0^3} + \frac{4\delta}{\omega_0^6} \quad (45)$$

for all $t \geq T_1, i = 1,2,3$. Let $\epsilon_{sum}(0) = |\epsilon_1(0)| + |\epsilon_2(0)| + |\epsilon_3(0)|$. It follows that

$$|[e^{\omega_0 A_\epsilon t}\epsilon(0)]_i| \leq \frac{\epsilon_{sum}(0)}{\omega_0^3} \quad (46)$$

for all $t \geq T_1, i = 1,2,3$. From (35), one has

$$|\epsilon_i(t)| \leq |[e^{\omega_0 A_\epsilon t}\epsilon(0)]_i| + |p_i(t)| \quad (47)$$

Let $\tilde{\xi}_{sum}(0) = |\tilde{\xi}_1(0)| + |\tilde{\xi}_2(0)| + |\tilde{\xi}_3(0)|$. According to $\epsilon_i(t) = \frac{\tilde{\xi}_i(t)}{\omega_0^{i-1}}, i = 1,2,3$ and (45)-(47), we have

$$|\tilde{\xi}_i(t)| \leq |\frac{|\tilde{\xi}_{sum}(0)|}{\omega_0^3} + \frac{3\delta}{\omega_0^{4-i}} + \frac{4\delta}{\omega_0^{7-i}} = \sigma_i \quad (48)$$

for all $t \geq T_1, i = 1,2,3$. Q.E.D. □

The results indicate that under the assumption of the boundedness of θ, the estimation error of ESO is bounded. Generally, the larger the bandwidth, the more accurate the estimation. However, a large bandwidth will increase noise sensitivity. Therefore, a proper bandwidth should be selected. By replacing the true value d, Eq.(5) can be rewritten as follows:

$$M(q)\ddot{q} + C(q,\dot{q})\dot{q} + G(q) = u + \hat{x}_3 \quad (49)$$

Finally, the appropriate bandwidth $\omega_0 = 15$ is determined.

4 Simulation results

The simulation duration is 10 s, and the simulation step is set to 0.01s. The simulation results of joint angle trajectory tracking are depicted in Fig.4. The ESO is applied to observe the lumped parameter disturbance caused by internal and external uncertainty disturbances such as joint friction and external enhancement of the anti-interference ability of the system. The simulation results show that the steady-state errors of the seven joints can be controlled within 0.05 °, which exhibits that the proposed HOFA control strategy has excellent dynamic and steady-state characteristics.

5 Conclusion

This study proposes a joint trajectory tracking control approach for the 7-DOF manipulator utilizing the HOFA system model and designing the trajectory tracking controller through direct parameterization. An ESO is implemented to estimate and compensate for the lumped disturbance and manage internal and external uncertainties in the manipulator control system. The compensated control strategy enables the system to follow the desired target trajectory while meeting performance criteria. Simulation results demonstrate the effectiveness and robustness of the proposed HOFA control method. Future experiments will validate the proposed theory using real robotic arm hardware platform parameters.

References

[1] Lee J K, Kim K, et al. Force-reflecting servo manipulators for remote handling task in a radioactive environment[C]. *2007 International Conference on Control, Automation and Systems*, 2007: 1025-1028.

[2] Santibañez V, Camarillo K, Moreno-Valenzuela J, et al. A practical PID regulator with bounded torques for robot manipulators[J]. *International Journal of Control, Automation and Systems*, 2010, 8: 544-555.

[3] Wang W, Xie B, et al. Adaptive backstepping control of uncertain gear transmission servosystems with asymmetric deadzone nonlinearity[J]. *IEEE Transactions on Industrial Electronics*, 2018, 66(5): 3752-3762.

[4] Tran T T, Ge S S, He W. Adaptive control for an uncertain robotic manipulator with input saturations[J]. *Control Theory and Technology*, 2016, 14(2): 113-121.

[5] Zhang S, Zhao Y, Lee J. Control of 3-DOF robotic manipulator by neural network based fuzzy-PD[J]. *International Journal of Precision Engineering and Manufacturing*, 2019, 20: 2109-2118.

[6] G. R. Duan. High-order System Approaches: I. Fully-actuated Systems and Parametric Designs[J]. *Acta Automatica Sinica*, 2020, 46(7): 1333-1345.

[7] G. R. Duan. High-order System Approaches: II. Controllability and Full-actuation[J]. *Acta Automatica Sinica*, 2020, 46(8): 1571-1581.

[8] G. R. Duan. High-order System Approaches: III. Observability and Observer Design[J]. *Acta Automatica Sinica*, 2020, 46(9): 1885-1895.

[9] G. R. Duan. High-order fully actuated system approaches: Part I. Models and basic procedure[J]. *International Journal of Systems Science*, 2021, 52(2): 422-435.

[10] G. R. Duan. High-order fully actuated system approaches: Part IV. Adaptive control and high-order backstepping[J]. *International Journal of Systems Science*, 2021, 52(5): 972-989.

[11] Li M, Yin H, Ding T, et al. Air flow rate and pressure control approach for the air supply subsystems in PEMFCs[J]. *ISA transactions*, 2022, 128: 624-634.

[12] Zheng Q, Dong L, Lee D H, et al. Active disturbance rejection control for MEMS gyroscopes[C]. *2008 American control conference. IEEE*, 2008: 4425-4430.

[13] Li C, Zhao H, Liu H, et al. Gas supply control and experimental validation for polymer electrolyte membrane fuel cells[J]. *Mechatronics*, 2023, 91: 102958.

[14] G. R. Duan. High-order fully actuated system approaches: Part III. Robust control and high-order backstepping[J]. *International Journal of Systems Science*, 2021, 52(5): 952-971.

[15] Han J. From PID to active disturbance rejection control[J]. *IEEE transactions on Industrial Electronics*, 2009, 56(3): 900-906.

[16] Talole S E, Kolhe J P, Phadke S B. Extended-state-observer-based control of flexible-joint system with experimental validation[J]. *IEEE Transactions on Industrial Electronics*, 2009, 57(4): 1411-1419.

[17] Zheng Q, Chen Z, Gao Z. A practical approach to disturbance decoupling control[J]. *Control engineering practice*, 2009, 17(9): 1016-1025.

Proceedings of the 3rd Conference on Fully Actuated System Theory and Applications
May 10-12, 2024, Shenzhen, China

Algebraic differentiator based fractional order controller by high-order fully actuated system approach

Yan-Qiao Wei[1], Yan-Hai Wang[1], Da-Yan Liu[2], Chang-Chun Hua[1]

1. School of Electrical Engineering, Yanshan University, Qinhuangdao, 066004, Hebei, China
E-mail: weiyanqiao@ysu.edu.cn;1716694429@qq.com;cch@ysu.edu.cn

2. INSA Centre Val de Loire, Université d'Orléans, PRISME EA 4229, Bourges Cedex 18022, France
E-mail: dayan.liu@insa-cvl.fr

Abstract: This paper considers a problem on the design of algebraic differentiator based fractional order controller by using the high-order fully actuated (HOFA) system approach. First, the considered nonlinear system is transformed into a HOFA system model. Second, a fractional order controller involving the Riemann-Liouville fractional sequential derivatives is directly written out for the HOFA system model in the framework of the closed-loop fractional order linear time invariant (LTI) system. Then, the algebraic integral formulas of the unknown derivatives are derived by applying the modulating functions method. Finally, an example is provided to illustrate the efficiency of the proposed method with noisy observation.

Key Words: Nonlinear control system, high-order fully actuated system, fractional order controller, algebraic differentiator.

1 Introduction

In reality, almost all physical systems are intrinsically nonlinear. Based on the state-space models, many efforts have been devoted to nonlinear control systems during the past decades. Though, the problems on the nonlinear control systems are still challenging. The high-order fully actuated (HOFA) system approach was raised from the fact that many practical fully actuated systems are governed by certain physical laws, which are usually second- or high-order differential equations, such as Newton's laws, Kirchhoff's laws, etc. [1,2]. By applying the HOFA system approach, the controller of a nonlinear system can be immediately written out as soon as a single HOFA system model or a set of HOFA system models are derived in [3–5]. Within the framework of HOFA system approach, considerable contributions on theories and applications have emerged in the most recent years [6–9].

As an extension of the classical calculus, fractional calculus has the ability to model some complex physical phenomena more accurately [10, 11]. In the field of control engineering, more and more researchers have realized the superior performance of controllers with fractional order operators, such as providing flexible stability margin and enhanced robustness [12–14]. However, the implementation of fractional order controllers is not easy due to the singularities and long-memory characteristics of the fractional order operators [15, 16]. Meanwhile, the adoption of inappropriate differentiators may amplify the effects of measurement noises caused by practical sensors [17]. Fortunately, a series of recent works on the modulating functions based algebraic differentiators have shown several advantages such as fast-convergence, robustness against sensor measurement noises, independence of initial conditions, and so on [18–22]. Inspired by the above mentioned works, this paper intends to design an algebraic differentiator based fractional order controller by combining the HOFA system approach with the modulating functions method, where the following symbols introduced in [1] are useful:

$$x^{(0\sim n)} := \begin{bmatrix} x \\ \dot{x} \\ \vdots \\ x^{(n)} \end{bmatrix}, \quad x_{i\sim j}^{(0\sim n)} := \begin{bmatrix} x_i^{(0\sim n)} \\ x_{i+1}^{(0\sim n)} \\ \vdots \\ x_j^{(0\sim n)} \end{bmatrix}, j \geq i.$$

2 Problem formulation

Consider the nonlinear system model as follows [1]:

$$x^{(m_c)} = F(x^{(0\sim m_c-1)}) + G(x^{(0\sim m_c-1)})u, \qquad (1)$$

where $x \in \mathbb{R}^r$, and m_c is a positive integer. Assumed that (1) satisfies the following conditions:

(C_1) : $F(x^{(0\sim m_c-1)})$ is a continuously differentiable vector-valued function of $x^{(0\sim m_c-1)}$,

(C_2) : $\frac{r}{2} \leq rank(G(x^{(0\sim m_c-1)})) \leq r$.

The objective of this work is to design an algebraic differentiator based fractional order controller u for the system (1). By denoting $\alpha \in \mathbb{R}_+$ as the fractional order and $\lceil \alpha \rceil$ as the smallest integer such that $\lceil \alpha \rceil \geq \alpha$, we introduce some basic concepts on the Riemann-Liouville fractional order operators in the following.

Definition 1 *[10] Let l be the smallest integer such that $l \geq \alpha$. The Riemann-Liouville fractional derivative of a function f is defined as follows: $\forall\, t \in \mathbb{R}_+$,*

$$\mathrm{D}_t^{\alpha} f(t) := \frac{d^l}{dt^l} \left\{ \mathrm{D}_t^{\alpha-l} f(t) \right\},$$

where $\mathrm{D}_t^{\alpha-l}$ refers to the Riemann-Liouville fractional integral operator.

Based on the above definition, the Riemann-Liouville fractional sequential derivative is defined as follows.

Definition 2 *[10] Let $k \in \mathbb{N}$, the Riemann-Liouville fractional sequential derivative of a function f is defined as fol-*

This work was supported by National Natural Science Foundation of China (No. 62303397), Natural Science Foundation of Hebei Province of China (No. F2021203028), Hebei innovation capability improvement plan project of China (No. 22567619H), and was supported by the project APR-IA 2021: COVEMR of the region of Centre Val de Loire, France.

lows: $\forall\, t \in \mathbb{R}_+$,

$$\mathcal{D}_t^{k\alpha} f(t) := \begin{cases} f(t), & \text{for } k = 0, \\ \mathrm{D}_t^{\alpha}\left\{\mathcal{D}_t^{(k-1)\alpha} f(t)\right\}, & \text{for } k \geq 1. \end{cases} \quad (2)$$

3 Main results

The main results on the proposed fractional order controller are introduced in this section.

3.1 Fractional order controller

Similar as done in [23], a fractional order controller is provided in the following theorem by applying the HOFA system approach. Different from [23], the proposed controller is given based on the fractional sequential derivatives of Riemann-Liouville type instead of Caputo type.

Theorem 1 *For the system (1) fulfilling* (C_1) *and* (C_2)*, let* $r, s \in \mathbb{N}^*$, $0 < \alpha < 1$, $\bar{\alpha} = [\alpha_0, \ldots, \alpha_i, \ldots, \alpha_{s-1}]^\top \in \mathbb{R}^{s\times 1}$ *with* $\alpha_i = i\alpha$ *and* $0 < \alpha_{s-1} < 2m_c$*. If there exists a nonsingular matrix* $Q(x) \in \mathbb{R}^{r\times r}$ *such that:*

$$z = \begin{bmatrix} z_a \\ z_b \end{bmatrix} = Q(x)x \in \mathbb{R}^r, z_a \in \mathbb{R}^{r_0\times 1}, z_b \in \mathbb{R}^{r_c\times 1}, \quad (3)$$

with $r_0 = r - r_c \leq r$*, the corresponding HOFA system model of (1) is given as follows:*

$$z_a^{(2m_c)} = h(z_a^{(0\sim 2m_c-1)}, z_b) + L(z_a^{(0\sim 2m_c-1)}, z_b)u, \quad (4)$$

where $h(z_a^{(0\sim 2m_c-1)}, z_b) \in \mathbb{R}^{r_0\times 2m_c-1}$ *is a vector function, and* $L(z_a^{(0\sim 2m_c-1)}, z_b) \in \mathbb{R}^{r_0\times r_0}$ *is a matrix function fulfilling:*

$$\det L(z_a^{(0\sim 2m_c-1)}, z_b) \neq 0. \quad (5)$$

If there exists the following vector $z_a^{(\bar{\alpha})}$*:*

$$z_a^{(\bar{\alpha})} = \begin{bmatrix} z_a \\ \mathcal{D}_t^{\alpha_1} z_a \\ \vdots \\ \mathcal{D}_t^{\alpha_{s-1}} z_a \end{bmatrix} \in \mathbb{R}^{sr},$$

and the matrix $A_{\bar{\alpha}} = \left[A_{\alpha_0}, A_{\alpha_1}, \ldots, A_{\alpha_{s-1}}\right]$ *with* $A_{\alpha_i} \in \mathbb{R}^{r_0\times r_0}$ *for* $i = 0, 1, \ldots, s-1$*, the fractional order controller* u *given by*

$$\begin{cases} u := -L^{-1}\left(z_a^{(0\sim 2m_c-1)}, z_b\right)\left(A_{\bar{\alpha}} z_a^{(\bar{\alpha})} + u^*\right), \\ u^* := h\left(z_a^{(0\sim 2m_c-1)}, z_b\right) - \nu^*, \end{cases} \quad (6)$$

with an external input $\nu^* \in \mathbb{R}^{r_0\times 1}$ *can lead to a closed-loop fractional order LTI system of (4) as follows:*

$$z_a^{(2m_c)} + \sum_{i=0}^{s-1} A_{\alpha_i} \mathcal{D}_t^{\alpha_i} z_a = \nu^*. \quad (7)$$

In order to guarantee the stability of the closed-loop fractional order LTI system (7), the matrix $A_{\bar{\alpha}}$ is chosen such that the following condition is fulfilled [23]:

$$|\arg(eig(A_c))| > \frac{\alpha\pi}{2}, \quad (8)$$

where

$$A_c := \begin{bmatrix} 0 & I_{r_0} & 0 & 0 \\ 0 & 0 & \ldots & 0 \\ 0 & 0 & \ldots & I_{r_0} \\ -A_{\alpha_0} & -A_{\alpha_1} & \ldots & -A_{\alpha_{s-1}} \end{bmatrix} \in \mathbb{R}^{r_c\times r_c},$$

with $r_c = sr_0$. Thus, the derivation of $z_a^{(0\sim 2m_c-1)}$ for the fractional order controller u becomes the main task of this work.

3.2 Algebraic integral formulas of $z_a^{(0\sim 2m_c-1)}$

In this subsection, the algebraic integral formulas of $z_a^{(0\sim 2m_c-1)}$ are derived for the fractional order controller (6) of the system (7).

Theorem 2 *Let* $t, T \in \mathbb{R}_+$*,* t_0 *be* $\max\{0, t-T\}$*,* α *be a real number in* $]0, 1[$ *and* ϕ_l *for* $l = 0, \ldots, 2m_c - 1$ *be a family of modulating functions satisfying the following properties:* $\forall j \in \{0, \ldots, 2m_c - 1\}$,

- $(P_1) : \phi_l \in \mathcal{C}^{2m_c}([0, t - t_0])$,
- $(P_2) : \phi_l^{(j)}(0) = 0$,
- $(P_3) : \phi_l^{(j)}(t - t_0) = 1$ *if* $j = l$, $\phi_l^{(j)}(t - t_0) = 0$ *else.*

Then, for the system (4), $z_a^{(0\sim 2m_c-1)}$ *can be given by the formulas as follows: for* $l = 0, \ldots, 2m_c - 1$,

$$\begin{aligned} & z_a^{(2m_c-1-l)}(t) \\ &= (-1)^l \left\{ \int_{t_0}^{t} \phi_l(\tau - t_0)\nu^*(\tau)d\tau \right. \\ &\quad - \int_{t_0}^{t} \phi_l^{(2m_c)}(\tau - t_0) z_a(\tau)d\tau \\ &\quad \left. - \int_{t_0}^{t} \phi_l(\tau - t_0)\left[\sum_{i=0}^{s-1} A_{\alpha_i} \mathcal{D}_\tau^{\alpha_i} z_a(\tau)\right] d\tau \right\}. \end{aligned} \quad (9)$$

Proof. The proof is given by following the steps below [18].

Step 1: Multiply and integration. For $l = 0, \ldots, 2m_c - 1$, we multiply the modulating functions ϕ_l to both side of (7) and take integration from t_0 to t. Then, we can get: for $l = 0, \ldots, 2m_c - 1$,

$$\begin{aligned} & \int_{t_0}^{t} \phi_l(\tau - t_0) z_a^{(2m_c)}(\tau)d\tau \\ &\quad + \int_{t_0}^{t} \phi_l(\tau - t_0)\left[\sum_{i=0}^{s-1} A_{\alpha_i} \mathcal{D}_\tau^{\alpha_i} z_a(\tau)\right] d\tau \\ &\quad = \int_{t_0}^{t} \phi_l(\tau - t_0)\nu^*(\tau)d\tau. \end{aligned} \quad (10)$$

Step 2: Application of integration by parts. By applying $2m_c$ times integration by parts formula to the first term of (10), we have: for $l = 0, \ldots, 2m_c - 1$,

$$\begin{aligned} & \int_{t_0}^{t} \phi_l(\tau - t_0) z_a^{(2m_c)}(\tau)d\tau \\ &\quad = (-1)^{2m_c} \int_{t_0}^{t} \phi_l^{(2m_c)}(\tau - t_0) z_a(\tau)d\tau \\ &\quad + \sum_{j=0}^{2m_c-1} (-1)^j \left[\phi_l^{(j)}(\tau - t_0) z_a^{(2m_c-1-j)}(\tau)\right]_{\tau=t_0}^{\tau=t}. \end{aligned} \quad (11)$$

Then, we get: for $l = 0, \ldots, 2m_c - 1$,

$$\begin{aligned}(-1)^{2m_c} &\int_{t_0}^{t} \phi_l^{(2m_c)}(\tau - t_0) z_a(\tau) d\tau \\ &+ \sum_{j=0}^{2m_c-1} (-1)^j \left[\phi_l^{(j)}(\tau - t_0) z_a^{(2m_c-1-j)}(\tau)\right]_{\tau=t_0}^{\tau=t} \\ &+ \int_{t_0}^{t} \phi_l(\tau - t_0) \left[\sum_{i=0}^{s-1} A_{\alpha_i} \mathcal{D}_\tau^{\alpha_i} z_a(\tau)\right] d\tau \\ &= \int_{t_0}^{t} \phi_l(\tau - t_0) \nu^*(\tau) d\tau. \end{aligned} \tag{12}$$

Step 3: Elimination of undesired terms. Thanks to (P_1) and (P_2) satisfied by ϕ_l, (12) becomes:

$$\begin{aligned}&\int_{t_0}^{t} \phi_l^{(2m_c)}(\tau - t_0) z_a(\tau) d\tau \\ &+ \sum_{j=0}^{2m_c-1} (-1)^j \phi_l^{(j)}(t - t_0) z_a^{(2m_c-1-j)}(t) \\ &+ \int_{t_0}^{t} \phi_l(\tau - t_0) \left[\sum_{i=0}^{s-1} A_{\alpha_i} \mathcal{D}_\tau^{\alpha_i} z_a(\tau)\right] d\tau \\ &= \int_{t_0}^{t} \phi_l(\tau - t_0) \nu^*(\tau) d\tau, \end{aligned} \tag{13}$$

where the terms involving the initial conditions of z_a are eliminated. Then, by applying the property (P_3) of ϕ_l to (13), we obtain (9) and complete the proof. ■

In this paper, the modulating functions ϕ_l required by Theorem 2 are constructed as follows [18]: for $l = 0, \ldots, 2m_c - 1$,

$$\phi_l(\tau - t_0) = \sum_{j=0}^{2m_c-1} c_{l,j} (\tau - t_0)^{2m_c+j+1}, \tag{14}$$

with $\tau \in [t_0, t]$. For $l = 0, \ldots, 2m_c - 1$, the coefficient vectors $C_l = (c_{l,0}, \ldots, c_{l,2m_c-1})^\top$ are the solutions of the algebraic systems as follows: for $l = 0, \ldots, 2m_c - 1$,

$$B_l C_l = d_l, \tag{15}$$

where $B_l \in \mathbb{R}^{2m_c \times 2m_c}$ is defined by: for $k = 0, \ldots, 2m_c - 1$ and $j = 0, \ldots, 2m_c - 1$

$$B_l(k, j) = \frac{(2m_c + j + 1)!}{(2m_c + j - k + 1)!} (t - t_0)^{2m_c+j-k+1}, \tag{16}$$

and $d_l \in \mathbb{R}^{2m_c \times 1}$ is defined by: $d_l(k) = 1$ if $l = k$, $d_l(k) = 0$ else.

4 Illustrative example

Similar as the previous works on algebraic differentiators [18–20, 22], the proposed formulas are also applicable in noise measurement environment.

Example: Consider the following nonlinear system [1]:

$$\begin{cases} \dot{x}_1 = x_1 + x_1 x_4 + x_3 u_1 + u_2, \\ \dot{x}_2 = x_2 e^{x_3} + u_1, \\ \dot{x}_3 = x_2 + x_3^2, \\ \dot{x}_4 = x_1 + x_2 - x_4 + x_1 x_4 + (1 + x_3) u_1 + u_2. \end{cases} \tag{17}$$

We can learn from (17) that $m_c = 1$ and $r = 2$. The system (17) matches the form of (1) by defining:

$$x = \begin{bmatrix} x_1 \\ x_2 \\ x_3 \\ x_4 \end{bmatrix}, \quad F(x) = \begin{bmatrix} x_1 + x_1 x_4 \\ x_2 e^{x_3} \\ x_2 + x_3^2 \\ x_1 + x_2 - x_4 + x_1 x_4 \end{bmatrix},$$

$$G(x) = \begin{bmatrix} x_3 & 1 \\ 1 & 0 \\ 0 & 0 \\ 1 + x_3 & 1 \end{bmatrix}, \quad u = \begin{bmatrix} u_1 \\ u_2 \end{bmatrix}.$$

By applying the transformation introduced in [1], we get:

$$z_{1\sim4} = Q x_{1\sim4}, \tag{18}$$

with

$$Q = \begin{bmatrix} -1 & -1 & 0 & 1 \\ 0 & 0 & 1 & 0 \\ 0 & 1 & 0 & 0 \\ 1 & 0 & 0 & 0 \end{bmatrix},$$

and the corresponding HOFA system model is:

$$\ddot{z}_{1\sim2} = h\left(z_{1\sim2}^{(0\sim1)}, z_3, z_4\right) + L\left(z_{1\sim2}^{(0\sim1)}, z_3, z_4\right) u, \tag{19}$$

where

$$L\left(z_{1\sim2}^{(0\sim1)}, z_3, z_4\right) = \begin{bmatrix} -z_2 - e^{z_2} & -1 \\ 1 & 0 \end{bmatrix}, \tag{20}$$

and

$$h\left(z_{1\sim2}^{(0\sim1)}, z_3, z_4\right) = \begin{bmatrix} -\dot{z}_1 - \zeta z_4 - z_3(e^{2z_2} + e^{z_2}\dot{z}_2) \\ 2z_2\dot{z}_2 + z_3 e^{z_2} \end{bmatrix}, \tag{21}$$

with $\zeta = 1 + z_1 + z_3 + z_4$. Let α be $1/2$ and $\bar{\alpha}$ be $(0, \alpha, 2\alpha, 3\alpha)^\top$, i.e., $s = 4$. According to (6), the fractional order controller can be designed as follows:

$$\begin{cases} u = -L^{-1}\left(z_{1\sim2}^{(0\sim1)}, z_3, z_4\right)\left(A_{\bar{\alpha}} z_{1\sim2}^{(\bar{\alpha})} + u^*\right), \\ u^* = h\left(z_{1\sim2}^{(0\sim1)}, z_3, z_4\right). \end{cases} \tag{22}$$

Let $A_{\bar{\alpha}}$ be given by the following matrices such that (8) is fulfilled:

$$A_{\alpha_0} = \begin{bmatrix} -0.2204 & -39.3959 \\ 1.5141 & -1.8611 \end{bmatrix},$$

$$A_{\alpha_1} = \begin{bmatrix} -77.3649 & -76.1591 \\ -1.3837 & -3.9031 \end{bmatrix},$$

$$A_{\alpha_2} = \begin{bmatrix} 150.3091 & -108.4296 \\ 4.6048 & -5.5316 \end{bmatrix},$$

$$A_{\alpha_3} = \begin{bmatrix} -0.8857 & -55.4753 \\ 2.8862 & -3.9470 \end{bmatrix}.$$

The pole location of A_c is depicted in Fig. 1.

Let the observations of z_1 and z_2 be corrupting by zero-mean white Gaussian noises with a variance 0.0005 on $[0, 5]$ and the sampling period T_s be 0.0005. The exogenous input signal v^* is $(3\sin(5t), 5\sin(10t))^\top$ as depicted in Fig.

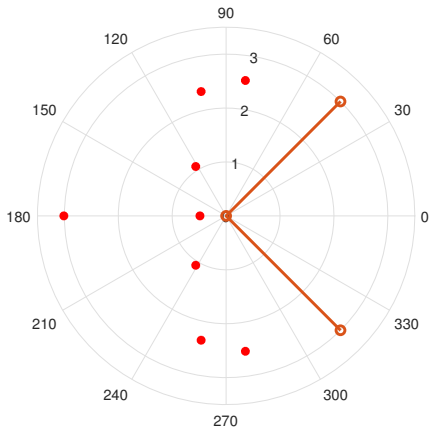

Fig. 1: Location of the desired eigenvalues.

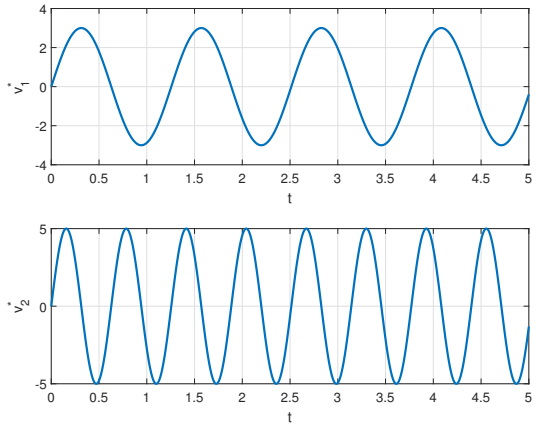

Fig. 2: Exogenous input signal v^*.

2. The initial value of x is given by $[0.01, 0.01, 0.01, 0.01]^\top$. By taking $T = 1.5$ in Theorem 2, $z_{1\sim 2}^{(0\sim 1)}$ is estimated online by using (9). The noisy observation and estimation of $z_{1\sim 2}$ are depicted in Fig. 3. To illustrate the performance of the proposed algebraic estimation method, the classical numerical difference method is adopted for comparison [24]. Then, the estimations of $z_1^{(1)}$ and $z_2^{(1)}$ are depicted in Fig. 4 and Fig. 5, respectively. The corresponding trajectories of x are shown in Fig. 6. Hence, the efficiency of the proposed algebraic differentiator based fractional order controller is verified in a noisy environment.

5 Conclusion

In this paper, a fractional order controller u designed by the HOFA system approach was studied. To obtain the fractional order controller u, the algebraic integral formulas of $z_a^{(0\sim 2m_c-1)}$ were derived by applying the modulating functions method, where the Riemann-Liouville fractional sequential derivatives of z_a are involved. A simulation example was given to illustrate the proposed results. More efforts on the implementation of fractional order controllers for HOFA system models will be devoted in future works.

References

[1] G. Duan, "High-order fully actuated system approaches: Part i. models and basic procedure," *International Journal of Systems Science*, vol. 52, no. 2, pp. 422–435, 2021.

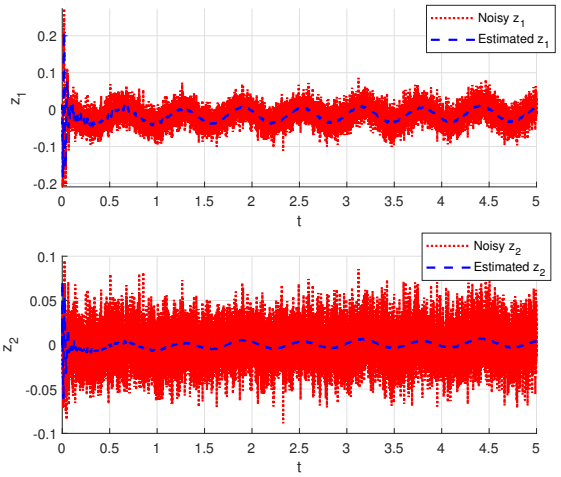

Fig. 3: Noisy observation and estimation of $z_{1\sim 2}$.

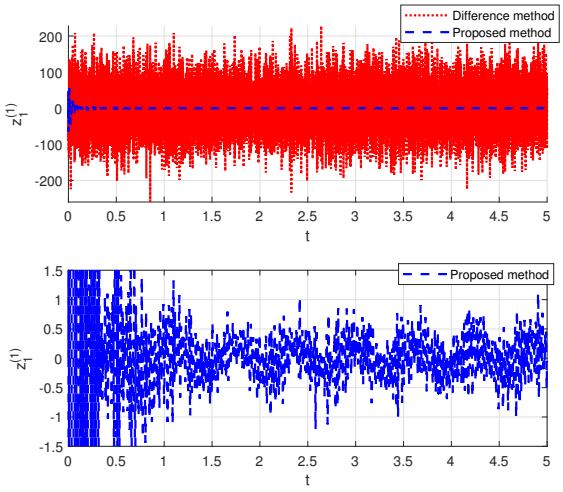

Fig. 4: Estimation of $z_1^{(1)}$.

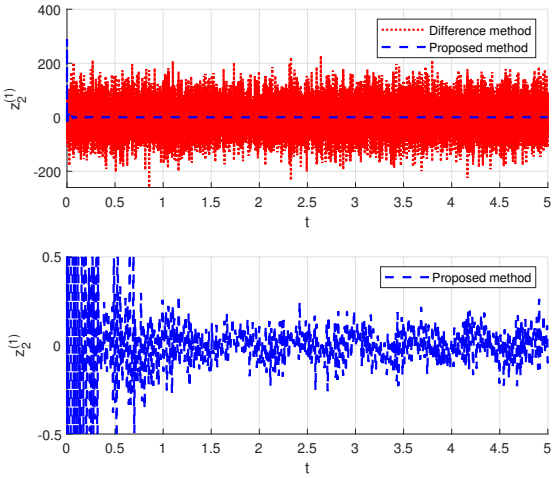

Fig. 5: Estimation of $z_2^{(1)}$.

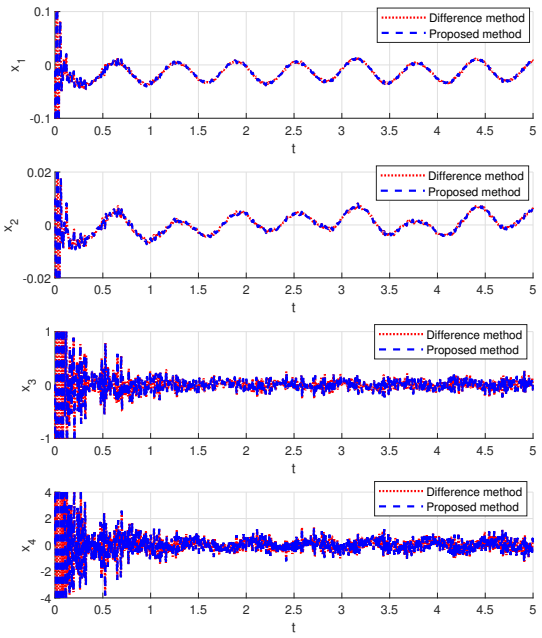

Fig. 6: Trajectories of x.

[2] G. Duan, "High-order fully actuated system approaches: part vii. controllability, stabilisability and parametric designs," *International Journal of Systems Science*, vol. 52, no. 14, pp. 3091–3114, 2021.

[3] D. Gu and S. Wang, "A high-order fully actuated system approach for a class of nonlinear systems," *Journal of Systems Science and Complexity*, vol. 35, no. 2, pp. 714–730, 2022.

[4] F. Xiao and L. Chen, "Attitude control of spherical liquid-filled spacecraft based on high-order fully actuated system approaches," *Journal of Systems Science and Complexity*, vol. 35, no. 2, pp. 471–480, 2022.

[5] P. Ning, C. Hua, and R. Meng, "Adaptive control for a class of nonlinear time-delay system based on the fully actuated system approaches," *Journal of Systems Science and Complexity*, vol. 35, no. 2, pp. 522–534, 2022.

[6] L. Zhang, L. Zhu, and C. Hua, "Practical prescribed time control based on high-order fully actuated system approach for strong interconnected nonlinear systems," *Nonlinear Dynamics*, vol. 110, no. 4, pp. 3535–3545, 2022.

[7] F. Adıgüzel and Y. Yalçın, "Immersion and invariance disturbance observer-based nonlinear discrete-time control for fully actuated mechanical systems," *International Journal of Systems Science*, vol. 53, no. 2, pp. 388–401, 2022.

[8] M. Cai, X. He, and D. Zhou, "Self-healing fault tolerant control for high-order fully-actuated systems against sensor faults: A redundancy framework," *IEEE Transactions on Cybernetics*, 2023.

[9] Q. Liu, L. Zhang, B. Sun, Y. Xiao, and G. Fan, "Fixed-time disturbance observer-based attitude prescribed performance predictive control for flexible spacecraft," *IEEE Transactions on Aerospace and Electronic Systems*, 2024.

[10] I. Podlubny, "Fractional differential equations," *Academic Press, London*, p. E2, 1999.

[11] M. Shitikova, "Fractional operator viscoelastic models in dynamic problems of mechanics of solids: A review," *Mechanics of solids*, pp. 1–33, 2022.

[12] I. Podlubny, "Fractional-order systems and $pi^{\lambda}d^{\mu}$ - controllers," *IEEE Transactions on automatic control*, vol. 44, no. 1, pp. 208–214, 1999.

[13] M. Xiao, B. Tao, W. X. Zheng, and G. Jiang, "Fractional-order pid controller synthesis for bifurcation of fractional-order small-world networks," *IEEE Transactions on Systems, Man, and Cybernetics: Systems*, 2019.

[14] L. Liu, D. Xue, and S. Zhang, "General type industrial temperature system control based on fuzzy fractional-order pid controller," *Complex & Intelligent Systems*, vol. 9, no. 3, pp. 2585–2597, 2023.

[15] I. Petráš, *Fractional-order nonlinear systems: modeling, analysis and simulation*. Springer Science & Business Media, 2011.

[16] D. Xue, *Fractional-order Control Systems - Fundamentals and Numerical Implementations*. Berlin: de Gruyter Press, 2017.

[17] A. Othmane, L. Kiltz, and J. Rudolph, "Survey on algebraic numerical differentiation: historical developments, parametrization, examples, and applications," *International Journal of Systems Science*, vol. 53, no. 9, pp. 1848–1887, 2022.

[18] D.-Y. Liu, Y. Tian, D. Boutat, and T.-M. Laleg-Kirati, "An algebraic fractional order differentiator for a class of signals satisfying a linear differential equation," *Signal Processing*, vol. 116, pp. 78–90, 2015.

[19] D.-Y. Liu, G. Zheng, D. Boutat, and H.-R. Liu, "Non-asymptotic fractional order differentiator for a class of fractional order linear systems," *Automatica*, vol. 78, pp. 61–71, 2017.

[20] Y.-Q. Wei, D.-Y. Liu, D. Boutat, H.-R. Liu, and Z.-H. Wu, "Modulating functions based model-free fractional order differentiators using a sliding integration window," *Automatica*, vol. 130, p. 109679, 2021.

[21] Y.-Q. Wei, D.-Y. Liu, D. Boutat, H.-R. Liu, and C. Lv, "Modulating functions based differentiator of the pseudo-state for a class of fractional order linear systems," *Journal of Computational and Applied Mathematics*, vol. 384, p. 113161, 2021.

[22] Z.-B. Wang, D.-Y. Liu, D. Boutat, X. Zhang, and P. Shi, "Nonasymptotic fractional derivative estimation of the pseudo-state for a class of fractional-order partial unknown nonlinear systems," *IEEE Transactions on Cybernetics*, 2023.

[23] Y.-Q. Wei, C.-C. Hua, and D.-Y. Liu, "Fractional order controller design for a class of nonlinear systems by high-order fully actuated system approach," in *2022 China Automation Congress (CAC)*. IEEE, 2022, pp. 2439–2443.

[24] W. Y. Yang, W. Cao, J. Kim, K. W. Park, H.-H. Park, J. Joung, J.-S. Ro, H. L. Lee, C.-H. Hong, and T. Im, *Applied numerical methods using MATLAB*. John Wiley & Sons, 2020.

Proceedings of the 3rd Conference on Fully Actuated System Theory and Applications
May 10-12, 2024, Shenzhen, China

Angle Attitude Control for Motion Platform Driven by Pneumatic Muscle Actuators

Yipeng Cao[1], Li Li[1], Chao Liu[1], Jiaping Qiang[1], Cui-Hua Zhang[1]
1. School of Electrical Engineering, Yanshan University, Qinhuangdao 066004, China
E-mail: yipeng.cao@stumail.ysu.edu.cn, lili@ysu.edu.cn, lc2019@stumail.ysu.edu.cn, qiangjiaping@stumail.ysu.edu.cn, cuihuazhang@ysu.edu.cn

Abstract: In this paper, angle attitude control is investigated for a pneumatic motion platform driven by pneumatic puscle actuators (PMAs) with unknown system parameters and time-varying disturbances. A nonlinear disturbance observer is constructed to observe the lumped disturbances, which consist of external time-varying disturbances and nonlinearity. In order to improve tracking control accuracy, an adaptive parameter estimation method based on estimation error is designed to ensure that the estimated value converges near the true value. A novel practical prescribed-time control is designed to make the tracking error converge to a prescribed performance boundary in a prescribed time, which is independent of the initial conditions. A sufficient condition of the prescribed-time convergence for PMAs system is given by the Lyapunov method. Finally, a series of experiments are provided to verify the effectiveness of the proposed control method.

Key Words: Pneumatic muscle actuators, disturbance observer, parameter estimation, adaptive control, prescribed-time control

1 Introduction

With the rapid development of artificial intelligence and robotics technology, robots are widely used in a variety of complex scenarios [1]-[3], which can be mainly divided into rigid robots and flexible robots. Compared with rigid robots, flexible robots have significant advantages in terms of human-robot safety and robustness to unknown environments, and are more capable of meeting the urgent needs of the next-generation smart revolution. As a kind of soft actuator, pneumatic muscle actuators (PMAs) with bionic properties inspired by human muscles are widely used in the mechanical structure design of various flexible robots because of their advantages of lightness, safe operation and fast response [4].

However, it is noted that the control difficulties of PMAs mainly include model inaccuracy, strong nonlinearity, hysteresis, and disturbances [5], which is a challenge to further improve the precision of the pneumatic motion control driven by PMAs. The existing control methods mainly include sliding-mode control approach [6], active disturbance rejection control approach [7] and model predictive control approach [8]. In the practical application driven by PMAs, it is very important to achieve the ideal control accuracy in a very short control response time. In the past few decades, finite-time control [9], fixed-time control [10] and prescribed-time control [11] are widely used in time-critical applications such as target interception and spacecraft docking. The prescribed time control can set the convergence time in advance, which is independent of the initial conditions and parameters. In [12], Song proposes a prescribed finite-time control method with regular state feedback based on time-varying scaling functions. In addition, research on the prescribed time control of PMAs is limited, and existing methods cannot maintain control of the system beyond the preset time interval. Therefore, it is of great theoretical and practical significance to develop a more practical prescribed time control method to make the system run in infinite time interval.

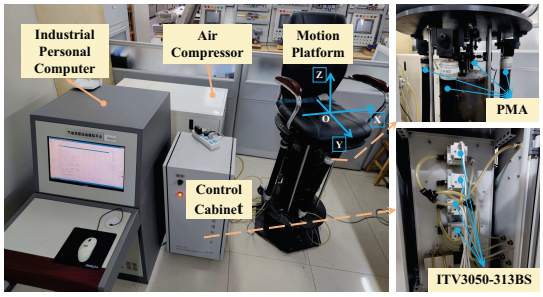

Fig. 1: Structure schematic of the experimental platform

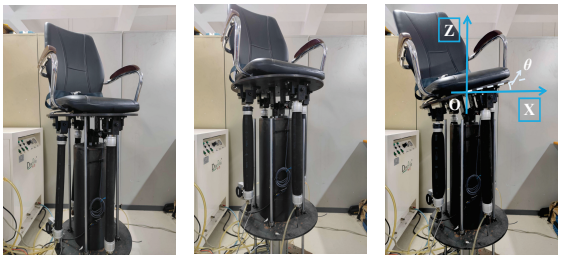

(a) Initial period (b) Preloaded period (c) Simulation period

Fig. 2: Movement process of the pneumatic motion platform

It is worth noting that the PMAs system is a fully-actuated system (FAS), that is, the number of system inputs is equal to the number of controlled degrees of freedom. The objective of this paper is to investigate the angle attitude control of the pneumatic motion platform driven by PMAs with unknown parameters and time-varying disturbances. The main contributions of this paper are summarized as follows:

i The unknown system parameters are estimated by an improved adaptive algorithm based on the parameter estimation error.

ii A nonlinear disturbance observer (NDOB) is constructed

The authors would like to thank the anonymous reviewers for their detailed comments that helped to improve the quality of the paper. The work was supported by the National Natural Science Foundation of China (61773334), and the Key Laboratory of Intelligent Rehabilitation and Neuroregulation of Hebei Province (22567619H).

to observe the time-varying disturbances.

iii An adaptive practical prescribed-time control (APPTC) method is designed to make the tracking error converge to a prescribed performance boundary in a prescribed time, which is independent of the initial conditions.

2 Problem formulation and preliminaries

2.1 Experimental platform

As shown in Fig. 1, a pneumatic motion platform driven by PMAs is shown in Fig. 1. The motion simulation platform can be used for simulated training systems and remote operating systems such as driving body simulators for airplanes, tanks and automobiles, which consists of four parts: a motion platform, an industrial control computer (610H, Advantech), a control cabinet and an air compressor (DA7003CS, DYNAIR). The motion platform is composed of a D/A card, a counting card, a cylinder (DA7003CS, DYNAIR), four PMAs (DMSP40, Festo) and two angle sensors (E6B2-CWZ3E, OMRON). The industrial control computer is used to produce control voltage signals. A proportional directional control valve (MPYE-5-3/8-010-B, Festo) and four pressure proportional valves (ITV3050-313BS, SMC) are integrated in the control cabinet to regulate the internal pressures of cylinder and four PMAs. Moreover, the air compressor is utilized to compress air.

As shown in Fig. 2, the motion process of the pneumatic motion platform mainly has three periods: initial period, preloaded period and motion simulation period. In the initial period shown in Fig. 2(a), the parameter initialization operation is accomplish and the cylinder and PMAs are not injected with compressed air. In the preloaded period shown in Fig. 2(b), the cylinder drives the motion platform to rise to the specified height along the Z-axis, and the preloaded voltages cause four pressure proportional valves to generate preloaded internal pressures. Then, two groups of PMAs use the preloaded internal pressures to generate the preloaded pulling forces. In the motion simulation period shown in Fig. 2(c), one group of PMAs maintains the preloaded state, and the internal pressure of the other group of PMAs is regulated by the change of the control voltages in the pressure proportional valves. Then, PMAs generate different pulling forces and displacements through different internal pressures, resulting in a single-degree-of-freedom deflection motion. The maximum deflection angle of the motion platform is 15°.

2.2 System description

From [13], the following dynamic system model driven by a group of PMAs is shown as

$$\begin{aligned}\ddot{\theta}(t) = &-\frac{b_v}{J}\dot{\theta}(t) + \frac{2\upsilon_0 u_0 r^2(2\epsilon_1\sigma_0+\epsilon_2)L_0^{-1}}{J}\theta(t)\\ &+\frac{2\upsilon_0\upsilon_u r(\epsilon_1\sigma_0^2+\epsilon_2\sigma_0+\epsilon_3)}{J}u(t)\\ &+\frac{2\upsilon_0\upsilon_u\epsilon_1 r^3 L_0^{-2}\theta^2(t)u(t)+\omega(t)}{J}.\end{aligned} \tag{1}$$

where $\theta(t)$ represents the deflection angle of the pneumatic motion platform driven by PMAs, $u(t)$ represents the control voltage signal, $\omega(t)$ represents the unknown nonlinearity, b_v represents the damping coefficient during deflection,

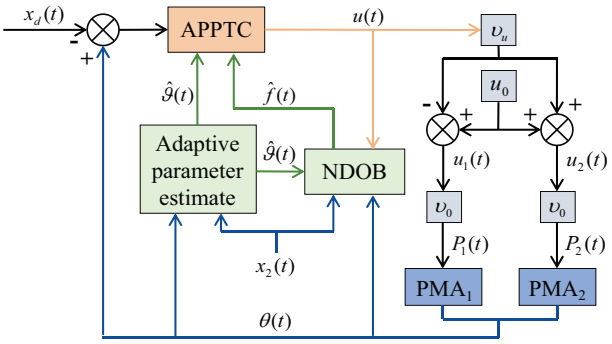

Fig. 3: Control block diagram of the proposed method

u_0 represents the preloaded voltage, υ_0 represents the proportionality coefficient of input pressure to input voltage, υ_u represents the voltage distribution coefficient, ϵ_1, ϵ_2 and ϵ_3 represent the known parameters of the dynamic model, J represents the moment of inertia, L_0 represents the initial length of PMAs, σ_0 represents the contraction coefficient of PMAs in preloaded state, and r represents the moment arm during deflection. Let $x_1(t) = \theta(t)$ and $x_2(t) = \dot{\theta}(t)$, the state space equations of system (1) are described as

$$\begin{cases}\dot{x}_1(t) = x_2(t)\\ \dot{x}_2(t) = b_1 x_1(t) + b_2 x_2(t) + b_0 u(t) + f(t)\end{cases} \tag{2}$$

with b_0 is an adjustable parameter and $f(t) = (b-b_0)u(t) + \varpi(t)$, where

$$\begin{aligned} b_1 &= \frac{2\upsilon_0 u_0 r^2(2\epsilon_1\sigma_0+\epsilon_2)L_0^{-1}}{J},\ b_2 = -\frac{b_v}{J},\\ b &= \frac{2\upsilon_0\upsilon_u r(\epsilon_1\sigma_0^2+\epsilon_2\sigma_0+\epsilon_3)}{J},\\ \varpi(t) &= \frac{2\upsilon_0\upsilon_u\epsilon_1 r^3 L_0^{-2}x_1^2(t)u(t)+\omega(t)}{J}.\end{aligned}$$

Before the specific method design, we first introduce a definition and an assumption.

Definition 1 *There is a system defined as*

$$\dot{\chi} = f(t;\chi;\varphi) \tag{3}$$

where χ is a state variable, $f : R_+ \times R^n \to R^n$ is a nonlinear function and piecewise continuous in time t for all parameter φ. Let $\Phi \subset R^m$ be a set of parameters. System (3) is said to be practical prescribed time stable, if for all $t \geq T$ and $\chi(0) = \chi_0 \in R^n$, there exist $\varphi \subset \Phi$ such that $\|\chi(t,\varphi)\| < \varepsilon$ for any given positive scalars $\varepsilon > 0$ and $T > 0$.

Assumption 1 *Note that $f(t)$ is continuously differentiable and bounded, which is treated as a lumped disturbance of the system (2). Thus, there exist positive constants d_{f1} and d_{f2} such that $|f(t)| \leq d_{f1}$ and $|\dot{f}(t)| \leq d_{f2}$ hold.*

3 Controller Design

As shown in Fig. 3, APPTC method is proposed to realize the attitude control of PMAs system.

3.1 Adaptive parameter estimation error acquisition

We will design a unified adaptive law to estimate unknown parameters b_1 and b_2, which is convenient for the subsequent development of NDOB and APPTC. Define $\psi(t) = [x_1(t),\ x_2(t)]^T$ and $\vartheta = [b_1,\ b_2]$, the second equation of (2) can be represented as a compact form as

$$\dot{x}_2(t) = \vartheta\psi(t) + b_0 u + f(t), \tag{4}$$

where ϑ is unknown system parameter vector.

Based on (4), an explicit expression of the error $\tilde{\vartheta} = \vartheta - \hat{\vartheta}$ will be obtained using the filter operation. To avoid the use of $\dot{x}_2(t)$, $\dot{\psi}(t)$ and $\dot{u}(t)$, the following three variables through the low-pass filter are expressed as

$$\begin{cases} k\dot{x}_{2r}(t) + x_{2r}(t) = x_2(t), x_{2r}(0) = 0 \\ k\dot{\psi}_r(t) + \psi_r(t) = \psi(t), \psi_r(0) = 0 \\ k\dot{u}_r(t) + u_r(t) = u(t), u_r(0) = 0 \end{cases} \tag{5}$$

where $k > 0$ is a filtered parameter. $x_{2r}(t)$, $\psi_r(t)$ and $u_r(t)$ are filtered variables. Then the following dummy variable f_r is defined as

$$k\dot{f}_r(t) + f_r(t) = f(t), f_r(0) = 0 \tag{6}$$

where f_r is only used for analysis and does not need to be calculated online. Based on the (4)-(6), one has that

$$\dot{x}_{2r}(t) = \frac{x_2 - x_{2r}}{k} = \vartheta\psi_r(t) + b_0 u_r + f_r(t) \tag{7}$$

Define intermediate matrix P_1 and vector Q_1, one can be calculated by

$$\begin{cases} \dot{P}_1(t) = -lP_1(t) + \psi_r(t)\psi_r(t)^T, \\ \dot{Q}_1(t) = -lQ_1(t) + \psi_r(t)[(x_2(t) - x_{2r}(t))/k - b_0 u_r] \end{cases}$$

where $P_1(0) = 0$ and $Q_1(0) = 0$, and $l > 0$ is a positive scalar to guarantee the boundedness of P_1 and Q_1. Then, the solution of P_1 and Q_1 can be calculated as

$$\begin{cases} P_1(t) = \int_0^t e^{-l(t-s)}\psi_r(s)\psi_r(s)^T ds, \\ Q_1(t) = \int_0^t e^{-l(t-s)}\psi_r(s)[(x_2(t) - x_{2r}(t))/k - b_0 u_r]ds \end{cases}$$

Combining with (7), the following relationship between P_1 and Q_1 is expressed as

$$Q_1(t) = P_1(t)\vartheta^T - \Delta(t)$$

where $\Delta(t) = -\int_0^t e^{-l(t-s)}\psi_s(r)f_r(s)ds$ is bounded because the $\psi(t)$, $\psi_r(t)$ and lumped disturbances $f(t)$, $f_r(t)$ are bounded. Hence, there exists $|\Delta(t)| \le d_\Delta$ for a positive scalar $d_\Delta > 0$.

Then, another online calculated vector H_1 associated with P_1 and Q_1 is expressed as

$$\begin{aligned} H_1(t) &= P_1(t)\hat{\vartheta}^T - Q_1(t) = P_1(t)\hat{\vartheta}^T - P_1(t)\vartheta^T + \Delta(t) \\ &= -P_1(t)\tilde{\vartheta}^T + \Delta(t) \end{aligned} \tag{8}$$

where $\hat{\vartheta}$ represents the estimate of the unknown parameter ϑ, and $\tilde{\vartheta} = \vartheta - \hat{\vartheta}$ represents the estimation error.

It can be seen that the online calculated vector H_1 in (8) associated with P_1 and Q_1 contains information of the estimation error $\tilde{\vartheta}$. Therefore, driving the designed adaptive law by using H_1 can ensure the convergence of parameter estimation while improving the control performance of the system.

In addition, appropriate excitation condition needs to be imposed in adaptive control to ensure the convergence of parameter estimation. As shown in the proof of [14], the intermediate matrix P_1 is positive definite and satisfies the minimum eigenvalue $\lambda_{min}(P_1) > \phi > 0$, which is related to the standard persistent excitation condition. The research case in this paper is able to ensure that there is a persistent excitation condition in the designed adaptive update law.

3.2 NDOB design

In this subsection, motivated by [17], the NDOB is designed to estimate the lumped disturbances $f(t)$ for more accurate attitude control. The specific design is as follows

$$\begin{cases} \hat{f}(t) &= f_z(t) + \kappa(t)x_2(t) \\ \dot{f}_z(t) &= -\kappa(t)(\hat{b}_1 x_1(t) + \hat{b}_2 x_2(t) \\ &\quad + b_0 u(t) + \hat{f}(t)) - \dot{\kappa}(t)x_2(t) \\ \kappa(t) &= \kappa_1(1 - e^{-\kappa_2 t}) \end{cases} \tag{9}$$

where $\hat{f}(t)$ is estimate value of $f(t)$, $\kappa(t)$ is a nonlinear function with $\kappa_1 > 0,\ \kappa_2 > 0$, and $\tilde{f}(t)$ is disturbance estimation error with

$$\begin{aligned} \dot{\tilde{f}}(t) &= \dot{f}(t) - \dot{\hat{f}}(t) \\ &= \dot{f}(t) - \dot{f}_z(t) - \dot{\kappa}(t)x_2(t) - \kappa(t)\dot{x}_2(t) \\ &= \kappa(t)\big((\hat{b}_1 - b_1)x_1(t) + (\hat{b}_2 - b_2)x_2(t) \\ &\quad + \hat{f}(t) - f(t)\big) + \dot{f}(t) \\ &= \kappa(t)(-\tilde{\vartheta}\psi(t) - \tilde{f}(t)) + \dot{f}(t) \end{aligned}$$

3.3 APPTC method design

In order to improve the control accuracy while reducing the overshoot and response time in the attitude control of pneumatic motion platforms, APPTC method is proposed in this subsection.

Based on the user-assigned settling time T and performance boundary ε, the designed time-varying function $\eta(t)$ is expressed as

$$\eta(t) = \begin{cases} a(e^{-t} - e^{-T})^{2p} + \varepsilon, & t \in [0,\ T) \\ \varepsilon, & t \in [T,\ \infty) \end{cases} \tag{10}$$

with $a > 0$, where $0 < T < \infty$ and $0 < \varepsilon < \infty$. p is a positive integer with $2p > n + 1$, which ensures that $\eta^{(i)}(t)(i = 0,\ 1, ...,\ n)$ is continuously differentiable. Let $z_1(t) = x_1(t) - x_d(t)$ with $z_1(t)$ is tracking error, if the following

$$-\eta(t) < z(t) < \eta(t) \tag{11}$$

is satisfied. Based on (10) and (11), one has that

$$|z_1(t)| < \varepsilon,\ \forall t \ge T$$

Then, define a performance function $\gamma(t)$ that is represented as

$$\gamma(t) = c(\eta(t) - z_1(t))(\eta t + z_1(t)) = c(\eta^2(t) - z_1^2(t))$$

where c is a positive constant. $\eta(t) - z_1(t)$ and $\eta(t) + z_1(t)$ are regarded as two distances from constraint boundaries $\eta(t)$ and $-\eta(t)$ to tracking error $z_1(t)$. Different from [15], the deferred constraint boundary in (11) can be changed by adjusting parameter a in the designed time-varying function $\eta(t)$, which avoids the infinity of $\gamma(t)$ caused by the infinity of $\eta(t)$ in time $[0, T)$ and reduces the complexity of analysis.

Further, the transformed variable $\xi_1(t)$ is constructed as

$$\xi_1(t) = \frac{z_1(t)}{c(\eta^2(t) - z_1^2(t))}$$

It is noted that the variable $\xi_1(t)$ exhibits the following two properties. The first property is that $\xi_1(t) = 0$ if and only if $z_1(t) = 0$. The second property is that $\xi_1 \to \infty$ when $z_1(t) \to \eta(t)$ or $z_1(t) \to -\eta(t)$.

Before the subsequent design, a crucial lemma based on the properties of $\xi_1(t)$ is given.

Lemma 1 *[15] If $\xi_1 \in L_\infty$, then $|z_1(t)| < \eta(t)$ holds for all $t \in [0, \infty)$.*

Differentiating $\xi_1(t)$ with respect to time, it is obtained that

$$\dot{\xi}_1(t) = \Big(\frac{1}{\gamma(t)} + \frac{2cz_1^2(t)}{\gamma(t)}\Big)\dot{z}_1(t) - \frac{2c\eta(t)\dot{\eta}(t)z_1(t)}{\gamma^2(t)} \quad (12)$$

Combining with (2) and (12), the $\dot{\xi}_1(t)$ is rewritten as

$$\dot{\xi}_1(t) = \mu(x_2(t) - \dot{x}_d(t)) + \nu$$

where

$$\mu = \frac{1}{\gamma(t)} + \frac{2cz_1^2(t)}{\gamma(t)},\ \nu = -\frac{2c\eta(t)\dot{\eta}(t)z_1(t)}{\gamma^2(t)}$$

It can be easily that μ is strictly positive. Meanwhile, the system (2) is converted into the following form

$$\begin{cases} \dot{\xi}_1(t) = \mu(x_2(t) - \dot{x}_d(t)) + \nu \\ \dot{x}_1(t) = x_2(t) \\ \dot{x}_2(t) = b_1x_1(t) + b_2x_2(t) + b_0u(t) + f(t) \end{cases} \quad (13)$$

Further, it is only necessary to focus on the design of controller $u(t)$ to stabilize the transformed system (13) to ensure the deferred tracking error constraint given in (11). The controller $u(t)$ will be designed by an backstepping method. First, the transformed coordinate is represented as follows

$$\xi_2(t) = x_2(t) - \alpha(t)$$

with the virtual controller $\alpha(t)$ derived as

$$\alpha = -\frac{k_1}{\mu}\xi_1 - \mu\xi_1\dot{x}_d^2 - \frac{\nu^2}{\mu}\xi_1$$

Note that the adaptive updating law for parameter estimation is constructed as

$$\dot{\hat{\vartheta}} = \Gamma(\xi_2(t)\psi(t) + \kappa(t)\hat{f}(t)\psi(t) - \sigma H_1(t)) \quad (14)$$

where $\Gamma > 0$ is an adaptive gain vector and $\sigma > 0$ is a learning gain. Hence, the final control law is designed as

$$u = \frac{1}{b_0}(\dot{\alpha} - k_2\xi_2 - \hat{\vartheta}\psi - \hat{f} - \mu\xi_1^2\xi_2) \quad (15)$$

where $k_2 > 0$ is another adjustable control parameter. Then, define

$$\begin{aligned} V &= V_1 + V_2 + V_3 + V_4 \\ &= \frac{1}{2}\xi_1^2 + \frac{1}{2}\xi_2^2 + \frac{1}{2}\tilde{\vartheta}\Gamma^{-1}\tilde{\vartheta}^T + \frac{1}{2}\tilde{f}^2 \end{aligned}$$

It can be derived that

$$\begin{aligned} \dot{V} &\le -k_1\xi_1^2 - (k_2 - \frac{\delta}{2})\xi_2^2 - (\phi - \frac{\sigma}{2\delta} - \frac{\kappa d_{f1}}{2\delta})\|\tilde{\vartheta}\|^2 \\ &\quad - (\kappa - \frac{1}{\delta})\tilde{f}^2 + \frac{\delta}{2}(\sigma\|\Delta\|^2 + \kappa d_{f1}\|\psi\|^2 + d_{f2}^2) + \frac{3}{4} \\ &\le -\varphi V + \varrho \end{aligned}$$

with

$$\begin{aligned} \varphi = \min\Bigg\{ & 2k_1, 2(k_2 - \frac{\delta}{2}), \\ & 2(\phi - \frac{\sigma}{2\delta} - \frac{\kappa d_{f1}}{2\delta})\Big/\lambda_{\max}(\Gamma^{-1}), 2(\kappa - \frac{1}{\delta})\Bigg\}, \\ \varrho = \frac{\delta}{2}(\sigma\|\Delta\|^2 + \kappa d_{f1}\|\psi\|^2 + d_{f2}^2) + \frac{3}{4} \end{aligned}$$

where φ is a positive scalar for any control parameter $k_2 > \frac{\delta}{2}$ and $\delta > \max\Big\{\frac{1+\kappa d_{f1}}{2\phi}, \frac{1}{\kappa}\Big\}$, and χ is an another positive scalar. Subsequently, the following theorem will be further elaborated.

Theorem 1 *Consider the system (13) with parameter estimation updating law (14) and adaptive control law (15), then*

(i) The closed loop system is stable. And the disturbance estimation error $\tilde{f}(t)$ and parameter estimation error $\tilde{\vartheta}$ converges to a small compact set

(ii) The tracking error $z_1(t)$ will converge to the preset performance region $\Omega = \{z_1 \in R : |z_1(t) < \varepsilon|\}$ within prescribed settling time T , where ε and T are all predetermined by users.

Proof.

(i) Integrating over $\dot{V} \le -\varphi V + \varrho$ yields $V \le e^{-\varphi t}V(0) + \frac{\varrho}{\varphi}(1 - e^{-\varphi t}) \le V(0) + \frac{\varrho}{\varphi}$. Thus, there exists $V \in L_\infty$ for any bounded initial conditions, in which implies $\xi_1 \in L_\infty$ and $\xi_2 \in L_\infty$. Therefore, the signals ξ_1 and ξ_2 are ultimately uniformly bounded and the closed-loop system (13) is stable. At the same time, it is concluded that the disturbance estimation error $\tilde{f}(t)$ and parameter estimation error $\tilde{\vartheta}$ are ultimately uniformly bounded. The proof is completed.

(ii) From Lemma 1, it is obtained that $-\eta(t) < z_1(t) < \eta(t)$ since ξ_1 is bounded. Thus, we can infer that the tracking error $|z_1(t)| < \varepsilon$ within time $t \ge T$ by the design of $\eta(t)$. That is, the tracking error $z_1(t)$ converges to the preset performance region $\Omega = \{z_1 \in R : |z_1(t) < \varepsilon|\}$ within the prescribed settling time T.

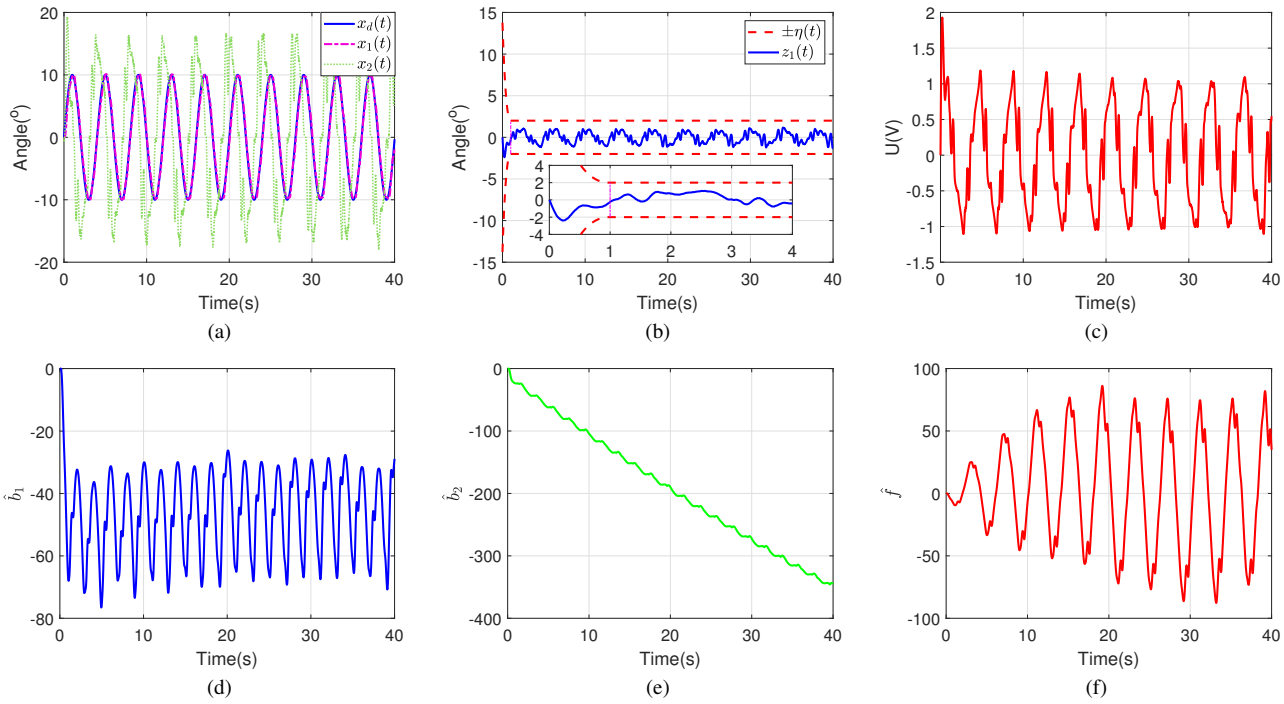

Fig. 4: Tracking control experiment results. (a) Deflection angle $x_1(t)$ and angular velocity $x_2(t)$. (b) Tracking error signal $z_1(t)$. (c) Control voltage signal $u(t)$. (d) Estimated parameter $\hat{b}_1$. (e) Estimated parameter $\hat{b}_2$. (f) Disturbance estimation signal $\hat{f}(t)$ by NDOB.

4 Experimental results and analysis

In this paper, attitude control is studied for the pneumatic motion platform based on PMAs. In order to further explore the effectiveness of the proposed control method, a series of tracking control experiments are carried out on the pneumatic motion platform. The desired signal $x_d(t)$ is selected as a sinusoidal signal with 0.25 Hz frequencies and 10° amplitudes for a group of PMAs. The sampling interval is 0.01 s in all tracking control experiments. The proportional coefficient of the pressure proportional valves is $\upsilon_0 = 0.09$. The preloaded voltage u_0 is 2 V and the voltage distribution coefficient is set as $\upsilon_u = 1$.

In the experiment, the observer parameters are selected as $k_1 = 36$, $k_2 = 26$, $\kappa_1 = 0.5$ and $\kappa_2 = 0.2$. And the parameters of APPTC method are designed as $T = 1$, $\varepsilon = 2$, $a = 80$, $c = 80$, $\Gamma = [1\ 4]$, $l = 1$, $\sigma = 0.01$ and $k = 0.02$. As shown in Fig. 4(a), the deflection angle $x_1(t)$ and $x_2(t)$ of PMAs are presented, which also implies the experimental result of tracking control. To show the control performance of APPTC method more clearly, the tracking error $z_1(t)$ is shown in Fig. 4(b). It can be seen that $z_1(t)$ converges to a bounded region $|z_1(t)| < \varepsilon$ for $t > T$, where the settling time $T = 1$ s and the performance boundary $\varepsilon = 2$ are all prescribed. As shown in Fig. 4(c), the maximum control voltage signal $u(t)$ does not exceed 2 V, in which the peak voltage generated is to make the deflection angle $x_1(t)$ to track the desired signal $x_d(t)$ quickly. Moreover, the estimation values $\hat{b}_1$ and $\hat{b}_2$ of the unknown parameters are indicated in Fig. 4(d) and Fig. 4(e), respectively. Based on the tracking results in Fig. 6, it is confirmed that $\hat{b}_1$ and $\hat{b}_2$ converge to the bounded regions near the true values, that is, the validity of the designed parameter update law (14) based on the estimated error is verified. In Fig. 4(f), the disturbance value $\hat{f}(t)$ estimated by the designed NDOB (9) is given, which presents a periodic change trend.

5 Conclusion

In this paper, we have investigated the angle attitude control for the pneumatic motion platform driven by PMAs with unknown system parameters and time-varying disturbances. NDOB has been designed to observe the lumped disturbance consists of external time-varying disturbances and nonlinearity. For ensuring that the estimated value converges near the true value, the adaptive parameter estimation method based on estimation error has been designed to improve tracking control accuracy. Subsequently, the observed lumped disturbances of PMAs system have been compensated by the designed APPTC law while the tracking error converges to a prescribed performance boundary in a prescribed time. Then, the convergence analyses of NODB and PMAs system have been given. Finally, experimental results have demonstrated the effectiveness of the proposed method. In the future work, since PMAs system is a FAS, we hope to use the FAS approach [16] to analyze the motion control problem driven by PMAs.

References

[1] K. Wen, T. S. Nguyen, D. Harton, T. Laliberte, C. Gosselin, A backdrivable kinematically redundant (6+3)-degree-of-freedom hybrid parallel robot for intuitive sensorless physical human-robot interaction. *IEEE Transactions on Robotics*, 37(4): 1222-1238, 2021.

[2] Z. Gong, Z. Nie, Q. Liu, X. J. Liu, Design and control of a multi-mobile-robot cooperative transport system based on a novel six degree-of-freedom connector. *ISA Transactions*, 139: 606-620, 2023.

[3] B. Jamil, G. Yoo, Y. Choi, H. Rodrigue, Hybrid robotic manipulator using sensorized articulated segment joints with soft inflatable rubber bellows. *IEEE Transaction on Industrial Electronics*, 69(10): 10259-10269, 2022.

[4] A. Miriyev, K. Stack, H. Lipson, Soft material for soft actuators, *Nature Communications*, 8, 2017.

[5] J. Zhang *et al.*, Robotic artificial muscles: current progress and future perspectives. *IEEE Transactions on Robotics*, 35(3): 761-781, 2019.

[6] J. Huang, Y. Cao, Y. Wang, Adaptive proxy-based sliding mode control for a class of second-order nonlinear systems and its application to pneumatic muscle actuators. *ISA Transactions*, 124: 395-402, 2020.

[7] L. Li , Y. Cao , L. Zhao, Output-based event-triggered tracking control for networked pneumatic muscle actuators system with packet disorders. *Nonlinear Dynamics*, 111(7): 6363-6378, 2023.

[8] J. Huang, Y. Cao, C. Xiong, H. Zhang, An echo state gaussian process-based nonlinear model predictive control for pneumatic muscle actuators. *IEEE Transactions on Automation Science and Engineering*, 16(3): 1071-1084, 2019.

[9] M. Basin, C. B. Panathula, Y. B. Shtessel, Adaptive uniform finite-/fixedtime convergent second-order sliding-mode control. *International Journal of Control*, 89(9): 1777-1787, 2016.

[10] D. Gmez-Gutirrez, On the design of non-autonomous fixed-time controllers with a predefined upper bound of the settling time. *International Journal of Robust and Nonlinear Control*, 30: 3817-3885, 2020.

[11] H. M. Becerra, C. R. Vzquez, G. Arechavaleta, J. Delfin, Predefined time convergence control for high-order integrator systems using time base generators. *IEEE Transactions on Control Systems Technology*, 26(5): 1866-1873, 2018.

[12] Y. Song, Y. Wang, M. Krstic, Time-varying feedback for stabilization in prescribed finite time. *International Journal of Robust and Nonlinear Control*, 29(3): 618-633, 2019.

[13] H. Yang, Y. Yu, J. Zhang, Angle tracking of a pneumatic muscle actuator mechanism under varying load conditions. *Control Engineering Practice*, 61: 1-10, 2017.

[14] J. Na, M. N. Mahyuddin, G. Herrmann, X. Ren, P. Barber, Robust adaptive finite-time parameter estimation and control for robotic systems. *International Journal of Robust and Nonlinear Control*, 25(16): 3045?3071, 2015.

[15] Y. Cao, J. Cao, Y. Song, Practical prescribed time tracking control over infinite time interval involving mismatched uncertainties and non-vanishing disturbances. *Automatica*, 136: 110050, 2022.

[16] G. Duan, High-order fully actuated system approaches: Part I. Models and basic procedure. *International Journal of Systems Science*, 52(2): 422-435, 2021.

[17] R. Zhang, B. Xu, P. Shi, Output feedback control of micromechanical gyroscopes using neural networks and disturbance observer. *IEEE Transactions on Neural Networks and Learning Systems*, 33(3): 962-972, 2022.

Proceedings of the 3rd Conference on Fully Actuated System Theory and Applications
May 10-12, 2024, Shenzhen, China

Observed State-Dependent Adaptive Control for Thermoacoustic Instability in Aeroengine Oscillating Combustion with Unknown Thermal Inertia

Yuzhuo Zhao[1], Dan Ma[2*]

1. College of Information Science and Engineering Northeastern University, Shenyang 110819, China;
2. State Key Laboratory of Synthetical Automation for Process Industries and College of Information Science and Engineering Northeastern University, Shenyang 110819, China;
E-mail: madan@mail.neu.edu.cn

Abstract: Thermoacoustic instability is the main form of combustion instability in aeroengine. For the thermoacoustic system with coupling between sound field and unknown nonlinear flame heat release, an active control method based on the fully actuated system method and a time-delay neural network (NN) state observer is proposed for one acoustic mode. Firstly, a time-delay NN observer is proposed, which addresses the shortcomings of the linear observer in observing nonlinear systems and extends the NN observer to time-delay nonlinear systems. Subsequently, the finite covering lemma is combined with the radial basis neural network (RBF NN) to approximate the unknown nonlinear heat release with the unknown thermal inertia. Then, based on the fully actuated system approach, an adaptive active control strategy is proposed, which ensures that the pressure and velocity of the thermoacoustic system, as well as the observation errors of the pressure and velocity, converge to a small neighborhood about the origin. Finally, the feasibility and effectiveness of the adaptive active control method based on the time-delay NN observer are verified through the coupling of the Culick acoustic motion model and the nonlinear flame response to form the thermoacoustic system.

Key Words: Adaptive Control, Fully Actuated Systems Approach, Nonlinear Time-Delay Systems, Time-Delay Neural Network State Observer

1 Introduction

The combustion chamber is one of the core components of aircraft engines, whose main task is to convert chemical energy into thermal energy. However, a small energy conversion in the combustion chamber may generate random fluctuations or noise, leading to combustion instability. The main form of combustion instability in aircraft engines is thermoacoustic instability [1], which is essentially the coupling of the heat release rate and the pressure, and the process of thermal power conversion (thermal and acoustic energy). Initially, the phenomenon of thermoacoustic instability is discovered by Higgins [2] in experiments. Subsequently, the thermoacoustic system is first scientifically described, and the "Rayleigh criterion" is proposed [3]. On this basis, mathematical models for thermoacoustic instability corresponding to different combustion situations [4, 5] are provided. In 1976, the second-order nonlinear dynamics model (Culick model) is proposed by using the Galerkin method [6], which is extended to the third-order nonlinear dynamics model [7].

However, in the Culick model, only the impact of acoustic motion on the model is considered, while the effects of flame combustion response and fluid dynamics instability are not taken into account. In this regard, Meng et al. [8] applied the $n-\tau$ model of combustion response [9] to the acoustic model based on the Culick acoustic model through the source term. However, with the development of computer simulation technology and a large number of experimental studies, it has been found that the unbounded nature of the $n-\tau$ flame response model can lead to divergent results, which increasingly cannot meet the needs of actual working conditions. Therefore, a nonlinear delayed flame response model [10] is proposed, which utilizes the arctangent function to ensure that the final result does not diverge and reaches a finite value. However, the above heat release models are not derived from physical principles, but are obtained through experiments and other means, and nonlinear convection and other factors are ignored in the models. Therefore, it is difficult to provide an accurate model for heat release. So, the unknown nonlinear function is considered to describe the coupling between the flame combustion response and the sound field.

At present, in order to suppress the phenomenon of thermoacoustic instability, both the passive control and the active control have received attention. Among them, the passive control mainly suppresses combustion instability by changing the structure of the combustion chamber or replacing propellants [11, 12]. The advantages of the passive control are its simple structure and good reliability, but its applicability is limited, the development cycle is long, and the development cost is high. Tsien [13] first applied control theory to suppress combustion instability in rocket engines. Subsequently, the proportional integral derivative (PID) controller [14], the feedback controller [15] and the optimal controller [16] are proposed to suppress thermoacoustic instability.

It is worth noting that through the concept and description of the high-order fully actuated system proposed in [17], we find that the thermoacoustic system is a typical type of the fully actuated system. Obviously, designing an active control strategy based on the fully actuated system method can not only reduce the complexity of controller design, but also facilitate the implementation of actual physical system design. Based on the high-order fully actuated system method [18], it is easy to design a controller to eliminate any measurable nonlinear terms and transform the closed-loop system into a linear system with the required characteristic struc-

This work is supported by NSFC under Grant U23A20324.

ture. This result also extends to the uncertain nonlinear system and proposes the adaptive controller [19] and the robust controller [20]. The related work has also been applied to the robust stabilization of thermoacoustic systems in the Rijke tube [21].

It is worth mentioning that the control methods proposed above are all state feedback control strategies, which rely on all states of the system. However, for the thermoacoustic system in the combustion chamber of aircraft engines, it only measures the fluctuation of pressure, and the fluctuation of velocity is difficult to measure. Therefore, the above control strategies are not applicable to thermoacoustic systems where only pressure fluctuations can be measured. To overcome this difficulty, the linear observer [22], the fuzzy observer [23], and the NN observer [24] have been proposed for nonlinear systems with unmeasurable states. However, it must be said that the linear observer ignores the nonlinear structure of the system, resulting in larger observation errors compared to the fuzzy or NN observer. However, the heat release in thermoacoustic systems has a time delay, so the fuzzy observer and the NN observer are not applicable. Therefore, a time-delay NN observer is proposed to overcome the drawbacks of the linear observer and extends the nonlinear observer to time-delay systems.

An adaptive active control strategy is proposed based on the fully actuated system method and the time-delay NN observer for the thermoacoustic system of an aircraft engine combustion chamber to ensure that the pressure and the velocity and the observation errors of the pressure and the velocity converge to a small neighborhood about the origin. The main contributions of this article include: 1)The finite covering lemma and the RBF NN are combined to approximate the unknown nonlinear heat release with the time delay from fuel injection to combustion. 2) A time-delay NN observer is proposed to overcome the shortcomings of the linear observer and extends the nonlinear observer to time-delay systems.

2 System Statements and Preliminaries

2.1 Model of the Thermoacoustic unstable System

Thermoacoustic instability is the main form of combustion instability in aircraft engines. According to the thermoacoustic unstable model with flame combustion effects in [8], a second-order nonlinear time-delay system with one acoustic mode is represented as

$$\begin{cases} \ddot{\eta}_1 + {\omega_1}^2 \eta_1 = F_1(\eta_1, \dot{\eta}_1) + Q_1\left(\eta_1(t-\tau)\right) + Bu_1, \\ y = \bar{p}\psi_1(x)\,\eta_1, \end{cases} \tag{1}$$

where $F_1 = -D_{11}\dot{\eta}_1 - E_{11}\eta_1 - A_{111}\dot{\eta}_1\dot{\eta}_1 - B_{111}\eta_1\eta_1 - R_{1111}\dot{\eta}_1\dot{\eta}_1\dot{\eta}_1 - S_{1111}\eta_1\eta_1\eta_1$, $B = \frac{\bar{a}^2}{\bar{p}E_1^2}\psi_1(r)$, η_1 and $\dot{\eta}_1$ respectively represent the amplitude of the pressure fluctuation and the velocity fluctuation; ω_1 is the natural frequency; $D_{11}, E_{11}, A_{111}, B_{111}, R_{1111}, S_{1111}$ are coefficients related to the motion of sound waves; $\bar{a}$ represents the speed of sound in the mixture; $\bar{P}$ represents the average pressure of the combustion chamber; E_1 represents the Euclidean norm; $\psi_1(x) = cos\frac{\pi x}{L}$ and $\psi_1(r) = cos\frac{\pi r}{L}$ are basis functions, x and r are the positions of the sensor and the actuator, respectively; L is the length of the combustion chamber; $Q_1\left(\eta_1(t-\tau)\right)$ is the heat release model related to the pressure amplitude with the unknown thermal inertia τ, where τ is the convective time from fuel injection to its combustion with upper bound τ_M. Due to the fact that the existing heat release models are not mechanistic models, but approximate models obtained through experiments, and a large number of experiments have shown that nonlinear factors are ignored in the models. Therefore, without loss of generality, an unknown nonlinear heat release with the unknown thermal inertia is considered in this paper. The system output y is the pressure fluctuation in the combustion chamber, and only the pressure fluctuation y is measurable directly.

According to [8], η_1 and $\dot{\eta}_1$ are the amplitude of the pressure and the velocity obtained through the Galerkin method, respectively. What's more, the pressure p and the velocity v_g are respectively represented as

$$p = \bar{p}\psi_1(x)\,\eta_1, \tag{2}$$

$$v_g = \frac{\nabla\psi_1(x)}{\bar{\gamma}k_1^2}\dot{\eta}_1, \tag{3}$$

where $k_1 = \frac{\pi}{L}$, $\nabla\psi_1^2(x) + k_1^2\psi_1^2(x) = 0$, $\bar{\gamma}$ represents the specific heat ratio.

The control gain B of the thermoacoustic system (1) is reversible, so the thermoacoustic system (1) is a second-order fully actuated system. Therefore, by using the standard description in [18], the thermoacoustic system (1) can be rewritten as

$$\begin{cases} \eta_1^{(2)} = f_1\left(\eta_1^{(0\sim1)}\right) + Q_1\left(\eta_1^{(0\sim1)}(t-\tau)\right) + Bu_1, \\ y = C\eta_1^{(0\sim1)}, \end{cases} \tag{4}$$

where $\ddot{\eta}_1 = \eta_1^{(2)}(t)$, $f_1\left(\eta_1^{(0\sim1)}\right) = F_1 - {\omega_1}^2\eta_1(t)$, $\eta_1^{(0\sim1)} = \begin{bmatrix} \eta_1 \\ \dot{\eta}_1 \end{bmatrix}$, $C = \begin{bmatrix} \bar{p}\psi_1(x) & 0 \end{bmatrix}$.

2.2 Preliminaries

Lemma 1 [25]: Supposing that $Q_1\left(\eta_1^{(0\sim1)}\right) : \Omega_{\eta_1^{(0\sim1)}} \to \mathbb{R}$ is a smooth function on compact set $\Omega_{\eta_1^{(0\sim1)}} \subset \mathbb{R}^n$, and for a constant time-delay $\tau \in [0, \tau_M]$, $\eta_1^{(0\sim1)} = \eta_1^{(0\sim1)}(t-\tau)$ is uniformly continuous with respect to t. Then, for any parameter $\delta_1 > 0$, there exists a finite partition of $[0, \tau_M]$, independent of t

$$0 \le t_1 \le t_2 \le \ldots \le t_m \le \tau_M$$

from which a point

$$\bar{\tau} \in \{t_1, \ldots, t_m\}$$

can be extracted, such that

$$|Q_1\left(\eta_1^{(0\sim1)}(t-\tau)\right) - Q_1\left(\eta_1^{(0\sim1)}(t-\bar{\tau})\right)| < \delta_1, \ \ \forall t \ge 0.$$

Remark 1: Since τ represents an unknown constant time-delay, the RBF NN cannot directly approximate the unknown nonlinear function $Q_1\left(\eta_1^{(0\sim1)}(t-\tau)\right)$. Therefore, using Lemma 1, the unknown nonlinear function $Q_1\left(\eta_1^{(0\sim1)}(t-\tau)\right)$ can be rewritten as

$Q_1\left(\eta_1^{(0\sim1)}(t-\tau)\right) = Q_1\left(\eta_1^{(0\sim1)}(t-\bar{\tau})\right) + \delta_1,\ \ \forall t \geq 0$, then the RBF NN is used to approximate the unknown nonlinear function $Q_1\left(\eta_1^{(0\sim1)}(t-\bar{\tau})\right)$ with time-delay $\bar{\tau}$, where $\bar{\tau} \in \{t_1, \ldots, t_m\} \in [0, \tau_M]$.

The control objective is to design an adaptive control method based on the time-delay NN state observer and the fully actuated system approach, so that the pressure p and the velocity v_g and the observation errors of the pressure $\tilde{p}$ and the velocity $\tilde{v}_g$ of the thermoacoustic system are bounded.

3 Time-Delay NN State Observer Design

According to Lemma 1, $Q_1\left(\eta_1^{(0\sim1)}(t-\tau)\right)$ can be expressed as

$$Q_1\left(\eta_1^{(0\sim1)}(t-\tau)\right) = Q_1\left(\eta_1^{(0\sim1)}(t-\bar{\tau})\right) + \delta_1, \quad (5)$$

where $\delta_1 > 0$.

Therefore, using the RBF NN [26] to approximate the unknown nonlinear function $Q_1\left(\eta_1^{(0\sim1)}(t-\bar{\tau})\right)$, and $Q_1\left(\eta_1^{(0\sim1)}(t-\bar{\tau})\right)$ can be represented as

$$\begin{aligned} Q_1\left(\eta_1^{(0\sim1)}(t-\bar{\tau})\right) =& W_1^T S_1\left(\eta_1^{(0\sim1)}(t-\bar{\tau})\right) \\ &+ \varepsilon_1\left(\eta_1^{(0\sim1)}(t-\bar{\tau})\right), \end{aligned} \quad (6)$$

where $S_i^T\left(\eta_1^{(0\sim1)}(t-\bar{\tau})\right) S_i\left(\eta_1^{(0\sim1)}(t-\bar{\tau})\right) \leq N_1$, W_1 and N_1 respectively are the weight vector and the node number of the RBF NN, $\varepsilon_1\left(\eta_1^{(0\sim1)}(t-\bar{\tau})\right) \leq \bar{\varepsilon}_1, \bar{\varepsilon}_1 > 0$.

Since all states in the system (1) are unmeasurable, a time-delay NN state observer is designed as,

$$\begin{aligned} \dot{\hat{\eta}}_1^{(0\sim1)} =& \begin{bmatrix} 0 \\ f_1\left(\hat{\eta}_1^{(0\sim1)}\right) \end{bmatrix} + \begin{bmatrix} 0 \\ \hat{W}_1^T S_1\left(\hat{\eta}_1^{(0\sim1)}(t-\bar{\tau})\right) \end{bmatrix} \\ &+ \begin{bmatrix} 0 \\ Bu_1 \end{bmatrix} + \begin{bmatrix} 0 & 1 \\ 0 & 0 \end{bmatrix} \hat{\eta}_1^{(0\sim1)} \\ &+ \mathrm{L}\left(y - C\hat{\eta}_1^{(0\sim1)}\right), \end{aligned} \quad (7)$$

where $\hat{W}_1$, $\hat{\eta}_1^{(0\sim1)}$ are the estimations of W_1, $\eta_1^{(0\sim1)}$, respectively. $L = \begin{bmatrix} l_1 \\ l_2 \end{bmatrix}$ is the matrix of parameters to be designed, where the parameters $l_i (i = 1, 2)$ are selected so that the matrix H is Hurwitz. If Γ and Q are positive definite matrices, then

$$H^T\Gamma + \Gamma H = -Q, \quad (8)$$

where $H = \begin{bmatrix} -l_1 & 1 \\ -l_2 & 0 \end{bmatrix}$.

The closed-loop system (4) can be also described by the following state-space form:

$$\begin{aligned} \dot{\eta}_1^{(0\sim1)} =& \begin{bmatrix} 0 \\ Q_1\left(\eta_1^{(0\sim1)}(t-\tau)\right) \end{bmatrix} + \begin{bmatrix} 0 & 1 \\ 0 & 0 \end{bmatrix} \eta_1^{(0\sim1)} \\ &+ \begin{bmatrix} 0 \\ f_1\left(\eta_1^{(0\sim1)}\right) \end{bmatrix} - \begin{bmatrix} 0 \\ Bu_1 \end{bmatrix}. \end{aligned} \quad (9)$$

Combining (7) and (9), the error system can be described by the following state-space form:

$$\begin{aligned} \dot{\tilde{\eta}}_1^{(0\sim1)} =& \begin{bmatrix} 0 \\ f_1\left(\eta_1^{(0\sim1)}\right) - f_1\left(\hat{\eta}_1^{(0\sim1)}\right) \end{bmatrix} + H\tilde{\eta}_1^{(0\sim1)} \\ &+ \begin{bmatrix} 0 \\ Q_1\left(\eta_1^{(0\sim1)}(t-\tau)\right) - \hat{W}_1^T S_1\left(\hat{\eta}_1^{(0\sim1)}(t-\bar{\tau})\right) \end{bmatrix}, \end{aligned} \quad (10)$$

where $\tilde{\eta}_1^{(0\sim1)} = \eta_1^{(0\sim1)} - \hat{\eta}_1^{(0\sim1)}$ is an observation error.

One of our control objectives is that the pressure p and the velocity v_g are bounded. It can be inferred from (2) and (3) that the pressure p and the velocity v_g are related to $\eta_1^{(0\sim1)}$, therefore, it is only necessary to prove that $\eta_1^{(0\sim1)}$ is bounded. But the boundedness of states $\eta_1^{(0\sim1)}$ cannot be directly proven. Since $\eta_1^{(0\sim1)} = \tilde{\eta}_1^{(0\sim1)} + \hat{\eta}_1^{(0\sim1)}$, as long as the observation error $\tilde{\eta}_1^{(0\sim1)}$ and the estimation of the state $\hat{\eta}_1^{(0\sim1)}$ are proven to be bounded, then the state $\eta_1^{(0\sim1)}$ in the system (1) has been proven to be bounded.

For the error system (10), choose Lyapunov function

$$V_0 = (\tilde{\eta}_1^{(0\sim1)})^T \Gamma \tilde{\eta}_1^{(0\sim1)}. \quad (11)$$

where $\Gamma = \begin{bmatrix} \Gamma_1 \\ \Gamma_2 \end{bmatrix}, \Gamma_1, \Gamma_2 \in \mathbb{R}^{2\times1}$.

According to (10), the derivative of V_0 is

$$\begin{aligned} \dot{V}_0 =& 2(\tilde{\eta}_1^{(0\sim1)})^T \Gamma_2\left(f_1\left(\eta_1^{(0\sim1)}\right) - f_1\left(\hat{\eta}_1^{(0\sim1)}\right)\right) \\ &+ 2(\tilde{\eta}_1^{(0\sim1)})^T \Gamma_2 Q_1\left(\eta_1^{(0\sim1)}(t-\tau)\right) \\ &- 2(\tilde{\eta}_1^{(0\sim1)})^T \Gamma_2 \hat{W}_1^T S_1\left(\hat{\eta}_1^{(0\sim1)}(t-\bar{\tau})\right) \\ &+ (\tilde{\eta}_1^{(0\sim1)})^T (H^T\Gamma + \Gamma H)\tilde{\eta}_1^{(0\sim1)}. \end{aligned} \quad (12)$$

Since the function $f_1\left(\eta_1^{(0\sim1)}\right)$ satisfies the Lipschitz condition, we have

$$\begin{aligned} \|f_1\left(\eta_1^{(0\sim1)}\right) - f_1\left(\hat{\eta}_1^{(0\sim1)}\right)\| &\leq \alpha\|\eta_1^{(0\sim1)} - \hat{\eta}_1^{(0\sim1)}\| \\ &= \alpha\|\tilde{\eta}_1^{(0\sim1)}\|, \end{aligned} \quad (13)$$

where $\alpha > 0$.

Combining (5) and (6), the unknown nonlinear function $Q_1\left(\eta_1^{(0\sim1)}(t-\tau)\right) - \hat{W}_1^T S_1\left(\hat{\eta}_1^{(0\sim1)}(t-\bar{\tau})\right)$ in (10) can be rewritten as

$$\begin{aligned} & Q_1\left(\eta_1^{(0\sim1)}(t-\tau)\right) - \hat{W}_1^T S_1\left(\hat{\eta}_1^{(0\sim1)}(t-\bar{\tau})\right) \\ =& W_1^T S_1\left(\eta_1^{(0\sim1)}(t-\bar{\tau})\right) - \hat{W}_1^T S_1\left(\hat{\eta}_1^{(0\sim1)}(t-\bar{\tau})\right) \\ &+ \delta_1 + \bar{\varepsilon}_1 \\ =& W_1^T\left(S_1\left(\eta_1^{(0\sim1)}(t-\bar{\tau})\right) - S_1\left(\hat{\eta}_1^{(0\sim1)}(t-\bar{\tau})\right)\right) \\ &+ \tilde{W}_1^T S_1\left(\hat{\eta}_1^{(0\sim1)}(t-\bar{\tau})\right) + \delta_1 + \bar{\varepsilon}_1, \end{aligned} \quad (14)$$

where $\tilde{W}_1 = W_1 - \hat{W}_1$.

Based on the Young's inequality and (14), we have

$$\begin{aligned}
&2(\tilde{\eta}_1^{(0\sim1)})^T\Gamma_2 Q_1\left(\eta_1^{(0\sim1)}(t-\tau)\right)\\
&-2(\tilde{\eta}_1^{(0\sim1)})^T\Gamma_2\hat{W}_1^T S_1\left(\hat{\eta}_1^{(0\sim1)}(t-\bar{\tau})\right)\\
\leq&4a_0\|\Gamma_2\|^2\left\|\tilde{\eta}_1^{(0\sim1)}\right\|^2+\frac{1}{a_0}\left(\delta_1^2+\bar{\varepsilon}_1^2\right)\\
&+\frac{1}{a_0}N_1\left\|W_1^T\right\|^2+\frac{1}{a_0}N_1\left\|\tilde{W}_1^T\right\|^2. \qquad (15)
\end{aligned}$$

According to (8),(13) and (15), (12) can be inferred as

$$\begin{aligned}
\dot{V}_0\leq&2\alpha\|\Gamma_2\|^2\|\tilde{\eta}_1^{(0\sim1)}\|^2-(\tilde{\eta}_1^{(0\sim1)})^T Q\tilde{\eta}_1^{(0\sim1)}\\
&+4a_0\|\Gamma_2\|^2\left\|\tilde{\eta}_1^{(0\sim1)}\right\|^2+\frac{1}{a_0}\left(\delta_1^2+\bar{\varepsilon}_1^2\right)\\
&+\frac{1}{a_0}N_1\left\|W_1^T\right\|^2+\frac{1}{a_0}N_1\left\|\tilde{W}_1^T\right\|^2\\
\leq&-\lambda_0\left\|\tilde{\eta}_1^{(0\sim1)}\right\|^2+\frac{1}{a_0}N_1\left\|\tilde{W}_1^T\right\|^2+\Delta_0, \qquad (16)
\end{aligned}$$

where

$$\begin{aligned}
\lambda_0=&\lambda\min Q-4a_0\|\Gamma_2\|^2-2\alpha\|\Gamma_2\|^2,\\
\Delta_0=&\frac{1}{a_0}\left(\delta_1^2+\bar{\varepsilon}_1^2\right)+\frac{1}{a_0}N_1\left\|W_1^T\right\|^2.
\end{aligned}$$

According to (16), if $\frac{1}{a_0}N_1\left\|\tilde{W}_1^T\right\|^2$ is bounded, then the observation error $\tilde{\eta}_1^{(0\sim1)}$ is bounded. Therefore, to design a controller based on the fully actuated system approach not only the boundedness of the state estimation $\hat{\eta}_1^{(0\sim1)}$ is ensured, but also $\frac{1}{a_0}N_1\left\|\tilde{W}_1^T\right\|^2$ is ensured to be bounded. Thereby, the boundedness of the observation error $\tilde{\eta}_1^{(0\sim1)}$ is ensured.

4 Adaptive Controller Design Based on the Fully Actuated System approach

In the paper, we introduce the following notations $A^{0\sim1}=[A_0\ A_1]$, $P\left(A^{0\sim1}\right)=[P_1\ P_2]$, $P_1,P_2\in\mathbb{R}^{2\times1}$, and $\Phi\left(A^{0\sim1}\right)=\begin{bmatrix}0&1\\-A_0&-A_1\end{bmatrix}$. $P\left(A^{0\sim1}\right)=P$, and $\Phi\left(A^{0\sim1}\right)=\Phi$.

Based on the fully actuated system approach, for the system (7), an adaptive control law is designed as

$$u_1=-B^{-1}\left(A^{0\sim1}\hat{\eta}_1^{(0\sim1)}+u_1^*\right), \qquad (17)$$

$$\begin{aligned}
u_1^*=&f_1\left(\hat{\eta}_1^{(0\sim1)}\right)+\hat{W}_1^T S_1\left(\hat{\eta}_1^{(0\sim1)}(t-\bar{\tau})\right)\\
&+\frac{3}{4}P_2^T\hat{\eta}_1^{(0\sim1)}, \qquad (18)
\end{aligned}$$

$$\dot{\hat{W}}_1=P_2^T\hat{\eta}_1^{(0\sim1)}S_1\left(\hat{\eta}_1^{(0\sim1)}(t-\bar{\tau})\right)-\kappa_1\hat{W}_1, \qquad (19)$$

where κ_1 is a design parameter.

Substituting (17) and (18) into (7) yields

$$\begin{aligned}
\dot{\hat{\eta}}_1^{(0\sim1)}=&\Phi\left(A^{0\sim1}\right)\hat{\eta}_1^{(0\sim1)}+\mathrm{L}\left(y-C\hat{\eta}_1^{(0\sim1)}\right)\\
&-\begin{bmatrix}0\\\frac{3}{4}P_2^T\hat{\eta}_1^{(0\sim1)}\end{bmatrix}. \qquad (20)
\end{aligned}$$

Thus, we choose the Lyapunov function candidate as follows:

$$V_1=\left(\hat{\eta}_1^{(0\sim1)}\right)^T P\left(A^{0\sim1}\right)\hat{\eta}_1^{(0\sim1)}+\frac{1}{2}\tilde{W}_1^T\tilde{W}_1. \qquad (21)$$

Then, the derivative of (21) along with (20) is

$$\begin{aligned}
\dot{V}_1=&\left(\hat{\eta}_1^{(0\sim1)}\right)^T\left(\Phi^T P+P\Phi\right)\hat{\eta}_1^{(0\sim1)}-\dot{\hat{W}}_1^T\tilde{W}_1\\
&-\frac{3}{2}\left(\hat{\eta}_1^{(0\sim1)}\right)^T P_2P_2^T\hat{\eta}_1^{(0\sim1)}\\
&+2\left(\hat{\eta}_1^{(0\sim1)}\right)^T PL\left(y-C\hat{\eta}_1^{(0\sim1)}\right). \qquad (22)
\end{aligned}$$

Based on the Young's inequality, we have

$$\begin{aligned}
2\left(\hat{\eta}_1^{(0\sim1)}\right)^T PL\left(y-C\hat{\eta}_1^{(0\sim1)}\right)\leq&\left(\hat{\eta}_1^{(0\sim1)}\right)^T P_2P_2^T\hat{\eta}_1^{(0\sim1)}\\
&+\frac{\|P\|^2\|L\|^2\left\|\tilde{\eta}_1^{(0\sim1)}\right\|^2}{P_2^TP_2}. \qquad (23)
\end{aligned}$$

Substituting (19) and (23) into (22), we have

$$\begin{aligned}
\dot{V}_1\leq&\left(\hat{\eta}_1^{(0\sim1)}\right)^T\left(\Phi^T P+P\Phi\right)\hat{\eta}_1^{(0\sim1)}+\kappa_1\tilde{W}_1^T\hat{W}_1\\
&-\frac{1}{2}\left(\hat{\eta}_1^{(0\sim1)}\right)^T P_2P_2^T\hat{\eta}_1^{(0\sim1)}+\frac{\|P\|^2\|L\|^2\left\|\tilde{\eta}_1^{(0\sim1)}\right\|^2}{P_2^TP_2}\\
&-P_2^T\hat{\eta}_1^{(0\sim1)}\tilde{W}_1^T S_1\left(\hat{\eta}_1^{(0\sim1)}(t-\bar{\tau})\right). \qquad (24)
\end{aligned}$$

Based on the Young's inequality, we have

$$\kappa_1\tilde{W}_1^T\hat{W}_1\leq-\frac{\kappa_1}{2}\left\|\tilde{W}_1\right\|^2+\frac{\kappa_1}{2}\|W_1\|^2. \qquad (25)$$

$$\begin{aligned}
&-P_2^T\hat{\eta}_1^{(0\sim1)}\tilde{W}_1^T S_1\left(\hat{\eta}_1^{(0\sim1)}(t-\bar{\tau})\right)\\
&\leq\frac{1}{2}\left\|\tilde{W}_1\right\|^2N_1+\frac{1}{2}\left(\hat{\eta}_1^{(0\sim1)}\right)^T P_2P_2^T\hat{\eta}_1^{(0\sim1)}. \qquad (26)
\end{aligned}$$

Substituting (25) and (26) into (24) yields

$$\begin{aligned}
\dot{V}_1\leq&\left(\hat{\eta}_1^{(0\sim1)}\right)^T\left(\Phi^T P+P\Phi\right)\hat{\eta}_1^{(0\sim1)}+\frac{\kappa_1}{2}\|W_1\|^2\\
&-(\frac{\kappa_1}{2}-\frac{1}{2}N_1)\left\|\tilde{W}_1\right\|^2+\frac{\|P\|^2\|L\|^2\left\|\tilde{\eta}_1^{(0\sim1)}\right\|^2}{P_2^TP_2}. \qquad (27)
\end{aligned}$$

5 Stability Analysis of Closed-Loop Systems

Theorem 1: Consider the thermoacoustic system (1). For any parameter W_1, if there exists a matrix $A^{0\sim n-1}$ to make the matrix $\Phi\left(A^{0\sim n-1}\right)$ stable, and $\Phi\left(A^{0\sim n-1}\right)$, $P\left(A^{0\sim n-1}\right)$ satisfying

$$\Phi^T P+P\Phi\leq-mP \qquad (28)$$

then the time-delay NN state observer (7) and the adaptive control laws (17)-(19) can make sure that the pressure p and the velocity v_g and the observation errors of the pressure and

the velocity amplitudes $\tilde{p}, \tilde{v}_g$ of the thermoacoustic system are bounded.

Proof: The Lyapunov function candidate is chosen as,

$$V = V_0 + V_1. \tag{29}$$

From (16) and (27), $\dot{V}$ can be inferred as

$$\begin{aligned}\dot{V} \leq & -\lambda_0 \left\| \tilde{\eta}_1^{(0\sim1)} \right\|^2 + \frac{1}{a_0} N_1 \left\| \tilde{W}_1^T \right\|^2 + \Delta_0 \\ & + \left(\hat{\eta}_1^{(0\sim1)} \right)^T \left(\Phi^T P + P\Phi \right) \hat{\eta}_1^{(0\sim1)} + \frac{\kappa_1}{2} \|W_1\|^2 \\ & - \left(\frac{\kappa_1}{2} - \frac{1}{2} N_1 \right) \left\| \tilde{W}_1 \right\|^2 + \frac{\|P\|^2 \|L\|^2 \left\| \tilde{\eta}_1^{(0\sim1)} \right\|^2}{P_2^T P_2}\end{aligned} \tag{30}$$

Substituting (28) into (30) yields

$$\begin{aligned}\dot{V} \leq & -\lambda \left\| \tilde{\eta}_1^{(0\sim1)} \right\|^2 - \left(\frac{\kappa_1}{2} - \frac{1}{2} N_1 - \frac{1}{a_0} N_1 \right) \left\| \tilde{W}_1 \right\|^2 \\ & - m \left(\hat{\eta}_1^{(0\sim1)} \right)^T P \hat{\eta}_1^{(0\sim1)} + \Delta \\ \leq & -cV + \Delta,\end{aligned} \tag{31}$$

where

$$\begin{aligned}& \lambda = \lambda_0 - \frac{\|P\|^2 \|L\|^2}{P_2^T P_2} > 0, \Delta = \frac{\kappa_1}{2} \|W_1\|^2 + \Delta_0, \\ & c = \min \left\{ \frac{\lambda}{\|\Gamma\|^2}, 2\left(\frac{\kappa_1}{2} - \frac{1}{2} N_1 - \frac{1}{a_0} N_1 \right), m \right\}, \\ & \frac{\kappa_1}{2} - \frac{1}{2} N_1 - \frac{1}{a_0} N_1 > 0.\end{aligned}$$

According to (29) and (31), we know that $\tilde{W}_1, \hat{\eta}_1^{(0\sim1)}$, and $\tilde{\eta}_1^{(0\sim1)}$ are bounded, and thus the system state $\eta_1^{(0\sim1)}$ is bounded. (Due to $\eta_1^{(0\sim1)} = \tilde{\eta}_1^{(0\sim1)} + \hat{\eta}_1^{(0\sim1)}$, $\eta_1^{(0\sim1)}$ is bounded.) It can be inferred from (2) and (3) that the pressure p and the velocity v_g and the observation errors of pressure and velocity amplitudes $\tilde{p}, \tilde{v}_g$ are bounded ($\tilde{p} = p - \hat{p}, \tilde{v}_g = v_g - \hat{v}_g$). The proof is thus completed.

6 Simulation Results

In actual combustion chambers, the heat release not only has nonlinear effects, but also reaches a saturation state when it reaches a certain degree. Therefore, according to [10], the heat release model $Q_1\left(\eta_1(t-\tau)\right)$ is given as follows,

$$Q_1\left(\eta(t-\tau)\right) = \frac{\beta}{k_c} \arctan\left(k_c \dot{\eta}_1\left(t-\tau\right)\right) \tag{32}$$

where $\beta = 1$ is a dimensionless constant, and $k_c = 0.5$ is a parameter used to describe the nonlinear saturation of flames.

The control parameters are chosen as $\kappa_1 = 5$, $\hat{W}_1 = \begin{bmatrix} 0.01 & 0.01 & 0.01 & 0.01 & 0.01 \end{bmatrix}^T$, and $\eta_1^{(0\sim1)}(0) = \begin{bmatrix} 0.3 & 0 \end{bmatrix}^T$. According to [21], we have $A_1^{0\sim1} = \begin{bmatrix} 2 & 2 \end{bmatrix}$, $P_{12}^T = \begin{bmatrix} 0.25 & 0.375 \end{bmatrix}$. Base on [8], the physical parameters are given in Table 1.

Fig. 1 illustrates the trajectory of the velocity and pressure p, v_g and the estimations of the velocity and the pressure $\hat{p}, \hat{v}_g$ for the thermoacoustic system with one acoustic mode. Obviously, under the proposed adaptive control, the estimations of states $\hat{p}, \hat{v}_g$ can effectively track the motion trajectory of the system velocity and pressure p, v_g. It can be clearly seen from Fig. 2 that the observation errors $\tilde{p}, \tilde{v}_g$ can converge to a small region about the origin. The control law and the adaptive law are shown in Fig. 3 and Fig. 4, respectively.

Table 1: physical parameters.

Parameter	Value	Parameter	Value
D_{11}	-0.01	E_{11}	-0.005
A_{111}	0	B_{111}	0
R_{1111}	-0.16525	S_{1111}	0.019
ω_1	1	L	$0.762m$
$\bar{a}$	$0.762m/\pi$	τ_M	$0.8s$
$\bar{P}$	$5.5atm$	$\bar{\gamma}$	1.23

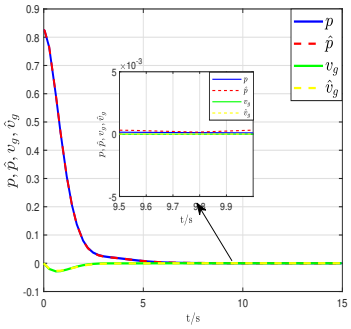

Fig. 1: The pressure and velocity p, v_g and the estimations of pressure and velocity $\hat{p}, \hat{v}_g$.

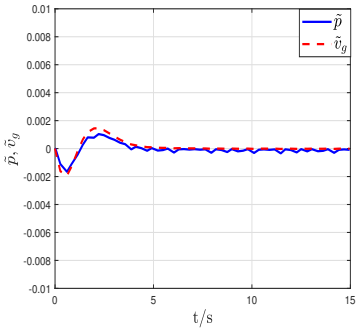

Fig. 2: The observer errors of the pressure and velocity $\tilde{p}, \tilde{v}_g$.

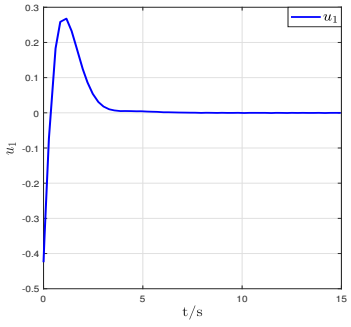

Fig. 3: The control law u_1.

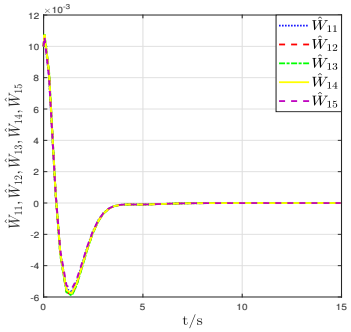

Fig. 4: The adaptive law $\hat{W}_1$.

7 Conclusion

An adaptive active control strategy based on a time-delay NN state observer was proposed for the thermoacoustic system with the unknown nonlinear flame heat release in the combustion chamber of an aircraft engine. For the nonlinear system with state time-delay, the time-delay NN state observer has better effectiveness and smaller observation errors compared to the linear observer. In addition, instead of the traditional Krasovskii functional, the finite covering lemma was combined with the RBF NN to approximate the unknown nonlinear heat release with the time delay. An adaptive active control was proposed based on the fully actuated system method to ensure that the pressure and the velocity fluctuations of the thermoacoustic system, as well as the observation errors of the pressure and the velocity fluctuations, converged to a small neighborhood around the origin. Finally, the feasibility and effectiveness of the design method were verified through simulation results.

References

[1] X. M. Huang, W. T. Baumann, Reduced-order modeling of dynamic heat release for thermoacoustic instability prediction. *Combustion Science and Technology*, 2007, 179(3): 617-636.

[2] B. Higgins, On the sound produced by a current of hy-drogen gas passing through a tube. *Journal of Natural Philosophy and Chemical Arts*, 1802, 1: 129-131.

[3] L. Rayleigh, The explanation of certain acoustical phenomena. *Nature*, 1878, 18: 319-321.

[4] A. A. Putnam, W. R. Dennis, Burner oscillations of the Gauze-Tone type. *Journal of the Acoustical Society of America*, 1954, 26(5): 716-725.

[5] J. Cohen, A. Torger, Experimental investigation of near-blowout instabilities in a lean, premixed step com-bustor. *AIAA 34th Aerospace Sciences Meeting and Exhibit. Reno: AIAA*, 1996: 1-13.

[6] F. E. C. Culick, Nonlinear behavior of acoustic waves in combustion chambersŁI. *Acta Astronautica*, 1976, 3(9-10): 716-734.

[7] V. Yang, F. E. C. Culick, Third-order nonlinear acoustic waves and triggering of pressure oscillations in combustion chambers. Part I: Longitudinal modes. *AIAA/SAE/ASME/ASEE 23rd Joint Propulsion Con-ference. San Diego: AIAA*, 1987, 3: 715-734.

[8] X. Meng, D. Ma, H. J. Lin, and C. Chen, Prescribed performance control of thermoacoustic instability in aero-engine combustion chambers. *Acta Aeronautica et Astronautica Sinica*, 2023, 44(17): 128182-128182.

[9] R. A. Battista, L. H. Caveny, and I. A. Gostintsev, Theory of dynamic extinguishment of solid propellants with special reference to nonsteady heat feedback law. *Journal of Spacecraft Rockets*, 1951, 8(3): 251-258.

[10] F. Gant, G. Ghirardo, and M. R. Bothien, On the importance of time delay and noise in thermoacoustic modeling. *Journal of Sound and Vibration*, 2021, 501(4): 116067.

[11] A. Cellier, C. J. Lapeyre, and G. Ztarlik, Detection of precursors of combustion instability using convolutional recurrent neural networks. *Combustion and Flame*, 2021, 233(3): 1-11.

[12] P. J. Milan, J. P. Hickey, and X. Wang, Deep-learning accelerated calculation of real-fluid properties in numerical simulation of complex flowfields. *Journal of Computational Physics*, 2021, 444: 1-25.

[13] S. Tsien, Servo-stabilization of combustion in rocket motors. *Journal of the American Rocket Society*, 1952, 22: 256-262.

[14] Y. Fung, V. Yang,and A. Sinha, Active control of combustion instabilities with distributed actuators. *Combustion Science and Technology*, 1991, 78: 217-245.

[15] B. M. Moran, A. Saurabh, and C. O. Paschereit, Effect of phase-shift feedback on thermoacoustic coupling. *IFAC-Papersonline*, 2016, 49(10): 65-70.

[16] A. M. Annaswamy, M. Fleifil, and J. W. Rumsey, Thermoacoustic instability: model-based optimal control designs and experimental validation. *IEEE Transactions on Control Systems Technology*, 2000, 8(6): 905-918.

[17] G. R. Duan, High-order fully actuated system approaches: Part I Models and basic procedure. *International Journal of Systems Science*, 2021, 52(2): 422-435.

[18] G. R. Duan, High-order fully actuated system approaches: Part II. Generalized strict-feedback systems. *International Journal of Systems Science*,2021, 52(3): 437-454.

[19] G. R. Duan, High-order fully actuated system approaches: Part IV. Adaptive control and high-order back-stepping. *International Journal of Systems Science*, 2021, 52(5): 972-989.

[20] G. R. Duan, High-order fully actuated system approaches: Part III. Robust control and high-order backstepping. *International Journal of Systems Science*, 2021, 52(5): 952-971.

[21] Y. Z. Zhao, D. Ma, H. W. Ma, Adaptive neural network control of thermoacoustic instability in Rijke tube: A fully actuated system approach. *Journal of Systems Science and Complexity*, 2022, 35(2): 586-603.

[22] Y. J. Liu, S. C. Tong, D. Wang, T. S. Li, and C. L. P . Chen, Adaptive neural output feedback controller design with reduced-order observer for a class of uncertain nonlinear SISO systems. *IEEE Trans. Neural Netw.*, 2011, 22(8): 1328-1334.

[23] T. Gao, T. Li, Y. J. Liu, S. Tong and F. Sun, Observer-based adaptive fuzzy control of nonstrict feedback nonlinear systems with function constraints. *IEEE Transactions on Fuzzy Systems*, 2023, 31(8): 2556-2567.

[24] Y. Zhan, X. Li and S. Tong, Observer-based decentralized control for non-strict-feedback fractional-order nonlinear large-scale systems with unknown dead zones. *IEEE Transactions on Neural Networks and Learning Systems*, 2023, 34(10): 7479-7490.

[25] X. Y. Zhang, Y. Wang, and X. K. Chen, Decentralized adaptive neural approximated inverse control for a class of large-scale nonlinear hysteretic systems with time delays. *IEEE Transactions on Systems, Man, and Cybernetics: Systems*, 2019, 49(12): 2424-2437.

[26] R. M. Sanner and J. E. Slotine, Gaussian networks for direct adaptive control. *IEEE Transactions on Neural Networks*, 1992, 3(6): 837-863.

Proceedings of the 3rd Conference on Fully Actuated System Theory and Applications
May 10-12, 2024, Shenzhen, China

Robust Prescribed-Time Global Control For the Elliptical Orbital Rendezvous System: A Fully Actuated System Approach

Shunli Li [1], Guangren Duan[1,2]

1. Center for Control Theory and Guidance Technology, Harbin Institute of Technology, Harbin 150001, P. R. China
E-mail: 21B904006@stu.hit.edu.cn, duangr@sustech.edu.cn

2. Shenzhen Key Laboratory of Control Theory and Intelligent Systems, Southern University of Science and Technology, Shenzhen 518055, P. R. China
E-mail: duangr@sustech.edu.cn

Abstract: The robust prescribed-time global control for the elliptical orbital rendezvous system is investigated under a class of time-varying disturbances. The elliptical orbital rendezvous system formulated by Newton's equation turns out to be a fully actuated system (FAS), thereby the idea of FAS approaches is applied to facilitate the controller design. Based on the parametric Lyapunov equation, a time-varying high-gain feedback is constructed such that the target spacecraft is captured successfully by the arbitrarily positioned chaser spacecraft within any prescribed time, that is, the origin of the closed-loop system is globally finite-time attractive within any prescribed time. In the absence of disturbances, the closed-loop system is strengthened to be globally finite-time stable with any prescribed time. Notably, the attractive result of the perturbed system implies the globally almost disturbance decoupling to such a class of disturbances. Comparative simulations verify the effectiveness of our approach.

Key Words: Elliptical Orbital Rendezvous, FAS Approach, Prescribed-Time Control, Parametric Lyapunov Equation, Time-Varying Feedback

1 Introduction

Spacecraft on-orbit operation and service, including repairing, saving, docking, and large structure assembling rely heavily on the technology of autonomous rendezvous [1, 2]. The spacecraft rendezvous system is characterized by a target spacecraft in a circular or elliptical orbit and another chaser spacecraft actively engaged with it, whose visualized sketch is depicted in Fig. 1. In the rotating frame XYZ, the

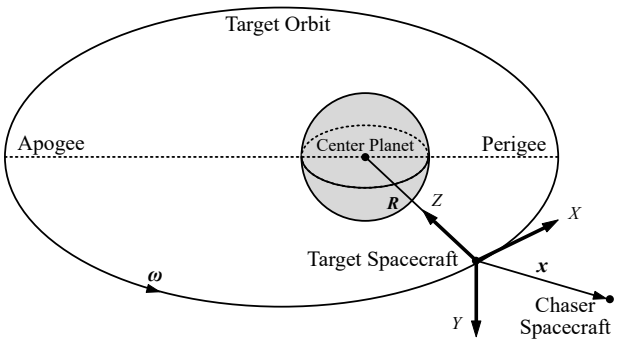

Fig. 1: Elliptical orbital rendezvous system and coordinates

relative motion between the chaser spacecraft and the target can be described by the nonlinear differential equation [3] (Newton's equation) for which the linearized equations are known as the Hill–Clohessy–Wiltshire equation [4] or the Tschauner–Hempel equation [2]. Notably, by employing three independent control accelerations (or thrusts) as control signals for the rendezvous system, the spacecraft rendezvous system can be classified as a fully actuated system (FAS), aligning with the definition of FASs (see [5, 6]). This characterization implies that the idea of FAS approaches can be applied in the control of the spacecraft rendezvous system.

Recently, the FAS approach [5–9] has attracted much more attention within the realm of nonlinear control. A variety of intricate problems including robust backstepping control with the weakened differential explosion [6, 10], disturbance attenuation [7], stabilization of nonholonomic systems [8], robust stabilization of a class of cascade systems [9], and fault-tolerant control of uncertain FASs [11], were studied by FAS approaches. The fundamental characteristic of FASs lies in their inherent fully actuated nature, where each degree of freedom possesses a direct control mechanism. This distinctive feature makes the FAS approach a direct and simplified methodology, especially effective in designing controllers with robustness against disturbances.

The rendezvous problem can be abstracted to a basic stabilization problem of the rendezvous system, in which other possible requirements such as robustness to disturbance [12], actuator saturation [13], lower thrust [14], fuel optimization [15], and optimal guidance [16] are also involved. Parallel to these problems, finite-time control of the rendezvous system has emerged as a highly active research area. For the circular orbital rendezvous system with bounded inputs, the finite-time stabilization was achieved by a class of time-varying high-gain feedback in [17], the nonsingular terminal sliding mode control in [18], and the dynamic event-triggered control and self-triggered control in [19]. For the elliptical orbital rendezvous system with bounded inputs, the fixed-time stabilization was achieved by the smooth periodic delayed feedback in [20].

We proceed to introduce the existing finite-time control approach briefly, particularly the time-varying feedback approach. In [21, 22], prescribed-time stabilization of a class of nonlinear normal form systems was originally achieved based on a time-varying high-gain that grows unbounded towards the terminal time. In [23], prescribed-time stabilization of generalized strict-feedback-like systems was

This work is supported by Science Center Program of the National Natural Science Foundation of China under grant 62188101, Major Program of National Natural Science Foundation of China under grants 61690210, 61690212, National Natural Science Foundation of China under grant 61333003.

achieved with the development of a class of dynamic high-gains and a state scaling process. Based on parametric Lyapunov equations (PLEs), another time-varying high-gain feedback method was designed in [17] to achieve the finite-time stabilization of linear systems with bounded input, and then this idea was generated in [24] to achieve the prescribed-time stabilization for a class of lower-triangular nonlinear systems.

This paper focuses on the robust prescribed-time global control for the elliptical orbital rendezvous system. A class of time-varying disturbances caused by the gravitational force of other stars is incorporated and further assumed to be piecewise continuous. With three independent control accelerations (or thrusts) being used as the control input, the elliptical orbital rendezvous system formulated by Newton's equation turns out to be an FAS, thereby the idea of FAS approaches in [6] is used to facilitate the controller design. In addition, motivated by the time-varying high-gain feedback approach in [17], a prescribed-time controller is designed for the perturbed rendezvous system such that the target spacecraft is captured successfully by the arbitrarily positioned chaser spacecraft within the prescribed time, that is, the origin of the closed-loop system is globally finite-time attractive within any prescribed-time.

We should highlight the contributions now. Firstly, our approach retains the control-oriented characteristic inherent in FAS approaches, noting that the controller is designed based on the FAS model. Secondly, our approach achieves an attractive result even in the presence of disturbances, which is not included in the analysis of [17]. Thirdly, our consideration of a piecewise continuous disturbance in this work is comparatively weaker than the one in [6]. It is important to acknowledge that our approach is motivated by the FAS approach [6] and the prescribed-time control approach [17].

Notations: A function $\boldsymbol{f}(x) : D \to \mathbb{R}^m$ is said to be $\mathcal{C}^n$ on a domain (open and connected set) $D \subset \mathbb{R}^n$ if it is n times continuously differentiable for some integer $n \geq 1$. $\boldsymbol{I}_r$ denotes the identity matrix with the dimension being r. $\boldsymbol{0}_r$ denotes the zero matrix with the dimension being r. $\det \boldsymbol{A}$ represents the determinant of the square matrix $\boldsymbol{A}$. $\mathrm{tr}(\boldsymbol{A})$ denotes the trace of a matrix $\boldsymbol{A}$. $\lambda_{\min}(\boldsymbol{A})$ and $\lambda_{\max}(\boldsymbol{A})$ represent the minimal and maximal eigenvalues of the symmetric matrix $\boldsymbol{A}$. We use $\mathrm{blockdiag}(\boldsymbol{A}_1, \boldsymbol{A}_2, \ldots, \boldsymbol{A}_n)$ to denote a diagonal matrix whose ith diagonal element is the matrix $\boldsymbol{A}_i$.

2 Preliminary Knowledge

We firstly recall the definition of finite-time stability.

Definition 1. *[25] The equilibrium $\boldsymbol{x} = \boldsymbol{0}$ of $\dot{\boldsymbol{x}} = \boldsymbol{f}(\boldsymbol{x}, t)$ is said to be globally finite-time stable with the convergence time $T(\boldsymbol{x}_0) > 0$ (denoted by T-GFTS) if it is stable in the Lyapunov sense and the origin is globally attractive with the convergence time $T(\boldsymbol{x}_0)$ (denoted by T-GFTA), namely, $\forall \boldsymbol{x}_0 \in \mathbb{R}^n \Rightarrow \lim_{t \to T} \|\boldsymbol{x}(t)\| = 0$.*

We proceed to recall some approaches regarding parametric Lyapunov equations. The following lemma is modified from the lemma 3 in [24], whose proof can be conducted in the same way.

Lemma 1. *[24] Consider the linear system $(\boldsymbol{\Phi}, \boldsymbol{B}) \in (\mathbb{R}^{nr \times nr}, \mathbb{R}^{nr \times r})$ with*

$$\boldsymbol{\Phi} = \begin{bmatrix} \boldsymbol{0} & \boldsymbol{I}_r & & \\ & \ddots & \ddots & \\ & & \boldsymbol{0} & \boldsymbol{I}_r \\ & & & \boldsymbol{0} \end{bmatrix}, \ \boldsymbol{B} = \begin{bmatrix} \boldsymbol{0} \\ \vdots \\ \boldsymbol{0} \\ \boldsymbol{I}_r \end{bmatrix}. \tag{1}$$

The following PLE

$$\boldsymbol{\Phi}^{\mathrm{T}} \boldsymbol{P} + \boldsymbol{P} \boldsymbol{\Phi} - \boldsymbol{P} \boldsymbol{B} \boldsymbol{B}^{\mathrm{T}} \boldsymbol{P} = -\gamma \boldsymbol{P} \tag{2}$$

has a unique positive definite solution if and only if $\gamma > 0$. Assume that $\gamma > 0$ is satisfied, then,

1) the positive definite solution $\boldsymbol{P}(\gamma)$ can be given by

$$\boldsymbol{P}(\gamma) = \gamma \boldsymbol{L}_n \boldsymbol{P}_n \boldsymbol{L}_n, \tag{3}$$

where $\boldsymbol{L}_n = \mathrm{blockdiag}(\gamma^{n-1} \boldsymbol{I}_r, \gamma^{n-2} \boldsymbol{I}_r, \cdots, \boldsymbol{I}_r)$ and $\boldsymbol{P}_n = \boldsymbol{P}(1)$;

2) there hold

$$0 < \frac{\boldsymbol{P}(\gamma)}{n\gamma} \leq \frac{\mathrm{d}\boldsymbol{P}(\gamma)}{\mathrm{d}\gamma} \leq \frac{\delta_{\mathrm{c}} \boldsymbol{P}(\gamma)}{n\gamma}, \ \forall \gamma > 0, \tag{4}$$

$$\mathrm{tr}(\boldsymbol{B}^{\mathrm{T}} \boldsymbol{P} \boldsymbol{B}) = n\gamma, \tag{5}$$

where $\delta_{\mathrm{c}} = n\left(1 + \lambda_{\max}(\boldsymbol{E}_n + \boldsymbol{P}_n \boldsymbol{E}_0 \boldsymbol{P}_n^{-1})\right)$ with $\boldsymbol{E}_n = \mathrm{blockdiag}((n-1)\boldsymbol{I}_r, (n-2)\boldsymbol{I}_r, \cdots, \boldsymbol{I}_r, \boldsymbol{0})$.

3 FAS Model and Problem Formulation

The relative motion of chaser spacecraft in the inertial frame can be captured by

$$\frac{\mathrm{d}^2 \boldsymbol{x}}{\mathrm{d}t^2} = -\mu \left(\frac{\boldsymbol{R} + \boldsymbol{x}}{|\boldsymbol{R} + \boldsymbol{x}|^3} - \frac{\boldsymbol{R}}{|\boldsymbol{R}|^3} \right) + \boldsymbol{u} + \boldsymbol{d}(t), \tag{6}$$

where $\boldsymbol{x} \in \mathbb{R}^3$ is the vector from target spacecraft to chaster spacecraft, $\boldsymbol{R} \in \mathbb{R}^3$ is the vector from center of gravity to target spacecraft with $\boldsymbol{R} = [0, 0, -R]^{\mathrm{T}}$ and R being the distance from the center of gravity to the target spacecraft, μ is the gravity constant, $\boldsymbol{u} \in \mathbb{R}^3$ is the acceleration vector due to thrust forces on the chaser spacecraft, and $\boldsymbol{d}(t)$ denotes the external time-varying disturbance due to the gravitational force of other stars or other situations. System (6) is formulated by the well-known Newton's equation.

As shown in Fig. 1, fix the rotating frame XYZ at the center of mass of the target spacecraft. For a vector $\boldsymbol{\chi}$, the derivative $\mathrm{d}\boldsymbol{\chi}/\mathrm{d}t$ in the inertial frame and the derivative $\mathrm{d_r}\boldsymbol{\chi}/\mathrm{d_r}t$ in the rotating frame satisfy

$$\frac{\mathrm{d}\boldsymbol{\chi}}{\mathrm{d}t} = \frac{\mathrm{d_r}\boldsymbol{\chi}}{\mathrm{d_r}t} + \boldsymbol{\omega} \times \boldsymbol{\chi},$$

where $\boldsymbol{\omega}$ is the angular velocity of the rotating frame, and

$$\boldsymbol{\omega} = [0, -\omega, 0]^{\mathrm{T}}$$

with ω being the orbital rate of the rotating frame. As a result, along with (6), the relative motion of chaser spacecraft in the rotating frame can be formulated as

$$\begin{aligned} \frac{\mathrm{d_r}^2 \boldsymbol{x}}{\mathrm{d_r}t^2} = &-\mu \left(\frac{\boldsymbol{R} + \boldsymbol{x}}{|\boldsymbol{R} + \boldsymbol{x}|^3} - \frac{\boldsymbol{R}}{|\boldsymbol{R}|^3} \right) + \boldsymbol{u} + \boldsymbol{d}(t) \\ &- \left(2\boldsymbol{\omega} \times \frac{\mathrm{d_r}\boldsymbol{x}}{\mathrm{d_r}t} + \frac{\mathrm{d}\boldsymbol{\omega}}{\mathrm{d}t} \times \boldsymbol{x} + \boldsymbol{\omega} \times \boldsymbol{\omega} \times \boldsymbol{x} \right). \end{aligned} \tag{7}$$

We now recapitulate the remaining parameters and symbols of the target orbit. Let a be the semimajor axis and e be the eccentricity of the target obit. According to [3], there yields

$$\begin{cases} T_{\mathrm{t}} &= 2\pi\sqrt{\frac{a^3}{\mu}}, \\ h &= \sqrt{\mu\left(1-e^2\right)a}, \end{cases} \tag{8}$$

where T_{t} is the period of the target orbit, and h is the orbital angular momentum of the target spacecraft. We point out that T_{t} and h are constant parameters. Besides, we know from [3] that

$$R = \frac{a\left(1-e^2\right)}{1+e\cos\theta}, \tag{9}$$

where θ is true anomaly of the target orbit. Let t_{p} be the time when the target spacecraft arrives at the perigee. At time t_{p}, the triple including the true anomaly θ, eccentric anomaly E, and mean anomaly M are equal to zero. The relation between these anomalies can be formulated as [3]

$$\begin{cases} M &= \frac{2\pi}{T_{\mathrm{t}}}\left(t-t_{\mathrm{p}}\right), \\ M &= E - e\sin E, \\ \tan\frac{\theta}{2} &= \sqrt{\frac{1+e}{1-e}}\tan\frac{E}{2}. \end{cases} \tag{10}$$

Clearly, these three anomalies M, E, θ are time-varying and one-to-one with respect to t. By the law of conservation of angular momentum $R^2\omega = h$, we obtain

$$\omega = h/R^2. \tag{11}$$

To this section end, the elliptical orbital rendezvous problem shall be abstract to the control problem. For simplicity, we denote $\dot{\boldsymbol{x}} \triangleq \mathrm{d_r}\boldsymbol{x}/\mathrm{d_r}t$, $\ddot{\boldsymbol{x}} \triangleq \mathrm{d_r^2}\boldsymbol{x}/\mathrm{d_r}t^2$, and

$$\begin{aligned} \boldsymbol{f}(\boldsymbol{x}^{(0\sim1)},t) \triangleq &-\mu\left(\frac{\boldsymbol{R}+\boldsymbol{x}}{|\boldsymbol{R}+\boldsymbol{x}|^3}-\frac{\boldsymbol{R}}{|\boldsymbol{R}|^3}\right) \\ &-\left(2\boldsymbol{\omega}\times\dot{\boldsymbol{x}}+\frac{\mathrm{d}\boldsymbol{\omega}}{\mathrm{d}t}\times\boldsymbol{x}+\boldsymbol{\omega}\times\boldsymbol{\omega}\times\boldsymbol{x}\right), \end{aligned}$$

where $\boldsymbol{x}^{(0\sim1)} = \left[\begin{array}{cc}\boldsymbol{x}^{\mathrm{T}} & \dot{\boldsymbol{x}}^{\mathrm{T}}\end{array}\right]^{\mathrm{T}}$. Then, system (7) can be written in the form of FAS model, namely,

$$\ddot{\boldsymbol{x}} = \boldsymbol{f}(\boldsymbol{x}^{(0\sim1)},t) + \boldsymbol{u} + \boldsymbol{d}(t), \tag{12}$$

where $\boldsymbol{u}$ turns out to be the control input, $\boldsymbol{f}: \mathbb{R}^6\times\mathbb{R}_{\geq0}\to\mathbb{R}^3$ is a C^∞ function with $\boldsymbol{f}(\boldsymbol{0},t) = 0$, $\forall t \geq 0$, and the disturbance $\boldsymbol{d}(t)$ satisfies

Assumption 1. *$\boldsymbol{d}: \mathbb{R}_{\geq0}\to\mathbb{R}^3$ is an unknown piecewise continuous function.*

Remark 1. *In view of (9), (10), and (11), the terms $\boldsymbol{R} = \boldsymbol{R}(\theta)$ and $\boldsymbol{\omega} = \boldsymbol{\omega}(\theta)$ are time-varying and thus the vector field $\boldsymbol{f}$ is in the time-varying case $\boldsymbol{f}(\boldsymbol{x}^{(0\sim1)},t)$. According to the definition of FAS in [5, 6], system (1) is a single-order FAS. In addition, the disturbance $\boldsymbol{d}(t)$ is only required to be piecewise continuous, which is weaker than the one in [6].*

By noting the practical task is that the target spacecraft could be captured successfully by the arbitrarily positioned chaser spacecraft within any prescribed time, we now highlight the main problem.

Problem 1. *Let $T > 0$ be a prescribed constant. Find a bounded control input $\boldsymbol{u}(\boldsymbol{x}^{(0\sim1)},t)$ such that the origin of the closed-loop system consisting of system (12) and $\boldsymbol{u}$ is T-GFTA. In addition, in the absence of $d(t)$, namely, $d(t) = 0$, system (12) is T-GFTS.*

4 Main Results

When it concerns the elliptical orbital rendezvous system, the associated PLE (2) is formed by

$$\boldsymbol{\Phi} = \begin{bmatrix}\boldsymbol{0} & \boldsymbol{I}_3 \\ \boldsymbol{0} & \boldsymbol{0}\end{bmatrix}, \quad \boldsymbol{B} = \begin{bmatrix}\boldsymbol{0} \\ \boldsymbol{I}_3\end{bmatrix}. \tag{13}$$

Then, we state the main results as follows.

Theorem 1. *Let $T > 0$ be a prescribed constant. Choose γ_0 as*

$$\gamma_0 = \frac{n+\delta_{\mathrm{c}}}{(1-s)nT}, \tag{14}$$

where $s \in (0,1)$ is a prescribed constant, and δ_{c} is given in (4). If we design the time-varying state feedback

$$\begin{cases} \boldsymbol{u}(t) &= \boldsymbol{v}(t) - \boldsymbol{f}(\boldsymbol{x}^{(0\sim1)},t), \\ \boldsymbol{v}(t) &= -\boldsymbol{B}^{\mathrm{T}}\boldsymbol{P}(\gamma(t))\boldsymbol{x}^{(0\sim1)}(t), \\ \gamma(t) &= \frac{T}{T-t}\gamma_0,\ \forall t\in[0,T), \end{cases} \tag{15}$$

where $\boldsymbol{P}(\gamma(t))$ is the unique positive definite solution to the PLE (2) with the pair $(\boldsymbol{\Phi},\boldsymbol{B})$ given by (13). Then the point $\boldsymbol{x}^{(0\sim1)} = \boldsymbol{0}$ of the closed-loop system consisting of (12) and (15) is T-GFTA and the input $\boldsymbol{u}(t)$ is bounded on the time interval $[0,T)$. In addition, in the absence of $d(t)$, that is, $d(t) = 0$, the closed-loop system is T-GFTS.

Proof. For simplicity, we omit the domain $[0,T)$ unless otherwise stated. The closed-loop system consisting of (12) and (15) turns out to be $\ddot{\boldsymbol{x}} = -\boldsymbol{B}^{\mathrm{T}}\boldsymbol{P}\boldsymbol{x}^{(0\sim1)} - \boldsymbol{d}(t)$, which can be written in the state-space form as

$$\dot{\boldsymbol{x}}^{(0\sim1)} = \left(\boldsymbol{\Phi} - \boldsymbol{B}\boldsymbol{B}^{\mathrm{T}}\boldsymbol{P}\right)\boldsymbol{x}^{(0\sim1)} + \boldsymbol{B}\boldsymbol{d}(t), \tag{16}$$

with $(\boldsymbol{\Phi},\boldsymbol{B})$ given by (13). Define a function $V(\boldsymbol{x}^{(0\sim1)},t): \mathbb{R}^6\times[0,T)\to\mathbb{R}_{\geq0}$ as

$$V(\boldsymbol{x}^{(0\sim1)},t) \triangleq \gamma\left(\boldsymbol{x}^{(0\sim1)}\right)^{\mathrm{T}}\boldsymbol{P}(\gamma)\boldsymbol{x}^{(0\sim1)}.$$

The derivative of $V(\boldsymbol{x}^{(0\sim1)},t)$ along the trajectory of the closed-loop system (16) is evaluated as

$$\begin{aligned} \dot{V} &= \dot{\gamma}\left(\boldsymbol{x}^{(0\sim1)}\right)^{\mathrm{T}}\boldsymbol{P}\boldsymbol{x}^{(0\sim1)} + \gamma\dot{\gamma}\left(\boldsymbol{x}^{(0\sim1)}\right)^{\mathrm{T}}\frac{\mathrm{d}\boldsymbol{P}}{\mathrm{d}\gamma}\boldsymbol{x}^{(0\sim1)} \\ &\quad + \gamma\left(\boldsymbol{x}^{(0\sim1)}\right)^{\mathrm{T}}\left[\left(\boldsymbol{\Phi}-\boldsymbol{B}\boldsymbol{B}^{\mathrm{T}}\boldsymbol{P}\right)^{\mathrm{T}}\boldsymbol{P} + \right. \\ &\quad \left.\boldsymbol{P}\left(\boldsymbol{\Phi}-\boldsymbol{B}\boldsymbol{B}^{\mathrm{T}}\boldsymbol{P}\right)\right]\boldsymbol{x}^{(0\sim1)} + 2\gamma\boldsymbol{d}^{\mathrm{T}}(t)\boldsymbol{B}^{\mathrm{T}}\boldsymbol{P}\boldsymbol{x}^{(0\sim1)} \\ &\leq \frac{n+\delta_{\mathrm{c}}}{n\gamma}\dot{\gamma}V - \gamma V - \gamma\left(\boldsymbol{x}^{(0\sim1)}\right)^{\mathrm{T}}\boldsymbol{P}\boldsymbol{B}\boldsymbol{B}^{\mathrm{T}}\boldsymbol{P}\boldsymbol{x}^{(0\sim1)} \\ &\quad + 2\gamma\left\|\boldsymbol{B}^{\mathrm{T}}\boldsymbol{P}\boldsymbol{x}^{(0\sim1)}\boldsymbol{d}(t)\right\|, \end{aligned} \tag{17}$$

where (2) and (4) are used. It follows from the Yong's inequality that

$$2\left\|\boldsymbol{B}^{\mathrm{T}}\boldsymbol{P}\boldsymbol{x}^{(0\sim1)}\boldsymbol{d}\right\| \leq \left(\boldsymbol{x}^{(0\sim1)}\right)^{\mathrm{T}}\boldsymbol{P}\boldsymbol{B}\boldsymbol{B}^{\mathrm{T}}\boldsymbol{P}\boldsymbol{x}^{(0\sim1)} + \|\boldsymbol{d}\|^2.$$

Then, $\dot{V}(\boldsymbol{x}^{(0\sim1)},t)$ in (17) can be continued as

$$\begin{aligned}\dot{V} &\leq \frac{n+\delta_{\mathrm{c}}}{n\gamma}\dot{\gamma}V-\gamma V+\gamma\left\|\boldsymbol{d}(t)\right\|^2\\ &=\frac{1}{\alpha\gamma}\left(\dot{\gamma}-\alpha\gamma^2\right)V+\gamma\left\|\boldsymbol{d}(t)\right\|^2. \end{aligned}\tag{18}$$

where $\alpha \triangleq n/\left(n+\delta_{\mathrm{c}}\right)$. By using the definition of γ_0, $\gamma(t)$ in (14) and (15), we obtain

$$\dot{\gamma}-\alpha\gamma^2=-\alpha s\gamma^2.$$

Define $d_{\mathrm{m}} \triangleq \sup_{0\leq t\leq T}\left\|\boldsymbol{d}(t)\right\|^2$. Then $\dot{V}(\boldsymbol{x}^{(0\sim1)},t)$ in (18) can be continued as

$$\dot{V}\leq -s\gamma(t)V+d_{\mathrm{m}}\gamma(t),$$

which, by the comparison lemma, implies

$$V\leq\left(\frac{T-t}{T}\right)^{s\gamma_0 T}V_0+\frac{d_{\mathrm{m}}}{s},\tag{19}$$

where $V_0 \triangleq V(\boldsymbol{x}^{(0\sim1)}(0),0)$. Observe that

$$V(\boldsymbol{x}^{(0\sim1)},t)\geq\lambda_{\min}(\boldsymbol{P}(\gamma_0))\gamma(t)\left\|\boldsymbol{x}^{(0\sim1)}\right\|^2,\tag{20}$$

$$V_0\leq\lambda_{\max}(\boldsymbol{P}(\gamma_0))\gamma_0\left\|\boldsymbol{x}^{(0\sim1)}(0)\right\|^2,\tag{21}$$

where $\mathrm{d}\boldsymbol{P}(\gamma)/\mathrm{d}\gamma>0$ in (4) and $\gamma\geq\gamma_0$ are used in (20). Let $\sigma_1 \triangleq \lambda_{\min}(\boldsymbol{P}(\gamma_0))$ and $\sigma_2 \triangleq \lambda_{\max}(\boldsymbol{P}(\gamma_0))$. Combined (19), (20), and (21) obtains

$$\begin{aligned}\left\|\boldsymbol{x}^{(0\sim1)}(t)\right\|^2 \leq\ & \frac{\sigma_2}{\sigma_1}\left(\frac{T-t}{T}\right)^{s\gamma_0T+1}\left\|\boldsymbol{x}^{(0\sim1)}(0)\right\|^2\\ &+\frac{1}{s\sigma_1\gamma_0}\frac{T-t}{T}d_{\mathrm{m}}.\end{aligned}\tag{22}$$

In view of $\lim_{t\to T}\left\|\boldsymbol{x}^{(0\sim1)}(t)\right\|=0$, the point $\boldsymbol{x}^{(0\sim1)}=\boldsymbol{0}$ of the closed-loop system of (16) is T-GFTA.

The boundedness of $\boldsymbol{u}(t)$ should be revealed. It follows from (3) and (5) that

$$\begin{aligned}\left\|\boldsymbol{v}(t)\right\|^2 &=\left(\boldsymbol{x}^{(0\sim1)}\right)^{\mathrm{T}}\boldsymbol{P}\boldsymbol{B}\boldsymbol{B}^{\mathrm{T}}\boldsymbol{P}\boldsymbol{x}^{(0\sim1)}\\ &\leq\lambda_{\max}(\boldsymbol{P}^{\frac{1}{2}}\boldsymbol{B}\boldsymbol{B}\boldsymbol{P}^{\frac{1}{2}})\left(\boldsymbol{x}^{(0\sim1)}\right)^{\mathrm{T}}\boldsymbol{P}^{\frac{1}{2}}\boldsymbol{P}^{\frac{1}{2}}\boldsymbol{x}^{(0\sim1)}\\ &\leq\mathrm{tr}\left(\boldsymbol{P}^{\frac{1}{2}}\boldsymbol{B}\boldsymbol{B}^{\mathrm{T}}\boldsymbol{P}^{\frac{1}{2}}\right)\left(\boldsymbol{x}^{(0\sim1)}\right)^{\mathrm{T}}\boldsymbol{P}\boldsymbol{x}^{(0\sim1)}\\ &=\mathrm{tr}\left(\boldsymbol{B}^{\mathrm{T}}\boldsymbol{P}\boldsymbol{B}\right)\left(\boldsymbol{x}^{(0\sim1)}\right)^{\mathrm{T}}\boldsymbol{P}\boldsymbol{x}^{(0\sim1)}\\ &=nV(\boldsymbol{x}^{(0\sim1)},t),\end{aligned}$$

which together with (19) implies

$$\left\|\boldsymbol{v}(t)\right\|^2\leq n\left(\frac{T-t}{T}\right)^{s\gamma_0T}V_0+\frac{nd_{\mathrm{m}}}{s}.\tag{23}$$

In view of the boundedness of $\boldsymbol{x}^{(0\sim1)}(t)$ in (22), $\boldsymbol{f}(\boldsymbol{x}^{(0\sim1)}(t),t)$ is bounded on the time interval $[0,T)$ owing to the continuity, which, together with the boundedness of $\boldsymbol{v}(t)$ in (23), implies that the control input $\boldsymbol{u}(t)$ is bounded on the time interval $[0,T)$.

When it concerns $d(t)=0$, substituting $d_{\mathrm{m}}=0$ into (22) leads to

$$\left\|\boldsymbol{x}^{(0\sim1)}(t)\right\|^2\leq\frac{\sigma_2}{\sigma_1}\left(\frac{T-t}{T}\right)^{s\gamma_0T+1}\left\|\boldsymbol{x}^{(0\sim1)}(0)\right\|^2,\tag{24}$$

which implies that the equilibrium $\boldsymbol{x}^{(0\sim1)}=\boldsymbol{0}$ of the closed-loop system (16) is Lyapunov stable and $\lim_{t\to T}\left\|\boldsymbol{x}^{(0\sim1)}(t)\right\|=0$. This proof is finished. □

Remark 2. *In the absence of $\boldsymbol{d}(t)$, the bounded results of $\boldsymbol{x}^{(0\sim1)}(t)$ in (22) is strengthened to the Lyapunov stable case (24), which results in the stabilization result for system (6).*

Remark 3. *Denote the trajectory of the closed-loop system (16) with and without $\boldsymbol{d}(t)$ as $\boldsymbol{x}^{(0\sim1)}(t)$ and $\boldsymbol{x}_*^{(0\sim1)}(t)$, respectively. By checking that $\lim_{t\to T}\left\|\boldsymbol{x}^{(0\sim1)}(t)\right\| = \lim_{t\to T}\left\|\boldsymbol{x}_*^{(0\sim1)}(t)\right\|=0$, it can be concluded that the disturbance $\boldsymbol{d}(t)$ is globally almost decoupled by the developed controller (15).*

5 Simulations

In this section, some comparative simulations are provided to verify the effectiveness of robust prescribed-time control for the elliptical orbital rendezvous system. We point out that the original plant (7) is chosen as the simulation plant. Some key parameters of the target orbital are listed in Table 1 [13]. Among these parameters, $a, e, \mu, t_{\mathrm{p}}$ are basic parameters of the target orbit, but T_{t}, h are calculated by (8). By using Lemma 1, the employed controller (15) can be written as

Table 1: Parameters of the target orbit

Parameters	Symbol	Values
Semimajor axis	a	$2.4616\times10^7\mathrm{m}$
Eccentricity	e	0.073074
Gravity constant	μ	$3.986\times10^{14}\mathrm{m}^3/\mathrm{s}^2$
Time at perigee	t_{p}	0s
Angular momentum	h	$6.672\times10^{10}\mathrm{m}^2/\mathrm{s}$
Period	T_{t}	38436s

$$\boldsymbol{u}(t)=-\boldsymbol{B}^{\mathrm{T}}\gamma\boldsymbol{L}_n(\gamma)\boldsymbol{P}_n\boldsymbol{L}_n(\gamma)\boldsymbol{x}^{(0\sim1)}(t)-\boldsymbol{f}(\boldsymbol{x}^{(0\sim1)},t)$$

where $\boldsymbol{P}_n$ and $\boldsymbol{L}_n(\gamma)$ are given by

$$\boldsymbol{P}_n=\begin{bmatrix}\boldsymbol{I}_3 & \boldsymbol{I}_3\\ \boldsymbol{I}_3 & 2\boldsymbol{I}_3\end{bmatrix},\ \boldsymbol{L}_n(\gamma)=\begin{bmatrix}\gamma\boldsymbol{I}_3 & \boldsymbol{0}\\ \boldsymbol{0} & \boldsymbol{I}_3\end{bmatrix}.$$

For a clear interpretation, we partition the vector $\boldsymbol{x}$ in the rotating frame XYZ as $\boldsymbol{x}=\begin{bmatrix}x_1 & x_2 & x_3\end{bmatrix}^{\mathrm{T}}$ and choose three types of initial conditions

$$\begin{aligned}\boldsymbol{x}_{0,1}&=[1000,-3,100,10000,3,-3]^{\mathrm{T}},\\ \boldsymbol{x}_{0,2}&=[2000,-6,200,20000,6,-6]^{\mathrm{T}},\\ \boldsymbol{x}_{0,3}&=[5000,-15,500,50000,15,-15]^{\mathrm{T}},\end{aligned}$$

and two types of disturbances

$$\begin{aligned}\boldsymbol{d}_1(t)&=[\mathrm{e}^{0.01t},3tx_2(t),100]^{\mathrm{T}},\\ \boldsymbol{d}_2&=[200,200,100]^{\mathrm{T}}.\end{aligned}$$

5.1 Cases Under Various T

We consider three cases regarding various prescribed times T, whose simulation parameters are listed as follows,

Case 1: $T = 1, \gamma_0 = 10, \boldsymbol{x}^{(0\sim1)}(0) = \boldsymbol{x}_{0,1}, \boldsymbol{d} = \boldsymbol{d}_1(t)$;
Case 2: $T = 2, \gamma_0 = 10, \boldsymbol{x}^{(0\sim1)}(0) = \boldsymbol{x}_{0,1}, \boldsymbol{d} = \boldsymbol{d}_1(t)$;
Case 3: $T = 5, \gamma_0 = 10, \boldsymbol{x}^{(0\sim1)}(0) = \boldsymbol{x}_{0,1}, \boldsymbol{d} = \boldsymbol{d}_1(t)$.

The simulation results including the state response and inputs are printed in Figs. 2-4. As observed, any states of $\boldsymbol{x}^{(0\sim1)}(t)$ converge to the origin within the prescribed time T, and in the meantime, the input $\boldsymbol{u}(t)$ is bounded, which validates the attractive results in Theorem 1.

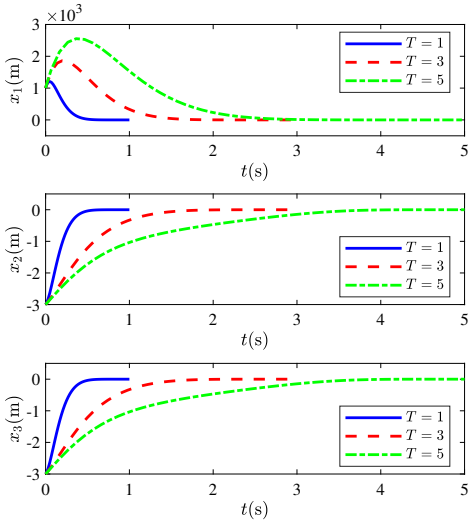

Fig. 2: The response $\boldsymbol{x}(t)$ under various T

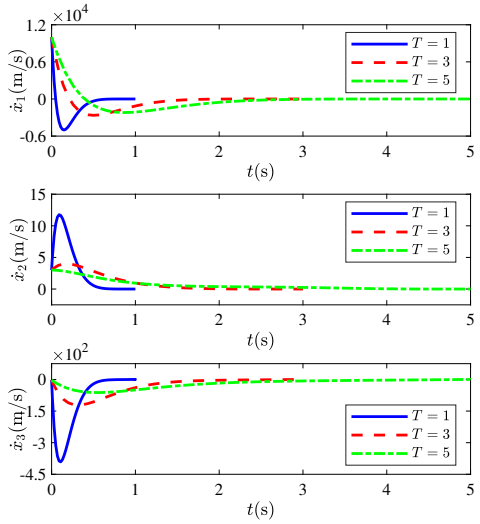

Fig. 3: The response $\dot{\boldsymbol{x}}(t)$ under various T

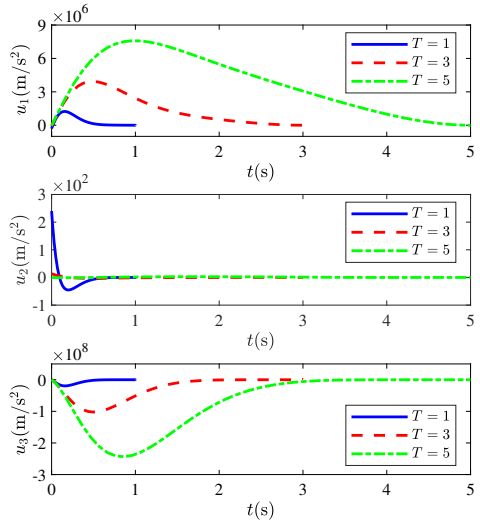

Fig. 4: Control input $\boldsymbol{u}(t)$ under various T

5.2 Cases Under Various $\boldsymbol{d}(t)$

We consider three cases regarding various disturbances $\boldsymbol{d}(t)$, whose simulation parameters are listed as follows,

Case 4: $T = 5, \gamma_0 = 10, \boldsymbol{x}^{(0\sim1)}(0) = \boldsymbol{x}_{0,1}, \boldsymbol{d} = \boldsymbol{d}_1(t)$;
Case 5: $T = 5, \gamma_0 = 10, \boldsymbol{x}^{(0\sim1)}(0) = \boldsymbol{x}_{0,1}, \boldsymbol{d} = \boldsymbol{d}_2$;
Case 6: $T = 5, \gamma_0 = 10, \boldsymbol{x}^{(0\sim1)}(0) = \boldsymbol{x}_{0,1}, \boldsymbol{d} = \boldsymbol{0}$.

The time-varying disturbance $\boldsymbol{d}_1(t)$ and the constant disturbance $\boldsymbol{d}_2$ are considered in Case 4 and Case 5 respectively. The trajectory $\boldsymbol{x}(t)$ converges to the origin in any cases, whose simulation results are printed in the rotating frame and captured by Fig. 5. By comparing these three cases, we obtain that the disturbance $\boldsymbol{d}_1(t)$ and $\boldsymbol{d}_2$ are almost disturbance decoupled, which verifies the results in Remark 3. However, it is clear that the attractive performance relies on the form of disturbances.

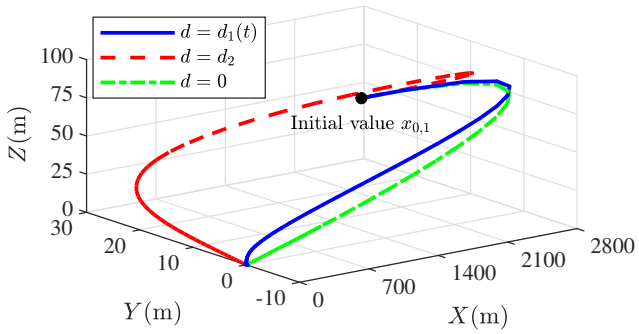

Fig. 5: Trajectory $\boldsymbol{x}(t)$ in the rotating frame under various $\boldsymbol{d}(t)$

5.3 Cases Under Various γ_0

We consider three cases regarding various initial gains γ_0, whose simulation parameters are listed as follows,

Case 7: $T = 5, \gamma_0 = 10, \boldsymbol{x}^{(0\sim1)}(0) = \boldsymbol{x}_{0,1}, \boldsymbol{d} = \boldsymbol{d}_1(t)$;
Case 8: $T = 5, \gamma_0 = 20, \boldsymbol{x}^{(0\sim1)}(0) = \boldsymbol{x}_{0,1}, \boldsymbol{d} = \boldsymbol{d}_1(t)$;
Case 9: $T = 5, \gamma_0 = 50, \boldsymbol{x}^{(0\sim1)}(0) = \boldsymbol{x}_{0,1}, \boldsymbol{d} = \boldsymbol{d}_1(t)$.

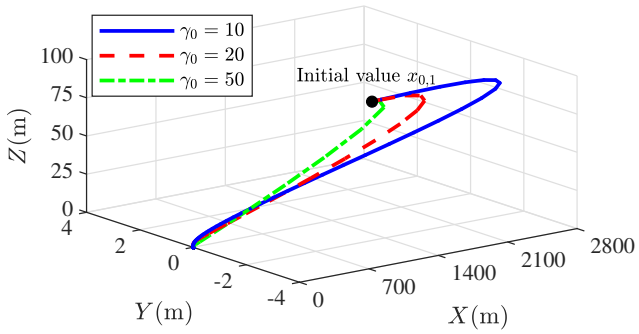

Fig. 6: Trajectory $\boldsymbol{x}(t)$ in the rotating frame under various γ_0

The trajectory $\boldsymbol{x}(t)$ converges to the origin in any case, whose simulation results are printed in the rotating frame and captured by Fig. 6. It is worth mentioning that the overshoots, particularly in the coordinate X (namely, the component x_1), are distinct under the different γ_0.

5.4 Cases Under Various $\boldsymbol{x}^{(0\sim1)}(0)$

We consider three cases regarding various initial values $\boldsymbol{x}_0$, whose simulation parameters are listed as follows,

Case 10: $T = 5, \gamma_0 = 20, \boldsymbol{x}^{(0\sim1)}(0) = \boldsymbol{x}_{0,1}, \boldsymbol{d} = \boldsymbol{d}_1(t)$;
Case 11: $T = 5, \gamma_0 = 20, \boldsymbol{x}^{(0\sim1)}(0) = \boldsymbol{x}_{0,2}, \boldsymbol{d} = \boldsymbol{d}_1(t)$;
Case 12: $T = 5, \gamma_0 = 20, \boldsymbol{x}^{(0\sim1)}(0) = \boldsymbol{x}_{0,3}, \boldsymbol{d} = \boldsymbol{d}_1(t)$.

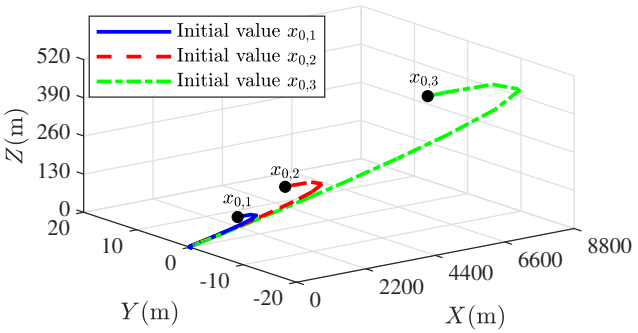

Fig. 7: Trajectory $\boldsymbol{x}(t)$ under various $\boldsymbol{x}^{(0\sim1)}(0)$

The trajectory $\boldsymbol{x}(t)$ converges to the origin in any case, whose simulation results are printed in the rotating frame and captured by Fig. 7. The demands for a large initial condition $\boldsymbol{x}_0$ in practical applications can be met by our approach owing to the global results in Theorem 1.

6 Conclusion

The robust prescribed-time global control for the elliptical orbital rendezvous system is studied, where the involved time-varying disturbances (concerning time only) is assumed to be piecewise continuous merely. With three independent control accelerations (or thrusts) being used as the control input, the elliptical orbital rendezvous system formulated by Newton's equation turns out to be an FAS, thereby the idea of FAS approaches is used to facilitate the controller design. In addition, motivated by the time-varying high-gain feedback approach, a prescribed-time controller is designed for the perturbed rendezvous system such that the target spacecraft is captured successfully by the arbitrarily positioned chaser spacecraft within the prescribed time, that is, the origin of the closed-loop system is globally finite-time attractive within any prescribed time.

References

[1] M. E. Polites, Technology of automated rendezvous and capture in space, *Journal of Spacecraft and Rockets*, 36(2): 280–291, 1999.

[2] T. E. Carter, State transition matrices for terminal rendezvous studies: brief survey and new example, *Journal of Guidance, Control, and Dynamics*, 21(1): 148–155, 1998.

[3] H. D. Curtis, *Orbital mechanics for engineering students*. Oxford: Butterworth-Heinemann, 2013.

[4] W. Clohessy and R. Wiltshire, Terminal guidance system for satellite rendezvous, *Journal of the Aerospace Sciences*, 27(9): 653–658, 1960.

[5] G. R. Duan, High-order fully actuated system approaches: Part I. Models and basic procedure, *International Journal of Systems Science*, 52(2): 422–435, 2021.

[6] G. R. Duan, High-order fully actuated system approaches: Part III. Robust control and high-order backstepping, *International Journal of Systems Science*, 52(5): 952–971, 2021.

[7] G. R. Duan, High-order fully-actuated system approaches: Part VI. Disturbance attenuation and decoupling, *International Journal of Systems Science*, 52(10):2161–2181, 2021.

[8] G. R. Duan, Brockett's first example: An FAS approach treatment, *Journal of Systems Science and Complexity*, 35(2): 441–456, 2022.

[9] G. R. Duan, Robust stabilization of time-varying nonlinear systems with time-varying delays: A fully actuated system approach, *IEEE Transactions on Cybernetics*, 53(12): 7455–7468, 2023.

[10] W. Z. Liu, G. R. Duan, and M. Z. Hou, High-order robust command filtered backstepping design for strict-feedback systems: A high-order fully actuated system approach, *International Journal of Robust and Nonlinear Control*, 32(18): 10251–10270, 2022.

[11] M. Cai, X. He, and D. Zhou, An active fault tolerance framework for uncertain nonlinear high-order fully-actuated systems, *Automatica*, 152: 110969, 2023.

[12] Y. Wang and H. Ji, Integrated relative position and attitude control for spacecraft rendezvous with ISS and finite-time convergence, *Aerospace Science and Technology*, 85: 234–245, 2019.

[13] B. Zhou, Z. Lin, and G. R. Duan, Lyapunov differential equation approach to elliptical orbital rendezvous with constrained controls, *Journal of Guidance, Control, and Dynamics*, 34(2): 345–358, 2011.

[14] S. Narayanaswamy and C. J. Damaren, Equinoctial Lyapunov control law for low-thrust rendezvous, *Journal of Guidance, Control, and Dynamics*, 46(4): 781–795, 2023.

[15] R. Epenoy, Fuel optimization for continuous-thrust orbital rendezvous with collision avoidance constraint, *Journal of Guidance, Control, and Dynamics*, 34(2): 493–503, 2011.

[16] G. Boyarko, O. Yakimenko, and M. Romano, Optimal rendezvous trajectories of a controlled spacecraft and a tumbling object, *Journal of Guidance, Control, and dynamics*, 34(4): 1239–1252, 2011.

[17] B. Zhou, Finite-time stabilization of linear systems by bounded linear time-varying feedback, *Automatica*, 113: 108760, 2020.

[18] S. He, D. Lin, and J. Wang, Autonomous spacecraft rendezvous with finite time convergence, *Journal of the Franklin Institute*, 352(11): 4962–4979, 2015.

[19] K. Zhang, Y. Liu, and J. Tan, Semiglobal finite-time stabilization of saturated spacecraft rendezvous system by dynamic event-triggered and self-triggered control, *IEEE Transactions on Aerospace and Electronic Systems*, 58(6): 5030–5042, 2022.

[20] Z. Zhang, H. Jiang, and X. Yang, Fixed-time stabilization of periodic linear systems and its application to the elliptical spacecraft rendezvous, *Journal of the Franklin Institute*, 360(12): 7832–7850, 2023.

[21] Y. Song, Y. Wang, J. Holloway, and M. Krstic, Time-varying feedback for regulation of normal-form nonlinear systems in prescribed finite time, *Automatica*, 83: 243–251, 2017.

[22] Y. Song, Y. Wang, and M. Krstic, Time-varying feedback for stabilization in prescribed finite time, *International Journal of Robust and Nonlinear Control*, 29(3): 618–633, 2019.

[23] P. Krishnamurthy, F. Khorrami, and M. Krstic, A dynamic high-gain design for prescribed-time regulation of nonlinear systems, *Automatica*, 115: 108860, 2020.

[24] B. Zhou and Y. Shi, Prescribed-time stabilization of a class of nonlinear systems by linear time-varying feedback, *IEEE Transactions on Automatic Control*, 66(12): 6123–6130, 2021.

[25] B. Zhou, Finite-time stability analysis and stabilization by bounded linear time-varying feedback, *Automatica*, 121: 109191, 2020.

Proceedings of the 3rd Conference on Fully Actuated System Theory and Applications
May 10-12, 2024, Shenzhen, China

Fully Actuated System Approach-Based Adaptive Event-Triggered Control for Nonlinear Switched Systems

Chengyuan Yan, Jianwei Xia*, Wei Sun

1. School of Mathematics Science, Liaocheng University, Liaocheng, 252000, P. R. China
E-mail: yanchengyuansd@163.com;njustxjw@126.com;sunw8617@163.com

Abstract: In this paper, an event-triggered control scheme for nonlinear switched system is proposed based on the fully actuated system approach. By integrating the switching signal information into the event-triggered mechanism (ETM), a mode-dependent event-triggered controller is designed to save communication resources. In addition, neural network is used to approximate the unknown nonlinear dynamics of the system. By combining the fully actuated system approach with mode-dependent ETM, the computational complexity is reduced. The proposed scheme guarantees that all the signals in the closed-loop system remain bounded. Finally, the effectiveness of the proposed control scheme is proved by example.

Key Words: Neural network, Event-triggered control, Nonlinear switched system.

1 Introduction

In recent years, the control problem of nonlinear systems has received extensive attention. Therefore, the stability of nonlinear systems has become a key problem that researchers need to solve. Many scholars have studied the stability of nonlinear systems and achieved fruitful results [1-4]. Nevertheless, all of the aforementioned outcomes require the conversion of the second-order system into the form of a first-order state space, which increases the computational complexity and wastes resources. In order to solve the problem, high-order fully actuated (HOFA) systems theory was proposed in [5–7]. Compared with the first-order state-space form, the HOFA systems can not only greatly simplify the controller design but also ensure the full-actuation characteristic of the system.

The existence of uncertainty problems in practical applications is widespread, which is solved by adaptive control design for uncertain nonlinear systems. And fuzzy logic system and NN are also used to approximate unknown continuous nonlinear functions [8–12]. Reference [8] considered the problem of adaptive NN control for nonlower triangular nonlinear systems with unmodeled dynamics and additional disturbances. However, these excellent results do not take into account energy consumption and communication burden.

Event-triggered control (ETC) has received a lot of attention due to their ability to conserve resources [13–16]. When we consider the ETC of switched system, it is inevitable to solve asynchronous switching problems between mode-dependent controllers and subsystems caused by triggering and switching. However, strict assumptions in the control design have been made to avoid asynchronous switching in many papers. In addition, the above ETC only applies to general first-order nonlinear systems, and cannot be directly applied to high-order fully actuated systems. Therefore, it is necessary to study ETC for HOFA nonlinear switched systems.

Inspired by the above analysis, this brief considers adaptive ETC for nonlinear switched system based on fully actuated system method. The innovations of the brief are shown as follows

(1) Compared with the above papers, the proposed ETM can be directly applied to HOFA systems, which not only successfully save resources, but also ensure that the state of the system is bounded.

(2) Combining fully actuated system approach with model-dependent ETM, the computational complexity is reduced.

(3) NN is utilized to estimate the unknown nonlinear functions, which is more convenient for controller design.

2 Problem formulation and preliminaries

Consider a single-link FJ robot system whose manipulators with an elastic revolute joint is actuated by a brushed direct current motor that can be given by

$$\begin{cases} M^{\sigma}\ddot{q}_1 + mgl^{\sigma}\sin(q_1) = K(q_2 - q_1), \\ J\ddot{q}_2 + B\dot{q}_2 - K(q_1 - q_2) = K_T I, \\ L\dot{I} + RI + K_B\dot{q}_2 = u, \end{cases} \tag{1}$$

where q_1 and q_2 are the angular position on the link and motor sides, respectively. M and m represent the load and link masses, respectively. l is the link length, g is the gravitational acceleration, K is stiffness coefficient of the torsional spring, J is the rotor inertia, B is the coefficient of viscous friction. K_T and K_B are torque constant of the direct current motor and back-emf coefficient, respectively. L, I and R are the armature inductance, current, and resistance, respectively. u is the torque input. $\sigma(t) : [0, \infty) \to M = \{1, 2, \cdots, m\}$ is the switching signal.

Obviously, the above system is a second-order system, and the proposed high-order ETC backstepping can deal with it directly without transforming it into a first-order state space form. Let $x_1 = q_1$, $x_2 = q_2$, $x_3 = I$. Then the system (1) can be converted to the following form

$$\begin{cases} x_1^{(m_1)} = f_1^{\sigma}(x_1^{(0\sim m_1-1)}) + g_1^{\sigma}(x_1^{(0\sim m_1-1)})x_2, \\ x_2^{(m_2)} = f_2^{\sigma}(x_i^{(0\sim m_i-1)}|_{i=1\sim 2}) + g_2^{\sigma}(x_i^{(0\sim m_i-1)}|_{i=1\sim 2})x_3, \\ x_3^{(m_3)} = f_3^{\sigma}(x_i^{(0\sim m_i-1)}|_{i=1\sim 3}) + g_3^{\sigma}(x_i^{(0\sim m_i-1)}|_{i=1\sim 3})u, \end{cases} \tag{2}$$

where x_i $(i = 1, 2, 3)$ and u denote the system state, input, respectively. m_i $(i = 1, 2, 3)$ are positive integers, and

$m_1 = 2, m_2 = 2, m_3 = 1$. $f_i^\sigma(x_i^{(0\sim m_i-1)}|_{i=1\sim i})$ are sufficiently smooth nonlinear functions. $g_i^\sigma(x_i^{(0\sim m_i-1)}|_{i=1\sim i})$ are control gain functions, and satisfies full-actuation conditions. And $f_1^\sigma(x_1^{(0\sim m_1-1)}) = -\frac{mgl^\sigma}{M^\sigma}sin(x_1) - \frac{K}{M^\sigma}x_1$, $f_2^\sigma(x_i^{(0\sim m_i-1)}|_{i=1\sim 2}) = \frac{K}{J}x_1 - \frac{B}{J}\dot{x}_2 - \frac{K}{J}x_2$, $f_3^\sigma(x_i^{(0\sim m_i-1)}|_{i=1\sim 3}) = -\frac{K_B}{L}\dot{x}_2 - \frac{R}{L}x_3$, $g_1^\sigma(x_1^{(0\sim m_1-1)}) = \frac{K}{M^\sigma}$, $g_2^\sigma(x_i^{(0\sim m_i-1)}|_{i=1\sim 2}) = \frac{K_T}{J}$, $g_3^\sigma(x_i^{(0\sim m_i-1)}|_{i=1\sim 3}) = \frac{1}{L}$. $\sigma(t) : [0,\infty) \to M = \{1, 2, \cdots, m\}$ is the switching signal. In the next, make some necessary symbols, full-actuation assumptions and lemmas.

In the paper, I_n represents the identity matrix and

$$x^{(0\sim n)} = \begin{bmatrix} x \\ \dot{x} \\ \vdots \\ x^{(n)} \end{bmatrix},$$

$$I_n^\circ = \begin{bmatrix} 0 & 0 & 1 \\ 0 & \iddots & 0 \\ 1 & 0 & 0 \end{bmatrix},$$

$$x_{i\sim j}^{(0\sim n)} = \begin{bmatrix} x_i^{(0\sim n)} \\ x_{i+1}^{(0\sim n)} \\ \vdots \\ x_j^{(0\sim n)} \end{bmatrix}, j \geq i$$

$$A^{0\sim n-1} = \begin{bmatrix} A_0 & A_1 & \dots & A_{n-1} \end{bmatrix},$$

$$\Phi(A^{0\sim n-1}) = \begin{bmatrix} 0 & I & & \\ & & \ddots & \\ & & & I \\ -A_0 & -A_1 & \dots & A_{n-1} \end{bmatrix}.$$

Assumption 1. [6] $g_k^p(x_i^{(0\sim m_i-1)}|_{i=1\sim k}) \neq 0, k = 1, \cdots, n, p \in M$.

Assumption 2. [9] The desired signal $y_d(t)$ and $\dot{y}_d(t)$ are known, continuous and bounded.

Lemma 1.[3] Let $f(x)$ be a continuous function which is defined on a compact set Ξ, there is NN such that the following inequality holds

$$f(x) = W^{*T}S(x) + \varepsilon(x), \tag{3}$$

where $\varepsilon(x)$ represents the approximation error with $|\varepsilon(x)| \leq \overline{\varepsilon}$ and $\overline{\varepsilon} > 0$ is positive constant.

Lemma 2.[15] For $\forall \epsilon > 0$ and $\sigma \in R$, it can be concluded that

$$0 \leq |\sigma| - \sigma \tanh(\frac{\sigma}{\epsilon}) \leq 0.2785\epsilon. \tag{4}$$

Lemma 3.[6] When the matrix $A^{0\sim n-1}$ is chosen to make the matrix $\Phi(A^{0\sim n-1})$ stable, it follows from the Lyapunov Theorem that there exists a positive definite matrix $P(A^{0\sim n-1})$ satisfying

$$\begin{aligned} &\Phi(A_i^{0\sim 1})^T P_i(A_i^{0\sim 1}) + P_i(A_i^{0\sim 1})\Phi(A_i^{0\sim 1}) \\ &= -\mu_i I_i, \end{aligned} \tag{5}$$

where $\mu_i > 0$ is a constant and $i = 1, \cdots, n$.

3 Controller Design and Stability Analysis

At the beginning of high-order ETC backstepping design, we give the some notations. Define

$$P_i(A_i^{0\sim 1}) = \begin{bmatrix} P_{iF}(A_i^{0\sim 1}) & P_{iL}(A_i^{0\sim 1}) \end{bmatrix},$$

$$\tilde{P}_i(A_i^{0\sim 1}) = I_2^\circ P_i^T(A_i^{0\sim 1}),$$

$$\tilde{P}_i^{-1}(A_i^{0\sim 1}) = \begin{bmatrix} Q_{i11}(A_i^{0\sim 1}) & Q_{i12}(A_i^{0\sim 1}) \\ Q_{iF}(A_i^{0\sim 1}) & Q_{iL}(A_i^{0\sim 1}) \end{bmatrix},$$

where $i = 1, \cdots, 3$, and $Q_{iL}(A_i^{0\sim 1}) \neq 0$.

Step 1: Firstly, the following coordinate transformation is defined as

$$e_1^{(0\sim 1)} = x_1^{(0\sim 1)} - y_d^{(0\sim 1)}, \tag{6}$$

$$\tilde{P}_2(A_2^{0\sim 1})e_2^{(0\sim 1)} = x_2^{(0\sim 1)} - \begin{bmatrix} \alpha_1 \\ 0 \end{bmatrix}.$$

Based on the above notations, one has

$$\begin{aligned} P_{2L}^T(A_2^{0\sim 1})e_2^{(0\sim 1)} &= x_2 - \alpha_1, \\ P_{2F}^T(A_2^{0\sim 1})e_2^{(0\sim 1)} &= \dot{x}_2. \end{aligned} \tag{7}$$

From (2) and (6), the time derivative of e_1 is

$$\begin{aligned} \ddot{e}_1 =& f_1^p(x_1^{(0\sim 1)}) + g_1^p(x_1^{(0\sim 1)})P_{2L}^T(A_2^{0\sim 1}) \\ &\times e_2^{(0\sim 1)} + g_1^p(x_1^{(0\sim 1)})\alpha_1. \end{aligned} \tag{8}$$

Choose virtual controller α_1 as

$$\begin{aligned} \alpha_1 =& -\frac{1}{g_1}(A_1^{(0\sim 1)}e_1^{(0\sim 1)} + \frac{1}{2a_1^2}P_{1L}^T(A_1^{0\sim 1})e_1^{(0\sim 1)} \\ &\times \hat{\theta}_1 S_1^T S_1 + \frac{1}{2}P_{1L}^T(A_1^{0\sim 1})e_1^{(0\sim 1)}), \end{aligned} \tag{9}$$

where $g_1 = \max_{p\in M}\{g_1^p, \}$. Then, (8) can be expressed in the state-space form

$$\dot{e}_1^{(0\sim 1)} = s_1^p \Phi(A_1^{0\sim 1})e_1^{(0\sim 1)} + \begin{bmatrix} 0 \\ H_1^p \end{bmatrix}$$

where $s_1^p = \{g_1^p/g_1, p \in M\}$, $H_1^p = f_1^p(x_1^{(0\sim 1)}) + g_1^p(x_1^{(0\sim 1)})P_{2L}^T(A_2^{0\sim 1})e_2^{(0\sim 1)} - \frac{1}{2}P_{1L}^T(A_1^{0\sim 1})e_1^{(0\sim 1)} - \frac{1}{2a_1^2}P_{1L}^T(A_1^{0\sim 1})e_1^{(0\sim 1)}\hat{\theta}_1 S_1^T S_1$.

The Lyapunov candidate function V_1 is designed as

$$V_1 = (e_1^{(0\sim 1)})^T P_1(A_1^{0\sim 1})e_1^{(0\sim 1)} + \frac{1}{2}\tilde{\theta}_1^2, \tag{10}$$

where $\theta_1 = \max_{p\in M}\{\|W_1^p\|^2\}$ and $\tilde{\theta}_1 = \theta_1 - \hat{\theta}_1$.

The derivative of V_1 can be derived as

$$\begin{aligned} \dot{V}_1 \leq& -\mu_1 s_{1,m}(e_1^{(0\sim 1)})^T e_1^{(0\sim 1)} - \tilde{\theta}_1\dot{\hat{\theta}}_1 \\ &+ 2P_{1L}^T(A_1^{0\sim 1})e_1^{(0\sim 1)} f_1^p(x_1^{(0\sim 1)}) \\ &- P_{1L}^T(A_1^{0\sim 1})e_1^{(0\sim 1)}(e_1^{(0\sim 1)})^T P_{1L}(A_1^{0\sim 1}) \\ &+ 2P_{1L}^T(A_1^{0\sim 1})e_1^{(0\sim 1)} g_1^p(x_1^{(0\sim 1)})P_{2L}^T(A_2^{0\sim 1})e_2^{(0\sim 1)} \\ &- P_{1L}^T(A_1^{0\sim 1})e_1^{(0\sim 1)}\frac{1}{a_1^2}P_{1L}^T(A_1^{0\sim 1})e_1^{(0\sim 1)}\hat{\theta}_1 S_1^T S_1 \end{aligned} \tag{11}$$

where $s_{1,m} = \min_{p\in M}\{s_1^p\}$. With the help of NN and Young's inequality, one gets

$$\begin{aligned}
&P_{1L}^T(A_1^{0\sim1})e_1^{(0\sim1)}F_1^p(X_1)\\
=&P_{1L}^T(A_1^{0\sim1})e_1^{(0\sim1)}(W_1^TS_1(X_1)+\varepsilon_1)\\
\leq&\frac{(P_{1L}^T(A_1^{0\sim1})e_1^{(0\sim1)})^2\theta_1S_1^T(X_1)S_1(X_1)}{2a_1^2}+\frac{1}{2}a_1^2\\
&+\frac{1}{2}P_{1L}^T(A_1^{0\sim1})e_1^{(0\sim1)}P_{1L}^T(A_1^{0\sim1})e_1^{(0\sim1)}+\frac{1}{2}\bar{\varepsilon}_1^2, \quad (12)
\end{aligned}$$

where $F_1^p(X_1) = f_1^p(x_1^{(0\sim1)})$, a_1 is a constant.

The adaptive law $\hat{\theta}_1$ is designed as

$$\dot{\hat{\theta}}_1 = \frac{1}{a_1^2}P_{1L}^T(A_1^{0\sim1})e_1^{(0\sim1)}P_{1L}^T(A_1^{0\sim1})e_1^{(0\sim1)}S_1^TS_1 - l_1\hat{\theta}_1. \quad (13)$$

Replacing (12) and (13) into (11), one gives

$$\begin{aligned}
\dot{V}_1 \leq&-\mu_1s_{1,m}(e_1^{(0\sim1)})^Te_1^{(0\sim1)}-\frac{1}{2}l_1\tilde{\theta}_1^2+a_1^2+\bar{\varepsilon}_1^2+\frac{1}{2}l_1\theta_1^2\\
&+2P_{1L}^T(A_1^{0\sim1})e_1^{(0\sim1)}g_1^p(x_1^{(0\sim1)})P_{2L}^T(A_2^{0\sim1})e_2^{(0\sim1)}. \quad (14)
\end{aligned}$$

Step 2: From (2) and (7), the time derivative of e_2 is

$$\begin{aligned}
\ddot{e}_2 =&Q_{2F}(A_2^{0\sim1})(\dot{x}_2-\dot{\alpha}_1)+Q_{2L}(A_2^{0\sim1})f_2^p(x_2^{(0\sim1)})\\
&+Q_{2L}(A_2^{0\sim1})g_2^p(x_2^{(0\sim1)})\tilde{P}_3(A_3^{(0\sim1)})e_3^{(0\sim1)}\\
&+Q_{2L}(A_2^{0\sim1})g_2^p(x_2^{(0\sim1)})\alpha_2. \quad (15)
\end{aligned}$$

Choose virtual controller α_2 as

$$\begin{aligned}
\alpha_2 =&-\frac{1}{Q_{2L}(A_2^{0\sim1})g_2}(A_2^{(0\sim1)}e_2^{(0\sim1)}+\frac{1}{2a_2^2}\\
&\times P_{2L}^T(A_2^{0\sim1})e_2^{(0\sim1)}\hat{\theta}_2S_2^TS_2+\frac{1}{2}P_{2L}^T(A_2^{0\sim1})e_2^{(0\sim1)}), \quad (16)
\end{aligned}$$

where $g_2 = \max_{p\in M}\{g_2^p\}$. And (15) can be expressed in the state-space form

$$\dot{e}_2^{(0\sim1)} = s_2^p\Phi(A_2^{0\sim1})e_2^{(0\sim1)}+\begin{bmatrix}0\\H_2^p\end{bmatrix}$$

where $s_2^p = \{g_2^p/g_2, p \in M\}$, $H_2^p = Q_{2F}(A_2^{0\sim1})(\dot{x}_2-\dot{\alpha}_1)+Q_{2L}(A_2^{0\sim1})f_2(x_2^{(0\sim1)})-\frac{1}{2a_2^2}P_{2L}^T(A_2^{0\sim1})e_2^{(0\sim1)}\hat{\theta}_2S_2^TS_2-\frac{1}{2}P_{2L}^T(A_2^{0\sim1})e_2^{(0\sim1)}+Q_{2L}(A_2^{0\sim1})g_2^p(x_2^{(0\sim1)})\tilde{P}_3(A_3^{(0\sim1)})e_3^{(0\sim1)}$.

The Lyapunov function candidate V_2 is presented as

$$V_2 = V_1+(e_2^{(0\sim1)})^TP_2(A_2^{0\sim1})e_2^{(0\sim1)}+\frac{1}{2}\tilde{\theta}_2^2. \quad (17)$$

Taking the derivative of V_2, one has

$$\begin{aligned}
\dot{V}_2 =&\dot{V}_1-s_{2,m}\mu_2(e_2^{(0\sim1)})^Te_2^{(0\sim1)}+2P_{2L}^T(A_2^{0\sim1})e_2^{(0\sim1)}\\
&\times(Q_{2F}(A_2^{0\sim1})(\dot{x}_2-\dot{\alpha}_1)+Q_{2L}(A_2^{0\sim1})f_2^p(x_2^{(0\sim1)}))\\
&+2P_{2L}^T(A_2^{0\sim1})e_2^{(0\sim1)}Q_{2L}(A_2^{0\sim1})g_2^p(x_2^{(0\sim1)})\tilde{P}_3(A_3)\\
&\times e_3-P_{2L}^T(A_2^{0\sim1})e_2^{(0\sim1)}\frac{1}{a_2^2}P_{2L}^T(A_2^{0\sim1})e_2^{(0\sim1)}\hat{\theta}_2S_2^TS_2\\
&-P_{2L}^T(A_2^{0\sim1})e_2^{(0\sim1)}(e_2^{(0\sim1)})^TP_{2L}(A_2^{0\sim1})-\tilde{\theta}_2\dot{\hat{\theta}}_2. \quad (18)
\end{aligned}$$

And similar to the (12), one gets

$$\begin{aligned}
&P_{2L}^T(A_2^{0\sim1})e_2^{(0\sim1)}F_2^p(X_2)\\
=&P_{2L}^T(A_2^{0\sim1})e_2^{(0\sim1)}(W_2^{pT}S_2(X_2)+\varepsilon_2)\\
\leq&\frac{(P_{2L}^T(A_2^{0\sim1})e_2^{(0\sim1)})^2\theta_2S_2^T(X_2)S_2(X_2)}{2a_2^2}+\frac{1}{2}a_2^2\\
&+\frac{1}{2}P_{2L}^T(A_2^{0\sim1})e_2^{(0\sim1)}P_{2L}^T(A_2^{0\sim1})e_2^{(0\sim1)}+\frac{1}{2}\bar{\varepsilon}_2^2 \quad (19)
\end{aligned}$$

where $F_2^p(X_2) = Q_{2F}(A_2^{0\sim1})(\dot{x}_2-\dot{\alpha}_1)+Q_{2L}(A_2^{0\sim1})f_2^p(x_2^{(0\sim1)})+P_{2L}^T(A_2^{0\sim1})e_2^{(0\sim1)}$, a_2 is a constant.

The adaptive law $\hat{\theta}_2$ is designed as

$$\dot{\hat{\theta}}_2 = \frac{1}{a_2^2}P_{2L}^T(A_2^{0\sim1})e_2^{(0\sim1)}P_{2L}^T(A_2^{0\sim1})e_2^{(0\sim1)}S_2^TS_2 - l_2\hat{\theta}_2. \quad (20)$$

Replacing (19) and (20) into (18), one gives

$$\begin{aligned}
\dot{V}_2 \leq&-\sum_{i=1}^{2}s_{i,m}\mu_i(e_i^{(0\sim1)})^Te_i^{(0\sim1)}+\sum_{i=1}^{2}(a_i^2+\bar{\varepsilon}_i^2+\frac{1}{2}l_i\theta_i^2)\\
&+2P_{2L}^T(A_2^{0\sim1})e_2^{(0\sim1)}g_2^pP_3(A_3)e_3-\sum_{i=1}^{2}\frac{l_i}{2}\tilde{\theta}_i^2 \quad (21)
\end{aligned}$$

Step 3: The HOFA adaptive event-triggered controller is designed as follows

$$\begin{aligned}
v(t) =&-(1+\gamma)(\alpha_3\tanh(\frac{e_3P_3g_3^p(x_i^{(0\sim m_i-1)}|_{i=1\sim3})\alpha_3Q_3}{\epsilon})\\
&+\bar{m}\tanh(\frac{e_3P_3g_3^p(x_i^{(0\sim m_i-1)}|_{i=1\sim3})\bar{m}Q_3}{\epsilon}), \quad (22)\\
u(t) =&v(t_k), \qquad t_k\leq t<t_{k+1}, \quad (23)\\
t_{k+1} =&\inf\{t\in R||\eta(t)|\geq\gamma|u(t)|+d\}, \quad (24)
\end{aligned}$$

where $\eta(t) = u(t)-v(t)$, $d>0$, $\epsilon>0$, $0<\gamma<1$ and $\bar{m}>\frac{d}{1-\gamma}$ are design parameters. Then, we can get following equations

$$P_3(A_3) = \tilde{P}_3(A_3)\in R, \tilde{P}_3^{-1}(A_3) = Q_3(A_3). \quad (25)$$

From (2), the time derivative of e_3 is

$$\begin{aligned}
\dot{e}_3 =&Q_3(A_3)(f_3^p(x_i^{(0\sim m_i-1)}|_{i=1\sim3})-\dot{\alpha}_2)\\
&+Q_3(A_3)g_3^p(A_3)(x_i^{(0\sim m_i-1)}|_{i=1\sim3})u\\
&+Q_3(A_3)g_3^p(A_3)(x_i^{(0\sim m_i-1)}|_{i=1\sim3})\alpha_3\\
&-Q_3(A_3)g_3^p(A_3)(x_i^{(0\sim m_i-1)}|_{i=1\sim3})\alpha_3. \quad (26)
\end{aligned}$$

Choose virtual controller α_3 as

$$\begin{aligned}
\alpha_3 =&-\frac{1}{Q_3(A_3)g_3}(A_3e_3+\frac{1}{2a_3^2}P_3^T\\
&\times(A_3)e_3\hat{\theta}_3S_3^TS_3+\frac{1}{2}P_3^T(A_3)e_3), \quad (27)
\end{aligned}$$

where $g_3 = \max_{p\in M}\{g_3^p\}$. And we can obtain the state-space form

$$\dot{e}_3 = s_3^p\Phi(A_3)e_3+H_3^p \quad (28)$$

where $s_3^p = \{g_3^p/g_3, p \in M\}$, $H_3^p = -A_3e_3 - \frac{1}{2a_3^2}P_3^T(A_3)e_3 + Q_3(A_3)g_3^p(A_3)(x_i^{(0\sim m_i-1)}|_{i=1\sim3})u + Q_3(A_3)(f_3^p(x_i^{(0\sim m_i-1)}|_{i=1\sim3}) - \dot{\alpha}_2) - \frac{1}{2}P_3^T(A_3)e_3\hat{\theta}_3S_3^T \times S_3 - Q_3(A_3)g_3^p(A_3)(x_i^{(0\sim m_i-1)}|_{i=1\sim3})\alpha_3$.

The Lyapunov function candidate V_3 is designed as

$$V_3 = V_2 + e_3P_3(A_3)e_3 + \frac{1}{2}\tilde{\theta}_3^2. \tag{29}$$

Taking the derivative of V_3, we obtain

$$\begin{aligned}\dot{V}_3 = &\dot{V}_2 - s_{3,m}\mu_3e_3^Te_3 - \frac{1}{a_3^2}P_3^T(A_3)e_3P_3^T(A_3)e_3\hat{\theta}_3 \\ &\times S_3^TS_3 + 2P_3^Te_3(Q_3(A_3)f_3^p(x_i^{(0\sim m_i-1)}|_{i=1\sim3} \\ &-Q_3(A_3)\dot{\alpha}_{3-1}) + 2P_3^Te_3Q_3(A_3)g_3^p(A_3)u \\ &- P_3^T(A_3)e_3Q_3(A_3)g_3^p(A_3)(x_i^{(0\sim m_i-1)}|_{i=1\sim3})\alpha_3 \\ &- P_3^T(A_3)e_3P_3^T(A_3)e_3 - \tilde{\theta}_3\dot{\hat{\theta}}_3.\end{aligned} \tag{30}$$

And similar to the (12), one gets

$$\begin{aligned}&P_3^T(A_3)e_3F_3^p(X_3) \\ =&P_3^T(A_3)e_3(W_3^{pT}S_3(X_3) + \varepsilon_3) \\ \leq&\frac{(P_3^T(A_3)e_3)^2\theta_3S_3^T(X_3)S_3(X_3)}{2a_3^2} + \frac{1}{2}a_3^2 + \frac{1}{2}\bar{\varepsilon}_3^2 \\ &+ \frac{1}{2}P_3^T(A_3)e_3P_3^T(A_3)e_3\end{aligned} \tag{31}$$

where $F_3^p(X_3) = Q_3(A_3)(f_3^p(x_i^{(0\sim m_i-1)}|_{i=1\sim3}) - \dot{\alpha}_2) + P_{2L}^T(A_2^{0\sim1})e_2^{(0\sim1)}$, a_3 is a constant.

The adaptive law $\hat{\theta}_3$ is designed as

$$\dot{\hat{\theta}}_3 = \frac{1}{a_3^2}P_3^T(A_3)e_3P_3^T(A_3)e_3S_3^TS_3 - l_3\hat{\theta}_3. \tag{32}$$

From (22)-(24), we have $v(t) = (1 + \gamma\lambda_1(t))u(t) + \lambda_2(t)d$, $\forall t \in [t_k, t_{k+1})$, where $\lambda_1(t) \in [-1, 1]$, $\lambda_2(t) \in [-1, 1]$. Then, we can get

$$u(t) = \frac{v(t)}{1 + \gamma\lambda_1(t)} - \frac{\lambda_2(t)d}{1 + \gamma\lambda_1(t)}. \tag{33}$$

According to $\frac{Q_3(A_3)P_3(A_3)A_3g_3^p(x_i^{(0\sim m_i-1)}|_{i=1\sim3})v(t)}{1+\gamma\lambda_1(t)} \leq \frac{Q_3(A_3)P_3(A_3)A_3g_3(x_i^{(0\sim m_i-1)}|_{i=1\sim3})v(t)}{1+\gamma}$, $Q_3(A_3)P_3(A_3)A_3g_3^p(x_i^{(0\sim m_i-1)}|_{i=1\sim3})|\frac{\lambda_2d}{1+\gamma\lambda_1(t)}| \leq Q_3(A_3)P_3(A_3)A_3g_3^p(x_i^{(0\sim m_i-1)}|_{i=1\sim3})\frac{d}{1-\lambda}$, $\bar{m} > \frac{d}{1-\gamma}$, it yields

$$\begin{aligned}\dot{V}_3 \leq &-\sum_{i=1}^{3}s_{i,m}\mu_i(e_i^{(0\sim1)})^Te_i^{(0\sim1)} + 0.2785\epsilon \\ &-\sum_{i=1}^{3}\frac{l_i}{2}\tilde{\theta}_i^2 + \sum_{i=1}^{3}(a_i^2 + \bar{\varepsilon}_i^2 + \frac{1}{2}l_i\theta_i^2).\end{aligned} \tag{34}$$

Theorem 1: Consider the system (1) under the Assumption 1-2, the virtual controller (9), (16) and (27), the actual controller (23) and the adaptive law (13), (20) and (32) are designed. Then, the following statements holds: (1) all signals in closed-loop system are bounded; (2) the event-triggered condition is Zeno-free.

Proof: We prove the result of the theorem in the following. Let $V = V_n$. Then we can get

$$\begin{aligned}\dot{V} =&\dot{V}_3 \\ \leq&-\sum_{i=1}^{3}s_{i,m}\mu_i(e_i^{(0\sim1)})^Te_i^{(0\sim1)} + 0.2785\epsilon \\ &-\sum_{i=1}^{3}\frac{l_i}{2}\tilde{\theta}_i^2 + \sum_{i=1}^{3}(a_i^2 + \bar{\varepsilon}_i^2 + \frac{1}{2}l_i\theta_i^2) \\ \leq&-DV(t) + C,\end{aligned} \tag{35}$$

where $D = \min\{\frac{s_{i,m}\mu_i}{\lambda_{\min}(P_i)}, l_i, i = 1, \cdots, 3\}$, $C = \sum_{i=1}^{3}(a_i^2 + \bar{\varepsilon}_i^2 + \frac{1}{2}l_i\theta_i^2)$. According to (**??**), the following inequality holds

$$0 \leq V(t) \leq \frac{C}{D} + (V(0) - \frac{C}{D})e^{-Dt}, \tag{36}$$

which means that all signals in closed-loop system can converge to a small neighborhood of zero. Next, we will prove that the designed ETC is Zeno-free.

From $\eta(t) = u(t) - v(t)$, $\forall t \in [t_k, t_{k+1})$, we have

$$\tfrac{d}{dt}|\eta| = \tfrac{d}{dt}(\eta \times \eta)^{\frac{1}{2}} = sign(\eta)\dot{\eta} \leq \varpi.$$

where ϖ is a constant. Since $\eta(t_k) = 0$ and $\lim_{t\to t_{k+1}}\eta(t) = (\gamma|u(t)| + d)$ thus $t_{k+1} - t_k \geq (\gamma|u(t)| + d)/\varpi > 0$.

This proof is completed.

4 Simulation Example

In simulations, the parameters of the system are choose as follows: $M^1 = 1$, $M^2 = 2$, $mgl^1 = 1$, $mgl^2 = 2$, $K_0 = 2$, $J = 1$, $B = 0.9$, $K_T = 1$, $L = 0.125$, $R = 25$ and $K_B = 1$.

The design parameters are chosen as $a_1 = 100$, $\mu_1 = 0.16$, $l_1 = 10$, $a_2 = 20$, $\mu_2 = 0.16$, $l_2 = 120$, $a_3 = 15$, $\mu_3 = 112$, $l_3 = 110$, $\bar{m} = 1.1$, $d = 0.5$, $\gamma = 0.5$, $\epsilon = 7$. The initial conditions are chosen as $x_1(0) = 0.11$, $\dot{x}_1(0) = -0.12$, $x_2(0) = 0.02$, $\dot{x}_2(0) = 0.02$, $x_3(0) = 0.05$, $\hat{\theta}_1(0) = 0.04$, $\hat{\theta}_2(0) = 0.55$, $\hat{\theta}_3(0) = 1.64$. In order to satisfy (5), some matrixes are designed as follows.

$$P_1(A_1^{(0\sim1)}) = \begin{bmatrix}68.2 & 0.40\\ 0.40 & 3.36\end{bmatrix};\quad A_1 = \begin{bmatrix}20 & 0.4\end{bmatrix};$$

$$P_2(A_2^{(0\sim1)}) = \begin{bmatrix}0.2107 & 0.0198\\ 0.0198 & 0.0399\end{bmatrix}; A_2 = \begin{bmatrix}4.04 & 0.4\end{bmatrix};$$

$$P_3(A_3) = \begin{bmatrix}7\end{bmatrix};\qquad A_3 = \begin{bmatrix}8\end{bmatrix}.$$

The simulation results are shown in Figs. 1-8. Fig. 1 exhibits the trajectories of q_1 and y_d. Fig. 2 displays the trajectories of $\dot{q}_1$ and $\dot{y}_d$. Fig. 3 displays the trajectories of $q_1 - y_d$. Fig. 4 displays the trajectories of $\dot{q}_1 - \dot{y}_d$. Fig. 5 displays the trajectories of q_2, $\dot{q}_2$ and I. Fig. 6 displays adaptive laws. Fig. 7 displays the trajectories of actual input u. The trajectory of time interval of event-triggered is shown in Fig. 8.

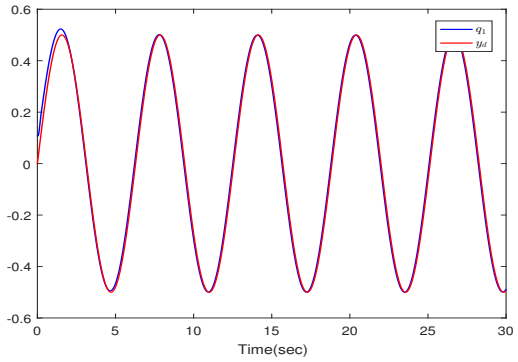

Fig. 1: The trajectories of q_1 and y_d.

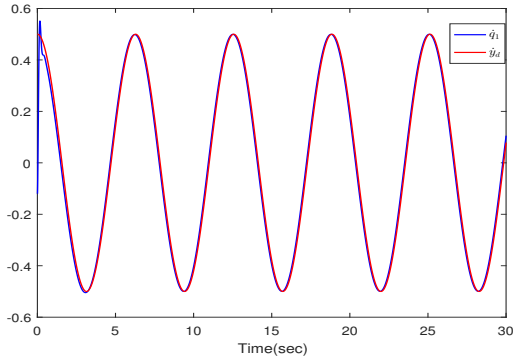

Fig. 2: The trajectories of $\dot{q}_1$ and $\dot{y}_d$.

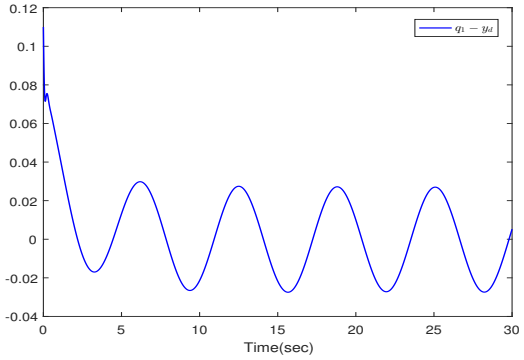

Fig. 3: The trajectory of $q_1 - y_d$.

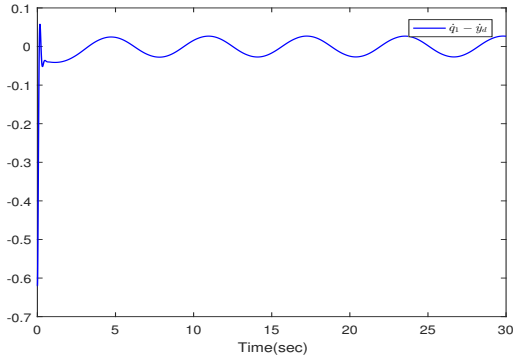

Fig. 4: The trajectory of $\dot{q}_1 - \dot{y}_d$.

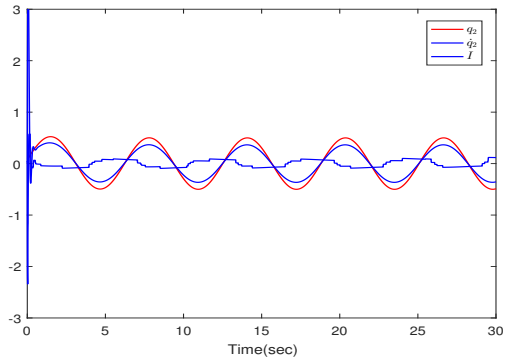

Fig. 5: The trajectories of q_2, $\dot{q}_2$ and I.

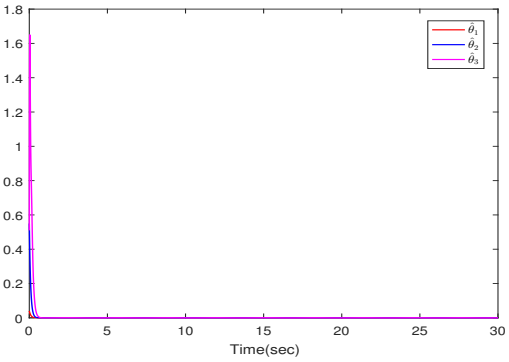

Fig. 6: The trajectories of adaptive laws.

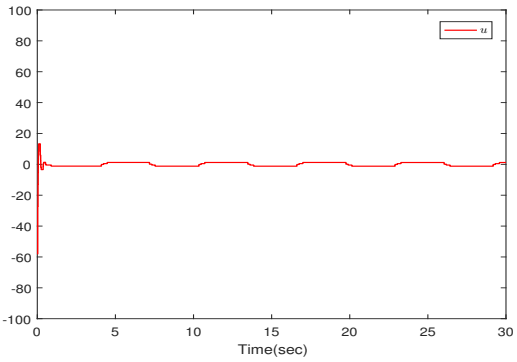

Fig. 7: The trajectory of u.

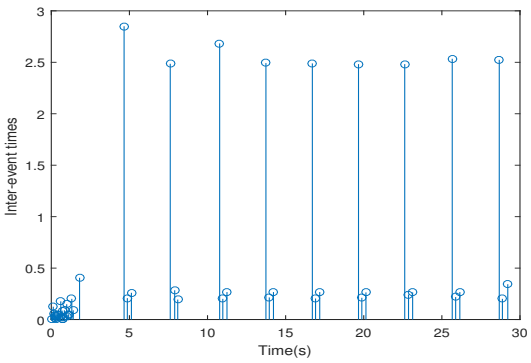

Fig. 8: The trajectory of time interval of event-triggered.

5 Conclusion

In this paper, the control problem of nonlinear switched systems is studied by using HOFA systems methods, which doesn't have to convert the system into a first-order system.

NN is introduced to deal with the unknown nonlinear functions. An adaptive event-triggered HOFA system control scheme is proposed by using HOFA system backstepping and event-triggered strategy. The proposed event-triggered controller guarantees that system states converge to a small neighborhood of zero. Finally, a single-link FJ robot example proves the validity of the proposed control scheme.

References

[1] K. K. Sun, S. S. Mou, J. B. Qiu, T. Wang and H. J. Gao, "Adaptive fuzzy control for nontriangular structural stochastic switched nonlinear systems with full state constraints," *IEEE Transactions on Fuzzy Systems*, vol. 27, no. 8, pp. 1587-1601, 2019.

[2] X. D. Zhao, X. Y. Wang, S. Zhang and G. D. Zong, "Adaptive neural backstepping control design for a class of nonsmooth nonlinear systems," *IEEE Transactions on Systems, Man, and Cybernetics: Systems*, vol. 49, no. 9, pp. 1820-1831, 2019.

[3] G. D. Zong, Q. Xu, X. D. Zhao, S. -F. Su and L. M. Song, "Output-feedback adaptive neural network control for uncertain nonsmooth nonlinear systems with input deadzone and saturation", *IEEE Transactions on Cybernetics*, vol. 53, no. 9, pp. 5957-5969, 2023.

[4] S. Ling, H. Wang and P. X. Liu, "Adaptive fuzzy tracking control of flexible-joint robots based on command filtering", *IEEE Transactions on Industrial Electronics*, vol. 67, no. 5, pp. 4046-4055, 2019.

[5] G. R. Duan, "High-order fully actuated system approaches: Part II. Generalized strict-feedback systems," *International Journal of Systems Science,* vol. 52, no. 3, pp. 437-454, 2021.

[6] G. R. Duan, "High-order fully actuated system approaches: Part IV. Adaptive control and high-order backstepping," *International Journal of Systems Science,* vol. 52, no. 5, pp. 972-989, 2021.

[7] G. R. Duan, "High-order fully actuated system approaches: Part V. Robust adaptive control," *International Journal of Systems Science,* vol. 52, no. 10, pp. 2129-2143, 2021.

[8] J. W. Xia, Y. X. Lian, S. -F. Su, H. Shen, and G. L. Chen, "Observer-based event-triggered adaptive fuzzy control for unmeasured stochastic nonlinear systems with unknown control directions," *IEEE Transactions on Cybernetics,* vol. 52, no. 10, pp. 10655-10666, 2022.

[9] C. C Yan, J. W. Xia, J. H. Park, W. Sun and X. P. Xie, "Observer-based adaptive optimized control for uncertain cyclic switched nonlinear systems: reinforcement learning algorithm approach," *IEEE Transactions on Circuits and Systems I: Regular Papers,* DOI: 10.1109/TCSI.2023.3332086.

[10] S. Li, C. K. Ahn and Z. R. Xiang, "Command-filter-based adaptive fuzzy finite-time control for switched nonlinear systems using state-dependent switching method," *IEEE Transactions on Fuzzy Systems,* vol. 29, no. 4, pp. 833-845, 2021.

[11] H. Q. Wang, P. Shi, H. Y. Li and Q. Zhou, "Adaptive neural tracking control for a class of nonlinear systems with dynamic uncertainties," *IEEE Transactions on Cybernetics,* vol. 47, no. 10, pp. 3075-3087, 2017.

[12] N. Zhang, J. W. Xia, J. H. Park, J. Zhang, H. Shen, "Improved disturbance observer-based fixed-time adaptive neural network consensus tracking for nonlinear multi-agent systems," *Neural Networks,* vol. 162, pp. 490-501, 2023.

[13] C. Y. Yan, J. W. Xia, J. H. Park and X. P. Xie, "Reinforcement learning-based adaptive event-triggered fuzzy control for cyclic switched stochastic nonlinear systems with actuator faults," *IEEE Transactions on Fuzzy Systems,* vol. 32, no. 3, pp. 1131-1143, 2024.

[14] X. L. Wang, H. S. Su, X. F. Wang and G. R. Chen, "Fully distributed event-triggered semiglobal consensus of multi-agent systems with input saturation," *IEEE Transactions on Industrial Electronics,* vol. 64, no. 6, pp. 5055-5064, 2017.

[15] L. Xing, C. Wen, Z. Liu, H. Su and J. Cai, "Event-triggered adaptive control for a class of uncertain nonlinear systems," *IEEE Transactions on Automatic Control,* vol. 62, no. 4, pp. 2071-2076, 2017.

[16] R. N. Yang, G. T. Li, Y. Z. Zhu and G. -P. Liu, "Event-triggered control for networked predictive control systems with time delay and external disturbance," *IEEE Transactions on Control of Network Systems,* vol. 10, no. 4, pp. 2120-2129, 2023.

Proceedings of the 3rd Conference on Fully Actuated System Theory and Applications
May 10-12, 2024, Shenzhen, China

Adaptive Fixed-Time Control for High-Order Fully Actuated System with Input Saturation

Ping Wang [1], Guangren Duan[1,2]

1. Center for Control Science and Technology, Southern University of Science and Technology, Shenzhen 518055, P. R. China
E-mail: pingwang0906@126.com

2. Center for Control Theory and Guidance Technology, Harbin Institute of Technology, Harbin 150001, P. R. China
E-mail: g.r.duan@hit.edu.cn

Abstract: This paper studies the fixed-time (FxT) tracking control problem of an uncertain high-order fully actuated (HOFA) system with parameter uncertainty, external disturbance, and input saturation. Firstly, to tackle the impact of the input saturation on the system, a hyperbolic tangent function is introduced to approximate the saturation function. Subsequently, utilizing the HOFA system method, an intermediate control variable with adaptive laws and a tracking error fractional order term is designed, which can effectively compensate for system parameter uncertainty and external disturbances, while promoting the FxT stability of the system. Based on this, a FxT controller is then constructed, incorporating an adaptive law designed to effectively manage the uncertainty in the input matrix resulting from the estimation of the saturation function. By employing FxT stability theory, the designed adaptive controller guarantees the boundedness of all system states, while ensuring that the tracking error converges to a small neighborhood of the origin within a fixed time. Finally, the effectiveness of the proposed control scheme is verified by simulating a three degree of freedom marine surface vessel system model.

Key Words: High-Order Fully Actuated System, Fixed-Time Stability, Input Saturation, Marine Surface Vessel

1 Introduction

Over the past few decades, considerable research attention has been dedicated to the analysis and synthesis of nonlinear systems due to the prevalence of nonlinearity in practical systems [1]. In existing results, many effective controller design methods have been proposed to improve the performance of nonlinear systems, such as feedback linearization [2], adaptive control [3], backstepping control [4], etc. Following this line, numerous meaningful studies have been conducted from diverse perspectives to explore nonlinear system control [5–9]. However, existing results rely on the first-order state space model of the system, which is suitable for state response analysis but not suitable for controller design [10]. Especially for increasingly complex and uncertain nonlinear systems, there is still an anticipation for the development of more efficient techniques to design controllers.

Most real-world physical systems are directly modeled based on specific physical laws, and their models are mostly described using second-order or higher-order differential equations. Based on this fact, the high-order fully actuated (HOFA) system method first presented by Duan in recent years has provided a new research perspective for nonlinear control systems [10–12]. In comparison to the first-order state space scheme, the HOFA system method not only greatly simplifies the controller design and ensures the full-actuation characteristics of the system, but also has a clearer physical background [13]. Therefore, since its inception, the HOFA method has received widespread attention from scholars in terms of control theory and applications [14–24]. These studies encompass adaptive control [14, 15], robust control [16], fault-tolerant control [17, 18], predictive control [19, 20], finite-time control [21, 22], and their applications in spacecraft [23, 24] and other various domains.

It should be noted that the aforementioned research results and their references have either focused solely on achieving infinite-time convergence or finite-time convergence. While finite-time stability [21, 22] ensures that the system trajectory converges within a finite time, its settling time depends on the initial values, which limits its practical applicability [25–27]. In order to address these limitations, fixed-time (FxT) stability was proposed in [28], wherein the settling time is a constant regardless of the initial conditions, making it better suited for real-time implementation. However, to the best of the author's knowledge, no research has achieved adaptive FxT control based on the HOFA method.

Based on the above discussions, this paper aims to handle the adaptive FxT tracking problem for the HOFA system with parameter uncertainty and input saturation. The main contributions of this paper are as follows:

(i) The adaptive FxT tracking control of uncertain nonlinear systems is achieved for the first time using the HOFA system method, expanding the applicability of this approach.

(ii) The presented control scheme is directly based on the high-order system model derived from physical laws, making it more convenient for controller design while reducing the burden of system conversion. Furthermore, in contrast to the existing FxT control algorithms [25–27] based on backstepping, the proposed control strategy in this paper also eliminates repeated derivation of the virtual controller, resulting in reduced computational complexity.

(iii) This paper takes into account not only system uncertainty but also input saturation. Typically, it may generate large control actions to maintain acceptable performance within a fixed time, making it essential to address this issue. To mitigate the effects of saturation, the hyperbolic tangent function is employed to approximate the saturation function, and by utilizing the mean value theorem, the adverse impact caused by input saturation can be effectively mitigated,

This work was supported in part by Shenzhen Key Laboratory of Control Theory and Intelligent Systems ZDSYS20220330161800001, the Major Program of National Natural Science Foundation of China (61690210, 61690212), the National Natural Science Foundation of China (61333003), and the Science Center Program of the National Natural Science Foundation of China under grant No. 62188101.

which extends existing control algorithms [10–24] without considering saturation.

2 Problem Formulation and Preliminaries

2.1 Mathematical Preliminaries

Notations: Throughout this paper, the argument (s) in a function or variable will be dropped if no confusion is likely to occur. For any variable $x \in R^m$, $x^{(n)}$ denotes its nth derivative, and $x^{(0\sim n-1)} = [x^T \ \ \dot{x}^T \ \ \cdots \ \ x^{(n-1)T}]^T \in R^{nm}$. For a set of constants A_i,

$$A^{0\sim n-1} = [A_0 \ \ A_1 \ \ \cdots \ \ A_{n-1}] \in R^{1\times n},$$

$$\Phi(A^{0\sim n-1}) = \begin{bmatrix} 0 & I & & \\ & & \ddots & \\ & & & I \\ -A_0 & -A_1 & \cdots & -A_{n-1} \end{bmatrix} \in R^{n\times n}.$$

I_m denotes the m-dimensional identity matrix.

Furthermore, we provide the following lemmas for controller design.

Lemma 1. [26] For $\forall x \in R$ and any constant $\sigma > 0$, it has $0 \le |x| - \frac{x^2}{\sqrt{x^2+\sigma^2}} < \sigma$.

Lemma 2. [11] For a matrix $A \in R^{n\times n}$, if its eigenvalues satisfy $\lambda_i(A) < -\gamma$ for $i = 1, \cdots, n$ with $\gamma > 0$, then there exists a positive definite matrix $P \in R^{n\times n}$ such that $A^T P + PA < -\gamma P$.

Lemma 3. [11] For any positive constant $\kappa > 0$, there always exists a set of constants $A_i \in R$ with $i = 0, \cdots, n-1$ that make $\lambda_i(\Phi(A^{0\sim n-1})) < -\frac{\kappa}{2}$ hold, where $i = 1, \cdots, n$.

On the basis of Lemmas 2 and 3, we can obtain that, for any $\kappa > 0$, there exists a positive definite matrix $P(A^{0\sim n-1})$ such that $\Phi^T(A^{0\sim n-1})P(A^{0\sim n-1}) + P(A^{0\sim n-1})\Phi(A^{0\sim n-1}) \le -\kappa P(A^{0\sim n-1})$. Next, for the subsequently controller design, we will define

$$P_L(A^{0\sim n-1}) = P(A^{0\sim n-1}) \begin{bmatrix} 0_{n-1} \\ I \end{bmatrix}. \tag{1}$$

Lemma 4. [11] For any selected matrix $F \in R^{n\times n}$, all matrices $A^{0\sim n-1}$ and $\Lambda \in R^{n\times n}$ satisfying $\det \Lambda \neq 0$ and $\Phi(A^{0\sim n-1}) = \Lambda F \Lambda^{-1}$ are derived by the equation $A^{0\sim n-1} = -ZF^n\Lambda^{-1}(Z, F)$ with

$$\Lambda(Z, F) = \begin{bmatrix} Z \\ ZF \\ \cdots \\ ZF^{n-1} \end{bmatrix},$$

where $Z \in R^{1\times n}$ is a design parameter matrix satisfying $\det \Lambda(Z, F) \neq 0$.

Lemma 5. [25] For any $x_i \in R$, $i = 1, 2, \cdots, n$, when $p \in (0, 1)$, there is $\big(\sum_{i=1}^n |x_i|\big)^p \le \sum_{i=1}^n |x_i|^p \le n^{1-p}\big(\sum_{i=1}^n |x_i|\big)^p$.

Lemma 6. [26] For $x, y \in R^n$, the Cauchy–Schwarz inequality $(x^T y)^2 \le \|x\|^2\|y\|^2$ holds. In particular, for $y_i > 0$, the inequality $\big(\sum_{i=1}^n y_i\big)^2 = \big(\sum_{i=1}^n 1 \cdot y_i\big)^2 \le n\big(\sum_{i=1}^n y_i^2\big)$ is further satisfied.

Lemma 7. [25] For a nonlinear dynamic $\dot{x} = f(t, x)$ with x_0 being the initial value, let the origin be its equilibrium point. If a continuous positive definite function $V(x) : R^n \to R_+ \cup \{0\}$ and scalars $c, b > 0$, $0 < \mu_1 < 1$ and $\mu_2 > 1$ satisfies (i) $V(x) = 0$ if and only if $x = 0$; (ii) $\dot{V} \le -cV^{\mu_1}(x) - bV^{\mu_2}(x) + \vartheta$, then the following two types of stability properties can be obtained: (1) when $\vartheta = 0$, the dynamic $\dot{x} = f(t, x)$ is globally FxT stable with the settling time being $T_f \le T_m = \frac{1}{c(1-\mu_1)} + \frac{1}{b(\mu_2-1)}$; (2) when $\vartheta \in (0, +\infty)$, the dynamic $\dot{x} = f(t, x)$ is practically FxT stable with T_f being estimated as $T_f \le T_m = \frac{1}{c\beta(1-\mu_1)} + \frac{1}{b\beta(\mu_2-1)}$ and the residual set of the solution $x(t)$ is

$$\Omega = \Big\{ \lim_{t\to T_f} x | V \le \min\Big\{ c^{-\frac{1}{\mu_1}}\Big(\frac{\vartheta}{1-\beta}\Big)^{\frac{1}{\mu_1}}, b^{-\frac{1}{\mu_2}}\Big(\frac{\vartheta}{1-\beta}\Big)^{\frac{1}{\mu_2}} \Big\} \Big\}$$

with $0 < \beta < 1$ being a constant.

2.2 Problem Formulation

In this paper, we consider the following HOFA system

$$\begin{aligned} x^{(n)} &= G(x^{(0\sim n-1)})u^s + f(x^{(0\sim n-1)}) + \psi(x^{(0\sim n-1)})\theta + d(t), \\ y &= x, \end{aligned} \tag{2}$$

where $x = [x_1, \cdots, x_m]^T \in R^m$ and $y \in R^m$ denote the state vector and output vector, respectively. $f = [f_1, \cdots, f_m]^T$ is a known sufficiently smooth function vector, $\psi \in R^{m\times r}$ denotes the known nonnegative function matrix, $\theta = [\theta_1 \ \cdots \ \theta_r]^T \in R^r$ is an unknown constant vector, $d = [d_1, \cdots, d_m]^T \in R^m$ represents the unknown time-varying disturbance vector, $G = [g_1^T, ..., g_m^T]^T \in R^{m\times m}$ is the smooth function matrix with $g_k \in R^{1\times m}$, $k = 1, \cdots, m$, and $\det(G(\cdot)) \neq 0$, which is the controllability rank condition. Additionally, $u^s = [u_1^s, u_2^s, \cdots, u_m^s]^T \in R^m$ denotes the control force subject to the saturation constraint. The saturation function $u_k^s = \text{sat}(u_k)$ has the following definition:

$$u_k^s = \text{sat}(u_k) = \begin{cases} u_{kM}, & u_k \ge u_{kM}, \\ u_k, & u_{km} < u_k < u_{kM}, \\ u_{km}, & u_k \le u_{km}, \end{cases} \tag{3}$$

where $k = 1, \cdots, m$, $u_{kM} > 0$ and $u_{km} < 0$ are two known constants, u_k is the actual control input to be designed.

Problem 1. Set the desired system output trajectory as y_d. This paper aims to design an adaptive FxT controller for system (2) such that: (i) the system output tracking error converges to a sufficiently small neighborhood of the origin within a fixed time; (ii) all signals of the closed-loop system are bounded.

For the above control objective, we first provide the following commonly used assumptions.

Assumption 1. The disturbance vector $d(t)$ is bounded by an unknown constant $\bar{d} > 0$, that is, $\|d(t)\| \le \bar{d}, \forall t \ge 0$.

Assumption 2. The trajectory $y_d = [y_{1d}, \cdots, y_{md}]^T$ is available and its nth derivative is bounded and known.

Next, to facilitate the subsequent controller design, similar to [5], we will introduce a smooth function $H(u_k)$ to approximate the saturation $\text{sat}(u_k)$, which is defined as

$$H(u_k) = \begin{cases} u_{kM}\tanh\big(\frac{u_k}{u_{kM}}\big), & u_k \ge 0, \\ u_{km}\tanh\big(\frac{u_k}{u_{km}}\big), & u_k < 0. \end{cases} \tag{4}$$

Then, by using the Lagrange mean value theorem yields

$$u_k^s = \text{sat}(u_k) = H(u_k) + \varsigma(u_k) = H'_{u_k}u_k + \varsigma(u_k), \tag{5}$$

where the error $\varsigma(u_k) = \text{sat}(u_k) - H(u_k)$ satisfies $|\varsigma(u_k)| \leq \max\{u_{kM}(1-\tanh(1)), u_{km}(\tanh(1)-1)\} \triangleq \varsigma_{kM}$, $H'_{u_k} = \frac{\partial H(u_k)}{\partial u_k}|_{u_k=u'_k}$ and $u'_k = \pi_k u_k + (1-\pi_k)u_{k0}$ with $u_{k0} = 0$, $0 < \pi_k < 1$ and $0 < \underline{H}_{km} \leq H'_{u_k} \leq 1$. Based on the above preparation, it is easy to obtain that there exist two unknown constants $\varsigma_M > 0$ and $\underline{H}_m > 0$ such that

$$|\varsigma(u_k)| \leq \max\{\varsigma_{kM}\} \leq \varsigma_M,\ k = 1, 2, \cdots, m,$$
$$H'_{u_k} \geq \min\{\underline{H}_{km}\} \geq \underline{H}_m. \tag{6}$$

Let the augmented vectors $u = [u_1, \cdots, u_m]^T$, $H'_u = \text{diag}\{H'_{u_1}, \cdots, H'_{u_m}\}$, $\bar{\varsigma}(u) = [\varsigma(u_1), \varsigma(u_2), \cdots, \varsigma(u_m)]^T$. Then, by using Eq. (5), the system (2) can be rewritten as:

$$\begin{aligned} x^{(n)} =& G(x^{(0\sim n-1)})H_u^{'}u + f(x^{(0\sim n-1)}) \\ &+ \psi(x^{(0\sim n-1)})\theta + d(t) + G(x^{(0\sim n-1)})\bar{\varsigma}(u), \end{aligned} \tag{7}$$

which will be used for the design of the actual controller u.

3 Controller Design

In this section, a FxT controller will be designed for the system (7) by utilizing the HOFA system approach.

Firstly, introduce the following coordinate transformation:

$$e^{(0\sim n-1)} = y^{(0\sim n-1)} - y_d^{(0\sim n-1)}. \tag{8}$$

From equations (2) and (7), it can be concluded that

$$\begin{aligned} e^{(n)} =& G(x^{(0\sim n-1)})H_u^{'}u + f(x^{(0\sim n-1)}) + \psi(x^{(0\sim n-1)})\theta \\ &+ d(t) + G(x^{(0\sim n-1)})\bar{\varsigma}(u) - y_d^{(n)}. \end{aligned} \tag{9}$$

As a result of the impact of input saturation, the system (7) or (9) exhibits an unknown input matrix $H_u^{'}$ and produces an additional term of uncertainty $G(x^{(0\sim n-1)})\bar{\varsigma}(u)$. To this end, first introduce the following unknown constant vector

$$\rho = [\rho_1, \rho_2]^T = \left[\frac{1}{\underline{H}_m}, \frac{\varsigma_M}{\underline{H}_m}\right]^T. \tag{10}$$

Subsequently, let the estimated signals of unknown parameter vectors $\theta \in R^r$, $\rho \in R^2$ and unknown constant $\bar{d}$ be $\hat{\theta} = [\hat{\theta}_1\ \hat{\theta}_2\ \cdots\ \hat{\theta}_r]^T$, $\hat{\rho} = [\hat{\rho}_1\ \hat{\rho}_2]^T$ and $\hat{d}$, respectively. And introduce the mathematical symbols

$$\begin{aligned} &\xi = e^{(0\sim n-1)^T} e^{(0\sim n-1)}, \\ &Z = \left(e^{(0\sim n-1)}\right)^T \left(P_L(A^{0\sim n-1}) \otimes I_m\right) \end{aligned} \tag{11}$$

with $P_L(A^{0\sim n-1})$ being defined in equation (1).

Next, in view of the uncertainty of the control gain matrix $H_u^{'}$, before designing the controller u, we first construct a intermediate control variable α on the basis of the HOFA idea and FxT stability theory for the system (9):

$$\begin{aligned} \alpha =& (A^{0\sim n-1} \otimes I_m)e^{(0\sim n-1)} - y_d^{(n)} + f(\cdot) + \psi(\cdot)\hat{\theta} \\ &+ \varphi(\cdot)\hat{d} + \lambda_{\max}(P)(A^{0\sim n-1} \otimes I_m)e^{(0\sim n-1)}\xi \\ &+ (A^{0\sim n-1} \otimes I_m)e^{(0\sim n-1)}\left(\lambda_{\min}(P)\xi\right)^{\mu-1}\eta(\cdot), \end{aligned} \tag{12}$$

and concurrently design the adaptive laws $\dot{\hat{\theta}}$ and $\dot{\hat{d}}$ with the following updated form

$$\begin{aligned} \dot{\hat{\theta}} &= \psi(\cdot)^T Z^T - \delta_{\theta_1}\hat{\theta} - \delta_{\theta_2}F_\theta, \\ \dot{\hat{d}} &= \varphi(\cdot)^T Z^T - \delta_{d_1}\hat{d} - \delta_{d_2}\hat{d}^3, \end{aligned} \tag{13}$$

where $\lambda_{\min}(P)$ and $\lambda_{\max}(P)$ denote the minimum and maximum eigenvalue of matrix $P(A^{0\sim n-1})$ defined in Lemma 3, respectively, $\delta_{\theta_1} > 0$, $\delta_{\theta_2} > 0$, $\delta_{d_1} > 0$, $\delta_{d_2} > 0$ and $\mu \in (0,1)$ are the design parameters. The functions F_θ, $\varphi(\cdot)$ and $\eta(\cdot)$ are defined as $F_\theta = \left[\hat{\theta}_1^3\ \hat{\theta}_2^3\ \cdots\ \hat{\theta}_r^3\right]^T$, and

$$\varphi(\cdot) = \frac{Z^T}{\sqrt{\|Z\|^2 + \sigma^2}},$$
$$\eta(\cdot) = \begin{cases} 1, & \text{if } \|e^{(0\sim n-1)}\| \geqslant \epsilon, \\ \sum_{j=1}^{n} \varrho_j \xi^{j-\frac{3}{4}}(\epsilon^2)^{-j+\frac{3}{4}}, & \text{otherwise,} \end{cases}$$

where σ has the same properties as defined in Lemma 1, $\epsilon > 0$ is a small constant, and the selection of coefficients ϱ_j are the same as the method in reference [26].

Now, based on the above preparations, the actual controller u is designed as

$$u = -G^{-1}(x^{(0\sim n-1)})Z^T\Psi^T\hat{\rho}, \tag{14}$$

with the adaptive law $\dot{\hat{\rho}}$ being chosen as

$$\dot{\hat{\rho}} = \|Z\|^2\Psi - \delta_{\rho_1}\hat{\rho} - \delta_{\rho_2}F_\rho, \tag{15}$$

where δ_{ρ_1} and δ_{ρ_2} are two positive design parameters, and the functions F_ρ and Ψ are $F_\rho = [\hat{\rho}_1^3\ \ \hat{\rho}_2^3]^T$ and

$$\Psi = \left[\frac{\|\alpha\|^2}{\sqrt{\|Z\alpha\|^2 + \sigma^2}}, \frac{\|G(\cdot)\|^2}{\sqrt{\|ZG\|^2 + \sigma^2}}\right]^T. \tag{16}$$

4 Stability Analysis and Main Results

Based on the above designed FxT controller with adaptive laws, the stability of the closed-loop system will be provided.

Theorem 1. For the HOFA model (2) with parameter uncertainty and input saturation, under Assumptions 1-2, the designed controller (14) with the intermediate control signal (12) and adaptive laws (13) and (15) can ensure that the closed-loop system is FxT stable and all signals are bounded. Furthermore, there exists a fixed time T_f, such that the system tracking error $e = y - y_d$ is bounded by

$$\|e\| \leq \sqrt{\frac{2\min\left\{\alpha_1^{-\frac{4}{3}}\left(\frac{C}{1-\beta}\right)^{\frac{4}{3}}, \alpha_2^{-\frac{1}{2}}\left(\frac{C}{1-\beta}\right)^{\frac{1}{2}}\right\}}{\lambda_{\min}(P)}}, \tag{17}$$

where positive constants α_1, α_2 and C are defined in (32), $\beta \in (0,1)$ are defined in (33) for the stability analysis.

Proof. Let the estimation error variables $\tilde{\theta} = \theta - \hat{\theta}$, $\tilde{d} = \bar{d} - \hat{d}$ and $\tilde{\rho} = \rho - \hat{\rho}$. Then, combining the above equations (9) and (12)-(16), we can obtain the following closed-loop system

$$\begin{aligned} &e^{(n)} + (A^{0\sim n-1} \otimes I_m)e^{(0\sim n-1)} \\ &+ \lambda_{\max}(P)(A^{0\sim n-1} \otimes I_m)e^{(0\sim n-1)}\xi \\ &+ (A^{0\sim n-1} \otimes I_m)e^{(0\sim n-1)}\left(\lambda_{\min}(P)\xi\right)^{\mu-1}\eta \\ =& -G(\cdot)H_u^{'}G(\cdot)^{-1}Z^T\Psi^T\hat{\rho} + \psi(\cdot)\tilde{\theta} \\ &+ G(x^{(0\sim n-1)})\bar{\varsigma}(u) + d(t) - \varphi(\cdot)\hat{d} + \alpha. \end{aligned} \tag{18}$$

This can be further rewritten as the state-space form

$$\begin{aligned} \dot{e}^{(0\sim n-1)} =& \left(\Phi(\cdot) \otimes I_m\right)e^{(0\sim n-1)} \\ &+ \lambda_{\max}(P)\left(\Phi(\cdot) \otimes I_m\right)e^{(0\sim n-1)}\xi \\ &+ \left(\Phi(\cdot) \otimes I_m\right)e^{(0\sim n-1)}\left(\lambda_{\min}(P)\xi\right)^{\mu-1}\eta \end{aligned}$$

$$+\begin{bmatrix} 0_{(n-1)m} \\ d(t)-\varphi(\cdot)\hat{d}+\psi(\cdot)\tilde{\theta} \end{bmatrix} + \begin{bmatrix} 0_{(n-1)m} \\ -GH_u^{'}G^{-1}Z^T\Psi^T\hat{\rho}+G\bar{\varsigma}(u)+\alpha \end{bmatrix}. \quad (19)$$

where $\Phi(\cdot)=\Phi(A^{0\sim n-1})$. Next, select the Lyapunov function for the system (19) as

$$V=\frac{1}{2}\big(e^{(0\sim n-1)}\big)^T\big(P(A^{0\sim n-1})\otimes I_m\big)e^{(0\sim n-1)} + \frac{1}{2}\tilde{\theta}^T\tilde{\theta}+\frac{1}{2}\tilde{d}^2+\frac{1}{2}\underline{H}_m\tilde{\rho}^T\tilde{\rho}. \quad (20)$$

By using equation (19), the time derivative of V is

$$\begin{aligned}\dot{V}=&\frac{1}{2}\big(e^{(0\sim n-1)}\big)^T\Big[\big(P(\cdot)\otimes I_m\big)\big(\Phi(\cdot)\otimes I_m\big) +\big(\Phi(\cdot)\otimes I_m\big)^T\big(P(\cdot)\otimes I_m\big)\Big]e^{(0\sim n-1)}\times\Big[1+\lambda_{\max}(P)\xi \\ &+\big(\lambda_{\min}(P)\xi\big)^{\mu-1}\eta\Big]+Z\big[d(t)-\varphi(\cdot)\hat{d}+\psi(\cdot)\tilde{\theta}\big] \\ &+Z\big[G\bar{\varsigma}(u)+\alpha-GH_u^{'}G^{-1}Z^T\Psi^T\hat{\rho}\big] \\ &-\dot{\hat{\theta}}^T\tilde{\theta}-\tilde{d}\dot{\hat{d}}-\underline{H}_m\dot{\hat{\rho}}^T\tilde{\rho}. \end{aligned} \quad (21)$$

Based on the definition $\varphi(\cdot)$ in equation (12), it follows from Assumption 1 and Lemma 1 that

$$\begin{aligned}Z\big[d(t)-\varphi(\cdot)\hat{d}\big]&\le\|Z\|\bar{d}-Z\varphi(\cdot)\hat{d} \\ &\le Z\varphi(\cdot)\tilde{d}+\sigma\bar{d}. \end{aligned} \quad (22)$$

Similarly, combining (5), (6), (10), (16) and Lemma 1 yields

$$\begin{aligned}&Z\big[G\bar{\varsigma}(u)+\alpha-GH_u^{'}G^{-1}Z^T\Psi^T\hat{\rho}\big] \\ &\le\frac{\|Z\|^2\|G\|^2\varsigma_M}{\sqrt{\|Z\|^2\|G\|^2+\sigma^2}}+\varsigma_M\sigma \\ &\quad+\frac{\|Z\|^2\|\alpha\|^2}{\sqrt{\|Z\|^2\|\alpha\|^2+\sigma^2}}+\sigma-\underline{H}_m\|Z\|^2\Psi^T\hat{\rho} \\ &\le\underline{H}_m\|Z\|^2\Psi^T\tilde{\rho}+\varsigma_M\sigma+\sigma. \end{aligned} \quad (23)$$

According to Lemma 3 and substituting equations (22) and (23) into (21) yields

$$\begin{aligned}\dot{V}\le&-\frac{1}{2}\kappa\big(e^{(0\sim n-1)}\big)^TPe^{(0\sim n-1)}\times\Big[1+\lambda_{\max}(P)\xi \\ &+\big(\lambda_{\min}(P)\xi\big)^{\mu-1}\eta\Big]+Z\varphi(\cdot)\tilde{d}+Z\psi(\cdot)\tilde{\theta} \\ &+\underline{H}_m\|Z\|^2\Psi^T\tilde{\rho}+\varsigma_M\sigma+\sigma+\sigma\bar{d} \\ &-\dot{\hat{\theta}}^T\tilde{\theta}-\tilde{d}\dot{\hat{d}}-\underline{H}_m\dot{\hat{\rho}}^T\tilde{\rho}. \end{aligned} \quad (24)$$

From adaptive laws (13) and (15), we can further obtain that

$$\begin{aligned}\dot{V}\le&-\frac{1}{2}\kappa\big(e^{(0\sim n-1)}\big)^TPe^{(0\sim n-1)}\times\Big[1+\lambda_{\max}(P)\xi \\ &+\big(\lambda_{\min}(P)\xi\big)^{\mu-1}\eta\Big]+\tilde{d}\big(\delta_{d_1}\hat{d}+\delta_{d_2}\hat{d}^3\big) \\ &+\big(\delta_{\theta_1}\hat{\theta}^T+\delta_{\theta_2}F_\theta^T\big)\tilde{\theta}+\underline{H}_m\big(\delta_{\rho_1}\hat{\rho}^T+\delta_{\rho_2}F_\rho^T\big)\tilde{\rho} \\ &+(1+\varsigma_M+\bar{d})\sigma. \end{aligned} \quad (25)$$

Note that $\mu\in(0,1)$ means $\mu-1<0$, and $\lambda_{\min}(P)\xi\le\big(e^{(0\sim n-1)}\big)^TP(\cdot)e^{(0\sim n-1)}\le\lambda_{\max}(P)\xi$ holds, where ξ is defined in (11). Then, it can be obtained that

$$\begin{aligned}&-\frac{1}{2}\kappa\big(e^{(0\sim n-1)}\big)^TP(\cdot)e^{(0\sim n-1)}\lambda_{\max}(P)\xi \\ &\le-2\kappa\Big(\frac{1}{2}\big(e^{(0\sim n-1)}\big)^TP(\cdot)e^{(0\sim n-1)}\Big)^2, \end{aligned} \quad (26)$$

$$\begin{aligned}&-\frac{1}{2}\kappa\big(e^{(0\sim n-1)}\big)^TP(\cdot)e^{(0\sim n-1)}\big(\lambda_{\min}(P)\xi\big)^{\mu-1} \\ &\le-2^{\mu-1}\kappa\Big(\frac{1}{2}\big(e^{(0\sim n-1)}\big)^TP(\cdot)e^{(0\sim n-1)}\Big)^{\mu}. \end{aligned} \quad (27)$$

Furthermore, the following inequalities can be obtained, and their proof are provided in the appendix.

$$\begin{aligned}&\tilde{d}\big(\delta_{d_1}\hat{d}+\delta_{d_2}\hat{d}^3\big) \\ &\le-\frac{\delta_{d_1}}{8}\tilde{d}^2-\tau_1\Big(\frac{1}{2}\tilde{d}^2\Big)^{\frac{3}{4}}-\delta_{d_2}\Big(1-\frac{9\epsilon^{4/3}}{4}\Big)\tilde{d}^4+c_1, \end{aligned} \quad (28)$$

$$\begin{aligned}\big(\delta_{\theta_1}\hat{\theta}^T+\delta_{\theta_2}F_\theta^T\big)\tilde{\theta}\le&-\frac{\delta_{\theta_1}}{8}\tilde{\theta}^T\tilde{\theta}-\tau_1\Big(\frac{1}{2}\tilde{\theta}^T\tilde{\theta}\Big)^{\frac{3}{4}} \\ &-\frac{\delta_{\theta_2}}{r}\Big(1-\frac{9\epsilon^{4/3}}{4}\Big)(\tilde{\theta}^T\tilde{\theta})^2+c_2, \end{aligned} \quad (29)$$

$$\begin{aligned}\big(\delta_{\rho_1}\hat{\rho}^T+\delta_{\rho_2}F_\rho^T\big)\tilde{\rho}\le&-\frac{\delta_{\rho_1}}{8}\tilde{\rho}^T\tilde{\rho}-\tau_1\Big(\frac{1}{2}\tilde{\rho}^T\tilde{\rho}\Big)^{\frac{3}{4}} \\ &-\frac{\delta_{\rho_2}}{r}\Big(1-\frac{9\epsilon^{4/3}}{4}\Big)(\tilde{\rho}^T\tilde{\rho})^2+c_3, \end{aligned} \quad (30)$$

with τ_1, ϵ, c_1, c_2 and c_3 being appropriate positive constants. For $\|e^{(0\sim n-1)}\|\geqslant\epsilon$, substituting (26)-(30) into (25) yields

$$\begin{aligned}\dot{V}\le&-2\kappa\Big(\frac{1}{2}\big(e^{(0\sim n-1)}\big)^TP(\cdot)e^{(0\sim n-1)}\Big)^2 \\ &-2^{\mu-1}\kappa\Big(\frac{1}{2}\big(e^{(0\sim n-1)}\big)^TP(\cdot)e^{(0\sim n-1)}\Big)^{\mu}-\tau_1\Big(\frac{1}{2}\tilde{d}^2\Big)^{\frac{3}{4}} \\ &-\tau_1\Big(\frac{1}{2}\tilde{\theta}^T\tilde{\theta}\Big)^{\frac{3}{4}}-\underline{H}_m\tau_1\Big(\frac{1}{2}\tilde{\rho}^T\tilde{\rho}\Big)^{\frac{3}{4}}-\delta_{d_2}\Big(1-\frac{9\epsilon^{4/3}}{4}\Big)\tilde{d}^4 \\ &-\frac{\delta_{\theta_2}}{r}\Big(1-\frac{9\epsilon^{4/3}}{4}\Big)(\tilde{\theta}^T\tilde{\theta})^2-\frac{\underline{H}_m\delta_{\rho_2}}{r}\Big(1-\frac{9\epsilon^{4/3}}{4}\Big)(\tilde{\rho}^T\tilde{\rho})^2 \\ &+(1+\varsigma_M+\bar{d})\sigma+c_1+c_2+\underline{H}_mc_3. \end{aligned} \quad (31)$$

Now, select $\mu=\frac{3}{4}$ and ϵ satisfying $1-\frac{9\epsilon^{4/3}}{4}>0$. Subsequently, let $\alpha_1=\min\{2^{\mu-1}\kappa,\tau_1,\underline{H}_m\tau_1\}$, $\varpi=1-\frac{9\epsilon^{4/3}}{4}$ and $\alpha_2=\frac{1}{4}\min\{2\kappa,4\delta_{d_2}\varpi,\frac{4\delta_{\theta_2}}{r}\varpi,\frac{4\delta_{\rho_2}}{r\underline{H}_m}\varpi\}$. Then, based on the definition of V, the inequality (31) will further satisfy

$$\dot{V}\le-\alpha_1V^{\frac{3}{4}}-\alpha_2V^2+C, \quad (32)$$

where $C=(1+\varsigma_M+\bar{d})\sigma+c_1+c_2+\underline{H}_mc_3$. Therefore, it follows from Lemma 7 that the closed-loop system (19) is FxT stable with $\mu_1=3/4$, $\mu_2=2$, $c=\alpha_1$, $b=\alpha_2$ and $\vartheta=C$. This further means that there exist a analysis constant $0<\beta<1$ and a fixed-time T_f satisfying $T_f\le T_m=\frac{4}{\beta\alpha_1}+\frac{1}{\beta\alpha_2}$, so that the function V converge to the set

$$V\le\min\Big\{\alpha_1^{-\frac{4}{3}}\Big(\frac{C}{1-\beta}\Big)^{\frac{4}{3}},\alpha_2^{-\frac{1}{2}}\Big(\frac{C}{1-\beta}\Big)^{\frac{1}{2}}\Big\}, \quad (33)$$

which indicates that V is bounded. From the definition of V, it can deduce that all variables $e^{(0\sim n-1)}$, $\tilde{\theta}$, $\tilde{d}$ and $\tilde{\rho}$ of the closed-loop system are also bounded. Because

$$\begin{aligned}\frac{1}{2}\lambda_{\min}(P)\|e\|^2&\le\frac{1}{2}\lambda_{\min}(P)\|e^{(0\sim n-1)}\|^2 \\ &\le\frac{1}{2}\big(e^{(0\sim n-1)}\big)^T\big(P(A^{0\sim n-1})\otimes I_m\big)e^{(0\sim n-1)}\le V, \end{aligned}$$

combined with inequality (33), it is evident that the inequality (17) holds. This completes the stability proof. □

Remark 1. The purpose of designing function η in (12) is to prevent the singularity of term $\left(\lambda_{\min}(P)\xi\right)^{\mu-1}e^{(0\sim n-1)}\eta$. By observing the definition of η, it becomes evident that term $\left(\lambda_{\min}(P)\xi\right)^{\mu-1}e^{(0\sim n-1)}\eta$ is continuous along the boundary $\|e^{(0\sim n-1)}\| = \epsilon$, effectively avoiding the chatting phenomenon. Furthermore, when $\|e^{(0\sim n-1)}\| < \epsilon$ holds, an extra term

$$\begin{aligned} H_e =& \frac{1}{2}\kappa\left(e^{(0\sim n-1)}\right)^T Pe^{(0\sim n-1)}\left(\lambda_{\min}(P)\xi\right)^{\mu-1} \\ &- \frac{1}{2}\kappa\left(e^{(0\sim n-1)}\right)^T Pe^{(0\sim n-1)}\left(\lambda_{\min}(P)\xi\right)^{\mu-1} \\ &\times \sum_{j=1}^{n}\varrho_j\xi^{j-\frac{3}{4}}(\epsilon^2)^{-j+\frac{3}{4}} \end{aligned}$$

emerges in inequality (31). Since $\|e^{(0\sim n-1)}\| < \epsilon$ is met, there exists a small constant $\bar{\epsilon}$ that ensures $\|H_e\| \le \bar{\epsilon}$. As a result, inequality (31) continues to hold with only a minimal increase in the constant term C.

5 Example and Simulation

In this section, the proposed HOFA fixed-time control scheme will be applied to a marine vessel to verify the effectiveness of the algorithm. The kinematics and kinetics of the ship can be described as [29]

$$\begin{aligned} \dot{\eta} &= R(\phi)\nu, \\ M\dot{\nu} &= g(\nu) + \Phi(\eta,\nu)\theta + u^s + \omega(t), \end{aligned} \tag{34}$$

where $\eta = [x, y, \phi]^T$ with (x, y) being the position information and ϕ being the heading angle in the earth-fixed coordinate, $\nu = [\tau, \upsilon, r]^T$ with τ, υ and r being its surge, sway and yaw velocities respectively in the body-frame, the vector $\omega = [\omega_\tau, \omega_\upsilon, \omega_r]^T$ is the unknown disturbances induced by the wind, waves and ocean currents, $g(\nu)$ and $\Phi(\eta,\nu)$ denote the known nonlinear functions, θ is the unknown parameter vector, $u^s = [u^s_\tau, u^s_\upsilon, u^s_r]^T$ denotes the control force subject to input saturation as defined in (3), that is, $u^s = H'_u u + \bar{\varsigma}(u)$. The matrix $R(\phi)$ denotes a rotate matrix described by

$$R(\phi) = \begin{bmatrix} \cos(\phi) & -\sin(\phi) & 0 \\ \sin(\phi) & \cos(\phi) & 0 \\ 0 & 0 & 1 \end{bmatrix}. \tag{35}$$

The definitions and meanings of the inertia matrix M with $M = M^T > 0$, the functions $g(\nu)$ and $\Phi(\eta,\nu)$ are the same as in [29]. From the system equation (34), we can obtain

$$\ddot{\eta} = -rRS\nu + RM^{-1}(g(\nu) + \Phi(\eta,\nu)\theta + u^s + \omega), \tag{36}$$

where $\dot{R} = -rRS$ with $S = \text{diag}\{\bar{S}, 0\}$ and $\bar{S} = \begin{bmatrix} 0 & 1 \\ -1 & 0 \end{bmatrix}$ is used to get the above equation.

Note that $\nu = R^{-1}(\phi)\dot{\eta}$, indicating that ν depends on η and $\dot{\eta}$. Let $f(\eta,\dot{\eta}) = -rRS\nu + RM^{-1}g(\nu)$, $\psi(\eta,\dot{\eta}) = RM^{-1}\Phi(\eta,\nu)$, $G(\eta,\dot{\eta}) = RM^{-1}$ and $d(t) = RM^{-1}\omega$. Then the above system (36) can be further written as

$$\ddot{\eta} = f(\eta,\dot{\eta}) + \psi\theta + G(\eta,\dot{\eta})u^s + d(t). \tag{37}$$

From the definitions of R and M, $\det(G) \neq 0$ can be obtained, and there exists an unknown constant $\bar{d} > 0$ that holds $\|d(t)\| \le \bar{d}$. Therefore, system (36) is a HOFA with the same properties as the studied system (2).

Next, we select the trajectory of the desired system output as $\eta_d = [0.2t + 3, 0.2t + 3, \pi/4]^T$. The external disturbance is chosen as $\omega(t) = [0.1\sin(0.1t), 0.1\cos(0.1t), 0.1\sin(0.02t)]^T$. The parameters of the saturation constraint are chosen as $u_{\tau M} = 10$, $u_{\tau m} = -10$, $u_{\upsilon M} = 10$, $u_{\upsilon m} = -10$, $u_{rM} = 10$, $u_{rm} = -10$. Based on the design process presented in Section III, the fixed-time HOFA controllers similar to the form of (14) with adaptive laws (13) and (15) can be constructed. For simulation, choose the initial value to be $\eta(0) = [3, 2, 0]^T$, $\nu(0) = [0, 0, 0]^T$, $\hat{\theta}(0) = [0.5]_{7\times1}$, $\hat{d}(0) = 0$ and $\hat{\rho}(0) = [0.1, 0.1]^T$. Let the design parameters be $\delta_{\theta_1} = 2$, $\delta_{\theta_2} = 0.1$, $\delta_{d_1} = 0.5$, $\delta_{d_2} = 0.002$, $\delta_{\rho_1} = 0.02$ and $\delta_{\rho_2} = 0.001$. Additionally, according to Lemma 4, select $Z = [1,\ 1]$ and $F = \begin{bmatrix} -3 & -1.5 \\ 1.5 & -3 \end{bmatrix}$. Then, we have $\Lambda(Z,F) = \begin{bmatrix} 1 & 1 \\ -1.5 & -4.5 \end{bmatrix}$. Hence, we further obtain $A^{0\sim1} = -ZF^2\Lambda^{-1} = [11.25\ 6]$, and $\Phi(A^{0\sim1}) = \begin{bmatrix} 0 & 1 \\ -11.25 & -6 \end{bmatrix}$. By selecting $\kappa = 4$ and solving the equation $\Phi(A^{0\sim1})^T P(A^{0\sim1}) + P(A^{0\sim1})\Phi(A^{0\sim1}) \le -\kappa P(A^{0\sim1})$, we have $P(A^{0\sim1}) = \begin{bmatrix} 11.2 & 2 \\ 2 & 0.6 \end{bmatrix}$. Using the above given controller parameters and these initial values, the simulation results are shown in Figs. 1-3 (Due to limited space, only selected key curves are displayed here).

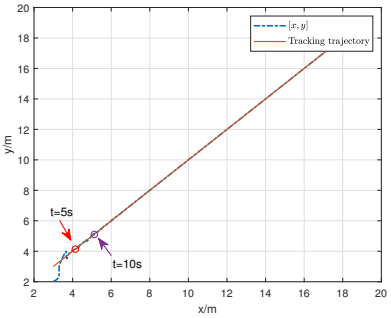

Fig. 1: The trajectories of system output and tracking signal

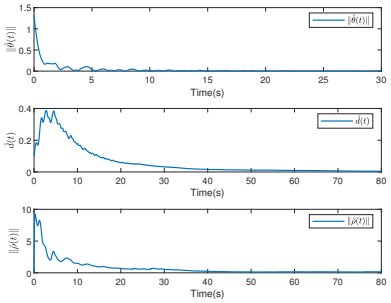

Fig. 2: The trajectories of adaptive laws

Fig. 1 shows the curves of position information $[x, y]$ of

the system and the tracking trajectory $\eta_d = [0.2t+3, 0.2t+3]$, indicating that the system output can quickly track the desired trajectory. From the trajectories of the adaptive law norms $\|\hat{\theta}\|$, $\hat{d}$ and $\|\hat{\rho}\|$ shown in Fig. 2, it can be concluded that all adaptive signals are all bounded. The trajectories of control input signals in three different directions are demonstrated in Fig. 3, which implies the control input is also bounded. This further implies the boundedness of other state signals. From Figs.1-3, the effectiveness of the proposed algorithm is verified.

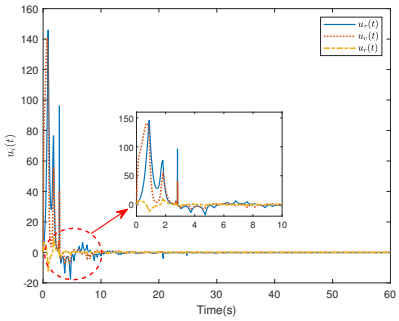

Fig. 3: The trajectory of the actual input signal

6 Conclusions

The FxT stability of an uncertain nonlinear system with input saturation, parameter uncertain and external disturbance has been investigated using the HOFA system approach. A hyperbolic tangent function has been employed to approximate the saturation function. Then, by introducing a special order of tracking error and combined with the adaptive techniques, a controller has been designed to ensure the FxT stability. The proposed algorithm achieves FxT stability of an uncertain higher-order system for the first time based on the fully actuated system method, expanding the adaptability of this method. Future work will study the FxT formation problem of multiple HOFA systems.

7 Appendix

*P*art I: Proof of inequality (28)

Based on the error signal $\tilde{d} = \bar{d} - \hat{d}$, using Lemma 4 yields

$$\delta_{d_1}\tilde{d}\hat{d} = \delta_{d_1}\tilde{d}(\bar{d}-\tilde{d}) \leq -\frac{\delta_{d_1}}{2}\tilde{d}^2 + \frac{\delta_{d_1}}{2}\bar{d}^2. \tag{38}$$

It follows from the complete square formula that

$$\begin{aligned} -\frac{\delta_{d_1}}{2}\tilde{d}^2 =& -\frac{\delta_{d_1}}{4}\tilde{d}^2 + \frac{1}{2\sqrt{2}}\frac{\tau_1^2}{\delta_{d_1}}|\tilde{d}| - \tau_1\Big(\frac{1}{2}\tilde{d}^2\Big)^{\frac{3}{4}} \\ & - \frac{1}{4}\Big(\sqrt{\delta_{d_1}}|\tilde{d}| - 2^{\frac{1}{4}}\frac{\tau_1}{\sqrt{\delta_{d_1}}}\sqrt{|\tilde{d}|}\Big)^2, \end{aligned} \tag{39}$$

where τ_1 is a positive constant to be selected. Furthermore, using Young inequality further yields

$$\frac{1}{2\sqrt{2}}\frac{\tau_1^2}{\delta_{d_1}}|\tilde{d}| \leq \frac{\delta_{d_1}}{8}\tilde{d}^2 + \frac{\tau_1^4}{4\delta_{d_1}^3}. \tag{40}$$

Substituting inequalities (39) and (40) into (38), we have

$$\delta_{d_1}\tilde{d}\hat{d} \leq -\frac{\delta_{d_1}}{8}\tilde{d}^2 - \tau_1\Big(\frac{1}{2}\tilde{d}^2\Big)^{\frac{3}{4}} + \frac{\tau_1^4}{4\delta_{d_1}^3} + \frac{\delta_{d_1}}{2}\bar{d}^2. \tag{41}$$

Next, for the term $\delta_{d_2}\tilde{d}\hat{d}^3$, we can obtain that

$$\begin{aligned} \delta_{d_2}\tilde{d}\hat{d}^3 &= \delta_{d_2}\tilde{d}(\bar{d}-\tilde{d})^3 \\ &= \delta_{d_2}\tilde{d}(\bar{d}^3 - 3\bar{d}^2\tilde{d} + 3\bar{d}\tilde{d}^2 - \tilde{d}^3) \\ &= -\delta_{d_2}\tilde{d}^4 + \delta_{d_2}\tilde{d}\bar{d}^3 - 3\delta_{d_2}\tilde{d}^2\bar{d}^2 + 3\delta_{d_2}\bar{d}\tilde{d}^3. \end{aligned} \tag{42}$$

For terms $\delta_{d_2}\tilde{d}\bar{d}^3$ and $-3\delta_{d_2}\tilde{d}^2\bar{d}^2$ of the above equation, it can be obtained from the Young inequality that:

$$\delta_{d_2}\tilde{d}\bar{d}^3 \leq 3\delta_{d_2}\tilde{d}^2\bar{d}^2 + \frac{\delta_{d_2}}{12}\bar{d}^4, \tag{43}$$

$$-3\delta_{d_2}\tilde{d}^2\bar{d}^2 \leq 3\delta_{d_2}\frac{3\epsilon^{4/3}}{4}|\tilde{d}^3|^{\frac{4}{3}} + 3\delta_{d_2}\frac{1}{4\epsilon^4}\bar{d}^4. \tag{44}$$

Combining inequalities (43) and (44), we have

$$\delta_{d_2}\tilde{d}\hat{d}^3 \leq -\delta_{d_2}\Big(1 - \frac{9\epsilon^{4/3}}{4}\Big)\tilde{d}^4 + \frac{\delta_{d_2}}{12}\bar{d}^4 + 3\delta_{d_2}\frac{1}{4\epsilon^4}\bar{d}^4. \tag{45}$$

Then, based on inequalities (41) and (45), we can obtain that

$$\begin{aligned} &\tilde{d}\big(\delta_{d_1}\hat{d} + \delta_{d_2}\hat{d}^3\big) \\ &\leq -\frac{\delta_{d_1}}{8}\tilde{d}^2 - \tau_1\Big(\frac{1}{2}\tilde{d}^2\Big)^{\frac{3}{4}} - \delta_2\Big(1 - \frac{9\epsilon^{4/3}}{4}\Big)\tilde{d}^4 + c_1, \end{aligned} \tag{46}$$

where c_1 is a positive constant with the following definition

$$c_1 = \frac{\tau_1^4}{4\delta_{d_1}^3} + \frac{\delta_{d_1}}{2}\bar{d}^2 + \frac{\delta_{d_2}}{12}\bar{d}^4 + 3\delta_{d_2}\frac{1}{4\epsilon^4}\bar{d}^4.$$

This proves the inequality (28).

*P*art II: Proof of inequalities (29) and (30)

From the definitions of θ, $\hat{\theta}$ and F_θ in Section III, one has

$$\big(\delta_{\theta_1}\hat{\theta}^T + \delta_{\theta_2}F_\theta^T\big)\tilde{\theta} = \sum_{j=1}^{r}\big(\delta_{\theta_1}\hat{\theta}_j\tilde{\theta}_j + \delta_{\theta_2}\hat{\theta}_j^3\tilde{\theta}_j\big). \tag{47}$$

For each term in equation (47), by using steps similar to inequality (46), we can deduce

$$\begin{aligned} &\delta_{\theta_1}\hat{\theta}_j\tilde{\theta}_j + \delta_{\theta_2}\hat{\theta}_j^3\tilde{\theta}_j \\ &\leq -\frac{\delta_{\theta_1}}{8}\tilde{\theta}_j^2 - \tau_1\Big(\frac{1}{2}\tilde{\theta}_j^2\Big)^{\frac{3}{4}} - \delta_{\theta_2}\Big(1 - \frac{9\epsilon^{4/3}}{4}\Big)\tilde{\theta}_j^4 + c_{2j}, \end{aligned} \tag{48}$$

with $c_{2j} = \frac{\tau_1^4}{4\delta_{\theta_1}^3} + \frac{\delta_{\theta_1}}{2}\theta^2 + \frac{\delta_{\theta_2}}{12}\theta^4 + 3\delta_{\theta_2}\frac{1}{4\epsilon^4}\theta^4$. This together with Lemmas 5 and 6 mean that (47) satisfies

$$\begin{aligned} \big(\delta_{\theta_1}\hat{\theta}^T + \delta_{\theta_2}F_\theta^T\big)\tilde{\theta} \leq& \sum_{j=1}^{r}\Big(-\frac{\delta_{\theta_1}}{8}\tilde{\theta}_j^2 - \tau_1\Big(\frac{1}{2}\tilde{\theta}_j^2\Big)^{\frac{3}{4}} \\ & - \delta_{\theta_2}\Big(1 - \frac{9\epsilon^{4/3}}{4}\Big)\tilde{\theta}_j^4 + c_{2j}\Big) \\ \leq& -\frac{\delta_{\theta_1}}{8}\tilde{\theta}^T\tilde{\theta} - \tau_1\Big(\frac{1}{2}\tilde{\theta}^T\tilde{\theta}\Big)^{\frac{3}{4}} \\ & - \frac{\delta_{\theta_2}}{r}\Big(1 - \frac{9\epsilon^{4/3}}{4}\Big)(\tilde{\theta}^T\tilde{\theta})^2 + c_2. \end{aligned} \tag{49}$$

This proves that inequality (29) holds. Similarly, the inequality (30) regarding the adaptive law $\hat{\rho}$ also holds.

References

[1] M. Krstic, I. Kanellakopoulous, and P. Kokotovic, *Nonlinear and Adaptive Control Design*, New York, NY, USA: Wiley, 1995.

[2] J. de Jesús Rubio, Robust feedback linearization for nonlinear processes control, *ISA Transactions*, 74: 155–164, 2018.

[3] P. V. Kokotović, *Foundations of adaptive control*, Springer-Verlag, 1991.

[4] J. Tsinias, Existence of control Lyapunov functions and applications to state feedback stabilizability of nonlinear systems, *SIAM Journal on Control and Optimization*, 29(2): 457–473, 1991.

[5] H. F. Min, S. Y. Xu, and Z. Q. Zhang, Adaptive finite-time stabilization of stochastic nonlinear systems subject to full-state constraints and input saturation, *IEEE Transactions on Automatic Control*, 66(3): 1306-1313, 2021.

[6] P. Wang, C. Yu, and J. Sun, Quantized feedback control for nonlinear feedforward systems with unknown output functions and unknown control coefficients, *International Journal of Robust and Nonlinear Control*, 29(12): 4002-4021, 2019.

[7] Y. Z. Wang, C. Y. Wen C, X. Li, Event-based model reference adaptive tracking, *IEEE Transactions on Automatic Control*, 68(12): 8201-8207, 2023.

[8] P. Wang, C. P. Yu, and Y.-J. Pan, Finite-time output feedback cooperative formation control for marine surface vessels with unknown actuator faults, *IEEE Transactions on Control of Network Systems*, 10(2): 887-899, 2023.

[9] Y. Xu, Z. G. Wu, Y. J, Pan. Adaptive output observers-based distributed tracking, *Automatica*, 2024, 161: 111489.

[10] G. R. Duan, High-order fully actuated system approaches: Part I. models and basic procedure, *International Journal of Systems Science*, 52(2): 422–435, 2021.

[11] G. R. Duan, High-order fully actuated system approaches: Part V. Robust adaptive control, *International Journal of Systems Science*, 52(10): 2129–2143, 2021.

[12] G. R. Duan, High-order fully actuated system approaches: Part VII. controllability, stabilisability and parametric designs, *International Journal of Systems Science*, 52(14): 3091–3114, 2021.

[13] G. R. Duan, High-order fully actuated system approaches: Part II. Generalized strict feedback systems, *International Journal of Systems Science*, 52(3): 437–454, 2021.

[14] R. X. Dong, C. C. Hua, K. Li, and R. Meng, Adaptive Fault-Tolerant Control for High-Order Fully Actuated System with Full-State Constraints, *Journal of the Franklin Institute*, on line, 2023.

[15] C. G. Liu, X. P. Liu, H. Q. Wang, Y. C. Zhou, and C. Gao, Adaptive control for unknown HOFA nonlinear systems without overparametrization, *International Journal of Robust and Nonlinear Control*, 33: 3640-3660, 2023.

[16] G. T. Tian, and G. R. Duan, Robust model reference tracking for uncertain second-order nonlinear systems with application to robot manipulator, *International Journal of Robust and Nonlinear Control*, 33(3): 1750-1771, 2023.

[17] M. Cai, X. He, and D. H. Zhou, An active fault tolerance framework for uncertain nonlinear high-order fully-actuated systems, *Automatica*, 152: 110969, 2023.

[18] M. Cai, X. He, and D. H. Zhou, Low-power fault tolerant control for nonideal high-order fully-actuated systems, *IEEE Transactions on Systems, Man, and Cybernetics: Systems*, 2023, doi: 10.1109/TSMC.2023.3257315.

[19] D. W. Zhang, G. P. Liu, and L. Cao, Proportional integral predictive control of networked high-order fully actuated networked multiagent systems with communication delays, *IEEE Transactions on Systems, Man, and Cybernetics: Systems*, 53(2): 801-812, 2023.

[20] D. W. Zhang and G. P. Liu, Predictive control for networked high-order fully actuated systems subject to communication delays and external disturbances, *ISA Transactions*, 2023, doi: 10.1016/j.isatra.2023.03.041.

[21] Q. Huang and Y. Zhang, Finite-time attitude tracking for fully-actuated flexible spacecraft without angular velocity measurements," in *Proceedings of 2023 Conference on Fully Actuated System Theory and Applications*, 2023: 1061-1066.

[22] D. Wang, Y. H. Wu, X. R. Chen, Y. Q. Zhang, S. H. Liu, and Y. H. Mao, Fully actuated system based spacecraft attitude finite time control, in *Proceedings of 2023 Conference on Fully Actuated System Theory and Applications*, 2023: 100-105.

[23] S. Lu, K. Tsakalis, and Y. Chen, Development and application of a novel high-order fully actuated system approach-Part I: 3-DOF quadrotor control, *IEEE Control Systems Letters*, 7: 1177-1182, 2023.

[24] T. Y. Zhao and G. R. Duan, Fully actuated system approach to attitude control of flexible spacecraft with nonlinear time-varying inertia, *Science China-Information Sciences*, 65(11): 212201, 2022.

[25] P. Wang, C. Yu, M. Lv and J. Cao, Adaptive fixed-time optimal formation control for uncertain nonlinear multiagent systems using reinforcement learning, *IEEE Transactions on Network Science and Engineering*, 11(2): 1729-1743, 2024.

[26] X. Jin, Adaptive fixed-time control for MIMO nonlinear systems with asymmetric output constraints using universal barrier functions, *IEEE Transactions on Automatic Control*, 64(7): 3046-3053, 2019.

[27] F. Wang, and G. Lai, Fixed-time control design for nonlinear uncertain systems via adaptive method, *Systems & Control Letters*, 140(7): 104704, 2020.

[28] A. Polyakov, Nonlinear feedback design for fixed-time stabilization of linear control systems, *IEEE Transactions on Automatic Control*, 57(8): 2106-2110,2012.

[29] R. Skjetne, T. I. Fossen, and P. V. Kokotovic, Adaptive maneuvering, with experiments, for a model ship in a marine control laboratory, *Automatica*, 41(2): 289-298, 2005.

Proceedings of the 3rd Conference on Fully Actuated System Theory and Applications
May 10-12, 2024, Shenzhen, China

DC-Link Voltage Control of Three-Phase AC/DC Converters with Current Constraints

Cheng Fu[1], Zicheng Zhang[1], Le Chang[2], Guanguan Zhang[1,*]

1. School of Control Science and Engineering, Shandong University, 250061 Jinan, China
E-mail: cfu@mail.sdu.edu.cn; zhangzc199105@163.com; ggzh@sdu.edu.cn

2. College of Electric Power Engineering, Shanghai University of Electric Power, Shanghai 200090, China
E-mail: lchang@shiep.edu.cn

Abstract: For three-phase AC/DC converters, the fast dynamic response of the DC-link voltage usually involves overlarge transient grid currents. Hence, users have to choose conservative control parameters to restrict the transient current, but this choice sacrifices dynamic performances to some extent. In this paper, a single-loop structure current-constrained control strategy is proposed to achieve fast dynamic performance of the DC-link voltage. In the controller, it introduces a nonlinear variable gain, acting as the penalty term, to regulate the control action as the current approaches its limit. Rigorous stability analysis is conducted for the closed-loop control system. Test results demonstrate that the proposed method successfully constrains the current within a safe threshold while achieving fast dynamic performance.

Key Words: Current constraint, nonlinear variable gain, single-loop structure, three-phase AC/DC converter.

1 Introduction

Three-phase AC/DC converters serve as vital interfaces connecting renewable energies to the public grid. One of the primary control objectives for three-phase AC/DC converters is to regulate the DC-link voltage to its reference value. For most applications, delivering a fast dynamic response of the DC-link voltage is crucial for ensuring the stable operation of loads [1]. However, a fast voltage dynamic response is usually accompanied by overlarge transient grid currents, which may result in equipment shutdown due to over-current protection and pose risks to power devices safety [2].

In general, the voltage regulation of three-phase AC/DC converters is controlled by a dual-loop structure, including the outer voltage and inner power/current loops. Linear proportional-integral (PI) methods are popular for these two loops due to its ease of implementation. Since the PI methods are developed based on the bounded operating horizon, their dynamic performance degrades when the system is exposed to large system uncertainties. To accommodate a wide range of operating conditions, several nonlinear control methods are introduced for these two loops, such as the sliding-mode control (SMC) [3], the passive-based control (PBC) [4], and the backstepping control (BSC) [5]. Under the dual-loop structure, the users usually set a soft limiter to restrict the current reference generated from the outer voltage loop to a safe threshold [6]. Thereafter, the inner current loop is designed to track the restricted reference to avoid overlarge transient grid currents. However, the current constraint cannot be strictly guaranteed. There is still some chance for the current to exceed the safe threshold, especially in the case of high control gains. Therefore, it is needed to choose conservative control gains to avoid the overlarge transient current, which sacrifices the dynamic response to some extent [7]. It is meaningful to design a control strategy for AC/DC converters to obtain a fast dynamic response while satisfying current constraints.

This work was supported in part by the National Natural Science Foundation of China under Grant 62273205 and Grant 62188101. (Corresponding authors: Guanguan Zhang.)

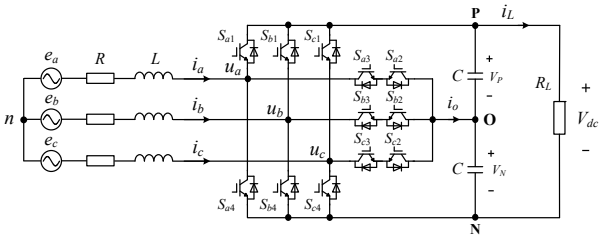

Fig. 1: Circuit structure of the three-phase AC/DC converter.

Inspired by the aforementioned methods, a simple current-constrained control is proposed to regulate the DC-link voltage of AC/DC converters. The contributions are given as follows.

1) It incorporates a nonlinear variable gain into the controller, as gird currents approach the safe threshold, the nonlinear gain is automatically adjusted to restrict the current promptly.
2) Unlike the cascade control structure results, a single-loop structure is utilized to regulate the DC-link voltage, which simplifies the control structure and requires fewer tuned parameters.
3) Theoretical analysis and test results demonstrate that the proposed strategy achieve a fast voltage dynamic response while avoiding overlarge transient grid currents.

2 System Description and Modeling

Fig. 1 shows the circuit structure of the three-phase AC/DC converter operating as a rectifier. It is connected to the grid through the filter inductor L and the line resistor R. The AC/DC converter employs a three-level T-type structure with two capacitors of equal capacitance C. The voltages across the capacitors are denoted as V_P and V_N, respectively. Table I presents an overview of the remaining system variables.

Next, we will give the mathematical model of the AC/DC converter and introduce the control objective. Note that the system modeling is built under some standard assumptions,

Table 1: System variables and parameters.

Variables	Description
$e_a,\ e_b, e_c$	Grid voltages in the abc reference frame
e_d, e_q	Grid voltages in the dq reference frame
$i_a,\ i_b, i_c$	Grid currents in the abc reference frame
i_d, i_q	Grid currents in the dq reference frame
$u_a,\ u_b, u_c$	Converter voltages in the abc reference frame
u_d, u_q	Converter voltages in the dq reference frame
V_{dc}, V_{dc}^*	DC-link voltage and its reference

such as balanced grid voltages and ignoring power losses.

2.1 System Modeling

Using the law of power conservation and instantaneous power theory, the DC-link mathematical model is built as

$$C\dot{V}_{dc} = \frac{3e_d}{V_{dc}} i_d - 2\frac{V_{dc}}{R_L} \tag{1}$$

where R_L represents the equivalent load resistance.

Define $U = 0.5V_{dc}^2$, the DC-link model is rewritten as

$$\dot{U} = \frac{3e_d}{C} i_d - \frac{4}{CR_L} U. \tag{2}$$

Using the Kirchhoff's Voltage Law, the ac-side mathematical model is built as

$$\begin{cases} L\dot{i}_a = e_a - Ri_a - u_a - u_{on} \\ L\dot{i}_b = e_b - Ri_b - u_b - u_{on} \\ L\dot{i}_c = e_c - Ri_c - u_c - u_{on} \end{cases} \tag{3}$$

in the abc reference frame.

Typically, the ac-side mathematical model is transformed from the abc axis to the dq axis to facilitate the control design [8]. The transformation matrix is expressed as

$$T = \frac{2}{3}\begin{bmatrix} \cos\omega t & \cos\left(\omega t - \frac{2\pi}{3}\right) & \cos\left(\omega t + \frac{2\pi}{3}\right) \\ -\sin\omega t & -\sin\left(\omega t - \frac{2\pi}{3}\right) & -\sin\left(\omega t + \frac{2\pi}{3}\right) \end{bmatrix}.$$

Then, the ac-side model in the dq-axis can be written as

$$L\dot{i}_d = -Ri_d + \omega L i_q + e_d - u_d \tag{4}$$

$$L\dot{i}_q = -Ri_q - \omega L i_d + e_q - u_q \tag{5}$$

in which ω is the grid angle frequency.

For the AC/DC converter acting as a rectifier, i_q is controlled to zero to achieve the unit power factor. In fact, this issue has been well addressed in existing literature. Here, a traditional PI method is adopted to control i_q for the purpose of achieving this goal simply and efficiently. Under this condition, the amplitude of grid currents is determined by i_q, i.e., limiting $|i_d|$ prevents overlarge grid currents.

Combining (2) and (4), the model for regulating the DC-link voltage is described as follows:

$$\begin{cases} \dot{U} = \dfrac{3e_d}{C} i_d - \dfrac{4}{CR_L} U \\ \dot{i}_d = -\dfrac{R}{L} i_d + \omega i_q + \dfrac{1}{L} e_d - \dfrac{1}{L} u_d \end{cases}. \tag{6}$$

The main control objective is to regulate the DC-link voltage to its reference with a fast dynamic response. In the meantime, the d-axis current is required to satisfy the constraint condition $|i_d| < I_s$, so as to avoid overlarge grid currents and ensure the safe operation of converters. $I_s > 0$ is the safety threshold of grid currents and selected as around 2 times rated currents.

2.2 Preliminaries

Before the control design, we introduce the following lemma that is used to complete the stability analysis of the closed-loop control system.

Lemma 1: [9] (Barbashin's theorem) For an autonomous system

$$\dot{x} = f(x) \tag{7}$$

where $f : D \to \mathbb{R}^n$ is a locally Lipschitz map from a domain $D \subset \mathbb{R}^n$ to $\mathbb{R}^n$. Let $x = 0$ be an equilibrium point for (7) and D be a domain containing $x = 0$. Let $V : D \to \mathbb{R}$ be a continuously differentiable function such that $V(x)$ is positive definite and $\dot{V}(x)$ is negative semidefinite in D. Let $S = \{x \in D | \dot{V}(x) = 0\}$ and suppose no solution can stay identically in S, other than the trivial solution $x(t) \equiv 0$ holds identically for all time. Then, $x = 0$ is asymptotically stable.

3 Current-Constrained Control

In this section, a simple current-constrained control is developed for the AC/DC converter to regulate the DC-link voltage.

Define the DC-link voltage and d-axis current tracking errors as follows:

$$e_1 = U^* - U,\ e_2 = -i_d + \frac{4U^*}{3e_d R_L} \tag{8}$$

in which $U^* = 0.5(V_{dc}^*)^2$ is the reference of U. Then, taking the derivative of (8) yields that

$$\begin{cases} \dot{e}_1 = -\dfrac{3e_d}{C} i_d + \dfrac{4}{CR_L} U \\ \quad = -\dfrac{4}{CR_L} e_1 + \dfrac{3e_d}{C} e_2 \\ \dot{e}_2 = \dfrac{R}{L} i_d - \omega i_q - \dfrac{1}{L} e_d + \dfrac{1}{L} u_d \end{cases}. \tag{9}$$

As per (8), it is clear that

$$i_d \in (-I_s,\ I_s) \Leftrightarrow e_2 \in \left(\underline{E}, \overline{E}\right) \tag{10}$$

where $\underline{E} = -I_s + \frac{4U^*}{3e_d R_L}$ and $\overline{E} = I_s + \frac{4U^*}{3e_d R_L}$. Based on (6) and instantaneous power theory, $\frac{4U^*}{3e_d R_L}$ is the steady-state value of the d-axis current, thus it yields $\underline{E} < 0$ and $\overline{E} > 0$.

Based on (8)–(10), the control objective is equal to design a controller u_d such that e_1 tends to zero with $e_2 \in \left(\underline{E}, \overline{E}\right)$. In order to satisfy the current constraint, the key is to establish a punishment mechanism for d-axis current in the controller. Here, the current-constrained voltage controller is constructed as

$$u_d = -k_1 e_1 - \left[k_2 + \frac{\eta}{I_s^2 - i_d^2}\right] e_2 - Ri_d + \omega L i_q + e_d \tag{11}$$

where k_1, k_2, and η are positive parameters.

Remark 1: In the designed controller (11), a nonlinear variable gain $\frac{\eta}{I_s^2-i_d^2}$ is introduced as the punishment mechanism of d-axis current. In particular, when $|i_d|$ tends to the safety threshold I_s, this nonlinear gain increases automatically. In this manner, the control action will be adjusted to limit the current in time.

Theorem 1: If $i_d(0) \in (-I_s,\ I_s)$, i.e., $e_2(0) \in (\underline{E},\ \overline{E})$, then the DC-link voltage tracks its reference value, while the current constraint condition $|i_d| < I_s$ is not violated.

Proof: For any given initial state $e(0) = (e_1(0), e_2(0)) \in G,\ \mathbb{R} \times (\underline{I},\ \bar{I})$, let $[0, T)$ be the largest time interval that satisfies $e_2(t) \in G$, where T is a positive constant or $T = +\infty$. Since the choice of initial state $e(0) \in G$, the time interval $[0, T)$ does exist.

Step 1: Prove that $|e_1(t)| \le N$ for $t \in [0, T)$, in which N will be specified later.

In the time interval $[0, T)$, substituting (11) into (9), the error closed-loop system is described by

$$\begin{cases} \dot{e}_1 = -\dfrac{4}{CR_L}e_1 + \dfrac{3e_d}{C}e_2 \\ \dot{e}_2 = \dfrac{1}{L}\left(-k_1 e_1 - \left[k_2 + \dfrac{\eta}{I_s^2 - i_d^2}\right]e_2\right) \\ \quad = \dfrac{1}{L}\left(-k_1 e_1 - \left[k_2 + \dfrac{\eta}{\left(\overline{E} - e_2\right)\left(e_2 - \underline{E}\right)}\right]e_2\right) \end{cases}. \tag{12}$$

Choose the Lyapunov function candidate as

$$V = \frac{k_1 C}{2 \cdot 3e_d L}e_1^2 + \frac{1}{2}e_2^2. \tag{13}$$

Note that the vector field of (12) is continuously differentiable in G. Taking the derivative of V in the time interval $t \in [0, T)$, it yields that

$$\begin{aligned} \dot{V} =& \frac{k_1 C}{3e_d L}e_1\dot{e}_1 + e_2\dot{e}_2 \\ =& \frac{k_1 C}{3e_d L}e_1\left(-\frac{4}{CR_L}e_1 + \frac{3e_d}{C}e_2\right) \\ & -\frac{k_1}{L}e_1 e_2 - \frac{1}{L}\left[k_2 + \frac{\eta}{\left(\overline{E} - e_2\right)\left(e_2 - \underline{E}\right)}\right]{e_2}^2 \\ =& -\frac{4k_1}{3e_d R_L L}e_1^2 - \frac{1}{L}\left[k_2 + \frac{\eta}{\left(\overline{E} - e_2\right)\left(e_2 - \underline{E}\right)}\right]e_2^2 \\ \le& -\frac{4k_1}{3e_d R_L L}e_1^2 - \frac{k_2}{L}e_2^2. \end{aligned} \tag{14}$$

From (14), it is obtained that $\dot{V} \le 0$ and $V(t) \le V(0)$, $t \in [0, T)$. Therefore, we have

$$\begin{aligned} & \frac{k_1 C}{2 \cdot 3e_d L}e_1^2(t) + \frac{1}{2}e_2(t)^2 \le V(0) \\ \Rightarrow & |e_1(t)| \le \left(\frac{2 \cdot 3e_d L}{k_1 C}V(0)\right)^{\frac{1}{2}},\ t \in [0, T). \end{aligned} \tag{15}$$

Denote $N = (2 \cdot 3e_d L/(k_1 C)V(0))^{\frac{1}{2}}$. It is concluded that if $e(0) \in G$, then $|e_1(t)| \le N$, $t \in [0, T)$.

Step 2: Prove the proposition as follows: *If $e(0) \in G$, then there exist $E_1 \in (0, \overline{E})$ and $E_2 \in (\underline{E}, 0)$ such that $e_2(t)\dot{e}_2(t) \le 0$, when $e(t) \in [-N, N] \times ([E_1, \overline{E}) \cup (\underline{E}, E_2])$, $t \in [0, T)$.*

Let $E_1 = \max\left\{e_2(0), (\kappa/(\eta + \kappa))\overline{E}\right\}$, $\kappa = k_1 N(\overline{E} - \underline{E})$. For $t \in [0, T)$, if $e_2(t) \in [E_1, \overline{E})$, then we have

$$\begin{aligned} \dot{e}_2(t) &\le \frac{1}{L}\left(k_1 N - \frac{\eta e_2(t)}{\left(\overline{E} - e_2(t)\right)\left(e_2(t) - \underline{E}\right)}\right) \\ &\le \frac{1}{L}\left(k_1 N - \frac{\eta e_2(t)}{\left(\overline{E} - e_2(t)\right)\left(\overline{E} - \underline{E}\right)}\right), \end{aligned} \tag{16}$$

and

$$\begin{aligned} k_1 N\left(\overline{E} - \underline{E}\right)\left(\overline{E} - e_2(t)\right) &\le k_1 N\left(\overline{E} - \underline{E}\right)\left(\overline{E} - E_1\right) \\ &\le k_1 N\left(\overline{E} - \underline{E}\right)\left(\overline{E} - \frac{\kappa}{\eta + \kappa}\overline{E}\right). \\ &\le \frac{\kappa\eta}{\eta + \kappa}\overline{E} \le \eta e_2(t) \end{aligned} \tag{17}$$

From (16) and (17), it is obtained that $e_2(t)\dot{e}_2(t) \le 0$ if $e_2(t) \in [E_1, \overline{E})$, $t \in [0, T)$.

Let $E_2 = \min\left\{e_2(0), (\kappa/(\eta + \kappa))\underline{E}\right\}$. For $t \in [0, T)$, if $e_2(t) \in (\underline{E}, E_2]$, then we have

$$\begin{aligned} \dot{e}_2(t) &\ge -\frac{1}{L}\left(k_1 N + \frac{\eta e_2(t)}{\left(\overline{E} - e_2(t)\right)\left(e_2(t) - \underline{E}\right)}\right) \\ &\ge -\frac{1}{L}\left(k_1 N + \frac{\eta e_2(t)}{\left(\overline{E} - \underline{E}\right)\left(e_2(t) - \underline{E}\right)}\right), \end{aligned} \tag{18}$$

and

$$\begin{aligned} k_1 N\left(\overline{E} - \underline{E}\right)\left(e_2(t) - \underline{E}\right) &\le k_1 N\left(\overline{E} - \underline{E}\right)\left(E_2 - \underline{E}\right) \\ &\le k_1 N\left(\overline{E} - \underline{E}\right)\left(\frac{\kappa}{\eta + \kappa}\underline{E} - \underline{E}\right). \\ &\le \frac{-\eta\kappa}{\eta + \kappa}\underline{E} \le -\eta e_2(t) \end{aligned} \tag{19}$$

From (18) and (19), it is obtained that $e_2(t)\dot{e}_2(t) \le 0$ if $e_2(t) \in (\underline{E}, E_2]$, $t \in [0, T)$. This completes the proposition.

Based on Steps 1–2, it is obtained that

$$e(t) = (e_1(t), e_2(t)) \in [-N, N] \times [E_2, E_1],\ t \in [0, T), \tag{20}$$

for any given $e(0) \in G$. Using the well-known continuation theorem of solution and the definition of the time interval $[0, T)$, it gets $T = +\infty$, i.e., the current constraints $|i_d| < I_s$ is guaranteed and the inequality (14) holds all the time. Using Lemma 1, the closed-loop system (12) with (11) is asymptotically stable, i.e., the tracking error of the DC-link voltage converges to zero exponentially. This completes the proof of Theorem 1. ■

Remark 2: Fig. 2 illustrates the control diagram of the proposed current-constrained control. The proposed strategy employs a single-loop structure to regulate the DC-link voltages. In comparison to the existing works that employ a cascaded control structure, the proposed strategy has fewer parameters and is more practical to implement. Additionally, the proposed strategy integrates a nonlinear variable gain in the controller. As the d-axis current approaches the safe threshold, the nonlinear gain is automatically adjusted to timely limit the current.

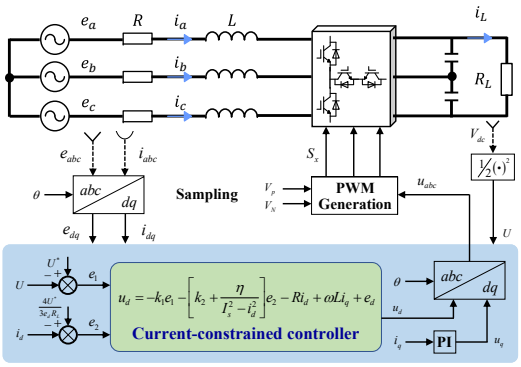

Fig. 2: Control diagram of the proposed strategy for the AC/DC converter.

Table 2: System parameters of the tested AC/DC converter.

Parameters	Symbol	Value
Rated power	S_r	2 kW
Grid voltage	$e_{a,b,c}$	110 Vrms
Grid angle frequency	ω	100π rad/s
DC-link voltage reference	V_{dc}^*	350 V
DC-link capacitor	C	1100 μF
DC-link load resistance	R_L	100 Ω
Filter inductance	L	3 mH
Line resistance	R	0.3 Ω
Switching frequency	T_f	10 kHz
Current safety threshold	I_s	15 A

4 Performance Validations

In this section, the proposed current-constrained control strategy is implemented on MATLAB/Simulink to verify its effectiveness. Table 2 summarizes the system parameters of the tested AC/DC converter. The control parameters are set as $k_1 = 0.2$, $k_2 = 30$, and $\eta = 1200$. Additionally, the traditional dual-loop PI method is implemented for the comparison, with a soft limiter of 15 A. Moreover, the PI method uses two sets of parameters: one set with high-gain parameters to achieve fast dynamic performance, and another set with conservative-gain parameters to ensure the current constraint condition is not violated. Details are given in Appendix.

4.1 DC-Link Voltage Regulation

The dynamic behavior of various control schemes is evaluated in this test as the DC-link voltage is regulated from 320 V to 350 V. Figs. 3–4 show the corresponding response waveforms including the DC-link voltage, d-axis current, and grid currents. Both the high-gain PI method and the proposed strategy exhibit fast dynamic response for the DC-link voltage, with a similar settling time (<8 ms). However, the transient d-axis current of the high-gain PI exceeds the safety threshold. Correspondingly, the grid currents exceed the safety threshold, see Fig. 4(b). This situation could result in equipment shutdown due to over-current protection and potentially lead to a risk of hardware damage. In contrast, the proposed strategy effectively limits the current amplitude

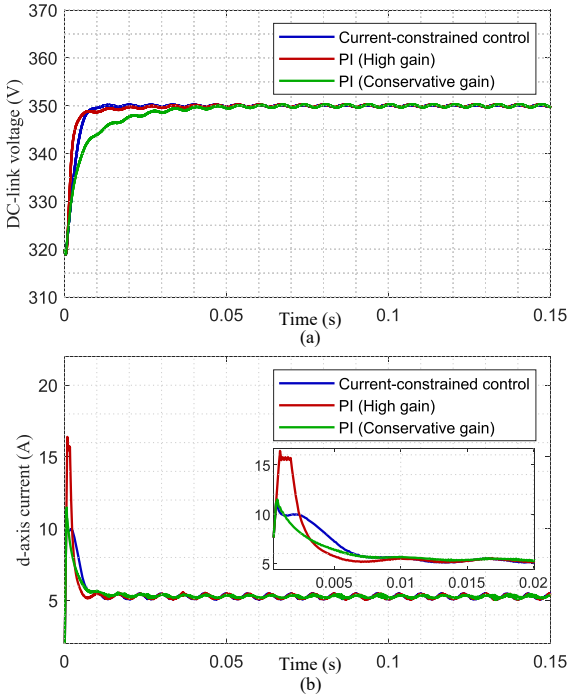

Fig. 3: DC-link voltage and d-axis current waveforms when the DC-link voltage is regulated from 320 V to 350 V. (a) DC-link voltage; (b) d-axis current.

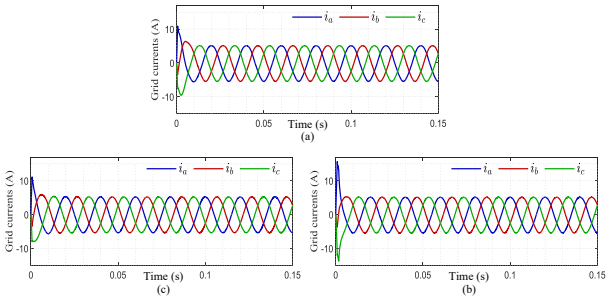

Fig. 4: Grid currents waveforms when the DC-link voltage is regulated from 320 V to 350 V. (a) Current-constrained control; (b) PI (High gain); (c) PI (Conservative gain).

while delivering a rapid voltage response. Employing a conservative gain to adjust the transient current of the PI method to match the proposed strategy will significantly slow down the DC-link voltage response, resulting in a settling time of 30 ms.

4.2 Load Disturbances

In this case, the load R_L changes from 100 Ω to 60 Ω to verify the dynamic performance against load disturbances. Figs. 5(a) and (b) display the response waveforms of the DC-link voltage and the d-axis current, respectively. All three methods restore the DC-link voltage to its reference value after load disturbances, but they exhibit distinct dynamic responses. Compared to the high-gain and conservative-gain PI methods, the proposed current-constrained control strategy exhibits faster dynamic response speed and smaller voltage drop. At the same time, there is no violation of the current constraint.

Recently, the fully actuated system approach has liberated

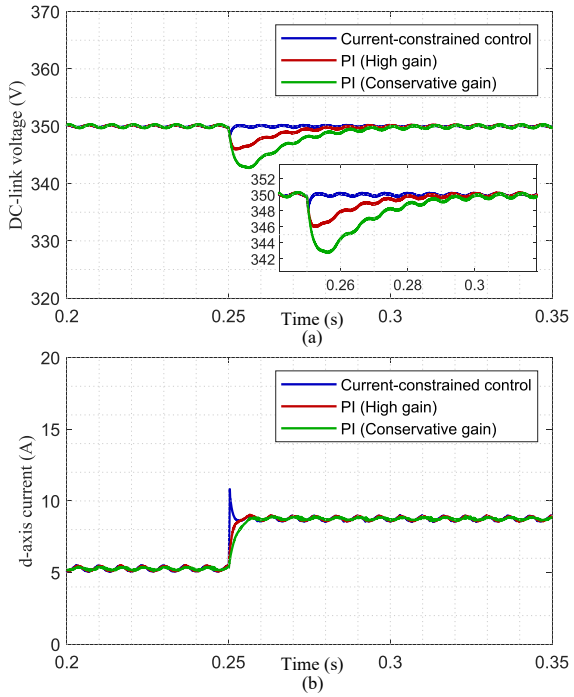

Fig. 5: DC-link voltage and d-axis current waveforms when the load changes from 100 Ω to 60 Ω. (a) DC-link voltage; (b) d-axis current.

itself from the constraints of state-space models and demonstrated superiority in handling nonlinearities and time-delays [10, 11]. In the future, the author will attempt to employ the fully actuated system approaches to address the control issues of converters with current constraints.

5 Conclusion

This paper has proposed a simple current-constrained voltage control strategy for three-phase AC/DC converters. Initially, an error dynamic system of the converter was built and the current constraint issue is transformed into limitation on the tracking error of the d-axis current. Subsequently, a single-loop controller with nonlinear variable gain was designed to regulate the DC-link voltage to its reference. The grid current was restricted within a safe threshold through automatic regulation of the nonlinear gain. Theoretical analysis and test results demonstrated the effectiveness and superiority of the proposed control strategy.

Appendix

In the test, two sets of PI parameters used for comparisons are given as follows:

Hign gain parameters: $K_{PV} = 0.6$, $K_{IV} = 80$, $K_{PI} = 60$, $K_{PI} = 80$, and $K_{II} = 750$;

Conservative gain parameters: $K_{PV} = 0.4$, $K_{IV} = 50$, $K_{PI} = 60$, and $K_{II} = 700$.

References

[1] L. Wu, J. Liu, S. Vazquez, and S. K. Mazumder, "Sliding mode control in power converters and drives: A review," *IEEE/CAA Journal of Automatica Sinica*, vol. 9, no. 3, pp. 392–406, 2022.

[2] T. Wang, Z. Q. Zhu, N. M. A. Freire, D. A. Stone, and M. P. Foster, "Generalized predictive dc-link voltage control for grid-connected converter," *IEEE Journal of Emerging and Selected Topics in Power Electronics*, vol. 10, no. 2, pp. 1489–1506, 2022.

[3] H. Lin, Y. Yin, X. Shen, A. M. Alcaide, J. Liu, J. I. Leon, S. Vazquez, L. G. Franquelo, and L. Wu, "Fuzzy logic system-based sliding-mode control for three-level NPC converters," *IEEE Transactions on Transportation Electrification*, vol. 8, no. 3, pp. 3307–3319, 2022.

[4] Y. Jiang, C. Qin, X. Xing, X. Li, and C. Zhang, "A hybrid passivity-based control strategy for three-level T-type inverter in LVRT operation," *IEEE Journal of Emerging and Selected Topics in Power Electronics*, vol. 8, no. 4, pp. 4009–4024, December 2020.

[5] C. Fu, C. Zhang, G. Zhang, and Q. Su, "Finite-time adaptive fuzzy control for three-phase PWM rectifiers with improved output performance," *IEEE Transactions on Circuits and Systems II: Express Briefs*, vol. 70, no. 8, pp. 3044–3048, 2023.

[6] C. Fu, C. Zhang, G. Zhang, C. Zhang, and Q. Su, "Finite-time command filtered control of three-phase ac/dc converter under unbalanced grid conditions," *IEEE Transactions on Industrial Electronics*, vol. 70, no. 7, pp. 6876–6886, 2023.

[7] T. Guo, Z. Wang, X. Wang, S. Li, and Q. Li, "A simple control approach for buck converters with current-constrained technique," *IEEE Transactions on Control Systems Technology*, vol. 27, no. 1, pp. 418–425, 2019.

[8] J. Lin, M. Su, W. Xiong, S. Xie, Y. Sun, and Y. Zhang, "Conductance emulating control strategy for three-phase current source rectifier under unbalanced grid voltages," *IEEE Transactions on Circuits and Systems II: Express Briefs*, vol. 69, no. 6, pp. 2837–2841, 2022.

[9] H. K. Khalil, *Nonlinear systems*, 3rd ed. Englewood Cliffs, NJ, USA: Prentice-Hall: Pearson, 2002.

[10] G. Duan, "High-order fully actuated system approaches: Part I. Models and basic procedure," *International Journal of Systems Science*, vol. 52, no. 2, pp. 422–435, 2021.

[11] ——, "High-order fully actuated system approaches: Part II. Generalized strict-feedback systems," *International Journal of Systems Science*, vol. 52, no. 3, pp. 437–454, 2021.

Proceedings of the 3rd Conference on Fully Actuated System Theory and Applications
May 10-12, 2024, Shenzhen, China

Integrated Guidance and Control Design Subject to Actuator Saturation Based on Fully Actuated System Approach

Lin Yang[1], Yuanlong Li[1]*

1. Department of Automation, Shanghai Jiao Tong University, and Key Laboratory of System Control and Information Processing, Ministry of Education of China, and Shanghai Engineering Research Center of Intelligent Control and Management, Shanghai 200240, P. R. China
E-mail: yanglin123@sjtu.edu.cn, liyuanlong0301@sjtu.edu.cn

Abstract: Based on fully actuated system approach, this paper proposes a design scheme for integrated guidance and control systems subject to actuator saturation. By elimination elevation-order way, the integrated guidance and control model in the pitch channel is transformed into a high-order fully actuated system with uncertain disturbances and actuator saturation. Firstly, a disturbance observer is constructed to estimate the disturbances generated by model nonlinearities, unknown target maneuvers, variations of aerodynamic parameters, etc. Then, an observer-based fully actuated controller is designed to stabilize the integrated guidance and control system and perform disturbance attenuation. Since the missile's deflection angle for pitch control is constrained by actuator saturation, an anti-windup compensator is introduced into the designed fully actuated controller to reduce the negative impact of saturation. Moreover, the stability conditions of the closed-loop system are established by the Lyapunov stability theory and the invariant set principle. Finally, a numerical simulation is provided to verify the effectiveness of the proposed design scheme.

Key Words: Fully Actuated System Approach, Integrated Guidance and Control, Actuator Saturation, Anti-windup Compensator

1 Introduction

Integrated guidance and control (IGC) design has become the mainstream solution to the missile-target interception [1]. The strategy of IGC design considers the guidance loop and the control loop as a whole. According to the missile's dynamics and the relative kinematics between missile and target, the control input of missile is directly designed to realize the target interception. Based on the sliding-mode control approach, Reference [2] proposed an adaptive sliding mode IGC design scheme that can adaptively estimate the upper bound of the uncertainties existing in system, thereby achieving robust tracking of the missile to the target. In [3], the IGC model is transformed into a linear system with uncertain disturbances, and a disturbance observer-based controller is designed to implement the guidance and control of missile. In [4], the unknown states and uncertain disturbances existing in IGC system are estimated by constructing an extended observer, and an observer-based backstepping control strategy is presented to robustly stabilize the system.

Even though the control approaches mentioned above have achieved many valuable results in IGC design, these approaches generally have some shortcomings, such as complex design process of controller, harsh stability conditions, and high requirements for model accuracy. Recently, Reference [5] pioneered the fully actuated system approach for nonlinear control problems. Based on the fully actuated system approach, the controller can be directly designed according to the characteristic structure of the desired closed-loop system, greatly reducing the design complexity of nonlinear controllers. Nowadays, the fully actuated system approach is mainly applied in the attitude and orbit control of spacecraft [6, 7], and is rarely applied in IGC design. Based on the fully actuated system approach, Reference [8] designed a three-dimensional interception guidance law for the missile system subject to the terminal impact-angle constraint. However, Reference [8] only considers the guidance process and does not consider the missile control issues.

On the other hand, since the physical limitation of missile's control surface, the deflection angle for pitch control will be constrained by saturated actuator. An effective method for handling actuator saturation is anti-windup design [9], also known as the two-step method. The first step is to design a controller without considering actuator saturation, and the second step is to design a compensator to alleviate the negative impact of saturation. Since the compensator is not functional if the actuator is not saturated, the performance of the nominal system is not affected by the compensator. Moreover, the introduction of anti-windup compensator will not modify the designed controller gain, so this method is able to deal with the saturated control problem of high-order fully actuated system (HOFAS).

Based on the above discussions, this paper studies the IGC design problem with actuator saturation through the fully actuated system approach. Firstly, the two-dimensional IGC model in the pitching channel is established, and further is transformed into a HOFAS by elimination elevation-order way. Secondly, a disturbance observer is constructed to estimate the disturbances caused by the aerodynamic parameters, model nonlinearities and target unknown maneuvers, and an observer-based fully actuated controller is designed to stabilize the HOFAS. Finally, an anti-windup compensator is introduced into the designed fully actuated controller to reduce the negative impact of actuator saturation on system performance. The stability of the closed-loop system is guaranteed by a set of matrix inequalities.

The remainder of this paper is organized as follows. Section 2 gives the IGC model. In Section 3, the control scheme is presented and the stability of the closed-loop system is analyzed. In Section 4, the effectiveness of the proposed method is validated by a numerical simulation. Section 5 concludes this paper.

This work is supported by the Science Center Program of National Natural Science Foundation of China under Grant Nos. 62188101 and National Natural Science Foundation of China under Grant Nos. 62373249.

2 Model Derivation

During the endgame phase, the missile's guidance and control problem can be treated as a planar one, and the corresponding geometric structure of missile-target engagement is shown in Fig. 1. The coordinate systems O-X_IZ_I and O-$X_{II}Z_{II}$ represent the inertial reference frame and the line-of-sight (LOS) reference frame respectively, where the LOS reference frame is defined to be rotated from the inertial reference frame by q_0. M and T denote the missile and the target, respectively. R is the relative distance between the missile and the target, z is the lateral distance between the missile and the target perpendicular to the X_{II}-axis, and q is the LOS angle. The velocities of the missile and the target are V_M and V_T, their accelerations are a_M and a_T, and their flight path angles are θ_M and θ_T. In addition, a_{MN} and a_{TN} represent the acceleration normal to the LOS of the missile and the target, respectively.

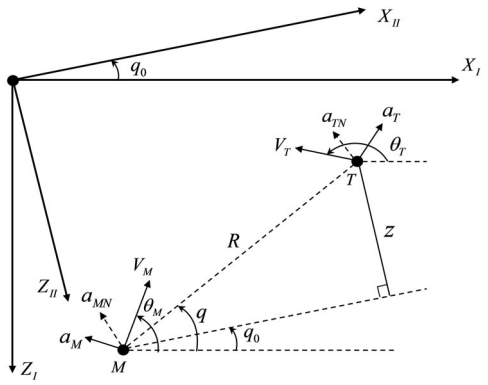

Fig. 1: Geometric structure of missile-target engagement

Letting $z_1 = z$ and $z_2 = \dot{z}$, the relative kinematics equation between the missile and the target is modeled as

$$\begin{cases} \dot{z}_1 = z_2, \\ \dot{z}_2 = a_T \cos(\theta_T - q_0) - a_M \cos(\theta_M - q_0), \\ \dot{\theta}_M = a_M / V_M, \\ \dot{\theta}_T = a_T / V_T. \end{cases} \tag{1}$$

Based on the model in [3], the dynamics equation of the missile is described as

$$\begin{cases} \alpha = \vartheta - \theta_M, \\ \dot{\alpha} = \frac{1}{mV_M}(mg\cos\theta_M - Y) + \omega_z + d_\alpha, \\ \dot{\vartheta} = \omega_z, \\ J_z\dot{\omega}_z = M_0 + M_{\delta_z}\delta_z + J_z d_{\omega_z}, \end{cases} \tag{2}$$

where α, ϑ and ω_z are the attack angel, the pitch angel and the pitch angular rate, respectively. m is the missile mass, g is the gravitational acceleration and Y is the lift force. J_Z is the moment of inertia about Z_{II}-axis, and δ_z is the deflection angle for pitch control. d_α and d_{ω_z} are the bounded uncertainties caused by unknown target maneuver, unmodeled dynamics and external disturbances. $M_0 = M_\alpha\alpha + M_{\omega_z}\omega_z$ is the pitch angular acceleration generated by the attack angle and pitch angle. The lift force Y and these parameters M_α, M_{ω_z} and M_{δ_z} have the following form

$$\begin{cases} Y = 57.3QS\left(L_\alpha\alpha + L_{\delta_z}\delta_z\right), \\ M_\alpha = 57.3QSm_z^\alpha, \\ M_{\omega_z} = QSL^2 m_z^\alpha / V_M, \\ M_{\delta_z} = 57.3QSLm_z^{\delta_z}, \end{cases}$$

where $Q = 0.5\rho V_M^2$ is the dynamic pressure, S is the aerodynamics reference area, and L is the aerodynamics reference length. L_α and L_{δ_z} are the derivatives of the lift force with respect to α and δ_z, respectively. Moreover, m_z^α, $m_z^{\omega_z}$ and $m_z^{\delta_z}$ are the derivatives of the pitch moment with respect to α, ω_z and δ_z. Without loss of generality, it is assumed that the aerodynamic force generated by the deflection angle is negligible and the nonlinearities are treated as bounded uncertainties. Denoting $z_3 = \alpha$, $z_4 = \omega_z$, $b = M_{\delta_z}$ and $u = \delta_z$, it follows from equations (1) and (2) that the IGC model can be represented by the following system

$$\begin{cases} \dot{z}_1 = z_2, \\ \dot{z}_2 = a_{23}z_3 + d_2, \\ \dot{z}_3 = a_{33}z_3 + z_4 + d_3, \\ \dot{z}_4 = a_{43}z_3 + a_{44}z_4 + bu + d_4, \end{cases} \tag{3}$$

where

$$\begin{aligned} a_{23} &= -57.3QSL_\alpha\cos(\theta_M(0) - q_0)/m, \\ a_{33} &= -57.3QSL_\alpha/mV_M, \\ a_{43} &= 57.3QSLm_z^\alpha/J_z, \\ a_{44} &= QSL^2 m_z^{\omega_z}/J_z V_M, \\ d_2 &= \left(\cos(\theta_M - q_0) - \cos(\theta_{M0} - q_0)\right)V_M a_{33} z_3 \\ &\quad + \cos(\theta_M - q_0)V_M d_3 + \cos(\theta_T - q_0)a_T, \\ d_3 &= g\cos\theta_M/V_M + d_\alpha, \\ d_4 &= d_{\omega_z}, \\ b &= 57.3QSLm_z^{\delta_z}/J_z. \end{aligned}$$

To complete the IGC design, we give the following assumptions.

Assumption 1. *During the endgame phase, the missile does not have engine thrust, that is, the velocity V_M is constant.*

Assumption 2. *Since the physical limitation of actuator, the deflection angle for pitch control will be constrained by the executable displacement of rudder surface. Assume that the actual control input of system (3) is defined by*

$$\mathrm{sat}(u) = \begin{cases} u_{\lim}, & u \geq u_{\lim}, \\ -u_{\lim}, & u \leq -u_{\lim}, \\ u, & u_{\lim} > u > -u_{\lim}, \end{cases}$$

where $u_{\lim}$ is the maximum amplitude of actuator.

Assumption 3. *The disturbances $d_i(t)$ and their arbitrary-order time derivatives are bounded, namely, there exist constants $d_{ij}^{\max} > 0$ such that*

$$\left|\frac{d^j d_i(t)}{dt^j}\right| \leq d_{ij}^{\max},\ i = 2,3,4,\ j = 0,1,2\cdots$$

The IGC model (3) is a first-order under-actuated system, which can be converted to a HOFAS by elimination

elevation-order way. Calculating the second order, third order and fourth order derivatives of z_1 yields that

$$\begin{cases} z_1^{(2)} = a_{23}z_3 + d_2, \\ z_1^{(3)} = a_{23}\left(a_{33}z_3 + z_4 + d_3\right) + \dot{d}_2, \\ z_1^{(4)} = a_{23}[a_{33}\left(a_{33}z_3 + z_4 + d_3\right) + a_{43}z_3 \\ \qquad + a_{44}z_4 + b\,\mathrm{sat}(u) + d_4 + \dot{d}_3] + d_2^{(2)}. \end{cases} \tag{4}$$

It follows from equations (3) and (4) that

$$\begin{cases} z_2 = \dot{z}_1, \\ z_3 = \dfrac{z_1^{(2)} - d_2}{a_{23}}, \\ z_4 = \dfrac{z_1^{(3)} - \dot{d}_2}{a_{23}} - a_{33}\dfrac{z_1^{(2)} - d_2}{a_{23}} - d_3. \end{cases} \tag{5}$$

According to equations (4) and (5), the states z_2, z_3 and z_4 can be replaced by the functions related to $z_1^{(i)}$, and a high-order model of z_1 is described by

$$\begin{aligned} z_1^{(4)} =& \left(a_{33} + a_{44}\right) z_1^{(3)} + \left(a_{43} - a_{33}a_{44}\right) z_1^{(2)} + d_2^{(2)} \\ & - \left(a_{33} + a_{44}\right) \dot{d}_2 + \left(a_{44}a_{33} - a_{43}\right) d_2 + a_{23}\dot{d}_3 \\ & + a_{23}d_4 - a_{44}a_{23}d_3 + a_{23}b\,\mathrm{sat}(u). \end{aligned} \tag{6}$$

Letting $a_0 = a_1 = 0$, $a_2 = a_{43} - a_{33}a_{44}$, $a_3 = a_{33} + a_{44}$, $\hat{b} = a_{23}b$ and $d = \ddot{d}_2 - \left(a_{33} + a_{44}\right)\dot{d}_2 + \left(a_{44}a_{33} - a_{43}\right) d_2 + a_{23}\dot{d}_3 + a_{23}d_4 - a_{44}a_{23}d_3$, system (6) is rewritten as the following standard HOFAS

$$z_1^{(4)} = \sum_{i=0}^{3} a_i z_1^{(i)} + \hat{b}\,\mathrm{sat}(u) + d. \tag{7}$$

3 Main Results

The IGC design mainly includes three steps. In the first step, we construct a disturbance observer to estimate the bounded disturbance d. In the second step, an observer-based fully actuated controller is designed to stabilize system (7) and perform disturbance attenuation. In the third step, an anti-windup compensator is introduced into the designed fully actuated controller to reduce the negative impact of saturation.

Step 1. Considering HOFAS (7), we design a disturbance observer as

$$\begin{cases} \hat{d} = \delta + \mu z_1^{(3)},\ \delta(0) = -\mu z_1^{(3)}(0), \\ \dot{\delta} = -\mu^2 z_1^{(3)} - \mu\left(\delta + \sum_{i=0}^{3} a_i z_1^{(i)} + \hat{b}\,\mathrm{sat}(u)\right), \end{cases} \tag{8}$$

where $\mu > 0$ is the observer gain and δ is the observer variable. The estimation error is defined by $\tilde{d} = d - \hat{d}$, and the error dynamic equation is computed by

$$\begin{aligned} \dot{\tilde{d}} &= \dot{d} - \dot{\hat{d}} \\ &= \dot{d} - \left(\dot{\delta} + \mu z_1^{(4)}\right) \\ &= \dot{d} - \mu\left(z_1^{(4)} - \mu z_1^{(3)} - \left(\delta + \sum_{i=0}^{3} a_i z_1^{(i)} + \hat{b}\,\mathrm{sat}(u)\right)\right) \\ &= \dot{d} - \mu\tilde{d}. \end{aligned} \tag{9}$$

It can be obtained from equation (9) that if the disturbance d is constant (i.e., $\dot{d} = 0$), the estimation error $\tilde{d}$ will converge to 0. If the disturbance d is time-varying, there exists a scalar $\tilde{d}_{\max} \geq 0$ such that $|\tilde{d}| \leq \tilde{d}_{\max}$ due to the assumption that $\dot{d}$ is bounded.

Step 2. Based on observer (8), a fully actuated controller involving disturbance estimation is designed as

$$\begin{cases} u = -\hat{b}^{-1}\left(\sum_{i=0}^{3} a_i z_1^{(i)} + v + \hat{d}\right), \\ v = \sum_{i=0}^{3} k_i z_1^{(i)}, \end{cases} \tag{10}$$

where k_i is the feedback gain to be designed.

Step 3. In order to reduce the negative impact of saturation, an anti-windup compensator $\eta = -\lambda\xi$ is introduced into controller (10), where $\lambda \geq 0$ is a scalar and $\xi = u - \mathrm{sat}(u)$. Then, controller (10) becomes

$$\begin{cases} u = -\hat{b}^{-1}\left(\sum_{i=0}^{3} a_i z_1^{(i)} + v + \hat{d}\right) - \lambda\xi, \\ v = \sum_{i=0}^{3} k_i z_1^{(i)}. \end{cases} \tag{11}$$

Under controller (11), we can obtain the closed-loop system in the following form

$$z_1^{(4)} = -\sum_{i=0}^{3} k_i z_1^{(i)} - \hat{b}(1+\lambda)\xi + \tilde{d}. \tag{12}$$

In what follows, we will give the parametric design method of feedback gain k_i such that the nominal closed-loop system have the desired characteristic structure. Denoting $x = [z_1\ \dot{z}_1\ z_1^{(2)}\ z_1^{(3)}]^{\mathrm{T}}$, system (12) is equivalent to

$$\begin{cases} \dot{x} = \Phi\left(k_{0\sim3}\right) x - B\xi + E\tilde{d}, \\ u = -\hat{b}^{-1}(Kx + \hat{d}), \end{cases} \tag{13}$$

where

$$\begin{aligned} &\Phi\left(k_{0\sim3}\right) = \begin{bmatrix} 0 & 1 & 0 & 0 \\ 0 & 0 & 1 & 0 \\ 0 & 0 & 0 & 1 \\ -k_0 & -k_1 & -k_2 & -k_3 \end{bmatrix}, \\ &B = \begin{bmatrix} 0_{1\times3} & \hat{b} \end{bmatrix}^{\mathrm{T}},\quad E = \begin{bmatrix} 0_{1\times3} & 1 \end{bmatrix}^{\mathrm{T}}, \\ &K = \begin{bmatrix} k_0 & k_1 & k_2 + a_2 & k_3 + a_3 \end{bmatrix}. \end{aligned}$$

Lemma 1. *[10] Assume that there exists matrices F, $V \in R^{4\times4}$ satisfying $\Phi(k_{0\sim3})V = VF$, then the feedback gain k_i can be computed by*

$$\begin{bmatrix} k_0 & k_1 & k_2 & k_3 \end{bmatrix} = -ZF^4V^{-1}, \tag{14}$$

where $Z \in R^{1\times4}$ satisfies $\det(V) \neq 0$ with

$$V = V(Z,F) = \begin{bmatrix} Z \\ ZF \\ ZF^2 \\ ZF^3 \end{bmatrix}.$$

Since the missile does not have engine thrust during the endgame phase, to reduce the requirement on acceleration, the following desired control performance is taken into account: the LOS angle q converges slowly to the expected value, and the LOS angular rate $\dot{q}$ converges quickly to 0. Therefore, the desired closed-loop poles are selected as $s_1 = -\rho_1$, $s_2 = -\rho_2$ and $s_3, s_4 = -\rho_3 \pm jv$, where $\rho_3 > \rho_2 > \rho_1 > 0$. Thus, matrix F is determined by

$$F = \mathrm{diag}\left\{-\rho_1, -\rho_2, \begin{bmatrix} -\rho_3 & -v \\ v & -\rho_3 \end{bmatrix}\right\}.$$

Based on the results in Lemma 1, letting $Z = [1 \;\; 1 \;\; 1 \;\; 1]$, substituting the expressions of Z and F into (14) yields

$$\begin{aligned} k_0 &= \rho_1\rho_2\rho_3^2 + \rho_1\rho_2/25, \\ k_1 &= \rho_1/25 + \rho_2/25 + \rho_1\rho_3^2 + \rho_2\rho_3^2 + 2\rho_1\rho_2\rho_3, \\ k_2 &= \rho_1\rho_2 + 2\rho_1\rho_3 + 2\rho_2\rho_3 + \rho_3^2 + 1/25, \\ k_3 &= \rho_1 + \rho_2 + 2\rho_3. \end{aligned}$$

Meanwhile, the feedback gain matrix K is

$$\begin{aligned} K = \big[&\rho_1\rho_2\rho_3^2 + \rho_1\rho_2/25,\ \rho_1/25 + \rho_2/25 + \rho_1\rho_3^2 \\ &+ \rho_2\rho_3^2 + 2\rho_1\rho_2\rho_3,\ \rho_1\rho_2 + 2\rho_1\rho_3 + 2\rho_2\rho_3 \\ &+\rho_3^2 + 1/25 + a_2,\ \rho_1 + \rho_2 + 2\rho_3 + a_3\big]. \end{aligned}$$

Using the parametric design method in Lemma 1, we can obtain the feedback gain K such that the closed-loop matrix $\Phi(k_{0\sim3})$ is Hurwitz. However, the closed-loop system (13) may still be unstable due to the existence of q and $\tilde{d}$. In the following parts, we will give the stability conditions of the closed-loop system (13). Given that d and $\tilde{d}$ are bounded, the disturbance estimation $\hat{d}$ is also bounded, so there exists a scalar $\hat{d}_{\max} \geq 0$ such that $|\hat{d}| \leq \hat{d}_{\max}$. The saturation constraint $|u| \leq u_{\max}$ implies $|Kx| \leq u_{\lim}^* = |\hat{b}|u_{\lim} - \hat{d}_{\max}$. To ensure that the control input u is bounded, a time-varying saturation coefficient $g(t)$ is employed to describe the nonlinear saturation function $\mathrm{sat}(u)$, i.e., $\mathrm{sat}(u) = g(t)u$, where

$$g(t) = \begin{cases} 1, & |Kx| \leq u_{\lim}^*, \\ u_{\lim}/|u|, & |Kx| > u_{\lim}^*. \end{cases}$$

Assume that there exists a scalar $g_d \in (0,\ 1]$ satisfying $|u| \leq u_{\lim}/g_d$, then we have $g \in [g_d,\ 1]$. The actuator saturation constraint can be transformed into the following constraint on state space

$$|Kx| \leq \hat{b}u_{\lim}\left(1 + \lambda\left(1 - g_d\right)\right)/g_d - \hat{d}_{\max}.$$

Thus, the feasible set of the system state is determined by $\mathcal{L}(H) = \left\{x \in R^4 : |Hx| \leq 1\right\}$, where

$$H = \frac{Kg_d}{\hat{b}u_{\lim}\left(1 + \lambda\left(1 - g_d\right)\right) - \hat{d}_{\max}g_d}.$$

Selecting a Lyapunov function $V = (x^{\mathrm{T}}x + \tilde{d}^{\mathrm{T}}\tilde{d})/2$, its a level set is defined by $\varepsilon(\rho) = \{V \in R : V \leq \rho\}$. Similarly, we also define another level set as $\varepsilon(\rho^*) = \{x \in R^4 : x^{\mathrm{T}}x \leq \rho^*\}$, where $\rho^* = 2\rho - \tilde{d}_{\max}^2$. It is obvious that $\varepsilon(\rho^*) \subseteq \varepsilon(\rho)$.

Lemma 2. *[11] The constraint $|u| \leq u_{\lim}/g_d$ can be interpreted into a sector nonlinearity condition. Denoting $S = 1 - g_d$, the following inequality holds*

$$q^{\mathrm{T}}M(Su - \xi) \geq 0, \;\; \forall M > 0. \tag{15}$$

Theorem 1. *Under the saturation constraints characterized by the polyhedron $\mathcal{L}(H)$, the closed-loop system (13) is uniform ultimate bounded within the invariant set $\varepsilon(\rho)$, if there exists a observer gain $\mu > 0$ and a compensator gain $\lambda > 0$ such that*

$$\begin{bmatrix} 1 & \rho^*H \\ \rho^*H^T & \rho^*I_4 \end{bmatrix} > 0, \tag{16}$$

$$\Phi + \frac{1}{2}\left((1+\lambda)BB^T + \left(1 + \hat{b}^{-1}MS + \gamma\right)I\right) < 0, \tag{17}$$

$$1 + \lambda - 2M(1 + \lambda S) + \hat{b}^{-1}MS\left(KK^T + 2\right) < 0, \tag{18}$$

$$1 + E^TE + \hat{b}^{-1}MS - 2\mu + \gamma < 0, \tag{19}$$

where $\gamma > 0$ is a scalar. Furthermore, the system state can converge to an arbitrarily small bounded region by increasing the scalar γ.

Proof. Given the quadratic Lyapunov function $V = (x^{\mathrm{T}}x + \tilde{d}^{\mathrm{T}}\tilde{d})/2$, its time derivative is computed by

$$\begin{aligned} \dot{V} = {} & x^T\Phi x - x^TB(1+\lambda)\xi + x^TE\tilde{d} \\ & - \mu\tilde{d}^T\tilde{d} + \tilde{d}^T\dot{d}. \end{aligned} \tag{20}$$

Based on inequality (15) in Lemma 2, it follows from equation (20) that

$$\begin{aligned} \dot{V} \leq {} & x^T\Phi x - x^TB(1+\lambda)\xi + x^TE\tilde{d} - \mu\tilde{d}^T\tilde{d} \\ & + \tilde{d}^T\dot{d} + \xi^TM(Su - \xi). \end{aligned} \tag{21}$$

Substituting $u = -\hat{b}^{-1}(Kx + \hat{d}) - \lambda\xi$ and $\hat{d} = d - \tilde{d}$ into inequality (21) yields that

$$\begin{aligned} \dot{V} \leq {} & x^T\Phi x - x^TB(1+\lambda)\xi + x^TE\tilde{d} - \hat{b}^{-1}MS\xi^TKx \\ & - M(\lambda S + 1)\xi^T\xi + \hat{b}^{-1}MS\xi^T\tilde{d} - \hat{b}^{-1}MS\xi^Td \\ & - \mu\tilde{d}^T\tilde{d} + \tilde{d}^T\dot{d}. \end{aligned} \tag{22}$$

In view of Young's inequality, we have

$$-(1+\lambda)x^TB\xi \leq \frac{1+\lambda}{2}\left(x^TBB^Tx + \xi^T\xi\right), \tag{23}$$

$$x^TE\tilde{d} \leq \frac{1}{2}\left(x^Tx + \tilde{d}^TE^TE\tilde{d}\right), \tag{24}$$

$$-\hat{b}^{-1}MS\xi^TKx \leq \frac{1}{2}\hat{b}^{-1}MS\left(x^Tx + \xi^TKK^T\xi\right), \tag{25}$$

$$\hat{b}^{-1}MS\xi^T\tilde{d} \leq \frac{1}{2}\hat{b}^{-1}MS\left(\xi^T\xi + \tilde{d}^T\tilde{d}\right), \tag{26}$$

$$-\hat{b}^{-1}MS\xi^Td \leq \frac{1}{2}\hat{b}^{-1}MS\left(\xi^T\xi + d^Td\right), \tag{27}$$

$$\tilde{d}^T\dot{d} \leq \frac{1}{2}\left(\tilde{d}^T\tilde{d} + \dot{d}^T\dot{d}\right). \tag{28}$$

Combining equalities (22)-(28), it is obtained that

$$\begin{aligned} \dot{V} \leq {} & x^TQ_1x + \xi^TQ_2\xi + \tilde{d}^TQ_3\tilde{d} \\ & + \frac{1}{2}\hat{b}^{-1}MSd^Td + \frac{1}{2}\dot{d}^T\dot{d}, \end{aligned} \tag{29}$$

where

$$Q_1 = \Phi + \frac{1}{2}\left[(1+\lambda)BB^T + 1 + \hat{b}^{-1}MS\right]I,$$
$$Q_2 = \frac{1}{2}\left[1+\lambda-2M(1+\lambda S)+\hat{b}^{-1}MS(KK^T+2)\right],$$
$$Q_3 = \frac{1}{2}\left(1+E^TE+\hat{b}^{-1}MS-2\mu\right).$$

It follows inequalities (17)-(19) that $Q_1 < -\gamma I/2$, $Q_2 < 0$ and $Q_3 < -\gamma/2$. Moreover, according to the assumption that the disturbance d and its derivative $\dot{d}$ are bounded, there exists a constant C such that

$$\hat{b}^{-1}MSd^Td + \dot{d}^T\dot{d} \le C. \tag{30}$$

It can be inferred form inequalities (29) and (30) that

$$\dot{V} \le -\gamma V + C. \tag{31}$$

We can derive from inequality (31) that $\dot{V} < 0$ if $\gamma > C/\rho$ and $V(0) = \rho$. Thus, the level set $\varepsilon(\rho)$ is an invariant set, and further it can be concluded that $\varepsilon(\rho^*)$ is an invariant set. Moreover, inequality (17) is equivalent to $\varepsilon(\rho^*) \subseteq \mathcal{L}(H)$, which implies that the system state will remain within the feasible set $\mathcal{L}(H)$ if the initial state is within the level set $\varepsilon(\rho^*)$. Based on the comparison lemma, inequality (31) is equivalent to

$$0 \le V(t) \le \frac{C}{\gamma} + \left(V(0) - \frac{C}{\gamma}\right)e^{-\gamma t}. \tag{32}$$

Furthermore, it can be derived from inequality (32) that

$$\|x\| \le \sqrt{\frac{2C}{\gamma} + 2\left(V(0) - \frac{C}{\gamma}\right)e^{-\gamma t}}. \tag{33}$$

It is concluded from inequality (33) that the state x can converge to an arbitrarily small bounded region by increasing the value of γ. □

4 Numerical Simulation

According to the model in [3], the corresponding aerodynamic parameters of the missile are as follows

$$\frac{-57.3QSc_y^{\alpha}}{mV_M} = -0.3487, \quad \frac{57.3QSLm_z^{\alpha}}{J_z} = 17.801,$$
$$\frac{QSL^2m_z^{\omega_z}}{J_zV_M} = -0.2741, \quad \frac{57.3QSLm_z^{\delta_z}}{J_z} = -31.267.$$

Consider that the deflection angle for control is constrained by $|\delta_z| \le 10^\circ$ and the known maneuver of target is $a_t = 0$. The initial states of missile and target are shown in Table 1.

Table 1: The initial states of missile and target

Distance	**LOS angle**	**Missile velocity**	**Target velocity**
R_0	q_0	V_{M0}	V_{T0}
$10Km$	20°	$500m/s$	$250m/s$
Attack angel	**Pitch angel of missile**	**Pitch angel of target**	**Pitch rate of missile**
α_0	θ_{M0}	θ_{T0}	ω_{z0}
0°	45°	125°	$0\ ^\circ/s$

Based on the proposed parametric design method of feedback gain, the desired closed-loop eigenvalues are chosen as $s_1 = -1$, $s_2 = -2$ and $s_{3,4} = -4 \pm j$, and the feedback gain matrix is calculated as $K = [34\ 67\ 60.8966\ 11.6228]$. The observer gain is designed as $\mu = 2$, and the simulation is firstly completed with the compensator gain $\lambda = 0$. Fig. 2 shows the relative motion between the missile and the target, indicating that the missile successfully intercepts the target. As shown in Fig. 3, the lateral distance and the lateral acceleration between the missile and the target gradually converge to 0, and the LOS angle remains stable during missile interception. Fig. 4 shows that the attack angle, the pitch angular rate, and the deflection angle of the missile gradually converge to the expected values. Fig. 5 depicts the trajectories of disturbance d and its estimation $\hat{d}$, indicating that the designed disturbance observer can accurately estimate the uncertain disturbance d. From the simulation results, it can be concluded that the proposed IGC design scheme in this paper is effective.

In what follows, to demonstrate the effect of anti-windup compensator on system performance, different compensator gains will be selected for comparative simulation. The compensator gain λ is chosen as 0, 1 and 5, respectively. Fig. 6 and Fig .7 show the lateral distance and the deflection angle for control with different compensator gains. It can be seen from the two figures that compared to $\lambda = 0$, selecting a compensator gain $\lambda = 1$ can effectively improve the transient performance of the closed-loop system and reduce the duration of saturation. Furthermore, as the compensator gain increases to $\lambda = 5$, the transient performance of the closed-loop system is further improved, and the duration of saturation is further reduced. Therefore, the introduction of anti-windup compensator can effectively reduce the negative impact of saturation, and improve the transient performance of closed-loop system.

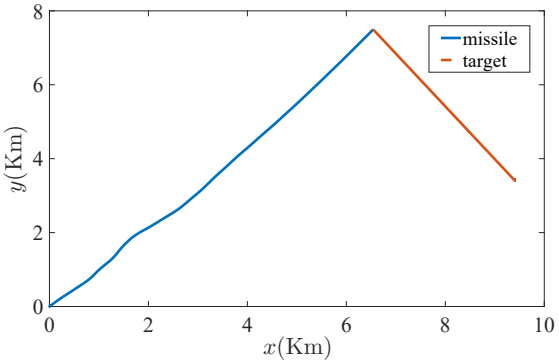

Fig. 2: Missile-target interception geometry.

5 Conclusion

This paper proposes a IGC design scheme that combines disturbance observer, fully actuated controller, and anti-windup compensator. Firstly, the IGC model is established and is further transformed into a HOFAS with disturbances and actuator saturation. Then, a disturbance observer-based controller is designed to stabilize the IGC system. Finally, an anti-windup compensator is introduced to improve the control performance. The effectiveness of the proposed design

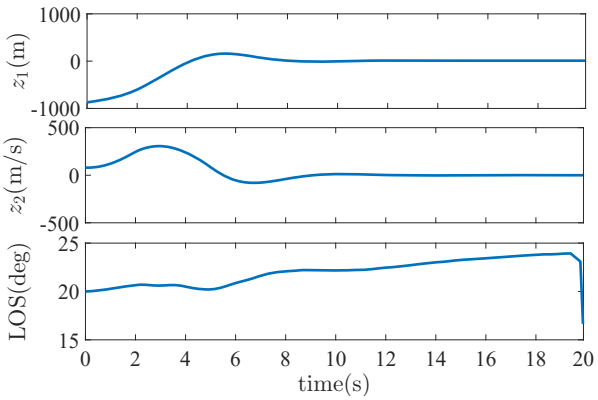

Fig. 3: Missile-target lateral distance, lateral relative velocity and LOS angle.

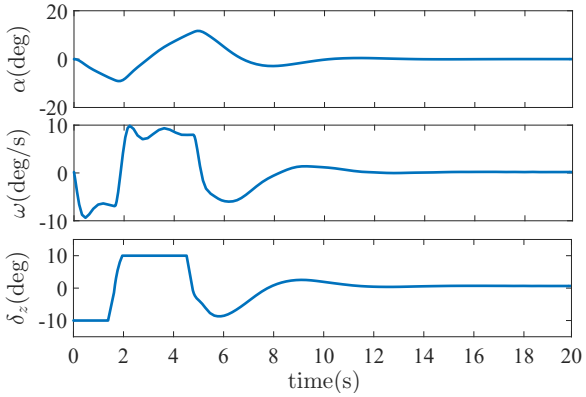

Fig. 4: Attack angle, pitch angular rate and deflection angle of missile.

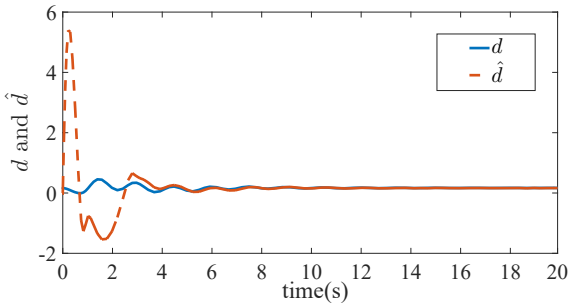

Fig. 5: Disturbance d and its estimation $\hat{d}$.

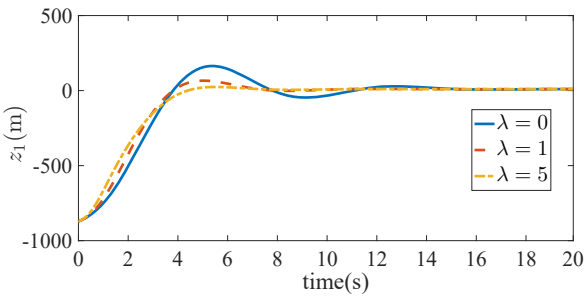

Fig. 6: Lateral distance between missile and target.

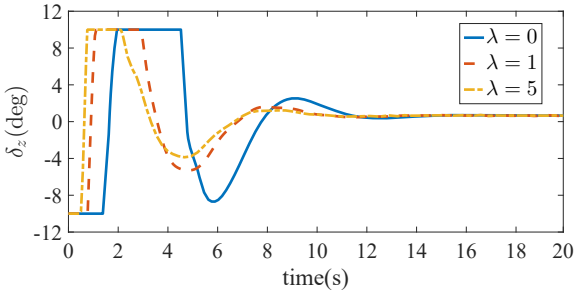

Fig. 7: Deflection angle of missile for control.

scheme is verified through a numerical simulation.

References

[1] D. E. Williams, J. Richman, B. Friedland. Design of an integrated strapdown guidance and control system for a tactical missile. *Proceedings of AIAA Guidance and Control Conference. Gatlinburg. USA: AIAA*, 1983: 57-66.

[2] D. K. Chwa, J. Y. Choi. Adaptive nonlinear guidance law considering control loop dynamics. *IEEE Transactions on Aerospace and Electronic Systems*, 2003, 39(4): 1134-1143.

[3] J. G. Guo, Y. Xiong, J. Zhou. A new sliding mode control design for integrated missile guidance and control system, *Aerospace Science and Technology*, 2018, 78: 54-61.

[4] X. L. Shao, H. L. Wang. Back-stepping active disturbance rejection control design for integrated missile guidance and control system via reduced-order ESO. *ISA Transactions*, 2015, 57:10-22.

[5] G. R. Duan. High-order fully actuated system approaches: Part I. Models and basic procedure. *International Journal of Systems Science*, 2021, 52(2): 422–435.

[6] D. W. Zhang, G. P. Liu, L. Cao. Proportional integral predictive control of high-order fully actuated networked multiagent systems with communication delays. *IEEE Transactions on Systems, Man, and Cybernetics: Systems*, 2022, 53(2): 801–812.

[7] D. W. Zhang, G. P. Liu, L. Cao. Coordinated control of high-order fully actuated multiagent systems and its application: a predictive control strategy. *IEEE/ASME Transactions on Mechatronics*, 2022, 27(6): 4362–4372.

[8] S. W. Chen, W. Wang, J. F. Fan, et al. Impact angle constraint guidance law using fully-actuated system approach. *Aerospace Science and Technology*, 2023, 136: 1270-1285.

[9] G. Grimm, J. Hatfield, I. Postlethwaite, et al. Anti-windup for stable linear systems with input saturation: an LMI-based synthesis. *IEEE Transactions on Automatic Control*, 2003, 48(9): 1509-1525.

[10] G. R. Duan. High-order fully actuated system approaches: Part I. Fully actuated systems and parametric designs. *Acta Automatica*, 2020, 46(7): 1333–1345.

[11] S. Tarbouriech, G. Garcia, J. M. Gomes da Silva. Stability and stabilization of linear systems with saturating actuators. London: *Springer*, 2011.

Proceedings of the 3rd Conference on Fully Actuated System Theory and Applications
May 10-12, 2024, Shenzhen, China

Planned Fully Actuated Attitude Control Strategy for Flexible Spacecraft

Dian Wang[1],Yunhua Wu[1,*], Songjing Ma[1],Xun Zeng[1]

1. College of Astronautics, Nanjing University of Aeronautics and Astronautics, Nanjing 210006
E-mail: yunhuawu@nuaa.edu.cn

Abstract: This paper addresses the problem of attitude control of flexible spacecraft. Considering the nonlinear system under external disturbance and model uncertainty, an attitude controller based on Fully Actuated System (FAS) theory and Sinusoidal angular acceleration attitude path can be designed to achieve the attitude maneuver with minimal residual vibration. Compared to traditional controllers, FAS is often more immune to the nonlinear factors and its control law is easier to design. FAS compound with Extended disturbance observer is designed to achieve the desired linear system when compensating for the lumped disturbance and adverse nonlinearity. Moreover, the planned smooth path can suppress the flexible vibration to great extent. Simulations show that the proposed method is tolerant to the external disturbance. And it can make the modal response superior with fast convergence and small oscillation which means our algorithm can achieve quality dynamic character in a short time. This explores the application of flexible spacecraft control of FAS.

Key Words: Flexible Spacecraft, Attitude Control, Fully Actuated System, Attitude path planning, Extended disturbance observer

1 Introduction

Due to the dynamic interactions between rigid motion and flexible deformation, unlike rigid spacecraft, flexible spacecraft exhibit structural vibrations and mode couplings that must be carefully managed to achieve precise attitude control and stabilization. The demand for agile spacecraft has led to advancements in attitude control systems, particularly for flexible structures such as solar arrays, which deform elastically as the spacecraft maneuvers and is exposed to environmental disturbances.

For the attitude control of flexible spacecraft, in the state space approach, the high-dimensional state space model corresponding to the rigid body motions and elastic modes is difficult to compute, the nonlinear dynamics of the under-actuated system cannot be adequately captured, and designing the control law is cumbersome. Against this background, Fully Actuated System (FAS) theory was developed. FAS[1] was first proposed by Duan in 2020 for the problem of the state space method. Unlike the state-space method, the FAS theory guarantees that a mathematically fully actuated structure can be constructed to compensate for the dynamic properties of the system, regardless of the complexity of the nonlinear terms, when the physical context remains. The controller based on FAS can achieve any quality dynamic performance only if the control parameters are chosen appropriately theoretically. However, it's the wide degree of design freedom that raises the problem of the difficulty in the selection of the design parameters.

Since the birth of FAS theory, there have been many researches on FAS control t application in spacecraft control since the birth of FAS. Duan proposed a generalized PID control in the tracking problem[3], developed[4] an anti-disturbance robust controller for models subject to external disturbances, and optimal control[5] for spacecraft attitude stabilization. Moreover, FAS is applied in attitude control of rigid spacecraft[6], liquid-filled spacecraft[7], and tracking control for rigid spacecraft with actuator saturation. Although the FAS-based attitude control for spacecraft has been researched for some time, the problem of vibration suppression in attitude control of flexible spacecraft hasn't been solved well.

At the same time, external disturbances, and inertia uncertainty are considered, making the proposed method more applicable in practice. The main contributions are summarized as follows:

1) The attitude system of the flexible spacecraft is built based on the FAS, which makes for the control algorithm design. We will investigate how tolerant the algorithm based on FAS is to external disturbance.

2) An attitude-planned path-integrated compound algorithm based on FAS and the Extended disturbance observer (EDO) from the Anti-disturbance rejection control (ADRC) technique has been designed. The controller developed includes two parts, one FAS to achieve linear equivalence, and the other auxiliary algorithm to achieve the vibration suppression.

2 Problem Formulation

2.1 Spacecraft Attitude Kinematics and Dynamics

Under the assumption that the power demanded by the flexible spacecraft is 1kW, the geometric parameters of the simplified model are designed according to the power generation efficiency of the solar panel of about 140-150W/m^2, as shown in Fig. 1. The satellite body and solar panels will be made of aluminum honeycomb, while the supporting structure will be made of carbon fiber.

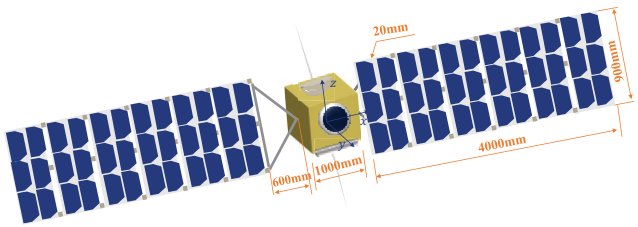

Fig.1 Spacecraft with flexible solar panels

Put $\boldsymbol{\theta}_s = [\varphi, \theta, \psi]^{\mathrm{T}}$, with the roll angle, the pitch angle and the yaw angle denoted by φ, θ, ψ . $\boldsymbol{N}(\boldsymbol{\theta}_s)$ denotes coordinate transformation matrix from $\boldsymbol{\omega}$ to $\dot{\boldsymbol{\theta}}_s$ of the spacecraft.The flexible spacecraft fully actuated attitude

This work is supported by National Natural Science Foundation (NNSF) of China under Grant No.61973153.

*Corresponding author at: College of Astronautics, Nanjing University of Aeronautics and Astronautics, Nanjing 210006, China.
E-mail address: yunhuawu@nuaa.edu.cn (Y. H. Wu).

dynamic system with inertia uncertainty and external disturbance can be written in the following second-order matrix form (Duan, 2020[1])

$$\ddot{\boldsymbol{\theta}}_s = \boldsymbol{f}(\boldsymbol{\theta}_s, \dot{\boldsymbol{\theta}}_s) + \boldsymbol{B}(\boldsymbol{\theta}_s, \dot{\boldsymbol{\theta}}_s)\boldsymbol{u} \tag{1}$$

Where

$$\begin{aligned}
&\boldsymbol{B}(\boldsymbol{\theta}_s, \dot{\boldsymbol{\theta}}_s) = \boldsymbol{N}(\boldsymbol{J}_0 - \boldsymbol{\delta}^{\mathrm{T}}\boldsymbol{\delta})^{-1} \\
&\boldsymbol{f}(\boldsymbol{\theta}_s, \dot{\boldsymbol{\theta}}_s) = \boldsymbol{f}_1 + \boldsymbol{f}_2 + \boldsymbol{f}_3 + \boldsymbol{f}_4 \\
&\boldsymbol{f}_1 = -\boldsymbol{B}(\boldsymbol{\omega} \times \boldsymbol{J}\boldsymbol{\omega}) + \dot{\boldsymbol{N}}\boldsymbol{N}^{-1}\dot{\boldsymbol{\theta}}_S \\
&\boldsymbol{f}_2 = \boldsymbol{B}[(-\boldsymbol{\omega} \times \boldsymbol{\delta}^{\mathrm{T}}\dot{\boldsymbol{\eta}}) + \boldsymbol{\delta}^{\mathrm{T}}(\boldsymbol{C}\dot{\boldsymbol{\eta}} + \boldsymbol{K}\boldsymbol{\eta})] \\
&\boldsymbol{f}_3 = \boldsymbol{B}\boldsymbol{d} \\
&\boldsymbol{f}_4 = \boldsymbol{B}(-\Delta\boldsymbol{J}\dot{\boldsymbol{\omega}} - \boldsymbol{\omega} \times \Delta\boldsymbol{J}\boldsymbol{\omega})
\end{aligned} \tag{2}$$

where $\boldsymbol{\omega} = [\omega_x \ \omega_y \ \omega_z]^{\mathrm{T}} \in \mathbf{R}^3$ denotes the angular velocity vector of spacecraft respect to the inertia system, $\boldsymbol{u} \in \mathbf{R}^3$ is the control torque vector, $\boldsymbol{d} \in \mathbf{R}^3$ denotes the disturbance torque vector constituted by the environmental disturbance and unmodeled dynamics. $\boldsymbol{J} \in \mathbf{R}^{3\times3}$ denotes the positive definite inertia matrix of the spacecraft, with the nominal inertia matrix of the spacecraft $\boldsymbol{J}_0$ and the inertia uncertainty $\Delta\boldsymbol{J}$ from onboard payload motions, fuel consumptions and etc. $\boldsymbol{\eta} \in \mathbf{R}^{\mathrm{n}}$ is elastic modal coordinate vector of the solar wings, $\delta \in \mathbf{R}^{\mathrm{n}\times3}(i = 1, 2, ...m)$ is the coupling matrix between the rigid dynamics and flexible modal of the solar wings, $\boldsymbol{C} = diag\left\{2\xi\omega_n\right\} \in \mathbf{R}^{\mathrm{n}\times\mathrm{n}}$ is the damping matrix of flexible appendage, $\boldsymbol{K} = diag\left\{\omega_n^2\right\} \in \mathbf{R}^{\mathrm{n}\times\mathrm{n}}$ is the stiffness matrix of flexible appendage, with damping ratio ξ, modal frequency ω_n.

Besides rigid attitude motion $\boldsymbol{f}_1$, the lumped nonlinearity $\boldsymbol{f}(\boldsymbol{\theta}_s, \dot{\boldsymbol{\theta}}_s) \in \mathbf{R}^3$ is a continuous vector function that consists of nonlinear vibration from rigid-flexible coupling $\boldsymbol{f}_2$, external environmental disturbance $\boldsymbol{f}_3$, and nonlinearity from inertia uncertainty $\boldsymbol{f}_4$, respectively. $\boldsymbol{B}(\boldsymbol{\theta}_s, \dot{\boldsymbol{\theta}}_s) \in \mathbf{R}^{3\times3}$ is a continuous vector function, satisfying the fully actuated condition $\det(\boldsymbol{B}(\boldsymbol{\theta}_s, \dot{\boldsymbol{\theta}}_s)) \neq 0, \forall \boldsymbol{\theta}_s^{(i)} \in \mathbf{R}^{3\times1}, i = 0, 1, 2.$

2.2 Attitude path planning

To ensure timely payload entry into operations, the spacecraft attitude maneuver must achieve high stability control within a short time after positioning, so the settling time must be shortened. Different attitude planning trajectories, such as triangular angular velocity, trapezoidal angular velocity, and sinusoidal angular acceleration trajectories, are designed as desired orientations around the Euler Axis for the flexible spacecraft attitude controller based on the fully actuated system (FAS) theory. Different trajectories combined with the controller are compared for maneuver performance with bending inhibition performance.

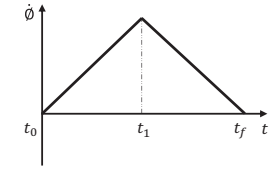

a. Triangular attitude angular velocity path

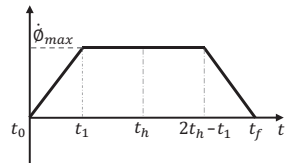

b. Trapezoidal attitude angular velocity path

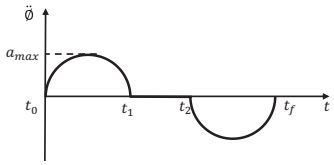

c. Sinusoidal attitude angular acceleration path

Fig. 2 Planned attitude path

2.2.1 Triangular attitude angular velocity path

Under time-optimal control, given the desired attitude angle ϕ_f, relation between angular velocity $\dot{\phi}$ and control amplitude u is shown in Fig.2.a, where t_1 is the time corresponding to $\phi = 0.5\phi_f$, $t_f = 2t_1$ is the completed time of the maneuver.

For large-angle maneuvering, the angular velocity, acceleration are limited by the angular momentum law $\dot{\phi}_{\max} = h_{\max} / J_{\max}$, $\ddot{\phi}_{\max} = u_{\max} / J_{\max}$, where $\dot{\phi}_{\max}$ is the maximum angular velocity; $J_{\max}$ is the rotational inertia of the rotating axis, and $h_{\max}$, $u_{\max}$ are the maximum angular momentum, output torque that actuator can provide.

The triangular path of the spacecraft attitude angular velocity during and after the maneuver is

$$\begin{cases}
\dot{\phi} = \ddot{\phi}_{\max} t & 0 \le t < t_1 \\
\dot{\phi} = 2\ddot{\phi}_{\max}\sqrt{(\phi_f - \phi_0)/\ddot{\phi}_{\max}} - \ddot{\phi}_{\max} t & t_1 \le t < t_f \\
\dot{\phi} = 0 & t \ge t_f
\end{cases} \tag{3}$$

where ϕ is the maneuver angle; ϕ_0, ϕ_f is the initial angle; is the target angle and t is the control time. The spacecraft maneuver is to use maximum actuator output torque to accelerate the spacecraft to $(\phi_0 + \phi_f)/2$, then decelerate with maximum torque.

2.2.2 Trapezoidal attitude angular velocity path

Given the maximum angular velocity constraint, the time-optimal maneuver about the instantaneous Euler rotation axis is shown in Fig.2.b, where the angular velocity profile is trapezoidal. The angular velocity profile is trapezoidal, where $t_1 = \dot{\phi}_{\max} / \ddot{\phi}_{\max}$ indicates the end of acceleration, $2t_h - t_1$ indicates the start of deceleration (reverse acceleration), and $2t_h$ is the uniform speed time. The spacecraft is accelerated by the maximum output torque of the actuator first, and when the actual angular velocity

reaches the maximum angular velocity constraint $\dot{\phi}_{\max}$, the output torque of the actuator is zero and the angular acceleration is zero, and at this time spacecraft maintains the constant speed and decelerates at the moment of $2t_h - t_1$ with the maximum angular acceleration in the reverse direction. Since the maximum torque and the maximum reverse torque generated by the actuator in a given direction are constants of equal amplitude, the acceleration time and deceleration time are equal, and the attitude velocity motion equation can be expressed as

$$\begin{cases} \dot{\phi}=\ddot{\phi}_{\max} t & 0\le t<t_1 \\ \dot{\phi}=\dot{\phi}_{\max} & t_1\le t<2t_h-t_1 \\ \dot{\phi}=\ddot{\phi}_{\max}(2t_h-t) & 2t_h-t_1\le t<t_f \\ \dot{\phi}=0 & t\ge t_f \end{cases} \tag{4}$$

where $t_f, \phi, \phi_0, \phi_f$ are defined as above; t_h satisfies the constraint

$$\ddot{\phi}_{\max} t_1^2 + 2\ddot{\phi}_{\max} t_1 (t_h - t_1) + \varphi_0 = \varphi_f .$$

3.2.3 Sinusoidal attitude angular acceleration path

The time-optimal attitude maneuver planned path strategy involves a step change in the control torque during the maneuver, which tends to excite low-frequency vibrations in the flexible structure, which can negatively affect the maneuver performance. To solve this problem, a simple form of sinusoidal angular acceleration is used for maneuver path design, as shown in Fig.2.c, considering both pointing accuracy and computational complexity.

The sinusoidal path of the spacecraft attitude angular velocity and acceleration during and after the maneuver is

$$\begin{cases} \ddot{\phi}=\ddot{\phi}_{\max}\sin(\dfrac{\pi}{t_1}t) & 0\le t<t_1 \\ \ddot{\phi}=0 & t_1\le t<t_2 \\ \ddot{\phi}=-\ddot{\phi}_{\max}\sin(\dfrac{\pi}{t_1}(t-t_2)) & t_2\le t<t_f \\ \ddot{\phi}=0 & t\ge t_f \end{cases} \tag{5}$$

where t_1, t_2, t_f represent the end moments of acceleration, uniform velocity, and deceleration respectively, satisfying

$$\begin{cases} t_1=\dfrac{\pi h_{\max}}{2u_{\max}} \\ t_2=\dfrac{\phi_f \cdot J_{\max}}{h_{\max}} \\ t_f=\dfrac{\pi h_{\max}}{2u_{\max}}+\dfrac{\phi_f \cdot J_{\max}}{h_{\max}} \end{cases}$$

where $h_{\max}, u_{\max}, J_{\max}, \phi_f$ are defined as above.

3 Controller Design

In this section, the proposed planned smooth maneuver path and FAS-based control scheme for flexible spacecraft will be introduced in detail, as shown in Fig.3. The controller comprises two parts: one for parametric method designed linear feedback about the state error between the real attitude $\boldsymbol{\theta}_s, \dot{\boldsymbol{\theta}}_s$ and the planned attitude $\boldsymbol{\theta}_d, \dot{\boldsymbol{\theta}}_d$, and one for nonlinear compensation of the lumped disturbance, which is composed of external environmental disturbance and flexible vibration, depending on the estimated state by an extended disturbance observer.

3.1 Extended Disturbance Observer (EDO) Design

Here, the ESO technique from ADRC is employed, with $\boldsymbol{z}_3 = \boldsymbol{f}(\boldsymbol{\theta}_s, \dot{\boldsymbol{\theta}}_s)$ treated as an additional state variable. $\boldsymbol{z}_1 = \boldsymbol{\theta}_s$, $\boldsymbol{z}_2 = \dot{\boldsymbol{\theta}}_s$, $\boldsymbol{z}_3 = \boldsymbol{f}'$ assumed, let $\dot{\boldsymbol{z}}_3 = \boldsymbol{g}(t)$, following the assumption that $\boldsymbol{g}(t)$ is unknown and bounded. Then, Eq. (1) can be expressed as:

$$\begin{cases} \dot{\boldsymbol{z}}_1=\boldsymbol{z}_2, \\ \dot{\boldsymbol{z}}_2=\boldsymbol{z}_3+\boldsymbol{B}\boldsymbol{u}+\boldsymbol{f}_1, \\ \dot{\boldsymbol{z}}_3=\boldsymbol{g}(t). \end{cases} \tag{6}$$

A parallel system of the EDO is designed based on the dynamic model of the original system.

$$\begin{cases} \dot{\hat{\boldsymbol{z}}}_1=\hat{\boldsymbol{z}}_2+\beta_1\boldsymbol{g}_1(\boldsymbol{e}_1), \\ \dot{\hat{\boldsymbol{z}}}_2=\hat{\boldsymbol{z}}_3+\boldsymbol{B}\boldsymbol{u}+\boldsymbol{f}_1+\beta_2\boldsymbol{g}_2(\boldsymbol{e}_1) \\ \dot{\hat{\boldsymbol{z}}}_3=\beta_3\boldsymbol{g}_3(\boldsymbol{e}_1). \end{cases} \tag{7}$$

where $\hat{\boldsymbol{z}}_1$, $\hat{\boldsymbol{z}}_2$ and $\hat{\boldsymbol{z}}_3$ are the estimates of $\boldsymbol{z}_1, \boldsymbol{z}_2$ and $\boldsymbol{z}_3$ respectively, and $\boldsymbol{g}_i(\bullet)$ is a modified exponential weighting function dependent on $\boldsymbol{e}_1$. Function $\boldsymbol{g}_i(\bullet)$ is defined as

$$g_i(e,\alpha_i,\delta)=\begin{cases} |e|^{\alpha_i}\,\mathrm{sgn}(e), & |e|>\delta \\ \dfrac{e}{\delta^{1-\alpha_i}}, & |e|\le\delta \end{cases}$$

α_i is selected from the range of 0 to 1, enabling g_i a high gain for small errors. Additionally, a small positive δ is used to restrict the gain in the source neighborhood.

If $\boldsymbol{e}_1 = \hat{\boldsymbol{z}}_1 - \boldsymbol{z}_1$, observation error dynamic can be defined from the parallel systems from Eqs.(8-9).

$$\begin{cases} \dot{\boldsymbol{e}}_1 = \boldsymbol{e}_2 + \beta_1 g_1(\boldsymbol{e}_1) \\ \dot{\boldsymbol{e}}_2 = \boldsymbol{e}_3 + \boldsymbol{B}\boldsymbol{u} + \boldsymbol{f}_1 + \beta_2 g_2(\boldsymbol{e}_1) \\ \dot{\boldsymbol{e}}_3 = \beta_3 g_3(\boldsymbol{e}_1) - \boldsymbol{g}(t). \end{cases}$$

Problem 1: Given the FAS system, find appropriate observer parameter $\beta_1, \beta_2, \beta_3$ such that

$$\lim_{x\to\infty} \boldsymbol{e}_3(t) = \lim_{x\to\infty} [\hat{\boldsymbol{z}}_3 - \boldsymbol{z}_3] = 0 \tag{8}$$

3.2 Controller Design

The observer mentioned above uses $\hat{\boldsymbol{z}}_1$, $\hat{\boldsymbol{z}}_2$ and $\hat{\boldsymbol{z}}_3$ to estimate $\boldsymbol{\theta}_s$, $\dot{\boldsymbol{\theta}}_s$, and $\boldsymbol{f}'$ respectively. Taking the FAS approach, the following ADRC controller can be proposed, whose architecture is shown in Figure 3. Control torque can be expressed as Eq. (9).

$$\boldsymbol{u} = \boldsymbol{u}_f + \boldsymbol{u}_d, \tag{9}$$

To compensate for the lumped disturbance $\boldsymbol{f}'$, the control $\boldsymbol{u}_d$ introduces an estimated state $\hat{\boldsymbol{z}}_3$ that accounts for ambiguity and uncertainty of $\boldsymbol{f}'$.

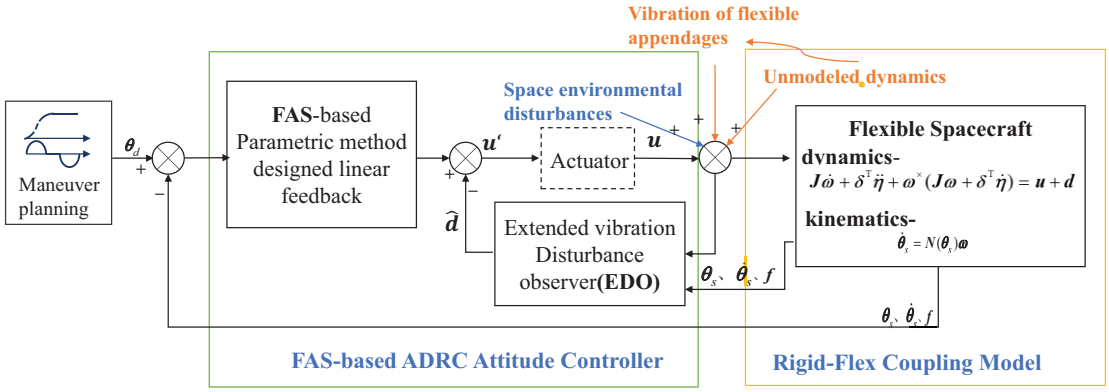

Fig. 3 FAS-based ADRC controller architecture

$$\boldsymbol{u}_d = -\boldsymbol{B}(\boldsymbol{\theta}_s)^{-1}\hat{\boldsymbol{z}}_3, \tag{10}$$

The state feedback term $\boldsymbol{u}_f$ is implemented using the PD strategy, which plays the role of the tracking differentiator in traditional ADRC.

$$\boldsymbol{u}_f = -\boldsymbol{B}(\boldsymbol{\theta}_s)^{-1}(\boldsymbol{A}_0\boldsymbol{\theta}_s + \boldsymbol{A}_1\dot{\boldsymbol{\theta}}_s) + \boldsymbol{v}_{ex} \tag{11}$$

where $\boldsymbol{A}_0$ and $\boldsymbol{A}_1$ are the feedback gain matrices to be designed, and $\boldsymbol{v}_{ex}$ is the external input feedforward control signal. By applying the controller (11)- (13) to the FAS model (3), the following constant linear closed-loop system can be obtained

$$\ddot{\boldsymbol{\theta}}_s + \boldsymbol{A}_1\dot{\boldsymbol{\theta}}_s + \boldsymbol{A}_0\boldsymbol{\theta}_s = \boldsymbol{e}_3 + \boldsymbol{B}\boldsymbol{v}_{ex}. \tag{12}$$

Since the proposed method has a feedforward control part $\boldsymbol{u}_d$ for nonlinear compensation of lumped nonlinearity, external input $\boldsymbol{v}_{ex}$ is not considered, the system (14) can be converted into the state-space form

$$\dot{\boldsymbol{\theta}}_s^{(0\sim1)} = \Phi(\boldsymbol{A}_{0\sim1})\boldsymbol{\theta}_s^{(0\sim1)} + \begin{bmatrix}\boldsymbol{O}_{3\times3}\\ \boldsymbol{e}_3\end{bmatrix}, \tag{13}$$

where $\boldsymbol{\Phi}(\boldsymbol{A}_{0\sim1}) = \begin{bmatrix}\boldsymbol{O}_{3\times3} & \boldsymbol{I}_{3\times3}\\ -\boldsymbol{A}_0 & -\boldsymbol{A}_1\end{bmatrix}$. Select the coefficient matrices $\boldsymbol{A}_{0\sim1}$, making $\boldsymbol{\Phi}(\boldsymbol{A}_{0\sim1})$ stable.

3.3 Parametric Design of $\boldsymbol{A}_{0\sim1}$

The closed-loop system (15), when the external signal $\boldsymbol{v}_{ex}$ is removed and the disturbance estimation error $\boldsymbol{e}_3 \to 0$, is as follows.

$$\ddot{\boldsymbol{\theta}}_s + \boldsymbol{A}_1\dot{\boldsymbol{\theta}}_s + \boldsymbol{A}_0\boldsymbol{\theta}_s = \boldsymbol{0} \tag{14}$$

Process: Following the FAS approach[16], the matrices are designed using parametric design method. An arbitrary nonsingular parameter matrix $\boldsymbol{Z} \in \mathbf{R}^{3\times6}$, Hurwitz matrix $\boldsymbol{F} \in \mathbf{R}^{6\times6}$ are introduced, satisfying $\det\boldsymbol{V}(\boldsymbol{Z},\boldsymbol{F}) \neq 0$. Here the nonsingular matrix $\boldsymbol{V} \in \mathbf{R}^{6\times6}$ is given by $\boldsymbol{V} = (\boldsymbol{Z}\ \boldsymbol{ZF})^{\mathrm{T}}$ to make $\dot{\boldsymbol{\theta}}_s^{(0\sim1)} = \boldsymbol{VFV}^{-1}\boldsymbol{\theta}_s^{(0\sim1)}$. Matrices $\boldsymbol{A}_{0\sim1}$ satisfy

$$\Phi(\boldsymbol{A}_{0\sim1}) = \boldsymbol{VFV}^{-1} \tag{15}$$

where $\boldsymbol{A}_{0\sim1} = \boldsymbol{ZF}^2\boldsymbol{V}^{-1}$.

Design the feedback controller $\boldsymbol{u}_f$

$$\boldsymbol{u}_f = \boldsymbol{B}(\boldsymbol{\theta}_s)^{-1}\boldsymbol{ZF}^2\boldsymbol{V}^{-1}[\boldsymbol{\theta}_s\ \ \dot{\boldsymbol{\theta}}_s]^{\mathrm{T}} \tag{16}$$

4 Numerical Simulation

In the section, some simulation examples are performed to study the planned maneuver strategy proposed control law. Attitude paths such as triangle attitude angular velocity path, trapezoidal attitude angular velocity path, and sinusoidal attitude angular acceleration path are integrated with the proposed controller to discover what combination can achieve both maneuverability and flexural vibration suppression. Furthermore, to verify the robustness to disturbance of the proposed method, 4 cases with different disturbances are applied.

The rigid-flexible coupling dynamics model of the flexible spacecraft in Fig.1 is based on the mode truncation method. The first four order dynamic characteristics are selected due to the high energy concentration in lower order modes. The spacecraft in Fig.1 dynamics and external environmental disturbance are listed in Table 1.

Table 1. The main parameters of the flexible spacecraft

Description	Value
Moments of inertia(kg.m^2)	$\boldsymbol{J} = \mathrm{diag}([87,100,96])$
Inertia uncertainty(kg.m^2)	$\Delta\boldsymbol{J} = 0.2\boldsymbol{J}$
Coupling matrix	$\boldsymbol{\delta} = \begin{bmatrix}1.3523 & 1.2784 & 2.1553\\ -1.1519 & 1.0176 & -1.2724\\ 2.2167 & 1.5891 & -0.8324\\ 1.23637 & -1.6537 & 1.2251\end{bmatrix}$
Number of considered elastic mode	$N = 4$
Natural frequency(rad/s)	$\boldsymbol{\Lambda}$ = [1.736, 10.859, 22.365, 29.892]
Damping ratios	$\xi_1 = \xi_2 = \xi_3 = \xi_4 = 0.01$
Disturbance Torque	$\boldsymbol{d} = 10^{-4}\begin{bmatrix}3\cos(0.1t)+4\\ 1.5\sin(0.1t)+3\cos(0.1t)\\ 3\sin(0.1t)+1\end{bmatrix}$

For the initial instantaneous Euler-rotation-axis angle of the flexible spacecraft $\phi_0 = 0\,\mathrm{deg}$, whose corresponding Euler angle attitude $\boldsymbol{\theta}_0 = [0,0,0]\,\mathrm{deg}$, $\dot{\boldsymbol{\theta}}_0 = [0,0,0]\,\mathrm{deg/s}$, the desired attitude $\phi_f = 37\,\mathrm{deg}$, $\boldsymbol{\theta}_d = [20,14,30]\,\mathrm{deg}$, $\dot{\boldsymbol{\theta}}_d = [0,0,0]\,\mathrm{deg/s}$, rela -tive control parameters are selected, the parameters for the observer: $\beta_0, \beta_1, \beta_2 = [50,150,500]$, $\delta = 0.01$, $\alpha_1 = 0.25$, $\alpha_2 = 0.5$; Parameters for controller:

$$\boldsymbol{F}=\begin{bmatrix}\boldsymbol{O}_{3\times3} & \boldsymbol{I}_{3\times3}\\ \mathrm{diag}([-10,-7,-5]) & \mathrm{diag}([-7,-11,-2])\end{bmatrix},$$

$\boldsymbol{Z}=\begin{bmatrix}\mathrm{diag}([-10,-7,-5])\ \mathrm{diag}([-7,-11,-2])\end{bmatrix}$, in the case in the case where the output capacity of actuator is $\boldsymbol{u}_{\max}=1.5\mathrm{Nm}$, maximum momentum $\boldsymbol{h}_{\max}$ is 2.5 $\mathrm{N}\cdot\mathrm{m}\cdot\mathrm{s}$, which can be provided by hybrid actuator, $\boldsymbol{J}_{\max}$ is 100 $\mathrm{kg}\cdot\mathrm{m}^2$.

4.1 Performance Analysis

Under the attitude path-based attitude controller, attitude response and structural dynamics of flexible spacecraft are depicted by Figs.4-8. Euler angle and attitude angular velocity response in the controlled system are shown in Figs.4-5. The controlled elastic modes arising from solar wings are shown in Figs.7-8.

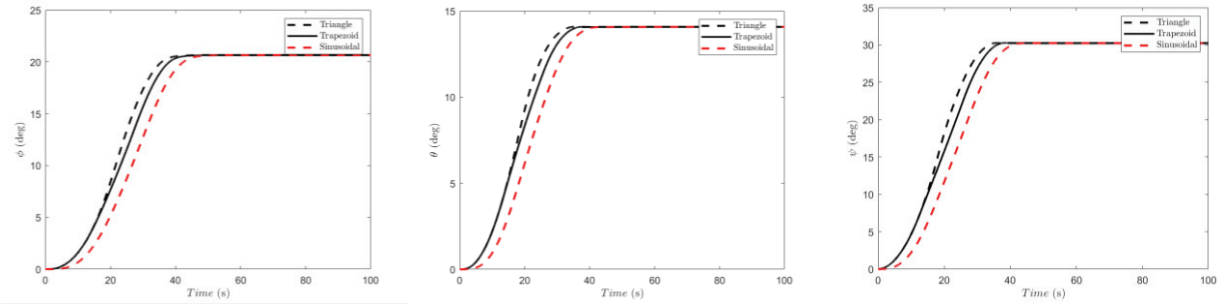

a. roll direction φ b. pitch direction θ c. yaw direction ψ

Fig. 4 Euler angle

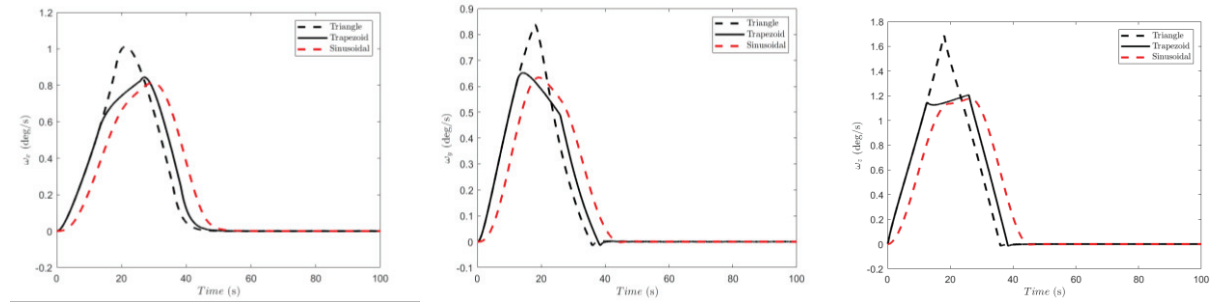

a. roll direction $\dot{\varphi}$ b. pitch direction $\dot{\theta}$ c. yaw direction $\dot{\psi}$

Fig.5 Angle velocity

It's evident that the closed-loop system based on the triangular angular velocity trajectory has a significantly faster maneuvering time than the controlled systems following the other two attitude paths, and that following trapezoidal trajectory takes seconds. As also reflected in Fig.5, the maximum attitude angular velocity of triangular path-based system during the maneuver is much higher than that of the closed-loop system under the other two paths.

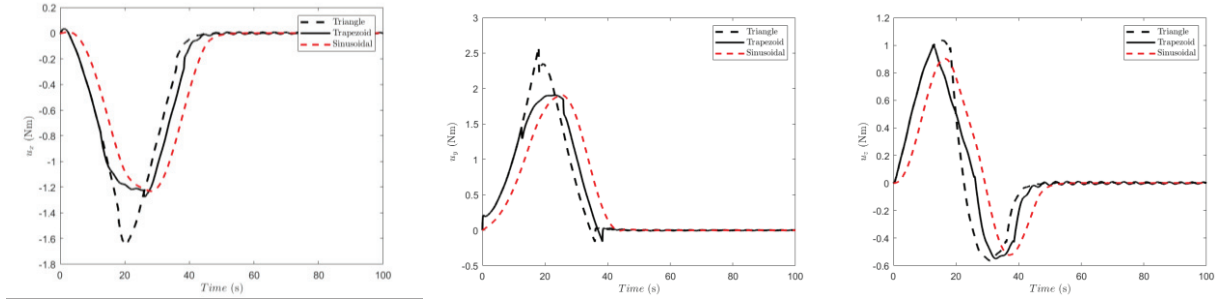

a. roll direction b. pitch direction c. yaw direction

Fig.6 Control input

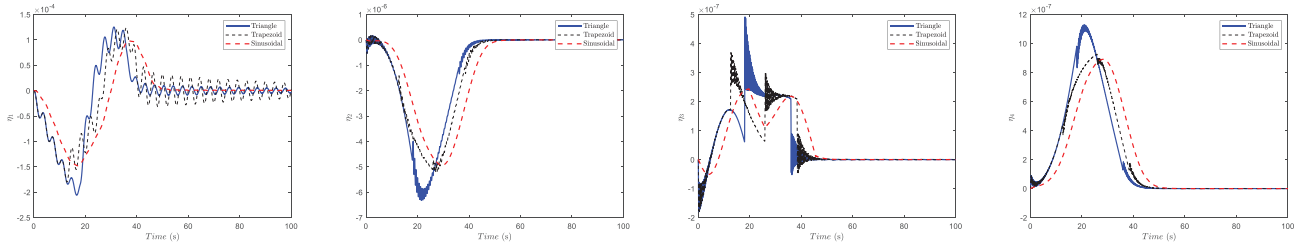

a.1st order b. 2nd order c. 3rd order d. 4th order

Fig.7 Modal displacement

Besides, attitude angular velocity trajectory of closed loop system following trapezoidal path and that following sinusoidal path approximate. Correspondingly, as shown in Fig.6, control torque amplitudes of the trapezoidal path and

sinusoidal path closed-loop attitude systems are close, but the sinusoidal path output torque is smoother than that of the trapezoidal path, which is more conducive to high-precision attitude pointing and high-stability attitude maneuvering.

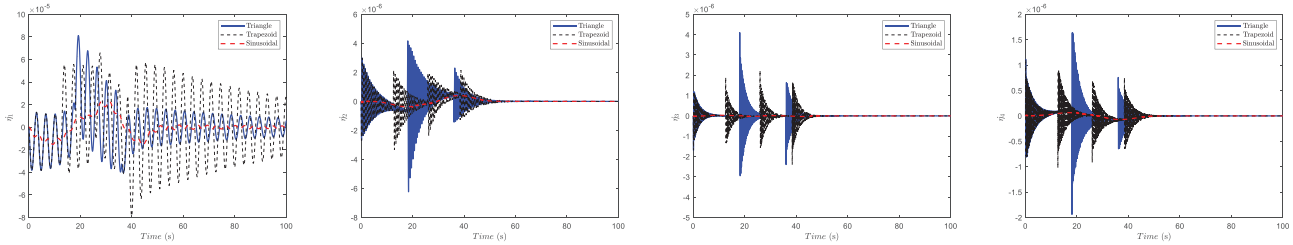

a.1st order b. 2nd order c. 3rd order d. 4th order

Fig.8 Modal velocity

As depicted in Figs.7-8, it's found that as the modal order increases, the modal response amplitude decreases, which confirms the validity of the previous proposal to consider only the first four orders of modes in the structural dynamics of flexural spacecraft.

It's observed that though the modal displacement response of the closed-loop system based on the sinusoidal path lags behind that of the other two paths, the closed-loop system exhibits the strongest vibration suppression, achieving high steady-state accuracy of the first four orders of modal displacements and modal velocities. It's noted that the modal responses have no jitter like that of the other two paths, which can be attributed to the planned gentle sinusoidal attitude angular acceleration. The jitter on modal responses arises from the rigid maneuver, which validates the sinusoidal attitude path can minimizes the excitation from attitude motions on the flexible attachments during rigid orientation.

4.2 Robustness to External Disturbance Analysis

Table 2. Cases the spacecraft may encounter

Case	Disturbance	Potential Expn
1	No	\
2	Harmonic $\boldsymbol{d}_h$	$10^{-3}\begin{bmatrix}3\cos(0.1t)+4\\1.5\sin(0.1t)+3\cos(0.1t)\\3\sin(0.1t)+1\end{bmatrix}$
3	Gaussian $\boldsymbol{d}_g$	$10^{-3}rand(4,1)$
4	Harmonic + Gaussian $\boldsymbol{d}_m$	$\boldsymbol{d}_h+\boldsymbol{d}_m$

The issue of disturbance rejection is especially noticeable for low-Earth orbiting satellites, which operate at altitudes where their dynamics are significantly influenced by most of the jamming. Therefore, we will investigate the robustness of the proposed control scheme to various external disturbances, as shown in Table 2. The table corresponds to different cases in which the flexible spacecraft will be subjected to disturbances.

The simulation results for the attitude control and vibration suppression of flexible spacecraft under the proposed method are presented in Figs 9-13 in four different cases.

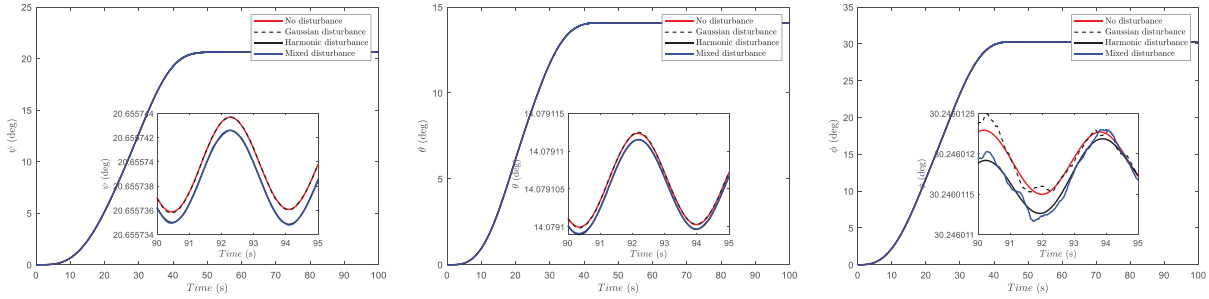

a. roll direction φ b. pitch direction θ c. yaw direction ψ

Fig. 9 Euler angle

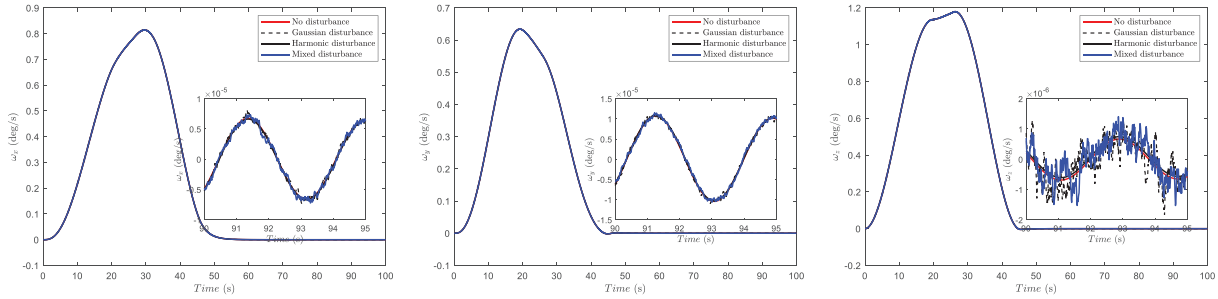

a. roll direction $\dot{\varphi}$ b. pitch direction $\dot{\theta}$ c. yaw direction $\dot{\psi}$

Fig.10 Angle velocity

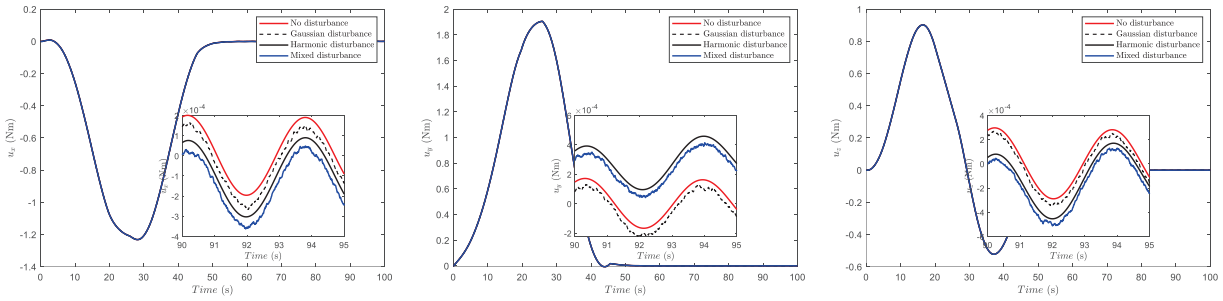

a. roll direction b. pitch direction c. yaw direction

Fig.11 Control input

As shown in Figs 9-13, attitude control and vibration suppression for flexible spacecraft show modestly strong robustness in four cases under the proposed method. Notably, the system under the method behaves differently in robustness to different disturbances, which perform better with harmonic disturbance than Gaussian disturbance and mixed disturbance, shown obviously in Figs 9-13.

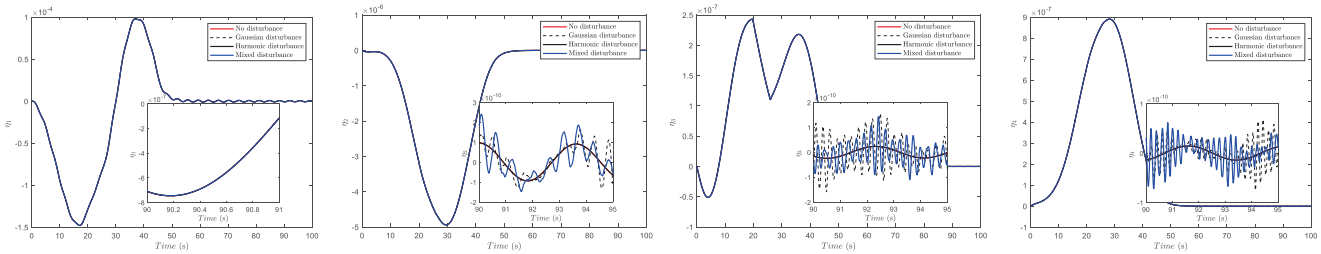

a.1st order b. 2nd order c. 3rd order d. 4th order

Fig.12 Modal displacement

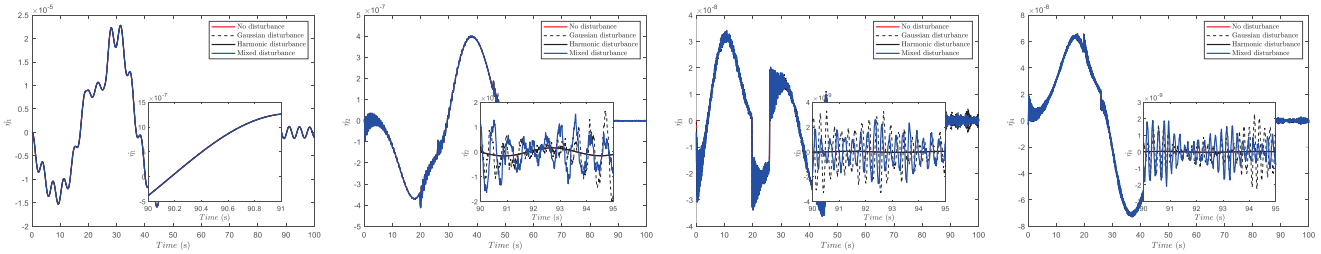

a.1st order b. 2nd order c. 3rd order d. 4th order

Fig.13 Modal velocity

It's obvious that, from the attitude response to the elastic vibration response, the amplitudes are approximately equal under the four cases, which means whether disturbance or not, whatever type of disturbance, the proposed method is so robust that the static and dynamic performance keep stable.

5 Conclusion

In this paper, a sinusoidal-path integrated controller is proposed for attitude control of flexible spacecraft subject to unknown inertia parameters and external disturbances. To handle the nonlinearity of flexible spacecraft, a potential controller based on a fully actuated system (FAS) is constructively developed, whereby a compound ADRC controller that integrates FAS and Extended disturbance observer is further derived to deal with the nonlinearity caused by the external disturbance and achieve high precision pointing. It is shown that the proposed control algorithm can steer the spacecraft to the desired orientation with minimal residual vibration despite the presence of external disturbances and system uncertainty. By leveraging the inherent dynamics of the vehicle's attitude path, this method optimizes control torque usage, enabling more efficient and reliable spacecraft maneuvers, and ultimately enhancing the success of space missions.

References

[1] M. Golestani, W. Zhang, Y. Yang, et al. Disturbance observer-based constrained attitude control for flexible spacecraft. *IEEE Transactions on Aerospace and Electronic Systems*, 2022, 59(2): 963-972.

[2] G. Duan. High-Order Fully Actuated System Approaches: Part I. Models and Basic Procedure. *International Journal of Systems Science*, 2021, 52(2): 422-435.

[3] G. Duan. High-Order Fully Actuated System Approaches: Part IX. Generalized PID control and Model Reference Tracking. *International Journal of Systems Science*, 2022, 53(3): 652-674.

[4] G. Duan. High-Order Fully Actuated System Approaches: Part VI. Disturbance Attenuation and Decoupling. *International Journal of Systems Science*, 2021, 52(10): 2161-2181.

[5] G. Duan. High-Order Fully Actuated System Approaches: Part VIII. Optimal Control with Application in Spacecraft Attitude Stabilization. *International Journal of Systems Science*, 2022, 53(1): 54-73.

[6] D. Wang, Y. Wu, X. Chen, et al. Fully Actuated System Based Spacecraft Attitude Finite Time Control//*2023 2nd Conference on Fully Actuated System Theory and Applications (CFASTA)*. IEEE, 2023: 100-105

[7] F.Z. Xiao, L.Q. Chen. Attitude Control of Spherical Liquid-Filled Spacecraft Based on High-Order Fully Actuated System Approaches. *Journal of Systems Science and Complexity*, 2022, 35(2): 471-480.

Proceedings of the 3rd Conference on Fully Actuated System Theory and Applications
May 10-12, 2024, Shenzhen, China

Robust multi-mobile robot formation control: A fully actuated system control approach

Zhihao Liu[1], Peng Li[1]

1. School of Mechanical Engineering and Automation, Harbin Institute of Technology (Shenzhen), Shenzhen 518055, P. R. China
E-mail: liuzhihaotina@163.com / lipeng2020@hit.edu.cn

Abstract: In this paper, a control law for a multi-mobile robot formation system with the leader-follower's distance-angle tracking method is developed based on the theory of fully actuated system (FAS), where the stability under disturbance is also characterized. Firstly, the dynamic error model of the target robot formation system with disturbance is established. Once the second-order nonlinear differential equation is obtained, it will be transformed into a linear time-invariant one by deploying the fully actuated system technique. Consequently, a control law is designed to eliminate the uncertainty and drive the error dynamic to converge to zero. Finally, the robot team can move forward along the desired trajectory in the predetermined formation. At the same time, the effectiveness of the proposed method is examined by extensive numerical experiments in comparison with the conventional sliding mode control (SMC). The simulation results show that the fully actuated parameter design method has better stability and faster convergence. Moreover,the proposed method shows higher robustness against disturbance.

Key Words: Fully actuated system, linear time-invariant system, distance-angle, multi-mobile robot formation

1 Introduction

With the rapid improvement of productivity, the dependence on the work of robots is consistently increasing especially for those complex and huge engineering tasks. Multi-mobile robot collaboration can handle work that cannot be achieved by a single robot [1]. Formation control is widely used not only in industrial production and military fields [2], but also in application scenarios such as UAV aerial performances with the popularization of unmanned aerial vehicles (UAVs) in recent years [3, 4]. Therefore, the study of formation control has important theoretical and practical value.

The control methods of robot formation are mainly divided into five categories: leader-follower, behavior-based, artificial potential, virtual structure, and graph theory. The leader-follower method transforms the formation control problem into the orientation and distance problem of the follower relative to the leader, which is convenient for the standard control theory to study and analyze its stable tracking error [5]. Therefore, the robot formation model in this paper is established and analyzed by the leader-follower method based on distance-angle [6, 7]. From the perspective of multi-robot system control, it is mainly divided into two categories: centralized control and distributed control. In distributed control, each robot only needs to interact with a few neighboring robots with its pose and other information, which reduces the amount of computation and the communication burden of a single robot. The advantages of distributed control, such as good adaptability and fault tolerance, make the research hotspots on multi-robot formation information interaction biased towards it. Thus, this paper uses a relatively simple distributed control to achieve the formation target, which not only reduces the amount of communication, but also helps to reduce the error and make it more flexible.

The robot model used in this paper is a common second-order dynamics model. The high-order system approach proposed in [8] can be used to design the control law to obtain a linear constant closed-loop system, which has a better effect on the control problem of general nonlinear systems than that of state-space technique. Reference [9] pointed out some problems of the controllability of the first-order dynamical system based on the state-space model, and then defined the complete controllability of the dynamics system with more general applicability and its relationship with the fully actuated system (FSA). Also, it proved that a fully actuated system can be transformed into a linear time-invariant closed-loop system with the desired characteristic structure by appropriately selecting a nonlinear state feedback control law. In this paper, the control model of the fully actuated system (FAS) proposed in [8] is used to achieve the control law, with the target nonlinear system being described through variable elimination and model transformation. An obvious advantage of this method is that a linear constant closed-loop system can always be obtained from arbitrarily assignable feature structures. This convenience helps to deal with many control problems, such as observer design [10], robust control [11], adaptive control [12], robust adaptive control [13], disturbance attenuation [14], and optimal control [15].

However, it is worth noting that the FAS technique requires accurate knowledge of system dynamics. Although it is robust to small modeling errors, it is not suitable for large uncertainty, such as the lack of dynamic details known, and the closed-loop system will be affected by the uncertainty characteristics [16]. Therefore, there exist some difficulties using FAS to achieve the formation. One is that the overshoot may be large and even lead to divergence, especially when each agent suffered both random and time-varying disturbance. This article manages to overcome it through suitably setting the limitations of the acceleration and velocity . Additionally, the formation model is coupled with only two separate control inputs, which makes it difficult to use fully actuated system technique to design the control law. This paper manages to find two suitable control variables and transform the dynamic error model into a fully actuated system.

*This work is partly supported by National Natural Science Foundation (NNSF) of China (Grant 62303133 and 62188101) and partly by the Guangdong Basic and Applied Basic Research Foundation (Grant 2021A1515110262, 2022A1515011274).

In this work, under a second-order error model of the leader-follower's distance-angle tracking formation, a control law is proposed deploying the fully actuated design approach. The uncertainty including the nonlinear term of the original system is eliminated by using the fully actuated characteristics, so as to obtain a linear time-invariant error system with asymptotic convergence and consequently to achieve the goal of formation control. The main contributions of this paper are as follows

(1) The nonlinear control method based on the theory of fully actuated system is applied to the multi-robot formation through the leader-follower control based on the distance-angle method.

(2) Considering both the random and the time-varying disturbance of each agent under the formation, the robustness of the fully actuated system control approach is confirmed though simulation.

(3) Combined with the theory of the fully actuated system, the acceleration and velocity are limited considering the control and safety of formation.

The rest of this paper is arranged as follows: Section 2 introduces a distance-angle-based leader-follower dynamic error model and the design formula of the conventional sliding mode control with its stability proof. In Section 3, a second-order fully actuated system model is established by designing a control law to ensure that the linear system obtained is stable and convergent. In Section 4, a specific example is simulated, and the simulation results of fully actuated system (FAS) and sliding mode control (SMC) under disturbance are given, which verifies the effectiveness of the fully actuated system technique. Finally, conclusions and prospects are summarized in Section 5.

Symbol description: I_n indicates a nth order identity matrix, and $0_{m\times n}$ represents a zero matrix with n columns and m rows. $\|\cdot\|_\infty$ represents the vector infinite norm.

2 Problem Formulation and Preliminaries

In this section, the dynamic model of the leader-follower system considering uncertainty and the error differential equation are established. Subsequently, the theoretical strategy of the conventional sliding mode control and the proof of its stability are given.

2.1 Dynamic error model of the leader-follower system

In this paper, the distance-angle control structure of the leader-follower framework is considered, where the ith robot is selected as the leader and the kth robot is selected as the follower. When the leader moves along the desired trajectory, the follower needs to maintain the desired relative position and relative phase angle to follow the leader and achieve the desired formation movement. The structure of the model is shown in Fig. 1.

As shown in Fig. 1, the relative distance l_{ik} between the leader i and the follower k is defined as the distance from the center of the leader i to the front sensor of the follower k. Its calculation formula is as follows

$$l_{ik} = \sqrt{(x_i - x_k - r\cos\theta_k)^2 + (y_i - y_k - r\sin\theta_k)^2}, \quad (1)$$

where (x_i, y_i) and (x_k, y_k) respectively represent the central coordinate position of the leader i and the follower k, and r represents the radius of the robots. θ_i and θ_k represent the azimuth angle of i and k, respectively.

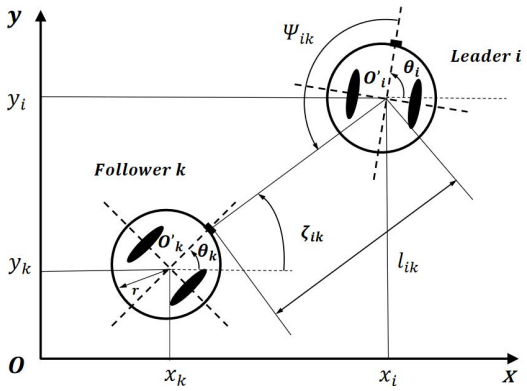

Fig. 1: Schematic diagram of the relevant parameters between robot i and k.

The relative phase angle Ψ_{ik} between i and k in Fig. 1 is defined as

$$\Psi_{ik} = \pi + \varsigma_{ik} - \theta_i, \quad (2)$$

where ς_{ik} is described and calculated as

$$\varsigma_{ik} = \arctan\frac{y_i - y_k - r\sin\theta_k}{x_i - x_k - r\cos\theta_k}.$$

Taking the second derivative of l_{ik} and Ψ_{ik} , defining $W_{ik} = [l_{ik},\ \Psi_{ik}]^T$, and considering the uncertainty (which will be described in more detail in subsection 2.2), the state space expression for the dynamical model of the leader-follower formation system is

$$\ddot{W}_{ik} = G_{ik}u_{ik} + d_{ik}\left(W_{ik}, \dot{W}_{ik}, t\right). \quad (3)$$

In equation (3), defining $\varphi_{ik} = \Psi_{ik} + \theta_i - \theta_k$, $F_{ik} = [F_1,\ F_2]^T$, and $P_{ik} = [P_1,\ P_2]^T$, then each parameter matrix is described as follows

$$G_{ik} = \begin{bmatrix} \cos\varphi_{ik} & r\sin\varphi_{ik} \\ -\dfrac{\sin\varphi_{ik}}{l_{ik}} & \dfrac{r\cos\varphi_{ik}}{l_{ik}} \end{bmatrix}, L_{ik} = \begin{bmatrix} -\cos\Psi_{ik} & 0 \\ \dfrac{\sin\Psi_{ik}}{l_{ik}} & -1 \end{bmatrix},$$

$$\Delta'_i = I_2 + \Delta_i,$$

$$d_{ik}\left(W_{ik}, \dot{W}_{ik}, t\right) = G_{ik}\Delta_k u_k + L_{ik}\Delta'_i u_i + F_{ik} + P_{ik},$$

$$\begin{aligned} F_1 =& (\Psi_{ik})^2 l_{ik} + 2\Psi_{ik}\dot{\theta}_i l_{ik} + \left(\dot{\theta}_i\right)^2 l_{ik} - r\cos\varphi_{ik}\left(\dot{\theta}_k\right)^2 \\ &- \left(\dot{y}_k\dot{\theta}_k - \dot{y}_i\dot{\theta}_i\right)\cos\left(\Psi_{ik} + \theta_i\right) + \left(\dot{x}_k\dot{\theta}_k - \dot{x}_i\dot{\theta}_i\right)\sin\left(\Psi_{ik} + \theta_i\right), \end{aligned}$$

$$\begin{aligned} F_2 =& -\frac{(\dot{y}_k\dot{\varphi}_{ik} - \Psi_{ik}\dot{y}_i)\sin\left(\Psi_{ik} + \theta_i\right)}{l_{ik}} - \frac{\dot{l}_{ik}r\dot{\theta}_k\cos\varphi_{ik}}{l_{ik}^2} \\ &- \frac{(\dot{x}_k\dot{\varphi}_{ik} - \Psi_{ik}\dot{x}_i)\cos\left(\Psi_{ik} + \theta_i\right)}{l_{ik}} - \frac{r\dot{\theta}_k\dot{\varphi}_{ik}\sin\varphi_{ik}}{l_{ik}} \\ &+ \frac{\dot{l}_{ik}\left((\dot{y}_i - \dot{y}_k)\cos\left(\Psi_{ik} + \theta_i\right) - (\dot{x}_i - \dot{x}_k)\sin\left(\Psi_{ik} + \theta_i\right)\right)}{l_{ik}^2}, \end{aligned}$$

$$\begin{aligned} P_1 =& -(\pi_{ix} - \pi_{kx})\cos\left(\Psi_{ik} + \theta_i\right) + r\pi_{k\theta}\sin\left(\varphi_{ik}\right) \\ &- \left(\pi_{iy} - \pi_{ky}\right)\sin\left(\Psi_{ik} + \theta_i\right), \end{aligned}$$

$$\begin{aligned} P_2 =& \frac{(\pi_{ix} - \pi_{kx})\sin\left(\Psi_{ik} + \theta_i\right)}{l_{ik}} - \pi_{i\theta} \\ &- \frac{\left(\pi_{iy} - \pi_y\right)\cos\left(\Psi_{ik} + \theta_i\right) - r\pi_{k\theta}\cos\varphi_{ik}}{l_{ik}}. \end{aligned}$$

Note: This paper makes the following assumptions about the leader-follower system:

1) There is no communication delay between the leader and the follower.

2) Each robot can detect its own pose and velocity.

3) The leader can transmit its pose and velocity to each of its followers precisely through communication.

Define $W_{ik}^* = \left[l_{ik}^* \ \Psi_{ik}^*\right]^T$ as the desired relative position and phase angle that the follower k expects to maintain with the leader i, and

$$We_{ik} = W_{ik} - W_{ik}^* = \left[l_{ik} - l_{ik}^* \ \Psi_{ik} - \Psi_{ik}^*\right]^T,$$

is the error state variable of the formation system. Then the state space expression for the dynamic error model of the leader-follower formation system is

$$\ddot{W}e_{ik} = G_{ik}u_{ik} + d_{ik}\left(We_{ik}, \dot{W}e_{ik}, t\right). \tag{4}$$

2.2 Uncertainty in multi-robot formation

In the formation system dynamics error model (4) proposed in this paper, $d_{ik} = d_{ik}\left(We_{ik}, \dot{W}e_{ik}, t\right)$ represents the uncertainty existing in the system, including four parts: $G_{ik}\Delta_k u_k$, $L_{ik}\Delta_i' u_i$, P_{ik}, and F_{ik}. Specifically:

1) $G_{ik}\Delta_k u_k$ indicates the change in the parameter of the follower k itself.

2) $L_{ik}\Delta_i' u_i$ indicates the changes of the control quantity information of the leader i and its parameter change that affect the followers.

3) P_{ik} denotes the set of external disturbance to which the leader i and the follower k are subjected.

4) F_{ik} represents the set of the part related to the state of the system.

While $G_{ik}\Delta_k u_k$, $L_{ik}\Delta_i' u_i$, and P_{ik} are disturbance items, F_{ik} is the nonlinear term of the system itself.

2.3 Sliding Mode Control (SMC) theory and strategy

The sliding mode control (SMC) forces the states of a system to move on a certain sliding mode surface and finally converge to zero [17]. SMC has good robustness to disturbance, since the designed sliding mode surface equation is only related to the states, and has nothing to do with other parameters of the system or external disturbance [18].

Hypothesis 1: There is an unknown constant $d_{ik}^* > 0$ that makes the uncertainty d_{ik} in the system (4) satisfy $\|d_{ik}\|_\infty \leq d_{ik}^*$, i.e, the uncertainty is bounded.

Design conventional sliding surface equation for the formation system

$$S_{ik} = \bar{J}_{ik}We_{ik} + \bar{K}_{ik}\dot{W}e_{ik}, \tag{5}$$

where $S_{ik} \in R^{2\times 1}$, $\bar{J}_{ik}$ and $\bar{K}_{ik}$ are the 2nd-order positive definite matrices to be designed.

Correspondingly, the conventional sliding mode control law of the system is designed as follows

$$u_k = -\left(\bar{K}_{ik}G_{ik}\right)^{-1}\left[\bar{\kappa}_{ik}sat\left(S_{ik}\right) + \bar{\eta}_{ik}S_{ik} + \bar{J}_{ik}\dot{W}e_{ik}\right], \tag{6}$$

where $\bar{\kappa}_{ik}$ and $\bar{\eta}_{ik}$ are the parameters to be designed. Especially, considering that the discontinuity of the $sgn(\cdot)$ function at the origin may affect the stability of the system, it is replaced by the saturation function $sat(\cdot)$, which is described as

$$sat\left(S\right) = \begin{cases} 1, & S > \delta, \\ kS, & |S| \leq \delta,\ k = \dfrac{1}{\delta}, \\ -1, & S < -\delta, \end{cases}$$

where δ is defined as a very small number.

Consider a positive definite Lyapunov function and its derivative

$$V = \frac{1}{2}S_{ik}^T S_{ik},$$

$$\begin{aligned} \dot{V} &= S_{ik}^T\dot{S}_{ik} \\ &= S_{ik}^T\left(\bar{J}_{ik}\dot{W}e_{ik} + \bar{K}_{ik}\ddot{W}e_{ik}\right) \\ &= S_{ik}^T\left(\bar{J}_{ik}\dot{W}e_{ik} + \bar{K}_{ik}\left(G_{ik}u_k + d_{ik}\right)\right) \\ &= S_{ik}^T\left(-\bar{\kappa}_{ik}sat\left(S_{ik}\right) - \bar{\eta}_{ik}S_{ik} + \bar{K}_{ik}d_{ik}\right). \end{aligned}$$

While choosing $\bar{\kappa}_{ik} > \|\bar{K}_{ik}\|_\infty d_{ik}^*$, $\dot{V}$ is negative definite, the system is asymptotically stable according to Lyapunov theorem.

Especially, if d_{ik} is known, design

$$u_k = -\left(\bar{K}_{ik}G_{ik}\right)^{-1}\left[\bar{\kappa}_{ik}sat\left(S_{ik}\right) + \bar{\eta}_{ik}S_{ik} + \bar{J}_{ik}\dot{W}e_{ik} + \bar{K}_{ik}d_{ik}\right],$$

then

$$\dot{V} = S_{ik}^T\left(-\bar{\kappa}_{ik}sat\left(S_{ik}\right) - \bar{\eta}_{ik}S_{ik}\right).$$

$\dot{V}$ is negative definite. Similarly, the system is stable.

3 Modeling of the Fully Actuated System (FAS) Approach

For the sake of convenience, the system (4) is recalled as

$$\ddot{W}e_{ik} = G_{ik}u_{ik} + d_{ik}\left(We_{ik}, \dot{W}e_{ik}, t\right). \tag{7}$$

For system (7), it is easy to prove that $\det\left(G_{ik}\right) \neq 0$, $\forall t > 0$, due to the fact that

$$\det\left(G_{ik}\right) = \begin{bmatrix} \cos\varphi_{ik} & r\sin\varphi_{ik} \\ -\dfrac{\sin\varphi_{ik}}{l_{ik}} & \dfrac{r\cos\varphi_{ik}}{l_{ik}} \end{bmatrix} = \frac{r^2}{l_{ik}} \neq 0.$$

Therefore according to [8], the system is fully actuated. Consequently, the system can be converted into a desired linear time-invariant one by designing a suitable control law. For the two-dimensional higher-order equation of states (7), extend it to a four-dimensional first-order system, defining $Z_1 = We_{ik}$, $Z_2 = \dot{W}e_{ik}$, which means $\dot{Z}_1 = \dot{W}e_{ik} = Z_2$ and the state is

$$Z = \begin{bmatrix} We_{ik} \\ \dot{W}e_{ik} \end{bmatrix} = \begin{bmatrix} Z_1 \\ Z_2 \end{bmatrix} = \begin{bmatrix} l_{ik} - l_{ik}^* \\ \Psi_{ik} - \Psi_{ik}^* \\ \dot{l}_{ik} - \dot{l}_{ik}^* \\ \Psi_{ik} - \Psi_{ik}^* \end{bmatrix}.$$

Then the error system (7) can be described as

$$\dot{Z} = \begin{bmatrix} \dot{W}e_{ik} \\ \ddot{W}e_{ik} \end{bmatrix} = \begin{bmatrix} 0_{2\times 2} & I_2 \\ 0_{2\times 2} & 0_{2\times 2} \end{bmatrix}\begin{bmatrix} Z_1 \\ Z_2 \end{bmatrix} + \begin{bmatrix} 0_{2\times 2} \\ G_{ik}u_k \end{bmatrix} + \begin{bmatrix} 0_{2\times 1} \\ d_{ik} \end{bmatrix},$$

where $u_k \in R^{2\times 1}$ is the control input to be designed, $G_{ik} \in R^{2\times 2}$ is the matrix of known parameters related to the relative distance, relative angle, and radius of the robots, and $d_{ik} =$

$d_{ik}\left(We_{ik}, \dot{We}_{ik}, t\right) \in R^{2\times1}$ is the uncertainty, whose detailed calculation formula has already been shown in subsection 2.1.

By designing the control law

$$u_k = G_{ik}^{-1}\left(-d_{ik} - A_1\dot{We}_{ik} - A_0We_{ik} + B_1v\right),$$

one can obtain the following linear time-invariant system

$$\begin{aligned}\dot{Z} &= \begin{bmatrix} 0_{2\times2} & I_2 \\ -A_0 & -A_1 \end{bmatrix} Z + \begin{bmatrix} 0_{2\times2} \\ B_1 \end{bmatrix} v \\ &= AZ + Bv,\end{aligned} \tag{8}$$

where

$$A = \begin{bmatrix} 0_{2\times2} & I_2 \\ -A_0 & -A_1 \end{bmatrix},\ B = \begin{bmatrix} 0_{2\times2} \\ B_1 \end{bmatrix},$$

in which A_1, $A_0 \in R^{2\times2}$, $B_1 \in R^{2\times2}$, and $v \in R^{2\times2}$, which all can be arbitrarily chosen. By selecting the four matrices appropriately, the system (8) can be controllable. In particular, if $B_1 = 0_{2\times2}$, with A_1 and $A_0 \in R^{2\times2}$ properly selected, the matrix A in equation (8) can be Hurwitz. Then the system is stable consequently. Particularly, in this article, $A_1 = 12I_2$, $A_0 = 36I_2$, $B_1 = 0_{2\times2}$. Consequently, it holds that

$$A = \begin{bmatrix} 0_{2\times2} & I_2 \\ -36I_2 & -12I_2 \end{bmatrix},\ B = 0_{4\times2}.$$

and the system (8) is then transformed into the following system

$$\dot{Z} = \begin{bmatrix} 0_{2\times2} & I_2 \\ -36I_2 & -12I_2 \end{bmatrix} Z. \tag{9}$$

Considering that

$$\begin{aligned}|\lambda I_4 - A| &= \begin{vmatrix} \lambda I_2 & -I_2 \\ 36I_2 & (\lambda+12)I_2 \end{vmatrix} \\ &= \left(\lambda^2 + 12\lambda + 36\right)^2 I_2 \\ &= 0.\end{aligned}$$

It can be seen that the eigenvalues of A are all -6, which means A is Hurwitz. Based on Routh-Hurwitz stability criterion, one can conclude that the linear time-invariant (LTI) system (9) is stable. Thus ultimately, the states

$$Z = \begin{bmatrix} We_{ik} \\ \dot{We}_{ik} \end{bmatrix} = \begin{bmatrix} Z_1 \\ Z_2 \end{bmatrix} = \begin{bmatrix} l_{ik} - l_{ik}^* \\ \Psi_{ik} - \Psi_{ik}^* \\ \dot{l}_{ik} - \dot{l}_{ik}^* \\ \dot{\Psi}_{ik} - \dot{\Psi}_{ik}^* \end{bmatrix} = 0.$$

In this paper, each follower follows only one leader. Consequently, each follower maintains the desired relative distance and angle with their respective leader, which means the formation is achieved that the robot team moves in the desired formation following the main leader moving along the expected trajectory.

4 Simulation Verification and Application

To verify the effectiveness of the designed scheme, a robot team with a distributed structure is used. The robot formation system consists of 8 robots with a radius of $0.2m$ and a virtual robot, which is the main leader and is numbered as 0th. The eight robots have their own leader respectively. The leader transmits its pose and velocity to the follower in one direction. Define that, if row $j+1$ in column $i+1$ is equal to 1, it means that the ith robot transmits the information such as its own pose and velocity to the jth robot. The communication matrix is as follows

$$Con = \begin{bmatrix} C_1 & 0_{5\times4} \\ C_2 & 0_{4\times4} \end{bmatrix},$$

where

$$C_1 = \begin{bmatrix} 0&0&0&0&0 \\ 1&0&0&0&0 \\ 0&1&0&0&0 \\ 0&1&0&0&0 \\ 0&1&0&0&0 \end{bmatrix},\ C_2 = \begin{bmatrix} 0&0&0&0&1 \\ 0&0&0&0&1 \\ 0&0&1&0&0 \\ 0&0&0&1&0 \end{bmatrix}.$$

The specific distributed communication topology is depicted as follows

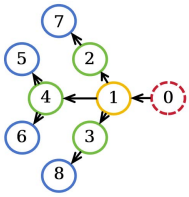

Fig. 2: Formation communication topology diagram.

Referring to [19], while the speed of the 0th virtual robot is

$$v_0 = \left[\sqrt{b\left(\cos(bt)^2 + 1\right)} \quad -b\sin(bt)/\left(\cos(bt)^2 + 1\right)\right]^T,$$

where $b = 0.05$, the robot team will move along the sinusoidal trajectory as shown in Fig. 3. The velocity v_0 is differentiated to get the acceleration of the 0th virtual robot.

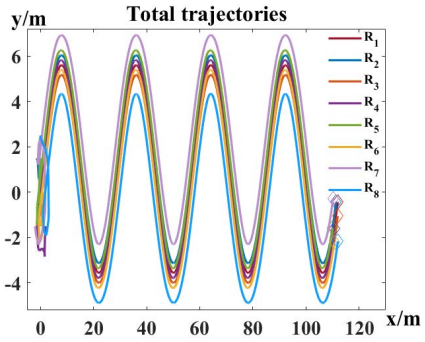

Fig. 3: Formation trajectories.

The disturbance parameters are set as follows

$$\Delta_k = \begin{bmatrix} 0.3rand() - 0.15 & 0 \\ 0 & 0.3rand() - 0.15 \end{bmatrix},$$

$$\pi_{kx} = \pi_{ky} = \pi_{k\theta} = 0.1\sin(2\pi t),$$

where k=1, ..., 8, and $rand()$ produces a random number ranging from 0 to 1 each time.

The initial pose of every robot, the initial relative distance and angle between every follower and their respective leader, and the desired ones are shown in Table 1-3, respectively.

Table 1: Initial poses

$q_i = [x_i \ y_i \ \theta_i]^T$ /(m m rad)	
	$q_0 = [1 \quad 1 \quad \pi/4]^T$
	$q_1 = [0 \quad 0 \quad \pi/4]^T$
	$q_2 = [-1.3 \quad 1.5 \quad 0]^T$
	$q_3 = [1.3 \quad -1.5 \quad \pi]^T$
	$q_4 = [2 \quad -1.5 \quad \pi/3]^T$
	$q_5 = [0 \quad 1.5 \quad \pi/3]^T$
	$q_6 = [0 \quad -1.5 \quad \pi/6]^T$
	$q_7 = [-2 \quad -1.5 \quad -\pi/4]^T$
	$q_8 = [0 \quad 2.5 \quad -\pi/6]^T$

Table 2: Initial relative distances and angles

$W_{ik} = [l_{ik} \ \psi_{ik}]^T$ /(m rad)	
	$W_{01} = [1.2142 \quad 3.1416]^T$
	$W_{12} = [1.3601 \quad -3.8178]^T$
	$W_{13} = [1.3601 \quad 3.5125]^T$
	$W_{14} = [0.9840 \quad 4.9343]^T$
	$W_{45} = [3.1985 \quad -4.1729]^T$
	$W_{46} = [1.3295 \quad 0.9925]^T$
	$W_{27} = [2.1907 \quad -0.6996]^T$
	$W_{38} = [3.0595 \quad 3.9465]^T$

Table 3: Desired relative distances and angles

$W^*_{ik} = [l^*_{ik} \ \psi^*_{ik}]^T$ /(m rad)	
	$W^*_{01} = [1 \quad \pi]^T$
	$W^*_{12} = [0.5 \quad \pi/1.5]^T$
	$W^*_{13} = [0.5 \quad -\pi/1.5]^T$
	$W^*_{14} = [1.5 \quad -\pi]^T$
	$W^*_{45} = [0.5 \quad \pi/1.5]^T$
	$W^*_{46} = [0.5 \quad -\pi/1.5]^T$
	$W^*_{27} = [1 \quad \pi/1.5]^T$
	$W^*_{38} = [1 \quad -\pi/1.5]^T$

Considering the safety issues, limitations are applied to the velocities together with the control inputs of the robot which are the accelerations. The maximum control inputs are the maximum accelerations, with the maximum linear acceleration being $50m/s^2$, and the maximum angular acceleration being $10\pi rad/s^2$. Simultaneously, the maximum linear velocity is $5m/s$, and the maximum angular velocity is $\pi rad/s$. That is, this paper sets $\|u_{kl}\|_\infty \leq 50$, $\|u_{kw}\|_\infty \leq 10\pi$, $\|v_l\|_\infty \leq 5$, $\|v_w\|_\infty \leq \pi$, where respectively, u_{kl} and u_{kw} represent linear acceleration and angular acceleration, and v_l and v_w represent linear velocity and angular velocity.

For sliding mode control (SMC), design

$$\bar{J}_{ik} = 4000I_2, \ \bar{K}_{ik} = 5000I_2, \ \bar{\kappa}_{ik} = \bar{\eta}_{ik} = 12I_2.$$

For fully actuated system (FAS) , design

$$A_1 = 12I_2, A_0 = 36I_2.$$

Simulation results are shown in Fig. 4-8, where it can be seen that by deploying the FAS technique, the error convergence speed is faster, and the robustness against disturbance is higher. The steady state error is reduced, and the fluctuation of the control input is suppressed. In addition, the parameter design of FAS is more straight forward and simpler.

1) The relative distance errors and relative angle errors are shown in Fig. 4-5.

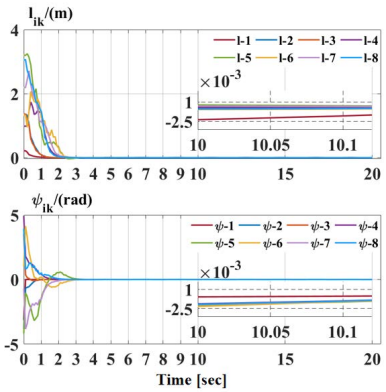

Fig. 4: FAS state errors.

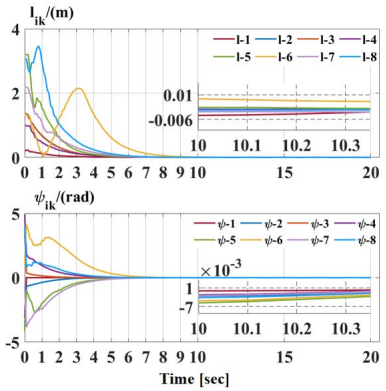

Fig. 5: SMC state errors.

2) The control inputs are shown in Fig. 6-7.

3) Additionally, the state errors with the disturbance term not removed is also given in this paper, as shown in Fig. 8.

As can be seen from the comparison of Fig. 4 and Fig. 5, the FAS control method has a faster convergence speed, less overshoot, and smaller stability error. From the comparison of the control input curves in Fig. 6 and Fig. 7, it can be seen that the control input of the FAS control method converges to a stable value faster, and the stability fluctuation is smaller, which means that the performance of FAS control is better. From Fig. 8, it can be concluded that FAS is more robust than SMC in response to disturbance especially on the distance errors since the fluctuations are smaller.

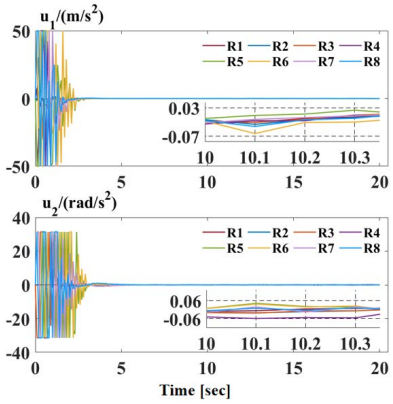

Fig. 6: FAS control inputs.

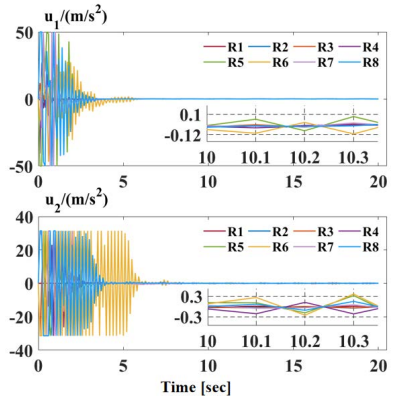

Fig. 7: SMC control inputs.

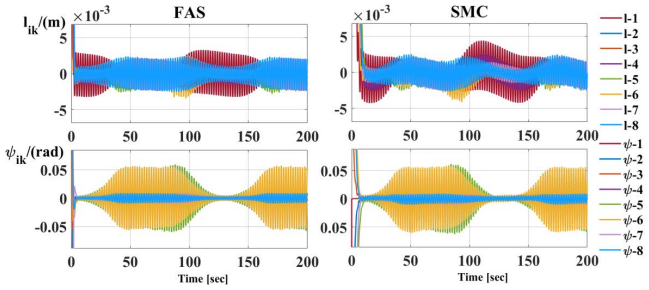

Fig. 8: The state errors in 200 seconds.

5 Conclusion and Future Work

It is difficult to establish a suitable high-order system for formation using the theory of fully actuated system. This paper succeeds in establishing a suitable robot formation error system based on the distance-angle and converting it into a linear stationary system through the design method of FAS. In this paper, the dynamic error system model of the robot formation is transformed into a high-order fully actuated system. Subsequently, the target closed-loop system is converted into a linear time-invariant one with the coefficient matrix being Hurwitz, so that the error converges to zero ultimately. Compared with the conventional sliding mode control (SMC) method, the fully actuated system (FAS) control method performs a faster convergence speed, higher robustness against disturbance, and less fluctuation of the control input in steady state.

Future research efforts will be devoted to considering obstacle avoidance and possible collisions between robots. The disturbance observers will be designed in the future to estimate the disturbance and then eliminate the effects of disturbance as effectively as possible.

References

[1] Y. Toda and N. Kubota. Self-Localization Based on Multiresolution Map for Remote Control of Multiple Mobile Robots, *IEEE Transactions on Industrial Informatics*, 9(3): 1772-1781, 2013.

[2] Lee C.E, Im H.J, Lim J.M, et al. Seamless Routing and Cooperative Localization of Multiple Mobile Robots for Search and Rescue Application, *ETRI Journal*, 37(2): 262-272, 2015.

[3] Juan Li, Ruikun Yuan, Honghan Zhang. Research on Multi-AUV Formation Control Algorithm Based on Leader-follower Method, *Chinese Journal of Scientific Instrument*, V40(06): 240-249, 2019.

[4] Lei Ji, Chunxia Fan. Multi-UAV Formation Control Method Based on Stochastic Delay, *Journal of Applied Sciences*, 037(004): 551-564, 2019.

[5] CHEN J, SUN D, YANG J, et al. Leader-follower formation control of multiple nonholonomic mobile robots incorporating a receding-horizon scheme, *Internatinal Journal of Robotics Research*, 29(6): 727-747, 2010.

[6] Lu Yu. Multi-robot sliding mode formation control based on disturbance observer. *North China Electric Power University (Beijing)*, 2017: 6-24.

[7] Jiarong Chen. Research on formation control of leader-follower robot based on second-order sliding mode algorithm. *North China Electric Power University (Beijing)*, 2021: 5-13.

[8] Duan Guang-Ren. High-order system approaches: I. Fullyactuated systems and parametric design. *Acta Automatica Sinica*, 46(7): 1333-1345, 2020.

[9] Duan Guang-Ren. High-order system approaches: II. Controllability and fully-actuation. *Acta Automatica Sinica*, 46(8): 1571-1581, 2020.

[10] Duan G R, High-order system approaches: III. Observability and observer design, *Acta Automatica Sinica*, 46(9): 1885-1895, 2020.

[11] Duan G R, High-order fully actuated system approaches: Part III. Robust control and high-order backstepping, *International Journal of Systems Science*, 52(5): 952-971, 2021.

[12] Duan G R, High-order fully actuated system approaches: Part IV. Adaptive control and high order backstepping, *International Journal of Systems Science*, 52(5): 972-989, 2021.

[13] Duan G R, High-order fully actuated system approaches: Part V. Robust adaptive control, *International Journal of Systems Science*, 52(10): 2129-2143, 2021.

[14] Duan G R, High-order fully-actuated system approaches: Part VI. Disturbance attenuation and decoupling, *International Journal of Systems Science*, 52(10): 2161-2181, 2021.

[15] Duan G R, High-order fully actuated system approaches: Part VIII. Optimal control with application in spacecraft attitude stabilisation, *International Journal of Systems Science*, 53(1): 54-73, 2022.

[16] Qin Z, Ren G D. Fully Actuated System Approach for 6DOF Spacecraft Control Based on Extended State Observer, *Journal of Systems Science and Complexity*, 35(2): 604-622, 2022.

[17] Peng Li. *Research and application of traditional and high-order sliding mode control*. National University of Defense Technology, 2012: chapter 2.

[18] Feng Chen. *Research on sliding mode variable structure control theory and its application in robot*. Jiangnan University, 2008: chapter 2.

[19] Qing Han. *Research on Robot Formation Control Method*. Shanghai: Shanghai Jiao Tong University Press, 2020: 23-27.

Proceedings of the 3rd Conference on Fully Actuated System Theory and Applications
May 10-12, 2024, Shenzhen, China

Sliding Mode Control for Tower Crane with Double Spherical Pendulum and Variable Cable Length

Gang Li[1,2], Xin Ma[1,2]*, Jing Li[3], Yibin Li[1,2]

1. Center for Robotics, School of Control Science and Engineering, Shandong University, Jinan 250061, China

2. Engineering Research Center of Intelligent Unmanned System, Ministry of Education, Jinan 250061, China

3. Shandong Fenghui Equipment Technology Co. LTD, Jinnan 250200, China
E-mail: maxin@sdu.edu.cn

Abstract: The complex dynamics of the double spherical pendulum with variable cable length present a significant challenge in controlling the swing of underactuated tower cranes. In this article, we present a sliding mode anti-sing controller for the underactuated seven degrees of freedom (7-DOF) tower crane with the double spherical pendulum and cable length variations. The underactuated 7-DOF tower crane model provides a comprehensive representation of the dynamics involved in jib slewing, trolley movement, cable length variations, hook swing, and payload swing. Utilizing the elimination method, a fully actuated system model is obtained from the underactuated 7-DOF tower crane model. Based on the fully actuated system model, we designed a sliding mode controller to effectively suppress both hook swing and payload swing. The theoretical analysis and experimental results demonstrate the accuracy of the 7-DOF tower crane dynamic model and the effectiveness of the sliding mode controller.

Key Words: Full actuated system model, Sliding mode control, 7-DOF Tower crane system, Anti-swing control.

1 Introduction

Tower cranes are typically used in the construction industry for lifting and transporting materials, including concrete, steel, and other building materials [1]. Tower cranes are the underactuated systems, which have fewer control inputs than the number of degrees of freedom (DOF) in the system [2]. Not all DOFs can be directly controlled simultaneously in underactuated tower cranes. This is because tower cranes have a limited number of controllers that can only control the trolley moving, jib slewing and payload hoisting, but lack the controller for the hook/payload swing directly. It is necessary to design the control strategies that effectively manage the tower crane, ensuring stability and safety throughout its operation.

In practices, the double spherical pendulum motion which may happen when jib slews and trolley moves to transport the large-size payload (e.g. distributed-mass beam) [3]. Furthermore, the lengths of the suspension cables are adjusted to lift or lower the payload. The tower crane with its variable cable lengths and double spherical pendulum effect constitutes a complex multi-input multi-output electromechanical system. This system features three inputs, including the jib controller, trolley controller, and cable controller, and seven DOFs, which encompass jib slewing, trolley movement, payload hoisting/lowering, and payload/hook spherical swing. Designing effective controllers that can counteract swinging motion while ensuring stability and safety is indeed a complex task in the 7-DOF tower crane system.

After decades of in-depth research, numerous remarkable results have been published regarding the control of underactuated tower crane systems with single spherical pendulum effect. Various anti-swing controllers are designed for the 4-DOF tower crane with single spherical pendulum and fixed cable length, including sliding mode control [4,5], fault-tolerant control [6], proportional integral derivative control [7], and observer-based nonlinear control [8], et.al. As the suspension cable length is time-varying, the anti-swing control performance of the aforementioned methods based on fixed cable lengths fails to work effectively. To solve anti-swing control problem of 5-DOF tower crane with single spherical pendulum and varying cable length, several control methods have been developed, including optimization trajectory planning [9], active disturbance rejection control [10], model predictive control [11], neural network system estimation based input shaping control [12,13], and adaptive control [14,15], et.al. However, these control methods belong to single spherical pendulum tower crane model while ignoring the hook swing motion.

Recently, some research works focus on complicated double spherical pendulum dynamic and controller design in 6-DOF tower crane with fixed cable lengths. Some open-loop controllers, such as input shaper [16], smoother [17] and trajectory planners [18,19] are designed for the 6-DOF tower crane. However, these open-loop control methods are very sensitive to the disturbances. By incorporating state feedback, several closed-loop control techniques, including energy analysis-based (EAB) control [20], neural network triggered control [21], adaptive tracking control [22,23], and active disturbance rejection control [24], significantly enhance the tower crane system's robustness to disturbances. The existing tower crane controllers typically consider 6-DOF (e.g., payload/hook spherical swing, trolley moving, and jib slewing), but often neglect the variable cable lengths, which can significantly impact the swing frequencies. The

* This work is supported by the Science Center Program of National Natural Science Foundation of China under Grant 62188101, Key Research and Development Project of Shandong Province under Grant 2021CXGC010701, Central Guidance for Local Scientific and Technological Development Funding Projects of Shandong Province under Grant YDZX2023042, and the Joint Fund of the National Nature Science Foundation of China and Shandong Province under Grant U1706228.

controller design for the tower crane with double spherical pendulum effect requires further improvement.

In order to solve the above issues, this paper proposes a sliding mode anti-swing control method for 7-DOF tower crane with variable cable lengths. Firstly, a underactuated dynamic model of 7-DOF tower crane is established by using Lagrange's modeling methods. Then, a fully actuated system model of 7-DOF tower crane is obtained from the underactuated model by utilizing the elimination method. After, a sliding mode anti-swing controller is designed based on the fully actuated system model of 7-DOF tower crane. At last, the effectiveness of the proposed sliding mode anti-swing controller is verified by hardware experiments.

The main contribution is outlined as follows:

1) This paper establishes a underactuated 7-DOF tower crane with variable cable lengths and double spherical pendulum effects.

2) This paper presents a sliding mode anti-swing control method that effectively addresses the challenges in 7-DOF tower crane systems. This control method utilizes three inputs to simultaneously regulate seven system outputs.

2 Dynamics Model of 7-DOF Tower Crane

The 7-DOF tower crane model is illustrated in Fig. 1. Table 2 presents its system parameters in full detail.

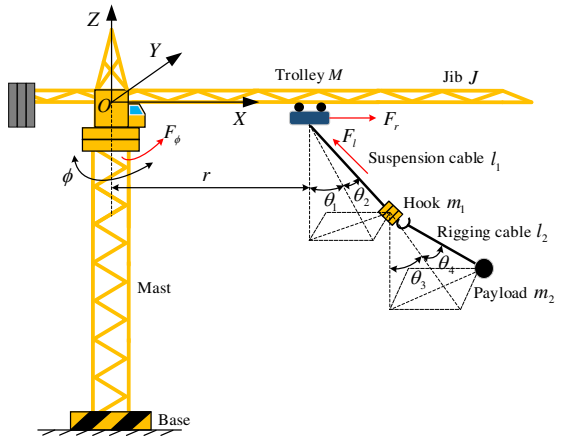

Fig. 1: Model of 7-DOF tower crane

Table 1: Nomenclature of 7-DOF Tower Crane Parameters

Para.	Parameter definition	Units
M,m_1,m_2	Trolley, hook and payload masses	kg
J	Jib inertia moment	kg·m^2
l_1,l_2	Suspension and rigging cable lengths	m
ϕ	Jib slewing angles	deg
r	Trolley translation displacements	m
θ_1,θ_2	Hook swing angles	deg
θ_3,θ_4	Payload swing angles	deg
F_ϕ,F_r,F_l	Resultant torques/forces controlling jib, trolley and suspension cable	N·m, N
g	Gravity constant	m/s^2

The position vectors of trolley, hook and payload are expressed as follows

$$p_M = \begin{bmatrix} r & 0 & 0 \end{bmatrix}^T \tag{1}$$

$$p_1 = \begin{bmatrix} x + l_1 s_1 c_2 & l_1 s_2 & -l_1 c_1 c_2 \end{bmatrix}^T \tag{2}$$

$$p_2 = \begin{bmatrix} x + l_1 s_1 c_2 + l_2 s_3 c_4 & l_1 s_2 + l_2 s_4 & -l_1 c_1 c_2 - l_2 c_3 c_4 \end{bmatrix}^T \tag{3}$$

where s_i, c_i are the abbreviation for $\sin\theta_i, \cos\theta_i$, i=1~4.

The angular velocity vector of the jib slewing is given as

$$v_j = \begin{bmatrix} 0 & 0 & \dot{\phi} \end{bmatrix}^T . \tag{4}$$

The velocity vectors of trolley, hook and payload are calculated as

$$v_M = \frac{\mathrm{d}p_M}{\mathrm{d}t} + v_j \times p_M \tag{5}$$

$$v_1 = \frac{\mathrm{d}p_1}{\mathrm{d}t} + v_j \times p_1 \tag{6}$$

$$v_2 = \frac{\mathrm{d}p_2}{\mathrm{d}t} + v_j \times p_2 . \tag{7}$$

The entire kinetic energy of the 7-DOF tower crane is obtained by using the velocity vectors (5)-(7) as follows:

$$K = \frac{1}{2} J \dot{\phi}^2 + \frac{1}{2} M v_M^T v_M + \frac{1}{2} m_1 v_1^T v_1 + \frac{1}{2} m_2 v_2^T v_2 . \tag{8}$$

The potential energy of the 7-DOF tower crane is given as

$$P = -m_1 g l_1 c_1 c_2 - m_2 g \left(l_1 c_1 c_2 + l_2 c_3 c_4 \right) . \tag{9}$$

We define the Lagrange's function $L = K - P$ and calculate the following Lagrange's equations

$$\begin{cases} \dfrac{\mathrm{d}}{\mathrm{d}t}\dfrac{\partial L}{\partial \dot{\eta}} - \dfrac{\partial L}{\partial \eta} = F_\eta, \eta = \phi, r, l_1, \\ \dfrac{\mathrm{d}}{\mathrm{d}t}\dfrac{\partial L}{\partial \dot{\theta}_i} - \dfrac{\partial L}{\partial \theta_i} = -d_i \dot{\theta}_i, i = 1,2,3,4. \end{cases} \tag{10}$$

The dynamic model of 7-DOF tower crane can be obtained from (10) as

$$\begin{aligned}
&\left[J + \left(M + m_1 + m_2 \right) r^2 + \left(m_1 + m_2 \right) l_1^2 + m_2 l_2^2 - m_2 c_3^2 \right. \\
&\cdot c_4^2 l_2^2 + 2 m_2 s_2 s_4 l_1 l_2 - \left(m_1 + m_2 \right) c_1^2 c_2^2 l_1^2 + 2 m_2 s_3 c_4 r l_2 \\
&+ 2 \left(m_1 + m_2 \right) s_1 c_2 r l_1 + 2 m_2 s_1 c_2 s_3 c_4 l_1 l_2 \left. \right] \ddot{\phi} - \left[\left(m_1 + m_2 \right) \right. \\
&\cdot s_2 l_1 + m_2 s_4 l_2 \left. \right] \ddot{r} - \left[\left(m_1 + m_2 \right) c_1 c_2 s_2 l_1^2 + m_2 c_1 c_2 s_4 l_1 l_2 \right] \ddot{\theta}_1 \\
&+ \left[\left(m_1 + m_2 \right) s_2 r - m_2 l_2 \left(s_1 c_2 s_4 + s_2 s_3 c_4 \right) \right] \ddot{l}_1 \\
&+ \left[\left(m_1 + m_2 \right) \left(s_1 l_1^2 + c_2 l_1 r \right) + m_2 l_1 l_2 \left(c_2 s_3 c_4 + s_1 s_2 s_4 \right) \right] \ddot{\theta}_2 \\
&- \left[m_2 \left(s_2 l_1 + s_4 l_2 \right) c_3 c_4 l_2 \right] \ddot{\theta}_3 + \left[m_2 l_2 \left(s_3 l_2 + c_4 r \right) + m_2 l_1 l_2 \right. \\
&\cdot \left(s_1 c_2 c_4 + s_2 s_3 s_4 \right) \left. \right] \ddot{\theta}_4 + \left[2 \left(M + m_1 + m_2 \right) r + 2 s_1 c_2 l_1 \right. \\
&\cdot \left(m_1 + m_2 \right) + 2 m_2 s_3 c_4 l_2 \left. \right] \dot{\phi} \dot{r} + \left[2 m_2 l_2 \left(s_2 s_4 + s_1 c_2 s_3 c_4 \right) \right. \\
&+ 2 \left(m_1 + m_2 \right) l_1 \left(s_1^2 + c_1^2 s_2^2 \right) + 2 \left(m_1 + m_2 \right) s_1 c_2 r \left. \right] \dot{\phi} \dot{l}_1 \\
&+ \left[2 \left(m_1 + m_2 \right) c_1 c_2 r l_1 + 2 \left(m_1 + m_2 \right) c_1 s_1 c_2^2 l_1^2 + 2 m_2 c_1 c_2 \right. \\
&\cdot s_3 c_4 l_1 l_2 \left. \right] \dot{\phi} \dot{\theta}_1 + \left[2 m_2 c_2 s_4 l_1 l_2 + 2 \left(m_1 + m_2 \right) c_1^2 c_2 s_2 l_1^2 \right. \\
&- 2 \left(m_1 + m_2 \right) s_1 s_2 l_1 r - 2 m_2 s_1 s_2 s_3 c_4 l_1 l_2 \left. \right] \dot{\phi} \dot{\theta}_2 \\
&+ \left[2 m_2 c_3 c_4 r l_2 + 2 m_2 c_3 s_3 c_4^2 l_2^2 + 2 m_2 s_1 c_2 c_3 c_4 l_1 l_2 \right] \dot{\phi} \dot{\theta}_3 \\
&+ \left[2 m_2 s_2 c_4 l_1 l_2 + 2 m_2 c_3^2 s_4 c_4 l_2^2 - 2 m_2 s_3 s_4 l_2 r - 2 m_2 s_1 c_2 \right. \\
&\cdot s_3 s_4 l_1 l_2 \left. \right] \dot{\phi} \dot{\theta}_4 - \left[2 \left(m_1 + m_2 \right) c_1 c_2 s_2 l_1 + 2 m_2 c_1 c_2 s_4 l_2 \right] \dot{l}_1 \dot{\theta}_1 \\
&+ \left[\left(m_1 + m_2 \right) s_1 c_2 s_2 l_1^2 + m_2 s_1 c_2 s_4 l_1 l_2 \right] \dot{\theta}_1^2 + \left[2 \left(m_1 + m_2 \right) \right. \\
&\cdot \left(s_1 l_1 + c_2 x \right) + 2 m_2 c_2 s_3 c_4 l_2 + 2 m_2 s_1 s_2 s_4 l_2 \left. \right] \dot{l}_1 \dot{\theta}_2 + \dot{\theta}_1 \dot{\theta}_2 \\
&\cdot \left[2 \left(m_1 + m_2 \right) c_1 s_2^2 l_1^2 + 2 m_2 c_1 s_2 s_4 l_1 l_2 \right] + \left[m_2 s_1 c_2 s_4 l_1 l_2 \right. \\
&- \left(m_1 + m_2 \right) s_2 l_1 r - m_2 s_2 s_3 c_4 l_1 l_2 \left. \right] \dot{\theta}_2^2 + \left[m_2 s_3 c_4 s_4 l_2^2 \right. \\
&+ m_2 s_2 s_3 c_4 l_1 l_2 \left. \right] \dot{\theta}_3^2 + \left[2 m_2 c_3 s_4^2 l_2^2 + 2 m_2 s_2 c_3 s_4 l_1 l_2 \right] \dot{\theta}_3 \dot{\theta}_4 \\
&+ \left[m_2 s_2 s_3 c_4 l_1 l_2 - m_2 s_4 l_2 r - m_2 s_1 c_2 s_4 l_1 l_2 \right] \dot{\theta}_4^2 = F_\phi
\end{aligned} \tag{11}$$

$$
\begin{aligned}
&(M+m_1+m_2)\ddot{r}-\left[(m_1+m_2)s_2l_1+m_2s_4l_2\right]\\
&\cdot\ddot{\phi}+(m_1+m_2)s_1c_2\ddot{l}_1+(m_1+m_2)c_1c_2l_1\ddot{\theta}_1\\
&-(m_1+m_2)s_1s_2l_1\ddot{\theta}_2+m_2c_3c_4l_2\ddot{\theta}_3-m_2s_3s_4\\
&\cdot l_2\ddot{\theta}_4-\left[(m_1+m_2)s_1c_2l_1(M+m_1+m_2)r\right.\\
&\left.+m_2s_3c_4l_2\right]\dot{\phi}^2-2(m_1+m_2)c_2l_1\dot{\phi}\dot{\theta}_2-2m_2c_4\\
&\cdot l_2\dot{\phi}\dot{\theta}_4-2(m_1+m_2)s_2\dot{\phi}\dot{l}_1+2(m_1+m_2)c_1c_2\\
&\cdot\dot{l}_1\dot{\theta}_1-2(m_1+m_2)s_1s_2\dot{l}_1\dot{\theta}_2-(m_1+m_2)s_1c_2\\
&\cdot l_1\dot{\theta}_1^2-2(m_1+m_2)c_1s_2l_1\dot{\theta}_1\dot{\theta}_2-m_2s_3c_4l_2\dot{\theta}_3^2\\
&-2m_2c_3s_4l_2\dot{\theta}_3\dot{\theta}_4-m_2s_3c_4l_2\dot{\theta}_4^2=F_r
\end{aligned}
\tag{12}
$$

$$
\begin{aligned}
&\left[(m_1+m_2)s_2r-m_2s_1c_2s_4l_2+m_2s_2s_3c_4\right]\ddot{\phi}\\
&+(m_1+m_2)s_1c_2r+(m_1+m_2)\ddot{l}_1+m_2s_{1-3}c_2\\
&\cdot c_4\ddot{\theta}_3+m_2l_2\left(s_2c_4-c_{1-3}c_2s_4\right)\ddot{\theta}_4+2s_2\dot{\phi}\dot{r}\\
&\cdot(m_1+m_2)-\left[(m_1+m_2)\left(c_1^2s_2^2+s_1^2\right)l_1\right.\\
&\left.+m_2s_2s_4l_2+(m_1+m_2)s_1c_2r+m_2s_1c_2s_3c_4l_2\right]\dot{\phi}^2\\
&+2(m_1+m_2)c_1s_2c_2l_1\dot{\phi}\dot{\theta}_1-2(m_1+m_2)s_1l_1\dot{\phi}\dot{\theta}_2\\
&+2m_2s_2c_3c_4l_2\dot{\phi}\dot{\theta}_3-2m_2\left(s_1c_2c_4+s_2s_3s_4\right)l_2\dot{\phi}\dot{\theta}_4\\
&-(m_1+m_2)c_2^2l_1\dot{\theta}_1^2-(m_1+m_2)l_1\dot{\theta}_2^2-m_2l_2c_{1-3}\\
&\cdot c_2c_4\dot{\theta}_3^2-2m_2l_2s_{1-3}c_2s_4\dot{\theta}_3\dot{\theta}_4-m_2l_2\\
&\cdot\left(s_2s_4+c_{1-3}c_2c_4\right)\dot{\theta}_4^2-(m_1+m_2)gc_1c_2=F_l
\end{aligned}
\tag{13}
$$

$$
\begin{aligned}
&-\left[(m_1+m_2)c_1c_2s_2l_1^2+m_2c_1c_2s_4l_1l_2\right]\ddot{\phi}\\
&+(m_1+m_2)c_1c_2l_1\ddot{r}+(m_1+m_2)c_2^2l_1^2\ddot{\theta}_1\\
&+m_2c_{1-3}c_2c_4l_1l_2\ddot{\theta}_3+m_2s_{1-3}c_2s_4l_1l_2\ddot{\theta}_4\\
&-2(m_1+m_2)c_1s_2c_2l_1\dot{\phi}\dot{l}_1-\left[(m_1+m_2)c_1c_2l_1r\right.\\
&\left.+(m_1+m_2)s_1c_1c_2^2l_1^2+m_2c_1c_2s_3c_4l_1l_2\right]\dot{\phi}^2\\
&-2(m_1+m_2)c_1c_2^2l_1^2\dot{\phi}\dot{\theta}_2-2m_2c_1c_2c_4l_1l_2\dot{\phi}\dot{\theta}_4\\
&+2(m_1+m_2)c_2^2l_1\dot{l}_1\dot{\theta}_1-2(m_1+m_2)c_2s_2l_1^2\dot{\theta}_1\dot{\theta}_2\\
&+m_2s_{1-3}c_2c_4l_1l_2\dot{\theta}_3^2-2m_2c_{1-3}c_2s_4l_1l_2\dot{\theta}_3\dot{\theta}_4\\
&+m_2s_{1-3}c_2c_4l_1l_2\dot{\theta}_4^2+(m_1+m_2)gs_1c_2l_1=-d_1\dot{\theta}_1
\end{aligned}
\tag{14}
$$

$$
\begin{aligned}
&\left[(m_1+m_2)s_1l_1^2+(m_1+m_2)c_2l_1r+m_2\right.\\
&\left.\cdot\left(c_2s_3c_4+s_1s_2s_4\right)l_1l_2\right]\ddot{\phi}-(m_1+m_2)s_1s_2l_1\ddot{r}\\
&+(m_1+m_2)l_1^2\ddot{\theta}_1-m_2s_{1-3}s_2c_4l_1l_2\ddot{\theta}_3+m_2l_1l_2\\
&\cdot\left(c_2c_4+c_{1-3}s_2s_4\right)\ddot{\theta}_4+2(m_1+m_2)c_2l_1\dot{\phi}\dot{r}\\
&+\left[(m_1+m_2)s_1s_2l_1r-m_2c_2s_4l_1l_2-(m_1+m_2)\right.\\
&\left.\cdot c_1^2s_2c_2l_1^2+m_2s_1s_2s_3c_4l_1l_2\right]\dot{\phi}^2+2(m_1+m_2)s_1\\
&\cdot l_1\dot{\phi}\dot{l}_1+2(m_1+m_2)c_1c_2^2l_1^2\dot{\phi}\dot{\theta}_1+2m_2c_2c_3c_4l_1l_2\\
&\cdot\dot{\phi}\dot{\theta}_3+2m_2l_1l_2\left(s_1s_2c_4-c_2s_3s_4\right)\dot{\phi}\dot{\theta}_4+2l_1\dot{l}_1\dot{\theta}_2\\
&\cdot(m_1+m_2)+(m_1+m_2)c_2s_2l_1^2\dot{\theta}_1^2+m_2c_{1-3}s_2\\
&\cdot c_4l_1l_2\dot{\theta}_3^2+2m_2s_{1-3}s_2s_4l_1l_2\dot{\theta}_3\dot{\theta}_4+m_2l_1l_2\dot{\theta}_4^2\\
&\cdot\left(c_{1-3}s_2c_4-c_2s_4\right)+(m_1+m_2)gc_1s_2l_1=-d_2\dot{\theta}_2
\end{aligned}
\tag{15}
$$

$$
\begin{aligned}
&-\left[m_2c_3c_4s_4l_2^2+m_2s_2c_3c_4l_1l_2\right]\ddot{\phi}+m_2c_3c_4l_2\ddot{r}\\
&+m_2s_{1-3}c_2c_4l_2\ddot{l}_1+m_2c_{1-3}c_2c_4l_1l_2\ddot{\theta}_1+m_2c_4^2l_2^2\ddot{\theta}_3\\
&-\left[m_2c_3c_4l_2r+m_2c_3s_3c_4^2l_2^2+m_2s_1c_2c_3c_4l_1l_2\right]\dot{\phi}^2\\
&-m_2s_{1-3}s_2c_4l_1l_2\ddot{\theta}_2-2m_2s_2c_3c_4l_2\dot{\phi}\dot{l}_1-2m_2c_2\\
&\cdot c_3c_4l_1l_2\dot{\phi}\dot{\theta}_2-2m_2c_3c_4^2l_2^2\dot{\phi}\dot{\theta}_4+2m_2c_{1-3}c_2c_4\\
&\cdot l_2\dot{l}_1\dot{\theta}_1-2m_2s_{1-3}s_2c_4l_2\dot{l}_1\dot{\theta}_2-m_2s_{1-3}c_2c_4l_1l_2\dot{\theta}_1^2\\
&-2m_2c_{1-3}s_2c_4l_1l_2\dot{\theta}_1\dot{\theta}_2-m_2s_{1-3}c_2c_4l_1l_2\dot{\theta}_2^2\\
&-2m_2c_4s_4l_2^2\dot{\theta}_3\dot{\theta}_4+m_2gs_3c_4l_2=-d_3\dot{\theta}_3
\end{aligned}
\tag{16}
$$

$$
\begin{aligned}
&\left[m_2s_3l_2^2+m_2c_4l_2r+m_2\left(s_1c_2c_4+s_2s_3s_4\right)l_1l_2\right]\\
&\cdot\ddot{\phi}-m_2s_3s_4l_2\ddot{r}+\left[m_2s_2c_4l_2-m_2c_{1-3}c_2s_4l_2\right]\ddot{l}_1\\
&+m_2s_{1-3}c_2s_4l_1l_2\ddot{\theta}_1+m_2l_1l_2\left(c_2c_4+c_{1-3}s_2s_4\right)\ddot{\theta}_2\\
&+m_2l_2^2\ddot{\theta}_4+2m_2c_4l_2\dot{\phi}\dot{r}+\left[m_2s_3s_4l_2r-m_2s_2c_4\right.\\
&\left.\cdot l_1l_2-m_2c_3^2c_4s_4l_2^2+m_2s_1c_2s_3s_4l_1l_2\right]\dot{\phi}^2+2m_2\\
&\cdot c_1c_2c_4l_1l_2\dot{\phi}\dot{\theta}_1+2m_2\left(s_1c_2c_4+s_2s_3s_4\right)l_2\dot{\phi}\dot{l}_1\\
&+2m_2l_1l_2\left(c_2s_3s_4-s_1s_2c_4\right)\dot{\phi}\dot{\theta}_2+2m_2c_3c_4^2l_2^2\dot{\phi}\dot{\theta}_3\\
&+2m_2l_2s_{1-3}c_2s_4\dot{l}_1\dot{\theta}_1+2m_2l_2\left(c_2c_4+c_{1-3}s_2s_4\right)\\
&\cdot\dot{l}_1\dot{\theta}_2+m_2c_{1-3}c_2s_4l_1l_2\dot{\theta}_1^2-2m_2s_{1-3}s_2s_4l_1l_2\dot{\theta}_1\dot{\theta}_2\\
&+m_2s_4c_4l_2^2\dot{\theta}_3^2+m_2l_1l_2\left(c_{1-3}c_2s_4-s_2c_4\right)\dot{\theta}_2^2\\
&+m_2gc_3s_4l_2=-d_4\dot{\theta}_4
\end{aligned}
\tag{17}
$$

where $F_\phi=F_{\phi a}-F_{\phi f}$, $F_r=F_{ra}-F_{rf}$, $F_l=F_{la}-F_{lf}$. $F_{\phi a}, F_{ra}$ and F_{la} represent the actuating torques/forces of jib, trolley and suspension cable, respectively. $F_{\phi f}, F_{rf}$ and F_{lf} are the friction torques/forces of the jib, trolley and suspension cable [22,23,25]. $d_i(i=1,2,3,4)$ represents the damping gains. s_{1-3}, c_{1-3} are the abbreviation for $\sin(\theta_1-\theta_3), \cos(\theta_1-\theta_3)$.

Based on the fact of small swing angles, we can obtain the linearization dynamic model of 7-DOF tower crane from (11)-(17) that

$$
\begin{aligned}
&\left[J+(M+m_1+m_2)r^2+2m_2\theta_3rl_2+2(m_1+m_2)\theta_1rl_1\right]\\
&\cdot\ddot{\phi}-\left[(m_1+m_2)\theta_2l_1+m_2\theta_4l_2\right]\ddot{r}+\left[2(M+m_1+m_2)r\right.\\
&\left.+2(m_1+m_2)l_1\theta_1+2m_2l_2\theta_3\right]\dot{\phi}\dot{r}+(m_1+m_2)\theta_2r\ddot{l}_1+m_2\\
&\cdot l_2r\ddot{\theta}_4+(m_1+m_2)l_1r\ddot{\theta}_2+2(m_1+m_2)\theta_1r\dot{\phi}\dot{l}_1+2m_2l_2r\dot{\phi}\dot{\theta}_3\\
&+2(m_1+m_2)l_1r\dot{\phi}\dot{\theta}_1+2(m_1+m_2)r\dot{l}_1\dot{\theta}_2=F_\phi
\end{aligned}
\tag{18}
$$

$$
\begin{aligned}
&-\left[(m_1+m_2)\theta_2l_1+m_2\theta_4l_2\right]\ddot{\phi}-(M+m_1+m_2)\ddot{r}\\
&+(m_1+m_2)\theta_1\ddot{l}_1+(m_1+m_2)l_1\ddot{\theta}_1+m_2l_2\ddot{\theta}_3\\
&-\left[(M+m_1+m_2)r+(m_1+m_2)l_1\theta_1+m_2l_2\theta_3\right]\dot{\phi}^2\\
&-2(m_1+m_2)\theta_2\dot{\phi}\dot{l}_1-2(m_1+m_2)l_1\dot{\phi}\dot{\theta}_2-2m_2l_2\dot{\phi}\dot{\theta}_4\\
&+2(m_1+m_2)\dot{l}_1\dot{\theta}_1=F_r
\end{aligned}
\tag{19}
$$

$$
\begin{aligned}
&(m_1+m_2)\theta_2r\ddot{\phi}+(m_1+m_2)\theta_1\ddot{r}+(m_1+m_2)\ddot{l}_1\\
&-(m_1+m_2)\theta_1r\dot{\phi}^2+2(m_1+m_2)\theta_2\dot{\phi}\dot{r}\\
&-2(m_1+m_2)g=F_l
\end{aligned}
\tag{20}
$$

$$
\begin{aligned}
&-\left[(m_1+m_2)\theta_2l_1^2+m_2\theta_4l_1l_2\right]\ddot{\phi}+(m_1+m_2)l_1\ddot{r}\\
&+(m_1+m_2)l_1^2\ddot{\theta}_1+m_2l_1l_2\ddot{\theta}_3-2(m_1+m_2)\theta_2l_1\dot{\phi}\dot{l}_1\\
&-\left[(m_1+m_2)l_1r+(m_1+m_2)l_1^2\theta_1+m_2l_1l_2\theta_3\right]\dot{\phi}^2\\
&-2(m_1+m_2)l_1^2\dot{\phi}\dot{\theta}_2-2m_2l_1l_2\dot{\phi}\dot{\theta}_4+2(m_1+m_2)\\
&\cdot l_1\dot{l}_1\dot{\theta}_1+(m_1+m_2)g\theta_1l_1=-d_1\dot{\theta}_1
\end{aligned}
\tag{21}
$$

$$
\begin{aligned}
&\left[(m_1+m_2)\theta_1l_1^2+(m_1+m_2)l_1r+m_2\theta_3l_1l_2\right]\ddot{\phi}\\
&+(m_1+m_2)l_1^2\ddot{\theta}_2+m_2l_1l_2\ddot{\theta}_4+2(m_1+m_2)l_1\dot{\phi}\dot{r}\\
&-\left[(m_1+m_2)l_1^2\theta_2+m_2l_1l_2\theta_4\right]\dot{\phi}^2+2m_2l_1l_2\dot{\phi}\dot{\theta}_3\\
&+2(m_1+m_2)\theta_1l_1\dot{\phi}\dot{l}_1+2(m_1+m_2)l_1^2\dot{\phi}\dot{\theta}_1\\
&+2(m_1+m_2)l_1\dot{l}_1\dot{\theta}_2+(m_1+m_2)g\theta_2l_1=-d_2\dot{\theta}_2
\end{aligned}
\tag{22}
$$

$$
\begin{aligned}
&m_2 l_2 \ddot{r} - \left[m_2 \theta_4 l_2^2 + m_2 \theta_2 l_1 l_2 \right] \ddot{\phi} + m_2 l_2 \left(\theta_1 - \theta_3 \right) \ddot{l}_1 \\
&+ m_2 l_1 l \ddot{\theta}_1 + m_2 l_2^2 \ddot{\theta}_3 - \left[m_2 l_2 r + m_2 l_2^2 \theta_3 + m_2 l_1 l_2 \theta_1 \right] \\
&\cdot \dot{\phi}^2 - 2 m_2 \theta_2 l_2 \dot{\phi} \dot{l}_1 - 2 m_2 l_1 l_2 \dot{\phi} \dot{\theta}_2 - 2 m_2 l_2^2 \dot{\phi} \dot{\theta}_4 \\
&+ 2 m_2 l_2 \dot{l}_1 \dot{\theta}_1 + m_2 g \theta_3 l_2 = -d_3 \dot{\theta}_3
\end{aligned} \tag{23}
$$

$$
\begin{aligned}
&\left[m_2 \theta_3 l_2^2 + m_2 l_2 r + m_2 \theta_1 l_1 l_2 \right] \ddot{\phi} + m_2 l_2 \left(\theta_2 - \theta_4 \right) \ddot{l}_1 \\
&+ m_2 l_1 l_2 \ddot{\theta}_2 + m_2 l_1^2 \ddot{\theta}_4 - \left[m_2 l_2^2 \theta_4 + m_2 l_1 l_2 \theta_2 \right] \dot{\phi}^2 \\
&+ 2 m_2 l_2 \dot{\phi} \dot{r} + 2 m_2 \theta_1 l_2 \dot{\phi} \dot{l}_1 + 2 m_2 l_1 l_2 \dot{\phi} \dot{\theta}_1 + 2 m_2 l_1^2 \dot{\phi} \dot{\theta}_3 \\
&+ 2 m_2 l_2 \dot{l}_1 \dot{\theta}_2 + m_2 g \theta_4 l_2 = -d_4 \dot{\theta}_4
\end{aligned} \tag{24}
$$

By using the elimination method, (18)-(24) can be rewritten as the full actuated system form [26]

$$
M_a \ddot{q}_a + N = U \tag{25}
$$

where q_a, U, M_a, N are defined as

$$
q_a = \begin{bmatrix} \phi \\ r \\ l_1 \end{bmatrix}, U = \begin{bmatrix} F_\phi \\ F_r \\ F_l \end{bmatrix}, M_a = \begin{bmatrix} m_{11} & m_{12} & m_{13} \\ m_{21} & m_{22} & m_{23} \\ m_{31} & m_{32} & m_{33} \end{bmatrix}, N = \begin{bmatrix} N_1 \\ N_2 \\ N_3 \end{bmatrix}
$$

with $m_{11} = J + Mr^2 + m_2 \theta_3 r l_2 + \left(m_1 + m_2 \right) \theta_1 r l_1$, $m_{22} = M$,

$m_{12} = m_{21} = -\left[m_2 \theta_4 l_2 + \left(m_1 + m_2 \right) \theta_2 l_1 \right]$, $m_{33} = m_1 + m_2$,

$m_{13} = m_{31} = \left(m_1 + m_2 \right) \theta_2 r$, $m_{23} = m_{32} = \left(m_1 + m_2 \right) \theta_1$, ,

$$
\begin{aligned}
N_1 &= 2\left[\left(M + m_1 + m_2 \right) r + m_2 \theta_3 l_2 + \left(m_1 + m_2 \right) \theta_1 l_1 \right] \dot{\phi} \dot{r} \\
&+ \left[m_2 \theta_4 r l_2 + \left(m_1 + m_2 \right) \theta_2 r l_1 \right] \dot{\phi}^2 - \left(m_1 + m_2 \right) g r \theta_2 - r d_2 \dot{\theta}_2 / l_1 ,
\end{aligned}
$$

$$
N_2 = M r \dot{\phi}^2 - \left(m_1 + m_2 \right) g \theta_1 - d_1 \dot{\theta}_1 / l_1 ,
$$

$$
N_3 = -\left(m_1 + m_2 \right) \theta_1 r \dot{\phi}^2 + 2 \left(m_1 + m_2 \right) \theta_2 \dot{\phi} \dot{r} - 2 \left(m_1 + m_2 \right) g .
$$

3 Sliding Mode Controller Design

This section provides the sliding mode controller design for the 7-DOF tower crane system. Fig. 2 is a block diagram of the proposed controller.

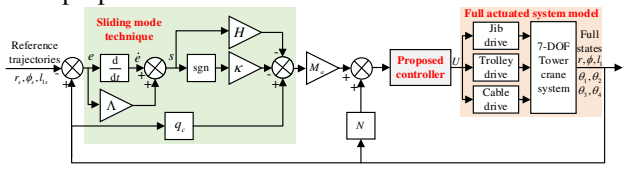

Fig. 2: Block diagram of the proposed controller.

A group of error signals e_ϕ, e_r, e_l about full state variables are defined as follows

$$
e = \begin{bmatrix} e_\phi \\ e_r \\ e_l \end{bmatrix} = \begin{bmatrix} \phi - l_1 \theta_2 - l_2 \theta_4 - \phi_s \\ r - l_1 \theta_1 - l_2 \theta_3 - r_s \\ l_1 - l_{1s} \end{bmatrix} \tag{26}
$$

where ϕ_s, r_s, l_{1s} are reference trajectory, which be selected to satisfy the following conditions.

$$
\begin{cases}
\phi_s, \dot{\phi}_s, \ddot{\phi}_s, r_s, \dot{r}_s, \ddot{r}_s, l_1, \dot{l}_1, \ddot{l}_1 \in \mathcal{L}_\infty , \\
\phi_s(0) = \phi_i, \dot{\phi}_s(0) = \ddot{\phi}_s(0) = 0, \\
r_s(0) = r_i, \dot{r}_s(0) = \ddot{r}_s(0) = 0, \\
l_1(0) = l_{1i}, \dot{l}_1(0) = \ddot{l}_1(0) = 0, \\
\phi_s(t) = \phi_d, \dot{\phi}_s(t) = \ddot{\phi}_s(t) = 0, \\
r_s(t) = r_d, \dot{r}_s(t) = \ddot{r}_s(t) = 0, \\
l_1(t) = l_{1d}, \dot{l}_1(t) = \ddot{l}_1(t) = 0, t \geq t_d ,
\end{cases} \tag{27}
$$

where ϕ_i / ϕ_d, r_i / r_d and l_{1i} / l_{1d} are the initial/target position of the actuators. t_d is the transportation time.

Based on the error signals (26), we construct the sliding mode surface as follows

$$
s = \begin{bmatrix} s_\phi & s_r & s_l \end{bmatrix}^T = \dot{e} + \Lambda e \tag{28}
$$

where $\Lambda = \mathrm{diag}\left\{ k_\phi, k_r, k_l \right\}$ are the positive control gain matrix. Taking the time derivative of (28), we can obtain that

$$
\dot{s} = \ddot{q}_a - q_c \tag{29}
$$

where $q_c \in \mathbb{R}^{3\times 1}$ can be expressed as

$$
q_c = \begin{bmatrix} \ddot{l}_1 \theta_2 + 2 \dot{l}_1 \dot{\theta}_2 + l_1 \ddot{\theta}_2 + l_2 \ddot{\theta}_4 + \ddot{\phi}_s - k_\phi \dot{e}_\phi \\ \ddot{l}_1 \theta_1 + 2 \dot{l}_1 \dot{\theta}_1 + l_1 \ddot{\theta}_1 + l_2 \ddot{\theta}_3 + \ddot{r}_s - k_r \dot{e}_r \\ \ddot{l}_{1s} - k_l \dot{e}_l \end{bmatrix} .
$$

Based on full actuated system model (25) and sliding mode surface (28)-(29), a sliding mode control method is designed for 7-DOF tower crane as follows

$$
U = N + M_a \left[q_c - \kappa \, \mathrm{sgn}(s) - H s \right] \tag{30}
$$

where $\kappa = \mathrm{diag}\left\{ k_1, k_2, k_3 \right\}$ and $H = \mathrm{diag}\left\{ \eta_1, \eta_2, \eta_3 \right\}$ are the positive gain matrices.

4 Closed-loop System Stability Analysis

Theorem 1. By using the proposed siding mode controller (30), the jib slewing angles ϕ, trolley moving displacements r, suspension cable lengths l_1, hook swing angles θ_1, θ_2 and payload swing angles θ_3, θ_4 are converged to their desired values, one has that

$$
\phi \to \phi_s, r \to r_s, l_1 \to l_{1s}, \theta_i \to 0, i = 1,2,3,4 . \tag{31}
$$

Proof. At first, a positive scalar function $V(t)$ is constructed as

$$
V = \frac{1}{2} s^T s . \tag{32}
$$

Taking the time derivative of (32) and using (25), (29)-(30), we have

$$
\begin{aligned}
\dot{V} &= s^T \dot{s} \\
&= s^T \left(\ddot{q}_a - q_c \right) \\
&= s^T \left[M_a^{-1} \left(U - N \right) - q_c \right] \\
&= -s^T \kappa \, \mathrm{sgn}(s) - s^T H s \\
&\leq -k_1 \left| s_\phi \right| - k_2 \left| s_r \right| - k_3 \left| s_l \right| - \eta_1 s_\phi^2 - \eta_2 s_r^2 - \eta_3 s_l^2 \\
&\leq -\eta_1 s_\phi^2 - \eta_2 s_r^2 - \eta_3 s_l^2 \leq 0
\end{aligned} \tag{33}
$$

which indicates that $V(t) \leq V(0) \in \mathcal{L}_\infty$. Moreover, we can get from (32) that

$$
s_\phi, s_r, s_l \in \mathcal{L}_\infty . \tag{34}
$$

By substituting (32) into (33), we can obtain that

$$
\dot{V} \leq -2 \min\left\{ \eta_1, \eta_2, \eta_3 \right\} V . \tag{35}
$$

By using the Bellman-Gronwall inequality [27] and (35), we can get

$$
V(t) \leq V(0) e^{-2 \min\{\eta_1, \eta_2, \eta_3\} t}, \forall t \geq 0 . \tag{36}
$$

We can obtain from (36) that

$$
\lim_{t \to \infty} V = 0 \Rightarrow \lim_{t \to \infty} s_\phi = 0, \lim_{t \to \infty} s_r = 0, \lim_{t \to \infty} s_l = 0 \tag{37}
$$

which indicates that sliding mode surface s are converged to zero.

We can get from (28) and (37) that the error signals e_ϕ, e_r, e_l are converged to zero. Furthermore, it can be obtained that

$$e_\phi = 0, e_r = 0, e_l = 0$$
$$\Rightarrow \phi = \phi_s, r = r_s, l_1 = l_{1s}, \theta_i = 0, i = 1 \sim 4. \quad (38)$$

So far, theorem 1 is proved. □

5 Experiment Results and Analysis

7-DOF tower crane hardware platform is shown in Fig. 3. The system parameters of the hardware platform and initial/desired values of actuators are provided as follows $M = 3\text{kg}, m_1 = 0.8\text{kg}, m_2 = 0.5\text{kg}, J = 5.6\text{kg}\cdot\text{m}^2, l_2 = 0.2\text{m}$, $g = 9.8\,\text{m/s}^2, d_j = 0.1, j = 1,2,3,4, \phi_i = 0\text{deg}, \phi_d = 50\text{deg}$, $r_i = 0.15\text{m}, r_d = 0.65\text{m}, l_{1i} = 0.1\text{m}, l_{1d} = 0.5\text{m}$.

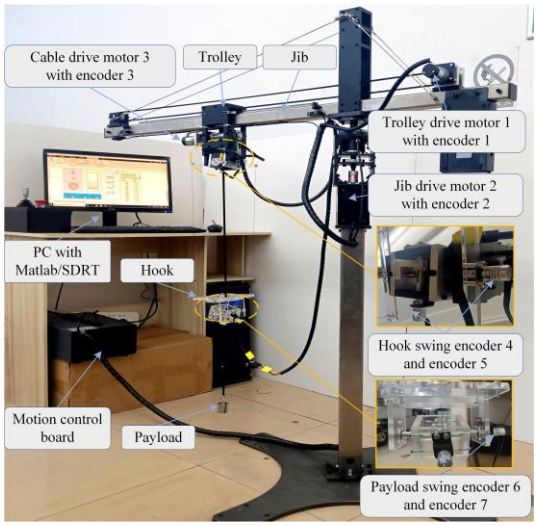

Fig. 3: Hardware platform of the 7-DOF tower crane system

Based on (27), the reference trajectory ϕ_s, r_s, l_{1s} are selected in [19]. The control gains of the proposed sliding mode controller are set as $k_\phi = 10, k_r = 10, k_l = 5$, $\kappa = \text{diag}\{5,5,5\}$, $H = \text{diag}\{5,5,5\}$.

The energy analysis based (EAB) controller [20] is selected as the comparative control method. However, The EAB controller does not account for changes in the length of the suspension cable. To ensure a fair comparison, we incorporate the following proportional-differential controller to control the suspension cable length variations: $F_l = -k_p e_l - k_d \dot{e}_l - (m_1 + m_2)g$. It allows us to directly compare the control performance of the proposed controller and comparative controller.

Fig. 4 is the experiment results. Both controllers enable the trolley and jib to transfer from the initial position to the final position without any overshoot. The payload is lowered accurately to the target location. However, the proposed sliding mode controller has more accurate positioning control performance than EAB controller. Experimental results confirm the presence of double spherical pendulum dynamic behavior during the trolley and jib motion process.

The anti-swing control performance of the EAB and proposed controller is shown in Fig. 5. Specially, the maximum payload swing angles by using the proposed sliding model controller are 2.27 degrees and 2.96 degrees for θ_3 and θ_4, respectively. In contrast, the EAB controller exhibits maximum payload swing angles are 4.25 degrees and 3.63 degrees for θ_3 and θ_4, respectively. Furthermore, the EAB controller exhibits residual swing even after the trolley and jib have reached the target location. The experimental results indicate that the proposed controller outperforms the EAB controller in terms of anti-swing control performance.

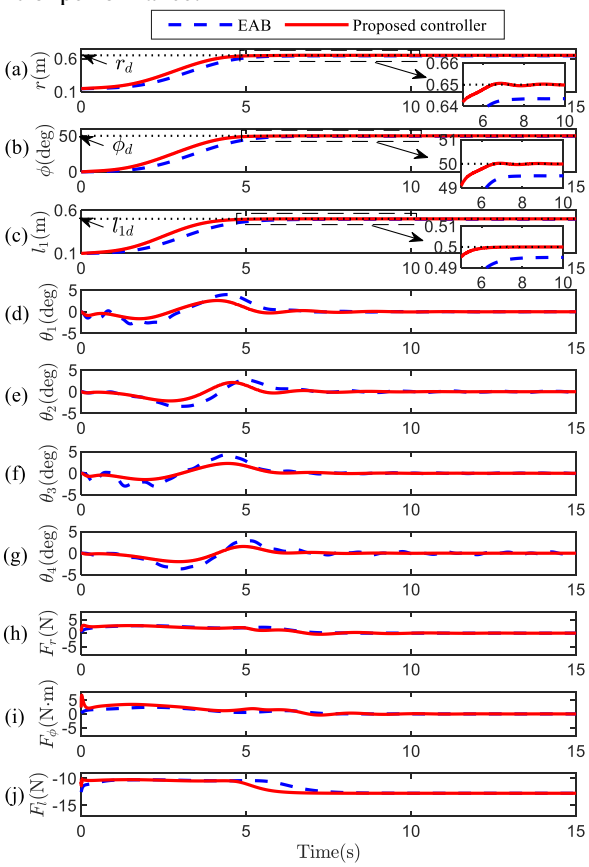

Fig. 4: Experiment results: (a) trolley displacement, (b) jib slewing angle, (c) suspension cable length, (d) hook swing angle 1, (e) hook swing angle 2, (f) payload swing angle 3, (g) payload swing angle 4, (h) trolley controller, (i) jib controller, (j) suspension cable controller.

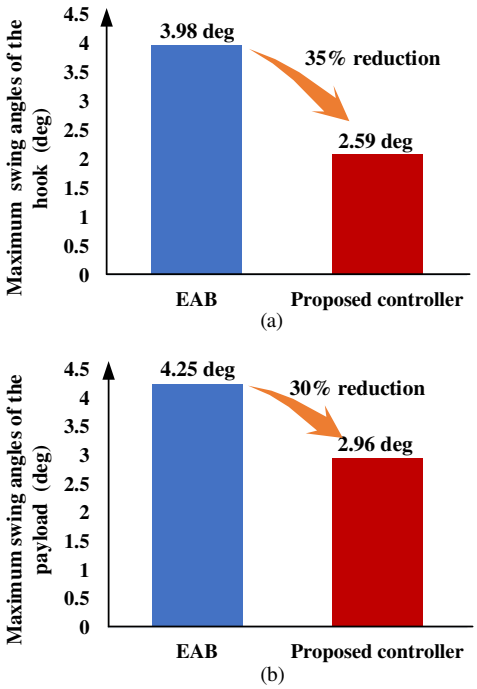

Fig. 5: Anti-swing control performance of the two controllers: (a) maximum swing angles of the hook, (b) maximum swing angles of the payload.

6 Conclusions

In this article, we present a 7-DOF tower crane system model that accounts for the effects of the double spherical pendulum and varying cable lengths. To our knowledge, this is the first 7-DOF dynamic model for tower cranes, incorporating the motion of the boom slewing, trolley movement, cable length variations, hook swing, and payload swing. Leveraging this model, we design an anti-swing control approach based on sliding mode techniques to achieve precise positioning and swing suppression. In the future, we aim to develop a robust controller for the 7-DOF tower crane that accounts for parameter uncertainties and external disturbances.

References

[1] H. Shi, R. Li, X. Bai, Y. Zhang, L. Min, D. Wang, X. Lu, Y. Yan, and Y. Lei, A review for control theory and condition monitoring on construction robots, *Journal of Field Robotics*, 2023, 40(4): 934-954.

[2] B. Lu and Y. Fang, Online trajectory planning control for a class of underactuated mechanical systems, *IEEE Transactions on Automatic Control*, 2024, 69(1): 442-448.

[3] G. Li, X. Ma and Y. Li, Adaptive anti-swing control for 7-DOF overhead crane with double spherical pendulum and varying cable length, *IEEE Transactions on Automation Science and Engineering,* early access, 2023, 1-12, doi: 10.1109/TASE.2023.3309937.

[4] P. V. Trieu, H. M. Cuong, H. Q. Dong, N. H. Tuan, and L. A. Tuan. Adaptive fractional-order fast terminal sliding mode with fault-tolerant control for underactuated mechanical systems: application to tower cranes, *Automation in Construction*, 2021, 123, Art. no. 103533.

[5] M. Zhang and X. Jing, Model-free saturated PD-SMC method for 4-DOF tower crane systems, *IEEE Transactions on Industrial Electronics*, vol. 69, no. 10, pp. 10270-10280, Oct. 2022.

[6] J. Xia, H. Ouyang, M. Zhang, Fault-tolerant controller design based on adaptive backstepping for tower cranes with actuator faults, *ISA Transactions*, early access, 2023, 1-9, doi: 10.1016/j.isatra.2023.12.032.

[7] N. Sun, Y. Wu, H. Chen and Y. Fang, Antiswing cargo transportation of underactuated tower crane systems by a nonlinear controller embedded with an integral term, *IEEE Transactions on Automation Science and Engineering*, 2019, 16(3): 1387-1398.

[8] T. Yang, N. Sun, H. Chen and Y. Fang, Observer-based nonlinear control for tower cranes suffering from uncertain friction and actuator constraints with experimental verification, *IEEE Transactions on Industrial Electronics*, 2021, 68(7): 6192-6204.

[9] M. Burkhardt, A. Gienger and O. Sawodny, Optimization-based multipoint trajectory planning along straight lines for tower cranes, *IEEE Transactions on Control Systems Technology*, 2024, 32(1): 290-297.

[10] R. C. Roman, R. E. Precup, and E. M. Petriu, Hybrid data-driven fuzzy active disturbance rejection control for tower crane systems, *European Journal of Control*, 2021, 58: 373-387.

[11] M. Böck and A. Kugi, Real-time nonlinear model predictive path-following control of a laboratory tower crane, *IEEE Transactions on Control Systems Technology*, 2014, 22(4): 1461-1473.

[12] S. M. Fasih ur Rehman, Z. Mohamed, A. R. Husain, H. I. Jaafar, M. H. Shaheed, and M. A. Abbasi, Input shaping with an adaptive scheme for swing control of an underactuated tower crane under payload hoisting and mass variations, *Mechanical Systems and Signal Processing*, 2022, 175, Art. no. 109106.

[13] S. M. Fasih ur Rehman, Z. Mohamed, A. R. Husain, L. Ramli, M. A. Abbasi, W. Anjum, and M. H. Shaheed. Adaptive input shaper for payload swing control of a 5-DOF tower crane with parameter uncertainties and obstacle avoidance, *Automation in Construction*, 2023, 154, Art. no. 104963.

[14] M. Zhang, Y. Zhang, B. Ji, C. Ma, and X. Chen. Adaptive sway reduction for tower crane systems with varying cable lengths, *Automation in Construction*, 2020, 119, Art. no. 103342.

[15] Y. Wu, N. Sun, H. Chen and Y. Fang, Adaptive output feedback control for 5-DOF varying-cable-length tower cranes with cargo mass estimation, *IEEE Transactions on Industrial Informatics*, 2021, 17(4): 2453-2464.

[16] J. Vaughan, D. Kim and W. Singhose, Control of tower cranes with double-pendulum payload dynamics, *IEEE Transactions on Control Systems Technology*, 2010, 18(6): 1345-1358.

[17] J. Peng, J. Huang and W. Singhose, Payload twisting dynamics and oscillation suppression of tower cranes during slewing motions, Nonlinear Dynamics, 2019, 98: 1041–1048.

[18] H. Ouyang, T. Tian, L. Yu, and G. Zhang, Motion planning approach for payload swing reduction in tower cranes with double-pendulum effect, *Journal of the Franklin Institute*, 2020, 357(13): 8299-8320.

[19] G. Li, X. Ma, Z. Li and Y. Li, Time-Polynomial-Based optimal trajectory planning for double-pendulum tower crane with full-state constraints and obstacle avoidance, *IEEE/ASME Transactions on Mechatronics*, 2023, 28(2): 919-932.

[20] H. Ouyang, T. Tian, L. Yu and G. Zhang, Load swing rejection for double-pendulum tower cranes using energy-shaping-based control with actuator output limitation, *ISA Transactions*, 2020, 101: 246-255.

[21] M. Zhang, X. Jing, W. Huang, Q. Lu, J. Chen, Z. Chen, Robust fault accommodation approach for double-pendulum tower cranes via adaptive neural network-triggered control, *Nonlinear Dynamics*, 2023, 111: 19993–20013.

[22] H. Ouyang, Z. Tian, L. Yu, and G. Zhang, Adaptive tracking controller design for double-pendulum tower cranes, *Mechanism and Machine Theory*, 2020, 153, Art. no. 103980.

[23] M. Zhang and X. Jing, Adaptive neural network tracking control for double-pendulum tower crane systems with nonideal inputs, *IEEE Transactions on Systems, Man, and Cybernetics: Systems*, 2022, 52(4): 2514-2530.

[24] X. Kang, L. Chai, and H. Liu, Anti-swing and positioning for double-pendulum tower cranes using improved active disturbance rejection controller, *International Journal of Control, Automation and Systems*, 2023, 21: 1210–1221.

[25] G. Li, X. Ma and Y. Li, Robust command shaped vibration control for stacker crane subject to parameter uncertainties and external disturbances, *IEEE Transactions on Industrial Electronics*, early access, 2024, 1-13, doi: 10.1109/TIE.2024.3366197.

[26] G. R. Duan, High-order fully actuated system approaches: Part I. models and basic procedure, *International Journal of System Science*, 2021, 52(2): 422–435.

[27] H. K. Khalil, Nonlinear Systems, 3rd ed. Englewood Cliffs, NJ, USA: Prentice–Hall, 2002.

Proceedings of the 3rd Conference on Fully Actuated System Theory and Applications
May 10-12, 2024, Shenzhen, China

Dynamic modeling and analysis of wafers in near-field acoustic levitation

Lipeng Wang[1], Jiang Wu[1,*], Chengqi Pan[2]

1. Center for robotics, School of Control Science and Technology, Shandong University, Jinan 250061
E-mail: l_ipeng_w@mail.sdu.edu.cn, wujiang@sdu.edu.cn

2. School of Mechanical engineering, Shandong University, Jinan 250061
E-mail: 202334425@mail.sdu.edu.cn

Abstract: The application of near-field acoustic levitation (NFAL) is increasing in popularity due to its practical applications in industry. This article presents a fluid-structure coupling model based on finite element analysis (FEA) for the dynamic analysis of wafers in NFAL. Initially, the one-eighth spherical shape equivalent model of NFAL was developed. Based on this model, static and transient investigations were conducted, respectively. Subsequently, various conditions that impact the wafer in NFAL, including deviation, initial velocity, and oscillation, were investigated. Finally, a mass-spring system with a single degree of freedom was explored. These results validated the feasibility of the wafer manipulation in NFAL and provided a practical method for dynamic modeling and analysis of wafers in NFAL.

Key Words: Dynamic modeling, finite element analysis, near-field acoustic levitation, wafer manipulation, fully actuated system theory

1 Introduction

Wafer accurate manipulation has become significantly crucial in the semi-conductor manufacturing industry [1,2], especially as the geometric feature dimensions of microchips continue to decrease. Conventional methods for manipulating wafers involve utilizing grippers equipped with mechanical stages or negative pressure adsorption [3,4]. However, owing to the susceptibility of wafer surfaces, mechanical contact, clamping, or adsorption during manipulation may inevitably cause surface scratches and the accumulation of particles/dust, especially when a slippery surface exists [5]. Particles produced during abrasion can adhere to the wafer and affect further processing [6]. Meanwhile, the negative pressure, whose intensity is difficult to control, easily causes stress concentration and even fracture because of wafer's fragility [7–9]. Thus, contactless levitation for wafer manipulation is gaining increasing attention owing to its security and micro-maneuverability features in industrial application.

Contactless manipulation methods typically include aerodynamic, magnetic, and acoustic levitations [10–12]. Air pumps are used to generate high-speed airflow in relation to aerodynamic levitation [13]. Featuring a powerful force and exceptionally precise manipulation, aerodynamic levitation is widely employed in industrial fields, e.g. air bearings, porous levitation stages, and chemical reactions [14–16]. However, the poor controllability due to its relatively high speed also increases the risk of fractures. Regarding magnetic levitation, the levitated objects should be magnetic or magnetically sensitive, so additional magnetic tray is required to hold the wafer; this likely causes the scratching between the tray and the wafer [17,18]. Acoustic levitation, including nodal acoustic levitation (NOAL) and near-field acoustic levitation (NFAL), generates a manipulable physical field by employing high-frequency vibrations to squeeze the air and avoids the usage of additional components (e.g. magnetic tray) [18]. The unique characteristics of acoustic levitation contribute to it being an attractive method for wafer contactless manipulations.

Comprising the exciter and the reflector, NOAL is typically utilized to capture/manipulate lightweight particles with dimensions smaller than 1/8 of the wavelength, e.g., tiny balls, liquid drops, or insects [19–21]; thus, it is not applicable for wafers to be levitated in a NOAL manner. In contrast to nodal capturing levitation, NFAL not only shares unique advantages for objects with a large diameter–thickness ratio (e.g. glass pane or silicon chip), also generates circumferential forces capable of rotating the levitated objects [22,23]. Thus, to a large extent, NFAL is suitable for wafer manipulations. Hashimoto and Koyama et al. [24,25] initially introduced the ultrasonic air squeeze gap model, investigated its ultrasonic vibration properties, and verified the correlation between levitation heights and acoustic variables (e.g. modes, wavelengths, frequencies, and amplitudes). Bucher et al. [26,27] developed a dynamic equivalent model for air squeeze gap with high-frequency excitation. Via investigation of the effects of air viscosity and compressibility on air gap films, they presented a method for assessing the dynamic behavior of air gap films. Melikhov et al. [28] derived the hydrodynamic governing equations incorporating nonlinear boundary conditions. A prognostic model was developed for estimating the pressure distribution in the air gap utilizing these modified equations. However, the intricate and nonlinear nature of the governing equations for acoustic air gaps continues to provide

* This work was supported in part by the Science Center Program of National Natural Science Foundation of China (NSFC) (No. 62188101), NSFC (No. 52105029 and No. 52375551), Natural Science Foundation of Shandong Province (ZR2021QE020), Taishan Scholar Foundation of Shandong Province (tsqn202306052), and Shandong Provincial Major Scientific and Technological Innovation Project (2021CXGC011207).

challenges for NFAL in constructing a precise feedback model.

In this study, a finite element analysis (FEA) model has been developed to investigate the fluid-structure coupling dynamic characteristics of fluid-structure coupling in the NFAL for the wafer. The stability of wafers in near-field acoustic levitation is evaluated via static and transient analyses.

2 Theoretical principle

Fig. 1 shows a schematic of the configuration [see Fig. 1(a)] and a simplified model [see Fig. 1(b)] of near-field acoustic levitation. To achieve non-contact manipulation of wafers, standing waves (SWs) are typically utilized to generate flexural vibrations in NFAL owing to its excellent controllability and stability. High-frequency SW vibrations generated a thin film of air with alternating high- and low-pressure areas, as shown in Fig. 1(a), which served as the wafer's levitation force. As shown in Fig. 1(b), the irradiator is assumed to be vibrating in harmonic motion as $u(r,t)$ and the height of the wafer levitation is represented as $h(t)$. The levitation process is classified as adiabatic because it involves minimal heat transfer and the absorption of acoustic in levitation is ignored. Based on the above assumptions, the Rayleigh radiation pressure in an ideal air gap on a fully reflecting object can be estimated as [29]:

$$\overline{p} = \langle p - p_0 \rangle = \frac{1+\gamma}{2}\left(1+\frac{\sin(2kh)}{2kh}\right)\langle E \rangle \tag{1}$$

where, p_0 represents the reference air pressure, γ denotes the molar heat capacity ratio of the air, k (= ω/c) means the wave number, in which ω is the angular frequency of the wave, and c is the sound velocity, h denotes the levitation distance between vibration source and wafer, and <E> is the time-averaged energy of the wave, respectively. The <E> can be calculated as [29]:

$$\langle E \rangle = \left(a_h^2/4\right)\left(\rho_0\omega^2/\sin^2 kh\right) \tag{2}$$

Here, a_h denotes the vibration amplitude of the irradiator plate.

The analytical calculation of the levitation force varies significantly under different boundary conditions in SWs-inspired NFAL. Considering the theory of mathematical models based on acoustic radiation pressure, the levitation force of the air squeeze film could be estimated as:

$$F = \iint_s \overline{p}\,\mathrm{d}S = \int_0^{2\pi}\mathrm{d}\theta\int_0^r \frac{\gamma+1}{8}\frac{a_h^2\rho_0 c^2}{h^2} r\,\mathrm{d}r \tag{3}$$

where, r (=100 mm) denotes the radius of the wafer, and s means the integral area. From eq. 3, it is clear to see that the levitation force is reversely proportional to the square of the levitation distance h and proportional to the square of the vibration amplitude a_0.

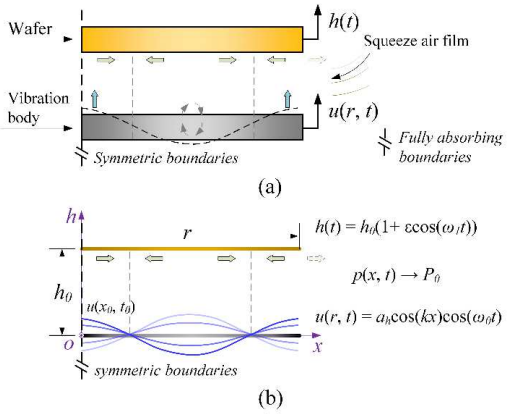

Fig. 1 Schematic of the near-field acoustic levitation (a) and a simplified mathematical model.

3 Simplified modeling of the NEAL

In terms of NFAL modeling, it is crucial to consider both the acoustic and structural fields induced by high-frequency vibrations. As a preliminary method, finite element analysis (FEA) provides efficient and convenient advantages for evaluating the interaction between fluid and solid fields. The acoustic property of the air gap was explored via acousto-structural coupling analysis and the transient analysis was implemented with ANSYS (ver. 14.5, ANSYS Inc., Canonsburg, USA). Fig. 2(a) illustrates a FEA model of the free acoustic field in the form of a one-eighth spherical shape with a radius of 150 mm, wherein the vibrating body is surrounded by air. In contrast to Fig. 2(a), Fig. 2(b) shows the NFAL model where both the wafer and the vibrating body are positioned in the air. The element or the air is FLUID30, while that of both the vibrating bodies and the wafer is SOLID45. The fluid-structure interface (FSI) condition is set to the boundaries among the air, the irradiators, and the wafer, while the absorbing boundary condition and symmetric boundary condition is set to the spherical surfaces and symmetry planes, respectively. To simplify the calculation, the same velocity excitation conditions are set to the vibrating bodies.

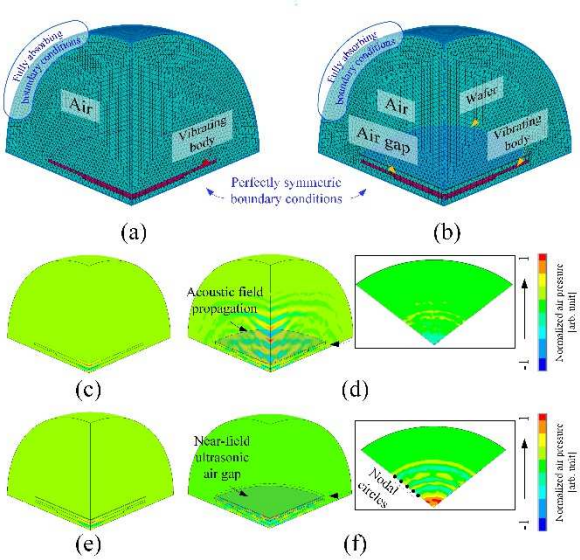

Fig. 2 FEA model of (a) the free acoustic field and (b) the NFAL, (c) and (d) show the air pressure distribution of the free acoustic field over time, while (e) and (f) represent the air pressure distribution in the NFAL, respectively.

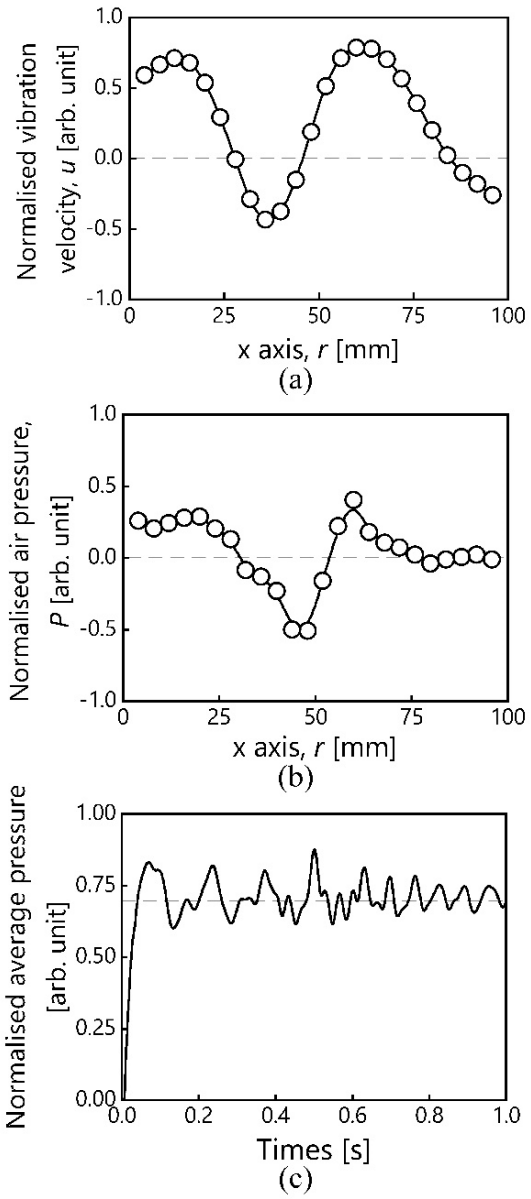

Fig. 3 (a) The x-axis vibration velocity, (b) air pressure, and (c) the time-averaged pressure of the air gap between the wafer and the vibrating body, respectively.

Fig. 2(c) and (d) show the initial distribution of air pressure in the free acoustic field and the distribution after approximately five vibration cycles, respectively. The high- and low-pressure areas disperse in all spatial directions along the vibrating wave and decrease in intensity as they propagate. Thus, it is not suitable for levitating wafers. Fig. 2(e) and (f) illustrates the air pressure variations in NFAL. It can be observed that the air pressure is constrained to the area between the wafer and the vibrating body, which is distinct from free fields. Additionally, the NFAL method provides a higher time-averaged air pressure, which makes it an exceptionally promising approach for levitating wafers.

Subsequently, the transient analysis was conducted utilizing the FEA model of NFAL. Fig. 3 (a) illustrates the vibration velocity distribution along the x-axis from the center to the periphery of the vibrating body. On the surface of the vibrating body, the SW is observed to be generated. Fig. 3(b) donates the distribution of air pressure at the same positions as the vibration velocity. It can be found that the air pressure exhibited similar distributional trends to vibration velocities; this indicates that the intended distribution of air pressure may be modulated by generating various vibrating patterns, and that the higher air pressure values can be achieved by altering the vibration amplitude. As shown in Fig. 3(c), the time-averaged pressure of the air gap increases rapidly and oscillates around a steady value. The levitation height of the wafer in the NFAL demonstrates characteristics similar to the time-averaged air pressure, based on its operating principle.

4 Stability analysis of the NFAL

On the one hand, because of the relatively small air damping coefficient, any tilt or disturbance on the irradiator surface of the vibrating body might result in the wafer being positioned off-center or slipping off. On the other hand, there existed a vertical levitation force and two orthogonal acoustic viscous forces due to the presence of acoustic velocity gradients in the squeezing air gap. When the wafer deviates from the center of the vibrating body, the geometrical boundary conditions and the asymmetry of the air pressure distribution in the air film tend to be altered. Thus, it is essential to consider both the initial and boundary conditions while evaluating the stability of the levitating wafer.

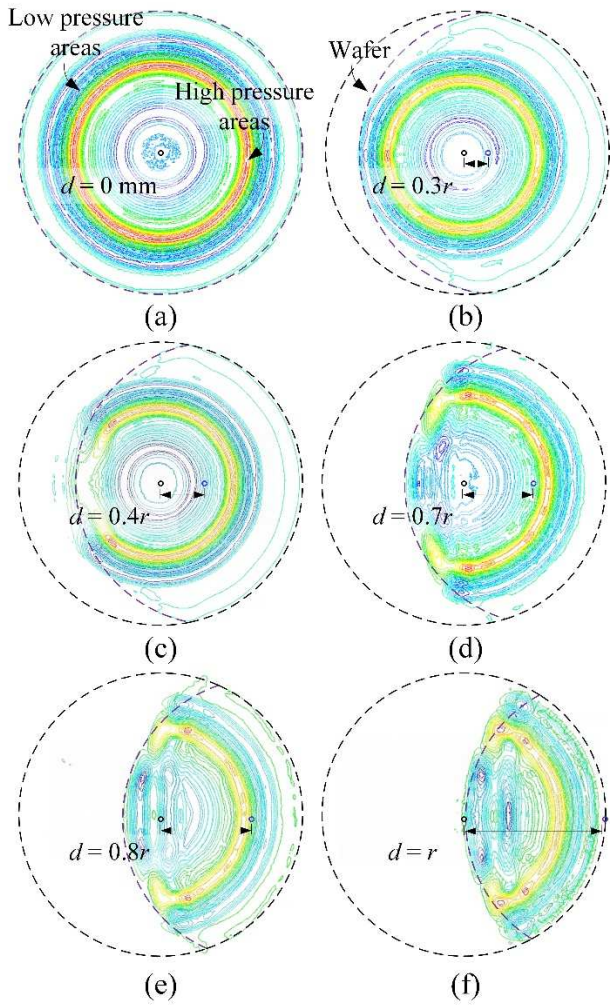

Fig. 4 Pressure distribution of the air squeeze film when the relative position deviation d between the wafer and the vibrating body equals (a) 0 mm, (b) 0.3r, (c) 0.4r, (d) 0.7r, (e) 0.8r, and (f) r, respectively. Here, r (= 100mm) denotes radius of the wafer.

4.1 Positional deviation of the wafer

In terms of geometric boundaries, the relative position between the wafer and the vibrating body strongly impacts the pressure distribution and levitation of NFAL. As shown in Fig. 4(a), the air pressure distribution was evaluated using the FEA method. Initially, there was no positional deviation (d = 0mm) between the wafer and the center of the vibrating body. It can be found that there is an alternating distribution of low- and high-pressure areas. When d increases to 0.3r, while the change in boundary conditions leads to a decrease in the intensity of the fringe acoustic field, the pressure distribution remains mostly unchanged. As shown in Fig. 4(c), when d increases to 0.4r, the majority of the wafer's surface keeps in contact with the air squeeze film owing to the air viscosity force. However, the decrease in pressure at the periphery of the air squeeze film might result in the tilting of the wafer or its potential interaction with the vibrating body's surface. Thus, the wafer may exist in the condition of instability. Figures 4(d) to (f) demonstrate a consistent rise in the positional deviation between the wafer and the center of the vibrating body, ranging from 0.7 times the radius (0.7r) to the whole radius (r). New sound pressure zones are formed to the right of the vibrating body due to the squeezing between the tilted wafer and the remaining air gap. Moreover, the overlapping area between the wafer and vibrating body decreases, inevitably reducing the wafer's levitation capacity.

It is worth mentioning that these results are achieved in the static statue, which means the speed or the acceleration of the wafer is not considered. Meanwhile, the change in the wafer's gesture is not considered. The relatively low sound pressure results in the reduction of levitation height, which is, however, a cause of the enhancement in the squeezing effect. Thus, oscillatory motion of the wafer occurs when the wafer's position remains close to the center of the vibrating body.

4.2 Initial velocity of the wafer

The wafer's stability of levitation is influenced by its gesture. Both the tilted irradiator surface of the vibrating body and the asymmetric air pressure might potentially result in the tipping of the wafer. However, the angle of tilt in relation to the dimension of the wafer remains minimal. An excessive angle might cause the wafer to come into contact with the vibrating body's surface, thereby hindering the effectiveness of near-field acoustic levitation. To simplify the model, wafer tilt is considered equivalent to both initially velocity and positional offset conditions. As shown in Fig. 5(a), the deviation of the wafer from the center of the vibrating body is approximately 0.3r, and the initial velocity of the wafer is set to 10mm/s. The radius of the circular air area surrounding the wafer is equal to twice the wafer's radius.

Fig. 5(a) to (f) illustrate the variation in pressure of the air squeeze film as the wafer is moving translationally, respectively. Initially, it can be observed that high- and low-pressure areas shift to the right with the wafer [see Fig. 5(a) and (b)]. With an increasing deviation, the right side of the wafer experiences compression, resulting in the formation of the new areas with high pressure [see Fig. 5(c) to (e)]. Finally, as shown in Fig. 5(f), an extreme deviation in the wafer will cause the air squeeze film to be destroyed.

4.3 Oscillation of the wafer in NFAL

It has been reported that the dynamic response of NFAL is influenced by the surrounding fluid and the forces acting on a levitating object can be decomposed into levitation forces caused by the compressibility of the fluid and damping forces associated with the viscosity of the fluid [26,27]. According to eq. 1to 3, when the air pressure is defined by $p(x,t)$, the levitation height can be estimated as [30,31]:

$$h(t) = h_0(1 + \varepsilon\cos(\omega_1 t)) \tag{4}$$

And the fully absorbing boundary conditions:

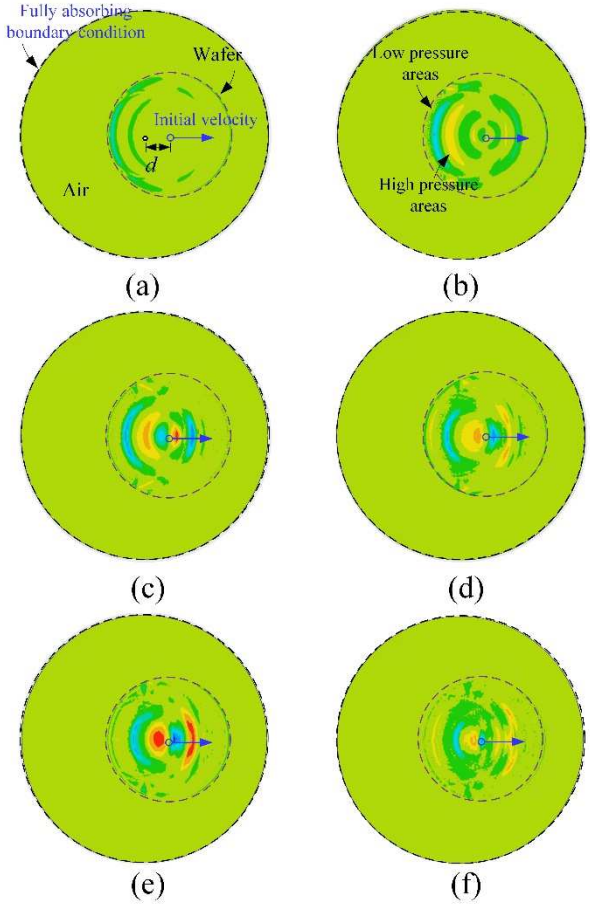

Fig. 5 Pressure distribution of the air squeeze film considering initial velocity conditions

$$\left.\frac{\partial p(x,t)}{\partial x}\right|_{x=0} = 0, \quad p(x=r,t) = p_0 \tag{5}$$

Here, h_0 represents a constant related to the levitation height, ε denotes the minimum value, and ω_1 means the angular frequency of the wafer.

Therefore, when considering acoustic viscous forces, the levitation of wafer in the NFAL may be represented as a spring-mass model with a single degree of freedom. The oscillation frequency of the wafer can be estimated as:

$$f_1 = \frac{1}{2\pi}\sqrt{\frac{k}{m}} = \frac{\omega_1}{2\pi} \tag{6}$$

And, k can be calculated by:

$$k = F / h \tag{7}$$

Here, m denotes the mass of the wafer, and k means the equivalent spring coefficient. Based on eqs. 1 to 4, it can be found that k is time-varying and strongly nonlinear; this makes it challenging for designing control and feedback systems.

5 Conclusions and discussion

This article presented a finite element analysis model to investigate the dynamic characteristics of fluid-structure coupling in the NFAL for the wafer. Through dynamic modeling and analysis of the wafer, we have drawn the following conclusions.

(1) In contract to free acoustic fields, the near-field acoustic levitation provided a higher time-averaged air pressure, which makes it an exceptionally promising approach for levitating wafers.

(2) The static analysis indicates that the ultrasonic air film can maintain stability even if the wafer is slightly off-center from the vibrating body.

(3) When the wafer has an initial velocity, the pressure distribution of the air squeeze gap will move translationally alongside the wafer within a limited region because of air viscosity.

(4) Wafer levitation could be modeled as a mass-spring system with a single degree of freedom, and control algorithms may be developed based on fully actuated system theory.

These conclusions validate the feasibility of the wafer manipulation in NFAL and provides a referable method for dynamic modeling and analysis of wafers in NFAL.

References

[1] Y. Daigo, T. Watanabe, A. Ishiguro, S. Ishii, and Y. Moriyama, “Influence and suppression of harmful effects due to by-product in CVD reactor for 4h-sic epitaxy,” *IEEE Trans. Semicond. Manuf.*, vol. 34, no. 3, pp. 340–345, Aug. 2021.

[2] S. Koch, M. Kleindienst, J. A. Moreno, and M. Horn, “Sliding mode control of a distributed-parameter wafer spin clean process,” *IEEE Trans. Control Syst. Technol.*, vol. 29, no. 5, pp. 2271–2278, Sep. 2021.

[3] Z. Dong and Y. Lin, “Ultra-thin wafer technology and applications: a review,” *Mater. Sci. Semicond. Process.*, vol. 105, art.no. 104681, Apr. 2020.

[4] H. Cheng, H. Chen and B. W. Mooring, “Accuracy analysis of dynamic-wafer-handling robotic system in semiconductor manufacturing,” *IEEE Trans. Ind. Electron*., vol. 61, no. 3, pp. 1402–1410, Mar. 2014.

[5] G. Laurent, A. Delettre, and N. L. Fort-Piat, “A new aerodynamic- traction principle for handling products on an air cushion,” *IEEE Trans. Robot.*, vol. 27, no. 2, pp. 379–384, Apr. 2011.

[6] S. H. Woo, J. Lee, and S. J. Yook, “Effect of a trap zone in reducing nanoparticle contamination of wafers and photomasks in parallel airflowp,” *IEEE Trans. Semicond. Manuf.*, vol. 31, no. 1, pp. 87–96, Feb. 2018.

[7] Z. Dong and Y. Lin, “Ultra-thin wafer technology and applications: a review,” *Mater. Sci. Semicond. Process.*, vol. 105, art.no. 104681, Apr. 2020.

[8] H. Cheng, H. Chen and B. W. Mooring, “Accuracy analysis of dynamic-wafer-handling robotic system in semiconductor manufacturing,” *IEEE Trans. Ind. Electron*., vol. 61, no. 3, pp. 1402–1410, Mar. 2014.

[9] C. Ming and D. Cui. “Wafer-handling robots and applications,” *Recent Pat. Eng*., vol. 3, no. 3, pp. 170–177, Jun. 2009.

[10] S. Howimanporn, S. Chookaew, and S. Chaiyaporn, “Experimental and implementation of robust control via floating air levitation and balancing rotary inverted pendulum,” *J. Phys. Conf. Ser*., vol. 1733, no. 1, art.no. 012013, Jan. 2021.

[11] A. E. Hajjaji and M. Ouladsine, “Modeling and nonlinear control of magnetic levitation systems,” *IEEE Trans. Ind. Electron*., vol. 48, no. 4, pp. 831-838, Aug. 2001.

[12] D. Koyama, Y. Wada, K. Nakamura, M. Nishikawa, T. Nakagawa, and H. Kihara, “An ultrasonic air pump using an acoustic traveling wave along a small air gap,” *IEEE Trans. Ultrason. Ferroelectr. Freq. Control*, vol. 57, no. 1, pp. 253–261, Jan. 2010.

[13] X. Brun and N. Shreyes, “Analysis of stresses and breakage of crystalline silicon wafers during handling and transport,” *Sol. Energy Mater. Sol. Cells*, vol. 93, no. 8, pp. 1238–1247, Aug. 2009.

[14] J. Wang, Y. He, C. Zhang, L. Gu, P. Li, D. Zheng, L. Wang, and Y. Mao, “A unified model for large-scale thickness measurement of lubricating film based on ultrasonic lag phase slope,” *Ultrasonics*, vol. 131, art. no. 106956, May 2023

[15] Y. Xiao, Y. Yang, C. Liu, and J. Rodriguez, “Design and Analysis of a Wireless Ultrasonic Motor Drive System,” *IEEE Trans. Power Electron.*, vol. 38, no. 10, PP. 12309 – 12314, Jul. 2023.

[16] C. An, T. Wang, X. Chen, X. Han, S. Wu, Q. Deng, L. Zhao, and N. Hu, “Ultrasonic-assisted preparation of two-dimensional materials for electrocatalysts,” *Ultrason. Sonochem.*, vol. 98, art. no. 106503, Jun 2023.

[17] C. Peng, M. Zhu, K. Wang, Y. Ren, and Z. Deng, “A two-stage synchronous vibration control for magnetically suspended rotor system in the full speed range,” *IEEE Trans. Ind. Electron.*, vol. 67, no. 1, pp. 480–489, Jan. 2020.

[18] L. Zhou and D. L. Trumper, “Magnetically levitated linear stage with linear bearing-less slice hysteresis motors,” *IEEE/ASME Trans. Mechatron*., vol. 26, no. 2, pp. 1084–1094, Apr. 2021.

[19] M. Röthlisberger, G. Schmidli, M. Schuck, and J. W. Kolar, "Multi-frequency acoustic levitation and trapping of particles in all degrees of freedom," IEEE Trans. Ultrason. Ferroelectr. Freq. Control, vol. 69, no. 4, pp. 1572–1575, Apr. 2022.

[20] D. Geng, N. Yan, W. Xie, Y. Lü, and B. Wei, “Extraordinary Solidification Mechanism of Liquid Alloys Under Acoustic Levitation State,” *Adv. Mater.*, vol. 35, no, 50, art.no. 2206464, Oct. 2022.

[21] W.J. Xie, C.D. Cao, Y.J. Lü, Z.Y. Hong, and B.Wei, “Acoustic method for levitation of small living animals,” *Appl. Phys. Lett.*, vol.89, art. no. 214102, Nov. 2006.

[22] S. Ueha, Y. Hashimoto, and Y. Koike, “Non-contact transportation using near-field acoustic levitation,” *Ultrasonics*, vol. 38, no. 1, pp. 26–32, Mar. 2000.

[23] R. Gabai, R. Shaham, S. Davis, N. Cohen, and I. Bucher, "A contactless stage based on near-field acoustic levitation for object handling and positioning—concept, design, modeling, and experiments," *IEEE/ASME Trans. Mechatron*., vol. 24, no. 5, pp. 1954–1963, Oct. 2019.

[24] D. Koyama, K. Nakamura, Non-contact ultrasonic transportation of small objects over long distances in air using a bending vibrator and reflector, *IEEE Transactions on Ultrasonics, Ferroelectrics, and Frequency Control*, 2010, 57(5): 1152–1159.

[25] K. Masuda, D. Koyama, M. Matsukawa, Noncontact transportation of planar object in an ultrasound waveguide, *IEEE Transactions on Ultrasonics, Ferroelectrics, and Frequency Control*, 2018, 65(11): 2160–2166.

[26] D. Ilssar and I. Bucher, "On the slow dynamics of near-field acoustically levitated objects under High excitation frequencies," *J. Sound. Vib.*, vol. 354, pp: 154–166, Oct. 2015.

[27] D. Ilssar, I. Bucher, and H. Flashner, "Modeling and closed loop control of near-field acoustically levitated objects," *Mech. Syst. Signal. Process.,* vol.85, pp: 367–381, Feb. 2017.

[28] I. Melikhov, S. Chivilikhin, A. Amosov, and R. Jeanson, "Viscoacoustic model for near-field ultrasonic levitation," *Phys. Rev. E*, vol. 94, no. 5, art. no. 053103, Nov. 2016.

[29] S. Zhao and J. Wallaschek, "A standing wave acoustic levitation system for large planar objects," *Arch. Appl. Mech.*, vol. 81, pp: 123–139, Dec. 2009.

[30] H. Li, Y. Wang, Y. Li, W. Sun, Y. Shen, and Q. Zeng, "The levitation and driving performance of a contact-free manipulation device actuated by ultrasonic energy," *Int. J. Mech. Sci.*, vol. 225, art. no. 107358, May 2022.

[31] J.Hu, K. Nakamura, and S. Ueha, "Stability Analysis of an Acoustically Levitated Disk," *IEEE Trans. Ultrason. Ferroelectr Freq. Control*, vol. 50, no. 2, pp: 117–127, Feb. 2003.

Proceedings of the 3rd Conference on Fully Actuated System Theory and Applications
May 10-12, 2024, Shenzhen, China

An FASA Based Fixed-Time Sliding Mode Control for Robotic Manipulator

Yu Zhang[1], Fanwei Meng[1], Bin Li[2]

1. School of Control Engineering, Northeastern University at Qinhuangdao, Qinhuangdao 066004, P. R. China
E-mail: 2272330@stu.neu.edu.cn, mengfanwei@neuq.edu.cn

2. School of Aeronautics and Astronautics, Sichuan University, Chengdu 610065, P. R. China
E-mail: bin.li@scu.edu.cn

Abstract: This paper investigates the fixed-time tracking error control for the robotic system with external disturbances based on the fully-actuated system approach (FASA). Firstly, a fixed-time sliding function is introduced and the fixed-time convergence of the sliding phase is verified. Secondly, combining the structure of the sliding function and the FASA, a fixed-time sliding mode controller (FSMC) is proposed. The stability of the system and the fixed-time convergence of the tracking error are proven. Finally, numerical simulation is carried out and experimental studies are provided by using a Franka manipulator for demonstrating the effectiveness of the proposed control method.

Key Words: Fully-actuated system, Fixed-time stability, Robotic manipulator, Sliding mode control

1 Introduction

In recent years, the manipulator of robotics has received widespread attention from researchers, and lots of control methods have been proposed to solve industrial problems[1]. With the uncertainty of the model, a control law should be designed to overcome the effect of these uncertainties. To the requirement of the convergence speed, the convergence time should be taken into consideration[2].

The tracking control problem of the robotic manipulator has been researched for many years. The sliding mode control is one of the commonly used control methods because of its strong robustness to external disturbance. In [3], a sliding mode manifold and a reaching law were proposed to realize the constraint tracking control of industrial robots. To overcome external disturbances and the effect of the chattering phenomenon in sliding mode control, a robust composite high-order super-twisting sliding mode controller was proposed in [4]. For the regulation of robotic arms with deadzone and gravity, a sliding mode controller was designed to guarantee the tracking error converging to zero in [5]. Most controllers only realize the asymptotic convergence of the tracking error. However, fast convergence is necessary in practical industrial applications.

Convergence speed is an important indicator of control systems. In [6], a new terminal sliding mode control approach was developed for robotic manipulators based on finite-time stability theory but ignoring external disturbances. In [7], to eliminate the effect of the uncertainty and external disturbances, the finite-time stability theory and the neural network were applied in the design of the sliding mode control strategy to improve the tracking performance of the robotic manipulators. In [8], a robust $H\infty$ finite-time tracking controller was proposed for robotic manipulators based on time delay estimation. However, the convergence time of the finite-time stability always depends on the initial conditions of the system. Therefore, the fixed-time stability theory was proposed to overcome this drawback. The fixed-time control algorithm of the robotic manipulator has been designed extensively in recent years. In [9], the author proposed a fixed-time control method considering the input saturation, output saturation, and system uncertainty, which realized fixed-time convergence. In [10], an adaptive neural fixed-time sliding mode controller was created for a class of uncertain robotic manipulators subject to input saturation and prescribed constraints. In [11], the adaptive fixed-time non-singular terminal sliding mode controller for the application of uncertain and disturbed robotic manipulators under the condition of actuator failures was proposed. However, due to the requirement to transform the system into a first-order state-space model, the design of the controller becomes more complex.

To solve this problem, the full-actuated system approach (FASA) was proposed by Duan in 2021, which opened up a new direction for solving control problems. Modeling the system as a first-order system will disrupt the full-actuated property of the system. It will bring many design challenges, such as system decoupling. In some complicated conditions, the system may not realize the local stabilization. Different from first-order system approaches, FASA makes use of the full-actuation property, which allows us to eliminate all the nonlinear dynamics [12] and makes the design of the controller convenient. So far, many researchers have studied its applications. In [13], FASA was applied in the adaptive control and high-order backstepping. In [14] and [15], FASA was expanded to the robust adaptive control and the optimal control, respectively. In [16], FASA was used to structure an adaptive fault-tolerant controller to realize the full-state constraints. In [17], a second-order quaternion system of rigid spacecraft attitude dynamics was derived based on the fully actuated system approach, which control strategy could control the scalar quaternion to reach the desired value and be used to deal with the unwinding phenomenon. In [18], a control parameterization method was adopted to optimize the parameter matrices of FASA based controller with the actuator saturation. To our knowledge, there is currently no combination of fixed-time stability theory, sliding mode control, and FASA.

In this paper, the parameter uncertainties and external disturbances are taken into consideration. A controller based on FASA is proposed for an n-link robotic manipulator. The

main contributions are as follows:

(I) The robotic manipulator system is transformed into a standard full-actuated system, which will make the controller design convenient.

(II) A fixed-time sliding mode controller (FSMC) is proposed based on FASA, which makes the tracking errors converge to the small neighborhood of zero within a fixed time.

(III) The proposed control algorithm is applied in the experiment with a Franka manipulator. Experimental results verify the effectiveness of this algorithm.

The rest parts of this paper are organized as follows: Section 2 gives the preliminaries and problem formulation. Section 3 introduces the sliding function and the FSMC. Section 4 and Section 5 present the simulation and experiment results, respectively. Finally, Section 6 concludes this paper.

2 Preliminaries and Problem Formulation

2.1 Preliminaries

The notation $\|\cdot\|$ denotes the Euclidean norm of a vector or the induced norm of a matrix. For the vector $\boldsymbol{x} = [x_1, x_2, \ldots, x_r]^\top \in \mathbb{R}^r$ and $k > 0$, $\boldsymbol{x}^{(0\sim n-1)} = \left[\boldsymbol{x}, \dot{\boldsymbol{x}}, \ldots, \boldsymbol{x}^{(n-1)}\right]^\top \in \mathbb{R}^{n\times r}$ and $\mathrm{sig}^k(\boldsymbol{x}) = \left[\mathrm{sig}^k(x_1), \mathrm{sig}^k(x_2), \ldots, \mathrm{sig}^k(x_r)\right]^\top \in \mathbb{R}^r$, where $\mathrm{sig}^k(x_i) = \mathrm{sign}(x_i)\,|x_i|^k, i = 1, 2, \ldots, r$.

Consider the following nonlinear system:

$$\dot{\boldsymbol{x}} = \boldsymbol{p}\left(\boldsymbol{x}\left(t\right)\right), \quad \boldsymbol{x}\left(0\right) = \boldsymbol{x}_0 \tag{1}$$

where $\boldsymbol{x} \in \mathbb{R}^r$ is the system state, and $\boldsymbol{p}$: $\mathbb{R}^r \to \mathbb{R}^r$ is a nonlinear function, with $\boldsymbol{p}(\boldsymbol{x}_0) = \boldsymbol{0}$.

Definition 1 ([19], [20]) *System* (1) *is globally finite-time stable if it is Lyapunov stable and for all $\boldsymbol{x}_0 \in \mathbb{R}^r$ there exists $T(\boldsymbol{x}_0) \geq 0$ dependent on the initial conditions such that, for any $\boldsymbol{x}(\cdot)$ solution of (4) with $\boldsymbol{x}(0) = \boldsymbol{x}_0$, $\lim_{t\to T(\boldsymbol{x}_0)} \|\boldsymbol{x}(t)\| = 0$, i.e. $\|\boldsymbol{x}(t)\| \equiv 0$ for all $t \geq T(\boldsymbol{x}_0)$. The function T is called the settling time.*

Definition 2 ([21]) *The origin of* (1) *is said to be fixed-time stable if it is globally finite-time stable and the settling-time function $T\left(\boldsymbol{x}_0\right)$ is bounded, i.e., $\exists T_{bound} > 0$: $T\left(\boldsymbol{x}_0\right) \leq T_{bound}, \forall \boldsymbol{x}_0 \in \mathbb{R}^r$.*

Lemma 1 ([22]) *Consider the system* (1)*. If there exists a positive definite continuous function V: $\mathbb{R}^r \to \mathbb{R}$ such that*

$$\dot{V}\left(\boldsymbol{x}\left(t\right)\right) \leq -c_1 V^{l_1}\left(\boldsymbol{x}\left(t\right)\right) - c_2 V^{l_2}\left(\boldsymbol{x}\left(t\right)\right) \tag{2}$$

where $c_1 > 0, c_2 > 0$, $0 < l_1 < 1$, $l_2 > 1$, then system (1) *is globally fixed-time stable and the settling time is bounded by*

$$T\left(\boldsymbol{x}\left(0\right)\right) \leq \frac{1}{c_1\left(1 - l_1\right)} + \frac{1}{c_2\left(l_2 - 1\right)} \tag{3}$$

Lemma 2 ([23]) *For any nonnegative scalars χ_1, χ_2, …, χ_r, there are two inequalities hold for $0 < p < 1$ and $q > 1$, respectively.*

$$\sum_{i=1}^{r} \chi_i^p \geq \left(\sum_{i=1}^{r} \chi_i\right)^p$$

$$\sum_{i=1}^{r} \chi_i^q \geq n^{1-q}\left(\sum_{i=1}^{r} \chi_i\right)^q$$

In [12], [24] and [25], it has been shown that fully-actuated systems physically exist and most nonlinear systems such as (1) can be either physically modeled as or converted into fully-actuated systems with uncertainties as follows

$$\boldsymbol{x}^{(n)} = \boldsymbol{f}(\boldsymbol{x}^{(0\sim n-1)}) + \Delta\boldsymbol{f}(\boldsymbol{x}^{(0\sim n-1)}) + \boldsymbol{L}(\boldsymbol{x}^{(0\sim n-1)})\boldsymbol{u} \tag{4}$$

where $\boldsymbol{x}, \boldsymbol{u} \in \mathbb{R}^r$ are the state vector and the control input vector, respectively, $\boldsymbol{f}(\boldsymbol{x}^{(0\sim n-1)}) \in \mathbb{R}^r$ is a continuous vector function, $\Delta\boldsymbol{f}(\boldsymbol{x}^{(0\sim n-1)}) \in \mathbb{R}^r$ is the nonlinear uncertainty of the system, and $\boldsymbol{L}(\boldsymbol{x}^{(0\sim n-1)}) \in \mathbb{R}^r$ denotes a continuous matrix function satisfying the following fully-actuated assumption:

Assumption 1 ([25]) *det*$\boldsymbol{L}(\boldsymbol{x}^{(0\sim n-1)}) \neq 0, \forall \boldsymbol{x}^{(i)} \in \mathbb{R}^r, i = 0, 1, \ldots, n-1$.

2.2 Problem Formulation

The dynamic equation of an n-link robotic manipulator is described as

$$\boldsymbol{M}\left(\boldsymbol{q}\right)\ddot{\boldsymbol{q}} + \boldsymbol{C}\left(\boldsymbol{q}, \dot{\boldsymbol{q}}\right)\dot{\boldsymbol{q}} + \boldsymbol{G}\left(\boldsymbol{q}\right) = \boldsymbol{u}\left(t\right) + \boldsymbol{d}\left(t\right) \tag{5}$$

where $\boldsymbol{q}, \dot{\boldsymbol{q}}, \ddot{\boldsymbol{q}} \in \mathbb{R}^r$ represent the joint position vector, joint velocity vector, and joint acceleration vector, respectively. $\boldsymbol{M}(\boldsymbol{q}) \in \mathbb{R}^{r\times r}$ is the inertia matrix, $\boldsymbol{C}(\boldsymbol{q}, \dot{\boldsymbol{q}}) \in \mathbb{R}^{r\times r}$ denotes the Coriolis force and centrifugal force matrix, $\boldsymbol{G}(\boldsymbol{q}) \in \mathbb{R}^r$ is the gravity matrix, and $\boldsymbol{u} \in \mathbb{R}^r$ denotes the control torque which needs to be designed.

In the paper, to simplify subsequent writing, $\boldsymbol{M}\left(\boldsymbol{q}\right)$, $\boldsymbol{C}\left(\boldsymbol{q}, \dot{\boldsymbol{q}}\right)$, and $\boldsymbol{G}\left(\boldsymbol{q}\right)$ are replaced by $\boldsymbol{M}$, $\boldsymbol{C}$, and $\boldsymbol{G}$. Considering the existed uncertainty in the $\boldsymbol{C}$ and $\boldsymbol{G}$, we have

$$\boldsymbol{C} = \boldsymbol{C}_0 + \Delta\boldsymbol{C}$$
$$\boldsymbol{G} = \boldsymbol{G}_0 + \Delta\boldsymbol{G}$$

where $\boldsymbol{C}_0$, $\boldsymbol{G}_0$ denote the nominal parts, $\Delta\boldsymbol{C}$, $\Delta\boldsymbol{G}$ are the uncertain parts of $\boldsymbol{C}$ and $\boldsymbol{G}$, respectively. Then (5) can be rewritten as

$$\boldsymbol{M}\ddot{\boldsymbol{q}} + (\boldsymbol{C} + \Delta\boldsymbol{C})\dot{\boldsymbol{q}} + (\boldsymbol{G} + \Delta\boldsymbol{G}) = \boldsymbol{u}\left(t\right) + \boldsymbol{d}\left(t\right) \tag{6}$$

Assumption 2 *The desired trajectory $\boldsymbol{q}_d$ is second-order differentiable and bounded. Furthermore, its derivative $\dot{\boldsymbol{q}}_d$ and second-order derivative $\ddot{\boldsymbol{q}}_d$ are bounded.*

The tracking error signal can be defined as follows:

$$\begin{cases} \boldsymbol{e} = [e_1, e_2, \ldots, e_n]^\top = \boldsymbol{q} - \boldsymbol{q}_d \\ \dot{\boldsymbol{e}} = [\dot{e}_1, \dot{e}_2, \ldots, \dot{e}_n]^\top = \dot{\boldsymbol{q}} - \dot{\boldsymbol{q}}_d \\ \ddot{\boldsymbol{e}} = [\ddot{e}_1, \ddot{e}_2, \ldots, \ddot{e}_n]^\top = \ddot{\boldsymbol{q}} - \ddot{\boldsymbol{q}}_d \end{cases} \tag{7}$$

where $\boldsymbol{e}$, $\dot{\boldsymbol{e}}$, $\ddot{\boldsymbol{e}}$ are the desired joint position error vector, velocity error vector and acceleration error vector, respectively. Combining (6) and (7), we can obtain that

$$\ddot{\boldsymbol{e}} = \boldsymbol{f}\left(\boldsymbol{e}, \dot{\boldsymbol{e}}\right) + \Delta\boldsymbol{f}\left(\boldsymbol{e}, \dot{\boldsymbol{e}}\right) + \boldsymbol{M}^{-1}\boldsymbol{u}(t) - \ddot{\boldsymbol{q}}_d \tag{8}$$

where

$$\boldsymbol{f}\left(\boldsymbol{e}, \dot{\boldsymbol{e}}\right) = \boldsymbol{M}^{-1}\left[-\boldsymbol{C}(\dot{\boldsymbol{e}} + \dot{\boldsymbol{q}}_d) - \boldsymbol{G}\right]$$
$$\Delta\boldsymbol{f}\left(\boldsymbol{e}, \dot{\boldsymbol{e}}\right) = \boldsymbol{M}^{-1}\left[\boldsymbol{d} - \Delta\boldsymbol{C}(\dot{\boldsymbol{e}} + \dot{\boldsymbol{q}}_d) - \Delta\boldsymbol{G}\right]$$

Therefore, system (8) satisfies the form of the fully-actuated tracking system proposed in [25] as follows:

$$\begin{aligned}\boldsymbol{e}^{(n)} =&\boldsymbol{f}(\boldsymbol{e}^{(0\sim n-1)},t)+\Delta\boldsymbol{f}(\boldsymbol{e}^{(0\sim n-1)},t)\\&+\boldsymbol{L}(\boldsymbol{e}^{(0\sim n-1)},t)\boldsymbol{u}(t)-(\boldsymbol{q}_d)^{(n)}\end{aligned}\tag{9}$$

The aim of our work is to design a FASA based FSMC to minimize the tracking error.

3 Sliding Function and FSMC Design

To achieve the fixed-time convergence, the sliding function we designed is as follows:

$$\boldsymbol{s}=\dot{\boldsymbol{e}}+\boldsymbol{H}(\boldsymbol{e})\tag{10}$$

$$\boldsymbol{H}_i(\boldsymbol{e})=\begin{cases}a_1\operatorname{sig}^{n_1}(e_i)+a_2\operatorname{sig}^{n_2}(e_i), & |e_i|\geq\varepsilon\\ l_1e_i+l_2e_i^3, & |e_i|<\varepsilon\end{cases}$$
$$i=1,2,\ldots,n$$

where $a_1>0$, $a_2>0$, $0<n_1<1$, $n_2>1$, and $l_1=\frac{a_1(3-n_1)}{2}\varepsilon^{n_1-1}+\frac{a_2(3-n_2)}{2}\varepsilon^{n_2-1}$, $l_2=\frac{a_1(n_1-1)}{2}\varepsilon^{n_1-3}+\frac{a_1(n_2-1)}{2}\varepsilon^{n_2-3}$ can guarantee $\boldsymbol{s}$ and its derivatives continuous.

Theorem 1 *Considering the fully-actuated system* (8) *with the sliding function* (10)*, $\boldsymbol{e}$ and $\dot{\boldsymbol{e}}$ can converge to $\boldsymbol{\Omega}_1=\left\{\boldsymbol{e}|\,\|\boldsymbol{e}\|\leq\sqrt{3}\varepsilon\right\}$ and $\boldsymbol{\Omega}_2=\left\{\dot{\boldsymbol{e}}|\,\|\dot{\boldsymbol{e}}\|\leq a_1\sqrt{3}\varepsilon^{n_1}+a_2\sqrt{3}\varepsilon^{n_2}\right\}$ within a fixed time when $\boldsymbol{s}=\boldsymbol{0}$, respectively. The settling time $T_{set1}\leq T_1=\frac{1}{m_1(1-h_1)}+\frac{1}{m_2(h_2-1)}$, where $m_1=a_12^{\frac{n_1+1}{2}}$, $m_2=a_22^{\frac{n_2+1}{2}}n^{\frac{1-n_2}{2}}$, $h_1=\frac{n_1+1}{2}$, and $h_2=\frac{n_2+1}{2}$.*

Proof. When $\boldsymbol{s}=\boldsymbol{0}$, according to (10), we can obtain that

$$\dot{\boldsymbol{e}}=-a_1\operatorname{sig}^{n_1}(\boldsymbol{e})-a_2\operatorname{sig}^{n_2}(\boldsymbol{e})\tag{11}$$

The Lyapunov function we selected is

$$V_1=\frac{1}{2}\boldsymbol{e}^\top\boldsymbol{e}\tag{12}$$

Combining (11) and the time derivative of (12), it has

$$\begin{aligned}\dot{V}_1&=\boldsymbol{e}^\top\left[-a_1\operatorname{sig}^{n_1}(\boldsymbol{e})-a_2\operatorname{sig}^{n_2}(\boldsymbol{e})\right]\\&=-a_1\boldsymbol{e}^\top\operatorname{sig}^{n_1}(\boldsymbol{e})-a_2\boldsymbol{e}^\top\operatorname{sig}^{n_2}(\boldsymbol{e})\\&\leq-a_12^{\frac{n_1+1}{2}}V_1^{\frac{n_1+1}{2}}-a_22^{\frac{n_2+1}{2}}n^{\frac{1-n_2}{2}}V_1^{\frac{n_2+1}{2}}\\&=-m_1V_1^{h_1}-m_2V_1^{h_2}\end{aligned}\tag{13}$$

where we define $m_1=a_12^{\frac{n_1+1}{2}}$, $m_2=a_22^{\frac{n_2+1}{2}}n^{\frac{1-n_2}{2}}$, $h_1=\frac{n_1+1}{2}$, and $h_2=\frac{n_2+1}{2}$, we can calculate that the settling time of $\boldsymbol{e}$ and $\dot{\boldsymbol{e}}$ converging to $\boldsymbol{\Omega}_1$ and $\boldsymbol{\Omega}_2$ is less than $\frac{1}{m_1(1-h_1)}+\frac{1}{m_2(h_2-1)}$.

Taking the time derivative of (10) into (8), we have

$$\dot{\boldsymbol{s}}=\boldsymbol{f}_1+\Delta\boldsymbol{f}_1+\boldsymbol{M}^{-1}\boldsymbol{u}(t)-\ddot{\boldsymbol{q}}_d\tag{14}$$

where

$$\begin{aligned}\boldsymbol{f}_1&=\boldsymbol{M}^{-1}\left[-\boldsymbol{C}\left(\boldsymbol{s}-\boldsymbol{H}+\dot{\boldsymbol{q}}_d\right)-\boldsymbol{G}\right]+\dot{\boldsymbol{H}}\\\Delta\boldsymbol{f}_1&=\Delta\boldsymbol{f}=\boldsymbol{M}^{-1}\left[\boldsymbol{d}-\Delta\boldsymbol{C}(\boldsymbol{s}-\boldsymbol{H}+\dot{\boldsymbol{q}}_d)-\Delta\boldsymbol{G}\right]\end{aligned}$$

Assumption 3 *There exists a non-negative scalar $\boldsymbol{\gamma}$ such that the nonlinear uncertainty $\Delta\boldsymbol{f}(\boldsymbol{e},\dot{\boldsymbol{e}})\in\mathbb{R}^r$ satisfies*

$$\|\Delta\boldsymbol{f}(\boldsymbol{e},\dot{\boldsymbol{e}})\|\leq\gamma$$

Then, we need to design the FSMC to guarantee the system states reaching the sliding surface within a fixed time. Based on this idea, the FASA based FSMC we designed is as follows:

$$\begin{aligned}&\boldsymbol{u}(t)=-\boldsymbol{M}\left[\boldsymbol{A}\boldsymbol{s}+\boldsymbol{u}^*(t)\right]\\&\boldsymbol{u}^*(t)=\boldsymbol{f}_1+\gamma\boldsymbol{g}(\boldsymbol{s})-\ddot{\boldsymbol{q}}_d+\beta_1\operatorname{sig}^{n_3}(\boldsymbol{s})+\beta_2\operatorname{sig}^{n_4}(\boldsymbol{s})\end{aligned}\tag{15}$$

where $\beta_1>0$, $\beta_2>0$, $0<n_3<1$, $n_4>1$, $\boldsymbol{A}\in\mathbb{R}^{r\times r}$ is a positive definite matrix, and a boundary layer is introduced to overcome the chattering problem. Thus, $\boldsymbol{g}(\boldsymbol{s})$ is designed as

$$\boldsymbol{g}(\boldsymbol{s})=\begin{cases}\frac{\boldsymbol{s}}{\|\boldsymbol{s}\|}, & \|\boldsymbol{s}\|\geq\alpha\\ \frac{\boldsymbol{s}}{\alpha}, & \|\boldsymbol{s}\|<\alpha\end{cases}\tag{16}$$

Theorem 2 *Consider the fully-actuated tracking system* (8) *with the FSMC* (15)*. $\boldsymbol{s}$ will converge to $\boldsymbol{\Omega}_3=\left\{\boldsymbol{s}|\,\|\boldsymbol{s}\|\leq\alpha\right\}$ with the settling time $T_{set2}\leq T_2=\frac{1}{m_3(1-h_3)}+\frac{1}{m_4(h_4-1)}$, where $m_3=\beta_12^{\frac{n_3+1}{2}}$, $h_3=\frac{n_3+1}{2}$, $m_4=\beta_22^{\frac{n_4+1}{2}}n^{\frac{1-n_4}{2}}$, and $h_4=\frac{n_4+1}{2}$.*

Proof. we select the following Lyapunov function

$$V_2=\frac{1}{2}\boldsymbol{s}^\top\boldsymbol{s}\tag{17}$$

Combining the FSMC (15) and the time derivative of (17), we can obtain that

$$\begin{aligned}\dot{V}_2&=\boldsymbol{s}^\top\left[-\beta_1\operatorname{sig}^{n_3}(\boldsymbol{s})-\beta_2\operatorname{sig}^{n_4}(\boldsymbol{s})-\boldsymbol{A}\boldsymbol{s}\right]\\&=-\beta_1\boldsymbol{s}^\top\operatorname{sig}^{n_3}(\boldsymbol{s})-\beta_2\boldsymbol{s}^\top\operatorname{sig}^{n_4}(\boldsymbol{s})-\boldsymbol{s}^\top\boldsymbol{A}\boldsymbol{s}\\&\leq-\beta_1\boldsymbol{s}^\top\operatorname{sig}^{n_3}(\boldsymbol{s})-\beta_2\boldsymbol{s}^\top\operatorname{sig}^{n_4}(\boldsymbol{s})\\&\leq-\beta_12^{\frac{n_3+1}{2}}V_2^{\frac{n_3+1}{2}}-\beta_22^{\frac{n_4+1}{2}}n^{\frac{1-n_4}{2}}V_2^{\frac{n_4+1}{2}}\\&=-m_3V_2^{h_3}-m_4V_2^{h_4}\end{aligned}\tag{18}$$

where $m_3=\beta_12^{\frac{n_3+1}{2}}$, $m_4=\beta_22^{\frac{n_4+1}{2}}n^{\frac{1-n_4}{2}}$, $h_3=\frac{n_3+1}{2}$ and $h_4=\frac{n_4+1}{2}$. According to Lemma 1, $\boldsymbol{s}$ will converge to $\boldsymbol{\Omega}_3$ within the settling time $T_{set2}\leq T_2=\frac{1}{m_3(1-h_3)}+\frac{1}{m_4(h_4-1)}$.

Theorem 3 *When $\boldsymbol{\Omega}_3=\{\boldsymbol{s}|\,\|\boldsymbol{s}\|\leq\alpha\}$, we will obtain the following conclusion:*

$\boldsymbol{e}$ and $\dot{\boldsymbol{e}}$ will converge to $\boldsymbol{\Omega}_1$ and $\boldsymbol{\Omega}_4=\left\{\dot{\boldsymbol{e}}|\,\|\dot{\boldsymbol{e}}\|\leq\alpha+\sqrt{3}a_1\varepsilon^{n_1}+\sqrt{3}a_2\varepsilon^{n_2}\right\}$ within the fixed time, respectively.

Proof. If $\|\boldsymbol{e}\|\geq1$, with (10) and (12), we have

$$\begin{aligned}\dot{V}_1&=\boldsymbol{e}^\top\left[-a_1\operatorname{sig}^{n_1}(\boldsymbol{e})-a_2\operatorname{sig}^{n_2}(\boldsymbol{e})+\boldsymbol{s}\right]\\&\leq-a_1\boldsymbol{e}^\top\operatorname{sig}^{n_1}(\boldsymbol{e})-a_2\boldsymbol{e}^\top\operatorname{sig}^{n_2}(\boldsymbol{e})+\|\boldsymbol{e}\|\alpha\\&\leq-a_12^{\frac{n_1+1}{2}}V_1^{\frac{n_1+1}{2}}-2^{\frac{n_2+1}{2}}\left(a_2n^{\frac{1-n_2}{2}}-\alpha\right)V_1^{\frac{n_2+1}{2}}\end{aligned}\tag{19}$$

Define $k_1=2^{\frac{n_2+1}{2}}\left(a_2n^{\frac{1-n_2}{2}}-\alpha\right)$. We obtain the settling time $T_{set3_1}\leq\frac{1}{m_1(1-h_1)}+\frac{1}{k_1(h_2-1)}$. Similarly, if $\|\boldsymbol{e}\|<1$,

we can obtain

$$\begin{aligned}\dot{V}_1 &= \boldsymbol{e}^\top \left[-a_1 \operatorname{sig}^{n_1}(\boldsymbol{e}) - a_2 \operatorname{sig}^{n_2}(\boldsymbol{e}) + \boldsymbol{s}\right] \\ &\leq -a_1 \boldsymbol{e}^\top \operatorname{sig}^{n_1}(\boldsymbol{e}) - a_2 \boldsymbol{e}^\top \operatorname{sig}^{n_2}(\boldsymbol{e}) + \|\boldsymbol{e}\|\alpha \\ &\leq -a_1 2^{\frac{n_1+1}{2}} V_1^{\frac{n_1+1}{2}} - a_2 2^{\frac{n_2+1}{2}} n^{\frac{1-n_2}{2}} V_1^{\frac{n_2+1}{2}} + \|\boldsymbol{e}\|\alpha \\ &\leq -\left(a_1 2^{\frac{n_1+1}{2}} - \alpha 2^{\frac{1}{4}}\right) V_1^{\frac{1}{4}} - a_2 2^{\frac{n_2+1}{2}} n^{\frac{1-n_2}{2}} V_1^{\frac{n_2+1}{2}}\end{aligned} \tag{20}$$

Define $k_2 = \left(a_1 2^{\frac{n_1+1}{2}} - \alpha 2^{\frac{1}{4}}\right)$. The settling time $T_{set3_2} \leq \frac{1}{k_2(1-h_1)} + \frac{1}{m_2(h_2-1)}$. According to Lemma 1, $\boldsymbol{e}$ and $\dot{\boldsymbol{e}}$ will converge to $\boldsymbol{\Omega}_1$ and $\boldsymbol{\Omega}_4$ respectively with the settling time $T_{set3} \leq \max\{T_{set3_1}, T_{set3_2}\}$, which indicates the total settling time $T_{total} \leq \max\{T_{set3_1}, T_{set3_2}\} + \frac{1}{m_3(1-h_3)} + \frac{1}{m_4(h_4-1)}$.

4 Simulation Results

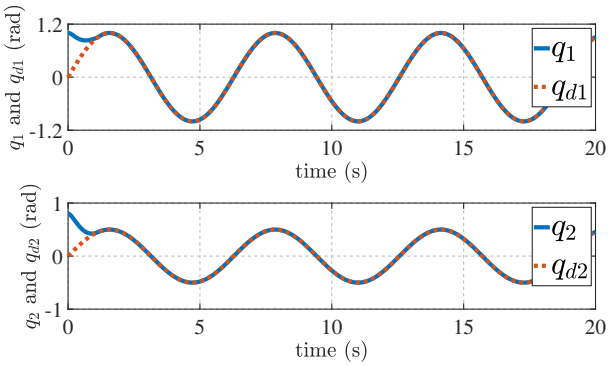

Fig. 1: Trajectories of $\boldsymbol{q}$ and desired signal $\boldsymbol{q}_d$

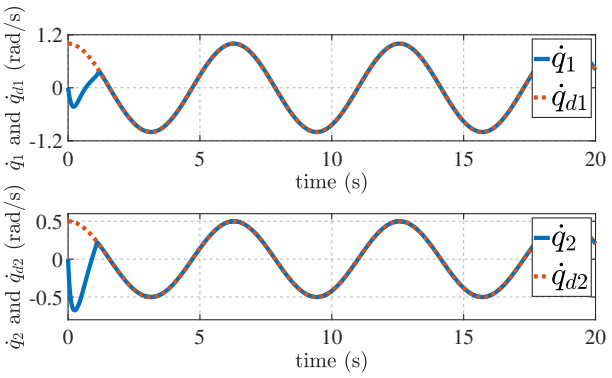

Fig. 2: Trajectories of $\dot{\boldsymbol{q}}$ and desired signal $\dot{\boldsymbol{q}}_d$

In this section, the numerical simulation on a two-DOF robotic manipulator is presented to verify the effectiveness of the proposed control method. The inertia matrix $\boldsymbol{M}(\boldsymbol{q})$, the Coriolis force and centrifugal force matrix $\boldsymbol{C}(\boldsymbol{q}, \dot{\boldsymbol{q}})$, and the gravity matrix $\boldsymbol{G}(\boldsymbol{q})$ are given as follows

$$\boldsymbol{M} = \begin{bmatrix} M_{11} & M_{12} \\ M_{21} & M_{22} \end{bmatrix}$$

$$\boldsymbol{C} = \begin{bmatrix} C_{11} & C_{12} \\ C_{21} & C_{22} \end{bmatrix}$$

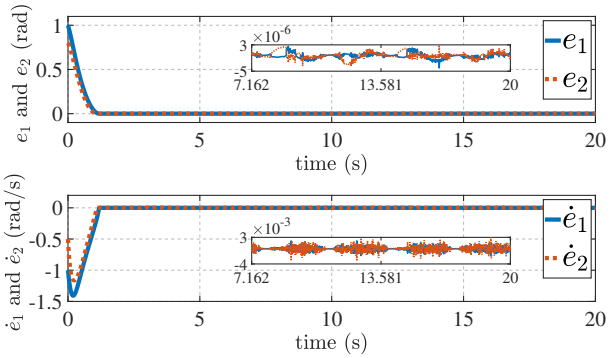

Fig. 3: The tracking error

$$\boldsymbol{G} = \begin{bmatrix} G_{11} \\ G_{21} \end{bmatrix}$$

where

$$\begin{aligned} M_{11} &= m_1 l_1^2 + m_2(l_1^2 + l_2^2 + 2l_1 l_2 \cos q_2) \\ M_{12} &= m_2(l_2^2 + l_1 l_2 \cos q_2) \\ M_{21} &= m_2(l_2^2 + l_1 l_2 \cos q_2) \\ M_{22} &= m_2 l_2^2 \\ C_{11} &= -m_2 l_1 l_2 \dot{q}_2 \sin q_2 \\ C_{12} &= -m_2 l_1 l_2 (\dot{q}_1 + \dot{q}_2) \sin q_2 \\ C_{21} &= -m_2 l_1 l_2 \dot{q} \sin q_2 \\ C_{22} &= 0 \\ G_{11} &= (m_1 l_2 + m_2 l_1) g \cos q_1 + m_2 l_2 g \cos(q_1 + q_2) \end{aligned}$$

with $m_1 = 1$kg, $m_2 = 2$kg, and $l_1 = 0.5$m, $l_1 = 1$m being the i th $(i = 1, 2)$ link's mass and length, respectively.

The external disturbances are given as

$$\boldsymbol{d} = \begin{bmatrix} 0.2\sin(pt) \\ 0.2\cos(pt) \end{bmatrix}$$

where $p = 0.05$.

The uncertain parts of $\boldsymbol{C}$ and $\boldsymbol{G}$ are as follows

$$\Delta \boldsymbol{C} = \begin{bmatrix} 0.1719 & 0.2529 \\ -0.1720 & 0.0677 \end{bmatrix} \times \sin(t)$$

$$\Delta \boldsymbol{G} = \begin{bmatrix} 0.0295 \\ 0.1425 \end{bmatrix} \times \sin(t)$$

The desired trajectories are given as $q_{d1} = q_{d2} = [\sin(t),\ 0.5\sin(t)]^\top$. The parameters of the proposed controller are set as $a_1 = a_2 = 2$, $\beta_1 = \beta_2 = 0.5$, $n_1 = n_3 = \frac{1}{2}$, $n_2 = n_4 = \frac{3}{2}$, $\varepsilon = 10^{-4}$, $\alpha = 0.001$ and $\boldsymbol{A} = \operatorname{diag}(4,\ 4)$.

According to Theorem 2 and 3, we can calculate the total settling time $T_{total1} \leq 7.162s$. The corresponding tracking trajectories are shown in Fig. 1 and Fig. 2. It can be seen that q_1, q_2, $\dot{q}_1$ and $\dot{q}_2$ have tracked their respective desired trajectories when $t \geq 7.162s$. The tracking errors converge to the small neighborhood of zero when $t \geq 7.162s$ according to Fig. 3, which means the fixed-time convergence is achieved.

5 Experiment

In this part, we use a Franka manipulator to demonstrate the effectiveness of the proposed control method by experiment. Franka manipulator is made up of seven joints and

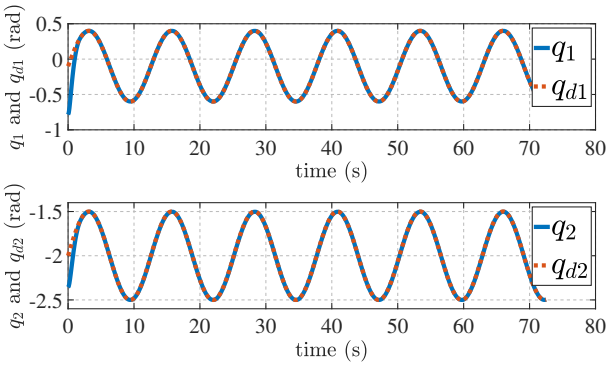

Fig. 4: Trajectories of $\boldsymbol{q}$ and desired signal $\boldsymbol{q}_d$

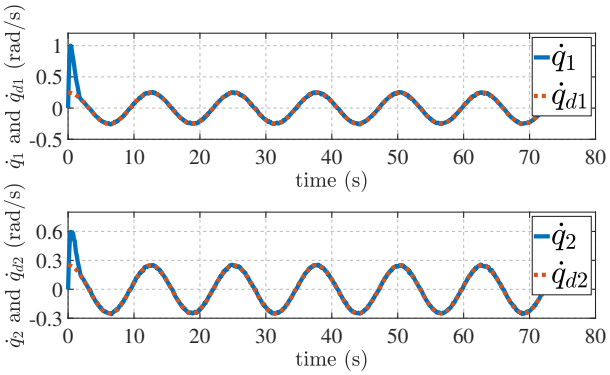

Fig. 5: Trajectories of $\dot{\boldsymbol{q}}$ and desired signal $\dot{\boldsymbol{q}}_d$

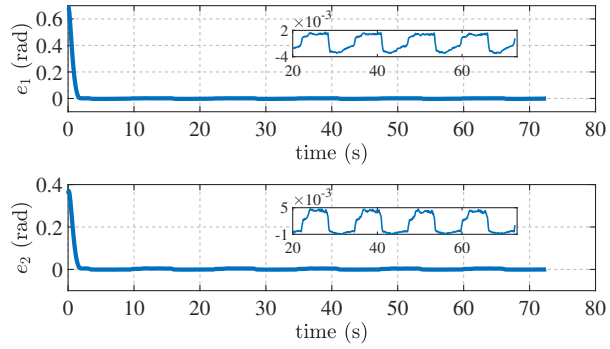

Fig. 6: The tracking error of $\boldsymbol{e}$

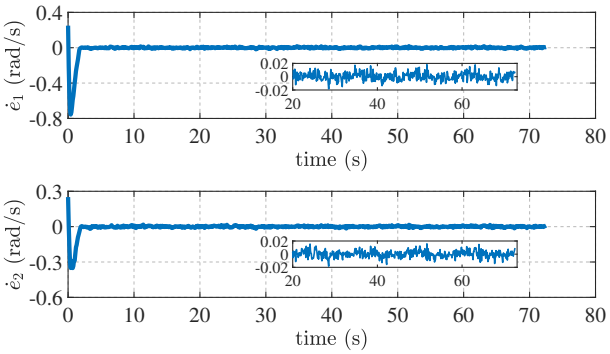

Fig. 7: The tracking error of $\dot{\boldsymbol{e}}$

torque sensors are equipped at each joint, which is applied in the rescue industry, human-machine collaboration production, and service industry. For simplicity and without loss of generality, we select two joints to finish this experiment. Considering the joint space limitation, the desired trajectories of q_{d1} and q_{d2} are given as

$$\begin{cases} q_{d1} = 0.5\sin(0.5t) - 0.1 \\ q_{d2} = 0.5\sin(0.5t) - 2 \end{cases} \tag{21}$$

The initial conditions of $\boldsymbol{q}$ and $\dot{\boldsymbol{q}}$ are given as $\boldsymbol{q}(0) = [-0.784316 \ -2.36229]^\top$ and $\dot{\boldsymbol{q}}(0) = [0 \ 0]^\top$, respectively. The parameters of controller are selected as $a_1 = a_2 = 1$, $\beta_1 = \beta_2 = 0.3$, $\gamma = 2$, $\alpha = 0.001$, $\varepsilon = 0.01$, and $\boldsymbol{A} = \mathrm{diag}(2,\ 2)$.

We can calculate the settling time $T_{total2} \leq 19.269$ s according to Theorem 2 and 3. Fig. 4 and Fig. 5 present the trajectories of $\boldsymbol{q}$, $\dot{\boldsymbol{q}}$ and their desired signals $\boldsymbol{q}_d$, $\dot{\boldsymbol{q}}_d$. It achieves well tracking performance of $\boldsymbol{q}$ and $\dot{\boldsymbol{q}}$. Fig. 6 and Fig. 7 show the tracking error of $\boldsymbol{e}$ and $\dot{\boldsymbol{e}}$, respectively. $\boldsymbol{e}$ and $\dot{\boldsymbol{e}}$ can converge to a small neighbourhood of zero within the fixed time T_{total2}, respectively.

6 Conclusion

In this paper, a FASA based FSMC is proposed for a robotic system with uncertainties and external disturbances. The standard full-actuated system form of the robotic system can contribute to the design of the controller. The FSMC can achieve tracking error converging to the small region within a fixed time. Finally, numerical simulation is carried out and experimental studies are conducted using a Franka manipulator to demonstrate the effectiveness of the proposed control method. However, the upper bounds of disturbances and uncertainties are generally unknown. In the future, we will combine the neural network and FASA to estimate the uncertainties and external disturbances.

References

[1] X. Qiu, C. Hua, J. Chen, Y. Zhang, and X. Guan, Event-triggered based adaptive neural network control of a robotic manipulator with output constraints and disturbance. *International Journal of Systems Science*, 2021, 52(12): 2415–2426.

[2] C. Zhu, Y. Jiang, and C. Yang, Fixed-time neural control of robot manipulator with global stability and guaranteed transient performance. *IEEE Transactions on Industrial Electronics*, 2022, 70(1): 803-812.

[3] Y. Xu, R. Liu, J. Liu, and J. Zhang, A novel constraint tracking control with sliding mode control for industrial robots. *International Journal of Advanced Robotic Systems*, 2021, 18(4): 17298814211029778.

[4] S. Tayebi-Haghighi, F. Piltan, and J. M. Kim, Robust composite high-order super-twisting sliding mode control of robot manipulators. *Robotics*, 2018, 7(1): 13.

[5] J. de Jesús Rubio, Sliding mode control of robotic arms with deadzone. *IET Control Theory & Applications*, 2017, 11(8): 1214-1221.

[6] D. Zhao, S. Li, and F. Gao, A new terminal sliding mode control for robotic manipulators. *International Journal of control*, 2009, 82(10): 1804-1813.

[7] H. Liu, and T. Zhang, Neural network-based robust finite-time control for robotic manipulators considering actuator dynamics. *Robotics and Computer-Integrated Manufacturing*, 2013, 29(2): 301-308.

[8] T. Zhang, and A. Zhang, Robust finite-time tracking control for robotic manipulators with time delay estimation. *Mathematics*, 2020, 8(2): 165.

[9] W. He, F. Kang, L. Kong, Y. Feng, G. Cheng, and C. Sun, Vibration control of a constrained two-link flexible robotic manipulator with fixed-time convergence. *IEEE Transactions on Cybernetics*, 2021, 52(7): 5973-5983.

[10] Y. Wu, H. Fang, T. Xu, and F. Wan, Adaptive neural fixed-time sliding mode control of uncertain robotic manipulators with input saturation and prescribed constraints. *Neural Processing Letters*, 2022, 54(5): 3829-3849.

[11] S. Ahmed, A. T. Azar, and M. Tounsi, Adaptive Fault Tolerant Non-Singular Sliding Mode Control for Robotic Manipulators Based on Fixed-Time Control Law. *Actuators. MDPI*, 2022, 11(12): 353.

[12] G. Duan, High-order fully actuated system approaches: Part I. Models and basic procedure. *International Journal of Systems Science*, 2021, 52(2): 422-435.

[13] G. Duan, High-order fully actuated system approaches: Part IV. Adaptive control and high-order backstepping. *International Journal of Systems Science*, 2021, 52(5): 972-989.

[14] G. Duan, High-order fully actuated system approaches: Part V. Robust adaptive control. *International Journal of Systems Science*, 2021, 52(10): 2129-2143.

[15] G. Duan, High-order fully actuated system approaches: Part VIII. Optimal control with application in spacecraft attitude stabilisation. *International Journal of Systems Science*, 2022, 53(1): 54-73.

[16] R. Dong, C. Hua, K. Li, and R. Meng, Adaptive Fault-Tolerant Control for High-Order Fully Actuated System with Full-State Constraints. *Journal of the Franklin Institute*, 2023.

[17] F. Z. Xiao, and L. Q. Chen, Fully actuated systems in terms of quaternions for spacecraft attitude control. *Acta Astronautica*, 2023, 209: 1-5.

[18] G. Liu, K. Zhang, and B. Li, Fully-actuated system approach based optimal attitude tracking control of rigid spacecraft with actuator saturation. *Journal of Systems Science and Complexity*, 2022, 35(2): 688-702.

[19] S. P. Bhat, and D. S. Bernstein, Finite-time stability of continuous autonomous systems. *SIAM Journal on Control and optimization*, 2000, 38(3): 751-766.

[20] Y. Hong, J. Wang, and D. Cheng, Adaptive finite-time control of nonlinear systems with parametric uncertainty. *IEEE Transactions on Automatic control*, 2006, 51(5): 858-862.

[21] A. Polyakov, Nonlinear feedback design for fixed-time stabilization of linear control systems. *IEEE transactions on Automatic Control*, 2011, 57(8): 2106-2110.

[22] M. Van, Y. Sun, S. Mcllvanna, M. N. Nguyen, M. O. Khyam, and D. Ceglarek, Adaptive Fuzzy Fault Tolerant Control for Robot Manipulators with Fixed-Time Convergence. *IEEE Transactions on Fuzzy Systems*, 2023.

[23] Z. Zuo, and L. Tie, A new class of finite-time nonlinear consensus protocols for multi-agent systems. *International Journal of Control*, 2014, 87(2): 363-370.

[24] G. Duan, High-order fully actuated system approaches: Part II. Generalized strict-feedback systems. *International Journal of Systems Science*, 2021, 52(3): 437-454.

[25] G. Duan, High-order fully actuated system approaches: Part III. Robust control and high-order backstepping. *International Journal of Systems Science*, 2021, 52(5): 952-971.

Proceedings of the 3rd Conference on Fully Actuated System Theory and Applications
May 10-12, 2024, Shenzhen, China

The Robust PI control of A Magnetically Levitated Planar Motor with Output Constrains

Xiang Chen, Tuopu Na, Chenglong Ma, Lei Ning, Bo Zhao

School of Instrumentation Science and Engineering, Harbin Institute of Technology, Harbin 150001
E-mail: natuopu@hit.edu.cn

Abstract: The magnetically levitated planar motor is utilized in precision industries, such as chip manufacturing, which encounters challenges in designing a high-performance motion controller. This paper proposes the robust PI controller to ensure the tracking error to a finite set within a specified time, even under conditions of uncertain mathematical models, actuator faults and output constraints. Moreover, the proposed approach utilizes a simple and computationally efficient controller structure, without complex adaptive strategies, observers and filters. Simulation results provide further support for the established theoretical findings.

Key Words: Magnetically levitated planar motor, output constraint, actuator faults, prescribed time, specified accuracy.

1 Introduction

The permanent magnet planar motors can achieve high-precision, multi-degree-of-freedom operations without the need for bearings, motor reducers, gears, and other mechanical components, which are free from the constraints of mechanical transmission structures and cables [1]. The maglev servo system provides possibilities for complex motion trajectories and exhibits high adaptability in special processing environments such as vacuum, facilitating its application in EUV lithography equipment [2,3]. However, the uncertain mathematical model inevitably poses challenges in the design of motion controllers.

Currently, the PID control is the primary feedback control method in precision motion control, which exhibits strong robustness and ease of parameter tuning [4-6]. Based on adaptive laws, [7] proposes an adaptive PID control strategy for magnetic levitation systems, improving control performance through online adjustments of the adaptive PID controller parameters. However, the PID amplifies the high frequency noise when it suppresses the low frequent disturbance. [8] and [9] apply model predictive control to the maglev servo system, which can realize efficient and fast control. However, this method has high requirements for the model accuracy. [10] combines adaptive robust control and iterative learning control to ensure the magnetic levitated planar motor has excellent tracking performance. Based on [10], [11] utilizes gated recurrent neural networks for trajectory prediction and compensation in a feedforward control structure, which effectively regulates both steady and transient characteristics. [12] proposes the adaptive sliding-mode technique based on disturbance compensation for magnetic levitation systems, aiming to suppress disturbances and enhance dynamic response capabilities. However, the complex control strategy will hinder efficient controller operation, requiring high computational performance.

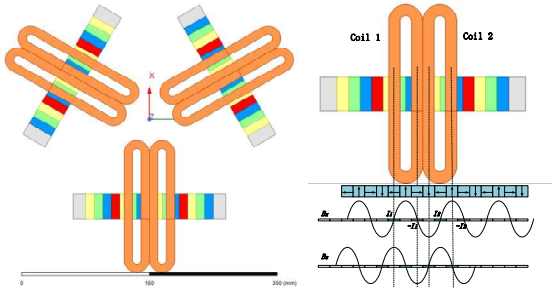

(a) (b)

Fig.1(a): Magnetic levitation planar motor structure. (b) The relation between the magnetic field and coil current

Recently, the prescribed performance control has been extensively researched, which allows for the predefinition of tracking performance, including convergence speed, overshoot, and accuracy [13]-[18]. However, due to the need for magnetic levitation planar motor to move strictly within the specified range, output constraint is necessary. [19]-[21] indicate that the barrier function can effectively constrain the output. [22] combines prescribed performance control with barrier functions to constrain the output, ensuring that trajectory errors are within a predetermined set.

This paper proposes a Robust PI control approach based on Prescribed Performance Control and the barrier function. It has the following advantages:

1） The proposed controller design principle is similar to the traditional PI controller, featuring a simple structure that ensures high computational efficiency.
2） The proposed controller ensures the convergence of tracking error under output constraints and low driver precision.
3） The proposed controller ensures the speed and accuracy of error convergence under model uncertainties and uncertain disturbances.

*This work is supported by National Natural Science Foundation of China under Grant 52207005.

2 System Description and Problem Formulation

2.1 System description

The structure of the magnetic levitation planar motor comprises three submotors denoted A, B and C, as depicted in Fig.1(a), where each adjacent coil shares a common magnet, providing independent controllable thrust in both the vertical and horizontal directions. The magnetic fields in the x- and z-directions of the submotor A manifest as sinusoidal waves with a period of 4τ, as illustrated in Fig.1(b). Coils 1 and 2 are separated by 3τ in the magnetic field. The current I_1 and I_2 are energized in the coils positioned beneath the Halbach PM array. Thereby, when Coil 1 generates zero force, Coil 2 is positioned to generate maximal force, and vice versa. The functional relation between force and current is presented by

$$\begin{bmatrix} F_{v1} \\ F_{h1} \end{bmatrix} = K_F \begin{bmatrix} 1 & 0 \\ 0 & 1 \end{bmatrix} \begin{bmatrix} i_{Q1} \\ i_{D1} \end{bmatrix} \tag{1}$$

Where K_F is presented by [23]

$$K_F = \frac{6\mu_0 K(1,1) l_c \tau_r}{b_c h_c \pi} \sinh\left(\frac{\pi h_c}{2\tau_r}\right) \sin\left(\frac{\pi b_c}{2\tau_r}\right) \sin\left(\frac{\pi \omega_c}{2\tau_r}\right) e^{-\frac{\pi\left(h_g + h_m + h_c/2\right)}{\tau_r}} \tag{2}$$

The decomposition method is expressed as [24]

$$\begin{bmatrix} i_{Q1} \\ i_{D1} \end{bmatrix} = \begin{bmatrix} \sin\left(\frac{\pi}{2\tau} x_c\right) & \sin\left(\frac{\pi}{2\tau} x_c + \frac{\pi}{2\tau} d\right) \\ \cos\left(\frac{\pi}{2\tau} x_c\right) & \cos\left(\frac{\pi}{2\tau} x_c + \frac{\pi}{2\tau} d\right) \end{bmatrix} \begin{bmatrix} I_1 \\ I_2 \end{bmatrix} \tag{3}$$

where d is the distance between the center of two coils.

The same analytical approach reveals that the forces of submotors B and C are similar to (1). By referencing [10], the dynamic equations for the three degrees of freedom can be formulated as:

$$M \begin{bmatrix} \ddot{x} \\ \ddot{y} \\ \ddot{z} + g \end{bmatrix} = K_F Q N^{-1} \begin{bmatrix} u_x \\ u_y \\ u_z \end{bmatrix} \tag{4}$$

$$Q = \begin{bmatrix} 1 & -\sin 30^\circ & -\sin 30^\circ & 0 & 0 & 0 \\ 0 & \cos 30^\circ & -\cos 30^\circ & 0 & 0 & 0 \\ 0 & 0 & 0 & 1 & 1 & 1 \end{bmatrix}$$

$$N = \begin{bmatrix} \frac{1}{3} & \frac{1}{3} & \frac{1}{3} & 0 & 0 & 0 \\ 0 & \frac{1}{2} & \frac{1}{2} & 0 & 0 & 0 \\ 0 & 0 & 0 & \frac{1}{3} & \frac{1}{3} & \frac{1}{3} \end{bmatrix}$$

where N^{-1} is the pseudo-inverse of N. M is the mass of the motor. The purpose of this article is to design u_x to ensure that the motor position x accurately tracks the desired trajectory x_d. Referring to [10], The state-space form is

$$\begin{cases} \dot{x}_1 = x_2 \\ \dot{x}_2 = \theta_1 u + \Delta(x_1, x_2) + \theta_2 \\ y = x_1 \end{cases} \tag{5}$$

where $x = [x_1 \quad x_2] \in \Re^2$ are the x-direction position and velocity of the magnetically levitated planar motor respectively. $\theta_1 = \left(NQ^{-1}K_F^{-1}M\right)^{-1}$ is unknow function related to the distance x. $u \in \Re$ is input signal. $y \in \Re$ is output signal. $\Delta(x_1, x_2)$ is the lumped uncertainty. θ_2 is the disturbance.

Assumption 1. θ_1 , θ_2 and $\Delta(x_1, x_2)$ are bounded time-varying function.

2.2 Actuator faults

As a high-precision motion platform, the magnetic levitation planar motor imposes extremely stringent performance requirements on its driver. Currently, existing drivers are unable to perfectly amplify the driving signals, leading to compromised output currents and resulting in system malfunctions. Therefore, it is imperative to anticipate and address such situations:

$$u = P(t)\eta \tag{6}$$

where $\eta \in \Re$ represents the drive input signal. $P(t)$ represents the degree of nonlinearity. When $P(t)$=1, the driver operates perfectly. When $P(t)$<1, the driver suffers from output losses. In practice, the output of the actuator is continuous. Thus, the unknow function $P(t)$ is considered bounded and continuous.

2.3 Output constraints

Due to the end effects of the Halbach magnet array, the motion range of the planar motor needs to be constrained such that

$$\underline{v}(t) < y(t) < \bar{v}(t), \quad t \geq 0, \tag{7}$$

where $\underline{v}(t)$ and $\bar{v}(t)$ represent the boundary constraints in the x-direction for motion.

Assumption 2. The functions $\underline{v}(t)$, $\bar{v}(t)$, $\underline{\dot{v}}(t)$, and $\bar{\dot{v}}(t)$ are bounded for all t $\geqslant$ 0. Furthermore, positive constants $\bar{\alpha}$ and $\underline{\alpha}$ exist such that

$$\underline{\alpha} < \bar{v}(t) - \underline{v}(t) < \bar{\alpha}, \quad t \geq 0, \tag{8}$$

2.4 Problem formulation

Problem 1. Considering the stringent requirements for positioning accuracy and response speed in magnetic levitation systems, as well as the challenges posed by insufficient driver precision and the influence of end effects. The objective is to design the controller ensuring:

- The motion trajectory can follow the given signal, and the bounded tracking error is expressed as follows:

$$\lim_{t\to\infty} \sup\left|y(t) - r(t)\right| = \lim_{t\to\infty} \sup\left|e_1(t)\right| < \delta \tag{9}$$

  where $r(t)$ and δ are the reference trajectory and predefined accuracy respective.
- All signals are bounded in the magnetic levitation system.

Assumption 3. The reference trajectory $r(t)$ is belong to the set $(\underline{\alpha}, \bar{\alpha})$.

3 Controller Design

Design a function as follow:

$$\phi(t) = \begin{cases} \cos^2(\frac{\pi}{2}\frac{t}{t_s}), & t < t_s \\ 0 & \text{else} \end{cases} \tag{10}$$

where $t_s > 0$ denotes a design parameter.

Design a performance function as follow:

$$\varphi_i(t) = \varphi_1\phi(t) + \varphi_2 \tag{11}$$

Where φ_1 and φ_2 are the predefined positive constant such that

$$\left|e_1(0)\right| < \varphi_1 \quad \varphi_1 + \varphi_2 \leq 1 \tag{12}$$

Considering output constraints, define the boundary conditions for the error as follow:

$$\underline{v}(t) - r(t) < e_1(t) < \bar{v}(t) - r(t) \tag{13}$$

To further refine the precision of adjustment in tracking accuracy, we construct

$$\begin{aligned} \bar{\beta}(t) &= \varphi_i(t)(\bar{v}(t) - r(t)) \\ \underline{\beta}(t) &= \varphi_i(t)(\underline{v}(t) - r(t)) \end{aligned} \tag{14}$$

Lemma 1. If

$$\underline{\beta}(t) < e_1(t) < \bar{\beta}(t), \quad t \geq 0 \tag{15}$$

is guaranteed, (9) is ensured.

Proof. Based on (10) – (14), it further obtains that

$$\underline{v}(t) - r(t) < \underline{\beta}(t) < \bar{\beta}(t) < \bar{v}(t) - r(t), \quad t \geq 0 \tag{16}$$

Based on assumption 2 and 3, it can be obtained that

$$\begin{aligned} 0 < \bar{v}(t) - r(t) < \bar{\alpha} \\ -\bar{\alpha} < \underline{v}(t) - r(t) < 0 \end{aligned} \tag{17}$$

Based on (11) and (14), it can be derived that

$$\begin{aligned} \bar{\beta}(t) &\leq \bar{\alpha}(\varphi_1\phi(t) + \varphi_2) \\ \underline{\beta}(t) &\geq -\bar{\alpha}(\varphi_1\phi(t) + \varphi_2) \end{aligned} \tag{18}$$

In case of (15), it holds that

$$-\bar{\alpha}\ (\varphi_1\phi(t) + \varphi_2) < e_1(t) < \bar{\alpha}\ (\varphi_1\phi(t) + \varphi_2) \tag{19}$$

Based on (12), the tracking error *e(t)* will be bounded. This completes the proof.

Design a barrier function to ensure (15) as follow:

$$A_1(t) = \ln(\frac{e_1(t) - \underline{\beta}(t)}{\bar{\beta}(t) - e_1(t)}) \tag{20}$$

The virtual control law is designed as follow

$$\gamma(t) = -c_1 A_1(t) \tag{21}$$

where c_1 is the predefined positive constant. The velocity error is presented as

$$e_2(t) = x_2(t) - \gamma(t) \tag{22}$$

Considering the actuator error, design the actual control law to constrain $e_2(t)$ as follow

$$\begin{aligned} \eta(t) &= -c_2 A_2(t) - c_3 \int_0^t A_2(t) d\tau \\ A_2 &= \tan(\frac{\pi}{2}\frac{e_2(t)}{k}) \end{aligned} \tag{23}$$

where c_2>0, c_3>0, and $|e_2(0)|$<k are the design parameters.

4 Stability Analysis

Theorem 1. Consider the magnetic levitation system (5) under Assumptions1, 2, 3 and 4. The proposed controller in (10)-(14) and (20)-(23) solve Problem 1.

Proof. It begins by assuming the existence of tracking errors that do not satisfy the following inequality:

$$\underline{\beta}(t) < e_1(t) < \bar{\beta}(t) \quad \left|e_2(t)\right| < k \quad t > 0 \tag{24}$$

This implies that the error at least satisfies the following conditions:

$$\begin{cases} \lim\limits_{x\to t_1} e_1(t) = \underline{\beta}(t_1) \\ \lim\limits_{x\to t_1} e_1(t) = \overline{\beta}(t_1) \\ \lim\limits_{x\to t_1} |e_2(t)| = k \end{cases} \tag{25}$$

where t_1 is the first time of the violation of (24). Then, it can be derived that

$$\underline{\beta}(t) < e_1(t) < \overline{\beta}(t) \qquad |e_2(t)| < k \quad t < t_1 \tag{26}$$

Subsequently, the following proof process relies on seeking a contradiction to demonstrate the (26) is not valid. The following proof omits the time or state dependence of certain functions for the convenience of analysis.

***Step 1*:** To analyze the position error, define the Lyapunov function as follow:

$$V_1 = \frac{1}{2} A_1^{\,2} \tag{27}$$

Differentiating (27) as follows:

$$\begin{aligned} \dot{V}_1 &= A_1 \cdot \frac{(\dot{e}_1 - \dot{\underline{\beta}})(\overline{\beta} - e_1) - (e_1 - \underline{\beta})(\dot{\overline{\beta}} - \dot{e}_1)}{(e_1 - \underline{\beta})(\overline{\beta} - e_1)} \\ &= A_1 \cdot \omega_1 \cdot (\dot{e}_1(\overline{\beta} - \underline{\beta}) + e_1(\dot{\underline{\beta}} - \dot{\overline{\beta}}) - \dot{\underline{\beta}}\overline{\beta} - \underline{\beta}\dot{\overline{\beta}}) \\ \omega_1 &= \frac{1}{(e_1 - \underline{\beta})(\overline{\beta} - e_1)} \end{aligned} \tag{28}$$

Based on (13) and (22), it can be derived that

$$\dot{e}_1 = e_2 - \dot{r} - c_1 A_1 \tag{29}$$

Inserting (29) into (28) yields

$$\begin{aligned} \dot{V}_1 &= A_1 \cdot \omega_1 \cdot (\overline{\beta} - \underline{\beta}) \cdot (I_1 - c_1 A_1) \\ I_1 &= e_2 - \dot{r} + \frac{\dot{\underline{\beta}} - \dot{\overline{\beta}}}{\overline{\beta} - \underline{\beta}} \cdot e_1 + \frac{\underline{\beta}\dot{\overline{\beta}} - \dot{\underline{\beta}}\overline{\beta}}{\overline{\beta} - \underline{\beta}} \end{aligned} \tag{30}$$

Then, the proof of the boundedness of I_1 is presented as follow:

1) Based on (26), e_1 and e_2 are bounded.

2) Based on assumption 2, 3 and (11), $\overline{\beta}$, $\dot{\overline{\beta}}$, $\underline{\beta}$, $\dot{\underline{\beta}}$ and $\dot{r}$ are bounded. Thus $\dot{\underline{\beta}} - \dot{\overline{\beta}}$ and $\underline{\beta}\dot{\overline{\beta}} - \dot{\underline{\beta}}\overline{\beta}$ are bounded. From (16), we know $0 < \overline{\beta} - \underline{\beta} < \overline{v}(t) - r(t)$.

Thus, I_1 is bounded as follow:

$$|I_1| < \overline{I}_1 \quad t < t_1 \tag{31}$$

where $\overline{I}_1$ is a constant.

Recalling (15), we know $\omega_1 \cdot (\overline{\beta} - \underline{\beta}) > 0$. Substituting (31) into (30) yields

$$\dot{V}_1 < |A_1| \cdot \omega_1 \cdot (\overline{\beta} - \underline{\beta}) \cdot (|I_1| - c_1 A_1) \quad t < t_1 \tag{32}$$

From (32), we know $\dot{V}_1 < 0$ when $|A_1| > \overline{I}_1 / c_1$. Based on (27), it can be obtained that

$$|A_1(t)| \le \left\{ |A_1(0)|, \quad \frac{\overline{I}_1}{c_1} \right\} \qquad t < t_1 \tag{33}$$

Recall that A_1 is the barrier function, indicating that e_1 will not approach to $\overline{\beta}$ or $\underline{\beta}$.

***Step 2*:** To analyze the velocity error, define the Lyapunov function as follow:

$$V_2 = \frac{1}{\pi} A_2^{\,2} \tag{34}$$

Differentiating (34) yields

$$\dot{V}_2 = \frac{1}{k} A_2 \cdot \frac{1}{\cos^2(\frac{\pi}{2} \cdot \frac{e_2}{k})} \dot{e}_2 \tag{35}$$

Based on (5) and (23), Differentiating (22) yields

$$\dot{e}_2(t) = \theta_1 \cdot (-c_2 A_2(t) - c_3 \int_0^t A_2(t) d\tau) + \Delta(x_1, x_2) + \theta_2 - \dot{\gamma} \tag{36}$$

Inserting (36) into (35) yields

$$\dot{V}_2 = \frac{1}{k} A_2 \cdot \frac{1}{\cos^2(\frac{\pi}{2} \cdot \frac{e_2}{k})} (I_2 - \theta_1 c_2 A_2) \tag{37}$$

where

$$I_2 = \theta_2 - \dot{\gamma} + \Delta(x_1, x_2) - \theta_1 \cdot c_3 \int_0^t A_2(t) d\tau \tag{38}$$

By using the mean value theorem for integrals, it can be derived that

$$c_3 \int_0^t A_2(t) d\tau = -c_3 A_2(\varepsilon), \quad \varepsilon \in [0, \quad t], \quad t < t_1 \tag{40}$$

Inserting (40) into (38) yields

$$I_2 = \theta_2 - \dot{\gamma} + \Delta(x_1, x_2) - \theta_1 c_3 A_2(\varepsilon) \tag{41}$$

Recalling (28), we know $\dot{\gamma}$ is bounded during $t<t_1$. Based on (5), θ_1, θ_2 and $\Delta(x_1, x_2)$ are bounded. There exists the constant $\overline{\theta}_1$, $\underline{\theta}_1$ such that $\underline{\theta}_1 < |\theta_1| < \overline{\theta}_1$. Based on (26) and the

continuity of A_2, it can be shown $A_2(\varepsilon)$ is bounded. Thus, it can be derived that I_2 is bounded as $t<t_1$ as follow:

$$|I_2| < \bar{I}_2 \quad t < t_1 \tag{42}$$

where $\bar{I}_2$ is a constant.

Recalling (37), it can be derived that

$$\dot{V}_2 < \frac{1}{k}|A_2| \cdot \frac{1}{\cos^2(\frac{\pi}{2} \cdot \frac{e_2}{k})}(\bar{I}_2 - \underline{\theta}_1 c_2 A_2) \tag{43}$$

From (43), we know $\dot{V}_2 < 0$ when $|A_2| > \bar{I}_2 / \underline{\theta}_1 c_2$. Based on (34), it can be obtained that

$$|A_2(t)| \le \left\{ |A_2(0)|, \quad \frac{\bar{I}_2}{\theta_1 c_2} \right\} \qquad t < t_1 \tag{44}$$

Recall that A_2 is the barrier function, indicating that e_2 will not approach to k or $-k$.

Based on (33) and (44), The scenario described by (25) will not occur and (24) holds consistently.

***Step 3*:** Taking（25）as a result, we can proof that all closed-loop signals are bounded as follow:

Since e_1 and e_2 are bounded, it follows that A_1 and A_2 are also bounded. Consequently, the virtual control signals γ and the actual input signals η are bounded. Based on (13) and (22), it can be deduced that x_1 and x_2 are bounded. The proof is completed.

5 Simulation Study

In this section, the accuracy of the theoretical derivations is verified through the simulation. Based on the state-space form (5), set the thrust coefficient associated with position , external disturbance and lumped uncertainty as follow:

$$\begin{aligned} &\frac{1}{\theta_1} = 0.5 + 0.1\sin(0.2x_1) \\ &\theta_2 = 0.1\sin(0.2t) \\ &\Delta(x_1, x_2) = 0.2(x_1 + x_2)\sin(0.3t) \end{aligned} \tag{45}$$

The position constraint of magnetic levitation planar motor is presented as follow:

$$\begin{aligned} &\underline{v}(t) = -1.5 - (0.6t) \\ &\bar{v}(t) = 1.5 - (0.6t) \end{aligned} \tag{46}$$

The reference trajectory is shown as follow:

$$r(t) = \sin(0.6t) - t/6 \tag{47}$$

The prescribed accuracy is specified as follow:

$$\limsup_{x \to \infty} |e_1(t)| \le 0.02 \tag{48}$$

The situation of actuator faults is specified as follow:

$$P(t) = 0.6 + 0.1\sin(t) \tag{49}$$

In order to solve problem 1, the controller is designed based on the above analysis. The parameters of the performance function and the values of the control gains are presented as follow:

$$\varphi_1 = 0.98 \quad \varphi_2 = 0.02 \quad k = 0.05 \quad c_1 = 3 \quad c_2 = c_3 = 20 \tag{50}$$

Set $x_1(0) = 0.4$, $x_2(0) = -1.6$. The simulation results are shown in Fig.2-5. From the Fig.2 and Fig.3, the state variable, the virtual control law and are bounded signals. Although under actuator faults, the position of maglev planar motor remains constrained. From the Fig.4 and Fig.5, it can be derived that the tracking performances satisfy the predefined accuracy.

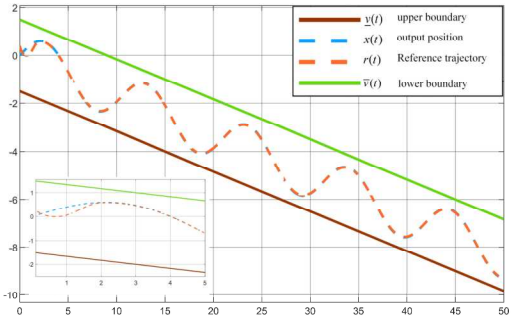

Fig.2 The constrained x-position of magnetic levitation plane motor

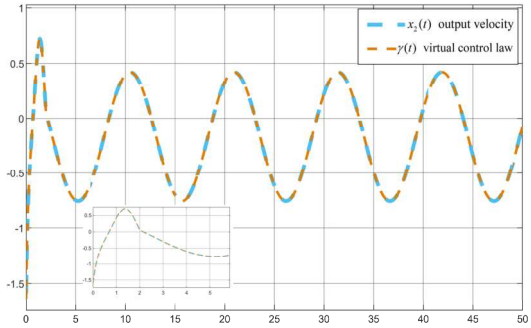

Fig.3 The virtual control law and velocity

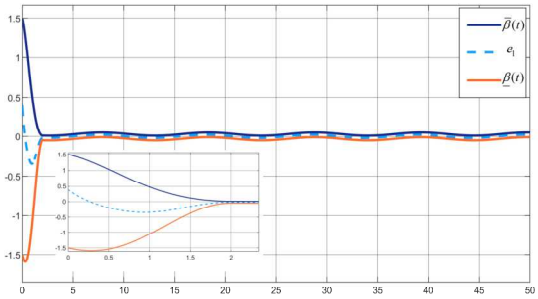

Fig.4 The tracking error under the imposed boundary

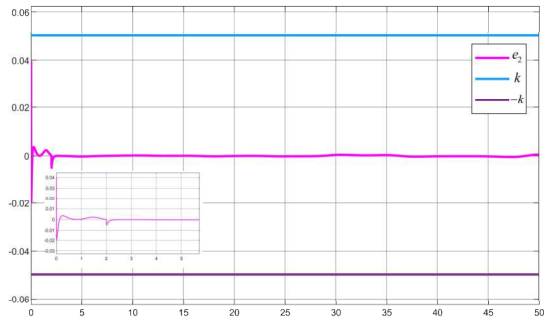

Fig.5 The tracking error under the imposed boundary

6 Conclusion

The paper designs a robust PI controller for the magnetic levitation planar motor with actuator faults, which can deal with the problem of unknown nonlinear dynamics model and external unknown disturbances. The presented PI controller can achieve the tracking accuracy within the prescribed time. Moreover, it ensures all the closed loop signals are bounded without violation of the output constraint. The presented control can achieve high computational efficiency without a complex structure, which is critical for realizing real-time control of the magnetically levitated planar motor.

References

[1] J. W. Jansen, C. M. M. van Lierop, E. A. Lomonova and A. J. A. Vandenput, Magnetically Levitated Planar Actuator With Moving Magnets, IEEE Transactions on Industry Applications, vol. 44, no. 4, pp. 1108-1115, July-aug. 2008.

[2] Y. Zhang, K. Ding and S. Du, Design Study of a High Loading Superconducting Magnetically Levitated Planar Motor, in IEEE Transactions on Applied Superconductivity, vol. 31, no. 5, pp. 1-4, Aug. 2021, Art no. 3601504.

[3] S. Zhang, X. Dang, K. Wang, J. Huang, J. Yang and G. Zhang, An Analytical Approach to Determine Coil Thickness for Magnetically Levitated Planar Motors, IEEE/ASME Transactions on Mechatronics, vol. 22, no. 1, pp. 572-580, Feb. 2017.

[4] A. Mughees and S. A. Mohsin, "Design and Control of Magnetic Levitation System by Optimizing Fractional Order PID Controller Using Ant Colony Optimization Algorithm," in IEEE Access, vol. 8, pp. 116704-116723, 2020.

[5] C. Sourkounis, PID-State Torque Control in Electromechanical Drive Systems Under Stochastic Load, IEEE Transactions on Industry Applications, vol. 48, no. 1, pp. 20-27, Jan.-Feb. 2012.

[6] L. Song et al., Motion Control of Capsule Robot Based on Adaptive Magnetic Levitation Using Electromagnetic Coil, IEEE Transactions on Automation Science and Engineering, vol. 20, no. 4, pp. 2720-2731, Oct. 2023.

[7] C. -M. Lin, M. -H. Lin and C. -W. Chen, SoPC-Based Adaptive PID Control System Design for Magnetic Levitation System, IEEE Systems Journal, vol. 5, no. 2, pp. 278-287, June 2011.

[8] J. Wang, L. Chen and Q. Xu, Disturbance Estimation-Based Robust Model Predictive Position Tracking Control for Magnetic Levitation System, IEEE/ASME Transactions on Mechatronics, vol. 27, no. 1, pp. 81-92, Feb. 2022.

[9] F. Xu, Y. Shi, K. Zhang and X. Xu, Real-Time Application of Robust Offset-Free MPC in Maglev Planar Machine, IEEE Transactions on Industrial Electronics, vol. 70, no. 6, pp. 6121-6130, June 2023.

[10] C. Hu, Z. Wang, Y. Zhu, M. Zhang and H. Liu, Performance-Oriented Precision LARC Tracking Motion Control of a Magnetically Levitated Planar Motor With Comparative Experiments, IEEE Transactions on Industrial Electronics, vol. 63, no. 9, pp. 5763-5773, Sept. 2016.

[11] C. Hu, T. Ou, Y. Zhu and L. Zhu, GRU-Type LARC Strategy for Precision Motion Control With Accurate Tracking Error Prediction, IEEE Transactions on Industrial Electronics, vol. 68, no. 1, pp. 812-820, Jan. 2021.

[12] J. Kang, X. Huang, C. Xia, D. Huang and F. Wang, Ultralocal Model-Free Adaptive Supertwisting Nonsingular Terminal Sliding Mode Control for Magnetic Levitation System, IEEE Transactions on Industrial Electronics, vol. 71, no. 5, pp. 5187-5194, May 2024.

[13] Z. Gao, Y. Zhang and G. Guo, Finite-Time Fault-Tolerant Prescribed Performance Control of Connected Vehicles With Actuator Saturation, IEEE Transactions on Vehicular Technology, vol. 72, no. 2, pp. 1438-1448, Feb. 2023.

[14] H. Ma, Q. Zhou, H. Li and R. Lu, Adaptive Prescribed Performance Control of A Flexible-Joint Robotic Manipulator With Dynamic Uncertainties, IEEE Transactions on Cybernetics, vol. 52, no. 12, pp. 12905-12915, Dec. 2022.

[15] P. K. Mishra and P. Jagtap, Approximation-Free Prescribed Performance Control With Prescribed Input Constraints, IEEE Control Systems Letters, vol. 7, pp. 1261-1266, 2023.

[16] S. Gao, Y. Hou, H. Dong, Y. Yue and S. Li, Global Nested PID Control of Strict-Feedback Nonlinear Systems With Prescribed Output and Virtual Tracking Performance, IEEE Transactions on Circuits and Systems II: Express Briefs, vol. 67, no. 2, pp. 325-329, Feb. 2020.

[17] S. Gao, H. Dong, B. Ning and Q. Zhang, Cooperative Prescribed Performance Tracking Control for Multiple High-Speed Trains in Moving Block Signaling System, IEEE Transactions on Intelligent Transportation Systems, vol. 20, no. 7, pp. 2740-2749, July 2019.

[18] S. Gao, M. Li, Y. Zheng and H. Dong, Expansive Errors-Based Fuzzy Adaptive Prescribed Performance Control by Residual Approximation, IEEE Transactions on Fuzzy Systems, vol. 30, no. 7, pp. 2736-2746, July 2022.

[19] B. Li, S. Wen, Z. Yan, G. Wen and T. Huang, A Survey on the Control Lyapunov Function and Control Barrier Function for Nonlinear-Affine Control Systems, IEEE/CAA Journal of Automatica Sinica, vol. 10, no. 3, pp. 584-602, March 2023.

[20] M. Ghanbarpour, A. Isaly, R. G. Sanfelice and W. E. Dixon, Optimal Safety for Constrained Differential Inclusions Using Nonsmooth Control Barrier Functions, IEEE Control Systems Letters, vol. 7, pp. 1303-1308, 2023.

[21] S. Farzan, V. Azimi, A. -P. Hu and J. Rogers, Adaptive Control of Wire-Borne Underactuated Brachiating Robots Using Control Lyapunov and Barrier Functions, IEEE Transactions on Control Systems Technology, vol. 30, no. 6, pp. 2598-2614, Nov. 2022.

[22] Jin-Xi Zhang, Guang-Hong Yang, Fault-tolerant output-constrained control of unknown Euler–Lagrange systems with prescribed tracking accuracy, Automatica, Volume 111, 108606, 2020.

[23] J. W. Jansen, C. M. M. van Lierop, E. A. Lomonova and A. J. A. Vandenput, Modeling of Magnetically Levitated Planar Actuators With Moving Magnets, IEEE Transactions on Magnetics, vol. 43, no. 1, pp. 15-25, Jan. 2007.

[24] D. L. Trumper, Won-Jong Kim and M. E. Williams, Design and analysis framework for linear permanent-magnet machines, IEEE Transactions on Industry Applications, vol. 32, no. 2, pp. 371-379, March-April 1996.

Proceedings of the 3rd Conference on Fully Actuated System Theory and Applications
May 10-12, 2024, Shenzhen, China

Wave Motion Compensation Controller Design for a Catamaran Upper Platform in the Presence of External Disturbance

Junyu Shen[1,2], Rongji Yin[1], Yao Yu[1], Rijie Zeng[1], Zhihuan Hu[1], Weidong Zhang[1], Jinhui Lu[3], Wei Xie[1]

1. Department of Automation, Shanghai Jiao Tong University, Shanghai, China
E-mail: {sjy_nova, rj-yin, franco1in}@sjtu.edu.cn, 2254502536@qq.com, {scarlet, wdzhang, weixie}@sjtu.edu.cn

2. SJTU Yazhou Bay Institute of Deepsea Sci-Tech, Shanghai Jiao Tong University, Hainan, China

3. National Engineering Research Center of Ship & Shipping Control System, Shanghai, China
E-mail: lu.jinhui@coscoshipping.com

Abstract: This paper presents a nonlinear controller for the upper platform of a catamaran in the presence of external time-varying disturbance induced by wind or wave. To handle disturbances, an observer is employed. Designed using the backstepping method, the controller effectively maintains the platform within a small neighborhood of 10^{-3}(m or rad) of the desired attitude and the observer monitors external disturbance in real time. Simulation results validate the strategy, demonstrating the platform's ability to consistently maintain an ideal posture in the presence of dynamic disturbance.

Key Words: catamaran, disturbance observer, adaptive controller.

1 Introduction

In the field of ship control, improving the stability of ship navigation is of great importance [1]. Wave compensation can enhance the safety, stability and comfort of navigation at sea, and plays a vital role in offshore operations and voyages [2]. Implementing wave compensation improves safety by reducing the risks caused by wave-induced motions, making ship voyages smoother and minimizing discomfort and seasickness to the maximum extent [3, 4].

In existing technologies, roll stabilizing fins [5, 6] and shifting mass [7] are utilized to make ships more steady during navigation. The principle of roll stabilizing fins works by generating hydrodynamic lift to counteract the rolling motion of the hull, thereby enhancing ship's stability and comfort [8]. This technique has been widely applied in large vessels, yachts and other areas. Shifting mass method is to strategically move weight within the ship to alter the center of gravity and produce a counter moment canceling out the lateral sway caused by waves [9, 10]. However, both roll stabilizing fins and shifting mass can only compensate for the roll motion of ships.

Inspired by [11], this paper proposes a new catamaran structure compared to traditional fixed connection ones. The catamaran structure, namely the combination of an upper platform and two symmetrical lower hulls through the connection of hinges and hydraulic actuators, enables relative motions between the hulls and the upper platform, as shown in Fig. 1. This design achieves real-time compensation for the upper platform's heave, pitch and roll motions, allowing the catamaran to adapt to the complex sea wave environments. Regarding this structure, a robust adaptive controller is proposed in the presence of time-varying disturbance to improve the stability of the upper platform of catamaran. Furthermore, a disturbance observer is designed and incorporated to estimate disturbance that may result from unmodeled dynamics and external environment. The controller effectively maintains the platform within a small neighborhood of the desired attitude, achieving global stability. Simulation results are presented to validate the efficacy and performance of the proposed control strategy.

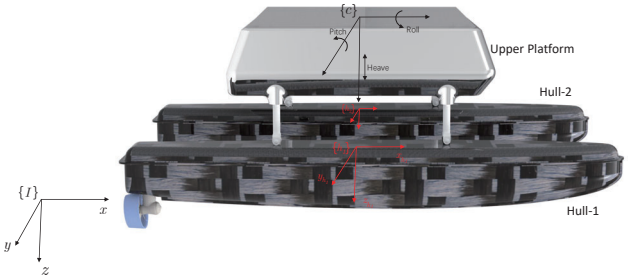

Fig. 1: Illustration of Catamaran.

The remainder of this paper is organized as follows. Section 2 introduces the notations used throughout this paper. The dynamic model of the catamaran upper platform and control problem are presented in Section 3. A nonlinear disturbance observer is given in Section 4. Section 5 presents control scheme and stability analysis. Simulation results are shown in Section 6. Section 7 summarizes the contents of this work.

2 Notation

The following notations are used throughout this paper. $\mathbb{R}^n$ represents the n-dimensional Euclidean space. A diagonal matrix $\mathbf{P} \in \mathbb{R}^{n\times n}$ with all diagonal elements are positive can be viewed as an element of the special matrix group $\mathcal{D}(n)$. $||\cdot||$ represents 2-norm of a vector or Frobenius norm of a matrix. For a matrix $\mathbf{A} \in \mathbb{R}^{n\times n}$ and a vector $x \in \mathbb{R}^n$, we have $||\mathbf{A}x|| \leq ||\mathbf{A}||\,||x||$ since the Frobenius norm of matrices is compatible with the 2-norm of vectors. Table 1 summarizes some main symbols and their corresponding descriptions used in the follows.

*This work is supported in part by the Science Center Program of National Natural Science Foundation of China under Grant 62188101, and in part by the Young Elite Scientists Sponsorship Program by CAST under Grant 2022QNRC001.

Table 1: Symbols summary

$\{I\}$	inertial frame
$\{c\},\ \{h_1\},\ \{h_2\}$	body frames
$\mathbf{q}$	attitude of the upper platform
$\mathbf{M}$	mass matrix of the upper platform
$\mathbf{d},\ \dot{\mathbf{d}}$	disturbance and its derivative
$\mathbf{G}$	gravity vector of the upper platform
$\mathbf{u}$	input force
$k_1,\ k_2,\ k_d$	positive control gains

3 Problem Formulation

This section presents the model of the catamaran upper platform, and formulates the control problem.

3.1 Catamaran Upper Platform Model

The catamaran upper platform, shown in Fig. 1, is modeled under forces and torques generated by four hydraulic actuators and external disturbances. Considering a fixed inertia frame $\{I\}$, a body-fixed frame $\{h_1\}$ attached to the Hull-1's center of mass, a body-fixed frame $\{h_2\}$ attached to the Hull-2's center of mass and a body-fixed frame $\{c\}$ attached to the center of mass of the upper platform, the dynamic equation is given by

$$\ddot{\mathbf{q}} = \mathbf{M}_t\mathbf{u} + \mathbf{M}^{-1}\mathbf{G} + \mathbf{M}^{-1}\mathbf{d} \tag{1}$$

where $\mathbf{q}$ is the attitude of the upper platform representing heave, pitch and roll motions, $\mathbf{M}_t$ is a 3×4 matrix which is related to both the specific parameters of the upper platform and the motions of the two hulls, $\mathbf{u} = [u_1,\ u_2,\ u_3,\ u_4]^\top$ represents the input forces generated by the 4 hydraulic actuators, $\mathbf{M} = \text{diag}(M,\ I_x,\ I_y)$ is a diagonal matrix with M being the mass of the upper platform and I_x and I_y being moments of inertia for roll and pitch, respectively, $\mathbf{G} = [Mg,\ 0,\ 0]^\top$ denotes the gravity vector of the upper platform, $\mathbf{d} = [d_1,\ d_2,\ d_3]^\top$ represents time-varying disturbance.

Assumption 1. *The disturbance* $\mathbf{d}$ *is an unknown, bounded and time-varying parameter. In addition,* $\mathbf{d}$ *is Lipschitz continuous whose derivative,* $\dot{\mathbf{d}}$*, is bounded, time-varying and satisfies*

$$||\dot{\mathbf{d}}|| \leq \zeta \tag{2}$$

for a known positive scalar ζ*.*

3.2 Control Objective

Let $\mathbf{q}_d = [z_d,\ \phi_d,\ \theta_d]^\top$ be a constant vector which represents the desired value of $\mathbf{q}$. The goal is to maintain the upper platform's attitude precisely at the desired attitude $\mathbf{q}_d$. To achieve this goal, the control objective is to design a control law that eliminates the heave, roll, and pitch motions of the upper platform, while minimizing the position error $||\mathbf{q} - \mathbf{q}_d||$ as much as possible.

4 Disturbance Observer

In order to estimate unknown external disturbance in real-time, a disturbance observer is employed to estimate $\mathbf{d}$. The following auxiliary variable is defined as

$$\boldsymbol{\xi} = \mathbf{d} - k_d\dot{\mathbf{q}} \tag{3}$$

where $k_d \in \mathbb{R}^+$ is a designed parameter. The time derivative of $\boldsymbol{\xi}$ is

$$\dot{\boldsymbol{\xi}} = \dot{\mathbf{d}} - k_d(\mathbf{M}_t\mathbf{u} + \mathbf{M}^{-1}\mathbf{G} + \mathbf{M}^{-1}\mathbf{d}) \tag{4}$$

The estimate of $\dot{\boldsymbol{\xi}}$ is chosen as

$$\dot{\hat{\boldsymbol{\xi}}} = -k_d(\mathbf{M}_t\mathbf{u} + \mathbf{M}^{-1}\mathbf{G} + \mathbf{M}^{-1}(\hat{\boldsymbol{\xi}} + k_d\dot{\mathbf{q}})) \tag{5}$$

where $\hat{\boldsymbol{\xi}}$ is the estimate of $\boldsymbol{\xi}$. Invoking (3), the estimate of time-varying disturbance $\mathbf{d}$ is

$$\hat{\mathbf{d}} = \hat{\boldsymbol{\xi}} + k_d\dot{\mathbf{q}} \tag{6}$$

Two error parameters are defined as

$$\tilde{\mathbf{d}} = \mathbf{d} - \hat{\mathbf{d}} \tag{7}$$

and

$$\tilde{\boldsymbol{\xi}} = \boldsymbol{\xi} - \hat{\boldsymbol{\xi}} \tag{8}$$

Based on (3) and (6), one has

$$\tilde{\boldsymbol{\xi}} = \tilde{\mathbf{d}} \tag{9}$$

Taking the time derivative of (8) and considering (4) and (5) yield

$$\dot{\tilde{\boldsymbol{\xi}}} = \dot{\mathbf{d}} - k_d\mathbf{M}^{-1}\tilde{\boldsymbol{\xi}} \tag{10}$$

Due to $\tilde{\boldsymbol{\xi}} = \tilde{\mathbf{d}}$, one has

$$\dot{\tilde{\mathbf{d}}} = \dot{\mathbf{d}} - k_d\mathbf{M}^{-1}\tilde{\mathbf{d}} \tag{11}$$

Lemma 1. *The estimation error* $\dot{\tilde{\mathbf{d}}}$*, given by (11), is stable and satisfies*

$$||\tilde{\mathbf{d}}|| \leq \frac{\zeta}{k_d\alpha} \tag{12}$$

where $\alpha = \min\{M^{-1},\ I_x^{-1},\ I_y^{-1}\}$.

Proof: A Lyapunov function candidate is defined as

$$V_d = \frac{1}{2}\tilde{\mathbf{d}}^\top\tilde{\mathbf{d}} \tag{13}$$

Based on (11) and **Assumption** 1, the time derivative of V_d is

$$\begin{aligned}\dot{V}_d &= \tilde{\mathbf{d}}^\top(\dot{\mathbf{d}} - k_d\mathbf{M}^{-1}\tilde{\mathbf{d}}) \\ &\leq -k_d\alpha||\tilde{\mathbf{d}}||^2 + \zeta||\tilde{\mathbf{d}}|| \\ &= -||\tilde{\mathbf{d}}||(k_d\alpha||\tilde{\mathbf{d}}|| - \zeta)\end{aligned}$$

The previous proof shows that $\dot{V}_d$ is strictly negative in the region of space defined by $||\tilde{\mathbf{d}}|| > \frac{\zeta}{k_d\alpha}$. This implies the estimation error $\tilde{\mathbf{d}}$ can be driven to arbitrarily small value by increasing k_d or decreasing ζ through considering slowly time-varying disturbance. Furthermore, when $\zeta = 0$, meaning the disturbance term $\tilde{\mathbf{d}}$ is assumed to be constant, the estimation error $\tilde{\mathbf{d}}$ achieves global exponential stability at the origin. □

5 Controller Design

In this section, a robust nonlinear control scheme is developed for the upper platform of the catamaran, which can compensate for external environmental disturbance. Referring to the standard backstepping control design method [15], a position error $\mathbf{z}_1 \in \mathbb{R}^3$ is defined as

$$\mathbf{z}_1 = \mathbf{q} - \mathbf{q}_d \tag{14}$$

Since $\mathbf{q}_d$ is a constant vector, computing the time derivative of $\mathbf{z}_1$ yields

$$\dot{\mathbf{z}}_1 = \dot{\mathbf{q}} \tag{15}$$

A Lyapunov function candidate is defined as

$$V_1 = \frac{1}{2}\mathbf{z}_1^\top \mathbf{z}_1 \tag{16}$$

Computing the time derivative of (16) yields

$$\dot{V}_1 = -W_1(\mathbf{z}_1) + \mathbf{z}_1^\top(k_1\mathbf{z}_1 + \dot{\mathbf{q}}) \tag{17}$$

where $W_1(\mathbf{z}_1) = k_1\mathbf{z}_1^\top\mathbf{z}_1$ with $k_1 \in \mathbb{R}^+$. Following the backstepping technique, $\mathbf{z}_2$ is denoted as

$$\mathbf{z}_2 = k_1\mathbf{z}_1 + \dot{\mathbf{q}} \tag{18}$$

The second Lyapunov function candidate is defined as

$$V_2 = V_1 + \frac{1}{2}\mathbf{z}_2^\top \mathbf{z}_2 \tag{19}$$

and its time derivative is

$$\begin{aligned}\dot{V}_2 = &-W_2(\mathbf{z}_1, \mathbf{z}_2) + \mathbf{z}_2^\top(\mathbf{z}_1 + k_2\mathbf{z}_2 + k_1\dot{\mathbf{z}}_1 \\ &+ \mathbf{M}_t\mathbf{u} + \mathbf{M}^{-1}\mathbf{G} + \mathbf{M}^{-1}\mathbf{d})\end{aligned} \tag{20}$$

where $W_2(\mathbf{z}_1, \mathbf{z}_2) = k_1\mathbf{z}_1^\top\mathbf{z}_1 + k_2\mathbf{z}_2^\top\mathbf{z}_2$

A Lyapunov function is presented as

$$V_3 = V_2 + V_d \tag{21}$$

where V_d is given by (13). Considering (20) and (11), the time derivative of V_3 is given by

$$\begin{aligned}\dot{V}_3 = &-W_3(\mathbf{z}_1, \mathbf{z}_2, \tilde{\mathbf{d}}) + \tilde{\mathbf{d}}^\top(\dot{\mathbf{d}} + \mathbf{M}^{-1}\mathbf{z}_2) \\ &+ \mathbf{z}_2^\top(\mathbf{z}_1 + k_2\mathbf{z}_2 + k_1\dot{\mathbf{z}}_1 + \mathbf{M}^{-1}\mathbf{G} \\ &+ \mathbf{M}^{-1}\hat{\mathbf{d}} + \mathbf{M}_t\mathbf{u})\end{aligned} \tag{22}$$

where $W_3(\mathbf{z}_1, \mathbf{z}_2, \tilde{\mathbf{d}}) = k_1\mathbf{z}_1^\top\mathbf{z}_1 + k_2\mathbf{z}_2^\top\mathbf{z}_2 + k_d\tilde{\mathbf{d}}^\top\mathbf{M}^{-1}\tilde{\mathbf{d}}$. The input is selected as

$$\mathbf{u} = -\mathbf{M}_t^\dagger(\mathbf{z}_1 + k_2\mathbf{z}_2 + k_1\dot{\mathbf{z}}_1 + \mathbf{M}^{-1}\mathbf{G} + \mathbf{M}^{-1}\hat{\mathbf{d}}) \tag{23}$$

where $\mathbf{M}_t^\dagger$ denotes the Moore-Penrose inverse matrix of $\mathbf{M}_t$. Substituting (23) into (22) yields

$$\dot{V}_3 = -W_3(\mathbf{z}_1, \mathbf{z}_2, \tilde{\mathbf{d}}) + \tilde{\mathbf{d}}^\top(\dot{\mathbf{d}} + \mathbf{M}^{-1}\mathbf{z}_2) \tag{24}$$

Theorem 1. *The dynamic model of the catamaran upper platform is given by (1), with $\mathbf{q}_d$ representing the desired trajectory. For the closed-loop system formed by substituting the control input (23) and disturbance observer (6), the position error $\mathbf{z}_1$ can be proven to be bounded in the presence of unknown time-varying disturbance $\mathbf{d}$.*

Proof: Since $\mathbf{M}^{-1}$ is a bounded, constant matrix, $||\mathbf{M}^{-1}||$ is also bounded within a range $c_1 \le ||\mathbf{M}^{-1}|| \le c_2$, where c_1 and c_2 are positive. Based on **Assumption** 1 and applying Young's inequality, one has

$$\begin{aligned}\tilde{\mathbf{d}}^\top\dot{\mathbf{d}} &\le \frac{1}{2}||\tilde{\mathbf{d}}||^2 + \frac{1}{2}||\dot{\mathbf{d}}||^2 \\ &\le \frac{1}{2}||\tilde{\mathbf{d}}||^2 + \frac{\zeta^2}{2}\end{aligned} \tag{25}$$

$$\begin{aligned}\tilde{\mathbf{d}}^\top\mathbf{M}^{-1}\mathbf{z}_2 &\le \frac{1}{2}||\tilde{\mathbf{d}}||^2 + \frac{1}{2}||\mathbf{M}^{-1}||^2||\mathbf{z}_2||^2 \\ &\le \frac{1}{2}||\tilde{\mathbf{d}}||^2 + \frac{c_2}{2}||\mathbf{z}_2||^2\end{aligned} \tag{26}$$

Utilizing (24), (25) and (26), V_3 can be upper bounded as

$$\begin{aligned}\dot{V}_3 &\le -k_1||\mathbf{z}_1||^2 - (k_2 - \frac{c_2^2}{2})||\mathbf{z}_2||^2 - (k_d c_1 - 1)||\tilde{\mathbf{d}}||^2 + \frac{\zeta^2}{2} \\ &\le -\lambda||\mathbf{z}||^2 + \frac{\zeta^2}{2}\end{aligned} \tag{27}$$

where $k_2 \ge c_2^2/2$, $k_d \ge 1/c_1$, $\mathbf{z} = [\mathbf{z}_1^\top, \mathbf{z}_2^\top, \boldsymbol{\xi}^\top]^\top$ and $\lambda = \min\{k_1,\ k_2 - c_2^2/2,\ k_d c_1 - 1\}$. Furthermore, it can be shown that $\dot{V}_3$ is strictly negative in the region where $||\mathbf{z}|| > \zeta/\sqrt{2\lambda}$, leading to the conclusion that z is uniformly bounded. □

6 Simulation Results

To validate the efficacy of the proposed controller, simulation results are presented in this section. The parameters of the system are given in Table 2.

The six degree-of-freedom motion of the catamaran hulls was obtained through MATLAB calculations based on the PM random wave spectrum. The resulting hull motion data, which will be utilized in subsequent simulations, are presented in Fig. 2. However, when a catamaran is sailing or turning, there will be surge and yaw motions on the platform. So for the upper platform control, only the heave, roll and pitch motions are compensated.

Table 2: Parameters of Catamaran Upper Platform

Parameter	Value(Unit)
M	100(kg)
I_x	11(kg·m^2)
I_y	21(kg·m^2)

Inspired by the works in [16] and [17], the external disturbance is modeled as first order Markov processes of the form

$$\dot{\mathbf{d}} = \mathbf{T}^{-1}(-\mathbf{d} + \mathbf{\Lambda}\,\boldsymbol{\omega}) \tag{28}$$

where $\mathbf{T} \in \mathbb{R}^{3\times3}$ is a diagonal time constant matrix, $\boldsymbol{\omega} \in \mathbb{R}^3$ is zero-mean white Gaussian noise, and $\mathbf{\Lambda} \in \mathbb{R}^{3\times3}$ is a diagonal matrix that scales $\boldsymbol{\omega}$. The initial value of the process is set to $\mathbf{d}_0 = [1/3,\ -2/3,\ -1/3]^\top$. For $\mathbf{T} = \text{diag}(5,\ 20,\ 20)$, $\mathbf{\Lambda} = \text{diag}(50,\ 50,\ 50)$, the resulting time-varying disturbance is displayed in Fig. 3.

The desired position and attitude of catamaran upper platform with respect to inertia frame $\{I\}$ is

$$\mathbf{q}_d = [-0.7,\ 0,\ 0]^\top$$

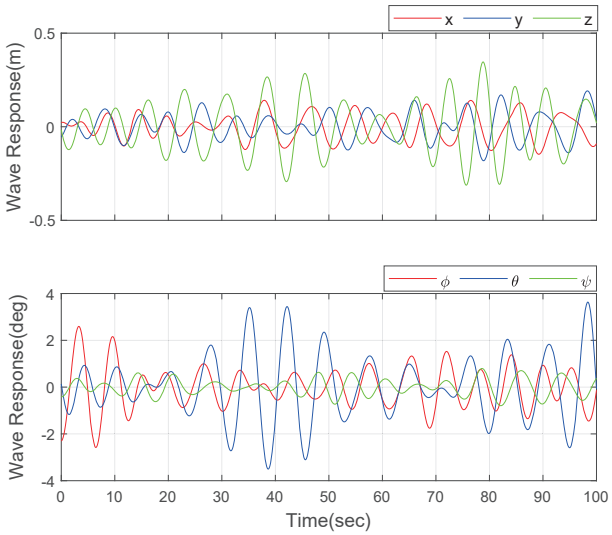

Fig. 2: Position and attitude of the hull.

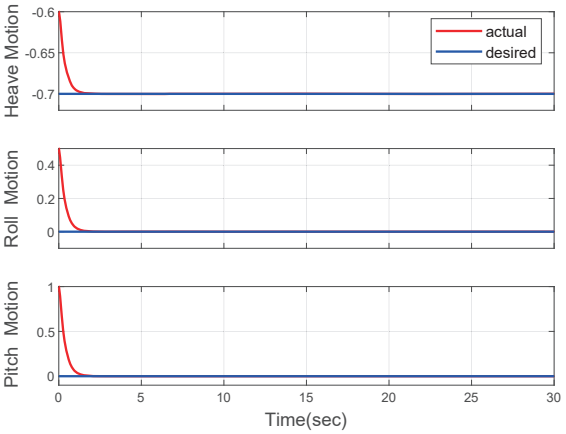

Fig. 4: Actual and desired attitude of the upper platform.

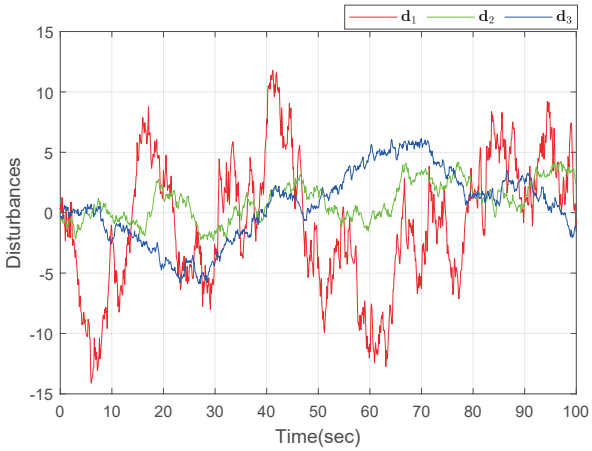

Fig. 3: External disturbance.

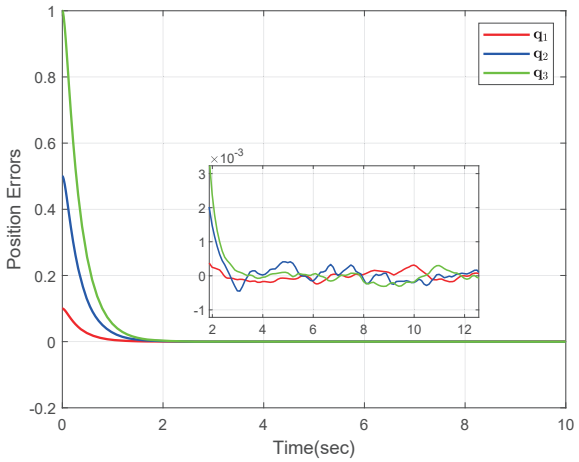

Fig. 5: Position error of the upper platform.

and the initial state of the catamaran upper platform is

$$\mathbf{q} = [-0.6,\ 0.5,\ 1]^\top$$

Simulation results are given from Fig. 4 to Fig. 8.

Fig. 4 shows the actual and desired heave, roll and pitch motions of the upper platform on a catamaran under the influence of the controller. As can be seen, the actual trajectory fluctuations of the platform stabilize across all degrees of motion within 5 seconds. However, due to time-varying disturbance $\mathbf{d}$, there persists slight amplitude of oscillation, as shown in Fig. 5.

Fig. 6 shows the output force generated by the hydraulic actuator. Owing to the large position error at the beginning, the input force is also relatively large. The hydraulic actuators equipped on the catamaran has an output of at least 10^4N, so a force of 10^3N is completely within the output range of the hydraulic actuator. Once the platform becomes relatively steady, the oscillation amplitude of the force is primarily employed to counteract the external disturbance.

Fig. 7 presents the disturbance observer's tracking of time-varying disturbance. It can be observed that the lag between $\mathbf{d}$ and its estimate are very small, implying the disturbance observer has rapid convergence and estimation capabilities. This demonstrates the strong robustness of the proposed disturbance observer design. Due to the observation delay of the observer, there is an error between $\mathbf{d}$ and its estimated value. The estimated error results are presented in Fig. 8.

Overall, the small position errors and rapid convergence to steady state validate the effectiveness of the proposed control strategy in achieving attitude control on the upper platform of the catamaran.

7 Conclusions

This paper proposes an adaptive robust control strategy with integrated disturbance compensation to stabilize the upper platform of catamaran under time-varying disturbance. Through stability analysis, the designed controller has been proven to maintain the upper platform within small neighborhood of 10^{-3}(m or rad) of the ideal attitude. The controller demonstrates precise and fast compensation for random wave excitation, providing an active motion control solution to significantly enhance stability of the catamaran upper platform in different sea conditions. Simulation results are given and analyzed, validating the efficacy of the proposed control laws. There are some shortcomings, such as the simulation being ideal compared to its actual conditions

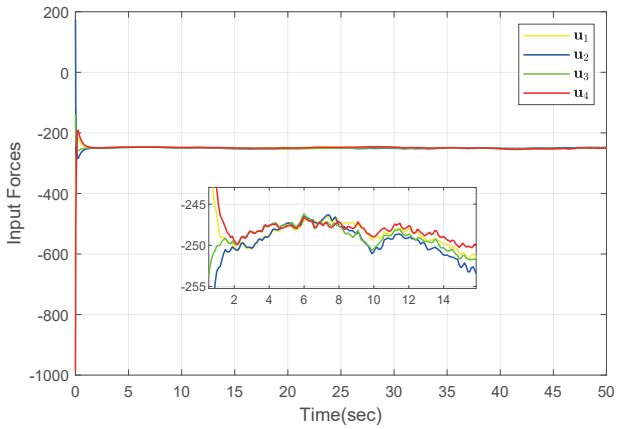

Fig. 6: Actuator forces.

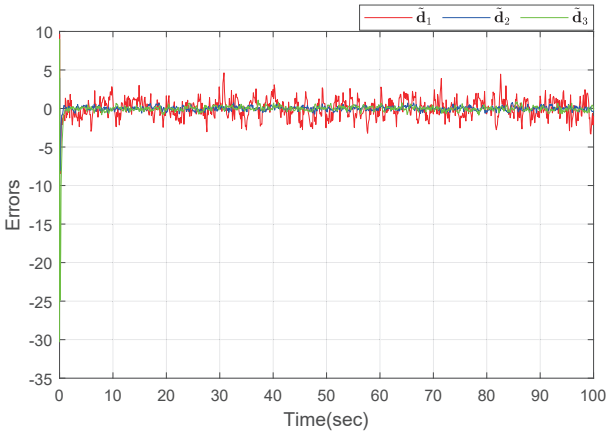

Fig. 8: Disturbance observe errors.

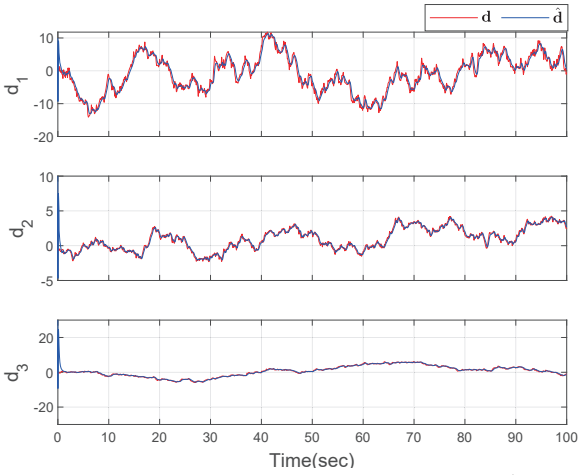

Fig. 7: Disturbance $\mathbf{d}$ and its estimated values $\hat{\mathbf{d}}$.

and the delay of hydraulic actuator output not being taken into account. After the future ship is built, we will test it in reality.

References

[1] W.-Y. Dzan, S.-Y. Chang, and K.-C. Hsu, "Designing and building of a catamaran and its stability analysis," in *2013 Second International Conference on Robot, Vision and Signal Processing*. IEEE, 2013, pp. 148–152.

[2] G. Tang, P. Lu, X. Hu, and S. Men, "Control system research in wave compensation based on particle swarm optimization," *Scientific Reports*, vol. 11, no. 1, p. 15316, 2021.

[3] Y. Cai, S. Zheng, W. Liu, Z. Qu, J. Zhu, and J. Han, "Sliding-mode control of ship-mounted stewart platforms for wave compensation using velocity feedforward," *Ocean Engineering*, vol. 236, p. 109477, 2021.

[4] Y. Hu, L. Tao, and W. Lv, "Anti-pendulation analysis of parallel wave compensation systems," *Proceedings of the Institution of Mechanical Engineers, Part M: Journal of Engineering for the Maritime Environment*, vol. 230, no. 1, pp. 177–186, 2016.

[5] S. Karakas, E. Ucer, and E. Pesman, "Control design of fin roll stabilization in beam seas based on lyapunov's direct method," *Polish Maritime Research*, vol. 19, no. 2, pp. 25–30, 2012.

[6] S. Lee, K.-P. Rhee, and J.-W. Choi, "Design of the roll stabilization controller, using fin stabilizers and pod propellers," *Applied Ocean Research*, vol. 33, no. 4, pp. 229–239, 2011.

[7] W.-C. Tiao, "Preliminary assessments of the anti-roll tank as a wave energy converter," *Ships and Offshore Structures*, vol. 8, no. 5, pp. 488–496, 2013.

[8] L. Lihua, Z. Peng, Z. Songtao, J. Ming, and Y. Jia, "Simulation analysis of fin stabilizer on ship roll control during turning motion," *Ocean Engineering*, vol. 164, pp. 733–748, 2018.

[9] J. Virgili-Llop, H. C. Polat, and M. Romano, "Attitude stabilization of spacecraft in very low earth orbit by center-of-mass shifting," *Frontiers in Robotics and AI*, vol. 6, p. 7, 2019.

[10] Y. Hirakawa, T. Hirayama, K. Kakizoe, T. Takayama, S. Funamizu, N. Okada, and A. Yamane, "Sea trial of prototype vertical weight stabilizer (vws) anti-rolling system for small ships," *Journal of Marine Science and Technology*, vol. 19, pp. 292–301, 2014.

[11] J. Han, S. Kanno, A. Mochizuki, D. Kitazawa, T. Maeda, and H. Itakura, "Study on attitude control of a cabin-suspended catamaran by using a double-loop control system," in *International Conference on Offshore Mechanics and Arctic Engineering*, vol. 58882. American Society of Mechanical Engineers, 2019, p. V009T13A053.

[12] P. A. Ioannou and J. Sun, *Robust adaptive control*. PTR Prentice-Hall Upper Saddle River, NJ, 1996, vol. 1.

[13] M. Labbadi and M. Cherkaoui, "Robust adaptive nonsingular fast terminal sliding-mode tracking control for an uncertain quadrotor uav subjected to disturbances," *ISA transactions*, vol. 99, pp. 290–304, 2020.

[14] W. Xie, J. Reis, D. Cabecinhas, and C. Silvestre, "Design and experimental validation of a nonlinear controller for underactuated surface vessels," *Nonlinear Dynamics*, vol. 102, pp. 2563–2581, 2020.

[15] S. Vaidyanathan and A. T. Azar, *Backstepping control of nonlinear dynamical systems*. Academic Press, 2020.

[16] K. D. von Ellenrieder, "Dynamic surface control of trajectory tracking marine vehicles with actuator magnitude and rate limits," *Automatica*, vol. 105, pp. 433–442, 2019.

[17] J. Refsnes, A. J. Sorensen, and K. Y. Pettersen, "A 6 dof nonlinear observer for auvs with experimental results," in *2007 Mediterranean Conference on Control & Automation*. IEEE, 2007, pp. 1–7.

Proceedings of the 3rd Conference on Fully Actuated System Theory and Applications
May 10-12, 2024, Shenzhen, China

Adaptive Tracking Control for State-Constrained Fully Actuated Systems And Its Application to Overhead Cranes

Yang Gao[1], Zhongcai Zhang[2], Peng Huang[2], and Yuqiang Wu[2]
[1]School of Automation, Southeast University, Nanjing 210096, P. R. China
[2]School of Engineering, Qufu Normal University, Rizhao 276826, P. R. China
E-mail: zhangzhongcai68@126.com

Abstract: This paper investigates the adaptive tracking problem for a class of fully actuated systems (FASs) subject to state constraints, external disturbance, and model uncertainties. Through the utilization of carefully designed auxiliary signals, the issue of full-state constraints in FAS is reduced to a constraint problem for a coupled variable. This transformation enables the direct proposal of the controller without involving recursive design. The proposed control method is applied to crane system, and its feasibility and efficacy are verified through simulation.

Key Words: Fully actuated system, state constraints, adaptive tracking control, underactuated overhead crane

1 Introduction

Over the last few decades, state-space methodologies have been the dominant paradigm in control systems. However, the process of designing controllers within the state-space framework may be cumbersome, potentially overlooking the inherent high-order fully actuated characteristics of a system. Seeking an alternative approach, researchers have explored various avenues.

In recent developments, alongside the state-space approach, the fully actuated system (FAS) approach has emerged. Duan's contributions [1–5] established the theoretical framework for the FAS approach, leading to subsequent studies with impressive outcomes [7–9]. The term "FAS" initially referred to a specific component of physical systems and underwent mathematical generalization by Duan. At the present time, FAS approach has become an universal method for nonlinear control. This evolution is motivated by the fact that many nonlinear systems can be naturally modeled as FASs at the physical level, and the majority of the remaining systems can be transformed into FASs. When a known nonlinear plant is modeled or converted into a FAS, the inherent full-actuation property allows for the partial or complete elimination of nonlinear dynamics. Then one gets a linear or "close to" linear closed-loop system, enabling the direct proposal of control laws. However, considering state constraints and model uncertainties, the direct formulation of controller faces challenges.

The issue of state constraints are commonly encountered in systems due to security considerations. Barrier Lyapunov function (BLF) approach is the mainstream method to deal with the state-constrained control problem of nonlinear systems at present. During the control design process based on BLF method, some constraint-related auxiliary terms (barrier terms) are used to construct Lyapunov functions, based on which barrier function terms can be integrated into the control law to guarantee the state constraints [10, 11]. Besides the BLF method, the investigations [12, 13] employed transformations based on state-dependent functions for crane systems. As a result, the constraints were ensured by guaranteeing the boundedness of the new coordinates. It should be pointed out that the implementation of the above method is based on backstepping design. Backstepping design can face an explosion of complexity due to repeated differentiation of virtual controllers. Therefore, a natural question arises, whether a general controller can be proposed for constrained FAS without recursive design procedures?

In this paper, a non-recursive adaptive tracking control for a class of state-constrained FASs is studied in the presence of disturbance and model uncertainties. The main contributions of this paper can be summarized by the following aspects:

(i) By elaborately designing auxiliary signals, the full-state constraints of FAS is transformed into the constraint issue of a coupled variable. This approach eliminates the use of backstepping method and simplifies the control design process.

(ii) The proposed controller is applied to the underactuated crane. It has been demonstrated by simulation that the developed controller achieves precise position tracking while also ensuring that all states remain within predetermined limits.

Notations

In this paper, the following notations are used. For integers $i > j \geq 0$, $\mathcal{A}_i^j$ and C_i^j represent the number of permutations and combinations respectively, i.e. $\mathcal{A}_i^j = i!/(i-j)!$ and $C_i^j = \mathcal{A}_i^j/(j!)$. $x^{(i)}$ denotes the $i-$th derivative of x, specially, $x^{(0)} = x$. Further, $x^{(0\sim i)} = [x, x^{(1)}, \cdots, x^{(i)}]^T$.

2 Problem formulation

Consider the following perturbed FAS as

$$x^{(n)} = f(x^{(0\sim n-1)}, t) + g(x^{(0\sim n-1)}, t)u + d(t) \quad (1)$$

subjected to the full-state constraints:

$$x^{(i)} \in \Omega_i = \{|x^{(i)}| < k_{ai}, i = 0, 1, \cdots, n-1\} \quad (2)$$

where u is the control input, f and g denote the uncertain nonlinear functions, d stands for the external disturbance, and $k_{ai} > 0$ are constraint constants.

This work was supported in part by the National Natural Science Foundation of China (62173207, 62073187, and 62073189), the Science Center Program of the National Natural Science Foundation of China (62188101), the China Postdoctoral Science Special Foundation (2023T160334), the Youth Innovation Team Project of Colleges and Universities in Shandong Province (2022KJ176), and the Graduate Teaching Case Base Project of Shandong Province (SDYAL20109).

The control objective is to develop an adaptive tracking controller such that: 1) all signals in the closed-loop system are bounded; 2) reference signal x_d can be tracked by x, and 3) system states $x^{(i)}$ satisfy the constraints in (2).

Assumption 1. For $i \geq 1$, states $x^{(i)}$ satisfy $x^{(i)}(0) = 0$.

Assumption 2. For functions $f(x^{(0\sim n-1)}, t)$ and $g(x^{(0\sim n-1)}, t)$, there holds that $|f(x^{(0\sim n-1)}, t)| \leq a\varphi(x^{(0\sim n-1)}, t)$ and $0 < \underline{g} \leq g(x^{(0\sim n-1)}, t) \leq \bar{g}$ where a, $\underline{g}$, and $\bar{g}$ are positive constants. Additionally, $\varphi(x^{(0\sim n-1)}, t)$ is a known function.

Assumption 3. The disturbance d is assumed to satisfy $|d| \leq D$ with D being an unknown constant.

3 Main results

3.1 Auxiliary variable design

In this section, we introduce three auxiliary signals. The first one is constructed as

$$\zeta(t) = \begin{cases} \sum\limits_{i=1}^{n+1} \sigma_i (\frac{t}{T})^{n+i}, & 0 \leq t \leq T \\ 1, & t \geq T \end{cases} \tag{3}$$

where $T > 0$ is a preassigned time configured by users and $\sigma_i > 0$ will be designed later. For the sake of simplicity, we define $\sigma = [\sigma_1, \sigma_2, \cdots, \sigma_{n+1}]^T \in R^{n+1}$, $b = [1, 0, \cdots, 0]^T \in R^{n+1}$, and

$$A = \begin{bmatrix} \mathcal{A}_{n+1}^0 & \mathcal{A}_{n+2}^0 & \cdots & \mathcal{A}_{2n+1}^0 \\ \mathcal{A}_{n+1}^1 & \mathcal{A}_{n+2}^1 & \cdots & \mathcal{A}_{2n+1}^1 \\ \vdots & \vdots & & \vdots \\ \mathcal{A}_{n+1}^n & \mathcal{A}_{n+2}^n & \cdots & \mathcal{A}_{2n+1}^n \end{bmatrix}. \tag{4}$$

Then one has the following proposition.

Proposition 1: For auxiliary signal (3), if parameters σ_i are solved by $\sigma = A^{-1}b$, then $\zeta(t)$ satisfies: a) $\zeta(0) = \zeta^{(i)}(0) = 0$; b) $\lim\limits_{t\to T} \zeta(t) = \zeta(T) = 1$, $\lim\limits_{t\to T} \zeta^{(i)}(t) = \zeta^{(i)}(T) = 0$ $(i = 0, \cdots, n)$.

Now, let us introduce the second auxiliary signal

$$y_d = \zeta(x_d - x_0) + x_0.$$

Based on proposition 1, one figures out that y_d and its derivatives up to the $n-$th order are continuous. Further, it can be found that $\lim_{t\to T} y_d^{(i)}(t) = y_d^{(i)}(T) = x_d^{(i)}(T)$ for $t \in [0, T]$ and $y_d^{(i)}(t) = x_d^{(i)}$ for $t \in [T, \infty)$, where $i = 0, \cdots, n$. Therefore, the tracking issue for x_d can be achieved by forcing $x^{(i)}$ tracking $y_d^{(i)}$.

Define $e = x - y_d$ and construct the final auxiliary signal as $S = \sum\limits_{r=0}^{n-1} C_{n-1}^r \lambda_1^{n-r-1} \lambda_2^r e^{(r)}$ with $\lambda_1 > 0$ and $\lambda_2 > 0$.

Proposition 2: For coupled variable S, the following inferences are true: 1) $S(0) = 0$; 2) if $S \to 0$, then $e^{(i)} \to 0$ $(i = 0, \cdots, n)$; 3) For a positive constant k, if $|S| \leq k$, then $|e^{(i)}| \leq \varepsilon_i$ for $t \geq 0$ where $\varepsilon_i = (\frac{2}{\lambda_2})^i \frac{k}{\lambda_1^{n-i-1}}$ $(i = 0, \cdots, n)$.

3.2 Control design

Based upon the above-mentioned analysis, the tracking controller and the adaptive laws are given as

$$\begin{aligned} u =& -\frac{\hat{p}}{\lambda_2^{n-1}} \alpha_u \tanh\Big(\frac{g_2 \hat{p} \alpha_u S}{\delta(t)}\Big) \\ \alpha_u =& \sum_{r=0}^{n-2} C_{n-1}^r \lambda_1^{n-r-1} \lambda_2^r e^{(r+1)} - \lambda_2^{n-1} y_d^{(n)} + \frac{\gamma S}{k^2 - S^2} \\ &+ \lambda_2^{n-1} \hat{a} \varphi \tanh\Big(\frac{g_1 S}{\delta(t)}\Big) + \lambda_2^{n-1} \hat{D} \tanh\Big(\frac{g_2 S}{\delta(t)}\Big) \\ \dot{\hat{a}} =& \lambda_2^{n-1} g_1 S \tanh\Big(\frac{g_1 S}{\delta(t)}\Big) \\ \dot{\hat{D}} =& \lambda_2^{n-1} g_2 S \tanh\Big(\frac{g_2 S}{\delta(t)}\Big) \\ \dot{\hat{p}} =& |g_2 S \alpha_u| \end{aligned} \tag{5}$$

where

$$g_1 = \frac{\varphi}{k^2 - S^2},\ g_2 = \frac{1}{k^2 - S^2},\ p = \frac{1}{\underline{g}},$$

$\mu > 0$ and $k > 0$ are design parameters, and $\delta(t)$ is a continuous function satisfying $\lim\limits_{t\to\infty} \int_0^t \delta(t) d\tau < \infty$. In addition, $\hat{a}$, $\hat{D}$, and $\hat{p}$ are estimations of a, D, and p, respectively.

3.3 Stability analysis

This section begins by presenting the main results of this article, followed by a comprehensive stability analysis.

Theorem 1. For the FAS (1) with Assumptions 1-3 being satisfied, if the initial condition $x(0)$ satisfies $x(0) \in \Omega_0$, and designed adaptive control law (5) is applied, then the control objectives 1)-3) are achieved.

Proof: Consider the Lyapunov function as

$$V = \frac{1}{2} \ln \frac{k^2}{k^2 - S^2} + \frac{1}{2}\tilde{a}^2 + \frac{1}{2}\tilde{b}^2 + \frac{\underline{g}}{2}\tilde{p}^2 \tag{6}$$

where $\tilde{a} = a - \hat{a}$, $\tilde{D} = D - \hat{D}$, and $\tilde{p} = p - \hat{p}$.

Taking the derivative of V with respect to time obtains

$$\begin{aligned} \dot{V} =& \frac{S}{k^2 - S^2}\Big(\sum_{r=0}^{n-2} C_{n-1}^r \lambda_1^{n-r-1} \lambda_2^r e^{(r+1)} + \lambda_2^{n-1} f \\ &+ \lambda_2^{n-1} d + \lambda_2^{n-1} g u - \lambda_2^{n-1} y_d^{(n)}\Big) - \tilde{a}\dot{\hat{a}} - \tilde{D}\dot{\hat{D}} \\ &- \underline{g}\tilde{p}\dot{\hat{p}}. \end{aligned} \tag{7}$$

Inserting (5) into (7) follows that

$$\dot{V} \leq -\frac{\gamma S^2}{(k^2 - S^2)^2} + (a\lambda_2^{n-1} + D\lambda_2^{n-1} + \underline{g}) k_* \delta, \tag{8}$$

which immediately implies that

$$\begin{aligned} V(t) + \gamma \int_0^t \Big(\frac{S}{k^2 - S^2}\Big)^2 d\tau \leq V(0) \\ + (a + D + \underline{g}) k_* \int_0^t \delta d\tau < +\infty. \end{aligned} \tag{9}$$

Therefore, it can be obtained that $V \in L_\infty \Rightarrow |S| < k$, $\hat{a} \in L_\infty$, $\hat{D} \in L_\infty$, and $\hat{p} \in L_\infty$. Furthermore, it can be concluded from Proposition 2 that $|S| < k \Rightarrow |e^{(i)}| < \varepsilon_i$, which

implies $u \in L_\infty$. The objective 1) is obtained. Moreover, $\frac{\partial}{\partial t}(\frac{S}{k^2-S^2}) = \frac{(k^2+S^2)\dot{S}}{k^2-S^2} \in L_\infty$. Noticed that $\frac{S}{k^2-S^2} \in L_2$, then $\frac{S}{k^2-S^2} \to 0 \Rightarrow S \to 0 \Rightarrow e^{(i)} \to 0$. Thus, the objective 2) is achieved. For objective 3), one defines $\bar{y}_d^{(i)} = \max\{|y_d^{(i)}(t)|\}$, and chooses $k < \min\{\frac{\lambda_2^i \lambda_1^{n-i-1}}{2^i}(k_{ai} - \bar{y}_d^i)\}$ $(i = 0, 1, \cdots n-1)$. Then, one has $|x^{(i)}| < |e^{(i)}| + \bar{y}_d^{(i)} < k_{ai}$. The proof of Theorem 1 is completed. □

4 Application to the overhead crane

4.1 System transformation

In this section, a practical example of the underactuated overhead crane systems is employed, whose dynamic model is described as follows:

$$\begin{aligned}(M+m)\ddot{x} + ml\ddot{\theta}\cos\theta - ml\dot{\theta}^2\sin\theta = F + d,\\ ml^2\ddot{\theta} + ml\ddot{x}\cos\theta + mgl\sin\theta = 0\end{aligned} \tag{10}$$

where x and θ denote the trolley position and swing angle of the rope, respectively, M and m denote the trolley mass and the payload mass, respectively, l is the cable length, g represents the gravity acceleration, and F is the control input. $d(t)$ is the friction, and it can be modeled as

$$d = -f_1 \tanh(\dot{x}/v_1) + f_2|\dot{x}|\dot{x}$$

where $f_1 \in R$, $f_2 \in R$, and $v_1 \in R$ are friction-related parameters.

Similar to [14], the following auxiliary variables are introduced:

$$\begin{aligned}&\mu(\theta) = l\ln(\frac{1}{\cos(\theta)} + \tan(\theta)),\ \xi_1 = x + \mu(\theta),\\ &\xi_2 = \dot{x} + \frac{l\dot{\theta}}{\cos(\theta)},\ \xi_3 = -g\tan(\theta),\ \xi_4 = -\frac{g\dot{\theta}}{\cos^2(\theta)},\\ &\varsigma = \frac{g}{(M + m\sin^2(\theta))l\cos(\theta)}.\end{aligned} \tag{11}$$

Then, one gets the remodeling of (10)

$$\begin{aligned}\dot{\xi}_1 &= \xi_2\\ \dot{\xi}_2 &= \Big(1 - \frac{l\xi_4^2}{(\xi_3^2 + g^2)^{1.5}}\Big)\xi_3\\ \dot{\xi}_3 &= \xi_4\\ \dot{\xi}_4 &= \varsigma u + v(t)\phi\end{aligned} \tag{12}$$

where

$$\begin{aligned}v(t) =& \Big[-\frac{f_1\tanh(\frac{\dot{x}}{v_1})}{(m\sin^2(\theta)+M)l}, \frac{f_2}{(m\sin^2(\theta)+M)l},\\ &\frac{M+m}{(m\sin^2(\theta)+M)l}, \frac{m}{(m\sin^2(\theta)+M)l}\Big]\\ \phi =& \Big[\frac{g}{\cos(\theta)}, \frac{g|\dot{x}|\dot{x}}{\cos(\theta)}, \frac{g^2\tan(\theta)}{\cos(\theta)}, \frac{gl\dot{\theta}^2\sin(\theta)}{\cos(\theta)}\Big]^T.\end{aligned}$$

When ξ_4 is confined in a narrow interval, the following result holds:

$$\begin{aligned}&\frac{l\xi_4^2}{(g^2+\xi_3^2)^{3/2}} \le \frac{l\xi_4^2}{g^3} \approx 0.001l\xi_4^2 \ll 1\\ &\Rightarrow \xi_3 \approx \xi_3\Big(1 - \frac{l\xi_4^2}{(\xi_3^2+g^2)^{1.5}}\Big).\end{aligned}$$

Hence, (12) can be rewritten as

$$\xi_1^{(4)} = \varsigma u + v(t)\phi. \tag{13}$$

The control goal in this section is to use adaptive controller (5) to make the trolley move to the desired potion p_d while suppressing rope swing, and meanwhile other states are also expected to be satisfied some certain constraints.

It can be derived from Proposition 1 that

$$y_d = \zeta(p_d - x_0) + x_0 \tag{14}$$

where

$$\zeta(t) = \begin{cases}\frac{126t^5}{T^5} - \frac{420t^6}{T^6} + \frac{540t^7}{T^7} - \frac{315t^8}{T^8} + \frac{70t^9}{T^9}, 0 \le t \le T\\ 1, \qquad t \ge T.\end{cases}$$

Further, by taking $f = v(t)\phi$, $a = \sup_{t>0}\|v(t)\|$, $\varphi = \|\phi\|$, and $\underline{g} = \frac{g}{(M+m)l}$, the control design in section 3 can be applied. For tracking error $e = \xi_1 - y_d$, one has $e^{(i)} \to 0 \Rightarrow \theta \to 0 \Rightarrow x \to p_d$. Meanwhile, if $|\xi_1^{(2)}| < k_{a2}$ is ensured, one obtains $|\theta| < \arctan(\frac{k_{a2}}{g}) \triangleq k_{b2}$, which means rope swing is suppressed in the whole control process. Similarly, by configuring $k_{b2} < \frac{\pi}{2}$, it can be induced that $|\dot{\theta}| < \frac{k_{a3}}{g} \triangleq k_{b3}$, $|\dot{x}| < k_{a1} + l\frac{k_{a2}}{g\cos(k_{b2})} \triangleq k_{b1}$, and $|x| < k_{a0} + \mu(k_{b2}) \triangleq k_{b0}$.

4.2 Simulation analysis

The physical parameters of the system are set as $M = 24$ kg, $m = 12$ kg, $l = 8$ m, $g = 9.8$ m/s^2, $f_1 = 5.4$, $f_2 = 1$, and $v_1 = 0.01$. The desired position is set as $p_d = 10$ m. T is set as $T = 7$ s, then it can be calculated that $\bar{y}_d = \sup_{t\ge0}|y_d(t)| = 10$, $\bar{y}_d^{(1)} = \sup_{t\ge0}|y_d^{(1)}(t)| = 3.52$, $\bar{y}_d^{(2)} = \sup_{t\ge0}|y_d^{(2)}(t)| = 1.92$, $\bar{y}_d^{(3)} = \sup_{t\ge0}|y_d^{(3)}(t)| = 2.3$. Therefore if k_{ai} are taken as $k_{a0} = 10.4$, $k_{a1} = 4$, $k_{a2} = 2.4$, and $k_{a3} = 2.7$, the states of crane system (10) satisfy $|\theta| < 0.2407$ rad (13.7624 deg), $|x| < 12.3403$ m, $|\dot{x}| < 6.0171$ m/s, and $|\dot{\theta}| < 0.2755$ rad/s (15.785 deg/s). To achieve the above configuration, λ_1, λ_2, and k can be chosen as $\lambda_1 = 2$, $\lambda_2 = 3$, and $k = 3$. The other parameters are set as $\gamma = 0.01$, $\lambda_2 = 4$, $\delta(t) = e^{-0.2t}$, $x(0) = \theta(0) = \dot{x}(0) = \dot{\theta}(0) = 0$.

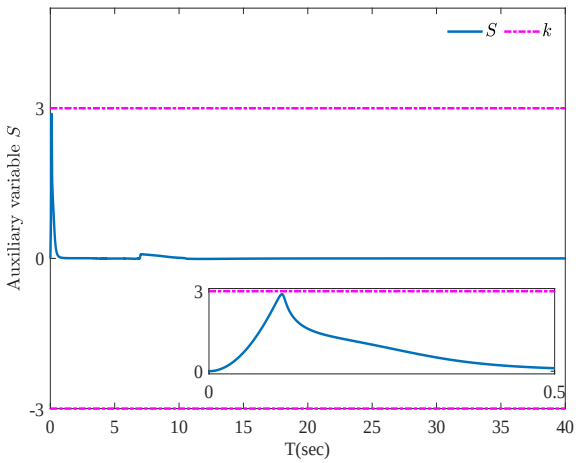

Fig. 1 Constrained auxiliary signal S

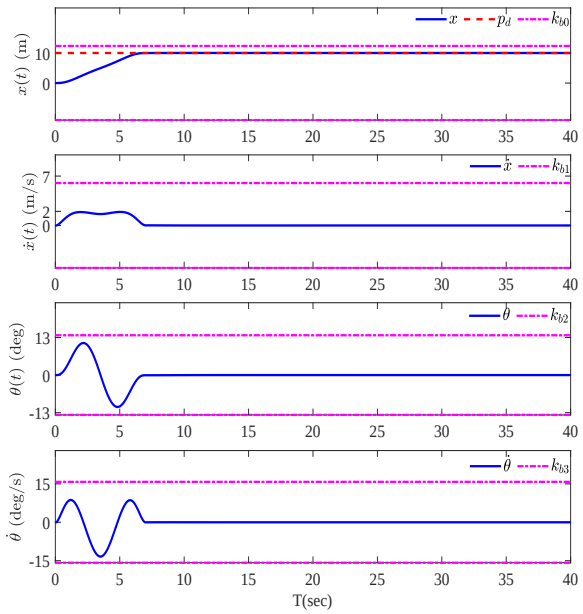

Fig. 2 The position tracking of trolley.

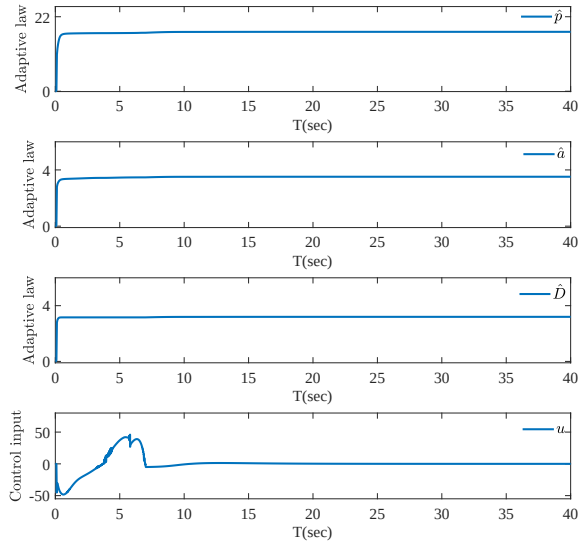

Fig. 3 The adaptive laws and control input.

The simulation results are depicted in Figs. 1-3. Fig. 1 plots the closed-loop response of the auxiliary signal S. It is evident that the desired constraint is guaranteed and S tends to zero asymptotically. Consequently, as shown in Fig. 2, the trolley and payload can be adjusted to the desired position p_d with the full-state constraints being not violated. Meanwhile, swing angel θ is compelled to converge to zero. Fig. 3 illustrates the boundedness of adaptive laws and controller.

5 Conclusion

In this paper, the adaptive tracking problem for a class of FASs with state constraints, external disturbance and model uncertainties is studied. The constraints of full-state variables are realized by guaranteeing the constraint of a coupled variable, simplifying the overall control design process. In this way, steady-state tracking performance can be ensured without violating the full-state constraints. Finally, the control algorithm is successfully applied to the underactuated crane system. Simulation result shows that the proposed control strategy has a favorable control performance.

References

[1] G. R. Duan, High-order fully actuated system approaches: Part I. Models and basic procedure, *International Journal of Systems Science*, 52(2): 422-435, 2021.

[2] G. R. Duan, High-order fully actuated system approaches: Part II. Generalized strict-feedback systems, *International Journal of Systems Science*, 52(3): 437-454, 2021.

[3] G. R. Duan, High-order fully actuated system approaches: Part VII. Controllability, stabilisability and parametric designs, *International Journal of Systems Science*, 52(14): 3091-3114, 2021.

[4] G. R. Duan, High-order fully actuated system approaches: Part VIII. Optimal control with application in spacecraft attitude stabilisation, *International Journal of Systems Science*, 53(1): 54-73, 2021.

[5] G. R. Duan, High-order fully-actuated system approaches: Part IX. Generalised PID control and model reference tracking, *International Journal of Systems Science*, 53(3): 652-674, 2022.

[6] G. R. Duan, High-order fully actuated system approaches: Part X. Basics of discrete-time systems, *International Journal of Systems Science*, 53(4), 810-832, 2022.

[7] G. P. Liu, Coordination of networked nonlinear multi-agents using a high-order fully actuated predictive control strategy, *IEEE/CAA Journal of Automatica Sinica*, 9(4): 615-623, 2022.

[8] G.-R. Duan, Robust stabilization of time-varying nonlinear systems with time-varying delays: a fully actuated system approach, *IEEE Transactions on Cybernetics*, 53(12): 7455-7468, 2023.

[9] G.-R. Duan, Substability and substabilization: control of subfully actuated systems, *IEEE Transactions on Cybernetics*, 53(11): 7309-7322, 2023.

[10] K. B. Ngo, R. Mahony, and Z. P. Jiang, Integrator backstepping using barrier functions for systems with multiple state constraints, in *Proceedings of the 44th IEEE Conference on Decision and Control*, IEEE, 2005: 8306-8312.

[11] Z. Zhang, Y. Gao, W. Sun and Y. Wu, Event-based nonsingular fixed-time tracking control of an uncertain manipulator system subject to full-state static constraints, *IEEE Transactions on Cybernetics*, to be published, doi: 10.1109/TCYB.2023.3289947.

[12] J. S. Huang, W. Wang, and J. Zhou, Adaptive control design for underactuated cranes with guaranteed transient performance: theoretical design and experimental verification, *IEEE Transactions on Industrial Electronics*, 69(3): 2822-2832, 2022.

[13] Y. Yang, X. Ye, B. Wen, J. Huang, and X. Su, Adaptive control design for uncertain underactuated cranes with nonsmooth input nonlinearities, *IEEE Transactions on Systems, Man, and Cybernetics: Systems*, 53(2): 1074-1083, 2023.

[14] X. Wu, K. Xu, and X. He, Disturbance-observer-based nonlinear control for overhead cranes subject to uncertain disturbances, *Mechanical Systems and Signal Processing*, 139: 106631, 2020.

Proceedings of the 3rd Conference on Fully Actuated System Theory and Applications
May 10-12, 2024, Shenzhen, China

Prescribed-Time Stabilization of Switched Nonholonomic Systems with Asymmetric Constraints

Siquan Li[1], Xujing Mao[2], Yanling Shang[1], Fangzheng Gao[1], Jiacai Huang[1]

1. School of Automation, Nanjing Institute of Technology, Nanjing 211167, China
E-mail: gaofz@126.com, gaofz@njit.edu.cn

2. The King's School, North Parramatta NSW 2151, Australia

Abstract: The problem of prescribed-time stabilization (PTS) is addressed for a kind of nonholonomic systems (NSs) with switched chain structures and asymmetric output constraints. A tan-type Barrier Lyapunov Function (BLF) is exploited to handle the obstacle caused by the asymmetric output constraints. By suitably introducing the time-varying function into the virtual (actual) controllers, a non-scaling design scheme for state feedback is developed to forces the states of the closed-loop system (CLS) to zero in any prescribed finite time without disobeying the constraints.

Key Words: switched nonholonomic systems; asymmetric constraints; Barrier Lyapunov Function; prescribed-time stabilization (PTS)

1 Introduction

Nonholonomic systems (NSs) have received much attention in the last decades due to their widespread practical applications[1]. However, the existence of nonholonomic constraint such systems not to meet the famous Brockett necessary condition, leading to their stabilization challenging [2]. Thanks to the constructive methods of discontinuous time-invariant feedback [3], smooth time-varying feedback [4] and hybrid feedback [5], many important results have been obtained [6–9].

From the point of view of convergence rate, the existing stabilization results can be divided into infinite-time stabilization (e.g., asymptotic or exponential stabilization) and finite-time stabilization. By comparison, the latter is more desired because it exhibits the appealing features of fast convergence and good disturbance rejection [10–14]. However, the existing results on finite-time stabilization suffer from shortcoming of the settling time heavily relying on initial system conditions. To address these, Andrieu *et al.* in [15] put the idea of fixed-time stability that the involved settling time function is irrespective of initial system conditions. Soon afterwards, the study on fixed-time control has become a popular topic [16–24]. Roughly speaking, the existing methods on the topic of fixed-time control come down to two kinds: the bi-limit homogeneous-based one [15, 16] and the Lyapunov-based one [17–25]. It is emphasized that the both methods suffer from some inherent defects, that is, the upper bound of the settling time (UBST) in the former exists but is unknown, and the UBST in the latter is bounded and adjustable, but it is so hard to be prespecified discretionarily in the light of requirements because the derived settling time functions currently depend on a few design parameters, whose selections are laborious to meet the prespecified settling time requirements [26].

However, prespecifiable settling time is indeed expected by some practical applications. This fact urges that the prescribed-time stability [27](also called predefined-time stability [28]), where the UBST can be selected by the user, has been drew into to study the stabilization problem of the considered systems [29–34]. For the nonholonomic systems with dynamics of single-mode structure, the PTS were also addressed in [35–38]. But due to the hybrid features leading to the control design for switched systems challenging, the research on PTS of nonholonomic systems with dynamics of multi-mode switching structures has received less attention. Moreover, as we know, one often faces certain constraints that represent physical limitations and performance requirements in solving practical control engineering problems. For instance, the position of an indoor robot ought to be constrained so that it can always work in some reasonable area. Violation of the constraints may give rise to system damage, unpredictability danger or performance degradation. [

Motivated by the above considerations, in this paper we concentrate on studying the PTS problem for a kind of NSs with switched chain structures and asymmetric output constraints. The contributions are highlighted as follows. (i) Different from the existing results mainly concerning NSs with dynamics of single-mode structure, the paper addresses NSs with dynamics of multi-mode switching structures making the studied systems more practical and general; (ii) A novel non-scaling transformation-based design is presented for switched NSs by employs the given time-varying function scaling the virtual (scaling) controllers. As a result, the computation burden of the time-varying scaling function is reduced to a large extent, leading to a simpler controller.

Notations. The notations adopted in this paper are fairly standard. Specifically, for a vector $z = (z_1, \ldots, z_n)^T \in \mathbb{R}^n$, denote $\bar{z}_j = (z_1, \ldots, z_j)^T \in \mathbb{R}^j$, $j = 1, \ldots, n$, and define $\lceil z \rceil^\delta$ as $\lceil z \rceil^\delta = \mathrm{sign}(z)|z|^\delta$.

2 Problem formulation and preliminaries

2.1 Problem formulation

Consider the following kind of uncertain NSs with switched chain structures

$$\begin{cases} \dot{\zeta}_i = u_{0\sigma(t)}\zeta_{i+1} + \Phi_{i\sigma(t)}(\zeta_0, \bar{\zeta}_i), \\ \dot{\zeta}_n = u_{1\sigma(t)} + \Phi_{n\sigma(t)}(\zeta_0, \bar{\zeta}_n), \\ \dot{\zeta}_0 = u_{0\sigma(t)}, \quad i = 1, \ldots, n-1, \end{cases} \tag{1}$$

This work was partially supported by the National Natural Science Foundation of China under Grant 61873120, the National Natural Science Foundation of Jiangsu Province under Grants BK20201469 and BE2021016-5 and the Qing Lan project of Jiangsu Province.

where $(\zeta_0,\zeta)^T=(\zeta_0,\zeta_1,\ldots,\zeta_n)^T\in\mathbb{R}^{n+1}$ is the system state (vector) and $\sigma(t):[0,+\infty)\to\mathbb{M}=\{1,2,\ldots,s\}$ is the piecewise continuous switching signal. For any $k\in\mathbb{M}$ and $i=1,\ldots,n$, $\Phi_{ik}:\mathbb{R}\times\mathbb{R}^i\to\mathbb{R}$ are continuous functions satisfying $\Phi_{ik}(\zeta_0,0)=0$.

Due to physical or performance limitations, this paper supposes the output y suffering from the following time-varying constraints

$$\Omega_i=\{\zeta_i(t):-k_{i1}(t)<\zeta_i(t)<k_{i2}(t)\},\ \ i=0,1, \quad (2)$$

with some pre-specified positive functions $k_{i1}(t)$ and $k_{i2}(t)$.

The control goal of this paper is to present a common state feedback controller which stabilizes system (1) within pre-scribed finite time T_p via the following following assumption.

Assumption 1. The time-varying output constraints $k_{ij}(t)$ $(i=0,1,\ j=1,2)$ are continuous differentiable and there are positive constants $\underline{k}_{i1}$, $\underline{k}_{i2}$, $\overline{k}_{i3}$ and $\overline{k}_{i4}$ such that $\underline{k}_{i1}\le k_{i1}(t)$, $\underline{k}_{i2}\le k_{i2}(t)$, $|\dot{k}_{i1}(t)|\le\overline{k}_{i3}$ and $|\dot{k}_{i2}(t)|\le\overline{k}_{i4}$.

Assumption 2. There are smooth functions $\varphi_{ik}\ge 0$ and a constant $\tau\in(0,1/n)$ such that

$$|\Phi_{ik}(\zeta_0,\bar{\zeta}_i)|\le\varphi_{ik}(\zeta_0,\bar{\zeta}_i)\sum_{j=1}^{i}|\zeta_j|^{\frac{\lambda_i-\tau}{\lambda_j}}, \quad (3)$$

where $\lambda_i=1-(i-1)\tau>0$, $i=1,\ldots,n$.

2.2 Preliminary results

Consider the nonlinear system

$$\dot{z}=\mu(t,z),\ \ z(0)=z_0,\ \ \mu(t,0)=0 \quad (4)$$

where $\mu:\mathbb{R}^+\times\mathbb{R}^n\to\mathbb{R}^n$ is a (discontinuous) nonlinear vector field on an open neighborhood U of the origin.

Definition 1[10]**.** The origin of system (4) is named finite-time stable if it is asymptotically stable and for any $z_0\in\mathbb{R}^n$, a settling time function $T:\mathbb{R}^n\setminus\{0\}\to(0,\infty)$ exists such that every solution $z(t,z_0)$ of (4) satisfies $z(t,z_0)=0,\forall\, t\ge T(z_0)$.

Definition 2[32]**.** The origin of system (4) is named global prescribed-time stable if it is finite-time stable and a tunable designing parameter $\vartheta\in\mathbb{R}$ exists to ensure $T(z_0)\le T_p$ for any prescribed finite time $T_p>0$ and any $z_0\in\mathbb{R}^n$.

Lemma 1[10]**.** For system (4), if there exists a C^1 and positive definite function $V(z)$ defined $\mathbb{R}^n$, some real numbers $c>0$ and $0<\alpha<1$ such that $\dot{V}(z)\le -cV^{\alpha}(z),\ \ \forall\, z\in\mathbb{R}^n$. Then, the origin of system (4) is globally finite-time stable with $T(z_0)\le\frac{V^{1-\alpha}(0)}{c(1-\alpha)},\ \forall\, z\in\mathbb{R}^n$.

Lemma 2[39]**.** For $\zeta_1\in\mathbb{R}$, $\zeta_2\in\mathbb{R}$, and a constant $m\ge 1$, one has (i)$|\zeta_1+\zeta_2|^m\le 2^{m-1}|\zeta_1^m+\zeta_2^m|$; (ii)$(|\zeta_1|+|\zeta_2|)^{1/m}\le|\zeta_1|^{1/m}+|\zeta_2|^{1/m}\le 2^{(m-1)/m}(|\zeta_1|+|\zeta_2|)^{1/m}$.

Lemma 3[39]**.** If c,d are positive constant and $\gamma(\zeta_1,\zeta_2)>0$ are real-valued function, then one has $|\zeta_1|^c|\zeta_2|^d\le\frac{c}{c+d}\gamma(\zeta_1,\zeta_2)|\zeta_1|^{c+d}+\frac{d}{c+d}\gamma^{-c/d}(\zeta_1,\zeta_2)|\zeta_2|^{c+d}$.

Lemma 4[40]**.** For $\zeta_1\in\mathbb{R}$, $\zeta_2\in\mathbb{R}$ and constant $0<m\le 1$ and $a>0$, one has $|\lceil\zeta_1\rfloor^{am}-\lceil\zeta_2\rfloor^{am}|\le 2^{1-m}|\lceil\zeta_1\rfloor^{a}-\lceil\zeta_2\rfloor^{a}|^m$.

3 Prescribed-time stabilization

In this section, a non-scaling control strategy is designed to achieve the stabilization task of system (1) within any given prescribed finite time $T_p>0$.

3.1 A scaling function

For the object of this paper, we introduce the following switched scaling function:

$$\digamma_1=\begin{cases}\Gamma_1, & t<T_{s1},\\ 1, & \text{otherwise},\end{cases} \quad (5)$$

where

$$\Gamma_1=\frac{T_{s1}}{T_{s1}-t}, \quad (6)$$

with the positive design parameter T_{s1} satisfying $0<T_{s1}<T_p$.

To avoid the state ζ_i violating the constraints , an asymmetric BLF function $V_{bi}:\Omega_i\to\mathbb{R}$ is given as follows:

$$V_{bi}(\zeta_i)=\frac{k_{bi}^2}{\pi}\tan\left(\frac{\pi\zeta_i^2}{2k_{bi}^2}\right), \quad (7)$$

where $k_{bi}=k_{i2}$, if $\zeta_i>0$, otherwise $k_{bi}=k_{i1}$.

It is clear that the function $V_{bi}(\zeta_i)$ is positive definite on Ω_i and satisfies $V_{bi}(\zeta_i)\to\infty$ as $\zeta_i\to -k_{i1}$ or $\zeta_i\to k_{i2}$. Besides, differentiating the function $V_{bi}(x_i)$ obtains that

$$\begin{aligned}\frac{\partial V_{bi}(\zeta_i)}{\partial\zeta_i}&=\Lambda_{bi}(\zeta_i)\zeta_i,\\ \frac{\partial V_{bi}(\zeta_i)}{\partial k_{bi}}&=\frac{2k_{bi}}{\pi}\tan\left(\frac{\pi\zeta_i^2}{2k_{bi}^2}\right)-\frac{1}{k_{bi}}\Lambda_{bi}(\zeta_i)\zeta_i^2,\end{aligned} \quad (8)$$

with $\Lambda_{bi}(\zeta_i)$ defined as

$$\Lambda_{bi}(\zeta_i)=\begin{cases}\sec^2\left(\frac{\pi\zeta_i^2}{2k_{i2}^2}\right), & \zeta_i>0,\\ \sec^2\left(\frac{\pi\zeta_i^2}{2k_{i1}^2}\right), & \zeta_i\le 0.\end{cases} \quad (9)$$

3.2 PTS of the ζ-subsystem

Take the common control u_{0c} for each subsystem $k\in\mathbb{M}$ as

$$u_{0c}=(|\operatorname{sign}(\zeta_0(0))|-\operatorname{sign}(\zeta_0(0))-1)\,c_0^*, \quad (10)$$

where $c_0^*>0$ is a design constant. As a consequence, the following result is reaped by simple mathematical derivations.

Proposition 1. *Under (10), the solution of the ζ_0-subsystem $\zeta_0(t)$ is well-defined on $[0,T_p)$.*

For simplicity, without loss of generality, in later use we assume $\zeta_0(0)<0$, that is, the sign of u_0 is positive. Then, Under (6), the ζ-subsystem is rewritten as

$$\begin{cases}\dot{\zeta}_i=h_i\zeta_{i+1}+\Phi_{i\sigma(t)}(\zeta_0,\bar{\zeta}_i),\\ \ \ i=1,\ldots,n-1,\\ \dot{\zeta}_n=h_nu_{1\sigma(t)}+\Phi_{n\sigma(t)}(\zeta_0,\bar{\zeta}_n),\end{cases} \quad (11)$$

with $h_i=c_0^*$, $i=1,\ldots,n-1$ and $h_n=1$.

Next a common state feedback controller u_{1c} will be developed to stabilize system (11) within a settling time T_1 ($T_{s1}<T_1<T_p$) by the recursive idea.

Step 1. Select $V_1 = V_{b1}$ as as the common Lyapunov function for this step. Then, for each subsystem k of switched system (10), applying Assumptions 1-2 gives

$$\dot{V}_1 \leq \Lambda_{b1}(\zeta_1)\left(h_1\zeta_1(\zeta_2-\zeta_2^*)+h_1\zeta_1\zeta_2^*+|\zeta_1|^{2-\tau}\tilde{\varphi}_{1k}\right), \tag{12}$$

where ζ_2^* is the virtual controller of ζ_2.

Take the common ζ_2^* for each subsystem $k \in \mathbb{M}$ as

$$\zeta_2^* = -\digamma_1\beta_1\lceil\zeta_1\rfloor^{\lambda_2}, \tag{13}$$

where

$$\beta_1 \geq \max_{k\in\mathbb{M}}\frac{1+c+\varphi_{1k}}{h_1}, \tag{14}$$

is a smooth function independent of k and c is a positive constant. Then, by substituting (13) into (12), one has

$$\dot{V}_1 \leq -(1+c)\Lambda_{b1}(\zeta_1)(\zeta_1)|\zeta_1|^{2-\tau}+\Lambda_{b1}(\zeta_1)h_1\zeta_1\left(\zeta_2-\zeta_2^*\right). \tag{15}$$

Step 2. Define $z_2 = \lceil\zeta_2\rfloor^{\frac{1}{\lambda_2}} - \lceil\zeta_2^*\rfloor^{\frac{1}{\lambda_2}}$ and take the common Lyapunov function $V_2 = V_1 + W_2$ with

$$W_2 = \int_{\zeta_2^*}^{\zeta_2}\left[\lceil s\rfloor^{\frac{1}{\lambda_2}} - \lceil\zeta_2^*\rfloor^{\frac{1}{\lambda_2}}\right]^{2-\lambda_2} ds. \tag{16}$$

From

$$\begin{cases} \dfrac{\partial W_2}{\partial\zeta_2} &= \lceil z_2\rfloor^{2-\lambda_2}, \\ \dfrac{\partial W_2}{\partial\theta} &= -(2-\lambda_2)\dfrac{\partial\left(\lceil\zeta_2^*\rfloor^{\frac{1}{\lambda_2}}\right)}{\partial\theta} \\ & \quad \times\displaystyle\int_{\zeta_2^*}^{\zeta_2}\left|\lceil s\rfloor^{\frac{1}{\lambda_2}} - \lceil\zeta_2^*\rfloor^{\frac{1}{\lambda_2}}\right|^{1-\lambda_2} ds, \end{cases} \tag{17}$$

where $\theta = t$ or $\theta = \zeta_1$, a direct calculation gives

$$\begin{aligned} \dot{V}_2 \leq\ & -(1+c)\digamma_1\Lambda_{b1}(\zeta_1)|\zeta_1|^{2-\tau} \\ & +\Lambda_{b1}(\zeta_1)h_1\zeta_1\left(\zeta_2-\zeta_2^*\right)+\lceil z_2\rfloor^{2-\lambda_2}h_2\zeta_3 \\ & +\lceil z_2\rfloor^{2-\lambda_2}\Phi_{2k}+\frac{\partial W_2}{\partial\zeta_1}(h_{1k}\zeta_2+\Phi_{1k})+\frac{\partial W_2}{\partial t}. \end{aligned} \tag{18}$$

Based on the fact $\digamma_1 \geq 1$ for all $t \geq 0$, we give the following estimates for some terms of (18). First, from the definitions of z_2 and ζ_2^* and Lemma 4, one has

$$\begin{aligned} |\zeta_2-\zeta_2^*| &\leq 2^{1-\lambda_2}\left|\lceil\zeta_2\rfloor^{\frac{1}{\lambda_2}} - \lceil\zeta_2^*\rfloor^{\frac{1}{\lambda_2}}\right|^{\lambda_2} \\ &= 2^{1-\lambda_2}|z_2|^{\lambda_2}. \end{aligned} \tag{19}$$

Thus, from (19) and Lemma 3, it is obtained that

$$\Lambda_{b1}(\zeta_1)\lceil z_1\rfloor^{2-\lambda_1}h_{1k}\left(\zeta_2-\zeta_2^*\right) \leq \frac{1}{4}|z_1|^{2-\tau}+|z_2|^{2-\tau}\varrho_{21k}, \tag{20}$$

where $\varrho_{21k} \geq 0$ is a smooth function.

Secondly, from Assumption 2 and Lemma 2, one gets

$$\begin{aligned} |\Phi_{2k}| &\leq \varphi_{2k}\left(|\zeta_1|^{\frac{\lambda_2-\tau}{\lambda_1}}+|\zeta_2|^{\frac{\lambda_2-\tau}{\lambda_2}}\right) \\ &\leq \varphi_{2k}\left(|\zeta_1|^{\lambda_2-\tau}+|z_2|^{\lambda_2-\tau}+\digamma_1\beta_1|\zeta_1|^{\lambda_2-\tau}\right). \end{aligned} \tag{21}$$

Using (21) and Lemma 3 yields

$$\lceil z_2\rfloor^{2-\lambda_2}\Phi_{2k} \leq \frac{1}{4}|\zeta_1|^{2-\tau}+\digamma_1^{\frac{2-\tau}{1+\tau}}|z_2|^{2-\tau}\varrho_{22k}, \tag{22}$$

where $\varrho_{22k} \geq 0$ is a smooth function.

Finally, notice that

$$\int_{\zeta_2^*}^{\zeta_2}\left|\lceil s\rfloor^{\frac{1}{\lambda_2}} - \lceil\zeta_2^*\rfloor^{\frac{1}{\lambda_2}}\right|^{1-\lambda_2} ds \leq 2^{1-\lambda_2}|z_2|, \tag{23}$$

$$\begin{aligned} \left|\frac{\partial\left(\lceil\zeta_2^*\rfloor^{\frac{1}{\lambda_2}}\right)}{\partial\zeta_1}\right| &\leq \digamma_1^{\frac{1}{\lambda_2}}\left|\frac{\partial\beta_1^{\frac{1}{\lambda_2}}}{\partial\zeta_1}\right||\zeta_1|+\digamma_1^{\frac{1}{\lambda_2}}\beta_1^{\frac{1}{\lambda_2}} \\ &\leq \digamma_1^{\frac{1}{\lambda_2}}\varpi_{21}, \end{aligned} \tag{24}$$

$$\begin{aligned} \left|\frac{\partial\left(\lceil\zeta_2^*\rfloor^{\frac{1}{\lambda_2}}\right)}{\partial t}\right| &\leq \frac{2}{T_{s1}\lambda_2}\digamma_1^{\frac{1+\lambda_2}{\lambda_2}}\beta_1^{\frac{1}{\lambda_2}}|\zeta_1| \\ &\leq \digamma_1^{\frac{1+\lambda_2}{\lambda_2}}|\zeta_1|\varpi_{22}, \end{aligned} \tag{25}$$

where ϖ_{21} and ϖ_{22} are some nonnegative smooth functions.

Then, from (23), (24), (25) and Lemma 3, one arrives

$$\frac{\partial W_2}{\partial\zeta_1}(h_{1k}\zeta_2+\Phi_{1k}) \leq \frac{1}{4}|\zeta_1|^{2-\tau}+\digamma_1^{\frac{2-\tau}{1-\tau}}|z_2|^{2-\tau}\varrho_{23k}, \tag{26}$$

$$\frac{\partial W_2}{\partial t} \leq \frac{1}{4}|\zeta_1|^{2-\tau}+\digamma_1^{\frac{(2-\tau)^2}{(1-\tau)^2}}|z_2|^{2-\tau}\varrho_{24k}, \tag{27}$$

where $\varrho_{23k} \geq 0$ and $\varrho_{24k} \geq 0$ are smooth functions.

As a result, by choosing $\varrho_2 \geq \max_{k\in\mathbb{M}}\varrho_{21k}+\varrho_{22k}+\varrho_{23k}+\varrho_{24k}$ being a smooth function and letting

$$\gamma_2 = \max\left\{1, \tfrac{2-\tau}{1+\tau}, \tfrac{2-\tau}{1-\tau}, \tfrac{(2-\tau)^2}{(1-\tau)^2}\right\}, \tag{28}$$

for every $k \in \mathbb{M}$ one has

$$\begin{aligned} & h_{1k}\zeta_1\left(\zeta_2-\zeta_2^*\right)+\lceil z_2\rfloor^{2-\lambda_2}\Phi_{2k}+\frac{\partial W_2}{\partial t} \\ & +\frac{\partial W_2}{\partial\zeta_1}(h_{1k}\zeta_2+\Phi_{1k}) \leq |\zeta_1|^{2-\tau}+\digamma_1^{\gamma_2}|z_2|^{2-\tau}\varrho_2. \end{aligned} \tag{29}$$

Substituting (29) into (18) yields

$$\dot{V}_2 \leq -c\digamma_1\Lambda_{b1}|\zeta_1|^{2-\tau}+\lceil z_2\rfloor^{2-\lambda_2}h_2\zeta_3+\digamma_1^{\gamma_2}|z_2|^{2-\tau}\varrho_2. \tag{30}$$

Hence, the virtual controller designed as

$$\zeta_3^* = -\digamma_1^{\gamma_2}\lceil z_2\rfloor^{\lambda_2-\tau}\beta_2, \tag{31}$$

with $\beta_2 \geq \max_{k\in\mathbb{M}}\frac{c+\varrho_2}{h_2}$, which together with the fact that $\digamma_1 \geq 1$ for all $t \geq 0$ is such that

$$\dot{V}_2 \leq -c\digamma_1\Lambda_{b1}(|\zeta_1|^{2-\tau}+|z_2|^{2-\tau})+\lceil z_2\rfloor^{2-\lambda_2}h_2(\zeta_3-\zeta_3^*). \tag{32}$$

Following the same arguments of Step 2, for Step i ($i = 2,\ldots,n$), we can find a C^1 and positive definite common Lyapunov function $V_i = V_1 + \sum_{j=2}^{i}W_j$ with

$$W_j = \int_{\zeta_j^*}^{\zeta_j}\left[\lceil s\rfloor^{\frac{1}{\lambda_j}} - \lceil\zeta_j^*\rfloor^{\frac{1}{\lambda_j}}\right]^{2-\lambda_j}\mathrm{d}s, \tag{33}$$

and a group of continuous virtual controllers $\zeta_{j+1}^* = -\digamma_1^{\gamma_j}\lceil z_j\rfloor^{\lambda_j-\tau}\beta_j$, $j = 1,\ldots,n$, such that

$$\dot{V}_j \leq -c\digamma_1\sum_{j=1}^{i}|z_j|^{2-\tau}+\lceil z_j\rfloor^{2-\lambda_j}h_{jk}(\zeta_{j+1}-\zeta_{j+1}^*). \tag{34}$$

where $z_1 = \zeta_1$. Consequently, the following result is obtained.

Theorem 1. Considering system (11) under Assumptions 1 and 2, the common state feedback controller $u_{1c} = \zeta_{n+1}^*$ with a properly selection of the design parameters renders renders the following conclusions hold.

(i) The state ζ_1 keeps in the set Ω_1 for all $t \geq 0$ without violating the constraints.

(ii) The equilibrium at the origin is prescribed-time stable within any given settling time T_1.

Proof. First, since for all $\theta \in (0, 1)$,

$$\tan\left(\frac{\pi\theta}{2}\right) \leq \frac{\pi\theta}{2}\sec\left(\frac{\pi\theta}{2}\right) \leq \frac{\pi\theta}{2}\sec^2\left(\frac{\pi\theta}{2}\right) \tag{35}$$

holds, and then we have

$$V_{b1} = \frac{k_{b1}^2}{\pi}\tan\left(\frac{\pi\zeta_1^2}{2k_{b1}^2}\right) \leq \frac{1}{2}\Lambda_{b1}(\zeta_1)|\zeta_1|^2. \tag{36}$$

Moreover, by Lemma 4, W_j can be calculated as

$$\begin{aligned} W_j &= \int_{\zeta_2^*}^{\zeta_j} \left[\lceil s\rceil^{\frac{1}{\lambda_j}} - \lceil\zeta_j^*\rceil^{\frac{1}{\lambda_j}}\right]^{2-\lambda_j} \mathrm{d}s. \\ &\leq |z_j|^{2-\lambda_j}|\zeta_j - \zeta_j^*| \\ &\leq 2^{1-\lambda_j}|z_j|^2. \end{aligned} \tag{37}$$

Therefore the following estimation is obtained.

$$\begin{aligned} V_n^{\frac{2-\tau}{2}} &= \left(V_{b1} + \sum_{j=2}^{n} W_j\right)^{\frac{2-\tau}{2}} \\ &\leq \Lambda_{b1}(\zeta_1)|\zeta_1|^{2-\tau} + \sum_{j=2}^{n}|z_j|^{2-\tau}. \end{aligned} \tag{38}$$

which together with (32) leads to

$$\dot{V}_n \leq -c\digamma_1 V_n^{\frac{2-\tau}{2}}. \tag{39}$$

When $\digamma_1 = \Gamma_1$, (39) indicates the equilibrium at the origin is prescribed-time stable and the convergence time satisfies

$$T_a \leq T_{s1}\left(1 - exp\left(-\frac{2V_n^{\frac{\tau}{2}}(0)}{c\tau T_{s1}}\right)\right) < T_{s1}. \tag{40}$$

When $t \geq T_{s1}$, one has $\digamma_1 = 1$. In this case (39) indicates that system states remain to the origin for all $t \geq T_{s1}$. As a result, it is concluded that the equilibrium at the origin is prescribed-time stable within any given settling time T_1.

3.3 PTS of the ζ_0-subsystem

Since $\dot{\zeta}(t) \equiv 0$, then we have that $\zeta(t)$ keeps zero for all $t \geq T_1$. As a result, to achieve the PTS task of system (1), we next only need to stabilize the ζ_0-subsystem in a prescribed time $T_2 \leq (1-\varepsilon)T_p$. Similar as that in Subsection 3.1, introduce

$$\Gamma_2 = \frac{T_{s2}}{T_{s2} - t}, \tag{41}$$

with the positive design parameter T_{s2} satisfying $0 < T_{s2} < T_2$.

Take the candidate common Lyapunov function V_0 as $V_0 = \zeta_0^2/2$ and select

$$u_{0c} = -\digamma_2\kappa\lceil\zeta_0\rceil^{1-\omega}, \tag{42}$$

with κ and $\omega \in (0, 1)$ being positive constants, one obtains

$$\dot{V}_0 \leq -\kappa\digamma_2(\zeta_0)|\zeta_0|^{2-\omega}. \tag{43}$$

Theorem 2. For the ζ_0-subsystem of (1), the common state feedback controller (47) drives the state ζ_0 to zero within the prescribed finite time T_2 without violating the constraints.

Proof. This proof follows the same line of that of Theorem 1.

Till now, the state feedback design for PTS of the system (1) is completed. Accordingly, the following theorem is stated to sum up the result.

Theorem 3. Consider the system (1) satisfying Assumptions 1 and 2. If the switching control strategy

$$u_{0c} = \begin{cases} u_{0c}\,|_{(6)}, & t < \varepsilon T_p, \\ u_{0c}\,|_{(38)}, & t \geq \varepsilon T_p, \end{cases} \tag{44}$$

$$u_{1c} = \zeta_{n+1}^*, \tag{45}$$

with a properly selection of the design parameters is applied, then the states of the CLS are driven to zero within any prescribed finite time T_p.

Proof. The results hold readily from the results of Theorems 1 and 2.

4 Conclusions

Based on the tan-type Barrier Lyapunov Function (BLF) to handle the the asymmetric constraints, a non-scaling design is developed for a kind of switched NSs with asymmetric output constraints . The suitable switching mechanism makes the proposed control scheme achieving the prescribed-time stabilization, leading to a simpler controller. Extension of this result with partial state information is one of our future research topics.

References

[1] R.M. Murray, S.S. Sastry, Nonholonomic motion planning: steering using sinusoids, IEEE Trans. Autom. Control 38(5)(1993) 700–716.

[2] R.W. Brockett, Asymptotic stability and feedback stabilization, Diff. Geom. Control Theory 27(1)(1983) 181–191.

[3] A. Astolfi, Discontinuous control of nonholonomic systems, Syst. Control Lett. 27(1)(1996) 37–45.

[4] C. Samson, Control of chained system: application to path following and time-varying point-stabilization of mobile robots, IEEE Trans. Autom. Control 40(1)(1995) 64–77.

[5] I. Kolmanovsky, N.H. McClamroch, Hybrid feedback laws for a class of cascade nonlinear control systems, IEEE Trans. Autom. Control 41(9)(1996) 1271–1282.

[6] Z.P. Jiang, Robust exponential regulation of nonholonomic systems with uncertainties, Automatica 36(2)(2000) 189–209.

[7] Y.P. Tian, S. Li, Exponential stabilization of nonholonomic dynamic systems by smooth time-varying control, Automatica 38(8)(2002) 1139–1146.

[8] Z.G. Liu, Y.Q. Wu, Z.Y. Sun, Output feedback control for a class of high-order nonholonomic systems with complicated nonlinearity and time-varying delay, J. Franklin Inst. 354(11)(2017) 4289–4310.
[9] H. Wang, Q. Zhu, Adaptive output feedback control of stochastic nonholonomic systems with nonlinear parameterization, Automatica 98(2018) 247–255.
[10] S. P. Bhat, D.S. Bernstein, Finite-time stability of continuous autonomous systems, SIAM J. Control Optim. 38(3) (2000) 751–766.
[11] F. Gao, Y. Wu, Z. Zhang. Finite-time stabilization of uncertain nonholonomic systems in feedforward-like form by output feedback, ISA Trans. 59(2015) 125–132.
[12] X.J. Xie, G.J. Li, Finite-time output-feedback stabilization of high-order nonholonomic systems, Int. J. Robust Nonlinear Control 29(9)(2019) 2695–2711.
[13] Z.Y. Sun, L.R. Xue, K. Zhang, A new approach to finite-time adaptive stabilization of high-order uncertain nonlinear system, Automatica 58 (2015) 60–66.
[14] J. Fu, R. Ma, T. Chai, Adaptive finite-time stabilization of a class of uncertain nonlinear systems via logic-based switchings, IEEE Trans. Autom. Control 62(11) (2017) 5998–6003.
[15] V. Andrieu, L. Praly, A. Astolfi, Homogeneous approximation, recursive observer design, and output feedback, SIAM J. Control Optim. 47(4)(2008) 1814–1850.
[16] B. Tian, Z. Zuo, X. Yan, H. Wang, A fixed-time output feedback control scheme for double integrator systems, Automatica 80(2017) 17–24.
[17] A. Polyakov, Nonlinear feedback design for fixed-time stabilization of linear control systems, IEEE Trans. Autom. Control 57(8)(2012) 2106–2110.
[18] F. Gao, Y. Wu, Z. Zhang, Y. Liu, Global fixed-time stabilization for a class of switched nonlinear systems with general powers and its application, Nonlin. Anal. Hybrid Syst. 31(2019)56–68.
[19] F. Gao, C. Zhu, J. Huang, Y. Wu, Global fixed-time output feedback stabilization of perturbed planar nonlinear Systems, IEEE Trans. Circuits Syst. II, Exp. Briefs 68(2) (2021) 707–711.
[20] M. Defoort, G. Demesure, Z. Zuo, A. Polyakov, M. Djemai, Fixed-time stabilisation and consensus of non-holonomic systems, IET Control Theory Appl. 10(18)(2016) 2497–2505.
[21] Z. Zuo, B. Tian, M. Defoort, Z. Ding, Fixed-time consensus tracking for multi-agent systems with high-order integrator dynamics, IEEE Trans. Autom. Control 63(2)(2018) 563–570.
[22] B. Ning, Q.L. Han, Prescribed finite-time consensus tracking for multi-agent systems with nonholonomic chained-form dynamics, IEEE Trans. Autom. Control 64(4)(2019) 1686–1693.
[23] F. Gao, J. Huang, X. Shi, X. Zhu, Nonlinear mapping-based fixed-time stabilization of uncertain nonholonomic systems with time-varying state constraints, J. Franklin Inst. 357(11) (2020) 6653–6670.
[24] F. Gao, J. Huang, X. Zhu, Y. Wu, Output feedback stabilization via nonlinear mapping for time-varying constrained nonholonomic systems in prescribed finite time, Information Sciences, 2021, 550: 297-312.
[25] F. Gao, Y. Wu, J. Huang, Y. Liu, Output feedback stabilization within prescribed finite time of asymmetric time-varying constrained nonholonomic systems, Int. J. Robust Nonlin. Control 31(2)(2021) 427–446.
[26] Y. Cao, C. Wen, S. Tan, Y. Song, Prespecifiable fixed-time control for a class of uncertain nonlinear systems in strict-feedback form, Int. J. Robust Nonlin. Control 30(3)(2020) 1203–1222.
[27] Y. Song, Y. Wang, J. Holloway, M. Krstic, Time-varying feedback for regulation of normal-form nonlinear systems in prescribed finite time, Automatica 83(2017) 243–251.
[28] J.D. Sánchez-Torres, D. Gómez-Gutiérrez, E. López, A. G. Loukianov, A class of predefined-time stable dynamical systems, IMA J. Math. Control Inf. 35(1) (2018): i1–i29.
[29] F. Gao, Y. Wu, Z. Zhang, Global fixed-time stabilization of switched nonlinear systems: a time-varying scaling transformation approach, IEEE Trans. Circuits Syst. II, Exp. Briefs 66(11) (2019) 1890–1894.
[30] P. Krishnamurthy, F. Khorrami, M. Krstic, A dynamic high-gain design for prescribed-time regulation of nonlinear systems, Automatica 115 (2020) 108860.
[31] B. Zhou, Y. Shi, Prescribed-time stabilization of a class of nonlinear systems by linear time-varying feedback. IEEE Transactions on Automatic Control, 66(12)(2021): 6123-6130.
[32] R. I. V. Kairuz, Y. ORlov, L. T. Aguilar, Prescribed-time stabilization of controllable planar systems using switched state feedback, IEEE Control Syst. Lett. 5(6)(2021): 2048–2053.
[33] W. Li, M. Krstic, Stochastic nonlinear prescribed-time stabilization and itnverse optimality, IEEE Trans. Autom. Control, doi: 10.1109/TAC.2021.3061646.
[34] C. C. Hua, P. Ning, K. Li, Adaptive prescribed-time control for a class of uncertain nonlinear systems, IEEE Trans. Autom. Control, doi: 10.1109/TAC.2021.3130883.
[35] X. Chen, X. Zhang, Output-feedback control strategies of lower-triangular nonlinear nonholonomic systems in any prescribed finite time, Int. J. Robust Nonlin. Control 29(4)(2019) 904–918.
[36] J.D. Sánchez-Torres, M Defoort, A.J. Munoz-Vázquez, Predefined-time stabilisation of a class of nonholonomic systems, Int. J. Control 93(12)(2020) 2941–2948.
[37] D. Hou, F. Gao, J. Y. Wu, A switching-based state-scaling design for prescribed-time stabilization of nonholonomic systems with actuator dead-zones, Aerosp. Sci. Technol. 118(2021) 106986.
[38] K. K. Zhang, B. Zhou, M. Hou, G.R. Duan, Prescribed-time control of high-order nonholonomic systems in chained form by time-varying feedback. Syst. & Control Lett., 2022, 166: 105307.
[39] C. Qian, W. Lin, A continuous feedback approach to global strong stabilization of nonlinear systems, IEEE Trans. Autom. Control 46(7)(2001) 1061–1079.
[40] S. Ding, W.H. Chen, K. Mei, D. Murray-Smith, Disturbance observer design for nonlinear systems represented by input-output models, IEEE Trans. Indust. Elec. 67(2)(2020) 1222–1232.

Proceedings of the 3rd Conference on Fully Actuated System Theory and Applications
May 10-12, 2024, Shenzhen, China

Sliding Mode Based Incremental Tracking Control of High-Order Fully Actuated Systems with Application

YU Miao[1], HOU Mingzhe[1], TAN Feng[1]
1. Center for Control Theory and Guidance Technology, Harbin Institute of Technology, Harbin, 150001, China
E-mail: hithyt@hit.edu.cn

Abstract: This paper proposes a sliding-mode based incremental tracking control method for the high-order fully actuated (HOFA) system. It is ensured that the tracking error converges to zero within the given settling time which is exactly user-assignable and maintains there from then on. By designing the desired tracking error trajectory, the reaching phase of the sliding mode is eliminated, and by adopting the basic principle of the INDI control strategy, the proposed control method only needs relatively limited model information, improving the robustness of the system against model uncertainties. The proposed approach is finally applied to the attitude tracking control of the high speed aircraft and the effectiveness of the design is verified by numerical simulation results.

Key Words: Incremental control, sliding mode control, high-order fully actuated (HOFA) system, attitude tracking control

1 Introduction

As an important one of the nonlinear control approaches, Nonlinear Dynamic Inversion (NDI) based on output feedback linearization has been widely used in the flight control [1–3] . However, NDI depends on the accurate model of the control system. When appearing modeling uncertainties, its robustness will deteriorate. In order to overcome shortcoming of NDI, the Incremental Nonlinear Dynamic Inversion (INDI) control method is proposed. As a simplified or enhanced NDI [4], this method is a sensor-based variation of the Nonlinear Dynamic Inversion control method. The theoretical development of the incremental control can be dated back to the late 1990s, started with the work from Smith [5] for NDI-based flight control. The main advantage of the INDI is that it is weak model dependent and thus has good robustness against model uncertainties. The INDI control has been widely used for flight control applications [6–12].

Adopting the core idea of INDI, other incremental control strategies have emerged, where a typical one is the sliding mode based incremental control. Refs.[13–15] investigate the sliding mode based incremental fault-tolerant control methods and their applications. Due to its good robustness against model uncertainties, the sliding mode based incremental control have also been widely used to the control of aircrafts, for example, [16] considers the sliding mode based incremental control of rotor-crafts, [17] blended-wing-body aircrafts, [18] tailless aircrafts and [19] morphing-wing aircrafts. However, the existing sliding mode based incremental control methods cannot ensure that the tracking error converges to zero within the given settling time which is exactly user-assignable and maintains there from then on.

Recently, high-order fully actuated (HOFA) model is proposed by Duan [20] to serve as a general model for control systems. Different from the state-space model, the HOFA model with a huge advantage of the full-actuation feature can easily eliminate the complicated nonlinear terms which are measurable. And many kinds of nonlinear systems in the state-space form can also be converted into HOFA form. Due to the full-actuation feature, the HOFA model is especially effective and convenient in tackling with nonlinear control problems. Some demonstrations can be found in [21] for adaptive control, [22] for robust control, [23] for optimal control and [24] for disturbance rejection control.

Motivated by the above discussions and based on our previous work [25], this paper proposes a novel sliding mode based incremental control approach for the HOFA system which could ensure that the tracking error converges to zero within the given settling time which is exactly user assignable and maintains there from then on. As a combination between incremental control and sliding mode control (SMC), the proposed approach has less model dependence by substituting a portion of the model information with acceleration measurement, and thus reduces the influence of model uncertainty on the system response. It possesses many merits such as good robustness, simplicity, and effectiveness to apply sliding mode based incremental control approach to the HOFA system. The main contributions of this paper can be summarized as follows. Firstly, the incremental control oriented model is established via expanding the HOFA model by the first-order Taylor series. Then a desired output tracking error trajectory which becomes zero after the user-assigned settling time is designed, based on which the sliding mode vector is constructed. Further, the sliding mode based incremental control law is designed to ensure that the sliding mode vector and thus the error between the output tracking error and the desired output tracking error maintains zero all the time, as a result, the output tracking error becomes zero after the settling time as desired output tracking error trajectory does. Finally, the proposed method is applied to the attitude control of high speed aircrafts and the effectiveness of the design is illustrated by simulation results.

The rest of this paper is structured as follows, a review of the INDI strategy and the problem formulation are presented in Section 2. In Section 3, the sliding mode based incremental control design for the HOFA system is given. Application to the attitude tracking control of high speed aircrafts and the effectiveness varication of the design result by nu-

This work was supported by the National Natural Science Foundation of China under Grant Number 62073096, the Science Center Program of National Natural Science Foundation of China under Grant Number 62188101, and the Heilongjiang Touyan Team Program. (Corresponding author: Mingzhe Hou).

merical simulations are given in Section 4. And conclusions are presented in Section 5.

2 Review of INDI and Problem Formulation

This section gives a brief review of the INDI control framework and then introduces the problem to be solved in the next section.

2.1 Review of INDI

Consider a class of nonlinear multiple-input multiple-output (MIMO) systems of the form

$$\dot{x} = f(x) + G(x)u, \tag{1}$$
$$y = h(x), \tag{2}$$

where $x \in R^n$ is the state vector, $u \in R^m$ is the input vector, and $y \in R^m$ is the output vector.

Instead of the total input vector u directly, the Incremental Nonlinear Dynamic Inversion (INDI) is based on the computation of the demanded control increment. To do so, the nonlinear MIMO system (1) is approximated by the first-order terms of its Taylor series expansion. Let x_0 and u_0 respectively represent the values of x and u at the last sampling time. For x and u in the neighborhoods of x_0 and u_0,

$$\begin{aligned}\dot{x} =& \dot{x}_0 + \frac{\partial}{\partial x}[f(x) + G(x)u]|_{\substack{x=x_0\\u=u_0}}(x - x_0) \\ &+ \frac{\partial}{\partial u}[f(x) + G(x)u]|_{\substack{x=x_0\\u=u_0}}(u - u_0) + o \\ \approx& \dot{x}_0 + \frac{\partial}{\partial x}[f(x) + G(x)u]|_{\substack{x=x_0\\u=u_0}}(x - x_0) \\ &+ G(x_0)(u - u_0),\end{aligned} \tag{3}$$

where $\dot{x}_0 = f(x_0) + g(x_0)u_0$, and o represents the higher order term that can be neglected.

For very small time increments (high sampling frequencies of the controller), it is reasonable to assume that u can change significantly faster than x, therefore, the assumption $\Delta x = x - x_0 = 0$ can be made. Considering this, (3) is further simplified as

$$\dot{x} \approx \dot{x}_0 + G(x_0)\Delta u, \tag{4}$$

where $\Delta u = u - u_0$.

When $\det G(x_0) \neq 0$, let

$$\Delta u = G^{-1}(x_0)(v - \dot{x}_0), \tag{5}$$

where v is an auxiliary control vector to be designed, then one can obtain a linear system $\dot{x} = v$. Once v is determined, the incremental control input can be computed by (5) and the total control input can be computed by

$$u = u_0 + \Delta u = u_0 + G^{-1}(x_0)(v - \dot{x}_0). \tag{6}$$

From this equation, the main advantage of the INDI can be clearly known: the control law does not depend on f anymore, which means that the designed controller is insensitive to a part of the model, improving the robustness of the system against model uncertainties.

2.2 Problem Formulation

Consider the following general HOFA system model with multiple orders [26]:

$$\begin{bmatrix} x_1^{(n_1)} \\ x_2^{(n_2)} \\ \vdots \\ x_m^{(n_m)} \end{bmatrix} = \begin{bmatrix} f_1(x_j^{(0\sim n_j-1)}|_{j=1\sim m}) \\ f_2(x_j^{(0\sim n_j-1)}|_{j=1\sim m}) \\ \vdots \\ f_m(x_j^{(0\sim n_j-1)}|_{j=1\sim m}) \end{bmatrix} + B(\cdot)u, \tag{7}$$

where $u \in R^r$ is the control input; $x_j \in R^{r_j}, j = 1, 2, \ldots, m$, are a set of vectors of proper dimensions with $r_1 + r_2 + \ldots + r_m = r$; $n_j, j = 1, 2, \ldots, m$, are a set of integers; $x = [x_1^{\mathrm{T}}, x_2^{\mathrm{T}}, \cdots, x_m^{\mathrm{T}}]^{\mathrm{T}}$ represents the system output; $x_j^{(n_j)}|_{j=1\sim m} = [(x_1^{(n_1)})^{\mathrm{T}}, (x_2^{(n_2)})^{\mathrm{T}}, \cdots, (x_m^{(n_m)})^{\mathrm{T}}]^{\mathrm{T}}$, $x_j^{(0\sim n_j-1)} = [x_j^{\mathrm{T}}, \dot{x}_j^{\mathrm{T}}, \cdots, (x_j^{(n_m-1)})^{\mathrm{T}}]^{\mathrm{T}}$ and $x_j^{(0\sim n_j-1)}|_{j=1\sim m} = [(x_1^{(0\sim n_1-1)})^{\mathrm{T}}, (x_2^{(0\sim n_2-1)})^{\mathrm{T}}, \cdots, (x_m^{(0\sim n_m-1)})^{\mathrm{T}}]^{\mathrm{T}}$; f_j are known r_j-dimensional smooth functions defined on R^μ with $\mu = \sum_{j=1}^m r_j n_j$; B is known $r \times r-$dimensional smooth function defined on R^μ. It is assumed in this paper that $\det B(\cdot) \neq 0$ for all $\cdot \in R^\mu$. For convenience, $x_j^{(0\sim n_j-1)}|_{j=1\sim m}$ is sometimes denoted by X in the following derivation. Denote $f(X) = [(f_1(X))^{\mathrm{T}}, (f_2(X))^{\mathrm{T}}, \cdots, (f_m(X))^{\mathrm{T}}]^{\mathrm{T}}$, then (7) can be compactly written as

$$x_j^{(n_j)}|_{j=1\sim m} = f(X) + B(X)u. \tag{8}$$

In this paper, the basic principle of INDI is used in the sliding mode control of the above HOFA system to achieve the following design objective: Given a $m-$dimensional reference signal $x_d(t)$ with $x_{jd}(t)$ of dimension r_j belonging to $C^{n_j}, j = 1, 2, 3 \cdots, m$ and satisfying that $x_{jd}^{(k)}(t), k = 0, 1, \cdots, n_j$ are all bounded, and a settling time $T_f > 0$, design a sliding mode based incremental control law u for the HOFA system (8) such that all the signals in the closed loop system are bounded, and the tracking error $e = x - x_d$ equals to zero when $t \geq T_f$.

3 Sliding Mode Based Incremental Control Design for the HOFA System

First of all, the HOFA system (8) is expanded by the first-order Taylor series around the point at the last sampling time (denoted by the subscript 0)

$$\begin{aligned}x_j^{(n_j)}|_{j=1\sim m} =& x_{j0}^{(n_j)}|_{j=1\sim m} \\ &+ \frac{\partial}{\partial X}[f(X) + B(X)u]|_{\substack{X=X_0\\u=u_0}}(X - X_0) \\ &+ \frac{\partial}{\partial u}[f(X) + B(X)u]|_{\substack{X=X_0\\u=u_0}}(u - u_0) \\ &+ o,\end{aligned} \tag{9}$$

with

$$x_{j0}^{(n_j)}|_{j=1\sim m} = f(X_0) + B(X_0)u_0. \tag{10}$$

Omitting the high-order terms, one has that

$$\begin{aligned} x_j^{(n_j)}|_{j=1\sim m} \approx & x_{j0}^{(n_j)}|_{j=1\sim m} \\ & + \frac{\partial}{\partial X}[f(X)+B(X)u]|_{\substack{X=X_0\\u=u_0}}(X-X_0) \\ & + B(X_0)(u-u_0). \end{aligned} \tag{11}$$

Considering the high sampling frequencies of the controller, it is assumed that $X - X_0 = 0$, then (11) can be written as follows

$$x_j^{(n_j)}|_{j=1\sim m} \approx x_{j0}^{(n_j)}|_{j=1\sim m} + B(X_0)(u-u_0). \tag{12}$$

Define

$$z = e - e_d, \tag{13}$$

where e_d is the desired tracking error trajectory to be designed, $e_d = [e_{1d}^{\mathrm{T}}, e_{2d}^{\mathrm{T}}, \cdots, e_{md}^{\mathrm{T}}]^{\mathrm{T}}$ where r_j-dimensional $e_{jd}, j = 1, 2, \cdots, m$, are such that: $e_{jd}(t), \dot{e}_{jd}(t)$, $\cdots$, $e_{jd}^{(n_j)}(t)$ are all bounded; $e_{jd}(0) = e_j(0)$, $\dot{e}_{jd}(0) = \dot{e}_j(0)$, $\cdots$, $e_{jd}^{(n_j-1)}(0) = e_j^{(n_j-1)}(0)$; $e_{jd}(t) = \dot{e}_{jd}(t) = \cdots = e_{jd}^{(n_j-1)}(t) = 0$ when $t \geq T_f$. It is noted that e_{jd} can be designed by all kinds of curve interpolation methods, with $t = 0$ and $t = T_f$ being the interpolation nodes. For example, we can design $e_{jd}, j \in \{1, 2, \cdots, m\}$ as follows

$$e_{jd} = \begin{cases} b_{j0} + b_{j1}t + \cdots + b_{j(2n_j-1)}t^{2n_j-1}, & if\ 0 \leq t \leq T_f, \\ 0, & if\ t > T_f, \end{cases}$$

where $b_{j0}, b_{j1}, \cdots, b_{j(n_j+1)}, \cdots, b_{j(2n_j-1)}$ are determined by

$$\begin{aligned} & b_{j0} = e_j(0), b_{j1} = \dot{e}_j(0), \\ & b_{j2} = -(2n_j-1)(e_j(0)/T_f^2) - 2n_j(\dot{e}_j(0)/T_f), \\ & b_{j3} = (2n_j-2)(e_j(0)/T_f^3) + (2n_j-3)(\dot{e}_j(0)/T_f^2), \\ & \quad \vdots \\ & b_{j(n_j+1)} = (-1)^{n_j}[n_j(e_j(0)/T_f^{n_j+1}) + (n_j-1)\dot{e}_j(0)/T_f^{n_j}], \\ & \quad \vdots \\ & b_{j(2n_j-1)} = 2(e_j(0)/T_f^{2n_j-1}) + \dot{e}_j(0)/T_f^{2n_j-2}. \end{aligned} \tag{14}$$

From (13), we can obtain that

$$z_j^{(n_j)}|_{j=1\sim m} = e_j^{(n_j)}|_{j=1\sim m} - e_{jd}^{(n_j)}|_{j=1\sim m}. \tag{15}$$

Define the sliding mode variable as

$$\begin{aligned} s_j = & z_j^{(n_j-1)} + C_{j(n_j-2)}z_j^{(n_j-2)} + \cdots \\ & + C_{j0}z_j, \ \ j = 1, 2, \cdots, m, \end{aligned} \tag{16}$$

where $C_{j0}, C_{j1}, \cdots, C_{j(n_j-2)}$ are design parameter matrices such that

$$\Phi_j = \begin{bmatrix} 0 & I & 0 & \cdots & 0 \\ 0 & 0 & I & \cdots & 0 \\ \vdots & \vdots & \vdots & \ddots & \vdots \\ 0 & 0 & 0 & \cdots & I \\ C_{j0} & C_{j1} & C_{j2} & \cdots & C_{j(n_j-2)} \end{bmatrix}, \tag{17}$$

for $j = 1, 2, \cdots, m$ are all Hurwitz matrices. It is easy to obtain that $s_j(0) = 0$ since $z_j(0), \dot{z}_j(0), \cdots, z_j^{(n_j-1)}(0)$ are all zero. Then we can obtain that

$$\begin{aligned} \dot{s}_j|_{j=1\sim m} = & z_j^{(n_j)}|_{j=1\sim m} + C_{j(n_j-2)}z_j^{(n_j-1)}|_{j=1\sim m} \\ & + \cdots + C_{j0}\dot{z}_j|_{j=1\sim m} \\ = & e_j^{(n_j)}|_{j=1\sim m} - e_{jd}^{(n_j)}|_{j=1\sim m} \\ & + C_{j(n_j-2)}z_j^{(n_j-1)}|_{j=1\sim m} \\ & + \cdots + C_{j0}\dot{z}_j|_{j=1\sim m} \\ = & x_j^{(n_j)}|_{j=1\sim m} - x_{jd}^{(n_j)}|_{j=1\sim m} \\ & - e_{jd}^{(n_j)}|_{j=1\sim m} + C_{j(n_j-2)}z_j^{(n_j-1)}|_{j=1\sim m} \\ & + \cdots + C_{j0}\dot{z}_j|_{j=1\sim m}. \end{aligned} \tag{18}$$

Substituting (12) into (18) yields that

$$\begin{aligned} \dot{s}_j|_{j=1\sim m} = & x_{j0}^{(n_j)}|_{j=1\sim m} + B(X_0)(u-u_0) \\ & - x_{jd}^{(n_j)}|_{j=1\sim m} - e_{jd}^{(n_j)}|_{j=1\sim m} \\ & + C_{j(n_j-2)}z_j^{(n_j-1)}|_{j=1\sim m} \\ & + \cdots + C_{j0}\dot{z}_j|_{j=1\sim m} \\ = & x_{j0}^{(n_j)}|_{j=1\sim m} + B(X_0)(u-u_0) + \eta, \end{aligned} \tag{19}$$

where

$$\begin{aligned} \eta = & - x_{jd}^{(n_j)}|_{j=1\sim m} - e_{jd}^{(n_j)}|_{j=1\sim m} \\ & + C_{j(n_j-2)}z_j^{(n_j-1)}|_{j=1\sim m} \\ & + \cdots + C_{j0}\dot{z}_j|_{j=1\sim m}. \end{aligned} \tag{20}$$

For $\det B(X_0) \neq 0$, the incremental control input is designed as

$$u - u_0 = -B^{-1}(X_0)(x_{j0}^{(n_j)}|_{j=1\sim m} + \eta + Ks_j|_{j=1\sim m}), \tag{21}$$

where $K = \mathrm{diag}(K_1, K_2, \cdots, K_m)$ with $K_j \in R^{r_j\times r_j}, j = 1, 2, \cdots, m$ being positive definite design parameter matrices. As a result, the final sliding mode based incremental control law is as follows

$$\begin{aligned} u = & - B^{-1}(X_0)(x_{j0}^{(n_j)}|_{j=1\sim m} + \eta + Ks_j|_{j=1\sim m}) \\ & + u_0, \end{aligned} \tag{22}$$

and the following closed-loop dynamic equation can be obtained

$$\dot{s}_j|_{j=1\sim m} = -Ks_j|_{j=1\sim m}, \tag{23}$$

The incremental controller structure is presented in Fig.1.

Choose

$$V = \frac{1}{2}s_j^{\mathrm{T}}|_{j=1\sim m}s_j|_{j=1\sim m}, \tag{24}$$

as the Lyapunov function, then the time derivative of V along the closed-loop dynamic equation is

$$\begin{aligned} \dot{V} = & s_j^{\mathrm{T}}|_{j=1\sim m}\dot{s}_j|_{j=1\sim m} \\ = & - s_j^{\mathrm{T}}|_{j=1\sim m}Ks_j|_{j=1\sim m} \leq 0. \end{aligned} \tag{25}$$

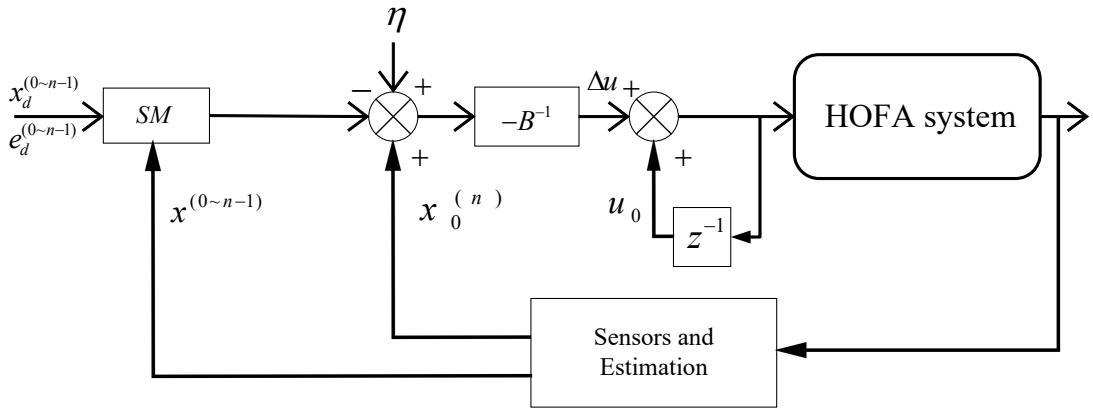

Fig. 1: Sliding mode based incremental control block diagram of the HOFA system.

Since $s_j(0)|_{j=1\sim m}=0$, one has that $V(0)=0$, as a result, $V(t)=0$ for $t\geq 0$, which in turn means that $s_j(t)|_{j=1\sim m}=0$ for $t\geq 0$, or equivalently, $s_j(t)=0, j=1,2,\cdots,m$ for $t\geq 0$. From (16), one can obtain that, for any $j\in\{1,2,\cdots,m\}$,

$$z_j^{(1\sim n_j-1)}=\Phi_j z_j^{(0\sim n_j-2)}+B_j s_j, \tag{26}$$

where $B_j=[0_{r_j\times r_j},\ 0_{r_j\times r_j},\ \cdots,\ I_{r_j\times r_j}]^{\mathrm{T}}$. Considering that Φ_j is Hurwitz, one has that $z_j^{(0\sim n_j-2)}=0$ and thus $z_j=0$ for $t\geq 0$. Therefore, $e_j(t)=e_{jd}(t)$ for $t\geq 0$. This means that the tracking error $e_j(t)=0$ for $t\geq T_f$ since $e_{jd}(t)=0$ for $t\geq T_f$.

It is noted, by designing the desired tracking error trajectory, it is ensured that $s_j(0)|_{j=1\sim m}=0$, this means that the reaching phase of the sliding mode is eliminated. Additionally, by adopting the basic principle of the INDI, the proposed control law does not depend on f anymore, which means that it only needs relatively limited model information, improving the robustness of the system against model uncertainties.

4 Application to the Attitude Control of High Speed Aircrafts

Consider control of the high speed aircraft attitude system given in [27]. Define

$$x=\begin{bmatrix}\gamma\\ \psi\\ \vartheta\end{bmatrix}, u=\begin{bmatrix}\delta_x\\ \delta_y\\ \delta_z\end{bmatrix}, \tag{27}$$

where γ,ψ and ϑ are respectively the roll angle, the yaw angle and the pitch angle; δ_x,δ_y and δ_z are the deflection angles of the control surfaces. The simplified dynamic model for the attitude system of the high speed aircraft can be written in the following HOFA system form:

$$\ddot{x}=D(x,\dot{x})+G(x)u, \tag{28}$$

where $D(x,\dot{x})=F(x,\dot{x})+qslB(x)m_0, G(x)=qslB(x)T$ (q is the dynamical pressure, s is the reference area and l is the reference length) with

$$\begin{aligned}
B(x) &= \begin{bmatrix}\frac{1}{J_x} & -\frac{tan(\vartheta)cos(\gamma)}{J_y} & \frac{tan(\vartheta)sin(\gamma)}{J_z}\\ 0 & \frac{cos(\gamma)}{J_y cos(\vartheta)} & -\frac{sin(\gamma)}{J_z cos(\vartheta)}\\ 0 & \frac{sin(\gamma)}{J_y} & \frac{cos(\gamma)}{J_z}\end{bmatrix},\\
m_0 &= \begin{bmatrix}m_x(V,\alpha,\beta,\omega_x,\omega_y,\omega_z,0,0,0)\\ m_y(V,\alpha,\beta,\omega_x,\omega_y,\omega_z,0,0,0)\\ m_z(V,\alpha,\beta,\omega_x,\omega_y,\omega_z,0,0,0)\end{bmatrix},\\
T &= \begin{bmatrix}\frac{\partial m_x}{\partial\delta_x} & \frac{\partial m_x}{\partial\delta_y} & \frac{\partial m_x}{\partial\delta_z}\\ \frac{\partial m_y}{\partial\delta_x} & \frac{\partial m_y}{\partial\delta_y} & \frac{\partial m_y}{\partial\delta_z}\\ \frac{\partial m_z}{\partial\delta_x} & \frac{\partial m_z}{\partial\delta_y} & \frac{\partial m_z}{\partial\delta_z}\end{bmatrix},
\end{aligned} \tag{29}$$

and

$$F(x,\dot{x})=[f_1(x,\dot{x}),\ f_2(x,\dot{x}),\ f_3(x,\dot{x})]^{\mathrm{T}} \tag{30}$$

with

$$\begin{cases}
f_1 = \Theta(0,1,0)\dot{\vartheta}^2\sin\gamma\cos\gamma\\
\quad -\Theta(\sin^2\vartheta,\cos^2\vartheta,\sin^2\vartheta)\dot{\psi}^2\sin\gamma\cos\gamma\\
\quad -\Theta_0(\vartheta,\gamma)\frac{1}{\cos\vartheta}\dot{\psi}\dot{\vartheta}-\frac{1}{\cos\vartheta}\dot{\psi}\dot{\vartheta}\\
\quad +\Theta(1,0,1)\dot{\gamma}\dot{\psi}\sin\vartheta\sin\gamma\cos\gamma\\
\quad +[\Theta(\sin^2\gamma,0,-\cos^2\gamma)+1]\dot{\gamma}\dot{\vartheta}tan\vartheta\\
f_2 = [\Theta(-\sin\gamma,0,\cos\gamma)\frac{\cos\gamma}{\cos\vartheta}-\frac{1}{\cos\vartheta}]\dot{\gamma}\dot{\vartheta}\\
\quad +\Theta(\sin\gamma,0,-\cos\gamma)\dot{\psi}^2\sin\vartheta\sin\gamma\\
\quad +\Theta(-\sin\gamma,0,\cos\gamma)\dot{\vartheta}\dot{\psi}\tan\vartheta\cos\gamma\\
\quad -\Theta(\sin\gamma,0,-\cos\gamma)\dot{\psi}\dot{\gamma}\sin\gamma+\dot{\psi}\dot{\vartheta}\tan\vartheta\\
f_3 = \Theta(1,0,1)(\dot{\psi}\sin\vartheta+\dot{\gamma})\dot{\vartheta}\sin\gamma\cos\gamma\\
\quad +\Theta(\cos^2\gamma,0,-\sin^2\gamma)\dot{\psi}^2\sin\vartheta\cos\vartheta\\
\quad +(\Theta(\cos^2\gamma,0,-\sin^2\gamma)+1)\dot{\psi}\dot{\gamma}\cos\vartheta
\end{cases},$$

where V is the velocity, w_x,w_y and w_z are the attitude angular velocity; α,β are respectively the angle of attack and the angle of sideslip, and the Θ function is defined by ([28])

$$\Theta(\xi,\zeta,\tau)=\frac{J_x-J_y}{J_z}\xi+\frac{J_y-J_z}{J_x}\zeta+\frac{J_z-J_x}{J_y}\tau, \tag{31}$$

where ξ, ζ and τ are the variables of the function; J_x, J_y, J_z are the rotary inertia corresponding to the body coordinate.

The objective is to design an attitude control law based on the model (28) to drive x to track the given reference signal $x_d = [\gamma_d, \psi_d, \vartheta_d]^{\mathrm{T}}$.

Expanding system (28) by the first-order Taylor series, one can obtain that

$$\ddot{x} \approx \ddot{x}_0 + G(x_0)(u - u_0), \tag{32}$$

where x_0, $\ddot{x}_0$ and u_0 are all obtained at the last sampling time.

According to the derivation of the sliding mode based incremental control in the previous section, the sliding mode variable is designed as

$$s = \dot{z} + Cz. \tag{33}$$

where $C = \mathrm{diag}(c_1, c_2, c_3)$ with c_1, c_2, c_3 being positive design parameters, $z = x - x_d - e_d$, and e_d is designed as follows

$$e_d = \begin{cases} b_0 + b_1 t + b_2 t^2 + b_3 t^3, & if\ 0 \le t \le T_f, \\ 0, & if\ t > T_f, \end{cases} \tag{34}$$

with

$$\begin{aligned} b_0 &= e(0), b_1 = \dot{e}(0), \\ b_2 &= -3(e(0)/T_f^2) - 2(\dot{e}(0)/T_f), \\ b_3 &= 2(e(0)/T_f^3) + (\dot{e}(0)/T_f^2). \end{aligned} \tag{35}$$

The final sliding mode based incremental control law is as follows

$$u = u_0 - G^{-1}(x_0)(\ddot{x}_0 - \ddot{x}_d - \ddot{e}_d + C\dot{z} + Ks). \tag{36}$$

In order to identify the performance of the obtained sliding mode based incremental attitude controller, the 6-DOF numerical simulation is carried out on the Winged-Cone hypersonic aircraft model. The equations to compute the aerodynamic moments and forces and the other parameters about the aircraft can be found in [29].

In the simulation, the initial values of roll, yaw and pitch angles are respectively set as $-3°, 1°$ and $2.4°$; the initial value of roll, yaw and pitch angular rates are all set as 0; the design parameters are set as follows: $C = \mathrm{diag}(10, 10, 10)$, $K = \mathrm{diag}(10, 10, 10)$, $T_f = 2s$; the attitude reference signal is taken as $x_d = [0, 0, \vartheta_d]^{\mathrm{T}}$ with ϑ_d being generated by the guidance system; the simulation step is set as $T = 0.01$s; and the angular accelerations $\ddot{x}_0$ are computed by

$$\ddot{x}[k] = \frac{\dot{x}[k] - \dot{x}[k-1]}{T}. \tag{37}$$

The simulation results are shown in Figs.2 to Figs.4. It is easy to see that the reference signals are tracked very well with the tracking error being zero when $t \ge T_f$. The simulation results show the effectiveness of the control method proposed in this paper.

5 Conclusion

In this paper, a sliding mode based incremental output tracking control method is proposed for the HOFA system. It is proved that the proposed control method could ensure that the tracking error equal to zero after the user-assigned settling time. The proposed approach is further applied to the attitude tracking control of some high speed aircraft. The simulation results show the effectiveness of the obtained results.

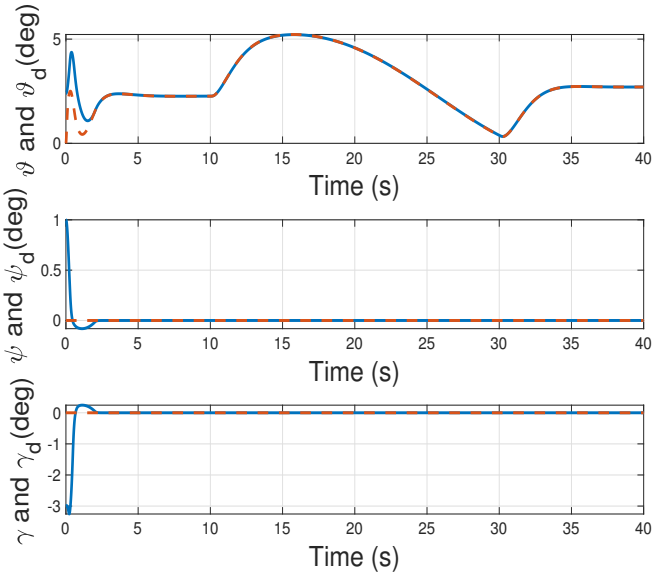

Fig. 2: The attitude angles and their reference signals.

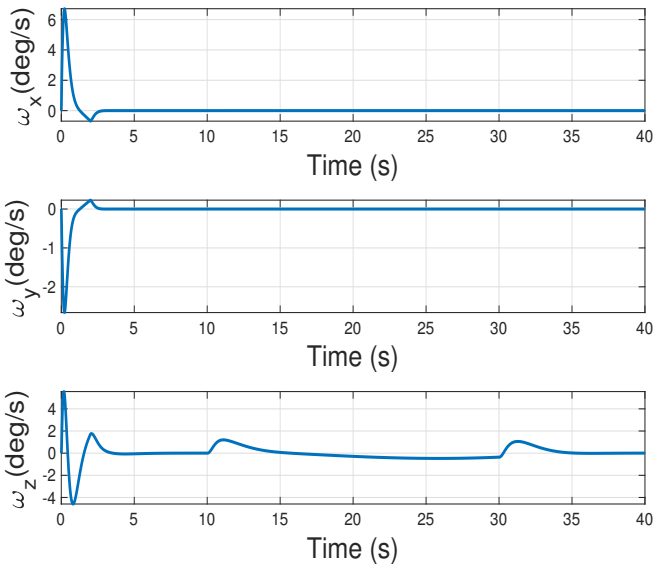

Fig. 3: The attitude angular velocities.

References

[1] R. Costa, Q. P. Chu, J. A. Mulder, "Reentry flight controller design using Nonlinear Dynamic Inversion," Journal of Spacecraft and Rockets, vol. 40, no. 1, pp. 64-71, Sep. 2003.

[2] S. H. Lane, R. F. Stengel, "Flight control design using Nonlinear Inverse Dynamics," Automatica, vol. 24, no. 4, pp. 471-483, Jul. 1998.

[3] T. Lombaerts, J. Kaneshige, S. Schuet, G. Hardy, B. L. Aponso, K. H. Shish, "Nonlinear Dynamic Inversion based attitude control for a hovering quad tiltrotor eVTOL vehicle," AIAA Scitech 2019 Forum, Jan. 2019.

[4] A. J. Ostroff, B. J. Bacon, "Enhanced NDI strategies for

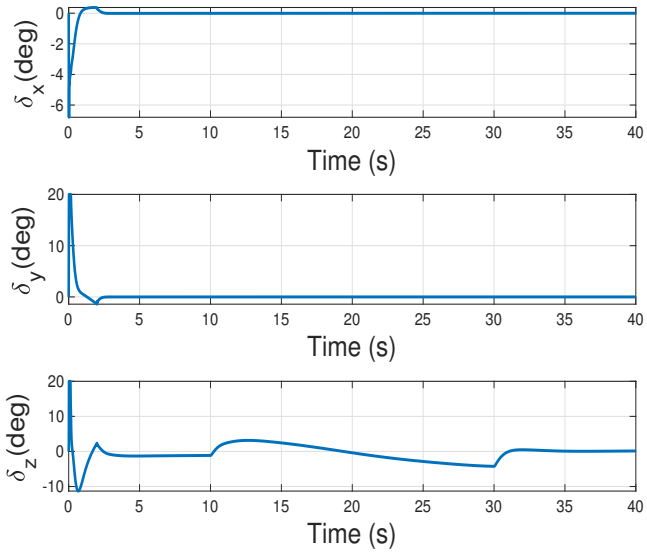

Fig. 4: The deflection angles of the control surfaces.

reconfigurable flight control," Proceedings of the American Control Conference, pp. 3631-3636, Aug. 2002.

[5] P. R. Smith, "A simplified approach to Nonlinear Dynamic Inversion based flight control," AIAA Atmospheric Flight Mechanics Conference, American Institute of Aeronautics and Astronautics, Aug. 1998.

[6] S. Sieberling, Q. P. Chu, J. A. Mulder, "Robust flight control using Incremental Nonlinear Dynamic Inversion and angular acceleration prediction," Journal of Guidance, Control and Dynamics, vol. 33, no. 6, pp. 1732-1742, Nov. 2010.

[7] J. Chang, Z. Guo, R. D. Breuker, X. Wang, "Predictor-based adaptive Incremental Nonlinear Dynamic Inversion for fault-tolerant flight control," IFAC-Papers OnLine, vol. 55, no. 6, pp. 730-736, Jun. 2022.

[8] E. Safwata, W. Zhanga, A. Kamelb, M. Kassemc, "Robustness analysis of modified Incremental Nonlinear Dynamic Inversion for small UAVs," Automatic Control and Computer Sciences, vol. 54, no. 2, pp. 128-138, Mar. 2020.

[9] S. Zhang, W. Han, Y. Zhang, "Finite time convergence Incremental Nonlinear Dynamic Inversion-based attitude control for flying-wing aircraft with actuator faults," Actuators, vol. 9, no. 70, pp. 1-21, Aug. 2020.

[10] T. J. L. Cervantes, S. H. Choi, B. S. Kim, "Flight control design using Incremental Nonlinear Dynamic Inversion with fixed-lag smoothing estimation." Int. J. Aeronaut. Space, vol. 21, no. 4, pp. 1047-1058, Jan. 2020.

[11] J. Chang, R. D. Breuker, X. Wang, "Adaptive nonlinear incremental flight control for systems with unknown control effectiveness," IEEE Trans. Ind. Electron, vol. 59, no. 1, pp. 862-867, Feb. 2023.

[12] X. Zhang, M. Ran, "Meta-Learning-Based Incremental Nonlinear Dynamic Inversion control for quadrotors with disturbances," Appl. Sci, vol. 13, no. 11844, pp. 1-16, Oct. 2023.

[13] X. Wang, E. J. van Kampen, Q. Chu, P. Lu, "Incremental sliding-mode fault-tolerant flight control," J. Guid. Control Dyn, vol. 42, no. 2, pp. 244-259, Feb. 2019.

[14] X. Wang, S. Sun, E. J. van Kampen, Q. Chu, "Quadrotor Fault Tolerant Incremental Sliding Mode Control driven by Sliding Mode Disturbance Observers," Aerospace Science and Technology, vol. 87, pp. 417-430, Apr. 2019.

[15] X. Wang, E.-J. van Kampen, Q. Chu, P. Lu, "Quadrotor fault-tolerant incremental nonsingular terminal sliding mode control," Aerospace Science and Technology, vol. 95, pp. 1-14, Oct. 2019.

[16] M. Cho, U. Jung, J. An, Y. Choi, C. Kim, "Adaptive trajectory tracking control for rotorcraft using incremental backstepping sliding mode control strategy," Int. J. Aerospace Engineering, vol. 2021, pp. 1-15, Jul. 2021.

[17] S. Liu, J. F. Whidborne, "Observer-Based incremental backstepping sliding-mode fault-tolerant control for blended-wing-body aircrafts," Neurocomputing, vol. 424, no. 2021, pp. 546-561, Aug. 2021.

[18] Z. He, J. Hu, Y. Wang, J. Cong, L. Han, M. Su, "Incremental backstepping sliding-Mode trajectory control for tailless aircraft with stability enhancer," Aerospace, vol. 9, no. 352, pp. 1-22, Jun. 2022.

[19] J. Liu, J. Shan, J. Wang, J. Rong, "Incremental sliding-mode control and allocation for morphing-wing aircraft fast manoeuvring," Aerospace Science and Technology, vol. 131, pp. 1-15, Oct. 2022.

[20] G. Duan, "High-order system approaches - I. Fully actuated systems and parametric designs," Acta Automatica Sinica, vol. 46, no. 7, pp. 1333-1345, Jul. 2020.(in Chinese)

[21] G. Duan, "High-order fully actuated system approaches: Part IV. Adaptive control and high-order backstepping," Int. J. Syst. Sci., vol. 52, no. 5, pp. 972-989, Apr. 2021.

[22] G. Duan, "High-order fully actuated system approaches: Part III. Robust control and high-order backstepping," Int. J. Syst. Sci., vol. 52, no. 5, pp. 952-971, Apr. 2021.

[23] G. Duan, "High-order fully actuated system approaches: Part VIII. optimal control with application in spacecraft attitude stabilisation," Int. J. Syst. Sci., vol. 53, no. 1, pp. 54-73, Jun.2022.

[24] G. Duan, "High-order fully-actuated system approaches: Part VI. Disturbance attenuation and decoupling," Int. J. Syst. Sci., vol. 52, no. 10, pp. 2161-2181, Jul. 2021.

[25] M. Hou, F. Tan, F. Han, G. Duan, "Adaptive sliding mode control of uncertain nonlinear systems with preassigned settling time and its applications," Int J Robust Nonlinear Control, vol. 29, no. 18, pp. 6438-6462, Sep. 2019.

[26] G. Duan, "High-order fully actuated system approaches: part VII. Controllability, stabilisability and parametric designs," Int. J. Syst. Sci., vol. 52, no. 14, pp. 3091-3114, Oct. 2021.

[27] M. Hou, S. Wang, G. Duan, F. Tan and Y. Liu, "Practical Finite-Time Control of Missiles-A Terminal Sliding Mode Approach," Proceedings of the 36th Chinese Control Conference, Jul. 2017.

[28] G. Duan, "Missile attitude control-A direct parametric approach," in Proceedings of the 33rd Chinese Control Conference, pp. 2414-2421, Jul. 2014.

[29] P. Wang, "Research on Attitude Control Method for Hypersonic Cruise Vehicle," Hunan: National University of Defense Technology, Oct. 2013.

Proceedings of the 3rd Conference on Fully Actuated System Theory and Applications
May 10-12, 2024, Shenzhen, China

High-Order Sliding Mode Control for Flexible Servo Systems using Fully Actuated System Approach

Yuzhong Wang[1], Guangren Duan[1,2]*, Ping Li[1]

1. the Center for Control Science and Technology, Southern University of Science and Technology, Shenzhen, P. R. China
E-mail: wangyz3@sustech.edu.cn,
E-mail: lip3@sustech.edu.cn

2. the Center for Control Theory and Guidance Technology, Harbin Institute of Technology, Harbin, P. R. China
E-mail: duangr@sustech.edu.cn

Abstract: This paper presents a high-order sliding mode control scheme for servo systems with the unknown disturbance via the fully actuated system (FAS) approach. Firstly, a three-order sliding surface based on the FAS approach is developed, and the integral part of the sliding surface contains the dynamical compensator, which can optimize the control performance of the system. Then, the asymptotical stability for sliding mode dynamics is ensured based on the Lyapunov technology. In addition, a sliding mode controller is proposed such that the unknown disturbance can be compensated and the trajectories of the system can be driven onto the sliding surface in a finite time. Finally, the effectiveness of the proposed approach is validated through comparative simulations.

Key Words: Sliding mode control (SMC), FAS approach, the unknown disturbance, the dynamical compensator.

1 Introduction

Servo systems play a pivotal role in diverse processes, encompassing industrial applications and mechatronic systems. Wherein, velocity control assumes paramount significance. Consequently, numerous studies are dedicated to designing velocity control schemes that achieve regulation, tracking accuracy, robustness, and energy efficiency [1, 2]. Several advanced control algorithms, including proportional-integral-derivative (PID) control [3, 4], sliding mode control (SMC) [5], and adaptive control [6] etc. have been employed to enhance the control performance of servo systems. Servo systems pertain to a category of underactuated mechanical systems where the dimension of control input is less than the degrees of freedom in motion [7]. The presence of underactuation poses challenges and complexities in designing and analyzing control systems. Servo systems inevitably encounter parameter uncertainties and unknown disturbances due to environmental changes [8]. Although high-gain feedback control is commonly employed to enhance disturbance rejection, it can potentially induce mechanical resonance and even lead to equipment damage. To deal with this problem, a state feedback controller with a dynamical compensator is proposed based on the fully actuated system (FAS) approach. However, unknown disturbances still cannot be fully compensated.

The SMC algorithm is highly effective and robust, as it demonstrates insensitivity to model uncertainties, external disturbances, and parameter variations [9–12]. Over the past few decades, SMC has been extensively applied in various physical systems such as robot manipulators, automotive engines, and power systems [12–14]. Consequently, the design problem of SMC has garnered significant attention with notable achievements for both linear and nonlinear systems[15–17]. In [16], a design method for sliding mode control is developed for a class of fully nonlinear systems in generalized regular form, considering both input distribution uncertainty and system uncertainties. Based on the generalized regular form, a new nonlinear sliding surface is developed, and the uniform ultimate stability of the corresponding sliding mode dynamics is analyzed. However, the research on sliding mode control of nonlinear systems is still not very sufficient.

As widely acknowledged, the physical world is predominantly governed by a set of fundamental physical laws. These laws have been employed to construct various basic second-order systems for modeling purposes, typically characterized as fully actuated [18]. Consequently, approaches towards higher order fully actuated (HOFA) systems have gradually emerged [18–20]. According to the FAS approach, a majority of physical nonlinear systems can be represented as a fully actuated model, which serves as an alternative system description form and offers enhanced universality, simplicity, and flexibility for the design and analysis of nonlinear systems. Thus, the HOFA system approach has received wide research [21–27]. Therein, the focus of [21] is on the cooperative control of high-order fully actuated networked multiagent systems (HOFA-NMASs). For effectively facilitating cooperation among HOFA-NMASs and actively compensating for communication delays, a proportional-integral (PI) predictive control scheme is proposed. Moreover, [22] develops an optimal tracking control strategy for a discrete-time nonlinear time-varying FAS with full state constraints and time-varying delays. To achieve this, a predictive controller by integrating the predictive control scheme and the constraint elimination technique into FAS approaches is designed. In addition, [25] investigates the problem of adaptive event-triggered control for a class of uncertain HOFA systems. An adaptive technique is employed to estimate the unknown parameters, while concurrently co-designing the controller and its event-triggered mechanism in order to optimize energy efficiency during signal transmission.

This work has been partially supported by Shenzhen Key Laboratory of Control Theory and Intelligent Systems ZDSYS20220330161800001, Shenzhen Science and Technology Program under grant No. KQTD20221101093557010 and the 8th batch of post-doctoral Innovative Talent Support Program BX20230150.

Motivated by the above discussions, this paper studies high-order sliding mode control for FS systems with the unknown disturbance using the FAS approach. The typical characteristics of FS systems are described by a two-mass system (TMS) model [27]. The main contributions of this study are summarized as follows:

1) A three-order sliding surface based on the FAS approach is proposed, and the dynamical compensator is added in the integral part of the sliding surface, which can optimize the control performance of the system.

2) The asymptotical stability for sliding mode dynamics is ensured based on the Lyapunov technology. Then, a sliding mode controller based on the FAS approach is proposed to match the unknown disturbance.

Notation: In this paper, R^r stands for the r-dimensional Euclidean space; $P < 0$ is a negative definite matrix.

2 System descriptions

2.1 HOFA model with uncertain nonlinearity

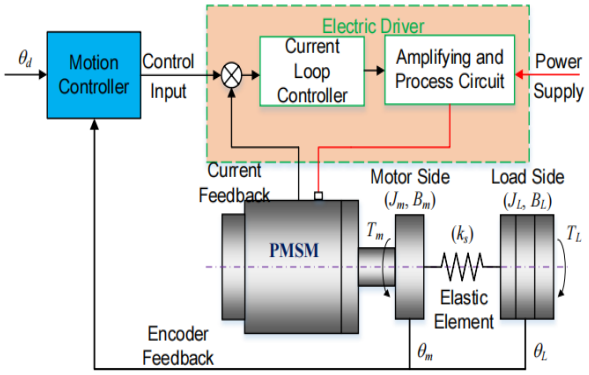

Fig. 1: The diagram of TMS configuration.

The diagram of the TMS configuration is depicted in Fig. 1, comprising two main components: the mechanical subsystem and the electrical subsystem. In the mechanical subsystem, a spring connects the driving shaft and the load shaft, with negligible impact on modeling due to its low damping factor. The electrical subsystem employs a permanent magnetic synchronous motor (PMSM) for supplying driving torque, while the servo driver operates in torque control mode. Typically, achieving a control bandwidth exceeding 1000 Hz through current closed-loop enables significantly faster response compared to the mechanical subsystem. Consequently, neglecting current-loop dynamics simplifies TMS modeling [27].

$$\begin{cases} J_L\ddot{\theta}_L + B_L\dot{\theta}_L + T_L = K_s\left(\theta_m - \theta_L\right) \\ J_m\ddot{\theta}_m + B_m\dot{\theta}_m + K_s\left(\theta_m - \theta_L\right) = u, \end{cases} \tag{1}$$

where θ_L denotes the motor shaft, θ_m is load shaft position, J_L is the moment of inertia of motor, J_m is the moment of inertia of load, B_L is the damping coefficient of motor, B_m is the damping coefficient of load, K_s and T_L are the stiffness of spring and denotes the external disturbance, respectively, u is the control input torque.

Based on [27], the following HOFA model can be obtained:

$$\theta_L^{(4)} = -\beta_3\dddot{\theta}_L - \beta_2\ddot{\theta}_L - \beta_1\dot{\theta}_L + b_0u - d_1, \tag{2}$$

where

$$\begin{cases} \beta_1 = \frac{1}{J_mJ_L}K_s\left(B_m + B_L\right) \\ \beta_2 = \frac{1}{J_mJ_L}\left(K_sJ_m + K_sJ_L + B_mB_L\right) \\ \beta_3 = \frac{1}{J_mJ_L}\left(J_mB_L + B_mJ_L\right) \\ b_0 = \frac{K_s}{J_mJ_L}. \end{cases}$$

d_1 represents the external disturbance given by

$$d_1 = \frac{1}{J_mJ_L}\left(J_m\ddot{T}_L + B_m\dot{T}_L + K_sT_L\right).$$

Assumption 1 *[25]*
1). The system states θ_L, $\dot{\theta}_L$, θ_m, and $\dot{\theta}_m$ are measurable;
2). The system parameters are constants and their deviations are bounded;
3). The load disturbance is bounded and differentiable.
4). d_1 is a bounded external disturbance satisfying $\|d_1\| \leq d_{\max}$.

Remark 1 *It can be seen that the HOFA model is same as the literature [27]. A state feedback control law with a dynamical compensator is proposed for the HOFA system (2) in [27]. However, the external disturbance is not well compensated by the proposed controller in [27]. To deal with this problem, a sliding mode control method based on the HOFA approach is developed in this paper.*

2.2 Three-order sliding surface

In the following, the three-order sliding function is designed as

$$s(t) = \dddot{\theta}_L + \int_0^t \sum_{i=0}^{3} k_i\theta_L^{(i)}(v) - K_\omega\omega(v)\,dv, \tag{3}$$

where $\dot{\omega} = a_\omega\omega + b_x\theta$, $\theta = \begin{bmatrix} \theta_L & \dot{\theta}_L & \ddot{\theta}_L & \dddot{\theta}_L \end{bmatrix}^T$, $K_\omega = \begin{bmatrix} k_{\omega1} & k_{\omega2} & k_{\omega3} & k_{\omega4} \end{bmatrix}^T$.

Then, we have

$$\dot{s}(t) = \theta_L^{(4)} + \sum_{i=0}^{3} k_i\theta_L^{(i)} - K_\omega\omega, \tag{4}$$

When $s(t) = \dot{s}(t) = 0$, an equivalent control law can be developed:

$$u_{eq} = \frac{1}{b_0}\left(\sum_{i=1}^{3}\beta_i\theta_L^{(i)} - \sum_{i=0}^{3}k_i\theta_L^{(i)} + K_\omega\omega + d_1\right), \tag{5}$$

Then, the sliding mode dynamics is obtained as:

$$\theta_L^{(4)} = -\sum_{i=0}^{3}k_i\theta_L^{(i)} + K_\omega\omega, \tag{6}$$

Let $k_{x0} = -\frac{1}{b_0}k_0$, $k_{xi} = \frac{1}{b_0}(\beta_i - k_i)$, $i = 1, 2, 3$. The closed-loop system (6) can be transformed as:

$$\begin{bmatrix} \dot{\theta} \\ \dot{\omega} \end{bmatrix} = \begin{bmatrix} A + BK_x & K_\omega \\ b_x & a_\omega \end{bmatrix}\begin{bmatrix} \theta \\ \omega \end{bmatrix}, \tag{7}$$

where

$$A = \begin{bmatrix} 0 & 1 & 0 & 0 \\ 0 & 0 & 1 & 0 \\ 0 & 0 & 0 & 1 \\ 0 & -\beta_1 & -\beta_2 & -\beta_3 \end{bmatrix}, B = \begin{bmatrix} 0 \\ 0 \\ 0 \\ b_0 \end{bmatrix},$$

$$K_x = \begin{bmatrix} k_{x0} & k_{x1} & k_{x2} & k_{x3} \end{bmatrix}.$$

Remark 2 *In this paper, a three-order sliding surface based on the HOFA system approach is proposed. At the same time, the pole assignment component and the dynamical compensator are added in the integral part of the sliding surface. This not only ensures the stability of the system, but also optimizes the control performance of the system through the dynamic compensator.*

2.3 Stability analysis

In the theorems, the asymptotic stability of the closed-loop system (7) is guaranteed based on the Lyapunov technology. Then, the state trajectories of the closed-loop system (6) can be driven onto the sliding surface in a finite time.

Theorem 1. Consider HOFA system (2). For given vector b_x, matrices A, B, K_ω , if there exist a positive matrix $P > 0$ such that the following inequality holds

$$\frac{1}{2}\begin{bmatrix} A+BK_x & BK_\omega \\ b_x & a_\omega \end{bmatrix}^T P + \frac{1}{2}P\begin{bmatrix} A+BK_x & BK_\omega \\ b_x & a_\omega \end{bmatrix} < 0, \tag{8}$$

then the closed-loop system (7) can asymptotically stabilize.

Proof. Choose the following Lyapunov function

$$V(t) = \frac{1}{2}\begin{bmatrix} \theta_L \\ \omega \end{bmatrix}^T P \begin{bmatrix} \theta_L \\ \omega \end{bmatrix}. \tag{9}$$

Then, we have

$$\begin{aligned}\dot{V}(t) =& \frac{1}{2}\begin{bmatrix} \theta \\ \omega \end{bmatrix}^T \begin{bmatrix} A+BK_x & BK_\omega \\ b_x & a_\omega \end{bmatrix}^T P \begin{bmatrix} \theta \\ \omega \end{bmatrix} \\ &+ \frac{1}{2}\begin{bmatrix} \theta \\ \omega \end{bmatrix}^T P \begin{bmatrix} A+BK_x & BK_\omega \\ b_x & a_\omega \end{bmatrix}\begin{bmatrix} \theta \\ \omega \end{bmatrix}.\end{aligned} \tag{10}$$

Based on (8), we get $\dot{V}(t) < 0$ when $\begin{bmatrix} \theta \\ \omega \end{bmatrix} \neq 0$. Thus, the asymptotic stability of the system (2) can be guaranteed. This completes the proof.

Remark 3 *Note that the first-order dynamical compensator is applied as an illustrative example in [27], and $K_\omega = k_{\omega 1}$, $a_\omega = a_{\omega 1}$, $b_x = \begin{bmatrix} b_{x1} & b_{x2} & b_{x3} & b_{x4} \end{bmatrix}$ are obtained. By using the method in [27], the system (6) can be transformed into the following HOFA model:*

$$\theta_L^{(5)} + \sum_{i=0}^{4}\gamma_i\theta_L^{(i)} = 0, \tag{11}$$

with

$$\begin{cases} \gamma_0 = b_0 b_{x1} a_{\omega 1} - b_0 k_{\omega 1} b_{x1} \\ \gamma_1 = -b_0 k_{x1} - (\beta_1 - b_0 k_{x2})\, a_{\omega 1} - b_0 k_{\omega 1} b_{x2} \\ \gamma_2 = \beta_1 - b_0 k_{x2} - (\beta_2 - b_0 k_{x3})\, a_{\omega 1} - b_0 k_{\omega 1} b_{x3} \\ \gamma_3 = \beta_2 - b_0 k_{x3} - (\beta_3 - b_0 k_{x3})\, a_{\omega 1} - b_0 k_{\omega 1} b_{x3} \\ \gamma_4 = \beta_3 - b_0 k_{x4} - a_{\omega 1}. \end{cases} \tag{12}$$

Then, the characteristic polynomial can be designed as

$$s^5 + \sum_{i=0}^{4}\gamma_i s^i = \prod_i^5 (s+\lambda_i), \tag{13}$$

with $s_i = -\lambda_i$, $\lambda_i > 0$, $i = 1, 2, 3, 4, 5$.

The control gains can be deduced as

$$\begin{cases} k_{\omega 1} = -\frac{1}{b_0 b_{x1}}\gamma_0 \\ k_{x1} = -\frac{1}{b_0}\gamma_1 - k_{\omega 1} b_{x2} \\ k_{x2} = -\frac{1}{b_0}(\gamma_2 - \beta_1) - k_{\omega 1} b_{x3} \\ k_{x3} = -\frac{1}{b_0}(\gamma_3 - \beta_2) - k_{\omega 1} b_{x4} \\ k_{x4} = -\frac{1}{b_0}(\gamma_4 - \beta_3), \end{cases} \tag{14}$$

where b_{xi}, $i = 1, 2, 3, 4$, are arbitrarily given parameters satisfying $b_{x1} \neq 0$. Thus, the explicit solution of the control gains can still be obtained in this paper.

2.4 SMC law synthesis

In this subsection, the state trajectories of the closed-loop system (7) can be driven onto the sliding surface in a finite time and maintain there by the developed SMC law.

Theorem 2. Consider HOFA system (2). For given positive constants $d_{\max} > 0$ and $\varrho > 0$, if the sliding surface is designed as (3), then the state trajectories of the closed-loop system in (6) can be driven onto the sliding surface $s(t) = 0$ in a finite time by the following SMC law:

$$\begin{aligned}u(t) =& \frac{1}{b_0}(\sum_{i=0}^{3}\beta_i\theta_L^{(i)}(t) - \sum_{i=0}^{3}k_i\theta_L^{(i)} + K_\omega\omega(t) \\ &- (d_{\max} + \varrho)\mathrm{sign}(s(t))).\end{aligned} \tag{15}$$

Proof. Choose the following Lyapunov function:

$$V(t) = \frac{1}{2}s^T(t)s(t). \tag{16}$$

Then, we have

$$\begin{aligned}\dot{V}(t) =& s^T(t)\dot{s}(t) \\ =& s^T(t)(\theta_L^{(4)} + \sum_{i=0}^{3}k_i\theta_L^{(i)} - K_\omega\omega) \\ =& s^T(t)(-\beta_3\dddot{\theta}_L - \beta_2\ddot{\theta}_L - \beta_1\dot{\theta}_L + b_0 u \\ &- d_1 + \sum_{i=0}^{3}k_i\theta_L^{(i)} - K_\omega\omega) \\ =& s^T(t)(-\beta_3\dddot{\theta}_L - \beta_2\ddot{\theta}_L - \beta_1\dot{\theta}_L + \sum_{i=0}^{3}\beta_i\theta_L^{(i)} \\ &- \sum_{i=0}^{3}k_i\theta_L^{(i)} + K_\omega\omega - (d_{\max} + \varrho)\mathrm{sign}(s(t)) \\ &- d_1 + \sum_{i=0}^{3}k_i\theta_L^{(i)} - K_\omega\omega) \\ \leq& -\varrho\|s(t)\|, \quad \forall\|s(t)\| \neq 0.\end{aligned} \tag{17}$$

Thus, the closed-loop system (6) states will be driven into sliding surface in a finite time. This completes the proof.

Remark 4 *Different with the literature [27], based on the FAS approach, a sliding mode control with a first-order dynamical compensator law is designed in (15). The external disturbance can be matched by $d_{\max}\mathrm{sign}(s(t))$.*

3 Experimental Results

To verify the effectiveness of the proposed method, the controller algorithm is implemented using the function of MATLAB/ Simulink module in this section.

The system parameters are same as [27]. The proposed approach is demonstrated to be superior through a comparison with the following two control approaches.

When we choose a sine disturbance, the results of the comparison are shown in Figs. 2-4.

S-FAS approach This approach has been used in [27]. Output position and output velocity under sine disturbance are shown in Figs. 2-3. We can see from the picture, and the curve fluctuations of output position and output velocity are very large.

DCSMC-FAS approach This is the proposed SMC-FAS approach based on a dynamical compensator. The SMC law is developed in (15). The results shows that the curve fluctuations of output position and output velocity are very small.

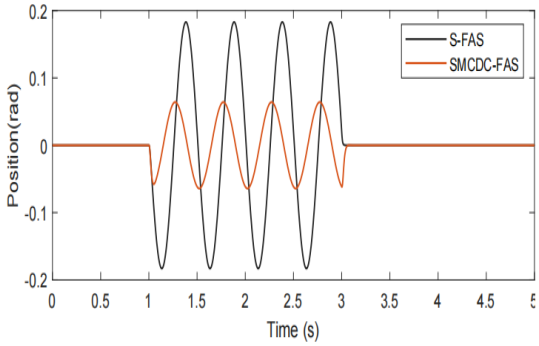

Fig. 2: Output position under sine disturbance.

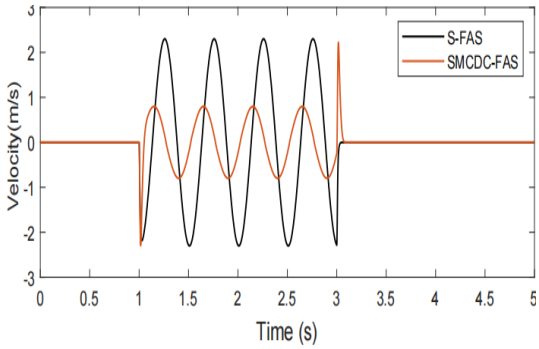

Fig. 3: Output velocity under sine disturbance.

When we choose a ramp disturbance, the results of the comparison are shown in Figs. 5-6.

S-FAS approach Output position under ramp disturbance is ploted in Figs. 5-6. Similarly, the curve fluctuations of output position is very large.

DCSMC-FAS approach This is the proposed SMC-FAS approach based on a dynamical compensator. The SMC law is developed in (15). The results shows that the curve fluctuations of output position is very small.

4 Conclusions

In this paper, the high-order SMC for FS systems with unknown disturbance via the FAS approach has been studied.

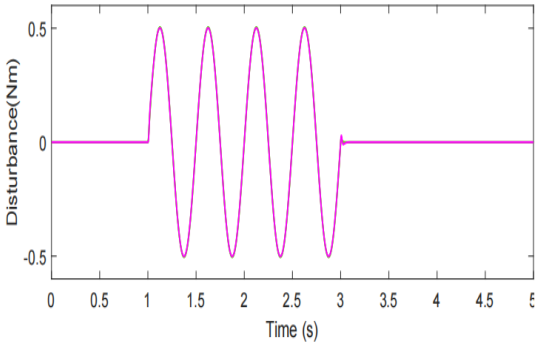

Fig. 4: Sine disturbance.

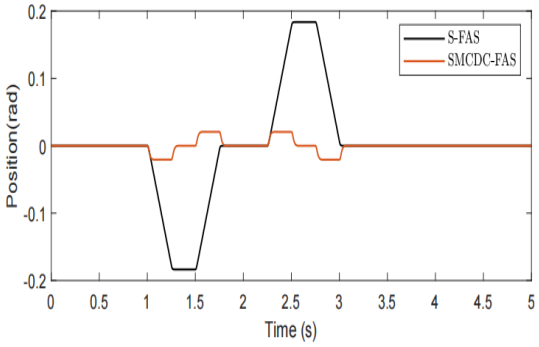

Fig. 5: Output position under ramp disturbance.

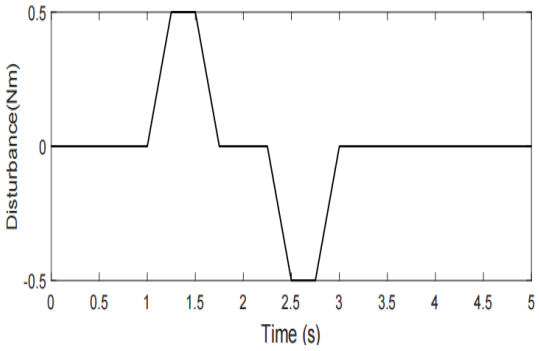

Fig. 6: Ramp disturbance.

The three-order sliding surface with the dynamical compensator has been designed. Then, the asymptotical stability of sliding mode dynamics has been obtained based on the Lyapunov technology even if there exists the unknown disturbance. Then, a sliding mode controller has been proposed such that the trajectories of the system can be driven onto the sliding surface in a finite time. Finally, a comparative simulation has been developed to illustrate the effectiveness of the proposed approach.

On the other hand, the small embedded microprocessors have been widely applied in industrial equipment, including the FS systems. Thus, the FS systems can be treated as networked control systems, which are often implemented over networks, where controllers communicate with actuators and/or sensors through shared networks. In such implementation, a control task consists of sampling physical signals. However, the network communication resources are usually limited. Thus, in future studies, the proposed method can be extended to event-triggered sliding mode control for

flexible servo systems using the FAS approach.

References

[1] A Ramírez, R Garrido, and S Mondié, "Velocity control of servo systems using an integral retarded algorithm," *ISA Transactions*, vol. 458, pp. 357C366, 2015.

[2] P. Li and G. Duan, "High-order fully actuated control approaches of flexible servo systems based on singular perturbation theory," *IEEE/ASME Transactions on Mechatronics*, vol. 28, no. 6, pp. 3386-3397, 2023.

[3] G. Zhang and J. Furusho, "Speed control of two-inertia system by PI/PID control," *IEEE Trans. Ind. Electron.*, vol. 47, no. 3, pp. 603C609, 2000.

[4] G. Pratt, P. Willisson, C. Bolton, and A. Hofman, "Late motor processing in low-impedance robots: Impedance control of series-elastic actuators," *Proc. Amer. Control Conf.*, Boston, MA, USA, 2004, pp. 3245C3251.

[5] V. Q. Leu, H. H. Choi and J. -W. Jung, "Fuzzy sliding mode speed controller for PM synchronous motors with a load torque observer," *IEEE Transactions on Power Electronics*, vol. 27, no. 3, pp. 1530-1539, 2012.

[6] Y. Wang, C. Wen, and X. Li, "Event-Based Model Reference Adaptive Tracking," *IEEE Transactions on Automatic Control*, doi: 10.1109/TAC.2023.3292745, 2023.

[7] K. Rsetam, Z. Cao and Z. Man, "Design of robust terminal sliding mode control for underactuated flexible joint robot," *IEEE Transactions on Systems, Man, and Cybernetics: Systems*, vol. 52, no. 7, pp. 4272-4285, 2022.

[8] H. Wang, Y. Pan, S. Li and H. Yu, "Robust sliding mode control for robots driven by compliant actuators," *IEEE Transactions on Control Systems Technology*, vol. 27, no. 3, pp. 1259-1266, 2019.

[9] Y. Xia, and Y. Jia, "Robust sliding-mode control for uncertain time-delay systems: an LMI approach," *IEEE Transactions on Automatic Control*, vol. 48, no. 6, pp. 1086-1091, 2003.

[10] Y. H. Roh, J. H. Oh, and E. Usai, "Robust stabilization of uncertain input-delay systems by sliding mode control with delay compensation," *Automatica,* vol. 35, no. 11, pp. 1861-1865, 1999.

[11] Y. G. Niu and C. W. D. Ho, "Robust observer design for It stochastic time-delay systems via sliding mode control," *Systems & Control Letters,* vol. 55, no. 10, pp. 781-793, 2006.

[12] G. Bartolini, A. Pisano, E. Punta, and U. Elio, "A survey of applications of second-order sliding mode control to mechanical systems," *International Journal of control*, vol. 76, pp. 875-892, 2003.

[13] S. Islam, P. X. Liu, and J. Chen, "Robust sliding mode control for robot manipulators," *IEEE Transactions on industrial electronics*, vol. 58, no. 6, pp. 2444-2453, 2010.

[14] L. Wang, T. Chai, and L. Zhai, "Neural-network-based terminal sliding-mode control of robotic manipulators including actuator dynamics," *IEEE Transactions on industrial electronics*, vol. 56, no. 9, pp. 3296-3304, 2009.

[15] Y. Zhao, X. Li and S. Song. "Observer-based sliding mode control for stabilization of mismatched disturbance systems with or without time delay," *IEEE Transactions on Systems, Man, and Cybernetics: Systems*, vol. 51, no. 12, pp. 7337-7345, 2021.

[16] Z. Mao, X. -G. Yan, B. Jiang and S. K. Spurgeon. "Sliding mode control of nonlinear systems with input distribution uncertainties," *IEEE Transactions on Automatic Control*, vol. 68, no. 10, pp. 6208-6215, 2023.

[17] B. Lu, Y. Fang and N. Sun. "Continuous sliding mode control strategy for a class of nonlinear underactuated systems," *IEEE Transactions on Automatic Control*, vol. 63, no. 10, pp. 3471-3478, 2018.

[18] R. G. Duan, "High-order system approaches: I. Full-actuation and parametric design," *Acta Automatica Sinica*, vol. 46, no. 7, pp. 1333-1345, 2020.

[19] R. G. Duan, "High-order system approaches: II. Controllability and fully-actuation," *Acta Automatica Sinica*, vol. 46, no. 8, pp. 1571-1581, 2020.

[20] R. G. Duan, "High-order system approaches: III. observability and observer design," *Acta Automatica Sinica*, vol. 46, no. 9, pp. 1885-1895, 2020.

[21] D. -W. Zhang, G. -P. Liu and L. Cao, "Proportional integral predictive control of high-order fully actuated networked multiagent systems with communication delays," *IEEE Transactions on Systems, Man, and Cybernetics: System*, vol. 53, no. 2, pp. 801-812, 2023.

[22] X. Wang and G. Duan, "Fully actuated system approaches: Predictive elimination control for discrete-time nonlinear time-varying systems with full state constraints and time-varying delays," *IEEE Transactions on Circuits and Systems I: Regular Papers*, DOI: 10.1109/TCSI.2023.3323454, 2023.

[23] Q. Huang, J. Sun and C. Zhang, "High-order fully actuated system approach to robust control of impulsive systems," *IEEE Transactions on Circuits and Systems II: Express Briefs*, DOI: 10.1109/TCSII.2023.3324199., 2023.

[24] D. -W. Zhang, G. -P. Liu and L. Cao, "Secure predictive coordinated control of high-order fully actuated networked multiagent systems under random DoS attacks," *IEEE Transactions on Cybernetics*, DOI: 10.1109/TCYB.2023.3324179., 2023.

[25] R. Meng, C. Hua, K. Li and P. Ning, "Adaptive event-triggered control for uncertain high-order fully actuated system," *IEEE Transactions on Circuits and Systems II: Express Briefs*, vol. 69, no. 11, pp. 4438-4442, 2022.

[26] Y. Wang, G. Duan and P. Li, "Event-triggered aAdaptive sliding mode control of uncertain nonlinear systems based on fully actuated system approach," *IEEE Transactions on Circuits and Systems II: Express Briefs*, doi: 10.1109/TCSI-I.2024.3353316, 2024.

[27] P. Li and G. Duan, "High-order fully actuated control approach for flexible servo systems using dynamical compensator," *2023 2nd Conference on Fully Actuated System Theory and Applications (CFASTA)*, Qingdao, China, pp. 862-867, 2023.

Proceedings of the 3rd Conference on Fully Actuated System Theory and Applications
May 10-12, 2024, Shenzhen, China

A Fully Actuated System Approach to Control of the 3D Cubli: Theory and Experiments

Zhijie Liu[1], Fuxing Yao[1], Guangren Duan[1,2], and He Kong[1]

1. Shenzhen Key Laboratory of Control Theory and Intelligent Systems, Southern Uni. of Sci. and Tech., Shenzhen 518055, China
E-mail: 12332642,12331363@mail.sustech.edu.cn; kongh@sustech.edu.cn

2. Center for Control Theory and Guidance Technology, Harbin Institute of Technology, Harbin 150001, China
E-mail: g.r.duan@hit.edu.cn/duangr@sustech.edu.cn

Abstract: The 3D Cubli is an interesting underactuated mechatronics system that has reaction wheels mounted on three of its faces and can balance on its corner or edge by applying controlled torques to the reaction wheels. Control of the 3D Cubli has attracted much attention in the literature, yet remains challenging due to strong nonlinearity and coupling inherent in the system, as well as adverse effects from external disturbances, unknown friction and other unmodeled dynamics that further intensify the difficulty of regulating system attitude. To address the above issues, this paper is concerned with high-order fully actuated (HOFA) system approach to control of the 3D Cubli. First, by adopting the concepts and tools from the recently developed fully actuated system approach, we transform the system dynamics of the Cubli into a nonlinear HOFA model. We leverage the full actuation property of the latter model to design a baseline controller to eliminate the nonlinearities inherent in the Cubli system. Second, a nonlinear observer is developed to estimate the additive system disturbance in real time. The estimated disturbance is then used to enhance the performance of the baseline controller. The stability of the closed-loop system has been rigorously established. Compared to the linearization-based LQR strategy, the proposed framework exhibits significantly better performance in hardware experiments that were conducted on a self-built 3D Cubli platform by the authors.

Key Words: HOFA system approaches, Underactuated Cubli, Nonlinear systems, Unmodeled dynamics, Nonlinear observer

1 Introduction

Control of underactuated systems has received much attention in the robotics and control community [1–3]. The 3D Cubli, introduced in [4], is an interesting underactuated mechatronics system that has reaction wheels mounted on three of its faces and can balance on its corner or edge by applying torques to the reaction wheels. Due to the potential applications (e.g., in space exploration [5]), control of the 3D Cubli has aroused considerable interest recently. A number of controller design frameworks have been proposed and examined for the 3D Cubli, including backstepping-based control [6], Linear Quadratic Regulator (LQR) [7, 8], etc.

In particular, Muehlebach et al. suggested a backstepping-based control scheme for the underactuated 3D Cubli system, which ensures the global stability of the system [6]. Gajamohan et al. designed a LQR-based controller for the 2D Cubli system and verified the effectiveness of this strategy through an experimental platform [7]. Furthermore, Gajamohan et al. employed a frequency-domain-based method to identify the parameters of the 3D Cubli, and achieved corner balancing based on the LQR-based controller, which was also validated through a 3D Cubli hardware system [8]. Recently, Hofer et al. introduced the one-wheel Cubli, a 3D inverted pendulum that can balance with a single reaction wheel [9]. They rederived the model of the system dynamics utilizing first principles and designed an LQR-based controller to stabilize the system in its upright equilibrium state.

This paper is concerned with control of the underactuated 3D Cubli that is influenced by unmodeled dynamics. Our interest in considering the above scenario is motivated by the fact that the motor within the Cubli system might experience unknown friction [10–12] or the system might not be perfectly built (in our self-built Cubli, the flying wheels are not installed symmetrically, resulting in structural imbalance).

Toward the goal of achieving satisfactory performance under unmodeled dynamics, we propose a fully actuated system approach to control the 3D Cubli. First, based on the concepts and tools from the recently developed fully actuated system approach [13–16], we transform the system dynamics of the Cubli into a nonlinear high-order fully actuated (HOFA) model. By leveraging the full actuation property of the latter model, we design a baseline controller to eliminate the nonlinearities inherent in the system. Afterward, a nonlinear observer is developed to estimate the additive system disturbance in real-time. The estimated disturbance is used to enhance the performance of the baseline controller. The stability of the closed-loop system has been rigorously established. Compared to the linearization-based LQR strategy [8], the proposed framework exhibits significantly better performance in hardware experiments that were conducted on our 3D Cubli platform.

2 Problem Formulation and Preliminaries

Consider the Cubli system depicted in Fig. 1. Table. 1 contains notations used in this paper, where $i = x, y, z$ and $j = 1, 2, 3$. Define $\mathbf{\Theta}_\omega \triangleq \mathrm{diag}(\Theta_{\omega 1}, \Theta_{\omega 2}, \Theta_{\omega 3})$ and $\hat{\mathbf{\Theta}}_0 \triangleq \mathbf{\Theta}_0 - \mathbf{\Theta}_{\mathrm{w}}$. The Lagrangian of the Cubli system is given by:

$$\begin{aligned}\mathcal{L} = &\frac{1}{2}\boldsymbol{\omega}_{\mathrm{h}}^{\mathrm{T}}\hat{\mathbf{\Theta}}_0\boldsymbol{\omega}_{\mathrm{h}} + \frac{1}{2}(\boldsymbol{\omega}_{\mathrm{h}} + \boldsymbol{\omega}_{\mathrm{w}})^{\mathrm{T}}\mathbf{\Theta}_{\mathrm{w}}(\boldsymbol{\omega}_{\mathrm{h}} + \boldsymbol{\omega}_{\mathrm{w}}) \\ &+ \boldsymbol{m}^{\mathrm{T}}\boldsymbol{g}.\end{aligned} \tag{1}$$

Based on Eq. (1), we can calculate the generalized momenta for the full Cubli system:

Zhijie Liu and Fuxing Yao contributed equally to this work. This work was supported by the Science, Technology, and Innovation Commission of Shenzhen Municipality, China, under Grant No. ZDSYS20220330161800001, and the Shenzhen Science and Technology Program under Grant No. KQTD20221101093557010. This work was also supported by the Science Center Program of the National Natural Science Foundation of China (NSFC) under Grant No. 62188101, as well as the NSFC under Grant No. 62350055.

Table 1: Relevant Parameters and Variables of the Cubli

Symbol	Description	Unit
$\boldsymbol{\Theta}_0$	Total moment of inertia of the Cubli	$\mathrm{kg}\cdot\mathrm{m}^2$
$\boldsymbol{\Theta}_{\mathrm{w}j}$	Moment of inertia of each reaction wheel	$\mathrm{kg}\cdot\mathrm{m}^2$
$\boldsymbol{m}$	Position vector from O to the center of gravity multiplied by the total mass	$\mathrm{kg}\cdot\mathrm{m}$
$\boldsymbol{g}$	Gravity vector	$\mathrm{m/s}^2$
$\boldsymbol{\omega}_{\mathrm{h}}$	Body angular velocity	$\mathrm{rad/s}$
$\boldsymbol{\omega}_{\mathrm{w}}$	Reaction wheel angular velocity	$\mathrm{rad/s}$
$\boldsymbol{T}$	Torque vector	$\mathrm{N}\cdot\mathrm{m}$
$\boldsymbol{D}$	Unmodeled dynamics	$\mathrm{N}\cdot\mathrm{m}$

$$\boldsymbol{p}_{\boldsymbol{\omega}_{\mathrm{h}}} \triangleq \frac{\partial \mathcal{L}^{\mathrm{T}}}{\partial \boldsymbol{\omega}_{\mathrm{h}}} = \hat{\boldsymbol{\Theta}}_0 \boldsymbol{\omega}_{\mathrm{h}} + \boldsymbol{\Theta}_{\mathrm{w}}(\boldsymbol{\omega}_{\mathrm{h}} + \boldsymbol{\omega}_{\mathrm{w}}), \tag{2}$$

$$\boldsymbol{p}_{\boldsymbol{\omega}_{\mathrm{w}}} \triangleq \frac{\partial \mathcal{L}^{\mathrm{T}}}{\partial \boldsymbol{\omega}_{\mathrm{w}}} = \boldsymbol{\Theta}_{\mathrm{w}}(\boldsymbol{\omega}_{\mathrm{h}} + \boldsymbol{\omega}_{\mathrm{w}}), \tag{3}$$

From Eqs. (1)-(3), based on the Euler-Lagrange equations, the dynamic model of the Cubli system can be established:

$$\dot{\boldsymbol{p}}_{\boldsymbol{\omega}_{\mathrm{h}}} = -\boldsymbol{\omega}_{\mathrm{h}} \times \boldsymbol{p}_{\boldsymbol{\omega}_{\mathrm{h}}} + \boldsymbol{m} \times \boldsymbol{g}, \tag{4}$$

$$\dot{\boldsymbol{p}}_{\boldsymbol{\omega}_{\mathrm{w}}} = \boldsymbol{T} + \boldsymbol{D}, \tag{5}$$

where $\boldsymbol{D}$ stands for the unmodeled dynamics. We make the following assumption for $\boldsymbol{D}$.

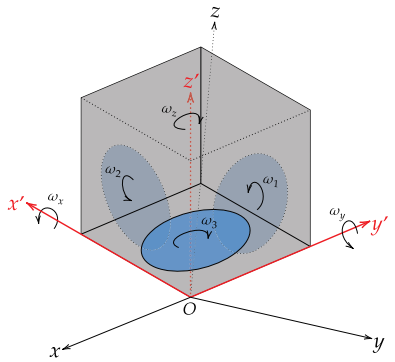

Fig. 1: Schematic diagram of the Cubli system. Note that 1) i and i' stand for the principle axis of the body fixed frame and inertial frame; 2) $\boldsymbol{O}$ denote the common origin of two coordinate systems.

Assumption 1. The unmodeled dynamics $\boldsymbol{D} \in \mathbb{R}^3$ is continuous, smooth, and bounded, and there exists a positive-definite scalar vector ρ such that the 1st order derivative of unmodeled dynamics satisfies: $\|\dot{\boldsymbol{D}}\| \leq \rho$.

3 Main Results

3.1 A HOFA Model for 3D Cubli

Based on the FA system approach [13–16], we next transform the Cubli system into a FA model. Firstly, based on Coriolis Theorem [17], Eq. (4) can be converted into:

$${}^{I}\dot{\boldsymbol{p}}_{\boldsymbol{\omega}_{\mathrm{h}}} = \boldsymbol{R}_B^I \dot{\boldsymbol{p}}_{\boldsymbol{\omega}_{\mathrm{h}}} + {}^{I}\boldsymbol{\omega}_{\mathrm{h}} \times {}^{I}\boldsymbol{p}_{\boldsymbol{\omega}_{\mathrm{h}}} = {}^{I}\boldsymbol{m} \times {}^{I}\boldsymbol{g}. \tag{6}$$

By inspecting Eq. (6), we know that the third element of the vector ${}^{I}\dot{\boldsymbol{p}}_{\boldsymbol{\omega}_{\mathrm{h}}}$ is always zero. Hence, one can extract the first two elements of ${}^{I}\boldsymbol{p}_{\boldsymbol{\omega}_{\mathrm{h}}}$ by denoting

$$\boldsymbol{x}_1 \triangleq \begin{bmatrix} {}^{I}\boldsymbol{p}_{\boldsymbol{\omega}_{\mathrm{h}}1} & {}^{I}\boldsymbol{p}_{\boldsymbol{\omega}_{\mathrm{h}}2} \end{bmatrix}^{\mathrm{T}} = \boldsymbol{N}\, {}^{I}\boldsymbol{p}_{\boldsymbol{\omega}_{\mathrm{h}}}, \tag{7}$$

where

$$\boldsymbol{N} = \begin{bmatrix} 1 & 0 & 0 \\ 0 & 1 & 0 \end{bmatrix}.$$

We also introduce matrix $\boldsymbol{M} = \begin{bmatrix} 0 & 1 \\ -1 & 0 \end{bmatrix}$ such that the cross product $\boldsymbol{a} \times \boldsymbol{b}$ of vectors $\boldsymbol{a}$ and $\boldsymbol{b}$ satisfies

$$\boldsymbol{N}(\boldsymbol{a} \times \boldsymbol{b}) = -\boldsymbol{a}_3 \boldsymbol{M}\boldsymbol{N}\boldsymbol{b} + \boldsymbol{b}_3 \boldsymbol{M}\boldsymbol{N}\boldsymbol{a}. \tag{8}$$

In light of (6), (8) and Coriolis Theorem, deriving the 1st order of derivatives of x_1 w.r.t. time yields:

$$\begin{aligned} \dot{\boldsymbol{x}}_1 &= \boldsymbol{N}\, {}^{I}\dot{\boldsymbol{p}}_{\boldsymbol{\omega}_{\mathrm{h}}} = \boldsymbol{N}({}^{I}\boldsymbol{m} \times {}^{I}\boldsymbol{g}) \\ &= -{}^{I}\boldsymbol{m}_3 \boldsymbol{M}\boldsymbol{N}\, {}^{I}\boldsymbol{g} - |\boldsymbol{g}|\, \boldsymbol{M}\boldsymbol{N}\, {}^{I}\boldsymbol{m} \\ &= -|\boldsymbol{g}|\, \boldsymbol{M}\boldsymbol{N}\, {}^{I}\boldsymbol{m}. \end{aligned} \tag{9}$$

One can also calculate the second and third orders of derivatives of x_1 w.r.t. time, and obtain:

$$\begin{aligned} \ddot{\boldsymbol{x}}_1 &= -|\boldsymbol{g}|\, \boldsymbol{M}\boldsymbol{N}\, {}^{I}\dot{\boldsymbol{m}} \\ &= -|\boldsymbol{g}|\, \boldsymbol{M}\boldsymbol{N}(\boldsymbol{R}_B^I \dot{\boldsymbol{m}} + {}^{I}\boldsymbol{\omega}_{\mathrm{h}} \times {}^{I}\boldsymbol{m}) \\ &= -|\boldsymbol{g}|\, \boldsymbol{M}\boldsymbol{N}({}^{I}\boldsymbol{\omega}_{\mathrm{h}} \times {}^{I}\boldsymbol{m}), \end{aligned} \tag{10}$$

and

$$\begin{aligned} \boldsymbol{x}_1{}^{(3)} &= -|\boldsymbol{g}|\, \boldsymbol{M}\boldsymbol{N}({}^{I}\dot{\boldsymbol{\omega}}_{\mathrm{h}} \times {}^{I}\boldsymbol{m} + {}^{I}\boldsymbol{\omega}_{\mathrm{h}} \times {}^{I}\dot{\boldsymbol{m}}) \\ &= -|\boldsymbol{g}|\, \boldsymbol{M}\boldsymbol{N}({}^{I}\dot{\boldsymbol{\omega}}_{\mathrm{h}} \times {}^{I}\boldsymbol{m}) \\ &\quad -|\boldsymbol{g}|\, \boldsymbol{M}\boldsymbol{N}[{}^{I}\boldsymbol{\omega}_{\mathrm{h}} \times ({}^{I}\boldsymbol{\omega}_{\mathrm{h}} \times {}^{I}\boldsymbol{m})]. \end{aligned} \tag{11}$$

Then, by utilizing (2) and (3) , one has:

$$\boldsymbol{\omega}_{\mathrm{h}} = \hat{\boldsymbol{\Theta}}_0^{-1}(\boldsymbol{p}_{\boldsymbol{\omega}_{\mathrm{h}}} - \boldsymbol{p}_{\boldsymbol{\omega}_{\mathrm{w}}}). \tag{12}$$

Deriving the 1st order of derivatives of $\boldsymbol{\omega}_{\mathrm{h}}$ w.r.t. time and using (4), (5) and (12) gives

$$\begin{aligned} \dot{\boldsymbol{\omega}}_{\mathrm{h}} &= \hat{\boldsymbol{\Theta}}_0^{-1}(\dot{\boldsymbol{p}}_{\boldsymbol{\omega}_{\mathrm{h}}} - \dot{\boldsymbol{p}}_{\boldsymbol{\omega}_{\mathrm{w}}}) = \hat{\boldsymbol{\Theta}}_0^{-1}(\dot{\boldsymbol{p}}_{\boldsymbol{\omega}_{\mathrm{h}}} - \boldsymbol{T} - \boldsymbol{D}) \\ &= \hat{\boldsymbol{\Theta}}_0^{-1}(-\boldsymbol{\omega}_{\mathrm{h}} \times \boldsymbol{p}_{\boldsymbol{\omega}_{\mathrm{h}}} + \boldsymbol{m} \times \boldsymbol{g} - \boldsymbol{T} - \boldsymbol{D}). \end{aligned} \tag{13}$$

One can project $\dot{\boldsymbol{\omega}}_{\mathrm{h}}$ in the inertial frame, and then construct a HOFA controller utilizing the FA system approach [13–16] for the Cubli system with unmodeled dynamics as follows:

$$\boldsymbol{T} = -\boldsymbol{\omega}_{\mathrm{h}} \times \boldsymbol{p}_{\boldsymbol{\omega}_{\mathrm{h}}} + \boldsymbol{m} \times \boldsymbol{g} - \boldsymbol{\Theta}_0 (\boldsymbol{R}_B^I)^{\mathrm{T}}\, {}^{I}\boldsymbol{v}, \tag{14}$$

where ${}^{I}\boldsymbol{v}$ is a reference input vector, whose specific form can be expressed as:

$${}^{I}\boldsymbol{v} = \boldsymbol{R}_B^I \hat{\boldsymbol{\Theta}}_0^{-1} \boldsymbol{D} + \dot{\boldsymbol{\omega}}_{\mathrm{h}}. \tag{15}$$

Then, substituting Eqs. (15) and (8) into Eq. (11) yields:

$$\begin{aligned} \boldsymbol{x}_1^{(3)} &= -|\boldsymbol{g}|\, \boldsymbol{M}\boldsymbol{N}[({}^{I}\boldsymbol{v} - \boldsymbol{R}_B^I \hat{\boldsymbol{\Theta}}_0^{-1}\boldsymbol{D}) \times {}^{I}\boldsymbol{m}] \\ &\quad -|\boldsymbol{g}|\, \boldsymbol{M}\boldsymbol{N}[{}^{I}\boldsymbol{\omega}_{\mathrm{h}} \times ({}^{I}\boldsymbol{\omega}_{\mathrm{h}} + {}^{I}\boldsymbol{m})] \\ &= |\boldsymbol{g}|\, [{}^{I}\boldsymbol{m}_3 \boldsymbol{N}({}^{I}\boldsymbol{v} - \boldsymbol{R}_B^I \hat{\boldsymbol{\Theta}}_0^{-1}\boldsymbol{D})] \\ &\quad -|\boldsymbol{g}|\, ({}^{I}\boldsymbol{v}_3 \boldsymbol{N}\, {}^{I}\boldsymbol{m} + \boldsymbol{M}\boldsymbol{N}\, {}^{I}\tilde{\boldsymbol{\omega}}_{\mathrm{h}}\, {}^{I}\tilde{\boldsymbol{\omega}}_{\mathrm{h}}\, {}^{I}\boldsymbol{m}). \end{aligned} \tag{16}$$

Based on Eq. (16), one can establish the relationship between the reference input vector ${}^{I}\boldsymbol{v}$ and the virtual variable $\boldsymbol{x}_1^{(3)}$:

$$\begin{aligned} \boldsymbol{N}\, {}^{I}\boldsymbol{v} = &\frac{1}{{}^{I}\boldsymbol{m}_3}\left(\frac{\boldsymbol{z}}{|\boldsymbol{g}|} + {}^{I}\boldsymbol{v}_3 \boldsymbol{N}\, {}^{I}\boldsymbol{m}\right) \\ &+ \frac{1}{{}^{I}\boldsymbol{m}_3} \boldsymbol{M}\boldsymbol{N}\, {}^{I}\tilde{\boldsymbol{\omega}}_{\mathrm{h}}\, {}^{I}\tilde{\boldsymbol{\omega}}_{\mathrm{h}}\, {}^{I}\boldsymbol{m}, \end{aligned} \tag{17}$$

within which $\boldsymbol{z} = \boldsymbol{x}_1^{(3)} + |\boldsymbol{g}|\,{}^I\boldsymbol{m}_3\boldsymbol{N}\boldsymbol{R}_B^I\hat{\boldsymbol{\Theta}}_0^{-1}\boldsymbol{D}$. In accordance with Eqs. (15) and (17), the following linear FA system can be derived:

$$\begin{cases} \boldsymbol{x}_1^{(3)} = \boldsymbol{z} - |\boldsymbol{g}|\,{}^I\boldsymbol{m}_3\boldsymbol{N}\boldsymbol{R}_B^I\hat{\boldsymbol{\Theta}}_0^{-1}\boldsymbol{D}, \\ {}^I\dot{\boldsymbol{\omega}}_{\mathrm{h3}} = {}^I\boldsymbol{v}_3 - \boldsymbol{P}\boldsymbol{R}_B^I\hat{\boldsymbol{\Theta}}_0^{-1}\boldsymbol{D}. \end{cases} \tag{18}$$

where $\boldsymbol{P} = \begin{bmatrix} 0 & 0 & 1 \end{bmatrix}$.

3.2 Observer Design for Disturbance Estimation

Note that Eq. (18) can be rewritten in the following form:

$$\dot{\boldsymbol{\xi}} = \boldsymbol{\tau} + \boldsymbol{\Upsilon}\boldsymbol{R}_B^I\hat{\boldsymbol{\Theta}}_0^{-1}\boldsymbol{D} = \boldsymbol{\tau} + \boldsymbol{\mathfrak{D}}, \tag{19}$$

with

$$\begin{cases} \dot{\boldsymbol{\xi}} \triangleq \begin{bmatrix} \boldsymbol{x}_1^{(3)} & {}^I\dot{\boldsymbol{\omega}}_{\mathrm{h3}} \end{bmatrix}^{\mathrm{T}}, \boldsymbol{\tau} \triangleq \begin{bmatrix} \boldsymbol{z} & {}^I\boldsymbol{v}_3 \end{bmatrix}^{\mathrm{T}}, \\ \boldsymbol{\Upsilon} \triangleq \begin{bmatrix} -|\boldsymbol{g}|\,{}^I\boldsymbol{m}_3\boldsymbol{N} & -\boldsymbol{P} \end{bmatrix}^{\mathrm{T}}, \\ \boldsymbol{\mathfrak{D}} = \boldsymbol{\Upsilon}\boldsymbol{R}_B^I\hat{\boldsymbol{\Theta}}_0^{-1}\boldsymbol{D}. \end{cases}$$

For the linear closed-loop system (19), one can design a nonlinear observer $\hat{\boldsymbol{\mathfrak{D}}}$ estimate the unmodeled dynamics [18]:

$$\dot{\hat{\boldsymbol{\mathfrak{D}}}} = \boldsymbol{\Xi}\dot{\boldsymbol{\xi}} - \boldsymbol{\Xi}(\hat{\boldsymbol{\mathfrak{D}}} + \boldsymbol{\tau}), \tag{20}$$

within which $\boldsymbol{\Xi} \in \mathbb{R}^{3\times3}$ represents a matrix to be designed to guarantee the stability of the estimation error.

Note, however, that the observer in the form of (20) contains unmeasurable state variables $\dot{\boldsymbol{\xi}}$ such that it cannot be applied in practice. To handle this issue and eliminate the necessity of unmeasurable information, we propose to reconstruct the observer as follows:

$$\begin{cases} \hat{\boldsymbol{\mathfrak{D}}} = \boldsymbol{\Psi} + \boldsymbol{Z}, \\ \dot{\boldsymbol{\Psi}} = -\boldsymbol{\Xi}(\boldsymbol{\tau} + \boldsymbol{\Psi} + \boldsymbol{Z}), \end{cases} \tag{21}$$

where $\boldsymbol{Z} = \int_0^t \boldsymbol{\Xi}\dot{\boldsymbol{\xi}}dt$. In the meantime, solving for the first-order derivative of $\boldsymbol{Z}$ w.r.t. time yields:

$$\frac{\partial \boldsymbol{Z}}{\partial t} = \frac{\partial \boldsymbol{Z}}{\partial \boldsymbol{\xi}}\frac{\partial \boldsymbol{\xi}}{\partial t} = \frac{\partial \boldsymbol{Z}}{\partial \boldsymbol{\xi}}\dot{\boldsymbol{\xi}} = \boldsymbol{\Xi}\dot{\boldsymbol{\xi}}. \tag{22}$$

Denote $\boldsymbol{\Xi}$ as a gain matrix to be designed. We then define the structure of $\boldsymbol{Z}$ as:

$$\boldsymbol{Z} = \boldsymbol{\Xi}\boldsymbol{\xi}. \tag{23}$$

We then have the following sufficient condition for the Lyapunov stability of the nonlinear observer (21) and (23).

Theorem 1. Consider the linear FA system with unmodeled dynamics $\boldsymbol{\mathfrak{D}}$ presented in Eq. (19). Given Assumption 1, if the nonlinear observer takes the forms as in Eq. (21), and the vector $\boldsymbol{Z}$ related to this observer $\hat{\boldsymbol{\mathfrak{D}}}$ is provided by Eq. (23) with $\boldsymbol{\Xi}$ being select as a diagonal matrix that satisfies the following condition

$$\begin{cases} \boldsymbol{\Xi} = \mathrm{diag}(\Xi_1, \Xi_2, \Xi_3), \\ \Xi_j > 0,\ j = 1, 2, 3, \end{cases} \tag{24}$$

then the estimation error of the nonlinear observer (21) is globally uniformly bounded.

Proof. Firstly, we define the estimation error of the nonlinear observer $\hat{\boldsymbol{\mathfrak{D}}}$ as follows

$$\tilde{\boldsymbol{\mathfrak{D}}} = \hat{\boldsymbol{\mathfrak{D}}} - \boldsymbol{\mathfrak{D}}, \quad \dot{\tilde{\boldsymbol{\mathfrak{D}}}} = \dot{\hat{\boldsymbol{\mathfrak{D}}}} - \dot{\boldsymbol{\mathfrak{D}}}. \tag{25}$$

Based on (19), (21), (22) and (25), one can then calculate the 1st order derivative of the nonlinear observer $\dot{\hat{\boldsymbol{\mathfrak{D}}}}$ w.r.t. time and obtain the following results:

$$\begin{aligned} \dot{\hat{\boldsymbol{\mathfrak{D}}}} &= \dot{\boldsymbol{\Psi}} + \frac{\partial \boldsymbol{Z}}{\partial t} \\ &= -\boldsymbol{\Xi}(\boldsymbol{\tau} + \boldsymbol{\Psi} + \boldsymbol{Z}) + \boldsymbol{\Xi}\dot{\boldsymbol{\xi}} \\ &= -\boldsymbol{\Xi}(\boldsymbol{\tau} + \hat{\boldsymbol{\mathfrak{D}}}) + \boldsymbol{\Xi}(\boldsymbol{\tau} + \boldsymbol{\mathfrak{D}}) \\ &= -\boldsymbol{\Xi}\tilde{\boldsymbol{\mathfrak{D}}}. \end{aligned} \tag{26}$$

For the nonlinear observer (21) presented above, one can establish a Lyapunov candidate function $V(t)$ as follows:

$$\mathcal{V}(t) = \frac{1}{2}\tilde{\boldsymbol{\mathfrak{D}}}^{\mathrm{T}}\tilde{\boldsymbol{\mathfrak{D}}} \tag{27}$$

In accordance with Eqs. (25)-(27), computing the 1st order derivative of the Lyapunov function $V(t)$ mentioned above w.r.t. time yields:

$$\dot{\mathcal{V}}(t) = \tilde{\boldsymbol{\mathfrak{D}}}^{\mathrm{T}}\dot{\tilde{\boldsymbol{\mathfrak{D}}}} = -\tilde{\boldsymbol{\mathfrak{D}}}^{\mathrm{T}}\boldsymbol{\Xi}\tilde{\boldsymbol{\mathfrak{D}}} - \tilde{\boldsymbol{\mathfrak{D}}}^{\mathrm{T}}\dot{\boldsymbol{\mathfrak{D}}}. \tag{28}$$

By utilizing the Cauchy-Schwarz inequality and Eq. (27), the following results from Eq. (28) can be furthen derived:

$$\begin{aligned} \dot{V}(t) &\le -\Xi_{\min}\tilde{\boldsymbol{\mathfrak{D}}}^{\mathrm{T}}\tilde{\boldsymbol{\mathfrak{D}}} + \varepsilon\tilde{\boldsymbol{\mathfrak{D}}}^{\mathrm{T}}\tilde{\boldsymbol{\mathfrak{D}}} + \dot{\boldsymbol{\mathfrak{D}}}^{\mathrm{T}}\dot{\boldsymbol{\mathfrak{D}}}\big/4\varepsilon \\ &\le -(\Xi_{\min} - \varepsilon)\tilde{\boldsymbol{\mathfrak{D}}}^{\mathrm{T}}\tilde{\boldsymbol{\mathfrak{D}}} + \eta^2/4\varepsilon \\ &= -\alpha V(t) + \gamma. \end{aligned} \tag{29}$$

within which 1) ε represents an external tuning parameter that is positive and bounded; 2) $\alpha = \Xi_{\min} - \varepsilon$ and $\gamma = \eta^2/4\varepsilon$; 3) η stands for a positive scalar that is always no less than the upper bound $\|\dot{\boldsymbol{\mathfrak{D}}}\|_{\max}$ of the 1st order derivative $\dot{\boldsymbol{\mathfrak{D}}}$ of the comprehensive uncertain dynamics $\boldsymbol{\mathfrak{D}}$. Since both ε and η are all positive and bounded, γ is always positive and bounded. Moreover, if α is positive-definite diagonal matrix, i.e., $\forall\, \Xi_j > \varepsilon, (j = 1, 2, 3)$, then the nonlinear observer (21) is Lyapunov stable.

In addition, the external parameter ε can be selected as a sufficiently small scalar, such that $\varepsilon \to 0$. Therefore, The range of admissible values for Ξ_j can be extended to:

$$\Xi_j > 0,\ (j = 1, 2, 3). \tag{30}$$

Then, one can multiply both sides of Eq. (29) by $e^{\alpha t}$ and conduct the integration operation over the closed interval $[0, t]$ to further derive the following conclusion:

$$\begin{aligned} &\frac{\partial}{\partial t}(Ve^{\alpha t}) \le \gamma e^{\alpha t} \Rightarrow \\ &\qquad 0 \le V(t) \le \frac{\gamma}{\alpha} + \left[V(0) - \frac{\gamma}{\alpha}\right]e^{-\alpha t}. \end{aligned} \tag{31}$$

Based on Eqs. (27) and (31), one can derive:

$$|\tilde{\boldsymbol{\mathfrak{D}}}| \le \sqrt{\frac{2\gamma}{\alpha} + 2\left[V(0) - \frac{\gamma}{\alpha}\right]e^{-\alpha t}}. \tag{32}$$

This implies that for any given arbitrarily positive scalar $\mathcal{X} \in \mathbb{R}^+ > \sqrt{2\gamma/\alpha}$, there exists a $\mathfrak{T} > 0$ such that $|\tilde{\mathfrak{D}}| \leq \mathcal{X}$ holds for any $t > \mathfrak{T}$. Consequently, $\tilde{\mathfrak{D}}$ is globally uniformly ultimate boundeded. The proof is now completed. □

Remark 1. Note that, both the unmodeled dynamics $\boldsymbol{D}$ and its derivative $\dot{\mathfrak{D}}$ are all bounded. In addition, the each element within $\boldsymbol{\Upsilon}$ and $\hat{\boldsymbol{\Theta}}_0^{-1}$ are bounded scalars, while $\boldsymbol{R}_B^I$ represents a rotation matrix that preserves the vector's length. Hence, it can be deduced that the newly introduced unmodeled dynamics $\mathfrak{D}$ and its derivative $\dot{\mathfrak{D}}$ are also bounded.

Remark 2. Note that $\mathcal{X}$ can be made sufficiently small by appropriately selecting the parameters Ξ_j, $(j = 1, 2, 3)$ while ensuring that conditions in (24) hold. Moreover, it should be remarked that the choice $\boldsymbol{Z} = \boldsymbol{\Xi}\boldsymbol{\xi}$ is only a viable choice (there might be other possibilities) for achieving the Lyapunov stability of the nonlinear observer (21).

3.3 Controller Design

A controller development process for the linear FA system (18) and (19) is provided as follows. Firstly, we introduce a new state variable, denoted as $\boldsymbol{x}$, for the closed-loop control system mentioned above:

$$\boldsymbol{x} \triangleq \left[\begin{array}{cccc} \boldsymbol{x}_1 & \dot{\boldsymbol{x}}_1 & \ddot{\boldsymbol{x}}_1 & {}^I\boldsymbol{\omega}_{\mathrm{h}3} \end{array} \right]^{\mathrm{T}}. \tag{33}$$

Based on the state variable $\boldsymbol{x}$, one can define the control objective $\boldsymbol{x}_{\mathrm{d}}$ of the Cubli system as:

$$\lim_{t\to\infty} \boldsymbol{x} = \left[\begin{array}{cccc} \boldsymbol{x}_{1\mathrm{d}} & \dot{\boldsymbol{x}}_{1\mathrm{d}} & \ddot{\boldsymbol{x}}_{1\mathrm{d}} & {}^I\boldsymbol{\omega}_{\mathrm{h}3\mathrm{d}} \end{array} \right]^{\mathrm{T}} = \boldsymbol{x}_{\mathrm{d}}, \tag{34}$$

within which $\boldsymbol{x}_{1\mathrm{d}}$ and ${}^I\boldsymbol{\omega}_{\mathrm{h}3\mathrm{d}}$ indicate the desired trajectories of $\boldsymbol{x}_1$ and ${}^I\boldsymbol{\omega}_{\mathrm{h}3}$, respectively.

Denote the error signal as $\boldsymbol{e} \triangleq \boldsymbol{x} - \boldsymbol{x}_{\mathrm{d}}$. Further, in light of Eqs. (33), (34) and the error signal $\boldsymbol{e}$, Eq. (19) can be rewritten in a state-space form as:

$$\dot{\boldsymbol{e}} = \boldsymbol{A}\boldsymbol{e} + \boldsymbol{B}\boldsymbol{u}, \tag{35}$$

where $\boldsymbol{u} = \boldsymbol{\tau} + \mathfrak{D} + \boldsymbol{\epsilon}$; $\boldsymbol{\epsilon} \in \mathbb{R}^{3\times 1}$ represents the tracking vector, and $\boldsymbol{A} \in \mathbb{R}^{7\times 7}$, $\boldsymbol{B} \in \mathbb{R}^{7\times 3}$ can be expressed as:

$$\boldsymbol{A} = \left[\begin{array}{cccc} \boldsymbol{0}_{2\times 2} & \boldsymbol{I}_{2\times 2} & \boldsymbol{0}_{2\times 2} & \boldsymbol{0}_{2\times 1} \\ \boldsymbol{0}_{2\times 2} & \boldsymbol{0}_{2\times 2} & \boldsymbol{I}_{2\times 2} & \boldsymbol{0}_{2\times 1} \\ \boldsymbol{0}_{2\times 2} & \boldsymbol{0}_{2\times 2} & \boldsymbol{0}_{2\times 2} & \boldsymbol{0}_{2\times 1} \\ \boldsymbol{0}_{1\times 2} & \boldsymbol{0}_{1\times 2} & \boldsymbol{0}_{1\times 2} & 0 \end{array} \right],$$

$$\boldsymbol{B} = \left[\begin{array}{c} \boldsymbol{0}_{4\times 3} \\ \boldsymbol{I}_3 \end{array} \right], \boldsymbol{\epsilon} = \left[\begin{array}{cc} \boldsymbol{x}_{1\mathrm{d}}^{(3)} & {}^I\dot{\boldsymbol{\omega}}_{\mathrm{h}3\mathrm{d}} \end{array} \right]^{\mathrm{T}}.$$

Therefore, one can define a quadratic cost function $J(t) = \int_0^\infty \boldsymbol{e}^{\mathrm{T}}\boldsymbol{Q}\boldsymbol{e} + \boldsymbol{u}^{\mathrm{T}}\boldsymbol{R}\boldsymbol{u}dt$ by appropriately selecting matrices $\boldsymbol{Q} \in \mathbb{R}^{7\times 7}$ and $\boldsymbol{R} \in \mathbb{R}^{3\times 3}$. Then the associated LQR gain can be obtained as

$$\boldsymbol{K} \in \mathbb{R}^{3\times 7} = \left[\begin{array}{cccc} \boldsymbol{A}_0 & \boldsymbol{A}_1 & \boldsymbol{A}_2 & \boldsymbol{0}_{2\times 1} \\ \boldsymbol{0}_{1\times 2} & \boldsymbol{0}_{1\times 2} & \boldsymbol{0}_{1\times 2} & A_\omega \end{array} \right].$$

Subsequently, the control input $\boldsymbol{u}$ can be determined as [19]:

$$\boldsymbol{u} = -\boldsymbol{K}\boldsymbol{e}.$$

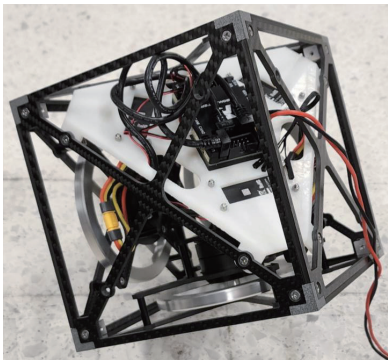

Fig. 2: Self-constructed 3D Cubli experimental setup.

Based on Eq. (19), (21) and (35), substituting $\boldsymbol{u}$, $\hat{\mathfrak{D}}$ and $\boldsymbol{\epsilon}$ into $\boldsymbol{\tau}$ yields:

$$\boldsymbol{\tau} = \left[\begin{array}{cc} \boldsymbol{z} & {}^I\boldsymbol{v}_3 \end{array} \right]^{\mathrm{T}} = -\boldsymbol{K}\boldsymbol{e} - \hat{\mathfrak{D}} - \boldsymbol{\epsilon}. \tag{36}$$

Following this, one can substitute $\boldsymbol{N}\boldsymbol{\tau}$ (i.e., $\boldsymbol{z}$) and $\boldsymbol{P}\boldsymbol{\tau}$ (i.e., ${}^I\boldsymbol{v}_3$) into Eq. (17) and get ${}^I\boldsymbol{v}_1$ and ${}^I\boldsymbol{v}_2$. The last step in the controller development is to substitute the reference input vector ${}^I\boldsymbol{v}$ into the HOFA controller $\boldsymbol{T}$ in Eq. (14).

Based on the above steps, one can derive the following closed-loop feedback system:

$$\begin{aligned} \dot{\boldsymbol{e}} &= \boldsymbol{A}\boldsymbol{e} - \boldsymbol{B}\boldsymbol{K}\boldsymbol{e} + \boldsymbol{B}(\mathfrak{D} - \hat{\mathfrak{D}}) \\ &= (\boldsymbol{A} - \boldsymbol{B}\boldsymbol{K})\boldsymbol{e} - \boldsymbol{B}\tilde{\mathfrak{D}} \\ &= \tilde{\boldsymbol{A}}\boldsymbol{e} - \boldsymbol{B}\tilde{\mathfrak{D}}. \end{aligned} \tag{37}$$

If one selects the gain matrix $\boldsymbol{K}$ such that $\tilde{\boldsymbol{A}}$ is Hurwitz stable, then the closed-loop system is essentially comprised of a stable system with bounded noise. Therefore, existing tools in set theory can be used to characterize the attraction and positive invariant property of the closed-loop state. Detailed discussions on these are skipped here due to limited space.

4 Experiments and Results

In this section, we carry out experimental studies to validate the effectiveness and advantages of the proposed framework, in comparison to the linearization-based LQR approach [8]. Towards this goal, we have built a 3D Cubli in-house as depicted in Fig. 2. The system parameters of the 3D underactuated Cubli system are determined as:

$$\hat{\boldsymbol{\Theta}}_0 = 10^{-3} \times \left[\begin{array}{ccc} 16 & -5.6 & -5.6 \\ -5.6 & 16 & -5.6 \\ -5.6 & -5.6 & 16 \end{array} \right], \boldsymbol{g} = \left[\begin{array}{c} 0 \\ 0 \\ -9.8 \end{array} \right],$$

$$\boldsymbol{m} = \left[\begin{array}{c} 0.0787 \\ 0.0787 \\ 0.0787 \end{array} \right], \boldsymbol{\Theta}_{\mathrm{w}} = 1.811 \times 10^{-4}\, \boldsymbol{I}_{3\times 3}.$$

For a fair comparison, the control gains for the proposed HOFA approach and the linearization-based LQR framework have been fine tuned until the control performance cannot be further improved. Specifically, the gains for the proposed HOFA controller with nonlinear observer are denoted as: $\boldsymbol{A}_0 = 200\, \boldsymbol{I}_{2\times 2}$, $\boldsymbol{A}_1 = 50\, \boldsymbol{I}_{2\times 2}$, $\boldsymbol{A}_2 = 10\, \boldsymbol{I}_{2\times 2}$,

Table 2: Quantitative indicators (bold means better)

Controllers $\times 10^{-3}$	$e_{\mathrm{p}\,\max}$ (rad)	$e_{\mathrm{r}\,\max}$ (rad)	$e_{\mathrm{x}\,\max}$ (rad/s)	$e_{\mathrm{y}\,\max}$ (rad/s)	$e_{\mathrm{z}\,\max}$ (rad/s)	$e_{1\,\max}$ (rad/s)	$e_{2\,\max}$ (rad/s)	$e_{3\,\max}$ (rad/s)	$T_{1\,\max}$ $(\mathrm{N}\cdot\mathrm{m})$	$T_{2\,\max}$ $(\mathrm{N}\cdot\mathrm{m})$	$T_{3\,\max}$ $(\mathrm{N}\cdot\mathrm{m})$
Proposed controller	**9.3**	**7.4**	**83.8**	**85.5**	**114.8**	**11741.1**	**9924.4**	**17911**	**137.4**	**128.4**	**238.7**
LQR-based controller	16.7	10.7	111.3	114.9	189	17455	19028.8	34414.5	147.9	141	266.5

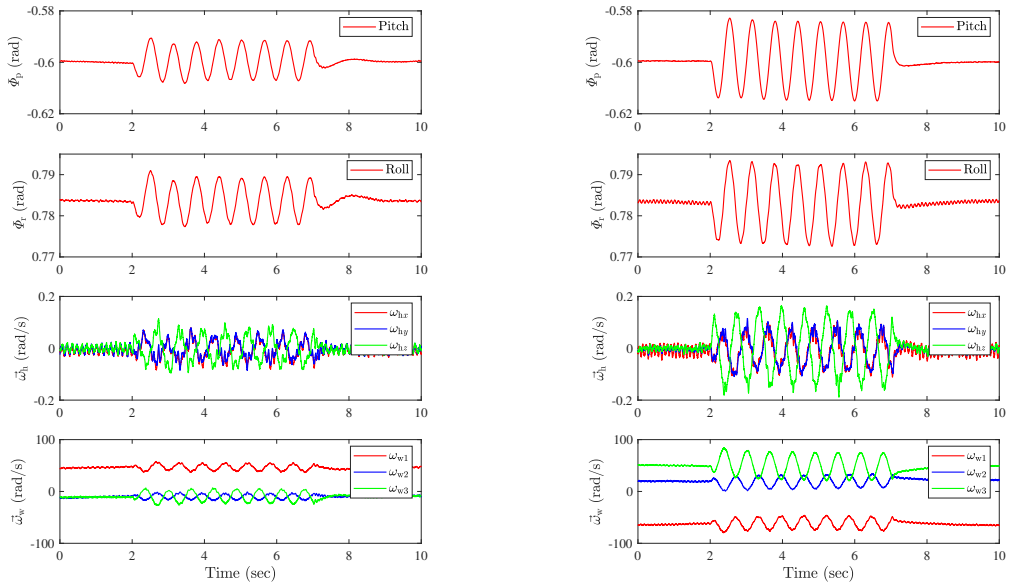

(a) Results of the proposed HOFA controller. (b) Results of the LQR-Based controller.

Fig. 3: Control inputs of the two controllers

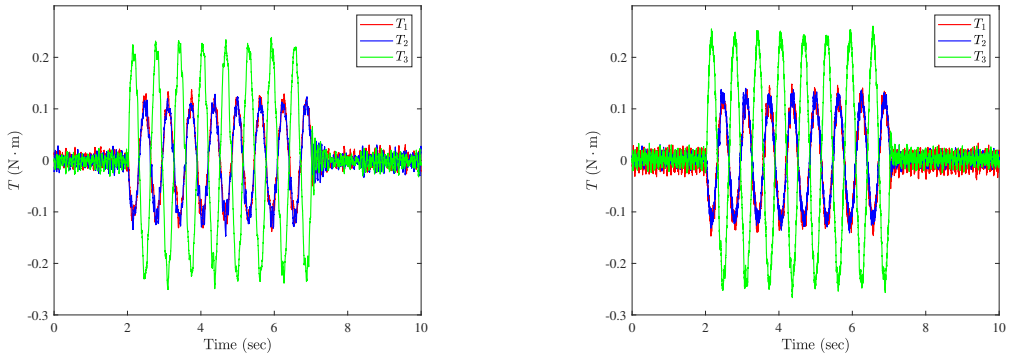

(a) Results of the proposed HOFA controller. (b) Results of the LQR-Based controller.

Fig. 4: Experimental performance under the implementation of the two controllers

$A_\omega = 10$, $\boldsymbol{\Xi} = \mathrm{diag}(30,\ 30,\ 30)$.Note that the control gains for the LQR-based controller are intricate. Due to space constraints, these parameters cannot be provided herein.

During our experiment, disturbances with magnitudes of $0.1\ \mathrm{N}\cdot\mathrm{m}$, $0.1\ \mathrm{N}\cdot\mathrm{m}$, and $0.2\ \mathrm{N}\cdot\mathrm{m}$ are respectively applied to the Cubli system in each of the three directions as $\boldsymbol{D}_1$, $\boldsymbol{D}_2$ and $\boldsymbol{D}_3$ after this experimental system stabilized for 2 seconds to emphasize the effectiveness and robustness of each controller. These disturbances are removed after 7 seconds later. The outcomes of these experiments can be depicted in Figs. 3-5. In addition, a series of quantitative indicators that can better justify the performance of each controller are defined as:

1) $e_{\mathrm{p}\,\max}$ indicates the maximum pitch angle error.
2) $e_{\mathrm{r}\,\max}$ indicates the maximum roll angle error.
3) $e_{i\,\max}, (i = x, y, z)$ stands for the maximum body angular velocity error in the ith direction.
4) $e_{j\,\max}, (j = 1, 2, 3)$ stands for the maximum angular velocity error of the jth reaction wheel.
5) $T_{j\,\max}$ represents the maximum torque applied by the jth reaction wheel.

Based on the observations from Figs. 3-5, detailed numerical values of the quantitative performance indicators for the HOFA controller with nonlinear observer and the LQR-based controller are provided in Table 2. More quantitatively, the following conclusions can be drawn (i.e., after 2 seconds when the system stabilizes):

1) The observer accurately tracks these unmodeled uncertainties in various directions and provides timely feedback to the HOFA controller to compensate for them. The estimated curve is almost consistent with the actual disturbance variation curve. This fact indicates that the proposed nonlinear observer possesses excellent tracking accuracy.

2) Compared with the LQR-based controller, the HOFA

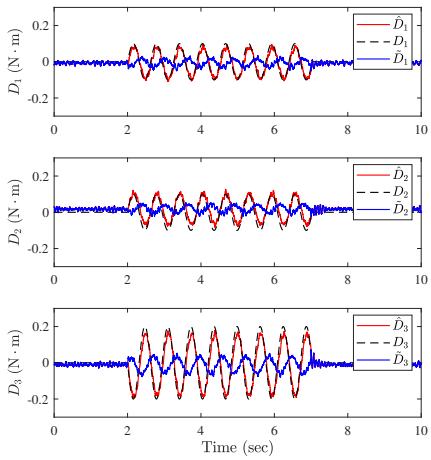

Fig. 5: Observer tracking performance of the proposed HOFA Controller.

controller can reduce the oscillation magnitudes of the Cubli experimental platform (i.e., the pitch angle and the roll angle). Its anti-disturbance capability increases by at least 30.8%. This sufficiently underscores the effective suppression of oscillation magnitudes of the pitch and roll angles in the Cubli system manipulated by the HOFA controller. Subsequent to the elimination of disturbances, these two system states rapidly stabilize and converge to the desired angles.

3) The oscillation magnitudes of each body angular velocity under the manipulation of the HOFA controller are significantly smaller than those under the control of the LQR-based controller. It can be summarized that the body angular velocities under the proposed controller are attenuated by at least 24.7%. In other words, the proposed controller can achieve smaller body angular velocities, which contributes to stabilize the entire system.

In conclusion, the comprehensive analysis in Table 2 and Figs 3-5 reveal that the HOFA controller with nonlinear dynamics exhibits better performance compared to the LQR scheme, especially in terms of robustness against unmodeled uncertainties.

5 Conclusion

In this paper, we have proposed an HOFA system approach to control of underactuated 3D Cublis with unmodeled dynamics. Inspired by the FA system approaches, we transformed the intricate underactuated model into a nonlinear FA system, without using any linearization or approximation. Based on the obtained FA system, a nonlinear observer was then designed to track the unknown disturbance, with a rigorous estimation error stability guarantee. Furthermore, through the construction of the tracking error signal, we developed a HOFA feedback controller for the 3D Cubli system. Thorough experimental studies have been carried out to validate and illustrate the improved performance of the proposed control scheme, compared to the existing linearization-based LQR approach.

References

[1] V. Klemm, A. Morra, C. Salzmann, F. Tschopp, K. Bodie, L. Gulich, N. Küng, D. Mannhart, C. Pfister, M. Vierneisel, F. Weber, R. Deuber, and R. Siegwart. Ascento: A two-wheeled jumping robot. In *IEEE Int. Conf. Robot. Autom.*, pages 7515–7521, May 2019.

[2] H. Shi, R. Li, X. Bai, Y. Zhang, L. Min, D. Wang, X. Lu, Y. Yan, and Y. Lei. A review for control theory and condition monitoring on construction robots. *J. Field Robot.*, 40:934 – 954, Jan 2023.

[3] H. Chen and N. Sun. An output feedback approach for regulation of 5-dof offshore cranes with ship yaw and roll perturbations. *IEEE Trans. Ind. Electron.*, 69(2):1705–1716, Feb 2022.

[4] A. W. Koenig, M. Pavone, J. C. Castillo-Rogez, and I. A. D. Nesnas. A dynamical characterization of internally-actuated microgravity mobility systems. In *IEEE Int. Conf. Robot. Autom.*, pages 6618–6624, 2014.

[5] M. Pavone, J. C. Castillo-Rogez, I. A. D. Nesnas, J. A. Hoffman, and N. J. Strange. Spacecraft/rover hybrids for the exploration of small solar system bodies. In *IEEE Aerospace Conference*, pages 1–11, 2013.

[6] M. Muehlebach and R. D'Andrea. Nonlinear analysis and control of a reaction-wheel-based 3-D inverted pendulum. *IEEE Trans. Control Syst. Technol.*, 25(1):235–246, Jan 2017.

[7] M. Gajamohan, M. Merz, I. Thommen, and R. D'Andrea. The cubli: A cube that can jump up and balance. In *IEEE/RSJ Int. Conf. Intell. Robot. Syst.*, pages 3722–3727, Dec 2012.

[8] M. Gajamohan, M. Muehlebach, T. Widmer, and R. D'Andrea. The cubli: A reaction wheel based 3D inverted pendulum. In *European Control Conference*, pages 268–274, Dec 2013.

[9] M. Hofer, M. Muehlebach, and R. D'Andrea. The one-wheel cubli: A 3D inverted pendulum that can balance with a single reaction wheel. *Mechatron.*, 91(10):102965, Oct. 2023.

[10] H. Kong and S. Sukkarieh. An internal model approach to estimation of systems with arbitrary unknown inputs. *Automatica*, 108(8):108482, Oct 2019.

[11] H. Kong. Noise covariance estimation via autocovariance least-squares with deadbeat filters. *Automatica*, 153(7):111049, Jul 2023.

[12] H. Kong, S. Sukkarieh, T. J. Arnold, T. Chen, B. Mu, and W. Zheng. Identifiability analysis of noise covariances for lti stochastic systems with unknown inputs. *IEEE Trans. Autom. Control.*, 68(7):4459–4466, Sep 2023.

[13] G. Duan. High-order fully actuated system approaches: Part II. generalized strict-feedback systems. *Int. J. Syst. Sci.*, 52(3):437–454, Oct 2021.

[14] G. R. Duan. High-order fully actuated system approaches: Part I. models and basic procedure. *Int. J. Syst. Sci.*, 52(2):422–435, Feb 2021.

[15] G. R. Duan. High-order fully actuated system approaches: Part VII. controllability, stability and parametric designs. *Int. J. Syst. Sci.*, 52(6):1285–1302, Sep 2021.

[16] G. R. Duan. High-order fully actuated system approaches: Part IX. generalized PID control and model reference tracking. *Int. J. Syst. Sci.*, 53(3):652–674, Mar 2021.

[17] M. H. Zhang and X. J. Jing. Adaptive neural network tracking control for double-pendulum tower crane systems with nonideal inputs. *IEEE Trans. Syst. Man Cybern. Syst.*, 52(4):2514–2530, Apr. 2022.

[18] W. H. Chen. A nonlinear disturbance observer for robotic manipulators. *IEEE Trans. Ind. Electron.*, 47(4):932–938, Apr 2000.

[19] G. R. Duan. *Linear System Theory (Volume II)*. Science Press, Beijing, 3rd edition, 2016.

Proceedings of the 3rd Conference on Fully Actuated System Theory and Applications
May 10-12, 2024, Shenzhen, China

Stabilization Control of Second-order Nonholonomic System with High-Order Fully Actuated System Approach

Qi Pan[1], Xiuhui Peng[1], Xueyan Wang[1]

1. College of Automation Engineering, Nanjing University of Aeronautics and Astronautics, Nanjing 211106, P. R. China
E-mail: yunqi11070613@gmail.com, xhpeng@nuaa.edu.cn,xueyanwang@nuaa.edu.cn

Abstract: This paper explores the stabilization of a category of second-order nonholonomic systems through a high-order fully actuated system approach. To begin with, explicit constructions of system state and control input transformations are devised to convert the second-order nonholonomic system into a second-order canonical chained form. Subsequently, within the framework of the fully actuated system, the stabilization quandary is tackled by formulating a straightforward, continuous, and smooth stabilizing controller, along with delineating the associated region of attraction. Lastly, numerical simulation of second-order nonholonomic unmanned vehicle control systems is provided to exhibit the efficacy of the proposed methodology.

Key Words: Second-order nonholonomic systems, stabilization control, fully actuated system approach, region of attraction

1 Introduction

In recent years, research endeavors aimed at controlling trajectory tracking and pose stabilization of nonholonomic systems have experienced a discernible upsurge. A considerable body of research has been accumulated, primarily concentrating on first-order nonholonomic systems that adhere to classical nonholonomic velocity relations [1, 2, 3]. Nevertheless, there exists another class of systems, namely the second-order nonholonomic system, which is even more crucial and ubiquitous. Due to a complexity distinct from that of first-order systems, this characteristic renders the control of second-order nonholonomic systems more challenging.

As the demand for motion control in complex mechanical systems and robotic systems increases, numerous investigations on first-order nonholonomic systems have been carried out. In [4], a class of $SE(2)$ unmanned vehicle tracking and stabilization problems with first-order nonholonomic constraints are solved, and global exponential stability and tracking are achieved. For hardware restriction and disturbance, reference [5] converts the first-order nonholonomic system of the control moment gyroscope into a chain system, and then performs nonlinear control. Based on these foundations, for under-actuated parallel robots and manipulators, a hierarchical sliding film controller is designed to achieve steady-state motion control, and a particle swarm optimization algorithm is used to calculate the target angle according to geometric constraints in [6] and [7], respectively.

On the basis of first-order nonholonomic systems, the research on second-order nonholonomic systems is in full swing. References [8] and [9] establish essential conditions for identifying underactuated manipulators with dynamic equations seen as nonholonomic constraints and demonstrate that feedback stabilization to a single point is unfeasible, proposing stabilization to an equilibrium manifold instead. In [10], a specific class of second-order nonholonomic systems has been explored, offering a discontinuous controller for exponential stabilization. Building on these foundations, an advanced controller is designed for trajectory tracking and robust control under uncertainties through the transformation of error models and the application of second-order sliding mode control in [11] and [12], respectively. Most recently, a control method for two-dimensional underactuated robots has been innovated in [13], emphasizing simplicity and efficiency in control through smart optimization, applicable even with passive links.

Recently, a methodology known as the High-Order Fully Actuated (HOFA) system approach has been investigated in [14, 15, 16], which has been expanded to discrete-time systems [17], time-varying and time-delay systems [18]. Considering fundamental physical principles such as Newton's laws, the principle of momentum, Euler's equations, and Lagrange's equations, which typically exhibit second-order characteristics, the transition to a state-space representation often simplifies these systems to first-order [19]. This simplification, while facilitating the consolidation of state variables into state vectors, sometimes overlooks the inherent complexity of the systems. Against this backdrop, the concept of "fully-actuated" systems has been introduced in [14], offering a fresh perspective by transforming a first-order system into a second-order fully-actuated model or even a higher-order one. This approach not only leverages the strengths of higher-order dynamics but also addresses some limitations of the traditional state-space method.

The HOFA system approach is particularly valuable for nonholonomic systems where smooth or continuous stabilizing controllers are often non-existent. For completely controllable systems, a global HOFA model enables a simple design of a globally exponentially stabilizing controller, as demonstrated in [20]. Similarly, for locally controllable systems, a local HOFA model facilitates the design of a locally exponentially stabilizing controller. In the case of sub-controllable systems, a sub-HOFA model aids in determining the region of exponential attraction within the initial state space, allowing for the straightforward design of a sub-stabilizing controller, also discussed in [20]. Notably, reference [21] applies the HOFA system approach to Brockett's first example system, while reference [22] extends this treatment to Brockett's second example system, using the HOFA system approach.

In light of the preceding discussions, few studies have

This work was supported in part by the National Natural Science Foundation of China under Grant 62103189, in part by the Science Center Program of National Natural Science Foundation of China under Grant 62188101.

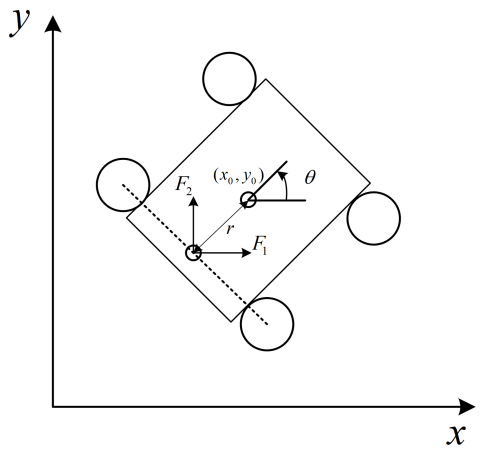

Fig. 1: Model of an unmanned vehicle

concentrated on the stabilization control for the second-order nonholonomic systems, especially those adopting a HOFA system approach for more efficient problem-solving. Meanwhile, the existing HOFA approach has solved first-order nonholonomic systems as illustrated in Brockett's first example [21] and second example [22]. Building upon the research conducted on first-order nonholonomic systems, this paper extends its findings to second-order nonholonomic systems, offering the following contributions. Initially, a second-order chain canonical system is explored and an example of an unmanned vehicle model moving in the horizontal plane is further given. In pursuit of this objective, a general HOFA controller is designed to ensure the system variables and control inputs of the system exponentially converge to zero, alongside the development of a specialized controller tailored to stabilize the unmanned vehicle in the horizontal plane. Furthermore, methods for determining fairly large attraction regions and defining generalized parameters are concurrently presented.

The structure of the subsequent sections of this paper is organized as follows. Section 2 presents the problem description. Section 3 delineates the canonical second-order chained form, the design of the stabilization controller, and the region of attraction. Section 4 conducts numerical simulations. Finally, section 5 provides conclusions for this work.

2 Problem Statement

Consider a second-order nonholonomic unmanned vehicle [23] moving within a horizontal plane, as depicted in Fig.1. Its mass and moment of inertia are m and I, respectively. In the inertial coordinate system, let (x, y, θ) be the position and attitude angle of the center of mass of the unmanned vehicle. The external force along the x-axis and y-axis directions of the inertial coordinate exerts on the unmanned vehicle is (F_1, F_2). The distance between the external force application point and the center of mass of the moving unmanned vehicle is r. The motion of an unmanned vehicle is governed by the following equation

$$\begin{aligned} m\ddot{x} &= F_1 \\ m\ddot{y} &= F_2 \\ I\ddot{\theta} &= F_1 r\sin\theta - F_2 r\cos\theta \end{aligned} \tag{1}$$

In consideration of practical situations, the attitude angle θ of the unmanned vehicle is restricted to $(-\pi/2, \pi/2)$. The control objective of the paper is to make the unmanned vehicle move to the origin and the attitude angle also converges to zero, namely

$$\begin{aligned} &\lim_{t\to\infty} x \to 0 \\ &\lim_{t\to\infty} y \to 0 \\ &\lim_{t\to\infty} \theta \to 0 \end{aligned} \tag{2}$$

3 Main Results

This section will detail the findings from three main subsections. Firstly, an analysis is conducted on the coordinate transformation of the typical chained nonholonomic systems in second-order form. Subsequently, control laws are designed for the transformed system using the HOFA system approach. Finally, to circumvent singularities, the broad attraction regions for the initial values are discussed.

3.1 Canonical second-order chained form

It is well known that standard second-order nonholonomic systems can be recast into the subsequent universal form [10]

$$\begin{aligned} \ddot{x}_1 &= u_1 \\ \ddot{x}_2 &= u_2 \\ \ddot{x}_3 &= \alpha(x_2)u_1 + \beta(x_2)u_2 \end{aligned} \tag{3}$$

where $\alpha(x_2)$, $\beta(x_2)$ are second-order differentiable functions of x_2. By employing (3), (1) can be expressed as

$$\begin{aligned} \ddot{x} &= u_1 \\ \ddot{\theta} &= u_2 \\ \ddot{y} &= u_1\tan\theta - u_2 I/(rm)\sec\theta \end{aligned} \tag{4}$$

with $u_1 = \frac{F_1}{m}, u_2 = \frac{r}{I}(F_1\sin\theta - F_2\cos\theta)$.

Lemma 1 Model (4) can be transformed into the subsequent second-order chained form

$$\ddot{y}_1 = v_1 \tag{5a}$$
$$\ddot{y}_2 = v_2 \tag{5b}$$
$$\ddot{y}_3 = y_2 v_1 \tag{5c}$$

with the following specified coordinate and input feedback transformations

$$\begin{aligned} y_1 &= x + I/(rm)(\cos\theta - 1) \\ y_2 &= \tan\theta \\ y_3 &= y + I/(rm)\sin\theta \\ v_1 &= -I/(rm)\dot{\theta}^2\cos\theta + u_1 - \\ &\quad u_2 I/(rm)\sin\theta \\ v_2 &= \sec^2\theta(u_2 + 2\dot{\theta}^2\tan\theta) \end{aligned} \tag{6}$$

Proof. Equation (5) can be obtained by simply differentiating equation (6) twice while using equation (4). □

Remark 1 The singular points occur at $\theta \neq \pi/2$. When θ closely approaches these singular points, equation (4) can be rewritten in an alternative form as follows

$$\begin{aligned} \ddot{y} &= u_1 \\ \ddot{\theta} &= u_2 \\ \ddot{x} &= u_1\cot\theta + u_2 I/(rm)\csc\theta \end{aligned} \tag{7}$$

with $u_1 = \frac{F_2}{m}, u_2 = \frac{r}{I}(F_1 \sin\theta - F_2 \cos\theta)$. Equation (6) can be converted into the second-order chained form using the subsequent coordinate transformations

$$\begin{aligned} y_1 &= y + I/(rm)\sin\theta \\ y_2 &= \cot\theta \\ y_3 &= x + I/(rm)(\cos\theta - 1) \\ v_1 &= -I/(rm)\dot{\theta}^2 \sin\theta + u_1 + \\ &\quad u_2 I/(rm)\cos\theta \\ v_2 &= -\csc^2\theta(u_2 - 2\dot{\theta}^2 \cot\theta) \end{aligned} \tag{8}$$

The singular point of the new transformation is $\theta = 0$. Combining the above two coordinate transformation methods and their respective advantages and disadvantages, we can choose the appropriate transformation at the right time. In order to avoid singular points, for example, when the angle is close to $\pi/2$, select transformations (8), and when it is close to 0, switch to transformations (6).

3.2 Controller Design

Based on the coordinate transformation above, the derivation of the HOFA model and the design of the fully actuated controller for the system will be conducted. To begin with, let us construct the HOFA model based on the system (5). By examining the equations (5a) and (5c), we obtain

$$\ddot{y}_3 = y_2 \ddot{y}_1 \tag{9}$$

and when $\ddot{y}_1 \neq 0$, it gives

$$y_2 = \frac{\ddot{y}_3}{\ddot{y}_1} \tag{10}$$

Differentiating the equation (5c) with respect to time, yield

$$\dddot{y}_3 = \dot{y}_2 v_1 + y_2 \dot{v}_1 \tag{11}$$

when $\ddot{y}_1 \neq 0$,

$$\dot{y}_2 = \frac{\dddot{y}_3 - y_2 \dot{v}_1}{v_1} \tag{12}$$

Then, continue to differentiate the equation (11),

$$\begin{aligned} {y_3}^{(4)} &= \ddot{y}_2 v_1 + 2\dot{y}_2 \dot{v}_1 + y_2 \ddot{v}_1 \\ &= 2\dot{y}_2 \dot{v}_1 + y_2 \ddot{v}_1 + \ddot{y}_1 v_2 \end{aligned} \tag{13}$$

On the other side, it can be derived from the equation (5a) that

$${y_1}^{(4)} = \ddot{v}_1 \tag{14}$$

Combining the aforementioned equation with equation (13), yields the subsequent fully actuated system

$$\begin{bmatrix} y_1^{(4)} \\ y_3^{(4)} \end{bmatrix} = \begin{bmatrix} 0 \\ 2\dot{y}_2 \dot{v}_1 \end{bmatrix} + \begin{bmatrix} 1 & 0 \\ y_2 & \ddot{y}_1 \end{bmatrix} \begin{bmatrix} \ddot{v}_1 \\ v_2 \end{bmatrix} \tag{15}$$

with the following feasibility constraint

$$\ddot{y}_1 \neq 0 \tag{16}$$

Next, based upon the aforementioned HOFA model (15), following the standard HOFA system approach, a continuous, and smooth controller can be established as follows

$$\begin{bmatrix} \ddot{v}_1 \\ v_2 \end{bmatrix} = -B^{-1}(A + \begin{bmatrix} b_3 y_1^{(3)} + b_2 y_1^{(2)} + b_1 y_1^{(1)} + b_0 y_1 \\ c_3 y_3^{(3)} + c_2 y_3^{(2)} + c_1 y_3^{(1)} + c_0 y_3 \end{bmatrix}) \tag{17}$$

with coefficients $b_i, c_i, i \in \{0,1,2,3\}$ are positive constant, $A = \begin{bmatrix} 0 \\ 2\dot{y}_2 \dot{v}_1 \end{bmatrix}$, $B = \begin{bmatrix} 1 & 0 \\ y_2 & \ddot{y}_1 \end{bmatrix}$, which results in a closed-loop system composed of

$$y_1^{(4)} + b_3 {y_1}^{(3)} + b_2 {y_1}^{(2)} + b_1 {y_1}^{(1)} + b_0 y_1 = 0 \tag{18a}$$

$$\ddot{y}_1 \neq 0 \tag{18b}$$

and

$${y_3}^{(4)} + c_3 y_3^{(3)} + c_2 y_3^{(2)} + c_1 y_3^{(1)} + c_0 y_3 = 0 \tag{19}$$

To enhance the concreteness and intuitiveness of the control law representation for facilitating subsequent proofs, equation (17) is reformulated as follows

$$\ddot{v}_1 = -b_3 y_1^{(3)} - b_2 y_1^{(2)} - b_1 y_1^{(1)} - b_0 y_1 \tag{20}$$

Up to this point, due to the equivalent coordinate transformation, the control law of the original system u_1, u_2 or F_1, F_2 can be derived from the inverse transformation of v_1, v_2.

In the forthcoming subsection, an elaboration on the region of attraction ensues, defining it as a domain within the initial state space wherein system trajectories, governed by the controller (17), exhibit exponential convergence towards the origin.

3.3 Region of Attraction

In order to achieve controller effectiveness and convergence, it is necessary to consider the controller's region of attraction due to the uniqueness of the HOFA approach. It has been proven that the fully actuated controller can achieve smooth and stable control for systems with the initial value set within the attraction region.

Considering the system (18), it should be noted that

$$y_1^{(4)} + b_3 {y_1}^{(3)} + b_2 {y_1}^{(2)} + b_1 {y_1}^{(1)} + b_0 y_1 = 0 \tag{21}$$

can be expressed in the state-space form

$$\begin{bmatrix} {y_1}^{(1)} \\ {y_1}^{(2)} \\ {y_1}^{(3)} \\ {y_1}^{(4)} \end{bmatrix} = \phi \begin{bmatrix} y_1 \\ {y_1}^{(1)} \\ {y_1}^{(2)} \\ {y_1}^{(3)} \end{bmatrix} \tag{22}$$

where

$$\phi = \begin{bmatrix} 0 & 1 & 0 & 0 \\ 0 & 0 & 1 & 0 \\ 0 & 0 & 0 & 1 \\ -b_0 & -b_1 & -b_2 & -b_3 \end{bmatrix} \tag{23}$$

Clearly, the solution of the system (22) is given by

$$\begin{bmatrix} y_1 \\ {y_1}^{(1)} \\ {y_1}^{(2)} \\ {y_1}^{(3)} \end{bmatrix} = e^{\phi t} \begin{bmatrix} x_0 \\ y_0 \\ p_0 \\ q_0 \end{bmatrix} \tag{24}$$

where $x_0 = y_1(0)$, $y_0 = {y_1}^{(1)}(0)$, $p_0 = {y_1}^{(2)}(0)$, and $q_0 = {y_1}^{(3)}(0)$ are the system initial values.

As is well-known

$$e^{At} = L^{-1}[(SI - A)^{-1}] \tag{25}$$

Concerning the feasibility constraint $\ddot{y}_1 = 0$, using (25) and then expanding the third term in (22), easily get $\ddot{y}_1 = 0$ is equal to

$$f(t)x_0 + g(t)y_0 + \alpha(t)p_0 + \beta(t)q_0 = 0 \tag{26}$$

and

$$\begin{aligned} b_3 &= d_0 + d_1 + d_2 + d_3 \\ b_2 &= d_0d_1 + d_0d_2 + d_0d_3 + d_1d_2 + d_1d_3 + d_2d_3 \\ b_1 &= d_0d_1d_2 + d_0d_1d_3 + d_0d_2d_3 + d_1d_2d_3 \\ b_0 &= d_0d_1d_2d_3 \end{aligned}$$

where d_0, d_1, d_2, d_3 are four positive scalars and $d_0 > d_1 > d_2 > d_3$.

$$\begin{aligned} f(t) =& \frac{d_0\, {d_1}^2\, d_2\, d_3\, \mathrm{e}^{-d_1 t}}{(d_0 - d_1)\,(d_1 - d_2)\,(d_1 - d_3)} \\ &- \frac{{d_0}^2\, d_1\, d_2\, d_3\, \mathrm{e}^{-d_0 t}}{(d_0 - d_1)\,(d_0 - d_2)\,(d_0 - d_3)} \\ &- \frac{d_0\, d_1\, {d_2}^2\, d_3\, \mathrm{e}^{-d_2 t}}{(d_0 - d_2)\,(d_1 - d_2)\,(d_2 - d_3)} \\ &+ \frac{d_0\, d_1\, d_2\, {d_3}^2\, \mathrm{e}^{-d_3 t}}{(d_0 - d_3)\,(d_1 - d_3)\,(d_2 - d_3)} \end{aligned} \tag{27}$$

$$\begin{aligned} g(t) =& \frac{\mathrm{e}^{-d_1 t}\,\left(d_0\, {d_1}^2\, d_2 + d_0\, {d_1}^2\, d_3 + {d_1}^2\, d_2\, d_3\right)}{(d_0 - d_1)\,(d_1 - d_2)\,(d_1 - d_3)} \\ &- \frac{\mathrm{e}^{-d_0 t}\,\left({d_0}^2\, d_1\, d_2 + {d_0}^2\, d_1\, d_3 + {d_0}^2\, d_2\, d_3\right)}{(d_0 - d_1)\,(d_0 - d_2)\,(d_0 - d_3)} \\ &- \frac{\mathrm{e}^{-d_2 t}\,\left(d_0\, d_1\, {d_2}^2 + d_0\, {d_2}^2\, d_3 + d_1\, {d_2}^2\, d_3\right)}{(d_0 - d_2)\,(d_1 - d_2)\,(d_2 - d_3)} \\ &+ \frac{\mathrm{e}^{-d_3 t}\,\left(d_0\, d_1\, {d_3}^2 + d_0\, d_2\, {d_3}^2 + d_1\, d_2\, {d_3}^2\right)}{(d_0 - d_3)\,(d_1 - d_3)\,(d_2 - d_3)} \end{aligned} \tag{28}$$

$$\begin{aligned} \alpha(t) =& \frac{{d_1}^2\, \mathrm{e}^{-d_1 t}\,(d_0 + d_2 + d_3)}{(d_0 - d_1)\,(d_1 - d_2)\,(d_1 - d_3)} \\ &- \frac{{d_0}^2\, \mathrm{e}^{-d_0 t}\,(d_1 + d_2 + d_3)}{(d_0 - d_1)\,(d_0 - d_2)\,(d_0 - d_3)} \\ &- \frac{{d_2}^2\, \mathrm{e}^{-d_2 t}\,(d_0 + d_1 + d_3)}{(d_0 - d_2)\,(d_1 - d_2)\,(d_2 - d_3)} \\ &+ \frac{{d_3}^2\, \mathrm{e}^{-d_3 t}\,(d_0 + d_1 + d_2)}{(d_0 - d_3)\,(d_1 - d_3)\,(d_2 - d_3)} \end{aligned} \tag{29}$$

$$\begin{aligned} \beta(t) =& \frac{{d_1}^2\, \mathrm{e}^{-d_1 t}}{(d_0 - d_1)\,(d_1 - d_2)\,(d_1 - d_3)} \\ &- \frac{{d_0}^2\, \mathrm{e}^{-d_0 t}}{(d_0 - d_1)\,(d_0 - d_2)\,(d_0 - d_3)} \\ &- \frac{{d_2}^2\, \mathrm{e}^{-d_2 t}}{(d_0 - d_2)\,(d_1 - d_2)\,(d_2 - d_3)} \\ &+ \frac{{d_3}^2\, \mathrm{e}^{-d_3 t}}{(d_0 - d_3)\,(d_1 - d_3)\,(d_2 - d_3)} \end{aligned} \tag{30}$$

Next, a brief explanation of the properties of the attraction region and how to obtain values within the attraction region.

Firstly, collect and simplify equation (27)-(30) can obtain

$$\begin{aligned} &\frac{e^{-d_0 t}}{(d_0 - d_1)(d_0 - d_2)(d_0 - d_3)} A_1 \\ &\frac{e^{-d_1 t}}{(d_0 - d_1)(d_1 - d_2)(d_1 - d_3)} A_2 \\ &\frac{e^{-d_2 t}}{(d_0 - d_2)(d_1 - d_2)(d_2 - d_3)} A_3 \\ &\frac{e^{-d_3 t}}{(d_0 - d_3)(d_1 - d_3)(d_2 - d_3)} A_4 \end{aligned} \tag{31}$$

with

$$\begin{aligned} A_1 &= a_{11}x_0 + a_{12}y_0 + a_{13}p_0 + a_{14}q_0 \\ A_2 &= a_{21}x_0 + a_{22}y_0 + a_{23}p_0 + a_{24}q_0 \\ A_3 &= a_{31}x_0 + a_{32}y_0 + a_{33}p_0 + a_{34}q_0 \\ A_4 &= a_{41}x_0 + a_{42}y_0 + a_{43}p_0 + a_{44}q_0 \end{aligned} \tag{32}$$

Now to find the attraction region is to find the region where $\ddot{y}_1 \neq 0$, that is make the sum of the four formulas of (31) not equal to zero. Without sacrificing generality, we initially assume the determination of the region's positive part. Due to the fact that $d_0 > d_1 > d_2 > d_3 > 0$ and $e^{-d_i t} > 0$, $i \in \{0, 1, 2, 3\}$, so the first parts of (31) are greater than zero. For more convenient expression, the second parts of (31) are rewritten into matrix form,

$$\begin{bmatrix} a_{11} & a_{12} & a_{13} & a_{14} \\ a_{21} & a_{22} & a_{23} & a_{24} \\ a_{31} & a_{32} & a_{33} & a_{34} \\ a_{41} & a_{42} & a_{43} & a_{44} \end{bmatrix} \begin{bmatrix} x_0 \\ y_0 \\ p_0 \\ q_0 \end{bmatrix} \leq 0 \tag{33}$$

It is patently evident that (33) represents a polyhedron in a geometric sense, and the symbol R is used to represent this part of the area. The area inside the polyhedron is the feasible region where the closed-loop system (18) is established. Without loss of generality, feasible points satisfying sufficient conditions can be directly found by substituting appropriate values as long as the equation is satisfied.

3.4 Stability analysis

Based on the attraction region of the designed system, this subsection analyzes the stability of the system. The main results are stated in the following theorem.

Theorem 1 For the coefficients b_3, b_2, b_1, b_0 in (18), and design the controller for the system (5) as (17). The system variables and control inputs all can converge to zero exponentially provided that the control system initial values are chosen from the attraction region and the polynomial $s^4 + c_3 s^3 + c_2 s^2 + c_1 s + c_0$ has four distinct roots which are both less than $-d_0$.

Proof. Since $y_3(t), \dot{y}_3(t), \ddot{y}_3(t), \dddot{y}_3(t)$ are the system variables of the closed-loop linear system (19), and $c_i, i \in \{0, 1, 2, 3\}$ are both positive, both $y_3(t), \dot{y}_3(t), \ddot{y}_3(t)$ and $\dddot{y}_3(t)$ converge to zero exponentially. Moreover, as previously demonstrated, provided that the system's initial values $x_0 = y_1(0)$, $y_0 = \dot{y}_1(0)$, $p_0 = \ddot{y}_1(0)$, and $q_0 = \dddot{y}_1(0)$ are chosen from within the attraction region R, the system variables $y_1(t)$, $\dot{y}_1(t)$, $\ddot{y}_1(t)$, and $\dddot{y}_1(t)$ satisfy the closed-loop subsystem (18). Consequently, $y_1(t)$, $\dot{y}_1(t)$, $\ddot{y}_1(t)$, $\dddot{y}_1(t)$,

and $v_1 = \ddot{y}_1$ also converge to zero exponentially. Thus, the second conclusion is verified.

Subsequently, from equation (20), it follows that the exponential convergence of $y_1(t)$, $\dot{y}_1(t)$, $\ddot{y}_1(t)$, and $\dddot{y}_1(t)$ immediately implies the exponential convergence of $\ddot{v}_1$. Next, when the polynomial $s^4 + c_3 s^3 + c_2 s^2 + c_1 s + c_0$ has four distinct roots which are both less than $-d_0$, the exponential decay rates of all orders of derivatives of y_3 are faster than those of y_1. Thus, by equation (10), it follows that y_2 converges to zero exponentially. According to equation (5), (10) and (12), when $\ddot{y}_1 \neq 0$, equation (12) can be rewritten as

$$\dot{y}_2 = \frac{\dddot{y}_3 - \frac{\ddot{y}_3}{\ddot{y}_1}\dddot{y}_1}{\ddot{y}_1} \tag{34}$$

Obviously, $\dot{y}_2$ also converges to zero exponentially.

Ultimately, with equation (17) and the preceding convergence analysis in consideration, v_2 exhibits exponential convergence towards zero. Consequently, the comprehensive proof is concluded, elucidating that the designed smooth and progressive controller (17) indeed renders the closed-loop system exponentially stable, owing to its notably vast region of attraction. □

4 Simulation

In this section, numerical simulations of the proposed controller are presented to substantiate its control efficacy and stability.

Case 1, apply control law (17) to simulate the system (5). According to Theorem 1, the initial values are chosen as $y_1(0) = 3$, ${y_1}^{(1)}(0) = -\frac{55}{24}$, ${y_1}^{(2)}(0) = 2$, and ${y_1}^{(3)}(0) = -2$. At the same time, $y_2(0) = -1$, $y_3(0) = 0.1516$, ${y_2}^{(1)}(0) = 0$, ${y_3}^{(1)}(0) = 0$.

Then, the controller parameters in (17) are chosen as

$$b_3 = 4, b_2 = 6, b_1 = 4, b_0 = 1$$

$$c_3 = \frac{24}{5}, c_2 = \frac{216}{25}, c_1 = \frac{864}{125}, c_0 = \frac{1296}{625}$$

Using the initial values described above, we conducted simulations for stabilizing the transformed model, and the results are depicted in Fig. 2. It is evident from the figures that system variables and the control variables all converge to zero within a finite time.

Case 2, apply controller (17) to simulate the system (1). The physical parameters of system (1) are taken as

$$m = 1, I = 1.2, r = 1$$

According to Theorem 1, the initial values are chosen as $x(0) = 3.3516$, ${x}^{(1)}(0) = -\frac{55}{24}$, $v_1(0) = 2$, and ${v_1}^{(1)}(0) = -2$. At the same time, $y(0) = 1$, $\theta(0) = -\frac{\pi}{4}$, ${y}^{(1)}(0) = 0$, $\theta^{(1)}(0) = 0$.

When employing the same parameters in the controller (17) as described previously, and utilizing the aforementioned initial values, simulations were conducted to stabilize the initial model. As the outcomes illustrated in Fig. 3, both system variables and control variables exhibit convergence to zero within a finite time frame.

Remark 2 In fact, the initial system and the transformed system are equivalent in theory. However, by comparing the

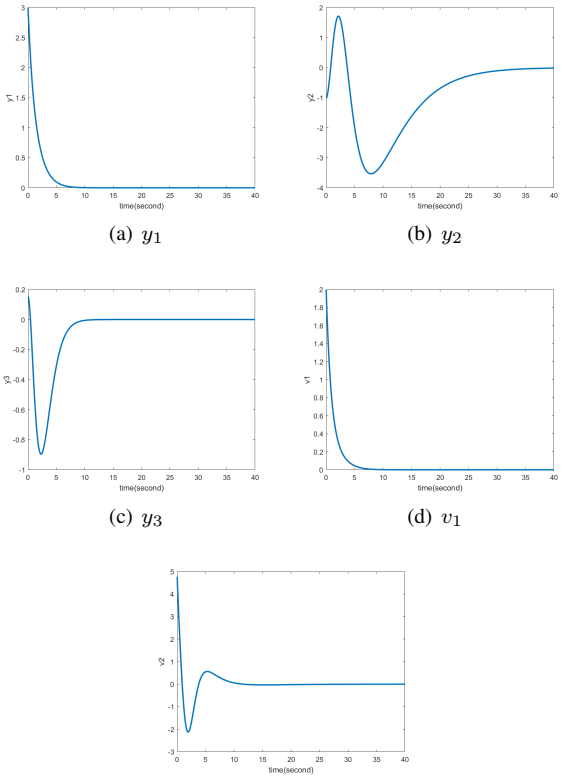

(a) y_1 (b) y_2 (c) y_3 (d) v_1 (e) v_2

Fig. 2: results of transformed system

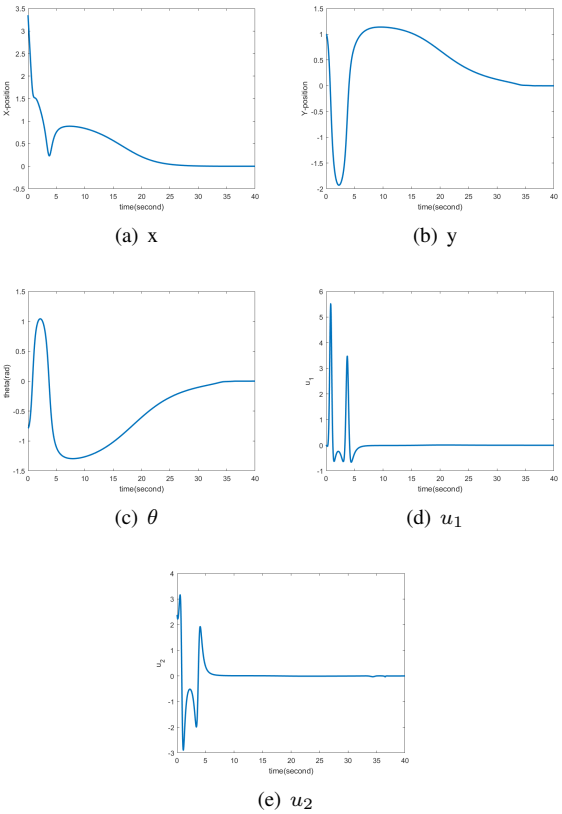

(a) x (b) y (c) θ (d) u_1 (e) u_2

Fig. 3: results of initial system

two situations of Fig.2 and Fig.3, it is not difficult to find that the position, attitude angle, and control law of the system change more smoothly after the transformation. The main reason is the introduction of tangent transformation during the coordinate transformation process of the original system. Thus, it is affected by the $\theta, \tan\theta$ when transforming back to the original system.

5 Conclusion

The stabilization of a category of second-order nonholonomic systems through a HOFA system approach has already been realized in this paper. The methodology commenced with the construction of explicit system state and control input transformations aimed at converting the second-order nonholonomic system into a second-order canonical chained form. Subsequently, the stabilization problem has been tackled utilizing the fully actuated system approach, culminating in the design of a straightforward, continuous, and smooth sub-stabilizing controller. Additionally, the corresponding region of attraction has been characterized and it can be found that the size of the attraction region is large enough. Finally, the simultaneous stabilization of the position and attitude of the second-order nonholonomic unmanned vehicle was achieved through numerical simulation, confirming the effectiveness of the method in this paper.

References

[1] Richard M Murray. "Control of nonholonomic systems using chained form". In: *Fields Inst. Commun.* 1 (1993), pp. 219–245.

[2] Andrew Richard Teel, Richard Martin Murray, and Greg Walsh. "Nonholonomic control systems: From steering to stabilization with sinusoids". In: *[1992] Proceedings of the 31st IEEE Conference on Decision and Control*. IEEE. 1992, pp. 1603–1609.

[3] LV Kolmanovksy, Mahmut Reyhanoglu, and N Harris McClamroch. "Discontinuous feedback stabilization of nonholonomic systems in extended power form". In: *Proceedings of 1994 33rd IEEE Conference on Decision and Control*. Vol. 4. IEEE. 1994, pp. 3469–3474.

[4] Reza Olfati-Saber. "Near-identity diffeomorphisms and exponential/spl epsi/-tracking and/spl epsi/-stabilization of first-order nonholonomic se (2) vehicles". In: *Proceedings of the 2002 american control conference (ieee cat. no. ch37301)*. Vol. 6. IEEE. 2002, pp. 4690–4695.

[5] Shota Washizu et al. "Nonlinear control for first-order nonholonomic system with hardware restriction and disturbance". In: *2015 10th Asian Control Conference (ASCC)*. IEEE. 2015, pp. 1–6.

[6] Mohammad Reza J Harandi and Hamid D Taghirad. "Motion control of an underactuated parallel robot with first order nonholonomic constraint". In: *2017 5th RSI International Conference on Robotics and Mechatronics (ICRoM)*. IEEE. 2017, pp. 582–587.

[7] Xu-Zhi Lai et al. "A simple and quick control strategy for a class of first-order nonholonomic manipulator". In: *Nonlinear Dynamics* 85 (2016), pp. 2261–2276.

[8] Giuseppe Oriolo and Yoshihiko Nakamura. "Control of mechanical systems with second-order nonholonomic constraints: Underactuated manipulators". In: *Proceedings of the 30th IEEE Conference on Decision and Control*. Vol. 3. Brighton, UK: IEEE. 1991, pp. 2398–2403.

[9] Giuseppe Oriolo and Yoshihiko Nakamura. "Free-joint manipulators: motion control under second-order nonholonomic constraints." In: *IROS*. Vol. 91. 1991, pp. 1248–1253.

[10] WL Xu and Bao Li Ma. "Stabilization of second-order nonholonomic systems in canonical chained form". In: *Robotics and Autonomous Systems* 34.4 (2001), pp. 223–233.

[11] Bao Li Ma and Shiu Kit Tso. "Unified controller for both trajectory tracking and point regulation of second-order nonholonomic chained systems". In: *Robotics and Autonomous Systems* 56.4 (2008), pp. 317–323.

[12] Antonella Ferrara, Luisa Giacomini, and Claudio Vecchio. "Control of nonholonomic systems with uncertainties via second-order sliding modes". In: *International Journal of Robust and Nonlinear Control: IFAC-Affiliated Journal* 18.4-5 (2008), pp. 515–528.

[13] Jundong Wu et al. "A general position control method for planar underactuated manipulators with second-order nonholonomic constraints". In: *IEEE Transactions on Cybernetics* 51.9 (2019), pp. 4733–4742.

[14] Guangren Duan. "High-order fully actuated system approaches: Part I. Models and basic procedure". In: *International Journal of Systems Science* 52.2 (2021), pp. 422–435.

[15] Guangren Duan. "High-order fully actuated system approaches: Part II. Generalized strict-feedback systems". In: *International Journal of Systems Science* 52.3 (2021), pp. 437–454.

[16] Guangren Duan. "High-order fully actuated system approaches: Part III. Robust control and high-order backstepping". In: *International Journal of Systems Science* 52.5 (2021), pp. 952–971.

[17] Guangren Duan. "High-order fully actuated system approaches: Part X. Basics of discrete-time systems". In: *International Journal of Systems Science* 53.4 (2022), pp. 810–832.

[18] Guangren Duan. "Discrete-time delay systems: part 1. Global fully actuated case". In: *Science China Information Sciences* 65.8 (2022), p. 182201.

[19] Rudolf Emil Kalman. "Mathematical description of linear dynamical systems". In: *Journal of the Society for Industrial and Applied Mathematics, Series A: Control* 1.2 (1963), pp. 152–192.

[20] Guangren Duan. "High-order fully actuated system approaches: part VII. Controllability, stabilisability and parametric designs". In: *International Journal of Systems Science* 52.14 (2021), pp. 3091–3114.

[21] Guang-Ren Duan. "Brockett's first example: An FAS approach treatment". In: *Journal of Systems Science and Complexity* 35.2 (2022), pp. 441–456.

[22] Guang-Ren Duan. "Brockett's Second Example: A FAS Approach Treatment". In: *Journal of Systems Science and Complexity* 36.5 (2023), pp. 1789–1808.

[23] Roy Featherstone. *Rigid body dynamics algorithms*. Springer, 2014.

Proceedings of the 3rd Conference on Fully Actuated System Theory and Applications
May 10-12, 2024, Shenzhen, China

Fully-Actuated Sliding Mode Synchronization Control for H-type Linear Motor System

Xiaolei Li*, Feilong Tang, Jiawei Liu, Zhihua Xiang
School of Astronautics, Harbin Institute of Technology, Harbin 150001, China
E-mail: xiaoleili@hit.edu.cn

Abstract: This article proposes a fully-actuated sliding mode synchronization control to realize high-precision tracking motion for an H-type linear motor system. Firstly, a dynamic model of the H-type linear motor system is presented, which establishes the relationship between the thrust difference and synchronization error. Secondly, utilizing the fully-actuated system theory, the dynamic model is transformed into a fully-actuated model instead of directly controlling the original model. Then, a fully actuated sliding mode synchronous controller is designed via sliding mode control and pole configuration to enhance control performance. To compensate for external disturbances and model uncertainties, an extended state observer is developed to achieve effective synchronous control for H-type linear motor system. Finally, comparative experiments are conducted on the H-type linear motor system to validate the effectiveness of the proposed method.

Key Words: H-type linear motor system, fully-actuated system theory, fully-actuated sliding mode control, extended state observer

1 Introduction

The H-type linear motor system (HLMS) has a wide applications for the fields of servo control [1, 2], such as, precise computer numerical control machines, surface mounted technology machines, lithography machines, and other applications related to linear motion owing to its high thrust, precision, and low vibration. In precise electromechanical equipment, permanent magnet linear synchronous motors (PMLSM), with their direct driving characteristics, eliminate the requirement of converting rotating motion into linear motion, thus greatly improving work efficiency [3]. They are commonly used as actuators to push the gantry stage to the designated position or track the specified trajectory. In the dual driven HLMS, synchronous control of two PMLSMs is crucial, which can reduce platform oscillation, increase stability, and improve thrust and bandwidth. Based on this, extensive researches have been conducted on the synchronous control of HLMS.

In terms of synchronous control of dual PMLSMs, Lin proposed a cross-coupled intelligent complementary sliding mode controller for the synchronous control of dual linear motors servo system [2]. He *et al*. adopted a synchronous planning control mode and an overall decoupling control mode to synchronously control the two axes. This achieves high-speed and high-precision control of the Y-direction bilinear motor, allowing simultaneous control of both axes during high-speed motion [3]. Li proposed a scheme that directly incorporates additional rotational dynamics, synchronizes the motion of two parallel motors, adjusts internal forces, and addresses parameter uncertainty [4]. Li developed a sliding mode state observer to replace sensors, resulting in a significant reduction in system chattering and achieving excellent control accuracy [5]. In order to guarantee the desired tracking performance of a linear motor control system, Sun *et al*. proposed a novel discrete-time fractional-order sliding mode control scheme [6, 7]. By combining classic cross-coupling with virtual line axis control, Chen utilized model predictive torque control to enhance dynamic response even further [8]. Shi adopted adaptive robust control to mitigate interference from measurement noise and achieve model compensation [9, 10]. Xie proposed a composite synchronous control scheme for a generalized model of dual parallel motion systems to address the issue of coupling effects [11].

In recent years, there has been flourishing development in the high-order fully-actuated (HOFA) theory since Duan's work [12–14]. HOFA is a method for eliminating state variables and increasing the system's order, which can organize the state and control variables of the under-actuated system into a single equation. Moreover, the HOFA method utilizes control variables to compensate for the known nonlinear items and original dynamics of the system, effectively transforming it into a linear system. By using the HOFA method, the new linear system can be configured with arbitrary poles to achieve a stable state in the closed-loop system. Duan proposed a generalized form of a strict feedback system and transformed it into a recursive solution of the HOFA model, which was proven to be more effective than the backstepping method [15, 16]. Duan addressed the problem of state feedback disturbance attenuation in HOFA systems with deterministic disturbances [17]. Wang designed state feedback control laws and virtual control laws [18]. By utilizing the approximate disturbance decoupling method to address unknown disturbances, Zhao developed a model for the motion of a fully-actuated system (FAS) in a six-degrees of freedom spacecraft and designed an extended state observer to estimate the total disturbance [19].

An accurate mathematical model is necessary for fully-actuated system theory to establish preferable closed-loop dynamic characteristics. However, when system model is not accurate enough, the control performance will be very poor. To tackle this issue, a fully-actuated sliding mode control (FASMC) is designed to enhance system robustness, and an extended state observer (ESO) is employed to compensate model uncertainties within a specific bandwidth.

This work was supported in part by the National Natural Science Foundation of China under Grant 62303139, in part by the Science Center Program of National Natural Science Foundation of China under Grant 62188101, and in part by the Heilongjiang Touyan Team Program. (Corresponding author: Xiaolei Li.)

The remainder of this article is as follows: In section 2, a physical model of the system will be developed, and the model will be converted into a FAS model through appropriate simplification and linear transformation. Section 3 will involve conducting a proof of the combination and stability of FASMC with ESO. Section 4 is to design experiments to validate the effectiveness of the algorithm. Section 5 provides conclusions.

2 System Model

2.1 Basic Physical Model

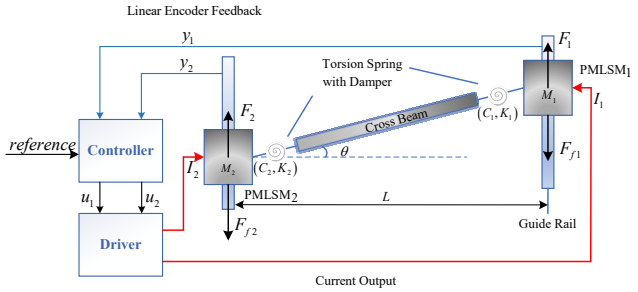

Fig. 1: The diagram of HLMS structure

The mechanical structure and electrical connection of the HLMS are illustrated in Fig. 1. In terms of the mechanical structure, both sides of the stage are equipped with linear motors that have nearly identical specifications. Crossbeams are used to establish mechanical coupling in the middle section. When the two motors operate asynchronously, synchronization errors occur, leading to deformation in both the beam and its connection with the motor.

The inclination angle of the crossbeam can be determined using a geometric relationship as

$$\theta = \arctan \frac{y_1 - y_2}{L} \approx \frac{y_1 - y_2}{L} \tag{1}$$

where θ represents the inclination angle of the crossbeam, y_1, y_2 stand for the displacement of PMLSM1 and PMLSM2, and L is the length of the crossbeam.

According to Lagrange's theorem and geometric relationships, the dynamic equation of the system is shown as

$$\begin{aligned} m_1\ddot{y}_1 &= -K_1\theta - C_1\dot{\theta} + F_1 - F_{f1} \\ m_2\ddot{y}_2 &= K_2\theta + C_2\dot{\theta} + F_2 - F_{f2} \\ J\ddot{\theta} &= -K\theta - C\dot{\theta} + \frac{1}{2}L\left(F_1 - F_2\right) \end{aligned} \tag{2}$$

where m_1, m_2 represent the equivalent mass of the dual motor system, $K_i, C_i (i = 1, 2)$ express the equivalent spring stiffness coefficient and equivalent damping coefficient at the connection between the crossbeam and the motors, respectively. $F_i, F_{fi} (i = 1, 2)$ are the electromagnetic thrust and frictional disturbance, separately. J indicates the equivalent moment of inertia of the crossbeam satisfying $J = \frac{1}{12} m_b L^2$, and m_b represents the equivalent mass of the crossbeam.

The friction disturbance is

$$F_{fi}\left(y, \dot{y}\right) = \mu_k m_i g sign\left(\dot{y}_i\right) + k_v \dot{y}_i, \quad \dot{y}_i \neq 0 \tag{3}$$

where μ_k indicates the static friction coefficient, k_v is the damping friction coefficient, m_i, g denote equivalent mass and gravitational acceleration, respectively. It can be found that friction is influenced by velocity. Furthermore, the disturbance also arises from the nonlinear characteristics of the stator magnetic field.

2.2 Fully-Actuated Dynamics Model

Based on the basic physical model above, it is challenging to analyze and control. Therefore, the following assumption can be made.

Assumption 1 *The holistic method is used to analyze the bilateral linear motor and the middle crossbeam. The research object is the y-axis coordinate of the midpoint of the crossbeam, and the external force acting on the system is simplified as the electromagnetic thrust and friction force on both sides. The simplified equation is shown as*

$$\begin{aligned} \left(m_1 + m_b + m_2\right)\ddot{y} &= F_1 + F_2 - F_{f1} - F_{f2} \\ J\ddot{\theta} &= -\left(K\theta + C\dot{\theta}\right) + \tfrac{1}{2}L\left(F_1 - F_2\right) \end{aligned} \tag{4}$$

The system's structure is divided into two parts: the position control subsystem and the synchronous control subsystem. These are controlled by the combined thrust force of two motors and the differential force of the two motors. According to **Assumption 1**, the controlled degree of freedom is reduced by one compared to the original system, which can be transformed into a fully-actuated system by the formula as

$$\begin{cases} u_c = \frac{(F_1 + F_2)}{2} \\ u_d = F_1 - F_2 \end{cases} \Leftrightarrow \begin{cases} F_1 = u_c + \frac{1}{2}u_d \\ F_2 = u_c - \frac{1}{2}u_d \end{cases} \tag{5}$$

where u_c denotes the common mode thrust of two actual electromagnetic thrusts F_1, F_2, and u_d indicates the differential mode thrust.

For tracking control, an error dynamics equation can be established as

$$\begin{aligned} \ddot{e}_y &= \ddot{y}_r + \tfrac{1}{m}\left(F_{f1} + F_{f2}\right) - \tfrac{2}{m}u_c \\ \ddot{\theta} &= -\tfrac{1}{J}\left(K\theta + C\dot{\theta}\right) + \tfrac{L}{2J}u_d \end{aligned} \tag{6}$$

where the error variable is $e_y = y_r - y$, and y_r is the reference input position of the linear motor. The total mass of the system is $m = m_1 + m_b + m_2$, which stands for the sum of the masses of the moving parts of the entire system.

Remark 1 *An analysis is conducted for equation (4): when a single-axis drive is used (such as when $F_2 = 0$), it is necessary to employ a control effect to simultaneously manage two degrees of freedom, y and θ, leading to an under-actuated system. When the double-axis drive with u_c and u_d is employed to the HLMS, it becomes fully-actuated without additional conversion, which facilitates the controller design.*

3 Main Results

3.1 Fully-actuated System Control

The conventional FAS approach adopts a method of reducing states and increasing orders. This transforms the low-order under-actuated system into a HOFA system, eliminates

the nonlinear system dynamics, converts it into a linear fully-actuated structure, and employs pole configuration for stabilization control. In Section II, the model has been established as FAS, which can utilize this theory to eliminate the nonlinear components of each control subsystem. For position and synchronization control channels, the theory of conventional FAS approach is actually equivalent to PD control with feedforward control. Based on the equations (4) and (5), the following controllers can be designed

$$\begin{aligned} u_{c_{FA}} &= \tfrac{m}{2}\ddot{y}_r + \tfrac{1}{2}\left(F_{f1} + F_{f2}\right) - a_0 e_y - a_1 \dot{e}_y \\ u_{d_{FA}} &= \tfrac{2}{L}\left(K\theta + C\dot{\theta}\right) - b_0\theta - b_1\dot{\theta} \end{aligned} \tag{7}$$

where $a_0 = -\frac{1}{2}mk_0, a_1 = -\frac{1}{2}mk_1, b_0 = \frac{2J}{L}l_0$ and $b_1 = \frac{2J}{L}l_1$ that can be used to adjust the pole positions of the position and synchronization control subsystem. The remaining portion of the equation (7) is utilized to incorporate the feedforward component, which helps to eliminate the known components and nonlinearity of the model, thereby facilitating pole configuration.

The poles of two subsystems are given as

$$\begin{aligned} \lambda_{c1,2} &= \tfrac{-k_1 \pm \sqrt{k_1^2 - 4k_0}}{2} \\ \lambda_{d1,2} &= \tfrac{-l_1 \pm \sqrt{l_1^2 - 4l_0}}{2} \end{aligned} \tag{8}$$

where, $\lambda_{c1,2}$, $\lambda_{d1,2}$ express the poles of position and synchronous loop, respectively. Pole configuration of two subsystem can be adjusted by changing the values of parameters k_0, k_1, l_0 and l_1.

3.2 Fully-actuated Sliding Mode Control

Based on the above analysis, the synchronous control system can be decomposed into the position subsystem and the synchronization subsystem. Then, HLMS can be transformed into a fully-actuated linear system with poles represented by equation (8) using the theory of FAS. However, in the application of control theory for FAS, there may be situations where the system order is too high, leading to increased model uncertainty and noise. Hence, sliding mode control can reduce the system's order. On the other hand, sliding mode control can enhance robustness and increase convergence speed in the second-order control system (9). The original system structure uses a controller (7) that is configured as

$$\ddot{x} + k_1\dot{x} + k_0 x = b u_{smc} \tag{9}$$

where u_{smc} is a sliding mode controller based on the fully-actuated control (7) design mentioned above. b represents the coefficient of control input. Consider the sliding mode variable to the following structure for the linear second-order system (9)

$$s = C_x x + \dot{x} \tag{10}$$

Choose appropriate parameters C_x, η can ensure that the following results are valid

$$\dot{s} + \eta s = \ddot{x} + \left(C_x + \eta\right)\dot{x} + C_x \eta x \tag{11}$$

If the following equation is satisfied

$$\begin{aligned} k_1 &= C_x + \eta \\ k_0 &= C_x \eta \end{aligned} \tag{12}$$

then the dynamic equation (10) of the sliding surface is equivalent to equation (9).

In order to improve the convergence speed, the following control law

$$u_{smc} = \frac{\eta}{b}s - k\left(|s|^{\frac{1}{2}} + k_s\right)\operatorname{sgn}(s) - rs \tag{13}$$

is designed to make the state s of the subsystem converge to 0, and when $s = 0$, the state variable x exponentially converges to 0. In equation (13), $k, k_s, r \in R$ are adjustable parameters. By integrating the position control subsystem and synchronous control subsystem (4), and employing fully-actuated sliding mode control (FASMC), based on the established error dynamics equation (6), it can be derived that. Firstly, the known nonlinear and poles of the system are eliminated using FAS theory shown in (7), and the poles are reconfigured to a stable state. By pole configuration, the original system was restructured into a system with the configuration as

$$\begin{aligned} \ddot{e}_y + k_1\dot{e}_y + k_0 e_y &= b_c u_{c_s} \\ \ddot{\theta} + l_1\dot{\theta} + l_0\theta &= b_d u_{d_s} \end{aligned} \tag{14}$$

where $b_c = -\frac{2}{m}, b_d = \frac{L}{2J}$, according to the sliding mode FAS theory mentioned above. Let the sliding mode variable be equation (15), utilizing FASMC (13), it can be inferred the controllers is shown in (16), respectively.

$$\begin{aligned} s_c &= C_c e_y + \dot{e}_y \\ s_d &= C_d\theta + \dot{\theta} \end{aligned} \tag{15}$$

$$\begin{aligned} u_{c_s} &= \tfrac{\eta_y}{b_c}s_c - k_c\left(|s_c|^{\frac{1}{2}} + k_{cs}\right)\operatorname{sgn}(s_c) - r_c s_c \\ u_{d_s} &= \tfrac{\eta_\theta}{b_d}s_d - k_d\left(|s_d|^{\frac{1}{2}} + k_{ds}\right)\operatorname{sgn}(s_d) - r_d s_d \end{aligned} \tag{16}$$

where

$$\begin{aligned} C_c + \eta_y &= k_1 \quad C_c\eta_y = k_0 \\ C_d + \eta_\theta &= l_1 \quad C_d\eta_\theta = l_0 \end{aligned}$$

The parameters k_d, r_d, k_c, and r_c are adjustable, which can be used to modify the approaching rate of control and robustness of system. Finally, by combining equations (7) and (16), the final control quantity is given as

$$\begin{aligned} u_c &= u_{c_{FA}} + u_{c_s} \\ u_d &= u_{d_{FA}} + u_{d_s} \end{aligned} \tag{17}$$

According to [20], it is evident that the system (6) is stable. This is the ultimate solution for the theory of FASMC, and achieving its stability is straightforward.

3.3 ESO-based Robust FASMC

It is noteworthy that the above process of controller design, is based on an ideal model and does not account for model uncertainty and external disturbances. In most practical systems, model uncertainty and external disturbances always exist. These factors not only affect control effectiveness but can also lead to system instability at times. To deal with them, an ESO-based control scheme is proposed to achieve better control performance.

For the nonlinear single degree of freedom FAS as equation (18), the general structure of the linear observer is to first establish the observation error for the known variables.

$$\begin{aligned} \dot{x}_1 &= x_2 \\ \dot{x}_2 &= f(x) + bu + d(x,t) \end{aligned} \tag{18}$$

where x_1, x_2 represents the system state variable. $f(x)$ is the function of x_1, x_2. The use of ESO aims to address uncertainties in system modeling and external disturbances $d(x,t)$. The expanded state is used to estimate the total system disturbance, and the control compensates the system to match the nominal model. Then, set the expanded state as $x_3 = d(x,t)$. The second-order system can be represented in the following form

$$\begin{cases} \dot{x}_1 = x_2 \\ \dot{x}_2 = f(x) + bu + x_3 \\ \dot{x}_3 = h(t) \end{cases} \tag{19}$$

The three states observed by the designed ESO are z_i, where $i = 1, 2, 3$. Define e_{oi} as the observation error of the observer, where $i = 1, 2, 3$. $h(t)$ is a bounded function. The observation error signal is calculated

$$e_{oi} = x_i - z_i, i = 1, 2, 3 \tag{20}$$

the structure of ESO is as follows

$$\begin{aligned} \dot{z}_1 &= z_2 + \alpha_1 e_{o1} \\ \dot{z}_2 &= z_3 + \alpha_2 e_{o1} + \beta_1 e_{o2} + f(x) + bu \\ \dot{z}_3 &= \alpha_3 e_{o1} + \beta_2 e_{o2} \end{aligned} \tag{21}$$

where $\alpha_1, \alpha_2, \alpha_3$ stand for the gain for adjusting position observation error, and β_1, β_2 represent the gain for adjusting velocity observation error. According to [21], it can be found that the error dynamics system of equations (19) − (21) converge to the origin. Similarly, ESO can be used to calculate the total disturbance of the position and synchronization control subsystem, represented by z_{c3} and z_{d3} respectively. The compensation for the estimated system disturbance is in the following form

$$u_t = u - \frac{1}{b} z_3 \tag{22}$$

where u_t is the control quantity after compensation, u is the output generated by FASMC as shown in (13). $b_c = -\frac{2}{m}$ and $b_d = \frac{L}{2J}$ are the control input coefficient of the position and synchronization control subsystem respectively.

Theorem 1 *The closed-loop system's control variable (22), composed of FASMC (13) and LESO (21), can ultimately maintain the stability and ensure robustness of HLMS. The control expression with disturbance observer is organized in the equations (23),*

$$\begin{aligned} u_c =& \frac{m}{2}\ddot{y}_r + \frac{1}{2}(F_{f1} + F_{f2}) - a_0 e_y - a_1 \dot{e}_y + \\ & \frac{\eta_y}{b_c} s_c - k_c \left(|s_c|^{\frac{1}{2}} + k_{cs} \right) \operatorname{sgn}(s_c) - r_c s_c + \frac{m}{2} z_{c3} \\ u_d =& \frac{2}{L}\left(K\theta + C\dot{\theta} \right) - b_0 \theta - b_1 \dot{\theta} + \\ & \frac{\eta_\theta}{b_d} s_d - k_d \left(|s_d|^{\frac{1}{2}} + k_{ds} \right) \operatorname{sgn}(s_d) - r_d s_d - \frac{2J}{L} z_{d3} \end{aligned} \tag{23}$$

Proof 1 *Firstly, by combining equations (9), (13), (19) and (21), the error dynamics equation of the system is established. The error system form is organized using a fully actuated sliding mode controller and an extended state observer*

$$\begin{aligned} \begin{bmatrix} \dot{x} \\ \dot{e}_o \end{bmatrix} &= \begin{bmatrix} A & B_e \\ 0 & A_e \end{bmatrix} \begin{bmatrix} x \\ e_o \end{bmatrix} \\ &+ B_s \left(|s|^{\frac{1}{2}} + k_s \right) \operatorname{sgn}(s) + B_h h(t) \end{aligned} \tag{24}$$

where $x = \begin{bmatrix} x_1 & x_2 \end{bmatrix}^T, e_o = \begin{bmatrix} e_{o1} & e_{o2} & e_{o3} \end{bmatrix}^T$ *is the augmented state variable in the system.* $B_h = \begin{bmatrix} 0 & 0 & 0 & 0 & 1 \end{bmatrix}^T, B_s = \begin{bmatrix} 0 & -bk & 0 & 0 & 0 \end{bmatrix}^T$ *represent input matrix of perturbation term and nonlinear components of FASMC. The remaining parts are defined as*

$$A = \begin{bmatrix} 0 & 1 \\ -brC_x & -br \end{bmatrix}, A_e = \begin{bmatrix} -\alpha_1 & 1 & 0 \\ -\alpha_2 & -\beta_1 & 1 \\ -\alpha_3 & -\beta_2 & 0 \end{bmatrix}$$

$$B_e = \begin{bmatrix} 0 & 0 & 0 \\ 0 & 0 & 1 \end{bmatrix}$$

For the observation error subsystem

$$\dot{e}_o = A_e e_o + B_h h(t)$$

choose the Lyapunov function in this form

$$V_e = e_o^T P_e e_o$$

where P_e *is a symmetric positive definite matrix that satisfies the Lyapunov equation* $A_e^T P_e + P_e A_e = -Q_e$*, and* Q_e *is a positive definite matrix. Find the derivative of the energy function with respect to time*

$$\begin{aligned} \dot{V}_e &= -e_o^T Q_e e_o + 2h B_h^T P_e e_o \\ &\le -\lambda_{\min}(Q_e) \|e_o\|^2 + 2 \left\| B_h^T P_e \right\| \|e_o\| \|h\| \\ &\le -\left(\lambda_{\min}(Q_e) \|e_o\| - 2 \left\| B_h^T P_e \right\| \|h\| \right) \|e_o\| \end{aligned}$$

If h *is bounded and satisfies* $\|e_o\| \ge \frac{2\|P_e B_h\| \|h\|}{\lambda_{\min}(Q)}$*,* $\dot{V}_e \le 0$*. Then, it can be observed that the norm of the observation error tends to decrease. However, under this condition, it may not converge to* 0*. This means that observation errors always exist. Due to the presence of observation errors caused by disturbances, the sign term in sliding mode control can effectively reduce this residual uncertainty at a minimal cost. By adjusting the parameter* k_s *to an appropriate range, system stability can be achieved, and control performance can be guaranteed. Select the appropriate parameters to meet*

$$\dot{s} + \eta s = bu$$

Put it into equation (22)

$$\dot{s} = -brs - bk\left(|s|^{\frac{1}{2}} + k_s \right) \operatorname{sgn}(s) + e_{o3}$$

If $bkk_s > \|e_{o3}\|_\infty$ *is satisfied,* $\dot{s} \le 0$*. Then* s *can converge to* 0 *in finite time. According to the relationship between* s *and the system state, the system state also converges to the equilibrium point.* ■

Remark 2 *Significantly, employing this method to observe disturbances results in a limited observation errors. Since matrix* $P_e, B_h, and Q$ *are constant matrices, the factors influencing this limit are contained in the rate of change* h *of the lumped disturbance* d*. When estimating static disturbances, setting* $h = 0$ *can lead to an unbiased estimation. When there are significant changes in model uncertainty or external disturbances and they exhibit a certain degree of variation, the extended observer experiences significant observation errors. Due to the bandwidth limitation of ESO, it is necessary to incorporate as much known nonlinear model information as possible into the feedforward control. This will enable ESO to better observe and alleviate the influence of unknown disturbances.*

4 Experimental Results

4.1 Experimental Platform

As shown in Fig. 2, Akribis's HLMS is equipped with PMLSMs on both sides of the stage. The permanent magnets are affixed to the grooves of the marble platform, and the motor coils on both sides of the crossbeam are energized to produce electromagnetic thrust, propelling the platform to move in a straight line. Both motors are equipped with AC servo drives for power delivery. The controller on the communication line is implemented on the TwinCat platform in Beckhoff's industrial control computer and programmed using the ST language of the IEC61131-3 protocol. The industrial computer can receive the position measurement signal with a resolution of $0.1\mu m$ feedback from the grating ruler, establish a feedback control loop, and transmit current instructions to the driver through the EtherCat network port. Forces are generated on both sides of the beam. PMLSM1 experiences electromagnetic thrust, friction resistance, and conduction force from the beam, and the same applies to PMLSM2.

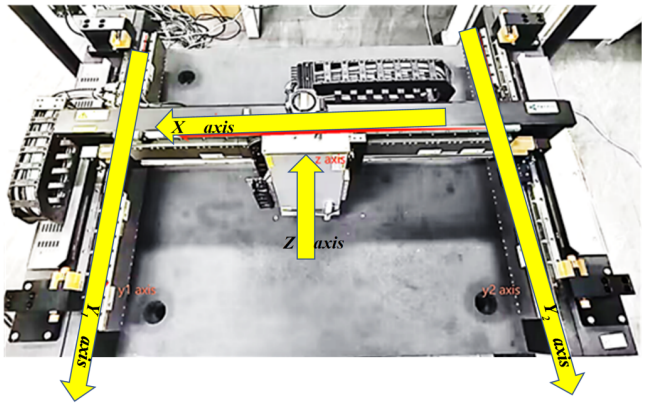

Fig. 2: The diagram of HLMS platform

4.2 Positioning Motion Control

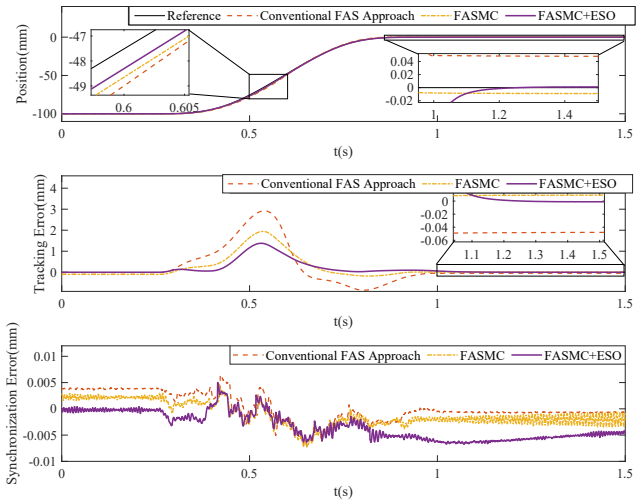

Fig. 3: Comparison of three control strategies in positioning control

A step signal with the amplitude of $100mm$ and the S-shaped speed profile, is utilized in this experiment to evaluate the positioning performance of the controllers. The experimental results are depicted in Fig. 3. From the standpoint of rise time and overshoot, the three control methods exhibit similar rise times and no overshoot. In terms of tracking error, a conventional fully actuated controller has a static error of about $0.6\mu m$, while a fully actuated SMC controller has a static error of about $10\mu m$. However, using a FASMC with ESO controller can reduce the static error to about $15\mu m$. In terms of synchronization errors, the conventional FAS control performs well, and the synchronization error stabilizes at about $0.9\mu m$. The FASMC method exhibits strong oscillations due to the presence of symbol terms during control. In contrast, the FASMC with ESO control method can partially mitigate the oscillation issue associated with FASMC method, leading to a gradual reduction in synchronization error towards 0. Overall, FASMC with ESO performs significant advantages in positioning accuracy compared to the conventional FAS control and SMC. In terms of synchronization errors caused by positioning, the FASMC with ESO method can mitigate the synchronization error oscillation issue associated with the FASMC method.

4.3 Tracking Motion Control

The experiment uses a sine signal with the amplitude of $40mm$ and the angular velocity of $\omega = \pi rad/s$ as the tracking signal. The experimental results of the three control methods are shown in Fig. 4. It is evident that in terms of tracking error, the conventional FAS control exhibits the maximum tracking error of $124.3\mu m$, the FASMC method demonstrates a better tracking effect of $67.5\mu m$, and the FASMC with ESO control method can achieve the best tracking error of $14.3\mu m$. In Fig. 5, it is evident that ESO reduces control oscillation to a certain extent. At the same time, in terms of synchronization error performance, the FASMC with ESO control method exhibits similar synchronization error amplitudes to those of the conventional FAS control and FASMC method. Overall, in terms of tracking performance, the FASMC with ESO control method performs equally well in tracking motion compared to conventional FAS control and FASMC methods, and excels in reducing tracking errors.

To quantify the control performance, the tracking error magnitudes of three controllers are presented in Table 1. These errors represent the positioning error in the positioning control experiment, the tracking error and the synchronization error in the tracking control experiment, as illustrated in the table. By comparison, FASMC with ESO can achieve a balance between tracking performance and synchronization performance. It is evident that FASMC with ESO demonstrates a significant improvement in control accuracy for both position and tracking control. This indirectly indicates its strong ability to compensate for disturbances. In addition, *Synchr Error* is an abbreviation for synchronization error of HLMS.

5 Conclusion

This article proposes fully-actuated sliding mode synchronization control approach with ESO for HLMS. For addressing the synchronization control issue, a fully-actuated error dynamics model is presented, whose u_c and u_d can explicitly express the synchronization dynamics of HLMS. To

Table 1: Tracking Error of Three Control Strategies

Control Strategies	Conventional FAS Control	FASMC	FASMC+ESO
Positing Error	$50\mu m$	$10\mu m$	$0.6\mu m$
Tracking Error	$124.3\mu m$	$67.5\mu m$	$14.3\mu m$
Synchr Error	$15.2\mu m$	$14.8\mu m$	$16.1\mu m$

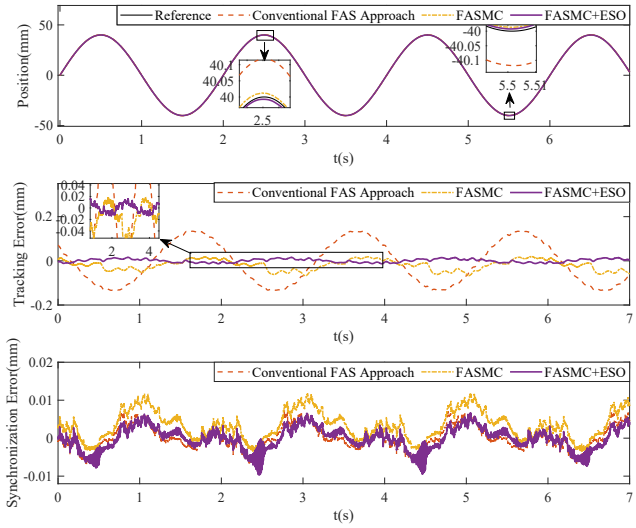

Fig. 4: Comparison of tracking sinusoidal signal

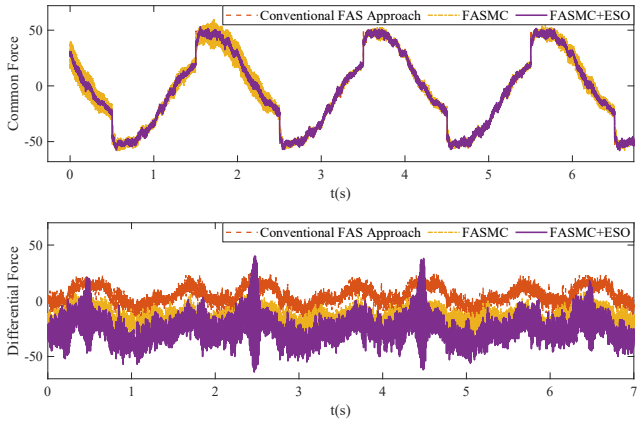

Fig. 5: Common mode and differential mode control inputs

achieve better control performance, FASMC approach is designed with the preferable robustness. Additionally, the ESO is raised to enhance the capabilities of disturbance observation and compensation of HLMS. According to experimental results, FASMC with ESO can significantly improve tracking motion control performance, compared with the conventional FAS control and FASMC.

References

[1] C. Bai, Z. Yin, Y. Zhang and J. Liu, "Robust Predictive Control for Linear Permanent Magnet Synchronous Motor Drives Based on an Augmented Internal Model Disturbance Observer," in *IEEE Transactions on Industrial Electronics*, vol. 69, no. 10, pp. 9771-9782, Oct. 2022

[2] F.-J.Lin, P. -H. Chou, C. -S. Chen and Y. -S. Lin, "DSP-Based Cross-Coupled Synchronous Control for Dual Linear Motors via Intelligent Complementary Sliding Mode Control," in *IEEE Transactions on Industrial Electronics*, vol. 59, no. 2, pp. 1061-1073, Feb. 2012.

[3] Y. He et al., "Research on Dual-Linear Motor Synchronous Control in the High-precision Gantry Motion Platform," *2017 IEEE 19th Electronics Packaging Technology Conference (EPTC)*, Singapore, pp. 1-5, 2017.

[4] C. Li, C. Li, Z. Chen and B. Yao, "Advanced Synchronization Control of a Dual-Linear-Motor-Driven Gantry With Rotational Dynamics" in *IEEE Transactions on Industrial Electronics*, vol. 65, no. 9, pp. 7526-7535, Sept. 2018.

[5] Z. Li, S. Zhou, Y. Xiao and L. Wang, "Sensorless Vector Control of Permanent Magnet Synchronous Linear Motor Based on Self-Adaptive Super-Twisting Sliding Mode Controller," in *IEEE Access*, vol. 7, pp. 44998-45011, 2019.

[6] G. Sun, L. Wu, Z. Kuang, Z. Ma, J. Liu, "Practical tracking control of linear motor via fractional-order sliding mode,". *Automatica*, vol. 94, p. 221-235, 2018.

[7] G. Sun, Z. Ma and J. Yu, "Discrete-Time Fractional Order Terminal Sliding Mode Tracking Control for Linear Motor," in *IEEE Transactions on Industrial Electronics*, vol. 65, no. 4, pp. 3386-3394, April 2018.

[8] Y. Chen, Z. Dong and C. Liu, "Combined Cross-Coupled and Electronic Virtual Line Shafting Control for Dual-Motor System," *IECON 2022 – 48th Annual Conference of the IEEE Industrial Electronics Society*, Brussels, Belgium, pp. 1-6, 2022.

[9] P. Shi, W. Sun, X. Yang, I. J. Rudas and H. Gao, "Master-Slave Synchronous Control of Dual-Drive Gantry Stage With Cogging Force Compensation," in *IEEE Transactions on Systems, Man, and Cybernetics: Systems*, vol. 53, no. 1, pp. 216-225, Jan. 2023.

[10] P. Shi, W. Sun and X. Yang, "RBF Neural Network-Based Adaptive Robust Synchronization Control of Dual Drive Gantry Stage With Rotational Coupling Dynamics," in *IEEE Transactions on Automation Science and Engineering*, vol. 20, no. 2, pp. 1059-1068, April 2023.

[11] B. Xie, L. Lei, Y. Yao and Y. Li, "Advanced Synchronous Control of Dual Parallel Motion Systems," in *IEEE Transactions on Industrial Electronics*, vol. 70, no. 2, pp. 1270-1281, Feb. 2023.

[12] G. Duan,"High-order System Approaches: I. Fully-actuated Systems and Parametric Designs,". *Acta Automatica Sinica*, 46(7): 1333-1345, 2020.

[13] G. Duan,"High-order system approaches: II. Controllability and full-actuation". *Acta Automatica Sinica*, 46(8): 15711581 , 2020.

[14] G. Duan,"High-order System Approaches: III. Observability and Observer Design". *Acta Automatica Sinica*, 46(9): 1885-1895, 2020.

[15] G. Duan, "High-order fully actuated system approaches: Part I. Models and basic procedure,". *International Journal of Systems Science*, vol. 52, no. 2, pp. 422-435, 2021

[16] G. Duan, "High-order fully actuated system approaches: Part II. Generalized strict-feedback systems,". *International Journal of Systems Science*, vol. 52, no. 3, pp. 437-454, 2021

[17] G. Duan, "High-order fully-actuated system approaches: Part VI. Disturbance attenuation and decoupling,". *International Journal of Systems Science*, vol. 52, no. 10, pp. 2161-2181, 2021

[18] N. Wang, X Liu, C Liu. "Almost Disturbance Decoupling for HOFA Nonlinear Systems with Strict-Feedback Form,". *Journal of Systems Science and Complexity*, 2022

[19] Q. Zhao , G.Duan ."Fully Actuated System Approach for 6DOF Spacecraft Control Based on Extended State Observer,".*Journal of Systems Science and Complexity*, 2022

[20] H. Khalil, "Nonlinear Systems (3rd Ed.)," 2002.

[21] Y. Li, P. Tan, J. Liu, and Z. Chen, "A Super-Twisting Extended State Observer for Nonlinear Systems,". *Mathematics*, vol. 10, no. 19, p. 3584, 2022

Proceedings of the 3rd Conference on Fully Actuated System Theory and Applications
May 10-12, 2024, Shenzhen, China

Prescribed-Time Tracking Control for Autonomous Underwater Vehicles

Shihui Jiang, Jing Fang, Xing Liu, Jinhong Yang, Liming Hao
CSSC Systems Engineering Research Institute, Beijing, P. R. China
E-mail: shihuijiang@hotmail.com, fangjing1_cssc@hotmail.com, liuxing_cssc@hotmail.com, yangjinhong_cssc@hotmail.com, haoliming_cssc@hotmail.com

Abstract: An uncertain ocean environment is a huge challenge for tracking control of autonomous underwater vehicles (AUVs) because the unknown external disturbance degrades the control performance. Motivated by this point, this paper proposes prescribed-time tracking control (PTC) with adaptive disturbance observer (ADO) for 4-DOF autonomous underwater vehicles, which ensures trajectory tracking convergence time within the range of a prescribed time under such an uncertain environment. By coupling a settling time function to construct prescribed-time transformation into the Lyapunov function and introducing a new transformed error, the convergence of the system error is provable. The simulation results validate the effectiveness of the proposed control scheme.

Key Words: Autonomous underwater vehicles (AUVs), Prescribed-time tracking control (PTC), Adaptive disturbance observer

1 Introduction

The ocean is home to abundant food and natural resources, many of which remain unexplored. Autonomous underwater vehicles (AUVs) are typical marine mechatronics systems that are utilized for exploration in these hostile working environments [1–4]. In recent years, a growing number of researchers have focused on the field of underwater exploration using AUVs [5].

However, the tracking control technique of AUVs is a challenging endeavor, largely due to the highly nonlinear dynamics and unknown uncertainties of the system dynamics. Furthermore, the complex ocean environment adds disturbances to the maneuvering of AUVs. Given these challenges, there is a need for a control scheme that provides robustness against uncertainties and disturbances.

To mitigate potential negative effects from unknown disturbances and unmodeled dynamics, some robust trajectory tracking controllers for AUVs have been developed, such as sliding mode control (SMC) [6, 7] and robust PID [8]. However, the above methods are based on the worst-case uncertainties, which are too conservative and limit a better control performance. Disturbance observer (DO) provides an alternative way to attenuate the influence of these uncertainties. A variety of DO has been proposed in the literature, like nonlinear observer [9], sliding mode observer [10], data-driven observer [11], and so on. Nevertheless, most of them require that the first-order derivative of the disturbance tends to be zero, which does not conform to the features of ocean environments exactly. To address the fast-varying uncertainties, an adaptive disturbance observer is adopted to estimate the ocean uncertainties in this study.

Furthermore, the convergence speed is a critical performance metric for AUV trajectory tracking to achieve time-critical tasks, that is, some tasks must be completed in a given time interval. To address this issue, various research has been proposed based on finite-time or fixed-time theories [12, 13], which have a wide range of applications [14, 15]. Although this fixed/finite-time stability can guarantee convergence speed and enhance disturbance rejection performance, these control schemes bring implicit convergence time, which is not beneficial in practical AUV applications. Prescribed-time control (PTC) provides an effective way to address the explicit convergence time determined by engineers.

Driven by the foregoing literature, we propose a new prescribed time trajectory tracking control coupling with an adaptive disturbance observer to address trajectory tracking control of AUVs subject to external disturbances. The main contributions in this paper are twofold:

1) A novel speed function is introduced to achieve the prescribed-time control for AUVs. Compared with finite-time or fixed-time controllers, the convergence time of PTC can be determined by directly setting one parameter rather than estimating convergence time and range by complex formulations.

2) The adaptive disturbance observer is first introduced to AUV control. In comparison with conventional disturbance observers, the ADO enjoys better disturbance attenuation performance.

This paper is organized as follows. The kinematics and kinetics for AUVs are introduced in Section 2. Section 3 designs the prescribed-time tracking controller with ADO. Then, simulation results demonstrate the effectiveness of the proposed scheme in Section 4. Section 5 gives the conclusion.

2 AUV Modelling

Referring to Fig. 1, B-Frame and I-Frame are the body-fixed frame and the inertial reference frame, respectively. Denote the vehicle position in I-Frame as $[x, y, z]^{\mathrm{T}}$, the attitude in I-Frame as ψ, the linear velocity in B-Frame as $[v_x, v_y, v_z]^{\mathrm{T}}$, and the angular velocity in B-Frame as $[\omega_x, \omega_y, \omega_z]^{\mathrm{T}}$. According to [16, 17], the roll and pitch angles are considerably small, i.e., $\omega_x \approx 0$ and $\omega_y \approx 0$. Consequently, for simplification, the reduced-order (4DOF) AUV model is adopted in this study. Denote $\boldsymbol{\eta} = [x, y, z, \psi]^{\mathrm{T}}$, $\boldsymbol{v} = [v_x, v_y, v_z, \omega]^{\mathrm{T}}$. One can obtain its kinematics, i.e., the transformation relationship from B-Frame to I-Frame as follows:

$$\dot{\boldsymbol{\eta}} = \boldsymbol{J}(\boldsymbol{\eta})\boldsymbol{v}, \tag{1}$$

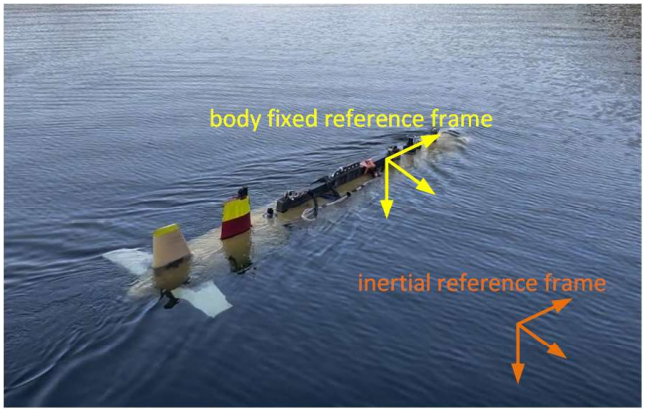

Fig. 1: Two reference frames for AUV

where

$$\boldsymbol{J}(\boldsymbol{\eta}) = \begin{bmatrix} \cos\psi & -\sin\psi & 0 & 0 \\ \sin\psi & \cos\psi & 0 & 0 \\ 0 & 0 & 1 & 0 \\ 0 & 0 & 0 & 1 \end{bmatrix}. \tag{2}$$

Moreover, the dynamics of AUVs in B-Frame are formulated as follows:

$$\boldsymbol{M}\dot{\boldsymbol{v}} + \boldsymbol{C}(v)\boldsymbol{v} + \boldsymbol{D}(v)\boldsymbol{v} = \boldsymbol{\tau} + \boldsymbol{d}, \tag{3}$$

where $\boldsymbol{M} \in \mathbb{R}^{4\times4}$ is the inertial matrix of the reduced-order AUV model; $\boldsymbol{C}(\boldsymbol{v})$ denotes the matrix of Coriolis and Centripetal forces; $\boldsymbol{D}(\boldsymbol{v})$ is the hydrodynamic damping matrix including linear and quadratic drag vector. The control forces and moments are grouped in the vector $\boldsymbol{\tau} = [\tau_x, \tau_y, \tau_z, \tau_w]^{\mathrm{T}}$, which denotes the propulsion forces and moments acting on the AUV; $\boldsymbol{d} = [d_1, d_2, d_3, d_4]$ represents the lumped external disturbances.

Due to parasite dynamics, parameter uncertainties, and the hydrodynamic ocean environment, $\boldsymbol{M}$, $\boldsymbol{C}$, and $\boldsymbol{D}$ are rewritten as:

$$\begin{aligned} \boldsymbol{M} &= \boldsymbol{M}_0 + \Delta\boldsymbol{M}, \\ \boldsymbol{C} &= \boldsymbol{C}_0 + \Delta\boldsymbol{C}, \\ \boldsymbol{D} &= \boldsymbol{D}_0 + \Delta\boldsymbol{D}, \end{aligned}$$

where $\boldsymbol{M}_0$, $\boldsymbol{C}_0$, $\boldsymbol{D}_0$ indicate the nominal values of $\boldsymbol{M}$, $\boldsymbol{C}$, $\boldsymbol{D}$, respectively; $\Delta\boldsymbol{M}$, $\Delta\boldsymbol{C}$, $\Delta\boldsymbol{D}$ denote the offset of $\boldsymbol{M}$, $\boldsymbol{C}$, $\boldsymbol{D}$, respectively.

Using the above equations, we have

$$\boldsymbol{M}_0\dot{\boldsymbol{v}} + \boldsymbol{C}_0(v)\boldsymbol{v} + \boldsymbol{D}_0(v)\boldsymbol{v} = \boldsymbol{\tau} + \boldsymbol{d}_\zeta, \tag{4}$$

where $\boldsymbol{d}_\zeta = -\Delta\boldsymbol{M} - \Delta\boldsymbol{C} - \Delta\boldsymbol{D} + \boldsymbol{d}$.

The nominal system parameters are given by

$$\boldsymbol{M}_0 = diag[-X_u, -Y_v, -Z_w, -N_r], \tag{5}$$

$$\boldsymbol{C}_0(\boldsymbol{v}) = \begin{bmatrix} 0 & 0 & 0 & -mv_y \\ 0 & 0 & 0 & -mv_x \\ 0 & 0 & 0 & 0 \\ -mv_y & -mv_x & 0 & 0 \end{bmatrix}, \tag{6}$$

$$\boldsymbol{D}_0(\boldsymbol{v}) = \boldsymbol{D}_1(\boldsymbol{v}) + \boldsymbol{D}_2(\boldsymbol{v}), \tag{7}$$

where m and I_z are the mass and the movement inertial of the AUV, respectively; X_u, Y_v, Z_w and N_r denote the parameters associated with the added mass effects; $\boldsymbol{D}_1(\boldsymbol{v})$ and $\boldsymbol{D}_2(\boldsymbol{v})$ are linear and quadratic hydrodynamic damping matrix, given by:

$$\begin{aligned} \boldsymbol{D}_1(\boldsymbol{v}) &= \begin{bmatrix} X_u & 0 & 0 & 0 \\ 0 & Y_v & 0 & 0 \\ 0 & 0 & Z_w & 0 \\ 0 & 0 & 0 & N_r \end{bmatrix}, \\ \boldsymbol{D}_2(\boldsymbol{v}) &= \begin{bmatrix} X_{u|u|}|v_x| & 0 & 0 & 0 \\ 0 & Y_{v|v|}|v_y| & 0 & 0 \\ 0 & 0 & Z_{w|w|}|v_z| & 0 \\ 0 & 0 & 0 & N_{r|r|}|w| \end{bmatrix}, \end{aligned} \tag{8}$$

where $X_{u|u|}$, $Y_{v|v|}$, $Z_{w|w|}$ and $N_{r|r|}$ denote the parameters associated with the added mass effects.

The following assumption is used.

Assumption 1 *Each element d_{ζ_i} of the disturbance $\boldsymbol{d}_\zeta$, $i = 1, 2, 3, 4$, is bounded and Lipschitz continuous, that is, $\|d_{\zeta_i}\| \leq \bar{d}_{\zeta_i}$ and $\dot{d}_{\zeta_i} \leq \bar{\dot{d}}_{\zeta_i}$, $\bar{d}_{\zeta_i}$ and $\bar{\dot{d}}_{\zeta_i}$ are the unknown positive constants. These parameters typically depends on the marine situations.*

The control objective is to design a controller to make practical posture $\boldsymbol{\eta}$ of AUVs track the desired trajectory $\boldsymbol{\eta}_d$, that is, the tracking error $\boldsymbol{e}_\eta$ can converge into an arbitrarily small neighbourhood of zero under the external disturbances.

3 Prescribed-Time Tracking Control

To achieve the control objective, the prescribed-time controller with adaptive disturbance observer is put forward in this paper. To begin with, the design of adaptive disturbance observer is introduced to address the parasite dynamics of AUVs.

3.1 Adaptive Disturbance Observer

Before designing the controller, adaptive observers are constructed to estimate the complex disturbances, To address these disturbances, the adaptive observer is designed as follows [18]:

$$\dot{\hat{\boldsymbol{v}}} = \boldsymbol{f} + G(\boldsymbol{v} - \hat{\boldsymbol{v}}) + \hat{\boldsymbol{\zeta}} + K\dot{\hat{\boldsymbol{\zeta}}}, \tag{9a}$$

$$\dot{\hat{\boldsymbol{\zeta}}} = \Gamma K(\boldsymbol{v} - \hat{\boldsymbol{v}}), \tag{9b}$$

$$\hat{\boldsymbol{d}}_\zeta = G\boldsymbol{M}_0(\boldsymbol{v} - \hat{\boldsymbol{v}} + K\hat{\boldsymbol{\zeta}}), \tag{9c}$$

where $\boldsymbol{f} = {\boldsymbol{M}_0}^{-1}(\boldsymbol{\tau} - \boldsymbol{C}_0(v)\boldsymbol{v} - \boldsymbol{D}_0(v)\boldsymbol{v})$ and $\hat{\boldsymbol{v}}$ is the estimate of $\boldsymbol{v}$, respectively; $\hat{\boldsymbol{d}}_\zeta$ denotes the estimate of the lumped external disturbances $\boldsymbol{d}_\zeta$; and Γ, G are positive diagonal matrices to be designed.

The adaptive gain matrix K is updated as follows:

$$\dot{K} = -GK + 1. \tag{10}$$

According to (9), we can define the estimation errors for 4-DOF AUVs as $\tilde{\boldsymbol{d}}_\zeta = \hat{\boldsymbol{d}}_\zeta - \boldsymbol{d}_\zeta$. Then, one has

$$\dot{\tilde{\boldsymbol{d}}}_\zeta = -G\tilde{\boldsymbol{d}}_\zeta - \dot{\boldsymbol{d}}_\zeta \tag{11}$$

Remark 1 *Compared with the conventional nonlinear disturbance observer [19, 20], the ADOs not only possess a simple structure but also address the fast-varying disturbances, that is, $\dot{\boldsymbol{d}}_\zeta$ is not required to tend to zero.*

3.2 Prescribed-Time Control Design

Before designing prescribed-time control for AUVs, the following Lemma is presented to help controller design.

Lemma 1 *[21] If a speed function is constructed as follows:*

$$\rho(t) = \begin{cases} \frac{T^4(1+t^2)}{(1-k_f)(T-t)^4+k_f T^4(1+t^2)}, & \text{if } 0 \le t < T \\ \frac{1}{k_f}, & \text{if } t > T \end{cases} \tag{12}$$

where $k_f \ll 1$ is a user-determined parameter. Then, the following properties hold:

i) $\rho(t)$ is a positive and strict-increasing function for $t \in [0, T)$ and $\rho(0) = 1$ and for $t \in [T, \infty)$, $\rho(t) = \frac{1}{k_f}$, and $\rho(t) \in [1, \frac{1}{k_f}]$ for $\forall t \ge 0$.

ii) $\rho(t)$ is C^n for $\forall t \ge 0$ and $\dot{\rho}(t) \ge 0$ is continuous and bounded.

iii) $\dot{\rho}(t)/\rho(t)$ and $(d/dt)(\dot{\rho}(t)/\rho(t))$ are also continuously differentiable and bounded functions.

It is aimed at controlling the AUV to track a desired trajectory while cruising. To achieve this goal, a prescribed-time tracking controller with an adaptive disturbance observer is exploited in the following. In the following, we will integrate the adaptive disturbance observers into a prescribed performance control scheme using backstepping techniques.

Define the tracking position error and the velocity error as follows:

$$\begin{aligned} \boldsymbol{e}_\eta &= \boldsymbol{\eta}_d - \boldsymbol{\eta}, \\ \boldsymbol{e}_v &= \boldsymbol{\alpha}_1 - \boldsymbol{v}, \end{aligned} \tag{13}$$

where $\boldsymbol{\eta}_d$ is the desired posture and $\boldsymbol{\alpha}_1$ is an intermediate control vector to be designed.

According to the above definitions, the auxiliary errors are formulated as follows:

$$\begin{aligned} \boldsymbol{E}_\eta &= \rho \boldsymbol{e}_\eta, \\ \boldsymbol{E}_v &= \rho \boldsymbol{e}_v, \end{aligned} \tag{14}$$

Choose a Lyapunov function as follows.

$$V_1 = \frac{1}{2} \boldsymbol{E}_\eta^T \boldsymbol{E}_\eta. \tag{15}$$

To ensure the system stability, the intermediate control vector is designed as follows.

$$\boldsymbol{\alpha}_1 = \boldsymbol{J}(\eta)^{-1}(\boldsymbol{k}_1 \boldsymbol{e}_\eta + \dot{\boldsymbol{\eta}}_d + \frac{\dot{\rho}}{\rho} \boldsymbol{e}_\eta), \tag{16}$$

where $\boldsymbol{k}_1 > 0$ is the designed control parameter matrix with appropriate dimension.

Then, the derivative of (15) comes to

$$\begin{aligned} \dot{V}_1 &= \boldsymbol{E}_\eta^T \dot{\boldsymbol{E}}_\eta \\ &= \boldsymbol{E}_\eta^T (\dot{\rho} \boldsymbol{e}_\eta + \rho \dot{\boldsymbol{e}}_\eta) \\ &= \boldsymbol{E}_\eta^T (\dot{\rho} \boldsymbol{e}_\eta + \rho(\dot{\eta}_d - \boldsymbol{J}(\eta)(\boldsymbol{\alpha}_1 - \boldsymbol{e}_v))) \\ &= -\boldsymbol{E}_\eta^T \rho \boldsymbol{k}_1 \boldsymbol{e}_\eta + \boldsymbol{E}_\eta^T \rho \boldsymbol{J}(\eta) \boldsymbol{e}_v \\ &= -\boldsymbol{E}_\eta^T \boldsymbol{k}_1 \boldsymbol{E}_\eta + \boldsymbol{E}_\eta^T \boldsymbol{J}(\eta) \boldsymbol{E}_v \end{aligned} \tag{17}$$

Furthermore, we choose the overall Lyapunov function as follows:

$$V_2 = V_1 + \boldsymbol{E}_v^T \boldsymbol{E}_v + \tilde{\boldsymbol{d}}_\zeta^T \tilde{\boldsymbol{d}}_\zeta. \tag{18}$$

In light of the above equation, and substituting the estimation error dynamics (11) of the adaptive disturbance observer for external disturbances, we have

$$\begin{aligned} \dot{V}_2 &= \dot{V}_1 + \boldsymbol{E}_v^T \dot{\boldsymbol{E}}_v + \tilde{\boldsymbol{d}}_\zeta^T \dot{\tilde{\boldsymbol{d}}}_\zeta \\ &= -\boldsymbol{E}_\eta^T \boldsymbol{k}_1 \boldsymbol{E}_\eta + \boldsymbol{E}_\eta^T \boldsymbol{J}(\eta) \boldsymbol{E}_v + \boldsymbol{E}_v^T (\dot{\rho} \boldsymbol{e}_v + \rho(\dot{\boldsymbol{\alpha}}_1 \\ &\quad - \boldsymbol{M}_0^{-1}(\boldsymbol{\tau} + \boldsymbol{d}_\zeta - \boldsymbol{C}_0(v)\boldsymbol{v} - \boldsymbol{D}_0(v)\boldsymbol{v}))) \\ &\quad + \tilde{\boldsymbol{d}}_\zeta^T (-G \tilde{\boldsymbol{d}}_\zeta - \dot{\boldsymbol{d}}_\zeta). \end{aligned} \tag{19}$$

To validate the stability and the convergence, the controller is designed as follows

$$\begin{aligned} \boldsymbol{\tau} = \boldsymbol{M}_0(\dot{\boldsymbol{\alpha}}_1 + \frac{\dot{\rho}}{\rho} \boldsymbol{e}_v + \boldsymbol{k}_2 \boldsymbol{e}_v) - \hat{\boldsymbol{d}}_\zeta + \boldsymbol{C}_0(v)\boldsymbol{v} \\ + \boldsymbol{D}_0(v)\boldsymbol{v} + \boldsymbol{J}(\eta)\boldsymbol{e}_\eta, \end{aligned} \tag{20}$$

where $\boldsymbol{k}_2$ is the designed control parameter matrix.

In this way, $\dot{V}_2$ transform into

$$\begin{aligned} \dot{V}_2 = -\boldsymbol{k}_1 \boldsymbol{E}_\eta^T \boldsymbol{E}_\eta - \boldsymbol{k}_2 \boldsymbol{E}_v^T \boldsymbol{E}_v - G \tilde{\boldsymbol{d}}_\zeta^T \tilde{\boldsymbol{d}}_\zeta \\ + \boldsymbol{M}_0^{-1} \rho \boldsymbol{E}_v^T \tilde{\boldsymbol{d}}_\zeta - \tilde{\boldsymbol{d}}_\zeta^T \dot{\boldsymbol{d}}_\zeta, \end{aligned} \tag{21}$$

Utilizing Young's inequality and Assumption 1, one has

$$\begin{aligned} \rho \boldsymbol{E}_v^T \tilde{\boldsymbol{d}}_\zeta &\le \rho^2 \|\boldsymbol{E}_v^T \boldsymbol{E}_v\| + \frac{1}{4} \|\tilde{\boldsymbol{d}}_\zeta^T \tilde{\boldsymbol{d}}_\zeta\|, \\ -\tilde{\boldsymbol{d}}_\zeta^T \dot{\boldsymbol{d}}_\zeta &\le \|\tilde{\boldsymbol{d}}_\zeta^T \tilde{\boldsymbol{d}}_\zeta\| + \frac{\|\bar{\dot{\boldsymbol{d}}}_\zeta^T \bar{\dot{\boldsymbol{d}}}_\zeta\|}{4}. \end{aligned} \tag{22}$$

According to the above equations, the derivative of (21) comes to

$$\begin{aligned} \dot{V}_2 \le -\boldsymbol{k}_1 \boldsymbol{E}_\eta^T \boldsymbol{E}_\eta - (\boldsymbol{k}_2 - \boldsymbol{M}_0^{-1} \rho^2) \boldsymbol{E}_v^T \boldsymbol{E}_v \\ - (G - \frac{5}{4}) \tilde{\boldsymbol{d}}_\zeta^T \tilde{\boldsymbol{d}}_\zeta + \frac{\|\bar{\dot{\boldsymbol{d}}}_\zeta^T \bar{\dot{\boldsymbol{d}}}_\zeta\|}{4} \end{aligned} \tag{23}$$

where $\bar{\dot{\boldsymbol{d}}}_\zeta = [\bar{\dot{d}}_{\zeta_1}, \bar{\dot{d}}_{\zeta_2}, \bar{\dot{d}}_{\zeta_3}, \bar{\dot{d}}_{\zeta_4}]$ is the upper bound of the $\dot{\boldsymbol{d}}_\zeta$.

Theorem 1 *For the AUV system* (4)*, if Assumption 1 holds, the prescribed-time controller* (20) *coupled with adaptive disturbance observer* (9) *ensures that the closed-loop system is stable, and meanwhile the closed-loop system has the following properties.*

(1) The closed-loop system signals are ultimately uniformly bounded.

(2) The tracking error will converge to a pre-given compact set within a predefined time T.

4 Simulation Results

This section details the numerical simulations performed to assess the effectiveness of the proposed control scheme. To illustrate its robustness in the face of uncertainties in model parameters and unknown environmental disturbances, time-varying disturbances are introduced to the system. The nominal parameters of the 4DOF AUV used in the simulation runs are outlined in Table 1 [22]. The simulations are conducted using MATLAB/Simulink.

Table 1: Parameters of the AUV

Description	Value	Unit
m	14.7	kg
I_z	0.36	N ms^2
X_u	1.399	N
Y_v	14.6	N
Z_w	−12.21	N
N_r	2.435	N m
$X_{u\|u\|}$	9.895	N s/m
$Y_{v\|v\|}$	27.8	N s/m
$Z_{w\|w\|}$	28.23	N s/m
$N_{r\|r\|}$	8.261	N

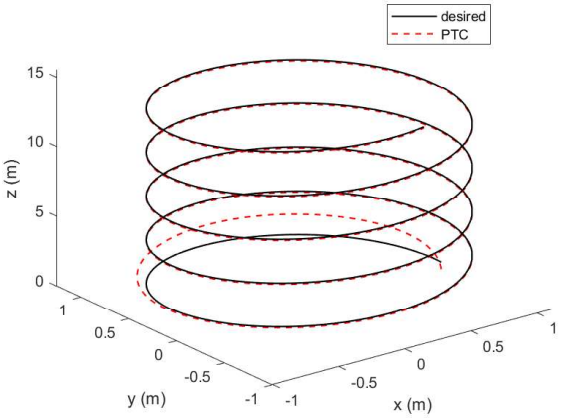

Fig. 2: Position evolution of AUV under PTC in 3D space.

The initial values is set to $\boldsymbol{\eta} = [0\text{m}, 0\text{m}, 0\text{m}, 0\,\text{rad}]$, and the desired trajectory is set to $x(t) = \cos(t)$, $y(t) = \sin(t)$, $z(t) = 0.5 + t/2$. The simulation time is $30s$.

Fig. 2 displays the tracking performance of AUV under PTC in 3D space. Clearly, the controlled AUV tracks the desired trajectory perfectly after a short transient response. Fig. 3 details the response of the AUV in every direction, including x, y, z and the yaw angle ψ. It can be seen that x, y, z and ψ converge to the reference signals within the prescribed time $4s$, which is determined by engineers with only one parameter. The corresponding control forces and moment are depicted in Fig. 4. Moreover, the estimation performance of the ADOs for system uncertainties and external disturbances are presented in Fig. 5, which demonstrates that the proposed ADO estimates the lumped disturbances fast and accurately. It can be concluded that the proposed PTC with ADO for AUVs performs well under complex system dynamics and environments.

5 Conclusion

In this paper, a prescribed-time controller with an adaptive disturbance observer is proposed for 3D trajectory tracking tasks of 4-degree-freedom AUVs. Under PTC, the tracking trajectory converges to the desired trajectory within a user-determined period by introducing a novel speed function, which greatly reduces the controller tuning time cost practically. To address the system uncertainties and environmental disturbances, ADOs are designed and combined into the controller, which compensates for the effects of unknown signals and boosts the robustness of the controller. Simula-

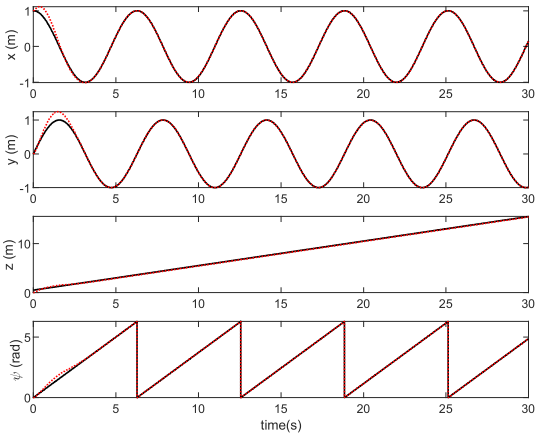

Fig. 3: Position and attitude evolution of AUV under PTC with respect to time.

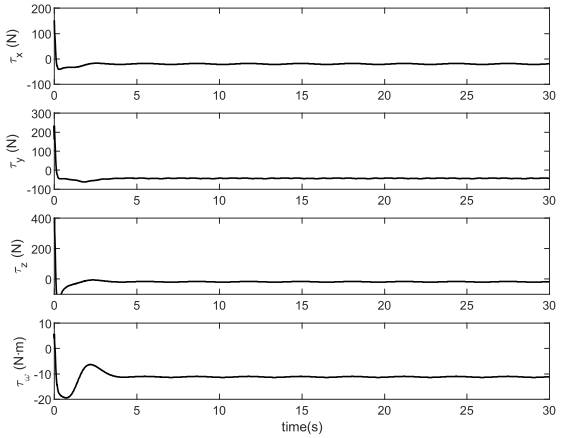

Fig. 4: The control forces and moment generated by PTC.

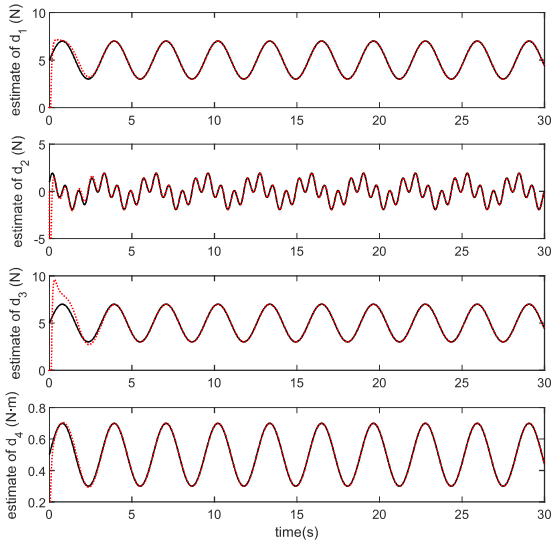

Fig. 5: Estimates of external disturbances of AUV under ADO.

tion results indicate that PTC with ADOs performs well for AUVs under complex environments.

References

[1] Y. Zhang, X. Liu, M. Luo, and C. Yang, "Bio-inspired approach for long-range underwater navigation using model predictive control," *IEEE transactions on cybernetics*, vol. 51, no. 8, pp. 4286–4297, 2019.

[2] Y. Shi, C. Shen, H. Fang, and H. Li, "Advanced control in marine mechatronic systems: A survey," *IEEE/ASME transactions on mechatronics*, vol. 22, no. 3, pp. 1121–1131, 2017.

[3] Y. Zhang, S. Oğuz, S. Wang, E. Garone, X. Wang, M. Dorigo, and M. K. Heinrich, "Self-reconfigurable hierarchical frameworks for formation control of robot swarms," *IEEE Transactions on Cybernetics*, 2023.

[4] J. Sverdrup-Thygeson, E. Kelasidi, K. Y. Pettersen, and J. T. Gravdahl, "The underwater swimming manipulator-a bio-inspired auv," in *2016 IEEE/OES Autonomous Underwater Vehicles (AUV)*. IEEE, 2016, pp. 387–395.

[5] A. Sahoo, S. K. Dwivedy, and P. Robi, "Advancements in the field of autonomous underwater vehicle," *Ocean Engineering*, vol. 181, pp. 145–160, 2019.

[6] T. Elmokadem, M. Zribi, and K. Youcef-Toumi, "Trajectory tracking sliding mode control of underactuated auvs," *Nonlinear Dynamics*, vol. 84, pp. 1079–1091, 2016.

[7] A. S. Tijjani, A. Chemori, and V. Creuze, "Robust adaptive tracking control of underwater vehicles: Design, stability analysis, and experiments," *IEEE/ASME Transactions on Mechatronics*, vol. 26, no. 2, pp. 897–907, 2020.

[8] J. Guerrero, J. Torres, V. Creuze, A. Chemori, and E. Campos, "Saturation based nonlinear pid control for underwater vehicles: Design, stability analysis and experiments," *Mechatronics*, vol. 61, pp. 96–105, 2019.

[9] G. V. Lakhekar, L. M. Waghmare, and R. G. Roy, "Disturbance observer-based fuzzy adapted s-surface controller for spatial trajectory tracking of autonomous underwater vehicle," *IEEE Transactions on Intelligent Vehicles*, vol. 4, no. 4, pp. 622–636, 2019.

[10] B. Su, H.-b. Wang, and Y. Wang, "Dynamic event-triggered formation control for auvs with fixed-time integral sliding mode disturbance observer," *Ocean Engineering*, vol. 240, p. 109893, 2021.

[11] Z. Peng, D. Wang, and J. Wang, "Data-driven adaptive disturbance observers for model-free trajectory tracking control of maritime autonomous surface ships," *IEEE Transactions on Neural Networks and Learning Systems*, vol. 32, no. 12, pp. 5584–5594, 2021.

[12] A. Polyakov, "Nonlinear feedback design for fixed-time stabilization of linear control systems," *IEEE transactions on Automatic Control*, vol. 57, no. 8, pp. 2106–2110, 2011.

[13] T. Zhang, S. Jiang, D. Shen, and H. Xu, "Adaptive finite-time fuzzy control for hybrid levitation system of maglev trains with active anti-lock constraints," *Journal of the Franklin Institute*, vol. 360, no. 4, pp. 2635–2659, 2023.

[14] S. Jiang, D. Shen, T. Zhang, and H. Xu, "Nonlinear robust composite levitation control for high-speed ems trains with input saturation and track irregularities," *IEEE Transactions on Intelligent Transportation Systems*, vol. 23, no. 11, pp. 20 323–20 336, 2022.

[15] T. Zhang, D. Shen, S. Jiang, and H. Xu, "Adaptive fixed-time antilock control of levitation system of high-speed maglev train," *IEEE Transactions on Intelligent Vehicles*, vol. 8, no. 5, pp. 3394–3404, 2011.

[16] T. I. Fossen, "Guidance and control of ocean vehicles," *University of Trondheim, Norway, Printed by John Wiley & Sons, Chichester, England, ISBN: 0 471 94113 1, Doctors Thesis*, 1999.

[17] ——, "Marine control systems–guidance. navigation, and control of ships, rigs and underwater vehicles," *Marine Cybernetics, Trondheim, Norway, Org. Number NO 985 195 005 MVA, www. marinecybernetics. com, ISBN: 82 92356 00 2*, 2002.

[18] G. Wang, M. Chadli, and M. V. Basin, "Practical terminal sliding mode control of nonlinear uncertain active suspension systems with adaptive disturbance observer," *IEEE/ASME Transactions On Mechatronics*, vol. 26, no. 2, pp. 789–797, 2020.

[19] W.-H. Chen, D. J. Ballance, P. J. Gawthrop, and J. O'Reilly, "A nonlinear disturbance observer for robotic manipulators," *IEEE Transactions on industrial Electronics*, vol. 47, no. 4, pp. 932–938, 2000.

[20] A. Mohammadi, M. Tavakoli, H. J. Marquez, and F. Hashemzadeh, "Nonlinear disturbance observer design for robotic manipulators," *Control Engineering Practice*, vol. 21, no. 3, pp. 253–267, 2013.

[21] K. Zhao, Y. Song, T. Ma, and L. He, "Prescribed performance control of uncertain euler–lagrange systems subject to full-state constraints," *IEEE transactions on neural networks and learning systems*, vol. 29, no. 8, pp. 3478–3489, 2017.

[22] R. R. Bharti, J. Narayan, and S. K. Dwivedy, "Robust tracking control for underactuated autonomous underwater vehicles," in *2022 IEEE 19th India Council International Conference (INDICON)*. IEEE, 2022, pp. 1–6.

Proceedings of the 3rd Conference on Fully Actuated System Theory and Applications
May 10-12, 2024, Shenzhen, China

Stackelberg Differential Game-based Hierarchical Approximate Optimal Interaction Control of Human-Centered Reconfigurable Robot Manipulator Systems

Tianjiao An[1], Haoyu Yan[1], Bing Ma[1], Hucheng Jiang[1], Bo Dong[1]
1. Department of Control Science and Engineering, Changchun University of Technology, Changchun 130012, China
E-mail: dongbo@ccut.edu.cn

Abstract: This paper proposes a Stackelberg game-based approximate optimal interaction control approach for human-centered reconfigurable robot manipulator (RRM) systems. Joint torque feedback technique is utilized to form the RRM dynamic model. According to differential game, the RRM's optimal control issue is transformed into a Stackelberg game issue between the human and the RRM. By the adaptive dynamic programming (ADP) algorithm, the cost functions of human as well as RRM are developed by critic neural network (NN) and implement to solve Hamilton-Jacobian (HJ) equations, which facilitate the acquisition of Stackelberg equilibrium. The position tracking error is ultimately uniformly bounded (UUB) according to the Lyapunov theory. Experiment results demonstrate the effectiveness of the proposed method.

Key Words: Adaptive dynamic programming, Reconfigurable robot manipulators, Human-robot collaboration, Stackelberg differential game, Interaction Control

1 Introduction

Since human-robot collaboration (HRC) combines the high precision and efficiency of robots with the high flexibility and intellectuality of humans, collaborative robots (also known as cobots) have been continually developed and widely adapted to medical, industrial, pension and other daily circumstances. Particularly, the nontrivial application of cobots such as rehabilitate stroke patients, assist transportations, etc is human-centered robotic systems where assists humans or acts instructions. Reconfigurable cobot with the properties of well disassembly and mezzo size came into being, that can recombine and reconfigure its own configuration according to different human-centered collaborative task requirements.

Compared with common robot-centered collaborative tasks, human-centered robotic systems draws on expertise and experience of human that is with higher security and intuitiveness, therefore, it is extensively applied in cooperative carrying heavy objects, teleoperation, assisted manipulator production and manufacturing, and other occasions. When human and robot collaborate with each other, bilateral participants (players) make decisions based on each other's strategy, whereafter, game theory has been utilized to describe the interaction process between robot and human/environment, that quantifying the indescribable interaction behavior. Notable Nash equilibrium of zero-sum [1], nonzero-sum [2] game and Pareto equilibrium of cooperative game [3] are achieved equilibrium by adopting different strategies among the participants. It is worth emphasizing that in Nash as well as Pareto equilibrium, every player in a dynamic system is with fair access to the information, however, in human-dominated collaborative tasks, human possesses absolute dominance over robot that can perceive the entirely information of the robot, on the contrary, the robotic systems can but response to the human's action therewith, in consequence, the aforementioned game-based methods with equal roles between players are not appropriate.

Stackelberg game was proposed by the German economist Stackelberg in 1934 and widely used to solve various economic problems [4]. Subsequent applications have been made in other fields such as nonlinear dynamics, biology, and decision processes. Stackelberg game involves two types of players, the leader and the follower, that the main feature is to address successive decision processes and the leader prioritizes the strategy over the decision maker. The follower then attempts to optimize the strategy based on the leader's response. In the meantime, the leader makes the best response corresponding to the follower's strategy according to the perceived policy. When humans initiatively interact with reconfigurable cobots, different reconfigurable robot manipulator (RRM)'s subsystem and its relevant interaction torque are deemed as hierarchical control policy in Stackelberg game. For the sake of obtaining the optimal control strategy for bilateral human and robotic systems respectively, the Stackelberg equilibrium solution of the dynamic system needs to be solved. Adaptive dynamic programming (ADP), proposed by Professor Werbos can obtain the optimal controller of the nonlinear system according to the highly nonlinear partial differential HJB equation to be solved, that is widely applied in scope of continuous time [5], discrete time [6], data driven [7], input/output constraint [8], actuator/sensor failure [9], uncertain disturbance [10] systems. Unfortunately, up to now, the most of existing methods for dealing with optimal interaction control are with the same access between the human as well as the robot. Thereupon, it leaves a seminal project to investigate the hierarchical game for human-centered collaborative issue and then address the Stackelberg differential game-based approximate optimal interaction control problem.

Motivated by above, a Stackelberg game-based approximate optimal interaction control approach is assessed for human-centered RRM systems.

The work is supported by National Natural Science Foundation of China (62173047), Scientific Technological Development Plan Project in Jilin Province of China (20220201038GX), Key Laboratory of Advanced Structural Materials (Changchun University of Technology), Ministry of Education, China (ASM-202202).

2 Dynamic analysis

2.1 RRM's dynamic model

On the basis of JTF technique, the ith RRM subsystem dynamic model is:

$$I_{im}\gamma_i\ddot{q}_i+\frac{\tau_{is}}{\gamma_i}+f_{ir}(q_i,\dot{q}_i)+I_i(q,\dot{q},\ddot{q})=\tau_i+\left[J_i^T f_{hu}\right]_i, \quad (1)$$

where subscript i is the ith joint subsystem, I_{im} indicates motor's moment of inertia, γ_i is gear ratio, q_i means the joint position, τ_{is} denotes coupled joint torque, $f_{ir}(q_i,\dot{q}_i)$ means joint friction, $I_i(q,\dot{q},\ddot{q})$ represents IDC effect, τ_i means control torque, J_i is Jacobi matrix, f_{hu} is human force input, and $[.]_i$ means the ith element of the vector.

1) Joint friction

$f_{ir}(q_i,\dot{q}_i)$ can be expressed as:

$$\begin{aligned} f_{ir}(q_i,\dot{q}_i) =& \hat{f}_{ib}\dot{q}_i+(\hat{f}_{is}e^{(-\hat{f}_{i\tau}\dot{q}_i^2)}+\hat{f}_{ic})\mathrm{sgn}(\dot{q}_i) \\ &+f_{ip}(q_i,\dot{q}_i)+Y_i(\dot{q}_i)\tilde{F}_{ir}, \end{aligned} \quad (2)$$

in which

$$Y_i(\dot{q}_i)=\left[f_{ib}-\hat{f}_{ib},f_{ic}-\hat{f}_{ic},f_{is}-\hat{f}_{is},f_{i\tau}-\hat{f}_{i\tau}\right]^T, \quad (3)$$

where $f_{ip}(q_i,\dot{q}_i)$ means position dependency friction, $f_{ib},f_{i\tau}$ are viscous as well as Stribect friction parameters, f_{is},f_{ic} denote static as well as Coulomb friction effect. Furthurmore, $\hat{f}_{ib},\hat{f}_{ic},\ \hat{f}_{is},\hat{f}_{i\tau}$ are the estimated values of $f_{ib},f_{ic},f_{is},f_{i\tau}$.

2) IDC effect

IDC is coupled among joint modules that formulates as:

$$\begin{aligned} I_i &= I_{im}\sum_{j=1}^{i-1}v_{mi}^T v_{lj}\ddot{q}_j+I_{im}\sum_{j=2}^{i-1}\sum_{k=1}^{j-1}v_{mi}^T(v_{lk}\times v_{lj})\dot{q}_k\dot{q}_j \\ &= I_{im}\sum_{j=1}^{i-1}D_j^i\ddot{q}_j+I_{im}\sum_{j=2}^{i-1}\sum_{k=1}^{j-1}\Theta_{kj}^i\dot{q}_k\dot{q}_j \\ &= \sum_{j=1}^{i-1}\left[I_{im}\hat{D}_j^i,I_{im}\right]\left[\ddot{q}_j,\tilde{D}_j^i\ddot{q}_j\right]^T \\ &\quad+\sum_{j=2}^{i-1}\sum_{k=1}^{j-1}\left[I_{im}\hat{\Theta}_{kj}^i,I_{im}\right]\left[\ddot{q}_j,\tilde{\Theta}_{kj}^i\dot{q}_k\dot{q}_j\right]^T, \end{aligned} \quad (4)$$

in which v_{mi},v_{lj},v_{lk} are unit vectors along with ith, jth and kth joint rotation axes. Accordingly, we have $D_j^i=v_{mi}^T v_{lj}$ and $\Theta_{kj}^i=v_{mi}^T(v_{lk}\times v_{lj})$. Moreover, we also have the relations that $\hat{D}_j^i=D_j^i-\tilde{D}_j^i$ and $\hat{\Theta}_{kj}^i=\Theta_{kj}^i-\tilde{\Theta}_{kj}^i$, in which $\hat{D}_j^i,\hat{\Theta}_{kj}^i$ denote the estimated values of D_j^i,Θ_{kj}^i as well as $\tilde{D}_j^i,\tilde{\Theta}_{kj}^i$ are alignment errors.

Define state vector $x_i=[x_{i1},x_{i2}]^T=[q_i,\dot{q}_i]^T$ and the control input $u_i=\tau_i$, $h_i=\left[J_i^T f\right]_i$. One has the ith subsystem state space:

$$\begin{cases}\dot{x}_{i1}=x_{i2}\\ \dot{x}_{i2}=\ell_i(x)+g_i u_i+h_i\end{cases}, \quad (5)$$

where

$$g_i=(I_{im}\gamma_i)^{-1}$$

$$\ell_i=-g_i\begin{pmatrix}(\hat{f}_{is}e^{(-\hat{f}_{i\tau}\dot{x}_{i1}^2)}+\hat{f}_{ic})\mathrm{sgn}(x_{i2})+f_{ip}(x_{i1},x_{i2})\\ +\hat{f}_{ib}x_{i2}+Y_i(x_{i2})\tilde{F}_{ir}+\dfrac{\tau_{is}}{\gamma_i}+I_i(x,\dot{x},\ddot{x})\end{pmatrix}. \quad (6)$$

2.2 Human limb model as well as motion intention estimation

f_{hu} is regarded as only external force exerting on the manipulator's end-effector in the human-centered robotic systems. The interaction control transfers human force input into motion commands of human-centered robotic systems:

$$-C_H\dot{c}+G_H(c_d-c)=f_{hu}, \quad (7)$$

where C_H, G_H denote human's damper, spring matrices, c represents RRM actual position in Cartesian space that formulates as $c(t)=\xi(q)$, $q(t)=[q_1,\cdots,q_i,\cdots,q_n]^T$ represents joint space's position, $\xi(\cdot)$ means mapping matrix, c_d is the motion intention.

c_d is formulated as:

$$c_d=\Lambda(f_{hu},c,\dot{c}), \quad (8)$$

where $\Lambda(f_{hu},c,\dot{c})$ represents unknown nonlinear function.

On account of c_d is unknown because of human's intention, according to the RBFNN, the human motion intention while interacting with an RRM system and its estimation are represented as:

$$c_d=W_h^T\psi(f,z,\dot{z})+\varepsilon,\hat{c}_d=\hat{W}_h^T\psi(f,z,\dot{z}), \quad (9)$$

where ε means estimation error, $\hat{W}_h$ represents estimated value of W_h, as well as ψ is Gaussian function.

On the basis of the cost function respect to the interaction force $E_{hu}=\frac{1}{2}\left\|f_{hu}^2\right\|$, the RRM can actively move toward subjective human's intention. Thus, one can obtain:

$$\dot{\hat{W}}_h=-\alpha'\frac{\partial E_{hu}}{\partial\hat{W}_h}=-\alpha' f_{hu}G_H\psi=-\alpha_{hu}f_{hu}\psi, \quad (10)$$

where α' is a positive scalar, $\alpha_{hu}=\alpha' G_H$.

We can get $\hat{W}_h$ as

$$\hat{W}_h(t)=\hat{W}_h(0)-\alpha_{hu}\int_0^t(f_{hu}(v)\psi(v))\,dv. \quad (11)$$

The control object includes optimally ensuring RRM systems' tracking error under human-centered collaborative task is UUB. Therefore, a Stackelberg game-based hierarchical optimal control approach is presented in next section.

3 Stackelberg game-based hierarchical approximate optimal control approach of human-centered RRM system

3.1 Derivation of Stackelberg differential game

Define the cost function of RRM system and human respectively as:

$$V_{iF}(\dot{e}_i,u_i,h_i)=\int_t^{\infty} r_{iF}(\dot{e}_i,u_i,h_i)d\tau \\ =\int_t^{\infty}\left(\dot{e}_i^T Q_{iF}\dot{e}_i+u_i^T R_{iFu}u_i+h_i^T R_{iFh}h_i\right)d\tau, \tag{12}$$

$$V_{iL}(\dot{e}_i,u_i,h_i)=\int_t^{\infty} r_{iL}(\dot{e}_i,u_i,h_i)d\tau \\ =\int_t^{\infty}\left(\dot{e}_i^T Q_{iL}\dot{e}_i+u_i^T R_{iLu}u_i+h_i^T R_{iLh}h_i\right)d\tau. \tag{13}$$

where r_{iF} and r_{iL} are the utility functions of follower and leader respectively. The position error is $e_i=x_{i1}-x_{id}$ and the velocity error vector means $\dot{e}_i=x_{i2}-\dot{x}_{id}$, $x_{id}=\hat{q}_i(t)$ represents estimated human motion. $Q_{iF},Q_{iL},R_{iFi},R_{iLi}$, R_{iFh},R_{iLh} are determined positive definite matrices.

The RRM system expects to seek the optimal response to the human base on the system's state. Define the follower's optimal cost function:

$$V_{iF}^*(\dot{e}_i,u_i,h_i)=\min_{u_i}\int_t^{\infty} r_{iF}(\dot{e}_i,u_i,h_i)d\tau. \tag{14}$$

Then, using the infinitesimal version of (12) with (1) and (5), the follower's Hamiltonian function is expressed as:

$$H_{iF}(\dot{e}_i,u_i,h_i,\nabla V_{iF})=r_{iF}(\dot{e}_i,u_i,h_i) \\ +\nabla V_{iF}\left(\ell_i(x)+g_iu_i+h_i\right). \tag{15}$$

According to the stationary condition $\frac{\partial H_{iF}}{\partial u_i}=0$, the local follower's optimal control policy is given by:

$$u_i^*=-\frac{1}{2}R_{iFu}^{-1}g_i^T\nabla V_{iF}^*. \tag{16}$$

Subsequently, we define the costate $\hbar$ considering the future effect from the follower, then, the leader makes response when making actions. It guarantees the human's requirement for the RRM's cost function.

$$\dot{\hbar}_{i1}=-\frac{\partial H_{iF}}{\partial \dot{e}_i} \\ =-\nabla\ell_i^T\nabla V_{iF}^*-2Q_{iF}\dot{e}_i-\nabla g_i^T\nabla V_{iF}^*u_i-\nabla V_{iF}^*h_i. \tag{17}$$

According to the costate (17) and the modified dynamic system $\dot{x}_{i2}=\ell_i(x)+g_iu_i^*+h_i$, we can obtain the leader's optimal cost function:

$$V_{iL}^*(\dot{e}_i,u_i,h_i)=\min_{h_i}\int_t^{\infty}\left(r_{iL}(\dot{e}_i,u_i,h_i)+\lambda_i^T\dot{\hbar}_{i1}\right)d\tau, \tag{18}$$

where λ_i means the Lagrange multiplier with respect to (17).

To the same, we can obtain the leader's Hamiltonian function and optimal control policy:

$$H_{iL}(\dot{e}_i,u_i,h_i,\nabla V_{iL})=r_{iL}(\dot{e}_i,u_i,h_i) \\ +\nabla V_{iL}\left(\ell_i(x)+g_iu_i+h_i\right)+\lambda_i^T\dot{\hbar}_{i1}, \tag{19}$$

$$\frac{\partial H_{iL}}{\partial \dot{e}_i}=0\rightarrow h_i^*=-\frac{1}{2}R_{iLh}^{-1}\left(\nabla V_{iL}^*-\nabla V_{iF}^*\lambda_i\right). \tag{20}$$

The related costate can be demonstrated as:

$$\dot{\hbar}_{i2}=-\left(\frac{\partial H_{iL}}{\partial \dot{e}_i}\right)^T=-\nabla\ell_i^T\nabla V_{iL}^*-2Q_{iL}\dot{e}_i+\frac{\partial\dot{\hbar}_1}{\partial\dot{e}_i}\lambda_i, \tag{21}$$

$$\dot{\lambda}_i=-\left(\frac{\partial H_{iL}}{\partial V_{iF}^*}\right)^T=-\frac{1}{2}g_i(x_i)R_{iFu}^{-1}R_{iLu}R_{iFu}^{-1}\nabla V_{iF}^* \\ +\frac{1}{2}g_i(x_i)R_{iFu}^{-1}g_i^T(x_i)\nabla V_{iL}^*+\nabla\ell_i^T\lambda_i+\nabla g_iu_i\lambda_i+h_i\lambda_i. \tag{22}$$

Afterwards, by substituting (16) and (20) into the Hamiltonian functions (15) and (19), the coupled HJ equations are:

$$0=r_{iF}(\dot{e}_i,u_i^*,h_i^*)+\nabla V_{iF}\left(\ell_i(x)+g_iu_i+h_i\right), \tag{23}$$

$$0=r_{iL}(\dot{e}_i,u_i^*,h_i^*)+\nabla V_{iL}\left(\ell_i(x)+g_iu_i+h_i\right)+\lambda_i^T\dot{\hbar}_{i1}. \tag{24}$$

As (23) and (24) can be deduced to obtain ∇V_{iF}^* and ∇V_{iL}^*, the required Stackelberg optimal solution can be derived. However, in the framework of the Stackelberg differential game the issue is transformed to optimally ensure RRM position tracking under the HRC task and the end-effector can actively move toward its human partner's intended position. As the coupled HJ equations with costates are difficult to solve, we use critic NN approach to deal with it.

3.2 Approximate solution of the Stackelberg game-based hierarchical optimal interaction control via the implementation of critic NN

Decomposition (16), one can represent as:

$$u_i^*=u_{i1}+u_{i2}^*, \tag{25}$$

where u_{i1} is dealing with $\ell_i(x)$, and u_{i2}^* is the optimal compensation of human-centered collaborative tasks.

According to (5), u_{i1} can be designed as:

$$u_{i1}=-\begin{pmatrix}-\left(\hat{f}_{is}e^{\left(-\hat{f}_{i\tau}x_{i2}^2\right)}+\hat{f}_{ic}\right)\mathrm{sgn}(x_{i2})\\ -\hat{f}_{ib}x_{i2}-g_i^{-1}\ddot{x}_{id}-\dfrac{\tau_{is}}{\gamma_i}\end{pmatrix}. \tag{26}$$

The optimal compensation control issue is then transformed into a Stackelberg game-based hierarchical optimal control approach.

The critic NN is developed to approximate the cost functions (14) and (18):

$$V_{im}{}^*(\dot{e}_i)=W_{im}^T\phi_{im}(\dot{e}_i)+\varepsilon_{im},m=F,L, \tag{27}$$

where W_{im} denotes the critic NN vector, ε_{im} is the finite approximate error, as well as $\phi_{im}(\dot{e}_i)$ represents activation function.

The gradient of the (27) is as follow equation:

$$\nabla V_{im}{}^*(\dot{e}_i)=\nabla\phi_{im}(\dot{e}_i)W_{im}+\nabla\varepsilon_{im},m=F,L, \tag{28}$$

where $\nabla\phi_{im}(\dot{e}_i)=\partial\phi_{im}(\dot{e}_i)/\partial\dot{e}_i$ denotes gradient of the activation function, $\nabla\varepsilon_{im}$ means gradient error.

By substituting (28) into (16) and (20), the optimal control and interaction torque are given by:

$$u_{i2}^{*}=-\frac{1}{2}R_{iFu}^{-1}g_{i}^{T}\left(\nabla\phi_{iF}(\dot{e}_{i})W_{iF}+\nabla\varepsilon_{iF}\right), \tag{29}$$

$$\begin{aligned}h_{i}^{*}=&-\frac{1}{2}R_{iLh}^{-1}g_{i}^{T}\left(\nabla\phi_{iL}(\dot{e}_{i})W_{iL}+\nabla\varepsilon_{iL}\right)\\&+\frac{1}{2}R_{iLh}^{-1}\left(\nabla\phi_{iF}(\dot{e}_{i})W_{iF}+\nabla\varepsilon_{iF}\right)\lambda_{i}.\end{aligned} \tag{30}$$

Substituting (29), (30) into (15) and (19), one yields:

$$\begin{aligned}&H_{iF}(\dot{e}_{i},u_{i},h_{i},W_{iF})=r_{iF}(\dot{e}_{i},u_{i},h_{i})\\&+\nabla\phi_{iF}(\dot{e}_{i})W_{iF}\left(\ell_{i}(x)+g_{i}u_{i}+h_{i}\right)=e_{iHF},\end{aligned} \tag{31}$$

$$\begin{aligned}&H_{iL}(\dot{e}_{i},u_{i},h_{i},W_{iL})=r_{iL}(\dot{e}_{i},u_{i},h_{i})+\nabla\phi_{iL}(\dot{e}_{i})W_{iL}\\&\begin{pmatrix}\ell_{i}(x)+h_{i}\\+g_{i}u_{i}\end{pmatrix}+\begin{pmatrix}-\nabla\ell^{T}\nabla\phi_{iL}(\dot{e}_{i})W_{iL}-2Q_{iF}\dot{e}_{i}-\nabla g_{i}^{T}\\\nabla\phi_{iL}(\dot{e}_{i})W_{iL}u_{i}-\nabla\phi_{iL}(\dot{e}_{i})W_{iL}h_{i}\end{pmatrix}\\&\lambda_{i}=e_{iHL}.\end{aligned} \tag{32}$$

where e_{iHF} and e_{iHL} denote residual error.

The estimated optimal cost function is:

$$\hat{V}_{im}^{*}(\dot{e}_{i})=\hat{W}_{im}^{T}\phi_{im}(\dot{e}_{i}),m=F,L. \tag{33}$$

Based on (29), (30) and (33), the approximate optimal control is:

$$\hat{u}_{i2}^{*}=-\frac{1}{2}R_{iFu}^{-1}g_{i}^{T}\left(\nabla\phi_{iF}(\dot{e}_{i})\hat{W}_{iF}\right), \tag{34}$$

$$\begin{aligned}\hat{h}_{i}^{*}=&\frac{1}{2}R_{iLh}^{-1}g_{i}^{T}\left(\nabla\phi_{iL}(\dot{e}_{i})\hat{W}_{iL}\right)\\&+\frac{1}{2}R_{iLh}^{-1}\left(\nabla\phi_{iF}(\dot{e}_{i})\hat{W}_{iF}\right)\lambda_{i}.\end{aligned} \tag{35}$$

Applying (34) and (35) into (31) and (32), the approximated Hamiltonian functions are given by:

$$\begin{aligned}&\hat{H}_{iF}(\dot{e}_{i},\hat{u}_{i},\hat{h}_{i},\hat{W}_{iF})=r_{iF}(\dot{e}_{i},\hat{u}_{i},\hat{h}_{i})\\&+\nabla\phi_{iF}(\dot{e}_{i})\hat{W}_{iF}\left(\ell_{i}(x)+g_{i}\hat{u}_{i}+\hat{h}_{i}\right)=e_{iF},\end{aligned} \tag{36}$$

$$\begin{aligned}&\hat{H}_{iL}(\dot{e}_{i},\hat{u}_{i},\hat{h}_{i},\hat{W}_{iL})=r_{iL}(\dot{e}_{i},\hat{u}_{i},\hat{h}_{i})+\nabla\phi_{iL}(\dot{e}_{i})\hat{W}_{iL}\\&\begin{pmatrix}\ell_{i}(x)+\hat{h}_{i}\\+g_{i}\hat{u}_{i}\end{pmatrix}+\begin{pmatrix}-\nabla\ell^{T}\nabla\phi_{iL}(\dot{e}_{i})\hat{W}_{iL}-2Q_{iF}\dot{e}_{i}-\nabla g_{i}^{T}\\\nabla\phi_{iL}(\dot{e}_{i})\hat{W}_{iL}\hat{u}_{i}-\nabla\phi_{iL}(\dot{e}_{i})\hat{W}_{iL}\hat{h}_{i}\end{pmatrix}\\&\lambda_{i}=e_{iL}.\end{aligned} \tag{37}$$

The approximated Hamiltonian error functions e_{iF} and e_{iL} are defined as follow equation:

$$e_{im}=\hat{H}_{im}-H_{im},m=F,L, \tag{38}$$

where $e_{im}=\hat{H}_{im},m=F,L$ is obtained using (31), (32), (36) and (37).

When defining the vector estimate error $\tilde{W}_{im}=W_{im}-\hat{W}_{im}$, it can be deduced that $e_{im}=e_{iHm}-\tilde{W}_{im}^{T}\nabla\phi_{im}(\dot{e}_{im})\ddot{e}_{im}$, by combining (31), (32), (36), (37) with (38). Base on gradient decent algorithm, define residual error function $E_{im}=\frac{1}{2}e_{im}^{2}$, which is minimized for adjusting critic NN weights. The update law is designed as:

$$\dot{\hat{W}}_{im}=-\varsigma_{im}e_{im}\nabla\phi_{im}(\dot{e}_{i})\ddot{e}_{i}, \tag{39}$$

where ς_{im} is the updated rate of the critic NN. ξ_{im} is denoted as $\nabla\phi_{im}(\dot{e}_{im})\ddot{e}_{im}$, and a positive constant ξ_{iLm} and $\|\xi_{im}\|\leq\xi_{iLm}$ is assumed. Hence, one obtains:

$$\begin{aligned}\dot{\tilde{W}}_{im}=&-\dot{\hat{W}}_{im}=\varsigma_{im}e_{im}\nabla\phi_{im}(\dot{e}_{im})\ddot{e}_{im}\\=&\varsigma_{im}(e_{iHm}-\tilde{W}_{im}^{T}\xi_{im})\xi_{im}.\end{aligned} \tag{40}$$

Theorem 1: Considered V_{im} which is approximated by (27), with W_{im}, and $\hat{V}_{im}$ given by (33) built with $\hat{W}_{im}$, if the weight of the critic NN is updated by (39), then the weight approximation error is UUB.

Proof: Choose Lyapunov function candidate:

$$L_{im}(t)=\frac{1}{2\varsigma_{im}}\tilde{W}_{im}^{T}\tilde{W}_{im},m=F,L. \tag{41}$$

The time derivative of $L_{im}(t)$ is:

$$\begin{aligned}\dot{L}_{im}(t)=&\frac{1}{\varsigma_{im}}\tilde{W}_{im}^{T}\dot{\tilde{W}}_{im}=\tilde{W}_{im}^{T}\left(e_{iHm}-\tilde{W}_{im}^{T}\xi_{im}\right)\xi_{im}\\=&\tilde{W}_{im}^{T}\left(e_{iHm}-\tilde{W}_{im}^{T}\xi_{im}\right)\xi_{im}\\=&\tilde{W}_{im}^{T}e_{iHm}\xi_{im}-\left\|\tilde{W}_{im}^{T}\xi_{im}\right\|^{2}\\\leq&\frac{1}{2}e_{iHm}^{2}-\frac{1}{2}\left\|\tilde{W}_{im}^{T}\xi_{im}\right\|^{2},m=F,L,\end{aligned} \tag{42}$$

where $\dot{L}_{im}(t)\leq 0$ when error function $\dot{e}_{im}$ lies outside $\Omega_{im}=\left\{\tilde{W}_{im}:\left\|\tilde{W}_{im}\right\|\leq\frac{e_{iHm}}{\xi_{iLm}}\right\}$. The proof is completed.

Based on (26) and the hierarchical optimal interaction control (34), $\hat{u}_{i}^{*}$ is given as follows:

$$\begin{aligned}\hat{u}_{i}^{*}=&u_{i1}+\hat{u}_{i2}^{*}\\=&-\begin{pmatrix}-\left(\hat{f}_{is}e^{\left(-\hat{f}_{i\tau}x_{i2}^{2}\right)}+\hat{f}_{ic}\right)\mathrm{sgn}(x_{i2})\\-\hat{f}_{ib}x_{i2}-g_{i}^{-1}\ddot{x}_{id}-\frac{\tau_{is}}{\gamma_{i}}\end{pmatrix}\\&-\frac{1}{2}R_{iFu}^{-1}g_{i}^{T}\left(\nabla\phi_{iF}(\dot{e}_{i})\hat{W}_{iF}\right).\end{aligned} \tag{43}$$

Theorem 2: Considered RRM system (1), the position tracking error of the closed-loop system is UUB under the human-centered collaborative task, by the developed Stackelberg game-based hierarchical approximate optimal control policy derived in (43).

Proof: Define the Lyapunov function:

$$V_{Ly}=\sum_{i=1}^{n}V_{iLy}=\sum_{i=1}^{n}\sum_{m}^{L,F}V_{im}^{*}. \tag{44}$$

Derivative (44) as follow equation:

$$\dot{V}_{Ly}(t)=\sum_{i=1}^{n}\sum_{m}^{L,F}\left(\left(\nabla V_{im}^{*}\right)^{T}\left(\ell_{i}(x)+g_{i}u_{i}+h_{i}-\ddot{x}_{id}\right)\right). \tag{45}$$

According to coupled HJ equations in (23) and (24), they are with follow equations:

$$(\nabla V_{iF}^{*})^{T}\left(\ell_i(x)-\ddot{x}_{id}\right)=-\dot{e}_i^{T}Q_{iF}\dot{e}_i+\frac{1}{4}(\nabla V_{iF}^{*})^{T} g_i R_{iFu}^{-1}g_i^{T}(\nabla V_{iF}^{*})+\frac{1}{4}(\nabla V_{iF}^{*})^{T}h_i R_{iFh}^{-1}h_i^{T}(\nabla V_{iF}^{*}). \tag{46}$$

$$(\nabla V_{iL}^{*})^{T}\left(\ell_i(x)-\ddot{x}_{id}\right)=-\dot{e}_i^{T}Q_{iL}\dot{e}_i+\frac{1}{4}(\nabla V_{iL}^{*})^{T} g_i R_{iLu}^{-1}g_i^{T}(\nabla V_{iL}^{*})+\frac{1}{4}(\nabla V_{iL}^{*})^{T}h_i R_{iLh}^{-1}h_i^{T}(\nabla V_{iL}^{*})+\lambda_i^{T}\dot{h}_{i1}. \tag{47}$$

Combining (46), (47) into (45), we obtain:

$$\dot{V}_{iLy}(t)=-\dot{e}_i^{T}\left(Q_{iF}+Q_{iL}\right)\dot{e}_i+\frac{1}{4}(\nabla V_{iF}^{*})^{T} g_i R_{iFu}^{-1}g_i^{T}(\nabla V_{iF}^{*})+\frac{1}{4}(\nabla V_{iF}^{*})^{T}h_i R_{iFh}^{-1}h_i^{T}(\nabla V_{iF}^{*})+\frac{1}{4}(\nabla V_{iL}^{*})^{T} g_i R_{iLu}^{-1}g_i^{T}(\nabla V_{iL}^{*})+\frac{1}{4}(\nabla V_{iL}^{*})^{T}h_i R_{iLh}^{-1}h_i^{T}(\nabla V_{iL}^{*})+\lambda_i^{T}\dot{h}_{i1}+(\nabla V_{iF}^{*}+\nabla V_{iL}^{*})^{T}(g_i u_i+h_i). \tag{48}$$

Considering (48), one obtains:

$$\dot{V}_{iLy}(t)=-\dot{e}_i^{T}\left(Q_{iF}+Q_{iL}\right)\dot{e}_i-(\nabla V_{iF}^{*})^{T}\left(g_i(u_i^{*}-u_i)\right)-(\nabla V_{iL}^{*})^{T}\left(h_i^{*}-h_i\right)+\frac{1}{4}(\nabla V_{iF}^{*})^{T} g_i R_{iFu}^{-1}g_i^{T}(\nabla V_{iF}^{*})+\frac{1}{4}(\nabla V_{iF}^{*})^{T}h_i R_{iFh}^{-1}h_i^{T}(\nabla V_{iF}^{*})+\frac{1}{4}(\nabla V_{iL}^{*})^{T} g_i R_{iLu}^{-1}g_i^{T}(\nabla V_{iL}^{*})+\frac{1}{4}(\nabla V_{iL}^{*})^{T}h_i R_{iLh}^{-1}h_i^{T}(\nabla V_{iL}^{*})+\lambda_i^{T}\dot{h}_{i1}. \tag{49}$$

Then, substituting (45) into (49), one yields:

$$\begin{aligned}\dot{V}_{iLy}(t)=&-\dot{e}_i^{T}\left(Q_{iF}+Q_{iL}\right)\dot{e}_i+\frac{1}{4}(\nabla V_{iF}^{*})^{T} g_i R_{iFu}^{-1}g_i^{T}(\nabla V_{iF}^{*})+\frac{1}{4}(\nabla V_{iF}^{*})^{T}h_i R_{iFh}^{-1}h_i^{T}(\nabla V_{iF}^{*})+\frac{1}{4}(\nabla V_{iL}^{*})^{T} g_i R_{iLu}^{-1}g_i^{T}(\nabla V_{iL}^{*})+\frac{1}{4}(\nabla V_{iL}^{*})^{T}h_i R_{iLh}^{-1}h_i^{T}(\nabla V_{iL}^{*})\\&+\lambda_i^{T}\dot{h}_{i1}+\frac{1}{2}\left(\nabla\phi_{iF}(\dot{e}_i)\hat{W}_{iF}+\nabla\varepsilon_{iF}\right)^{T}\left(g_i R_{iFu}^{-1}\right.\\&\left.(g_i^{T}\nabla\phi_{iF}^{T}\tilde{W}_{iF}+g_i^{T}\nabla\varepsilon_{iF})\right)+\frac{1}{2}(\nabla\phi_{iL}(\dot{e}_i)\hat{W}_{iL}+\nabla\varepsilon_{iL})^{T}\\&\left(R_{iLh}^{-1}\left(\nabla\phi_{iL}^{T}\tilde{W}_{iL}+\nabla\varepsilon_{iL}\right)\right)\\=&-\dot{e}_i^{T}\left(Q_{iF}+Q_{iL}\right)\dot{e}_i+\Pi_{iJ},\end{aligned} \tag{50}$$

in which Π_{iJ} has up-bound:

$$\Pi_{iJ}\le\pi_{iJ}, \tag{51}$$

where π_{iJ} is a constant.

Combining (50), $\dot{V}_{Ly}(t)$ has:

$$\begin{aligned}\dot{V}_{iLy}(t)&\le-\dot{e}_i^{T}\left(Q_{iF}+Q_{iL}\right)\dot{e}_i+\pi_{iJ}\\&\le-\lambda_{\min}\left(Q_{iF}+Q_{iL}\right)\|\dot{e}_i\|^{2}+\pi_{iJ}.\end{aligned} \tag{52}$$

If $\dot{e}_i$ lies outside:

$$\Omega_i=\left\{\dot{e}_i:\|\dot{e}_i\|\le\sqrt{\frac{\pi_{iJ}}{\lambda_{\min}(Q_{iF}+Q_{iL})}}\right\}, \tag{53}$$

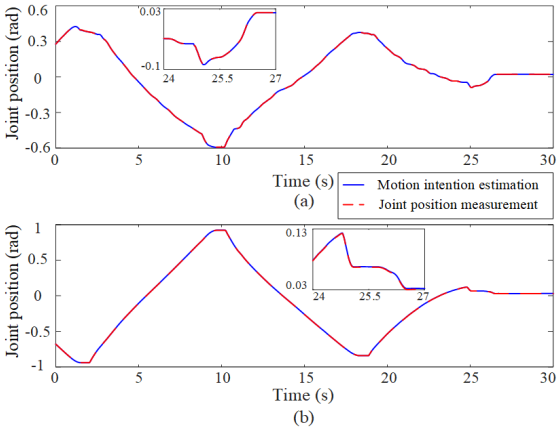

Fig. 1: Motion intention estimation and position tracking under handshaking tasks via proposed control approach (a) joint one (b) joint two.

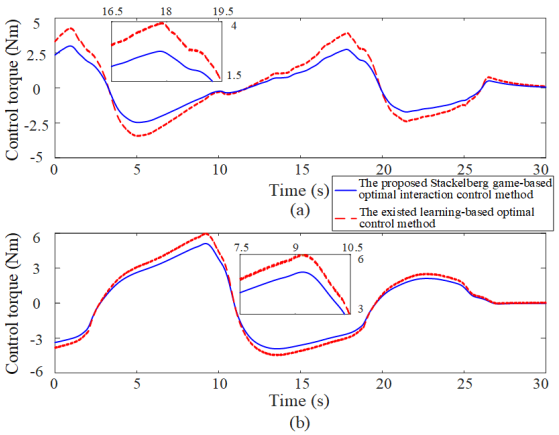

Fig. 2: Control torque under handshaking tasks via existed and proposed control method (a) joint one (b) joint two.

(45) is negative. Hence, we have $\dot{V}_{Ly}(t)<0$ for any $\dot{e}_i\neq 0$ when (53) is satisfied. The position tracking error under human-centered collaborative task is UUB under (43). This proof is completed.

4 Experiments

The proposed Stackelberg game-based approximate optimal interaction control approach method is verified by 2-DOF RRM experimental platform. Two kinds of control methods are utilized to demonstrate the effectiveness of the developed method: the existed ADP-based optimal control without Stackelberg game method, and the proposed Stackelberg game-based hierarchical optimal interaction control approach.

Fig. 1 is position tracking curves under handshaking tasks, obtained by the proposed Stackelberg game-based approximate optimal interaction control approach. Fig. 2 is control torque under handshaking tasks via existed optimal control method and the proposed Stackelberg game-based approximate optimal interaction control approach. Using the Stackelberg game-based approximate optimal interaction control approach, the instant increase of control torques is restrained within safe limits. Fig. 3 is the initiative interaction torque curves under handshaking tasks by

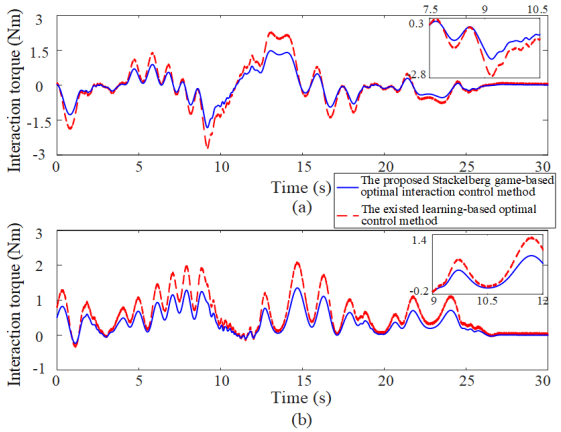

Fig. 3: Interaction torque under handshaking tasks via existed and proposed control method (a) joint one (b) joint two.

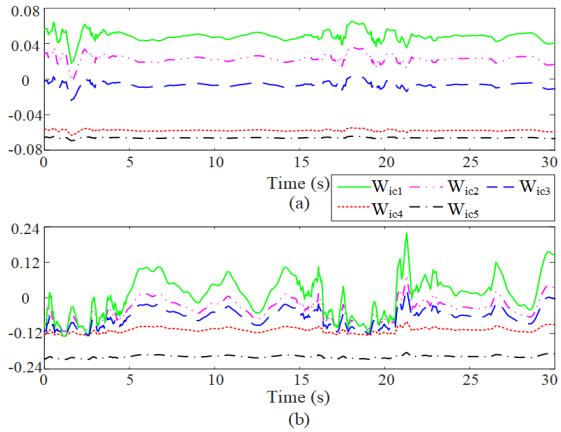

Fig. 4: NN curves under handshaking tasks via proposed Stackelberg game-based hierarchical optimal interaction control approach (a) joint one (b) joint two.

the existed optimal control method as well as the developed Stackelberg game-based approximate optimal interaction control approach. The existed learning-based optimal control method is without hierarchical level, therefore the interaction torque is a touch of quavering and massive than the proposed method. It can be seen that the value of interaction torque keeps within a reasonable range during handshaking tasks, under the Stackelberg game-based approximate optimal interaction control approach, and without strong chattering phenomenon. This is because Stackelberg game technique, which guarantees security of the human. Fig. 4 shows the critic NN weight curves under handshaking obtained by the proposed Stackelberg game-based approximate optimal interaction control approach. According to the figure, the weight can reflect the human intention in real time.

5 Conclusion

A Stackelberg game-based approximate optimal interaction control approach is presented for human-centered RRM systems. JTF technique is utilized to form the RRM dynamic model. The major objective of optimal control with HRC is transformed into approximating Stackelberg equilibrium by adopting Stackelberg game governed between the human and the RRM that are regarded as players with different hierarchical level in interaction process. On the basis of the ADP, the approximate optimal interaction control policy with HRC task is developed via critic NN-based Stackelberg game manner for addressing HJ equations. The position tracking error is UUB according to the Lyapunov theory. Experiment results demonstrate the effectiveness of the proposed method.

References

[1] S. Xue, B. Luo, D. Liu, Y. Yang, Constrained Event-Triggered H∞ Control Based on Adaptive Dynamic Programming With Concurrent Learning, IEEE Transactions on Systems, Man, and Cybernetics: Systems, 52(1):357-369, 2022.

[2] T. An, X. Zhu, M. Zhu, B. Ma, B. Dong, Fuzzy Logic Nonzero-sum Game-Based Distributed Approximated Optimal Control of Modular Robot Manipulators with Human-robot Collaboration, Neurocomputing, 543:126276, 2023.

[3] T. An, Y. Wang, G. Liu, Y. Li, B. Dong, Cooperative Game-Based Approximate Optimal Control of Modular Robot Manipulators for Human–Robot Collaboration, IEEE Transactions on Cybernetics, 53(7):4691-4703, 2023.

[4] M. Lin, B. Zhao, D. Liu, Event-Triggered Robust Adaptive Dynamic Programming for Multiplayer Stackelberg–Nash Games of Uncertain Nonlinear Systems, IEEE Transactions on Cybernetics, 54(1):273-286, 2024.

[5] L. Zhang, S. Zhuang, R. Braatz, Switched Model Predictive Control of Switched Linear Systems: Feasibility, Stability and Robustness, Automatica, 67:8-21, 2016.

[6] L. Zhang, S. Zhuang, P. Shi, Non-Weighted Quasi-Time-Dependent H∞ Filtering for Switched Linear Systems with Persistent Dwell-Time, Automatica, 54:201-209, 2015.

[7] B. Cai, J. Yang, S. Yuan, Y. Shi, L. Zhang, Estimation for Fuzzy Semi-Markov Jump Systems with Indirectly Accessible Mode Information and Nonideal Data Transmission, IEEE Transactions on Systems, Man, and Cybernetics: Systems, 51(7):4016-4027, 2019.

[8] Y. Lv, J. Na, X. Zhao, Y. Huang, X. Ren, Multi-H∞ Controls for Unknown Input-Interference Nonlinear System With Reinforcement Learning, IEEE Transactions on Neural Networks and Learning Systems, 34,(9):5601-5613, 2023.

[9] S. Zhang, B. Zhao, D. Liu, Y. Zhang, Event-Triggered Decentralized Integral Sliding Mode Control for Input-Constrained Nonlinear Large-Scale Systems With Actuator Failures, IEEE Transactions on Systems, Man, and Cybernetics: Systems, doi: 10.1109/TSMC.2023.3331150.

[10] Y. Zhang, B. Zhao, D. Liu, S. Zhang, Adaptive Dynamic Programming-Based Event-Triggered Robust Control for Multiplayer Nonzero-Sum Games With Unknown Dynamics, IEEE Transactions on Cybernetics, 53(8):5151-5164, 2023.

Proceedings of the 3rd Conference on Fully Actuated System Theory and Applications
May 10-12, 2024, Shenzhen, China

Tracking Ability of High-Order Fully Actuated Iterative Learning Control

Zeyi Zhang[1], Hao Jiang[1], Dong Shen[1]
1. School of Mathematics, Renmin University of China, Beijing 100872, P. R. China
E-mail: {zhzy, jiangh, dshen}@ruc.edu.cn

Abstract: This article investigates the tracking ability of iterative learning control (ILC) for a class of affine high-order fully actuated (HOFA) systems. Tracking ability refers to the property that the system can track any desired output trajectory. The emerging HOFA system theory is a control-oriented approach. Under this theory framework, we present an iterative HOFA system model, and find that the tracking ability of the HOFA system is solely related to the measurement matrix due to the fully actuated characteristic. To achieve the tracking ability of HOFA systems, we propose an ILC scheme by a HOFA control approach, including HOFA feedback and learning-based feedforward. By using the proportional update law, the tracking ability of the HOFA system is achieved, that is, the actual output of the system asymptotically tracks to the desired output. In addition, we verify the proposed scheme through numerical simulations.

Key Words: High-order fully actuated systems, iterative learning control, trajectory tracking, tracking ability

1 Introduction

Iterative learning control (ILC) is an intelligent control method which is widely used in robotics, chemical plants, and traffic control [1–3]. Iterative system means that a system operates in a finite time interval, resets, and then operates again. This iterative system generates a lot of historical data. ILC controller can learn from the data and improve the transient performance. With the increase of iterations, ILC can achieve high-accuracy trajectory tracking in the whole time interval.

ILC is usually used to achieve perfect trajectory tracking, depending on the tracking ability. The tracking ability, we refer to the ability of an iterative system to track any desired output trajectory. It can be studied by determining the output range of the system. This problem, also referred to as learning ability of ILC, has been reported in much literature in recent years [4–15]. In [4–6], the authors analyze the relation between tracking ability and system matrices (input-output matrix and feedforward matrix) for discrete-time state-space models. The results are generalized to discrete-time affine nonlinear systems with iteration-varying trial lengths [7], and further, to linear systems with delay and varying length [8]. Under fading communication, the authors of [9] provide techniques that trade off tracking ability and convergence speed. In [10], a data-driven criteria approach is proposed to judge whether a given desired output can be perfectly tracked. For the desired output that can not be perfectly tracked, the authors of [11] present a data-driven solution achieving the least-square approximation of the desired output. The tracking ability of discrete-time linear systems is intensively studied in [12] through the lens of linear algebraic equations. For continuous-time systems, the authors of [13] analyze the tracking ability of linear systems based on frequency domain algebraic equations. The tracking ability of linear fractional-order and distributed-order fractional systems are studied in [14, 15], respectively. These studies, all published in the last three years, show that this emerging problem has attracted the attention of researchers. Moreover, except for [13], which uses the transfer function model, the rest use the first/fractional-order state space model.

High-order fully actuated (HOFA) system is a common model oriented for control design. Many basic physical laws exist in the HOFA form. Controllable linear systems, pseudo-strict-feedback systems, and feedback linearisation systems can be transformed into HOFA systems [16–19]. This theory shows its superiority in dealing with a series of complex problems such as nonlinearity, time-varying and delays. For example, predictive control and coordinated control based on HOFA systems are studied in [20–22]. Fault-tolerant control problems are investigated in [23–26]. In [27], the authors present practical prescribed time control design based on HOFA system approach. In addition, the application of HOFA system in spacecraft, DC microgrids, and quadrotor can be seen in [28–30]. Following the widespread adoption of HOFA system approach, this paper investigates the iterative learning control of HOFA system, which is still a blank.

In this paper, we analyze the tracking ability of HOFA systems and propose the HOFA–ILC scheme (HOFAILC) to achieve the tracking task. First, we introduce the iterative HOFA system model, whose repetitive characteristics are analyzed. The corresponding assumptions are given. Then, we use the lifting technique to determine the tracking ability of the system. We find that the HOFA systems can achieve arbitrary state trajectories, resulting that the tracking ability relies solely on the measurement matrix. Finally, the HOFAILC is proposed to achieve the tracking ability. The HOFAILC consists of two parts : the HOFA state feedback is designed to improve the closed-loop performance of the system; a proportional (P)-type ILC scheme is used to learn from the previous iteration for generating feedforward signal. This provides an asymptotic convergence of the actual output to the desired output.

This work was supported by the National Natural Science Foundation of China (62173333, 12271522) and Beijing Natural Science Foundation (Z210002).

Organization. Section 2 describes the system model, assumptions and problem formulation. Section 3 gives the results of the problem. Numerical examples are illustrated in Section 4. Finally, the conclusion is in Section 5.

Notation. **span**(M) denotes the linear space spanned by the columns of matrix M. **rank**(M) is the rank of matrix M. I is the identical matrix. $\rho(M)$ is the spectral radius of matrix M.

2 Problem Formulation

In this section, we introduce the iterative HOFA system, related assumptions, and the definitions about the tracking ability.

2.1 System Description

According to the step backward discrete-time HOFA models [31], we give the iterative discrete-time HOFA system:

$$\begin{aligned} x_{k,t+1} &= f(x_{k,t}^{[0\sim\tau-1]}, t) + B(x_{k,t}^{[0\sim\tau-1]})u_{k,t}, \\ y_{k,t} &= C_t x_{k,t}, \end{aligned} \tag{1}$$

where $k = 0, 1, \cdots$ is the iteration index, $t = 0, 1, \cdots, N$ denotes the time instant, and N is the trial length. $x_{k,t} \in \mathbb{R}^r, u_{k,t} \in \mathbb{R}^r$, and $y_{k,t} \in \mathbb{R}^m$ are the system state, input, and output, respectively. $f(\cdot) \in \mathbb{R}^r$ is a nonlinear vector function. $B(\cdot) \in \mathbb{R}^{r\times r}$ is a nonlinear matrix function. C_t is the time-varying measurement matrix. The vector $x_{k,t}^{[0\sim\tau-1]} = [x_{k,t}^T, x_{k,t-1}^T, \ldots, x_{k,t-\tau+1}^T]^T$.

Assumption 1. *The initial values $x_{k,t}$, $t \leq 0$ are reset to fixed values.*

Remark 1. *The assumption of identical initial condition (i.i.c.) is common in the ILC field, and it is necessary to achieve perfect tracking [13]. Its implementation and relaxation have been widely studied as an important issue of ILC [32–34]. In the first-order state space model, only $x_{k,0}$ is usually involved. This paper, however, extends i.i.c. to be compatible with the HOFA system.*

The system (1) is fully actuated if it satisfies the following condition.

Condition 1. *[35]* $\det B(x_{k,t}^{[0\sim\tau-1]}) \neq 0$, $\forall x_{k,t}^{[0\sim\tau-1]} \in \mathbb{R}^{\tau r}$ *and* $\forall t \geq 0$.

This fully actuated characteristic facilitates constant linear closed-loop systems with arbitrarily assignable eigenstructures.

2.2 Tracking Ability

Denote the desired output as $y_{d,t}$, $t = 1, \ldots, N$. The control task is that the errors converge to zero as the iteration increases, i.e., $\lim_{k\to\infty} e_{k,t} = 0$, $t = 1, \ldots, N$, where $e_{k,t} = y_{k,t} - y_{d,t}$. In this way, for any predetermined tracking accuracy, there exists k_* such that the output of all time instants exactly track to the desired output for $k \geq k_*$. In particular, achieving zero-error tracking is called perfect tracking.

Definition 1. *For a desired output that can be perfectly tracked, we call it is* realizable*, i.e., $\{y_{d,t}\}_{t=1,\ldots,N}$ is realizable if there exists some $\{x_{d,t}\}_{t\leq N}$ and $\{u_{d,t}\}_{t=0,\ldots,N-1}$ such that*

$$\begin{aligned} x_{d,t+1} &= f(x_{d,t}^{[0\sim\tau-1]}, t) + B(x_{d,t}^{[0\sim\tau-1]})u_{d,t}, \\ y_{d,t} &= C_t x_{d,t}. \end{aligned}$$

Definition 2. *The system* (1) *has complete tracking ability if any desired output $y_{d,t} \in \mathbb{R}^m$, $t = 1, \ldots, N$ is realizable. Otherwise, it has incomplete tracking ability.*

Define the output trajectory space

$$\mathfrak{Y} = \left\{ [y_{k,1}^T, y_{k,2}^T, \cdots, y_{k,N}^T]^T \,\middle|\, y_{k,t} \text{ is generated by (1)} \right\}$$

of system (1). The system (1) has complete tracking ability if $\mathfrak{Y} = \mathbb{R}^{mN}$, and has incomplete tracking ability if $\mathfrak{Y} \subsetneq \mathbb{R}^{mN}$.

3 Main Results

In this section, we use the HOFA control method to study the tracking ability and achieve it.

Set $1 \leq \varpi \leq \tau$, and $A_0, A_1, \cdots, A_{\varpi-1} \in \mathbb{R}^{r\times r}$ are ϖ arbitrarily given matrices. Then the HOFAILC controller is given as

$$u_{k,t} = B^{-1}(\cdot)[-f(x_{k,t}^{[0\sim\tau-1]}, t) + \sum_{i=0}^{\varpi-1} A_i x_{k,t-i} + v_{k,t}], \tag{2}$$

where $v_{k,t}$ is the learning control input to be designed. Using this controller, the following closed-loop iterative HOFA system is obtained as

$$x_{k,t+1} = \sum_{i=0}^{\varpi-1} A_i x_{k,t-i} + v_{k,t}. \tag{3}$$

This constant linear system can be transformed to a more simple form by utilizing the lifting technique, which is a common trick to represent ILC systems and analyze convergence. In specific, due to the finite length of the trial, we stack variables in the time domain over time. As a result, we can highlight the system dynamics along the iteration axis.

From (3), we derive the relation between state and learning control input. Denote $A_{[i_1,i_2,\ldots,i_n]}^{[j_1,j_2,\ldots,j_n]} \triangleq A_{i_1}^{j_1} A_{i_2}^{j_2} \cdots A_{i_n}^{j_n}$, we give some examples

$$\begin{aligned} x_{k,1} &= \sum_{i=0}^{\varpi-1} A_i x_{k,-i} + v_{k,0}, \\ x_{k,2} &= A_{[0,\varpi-1]}^{[1,1]} x_{k,1-\varpi} + \sum_{i=1}^{\varpi-2} (A_{i+1} + A_{[0,i]}^{[1,1]}) x_{k,-i} \\ &\quad + (A_1 + A_0^2) x_{k,0} + A_0 v_{k,0} + v_{k,1}, \\ x_{k,3} &= (A_1 + A_0^2) A_{\varpi-1} x_{k,1-\varpi} \\ &\quad + (A_{[0,\varpi-2]}^{[2,1]} + A_{[0,\varpi-2]}^{[1,1]} + A_{[0,\varpi-1]}^{[1,1]}) x_{k,2-\varpi} \\ &\quad + \sum_{i=1}^{\varpi-3} (A_{i+2} + A_{[0,i+1]}^{[1,1]} + A_{[0,i,1,i]}^{[2,1,1,1]}) x_{k,-i} \\ &\quad + (A_0^3 + A_{[1,0]}^{[1,1]} + A_{[0,1]}^{[1,1]} + A_2) x_{k,0} + v_{k,2} \\ &\quad + A_0 v_{k,1} + (A_0^2 + A_1) v_{k,0}, \\ x_{k,4} &= (A_0^3 + A_{[1,0]}^{[1,1]} + A_{[0,1]}^{[1,1]} + A_2) A_{\varpi-1} x_{k,1-\varpi} \\ &\quad + (((A_0^2 + A_0 + A_1) A_0 + A_2) A_{\varpi-2} \end{aligned}$$

$$
\begin{aligned}
&\quad + (A_0^2 + A_1)A_{\varpi-1})x_{k,2-\varpi} \\
&+ (A_{[0,\varpi-1]}^{[1,1]} + (A_0^2 + A_1)A_{\varpi-2} \\
&\quad + (A_{[0,\varpi-3,1]}^{[3,1,1]} + A_{[1,0]}^{[1,1]} + A_2^1)A_{\varpi-3})x_{k,3-\varpi} \\
&+ \sum_{i=1}^{\varpi-4} (A_{[0,i+2]}^{[1,1]} + (A_1 + A_0^2)A_{i+1}^1 \\
&\quad + A_{[0,i,1,i]}^{[3,1,1,1]} + A_{[1,0,i]}^{[1,1,1]} + A_{[2,i]}^{[1,1]} x_{k,-i})x_{k,-i} \\
&+ (A_0^4 + A_{[0,1,0]}^{1,1,1} + A_{[0,2]}^{[1,1]} + A_{[2,0]}^{[1,1]} \\
&\quad + A_{[0,1]}^{[2,1]} + A_{[1,0]}^{[1,2]} + A_1^2 + A_3)x_{k,0} \\
&+ v_{k,3} + A_0 v_{k,2} + (A_0^2 + A_1)v_{k,1} \\
&+ (A_0^3 + A_{[0,1]}^{[1,1]} + A_{[1,0]}^{[1,1]} + A_2)v_{k,0}, \\
&\vdots
\end{aligned}
$$

We conclude that $x_{k,t}$ is a combination of initial values $x_{k,i}$, $i \le 0$, and inputs $u_{k,i}$, $i \le t-1$, then we have the following matrix representation: Denote super-vectors

$$
\begin{aligned}
Y_k &= [y_{k,1}^T, y_{k,1}^T, \cdots, y_{k,N}^T]^T \in \mathbf{R}^{mN}, \\
X_\circ &= [x_{k,0}^T, x_{k,-1}^T, \cdots, x_{k,\varpi-1}^T]^T \in \mathbf{R}^{r\varpi}, \\
X_k &= [x_{k,1}^T, x_{k,2}^T, \cdots, x_{k,N}^T]^T \in \mathbf{R}^{rN}, \\
V_k &= [v_{k,0}^T, v_{k,0}^T, \cdots, v_{k,N-1}^T)]^T \in \mathbf{R}^{rN},
\end{aligned}
$$

we have an algebraic representation between output trajectory and state trajectory, and that of state trajectory and input trajectory.

$$
\begin{aligned}
X_k &= \mathcal{S}V_k + \mathcal{M}X_\circ, \\
Y_k &= \mathcal{C}X_k,
\end{aligned}
\tag{4}
$$

where $\mathcal{S}$ is a block Toeplitz matrix

$$
\mathcal{S} = \begin{pmatrix} S_1 & O & \cdots & O \\ S_2 & S_1 & \cdots & O \\ \vdots & \vdots & \ddots & \vdots \\ S_N & S_{N-1} & \cdots & S_1 \end{pmatrix}
$$

with $S_1 = I$, $S_2 = A_0$, $S_3 = A_0^2 + A_1$, $S_4 = A_0^3 + A_{[0,1]}^{[1,1]} + A_{[1,0]}^{[1,1]} + A_2$, $\cdots$. $\mathcal{C} = \text{diag}\{C_1, C_2, \ldots, C_N\} \in \mathbb{R}^{mN \times rN}$. The elements of matrix $\mathcal{M}$ are constructed by A_i, $i = 0, \ldots, \varpi - 1$.

Now we have the following result.

Theorem 1. *Let system* (1) *with Assumption 1 satisfy fully actuated Condition 1, it has the complete tracking ability* $\mathcal{Y} = \mathbb{R}^{mN}$ *if and only if* $\mathcal{C}$ *is of full row rank.*

Proof. Note that $\mathcal{S}$ is non-singular, thus any state trajectory X_k can be realized by some V_k for any initial value $X_\circ$. That is, X_k can take any vector in $\mathbb{R}^{rN}$. The output trajectory space $\mathcal{Y} = \{Y_k | Y_k = \mathcal{C}X_k\}$ is thus equal to $\mathbf{span}(\mathcal{C})$. One can check that $\mathbf{span}(\mathcal{C}) = \mathbb{R}^{mN}$ if and only if $\mathbf{rank}(\mathcal{C}) = mN$, if and only if $\mathcal{C}$ is of full row rank. □

We notice that $\mathbf{rank}(\mathcal{C}) = mN$ if and only if $\mathbf{rank}(C_t) = m$, $t = 1, 2, \ldots, N$. The measurement matrix C_t measures the state at time t,which falls within the measurement range of the sensor. Thanks to the fully actuated characteristic, any state can be reached, hence, any output within the measurement range can also be realized, i.e., $\mathcal{Y} = \mathbf{span}(\mathcal{C})$. In short, when the sensors have sufficient measurement range, the system has a complete tracking ability.

The above discussion implies that the system (1) can provide arbitrary trajectory tracking within the measurement range of the sensors, which is guaranteed by the fully actuated condition. This reminds engineers that for the HOFA system, as long as the desired output within the measurement range is selected, the existence of perfect tracking can be guaranteed, even if the system has incomplete tracking ability. On the other hand, fully actuated characteristics are difficult to maintain when using state-space models [16]. Hence, the findings illustrate the analytical convenience of HOFA approach over state space approach.

3.1 Update of Learning Control Input

We have analyzed the tracking ability and tracking range of the HOFA system. To implement the tracking ability, we now design the update law of the learning control input in HOFAILC which is actually the feedforward signal.

The P-type learning update law is given as

$$
v_{k+1,t} = v_{k,t} - L_t e_{k,t+1}, \tag{5}
$$

where L_t is the time-varying learning gain matrix. This scheme has the advantages of simple structure, high computational efficiency and only error requirement. The convergence along the iteration axis of the HOFAILC is provided by the following theorem.

Theorem 2. *Suppose that system* (1) *with Assumption 1 satisfies Condition 1 and has the complete tracking ability. We apply the HOFAILC* (2) *and* (5)*, then, for any desired output* $y_{d,t}$*, the error converges to zero as* k *tends to infinity if and only if* $\rho(I - C_t L_t) < 1$.

Proof. We derive the lifted representation for the update law (5):

$$
V_{k+1} = V_k - LE_k,
$$

where the matrix $L = \text{diag}\{L_1, L_2, \cdots, L_N\}$ and the super-vector $E_k = [e_{k,1}^T, e_{k,1}^T, \cdots, e_{k,N}^T]^T$.

Denote $\mathcal{H} = \mathcal{CS}$, $Y_d = [y_{d,1}^T, y_{d,1}^T, \cdots, y_{d,N}^T]^T$, considering the lifted form (4) of closed-loop system (3), we obtain the evolution of lifted error

$$
\begin{aligned}
E_{k+1} &= Y_{k+1} - Y_d = \mathcal{H}(V_k - LE_k) + \mathcal{CM}X_0 - Y_d \\
&= (I - \mathcal{H}L)E_k.
\end{aligned}
$$

Since $\mathcal{C}$ is of full row rank, $\mathcal{H}$ is of full row rank. The sequence E_k converges to zero if and only if $\rho(I - \mathcal{H}L) < 1$ [36]. The matrix $\mathcal{H}L$ is lower triangular, and the sub-block on its diagonal is $C_t L_t$. Hence, the eigenvalues of $I - \mathcal{H}L$ are the eigenvalues of $I - C_t L_t$, $t = 1, 2, \ldots, N$, which means that $\rho(I - \mathcal{H}L) < 1$ if and only if $\rho(I - C_t L_t) < 1$, $t = 1, 2, \ldots, N$. The proof is completed. □

4 Numerical Examples

4.1 Example 1

We give an example of the difference between a HOFA model and a state-space model when designing an ILC con-

troller. Consider an externally-driven spring mass system whose dynamics are given by

$$m\ddot{q} + c\dot{q} + kq = u \tag{6}$$

which is fully actuated. Here, m is the mass, q is the displacement of the mass, c is the coefficient of viscous friction, k is the spring constant, and u is the applied force.

We consider discretization of system (6). For example, we discretize it in central difference format:

$$\ddot{q}(t\delta) = \frac{q((t+1)\delta) - 2q(t\delta) + q((t-1)\delta)}{\delta^2},$$
$$\dot{q}(t\delta) = \frac{q((t+1)\delta) - q((t-1)\delta)}{2\delta},$$

which derives an iterative discrete-time fully actuated system

$$x_{k,t+1} + \frac{2k-4m}{2m+c\delta}x_{k,t} + \frac{2m-c\delta}{2m+c\delta}x_{k,t-1} = \frac{2\delta^2}{2m+c\delta}u_{k,t}. \tag{7}$$

In general, the value of $x_{k,t} = q_k(t\delta)$ can be measured directly. Hence, the desired output is given as displacement, that is, $x_{d,t}$ is expected to be tracked by $x_{k,t}$. Moreover, the system (7) has complete tracking ability. The HOFAILC can be applied. The displacement error can be directly used in the update law. In short, we can easily implement arbitrary displacement trajectories with this model and HOFAILC. Moreover, we can achieve the tracking task of displacement by a simple P-type ILC scheme:

$$u_{k+1,t} = u_{k,t} - K_p(x_{k,t+1} - x_{d,t+1}).$$

The convergence proof can follow the study in [8].

Now we use the state space model to design the controller. Set $x = [q, \dot{q}]$ as the state, system (6) is identical to the system:

$$\dot{x} = \begin{bmatrix} 0 & 1 \\ -k/m & -c/m \end{bmatrix} x + \begin{bmatrix} 0 \\ 1/m \end{bmatrix} u.$$

We discretize the above model using Euler's method to have

$$\begin{aligned} x_{k,t+1} &= \begin{bmatrix} 1 & \delta \\ -k\delta/m & -c\delta/m+1 \end{bmatrix} x_{k,t} + \begin{bmatrix} 0 \\ \delta/m \end{bmatrix} u_{k,t} \\ &= \mathsf{A}x_{k,t} + \mathsf{B}u_{k,t}, \\ y_{k,t} &= \mathsf{C}x_{k,t} \end{aligned}$$

where $x_{k,t} = [q_k(t\delta), \dot{q}_k(t\delta)]$, and B is an overdetermined matrix. We discuss three cases.

Case 1. If the measurement matrix is $\mathsf{C} = [1 \quad 0]$, which coincides with reality, then $\mathsf{CB} = 0$ causes the system to lose full tracking ability [5]. Since $\mathsf{CAB} = \delta^2/m \neq 0$, the relative degree of the system is 2. Thus, $y_{k,2}, y_{k,3}, \cdots, y_{k,N}$ can track any desired output, which can be realized by the following P-type update law:

$$u_{k+1,t} = u_{k,t} - K_p(q_k((t+2)\delta) - q_d((t+2)\delta),$$

where $q_d(t)$ is the desired displacement. However, the tracking of $y_{k,1}$ is neglected.

Case 2. If the measurement matrix is $\mathsf{C} = [0 \quad 1]$, then $\mathsf{CB} \neq 0$ causes the system to have full tracking ability [5]. The desired output $\dot{q}_d(t)$ is for velocity. The velocity error converges to zero instead of the displacement error. The P-type update law is given by

$$u_{k+1,t} = u_{k,t} - K_p(\dot{q}_k((t+1)\delta) - \dot{q}_d((t+1)\delta)).$$

However, the velocity must be accessible either directly or through the difference in displacements. This approach also amplifies the noise.

Case 3. If the measurement matrix is $\mathsf{C} = \left[\begin{smallmatrix} 1 & 0 \\ 0 & 1 \end{smallmatrix}\right]$, setting the desired trajectories for both displacement and velocity can create unachievable problems. For example, set $N = 2$, we have the lifted system

$$\begin{bmatrix} y_{k,1} \\ y_{k,2} \end{bmatrix} = \begin{bmatrix} 0 & 0 \\ \delta/m & 0 \\ \delta^2/m & 0 \\ -c\delta^2/m^2 & \delta/m \end{bmatrix} \begin{bmatrix} u_{k,0} \\ u_{k,1} \end{bmatrix}.$$

Therefore, any desired output meeting $y_{k,1}(1) \neq 0$ can not be tracked.

These three cases show that the state space model brings some inconvenience and challenges for the design of the controller. With HOFA model, we give inputs directly by utilizing displacement errors.

4.2 Example 2

We verify the convergence of HOFAILC scheme. Given the following HOFA system

$$\begin{aligned} x_{k,t+1} &= \frac{x_{k,t}}{2} - \frac{\sin(x_{k,t})}{100} - x_{k,t-1} + 0.1u_{k,t}, \\ y_{k,t} &= x_{k,t}, \end{aligned} \tag{8}$$

with initial values $x_{k,t} = 0$, $t \leq 0$. The desired output is $y_{d,t} = 30\sin(0.3t) + 5\cos(0.1t)$, the trial length $N = 50$, and the number of iterations is 10.

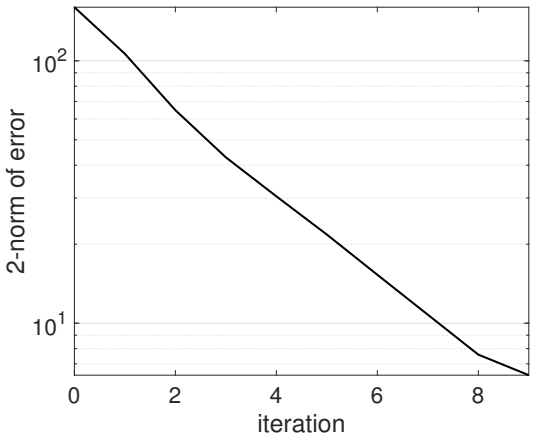

Fig. 1: Performance profile along the iteration axis

The HOFAILC is designed as: Set the initial iteration input $v_{0,t} = 0$, the input is given as

$$u_{k,t} = 10(-\frac{x_{k,t}}{2} + \frac{\sin(x_{k,t})}{100} + x_{k,t-1} + 0.5x_{k,t} + v_{k,t}),$$
$$v_{k+1,t} = v_{k,t} - 0.2e_{k,t}.$$

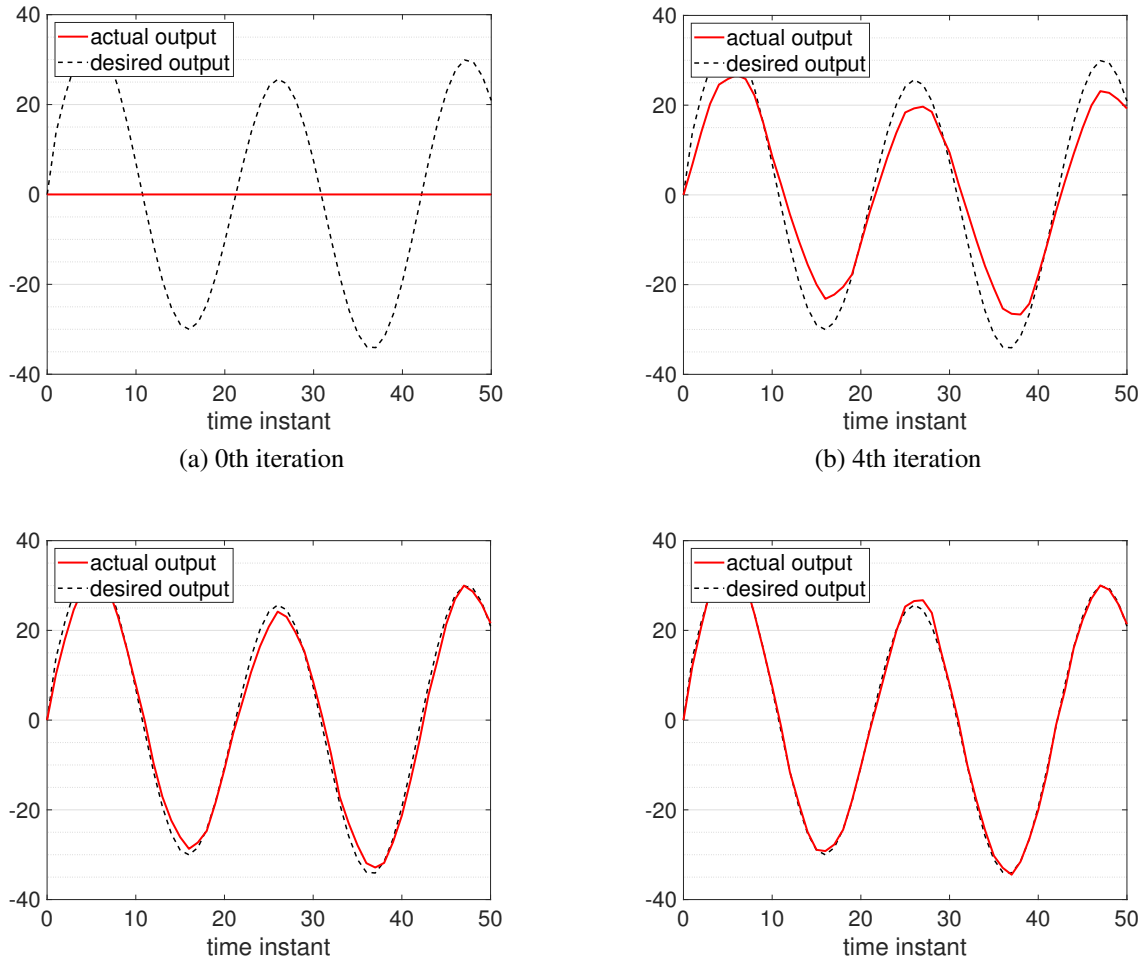

(a) 0th iteration (b) 4th iteration

(c) 7th iteration (d) 10th iteration

Fig. 2: Output trajectories of ILC at the (a) 0th, (b) 4th, (c) 7th, and (d) 10th iterations. The black dash lines and red solid lines are the desired outputs and output trajectories, respectively.

The learning gain matrix $L_t = 0.2$ derives $1 - C_t L_t = 0.8 < 1$ satisfying the spectral radius condition, which ensures the convergence of $v_{k,t}$. The HOFA feedback control contributes the closed-loop system

$$x_{k,t+1} = 0.5x_{k,t} + v_{k,t},$$
$$y_{k,t} = x_{k,t},$$

which coincides with a state space model.

Fig. 1 shows that the l_2 norm $\|E_k\|$ of the lifted error exponentially converges to zero. The performance index $\|E_k\|$ indicates the overall performance of the system tracking task. This verifies the effectiveness of HOFAILC and Theorem 2.

In Fig. 2, we show that the output of system (8) controlled by the HOFAILC gradually approaches the desired output from the initial iteration to the 10th iteration. Few iterations improve the transient performance. In the 10th iteration, the actual output has accurately tracked the desired output. This demonstrates the ability of HOFAILC to track with high precision.

5 Conclusion

In this paper, we described the trajectory tracking problem of ILC on HOFA systems. We establish an iterative HOFA system model. For the model, we analyzed the tracking ability of the system through a HOFA control approach. We found that the tracking ability of the HOFA system is only related to the measurement matrix. In other words, the system can achieve any desired output in measurement range thanks to the fully actuated characteristic of the system. We designed a HOFA–ILC scheme to iteratively update the input, and finally achieve perfect trajectory tracking.

The HOFA system is a powerful tool to analyze nonlinear systems, and we expect to analyze the tracking ability of ILC for sub-HOFA systems. Considering that ILC compensates nicely for repetitive disturbance and requires low system knowledge, this will help to relax the requirement of state and system dynamics knowledge in the HOFA system approach, which is left for future work.

References

[1] M. Sun, S. Ge, and I. Mareels, "Adaptive repetitive learning control of robotic manipulators without the requirement for initial repositioning," *IEEE Transactions on Robotics*, vol. 22, no. 3, pp. 563–568, 2006.

[2] D. A. Bristow, M. Tharayil, and A. G. Alleyne, "A survey of iterative learning control," *IEEE Control Systems*, vol. 26, no. 3, pp. 96–114, 2006.

[3] Y. Wang, F. Gao, and F. J. Doyle, "Survey on iterative learning control, repetitive control, and run-to-run control," *Journal of Process Control*, vol. 19, no. 10, pp. 1589–1600, 2009.

[4] Y. Z. Jian Liu and X. Ruan, "Iterative learning control for a class of uncertain nonlinear systems with current state feedback," *International Journal of Systems Science*, vol. 50, no. 10, pp. 1889–1901, 2019.

[5] J. Liu, X. Ruan, and Y. Zheng, "Iterative learning control for discrete-time systems with full learnability," *IEEE Transactions on Neural Networks and Learning Systems*, vol. 33, no. 2, pp. 629–643, 2022.

[6] J. Liu, X. Ruan, Y. Zheng, Y. Yi, and C. Wang, "Learning-ability of discrete-time iterative learning control systems with feedforward," *SIAM Journal on Control and Optimization*, vol. 61, no. 2, pp. 543–559, 2023.

[7] Y. Zhang, J. Liu, and X. Ruan, "Learning ability of iterative learning control system with a randomly varying trial length," *International Journal of Systems Science*, vol. 53, no. 4, pp. 870–882, Mar. 2022.

[8] H. Luo, J. Wang, and D. Shen, "Learning ability analysis for linear discrete delay systems with iteration-varying trial length," *Chaos, Solitons & Fractals*, vol. 171, p. 113428, Jun. 2023.

[9] D. Shen, G. Qu, and X. Yu, "Averaging techniques for balancing learning and tracking abilities over fading channels," *IEEE Transactions on Automatic Control*, vol. 66, no. 6, pp. 2636–2651, 2021.

[10] Y. Wu and D. Meng, "Data-based trackability criteria and control design for disturbed learning systems," *Automatica*, vol. 155, p. 111113, 2023.

[11] Z. Zhang, H. Jiang, D. Shen, and S. S. Saab, "Data-driven learning control algorithms for unachievable tracking problems," *IEEE/CAA Journal of Automatica Sinica*, vol. 11, no. 1, pp. 205–218, 2024.

[12] D. Meng and Y. Wu, "Control design for iterative methods in solving linear algebraic equations," *IEEE Transactions on Automatic Control*, vol. 67, no. 10, pp. 5039–5054, 2022.

[13] D. Meng and J. Zhang, "Fundamental trackability problems for iterative learning control," *IEEE/CAA Journal of Automatica Sinica*, vol. 10, no. 10, pp. 1933–1950, 2023.

[14] P. Gu, Y. Chen, and S. Tian, "Learnability of linear fractional-order ILC systems," *IEEE Transactions on Circuits and Systems II: Express Briefs*, vol. 68, no. 3, pp. 963–967, Mar. 2021.

[15] O. A. ngeles Ramrez, G. Fernndez-Anaya, A. J. Muoz-Vzquez, J. D. Snchez-Torres, and F. Melndez-Vzquez, "Iterative learning control applied to distributed-order linear time invariant MIMO systems to achieve learnability," *Asian Journal of Control*, vol. 25, no. 4, pp. 2508–2520, 2023.

[16] G. Duan, "High-order system approaches: I. Fully-actuated systems and parametric designs," *Acta Automatica Sinica*, vol. 46, no. 7, pp. 1333–1345, 2020.

[17] G. Duan, "High-order fully actuated system approaches: Part I. Models and basic procedure," *International Journal of Systems Science*, vol. 52, no. 2, pp. 422–435, 2021.

[18] G. Duan, "High-order fully actuated system approaches: Part II. Generalized strict-feedback systems," *International Journal of Systems Science*, vol. 52, no. 3, pp. 437–454, 2021.

[19] G. Duan, "High-order fully actuated system approaches: Part III. Robust control and high-order backstepping," *International Journal of Systems Science*, vol. 52, no. 5, pp. 952–971, 2021.

[20] D.-W. Zhang, G.-P. Liu, and L. Cao, "Coordinated control of high-order fully actuated multiagent systems and its application: A predictive control strategy," *IEEE/ASME Transactions on Mechatronics*, vol. 27, no. 6, pp. 4362–4372, 2022.

[21] G.-P. Liu, "Coordination of networked nonlinear multi-agents using a high-order fully actuated predictive control strategy," *IEEE/CAA Journal of Automatica Sinica*, vol. 9, no. 4, pp. 615–623, 2022.

[22] D.-W. Zhang and G.-P. Liu, "Predictive control for networked high-order fully actuated systems subject to communication delays and external disturbances," *ISA Transactions*, vol. 139, pp. 425–435, 2023.

[23] M. Cai, X. He, and D. Zhou, "Self-healing fault-tolerant control for high-order fully actuated systems against sensor faults: A redundancy framework," *IEEE Transactions on Cybernetics*, pp. 1–13, 2023.

[24] M. Cai, X. He, and D. Zhou, "An active fault tolerance framework for uncertain nonlinear high-order fully-actuated systems," *Automatica*, vol. 152, p. 110969, 2023.

[25] R. Dong, C. Hua, K. Li, and R. Meng, "Adaptive fault-tolerant control for high-order fully actuated system with full-state constraints," *Journal of the Franklin Institute*, vol. 360, no. 12, pp. 8062–8074, 2023.

[26] M. Cai, X. He, and D. Zhou, "Low-power fault-tolerant control for nonideal high-order fully actuated systems," *IEEE Transactions on Systems, Man, and Cybernetics: Systems*, vol. 53, no. 8, pp. 4875–4887, 2023.

[27] L. Zhang, L. Zhu, and C. Hua, "Practical prescribed time control based on high-order fully actuated system approach for strong interconnected nonlinear systems," *Nonlinear Dynamics*, vol. 110, no. 4, pp. 3535 – 3545, 2022.

[28] D.-W. Zhang and G.-P. Liu, "A high-order fully actuated predictive control approach for spacecraft flying-around," in *2023 2nd Conference on Fully Actuated System Theory and Applications (CFASTA)*, 2023, pp. 954–959.

[29] Y. Yu, G.-P. Liu, Y. Huang, and J. M. Guerrero, "Coordinated predictive secondary control for DC microgrids based on high-order fully actuated system approaches," *IEEE Transactions on Smart Grid*, vol. 15, no. 1, pp. 19–33, 2024.

[30] S. Lu, K. Tsakalis, and Y. Chen, "Development and application of a novel high-order fully actuated system approachPart I: 3-DOF quadrotor control," *IEEE Control Systems Letters*, vol. 7, pp. 1177–1182, 2023.

[31] G. Duan, "High-order fully actuated system approaches: Part X. Basics of discrete-time systems," *International Journal of Systems Science*, vol. 53, no. 4, pp. 810–832, 2022.

[32] M. Sun and D. Wang, "Iterative learning control with initial rectifying action," *Automatica*, vol. 38, no. 7, pp. 1177–1182, 2002.

[33] S. S. Saab, D. Shen, M. Orabi, D. Kors, and R. H. Jaafar, "Iterative learning control: Practical implementation and automation," *IEEE Transactions on Industrial Electronics*, vol. 69, no. 2, pp. 1858–1866, 2022.

[34] J. Xu and R. Yan, "On initial conditions in iterative learning control," *IEEE Transactions on Automatic Control*, vol. 50, no. 9, pp. 1349–1354, 2005.

[35] G. Duan, "Discrete-time delay systems: Part 1. Global fully actuated case," *Science China Information Sciences*, vol. 65, no. 8, p. 182201, Aug. 2022.

[36] D. Meng and K. L. Moore, "Robust iterative learning control for nonrepetitive uncertain systems," *IEEE Transactions on Automatic Control*, vol. 62, no. 2, pp. 907–913, 2017.

Proceedings of the 3rd Conference on Fully Actuated System Theory and Applications
May 10-12, 2024, Shenzhen, China

Robust Adaptive Control for a class of Nonlinear Uncertain HOFA Systems with Actuator Attacks

Cunfu Qin[1], Xiao Wang[1], Ping Zhao[1]
1. School of Information Science and Engineering, Shandong Normal University, Jinan 250358, P. R. China
E-mail: zhaoping@amss.ac.cn

Abstract: In this paper, a robust adaptive controller is proposed for a class of nonlinear uncertain High-order Fully Actuated (HOFA) systems in the presence of actuator attacks. Specifically, a parameterizable adaptive controller is designed to address actuator attacks and nonlinear uncertainties. By employing Lyapunov stability theory, it is demonstrated that the designed robust adaptive controller can guarantee the stability of the closed-loop system. Finally, the effectiveness of the proposed algorithm is verified through the simulation of a numerical example.

Key Words: Robust Adaptive Controller, High-order Fully Actuated (HOFA) Systems, Nonlinear Uncertainty, Actuator Attacks

1 Introduction

The state space method has been proven to be a highly effective approach for studying nonlinear systems, and the method has significant practical implications in the domains of control engineering, dynamics analysis, circuit design, and related fields. In the field of control system theory, many scholars have focused their research on the state space method or have applied it within the framework of first-order systems [1]. This includes the analysis of Lyapunov stability theory [2], the Pontryagin's maximum principle [3], the Kalman filter [4] and so on. The analysis and design of controllers for nonlinear systems have attracted significant attention from scholars due to the prevalence of such systems. Regarding nonlinear systems, there have been many outstanding research results [5–8]. In [9] , the adaptive fuzzy sliding mode control problem of nonlinear systems was examined. Further, Wen, Chen and Ge investigated a nonlinear strict feedback system using the backstepping control method in [10]. In [11], the issue of asymptotic tracking of nonlinear systems is discussed.

Unlike traditional first-order state space models, HOFA systems represent a completely new model suitable for designing controllers. This model was initially proposed by Duan in 2020, who highlighted that the HOFA system serves as a descriptive framework for dynamic systems and a control-oriented model [12]. In recent years, extensive research on the HOFA system has led to significant advancements and notable achievements. Duan generalized physical concepts to fully actuated systems and introduced a HOFA system model to describe the dynamic system in [1, 12]. Duan established a connection between the generalized form of strict feedback systems and HOFA systems in [13]. In [14], a robust control method was proposed to address the challenges posed by the HOFA systems with nonlinear uncertainties. An adaptive control method was proposed in [15] to address a set of unknown parameters. Furthermore, in [16, 17], the application of robust adaptive control was explored to address the challenges posed by the presence of nonlinear uncertainties and unknown parameter vectors in HOFA systems, and the effectiveness of both robust adaptive control and disturbance rejection control was demonstrated and validated. In [18–21], Duan also developed other aspects of HOFA systems, such as the stability problem, optimal control problem, generalized PID control problem, and discrete-time models. Furthermore, the fault-tolerant control and event-triggered control issues of HOFA systems have been investigated in [22, 23].

Cyber-physical systems (CPSs) are found in numerous automation industries, including aerospace, automotive, energy, manufacturing, and transportation etc. The security of CPSs is of utmost importance, and extensive research on CPSs attacks has consistently been a prominent and pressing concern in the field. Based on the method of execution, there are two common types of cyber-attacks: deception attacks and denial of service attacks. Deception attacks have the potential to compromise data integrity through the alteration of data packets, while denial of service attacks can disrupt data availability by blocking information flow [24]. When a control system experiences a cyber-attack, it can significantly impair the system's performance. Therefore, it is imperative to develop a control algorithm that can effectively restore the system's performance. To date, a substantial body of literature has been published on the topic of cyber-attacks on control systems, yielding a multitude of promising findings [25–34]. For instance, Zhang, Wang and Liu et al. investigated recoverable cyber-attacks on nonlinear multi-agent systems in [27]. In [30], the issue of false data injection in networked systems was discussed. In [34], Yucelen, Haddad and Feron introduced an adaptive control algorithm aimed at mitigating sensor attacks. This algorithm ensures that the linear dynamic system remains stable in the presence of sensor attacks. It can be seen that the issue of cyber-attacks within the framework of state space has been deeply studied by numerous scholars, and many outstanding findings have been achieved.

Up to now, despite the existence of numerous research findings on control systems affected by cyber-attacks in state space, there remains a scarcity of studies focusing on HOFA systems impacted by cyber-attacks. Based on the aforementioned research findings, this paper introduces a robust adaptive control algorithm for a specific category of uncertain HOFA systems with time-invariant actuator attacks. The algorithm not only mitigates the impact of nonlinear uncer-

This work is supported by the Natural Science Foundation of Shandong Province under Grant ZR2017JL028.

tainties in the system but also guarantees the stability of the system in the presence of actuator attacks.

Notation: In this paper, $\mathbb{R}^r$ denotes the r-dimensional real vectors. The notation $\mathbb{R}^{r\times r}$ represents the set of $r \times r$ real matrix. $\|\cdot\|$ is used to denote the Euclidean norm. The notation $x^{(i)}$ represents the i-th derivative of $x \in \mathbb{R}^r$. P and Φ represent the matrices $P(A^{(0\sim m-1)})$ and $\Phi(A^{(0\sim m-1)})$, respectively. The notation $\lambda_{\max}(\cdot)$ is used to represent the maximum eigenvalue of a matrix. $\lambda_i(A)$ represents the i-th eigenvalue of matrix A. Both blank matrices and 0 represent null matrices. In addition, we will use the following symbols:

$$\|x\| = (x^T x)^{\frac{1}{2}},$$

$$\|x^{(0\sim m-1)}\|_P = ((x^{(0\sim m-1)})^T P x^{(0\sim m-1)})^{\frac{1}{2}},$$

$$A^{(0\sim m-1)} = [A_0, A_1, \cdots, A_{m-1}] \in \mathbb{R}^{r\times mr},$$

$$A^{(0\sim m-1)}x^{(0\sim m-1)} = A_0 x + A_1 \dot{x} + \cdots + A_{m-1}x^{(m-1)},$$

$$x^{(0\sim m-1)} = \begin{bmatrix} x \\ \dot{x} \\ \ddot{x} \\ \vdots \\ x^{(m-1)} \end{bmatrix} \in \mathbb{R}^{mr},$$

$$\Phi = \begin{bmatrix} 0 & I & & \\ & & \ddots & \\ & & & I \\ -A_0 & -A_1 & \dots & -A_{m-1} \end{bmatrix} \in \mathbb{R}^{mr\times mr},$$

where P refers to some symmetric positive definite matrix, $x \in \mathbb{R}^r, A_i \in \mathbb{R}^{r\times r}, i = 0, 1\cdots m-1$.

2 Problem Formulation and Preliminaries

Consider a class of nonlinear uncertain HOFA systems of the following form

$$\begin{aligned} x^{(m)} &= g(x^{(0\sim m-1)}) + b(x^{(0\sim m-1)})u(t) \\ &\quad + \Delta g(x^{(0\sim m-1)}), \end{aligned} \tag{1}$$

where $x \in \mathbb{R}^r, \dot{x}, \dots x^{(m)}$ represent the state vector and its derivatives of each order, $u(t) \in \mathbb{R}^r$ refers to the control input, $g(x^{(0\sim m-1)}) \in \mathbb{R}^r$ denotes a nonlinear vector function of known form, $b(x^{(0\sim m-1)}) \in \mathbb{R}^{r\times r}$ refers to a nonlinear gain matrix of known form, $\Delta g(x^{(0\sim m-1)}) \in \mathbb{R}^r$ is the nonlinear uncertainty of the system.

Due to the presence of fundamental physical laws, numerous systems can be effectively represented and analyzed as HOFA systems. As a result, HOFA systems are very vulnerable to attacks. In this paper, we make the assumption that the compromised control input is available and can be used. Furthermore, we consider the specific form of the compromised control input as

$$\tilde{u}(t) = u(t) + \delta_a, t \geq 0, \tag{2}$$

where $\tilde{u}(t)$ represents the control input following an actuator attack. δ_a is a vector of unknown bounded constants representing time-invariant actuator attacks.

Our control objective is to develop a robust adaptive controller for the HOFA system (1) with actuator attacks so that the closed-loop system signals are bounded.

In order to achieve the control objective, we present the following assumptions and lemmas.

Assumption 1. ([14]) Det $b(x^{(0\sim m-1)}) \neq 0, \forall x^{(i)} \in \mathbb{R}^r, i = 0, 1, \dots, m-1$. This is the basic assumption of HOFA systems.

Assumption 2. ([16]) The nonlinear uncertainty system (1) possess a non-negative continuous scalar function $\omega(x^{(0\sim m-1)})$ that satisfies

$$\|\Delta g(x^{(0\sim m-1)})\| \leq \omega(x^{(0\sim m-1)}). \tag{3}$$

Lemma 1. ([16]) If there exists a value σ such that $\mathrm{Re}\lambda_i(A) < -\frac{\sigma}{2}$, then there exists a positive definite matrix $P \in \mathbb{R}^{n\times n}$ such that satisfies $A^T P + PA \leq -\sigma P$, where σ is a positive constant and A is an $n \times n$ real matrix.

Lemma 2. ([16]) For any $\mu > 0$, there exists a set of matrices $A_i \in \mathbb{R}^{r\times r}, i = 0, 1, \dots, m-1$ satisfying

$$Re\lambda_i(\Phi(A^{(0\sim m-1)})) < -\frac{\mu}{2}, i = 1, 2, \dots, mr. \tag{4}$$

Based on Lemma 1 and Lemma 2, for any $\mu > 0$, there exists a positive definite matrix $P(A^{(0\sim m-1)})$ such that

$$\Phi^T P + P\Phi \leq -\mu P, \tag{5}$$

where $P \triangleq P(A^{(0\sim m-1)}) = [P_1, P_2, \dots, P_m], P_i \in \mathbb{R}^{mr\times r}$. Besides, we define the symbol

$$P_L \triangleq P_L(A^{(0\sim m-1)}) = P(A^{(0\sim m-1)}) \begin{bmatrix} 0 \\ I_r \end{bmatrix} = P_m.$$

Lemma 3. ([16]) For an arbitrarily chosen matrix $E \in \mathbb{R}^{mr\times mr}$ and a nonsingular matrix $V \in \mathbb{R}^{mr\times mr}$, the parametric solutions of $A^{(0\sim m-1)}$ and $\Phi(A^{(0\sim m-1)})$ satisfies

$$\Phi(A^{(0\sim m-1)}) = VEV^{-1},$$

$$A^{(0\sim m-1)} = -ZE^m V^{-1}(Z, E),$$

$$V(Z, E) = \begin{bmatrix} Z \\ ZE \\ \vdots \\ ZE^{m-1} \end{bmatrix},$$

where $Z \in \mathbb{R}^{r\times mr}$ is an appropriate parameter matrix satisfying

$$DetV(Z, E) \neq 0.$$

Lemma 4. For two real numbers m and n, and $n > 0$, the following inequality holds

$$m - \frac{m^2}{4n} \leq n.$$

3 Robust Adaptive controller Design and Stability Analysis

3.1 Controller Design

In this section, we present the robust adaptive control algorithm for the nonlinear uncertain HOFA system (1) considering time-invariant actuator attack (2). The controller is

designed as follows:

$$\begin{cases} u = -b^{-1}(x^{(0\sim m-1)})[v_0 + v_1] - \hat{\delta}_a, \\ v_0 = g(x^{(0\sim m-1)}) + A^{(0\sim m-1)}x^{(0\sim m-1)}, \\ v_1 = \dfrac{\omega^2(x^{(0\sim m-1)})}{4\varpi} P_L^T(A^{(0\sim m-1)})x^{(0\sim m-1)}, \\ \dot{\hat{\delta}}_a = \Gamma b^T(x^{(0\sim m-1)})P_L^T x^{(0\sim m-1)} - \Gamma\hat{\delta}_a, \end{cases} \tag{6}$$

where ϖ is a suitably chosen positive real number. Γ is a positive definite matrix of appropriate dimensions. The role of v_0 is to eliminate the nonlinear terms in the system in order to obtain a linear constant closed-loop system. On the other hand, the roles of v_1 and adaptive law are to suppress the effects of nonlinear uncertainty and actuator attacks in the system.

By incorporating the controller (6) into the HOFA system (1), we can derive the closed-loop system as follows:

$$\begin{aligned} x^{(m)} &= -A^{(0\sim m-1)}x^{(0\sim n-1)} + b(x^{(0\sim m-1)})\tilde{\delta}_a \\ &\quad -\frac{\omega^2(x^{(0\sim m-1)})}{4\varpi} P_L^T(A^{(0\sim m-1)})x^{(0\sim m-1)} \\ &\quad +\Delta g(x^{(0\sim m-1)}), \end{aligned} \tag{7}$$

where $\tilde{\delta}_a = \delta_a - \hat{\delta}_a$,

$$\dot{\tilde{\delta}}_a = \Gamma\hat{\delta}_a - \Gamma b^T(x^{(0\sim m-1)})P_L^T x^{(0\sim m-1)}. \tag{8}$$

Furthermore, we can get the following state-space form

$$\begin{aligned} \dot{x}^{(0\sim m-1)} &= \Phi(A^{(0\sim m-1)})x^{(0\sim m-1)} \\ &\quad + \begin{bmatrix} 0 \\ \phi_\delta(x^{(0\sim m-1)}) + \phi_u(x^{(0\sim m-1)}) \end{bmatrix}, \end{aligned} \tag{9}$$

where $\phi_\delta(x^{(0\sim m-1)}) = b(x^{(0\sim m-1)})\tilde{\delta}_a, \phi_u(x^{(0\sim m-1)}) = \Delta g(x^{(0\sim m-1)}) - \dfrac{\omega^2(x^{(0\sim m-1)})}{4\varpi} P_L^T(A^{(0\sim m-1)})x^{(0\sim m-1)}$.

Then, we can get the following theorem:

Theorem 1. Under Assumptions 1-2, choose appropriate positive real numbers μ and ϖ, and let $A^{(0\sim m-1)} \in \mathbb{R}^{r\times mr}$ satisfy condition (4). The control law (6) ensures that the signals of the closed-loop systems (8) and (9) are all bounded.

Remark 1. When designing the controller (6), we can appropriately select values for ϖ and Γ to minimize the bound of the closed-loop system state $x^{(0\sim n-1)}$ and the estimation error $\tilde{\delta}_a$.

3.2 Stability analysis

To establish the validity of Theorem 1, we select a Lyapunov function candidate in the following format:

$$V = \frac{1}{2}(x^{(0\sim m-1)})^T P x^{(0\sim m-1)} + \frac{1}{2}\tilde{\delta}_a^T\Gamma^{-1}\tilde{\delta}_a, \tag{10}$$

where $P = P(A^{(0\sim m-1)})$ is a positive definite matrix satisfying inequality (5).

Based on equations (8) and (9), the time derivative of equation (10) can be expressed as

$$\begin{aligned} \dot{V} &= \frac{1}{2}(\dot{x}^{(0\sim m-1)})^T P x^{(0\sim m-1)} - \tilde{\delta}_a^T\Gamma^{-1}\dot{\hat{\delta}}_a \\ &\quad +\frac{1}{2}(x^{(0\sim m-1)})^T P\dot{x}^{(0\sim m-1)} \\ &= \frac{1}{2}(x^{(0\sim m-1)})^T(\Phi^T P + P\Phi)x^{(0\sim m-1)} \\ &\quad -\tilde{\delta}_a^T\Gamma^{-1}\dot{\hat{\delta}}_a + (x^{(0\sim m-1)})^T P\cdot \\ &\quad \begin{bmatrix} 0 \\ \phi_\delta(x^{(0\sim m-1)}) + \phi_u(x^{(0\sim m-1)}) \end{bmatrix} \\ &= \frac{1}{2}(x^{(0\sim m-1)})^T(\Phi^T P + P\Phi)x^{(0\sim m-1)} \\ &\quad +(x^{(0\sim m-1)})^T P_L\phi_\delta(x^{(0\sim m-1)}) \\ &\quad +(x^{(0\sim m-1)})^T P_L\phi_u(x^{(0\sim m-1)}) \\ &\quad -\tilde{\delta}_a^T\Gamma^{-1}\dot{\hat{\delta}}_a. \end{aligned} \tag{11}$$

According to Equation (3) and Lemma 4, one can derive that

$$\begin{aligned} & (x^{(0\sim m-1)})^T P_L\phi_u(x^{(0\sim m-1)}) \\ =\ & (x^{(0\sim m-1)})^T P_L\Delta g \\ & -\frac{1}{4\varpi}\omega^2(x^{(0\sim m-1)})[(x^{(0\sim m-1)})^T P_L P_L^T x^{(0\sim m-1)}] \\ =\ & (x^{(0\sim m-1)})^T P_L\Delta g \\ & -\frac{1}{4\varpi}\omega^2(x^{(0\sim m-1)})\|P_L^T x^{(0\sim m-1)}\|^2 \\ \le\ & \|\Delta g\|\|P_L^T x^{(0\sim m-1)}\| \\ & -\frac{1}{4\varpi}\omega^2(x^{(0\sim m-1)})\|P_L^T x^{(0\sim m-1)}\|^2 \\ \le\ & \omega(x^{(0\sim m-1)})\|P_L^T x^{(0\sim m-1)}\| \\ & -\frac{1}{4\varpi}\omega^2(x^{(0\sim m-1)})\|P_L^T x^{(0\sim m-1)}\|^2 \\ \le\ & \varpi. \end{aligned} \tag{12}$$

Substituting (5), (6) and (12) into (11), we have

$$\begin{aligned} \dot{V} &= \frac{1}{2}(x^{(0\sim m-1)})^T(\Phi^T P + P\Phi)x^{(0\sim m-1)} \\ &\quad -\frac{1}{4\varpi}\omega^2(x^{(0\sim m-1)})\|P_L^T x^{(0\sim m-1)}\|^2 \\ &\quad -\tilde{\delta}_a^T\Gamma^{-1}[\dot{\hat{\delta}}_a - \Gamma b^T(x^{(0\sim m-1)})P_L^T x^{(0\sim m-1)}] \\ &\quad +(x^{(0\sim m-1)})^T P_L\Delta g \\ &\le -\frac{\mu}{2}(x^{(0\sim m-1)})^T P x^{(0\sim m-1)} + \varpi \\ &\quad -\frac{1}{2}\tilde{\delta}_a^T\tilde{\delta}_a + \frac{1}{2}\delta_a^T\delta_a \\ &\le -\alpha V + \beta, \end{aligned} \tag{13}$$

where $\alpha = \min\{\mu, \dfrac{1}{\lambda_{\max(\Gamma^{-1})}}\}$, $\beta = \dfrac{1}{2}\delta_a^T\delta_a + \varpi$.

Thus, it can be verified that $0 \le V \le e^{-\alpha t}(V_{(0)} - \dfrac{\beta}{\alpha}) + \dfrac{\beta}{\alpha}$ from inequality (13), which means that the states and errors of the closed-loop systems are bounded.

If the uncertain nonlinearity of the HOFA system (1) satisfies Assumption 3 below, we can get Corollary 1.

Assumption 3. ([16]) The nonlinear uncertainty system (1) possess a non-negative continuous scalar function

$\omega(x^{(0\sim m-1)})$ that satisfies

$$\|\Delta g(x^{(0\sim m-1)})\| \leq \omega(x^{(0\sim m-1)})\|P_L^T(x^{(0\sim m-1)})\|. \quad (14)$$

Corollary 1. Letting the HOFA system (1) satisfies Assumption 1 and Assumption 3, the control law (15) can ensure that when time goes to infinity, $\|x^{(0\sim m-1)}\| \to 0$ and $\|\tilde{\delta}_a\|$ is bounded. The control law is given by

$$\begin{cases} u = -b^{-1}(x^{(0\sim m-1)})[v_0 + v_1] - \hat{\delta}_a, \\ v_0 = g(x^{(0\sim m-1)}) + A^{(0\sim m-1)}x^{(0\sim m-1)}, \\ v_1 = \dfrac{1}{\varpi}\omega(x^{(0\sim m-1)})P_L^T(A^{(0\sim m-1)})x^{(0\sim m-1)}, \\ \dot{\hat{\delta}}_a = \Gamma b^T(x^{(0\sim m-1)})P_L^T x^{(0\sim m-1)}, \end{cases} \quad (15)$$

where ϖ is a suitably chosen positive real number satisfying $\varpi \leq 1$; Γ is a positive definite matrix of appropriate dimensions.

Proof: Under the control law (15), we can get the following closed-loop system:

$$\begin{aligned} x^{(m)} = & - A^{(0\sim m-1)}x^{(0\sim m-1)} + b(x^{(0\sim m-1)})\tilde{\delta}_a \\ & - \frac{1}{\varpi}\omega(x^{(0\sim m-1)})P_L^T(A^{(0\sim m-1)})x^{(0\sim m-1)} \\ & + \Delta g(x^{(0\sim m-1)}), \end{aligned} \quad (16)$$

which can be equivalently expressed as

$$\begin{aligned} \dot{x}^{(0\sim m-1)} &= \Phi(A^{(0\sim m-1)})x^{(0\sim m-1)} \\ &\quad + \begin{bmatrix} 0 \\ \phi_\delta(x^{(0\sim m-1)}) + \phi_{u1}(x^{(0\sim m-1)}) \end{bmatrix}, \end{aligned} \quad (17)$$

where $\phi_\delta(x^{(0\sim m-1)}) = b(x^{(0\sim m-1)})\tilde{\delta}_a, \phi_{u1}(x^{(0\sim m-1)}) = \Delta g(x^{(0\sim m-1)}) - \dfrac{1}{\varpi}\omega(x^{(0\sim m-1)})P_L^T(A^{(0\sim m-1)})x^{(0\sim m-1)}$.

We can choose the same Lyapunov function as in (10). In view of equations (15) and (17), we can obtain

$$\begin{aligned} \dot{V} &= \frac{1}{2}(\dot{x}^{(0\sim m-1)})^T P x^{(0\sim m-1)} \\ &\quad + \frac{1}{2}(x^{(0\sim m-1)})^T P \dot{x}^{(0\sim m-1)} - \tilde{\delta}_a^T \Gamma^{-1}\dot{\hat{\delta}}_a \\ &= \frac{1}{2}(x^{(0\sim m-1)})^T(\Phi^T P + P\Phi)x^{(0\sim m-1)} \\ &\quad + (x^{(0\sim m-1)})^T P_L \phi_\delta(x^{(0\sim m-1)}) - \tilde{\delta}_a^T\Gamma^{-1}\dot{\hat{\delta}}_a \\ &\quad + (x^{(0\sim m-1)})^T P_L \phi_{u1}(x^{(0\sim m-1)}). \end{aligned} \quad (18)$$

Based on Assumption 2, we can prove

$$\begin{aligned} & (x^{(0\sim m-1)})^T P_L \phi_{u1}(x^{(0\sim m-1)}) \\ = \; & (x^{(0\sim m-1)})^T P_L \Delta g \\ & - \frac{1}{\varpi}\omega(x^{(0\sim m-1)})[(x^{(0\sim m-1)})^T P_L P_L^T x^{(0\sim m-1)}] \\ \leq \; & \|\Delta g\|\|P_L^T x^{(0\sim m-1)}\| \\ & - \frac{1}{\varpi}\omega(x^{(0\sim m-1)})\|P_L^T x^{(0\sim m-1)}\|^2 \\ \leq \; & \omega(x^{(0\sim m-1)})\|P_L^T x^{(0\sim m-1)}\|^2 \\ & - \frac{1}{\varpi}\omega(x^{(0\sim m-1)})\|P_L^T x^{(0\sim m-1)}\|^2 \\ = \; & - \frac{1-\varpi}{\varpi}\omega(x^{(0\sim m-1)})\|P_L^T x^{(0\sim m-1)}\|^2. \end{aligned} \quad (19)$$

From lemma 2 and equation (19), we can obtain

$$\begin{aligned} \dot{V} &\leq -\frac{\mu}{2}(x^{(0\sim m-1)})^T P x^{(0\sim m-1)} \\ &\quad - \frac{1-\varpi}{\varpi}\omega(x^{(0\sim m-1)})\|P_L^T x^{(0\sim m-1)}\|^2 \\ &\quad - \tilde{\delta}_a^T\Gamma^{-1}[\dot{\hat{\delta}}_a - \Gamma b^T(x^{(0\sim m-1)})P_L^T x^{(0\sim m-1)}] \\ &\leq -\frac{\mu}{2}(x^{(0\sim m-1)})^T P x^{(0\sim m-1)} \\ &\quad - \frac{1-\varpi}{\varpi}\omega(x^{(0\sim m-1)})\|P_L^T x^{(0\sim m-1)}\|^2 \\ &\leq -\frac{\mu}{2}\|x^{(0\sim m-1)}\|_P \\ &\quad - \frac{1-\varpi}{\varpi}\omega(x^{(0\sim m-1)})\|P_L^T x^{(0\sim m-1)}\|^2 \\ &\leq 0. \end{aligned} \quad (20)$$

Thus, according to the Lyapunov stability analysis, the corollary 1 holds.

4 Simulation

In this section, we present a numerical example to illustrate the effectiveness of the proposed method for nonlinear uncertain HOFA systems with actuator attacks. Now, let us consider the HOFA system model [36] given by

$$\ddot{x} = g(x^{(0\sim 1)}) + b(x^{(0\sim 1)})u + \Delta g(x^{(0\sim 1)}), \quad (21)$$

where $x \in \mathbb{R}^2$ represents the state, $u \in \mathbb{R}^2$ represents the control input, $g(x^{(0\sim 1)}) \in \mathbb{R}^2$ denotes the nonlinear vector function, $b(x^{(0\sim n-1)}) \in \mathbb{R}^{2\times 2}$ refers to the nonlinear gain matrix, $\Delta g(x^{(0\sim 1)}) \in \mathbb{R}^2$ is the nonlinear uncertainty of the system, and their specific forms are

$$g(x^{(0\sim 1)}) = -M^{-1}(x^{(0\sim 1)})D(x^{(0\sim 1)})\dot{x},$$

$$b(x^{(0\sim 1)}) = M^{-1}(x^{(0\sim 1)}),$$

$$\Delta g(x^{(0\sim 1)}) = 0.05(3x + 2\dot{x}),$$

$$D(x^{(0\sim 1)}) = -15.1875\sin(x_2)\begin{bmatrix} \dot{x}_2 & \dot{x}_1 + \dot{x}_2 \\ \dot{x}_1 & 0 \end{bmatrix},$$

$$M(x^{(0\sim 1)}) = \begin{bmatrix} 30.375 & 15.1875 \\ 15.1875 & 0 \end{bmatrix}\cos(x_2) + \begin{bmatrix} 50.625 & 10.125 \\ 10.125 & 10.125 \end{bmatrix}.$$

In order to deal with the nonlinear uncertain HOFA system (21) with actuator attacks, the robust adaptive controller is designed as

$$\begin{cases} u = -M(x^{(0\sim 1)})[v_0 + v_1] - \hat{\delta}_a, \\ v_0 = -M^{-1}(x^{(0\sim 1)})D(x^{(0\sim 1)})\dot{x} + A^{(0\sim 1)}x^{(0\sim 1)}, \\ v_1 = \dfrac{1}{4\varpi}\omega^2(x^{(0\sim 1)})P_L^T(A^{(0\sim 1)})x^{(0\sim 1)}, \\ \dot{\hat{\delta}}_a = \Gamma(M^{-1}(x^{(0\sim 1)}))^T P_L^T x^{(0\sim 1)} - \Gamma\hat{\delta}_a, \end{cases} \quad (22)$$

where $\omega(x^{(0\sim 1)}) = 0.05(3\|x\| + 2\|\dot{x}\|)$, $\varpi = 10^{-4}$, $\Gamma = \begin{bmatrix} 1 & 0 \\ 0 & 1 \end{bmatrix}$.

According to Lemma 2 and Lemma 3, we can get $\mu = 8$,

$$A_0 = \begin{bmatrix} 24 & 21 \\ -16 & 56 \end{bmatrix}, A_1 = \begin{bmatrix} 11 & 3 \\ -2 & 15 \end{bmatrix},$$

$$\Phi_{(A^{(0\sim1)})} = \begin{bmatrix} 0 & 0 & 1 & 0 \\ 0 & 0 & 0 & 1 \\ -24 & -21 & -11 & -3 \\ 16 & -56 & 2 & -15 \end{bmatrix}.$$

Furthermore, by solving the Lyapunov equation $(\Phi(A^{(0\sim1)}) + \frac{\mu}{2}I)^T P + P(\Phi(A^{(0\sim1)}) + \frac{\mu}{2}I) = -0.001I$, we can get

$$P = 10^{-3} \begin{bmatrix} 148.39 & -75.09 & 17.5 & -10.88 \\ -75.09 & 67.88 & -9.38 & -8.37 \\ 17.5 & -9.38 & 2.18 & -1.36 \\ -10.88 & 8.37 & -1.36 & 1.18 \end{bmatrix},$$

$$P_L^T = 10^{-3} \begin{bmatrix} 17.5 & -9.38 & 2.18 & -1.36 \\ -10.88 & 8.37 & -1.36 & 1.18 \end{bmatrix}.$$

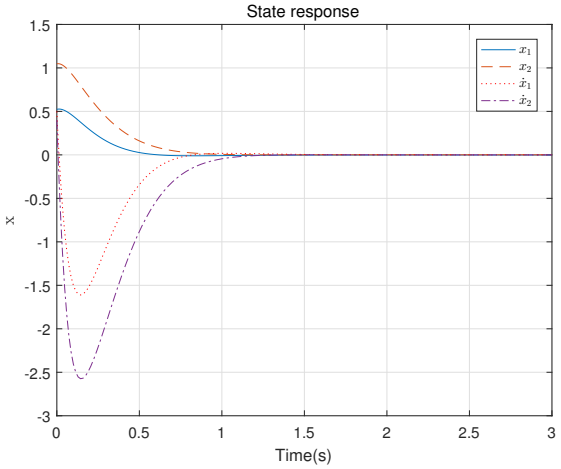

Fig. 1: Response of x, $\dot{x}$

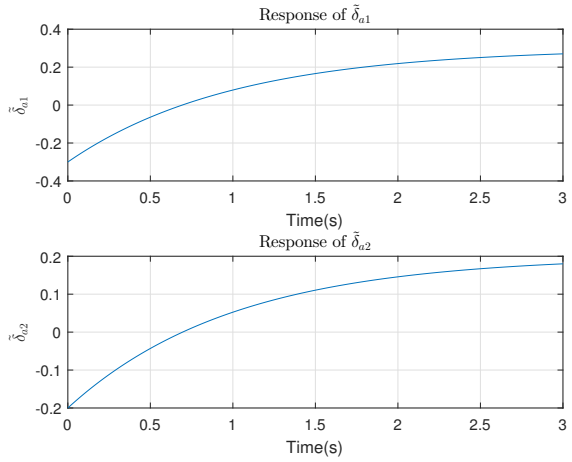

Fig. 2: Response of $\tilde{\delta}_a$

In order to establish the validity of Theorem 1, it is postulated that the actuator attacks, which is both time-invariant and input-independent, can be represented by the vector $[\delta_{a1(0)}, \delta_{a2(0)}] = [0.3, 0.2]$. The initial values are given by $[x_{1(0)}, x_{2(0)}, \dot{x}_{1(0)}, \dot{x}_{2(0)}] = [\frac{\pi}{6}, \frac{\pi}{3}, 0.5, 0.4]$ and $[\hat{\delta}_{a1(0)}, \hat{\delta}_{a2(0)}] = [0.6, 0.4]$. The simulation results are depicted in Fig. 1 to Fig. 3. Fig. 1 illustrate the trajectories of the state response x and $\dot{x}$, respectively. Fig. 2 shows the errors signals of system (8). The control input u is plotted in fig. 3. Based on the simulation results, it is evident that the signals of the closed-loop systems (8) and (9) are all bounded. Therefore, the effectiveness of the robust adaptive control strategy proposed in this paper has been demonstrated.

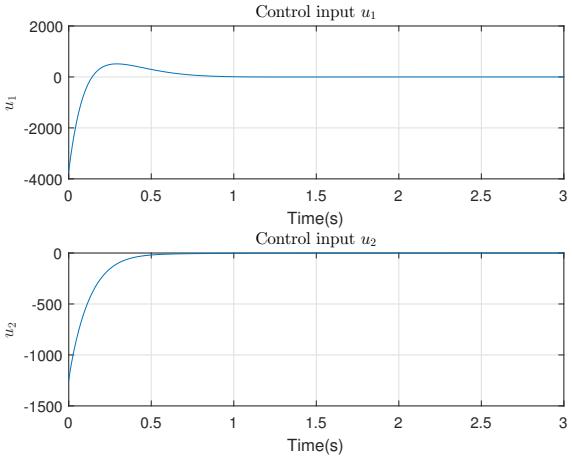

Fig. 3: Control input u

5 Conclusion

Cyber-physical systems exist in many fields. System performance will be significantly affected when a cyber-attack occurs on the system. How to ensure the stable operation of the system is an issue worth considering. This paper proposes a robust adaptive control algorithm to solve the actuator attack problem in the field of HOFA systems. First of all, the control algorithm can deal with uncertainties in the system. When actuator attacks occur in the HOFA system, the controller designed in this paper can effectively mitigate the impact of actuator attacks on the system. Finally, the algorithm's effectiveness is verified through simulation. In order to further advance research in this field, it is recommended to explore the possibility of expanding the research direction to include time-varying and input-dependent actuator attacks.

References

[1] G. R. Duan, High-order fully actuated system approaches: Part I. Models and basic procedure. *International Journal of Systems Science*, 2021, 52(2): 422–435.

[2] A. Lyapunov, The general problem of the stability of motion. *International journal of control*, 1992, 55(3): 531–534.

[3] L. Pontryagin, Optimal regulation processes. *Uspekhi Matematicheskikh Nauk*, 1959, 14(1): 3–20.

[4] R. Kalman, A new approach to linear filtering and prediction problems. *Journal of Basic Engineering Transactions*, 1960, 82(1): 35–45.

[5] C. Hua, K. Li, and X. Guan, Leader-following output consensus for high-order nonlinear multiagent systems. *IEEE Transactions on Automatic Control*, 2018, 64(3): 1156–1161.

[6] M. Li and Z. Xiang, Adaptive neural network tracking control for a class of switched nonlinear systems with input delay. *Neurocomputing*, 2019, 366: 284-294.

[7] X. Li, J. He, C. Wen, and X. Liu, Backstepping-based adaptive control of a class of uncertain incommensurate fractional-order nonlinear systems with external disturbance. *IEEE Transactions on Industrial Electronics*, 2021, 69(4): 4087-4095.

[8] J. Ma, J. Park, and S. Xu, Command-filter-based finite-time adaptive control for nonlinear systems with quantized input. *IEEE Transactions on Automatic Control*, 2020, 66(5): 2339-2344.

[9] B. Yoo and W. Ham, Adaptive fuzzy sliding mode control of nonlinear system. *IEEE Transactions on fuzzy systems*, 1998, 6(2): 315-321.

[10] G. Wen, C. Chen, and S. Ge, Simplified optimized backstepping control for a class of nonlinear strict-feedback systems with unknown dynamic functions. *IEEE Transactions on Cybernetics*, 2020, 51(9): 4567-4580.

[11] N. Xu, X. Zhao, G. Zong, and Y. Wang, Adaptive control design for uncertain switched nonstrict-feedback nonlinear systems to achieve asymptotic tracking performance. *Applied Mathematics and Computation*, 2021, 408: 126344.

[12] G. R. Duan, High-order system approaches - I. Full-actuation and parametric design. *Acta Automatica Sinica*, 2020, 46(7): 1333-1345.

[13] G. R. Duan, High-order fully actuated system approaches: Part II. Generalized strict-feedback systems. *International Journal of Systems Science*, 2021, 52(3): 437-454.

[14] G. R. Duan, High-order fully actuated system approaches: Part III. Robust control and high-order backstepping. *International Journal of Systems Science*, 2021, 52(5): 952-971.

[15] G. R. Duan, High-order fully actuated system approaches: Part IV. Adaptive control and high-order backstepping. *International Journal of Systems Science*, 2021, 52(5): 972-989.

[16] G. R. Duan, High-order fully actuated system approaches: Part V. Robust adaptive control. *International Journal of Systems Science*, 2021, 52(10): 2129-2143.

[17] G. R. Duan, High-order fully-actuated system approaches: Part VI. Disturbance attenuation and decoupling. *International Journal of Systems Science*, 2021, 52(10): 2161-2181.

[18] G. R. Duan, High-order fully actuated system approaches: part VII. Controllability, stabilisability and parametric designs. *International Journal of Systems Science*, 2021, 52(14): 3091-3114.

[19] G. R. Duan, High-order fully actuated system approaches: Part VIII. Optimal control with application in spacecraft attitude stabilisation. *International Journal of Systems Science*, 2022, 53(1): 54-73.

[20] G. R. Duan, High-order fully-actuated system approaches: Part IX. Generalised PID control and model reference tracking. *International Journal of Systems Science*, 2022. 53(3): 652-674.

[21] G. R. Duan, High-order fully actuated system approaches: Part X. Basics of discrete-time systems. *International Journal of Systems Science*, 2022. 53(4): 810-832.

[22] M. Cai, X. He, and D. Zhou, Fault-tolerant tracking control for nonlinear observer-extended high-order fully-actuated systems. *Journal of the Franklin Institute*, 2023, 360(1): 136-153.

[23] R. Meng, C. Hua, K. Li, and P. Ning, Adaptive event-triggered control for uncertain high-order fully actuated system. *IEEE Transactions on Circuits and Systems II: Express Briefs*, 2022, 69(11): 4438-4442.

[24] A. Teixeira, I. Shames, H. Sandberg, and K. Johansson, A secure control framework for resource-limited adversaries. *Automatica*, 2015, 51: 135-148.

[25] H. Fawzi, P. Tabuada, and S. Diggavi, Secure estimation and control for cyber-physical systems under adversarial attacks. *IEEE Transactions on Automatic control*, 2014, 59(6): 1454-1467.

[26] J. Weimer, N. Bezzo, M. Pajic, G. Pappas, O. Sokolsky, and I. Lee, Resilient parameter-invariant control with application to vehicle cruise control. *Control of Cyber-Physical Systems*, 2013: 197-216.

[27] W. Zhang, Z. Wang, Y. Liu, D. Ding, and F. Alsaadi, Sampled-data consensus of nonlinear multiagent systems subject to cyber attacks. *International Journal of Robust and Nonlinear Control*, 2018, 28(1): 53-67.

[28] D. Ding, Z. Wang, Q. Han, and G. Wei, Security control for discrete-time stochastic nonlinear systems subject to deception attacks. *IEEE Transactions on Systems, Man, and Cybernetics: Systems*, 2016, 48(5): 779-789.

[29] L. Ma, Z. Wang, H. Lam, and N. Kyriakoulis, Distributed event-based set-membership filtering for a class of nonlinear systems with sensor saturations over sensor networks. *IEEE transactions on cybernetics*, 2016, 47(11): 3772-3783.

[30] Z. Pang, L. Fan, Z. Dong, Q. Han, and G. Liu, False data injection attacks against partial sensor measurements of networked control systems. *IEEE Transactions on Circuits and Systems II: Express Briefs*, 2021, 69(1): 149-153.

[31] J. Liu, E. Tian, X. Xie, and H. Lin, Distributed event-triggered control for networked control systems with stochastic cyber-attacks. *Journal of the Franklin Institute*, 2019, 356(17): 10260-10276.

[32] L. Hu, Z. Wang, Q. Han, and X. Liu, State estimation under false data injection attacks: Security analysis and system protection. *Automatica*, 2018, 87: 176-183.

[33] D. Ding, Z. Wang, D. Ho, and G. Wei, Observer-based event-triggering consensus control for multiagent systems with lossy sensors and cyber-attacks. *IEEE transactions on cybernetics*, 2016, 47(8): 1936-1947.

[34] T. Yucelen, W. Haddad, and E. Feron, Adaptive control architectures for mitigating sensor attacks in cyber-physical systems. *Cyber-Physical Systems*, 2016, 2(1-4): 24-52.

[35] F. Li and Y. Tang, False data injection attack for cyber-physical systems with resource constraint. *IEEE transactions on cybernetics*, 2018, 50(2): 729-738.

[36] G. Tian and G. Duan, Robust model reference tracking for uncertain second-order nonlinear systems with application to robot manipulator. *International Journal of Robust and Nonlinear Control*, 2023, 33(3): 1750-1771.

Proceedings of the 3rd Conference on Fully Actuated System Theory and Applications
May 10-12, 2024, Shenzhen, China

Adaptive Iterative Learning Control for Permanent Magnet Synchronous Motors with Uncertainties

Ke Yang, Xuefang Li*
School of Intelligent Systems Engineering, Shenzhen Campus of Sun Yat-Sen University, Shenzhen 518000, P. R. China
E-mail: lixuef25@mail.sysu.edu.cn

Abstract: This paper proposes a novel adaptive iterative learning control (AILC) strategy for position tracking of permanent magnet synchronous motor (PMSM) servo systems. The primary objective of this paper is to achieve precise position tracking control in the presence of both the load disturbances and the friction forces. The designed control scheme compensates for the load disturbance indirectly by adjusting the desired control input in the controller. Moreover, an adaptive parametric update law is employed to estimate the unknown parameters. The convergence properties of the proposed control algorithms are analyzed using the composite energy function (CEF) methodology. Additionally, the effectiveness of the proposed method for the PMSM system is validated through simulations conducted in MATLAB.

Key Words: Adaptive Iterative Learning Control, Permanent magnet synchronous motor (PMSM), Composite Energy Function

1 Introduction

Permanent magnet synchronous motor (PMSM) servo systems have been extensively used in various high-precision motion control applications because of their attractive advantages including a compact structure, high power density, high efficiency and reliability, etc.,[1]. Research in PMSM control typically focuses on two primary aspects enhancing motor disturbance rejection capabilities and improving rotor tracking performance. Both rotor speed and position tracking control are crucial, with a particular emphasis on high-precision position control. Precise control over the rotor's position directly impacts the system's accuracy, stability, and dynamic performance.

In practical PMSM implementations, external nonlinear disturbances, such as the load disturbances and the friction forces, wield a substantial impact on position control. Load disturbances materialize from abrupt alterations in external load, while friction forces, stemming from transmission gears, would degrade the system's performance, both of them potentially culminating in undesirable vibrations [2]. Optimizing motor position control, particularly in high-precision position tracking, demands effective compensation for load disturbances and friction forces. Various control techniques, such as model predictive control (MPC) [3], high-order sliding-mode control [4], and fuzzy sliding-mode control [5], have been proposed in the literature. Despite its optimal solutions within specific control intervals, the MPC-based approach exhibits poor real-time performance and incurs high computational costs in practical applications [6]. On the other hand, the high-order sliding mode controller facilitates rapid achievement of desired performance in motor systems [7]. However, the specific switching logic in the sliding mode reaching law induces chattering in the control input, adversely affecting overall control effectiveness [8]. The intricacies of the PMSM system, characterized by complex dynamics, present challenges in adjusting fuzzy rule parameters to adapt to system variations. Furthermore, the lack of robustness in the face of motor system parameter changes deteriorates the application of fuzzy sliding mode control [9]. In summary, while the methods above offer effective approaches for addressing compensation uncertainties in motor position control, challenges related to real-time performance, computational costs, and robustness need to be carefully addressed for practical implementation in high-precision applications.

In practical applications, the maneuver of the PMSM rotor position notably demonstrates repetition. Learning control approaches enhance tracking accuracy by updating the control input with the data generated from the previous trails or periods [10]. Two widely utilized methods are repetitive learning control (RLC) and iterative learning control (ILC), both commonly applied in periodic trajectory tracking tasks. RLC is employed for achieving high-precision tracking control in the infinite time domain [11]. On the other hand, ILC is utilized for performing tracking tasks within finite time intervals [12]. In [13], it presents an improved adaptive iterative learning current control approach for interior permanent magnet synchronous motor (IPMSM) drives, greatly improving performance in dynamic and steady-state scenarios. In [14], the proposed adaptive ILC-based method for sensorless PMSM drives does not require the offline detection and the discrimination of harmonic frequencies, which has a strong suppression ability for the estimated rotor position harmonic error. In [15], an adaptive PD-type ILC approach is proposed to improve the PMSM position tracking in the presence of friction uncertainty. However, the majority of the aforementioned works employ the ILC approach to address periodic disturbances, combined with other control algorithms to handle non-periodic uncertainties, which complicates the control systems significantly. To simultaneously address the load disturbances with periodic tracking trajectories and the non-periodic friction disturbances, it is worth developing an effective strategy based on ILC.

This paper proposes a novel position tracking control scheme for PMSM based on an adaptive iterative learning control (AILC) method within the finite-time domain, in the presence of both the load disturbances and the friction

This work is supported by the National Natural Science Foundation of China (Grant No. 62373385), the Natural Science Foundation of Guangdong Province (Grant No. 2022A1515010881), the Shenzhen Science and Technology Program(Grant No. 202305063000008, 20231121093427001)
*Corresponding author

forces. The proposed control scheme indirectly compensates for load disturbances by adjusting the desired control input in the controller. Moreover, an adaptive parametric update law is employed to estimate the unknown parameters, effectively mitigating the impact of friction forces. The controller gradually adjusts by learning and adapting to compensate for disturbances. This enables accurate position tracking control of PMSM, even in challenging scenarios where both the load disturbances and the friction forces coexist.

This paper is organized as follows. Section II provides an introduction to the dynamics of the PMSM and formulates the position tracking control problem. Section III shows the design of the AILC controller, along with the observer for estimating unmeasurable states in the friction model and the adaptively updated laws for estimating unknown parameters in the system. The convergence analysis of the proposed control scheme is presented in section IV. Section V presents the simulation on MATLAB to validate the proposed method in the PMSM system and Section VI is a conclusion for the whole paper.

2 Problem formulation

The mathematical dynamics of the PMSM in the rotating $d-q$ reference frame is described as [16]

$$\begin{cases} \dot{\theta} = \omega, \\ \dot{\omega} = g_1 i_q - g_2 \omega - g_3 T_L(\theta) - g_1 F_f, \\ \dot{i_q} = -g_4 i_q + g_5 \omega + g_6 u_q - g_7 \omega i_d, \\ \dot{i_d} = -g_4 i_d + g_6 u_d + g_7 \omega i_q, \end{cases} \tag{1}$$

where $g_1 \triangleq \frac{3n_p\varphi_f}{2J}, g_2 \triangleq \frac{B}{J}, g_3 \triangleq \frac{1}{J}$, $g_4 \triangleq \frac{R}{L}, g_5 \triangleq \frac{n_P\varphi_f}{L}, g_6 \triangleq \frac{1}{L}, g_7 \triangleq n_P$, θ is rotor position, ω is rotor angular speed, i_q, i_d are the stator currents of the d-axis and q-axis, u_q, u_d are the stator voltages of the d-axis and q-axis. R is the stator resistance, L is the stator inductance, J is the moment of inertia, B is the equivalent damping coefficient, n_p is the number of pole pairs, φ_f is the flux linkage. All the above motor parameters are known. $T_L(\theta)$ is load torque related to motor rotor position θ, F_f is friction torque generated by friction force during the motor operation.

It is now recognized that the two high-performance control strategies for PMSM systems are field-oriented control (FOC) and direct torque control (DTC) [17]. In this section, the FOC scheme is adopted, which commonly employs a conventional cascade control structure. In this setup, the inner loop handles current control, while the outer loop manages speed and position control. When performing position control in the outer loop, the q-axis current i_q works as a control input, and the motor rotor position θ and speed ω both work as state variables. Consequently, we consider the following position mechanical dynamics for the controller design in the iteration domain, and the subscript k is the iteration index

$$\begin{cases} \dot{\theta}_k = \omega_k, \\ \dot{\omega}_k = g_1 i_{q,k} - g_2 \omega_k - g_3 T_L(\theta_k) - g_1 F_{f,k}, \end{cases} \tag{2}$$

where θ_k is position state, ω_k is speed state, $i_{q,k}$ is the q-axis current. $T_L(\theta_k)$ is the load torque dependent on position state, $F_{f,k}$ is friction torque.

Define $x_{1,k} = \theta_k$, $x_{2,k} = \omega_k$, and $u_k = i_{q,k}$, the above-mentioned equation is rewritten as follows

$$\begin{cases} \dot{x}_{1,k} = x_{2,k}, \\ \dot{x}_{2,k} = g_1 u_k - g_2 x_{2,k} - g_3 T_L(x_{1,k}) - g_1 F_{f,k}, \end{cases} \tag{3}$$

where $T_L(x_{1,k})$ represents the position-dependent load torque. To accurately describe the friction process, this paper adopts the dynamic LuGre model, which closely resembles real-world friction phenomena, to model friction torque. By utilizing this friction model, the nonlinear characteristics of friction in the PMSM system can be effectively compensated for. Thus the friction torque $F_{f,k}$ in PMSM system can be accurately described by the LuGre model [18]

$$\begin{cases} F_{f,k} = \rho_0 z_k + \rho_1 \dot{z_k} + \rho_2 x_{2,k}, \\ \dot{z}_k = x_{2,k} - \phi(x_{2,k}) \left| x_{2,k} \right| z_k, \\ \phi(x_{2,k}) = F_c + (F_s - F_c)^{-(x_{2,k}/\omega_s)^2}. \end{cases} \tag{4}$$

For the friction model (4), the nonlinear function $\phi(x_{2,k})$ is used to model the Stribeck effect, which is assumed to be strictly positive. However, the stiffness coefficient ρ_0, the damping coefficient ρ_1, and the viscous coefficient ρ_2 are unknown. z is an unmeasurable state associated with the motor rotor state. F_c, F_s are the coulomb friction torque and stiction friction torque and ω_s is the characteristic Stribeck angular velocity.

According to the first and second formulas in (4), the above friction model (4) can be streamlined, yielding the subsequent expression for the friction torque

$$F_{f,k} = \rho_0 z_k - \rho_1 \left| x_{2,k} \right| \phi(x_{2,k}) z_k + \rho x_{2,k}, \tag{5}$$

$$\rho = \rho_1 + \rho_2. \tag{6}$$

For the system (3), define $x_{1,r}$ as a periodic position reference trajectory that will be tracked. The reference velocity trajectory $x_{2,r} = \dot{x}_{1,r}$, is also periodic with the same period. The expected reference tracking trajectory model is as follows, which is generated by

$$\begin{cases} \dot{x}_{1,r} = x_{2,r}, \\ \dot{x}_{2,r} = g_1 u_r - g_2 x_{2,r} - g_3 T_L(x_{1,r}), \end{cases} \tag{7}$$

where u_r is the periodic desired control input to the reference model.

The main objective of this paper is to develop an adaptive iterative learning controller u_k for position tracking in the PMSM systems, which enables the rotor position $x_{1,k}$ to precisely track a periodic reference trajectory $x_{1,r}$ in the presence of the uncertainty $T_L(x_{1,k})$ and friction disturbance $F_{f,k}$. To facilitate the controller design and analysis, the following assumptions are imposed.

Assumption 1: The initial states of the system (3) can be aligned with the initial value of the desired trajectories, namely, $x_{1,k}(0) = x_{1,r}(0)$ and $x_{2,k}(0) = x_{2,r}(0)$.

Assumption 2: $T_L(\cdot)$ is Lipschitz continuous function such that for all $x_{1,k1}, x_{1,k2} \in R$, $|T_L(x_{1,k1}) - T_L(x_{1,k2})| \leq \eta |x_{1,k1} - x_{1,k2}|$, where η is a positive constant.

Remark 1: In the PMSM system, position-dependent load disturbances are typically subjected to physical limits and mechanical constraints, leading to an upper bound on their rate of change. This implies that, for a given range of rotor position variations, the change rate of load disturbances is bounded. In this paper, $T_L(x_1)$ is bounded load torque and the Lipschitz continuous is commonly used [19].

3 Controller Design

When designing the controller of high-order systems, the linear filter error is introduced to reduce the system's order and simplify the design process [20]. Accordingly, define $e_{1,k}$ as the position tracking error, $e_{2,k}$ as the speed tracking error, and s_k as the filter error. The defined errors are as follows

$$\begin{cases} e_{1,k} = x_{1,k} - x_{1,r}, \\ e_{2,k} = x_{2,k} - x_{2,r}, \\ s_k = \dot{e}_{1,k} + \lambda e_{1,k}. \end{cases} \tag{8}$$

To decouple the dynamics of the friction model (5) with unknown parameters ρ_0 and ρ_1, we introduce the variables $z_{0,k}$ and $z_{1,k}$, representing specific instances of the general variable z_k associated with ρ_0 and ρ_1, respectively. This enables a clear distinction and independent treatment of these parameters throughout the analysis. To facilitate the AILC design, we rewrite the second formula in the nonlinear model (3) into the parameterized form

$$\dot{x}_{2,k} = g_1 u_k + \Theta_k \mathbf{f}(x_{2,k}) - g_3 T_L(x_{1,k}), \tag{9}$$

where $\Theta \triangleq \begin{bmatrix} \sigma_0 & \sigma_1 & \sigma_2 \end{bmatrix}$ is unknown, and $\sigma_0 = -g_1\rho$, $\sigma_1 = g_1\rho_1$, $\sigma_2 = -g_1\rho - g_2$, the known nonlinear system function $\mathbf{f}(x_{2,k}) \triangleq \begin{bmatrix} z_{0,k} & |x_{2,k}|\,\phi(x_{2,k})z_{1,k} & x_{2,k} \end{bmatrix}^T$, given that the unmeasurable state z_k can be estimated. Both g_1, g_3 are the known PMSM parameters, $T_L(x_{1,k})$ is a nonparametric load disturbance dependent on state $x_{1,k}$.

The load disturbance $T_L(x_{1,k})$ can be considered as a time-varying disturbance with a periodic trajectory. However, its specific characteristics are unknown and difficult to model accurately. To address this issue, one effective approach is to introduce the estimation of the expected control input in the controller. This allows for an indirect suppression of the uncertainties caused by the load disturbance, thereby enhancing the robustness of the system.

For the PMSM system (9),the following AILC law can be developed if $\mathbf{f}(x_{2,k})$ is known

$$\begin{aligned} u_k =& \hat{u}_{r,k} - \frac{1}{g_1}(\hat{\Theta}_k \mathbf{f}(x_{2,k}) + g_2 x_{2,r} + \lambda e_{2,k} \\ &+ p e_{1,k} + \frac{\hat{\eta}_{1,k}}{4p\lambda} s_k), \end{aligned} \tag{10}$$

where $\hat{u}_{r,k}$ is the estimate of desired control input $u_{r,k}$, and $\hat{\Theta}_k$ is the estimate of the parametric uncertainty, $\hat{\eta}_{1,k}$ is the estimate of the gain $\eta_{1,k}$ associated with η. The parameters λ and p denote the gain coefficients for the corresponding error terms $e_{2,k}$ and $e_{1,k}$.

The updating law for $\hat{\Theta}_k$ is developed as follows

$$\hat{\Theta}_k(t) = \hat{\Theta}_{k-1}(t) + \hat{\mathbf{f}}(x_2)^T \Gamma s_k, \tag{11}$$

$$\hat{\Theta}_{-1}(t) = \mathbf{0}, \quad t \in [0, T] \tag{12}$$

where $\Gamma \triangleq \text{diag}\{r_1, r_2, r_3\}$ is the diagonal learning gain matrix with positive diagonal elements, $\hat{\mathbf{f}}(x_{2,k})$ is the estimate of the system function $\mathbf{f}(x_{2,k})$.

Thus the nonparametric uncertainty $T_L(x_{1,k})$ is addressed by utilizing the periodic characteristics of the expected trajectory $u_{r,k}$. The adaptive law updates $\hat{u}_{r,k}(t)$ as follows

$$\hat{u}_{r,k}(t) = \hat{u}_{r,k-1}(t) - \mu_0 s_k, \tag{13}$$

$$\hat{u}_{r,-1}(t) = 0, \quad t \in [0, T] \tag{14}$$

where $\mu_0 > 0$ is learning gain.

Also, design adaptive law in the iteration domain of the unknown coefficient $\eta_{1,k}$ as follows

$$\hat{\eta}_{1,k}(t) = \hat{\eta}_{1,k-1}(t) + \mu_1 s_k^2, \tag{15}$$

$$\hat{\eta}_{1,-1}(t) = 0, \quad t \in [0, T] \tag{16}$$

where $\mu_1 > 0$ is learning gain.

However, the premise of designing the controller (10) relies on the assumption that the function $\mathbf{f}(x_{2,k})$ is known. The LuGre friction model (4) indicates that z_k is an unmeasurable state associated with $\mathbf{f}(x_{2,k})$. This contradicts the prerequisite that function $\mathbf{f}(x_{2,k})$ is known.

To obtain information about the function $\mathbf{f}(x_{2,k})$, a dual-observer is designed to estimate $z_{0,k}$ and $z_{1,k}$ separately [21],

$$\hat{z}_{0,k}(t) = \hat{z}_{0,k-1}(t) + s_k, \tag{17}$$

$$\hat{z}_{0,-1}(t) = 0, \quad t \in [0, T], \tag{18}$$

$$\hat{z}_{1,k}(t) = \hat{z}_{1,k-1}(t) + \phi(x_{2,k})|x_{2,k}|s_k, \tag{19}$$

$$\hat{z}_{1,-1}(t) = 0, \quad t \in [0, T]. \tag{20}$$

After obtaining the estimate of $z_{0,k}$ and $z_{1,k}$, rewrite $\mathbf{f}(x_{2,k})$ in (10) as $\hat{\mathbf{f}}(x_{2,k})$, and the estimated function $\hat{\mathbf{f}}(x_{2,k}) \triangleq \begin{bmatrix} \hat{z}_{0,k} & |x_{2,k}|\,\phi(x_{2,k})\hat{z}_{1,k} & x_{2,k} \end{bmatrix}^T$.

The final proposed controller algorithm is as follows

$$\begin{aligned} u_k =& \hat{u}_{r,k} - \frac{1}{g_1}(\hat{\Theta}_k \hat{\mathbf{f}}(x_{2,k}) + g_2 x_{2,r} + \lambda e_{2,k} \\ &+ p e_{1,k} + \frac{\hat{\eta}_{1,k}}{4p\lambda} s_k). \end{aligned} \tag{21}$$

With the proposed AILC scheme, we have the following result in theorem 1.

Theorem 1: For system (4) under Assumptions $1-2$, the proposed controller (21) with the updating laws $(11)-(20)$ ensures that both the filter error s_k and the position tracking error $e_{1,k}$ converge to zero pointwisely as $k \to \infty$.

4 Convergence analysis

To carry out the convergence analysis, the designed CEF is as follows, $t \in [0, T]$

$$\begin{aligned} E_k(t) =& \frac{1}{2}s_k^2 + \frac{1}{2}pe_{1,k}^2 + \frac{1}{2}\int_0^t \tilde{\Theta}_k \Gamma^{-1} \tilde{\Theta}_k^T d\tau + \frac{\sigma_0}{2}\int_0^t \tilde{z}_{0,k}^2 d\tau \\ &+ \frac{\sigma_1}{2}\int_0^t \tilde{z}_{1,k}^2 d\tau + \frac{g_1}{2\mu_0}\int_0^t \tilde{u}_{r,k}^2 d\tau + \frac{1}{2\mu_1}\frac{1}{4p\lambda}\int_0^t \tilde{\eta}_{1,k}^2 d\tau, \end{aligned} \tag{22}$$

where $\tilde{\Theta}_k$, $\tilde{z}_{0,k}$, $\tilde{z}_{1,k}$, $\tilde{u}_{r,k}$, $\tilde{\eta}_{1,k}$, which defined as $\tilde{\Theta}_k \triangleq \Theta_k - \hat{\Theta}_k$, $\tilde{z}_{0,k} \triangleq z_{0,k} - \hat{z}_{0,k}$, $\tilde{z}_{1,k} \triangleq z_{1,k} - \hat{z}_{1,k}$, $\tilde{u}_{r,k} \triangleq u_{r,k} - \hat{u}_{r,k}$, $\tilde{\eta}_{1,k} \triangleq \eta_{1,k} - \hat{\eta}_{1,k}$ represent the estimation errors.

Proof of Theorem 1: The proof is divided into two parts. The first part illustrates the nonincreasing property of the composite energy function (CEF) along the iteration axis. The second part focuses on demonstrating the convergence of both filter error and tracking error.

Part I. The difference of the CEF: For a given $t \in [0, T]$, the difference of the CEF at two consecutive iterations is at

two consecutive iterations is defined as

$$\begin{aligned}\Delta E_k =& E_k - E_{k-1}\\ =&\frac{1}{2}s_k^2 - \frac{1}{2}s_{k-1}^2 + \frac{1}{2}pe_{1,k}^2 - \frac{1}{2}pe_{1,k-1}^2\\ &+ \frac{1}{2}\int_0^t (\tilde{\Theta}_k\Gamma^{-1}\tilde{\Theta}_k^T - \tilde{\Theta}_{k-1}\Gamma^{-1}\tilde{\Theta}_{k-1}^T)d\tau\\ &+ \frac{\sigma_0}{2}\int_0^t (\tilde{z}_{0,k}^2 - \tilde{z}_{0,k-1}^2)d\tau + \frac{\sigma_1}{2}\int_0^t (\tilde{z}_{1,k}^2 - \tilde{z}_{1,k-1}^2)d\tau\\ &+ \frac{g_1}{2\mu_0}\int_0^t (\tilde{u}_{r,k}^2 - \tilde{u}_{r,k-1}^2)d\tau\\ &+ \frac{1}{2\mu_1}\frac{1}{4p\lambda}\int_0^t (\tilde{\eta}_{1,k}^2 - \tilde{\eta}_{1,k-1}^2)d\tau.\end{aligned} \tag{23}$$

The first term and the third term in (22) can be rewritten as

$$\frac{1}{2}s_k^2 + \frac{1}{2}pe_{1,k}^2 = \int_0^t (s_k\dot{s}_k + pe_{1,k}\dot{e}_{1,k})d\tau. \tag{24}$$

To simplify the process, use $L_k(t)$ to represent the right formula in (26) and can derive that

$$\begin{aligned}L_k(t) =& \int_0^t (s_k\dot{s}_k + pe_{1,k}\dot{e}_{1,k})d\tau\\ =&\int_0^t s_k[g_1u_k + \Theta_k\mathbf{f}(x_{2,k}) - g_3T_L(x_{1,k}) - g_1u_r + g_2x_{2,r}\\ &+ g_3T_L(x_{1,r}) + \lambda e_{2,k}] + pe_{1,k}[s_k - \lambda e_{1,k}]d\tau\\ =&\int_0^t s_k[g_1u_k + \Theta_k\mathbf{f}(x_{2,k}) - g_1u_r + g_2x_{2,r} + \lambda e_{2,k}\\ &- g_3(T_L(x_{1,k}) - T_L(x_{1,r}))] + pe_{1,k}s_k - p\lambda e_{1,k}^2d\tau\\ \le&\int_0^t s_k[g_1u_k + \Theta_k\mathbf{f}(x_{2,k}) - g_1u_r + g_2x_{2,r} + \lambda e_{2,k}\\ &+ g_3|(T_L(x_{1,k}) - T_L(x_{1,r}))|] + pe_{1,k}s_k - p\lambda e_{1,k}^2d\tau\\ \le&\int_0^t s_k(g_1u_k + \Theta_k\mathbf{f}(x_{2,k}) - g_1u_r + g_2x_{2,r} + \lambda e_{2,k} + pe_{1,k})\\ &+ g_3\eta|x_{1,k} - x_{1,r}|s_k - p\lambda e_{1,k}^2d\tau\\ =&\int_0^t s_k(g_1u_k + \Theta_k\mathbf{f}(x_{2,k}) - g_1u_r + g_2x_{2,r} + \lambda e_{2,k} + pe_{1,k})\\ &- [p\lambda e_{1,k}^2 - g_3\eta\cdot sign(e_{1,k})\cdot e_{1,k}s_k + \frac{g_3^2\eta^2}{4p\lambda}s_k^2] + \frac{g_3^2\eta^2}{4p\lambda}s_k^2d\tau\\ \le&\int_0^t s_k(g_1u_k + \Theta_k\mathbf{f}(x_{2,k}) - g_1u_r + g_2x_{2,r} + \lambda e_{2,k}\\ &+ pe_{1,k} + \frac{g_3^2\eta^2}{4p\lambda}s_k)d\tau,\end{aligned} \tag{25}$$

where the $sign(\cdot)$ is a sign function, that returns the sign of a real number.

Substitute the AILC controller (21) into the above (25) yieds as follows, where $\eta_1 = g_3^2\eta^2$

$$\begin{aligned}\frac{1}{2}s_k^2 + \frac{1}{2}pe_{1,k}^2 =& \int_0^t (s_k\dot{s}_k + pe_{1,k}\dot{e}_{1,k})d\tau\\ \le&\int_0^t s_k(g_1u_k + \Theta_k\mathbf{f}(x_{2,k}) - g_1u_r + g_2x_{2,r}\\ &+ \lambda e_{2,k} + pe_{1,k} + \frac{1}{4p\lambda}\eta_1s_k)d\tau\\ \le&\int_0^t s_k[\Theta_k(t)\mathbf{f}(x_{2,k})\\ &- \hat{\Theta}_k\hat{\mathbf{f}}(x_{2,k}) - g_1\tilde{u}_r + \frac{1}{4p\lambda}\tilde{\eta}_{1,k}s_k]d\tau.\end{aligned} \tag{26}$$

Simplify the term which is related to friction parameters in (22), where updating law (11) is used

$$\begin{aligned}&\frac{1}{2}\int_0^t (\tilde{\Theta}_k\Gamma^{-1}\tilde{\Theta}_k^T - \tilde{\Theta}_{k-1}\Gamma^{-1}\tilde{\Theta}_{k-1}^T)d\tau\\ &= \frac{1}{2}\int_0^t (\tilde{\Theta}_k + \tilde{\Theta}_{k-1})\Gamma^{-1}(\tilde{\Theta}_k^T - \tilde{\Theta}_{k-1}^T)d\tau\\ &= \frac{1}{2}\int_0^t (2\tilde{\Theta}_k + \tilde{\Theta}_{k-1} - \tilde{\Theta}_k)\Gamma^{-1}(\tilde{\Theta}_k^T - \tilde{\Theta}_{k-1}^T)d\tau\\ &= \frac{1}{2}\int_0^t 2\tilde{\Theta}_k\Gamma^{-1}(\tilde{\Theta}_k^T - \tilde{\Theta}_{k-1}^T)\\ &\quad + (\tilde{\Theta}_{k-1} - \tilde{\Theta}_k)\Gamma^{-1}(\tilde{\Theta}_k^T - \tilde{\Theta}_{k-1}^T)d\tau\\ &\le \int_0^t \tilde{\Theta}_k\Gamma^{-1}(\tilde{\Theta}_k^T - \tilde{\Theta}_{k-1}^T)d\tau\\ &= \int_0^t \tilde{\Theta}_k\Gamma^{-1}(\hat{\Theta}_{k-1}^T - \hat{\Theta}_k^T)d\tau\\ &= -\int_0^t \tilde{\Theta}_k\hat{\mathbf{f}}(x_{2,k})s_kd\tau.\end{aligned} \tag{27}$$

The other terms in (22) about the state $z_{0,k}$ can be simplify by using updating law (18) as follows

$$\begin{aligned}&\frac{\sigma_0}{2}\int_0^t (\tilde{z}_{0,k}^2 - \tilde{z}_{0,k-1}^2)d\tau\\ &= \frac{\sigma_0}{2}\int_0^t (\tilde{z}_{0,k} - \tilde{z}_{0,k-1})((\tilde{z}_{0,k} + \tilde{z}_{0,k-1}))d\tau\\ &= \frac{\sigma_0}{2}\int_0^t (\tilde{z}_{0,k} - \tilde{z}_{0,k-1})((2\tilde{z}_{0,k} + \tilde{z}_{0,k-1} - \tilde{z}_{0,k}))d\tau\\ &\le \frac{\sigma_0}{2}\int_0^t 2\tilde{z}_{0,k}(\tilde{z}_{0,k} - \tilde{z}_{0,k-1})d\tau\\ &= \sigma_0\int_0^t \tilde{z}_{0,k}(\hat{z}_{0,k-1} - \hat{z}_{0,k})d\tau\\ &= -\sigma_0\int_0^t \tilde{z}_{0,k}s_kd\tau.\end{aligned} \tag{28}$$

Do the same simplification like (28) for the term related to $z_{1,k}$ in (22), so that

$$\frac{\sigma_1}{2}\int_0^t (\tilde{z}_{1,k}^2 - \tilde{z}_{1,k-1}^2)d\tau \le -\sigma_1\int_0^t \tilde{z}_{1,k}\phi(x_{2,k})|x_{2,k}|s_kd\tau. \tag{29}$$

Combining (28) and (29), we have

$$\begin{aligned}&\frac{\sigma_0}{2}\int_0^t (\tilde{z}_{0,k}^2 - \tilde{z}_{0,k-1}^2)d\tau + \frac{\sigma_1}{2}\int_0^t (\tilde{z}_{1,k}^2 - \tilde{z}_{1,k-1}^2)d\tau\\ &\le -\sigma_0\int_0^t \tilde{z}_{0,k}s_kd\tau - \sigma_1\int_0^t \tilde{z}_{1,k}\phi(x_{2,k})|x_{2,k}|s_kd\tau\\ &= -\int_0^t \Theta_k\tilde{\mathbf{f}}(x_{2,k})s_kd\tau,\end{aligned} \tag{30}$$

where $\tilde{\mathbf{f}}(x_{2,k}) \triangleq \mathbf{f}(x_{2,k}) - \hat{\mathbf{f}}(x_{2,k})$.

The second to last term in (22) becomes like follows, where updating law (13) is used

$$\begin{aligned}
&\frac{g_1}{2\mu_0}\int_0^t(\tilde{u}_{r,k}^2-\tilde{u}_{r,k-1}^2)d\tau \\
&=\frac{g_1}{2\mu_0}\int_0^t(\tilde{u}_{r,k}-\tilde{u}_{r,k-1})(\tilde{u}_{r,k}+\tilde{u}_{r,k-1})d\tau \\
&=\frac{g_1}{2\mu_0}\int_0^t(\tilde{u}_{r,k}-\tilde{u}_{r,k-1})(2\tilde{u}_{r,k}+\tilde{u}_{r,k-1}-\tilde{u}_{r,k})d\tau \\
&\le\frac{g_1}{2\mu_0}\int_0^t 2\tilde{u}_{r,k}(\tilde{u}_{r,k}-\tilde{u}_{r,k-1})d\tau \\
&=\frac{g_1}{\mu_0}\int_0^t \tilde{u}_{r,k}(\hat{u}_{r,k-1}-\hat{u}_{r,k})d\tau \\
&=g_1\int_0^t \tilde{u}_{r,k}s_k d\tau.
\end{aligned} \tag{31}$$

The last term in (22) holds as follows, where updating law (15) is used

$$\begin{aligned}
&\frac{1}{2\mu_1}\frac{1}{4p\lambda}\int_0^t(\tilde{\eta}_{1,k}^2-\tilde{\eta}_{1,k-1}^2)d\tau \\
&=\frac{1}{2\mu_1}\frac{1}{4p\lambda}\int_0^t(\tilde{\eta}_{1,k}-\tilde{\eta}_{1,k-1})(\tilde{\eta}_{1,k}+\tilde{\eta}_{1,k-1})d\tau \\
&=\frac{1}{2\mu_1}\frac{1}{4p\lambda}\int_0^t(\tilde{\eta}_{1,k}-\tilde{\eta}_{1,k-1})(2\tilde{\eta}_{1,k}+\tilde{\eta}_{1,k-1}-\tilde{\eta}_{1,k})d\tau \\
&\le\frac{1}{2\mu_1}\frac{1}{4p\lambda}\int_0^t 2\tilde{\eta}_{1,k}(\tilde{\eta}_{1,k-1}-\tilde{\eta}_{1,k})d\tau \\
&=\frac{1}{\mu_1}\frac{1}{4p\lambda}\int_0^t \tilde{\eta}_{1,k}(\hat{\eta}_{1,k-1}-\hat{\eta}_{1,k})d\tau \\
&=-\frac{1}{4p\lambda}\int_0^t \tilde{\eta}_{1,k}s_k^2 d\tau.
\end{aligned} \tag{32}$$

Finally, according to (23) and combining the above expressions (26), (27), (30), (31) and (32) , it holds that

$$\begin{aligned}
\Delta E_k =& E_k - E_{k-1} \\
\le& \int_0^t s_k(t)[\Theta_k\mathbf{f}(x_{2,k})-\hat{\Theta}_k\hat{\mathbf{f}}(x_{2,k}) \\
&-g_1\tilde{u}_{r,k}+\frac{1}{4p\lambda}\tilde{\eta}_{1,k}s_k]d\tau \\
&-\int_0^t\tilde{\Theta}_k\hat{\mathbf{f}}(x_{2,k})s_k d\tau-\int_0^t\Theta_k\tilde{\mathbf{f}}(x_{2,k})s_k d\tau \\
&+g_1\int_0^t\tilde{u}_{r,k}s_k d\tau-\frac{1}{4p\lambda}\int_0^t\tilde{\eta}_{1,k}s_k^2 d\tau \\
&-\frac{1}{2}s_{k-1}^2-\frac{1}{2}pe_{1,k-1}^2 \\
\le& -\frac{1}{2}s_{k-1}^2-\frac{1}{2}pe_{1,k-1}^2 \\
\le& 0.
\end{aligned} \tag{33}$$

Part II. Convergence property of tracking error: At iteration number $i = 0$, $\hat{\Theta}_{-1}(t) = 0$, $\hat{z}_{0,-1} = 0, \hat{z}_{1,-1} = 0$, $\hat{u}_{r,-1} = 0$ and $\hat{\eta}_{1,-1} = 0$ thus E_0 is boundedness. Applying (33) repeatedly we have

$$E_k = E_0 + \sum_{i=1}^{k}\Delta E_i, \tag{34}$$

$$\lim_{k\to\infty}E_k \le E_0 - \lim_{k\to\infty}\sum_{i=1}^{k-1}(\frac{1}{2}s_i^2) - \lim_{k\to\infty}\sum_{i=1}^{k-1}(\frac{1}{2}pe_{1,i}^2). \tag{35}$$

Consider the positiveness of E_k and boundedness of E_0, filter error s_k, and position tracking error $e_{1,k}$ both converge to zero pointwisely as $k \to \infty$.

5 Simulation Results

In this section, simulations are conducted in MATLAB to show the effectiveness of the proposed AILC Scheme in the PMSM system. The motor parameters employed in the simulation are described in Table 1

Table 1: Parameters of the PMSM

Names	Parameters	Values
Moment of Inertia	$J(kg\times m^2)$	1.95×10^{-3}
Flux linkage	$\varphi_f(Wb)$	$4.73\times10-4$
Pole Paris	n_p	4
Equivalent damping coefficient	B	2.53×10^{-4}
Stator Resistance	$R(\Omega)$	0.53
Stator Inductance	$L(mH)$	3.7×10^{-4}
Load Torque	$TL(Nm)$	$0.5sin(x_1)$
Stiffness Coefficient	ρ_0	0.5
Damping Coefficient	ρ_1	0.3
Vicious Coefficient	ρ_2	0.01
Column Friction Torque	$F_c(Nm)$	0.25
Stiction Friction Torque	$F_s(Nm)$	0.34
Stribeck Angular Velocity	$\omega_s(rad/s)$	0.01

The reference trajectory of the rotor position is given by $x_{1,r} = 0.2\pi sin(2\pi t)$, with a period T= 2π. In the scheme, the learning gain is selected as Γ =diag$\{0.5, 0.01, 0.05\}$. Other gains are set as $\lambda = 5$, $p = 5$, and in the updated law (13) and (15), where $\mu_0 = 0.01$, $\mu_1 = 0.01$.

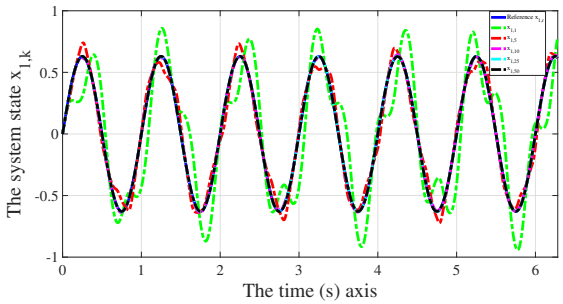

Fig. 1: Variation of PMSM state $x_{1,k}$ in iteration domian

The simulation results are illustrated in Figs. 1-3. Fig. 1 illustrates the evolving rotor position trajectory across iterations, gradually converging to the desired reference with increasing iteration numbers. Examining the system's tracking performance at the first iteration, it is evident that the system state $x_{1,k}$ at the initial iteration deviates from the reference $x_{1,r}$. However, the 50th iteration tracking trajectory shows that the disparity between the output trajectory and the reference $x_{1,r}$ becomes invisible.

Specifically, Fig. 2 and Fig. 3 provide a more detailed insight into the performance of the proposed controller. Fig. 2 showcases the convergence of the filter error, emphasizing the progressive reduction of error values over successive iterations. Simultaneously, Fig. 3 presents the position tracking error, illustrating a trend of error reduction with the increasing iteration numbers. This consistent convergence towards zero for both errors illustrates the efficacy of the proposed

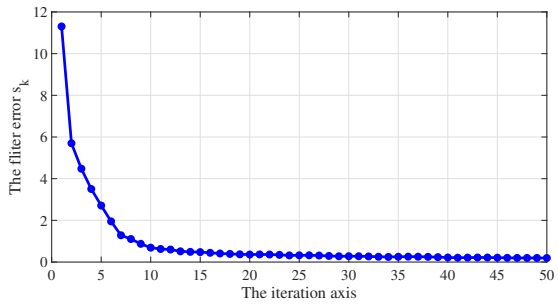

Fig. 2: Maximum filter error along the iteration axis

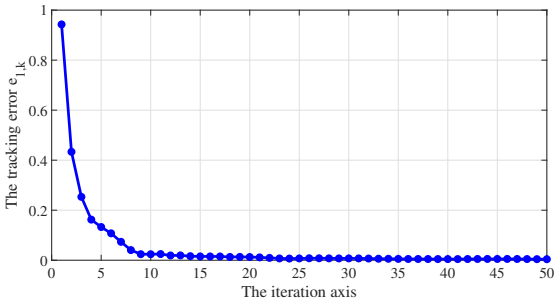

Fig. 3: Maximum tracking error along the iteration axis

AILC scheme. The AILC scheme is thereby convincingly demonstrated through the mitigation of these considered disturbances, validating its effectiveness in achieving desired control objectives.

6 Conclusion

In this article, a novel design scheme of CEF-based AILC for the precise tracking of PMSM rotor position with the load disturbances and friction forces is proposed. The scheme incorporates compensatory strategies to address the load disturbances, while a parametric update law is employed to estimate the unknown parameters within the friction model. This research contributes valuable insights into the application of AILC for systems with unknown parameters and complex dynamics. Future work may focus on further refinement of the proposed scheme and its application in real-world scenarios, solidifying its potential for practical implementations.

References

[1] J. Na, Q. Chen, X. Ren, and Y. Guo, "Adaptive prescribed performance motion control of servo mechanisms with friction compensation," *IEEE Transactions on Industrial Electronics*, vol. 61, no. 1, pp. 486–494, 2013.

[2] C.-C. Liu, M.-S. Tsai, and C.-C. Cheng, "Development of a novel transmission engaging model for characterizing the friction behavior of a feed drive system," *Mechanism and Machine Theory*, vol. 134, pp. 425–439, 2019.

[3] C. Gong, Y. Hu, K. Ni, J. Liu, and J. Gao, "Sm load torque observer-based fcs-mpdsc with single prediction horizon for high dynamics of surface-mounted pmsm," *IEEE Transactions on Power Electronics*, vol. 35, no. 1, pp. 20–24, 2019.

[4] A. K. Junejo, W. Xu, C. Mu, M. M. Ismail, and Y. Liu, "Adaptive speed control of pmsm drive system based a new sliding-mode reaching law," *IEEE Transactions on Power Electronics*, vol. 35, no. 11, pp. 12 110–12 121, 2020.

[5] V. Q. Leu, H. H. Choi, and J.-W. Jung, "Fuzzy sliding mode speed controller for pm synchronous motors with a load torque observer," *IEEE Transactions on Power Electronics*, vol. 27, no. 3, pp. 1530–1539, 2012.

[6] X. Sun, M. Wu, G. Lei, Y. Guo, and J. Zhu, "An improved model predictive current control for pmsm drives based on current track circle," *IEEE Transactions on Industrial Electronics*, vol. 68, no. 5, pp. 3782–3793, 2020.

[7] Q. Wang, H. Yu, M. Wang, and X. Qi, "An improved sliding mode control using disturbance torque observer for permanent magnet synchronous motor," *IEEE access*, vol. 7, pp. 36 691–36 701, 2019.

[8] G. Bartolini, A. Ferrara, E. Usai, and V. I. Utkin, "On multi-input chattering-free second-order sliding mode control," *IEEE transactions on automatic control*, vol. 45, no. 9, pp. 1711–1717, 2000.

[9] Q. N. Khanh, N. D. That, Q. N. Hong, and Q. P. Ha, "Fpga-based fuzzy sliding mode control for sensorless pmsm drive," in *2012 IEEE International Conference on Automation Science and Engineering (CASE)*. IEEE, 2012, pp. 172–177.

[10] Q. Chen, X. Yu, M. Sun, C. Wu, and Z. Fu, "Adaptive repetitive learning control of pmsm servo systems with bounded non-parametric uncertainties theory and experiments," *IEEE Transactions on Industrial Electronics*, vol. 68, no. 9, pp. 8626–8635, 2020.

[11] J.-X. Xu and R. Yan, "On repetitive learning control for periodic tracking tasks," *IEEE Transactions on Automatic Control*, vol. 51, no. 11, pp. 1842–1848, 2006.

[12] D. A. Bristow, M. Tharayil, and A. G. Alleyne, "A survey of iterative learning control," *IEEE control systems magazine*, vol. 26, no. 3, pp. 96–114, 2006.

[13] S. A. Q. Mohammed and K.-B. Lee, "Improved adaptive iterative learning current control approach for ipmsm drives," *Journal of Power Electronics*, vol. 23, no. 2, pp. 284–295, 2023.

[14] G. Bi, G. Zhang, G. Wang, Q. Wang, Y. Hu, and D. Xu, "Adaptive iterative learning control-based rotor position harmonic error suppression method for sensorless pmsm drives," *IEEE Transactions on Industrial Electronics*, vol. 69, no. 11, pp. 10 870–10 881, 2022.

[15] S. Riaz, R. Qi, O. Tutsoy, and J. Iqbal, "A novel adaptive pd-type iterative learning control of the pmsm servo system with the friction uncertainty in low speeds," *PloS one*, vol. 18, no. 1, p. e0279253, 2023.

[16] Y. X. Su, C. H. Zheng, and B. Y. Duan, "Automatic disturbances rejection controller for precise motion control of permanent-magnet synchronous motors," *IEEE Transactions on Industrial Electronics*, vol. 52, no. 3, pp. 814–823, 2005.

[17] M. Merzoug and F. Naceri, "Comparison of field-oriented control and direct torque control for permanent magnet synchronous motor (pmsm)," *International Journal of Electrical and Computer Engineering*, vol. 2, no. 9, pp. 1797–1802, 2008.

[18] C. Canudas de Wit, H. Olsson, K. Astrom, and P. Lischinsky, "A new model for control of systems with friction," *IEEE Transactions on Automatic Control*, vol. 40, no. 3, pp. 419–425, 1995.

[19] M. Sun, H. Li, and Y. Li, "A unified design approach to repetitive learning control for systems subject to fractional uncertainties," *Journal of Dynamic Systems, Measurement, and Control*, vol. 140, no. 6, p. 061003, 2018.

[20] W. E. Dixon, A. Behal, D. M. Dawson, and S. P. Nagarkatti, *Nonlinear control of engineering systems a Lyapunov-based approach*. Springer Science & Business Media, 2003.

[21] W. Zhang, M. Li, Y. Gao, and Y. Chen, "Periodic adaptive learning control of pmsm servo system with lugre model-based friction compensation," *Mechanism and Machine Theory*, vol. 167, p. 104561, 2022.

Proceedings of the 3rd Conference on Fully Actuated System Theory and Applications
May 10-12, 2024, Shenzhen, China

Hierarchical Robust Control for Unmanned Quadrotor Transportation Systems: Exploiting Beneficial State-Coupling

Lincong Han, Menghua Zhang*
1. School of Electrical Engineering, University of Jinan, Jinan 250000, P. R. China
E-mail: zhangmenghua@mail.sdu.edu.cn

Abstract: Quadrotor has been widely used because of its high maneuverability and its ability to take off in limited space. It is very challenging to eliminate the swing in the course of its dispatching task because there is no direct control of the payload. The quadrotor transport system has to realize not only the control of the position and load of the outer loop, but also the control of the attitude of the inner loop, which shows the cascaded underactuated–underactuated property. This feature makes the quadrotor precise positioning and effectively restrain the load swing become extremely difficult.This paper presents a nonlinear hierarchical control scheme for quadrotor transport system, which makes full use of the cascading characteristics of the system and separates the inner loop and outer loop controller design to facilitate the design process. To be more specific, in the outer loop subsystem, a virtual control vector is designed based on the proposed energy storage function, and a saturation function is introduced to make the desired attitude unaffected by any singularity. For the inner loop, a geometric attitude tracking controller based on the body coordinate system is designed to drive the quadrotor to achieve the desired attitude. Based on that, a new control method which makes full use of the coupling effect is proposed, which not only achieves the precise positioning of the quadrotor, but also achieves the effective load swing elimination.

Key Words: Underactuated systems, Quadrotor, Coupling effect, Energy analysis

1 Introduction

Recently, unmanned aerial vehicles (UAVs) have received extensive attention from the mechatronic engineering community. Among the many applications, air cargo transportation is an important application, which has received extensive attention in recent years. The conventional approach is to grasp the payload through a gripper equipped on the quadrotor [1], but the load increases the inertia of the whole system, which makes the attitude change response slow [2]. Another, more interesting method of transport is to dangle the payload underneath the quadcopter using a cable. In contrast, this method allows the quadrotor to still maintain good agility when transporting large objects [3]. Therefore, it is of practical engineering and theoretical significance to study the cable-suspended payload-quadrotor system.

Up to now, the control problem of quadrotor is still a fairly open topic. With the exception of open-loop approach, almost all previous schemes required full state feedback [4]. Compared to quadrotor control without suspension payloads, the work presented in this paper is more challenging due to the addition of system degrees of freedom [5] and the newly introduced payload swing suppression objective, still having the same control input. Theoretical analysis and simulation results show that the designed controller can realize accurate positioning of the quadrotor and restrain the load swing at the same time, thus improving the safety and transportation efficiency of the system. Specifically, through dynamic analysis using the Lagrange method, we know that the inner and outer loop of the cascade are coupled by a nonlinear interconnect term [6]. For the outer loop, a new energy storage function is constructed and analyzed, and a simple virtual control vector is constructed. Then, the thrust input and desired attitude of the quadrotor were derived, and the inner loop was driven by the non-coordinate geometric tracking controller on the Lie Group [7] to achieve the desired attitude. At the same time, the control framework of coupling effect identification and coupling effect utilization is introduced to make the system have better transient characteristics. Lyapunov techniques and LaSalle invariance theorem are used to ensure the stability of the integral closed loop system.

Therefore, the main contributions of this paper are as follows.

1) Different from the existing results, there is no singularity in the design of saturated virtual control input considering the saturation problem of motor input in the actual situation.

2) Due to careful mathematical treatment, and the treatment of the coupling terms between the inner and outer rings, this allows us to construct the control law of the inner and outer rings separately, so long as both subsystems are asymptotically stable, the asymptotic stability of the whole system can be theoretically guaranteed.

3) Coupling effect identification and coupling effect utilization control are introduced to improve the transient characteristics of the system by judging whether coupling is beneficial and applying beneficial coupling terms to the system.

The rest of this article is arranged as follows. In the Section 2, we model an unmanned quadrotor transport system. Then, the development of the controller is introduced in detail in Section 3. The Section 4 is the simulation result. Finally, the Section 5 summarizes and looks forward to the work of this paper.

2 Dynamics Analysis and Error Definition

Consider the fully dynamic unmanned quadrotor transport system shown in Fig. 1. Based on Lagrange modeling technique, we can use the following dynamic equation to represent the system:

This work was supported in part by the National Natural Science Foundation of China under Grant No. 62273163, the Taishan Scholar Foundation of Shandong Province under Grant No. tsqn202312212, the Outstanding Youth Foundation of Shandong Province Under Grant No. ZR2023YQ056, the Key RD Project of Shandong Province under Grant No. 2022CXGC010503.(Corresponding author: M. Zhang)

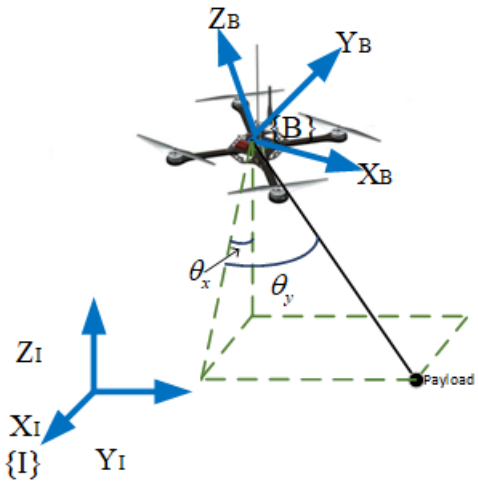

Fig. 1: quadrotor transportation system.

$$\boldsymbol{M_c}(\boldsymbol{q})\ddot{\boldsymbol{q}} + \boldsymbol{V_c}(\boldsymbol{q},\dot{\boldsymbol{q}})\dot{\boldsymbol{q}} + \boldsymbol{G}(\boldsymbol{q}) = \boldsymbol{u} + \boldsymbol{F_r} \tag{1}$$

$$\dot{\boldsymbol{R}} = \boldsymbol{R}sk(\boldsymbol{\Omega}) \tag{2}$$

$$\boldsymbol{J}\dot{\boldsymbol{\Omega}} + sk(\boldsymbol{\Omega})\boldsymbol{J}\boldsymbol{\Omega} = \boldsymbol{\tau} \tag{3}$$

Where (1) represents the outer loop dynamics model, which includes quadrotor translation and payload swing; (2) and (3) represent the dynamics model of the inner loop, showing the attitude characteristics. $sk(\cdot) : \mathbb{R}^{\boldsymbol{3}} \rightarrow so(3)$ transform a vector into a skew-symmetric matrix. $\boldsymbol{q}(t) \in \mathbb{R}^5$ represents the state vector of the outer loop, and $\boldsymbol{M_c}(q), \boldsymbol{V_c}(q,\dot{q}) \in \mathbb{R}^{5\times5}, \boldsymbol{G}(q)$,and $\boldsymbol{u} \in \mathbb{R}^5$ represent the inertia matrix, the centripetal-Coriolis matrix, the gravity vector, and the resultant force applied to the outer loop subsystem, and $\boldsymbol{F_r}$ represent air resistance vector, respectively. The above symbols are expressed in detail as follows:

$$\boldsymbol{q} = [\boldsymbol{\xi}^T, \theta_x, \theta_y]^T \tag{4}$$

$$\boldsymbol{M_c} = \begin{bmatrix} m_{c11} & 0 & 0 & m_{c14} & m_{c15} \\ 0 & m_{c22} & 0 & 0 & m_{c25} \\ 0 & 0 & m_{c33} & m_{c34} & m_{c35} \\ m_{c41} & 0 & m_{c43} & m_{c44} & 0 \\ m_{c51} & m_{c52} & m_{c53} & 0 & m_{c55} \end{bmatrix} \tag{5}$$

$m_{c11} = m_{c22} = m_{c33} = M + m, m_{c44} = ml^2C_y^2,$
$m_{c55} = ml^2, m_{c41} = m_{c14} = mlC_xC_y,$
$m_{c43} = m_{c34} = mlS_xC_y, m_{c51} = m_{c15} = -mlS_xS_y,$
$m_{c52} = m_{c25} = mlC_y, m_{c53} = m_{c35} = mlC_xS_y$

$$\boldsymbol{V_c} = \begin{bmatrix} 0 & 0 & 0 & V_{c14} & V_{c15} \\ 0 & 0 & 0 & 0 & V_{c25} \\ 0 & 0 & 0 & V_{c34} & V_{c35} \\ 0 & 0 & 0 & V_{c44} & V_{c45} \\ 0 & 0 & 0 & V_{c54} & 0 \end{bmatrix} \tag{6}$$

$V_{c14} = -ml\dot{\theta}_xS_xC_y - ml\dot{\theta}_yC_xS_y, V_{c44} = -ml^2\dot{\theta}_yC_yS_y,$
$V_{c34} = ml\dot{\theta}_xC_xC_y - ml\dot{\theta}_yS_xS_y, V_{c54} = ml^2\dot{\theta}_xC_yS_y,$
$V_{c15} = -ml\dot{\theta}_xC_xS_y - ml\dot{\theta}_yS_xC_y, V_{c25} = -ml\dot{\theta}_yS_y,$
$V_{35} = -ml\dot{\theta}_xS_xS_y + ml\dot{\theta}_yC_xC_y, V_{c45} = -ml^2\dot{\theta}_xC_yS_y$

$$\boldsymbol{G} = [0, 0, 0, mglS_xC_y, mglC_xS_y]^T \tag{7}$$

$$\boldsymbol{u} = [(fRe_3 - (M+m)ge_3)^T, 0, 0]^T \tag{8}$$

$$\boldsymbol{F_r} = [f_{rx}, f_{ry}, f_{rz}, f_{r\theta_x}, f_{r\theta_y}]^T \tag{9}$$

$$\boldsymbol{e_3} = [0, 0, 1]^T \tag{10}$$

where $\boldsymbol{\xi}(t) = [x(t), y(t), z(t)]^T \in \mathbb{R}^3$represents the position of the quadrotor's center of mass in the inertial coordinate system; $\theta_x(t) \in \mathbb{R}$ and $\theta_y(t) \in \mathbb{R}$ are the motion of the projection signal; $\boldsymbol{R}(t) \in SO(3)$ is the rotation matrix of the quadrotor from fixed coordinate frame to inertial coordinate frame; $\boldsymbol{\Omega}(t) \in \mathbb{R}^3$ represents the angular velocity of the quadrotor in the body coordinate frame; $M \in \mathbb{R}$ and $m \in \mathbb{R}$ represent the mass of quadrotor and payload, respectively; $l \in \mathbb{R}$ is the length of rope; $g \in \mathbb{R}$ is the gravitational acceleration; $\boldsymbol{J} \in \mathbb{R}^{3\times3}$ is the inertia moment of the quadrotor in body coordinate system; C_x, C_y, S_x and S_y are abbreviations of $\cos(\theta_x), \cos(\theta_y), \sin(\theta_x)$, and $\sin(\theta_y)$, respectively.

As mentioned above, there are two main control objectives of the quadrotor lifting system, which are to ensure that the quadrotor reaches the target position $\xi_d = [x_d, y_d, z_d]^T \in \mathbb{R}^3$ accurately and to suppress the payload swing $\xi \rightarrow \xi_d, \Theta \rightarrow 0_{2\times1}$, the target can also be expressed in the following form:

$$\boldsymbol{q} \rightarrow \boldsymbol{q_d} = [\xi_d^T, 0, 0]^T \tag{11}$$

In order to facilitate the subsequent controller design and analysis, the outer loop tracking error $\boldsymbol{e_q}(t), \dot{\boldsymbol{e}}_{\boldsymbol{q}}(t) \in \mathbb{R}^5$ is defined as

$$\boldsymbol{e_q} = \boldsymbol{q} - \boldsymbol{q_d} = [\boldsymbol{e_\xi}^T, \boldsymbol{\Theta}^T]^T \tag{12}$$

$$\dot{\boldsymbol{e}}_{\boldsymbol{q}} = [\dot{\boldsymbol{e}}_{\boldsymbol{\xi}}{}^T, \dot{\boldsymbol{\Theta}}^T]^T = [\dot{\boldsymbol{\xi}}^T, \dot{\boldsymbol{\Theta}}^T]^T \tag{13}$$

Then,the outer loop dynamics (1) can be reorganized as

$$\dot{\boldsymbol{e}}_{\boldsymbol{q}} = \boldsymbol{e}_{\dot{\boldsymbol{q}}} \tag{14}$$

$$\boldsymbol{e}_{\dot{\boldsymbol{q}}} = \boldsymbol{M_c^{-1}}(\boldsymbol{u} - \boldsymbol{V_c}\boldsymbol{e}_{\dot{\boldsymbol{q}}} - \boldsymbol{G}) \tag{15}$$

For the inner loop subsystem, define the attitude tracking error $\boldsymbol{e_R}(t) \in \mathbb{R}^3$ and the angular velocity tracking error $\boldsymbol{e_R}(t) \in \mathbb{R}^3$as

$$\boldsymbol{e_R} = \frac{1}{2}vex(\boldsymbol{R_d}{}^T\boldsymbol{R} - \boldsymbol{R}^T\boldsymbol{R_d}) \tag{16}$$

$$\boldsymbol{e_\Omega} = \boldsymbol{\Omega} - \boldsymbol{R}^T\boldsymbol{R_d}\boldsymbol{\Omega_d} \tag{17}$$

where $vex(\cdot) : so(3) \rightarrow \mathbb{R}^3$ is the inverse operation of $sk(\cdot)$, $\boldsymbol{R_d} \in \mathbb{R}^{3\times3}, \boldsymbol{\Omega_d} \in \mathbb{R}^3$ are the desired attitude and desired angular velocity of the quadrotor respectively, which will be determined later. The derivative of $\boldsymbol{e_R}$ and $\boldsymbol{e_\Omega}$ with respect to time is as follows:

$$\dot{\boldsymbol{e}}_{\boldsymbol{R}} = \frac{1}{2}vex(\boldsymbol{R_d}{}^T\boldsymbol{R}sk(\boldsymbol{e_\Omega}) + sk(\boldsymbol{e_\Omega})\boldsymbol{R}^T\boldsymbol{R_d})) \tag{18}$$

$$\boldsymbol{J}\dot{\boldsymbol{e}}_{\boldsymbol{\Omega}} = \boldsymbol{\tau} - sk(\boldsymbol{\Omega})\boldsymbol{J}\boldsymbol{\Omega} + \boldsymbol{J}(sk(\Omega)\boldsymbol{R}^T\boldsymbol{R_d}\boldsymbol{\Omega_d} - \boldsymbol{R}^T\boldsymbol{R_d}\dot{\boldsymbol{\Omega}}_{\boldsymbol{d}}) \tag{19}$$

Then, a nonlinear control scheme is designed for the quadrotor transport system with cascade structure of (12), (13), (18) and (19) to achieve the control objective. It is worth pointing out that the inner loop subsystem and the

outer loop subsystem are coupled by the nonlinear interconnect term, which is caused by the rotation matrix R appearing in (8).

Remark 1: It can be seen from (1)-(3) that the full dynamics of the quadrotor transport system presents eight degrees of freedom.

Remark 2: With four control inputs consisting of $f \in \mathbb{R}$and $\boldsymbol{\tau} \in \mathbb{R}^3$, the quadrotor itself is underactuated and provides the driving force for the entire transportation system, presenting a "double" underactuated characteristic. This is quite different from other underactuated systems where the drive part is fully actuated, because the outer loop control input $\boldsymbol{u}(t)$is not only related to the thrust $f(t)$, And directly depends on the attitude of the quadrotor $\boldsymbol{R}(t)$determined by the moment $\boldsymbol{\tau}(t)$.

3 CONTROL DEVELOPMENT

The total energy in the outer loop subsystem consists of kinetic energy and potential energy, which are expressed as follows:

$$E = \frac{1}{2}\dot{\boldsymbol{q}}^T \boldsymbol{M_c}\dot{\boldsymbol{q}} + mgl(1 - C_x C_y) \tag{20}$$

The derivative of (20) can be derived as follows:

$$\begin{aligned}\dot{E} &= \dot{\boldsymbol{q}}^T(\boldsymbol{M_c}\ddot{\boldsymbol{q}} + \tfrac{1}{2}\dot{\boldsymbol{M}}_{\boldsymbol{c}}\dot{q}) + mgl(\dot{\theta}_x S_x C_y + \dot{\theta}_y C_x S_y) \\ &= \dot{\boldsymbol{e}}_{\boldsymbol{\xi}}{}^T[f\boldsymbol{R}\boldsymbol{e_3} - (M+m)g\boldsymbol{e_3}]\end{aligned} \tag{21}$$

Furthermore, in order to construct the "shaped" energy storage function, define the following auxiliary function:

$$\boldsymbol{E_s} = [k_{px}, k_{py}, k_{pz}]\boldsymbol{A} \tag{22}$$

where k_{px}, k_{py} and k_{pz} are positive control gains, and vector $\boldsymbol{A} \in \mathbb{R}^3$ is represented by the following form:

$$\boldsymbol{A} = [\ln\cosh(e_x), \ln\cosh(e_y), \ln\cosh(e_z)]^T \tag{23}$$

According to (20) and (22), the total energy storage function is constructed as

$$V = E + E_s \tag{24}$$

Taking the time derivative of (21) and utilizing (24), We can get the following results:

$$\begin{aligned}\dot{V} &= \dot{E} + [k_{px}, k_{py}, k_{pz}]\dot{A} \\ &= \dot{\boldsymbol{e}}_{\boldsymbol{\xi}}{}^T[f\boldsymbol{R}\boldsymbol{e_3} - (M+m)g\boldsymbol{e_3} + k_p\boldsymbol{B}]\end{aligned} \tag{25}$$

wherein $k_p = diag([k_{px}, k_{py}, k_{pz}]) \in \mathbb{R}^{3\times3}$ is a positive definite diagonal matrix, and $\boldsymbol{B} \in \mathbb{R}^3$ is defined in the following form:

$$\boldsymbol{B} = [\tanh(e_x), \tanh(e_y), \tanh(e_z)]^T \tag{26}$$

To deal with the coupling term, fRe_3 can be divided into the following two parts:

$$\begin{aligned}f\boldsymbol{R}\boldsymbol{e_3} &= \tfrac{f}{\boldsymbol{e_3}^T\boldsymbol{R_d}^T\boldsymbol{R}\boldsymbol{e_3}}[(\boldsymbol{e_3}^T\boldsymbol{R_d}^T\boldsymbol{R}\boldsymbol{e_3})\boldsymbol{R}\boldsymbol{e_3} - \boldsymbol{R_d}\boldsymbol{e_3}] \\ &+ \tfrac{f}{\boldsymbol{e_3}^T\boldsymbol{R_d}^T\boldsymbol{R}\boldsymbol{e_3}}\boldsymbol{R_d}\boldsymbol{e_3}\end{aligned} \tag{27}$$

where the signal $\boldsymbol{\Delta}(t) = [\Delta_1, \Delta_2, \Delta_3]^T \in \mathbb{R}^3$ and the to-be-constructed virtual control vector $\boldsymbol{f_d} = [f_{d1}, f_{d2}, f_{d3}]^T \in \mathbb{R}^3$ are defined as

$$\boldsymbol{\Delta} = \frac{f}{\boldsymbol{e_3}^T\boldsymbol{R_d}^T\boldsymbol{R}\boldsymbol{e_3}}[(\boldsymbol{e_3}^T\boldsymbol{R_d}^T\boldsymbol{R}\boldsymbol{e_3})\boldsymbol{R}\boldsymbol{e_3} - \boldsymbol{R_d}\boldsymbol{e_3}] \tag{28}$$

$$\boldsymbol{f_d} = \frac{f}{\boldsymbol{e_3}^T\boldsymbol{R_d}^T\boldsymbol{R}\boldsymbol{e_3}}\boldsymbol{R_d}\boldsymbol{e_3} \tag{29}$$

To make full use of beneficial coupling term, the definition of indicator for coupling term effects are purposed proposed and defined as follows

$$J_1 = \mathrm{sgn}[\dot{e}_x\Delta_1] \tag{30}$$

$$J_2 = \mathrm{sgn}[\dot{e}_y\Delta_2] \tag{31}$$

$$J_3 = \mathrm{sgn}[\dot{e}_z\Delta_3] \tag{32}$$

Based on the introduced coupling term effect indicator, the coupling term effect is defined in the following [10]

$$\begin{cases} J_1, J_2, J_3 < 0, \text{coupling effect is beneficial} \\ J_1, J_2, J_3 > 0, \text{coupling effect is detrimental} \\ J_1, J_2, J_3 = 0, \text{coupling effect is nil} \end{cases} \tag{33}$$

Furthermore, (29) implies that vectors $\boldsymbol{f_d}$ and $\boldsymbol{R_d}\boldsymbol{e_3}$ have the same direction; therefore, the desired unit direction vector $\boldsymbol{b_{3d}} = \boldsymbol{R_d}\boldsymbol{e_3} \in \mathbb{R}^3$ can be constructed as

$$\boldsymbol{b_{3d}} = \boldsymbol{R_d}\boldsymbol{e_3} = \frac{\boldsymbol{f_d}}{\|\boldsymbol{f_d}\|} \tag{34}$$

Substituting the results of (34) into (29) yields

$$\boldsymbol{f_d} = \frac{f\,\|\boldsymbol{f_d}\|}{\boldsymbol{f_d}^T\boldsymbol{R}\boldsymbol{e_3}}\frac{\boldsymbol{f_d}}{\|\boldsymbol{f_d}\|} = \frac{f\boldsymbol{f_d}}{\boldsymbol{f_d}^T\boldsymbol{R}\boldsymbol{e_3}} \tag{35}$$

indicating that

$$f = \boldsymbol{f_d}^T\boldsymbol{R}\boldsymbol{e_3} \tag{36}$$

It can be seen that as long as the virtual controller $f_d(t)$is designed, the real control $f$can be obtained directly through (36). Therefore, the core step is to design $f(t)$. For this, note from (25) and (27)that

$$\dot{V} = \dot{\boldsymbol{e}}_{\boldsymbol{\xi}}{}^T[\boldsymbol{f_d} + \boldsymbol{\Delta} - (M+m)g\boldsymbol{e_3} + \boldsymbol{K_p}\boldsymbol{B}] \tag{37}$$

construct $\boldsymbol{f_d}$ in the following saturated way:

$$\boldsymbol{f_d} = -\boldsymbol{K_p}\boldsymbol{B} + (M+m)ge_3 - \boldsymbol{K_d}\boldsymbol{C} - \boldsymbol{P} \tag{38}$$

where $\boldsymbol{K_d} = diag([k_{dx}, k_{dy}, k_{dz}]) \in \mathbb{R}^{3\times3}$ denotes a positive definite diagonal matrix. $\boldsymbol{C} \in \mathbb{R}^3$ and P is defined as follows:

$$\boldsymbol{C} = [\tanh(\dot{e}_x), \tanh(\dot{e}_y), \tanh(\dot{e}_z)]^T \tag{39}$$

$$\boldsymbol{P} = [p_1, p_2, p_3]^T \tag{40}$$

$$p_1 = \begin{cases} 0, & J_1 \le 0 \\ J_1\Delta_1, & J_1 > 0 \end{cases} \tag{41}$$

$$p_2 = \begin{cases} 0, & J_2 \le 0 \\ J_2\Delta_2, & J_2 > 0 \end{cases} \tag{42}$$

$$p_3 = \begin{cases} 0, & J_3 \le 0 \\ J_3\Delta_3, & J_3 > 0 \end{cases} \tag{43}$$

In order to avoid possible singularity problems in quadrotor attitude control, for the inner loop subsystem (18) and (19), we adopt the following control method [8]:

$$\begin{aligned}\boldsymbol{\tau} &= -\boldsymbol{k_R}\boldsymbol{e_R} - \boldsymbol{k_\Omega}\boldsymbol{e_\Omega} + sk(\boldsymbol{\Omega})\boldsymbol{J}\boldsymbol{\Omega} \\ &- \boldsymbol{J}(sk(\boldsymbol{\Omega})\boldsymbol{R}^T\boldsymbol{R_d}\boldsymbol{\Omega_d} - \boldsymbol{R}^T\boldsymbol{R_d}\dot{\boldsymbol{\Omega}}_{\boldsymbol{d}})\end{aligned} \tag{44}$$

where $\boldsymbol{K_R}, \boldsymbol{K_\Omega} \in \mathbb{R}^{3\times3}$ are positive constants. Considering the characteristic $\|\tanh(\ cdot)\| \leq 1$, we choose that the (38) control gains should meet the following conditions:

$$k_{pz} + k_{dz} \leq (M+m)g \tag{45}$$

to make the last term of f_d nonzero, implying that $\boldsymbol{f_d} = 0$; therefore, the desired direction vector b3d is free of any singularity problems on the basis of (34). In order to determine the expected attitude R_d, choose an arbitrary vector $\boldsymbol{b_1} \in \mathbb{R}^3$ not parallel to the $\boldsymbol{b_{3d}}$. Then, we can get the desired attitude:

$$\boldsymbol{R_d} = [\boldsymbol{b_{2d}} \times \boldsymbol{b_{3d}}; \boldsymbol{b_{2d}}; \boldsymbol{b_{3d}}] \tag{46}$$

where $\boldsymbol{b_{2d}} \in \mathbb{R}^3$ represents the direction of the body-fixed axes calculated as

$$\boldsymbol{b_{2d}} = \frac{\boldsymbol{b_{3d}} \times \boldsymbol{b_{1c}}}{\|\boldsymbol{b_{3d}} \times \boldsymbol{b_{1c}}\|} \tag{47}$$

Subsequently, we intend to rewrite the outer loop subsystem dynamics to separate out the coupling term. According to (8), (28), (29), the input $u$of the outer loop subsystem can be divided into the following three parts: [9]:

$$\boldsymbol{u} = \boldsymbol{u_d} - \boldsymbol{m_0} + \boldsymbol{\Delta_u} \tag{48}$$

where $\boldsymbol{u_d} = \mathbb{R}^5$ is derived from vector $\boldsymbol{f_d}, \boldsymbol{m_0} \in \mathbb{R}^5$represents the total mass of the quadrotor and payload, $\boldsymbol{\Delta_u} \in \mathbb{R}^5$represents the coupling term between the inner loop and the outer loop, whose concrete expression is:

$$\boldsymbol{u_d} = [\boldsymbol{f_d}^T, 0, 0]^T \tag{49}$$

$$\boldsymbol{m_0} = [0, 0, (M+m)g, 0, 0]^T \tag{50}$$

$$\boldsymbol{\Delta_u} = [\boldsymbol{\Delta}^T, 0, 0]^T \tag{51}$$

Substituting (48) into (13), one has

$$\dot{\boldsymbol{e}}_{\dot{\boldsymbol{q}}} = \boldsymbol{M}^{-1}(\boldsymbol{u_d} - \boldsymbol{u_m} - \boldsymbol{V_c}\dot{\boldsymbol{e}}_{\boldsymbol{q}} - \boldsymbol{G}) + \boldsymbol{M_c}^{-1}\boldsymbol{u_\Delta} \tag{52}$$

By defining $\boldsymbol{e}(t) = [\boldsymbol{e_q}^T(t), \dot{\boldsymbol{e}}_{\boldsymbol{q}}^T(t)]^T \in \mathbb{R}^{10}$, and then utilizing (14) and (52), it is derived that

$$\dot{\boldsymbol{e}} = \boldsymbol{\alpha}(\boldsymbol{e}, \boldsymbol{f_d}, \boldsymbol{\xi_d}) + \boldsymbol{\beta} \tag{53}$$

where $\boldsymbol{\alpha}(t) \in \mathbb{R}^{10}$ can be expressed as

$$\boldsymbol{\alpha} = \prod_{10}\dot{\boldsymbol{e}}_{\boldsymbol{q}} + \prod_{01}\boldsymbol{M_c}^{-1}(\boldsymbol{u_d} - \boldsymbol{u_m} - \boldsymbol{V_c}\dot{\boldsymbol{e}}_{\boldsymbol{q}} - \boldsymbol{G}) \tag{54}$$

and $\boldsymbol{\beta}(t) \in \mathbb{R}^{10}$ is the coupling term defined as follows:

$$\boldsymbol{\beta} = \prod_{01}\boldsymbol{M_c}^{-1}\boldsymbol{u_\Delta} \tag{55}$$

where matrices $\prod_{10}, \prod_{01} \in \mathbb{R}^{5\times5}$ are constants explicitly expressed as

$$\prod_{10} = \begin{bmatrix} I_{5\times5} \\ 0_{5\times5} \end{bmatrix}, \prod_{01} = \begin{bmatrix} 0_{5\times5} \\ I_{5\times5} \end{bmatrix} \tag{56}$$

where $I_{5\times5}$ stands for a $0_{5\times5}$ identity matrix, and 5×5 stands for a 5×5 zero matrix.

The procedure of stability proof is omitted because of paper space

4 Simulation Results

In order to verify the performance of the proposed control method, two sets of simulations are designed for verification. Among them, the first group will be compared and analyzed with PD control method; The second group further tested the robustness of the method against external interference. The system parameters in the experiment are as follows:

$M = 0.625kg, m = 0.075kg, g = 9.8kg \cdot m/s^2$,
$l = 0.535m, J = \mathrm{diag}(0.005, 0.005, 0.013)kg \cdot m^2$

In the first set of simulations, the control gain of the proposed control method is set as follows:

$$\boldsymbol{J} = diag([0.005, 0.005, 0.013])kg \cdot m^2 \tag{57}$$

$$\boldsymbol{K_p} = diag([2.7, 3.5, 4.9]) \tag{58}$$

$$\boldsymbol{K_d} = diag([3.7, 3.7, 3.6]) \tag{59}$$

$$\boldsymbol{K_R} = diag([6.6, 6.6, 6.3]) \tag{60}$$

$$\boldsymbol{K_\Omega} = diag([0.6, 0.6, 1]) \tag{61}$$

and vector $\boldsymbol{b_{1c}}$ is chosen as $[1, 0, 0]^T$ in this paper.

We compare the performance of the proposed controller with PD controller without any external disturbances. The quadrotor initial position is set as

$$\boldsymbol{\xi}(0) = [-0.5, 1.3, 1.0]^T \tag{62}$$

and the desired position is set as

$$\boldsymbol{\xi_d} = [0.5, 0.3, 1.5]^T \tag{63}$$

The results obtained are shown in Fig. 2 and Fig. 3, including the position of quadrotor, the swing Angle of the payload, the thrust $\boldsymbol{f_d}$ and torque $\tau(t)$. By comparing the simulation results of Fig. 2 and Fig. 3, it can be seen that this method has higher positioning accuracy, smaller payload swing, and almost higher transportation efficiency.

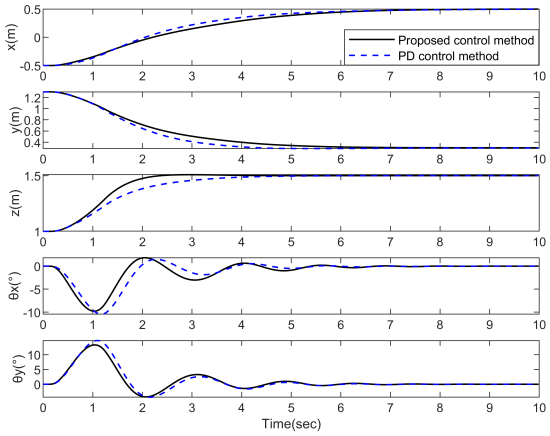

Fig. 2: Quadrotor position $\xi(t)$ and the payload swing angle $\Theta(t)$

In the simulation of the second set of robustness tests, the robustness of the system is tested by applying disturbance in different directions to the payload and the body respectively. The specific performance is shown in Fig. 4. In the process of quadrotor transport, even if the payload is disturbed at t_1,

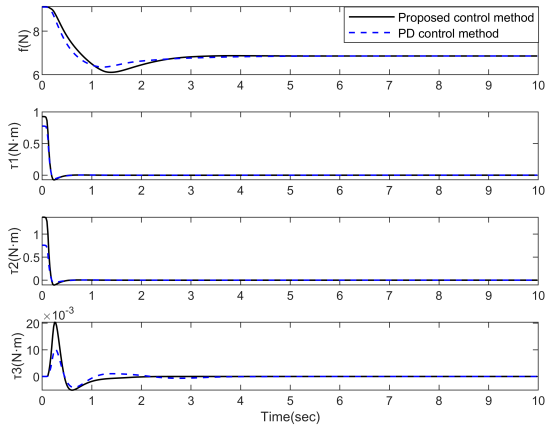

Fig. 3: Control inputs $f(t)$ and $\tau(t)$

the proposed algorithm can still ensure the accurate arrival of the aircraft to the target position and effectively suppress the payload swing. When t_2 and t_3 apply interference from different directions to the payload, the system can still quickly restore the equilibrium state; The position of the quadrotor is offset by interference at t_4 and t_5, but the proposed algorithm can still ensure the stability of the system.

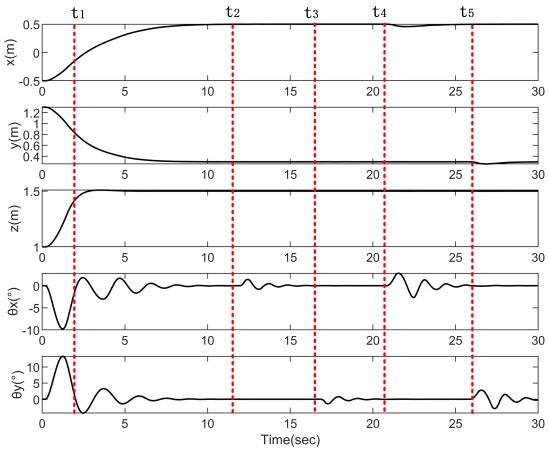

Fig. 4: Control inputs $f(t)$ and $\tau(t)$

In summary, the simulation results clearly show the superior performance of the method in suppressing the quadrotor payload swing. At the same time, it also shows strong robustness

5 Conclusion

For the unmanned quadrotor transport system, a hierarchical control scheme is proposed, which can effectively suppress and eliminate the load swing, ensure the accurate positioning of the quadrotor and handle the coupling term. The core contribution of this paper is the construction of formula based on the cascade system theory and the processing of inner and outer loop coupling terms. This allows us to design the inner loop and the outer loop respectively, which brings great convenience to the design and analysis of the controller. Simulation results show that this method has superior control performance.

References

[1] Y. Cao, M. Wang, and G. Li, "Flight dynamics modeling, trim, stability, and controllability of coaxial compound helicopters," Journal of Aerospace Engineering, vol. 36, 2021.

[2] W. Xu, H. Peng, and L. Yang,"Robust attitude control of a 3-DOF helicopter prototype subject to wind disturbance and communication delay." Transactions of the Institute of Measurement and Control, vol. 43, pp. 3071–3081, 2021.

[3] Z. Zuo, P. Ru, "adaptive tracking control of quad-rotor unmanned aircrafts." IEEE Transactions on Aerospace and Electronic Systems, vol. 50, pp. 3090–3101, 2014.

[4] H. Liu, X. Wang, and Y. Zhong, "Quaternion-based robust attitude control for uncertain robotic quadrotors," IEEE Transactions on Industrial Informatics, vol. 11, pp. 406–415, 2015.

[5] S. Yang, "Energy-based nonlinear adaptive control design for the quadrotor UAV system with a suspended payload," IEEE Transactions on Industrial Electronics, vol. 67, pp. 2054–2064, 2019.

[6] N. Cao,"Inner–outer loop control for quadrotor UAVs with input and state constraints." IEEE Transactions on Control Systems Technology, vol. 24, pp. 1797–1804, 2021. 2015.

[7] A. Akhtar, S.L. Waslander, "Controller class for rigid body tracking on $\mathsf{SO}(3)$," IEEE Transactions on Automatic Control, vol. 66, pp. 2234–2241, 2020.

[8] S. Gajbhiye, D. Cabecinhas, and C. Silvestre,"Geometric finite-time inner-outer loop trajectory tracking control strategy for quadrotor slung-load transportation." Nonlinear Dynamics, vol. 107, pp. 2291–2308, 2022.

[9] X. Liang, Y. Fang, and N. Sun,"Nonlinear hierarchical control for unmanned quadrotor transportation systems." IEEE Transactions on Industrial Electronics, vol. 65, pp. 3395–3405, 2017.

[10] M. Zhang, L. Zhang, and W. Huang,"Toward a Finite-Time Energy-Saving Robust Control Method for Active Suspension Systems: Exploiting Beneficial State-Coupling, Disturbance, and Nonlinearities." IEEE Transactions on Systems, Man, and Cybernetics: Systems, 2023.

Proceedings of the 3rd Conference on Fully Actuated System Theory and Applications
May 10-12, 2024, Shenzhen, China

Model Reference Adaptive Control for Multi-Variable Systems Using Available Signal for Feedback

Yingli Sang, Zhengqiang Zhang
the School of Engineering, Qufu Normal University, Rizhao 276826, P. R. China
E-mail: qufuzzq@126.com

Abstract: This paper develops a new model reference adaptive control for multi-variable systems with input disturbance. The controller structure is established by using reduced-order state observer and the direct estimate of nominal controller parameters. The output matching condition, new tracking error, estimate error as well as adaptive properties are developed depending on the available signals, rather than the state or output signals in the existing schemes. The new output matching condition is crucial to the analysis of model reference adaptive control output tracking. With this presented control design, the desired system properties are achieved including system stability and output tracking, and the simulation results indicate the disturbance rejection ability of the developed scheme.

Key Words: Adaptive Control, Model Reference Adaptive Control, Disturbance Rejection, Output Tracking

1 Introduction

Many scholars focus on the research of adaptive disturbance rejection control. The commonly used methods include active disturbance rejection control [1, 2], sliding mode control [3, 4], disturbance-observer-based control [5] and model reference adaptive control (MRAC) [6–9]. Model reference adaptive control is a valid anti-interference control method, which can realize system state or output tracking by designing a feedback controller, and is often used in aircraft model.

The existing feedback methods of model reference adaptive disturbance rejection feedback control schemes for multi-variable system are mainly state feedback [10, 11] and output feedback [12, 13]. In addition to these two feedback techniques, a new partial-state feedback MRAC scheme was put out in [14, 15] to solve system uncertainty for single-variable and multi-variable systems, respectively. The disturbance rejection issue can also be resolved by the partial state feedback MRAC. The partial-state feedback method was first used to solve disturbance rejection problem for single-variable systems in [16]. However, the research on partial-state feedback disturbance rejection control for multi-variable system is lacking.

It is challenging to study anti-disturbance control for multi-variable systems with unmatched disturbances. Since the disturbance does not occur in the input channel, a simple compensation term $-\alpha d(t)$, with constant matrix α, can not eliminate the effect of the disturbance. It is necessary to design a new disturbance compensation term. In addition, compared with single-input single-output (SISO) system, the high frequency gain K_p is a matrix rather than a constant which equals to the leading coefficient of molecular polynomial of the transfer function for SISO system. For multiple-input multiple-output system, a prior knowledge of the gain matrix K_p is more difficult to determine for stable adaptive law design. [17] used the condition that $K_p^T S_p^{-1} > 0$ is a symmetric matrix to relax the knowledge of K_p to solve the aircraft turbulence compensation problem using state feedback. To use less information about K_p for adaptive control, matrix decomposition technique was developed in [18]. Only the knowledge of leading principal minors is applied to design adaptive control. In [19], a stable adaptive control strategy was proposed relied on LDS decomposition of K_p. And, the matrix decomposition technique was utilized in dealing with disturbance problem in [20].

This paper develops a MRAC approach by using available signal for feedback. The novel control structure is designed, and the new feedback method adds the flexibility in feedback signal selection. For multi-variable systems in the presence of disturbances, the proposed new approach has forced us to reconsider the selection of auxiliary signals and estimation error. In addition, the new output matching conditions are established, which is crucial for constructing the tracking error. The adaptive law is designed based on LDS matrix decomposition, and its properties are verified. The designed MRAC scheme can guarantee the system stability, disturbance rejection and asymptotic output tracking.

2 Controller Structure Design

Consider a multi-variable linear time invariant uncertain system:

$$\dot{x}(t) = Ax(t) + Bu(t) + B_d d(t), y(t) = Cx(t), \quad (1)$$

where $x(t) \in \mathbb{R}^n$ is the system state, $u(t) \in \mathbb{R}^M$ is the input, and $y(t) \in \mathbb{R}^M$ is the output, matrices A, B, B_d, and C are unknown. The disturbance signal can be expressed as

$$d(t) = [d_1(t), \cdots, d_p(t)]^T, \quad (2)$$

$$d_i(t) = d_{i0} + \sum_{j=1}^{s_i} d_{ij} w_{ij}(t), \quad (3)$$

with unknown parameters $d_{ij}, i = 1, \cdots, p, j = 0, \cdots, s_i$ and known signals $w_{ij}(t)$. The system (1) has another form:

$$y(s) = G(s)u(s) + G_d(s)d(s), \quad (4)$$

with $G(s) = C(sI - A)^{-1}B$, $G_d(s) = C(sI - A)^{-1}B_d$. The objective of this paper is that developing an adaptive controller, whose feedback signals are available signals,

This work is supported by in part by the National Natural Science Foundation of China under Grant 62373214 ; in part by the Shandong Provincial Natural Science Foundation under Grant ZR2021ZD13; and in part by the Taishan Scholarship Project of Shandong Province.

makes the uncertain systems stable and achieves the output tracking between system and a reference model:

$$y_r(t) = W_r(s)[r](t), \tag{5}$$

where $W_r(s)$ is stable, and $r(t) \in \mathbb{R}^M$ is a bounded continuous function. The model reference adaptive control needs the following assumptions:

Assumption 1. The system is controllable and observable;

Assumption 2. Transfer matrix $G(s)$ has full rank and its modified left interactor matrix $\xi_r(s)$ is known, nonsingular matrix K_p satisfies $\lim_{s\to\infty} \xi_r(s)G(s) = K_p$, $N(s) = C\text{adj}(sI - A)B$ is stable;

Assumption 3. The relative degree of (A, B, C) is not greater than that of (A, B_d, C).

For designing the controller using available signal, the available signal has the following description:

$$y_a(t) = C_a x(t), \tag{6}$$

where $C_a \in \mathbb{R}^{q\times n}$. It has the input-output form: $y_a(s) = G_a(s)u(s) + G_{ad}(s)d(s)$. In addition, we add the assumption:

Assumption 4. (A, C_a) is observable.

Based on this assumption, we design the state observer using available signal $y_a(t)$. Finding a invertible matrix $P \in \mathbb{R}^{n\times n}$ guarantees $C_aP = [I_{q\times q}, 0]$. The controlled plant has the new form:

$$\dot{x}_a(t) = \begin{bmatrix} D_1 & D_2 \\ D_3 & D_4 \end{bmatrix} \begin{bmatrix} x_{a1}(t) \\ x_{a2}(t) \end{bmatrix} + \begin{bmatrix} E_1 \\ E_2 \end{bmatrix} u(t) + \begin{bmatrix} F_1 \\ F_2 \end{bmatrix} d(t). \tag{7}$$

with $x_a(t) = P^{-1}x(t) = [x_{a1}^T, x_{a2}^T]^T$, $x_{a1}(t) = y_a(t)$. To achieve feedback control using available signal $y_a(t)$, signal $y_a(t)$ is used to express $x_{a2}(t)$. According to the state observer theory, the estimate $\hat{x}_{a2}(t)$ is generated as $\dot{\hat{x}}_{a2}(t) = (D_4 - L_oD_2)\hat{x}_{a2}(t) + (D_3 - L_oD_1)y_a(t) + (E_2 - L_oE_1)u(t) + (F_2 - L_oF_1)d(t) + L_o\dot{y}_a(t)$, with matrix $L_o \in \mathbb{R}^{(n-q)\times q}$ making matrix $D_4 - L_oD_2$ stable. It follows that

$$\hat{x}_{a2}(t) = (sI - D_4 + L_oD_2)^{-1}\{((D_4 - L_oD_2)L_o + D_3 - L_oD_1)y_a(t) + (E_2 - L_oE_1)u(t) + (F_2 - L_oF_1)d(t)\} + L_oy_a(t) + e^{(D_4-L_oD_2)t}(\hat{x}_{a2}(0) - L_oy_a(0)). \tag{8}$$

From the observer, we have the result that

$$\lim_{t\to\infty} (\hat{x}_{a2}(t) - x_{a2}(t)) = 0. \tag{9}$$

From the definition of $x_a(t)$ in (7), $x_{a1}(t)$ equals to available signal $y_a(t)$, and

$$\lim_{t\to\infty} (\hat{x}_a(t) - x_a(t)) = 0, \tag{10}$$

is obtained, and then, with the transformation between $x_a(t)$ and $x(t)$,

$$\lim_{t\to\infty} (\hat{x}(t) - x(t)) = 0, \tag{11}$$

is established. According to the state feedback controller structure

$$u(t) = K_1^*x(t) + K_2^*r(t) + K_3^*d(t), \tag{12}$$

with $K_1^* \in \mathbb{R}^{M\times n}$, $K_2^* = K_p^{-1} \in \mathbb{R}^{M\times M}$, $K_3^* \in \mathbb{R}^{M\times p}$ and (8), the term $K_1^*x(t)$ can be expressed using available signal $y_a(t)$ as

$$\begin{aligned} &K_1^*x(t) = K_1^*\hat{x}(t) + K_1^*\delta_0(t) = K_1^*P\hat{x}_a(t) + K_1^*\delta_0(t) \\ &= Q_1y_a(t) + Q_2(sI - D_4 + L_oD_2)^{-1}\{((D_4 - \\ &L_oD_2)L_o + D_3 - L_oD_1)y_a(t) + (E_2 - L_oE_1)u(t) + \\ &(F_2 - L_oF_1)d(t)\} + Q_2L_oy_a(t) + \delta_1(t), \end{aligned} \tag{13}$$

with $K_1^*P = [Q_1, Q_2], Q_1 \in \mathbb{R}^{M\times q}, Q_2 \in \mathbb{R}^{M\times(n-q)}$, and exponentially decaying terms $\delta_0(t)$ and $\delta_1(t)$. The new controller structure is obtained as

$$\begin{aligned} &u(t) = \frac{M_1(s)}{\Lambda(s)}[y_a](t) + \frac{M_3(s)}{\Lambda(s)}[u](t) + \frac{M_4(s)}{\Lambda(s)}[d](t) + \\ &M_2y_a(t) + K_2^*r(t) + K_3^*d(t) + \delta_1(t), \end{aligned} \tag{14}$$

where $M_1 = Q_2\text{adj}(sI - D_4 + L_oD_2)((D_4 - L_oD_2)L_o + D_3 - L_oD_1) \in \mathbb{R}^{M\times q}$, $M_2 = Q_2L_o + Q_1 \in \mathbb{R}^{M\times q}$, $M_3 = Q_2\text{adj}(sI - D_4 + L_oD_2)(E_2 - L_oE_1) \in \mathbb{R}^{M\times M}$, $M_4 = Q_2\text{adj}(sI - D_4 + L_oD_2)(F_2 - L_oF_1) \in \mathbb{R}^{M\times p}$, $\Lambda(s) = \det(sI - D_4 + L_oD_2)$. The elements of matrices $M_1(s), M_3(s)$, and $M_4(s)$ are polynomials, which can separate the parameters from the operator "s". From (13) and (14), the structure of state-observer-based state feedback controller is changed. The full state feedback changes to partial-state feedback. Combining with the parametrization of signal

$$\begin{aligned} &d(t) = NW(t), \\ &W(t) = [1, W_1^T(t), \cdots, 1, W_p^T(t)]^T \in \mathbb{R}^{s+p}, \\ &W_i(t) = [w_{i1}(t), \cdots, w_{is_i}(t)]^T, \end{aligned} \tag{15}$$

where parameter matrix $N \in \mathbb{R}^{p\times(s+p)}$, and $s = s_1 + \cdots + s_p$. Ignoring the exponential decay term $\delta_1(t)$, we get the parameterized controller as

$$\begin{aligned} &u(t) = \frac{\Theta_1^*H_1(s)}{\Lambda(s)}[y_a](t) + \frac{\Theta_2^*H_2(s)}{\Lambda(s)}[u](t) + \frac{\Theta_3^*H_3(s)}{\Lambda(s)}\cdot \\ &[W](t) + \Theta_4^*y_a(t) + \Theta_5^*r(t) + \Theta_6^*W(t), \end{aligned} \tag{16}$$

where $H_1 = [I_q, sI_q, \cdots, s^{n-q-1}I_q]^T \in \mathbb{R}^{(n-q)q\times q}$, $H_2 = [I_M, sI_M, \cdots, s^{n-q-1}I_M]^T \in \mathbb{R}^{(n-q)M\times M}$, $H_3 = [I_{s+p}, sI_{s+p}, \cdots, s^{n-q-1}I_{s+p}]^T \in \mathbb{R}^{(n-q)(s+p)\times(s+p)}$, $\Theta_1^*H_1(s) = M_1(s)$ with parameter matrix $\Theta_1^* \in \mathbb{R}^{M\times(n-q)q}$, $\Theta_2^*H_2(s) = M_3(s)$ with parameter matrix $\Theta_2^* \in \mathbb{R}^{M\times(n-q)M}$ and $\Theta_3^*H_3(s)$ $[W](t) = M_4(s)[d](t)$ with parameter matrix $\Theta_3^* \in \mathbb{R}^{M\times(n-q)(s+p)}$, $\Theta_4^* = M_2$, $\Theta_5^* = K_2^* \in \mathbb{R}^{M\times M}$, and $\Theta_6^* = K_3^*N \in \mathbb{R}^{M\times(s+p)}$.

The designed controller relies on reduced-order state observer and state feedback control design. Because the close degree of state and the estimate of state converges to zero [17] and the state feedback controller has the ability of achieving output tracking, the new controller (16) has the same control performance. We have the following result.

Theorem 1. For the systems with known parameters and disturbance, the controller parameters exist and the controller (16) guarantees the boundedness of system signals and output tracking of plant and reference model.

The proof of this Theorem is divided into two parts. One is to verify the existence of controller parameters to achieve plant-model output tracking. The other is to ensure the boundedness of system signals. From the controller structure (16), the parameters Θ_i^*, $i = 1, \cdots, 6$, are related to state feedback controller parameters whose existence is verified in the previous work. Thus, the existence of the designed new controller parameters Θ_i^*, $i = 1, \cdots, 6$, can be guaranteed. From the output tracking property $y(t) - y_r(t) = \delta_2(t)$, the output signal is bounded with $\xi_r(s)[y - \delta_2](t) = r(t)$, exponential decay term $\delta_2(t)$ and $W_r(s) = \xi_r^{-1}(s)$. Combining with the system model (4), the boundedness of signals $x(t)$ and $u(t)$ is easily proved. According to the plant-model output tracking, a matching condition is established.

Corollary 1. The partial-state feedback controller parameters Θ_i^*, $i = 1, \cdots, 6$, satisfy

$$\begin{aligned}&\Lambda(s)I - \Theta_1^* H_1(s)G_a(s) - \Theta_2^* H_2(s) - \Theta_4^*\Lambda(s)G_a(s)\\&= \Theta_5^*\Lambda(s)\xi_r(s)G(s), \qquad (17)\\&\Theta_1^* H_1(s)G_{ad}(s)d(s) + \Theta_3^* H_3(s)W(s) + \Theta_4^*\Lambda(s)G_{ad}(s)d(s)\\&+ \Lambda(s)\Theta_5^*\xi_r(s)G_d(s)d(s) + \Theta_6^*\Lambda(s)W(s) = 0. \qquad (18)\end{aligned}$$

Corollary 1 is essential for establishing the output tracking error equation, and lays a foundation for designing a stable adaptive law.

3 Adaptive Control Design

In the above Section, the controller parameters are separated from signals. For uncertain systems, the parameters are unknown. Thus, it needs to be estimated and then we have the adaptive controller by estimating the controller parameters Θ_i^*, $i = 1, \cdots, 6$, as:

$$\begin{aligned}u(t) = {}&\hat{\Theta}_1(t)\frac{H_1(s)}{\Lambda(s)}[y_a](t) + \hat{\Theta}_2(t)\frac{H_2(s)}{\Lambda(s)}[u](t) +\\&\hat{\Theta}_3(t)\frac{H_3(s)}{\Lambda(s)}[W](t) + \hat{\Theta}_4(t)y_a(t) + \hat{\Theta}_5(t)r(t) +\\&\hat{\Theta}_6(t)W(t), \qquad (19)\end{aligned}$$

where $\hat{\Theta}_i(t)$ are estimates of $\Theta_i^*, i = 1, \cdots, 6$, in (16). Next, we will design adaptive law to update $\hat{\Theta}_i(t)$ to obtain the desired results. Operating $u(s)$ on both sides of (17), we have

$$\begin{aligned}u(s) = {}&\Theta_1^*\frac{H_1(s)}{\Lambda(s)}(y_a(s) - G_{ad}(s)d(s)) +\\&\Theta_2^*\frac{H_2(s)}{\Lambda(s)}u(s) + \Theta_4^*(y_a(s) - G_{ad}(s)d(s)) +\\&\Theta_5^*\xi_r(s)(y(s) - G_d(s)d(s)). \qquad (20)\end{aligned}$$

Combining with (18),

$$\begin{aligned}u(s) = {}&\Theta_1^*\frac{H_1(s)}{\Lambda(s)}y_a(s) + \Theta_2^*\frac{H_2(s)}{\Lambda(s)}u(s) + \Theta_4^* y_a(s) +\\&\Theta_5^*\xi_r(s)y(s) + \Theta_3^*\frac{H_3(s)}{\Lambda(s)}W(s) + \Theta_6^* W(s). \qquad (21)\end{aligned}$$

Based on the reference model $\xi_r(s)[y_r](t) = r(t)$ with $W_r(s) = \xi_r^{-1}(s)$, subtracting (19) from (21), a tracking error equation about parameter errors $\tilde{\Theta}_i(t) = \hat{\Theta}_i(t) - \Theta_i^*$ is shown as

$$\begin{aligned}&\Theta_5^*\xi_r(s)[e](t) = \tilde{\Theta}_1(t)\frac{H_1(s)}{\Lambda(s)}[y_a](t) + \tilde{\Theta}_2(t)\frac{H_2(s)}{\Lambda(s)}[u](t) +\\&\tilde{\Theta}_3(t)\frac{H_3(s)}{\Lambda(s)}[W](t) + \tilde{\Theta}_4(t)y_a(t) + \tilde{\Theta}_5(t)r(t) +\\&\tilde{\Theta}_6(t)W(t), \qquad (22)\end{aligned}$$

that is,

$$\Theta_5^*\xi_r(s)[e](t) = \tilde{\Theta}(t)\Upsilon(t), \qquad (23)$$

where $e(t) = y(t) - y_r(t)$, $\tilde{\Theta}(t) = [\tilde{\Theta}_1(t), \tilde{\Theta}_2(t), \tilde{\Theta}_3(t), \tilde{\Theta}_4(t), \tilde{\Theta}_5(t), \tilde{\Theta}_6(t)]$, $\Upsilon(t) = [\upsilon_1^T(t), \upsilon_2^T(t), \upsilon_3^T(t), y_a^T(t), r^T(t), W^T(t)]^T$, $\upsilon_1(t) = H_1(s)\Lambda^{-1}(s)[y_a](t)$, $\upsilon_2(t) = H_2(s)\Lambda^{-1}(s)[u](t)$, $\upsilon_3(t) = H_3(s)\Lambda^{-1}(s)[W](t)$, $u(t), y_a(t), W(t)$, and $y(t)$ derive from inverse laplace transform, and $\Theta_5^* = K_p^{-1}$. According to (23), we know that, in uncertain systems, the output tracking error $e(t)$ is related to the unknown constant matrix K_p, and it has the another description as

$$e(t) = \xi_r^{-1}(s)K_p[\tilde{\Theta}\Upsilon](t), \qquad (24)$$

where the prior knowledge of K_p is needed. We add the following assumption:

Assumption 5. The signs of leading principal minors α_i of matrix K_p, $i = 1, \cdots, M$, are known.

It is well known that an arbitrary matrix can be transformed into a diagonal matrix through elementary transformation. Hence, $LK_pU = D$ is achievable with unit lower triangular matrix L, diagonal matrix D and unit upper triangular matrix U. Then, the gain matrix K_p has a decomposition: $K_p = \bar{L}\bar{D}S$ where unit lower triangular matrix $\bar{L} = L^{-1}\bar{D}U^T\bar{D}^{-1}$, diagonal matrix $\bar{D} = \text{diag}\{\text{sign}[\alpha_1]\beta_1, \cdots, \text{sign}[\alpha_M\alpha_{M-1}^{-1}]\beta_M\}$, arbitrary $\beta_j > 0, j = 1, \cdots, M$, and symmetric and positive definite matrix $S = U^{-T}\beta^{-1}|D|U^{-1}$, $\beta = \text{diag}\{\beta_1, \cdots, \beta_M\}$. According to the above matrix decomposition, we have the new expression of error equation (23) as

$$\bar{L}^{-1}\xi_r(s)[e](t) = \bar{D}S\tilde{\Theta}(t)\Upsilon(t), \qquad (25)$$

where $\bar{L}^{-1} = I + Z$, $Z = [0, Z_2^*, \cdots, Z_M^*]^T$, $Z_i^* = [z_i^{*T}, 0]^T \in \mathbb{R}^M$, and $z_i^* = [z_{i1}^*, \cdots, z_{ii-1}^*]^T$, $i = 2, \cdots, M$. Choose a stable polynomial $f(s)$, whose degree equals to the maximum degree of polynomials in $\xi_r(s)$. Let $h(s) = f^{-1}(s)$, $\bar{e}(t) = h(s)\xi_r(s)[e](t) = [\bar{e}_1, \cdots, \bar{e}_M]^T$ and $\eta_k(t) = [\bar{e}_1, \cdots, \bar{e}_{k-1}]^T$, $k = 2, \cdots, M$, where $\bar{e}_i(t) = \sum_{j=1}^M h(s)\xi_{rij}(s)[e_j](t)$ and $\xi_{rij}(s)$ represents the element in row i and column j of the matrix $\xi_r(s)$. Equation (25) can be expressed as $\bar{e}(t) + Z\bar{e}(t) = \bar{D}Sh(s)[\tilde{\Theta}\Upsilon](t)$, which can be further expressed as $\bar{e}(t) + [0, z_2^{*T}\eta_2(t), \cdots, z_M^{*T}\eta_M(t)]^T = \bar{D}Sh(s)[\tilde{\Theta}\Upsilon](t)$, with unknown vector z_i^*, $i = 2, \cdots, M$, and matrix $\bar{D}S$. Introduce estimate error signal $\sigma(t) = \bar{e}(t) + [0, z_2^T(t)\eta_2(t), \cdots, z_M^T(t)\eta_M(t)]^T + \Phi(t)\varphi(t)$, where $z_i(t)$ and $\Phi(t)$ are estimates of z_i^* and $\bar{D}S$, and $\varphi(t) =$

$\hat{\Theta}(t)\tau(t) - h(s)[\hat{\Theta}\Upsilon](t)$, $\tau(t) = h(s)[\Upsilon](t)$, $\hat{\Theta}(t) = [\hat{\Theta}_1(t), \hat{\Theta}_2(t), \hat{\Theta}_3(t), \hat{\Theta}_4(t), \hat{\Theta}_5(t), \hat{\Theta}_6(t)]$. The estimate error equation can be expressed as

$$\begin{aligned}\sigma(t) =&[0, \tilde{z}_2^T(t)\eta_2(t), \cdots, \tilde{z}_M^T(t)\eta_M(t)]^T + \\ &\bar{D}S\tilde{\Theta}(t)\tau(t) + \tilde{\Phi}(t)\varphi(t),\end{aligned} \tag{26}$$

where $\tilde{z}_i(t) = z_i(t) - z_i^*$ and $\tilde{\Phi}(t) = \Phi(t) - \bar{D}S$. From estimate error equation (26), the adaptive law is designed by gradient algorithm as:

$$\dot{z}_i(t) = -\frac{\Gamma_i \sigma_i(t)\eta_i(t)}{m^2(t)}, i = 2, \cdots M, \tag{27}$$

$$\dot{\hat{\Theta}}(t) = -\frac{\bar{D}\sigma(t)\tau^T(t)}{m^2(t)}, \dot{\Phi}(t) = -\frac{\Gamma_\Phi \sigma(t)\varphi^T(t)}{m^2(t)}, \tag{28}$$

with diagonal positive definite matrices Γ_i and Γ_Φ, and $m^2(t) = 1 + \varphi^T(t)\varphi(t) + \tau^T(t)\tau(t) + \sum_{i=2}^{M} \eta_i^T(t)\eta_i(t)$. Then, we have the following properties of adaptive laws.

Lemma 1. (1) $\dot{z}_i(t) \in L^2$, $\dot{\hat{\Theta}}(t) \in L^2$, $\dot{\Phi}(t) \in L^2$ and $\sigma(t)m^{-1}(t) \in L^2$;
(2) $z_i(t)$, $\hat{\Theta}(t)$, $\Phi(t)$ and $\sigma(t)m^{-1}(t)$ are bounded.

The Lemma 1 can be proved by designing the positive definite function $V(\tilde{z}_i(t), \tilde{\Theta}(t), \tilde{\Phi}(t)) = \sum_{i=2}^{M} \tilde{z}_i^T(t)\Gamma_i^{-1} \cdot \tilde{z}_i(t) + \text{trace}[\tilde{\Theta}^T(t)S\tilde{\Theta}(t)] + \text{trace}[\tilde{\Phi}^T(t)\Gamma_\Phi^{-1}\tilde{\Phi}(t)]$. The derivative of $V(\cdot)$ is $\dot{V}(\cdot) = -2\sigma^T(t)\sigma(t)m^{-2}(t)$. Based on the $\bar{L}\bar{D}S$ matrix decomposition, adaptive law design and Lemma 1, the desired closed-loop system performance can be achieved.

Theorem 2. For uncertain systems satisfying Assumptions 1-5 with input disturbances, the adaptive controller (19) whose parameters are updated by adaptive laws (27) and (28) makes the closed-loop system stable and can realize asymptotic output tracking.

The proof of Theorem 2 omitted here depends on Small-Gain Lemma and Barbalat Lemma described in [21]. The control signal $u(t)$, output $y(t)$, and signal $\bar{e}(t)$ can be described using auxiliary signal $y_h(t) = F(s)[y](t)$ and bounded signals $r(t)$, $f(t)$ and various stable operators, where stable $F(s)$ satisfys $s\bar{F}(s) = 1 - F(s)$ and $F(s) = \bar{a}^l(s+\bar{a})^{-l}$, with the maximum degree l of polynomials in ξ_r and sufficiently large constant $\bar{a} > 0$. From the Small-Gain Lemma, the boundedness of $y_h(t)$ can be further obtained. Then, combining with signal properties in Lemma 1 and the stable filter, boundedness of closed-loop system signals and tracking property are further obtained.

4 Example

In this section, we use a linearized aircraft model [22] to illustrate the feasibility of this scheme:

$$\begin{bmatrix} \dot{v}_b \\ \dot{p}_b \\ \dot{r}_b \\ \dot{\phi} \\ \dot{\psi} \end{bmatrix} = \begin{bmatrix} -0.1386 & 14.326 & -219.04 & 32.167 & 0 \\ -0.0207 & -2.1692 & 0.9132 & 0.0003 & 0 \\ 0.0029 & -0.1644 & -0.1577 & -0.0049 & 0 \\ 0 & 1 & 0.0062 & 0 & 0 \\ 0 & 0 & 1 & 0 & 0 \end{bmatrix} \begin{bmatrix} v_b(t) \\ p_b(t) \\ r_b(t) \\ \phi(t) \\ \psi(t) \end{bmatrix} + \begin{bmatrix} 0.159 & 0.002 \\ 0.013 & 0.213 \\ -0.129 & 0.002 \\ 0 & 0 \\ 0 & 0 \end{bmatrix} \begin{bmatrix} d_r(t) \\ d_a(t) \end{bmatrix}$$

$$+ \begin{bmatrix} 0.13858 & -14.326 \\ 0.0207 & 2.1692 \\ -0.0029 & 0.16444 \\ 0 & -1 \\ 0 & 0 \end{bmatrix} \begin{bmatrix} v_w \\ p_w \end{bmatrix},$$

$$y = \begin{bmatrix} 1 & 0 & 0 & 0 & 0 \\ 0 & 0 & 0 & 0 & 1 \end{bmatrix} \begin{bmatrix} v_b(t) \\ p_b(t) \\ r_b(t) \\ \phi(t) \\ \psi(t) \end{bmatrix}, \tag{29}$$

where the state variables are lateral velocity, roll rate, yaw rate, roll angle, and yaw angle, respectively, the control input are the rudder position and aileron position, respectively, and we just consider the effect of lateral wind velocity v_w and roll gust velocity p_w on aircraft. In this simulation, the Assumptions 1-5 are satisfied, and K_p is nonsingular. With the choices of initial state $x(0) = [0.1, 0.2, 0.5, 0.1, 0.1]$, $\Lambda(s) = (s+1)^2$, $\xi_r(s) = \text{diag}\{(s+1), (s+1)^2\}$, $h(s) = (s+1)^{-2}$, $\Gamma_2 = 10$, $\Gamma_\Phi = \text{diag}\{1, 5\}$, $\bar{D} = \text{diag}\{2, 6\}$, $r(t) = [1, 0.1\text{sin}(0.2t)]^T$, $v_w(t) = 10 + 0.2\text{sin}(0.2\pi t)$, $p_w(t) = 0.5\text{sin}(0.2t)$, and partial state signal $y_a(t) = [v_b, \phi, \psi]^T$. The system response curves of the partial-state feedback control and output feedback control schemes are shown in Figures 1 and 2 with the same conditions, where the curves of $u(t)$ are shown in Figure 1, the curves of tracking error $e(t)$ are shown in Figure 2.

It follows from Figures 1 and 2 that the control input signals are bounded, the output tracking between system and reference model is achieved, and the new scheme enables faster tracking under the same conditions and initial values. In a word, the designed partial-state feedback disturbance rejection control scheme has the ability to make aircraft model stable and to reject turbulence disturbance.

5 Conclusion

This paper develops a disturbance rejection control scheme using partial-state feedback MRAC method for multivariable linear time-invariant system with disturbances. The nominal controller structure is proposed. The adaptive law is designed using $\bar{L}\bar{D}S$ matrix decomposition technique of K_p. In addition, some properties of adaptive law are given, which is crucial in stability analysis. The designed control scheme uses partial available signal for feedback and guarantees that system output asymptotically tracks the reference output $y_r(t)$. The simulation results demonstrate the feasibility of this control scheme. The proposed control method is potential, which can be extended to other control problems such as adaptive actuator failure compensation, time-delay systems and PDE systems.

References

[1] C. Liu, X. Yue, J. Zhang, and K. Shi, Active disturbance rejection control for delayed electromagnetic docking of spacecraft in elliptical orbits, IEEE Transactions on Aerospace and Electronic Systems, 58(3): 2257-2268, 2022.

[2] S. Shen, J. Xu, P. Chen, and Q. Xia, An intelligence attitude controller based on active disturbance rejection control technology for an unmanned helicopter, IEEE Transactions on Vehicular Technology, 72(3): 2936-2946, 2023.

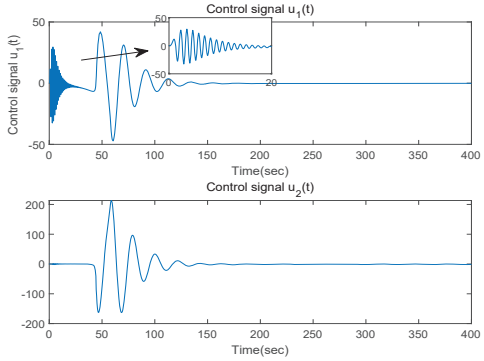

(a) Control signals of partial state feedback

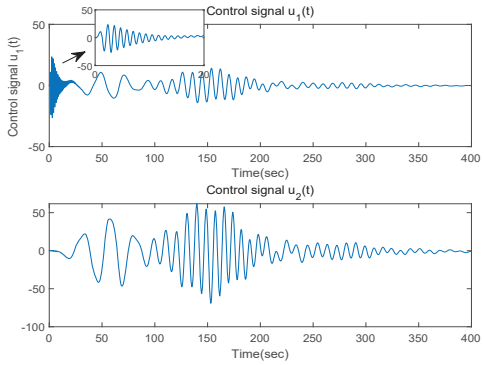

(b) Control signals of output feedback

Fig. 1: The curves of control signals.

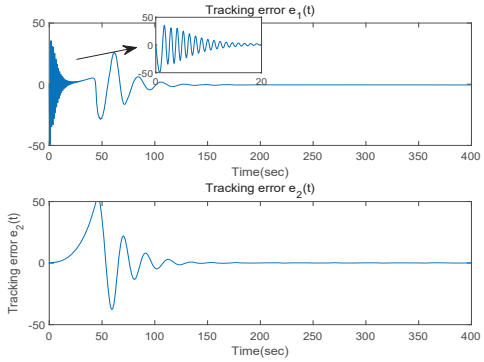

(a) Tracking error signals of partial state feedback

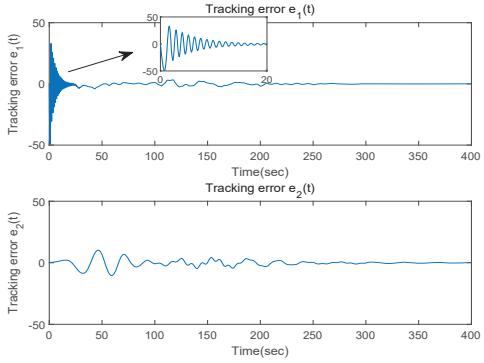

(b) Tracking error signals of output feedback

Fig. 2: The curves of tracking error signals .

[3] C. Jing, H. Xu, and X. Niu, Adaptive sliding mode disturbance rejection control with prescribed performance for robotic manipulators, ISA Transactions, 91: 41-51, 2019.

[4] S. A. Suhail, M. A. Bazaz, and S. Hussain, Adaptive sliding mode-based active disturbance rejection control for a quadcopter, Transactions of the Institute of Measurement and Control, 44(16): 3176-3190, 2022.

[5] W. Chen, J. Yang, L. Guo, and S. Li, Disturbance-observer-based control and related methods-an overview, IEEE Transactions on industrial Electronics, 63(2): 1083-1095, 2016.

[6] G. Kreisselmeier, and K. Narendra, Stable model reference adaptive control in the presence of bounded disturbances, *IEEE Transactions on Automatic Control*, 27(6): 1169-1175, 1982.

[7] A. Datta, and P. A. Ioannou, Performance analysis and improvement in model reference adaptive control, *IEEE Transactions on Automatic Control*, 39(12): 2370-2387, 1994.

[8] L. Wen, G. Tao, H. Yang, and Y. Zhang, An adaptive disturbance rejection control scheme for multivariable nonlinear systems, *International Journal of Control*, 89(3): 594-610, 2016.

[9] X. Liu, X. Ma, R. Feng, Y. Chen, Y. Shi, and S. Zheng, Model reference adaptive compensation and robust controller for magnetic bearing systems with strong persistent disturbances, *IEEE Transactions on Industrial Electronics*, 70(11): 10902-10911, 2023.

[10] G. Tao, X. Tang, and S. M. Joshi, Adaptive output rejection of unmatched input disturbances, *Systems and Control Letters*, 47(1): 25-35, 2002.

[11] J. Guo, and G. Tao, A discrete-time multivariable MRAC scheme applied to a nonlinear aircraft model with structural damage, *Automatica*, 53: 43-52, 2015.

[12] K. Narendra, and A. Annaswamy, Robust adaptive control in the presence of bounded disturbances, *IEEE Transactions on Automatic Control*, 31(4): 306-315, 1986.

[13] Y. Liu, and G. Tao, An adaptive disturbance rejection algorithm for MIMO systems with an aircraft flight control application, in *Proceedings of AIAA Guidance, Navigation, and Control Conference*, South Carolina, USA, 2007.

[14] G. Song, and G. Tao, Partial-state feedback model reference adaptive control scheme, *IEEE Transactions on Automatic Control*, 65(1): 44-57, 2020.

[15] G. Song, and G. Tao, Partial-state feedback multi-variable MRAC and reduced-order designs, *Automatica*, 129: 109622, 2021.

[16] Z. Zhang, Y. Sang, and X. Chen, Model reference adaptive disturbance rejection control using partial-state feedback, *Automatica*, 154: 111071, 2023.

[17] L. Wen, G. Tao, H. Yang, and Y. Yang, Aircraft turbulence compensation using adaptive multivariable disturbance rejection techniques, *Journal of Guidance, Control and Dynamics*, 38(5): 954-962, 2015.

[18] A. K. Imia, R. Costa, L. Hsu, G. Tao, and P. Kokotovic, Multivariable MRAC using high frequency gain matrix factorization, in *Proceedings of 40th IEEE Conference on Decision and Control*, Oriando, Florida, USA, 2001.

[19] J. X. Guo, G. Tao, and Y. Liu, A multivariable MRAC scheme with application to a nonlinear aircraft model, *Automatica*, 47(4): 804-812, 2011.

[20] L. Wen, G. Tao, and Y. Liu, Multivariable adaptive output rejection of unmatched input disturbances, *Int. J. Adapt. Control Signal Process.*, 30: 1203-1227, 2016.

[21] G. Tao, *Adaptive control design and analysis*. Hoboken, NJ, USA: Wiley, 2003.

[22] G. Tao, S. Chen, X. Tang, and S. M. Joshi, *Adaptive control of systems with actuator failures*. London, UK: Springer-Verlag, 2004.

Proceedings of the 3rd Conference on Fully Actuated System Theory and Applications
May 10-12, 2024, Shenzhen, China

Mitigation of Distribution Transformer Overloading with Rolling-Horizon Optimization of Vehicle-to-Grid Resource

Lin Xia[1], Xiao Hong[1], Xiaowei Sun[1], Qingxue Li[1], Hao Wu[1], Yingning Huo*[2], Guangchao Geng[3]

1. Hangzhou Power Supply Company, State Grid Zhejiang Electric Power Co., Ltd., Hangzhou 310020, P. R. China

2. Polytechnic Institute, Zhejiang University, Hangzhou 310015, P. R. China
E-mail: hyn27@zju.edu.cn

3. College of Electrical Engineering, Zhejiang University, Hangzhou 310027, P. R. China

Abstract: Electric vehicles (EVs) play a crucial role in the global transition to low-carbon and clean energy. Large amounts of uncontrolled EVs charging can cause short-term overloading problems with distribution transformers in some areas. EVs as a mobile energy storage component with Vehicle-to-Grid (V2G) capability can provide a solution to alleviate the overloading and aging problems of distribution transformers. This paper comprehensively considers the charging and discharging losses of EVs and the peak load of distribution transformers, with the constraint of EVs' own charging and discharging demands. The rolling-horizon optimization is employed to solve the model, which can adapt to dynamic changes in load conditions and provide rapid solutions. In this paper, the effectiveness of the proposed method is verified and the loads exceeding the capacity of the transformer are successfully shifted to other times and the charging needs of the users participating in the V2G program are met.

Key Words: electric vehicles, load shift,rolling-horizon optimization, Vehicle-to-Grid

1 Introduction

As global climate change and environmental pollution become increasingly severe, reducing greenhouse gas emissions and dependence on traditional petroleum fuels has become a global consensus [1]. Electric vehicles (EVs), as a novel form of transportation that uses electricity as a driving energy source and does not require traditional fuel engines, can achieve zero or low emissions during operation. However, the widespread adoption of EVs, while improving the environment, often leads to overload and aging problems in distribution transformers due to their large-scale and uncontrolled charging behavior [2].

EVs also have energy storage and vehicle-to-grid (V2G) capabilities, which can play a more active role in the energy system [3]. Through the energy storage function of EVs, they can be viewed as mobile energy storage devices that interact with the power grid. If the V2G feature is fully utilized to transfer power loads, it can greatly alleviate the overload pressure and aging problems caused by uncontrolled EV loads on distribution transformers [4].

It is projected that uncontrolled EV charging loads will lead to a peak load increase of up to 10% by 2030 [5]. V2G can mitigate the impacts caused by uncontrolled EV charging on the power grid and effectively reduce electricity pressure on the distribution network during peak load periods. If issues such as "range anxiety" and "minimum range" can be addressed, there will be a high willingness among EVs users to participate in V2G [6]

Existing research has made numerous innovative and practical contributions in the domain of coordinated control for EVs. The study documented [7] investigated optimization and coordination strategies for plug-in EVs, effectively reducing peak loads and the cost of grid expansion. A communication-free intelligent charging algorithm for EVs was proposed [8], which can effectively address distribution transformer overload issues even without centralized control. Reference [9] considered photovoltaic power and building demand forecasts, V2G and vehicle-to-building (V2B) capabilities of EVs, as well as the impact of power trading, to regulate the charging and discharging power of EVs. An intelligent framework for energy sharing among EVs was proposed [10], optimizing cost, time, system efficiency, user satisfaction, and social welfare through a two-tier matching approach. Reference [11] focused on the issue of distribution transformer overloads, determining the range of EVs that can be accommodated by monitoring key parameters and adopting corresponding charging control strategies. Reference [12] proposes a centralized control strategy based on smart meters, which enables effective management of the charging load for EVs.

In terms of improving EV users' participation in V2G systems, reference [13] established a real-time settlement system for V2G, which increased V2G participation rates. The simulation results showed that this system significantly improved user participation rates. A vehicular ad-hoc network system model was established and applied to the Texas power market in the study documented [14]. The results indicated that reducing battery costs, providing subsidies and incentive-based market products can increase user participation rates. The V2G-OLC algorithm proposed [15], it can effectively reduce EV users' charging costs, solving the problem of charging costs in the housing sector. In [16], a subsidy program designed for V2G services was proposed to compete with the renewable energy market.

In industry practice, EVs have been able to achieve bidirectional interaction with the power grid. Reference [17] introduces a configuration of an AC-DC converter for V2G technology, enabling the bidirectional flow of energy. Reference [18] presents a topology structure based on current-source-type converters and a unified control scheme based on active disturbance rejection control principles, demonstrating its effectiveness through experimental validation. A novel bidirectional DC/DC converter is developed in [19],

This work was supported by the project of the State Grid Zhejiang Electric Power Co. Ltd. (B311HZ23000Q).

which enables energy conversion and control at different voltage levels in EV systems.

Given the aforementioned discussions, this paper addresses the issue of transformer overload caused by a large number of uncontrollable EV charging. To tackle this problem, a rolling-horizon optimization model is proposed, which calculates the optimal control actions at each time step to adapt to system dynamics and environmental changes. This approach enables a rational regulation of V2G resources. Firstly, the paper classifies and defines the characteristics of uncontrollable EVs engaged in unregulated charging and controllable EVs participating in V2G. Subsequently, considering user demands, vehicle electrical characteristics, and substation capacity constraints, the objective function is formulated to minimize charging and discharging losses while incorporating a penalty term for maximum load. rolling-horizon optimization is performed upon the arrival of each EV to achieve the optimal control outcome at the current time. Simulation results demonstrate the efficacy of this method in effectively resolving the problem of transformer overload resulting from uncontrolled EV charging, while maintaining the overall load at a lower level.

This paper is structured as follows. Section II provides definitions of the controlled and uncontrollable EVs used in this study. Section III presents the proposed V2G control strategy using rolling-horizon optimization. In Section IV, the proposed method is simulated and analyzed using data from an industrial park in Shanghai. Finally, Section V summarizes the key findings and conclusions of this thesis.

2 Charging Modes for EVs

2.1 Problem Statement

When a large number of EVs enter the charging state, it may cause serious overload and aging issues for distribution transformers. In this paper, we propose a method based on rolling-horizon optimization to regulate V2G resources and alleviate the overload and aging problems of distribution transformers. Specifically, this method combines future grid load conditions and user demands to dynamically formulate corresponding charging and discharging strategies. By employing rolling-horizon optimization, intelligent management of charging and discharging behaviors can be achieved, effectively controlling the overload and aging problems of distribution transformers.

In power systems, proper protection of transformer mineral oil is particularly important. Prolonged operation under high loads can have adverse effects on the transformer itself, leading to a shortened lifespan [4]. Therefore, the objective of V2G charging and discharging control in this study is to reduce peak loads on distribution transformers and ensure their safe operation.

By implementing flexible scheduling of EV charging and discharging through V2G technology, power load can be dispersed in time and space. Consequently, the load on distribution transformers becomes more evenly distributed, avoiding damages caused by excessive peak loads and load fluctuations. Therefore, the V2G charging and discharging control strategy proposed in this paper aims to optimize the load distribution of the power system, reduce the load pressure on distribution transformers, mitigate the risk of overload, and delay the aging process.

2.2 Uncontrolled Charging

Uncontrolled EVs are considered as simple electrical devices in this paper, where they continuously charge at the rated power of the EV when plugged into a power source until the battery is full or the EV leaves the charging station [20]. As a result, the power level during the charging period and the charging duration of EV users cannot be adjusted and solely depend on the type of EV and the user's charging gun time.

However, the simultaneous connection of a large number of uncontrolled EVs for charging can lead to extremely high peak loads, often coinciding with the peak loads of other electrical devices. This seriously affects the safe operation of the power grid, particularly causing issues related to transformer overload and aging. To address this problem, measures need to be taken to mitigate the adverse effects of uncontrolled EV charging loads on distribution transformers.

2.3 Controlled Charging

In this paper, controlled EVs refer to a way of regulating charging and discharging power during the EV's stay by utilizing V2G technology. This means that we can reasonably allocate charging resources based on grid load conditions and user demand. Although the plug-in time of controlled EVs has a high degree of uncertainty, the charging and discharging time of EVs can be specified, and their behavior can be managed in an orderly manner through the use of corresponding schedulers.

The application of this V2G technology enables the power system to adjust and manage loads more flexibly, improve the reliability and stability of the power grid. Through intelligent scheduling algorithms and real-time monitoring systems, we can optimize the charging and discharging behavior of controlled EVs according to the actual situation, minimizing the impact on the power grid. The load that exceeds the carrying capacity of the distribution transformer can be transferred to the EVs, thereby achieving smooth regulation of the power load. The energy storage capabilities of EVs can be fully utilized to participate in power market transactions and regulation. This orderly management approach can meet the needs of users while alleviating pressure on the power system, achieving sustainable development and optimal operation of the power system [6]. Therefore, controlled EVs have significant potential and value in future energy planning and management.

3 Rolling-Horizon Optimization Strategy

3.1 General Overview of the Proposed Scheme

In this paper, we employ the rolling-horizon optimization method to address the issue of load exceeding transformer capacity and achieve control over V2G resources' charging and discharging. The unique aspect of the rolling-horizon optimization method lies in its ability to provide near-optimal solutions that are continuously updated and incorporate new information over time. Compared to other approaches for handling uncertain problems such as stochastic programming and robust optimization, the rolling-horizon optimization method demonstrates higher practicality and effectiveness in dealing with complex optimization prob-

lems. Through this method, we are able to find the optimal charging and discharging strategy in situations of excessive load, ensuring that the transformer's capacity is not overloaded. Additionally, the rolling-horizon optimization method possesses flexibility and can dynamically adjust with the incorporation of new information, thereby better adapting to complex real-world scenarios.

When a controllable EV is connected or when the load of the distribution transformer is excessive, the method proposed in this paper makes decisions based on the known future period information to allocate the control power of EVs for future periods, as illustrated in Fig. 1.

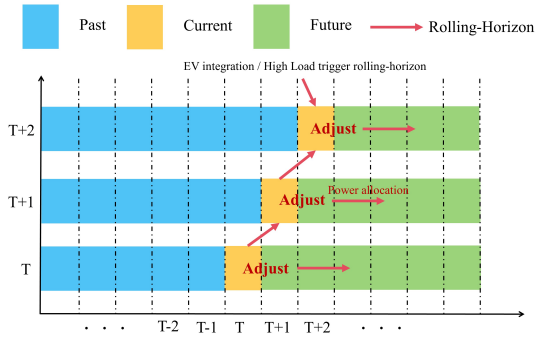

Fig. 1: Rolling-horizon optimization adjustment

It comprehensively considers factors such as the charging demand constraints of EVs, grid load conditions, and battery status to formulate the optimal charging and discharging strategy. The overall structure of the method is illustrated in Fig. 2. By utilizing the rolling-horizon optimization method, the charging and discharging plans can be dynamically adjusted based on real-time data, minimizing the occurrence of load exceeding transformer capacity as much as possible.

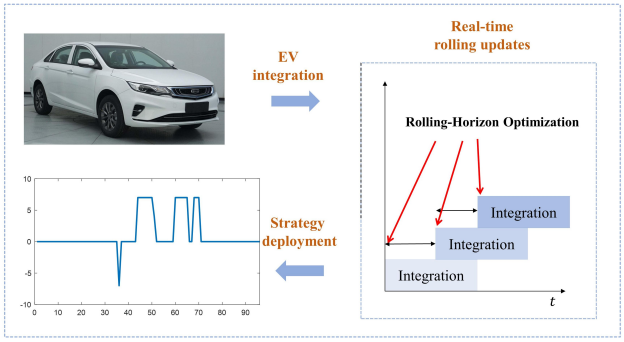

Fig. 2: Real-time rolling-horizon optimization framework

The key to the rolling horizon optimization method is to re-solving the problem at each time step and update it with new information. This iterative approach enables the optimization results to progressively approach the global optimum and adapt to dynamic changes in parameters. Through continuous iteration and updating, the rolling horizon optimization method can provide efficient and feasible charging and discharging control schemes in practical applications, ensuring that the load does not exceed the transformer capacity while meeting the charging needs of EV users. The aforementioned energy management strategy is implemented using an Mixed Integer Linear Programming based optimization method.

3.2 Optimization Model

3.2.1 Objective Function

The objective function is crucial in achieving overall control of EV loads. From the perspective of minimizing the energy loss during the charging and discharging processes of EVs and ensuring the safe operation of distribution transformers, ordered charging and discharging strategies are adjusted to mitigate the numerous problems caused by unregulated EV charging. This guarantees that the load does not exceed the capacity of the distribution transformer, with the formula represented by (1). The objective function of this model aims to minimize the energy loss during the charging and discharging processes of EVs, while considering the penalty for exceeding the load limit.

$$\min \quad (\sum_{i=1}^{N} P_i^{loss} + K * L_{max}) \tag{1}$$

where N represents the total number of controllable EVs, P_i^{loss} represents the energy loss during the charging and discharging processes, K represents the penalty term for exceeding the maximum load during regulation periods, L_{max} represents the maximum load during the regulation period for EVs.

3.2.2 Constraint

1) Charging adjustment period constraint

Considering the specific implementation of the charging and discharging control equipment and the practical solvability of this strategy, a day is divided into 96 independent regulation periods with a 15-minute interval. For instance, if 00:00-00:15 is considered as one regulation period, the arrival time of the EV user is treated as the first regulation period. The information of each arriving EV user is uploaded to the rolling horizon optimization model, followed by the issuance of strategies for the next 96 time points.

2) Distribution transformer capacity constraint

The future substation load for the regulation periods is obtained by summing the power curve of the future load profile and the power curve generated by the rolling horizon optimization strategy for EVs. The formula for calculating the substation load for the future regulation periods is given as equation (2):

$$L_t = \sum_{i=1}^{N} p_{i,t} + L_{pre,t} \qquad t = 1, 2, \cdots, T \tag{2}$$

where L_t is the total power of the distribution transformer at time t, $L_{pre,t}$ is the power of uncontrollable loads at time t, $p_{i,t}$ is the power of the formulated EV charging and discharging strategy, T is the total number of segmented charging and scheduling periods.

To ensure that the total load at any given time during the regulation period does not exceed the safe capacity of the distribution transformer, the formula is as follows:

$$L_t \leq \eta_1 S_T \qquad t = 1, 2, \cdots, T \tag{3}$$

where η_1 is the safety constraint percentage of the distribution transformer, S_T is the capacity of the distribution transformer in the substation.

3) Charging period constraint

To ensure that the charging and discharging strategy for EV users is not executed after they leave, the formula is represented as equation (4):

$$u_{i,t} = 0 \quad \mathrm{t} \geq t_{end} \tag{4}$$

where $u_{i,t}$ is a binary variable indicating the on-off control of the EV charging and discharging controller at time t, t_{end} represents the departure time when the user leaves.

4) Charging power limitation constraint

Based on the actual carrying capacity of the EV's power battery, the actual charging and discharging power of the EV is limited to a certain safe range, as represented by equation (5):

$$u_{i,t} * P_{\mathrm{i,min}} \leq |p_{i,t}| \leq u_t * P_{i,max} \qquad t = 1, 2, \cdots, T \tag{5}$$

where $P_{i,max}$ represents the maximum charging and discharging power that the EV battery can withstand, $P_{i,min}$ represents the minimum charging and discharging power limited by the control strategy for the EV.

5) User energy demand constraint

During the stay time of the EV user, it is necessary to meet the demand for charging capacity required for their own travel without exceeding the maximum capacity of their battery. The equation (6) is represented as follows:

$$C_i * SOC_{i,2} \leq C_i * SOC_{i,1} + \sum_{t=1}^{T} p_{i,t} u_t \eta \Delta t \leq C_i \tag{6}$$

where C_i represents the battery capacity of the i-th EV, $SOC_{i,1}$ represents the battery state of charge when user i arrives, $SOC_{i,2}$ represents the minimum required battery state of charge when user i leaves, η represents the charging and discharging efficiency of the EV, $Deltat$ represents the time interval of the regulation periods.

6) Battery SOC limitation constraint

During the stay time of the EV user, to prevent the situation where the discharge energy of the EV exceeds its remaining energy during the regulation process, a corresponding physical constraint is added. The equation (7) is represented as follows:

$$0 \leq C_i * SOC_{i,1} + \sum_{t=1}^{T_k} p_{i,t} u_{i,t} \eta \Delta t \qquad T_k = 1, 2, \cdots, T \tag{7}$$

where η represents the energy conversion efficiency of the charging and discharging process of EVs.

7) Maximum load penalty term

Considering the situation of high load rate on the distribution transformer, in order to ensure the safe operation of the power grid and reduce the aging of the transformer due to overload, a maximum load penalty term is introduced to minimize the maximum load during the regulation period. The formulas are given as equation (8) and equation (9):

$$L_{max} \geq \left(\frac{L_t - \eta_2 {}^{\star} S_T}{S_T}\right) \qquad t = 1, 2, \cdots, T \tag{8}$$

$$L_{max} \geq 0 \tag{9}$$

where η_2 represents the percentage constraint penalty term for the maximum load constraint during EV regulation period, L_{max} represents the maximum load during the regulation period.

8)Energy loss term

To avoid ineffective charging and discharging regulation under the rolling horizon optimization strategy for EVs, the energy loss generated during the charging and discharging process is included in the objective function. The equation (10) is represented as follows:

$$P_i^{loss} = \sum_{t=1}^{T} p_{i,t}(1 - \eta) \tag{10}$$

The overall rolling-horizon optimization process is illustrated in Fig. 3. This strategy solves the charging and discharging power of controllable EVs in different time periods based on the users' own demand information and corresponding transformer constraints. If the calculated charging and discharging strategy fails to meet the constraint requirements, all connected EVs will be re-planned and resolved. In case the constraints still cannot be satisfied after resolving all EVs, new arrivals of uncontrollable EVs will be rejected to ensure the safe operation of the distribution transformer.

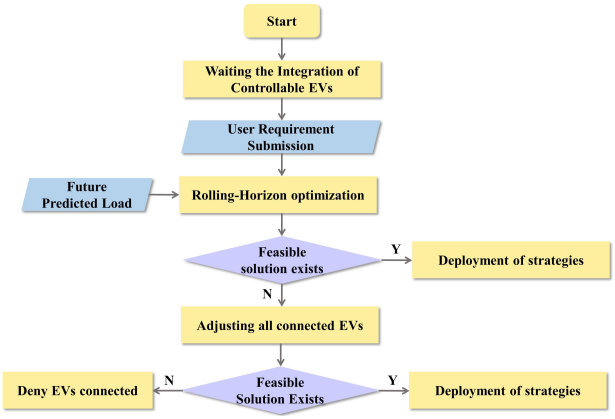

Fig. 3: Real-time rolling-horizon optimization strategy flow chart

4 Case Study

4.1 Data Preparation

The relevant scenario parameters of the industrial park selected in this paper are shown in Table 1. According to the literature [21], the travel patterns of EV users can be approximated as a normal distribution. It is assumed that the arrival time of EV users at the industrial park follows a normal distribution with a mean of 8 and a standard deviation of 1, limited to between 7:00 am and 9:00 am. At the same time, it is assumed that the departure time of EV users from the industrial park follows a normal distribution with a mean of 18 and a standard deviation of 1, limited to between 5:00 pm and 7:00 pm. To simulate the initial charging state of EVs, we set their charge state to follow a normal distribution with a mean of 0.4 and a standard deviation of 0.12, limited to between 0.1 and 0.6. In addition, we set the battery capacity of the EV to 42kWh, and its maximum charging and discharging power to 7kW. The parameters set can be seen in Table 2.

Table 1: Parameterization of the Selected Scenario

Parameter	Value	Parameter	Value
Transformer capacity	800 kVA	Time resolution	15min
EVs num	80	Maximum Load Penalty	1000

Table 2: EV Parameter Setting

Parameter	Distribution	Boundary
Arrival time	$N(8, 1^2)$	7-9
Departure time	$N(18, 1^2)$	17-19
Arrival SOC	$N(0.4, 0.1^2)$	0.1-0.6
Departure SOC	0.9	/
Battery capacity	$C = 42kWh$	/
Maximum charge and discharge power	$P = 7kW$	/
Charge efficiency	$\eta_1 = 0.95$	/

The industrial park data used in this study was obtained from a real industrial area located in Shanghai, China. The load data for one day was selected as the baseline load, which does not include the uncontrollable load of EVs.

Based on the parameter settings in Table 1 and Table 2, we conducted a simulation of the EVs under uncoordinated charging. The results are shown in Fig. 4. The EV load overlaid on top of the baseline load far exceeded the capacity of the distribution transformer. Long-term overloading can accelerate the aging and damage of internal components of the transformer, shorten its service life, and seriously affect the power supply quality.

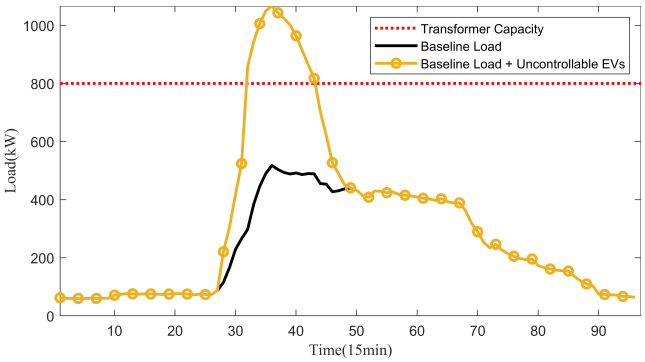

Fig. 4: Load profile graph after uncontrolled integration of EVs

Based on the generated EV behavior data, we selected 25% of the EVs as our controlled EVs. These EVs were regulated using the rolling-horizon optimization strategy. The results of this regulation are illustrated in Fig. 5. Through the application of the rolling-horizon optimization strategy, the excessive load that was originally beyond the capacity of the distribution transformer has been shifted to other time periods. This ensures the safe operation of the substation transformer while simultaneously meeting the self-charging needs of the participating V2G users.

When 50% of the EVs are selected as controlled EVs and participate in V2G regulation, the results, as shown in Fig. 6, demonstrate the effectiveness of the rolling-horizon optimization strategy in minimizing the overall load curve well below the rated capacity of the distribution transformer. This indicates that by regulating the charging and discharging behavior of EVs, it is possible to significantly reduce peak loads and ensure the safe operation of the distribution

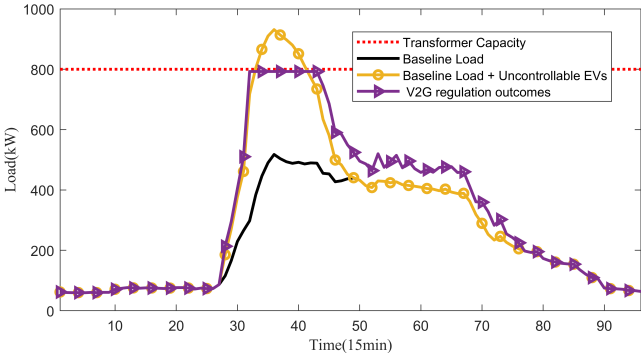

Fig. 5: Load profile graph after the integration of 25% controllable EVs

transformer. Furthermore, this regulation strategy also satisfies the self-charging requirements of V2G participants, thereby achieving load balancing and resource optimization objectives.

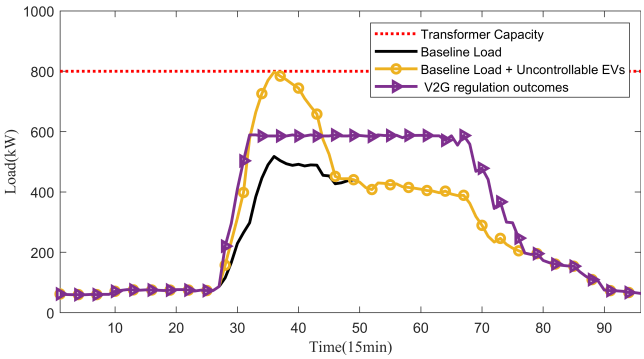

Fig. 6: Load profile graph after the integration of 50% controllable EVs

If all the EVs connected are controllable, the simulation results through the rolling-horizon optimization strategy are shown in Fig. 7. Although the simulation results appear similar to those obtained in Fig. 6, which involved 50% of the controlled EVs participating in the V2G program, the behavior of individual EVs is completely different. When all EVs participate in the V2G program, one of the target functions is to minimize losses. Therefore, EVs tend to discharge less and engage in more orderly charging regulation.

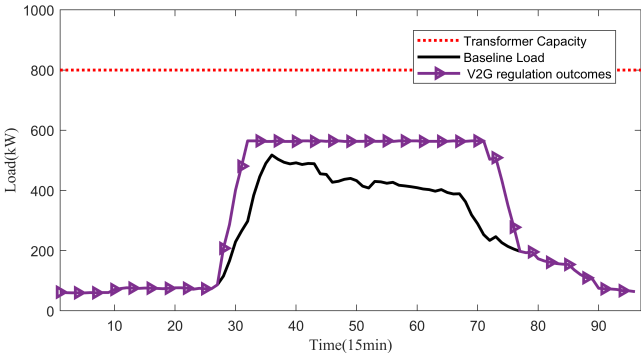

Fig. 7: Load profile graph after the integration of 100% controllable EVs

The load conditions under different percentages of controllable EVs are shown in Table 3. The research findings indicate that as the number of controllable EVs participating in the V2G program increases, the effectiveness of load

management in the distribution area also improves gradually. Experimental data reveals that as the number of controllable EVs increases, the peak load of the transformer gradually decreases, demonstrating the effectiveness of the rolling-horizon optimization strategy in optimizing and regulating the load of the power system. Therefore, in future power system planning, it is important to consider promoting and utilizing controllable EVs to further enhance the sustainability and economic benefits of the power system.

Table 3: EV Parameter Setting

Controllable EVs Ratio	Peak(kW)	Transformer Capacity Ratio
0%	1066.7	133.3%
25%	792.6	99.1%
50%	589.1	73.6%
100%	564.7	70.6%

5 Conclusion

This paper proposes a rolling-horizon optimization method utilizing V2G resources to reduce peak loads on distribution transformers. The paper first distinguishes between uncontrolled EVs with unordered charging and controllable EVs participating in V2G, defining their respective characteristics. Furthermore, considering the constraints of user demands for controllable EVs, vehicle electrical characteristics, and substation transformer capacity, an optimization model is proposed with the objective function of minimizing charging and discharging losses while incorporating a penalty term for maximum load. Real-time control is achieved through the rolling-horizon optimization approach at each EV's arrival to obtain the optimal solution for the current time period. Through simulation experiments, the effectiveness of this method in addressing the issue of overloaded distribution transformers under uncontrolled EV charging is validated, resulting in a lower overall load level.

References

[1] Yongxian Zhu, Steve Skerlos, Ming Xu, and Daniel R. Cooper. Reducing greenhouse gas emissions from U.S. light-duty transport in line with the 2 °c target. *Environmental Science and Technology*, 2021.

[2] Wenyi Du, Juan Ma, and Wanjun Yin. Orderly charging strategy of electric vehicle based on improved PSO algorithm. *Energy*, 271:127088, 2023.

[3] C. Pang, P. Dutta, and M. Kezunovic. BEVs/PHEVs as dispersed energy storage for v2b uses in the smart grid. *IEEE Transactions on Smart Grid*, 3(1):473–482, 2012.

[4] Radu Godina, Eduardo M.G. Rodrigues, João C.O. Matias, and João P.S. Catalão. Smart electric vehicle charging scheduler for overloading prevention of an industry client power distribution transformer. *Applied Energy*, 178:29–42, 2016.

[5] Cong Zhang, Jeffery B. Greenblatt, Pamela Macdougall, Samveg Saxena, and Aditya Jayam Prabhakar. Quantifying the benefits of electric vehicles on the future electricity grid in the midwestern united states. *Applied Energy*, 270, 2020.

[6] Joachim Geske and Diana Schumann. Willing to participate in vehicle-to-grid (V2G)? why not! *Energy Policy*, 120(SEP.):392–401, 2018.

[7] Zhuowei Luo, Zechun Hu, Yonghua Song, Zhiwei Xu, and Haiyan Lu. Optimal coordination of plug-in electric vehicles in power grids with cost-benefit analysis—part ii: A case study in china. *IEEE Transactions on Power Systems*, 28(4):3556–3565, 2013.

[8] Heyang Yu, Chuanzi Xu, Weifeng Wang, Guangchao Geng, and Quanyuan Jiang. Communication-free distributed charging control for electric vehicle group. *IEEE Transactions on Smart Grid*, pages 1–1, 2023.

[9] Peiman Mirhoseini and Navid Ghaffarzadeh. Economic battery sizing and power dispatch in a grid-connected charging station using convex method. *The Journal of Energy Storage*, 31:101651, 2020.

[10] Mohammed Shurrab, Shakti Singh, Hadi Otrok, Rabeb Mizouni, Vinod Khadkikar, and Hatem Zeineldin. A stable matching game for v2v energy sharing–a user satisfaction framework. *IEEE Transactions on Intelligent Transportation Systems*, 23(7):7601–7613, 2022.

[11] Arjun Visakh and Manickavasagam Parvathy Selvan. Analysis and mitigation of the impact of electric vehicle charging on service disruption of distribution transformers. *Sustainable Energy, Grids and Networks*, 35:101096, 2023.

[12] Jianping Li, Heyang Yu, Yingning Huo, Chuanzi Xu, Xinyu Xiang, and Guangchao Geng. Coordinated charging of electric vehicle group using smart meters. *2023 IEEE Industrial and Commercial Power System Asia*, pages 1148–1153, 2023.

[13] Yongpeng Shen, Ting He, Dongqi Liu, Yaohua Tang, and Yanfeng Wang. e-cny vehicle-to-grid real-time settlement system. *IEEE Journal of Emerging and Selected Topics in Industrial Electronics*, pages 1–10, 2023.

[14] Vivek Bhandari, Kaiyang Sun, and Frances Homans. The profitability of vehicle to grid for system participants - a case study from the electricity reliability council of texas. *Energy*, 153(JUN.15):278–286, 2018.

[15] Harun Turker and Seddik Bacha. Optimal minimization of plug-in electric vehicle charging cost with vehicle-to-home and vehicle-to-grid concepts. *IEEE Transactions on Vehicular Technology*, 2018.

[16] David B. Richardson. Encouraging vehicle-to-grid (V2G) participation through premium tariff rates. *Journal of Power Sources*, 243(dec.1):219–224, 2013.

[17] Zirui Jia and Liyuan Chen. Design of a bidirectional power interface for V2G technology with smaller dc-link capacitance. *International Journal of Smart Grid and Clean Energy*, (1), 2014.

[18] Yao Sun, Weixia Liu, Mei Su, Xing Li, Hui Wang, and Jian Yang. A unified modeling and control of a multi-functional current source-typed converter for V2G application. *Electric Power Systems Research*, 106:12–20, 2014.

[19] Ching-Ming Lai, Yu-Huei Cheng, Ming-Hua Hsieh, and Yuan-Chih Lin. Development of a bidirectional dc/dc converter with dual-battery energy storage for hybrid electric vehicle system. *IEEE Transactions on Vehicular Technology*, 67(2):1036–1052, 2018.

[20] Analysis and mitigation of the impact of electric vehicle charging on service disruption of distribution transformers. *Sustainable Energy, Grids and Networks*, 35:101096, 2023.

[21] John Brady and Margaret O'Mahony. Modelling charging profiles of electric vehicles based on real-world electric vehicle charging data. *Sustainable Cities and Society*, 26:203–216, 2016.

Proceedings of the 3rd Conference on Fully Actuated System Theory and Applications
May 10-12, 2024, Shenzhen, China

A Learning Controller for Periodic Disturbance Rejection of Uncertain Nonholonomic Systems

Li Liu[1], Yan Zhao[2], Jiangbo Yu[2], Chunxiao Wang[2], Xiao Yu[2]

1. School of Information and Electrical Engineering, Shandong Jianzhu University, Jinan 250101, P. R. China

2. School of Science, Shandong Jianzhu University, Jinan 250101, P. R. China

E-mail: zhaoyan@sdjzu.edu.cn

Abstract: A learning control approach is developed to tackle the robust stabilization problem for a class of chained-form nonholonomic systems with dynamic uncertainty and nonlinear parameterization. Different from the existing results, the additive periodic perturbations are allowed in the input channel, and a learning-based feedforward term is incorporated into the composite controller against unknown periodic dynamics with a known period. Moreover, a switching adaptive control strategy is constructed to get around the smooth stabilization burden associated with the nonholonomic systems due to Brockett's necessary condition. Numerical simulation results are presented to illustrate the performance of the proposed algorithm.

Key Words: Nonholonomic systems, Input-to-state stable (ISS), Iterative learning control (ILC), Periodic disturbance , Dynamic uncertainty

1 Introduction

The term "nonholonomic" originated in modern analytical mechanics. As described in [1], many plants are subject to the so-called nonholonomic (non-integrable) constrained in practical engineering applications, such as wheeled mobile robots [2] and vertical rolling unicycle cars [3]. Compared with traditional nonlinear systems, the existence of nonholonomic constraints limits the direct application of classical nonlinear methods, which makes the control theory research of nonholonomic systems more challenging. However, due to Brockett's condition [4], non-holonomic systems, although controllable, cannot be stabilized through a series of smooth continuous state feedbacks. This makes the stability control of such nonlinear systems an interesting and challenging area in the field of nonlinear control [5].

In almost all engineering control systems, the presence of disturbances, model uncertainties and nonlinear model parts are inevitable, which could influence system performance and lead to instability. Exogenous periodic disturbances commonly occur in repetitive robot tasks. For example, many industrial applications require robots to perform repetitious tasks (e.g., assembly, manipulation, inspection). When there is input disturbance, the control design of the system usually needs to make some compensation. Iterative learning control (ILC) is a powerful tool to deal with the periodic perturbations in [6] and [7]. The learning methods are proposed for periodic perturbations with known periods and unknown periods (see [8]). In [9], Ham et al. used a Lyapunov-based technique to study an ILC combined with a robust control design to achieve globally consistent final bounded link position tracking of a robot operator.

In this paper, we propose a repetitive learning controller for chained-form nonholonomic systems with exogenous periodic disturbances that satisfy the matching condition. The main work of this paper is as follows: (i) There are cascaded dynamic uncertainties and additional disturbances in the system, iterative learning control is used to compensate the additive periodic disturbances in the adaptive stability control framework of nonholonomic systems. (ii) This paper discusses the use of small gain conditions and parameter separation techniques to describe the growth of nonlinear drift. The proposed stability control scheme improves the existing results of robust stabilization of uncertain nonholonomic systems with external perturbations.

This work is supported in part by the National Natural Science Foundation of China under Grants 62076150, 62133008 and 62303280, in part by the National Natural Science Foundation of Shandong Province under Grants ZR2021MF009 and ZR2023MF055, in part by the Development Plan of Youth Innovation Team of University in Shandong Province under Grant 2021KJ067, in part by the Taishan Scholar Project of Shandong Province under Grant TSQN201812092.

2 Problem Formulation

In this paper, we study the global adaptive stabilizing control problem for the following class of nonholonomic uncertain systems:

$$\begin{cases} \dot{\eta} &= q(\eta, x, \theta) \\ \dot{x}_0 &= d_0(t)u_0 + \phi_0^d(u_0, x_0, \eta, \theta) \\ \dot{x}_i &= d_i(t)x_{i+1}u_0 + \phi_i^d(u_0, x_0, x, \eta, \theta) \\ \dot{x}_n &= d_n(t)\left(u + d(t)\right) + \phi_n^d(u_0, x_0, x, \eta, \theta) \end{cases} \tag{1}$$

where u_0, u are control inputs, $(x_0, x^{\mathrm{T}})^{\mathrm{T}} \in \mathcal{R}^{1+n}$ indicates the measurement status, $\eta \in \mathcal{R}^r$ is the remaining part of the unmeasurable state, representing the unmeasurable dynamic uncertainty. Moreover, $\theta \in \mathcal{R}^{n_\theta}$ is an unknown constant vector, and the functions $d_i(\cdot)$ and $\phi_i^d(\cdot)(i = 0, 1, \cdots, n)$ represent the virtual control factor and inputs and states driven uncertainties, respectively. Suppose $\phi_i^d(\cdot)(i = 0, 1, \cdots, n)$ and $q(\cdot)$ are unknown Lipschitz continuous functions that disappear at the origin.

The objective in this paper is to find, if possible, a partial state feedback control law of the following form

$$u_0 = \mu_0(x_0, x, \widehat{\theta}),\ u = \mu(x_0, x, \widehat{\theta}),\ \dot{\widehat{\theta}} = \nu(x_0, x, \widehat{\theta}), \tag{2}$$

such that not only $\big(\eta(t), x_0(t), x(t)\big)$ converge to zero as $t \to \infty$, and moreover, all signals in closed-loop system are bounded. Throughout the paper, the following assumptions are needed for the system (1):

(A1) For the η-subsystem in (1), there is an ISS-Lyapunov function $U_0(\eta)$ satisfying

$$\underline{\alpha}_\eta(\|\eta\|) \le U_0(\eta) \le \overline{\alpha}_\eta(\|\eta\|), \tag{3}$$

$$\frac{\partial U_0}{\partial \eta}\, q(\eta, x, \theta) \le -\alpha_0(\|\eta\|) + \sigma_0\gamma_0(|x_1|), \tag{4}$$

where $\underline{\alpha}_\eta(\cdot), \overline{\alpha}_\eta(\cdot), \alpha_0(\cdot), \gamma_0(\cdot) \in \mathcal{K}_\infty$, σ_0 is an unknown positive constant.

(A2) For each $i = 0, 1, \cdots, n$, there exist two known positive constants $c_{i1} > 0$ and $c_{i2} > 0$, satisfies

$$c_{i1} \le d_i(t) \le c_{i2}. \tag{5}$$

(A3) There exist known non-negative smooth functions $\varphi_0(\cdot)$, $\varphi_{ij}(\cdot)$ and $\psi_i(\cdot)$, with $\varphi_{ij}(0) = 0$ and $\psi_i(0, \cdots, 0) = 0$, $i = 0, 1, \cdots, n$, satisfies

$$\begin{aligned} |\phi_0^d(u_0, x_0, \eta, \theta)| &\le \theta_0|x_0|\varphi_0(x_0), \qquad (6)\\ |\phi_i^d(u_0, x_0, x, \eta, \theta)| &\le \theta_i \sum_{j=1}^{i} |x_j|\varphi_{ij}(\eta) \\ &\quad +\theta_i\psi_i(x_1, \cdots, x_i). \qquad (7) \end{aligned}$$

where $i = 1, \cdots, n$.

(A4) For the functions $\gamma_0(\cdot)$ and $\varphi_{ij}(\cdot)$ from **(A1)** and **(A3)**, the following local small-gain condition holds

$$\limsup_{s\to 0^+} \frac{\gamma_0(s)}{s^2} < +\infty, \tag{8}$$

$$\limsup_{s\to 0^+} \frac{\varphi_{ij}^2(s)}{\alpha_0(s)} < +\infty, \tag{9}$$

where $j = 1, \cdots, i$; $i = 1, \cdots, n$.

(A5) The additive disturbance $d(t)$ satisfies $|d(t)| \le \mu$, where $\mu > 0$ is unknown positive constant.

The following lemma is used for the control design.

Lemma 1[10]: For any $x, y \in \mathcal{R}$, there holds

$$2\,xy \le \frac{1}{\lambda}x^2 + \lambda y^2, \tag{10}$$

where $\lambda > 0$ is a constant.

3 Learning-based controller design and switching strategy

The design process is summarized in two separate phases. In the first stage, we design the control law u_0 to stabilize the x_0-subsystem. The second stage and then select control u so that the rest of the state converges to zero.

For convenience, we let the initial time be $t_0 = 0$, and we first consider the condition that $x_0(0) \neq 0$. In this case, the controller u_0 takes the following form

$$u_0 = x_0\beta_0(x_0, \widehat{\theta}_0),\ \dot{\widehat{\theta}}_0 = x_0^2\varphi_0(x_0), \tag{11}$$

where $\widehat{\theta}_0$ be the estimate of θ_0, $\beta_0(x_0, \widehat{\theta}_0) = -\sqrt{\lambda_0^2 + \varphi_0^2(x_0)\widehat{\theta}_0^2} - \lambda_0\varphi_0(x_0)\widehat{\theta}_0$, and $\lambda_0 > 0$ is to satisfy the design parameters $\lambda_0\, c_{01} > 1$.

Lemma 2: Assume that the control signal u_0 (11) is applied into the x_0-subsystem in (1). If $x_0(0) \neq 0$, the state $x_0(t)$ asymptotically converges to zero as t approaches infinity, but never reaches zero.

Proof: Substituting (11) into x_0-subsystem in (1), yields

$$\begin{aligned} \dot{x}_0 = &-d_0(t)x_0\sqrt{\lambda_0^2 + \varphi_0^2(x_0)\widehat{\theta}_0^2} - d_0(t)\lambda_0 x_0\varphi_0(x_0)\widehat{\theta}_0 \\ &+\phi_0^d(u_0, x_0, \eta, \theta). \end{aligned} \tag{12}$$

Then, we select the Lyapunov function

$$V_0(x_0) = \frac{1}{2}x_0^2 + \frac{c_{01}\lambda_0}{2}\widetilde{\theta}_0^2, \tag{13}$$

where $\widetilde{\theta}_0 = \theta_0 - \widehat{\theta}_0$ is the estimate error. Differentiating (13) along system trajectories yields

$$\begin{aligned} \dot{V}_0(x_0) &\le -c_{01}\lambda_0 x_0^2 + c_{01}\lambda_0\widetilde{\theta}_0\big(x_0^2\varphi_0(x_0) - \dot{\widehat{\theta}}_0\big) \\ &= -c_{01}\lambda_0 x_0^2. \end{aligned} \tag{14}$$

Hence, when $x_0(t) \to 0$ as $t \to \infty$, in view of LaSalle's Theorem [11], we can establish that $x_0(t)$ and $\widehat{\theta}_0(t)$ are bounded.

In terms of $\phi_0^d(0, 0, 0, \theta) = 0$, then, there exists a smooth function $\phi_0(u_0, x_0, \eta, \theta)$ such that

$$\phi_0^d(u_0, x_0, \eta, \theta) = x_0\phi_0(u_0, x_0, \eta, \theta). \tag{15}$$

Furthermore, combining the control law (11), we get

$$\begin{aligned} \dot{x}_0 = -x_0\Big(&d_0(t)\sqrt{\lambda_0^2 + \varphi_0^2(x_0)\widehat{\theta}_0^2} + d_0(t)\lambda_0\varphi_0(x_0)\widehat{\theta}_0 \\ &-\phi_0(u_0, x_0, \eta, \theta)\Big). \end{aligned} \tag{16}$$

Since $x_0(t)$ and $\widehat{\theta}_0(t)$ are bounded, we obtain the solution of (16) satisfying

$$x_0(t) = x_0(0)e^{-\int_0^t \chi(\tau)\mathrm{d}\tau}, \tag{17}$$

where $\chi(\tau) = d_0(\tau)\sqrt{\lambda_0^2 + \varphi_0^2(x_0(\tau))\widehat{\theta}_0^2(\tau)} + d_0(\tau)\lambda_0\varphi_0(x_0(\tau))\widehat{\theta}_0(\tau) - \phi_0(u_0(\tau), x_0(\tau), \eta(\tau), \theta)$.

It is known from (17) that there are two possible cases for $x_0(t) = 0$, i.e., $x_0(0) = 0$ and $t = \infty$. The proof is hence established.

In order to avoid the uncontrollable situation of the system, the following coordinate changes are introduced

$$z_i = \frac{x_i}{u_0^{n-i}},\ i = 1, \cdots, n. \tag{18}$$

Under this transformation defined in (18), the x-subsystem is transformed into

$$\begin{cases} \dot{z}_i &= d_i(t)z_{i+1} + \bar{\phi}_i^d(u_0, x_0, z, \eta, \theta), \\ \dot{z}_n &= d_n(t)\,(u + d(t)) + \bar{\phi}_n^d(u_0, x_0, z, \eta, \theta), \end{cases} \tag{19}$$

where $\bar{\phi}_i^d(u_0, x_0, z, \eta, \theta) = \frac{\phi_i^d(\cdot)}{u_0^{n-i}} - (n-i)\frac{\partial u_0}{\partial x_0}\, d_0(t)z_i - (n-i)\frac{1}{u_0}\frac{\partial u_0}{\partial \widehat{\theta}_0}x_0^2\varphi_0(x_0)z_i - (n-i)\frac{1}{u_0}\frac{\partial u_0}{\partial x_0}\phi_0^d(\cdot)z_i$, $i = 1, \cdots, n$.

In order to deal with the nonlinearities $\bar{\phi}_i^d(\cdot)(i = 1, \cdots, n)$, we give the following **Propositions 1**-**2**, and their proofs can be found in [12].

Proposition 1: For each $\bar{\phi}_i^d(u_0, x_0, z, \eta, \theta)(i = 1, \cdots, n)$, there holds

$$\begin{aligned} |\bar{\phi}_i^d(u_0, x_0, z, \eta, \theta)| \le\ &\theta^*\Big(\sum_{j=1}^{i}|z_j||u_0|^{i-j}\big(\varphi_{ij}(\eta) \\ &+\psi_{ij}(x_{[i]})\big)\Big) + \omega_i(x_0, \widehat{\theta}_0)|z_i|. \end{aligned} \tag{20}$$

Proposition 2: Introduce another ISS-Lyapunov function

$$\overline{V}_0(\eta) = \int_0^{V_0(\eta)} \rho(s)\mathrm{d}s$$

such that

$$\begin{aligned}\dot{\overline{V}}_0(\eta) \leq\ & -(1-\varepsilon)\rho\circ\underline{\alpha}_\eta(\|\eta\|)\alpha_0(\|\eta\|) \\ & +\sigma\xi_1^2\widehat{\gamma}_0(u_0,\xi_1),\end{aligned} \tag{21}$$

where $\rho(\cdot)$ is a smooth, non-decreasing function, $\widehat{\gamma}_0(\cdot)$ is a smooth nonnegative function, σ is an unknown positive constant, and ε satisfying $\varepsilon \in (0,1)$ is a positive constant.

Next, we use a recursive approach to describe the controller design process.

Step 1: Let α_1 be the first virtual control law, the error is $\xi_2 = z_2 - \alpha_1$, and denote $\xi_1 = z_1$. Then, we choose

$$V_1(\xi_1) = \overline{V}_0(\eta) + \frac{1}{2}\xi_1^2. \tag{22}$$

Differentiating (22) along system trajectories yields

$$\begin{aligned}\dot{V}_1 \leq\ & -(1-\varepsilon)\rho\circ\underline{\alpha}_\eta(\|\eta\|)\alpha_0(\|\eta\|) + \sigma\xi_1^2\widehat{\gamma}_0(u_0,\xi_1) \\ & +d_1(t)\xi_1\alpha_1 + \xi_1\bar{\phi}_1^d(\cdot) + d_1(t)\xi_1\xi_2.\end{aligned} \tag{23}$$

According to **Proposition 1** and **Lemma 1**, we can get

$$\begin{aligned}\xi_1\bar{\phi}_1^d(\cdot) \leq\ & \xi_1^2\psi_{11}(x_1)\theta^* + \xi_1^2\omega_1(x_0,\widehat{\theta}_0) + \frac{1}{4}\xi_1^4\theta^{*2} \\ & +\varphi_{11}^2(\eta).\end{aligned} \tag{24}$$

Denote

$$\Theta = \max\{\frac{1}{4}\theta^{*2}, \theta^*, \sigma, \theta_0^2\}, \tag{25}$$

and

$$\varrho_{11}(x_0,x_1) = \xi_1^2 + \psi_{11}(x_1), \tag{26}$$

we further get

$$\begin{aligned}|\xi_1||\bar{\phi}_1^d(\cdot)| \leq\ & \varphi_{11}^2(\eta) + \xi_1^2\varrho_{11}(x_0,x_1)\Theta \\ & +\xi_1^2\omega_1(x_0,\widehat{\theta}_0).\end{aligned} \tag{27}$$

Define the smooth function as follows

$$\begin{aligned}\varrho_{11}(x_0,\xi_1,\widehat{\theta}_0) &= \xi_1^2 + \psi_{11}(x_1) + \widehat{\gamma}_0(u_0,\xi_1), \\ \varrho_{12}(x_0,\widehat{\theta}_0) &= \omega_1(x_0,\widehat{\theta}_0),\end{aligned} \tag{28}$$

then, we get

$$\begin{aligned}\dot{V}_1 \leq\ & -(1-\varepsilon)\rho\circ\underline{\alpha}_\eta(\|\eta\|)\alpha_0(\|\eta\|) + d_1(t)\xi_1\xi_2 \\ & +d_1(t)\xi_1\alpha_1 + \varphi_{11}^2(\eta) + \xi_1^2\varrho_{11}(x_0,\xi_1,\widehat{\theta}_0)\Theta \\ & +\xi_1^2\varrho_{12}(x_0,\xi_1)\,.\end{aligned} \tag{29}$$

We introduce $\widehat{\Theta}(\cdot)$ to estimate Θ, and $\widetilde{\Theta}(\cdot) = \Theta - \widehat{\Theta}(\cdot)$ is the estimation error. Then, we augment the function (22) with $\widetilde{\Theta}^2$ in the form of

$$\overline{V}_1(\xi_1) = V_1 + \frac{1}{2}\widetilde{\Theta}^2. \tag{30}$$

After some simple calculations, we have

$$\begin{aligned}\dot{\overline{V}}_1 \leq\ & -(1-\varepsilon)\rho\circ\underline{\alpha}_\eta(\|\eta\|)\alpha_0(\|\eta\|) + d_1(t)\xi_1\xi_2 \\ & +d_1(t)\xi_1\alpha_1 + \varphi_{11}^2(\eta) + \xi_1^2\varrho_{11}(x_0,\xi_1,\widehat{\theta}_0)\widehat{\Theta} \\ & +\xi_1^2\varrho_{12}(x_0,\xi_1) + \widetilde{\Theta}(\xi_1^2\varrho_{11}(\cdot) - \dot{\widehat{\Theta}}).\end{aligned} \tag{31}$$

We choose the virtual control input α_1 as follows

$$\begin{aligned}\alpha_1(x_0,\widehat{\theta}_0,\widehat{\Theta},z_1) =\ & -\lambda_1\xi_1 - \frac{1}{c_{11}}\xi_1\varrho_{11}(x_0,\widehat{\theta}_0,z_1)\widehat{\Theta} \\ & -\frac{1}{c_{11}}\xi_1\varrho_{12}(x_0,\xi_1),\end{aligned} \tag{32}$$

and

$$\tau_1 = \xi_1^2\varrho_{11}(x_0,\widehat{\theta}_0,z_1), \tag{33}$$

where $\lambda_1 > 0$ is a design parameter determined later. A direct substitution leads to

$$\begin{aligned}\dot{\overline{V}}_1 \leq\ & -(1-\varepsilon)\rho\circ\underline{\alpha}_\eta(\|\eta\|)\alpha_0(\|\eta\|) + \varphi_{11}^2(\eta) \\ & -c_{11}\lambda_1\xi_1^2 + d_1(t)\xi_1\xi_2 + \widetilde{\Theta}(\tau_1 - \dot{\widehat{\Theta}}).\end{aligned} \tag{34}$$

Step i $(2 \leq i \leq n-1)$: In **Step** i, we denote $\xi_{i+1} = z_{i+1} - \alpha_i$, where α_i is the virtual control input, $i = 2,\cdots,n-1$. In this step, we provide a **Proposition 3**, which can be verified using a recursive manner, and its proof is omitted due to the space limits.

Proposition 3: For each $i = 2,\cdots,n-1$, there exist smooth functions α_i and τ_i in the form of

$$\begin{aligned}\alpha_i =\ & -\lambda_i\,\xi_i - \frac{1}{c_{i1}}\xi_i\varrho_{i1}(x_0,\widehat{\theta}_0,\widehat{\Theta},z_{[i]})\widehat{\Theta} \\ & -\frac{1}{c_{i1}}\xi_i\varrho_{i2}(x_0,\widehat{\theta}_0,\widehat{\Theta},z_{[i]}),\end{aligned} \tag{35}$$

$$\tau_i = \tau_{i-1} + \xi_i^2\varrho_{i1}(x_0,\widehat{\theta}_0,\widehat{\Theta},z_{[i]}) \tag{36}$$

with the design parameter $\lambda_i > 0$ and smooth nonnegative functions $\varrho_{i1}(x_0,\widehat{\theta}_0,\widehat{\Theta},z_{[i]})$, $\varrho_{i2}(x_0,\widehat{\theta}_0,\widehat{\Theta},z_{[i]})$, such that the time-derivative of Lyapunov function candidate

$$V_i = V_{i-1} + \frac{1}{2}\xi_i^2 \tag{37}$$

satisfies

$$\begin{aligned}\dot{V}_i \leq\ & -(1-\varepsilon)\rho\circ\underline{\alpha}_\eta(\|\eta\|)\alpha_0(\|\eta\|) \\ & -\sum_{j=1}^{i}\big(\lambda_j c_{j1} - (i-j)\big)\xi_j^2 \\ & +\sum_{j=1}^{i}\sum_{k=1}^{j}(i+1-j)\varphi_{jk}^2(\eta) + d_i(t)\xi_i\xi_{i+1} \\ & +\big(\widetilde{\Theta} + \sum_{j=2}^{i}\xi_j\frac{\partial\alpha_{j-1}}{\partial\widehat{\Theta}}\big)\big(\tau_i - \dot{\widehat{\Theta}}\big).\end{aligned} \tag{38}$$

Step n: In this step, we deal with the exogenous periodic disturbance. To this end, we choose Lyapunov function

$$\begin{aligned}V_n =\ & V_{n-1} + \frac{1}{2}\xi_n^2 + \frac{1}{2}\int_{t-T}^{t}\Big(\mathbf{sat}_\mu\big(d(s)\big) \\ & -\mathbf{sat}_\mu\big(\hat{d}(s)\big)\Big)^2\mathrm{d}s.\end{aligned} \tag{39}$$

where $\hat{d}(t) \in \mathcal{R}$ is a disturbance estimate that is updated according to the following iterative learning law

$$\hat{d}(t) = \begin{cases} 0, & t < 0, \\ \mathbf{sat}_\mu\big(\hat{d}(t-T)\big) + \xi_n, & t \geq 0, \end{cases} \tag{40}$$

and function $\mathbf{sat}_\mu(\cdot) \in \mathcal{R}$ is defined as

$$\mathbf{sat}_\mu(s) = \begin{cases} s, & |s| \le \mu, \\ \mu\,\mathrm{sign(s)}, & |s| \ge \mu, \end{cases} \tag{41}$$

and μ was defined in **(A5)**.

After some simple and direct calculations, the time-derivative of V_n is given

$$\begin{aligned} \dot{V}_n \le\ & -(1-\epsilon)\rho \circ \underline{\alpha}_\eta(\|\eta\|)\alpha_0(\|\eta\|) \\ & -\sum_{j=1}^{n-1}\big(\lambda_j c_{j1} - (n-j)\big)\xi_j^2 \\ & +\sum_{j=1}^{n}\sum_{k=1}^{j}(n+1-j)\varphi_{jk}^2(\eta) \\ & +\xi_n d_n(t)(u+\hat{d}(t)) + \xi_n^2\varrho_{n1}(x_0,\widehat{\theta}_0,\widehat{\Theta},z_{[n]})\widehat{\Theta} \\ & +\xi_i^2\varrho_{i2}(x_0,\widehat{\theta}_0,\widehat{\Theta},z_{[i]}) - \frac{1}{2}\xi_n^2 \\ & +\big(\widetilde{\Theta} + \sum_{j=2}^{i}\xi_j\frac{\partial\alpha_{j-1}}{\partial\widehat{\Theta}}\big)\big(\tau_i - \dot{\widehat{\Theta}}\big). \end{aligned} \tag{42}$$

As a result, we choose the the control law u in the form of

$$\begin{aligned} u =\ & -\lambda_n\,\xi_n - \frac{1}{c_{n1}}\xi_n\varrho_{n1}(x_0,\widehat{\theta}_0,\widehat{\Theta},z)\widehat{\Theta} \\ & -\frac{1}{c_{n1}}\xi_n\varrho_{n2}(x_0,\widehat{\theta}_0,\widehat{\Theta},z) - \hat{d}(t) \end{aligned} \tag{43}$$

$$\dot{\widehat{\Theta}} = \tau_n = \sum_{i=1}^{n}\xi_i^2\varrho_{i1}(x_0,\widehat{\theta}_0,\widehat{\Theta},z_{[i]}), \tag{44}$$

then, we gain

$$\begin{aligned} \dot{V}_n \le\ & -(1-\epsilon)\rho \circ \underline{\alpha}_\eta(\|\eta\|)\alpha_0(\|\eta\|) \\ & -\sum_{j=1}^{n}\big(\lambda_j c_{j1} - (n-j)\big)\xi_j^2 \\ & +\sum_{j=1}^{n}\sum_{k=1}^{j}(n+1-j)\varphi_{jk}^2(\eta) - \frac{1}{2}\xi_n^2. \end{aligned} \tag{45}$$

This completes the control design when $x_0(0) \neq 0$.

While $x_0(0) = 0$, we use the following switching control strategy. To this end, we consider the adaptive control law

$$u_0 = x_0\beta_0(x_0,\widehat{\theta}_0) + \bar{u}_0,\ \dot{\widehat{\theta}}_0 = x_0^2\varphi_0(x_0), \tag{46}$$

where $\beta_0(x_0,\widehat{\theta}_0)$ and $\widehat{\theta}_0$ are designed in (11), and $\bar{u}_0 > 0$ is a constant.

Select the Lyapunov function in (13), by means of the adaptive control law in (46), it can be verified that the time derivative satisfies

$$\dot{V}_0 \le -\lambda_0 x_0^2 + \bar{u}_0 x_0. \tag{47}$$

Then, we can conclude that x_0 and $\widehat{\theta}_0$ are bounded since $\lambda_0 > 0$ and $\bar{u}_0$ is a constant.

Additionally, we know from the following equation

$$\dot{x}_0 = d_0(t)\beta(x_0,\widehat{\theta}_0)x_0 + x_0\phi_0(u_0,x_0,\eta,\theta) + \bar{u}_0 \tag{48}$$

that the solution is

$$\begin{aligned} x_0(t) =\ & x_0(0)e^{-\int_0^t\chi(\tau)\mathrm{d}\tau} \\ & +\bar{u}_0 e^{-\int_0^t\chi(\tau)\mathrm{d}\tau}\int_0^t e^{\int_0^\tau\chi(s)\mathrm{ds}}\mathrm{d}\tau. \end{aligned} \tag{49}$$

Therefore, x_0 is known not to escape in finite time, and for any $t^* > 0$, $x_0(t^*) \neq 0$. Thus, the input state scaling of the control design can be resorted, and the control inputs u_0 and u are switched into to (11) and (43), respectively.

4 MAIN RESULTS

In this section, we analyze the behavior of the uncertain nonholonomic systems.

Theorem 1: If **Assumptions 1-4** are true, then the state-feedback laws (11) and (43) with a switching control strategy are used so that all signals in a nonholonomic system are bounded at $[0,\infty)$, and

$$\lim_{t\to\infty}\Big(|\eta(t)| + |x_0(t)| + |x(t)| + |\xi(t)|\Big) = 0. \tag{50}$$

Proof: Using **Lemma 2** and the local conditions (9), the expected function ρ satisfies the following formulathe

$$\frac{1-\varepsilon}{2}\rho \circ \underline{\alpha}_\eta(\|\eta\|)\alpha_0(\|\eta\|) \ge \sum_{j=1}^{n}\sum_{k=1}^{j}(n+1-j)\varphi_{jk}^2(\eta). \tag{51}$$

Choose the constants $(\lambda_1,\cdots,\lambda_n)$ satisfies

$$\lambda_j c_{j1} - n + j \ \ge\ 1,\ j = 1,\cdots,n. \tag{52}$$

Then, we can obtain that

$$\dot{V}_n \le -\sum_{j=1}^{n}\xi_j^2 - \frac{1-\varepsilon}{2}\rho \circ \underline{\alpha}_\eta(\|\eta\|)\alpha_0(\|\eta\|) - \frac{1}{2}\xi_n^2, \tag{53}$$

which implies that all signals in the closed-loop system are bounded. It follows that the closed-loop system has a unique solution that is defined for all $t > 0$, thus $T_f = \infty$. In addition, according to LaSalle's Theorem [11], it can be obtained that as t approaches infinity, the signals $\big(\eta(t), x_0(t), \xi(t)\big)$ converge to zero. In view of ξ_i and α_i in (35), we know that the variables $z_i(t)(i = 1,\cdots,n)$ are bounded, and using a recursive way, we can further prove that $z_i(t)(i = 1,\cdots,n)$ asymptotically converges to zero. Then, it can be obtained

$$\lim_{t\to\infty}\xi_i(t) = 0,\ i = 1,\cdots,n. \tag{54}$$

Furthermore, we from $x_i = z_i\,u_0^{n-i}\,(i = 1,\cdots,n)$ in (18) that

$$\lim_{t\to\infty}x_i(t) = 0,\ i = 1,\cdots,n. \tag{55}$$

This shows that the property (50) holds true.

5 SIMULATION

In this section, we will illustrate the presented control scheme using numerical simulation. Consider the system

$$\begin{cases} \dot{\eta} &= -k\,\eta + \sigma x_1,\ k > 0, \\ \dot{x}_0 &= u_0 + x_0, \\ \dot{x}_1 &= x_2 u_0 + \eta\,x_1^2, \\ \dot{x}_2 &= u + \sin(2\pi t), \end{cases} \tag{56}$$

where $\sigma > 0$ is an unknown constant, and $d(t) = \sin(2\pi t)$ denotes the periodic disturbance.

Using the control scheme proposed in **Section 3**, we can design the learning controller as follows. When $x_0(0) \neq 0$, we take

$$\begin{aligned} u &= -\lambda_2\xi_2 - \hat{d}(t) - \xi_2\varrho_{21}(x_0, \widehat{\Theta}, z)\widehat{\Theta} \\ &\quad -\xi_2\varrho_{22}(x_0, \widehat{\Theta}, z), \qquad (57) \\ \dot{\widehat{\Theta}} &= \xi_1^2\varrho_{11}(x_0, \widehat{\Theta}, z_{[1]}) + \xi_2^2\varrho_{21}(x_0, \widehat{\Theta}, z_{[2]}), \quad (58) \end{aligned}$$

with $z_1 = \frac{x_1}{u_0}$, $z_2 = x_2$, $\xi_1 = z_1$, $\xi_2 = z_2 - \alpha_1$, $\alpha_1 = -\lambda_1\xi_1 - \xi_1^2\widehat{\Theta} - \xi_1^2$, $\varrho_{21}(\cdot) = \frac{1}{4}\left(\frac{\partial\alpha_1}{\partial z_1}\right)^2\left(1 + x_1^2 + z_1^2\right)$, $\varrho_{22}(\cdot) = \frac{1}{4}\left(\frac{\partial\alpha_1}{\partial\widehat{\Theta}}\right)^2\xi_1^4 + \frac{1}{4}\xi_2^2\left(\frac{\partial\alpha_1}{\partial\widehat{\Theta}}\right)^2\varrho_{21}^2(\cdot)$, and

$$\hat{d}(t) = \begin{cases} 0, & t < 0, \\ \mathbf{sat}_\mu\left(\hat{d}(t-T)\right) + \xi_2, & t \geq 0. \end{cases} \qquad (59)$$

The simulations are performed by MATLAB with the following initial conditions: $\eta(0) = 0, x_0(0) = 1, x_1(0) = 1, x_2(0) = 0.5, \hat{\Theta}(0) = 0.5$, system parameters: $\sigma = 1$, and design parameters: $\lambda_1 = 2$, $\lambda_2 = 1$. Fig.1 shows that the closed-loop responses by use of the proposed methodology in the paper.

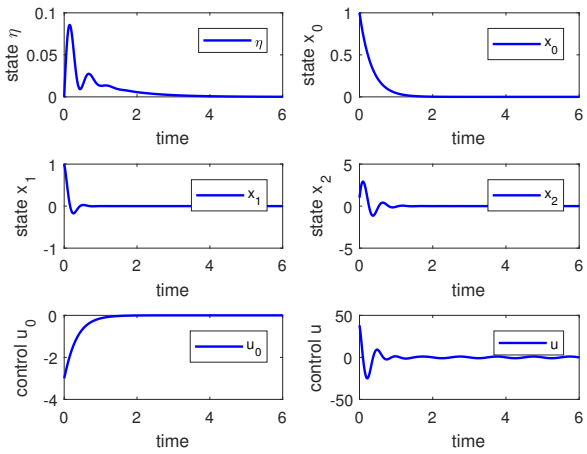

Fig.1 The responses in closed-loop system (56)-(58)

6 CONCLUSION

In this paper, we study the global robust stabilization problem for a class of nonholonomic systems with ISS dynamic uncertainties and non-zero periodic perturbations in the input channels. The iterative learning control is used to compensate the periodic disturbance, and the changing supply rate technique is used to deal with the unmeasured state. A switching adaptive control strategy is proposed to overcome the smooth stabilization burden associated with the nonholonomic systems. Finally, a numerical example is given to illustrate the performance of the proposed control method.

References

[1] R.M. Murray and S. Sastry, Nonholonomic motion planning: steering using sinusoids. *IEEE Transactions on Automatic Control*, 1993, 38(5): 700–716.

[2] Y.C. Chang and B.S. Chen, Robust tracking designs for both holonomic and nonholonomic constrained mechanical systems: adaptive fuzzy approach[J]. *IEEE Transactions on Fuzzy Systems*, 2000, 8(1): 46–66.

[3] M.M. Carlos, P.J. Javier, A.D. Adrian, and C.H. César, Velocity and position tracking controllers for wheeled mobile robots. *IFAC-PapersOnLine*, 2023, 56(2): 2158–2163.

[4] R.W. Brockett, Asymptotic stability and feedback stabilization. *Differential Geometric Control Theory*, 1983, 27(1): 181-191.

[5] A. Astolfi, Discontinuous control of nonholonomic systems. *Systems & Control Letters*, 1996, 27(1): 37–45.

[6] M. Sun and D. Wang, Sampled-data iterative learning control for non-linear systems with arbitrary relative degree. *Automatica*, 2001, 37(2): 283–289.

[7] D. Wang, On D-type and P-type ILC designs and anticipatory approach. *International Journal of Control*, 2000, 23(10): 890–901.

[8] Y.C. Man and Y.G. Liu, Global adaptive stabilisation for nonlinear systems with unknown control directions and input disturbance. *International Journal of Control*, 2016, 89(5): 1038–1046.

[9] C. Ham, Z. Qu, and R. Johnson, A nonlinear iterative learning control for robot manipulators in the presence ofactuator dynamics. *International Journal of Control, Automation, and Systems*, 2000, 15(3): 107–119.

[10] G. Hardy, J. Littlewood, G. Pólya, *Inequalities*, 2nd edition. Cambridge University Press, 1988.

[11] M. Krstić, I. Kanellakopoulos, P.V. Kokotović, *Nonlinear and Adaptive Control Design*. New York: Wiley, 1995.

[12] Y. Zhao and J.B. Yu, Adaptive output feedback stabilising control of uncertain chained-form non-holonomic systems. *International Journal of Control*, 2022, 95(11): 3070–3083.

Proceedings of the 3rd Conference on Fully Actuated System Theory and Applications
May 10-12, 2024, Shenzhen, China

Adaptive Fixed-time Fault-tolerant Control of Nonstrict-Feedback Nonlinear Systems

Jing Wu[1], Lantao Xing[1]
1. School of Control Science and Engineering, Shandong University, Jinan, 250000, P. R. China
E-mail: wujing1180@126.com, lantao.xing@sdu.edu.cn

Abstract: In this paper, a fixed-time fault-tolerant tracking control method for nonstrict-feedback nonlinear systems is proposed. Firstly, fuzzy logic systems are employed to approximate unknown nonlinear functions and handle nonstrict-feedback structures. Additionally, the command filter technique is utilized to address the issue of "complexity explosion". Furthermore, a novel adaptive estimation law is developed to effectively compensate for actuator faults. It is proved that the proposed fixed-time control method ensures a known and independent upper bound of dwell time and the boundedness of all signals in the closed-loop system can be ensured. Finally, a simulation example is presented to demonstrate the effectiveness of the proposed control method.

Key Words: Fixed-time Control, Fault-tolerant Control, Nonstrict-feedback Nonlinear System, Command Filter.

1 Introduction

In recent years, there has been significant attention devoted to the control of nonlinear systems. Compared to linear systems, the structure of nonlinear systems is more intricate, posing great challenges in controller design. Therefore, it is imperative in-depth research on designing effective control schemes for nonlinear systems [1–3]. In response to such issues, a range of nonlinear control algorithms have been proposed, including fuzzy control [4], sliding mode control [5] and adaptive backstepping control [6].

The study of nonstrict-feedback nonlinear systems is extensive due to their ability to describe a wide range of practical systems, such as electromechanical systems [7], aircraft systems [8]. Notably, the standard backstepping technique is not applicable to nonstrict-feedback nonlinear systems. Fortunately, Tong *et al.* [9] successfully addressed the tracking control problem of single-input single-output nonstrict-feedback nonlinear systems by leveraging the unique property of fuzzy logic systems (FLSs). Building upon this foundation, numerous adaptive backstepping control strategies have been developed for nonlinear systems with nonstrict-feedback structures, as evidenced in [10–12] and related references.

The above-mentioned references should be noted as being considered under ideal conditions. However, in practice scenarios, the actuator is susceptible to malfunctions due to various disturbing factors. In order to mitigate the adverse effects of actuator faults, fault-tolerant control has been emerged [13–16]. For instance, a solution for adaptive fault-tolerant control of nonlinear multiagent systems with intermittent actuator faults is presented in [15]. In [16], a robust output feedback fault-tolerant control of a Lipschitz nonlinear system is developed.

In addition, the rapid advancement of industry has resulted in increasingly stringent demands for system stability. Finite-time stabilization was proposed by S P Bhat *et al.* in [17], and since then, finite-time control has garnered significant attention due to its appealing transient performance and tracking capabilities. However, in the case of finite-time control, the upper bound of dwell time is often influenced by the initial state of the system [18–20]. To overcome this limitation, Polyakov *et al.* further introduced fixed-time stabilization in [21], where the upper bound of dwell time is no longer dependent on the initial state. Subsequently, numerous scholars have conducted research on fixed-time control of nonlinear systems [22–25].

Motivated by the aforementioned discussions, this study focuses on addressing the fixed-time fault-tolerant control problem of nonstrict-feedback nonlinear systems. The main contributions are outlined as follows:

(1) The system considered in this paper adopts a nonstrict-feedback form, which is effectively managed by the inherent properties of FLSs. Additionally, the utilization of command filter prevents repeated derivation of virtual controllers, while compensatory signals containing redundant terms are incorporated into nonlinear functions for approximation.

(2) The issue of actuator faults is properly resolved by introducing a novel adaptive parameter to define the lower bound of multiplicative fault. This incorporation results in the utilization of two adaptive laws throughout the entire control design process, thereby alleviating computational burden.

The remaining sections of the paper are structured as follows: Section II presents the system model and provides preliminary information. Section III introduces a fixed-time fault-tolerant control method, encompassing controller design and stability analysis of the closed-loop system. Section IV presents simulation result, while conclusions are drawn in Section V.

2 Problem Statement and Preliminaries

2.1 Problem Statement

In this paper, the following nonstrict-feedback nonlinear system is considered

$$\begin{cases} \dot{\xi}_i(t) = \xi_{i+1}(t) + F_i(\bar{\xi}(t)) + \Lambda_i(t), \\ \qquad i = 1, \cdots, n-1, \\ \dot{\xi}_n(t) = u_a(t) + F_n(\bar{\xi}(t)) + \Lambda_n(t), \\ y(t) = \xi_1(t), \end{cases} \tag{1}$$

This work was supported in part by the National Natural Science Foundation of China (Grant Number: 62203270, 20221017-10, 62188101), in part by the National Natural Science Foundation of Shandong Province (Grant Number: ZR2022MF227).

where $\bar{\xi}(t) = [\xi_1, \cdots, \xi_n]^T \in R^n$ stands for the state vector. $y(t)$ denotes the system output. $F_i(\bar{\xi})$ is an unknown continuous function. $\Lambda_i(t)$ represents bounded time-varying interference with an upper bound Λ_i^*. $u_a(t)$ is the control input that suffers actuator fault, and the fault model is given as [26]

$$u_a = \varpi(t, t_\varpi)u_s + \sigma(t, t_\sigma), \tag{2}$$

where u_s is the control input signal that is actually designed. $\varpi(t, t_\varpi) \in (0, 1]$ and $\sigma(t, t_\sigma)$ are multiplicative and additive faults, respectively. Correspondingly, t_ϖ and t_σ represent the instants when the multiplicative and additive faults happen.

The control goal is to construct an adaptive fault-tolerant controller such that the system output y can track the given signal y^* in a fixed time. In addition, all signals of the closed-loop system are bounded. To achieve this goal, two reasonable assumptions are provided.

Assumption 1. The reference trajectory $y^*(t)$ and its first order derivative $\dot{y}^*(t)$ are bounded.

Assumption 2. There exist unknown constant lower bound $\underline{\varpi}$ and upper bound σ^* such that $0 < \underline{\varpi} < \varpi \leq 1$ and $|\sigma(t, t_\sigma)| \leq \sigma^*$.

2.2 Preliminaries

1) Fixed-time control

The present section introduces a crucial definition and several indispensable lemmas.

Definition 1. [24] The origin of the system

$$\dot{x} = f(t, x),\ x(0) = x_0 \tag{3}$$

is practically fixed-time stable if it is finite-time stable and the setting time T is bounded, i.e., $\exists\ T_{\max}$, such that $T \leq T_{\max}$.

Lemma 1. [24] If a positive definite and radially unbounded function $U(x) : R^n \to R$ such that $U(x) = 0 \Rightarrow x = 0$ and

$$\dot{U}(x) \leq -\lambda_1 U^{p_1}(x) - \lambda_2 U^{p_2}(x) + \Delta, \tag{4}$$

where $\lambda_1 > 0$, $\lambda_2 > 0$, $p_1 > 1$ and $0 < p_2 < 1$, then system (3) is practical fixed-time stable. Moreover, it holds that

$$x \in \Big\{U(x) \leq \min\Big\{\Big(\frac{\Delta}{(1-\pi)\lambda_1}\Big)^{\frac{1}{p_1}}, \Big(\frac{\Delta}{(1-\pi)\lambda_2}\Big)^{\frac{1}{p_2}}\Big\}\Big\},$$

and the settling time $T \leq T_{\max} = \frac{1}{\lambda_1\pi(p_1-1)} + \frac{1}{\lambda_2\pi(1-p_2)}$ with $0 < \pi < 1$.

2) Fuzzy logic systems

The utilization of FLSs in subsequent control design is introduced for the purpose of approximating unknown nonlinear functions.

IF-THEN Rules: R^i: If ζ_1 is $\mathcal{F}_1^i$ and $\cdots$ and ζ_n is $\mathcal{F}_n^i$, then Υ is $\Gamma^i,\ i = 1, \cdots, n$.

The following expression about FLS is given

$$\Upsilon(\zeta) = \frac{\sum\limits_{i=1}^{N} s_i \prod\limits_{j=1}^{n} \varphi_{\mathcal{F}_j^i}(\zeta_j)}{\sum\limits_{i=1}^{N}[\prod\limits_{j=1}^{n} \varphi_{\mathcal{F}_j^i}(\zeta_j)]},$$

with $s_i = \max\limits_{\Upsilon \in R} \varphi_{\mathcal{F}_j^i}(\zeta_j)$. Denote $S = [s_1, \cdots, s_n]^T$, $\Psi(\zeta) = [\phi_1(\zeta), \cdots, \phi_n(\zeta)]^T$, $\phi_i(\zeta) = \frac{\prod\limits_{j=1}^{n} \varphi_{\mathcal{F}_j^i}(\zeta_j)}{\sum\limits_{i=1}^{N}[\prod\limits_{j=1}^{n} \varphi_{\mathcal{F}_j^i}(\zeta_j)]}$, then one has

$$\Upsilon(\zeta) = S^T\Psi(\zeta).$$

Lemma 2. [10] Let $\Upsilon(\zeta)$ be a continuous function defined on the compact set Ω, there exists a FLS $S^T\Psi(\zeta)$ such that

$$\sup_{\zeta \in \Omega} |\Upsilon(\zeta) - S^T\Psi(\zeta)| \leq \check{\varepsilon}$$

with $\check{\varepsilon} > 0$ being a constant.

Lemma 3. [24] For $o_i \in R$, if $0 < q \leq 1$, the following inequalities hold

$$\Big(\sum_{i=1}^{n} |o_i|\Big)^q \leq \sum_{i=1}^{n} |o_i|^q,$$
$$\Big(\sum_{i=1}^{n} |o_i|\Big)^2 \leq n\sum_{i=1}^{n} |o_i|^2. \tag{5}$$

3 Fixed-time Fault-tolerant Control Scheme

The first step involves defining the subsequent transformation

$$\begin{cases} \varsigma_1 = \xi_1 - y^*, \\ \varsigma_i = \xi_i - \bar{\beta}_i,\ i = 2, \cdots, n, \end{cases} \tag{6}$$

the output of the first-order command filter $\tau_i\dot{\bar{\beta}}_i + \bar{\beta}_i = \beta_i$, denoted as $\bar{\beta}_i$, serves as the input for the virtual controller β_i. Here, τ_i represents a parameter and $\bar{\beta}_i(0) = \beta_i(0)$ denotes its initial value. Subsequently, the compensating signals $\varrho_i,\ (i = 1, \cdots, n)$ are designed as

$$\begin{cases} \dot{\varrho}_1 = -\ell_1\varrho_1^3 + \varrho_2 + \bar{\beta}_2 - \beta_2 - l_1\text{sgn}(\varrho_1), \\ \dot{\varrho}_i = -\ell_i\varrho_i^3 - \varrho_{i-1} + \varrho_{i+1} + \bar{\beta}_{i+1} - \beta_{i+1} \\ \qquad - l_i\text{sgn}(\varrho_i), \\ \dot{\varrho}_n = -\ell_n\varrho_n^3 - \varrho_{n-1} - l_n\text{sgn}(\varrho_n), \end{cases} \tag{7}$$

where $\varrho_i(0) = 0$, ℓ_i and l_i are positive constants. Next, the compensated tracking errors χ_i are given as

$$\chi_i = \varsigma_i - \varrho_i,\ i = 1, \cdots, n. \tag{8}$$

Taking advantage of backstepping technique, the virtual controllers and actual controller are constructed as

$$\begin{cases} \beta_2 = -\Big(W_{11}(\frac{1}{2})^{\frac{3}{4}}\Xi_1(\chi_1) + \frac{W_{12}}{4}\chi_1^3 + \frac{\chi_1}{2} \\ \qquad + \frac{\chi_1\hat{\eta}}{2a_1^2\Psi_1^T(\bar{X}_1)\Psi_1(\bar{X}_1)}\Big), \\ \beta_{i+1} = -\Big(W_{i1}(\frac{1}{2})^{\frac{3}{4}}\Xi_i(\chi_i) + \frac{W_{i2}}{4}\chi_i^3 + \varsigma_{i-1} \\ \qquad + \frac{\chi_i}{2} + \frac{\chi_i\hat{\eta}}{2a_i^2\Psi_i^T(\bar{X}_i)\Psi_i(\bar{X}_i)}\Big), \\ \qquad i = 2, \cdots, n-2, \\ \beta_n = W_{n1}(\frac{1}{2})^{\frac{3}{4}}\Xi_n(\chi_n) + \frac{W_{n2}}{4}\chi_n^3 + \varsigma_{n-1} \\ \qquad + \frac{\chi_n}{2} + \frac{\chi_n\hat{\eta}}{2a_n^2\Psi_n^T(\bar{X}_n)\Psi_n(\bar{X}_n)}, \\ u_s = -\frac{\chi_n\hat{\kappa}^2\beta_n^2}{\sqrt{\chi_n^2\hat{\kappa}^2\beta_n^2 + \epsilon^2}}, \end{cases} \tag{9}$$

where W_{i1}, W_{i2}, a_i, ϵ are positive parameters, and $\Xi_i(\chi_i)$ is a piecewise function. If $\chi_i \geq 0$, $\Xi_i(\chi_i) = \sqrt{\chi_i}$; otherwise

$\Xi_i(\chi_i) = -\sqrt{|\chi_i|}$. Define a constant $\eta = \max\{\|S_i\|^2, i = 1, \cdots, n\}$ with $\tilde{\eta} = \hat{\eta} - \eta$, where $\hat{\eta}$ is the estimate of η. From $0 < \underline{\varpi} < \varpi$, we further define the unknown parameter $\kappa = \frac{1}{\underline{\varpi}}$. Moreover, adaptive laws $\dot{\hat{\eta}}$ and $\dot{\hat{\kappa}}$ are constructed as

$$\begin{cases} \dot{\hat{\eta}} = \sum\limits_{i=1}^{n} \frac{r_1 \chi_i^2}{2a_i^2 \Psi_i^T(\bar{X}_i)\Psi_i(\bar{X}_i)} - b_1\hat{\eta} - \frac{b_2}{r_1}\hat{\eta}^3, \\ \dot{\hat{\kappa}} = r_2\chi_n\beta_n - b_3\hat{\kappa} - \frac{b_4}{r_2}\hat{\kappa}^3 \end{cases} \tag{10}$$

with $r_1, r_2, b_1, b_2, b_3, b_4$ being known positive constants.

3.1 Control Design

Step 1: From (1) and (6), $\dot{\varsigma}_1$ is rewritten as $\dot{\varsigma}_1 = \varsigma_2 + \bar{\beta}_2 + F_1 + \Lambda_1 - \dot{y}^*$. Then, the combination of (7) yields

$$\dot{\chi}_1 = \varsigma_2 + \beta_2 + F_1 + \Lambda_1 - \dot{y}^* - \varrho_2 + l_1 \text{sgn}(\varrho_1) + \ell_1 \varrho_1^3.$$

Let $U_1 = \frac{1}{2}\chi_1^2 + \frac{1}{2r_1}\tilde{\eta}^2$, its derivative is

$$\begin{aligned} \dot{U}_1 \le{}& \chi_1\beta_2 + \chi_1\bar{F}_1 + \ell_1\chi_1(\varrho_1^3 - \varsigma_1^3) + 3\ell_1\chi_1\varrho_1\varsigma_1^2 \\ & - \chi_1\dot{y}^* - 3\ell_1\chi_1\varrho_1^2\varsigma_1 + \frac{l_1^2 + \Lambda_1^{*2}}{2} + \frac{\chi_1^2\varrho_1^2}{2} \\ & + \ell_1\chi_1^4 + \chi_1\chi_2 + \frac{\tilde{\eta}\dot{\hat{\eta}}}{r_1}, \end{aligned}$$

where $\bar{F}_1(X_1) = F_1 + \frac{\chi_1\varrho_1^2}{2} + \ell_1\varsigma_1^3 - \dot{y}^* - 3\ell_1\varrho_1\varsigma_1^2 + 3\ell_1\varrho_1^2\varsigma_1 - \ell_1\chi_1^3 + \frac{\chi_1}{2}$ denotes the unknown term and $X_1 = [\xi^T, y^*, \dot{y}^*, \varrho_1]^T$, which can be approached by FLSs, i.e., $\bar{F}_1(X_1) = S_1^T\Psi_1(X_1) + \delta_1(X_1)$ and $|\delta_1(X_1)| \le \bar{\delta}_1$ with $\bar{\delta}_1$ being the upper bound.

Applying the property $0 < \Psi_1^T(\cdot)\Psi_1(\cdot) \le 1$ of FLSs, the following inequality is valid

$$\begin{aligned} & \chi_1(S_1^T\Psi_1(X_1) + \delta_1(X_1)) \\ \le{}& \frac{\chi_1^2\eta\Psi_1^T(X_1)\Psi_1(X_1)}{2a_1^2} + \frac{a_1^2}{2} + \frac{\chi_1^2}{2} + \frac{\bar{\delta}_1^2}{2} \\ \le{}& \frac{\chi_1^2\eta}{2a_1^2\Psi_1^T(\bar{X}_1)\Psi_1(\bar{X}_1)} + \frac{a_1^2}{2} + \frac{\chi_1^2}{2} + \frac{\bar{\delta}_1^2}{2}, \end{aligned} \tag{11}$$

where $\bar{X}_1 = [\xi_1, y^*, \dot{y}^*, \varrho_1]^T$.

It is worth noting that $\ell_1\chi_1\varrho_1^3 - \ell_1\chi_1\varsigma_1^3 + 3\ell_1\chi_1\varrho_1\varsigma_1^2 - 3\ell_1\chi_1\varrho_1^2\varsigma_1 + \ell_1\chi_1^4 = \chi_1(\ell_1\varrho_1^3 - \ell_1\varsigma_1^3 + 3\ell_1\varrho_1\varsigma_1^2 - 3\ell_1\varrho_1^2\varsigma_1) + \ell_1\chi_1^4 = \ell_1\chi_1(\varrho_1 - \varsigma_1)^3 + \ell_1\chi_1^4 = -\ell_1\chi_1^4 + \ell_1\chi_1^4 = 0$, then the term $\ell_1\chi_1^3$ can be handled. Taking (9) and (11) into $\dot{U}_1$, one obtains

$$\begin{aligned} \dot{U}_1 \le{}& -W_{11}\Big(\frac{1}{2}\chi_1^2\Big)^{\frac{3}{4}} - W_{12}\Big(\frac{1}{2}\chi_1^2\Big)^2 + \chi_1\chi_2 + \Pi_1 \\ & + \frac{\tilde{\eta}}{r_1}\Big(\dot{\hat{\eta}} - \frac{r_1\chi_1^2}{2a_1^2\Psi_1^T(\bar{X}_1)\Psi_1(\bar{X}_1)}\Big), \end{aligned} \tag{12}$$

where $\Pi_1 = \frac{\Lambda_1^{*2}}{2} + \frac{a_1^2}{2} + \frac{\bar{\delta}_1^2}{2} + \frac{l_1^2}{2} > 0$ is a constant term.

Step i $(i = 2, \cdots, n-1)$**:** Taking (7) into $\dot{\chi}_i$, it is natural to obtain

$$\begin{aligned} \dot{\chi}_i = {}& \chi_{i+1} + F_i + \Lambda_i - \dot{\bar{\beta}}_i + \ell_i\varrho_i^3 + \beta_{i+1} \\ & + \varrho_{i-1} + l_i\text{sgn}(\varrho_i). \end{aligned}$$

Define $U_i = U_{i-1} + \frac{1}{2}\chi_i^2$, differentiating U_i with respect to time yields

$$\begin{aligned} \dot{U}_i \le{}& -\sum_{j=1}^{i-1} W_{j1}\Big(\frac{\chi_j^2}{2}\Big)^{\frac{3}{4}} - \sum_{j=1}^{i-1} W_{j2}\Big(\frac{\chi_j^2}{2}\Big)^2 - 3\ell_i\chi_i\varrho_i^2\varsigma_i \\ & + \frac{\tilde{\eta}}{r_1}\Big(\dot{\hat{\eta}} - \sum_{j=1}^{i-1}\frac{r_1\chi_j^2}{2a_j^2\Psi_j^T(\bar{X}_j)\Psi_j(\bar{X}_j)}\Big) + \chi_i\varsigma_{i-1} \\ & + \chi_i\bar{F}_i + \frac{\Lambda_i^{*2}}{2} + \ell_i\chi_i\varrho_i^3 + \chi_i\beta_{i+1} + \chi_i\chi_{i+1} \\ & + 3\ell_i\chi_i\varrho_i\varsigma_i^2 - \ell_i\chi_i\varsigma_i^3 + \frac{l_i^2}{2} + \ell_i\chi_i^4 + \Pi_{i-1}, \end{aligned}$$

where $\chi_i\varrho_{i-1} + \chi_{i-1}\chi_i = \chi_i(\varsigma_{i-1} - \chi_{i-1}) + \chi_{i-1}\chi_i = \chi_i\varsigma_{i-1}$, $\bar{F}_i(X_i) = F_i + \frac{\chi_i\varrho_i^2}{2} + \ell_i\varsigma_i^3 - \dot{\bar{\beta}}_i - 3\ell_i\varrho_i\varsigma_i^2 + 3\ell_i\varrho_i^2\varsigma_i - \ell_i\chi_i^3 + \frac{\chi_i}{2}$ represents the unknown function and $X_i = [\xi^T, y^*, \dot{y}^*, \varrho_1, \cdots, \varrho_i, \hat{\eta}]^T$. $S_i^T\Psi_i(X_i)$ can be utilized to approach the unknown term $\bar{F}_i$ and $|\delta_i(X_i)| \le \bar{\delta}_i$ with $\bar{\delta}_i$ being an error upper bound of $\delta_i(X_i)$. Similar to step 1, one has

$$\begin{aligned} & \chi_i S_i^T(X_i)\Psi_i(X_i) + \chi_i\delta_i(X_i) \\ \le{}& \frac{\eta\chi_i^2}{2a_i^2\Psi_i^T(\bar{X}_i)\Psi_i(\bar{X}_i)} + \frac{a_i^2}{2} + \frac{\chi_i^2}{2} + \frac{\bar{\delta}_i^2}{2}, \end{aligned} \tag{13}$$

where $\bar{X}_i = [{\xi_i}^T, y^*, \dot{y}^*, \varrho_1, \cdots, \varrho_i, \hat{\eta}]^T$. By calculation, one gets $\ell_i\chi_i\varrho_i^3 - \ell_i\chi_i\varsigma_i^3 + 3\ell_i\chi_i\varrho_i\varsigma_i^2 - 3\ell_i\chi_i\varrho_i^2\varsigma_i + \ell_i\chi_i^4 = \chi_i(\ell_i\varrho_i^3 - \ell_i\varsigma_i^3 + 3\ell_i\varrho_i\varsigma_i^2 - 3\ell_i\varrho_i^2\varsigma_i) + \ell_i\chi_i^4 = 0$. Considering (9) and (13) yields

$$\begin{aligned} \dot{U}_i \le{}& -\sum_{j=1}^{i} W_{j1}\Big(\frac{1}{2}\chi_j^2\Big)^{\frac{3}{4}} - \sum_{j=1}^{i} W_{j2}\Big(\frac{1}{2}\chi_j^2\Big)^2 + \chi_i\chi_{i+1} \\ & + \frac{\tilde{\eta}}{r_1}\Big(\dot{\hat{\eta}} - \sum_{j=1}^{i}\frac{r_1\chi_j^2}{2a_j^2\Psi_j^T(\bar{X}_j)\Psi_j(\bar{X}_j)}\Big) + \Pi_i \end{aligned}$$

with $\Pi_i = \Pi_{i-1} + \frac{a_i^2}{2} + \frac{l_i^2}{2} + \frac{\Lambda_i^{*2}}{2} + \frac{\bar{\delta}_i^2}{2}$.

Step n: As before, the time derivative of $\frac{1}{2}\chi_n^2$ is given as

$$\begin{aligned} \chi_n\dot{\chi}_n = {}& \chi_n(\varpi u_s + \sigma) + \chi_n F_n + \chi_n\Lambda_n - \chi_n\dot{\bar{\beta}}_n \\ & + \ell_n\chi_n\varrho_n^3 + \chi_n\varrho_{n-1} + l_n\chi_n\text{sgn}(\varrho_n). \end{aligned}$$

Define the Lyapunov function candidate as $U_n = U_{n-1} + \frac{1}{2}\chi_n^2 + \frac{\varpi}{2r_2}\tilde{\kappa}^2$, where $\hat{\kappa}$ is the estimate of κ with $\tilde{\kappa} = \hat{\kappa} - \kappa$. In conjunction with the previous step, there holds

$$\begin{aligned} \dot{U}_n \le{}& -\sum_{j=1}^{n-1} W_{j1}\Big(\frac{\chi_j^2}{2}\Big)^{\frac{3}{4}} - \sum_{j=1}^{n-1} W_{j2}\Big(\frac{\chi_j^2}{2}\Big)^2 + \chi_n\varpi u_s \\ & + \frac{\sigma^{*2}}{2} + \chi_n F_n + \chi_n^2 + \frac{\bar{\ell}_n^2}{2} - \chi_n\dot{\bar{\beta}}_n + \underline{\varpi}\frac{\tilde{\kappa}\dot{\hat{\kappa}}}{r_2} \\ & + \frac{\tilde{\eta}}{r_1}\Big(\dot{\hat{\eta}} - \sum_{j=1}^{n-1}\frac{r_1\chi_j^2}{2a_j^2\Psi_j^T(\bar{X}_j)\Psi_j(\bar{X}_j)}\Big) + \chi_{n-1}\chi_n \\ & + \ell_n\chi_n\varrho_n^3 + \frac{\chi_n^2\varrho_n^2}{2} + \frac{l_n^2}{2} + \Pi_{n-1} + \chi_n\varrho_{n-1}. \end{aligned}$$

Let $\bar{F}_n(X_n) = F_n + \frac{\chi_n\varrho_n^2}{2} + \ell_n\varsigma_n^3 - \dot{\bar{\beta}}_n - 3\ell_n\varrho_n\varsigma_n^2 + 3\ell_n\varrho_n^2\varsigma_n - \ell_n\chi_n^3 + \chi_n$, and $X_n = [\xi^T, y^*, \dot{y}^*, \varrho_1, \cdots, \varrho_n, \hat{\eta}]^T$. $\bar{F}_n$ can be utilized to approximate $S_n^T\Psi_n(X_n)$, and the below formula always holds

$$\begin{aligned} & \chi_n S_n^T(X_n)\Psi_n(X_n) + \chi_n\delta_n \\ \le{}& \frac{\eta\chi_n^2}{2a_n^2\Psi_n^T(\bar{X}_n)\Psi_n(\bar{X}_n)} + \frac{a_n^2}{2} + \frac{\chi_n^2}{2} + \frac{\bar{\delta}_n^2}{2}, \end{aligned} \tag{14}$$

where $\bar{X}_n = X_n$. Taking into account u_s in (9), $\chi_n \varpi u_s$ can be rewritten as

$$\begin{aligned}\chi_n \varpi u_s &\leq -\frac{\varpi \chi_n^2 \hat{\kappa}^2 \beta_n^2}{\sqrt{\chi_n^2 \hat{\kappa}^2 \beta_n^2 + \epsilon^2}} \\ &\leq \varpi \epsilon - \underline{\varpi} \chi_n \hat{\kappa} \beta_n.\end{aligned}$$

Consider $\dot{\hat{\kappa}}$ in (10), $\dot{U}_n$ has the following form

$$\begin{aligned}\dot{U}_n \leq & -\sum_{j=1}^{n-1} W_{j1} \Big(\frac{\chi_j^2}{2}\Big)^{\frac{3}{4}} - \sum_{j=1}^{n-1} W_{j2} \Big(\frac{\chi_j^2}{2}\Big)^2 - \frac{b_3}{r_2} \tilde{\kappa} \hat{\kappa} \\ & - \frac{b_4 \tilde{\kappa}}{r_2^2} \hat{\kappa}^3 + \frac{\Lambda_n^{*2}}{2} + \varsigma_{n-1} \chi_n + \Pi_{n-1} + \frac{\sigma^{*2}}{2} \\ & + \frac{\tilde{\eta}}{r_1} \Big(\dot{\hat{\eta}} - \sum_{j=1}^{n-1} \frac{r_1 \chi_j^2}{2 a_j^2 \Psi_j^T(\bar{X}_j) \Psi_j(\bar{X}_j)} \Big) + \varpi \epsilon \\ & + \frac{l_n^2}{2} + \chi_n \bar{F}_n - \chi_n \beta_n, \end{aligned} \tag{15}$$

where $-\chi_n \beta_n = -\underline{\varpi} \chi_n \hat{\kappa} \beta_n + \varpi \chi_n \tilde{\kappa} \beta_n$. Combining (9), (10), (14) and (15), one has

$$\begin{aligned}\dot{U}_n \leq & -\sum_{j=1}^{n} W_{j1} \Big(\frac{\chi_j^2}{2}\Big)^{\frac{3}{4}} - \sum_{j=1}^{n} W_{j2} \Big(\frac{\chi_j^2}{2}\Big)^2 - \frac{b_1}{r_1} \tilde{\eta} \hat{\eta} \\ & - \frac{b_2}{r_1^2} \tilde{\eta} \hat{\eta}^3 - \frac{b_3}{r_2} \tilde{\kappa} \hat{\kappa} - \frac{b_4}{r_2^2} \tilde{\kappa} \hat{\kappa}^3 + \Pi_n, \end{aligned} \tag{16}$$

where $\Pi_n = \Pi_{n-1} + \frac{\Lambda_n^{*2}}{2} + \frac{a_n^2}{2} + \frac{l_n^2}{2} + \frac{\bar{\delta}_n^2}{2} + \frac{\sigma^{*2}}{2}$ is a positive constant.

3.2 Stability Analysis

Theorem 1. The adaptive fault-tolerant controller designed in (9) ensures the boundedness of all signals in system (1), while achieving fixed-time stability for the output tracking error ς_1.

Proof. The processing of certain terms is necessary in order to reach fixed-time stability. Take $-\frac{b_1}{r_1} \tilde{\eta} \hat{\eta}$ in (16) for example, one can observe that

$$\begin{aligned}-\frac{b_1}{r_1} \tilde{\eta} \hat{\eta} &\leq -\frac{b_1}{2r_1} \tilde{\eta}^2 + \frac{b_1}{2r_1} \eta^2 \\ &\leq \hbar \Big(\frac{\tilde{\eta}^2}{2r_1}\Big)^{\frac{3}{4}} + \frac{b_1}{2r_1} \eta^2 + \frac{\hbar^4}{4b_1^3} \end{aligned} \tag{17}$$

with $\hbar > 0$ being a constant. The reason for obtaining the above inequality is that the term $-\frac{b_1}{2r_1} \tilde{\eta}^2$ satisfies the following formula

$$\begin{aligned}-\frac{b_1}{2r_1} \tilde{\eta}^2 &= -\frac{b_1}{4r_1} \tilde{\eta}^2 - \hbar \Big(\frac{\tilde{\eta}^2}{2r_1}\Big)^{\frac{3}{4}} + \frac{\hbar^2}{2\sqrt{2r_1 b_1}} |\tilde{\eta}| \\ &\quad - \frac{1}{4r_1} \Big(\sqrt{b_1} |\tilde{\eta}| - \hbar (2r_1)^{\frac{1}{4}} \sqrt{\frac{|\tilde{\eta}|}{b_1}} \Big)^2 \\ &\leq -\frac{b_1}{4r_1} \tilde{\eta}^2 - \hbar \Big(\frac{\tilde{\eta}^2}{2r_1}\Big)^{\frac{3}{4}} + \frac{b_1}{8r_1} \tilde{\eta}^2 + \frac{\hbar^4}{4b_1^3}. \end{aligned}$$

Similarly, it is easy to get $-\frac{b_3}{r_2} \tilde{\kappa} \hat{\kappa} \leq \hbar \Big(\frac{\tilde{\kappa}^2}{2r_2}\Big)^{\frac{3}{4}} + \frac{b_3}{2r_2} \kappa^2 + \frac{\hbar^4}{4b_3^3}$. The term $-\frac{b_2}{r_1^2} \tilde{\eta} \hat{\eta}^3$ can be rewritten as

$$-\frac{b_2}{r_1^2} \tilde{\eta} \hat{\eta}^3 = -\frac{b_2}{r_1^2} \tilde{\eta}^4 - \frac{3b_2}{r_1^2} \tilde{\eta}^3 \eta - \frac{3b_2}{r_1^2} \tilde{\eta}^2 \eta^2 - \frac{b_2}{r_1^2} \tilde{\eta} \eta^3. \tag{18}$$

Letting $\delta_1 = \frac{\tilde{\eta}^3}{\iota}$, $\delta_2 = \iota \eta$, $\theta_1 = \frac{4}{3}$, and $\theta_2 = 4$, one immediately has $\delta_1 \delta_2 \leq \frac{\delta_1^{\theta_1}}{\theta_1} + \frac{\delta_2^{\theta_2}}{\theta_2}$, i.e., $-\frac{3b_2}{r_1^2} \tilde{\eta}^3 \eta \leq \frac{9b_2}{4r_1^2 \iota^{\frac{4}{3}}} |\tilde{\eta}^3|^{\frac{4}{3}} + \frac{3b_2 \iota^4 \eta^4}{4r_1^2}$. In addition, $-\frac{b_2}{r_1^2} \tilde{\eta} \eta^3 \leq \frac{3b_2}{r_1^2} \tilde{\eta}^2 \eta^2 + \frac{b_2}{12r_1^2} \eta^4$ always holds. Thus, (18) becomes

$$\begin{aligned}-\frac{b_2}{r_1^2} \tilde{\eta} \hat{\eta}^3 \leq & -\frac{b_2}{r_1^2} \tilde{\eta}^4 + \frac{9b_2}{4r_1^2 \iota^{\frac{4}{3}}} |\tilde{\eta}^3|^{\frac{4}{3}} + \frac{b_2}{12r_1^2} \eta^4 \\ & + \frac{3b_2}{r_1^2} \tilde{\eta}^2 \eta^2 + \frac{3b_2 \iota^4 \eta^4}{4r_1^2}. \end{aligned} \tag{19}$$

Choose $\iota^{\frac{4}{3}} = 3$, (19) is changed to

$$-\frac{b_2}{r_1^2} \tilde{\eta} \hat{\eta}^3 \leq -b_2 \Big(\frac{\tilde{\eta}^2}{2r_1}\Big)^2 + \frac{61 b_2}{3r_1^2} \eta^4. \tag{20}$$

The identical computation yields

$$-\frac{b_4}{r_2^2} \tilde{\kappa} \hat{\kappa}^3 \leq -b_4 \Big(\frac{\tilde{\kappa}^2}{2r_2}\Big)^2 + \frac{61 b_4}{3r_2^2} \kappa^4. \tag{21}$$

The above deflations can be substituted into (16) to yield the following result

$$\begin{aligned}\dot{U}_n \leq & -\bar{\alpha}_1 \sum_{j=1}^{n} \Big(\frac{\chi_j^2}{2}\Big)^{\frac{3}{4}} - \bar{\alpha}_2 \sum_{j=1}^{n} \Big(\frac{\chi_j^2}{2}\Big)^2 - \hbar \Big(\frac{\tilde{\eta}^2}{2r_1}\Big)^{\frac{3}{4}} \\ & - \hbar \Big(\frac{\tilde{\kappa}^2}{2r_2}\Big)^{\frac{3}{4}} - b_2 \Big(\frac{\tilde{\eta}^2}{2r_1}\Big)^2 - b_4 \Big(\frac{\tilde{\kappa}^2}{2r_2}\Big)^2 + \bar{\Pi}_n, \end{aligned}$$

where $\bar{\alpha}_1 = \min\{W_{j1}\}$, $\bar{\alpha}_2 = \frac{1}{n} \min\{W_{j2}\}$ and $\bar{\Pi}_n = \Pi_n + \frac{61 b_2}{3r_1^2} \eta^4 + + \frac{61 b_4}{3r_2^2} \kappa^4 + \frac{\hbar^4}{4b_1^3} + + \frac{\hbar^4}{4b_3^3} + \frac{b_1}{2r_1} \eta^2 + \frac{b_3}{2r_2} \kappa^2$. Combining Lemma 3 comes to $-\sum_{j=1}^{n} \Big(\frac{\chi_j^2}{2}\Big)^{\frac{3}{4}} \leq -\Big(\sum_{j=1}^{n} \frac{\chi_j^2}{2}\Big)^{\frac{3}{4}}$ and $-\sum_{j=1}^{n} \Big(\frac{\chi_j^2}{2}\Big)^2 \leq -\Big(\sum_{j=1}^{n} \frac{\chi_j^2}{2}\Big)^2$, Then, $\dot{U}_n$ can be rewritten as

$$\dot{U}_n \leq -\nu_1 U_n^{\frac{3}{4}} - \nu_2 U_n^2 + \bar{\Pi}_n \tag{22}$$

with $\nu_1 = \min\{\bar{\alpha}_1, \hbar\}$ and $\nu_2 = \min\{\bar{\alpha}_2, b_2, b_4\}$. In a fixed time $T \leq T_{\max} = \frac{4}{\nu_1 \pi} + \frac{1}{\nu_2 \pi}$, it can be concluded that $|\chi_1| \leq \min\Big\{\sqrt{2\Big(\frac{\bar{\Pi}_n}{(1-\pi)\nu_2}\Big)^{\frac{1}{2}}}, \sqrt{2\Big(\frac{\bar{\Pi}_n}{(1-\pi)\nu_1}\Big)^{\frac{4}{3}}}\Big\}$. Then, the fixed-time convergence of χ_i can be obtained. Construct the following Lyapunov function

$$U_{n+1} = \sum_{i=1}^{n} \frac{1}{2} \varrho_i^2. \tag{23}$$

The derivative can be computed by combining (7)

$$\begin{aligned}\dot{U}_{n+1} &= -\sum_{i=1}^{n} \ell_i \varrho_i^4 + \sum_{i=2}^{n} \varrho_i (\bar{\beta}_i - \beta_i) - \sum_{i=1}^{n} l_i \varrho_i \mathrm{sgn}(\varrho_i) \\ &\leq -\sum_{i=1}^{n} \ell_i \varrho_i^4 + \sum_{i=2}^{n} |\varrho_i| |\bar{\beta}_i - \beta_i| - \sum_{i=1}^{n} l_i |\varrho_i|. \end{aligned}$$

By the aid of $|\bar{\beta}_i - \beta_i| \leq c_i$ with $c_i < l_i$ being a known constant, $\dot{U}_{n+1}$ can be shown as

$$\dot{U}_{n+1} \leq -\sum_{i=1}^{n} \ell_i \varrho_i^4 - \sum_{i=1}^{n} (l_i - c_i) |\varrho_i|$$

$$\leq -\bar{d}_1 U_{n+1}^2 - \bar{d}_2 U_{n+1}^{\frac{1}{2}}, \tag{24}$$

where $\bar{d}_1 = \min\{4\ell_i\}$, $\bar{d}_2 = \min\{\sqrt{2}(l_i - c_i)\}$ for $i = 1, \cdots, n$. Applying Lemma 1, the fixed-time convergence of ϱ_i can be certified. The stability of ς_i is guaranteed due to the relationship $\varsigma_i = \chi_i + \varrho_i$. When $U_n^2 > \frac{\bar{\Pi}_n}{\varsigma_2}$, it follows from $\dot{U}_n \leq -\varsigma_1 U_n^{\frac{3}{4}} - \varsigma_2 U_n^2 + \bar{\Pi}_n$ that $\dot{U}_n < 0$, which implies that U_n is bounded. Furthermore, the variables χ_i, $\hat{\eta}$ and $\tilde{\eta}$ are also bounded. Similarly, we can verify the boundedness of ϱ_i and ς_i. Consider the designed controllers, we establish the boundedness of β_i and u_s by combining Assumption 1, indicating that all signals remain within bounds.

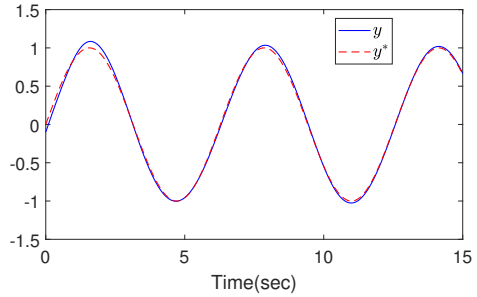

Fig. 1: System output y and tracking signal y^*

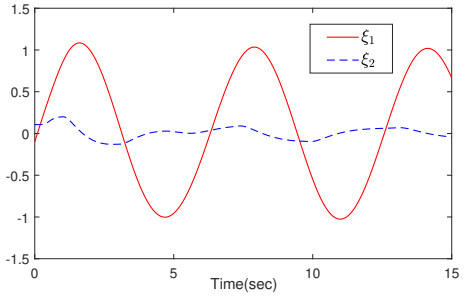

Fig. 2: System states ξ_1 and ξ_2

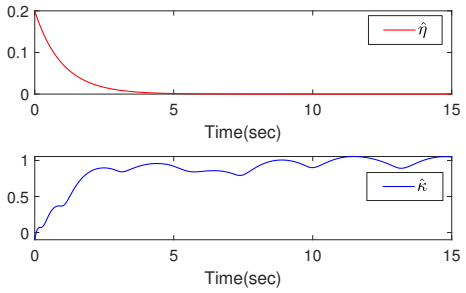

Fig. 3: Adaptive parameters $\hat{\eta}$ and $\hat{\kappa}$

4 Simulation Result

The above theoretical results are verified through a numerical example presented in this section. The system under consideration is a second-order nonstrict-feedback nonlinear system with actuator faults

$$\begin{cases} \dot{\xi}_1 = \xi_2 + F_1(\xi_1, \xi_2) + \Lambda_1(t), \\ \dot{\xi}_2 = u_a + F_2(\xi_1, \xi_2) + \Lambda_2(t), \\ y(t) = \xi_1(t), \end{cases} \tag{25}$$

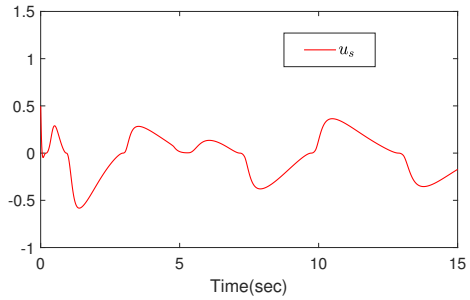

Fig. 4: System input u_s

where $F_1(\xi_1, \xi_2) = 0.05\xi_1 \sin \xi_2$, $F_2(\xi_1, \xi_2) = 0.025\xi_2 \sin \xi_1$, $\Lambda_1(t) = 0.95 \cos t$, $\Lambda_2(t) = 0.01 \sin t$. The multiplicative fault and additive fault are given as $\varpi = 0.75e^{-0.05t}$ and $\sigma = 0.04 \sin t$, respectively. The reference signal is $y^* = \sin t$.

The design parameters are chosen as $W_{11} = 1$, $W_{12} = 1$, $W_{21} = 10$, $W_{22} = 10$, $a_1 = 10$, $a_2 = 10$, $b_1 = 1$, $b_2 = 1$, $b_3 = 1$, $b_4 = 5$, $l_1 = 1$, $l_2 = 1$, $\epsilon = 0.1$, $r_1 = 10$, $\tau_1 = -1$, $\ell_1 = 1$, $\ell_2 = 1$, and $r_2 = 0.1$. The initial values are $\xi_1(0) = -0.1$, $\xi_2(0) = 0.1$, $\hat{\eta}(0) = 0.2$, $\hat{\kappa}(0) = -0.1$, $\varrho_1(0) = 0$, $\varrho_2(0) = 0$. It can be seen from Fig. 1 that y can track y^* well. Figs. 2-4 illustrate the boundedness of all the closed-loop signals.

5 Conclusions

This paper investigates adaptive fault-tolerant tracking control for nonstrict-feedback nonlinear systems with actuator faults. Based on the approximation of unknown nonlinear functions, FLSs are combined with command filtering to eliminate the redundant compensation signals. Additionally, efficient estimation of actuator fault parameters enable fault-tolerant control. The proposed control method guarantees convergence of the system output to the origin's neighborhood within a fixed time. The numerical example verifies the feasibility of this control method.

References

[1] T. P. Zhang, S. S. Ge, C. C. Hang, Adaptive neural network control for strict-feedback nonlinear systems using backstepping design, *Automatica*, 2000, 36(12): 1835-1846.

[2] X. D. Zhao, X. Y. Wang, S. Zhang, G. D. Zong, Adaptive neural backstepping control design for a class of nonsmooth nonlinear systems, *IEEE Transactions on Systems, Man, and Cybernetics: Systems*, 2019, 49(9): 1820-1831.

[3] Q. K. Shen, P. Shi, R. K. Agarwal, Y. Shi, Adaptive neural network-based filter design for nonlinear systems with multiple constraints, *IEEE Transactions on Neural Networks and Learning Systems*, 2021, 32(7): 3256-3261.

[4] T. Wang, J. Wu, Y. J. Wang, M. Ma, Adaptive fuzzy tracking control for a class of strict-feedback nonlinear systems with time-varying input delay and full state constraints, *IEEE Transactions on Fuzzy Systems*, 2020, 28(12): 3432-3441.

[5] H. Alwi, C. Edwards, Fault tolerant control using sliding modes with on-line control allocation, *Automatica*, 2008, 44(7): 1859-1866.

[6] L. T. Xing, C. Y. Wen, Y. Zhu, H. Y. Su, Z. Liu, Output feedback control for uncertain nonlinear systems with input quantization, *Automatica*, 2016, 65: 191-202.

[7] M. P. Aghababa, Adaptive control for electromechanical sys-

tems considering dead-zone phenomenon, *Nonlinear Dynamics*, 2014, 75(1-2): 157-174.

[8] F. Li, W. Guan, Q. Wang, X. H. Xu, Modeling and adaptive control of magneto-rheological buffer system for aircraft landing gear, *Applied Mathematical Modelling*, 2015, 39(9): 2509-2517.

[9] S. C. Tong, Y. M. Li, S. Sui, Adaptive fuzzy tracking control design for SISO uncertain nonstrict feedback nonlinear systems, *IEEE Transactions on Fuzzy Systems*, 2016, 24(6): 1441-1454.

[10] Y. M. Li, S. C. Tong, Adaptive fuzzy output-feedback stabilization control for a class of switched nonstrict-feedback nonlinear systems, *IEEE Transactions on Cybernetics*, 2017, 47(4): 1007-1016.

[11] H. Y. Li, L. Bai, Q. Zhou, R. Q. Lu, L. J. Wang, Adaptive fuzzy control of stochastic nonstrict-feedback nonlinear systems with input saturation, *IEEE Transactions on Systems, Man, and Cybernetics: Systems*, 2017, 47(8): 2185-2197.

[12] H. R. Ren, H. Ma, H. Y. Li, R. Q. Lu, A disturbance observer based intelligent control for nonstrict-feedback nonlinear systems, *Science China Technological Sciences*, 2023, 66: 456-467.

[13] K. K. Sun, L. Liu, J. B. Qiu, G. Feng, Fuzzy adaptive finite-time fault-tolerant control for strict-feedback nonlinear systems, *IEEE Transactions on Fuzzy Systems*, 2021, 29(4): 786-796.

[14] L. T. Xing, C. Y. Wen, Z. T. Liu, H. Y. Su, J. P. Cai, Adaptive compensation for actuator failures with event-triggered input, *Automatica*, 2017, 85: 129-136.

[15] W. Wu, Y. M. Li, S. C. Tong, Neural network output-feedback consensus fault-tolerant control for nonlinear multiagent systems with intermittent actuator faults, *IEEE Transactions on Neural Networks and Learning Systems*, 2023, 34(8): 4728-4740.

[16] H. Habibi, A. Yazdani, M. Darouach, H. Wang, T. Fernando, I. Howard, Observer-based sensor fault tolerant control with prescribed tracking performance for a class of nonlinear systems, *IEEE Transactions on Automatic Control*, 2023, 68(12): 8259-8266.

[17] S. P. Habibi, D. S. Bernstein, Continuous finite-time stabilization of the translational and rotational double integrators, *IEEE Transactions on Automatic Control*, 1998, 43(5): 678-682.

[18] H. Q. Wang, P. X. P. Liu, X. D. Zhao, X. P. Liu, Adaptive fuzzy finite-time control of nonlinear systems with actuator faults, *IEEE Transactions on Cybernetics*, 2020, 50(5): 1786-1797.

[19] D. Y. Jin, B. Niu, H. Q. Wang, D. Yang, A new adaptive DS-based finite-time neural tracking control scheme for nonstrict-feedback nonlinear systems, *IEEE Transactions on Systems, Man, and Cybernetics: Systems*, 2022, 52(2): 1014-1018.

[20] A. Q. Wang, L. Liu, J. B. Qiu, G. Feng, Finite-time adaptive fuzzy control for nonstrict-feedback nonlinear systems via an event-triggered strategy, *IEEE Transactions on Fuzzy Systems*, 2020, 28(9): 2164-2174.

[21] A. Polyakov, Nonlinear feedback design for fixed-time stabilization of linear control systems, *IEEE Transactions on Automatic Control*, 2012, 57(8): 2106-2110.

[22] X. Jin, Adaptive fixed-time control for MIMO nonlinear systems with asymmetric output constraints using universal barrier functions, *IEEE Transactions on Automatic Control*, 2019, 64(7): 3046-3053.

[23] H. B. Du, G. H. Wen, D. Wu, Y. Y. Cheng, J. H. Lu, Distributed fixed-time consensus for nonlinear heterogeneous multi-agent systems, *Automatica*, 2020, 113: 108797.

[24] K. X. Lu, Z. Liu, Y. N. Wang, C. L. P. Chen, Fixed-time adaptive fuzzy control for uncertain nonlinear systems, *IEEE Transactions on Fuzzy Systems*, 2021, 29(12): 3769-3781.

[25] D. S. Ba, Y. X. Li, S. C. Tong, Fixed-time adaptive neural tracking control for a class of uncertain nonstrict nonlinear systems, *Neurocomputing*, 2019, 363(12): 273-280.

[26] F. Wang, X. Zhang, Adaptive finite time control of nonlinear systems under time-varying actuator failures, *IEEE Transactions on Systems, Man, and Cybernetics: Systems*, 2019, 49(9): 1845-1852.

Proceedings of the 3rd Conference on Fully Actuated System Theory and Applications
May 10-12, 2024, Shenzhen, China

Bias-Policy Iteration Based Adaptive Dynamic Programming for Linear Fully Actuated Systems

Huaiyuan Jiang[1], Xuefei Yang[1], Chuanchuan Xu[2], Kangkang Zhang[3]

1. Center for Control Theory and Guidance Technology, Harbin Institute of Technology, P.O. Box 416, Harbin, 150001, China.
E-mail: huaiyuanjiang@hit.edu.cn, yangxuefei@hit.edu.cn,19b904066@stu.hit.edu.cn

2. Nanjing Research Institute of Electronic Engineering, Nanjing, 210000, China.
E-mail: chuanchuanxudr@163.com

3. Department of Mechanical Engineering, University of Hong Kong, Hong Kong, China.
E-mail: kangkang_kkz@163.com

Abstract: In this paper, the bias-policy iteration based optimal control of fully actuated systems is further reconsidered. With the help of the fully actuated property, a more neat bias-PI method for the fully actuated cases is established with the convergence proof. The data-driven implementation for the proposed algorithm is introduced accordingly. A numerical example verifies the effectiveness of the proposed results.

Key Words: Fully actuated systems, Adaptive dynamic programming, Data driven control, Bias-policy iteration

1 Introduction

Optimal control is a powerful mathematical and computational technique employed in control theory that ascertain the optimal way to manipulate the controlled dynamic systems and to ensure the achievement of desired performance metrics while minimizing associated costs or maximizing specific objectives [5]. Since in 1950s when the Pontryagin's Minimum Principle and Bellman's Dynamic Programming were formally established, the optimal control theory has attracted lots of interests from scientists and engineers in control community, and has soon been applied to numerous practical occasions, for example, aerospace, economics, electrical engineering, and robotics [7, 8].

While optimal control offers a powerful toolset for efficiently managing complex systems, its implementation such as dynamic programming can be challenging due to the "curse of dimensionality" problem [1]. In addition, the traditional optimal control techniques usually require the exact information of the parameters of the controlled systems during the full design process, while in practical engineering applications, the system information is not always available. Therefore, the design of data-driven based optimal control technique has become a hot topic in control community and been broadly studied in these years [6].

The adaptive dynamic programming (ADP) technique, as one of the typical data-driven optimal control methods, approximates the optimal controllers using the input and output data of the controlled systems, such that the need for system dynamics information during the controller design process is eliminated by imitating the learning behavior from biological systems, which allows the "curse of dimensionality" problem to be overcome. In recent years, scientists and engineers have paid close attention to the ADP technique, and fruitful results were proposed to solve optimal control issues for uncertain systems. For example, the nonlinear optimal control problem with constraint inputs [4], the H_∞ optimal control problem was solved by using ADP technique [9, 10], the optimal regulation problem [11], and many other occasions such as game problems [14], event-trigger control [13], optimal control for multi-agent systems [12], and so on [15, 16].

Usually there are two components that make up the iterative scheme of the ADP technique: the policy evaluation component, which assesses the performance index value under the specified control policy, and the policy improvement component, which enhances the control policy in light of the assessed estimated performance index [6]. With different execution order of these two components, the ADP methods may provides different benefits and inconvenience. For example, by initiating the algorithm with an admissible policy, the policy iteration based ADP method possesses a fast convergence speed, while the initial control policy is required to be admissible. Meanwhile, by using an initial semidefinite performance index value function, the value iteration based ADP method is easier to be initiated while the convergence may be slow. Over the past 15 years, lots of efforts was paid to remove the constraints and inconvenience in the ADP method, and fruitful results was proposed, for example, homotopic iteration method [20], the hybrid iteration method [21] and the bias-policy iteration (bias-PI) method [22]. However, all the method mentioned above have more complicated structure compared to the traditional ADP method, which will increase the computational burden more or less.

Recently, the analysis and control of fully actuated systems (FAS), has gained lots of attentions from control community [17–19]. As argued in [17], the FAS model can bring lots of benefit in cancelling the known nonlinearities in the system and hence to convert, to an extent, a nonlinear problem into a linear one. In [17], a nonlinear optimal controller in a state feedback form is obtained by effectively converting the nonlinear optimal control issue into a linear quadratic optimal control problem and the infinite-time output regulation

This work was supported in part by the National Natural Science Foundation of China under grant number 62303132, the Fundamental Research Funds for the Central Universities under grant number No.HIT.OCEF.2023007, in part by the Science Center Program of National Natural Science Foundation of China under Grant 62188101, and in part by the Heilongjiang Touyan Team Program. Corresponding author: Huaiyuan Jiang.

problem is also resolved after addressing the finite-time optimal tracking control problem. Interestingly, it is found that the fully actuated property may have potential advantage in simplifying the existing ADP method.

In this paper, the ADP method for FAS is further studied and the bias-PI algorithm for FAS is redesigned for solving the optimal control problem of FAS. First the traditional bias-PI method is briefly recalled, then by using the fully actuation property, a more neat bias-PI method for the fully actuated cases is then established with the convergence proof. The data-driven implementation for the proposed algorithm is introduced accordingly. A numerical example is finally introduced to verify the effectiveness of the proposed results.

The rest of this paper is organized as follows. The problem formation and related preliminaries for the controller design of linear optimal control problem are briefly introduced in Section 2. In Section 3, the existing result on bias-policy method and its generalization for the FAS case with convergence proof and data-driven implementation is given. A numerical example is introduced out in Section 4 to illustrate the effectiveness of the proposed algorithms. Finally, Section 5 concludes this paper.

2 Problem Formulation and Preliminaries

the following linear system

$$\dot{x} = Ax + Bu, \tag{1}$$

where $x \in \mathbb{R}^n$ denotes the state of the system, $u \in \mathbb{R}^m$ is the control input, and y the output of the system. In addition it is assumed that (A, B) is controllable. The design objective of the optimal control is to stabilizing system (13) while minimizing the following index function

$$J(x,u) = \int_0^\infty \left(x^{\mathrm{T}}Qx + u^{\mathrm{T}}Ru\right) \mathrm{d}t, \tag{2}$$

It is well known that by linear optimal control theory, the desired controller has the following form

$$u^* = -B^T P^* x, \tag{3}$$

where P^* is the positive definite solution of the following Riccati equation

$$A^{\mathrm{T}}P + PA - PBR^{-1}B^{\mathrm{T}}P + Q = 0. \tag{4}$$

On the other hand, due to the nonlinearity of the Riccati equation, the solution to (4) is usually hard to obtain analytically. So far many scholars have put their efforts on the numerical approximation methods for solving (4) and fruitful results were proposed. One of such methods known as the Kleinman iteration or the Policy Iteration method, is introduced as follows.

Lemma 1 *[3] Let K_0 be such that $A_0 = A - BK_0$ is Hurwitz, and P_k be the solution to the following Lyapunov equation, for $k \in \mathbb{Z}_+$,*

$$0 = A_{k-1}^{\mathrm{T}}P_k + P_k A_{k-1} + K_{k-1}RK_{k-1}^{\mathrm{T}} + Q, \tag{5}$$

with $A_{k-1} = A - BR^{-1}B^{\mathrm{T}}P_{k-1}$ for $k \geq 2$. Then there hold:

- *A_k is Hurwitz for $k \in \mathbb{Z}_+$;*
- *$P_k \geq P_{k+1} \geq P^*$ for $k \in \mathbb{Z}_+$;*
- *$\lim_{k\to\infty} P_k = P^*$.*

It is believed that to initiate the PI method, one needs to choose a stabilizing control gain K_0 which may be hard to obtain in practical usage. Recently several different approaches were emerged to further relax this condition, such as homotopic iteration method [20], the hybrid iteration method [21] and the bias-PI method [22]. However, all the method mentioned above have more complicated structure compared to the traditional PI method, which will increase the computational burden. Recently a novel system analysis approach called the full actuated system approach [17–19] was established and now attracts lots of attentions from control community. Interestingly, it is found that the fully actuated property may have potential advantage in simplify the above mentioned method. In the following, the bias-PI method for first-order fully actuated systems is considered and the following assumption is made.

Assumption 1 *B is of full rank with $m = n$.*

3 Bias-PI method for fully actuated systems

In this section, the bias-PI method for fully actuated systems is further studied, and a more neat result is proposed. First, the model based bias-PI method is recalled, and the convergence of the bias-PI method for the fully actuated systems is detailed analysed. Then the correspondent data-driven implementation for the proposed method is introduced accordingly.

3.1 Traditional Bias-PI method

By introducing the matrix operator $F_P^\gamma(M)$ as

$$\begin{aligned} F_P^\gamma(M) = &\left(A - BR^{-1}B^{\mathrm{T}}P - \frac{\gamma}{2}I_n\right)^{\mathrm{T}} M \\ &+ M\left(A - BR^{-1}B^{\mathrm{T}}P - \frac{\gamma}{2}I_n\right), \end{aligned}$$

and the following iteration scheme

$$P_{i+1} = P_i - \left(F_{P_i}^\gamma\right)^{-1}\left(F(P_i)\right), \tag{6}$$

the traditional PI method is modified as

$$\overline{A}_i^{\mathrm{T}}P_{i+1} + P_{i+1}\overline{A}_i + P_i BR^{-1}B^{\mathrm{T}}P_i + Q + \gamma P_i = 0, \tag{7}$$

with

$$\overline{A}_i = A - BR^{-1}B^{\mathrm{T}}P_i - \frac{\gamma}{2}I_n.$$

Notice that the existence of $(F_{P_i}^\gamma)^{-1}$ can be guaranteed if $\overline{A}_i$ keeps being Hurwitz during the iteration, which is a weaker condition compared to the traditional PI method that $A - BR^{-1}B^{\mathrm{T}}P_i$ is Hurwitz. By introducing an auxiliary iteration

$$\underline{A}_j^{\mathrm{T}}\underline{P}_{j+1} + \underline{P}_{j+1}\underline{A}_j + Q + \underline{P}_j BR^{-1}B^{\mathrm{T}}\underline{P}_j = 0, \tag{8}$$

where $\underline{A}_j = A - BR^{-1}B^{\mathrm{T}}\underline{P}_j - \frac{\gamma}{2}I_n$, and a correspondent parameter

$$\beta_i = \lambda_{\max}(P_i P_{i-1}^{-1}),\ i \in \mathbb{Z}_+, \tag{9}$$

the following results can be easily obtained.

Algorithm 1 Model-based Bias-PI Algorithm

Choose $P_0 > 0$ and $\gamma_0 > 0$ such that $A - BR^{-1}B^{\mathrm{T}}P_0 - \frac{\gamma_0}{2}I_n$ is Hurwitz. Set the approximation threshold ε such that $\frac{\lambda_{\min}(Q)}{\gamma_0} > \varepsilon > 0$ and let $\gamma = \gamma_0$. Set n_2 large enough such that $n_2 > \lambda_{\max}(P_0)$ and $n_2 > \lambda_{\max}(P^*)$, where P^* is the positive definite solution to (4). Let $n_1 > \frac{\lambda_{\max}(Q)}{\lambda_{\min}(Q)}n_2$ and set $i = 0$.
repeat
  if $\lambda_{\max}(P_i) > n_1$, **then**
    Let $\gamma_i = \gamma_{i-1}\frac{\beta_i - 1}{\beta_i}$, where β_i is defined by (9) and $P_{i,0} = P_i$. Set $j = 0$.
    repeat
      Solve (8) with $\gamma = \gamma_i$ to get $P_{i,j+1}$. Let $j = j + 1$.
    until $\lambda_{\max}(P_{i,j}) < n_2$.
    Let $P_i = P_{i,j}$.
  end if
  Let $\gamma_{i+1} = \gamma_i$, and solve (7) with $\gamma = \gamma_{i+1}$ to get P_{i+1}. Let $i = i + 1$.
until $\|P_i - P_{i-1}\| \le \varepsilon$.

Lemma 2 *Consider the matrix series $\{P_i\}$ generated by (7). If $P_0 > 0$ and $\gamma > 0$ are such that $A - BR^{-1}B^{\mathrm{T}}P_0 - \frac{\gamma}{2}I_n$ is Hurwitz, then the following two properties hold:*

1) $A - BR^{-1}B^{\mathrm{T}}P_i - \frac{\gamma}{2}I_n$ is Hurwitz for $i \in \mathbb{Z}_+$;
2) $P_{i+1} \le P_i$, if $P_i \le P_{i-1}$;
3) the series $\{P_i\}$ is convergent to the positive definite solution to (4) if it is bounded.

Lemma 3 *The matrix series $\{P_i\}$ generated by Algorithm 1 converges to the positive solution P^* to the ARE (4) as $i \to \infty$.*

Lemma 4 *By choosing ε and γ_0 properly such that $\varepsilon\gamma_0 I_n < Q$, the approximation of P^* denoted by $\hat{P}$ obtained by Algorithm 1 ensures that $A - BR^{-1}B^{\mathrm{T}}\hat{P}$ is Hurwitz.*

Notice that in Algorithm 1 an extra iteration scheme (8), which, however, adds some unnecessary computational burden to the algorithm. On the other hand, by taking the fully actuated property into consideration, the following result can be directly obtained.

Corollary 1 *Let $P_0 > 0$ and $\gamma > 0$ be such that $A - BR^{-1}B^{\mathrm{T}}P_0 - \frac{\gamma}{2}I_n$ is Hurwitz, and consider the matrix series $\{P_i\}$ generated by (7). If B is full of row rank, then the series $\{P_i\}$ is bounded.*

Proof. First, for any $P_0 > 0$ which satisfies that $A - BR^{-1}B^{\mathrm{T}}P_0 - \frac{\gamma}{2}I_n$ is Hurwitz, by

$$A^{\mathrm{T}}P^* + P^*A + Q - P^*BR^{-1}B^{\mathrm{T}}P^* = 0,$$

we have

$$\begin{aligned}0 =& \left(A - BR^{-1}B^{\mathrm{T}}P_0 - \frac{\gamma}{2}I_n\right)^{\mathrm{T}}P^* \\ &+ P^*\left(A - BR^{-1}B^{\mathrm{T}}P_0 - \frac{\gamma}{2}I_n\right) \\ &+ Q - P^*BR^{-1}B^{\mathrm{T}}P^* \\ &+ \gamma P^* + P^*BR^{-1}B^{\mathrm{T}}P_0 + P_0BR^{-1}B^{\mathrm{T}}P^*. \quad (10)\end{aligned}$$

Denote $\underline{\beta}_0$ as $\underline{\beta}_0 = \lambda_{\min}(P_0 (P^*)^{-1})$, where P^* is the positive definite solution to (4). Then we can easily obtain by $\lambda_{\min}(P_0 (P^*)^{-1} = \lambda_{\min}\left((P^*)^{-\frac{1}{2}}P_0 (P^*)^{-\frac{1}{2}}\right)$ that

$$\begin{aligned}&P_0 - \underline{\beta}_0 P^* \\ =&(P^*)^{\frac{1}{2}}\left((P^*)^{-\frac{1}{2}}P_0(P^*)^{-\frac{1}{2}} - \underline{\beta}_0 I_n\right)(P^*)^{\frac{1}{2}} \\ \ge&0. \quad (11)\end{aligned}$$

Then similar to the proof of (11), we have

$$P_0 - \underline{\beta}_0 P^* \ge 0.$$

Therefore, it follows from (7) and (10) that

$$\begin{aligned}&\underline{A}_0^{\mathrm{T}}(P_1 - \underline{\beta}_0 P^*) + (P_1 - \underline{\beta}_0 P^*)\underline{A}_0 \\ =& -(Q + P_0BR^{-1}B^{\mathrm{T}}P_0 + \gamma P_0) \\ &+ \underline{\beta}_0(Q - P^*BR^{-1}B^{\mathrm{T}}P^* + \gamma P^* \\ &+ P^*BR^{-1}B^{\mathrm{T}}P_0 + P_0BR^{-1}B^{\mathrm{T}}P^*). \quad (12)\end{aligned}$$

where $\underline{A}_0 = A - BR^{-1}B^{\mathrm{T}}P_0 - \frac{\gamma}{2}I_n$. If $\underline{\beta}_0 \ge 1$, then by (4) and (7) we directly obtain

$$\begin{aligned}&\underline{A}_0^{\mathrm{T}}(P_1 - P^*) + (P_1 - P^*)\underline{A}_0 \\ =& -\gamma(P_0 - P^*) - (P_0 - P^*)BR^{-1}B^{\mathrm{T}}(P_0 - P^*) \\ \le&0,\end{aligned}$$

which further indicates that $P_1 \ge P^*$.

If $\underline{\beta}_0 < 1$, then by (12) we have

$$\begin{aligned}&\underline{A}_0^{\mathrm{T}}(P_1 - \underline{\beta}_0 P^*) + (P_1 - \underline{\beta}_0 P^*)\underline{A}_0 \\ =& -((1 - \underline{\beta}_0)Q + (1 - \underline{\beta}_0)P_0BR^{-1}B^{\mathrm{T}}P_0 \\ &+ (\gamma P_0 - \underline{\beta}_0 P^*) + \underline{\beta}_0(P_0 - P^*)BR^{-1}B^{\mathrm{T}}(P_0 - P^*)) \\ <&0,\end{aligned}$$

which implies $(P_1 - \underline{\beta}_0 P^*) > 0$. Therefore, by denoting $\underline{\beta}_0^* = \min\left\{1, \underline{\beta}_0\right\}$ and repeating the above calculation recursively for $i \in \mathbb{Z}_+$, we have $P_i \ge \underline{\beta}_0^* P^*, \forall i \in \mathbb{Z}_+$.

If there exists an i_m such that $\beta_{i_m} \le 1$, then by Lemma 2, we have that $P_i \le P_{i-1}$ for $i \ge i_m$, which indicates that P_i is bounded. Now we assume that β_i defined by (9) satisfies that $\beta_i > 1$ for $i \in \mathbb{Z}_+$. It follows from $P_i \ge \underline{\beta}_0^* P^*$ that $P_i^{-1} \le \frac{1}{\underline{\beta}_0^*}(P^*)^{-1}$. Since B is full of row rank, we have $BR^{-1}B^{\mathrm{T}} > 0$. Therefore, by defining $\beta_b = \lambda_{\min}(BR^{-1}B^{\mathrm{T}}P^*)$ we have $BR^{-1}B^{\mathrm{T}} \ge \beta_b(P^*)^{-1} \ge \beta_b\underline{\beta}_0^* P_i^{-1}$. Since we have assumed that $\beta_i > 1$ for $i \in \mathbb{Z}_+$, by choosing $\overline{\beta}_{i+1}$ such that

$$\gamma\frac{\beta_i - \overline{\beta}_{i+1}}{\overline{\beta}_{i+1} - 1} = \beta_b\underline{\beta}_0^*,$$

we have

$$\begin{aligned}&(\overline{\beta}_{i+1} - 1)P_iBR^{-1}B^{\mathrm{T}}P_i - \gamma\frac{(\beta_i - \overline{\beta}_{i+1})}{\beta_i}P_i \\ =&(\overline{\beta}_{i+1} - 1)P_i\left(BR^{-1}B^{\mathrm{T}} - \gamma\frac{(\beta_i - \overline{\beta}_{i+1})}{\beta_i(\overline{\beta}_{i+1} - 1)}P_i^{-1}\right)P_i \\ \ge&(\overline{\beta}_{i+1} - 1)P_i\left(BR^{-1}B^{\mathrm{T}} - \gamma\frac{(\beta_i - \overline{\beta}_{i+1})}{(\overline{\beta}_{i+1} - 1)}P_i^{-1}\right)P_i \\ \ge&0.\end{aligned}$$

Therefore, it follows from (7) that

$$\begin{aligned}&\overline{A}_i^{\mathrm{T}}P_i+P_i\overline{A}_i\\=&P_iBR^{-1}B^{\mathrm{T}}P_i-Q-\gamma P_{i-1}\\&-\left(P_i-P_{i-1}\right)BR^{-1}B^{\mathrm{T}}\left(P_i-P_{i-1}\right).\end{aligned}\tag{13}$$

By (7) and (13)

$$\begin{aligned}&\overline{A}_i^{\mathrm{T}}(P_{i+1}-\overline{\beta}_{i+1}P_i)+(P_{i+1}-\overline{\beta}_{i+1}P_i)\overline{A}_i\\=&(\overline{\beta}_{i+1}-1)Q+\gamma(\overline{\beta}_{i+1}P_{i-1}-P_i)\\&+\overline{\beta}_{i+1}(P_i-P_{i-1})BR^{-1}B^{\mathrm{T}}(P_i-P_{i-1})\\&+(\overline{\beta}_{i+1}-1)P_iBR^{-1}B^{\mathrm{T}}P_i\\>&\overline{\beta}_{i+1}(P_i-P_{i-1})BR^{-1}B^{\mathrm{T}}(P_i-P_{i-1})\\&+\gamma\frac{\overline{\beta}_{i+1}}{\beta_i}(\beta_iP_{i-1}-P_i)-\gamma\frac{(\beta_i-\overline{\beta}_{i+1})}{\beta_i}P_i\\>&0,\end{aligned}\tag{14}$$

where $\overline{A}_i=A-BR^{-1}B^{\mathrm{T}}P_i-\frac{\gamma}{2}I_n$. Since in Lemma 2 it is proved that $\overline{A}_i$ is Hurwitz for $i\in\mathbb{Z}_+$, by (14) we have

$$P_{i+1}-\overline{\beta}_{i+1}P_i<0,$$

which implies that

$$\overline{\beta}_{i+1}>\lambda_{\max}(P_{i+1}P_i^{-1})=\beta_{i+1}.\tag{15}$$

Let $\beta_1^R=\beta_1>1$ and define $\left\{\beta_i^R\right\}$ for $i>1$ according to

$$\gamma\frac{\beta_i^R-\beta_{i+1}^R}{\beta_{i+1}^R-1}=\beta_b\underline{\beta}_0^*.\tag{16}$$

Similar to the proof of (15) we can show that for $i\in\mathbb{Z}_+$,

$$\beta_i\le\beta_i^R.$$

Notice that (16) is equal to

$$c(\beta_i^R-\beta_{i+1}^R)=\beta_{i+1}^R-1,$$

where $c=\frac{\gamma}{\beta_b\underline{\beta}_0^*}$. Then direct computation gives

$$\begin{aligned}\beta_{i+1}^R=&\frac{c\beta_i^R+1}{c+1}\\=&1+\frac{c}{c+1}\left(\beta_i^R-1\right)\\&\vdots\\=&1+\left(\frac{c}{c+1}\right)^i(\beta_1-1).\end{aligned}$$

By noticing $\beta_i\le\beta_i^R$, there holds

$$P_i\le\prod_{n=1}^i\beta_nP_0\le\prod_{n=1}^i\beta_n^RP_0.$$

In the meanwhile, by the fact that $\ln(1+x)<x$ holds for $x>0$, for $i\in\mathbb{Z}_+$, we have

$$\begin{aligned}&\ln\left(\prod_{n=1}^i\beta_n^R\right)\\=&\sum_{n=1}^i\ln\beta_n^R\\=&\sum_{n=1}^i\ln\left(1+\left(\frac{c}{c+1}\right)^{n-1}(\beta_1-1)\right)\\<&\sum_{n=1}^i\left(\frac{c}{c+1}\right)^{n-1}(\beta_1-1)\\=&\frac{1-\left(\frac{c}{c+1}\right)^i}{1-\frac{c}{c+1}}(\beta_1-1)\\<&\frac{1}{1-\frac{c}{c+1}}(\beta_1-1)\\=&(c+1)(\beta_1-1).\end{aligned}\tag{17}$$

Therefore, $\prod_{n=1}^i\beta_n<\prod_{n=1}^i\beta_n^R<\mathrm{e}^{(\beta_1-1)(c+1)}$, which implies that $\prod_{n=1}^i\beta_n$ is bounded. By the definition of β_i, we have

$$P_i\le\prod_{n=1}^i\beta_nP_0,$$

which implies that $\left\{P^i\right\}$ is bounded. The proof is thus finished. ■

Algorithm 2 Bias-PI Algorithm for Fully Actuated Systems

1: Choose $P_0=0$ and $\gamma>0$ such that $A-\frac{\gamma}{2}I_n$ is Hurwitz. Set the approximation threshold ε properly.
2: **repeat**
3: Solve (7) with to get P_{i+1}. Let $i=i+1$.
4: **until** $\|P_i-P_{i-1}\|\le\varepsilon$.

Theorem 1 *The matrix series $\{P_i\}$ generated by Algorithm 2 converges to the positive solution P^* to the ARE (4) as $i\to\infty$.*

The proof of Theorem 1 can be directly obtained by Lemma 2 and Corollary 1 and is thus omit here. Compared to the existing bias-PI algorithms such as Algorithm 1, it is obvious that Algorithm 2 has a more neat formation and is easier to be implemented. Similar to the existing bias-PI method based algorithm, Algorithm 2 only generates an approximation of the solution to (4), denoted by $\hat{P}=P_i$. However, the corresponding control gain $\hat{K}=-R^{-1}B^{\mathrm{T}}\hat{P}$ may not be able to ensure that $A-B\hat{K}$ is Hurwitz. Following the idea of Lemma 4, the following corollary is proposed.

Corollary 2 *By choosing ε and γ properly such that $\varepsilon\gamma I_n<Q$, the approximation of P^* denoted by $\hat{P}$ obtained by Algorithm 1 ensures that $A-BR^{-1}B^{\mathrm{T}}\hat{P}$ is Hurwitz.*

Remark 1 *The parameter γ in the proposed algorithm serves as an damping term that helps relaxing the convergence condition of the traditional PI method. Intuitively, a large γ slows the convergence speed of the proposed algorithm. For this concern, one may decrease γ during the iteration, only to ensuring that $A-BK-\frac{1}{2}\gamma I_n$ is Hurwitz.*

3.2 Data-driven implementation for Algorithm 2

In the following, the traditional data-driven implementation for Algorithm 2 is introduced. By noting (7) and letting $K_i = R^{-1}B^{\mathrm{T}}P_i$, the linear system described by (1) with the control input u can be formed as

$$\begin{aligned} & x^{\mathrm{T}}(t+\Delta t)P_{i+1}x(t+\Delta t) - x^{\mathrm{T}}(t)P_{i+1}x(t) \\ =& -\int_t^{t+\Delta t} x^{\mathrm{T}}(Q+K_i^{\mathrm{T}}RK_i+\gamma(P_i-P_{i+1}))x\mathrm{d}s \\ & +2\int_t^{t+\delta t}(u+K_ix)^{\mathrm{T}}RK_{i+1}x\mathrm{d}s, \quad i\geq 0, \end{aligned}$$

with $A_i = A - BK_i$. Therefore, one obtains

$$\begin{aligned} & x^{\mathrm{T}}(t+\delta t)P_{i+1}x(t+\delta t) - x^{\mathrm{T}}(t)P_{i+1}x(t) \\ =& -\int_t^{t+\delta t} x^{\mathrm{T}}(Q_i+\gamma P_i)x\mathrm{d}s - \gamma\int_t^{t+\delta t} x^{\mathrm{T}}P_{i+1}x\mathrm{d}s \\ & +2\int_t^{t+\delta t}(u+K_ix)^{\mathrm{T}}RK_{i+1}x\mathrm{d}s, \end{aligned} \tag{18}$$

where $Q_i = Q + K_i^{\mathrm{T}}RK_i$. By letting

$$\begin{aligned} \bar{x} &= [x_1^2, 2x_1x_2, \cdots, x_2^2, 2x_2x_3, \cdots, x_n^2], \\ \bar{P} &= [p_{11}, p_{12}, p_{13}, \cdots, P_{22}, p_{23}, \cdots, p_{nn}]^{\mathrm{T}}. \end{aligned}$$

we have by (18) that

$$\begin{aligned} & \left((\bar{x}(t+\delta t)-\bar{x}(t)) - \gamma\int_t^{t+\delta t}\bar{x}\mathrm{d}s\right)\bar{P}_{i+1} \\ =& \int_t^{t+\delta t}(x^{\mathrm{T}}\otimes x^{\mathrm{T}})\mathrm{d}s\mathrm{vec}(Q_i^{\gamma}) \\ & +2\int_t^{t+\delta t} x^{\mathrm{T}}\otimes\left((u+K_ix)^{\mathrm{T}}R\right)\mathrm{d}s\mathrm{vec}(K_{i+1}), \end{aligned}$$

with $Q_i^{\gamma} = Q_i + \gamma P_i$. For the time series $t_0 < t_1 < t_2 < t_3 < \cdots < t_l$, Define

$$\begin{aligned} \Xi_x &= \begin{bmatrix} \Xi_{1,x} & \Xi_{2,x} & \cdots & \Xi_{l,x} \end{bmatrix}^{\mathrm{T}}, \\ \Xi_{i,x} &= \left((\bar{x}(t_i)-\bar{x}(t_{i-1})) - \gamma\int_{t_{i-1}}^{t_i}\bar{x}\mathrm{d}s\right)^{\mathrm{T}}, i=1,...,l, \\ \mathcal{I}_x &= \begin{bmatrix} \int_{t_0}^{t_1} x\otimes x\mathrm{d}s & \cdots & \int_{t_{l-1}}^{t_l} x\otimes x\mathrm{d}s \end{bmatrix}^{\mathrm{T}}, \\ \mathcal{I}_u &= \begin{bmatrix} \int_{t_0}^{t_1} x\otimes u\mathrm{d}s & \cdots & \int_{t_{l-1}}^{t_l} x\otimes u\mathrm{d}s \end{bmatrix}^{\mathrm{T}}, \end{aligned}$$

and notice

$$\begin{aligned} & x^{\mathrm{T}}\otimes\left((u+K_ix)^{\mathrm{T}}R\right) \\ =& \left(x^{\mathrm{T}}\otimes x^{\mathrm{T}}\right)\left(I_n\otimes K_i^{\mathrm{T}}R\right) + \left(x^{\mathrm{T}}\otimes u^{\mathrm{T}}\right)(I_n\otimes R). \end{aligned}$$

Then there holds

$$\Theta_i\begin{bmatrix} \bar{P}_{i+1} \\ \mathrm{vec}(K_{i+1}) \end{bmatrix} = -\mathcal{I}_x\mathrm{vec}(Q_i^{\gamma}), \quad i\geq 0, \tag{19}$$

with $\Theta_i = [\Xi_x, -2\mathcal{I}_x\left(I_n\otimes K_i^{\mathrm{T}}R\right) - 2\mathcal{I}_u(I_n\otimes R)]$.

To ensure that the solution to (19) is unique, the following lemma is introduced.

Algorithm 3 Data-Driven Bias-PI Algorithm for Fully Actuated Systems

Choose $P_0 = 0$,K_0 and $\gamma > 0$ such that $A - BK_0 - \frac{\gamma}{2}I_n$ is Hurwitz. Set l large enough. During the time interval $[t_0, t_l]$, employ $u = -K_0x + e$ as the input on the time interval $[t_0, t_l]$, where e is the exploration noise. Compute Ξ_x, I_x and I_u until the rank condition in (20) is satisfied.
Set the approximation threshold ε which satisfies that $\frac{\lambda_{\min}(Q)}{\gamma} > \varepsilon > 0$ and set $i = 0$.
repeat
  Solve (19) to get (P_{i+1}, K_{i+1}), and let $i = i + 1$.
until $\|P_i - P_{i-1}\| \leq \varepsilon$.
Use $u(t) = -K_ix(t)$ as the approximated optimal control policy.

Lemma 5 *[2] If the following condition is satisfied*

$$rank(\mathcal{I}_x, \mathcal{I}_u) = \frac{n(n+1)}{2} + mn, \tag{20}$$

then the matrix Θ_i is of full column rank.

4 Simulation

A numerical example is presented to illustrate the effectiveness of the proposed allocation strategies. The plant model has dimensions $n = 4$ and $m = 4$ with the matrices used for the simulation being randomly generated and B being of full rank. The weight matrix is simplify chosen as $Q = R = I_4$ only for illustrative purpose. The traditional PI method and the proposed bias-PI method are separately used for solving the optimal control problem, the initial control gain is simply chosen as $K_0 = 0$. The input $u(t)$ is chosen such that

$$u(t) = 30\sum_{i=1}^{30}\sin(\omega_i t),$$

where ω_i are randomly chosen from $[-50, 50]$. The approximate error ε are set as $\varepsilon = 10^{-4}$. In addition, for the bias-PI method we choose $P_0 = 0$ and different values of γ for the algorithm. Then the system data on the time interval $[0, 1]$ are collected to generate the matrices I_x, I_u and Δ_x. After the data collection, the algorithms are executed and then the obtained control policy is applied to the system at $t = 1s$. The iteration convergence of different algorithm and the trajectories of the norm of system state by the controllers generated by different algorithms are given in Fig. 1.

Table 1: Convergence of Algorithm 3 with different γ.

γ	0 (PI)	γ^*	$5\gamma^*$	$10\gamma^*$
$\|\hat{P}-P^*\|$	13.596	0.0002	0.002	0.00004
Iterations	7 (FAIL)	26	29	74

To further show the influence of γ in Algorithm 3. We set $\gamma^* = \max\{2\lambda_{\max}(A), 0\}$ and re-execute Algorithm 3 with different γ. From Table 1, it can be seen that choosing a larger γ may increase the approximation error and the number of iterations. In the meanwhile, a small γ makes the condition $A - BK_0 - \frac{\gamma}{2}I_n$ being Hurwitz hard to satisfy. Therefore, the trade off should be taken into consideration when choosing γ for the bias-PI algorithm, which is the same with the result in [22].

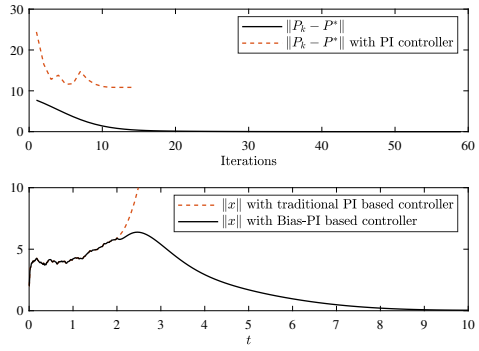

Fig. 1: Trajectories of the convergence error and the norm of the closed-loop system state

5 Conclusion

In this paper, the bias-policy iteration based optimal control of fully actuated linear systems is further reconsidered. With the help of the fully actuation property, a more neat bias-PI method for the fully actuated cases is established with the convergence proof. The data-driven implementation for the proposed algorithm is introduced accordingly. A numerical example verifies the effectiveness of the proposed results. In future, the authors will focus on the generalization of the proposed method to the practical complex systems.

References

[1] P. Werbos, *Beyond Regression: New Tools for Prediction and Analysis in the Behavioural Sciences*, Ph.D. Thesis, Harvard University, 1974.

[2] Y. Jiang, & Z. P. Jiang, Computational adaptive optimal control for continuous-time linear systems with completely unknown dynamics, *Automatica*, 48(10), 2699–2704, 2012.

[3] D. Kleinman, On an iterative technique for Riccati equation computations, *IEEE Transactions on Automatic Control*, 13(1), 114–115, 1968.

[4] M. Abu-Khalaf, & F. L. Lewis, Nearly optimal control laws for nonlinear systems with saturating actuators using a neural network HJB approach. *Automatica*, 41(5), 779–791, 2005.

[5] F. L. Lewis, D. Vrabie, & V. L. Syrmos, *Optimal Control*, John Wiley & Sons, 2012.

[6] D.Liu, S. Xue, B. Zhao, & Q. Wei, Adaptive dynamic programming for control: a survey and recent advances. *IEEE Transactions on Systems, Man, and Cybernetics: Systems*, 51(1), 142–160, 2020.

[7] D. Wang, H. He, & D. Liu, Adaptive critic nonlinear robust control: a survey. *IEEE Transactions on Cybernetics*, 47(10), 3429–3451, 2017.

[8] D. P. Bertsekas, *Dynamic Programming and Optimal Control*, Belmont, MA: Athena scientific, 1995.

[9] H. Jiang, B. Zhou, & G. P. Liu, H_∞ optimal control of unknown linear systems by adaptive dynamic programming with applications to time-delay systems, *International Journal of Robust and Nonlinear Control*, 31(12): 5602–5617, 2021.

[10] H. Modares, F. L. Lewis, & Z. P. Jiang, H_∞ tracking control of completely unknown continuous-time systems via off-policy reinforcement learning, *IEEE transactions on neural networks and learning systems*, 26(10), 2550–2562, 2015.

[11] W. Gao, & Z. P. Jiang, Adaptive dynamic programming & adaptive optimal output regulation of linear systems. *IEEE Transactions on Automatic Control*, 61(12), 4164–4169, 2016.

[12] Y. Jiang, W. Gao, J. Na, D. Zhang, T. T. Hämäläinen, V. Stojanovic, & F. L. Lewis, Value iteration and adaptive optimal output regulation with assured convergence rate, *Control Engineering Practice*, 121: 105042, 2022.

[13] B. Luo, Y. Yang, D. Liu, & H.-N. Wu, Event-triggered optimal control with performance guarantees using adaptive dynamic programming, *IEEE Transactions on Neural Networks and Learning Systems*, 31(1), 76–88, 2020.

[14] M. Li, J. Qin, N. M. Freris, & D. W. Ho, Multiplayer Stackelberg-Nash game for nonlinear system via value iteration-based integral reinforcement learning, *IEEE Transactions on Neural Networks and Learning Systems*, 33(4): 1429–1440, 2020.

[15] D. Wang, J. Wang, M. Zhao, P. Xin & J. Qiao, Adaptive Multi-Step Evaluation Design With Stability Guarantee for Discrete-Time Optimal Learning Control, *IEEE/CAA Journal of Automatica Sinica*, 10(9): 1797–1809, 2023.

[16] H. Su, H. Zhang, H. Jiang & Y. Wen, Decentralized Event-Triggered Adaptive Control of Discrete-Time Nonzero-Sum Games Over Wireless Sensor-Actuator Networks With Input Constraints, *IEEE Transactions on Neural Networks and Learning Systems*, 31(10): 4254–4266,2020.

[17] G. Duan, High-order fully actuated system approaches: Part VIII. Optimal control with application in spacecraft attitude stabilisation, *International Journal of Systems Science*, 53(1): 54–73, 2022.

[18] G. Duan, High-order fully actuated system approaches: Part I. Models and basic procedure. *International Journal of Systems Science*, 52(2): 422–435, 2021.

[19] G. Duan, High-order fully actuated system approaches: Part II. Generalized strict-feedback systems, *International Journal of Systems Science*, 52(3): 437-454, 2021.

[20] C. Chen, F. L. Lewis, & B. Li, Homotopic policy iteration-based learning design for unknown linear continuous-time systems, *Automatica*, 138: 110153, 2022.

[21] O. Qasem, W. Gao, & K. G. Vamvoudakis, Adaptive optimal control of continuous-time nonlinear affine systems via hybrid iteration, *Automatica*, 157: 111261, 2023.

[22] H. Jiang, & B. Zhou, Bias-policy iteration based adaptive dynamic programming for unknown continuous-time linear systems, *Automatica*, 136: 110058, 2022.

Proceedings of the 3rd Conference on Fully Actuated System Theory and Applications
May 10-12, 2024, Shenzhen, China

UUV Trajectory Tracking Control Based on Gaussian Process Model Predictive Control

Xiaoming Yan[1,2], Yang Liu[1,2]

1. National Key Laboratory of Autonomous Marine Vehicle Technology, Harbin Engineering University, Harbin 150001, China

2. Qingdao Innovation and Development Center of Harbin Engineering University, Qingdao, 266000, China
E-mail: yxming7654@163.com
E-mail: y_liu@hrbeu.edu.cn

Abstract: Aiming at the problem of Unmanned Underwater Vehicle (UUV) trajectory tracking control in three-dimension (3D) underwater environment, a trajectory tracking control method based on Gaussian Process Model Predictive Control (GP-MPC) method is proposed. By integrating the theory and methods of Gaussian Process (GP) with the framework of model predictive control to achieve modelling predictions of system uncertainty. Firstly, the mathematical model of UUV under five degrees of freedom is established and linearly discretized; Then, the model predictive controller is designed to achieve the tracking control of the desired trajectory and predict the unmodelled part of the UUV by using GP; Finally, the three-dimensional trajectory tracking simulation experiments are conducted to validate that the method has a better controlling effect compared with the traditional MPC method during the tracking process with uncertain model parameters.

Key Words: UUV, Model Predictive Control, Gaussian Process, Tracking Control

1 Introduction

With the advantages of flexibility and low cost, UUV has a wide application prospect in ocean exploration, seabed resource exploitation and seabed operation[1-2]. UUV trajectory tracking is the ability of a UUV, driven by a control system, to start from an initial position and accurately follow a desired trajectory to its destination. Currently, the main trajectory tracking control algorithms include: PID control, fuzzy control, neural network control, robust control, sliding mode control, backstepping control, model predictive control[3].

However, due to the highly non-linear UUV model and the complex underwater environment, a single control algorithm has certain limitations and is difficult to achieve accurate and stable tracking control of UUV[4]. In order to solve this problem, many scholars have carried out research on combining the advantages of different algorithms, and are committed to constructing a more integrated and highly robust hybrid control strategy, aiming at overcoming the shortcomings of a single algorithm and improving the performance of UUV trajectory tracking systems in complex underwater environments[5-7].

[8] designed fuzzy position and bow controllers based on the relative state error between the navigator and the reference trajectory by using the T-S fuzzy framework to cope with marine environment disturbances. [9] designed a global finite time control method by combining PID and sliding mode control, which ensures the global stability of all trajectory tracking errors in finite time under model parameter perturbation and unknown ocean current conditions. [10] proposes a 3D underwater trajectory tracking method for navigators based on model predictive control, which considers system inputs and state constraints, and employs a rolling time-domain implementation to improve robustness.

MPC is an advanced control strategy and widely used in automatic control systems. To effectively reduce the computational complexity of the algorithm, the [11] uses the Laguerre function to introduce the rolling optimization process of MPC, which reduces the computation time by transforming multiple control inputs of UUV into a small number of Laguerre coefficients for optimization. [12] combines nonlinear model predictive control with an event-triggered mechanism for 3D trajectory tracking, reducing the number of controller iterations while ensuring the tracking performance of the UUV.

In addition to this, serial control strategies are also widely used in this field. [13] solved the velocity jump problem during UUV motion by combining the kinematic control based on quantum particle swarm model predictive control and the dynamics control based on sliding mode control in series to satisfy the propeller constraints while solving the velocity jump problem during UUV motion. [14] based on adaptive dynamic sliding mode control algorithm for dynamics controller design, in series with MPC-based kinematics controller, effectively reduces the effect of wave disturbances and improves the robustness of the system.

Compared with the serial control, the approach using the dual closed-loop control framework requires two optimal control problems to be solved in each control cycle, which increases the amount of computation but provides a more flexible and precise control for the system and improves the robustness of the tracking control. [15] employs a dual-closed-loop model-based predictive control approach that transforms trajectory tracking control into a design problem of an outer-loop position controller and an inner-loop velocity controller, reducing algorithmic complexity and improving the convergence of the AUV trajectory. [16] proposes a dual closed-loop robust model predictive control method by incorporating state and input

*This work is supported by the Natural Science Foundation of Shandong Province under Grant ZR2022QE056; Natural Science Foundation of Heilongjiang Province under Grant LH2023F025; Research Fund from National Key Laboratory of Autonomous Marine Vehicle Technology 2023-SXJQR-SYSJJ04.

constraints, designing a nonlinear auxiliary control law in the dynamic controller, using the velocity increment as an input to make the velocity change smoother, and incorporating a finite time extended state observer to compensate for the model uncertainty problem.

Gaussian process model predictive control is an advanced control method that combines Gaussian process and model predictive control to effectively deal with nonlinearity, uncertainty and complexity [17]. By integrating the theory and methods of Gaussian processes with the framework of model predictive control to improve the accuracy of modelling system dynamics and uncertainty. [18] used effective sampling data to design a Gaussian process model based predictive control method to solve the problem of difficult modelling of sailboats, designed an adaptive weight term in the objective function and designed a heading compensated control method based on the deviation distance to improve the tracking accuracy. In the [19], by considering the residual uncertainty provided by the Gaussian process model, it was combined with the MPC to achieve a cautious control of a racing car, with significant improvements in performance and safety compared to the nominal controller. [20] transforms a nonlinear nonconvex problem into a convex one by deriving a GP-based local dynamics model, which achieves constraints on the control inputs and higher computational efficiency while ensuring trajectory tracking performance.

Based on the above discussion, to overcome the model uncertainty caused by the hydrodynamic effect and the ocean current during the high-speed movement of UUV, this paper presents a UUV 3D underwater trajectory tracking controller design based on a Gaussian process model predictive control method. The remainder of the paper is structured as follows: section 2 introduces the UUV mathematical model and its linear discretization; section 3 describes the model predictive controller design and the training of the Gaussian model for prediction of the unmodelled dynamics; section 4 conducts simulation experiments to numerically simulate the designed controller; and section 5 concludes the paper.

2 UUV Model

The UUV is assumed to be a rigid body, the origin of the inertial system coincides with the center of gravity of the UUV, and the UUV is symmetric left-right and up-down. At this point, the heeling angle is very small and can be ignored, so only five-degree-of-freedom mathematical model of UUV is considered. Based on the kinematics and dynamics equations of the UUV the model can be obtained as follows:

$$\begin{cases} \dot{\eta} = J(\eta)V \\ M\dot{V} + D(V)V + C(V)V + g(\eta) = \tau \end{cases} \tag{1}$$

where $\eta = [x \quad y \quad z \quad \theta \quad \psi]^T$ denotes the position and attitude of the UUV, $V = [u \quad v \quad w \quad q \quad r]^T$ denotes the velocity and angular velocity of the UUV, $\tau = [\tau_u \quad \tau_v \quad \tau_w \quad \tau_q \quad \tau_r]^T$ denotes the forces and moments on the UUV, $M = M_{RB} + M_A$ denotes the sum of the inertia matrix of the UUV itself and the additional inertia matrix of the hydrodynamics, $C(V) = C_{RB}(V) + C_A(V)$ represents the Coriolis inertial force matrix generated by the interaction between rigid body motion and fluid, $D(V)$ denotes the fluid damping matrix, and $g(\eta)$ denotes the restoring forces and moments.

Let $X = [\eta \quad V]^T$, $U = \tau$, a transformation of the above equation yields

$$\dot{X} = f(X,U) = \begin{cases} J(\eta)v \\ M^{-1}\left(\tau - D(v)v - C(v)v - g(\eta)\right) \end{cases} \tag{2}$$

Due to the limited resources of the controller on board the UUV, the nonlinear model in Eq.(2) is rewritten as a linear model to improve its computational efficiency. The first-order term is retained at the reference point (X_r, U_r) by Taylor series expansion.

$$\dot{X}_r = f(X_r, U_r) \tag{3}$$

$$\begin{aligned} \dot{X} = f(X_r,U_r) &+ \left.\frac{\partial f(X,U)}{\partial X}\right|_{\substack{X=X_r \\ U=U_r}} (X - X_r) \\ &+ \left.\frac{\partial f(X,U)}{\partial U}\right|_{\substack{X=X_r \\ U=U_r}} (U - U_r) \end{aligned} \tag{4}$$

The UUV linear error model can be obtained by subtracting equation (3) from equation (4)

$$\dot{X} - \dot{X}_r = \left.\frac{\partial f(X,U)}{\partial X}\right|_{\substack{X=X_r \\ U=U_r}} (X - X_r) + \left.\frac{\partial f(X,U)}{\partial U}\right|_{\substack{X=X_r \\ U=U_r}} (U - U_r) \tag{5}$$

Let $\dot{X}_e = \dot{X} - \dot{X}_r$, $U_e = U - U_r$, $A = \left.\frac{\partial f(X,U)}{\partial X}\right|_{\substack{X=X_r \\ U=U_r}}$, $B = \left.\frac{\partial f(X,U)}{\partial U}\right|_{\substack{X=X_r \\ U=U_r}}$, Then equation (5) can be rewritten as

$$\dot{X}_e = AX_e + BU_e \tag{6}$$

Then the model is discretized in terms of sampling time t_s and rewritten into state space method representation by the forward Eulerian method to provide a predictive model for subsequent linear model predictive controllers with the following expression

$$X_e(k+1) = A(k)X_e(k) + B(k)U_e(k) \tag{7}$$

where $A(k) = I + t_s A$, $B(k) = t_s B$.

3 Trajectory Tracking Controller Design

3.1 MPC Controller Design

The model predictive control consists of three main components, namely the predictive model, roll optimization and feedback correction. The design of the model predictive controller is based on the predictive model developed in the

previous section. Let the prediction time domain of MPC be N_p, and the control time domain be N_c.

This leads to the expression of the prediction equation at time k

$$\bar{X}(k+1)=\bar{A}(k)\bar{X}(k)+\bar{B}(k)\bar{U}(k) \tag{8}$$

where, $\bar{X}(k+1)=\begin{bmatrix} X(k+1|\ k) \\ X(k+2|\ k) \\ X(k+3|\ k) \\ \vdots \\ X(k+N_p|\ k) \end{bmatrix}$,

$$\bar{U}(k)=\begin{bmatrix} U(k+1) \\ U(k+2) \\ U(k+3) \\ \vdots \\ U(k+N_c-1) \end{bmatrix},\quad \bar{A}(k)=\begin{bmatrix} A \\ A^2 \\ A^3 \\ \vdots \\ A^{Np} \end{bmatrix}$$

$$\bar{B}(k)=\begin{bmatrix} B & \mathbf{0}_{5\times5} & \mathbf{0}_{5\times5} & \cdots & \mathbf{0}_{5\times5} \\ AB & B & \mathbf{0}_{5\times5} & \cdots & \mathbf{0}_{5\times5} \\ A^2B & AB & B & \cdots & \mathbf{0}_{5\times5} \\ \vdots & \vdots & \vdots & \ddots & \vdots \\ A^{N_p-1}B & A^{N_p-2}B & A^{N_p-3}B & \cdots & A^{N_p-N_c}B \end{bmatrix}.$$

Construct the cost function according to the set desired trajectory as

$$J=\left(\bar{X}(k+1)-\bar{X}_r(k+1)\right)^T Q\left(\bar{X}(k+1)-\bar{X}_r(k+1)\right) +\bar{U}(k)^T R\bar{U}(k) \tag{9}$$

where Q, R is the weight matrix; the first term represents the accumulation value of the error, the smaller the value the faster the convergence; the second term represents the accumulation value of the input, the smaller the value the less control energy consumption.

Considering the control input constraints $U_{\min}\le U\le U_{\max}$ in the actual operation process, the convex quadratic programming method that can effectively deal with the constraints is selected as the optimization algorithm for solving the problem, and its expression form after derivation is:

$$\begin{aligned} &\bar{U}^*(k)=\arg\min_{\bar{U}(k)}\frac{1}{2}\bar{U}^T(k)H(k)\bar{U}(k)+f^T(k)\bar{U}(k) \\ &\text{s.t. } X(k+1)=f\left(X(k),U(k)\right) \\ &\quad \bar{U}_{\min}\le\bar{U}(k)\le\bar{U}_{\max} \end{aligned} \tag{10}$$

where $\bar{U}^*(k)$ denotes the optimal control input at the current moment, $H(k)=2\left(\bar{B}^T(k)Q\bar{B}(k)+R\right)$,

$f(k)=2\bar{B}^T(k)Q\left(\bar{A}(k)\bar{X}(k)-\bar{X}_r(k)\right)$.

During each control cycle, the MPC uses the system state and model at the current moment to predict the system behavior at a future time, and by solving this optimization problem, the optimal sequence of control inputs is found and only the control inputs at the current moment are applied, allowing the UUV to better track the predefined desired trajectory.

3.2 GP-MPC Controller Design

The real model of the UUV system is assumed to be:

$$X(k+1)=f_t\left(X(k),U(k)\right) \tag{11}$$

For the part of the unmodelled dynamics caused by factors such as nonlinearities and disturbances in the system's own dynamics during practical applications, predictions are made by using GP, and the specific expressions of the constructed model are as follows:

$$\begin{aligned} X(k+1)=&f\left(X(k),U(k)\right) \\ &+B_d\left(d\left(X(k),U(k)\right)+w(k)\right) \end{aligned} \tag{12}$$

where $f\left(X(k),U(k)\right)$ is the nominal model based on the mechanism; $d\left(X(k),U(k)\right)$ is the unmodelled part to be predicted; $w(k)$ denotes gaussian noise with zero mean and diagonal matrix of variances, $w(k)\sim \mathrm{N}\left(0,\sigma^2\right)$;

$B_d=\left[0_{5*5};I_{5*5}\right]$.

To obtain the gaussian model, it is necessary to acquire valid sampled data for training. The control quantities generated by introducing the MPC controller of the nominal model are collected and acted on the real system to get the state output of the system.

The collected UUV state and control input data are used as training inputs S, and the deviation between the real model output and the nominal model output is calculated as the training output Ω, which can be described by the mean and covariance functions according to the definition of Gaussian Process.

$$\Omega\sim \mathrm{N}\left(0,K(S,S)+\sigma^2\right) \tag{13}$$

where $K(S,S)$ is kernel function.

The choice of the kernel function of GP has a significant impact on the model performance. The kernel function defines the correlation between data points in the input space and influences the predictive and generalization ability of the gaussian process model, the square exponential kernel function is chosen with the following expression:

$$K\left(s,\tilde{s}\right)=\sigma_f^2\exp\left(-\frac{1}{2}\left(s-\tilde{s}\right)^T L^{-1}\left(s-\tilde{s}\right)\right) \tag{14}$$

where $s,\tilde{s}$ denotes the two sampled data; the orthogonal diagonal length scale matrix L and the noise variance σ_f are hyperparameters of the Gaussian model.

The joint distribution of the training data and its output values for a given input s^* can be expressed as follows:

$$\begin{bmatrix}\Omega \\ f^*\end{bmatrix}\sim \mathrm{N}\left(\mathbf{0},\begin{bmatrix}K(S,S)+\sigma^2 & K\left(S,s^*\right) \\ K\left(s^*,S\right) & K\left(s^*,s^*\right)\end{bmatrix}\right) \tag{15}$$

The performance of the Gaussian Process is highly dependent on the choice of hyperparameters. Maximum

likelihood estimation with the increase of the sample size, the estimated value will gradually converge to the real parameters and the derivation process is relatively simple to ensure the accuracy of the estimation, compared with the Bayesian optimization of the computational cost is low, so the choice of maximum likelihood estimation of hyperparameters for optimization processing, the likelihood function is

$$\log p(\Omega|\ \sigma_f, L) = -\frac{1}{2}\Omega^T K_{s^*s^*}^{-1}\Omega - \frac{1}{2}\log\left|K_{s^*s^*}\right| - \frac{N}{2}\log(2\pi) \tag{16}$$

where the first term is the data term denoting the information provided through the observed data, which is used to adjust the fit of the Gaussian Process model to the observed data; the second term is the parameter term of the kernel function, which is used to describe the correlation between the observed data; the third term is the constant term.

Based on the above results, the mean and covariance functions can be obtained as:

$$\begin{aligned}\mu(s^*) &= K_{ss^*}\left(K_{s^*s^*} + I\sigma^2\right)^{-1}\Omega \\ \Sigma(s^*) &= K_{ss} - K_{ss^*}\left(K_{s^*s^*} + I\sigma^2\right)^{-1}K_{s^*s}\end{aligned} \tag{17}$$

The unmodelled part can therefore be approximated by a Gaussian process of the following form

$$d\left(X(k),U(k)\right) \sim \mathrm{N}\left(\mu(s^*),\Sigma(s^*)\right) \tag{18}$$

The predictive model is introduced into the nominal model and the model predictive control controller is applied for underwater 3D trajectory tracking with the following new expression.

$$\begin{aligned}&\bar{U}^*(k) = \arg\min_{\bar{U}(k)} \frac{1}{2}\bar{U}^T(k)H(k)\bar{U}(k) + f^T(k)\bar{U}(k) \\ &\text{s.t. } X(k+1) = f\left(X(k),U(k)\right) \\ &\qquad + B_d\left(d\left(X(k),U(k)\right) + w(k)\right) \\ &\bar{U}_{\min} \le \bar{U}(k) \le \bar{U}_{\max}\end{aligned} \tag{19}$$

4 Simulation Results and Analysis

Based on the analysis of the UUV trajectory tracking and the study of the controller, the Gaussian Process model predictive controller is simulated and designed. The parameters provided in the [11] are chosen for the nominal UUV model and a random offset between ±50% is introduced to the parameters in the real model.

Simulation time $t = 350s$, set the desired 3D trajectory as:

$$\begin{cases} x_r = 10\sin(0.04t) \\ y_r = 10\cos(0.04t) \\ z_r = -0.05t \end{cases} \tag{20}$$

Sampling time $t_s = 0.5$, $Q = 50 * diag(1,1,1,1,1,1,1,1,1,1)$, $R = 0.001 * diag(1,1,1,1,1,1)$, $N_p = 20$, $N_c = 20$, it is applied to the designed controller for simulation experiments. The controller simulation using the nominal model prediction was used to collect training data at 0~200s and the Gaussian Process model was added after 200s.

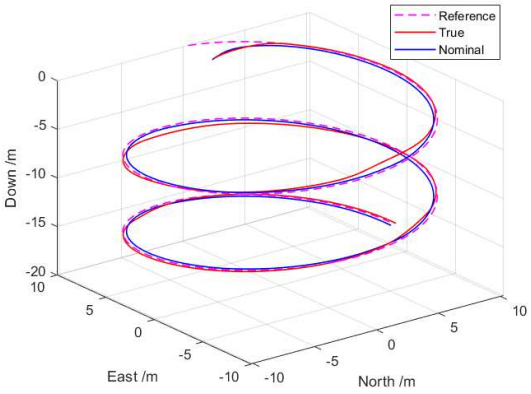

Fig. 1: 3D tracking trajectory

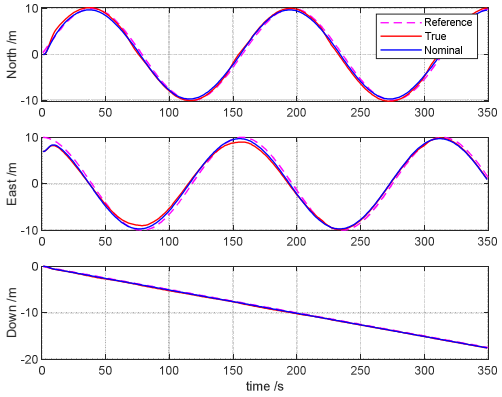

Fig. 2: UUV location comparison

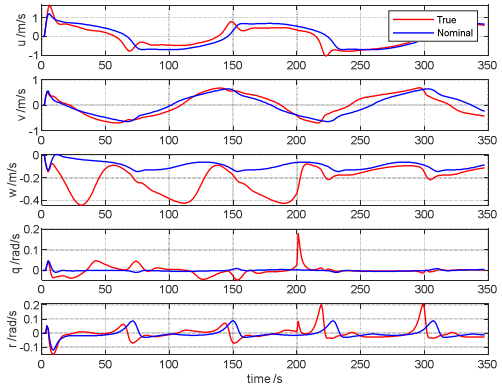

Fig. 3: Velocity profiles for each degree of freedom

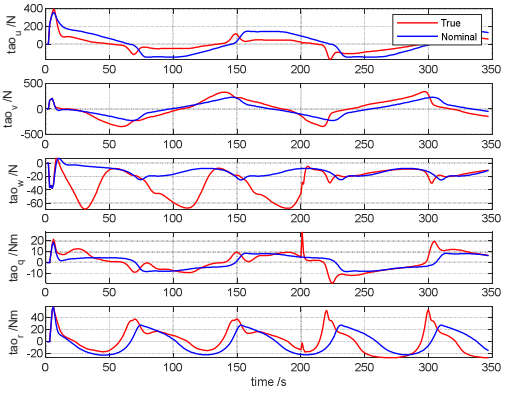

Fig. 4: Force and moment variation curves

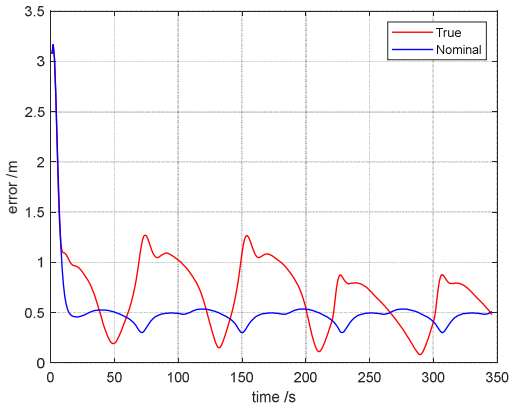

Figure. 5: Total error curve

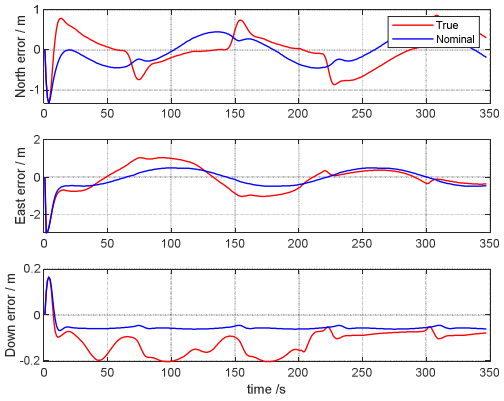

Figure. 6: Position error curve

The blue curve in the figure represents the controller control effect in the case of using the nominal model, and the red curve represents the control effect of using the nominal model output for the real system.

From Fig. 1 and Fig. 2, it can be intuitively seen that at 0~200s, due to the modelling error between the nominal model and the real system, when the controller output is applied to the real system, although the controller can still track the desired trajectory, but at this time, the control effect will be affected; at 200~350s, it can be seen that with the introduction of the Gaussian Process model, the trajectory of the UUV motion can be gradually approximated to the desired trajectory, and a better control effect can be achieved;

From Fig. 3 and Fig. 4, it can be seen that when the Gaussian Process is introduced in the 200s, the speed and control output will change suddenly due to the change of the prediction model, but after that, it can keep relatively stable change; from Fig. 5, it can be seen that after the introduction of the Gaussian process in the 200s, the maximal tracking error by the UUV will be 0.9 m from 1.3 m; From Fig. 6, it can be seen that the fluctuation of the change of the error in all directions is obvious after joining the Gaussian model become smaller, and the controller can achieve better stability.

5 Conclusion

1) In this paper, a five-degree-of-freedom mathematical model of UUV is established and linearly discretized, and then the model predictive control method is used to design the UUV trajectory tracking controller.

2) A Gaussian process is introduced to predict the uncertainty of the model parameters when the UUV is moving at high speed, and it is proved through simulation experiments that it can better achieve the underwater three-trajectory tracking task of the UUV compared with the traditional model predictive controller.

3) In the subsequent research, the problem of reduced computational efficiency due to the large amount of collected data as the task proceeds should also be considered.

References

[1] ER M J, GONG H B, LIU Y, et al. Intelligent Trajectory Tracking and Formation Control of Underactuated Autonomous Underwater Vehicles: A Critical Review. *IEEE Transactions on Systems Man Cybernetics-Systems*, 2024, 54(1): 543-555.

[2] BASHIR A, KHAN S, IQBAL N, et al. A Review of the Various Control Algorithms for Trajectory Control of Unmanned Underwater Vehicles. *Sustainability*, 2023, 15(20): 14691.

[3] ZHANG Y, LIU X, LUO M, et al. MPC-based 3-D trajectory tracking for an autonomous underwater vehicle with constraints in complex ocean environments. *Ocean Engineering*, 2019, 189: 106309.

[4] TIJJANI A S, CHEMORI A, CREUZE V. A survey on tracking control of unmanned underwater vehicles: Experiments-based approach. *Annual Reviews in Control*, 2022, 54: 125-47.

[5] BINGUL Z, GUL K. Intelligent-PID with PD Feedforward Trajectory Tracking Control of an Autonomous Underwater Vehicle. *Machines*, 2023, 11(2): 300.

[6] TANG J, DANG Z K, DENG Z C, et al. Adaptive fuzzy nonlinear integral sliding mode control for unmanned underwater vehicles based on ESO. *Ocean Engineering*, 2022, 266 (5): 113154.

[7] DONG B T, SHI Y, XIE W, et al. Learning-based robust optimal tracking controller design for unmanned underwater vehicles with full-state and input constraints. *Ocean Engineering*, 2023, 271: 113757.

[8] BAN H J, YANG X, LUO X Y, et al. Fuzzy-based Tracking Controller Design for Autonomous Underwater Vehicle. in *proceedings of the 36th Chinese Control Conference*, 2017: 4813-4818.

[9] YU H M, GUO C, YAN Z P. Globally finite-time stable three-dimensional trajectory-tracking control of underactuated UUVs. *Ocean Engineering*, 2019, 189: 106329.

[10] ZHANG Y D, LIU X F, LUO M Z, et al. MPC-based 3-D trajectory tracking for an autonomous underwater vehicle with constraints in complex ocean environments. *Ocean Engineering*, 2019, 189: 106309.

[11] ZHANG W, WANG Q, WU W H, et al. MPC for 3-D Trajectory Tracking of UUV with Constraints Using Laguerre Functions. in *proceedings of the OCEANS Hampton Roads Conference*, 2022: 1-6.

[12] ZHANG W, WANG Q, WU W H, et al. Event-trigger NMPC for 3-D trajectory tracking of UUV with external disturbances. *Ocean Engineering*, 2023, 283: 115050.

[13] GAN W Y, ZHU D Q, JI D X. QPSO-model predictive control-based approach to dynamic trajectory tracking control for unmanned underwater vehicles. *Ocean Engineering*, 2018, 158: 208-220.

[14] WANG X W, YAO X L, ZHANG L. Path Planning under Constraints and Path Following Control of Autonomous Underwater Vehicle with Dynamical Uncertainties and Wave

Disturbances. *Journal of Intelligent & Robotic Systems*, 2020, 99: 891-908.

[15] GONG P, YAN Z P, ZHANG W, et al. Trajectory tracking control for autonomous underwater vehicles based on dual closed-loop of MPC with uncertain dynamics. *Ocean Engineering*, 2022, 265: 112697.

[16] YAN Z P, YAN J Y, CAI S J, et al. Robust MPC-based trajectory tracking of autonomous underwater vehicles with model uncertainty. *Ocean Engineering*, 2023, 286(2): 115617.

[17] WANG J, FADER M T H, MARSHALL J A. Learning-based model predictive control for improved mobile robot path following using Gaussian processes and feedback linearization. *Journal of Field Robotics*, 2023, 40(5): 1014-1033.

[18] DONG Y Q, WU N L, QI J, et al. Predictive Course Control and Guidance of Autonomous Unmanned Sailboat Based on Efficient Sampled Gaussian Process. *Journal of Marine Science and Engineering*, 2021, 9(12): 1420.

[19] HEWING L, KABZAN J, ZEILINGER M N. Cautious Model Predictive Control Using Gaussian Process Regression. *IEEE Transactions on Control Systems Technology*, 2020, 28(6): 2736-2743.

[20] CAO G, LAI E M K, ALAM F. Gaussian Process Model Predictive Control of an Unmanned Quadrotor. in *2nd International Conference on Control, Automation and Robotics*, 2016: 200-206.

Proceedings of the 3rd Conference on Fully Actuated System Theory and Applications
May 10-12, 2024, Shenzhen, China

Low-cost adaptive obstacle avoidance trajectory control for express delivery drone

Yanhui Zhang[1,2], Yifan Zhang[1], Zheyu Tong[1], Hua Yang[1], Caisheng Wei[3], Weifang Chen[1]

1. School of Aeronautics and Astronautics, Zhejiang University, Hangzhou 310058, P. R. China
E-mail: yanhuizhang@zju.edu.cn

2. Department of Electrical and Computer Engineering, National University of Singapore, Singapore 117583, Singapore

3. School of Automation, Central South University, Changsha 410083, P. R. China

Abstract: This paper studies quadcopters' obstacle avoidance trajectory control (OATC) problem for express delivery. A new nonlinear adaptive learning controller that is low-cost and portable to different wheelbase sizes is proposed to adapt to large-angle maneuvers and load changes in UAV delivery missions. The controller consists of a nonlinear variable gain (NLVG) function and an extreme value search (ES) algorithm to reduce overshoot and settling time. Finally, simulations were conducted on a quadcopter to verify the effectiveness of the proposed control scheme under two typical collision-free trajectories.

Key Words: Adaptive Learning Control, Delivery Drone, Obstacle Avoidance

1 Introduction

The obstacle avoidance trajectory control (OATC) problem of the uncrewed aerial vehicle (UAV) has received significant attention recently in the real world (indoor and outdoor) as illustrated in [1]. In these scenarios, the drones that can avoid obstacles have more application value for many missions, such as exploration, swarms flight, and prevention-control of new coronavirus (see [2], [3], and references therein). Since drones are not limited by infrastructure such as light poles, streams, and walls, they can lower labor costs and reduce package delivery time [4]. Significantly, the demand for drone delivery tasks is increasing sharply, and it is vital to realize obstacle avoidance flight control in 3D airlines [5]. Hence, in the future scenario of dense air flight traffic, OATC between UAVs-UAVs and UAVs-MAVs (Manned Vehicle) will be sensitive.

In the last decades, several classical methodologies have been presented for OATC to achieve the flight control of quadcopters, such as detection and image processing in [6]. Also, for such UAV obstacle avoidance problems, some researchers have done some exciting work in the fields of motion planning for drones. Besides, some others focus on the controller problems, as our former work in [7] and W. Bao described in [8]. However, due to the varied layout and motors, quadcopters' parameters are different in practical scenarios. Hence, the controller transplant cost must be lowered to adapt to another flight platform. Thus, the NN controllers have yet to be used on a large scale in recent years. In recent years, some methods have been proposed to solve the problem (such as PID, ESC [9]). Some others designed the control system combined PID/MPC with robust control and learning-based adaptive control in [10] and [11]. Motivated by the observation above, this paper proposes NLVG-PID, which could reduce the overshoot of fixed-gains PID controllers. The main contributions of this work lie in: 1) The structure of the fixed-gain PID controller and the nonlinear dynamics and kinematics models are analyzed in this work. 2) The NLVG-PID controller of a delivery quadcopter is designed, and the extremum seeking is introduced to learn the optimal nonlinear PID parameter under boundary conditions. To our knowledge, this is the first NLVG-PID obstacle avoidance controller to be used in delivery drones. 3) A simulation was performed on a quadcopter to verify the effectiveness of the proposed control scheme under two typical collision-free trajectories.

The Scheme of quadcopter control system is described in Fig. 1.

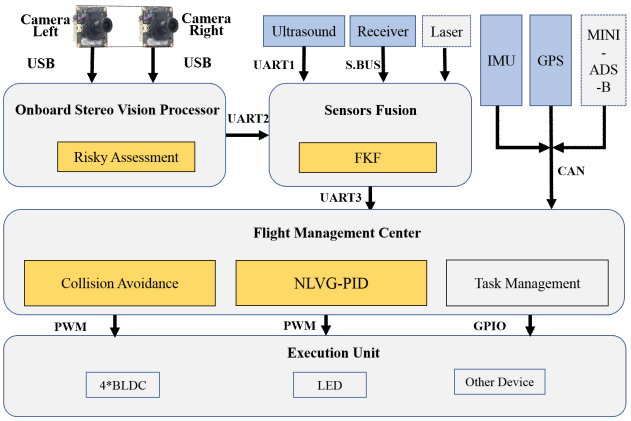

Fig. 1: Scheme of NLVG-PID 3D delivery drone system.

The remainder of this paper is organized as follows: Section 2, the mathematical model of dynamics, kinematics, and obstacle detection pipeline of the quadcopter are described in detail. In Section 3, the NLVG-PID framework and an ES method for boundary optimal parameter determination are developed. The stability analysis of the closed-loop system is also provided in this section. In Section 4, the quadcopter's NLVG-PID controller system has been verified in four-side route, 8-character route, and scenic spiral position tracking, respectively. Section 5 concludes this work.

2 Problem formulation

This paper assumes that the structure of the express delivery drone, an X-type quadcopter from [6], is known, but

This work was supported in part by the National Natural Science Foundation of China for the Near Space Research Program under Grant U20B2007 and Grant 12002306. The first author of this paper (Yanhui Zhang) gratefully acknowledges the support by the China Scholarship Council (grant number 202306320387).

the specific load weight and the precise model of the drone are unknown. Obstacle avoidance is performed in three-dimensional space. First, the threat area is circled in the top view, as shown in Fig.2. Avoid obstacles, and then choose whether to fly upward or downward according to the distance cost in Euclidean space.

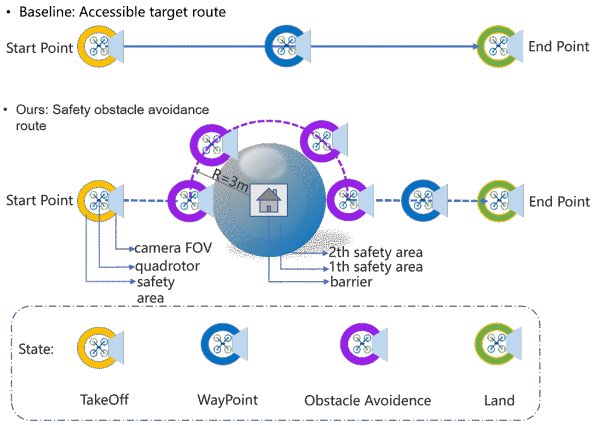

Fig. 2: Delivery drone 3D obstacle avoidance process.

To facilitate the analysis of the rotation and translation of the UAV, a coordinate system is depicted as shown in our former work [12], the $B = (X_B, Y_B, Z_B)$ denotes the body-fixed coordinate system (B-frame), $E = (X_E, Y_E, Z_E)$ is the earth inertial frame (E-frame), $V_E = (v_{ex}, v_{ey}, v_{ez})$ indicates the velocity of quadcopter in E-frame. The schematic diagram of the quadcopter control system includes the following components, as displayed in Fig. 1.

3 Controller design

In this paper, we defined basic PID controller as follows:

$$U(t)_j^{\text{PID}} = K_p^j \cdot e(t) + K_d^j \cdot \dot{e}(t) + K_i^j \cdot \int_0^t e(\tau) d\tau, \quad (1)$$

with $j \in [x, y, z, \psi]$ and

$$\begin{cases} e(t) = \zeta_{desire} - \zeta_{real}, \\ \dot{e}(t) = \dot{\zeta}_{desire} - \dot{\zeta}_{real}, \end{cases} \quad (2)$$

$\zeta_{desire}, \zeta_{real}$ are the desired value and the real value of ζ.

Remark 1 *It can be observed that the quadcopter system is highly nonlinear and strongly coupled.*

Remark 2 *It can be seen that the quadcopter system is highly nonlinear and strongly coupled. Usually, in order to reduce the complexity of control system design, channel decoupling is used to decouple the three-axis position and attitude control.*

3.1 NLVG-PID controller

Defining nonlinear variable gains $f_{K_p(e)}$ of P controller in channle j. Besides, δ_2 impact on $f_{K_p(e)}$. In order to improve the PID controller's fast control capability for errors of different sizes, nonlinear gain terms are used instead of the fixed terms K_p, K_i, K_d in (1). When the small error is close to zero, the value of the NLVG parameter reaches the lower limit $k_{\min} = [k_{p1}, k_{i1}, k_{d1}]$. In the case of large errors,

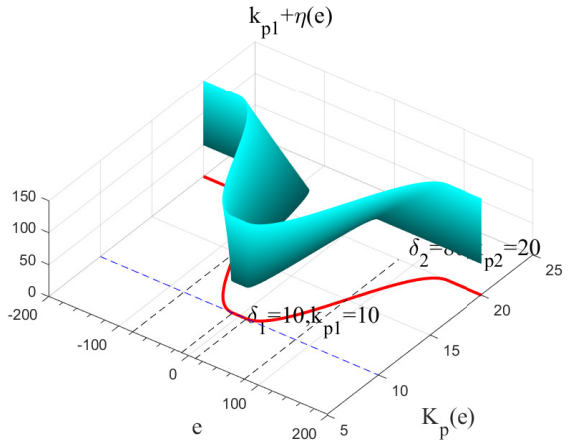

Fig. 3: The change process of NLVG-PID.

the upper limit $k_{\max} = [k_{p2}, k_{i2}, k_{d2}]$ is reached, as shown in Fig. 3. Hence, we design the control law as follows:

$$U(t)_j^{\text{NLVG-PID}} = f_{K_p}^j \cdot e(t) + f_{K_i}^j \cdot \dot{e}(t) + f_{K_d}^j \cdot \int_0^t e(\tau) d\tau, \quad (3)$$

where

$$f_{K_p}^j = \begin{cases} k_{p1}^j, & |e(t)| \in [0, \delta_{p1}), \\ k_{p1}^j + \eta_p^j, & |e(t)| \in [\delta_{p1}, \delta_{p2}], \\ k_{p1}^j + 2A_P^j, & |e(t)| \in (\delta_{p2}, +\infty), \end{cases} \quad (4)$$

and

$$\eta_p^j = -A_P^j \cdot \cos\left(\frac{2\pi}{\delta_{p2} - \delta_{p1}} |e(t)| - \delta_{p1}\right) + A_P^j, \quad (5)$$

where $\delta_1, \delta_2 \in \mathbb{R}^+$, which based on the performance metrics (13), as shown in Fig. 3. Likewise, the integral item is

$$f_{K_i}^j = \begin{cases} k_{i1}^j, & |\dot{e}(t)| \in [0, \delta_{i1}), \\ k_{i1}^j + \eta_i^j, & |\dot{e}(t)| \in [\delta_{i1}, \delta_{i2}], \\ k_{i1}^j + 2A_I^j, & |\dot{e}(t)| \in (\delta_{i2}, +\infty), \end{cases} \quad (6)$$

where

$$\eta_i^j = -A_I^j \cdot \cos\left(\frac{2\pi}{\delta_{i2} - \delta_{i1}} |\dot{e}(t)| - \delta_{i1}\right) + A_I^j, \quad (7)$$

and the differential item is

$$f_{K_d}^j = \begin{cases} k_{d1}^j, & |\int_0^t e(\tau)d\tau| \in [0, \delta_{d1}), \\ k_{d1}^j + \eta_d^j, & |\int_0^t e(\tau)d\tau| \in [\delta_{d1}, \delta_{d2}], \\ k_{d1}^j + 2A_D^j, & |\int_0^t e(\tau)d\tau| \in (\delta_{d2}, +\infty), \end{cases} \quad (8)$$

where

$$\eta_d^j = -A_D^j \cdot \cos\left(\frac{2\pi}{\delta_{d2} - \delta_{d1}} \left| \int_0^t e(\tau)d\tau \right| - \delta_{d1}\right) + A_D^j. \quad (9)$$

Remark 3 *The variables k_1 and $k_2 = k_1 + 2A^j$ in (8) are learning through the ES method [13].*

Defining the state vector of the quadcopter as:

$$X = \begin{bmatrix} \phi & \dot{\phi} & \theta & \dot{\theta} & \psi & \dot{\psi} & x & \dot{x} & y & \dot{y} & z & \dot{z} \end{bmatrix}^\top, \quad (10)$$

and the input vector of controller can be formulated as

$$\begin{aligned} U &= [U_x, U_y, U_z, U_\phi, U_\theta, U_\psi] \\ &= [\ddot{x}_{real}, \ddot{y}_{real}, F_t, \Gamma_x, \Gamma_y, \Gamma_z], \end{aligned} \tag{11}$$

where $U \in \mathbb{R}^6$, and

$$\begin{cases} U_x = \ddot{x}_{desire} + f^x_{K_p}(e_x) + f^x_{K_i}\left(\int e_x dt\right) + f^x_{K_d}(\dot{e}_x) \\ U_y = \ddot{y}_{desire} + f^y_{K_p}(e_y) + f^y_{K_i}\left(\int e_y dt\right) + f^y_{K_d}(\dot{e}_y) \\ U_z = f^z_{K_p}(e_z) + f^z_{K_i}\left(\int e_z dt\right) + f^z_{K_d}(\dot{e}_z) \\ U_\phi = f^\phi_{K_p}(e_\phi) + f^\phi_{K_i}(\dot{e}_\phi) + f^\phi_{K_d}\left(\int e_\phi dt\right) \\ U_\theta = f_{\theta 1}(e_\theta) + f_{\theta 2}(\dot{e}_\theta) + f_{\theta 3}\left(\int e_\theta dt\right) \\ U_\psi = f_{\psi 1}(e_\psi) + f_{\psi 2}(\dot{e}_\psi) + f_{\psi 3}\left(\int e_\psi dt\right). \end{cases} \tag{12}$$

where $e_i = e_{i,desire} - e_{i,real}$, and$i \in \{x, y, z, \phi, \theta, \psi\}$. In (12), $e_{i,real}$ is the real value of e_i, and $e_{i,desire}$ is the desire value of e_i.

3.2 ES in NLVG-PID

In ES, disturbance driving is used to find and maintain an extremum value for dynamic systems. This approach was first proposed by Leblanc, and the stability analysis of ES was first generally implemented by Krstic in [14]. We used the ES method to calculate the local optimal PID gain for the controller. The input is the step signal (e.g., maximum desired angle or position), while the output is the boundary of variable gains, where $\vec{K}_1 = (k_{p1}, k_{i1}, k_{d1})$ and $\vec{K}_2 = (k_{p2}, k_{i2}, k_{d2})$. $\vec{K} = (k_p, k_i, k_d)$. The cost function of drone performance during the time $t \in [t_0, t_f]$ can be defined as

$$\mathcal{J}(\vec{K}) = \frac{1}{t_f - t_o} \int_{t_0}^{t_f} e^2(t, \vec{K}) dt, \tag{13}$$

where $e(t, \vec{K})$ denotes the error in following the desired path with initial disturbance using parameters $\vec{K}$. Suppose the cost function gradient, $\nabla\mathcal{J}(\vec{K})$, is available and could iteratively improve the parameter of the NLVG-PID controller. The parameter iterate rule can be defined as

$$\vec{K}(t) = \vec{K}(t-1) - \alpha \nabla \mathcal{J}(K(\vec{t-1})), \tag{14}$$

where α denotes the step size of the parameter of the quadcopter at each step of the iteration, and $\vec{K}(t-1)$ denotes the parameter vector after $t-1$ times iterations. Then the key point is to estimate $\nabla\mathcal{J}(\vec{K}(t-1))$. That is

$$\nabla \mathcal{J}(\vec{K}) = \left(\frac{\partial}{\partial K_p}\mathcal{J}(\vec{K}), \frac{\partial}{\partial K_i}\mathcal{J}(\vec{K}), \frac{\partial}{\partial K_d}\mathcal{J}(\vec{K}) \right). \tag{15}$$

From (13), the derivative to the gains numerically can be computed as

$$2\frac{\partial}{\partial K} J(\vec{K}) \approx \frac{\mathcal{J}\left(\vec{K} + \delta \cdot \hat{U}_K\right) - \mathcal{J}\left(\vec{K} - \delta \cdot \hat{U}_K\right)}{\delta}, \tag{16}$$

where U_K is the unit vector in the K direction. When $\delta \to 0$, this approximation can minimize the cost function and optimize the local boundary PID parameters. The parameters are randomly initialized to positive numbers, and the periodic perturbation function is evaluated to evaluate the varying PID parameters and gradients of $\mathcal{J}(\vec{K})$. To avoid the cost function falling into a local optimum, the initial value of the optimization value needs to be randomly reset multiple times and compared to find the best result. By plotting the functional relationship between the cost function and the number of iterations, we can observe the convergence of the system and verify the working principle of this learning method.

3.3 Strategy planning of obstacle avoidance

The stereo cameras are used to detect the largest threat in the visual range of the cameras, which fuse with distance from the ultrasonic sensor to the obstacles Obj^j_{risky} front at the visual risk assessment models. The relative position of the quadcopter is $p = (x, y, z)$ and the direction is $v = (v_x, v_y, v_z)$. The l_s denotes the distance of the current position and the boundary safety position of quadcopter P^i_{safe}, and the safety radius R_{safe} of the generated 3D sphere Ω in intersecting line on the direction of the velocity vector, Bessel curve fitting is carried out by setting the trajectory of UAV that meets the dynamic constraints.

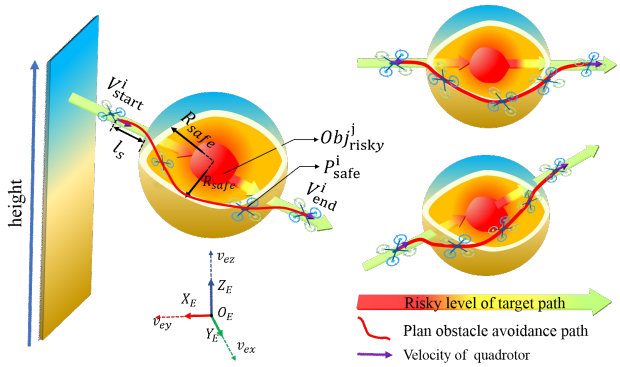

Fig. 4: Quadcopter path planning of free-collision in 3D space.

4 Simulation and results

A simulation experiment was established to verify the efficiency of the NLVG-PID controller. The specific test parameters are set as [12]. The rate inner loop controller is the lowest-level controller of the quadcopter. Aiming at the internal loop angle control's step response, PID control and NLVG-PID plus ES control simulation experiments were conducted. The results and analysis are shown in Fig. 5 and Table 4. It should be noted that the performance of the NLVG-PID controller uses three cost functions (IAE: integrated absolute error, ITAE: integration time and absolute error, ITSE: integrated time-weighted squared error), as set $t^{angle}_{peak1} = 0.15s$, $t^{position}_{peak2} = 0.37s$.

The initial parameters of the quadcopter can be determined as [6]. First, the inner loop controller parameters $K^\phi_{PID} = (8, 0.1, 5)$, $K^\theta_{PID} = (8, 0.1, 5)$, $K^\psi_{PID} = (8, 0.1, 5)$, and the outter loop position controller initial parameters are $K^\phi_{PID} = (5, 0.2, 5)$, $K^\theta_{PID} = (5, 0.2, 5)$, $K^\psi_{PID} = (5, 0.2, 5)$. Second, the scaler gains $\delta_1 = 0.01$, $\delta_2 = 0.838$, then the controller parameters are learned by ES in subsection 3.2. Moreover, the step size of this simulation is $\Delta t = 0.01s$; the total time is $T_{total} = 140s$.

Table 1: Results for fixed-PID and NLVG controller in step singal of quadcopter

Channel	PID			NLVG-PID (Ours)			Function
	IAE	ITAE	ITSE	IAE	ITAE	ITSE	-
ϕ	1025.01	5.10	185.75	933.8	4.71	156.42	attitude in x axis (^{o})
θ	1015.29	5.03	172.42	910.0	4.33	140.90	attitude in y axis (^{o})
x	94.82	0.47	0.92	86.32	0.43	0.78	position x
y	91.82	0.41	0.89	82.66	0.36	0.70	position y

* IAE $= \frac{1}{t_{peak}} \int_0^{t_{peak}} |e|dt$; ITAE $= \frac{1}{t_{peak}} \int_0^{t_{peak}} t|e|dt$; ITSE $= \frac{1}{t_{peak}} \int_0^{t_{peak}} te^2dt$.

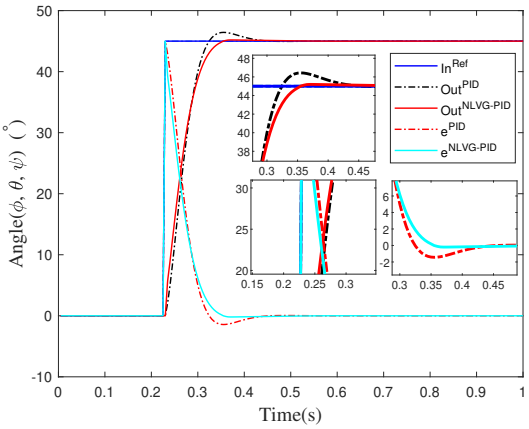

Fig. 5: Attitude controller step-response of PID and NLVG-PID

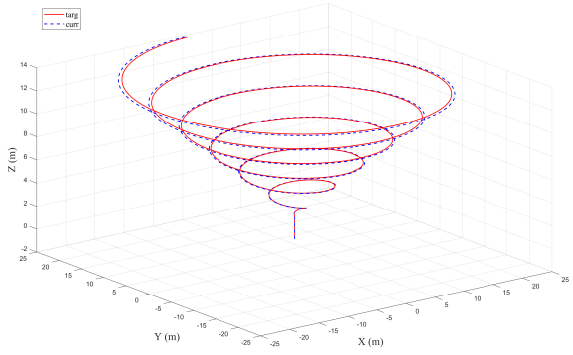

Fig. 6: Storm-type obstacle avoidance routes in 3D view.

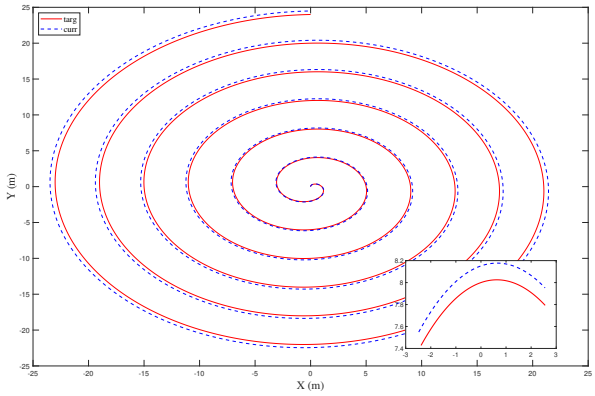

Fig. 7: b) Storm-type obstacle avoidance routes in X-Y view.

4.1 Example 1: Storm path following

To verify the effect of large-angle turning and small-angle adjustment of aircraft under the disturbance of obstacles, a storm airline is a continuous arc of increasing radius and height, designed as Fig. 7.

As shown in the Fig. 7-10, when the aircraft executes the takeoff command at t=20s, the attitude angle error is significant at this time. Then, PID and dynamic adaptive control algorithms are used for individual control. During the execution of the storm path, the attitude angle error decreases, and the control optimization effect is significantly improved. The Euler angle (ϕ, θ, ψ), the angle error $(\phi_{err}, \theta_{err}, \psi_{err})$, the position (X, Y, Z), and the position error $(X_{err}, Y_{err}, Z_{err})$ in OATC are described in Fig. 7-10, respectively. From these figures, it can be observed that the angle and position errors can lead to a fast convergence into the local neighborhood areas in both the fixed-gain PID controller and NLVG-PID. However, the proposed NLVG-PID with ES control systems can perform well in OATC missions. It should be noted that the altitude of these missions is to keep the same value as $10m$.

The desired trajectory path (Lissajous-type) of the quadcopter is depicted in Fig. 12, and the Euler angle and the position error in OATC are described in Fig. 12-16, respectively. As can be seen from these figures, using NLVG is better than PID in calculating a fast and smooth control output, thereby quickly tracking the desired command. It is worth noting that the height of this mission dynamically changes with the Lissajous-type path, which can verify that the proposed NLVG-PID performs well in periodic 3D path tracking.

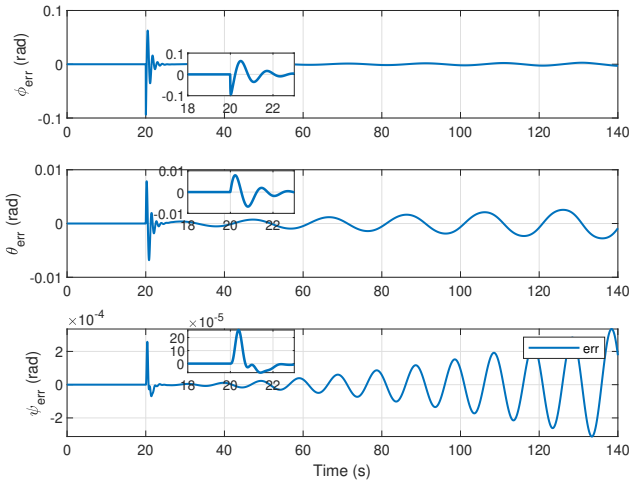

Fig. 8: PID: angle error of Storm-type path.

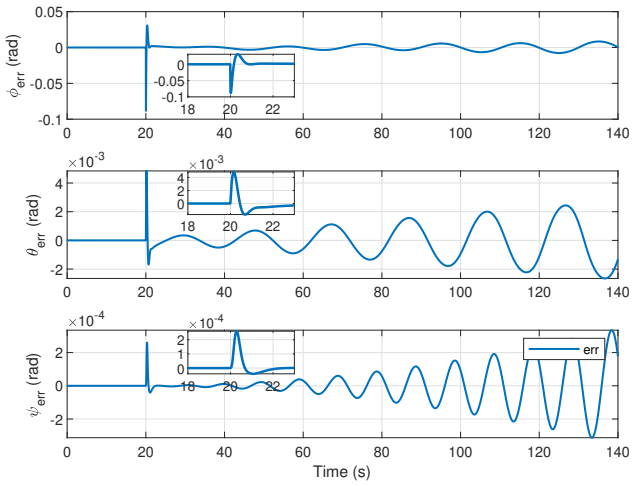

Fig. 9: NLVG-PID: angle error of Storm-type path.

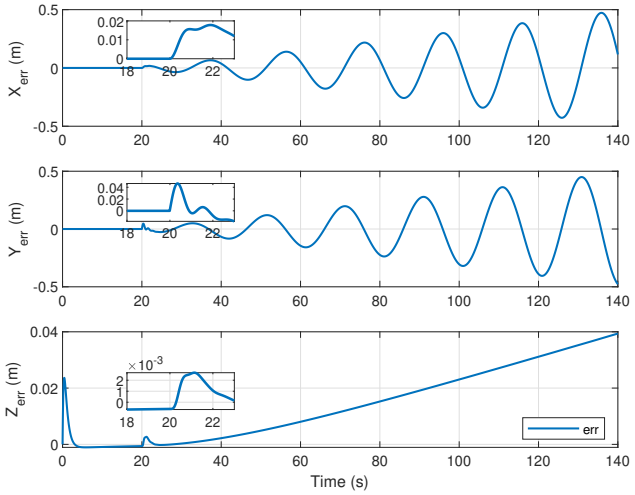

Fig. 10: PID: position error of the Storm-type path

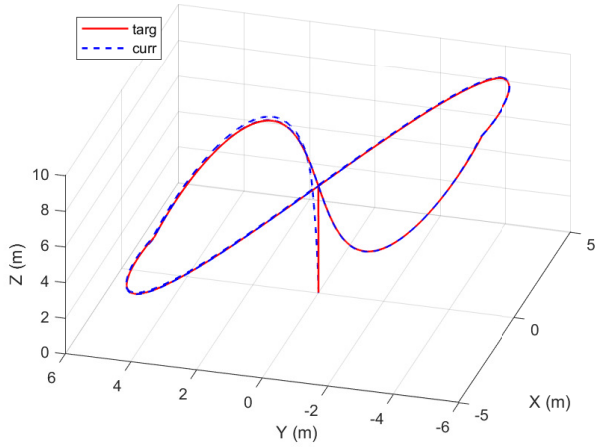

Fig. 11: Lissajous-type path in 3D view.

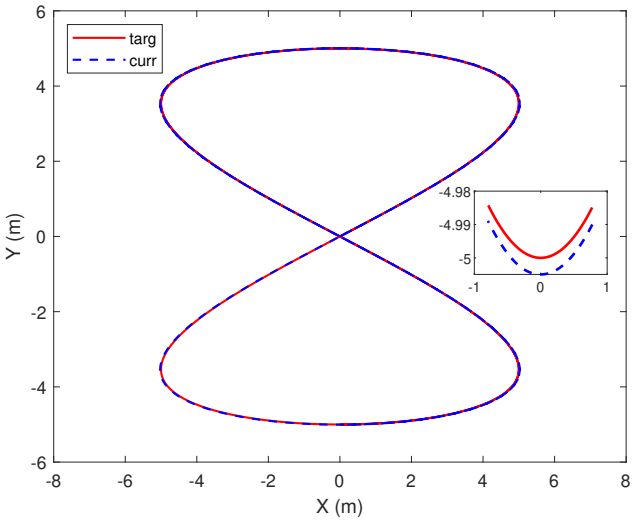

Fig. 12: Lissajous-type path in X-Y view.

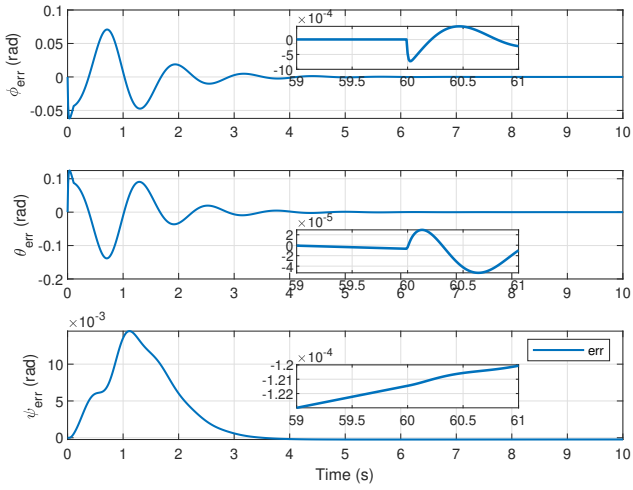

Fig. 13: PID: attitude angle error in Lissajous-type path.

4.2 Example 2: Lissajous curve following

This work designed a 3D-Lissajous curve to conduct flight simulation verification of the quadcopter's control performance under periodic disturbances.

As can be seen in Fig. 14, when the aircraft executes the takeoff command at t=0s, the position and attitude angle errors at the moment of takeoff are significant. Then, PID and dynamic adaptive control algorithms are used for control, respectively. During the execution of the Lissajous path, the attitude angle error is gradually reduced by about 50%, the position error is reduced by about 15%, and the control optimization effect is partially improved. Compared with Example 4.1, the path of Example 4.2 is more complex, and there are significant changes in height and position, so the effect improvement is slightly reduced.

5 Conclusion

This paper studies the active motion control problem of quadcopter obstacle avoidance. A new design scheme for adaptive learning control of flight controllers based on low-cost dynamic linear optimization under uncertain conditions with obstacles is proposed. First, an NLVG-PID controller is presented for the formulated UAV model. Furthermore, ES is used to learn optimal NLVG-PID parameters in offline

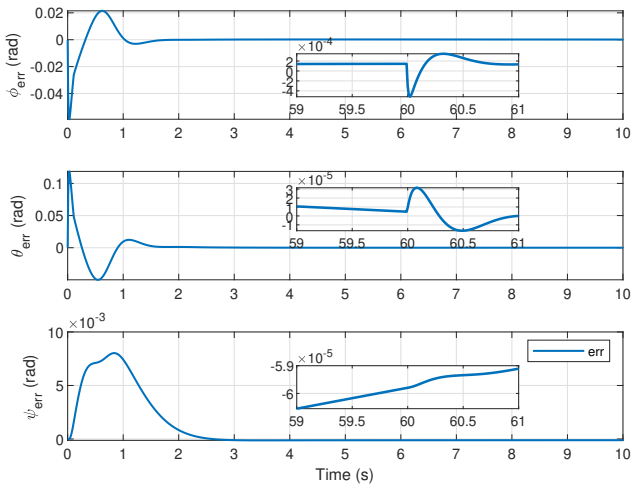

Fig. 14: NLVG-PID: attitude angle error in Lissajous-type path.

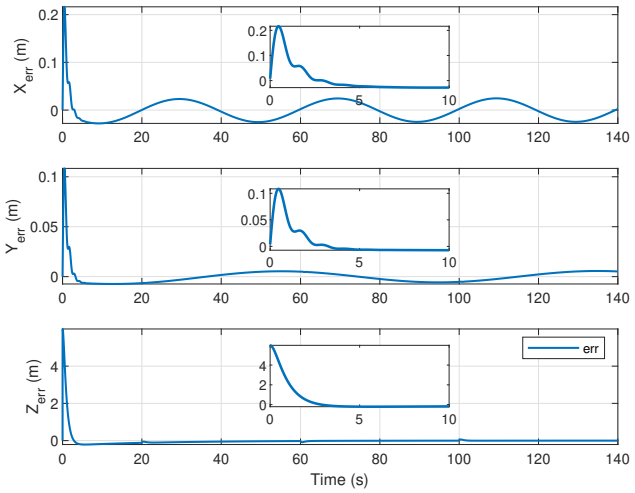

Fig. 15: PID: position errors in Lissajous-type path.

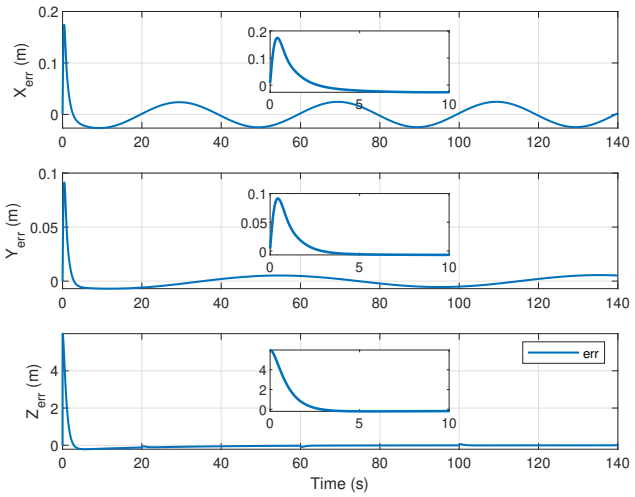

Fig. 16: NLVGPID: position errors in Lissajous-type path.

maximum or minimum error step signals. Numerical simulations were performed based on this design, and the results show that the proposed adaptive learning controller can reduce response overshoot and settling time in typical 3D path curves (such as storm paths).

References

[1] S. Bouabdallah, P. Murrieri, and R. Siegwart, "Design and control of an indoor micro quadrotor," *IEEE International Conference on Robotics and Automation, 2004. Proceedings. ICRA 04. 2004*, vol. 5, pp. 4393–4398 Vol.5, 2004.

[2] Y. Chen, D. Huang, N. Qin, and Y. Zhang, "Adaptive iterative learning control for a class of nonlinear strict-feedback systems with unknown state delays," *IEEE Transactions on Neural Networks and Learning Systems*, vol. 34, no. 9, pp. 6416–6427, 2023.

[3] Y. Zhang, J. Sun, H. Liang, and H. Li, "Event-triggered adaptive tracking control for multiagent systems with unknown disturbances," *IEEE Transactions on Cybernetics*, vol. 50, no. 3, pp. 890–901, 2020.

[4] Q. Xu and Y. Zhang, "Event-triggered nonlinear information fusion preview control of a two-degree-of-freedom helicopter system," *Aerospace Science and Technology*, vol. 140, p. 108474, 2023.

[5] B. J. Emran and H. Najjaran, "A review of quadrotor: An underactuated mechanical system," *Annual Reviews in Control*, vol. 46, pp. 165 – 180, 2018.

[6] Y. Zhang, T. Chen, S. Chen, and Z. Wang, "Assess-ranging-fuse: Obstacle detection based on stereo vision threat assessment and ultrasonic ranging," in *2020 Chinese Automation Congress (CAC)*, 2020, pp. 6186–6191.

[7] Y. Zhang, Y. Yang, W. Chen, and H. Yang, "Realtime brain-inspired adaptive learning control for nonlinear systems with configuration uncertainties," *IEEE Transactions on Automation Science and Engineering*, pp. 1–12, 2023.

[8] W. Bao and Z. Qi, "Challenges and perspectives of information and control technology for cislunar space exploration and development," *Guidance, Navigation and Control*, vol. 03, no. 02, p. 2350013, 2023.

[9] C. Yin, Y. Chen, and S.-m. Zhong, "Fractional-order sliding mode based extremum seeking control of a class of nonlinear systems," *Automatica*, vol. 50, no. 12, pp. 3173–3181, 2014.

[10] Z. Xing, Y. Zhang, and C.-Y. Su, "Active wind rejection control for a quadrotor uav against unknown winds," *IEEE Transactions on Aerospace and Electronic Systems*, vol. 59, no. 6, pp. 8956–8968, 2023.

[11] C. Wei, J. Luo, H. Dai, and G. Duan, "Learning-based adaptive attitude control of spacecraft formation with guaranteed prescribed performance," *IEEE Transactions on Cybernetics*, vol. 49, no. 11, pp. 4004–4016, 2019.

[12] Y. Zhang, H. Yang, Y. Chen, and W. Chen, "Adaptive extremum seeking controller via nonlinear variable gain for uncertainty model multirotor," in *2022 41st Chinese Control Conference (CCC)*, 2022, pp. 2308–2314.

[13] N. J. Killingsworth and M. Krstic, "Pid tuning using extremum seeking: online, model-free performance optimization," *IEEE Control Systems Magazine*, vol. 26, no. 1, pp. 70–79, 2006.

[14] M. Krstic and H.-H. Wang, "Stability of extremum seeking feedback for general nonlinear dynamic systems," *Automatica*, vol. 36, no. 4, pp. 595–601, 2000.

Proceedings of the 3rd Conference on Fully Actuated System Theory and Applications
May 10-12, 2024, Shenzhen, China

Adaptive Dynamic Programming-based Self-triggered Optimal Control for Nonzero-sum Games of Nonlinear Systems with Constrained State

Gan Zhi[1], Hanguang Su[1], Rui Wang[1], Dazhong Ma[1]
1. College of Information Science and Engineering, Northeastern University, Shenyang 110167, P. R. China
E-mail: 2271054@stu.neu.edu.cn

Abstract: Taking into account multiple control inputs problem in constrained states systems, based on the adaptive dynamic programming (ADP) approach, a sort of self-triggered control (STC) method has been proposed. The constraint boundary of the state constrained system is released by introducing a potential barrier function. Then, on the basis of event-triggered control (ETC) law, the STC strategy was obtained. The STC strategy was updated, if the time reached the triggering time calculated by the self-triggered mechanism. Next, the neural networks (NNs) are used to approach the optimal value function, and then an approximate self-triggered optimal policy is designed. To solve the problem of the persistence of excitation (PE) conditions, the experience replay (ER) method is combined with the weight updating rule, and the validity of the proposed method is proved by a example.

Key Words: Constrained states, adaptive dynamic programming (ADP), self-triggered control (STC), event-triggered control (ETC), neural networks (NNs).

1 Introduction

In recent decades, with the rapid development of modern industry, more transmission and computing resources required for control systems are needed. In many modern industry, the control target can be achieved by using limited acquiring and computing resources. This seriously restricts the performance of control systems. In the traditional control systems, most controllers require system information is transmitted through periodically sampled signals. Generally speaking, gathering more system information can contribute to correct control inputs, and controlled systems are improved promptly, which achieve better control effects. To achieve this, it is necessary to increase the sampling frequency. However, under limited transmission and computing resources, higher sampling frequency may exacerbate communication network congestion and occupy more computing resources. Therefore, how to balance system performance with transmission and computing resources has become an urgent problem of modern industry[1].

Event triggered control (ETC) methods[2] are considered to be an effective way to address the above issues. Under the ETC method, the control inputs will only be updated when the triggered condition is broken. ETC method greatly reduces trigger interval, thereby effectively alleviating the pressure of acquiring and computing resources. In previous work[1–3], it has been proven that the ETC method can reduce the system resource consumption with almost no impact on system performance.

Along with the widespread development of ETC, the so-called self-triggered control (STC) methods [4] have been proposed as an alternative solution to save the system resources. The fundamental difference between STC and ETC is that ETC is passive while STC is active[5]. In the STC, it is possible to pre-calculate the next triggering time according to the current triggering time and the relevant parameters of the system at this moment[6]. Between the two triggering moments, the sensors can be shut down for data collection, thereby further releasing the communication resources[6].

For many complex systems, multiple controllers are often needed to regulate system performance. In these optimal problems, multiple participants compete or cooperate to meet control objectives. This type of problem usually considered as a non-zero-sum (NZS) games[1], whose optimal solution can be obtained by solving the coupled Hamilton–Jacobi (HJ) equations to approach a set of Nash equilibrium. However, due to the high complexity of such problems, it's hard-pressed to calculate the coupled HJ equation solutions. Adaptive dynamic programming (ADP) algorithm has been widely applied in solving the HJ equations and has been proven to be an effective approach[7].

In the actual industrial process, due to the influence of actuator structure or system internal structure, the control inputs and system states are limited[7]. Once the system states are prevented from reaching the controller's design goal due to the system inherent constraints, the control effect will be severely affected[8].

To address the aforementioned issues, an ADP-based STC method is designed for getting the approximate Nash equilibriums in this paper. Moreover, in practical engineering, serious consequences are caused by adding random detection noise to the control inputs. In this paper, for eliminating the persistence of excitation (PE) conditions, we adopt experience replay (ER) method [9, 10].

The structure of the paper is introduced as follows. In Section 2, the controlled system with constrained states is introduced and we completes the system transition through the defined barrier function. In Section 3, the self-triggered rule and the optimal control policy are derived. After that, the realization of NNs is presented. In Section 4 , a simulation analysis is given on the basis of the proposed algorithm. The conclusions are set out in Section 5.

2 Statement of Problem and Transformation

Take into account the affine system with multiple controllers and state constraints with the form of

$$\dot{x}(t) = f(x(t)) + \sum_{j=1}^{N} g_j(x(t))u_j(t), \tag{1}$$

where $x(t) \in \mathbb{R}^n$ is the system state, $u_j \in \mathbb{R}^{m_j}, j \in \mathcal{N}$ is the control input of the jth controller. $f(x) : \mathbb{R}^n \to \mathbb{R}^n$ and $g_i(x) : \mathbb{R}^n \to \mathbb{R}^{n\times m_j}$ are the drift dynamics and the control input dynamics, respectively. According to[8], the transition between state constrained and unconstrained system through the defined barrier function is completed.

Definition 1 ([7, 8, 11]) *The interval reversible barrier function is defined as follows:*

$$\rho(r) = \ln\left(\frac{z}{y}\frac{y-r}{z-r}\right), \forall r \in (y, z), \tag{2}$$

where r is system state, y and z are the two boundaries of state r. The interval (y, z) is the reversible interval of the defined function.

Performing inverse operations on the potential barrier function (2) to obtain the inverse function

$$\rho^{-1}(s) = yz\frac{e^{\frac{s}{2}} - e^{-\frac{s}{2}}}{ye^{\frac{s}{2}} - ze^{-\frac{s}{2}}}, \quad \forall s \in \mathbb{R}. \tag{3}$$

The partial derivative of function (3) relative to the transformed variable s is

$$\frac{\mathrm{d}\rho(s)^{-1}}{\mathrm{d}s} = \frac{zy^2 - yz^2}{y^2e^s - 2yz + z^2e^{-s}}. \tag{4}$$

Definition 1 describes the basic relationship between the potential barrier function and its inverse function. The above functions can be used to achieve the conversion between constrained and unconstrained functions through coordinate inversion. Then, the undermentioned assumptions are prerequisites to explain the relevant properties of the conversion process.

Assumption 1 *When a constrained system (1) is in a stable state, the barrier function should satisfy*

$$\rho(0; y, z) = 0. \tag{5}$$

If the state x of the restricted function (1) approaches the limit boundary (y, z), the barrier function will approach infinity, which means that the barrier function satisfies

$$\begin{aligned} \lim_{x\to y^+} \rho(x; y, z) \to -\infty, \\ \lim_{x\to z^-} \rho(x; y, z) \to +\infty. \end{aligned} \tag{6}$$

Using the barrier function and its related assumptions, the process of converting the state constrained system to the unconstrained system will be shown as follows:

$$\begin{aligned} p_h &= \rho(x_h; y_h, z_h) \\ x_h &= \rho^{-1}(p_h; y_h, z_h) \end{aligned}, \tag{7}$$

where p_h is the h-th transformed state and its corresponding x_h are inverse functions of each other.

The converted system can be derived from p_h, this is

$$\begin{aligned} \dot{p}_h &= \frac{\dot{x}_h}{\frac{\mathrm{d}\rho^{-1}(p_h; y_h, z_h)}{\mathrm{d}p_h}} \\ &= F_h(p) + \sum_{j=1}^{N} G_{j,h}(p)u_j(t), \end{aligned} \tag{8}$$

where

$$\begin{aligned} &\dot{x}_h = f_h(x) + \sum_{j=1}^{N} g_{j,h}(x)u_j(t), \\ &F_h(p) = \rho_{ph} f_h\left(\left[\rho_1^{-1}(p_1)\cdots\rho_{pn}^{-1}(p_n)\right]\right), \\ &G_{j,h}(p) = \rho_{ph} g_{j,h}\left(\left[\rho_1^{-1}(p_1)\cdots\rho_{pn}^{-1}(p_n)\right]\right), \\ &\rho_{ph} = \frac{z_h^2e^{-ph} - 2y_hz_h + y_h^2e^{ph}}{z_hy_h^2 - y_hz_h^2}, \end{aligned}$$

Then, the unconstrained system is constructed as

$$\dot{p} = F(p) + \sum_{j=1}^{N} G_j(p)u_j(t), \tag{9}$$

where $p = [p_1, \ldots, p_n]^T$ is the unconstrained system state, $F(p) = [F_1(p), \ldots, F_n(p)]^T$, and $G(p) = [G_{j,1}(p), \ldots, G_{j,n}(p)]^T$.

For the unconstrained system (9), the performance index is defined as

$$\begin{aligned} J_i\big(p(0)\big) &= \int_0^\infty \left(p^TQ_ip + \sum_{j=1}^{N} u_j^TR_{ij}u_j\right)d\tau \\ &\triangleq \int_0^\infty \rho_i(p, u_1, \ldots, u_N)d\tau, \end{aligned} \tag{10}$$

where $\forall i \in \mathcal{N}$ and $\forall j \in \mathcal{N}$, $\rho_i(p, u_1, \ldots, u_N)$ is the utility function of the ith player, with $Q_i \in \mathbb{R}^{n\times n}$ a positive definite matrix and $R_{ij} \in \mathbb{R}^{m_j\times m_j}$ a symmetric positive definite matrix. Define the value function as

$$V_i(p(t)) = \int_t^\infty \left(p^TQ_ip + \sum_{j=1}^{N} u_j^TR_{ij}u_j\right)d\tau. \tag{11}$$

Definition 2 ([1, 12]) *The Nash equilibrium is defined as an optimal control policies $\{u_1^*, \ldots, u_N^*\}$. The the Nash equilibrium is met*

$$\begin{aligned} V_i^* &\triangleq V_i(p, u_1^*, \ldots, u_i^*, \ldots, u_N^*) \\ &\le V_i(p, u_1^*, \ldots, u_i, \ldots, u_N^*), i \in \mathbb{N}. \end{aligned} \tag{12}$$

Based on Definition 2, suppose the value function $V_i(x)$ is continuously differential, The following equation can be obtained by differentiating formula (11):

$$0 = p^TQ_ip + \sum_{j=1}^{N} u_j^TR_{ij}u_j + (\nabla V_i)^T\left(F(p) + \sum_{j=1}^{N} G_ju_j\right) \tag{13}$$

with $V_i(0) = 0$. According to (13), define the system Hamiltonian function as

$$
\begin{aligned}
&H_i(p, u_1, \ldots, u_N) \\
&= p^T Q_i p + \sum_{i=1}^{N} \boldsymbol{u}_j^T R_{ij} \boldsymbol{u}_j \\
&\quad + (\nabla V_i)^T \left(F(p) + \sum_{j=1}^{N} G_j \boldsymbol{u}_j \right).
\end{aligned} \tag{14}
$$

It is necessary that the Hamiltonian function satisfies $\frac{\partial H_i}{\partial u_i} = 0$ to make the system stable. Then, the optimal control policy is obtain as

$$
u_i^* = -\frac{1}{2} R_{ii}^{-1} G_i^T(p) \nabla V_i^*. \tag{15}
$$

According to (14) and (15), we can obtain

$$
\begin{aligned}
&H_i(p, u_1^*, ..., u_N^*, V_i^*) \\
&= p^T Q_i p + \sum_{j=1}^{N} u_j^{*T} R_{ij} u_j^* \\
&\quad + (\nabla V_i^*)^T \left(F(p) + \sum_{j=1}^{N} G_j(p) u_j^* \right) = 0, \\
&V_i^*(0) = 0.
\end{aligned} \tag{16}
$$

3 Self-Triggered Approximator Design

3.1 Event-Triggered Controller Design

In order to alleviate system communication congestion and reduce computing resources, an event triggered method has been introduced in this section. The method defines the triggering time as a monotonically increasing sequence$\{\tau_k\}_{k=0}^{\infty}$. Here τ_k also represents the k-th sampling time and satisfies $\tau_0 = 0$, $\tau_k \in \mathbb{R}^+$, $k \in \mathbb{N}$. The sampling state remains unchanged between two sampling moments. The event-triggered error is

$$
e(t) = \overline{p}_k - p(t), \quad t \in [\tau_k, \tau_{k+1}), \tag{17}
$$

where $\overline{p}_k = p(\tau_k)$.

In addition, due to the correlation between control law and sampling state, the control input should also stay the same until the next sampling time arrives. The ETC method is introduced into (15) for the event-triggered optimal control law

$$
u_i^*(\overline{p}_k) = -\frac{1}{2} R_{ii}^{-1} G_i^T(\overline{p}_k) \nabla V_i^*(\overline{p}_k), \quad t \in [\tau_k, \tau_{k+1}). \tag{18}
$$

3.2 Critic Neural Adaptive Design

In order to solve the HJ function, adaptive optimal controller and the optimal value function $V_i^*(p)$ is designed through NNs. The design process is as follows:

The optimal value function $V_i^*(p)$ is represented through NNs as

$$
V_i^*(p) = W_{ci}^T \phi_c(p) + \varepsilon_{ci}(p), \tag{19}
$$

where $W_{ci} \in \mathbb{R}^L$ is the ideal weight vector, $\phi_c(p) \in \mathbb{R}^L$ is the activation function, $\varepsilon_{ci}(p) \in \mathbb{R}$ is the NN approximation error. Furthermore, we can obtain the partial derivative of optimal value function, this is

$$
\nabla V_i^*(p) = \nabla \phi_c^{\mathsf{T}}(p) W_{ci} + \nabla \varepsilon_{ci}(p). \tag{20}
$$

Due to the unknown ideal weight, the estimation weight $\hat{W}_{ci}$ is designed to replace the ideal weight W_{ci}. We have

$$
\nabla \hat{V}_i(p) = \nabla \phi_c^{\mathsf{T}}(p) \hat{W}_{ci}. \tag{21}
$$

According to (18) and (21), the optimal control law is reconstructed as

$$
\hat{u}_i(\overline{p}_k) = -\frac{1}{2} R_{ii}^{-1} G_i^T(\overline{p}_k) \nabla \phi_c^T(\overline{p}_k) \hat{W}_{ci}, t \in [\tau_k, \tau_{k+1}). \tag{22}
$$

According to above equations, the approximate Hamiltonian error is constructed as follows:

$$
\begin{aligned}
&\hat{H}_i(p, \hat{u}_1(\overline{p}_k), ..., \hat{u}_N(\overline{p}_k), \hat{W}_{ci}) \\
&= p^T Q_i p + \sum_{j=1}^{N} \hat{u}_j^T(\overline{p}_k) R_{ij} \hat{u}_j(\overline{p}_k) \\
&\quad + \hat{W}_{ci}^T \nabla \phi_c(p) [F(p) + \sum_{j=1}^{N} G_j \hat{u}_j(\overline{p}_k)] \triangleq e_{ci}.
\end{aligned} \tag{23}
$$

Minimizing the approximate Hamiltonian error (23) is considered the goal of the critic weight $\hat{W}_{ci}$ updating. The objective function is defined as $E_{ci} = (1/2) e_{ci}^T e_{ci}$. ER technique is the effectual way for relaxation of PE. Inspired by the excellent achievements in[12], historical data is introduced into the updating rule of the critic weight. Based on the gradient descent algorithm, the updating law of the critic NN weight is designed as

$$
\begin{aligned}
\dot{\hat{W}}_{ci} =& \frac{\alpha_c \Upsilon_i}{\left(1 + \Upsilon_i^{\mathsf{T}} \Upsilon_i\right)^2} \left(\hat{W}_{ci}^{\mathsf{T}} \Upsilon_i + p^{\mathsf{T}} Q_i p + \sum_{j=1}^{N} \hat{u}_j^T R_{ij} \hat{u}_j \right) \\
&- \sum_{d=1}^{N_D} \frac{\alpha_c \Upsilon_{id}}{\left(1 + \Upsilon_{id}^{\mathsf{T}} \Upsilon_{id}\right)^2} (\hat{W}_{ci}^{\mathsf{T}} \Upsilon_{id} + p^{\mathsf{T}}(t_d) Q_i p(t_d) \\
&+ \sum_{j=1}^{N} \hat{u}_j^T \left(\overline{p}_k(t_d)\right) R_{ij} \hat{u}_j(\overline{p}_k(t_d)) \Bigg), \\
&t_d \in [\tau_k, \tau_{k+1}),
\end{aligned} \tag{24}
$$

where α_c is positive constant and represent the learning rate, $d \in \mathcal{N}_{\mathcal{D}}$ respect the index for storing historical data, $\Upsilon_i = \nabla \phi_c(p)(F(p) + \sum_{j=1}^{N} G_j(p) \hat{u}_j(\overline{p}_k))$, $\Upsilon_{id} = \nabla \phi_c(p(t_d))(F(p(t_d)) + \sum_{j=1}^{N} G_j(p(t_d)) \hat{u}_j(\overline{p}_k(t_d)))$.

The weight estimation error of the critic NN is defined as $\tilde{W}_{ci} = W_{ci} - \hat{W}_{ci}$. Inspired by [14], based on (24), we can find the dynamics of the critic network weight estimation

error is

$$\begin{aligned}\dot{\tilde{W}}_{ci} =& -\dot{\hat{W}}_{ci}\\ =& -\alpha_c(\Phi_i\Phi_i^{\mathsf{T}}+\sum_{d=1}^{N_r}\Phi_{id}\Phi_{id}^{\mathsf{T}})\tilde{W}_{ci}+\frac{\alpha_c\Phi_i}{1+\Upsilon_i^{\mathsf{T}}\Upsilon_i}\varepsilon_{Hi}\\ &+\sum_{d=1}^{N_r}\frac{\alpha_c\Phi_{id}}{1+\Upsilon_{id}^{\mathsf{T}}\Upsilon_{id}}\varepsilon_{Hid}, t, t_d\in[\tau_k,\tau_{k+1}),\end{aligned} \tag{25}$$

where

$\Phi_i=\frac{\Upsilon_i}{1+\Upsilon_i^{\mathsf{T}}\Upsilon_i}$,

$\Phi_{id}=\frac{\Upsilon_{id}}{1+\Upsilon_{id}^{\mathsf{T}}\Upsilon_{id}}$,

$\varepsilon_{Hi}=-\nabla\varepsilon_{ci}^{\mathsf{T}}(p)(F(p)+\sum^{N}G_j(p)\hat{u}_j(\bar{p}_k))$,

$\varepsilon_{Hid}=\nabla\varepsilon_{ci}^{\mathsf{T}}(p(t_d))\left(F(p(t_d))+\sum_{j=1}^{N}G_j(p(t_d))\hat{u}_j(\bar{p}_k)\right)$,

here ε_{Hi} and ε_{Hid} are the residual errors.

3.3 Stability Analysis

According to [12–14], the undermentioned assumptions are prerequisites to conduct stability analysis.

Assumption 2 *Without loss of generality, for any $p\in\Omega$ and the corresponding i-th critic NN, $G_j(p)$, $\nabla\mathbb{V}_i^*(p)$, W_{ci}, ϕ_c, ε_{ci}, $\nabla\phi_c$, $\nabla\varepsilon_{ci}$ are bounded. This is,*

$$\begin{gathered}\parallel G_j(p)\parallel\leq\bar{B}_{G_j},\ \parallel\nabla\mathbb{V}_i^*(p)\parallel\leq\bar{B}_{V_i},\\ \|W_{ci}\|\leq\bar{B}_{W_{ci}},\ \|\nabla\phi_c(p)\|\leq\bar{B}_{\phi_c},\\ \|\nabla\varepsilon_{ci}(x)\|\leq\bar{B}_{\varepsilon_{ci}},\ \|\nabla\varepsilon_{Hi}(x)\|\leq\bar{B}_{\varepsilon_{Hi}},\end{gathered}$$

where $\bar{B}_{G_j}$, $\bar{B}_{V_i}$, $\bar{B}_{W_{ci}}$, $\bar{B}_{\phi_c}$, $\bar{B}_{\varepsilon_{ci}}$ and $\bar{B}_{\varepsilon_{Hi}}$ are the boundary tangent of the relevant parameters that needs to be taken as positive value.

Assumption 3 *$F(p)$ is Lipschitz function, and $\|F(p)\|\leq L_F\|p\|$ with $F(0)=0$, where $L_F>0$.*

Assumption 4 *$u(p)$ is Lipschitz function. Specifically, it's means there exists a positive number L_u that makes*

$$u^*(p)-u^*(\bar{p}_k)\leq L_u\parallel p-\bar{p}_k\parallel.$$

Theorem 1 *Consider the system that needs to be adjusted as (9), for any i-th player and their corresponding NNs. Relevant Assumptions 2-4 are all met. The update pattern of optimal control law is set as (22), the critic NN weights adaptive laws are (24). The system state p of the transformed system (9) and the critic weight estimation error $\tilde{W}_c$ are met UUB, if the triggering condition is constructed as*

$$\parallel e(t)\parallel^2\leq\frac{\sum_{i=1}^{N}\beta(1-\alpha)\lambda_{\min}(Q_i)\parallel\bar{p}_k\parallel^2}{NL_u^2+\sum_{i=1}^{N}\beta\left(\frac{1}{\alpha}-1\right)\lambda_{\max}(Q_i)}=e_T, \tag{26}$$

where $\alpha\in(0,1)$ and e_T is the triggered threshold.

Due to space limitations, the proofs are omitted herein. The similar proof can be referenced[12].

3.4 Self-Triggered Rule

In this section, inspired by work [5], self-triggered rule is derived based on the above event triggering method. The system state p of the transformed system (9) will be proved to be UUB, under the self-triggered rule. The design process is as follows:

For any $t\in[\tau_k,\tau_{k+1})$, from the the event-triggered error (17), the time derivative of the event-triggered error is obtained as

$$\|\dot{e}(t)\|=\|\dot{p}\|. \tag{27}$$

According to (9) and (28), we have

$$\begin{aligned}\|\dot{e}(t)\|=&\parallel\dot{p}\parallel\\ \leq&\parallel F(p)\parallel+\sum_{i=1}^{N}G_i\parallel\hat{u}_i(\bar{p}_k)\parallel\\ \leq& L_F\parallel p\parallel+\sum_{i=1}^{N}G_i\parallel\hat{u}_i(\bar{p}_k)\parallel\\ \leq& L_F\|\bar{p}_k+e(t)\|+L_{gu}\\ \leq& L_F\|\bar{p}_k\|+L_F\|e(t)\|+L_{gu},\end{aligned} \tag{28}$$

where $L_{gu}=\sum_{i=1}^{N}\bar{G}_i\bar{u}_i$. Then, utilizing comparing lemma [15], we have

$$\parallel e(t)\parallel\leq\frac{L_F\parallel\bar{p}_k\parallel+L_{gu}}{L_F}(e^{L_F(t-\tau_k)}-1). \tag{29}$$

When $t=\tau_{k+1}$, the event-triggered condition (26) is violated, we obtain

$$\frac{L_F\parallel\bar{p}_k\parallel+L_{gu}}{L_F}(e^{L_F(\tau_{k+1}-\tau_k)}-1)>\sqrt{e_T}. \tag{30}$$

This indicates that the two sampling time intervals satisfy

$$\tau_{k+1}-\tau_k>\frac{\ln(1+(\frac{L_F\sqrt{e_T}}{L_F\|\bar{p}_k\|+L_{gu}}))}{L_F}. \tag{31}$$

Theorem 2 *Based on the above derivation and event-triggering rule (26). Relevant Assumptions 2-4 are all met. The update pattern of optimal control law is set as (22), the critic NN weights adaptive laws are (24). Then, the system state p of the transformed system (9) and the critic weight estimation error $\tilde{W}_c$ are met UUB, if the triggering law is constructed as*

$$t_{k+1}=t_k+\frac{\ln(1+(\frac{L_F\sqrt{e_T}}{L_F\|\bar{p}_k\|+L_{gu}}))}{L_F}. \tag{32}$$

Theorem 3 *Consider system (9) that have undergone barrier function transformation. Let the self-triggering condition is (32), the lower bound of sampled time interval $\Delta t_{\min}$ is given by*

$$\Delta t_{\min}\geq\frac{1}{L_F}\ln(1+(\frac{L_FE}{L_F+\frac{L_{gu}}{\Xi}}))>0, \tag{33}$$

where Ξ and E are positive constants.

Due to space limitations, the proofs are omitted herein.

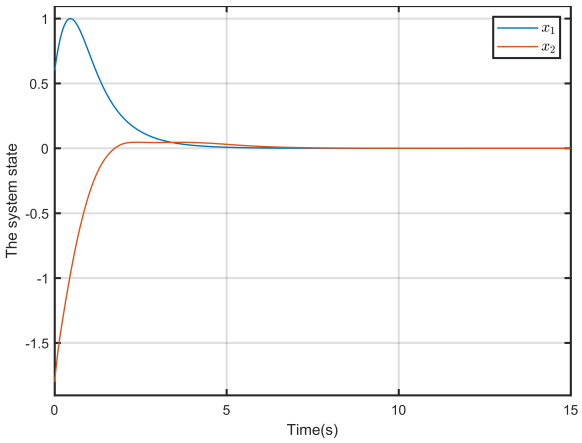

Fig. 1: Simulation results for the state.

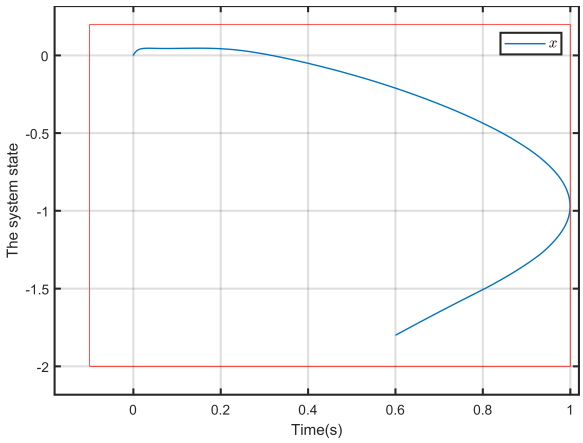

Fig. 2: The state trajectory and restricted scope.

4 Simulation

One simulation examples is employed to prove the effectiveness of the theoretical analysis provided above. Considering the two-order nonlinear system with three controllers. The system dynamics is formulated as

$$\dot{x} = f(x) + g_1(x)u_1 + g_2(x)u_2 + g_3(x)u_3, \tag{34}$$

where

$$f(x) = \begin{bmatrix} -1.2x_1 + 1.5x_2\sin(x_2) \\ 0.6x_1 - x_2 \end{bmatrix},$$

$$g_1(x) = \begin{bmatrix} 0 \\ 0.85\sin(x_2)\cos(x_2) \end{bmatrix},$$

$$g_2(x) = \begin{bmatrix} 0 \\ 0.8\sin(x_1)\cos(x_2) \end{bmatrix},$$

$$g_3(x) = \begin{bmatrix} 0 \\ 0.5\sin(x_2) \end{bmatrix},$$

the system state vector is $x = [x_1, x_2]^T \in \mathbb{R}^2$,and the two dimensional control input vector is written as $u_1 \in \mathbb{R}$, $u_2 \in \mathbb{R}$ and $u_3 \in \mathbb{R}$. Corresponding parameter matrix in value function are picked as $Q_1 = 2I_{2\times2}$, $Q_2 = 1.8I_{2\times2}$, $Q_3 = 0.3I_{2\times2}$, $R_{11} = 2I_{2\times2}$, $R_{12} = I_{2\times2}$, $R_{13} = 2I_{2\times2}$, $R_{21} = I_{2\times2}$, $R_{22} = 3I_{2\times2}$, $R_{23} = 2I_{2\times2}$, $R_{31} = 2I_{2\times2}$, $R_{32} = 2I_{2\times2}$ and $R_{33} = 2I_{2\times2}$. The upper and lower bounds of two state variables are set as $y_1 = -0.1$, $z_1 = 1$, $y_2 = -2$ and $z_2 = 0.2$, respectively.

The activation function is selected as $\phi_c(p) = [p^2{}_1, p_1p_2, p^2{}_2]^T$ to approximate the HJB equations. Then, the initial weights corresponding to the input vectors controlled by two controllers are $\hat{W}_{c1} = [-0.1087, 0.9035, 1.1240]^T$, $\hat{W}_{c2} = [-0.4240, -0.1375, 0.6420]^T$ and $\hat{W}_{c3} = [-0.2040, 0.1375, 0.0620]^T$, respectively. The learning rates of critic NN and the index of stored data are picked as $\alpha_1 = 0.4$, $\alpha_2 = 0.45$, $\alpha_2 = 0.5$ and $N_D = 24$.

The system state in Fig.1 converges to 0 in about 7 seconds Fig.1-2 collectively present the effectiveness of the state constrained method. The system state x_1 is limited within the set state limit range by the algorithm in this paper at about 0.5 seconds. Fig.3 (a) present the evolution of control strategies based on STC and the control inputs $u_i \in \mathbb{R}$ are piecewise continuous signals. In Fig.3 (b)-(d), the update trajectories of the critic weights

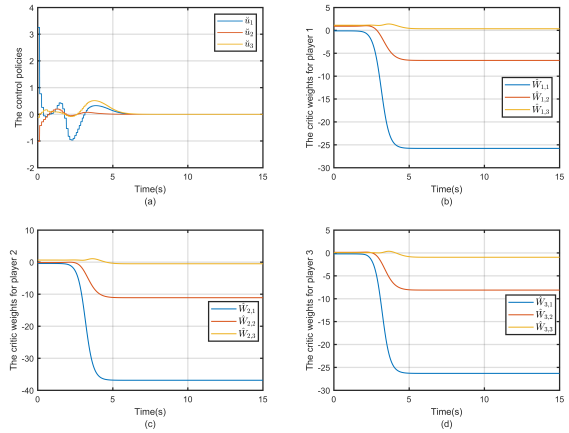

Fig. 3: The evolutionary trajectory of (a) controlled inputs; (b) the critic NN weight $\hat{W}_1$; (c) the critic NN weight $\hat{W}_2$; (b) the critic NN weight $\hat{W}_3$.

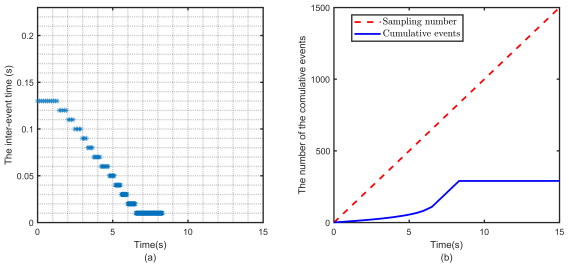

Fig. 4: The time interval of (a) the sampling period; (b) the cumulative number of the sampling.

$\hat{W}_1$, $\hat{W}_2$ and $\hat{W}_3$ are obtained. The critic weight vectors converge to $\hat{W}_{c1} = [-25.7793, -6.5604, 0.3565]^T$, $\hat{W}_{c2} = [-36.8728, -11.1066, -0.5157]^T$ and $\hat{W}_{c3} = [-26.3069, -8.1104, -0.9385]^T$, respectively. Fig.4(a) present the inter-event time. Because dead zone was set up, when the system states approach 0, the controller strategies are no longer updated and event triggering is no longer performed. Moreover, Fig.4(b) indicates that the number of the comulative events of self-triggered method greatly decreases the number of updating times. Consequently, the acquiring and computing resources can be saved.

5 Conclusion

In this work, the system with multiple control inputs and limited states are considered. An adaptive optimal self-triggered control method has been developed based on the ADP algorithm. Then, the approximate self-triggered optimal control is designed by approximating the optimal value function through the critic NN. The ER technology is combined with the weight updating law, in order to address the PE condition, Moreover, the effectiveness of the ADP based STC method was verified through the simulation example. Next, we will attempt to apply the algorithm to practical industrial processes in the future.

References

[1] H. Su, H. Zhang, S. Sun, Y. Cai, Integral reinforcement learning-based online adaptive event-triggered control for nonzero-sum games of partially unknown nonlinear systems, *Neurocomputing*, 2020, 377:243-255.

[2] X. Yang and H. He, Adaptive Critic Designs for Event-Triggered Robust Control of Nonlinear Systems With Unknown Dynamics, *IEEE Transactions on Cybernetics*, 2019, 49(6):2255-2267.

[3] M. Li, D. Wang, M. Zhao, J. Qiao, Event-triggered constrained neural critic control of nonlinear continuous-time multiplayer nonzero-sum games, *Information Sciences*, 2023, 631:412-428.

[4] W. P. M. H. Heemels, K. H. Johansson and P. Tabuada, An introduction to event-triggered and self-triggered control, *2012 IEEE 51st IEEE Conference on Decision and Control (CDC)*, Maui, HI, USA, 2012:3270-3285.

[5] Z. Ming, H. Zhang, Y. Yan and J. Sun, Self-Triggered Adaptive Dynamic Programming for Model-Free Nonlinear Systems via Generalized Fuzzy Hyperbolic Model, *IEEE Transactions on Systems, Man, and Cybernetics: Systems*, 2023, 53(5):2792-2801.

[6] L. Lu, J. M. Maciejowski, Self-triggered MPC with performance guarantee using relaxed dynamic programming, *Automatica*, 2020, 114.

[7] Q. Wei, J. Lu, T. Zhou, X. Cheng and F. -Y. Wang, Event-Triggered Near-Optimal Control of Discrete-Time Constrained Nonlinear Systems With Application to a Boiler-Turbine System, *IEEE Transactions on Industrial Informatics*, 2022, 18(6):3926-3935.

[8] Y. Yang, K. G. Vamvoudakis, H. Modares, Y. Yin and D. C. Wunsch, Safe Intermittent Reinforcement Learning With Static and Dynamic Event Generators, *IEEE Transactions on Neural Networks and Learning Systems*, 2020, 31(12):5441-5455.

[9] X. Yang and H. He, Adaptive Critic Learning and Experience Replay for Decentralized Event-Triggered Control of Nonlinear Interconnected Systems, *IEEE Transactions on Systems, Man, and Cybernetics: Systems*, 2020, 50(11):4043-4055.

[10] M. Lin, B. Zhao and D. Liu, Policy Gradient Adaptive Critic Designs for Model-Free Optimal Tracking Control With Experience Replay, *IEEE Transactions on Systems, Man, and Cybernetics: Systems*, 2022, 52(6):3692-3703.

[11] R. Song, L. Liu, L. Xia and F. L. Lewis, Online Optimal Event-Triggered $H\infty$ Control for Nonlinear Systems With Constrained State and Input, *IEEE Transactions on Systems, Man, and Cybernetics: Systems*, 2023, 53(1):131-141.

[12] Y. Zhang, B. Zhao, D. Liu and S. Zhang, Adaptive Dynamic Programming-Based Event-Triggered Robust Control for Multiplayer Nonzero-Sum Games With Unknown Dynamics, *IEEE Transactions on Cybernetics*, 2023, 53(8):5151-5164.

[13] Q. Zhao, J. Sun, G. Wang and J. Chen, Event-Triggered ADP for Nonzero-Sum Games of Unknown Nonlinear Systems, *IEEE Transactions on Neural Networks and Learning Systems*, 2022, 33(2):1905-1913.

[14] V. Narayanan, A. Sahoo, S. Jagannathan and K. George, Approximate Optimal Distributed Control of Nonlinear Interconnected Systems Using Event-Triggered Nonzero-Sum Games, *IEEE Transactions on Neural Networks and Learning Systems*, 2019, 30(5):1512-1522.

[15] H. Khalil, *Nonlinear Systems, 3rd ed*. Upper Saddle River, NJ, USA: Prentice-Hall, 2002,chapter 3.

Proceedings of the 3rd Conference on Fully Actuated System Theory and Applications
May 10-12, 2024, Shenzhen, China

Reinforcement Learning Control for a 2-DOF Flight Attitude Simulator

Yu Cai[1], Xiaojun Ban[1], Chengbao Zhou[2]

1. Center for Control Theory and Guidance Technology, Harbin Institute of Technology, Harbin 150001, P. R. China.
E-mail: 22S004074@stu.hit.edu.cn, banxiaojun@hit.edu.cn

2. Hangzhou Zhiyuan Research Institute Co., Ltd., Hangzhou 310024, China

Abstract: This paper focuses on the control problem for a two-degree-of-freedom flight simulator experimental setup, proposing a reinforcement learning-based flight attitude controller. The flight simulator aims to simulate the aircraft attitude control system, requiring consideration of its nonlinearity, model uncertainty, and the impact of external disturbances when designing the controller. Proximal Policy Optimization (PPO), as a policy gradient-based deep reinforcement learning algorithm, autonomously learns an approximately optimal controller based on a given objective function without the need for a mathematical model of the controlled object. Thanks to the application of the Actor-Critic framework and neural networks, the training of the two-degree-of-freedom flight simulator controller can rapidly converge within a short period. Simulations validate the generalization capability of the trained PPO controller and its robustness to external disturbances.

Key Words: Aircraft Control, Reinforcement Learning, Proximal Policy Optimization, Attitude Stabilization

1 Introduction

Rotary-wing aircrafts, due to their simple structure, low cost, and convenient usage, have gained widespread recognition and are extensively employed in various industries [1–3]. Due to the vertical takeoff and landing capabilities, ease of fabrication, remote control feasibility, and relatively low cost, rotary-wing small aircrafts find widespread applications in entertainment, aerial surveillance, search and rescue operations, as well as studies in control theory [4, 5]. Research on the control methods for their attitude is essential.

Flight attitude simulators serve as excellent experimental platforms to validate attitude control algorithms [6–8]. They enable convenient adjustments of the system's center of mass, thereby altering the parameters in the controlled object's dynamic equations, which serve as excellent experimental platforms for investigating strong robustness, adaptive attitude stability, and large-angle attitude adjustment control issues [9–11]. The flight attitude simulators possess characteristics such as inherent instability and nonlinearity, so that effective and feasible control strategies are required to ensure its stable operation.

In recent years, with the surge in artificial intelligence (AI), there has been extensive cross-disciplinary integration between the field of artificial intelligence and traditional control theory [12]. One particularly promising research direction is the application of reinforcement learning (RL) theory to the control systems of rotary-wing aircrafts. As a significant branch of machine learning, reinforcement learning plays a crucial role in various theoretical and technical domains, including control theory, industrial control, intelligent decision-making and financial management [13]. The foundational theory of reinforcement learning is based on Markov theory, where the problems of control and optimization are modeled and solved by introducing the concepts of "reward" and "action" using Markov decision processes. Built upon the framework of Markov decision processes, the fundamental principle of reinforcement learning involves optimizing the current agent's strategy through interaction with the environment, ultimately maximizing the expectation of cumulative rewards [14].

Thanks to the rapid development of computer hardware and software, researchers have extensively applied reinforcement learning and deep neural networks to approximate optimal controller solutions for complex nonlinear control systems. In [15], a dueling-double DQN algorithm is proposed, successfully achieving stable control of the magnetic levitation ball system. Reference [16] applies DDPG and RDPG algorithms to the vehicle's autonomous driving system, achieving good control performance. [17] utilizes the TD3 algorithm to guide PID controller parameter optimization, completing the design of a model-free controller for the aircraft's attitude system. Addressing the vibration control problem of a semi-driven suspension system in vehicles, [18] extensively utilizes the PPO algorithm for system control and tuning.

This paper focuses on a small 2-DOF flight attitude simulator suitable for studying the attitude control of rotor-type micro UAVs in a laboratory environment. Regarding the close-loop control system of the simulator, this paper first establishes the nonlinear dynamic model of its pitch channel. Subsequently, a PPO algorithm based on the Actor-Critic framework is employed for training and iteration of the stabilizing controller for the flight simulator system. Finally, simulations validate that the designed reinforcement learning controller exhibits good generalization capability and robustness to external disturbances.

The rest of this article is organized as follows: Section 2 sets up the nonlinear dynamic model of the 2-DOF flight attitude simulator. Controller design of the simulator based on PPO algorithm is introduced in Section 3 and simulation results are presented in Section 4. Finally, Section 5 summarizes the conclusion.

2 System Modeling

The mechanical structure of the two-degree-of-freedom flight attitude simulator mainly consists of a base, U-shaped frame, a swing arm, propellers, and other parts. Its simplified structural diagram is shown in Fig. 1. There is a motor at each end of the swing arm, with the directions of the two

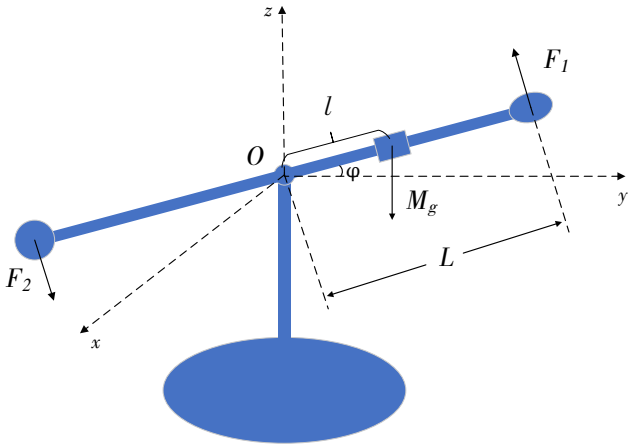

Fig. 1: Simplified diagram of the flight attitude simulator.

motors perpendicular to each other, each equipped with a propeller. These propellers drive the swing arm to perform pitch and yaw movements around the base. F_1 represents the lift of the propeller in the pitch direction, directed upward along the vertical swing rod, and F_2 represents the lift of the propeller in the yaw direction, pointing vertically outward from the paper. If only pitch motion is considered, the yaw direction needs to be kept stationary. The origin O of the coordinate system is chosen at the coincident position of the vertical rod and the swing arm, with the x-axis as horizontal, the z-axis as vertical, and the y-axis determined by the right-hand rule. The y-axis is defined as the zero position for pitch, and the pitch angle is considered positive in the counterclockwise direction (upward in the figure) in this paper.

In this research, we only consider the controller design for the pitch channel of the flight simulator, thus simplifying the spatial motion of the entire system to planar motion. Based on the force analysis of the simplified diagram and Newton's second law, the nonlinear dynamic model for the pitch channel of the flight simulator can be derived as

$$(J + Ml^2)\ddot{\phi} = -k\dot{\phi} - Mgl\cos\phi + F_1 L + d, \quad (1)$$

where ϕ is the pitch angle of swinging arm, J denotes the moment of inertia of the entire swinging arm relative to O, k is the rotational angular velocity damping coefficient, M represents the mass of the clump weight and g is the gravity acceleration, the distance from the counterweight block to O is denoted by l and the length of the swinging arm is denoted by L, d is regarded as the external disturbance. Table 1 illustrates the physical parameter values of the flight simulator.

Table 1: Physical Parameter Values of 2-DOF Flight Attitude Simulator

Parameter	Value
M	$0.3kg$
g	$9.8kg \cdot m^2$
k	$0.14N \cdot m \cdot s/rad$
J	$0.082kg \cdot m^2$
l	$0.051m$
L	$0.36m$

Choosing the state variables of the system as $x = [\phi \ \ \dot{\phi}]^\top$ and the control input as $u = F_1$, the affine nonlinear state-space model of the flight simulator is given by

$$\dot{x} = f(x) + g(x)u + d', \quad (2)$$

where

$$f(x) = \begin{bmatrix} \dot{x_2} \\ -\frac{kx_2 + Mgl\cos(x_1)}{J+Ml^2} \end{bmatrix},$$

$$g(x) = \begin{bmatrix} 0 \\ \frac{L}{J+Ml^2} \end{bmatrix},$$

$$d' = \begin{bmatrix} 0 \\ \frac{d}{J+Ml^2} \end{bmatrix}.$$

The control objective is that given the flight attitude simulator system (1) with time-varying external disturbances d, design a controller that stabilizes the state of close-loop system, which is

$$\lim_{t\to\infty} \phi = 0, \lim_{t\to\infty} \dot{\phi} = 0 \quad (3)$$

with an arbitrary initial pitch angle ϕ_0.

3 Controller Design

3.1 Reinforcement Learning and PPO Algorithm

The optimal control problem of the 2-DOF flight attitude simulator can be formulated as a Markov Decision Process (MDP). A MDP is generally defined by a quadruple consisting of $(\mathcal{S}, \mathcal{A}, \mathcal{R}, \mathcal{P})$, where $\mathcal{S}$ is a set of state space, $\mathcal{A}$ is a set of action space, $\mathcal{R}$ denotes the reward function space and $\mathcal{P}$ denotes the transition probability distribution [19]. Reinforcement learning (RL) is a method focusing on developing algorithms and models to enable machines or agents to learn and make decisions in a dynamic environment of MDP. The goal of reinforcement learning is to train the agent to learn a policy, which is a mapping from states s_t to actions a_t, that maximizes the expected cumulative reward over time. It can be particularly useful in scenarios where explicit mathematical solutions may be difficult to derive, and an agent needs to explore and learn optimal strategies through trial and error.

The expected cumulative reward function that RL aims to optimize can be described as [20]

$$J\left(\pi_{\theta_p}\right) = \mathbb{E}\left[\sum_{t=0}^{T} \gamma^t \mathcal{R}\left(s_t, a_t, s_{t+1}\right)\right], \quad (4)$$

where π_{θ_p} is the control policy parameterized by θ_p, T denotes the time horizon of the trajectory and γ is the discount factor. Based on the objective (4), the optimal policy for RL can be expressed by

$$\pi^*_{\theta_p} = \arg\max_{\theta_p} J(\pi_{\theta_p}). \quad (5)$$

The Proximal Policy Optimization (PPO) algorithm [21], which is commonly used in several research and applications, is a type of policy optimization algorithm based on gradient ascent, seeking the optimal gradient of the policy. PPO operates within the Actor-Critic framework, where the Actor learns decision actions, and the Critic learns the state

value function. This algorithm integrates the core ideas of Trust Region Policy Optimization (TRPO) [22], updating the policy within a trust region to ensure the safety of policy performance. PPO algorithm, as a reinforcement learning approach designed to handle continuous states and actions, is prone to be highly suitable for the controller training of the 2-DOF flight simulator.

Unlike TRPO and value-based RL algorithms, the simplicity of PPO lies in its novel clipped objective function, which can be formulated by

$$J(\theta_p) = \mathbb{E}\left[\min(r(\theta_p),\ c(r(\theta_p), 1-\varepsilon, 1+\varepsilon))\hat{A}_\pi(s_t, a_t)\right], \tag{6}$$

where

$$r(\theta_p) = \frac{\pi_{\theta_p}(a_t|s_t)}{\pi_{\theta'_p}(a_t|s_t)} \tag{7}$$

denotes the ratio of action probabilities between the new and old policies, $c(\cdot)$ is the clip function which restricts the adjusted probability ratio to the range of $(1-\varepsilon, 1+\varepsilon)$, preventing rapid updates of θ_p that could result in a significant difference between the new and old policies and $\hat{A}_\pi$ denotes the advantage function using the policy π. Implementing with the simple objective (6), solution to the PPO algorithm can be approached using most first-order optimization methods, such as Stochastic Gradient Descent (SGD), Momentum and Adam, which is particularly suitable for the utilization of neural network approximators.

According to [23], for the sake of reducing estimation variance, the advantage function $\hat{A}_\pi$ can be calculated using the Generalized Advantage Estimation (GAE) method. In this manner, the advantage function can be expressed by

$$\hat{A}_t = \delta_t + (\lambda\gamma)\delta_{t+1} + \cdots + (\lambda\gamma)^k\delta_{t+k}, \tag{8}$$

where

$$\delta_t = r_t + \gamma V(s_{t+1}) - V(s_t) \tag{9}$$

represents the Temporal Difference (TD) error [24], $V(s_t)$ denotes the state value function output by the critic network and λ is a hyperparameter. Overall, the pseudocode of PPO algorithm is detailed in Algorithm 1.

Algorithm 1 PPO algorithm using Actor-Critic framework

Initialize actor network $\pi_{\theta p_0}$ and critic network $V_{\theta v_0}$
Initialize learning rates of the actor and the critic α_p, α_v
Initialize buffer B with size D, and $\gamma, \epsilon, \lambda$
for $i \leq N$ **do**
  for $t = 0, 1, 2, \ldots, T$ **do**
    Choose action $a_t \sim \pi_\vartheta(a|s_t)$;
    Execute a_t into environment and get r_t, s_{t+1};
    Store transition (s_t, a_t, r_t, s_{t+1}) into buffer B;
    $i \leftarrow i + 1$
    $t \leftarrow t + 1$
    if $i \,\%\, D = 0$ **then**
      Compute The discounted reward $R_t = \sum_{j=0}^{M} \gamma^j r_j$
      for $k = 0, 1, 2, \ldots, K$ **do**
        Estimate the advantage $\hat{A}_p i$ using (8);
        Compute the ratio r_{θ_p} using (7);
        Update the actor network using (4) and (5);
        Update the critic network by
          $\theta_{v_{k+1}} = \arg\min_{\theta_{v_k}} \delta_t^2$.
      end for
    end if
  end for
end for

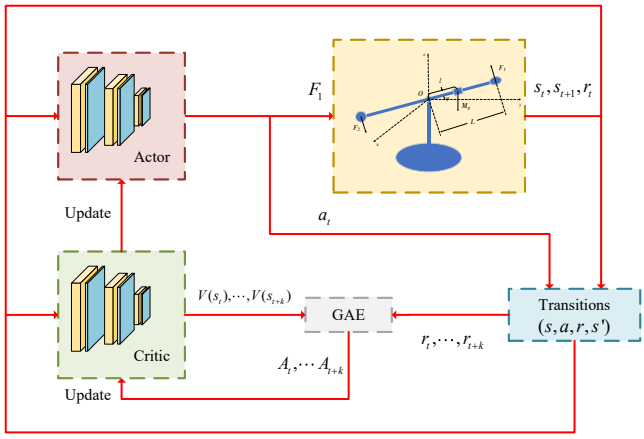

Fig. 2: Controller training block diagram of 2-DOF flight attitude simulator.

3.2 RL Controller Design

According to the described PPO algorithm in Algorithm 1, the training of the controller involves multiple interactions between the agent and the control system environment. The agent takes action a_t based on the current state s_t, and then receives feedback from the flight simulator system in the form of reward r_t and the next state s_{t+1}. The GAE (8) is calculated using the collected transitions, and weight updates are performed on the Actor and Critic networks based on the objective function. The controller training diagram of the 2-DOF flight attitude simulator is depicted in Fig. 2.

In the RL concept, the Actor network takes the observed state vectors as input and outputs the action vectors as control signals. Specifically, in the controller training of the 2-DOF flight attitude simulator, we define the state vector as $s_t = [\phi\ \ \dot{\phi}]^\top$ for observation, and the action vector is chosen as $a_t = F_1$. As a result, the structures of the Actor network and the Critic network are designed as the same fully connected neural network structure, which has two inputs and one output with two hidden layers of 64 units. According to the optimal control theory [25–27], the control objective or index should be a combination of quadratic forms of system states and control inputs. Consequently, the essential reward function is designed as the negative form of the optimal control index, which is expressed by

$$r_t = -c_1\phi^2 - c_2\dot{\phi}^2 - c_3F_1^2, \tag{10}$$

where $c_i, i = 1, 2, 3$ are positive constants which can be manipulated according to the required controller performance. The values of parameters involved in the controller and training process are collected in Table 2.

4 Simulation

The hardware used in the simulation is mainly a personal computer with an Intel i7-12700H CPU and a NVIDIA GeForce RTX3060 GPU. The simulation programs are running based on Python 3.10 and Pytorch 1.13.1.

Table 2: Training Parameter Values of PPO Controller

Parameter	Value	Parameter	Value
γ	0.99	N	250
λ	0.95	T	500
α_p	$5e^{-5}$	K	100
α_v	$5e^{-4}$	c_1	1
D	1000	c_2	0.1
ε	0.2	c_3	0.01

4.1 Controller Training

The time horizon of each training episode is 10s with a sample interval of 0.02s, which is, 500 timesteps in total. It should be noted that the model used in controller training is the nominal system without any external disturbances and model uncertainties, namely $d = 0$. Moreover, the pitch angle is limited by $\phi \in [-60°, 60°]$ and the episode is desired to be terminated if the angle is observed beyond the limitation during training. At the beginning of each episode, the pitch angle ϕ is set randomly in the range of $[-60°, 60°]$ and the angular velocity is set $\dot{\phi} = 0$. The agent is designed to choose actions within $F_1 \in [-1.5N, 4N]$ due to the restriction of actuator saturation.

The whole training process of the PPO controller lasts about half an hour, and the training curve is illustrated in Fig. 3. According to Fig. 3, the curve indicates that the performance of the controller fluctuates dramatically during the first 50 training epochs because PPO algorithm needs plenty of explorations at the beginning of training. However, the reward begins to converge after about 100 training epochs and stays steadily around -20 until the end of training process, which showcases the prominent stability of PPO algorithm in policy improvement after finding a relatively effective policy.

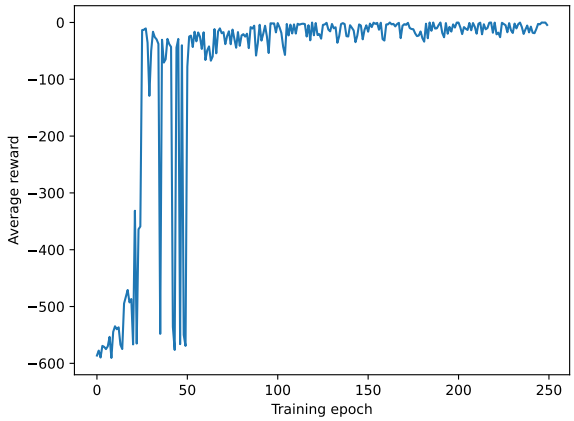

Fig. 3: Controller training curve.

4.2 Controller Test

After the controller of the 2-DOF flight attitude simulator is well-trained by PPO algorithm, the generation ability of the PPO controller is desired to be tested first. We design 10 independent tests, in which the initial pitch angle of the attitude simulator is chosen evenly between $[-85°, 85°]$. It is noteworthy that the angles ranged in $\pm[60°, 85°]$ have never been observed by the agent during training process. The external disturbances d is not involved in these tests as well.

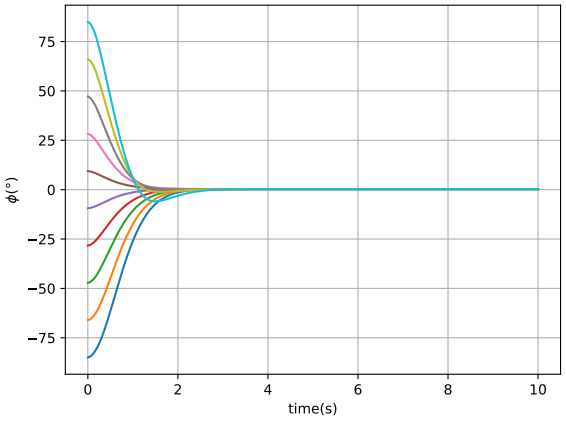

Fig. 4: Angular position responses with different initial angles.

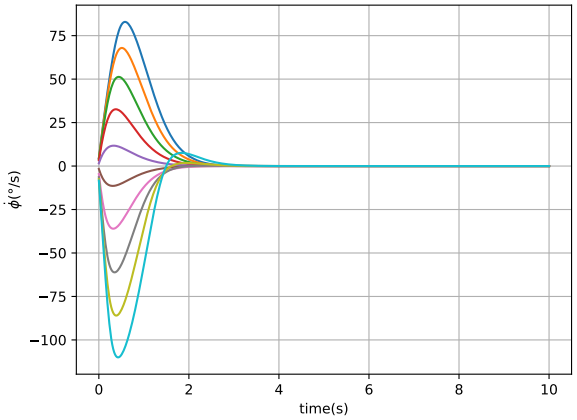

Fig. 5: Angular velocity responses with different initial angles.

The angular position and velocity responses of pitch tunnel of the flight attitude simulator are depicted in Fig. 4 and Fig. 5. It is shown that the trained PPO controller, regardless of whether the observed state is one encountered during the agent's training, demonstrates the ability to rapidly, smoothly, and stably achieve attitude stabilization control for the 2-DOF flight simulator. Only in one test, there is a little overshooting in the angle and angular velocity responses due to an excessively large initial angle $(85°)$ and the influence of the gravity on the clump weight. Nevertheless, such a extreme scenario is unlikely to occur in practical applications, so it has a minimal impact on the overall performance of the PPO controller.

4.3 Comparative Simulation

In order to show the effectiveness of our proposed controller, another two controllers for the 2-DOF flight attitude simulator are trained under the same conditions, including a PPO controller without GAE and a DDPG controller. The

initial state of the simulator is set as $\phi = -60°, \dot{\phi} = 0$, the angular position and velocity responses of systems controlled by the three different controllers are collected in Fig. 6 and Fig. 7.

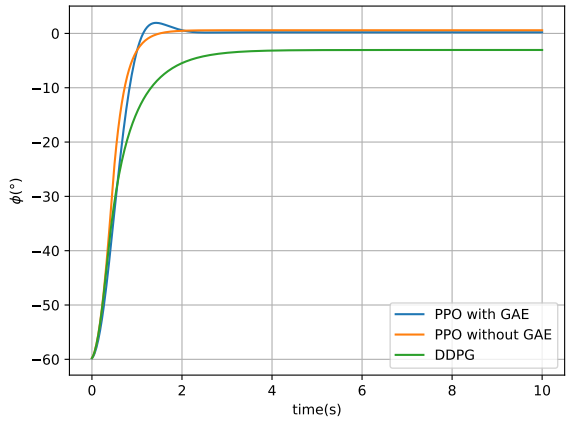

Fig. 6: Angular position responses using three different RL controllers.

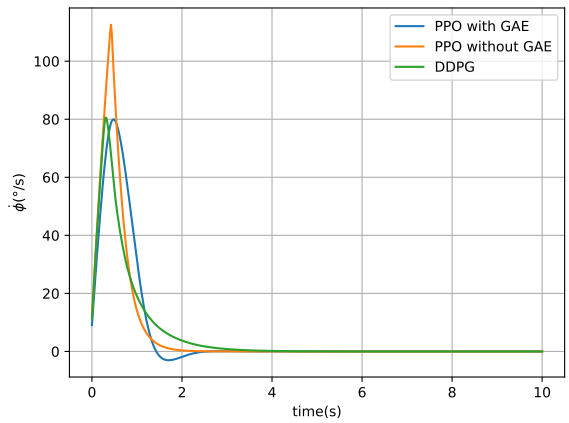

Fig. 7: Angular velocity responses using three different RL controllers.

According to Fig. 6, the DDPG controller is not well-trained under the same training epochs and other conditions, with a control error of $-4°$. In contrast, the PPO controllers do a relatively good job in stabilizing the closed-up systems. Although having a tiny overshoot at 1.7s, the PPO controller with GAE (8) reaches a control error of about $-0.2°$, while that of the PPO controller without GAE is around $1°$. In Fig. 7, the PPO controller without GAE witnesses a considerable velocity response at roughly $110°/s$ in the first second of the episode, which is not rational to achieve in real-world flight experiments. By comparison, the velocity response of PPO controller with GAE is much smoother, in line with the actual operating conditions of the simulator. Therefore, the proposed PPO controller equipped with GAE demonstrates a higher level of control accuracy and rationality in the flight attitude simulator system.

4.4 Robustness Assessment

Eventually, time-varying external disturbances are introduced to assess the robustness of the proposed PPO controller for the 2-DOF flight attitude simulator. The external disturbance d in (1) can be modeled as the sum of a slow time-varying signal and some noise, which can be expressed by

$$d = 0.2 \sin(0.4\pi t) + w_0, \tag{11}$$

where $w_0 \sim \mathcal{N}(0, \sigma)$ is the zero-mean Gaussian white noise and σ is the standard deviation of the noise.

In this test, we set the initial state of the flight attitude simulator as $\phi = -60°, \dot{\phi} = 0$. In comparison, the standard deviation of the disturbance signal introduced in the mechanism is designed to switch from $\sigma = 1$ to $\sigma = 5$, aiming to evaluating the PPO controller's tolerance to variations in disturbances. The angular position and velocity responses of the flight attitude simulator in presence of Gaussian white noise disturbances are illustrated in Fig. 8 and Fig. 9.

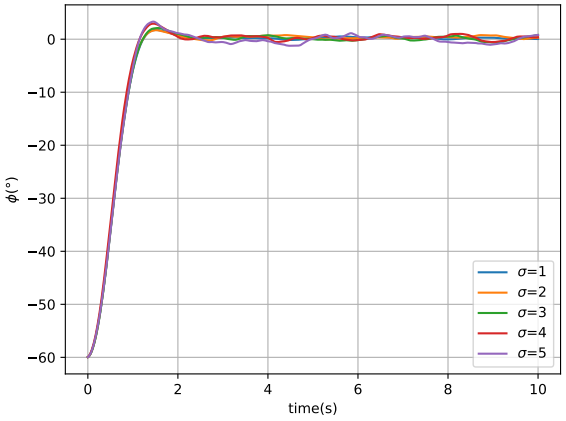

Fig. 8: Angular position responses with different Gaussian white noises.

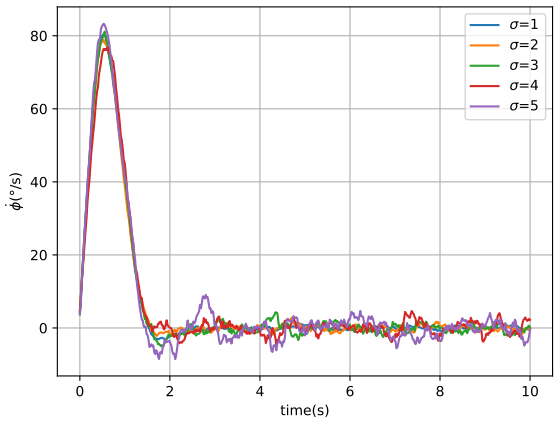

Fig. 9: Angular velocity responses with different Gaussian white noises.

The simulation results indicate that the introduction of external disturbances does indeed have a certain impact on the

controller's performance. This results in some overshooting in the angular position and introduces oscillations in the angular velocity of the flight simulator which increase with the growing standard deviation σ of the noise w_0. Nevertheless, the PPO controller can still stabilize the flight attitude simulator near the origin under the influence of noise with varying variances, with the maximum control angle error of around 1.8°. Consequently, the simulation demonstrates the robustness and effectiveness of the model-free flight attitude simulator controller trained using PPO algorithm.

5 Conclusion

This paper addresses the control issue of a 2-DOF flight attitude simulator system and achieves the design and training of a model-free approximate optimal controller based on the PPO algorithm. Due to the sensibility of the simulator's pitch channel to the gravitational effect of the clump weight, we initially establish a nonlinear dynamic model and introduce external disturbances. Subsequently, utilizing the Actor-Critic framework and neural networks, we devise a PPO controller training framework tailored to the dynamic model of flight attitude simulator and implement it. Finally, through sufficient simulations in different aspects, the proposed controller is validated to exhibit good generalization ability and robustness.

Our future work is to investigate robust approaches in response to disturbances of more complex forms, and then apply the controller to our real-world 2-DOF flight attitude simulator system to assess its effectiveness.

References

[1] S. A. Bortoff, "The university of toronto rc helicopter: a test bed for nonlinear control," in *Proceedings of the 1999 IEEE International Conference on Control Applications (Cat. No. 99CH36328)*, vol. 1. IEEE, 1999, pp. 333–338.

[2] Z. Zhou, G. Hu, C. Hu, C. Wen, and L. Chang, "A survey of belief rule-base expert system," *IEEE Transactions on Systems, Man, and Cybernetics: Systems*, vol. 51, no. 8, pp. 4944–4958, 2019.

[3] J. Lin, X. Wang, and X. Ban, "An unbiased pseudo-linear kalman filter based on three-dimensional angle of arrival," *Navigation Positioning and Timing*, vol. 10, pp. 77–85, 2023.

[4] T. Oktay and C. Sultan, "Simultaneous helicopter and control-system design," *Journal of Aircraft*, vol. 50, no. 3, pp. 911–925, 2013.

[5] K. Yu, X. Wang, and H. Lu, "Active-passive station tracking algorithm based on interactive multi-model," *Navigation Positioning and Timing*, vol. 10, pp. 72–80, 2023.

[6] L. Ren, X. Ban, F. Wu, and X. Huang, "Fuzzy learning controller design of 2-dof flight attitude simulator," *Electric Machines and Control*, vol. 23, pp. 127–134, 2019.

[7] Y. Yang, K. Deng, Y. Zuo, X. Ban, and X. Huang, "Parameter design and optimization of a flight attitude simulator system based on pilco framework," *Optics and Precision Engineering*, vol. 27, pp. 2365–2373, 2019.

[8] H. Yin, Y. Yang, Y. Zhao, Y. Liang, and X. Ban, "Self-tuning controller design for a 2-dof flight attitude simulator," *Electric Machines and Control*, vol. 22, pp. 105–112, 2018.

[9] G. Hoffmann, H. Huang, S. Waslander, and C. Tomlin, "Quadrotor helicopter flight dynamics and control: Theory and experiment," in *AIAA guidance, navigation and control conference and exhibit*, 2007, p. 6461.

[10] H. Shim, T. J. Koo, F. Hoffmann, and S. Sastry, "A comprehensive study of control design for an autonomous helicopter," in *Proceedings of the 37th IEEE conference on decision and control (Cat. No. 98CH36171)*, vol. 4. IEEE, 1998, pp. 3653–3658.

[11] H. Hung, H. Hsu, and T. Cheng, "Ieeeexample: Bstcontrol optimal sensing for tracking task by heterogeneous multi-uav systems," *IEEE Transactions on Control Systems Technology*, 2023.

[12] Z. Wang and T. Hong, "Reinforcement learning for building controls: The opportunities and challenges," *Applied Energy*, vol. 269, p. 115036, 2020.

[13] B. Kiumarsi, K. G. Vamvoudakis, H. Modares, and F. L. Lewis, "Optimal and autonomous control using reinforcement learning: A survey," *IEEE transactions on neural networks and learning systems*, vol. 29, no. 6, pp. 2042–2062, 2017.

[14] L. Buşoniu, T. De Bruin, D. Tolić, J. Kober, and I. Palunko, "Reinforcement learning for control: Performance, stability, and deep approximators," *Annual Reviews in Control*, vol. 46, pp. 8–28, 2018.

[15] Y. Yang, X. Ban, X. Huang, and C. Shan, "A dueling-double-deep q-network controller for magnetic levitation ball system," in *2020 39th Chinese Control Conference (CCC)*. IEEE, 2020, pp. 1885–1890.

[16] C. Chang, J. Tsai, J. Lin, and Y. Ooi, "Autonomous driving control using the ddpg and rdpg algorithms," *Applied Sciences*, vol. 11, no. 22, p. 10659, 2021.

[17] Z. Zhang, X. Li, J. An, W. Man, and G. Zhang, "Model-free attitude control of spacecraft based on pid-guide td3 algorithm," *International Journal of Aerospace Engineering*, vol. 2020, pp. 1–13, 2020.

[18] S. Han and T. Liang, "Reinforcement-learning-based vibration control for a vehicle semi-active suspension system via the ppo approach," *Applied Sciences*, vol. 12, no. 6, p. 3078, 2022.

[19] C. Wu, W. Pan, R. Staa, J. Liu, G. Sun, and L. Wu, "Deep reinforcement learning control approach to mitigating actuator attacks," *Automatica*, vol. 152, p. 110999, 2023.

[20] P. Duraisamy, M. Nagarajan Santhanakrishnan, and A. Rengarajan, "Design of deep reinforcement learning controller through data-assisted model for robotic fish speed tracking," *Journal of Bionic Engineering*, vol. 20, no. 3, pp. 953–966, 2023.

[21] J. Schulman, F. Wolski, P. Dhariwal, A. Radford, and O. Klimov, "Proximal policy optimization algorithms," *arXiv preprint arXiv:1707.06347*, 2017.

[22] V. Mnih, A. P. Badia, M. Mirza, A. Graves, T. Lillicrap, T. Harley, D. Silver, and K. Kavukcuoglu, "Asynchronous methods for deep reinforcement learning," in *International conference on machine learning*. PMLR, 2016, pp. 1928–1937.

[23] J. Schulman, P. Moritz, S. Levine, M. Jordan, and P. Abbeel, "High-dimensional continuous control using generalized advantage estimation," *arXiv preprint arXiv:1506.02438*, 2015.

[24] O. E. Egbomwan, S. Liu, and H. Chaoui, "Twin delayed deep deterministic policy gradient (td3) based virtual inertia control for inverter-interfacing dgs in microgrids," *IEEE Systems Journal*, 2022.

[25] F. L. Lewis, D. Vrabie, and V. L. Syrmos, *Optimal control*. John Wiley & Sons, 2012.

[26] Z. Feng, Z. Zhou, C. Hu, X. Ban, and G. Hu, "A safety assessment model based on belief rule base with new optimization method," *Reliability Engineering & System Safety*, vol. 203, p. 107055, 2020.

[27] S. Tang, Z. Zhou, C. Hu, J. Yang, and Y. Cao, "Perturbation analysis of evidential reasoning rule," *IEEE transactions on systems, man, and cybernetics: systems*, vol. 51, no. 8, pp. 4895–4910, 2019.

Proceedings of the 3rd Conference on Fully Actuated System Theory and Applications
May 10-12, 2024, Shenzhen, China

Adaptive Iterative Learning Control for Underactuated Systems with Unknown Input Distribution Matrices: Ensuring Input Continuity

Mali Yin, Xuefang Li*
School of Intelligent Systems Engineering, Shenzhen Campus of Sun Yat-Sen University, Shenzhen 518000, P. R. China
E-mail: lixuef25@mail.sysu.edu.cn

Abstract: This work investigates the adaptive iterative learning control (AILC) problem for a class of underactuated systems with unknown input distribution matrices. By introducing a newly designed control gain matrix, a novel AILC algorithm is proposed, which is able to deal with the unknown nonsquare control gain matrix effectively. Additionally, an auxiliary system is adopted to deal with the input saturation. The convergence of the proposed control algorithm is rigorously analyzed by using the composite energy function (CEF) method. The effectiveness is demonstrated through a numerical example.

Key Words: Adaptive iterative learning control, Underactuated systems, Unknown control gains, Input saturation, Input continuity.

1 Introduction

Since iterative learning control (ILC) was initially proposed by Arimoto et al. in 1984, it has become a research hotspot. ILC is one of the most effective control methods for dealing with control problems of systems that repeat operation within a finite interval. In the past four decades, ILC has formed a relatively complete theoretical framework [1–3]. Moreover, it has been widely applied in various fields, including robotics [4], intelligent manufacturing [5], etc. In the field of iterative learning control (ILC), there are two main design frameworks, namely conventional ILC (CILC) and adaptive ILC (AILC). For the former, both the controller design and convergence analysis are based on contraction mapping methods, which are usually applicable to globally Lipschitz continuous systems. For the latter, the control law is designed based on a Lyapunov-like theory, which is effective in dealing with locally Lipschitz continuous systems.

In the past two decades, the development of AILC theory has been the pursuit of many researchers, who have devoted themselves to its deepening and improvement. For example, in [6], researchers developed an AILC scheme considering the updating law of parameters on the time axis, aiming to connect the theories of ILC and adaptive control, and assuming that the unknown parameters remain constant. In addition, a new AILC algorithm was proposed in [2] and [7], where a parameter estimation mechanism was introduced along the iteration axis to cope with the uncertainty of time-varying parameters. A novel AILC method was designed based on the Barrier CEF method in [8] to handle state constraints and non-parametric uncertainties. A generalization of AILC to handle norm-bounded uncertainties was presented in [9]. However, it should be noted that the existing AILC research mainly focuses on Single Input Single Output (SISO) systems or Fully Actuated MIMO systems with known and invertible control gain matrices. The problem becomes highly challenging when the control gain matrix is unknown or the controlled system is underactuated.

In the field of AILC research, there is relatively little literature on the treatment of underactuated systems. For example, the pioneering study in [7] investigated ordinary nonlinear systems with non-square input distribution matrices and proposed an AILC design based on the Composite Energy Function (CEF) framework, where the input distribution matrix needs to satisfy the known and left invertible condition. The applicability of AILC was extended to nonlinear systems with non-parametric uncertainties in [10], also requiring the left invertibility of the input distribution matrix as a key prerequisite. In fact, similar assumptions, such as the invertibility or left invertibility of the input distribution matrix, have also appeared in other research reports, including [8, 11–14] and related citations. Due to the existence of a large number of underactuated systems in reality, most of them do not satisfy these assumptions, which significantly narrows down the applicability of AILC, limited to only a few nonlinear systems.

In practical applications, the input distribution matrix of many underactuated systems is either partially known or completely unknown. In the case of an unknown input distribution matrix, researchers in [15] developed an adaptive estimation algorithm for handling unknown input distribution matrices in discrete-time systems, which was later applied to continuous-time systems in [16], covering the case of unknown input distribution matrices. Additionally, an AILC method using fuzzy logic techniques was introduced in [17] to deal with the issue of unknown input distribution matrices in nonlinear systems, where fuzzy logic was used to approximate the uncertainties associated with the unknown input distribution matrix. However, in the existing literature, only a few studies have addressed the AILC design for nonlinear systems with unknown input distribution matrices. When faced with underactuated systems with unknown input distribution matrices, the AILC design becomes more challenging.

In this work, we focus on the AILC design for underactu-

This work is supported by the National Natural Science Foundation of China (Grant No. 62373385), the Natural Science Foundation of Guangdong Province (Grant No. 2022A1515010881), and the Shenzhen Science and Technology Program (Grant No. 202305063000008, 20231121093427001)

*Corresponding author

ated systems with unknown input distribution matrices and ensure the convergence of tracking error considering input saturation. Furthermore, although the controller in [18] addresses the issue of non-square control gain matrices, it may suffer from switching problems, which can lead to the discontinuity of the controller. In this research, we avoid the switching problem by introducing specially designed control gain matrices.

The structure of this paper is as follows. Section II introduces the problem formulation. Section III presents the AILC design and convergence analysis for underactuated systems with unknown input distribution matrices. Section IV provides a simulation example. Finally, Section V concludes the paper.

2 Problem Formulation

Consider the following MIMO nonlinear system

$$\dot{\mathbf{x}}_k = \mathbf{f}\left(\mathbf{x}_k, t\right)\Theta + A\left(\mathbf{x}_k, t\right)\mathrm{sat}\left(\mathbf{u}_k(t)\right) + \mathbf{w}^r, \quad (1)$$

where $k \in \mathbf{N}$ denotes the iteration index, $t \in [0, T]$, $T > 0$ represents the trial length, $\mathbf{x}_k$ is the measurable system state, $\mathbf{f}\left(\mathbf{x}_k, t\right) : \mathbf{R}^n \times \mathbf{R}^+ \to \mathbf{R}^{n\times p}$ is a known function, $\mathbf{w}^r$ is a known vector valued function, $\Theta \in \mathbf{R}^p$ is the unknown parametric uncertainties, $A\left(\mathbf{x}_k, t\right) \in \mathbf{R}^{n\times m}$ is the unknown control gain matrix, $\mathbf{u}_k(t) = \left[\mathbf{u}_{1,k}(t), \ldots, \mathbf{u}_{m,k}(t)\right]^T \in \mathbf{R}^m$ is the control input, and $\mathrm{sat}\left(\mathbf{u}_k(t)\right) = \left[\mathrm{sat}\left(\mathbf{u}_{1,k}(t)\right), \ldots, \mathrm{sat}\left(\mathbf{u}_{m,k}(t)\right)\right]^T$ is the saturation function that is defined as follows:

$$\mathrm{sat}\left(\mathbf{u}_{j,k}(t)\right) \triangleq \begin{cases} \mathrm{sign}\left(\mathbf{u}_{j,k}(t)\right)\mathbf{u}_{j,\max}, & \left|\mathbf{u}_{j,k}(t)\right| \geq \mathbf{u}_{j,\max} \\ \mathbf{u}_{j,k}(t), & \left|\mathbf{u}_{j,k}(t)\right| \leq \mathbf{u}_{j,\max}, \end{cases} \quad (2)$$

with $\mathbf{u}_{j,\max} > 0$ being the upper bound of the j th control input component $\mathbf{u}_{j,k}(t)$ imposed by either physical constraints or artificial limitations. For simplicity, we denote $\overline{\mathbf{u}}_k(t) \triangleq \mathrm{sat}\left(\mathbf{u}_k(t)\right)$ with $\bar{\mathbf{u}}_{j,k}(t) \triangleq \mathrm{sat}\left(\mathbf{u}_{j,k}(t)\right), j = 1, 2, \cdots, m$, namely, $\bar{\mathbf{u}}_k(t) = \left[\bar{\mathbf{u}}_{1,k}(t), \ldots, \bar{\mathbf{u}}_{m,k}(t)\right]^T$.For simplicity, let us denote $\mathbf{f}_k \triangleq \mathbf{f}\left(\mathbf{x}_k, t\right)$, $A_k \triangleq A\left(\mathbf{x}_k, t\right)$, $\bar{\mathbf{u}}_k \triangleq \bar{\mathbf{u}}_k(t)$.

The reference trajectory $\mathbf{x}_r \in \mathbf{R}^n$ is generated by the following reference model:

$$\dot{\mathbf{x}}_r = \mathbf{w}^r, \quad (3)$$

with $\mathbf{w}^r$ being continuous with respect to both $\mathbf{x}_r$ and t. The control objective of the present work is summarized as follows.

The control objective: For the system (1), the control objective is to determine a sequence of the control input $\mathbf{u}_k$ that are able to drive the system state $\mathbf{x}_k$ to accurately track a predefined reference trajectory $\mathbf{x}_r$, $\forall t \in [0, T]$ as the iteration index k goes to infinity.

To facilitate the controller design and analysis, the following assumptions are imposed to the system (1).

Assumption 1: The control gain matrix A_k is unknown but norm-bounded.

Assumption 2: The initial states of the system (1) can be aligned with the initial value of the desired trajectory, namely, $\mathbf{x}_k(0) = \mathbf{x}_r(0), \forall k \in \mathbf{Z}$.

Remark 1: The identical initialization condition (i.i.c.) is a common assumption in ILC area, which is imposed to guarantee the perfect tracking performance. In literature, there have been many works showing that the i.i.c. can be removed by sacrificing the tracking performance to some extent, while extra system information or additional control mechanisms are required [19, 20]. For the present work, the i.i.c. may be removed by combining the initial state learning or rectification techniques in [19, 20] with the proposed control approach.

Let $\mathbf{e}_k \triangleq \mathbf{x}_k - \mathbf{x}_r$ be the tracking error. The corresponding error dynamics can be derived as follows:

$$\begin{aligned} \dot{\mathbf{e}}_k =& \dot{\mathbf{x}}_k - \dot{\mathbf{x}}_r \\ =& \mathbf{f}_k\Theta + A_k\bar{\mathbf{u}}_k. \end{aligned} \quad (4)$$

Considering the fact that the control gain matrix A_k is unknown, the conventional design principle that involves A_k explicitly in the control algorithms is no longer applicable. In this work, inspired by this issue, the error dynamics are reformulated as follows:

$$\begin{aligned} \dot{\mathbf{e}}_k =& \dot{\mathbf{x}}_k - \dot{\mathbf{x}}_r \\ =& \mathbf{f}_k\Theta + B\bar{\mathbf{u}}_k + \left[A_k\bar{\mathbf{u}}_k - B\bar{\mathbf{u}}_k\right], \end{aligned} \quad (5)$$

where the term $B\bar{\mathbf{u}}_k$ is added and subtracted. Here, $B = E_{1j}G \in \mathbf{R}^{n\times m}$, E_{1j} represents the elementary row transformation matrix for swapping row 1 and row j, $G = \begin{bmatrix} I_m \\ 0 \end{bmatrix} \in \mathbf{R}^{n\times m}$ with I_m being the m-dimensional identity matrix. In this case, the matrix B can be regarded as a newly defined control gain matrix, while the originally unknown control gain matrix A_k is treated as a norm-bounded system uncertainty. Thus, the AILC design for systems with unknown control gain matrices is transformed into a design for systems with known but non-square control gain matrices. For the error dynamics in equation (5), based on Assumption 1 and the boundedness of $\bar{\mathbf{u}}_k$, it can be shown that the uncertainties satisfy the following inequality:

$$\left\|A_k\bar{\mathbf{u}}_k - B\bar{\mathbf{u}}_k\right\| \leqslant \varphi, \quad (6)$$

where $\varphi > 0$ is an unknown quantity. For simplicity, we denote $\omega_k \triangleq A_k\bar{\mathbf{u}}_k - B\bar{\mathbf{u}}_k$.

3 Controller Design and Convergence Analysis

To compensate for the impact of the input saturation, we introduce an auxiliary variable λ_k, which is generated by the following auxiliary system:

$$\begin{aligned} \dot{\lambda}_k =& -\nu\lambda_k + B\Delta\mathbf{u}_k, \\ \lambda_k(0) =& 0, \end{aligned} \quad (7)$$

where $\nu > 0$ is a tunable parameter to be designed, and $\Delta\mathbf{u}_k = \bar{\mathbf{u}}_k - \mathbf{u}_k$ represents the difference between the actual input and the unsaturated input. After introducing the auxiliary system, we incorporate tracking error by defining a new virtual tracking error as follows:

$$\tilde{\mathbf{e}}_k = \mathbf{e}_k - \lambda_k. \quad (8)$$

The dynamics of the corresponding virtual tracking error can be derived as follows:

$$\begin{aligned}\dot{\tilde{\mathbf{e}}}_k =&\dot{\mathbf{e}}_k - \dot{\lambda}_k \\ =&\mathbf{f}_k\Theta + B\bar{\mathbf{u}}_k + \omega_k + \nu\lambda_k - B\Delta\mathbf{u}_k \\ =&\mathbf{f}_k\Theta + B\mathbf{u}_k + \omega_k + \nu\lambda_k.\end{aligned} \tag{9}$$

Based on the virtual tracking error dynamics (9) and the inequality (6),we can develop an novel AILC algorithm as follows:

$$\mathbf{u}_k(t) = \begin{cases}\mathbf{u}_{1,k} + \mathbf{u}_{2,k} + \mathbf{u}_{3,k}, & \|\tilde{\mathbf{e}}_k\| \neq 0 \\ \mathbf{u}_k(t^-), & \|\tilde{\mathbf{e}}_k\| = 0,\end{cases} \tag{10}$$

where

$$\mathbf{u}_{1,k} = \frac{B^T}{\|BB^T\|}\left(-\nu\mathbf{e}_k - \mathbf{f}_k\hat{\Theta}_k\right), \tag{11}$$

$$\mathbf{u}_{2,k} = -\frac{P_k B^T\tilde{\mathbf{e}}_k}{\left\|\tilde{\mathbf{e}}_k^T B\right\|^2}\|\tilde{\mathbf{e}}_k\|\left\|\nu\mathbf{e}_k + \mathbf{f}_k\hat{\Theta}_k\right\|, \tag{12}$$

$$\mathbf{u}_{3,k} = -\frac{B^T\tilde{\mathbf{e}}_k}{\left\|\tilde{\mathbf{e}}_k^T B\right\|^2}\hat{\varphi}_k\tilde{\mathbf{e}}_k^T\text{sign}(\tilde{\mathbf{e}}_k), \tag{13}$$

$$P_k = \frac{\|B\|^2}{\|BB^T\|} + 1. \tag{14}$$

We define $\tilde{\mathbf{e}}_k = [\tilde{\mathbf{e}}_{1,k}, \ldots, \tilde{\mathbf{e}}_{n,k}]^T$. When $\|\tilde{\mathbf{e}}_k\| \neq 0$, let j denote the index of the first non-zero component in $\tilde{\mathbf{e}}_k$. This condition guarantees that the product $\tilde{\mathbf{e}}_k^T B$ forms a non-zero vector, which can be represented as $[\tilde{\mathbf{e}}_{j,k}(t), *]$, where the first component is non-zero, ensuring that the norm $\left\|\tilde{\mathbf{e}}_k^T B\right\| \neq 0$. The asterisk (*) represents any values that are not of concern in this analysis, as our focus is solely on demonstrating that the first element is non-zero to avoid singularity. Therefore, the corresponding controller will not encounter singularity issues in this case. Additionally, since $\|E_{1j}\| = 1$ and G is norm-bounded, it follows that B is also norm-bounded.

Remark 2: For the proposed control law (10), when the condition $\|\tilde{\mathbf{e}}_k\| = 0$ is satisfied, the value of the control input $\mathbf{u}_k(t)$ is equal to the left limit value at time t. This design aims to eliminate the discontinuity effects caused by control input switching in [18] and ensures the left continuity and stability of the control system. By maintaining the left limit value of the control input, we can avoid sudden changes in the control input, thereby improving the performance and robustness of the control system.

$\hat{\Theta}_k \in \mathbf{R}^p$ is the estimate of Θ generated by (15):

$$\begin{aligned}\hat{\Theta}_k(t) =&\hat{\Theta}_{k-1}(t) + \Gamma\mathbf{f}_k^T\tilde{\mathbf{e}}_k, \\ \hat{\Theta}_{-1}(t) =&0, t \in [0, T],\end{aligned} \tag{15}$$

with Γ being a positive definite learning gain matrix to be designed. $\hat{\varphi}_k$ is the estimate of the unknown quantity φ generated by (16):

$$\begin{aligned}\hat{\varphi}_k =&\hat{\varphi}_{k-1} + \gamma\tilde{\mathbf{e}}_k^T\text{sign}(\tilde{\mathbf{e}}_k), \\ \hat{\varphi}_{-1}(t) =&0, t \in [0, T],\end{aligned} \tag{16}$$

with $\gamma > 0$ being the learning gain to be determined.

With the proposed AILC law (10)- (16), we can obtain the following result.

Theorem 1: For the system (1) with the Assumptions 1-2, the proposed AILC algorithm (10)- (16) together with the auxiliary system (7) ensure that the tracking error $\mathbf{e}_k(t)$ converges to a neighborhood of the origin as the iteration number approaches to infinity.

To carry out the convergence analysis, the following CEF is developed:

$$E_k(t) = \frac{1}{2}\tilde{\mathbf{e}}_k^T\tilde{\mathbf{e}}_k + \frac{1}{2}\int_0^t \Phi_k^T\Gamma^{-1}\Phi_k d\tau + \frac{1}{2\gamma}\int_0^t \psi_k^2 d\tau, \tag{17}$$

where $\Phi_k = \hat{\Theta}_k - \Theta$ and $\psi_k = \hat{\varphi}_k - \varphi$ represent the estimation errors.

According to the reference [18], the inverse image of the set $\left\{\tau \in [0,t] \mid \left\|\tilde{\mathbf{e}}_k^T(\tau)\right\| \neq 0, t \in [0,T]\right\}$ is an open set over $[0,t]$, which can be divided into countable disjoint open intervals. Thus, there have only countable closed intervals on $[0,t]$ such that $\left\|\tilde{\mathbf{e}}_k^T(\tau)\right\| = 0$. we denote $Q \triangleq \left\{\tau \in [0,t] \mid \left\|\tilde{\mathbf{e}}_k^T(\tau)\right\| = 0, t \in [0,T]\right\} \triangleq \bigcup_{i=1}^{\infty}[a_{i,k}, b_{i,k}]$ and $S \triangleq \left\{\tau \in [0,t] \mid \left\|\tilde{\mathbf{e}}_k^T(\tau)\right\| \neq 0, t \in [0,T]\right\} \triangleq \bigcup_{i=1}^{\infty}(c_{i,k}, d_{i,k})$. Therefore, we can conclude that $Q \cup S = [0,t]$.

Proof of Theorem 1: The proof can be divided into three parts, each addressing a different aspect. The first part demonstrates the nonincreasing property of the CEF along the iteration axis. The second part establishes the convergence of the virtual tracking error. Finally, the third part shows the convergence of the tracking error.

Part I. The difference of CEF: For a given $t \in [0,T]$, the difference of the CEF at two consecutive iterations is

$$\begin{aligned}\Delta E_k =& E_k - E_{k-1} \\ =& \frac{1}{2}\tilde{\mathbf{e}}_k^T\tilde{\mathbf{e}}_k - \frac{1}{2}\tilde{\mathbf{e}}_{k-1}^T\tilde{\mathbf{e}}_{k-1} \\ &+ \frac{1}{2}\int_0^t \left(\Phi_k^T\Gamma^{-1}\Phi_k - \Phi_{k-1}^T\Gamma^{-1}\Phi_{k-1}\right)d\tau \\ &+ \frac{1}{2\gamma}\int_0^t \left(\psi_k^2 - \psi_{k-1}^2\right)d\tau.\end{aligned} \tag{18}$$

For the first term on the right hand side of (18), we have

$$\begin{aligned}\frac{1}{2}\tilde{\mathbf{e}}_k^T\tilde{\mathbf{e}}_k =& \int_0^t \tilde{\mathbf{e}}_k^T\dot{\tilde{\mathbf{e}}}_k d\tau \\ =& \int_S \tilde{\mathbf{e}}_k^T\dot{\tilde{\mathbf{e}}}_k d\tau + \int_Q \tilde{\mathbf{e}}_k^T\dot{\tilde{\mathbf{e}}}_k d\tau \\ =& \int_S \tilde{\mathbf{e}}_k^T\dot{\tilde{\mathbf{e}}}_k d\tau,\end{aligned} \tag{19}$$

where the i.i.c. in the Assumption 2 and (7) is adopted. We denote $\int_S \tilde{\mathbf{e}}_k^T\dot{\tilde{\mathbf{e}}}_k d\tau = \sum_{i=1}^{\infty}\int_{c_{i,k}}^{d_{i,k}} \tilde{\mathbf{e}}_k^T\dot{\tilde{\mathbf{e}}}_k d\tau$ and $\int_Q \tilde{\mathbf{e}}_k^T\dot{\tilde{\mathbf{e}}}_k d\tau = \sum_{i=1}^{\infty}\int_{a_{i,k}}^{b_{i,k}} \tilde{\mathbf{e}}_k^T\dot{\tilde{\mathbf{e}}}_k d\tau$.

By substituting the controller (10) into (9), it gives

$$\begin{aligned}\tilde{\mathbf{e}}_k^T\dot{\tilde{\mathbf{e}}}_k &= \tilde{\mathbf{e}}_k^T\mathbf{f}_k\Theta + \tilde{\mathbf{e}}_k^T\omega_k + \nu\tilde{\mathbf{e}}_k^T\lambda_k \\ &+ \frac{\tilde{\mathbf{e}}_k^TBB^T}{||BB^T||}\left[-\nu\mathbf{e}_k - \mathbf{f}_k\hat{\Theta}_k\right] \\ &- \frac{\tilde{\mathbf{e}}_k^TBP_kB^T\tilde{\mathbf{e}}_k}{||\tilde{\mathbf{e}}_k^TB||^2}||\tilde{\mathbf{e}}_k||||\nu\mathbf{e}_k + \mathbf{f}_k\hat{\Theta}_k|| \\ &- \frac{\tilde{\mathbf{e}}_k^TBB^T\tilde{\mathbf{e}}_k}{||\tilde{\mathbf{e}}_k^TB||^2}\hat{\varphi}_k\tilde{\mathbf{e}}_k^T\mathrm{sign}(\tilde{\mathbf{e}}_k).\end{aligned} \tag{20}$$

Due to the equation $\frac{BB^T}{||BB^T||} = \frac{BB^T}{||BB^T||} - I + I$, we can obtain the following inequality:

$$\begin{aligned}&\tilde{\mathbf{e}}_k^T\frac{BB^T}{||BB^T||}[-\nu\mathbf{e}_k - \mathbf{f}_k\hat{\Theta}_k] \\ &= \tilde{\mathbf{e}}_k^T(\frac{BB^T}{||BB^T||} - I + I)[-\nu\mathbf{e}_k - \mathbf{f}_k\hat{\Theta}_k] \\ &\leq -\nu\tilde{\mathbf{e}}_k^T\mathbf{e}_k - \tilde{\mathbf{e}}_k^T\mathbf{f}_k\hat{\Theta}_k \\ &+ ||\tilde{\mathbf{e}}_k||\left(\frac{||B||^2}{||BB^T||} + 1\right)||\nu\mathbf{e}_k + \mathbf{f}_k\hat{\Theta}_k|| \\ &= -\nu\tilde{\mathbf{e}}_k^T\mathbf{e}_k - \tilde{\mathbf{e}}_k^T\mathbf{f}_k\hat{\Theta}_k + P_k||\tilde{\mathbf{e}}_k||||\nu\mathbf{e}_k + \mathbf{f}_k\hat{\Theta}_k||.\end{aligned} \tag{21}$$

Moreover, the following equality holds:

$$-\frac{\tilde{\mathbf{e}}_k^TBB^T\tilde{\mathbf{e}}_k}{||\tilde{\mathbf{e}}_k^TB||^2} = -1, \tag{22}$$

$$\nu\tilde{\mathbf{e}}_k^T\lambda_k = \nu\tilde{\mathbf{e}}_k^T(\mathbf{e}_k - \tilde{\mathbf{e}}_k) = \nu\tilde{\mathbf{e}}_k^T\mathbf{e}_k - \nu\tilde{\mathbf{e}}_k^T\tilde{\mathbf{e}}_k. \tag{23}$$

And the following inequality holds:

$$\tilde{\mathbf{e}}_k^T\omega_k \leq ||\tilde{\mathbf{e}}_k||\varphi = \varphi\tilde{\mathbf{e}}_k^T\mathrm{sign}(\tilde{\mathbf{e}}_k), \tag{24}$$

where $\|\omega_k\| \leqslant \varphi$ presented in (6) is used. Consequently, by substituting (21)- (24) into (20), it yields

$$\begin{aligned}\tilde{\mathbf{e}}_k^T\dot{\tilde{\mathbf{e}}}_k \leq &- \nu\tilde{\mathbf{e}}_k^T\tilde{\mathbf{e}}_k + \nu\tilde{\mathbf{e}}_k^T\mathbf{e}_k + \varphi\tilde{\mathbf{e}}_k^T\mathrm{sign}(\tilde{\mathbf{e}}_k) \\ &- \nu\tilde{\mathbf{e}}_k^T\mathbf{e}_k - \tilde{\mathbf{e}}_k^T\mathbf{f}_k(\hat{\Theta}_k - \Theta) \\ &+ P_k||\tilde{\mathbf{e}}_k||||\nu\mathbf{e}_k + \mathbf{f}_k\hat{\Theta}_k|| \\ &- P_k||\tilde{\mathbf{e}}_k||||\nu\mathbf{e}_k + \mathbf{f}_k\hat{\Theta}_k|| \\ &- \hat{\varphi}_k\tilde{\mathbf{e}}_k^T\mathrm{sign}(\tilde{\mathbf{e}}_k) \\ &= -\nu\tilde{\mathbf{e}}_k^T\tilde{\mathbf{e}}_k - \psi_k\tilde{\mathbf{e}}_k^T\mathrm{sign}(\tilde{\mathbf{e}}_k) - \tilde{\mathbf{e}}_k^T\mathbf{f}_k\Phi_k.\end{aligned} \tag{25}$$

According to (25) and (19), we have

$$\begin{aligned}\frac{1}{2}\tilde{\mathbf{e}}_k^T\tilde{\mathbf{e}}_k &= \int_S\tilde{\mathbf{e}}_k^T\dot{\tilde{\mathbf{e}}}_k d\tau \\ &\leq \int_S[-\nu\tilde{\mathbf{e}}_k^T\tilde{\mathbf{e}}_k - \psi_k\tilde{\mathbf{e}}_k^T\mathrm{sign}(\tilde{\mathbf{e}}_k) - \tilde{\mathbf{e}}_k^T\mathbf{f}_k\Phi_k]d\tau.\end{aligned} \tag{26}$$

In terms of the third term of (18), we have that

$$\begin{aligned}&\Phi_k^T\Gamma^{-1}\Phi_k - \Phi_{k-1}^T\Gamma^{-1}\Phi_{k-1} \\ &= -\left(\hat{\Theta}_k - \hat{\Theta}_{k-1}\right)^T\Gamma^{-1}\left(\hat{\Theta}_k - \hat{\Theta}_{k-1}\right) \\ &- 2\left(\hat{\Theta}_{k-1} - \hat{\Theta}_k\right)^T\Gamma^{-1}\Phi_k \\ &= -\tilde{\mathbf{e}}_k^T\mathbf{f}_k\Gamma\mathbf{f}^T(\mathbf{x}_k)\tilde{\mathbf{e}}_k + 2\tilde{\mathbf{e}}_k^T\mathbf{f}_k\Phi_k \\ &\leq 2\tilde{\mathbf{e}}_k^T\mathbf{f}_k\Phi_k,\end{aligned} \tag{27}$$

where the updating law (15) is applied. Therefore, the third term on the right hand side of (18) becomes

$$\begin{aligned}&\frac{1}{2}\int_0^t\left(\Phi_k^T\Gamma^{-1}\Phi_k - \Phi_{k-1}^T\Gamma^{-1}\Phi_{k-1}\right)d\tau \\ &\leq \int_0^t\tilde{\mathbf{e}}_k^T\mathbf{f}_k\Phi_k d\tau \\ &= \int_S\tilde{\mathbf{e}}_k^T\mathbf{f}_k\Phi_k d\tau + \int_Q\tilde{\mathbf{e}}_k^T\mathbf{f}_k\Phi_k d\tau \\ &= \int_S\tilde{\mathbf{e}}_k^T\mathbf{f}_k\Phi_k d\tau.\end{aligned} \tag{28}$$

In addition, for the last term of (18), we have

$$\begin{aligned}&\frac{1}{2\gamma}\int_0^t(\psi_k^2 - \psi_{k-1}^2)d\tau \\ &\leq \frac{1}{2\gamma}\int_0^t 2\psi_k(\hat{\varphi}_k - \hat{\varphi}_{k-1})d\tau \\ &\leq \frac{1}{2\gamma}\int_0^t 2\psi_k\gamma\tilde{\mathbf{e}}_k^T\mathrm{sign}(\tilde{\mathbf{e}}_k)d\tau \\ &= \int_0^t\psi_k\tilde{\mathbf{e}}_k^T\mathrm{sign}(\tilde{\mathbf{e}}_k)d\tau \\ &= \int_S\psi_k\tilde{\mathbf{e}}_k^T\mathrm{sign}(\tilde{\mathbf{e}}_k)d\tau + \int_Q\psi_k\tilde{\mathbf{e}}_k^T\mathrm{sign}(\tilde{\mathbf{e}}_k)d\tau \\ &= \int_S\psi_k\tilde{\mathbf{e}}_k^T\mathrm{sign}(\tilde{\mathbf{e}}_k)d\tau,\end{aligned} \tag{29}$$

where the updating law (16) is applied. Finally, combining (26), (28), (29) with (18), we have

$$\begin{aligned}\Delta E_k(t) &\leq -\frac{1}{2}\tilde{\mathbf{e}}_{k-1}^T(t)\tilde{\mathbf{e}}_{k-1}(t) - \int_S\nu\tilde{\mathbf{e}}_k^T(\tau)\tilde{\mathbf{e}}_k(\tau)d\tau \\ &\leq -\frac{1}{2}\left\|\tilde{\mathbf{e}}_{k-1}(t)\right\|^2.\end{aligned} \tag{30}$$

Part II. Convergence of virtual tracking error: From (30), we can obtain the following inequality:

$$E_k(t) \leq E_0(t) - \frac{1}{2}\sum_{j=1}^k\|\tilde{\mathbf{e}}_{j-1}\|^2. \tag{31}$$

Note that $E_k(t)$ is positive. If $E_0(t)$ is bounded, we can obtain immediately from (31) that $\lim_{k\to\infty}\tilde{\mathbf{e}}_k(t) = 0, t \in [0, T]$.

The boundedness of $E_0(t)$ can be derived as follows:

$$E_0 = \frac{1}{2}\tilde{\mathbf{e}}_0^T\tilde{\mathbf{e}}_0 + \frac{1}{2}\int_0^t\Phi_0^T\Gamma^{-1}\Phi_0 d\tau + \frac{1}{2\gamma}\int_0^t\psi_0^2 d\tau. \tag{32}$$

If $\left\|\tilde{\mathbf{e}}_0^T(t)\right\| = 0$, we have that $\hat{\Theta}_0(t) = \Gamma\mathbf{f}_k^T\tilde{\mathbf{e}}_k(t) = 0$ and $\hat{\varphi}_0(t) = \gamma\tilde{\mathbf{e}}_0^T(t)\mathrm{sign}(\tilde{\mathbf{e}}_0(t)) = 0$. Thus, $\Phi_0 = -\Theta$ and $\psi_0 = -\varphi$. We can obtain the following equality:

$$\begin{aligned}E_0 &= \frac{1}{2}\tilde{\mathbf{e}}_0^T\tilde{\mathbf{e}}_0 + \frac{1}{2}\int_0^t\Phi_0^T\Gamma^{-1}\Phi_0 d\tau + \frac{1}{2\gamma}\int_0^t\psi_0^2 d\tau \\ &= \frac{1}{2}\int_0^t\Theta^T\Gamma^{-1}\Theta d\tau + \frac{1}{2\gamma}\int_0^t\varphi^2 d\tau.\end{aligned} \tag{33}$$

This implies that $E_0(t)$ is bounded. If $\left\|\tilde{\mathbf{e}}_0^T(t)\right\| \neq 0$, by utilizing the result shown in(25), the derivative of $E_0(t)$ with

respect to t can be calculated as

$$\begin{aligned}\dot{E}_0(t) &= \tilde{\mathbf{e}}_0(t)^T\dot{\tilde{\mathbf{e}}}_0(t) + \frac{1}{2}\Phi_0(t)^T\Gamma^{-1}\Phi_0(t) + \frac{1}{2\gamma}\psi_0^2(t)\\ &\le -\nu\tilde{\mathbf{e}}_0(t)^T\tilde{\mathbf{e}}_0(t) - \tilde{\mathbf{e}}_0(t)^T\mathbf{f}_0\Phi_0(t) + \frac{1}{2}\Phi_0(t)^T\Gamma^{-1}\Phi_0(t)\\ &- \psi_0(t)\tilde{\mathbf{e}}_0^T(t)\text{sign}(\tilde{\mathbf{e}}_0(t)) + \frac{1}{2\gamma}\psi_0^2(t).\end{aligned} \tag{34}$$

According to the fact that $\hat{\Theta}_{-1}(t) = 0$, we have that $\hat{\Theta}_0(t) = \Gamma\mathbf{f}_k^T\tilde{\mathbf{e}}_k(t)$, namely, $\tilde{\mathbf{e}}_k^T(t)\mathbf{f}_k = \hat{\Theta}_0^T(t)\Gamma^{-1}$. By applying the Young's inequality, we have that

$$\begin{aligned}&- \Theta^T(t)\Gamma^{-1}\Phi_0(t)\\ &\le \frac{1}{2}(\Theta^T(t)\Gamma^{-1}\Theta(t) + \Phi_0^T(t)\Gamma^{-1}\Phi_0(t)).\end{aligned} \tag{35}$$

Therefore, we can obtain the following inequality:

$$\begin{aligned}&- \tilde{\mathbf{e}}_0^T(t)\mathbf{f}_k\Phi_0(t) + \frac{1}{2}\Phi_0^T(t)\Gamma^{-1}\Phi_0(t) = -\hat{\Theta}_0(t)\Gamma^{-1}\Phi_0(t)\\ &- \frac{1}{2}\Phi_0^T(t)\Gamma^{-1}\Phi_0(t) + \Phi_0^T(t)\Gamma^{-1}\Phi_0(t)\\ &= -\frac{1}{2}\Phi_0^T(t)\Gamma^{-1}\Phi_0(t) - \Theta^T(t)\Gamma^{-1}\Phi_0(t)\\ &\le -\frac{1}{2}\Phi_0^T(t)\Gamma^{-1}\Phi_0(t)\\ &+ \frac{1}{2}(\Theta^T(t)\Gamma^{-1}\Theta(t) + \Phi_0^T(t)\Gamma^{-1}\Phi_0(t))\\ &= \frac{1}{2}\Theta^T(t)\Gamma^{-1}\Theta(t).\end{aligned} \tag{36}$$

According to the fact that $\hat{\varphi}_{-1}(t) = 0$, we have that $\hat{\varphi}_0(t) = \gamma\tilde{\mathbf{e}}_0^T(t)\text{sign}(\tilde{\mathbf{e}}_0(t))$. Therefore, we can obtain the following inequality:

$$\begin{aligned}&- \psi_0(t)\tilde{\mathbf{e}}_0^T(t)\text{sign}(\tilde{\mathbf{e}}_0(t)) + \frac{1}{2\gamma}\psi_0^2(t)\\ &= -\frac{1}{\gamma}\psi_0(t)\hat{\varphi}_0(t) + \frac{1}{2\gamma}\psi_0^2(t)\\ &= \frac{1}{2\gamma}\psi_0(t)(-\varphi(t) - \hat{\varphi}_0(t))\\ &= \frac{\varphi^2(t) - \hat{\varphi}_0^2(t)}{2\gamma}\\ &\le \frac{\varphi^2(t)}{2\gamma}.\end{aligned} \tag{37}$$

Finally, combining (36), (37) with (34), we have

$$\dot{E}_0(t) \le -\nu\tilde{\mathbf{e}}_0(t)^T\tilde{\mathbf{e}}_0(t) + \frac{1}{2}\Theta(t)^T\Gamma^{-1}\Theta(t) + \frac{1}{2\gamma}\varphi^2(t). \tag{38}$$

As a result, $\dot{E}_0(t)$ is negative whenever the condition $\nu\tilde{\mathbf{e}}_0(t)^T\tilde{\mathbf{e}}_0(t) > \frac{1}{2}\Theta(t)^T\Gamma^{-1}\Theta(t) + \frac{1}{2\gamma}\varphi^2(t)$ holds, which implies that $E_0(t)$ is bounded if $\left\|\tilde{\mathbf{e}}_0^T(t)\right\| \neq 0$. Therefore, $E_0(t)$ is bounded over the entire time interval $[0, T]$.

Part III. Convergence of actual tracking error: We have already analyzed the convergence of the virtual tracking error, and our objective is to achieve convergence of the actual tracking error. Therefore, it is necessary to analyze the properties of the auxiliary system. The Lyapunov function for the auxiliary system is defined as follows:

$$V_\lambda = \frac{1}{2}\|\lambda_k\|^2. \tag{39}$$

Taking the derivative of the Lyapunov function, we can obtain the following inequality:

$$\begin{aligned}\dot{V}_\lambda &= \lambda_k^T\dot{\lambda}_k\\ &= -\nu\|\lambda_k\|^2 + \lambda_k^TB\Delta\mathbf{u}_k\\ &\le -\nu\|\lambda_k\|^2 + \frac{1}{2}\|\lambda_k\|^2 + \frac{1}{2}\|B\Delta\mathbf{u}_k\|^2\\ &\le \left(-\nu + \frac{1}{2}\right)\|\lambda_k\|^2 + \frac{1}{2}\|B\Delta\mathbf{u}_k\|^2,\end{aligned} \tag{40}$$

where the Young's inequality (41) is used. The Young's inequality is given by:

$$\lambda_k^TB\Delta\mathbf{u}_k \le \frac{1}{2}\|\lambda_k\|^2 + \frac{1}{2}\|B\Delta\mathbf{u}_k\|^2. \tag{41}$$

Integrating both sides of inequality (40), we can obtain

$$\begin{aligned}&V_\lambda(T) - V_\lambda(0)\\ &\le \int_0^T\left(-\nu + \frac{1}{2}\right)\|\lambda_k\|^2d\tau + \int_0^T\frac{1}{2}\|B\Delta\mathbf{u}_k\|^2d\tau.\end{aligned} \tag{42}$$

Based on the fact that $\lambda_k(0) = 0$, we have $V_\lambda(0) = 0$. Therefore, we can obtain

$$\int_0^T\|\lambda_k\|^2d\tau \le \frac{1}{2c_\lambda}\int_0^T\|B\Delta\mathbf{u}_k\|^2d\tau, \tag{43}$$

where $c_\lambda = \nu - \frac{1}{2} > 0$. According to (30), we can obtain

$$\Delta E_k \le -\int_S\nu\tilde{\mathbf{e}}_k^T\tilde{\mathbf{e}}_kd\tau. \tag{44}$$

Furthermore, we can obtain

$$\int_S\nu\tilde{\mathbf{e}}_k^T\tilde{\mathbf{e}}_kd\tau \le E_{k-1} - E_k \le E_{k-1}. \tag{45}$$

That is

$$\int_S\|\tilde{\mathbf{e}}_k\|^2d\tau \le \frac{1}{\nu}E_{k-1}. \tag{46}$$

Since $\mathbf{e}_k = \tilde{\mathbf{e}}_k + \lambda_k$, we can obtain

$$\begin{aligned}&\int_0^T\|\mathbf{e}_k\|^2d\tau\\ &\le 2\left(\int_0^T\|\lambda_k\|^2d\tau + \int_0^T\|\tilde{\mathbf{e}}_k\|^2d\tau\right)\\ &= 2\left(\int_0^T\|\lambda_k\|^2d\tau + \int_S\|\tilde{\mathbf{e}}_k\|^2d\tau + \int_Q\|\tilde{\mathbf{e}}_k\|^2d\tau\right)\\ &= 2\left(\int_0^T\|\lambda_k\|^2d\tau + \int_S\|\tilde{\mathbf{e}}_k\|^2d\tau\right)\\ &\le \frac{1}{c_\lambda}\int_0^T\|B\Delta\mathbf{u}_k\|^2d\tau + \frac{2}{\nu}E_{k-1}.\end{aligned} \tag{47}$$

As k approaches infinity, we can obtain

$$\lim_{k\to\infty}\int_0^T\|\mathbf{e}_k\|^2d\tau \le \frac{1}{c_\lambda}\lim_{k\to\infty}\int_0^T\|B\Delta\mathbf{u}_k\|^2d\tau. \tag{48}$$

Since $\Delta E_k \le 0$ and E_0 is bounded, E_k is also bounded. Based on the boundedness of E_k and the controller (10), we can conclude the boundedness of the control input $\mathbf{u}_k$. Therefore, the boundedness of $\Delta\mathbf{u}_k$ can be derived from the fact that $\bar{\mathbf{u}}_k$ is bounded. As a result, we can conclude that the actual tracking error $\mathbf{e}_k$ converges to a neighborhood of the origin. ■

4 Simulation

In order to verify the effectiveness of the proposed AILC algorithm, this section presents a numerical example involving a nonlinear system. In this example, the control gain matrix for the system is unknown. Let us consider a nonlinear system, which is governed by the system (1) with

$$\mathbf{f}_k = \begin{bmatrix} \sin(\mathbf{x}_{1,k}) \\ 2\sin(\mathbf{x}_{2,k}) \end{bmatrix}, \quad \Theta = 1,$$
$$\mathbf{w}^r = \begin{bmatrix} \sin(t) \\ \cos(t) \end{bmatrix}, A_k = \begin{bmatrix} 1.2 & 0.3 \\ 0 & 0.5 \end{bmatrix},$$

where $\mathbf{x}_k = [\mathbf{x}_{1,k}, \mathbf{x}_{2,k}]^T$, and the upper bounds for the two control input components are set to $\mathbf{u}_{1,\max} = \mathbf{u}_{2,\max} = 0.5$. The control gain matrix A_k is assumed to be unknown but norm-bounded, satisfying the Assumption 1. The reference trajectory is assumed to be $\mathbf{x}_r(t) = [0.6 - \cos(t), \sin(t) + 0.5]^T$.

For the proposed controller (10) together with the updating laws (15) and (16), let us set the feedback gain $\nu = 0.9$, $\Gamma = 0.7$ and $\gamma = 0.7$. The convergence of the maximal tracking error $\mathbf{e}_{\max,k} = \max_{t\in[0,T]} |\mathbf{e}_{1,k}(t)| + \max_{t\in[0,T]} |\mathbf{e}_{2,k}(t)|$ is presented in Fig. 1. It is evident that with the proposed control method, even though the control gain matrix A_k is unknown, the maximal tracking error decreases significantly as the iteration number increases, dropping by 99.4% within 10 iterations.

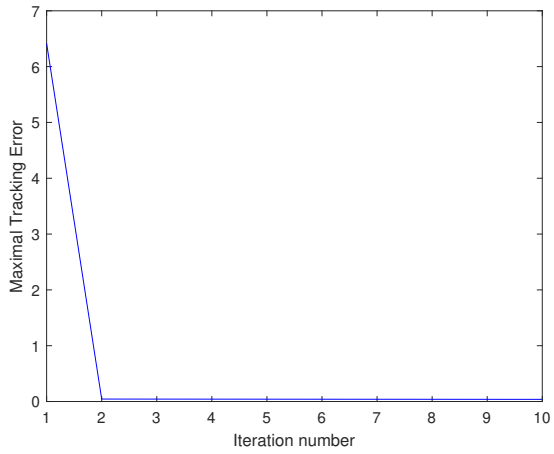

Fig. 1: The maximal tracking error profile along the iteration axis.

5 Conclusion

This paper investigates the design of adaptive iterative learning control (AILC) for underactuated systems with unknown input distribution matrices. A new AILC algorithm is proposed, which addresses the challenge of unknown input distribution matrices by introducing specially designed control gain matrices. These matrices transform the unknown input distribution matrices into system disturbances, and robust terms are incorporated into the controller to eliminate the unknownness of the input distribution matrices. Additionally, an auxiliary system related to the input is introduced to handle input saturation, enabling the system to track reference trajectories even in the presence of input saturation constraints. The convergence of the tracking error to a neighborhood of the origin is theoretically analyzed and proven through mathematical derivations. Finally, the effectiveness and performance of the proposed algorithm are validated through a simulation example.

References

[1] D. Bristow, M. Tharayil, and A. Alleyne, "A survey of iterative learning control," *IEEE Control Systems Magazine*, vol. 26, no. 3, pp. 96–114, 2006.

[2] J.-X. Xu and Y. Tan, "Linear and nonlinear iterative learning control," *Lecture Notes in Control and Information Sciences*, vol. 291, 06 2003.

[3] A. Tayebi, "Adaptive iterative learning control for robot manipulators," *Automatica*, vol. 40, no. 7, pp. 1195–1203, 2004.

[4] L. Consolini and C. M. Verrelli, "Learning control in spatial coordinates for the path-following of autonomous vehicles," in *2013 European Control Conference (ECC)*, 2013, pp. 1175–1180.

[5] S. Devasia, "Iterative machine learning for output tracking," *IEEE Transactions on Control Systems Technology*, vol. 27, no. 2, pp. 516–526, 2019.

[6] M. French and E. Rogers, "Nonlinear iterative learning by an adaptive lyapunov technique," in *Proceedings of the 37th IEEE Conference on Decision and Control (Cat. No.98CH36171)*, vol. 1, 1998, pp. 175–180 vol.1.

[7] J.-X. Xu and Y. Tan, "A composite energy function-based learning control approach for nonlinear systems with time-varying parametric uncertainties," *IEEE Transactions on Automatic Control*, vol. 47, no. 11, pp. 1940–1945, 2002.

[8] J.-X. Xu and X. Jin, "State-constrained iterative learning control for a class of mimo systems," *IEEE Transactions on Automatic Control*, vol. 58, no. 5, pp. 1322–1327, 2013.

[9] X. Li, D. Huang, B. Chu, and J.-X. Xu, "Robust iterative learning control for systems with norm-bounded uncertainties," *International Journal of Robust and Nonlinear Control*, vol. 26, no. 4, pp. 697–718, 2016.

[10] J.-X. Xu, X. Jin, and D. Huang, "Composite energy function-based iterative learning control for systems with nonparametric uncertainties," *International Journal of Adaptive Control and Signal Processing*, vol. 28, no. 1, pp. 1–13, 2014.

[11] D. Shen and J.-X. Xu, "Adaptive learning control for nonlinear systems with randomly varying iteration lengths," *IEEE Transactions on Neural Networks and Learning Systems*, vol. 30, no. 4, pp. 1119–1132, 2019.

[12] X. Jin, "Iterative learning control for mimo nonlinear systems with iteration-varying trial lengths using modified composite energy function analysis," *IEEE Transactions on Cybernetics*, vol. 51, no. 12, pp. 6080–6090, 2021.

[13] X. Li, D. Shen, and J.-X. Xu, "Adaptive iterative learning control for mimo nonlinear systems performing iteration-varying tasks," *Journal of the Franklin Institute*, vol. 356, no. 16, pp. 9206–9231, 2019.

[14] X. Jin, "Adaptive fixed-time control for mimo nonlinear systems with asymmetric output constraints using universal barrier functions," *IEEE Transactions on Automatic Control*, vol. 64, no. 7, pp. 3046–3053, 2019.

[15] W. Yan and M. Sun, "Adaptive iterative learning control of discrete-time varying systems with unknown control direction," *International Journal of Adaptive Control and Signal Processing*, vol. 27, no. 4, pp. 340–348, 2013.

[16] D. Shen and J.-X. Xu, "Adaptive learning control for nonlinear systems with randomly varying iteration lengths," *IEEE Transactions on Neural Networks and Learning Systems*, vol. 30, no. 4, pp. 1119–1132, 2019.

[17] C.-J. Chien, "A combined adaptive law for fuzzy iterative learning control of nonlinear systems with varying control tasks," *IEEE Transactions on Fuzzy Systems*, vol. 16, no. 1, pp. 40–51, 2008.

[18] X. Li and D. Huang, "Adaptive iterative learning control for nonsquare nonlinear systems with various nonrepetitive uncertainties: A unified approach," *IEEE Transactions on Automatic Control*, vol. 69, no. 3, pp. 1736–1743, 2024.

[19] Y. Chen, C. Wen, Z. Gong, and M. Sun, "An iterative learning controller with initial state learning," *IEEE Transactions on Automatic Control*, vol. 44, no. 2, pp. 371–376, 1999.

[20] M. Sun and D. Wang, "Iterative learning control with initial rectifying action," *Automatica*, vol. 38, no. 7, pp. 1177–1182, 2002.

Proceedings of the 3rd Conference on Fully Actuated System Theory and Applications
May 10-12, 2024, Shenzhen, China

Adaptive Neural Network Sliding Mode Vibration Control for Clamped Beam Systems with Input Saturation and Model Uncertainties

Shilun Li[1 2], Xiaohan Lin[1], Jun Wang[1], Chuankun Qu[1], Wei Chen[1]

1. Shanghai Aerospace Systems Engineering Institute, Shanghai 201109, P. R. China
E-mail: lishilun_liszt@163.com

2. Shanghai ASES Spaceflight Technology Co.Ltd, Shanghai 201108, P. R. China
E-mail: lishilun_liszt@163.com

Abstract: This paper presents a novel adaptive neural network nonsingular fast terminal sliding mode control method for flexible double-clamped beam systems with input saturation and distributed disturbance. Firstly, the ordinary differential equations of the beam system are provided. Secondly, a novel auxiliary function is employed to design a nonsingular fast terminal sliding mode controller, ensuring the stability of the closed-loop system under state constraints. Additionally, an adaptive neural network is proposed to handle possible unknown parts of the model parameters. It is demonstrated that the proposed control method can simultaneously address input saturation and distributed disturbance without requiring precise knowledge of the model. Finally, numerical simulation results illustrate the effectiveness of the proposed control approach.

Key Words: vibration control, nonsingular fast terminal sliding mode control, adaptive neuro-network control

1 Introduction

With the surge in aerospace advancements, heavy spacecraft and aircraft have garnered significant attention. However, vibrations caused by various factors during their operation pose a significant threat to their structural integrity. Active vibration control, due to its superior vibration suppression efficiency compared to passive methods, has become a key research focus. Given the high costs involved in research and experimental development, scientists are particularly interested in developing active vibration control techniques tailored for fundamental structural elements like beams and plates, as they form the backbone of complex aerospace structures and their stability is crucial for overall performance and safety [1–4].

Extensive research has been conducted on the control design and stability analysis of flexible mechanical systems leveraging partial differential equations (PDEs). In [5] an adaptive barrier control law is introduced to mitigate vibrations in Euler-Bernoulli beams with boundary output constraints. Additionally, [6] presents a restrained adaptive boundary iterative learning control approach utilizing a time-weighted composite energy function to address vibration control in the presence of aperiodic disturbances. However, these methods are limited in addressing nonlinearity arising from mid-plane stretching and actuator characteristics, crucial factors in practical applications [7–10]. Piezoelectric (PZT) actuators, known for their lightweight, low cost, and combined sensing and actuation capabilities, are widely employed and thus deserve consideration in modeling [11–13]. In [14–16], PDEs mathematical models for micro-scale beams are developed, incorporating both mid-plane stretching and PZT actuators based on the Hamiltonian principle. To simplify these models, the Galerkin projection method is employed, reducing the complexity of the PDEs to ordinary differential equations (ODEs), thereby facilitating further analysis and control design.

The sliding mode control (SMC) approach has garnered significant attention in vibration control systems due to its robust characteristics against model errors, parameter uncertainties, and external disturbances. However, the linear nature of the sliding mode design in SMC results in asymptotic convergence, limiting its performance. To enhance this convergence property, Terminal Sliding Mode Control (TSMC) has been proposed, incorporating a nonlinear sliding mode manifold to facilitate finite-time convergence to the equilibrium point [17]. In the realm of second-order sliding mode (SOSM) control, a novel approach has been introduced to address disturbances bounded by positive functions and sliding mode dynamics with mismatched terms [18]. Additionally, an advanced SOSM controller incorporating a saturation level has been developed to ensure global convergence and optimize dynamic performance [19]. Furthermore, research has focused on developing improved terminal sliding mode tracking controllers for third-order chained-form nonholonomic systems with unknown external disturbances [20]. These controllers aim to achieve finite-time convergence, enhancing the system's response. However, certain modified control laws still suffer from the singularity problem, particularly near the equilibrium point. To address this issue, a nonsingular fast terminal sliding mode control approach has been explored, aiming to eliminate potential singularities in uncertain nonlinear systems [21]. This method offers a promising solution to the singularity problem, but it may not guarantee constrained vibration amplitudes, potentially posing a risk of structural damage.

To mitigate this concern, alternative control design methodologies have been investigated. These approaches aim to incorporate constraints and safety considerations into the control framework, ensuring that the system operates within prescribed limits. While these methods may vary in their specific implementation, they generally focus on preventing state variables from violating predefined constraints

This work was partially supported by Shanghai Science and Technology Development Funds (Grant No.23YF1411100).

and enhancing the overall performance and safety of the vibration system.

In this paper, a novel vibration control strategy is proposed for a nonlinear double-clamped beam with a piezoelectric actuator. The control approach addresses model uncertainties, input saturation, and distributed disturbances. By utilizing the Galerkin projection method, the motion equations of the beam are transformed into nonlinear ordinary differential equations, enabling the design of tailored control laws. A fast nonsingular terminal sliding mode control law is introduced to ensure finite-time stability of the system. Additionally, an auxiliary system is designed to mitigate the saturation effects of the piezoelectric actuator. Furthermore, an adaptive radial basis function (RBF) neural network is integrated into the sliding mode control law to approximate unknown nonlinearities in the system model. This approach enhances the controller's adaptive capabilities and robustness. The proposed control laws guarantee finite-time convergence of system state variables and improve vibration suppression performance, making it suitable for practical applications with complex nonlinear dynamics.

The organization of the paper proceeds as follows: Section 2 delves into the background of the nonlinear flexible double-clamped beam system, laying the foundation for subsequent discussions. Section 3 presents the proposed control laws and their stability analysis, providing a rigorous mathematical framework for the control strategy. Section 4 presents simulation results that demonstrate the practical effectiveness of the proposed control laws. Finally, Section 5 summarizes the key findings and contributions of the paper, drawing conclusions on the overall performance and implications of the proposed approach.

2 Backgrounds and preliminaries

In this section, we present the mathematical formulation of the model for the nonlinear flexible doubly clamped beam system, along with assumptions that facilitate simplified analysis. Subsequently, we introduce relevant lemmas to support the subsequent controller design.

Figure 1 presents a typical nonlinear flexible beam structure with fixed ends and an overall length of L. Taking into account the unknown vibration disturbances that the beam may encounter in practical applications, we specifically designed and installed a layer of piezoelectric actuator on a specific region of the upper surface of the beam to achieve efficient vibration suppression. Furthermore, this paper focuses on discussing the distributed disturbance $d(x,t)$ along the length of the beam (the X-axis). This disturbance exhibits significant time-varying characteristics and has a considerable impact on the steady-state behavior and deformation of the beam.

Defining state variable $x_1(t)$ as the displacement of the piezoelectric actuator and $x_2(t)$ as the velocity of the piezoelectric actuator, we can approximately express the nonlinear differential equation for a doubly-clamped beam system that takes into account input saturation and disturbances.

$$\begin{aligned}\dot{x}_1(t) &= x_2(t)\\ \dot{x}_2(t) &= A(x_1,\delta_1) + B(\delta_1)\tau_{sat}(t) + C(\delta_1)\tilde{d_{x_1}}(,t)\end{aligned} \tag{1}$$

where

$$\begin{aligned}A(x_1(t),\delta_1) &= \frac{-EIx_1\int_0^L {\delta_1}''''(l_p)\mathrm{d}x}{\rho A\int_0^L \delta_1(l_p)\mathrm{d}x}\\ &+ \frac{\frac{EA}{2L}x_1^3(t)\int_0^L({\delta_1}'(l_p))^2{\delta_1}''(l_p)\mathrm{d}x}{\rho A\int_0^L \delta_1(l_p)\mathrm{d}x}\\ B(\delta_1) &= \frac{\varrho({\delta_1}'(l_p)(a) - {\delta_1}'(b))}{\rho A\int_0^L(\delta_1(l_p))^2\mathrm{d}x}\\ C(\delta_1) &= \frac{\int_0^L \delta_d(l_p)\mathrm{d}x}{\rho A\int_0^L \delta_1(l_p)\mathrm{d}x}\end{aligned} \tag{2}$$

where, E, A, and I represent the Young's modulus, cross-sectional area, and moment of inertia of the doubly-clamped beam, respectively. The coefficient ϱ denotes the input coefficient of the piezoelectric actuator, while l_p signifies the distance from the left end of the beam to the location where the piezoelectric actuator is installed, a and b represent the distances from the piezoelectric actuator to the left and right ends of the beam, respectively. δ_1 represents the first-order mode shape of the structure. δ_d represents the main shape of the spatially distributed disturbance. $\tilde{d_{x_1}}(t)$ represents the disturbance at location l_p. Moreover, $\tau_{sat}(t)$ represents the control input that accounts for input saturation.

In practical applications, the control voltage applied to the piezoelectric actuator is constrained due to limitations inherent in the piezoelectric layer. Consequently, this paper presents an input function that incorporates saturation effects, expressed as follows.

$$\tau_{sat}(t) = \begin{cases}\tau_{lim}, & \tau(t) > \tau_{lim}\\ \tau(t), & |\tau(t)| \le \tau_{lim}\\ -\tau_{lim}, & \tau(t) < -\tau_{lim}\end{cases} \tag{3}$$

where, $\tau_{sat}(t)$ represents the control input, $\tau(t)$ stands for the designed control command, and τ_{lim} denotes the saturation limit. The control input is constrained within the bounds of $-\tau_{lim}$ and τ_{lim}, ensuring that $\tau_{sat}(t)$ does not exceed the saturation limit.

Assumption 1. Concerning the unknown distributed disturbance $\tilde{d_{x_1}}(t)$ that varies both spatially and temporally, we make the reasonable assumption that there exists a positive constant $d_max \in \mathrm{R}^+$ such that the magnitude of this disturbance is always bounded by d_max, $|\tilde{d_{x_1}}(,t)| \le d_max$. This assumption is well-founded because the time-varying nature of $\tilde{d_{x_1}}(t)$ is constrained by its finite energy content.

Lemma 1. Assuming the existence of continuously differentiable and positive definite functions $V(z) : Z \to \mathbb{R}^+$ that satisfy the condition:

$$V(z) \to \infty \text{ as } |z| \to k_b \tag{4}$$

Given an initial condition $z(0) \in \mathcal{Z}$, if the following inequality is fulfilled:

$$\dot{V} = \frac{\partial V}{\partial z} \le -\mu V + C \tag{5}$$

where μ and C are positive constants, then $z(t)$ remains bounded and belongs to the set $\mathcal{Z}$ can be concluded.

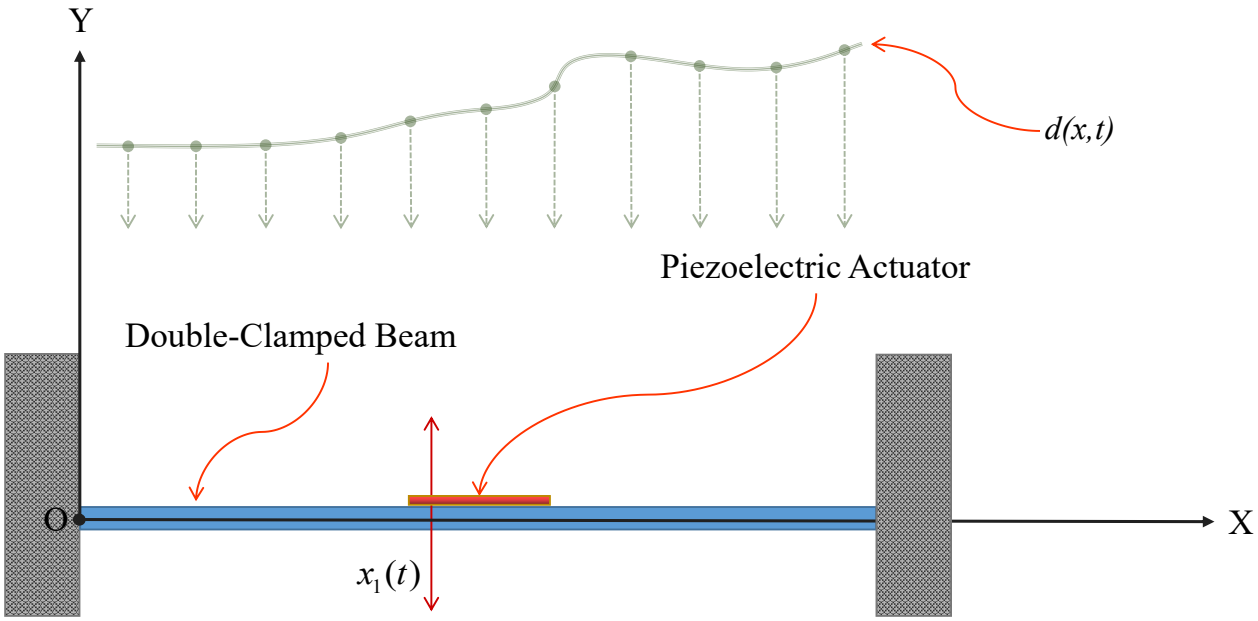

Fig. 1: Diagram of the object under control

3 Control law design

3.1 The nonsingular fast terminal sliding mode control law

In this subsection, a novel control law for the nonsingular fast terminal sliding mode is introduced, leveraging the capabilities of the RBF neural network. The selection of the nonsingular fast terminal sliding mode surface is formulated as follows:

$$s = x_1 + q_1|x_1|^{\iota}\text{sign}(x_1) + q_2|x_2|^{m/n}\text{sign}(x_2) \quad (6)$$

where q_1, q_2 are positive constants, the coefficients in the sliding mode surface satisfying $1 < m/n < 2$, $\iota > m/n$.

To address the issue of approximating the unknown component $A(x_1, \delta_1)$ within the double-clamped beam system, which poses challenges in practical measurements, we utilize an adaptive radial basis function (RBF) neural network. The choice of RBF neural network stems from its exceptional universal approximation capabilities and resilience against environmental noise, making it a suitable candidate for tackling this complex problem.

Figure 2 illustrates the architecture of the radial basis function (RBF) neural network, comprising three distinct layers: the input layer, the hidden layer, and the output layer.

Let $x = [x_1, x_2, .., x_n]$ represent the input vector. The activation function for the i-th node in the hidden layer is selected as a Gaussian function, which can be formally expressed as follows:

$$\varpi_{Ai}(l_p) = \exp\left(-\frac{\|x - b_i\|^2}{2g_i^2}\right), i = 1, 2, \cdots, n \quad (7)$$

where, the approximation properties of the RBF neural network are harnessed to estimate and compensate for the

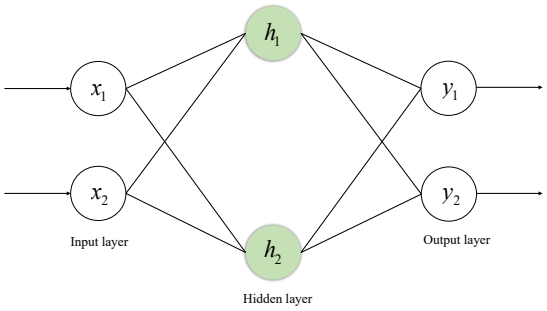

Fig. 2: The RBF neural network

unknown nonlinear elements in the system. Specifically, $A(x_1, \delta_1)$ is chosen as the approximating function, where b_i and g_i^2 represent the center and spread of the radial basis function, respectively. The mathematical representation of $A(x_1, \delta_1)$ is detailed below:

$$A(x_1, \delta_1) = H^{\mathrm{T}}\varpi_A(l_p) + \xi_A \quad (8)$$

where, H represents the optimal weighting matrix, while ξ_A stands for the approximation error associated with the RBF neural network. This error is bounded by ξ_m for both i=1 and i=2. The estimation of $A(x_1, \delta_1)$ can be expressed as follows:

$$\hat{A}(x_1, \delta_1) = \hat{H}^{\mathrm{T}}\varpi_A(l_p) \quad (9)$$

where $\hat{H}$ denotes the estimation of H. Taking into account the flexible double-clamped beam system outlined in (1), which incorporates model uncertainties, unknown distributed disturbances, and input saturation, the control law

can be formulated as follows:

$$\tau = -\frac{1}{C}[\hat{A}(l_p) + \frac{1}{q_2}\frac{n}{m}|x_2|^{1-m/n}(\dot{x}_1 + q_1\iota|x_1|^{\iota-1}\dot{x}_1 - k\vartheta) + q_3|s|^{\theta}\text{sign}(s) + q_4|s|^{\eta}\text{sign}(s)] \tag{10}$$

where

$$\dot{\hat{H}} = p_1 q_2 \frac{m}{n}|x_2|^{m/n-1} s\varpi_{A(l_p)} - p_1 p_2 \hat{H} \tag{11}$$

Furthermore, p_1 and p_2 are positive constants that contribute to the control law's performance. Assuming the validity of Assumption 1 for any given initial conditions, the proposed control strategy (10), coupled with the adaptive laws governing the RBF neural network, ensures that the system states asymptotically converge to a region close to zero. This convergence region can be made arbitrarily small by suitably adjusting the parameters q_3, q_4 and p_1, p_2

3.2 Stability analysis

The estimation error of the weighting vector can be defined as $\tilde{H} = H - \hat{H}$. The estimation error of $A(x_1, \delta_1)$ can be defined as $\tilde{A}(x_1, \delta_1) = A(x_1, \delta_1) - \hat{A}(x_1, \delta_1)$. Then, choose the Lyapunov function as follows, The estimation error for the weighting vector can alternatively be expressed as $\tilde{H} = H - \hat{H}$. Similarly, the estimation error for $\tilde{A}(x_1, \delta_1)$ can be represented as $\tilde{A}(x_1, \delta_1) = A(x_1, \delta_1) - \hat{A}(x_1, \delta_1)$. Subsequently, the Lyapunov function can be selected in the following manner:

$$\ell(t) = \frac{1}{2}s^2 + \frac{1}{2p_1}\tilde{H}^{\mathrm{T}}\tilde{H} + \frac{1}{2}\vartheta^2 \tag{12}$$

where $\dot{\vartheta} = -k_a\vartheta + k_b\Delta\tau$, $k_a > 0$, $k_b > 0$, ϑ represents the state of the system responsible for compensating for input saturation. $\Delta\tau = \tau_{sat} - \tau$. The time derivative of the Lyapunov function (12) can be formulated as follows:

$$\begin{aligned}\dot{\ell}(t) &= s\dot{s} + \vartheta\dot{\vartheta} + \frac{1}{p_1}\tilde{H}^{\mathrm{T}}\dot{\tilde{H}} \\ &= q_2\frac{m}{n}|x_2|^{m/n-1}(B(\delta_1)\Delta\tau + \tilde{A}(x_1,\delta_1) + \tilde{d} \\ &- q_3|s|^{\theta}\text{sign}(s) - q_4|s|^{\eta}\text{sign}(s)) + k\vartheta \\ &+ \vartheta(-k_a\vartheta + k_b\Delta\tau) - \frac{1}{p_1}\tilde{H}^{\mathrm{T}}\dot{\hat{H}}\end{aligned} \tag{13}$$

Then, the proposed control law (10) and (11) are incorporated into (13). Utilizing the Young's inequality, By applying the Young's inequality, (13) can be reformulated as follows,

$$\begin{aligned}\dot{\ell}(t) &\le q_2\frac{m}{n}|x_2|^{m/n-1}(B(\delta_1)\Delta\tau\cdot s + s\tilde{A}(x_1,\delta_1) + |s|D_m \\ &- q_3|s|^{\theta+1} - q_4|s|^{\eta+1}) + \frac{1}{2}k^2 + \frac{1}{2}\vartheta^2 - k_a\vartheta^2 + \frac{1}{2}k_b\vartheta^2 \\ &+ \frac{1}{2}\Delta\tau^2 + p_2\tilde{H}^{\mathrm{T}}\hat{H} - q_2\frac{m}{n}|x_2|^{m/n-1}s\tilde{H}^{\mathrm{T}}\varpi_{A(l_p)} \\ &= -\frac{1}{2}(2k_a - k_b^2 - 1)\vartheta^2 + p_2\tilde{H}^{\mathrm{T}}(H - \tilde{H}) + \frac{1}{2}\Delta\tau^2 \\ &- q_2\frac{m}{n}|x_2|^{m/n-1}s\xi_A + \frac{1}{2}k^2 + cs^2 + q_2\frac{m}{n}|x_2|^{m/n-1}\cdot \\ &(B(\delta_1)\Delta\tau\cdot s + |s|D_m - q_3|s|^{\theta+1} - q_4|s|^{\eta+1})\end{aligned} \tag{14}$$

Assuming the existence of a positive constant Φ such that $|D_m - \xi_A| \le \Phi$ holds, we proceed to define μ and Z as detailed below.

$$\begin{aligned}\mu &= \min(c, (2k_a - k_b^2 - 1), 2p_1p_2) \\ Z_1 &= \frac{1}{2}k^2 + \frac{1}{2}\Delta\tau^2 + q_2\frac{m}{n}|x_2|^{m/n-1}(B|s\Delta\tau| \\ &+ |s|\Gamma - q_3|s|^{\theta+1} - q_4|s|^{\eta+1}) \\ Z_2 &= q_2\frac{m}{n}|x_2|^{m/n-1}(q_3|s|^{\theta+1} + q_4|s|^{\eta+1})\end{aligned}$$

Then we have,

$$\dot{\ell}(t) = -\mu\ell(t) + Z_1 - Z_2 \tag{15}$$

Based on Assumption 1, choose parameters k_a, p_1, p_2 and k_b satisfying $p_1 > 0$, $p_2 > 0$ and $2k_a - k_b^2 > 1$, then we have $\dot{\ell} \le -\mu\ell + Z_1$ from (15), then, based on lemma 1, the system states asymptotically converge to a region close to zero. Relying on Assumption 1, we select parameters k_a, p_1, p_2 and k_b that fulfill the conditions $p_1 > 0$, $p_2 > 0$ and $2k_a - k_b^2 > 1$. As a result, from (15), we obtain $\dot{\ell} \le -\mu\ell + Z_1$. Utilizing Lemma 1, the system states asymptotically converge to a region near zero can be concluded.

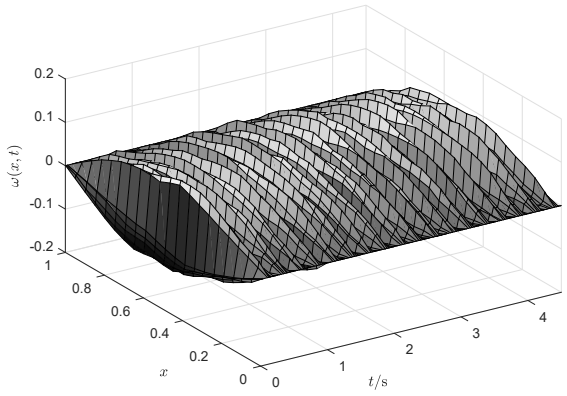

Fig. 3: The deflection of the double-clamped beam without control

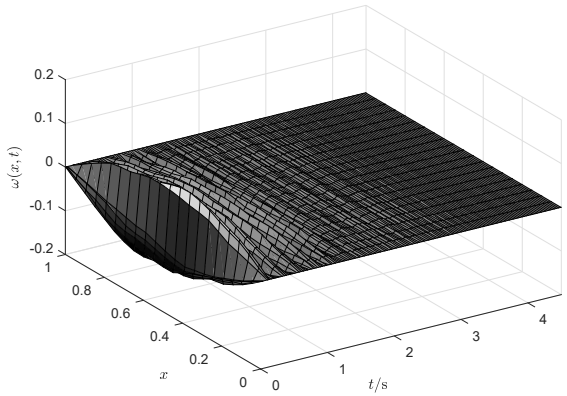

Fig. 4: The deflection of the beam with Adaptive NN NFTSMC control

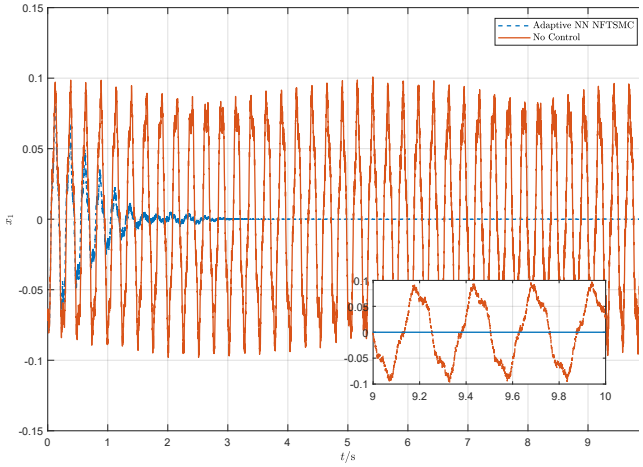

Fig. 5: The displacement of the beam at actuator position

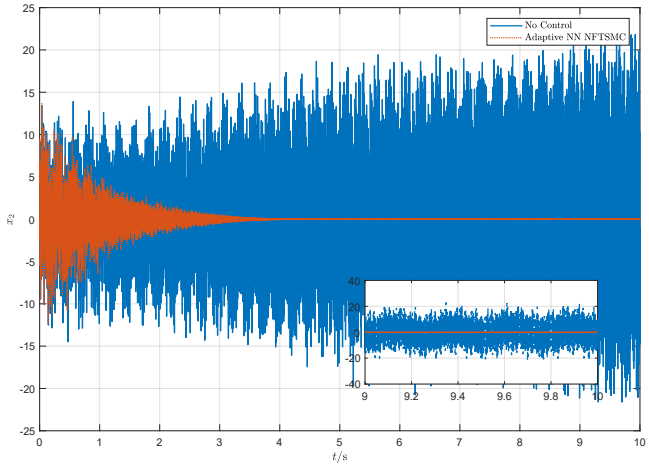

Fig. 6: The state response of the beam at actuator position

4 Simulation analysis

To demonstrate the efficacy of the adaptive neural network-based nonsingular fast terminal sliding mode control law (Adaptive NN NFTSMC) (10), numerical simulations are conducted for a double-clamped beam actuated by a piezoelectric actuator, considering input saturation and unknown distributed disturbances.

By selecting appropriate temporal and spatial step sizes for approximating the solution of the PDE system, the finite difference method is employed to demonstrate the effectiveness of the proposed control law (10).

To highlight the superiority of the proposed control laws, we compare their performance under two distinct scenarios. In the first scenario, the double-clamped beam vibrates freely, exposed to distributed disturbances without any control voltage $\tau_{sat}(t) = 0$. The displacement x_1 at the actuator position is presented in Figure 5, while the deflection output $\omega(x,t)$ of the beam system is displayed in Figure 3. Notably, there are prominent periodic vibrations with multiple frequencies along the beam, indicating the significant impact of distributed disturbances.

The deflections of the double-clamped beam, controlled by the proposed law (10), are depicted in Figures 4 to 6. As evident from Figures 3 to 6, the proposed control law (10) effectively suppresses vibrations. By leveraging the adaptive neural network NFTSMC law (10), we overcome the challenges posed by unknown dynamics in the double-clamped beam system. Despite potential estimation errors associated with the adaptive neural network, the proposed control law (10) demonstrates impressive performance in vibration suppression. Furthermore, with the assistance of the compensation system, the control law (10) introduced in this paper adeptly manages input saturation in the piezoelectric actuator.

5 Conclusion

This paper delves into the vibration control challenges encountered in a flexible double-clamped beam system. To address these challenges, an adaptive neural network-based nonsingular fast terminal sliding mode control scheme is proposed specifically tailored for the double-clamped beam. This approach effectively compensates for unknown dynamics within the system model, thereby suppressing vibrations in the beam. Simulation results demonstrate the exceptional performance of our proposed control in mitigating beam vibrations. Given the complexities associated with the control laws proposed, future work will focus on their practical implementation.

References

[1] Y. -R. Hu, and A. Ng, "Active robust vibration control of flexible structures," in *J. Sound Vib.*, vol. 288, no. 1-2, pp. 43-56, Nov. 2005.

[2] A. Baz, K. Imam, and J. McCoy, "Active vibration control of flexible beams using shape memory actuators," in *J. Sound Vib.*, vol. 140, no. 3, pp. 437-456, Aug. 1990.

[3] A. Preumont, *Vibration control of active structures: an introduction*, 4nd ed. Cham: Springer, 2018.

[4] T. Bailey and J. E. Hubbard, "Distributed piezoelectric-polymer active vibration control of a cantilever beam," in *J. Guid. Control Dyn.*, vol. 8, no. 5, pp. 605-611, May. 1985.
[5] W. He and S. S. Ge, "Vibration control of a flexible beam with output constraint," in *IEEE Trans. Ind. Electron.*, vol. 62, no. 5, pp. 5023-5030, Aug. 2015.
[6] W. He, T. Meng, D. Huang, and X. Li, "Adaptive boundary iterative learning control for an Euler–Bernoulli beam system with input constraint," in *IEEE Trans. Neural Netw. Learn Syst.*, vol. 29, no. 5, pp. 1539-1549, May. 2017.
[7] W. Xia, L. Wang, and L. Yin, "Nonlinear non-classical microscale beams: static bending, postbuckling and free vibration," in *Int. J. Eng. Sci.*, vol. 48, no. 12, pp. 2044-2053, Dec. 2010.
[8] M. Asghari, M. H. Kahrobaiyan, and M. T. Ahmadian, "A nonlinear Timoshenko beam formulation based on the modified couple stress theory," in *Int. J. Eng. Sci.*, vol. 48, no. 12, pp. 1749-1761, Dec. 2010.
[9] E. K. Dimitriadis, C. R. Fuller, and C. A. Rogers, "Piezoelectric actuators for distributed vibration excitation of thin plates," in *J. Vib. Acoust.*, vol. 113, no. 1, pp. 100-107, Jan. 1991.
[10] W. Sun, H. Gao, and B. Yao, "Adaptive Robust Vibration Control of Full-Car Active Suspensions With Electrohydraulic Actuators," in *IEEE Trans. Control Syst. Technol.*, vol. 21, no. 6, pp. 2417-2422, Nov. 2013
[11] L. Sui, X. Xiong, and G. Shi, "Piezoelectric actuator design and application on active vibration control," in *Phys. Proc.*, vol. 25, pp. 1388-1396, Apr. 2012.
[12] N. W. Hagood, W. H. Chung, and V. F. Andreas, "Modelling of piezoelectric actuator dynamics for active structural control," in *J. Intell. Material Syst. Structures*, vol. 1, no. 3, pp. 327-354, Jul. 1990.
[13] I. Bruant, L. Gallimard, and S. Nikoukar, "Optimal piezoelectric actuator and sensor location for active vibration control, using genetic algorithm," in *J. Sound Vib.*, vol. 329, no. 10, pp. 1615-1635, May. 2010.
[14] R. Vatankhah and M. H. Asemani, "Output feedback control of piezoelectrically actuated non-classical micro-beams using TS fuzzy model," in *J. Franklin Inst.*, vol. 354, no. 2, pp. 1042-1065, Jan. 2017.
[15] M. J. Shirazi, H. Salarieh, A. Alasty, and R. Shabani, "Tip tracking control of a micro-cantilever Timoshenko beam via piezoelectric actuator," in *J. Vib. Control*, vol. 19, no. 10, pp. 1561-1574, Jul. 2013.
[16] A. V. Moghaddam, A. Rajaei, R. Vatankhah, and M. R. Yazdia, "Terminal sliding mode control with non-symmetric input saturation for vibration suppression of electrostatically actuated nanobeams in the presence of Casimir force," in *Appl. Math. Model*, vol. 60, pp. 416-434, Aug. 2018.
[17] X. Bo, L. Zhang, and W. Ji. "Improved non-singular fast terminal sliding mode control with disturbance observer for PMSM drives." in *IEEE T TRANSP ELECTR*, pp. 2753-2762, July. 2021
[18] Q. Lei, and W. Zhang. "Adaptive non-singular integral terminal sliding mode tracking control for autonomous underwater vehicles." in *IET Contr. Theory Appl*, vol. 11, no. 8, pp.1293-1306, May. 2017
[19] S. Ding and S Li. "Second-order sliding mode controller design subject to mismatched term," in *Automatica*, vol. 77, pp. 388-392, Mar. 2017.
[20] Y. Feng, Z. Yu and Z. Man, "Non-singular terminal sliding mode control of rigid manipulators," in *Automatica*, vol. 38, no. 12, pp. 2159-2167, Dec. 2002.
[21] X. Lin, X. Shi, S. Li, S. K. Nguang, and L. Zhang. "Non-singular Fast Terminal Adaptive Neuro-sliding Mode Control for Spacecraft Formation Flying Systems," in *Complexity*, vol.2020, pp. 1-15, May. 2020.

Proceedings of the 3rd Conference on Fully Actuated System Theory and Applications
May 10-12, 2024, Shenzhen, China

Adaptive Dynamic Programming and Blockchain Technique-Based Smart Home Energy Management

Chujian Zeng[1], Bo Zhao[2]*, Derong Liu[3]

1. School of Automation, Guangdong University of Technology, Guangzhou 510006, China
E-mail: 1112104026@mail2.gdut.edu.cn

2. School of Systems Science, Beijing Normal University, Beijing 100875, China
E-mail: zhaobo@bnu.edu.cn

3. School of System Design and Intelligent Manufacturing, Southern University of Science and Technology, Shenzhen 518055, China
E-mail: liudr@sustech.edu.cn

Abstract: This paper focuses on developing an optimal energy storage strategy for smart home energy management using adaptive dynamic programming (ADP) and blockchain technique. The ADP-based self-learning algorithm is developed to generate an iterative control sequence for the battery as the electricity storage equipment. The algorithm takes real-time electricity prices, load demand, and battery power efficiency into account to establish an optimal performance index function. The goal is to minimize total electricity costs while maximizing the battery's lifespan. Additionally, the blockchain technique is employed to ensure transparent, tamper-proof and secure transaction data. A numerical simulation is provided to demonstrate the effectiveness of the proposed algorithm.

Key Words: Adaptive dynamic programming, energy management, optimal control, smart home, blockchain

1 Introduction

With the growing demand for smart grid implementation, smart home energy management systems have garnered increasing attention. Within these systems, the electricity storage equipments, i.e., batteries, play a vital role in effectively scheduling energy. They store energy during periods of low electricity costs and meet load demand during periods of high electricity costs. In the past decade, several approaches have been proposed in battery management [1–3]. However, these methods have overlooked the optimization of electricity costs and battery lifespan, which has hindered the effective utilization of battery management and control [4, 5].

Adaptive dynamic programming (ADP) has emerged as a powerful approach for solving the optimal control problem for smart home energy management systems [6–10]. Researchers have made significant progress in recent years. In [11], a self-learning scheme was developed for controlling and managing residential energy systems. Then, Wei *et al.* [12] extended the method to accommodate multiple battery systems with power constraints. The incorporation of renewable energy sources into household energy systems has significantly heightened the complexity of energy management and control. Liu *et al.* [13] proposed an action-dependent heuristic dynamic programming approach to enhance electricity efficiency in residential microgrids, then the energy scheduling problem was solved. However, the ledger of transactions has been stored in a centralized manner within the energy supplier, which raises concerns regarding individual privacy and storage security.

Blockchains are tamper-resistant and distributed data structures, or ledgers, which can offer secure data storage without requiring a central authority [14]. Unlike traditional centralized systems, where a single trusted entity manages the ledger, in blockchain networks, each participant holds a copy of the ledger and agrees on its valid state collectively through consensus mechanisms. Transactions within a blockchain are cryptographically linked to previous ones, ensuring the integrity and security of the network. This decentralized property allows every user in the network to independently validate the transactions, promoting transparency and providing reliable and tamper-proof records [15].

Additionally, blockchains which employ public-key cryptography is an asymmetric cryptographic method [16]. Each node in the network possesses a private key and a corresponding public key, consisting of numeric or alphanumeric characteristics. The public key is openly shared with other users, while the private key remains confidential. These keys are mathematically linked in such a way that data encrypted with one key can only be decrypted using its corresponding counterpart. The utilization of public-private key cryptography ensures the authentication of the source of transactions, and guarantee the actions to be performed by authorized users. This approach enhances privacy and security.

The objective of this paper is to develop an optimal energy storage strategy for smart home energy management. By formulating a suitable battery model for smart home energy systems, a performance index function is constructed by taking into account real-time electricity prices, load demand and battery power efficiency. Then, the iterative ADP algorithm is employed to derive the optimal control sequence for the battery. Moreover, we integrate blockchain technique to ensure individual privacy, tamper resistance and storage security [17].

The structure of this paper is organized as follows. Section 2 provides a problem formulation, including the construction of the battery model and the statement of optimization objectives. Section 3 discusses the system transformation

Corresponding author: Bo Zhao.

This work was supported in part by the National Key Research and Development Program of China under Grant 2021YFE0206100, in part by the National Natural Science Foundation of China under grants 62073085 and 61973330, in part by the Shenzhen Science and Technology Program under grant JCYJ20230807093513027, in part by the Fundamental Research Funds for the Central Universities under grant 1243300008, and in part by the Beijing Normal University Tang Scholar.

and the details of the iterative ADP algorithm. In Section 4, blockchain technique is introduced to ensure individual privacy, tamper-resistance, and storage security. Section 5 presents the numerical results to illustrate the effectiveness of the proposed algorithm. Finally, Section 6 concludes this paper.

2 Problem Formulation

Fig. 1 depicts the structure of smart home energy management systems, which consist of a battery model and a blockchain network. The optimization objectives are then introduced to guide the control and management of the system.

2.1 Smart Home Energy Management Systems

The smart home energy management systems are modeled as discrete systems with a time step of 1 hour. We assume that the home load P_{Lt} varies on an hourly basis. The battery is responsible for making decisions to meet the demand of the home load by considering the real-time electricity rate C_t.

2.2 Battery Model

Let E_{bt} be the battery energy at time instant t, then the battery model is written as [12]

$$E_{b(t+1)} = E_{bt} - P_{bt} \times \eta(P_{bt}), \tag{1}$$

where the battery operates in three modes, i.e., charging, discharging and idle modes corresponding to $P_{bt} < 0$, $P_{bt} > 0$ and $P_{bt} = 0$, respectively. The efficiency of battery charging/discharging is defined as $\eta(P_{bt}) = 0.898 - 0.173|P_{bt}|/P_{rate}$, where $P_{rate} > 0$ represents the rated power output of the battery.

The battery constraint is considered as

$$E_b^{\min} \le E_{bt} \le E_b^{\max}, \tag{2}$$

where $E_b^{\min}$ and $E_b^{\max}$ denote the minimum and maximum stored energies, respectively.

2.3 Optimization Objectives

Considering the home load and real-time electricity rate, the main objective of the optimal battery management is to determine the optimal action. In this context, let P_{Tt} be the power of home load at time instant t, and P_{gt} be the power obtained from the power grid.

In order to obtain the optimal control sequence, it is necessary to consider the load balance. To construct the home energy system, a delay is introduced into P_{bt} and expressed as $P_{Tt} = P_{b(t-1)} \times \eta(P_{b(t-1)}) + P_{gt}$. Let $P_{L(t-1)} = P_{Tt}$, the load balance is represented as

$$P_{L(t-1)} = P_{b(t-1)} \times \eta(P_{b(t-1)}) + P_{gt}, \tag{3}$$

where $P_{gt} \ge 0$.

To prolong the battery's lifespan, we aim to maintain the energy of the battery close to the half of the storage limit E_b^o as

$$E_b^o = \frac{1}{2}\big(E_b^{\min} + E_b^{\max}\big). \tag{4}$$

Inspired by [18], in order to minimize the total cost from the grid, the charging/discharging power of the battery, and extend the battery's lifespan, a performance index function is established as

$$\sum_{t=0}^{\infty} \gamma^i \Big(m_1 (C_t P_{gt})^2 + m_2 (E_{bt} - E_b^o)^2 + m_3 (P_{bt})^2 \Big), \tag{5}$$

where constants m_1, m_2 and $m_3 > 0$, $0 < \gamma < 1$ be the discount factor.

3 Iterative ADP Algorithm for Smart Home Energy Management System

In this section, an iterative ADP algorithm is proposed to derive the optimal control law for smart home energy management systems.

3.1 System Transformations

Letting $x_{1,t} = P_{gt}$, $x_{2,t} = E_{bt} - E_b^o$ and $u_t = P_{bt}$, based on (3), we have

$$x_{t+1} = F(x_t, u_t, t) = \begin{pmatrix} P_{Lt} - u_t \\ x_{2t} - u_t \eta(u_t) \end{pmatrix}, \tag{6}$$

where $x_t = [x_{1t}, x_{2t}]^{\mathsf{T}}$.

3.2 Optimality Principle

Let $\underline{u}_t = (u_t, u_{t+1}, \cdots)$ be the control sequence, and $M_t = \begin{bmatrix} m_1 C_t^2 & 0 \\ 0 & m_2 \end{bmatrix}$. The performance index function (5) is rewritten as

$$J(x_t, \underline{u}_t, t) = \sum_{t=0}^{\infty} \gamma^i U(x_i, u_i, i), \tag{7}$$

where the utility function is

$$U(x_t, u_t, t) = x_t^{\mathsf{T}} M_t x_t + m_3 u_t^{\mathsf{T}} u_t. \tag{8}$$

Let $\underline{\mathbb{U}}_t = \{\underline{u}_t : \underline{u}_t = (u_t, u_{t+1}, \cdots), u_{t+i} \in \mathbb{R}^m, i = 0, 1, ...\}$ be the control sequence set. Then, for an arbitrary control sequence $\underline{u}_t \in \underline{\mathbb{U}}_t$, the optimal performance index function can be expressed as

$$J^*(x_t, t) = \inf_{\underline{u}_t} \{J(x_t, \underline{u}_t, t) : \underline{u}_t \in \underline{\mathbb{U}}_t\}. \tag{9}$$

Based on Bellman's principle of optimality, the discrete-time Hamilton-Jacobi-Bellman equation is derived by

$$J^*(x_t, t) = \inf_{\underline{u}_t} \{U(x_t, u_t, t) + \gamma J^*(x_{t+1}, t+1)\}. \tag{10}$$

The optimal control sequence is derived by

$$u^*(x_t, t) = \arg\inf_{\underline{u}_t} \{U(x_t, u_t, t) + \gamma J^*(x_{t+1}, t+1)\}. \tag{11}$$

3.3 The Iterative ADP Algorithm

For any $k = 0, 1, \ldots,$ we define

$$\mathcal{U}_k = (u_k, u_{k+1}, ..., u_{k+\lambda-1}) \tag{12}$$

as the control sequence from k to $k + \lambda - 1$.

The utility function is obtained as

$$\Lambda(x_k, \mathcal{U}_k) = \sum_{\theta}^{\lambda-1} \gamma^\theta U(x_{k+\theta}, u_{k+\theta}, \theta). \tag{13}$$

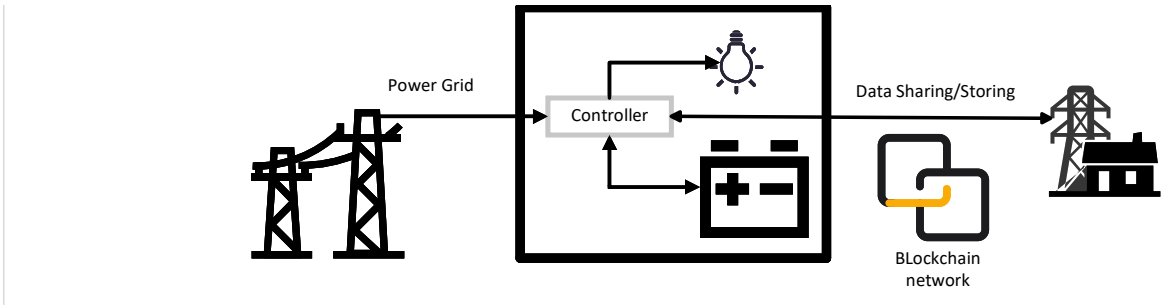

Fig. 1: Smart home energy management system.

The optimal performance index function is expressed as

$$J^*(x_k) = \min_{\underline{u}_t}\{\Lambda(x_k, \mathcal{U}_k) + \gamma^\theta J^*(x_{t+1}, t+1)\}. \quad (14)$$

The optimal control sequence is obtained as

$$\mathcal{U}^*(x_k) = \arg\min_{\underline{u}_t}\{\Lambda(x_k, \mathcal{U}_k) + \gamma^\theta J^*(x_{t+1}, t+1)\}. \quad (15)$$

Let $i = 0, 1, \ldots$ be the iteration index, $\Psi(x_t)$ be an arbitrary positive semidefinite function, define the initial performance index function $V_0(x_t) = \Psi(x_t)$. Then, the iterative value function and the iterative control sequence are derived by

$$V_{i+1}(x_t, t) = \min_{\mathcal{U}_k}\{\Lambda(x_k, \mathcal{U}_k) + \gamma^\theta V_i(x_{t+\theta})\}, \quad (16)$$

$$\mathcal{U}_i(x_k) = \arg\min_{\mathcal{U}_k}\{\Lambda(x_k, \mathcal{U}_k) + \gamma^\theta V_i(x_{t+\theta})\}. \quad (17)$$

For a new iteration index $j = 0, 1, \ldots, 23$,

$$\begin{aligned} V_i^{j+1}(x_k) &= \min_{u_k}\{U(x_k, u_k, j) + \gamma V_i^j(x_{k+1})\} \\ &= U(x_k, u_k^j, j) + \gamma V_i^j(x_{k+1})\}, \end{aligned} \quad (18)$$

and

$$u_i^j(x_k) = \arg\min_{u_k}\{U(x_k, u_k, j) + \gamma V_i^j(x_{k+1})\}. \quad (19)$$

3.4 Properties of the Iterative ADP Algorithm

In this subsection, we will demonstrate that as the iteration index i tends to infinity, the iterative performance index function and iterative control sequence will converge to their optimums, respectively.

Theorem 1 *For $i = 0, 1, \ldots,$ and $j = 0, 1, \ldots, 23$, $V_i^j(x_k)$ and $v_i^j(x_k)$ are obtained by (18) and (19). Then, the iterative control sequence can be expressed by*

$$\mathcal{U}_i(x_k) = \{u_i^{23}(x_k), \ldots, u_i^0(x_{k+23})\}. \quad (20)$$

Theorem 2 *For $i = 0, 1, \ldots,$ $V_{i+1}(x_k)$ and $\mathcal{U}_i(x_k)$ are obtained by (16) and (17). Then, the iterative performance index function $V_i(x_k)$ converges to the optimal performance index function, i.e.,*

$$\lim_{i\to\infty} V_i(x_k) = J^*(x_k). \quad (21)$$

Corollary 1 *For $i = 0, 1, \ldots,$ $V_{i+1}(x_k)$ and $\mathcal{U}_i(x_k)$ are obtained by (16). The iterative control law sequence $\mathcal{U}_i(x_k)$ converges to the optimal control law sequence, we have*

$$\lim_{i\to\infty} \mathcal{U}_i(x_k) = \mathcal{U}(x_k). \quad (22)$$

Specifically, the proofs of Theorems 1 and 2, and Corollary 1 have been provided in [18], and for the sake of brevity, they are omitted in this paper.

4 Blockchain Technique

The training and implementation of intelligent algorithms rely on the data provided by intelligent devices. Traditionally, a common approach for managing data is to use a centralized system with a trusted intermediary. A central authority is responsible for storing and safeguarding the valid state of the ledger while ensuring data integrity and currency. However, centralized systems suffer from significant drawbacks, notably a single point of failure. This vulnerability exposes them to technical malfunctions and malicious attacks, compromising the system security and reliability.

A blockchain is a shared and distributed database that provides secure storage of data without relying on a central authority. Multiple users are allowed to modify the ledger. Instead of being managed by a single trusted entity, each network participant maintains a copy of the ledger and reaches a consensus on its valid state. Therefore, the blockchain is potential to be utilized for communication among smart devices, the data transmission and storage purposes. In this work, the primary data stored in the blockchain is transaction information.

The algorithm process is presented in Algorithm 1. In Step 1, nodes generate pseudo-identities (public keys) and private keys using algorithms such as elliptic curve digital signatures. To preserve privacy, information interaction among nodes is carried out anonymously. In Step 2, the optimal control sequence is obtained using the ADP algorithm to allow the determination of the energy purchasing strategy. Step 3 involves nodes encrypting their transaction information using their private keys and broadcasting it to the network. In Step 4, nodes on the network validate the authenticity of the transactions. Step 5 entails grouping validated transactions together into blocks. During the block mining, miners compete to solve a computational puzzle known as proof-of-work, which requires high computational power, and to secure the network against malicious activities. In Step 6, the block is validated, by ensuring that it adheres to the consensus rules and contains accurate transaction information. The proposed verification mechanism is effective due to the irreversibility of the hash function. If the majority of nodes agree on the validity of the proposed block, they are added to the blockchain to become a permanent part of the distributed ledger.

Algorithm 1 Smart Home Energy Management Algorithm

Step 1: For all nodes, randomly generate a unique key pair P_i, S_i;

Step 2: Calculate the optimal control sequence and energy purchasing strategy.

Step 3: Node encrypts and broadcasts the actual energy purchase.

Step 4: Decrypt and verify the transaction from the node.

Step 5: Block formation.

Step 6: Block mining.

Step 7: Block validation.

Step 8: Consensus and block addition.

5 Numerical Analysis

This section aims to demonstrate the effectiveness of the developed method through a numerical experiment. Fig. 2 illustrates the load demand (in kW) for a duration of 168 hours, along with the corresponding real-time electricity rates (in cents) during the same period [18].

The capacity of the battery is set to 100 kWh, which is a typical value for common energy storage systems. The minimum and maximum energy levels of the battery are defined as $E_b^{\min} = 20$ kWh and $E_b^{\max} = 80$ kWh, respectively. For the battery, the rated power and the initial energy level are selected as 16.5 kW and 60 kWh, respectively. To formulate the performance index function (5), the coefficients m_1, m_2 and m_3 are set to 1, 0.5 and 0.2, respectively. The initial state x_0 is randomly assigned as $[8, 60]^{\mathsf{T}}$, where the first and the second elements represent the load demand and the energy level.

The optimal control strategy for the smart home energy management system is presented in Fig. 3. It can be observed that the battery charges during periods of low load demand and electricity rates, and discharges in an opposite scenario. This strategy enables efficient utilization of the energy storage system. The total cost incurred in one week with considering the electricity rates and load demands is 2671.54 cents. Fig. 4 illustrates the corresponding energy levels in the energy storage equipment throughout the week. It provides a visual representation on how the energy storage varies based on the charging and discharging actions determined by the optimal control strategy, respectively.

The transaction process is also provided. As shown in Fig. 5, the sender utilizes a private key to encrypt their transaction information to ensure its confidentiality and integrity. On the other hand, the receiver uses the corresponding public key to verify the authenticity of the information. Each transaction is securely recorded within a block in the blockchain. Once the optimal energy purchasing strategy is formulated and broadcasted in the blockchain network, all data recorded in the block, including transaction details, are maintained and accessible to all nodes. This ensures the privacy of each node through anonymous operations. Furthermore, the credibility of the recorded data is guaranteed by the transparent, traceable and tamper-resistant nature of the public data ledger provided by the blockchain. The decentralized and distributed nature of the blockchain network pre-

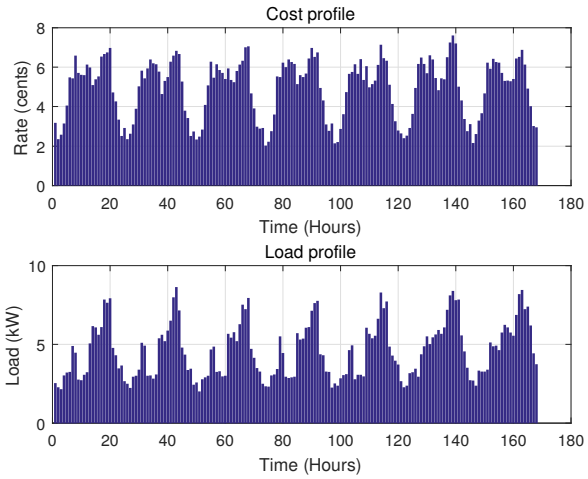

Fig. 2: Home load demand and electricity rate in 168 hours.

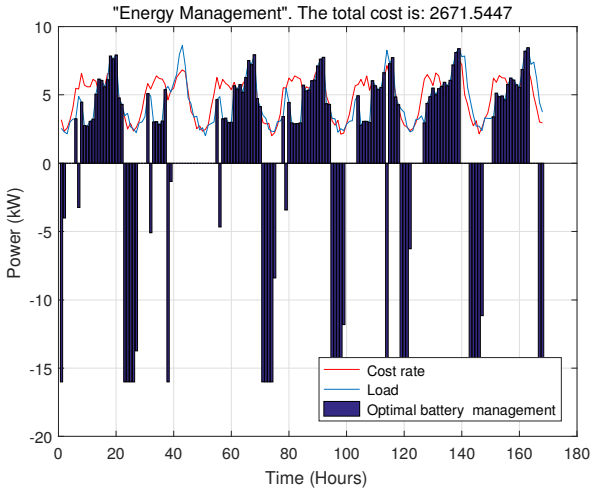

Fig. 3: Optimal battery management in 168 hours.

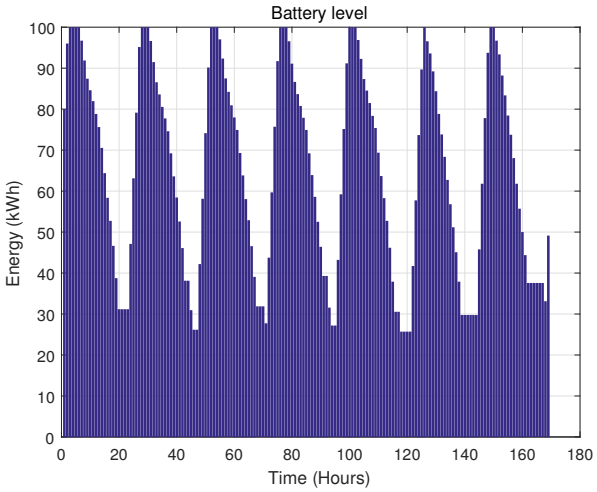

Fig. 4: Optimal battery level in 168 hours.



Fig. 5: Message signature.

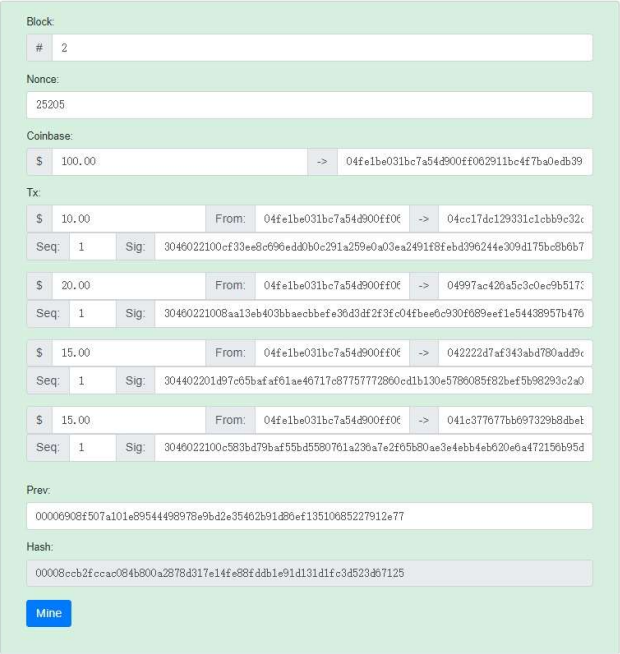

Fig. 6: The transaction record processes in the blockchain.

vents any single entity from manipulating or tampering with the recorded data, thereby enhancing the trust and credibility of the transactions.

6 Conclusion

This paper investigates an optimal control scheme for a smart home energy management system by incorporating the ADP and blockchain technique. The ADP-based self-learning algorithm is developed to generate the iterative control sequence for the battery. By considering real-time electricity prices and load demands, an optimal performance index function is established to minimize overall electricity costs and maximize the battery lifespan. Additionally, the blockchain technique is employed to ensure transparency, tamper-proofing, and data security for energy information. Numerical results are provided to validate the effectiveness of the proposed algorithm.

References

[1] H. J. Bergveld, W. S. Kruijt, P. H. Notten, H. J. Bergveld, W. S. Kruijt, and P. H. Notten, *Battery management systems*. Springer, 2002.

[2] Y. Wang, J. Tian, Z. Sun, L. Wang, R. Xu, M. Li, and Z. Chen, "A comprehensive review of battery modeling and state estimation approaches for advanced battery management systems," *Renewable and Sustainable Energy Reviews*, vol. 131, Art. no. 110015, 2020.

[3] F. Y. Melhem, O. Grunder, Z. Hammoudan, and N. Moubayed, "Optimization and energy management in smart home considering photovoltaic, wind, and battery storage system with integration of electric vehicles," *Canadian Journal of Electrical and Computer Engineering*, vol. 40, no. 2, pp. 128–138, 2017.

[4] P. Lazzeroni, S. Olivero, M. Repetto, F. Stirano, and M. Vallet, "Optimal battery management for vehicle-to-home and vehicle-to-grid operations in a residential case study," *Energy*, vol. 175, pp. 704–721, 2019.

[5] L. Bhamidi and S. Sivasubramani, "Optimal sizing of smart home renewable energy resources and battery under prosumer-based energy management," *IEEE Systems Journal*, vol. 15, no. 1, pp. 105–113, 2020.

[6] D. Liu, S. Xue, B. Zhao, B. Luo, and Q. Wei, "Adaptive dynamic programming for control: A survey and recent advances," *IEEE Transactions on Systems, Man, and Cybernetics: Systems*, vol. 51, pp. 142–160, Jan. 2020.

[7] D. Wang, N. Gao, D. Liu, J. Li, and F. L. Lewis, "Recent progress in reinforcement learning and adaptive dynamic programming for advanced control applications," *IEEE/CAA Journal of Automatica Sinica*, vol. 11, no. 1, pp. 18–36, 2023.

[8] D. Liu, Q. Wei, D. Wang, X. Yang, and H. Li, *Adaptive dynamic programming with applications in optimal control*. Springer, 2017.

[9] B. Zhao, G. Shi, and D. Liu, "Event-triggered local control for nonlinear interconnected systems through particle swarm optimization-based adaptive dynamic programming," *IEEE Transactions on Systems, Man, and Cybernetics: Systems.*, vol. 53, no. 12, pp. 7342 – 7353, 2023.

[10] B. Zhao, Y. Zhang, and D. Liu, "Adaptive dynamic programming-based cooperative motion/force control for modular reconfigurable manipulators: A joint task assignment approach," *IEEE Transactions on Neural Networks and Learning Systems.*, vol. 34, no. 12, pp. 10944 – 10954, 2023.

[11] T. Huang and D. Liu, "A self-learning scheme for residential energy system control and management," *Neural Computing and Applications*, vol. 22, no. 2, pp. 259–269, 2013.

[12] Q. Wei, D. Liu, G. Shi, and Y. Liu, "Multibattery optimal coordination control for home energy management systems via distributed iterative adaptive dynamic programming," *IEEE Transactions on Industrial Electronics*, vol. 62, no. 7, pp. 4203–4214, 2015.

[13] D. Liu, Y. Xu, Q. Wei, and X. Liu, "Residential energy scheduling for variable weather solar energy based on adaptive dynamic programming," *IEEE/CAA Journal of Automatica Sinica*, vol. 5, no. 1, pp. 36–46, 2017.

[14] K. Christidis and M. Devetsikiotis, "Blockchains and smart contracts for the internet of things," *IEEE Access*, vol. 4, pp. 2292–2303, 2016.

[15] S. Wen, W. Xiong, J. Tan, S. Chen, and Q. Li, "Blockchain enhanced price incentive demand response for building user energy network in sustainable society," *Sustainable Cities and Society*, vol. 68, Art. no. 102748, 2022.

[16] T. Wang, H. Hua, Z. Wei, and J. Cao, "Challenges of blockchain in new generation energy systems and future outlooks," *International Journal of Electrical Power & Energy Systems*, vol. 135, Art. no. 107499, 2022.

[17] Q. Wang and M. Su, "Integrating blockchain technology into the energy sectorfrom theory of blockchain to research and application of energy blockchain," *Computer Science Review*, vol. 37, Art. no. 100275, 2020.

[18] Q. Wei, D. Liu, Y. Liu, and R. Song, "Optimal constrained self-learning battery sequential management in microgrid via adaptive dynamic programming," *IEEE/CAA Journal of Automatica Sinica*, vol. 4, no. 2, pp. 168–176, 2016.

Proceedings of the 3rd Conference on Fully Actuated System Theory and Applications
May 10-12, 2024, Shenzhen, China

Dynamic SLAM Based on Neural Network and Depth Information

Aoqiang Liu, Shu Yang, Yuan Fan
School of Electrical Engineering and Automation, Anhui University, Hefei, Anhui 230601, P. R. China
E-mail: yuanf@ahu.edu.cn

Abstract: In the current Simultaneous Localization and Mapping (SLAM) framework, it is assumed that the environment remains static, meaning no changes in objects are detected. However, in real-world scenarios, encountering a dynamic environment where objects exhibit movement is inevitable. To address this issue, and we incorporate real-time object detection network You Only Look Once (YOLO) into our system to detect dynamic objects and mitigate their impact. Our approach utilizes an RGBD camera and develops an algorithm based on depth information to effectively distinguish between background and dynamic objects. By integrating an object detection thread into ORB-SLAM3, our system identifies dynamic objects within the environment while proposing a novel depth weight selection algorithm to maximize the number of static feature points for improved data associations. Finally, we evaluate tracking accuracy using publicly available TUM and BONN datasets.

Key Words: SLAM, YOLOV5, Depth Information

1 Introduction

SLAM (Simultaneous Localization and Mapping) is a widely adopted robotics and autonomous vehicle system to facilitate self-navigation and map creation in unfamiliar environments. The primary application areas of SLAM technology encompass AR/VR equipment, unmanned machines, and autonomous driving. Consequently, SLAM has garnered significant attention due to its immense value in enhancing the accuracy of the SLAM system. In the current vSLAM system, most detection scenarios assume static environments where no objects move within the scene. However, real-world environments predominantly consist of non-static elements or dynamic surroundings. Within dynamic environments, we categorize them into high-dynamic and low-dynamic settings. While existing vSLAM systems combined with target detection perform well in low-dynamic environments, they encounter substantial trajectory errors in high-dynamic settings.

To address this issue, researchers propose tracking only static feature points while disregarding dynamic feature points for dynamic problems. Even with dynamic feature points, there needs to be more data association for pose estimation within high-dynamic scenarios, resulting in significant trajectory errors. In object detection networks, instance segmentation has high accuracy. However, achieving a balance between detection accuracy and speed proves challenging with instance segmentation techniques such as Mask-RCNN and SegNet. In light of this challenge, we present a real-time approach that leverages RGB-D camera characteristics along with depth information provided by it to achieve an equivalent performance level as instance segmentation within a SLAM system. We propose an algorithm that separates background regions from dynamic targets by assigning each detection box a depth weight, ensuring the removal of only the feature points belonging to dynamic targets while retaining those associated with the background region. This ensures that sufficient feature points are available for matching purposes.
The main contributions of this paper are as follows:

- We propose a real-time visual SLAM system that operates effectively in high dynamic environments.
- We introduce a algorithm for utilizing depth values, enabling the distinction between background points and dynamic objects, the tracking accuracy can be improved by increasing the utilization of feature points.

2 Related Work

2.1 VSLAM

The first visual slam system for a monocular camera was developed by Davison et al[1].The first visual slam system based on keyframe bundle adjustment was developed by Klein et al. Mur-Artal et al.[2]. proposed a system with three threads called ORB-SLAM [3], subsequent versions of ORB-SLAM2[4],ORB-SLAM3 [5], and our system was developed on the basis of ORB-SLAM3. The ORB-SLAM3 adds two major innovations: a feature-based, tightly integrated visual-inertial SLAM that relies entirely on maximum a posteriori probability estimation. The second is the multi-map system, which depends on a new location identification method and improves recall rates.

2.2 Dynamic Object Recognition

Dynamic object recognition is vital in a highly dynamic environment in the SLAM system. The recognition of dynamic objects is divided into two stages and one-stage methods. Compared with the two-stage method, the one-stage method predicts the mask directly without region suggestion. Compared with the two methods, the two-stage method has higher detection and segmentation accuracy, but the speed is slower. The one-stage method is faster than the two-stage method, but the detection accuracy has an inevitable loss.

2.3 Dynamic SLAM

In the two-phase approach, both Mask-RCNN and Blend-Mask[6–13] demonstrate excellent performance. DynaSLAM[14], proposed by Berta Bescos et al., utilizes

This work was supported by the National Natural Science Foundation of China (61973002), and the Anhui Provincial Natural Science Foundation (2008085J32).

the Mask-RCNN network for semantic segmentation and achieves remarkable accuracy. DynaSLAM II[15] employs instance semantic segmentation, and ORB features to track dynamic objects. The optimization of static scenes and dynamic objects is carried out in conjunction with the camera and moving agent's trajectory through a novel beam adjustment proposal. However, including multiple view geometry stages introduces additional deceleration primarily due to the region growth algorithm. Background repair also introduces delays. The drawback of employing a two-stage approach is its inability to operate in real-time. In contrast, within the one-stage approach, Crowd-SLAM[16] demonstrates that an object detection-based method outperforms a semantic segmentation-based method when dealing with moving objects without predefined information. Nevertheless, feature points are abundant within the bounding box, which poses challenges; erasing all these points would result in insufficient data association for attitude estimation, leading to the failure of the SLAM system. To balance real-time system performance and detection accuracy, we selected YOLOV5 as our one-stage method for dynamic object recognition. Combining it with depth information provided by RGBD cameras, we retain feature points belonging to background regions within the detection box while eliminating only those associated with dynamic objects to establish the maximum data associations possible. Our system has been evaluated on TUM and BONN datasets, where results indicate comparable performance to instance segmentation methods.

3 Methodology

3.1 System Framework Overview

The framework of our proposed method is illustrated in Figure 1, which comprises four threads: Object detection, tracking, local mapping, and loop closing. The RGB-D image is initially inputted into the system and processed by object detection and tracking threads. The tracking thread initially extracts ORB feature points from the image. These points are combined with depth information from the RGB-D image and target detection information provided by the target detection thread. By doing so, dynamic objects within the image can be effectively separated from their background counterparts while ensuring that feature points belonging to these dynamic objects are eliminated to establish more robust data associations.

3.2 Dynamic Object Recognition

3.2.1 Depth Image

Depth image, also known as range image, refers to the image that takes the distance (depth) from the image collector to each point in the scene as the pixel value, which directly reflects the geometry of the visible surface of the scene. In the image frame provided by the depth data stream, each pixel represents the distance from the object closest to the camera plane to the object at the specified (x, y) coordinate in the depth sensor's field of view.The depth maps in the TUM dataset are stored in PNG format as 640x480 16-bit monochrome images. The depth images are scaled by a factor of 5000, i.e., a pixel value of 5000 in the depth image corresponds to a distance of 1 meter from the camera.For the place where the pixel value of the center point of the detection box is 0, the pixel value is supplemented.The pixel value supplement method is shown in the Figure 2:

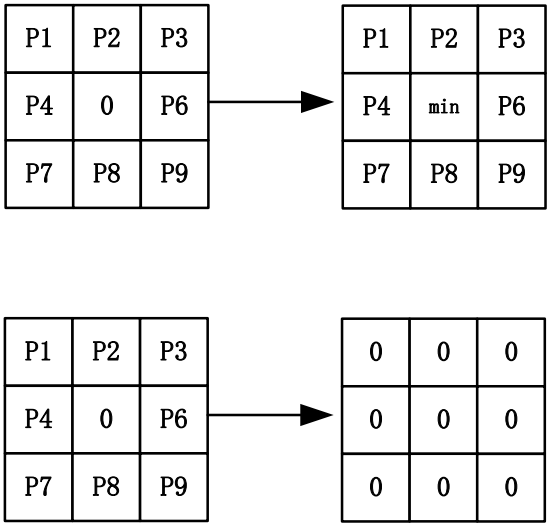

Fig. 2: The pixel value of the center point of the detection box is 0, and there are two cases. The first case is that the surrounding pixel value is not 0, and the pixel value is the minimum value of the surrounding pixel value except 0. In the second case, the surrounding pixel values are all 0, then the center point is 0

Where min is expressed as:

$$\min = \boldsymbol{min}\{\mathbf{P1}, \mathbf{P2}, \mathbf{P3}, \mathbf{P4}, \mathbf{P6}, \mathbf{P7}, \mathbf{P8}, \mathbf{P9}\}$$

3.2.2 Depth Weight

When there are moving objects in the environment, it can cause errors in our SLAM system, specifically in the matching of ORB feature points. We must identify and remove the feature points extracted from these objects to address this issue to reduce mismatches. However, using a Mask-RCNN network, such as DynaSLAM segmentation, can be time-consuming and affect real-time performance. Therefore, we use YOLOV5 as our target detection network and train it using the coco dataset. This allows the trained network to identify 80 categories, including people designated as dynamic objects. In some cases, relying solely on object detection algorithms to remove feature points can result in fewer remaining features or even an inability to extract them altogether, especially in highly dynamic environments where dynamic objects occupy a significant portion of the image. To address this issue, we use depth maps provided by RGBD cameras to jointly assess and assign a depth weight $\bar{d}_w$ to each detected area of a dynamic object. This effectively distinguishes the dynamic object from the background. The formula for $\bar{d}_w$ is as follows:

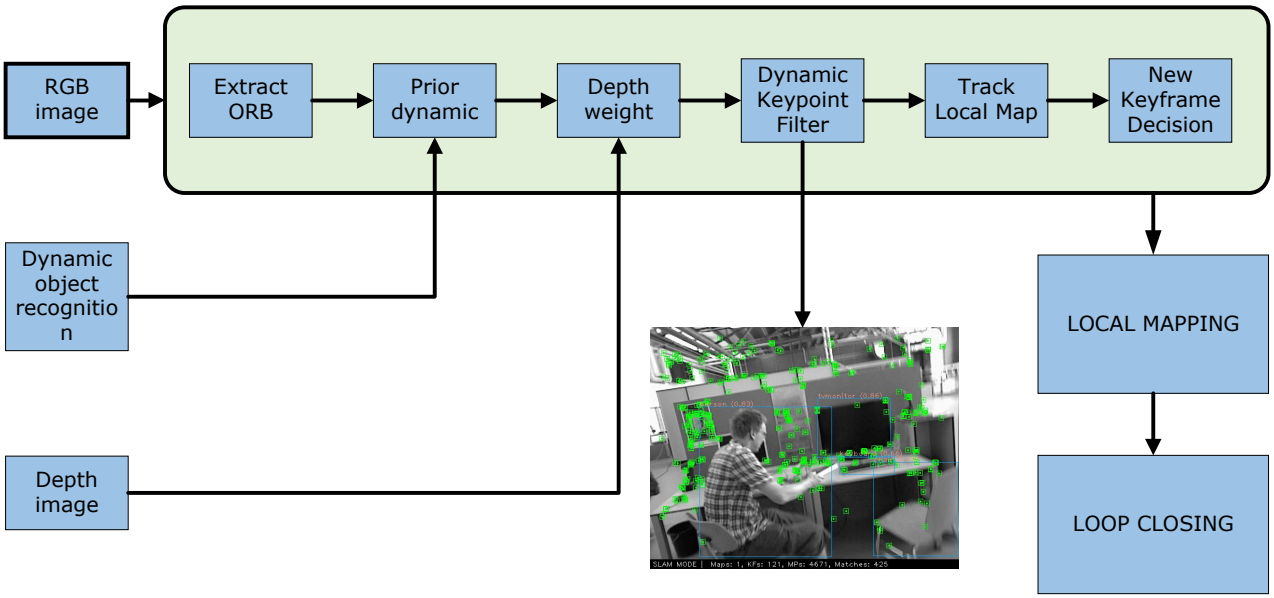

Fig. 1: This represents the framework of our system, where four primary threads operate concurrently. The object detection thread supplies dynamic target information from the image, while the Tracking thread incorporates depth data to eliminate dynamic feature points.

$$\bar{d}_w = \begin{cases} \text{if} \quad \mathrm{d_m} > 0, \quad \mathrm{d_c} > 0, \quad \mathrm{d_m} - \mathrm{d_c} > \sigma \\ \quad 0.3 * d_m + 0.7 * d_c \\ \text{if} \quad \mathrm{d_m} > 0, \quad \mathrm{d_c} > 0, \quad \mathrm{d_m} - \mathrm{d_c} < \sigma \\ \quad 1.1 * d_c \\ \text{if} \quad \mathrm{d_m} > 0, \quad \mathrm{d_c} = 0 \\ \quad d_{\max} \\ \text{if} \quad \mathrm{d_c} = 0, \quad \mathrm{d_c} = 0 \\ \quad max \end{cases} \tag{1}$$

where $\bar{d}_w$ is the depth weight of the bounding box, d_m is the maximum boundary depth, and d_c is the center depth. The physical meaning refers to the establishment of depth between a dynamic object and the background when there is a significant distance between them. A weighted average is then used to indicate that the dynamic object is closer to the background feature points, while retaining as many background feature points as possible. In cases where the dynamic object has a strong connection with the background, a depth weight of 1.1 times the depth value of the dynamic object is employed. However, in practical situations, there are points with invalid depth values which make it inconvenient for us to distinguish their significance. During conservative periods, when an invalid depth value occurs, it is represented using an invalid depth value. Specifically, if the central point's depth value is invalid, we search for and replace it with the minimum value among its surrounding points' depths; only if this substitution proves invalid will we consider the central point's own depth invalid. When both maximum and center depths represent potential background points due to close connectivity between a dynamic object and its background (with small differences in their depths), it becomes necessary to determine whether or not the center point represents a dynamic object and whether or not its corresponding depth matches that of its minimum bounding box; in such cases, we use this minimum bounding box's depth value instead of that of the center point itself. When the center depth and corner depth are not effective, the maximum depth is used for conservative reasons. These processing above steps ensure robustness in determining depth weights while adapting effectively within various dynamic environments.

4 Experiments and Results

To compare the proposed methodologies, we assess our system's performance using RGB-D and BONN datasets and evaluate the tracking capabilities of different SLAM systems through publicly available TUM datasets and Bonn datasets to quantify our system's effectiveness in highly dynamic scenarios.

4.1 Evaluation Metrics

In the experiment, we use absolute trajectory error (ATE) for comparison, which is very suitable for measuring the performance of VSLAM. ATE [43] is used to evaluate the global consistency of the estimated trajectory and compare the absolute distance between the translation component of the estimated trajectory and the real trajectory on the ground. Formula 2 writes the calculation of ATE at time step i:

$$ATE_i = E_i^{-1} T G_i \tag{2}$$

where E is the estimated trajectory, G represents the ground truth, and T is the transformation that aligns the two trajectories.

By comparing root mean square error (RMSE), standard deviation (STD), mean and median in ATE.

For a sequence of N postures, the RMSE of ATE is given

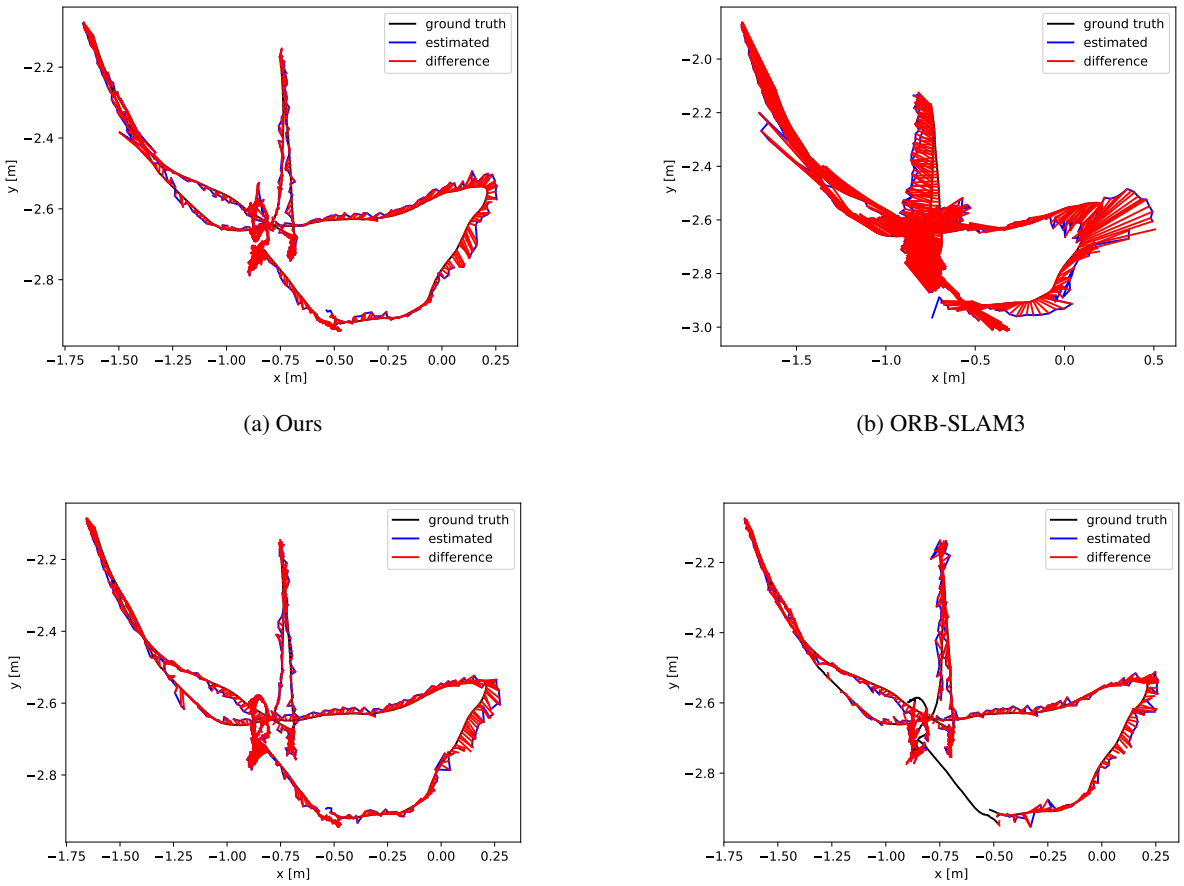

(a) Ours

(b) ORB-SLAM3

(c) DynaSLAM

(d) Crowd-SLAM

Fig. 3: TUM datasets absolute trajectory error

by equation 3

$$RMSE\left(ATE_{1:N}\right) = \sqrt{\frac{1}{N}\sum_{i=1}^{N}\left\|trans\left(ATE_i\right)\right\|^2} \quad (3)$$

The calculation of each sequence is performed through multiple iterations, as dynamic objects tend to amplify the uncertainty effect. Our method is compared against ORB-SLAM3, DynaSLAM, and Crowd-SLAM.

4.2 TUM Dataset

The TUM RGB-D dataset[17] comprises sequences of images captured by an RGB-D camera in a dynamic environment, accompanied by precise, accurate trajectories and camera parameters. Dynamic SLAM primarily serves to assess the performance in dynamic environments. We have selected data from static, low-dynamic, and high-dynamic environments to evaluate and test the system's capabilities. In the fr3/walking-halfspare sequence, two individuals traverse an office scene while manually moving the Asus Xtion sensor along three directions (xyz) while maintaining a consistent direction. This sequence was designed to gauge the robustness of visual SLAM and mileage computing methods when dealing with fast-moving dynamic objects across significant portions of the visible scene. We compared the motion trajectories of ORB-SLAM3, DynaSLAM, and Crowd-

Table 1: TUM Dataset Absolute Trajectory

	Sequence	fr2/d/w/p	fr3/s/h	fr3/s/s	fr3/w/half	fr3/s/xyz	fr3/w/xyz
Ours	RMSE	0.0767	0.0522	**0.0068**	**0.0286**	0.0144	**0.0151**
	Mean	0.0750	0.0306	**0.0060**	**0.0237**	0.0127	0.0133
	Median	0.0755	0.0196	**0.0053**	**0.0200**	0.0114	0.0121
	S.D.	**0.0162**	0.0422	**0.0032**	0.0165	0.0067	**0.0075**
ORB-SLAM3	RMSE	0.0753	**0.0188**	0.0094	0.1974	**0.0093**	0.2774
	Mean	0.0734	**0.0157**	0.0081	0.1850	**0.0080**	0.2158
	Median	0.0734	**0.0137**	0.0072	0.1753	**0.0071**	0.2065
	S.D.	0.0166	0.0103	0.0048	0.0688	**0.0048**	0.1742
DynaSLAM	RMSE	**0.0709**	0.0208	/	0.0289	0.0141	0.0153
	Mean	**0.0690**	0.0183	/	0.0242	0.0124	**0.0131**
	Median	**0.0671**	0.0163	/	0.0205	0.0112	0.0117
	S.D.	0.0166	**0.0099**	/	**0.0154**	0.0067	**0.0075**
Crowd-SLAM	RMSE	0.0741	0.0263	0.0119	0.0354	0.0185	0.0177
	Mean	0.0718	0.0243	0.0101	0.0307	0.0157	0.0153
	Median	0.0682	0.0244	0.0088	0.0275	0.0140	**0.0136**
	S.D.	0.0185	0.0100	0.006	0.0175	0.0097	0.0089

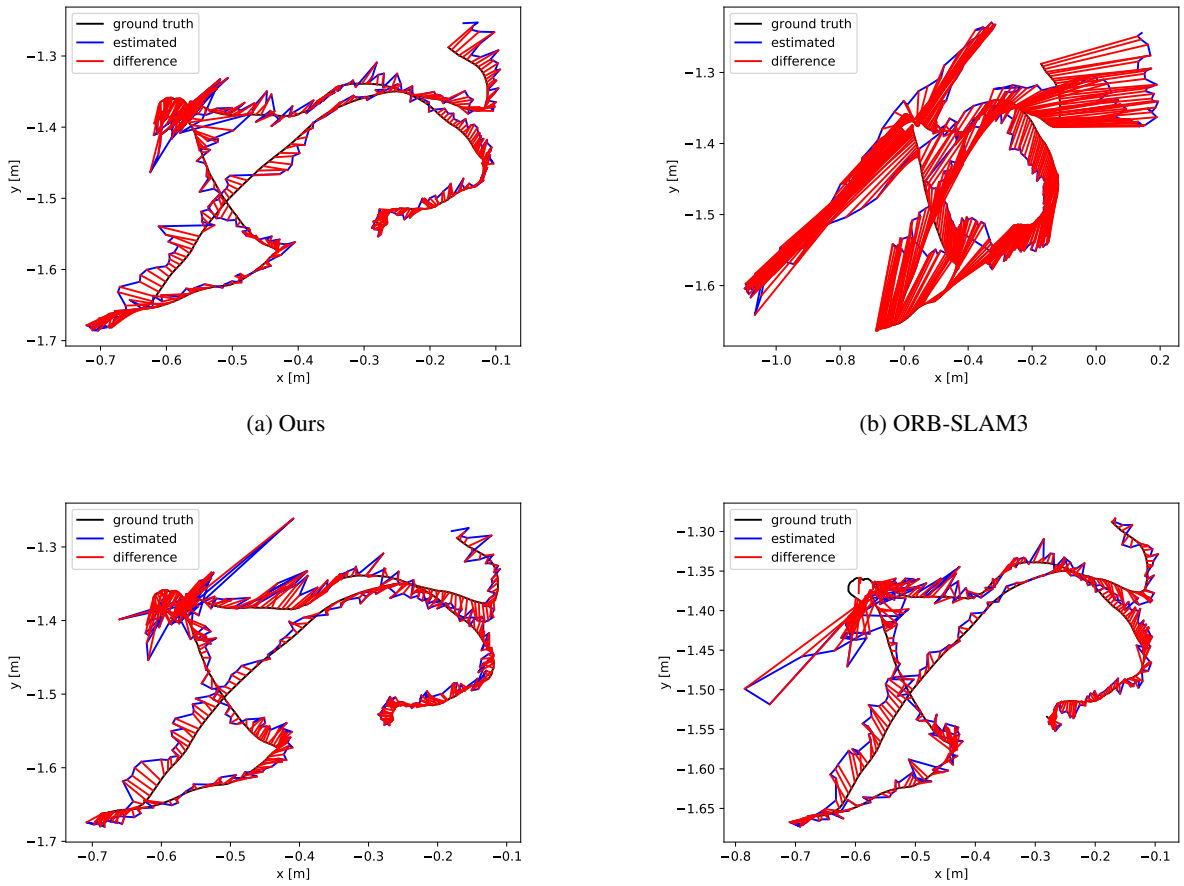

(a) Ours

(b) ORB-SLAM3

(c) DynaSLAM

(d) Crowd-SLAM

Fig. 4: Bonn datasets absolute trajectory error

SLAM. Figure 3 shows the motion of four different SLAM systems in fr3/w/half. TABLE 1 shows the running effects of different data sets on different SLAM systems. In fr3/s/h, and fr3/s/xyz, where static scenes are the majority, ORB-SLAM3 works best. For the high dynamic sequences fr2/d/w/p,fr3/s/s,fr3/w/half, and fr3/w/xyz, our method and DynaSLAM have good results, but our system is real-time.

4.3 Bonn RGB-D Dynamic Dataset

The Bonn dataset[18] is a highly dynamic sequence of individuals walking and performing various tasks, surpassing the TUM dataset in terms of challenging scenarios. It was recorded using an Asus Xtion Pro Live Sensor and an Optitrack Prime 13 motion capture system to provide accurate groundtruth data.

Moreover, it shares the same evaluation metrics as the TUM dataset. Among them, Figure 4 shows the trajectory errors of different SLAM in the bolloon/bolloon2 data set, and Table 2 shows the operation effects in three different sequences of bolloon, bolloon2, and crowd. In the crowd sequence, Crowd-SLAM handles crowded scenes better than our method, and in the balloon, balloon2 sequence, a man shooting a balloon scene, our method has a good effect with DynaSLAM.

Table 2: BONN Dataset Absolute Trajectory

Sequence		balloon2	crowd	balloon
Ours	RMSE	**0.0282**	0.0222	**0.0255**
	Mean	0.0248	0.0180	**0.0227**
	Median	**0.0211**	**0.0149**	**0.0225**
	S.D.	**0.0131**	0.0122	0.0101
ORB-SLAM3	RMSE	0.2126	0.8557	0.0554
	Mean	0.1649	0.7321	0.0414
	Median	0.1289	0.7278	0.0329
	S.D.	0.1342	0.4431	0.0368
DynaSLAM	RMSE	0.0292	**0.0207**	0.0271
	Mean	**0.0243**	0.0197	0.0252
	Median	0.0219	0.0166	0.0236
	S.D.	0.0162	0.0096	**0.0099**
Crowd-SLAM	RMSE	0.0308	**0.0181**	0.0303
	Mean	0.0256	**0.0153**	0.0268
	Median	0.0213	**0.0149**	0.0246
	S.D.	0.0149	**0.0079**	0.0128

5 Conclusions

We propose a visual SLAM system. Based on ORB-SLAM3, we add a method of target detection network combined with deep information, which makes the system robust in a highly dynamic environment. Compared with the existing SLAM system, our system has relatively high accuracy compared with the DynaSLAM system on TUM dataset. However, compared with DynaSLAM, our system has higher real-time performance. On BONN data set, crowd-SLAM achieves better results in Crowd environment, but our SLAM system achieves good accuracy in other sequences.

References

[1] A.J. Davison, I.D. Reid, N.D. Molton, O. Stasse,"MonoSLAM: Real-time single camera SLAM," *IEEE Transactions on Pattern Analysis and Machine Intelligence*,vol. 29, no. 6, pp. 1052–1067, 2007.

[2] G. Klein, D. Murray,"Parallel tracking and mapping for small AR workspaces," in *6th IEEE and ACM International Symposium on Mixed and Augmented Reality*,2007.

[3] R. Mur-Artal, J.M.M. Montiel, J.D. Tardós,"ORB-SLAM: a Versatile and Accurate Monocular SLAM System," *IEEE Transactions on Robotics*,vol. 31, no. 5, pp. 1147–1163, 2015.doi: 10.1109/TRO.2015.2463671

[4] R. Mur-Artal, J.D. Tardós,"ORB-SLAM2: an Open-Source SLAM System for Monocular, Stereo and RGB-D Cameras," *IEEE Transactions on Robotics*,vol. 33, no. 5, pp. 1255–1262, 2017.doi: 10.1109/TRO.2017.2705103

[5] C. Campos, R. Elvira, J.J. Gómez, J.M.M. Montiel, J.D. Tardós,"ORB-SLAM3: An Accurate Open-Source Library for Visual, Visual-Inertial and Multi-Map SLAM," *IEEE Transactions on Robotics*,vol. 37, no. 6, pp. 1874–1890, 2021.

[6] Z. Tian, C. Shen, H. Chen, T. He,"FCOS: Fully Convolutional One-Stage Object Detection," in *Proc. Int. Conf. Computer Vision (ICCV)*,2019.

[7] H. Chen, K. Sun, Z. Tian, C. Shen, Y. Huang, Y. Yan,"BlendMask: Top-Down Meets Bottom-Up for Instance Segmentation," in *Proc. IEEE Conf. Computer Vision and Pattern Recognition (CVPR)*,2020.

[8] R. Zhang, Z. Tian, C. Shen, M. You, Y. Yan,"Mask Encoding for Single Shot Instance Segmentation," in *Proc. IEEE Conf. Computer Vision and Pattern Recognition (CVPR)*,2020.

[9] Y. Liu, H. Chen, C. Shen, T. He, L. Jin, L. Wang,"ABCNet: Real-time Scene Text Spotting with Adaptive Bezier-Curve Network,"in *Proc. IEEE Conf. Computer Vision and Pattern Recognition (CVPR)*,2020.

[10] X. Wang, T. Kong, C. Shen, Y. Jiang, L. Li,"SOLO: Segmenting Objects by Locations,"*arXiv preprint arXiv:1912.04488*, 2019.

[11] X. Wang, R. Zhang, T. Kong, L. Li, C. Shen,"SOLOv2: Dynamic, Faster and Stronger,"*arXiv preprint arXiv:2003.10152*, 2020.

[12] Z. Tian, H. Chen, C. Shen,"DirectPose: Direct End-to-End Multi-Person Pose Estimation," *arXiv preprint arXiv:1911.07451*,2019.

[13] Z. Tian, C. Shen, H. Chen,"Conditional Convolutions for Instance Segmentation," *arXiv preprint arXiv:2003.05664*,2020.

[14] B. Bescos, JM. Fácil, J. Civera, J. Neira,"DynaSLAM: Tracking, Mapping and Inpainting in Dynamic Environments," *IEEE RA-L*,2018.

[15] B. Bescos, C. Campos, J.D. Tardos, J. Neira,"DynaSLAM II: Tightly-Coupled Multi-Object Tracking and SLAM," *IEEE Robotics and Automation Letters*,2021,doi: 10.1109/lra.2021.3068640

[16] J.C.V. Soares, M. Gattass, M.A. Meggiolaro, "Crowd-SLAM: Visual SLAM Towards Crowded Environments using Object Detection," *Journal of Intelligent & Robotic Systems*,vol. 102, no. 50,doi: https://doi.org/10.1007/s10846-021-01414-1,2021.

[17] J. Sturm, N. Engelhard, F. Endres, W. Burgard, D. Cremers, "A Benchmark for the Evaluation of RGB-D SLAM Systems,"in *Proc. of the International Conference on Intelligent Robot Systems (IROS)*,2012.

[18] E. Palazzolo, J. Behley, P. Lottes, P. Giguère, C. Stachniss, "ReFusion: 3D Reconstruction in Dynamic Environments for RGB-D Cameras Exploiting Residuals," in *Proc. of the International Conference on Intelligent Robot Systems (IROS)*,2019.

Proceedings of the 3rd Conference on Fully Actuated System Theory and Applications
May 10-12, 2024, Shenzhen, China

High-order Fully Actuated Approach for Output Position Control of Two Mass Systems based on Extended State Observer

Ping Li[1], Guang-ren Duan[1, 2], Bi Zhang[3], Yuzhong Wang[1]

1. Shenzhen Key Laboratory of Control Theory and Intelligent Systems, School of System Design and Intelligent Manufacturing, Southern University of Science and Technology, Shenzhen 518055, China
E-mail: lip3@susctech.edu.cn; duangr@sustech.edu.cn; wangyz3@susctech.edu.cn

2. Center for Control Theory and Guidance Technology, Harbin Institute of Technology, Harbin 150001, China
E-mail: g.r.duan@hit.edu.cn

3. Department of Mechanical and Energy Engineering, Southern University of Science and Technology, Shenzhen 518055, China
E-mail: zhangb@sustech.edu.cn

Abstract: This paper proposes a high-order fully actuated (HOFA) control approach for the output position control of two-mass systems (TMSs) based on extended state observer (ESO). TMSs belongs to a class of underactuated mechanical systems, which can be converted into an HOFA model using variable elimination. Based on the feature of HOFA model, it is extremely simple to solve the position control law such that a desired tracking error system can be achieved. To handle the control issues of high-order derivatives and unknown disturbances, a linear ESO is employed for state estimation and active disturbance rejection control, where the lumped disturbance is treated as an extended system state. The theoretical stability of control system is analyzed with the help of sliding manifold. Comparative simulations are performed to demonstrate the effectiveness of the proposed approach.

Key Words: Extended state observer (ESO), High-order fully actuated (HOFA) approach, Output position control, Two-mass system (TMS)

1 Introduction

With the rapid development of high-end automation equipment such as CNC machine tools, intelligent robots and aerospace vehicles, the performance requirement of motion control systems becomes higher and higher [1-3]. In industrial applications, servo motors have been widely applied for better dynamical properties due to their various advantages including fast response, low noise, low cost, high efficiency and torque to inertia ratio [4-6]. From the practical viewpoint, transmission parts, e.g., gear reducer, belt and ball screw are always applied in servo systems to facilitate the driving control, in which the motion axes should be connected by elastic couplings. These elastic elements in transmission system yield the so-called flexible servo (FS) system [7]. Two-mass system (TMS) is a popular model for the investigation of FS systems. In the presence of uncertainties and disturbances, high-gain control is one of the simplest and most effective ways to achieve the high control accuracy. However, applying high control gains is more likely to excite the mechanical resonance of TMS, which may deteriorate the achieved control performance, and even lead to instability. The high-performance controller design of TMSs is still a challenge task for control engineering practice.

*This work was supported in part by the National Natural Science Foundation of China (62203206, 61333003, 62163012); in part by the Major Program of the National Natural Science Foundation of China (61690210, 61690212); in part by the Shenzhen Key Laboratory of Control Theory and Intelligent Systems under Grant ZDSYS20220330161800001; in partly by Shenzhen Science and Technology Innovation Commission (JSGG20220831110605009); and in part by the Science Center Program of the National Natural Science Foundation of China under Grant 62188101.

There is no doubt that the cascaded P/PI controller plays a dominant place in industrial servo systems, which is composed of current, velocity and position control loops [8]. The cascaded control possesses many advantages such as simple structure, intuitive parameter tuning and acceptable control performance, but it is difficult to directly handle the mechanical resonance in the FS systems. Notch filter is the most applied technique to suppress the system vibrations at the resonant frequency in practice, which is a passive approach without an additional sensor. However, it is very difficult to obtain exact resonance frequency in actual systems due to the parameter uncertainties with environment change. The deviation between the notch frequency and the actual resonant frequency may induce serious system oscillations or even result in unstable system [9].

Different from the classical frequency-domain control design method, modern control theory based on state-space equation is a time-domain technique, which focuses on the system state analysis and response. State-space approach has stayed in an absolutely dominant place in the field of systems and control [10]. Based on the state-space framework, a variety of advanced methods have been investigated for the control design of TMSs, such as model predictive control (MPC) [11], sliding model control (SMC) [12], active disturbance rejection control (ADRC) [13], robust adaptive control [14]. Besides, artificial intelligent technologies like fuzzy logic and neural network have also been applied for the high-performance control of TMSs [15], [16]. It is worth noting that TMS is a classical underactuated mechanical systems, in which the number of control inputs is less than the motion degrees of freedom (DOFs). State-space approach transforms the original system into an augmented first-order system, which is quite

suitable for the solution of state observation and response, but does not provide much convenience for the controller design.

To overcome the drawbacks of first-order state-space method, a novel high-order fully actuated (HOFA) approach is proposed by Duan and has rapidly attracted widespread attention in researches [17-21]. The full-actuation feature of HOFA models ensures a more direct control strategy for a desired closed-loop response, rendering them particularly favorable in fields like mechanical engineering, aerospace, and electrical systems. As a practical numerical example, HOFA approach has been used to synthesize the control law of a compliant robot system in which the mechanical subsystem is formulated as a TMS model [18]. Furthermore, comparative experiments on an FS system driven by servo motor have been carried out to the effectiveness and superiority of HOFA approach [7], [22]. HOFA approach possesses many advantages such as simplicity, straightforward and effectiveness, but suffers from some practical issues since the direct derivatives of signals cannot be realized in physics. It seems that the high-order derivatives of signals can be obtained by using the entire system information based on the model transformation. However, the full-state feedback requires the additional sensor at the end effector, which may encounter the cost increase and assembly problems.

Motivated by the aforementioned difficulties, this article presents an HOFA approach for the output position control of TMSs based on extended state observer (ESO). Firstly, the dynamics of TMS is transformed into an HOFA model via variable elimination method. Then, the control law for trajectory tracking can be synthesized in a quite simple way for a desired tracking error system, in which the control gains are explicitly solve by using a bandwidth parametric method. To overcome the control issues of "differential explosion" and unknown disturbances, a linear ESO is constructed for online state estimation and disturbance compensation to improve the tracking control accuracy in the presence of uncertainties and disturbances. Furthermore, the theoretical stability is analyzed to ensure the practical exponential stability of the control system. Finally, comparative simulations have been carried out to verify the effectiveness of the proposed control approach.

2 Problem Formulation

Fig. 1 shows the schematic diagram of TMS. As presented in [22], the dynamical differential equation of TMS can be described as

$$J_L\ddot{\theta}_L + B_L\dot{\theta}_L + T_L = K_s(\theta_m - \theta_L), \tag{1}$$

$$J_m\ddot{\theta}_m + B_m\dot{\theta}_m + K_s(\theta_m - \theta_L) = T_m, \tag{2}$$

where θ_m and θ_L denote the angular position of motor and load, respectively, J_m and J_L are the moment of inertia of motor side and load side, respectively, B_m and B_L represent the viscous coefficient of motor side and load side, respectively, K_s is the transmission stiffness, T_m is the output torque of motor, T_L denotes the disturbance.

The control goal of this paper is to design a control law such that the system output θ_L can accurately track a given

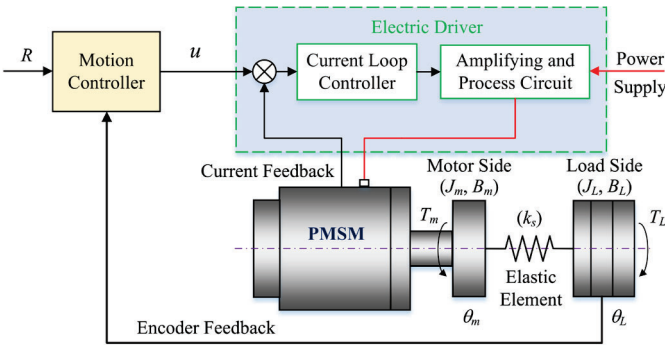

Fig. 1. The schematic diagram of TMS.

smooth reference trajectory θ_d. For the consideration of practical use, the proposed control scheme is expected to have simple structure and reliable control performance, with intuitive parameter tuning and easy implementation.

It should be noted that there inevitably exist various uncertainties and disturbances in actual systems. To facilitate the control system design and analysis, it is assumed that the plant parameters are bounded constants and the system disturbances is differential-bounded. Only the system output θ_L is the measured. The desired trajectory θ_d is smooth enough and its n-order derivatives are known in prior. In addition, the dynamics of internal current control loop can be ignored due to its much faster response than the mechanical subsystem [8], leading to that

$$u \approx T_m. \tag{3}$$

3 Controller Design

3.1 HOFA control approach

According to the variable elimination method in [22], it can be obtained from (1) that the variable θ_m and its first-order and second-order derivatives can be respectively expressed as

$$\theta_m = \left(J_L\ddot{\theta}_L + B_L\dot{\theta}_L + K_s\theta_L + T_L\right)/K_s, \tag{4}$$

$$\dot{\theta}_m = \left(J_L\dddot{\theta}_L + B_L\ddot{\theta}_L + K_s\dot{\theta}_L + \dot{T}_L\right)/K_s, \tag{5}$$

and

$$\ddot{\theta}_m = \left(J_L\theta_L^{(4)} + B_L\dddot{\theta}_L + K_s\ddot{\theta}_L + \ddot{T}_L\right)/K_s. \tag{6}$$

Applying the expressions (4)-(6) to eliminate the variables θ_m, $\dot{\theta}_m$ and $\ddot{\theta}_m$ in (2), yields the HOFA model of TMS as

$$\theta_L^{(4)} + a_3\dddot{\theta}_L + a_2\ddot{\theta}_L + a_1\dot{\theta}_L = b_0u - d_1 \tag{7}$$

where a_1, a_2, a_3, b_0 and d_1 are respectively given by

$$\begin{cases} a_1 = K_s(B_m + B_L)/(J_mJ_L), \\ a_2 = (K_sJ_m + K_sJ_L + B_mB_L)/(J_mJ_L), \\ a_3 = (J_mB_L + B_mJ_L)/(J_mJ_L), \\ b_0 = K_s/(J_mJ_L), \\ d_1 = \left(J_m\ddot{T}_L + B_m\dot{T}_L + K_sT_L\right)/(J_mJ_L). \end{cases} \tag{8}$$

With the fully actuated control property of HOFA model, the control law for the trajectory tracking of TMS in (1) and (2) can be designed as follows:

$$u = \frac{1}{b_0}\left(\sum_{i=1}^{3} a_i \theta_L^{(i)} - \sum_{j=0}^{3} k_j e_1^{(j)} + \theta_d^{(4)}\right), \tag{9}$$

where $e_1 \triangleq \theta_L - \theta_d$ is the tracking error, k_j $(j = 0, 1, 2, 3)$ are the positive control gains.

Substituting (9) into (7), yields the following tracking error system:

$$e_1^{(4)} + \sum_{j=0}^{3} k_j e_1^{(j)} = -d_1. \tag{10}$$

In this paper, the bandwidth parameterization method is used to design the control gains. We can prescribe the characteristic polynomial of (10) as

$$\lambda(s) = (s + \omega_c)^4, \tag{11}$$

where ω_c is the bandwidth parameter of the closed-loop system.

According to the relationship between (10) and (11), the control gains can be directly obtained as

$$k_i = \frac{4!}{i!\,(4-i)!}\,\omega_c^{4-i}, i = 0,1,2,3. \tag{12}$$

Remark 1: The controller (9) is a composite control scheme for trajectory tracking, which is constituted by two parts: one is the compensation control to remove the original dynamics, and the other is the control effort to yield the desired tracking error dynamics. Owing to the control property of the HOFA model (7), an explicit solution can be obtained in a quite simple way for the controller design of TMSs, in which the control gains are directly obtained via the bandwidth parametric method with only one parameter (ω_c) required to be tuned. That provides a great convenience for control engineering practice.

It is well-known that the ideal derivatives of signals are physically unrealizable and the numerical differentiation easily results in the "differential explosion" problem. Therefore, the high-order derivatives of system output θ_L cannot be directly obtained. The differential signals seem to be obtained via the model transformation. However, actual systems are inevitably subject to parameter uncertainties and unknown disturbances, which may have a significant impact on the state estimation, as well as the tracking accuracy.

3.2 HOFA control approach

Let $\boldsymbol{x} \triangleq [x_1\ x_2\ x_3\ x_4]^{\mathrm{T}} = \left[\theta_L\ \dot{\theta}_L\ \ddot{\theta}_L\ \dddot{\theta}_L\right]^{\mathrm{T}}$ be the state vector. The HOFA model (7) of TMS can be transformed into a state-space equation given by

$$\begin{cases} \dot{x}_1 = x_2, \\ \dot{x}_2 = x_3, \\ \dot{x}_3 = x_4, \\ \dot{x}_4 = \hat{b}_0 u + \Delta_1, \end{cases} \tag{13}$$

where $\hat{b}_0$ is the estimation value of b, $\tilde{b} \triangleq b - \hat{b}_0$ denotes the estimation error, $\Delta_1 \triangleq \tilde{b}u - (a_3 x_4 + a_2 x_3 + a_1 x_2) - d_1$ is the lumped disturbance.

Let $x_5 \triangleq \Delta_1$ be the extended system state, and define $h(t) = \dot{\Delta}_1$. Then, the system (13) can be written in an augmented state-space form as

$$\begin{cases} \dot{x}_1 = x_2, \\ \dot{x}_2 = x_3, \\ \dot{x}_3 = x_4, \\ \dot{x}_4 = \hat{b}_0 u + x_5, \\ \dot{x}_5 = h(t), \end{cases} \tag{14}$$

and the linear ESO can be constructed as

$$\begin{cases} \dot{\hat{x}}_1 = \hat{x}_2 + l_1(x_1 - \hat{x}_1), \\ \dot{\hat{x}}_2 = \hat{x}_3 + l_2(x_1 - \hat{x}_1), \\ \dot{\hat{x}}_3 = \hat{x}_4 + l_3(x_1 - \hat{x}_1), \\ \dot{\hat{x}}_4 = \hat{b}_0 u + \hat{x}_5 + l_4(x_1 - \hat{x}_1), \\ \dot{\hat{x}}_5 = l_5(x_1 - \hat{x}_1), \end{cases} \tag{15}$$

where $\hat{x}_i$ denote the observed values of x_i, l_i are the positive observer gains, $i = 1, 2, 3, 4, 5$.

Let $\tilde{x}_i \triangleq x_i - \hat{x}_i$ $(i = 1, 2, 3, 4, 5)$ be the state estimation errors. Subtracting (15) from (14) yields the state estimation error dynamics as

$$\begin{cases} \dot{\tilde{x}}_1 = \tilde{x}_2 - l_1\tilde{x}_1, \\ \dot{\tilde{x}}_2 = \tilde{x}_3 - l_2\tilde{x}_1, \\ \dot{\tilde{x}}_3 = \tilde{x}_4 - l_3\tilde{x}_1, \\ \dot{\tilde{x}}_4 = \tilde{x}_5 - l_4\tilde{x}_1, \\ \dot{\tilde{x}}_5 = h(t) - l_5\tilde{x}_1. \end{cases} \tag{16}$$

Applying the variable elimination method, the system (16) can be transformed into

$$\tilde{x}_1^{(5)} + \sum_{j=0}^{4} l_{5-j}\tilde{x}_1^{(j)} = h(t). \tag{17}$$

Similar to the closed-loop controller design, the bandwidth method is employed to design the observer gains. We can specify the characteristic polynomial of (17) as

$$\lambda(s) = (s + \omega_o)^5, \tag{18}$$

where ω_o represents the observer bandwidth parameter.

Combining (17) and (18), the observer gains can be explicitly solved as

$$l_i = \frac{5!}{i!\,(5-i)!}\,\omega_o^i, i = 1, 2, 3, 4, 5. \tag{19}$$

Lemma 1 [23]: Given that $h(t)$ is bounded, there exist some constants $\sigma_i > 0$ and a finite time $T_1 > 0$ such that

$$|\tilde{x}_i| \le \sigma_i, \sigma_i = \mathcal{O}\left(\frac{1}{\omega_o^c}\right), i = 1, 2, 3, 4, 5 \quad \forall t \ge T_1, \tag{20}$$

where $\mathcal{O}(\cdot)$ denotes an infinitesimal amount, c is a positive integer.

Remark 2: The result in *Lemma 1* shows that the estimation errors of system states are finally bounded by the observer bandwidth ω_o. For the bounded $h(t)$, the estimation errors are guaranteed to satisfy that $\tilde{x}_i \to 0$ $(i = 1, 2, 3, 4, 5)$ as $\omega_o \to 0$ and $t \to \infty$. Applying the estimated states for the controller design can effectively relieve the "differential explosion" problem in the HOFA approach. Besides,

the estimated value of the extended system state x_5 can serve as an adaptive law to bridge the gap between the nominal model and actual systems, which actively rejects the lumped disturbances such that an improve tracking control accuracy can be achieved.

3.3 HOFA control based on linear ESO

According to the variable elimination method in [22], it can be obtained from (1) that the variable θ_m and its first-order and second-order derivatives can be respectively expressed as

With the estimated values of system states and the lumped disturbance, the control law for trajectory tracking can be re-designed as

$$u = \frac{1}{\hat{b}_0}\left(-k_0 e_1 - \sum_{j=1}^{3} k_j \hat{e}_1^{(j)} + \hat{x}_5 + \theta_d^{(4)}\right), \tag{21}$$

where $\hat{e}_1^{(j)} \triangleq \hat{x}_i - \theta_d^{(j)}, i = 1,2,3.$

To facilitate the control system analysis, we can design the following sliding manifold.

$$p = \dddot{e}_1 + 3\omega_c \ddot{e}_1 + 3\omega_c^2 \dot{e}_1 + \omega_c^3 e_1 \tag{22}$$

Based on the Laplace transformation, the expression (22) can be rewritten as

$$e_1(s) = \frac{1}{(s+\omega_c)^3} p(s). \tag{23}$$

It is clear from (23) that e_1 is the low-pass filtered value of p satisfying $|e_1| \le \frac{1}{\omega_c^3}|p|$ overall the frequency ranges.

Theorem 1: Assume that $h(t)$ is bounded, the control law u (21) based on the linear ESO (15), with the control gains given by (12) and the observer gains given by (19), guarantees that the TMS in (1) and (2) has practical exponential stability. Furthermore, after the finite time T_1, there exists a constant $\delta \triangleq \sum_{i=1}^{3} k_i \sigma_{i+1} + \sigma_5$ such that

$$p(t) < e^{-\omega_c \Delta t} p(T_1) + \frac{\delta}{\omega_c}(1 - e^{-\omega_c \Delta t}), \tag{24}$$

where $\Delta t \triangleq t - T_1$.

Proof: Substituting (21) into (14) yields the tracking error system as

$$e_1^{(4)} + \sum_{i=0}^{3} k_i e_1^{(i)} = \sum_{j=1}^{3} k_j \tilde{x}_{i+1} + \tilde{x}_5. \tag{25}$$

Taking the derivative of p yields

$$\dot{p} = e_1^{(4)} + 3\omega_c \dddot{e}_1 + 3\omega_c^2 \ddot{e}_1 + \omega_c^3 \dot{e}_1, \tag{26}$$

Substituting (25) into (26) and applying the control gains in (12), yields

$$\dot{p} = -\omega_c p + \sum_{j=1}^{3} k_j \tilde{x}_{i+1} + \tilde{x}_5. \tag{27}$$

Applying the result in *Lemma 1*, after the finite time T_1, one has

$$\dot{p} \le -\omega_c p + \sum_{j=1}^{3} k_j \sigma_{j+1} + \sigma_5. \tag{28}$$

Integrating (28) over $[T_1\ t]$, yields

$$p(t) < e^{-\omega_c \Delta t} p(T_1) + \left(\sum_{i=1}^{3} k_i \sigma_{i+1} + \sigma_5\right) \int_{T_1}^{t} e^{-\omega_c (t-\tau)}\, d\tau, \tag{29}$$

which implies the inequality (24) is satisfied. According to the definition in [13], it is easy to ensure that the control system has practical exponential stability. The proof is completed.

Remark 3: The result in *Theorem 1* suggests that under the proposed controller (21), the sliding manifold p exponentially converges to a region around the origin at the convergence rate of ω_c, and its upper bound is determined by the controller bandwidth ω_c and the observer bandwidth ω_o simultaneously. It can be known from (20), (23) and (24) that applying larger ω_c and ω_o can significantly reduce the tracking error. Unfortunately, too large ω_c and ω_o will induce the ignored current-loop dynamics and discretization errors, which may deteriorate the achieved control performance and even damage the system stability. In practice, the parameters ω_c and ω_o should be carefully tuned with a trade-off between the tracking accuracy and the robust stability property.

4 Simulation Validation

In the section, the comparative simulations have been conducted to demonstrate the effectiveness of the proposed approach. The simulation program of control system is implemented via MATLAB/Simulink software on a computer with Intel i7-13700K CPU and 32 GB of RAM. The parameter values of TMS presented in (1) and (2) are shown in Table 1. Based on the normal parameters, it can be easily obtained that $a_1 = 2.0 \times 10^6$, $a_2 = 2.67 \times 10^5$, $a_3 = 20$ and $b_0 = 1.67 \times 10^9$.

Table 1 Parameter values of TMS

Parameters	Values
J_m	0.4×10^{-4} kg·m^2
B_m	6.0×10^{-4} Nm/(rad/s)
J_L	1.2×10^{-4} kg·m^2
B_L	6.0×10^{-4} Nm/(rad/s)
K_s	8 Nm/rad

We design the following two controller for comparison.

1) **C1:** This is the tracking control law (9) via the HOFA approach. In this control scheme, the derivatives of output position are estimated via a numerical method, in which a low-pass filter with a time constant 0.001 is applied for each derivative to attenuate the high-frequency noise and discretization errors. The closed-loop bandwidth parameter is set as $\omega_c = 160$ by trial-and-error tuning. It is clear from (12) that the control gains are set as $k_1 = 6.55 \times 10^8$, $k_2 = 1.64 \times 10^7$, $k_3 = 1.54 \times 10^5$ and $k_4 = 640$.

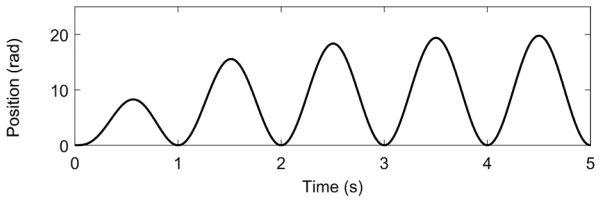

Fig. 2. Desired trajectory.

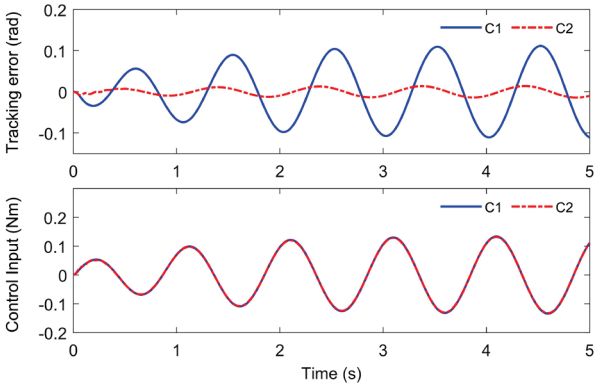

Fig. 3. Trajectory tracking under uncertain J_L.

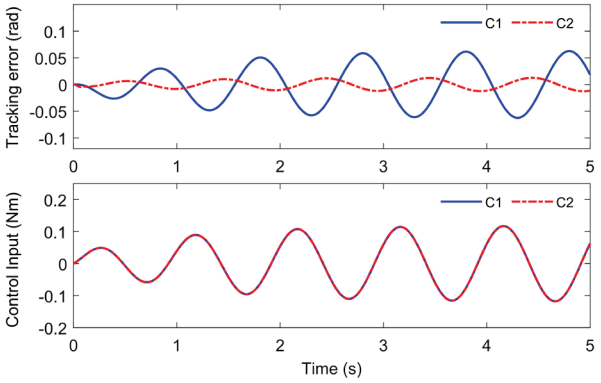

Fig. 4. Trajectory tracking under uncertain B_L.

2) **C2:** This is the proposed tracking control law (21) based on HOFA approach, where the system states and the lumped disturbance are estimated via the linear ESO (15). For fairness, the closed-loop bandwidth in this control scheme is chosen as the same to C1, i.e., $\omega_c = 160$. The observer bandwidth parameter is selected as $\omega_o = 1500$. By using the bandwidth parameterization method, it is easy to obtain the observer gains from (19).

4.1 Trajectory tracking with uncertainties

Shown in Fig. 2, a smooth trajectory designed as $\theta_d = 10(1-e^{-t})(1-\cos(2\pi t))$ rad is applied in this trajectory tracking control test. Two types of parameter uncertainties are tested: one is the uncertain J_L in which the load inertia is changed from $1.2\times10^{-4}\,\mathrm{kg\cdot m^2}$ to $2.4\times10^{-4}\,\mathrm{kg\cdot m^2}$, and the other is the uncertain B_L by injecting a damping force of $4.0\times10^{-4}\,\mathrm{Nm/(rad/s)}$ into the system.

Figs. 3 and 4 presents the tracking errors and control inputs of C1 and C2 under the uncertain J_L and B_L, respectively. It's can be seen that C2 has achieved a much better tracking accuracy than C1 under the two parameter uncertainties. The comparative trajectory tracking control test demonstrates the superiority of the proposed HOFA approach based on ESO.

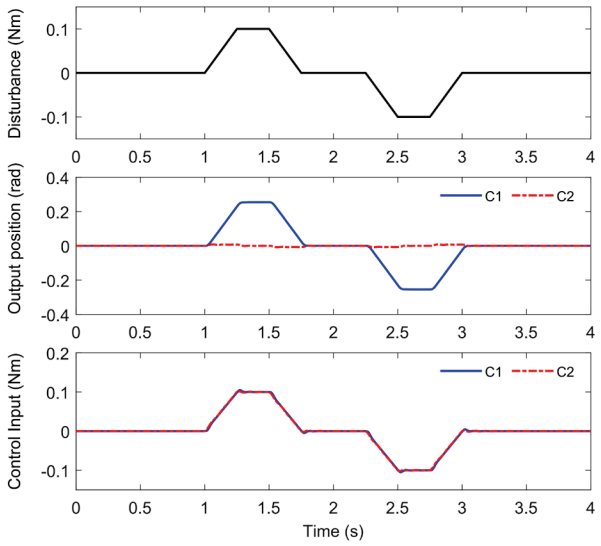

Fig. 5. Output regulation under trapezoidal disturbance.

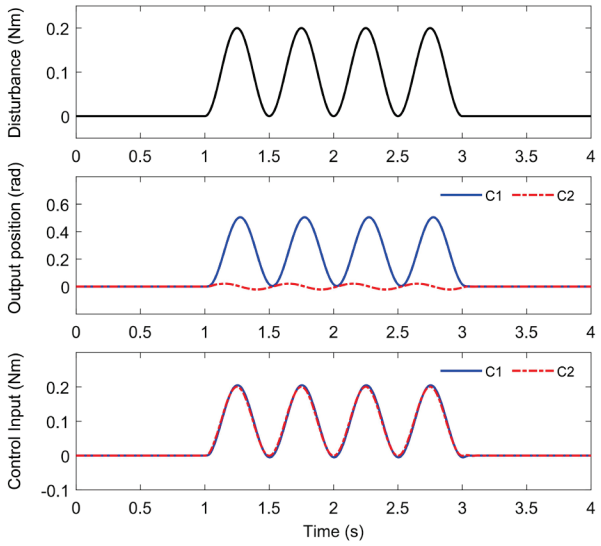

Fig. 6. Output regulation under sinusoidal disturbance.

4.2 Output regulation under disturbances

In the subsection, the output regulation test of C1 and C2 is carried out under two time-varying disturbances: one is the trapezoidal disturbance with a slope of $0.4\,\mathrm{Nm/s}$; the other is the sinusoidal disturbance given by $T_L = 0.1\sin(2\pi t)$ Nm.

The simulation results under the two added disturbances are shown in Figs. 5~6, respectively. It can be known that C2 has a much better control accuracy than C1 in the presence of both trapezoidal and sinusoidal disturbances, which demonstrates that C2 obtains a much better disturbance rejection performance. The reason can be attributed to that the linear ESO can accurately estimate the time-varying disturbances. When the estimated valued is employed for compensation control, the impact of disturbances can be significantly attenuated. As a result, C2 obviously improves the control accuracy under time-varying disturbances.

5 Conclusion

This paper proposes an HOFA approach for the output tracking control of TMSs based on ESO. The dynamics of TMS is a class of under-actuation mechanical systems, which can be transformed into an HOFA model via variable elimination method. Based on the full-actuation feature of HOFA model, the tracking control law can be synthesized in a very simple way to achieve a desired tracking error system, where the control gains are explicitly solved via the bandwidth parameterization method. To handle the signal differential problem, a linear ESO is constructed online state estimation and real-time disturbance compensation. The stability analysis has ensured the practical exponential stability of the control system. Comparative simulation results have demonstrated that the proposed HOFA approach based on ESO can achieve a much higher tracking accuracy than the standard one in the presence of parameter uncertainties and unknown disturbances.

References

[1] R. F. A. Khan, K. Rsetam, Z. Cao, and Z. Man, "Singular perturbation-based adaptive integral sliding mode control for fexible joint robots," *IEEE Trans. Ind. Electron.,* vol. 70, no. 10, pp. 10516-10525, Oct 2023.

[2] P. Li, L. Wang, G. Zhu, and M. Zhang, "Predictive active disturbance rejection control for servo systems with communication delays via sliding mode approach," *IEEE Trans. Ind. Electron.,* vol. 68, no. 12, pp. 12679-12688, Dec 2021.

[3] P. Li, G. Zhu, and M. Zhang, "Linear active disturbance rejection control for servo motor systems with input delay via internal model control rules," *IEEE Trans. Ind. Electron.,* vol. 68, no. 2, pp. 1077-1086, Feb. 2021.

[4] P. Li and G. Zhu, "IMC-based PID control of servo motors with extended state observer," *Mechatronics,* vol. 62, Oct. 2019, (Art. no. 102252).

[5] P. Li and G. Zhu, "Robust internal model control of servo motor based on sliding mode control approach," *ISA Trans.,* vol. 93, pp. 199-208, Oct. 2019.

[6] P. Li, K. Guo, and M. Zhang, "Linear active disturbance rejection control of servo systems via IMC principle with active damping and sliding mode techniques," *ISA Trans.,* vol. 129, pp. 663-672, Oct. 2022.

[7] P. Li and G. Duan, "High-order fully actuated control approaches of flexible servo systems based on singular perturbation theory," *IEEE-ASME Trans. Mechatron.,* vol. 26, no. 8, pp. 3386-3397, Dec. 2023.

[8] M. Yuan, C. Manzie, M. Good *et al.*, "A review of industrial tracking control algorithms," *Control Eng. Practice,* vol. 102, Sep. 2020, (Art. no. 104536).

[9] W. Bahn, T. Kim, S. Lee, and D. Cho, "Resonant frequency estimation for adaptive notch filters in industrial servo systems," *Mechatronics,* vol. 41, pp. 45-57, Feb. 2017.

[10] R. C. Dorf and R. H. Bishop, *Modern control systems*, 12th ed. Upper Saddle River, NJ, USA: Pearson, 2011.

[11] M. Cychowski and K. Szabat, "Efficient real-time model predictive control of the drive system with elastic transmission," *IET Contr. Theory Appl.,* vol. 4, no. 1, pp. 37-49, Jan 2010.

[12] C. Wang, F. Liu, J. Xu, and J. Pan, "An SMC-based accurate and robust load speed control method for elastic servo system," *IEEE Trans. Ind. Electron.,* vol. 71, no. 3, pp. 2300-2308, Mar 2024.

[13] P. Li, L. Wang, B. Zhong, and M. Zhang, "Linear active disturbance rejection control for two-mass systems via singular perturbation approach," *IEEE Trans. Ind. Inform.,* vol. 18, no. 5, pp. 3022-3032, May 2022.

[14] H. MoradiMaryamnegari and A. Khoshnood, "Robust adaptive vibration control of an underactuated flexible spacecraft," *J. Vib. Control,* vol. 25, no. 4, pp. 834-850, Feb. 2019.

[15] S. Ling, H. Wang, and P. Liu, "Adaptive fuzzy tracking control of flexible-joint robots based on command filtering," *IEEE Trans. Ind. Electron.,* vol. 67, no. 5, pp. 4046-4055, May. 2020.

[16] T. Orlowska-Kowalska and M. Kaminski, "FPGA implementation of the multilayer neural network for the speed estimation of the two-mass drive system," *IEEE Trans. Ind. Inform.,* vol. 7, no. 3, pp. 436-445, Aug. 2011.

[17] G. Duan, "High-order fully actuated system approaches: Part I. Models and basic procedure," *Int. J. Syst. Sci.,* vol. 52, no. 2, pp. 422-435, Jan. 2021.

[18] G. Duan, "High-order fully-actuated system approaches: Part II. Generalized strict-feedback systems," *Int. J. Syst. Sci.,* vol. 52, no. 3, pp. 437-454, Feb. 2021.

[19] G. Duan, "High-order fully actuated system approaches: Part III. Robust control and high-order backstepping," *Int. J. Syst. Sci.,* vol. 52, no. 5, pp. 952-971, Apr. 2021.

[20] G. Duan, "High-order fully actuated system approaches: part VII. Controllability, stabilisability and parametric designs," *Int. J. Syst. Sci.,* vol. 52, no. 14, pp. 3091-3114, Oct. 2021.

[21] Y. Wang, G. Duan, and P. Li, "Event-Triggered Adaptive Sliding Mode Control of Uncertain Nonlinear Systems Based On Fully Actuated System Approach," *IEEE Trans. Circuits Syst. II-Express Briefs,* pp. 1-5, 2024.

[22] P. Li and G. Duan, "High-order fully actuated control approach for flexible servo systems using dynamical compensator," in *Proc. 2nd Conf. Fully Actuated Syst. Theory App.*, Qingdao, China, 2023, pp. 862-867.

[23] F. Goforth, Q. Zheng, and Z. Gao, "A novel practical control approach for rate independent hysteretic systems," *ISA Trans.,* vol. 51, no. 3, pp. 477-484, May. 2012.

Proceedings of the 3rd Conference on Fully Actuated System Theory and Applications
May 10-12, 2024, Shenzhen, China

Tracking control of motion control systems with disturbance observer based on high-order fully actuated system approach

Rongmei Li[1], Xin Huo[1], Aijing Wu[1], Weizhen Liu[2]

1. Control and Simulation Center, Harbin Institute of Technology, Harbin 150080, P. R. China
E-mail: huoxin@hit.edu.cn

2. Shenzhen Key Laboratory of Control Theory and Intelligent Systems, Southern University of Science and Technology, Shenzhen 518055, China

Abstract: This paper investigates the tracking problem of motion control systems driven by permanent magnet synchronous motors (PMSMs) in the presence of unknown disturbances. In contrast to using the model of state space methods, this study adopts a different method by initially transforming the model of a motion control system driven by PMSM into a high-order fully actuated (HOFA) system. Subsequently, a controller is designed based on the HOFA system approach, and a closed-loop linear system with disturbances is obtained. To handle the impact of disturbances, a disturbance observer is employed to estimate the disturbance. The validity of the proposed algorithm is assessed through theoretical analysis, and a numerical simulation is also conducted to further support the findings, thereby underscoring the effectiveness of the proposed approach.

Key Words: Disturbance observer, High-order fully actuated system approach, Motion control systems, Tracking control

1 Introduction

In recent years, with the development of power electronic devices, alternating current (AC) drive systems have gradually gained attention due to their performance being comparable to direct current (DC) drive systems. As a driving force in AC drive systems, permanent magnet synchronous motors (PMSMs) have been widely applied in industrial drive systems [1], and electric vehicles [2] due to their high efficiency, high power density, and excellent dynamic response characteristics. However, due to factors such as the motor's inherent structure, the ripple torque is inevitably present. The ripple torque significantly affects the speed stability and position tracking accuracy of PMSM. Therefore, rejecting disturbances is essential to achieve high-precision control of the motor.

For time-periodic disturbances, learning control methods such as repetitive control [3, 4] and iterative learning [5, 6] have been used for disturbance parameter identification and rejection. The steady-state speed ripple periodic disturbance problem of servo system was investigated in [3]. Different from the fuzzy theory for mitigating periodic disturbances in [3], a novel method called the input matching least mean square (LMS) adaptive filter (IMLMS-AF) was introduced to address the challenges posed by spatially cyclic disturbances in [4]. The study conducted by Steinberg et al. in [5] was focused on investigating the effectiveness of iterative learning active flow control in mitigating the effects caused by periodic disturbances. In a related study, Wu and his collaborators [6] proposed a novel circularly orthogonal projection-based iterative learning control method to address spatially cyclic disturbances. Their method aims to tackle the challenges posed by such disturbances and enhance the control performance in the presence of spatial variations.

This work was partially supported by the National Natural Science Foundation of China under Grant 62373128, the Science Center Program of National Natural Science Foundation of China under Grant 62188101, the Natural Science Foundation of Heilongjiang Province of China under Grant LH2021F025, the Basic Research Plan of Shenzhen of China under Grant JCYJ20200109113429208, and the Heilongjiang Touyan Team Program.

Although the learning control methods obtain accurate information about the interference amplitude and location, it is not straightforward. For time-periodic disturbance, the control signal opposite to the disturbance is generally introduced into the traditional method of disturbance rejection and superimposed to counteract the effects of disturbance. For example, a novel composite controller was presented to improve the disturbance rejection property of the PMSM in the speed regulation problem in [7], and the estimated value of the designed extended state observer (ESO) was used in the feed-forward compensation. Furthermore, a composite terminal sliding mode control method based on disturbance observer was proposed in [8] to investigate the speed regulation problem of PMSM. A smaller value for the switching gain without sacrificing disturbance rejection performance was obtained by disturbance estimation for feed-forward compensation. For a high-order descriptor linear system, a controller composed of a decoupling controller and a disturbance observer was proposed in [9].

It is noteworthy that the majority of advanced control techniques developed for servo system rely on the utilization of first-order state-space models. The state-space approach primarily focuses on the state vector, making it highly suitable for response analysis. However, it does not offer significant convenience in deriving control laws [10–13]. Moreover, motion control systems are typically represented through physical laws such as Newton's law or Lagrange's equation. The inclusion of background information on system dynamics facilitates clear and straightforward control design and analysis. Nevertheless, when adopting the first-order system approach, all the relevant background information is omitted from the original model. In contrast to the conventional approach of employing first-order state space equations, Duan has put forth a pioneering method called the HOFA system approach. This novel approach offers a promising solution for addressing a wide range of control problems, such as fault-tolerant control [14, 15], predictive control [16, 17], event-triggered control [18] and so on. In addition to theoretical advancements, the practical application of the HOFA

system approach has also witnessed significant progress in the field of engineering. A HOFA control approach was proposed for flexible servo systems and the singular perturbation method was investigated to deal with the high-order derivative problem of signals in [19].

Motivated by the aforementioned researches, this article focuses on investigating the HOFA system approach to tackle the tracking control issue encountered in PMSM in the presence of unknown disturbances. The basic theory of HOFA system approach is introduced in Section 2. Then, the main results are detailed in Section 3. After designing the HOFA controller and the disturbance observer, the stability of the system is analysed. The numerical simulation is provided under the influence of disturbances in Section 4. Finally, Section 5 summarizes the whole paper.

2 Preliminaries of HOFA system approach

Consider a linear system based on the state-space form

$$\dot{x} = Ax + Bu. \tag{1}$$

where $x \in \mathbb{R}^n$ is the state vector, $u \in \mathbb{R}^r$ is the control input, $A \in \mathbb{R}^{n\times n}$ and $B \in \mathbb{R}^{n\times r}$ are the coefficient matrix. According to Theorem 2 in [11], the system (1) can be converted into the following linear HOFA system,

$$A_\mu z^\mu + A_{\mu-1} z^{\mu-1} + \ldots + A_1 \dot{z} + A_0 z = \tilde{B}u. \tag{2}$$

where z is a vector of r dimension, $A_i \in \mathbb{R}^{r\times r}, i = 0, 1, \ldots, \mu$ are the coefficient matrices. Besides

$$\tilde{B} = \begin{bmatrix} 1 & b_{12} & b_{13} & \cdots & b_{1r} \\ 0 & 1 & b_{23} & \cdots & b_{2r} \\ 0 & 0 & 1 & \cdots & b_{3r} \\ \vdots & \vdots & \vdots & \ddots & \vdots \\ 0 & 0 & 0 & \cdots & 1 \end{bmatrix}.$$

Once (2) is obtained and $\det\tilde{B} \neq 0$, a controller $u = -\tilde{B}^{-1}\left[\sum_{i=0}^{\mu-1} L_i z^{(i)} - v\right]$ can be directly given to get a closed-loop system as follows

$$\sum_{i=0}^{\mu} (L_i + A_i) z^{(i)} = v, \tag{3}$$

where $L_i, i = 0, 1, \ldots, \mu$ is the matrix that needs to be designed, v is external signal. The flexibility of the series of matrices L_i allows for the attainment of closed-loop systems exhibiting desired performance characteristics by selecting appropriate matrices. It becomes evident that employing full-actuation in the control of a HOFA system offers significant advantages and convenience.

3 Main Results

3.1 HOFA controller design

This paper aims at addressing the tracking problem of motion control system driven by a PMSM. The vector control structure of system model is illustrated in Fig. 1. I_q is the cross axis currents in the coordinate $d-q$ axis, ω is the controlled angular velocity, L is the motor inductance, J is the moment of inertia, D is the frictional coefficient, P_m is the

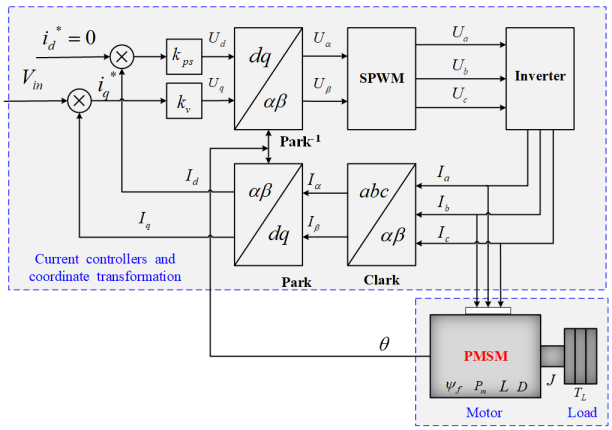

Fig. 1: Vector control system of PMSM.

number of motor poles, R is the equivalent resistance, k_{ps} is the driver amplification factor, k_v is the current amplification factor, and $u_q = k_{ps}k_v V_{in} - k_{ps}I_q$, V_{in} is represented as u as the control input in Fig. 1.

Taking $\dot{\theta} = \omega$, θ is the angular position. Then, the following HOFA system can be obtained.

$$\dddot{\theta} + a_2\ddot{\theta} + a_1\dot{\theta} = ku + a_3, \tag{4}$$

with

$$\begin{cases} a_1 = \frac{R+k_{ps}}{JL}D + \frac{3}{2JL}{P_m}^2{\psi_f}^2 \\ a_2 = \frac{D}{J} + \frac{R+k_{ps}}{L} \\ a_3 = -\frac{\dot{T}_L}{J} - \frac{R+k_{ps}}{L}\frac{T_L}{J} \\ k = \frac{3}{\sqrt{2}JL}P_m\psi_f k_{ps}k_v \end{cases}$$

By employing the output regulation theory, the state output controller u_f can be designed as follows.

$$u_f = -\frac{1}{k}\left(\sum_{i=0}^{3} l_i\theta^{(i)} + a_3\right), \tag{5}$$

where l_2, l_1, and l_0 are the designed parameters.

Let $u = u_f$ and substituting (5) into (4), it can be concluded that

$$\dddot{\theta} + \sum_{i=1}^{2}(a_i + l_i)\theta^{(i)} + l_0\theta = 0. \tag{6}$$

Considering θ_d is the designated position signal, and the controller u_0 is designed as

$$u_0 = \frac{1}{k}\left(\dddot{\theta}_d + \sum_{i=1}^{2}(a_i + l_i)\theta^{(i)} - \sum_{i=0}^{3} l_i\theta^{(i)} - a_3\right). \tag{7}$$

Let $u = u_0$ and substituting (7) into (4), one has

$$\dddot{e} + \sum_{i=1}^{2}(a_i + l_i)e^{(i)} + l_0 e = 0, \tag{8}$$

where $e = \theta - \theta_d$ is the tracking error. For ease of representation, let $E(e^{(0\sim3)}) = \dddot{e} + \sum_{i=1}^{2}(a_i + l_i)e^{(i)} + l_0 e$.

The characteristic equation of tracking error of the closed-loop system (8) can be expressed as

$$s^3 + \sum_{i=1}^{2}(a_i + l_i)s^i + l_0 = 0. \tag{9}$$

It is worth noting that the HOFA system approach provides a straightforward approach for the controller design and analysis of motion control systems. The full-actuation property allows compensating for all original dynamics and facilitates arbitrary placement of closed-loop poles, thereby achieving the desired closed-loop dynamics. That is, l_0, l_1, and l_2 are chosen under the guarantee all the roots of (9) have negative real part. However, this simple method requires high-order derivatives of the measured signals and desired trajectory, which can be challenging in practical applications due to discretization errors and measurement noise. Taking the derivative of the system's state $\dot{\omega}$ yields $\ddot{\omega}$, it can avoid the straight need for high-order signal derivatives.

3.2 Disturbance observer design

The attainment of these ideal results in Section 3.1 is contingent upon the accuracy of the system model. In general, it is not feasible to obtain complete information about the system in practical settings. Internal uncertainties and external disturbances can significantly impact estimation accuracy and control precision. Considering the disturbance in this paper, (4) can be rewritten as

$$\dddot{\theta} + a_2\ddot{\theta} + a_1\dot{\theta} = ku + a_3 + d. \tag{10}$$

If the estimation of disturbance $\hat{d}$ can be estimated by disturbance observer, the controller can be designed as follows to realize disturbance rejection.

$$u = u_0 - \frac{1}{k}\hat{d}. \tag{11}$$

The disturbance observer is designed in Theorem 1.

Theorem 1. If the disturbance d in (10) satisfies the following equation

$$\dddot{d} + \alpha_1\ddot{d} + \alpha_0\dot{d} = 0, \tag{12}$$

where α_1 and α_0 are parameters, then the disturbance observer can be designed as

$$\dddot{\hat{d}} + \alpha_1\ddot{\hat{d}} + \alpha_0\dot{\hat{d}} = \left(\beta_1\frac{d}{dt} + \beta_0\right)E(e^{(0\sim3)}), \tag{13}$$

to make the error of the observer converge to zero where the designed parameters β_1 and β_0 need to make all the roots of the following equation have negative real parts

$$s^2 + (\alpha_1 + \beta_1)\,s + (\alpha_0 + \beta_0) = 0. \tag{14}$$

Proof. Substituting (11) into (10), one has

$$E(e^{(0\sim3)}) = \tilde{d}, \tag{15}$$

where $\tilde{d} = d - \hat{d}$ is the error of disturbance observer.

From (12), (13) and (15), it can be got that

$$\dddot{\tilde{d}} + (\alpha_1 + \beta_1)\,\ddot{\tilde{d}} + (\alpha_0 + \beta_0)\,\tilde{d} = 0. \tag{16}$$

Obviously, (14) is the characteristic equation of (16). The error of the observer $\tilde{d}$ converges to zero when the parameter β_1 and β_0 are chosen to guarantee the roots of (14) have negative part. To enhance the clarity and comprehensibility of the designed controller, the control structure diagram is provided, as shown in Fig. 2, from which it can be seen that the controller (11) consists of three parts. The first part represents tracking performance, the second part removes tracking error when the disturbance is zero, and the third part compensates for the disturbance received. The parameters l_0, l_1 and l_2 that ensure the stability of the closed-loop system obtained by the HOFA system approach are used to design disturbance observers.

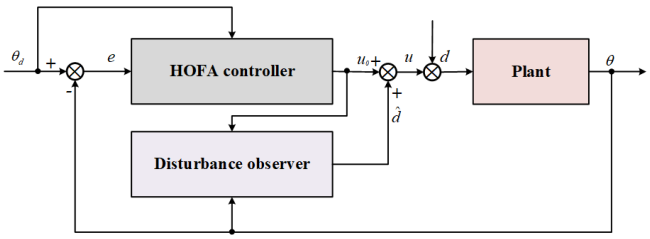

Fig. 2: Control structure of HOFA system approach with disturbance observer.

3.3 Stability analysis

Theorem 2. Under the controller (11) and the disturbance observer (13), the closed-loop system (6) with the disturbance satisfying (12) is stable and the tracking error is zero.

Proof. From (13), one has

$$\hat{d} = \left(\frac{\beta_1\frac{d}{dt} + \beta_0}{\frac{d^2}{dt^2} + \alpha_1\frac{d}{dt} + \alpha_0}\right)E(e^{(0\sim3)}). \tag{17}$$

Considering $d = 0$ and substitution of (11) into (4) yields

$$E(e^{(0\sim3)}) + \hat{d} = 0. \tag{18}$$

Substitution of (17) into (18) yields

$$\left(1 + \frac{\beta_1\frac{d}{dt} + \beta_0}{\frac{d^2}{dt^2} + \alpha_1\frac{d}{dt} + \alpha_0}\right)E(e^{(0\sim3)}) = 0. \tag{19}$$

Next, it can be derived that

$$\left(\frac{d^2}{dt^2} + (\alpha_1 + \beta_1)\frac{d}{dt} + (\alpha_0 + \beta_0)\right)E(e^{(0\sim3)}) = 0. \tag{20}$$

Thus the characteristic equation of (20) is

$$\begin{aligned}&\left(s^3 + \sum_{i=1}^{2}(a_i + l_i)s^i + l_0\right)\\ &\quad\times\left(s^2 + (\alpha_1 + \beta_1)\,s + (\alpha_0 + \beta_0)\right) = 0.\end{aligned} \tag{21}$$

According to the selection of parameter l_0, l_1, l_2, β_0 and β_1, all roots of (21) have negative real parts, and the system is asymptotically stable.

Next, considering $d \neq 0$, one has

$$\left(1 + \frac{\beta_1\frac{d}{dt} + \beta_0}{\frac{d^2}{dt^2} + \alpha_1\frac{d}{dt} + \alpha_0}\right)E(e^{(0\sim3)}) = d. \tag{22}$$

From (22), the transfer function from d to e can be obtained

as

$$\begin{aligned}\frac{E(s)}{D(s)} &= \left(s^2+\alpha_1 s+\alpha_0\right) \\ &\times \left(s^2+\left(\alpha_1+\beta_1\right)s+\left(\alpha_0+\beta_0\right)\right)^{-1} \\ &\times \left(s^3+\sum_{i=1}^{2}\left(a_i+l_i\right)s^i+l_0\right)^{-1}.\end{aligned} \tag{23}$$

According to [9], the following equation yields

$$\begin{aligned}e(\infty) &= \lim_{s\to 0} s\frac{E(s)}{D(s)}D(s) \\ &= \lim_{s\to 0} s\left(s^2+\alpha_1 s+\alpha_0\right)D(s) \\ &\times \left(s^2+\left(\alpha_1+\beta_1\right)s+\left(\alpha_0+\beta_0\right)\right)^{-1} \\ &\times \left(s^3+\sum_{i=1}^{2}\left(a_i+l_i\right)s^i+l_0\right)^{-1}.\end{aligned} \tag{24}$$

Since the poles of $D(s)$ and the zeros of the polynomial $s^2+\alpha_1 s+\alpha_0$ are equal, then $e(\infty)=0$ from (24).

4 Simulation

A numerical simulation is conducted to validate the effectiveness of the proposed scheme. The simulation is structured into two primary components. Firstly, it is demonstrated that the HOFA controller can achieve tracking errors converge to zero under the disturbance, similar to PID controller. Secondly, the simulation focuses on evaluating the observation performance of the disturbance observer designed based on the HOFA system approach.

4.1 Simulation Set-up

Through system identification in this paper, the plant model $P(s)$ is obtained, providing a comprehensive understanding of the turntable system dynamics. The model can be represented as

$$P(s)=\frac{92224}{s^2+514.5s+781.1} \tag{25}$$

In order to facilitate a comparative analysis with the classical PID controller, the following PID controller $K(s)$ is employed for the system.

$$K(s)=16.2279\times\frac{0.2756s+1}{0.0919s+1}\times\left(\frac{0.083s+1}{0.049s+1}\right)^5 \tag{26}$$

The parameters of the proposed HOFA system approach with disturbance observer in this paper during the numerical simulation are presented in Table 1.

Table 1: Parameters for Proposed Approach

Parameter	Setting Value	Parameter	Setting Value
k	92224	l_2	1
l_0	0.3×10^7	α_0	$(\pi/180)^2$
a_1	845.4125	α_1	1
a_2	514.625	$\alpha_0+\beta_0$	400
l_1	7.5×10^4	$\alpha_1+\beta_1$	40

According to [6], the spatially cyclic disturbance, which can be obtained by linear transformation of time and frequency, is considered in simulation. The frequencies of major disturbance harmonics are obtained as $f_1=\frac{1}{360^\circ}$, $f_2=\frac{1}{24^\circ}$ and $f_3=\frac{1}{10^\circ}$, with corresponding amplitudes of 1.8 Nm, 0.12 Nm and 0.05 Nm.

4.2 Results and Comparisons

First, this simulation aims to validate the effectiveness of the proposed HOFA approach by comparing it with PID control schemes under disturbance without disturbance observer.

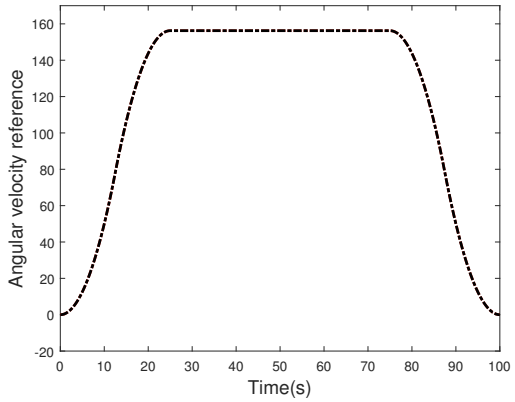

Fig. 3: The designated angular velocity signal ω.

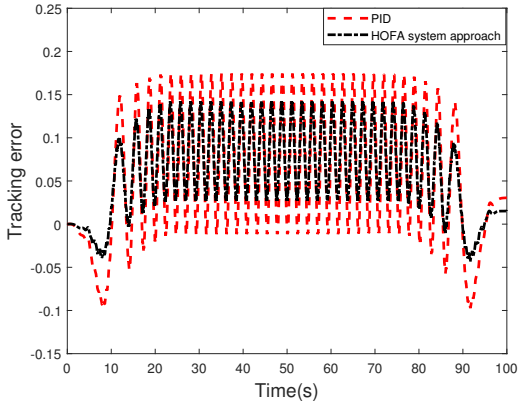

Fig. 4: The tracking error e under PID and HOFA system approach.

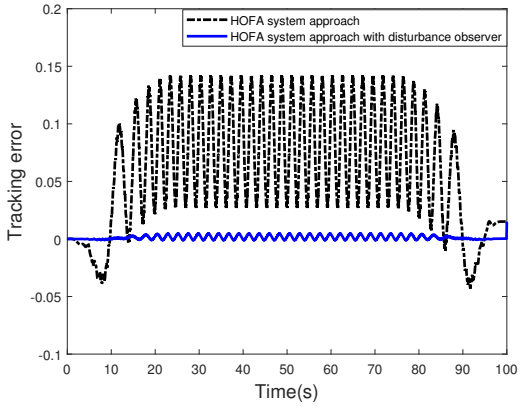

Fig. 5: The tracking error e under HOFA system approach with disturbance observer.

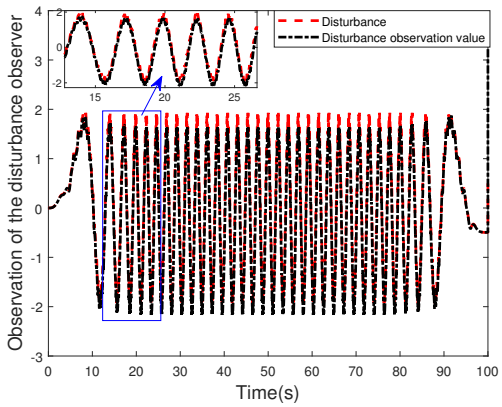

Fig. 6: Estimation of the disturbance d.

The designated sign ω is shown in Fig. 3. The tracking errors e of two distinct scenarios under PID controller and HOFA-based controller are shown in Fig. 4, from which it can be seen that using the HOFA system approach to design the controller can achieve tracking control like PID control. Furthermore, considering the flexibility provided by the HOFA system approach, the poles of the closed-loop system can be configured arbitrarily. This allows for the adjustment of parameter values l_0, l_1 and l_2, resulting in improved tracking performance.

Next, the controller with the disturbance observer is considered. Fig. 5 shows the tracking error under HOFA approach with disturbance. The blue line shows the tracking error under the controller (11) with the disturbance observer (13). From Fig. 5, the controllers with disturbance observers can better achieve tracking performance. That is, the disturbance observer can compensate for the errors caused by disturbances. The estimation of disturbance is shown in Fig. 6, and it can be concluded that the designed observer can estimate the disturbances by choosing appropriate parameters.

5 Conclusion

In this paper, the tracking problem has been investigated for a motion control system driven by PMSM under the unknown disturbance. This paper begins by presenting the modeling of the PMSM, employing a HOFA system model. Subsequently, by leveraging the HOFA system approach, a closed-loop linear system is derived, encompassing both tracking error and disturbance error. Then, a controller grounded in the HOFA system approach is proposed. The designed disturbance observer can estimate disturbances well. And the efficacy of the control algorithm is then substantiated through comprehensive simulation. Furthermore, considering the intricate nature of disturbances in actual systems, coupled with the existence of multiple unknown parameters, the design of controllers utilizing the HOFA system approach to achieve disturbance parameter identification emerges as a noteworthy topic for future study.

References

[1] H. Attar, A. T. Abu-Jassar, and V. Lyashenko et al. Proposed synchronous electric motor simulation with built-in permanent magnets for robotic systems. *SN Appl. Sci.* 5(160), 2023.

[2] W. Li, Y. He, Parameterization and Performance of Permanent Magnet Synchronous Motor for Vehicle Based on Motor-CAD and OptiSLang, *Wireless Communications and Mobile Computing*, 8217386, 2022.

[3] J. Wang, Fuzzy Adaptive Repetitive Control for Periodic Disturbance with Its Application to High Performance Permanent Magnet Synchronous Motor Speed Servo Systems, *Entropy*, 18(9): 261, 2016.

[4] Q. Liu, X. Huo, K. -Z. Liu and H. Zhao, A Parallelized Input Matching LMS Adaptive Filter for the Rejection of Spatially Cyclic Disturbances, *IEEE Transactions on Industrial Electronics*, 70(10): 10536–10545, 2023.

[5] S. J. Steinberg, M. Staats, W. Nitsche, and R. King, Iterative Learning Active Flow Control Applied to a Compressor Stator Cascade With Periodic Disturbances, *ASME. J. Turbomach*, 137(11): 111003, 2015.

[6] A. Wu, X. Huo, Q. Liu and J. Ma, Circularly Orthogonal Projection-Based Iterative Learning Control for Rejecting Spatially Cyclic Disturbances, *IEEE Transactions on Industrial Electronics*, doi: 10.1109/TIE.2023.3314901.

[7] S. Li, A speed control for a PMSM using finite-time feedback control and disturbance compensation, *Transactions of the Institute of Measurement and Control*, 32(2): 170–187, 2010.

[8] S. Li, M. Zhou and X. Yu, Design and Implementation of Terminal Sliding Mode Control Method for PMSM Speed Regulation System, *IEEE Transactions on Industrial Informatics*, 9(4): 1879–1891, 2013.

[9] Y. Liu, T. Zhang, J. Song and M. Junaid Khan, Controller design for high-order descriptor linear systems based on requirements on tracking performance and disturbance rejection, *Aerospace Science and Technology*, 13(7): 364–373, 2009.

[10] G. Duan, High-order fully actuated system approaches: Part I. Models and basic procedure, *International Journal of Systems Science*, 52(2): 422–435, 2021.

[11] G. Duan, High-order fully actuated system approaches: Part II. Generalized strict-feedback systems, *International Journal of Systems Science*, 52(3): 437–454, 2021.

[12] G. Duan, High-order fully actuated system approaches: part VII. Controllability, stabilisability and parametric designs, *International Journal of Systems Science*, 52(14), 3091–3114, 2021.

[13] L. Hu, G. Duan, M. Hou, Robust adaptive guaranteed cost tracking control for high-order nonlinear systems with uncertainties based on high-order fully actuated system approaches. *Int J Robust Nonlinear Control.* 33(13): 7583–7605, 2023.

[14] X. Liu, M. Chen, D. Zhou and L. Sheng, Fault-Tolerant Control of Stochastic High-Order Fully Actuated Systems, *IEEE Transactions on Cybernetics*, doi: 10.1109/TCYB.2023.3320441.

[15] X. Liu, M. Chen, L. Sheng, D. Zhou, Adaptive fault-tolerant control for nonlinear high-order fully-actuated systems, *Neurocomputing*, 495: 75–85, 2022.

[16] G. Liu, Predictive Control of High-Order Fully Actuated Nonlinear Systems with Time-Varying Delays. *J Syst Sci Complex* 35: 457–470, 2022.

[17] D. Zhang, G. Liu and L. Cao, Secure Predictive Coordinated Control of High-Order Fully Actuated Networked Multiagent Systems Under Random DoS Attacks, *IEEE Transactions on Cybernetics*, doi: 10.1109/TCYB.2023.3324179.

[18] R. Meng, C. Hua, K. Li and P. Ning, Adaptive Event-Triggered Control for Uncertain High-Order Fully Actuated System, *IEEE Transactions on Circuits and Systems II: Express Briefs*, 69(11): 4438–4442, 2022.

[19] P. Li and G. Duan, High-Order Fully Actuated Control Approaches of Flexible Servo Systems Based on Singular Perturbation Theory, *IEEE/ASME Transactions on Mechatronics*, 28(6): 3386–3397, 2023.

Proceedings of the 3rd Conference on Fully Actuated System Theory and Applications
May 10-12, 2024, Shenzhen, China

Gait Stability Control of Quadruped Robot by Composite Nonlinear Feedback and Model Predictive Control

Jiang Xu[1], Xiafu Peng[1],Xiao Yu[2], Weiyao Lan[1]

1. Department of Automation, Xiamen University, Xiamen 361005, P. R. China
E-mail: jiangxu@stu.xmu.edu.cn, xfpeng@xmu.edu.cn, wylan@xmu.edu.cn

2. Institute of Artificial Intelligence, Xiamen University, Xiamen 361005, P. R. China
E-mail: xiaoyu@xmu.edu.cn

Abstract: This paper investigates the gait stability control problem of the quadruped robot body. Due to the lack of action prediction in advance and effective adjustment of the motion state, it is difficult to enhance the body stability of the quadruped robot during its locomotion. A new control framework based on composite nonlinear feedback (CNF) is proposed, which is able to adjust the input torque of the system based on its current motion state. The controller consists of a model predictive control (MPC) and a nonlinear feedback part, which establishes a closed-loop system by state feedback. The error between the target state and the actual state is introduced to construct a nonlinear input compensation term, and the optimal input is solved, so as to form a composite nonlinear feedback control. The algorithm is also on the basis of the state estimation and the use of inertial measurement unit (IMU). The simulation results show that the performance on the body stability of the quadruped robot is improved and the robot appears adapt to more complex terrain during motion. The results illustrate the effectiveness of the proposed approach.

Key Words: Quadruped robot, stability control, nonlinear feedback, model predictive control

1 Introduction

The body stability of a quadruped robot during its motion is an essential issue, and the realization of various complex actions is based on the premise that the robot can steadily move. Motion control of quadruped robots must take into account the kinematics and dynamics of the robot, and the motion constraints of the robotic system should be considered. Thus, it is necessary to find a suitable control method to make the robot complete the specified task. For motion control, optimization methods for motion trajectory were proposed in [1, 2]. The optimization method developed in [1] combines with the estimation of sensors, and the method can achieve efficient and flexible motion control. Meanwhile, to address the uncertainty of robot motion, an approach that utilizes deep neural networks for motion control was introduced in [3].

However, the aforementioned works require accurate models and the parameters in the system need to be accurately calculated, which will increase the complexity of the calculation and reduce the practicability. In this context, model predictive control (MPC) is introduced into the motion control of quadruped robots [4]. Current MPC algorithms for quadruped robots facilitate high-level motion planning and trajectory generation for the robots, which can generate an optimal policy taking into account the dynamics and constraints [5]. Nevertheless, in terms of robot control alone, the stability of the robot body needs improvement. The idea of hierarchical control was presented in [6–8]. The robot dynamical model was hierarchically divided into multiple levels in [6], and the MPC method was used. The effectiveness of hierarchical model predictive control was verified by experiments in [7]. In [8], the authors proposed to employ deep reinforcement learning under the MPC framework to realize conversion between different modalities. Naturally, the learning method used in [9–11] were also feasible. A novel approach was presented that combines the robot dynamical model with machine learning techniques to optimize the MPC controller. The objective is to enhance the ability to adapt and perform effectively on slippery ground conditions [9]. The effectiveness of this learning-based approach was further confirmed in related studies [10, 11], where the control strategies and model parameters were optimized to improve performance.

For practical robotic control systems, the nonlinear dynamics of the system model cannot be neglected. In [12], a nonlinear optimization approach was proposed for optimizing the parameters of a quadruped robot. In addition, in [13] and [14], the composite nonlinear control methods contributed to improving the transient performance and maintaining the stability of the closed-loop system. The linear part of the controller is used to achieve the purpose of accurate tracking of the desired position. The nonlinear part can well compensate for the hysteresis and instability of the predicted output.

In this paper, a control framework of which is different from [14], is proposed. Our control scheme is based on MPC control algorithm, adding nonlinear input compensation to form a composite nonlinear feedback (CNF) control. In this way, the robot use the error between the current actual attitude information and the expected attitude information when it is moving, and adjust the input torque of the system. In the experiments on the Unitree A1 robot, the motion of the robot body stays in the range of $0.02\,\mathrm{rad}$, while the motion by the MPC control scheme only can stay in the range of $0.07\,\mathrm{rad}$. This demonstrates the improvement by our proposed approach.

The remainder of this paper is organized as follows. In Section 2, aiming at the existing problems, we propose a new control method to improve the robot's motion control

This work was supported in part by the National Natural Science Foundation of China under Grants 62273285 and 62173283, and in part by Innovation Fund for Production, Education and Research of Universities and Colleges, Ministry of Education, China, under Grant 2021ZYA02006.

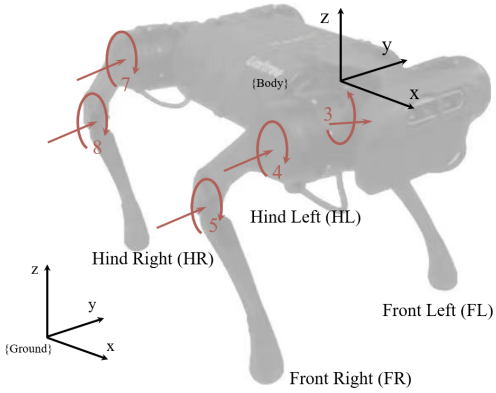

Fig. 1: Configuration of quadruped robot.

effect under limited conditions. Section 3 describes the design process of our specific control method. In Section 4, a simulation example is given. Section 5 concludes the paper.

2 Preliminaries

2.1 Lumped Mass Model of Bionic Quadruped Robot

The bionic quadruped robot needs high-frequency control input information for control, and the robot's control effect can be affected by the input generated by different control algorithms. We use the simplified model to construct the control algorithm in order to deal with an issue of the control algorithm's complexity. The bionic quadruped robot's limb weight is quite less than its body weight, so when it moves, its general moment of inertia and barycenter will not change greatly. We consider the bionic quadruped robot as a lumped mass model, since the following assumption is made.

Assumption 2.1 *The gimbal lock issue will not arise while the robot is moving.*

When an external force applies on a rigid body, theoretical mechanics states that the barycenter momentum (1) and angular momentum (2) both change.

$$m\ddot{\mathbf{p}} = \sum_{i=1}^{n_c} \mathbf{f}_i - \mathbf{c}_g \tag{1}$$

$$\frac{d}{dt}(\boldsymbol{I}\boldsymbol{\omega}) = \sum_{i=1}^{n_c} \mathbf{v}_i \times \mathbf{f}_i \tag{2}$$

where m is the robot's mass and n_c is the number of contacts. $\mathbf{p}$, $\mathbf{f}_i$ and $\mathbf{c}_g$ are the 3D robot position in the global coordinate system, the foot reaction force and the external force caused by gravity. (1) represents the influence of the resulting force of different points on the rigid body on the motion sense state of the rigid body. $\boldsymbol{I} \in \mathbb{R}^{3\times3}$ is the rotational inertia tensor, $\boldsymbol{\omega}$ is the angular velocity of the body in the world coordinate system, and $\mathbf{v}_i$ is the vector from the center of mass to the point of action.

The speed and rotation angle of the body are often the main state variables of bionic quadruple robots. Therefore, the Euler angle of the robot body $\boldsymbol{\Theta} \in \mathbb{R}^3$, the position information of the body in the world coordinate system $\mathbf{p} \in \mathbb{R}^3$, the euler angular velocity $\boldsymbol{\omega} \in \mathbb{R}^3$ and the velocity of the center of mass $\dot{\mathbf{p}} \in \mathbb{R}^3$ are selected to form a 12-dimensional vector $\left[\boldsymbol{\Theta}, \mathbf{p}, \boldsymbol{\omega}, \dot{\mathbf{p}}\right]^\top$. The desired state information is used to control the size of the given input through the handle, and the actual state information is calculated through the IMU. In particular, the following assumption on IMU is required.

Assumption 2.2 *There is no error between the measured information of IMU and the actual information.*

2.2 Problem Statement

This problem can be formally stated as follows. Consider a bionic quadruped robot controlled by a handle and moving on structured terrain. The IMU is placed at the barycenter of the robot, and the IMU is used to measure the angle, angular velocity, and linear velocity information of the robot. Encoders are included into the 12 joint motors, allowing for the measurement of the motor's speed and rotation angle.

The trajectory of the foot movement is set as a 5th order Bezier curve. Setting the control parameters of the handle, the desired motion state information can be generated by swinging the rocker forward.

The objective is to improve the performance of the actual motion states x when it tracks the desired motion states x_{ref}. That is, during the motion, the error $\|\mathrm{x}_{ref} - \mathrm{x}\|$ can be reduced. We aim to design an appropriate motor input torque $\mathbf{u}_{in}$ such that, within a certain period of time, the variation amplitude of $|\theta_{\max} - \theta_{\min}|$ and $|\phi_{\max} - \phi_{\min}|$ during the motion of the robot can be reduced.

3 Method

The design of the control law is divided into two parts: the model predictive control part and the nonlinear feedback control part. In this paper, the main role of MPC is to calculate the optimal input torques for the linear part. The nonlinear part mainly computes the compensated input torques.

The overall control scheme is described in Fig. 2.

3.1 Model Predictive Control

In order to precisely measure the robot's attitude change information in 3D space, we decompose the attitude change information in accordance with the sequence of first rotating ϕ angle around the x-axis, then rotating θ angle around the y-axis, and then rotating ψ angle around the z-axis, counterclockwise to the positive direction. The angle of rotation can be expressed as $\left[\phi, \theta, \psi\right]^\top \in \mathbb{R}^3$. The transition from the world coordinate system to the body coordinate system is represented by the rotation matrix $\boldsymbol{R}$.

$$\boldsymbol{R} = \boldsymbol{R}_z(\psi)\boldsymbol{R}_y(\theta)\boldsymbol{R}_x(\phi) \tag{3}$$

After inputting the parameters, the rotation matrix $\boldsymbol{R}$ is shown as follows.

$$\boldsymbol{R} = \begin{bmatrix} \cos\psi & -\sin\psi & 0 \\ \sin\psi & \cos\psi & 0 \\ 0 & 0 & 1 \end{bmatrix} \begin{bmatrix} \cos\theta & 0 & \sin\theta \\ 0 & 1 & 0 \\ -\sin\theta & 0 & \cos\theta \end{bmatrix} \begin{bmatrix} 1 & 0 & 0 \\ 0 & \cos\phi & -\sin\phi \\ 0 & \sin\phi & \cos\phi \end{bmatrix} \tag{4}$$

According to [15] and [16], since the bionic quadruple robot's roll angle ϕ and pitch angle θ during motion are small, they merely affect the computation and are thus ignored. Then, $\boldsymbol{R}$ becomes

$$\boldsymbol{R} = \boldsymbol{R}_z(\psi) = \begin{bmatrix} \cos\psi & -\sin\psi & 0 \\ \sin\psi & \cos\psi & 0 \\ 0 & 0 & 1 \end{bmatrix} \tag{5}$$

When the rotation matrix $\boldsymbol{R}$ is nonsingular, the link between the attitude angle of the body and the angular velocity in the world coordinate system can be found.

$$\begin{bmatrix} \dot{\phi} \\ \dot{\theta} \\ \dot{\psi} \end{bmatrix} = \begin{bmatrix} \cos\psi & \sin\psi & 0 \\ -\sin\psi & \cos\psi & 0 \\ 0 & 0 & 1 \end{bmatrix} \boldsymbol{\omega} = \boldsymbol{R}_z^{\top}(\psi)\boldsymbol{\omega} \quad (6)$$

The bionic quadruped robot's moment of inertia $\boldsymbol{I}_B$ in the body coordinate system may be calculated using SolidWorks 3D software. In the world coordinate system, the moment of inertia can be expressed as

$$\boldsymbol{I} = \boldsymbol{R}\boldsymbol{I}_B\boldsymbol{R}^{\top} \quad (7)$$

Use the simplified rotation matrix $\boldsymbol{R}$

$$\hat{\boldsymbol{I}} \approx \boldsymbol{R}_z(\psi)\boldsymbol{I}_B\boldsymbol{R}_z^{\top}(\psi) \quad (8)$$

The moment of inertia $\hat{\boldsymbol{I}}$ times the angular velocity $\boldsymbol{\omega}$ has the following differential term

$$\frac{d}{dt}(\hat{\boldsymbol{I}}\boldsymbol{\omega}) = \hat{\boldsymbol{I}}\dot{\boldsymbol{\omega}} + \boldsymbol{\omega} \times (\hat{\boldsymbol{I}}\boldsymbol{\omega}) \approx \hat{\boldsymbol{I}}\dot{\boldsymbol{\omega}} \quad (9)$$

where $\boldsymbol{\omega} \times (\hat{\boldsymbol{I}}\boldsymbol{\omega})$ can be deleted because it is quadratic.

Refer to the method of [17], the dymamics system can be expressed as

$$\frac{d}{dt}\begin{bmatrix} \boldsymbol{\Theta} \\ \mathbf{p} \\ \boldsymbol{\omega} \\ \dot{\mathbf{p}} \end{bmatrix} = \underbrace{\begin{bmatrix} \mathbf{0}_{3\times3} & \mathbf{0}_{3\times3} & \boldsymbol{R}_z^{\top}(\psi) & \mathbf{0}_{3\times3} \\ \mathbf{0}_{3\times3} & \mathbf{0}_{3\times3} & \mathbf{0}_{3\times3} & \mathbf{1}_{3\times3} \\ \mathbf{0}_{3\times3} & \mathbf{0}_{3\times3} & \mathbf{0}_{3\times3} & \mathbf{0}_{3\times3} \\ \mathbf{0}_{3\times3} & \mathbf{0}_{3\times3} & \mathbf{0}_{3\times3} & \mathbf{0}_{3\times3} \end{bmatrix}}_{\boldsymbol{A}} \begin{bmatrix} \boldsymbol{\Theta} \\ \mathbf{p} \\ \boldsymbol{\omega} \\ \dot{\mathbf{p}} \end{bmatrix} + \underbrace{\begin{bmatrix} \mathbf{0}_{3\times3} & \dots & \mathbf{0}_{3\times3} \\ \mathbf{0}_{3\times3} & \dots & \mathbf{0}_{3\times3} \\ \hat{\mathbf{I}}^{-1}[\mathbf{v}_1] & \dots & \hat{\mathbf{I}}^{-1}[\mathbf{v}_n] \\ \frac{\mathbf{1}_{3\times3}}{m} & \dots & \frac{\mathbf{1}_{3\times3}}{m} \end{bmatrix}}_{\boldsymbol{B}} \begin{bmatrix} f_1 \\ \dots \\ f_n \end{bmatrix} + \begin{bmatrix} 0 \\ \dots \\ \dots \\ \mathbf{g} \end{bmatrix} \quad (10)$$

To facilitate computation, $\mathbf{g}$ is included in the state variables

$$\frac{d}{dt}\begin{bmatrix} \boldsymbol{\Theta} \\ \mathbf{p} \\ \boldsymbol{\omega} \\ \dot{\mathbf{p}} \\ \mathbf{g} \end{bmatrix} = \underbrace{\begin{bmatrix} \mathbf{0}_{3\times3} & \mathbf{0}_{3\times3} & \boldsymbol{R}_z^{\top}(\psi) & \mathbf{0}_{3\times3} & \mathbf{0}_{3\times1} \\ \mathbf{0}_{3\times3} & \mathbf{0}_{3\times3} & \mathbf{0}_{3\times3} & \mathbf{1}_{3\times3} & \mathbf{0}_{3\times1} \\ \mathbf{0}_{3\times3} & \mathbf{0}_{3\times3} & \mathbf{0}_{3\times3} & \mathbf{0}_{3\times3} & \mathbf{0}_{3\times1} \\ \mathbf{0}_{3\times3} & \mathbf{0}_{3\times3} & \mathbf{0}_{3\times3} & \mathbf{0}_{3\times3} & \mathbf{d}_{3\times1} \\ \mathbf{0}_{1\times3} & \mathbf{0}_{1\times3} & \mathbf{0}_{1\times3} & \mathbf{0}_{1\times3} & \mathbf{0}_{1\times1} \end{bmatrix}}_{\boldsymbol{A}_c(\psi)} \times \begin{bmatrix} \boldsymbol{\Theta} \\ \mathbf{p} \\ \boldsymbol{\omega} \\ \dot{\mathbf{p}} \\ \mathbf{g} \end{bmatrix} + \underbrace{\begin{bmatrix} \mathbf{0}_{3\times3} & \dots & \mathbf{0}_{3\times3} \\ \mathbf{0}_{3\times3} & \dots & \mathbf{0}_{3\times3} \\ \hat{\mathbf{I}}^{-1}[\mathbf{v}_1] & \dots & \hat{\mathbf{I}}^{-1}[\mathbf{v}_n] \\ \frac{\mathbf{1}_{3\times3}}{m} & \dots & \frac{\mathbf{1}_{3\times3}}{m} \\ \mathbf{0}_{1\times3} & \dots & \mathbf{0}_{1\times3} \end{bmatrix}}_{\boldsymbol{B}_c(\mathbf{v}_1,\cdots,\mathbf{v}_n,\psi)} \begin{bmatrix} f_1 \\ \dots \\ f_n \end{bmatrix} \quad (11)$$

where $\mathbf{d}_{3\times1} = \begin{bmatrix} 0 & 0 & 1 \end{bmatrix}^{\top}$.

Simplify (11) yields

$$\dot{\mathrm{x}} = \boldsymbol{A}_c(\psi)\mathrm{x}(t) + \boldsymbol{B}_c(\mathbf{v}_1,\cdots,\mathbf{v}_n,\psi)\hat{\mathbf{f}}(t) \quad (12)$$

The discrete dynamics of the system can be expressed as

$$\frac{\mathrm{x}(p+1) - \mathrm{x}(p)}{\delta t} = \boldsymbol{A}_c\mathrm{x}(p) + \boldsymbol{B}_c\hat{\mathbf{f}}(p) \quad (13)$$

Write (13) in recursive form

$$\mathrm{x}(p+1) = (\delta t\boldsymbol{A}_c + E)\mathrm{x}(p) + \delta t\boldsymbol{B}_c\hat{\mathbf{f}}(p) \quad (14)$$

Let: $\delta t\boldsymbol{A}_c + \boldsymbol{E} = \tilde{\boldsymbol{A}}$, $\delta t\boldsymbol{B}_c = \tilde{\boldsymbol{B}}$. Iterating n times, we can get

$$\begin{aligned} \mathrm{x}(p+1) &= \tilde{\boldsymbol{A}}\mathrm{x}(p) + \tilde{\boldsymbol{B}}\hat{\mathbf{f}}(p) \\ \mathrm{x}(p+2) &= \tilde{\boldsymbol{A}}^2\mathrm{x}(p) + \tilde{\boldsymbol{A}}\tilde{\boldsymbol{B}}\hat{\mathbf{f}}(p) + \tilde{\boldsymbol{B}}\hat{\mathbf{f}}(p+1) \\ \mathrm{x}(p+3) &= \tilde{\boldsymbol{A}}^3\mathrm{x}(p) + \tilde{\boldsymbol{A}}^2\tilde{\boldsymbol{B}}\hat{\mathbf{f}}(p) + \tilde{\boldsymbol{A}}\tilde{\boldsymbol{B}}\hat{\mathbf{f}}(p+1) + \tilde{\boldsymbol{B}}\hat{\mathbf{f}}(p+2) \\ \mathrm{x}(p+n) &= \tilde{\boldsymbol{A}}^n\mathrm{x}(p) + \tilde{\boldsymbol{A}}^{n-1}\tilde{\boldsymbol{B}}\hat{\mathbf{f}}(p) + \cdots + \tilde{\boldsymbol{B}}\hat{\mathbf{f}}(p+n-1) \end{aligned} \quad (15)$$

Set $p = 0$, summarizing (15) as

$$\begin{bmatrix} \mathrm{x}(1) \\ \mathrm{x}(2) \\ \cdots \\ \mathrm{x}(n) \end{bmatrix} = \begin{bmatrix} \tilde{\boldsymbol{A}}^1 \\ \tilde{\boldsymbol{A}}^2 \\ \cdots \\ \tilde{\boldsymbol{A}}^n \end{bmatrix} \mathrm{x}(0) + \begin{bmatrix} \tilde{\boldsymbol{B}} & 0 & 0 & \cdots & 0 \\ \tilde{\boldsymbol{A}}\tilde{\boldsymbol{B}} & \tilde{\boldsymbol{B}} & 0 & \cdots & 0 \\ \tilde{\boldsymbol{A}}^2\tilde{\boldsymbol{B}} & \tilde{\boldsymbol{A}}\tilde{\boldsymbol{B}} & \tilde{\boldsymbol{B}} & \cdots & 0 \\ \cdots & \cdots & \cdots & \cdots & \cdots \\ \tilde{\boldsymbol{A}}^{n-1}\tilde{\boldsymbol{B}} & \tilde{\boldsymbol{A}}^{n-2}\tilde{\boldsymbol{B}} & \tilde{\boldsymbol{A}}^{n-3}\tilde{\boldsymbol{B}} & \cdots & \tilde{\boldsymbol{B}} \end{bmatrix} \begin{bmatrix} \hat{\mathbf{f}}(0) \\ \hat{\mathbf{f}}(1) \\ \hat{\mathbf{f}}(2) \\ \cdots \\ \hat{\mathbf{f}}(n-1) \end{bmatrix} \quad (16)$$

Simplify (16) as

$$\mathrm{X} = \boldsymbol{A}_{\mathrm{qp}}\mathrm{x}(0) + \boldsymbol{B}_{\mathrm{qp}}\mathbf{F} \quad (17)$$

In order to effectively manage the bionic quadriplegic robot, there should be as little difference as possible between the desired state $\mathrm{x}_{ref}(k+1)$ and real states $\mathrm{x}(k+1)$ of the system, along with as little energy waste and system input $\hat{\mathbf{f}}(k)$ that fits the motor's actual input. From these two perspectives, the cost function $\boldsymbol{Y}$ is defined as follows

$$\boldsymbol{Y} = \sum_{k=0}^{n-1} ||\mathrm{x}(k+1) - \mathrm{x}_{ref}(k+1)||_{\boldsymbol{Q}}^2 + ||\hat{\mathbf{f}}(k)||_{\boldsymbol{S}}^2 \quad (18)$$

where $\boldsymbol{Q}$ and $\boldsymbol{S}$ are weight matrices. Because the state variables x are not equivalent to the input force $\hat{\mathbf{f}}(k)$, and the important coefficient in the actual control is not the same, the weight can be adjusted to match the control parameters in different environments.

Arrange (17) to the cost function $\boldsymbol{Y}$ as

$$\begin{aligned} \boldsymbol{Y} =& (\mathrm{X} - \mathrm{X}_{ref})^{\top}\boldsymbol{Q}(\mathrm{X} - \mathrm{X}_{ref}) + \mathbf{F}^{\top}\boldsymbol{S}\mathbf{F} \\ =& [\boldsymbol{A}_{qp}\mathrm{x}(0) + \boldsymbol{B}_{qp}\mathbf{F} - \mathrm{X}_{ref}]^{\top}\boldsymbol{Q}[\boldsymbol{A}_{qp}\mathrm{x}(0) + \boldsymbol{B}_{qp}\mathbf{F} \\ & - \mathrm{X}_{ref}] + \mathbf{F}^{\top}\boldsymbol{S}\mathbf{F} \\ =& [\boldsymbol{A}_{qp}\mathrm{x}(0)]^{\top}\boldsymbol{Q}\boldsymbol{A}_{qp}\mathrm{x}(0) + (\boldsymbol{B}_{qp}\mathbf{F})^{\top}\boldsymbol{Q}\boldsymbol{B}_{qp}\mathbf{F} \\ & + 2[\boldsymbol{A}_{qp}\mathrm{x}(0)]^{\top}\boldsymbol{Q}\boldsymbol{B}_{qp}\mathbf{F} - 2[\boldsymbol{A}_{qp}\mathrm{x}(0)]^{\top}\boldsymbol{Q}\mathrm{X}_{ref} \\ & + \mathrm{X}_{ref}^{\top}\boldsymbol{Q}\mathrm{X}_{ref} - 2(\boldsymbol{B}_{qp}\mathbf{F})^{\top}\boldsymbol{Q}\mathrm{X}_{ref} + \mathbf{F}^{\top}\boldsymbol{S}\mathbf{F} \end{aligned} \quad (19)$$

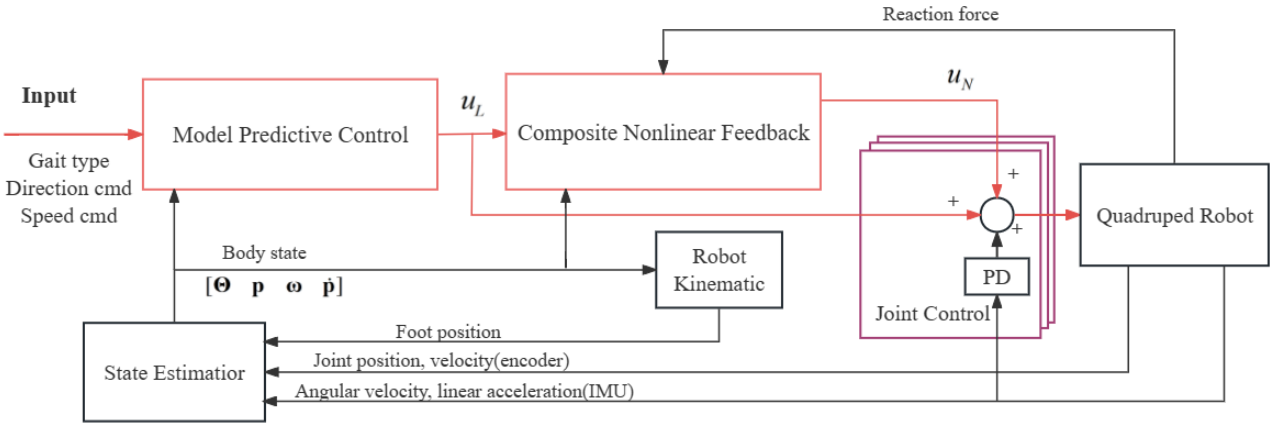

Fig. 2: Overall control scheme.

The current state $\mathrm{x}(0)$ can be obtained by IMU. The weight matrix $\boldsymbol{Q}$ and $\boldsymbol{S}$ are constant matrices, so three constant terms can be discarded and the remaining four terms can be reformulated for quadratic programming.

$$\begin{aligned}\boldsymbol{Y'} =&(\boldsymbol{B}_{qp}\mathbf{F})^{\top}\boldsymbol{Q}\boldsymbol{B}_{qp}\mathbf{F} + 2[\boldsymbol{A}_{qp}\mathrm{x}(0)]^{\top}\boldsymbol{Q}\boldsymbol{B}_{qp}\mathbf{F} \\ &- 2(\boldsymbol{B}_{qp}\mathbf{F})^{\top}\boldsymbol{Q}X_{ref} + \mathbf{F}^{\top}\boldsymbol{S}\mathbf{F}\end{aligned} \tag{20}$$

Formulate into quadratic programming form

$$\boldsymbol{Y'} = \frac{1}{2}\mathbf{F}^{\top}\boldsymbol{H}\mathbf{F} + \mathbf{F}^{\top}\boldsymbol{z} \tag{21}$$

where

$$\begin{aligned}\boldsymbol{H} =&2(\boldsymbol{B}_{qp}^{\top}\boldsymbol{Q}\boldsymbol{B}_{qp} + \boldsymbol{S}) \\ \boldsymbol{z} =&2\boldsymbol{B}_{qp}^{\top}\boldsymbol{Q}(\boldsymbol{A}_{qp}\mathrm{x}(0) - X_{ref})\end{aligned} \tag{22}$$

Let n denote the total number of prediction time steps, $\boldsymbol{A}qp$ is a $13n \times 13$ matrix; $\boldsymbol{B}qp$ is a $13n \times 12n$ matrix; $\boldsymbol{Q}$ is a $13n \times 13n$ matrix; $\boldsymbol{S}$ is a $12n \times 12n$ matrix; $\boldsymbol{H}$ is a $12n \times 12n$ matrix; $\boldsymbol{z}$ is a $13n \times 1$ matrix; X_{ref} is a $13n \times 1$ matrix.

In practical applications, considering the constraints of quadratic programming, it is required that the force exerted by the robot in the x-axis and y-axis directions must exceed the static friction force on the ground, while the force exerted in the z-axis direction must be less than the torque that the motors can provide.

$$\begin{cases} -\mu f_z \le f_x \le \mu f_z \\ -\mu f_z \le f_y \le \mu f_z \\ f_{\min} \le f_z \le f_{\max} \end{cases} \tag{23}$$

The final result can be obtained through a quadratic programming solver. The values obtained by quadratic programming solver represent the optimal values for the next n steps, where $\boldsymbol{F}$ contains n sets of solutions. Therefore, the first set of solutions $\hat{\mathbf{f}}(0)$ is chosen as the optimal linear input $\mathbf{u}_L$ for the system, i.e., $\hat{\mathbf{f}}(0) = \mathbf{u}_L$. Subsequently, this process is repeated to continually calculate the current optimal input torques.

3.2 Composite Nonlinear Feedback Control

In theory, MPC can provide globally optimal solutions, but this requires an accurate model and convex optimization problems. However, achieving this in practical applications is challenging, especially for complex systems like bionic quadruped robots. CNF can mitigate the impact force at the foot-ground contact by adjusting the system's damping, even when the model is not precise. As a result, CNF achieves smoother motion during locomotion compared to MPC alone.

The final performance of bionic quadruped robot control is influenced by two factors: firstly, the difference between the actual output torque and the input torque, and secondly, the difference between the desired motion state and the actual motion state. According to [18–20], nonlinear terms can be constructed for different cases. In our experiment, the nonlinear feedback control law is given by

$$\mathbf{u}_N = \rho[\hat{\mathbf{f}}(k), \mathbf{y}]\boldsymbol{B}^{\top}\boldsymbol{P}[\mathrm{x}(k) - \mathrm{x}_{ref}(k)] \tag{24}$$

where $\hat{\mathbf{f}}(k)$ represents the desired torque, $\mathbf{y}$ denotes the joint torque, which is the actual output in each control cycle, $\mathrm{x}(k)$ represents the current actual state of the robot, and $\mathrm{x}_{ref}(k)$ represents the desired robot state. $\boldsymbol{P}$ is a positive definite matrix, which is the solution of

$$(\boldsymbol{A} + \boldsymbol{B}\boldsymbol{G})^{\top}\boldsymbol{P} + \boldsymbol{P}(\boldsymbol{A} + \boldsymbol{B}\boldsymbol{G}) = -\boldsymbol{W} \tag{25}$$

where $\boldsymbol{W}$ is a positive definite matrix, $\boldsymbol{G}$ is the feedback gain matrix, which is obtained by solving for the desired poles of the system set at $(-1, j)$ and $(-1, -j)$. The selection of poles can be adjusted based on different desired states, and its value will affect the magnitude of the feedback gain matrix.

The non-linear coefficient $\rho[\hat{\mathbf{f}}(k), \mathbf{y}]$ is related to the difference between the actual output torque and the desired torque. By the property of the exponential function, as the difference between the actual torque and the desired torque increases, the absolute value of $\rho[\hat{\mathbf{f}}(k), \mathbf{y}]$ becomes larger; as the difference decreases, the absolute value of $\rho[\hat{\mathbf{f}}(k), \mathbf{y}]$ becomes smaller. α and β are used to control the magnitude of the non-linear input term, and different values can be chosen

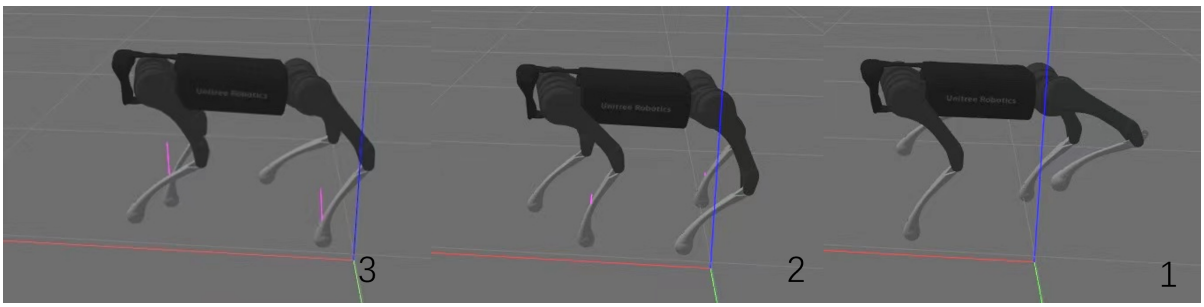

Fig. 3: Quadruped robot movement posture.

according to different situations.

$$\rho[\hat{\mathbf{f}}(k), \mathbf{y}] = -\beta e^{-\alpha|\mathbf{y}-\hat{\mathbf{f}}(k)|} \tag{26}$$

Combine (24) and (26), we obtain:

$$\mathbf{u}_N = -\beta e^{-\alpha|\mathbf{y}-\hat{\mathbf{f}}(k)|} \boldsymbol{B}^\top \boldsymbol{P}[\mathrm{x}(k) - \mathrm{x}_{ref}(k)] \tag{27}$$

At this point, the input $\mathbf{u}_{in}$ of the quadruped robot system is

$$\mathbf{u}_{in} = \mathbf{u}_L + \mathbf{u}_N \tag{28}$$

Algorithm 1: CNF and MPC control algorithm

Input :
Direction cmd, Speed cmd
Output:
Optimal torque $\mathbf{u}_{in}$

Establish the simple lumped mass model;
while *within physical limits* **do**
  Calculate the system rotation matrix $\boldsymbol{R}$;
  Figure out $\boldsymbol{A}_c(\psi)$, $\boldsymbol{B}_c(\mathbf{v}_1, \cdots, \mathbf{v}_n, \psi)$;
  Discretize the system and combine the system equations for the next n steps;
  Set the constraints of the solution;
  Solve for $\mathbf{u}_L$ with quadratic programming;
  Solve $\boldsymbol{P}$;
  Gets the current status $\mathrm{x}(k)$ from the IMU;
  Solve $\mathbf{u}_N$;
  $\mathbf{u}_{in} = \mathbf{u}_L + \mathbf{u}_N$
end

The proposed approach is summarized in Alogrithm 1. To improve the performance when the robot tracks the desired state, i.e., to minimize $\|\mathrm{x}_{ref} - \mathrm{x}\|$, the following two steps are taken: the MPC algorithm solves for the optimal input $\mathbf{u}_L$, and the CNF is used to calculate $\mathbf{u}_N$ by introducing the error between the expected and actual values. These steps together form $\mathbf{u}_{in}$, which reduces the variation of pitch angle $|\theta_{\max} - \theta_{\min}|$ and the variation of roll angle $|\phi_{\max} - \phi_{\min}|$ within a certain time period, thereby improve the stability of the robot during motion.

4 Experiment

To illustrate the effectiveness of the proposed method, we simulated the transformation of the roll angle and pitch angle of the body of the quadruped robot under the control of MPC and CNF-MPC in the ROS environment.

Table 1: Motor Parameters

Joint	K_p	K_d	Rotatable Angle(rad)
Hip	150	20	[-1.57,1.57]
Thight	150	20	[-1.57,1.57]
Calf	100	10	[-3.14,3.14]

Table 2: Comparison Between CNF-MPC and MPC

Euler Angle	MPC	CNF-MPC
Roll(rad)	[-0.034, 0.071]	[-0.014, 0.006]
Pitch(rad)	[-0.063, 0.056]	[-0.021, -0.007]

The strategy used in this work is illustrated in Algorithm 1. The effectiveness of the control is verified through the comparison between MPC and CNF-MPC algorithms. The quadruped robot is set to move at a speed of $0.5\,\mathrm{m/s}$ using a trot gait for straight-line and the motion period is set to $0.5\,\mathrm{s}$. The foot trajectory follows a $5th$ order Bezier curve. The prediction horizon is set to $n = 10$. At the beginning of control, the joint torque is 0, and the robot lies on the ground. It is necessary to complete some settings of the motor parameters of the robot's thighs, calves and hip joints, including gain coefficient K_p, differential coefficient K_d, motor motion angle limit protection, the specific motion parameters are listed in Table 1. Increasing the coefficients K_p and K_d will increase the motion speed and torque.

In order to make the experimental results more reliable, we make the environment of the robot consistent, receive the command at the same time, and compare the control effect of different control algorithms. Fig.3 shows the action of the robot in motion. The pitch angle and roll angle of the quadruped robot are calculated by the IMU sensor mounted on the body and only need to be read at any time when in use. Fig.4 shows the comparison of the roll angle of the original MPC algorithm with that of the CNF control under the same circumstances. Fig.5 shows the comparison of the pitch angle under the control of the original MPC algorithm and the CNF control in the same case.

Under the control of MPC algorithm and CNF-MPC algorithm, the changes of pitch angle and roll angle during the movement of the quadruped robot are shown in Table 2. It can be seen from the experimental results that under the control of MPC algorithm, the variation range of the roll angle of the robot is close to $0.1\,\mathrm{rad}$, but with the introduction of CNF control method, the stability of the robot body during movement has been significantly improved, and the motion range of the robot can be controlled within $0.02\,\mathrm{rad}$. Sim-

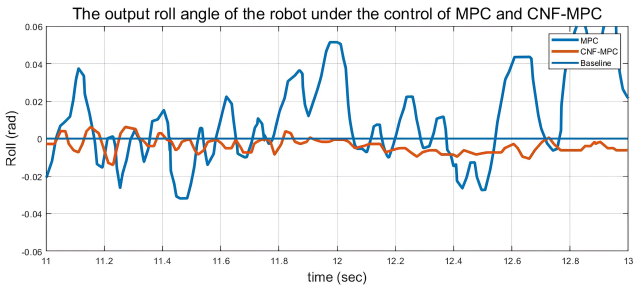

Fig. 4: Variation of roll angle under MPC and CNF-MPC.

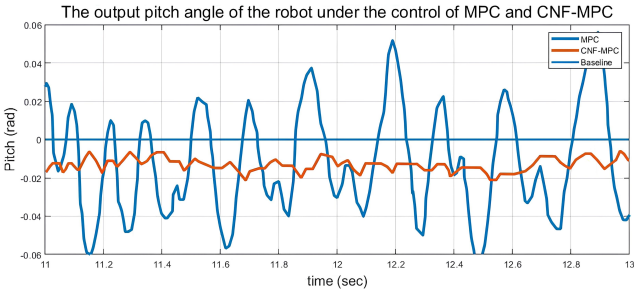

Fig. 5: Variation of pitch angle under MPC and CNF-MPC.

ilarly, under the control of MPC algorithm, the pitch angle of the quadruped robot changes at $0.12\,\mathrm{rad}$, but after the introduction of CNF control, the robot changes obviously become steady, and the stability of the body is well controlled, the change is within $0.02\,\mathrm{rad}$. This is also the improvement of the stability of the robotic system after using the CNF control.

5 Conclusions

Addressing the challenge of stability control for quadruped robots during motion, this paper proposes a controller capable of adjusting the optimal input torque of the system in different motion states to achieve better stability. To tackle the lack of motion prediction and effective adjustment of motion states during motion, an algorithm is proposed under the scheme of MPC that introduces CNF. By incorporating the deviation between the target state and the actual state, a nonlinear input compensation is constructed, and parameters are solved to form a composite nonlinear feedback control. Experimental results demonstrate that this method can improve the adaptability of quadruped robots to stable terrain during motion. In the future, we will validate the effectiveness of the controller through physical experiments.

References

[1] A. Skarlatos and T. Theodoulidis, "Calculation of the eddy-current flow around a cylindrical through-hole in a finite-thickness plate," *IEEE Transactions on Magnetics*, vol. 51, no. 9, pp. 1–7, 2015.

[2] A. Caccavale and M. Schwager, "A distributed algorithm for mapping the graphical structure of complex environments with a swarm of robots," in *2017 IEEE International Conference on Robotics and Automation (ICRA)*, 2017, pp. 1459–1466.

[3] A. Azari and C. Cavdar, "Self-organized low-power iot networks: A distributed learning approach," in *2018 IEEE Global Communications Conference*, 2018, pp. 1–7.

[4] J. Di Carlo, P. M. Wensing, B. Katz, G. Bledt, and S. Kim, "Dynamic locomotion in the mit cheetah 3 through convex model-predictive control," in *2018 IEEE/RSJ International Conference on Intelligent Robots and Systems*, 2018, pp. 1–9.

[5] J. JianJu and G. YunJian, "A enhanced self-assembly morphology distributed control algorithm of swarm robots," in *2017 2nd International Conference on Robotics and Automation Engineering (ICRAE)*, 2017, pp. 57–62.

[6] H. Li, R. J. Frei, and P. M. Wensing, "Model hierarchy predictive control of robotic systems," *IEEE Robotics and Automation Letters*, vol. 6, no. 2, pp. 3373 – 3380, 2021.

[7] A. Rigo, Y. Chen, S. K. Gupta, and Q. Nguyen, "Contact optimization for non-prehensile loco-manipulation via hierarchical model predictive control," 2022.

[8] S. Xu, L. Zhu, and C. P. Ho, "Learning efficient and robust multi-modal quadruped locomotion: A hierarchical approach," 2022, pp. 4649 – 4655.

[9] Z. Zhang, H. An, Q. Wei, and H. Ma, "Learning-based model predictive control for quadruped locomotion on slippery ground," 2022, pp. 47 – 52.

[10] H. Li, W. Yu, T. Zhang, and P. M. Wensing, "Zero-shot retargeting of learned quadruped locomotion policies using hybrid kinodynamic model predictive control," vol. 2022-October, 2022, pp. 11 971 – 11 977.

[11] U. A. Mishra, S. R. Samineni, P. Goel, C. Kunjeti, H. Lodha, A. Singh, A. Sagi, S. Bhatnagar, and S. Kolathaya, "Dynamic mirror descent based model predictive control for accelerating robot learning," in *2022 International Conference on Robotics and Automation (ICRA)*, 2022, pp. 1631–1637.

[12] Y.-H. Shin, S. Hong, S. Woo, J. Choe, H. Son, G. Kim, J.-H. Kim, K. Lee, J. Hwangbo, and H.-W. Park, "Design of kaist hound, a quadruped robot platform for fast and efficient locomotion with mixed-integer nonlinear optimization of a gear train," 2022, pp. 6614 – 6620.

[13] W. Lan and B. M. Chen, "On selection of nonlinear gain in composite nonlinear feedback control for a class of linear systems," in *2007 46th IEEE Conference on Decision and Control*, 2007, pp. 1198–1203.

[14] W. Lan, C. K. Thum, and B. M. Chen, "A hard-disk-drive servo system design using composite nonlinear-feedback control with optimal nonlinear gain tuning methods," *IEEE Transactions on Industrial Electronics*, vol. 57, no. 5, pp. 1735–1745, 2010.

[15] T. Horvat, K. Melo, and A. J. Ijspeert, "Model predictive control based framework for com control of a quadruped robot," vol. 2017-September, 2017, pp. 3372 – 3378.

[16] M. Chignoli and S. Kim, "Online trajectory optimization for dynamic aerial motions of a quadruped robot," vol. 2021-May, 2021, pp. 7693 – 7699.

[17] D. Kim, J. Di Carlo, B. Katz, G. Bledt, and S. Kim, "Highly Dynamic Quadruped Locomotion via Whole-Body Impulse Control and Model Predictive Control," *arXiv e-prints*, p. arXiv:1909.06586, Sep. 2019.

[18] B. M. Chen, T. H. Lee, K. Peng, and V. Venkataramanan, "Composite nonlinear feedback control for linear systems with input saturation: Theory and an application," *IEEE Transactions on Automatic Control*, vol. 48, no. 3, pp. 427 – 439, 2003.

[19] W. Lan and B. M. Chen, "On selection of nonlinear gain in composite nonlinear feedback control for a class of linear systems," in *2007 46th IEEE Conference on Decision and Control*, 2007, pp. 1198–1203.

[20] Z. Lin, M. Pachter, and S. Banda, "Toward improvement of tracking performance - nonlinear feedback for linear systems," *International Journal of Control*, vol. 70, no. 1, pp. 1 – 11, 1998.

Proceedings of the 3rd Conference on Fully Actuated System Theory and Applications
May 10-12, 2024, Shenzhen, China

Attitude Control of a Three-Cable-Driven Parallel Robot for Full-Mode Chattering Wind Tunnel Tests

Lei Zhan[1], Qi Lin[2], Weiyao Lan[1]

1. Department of Automation, Xiamen University, Xiamen 361005, P. R. China
E-mail: zhanlei@stu.xmu.edu.cn, wylan@xmu.edu.cn

2. College of Aeronautics and Astronautics, Xiamen University, Xiamen 361005, P. R. China
E-mail: qilin@xmu.edu.cn

Abstract: The purpose of this paper is to propose a kinematic attitude control method for the support system of wind tunnel full-mode flutter experiments. The support system discussed in this paper is a two-spring-three-Cable-driven parallel robot system (2S-3CDPRs). The paper utilizes the PID control strategy to achieve the desired attitude control. To begin, the paper establishes the kinematics and dynamics model of the aircraft model using the vector closure principle and Newton-Euler method. The mechanical system is then modeled using ADAMS software. The next step involves performing joint Simulink simulations with PID control to evaluate the effectiveness of the proposed method. Finally, the paper conducts experiments using a motion control card and applies Attitude and Heading Reference Systems (AHRS) to monitor the real-time attitude of the model. This step aims to further validate the practicality and excellent performance of the PID control method in adjusting the attitude of the support system. In summary, this paper presents a PID control-based kinematic attitude control method for the wind tunnel support system. The proposed method is evaluated through simulations and experiments, demonstrating its effectiveness and practical application in the context of the 2S-3CDPRs.

Key Words: Full-mode chattering, Under-constrained cable-driven parallel robot, Dynamic analysis, PID control

1 Introduction

Flutter is an aerodynamic phenomenon that can lead to serious damage to the structure of a vehicle. It is one of the key problems that must be solved in the process of aircraft design and development. In order to simulate the flutter phenomenon during the real flight of the aircraft in the wind tunnel, it is necessary to make the support system release five degrees of freedom to the whole aircraft model, and only constrain the degrees of freedom in the direction of the incoming flow from the wind tunnel. At the same time, the rigid body modal frequency of the support should be as low as possible to ensure that it is in the range of 1/10 to 1/3 of the model's intrinsic frequency [1]. This will effectively minimize the structural dynamic disturbances to the model itself and reduce the aerodynamic disturbances to the model. Therefore, it is necessary to use soft elastic support methods as much as possible, so cable traction parallel support techniques are widely used [2, 3].

The Cable-driven parallel robot system utilizes a cable to connect the mobile platform to the fixed base, and the position of the mobile platform is controlled through cable winding [4, 5]. This mechanism offers several advantages over other support systems, including high load capacity, low inertia, and a large working space. Furthermore, it boasts a low construction cost and easy installation in an open environment. By incorporating springs, the system undergoes significant changes in its static and dynamic characteristics, thereby improving the rigid body modal frequencies to meet the support requirements [6].

In the field of under-constrained Cable-driven parallel robot system, various control strategies have been proposed. Some of these include PI plus fuzzy control [7], active fault-tolerant control [8], partial-feedback linearized control combined with online trajectory planning [9], feedback linearized control [10, 11], and stationary-to-stationary trajectory planning control[12].

The outline of the article is as follows. Section II provides an explanation of the two-spring-three- Cable-driven parallel robot system (2S-3CDPRs) problem description and research methodology. Section III establishes the kinematic and dynamic models of the cable-driven parallel robot, compensating for the deformation length of the spring within the model. This compensation accounts for the deformation of the spring in the model. In Section IV, the mechanical model of the test mechanism is established in ADAMS, the model interface is set up, and co-simulation with Simulink is conducted to verify the excellent effect and practicability of the PID control method in the attitude control of 2S-3CDPRs. Finally, experimental validation is carried out. Section V provides the paper's conclusion.

2 Problem Description

In wind tunnel full-mode flutter experiments, there is a lack of data and control strategy studies regarding the application of two-spring-three-cable-driven parallel robots (2S-3CDPRs). To bridge this gap, this study proposes the utilization of PID controllers to precisely control the roll and pitch angles of the aircraft model. The objective is to enhance experimental stability and accuracy, while offering a novel solution for investigating the dynamic characteristics of aircraft in wind tunnel tests. In this paper, a PID controller is designed and optimized to regulate the roll and pitch angles of the aircraft model using a joint simulation of ADAMS and Simulink. Subsequently, the effectiveness and accuracy of the control strategy are experimentally validated.

3 Dynamic Model

The demand for support systems in wind tunnel full-mode flutter experiments has created a need for relevant experimental data and control experiments of support systems

This work was supported in part by the National Natural Science Foundation of China under Grants 62273285 and 12072304.

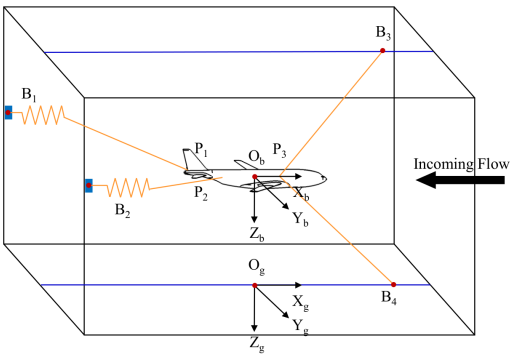

Fig. 1: Schematic diagram of 2S-3CDPRs

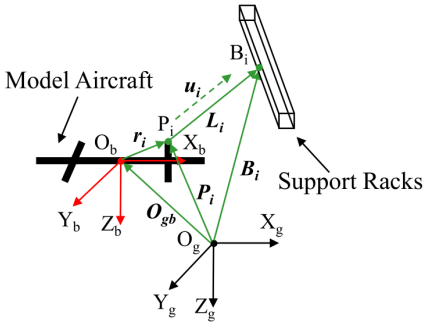

Fig. 2: Kinematics of an under-constrained CDPRs

incorporating two-spring-three- Cable-driven parallel robot system (2S-3CDPRs). In this paper, we present a design for a two-spring-three- Cable-driven parallel robot system (2S-3CDPRs), as shown in Fig. 1. The system mainly consists of one vertical cable (B_3B_4), two horizontal cables (B_1P_1, B_2P_2) equipped with series springs, the support frame, the transmission, the drive, the attitude detection module, and the control module. One end of the horizontal cables (B_1P_1, B_2P_2) is fixed on the horizontal pulley set at the rear end of the fuselage, while the other end is fixed on the slider of the transmission device on the frame. Vertical cables (B_3B_4) pass around the vertical pulley set at the front end of the fuselage and are fixed to the slider of the transmission device after passing around the fixed pulley on the frame. The motor drives the slider in the same direction or the opposite direction to control pitch and roll attitude. The spring is introduced to provide passive force to keep the cable in a certain tension [6].

3.1 Kinematic Model

To describe the kinematic modeling of the unconstrained cable traction parallel system, a dynamic coordinate system (fuselage coordinate system) and a static coordinate system (ground coordinate system) were established, as depicted in Fig. 2. The two short black rods on the airplane model in the figure represent the vertical pulley block at the front end of the fuselage and the horizontal pulley block at the rear end of the fuselage, respectively. Fig. 2 illustrates the fuselage coordinate system established on the aircraft model as $O_bX_bY_bZ_b$, with the origin O_b coinciding with the center of mass P of the aircraft model. The X_b axis aligns with the main axis of the fuselage, and its positive direction points towards the front end of the fuselage. The Z_b axis lies in the plane of symmetry of the aircraft model, perpendicular to the X_b axis, and its positive direction is directed towards the lower part of the aircraft model. The Y_b axis is perpendicular to the plane of symmetry of the aircraft model, and its positive direction follows the right-hand rule. The ground coordinate system $O_gX_gY_gZ_g$ is established with the geometric center of the bottom surface of the support frame as the origin. The positive direction of the Z_g axis corresponds to the direction of gravity, i.e., vertically downward; the positive direction of the X_g axis points towards the incoming flow from the wind tunnel; and the positive direction of theY_g axis hangs down from the X_g axis in accordance with the right-hand rule.

Assuming that all cables are under tension and considering that one cable at the front end of the fuselage is equivalent to two cables, we define L_i as the vector between the hinge point P_i of the ith cable, connecting the end-effector (i.e., the airplane model), and the fixed hinge point B_i (i.e., the fixed pulley) on the support frame. In the ground coordinate system, the cable vector Li can be expressed as

$$\boldsymbol{L}_i = \boldsymbol{B}_i - (\boldsymbol{X}_P + \boldsymbol{R}\boldsymbol{x}_{p_i}) \tag{1}$$

where $i \in \mathbb{R}$, $\boldsymbol{B}_i$ is the position vector of point B_i in the ground coordinate system, $\boldsymbol{X}_p$ is the position vector of point $\boldsymbol{Ob(P)}$ in the ground coordinate system, $\boldsymbol{x}_{pi}$ is the position vector of point P_i in the fuselage coordinate system, and $\boldsymbol{R}$ is the rotation matrix from the fuselage coordinate system to the ground coordinate system. The rotation matrix $\boldsymbol{R}$ is denoted as:

$$\boldsymbol{R} = \begin{bmatrix} c\theta c\varphi & s\phi s\theta c\varphi - c\phi s\varphi & c\phi s\theta c\varphi + s\phi s\varphi \\ c\theta s\varphi & s\phi s\theta s\varphi + c\phi c\varphi & c\phi s\theta s\varphi - s\phi c\varphi \\ -s\theta & s\phi c\theta & c\phi c\theta \end{bmatrix} \tag{2}$$

where in the rotation matrix $\boldsymbol{R}$, c represents the cos trigonometric function and s represents the sin trigonometric function ϕ, θ, and φ represent the roll angle, pitch angle, and yaw angle, respectively. These angles correspond to the independent rotations of the fuselage coordinate system relative to the positive directions of the X_g,Y_g,and Z_g axes in the ground coordinate system. The rotation order of matrix $\boldsymbol{R}$ is specified as Z-Y-X, indicating that the rotation occurs around the Z-axis first (yaw), followed by the Y-axis (pitch), and finally the X-axis (roll). This particular order of rotations determines the sequential application of rotations to determine the final orientation of the fuselage coordinate system with respect to the ground coordinate system.

Then, the length L_i of the ith cable can be expressed as:

$$\mathrm{L_i} = \sqrt{\boldsymbol{L}_i^T \boldsymbol{L}_i} \tag{3}$$

It follows from (1) and (3) that

$$\mathrm{L_i^2} = (\boldsymbol{L}_i)^T (\boldsymbol{B}_i - \boldsymbol{X}_P - \boldsymbol{R}\boldsymbol{x}_{pi}) \tag{4}$$

Derivating both sides of (4) with respect to time, simplifying can be obtained:

$$\mathrm{L_i}\dot{\mathrm{L}}_\mathrm{i} = (\boldsymbol{L}_i)^T \left(-\dot{\boldsymbol{X}}_P - \dot{\boldsymbol{R}}\boldsymbol{x}_{pi}\right) \tag{5}$$

$\dot{\boldsymbol{R}}$ is the time derivative of the rotation matrix $\boldsymbol{R}$ from the fuselage coordinate system to the ground coordinate system.

$$\dot{\boldsymbol{R}} = \boldsymbol{R}^{\circ}\boldsymbol{R} \tag{6}$$

$$\boldsymbol{R}^{\circ} = \omega^{\times} = \begin{bmatrix} 0 & -\omega_{\mathrm{z}} & \omega_{\mathrm{y}} \\ \omega_{\mathrm{z}} & 0 & -\omega_{\mathrm{x}} \\ -\omega_{\mathrm{y}} & \omega_{\mathrm{x}} & 0 \end{bmatrix} \tag{7}$$

$$\omega = \begin{bmatrix} \omega_{\mathrm{x}} & \omega_{\mathrm{y}} & \omega_{\mathrm{z}} \end{bmatrix}^{T} \tag{8}$$

ω is the angular velocity of the aircraft model in the ground coordinate system, and $\omega^{\times}$ is the antisymmetric matrix of ω.

Substituting (6) into (5), and then using $\boldsymbol{R}^{\circ} = \omega^{\times}$, we can get:

$$\mathrm{L_i}\dot{\mathrm{L}}_{\mathrm{i}} = (\boldsymbol{L}_i)^{T}\left(-\dot{\boldsymbol{X}}_P - \omega \times \boldsymbol{R}\boldsymbol{x}_{pi}\right) \tag{9}$$

Let $\boldsymbol{R}\boldsymbol{x}_{pi} = \boldsymbol{r}_i$, then

$$\mathrm{L_i}\dot{\mathrm{L}}_{\mathrm{i}} = (\boldsymbol{L}_i)^{T}\left(-\dot{\boldsymbol{X}}_P - \omega \times \boldsymbol{r}_i\right) \tag{10}$$

Simplifying (10), then

$$\mathrm{L_i}\dot{\mathrm{L}}_{\mathrm{i}} = -(\boldsymbol{L}_i)^{T}\dot{\boldsymbol{X}}_P - (\boldsymbol{r}_i \times \boldsymbol{L}_i)^{T}\omega \tag{11}$$

Write (11) in matrix form

$$\tilde{\boldsymbol{L}}\dot{\boldsymbol{L}} = -\tilde{\boldsymbol{J}}\dot{\boldsymbol{X}}_{\omega} \tag{12}$$

In (12), each matrix is defined in turn as

$$\begin{cases} \dot{\boldsymbol{L}} = \begin{bmatrix} \dot{\mathrm{L}}_1 & \dot{\mathrm{L}}_2 & \dot{\mathrm{L}}_3 & \dot{\mathrm{L}}_4 \end{bmatrix}^{T} \\ \tilde{\boldsymbol{L}} = \mathrm{diag}\begin{bmatrix} \mathrm{L}_1 & \mathrm{L}_2 & \mathrm{L}_3 & \mathrm{L}_4 \end{bmatrix} \\ \dot{\boldsymbol{X}}_{\omega} = \begin{bmatrix} \dot{\boldsymbol{X}}_P & \omega \end{bmatrix}^{T} = \begin{bmatrix} \boldsymbol{v} & \omega \end{bmatrix}^{T} \\ \tilde{\boldsymbol{J}} = \begin{bmatrix} \boldsymbol{L}_1 & \boldsymbol{L}_2 & \boldsymbol{L}_3 & \boldsymbol{L}_4 \\ \boldsymbol{r}_1 \times \boldsymbol{L}_1 & \boldsymbol{r}_2 \times \boldsymbol{L}_2 & \boldsymbol{r}_3 \times \boldsymbol{L}_3 & \boldsymbol{r}_4 \times \boldsymbol{L}_4 \end{bmatrix}^{T} \end{cases} \tag{13}$$

where $\dot{\boldsymbol{X}}_{\omega}$ is the velocity vector of the aircraft model, which contains the linear and angular velocities of the aircraft model with respect to the ground coordinate system, $\boldsymbol{v}$ and ω. Then, (12) can be written as

$$\dot{\boldsymbol{L}} = -\tilde{\boldsymbol{L}}^{-1}\tilde{\boldsymbol{J}}\dot{\boldsymbol{X}}_{\omega} = -\boldsymbol{J}\dot{\boldsymbol{X}}_{\omega} \tag{14}$$

where $\boldsymbol{J}$ is the Jacobi matrix (4×6) of the 2S-3CDPRs organization with the expression:

$$\boldsymbol{J} = \begin{bmatrix} \boldsymbol{u}_1 & \boldsymbol{u}_2 & \boldsymbol{u}_3 & \boldsymbol{u}_4 \\ \boldsymbol{r}_1 \times \boldsymbol{u}_1 & r_2 \times \boldsymbol{u}_2 & r_3 \times \boldsymbol{u}_3 & r_4 \times \boldsymbol{u}_4 \end{bmatrix}^{T} \tag{15}$$

Where $\boldsymbol{u}_i$ is the unit vector of the cable. Equation (14) relates the motion of the cable to the aircraft model through the Jacobi matrix. In the modeling of a spring that is equivalent to a cable, the Jacobi matrix does not include the rotation of the spring on the aircraft model. During the movement of the cable, the tension is transmitted to the spring, resulting in displacement in the direction of B_iP_i. To compensate for this displacement, ΔL_i is introduced, which is defined as the difference between the lengths of the ith spring in its initial state and after deformation due to the tension, given by ΔL_i = (t_{si}- t_{s0})/k_s, where t_{si} is the force generated by the deformation of the ith spring, t_{s0} is the initial preload of the ith spring, and k_s is the spring stiffness coefficient.

3.2 Dynamical Model

Number section and subsection headings consecutively in Arabic numbers and type them in bold. Avoid using too many capital letters. If any further subdivision of a subsection is needed the titles should be 10 point and flushed left.

The approach for modeling the dynamics of the two-spring-three-cable support system is outlined as follows:

1)The two cables connected to the tandem spring are treated as cables with lower stiffness.

2)Both the cable and the spring are assumed to be in a taut state and can be approximated as straight line segments.

3)In order to focus on the motion characteristics of the airplane model, the masses of the Kevlar cable and the spring are neglected, and the airplane model is simplified as a rigid body.

The dynamic equations of the airplane model are derived using the Newton-Euler method. The matrix form of these equations is presented as

$$\begin{bmatrix} m\boldsymbol{I}_{3\times3} & \boldsymbol{0}_{3\times3} \\ \boldsymbol{0}_{3\times3} & \boldsymbol{I}_p \end{bmatrix}\begin{bmatrix} \ddot{\boldsymbol{X}}_p \\ \dot{\omega} \end{bmatrix} + \begin{bmatrix} \boldsymbol{0}_{3\times1} \\ \omega \times \boldsymbol{I}_p\omega \end{bmatrix} - \begin{bmatrix} m\boldsymbol{g} \\ \boldsymbol{0}_{3\times1} \end{bmatrix} = \boldsymbol{J}^{T}\boldsymbol{T} \tag{16}$$

where the variables and matrices are defined as

$\boldsymbol{m}$: Mass of the aircraft model,

$\boldsymbol{I}_{3\times3}$: Unit matrix of size 3×3,

$\boldsymbol{I}_p$: Inertia matrix of the center of mass of the aircraft model,

$\boldsymbol{X}_p$: Position vector of the aircraft model,

ω: Angular velocity vector of the aircraft model,

$\boldsymbol{T}$: Vector of tension values of the cables,

$\boldsymbol{J}^{T}$: Structural matrix of the mechanism of the two-spring-three-cable support system.

It is stated that treating the two cables of the tandem springs as cables with lower stiffness does not affect the structural matrix $\boldsymbol{J}^{T}$. This implies that the assumption of lower stiffness for the cables does not alter the overall structure or arrangement of the system, and the matrix $\boldsymbol{J}^{T}$ remains unchanged.

The attitude vector of the airplane model, denoted as $\boldsymbol{X} = [\boldsymbol{X}_p\boldsymbol{\Phi}]^{T} = [\mathrm{x\ y\ z}\ \phi\ \theta\ \varphi]^{T}$, where $\boldsymbol{\Phi}$ represents the Euler angles $[\phi\ \theta\ \varphi]$ for roll, pitch, and yaw respectively. In accordance with the principle of rigid body rotation around a fixed point, the angular velocity vector of the airplane model can be expressed as:

$$\omega = \begin{bmatrix} \omega_x & \omega_y & \omega_z \end{bmatrix}^{T} = \boldsymbol{E}\dot{\boldsymbol{\Phi}} \tag{17}$$

ω represents the angular velocity vector and $\boldsymbol{E}$ denotes the mapping matrix that relates the time derivative of $\boldsymbol{\Phi}$ to the angular velocity vector, where

$$\boldsymbol{E} = \begin{bmatrix} \cos\theta\cos\varphi & -\sin\varphi & 0 \\ \cos\theta\sin\varphi & \cos\varphi & 0 \\ -\sin\theta & 0 & 1 \end{bmatrix} \tag{18}$$

Combining (17) with (16), we can express (16) in terms of the attitude vector of the airplane model as

$$\boldsymbol{M}(\boldsymbol{X})\ddot{\boldsymbol{X}} + \boldsymbol{C}(\boldsymbol{X},\boldsymbol{X})\dot{\boldsymbol{X}} - \boldsymbol{G}(\boldsymbol{X}) = \boldsymbol{J}^{T}\boldsymbol{T} \tag{19}$$

This equation establishes the relationship between the cable tension and the kinematics of the model, where

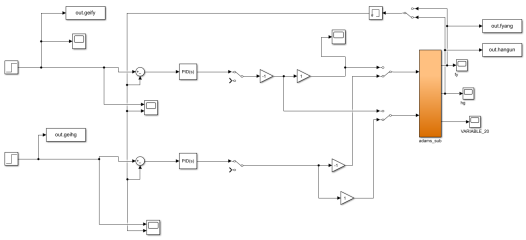

Fig. 3: System simulation structure

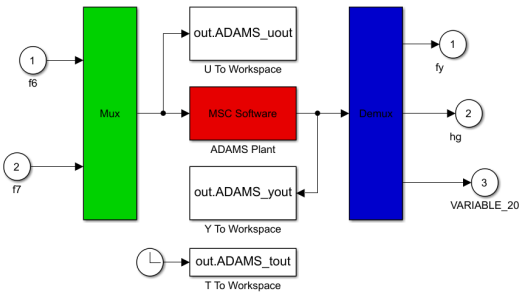

Fig. 4: Schematic diagram of ADMAS data exchange with Simulink

$$\begin{cases} \boldsymbol{G}(\boldsymbol{X}) = \begin{bmatrix} m\boldsymbol{g} \\ \boldsymbol{0}_{3\times 1} \end{bmatrix} \\ \boldsymbol{M}(\boldsymbol{X}) = \begin{bmatrix} m\boldsymbol{I}_{3\times 3} & \boldsymbol{0}_{3\times 3} \\ \boldsymbol{0}_{3\times 3} & \boldsymbol{I}_p\boldsymbol{E} \end{bmatrix} \\ \boldsymbol{C}(\boldsymbol{X}, \dot{\boldsymbol{X}}) = \begin{bmatrix} \boldsymbol{0}_{3\times 3} & \boldsymbol{0}_{3\times 3} \\ \boldsymbol{0}_{3\times 3} & \boldsymbol{I}_p\dot{\boldsymbol{E}} + (\boldsymbol{E}\dot{\boldsymbol{\Phi}}) \times \boldsymbol{I}_p\boldsymbol{E} \end{bmatrix} \end{cases} \tag{20}$$

4 Simulation and Experiment

4.1 Simulation Settings

ADAMS is especially suitable for simulating complex mechanical structures in robotic systems. On the other hand, Simulink is a dynamic system modeling and simulation tool within the MATLAB environment. It excels in the design, analysis, and implementation of control system algorithms. By combining these two engineering software programs, different modeling techniques that do not require mathematical models can be implemented [13].

The MSC Sofeware module is configured within the adams sub module. After completing the setup, a PID control system module is constructed, and simulation parameters are defined in Simulink. Finally, the entire system is co-simulated to observe its performance. The system's response curve is analyzed to verify the controller's performance, including aspects such as stability, speed, overshoot, and settling time. Based on the simulation results, PID parameters are adjusted iteratively until a satisfactory control effect is achieved. The system simulation structure is shown in Fig. 3.

The construction of the control system module and the setting of the simulation parameters are implemented in the "adams sub" module, as illustrated in Fig. 4.

The PID control principle is based on three fundamental mathematical operations on the system output error: proportional (P), integral (I), and derivative (D), which are used to dynamically adjust the output of the controller for precise control of the controlled process. The PID parameters, namely Kp (proportional gain), Ki (integral gain), and Kd (derivative gain), can be tuned manually using empirical methods, theoretical calculations (such as the Ziegler-Nichols method), trial-and-error techniques, fuzzy control rule self-tuning, or other methods [13, 14]. The schematic diagram of the system is illustrated in Fig. 5.

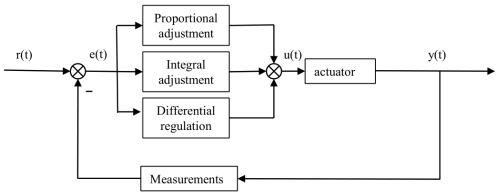

Fig. 5: Schematic diagram of PID system

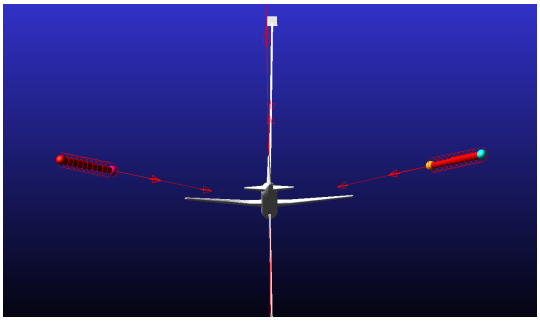

Fig. 6: Pitch dynamics simulation in ADAMS

The controller output can be expressed as:

$$u(t) = K_p e(t) + K_i \int e(t)dt + K_d \frac{de(t)}{dt} \tag{21}$$

4.2 Pitching Attitude Simulation

After repeated analysis and adjustment of the simulation results, the values of the PID controller parameters are finally determined as follows: the proportional gain K_p is set to 200, the integral gain K_i is set to 300, and the differential gain K_d is set to 0.0001, which achieves the ideal control effect. The pitch angle of the airplane model can be controlled by adjusting the same direction movement of the slider. The ADAMS simulation model of 2S-3CDPRs with a pitch angle ranging from 0° to +10° is depicted in Fig. 6, while the variation and expected values of the pitch angle are presented in Fig. 7.

Regarding the regulation of the roll attitude, the unidirectional pitch angle can reach 10°, allowing for an adjustment range of the pitch attitude angle between -10° and +10°.

4.3 Rolling Attitude Simulation

After repeated analysis and adjustment of the simulation results, the values of the PID controller parameters are finally determined as follows: the proportional gain K_p is set to 100, the integral gain K_i is set to 500, and the differential gain K_d is set to 0.001, which achieves the ideal control effect. The roll angle of the airplane model can be controlled by adjusting the opposite direction movement of the slider.

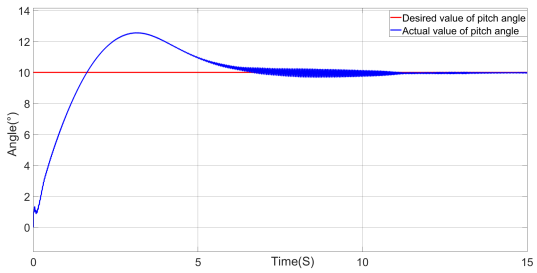

Fig. 7: PID control of pitch attitude angle response

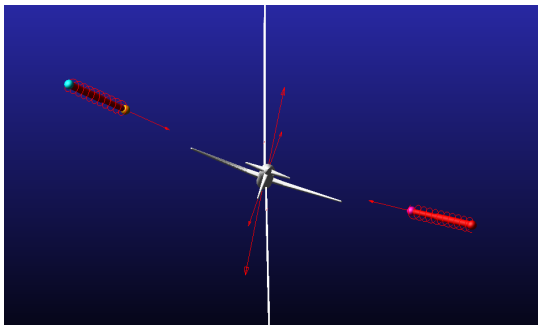

Fig. 8: Roll dynamics simulation in ADAMS

The ADAMS simulation model of 2S-3CDPRs with a roll angle ranging from 0° to +20° is depicted in Fig. 8, while the variation and expected values of the roll angle are presented in Fig. 9.

Regarding the regulation of the roll attitude, the unidirectional pitch angle can reach 20°, allowing for an adjustment range of the roll attitude angle between -20° and +20°.

4.4 Experimental Verification

The ground prototype built in the laboratory is shown in Fig. 10. The prototype uses a horizontal cable reconfiguration module firstly the cable is fixed to the slider of the ball screw, the upper computer inputs the motor control command, through the control card, the driver, and finally the motor drives the screw to drive the slider movement. During the movement, AHRS is used to measure the attitude.

To configure the motor driver before the experiment, follow these steps:

1)Set the servo motor to position control mode: Configure the servo motor to operate in position control mode. This mode allows for precise control of the motor's position and facilitates accurate positioning of the slider on the ball screw.

2)Adjust the electronic gears: Fine-tune the electronic

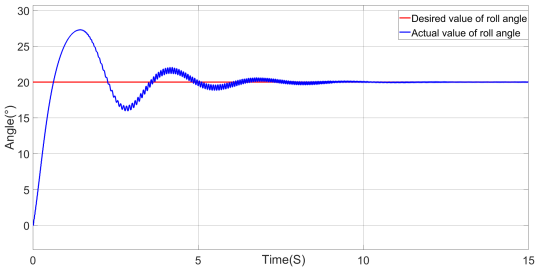

Fig. 9: PID control of roll attitude angle response

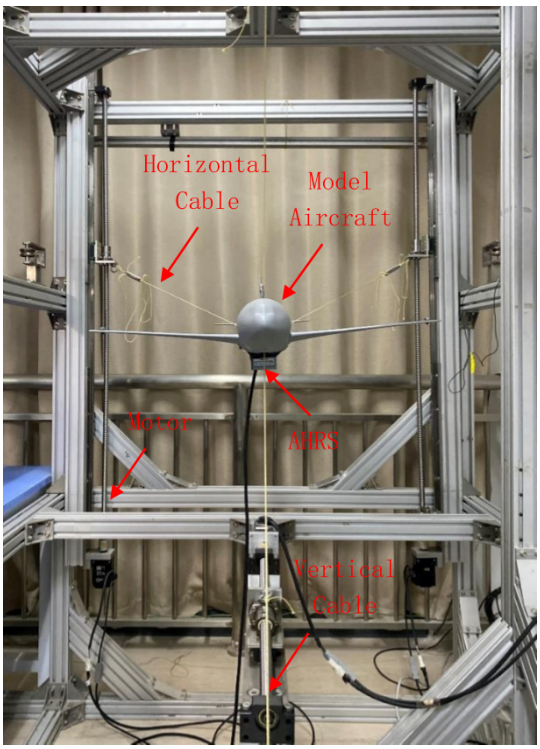

Fig. 10: 2S-3CDPRs test mechanism

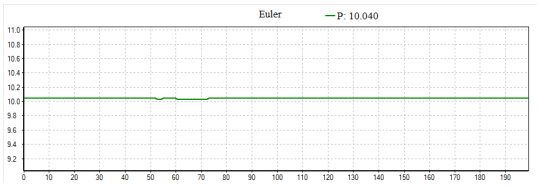

Fig. 11: Real-time monitoring of pitch attitude

gearing mechanism to achieve the desired motion characteristics.

Next, configure the control card parameters:

1)Set the closed-loop mode: Configure the control card to operate in closed-loop mode.

2)Adjust the PID parameters: Set the PID parameters on the control card to optimize the control system's performance.

The AHRS system is employed to monitor the attitude of the model. The control subsystem utilizes the AHRS measurements to make necessary adjustments to the model's attitude. The PID control algorithm, operating in position control mode, can effectively eliminate positional errors and maintain stability, ensuring that the slider accurately reaches the target position for adjusting the model's attitude.

4.5 Pitching Control

The method described involves controlling the isotropic motion of the slider to adjust the pitch angle of the aircraft model. At the initial moment, the model has a zero attitude, and commands are sent from the upper computer of the control system to the servo drive. The motor then operates according to these commands, propelling the slider in the same direction and at the same speed. As the slider moves, the pulleys adjust the spatial configuration of the horizontal

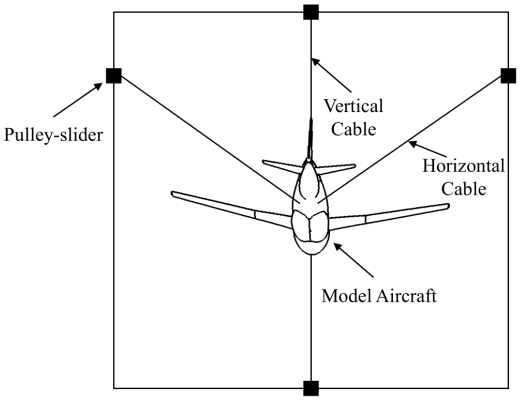

Fig. 12: Attitude of pitching

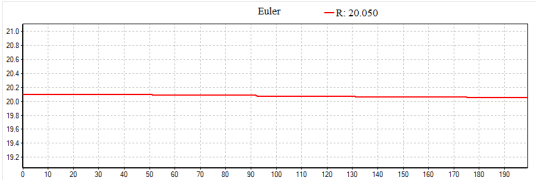

Fig. 13: Real-time monitoring of roll attitude

rope, thereby modifying the attitude of the aircraft model.

The Attitude and Heading Reference System (AHRS) monitors the model attitude in real time, and the pitch angle of the model after stabilization is shown in Fig. 11. Take Fig. 12 as an example, when looking from the back of the horizontal rope, the motion displacement of the left and right sliders away from the initial position is equal in size and direction.

4.6 Rolling Control

By controlling the isotropic motion of the slider, the pitch angle of the aircraft model can be controlled. Initially, the model is in a zero-attitude state. The upper computer of the control system sends commands to the servo drive, which in turn instructs the motor to move the slider in the desired direction and at a consistent speed. As the slider moves, the pulleys adjust the spatial configuration of the horizontal rope, thereby modifying the attitude of the aircraft model.

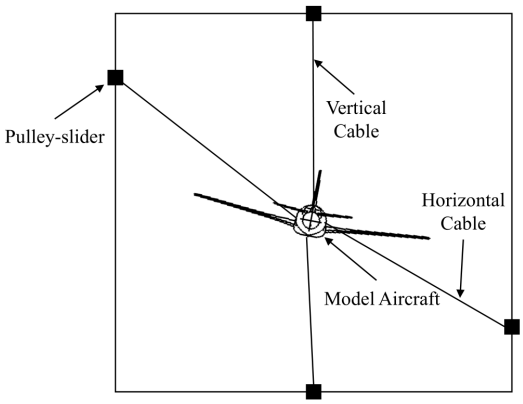

Fig. 14: Attitude of rolling

The Attitude and Heading Reference System (AHRS) monitors the model attitude in real time, and the roll angle of the model after stabilization is shown in Fig. 13. Taking Fig. 14 as an example, the left slider moves downward while the right slider moves upward.

5 Conclusion

The PID control strategy employed in the experiments has effectively achieved precise control of the attitude of the aircraft model within the cable-driven parallel robot mechanism. Furthermore, all attitudes reached the desired values and exhibited rapid stabilization. This demonstrates the potential for practical application and further development of this approach in controlling the attitude of aircraft models using rope-traction parallel robot mechanisms.

References

[1] B. Lu, X. Yang, J. Luo, et al, Suspension support system for full-mode flutter test in transonic wind tunnel. *Experimental Fluid Mechanics*, 2009, 23(3): 90–94.

[2] Z. Zhao, Y. Yan, K. Zeng, et al, Multi-body dynamic analysis of three-cable suspension system in full-mode vibration wind tunnel. *Journal of Aeronautics*, 2020,41(11):277–287.

[3] S. Cole, J. Garcia, Past, present, and future capabilities of the Transonic Dynamics Tunnel from an aeroelasticity perspective. *41st Structures, Structural Dynamics, and Materials Conference and Exhibit*, 2012: 1767.

[4] J. -P. Merlet and D. Daney, A portable, modular parallel wire crane for rescue operations, *2010 IEEE International Conference on Robotics and Automation*, 2010: 2834–2839.

[5] A. V. Maloletov, M. Y. Fadeev, A. S. Klimchik, Error analysis in solving the inverse problem of the cable-driven parallel underactuated robot kinematics and methods for their elimination, *IFAC–PapersOnLine*, 2019, 52(13): 1156–1161.

[6] P. Zhang, W. Lu, X. Lv, Analysis of main resonance response of suspension cables with additional spring protection device, *Journal of Vibration Engineering*, 2020, 33(3): 550–558.

[7] B. Zi, B. Y. Duan, J. L. Du, et al, Dynamic modeling and active control of a cable-suspended parallel robot, *Mechatronics*, 2008, 18(1): 1–12.

[8] S. M. Fazeli, M. Abedi, A. Molaei, et al, Active fault-tolerant control of cable-driven parallel robots, *Nonlinear Dynamics*, 2023, 111(7): 6335–6347.

[9] L. Scalera, A. Gasparetto, D. Zanotto, Design and experimental validation of a 3-DOF underactuated pendulum-like robot, *IEEE/ASME Transactions on Mechatronics*, 2019, 25(1): 217–228.

[10] J. Begey, L. Cuvillon, M. Lesellier, M. Gouttefarde and J. Gangloff, Dynamic control of parallel robots driven by flexible cables and actuated by position-controlled winches, *IEEE Transactions on Robotics*, 2018, 35(1): 286–293.

[11] A. A. Kumar, J. F. Antoine, G. Abba, Input-Output Feedback Linearization for the Control of a 4 Cable-Driven Parallel Robot, *IFAC–PapersOnLine*, 2019, 52(13): 707–712.

[12] E. Idà, T. Bruckmann and M. Carricato. Rest-to-rest trajectory planning for underactuated cable-driven parallel robots, *IEEE Transactions on Robotics*, 2019, 35(6): 1338–1351.

[13] A. Çakan and F. M. Botsalı, and M. Tınkır, Pid control of inverted pendulum using adams and matlab co-simulation, *Proceedings of the 4th international conference on control, mechatronics and automation*, 2016: 136–139.

[14] M. Carpio, R. Saltaren, J. Viola, C. Calderon, J. Guerra, Proposal of a decoupled structure of fuzzy-pid controllers applied to the position control in a planar cdpr, *Electronics*, 2021, 10(6): 745.

Proceedings of the 3rd Conference on Fully Actuated System Theory and Applications
May 10-12, 2024, Shenzhen, China

Modeling, simulation and experiment of an origami robot with a coupled bar-hinge mechanism

Junpeng Mai[1], Hanzhao Shao[2], Shaojie Liu[1], Yuanzhuo Zhang[3], Liangming Chen[1], and Huijuan Feng[3]

1. School of System Design and Intelligent Manufacturing and Shenzhen Key Laboratory of Control Theory and Intelligent Systems, Southern University of Science and Technology, Shenzhen 518055, P. R. China
E-mail: 12112316@mail.sustech.edu.cn; 12112313@mail.sustech.edu.cn; chenlm6@sustech.edu.cn

2. Department of Electronic and Electrical Engineering, Southern University of Science and Technology, Shenzhen 518055, P. R. China
E-mail: 12111024@mail.sustech.edu.cn;

3. Department of Mechnical and Energy Engineering, Southern University of Science and Technology, Shenzhen 518055, P. R. China
E-mail: 12110303@mail.sustech.edu.cn; fenghj@sustech.edu.cn

Abstract: This paper aims to analyze the motion behavior of an origami robot with a coupled bar-hinge mechanism. By disassembling the planar six-hinge mechanism into two planar four-hinge mechanisms with coupled motion, this paper derives the kinematics of the planar six-hinge mechanism based on the algebraic differential kinematics of the planar four-hinge motions. The rotational angle change and the moving step length of the origami robot are further calculated. Finally, the theoretical motion model is verified with the motion simulation data of the planar six-hinge mechanism origami robot in SolidWorks and the experimental data of the physical model. This verification proves the feasibility of the theoretical analysis, simulation model, and physical model.

Key Words: Origami robot, kinematics, modeling and simulation, bar-hinge mechanism, angle change

1 Introduction

Origami, an ancient art form from the East, has evolved over thousands of years. Initially, it served as a decorative paper folding technique. However, today, origami has transcended artistic boundaries to revolutionize engineering and design. The unique appeal of origami structures lies in their ability to transform two-dimensional materials into complex three-dimensional shapes while maintaining lightness and foldability. This transformative capability of origami structures has unveiled immense potential in various engineering applications, particularly robotics.

In robotic engineering, origami structures are favored for their flexibility, lightweight, and high reconfigurability. These properties streamline and economize robot designs and enhance robots' adaptability to diverse environments and tasks. A notable example is the modular robot named Pneumagami, powered by soft pneumatic actuators and incorporating construction principles inspired by origami[1]. This design approach results in a lightweight, robust robot that is particularly suitable for wearable robotics applications.

The application of origami structures in robotic leg design mainly showcases their advantages. Origami-inspired designs enable robotic legs that are lightweight yet robust, offering enhanced adaptability and mobility. For instance, using a self-locking foldable mechanism in robotic arms allows them to be folded flat and maintain high stiffness when deployed[2], facilitating mobile robots and uncrewed aerial vehicles (UAVs) to access confined spaces. This origami-inspired design balances being lightweight, compact, and scalable while maintaining kinematic behavior. Additionally, the design of deformable wheels based on origami structures, as showcased by Lee et al.[3], exemplifies the adaptability of origami in robotic locomotion, enabling robots to navigate through small gaps by altering the shape or size of their wheels.

This paper aims to analyze the motion state of a planar origami robot with a six-hinge mechanism according to the design given in [4]. The planar six-hinge mechanism is disassembled into a four-hinge mechanism, and constraint conditions are added. This paper focuses on the angle change and the moving step length of the six-hinge origami robot. Finally, the motion model is mutually verified based on theoretical analysis with the motion simulation data of the planar six-hinge mechanism origami robot in SolidWorks and the experimental data of the physical model.

Subsequently, the crank-rocker mechanism within the four-hinge setup is deliberated upon for selection as the robot's leg structure. This decision perfectly aligns with the objectives of achieving efficient, controlled movement in the robot's design. The crank facilitates effective rotation, while the rocker enables the robot's legs to achieve motion through its rotation.

2 Design

2.1 Mechanical Structure Analysis and Selection

The experimental plan involves using a steering motor to manipulate the folding and unfolding of an origami structure, which is crucial for the robot's movement. Inspiration for selecting an appropriate mechanical structure was drawn from the existing origami robot designed in [4]. The chosen structure is a planar six-hinge mechanism, evolving from the planar four-hinge mechanism.

This framework begins by analyzing the four-hinge mechanism using the Freudenstein equation. This analysis yields the input-output equation, laying the foundation for comprehending the motion behavior of the planar origami robot.

Subsequently, the crank-rocker mechanism within the four-hinge setup is deliberated upon for selection as the

This work is supported by Shenzhen Key Laboratory of Control Theory and Intelligent Systems under Grant ZDSYS20220330161800001 and College Students' Innovative and Entrepreneurial Training Program under Grant 2023X31.

robot's leg structure. This decision perfectly aligns with the objectives of achieving efficient, controlled movement in the robot's design. The crank facilitates effective rotation, while the rocker enables the robot's legs to achieve motion through its rotation.

2.2 Planar Six-hinge Mechanism Analysis and Modeling

An in-depth analysis and modeling of the planar six-hinge mechanism, a pivotal component of the experimental model, is undertaken. This mechanism, abstracted from the steering motor, swinging arms, and moving cardboard, embodies a crank-rocker mechanism within the hinge mechanism framework.

A comprehensive overview of the planar six-hinge mechanism has been commenced, elucidating its composition and categorization within the hinge mechanism domain. The model used in the experiment is depicted in Fig. 1. The top hinge, serving as the frame, intricately connects two flat four-hinge mechanisms on the left and right, resulting in a unified flat six-hinge mechanism.

Following this overview, a detailed symmetry analysis and derivation of kinematic equations are undertaken for the symmetrical planar four-hinge mechanism on both the left and right sides.

The kinematic equations are simplified to enhance modeling efficiency by introducing the tangent of half-angle parameters. This simplification strategy transforms complex trigonometric equations into more manageable algebraic forms, streamlining the analysis and simulation processes.

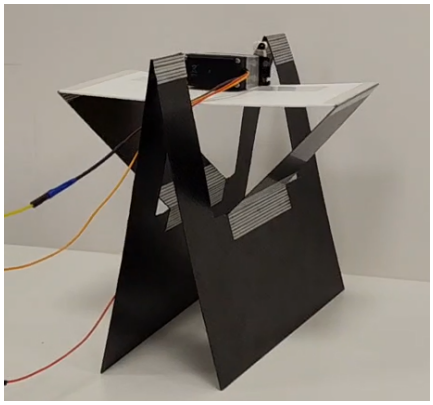

Fig. 1: The prototype of the designed origami robot

3 Modeling

3.1 Planar four-hinge mechanism

A conventional planar four-hinge structure is depicted in Fig. 2. Initially, the Freudenstein equation is employed to examine the planar four-hinge structure, where θ_1 serves as the input, and θ_4 as the output, resulting in an input-output equation:

$$k_1 cos(\theta_4) - k_2 cos(\theta_1) + k_3 = cos(\theta_1 - \theta_4) \quad (1)$$

where

$$k_1 = \frac{a_4}{a_1} \quad k_2 = \frac{a_4}{a_3} \quad k_3 = \frac{a_1^2 - a_2^2 + a_3^2 + a_4^2}{2a_1a_3}$$

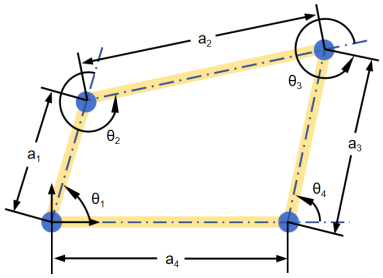

Fig. 2: Planar four-hinge mechanism

However, equations involving trigonometric functions can be challenging to manipulate. To address this, the tangent of half-angle parameter v_i is introduced to represent the four angles θ_i, i.e., $v_i = \tan\left(\frac{\theta_i}{2}\right)$. This transformation renders the equation purely algebraic, simplifying the solving process.

Let a_1, a_2, a_3, and a_4 denote the lengths of the hinges in the four-hinge mechanism in Fig. 2, with θ_1 as the input angle and θ_4 as the output angle. The input-output equation, as presented in [5], is

$$A_1A_2v_1^2v_4^2 + B_1B_2v_1^2 + C_1C_2v_4^2 - 8a_1a_3v_1v_4 + D_1D_2 = 0 \quad (2)$$

where

$$A_1 = a_1 - a_2 - a_3 + a_4, \quad A_2 = a_1 + a_2 - a_3 + a_4$$
$$B_1 = a_1 - a_2 + a_3 + a_4, \quad B_2 = a_1 + a_2 + a_3 + a_4$$
$$C_1 = a_1 - a_2 + a_3 - a_4, \quad C_2 = a_1 + a_2 + a_3 - a_4$$
$$D_1 = a_1 + a_2 - a_3 - a_4, \quad D_2 = a_1 - a_2 - a_3 - a_4$$

Similarly, according to [5], the input-output equations for θ_1-θ_2 and θ_1-θ_3 are derived by considering θ_1 as the input angle.

$$A_2B_1v_1^2v_3^2 + A_1B_2v_1^2 + C_1D_1v_3^2 + C_2D_2 = 0 \quad (3)$$

$$A_1B_1v_1^2v_2^2 + A_2B_2v_1^2 + C_1D_2v_2^2 + 8a_2a_4v_1v_2 + C_2D_1 = 0 \quad (4)$$

The equations of the planar four-hinge motion can be obtained by establishing the relationships among angles θ_1, θ_2, θ_3, and θ_4. Assuming that rod a_1 acts as the driver with an angular velocity of $\dot{\theta_1}$, variations in angles θ_2, θ_3, and θ_4 over time can be explored based on the time-dependent changes in θ_1. This elucidates the dynamic behavior of the system.

3.2 Planar six-hinge mechanism

The prototype utilized in our experiment, illustrated in Fig. 1, is an origami robot. In this design, the steering motor, which is the power source, is situated within a box at the top. The dynamic components of the hinge mechanism consist of two swinging arms connected to the steering motor. As the steering motor initiates rotation, it moves the swinging arms, propelling the cardboard structure to move. The in-motion cardboard effectively functions as the legs of the origami robot, resulting in the robot advancing with each rotation of the steering motor.

The structure can be abstracted as a planar six-hinge mechanism, as illustrated in Fig. 3. In this abstraction, the cardboard loaded with the steering motor serves as the frame in the hinge mechanism, while the swing arm of the steering motor functions as the connecting rod within the hinge mechanism. The movement of the cardboard, driven by the rotation of the steering motor swing arm, assumes the role of the connecting rod. This mechanism falls under the crank rocker mechanism within the hinge mechanism.

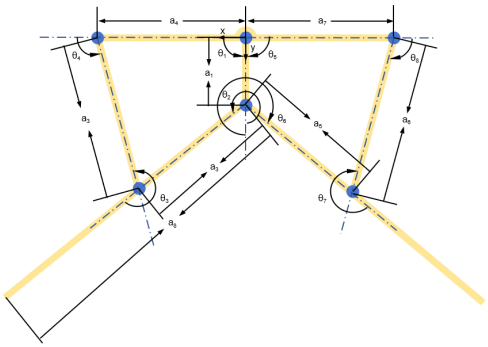

Fig. 3: Planar six-hinge mechanism in the origami robot

According to Fig. 3, it is evident that the planar six-hinge mechanism can be segmented into two planar four-hinge mechanisms on the left and right sides. The upper hinge functions as the frame, uniting the two symmetrical flat four-hinge mechanisms on the left and right, forming a cohesive flat six-hinge mechanism.

Based on the analysis of the motion equations of the four hinge mechanisms on the left and right sides of the symmetric plane, the motion state of one mechanism can be obtained by obtaining the motion state of the other mechanism because of its inherent symmetry.

Equations (1), (2), and (3) intricately capture the positional relationships involving link lengths and joint angles for both the left and right sides of the symmetrical four-hinge mechanism. The resolution of these equations facilitates the analysis and prediction of motion states and positions based on specified link lengths and initial conditions, leveraging the inherent symmetry between the left and proper planar four-hinge mechanisms.

As depicted in Fig. 3, a_1, a_2, a_3, a_4, a_5, a_6, and a_7 represent the lengths of the planar six-hinge connecting rod, with θ_1 denoting the input angle and θ_6, θ_7, θ_8 signifying the output angles. Then the deduced relationships are

$$A_1A_2v_5^2v_7^2 + B_1B_2v_5^2 + C_1C_2v_7^2 - 8a_1a_3v_5v_7 + D_1D_2 = 0 \tag{5}$$

$$A_2B_1v_5^2v_6^2 + A_1B_2v_5^2 + C_1D_1v_6^2 + C_2D_2 = 0 \tag{6}$$

$$A_1B_1v_5^2v_5^2 + A_2B_2v_5^2 + C_1D_2v_5^2 + 8a_2a_4v_5v_5 + C_2D_1 = 0 \tag{7}$$

$$v_5 = tan(\frac{\pi - \theta_1}{2}) \tag{8}$$

The above equations are the overall kinematic equations of the six-hinge origami robot.

4 Simulation

4.1 Setup

To ensure the composition of our flat six-hinge structure, which consists of two symmetrical crank-rocker mechanisms, and to verify our model's proper functionality, a Matlab simulation was initially conducted, and a SolidWorks model was created for validation. The construction of the model in SolidWorks facilitates the observation of motion animations. Leveraging the model motion animation feature allows for a more intuitive understanding of the effects resulting from parameter adjustments.

Using one of the planar four-hinge structures as an illustration, the rod length parameters we designate must satisfy the following conditions:

- The size should be convenient for creating a physical model, striking a balance between not being excessively large or small while accommodating the steering motor.
- The sum of the longest and shortest sides of the four hinges must be less than the sum of the other two sides to ensure the rotation of the planar four-hinge structure.
- a_2-a_1, a_3, a_4 must collectively form an acute triangle. The robot's legs can only move when a_2-a_1, a_3, and a_4 form an acute triangle.

Finally, the rod length parameters are set as shown in the following table:

Table 1: hinge Parameters

Parameter	Symbol	Value (cm)
Link 1	a_1	4
Link 2	a_2, a_5	10
Link 3	a_3, a_6	10
Link 4	a_4, a_7	9

4.2 MATLAB Simulation

In the mathematical modeling section, Equations (2)-(7) are analyzed using MATLAB.

Assuming the motor's angular velocity is 111 rad/s, the time required for the driving member a_1 to complete one rotation round is investigated. The variation in angles θ_2, θ_3, and θ_4 over time is examined with the change in θ_1 as the input.

In Equation (2), a value is assigned to v_1 at specific time points, allowing us to determine the corresponding value of v_4. However, as this equation is quadratic with one variable, two solutions for v_4 arise. This implies that, in certain instances, a specific value of v_1 corresponds to two distinct values of v_4. As v_1 progresses through time, two sets of v_2, v_3, and v_4 pairs associated with it exist, signifying that each time point corresponds to two distinct states of motion for the planar six-hinge structure.

Taking angle θ_2 as an example, as illustrated in Fig. 4, the red and blue lines represent the two solutions of v_2 derived from Equation (3), respectively.

When considered individually, the red and blue lines do not represent continuous curves of v_2 changes. Recognizing that the two solutions of v_2 correspond to the two distinct states of motion for the planar six hinges, it becomes evident that there must be two continuous curves of v_2 changes.

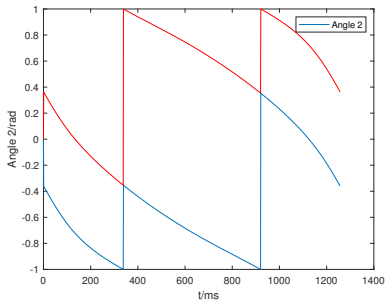

Fig. 4: Two solutions of angle θ_2 in a quadratic equation with one variable

Consequently, the red and blue lines are combined to form two continuous curves, each corresponding to a distinct motion state of the six-hinge. Similarly, the variations of v_3 and v_4 with time were obtained using MATLAB. The subsequent challenge involved determining which of the two solutions of the equation would be utilized as the data for the experiment.

The resolution involved a pragmatic approach. The motion of the two-dimensional six-hinge model was scrutinized, and the angle changes between the hinges during motion were recorded. Ultimately, the solution aligned with the actual motion state was selected based on the observed changes in angles between the hinges during the process.

The changes of v_2, v_3, v_4 with v_1 are depicted in Fig. 5, Fig. 6, Fig. 7.

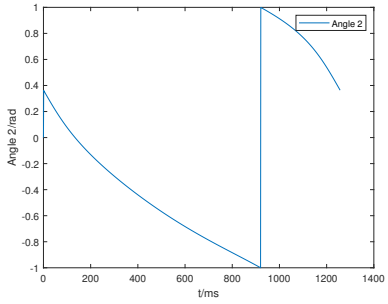

Fig. 5: Change of angle θ_2 over time

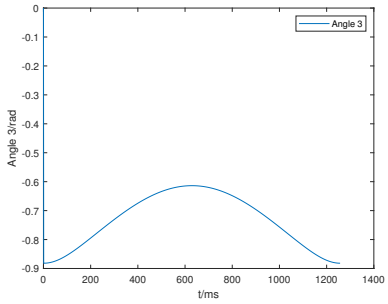

Fig. 6: Change of angle θ_3 over time

As the above image shows, the flat four-hinge structure conforms to a crank-rocker mechanism, where a_1 serves as the crank, a_2, and a_3 function as the rocker.

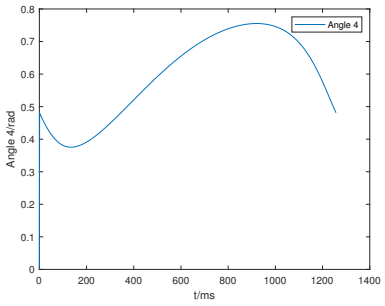

Fig. 7: Change of angle θ_4 over time

In Fig. 8, point A is designated as the origin of the coordinate system, and the model's displacement is computed for each revolution of the steering motor.

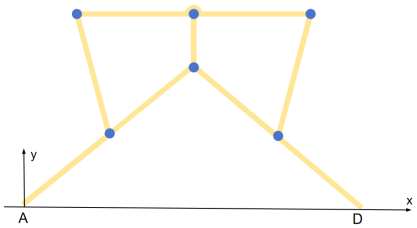

Fig. 8: Geometric relationship of the bars and hinges

Subsequently, the extent of forward movement for our model with each rotation of the steering motor can be determined, as illustrated in Fig. 9 and Fig. 10.

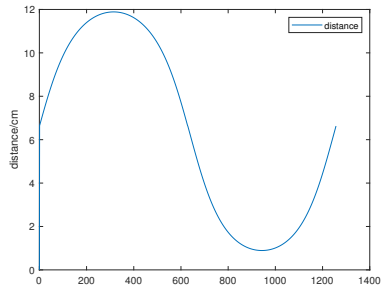

Fig. 9: Distance of point A and point D

4.3 SolidWorks Simulation

SolidWorks was chosen to simulate the planar six-hinge model. Following a successful model simulation, the data exported from SolidWorks was compared with those obtained from MATLAB modeling. The comparative results are presented in Fig. 11, Fig. 12, Fig. 13, and Fig. 14.

As evident from Fig. 11, Fig. 12, Fig. 13, and Fig. 14, the data acquired from SolidWorks simulation exhibits a high degree of consistency with the data obtained from MATLAB modeling, thereby mutually verifying their correctness. Nevertheless, owing to the constraints of SolidWorks exported data points, fewer data points from SolidWorks do not perfectly align with the data from MATLAB.

In the subsequent section, a physical model will be constructed for experiments, and data will be recorded to validate the accuracy of our modeling and simulation.

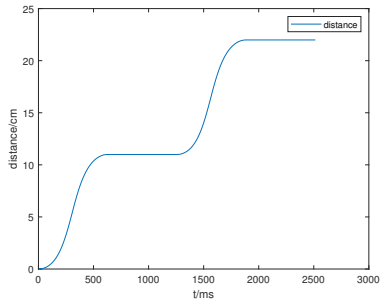

Fig. 10: Distance traveled by the robot

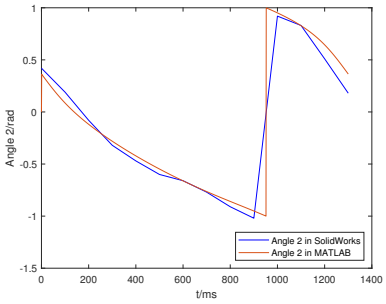

Fig. 11: Comparison of angle θ_2 in Matlab simulation and Solidworks

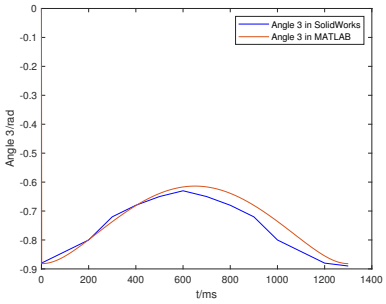

Fig. 12: Comparison of angle θ_3 in Matlab simulation and Solidworks

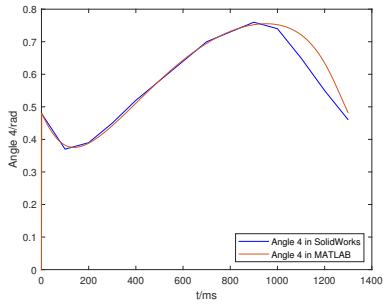

Fig. 13: Comparison of angle θ_4 in Matlab simulation and Solidworks

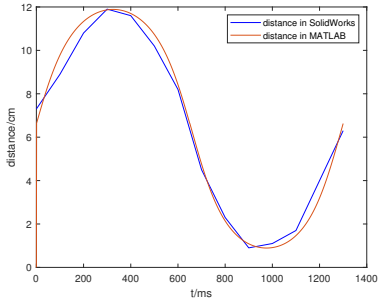

Fig. 14: Comparison of distance of point A and point D

5 Physical Experiment

5.1 Material selection of the robot's components

Specialized materials and laser-cutting machines were utilized to fabricate our prototype, ensuring strength and flexibility.

For the power source of our robot, we selected the 360-degree MG995 steering motor. The adoption of the MG995 steering motor as the robot's power supply offers three notable advantages: it enables a complete 360-degree rotation, facilitating the realization of a crank-rocker mechanism within the planar six-hinge; it provides robust torque, effortlessly propelling the movement of the robot's leg structure; and it does so at a low cost, ensuring sufficient performance for experimental purposes.

A suitable robotic arm was crafted using 3D printing to complement this choice and then affixed to the steering motor, as depicted in Fig. 15. This design ensures the arm's resilience, mitigating the risk of breakage or dislodgment during the rotation of the steering motor.



Fig. 15: Steering motor used in the design of the robot

In selecting the robot's framework, carbon fiber plates were used as the robot's skeleton, and 3D printing plates were used as the carrier of the steering motor. Carbon fiber plate and 3D printing board each have advantages: carbon fiber plate is thinner and lighter than 3D printing board, making the robot lighter and more accessible for the steering motor to drive the leg rotation; 3D printing plate is more rigid than carbon fiber plate, as the carrier of the steering motor is not easy to be bent by the steering motor.

The prototype is shown in Fig. 1. The robot skeleton is divided according to the location of the crease, and the carbon fiber plate is divided into individual parts using laser cutting. Use tape to splice parts where they need to be folded. This

splicing method dramatically reduces the resistance of the robot's joint parts during rotation. The experimental video is given in [6].

5.2 Physical experimental data

Recording the robot's movement in a video [6], images of the robot at different moments were presented for comparison in Fig. 16. The first and third pictures showcase the maximum and minimum distance between the robot's legs.

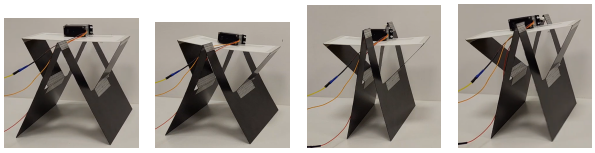

(a) t=0 s (b) t=0.5s (c) t=1.0s (d) t=1.5s

Fig. 16: Comparison of robots at different timese

With each rotation of the steering motor, the distance covered by the robot was meticulously recorded. The recording process was repeated 25 times, and the distances were averaged every five repetitions to obtain the average distance of the robot, as illustrated in Fig. 17.

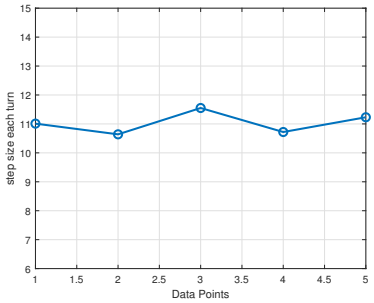

Fig. 17: Robot travel distance per steering motor rotation

Compared with Fig. 10, it is evident that the distance covered by the robot in the experiment is shorter than the distance calculated in the simulation. This discrepancy is primarily attributed to insufficient friction between the robot's legs and the ground. The friction deficiency causes the robot's front legs to slide backward as it moves forward, resulting in the actual distance of the robot's advance being less than anticipated.

6 Conclusion

In this paper, the design of a simple robot utilizing the planar six-hinge structure derived from origami-inspired robotics is presented. The modeling of the planar six-hinge structure is delved into, employing MATLAB and SolidWorks for simulation. The investigation focuses on the six-hinge origami robot's angle changes and step sizes. Subsequently, a prototype was fabricated using a steering motor, carbon fiber plate, and 3D printing plate, and the distance the robot covered with each forward step was recorded.

The data acquired from the experiment indicates consistency between our MATLAB and SolidWorks models, further validated by the real-world experiment. Ultimately, our motion model, grounded in theoretical analysis, is corroborated by motion simulation data and experimental data from the physical model in SolidWorks. This comprehensive validation process underscores the feasibility of our theoretical analysis, simulation, and physical models.

Acknowledgment

The authors would like to thank Jin Wei from Southern University of Science and Technology for the assistance in the design and manufacture of the robot.

References

[1] M. A. Robertson, Ö. C. Kara, and J. Paik, "Soft pneumatic actuator-driven origami-inspired modular robotic 'pneumagami'" The International Journal of Robotics Research, vol. 40, no. 1, pp. 72-85, Mar. 2020, doi: 10.1177/0278364920909905.

[2] S.-J. Kim, D.-Y. Lee, G.-P. Jung, and K.-J. Cho, "An origami-inspired, self-locking robotic arm that can be folded flat," Science Robotics, vol. 3, no. 16, Mar. 2018, doi: 10.1126/scirobotics.aar2915.

[3] "Deformable wheel robot based on origami structure," IEEE Conference Publication — IEEE Xplore. https://ieeexplore.ieee.org/document/6631383.

[4] G. Wang, "Origami Robots," Guanyun Wang, Dec. 2017. [Online]. Available: https://www.guanyundesign.com/Origami-Robots.

[5] J. J. Uicker, G. R. Pennock, and J. E. Shigley, Theory of Machines and Mechanisms, 5th ed. New York, NY, USA: Oxford University Press, 2017, pp. 12-13.

[6] https://www.bilibili.com/video/BV19Z421e7i3.

Proceedings of the 3rd Conference on Fully Actuated System Theory and Applications
May 10-12, 2024, Shenzhen, China

Fault estimation for unmanned surface vehicles based on adaptive observer

Feng Gao[1], Liheng Chen[2],

1. The College of Intelligent Systems Science and Engineering, Harbin Engineering University, Harbin 150001, P. R. China
E-mail: 2934793673@qq.com

2. the College of Intelligent Systems Science and Engineering, Harbin Engineering University, Harbin 150001, P. R. China
E-mail: clh114131@gmail.com

Abstract: This paper presents the design of an innovative adaptive observer method tailored specifically for unmanned surface vessels (USVs). The proposed method addresses several challenges inherent in the operation of USVs, including unknown sensor faults, unknown stuck actuator faults, and external disturbances. These issues, if left unaddressed, could significantly impact the performance and safety of USVs. The cornerstone of the proposed method is an online iterative adaptive mechanism, which is employed to reconstruct the states and faults of the USV. This mechanism leverages real-time data and iterative processes to adaptively update the state estimates and fault predictions, thereby enabling more accurate and timely fault detection and mitigation. In the final part of the article, we provide a comprehensive verification of the proposed design method. This is achieved through a detailed simulation analysis of the USVs model. The simulation results not only demonstrate the feasibility of the proposed method but also attest to its effectiveness in enhancing the reliability and safety of USVs.

Key Words: Sensor fault, actuator fault, adaptive observer, unmanned surface vessel

1 Introduction

As technology continues to advance at an unprecedented pace, unmanned surface vessels (USVs) are finding increasingly diverse applications, ranging from maritime safety patrols and marine observation to radar monitoring and beyond. However, the practical deployment of these vessels is not without its challenges. In particular, the failure of certain control components is an inevitability that can have serious implications for the safe operation of the vessel, potentially leading to severe accidents [1–6].

In light of these challenges, the primary focus of the research community has shifted towards the development and implementation of robust identification and estimation techniques for potential faults. The ultimate goal of these efforts is to enhance the dependability and stability of the USV systems [7–9]. One technique that has garnered significant attention is Fault Estimation (FE), owing to its ability to accurately report the relevant details of unidentified faults that have occurred [10–14]. For instance, one study provided an estimation of system faults with unknown actuator efficiency factors. However, it is important to note that unidentified faults in USVs are typically not static, but rather exhibit temporal variations, representing an open research direction that warrants further investigation.

On the other hand, the adaptive observer technique, despite its effectiveness in fault estimation, has seen limited application in USVs. The fault approximation of an adaptive observer relies on the difference of direct outputs. By utilizing an online updating adaptive mechanism for fault estimation, it is possible to obtain accurate observation results. As such, there is a clear and pressing need to design an adaptive strategy specifically tailored for USVs.

This work was supported in part by the National Natural Science Foundation of China (No. 62273114), in part by the Macao Young Scholars Program (No. AM2022004), in part by the China Postdoctoral Science Foundation (No. 2019M661255, No. 2021T140149). Corresponding author: Liheng Chen

In response to these challenges, this article proposes the design of an adaptive observer for USVs to address the FE problem. The study will investigate the FE problem of USVs with time-varying actuators and sensor faults, as well as external disturbances, within a unified system framework. The proposed observer will rely on an online adaptive mechanism for reconstructing faults, offering a promising solution to enhance the safety and reliability of USVs. This work is expected to contribute to the ongoing efforts to improve fault detection and handling in USVs, and hopefully, inspire further research in this critical area.

The structure of the paper is as follows. Section II introduces the model of unmanned surface vessels considered in this work. The main derivations are presented in The third part. Part IV provides a imitation validation of the recommended solution using an unmanned surface vessel model. Finally, the last section concludes the work conducted in this paper.

2 Model Conditions And Analysis

Considering a system of unmanned watercraft including sensors, actuators, and external interference failures as,

$$\begin{cases} \dot{x}(t) = & A_l x(t) + B_l u(t) + B_{la} f_c(t) + \\ & E_l w(t) \\ y(t) = & Gx(t) + D_{ls} f_m(t) \end{cases} \tag{1}$$

where $x(t) \in \mathbf{R}^m$ is the unmanned surface vessel system state, $u(t) \in \mathbf{R}^n$ is the control part, $y(t) \in \mathbf{R}^c$ is the output, $f_c(t) \in \mathbf{R}^c$ is the actuator fault, $f_m(t) \in \mathbf{R}^q$ is the sensor fault, $w(t) \in \mathbf{R}^a$ is the interference vector.

In the unmanned surface vessel, the system matrices A_l, B_l, G, D_{ls}, E_l are given by

$$A_l = \begin{bmatrix} -\frac{1}{T_a} & 0 & 0 & 0 & 0 \\ -\frac{K_a}{T_b} & -\frac{1}{T_b} & 0 & 0 & 0 \\ 0 & 1 & 0 & 0 & 0 \\ \omega^2 K_e & 0 & 0 & -2\zeta\omega & -\omega^2 \\ 0 & 0 & 0 & 1 & 0 \end{bmatrix}$$

$$E_l = \begin{bmatrix} 0 & \frac{1}{T_b} & 0 & 0 & 0 \\ 0 & 0 & 0 & \omega^2 & 0 \end{bmatrix}^T$$

$$B_l = \begin{bmatrix} \frac{K_b}{T_a} & \frac{K_c}{T_b} & 0 & \omega^2 K_d & 0 \end{bmatrix}^T$$

$$G = I_5$$

$$D_{ls} = \begin{bmatrix} 0 & 0 & 1 & 0 & 1 \end{bmatrix}^T$$

where T_a and T_b are time constants; K_a, K_b, K_c, K_d, K_e are known gains; ω and ζ are frequency and damping ratio. Hence, we have $m = 5$, $n = 1$, $a = 2$ in the unmanned surface vessel system.

In this article, the following hypotheses are considered: $Assumption$ 1: For each $i = 1, 2, ..., N$, The provided equation is correct,

$$rank\left(\begin{bmatrix} \gamma I_n - A_l & B_l & B_{la} & 0 & E_l \\ C & 0 & 0 & D_{ls} & 0 \end{bmatrix}\right) = n+q+m+s+a \tag{2}$$

3 Major Processes

3.1 System augmentation method

We will design a new augmentation method in this content that is used to analyze a novel vector constructed from the sensor fault and state vector. This method will help us gain a deeper understanding of the vector and may provide new perspectives and methods for addressing related issues.

The augmentation method is as follows:

$$\begin{cases} \bar{E}\dot{\bar{x}}(t) = \bar{A}_l \bar{x}(t) + B_l u(t) + B_{la} f_a(t) + E_l w(t) \\ y(t) = \bar{G}\bar{x}(t) \end{cases} \tag{3}$$

where

$$\begin{aligned} \bar{E} &= \begin{bmatrix} I_n & 0_{m\times q} \end{bmatrix} \in \mathbf{R}^{m\times(m+q)} \\ \bar{A}_l &= \begin{bmatrix} A_l & 0_{m\times q} \end{bmatrix} \in \mathbf{R}^{m\times(m+q)} \\ \bar{G} &= \begin{bmatrix} G & D_{ls} \end{bmatrix} \in \mathbf{R}^{c\times(m+q)} \\ \bar{x}(t) &= \begin{bmatrix} x^T(t) & {f_m}^T(t) \end{bmatrix}^T \in \mathbf{R}^{m+q} \end{aligned} \tag{4}$$

Then, a matrix $M_l \in \mathbf{R}^{(m+q)\times m}$ is defined as,

$$M_l = \begin{bmatrix} I_n \\ -D_{ls}^{\dagger} G + Z_l\left(I_p - D_{ls}{D_{ls}}^{\dagger}\right) G \end{bmatrix} \tag{5}$$

where $Z_l \in \mathbf{R}^{q+c}$ is an random matrix,${D_{ls}}^{\dagger} \in \mathbf{R}^{q+c}$ is the generalized inverse of D_{ls}. We opt for the specific format that${D_{ls}}^{\dagger} = \left({D_{ls}}^T D_s\right)^{-1} {D_{ls}}^T$ and $Z_l = 0_{q\times c}$, then $M_l = \begin{bmatrix} I_n \\ -\left({D_{ls}}^T D_{ls}\right)^{-1} {D_{ls}}^T G \end{bmatrix}$.

Multiplication of M to both sides of the first equation in (3),

$$\begin{cases} \bar{E}_g \dot{\bar{x}}(t) = \bar{A}_{lg}\bar{x}(t) + \bar{B}_{lg} u(t) + \bar{B}_{lag} f_a(t) + \bar{E}_l w(t) \\ y(t) = \bar{G}\bar{x}(t) \end{cases} \tag{6}$$

where

$$\begin{aligned} \bar{E}_g &= \begin{bmatrix} I_n & 0_{m\times q} \\ -\left(D_{ls}^T D_{ls}\right)^{-1} D_{ls}^T G & 0_{q\times q} \end{bmatrix} \in \mathbf{R}^{(m+q)\times(m+q)}, \\ \bar{A}_{lg} &= \begin{bmatrix} A_l & 0_{m\times q} \\ -\left(D_{ls}^T D_{ls}\right)^{-1} D_{ls}^T G & 0_{q\times q} \end{bmatrix} \in \mathbf{R}^{(m+q)\times(m+q)}, \\ \bar{B}_{lg} &= \begin{bmatrix} B_l \\ -\left(D_{ls}^T D_{ls}\right)^{-1} D_{ls}^T G B_l \end{bmatrix} \in \mathbf{R}^{(m+q)\times n}, \\ \bar{B}_{lag} &= \begin{bmatrix} B_{la} \\ -\left(D_{ls}^T D_{ls}\right)^{-1} D_{ls}^T G B_{la} \end{bmatrix} \in \mathbf{R}^{(n+s)\times s}. \\ \bar{E}_l &= \begin{bmatrix} E_l \\ -\left(D_{ls}^T D_{ls}\right)^{-1} D_{ls}^T G E_l \end{bmatrix} \in \mathbf{R}^{(m+q)\times a} \end{aligned} \tag{7}$$

It is given that $\bar{B}_{ld} = \begin{bmatrix} \bar{B}_{lg} & \bar{B}_{lag} \end{bmatrix} \in \mathbf{R}^{(m+q)\times(n+s)}$.

3.2 Adaptive observer design

$Assumption$ 2: The input $u(t)$ remains bounded and continuous for all time t,

$$\mu_{11} \leqslant \oint_t^{t+\Delta t} u^T(\rho) u(\rho)\, d\rho \leqslant \mu_{12} \tag{8}$$

where Δt, μ_{11} and μ_{12} are positive value.

According to the system augmentation scheme, the adaptive observer system is as follows.

$$\begin{cases} \dot{\theta}(t) = \bar{A}_{ls}\theta(t) + \bar{L}_{lp} y(t) + \bar{B}_{lg} u(t) + \bar{B}_{lag}\hat{f}_c(t) + \bar{E}_l \hat{w}(t) \\ \hat{\bar{x}}(t) = \theta(t) + \bar{L}_{ld} y(t) \end{cases} \tag{9}$$

where $\theta(t) \in \mathbf{R}^{m+q}$ is the temporary variable;$\hat{\bar{x}}(t) \in \mathbf{R}^{m+q}$ is the evaluation of $\bar{x}(t)$;$\hat{f}_c(t) \in \mathbf{R}^s$ is the evaluation of the actuator fault;$\bar{A}_{ls} \in \mathbf{R}^{(m+q)\times(m+q)}$, $\bar{L}_{lp} \in \mathbf{R}^{(m+q)\times c}$, $\bar{L}_{ld} \in \mathbf{R}^{(m+q)\times c}$ are the parameters that are designed.

The adaptive laws of $\hat{f}_{cl}(t)$ for $l = 1, 2, ..., s$ are as follows,

$$\dot{\hat{f}}_{cl}(t) = -\mu_{1l} S_{2l}\left(\bar{G}\hat{\bar{x}}(t) - y(t)\right) - \mu_{2l}\hat{f}_{cl}(t) \tag{10}$$

where S_{2l} is the lth row of the matrix $S_2 \in \mathbf{R}^{s\times c}$.

The adaptive laws of $\hat{w}_h(t)$ for $h = 1, 2, ..., a$ are as follows,

$$\dot{\hat{w}}_h(t) = -\omega_{1h} S_{1h}\left(\bar{G}\hat{\bar{x}}(t) - y(t)\right) - \omega_{2h}\hat{w}_h(t) \tag{11}$$

where S_{1h} is the hth row of the matrix $S_1 \in \mathbf{R}^{a\times c}$.

According to$Assumption$ 2, the adaptive rates (11) and (12) are bounded.The error variables are defined as follows,

$$\begin{aligned} \bar{e}_x(t) &= \hat{\bar{x}}(t) - \bar{x}(t), \\ e_f(t) &= \hat{f}_c(t) - f_c(t), \\ e_w(t) &= \hat{w}(t) - w(t) \end{aligned} \tag{12}$$

where $e_f(t) = \begin{bmatrix} e_{f1}(t) & e_{f2}(t) & ... & e_{fs}(t) \end{bmatrix}^T \in \mathbf{R}^s$, $e_w(t) = \begin{bmatrix} e_{w1}(t) & e_{w2}(t) & ... & e_{wa}(t) \end{bmatrix}^T \in \mathbf{R}^a$.Then,we have,

$$\begin{aligned} &\dot{\bar{e}}_x(t) = \dot{\hat{\bar{x}}}(t) - \dot{\bar{x}}(t) \\ &= \dot{\theta}(t) + \bar{L}_{ld}\dot{y}(t) - \dot{\bar{x}}(t) \\ &= \bar{A}_{ls}\hat{\bar{x}}(t) + \left(\bar{L}_{lp} - \bar{A}_{ls}\bar{L}_{ld}\right)\bar{G}\bar{x}(t) + \bar{B}_{lg} u(t) + \bar{B}_{lag}\hat{f}_c(t) \\ &+ \bar{E}_l\hat{w}(t) + \left(\bar{L}_{ld}\bar{G} - I_{m+q}\right)\dot{\bar{x}}(t) \end{aligned} \tag{13}$$

We make $\bar{L}_{ld}$ as,

$$\bar{L}_{ld} = \begin{bmatrix} 0 \\ \left(D_{ls}{}^{T} D_{ls}\right)^{-1} D_{ls}{}^{T} \end{bmatrix} \tag{14}$$

From (6) we know that,

$$\begin{aligned} &\left(\bar{L}_{ld}\bar{G} - I_{m+q}\right)\dot{\bar{x}}(t) \\ &= \begin{bmatrix} -I_n & 0 \\ \left(D_{ls}{}^{T} D_{ls}\right)^{-1} D_{ls}{}^{T} & 0 \end{bmatrix} \dot{\bar{x}}(t) \\ &= -\bar{A}_{lg}\bar{x}(t) - \bar{B}_{lg}u(t) - \bar{B}_{lag}f_c(t) - \bar{E}_l w(t) \end{aligned} \tag{15}$$

Substituting (14) into (16),

$$\begin{aligned} &\dot{\bar{e}}_x(t) = \dot{\hat{\bar{x}}}(t) - \dot{\bar{x}}(t) \\ &= \dot{\theta}(t) + \bar{L}_{ld}\dot{y}(t) - \dot{\bar{x}}(t) \\ &= \bar{A}_{ls}\hat{\bar{x}}(t) + \left(\bar{L}_{lp} - \bar{A}_{ls}\bar{L}_{ld}\right)\bar{G}\bar{x}(t) + \bar{B}_{lg}u(t) + \bar{B}_{lag}\hat{f}_c(t) \\ &+ \bar{E}_l\hat{w}(t) - \bar{A}_{lg}\bar{x}(t) - \bar{B}_{lg}u(t) - \bar{B}_{lag}f_c(t) - \bar{E}_l w(t) \\ &= \bar{A}_{ls}\hat{\bar{x}}(t) + \left(\bar{L}_{lp}\bar{G} - \bar{A}_{ls}\bar{L}_{ld}\bar{G} - \bar{A}_{lg}\right)\bar{x}(t) \\ &+ \bar{B}_{lag}e_f(t) + \bar{E}_l e_w(t) \end{aligned} \tag{16}$$

We make $\bar{A}_{ls}$ and $\bar{L}_{lp}$ as,

$$\bar{A}_{ls} = \bar{A}_{lg} - L_l\bar{C}, \bar{L}_{lp} = L_l + \bar{A}_{ls}\bar{L}_l w \tag{17}$$

where $L \in \mathbf{R}^{c\times(m+q)}$ is the gain matrix.Then we have,

$$\begin{aligned} &\dot{\bar{e}}_x(t) = \bar{A}_{ls}\hat{\bar{x}}(t) + \left(\bar{L}_{lp}\bar{G} - \bar{A}_{ls}\bar{L}_{ld}\bar{G} - \bar{A}_{lg}\right)\bar{x}(t) \\ &+ \bar{B}_{lag}e_f(t) + \bar{E}_l e_w(t) \\ &= \left(\bar{A}_{lg} - L_l\bar{G}\right)\bar{e}_x + \bar{B}_{lag}e_f(t) + \bar{E}_l e_w(t) \end{aligned} \tag{18}$$

$Theorem$ 1:Under the adaptive laws (11) and (12), If there are positive definite matrices $P_l \in \mathbf{R}^{(m+q)\times(m+q)}$ and $Q_l \in \mathbf{R}^{(m+q)\times(m+q)}$,matrices $S = \begin{bmatrix} S_1{}^{T} & S_2{}^{T} \end{bmatrix}^{T} \in \mathbf{R}^{(a+s)\times c}$ and $\bar{Y}_l \in \mathbf{R}^{(m+q)\times c}$, the following conditions hold,

$$\begin{aligned} &P_l\bar{A}_{lg} + \bar{A}_{lg}P_l - \bar{Y}_l\bar{G} - \bar{G}^T\bar{Y}_l^T + Q_l < 0, \\ &\begin{bmatrix} \bar{E}_l & \bar{B}_{lag} \end{bmatrix}^T P_l = S\bar{G} \end{aligned} \tag{19}$$

then the system (19) is almost surely asymptotically stable. Besides, it is chosen that $L_l = {P_l}^{-1}\bar{Y}_l$.

$Proof$. Design the following Lyapunov function,

$$V(t) = V_1(t) + V_2(t) + V_3(t) \tag{20}$$

where

$$\begin{aligned} V_1(t) &= \bar{e}_x^T(t) P \bar{e}_x(t), \\ V_2(t) &= \sum_{l=1}^{s} \frac{e_{fl}^2(t)}{\mu_{1l}}, \\ V_3(t) &= \sum_{h=1}^{a} \frac{e_{wh}^2(t)}{\omega_{1h}} \end{aligned} \tag{21}$$

Then, we have

$$\begin{aligned} &\dot{V}_1(t) = \bar{e}_x^T(t)\left[P_l\left(\bar{A}_{lg} - L_l\bar{G}\right) + \left(\bar{A}_{lg} - L_l\bar{G}\right)^T P_l\right]\bar{e}_x(t) \\ &+ 2\bar{e}_x^T(t) P_l \bar{B}_{lag} e_f(t) + 2\bar{e}_x^T(t) P_l \bar{E}_l e_w(t) \\ &\dot{V}_2(t) = \sum_{l=1}^{s} \frac{2e_{fl}(t)\dot{e}_{fl}(t)}{\mu_{1l}}, \dot{V}_3(t) = \sum_{h=1}^{a} \frac{2e_{wh}(t)\dot{e}_{wh}(t)}{\omega_{1h}} \end{aligned} \tag{22}$$

Noted at,

$$\begin{aligned} &\dot{V}_2(t) + 2\bar{e}_x^T(t) P_l \bar{B}_{lag} e_f(t) \\ &= \sum_{l=1}^{s} \frac{2e_{fl}(t)\dot{e}_{fl}(t)}{\mu_{1l}} + 2\sum_{l=1}^{s} e_{fl}\left(\bar{B}_{lag}^T P_l^T \bar{e}_x(t)\right)_l \\ &= \sum_{l=1}^{s} 2\left[\frac{e_{fl}(t)}{\mu_{1l}}\left(\dot{\hat{f}}_{cl}(t) - \dot{f}_{cl}(t)\right) + e_{fl}(t)\left(\bar{B}_{lag}^T P_l^T \bar{e}_x(t)\right)_l\right] \end{aligned} \tag{23}$$

where $\left(\bar{B}_{lag}^T P_l^T \bar{e}_x(t)\right)_l$ denotes the lth row of the vectri $\bar{B}_{lag}^T P_l^T \bar{e}_x(t)$.Consider (11) into (24),

$$\begin{aligned} &\dot{V}_2(t) + 2\bar{e}_x^T(t) P_l \bar{B}_{lag} e_f(t) \\ &= \sum_{l=1}^{s} 2\begin{bmatrix} -e_{fl}(t)\left(S_2\bar{G}\bar{e}_x(t)\right)_l + e_{fl}(t)\left(\bar{B}_{lag}^T P_l^T \bar{e}_x(t)\right)_l \\ -\frac{\mu_{2l}}{\mu_{1l}} e_{fl}(t)\hat{f}_{cl}(t) - \frac{1}{\mu_{1l}} e_{fl}(t)\dot{f}_{cl}(t) \end{bmatrix} \\ &= \sum_{l=1}^{s} 2\left[-\frac{\mu_{2l}}{\mu_{1l}} e_{fl}(t)\left(f_{cl}(t) + e_{fl}(t)\right) - \frac{1}{\mu_{1l}} e_{fl}(t)\dot{f}_{cl}(t)\right] \end{aligned} \tag{24}$$

Now consider the term $-\sum_{l=1}^{s} 2\frac{\mu_{2l}}{\mu_{1l}} e_{fl}(t)\left(f_{cl}(t) + e_{fl}(t)\right)$,

$$\begin{aligned} &-\sum_{l=1}^{s} 2\frac{\mu_{2l}}{\mu_{1l}} e_{fl}(t)\left(f_{cl}(t) + e_{fl}(t)\right) \\ &\leqslant \sum_{l=1}^{s}\left[\frac{\mu_{2l}}{\mu_{1l}} e_{fl}^2(t) + \frac{\mu_{2l}}{\mu_{1l}} f_{cl}^2(t) - \frac{2\mu_{2l}}{\mu_{1l}} e_{fl}^2(t)\right] \\ &\leqslant \sum_{l=1}^{s}\left[-\frac{\mu_{2l}}{\mu_{1l}} e_{fl}^2(t) + \frac{\mu_{2l}}{\mu_{1l}} f_{cl}^2(t)\right] \end{aligned} \tag{25}$$

Another term $-\sum_{l=1}^{s} \frac{2}{\mu_{1l}} e_{fl}(t)\dot{f}_{cl}(t)$, there exists a constant $0 < \varepsilon_1 < \mu_{2l}$,

$$\begin{aligned} &-\sum_{l=1}^{s} \frac{2}{\mu_{1l}} e_{fl}(t)\dot{f}_{cl}(t) \\ &\leqslant \sum_{l=1}^{s}\left[\frac{\varepsilon_1}{\mu_{1l}} e_{fl}^2(t) + \frac{1}{\mu_{1l}\varepsilon_1}\dot{f}_{cl}^2(t)\right] \\ &\leqslant \sum_{l=1}^{s}\left[\frac{\varepsilon_1}{\mu_{1l}} e_{fl}^2(t) + \frac{1}{\mu_{1l}\varepsilon_1}\bar{\dot{f}}_{cl}^2\right] \end{aligned} \tag{26}$$

where $\bar{f}_{cl}$ means the maximum of $f_{cl}(t)$, $\bar{\dot{f}}_{cl}$ means the maximum of $\dot{f}_{cl}(t)$. Then, we have,

$$\begin{aligned} &\dot{V}_2(t) + 2\bar{e}_x^T(t) P_l \bar{B}_{lag} e_f(t) \\ &\leqslant \sum_{l=1}^{s}\left[-\frac{\mu_{2l}}{\mu_{1l}} e_{fl}^2(t) + \frac{\mu_{2l}}{\mu_{1l}} f_{cl}^2(t) + \frac{\varepsilon_1}{\mu_{1l}} e_{fl}^2(t) + \frac{1}{\mu_{1l}\varepsilon_1}\bar{\dot{f}}_{cl}^2\right] \\ &\leqslant \sum_{l=1}^{s}\left[-\frac{\mu_{2l} - \varepsilon_1}{\mu_{1l}} e_{fl}^2(t) + \frac{\mu_{2l}}{\mu_{1l}}\bar{f}_{cl}^2 + \frac{1}{\mu_{1l}\varepsilon_1}\bar{\dot{f}}_{cl}^2\right] \end{aligned} \tag{27}$$

Considering term $V_3(t)$ and $2\bar{e}_x^T(t) P_l \bar{E}_l e_w(t)$ in (23),

$$\begin{aligned} &\dot{V}_3(t) + 2\bar{e}_x^T(t) P_l \bar{E}_l e_w(t) \\ &= \sum_{h=1}^{a} 2\left[\frac{e_{wh}(t)}{\omega_{1h}}\left(\dot{\hat{d}}_w(t) - \dot{d}_w(t)\right) + e_{wh}(t)\left(\bar{E}_l^T P_l^T \bar{e}_x(t)\right)_h\right] \end{aligned} \tag{28}$$

where $\left(\bar{E}^T P_l{}^T \bar{e}_x(t)\right)_h$ represents the hth row of the vector $\bar{E}_l{}^T P_l{}^T \bar{e}_x(t)$.With the adaptive law (12), we have,

$$\begin{aligned}&\dot{V}_3(t) + 2\bar{e}_x^T(t) P_l \bar{E}_l e_w(t)\\&= \sum_{h=1}^{a} 2\left[-\frac{\omega_{2h}}{\omega_{1h}} e_{wh}(t)\left(w_h(t) + e_{wh}(t)\right) - \frac{1}{\omega_{1h}} e_{wh}(t)\,\dot{w}_h(t)\right]\end{aligned} \tag{29}$$

Now consider the term $-\sum_{h=1}^{a} \frac{2\omega_{2h}}{\omega_{1h}} e_{wh}(t)\left(w_h(t) + e_{wh}(t)\right)$, that,

$$\begin{aligned}&-\sum_{h=1}^{a} \frac{2\omega_{2h}}{\omega_{1h}} e_{wh}(t)\left(w_h(t) + e_{wh}(t)\right)\\&\leqslant \sum_{h=1}^{a=1}\left[-\frac{\omega_{2h}}{\omega_{1h}} e_{wh}^2(t) + \frac{\omega_{2h}}{\omega_{1h}} w_h^2(t)\right]\end{aligned} \tag{30}$$

For the term $-\sum_{h=1}^{a} \frac{2}{\omega_{1h}} e_{wh}(t)\,\dot{w}_h(t)$, there exists a constant $0 < \varepsilon_2 < \omega_{2h}$,

$$\begin{aligned}&-\sum_{h=1}^{a} \frac{2}{\omega_{1h}} e_{wh}(t)\,\dot{w}_h(t)\\&\leqslant \sum_{h=1}^{a}\left[\frac{\varepsilon_2}{\omega_{1h}} e_{wh}^2(t) + \frac{1}{\omega_{1h}\varepsilon_2}\bar{\bar{w}}_h^2\right]\end{aligned} \tag{31}$$

where $\bar{w}_h$ means the maximum of $w_h(t)$, $\bar{\bar{w}}_h$ means the maximum of $\dot{w}_h(t)$. Therefore, we have,

$$\begin{aligned}&\dot{V}_3(t) + 2\bar{e}_x^T(t) P_l \bar{E}_l e_w(t)\\&\leqslant \sum_{h=1}^{a}\left[-\frac{\omega_{2h}}{\omega_{1h}} e_{wh}^2(t) + \frac{\omega_{2h}}{\omega_{1h}} w_h^2(t) + \frac{\varepsilon_2}{\omega_{1h}} e_{wh}^2(t) + \frac{1}{\omega_{1h}\varepsilon_2}\bar{\bar{w}}_h^2\right]\\&\leqslant \sum_{h=1}^{a}\left[-\frac{\omega_{2h} - \varepsilon_2}{\omega_{1h}} e_{wh}^2(t)\,\frac{\omega_{2h}}{\omega_{1h}}\bar{w}_h + \frac{1}{\omega_{1h}\varepsilon_2}\bar{\bar{w}}_h^2\right]\end{aligned} \tag{32}$$

Consider equations (20), (28), and (33),

$$\begin{aligned}&\dot{V}_1(t) + \dot{V}_2(t) + \dot{V}_3(t)\\&\leqslant -\bar{e}_x^T(t) Q_l \bar{e}_x(t) + \sum_{l=1}^{s}\left[-\frac{\mu_{2l} - \varepsilon_1}{\mu_{1l}} e_{fl}^2(t) + \frac{\mu_{2l}}{\mu_{1l}}\bar{f}_{al}^2 + \frac{1}{\mu_{1l}\varepsilon_1}\bar{\bar{f}}_{cl}^2\right]\\&+ \sum_{h=1}^{a}\left[-\frac{\omega_{2h} - \varepsilon_2}{\omega_{1h}} e_{wh}^2(t)\,\frac{\omega_{2h}}{\omega_{1h}}\bar{w}_h + \frac{1}{\omega_{1h}\varepsilon_2}\bar{\bar{w}}_h^2\right]\\&\leqslant -\alpha_0 V(t) + \beta\end{aligned} \tag{33}$$

where $\alpha_0 = \min\left\{\lambda_{\min}\left\{Q_l P_l^{-1}\right\}, \mu_{2l} - \varepsilon_1, \omega_{2h} - \varepsilon_2\right\}$, and $\beta = \sum_{l=1}^{s}\left[-\frac{\mu_{2l}-\varepsilon_1}{\mu_{1l}} e_{fl}^2(t) + \frac{\mu_{2l}}{\mu_{1l}}\bar{f}_{cl}^2 + \frac{1}{\mu_{1l}\varepsilon_1}\bar{\bar{f}}_{cl}^2\right] + \sum_{h=1}^{a}\left[-\frac{\omega_{2h}-\varepsilon_2}{\omega_{1h}} e_{wh}^2(t)\,\frac{\omega_{2h}}{\omega_{1h}}\bar{d}_w + \frac{1}{\omega_{1h}\varepsilon_2}\bar{\bar{d}}_w^2\right]$.

Thus, the error system (32) is asymptotically stable almost surely.

Remark 1:Please note that the matrix equality in Equation (33) cannot be solved directly using the MATLAB toolbox. The condition of the matrix equation can be formulated as the following LMI problem: minι, subject to

$$\begin{aligned}&\begin{bmatrix}-\iota \mathrm{I}_{m+q} & \left(\bar{B}_{ld}^T P_l - S\bar{G}\right)^T\\ * & -I_{a+s}\end{bmatrix} < 0\\&P_l \bar{A}_{lg} + \bar{A}_{lg}^T P_l - \bar{Y}_l \bar{G} - \bar{G}^T \bar{Y}_l{}^T + Q_l < 0\end{aligned} \tag{34}$$

where $L_l = P_l{}^{-1}\bar{Y}_l$.

Remark 2:In Theorem 1, alternatively, it has been determined that the evaluated errors are confined within a specific proximity to zero, which is influenced by the limits of the faults and the derivatives of the faults. However, based on (34), we can only make adjustments to the adaptive gains μ_{1l}, μ_{2l}, ω_{1h}, ω_{2h} to reduce the set of fault errors.Nevertheless, due to the sensitivity of the aforementioned scalars to system parameters, it becomes challenging to attain the desired estimated performance.

4 SIMULATION RESULTS

In this section, a model of an unmanned surface vessel is selected to validate the effectiveness of the design method. The model is as follows:

$$\begin{aligned}A_l &= \begin{bmatrix}-0.1000 & 0 & 0 & 0 & 0\\ -0.2760 & -0.6000 & 0 & 0 & 0\\ 0 & 1.0000 & 0 & 0 & 0\\ 0.6501 & 0 & 0 & -0.1180 & -0.3969\\ 0 & 0 & 0 & 1.0000 & 0\end{bmatrix},\\ B_l &= \begin{bmatrix}0.0078\\ -0.0126\\ 0\\ -0.0338\\ 0\end{bmatrix}, B_{la} = \begin{bmatrix}1\\0\\0\\0\\0\end{bmatrix}, G = I_5, D_{ls} = \begin{bmatrix}0\\0\\1\\0\\1\end{bmatrix},\\ E_l &= \begin{bmatrix}0 & 0\\ 0.6 & 0\\ 0 & 0\\ 0 & 0.3969\\ 0 & 0\end{bmatrix}\end{aligned} \tag{35}$$

The input, unknown actuator, sensor faults and external interference are considered as,

$$\begin{aligned}&u(t) = 0.1\sin t,\\&f_m(t) = \begin{cases}0.05t, & 0 \leqslant t \leqslant 10\\ 0.2\sin\left(0.9\left(t-10\right)\right) + 0.5, & t > 10\end{cases}\\&f_c(t) = 0.2\sin\left(1.2t\right)\\&w_1(t) = 0.6\sin\left(1.5t\right)\\&w_2(t) = 0.5\sin\left(1.2t\right)\end{aligned}$$

The matrix M in (5) is made as,

$$M_l = \begin{bmatrix}1 & 0 & 0 & 0 & 0\\ 0 & 1 & 0 & 0 & 0\\ 0 & 0 & 1 & 0 & 0\\ 0 & 0 & 0 & 1 & 0\\ 0 & 0 & 0 & 0 & 1\\ 0 & 0 & -0.5000 & 0 & -0.5000\end{bmatrix} \tag{36}$$

Based on equation (20), the observer parameters are de-

signed as follows,

$$L_l = \begin{bmatrix} 1.0998 & -0.0893 & -0.0474 & 0.4126 & 0.0292 \\ -0.2028 & 0.6783 & 0.2437 & 0.0412 & -0.2044 \\ -0.0790 & 0.6852 & 1.0261 & -0.0577 & 0.4722 \\ 0.4199 & -0.1473 & -0.3137 & 1.0997 & 0.1757 \\ 0.1668 & 0.3048 & -0.2746 & 0.2557 & 0.8180 \\ -0.0938 & -0.4215 & 0.4942 & -0.1490 & 0.5816 \end{bmatrix}$$

$$S = \begin{bmatrix} -0.0008 & -0.0011 & -0.0008 & -0.0006 & 0.0013 \\ -0.0009 & -0.0004 & -0.0013 & -0.0008 & -0.0002 \\ 0.0018 & 0.0011 & -0.0001 & -0.0011 & -0.0012 \end{bmatrix} \quad (37)$$

The adaptive gains are as follows:$\mu_1 = 10000, \mu_2 = 1, \omega_1 = 70000, \omega_2 = 1$.The results are shown in the following figures.

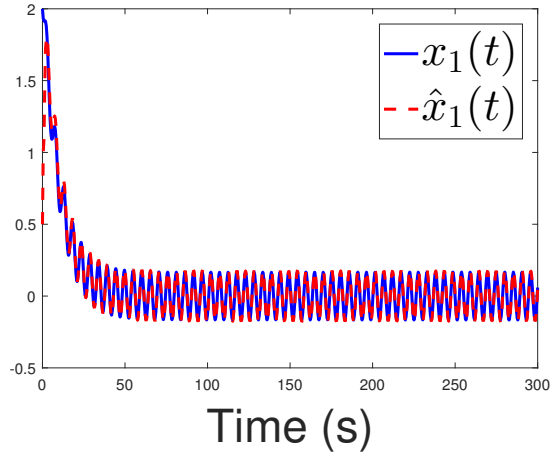

Fig. 1: State $x_1(t)$ and its estimation $\hat{x}_1(t)$

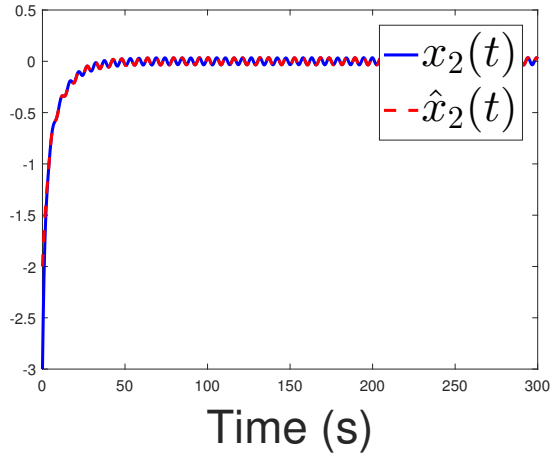

Fig. 2: State $x_2(t)$ and its estimation $\hat{x}_2(t)$

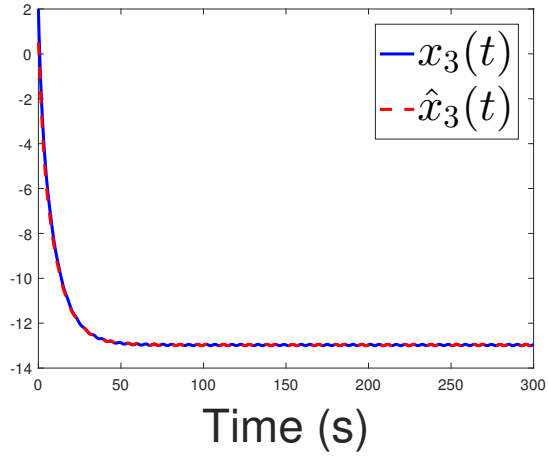

Fig. 3: State $x_3(t)$ and its estimation $\hat{x}_3(t)$

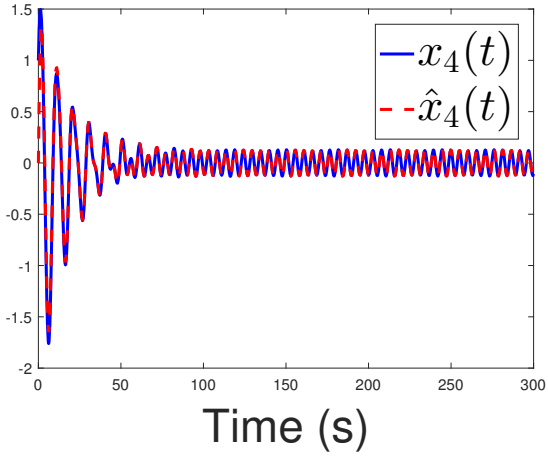

Fig. 4: State $x_4(t)$ and its estimation $\hat{x}_4(t)$

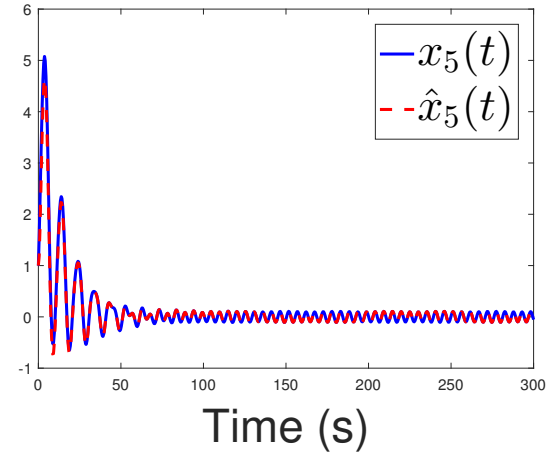

Fig. 5: State $x_5(t)$ and its estimation $\hat{x}_5(t)$

5 Conclusions

In this paper, we present a novel adaptive feedforward observer Fault Estimation (FE) approach, specifically designed for unmanned surface vessel systems that are prone to actuator and sensor faults. This adaptive mechanism is capable of adjusting its parameters based on the real-time data it receives, thereby enhancing the accuracy and reliability of the fault estimation process. The proposed mehtod significantly enhances the safety, reliability, and operational efficiency of unmanned surface vessel systems.

References

[1] H. Dong, Z. Wang, and H. Gao, Fault detection for Markovian jump systems with sensor saturations and randomly varying

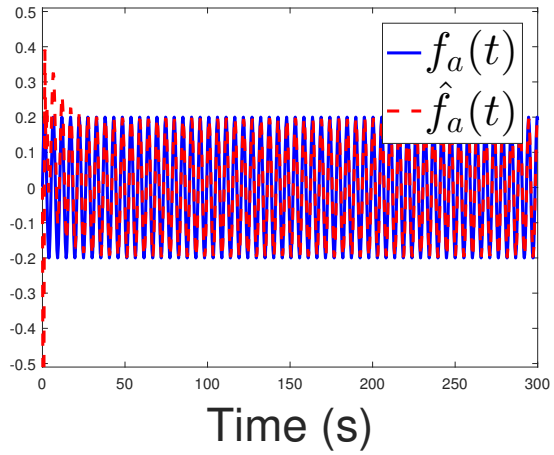

Fig. 6: Actuator fault $f_a\,(t)$ and its estimation $\hat{f}_a\,(t)$

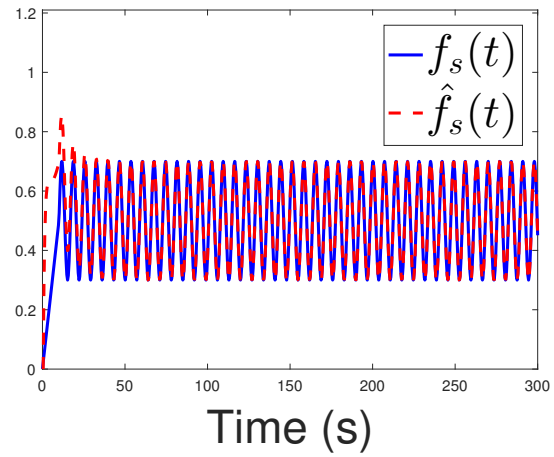

Fig. 7: Sensor fault $f_s\,(t)$ and its estimation $\hat{f}_s\,(t)$

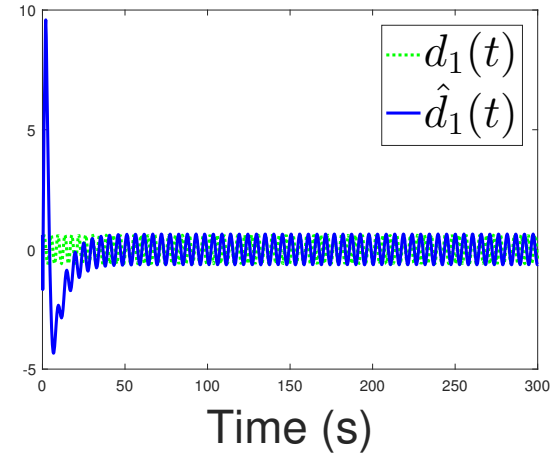

Fig. 8: External interference$d_1\,(t)$ and its estimation $\hat{d}_1\,(t)$

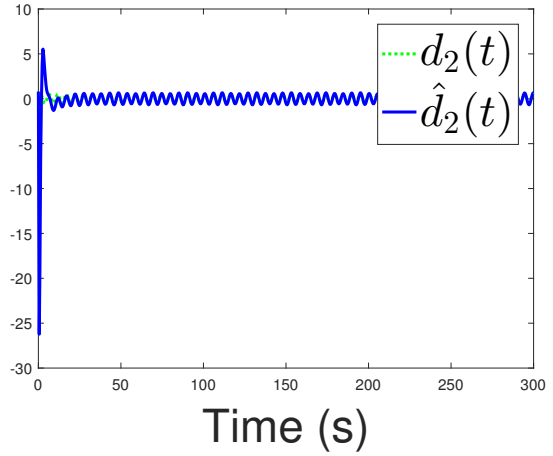

Fig. 9: External interference $d_2\,(t)$ and its estimation $\hat{d}_2\,(t)$

nonlinearities.*IEEE Trans. Circuits Syst. I, Reg. Papers*, 2012, 59(10): 2354-2362.

[2] L. Chen, M. Liu, X. Huang, S. Fu, and J. Qiu, Adaptive fuzzy sliding mode control for network-based nonlinear systems with actuator failures, *IEEE Trans. Fuzzy Syst*, 2018, 26(3): 1311-1323.

[3] Q. Zhang, H. Yu, and X. Wang,Integral terminal sliding mode control for a class of nonaffine nonlinear systems with uncertainty,*Mathematical Problems in Engineering*, 2013:1-11.

[4] E. Weyer, G. Szederknyi, and K. Hangos,Grey box fault detection of heat exchangers,*Control Engineering Practice*, 2000, 8(2): 121-131.

[5] S. Choy and E. Weyer,Reconfiguration schemes to mitigate faults in automated irrigation channels,*Control Engineering Practice*, 2008, 16(10):1184-1194.

[6] L. Wu, X. Yao, and X. W. Zheng,Generalized H 2 fault detection for two-dimensional Markovian jump systems,*Automatica*, 2012, 48(8): 1741-1750.

[7] M. Chadli, A. Abdo, and S. X. Ding,H_-/H_∞ fault detection filter design for discrete-time Takagi-Sugeno fuzzy system, *Automatica*, 2013, 49(7):1996-2005.

[8] M. Basin and P. Rodriguez-Ramirez, Sliding mode filter design for nonlinear polynomial systems with unmeasured states,*Information Sciences*, 2012, 204:82-91.

[9] C. Edwards, T. Lombaerts, and H. Smaili, Fault tolerant flight control,*Lecture Notes in Control and Information Sciences*, 2010, 399:1-560.

[10] T. Wang, J. Qiu, S. Fu, and W. Ji,Distributed fuzzy H_∞ filtering for nonlinear multirate networked double-layer industrial processes,*IEEE Trans. Ind. Electron*, 2017, 64(6):5203-5211.

[11] Z. Xiang, Y. N. Sun, and Q. Chen,Robust reliable stabilization of uncertain switched neutral systems with delayed switching,*Applied Mathematics and Computation*, 2011, 217(23):9835-9844.

[12] H. R. Karimi, M. Zapateiro, and N. Luo,A linear matrix inequality approach to robust fault detection filter design of linear systems with mixed time-varying delays and nonlinear perturbations,*Journal of the Franklin Institute*, 2010, 347(6):957-973.

[13] Y. Li, H. R. Karimi, M. Zhong, S. X. Ding, and S. Liu,Fault detection for linear discrete time-varying systems with multiplicative noise: the finite-horizon case,*IEEE Trans. Circuits Syst. I, Reg. Papers*, 2018, 65(10):3492-3505.

[14] H. Li, Z. Chen, L. Wu, H. K. Lam, and H. Du,Event-triggered fault detection of nonlinear networked systems,*IEEE Transactions on Cybernetics*, 2017, 47(4):1041-1052.

Proceedings of the 3rd Conference on Fully Actuated System Theory and Applications
May 10-12, 2024, Shenzhen, China

Research on Unmanned Surface Vessel Intrusion Evasion Strategy Based on Deep Reinforcement Learning

Changmao Wu, Liheng Chen
College of Intelligent Systems Science and Engineering, Harbin Engineering University, Harbin 150001, China.
E-mail: clh114131@gmail.com

Abstract: This paper focuses on the scenario where unmanned vessels (UAVs) from the red team need to break through the interception of unmanned vessels from the blue team, utilizing deep reinforcement learning technology to accomplish the intrusion evasion task. The study proposes a strategy with Multi-Agent Deep Deterministic Policy Gradient (MADDPG) reinforcement learning framework at its core. The paper presents a method for designing the state space based on the relative positions between the blue team's unmanned vessel and each red team's unmanned vessel. The speed of red team's unmanned vessels is considered as the action space for each agent. Additionally, reward functions are designed based on the goals of the intrusion evasion task to incentivize the red team's unmanned vessels to adopt expected behaviors. This ensures that the red team's unmanned vessels, while avoiding interception by the blue team's unmanned vessels, can successfully carry out the task of striking the target.

Key Words: Unmanned Surface Vessel, Deep Learning, Reinforcement Learning, Path Planning

1 Introduction

With the rapid development of new-generation technologies such as artificial intelligence, information networks, cloud computing, communication, and navigation, unmanned surface vessels (USVs) are undergoing a systematic, intelligent, and unmanned transformation as an emerging form of future maritime vessels. In various fields such as marine surveying, rescue operations, environmental monitoring, and military applications, the widespread use of USVs calls for in-depth research on their fully autonomous navigation and task execution capabilities. The complexity of maritime missions makes the intrusion evasion capability of USVs crucial[1].

Traditional path planning algorithms perform poorly when faced with the dynamic maritime environment and diverse mission requirements. Therefore, the introduction of intelligent algorithms, especially deep reinforcement learning, becomes an ideal choice[2]. The Multi-Agent Deep Deterministic Policy Gradient (MADDPG) algorithm, as a deep reinforcement learning framework for multi-agent environments, provides powerful intrusion evasion capabilities for USVs. Through MADDPG, USVs can perceive the environment in real-time and learn intrusion evasion strategies that adapt to dynamic conditions using deep neural networks.

This approach enables USVs not only to make real-time decisions based on changes in the maritime environment but also, through learning and iteration, automatically acquire optimal intrusion evasion strategies. This reduces redundancy, optimizes resource utilization, and enhances the accuracy of intrusion evasion and task execution efficiency. Research on USVs based on dynamic intrusion evasion and the MADDPG algorithm is significant in improving the intelligence, adaptability, and efficiency of intrusion evasion. This not only helps meet the demands of complex maritime missions but also drives the development of USV technology, providing unprecedented opportunities for the effective utilization of marine resources and environmental protection.

The study of dynamic intrusion evasion for multiple USVs is at the forefront of development, with researchers dedicated to addressing the challenges of collaborative work among multiple intelligent agents. Deep reinforcement learning is an internationally and domestically acclaimed research direction in the field of artificial intelligence. Internationally, researchers are committed to advancing algorithmic innovation, focusing on generalization capabilities and practical applications, particularly in areas such as robot control and autonomous driving.

Domestically, research emphasizes theoretical exploration, domain applications, and the integration of industry, academia, and research. Simultaneously, efforts are being made to promote open-source frameworks for deep reinforcement learning technology, supporting its widespread application in practical problem-solving. This global research trend indicates that deep reinforcement learning has immense potential in solving complex tasks and practical applications, contributing significant innovations and practical applications to the development of artificial intelligence technology[3].

The adoption of multi-agent reinforcement learning algorithms, such as MADDPG, aims to achieve distributed intrusion evasion of intelligent agents, with a focus on real-time perception, collaborative control, conflict avoidance, and collaborative task execution. Through simulation and field validation, the research aims to enhance the adaptability and efficiency of multi-USV systems in dynamic, complex maritime environments, laying a solid foundation for the future application of USV technology.

2 Design of Multi-Unmanned Surface Vessel Intrusion Evasion Methods

This chapter is designed for the scenario of multiple unmanned surface vehicles in breach missions, establishing

This work was supported in part by the National Natural Science Foundation of China (62273114), in part by the Macao Young Scholars Program (AM2022004), in part by the China Postdoctoral Science Foundation (2019M661255, 2021T140149).
Corresponding author: Liheng Chen.

basic settings for the application environment of multiple agents. Additionally, it involves designing the state space, action space, reward system, and essential functions for learning in the scenario that the multiple agents face.

2.1 Multiple-Agent Deep Deterministic Policy Gradient Algorithm

The Deep Deterministic Policy Gradient (DDPG) algorithm has achieved significant success in addressing the challenge of continuous action in unmanned surface vehicle (USV) missions. However, traditional DDPG algorithms face limitations when dealing with breach missions involving multiple USVs. In a multi-agent context, where each USV's strategy is constantly changing, the perception of the environment by each agent evolves, violating the fundamental assumption of deep reinforcement learning that assumes the environment is a Markovian environment[4]. This makes it challenging to effectively train the agents.

The utilization of the MADDPG (Multi-Agent Deep Deterministic Policy Gradient) algorithm in the study of unmanned surface vessel intrusion avoidance strategies is motivated by its advantageous characteristics within this context. MADDPG excels in facilitating multi-agent collaboration, adapting to dynamic environmental conditions inherent to maritime settings, and demonstrating scalability to accommodate varying numbers of agents. Moreover, drawing from the robustness of deep deterministic policy gradient algorithms, MADDPG ensures stability in multi-agent environments while leveraging the representational power of deep learning to effectively navigate complex state and action spaces. As such, MADDPG stands as a prominent choice for addressing the intricacies of unmanned surface vessel intrusion avoidance scenarios.

To address this issue, researchers have proposed the multi-Agent deep deterministic policy Gradient (MADDPG) algorithm, specifically tailored for breach applications involving multiple USVs. MADDPG introduces improvements suitable for multi-agent learning on top of DDPG. In MADDPG, if there are n USVs, each USV is equipped with a policy network and a target network. The critical aspect of MADDPG lies in its unique Critic component, which evaluates not only the actions of individual agents but also requires global information, including the actions of other USVs. Each USV can enhance the training of its actions based on its respective Critic, thus improving training effectiveness in a multi-agent environment. This innovation holds promise for achieving better performance in complex scenarios involving coordinated breach actions by unmanned surface vehicles.

MADDPG (Multi-Agent Deep Deterministic Policy Gradient) is a multi-agent reinforcement learning algorithm that extends the single-agent DDPG algorithm to address collaborative breach problems in a multi-agent environment. The Actor network for each USV i estimates its policy, selecting actions based on observed states. The formula is as follows, where s_i represents the observed state of the i-th USV, θ_i is the parameter of the i-th agent's policy network, and the output of the Actor network is the action[5].

$$a_i = \mu(s_i; \theta_i) \tag{1}$$

The Critic network is employed to estimate the value function for state-action pairs. Each agent has its own Critic network, and global information, including the actions of other agents, is taken into account. The Critic network for each USV i estimates the value function for state-action pairs, considering global information, which includes the actions of other USVs denoted by "o." The formula is as follows, where τ_i represents the parameters of the Critic network.

$$Q_i(s, a, o; \tau_i) \tag{1}$$

The formula for calculating the target value of the Critic network is as follows, where r_i represents the immediate reward and γ is the discount factor.

$$y_i = r_i + \gamma Q_i'(s', \mu_i'(s'; \theta_i'), o'; \tau_i') \tag{3}$$

The parameters τ_i of the Critic network are updated by minimizing the mean squared error loss function, as shown in the following formula.

$$\nabla_{\tau_i} J \approx \frac{1}{N} \sum_{i=1}^{N} \frac{1}{2} \left(y_i - Q_i \left(s, a, o; \tau_i \right) \right)^2 \tag{4}$$

The parameters θ_i of the Actor network are updated using the policy gradient method, as shown in the following formula, where $\nabla_{\theta_i} J$ represents the gradient of the Actor.

$$\nabla_{\theta_i} J \approx \frac{1}{N} \sum_{i=1}^{N} \nabla_a Q_i \left(s, a, o; \tau_i \right) \Big|_{a=\mu_i(s;\theta_i)} \nabla_{\theta_i} \mu_i \left(s; \theta_i \right) \tag{5}$$

In this formula framework, each unmanned ship selects actions based on its own Actor network, while the Critic network considers global information to evaluate the value function. Through collaborative learning, the MADDPG algorithm optimizes the multi-unmanned ship system. This integrated approach is expected to achieve better performance in tasks such as collaborative actions and path planning in unmanned ship scenarios.

2.2 Markov Decision Process (MDP) Modeling

In the deep reinforcement learning for unmanned ship breach missions, we consider the environment in which multiple agents operate as a Markov Decision Process. This process involves a set of interactive entities, namely the unmanned ship agents and the environment. The unmanned ship agents can make decisions based on the state of the environment and change the environment's state through corresponding actions. The environment in this decision-making process encompasses everything outside the unmanned ship agents, and its state changes with the actions of the unmanned ship agents. Simultaneously, unmanned ship agents can perceive changes in the environment's state and receive corresponding rewards based on these changes.

In the context of breach missions, we establish a Markov process-based unmanned ship breach model for each multi-agent. The strategy network of each unmanned ship agent, representing its path planning model, can make breach decisions based on the current environmental state. These decisions lead to changes in the environment's state, and the agents can perceive these changes and receive rewards accordingly, guiding them to perform breach tasks more effectively in complex scenarios. Such modeling facilitates the application of deep reinforcement learning algorithms in multi-agent collaborative breach

environments, enhancing the overall performance of unmanned ship teams[6].

Typically, this Markov Decision Process can be described using a quintuple, where the interpretation of each element is as follows:

State space S_i: Represents the set of environmental states where unmanned ship agent i of the red team is located. Considering the scenario with multiple agents, the state space is the collective set of states for all unmanned ship agents.

Action space A_i : Represents the set of actions for unmanned ship agent i of the red team. In the case of multiple agents, the action space is the collective set of actions for all unmanned ship agents.

Transition function P_i : This function describes the probability of transitioning from one state to another when agent i takes a certain action in a given state.

Reward function R_i: Provides rewards to agent i based on the actions it takes in different states.

Discount factor γ: Its value ranges between 0 and 1, representing the importance of future rewards in the current value. A smaller value indicates a greater emphasis on rewards in the current state, while a larger value indicates a greater emphasis on future rewards.

This quintuple provides a comprehensive framework, enabling deep reinforcement learning algorithms to learn and optimize the decision-making strategies of agents in complex unmanned ship breach scenarios[7]. This, in turn, enhances the overall performance and efficiency of the entire system.

2.3 State space design

In the context of unmanned ship breach missions, considering practicality and modeling convenience, we choose a spherical coordinate system as the environmental model, using only latitude and longitude for location and disregarding height. In this breach task environment, we have multiple unmanned ships, each of which needs to plan its own path to effectively complete the mission[8].

To simplify the model, we define the state space for each unmanned ship as the set of states for that particular ship, where the state format is the same for each unmanned ship. We use the term "Unmanned Ship Learning Robot" (USL) to refer to the collection of unmanned ship intelligent agents, with each unmanned ship agent belonging to this set.

For each unmanned ship agent belonging to the USL, assuming there are m blue team unmanned ships for interception, we define its state space as a 2+2+4*m-dimensional vector.

$$S_{\mathrm{i}} = [x, y, v_x, v_y, d_x^{i1}, \ldots, d_x^{ij}, \ldots, d_x^{im}, d_y^{\mathrm{i1}}, \ldots, d_y^{\mathrm{ij}}, \ldots, d_y^{im}, \ldots, d_{v_x}^{i1}, \ldots, d_{v_x}^{ij}, \ldots, d_{v_x}^{im}, d_{v_y}^{i1}, \ldots, d_{v_y}^{ij}, \ldots, d_{v_y}^{im}] \quad (6)$$

In this definition, x represents the horizontal coordinate relative to the destination, y represents the vertical coordinate relative to the destination, v_x represents the horizontal velocity of the current red team unmanned ship, and v_y represents the vertical velocity of the current red team unmanned ship. Simultaneously, d_x^{ij} represents the horizontal distance between the i-th red team unmanned ship agent and the j-th blue team unmanned ship, while d_y^{ij} represents the vertical distance. $d_{v_x}^{ij}$ represents the horizontal velocity difference between the i-th red team unmanned ship agent and the j-th blue team unmanned ship, and $d_{v_y}^{ij}$ represents the vertical velocity difference.

2.4 Action space design

Given the practical considerations and the requirements of model simulation, we define the actions of the red team unmanned ship agents as changes in their direction. In this breach mission, we assume that the velocity of the red team unmanned ships remains constant and moves at a predetermined speed. Therefore, we simplify the action setting for the red team unmanned ship agents to only involve changes in direction[9]. Specifically, we define the actions of the red team unmanned ship agents as follows:

$$A_i = [v_x, v_y] \quad (2)$$

According to the strategy learned during training, make corresponding changes to the direction of the red team unmanned ships at different times. This action definition, while remaining concise, meets the requirements of the red team unmanned ship breach mission. It allows the agents to flexibly make appropriate decisions based on the environmental state and the learned strategy, optimizing the effectiveness of the breach mission.

By adjusting the direction while maintaining a predetermined speed, the red team unmanned ship agents can effectively evade interception by blue team unmanned ships and maintain the continuity of movement during the breach process. The implementation of this action definition contributes to improving the adaptability and success rate of the red team unmanned ship agents in breach missions[10].

2.5 Reward function design

In the research on red team unmanned ship breach missions, a series of reward functions must be defined to guide the agent's learning towards the desired behavior. These functions should assign different rewards to the agent based on indicators such as the state of the red team unmanned ship, the distance to the target, and whether it is intercepted by the blue team unmanned ship, encouraging the agent to learn the expected behavior[11].

In the context of red team unmanned ship breach missions based on deep reinforcement learning, in addition to designing reward functions for the distance and direction of the red team unmanned ship to the target, it is also necessary to consider a reward function for avoiding the blue team unmanned ships. In the scenario, there are scenarios where blue team unmanned ships collide with red team unmanned ships, requiring the design of a reward function to guide the red team unmanned ship agent to successfully avoid the blue team unmanned ships and reach the target point.

Specifically, the following reward functions are defined: a penalty (reward = -1) is given when the red team unmanned ship collides with the blue team unmanned ship, and a reward (reward = 5) is given when the distance between the red team unmanned ship and the target is less than 50 km, considering the mission accomplished.

Through this reward function, when the distance from the red team unmanned ship to the target is greater than one hundred kilometers, it checks if the unmanned ship deviates too far from the target, deducting a certain reward if it is too

far. When the distance to the target is less than 100 km, it is considered that the red team unmanned ship has entered a relatively close range to the target, providing corresponding rewards and marking the distance as 1. In this close range to the target, if the red team unmanned ship collides with the blue team unmanned ship, a reward deduction is applied. If the status of the red team unmanned ship indicates no collision with the blue team unmanned ship and it has not entered the close range, but the distance to the target is reduced, it is considered that the red team unmanned ship is advancing towards the target, and a reward is given[12].

When the red team unmanned ship is close to the target, another set of reward functions is designed to reward the red team unmanned ship. When the distance from the red team unmanned ship to the target is less than 50 km, it is considered that the mission is accomplished, providing a relatively large reward. The construction of these reward functions effectively guides the learning of the red team unmanned ship agent, enabling it to form effective breach strategies in complex environments.

2.6 Training process of MADDPG algorithm.

M In the research on intrusion missions of unmanned surface vehicles (USVs) in the red team, traditional single-agent algorithms fail to effectively utilize the states and information of other agents, leading to suboptimal training outcomes. To address this issue, the Multi-Agent Deep Deterministic Policy Gradient (MADDPG) algorithm is introduced.

The MADDPG algorithm shares structural similarities with the traditional Deep Deterministic Policy Gradient (DDPG) algorithm. In the actor component, each red team USV agent outputs corresponding actions based on its local observations. However, in the critic component, MADDPG differs from traditional algorithms by requiring global information for evaluation. This enables better collaboration among red team USV agents. The application of MADDPG algorithm in the training process for intrusion missions of red team USVs is outlined as follows:

(1) Initialize the policy network and target network parameters for red team USV agents.

(2) Initialize the experience pool to store experiences during the training process.

(3) Scene initialization to obtain the initial state of red team USV agents.

(4) Use the MADDPG algorithm to select actions for red team USV agents corresponding to their states.

(5) Interact with the environment to receive rewards and obtain the next state.

(6) Repeat steps 4 and 5 until completing one training episode.

(7) Store samples in the experience pool.

(8) Select multiple samples from the experience pool, calculate, and update the target and policy networks.

(9) Repeat steps 1-8 until the training of red team USV agents is completed.

In the practical application of dynamic path planning for unmanned surface vehicles, the MADDPG algorithm enables USV agents to plan paths more efficiently in complex marine environments. By adapting to environmental changes and enhancing the accuracy and efficiency of path planning through the sharing and coordination of global information, USV agents can intelligently accomplish tasks, contributing to the development of unmanned surface vehicle technology.

Table 1: Experimental parameter settings

Parameters	Values
Number of unmanned vessels on the red side	2
Number of unmanned vessels on the blue side	4
Safe distance between unmanned vessels on the red side and those on the blue side	10Km
Speed of unmanned vessels on the red side	10Kn
Speed of unmanned vessels on the blue side	5Kn
Size of the experience pool	500000
Objective function updating coefficient	0.95
Learning rate of the actor network	0.0002
Learning rate of the critic network.	0.001

(1) Early Stage of Training:

In the initial training phase of the red team's unmanned boat assault mission, by observing the trajectory of the blue team's unmanned boat agents (as shown in the figure below), it is evident that the training level of the red team's unmanned boat trajectory is not yet sufficient at this stage. During this phase, guided by its strategy, the red team's unmanned boat agents maintain a relatively distant distance from the target, resulting in a relatively poor task completion. This indicates that the red team's unmanned boat agents have not fully mastered the complex interception strategy of the blue team's unmanned boat in the early stages, and their decision-making is limited by training data and experience.

In the figure, the trajectory of the red team's unmanned boat agents exhibits relatively conservative behavior. This may be attributed to the fact that the red team's unmanned boat agents have not fully adapted to the complexity of the assault mission in the early stages of training, leading to relatively conservative decision-making.

To enhance the effectiveness of assault, further training is needed to optimize the strategy. As training progresses, the red team's unmanned boat agents will gradually improve their route planning, adapt to more complex scenarios, and achieve a more effective assault effect. This highlights the importance of the training process and provides valuable insights for optimizing the dynamic path planning of the red team's unmanned boat.

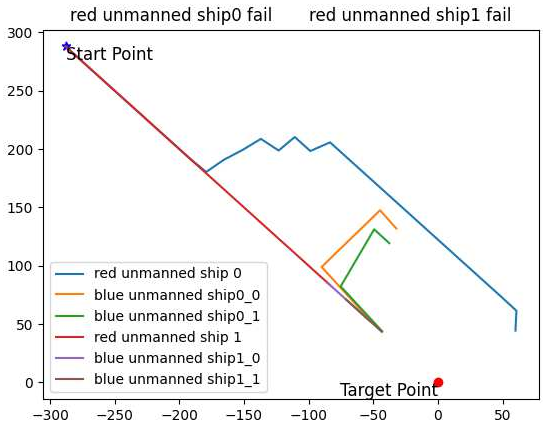

Fig. 1: Early stage of training

(2) Mid-Stage of Training:

In the mid-training phase of the red team's unmanned boat assault mission, as observed in the figure below, it is evident that the red team's unmanned boat assault algorithm has made significant progress after a certain degree of training. During this mid-training phase, the red team's unmanned boat agents, guided by the algorithm, demonstrate preliminary capabilities to make decisions based on the current state. Their trajectory shows a more flexible and proactive trend.

At this stage, the red team's unmanned boat agents successfully avoided the blue team's unmanned boats shown in the figure, approaching the red team's target more closely, and the effectiveness of path planning has significantly improved. The figure clearly illustrates that the red team's unmanned boat agents have acquired the ability to make decisions based on the current state in the mid-training phase, providing a beneficial foundation for subsequent training and path planning optimization. The learning performance of the red team's unmanned boat agents exhibits characteristics of adaptation to complex environments, laying a solid foundation for improving assault effectiveness and avoiding interception by the blue team's unmanned boats in more complex scenarios. This highlights the potential of deep reinforcement learning in the red team's unmanned boat assault mission and the gradual optimization process.

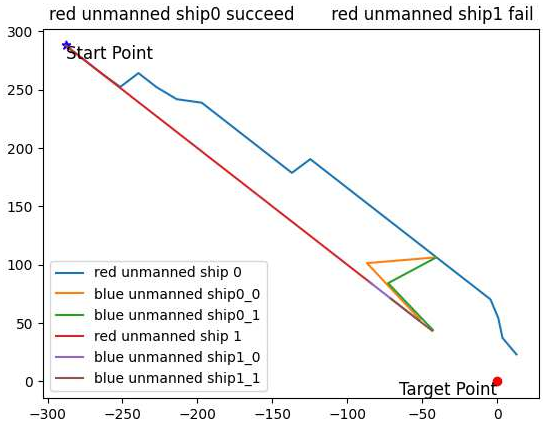

Fig. 2: Mid-stage of training

(3) Late Stage of Training:

In the late stage of training for the red team's unmanned boat assault mission, as observed in the figure below, it is evident that dynamic assault by unmanned boats has been thoroughly trained and is displaying a significant assault effect. At this stage, the red team's unmanned boat agents can make optimized action decisions in complex environments, successfully avoiding the blue team's unmanned boats and directly reaching the target. In the figure, the trajectory of the red team's unmanned boat agents exhibits more precise and focused assault behavior. At this point, the unmanned boat agents have successfully adapted to the complex dynamic assault task, and their decision-making has become more flexible and efficient.

The results in the late stage of training highlight the significant progress in dynamic assault by the red team's unmanned boats. With the deepening of training, the assault effectiveness of the red team's unmanned boat agents gradually improves, providing strong support for the research and practical application of unmanned boat dynamic path planning. This also demonstrates the potential of deep reinforcement learning in addressing multi-agent path planning problems. Through optimization in the late stage of training, the red team's unmanned boat agents can better adapt to environmental changes and achieve a higher level of assault effectiveness.

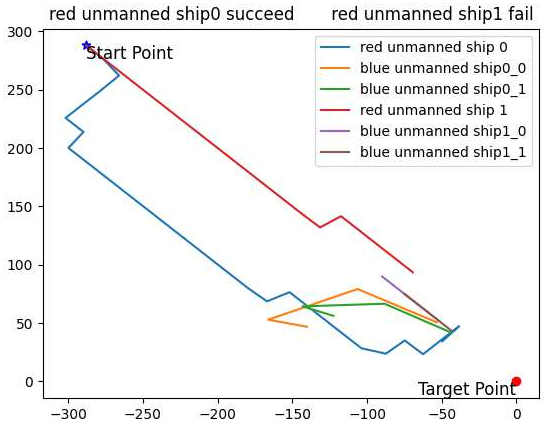

Fig. 3: Late stage of training

(4) Training Completion:

By observing the figure below, we can see that after training completion, the red team's unmanned boat dynamic assault algorithm has successfully formulated corresponding actions for unmanned boat agents based on the environmental state. Guided by this algorithm, the red team's unmanned boat agents have successfully completed the task of navigating through all the blue team's unmanned boats and reaching the target point.

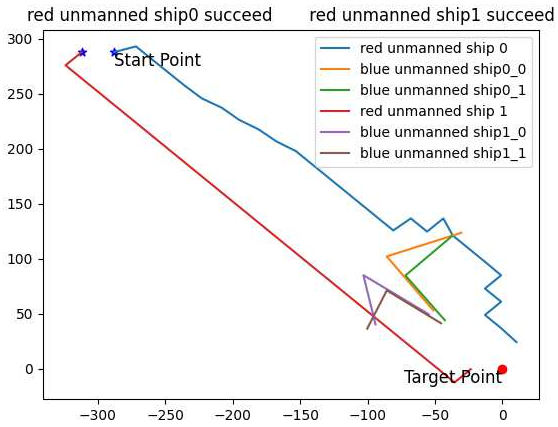

Fig. 4: Training completed.

The performance differences observed in different training stages reflect the gradual optimization of training effectiveness. In the early stages, due to the immaturity of the red team's unmanned boat dynamic assault algorithm, the unmanned boat agents struggled to accurately formulate action decisions based on the state, resulting in situations where they were distant from or deviated from the target. As training progressed, the algorithm gradually guided the red team's unmanned boat agents closer to the target, but the assault effectiveness remained moderate, making it difficult to reach the target point. Convergence in MADDPG means stable agent policies. It's checked by tracking policy changes over training. Factors like hyperparameters affect it.

In the late stages of training, the algorithm successfully guided two red team's unmanned boat agents to complete the assault task, but some red team's unmanned boat agents still faced interception by the blue team's unmanned boats. Ultimately, after training completion, the model could effectively guide multiple red team's unmanned boat agents to overcome blue team interception and reach the target point in the specified environment. This indicates that the application of deep reinforcement learning in dynamic path planning for the red team's unmanned boats provides an effective solution for enhancing dynamic assault effectiveness.

3 Conclusion

This paper focuses on the topic of dynamic assault by red team's unmanned boats. Through the idealized modeling of the red team's unmanned boat assault scenario, the paper successfully designs the state space and action space. On this basis, a reward function associated with the state space and action space is constructed to guide the training of the red team's unmanned boat agents. Simultaneously, a series of functions are defined to implement the perception of the environment by the red team's unmanned boat agents. The paper completes the training model for the red team's unmanned boat multi-agent dynamic assault scenario.

Through idealized modeling and training, this paper provides a beneficial research foundation for the dynamic path planning of red team's unmanned boats. The defined state space, action space, and reward function construct a complete training framework, enabling the red team's unmanned boat agents to learn effective path planning strategies in complex dynamic assault scenarios. This research holds significant importance for the application of deep reinforcement learning in unmanned boat technology, offering robust support for enhancing the performance of red team's unmanned boats in practical assault missions.

References

[1] HD. Silver, A. Huang, C. J. Maddison, A. Guez, L. Sifre, G. Van Den Driessche, et al., “Mastering chess and shogi by self-play with a general reinforcement learning algorithm,” *Nature*, vol. 529, no. 7587, pp. 484-489, 2016.

[2] V. Mnih, K. Kavukcuoglu, D. Silver, A. A. Rusu, J. Veness, M. G. Bellemare, et al., “Human-level control through deep reinforcement learning,” *Nature*, vol. 518, no. 7540, pp. 529-533, 2015.

[3] R. S. Sutton and A. G. Barto, *Reinforcement Learning: An Introduction*. MIT Press, 2018.

[4] S. Zhang and C. Miao, “Deep reinforcement learning in robotics: A review,” *IEEE Access*, vol. 6, pp. 36638-36647, 2018.

[5] T. Haarnoja, A. Zhou, P. Abbeel, and S. Levine, “Soft actor-critic: off-policy maximum entropy deep reinforcement learning with a stochastic Actor,” *arXiv preprint arXiv:1801.01290*, 2018.

[6] Y. Ma, M. Hu, and X. Yan, “Multi-objective path planning for unmanned surface vehicle with currents effects,” *ISA Transactions*, vol. 75, pp. 137-156, 2018.

[7] R. Polvara, et al., “Obstacle avoidance approaches for autonomous navigation of unmanned surface vehicles,” *The Journal of Navigation*, vol. 71, no. 1, pp. 241-256, 2018.

[8] B. Singh, R. Kumar, and V. P. Singh, “Reinforcement learning in robotic applications: A comprehensive survey,” *Artificial Intelligence Review*, pp. 1-46, 2022.

[9] X. Zhang, et al., “Decision-making for the autonomous navigation of maritime autonomous surface ships based on scene division and deep reinforcement learning,” *Sensors*, vol. 19, no. 18, p. 4055, 2019.

[10] J. B. Escario, J. F. Jimenez, and J. M. Giron-Sierra, “Optimisation of autonomous ship manoeuvres applying ant colony optimisation metaheuristic,” *Expert Systems with Applications*, vol. 39, no. 11, pp. 10120-10139, 2012

[11] B. C. Shah and S. K. Gupta, “Long-distance path planning for unmanned surface vehicles in complex marine environment,” *IEEE Journal of Oceanic Engineering,* vol. 45, no. 3, pp. 813-830, 2019.

[12] C. Wang, et al., “Autonomous navigation of UAVs in large-scale complex environments: A deep reinforcement learning approach,” *IEEE Transactions on Vehicular Technology*, vol. 68, no. 3, pp. 2124-2136, 2019

Proceedings of the 3rd Conference on Fully Actuated System Theory and Applications
May 10-12, 2024, Shenzhen, China

Path-following control of autonomous tugs based on Gaussian process regression and arithmetic optimization algorithm

Shijie Li[1,4], Yang Li[4], Xinjue Hu*[1,2,3], Jialun Liu[1,2,3], Muheng Wei[5]

1. State Key Laboratory of Maritime Technology and Safety, Wuhan University of Technology, Wuhan 430063, China
E-mail: {lishijie, jialunliu, huxinjue}@whut.edu.cn

2. Intelligent Transportation Systems Research Center, Wuhan University of Technology, Wuhan, 430063
E-mail: {jialunliu, huxinjue}@whut.edu.cn

3. National Engineering Research Center for Water Transport Safety, Wuhan, 430063, China
E-mail: {jialunliu, huxinjue}@whut.edu.cn

4. School of Transportation and Logistics Engineering, Wuhan 430063, China
E-mail: {lishijie, liyang123}@whut.edu.cn

5. ZhenDui Industry Artificial Intelligence Co. Ltd, Shenzhen 518101, China
E-mail: weimuheng@163.com

Abstract: Intelligent tugs with high autonomy are becoming a worldwide research focus, particularly for the needs of automated port operations. The path-following control of tug is an important part of intelligent tugs research. This paper proposes a path-following control method that combines Gaussian Process Regression (GPR) and Arithmetic Optimization Algorithm (AOA) for autonomous tugs. A GPR model is constructed to identify the correlation between the heading angle and the rotation angle of the azimuth thrusters, which acts as the prediction model in the path-following controller. The AOA is utilized to determine the optimal control inputs for each sampling interval, adopting the sine-cosine search strategy instead of addition and subtraction operations and introduces an inertia factor to improve the computational efficiency of AOA. A Line-of-Sight (LOS) algorithm is used as the guidance law to transform reference waypoints into reference heading angles, and the path-following controller is designed based on the GPR model and AOA. Simulation results show that the proposed method performs well in the path-following task without having prior knowledge regarding the hydrodynamic coefficients and ship parameters.

Key Words: Autonomous surface ships, path-following control, Gaussian process regression, arithmetic optimization algorithm

1 Introduction

A tug is a special type of vessel used mainly near the harbor and ports to assist the docking, towing, hauling, escorting, emergency rescue, and other assistance maneuvers for large cargo ships. It is usually equipped with two azimuth thrusters to provide propulsive forces and moments that result in surge, sway, and yaw motion. Unlike underactuated cargo ships that are equipped with propellers and rudders, a tug can be considered a fully-actuated system because the thrusters can provide forces in three Degrees-Of-Freedom (D-O-F) in the horizontal plane. Intelligent tugs with high autonomy are a growing area of research around the world, especially for the needs of automated port operations. Path following, as a basic task of ship motion control, is crucial for achieving autonomous navigation of intelligent tugs.

Researchers have made significant progress in path following control. Various control algorithms have been utilized by researchers for ship path following control, including PID [1], adaptive control [2], sliding mode control [3], model predictive control [4], and combination with machine learning techniques [5]. However, current research still needs to address some issues. On one hand, the effectiveness of commonly used model-based controller design is limited in nonlinear and uncertain navigation environments due to the inaccuracy of the system model. On the other hand, accurate mathematical models are difficult to obtain due to the coupled effects of hydrodynamic forces acting on the ship's hull and propulsion forces generated by its control actuators. Commonly used mathematical models for designing ship motion controllers include the Nomoto model [6], which only describes yaw movements, and the Maneuvering Modeling Group (MMG) model [7], which usually ignores the coupled effects between the ship's sway and yaw movements. It is important to strike a balance between model accuracy and controller design needs to allow for wider application of the models to different scenarios.

With the advancement of machine learning, researchers have proposed several data-driven modeling methods to deal with the difficulties in constructing mechanism mathematical models for ship movements. Gaussian Process Regression (GPR) is a nonparametric probabilistic modeling method suitable for small datasets [8]. It enables direct modeling of systems with unknown dynamics and can be integrated into a Model Predictive Control (MPC) framework to address various control problems [9, 10]. This also brings the problem of difficulty in solving the optimization problems formulated in MPC based on nonparametric models. Therefore, heuristic strategies offer a feasible solution. Metaheuristic optimization algorithms such as genetic algorithm (GA) [11], particle swarm optimization (PSO) algorithm [12], adaptive-mutation beetle swarm prediction ((AMBS-P) algorithm [5, 13] have been widely used in controller design of ships. These algorithms are useful for tuning controller parameters, identifying model parameters, and searching for feasible solutions for optimal controllers.

The Arithmetic Optimization Algorithm (AOA) [14] has received increased attention in recent years due to its promis-

This work was supported by National Key R&D Program of China (2022YFE0125200) , National Natural Science Foundation of China (52272425) and Natural Science Foundation of Hubei Province, China (2023AFB064).

*Corresponding author.

ing results in solving challenging optimization problems. It shows great potential in solving single-objective, multi-objective, discrete problems. In this paper, the AOA algorithm is incorporated with the model predictive control framework to search for optimal solutions for the rotation angles of thrusters.

This paper proposes a path-following control method that combines Gaussian Process Regression (GPR) and Arithmetic Optimization Algorithm (AOA) for autonomous tugs. A GPR model is constructed to identify the correlation between the heading angle and the rotation angle of the azimuth thrusters, which acts as the prediction model in the path-following controller. The arithmetic optimization algorithm is utilized to determine the optimal control inputs for each sampling interval. A Line-of-Sight (LOS) algorithm is used as the guidance law to transform reference waypoints into reference heading angles, and the path-following controller is designed based on the GPR model and AOA. Simulation results show that the proposed method performs well in the path-following task without having prior knowledge regarding the hydrodynamic coefficients and ship parameters.

The structure of this paper is as follows. Section 2 describes the characteristics of ship dynamics, LOS guidance strategy and the path following control problem. Section 3 gives the steps of model recognition based on Gaussian process regression. Section 4 introduces the design steps of the arithmetic optimization algorithm controller based on the GPR model. Section 5 presents the simulation results regarding the accuracy of the Gaussian process regression model and the path-following control performance. Section 6 gives conclusions and future research directions.

2 Preliminaries and problem description

2.1 Ship Dynamics

Fig. 1 gives the configuration of the tug and its coordinate system. It is equipped with two twin-screw azimuth thrusters located at the stern below the hull to provide propulsion and torque. This paper mainly considers its 3-DOF movements in surge, sway and yaw directions in a North-East-Down (NED) reference frame fixed to the ocean surface with its x-axis pointing North, y-axis pointing East, and z-axis pointing downwards. The position of the tug can be described as a vector $\boldsymbol{\eta} = [x, y, \psi]^T \in \mathbb{R}^3$, in which ψ represents the heading angle relative to North in the horizontal plane. The velocity of the ship includes its surge speed u towards the x-axis and the sway speed v towards the y-axis, as well as its yaw rate r. Therefore, the generated velocity vector $\boldsymbol{v} = [u, v, r]^T \in \mathbb{R}^3$. The evolution of the movements of the tug can be described as [15]:

$$\begin{cases} \dot{\boldsymbol{\eta}} = \begin{bmatrix} \cos(\psi) & -\sin(\psi) & 0 \\ \sin(\psi) & \cos(\psi) & 0 \\ 0 & 0 & 1 \end{bmatrix} \boldsymbol{v} \\ \boldsymbol{M}\dot{\boldsymbol{v}} = -\boldsymbol{C}(\boldsymbol{v})\boldsymbol{v} - \boldsymbol{D}(\boldsymbol{v})\boldsymbol{v} + \boldsymbol{\tau} + \boldsymbol{d} \end{cases} \tag{1}$$

in which matrices $\boldsymbol{M}$, $\boldsymbol{C}(\boldsymbol{v})$ and $\boldsymbol{D}(\boldsymbol{v})$ represent ship inertia coefficients, the Coriolis and centripetal matrix, and the damping matrix, respectively. The control forces and moments are expressed as $\boldsymbol{\tau} = [\tau_u, \tau_v, \tau_r]^T \in \mathbb{R}^3$, which are generated by its twin azimuth thrusters. Vector $\boldsymbol{d} = [d_x, d_y, d_\psi]^T \in \mathbb{R}^3$ represents the external disturbances.

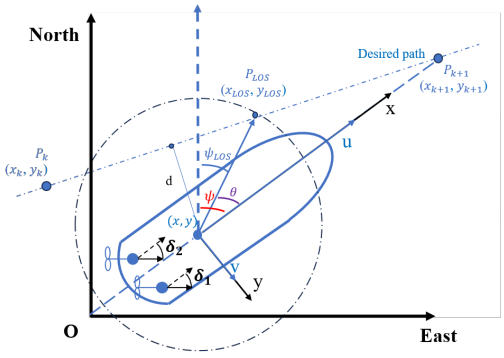

Fig. 1: Ship coordinate system

According to [15], the control forces and moments are generated by azimuth thruster rotation angles and speeds as follows:

$$\boldsymbol{\tau} = \begin{bmatrix} \cos(\delta_1) & \cos(\delta_2) \\ \sin(\delta_1) & \sin(\delta_2) \\ l_x \sin(\delta_1) - l_y \cos(\delta_1) & l_x \sin(\delta_2) + l_y \cos(\delta_2) \end{bmatrix} \boldsymbol{T} \tag{2}$$

where δ_1 and δ_2 represent the rotation angles of the starboard and port side thrusters, respectively. $\boldsymbol{T}$ represent the forces generated by each thruster. It can be seen that the changes of the heading angle of the tug is dependent on the coupled effects of rotation angles δ_1 and δ_2.

2.2 Problem description

Due to practical limitations, there are many coupled terms that cannot be directly measured to identify model parameters in (1). This paper utilizes GPR to exploit experimental data to build models for predicting the heading angle of the tug, given the prior knowledge that the its heading angle is determined by both thruster rotation angles. The design of a path-following controller requires a guidance strategy to generate suitable references as control objectives. The Line-Of-Sight (LOS) guidance strategy has been commonly used in path-following control problems, turning the reference path into a series of reference heading angles. This paper uses the LOS guidance strategy and transforms the path-following control into a heading control problem.

As illustrated in Fig.1, assuming that P_{k+1} is the current following path point and P_k is the previous path point, draw a circle with the current position (x, y) of the ship as the center and $R_{LOS} = n \times L_{pp}$. Parameter L_{pp} represents the length of the ship, and R_{LOS} represents the radius to intersect with the desired path, and select the point closer to P_{k+1} as the LOS point. The angle between the direction vector of the current ship's coordinates to the LOS point and north is the reference LOS angle ψ_{LOS}. θ is the yaw angle, and d is the shortest distance from the current ship position to the desired path. ψ_{LOS} can be calculated by:

$$\tan\left(\psi_{LOS}(t)\right) = \frac{\Delta y(t)}{\Delta x(t)} = \frac{y_{\mathrm{LOS}}(t) - y(t)}{x_{\mathrm{LOS}}(t) - x(t)} \tag{3}$$

The LOS point coordinates are represented by x_{LOS} and y_{LOS}, while the current ship coordinates are represented by

x and y. Then θ can be calculated from the error between the ship's current heading angle ψ and the reference angle ψ_{LOS}. The ship should continuously adjust its yaw angle towards 0, allowing it to automatically navigate along the calculated reference heading and follow the desired route indefinitely, achieving the goal of path-following. In other words, the objective of the path-following control is to ensure that the tug always follows the reference heading angle ψ_{LOS} by adjusting its rotation angles δ_1 and δ_2. The GPR are used to predict the ship's heading angle at time $k+1$ given its states and control inputs at time k which is expressed as follows:

$$\psi(k+1) = G_{\psi}(\psi(k), \delta_1(k), \delta_2(k)) \tag{4}$$

An optimization problem can be formulated based on the GPR model. The objective of this problem is to minimize the deviations of the predicted heading angles from the reference angle ψ_{LOS}. The AOA is incorporated to solve the formulated optimization problem.

3 Gaussian process regression

The GPR initially assumes that the the unknown function f follows a prior Gaussian process:

$$f(z) \sim \mathcal{GP}\left(0, k(z, z')\right) \tag{5}$$

in which,$z \in R^s$,$k(z, z')$ is a symmetric and positively definite kernel function. This paper chooses the Radial Basis Function (RBF):

$$k(z, z') = A\exp(\tfrac{-\|z-z'\|^2}{2l^2}) \tag{6}$$

in which A and l are hyperparameters that represent amplitude and length scales, respectively.

Assume that $Z = \{z_i \in \mathbf{R}^s, i = 1, 2, \cdots, N\}$ is the input training set, and $Y = \{y_i \in \mathbf{R}, i = 1, 2, \cdots, N\}$ is the corresponding set of observations. f_N is the real output set. $z_* \in \mathbf{R}^s$ is test point, $f_* = f(z_*)$. GPR uses Bayesian formula for posterior inference :

$$p(f_N, f_* \mid Y) = \tfrac{p(Y|f_N)p(f_N, f_*)}{\int\int p(Y|f_N)p(f_N, f_*)\mathrm{d}f_N\mathrm{d}f_*} \tag{7}$$

in which $p(f_N, f_*)$ is the Gaussian prior distribution, $p(Y|f_N)$ is the likelihood function, which is used to describe the observation noise. It is assumed that the observation noise in the environment is Gaussian white noise. Then $p(Y \mid f_N) = \mathcal{N}(f_N, \sigma^2 I)$, where $p(Y \mid f_N)$ is a Gaussian distribution, with the mean being the function value corresponding to the real output f_N and the variance being the noise variance, σ represents the standard deviation of the noise.$\boldsymbol{I}$ is the identity matrix.

The above results are integrated to obtain a prediction model :

$$\begin{cases} p(f_* \mid Y) = \int p(f_N, f_* \mid Y)\mathrm{d}f_N = \mathcal{N}\left(m^*, \Sigma^*\right) \\ m^* = \boldsymbol{K}_{*N}(\boldsymbol{K}_{NN} + \sigma^2\boldsymbol{I})^{-1}\boldsymbol{y} \\ \Sigma^* = k\left(z_*, z_*\right) - \boldsymbol{K}_{*N}(\boldsymbol{K}_{NN} + \sigma^2\boldsymbol{I})^{-1}\boldsymbol{K}_{N^*} \end{cases} \tag{8}$$

in which $\boldsymbol{K}_{N^*} = [k(z_*, z_1), k(z_*, z_2), \cdots, k(z_*, z_N)]^\top$ is the covariance vector. $\boldsymbol{K}_{*N} = \boldsymbol{K}_{N^*}^\top$, and $\boldsymbol{y} = [y_1, y_2, \cdots, y_N]^\top$ is the observation vector. m^* is predicted value at z_* with function f. Σ^* is is the predictive variance of f in z_*.

A GPR model can be constructed using data collected from simulated or real-world experiments. By setting reasonable excitation signal inputs, ship data can be collected more comprehensively, which can help establish a more accurate model. To establish the correlation between the heading angle ψ and rotation angles δ_1 and δ_2, it is essential to design two azimuth rotation angle commands δ_1 and δ_2 excitation signals to ensure they cover a broader input space. According to the physical limits of the actual ship, the δ_1 is randomly selected from a range of 0° to $+35^\circ$,the δ_2 is randomly selected form a range of -35° to 0°. The reason for this configuration is to prevent interference between the forces generated by the two azimuth thrusters, which could complicate the determination of the torque produced by each individual thruster. To account for the nonlinear, large time delay and large inertia characteristics of the ship's motion, the excitation signals are provided in a 5-second cycle with a 1-second sampling interval.

The dataset for GPR model identification is constructed as $\mathcal{X}_{\mathrm{Input}} = \left[\{\delta_1(i)_{i=1}^M\}, \{\delta_2(i)_{i=1}^M\}, \{\psi(i)_{i=1}^M\}\right]$ and $\mathcal{X}_{\mathrm{Output}} = \left[\{\{\psi(t+1)_{i=1}^M\}\right]$. Therefore, the GPR model G_ψ is a 3-input-1-output model. After sufficient data has been collected, the GPR model for yaw movements is represented as a function whose values are determined by a prior distribution. This function follows a prior Gaussian process (5) and use (7) for posterior inference. Finally, the prediction model G_ψ can be obtained based on (8).

4 Design steps of path-following controller

4.1 Arithmetic optimization algorithm

The AOA is a metaheuristic optimization algorithm, inspired by the use of arithmetic operators in solving arithmetic problems [14]. The process is divided into two stages: exploration and exploitation. During the exploration phase, the search is conducted using highly dispersed multiplication (M"$\times$") or division (D"$\div$") operators to ensure extensive coverage of search space. In the exploitation phase, the search is conducted using high-density subtraction (S"$-$") or addition (A"$+$") operators to improve accuracy of obtained solutions. This paper uses the model G_ψ to predict heading angles when given different candidate thruster rotation angles. The AOA is utilized to search for the optimal rotation angles that minimize the deviations between the predicted and reference heading angles. Fig. 2 shows the how the operators used converges to the optimal region. Parameters r_1,r_2 and r_3 are three random numbers in $[0, 1]$, r_1 is used to choose between the exploration phase and the exploitation phase, r_2 and r_3 play a role in selecting which operator to use. μ is a control parameter to adjust the search process. Through exploration phase and exploitation phase, operators D, M, S, and A continuously approach the feasible positions of the optimal solution. In AOA, the optimization process begins with a set of candidate solutions consists of a number of azimuth rotation angles. This assumes that $\delta_1 \in [0^\circ, +35^\circ]$ and $\delta_2 \in [-35^\circ, 0^\circ]$, each with a set of candidate solutions selected from their respective ranges.N is the number of candidate solutions in each group.

The transition between exploration phase and exploitation

phase is determined by r_1 and MOA (Math Optimizer Accelerated Function), when $r_1 > MOA$, AOA enters the exploration phase.Otherwise, AOA enters the exploitation phase.The mathematical expression of MOA is as follows:

$$MOA(t) = Min + t \times \left(\frac{Max - Min}{T_{max}}\right) \tag{9}$$

Among them, t is the current iteration number, T is the maximum iteration number, Max and Min are the maximum and minimum values of MOA which are set as 1 and 0.2, respectively.

In the exploration phase , mathematical calculations are performed by division (D) and multiplication (M) operators can yield high distribution values or decisions that conform to the exploration mechanism. The equation for updating the position during the exploration phase is as follow:

$$X_{i,j}(t+1) = \begin{cases} X_{best}(t_j) \div (MOP + \varepsilon) \\ \times((UB_j - LB_j) \times \mu + LB_j), r_2 < 0.5 \\ X_{best}(t_j) \times MOP \\ \times((UB_j - LB_j) \times \mu + LB_j), r_2 \geq 0.5 \end{cases} \tag{10}$$

Among them, ε represents a minimum value ($\varepsilon > 0$) . $X_{i,j}(t+1)$ is the j-th position of i-th solution in the next iteration. UB_j and LB_j represent the upper and lower bounds of the j-th position, respectively. $X_{best}(t_j)$ is the j-th position in the best-obtained solution so far. The MOP (Math Optimizer Probability) is a coefficient and calculated as follows:

$$MOP(t) = 1 - \frac{t^{\frac{1}{\alpha}}}{T^{\frac{1}{\alpha}}} \tag{11}$$

in which α is a sensitive parameter that represents the exploitation phase accuracy during the iteration process. $MOP(t)$ represents the function value at the t-th iteration. For the first operator (D), if $r_2 < 0.5$, the other operators will not explore until operator (D) reaches the optimal value for the current task. Otherwise, the second operator (M) will perform the current solving calculation task first.

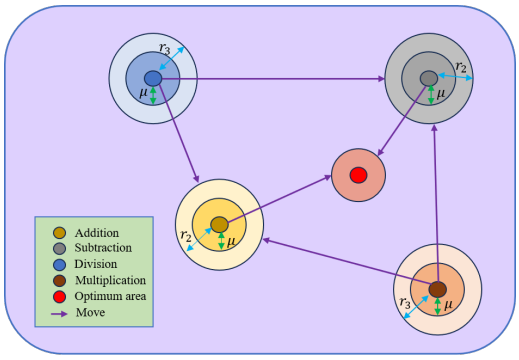

Fig. 2: Model for updating mathematical operators positions to the optimum area in AOA

In the exploitation phase, the algorithm uses subtraction (S) and addition (A) operators to get high-dense results expressed as follows:

$$X_{i,j}(t+1) = \begin{cases} X_{best}(t_j) - MOP \\ \times((UB_j - LB_j) \times \mu + LB_j), r_3 < 0.5 \\ X_{best}(t_j) + MOP \\ \times((UB_j - LB_j) \times \mu + LB_j), r_3 \geq 0.5 \end{cases} \tag{12}$$

4.2 Sine-cosine strategy and inertia factor

To enhance the search performance and convergence speed of AOA during later stages of algorithm iteration, this paper proposes replacing the addition and subtraction operation strategy with the sine cosine search strategy. Using the periodicity of sine and cosine functions to approximate the optimal solution is a more stable and accurate method than using addition (A) and subtraction (S) operators. This method also converges faster to obtain the global optimal solution.

As introduced in Section 4.1, the strategy for updating an individual's position is determined by the size of random values and the current individual. The optimal individual is guided by this position update mechanism, which is based on iterative updates of the current population and does not rely on historical information. Therefore, this paper introduces inertia factor inspired by the PSO algorithm, which allows the algorithm to learn from historical information of the previous generation during the iteration process. The inertia factor w is calculated as follows:

$$w = 1 - (\frac{t}{T_{max}})^2 \tag{13}$$

Consequently, the exploitation results are calculated as:

$$X_{i,j}(t+1) = \begin{cases} w \times X_{i,j}(t) + \mu \times sin(r_4) \\ \times |r_5 \times X_{best}(t_j) - X_{i,j}(t)|, r_3 < 0.5 \\ w \times X_{i,j}(t) + \mu \times cos(r_4) \\ \times |r_5 \times X_{best}(t_j) - X_{i,j}(t)|, r_3 \geq 0.5 \end{cases} \tag{14}$$

in which $r_4 \in [0, 2\pi]$, $r_5 \in [0, 2]$ and that they take random values. $X_{i,j}(t)$ is the j-th position of i-th solution at the current iteration count.

4.3 Path-following controller design

Based on the LOS guidance strategy that transforms a reference path into a series of reference heading angles, the AOA needs to calculate the required rotation angles in each sampling interval to ensure that the tug follows the reference heading angles to track the reference path.

Fig. 3 illustrates the control scheme of the proposed GPR-AOA path-following controller. Given the reference path, the tracking objectives of desired heading angles are determined based on the LOS guidance strategy. A predictive controller is formulated for heading control using the model G_ψ as the prediction model. An optimization problem is therefore formulated based on the current and reference states of the ship at each sampling interval. The AOA is employed to calculate the optimal control inputs for rotation angles. Algorithm 1 outlines the steps involved in the algorithmic process.

Firstly, initialize AOA parameters including α and μ, lower bound LB_j, upper bound UB_j,the number of candi-

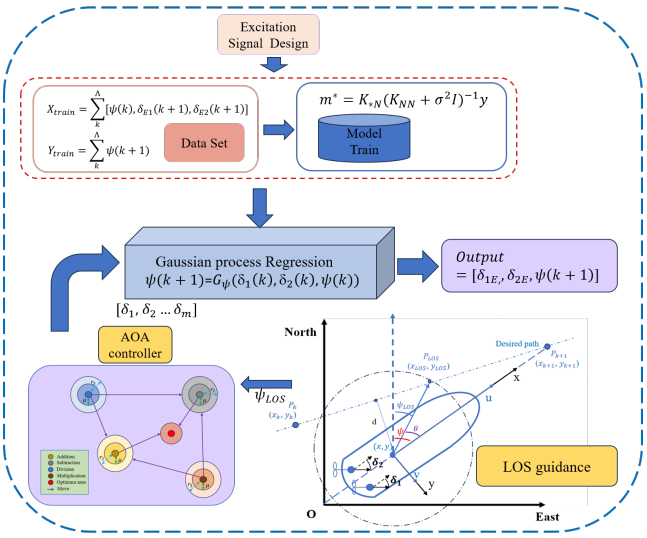

Fig. 3: Control scheme of GPR-AOA controller

date solutions N and maximum number of iterations T. At sampling interval k, given the current ship states including its current heading angle $\psi(k)$ and positions $x(k)$, $y(k)$ and its deviations from the reference path, use (3) to calculate the LOS angle $\psi_{LOS}(k)$. Randomly generated a number of candidate rotation angles are used as δ_1 and δ_2, the δ_1 is randomly selected from a range of $[0°,35°]$,the δ_2 is randomly selected form a range of $[-35°,0°]$.The initial candidate solution sequence and $\psi_{LOS}(k)$ are substituted into the model G_ψ to calculate and predict the heading angle $\hat{\psi}(k) = G_\psi(\delta_1(k), \delta_2(k), \psi(k))$ for the next sampling interval $k+1$. The AOA is used to minimize the error between the predicted heading angle $\hat{\psi}(k+1)$ and LOS angles $\psi_{LOS}(k+1)$. Therefore, the fitness function can be constructed as follows:

$$f(t) = |G_\psi(\delta_1, \delta_2, \psi(t)) - \psi_{LOS}| \tag{15}$$

Then the AOA optimization procedure initiates. While the maximum iteration T has not been reached, update the values of MOA ,MOP and w according to (9) ,(11)and (13) respectively, In each iteration, 5 random numbers are generated, and the value ranges of (r_1, r_2, r_3, r_4, r_5) are as described above, $r_1, r_2, r_3 \in [0,1]$,$r_4 \in [0, 2\pi]$, $r_5 \in [0,2]$. Guided by these random numbers, the operators D, M, sine function, and cosine function continuously update the positions of candidate solutions until they approach the current optimal solution based on (10)and (14). The AOA continuously calculates the fitness of each updated candidate solution and terminates when it satisfies the end criterion, which is exceeding the maximum number of iterations. It outputs the optimal solution $\delta_1^*(k)$ and $\delta_2^*(k)$ with the minimum fitness as the optimal control command for the rotation angles.

5 Simulation results

5.1 Simulation setup

A model-scaled tug is chosen as the target ship and its parameters can be found in Appendix A.We use a modular ship maneuvering model that have been validated in [16] as the simulation model.The relevant parameters of AOA used are given as $N = 5$, $\delta_1 \in [0°, +35°]$, $\delta_2 \in [-35°, 0°]$, $\alpha = 5$, $\mu = 0.499$, $T = 5$. And initialize ship status,including initial heading angle $\psi = 0°$ and initial angle of the azimuth thrusters $\delta_1 = 0°$ and $\delta_2 = 0°$.The initial position of the ship is the starting point of each path.The range of heading angle is $[0°, 360°]$.

Algorithm 1 The algorithmic steps of ship path-follow control method

```
Initialize AOA parameters: α,μ,LB_j,UB_j,N and T
Randomly given initial sequence δ1 and δ2
while Within the simulation duration do
    while t < T do
        Calculate the LOS angle use (3) based on the current ship status and target path
        Calculate fitness function values based on initial δ1,δ2 and model G_ψ use (15)
        Determine the optimal rotation angle (determine the current optimal value)
        Update the value of MOA according to (9)
        Updata the value of MOP according to (11)
        Updata the value of w according to (13)
        for i=1 to Solutions do
            for j=1 to Solutions do
                Generate random values (r1,r2,r3,r4,r5)
                if r1 > MOA then
                    Exploration phase
                    if r2 < 0.5 then
                        Apply the Division math operator (D"÷"). Update the ith solutions' positions using the first rule in(10)
                    else
                        Apply the Multiplication math operator (M"×"). Update the ith solutions' positions using the second rule in (10)
                    end if
                else
                    Exploitation phase
                    if r3 < 0.5 then
                        Apply the sine function. Update the ith solutions' positions using the first rule in (14)
                    else
                        Apply the cosine function. Update the ith solutions' positions using the second rule in (14)
                    end if
                end if
            end for
        end for
    end while
    t=t+1
    Return the best solution (X): δ1*(k) , δ2*(k)
end while
```

5.2 Prediction model evaluation

The paper uses excitation signals for thruster rotation angle, as introduced in Section 3, to conduct simulations with a time length of 10,000 seconds. A number of 7595 valid samples is chosen to create the dataset for identifying the model G_ψ.

The training set and test set were divided in a 7:3 ratio. Fig.4 shows the performance of G_ψ on the test set that 97.7% of the sample points have an error range of $[-4°, 4°]$. In this paper, RMSE(Root Mean Square Error), MAPE(Mean Absolute Percentage Error), and R^2(Coefficient of deter-

mination) are used as identification accuracy evaluation indicators. The model accuracy meets the requirements of controller design, as indicated by RMSE=1.399(heading error(deg)), MAPE=0.0379(heading error(deg)), and $R^2 = 0.9998$.The results show G_ψ has good accuracy.

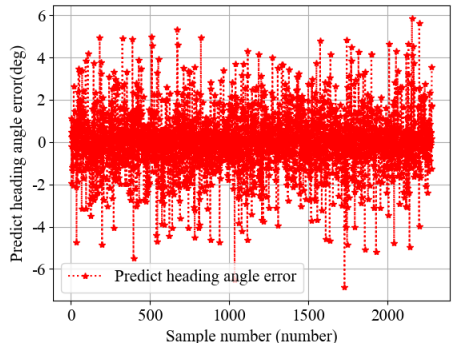

Fig. 4: Prediction error of G_ψ

5.3 Convergence of AOA

The AOA needs to calculate the optimal rotation angles at each sampling interval to ensure that the tugs follows the reference LOS angle to track the reference path. Fig. 5 gives the convergence of the fitness function over iterations in one sampling interval of the heading control simulations. It can be seen that the algorithm converges rapidly within 10 seconds, demonstrating its fast convergence speed and good solution accuracy.

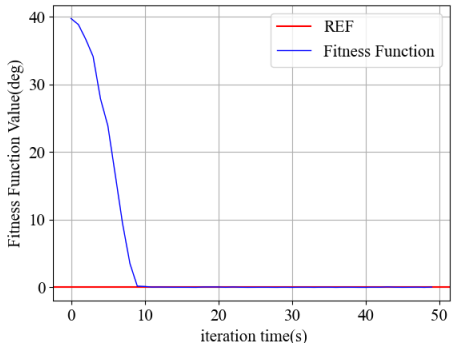

Fig. 5: Convergence of AOA

5.4 Straight path-following effect

A regular hexagon is set as the desired path which consists of a series of way points as :

$$\begin{aligned}[x(t), y(t)] = [&(60, 60), (110, 60), (160, 60),\\ &(185, 103.3), (210, 146.6), (185, 189.9),\\ &(160, 233.3), (110, 233.3), (60, 233.3),\\ &(35, 189.9), (10, 146.6), (35, 103.3), (60, 60)]\end{aligned} \tag{16}$$

In order to highlight the superiority of the controller designed in this paper in terms of control performance, simulation experiments were conducted to compare and verify it with the PID algorithm. Fig. 6 shows the simulated paths of the tug. The red line represents the desired path, while the blue and green lines represent the actual path. Under the control of GPR-AOA algorithm, ships can follow the expected path well, and its control effect is better than PID algorithm. Fig. 7 gives the changes of rotation angles over time. Fig. 8 illustrates the changes of heading angles and LOS angles. Under the control of GPR-AOA algorithm,it can be seen that the heading error converges quickly within 20 seconds. Among them, the maximum error of the heading angle and LOS angle is $19.91°$, the minimum error is $0°$, and the average error is $1.48°$. However, when using the PID algorithm, it still has significant errors,the maximum error of the heading angle and LOS angle is $21.91°$, the minimum error is $0°$, and the average error is $4.79°$. Fig. 9 shows the average computation times in each sampling interval. It is far less than the 1 seconds sampling interval, which is acceptable for practical implementations.

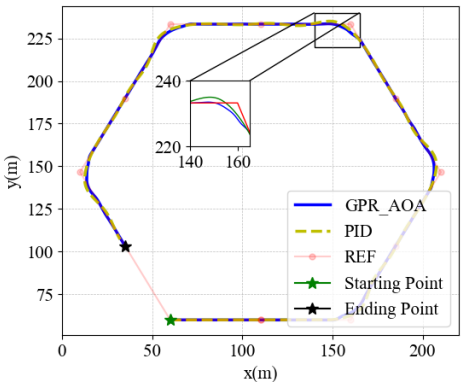

Fig. 6: Simulated path of tug in straight path-following

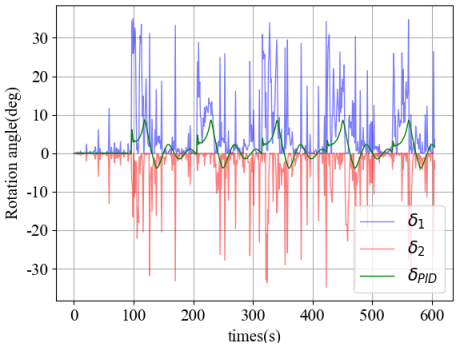

Fig. 7: Rotation angle of azimuth thrusters in straight path-following

5.5 Curved path-following effect

The reference curve path is set to a sine function path defined as:

$$\begin{cases} x(t) = 30 + 30 \times t \\ y(t) = 30 + 30 \times \sin(t) \end{cases} \tag{17}$$

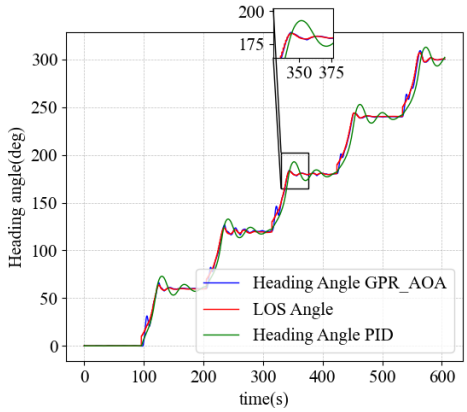

Fig. 8: Changes of heading angle in straight path-following

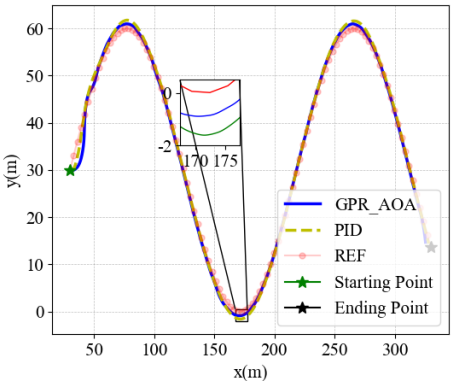

Fig. 10: Simulated path of tug in curved path-following

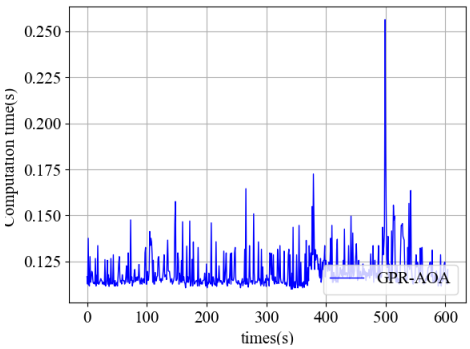

Fig. 9: Computation time in each sampling interval in straight path-following

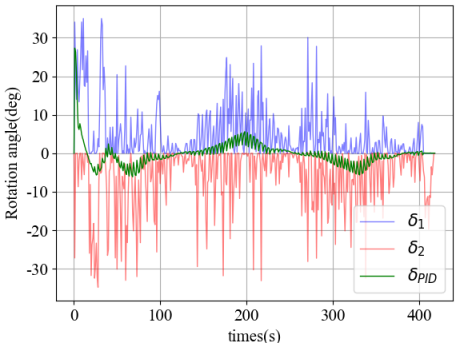

Fig. 11: Rotation angles of azimuth thrusters in curved path-following

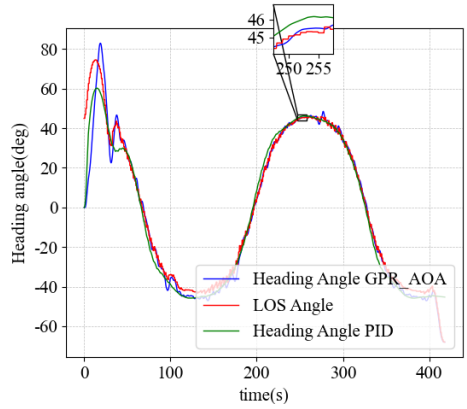

Fig. 12: Changes of heading angle in curved path-following

Fig. 10 gives the simulated paths of the tug when it follows a curved reference path. It can be seen that the ships controlled by GPR-AOA algorithm can better track and enter the reference path than ships controlled by PID algorithm. Fig. 11 gives the changes of rotation angles over time. Fig. 12 illustrates the changes of heading angles and LOS angles. The actual heading angle of a ship controlled by the GPR-AOA algorithm can maintain synchronous changes with the LOS angle. When the ship follows the reference path, the maximum error of the heading angle and LOS angle is $6.79°$, the minimum error is $0°$, and the average error is $1.78°$. The actual heading angle of the ship under PID algorithm control is not synchronized with the change of LOS angle, and there is a large error, the maximum error of the heading angle and LOS angle is $30.91°$, the minimum error is $0°$, and the average error is $4.59°$. Fig.13 shows the average computation times in each sampling interval. It is far less than the 1 seconds sampling interval, which is acceptable for practical implementations.

6 Conclusions and future work

This paper proposes an autonomous tug path tracking control method that combines GPR and AOA. Using the LOS algorithm as the guidance law, the path-following control problem is transformed into a heading control problem. A GPR model is constructed to identify the correlation between the heading angle and the rotation angle of the azimuth thrusters, which acts as the prediction model in the path-following controller.The AOA is utilized to determine the optimal control inputs. Compared with other control algorithms that require a large amount of parameter tuning, the proposed GPR-AOA controller has the characteristics of fast convergence speed and accuracy, and has good application value.

Future work will expand this research in several directions. Firstly, model-scaled ship experiments will be conducted in a real environment to further validate the effectiveness. Secondly, the potential of changing offline GPR identification to online identification will be investigated to further improve the control performance and data utilization. In ad-

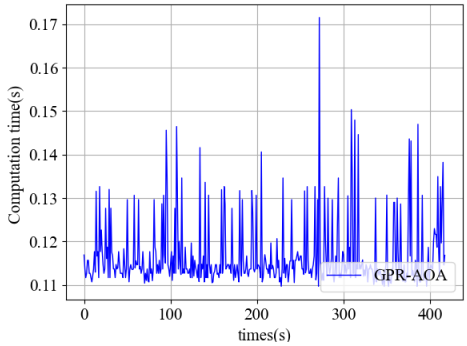

Fig. 13: Computation time in each sampling interval in curved path-following

dition, further improving the convergence speed and solution accuracy of the AOA.

References

[1] Q. Zhang, Z. Ding, and M. Zhang, "Adaptive self-regulation pid control of course-keeping for ships," *Polish Maritime Research*, vol. 27, no. 1, pp. 39–45, 2020.

[2] G. Zhang, X. Zhang, and Y. Zheng, "Adaptive neural path-following control for underactuated ships in fields of marine practice," *Ocean Engineering*, vol. 104, pp. 558–567, 2015.

[3] H. Zhang, X. Zhang, and R. Bu, "Sliding mode adaptive control for ship path following with sideslip angle observer," *Ocean Engineering*, vol. 251, p. 111106, 2022.

[4] H. He, T. Van Zwijnsvoorde, E. Lataire, and G. Delefortrie, "Model predictive controller for path following ships validated by experimental model tests," *Ocean Engineering*, vol. 288, p. 115971, 2023.

[5] L. Wang, S. Li, J. Liu, and Q. Wu, "Data-driven path-following control of underactuated ships based on antenna mutation beetle swarm predictive reinforcement learning," *Applied Ocean Research*, vol. 124, p. 103207, 2022.

[6] K. Nomoto, K. Taguchi, K. Honda, and S. Hirano, "On the steering qualities of ships," *Journal of Zosen Kiokai*, vol. 1956, no. 99, pp. 75–82, 1956.

[7] H. Yasukawa and Y. Yoshimura, "Introduction of mmg standard method for ship maneuvering predictions," *Journal of Marine Science and Technology*, vol. 20, no. 1, pp. 37–52, 2015.

[8] Z. L. Ouyang, S. Y. Liu, and Z. J. Zou, "Nonparametric modeling of ship maneuvering motion in waves based on gaussian process regression," *Ocean Engineering*, vol. 264, p. 112100, 2022.

[9] J. Caldwell and J. A. Marshall, "Towards efficient learning-based model predictive control via feedback linearization and gaussian process regression," in *2021 IEEE/RSJ International Conference on Intelligent Robots and Systems (IROS)*, pp. 4306–4311, IEEE, 2021.

[10] P. Xu, H. Qin, J. Ma, Z. Deng, and Y. Xue, "Data-driven model predictive control for ships with gaussian process," *Ocean Engineering*, vol. 268, p. 113420, 2023.

[11] D. K. Gupta, K. L. Vasudev, and S. K. Bhattacharyya, "Genetic algorithm optimization based nonlinear ship maneuvering control," *Applied Ocean Research*, vol. 74, pp. 142–153, 2018.

[12] M. Ryalat, H. S. Damiri, and H. ElMoaqet, "Particle swarm optimization of a passivity-based controller for dynamic positioning of ships," *Applied Sciences*, vol. 10, no. 20, 2020.

[13] L. Wang, S. Li, J. Liu, Q. Wu, and R. R. Negenborn, "Ship docking and undocking control with adaptive-mutation beetle swarm prediction algorithm," *Ocean Engineering*, vol. 251, p. 111021, 2022.

[14] L. Abualigah, A. Diabat, S. Mirjalili, M. Abd Elaziz, and A. H. Gandomi, "The arithmetic optimization algorithm," *Computer Methods in Applied Mechanics and Engineering*, vol. 376, p. 113609, 2021.

[15] T. I. Fossen, *Handbook of marine craft hydrodynamics and motion control*. John Wiley & Sons, 2011.

[16] X. You, X. Yan, J. Liu, S. Li, and Y. Liu, "A novel model-based parameters estimation combining local optimization and global optimization of nonlinear ship models with physical experiment dataset," 2023.

A Appendix A

Table 1: The dynamics parameter values of Qiuxin No.5 tug [16].

m_{11}	138.057 kg
m_{22}	106.600 kg
m_{33}	15.648 kgm^2
X_u	-8.986 kg/s
$X_{\|u\|u}$	-31.429 kg/s
X_{uuu}	-6.895 kg/s
Y_v	-71.904 kg/s
$Y_{\|v\|v}$	-77.643 kg/s
Y_{vvv}	-27.139 kg/s
$Y_{\|r\|v}$	-43.221 kg/s
N_r	-26.712 kg/s
$N_{\|r\|r}$	-9.828 kg/s
N_{rrr}	-9.232 kg/s
$N_{\|v\|r}$	-2.347 kg/s

Proceedings of the 3rd Conference on Fully Actuated System Theory and Applications
May 10-12, 2024, Shenzhen, China

Development and Verification of Semi-physical In-loop Real-time Control Experimental Platform for Harsh Sea Condition Floating Body Salvage

Xiaoning Zhao[1], Yougang Sun[1], Zhiqiang Xu[2], Zhenyu He[1]

1. Institute of Railway Transit, Tonji University, Shanghai 200092, China
E-mail: zhaoxiaoning@tongji.edu.cn; 21040@tongji.edu.cn; 2233466@tongji.edu.cn

2. Fishery Machinery and Instrument Research Institute, Chinese Academy of Fishery Sciences, Shanghai 200092, China
E-mail: xuzhiqiang@fmiri.ac.cn

Abstract: As a fully actuated system, the harsh sea condition floating body salvage equipment has been widely used in marine engineering and has become an important guaranteed equipment for marine development. Most of the current wave compensation control strategies of the salvage equipment ignore characteristics such as nonlinearity and time-delay, and most of them are verified by numerical simulation, which cannot effectively prove the effectiveness of the proposed control strategy in the actual situation. In view of the above problems, this paper develops a semi-physical in-loop real-time control experimental platform for harsh sea condition floating body salvage. Specifically, a harsh sea condition floating body salvage test-bed based on a 6-degree-of-freedom wave simulation platform is built. In the MATLAB/Simulink environment, a rapid control prototype host computer including is built to realize real-time control of semi-physical in-loop. The experimental results show that the developed platform fully considers the nonlinearity and time-delay, which can be used to develop and verify the control algorithm of harsh sea condition floating body salvage equipment quickly and accurately.

Key Words: Floating body salvage, wave compensation, nonlinear, time-delay, rapid control prototype

1 Introduction

The further development of marine resources makes the application of harsh sea condition floating body salvage equipment in marine engineering more and more extensive, shown in Fig.1, and it is one of the most important support equipment for marine development [1, 2]. Different from the ground operation, the ship will produce sway, surge, heave and roll, pitch, yaw six degrees of freedom motion under the action of waves, which seriously affects the stability of the floating body salvage equipment operation and may lead to a major accident of salvage failure, lifting cargo damage and even casualties [3, 4]. To ensure the safe operation of floating salvage equipment, the influence of waves must be suppressed [5, 6].

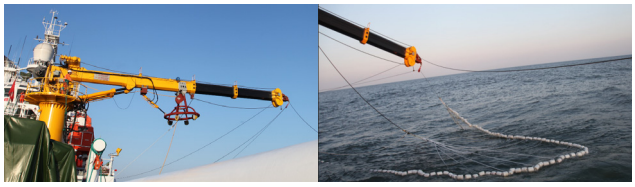

Fig. 1: Harsh sea condition floating body salvage equipment

In view of the above problems, domestic and foreign scholars have proposed wave compensation technology for harsh sea condition floating salvage equipment. Zhang [7] trained a neural network based on multivariate long-term and short-term memory to predict the heave and pitch motion of ships to achieve advanced compensation for wave interference. The simulation results show that the proposed method significantly reduces the standard deviation of heave and pitch of floating crane. Chen [8] proposed a heave prediction and control method of floating crane based on model predictive control, which predicts the heave displacement of the crane load in advance and takes it as the input of the position loop of the compensator. The simulation results show that the proposed controller has good predictive ability and control accuracy. Zinag [9] proposed a controller based on reinforcement learning, which uses a deep deterministic strategy gradient algorithm for active heave compensation. The simulation results show that the heave compensation performance of the proposed controller is about 10 % higher than that of the tuned servo differential controller. Liu [10] designed an adaptive wave compensation algorithm based on beetle antennae search algorithm and radial basis function neural network. The experimental results show that the designed algorithm can reduce the compensation error by about 40 % compared with the traditional method.

Although the above research results have achieved good wave compensation effect, most scholars use numerical simulation to verify the effectiveness of the proposed method, and only a few scholars have carried out sea wave compensation experiments. The numerical simulation is efficient and simple, but the simulation environment is too idealized to simulate the high nonlinearity, time-delay and strong coupling of the harsh sea condition floating body salvage equipment, and the control effect is not intuitive and reliable. The offshore experiment is intuitive and real, but the experiment cost and the risk are high. To ensure the stability and reliability of the equipment, industrial controllers such as PLC are often used. However, it is difficult to apply intelligent control technology based on computer science and artificial intelligence to solve the control problem of complex nonlinear equipment [11].

Semi-physical in-loop real-time control is between numerical simulation and physical experiment, which not only retains some physical characteristics in physical experiment, but also has the characteristics of high

efficiency and simplicity of numerical simulation. In principle, semi-physical in-loop real-time control can be divided into Rapid Control Prototype (RCP) and Hardware-in-the-loop (HIL) [12]. RCP helps users quickly build a virtual prototype controller to control the real controlled object. Correspondingly, HIL uses real controller hardware to control virtual controlled objects. At present, semi-physical in-loop real-time control has been widely studied and applied in aerospace [13], automobile [14], electric power [15] and other fields.

The mathematical model of harsh sea condition floating body salvage equipment is relatively complex, but the hardware structure is relatively simple. The difficulty lies in the algorithm design of the controller. Therefore, it is necessary to develop an experimental platform that can quickly verify the control algorithm. Based on the principle of RCP, this paper develops a semi-physical in-loop real-time control experimental platform for harsh sea condition floating body salvage. The specific work is to build a harsh sea condition floating body salvage experimental equipment based on a 6-degree-of-freedom wave simulation platform. In the MATLAB/Simulink environment, a rapid control prototype host computer including operation control and program design is built to realize the real-time control of the semi-physical in-loop. A series of experiments are carried out based on the experimental platform. The results show that the developed experimental platform for harsh sea condition floating body salvage can be used to develop and verify the control algorithm quickly and accurately.

The rest of this paper is as follows: section 2 introduces the design of the overall framework; section 3 introduces the construction of the hardware platform from two aspects of principle and physical object. In section 4, the construction of the software platform is introduced, and the complete use process is given. In section 5, a series of comparative experiments are carried out based on the developed experimental platform, which shows the superiority of the platform. Section 6 is a conclusion.

2 Overall Framework Design

The overall framework of the experimental platform, which consists of hardware including floating body salvage equipment and software developed in MATLAB/Simulink environment, as shown in Fig.2.

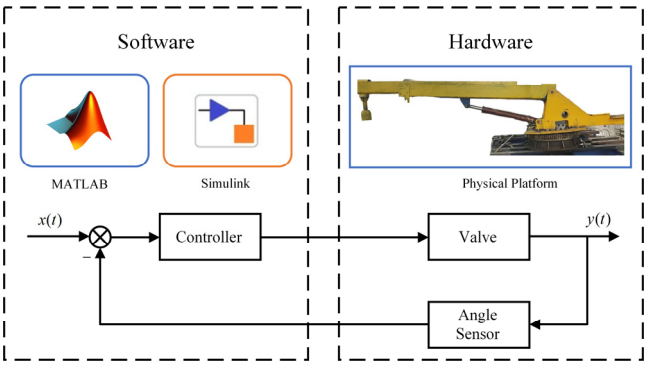

Fig. 2: Overall framework

Hardware platform includes actuator and sensor in the block diagram, which is composed of harsh sea condition floating body salvage equipment, servo valve, angle sensor and swing table.

Software platform includes the controller in the block diagram, which is composed of upper computer developed in MATLAB/Simulink environment.

Hardware as the real controlled object, software as the virtual controller, together constitute the semi-physical in-loop real-time control experimental platform based on rapid control prototype. The user can design the controller on software platform, to control the hardware of the harsh sea condition floating body salvage equipment in real time. In this way, the control algorithm can be verified accurately and intuitively.

3 Hardware Platform Design

Hardware principle of the experimental platform is shown in Fig.3. The Industrial Personal Computer (IPC) runs Windows operating system, which has rich hardware interfaces and high software compatibility. The Data Acquisition (DAQ) card is installed on the PCI slot of the IPC, which can receive control instruction and generate voltage signal to control the servo valve in real time. The servo valve receives the control signal to control the oil inlet and outlet of the hydraulic cylinder of the salvage equipment. The angle sensor can feedback the inclination data to IPC in real time and it is connected to the IPC through the COM port.

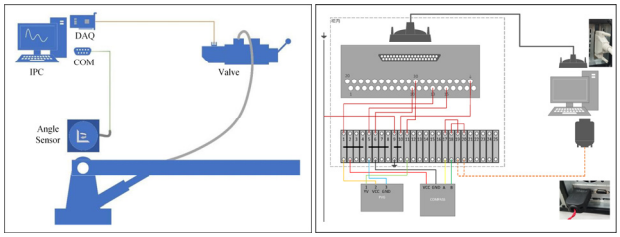

Fig. 3: Hardware principle of the experimental platform

DAQ card can be obtained from the IPC and provides a 12 V power supply to devices. The input and output of DAQ card is a 37-pin trapezoidal interface, which is connected to the wiring board in IPC. The board provides 12 V and 5 V power supply, power supply grounding and digital, analog, counter input and output interfaces. The servo valve is 11 ~ 32 V wide voltage input and the maximum current is 570 mA at 12 V voltage, which can be obtained from the 12 V power supply of DAQ card. Reference voltage control line is connected to the analog voltage output terminal of DAQ card. The tilt sensor has a wide voltage input of 9 ~ 36 V and the maximum co-group current is 40mA, which can directly obtain 12V power supply from DAQ card.

According to the hardware schematic diagram, the hardware platform is built in the laboratory, as shown in Fig.4.

The floating body salvage equipment is placed on a swing table supported by four hydraulic rods. By controlling the frequency and speed of the four hydraulic rods, the swing table can simulate the swing of the ship under different sea conditions. The angle sensor is installed behind the boom of the floating salvage equipment to detect and feedback the boom inclination angle in real time.

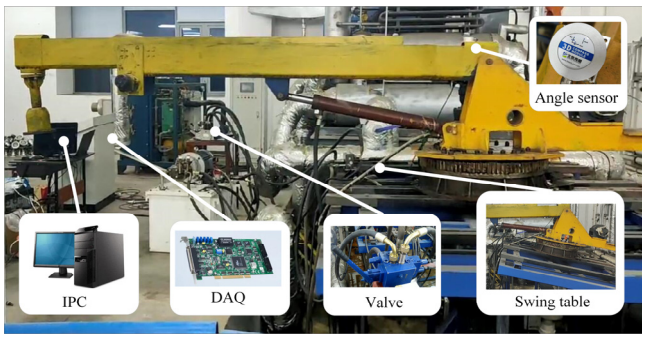

Fig. 4: Experimental equipment

4 Software Platform Development

Software platform is built in MATLAB/Simulink environment, including operation control, program design, communication, and result display functions. The software architecture is shown in Fig.5.

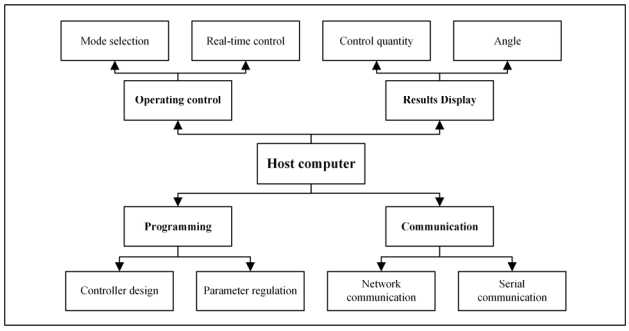

Fig. 5: Software architecture

Software interface is shown in Fig.6. The control panel is composed of a three-stage knob switch, a state indicator light, a slider control, and a dashboard, which integrates device start-stop, mode switching, manual operation and state indication functions. Using the three-stage knob switch can switch the device mode to Off, Manual and Auto. Different color of the indicator light indicates the current control state, which is gray when Off, green when Manual, and orange when Auto. In the manual mode, the control quantity can be adjusted by manually dragging the slider control. The dashboard indicates the current control quantity.

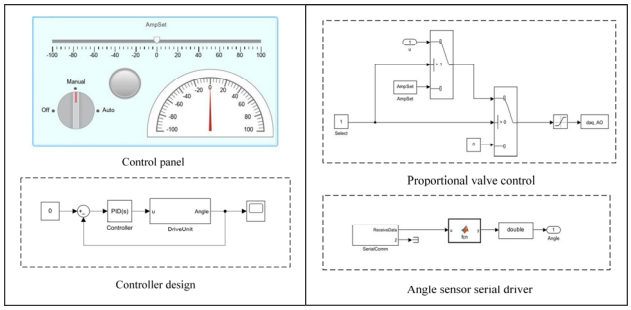

Fig. 6: Software interface

The core function block of the controller design part is DriveUnit, which can receive control quantity of the controller and output the boom inclination angle. The controller can be built based on Simulink. The output port and angle input port of the controller can be connected to DriveUnit. The program of the control panel is also associated to the block. The core function block of DriveUnit is composed of servo valve drive module and angle sensor drive module.

Considering the safety and hardware performance of the equipment operation, the operation process of the experimental platform is designed as shown in Fig.7.

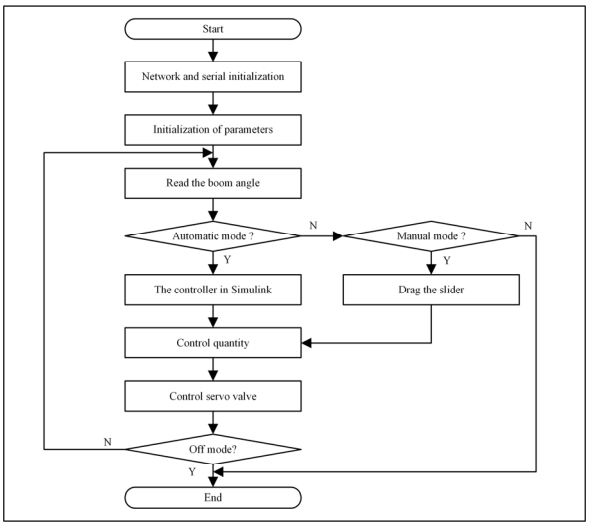

Fig. 7: Operation process

5 Experimental Verification

To verify the experimental platform developed in this paper, experiments under different working conditions were carried out on the swing table. The control goal of the harsh sea condition floating body salvage equipment is to always maintain the level of the boom when the swing table simulates the ship's rolling.

The swing platform is set to roll at a frequency of 0.2 Hz. The swing amplitude of working condition 1 is 5 °, and the swing amplitude of working condition 2 is 10 °. The swing curve of the swing table is shown in Fig.8.

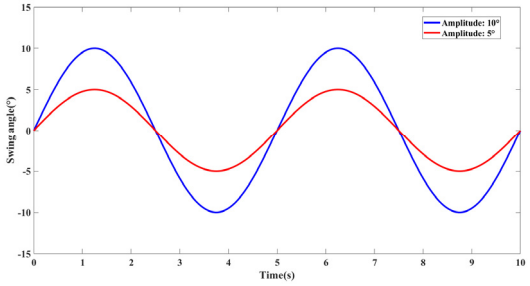

Fig. 8: Rocking table simulates ship rolling

5.1 Verification Experiment Based on PID Control

PID controller is built in the upper computer, and the experiment is carried out under working condition 1 and working condition 2 respectively. The experimental results are shown in Fig.9 and Fig.10.

The experimental results show that the vibration amplitude reaches ±7 ° and ±10 ° respectively under the two working conditions, and the oscillation is large during the adjustment process. The reason is that the hydraulic system

has problems such as high nonlinearity and dead zone characteristics, so the PID controller is difficult to stabilize the system.

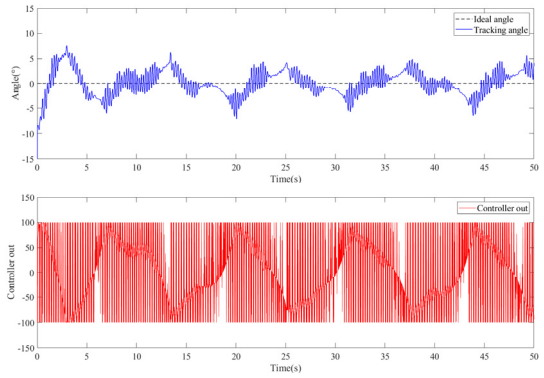

Fig. 9: PID control experiment under working condition 1

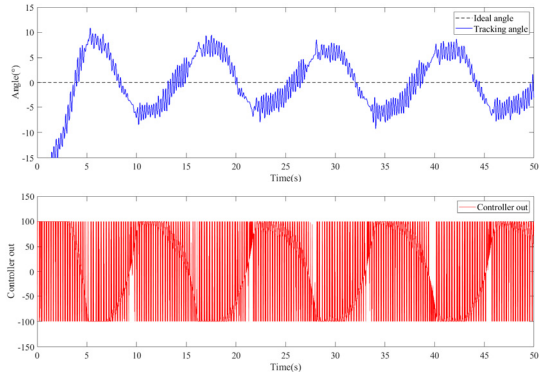

Fig. 10: PID control experiment under working condition 2

5.2 The Verification Experiment of Improved PID Control Based on Semi-physical In-loop Real-time Control Experimental Platform

Based on semi-physical in-loop real-time control experimental platform, the control algorithm can be simply improved and verified. Considering the dead zone characteristics of the servo valve, it can be identified and compensated by the experimental platform simply. The dead zone compensation principle of servo valve is shown in Fig.11.

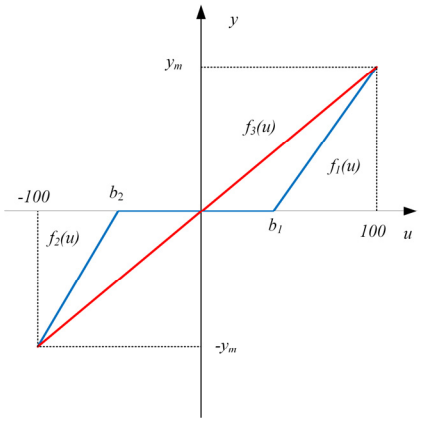

Fig. 11: Servo valve dead zone compensation principle

Where u is the input signal of the servo valve, y is the output flow of the servo valve, $f_1(u)$ and $f_2(u)$ are the input and output relationship of the servo valve before compensation, b_1 is the positive dead zone of the servo valve, b_2 is the reverse dead zone, $f_3(u)$ is the expected input and output relationship of the servo valve after compensation.

Based on the above principle, the dead zone compensation function is:

$$u_1 = \begin{cases} \dfrac{100 - b_1}{100} u_0 + b_1 & (u_0 > 0) \\ 0 & (u_0 = 0) \\ \dfrac{100 + b_2}{100} u_0 + b_2 & (u_0 < 0) \end{cases} \quad (1)$$

where u_0 is the original control quantity, u_1 is the actual control quantity after compensation.

The dead zone compensation function is written into the S-Function module in Simulink, and the experiment is carried out under condition 1 and condition 2 respectively. The experiment results are shown in Fig.12 and Fig.13.

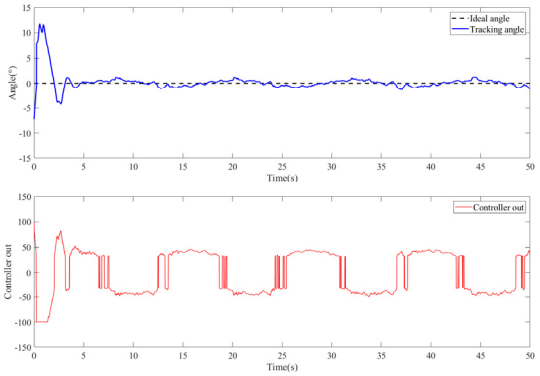

Fig. 12: Improved PID control under condition 1

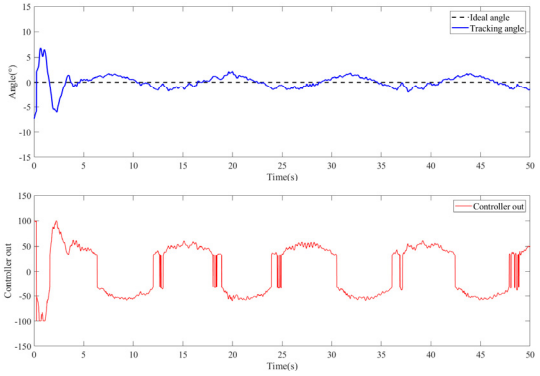

Fig. 13: Improved PID control under condition 2

The experimental results show that the vibration amplitude under the two working conditions is ±1 ° and ±2 ° respectively, and the oscillation during the adjustment process is small. The experimental results show that the control algorithm can be improved and verified by the experimental platform simply and quickly.

6 Conclusion

Based on rapid control prototype, this paper develops a semi-physical in-loop real-time control experimental platform for harsh sea condition floating body salvage. In terms of hardware, the harsh sea condition floating body salvage test-bed based on a 6-degree-of-freedom wave simulation platform is built. In terms of software, the upper computer software is developed in Simulink environment, which can facilitate the developers to build the control algorithm with rich module resources. In experiment, with the help of the semi-physical real-time control experimental platform for harsh sea condition floating body salvage, the control algorithm is simply improved. Compared with PID control, the improved PID control effect is significantly improved, which shows the superiority of the developed experimental platform. In the future, the experimental platform can be widely used in the research of active control algorithm of harsh sea condition floating body salvage equipment, such as neural network, genetic algorithm, and other intelligent control algorithms. The experimental platform will greatly improve the work efficiency and reliability in algorithm verification and parameter optimization.

References

[1] X. Liu, W. Li, W. Wang, and Z. Xu, "Control for the New Harsh Sea Conditions Salvage Crane Based on Modified Fuzzy PID," Asian Journal of Control, vol. 20, no. 4, pp. 1582–1594, 2018.

[2] Z. Ren, R. Skjetne, A. S. Verma, Z. Jiang, Z. Gao, and K. H. Halse, "Active heave compensation of floating wind turbine installation using a catamaran construction vessel," Mar. Struct., vol. 75, p. 102868, Jan. 2021.

[3] Z. Li, X. Ma, Y. Li, Q. Meng, and J. Li, "ADRC-ESMPC active heave compensation control strategy for offshore cranes," Ships Offshore Struct., vol. 15, no. 10, pp. 1098–1106, Nov. 2020.

[4] J. K. Woodacre, R. J. Bauer, and R. Irani, "Hydraulic valve-based active-heave compensation using a model-predictive controller with non-linear valve compensations," Ocean Eng., vol. 152, pp. 47–56, Mar. 2018.

[5] M. Li, P. Gao, J. Zhang, J. Gu, and Y. Zhang, "Study on the system design and control method of a semi-active heave compensation system," Ships Offshore Struct., vol. 13, no. 1, pp. 43–55, Jan. 2018.

[6] N. Xianliang, Z. Jiawen, and X. Jianan, "The heave motion estimation for active heave compensation system in offshore crane," in 2016 IEEE International Conference on Mechatronics and Automation, Harbin, Heilongjiang, China: IEEE, Aug. 2016, pp. 1327–1332.

[7] F. Zhang et al., "Semi-Active Heave Compensation for a 600-Meter Hydraulic Salvaging Claw System with Ship Motion Prediction via LSTM Neural Networks," J. Mar. Sci. Eng., vol. 11, no. 5, p. 998, May 2023.

[8] H. Chen, J. Xie, J. Han, W. Shi, J.-F. Charpentier, and M. Benbouzid, "Position Control of Heave Compensation for Offshore Cranes Based on a Particle Swarm Optimized Model Predictive Trajectory Path Controller," J. Mar. Sci. Eng., vol. 10, no. 10, Art. no. 10, Oct. 2022.

[9] S. Zinage and A. Somayajula, "Deep Reinforcement Learning Based Controller for Active Heave Compensation," IFAC-Pap., vol. 54, no. 16, pp. 161–167, Jan. 2021.

[10] J. Liu and X. Chen, "Adaptive Control Based on Neural Network and Beetle Antennae Search Algorithm for an Active Heave Compensation System," Int. J. Control Autom. Syst., vol. 20, no. 2, pp. 515–525, Feb. 2022.

[11] F. Zhang, J. Hou, D. Ning, W. Zhang, D. Wang, and Y. Gong, "Performance analysis of the passive heave compensator for hydraulic shipwreck lifting systems in twin-barge salvaging," Ocean Eng., vol. 280, p. 114469, Jul. 2023.

[12] A. Wu, J.-F. Mao, and X. Zhang, "An ADRC-Based Hardware-in-the-Loop System for Maximum Power Point Tracking of a Wind Power Generation System," IEEE Access, vol. 8, pp. 226119–226130, 2020.

[13] "Research of Rapid Control Prototyping for Flight Control System and Hardware-In-The Loop Test-All Databases." Accessed: Feb. 06, 2024.

[14] "Hardware-in-the-Loop Testing of a Hybrid Brake-by-Wire System for Electric Vehicles-Web of Science Core Collection." Accessed: Feb. 06, 2024.

[15] S. Dickler, T. Kallen, J. Zierath, and D. Abel, "Rapid control prototyping of model predictive wind turbine control toward field testing," J. Phys. Conf. Ser., vol. 1618, p. 022068, Sep. 2020.

Proceedings of the 3rd Conference on Fully Actuated System Theory and Applications
May 10-12, 2024, Shenzhen, China

Trajectory Tracking of Differential Driven AGV Based on Kalman Filter and Model Predictive Control

Zhihao Xu[1], Yue Jiang[1], Kai Peng[2], Hongxia Wang[1,*],

1. College of Electrical Engineering and Automation, Shandong University of Science and Technology, Qingdao 266590, P. R. China
E-mail: 925441069@qq.com; whx1123@163.com; sdustjiangyue@163.com

2. School of Power and Energy, Northwestern Polytechnical University, Xi'an, 710072, P. R. China
E-mail: pengkai@nwpu.edu.cn

Abstract: Trajectory tracking is one of the key technologies of automated guided vehicles. However, the existing relevant research seldom considers the influence of noise on tracking accuracy in the real environment. Considering the automated guided vehicle model with additive noise, a new trajectory tracking algorithm is proposed in this paper. In the algorithm, the initial state and control are first given. Then state estimation and optimal control are implemented alternatively. The former is realized by the Kalman filter and the latter is resorted to model predictive control. The algorithm can effectively reduce the influence of noises on trajectory tracking. Finally, the proposed algorithm is evaluated by simulation experiments.

Key Words: Kalman filter, model predictive control, trajectory tracking, Automatic Guided Vehicle

1 Introduction

The demand for modern automation equipment is increasing. As a flexible and intelligent autonomous navigation vehicle, AGV is crucial for optimizing production processes and improving production efficiency [1]. Trajectory tracking is the foundation of AGV, and it plays an important role in the study of AGV. Trajectory tracking not only ensures the stable operation of AGVs in complex environments but also improves the efficiency of their task execution. At present, many control methods have been applied to the trajectory tracking problem of AGV, including PID control, sliding mode control(SMC), and MPC [2]-[7].

The PID algorithm is relatively simple. The algorithm does not need the exact model of the system to realize the trajectory tracking function [8]. However, the parameter adjustment of a traditional PID controller is complicated, and the control parameters cannot be changed timely according to the change of state. This can lead to less-than-ideal tracking [9]. Therefore, researchers often combine PID with other algorithms to improve the control effect. For example, a PID controller based on an improved genetic Algorithm (IGA) was proposed by Yuan T et al. which adopted IGA to optimize PID parameters, thus improving tracking performance [10].

SMC is widely used in AGV systems for trajectory tracking because of its strong robustness and easy implementation [11]. A general rollover prevention control framework for high-speed wheeled mobile robots was proposed by Yan C et al., and an integral sliding mode wheel speed tracking controller was designed, which successfully realized rollover prevention in trajectory tracking and path following [12]. However, it is difficult to design a sliding mode control function and the system driven by SMC is susceptible to high-frequency perturbations [13].

MPC is an algorithm that obtains control inputs by solving constrained optimization problems [14]-[16]. The algorithm first predicts the output of the system, and then adjusts the control strategy according to the designed performance index, to realize the effective control of the system. Therefore, MPC has become one of the important methods to deal with trajectory tracking problems. The controller can guarantee the tracking accuracy and dynamic stability of the vehicle simultaneously. An algorithm combining model predictive control and delayed neural network was designed by Wang D et al. to solve the omnidirectional robot trajectory tracking problem under constraints [17]. A switched MPC framework was given by [18]. By selecting appropriate vehicle models and supervision schemes, the balance between MPC performance and computational cost was achieved, and accurate path tracking was realized.

However, the above trajectory tracking algorithms do not account for high-frequency noise in a real environment which can affect the accuracy of tracking. Therefore, this paper presents a new algorithm for tracking trajectories, taking into account the AGV model with additive Gaussian noise. The algorithm first initializes the state and control. The state and control after initialization are combined with the KF to estimate the state of the next moment. Then the optimal control at the next moment is solved according to the MPC and state estimated by the KF. The alternate execution of state estimation and control optimization reduces noise influence and improves trajectory tracking accuracy.

The rest of the paper is organized as follows: Section 2 presents the problem and kinematics equations of the system to be solved in this paper. Section 3 describes the detailed algorithm: the control strategy is adjusted by the method of MPC and KF alternating operation, and the trajectory tracking is realized. In section 4, the algorithm is verified by simulation experiments. Finally, the algorithm is summarized in Section 5. The trajectory tracking scheme of this paper is shown in Fig. 1.

This work was supported by the Original Exploratory Program Project of National Natural Science Foundation of China (62250056), the Joint Funds of the National Natural Science Foundation of China (U23A20325), the Major Basic Research of Natural Science Foundation of Shandong Province (ZR2021ZD14), and the High-level Talent Team Project of Qingdao West Coast New Area (RCTD-JC-2019-05).

*Corresponding Author.

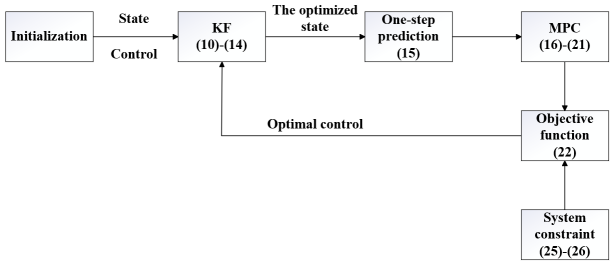

Fig. 1: The scheme of trajectory tracking

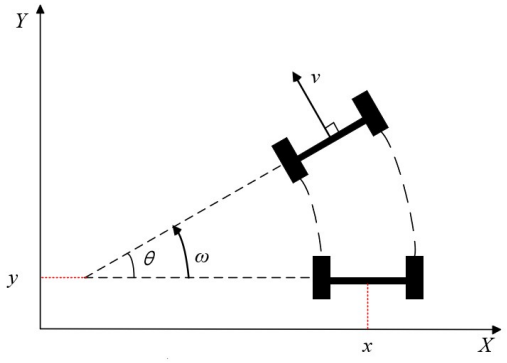

Fig. 2: Kinematic model for differential drive AGV

2 Problem Formulation

When the operation of AGV is disturbed by noise, the tracking will be biased. To deal with this problem, we consider a kinematic model with additive Gaussian noise.

Based on the differential drive AGV shown in Figure 2, the kinematic model established in this paper is as follows

$$\begin{bmatrix}\dot{x}\\ \dot{y}\\ \dot{\theta}\end{bmatrix} = \begin{bmatrix}cos\theta & 0\\ sin\theta & 0\\ 0 & 1\end{bmatrix}\begin{bmatrix}v\\ \omega\end{bmatrix} + W, \tag{1}$$

where x and y represent the abscissa and ordinate of the geometric center of the AGV, θ is the heading angle of the AGV, v is the velocity of the AGV, ω is the angular velocity of the AGV, W denotes the Gaussian noise during AGV operation.

System (1) can be expressed in a concise form as

$$\dot{X} = f(X, u) + W, \tag{2}$$

where state variable $X = \begin{bmatrix}x & y & \theta\end{bmatrix}^T$ and control input $u = \begin{bmatrix}v & \omega\end{bmatrix}^T$.

The state equation of the reference trajectory is set

$$\dot{X}_r = f(X_r, u_r), \tag{3}$$

where state variable $X_r = \begin{bmatrix}x_r & y_r & \theta_r\end{bmatrix}^T$ and control input $u_r = \begin{bmatrix}v_r & \omega_r\end{bmatrix}^T$.

3 A New Trajectory Tracking Method

In order to reduce the influence of noise on trajectory tracking accuracy, an alternate algorithm of MPC and KF is proposed in this paper.

3.1 Linearization of the Error Model

The Taylor series expansion is performed at the reference trajectory point

$$\begin{aligned}\dot{X} =& f(X_r, u_r) + \frac{\partial f(X_r, u_r)}{\partial X}(X - X_r)\\ &+ \frac{\partial f(X_r, u_r)}{\partial u}(u - u_r) + W.\end{aligned} \tag{4}$$

The result of subtracting (3) from (4) is

$$\begin{aligned}\dot{\tilde{X}} &= \dot{X} - \dot{X}_r\\ &= \frac{\partial f(X_r, u_r)}{\partial X}\tilde{X} + \frac{\partial f(X_r, u_r)}{\partial u}\tilde{u} + W,\end{aligned} \tag{5}$$

where $\tilde{X} = X - X_r$, $\tilde{u} = u - u_r$.

Discretize (5) using the forward Euler method

$$\tilde{X}(k+1) = A(k)\tilde{X}(k) + B(k)\tilde{u}(k) + W(k), \tag{6}$$

$A(k)$ and $B(k)$ are given as

$$A(k) = \begin{bmatrix}1 & 0 & -v_r(k)sin\theta_r(k)T\\ 0 & 1 & -v_r(k)cos\theta_r(k)T\\ 0 & 0 & 1\end{bmatrix}, \tag{7}$$

$$B(k) = \begin{bmatrix}cos\theta_r(k)T & 0\\ sin\theta_r(k)T & 0\\ 0 & T\end{bmatrix}, \tag{8}$$

where $W(k)$ represents Gaussian white noise with a mean of 0 and a covariance matrix of R_w, T is the sampling period.

Then the observation equation of the system is

$$Z(k) = H\tilde{X}(k) + V(k), \tag{9}$$

where $Z(k)$ is the measured value, H is the measurement matrix of the system, and $V(k)$ represents Gaussian white noise with a mean of 0 and a covariance matrix of R_v. In addition, $W(k)$ and $V(k)$ are mutually independent.

3.2 Alternating Operation of MPC and KF

In this algorithm, we first initialize the state and control. The state and control after initialization are $\hat{X}(k-1)$ and $\tilde{u}(k-1)$, respectively. Then we use the Kalman filter to estimate the state at the next moment.

The state equation and observation equation of the system are (6) and (9) respectively.

During the prediction phase of the Kalman filter, the formulas for system state estimation and covariance estimation are given by

$$\bar{X}(k) = A(k-1)\hat{X}(k-1) + B(k-1)\tilde{u}(k-1), \tag{10}$$

$$\bar{P}(k) = A(k)\hat{P}(k-1)A(k)^T + R_w. \tag{11}$$

where $\bar{X}$ represents the prior state estimate, $\hat{X}$ represents the posterior state estimate, $\bar{P}$ represents the prior error covariance, $\hat{P}$ represents the updated error covariance.

Subsequently, during the correction phase of the Kalman filter, the Kalman gain, updated state estimation, and updated error covariance are given by

$$K(k) = \bar{P}(k)H^T[H\bar{P}(k)H^T + R_v]^{-1}, \tag{12}$$

$$\hat{X}(k) = \bar{X}(k) + K(k)[H\bar{X}(k) - Z(k)], \tag{13}$$

$$\hat{P}(k) = [I - K(k)]\bar{P}(k), \tag{14}$$

where $\hat{X}(k)$ is the next moment state estimated by KF. According to the estimated state $\hat{X}(k)$ and MPC, we can solve the optimal control at the next moment.

In order to solve the optimal control using MPC, we need to make a one-step prediction of the estimated state

$$\bar{X}(k+1) = A(k)\hat{X}(k) + B(k)\tilde{u}(k). \tag{15}$$

According to equation (15), we construct a new state vector as follows

$$\xi(k) = \begin{bmatrix} \hat{X}(k) \\ \tilde{u}(k-1) \end{bmatrix}, \tag{16}$$

and we can establish a new state-space representation

$$\xi(k+1) = \tilde{A}(k)\xi(k) + \tilde{B}(k)\Delta u(k), \tag{17}$$

$$\eta(k) = \tilde{C}(k)\xi(k), \tag{18}$$

where

$$\tilde{A}(k) = \begin{bmatrix} A(k) & B(k) \\ 0 & I \end{bmatrix}, \tilde{B}(k) = \begin{bmatrix} B(k) \\ I \end{bmatrix}, \tilde{C}(k) = \begin{bmatrix} I & 0 \end{bmatrix},$$

$\Delta u(k)$ is the control increment at the moment k.And we define $\Delta u(k)$ as

$$\Delta u(k) = u(k) - u(k-1), \tag{19}$$

and we can obtain

$$\begin{aligned} \Delta u(k) &= (u(k) - u_r) - (u(k-1) - u_r) \\ &= \tilde{u}(k) - \tilde{u}(k-1). \end{aligned} \tag{20}$$

State prediction based on (17) yields the following equation, N_p is the forecast time horizon.

$$\begin{aligned}
\xi(k+1) =& \tilde{A}(k)\xi(k) + \tilde{B}(k)\Delta u(k) \\
\xi(k+2) =& \tilde{A}(k+1)\tilde{A}(k)\xi(k) \\
&+ \tilde{A}(k+1)\tilde{B}(k)\Delta u(k) \\
&+ \tilde{B}(k+1)\Delta u(k+1) \\
\xi(k+3) =& \tilde{A}(k+2)\tilde{A}(k+1)\tilde{A}(k)\xi(k) \\
&+ \tilde{A}(k+2)\tilde{A}(k+1)\tilde{B}(k)\Delta u(k) \\
&+ \tilde{A}(k+2)\tilde{B}(k+1)\Delta u(k+1) \\
&+ \tilde{B}(k+2)\Delta u(k+2) \\
&\vdots \\
\xi(k+N_p) =& \prod_{i=N_p-1}^{0} \tilde{A}(k+i)\xi(k) \\
&+ [\sum_{i=1}^{N_p-1} (\prod_{N_p-1}^{i} \tilde{A}(k+i))\tilde{B}(k+i-1) \\
&\times \Delta u(k+i-1)] + \tilde{B}(k+N_p-1) \\
&\times \Delta u(k+N_p-1).
\end{aligned}$$

According to (18), the new system output can be calculated as follows

$$\begin{aligned}
\eta(k+1) =& \tilde{C}(k)\xi(k+1) \\
=& \tilde{C}(k)\tilde{A}(k)\xi(k) + \tilde{C}(k)\tilde{B}(k)\Delta u(k) \\
\eta(k+2) =& \tilde{C}(k)\xi(k+2) \\
=& \tilde{C}(k)\tilde{A}(k+1)\tilde{A}(k)\xi(k) \\
&+ \tilde{C}(k)\tilde{A}(k+1)\tilde{B}(k)\Delta u(k) \\
&+ \tilde{C}(k)\tilde{B}(k)\Delta u(k+1) \\
\eta(k+3) =& \tilde{C}(k)\xi(k+3) \\
=& \tilde{C}(k)\tilde{A}(k+2)\tilde{A}(k+1)\tilde{A}(k)\xi(k) \\
&+ \tilde{C}(k)\tilde{A}(k+2)\tilde{A}(k+1)\tilde{B}(k)\Delta u(k) \\
&+ \tilde{C}(k)\tilde{A}(k+2)\tilde{B}(k+1)\Delta u(k+1) \\
&+ \tilde{C}(k)\tilde{B}(k+2)\Delta u(k+2) \\
&\vdots \\
\eta(k+N_p) =& \tilde{C}(k)\xi(k+N_p) \\
=& \prod_{i=N_p-1}^{0} \tilde{C}(k)\tilde{A}(k+i)\xi(k) \\
&+ [\sum_{i=1}^{N_p-1} (\prod_{N_p-1}^{i} \tilde{C}(k)\tilde{A}(k+i))\tilde{B}(k+i-1) \\
&\times \Delta u(k+i-1)] + \tilde{C}(k)\tilde{B}(k+N_p-1) \\
&\times \Delta u(k+N_p-1).
\end{aligned}$$

To make the relationship more explicit, we express the output of the system at future moments in the following form

$$Y(k) = \Psi(k)\xi(k) + \Theta(k)\Delta U(k), \tag{21}$$

where we set $A_1(k) = (\prod_{N_p-1}^{1} \tilde{A}(k+i))$, $A_2(k) = (\prod_{N_p-1}^{2} \tilde{A}(k+i))$,

$$\Theta(k) = \tilde{C}(k) \begin{bmatrix} \tilde{B}(k) & 0 & \cdots & 0 \\ \tilde{A}(k)\tilde{B}(k) & \tilde{B}(k+1) & \cdots & 0 \\ \cdots & \cdots & \ddots & \cdots \\ A_1(k)\tilde{B}(k) & A_2(k)\tilde{B}(k+1) & \cdots & \tilde{B}(k+N_p-1) \end{bmatrix},$$

$$\Delta U(k) = \begin{bmatrix} \Delta u(k) \\ \Delta u(k+1) \\ \cdots \\ \Delta u(k+N_c-1) \end{bmatrix}, Y(k) = \begin{bmatrix} \eta(k+1) \\ \eta(k+2) \\ \cdots \\ \eta(k+N_p) \end{bmatrix},$$

$$\Psi(k) = \begin{bmatrix} \tilde{C}(k)\tilde{A}(k) \\ \tilde{C}(k)\tilde{A}(k+1)\tilde{A}(k) \\ \cdots \\ \prod_{i=N_p-1}^{0} \tilde{C}(k)\tilde{A}(k+i) \end{bmatrix}.$$

In the process of AGV trajectory tracking, we obtain the control sequence by solving the objective function, thus ensuring that the AGV tracks the reference trajectory as accurately as possible. We define the objective function as

$$J(k) = Y^T Q Y + \Delta U(k)^T R \Delta U(k). \tag{22}$$

Substituting (21) into (22) yields

$$\begin{aligned} J(k) =&\Delta U(k)^T(\Theta(k)^TQ\Theta(k)+R)\Delta U(k) \\ &+2(\Psi(k)\xi(k))^TQ\Theta(k)\Delta U(k)+E, \end{aligned} \tag{23}$$

$$E =(\Psi(k)\xi(k))^TQ(\Psi(k)\xi(k)), \tag{24}$$

where Q and R are weighting matrices, E is a constant that can be neglected during the simplification process.

In the actual control system, we consider the constraints of control quantity and control increment to satisfy the requirements of AGV safety and stability. The constrained targets are given as

$$\begin{gathered} u_{min} \le u(k+t) \le u_{max}, \\ t=0,1,\cdots,N_c-1, \end{gathered} \tag{25}$$

$$\begin{gathered} \Delta u_{min} \le \Delta u(k+t) \le \Delta u_{max}, \\ t=0,1,\cdots,N_c-1, \end{gathered} \tag{26}$$

where u_{min} is the minimum control quantity, u_{max} is the maximum control quantity, Δu_{min} is the minimum control increment and Δu_{max} is the maximum control increment.

Since the solution of the objective function is the control increment, the constraint is written in the form of a control increment. In addition, we know the control quantity at the last moment. Therefore, the control quantity at the current moment can be expressed in the following form

$$u(k+t)=u(k+t-1)+\Delta u(k+t). \tag{27}$$

And we set

$$U(k-1)=1_{N_c}\otimes u(k-1), \tag{28}$$

$$\Upsilon=\begin{bmatrix} 1 & 0 & 0 & \cdots & 0 \\ 1 & 1 & 0 & \cdots & 0 \\ 1 & 1 & 1 & \cdots & 0 \\ \cdots & \cdots & \cdots & \ddots & \cdots \\ 1 & 1 & 1 & \cdots & 1 \end{bmatrix}_{N_c\times N_c} \otimes I, \tag{29}$$

where 1_{N_c} is an N_c-dimensional column vector with all elements equal to 1, $\otimes$ is Kronecker Product.

Therefore, (25) and (26) can be rewritten as

$$U_{min} \le \Upsilon\Delta U(k)+U(k-1) \le U_{max}, \tag{30}$$

$$\Delta U_{min} \le \Delta U(k) \le \Delta U_{max}, \tag{31}$$

where

$$U_{min}=1_{N_c}\otimes u_{min}, \tag{32}$$

$$U_{max}=1_{N_c}\otimes u_{max}, \tag{33}$$

$$\Delta U_{min}=1_{N_c}\otimes \Delta u_{min}, \tag{34}$$

$$\Delta U_{max}=1_{N_c}\otimes \Delta u_{max}. \tag{35}$$

We transform the objective function (22) into a QP problem and solve it in conjunction with constraints,

$$J=\Delta U(k)^TH(k)\Delta U(k)+g(k)\Delta U(k), \tag{36}$$

$$\begin{gathered} s.t. U_{min} \le \Upsilon\Delta U(k)+U(k-1) \le U_{max}, \\ \Delta U_{min} \le \Delta U(k) \le \Delta U_{max}, \end{gathered}$$

with

$$H(k)=\Theta(k)^TQ\Theta(k)+R, \tag{37}$$

$$g(k)=2(\Psi(k)\xi(k))^TQ\Theta(k). \tag{38}$$

By solving (36), a series of control increments in the control horizon can be obtained

$$\Delta U^*(k)=\begin{bmatrix}\Delta u^*(k) & \cdots & \Delta u^*(k+N_p-1)\end{bmatrix}^T. \tag{39}$$

Apply the first element $\Delta u^*(k)$ in (38) to the system. We can get the optimal control at k moment, that is

$$u^*(k)=u(k-1)+\Delta u^*(k). \tag{40}$$

In addition, we can also obtain the optimal $\tilde{u}^*$ at the moment k, that is

$$\tilde{u}^*(k)=\tilde{u}(k-1)+\Delta u^*(k). \tag{41}$$

and we can use $\tilde{u}^*(k)$ and the Kalman filter to estimate the state at the next moment.

Algorithm 1 Alternating Operation of MPC and KF

```
Define N as the maximum number of iterations
Initialize X̂(k−1), ũ(k−1)
while k ≤ N do
    Estimate X̂(k) based on KF
    Solving MPC based on X̂(k) yields Δu*(k)
    u*(k) ← u*(k−1) + Δu*(k)
    k ← k + 1
end while
```

4 Simulation

To demonstrate the effectiveness of the algorithm, we consider tracking different trajectories and compare the algorithm with the noise-disturbed MPC algorithm. We use MATLAB to conduct simulation experiments.

4.1 Tracking a Circular Trajectory

In the experiment, we set the sampling period T = 0.1, reference line velocity $v_r = 2$, reference angular velocity $\omega_r = 0.033\pi$, the initial state $X = \begin{bmatrix}-0.2 & 1 & 0.016\pi\end{bmatrix}^T$. We consider tracking the circular trajectory in Fig.3.

Fig.3 shows the tracking results of the two algorithms for the circular trajectory. It can be seen from the figure that under the influence of noise, the algorithm designed in this paper can successfully track the circular trajectory and is closer to the reference trajectory than the MPC algorithm. Fig.4 and Fig.5 show the circular trajectory tracking errors of the two algorithms under the influence of noise. It can be seen that the trajectory tracking error of this algorithm is always kept in a small range, and the error of this algorithm is smaller than that of the MPC algorithm.

4.2 Tracking a Straight Trajectory

In the experiment, we set the sampling period T = 0.1, reference line velocity $v_r = 2.5$, reference angular velocity $\omega_r = 0$, the initial state $X = \begin{bmatrix}0 & 0.5 & 0.016\pi\end{bmatrix}^T$.We consider tracking the straight trajectory in Fig.6.

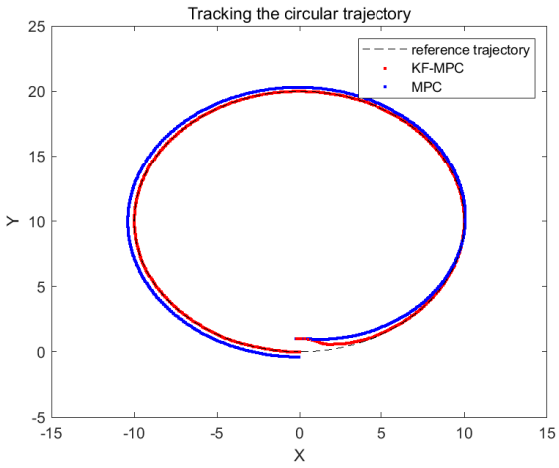

Fig. 3: Circular trajectory tracking

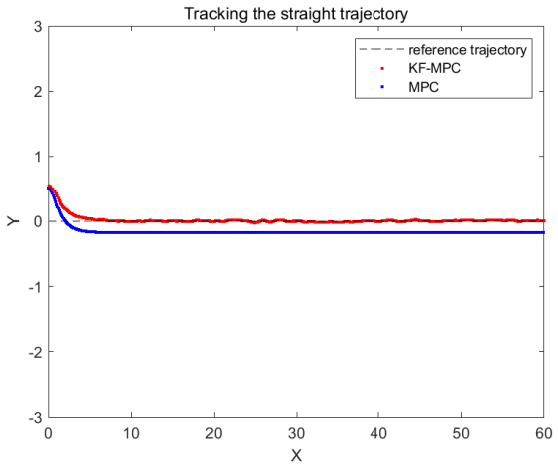

Fig. 6: Straight trajectory tracking

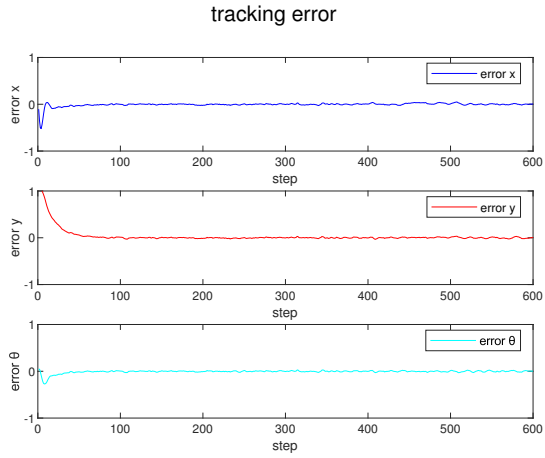

Fig. 4: Circular trajectory tracking error based on KF-MPC

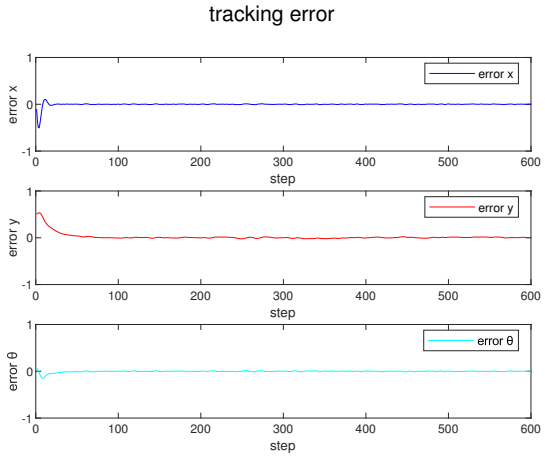

Fig. 7: Straight trajectory tracking error based on KF-MPC

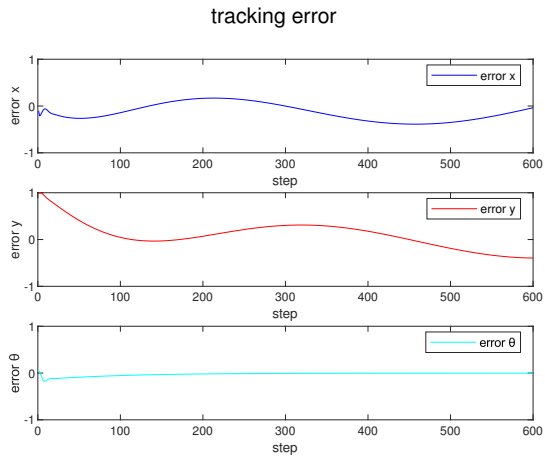

Fig. 5: Circular trajectory tracking error based on MPC

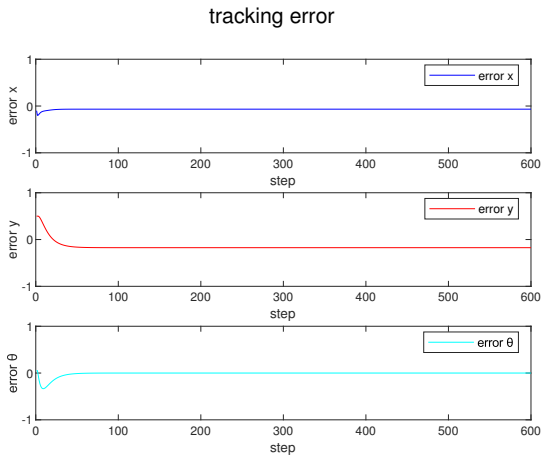

Fig. 8: Straight trajectory tracking error based on MPC

As can be seen from Fig.6, due to the influence of noise, only MPC can not accurately track the linear trajectory. However, the algorithm designed in this paper can effectively reduce the influence of noise, so that AGV can complete the tracking more accurately. Fig.7 and Fig.8 show the tracking errors of the two algorithms. It can be seen that the accuracy of the proposed algorithm is higher.

In summary, it can be seen from the above two sets of experiments that the algorithm can reduce the influence of noise on AGV, enable it to accurately track the reference trajectory, and control the error within a small range. Simulation results further prove the effectiveness of the proposed algorithm.

5 Conclusions

In this paper, an alternate algorithm of Kalman filter and model predictive control is proposed to reduce the influence of noise and improve the accuracy of trajectory tracking for differential drive AGV systems with additive Gaussian noise. The Kalman filter part of the algorithm can estimate the state and reduce the interference of noise. In the model predictive control part of the algorithm, we can get the optimal control at the current moment. In addition, the effectiveness of the proposed algorithm can be evaluated by the experimental results of tracking different trajectories. In conclusion, the algorithm achieves good results in trajectory tracking and provides an effective control strategy for practical application.

References

[1] H. Rashidi, F. Matinfar, and F. A. Parand. Automated guided vehicles - a review on applications, problem modeling and solutions. *Tarrahan Parseh Transportation Research Institute*, (3), 2021.

[2] H. Khodadadi and H. Ghadiri. Self-tuning pid controller design using fuzzy logic for half car active suspension system. *International Journal of Dynamics and Control*, 2016.

[3] S. T. Kao, W. J. Chiou, and M. T. Ho. Integral sliding mode control for trajectory tracking control of an omnidirectional mobile robot. *IEEE*, 2011.

[4] B. Moudoud, H. Aissaoui, and M. Diany. Fuzzy adaptive sliding mode controller for electrically driven wheeled mobile robot for trajectory tracking task. *Journal of Control and Decision*, pages 1–9, 2021.

[5] D. Chu, H. Li, C. Zhao, and T. Zhou. Trajectory tracking of autonomous vehicle based on model predictive control with pid feedback. *IEEE Transactions on Intelligent Transportation Systems*, 24(2):2239–2250, 2023.

[6] Z. Zuo, X. Yang, Z. Li, Y. Wang, Q. Han, L. Wang, and X. Luo. Mpc-based cooperative control strategy of path planning and trajectory tracking for intelligent vehicles. *IEEE Transactions on Intelligent Vehicles*, 6(3):513–522, 2021.

[7] H. Pang, N. Liu, C. Hu, and Z. Xu. A practical trajectory tracking control of autonomous vehicles using linear time-varying mpc method. *Proceedings of the Institution of Mechanical Engineers, Part D. Journal of Automobile Engineering*, (4):236, 2022.

[8] R. Marino, S. Scalzi, and M. Netto. Nested pid steering control for lane keeping in autonomous vehicles. *Control Engineering Practice*, 19(12):1459–1467, 2011.

[9] W. Farag. Complex trajectory tracking using pid control for autonomous driving. *International Journal of Intelligent Transportation Systems Research*, 18(2), 2019.

[10] T. Yuan, G. Guo, B. Du, Z. Zhao, and W. Xu. The adaptive sliding mode control using improved genetic algorithm tuning pid controller for the planetary rover. *Aircraft Engineering and Aerospace Technology*, 2021.

[11] T. Truong, A. T. Vo, and H. Kang. A backstepping global fast terminal sliding mode control for trajectory tracking control of industrial robotic manipulators. *IEEE Access*, 9:31921–31931, 2021.

[12] C. Yan, K. Shao, X. Wang, J. Zheng, and B. Liang. Reference governor-based control for active rollover avoidance of mobile robots. *2021 IEEE International Conference on Systems, Man, and Cybernetics (SMC)*, pages 429–435, 2021.

[13] X. Zhou and L. He. Sliding mode control for trajectory tracking of agv based on improved fast stationary power approach law. *Journal of Physics: Conference Series*, 2417(1):12–32, 2022.

[14] D. Q. Mayne, J. B. Rawlings, C. V. Rao, and P. O. M. Scokaert. Constrained model predictive control: Stability and optimality. *Automatica*, 36(6):789–814, 2000.

[15] K. Zhang, Q. Sun, and Y. Shi. Trajectory tracking control of autonomous ground vehicles using adaptive learning mpc. *IEEE Transactions on Neural Networks and Learning Systems*, 32(12):5554–5564, 2021.

[16] Z. Zhao, H. Liu, H. Chen, J. Hu, and H. Guo. Kinematics-aware model predictive control for autonomous high-speed tracked vehicles under the off-road conditions. *Mechanical Systems and Signal Processing*, 123:333–350, 2019.

[17] D. Wang, W. Wei, Y. Yeboah, Y. Li, and Y. Gao. A robust model predictive control strategy for trajectory tracking of omni-directional mobile robots. *Journal of Intelligent and Robotic Systems*, 98:439–453, 2020.

[18] M. Rokonuzzaman, N. Mohajer, and S. Nahavandi. Effective adoption of vehicle models for autonomous vehicle path tracking: a switched mpc approach. *Vehicle system dynamics*, 61(5):1236–1259, 2023.

Proceedings of the 3rd Conference on Fully Actuated System Theory and Applications
May 10-12, 2024, Shenzhen, China

Robust H_∞ Synchronization for Networked Re-Entrant Manufacturing Systems

Chenguang Liu[1], Qing Gao[2,3], Wei Wang[2,3], Jinhu Lü[2,3]

1. Institute of Artificial Intelligence, Beihang University, Beijing 100191, P. R. China
E-mail: chenguangliu@buaa.edu.cn

2. School of Automation Science and Electrical Engineering, Beihang University, Beijing 100191, P. R. China
E-mail: gaoqing@buaa.edu.cn

3. Zhongguancun Laboratory, Beijing, P. R. China

Abstract: This paper delves into the robust H_∞ synchronization for a type of networked re-entrant manufacturing systems (ReMSs). The dynamics of the considered networked ReMSs are described by nonlinear hyperbolic partial differential equations. Given the potential communication uncertainties and external disturbances in the production lines, a robust H_∞ synchronization criterion is derived for the networked ReMSs by utilizing an edge-dependent distributed adaptive strategy. A numerical simulation is utilized to validate the effectiveness of the developed adaptive scheme and the obtained criterion.

Key Words: Re-entrant manufacturing systems (ReMSs), networked control, robust synchronization, distributed adaptive contol.

1 Introduction

In recent decades, re-entrant manufacturing systems (ReMSs) have emerged as a prominent research focus, driven by the increasing need for elevated reliability, enhanced performance, and sustainability of re-entry features within work-in-progress across diverse highly automated industrial manufacturing processes, such as the chemical material production, the semiconductor wafer fabrication and the printed circuit board manufacturing [1–4].

Note that significant research results on discrete event-based ReMSs, such as the queuing networks [5, 6] and the Petri nets [7, 8], have been presented to date. However, the escalating number of processing steps, machines, and materials may impose a substantial increase in computational burdens and considerable time consumption on these discrete-event system models. To address these limitations, an alternative continuum approximation model characterized by hyperbolic conservative equation has emerged and been applied to describe ReMSs [9–11], which could effectively capture the re-entry feature and system dynamics with high complexity. In [10], a continuum ReMS with high re-entry feature was established by a nonlinear hyperbolic partial differential equation, and an even-triggered strategy was designed to guarantee the stability for such a highly ReMS by utilizing the logarithmic norm of the state. In [11], a type of highly ReMSs with local and nonlocal velocities was presented based on the conservation law, and the controllability and the stabilization were further studied by means of the Lyapunov function method.

In operational re-entrant manufacturing facilities, it is often essential to cooperatively synchronize production across different manufacturing lines to meet practical market requirements. This entails implementing a dynamic and highly adaptable control system spanning various production lines. The synthesis of synchronization control for networked control systems is directed towards attaining a shared consensus through a communication channel, which provides a feasible solution to reach this objective [12–15]. In [12], the authors studied the synchronization regulation control problem for networked distributed parameter systems by utilizing two distinct type of liner synchronization controllers with constant and adaptive edge-dependent feedback gains. In [13], the authors investigated the synchronization tracking problem for networked agent systems under the denial-of-service attacks, some synchronization criteria were derived for such a networked control system based on the hybrid control theory. In [14], the authors developed a distributed adaptive control strategy to guarantee the synchronization for a class of networked systems with unknown nonlinear dynamics. In [15], the authors focused on the synchronization for directed networked systems with heterogeneous nonlinear dynamics, and derived the some synchronization conditions for the networked control system based on the obtained robust stability results. Therefore, the networked control can be regarded as a viable method to guarantee synchronous production activities for the ReMSs. Furthermore, external disturbances are unavoidable in networked control for ReMSs, often resulting in compromised productivity or even complete disruption of production. Although the initial exploration of some control approaches, such as the event-triggered control [10] and the fuzzy control [16, 17], for ReMSs, the robust H_∞ synchronization for networked ReMSs has not yet been investigated.

In this paper, we make the first attempt to networked control for ReMSs comprising a three-tiered architecture and delve into the robust H_∞ synchronization for the networked ReMSs. The primary contributions of this paper are outlined as follows. Firstly, in contrast to uncoupled ReMSs [9–11], a three-tiered architecture for networked ReMSs with nonlinear dynamics and exogenous disturbances is established, which contains the production line, the manufacturing layer and the workshop layer. Secondly, given the communication uncertainties in the networked control system, the synchronization controllers with adaptive edge-dependent feedback gains are designed to ensure the H_∞ synchronization for the ReMSs. Finally, a numerical example is utilized to validate the effectiveness of the obtained results.

This work was supported in part by the National Key Research and Development Program of China under Grant 2022YFF0902800 and in part by the National Natural Science Foundation of China under Grant 92367204.

Notations: $\varphi_1(U), \varphi_2(U), \ldots, \varphi_r(U)$ denote the eigenvalues in descending order of the real symmetric matrix $U \in \mathbb{R}^{r\times r}$, where r is a positive integer.

2 System Modeling and Problem Formulation

In this paper, the networked ReMS is characterized by a three-tiered architecture, as illustrated in Fig. 1, encompassing the production line, the manufacturing layer and the workshop layer.

1) Production Line

The re-entrant manufacturing process implies that work-in-process repeatedly passes through the same workstation at different stages of the manufacturing flow. As illustrated in (c) of Fig. 1, a straightforward re-entrant production line, comprising multiple machines, buffers, and re-buffers, is depicted: the buffers hold work-in-process awaiting service at each machine, while the re-buffers hold work-in-process that are returned to each machine, awaiting subsequent service. Then, based on the mass conservation law, the dynamics of a re-entrant production line can be characterized by the following hyperbolic partial differential equation [9]:

$$\frac{\partial p(t,s)}{\partial t} + c\frac{\partial p(t,s)}{\partial s} = 0,$$

where $s \in [0,1]$ denotes the completion of products; the state variable $p(t,s) \in \mathbb{R}$ describes the production density at stage $s \in [0,1]$ and time $t \in [0,+\infty)$; $0 \leqslant c \in \mathbb{R}$ represents the velocity of a job moving in the production line.

2) Manufacturing Layer

To enhance production efficiency and mitigate the risk of production interruptions caused by machine failures, a manufacturing workshop is often equipped with multiple production lines, as illustrated in (b) of Fig. 1. Then, the dynamics of a workshop with n production lines can be characterized by the following equation:

$$\frac{\partial p_i(t,s)}{\partial t} = -c_i\frac{\partial p_i(t,s)}{\partial s} + \sum_{j=1}^{n} e_{ij}h_j(p_j(t,s)),$$

where $i,j = 1,2,...,n$, n is a positive scalar representing the number of production lines in a workshop; $e_{ij} \in \mathbb{R}$ denotes the coupled weight between ith and jth production lines; the nonlinear function $h_j(p_j(t,s))$ implies the coupling relationship between ith and jth production lines and satisfies

$$|h_j(\vartheta_1) - h_j(\vartheta_2)| \leqslant d_j|\vartheta_1 - \vartheta_2|,\ \forall\, \vartheta_1, \vartheta_2 \in \mathbb{R}, \quad (1)$$

where d_j is a positive scalar.

Take $p(t,s) = (p_1(t,s), p_2(t,s), \ldots, p_n(t,s))^T \in \mathbb{R}^n$, $E = (e_{ij})_{n\times n} \in \mathbb{R}^{n\times n}$, $0 \leqslant C = \mathrm{diag}(c_1, c_2, \ldots, c_n) \in \mathbb{R}^{n\times n}$, $h(p(t,s)) = (h_1(p_1(t,s)), \ldots, h_n(p_n(t,s)))^T \in \mathbb{R}^n$, then the workshop dynamics can be reformulated as

$$\frac{\partial p(t,s)}{\partial t} = -C\frac{\partial p(t,s)}{\partial s} + Eh(p(t,s)).$$

3) Workshop Layer

To achieve process specialization and cater to larger-scale production demands, a re-entrant manufacturing factory typically consists of multiple workshops, as illustrated in (a) of Fig. 1. Then, the dynamics of a ReMS composed of r manufacturing workshops, each of which equipped with n production lines can be established as

$$\frac{\partial \rho_k(t,s)}{\partial t} = -C\frac{\partial \rho_k(t,s)}{\partial s} + Eh(\rho_k(t,s)), \quad (2)$$

where $k = 1,2,\ldots,r$, r is a positive scalar representing the number of workshops; the state vector $\rho_k(t,s) = (\rho_{k1}(t,s), \rho_{k2}(t,s), \ldots, \rho_{kn}(t,s))^T \in \mathbb{R}^n$ denotes the product density of the kth workshop equipped with n production lines.

An undirected graph $\mathcal{F}(\mathcal{I}, \mathcal{J}, U)$ is assumed to characterize the communication topology for the networked ReMS (2). The node set $\mathcal{I} = \{1,2,\ldots,r\}$ represents the workshops, the edge set $\mathcal{J} \subset \mathcal{I}\times\mathcal{I}$ represents communication links among the networked ReMS (2), and $U(t)$ is the time-varying adjacency matrix of $\mathcal{F}$. The set of neighbors of the lth workshop is denoted by $\mathcal{K}_l = \{k \in \mathcal{I} : (l,k) \in \mathcal{J}\}$. The element $U_{kl}(t)$ of the weighted adjacent matrix $U(t)$, characterizing the underlying communication topology of all workshops, satisfies the following condition:

$$U_{kl}(t) = \begin{cases} U_{lk}(t), & \text{if } l \in \mathcal{K}_k, \\ -\sum\limits_{\substack{\epsilon=1 \\ \epsilon\neq k}}^{r} U_{k\epsilon}(t), & \text{if } l = k, \\ 0, & \text{otherwise.} \end{cases}$$

The exogenous disturbances are inevitable in networked control systems. Denote the bounded and square integrable function $\beta_k(t,s) \in \mathbb{R}^n$ as the external disturbance in the temporal-spatial domain, i.e.,

$$\int_0^{t^*}\int_0^{L} \beta_k^T(t,s)\beta_k(t,s)dsdt < \infty$$

for any $0 < t^* \in \mathbb{R}$ and $0 < L \leqslant 1$. Then, a more general model can be formulated as follows:

$$\begin{aligned}\frac{\partial \rho_k(t,s)}{\partial t} = &-C\frac{\partial \rho_k(t,s)}{\partial s} + Eh(\rho_k(t,s)) + \beta_k(t,s) \\ &+u_k(t,s), k = 1,2,\ldots,r, \end{aligned} \quad (3)$$

subject to the following initial and boundary conditions:

$$\begin{aligned}\rho_k(0,s) &= \rho_k^*(s), s \in [0,L], \\ \rho_k(t,0) &= 0,\ t \in [0,+\infty),\end{aligned}$$

where the $u_k(t,s)$ is the control input to be designed and the function $\rho_k^*(s)$ is continuous.

Now, the robust H_∞ synchronization problem of the networked system (3) can be formulated. Taking $\bar{\rho}(t,s) = \frac{1}{r}\sum\limits_{\epsilon=1}^{r}\rho_\epsilon(t,s)$, one obtains

$$\begin{aligned}\frac{\partial \bar{\rho}(t,s)}{\partial t} = &-C\frac{\partial \bar{\rho}(t,s)}{\partial s} + \frac{1}{r}\sum_{\epsilon=1}^{r} Eh(\rho_\epsilon(t,s)) + \frac{1}{r}\sum_{\epsilon=1}^{r}\beta_\epsilon(t,s) \\ &+\frac{1}{r}\sum_{\epsilon=1}^{r} u_\epsilon(t,s).\end{aligned}$$

Define $\alpha_k(t,s) = \rho_k(t,s) - \bar{\rho}(t,s)$, $k = 1,2,\ldots,r$, then the dynamics of synchronization error for the networked system (3) are presented as follows:

$$\frac{\partial \alpha_k(t,s)}{\partial t} = -C\frac{\partial \alpha_k(t,s)}{\partial s} + Eh(\rho_k(t,s)) + \beta_k(t,s)$$

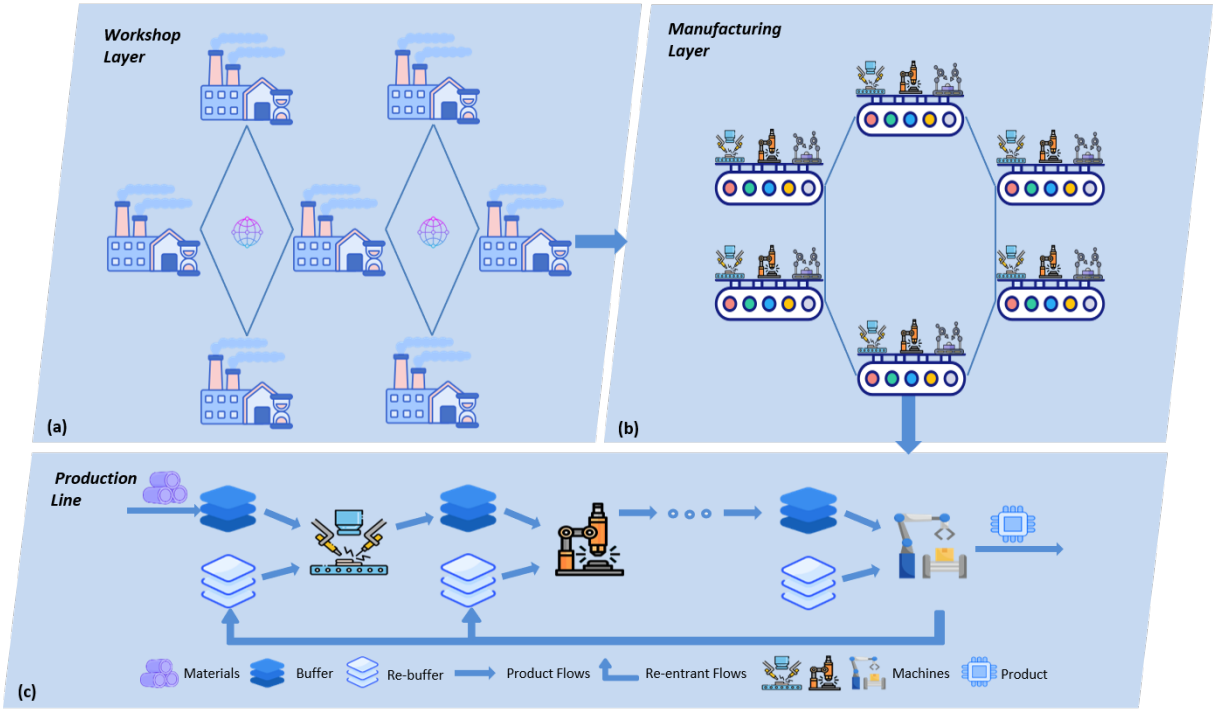

Fig. 1: Hierarchical architecture of ReMS.

$$+u_k(t,s)-\frac{1}{r}\sum_{\epsilon=1}^{r}Eh(\rho_\epsilon(t,s))$$
$$-\frac{1}{r}\sum_{\epsilon=1}^{r}\beta_\epsilon(t,s)-\frac{1}{r}\sum_{\epsilon=1}^{r}u_\epsilon(t,s). \tag{4}$$

For notational brevity, one denotes

$$\alpha(t,s)=(\alpha_1^T(t,s),\alpha_2^T(t,s),\dots,\alpha_r^T(t,s))^T,$$
$$\beta(t,s)=(\beta_1^T(t,s),\beta_2^T(t,s),\dots,\beta_r^T(t,s))^T.$$

Then the H_∞ disturbance attenuation for the error dynamics (4) is given by

$$\int_0^{t^*}\int_0^{L}\alpha^T(t,s)\alpha(t,s)dsdt$$
$$\leqslant\gamma^2\int_0^{t^*}\int_0^{L}\beta^T(t,s)\beta(t,s)dsdt+\mathcal{V}(\alpha(0,\cdot)) \tag{5}$$

for the time $t^*\in\mathbb{R}$, the attenuation index $0<\gamma\in\mathbb{R}$ and the positive functions $\mathcal{V}(\alpha(0,\cdot))>0$.

The purpose of this study is to formulate appropriate control inputs $u_k(t,s)$ for every workshop such that the errors $\alpha_k(t,s)$ in networked manufacturing system (4) reach the disturbance attenuation condition (5).

3 Main Results

Considering that the communication uncertainties caused by unreliable transmission or limited communication range, the following synchronization control schemes, which contain adaptive laws tuning coupling gains among workshops, are designed to guarantee the H_∞ synchronization for the ReMS (3):

$$u_k(t,s)=\sum_{l\in\mathcal{K}_k}U_{kl}(t)B[\rho_l(t,s)-\rho_k(t,s)], \tag{6}$$

where adaptive edge-dependent synchronization gains U_{kl} are given by

$$\dot{U}_{kl}(t)=v_{kl}\int_0^{L}[\rho_k(t,s)-\rho_l(t,s)]^THB[\rho_k(t,s)-\rho_l(t,s)]ds,$$

where $0<v_{kl}=v_{lk}\in\mathbb{R}$ are used to regulate the adaptive rates; $0<H=\mathrm{diag}(\mathcal{H}_1,\mathcal{H}_2,\dots,\mathcal{H}_n)\in\mathbb{R}^{n\times n}$; $B=\mathrm{diag}(b_1,b_2,\dots,b_n)\in\mathbb{R}^{n\times n}$ is a positive matrix indicating the interaction among production lines of different workshops.

To obtain the main results, a lemma is first introduced.

Lemma 3.1. [18] The following inequality holds:

$$\alpha^T(U\otimes B)\alpha\leqslant\varphi_2(U)\alpha^T(I_r\otimes B)\alpha,$$

where $\alpha=(\alpha_1^T,\alpha_2^T,\dots,\alpha_r^T)^T\in\mathbb{R}^{rn}$, $0<B\in\mathbb{R}^{n\times n}$, $\alpha_k\in\mathbb{R}^n$, $\sum_{k=1}^{r}\alpha_k=0$, and $U=(U_{kl})_{r\times r}\in\mathbb{R}^{r\times r}$ is an irreducible matrix satisfying $U_{kl}=U_{lk}\geqslant 0$ if $k\neq l$, and $U_{kl}=-\sum_{l=1,l\neq k}^{r}U_{kl}$ if $l=k$.

Then, the following result can be obtained.

Theorem 3.1. By utilizing the synchronization controller (6), the ReMS (3) can attain the robust H_∞ synchronization if the following condition holds:

$$HEE^TH+D+\frac{1}{\gamma^2}H^2+I_n+2\varphi_2(U^*)(HB)\leqslant 0, \tag{7}$$

where $U^*=(U_{kl}^*)_{r\times r}\in\mathbb{R}^{r\times r}$ is defined similar to $U(t)$.

Proof. The closed-loop networked control system, constituted by (4) and (6), is formulated as follows:

$$\frac{\partial\alpha_k(t,s)}{\partial t}=-C\frac{\partial\alpha_k(t,s)}{\partial s}+Eh(\rho_k(t,s))+\beta_k(t,s)$$
$$+\sum_{l=1}^{r}U_{kl}(t)B\left[\alpha_l(t,s)+\frac{1}{r}\sum_{\epsilon=1}^{r}\rho_\epsilon(t,s)\right]$$

$$
\begin{aligned}
&-\frac{1}{r}\sum_{\epsilon=1}^{r} Eh(\rho_\epsilon(t,s)) - \frac{1}{r}\sum_{\epsilon=1}^{r} u_\epsilon(t,s)\\
&-\frac{1}{r}\sum_{\epsilon=1}^{r} \beta_\epsilon(t,s)\\
=&-C\frac{\partial \alpha_k(t,s)}{\partial s} + Eh(\rho_k(t,s)) + \beta_k(t,s)\\
&-\frac{1}{r}\sum_{\epsilon=1}^{r} Eh(\rho_\epsilon(t,s)) - \frac{1}{r}\sum_{\epsilon=1}^{r} u_\epsilon(t,s)\\
&-\frac{1}{r}\sum_{\epsilon=1}^{r} \beta_\epsilon(t,s) + \sum_{l=1}^{r} U_{kl}(t) B\alpha_l(t,s). \quad (8)
\end{aligned}
$$

Further, the following Lyapunov function for the system (8) is selected:

$$
\begin{aligned}
\mathcal{V}(t) =& \sum_{k=1}^{r}\int_0^L \alpha_k^T(t,s) H \alpha_k(t,s) ds\\
&+\sum_{k=1}^{r}\sum_{l\in\mathcal{K}_k} \frac{(U_{kl}(t)-U_{kl}^*)^2}{2v_{kl}}. \qquad (9)
\end{aligned}
$$

Calculating the time derivative of (9), one derives

$$
\begin{aligned}
\dot{\mathcal{V}}(t) =& 2\sum_{k=1}^{r}\int_0^L \alpha_k^T(t,s) H\Big[-C\frac{\partial \alpha_k(t,s)}{\partial s} + Eh(\rho_k(t,s))\\
&-Eh(\bar{\rho}(t,s)) + Eh(\bar{\rho}(t,s)) - \frac{1}{r}\sum_{\epsilon=1}^{r} Eh(\rho_\epsilon(t,s))\\
&+\beta_k(t,s) - \frac{1}{r}\sum_{\epsilon=1}^{r}\beta_\epsilon(t,s) - \frac{1}{r}\sum_{\epsilon=1}^{r} u_\epsilon(t,s)\\
&+\sum_{l=1}^{r} U_{kl}(t) B\alpha_l(t,s)\Big] ds\\
&+\sum_{k=1}^{r}\sum_{l\in\mathcal{K}_k} \frac{(U_{kl}(t)-U_{kl}^*)\dot{U}_{kl}(t)}{v_{kl}}\\
=& 2\sum_{k=1}^{r}\int_0^L \alpha_k^T(t,s) HE\Big[h(\bar{\rho}(t,s)) - \frac{1}{r}\sum_{\epsilon=1}^{r} h(\rho_\epsilon(t,s))\Big] ds\\
&+2\sum_{k=1}^{r}\int_0^L \alpha_k^T(t,s) HE\big[h(\rho_k(t,s)) - h(\bar{\rho}(t,s))\big] ds\\
&-\frac{2}{r}\sum_{k=1}^{r}\sum_{\epsilon=1}^{r}\int_0^L \alpha_k^T(t,s) H[\beta_\epsilon(t,s) + u_\epsilon(t,s)] ds\\
&+2\sum_{k=1}^{r}\sum_{l=1}^{r} U_{kl}(t)\int_0^L \alpha_k^T(t,s) HB\alpha_l(t,s) ds\\
&-2\sum_{k=1}^{r}\int_0^L \alpha_k^T(t,s) HC\frac{\partial \alpha_k(t,s)}{\partial s} ds\\
&+2\sum_{k=1}^{r}\int_0^L \alpha_k^T(t,s) H\beta_k(t,s) ds\\
&+\sum_{k=1}^{r}\sum_{l\in\mathcal{K}_k}(U_{kl}(t)-U_{kl}^*)\int_0^L [\rho_k(t,s)-\rho_l(t,s)]^T\\
&\times HB[\rho_k(t,s)-\rho_l(t,s)] ds. \qquad (10)
\end{aligned}
$$

According to the boundary condition, one obtains

$$
\begin{aligned}
&-2\sum_{k=1}^{r}\int_0^L \alpha_k^T(t,s) HC\frac{\partial \alpha_k(t,s)}{\partial s} ds\\
=& 2\sum_{k=1}^{r}\int_0^L \frac{\partial \alpha_k^T(t,s)}{\partial s} HC\alpha_k(t,s) ds\\
&-2\sum_{k=1}^{r}\alpha_k^T(t,s) HC\alpha_k(t,s)|_{s=0}^{s=L}\\
=& 2\sum_{k=1}^{r}\int_0^L \frac{\partial \alpha_k^T(t,s)}{\partial s} HC\alpha_k(t,s) ds\\
&-2\sum_{k=1}^{r}\alpha_k^T(t,L) HC\alpha_k(t,L)\\
\leqslant& 2\sum_{k=1}^{r}\int_0^L \alpha_k^T(t,s) HC\frac{\partial \alpha_k(t,s)}{\partial s} ds. \qquad (11)
\end{aligned}
$$

Additionally, since

$$
\sum_{k=1}^{r}\alpha_k(t,s) = \sum_{k=1}^{r}\Big[\rho_k(t,s) - \frac{1}{r}\sum_{\epsilon=1}^{r}\rho_\epsilon(t,s)\Big] = 0,
$$

one derives

$$
\begin{aligned}
&\sum_{k=1}^{r}\alpha_k^T(t,s) HE\Big[h(\bar{\rho}(t,s)) - \frac{1}{r}\sum_{\epsilon=1}^{r} h(\rho_\epsilon(t,s))\Big] = 0,\\
&\frac{2}{r}\sum_{k=1}^{r}\sum_{\epsilon=1}^{r}\alpha_k^T(t,s) H[\beta_\epsilon(t,s) + u_\epsilon(t,s)] = 0. \qquad (12)
\end{aligned}
$$

From (1), one infers

$$
\begin{aligned}
&2\sum_{k=1}^{r}\int_0^L \alpha_k^T(t,s) HE\left[h(\rho_k(t,x)) - h(\bar{\rho}(t,s))\right] ds\\
\leqslant& \sum_{k=1}^{r}\int_0^L \alpha_k^T(t,s)(HEE^TH + D)\alpha_k(t,s) ds, \qquad (13)
\end{aligned}
$$

where $D = \mathrm{diag}(d_1^2, d_2^2, \ldots, d_n^2)$.

Further, according to (10)-(13), one has

$$
\begin{aligned}
\dot{\mathcal{V}}(t) \leqslant& -2\sum_{k=1}^{r}\sum_{\substack{l=1\\ l\neq k}}^{r}\big(U_{kl}(t)-U_{kl}^*\big)\int_0^L \alpha_k^T(t,s) HB\alpha_l(t,s) ds\\
&+\sum_{k=1}^{r}\sum_{\substack{l=1\\ l\neq k}}^{r}\big(U_{kl}(t)-U_{kl}^*\big)\int_0^L \alpha_k^T(t,s) HB\alpha_k(t,s) ds\\
&+\sum_{l=1}^{r}\sum_{\substack{k=1\\ k\neq l}}^{r}\big(U_{kl}(t)-U_{kl}^*\big)\int_0^L \alpha_l^T(t,s) HB\alpha_l(t,s) ds\\
&+\sum_{k=1}^{r}\int_0^L \alpha_k^T(t,s)(HEE^TH + D)\alpha_k(t,s) ds\\
&+2\sum_{k=1}^{r}\sum_{l=1}^{r} U_{kl}(t)\int_0^L \alpha_k^T(t,s) HB\alpha_l(t,s) ds\\
&+2\sum_{k=1}^{r}\int_0^L \alpha_k^T(t,s) H\beta_k(t,s) ds
\end{aligned}
$$

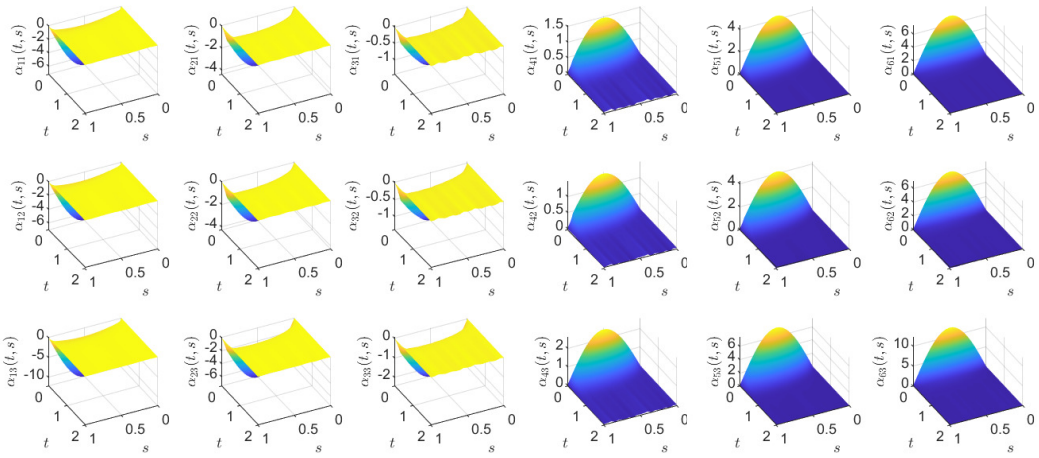

Fig. 2: Trajectories of $\alpha_{k1}(t,s), \alpha_{k2}(t,s)$ and $\alpha_{k3}(t,s), k = 1, 2, \ldots, 6$ under the synchronization controller (6).

$$
\begin{aligned}
&= -2\sum_{k=1}^{r}\sum_{l=1}^{r}\big(U_{kl}(t)-U_{kl}^{*}\big)\int_0^L \alpha_k^T(t,s)HB\alpha_l(t,s)ds \\
&\quad +\sum_{k=1}^{r}\int_0^L \alpha_k^T(t,s)(HEE^TH+D)\alpha_k(t,s)ds \\
&\quad +2\sum_{k=1}^{r}\sum_{l=1}^{r}U_{kl}(t)\int_0^L \alpha_k^T(t,s)HB\alpha_l(t,s)ds \\
&\quad +2\sum_{k=1}^{r}\int_0^L \alpha_k^T(t,s)H\beta_k(t,s)ds \\
&= \sum_{k=1}^{r}\int_0^L \alpha_k^T(t,s)(HEE^TH+D)\alpha_k(t,s)ds \\
&\quad +2\sum_{k=1}^{r}\sum_{l=1}^{r}U_{kl}^{*}\int_0^L \alpha_k^T(t,s)HB\alpha_l(t,s)ds \\
&\quad +2\sum_{k=1}^{r}\int_0^L \alpha_k^T(t,s)H\beta_k(t,s)ds. \qquad (14)
\end{aligned}
$$

Based on (14) and Lemma 3.1, one obtains

$$
\begin{aligned}
&\int_0^L \alpha^T(t,s)\alpha(t,s)ds-\gamma^2\int_0^L \beta^T(t,s)\beta(t,s)ds+\dot{\mathcal{V}}(t) \\
&\leqslant \int_0^L \alpha^T(t,s)\alpha(t,s)ds-\gamma^2\int_0^L \beta^T(t,s)\beta(t,s)ds \\
&\quad +\int_0^L \alpha^T(t,s)[I_r\otimes(HEE^TH+D)]\alpha(t,s)ds \\
&\quad +2\int_0^L \alpha^T(t,s)[U^*\otimes(HB)]\alpha(t,s)ds \\
&\quad +2\int_0^L \alpha^T(t,s)(I_r\otimes H)\beta(t,s)ds \\
&\leqslant \int_0^L \alpha^T(t,s)[I_r\otimes(HEE^TH+D)]\alpha(t,s)ds \\
&\quad +2\varphi_2(U^*)\int_0^L \alpha^T(t,s)[I_r\otimes(HB)]\alpha(t,s)ds \\
&\quad +\frac{1}{\gamma^2}\int_0^L \alpha^T(t,s)(I_r\otimes H^2)\alpha(t,s)ds \\
&\quad +\int_0^L \alpha^T(t,s)\alpha(t,s)ds \\
&\leqslant \int_0^L \alpha^T(t,s)\Big\{I_r\otimes\Big[HEE^TH+D+\frac{1}{\gamma^2}H^2+I_n \\
&\quad +2\varphi_2(U^*)(HB)\Big]\Big\}\alpha(t,s)ds. \qquad (15)
\end{aligned}
$$

It follows from (7) and (15) that

$$
\int_0^L \alpha^T(t,s)\alpha(t,s)ds \leqslant \gamma^2\int_0^L \beta^T(t,s)\beta(t,s)ds-\dot{\mathcal{V}}(t),
$$

which indicates that

$$
\begin{aligned}
&\int_0^{t^*}\int_0^L \alpha^T(t,s)\alpha(t,s)dsdt \\
&\leqslant \gamma^2\int_0^{t^*}\int_0^L \beta^T(t,s)\beta(t,s)dsdt+\mathcal{V}(\alpha(0,\cdot)). \qquad (16)
\end{aligned}
$$

Therefore, the proof of Theorem 3.1 is completed.

4 Numerical Illustration

In this section, the effectiveness of the developed synchronization control approach is demonstrated through an illustrative example of a networked ReMS comprising six workshops, each of which equipped with three production lines. The corresponding parameters of the networked system are given as follows.

$$
E=\begin{pmatrix}0.45 & 0.35 & 0.15\\ 0.35 & 0.55 & 0.25\\ 0.15 & 0.25 & 0.65\end{pmatrix}, \beta_k(t,s)=\begin{pmatrix}0.4\sin(4k\pi s)t\\ 0.4\sin(4k\pi s)t\\ 0.4\sin(4k\pi s)t\end{pmatrix},
$$

$$
C=\begin{pmatrix}0.5 & 0 & 0\\ 0 & 0.6 & 0\\ 0 & 0 & 0.4\end{pmatrix}, h(\rho_k)=\begin{pmatrix}0.25\tanh(\rho_{k1})\\ 0.45\tanh(\rho_{k2})\\ 0.35\tanh(\rho_{k3})\end{pmatrix}.
$$

Note that the functions $h_1(\rho_k), h_2(\rho_k), h_3(\rho_k)$ meet condition (1) with $d_1 = 0.25, d_2 = 0.45, d_3 = 0.35$, respectively. Taking

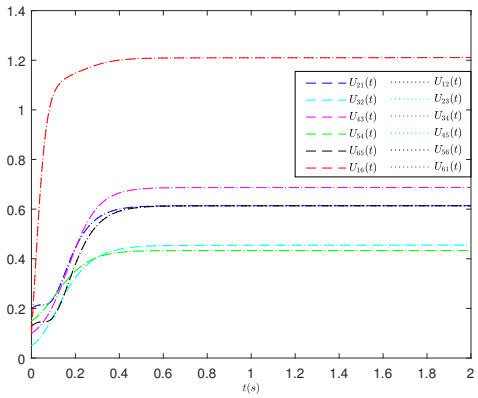

Fig. 3: Trajectories of $U_{kl}(t), k = 1, 2, \ldots, 6, l \in \mathcal{K}_k$.

$$U(0) = \begin{pmatrix} -0.3 & 0.2 & 0 & 0 & 0 & 0.1 \\ 0.2 & -0.25 & 0.05 & 0 & 0 & 0 \\ 0 & 0.05 & -0.15 & 0.1 & 0 & 0 \\ 0 & 0 & 0.1 & -0.25 & 0.15 & 0 \\ 0 & 0 & 0 & 0.15 & -0.28 & 0.13 \\ 0.1 & 0 & 0 & 0 & 0.13 & -0.23 \end{pmatrix},$$

one can obtain that $B = \mathrm{diag}(11.0078, 11.0216, 11.0679)$ and $\varphi_2(U^*) \leqslant -4.0833$ satisfying (7) by utilizing the MATLAB. Letting

$$U^* = \begin{pmatrix} -11 & 5 & 0 & 0 & 0 & 6 \\ 5 & -13 & 8 & 0 & 0 & 0 \\ 0 & 8 & -12 & 4 & 0 & 0 \\ 0 & 0 & 4 & -10 & 6 & 0 \\ 0 & 0 & 0 & 6 & -11 & 5 \\ 6 & 0 & 0 & 0 & 5 & -11 \end{pmatrix},$$

one has $\varphi_2(U^*) = -4.9818 < -4.0833$. Based on Theorem 3.1, the H_∞ synchronization is realized with the aid of the adaptive synchronization controller (6). Fig. 2 exhibits the trajectories of $\alpha_{k1}(t, s), \alpha_{k2}(t, s)$ and $\alpha_{k3}(t, s), k = 1, 2, \ldots, 6$ subject to the unanticipated disturbances $\beta_k(t, s)$ under the adaptive synchronization controller (6). Fig. 3 reveals the gradual convergence of $U_{kl}(t)$, $k = 1, 2, \ldots, 6$, $l \in \mathcal{K}_r$ to steady-state values, which indicates that the parameter adjustment laws are successfully implemented as the system achieves H_∞ synchronization.

5 Conclusion

The control of manufacturing systems is becoming increasingly critical in modern industry. In this paper, the robust H_∞ synchronization for the networked ReMSs comprising a three-tiered architecture has been investigated. Considering the potential communication uncertainties and external disturbances in the production lines, an edge-dependent distributed adaptive strategy has been utilized to address the robust H_∞ synchronization for networked ReMSs. A numerical simulation has been employed to validate the effectiveness of the obtained criterion and the developed adaptive strategy.

References

[1] S. Arima, A. Kobayashi, Y.-F. Wang, K. Sakurai, and Y. Monma, Optimization of re-entrant hybrid flows with multiple queue time constraints in batch processes of semiconductor manufacturing. *IEEE Transactions on Semiconductor Manufacturing*, 2015, 28(4): 528–544.

[2] J. Han, M. Cai, Y. Lin, W. Liu, X. Luo, H. Zhang, and M. Zhong, 3D re-entrant nanograss on microcones for durable superamphiphobic surfaces via laser-chemical hybrid method. *Applied Surface Science*, 2018, 456: 726–736.

[3] S.-G. Ko, T.-S. Yu, and T.-E. Lee, Wafer delay analysis and workload balancing of parallel chambers for dual-armed cluster tools with multiple wafer types. *IEEE Transactions on Automation Science and Engineering*, 2021, 18(3): 1516–1526.

[4] M. Ibrahim and S. Reveliotis, Throughput maximization of capacitated re-entrant lines through fluid relaxation. *IEEE Transactions on Automation Science and Engineering*, 2019, 16(2): 792–810.

[5] S. Kumar and P. R. Kumar, Queueing network models in the design and analysis of semiconductor wafer fabs. *IEEE Transactions on Robotics and Automation*, 2001, 17(5): 548–561.

[6] J. M. Harrison and L. M. Wein, Scheduling networks of queues: Heavy traffic analysis of a two-station closed network. *Operations Research*, 1990, 38(6): 1052–1064.

[7] C. Lin, M. Xu, D. C. Marinescu, F. Ren, and Z. Shan, A sufficient condition for instability of buffer priority policies in re-entrant lines. *IEEE Transactions on Automatic Control*, 2003, 48(7): 1235–1238.

[8] N. G. Odrey, J. D. Green, and A. Appello, A generalized Petri net modeling approach for the control of re-entrant flow semiconductor wafer fabrication. *Robotics and Computer-Integrated Manufacturing*, 2001, 17: 5–11.

[9] D. Armbruster, D. E. Marthaler, C. Ringhofer, K. Kempf, and T. Jo, A continuum model for a re-entrant factory. *Operations Research*, 2006, 54: 933–950.

[10] M. Diagne and I. Karafyllis, Event-triggered boundary control of a continuum model of highly re-entrant manufacturing systems. *Automatica*, 2021, 134: 109902.

[11] J. Chu, P. Shang, and Z. Wang, Controllability and stabilization of a conservation law modeling a highly re-entrant manufacturing system. *Nonlinear Analysis*, 2019, 189: 111577.

[12] M. A. Demetriou, Adaptation and optimization of synchronization gains in the regulation control of networked distributed parameter systems. *IEEE Transactions on Automatic Control*, 2015, 60(8): 2219–2224.

[13] Y. Wan, G. Wen, X. Yu, and T. Huang, Distributed consensus tracking of networked agent systems under denial-of-service attacks. *IEEE Transactions on Systems, Man, and Cybernetics: Systems*, 2021, 51(10): 6183–6196.

[14] A. Das and F. L. Lewis, Distributed adaptive control for synchronization of unknown nonlinear networked systems. *Automatica*, 2010, 46(12): 2014–2021.

[15] E. Panteley and A. Loria, Synchronization and dynamic consensus of heterogeneous networked systems. *IEEE Transactions on Automatic Control*, 2017, 62(8): 3758–3773.

[16] C. Zhang, Q. Gao, M. V. Basin, J. Lv, and H. Liu, Robust control of multi-line re-entrant manufacturing plants via stochastic continuum models. *IEEE Transactions on Automation Science and Engineering*, early access, Aug. 23, 2023, doi: 10.1109/TASE.2023.3305308.

[17] K. Zhang, M. V. Basin, Q. Gao, Y. Deng, and X. Song, Robust stability and fuzzy controller synthesis for a class of hybrid re-entrant manufacturing systems. *Discrete and Continuous Dynamical Systems-S*, 2023, 16: 1909-1928.

[18] C.-G. Liu, J.-L. Wang, and H.-N. Wu, Finite-time passivity for coupled fractional-order neural networks with multistate or multiderivative couplings. *IEEE Transactions on Neural Networks and Learning Systems*, 2023, 34(9): 5976–5987.

Proceedings of the 3rd Conference on Fully Actuated System Theory and Applications
May 10-12, 2024, Shenzhen, China

Structural Design and Kinematic Analysis of Fully Automated Material Handling Robots for Warehouse Logistics

Runchen Zhao, Haibo Du*, Xunhong Sun, Wenwu Zhu
School of Electrical and Automation Engineering, Hefei University of Technology, Hefei 230009, P. R. China
E-mail: haibo.du@hfut.edu.cn

Abstract: In order to enhance the material handling efficiency and intelligent capabilities of warehouse logistics environments, this article focuses on the research of fully automated material handling robots. The design principles and motion structure of the robot are introduced, with a particular emphasis on establishing the kinematic model of its upper structure based on an improved Denavit-Hartenberg (D-H) approach. Kinematic analysis, including both forward and inverse solutions, is performed by incorporating joint parameters, and the results are validated. This research provides a foundational basis for the control of fully automated material handling robots, contributing to advancements in the field of intelligent warehouse logistics.

Key Words: Warehouse Logistics, Fully Automated Material Handling Robots, Denavit-Hartenberg Method, Kinematic Analysis

1 Introduction

With the continuous progress and development of technology, robots have found extensive applications across various industries[1–5]. In today's diverse and complex industrial scenarios, such as manufacturing production plants, numerous situations require material handling, including the storage of raw materials, components, and finished products in warehouses. In such storage environments, traditional manual operations incur high costs, exhibit low efficiency, and pose potential risks, particularly when handling heavy loads. Consequently, substituting machines for manual labor is emerging as the predominant solution for the future.

In contemporary automated factories, common solutions for material handling include belt conveyors and guided vehicles[6]. Belt conveyors are frequently employed for small-item and low-speed transportation, yet they suffer from large spatial requirements and limited flexibility as they can only operate along fixed routes. In contrast, guided vehicles, while more agile and lightweight, lack autonomous path planning and obstacle avoidance capabilities. They require the pre-installation of tracks or magnetic strips, involving significant engineering efforts. Once deployed, altering the route necessitates substantial adjustments, resulting in significant resource wastage. Therefore, in modern flexible manufacturing environments, there is a pressing need for highly efficient, flexible, and autonomous intelligent material handling equipment.

Numerous studies have been conducted on automated handling devices. Lin Yuxin et al. designed an intelligent vehicle with a six-axis robotic arm and an automatic sorting cargo box based on the application of AGV (Automated Guided Vehicle) in small and medium-sized enterprises. This vehicle is capable of selectively gripping and loading goods using the robotic arm, achieving automation in the functions of loading, transporting, and unloading cargo [7]. Wei Liang et al. focused on automotive bodies and mapped the transport body, the operating mechanism of the transport body, and the entire transported vehicle into parallel mechanisms of dynamic and static platforms. Through structural synthesis, they devised a transport robot with a parallel transport mechanism, presenting a novel approach for the transport mechanism of transport robots [8]. Deng Yuxin et al. designed a wheeled line-following robot for intelligent logistics based on the STM32 chip. The compact and lightweight mechanical structure of the vehicle enables self-detection of cargo positions for pick-up and unloading, precise fixation of items, and autonomous recognition and guidance following predefined paths. The system achieves stable line-following control of the AGV (Automated Guided Vehicle) with differential drive, adjusting the path in real-time based on feedback information from sensors [9].

This paper presents a fully automated material handling robot that utilizes a two-stage telescopic structure to facilitate the handling and transfer of boxed materials stored on shelves in warehousing environments. The study employs an improved Denavit-Hartenberg (D-H) parameter method to establish the kinematic model of the fully automated material handling robot[10–13]. The kinematic forward and inverse solutions are obtained and validated for accuracy.

2 STRUCTURAL DESIGN

The mechanical structure of the fully automated material handling robot is illustrated in Fig. 1. The robot's main body comprises three components: the transfer mechanism, lifting mechanism, and the chassis of the vehicle body.

2.1 Transfer Mechanism

The robot's transfer mechanism incorporates commonly used mechanical transmission components such as chain wheel drive, belt wheel drive, slider guides, and rotary bearings, as shown in Fig. 2. During operation, the transfer arm is initially driven to extend a sufficient distance to the rear of the cargo box. At this point, the claws at the ends of the two arms rotate to a closed position, and the transfer mechanism as a whole adopts a clamping configuration to move the cargo box back onto the loading tray. Subsequently, the transfer mechanism rotates, orienting the entire structure towards the robot's own cargo tray. The transfer arm is then once again driven to place the cargo box onto the robot's cargo tray, and finally, the claws are rotated to an open posi-

This work was supported by the National Natural Science Foundation of China under Grants No.62073113, No.62003122.

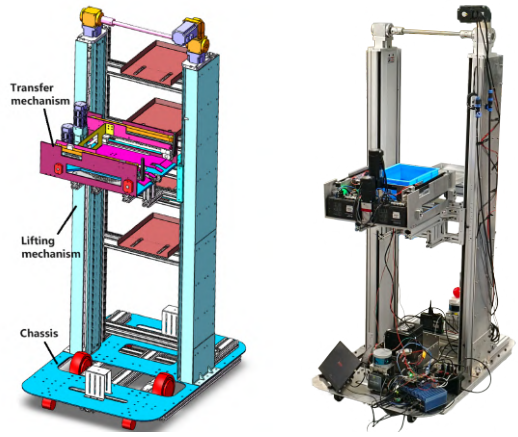

Fig. 1: Main Structure of Robot

tion, completing the transfer motion for a single cargo box.

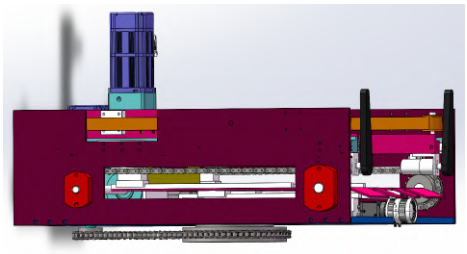

Fig. 2: Transfer Mechanism

The design of the two-stage telescopic mechanism is crucial for the transfer mechanism throughout the entire motion process. When the robot chassis is parked at a distance of 50mm from the shelf's side, in order to smoothly retrieve the cargo, the claws need to extend at least 520mm. When a servo motor serves as the driving source, conventional rotational-to-linear mechanisms like screw slides, gear racks, and others can be employed to fulfill the transmission requirements. Although these mechanisms can meet the travel distance requirement, their structural length exceeds 520mm, resulting in a larger volume for the transfer mechanism. Considering that the transfer mechanism needs to rotate as well, a larger volume would increase the distance from the rotation center to the lifting mechanism. This has a significant impact on the width and length design of the vehicle body chassis. In the case of a linear motor as the driving source, volume-related issues similarly arise. Hence, a two-stage telescopic design is necessary. The designed two-stage telescopic mechanism in this study is composed of a combination of belt pulleys and slide rails, utilizing chain drive to achieve the two-stage telescopic motion, as illustrated in Fig. 3.

2.2 Lifting Mechanism

The lifting mechanism of the robot adopts linear screw drive, connecting two screw modules together through a single servo motor, optical shaft, and coupling components. This mechanical arrangement achieves synchronization at the mechanical level, facilitating control. This design choice helps prevent coding errors and potential risks associated with occasional malfunctions in dual-motor drive configu-

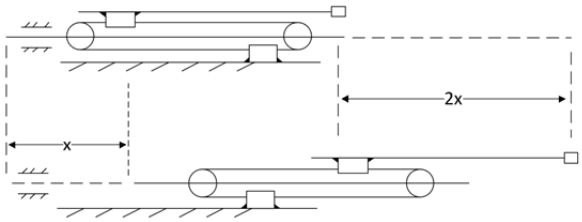

Fig. 3: Principle of Two-Stage Telescoping

rations, as illustrated in Fig. 4.

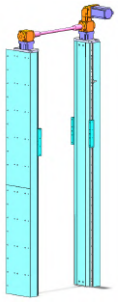

Fig. 4: Lifting Mechanism

2.3 Chassis Design

Analysis of the Motion Requirements for the Fully Automated Material Handling Robot reveals several key functionalities: achieving forward and turning capabilities, accomplishing in-place rotation, and traversing smoothly on mildly uneven surfaces. Common mobile robot chassis wheel systems are classified into three-wheel, four-wheel, and six-wheel structures, with wheels categorized as drive wheels and omnidirectional wheels. Due to the substantial overall load of the fully automated material handling robot, three-wheel or four-wheel structures often struggle to meet the load requirements. Therefore, the six-wheel structure is employed to ensure stability of the upper structure under heavy loads, thereby enhancing the overall mechanical lifespan. The wheel system, composed of the aforementioned drive wheels and omnidirectional wheels, is depicted in Fig. 5, where black shapes represent drive wheels and gray shapes represent omnidirectional wheels.



Fig. 5: Six-Wheel Chassis Structure

After opting for a six-wheel structure, the fully automated material handling robot requires the design of a locomotion system to fulfill its motion functionalities. The locomotion system chosen for the fully automated material handling robot in this study is the differential drive system. This system achieves the required motion functionalities by controlling the motion direction and speed of two drive wheels.

2.4 Analysis of Robot Motion Structure

Apart from the vehicle chassis, all other mechanisms are collectively referred to as the upper structure. In warehousing environments, cargo boxes, which bear materials, are typically placed on square-shaped shelves. Each shelf is divided into multiple layers. When the robot is tasked with handling and transferring items on the shelves, to maintain stable and coherent motions, it first needs to dock at one side of the shelf. Subsequently, the upper structure is controlled to execute the corresponding actions, as illustrated in Fig. 6. At this point, the motion of the fully automated material handling robot involves four degrees of freedom: the translational degree of freedom for lifting up and down, the rotational degree of freedom for the transfer mechanism, the translational degree of freedom for the extension of the transfer mechanism's loading arm, and the rotational degree of freedom for the gripper at the end of the arm. By controlling the rotation and movement of each axis, the effective handling of transferred goods can be achieved.

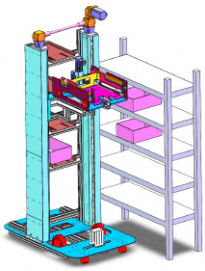

(a) Docking at the Target Position

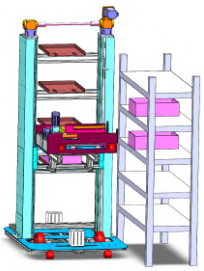

(b) Facing the Cargo Box

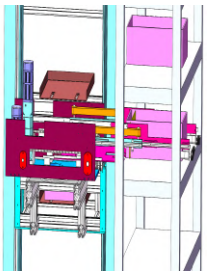

(c) Gripping the Cargo Box

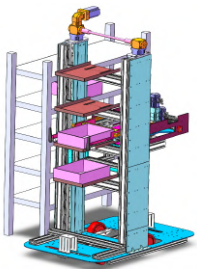

(d) Transferring the Cargo Box

Fig. 6: Material Retrieval Process of the Robot

During automatic control, the fully automated material handling robot docks at the target point based on a pre-set trajectory. To pick up a cargo box from the second shelf, as shown in Fig.6(a), the lifting mechanism first lowers the transfer mechanism and rotates it to align with the cargo box's position, as depicted in Fig.6(b). The pick-up arm then moves to lift and transport the cargo, as shown in Fig.6(c). After picking up the cargo box, the transfer mechanism rotates, coordinated with the lifting mechanism, to position the box directly over the robot's loading platform, as illustrated in Fig.6(d). This entire process requires the inverse kinematics of the various joint motions at the specified position points.

3 Kinematic Analysis and Simulation

3.1 Establishment of the Robot Denavit-Hartenberg Model

Based on the previous analysis of the motion structure of the fully automated material handling robot, when the robot is handling cargo, the chassis remains stationary. Therefore, the kinematic analysis of the robot can be simplified to focus on the upper structure. Since the robot has two arms, but the end rotation angles are opposite when gripping cargo, for the purpose of kinematic modeling and analysis, they are considered as a whole. The kinematic model of the robot is established using an improved Denavit-Hartenberg (D-H) method, as illustrated in Fig. 7.

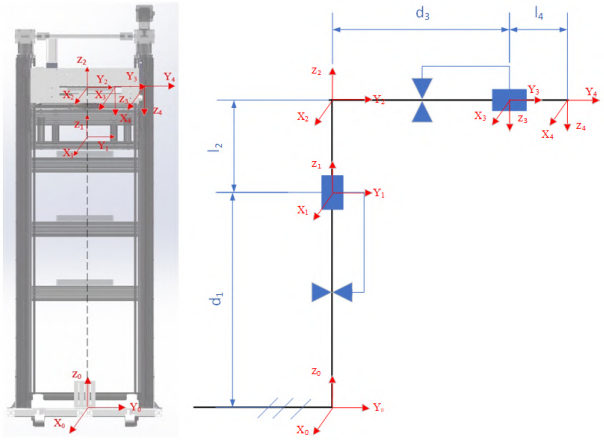

Fig. 7: Kinematic Model of the Robot

Based on the joint coordinate systems established in the figure, the Denavit-Hartenberg parameter table for each joint of the upper structure of the robot is presented in Table 1.

Table 1: Robot Denavit-Hartenberg Parameters

Joint i	**Twist Angle** $\alpha_{i-1}(^\circ)$	**Link Length** a_{i-1}(m)	**Joint Offset** d_i(m)	**Joint Angle** $\theta_i(^\circ)$
1	0	0	d_1	0
2	0	0	l_2	θ_2
3	0	-90	d_3	0
4	0	0	l_4	θ_4

Where l_2 and l_4 are constants determined by the mechanical design parameters of the robot, with specific values l_2 = 0.17m and l_4 = 0.01m. The movement range for each joint is determined based on the structural characteristics and dimensional parameters of the robot, as presented in Table 2.

Table 2: Joint Range of Motion

Parameter	$\boldsymbol{d_1}$(m)	$\boldsymbol{\theta_2}(^\circ)$	$\boldsymbol{d_3}$(m)	$\boldsymbol{\theta_4}(^\circ)$
Upper Limit	0.4	-90	0.225	0
Lower Limit	1.6	90	0.825	90

3.2 Forward Kinematic Analysis

The Denavit-Hartenberg parameter table for the robot effectively defines the relative pose relationships of the various joints in three-dimensional space.Using coordinate system

X_0-Y_0-Z_0 as the base coordinate system, it is possible to calculate the coordinate transformation matrix for the end-effector coordinate system relative to the base coordinate system. The coordinate transformation matrix between adjacent coordinate systems $\{O_{i-1}\}$ and $\{O_i\}$ can be obtained through four consecutive transformations based on the D-H parameters:

$$ {}^{i-1}_{i}T = R_X(\alpha_{i-1})D_X(a_{i-1})R_Z(\theta_i)D_Z(d_i) \tag{1} $$

The general expression for ${}^{i-1}_{i}T$ is:

$$ {}^{i-1}_{i}T = \begin{bmatrix} c\theta_i & -s\theta_i & 0 & a_{i-1} \\ s\theta_i c\alpha_{i-1} & c\theta_i c\alpha_{i-1} & -s\alpha_{i-1} & -s\alpha_{i-1}d_i \\ s\theta_i s\alpha_{i-1} & c\theta_i s\alpha_{i-1} & c\alpha_{i-1} & c\alpha_{i-1}d_i \\ 0 & 0 & 0 & 1 \end{bmatrix} \tag{2} $$

Where $c\alpha$ is an abbreviation for $\cos\alpha$, and $s\alpha$ is an abbreviation for $\sin\alpha$.

Substituting the joint parameters from the Denavit-Hartenberg parameter table into the expression yields the coordinate transformation matrix between adjacent joints:

$$ {}^{0}_{1}T = \begin{bmatrix} 1 & 0 & 0 & 0 \\ 0 & 1 & 0 & 0 \\ 0 & 0 & 1 & d_1 \\ 0 & 0 & 0 & 1 \end{bmatrix} \tag{3} $$

$$ {}^{1}_{2}T = \begin{bmatrix} c\theta_2 & -s\theta_2 & 0 & 0 \\ s\theta_2 & c\theta_2 & 0 & 0 \\ 0 & 0 & 1 & l_2 \\ 0 & 0 & 0 & 1 \end{bmatrix} \tag{4} $$

$$ {}^{2}_{3}T = \begin{bmatrix} 1 & 0 & 0 & 0 \\ 0 & 0 & 1 & d_3 \\ 0 & -1 & 0 & 0 \\ 0 & 0 & 0 & 1 \end{bmatrix} \tag{5} $$

$$ {}^{3}_{4}T = \begin{bmatrix} c\theta_4 & -s\theta_4 & 0 & 0 \\ s\theta_4 & c\theta_4 & 0 & 0 \\ 0 & 0 & 1 & l_4 \\ 0 & 0 & 0 & 1 \end{bmatrix} \tag{6} $$

The homogeneous transformation matrix ${}^{0}_{4}T$ for the robot end-effector relative to its base coordinate system can be obtained by multiplying ${}^{0}_{1}T$, ${}^{1}_{2}T$, ${}^{2}_{3}T$, ${}^{3}_{4}T$ together:

$$ {}^{0}_{4}T = \begin{bmatrix} r_{11} & r_{12} & r_{13} & p_x \\ r_{21} & r_{22} & r_{23} & p_y \\ r_{31} & r_{32} & r_{33} & p_z \\ 0 & 0 & 0 & 1 \end{bmatrix} \tag{7} $$

Where:

$$ \begin{aligned} &r_{11} = c\theta_2 c\theta_4, r_{12} = -c\theta_2 s\theta_4, r_{13} = -s\theta_2, \\ &r_{21} = s\theta_2 c\theta_4, r_{22} = -s\theta_2 s\theta_4, r_{23} = c\theta_2, \\ &r_{31} = -s\theta_4, r_{32} = -c\theta_4, r_{33} = 0, \\ &p_x = -l_4 s\theta_2 - d_3 s\theta_2, p_y = l_4 c\theta_2 + d_3 c\theta_2, \\ &p_z = d_1 + l_2, \end{aligned} \tag{8} $$

Formulas (3) - (8) constitute the forward kinematics equations for the fully automated material handling robot.

3.3 Inverse Kinematic Analysis

This subsection focuses on solving the inverse kinematics equations for the fully automated material handling robot. Assuming the desired end-effector pose is given by T_{end}, it is represented as:

$$ T_{end} = \begin{bmatrix} r_{11} & r_{12} & r_{13} & p_x \\ r_{21} & r_{22} & r_{23} & p_y \\ r_{31} & r_{32} & r_{33} & p_z \\ 0 & 0 & 0 & 1 \end{bmatrix} \tag{9} $$

Simultaneously, according to the forward kinematics equations, it can be noted that:

$$ T_{end} = {}^{0}_{4}T = {}^{0}_{1}T{}^{1}_{2}T{}^{2}_{3}T{}^{3}_{4}T \tag{10} $$

After joint computation, the result is:

$$ \begin{aligned} &d_1 = p_z - l_2, \\ &\theta_2 = \arccos(\frac{p_y}{\sqrt{p_x^2 + p_y^2}}), \\ &d_3 = \sqrt{p_x^2 + p_y^2} - l_4, \\ &\theta_4 = \arccos(-r_{32}) \end{aligned} \tag{11} $$

Where l_2 is a constant determined by the mechanical design parameters of the robot, with l_2 = 0.17 m. The above equation represents the solution to the inverse kinematics equations for the fully automated material handling robot.

3.4 Validation of Forward Kinematics

The method for validating forward kinematics involves comparing the results obtained from the homogeneous transformation matrices calculated based on the Denavit-Hartenberg modeling method with those obtained using the MATLAB Robotics Toolbox. The MATLAB Robotics Toolbox provides a robot teaching interface (as shown in Fig. 8) that allows for adjustments to the displacement of each joint of the robot.

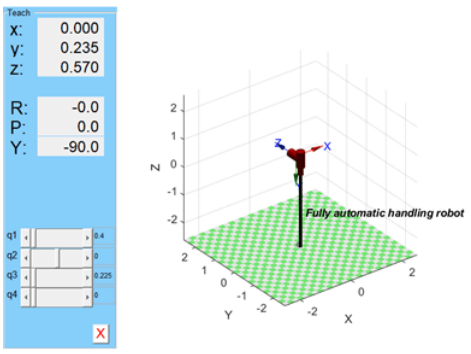

Fig. 8: MATLAB Robotics Teaching Interface

During the validation of the results obtained from forward kinematics analysis, joint displacement values for each joint of the robot were provided. These values were first substituted into the formulas to calculate the expected end-effector pose. The MATLAB Robotics Toolbox, on the other hand, provided results through the robot teaching interface after inputting the joint displacements. For ease of comparison,

this subsection presents only the comparison results for the end-effector position, as shown in Table 3.

From the table, it can be observed that, by providing four sets of different joint displacement variables, the end-effector positions obtained from the two methods are consistent. The slight differences in data are attributed to the limited precision of the MATLAB teaching interface. This confirms the accuracy of the forward kinematics analysis for the fully automated material handling robot in this study.

Table 3: Validation of Forward Kinematics Analysis Results

Joint Variables $[d_1,\theta_2,d_3,\theta_4]$	**Calculated position [x,y,z]**	**Taught position [x,y,z]**
[0.60,-90,0.30,0]	[0.3100,0.0000,0.7700]	[0.3098,0.0000,0.7694]
[0.80,-60,0.40,60]	[0.3551,0.2050,0.9700]	[0.3548,0.2032,0.9674]
[1.00,-45,0.50,45]	[0.3606,0.3606,1.1700]	[0.3612,0.3575,1.1660]
[1.20,0,0.60,90]	[0.0000,0.6100,1.3700]	[0.0000,0.6088,1.3670]

3.5 Validation of Inverse Kinematics

In this section, the correctness of the inverse kinematics analysis for the fully automated material handling robot is validated through motion planning. Utilizing the straight-line trajectory planning function in the MATLAB Robotics Toolbox, the motion planning is carried out based on the actual joint motion patterns for gripping cargo. The inverse solution algorithm used is the one derived from the inverse kinematics equations for the fully automated material handling robot as presented earlier. The correctness of the inverse kinematics analysis is demonstrated through the results of motion planning. Motion planning is divided into two processes: picking and delivering. For the picking process,the starting point coordinates are set as $P_{start1}[0.235, 0.000, 1.770]$, and the target point coordinates are set as $P_{end1}[0.000, 0.235, 1.370]$. The selection of target point coordinates is such that they are positioned at the center coordinates of the actual rear face of the cargo box on the shelf. The robot moves from the initial position to the target position after a given step length. The displacement variation curves of each joint with respect to the step length during the robot's motion planning process are shown in Fig. 9. The actual motion effects of the joints after every hundred steps are illustrated in Fig. 10.

For the delivery motion, the starting point coordinates are set as $P_{start2}[0.000, 0.235, 1.370]$, and the target point coordinates are set as $P_{end2}[-0.235, 0.000, 1.570]$. The selection of target point coordinates is positioned at the center coordinates of the actual rear face of the cargo box on the robot's loading platform. The displacement variation curves of each joint with respect to the step length are depicted in Fig. 11. The actual motion effects of the joints after every hundred steps are illustrated in Fig. 12.

In summary, the inverse kinematics solution developed for the fully automated material handling robot in Section C can assist the motion planner in MATLAB to generate displacement variation curves for each joint of the robot during the motion processes. This validates that the inverse kinematics equations derived in this paper are applicable to the operational phase of the fully automated material handling robot.

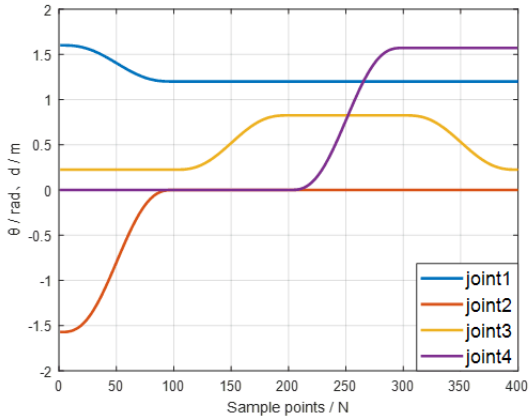

Fig. 9: Picking Movement

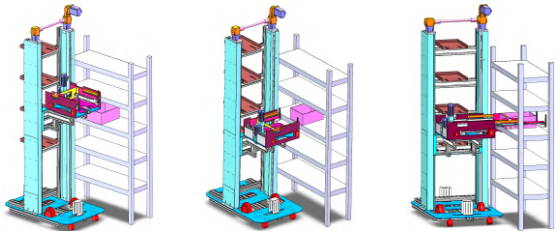

(a) Initial position (b) Sample points from 0 to 100 (c) Sample points from 100 to 200

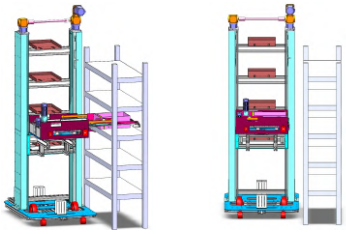

(d) Sample points from 200 to 300 (e) Sample points from 300 to 400

Fig. 10: Picking Movement Results

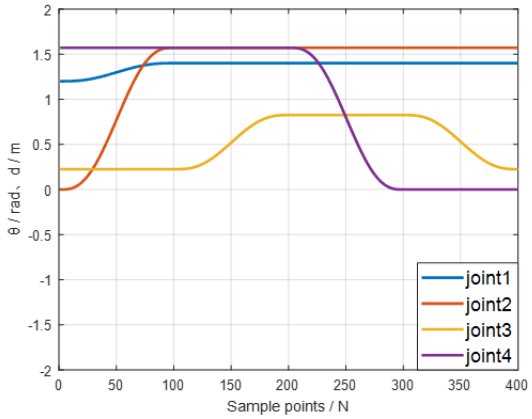

Fig. 11: Delivery Movement

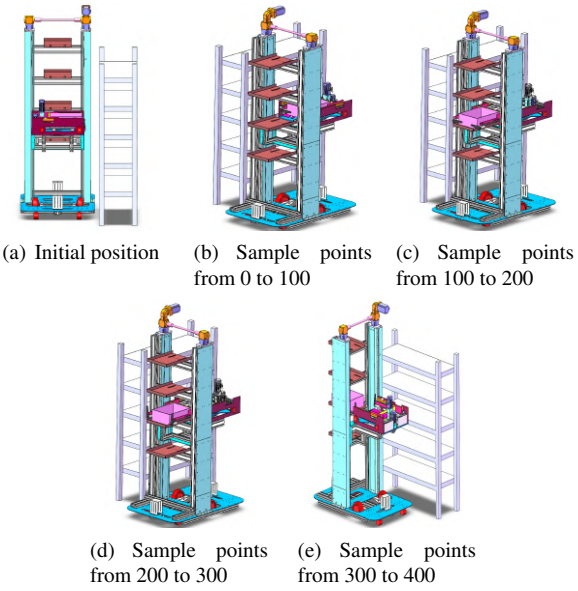

(a) Initial position (b) Sample points from 0 to 100 (c) Sample points from 100 to 200

(d) Sample points from 200 to 300 (e) Sample points from 300 to 400

Fig. 12: Delivering Movement Results

4 CONCLUSION

This paper focuses on the warehouse environment, using a fully automated material handling robot as the research subject. Initially, the robot underwent mechanical design, and an introduction to the motion structure was provided, including the transfer mechanism, lifting mechanism, and vehicle chassis. Subsequently, the robot's kinematic forward and inverse solutions were obtained based on an improved Denavit-Hartenberg parameter method. The correctness of both forward and inverse solutions was verified through MATLAB calculations, providing a foundation for the automatic control of the fully automated material handling robot.

References

[1] W. Qizhi and X. De, On the kinematics analysis and motion planning of the manipulator of a mobile robot, in *Proceedings of 23th Chinese Control and Decision Conference*, 2011: 4033-4037.

[2] Fang Yi, Wang Shuai, Bi Qiushi, Design and Technical of Wall-Climbing Robots, in *Journal of Bionic Engineering*, 2022, 19(4): 877-901.

[3] Mingliang zhang, Zhixin shi, Yufeng luo, Structural design and analysis of end-effector of Traditional Chinese medicine massage robot, in *Journal of Mechanical Transmission*, 2020, 44(6):6.

[4] Marc Raibert, Kevin Blankespoor, Gabriel Nelson, BigDog, the Rough-Terrain Quadruped Robot, in *The 17th World Congress of the International Federation of Automatic Control*, 2008:10822-10824.

[5] Yanjun Cao, An entanglement-clearing robot for power transmission line with composite clearing tool, in *Cyber Technology in Automation, Control, and Intelligent Systems*, 2015.

[6] Bingkun Zheng, Yizong Nai, Feng Ye, Design and Realization of AGV Control System Based on Magnetic Guidance , in *Automation and Instrumentation*, 2014,29(03):6-10.

[7] Yuxin Lin, Junhui Dai, Design of An Intelligent Vehicle for Automatic Manufacture System, in *Mechanical & Electrical Engineering Technology*,2018,47(02):7-10.

[8] Liang Wei, Lubin Hang, Xiaobo Huang, Weizhong Guo, An AGV Parallel Mechanism Unloading Device Constructed by Position and Orientation Characteristics(POC)Theory, in *Machinery Design & Manufacture*,2022,381(11):58-61.

[9] Yuxin Deng, Hongfang Chen, Shuang Zhang, Yu Wang, Chaowei Liang, Ruoshui Sun, Design of Wheeled Tracking Robot System for Intelligent Logistics, in *Tool Engineering*,2022,56(06):57-60.

[10] X. Jian, B. Huang, Y. Zhang, J. Li, X. Chen and S. Xu, Digital Control Method of Bucket Truck Based on DH Parameter Modeling, in *Proceedings of 5th International Conference on Mechatronics, Robotics and Automation*, 2022: 74-78.

[11] M. L. Strydom, A. Banach, J. Roberts, R. Crawford and A. T. Jaiprakash, Kinematic Model of the Human Leg Using DH Parameters, in *IEEE Access*, vol. 8, pp. 191737-191750, 2020.

[12] S. Pan, S. Guan and X. Li, Research on the Design and Control Scheme of Engineering Excavator Robot, in *Proceedings of 35th Chinese Control and Decision Conference*, 2023: 4948-4952.

[13] N. Xu, X. Peng, L. Peng, Z. Hou and M. Gui, Modeling and Kinematics Analysis of a Novel 5-DOF Upper Limb Exoskeleton Rehabilitation Robot,in *Proceedings of 39th Chinese Control Conference*, 2020: 1052-1057.

Proceedings of the 3rd Conference on Fully Actuated System Theory and Applications
May 10-12, 2024, Shenzhen, China

Identification Algorithm of the Industrial Dryers Based on Subspace

Ning Ding, Jianwei Ma*, Jiangrong Li
Yan'an University, Yan'an716000, China
E-mail: majianwei@yau.edu.cn

Abstract: In order to improve the product quality and reduce energy consumption, various modeling and control methods of the Industrial Dryers in drying process have been concepted according to complexity and nonlinearity. These methods usually dedicate to optimizing drying parameters, temperature controlling, system model identification, and neural network predictive control. This paper suggests a subspace identification method of Industrial Dryers system, which is based on the MOESP algorithm and the TN-MOESP algorithm. The paper conducted simulation experiments on two identification algorithms and tested the algorithms on an industrial drying machine dataset. Simulation results show that the MOESP algorithm is more accuracy, while the TN-MOESP algorithm has a faster identification speed.

Keywords: Industrial Dryer; Subspace Identification; MOESP Algorithm

1 Introduction

Industrial Dryers are important equipment, which is widely used in various fields such as food processing, metallurgy, chemical industry, and textile. However, how to reduce losses during the drying process and control the drying process remains a topic so that contemporary scholars need to explore further [1]. AS Mujumdar et al. proposed a method for determining the optimal drying parameters using two models. One model is used to model the moisture migration during isothermal drying, while the other model is applied to the process of temperature increase in roof tiles. By simultaneously using these two models, the drying process can be comprehensively characterized [2]. Abdenouri N et al. introduced a study of the thermal behavior and temperature control methods within a mixed solar drying machine. They established a state-space model based on the nonlinear least squares method and developed a fuzzy logic controller (FLC). Through simulation verification compared with traditional PI temperature controllers, the fuzzy logic controller exhibited good performance [3]. Platon R et al. applied a subtraction clustering algorithm to identify the target system model. They represented the industrial drying process as a first-order Sugeno system model with three inputs and one output, and evaluated its performance by comparing parameter searches using different step lengths [4]. Cubillos F A et al. explored the use of the Grey-Box Neural Model (GNM) in a Nonlinear Model Predictive Control (NMPC) scheme for a direct rotary dyeing machine. By combining the mass and energy balances of the rotary dryer with a feedforward neural network (FFNN), they constructed a neural network to estimate the drying rate and volumetric heat transfer coefficient. The results demonstrated that the GNM method accurately captured the dynamic behavior of the rotary dryer [5]. Abdel-Jabbar N M et al. presented a dynamic model of a fluidized bed dryer based on fundamental process principles. They introduced step changes in manipulated and load variables into a rigorous model and utilized the resulting data for offline model identification. Simulation results indicated that the model effectively reflected the dynamic characteristics of the fluidized bed drying process [6]. Berrada M et al. proposed a state variable model for the drying section of a paper machine. Based on the mass and energy balances of steam, paper, cylindrical heater walls, and moisture, this paper established six nonlinear partial differential equations. Through this model, operational parameters required to achieve the desired steam temperature and achieve effective drying can be determined [7]. Shahhosseini S et al. proposed an adaptive model for describing the dynamic behavior of a rotary sugar drying process by integrating online variable estimation and parameter identification techniques with physical laws. This model uses online measurements to estimate heat and mass transfer rates, thus accurately tracking the dynamic behavior of the rotary drying process [8]. These studies provide valuable references for the optimization design and control of industrial dryers, contributing to improving product quality, reducing energy consumption, and promoting the sustainable development of industrial production.

The main objective of this paper is to model and control the industrial drying process using subspace algorithms. This algorithm utilizes input-output data to identify the system model, moreover need not to understand the inherent relationships and logical connections between parameters, thus more easy to realize [9].

2 Problem Statement

The drying process of Industrial Dryers is characterized by complexity and nonlinearity, making the control of the drying process difficult. It is necessary to choose appropriate identification methods and techniques to obtain an accurate model that supports the optimization design and control of the system.

This paper chooses to extend the discrete-time state-space model and expands the general state-space model into a nonlinear state-space model:

$$x_{t+1} = f\left(x_t, u_t\right), \tag{1}$$

$$y_t = g\left(x_t, u_t\right), \tag{2}$$

Where $f(\bullet), g(\bullet)$ is a nonlinear vector function. For nonlinear functions, this paper chooses to represent them using multivariate polynomials. The following polynomial state-space model was proposed in reference [10]:

$$x_{t+1} = Ax_t + f\left(u_t\right), \tag{3}$$

$$y_t = Cx_t + g\left(u_t\right). \tag{4}$$

In which, $f(\bullet), g(\bullet)$ are multivariate polynomials of

total degree *d*. As this model satisfies input-output equations, any subspace method can be adopted to identify system parameters. In this paper, the MOESP algorithm and the tensor-network-based MOESP algorithm are employed for the identification of the Industrial Dryers [11].

3 Algorithm Introduction

3.1 MOESP Algorithm

Consider the following discrete-time state-space model:

$$x(k+1) = Ax(k) + Bu(k) + w(k), \tag{5}$$

$$y(k) = Cx(k) + Du(k) + v(k), \tag{6}$$

Assuming the current time is *k*, the past time is denoted as *p*, and the future time is denoted as *f*. By repeatedly applying the above equation, the following equation can be obtained:

$$y_f = \Gamma_f x(k) + H_f u_f + G_f w_f + v_f, \tag{7}$$

The vector u_f, w_f, v_f, y_f has the same stacking method. For the past time *p*, the input-output equation of the past time can be obtained in the same way:

$$y_p = \Gamma_p x(k-p) + H_p u_p + G_p w_p + v_p, \tag{8}$$

Other vectors and matrices are defined similarly to before. Then the past and future output equations are written in the Hankel matrix form, giving the following expression:

$$\begin{aligned} Y_f &= \Gamma_f X_f + H_f U_f + G_f W_f + V_f, \\ Y_p &= \Gamma_p X_p + H_p U_p + G_p W_p + V_p. \end{aligned} \tag{9}$$

For nonlinear extended state-space models, modifications need to be made to the traditional MOESP algorithm to adapt to the extended model. The following steps are the specific implementation process of the modified MOESP algorithm [11]:

Step1: Construct input-output Hankel matrices with a given number of blocks *k*.

Step2: Perform an LQ decomposition on the Hankel matrices.

$$\begin{pmatrix} U \\ Y \end{pmatrix} = \begin{pmatrix} L_{11} & 0 \\ L_{21} & L_{22} \end{pmatrix} \begin{pmatrix} Q_1^T \\ Q_2^T \end{pmatrix}$$

Step3: Perform SVD decomposition on L_{22}:

$$L_{22} = \begin{pmatrix} U_1 & U_2 \end{pmatrix} \begin{pmatrix} S_1 & 0 \\ 0 & 0 \end{pmatrix} \begin{pmatrix} V_1^T \\ V_2^T \end{pmatrix}$$

Step4: Determine the order of the system $n = rank\left(L_{22}\right)$

Step5: Construct the extended observability matrix $O_k = U_1 S_1^{1/2}$ and determine the value of $C = O_k\left(1:p,:\right)$.

Step6: Calculate *A* from $O_k\left(1:kp-p,:\right)A = O\left(p+1:kp,:\right)$.

Step7: Divide $U_2^T := \begin{pmatrix} L_1 & \cdots & L_k \end{pmatrix}$ into *k* blocks of size $\left(kp-n\right)\times p$.

Step8: Divide $U_2^T L_{21} L_{11}^{-1} := \begin{pmatrix} M_1 & \cdots & M_k \end{pmatrix}$ into *k* blocks of size $\left(kp-n\right)\times m^d$.

Step9: Definition $\overline{L}_i := \begin{pmatrix} L_i & \cdots & L_k \end{pmatrix}, i = 2,\ldots k$

Step10: Calculate the matrices *B* and *D* from the following equation:

$$\begin{pmatrix} L_1 & \overline{L}_2 O_{k-1} \\ L_2 & \overline{L}_3 O_{k-2} \\ \vdots & \vdots \\ L_{k-1} & \overline{L}_k O_1 \\ L_k & 0 \end{pmatrix} \begin{pmatrix} D \\ B \end{pmatrix} = \begin{pmatrix} M_1 \\ M_2 \\ \vdots \\ M_{k-1} \\ M_k \end{pmatrix} \tag{10}$$

3.2 TN-MOESP Algorithm

The difference between tensor network subspace identification and traditional subspace identification lies in the representation of the input part of the polynomial state-space model using tensor networks. The specific form is as follows:

$$x_{t+1} = Ax_t + \mathcal{B}u_t^d, \tag{11}$$

$$y_t = Cx_t + \mathcal{D}u_t^d, \tag{12}$$

Where $\mathcal{B}, \mathcal{D}$ are $d+1$-way tensors with dimensions $n\times m\times m\cdots\times m$ and $p\times m\times m\cdots\times m$. Another form of tensor representation is as follows:

$$x_{t+1} = Ax_t + Bu_t\ , \tag{13}$$

$$y_t = Cx_t + Du_t\ , \tag{14}$$

Where *B* and *D* are matrices reshaped from tensor $\mathcal{B}$, $\mathcal{D}$ into dimensions of $n\times m^d$ and $p\times m^d$, respectively, and u_t is defined as the *d*-th Kronecker product:

$$u_t = \overbrace{u_t \otimes u_t \otimes \cdots \otimes u_t}^{d} \in R^{m^d} \tag{15}$$

Similar to traditional subspace identification, the following tensor-based input-output equation can be obtained through iterative recursion:

$$Y_{0|k-1} = O_k X + P_k U_{0|k-1}, \tag{16}$$

Where *X* is the state vector, O_k is the extended observability matrix, P_k is the Toeplitz matrix, $Y_{0|k-1}$ and $U_{0|k-1}$ are block Hankel matrices. The difference between the TN-MOESP algorithm and the MOESP algorithm lies in the representation of the polynomial input using tensor networks. Therefore, the implementation process of the two algorithms is similar. Thus, the TN-MOESP (Tensor Network MOESP) algorithm based on tensor networks is implemented as follows, and detailed implementation procedures can be found in reference [11].

3.2.1 Construct a tensor network for matrix $U_{0|k-1}$

Matrix $U_{0|k-1}$ has dimensions $km^d \times N$, so it needs to be stored as a tensor network. The main idea behind constructing a tensor network is reshaping:

$$U := reshape(U_{0|k-1}, [m^d, kN]).$$

The reshaped matrix *U* consists of *kN* columns, each of which is a repeated left Kronecker product. Perform SVD decomposition on the reshaped matrix, where the resulting *U* is reshaped as $\mathcal{U}^{(i)}$ and *SV* is reshaped as $\mathcal{U}^{(i+1)}$, with

i ranging from 1 to *d*-1.The tensor network is constructed starting from $\mathcal{U}^{(1)}$ and building up to $\mathcal{U}^{(d)}$ .The matrix $U_{0|k-1}$ is ultimately constructed into a tensor network through the following reshaping process:

$$reshape(\mathcal{U}^{(d)},[r_d, mk, N, 1])$$

3.2.2 Compute L_{11}, L_{21}, L_{22}

Since the LQ decomposition in the MOESP algorithm cannot be computed in tensor network form, a more efficient SVD is used to decompose $U_{0|k-1}$:

$$U_{0|k-1} = WTQ^T = \begin{pmatrix} W_1 & W_2 \end{pmatrix} \begin{pmatrix} T_1 & 0 \\ 0 & 0 \end{pmatrix} \begin{pmatrix} Q_1^T \\ Q_2^T \end{pmatrix}, \quad (17)$$

Where matrices $W \in km^d \times N$, *T*, *Q* are respectively $N \times N$ diagonal and orthogonal matrices. Let $\mathcal{U}^{(1)} \cdots \mathcal{U}^{(d)}$ represent the tensor network of $U_{0|k-1}$. Tensor network $U_{0|k-1}$ is shaped into a matrix , then SVD decomposition is performed. The orthogonal factor W from equation (17) is shaped into the tensor network $\mathcal{W}^{(1)} \cdots \mathcal{W}^{(d)}$. The orthogonal factor W is calcuated in tensor network form , and finally, the required matrix factor L_{11}, L_{21}, L_{22} can be computed as:

$$L_{11} = W_1 T_1 \in R^{km^d \times r}, \quad (18)$$

$$L_{21} = Y_{0|k-1} Q_1 \in R^{kp \times r}, \quad (19)$$

$$L_{22} = Y_{0|k-1} Q_2 \in R^{kp \times kp}, \quad (20)$$

The tensor network of L_{11} can be easily found, as the first *d*-1 tensors are identical to the tensors of *W*, while the *d*-th tensor of L_{11} is the same as $\mathcal{W}^{(d)} \times_3 (T_1 \quad 0)^T$.

3.2.3 Compute matrices *A* and *C*

Once the matrix factor L_{11}, L_{21}, L_{22} is computed, the traditional MOESP algorithm can be used to find matrices *A* and *C*. Matrix L_{22} reveals the system order *n* and the extended observability matrix O_k as $U_1 S_1^{1/2}$, from which the first *p* rows are taken as the matrix *C*. Using the shift property of the extended observability matrix, matrix *A* can be obtained.

3.2.4 Compute $U_2^T L_{21} L_{11}^{-1}$

In the MOESP algorithm, it is necessary to compute the matrix $U_2^T L_{21} L_{11}^{-1}$, which represents the tensor network form of the left inverse of L_{11}. From equation (18), we know that $L_{11}^{-1} = T_1^{-1} W_1^T$ exists and $W_1^T W_1 = I_r$, where W_1 's transpose is obtained by permuting the second and third dimensions of each tensor in the network. Therefore, the tensor network of L_{11}^{-1} is obtained by replacing each tensor $\mathcal{W}^{(i)}$ with $\tilde{\mathcal{W}}^{(i)}$ and computing $\tilde{\mathcal{W}}^{(d)} \times_2 (T_1^{-1} \quad 0)$, where T_1^{-1} is obtained by reversing the diagonal elements. The tensor network of L_{11}^{-1} is then multiplied with $U_2^T L_{21}$ on the *d*-th tensor. In fact, the multiplication with T_1^{-1} can be combined with $U_2^T L_{21}$. This leads to the following theorem.

Theorem 1: Let $\tilde{\mathcal{W}}^{(i)} (i = 1, \ldots, d)$ be the tensor obtained by rearranging the two-dimensional and three-dimensional indices of the tensor $\mathcal{W}^{(i)} (i = 1, \ldots, d)$ after SVD decomposition. Then, the tensor network $\mathcal{M}^{(1)}, \ldots, \mathcal{M}^{(d)}$ corresponding to the matrix $U_2^T L_{21} L_{11}^{-1}$ is:

$$\mathcal{M}^{(i)} := \tilde{\mathcal{W}}^{(i)} \in R^{r_i \times 1 \times m \times r_{i+1} (i=1,\ldots,d-1)},$$

$$\mathcal{M}^{(d)} := \tilde{\mathcal{W}}^{(d)} \times_2 U_2^T L_{21} (T_1^{-1} \quad 0)^T \in R^{r_d \times (kp-n) \times km \times 1},$$

The matrix $U_2^T L_{21} L_{11}^{-1}$ is reshaped and divided into *k* blocks of size $(kp-n) \times m^d$ as follows:

$$reshape(\mathcal{M}^{(d)},[r_d, (kp-n), m, k, 1]),$$

$$permute(\mathcal{M}^{(d)},[1, 2, 4, 3, 5]),$$

$$reshape(\mathcal{M}^{(d)},[r_d, (kp-n)k, m, 1]).$$

3.2.5 Compute the tensor networks of *B*,*D*

To estimate the matrices *B* and *D*, it is necessary to solve the linear system (10). In the process, we need to compute the pseudo-inverse of a $k(kp-n) \times (p+n)$ matrix. If we denote this matrix pseudo-inverse as L^{-1} , then combining *D* and *B* yields:

$$\begin{pmatrix} D \\ B \end{pmatrix} = L^{-1} \begin{pmatrix} M_1 \\ M_2 \\ \\ M_{k-1} \\ M_k \end{pmatrix} \quad (21)$$

In the equation, *M* represents the partitioning of $U_2^T L_{21} L_{11}^{-1}$ into *k* blocks of size $(kp-n) \times m^d$. The tensor network representation of partitioning the $U_2^T L_{21} L_{11}^{-1}$ matrix has been obtained in the previous section. Therefore, contracting $\mathcal{M}^{(d)} \times_2 L^{-1}$ yields the tensor network representing the connection between *D* and *B*.

The above algorithm does not return separate tensor networks for *B* and *D*, which is not strictly required for simulating the model. In fact, using the connection of *B* and *D* within a single tensor network simplifies the simulation. There is no need to form repeated Kronecker products u_t , and only to contract u_t with each tensor in the network.

4 Simulation Verification

In this section, the source and purpose of each dataset will be introduced in turn, and the identification performance of the algorithm for the Industrial Dryers system will be validated by using two different datasets.

Dataset 1: This data set uses a known linear system state-space model, with random white noise as input, to generate 1000 sets of simulated input-output data. Its main purpose is to verify the performance and accuracy of the algorithm. The system matrix A, B, C, D of the state-space model used to generate this data set are:

$$A = \begin{bmatrix} 0.2128 & 0.1360 & 0.1979 & -0.0836 \\ 0.1808 & 0.4420 & -0.3279 & 0.2344 \\ -0.5182 & 0.1728 & -0.5448 & -0.3083 \\ 0.2252 & -0.0541 & -0.4679 & 0.8290 \end{bmatrix}$$

$$B = \begin{bmatrix} -0.0101 & 0.0317 & -0.9347 \\ -0.0600 & 0.5621 & 0.1657 \\ -0.3310 & -0.3712 & -0.5846 \\ -0.2655 & 0.4255 & 0.2204 \end{bmatrix}$$

$$C = \begin{bmatrix} 0.6557 & -0.2502 & -0.5188 & -0.1229 \\ 0.6532 & -0.1583 & -0.0550 & -0.2497 \end{bmatrix}$$

$$D = \begin{bmatrix} -0.4326 & 0.1253 & -1.1465 \\ -1.6656 & 0.2877 & 1.1909 \end{bmatrix}$$

Dataset 2: This dataset contains data from Industrial Dryers and has a size of 867*7. The first column represents the index, columns 2-4 represent the inputs, and columns 5-7 represent the outputs. The purpose of this dataset is to verify the identification performance and accuracy of the subspace identification algorithm for the Industrial Dryers system. This dataset is sourced from the STADIUS's Identification Database and can be downloaded from the following website: https://homes.esat.kuleuven.be/~smc/daisy/daisydata.html

4.1 Stability Analysis

Before conducting system simulation, it is important to analyze the stability of the system. The poles of the system for Dataset 1 and Dataset 2 separately are analyzed to understand the stability of the system.

From Figure 1 and Figure 2, it can be observed that both Data Set 1 and Data Set 2 have stable systems. However, the system identified from Data Set 2 in Figure 2 has more poles and they are closer to the unit circle. This is because the dynamic characteristics of the industrial dryer system are more complex, with multiple factors affecting system stability. In this study, a polynomial input model was chosen. As the polynomial degree (d) increases, more terms are included in the polynomial, providing more degrees of freedom to fit the dynamic characteristics of the real system, thus introducing more poles.

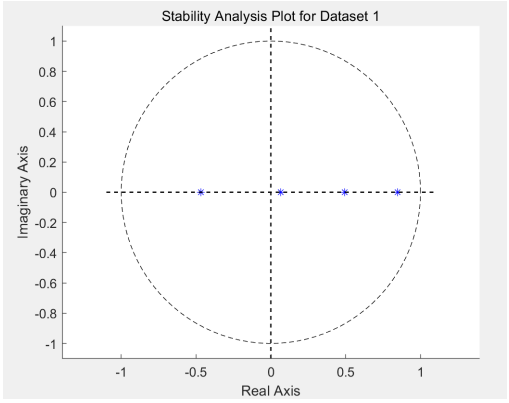

Fig. 1 :System Stability Plot of Dataset 1

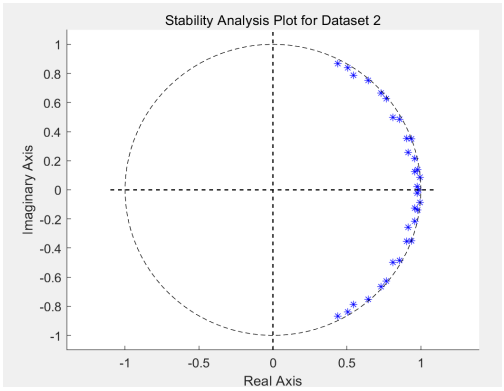

Fig. 2 :System Stability Plot of Dataset 2

4.2 System Simulation Analysis

Firstly, two algorithms were applied to identify dataset 1, and two indicators, running time and relative error were used to evaluate the performance and accuracy of the algorithms. The specific results are as follows:

Table 1: Performance comparison of the two algorithms based on dataset 1

d	MOESP		TN-MOESP	
	Running Time(s)	Relative Error	Running Time(s)	Relative Error
2	0.217486	2.8105e-14	0.165534	4.8409e-14
3	0.397300	4.5932e-14	0.232924	1.8994e-13
4	0.832095	6.7944e-14	0.315318	9.8961e-14
5	1.928801	1.4565e-13	0.349356	3.2373e-13
6	6.699844	5.2727e-13	0.401874	4.7239e-13
7	85.227359	6.4392e-12	0.497911	1.8134e-12

According to the results in the table, it can be observed that both algorithms can identify the system model with extremely small errors, indicating good data fitting performance and the ability to simulate the behavior of the system. However, there is a significant difference in running time between them. When the maximum nonlinearity order is set to d=7, the difference in running time is 171 times.

Next, two algorithms are used to simulate and verify the operation of Industrial Dryers. Before the simulation verification, it is necessary to analyze the outliers in the

Industrial Dryers data using the box plot method.

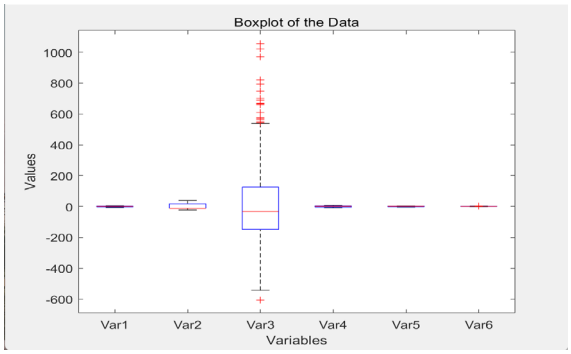

Fig. 3 :Boxplot of dataset 2

The box plot shows that the outliers mainly appear in the third variable. However, since the third variable is an input variable, retaining the outliers not only doesn't have negative impact on the system's performance and expected results but may also have a positive impact. These outliers are important for understanding the system or data distribution and keeping them can provide a more comprehensive data perspective. Therefore, it is reasonable not to perform outlier processing based on these considerations , and the data containing outliers continues to be used for analysis and research.

Next, dataset 2 is identified. Average relative error, runtime, and matching degree as evaluation metrics are used to assess the simulation of the drying process by two algorithms. The identification results are as follows:

Table 2 : Performance comparison of the two algorithms based on dataset 2

d	MOESP			TN-MOESP		
	Running Time(s)	MRE	Matching Degree	Running Time(s)	MRE	Matching Degree
1	0.1871	7.4654	0.88541			
2	0.2258	7.7029	0.85107	0.1418	7.7029	0.85107
3	0.3176	10.7943	0.39125	0.1375	10.7943	0.39125
4	0.6007	15.6412	0.05821	0.1791	22.7148	0.47733
5						
6	3.7978	3.4959	0.61282	0.2162	131.5653	0.3549
7	21.4062	10.5463	0.21013	0.2819	136.4194	0.11657
8	73.7989	2.0274	0.36121			

The blank spaces in the table are due to the inability to find a stable A matrix during identification, making the algorithm unfeasible. When d=1, the MOESP algorithm achieves the highest matching degree in simulating output, and when d=2, both algorithms reach a matching degree of 85% in simulating output. The figure below shows the simulation output plots of the two algorithms for d=1 and d=2, indicating a better match between the simulated output of the first two values of the system and the actual output. As the maximum non-linear order d increases, the simulation output of both algorithms deteriorates, but the TN-MOESP algorithm demonstrates stronger performance in identification speed.

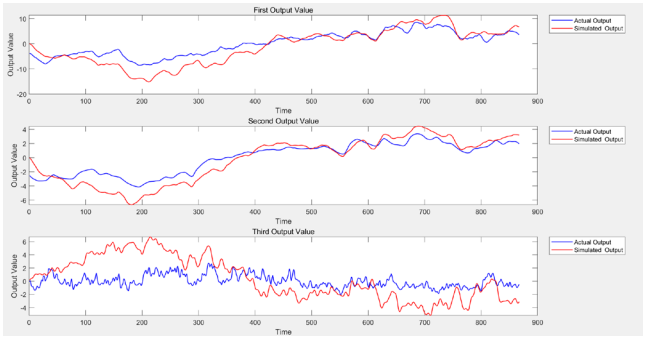

Fig. 4 :Simulated Output Plot based on MOESP Algorithm with d=1

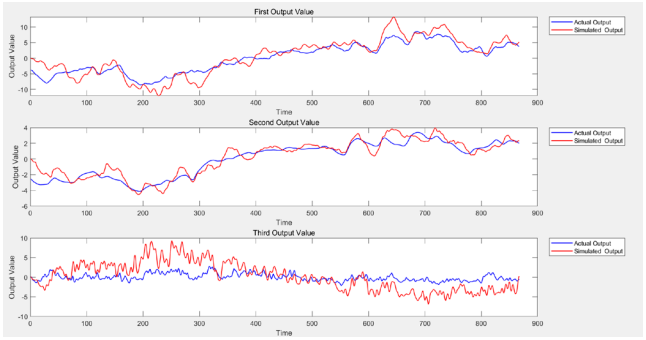

Fig. 5 :Simulated Output Plot based on MOESP Algorithm with d=2

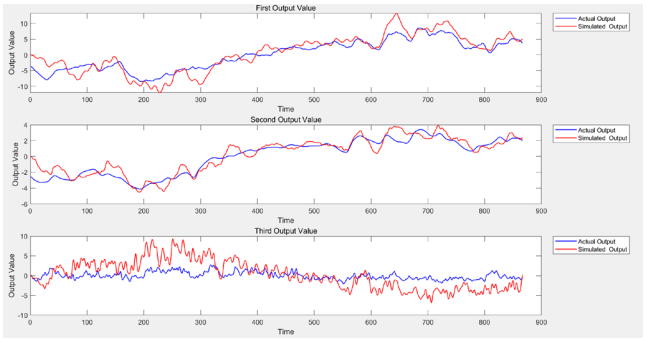

Fig. 6 :Simulated Output Plot based on TN-MOESP Algorithm with d=2

5 Conclusion

In view of the complexity and nonlinear characteristics of the drying process of Industrial Dryers and the difficulty of accurate control, this paper presents the simulation and control of Industrial Dryers based on subspace identification algorithm. Simulation results show that both MOESP algorithm and TN-MOESP algorithm have good performance and accuracy, and can simulate the behavior of Industrial Dryer system well. The matching degree and average relative error of the system are also within the acceptable range. MOESP algorithm has the highest matching degree, while TN-MOESP algorithm shows a faster speed in identification. The results provide strong support for improving the efficiency and accuracy of industrial production, and provide important reference significance for the control of complex systems.

References

[1] Mujumdar A S, Zhonghua W. Thermal drying technologies—Cost-effective innovation aided by mathematical modeling approach[J]. Drying technology, 2007, 26(1): 145-153.

[2] Vasić M, Radojević Z. Characterization of drying behavior and modeling of industrial drying process[C]//IOP Conference Series: Materials Science and Engineering. IOP Publishing, 2020, 916(1): 012124.
[3] Abdenouri N, Zoukit A, Salhi I, et al. Model identification and fuzzy control of the temperature inside an active hybrid solar indirect dryer[J]. Solar energy, 2022, 231: 328-342.
[4] Platon R, Amazouz M. Modeling of a drying process using subtractive clustering based system identification[C]//Proceedings Joint 9th IFSA World Congress and 20th NAFIPS International Conference (Cat. No. 01TH8569). IEEE, 2001: 2994-2999.
[5] Cubillos F A, Vyhmeister E, Acuna G, et al. Rotary dryer control using a grey-box neural model scheme[J]. Drying Technology, 2011, 29(15): 1820-1827.
[6] Abdel-Jabbar N M, Jumah R Y, Ali M Q A H. Multivariable process identification and control of continuous fluidized bed dryers[J]. Drying Technology, 2002, 20(7): 1347-1377.
[7] Berrada M, Tarasiewicz S, Elkadiri M E, et al. A state model for the drying paper in the paper product industry[J]. IEEE Transactions on Industrial Electronics, 1997, 44(4): 579-586.
[8] Shahhosseini S, Cameron I T, Wang F Y. A dynamic model with on-line identification for rotary sugar drying processes[J]. Drying Technology, 2001, 19(9): 2103-2129.
[9] Li H, Cai Y. N4SID based subspace identification method for normal temperature continuous transonic wind tunnel system[C]//2016 Chinese Control and Decision Conference (CCDC). IEEE, 2016: 1394-1398.
[10] J. Paduart, L. Lauwers, J. Swevers, K. Smolders, J. Schoukens, and R. Pintelon. Identification of nonlinear systems using Polynomial Nonlinear State Space models. Automatica, 46(4):647 – 656, 2010.
[11] Batselier K, Ko C Y, Wong N. Tensor network subspace identification of polynomial state space models[J]. Automatica, 2018, 95: 187-196.

Proceedings of the 3rd Conference on Fully Actuated System Theory and Applications
May 10-12, 2024, Shenzhen, China

Model Predictive Path Integral Control of a Temperature Profile in Tubular Chemical Reactor with Recycle

Ling Ai[1], Yingwei Chen[1], Yang Xu[2], Xueqin Chen[3], Kok Lay Teo[4]

1. Department of Automation, Harbin University of Science and Technology, Harbin 150080, P. R. China
E-mail: ailing@hrbust.edu.cn

2. Navigation College, Dalian Maritime University, Dalian 510330, P. R. China
E-mail: xuyang_dlmu@163.com

3. Research Center of Satellite Technology, Harbin Institute of Technology, Harbin 150010, P. R. China
E-mail: xueqin_chen@163.com

4. School of Mathematical Sciences, Sunway University, Bandar Sunway, 47500 Selangor Darul Ehsan, Malaysia
E-mail: K.L.Teo@curtin.edu.au

Abstract: Several non-isothermal dispersion reactions accounting for energy and mass transport in a recycle stream are carried out in tubular reactor with recycle. These processes often have spatiotemporal distribution, stochastic disturbances, and recycle loop dead-time characteristics, described by nonlinear parabolic partial differential equations (PDEs). This paper is devoted to the design of a model predictive path integral (MPPI) controller to stabilize the axial temperature profile control in tubular reactor. An array of reduced-order approximations by virtue of Karhunen-Loève decomposition (KLD), and then a nonlinear model suitable for control purposes is developed. Subsequently, the reduction model is embedded into the design of MPPI controller. Finally, the simulation results demonstrate that the MPPI controller presented a good behavior to eliminate the oscillations of the temperature profile in tubular reactor.

Key Words: Model Predictive Path Integral Control, Temperature Control, Model Reduction, Tubular Reactor with Recycle, Hopf Bifurcation Phenomenon

1 Introduction

Tubular reactors with recycle are extensively employed in a mass of chemical production process, such as fermentation process, hydrogenation process, and wastewater treatment [1]. The diverse product requirements bring the heterogeneous reaction mechanisms. The mathematical modeling of the transport-reaction processes, are commonly described by a calss of nonlinear partial differential equations (PDEs). The accurate model parameters are difficult to be derived via the first principle mechanism [2]. The inlet temperature and concentration disturbance caused by the recycle steams bring additional uncertainty and randomness [3–5]. The investigation of tubular reactors with recycle is particularly practical and meaningful and the correlative modeling and control techniques have been developed by leaps and bounds.

Model predictive control (MPC) has the ability to explicitly handle constraints and uncertainties. This intrinsic feature is especially beneficial for managing complicated chemical processes [6–8]. The model predictive output controller design with a discrete Luenberger observer is proposed to achieve optimal closed-loop system stabilization of a non-isothermal axial dispersion tubular reactor [9] and a coupled continuous stirred-tank reactor (CSTR) example is discussed later [10]. Furthermore, the spatiotemporal variables containing system characteristics are collected by sensors installed in the axial direction of the reactor. A batch of data-driven MPC algorithms have been studied through the analysis of spatiotemporal data-streams [11, 12]. Aim at the stabilisation issue of the oscillatory behaviour of a tubular reactor with recycle, a framework for linear MPC algorithm based on the Proper Orthogonal Decomposition (POD) and Trajectory Piecewise-Linear (TPWL) technique [13] and its adaptive linearization version [14] is proposed. Afterwards, they further developed a nonlinear MPC (NMPC) with a data-driven model reduction-based approach by POD and artificial neural networks (ANNs) techniques [15]. A robust multi-model NMPC for nonlinear convection-diffusion-reaction systems is presented, which is applied to the reactant concentration control issue of a tubular reactor with recycle[16].

In recent years, the innovative nonlinear identification techniques emerge in an endless stream, and some of which have been applied to the modeling issue of tubular reactors [17, 18]. Extreme learning machines (ELM) [23], one of the important procedures, has been employed for modeling nonlinear spatiotemporal distribution systems (SDSs) with the potential to be applied in the tubular reactors [19–21]. Besides, there have been reports of the design of NMPC with the use of ELM [22].

In this paper, a novel Model Predictive Path Integral (MPPI) controller is presented to regulate the temperature profile in a non-isothermal tubular reactor with recycle. The exothermic diffusion reaction described by a parabolic PDE is considered. Under the influence of recycle stream, the open-loop system may cause unstable oscillations, which are called hopf bifurcation phenomenon. The control objective is to stabilize the temperature profile to achieve optimal production output. The reduction model via Karhunen-Loève decomposition (KLD) and ELM techniques is constructed to meet the requirement of the control. The Path Integral Optimal Control (PIOC) is embedded to solve the nonlinear optimal problem.

In the following paper, the tubular reactor with recycle together with its dynamical models, including the nonlinear parabolic PDEs model is briefly described in section 2. Sec-

This work is supported by National Natural Science Foundation (NNSF) of China under Grant 61806060.

tion 3 is devoted to develop a MPPI controller to solve the temperature control problem, including providing KL-ELM based model reduction. In Section 4, simulation studies have been performed to reveal the controller performances. The conclusions are presented in Section 5.

2 Tubular reactor with recycle

The tubular reactors are widely used in continuous large-scale chemical processes, usually composed of several slender series or parallel pipes, resulting in axial lengths far greater than radial lengths [4]. A tubular reactor considered in this article is shown in Fig. 1. A first-order irreversible exothermic reaction of the form A $\rightarrow$ B, the reactant A conducts an exothermic reaction to generate product B. The surplus reactant A is separated, and then fed back to the inlet. A co-current cooling jacket that covers the exterior of the tubular reactor removes the reaction heat.

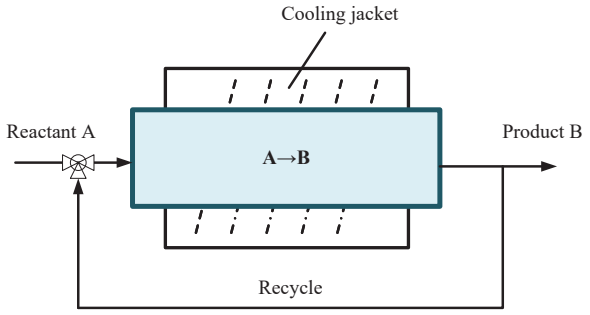

Fig. 1: The tubular reactor with recycle.

The principles of mass and energy conservation can be used to create the reaction process model, the normalization dynamic model described by partial differential equations (PDEs) is expressed as follows.

$$\begin{aligned}\frac{\partial C}{\partial t} &= \frac{1}{P_{eC}}\frac{\partial^2 C}{\partial x^2} - \frac{\partial C}{\partial x} - B_C C exp\left(\frac{\gamma T}{1+T}\right)\\ \frac{\partial T}{\partial t} &= \frac{1}{P_{eT}}\frac{\partial^2 T}{\partial x^2} - \frac{\partial T}{\partial x} - B_T B_C C exp\left(\frac{\gamma T}{1+T}\right)\\ &\quad + \beta_T\left(T_c - T\right)\end{aligned} \tag{1}$$

with the Danckwerts boundary conditions:

$$\begin{aligned}\left.\frac{\partial C}{\partial x}\right|_{x=0} &= P_{eC}\left[C(t,0) - (1-r)C_{in} - rC(t,1)\right]\\ \left.\frac{\partial C}{\partial x}\right|_{x=1} &= 0\\ \left.\frac{\partial T}{\partial x}\right|_{x=0} &= P_{eT}\left[T(t,0) - (1-r)T_{in} - rT(t,1)\right]\\ \left.\frac{\partial T}{\partial x}\right|_{x=1} &= 0\end{aligned} \tag{2}$$

where the dimensionless axial concentration $C(x,t)$ of reactor A and temperature $T(x,t)$ depend on time $t \in [0,+\infty)$ and position $x \in [0,1]$. C_{in} and T_{in} represent the input concentration and input temperature, respectively. The other process parameters of the tubular reactor are summarized in Table 1.

Table 1: The dimensionless parameters

Symbol	Definition	Value
P_{eC}	Peclet mass number	7.0
P_{eT}	Peclet energy number	7.0
B_C	pre-exponential factor	0.1
B_T	heat of reaction	2.5
γ	activation energy	10.0
β_T	heat transfer coefficient	2.0
r	recycle ratio	0.5

Assume m temperature sensors are arranged uniformly along the axial direction of the tubular reactor, and the concentration can only be measured at the inlet and outlet positions. The m zones cooling jacket T_c can be independent manipulated, let

$$T_c^k(t) = \mathbf{b}(\mathbf{x}) \cdot \mathbf{u}(\mathbf{t}) \tag{3}$$

where the control variables $\mathbf{u(t)} = [\mathbf{u_1(t)}, \ldots, \mathbf{u_m(t)}]^{\mathbf{T}}$, $\mathbf{b(x)} = [\mathbf{b_1(x)}, \ldots, \mathbf{b_m(x)}]^{\mathbf{T}}$, and $b_k(x) = H\left(x-(k-1)/m\right) - H\left(x-k/m\right)$, $H(\cdot)$ represents the standard Heaviside function.

The recirculating steam may occur Hopf bifurcation phenomenon in the open-loop system. Fig 2 displays the open-loop temperature profiles at zero inputs for a recycle ratio of $r = 0.5$. The investigation of how the recycle ratio affects the reaction process can be found in [4]. To stabilize the system, a genuine controller's design is necessary.

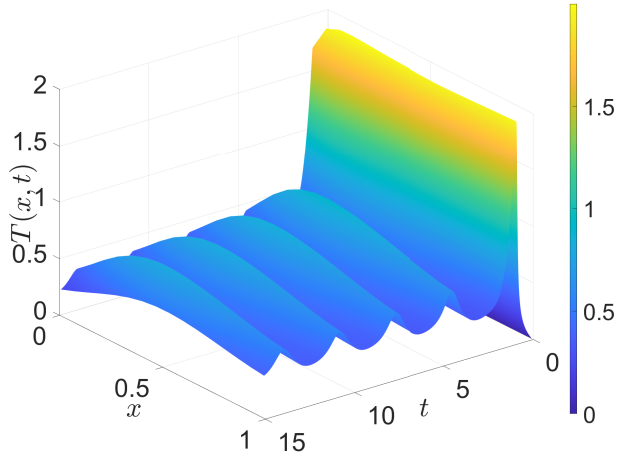

Fig. 2: The open-loop temperature profiles at zero inputs.

3 MPPI controller design

In this section, we synthesize and implement a MPPI controller on the tubular reactor with recycle. The original PDE model of the system might not feasible for direct controller development for the reason of its high dimensionality. Fortunately, model reduction via KLD can be employed to obtain the low-dimensional representation for parabolic systems. Subsequently, the nonlinear dynamics of the nominal system can be identified by ELM. On the basis of maintaining the accuracy of the original PDE model, the PIOC algorithm is utilized in conjunction with the development of a model

predictive controller to streamline the solution process of the rolling optimization problem.

3.1 Model reduction by KLD

According to the theory of spatiotemporal decomposition, the spatiotemporal variables $T(x,t)$ can be expanded into

$$T(x,t)=\sum_{i=1}^{+\infty}\phi_i(x)Y_i(t) \tag{4}$$

where $\phi_i(x)$ and $Y_i(t)$ represents the ith spatial basis function and the corresponding time-series, respectively. For parabolic systems with dominant modes, a limited class of spatial basis functions sloved by KLD are only required. Preserve the first n dominant modes that can maintain 99% energy of the system, then

$$T_n(x,t)\approx\mathbf{\Phi_n(x)Y(t)}, \tag{5}$$

$$\mathbf{Y(t)}\approx\mathbf{\Phi_n^T(x)T(x,t)}, \tag{6}$$

where $T_n(x,t)$ represents the n-order approximation of $T(x,t)$, $\mathbf{\Phi_n(x)}=[\phi_1(x),\cdots,\phi_n(x)]$ and $\mathbf{Y(t)}=[\mathbf{Y_1(t)},\cdots,\mathbf{Y_n(t)}]^\mathbf{T}$ represents the set of spatial basis function and the corresponding time-series,

3.2 KL-ELM modelling

Among numerous different nonlinear identification techniques, ELM is one type of highly efficient single hidden layer neural network (SLNN) algorithm. With the capacity to establish weights by Moore Penrose generalized inverse instead of gradient based backpropagation, ELM is capable of identifying nonlinearity more quickly. ELM algorithm conjunction with KLD can impactfully convert the high-dimensional system model into an appropriate low-dimensional control model. The reduced model by KLD can be written as

$$\mathcal{Y}_t=\mathrm{f}\left(\mathbf{X_t}\right) \tag{7}$$

where $\mathcal{Y}_t=[\hat{Y}_1(t),...,\hat{Y}_n(t)]$, $\hat{Y}_t^{(i)}=\hat{Y}_i(t)$, $\mathbf{X_t^{(i)}}=\left[\mathbf{Y_{t-1}^{(i)}},\ldots,\mathbf{Y_{t-n_y}^{(i)}},\mathbf{u_{t-1}^{(1)}},\ldots,\mathbf{u_{t-n_u}^{(1)}},\ldots,\mathbf{u_{t-1}^{(N_a)}},\ldots,\mathbf{u_{t-n_u}^{(N_a)}}\right]$.

The ith state variables $\mathbf{X_t^{(i)}}$ at time t by ELM algorithm are expressed as

$$\mathcal{Y}_t^{(i)}=\mathrm{G^T}\left(\alpha^{(\mathrm{i})}\mathrm{X_t^{(i)T}}+\eta^{(\mathrm{i})}\right)\beta^{(\mathrm{i})} \tag{8}$$

where $\alpha^{(i)}$ is the ith corresponding input weight coefficient matrix, $\eta^{(i)}$ is the ith corresponding bias term, $\beta^{(i)}$ is the ith corresponding output weight coefficient matrix, $G(\cdot)$ is the activation function.

An appropriate dataset is utilized as training data, and feature mapping and linear parameterization are applied to determine the time-seriesl's primary parameters, and finally the output of the associated time-series estimation is obtained. The network structure of ELM is fully connected, and the estimated value of each output layer node can be approximated by different model parameters. First, the hidden layer parameters α and η are randomly set, and then the hidden layer's output is obtain via mapping the training data to the feature space, let the number of the hidden layer nodes is N_h. The generated hidden layer parameters have a $[0,1]$ uniform distribution, the ith input weight coefficient matrix $\alpha^{(i)}=f_\alpha(\mathrm{rand}(N_h,n_y+N_a\times n_u))$, the ith bias term $\eta^{(i)}=f_\eta(\mathrm{rand}(N_h,1))$, where $\mathrm{rand}(p,q)$ represents $p\times q$-dimensional scalar matrix obeying by standard uniform distribution. the function f_α and f_η represent the relationship between the input weight matrix, bias vector and scalar matrix, respectively. Let the ith output of the hidden layer H^i, the random parameters $\alpha^{(i)}$ and $\eta^{(i)}$, then

$$H^{(i)}=G\left(\alpha^{(i)}\bar{X}_t^{(i)T}+\eta^(i)\right) \tag{9}$$

The purpose of linear parameterization is to solve for the output weight coefficients β. By minimizing the square of the fitting error, the optimal solution for the output weight coefficient is obtained, and the performance indicators are expressed as follows.

$$\min_\beta J=\left\|{H^{(i)}}^T\beta^{(i)}-\bar{Y}_t^{(i)}\right\|_2^2 \tag{10}$$

where $E={H^{(i)}}^T\beta^{(i)}-\bar{Y}_t^{(i)}$ represents i^{th} fitting error. According to the theory of unconditional optimization and the concept of matrix analysis, the optimal solution to the problem is obtained as

$$\hat{\beta}^{(i)}=H^{(i)*}\bar{Y}_t^{(i)} \tag{11}$$

where $H^{(i)*}$ represents the Moore Penrose generalized inverse of the ith hidden layer output. When $H^{(i)T}H^{(i)}$ is an invertible matrix, the optimal solution obtained by the projection method can be expressed as

$$\hat{\beta}^{(i)}=(H^{(i)T}H^{(i)})^{-1}H^{(i)T}\bar{Y}_t^{(i)} \tag{12}$$

3.3 Controller design

Along these lines, we will design a Model Predictive Path Integral (MPPI) controller of the nominal system. The MPPI algorithm was initially produced for an aggressive driving task [24] and recently was incorporated to the chemical process [25]. The control action is implemented on the cooling jacket to stabilize the temperature field in the tubular reactor. The stochastic optimum control challenge is to obtain the optimal control sequence $\mathbf{U}^*$ that minimizes the cost function of the expected trajectory S. Consider the following stochastic optimal control problem.

$$\min J=E(S)=E\left[\frac{1}{2}\sum_{p=1}^{N_p}\left\|\hat{\mathbf{Y}}(t+p)-\mathbf{w}(t+p)\right\|_2^2\right] \tag{13}$$

subject to

$$\hat{Y}_t^{(i)}=\mathrm{G^T}\left(\alpha^{(\mathrm{i})}\mathrm{X_t^{(i)T}}+\eta^{(\mathrm{i})}\right)\beta^{(\mathrm{i})}$$

and

$$\begin{aligned}\mathbf{u}_{\min}\le\mathbf{u}(t+c)\le\mathbf{u}_{\max}\\ \Delta\mathbf{u}_{\min}\le\Delta\mathbf{u}(t+c)\le\Delta\mathbf{u}_{\max},\quad c=1,\cdots,N_c\end{aligned}$$

where N_p and N_c represent the prediction horizon and the control horizon, $\mathbf{u}_{\min}$, $\mathbf{u}_{\max}$, and $\Delta\mathbf{u}_{\min}$, $\Delta\mathbf{u}_{\max}$ represent

the minimum and maximum values of the input and input increments, respectively. $\mathbf{U}^* = [\mathbf{u}^*(\mathbf{t}+\mathbf{1}), \cdots, \mathbf{u}^*(\mathbf{t}+\mathbf{N_c})]$. Consider a random input vector $\hat{\mathbf{u}} = \mathbf{u} + \delta\mathbf{u}$, and define

$$\delta\mathbf{u} = \frac{1}{\sqrt{\rho}} \frac{\epsilon}{\sqrt{\Delta t}} \tag{14}$$

where $\delta\mathbf{u}$ is iterative control vector, ρ is the perturbation hyperparameter, ϵ is the standard normal Gaussian random variable, Δt is the discrete time interval.

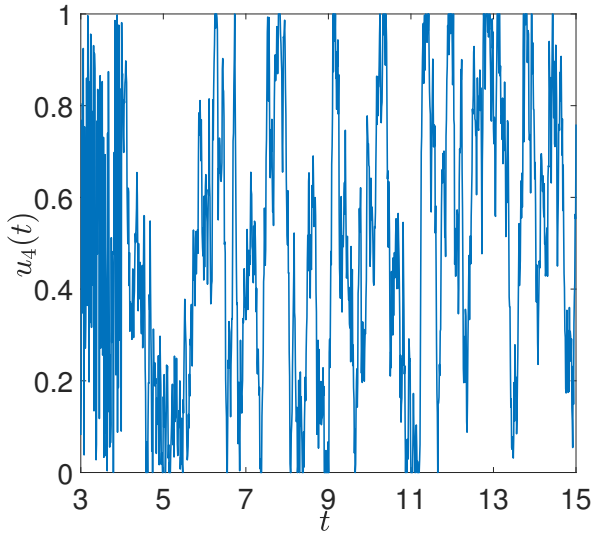

Fig. 3: The 4th random excitation input.

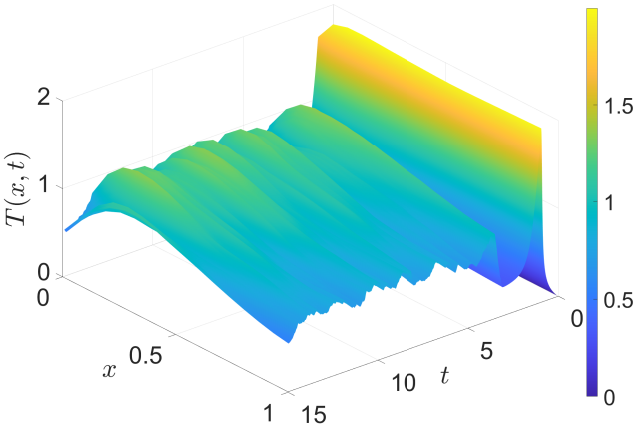

Fig. 4: The corresponding temperature profiles.

According to the importance sampling theorem [24, 25], several trajectories can be generated using forward sampling of the random diffusion process, and the operating costs of each trajectory at various time steps are evaluated to produce an ideal control rule based on Monte Carlo approximation. Therefore, the linear inverse Chapman-Kolmogorov equations derived from the stochastic Hamiltonian-Jacobi-Bellman (HJB) equations of system dynamics and cost functions can be converted into different modified trajectory cost functions via the generalized likelihood ratio between discrete diffusion processes by applying the Feynman-Kac theorem to the linear equations in conjunction with the generalized importance sampling theorem. The optimal control sequence U^* can be updated via the reward weighted mean of random variables, and then only the first input $\mathbf{u}^*(\mathbf{t}+\mathbf{1})$ is applied on the actual system. The control sequence scroll to the next time step in sequence, and enable the final control input to fill in the final part to achieve a hot start from portion that wasn't carried out in the previous round for the subsequent optimization. In light of the aforementioned theory, the iteration control sequence at time $t+p$ can be expressed as

$$\mathbf{u}^*(t+p) = \mathbf{u}(t+p) + \frac{E\left[\exp(-\frac{\tilde{S}(t+p)}{\lambda}) \cdot \delta\mathbf{u}(t+p)\right]}{E\left[\exp(-\frac{\tilde{S}(t+p)}{\lambda})\right]} \tag{15}$$

where $\tilde{S}$ represents the correction trajectory cost function, λ is the weighting coefficient. Let

$$q(t+p) = \frac{1}{2}\left\|\hat{\mathbf{y}}(t+p) - \mathbf{w}(t+p)\right\|_2^2 \tag{16}$$

where $q(t+p)$ is the operation cost function at time $t+p$, the relationship between the operation cost function $q(t+p)$ and the correction trajectory cost function $\tilde{S}$ can be expressed as

$$\tilde{S}(t+p) = \sum_{j=p}^{N_p} q(t+j) \tag{17}$$

so that

$$\mathbf{u}^*(t+p) = \mathbf{u}(t+p) + \frac{\sum_{k=1}^{K} \exp(-\frac{\tilde{S}_k(t+p)}{\lambda}) \cdot \delta\mathbf{u}_k(t+p)}{\sum_{k=1}^{K} \exp(-\frac{\tilde{S}_k(t+p)}{\lambda})} \tag{18}$$

where K is the number of random sampling, $\tilde{S}_k(t+p)$ is the Kth forward cost starting from time $t+p$, and then the control input $\mathbf{u}^*(t+1)$ is implemented to the system.

4 Simulation results

Consider 16 temperature sensors and 8 zones cooling jacket uniformly distributed along the axial direction in the tubular reactor in the simulation, and the chemical parameter values are shown in Table 1. The process data are sloved by Matlab PDE toolbox. the sampling period $\Delta t = 0.01$, and total simulation period $ts = 15$.

Three elements make up the random training incentive signal. There is no excitation signal present before $t = 3$, the excitation signal is set a random value in the interval [0,1] from $t = 3$ to 4, the excitation signal is set to meet the requirements $u_k(t+1) = u_k(t) + 0.1\tau_N, 0 \le u_k(t) \le 1$ for the remaining time, where τ_N is standard normal random number. The 4th random excitation input and the corresponding temperature profiles are shown in Fig 3 and Fig 4.

We pick the 900 temperature snapshots with the range of $[3, 12]$ as the training data-set, and other 300 temperature snapshots with the range of $[12, 15]$ as the test data-set. By adopting the first three dominant modes, the system's energy can be preserved to a maximum of 99%. The corresponding first three basis functions are shown in Fig 5.

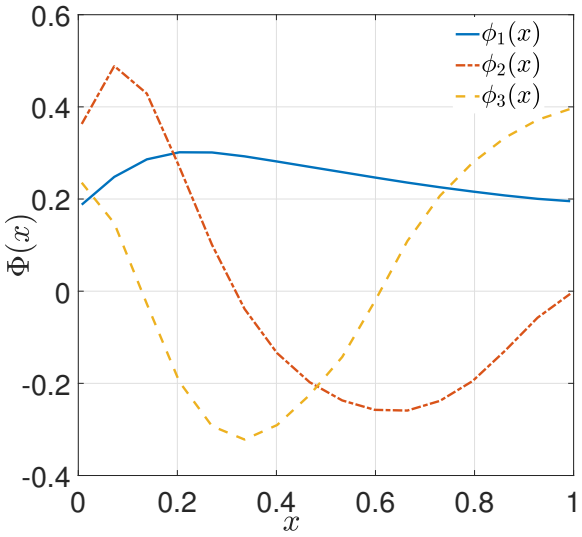

Fig. 5: The first three basis functions.

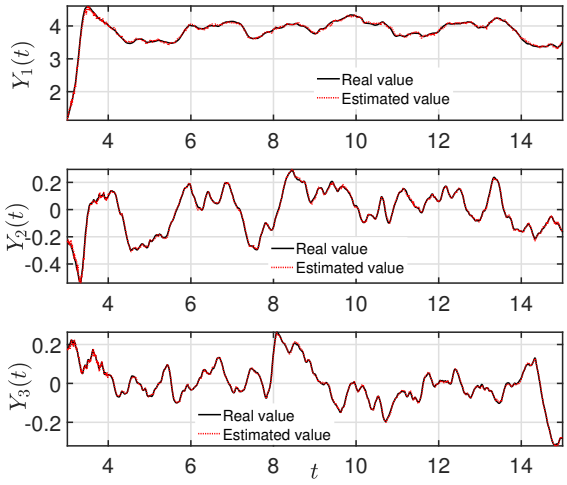

Fig. 6: The time-series of low-dimensional representation

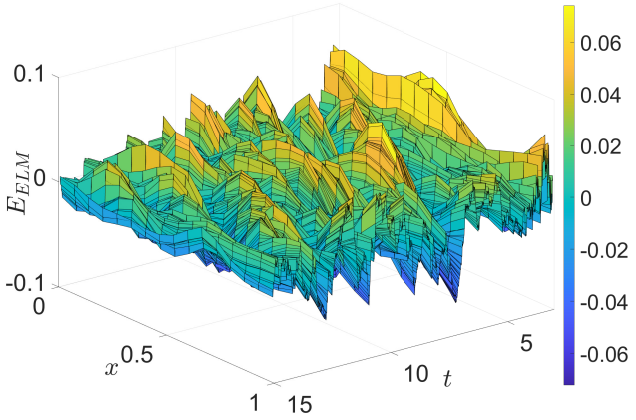

Fig. 7: The reconstruction error.

Subsequently, the corresponding low-dimensional time-series representations are identified by ELM with Sigmoid activation function. The high-dimensional temperature profiles can also be restored through inverse transformation of KLD. The time-series of low-dimensional representation and the reconstruction error are shown in Fig 6 and Fig 7.

Consider the following optimization problem

$$[\min J = \frac{1}{2}\sum_{p=1}^{N_P}\left\|\hat{T}(x,t_n+p) - T_{\text{ref}}(x,t_n+p)\right\|_2^2 \quad (19)$$

subject to

$$0 \le u_k \le 1 \quad |\Delta u_k| \le 0.1$$

Let recycle ratio $r = 0.5$, perturbation hyperparameter $1/\sqrt{\rho} = 0.15$, weighting coefficient $\lambda = 0.01$, prediction horizon $N_p = 4$, control horizon $N_c = 1$, number of sampling trajectories $N_k = 2000$. Give the temperature reference trajectory T_{ref}. Solving the aforementioned optimization problem with the proposed algroithm to obtain the U^*. The closed-loop control input and temperature profile are shown in Fig 8 and Fig 9.

From Fig 8 and Fig 9, the hopf bifurcation phenomenon has vanished, and the temperature field tends to asymptotically stabilize in $t = 5$, and converges in $t = 8$. The simulation results show that the developed MPPI controller has good control performance for the temperture control in tubular reactor with recycle.

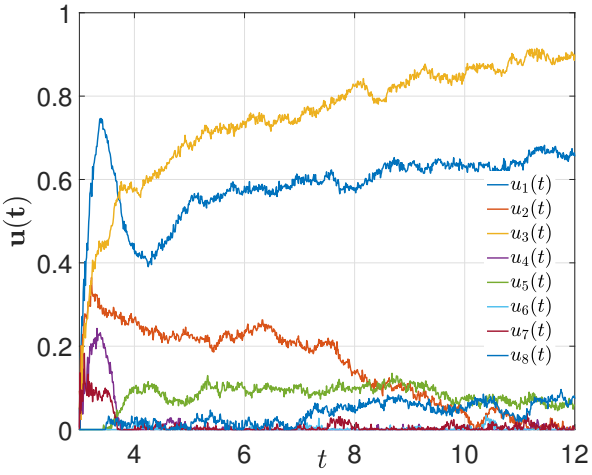

Fig. 8: The closed-loop control input.

5 Conclusions

In this paper, the results of applying Model Predictive Path Integral (MPPI) control techniques to the control of the temperature profile in tubular chemical reactor with recycle have been presented. The model reduction of state dimension via the Karhunen-Loève decomposition (KLD) and Extreme Learning Machine (ELM) technique was demonstrated to be simple and efficient. The reduced-order model is integrated into a nonlinear predictive control architecture. The simulation results indicate that the MPPI controller is able to stabilize the axial temperature profile control in tubular reactor, and eliminate the hopf bifurcation phenomenon. Meanwhile, the control constraints and disturbances can conveniently handled.

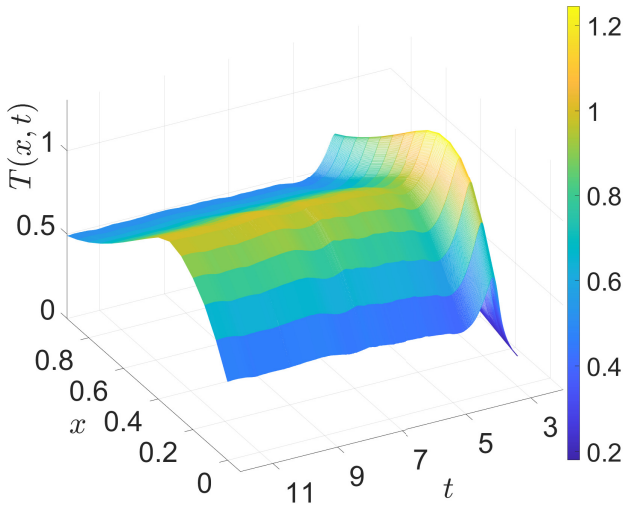

Fig. 9: The closed-loop temperature profile

Even if the presented MPPI controller show great potential and performance for dissipation reaction in tubular reactor, the convection dominated reactions can't yet be handled gracefully by the provided strategy. In a subsequent publication, we intend to incorporate a model reduction technique that can handle the convection dominated reactions into the MPPI control algorithms that are already in operation.

References

[1] C. S. Bildea, A. C. Dimian, S. C. Cruz, and P. D. Iedema, Design of tubular reactors in recycle systems. *Computers and Chemical Engineering*, 2004, 28(1): 63–72.

[2] X. G. Wang, B. H. Tian, C. H. Wang, abd J. H. Wu, Mathematical modelling of residence time distribution in tubular loop reactors. *The Canadian Journal of Chemical Engineering*, 2017, 95(6): 1101–1108.

[3] F. Reyes, and W. L. Luyben, Design and Control of Tubular Reactor Systems with Both Gas and Liquid Recycles. *Industrial & Engineering Chemistry Research*, 2001, 40(19): 4089–4101.

[4] C. Antoniades, and P. D. Christofides, Studies on Nonlinear Dynamics and Control of a Tubular Reactor with Recycle. *Nonlinear Analysis*, 2001, 47(9): 5933–5944.

[5] M. Berezowski, Application of Lyapunov's Methods for Analyzing the Stability of a Tubular Chemical Reactor with Recycle. *Chemistry Engineering Technology*, 2020, 43(12): 2523–2529.

[6] T. Tosukhowong, W. G. Xie, and J. H. Lee, Approximate Dynamic Programming Based Optimal Control Applied to an Integrated Plant with a Reactor and a Distillation Column with Recycle. *AICHE Journal*, 2009, 55(4): 919–930.

[7] S. V. Rakovic, Nonlinear Predictive Control for Trajectory Tracking and Path Following: An Introduction and Perspectivein *Handbook of Model Predictive Control*, S. V. Rakovic, and W. S. Levine. Eds. Switzerland: Springer-Verlag Press, 2019: 169–195.

[8] M. Schwenzer, M. Ay, T. Bergs, and D. Abel, Review on model predictive control: an engineering perspective. *The International Journal of Advanced Manufacturing Technology*, 2021, 117(5): 1327–1349.

[9] S. Khatibi, G. O. Cassol, and S. Dubljevic, Model predictive control of a non-isothermal axial dispersion tubular reactor with recycle. *Computers and Chemical Engineering*, 2021, 145(2): 107159.

[10] S. Khatibi, G. O. Cassol, S. Dubljevic, Linear Model Predictive Control for a Coupled CSTR and Axial Dispersion Tubular Reactor with Recycle. *Mathematics*, 2020, 8(5): 711.

[11] P. C. N. Verheijen, V. Breschi, M. Lazar, Handbook of linear data-driven predictive control: Theory, implementation and design. *Annual Reviews in Control*, 2023, 56(12): 100914.

[12] L. Ai, D. S. Zhang, K. L. Teo, and L. W. Deng, Generalized Predictive Temperature Control in Tubular Chemical Reactors by means of Proper Orthogonal Decomposition and Least Squares Support Vector Machine, in *Proceedings of 39th Chinese Control Conference*, 2020: 2407–2412.

[13] W. G. Xie, I. Bonis, and C. Theodoropoulos, Off-line model reduction for on-line linear MPC of nonlinear large-scale distributed systems. *Computers and Chemical Engineering*, 2011, 35(5): 750–757.

[14] I. Bonis, W. G. Xie, and C. Theodoropoulos, A linear model predictive control algorithm for nonlinear large-scale distributed parameter systems. *AICHE Journal*, 2012, 58(3): 801–811.

[15] W. G. Xie, I. Bonis, and C. Theodoropoulos, Data-driven model reduction-based nonlinear MPC for large-scale distributed parameter systems. *Journal of Process Control*, 2015, 35(11): 50–58.

[16] M. R. Garcia, C. Vilas, L. O. Santos, and A. A. Alonso, A robust multi-model predictive controller for distributed parameter systems. *Journal of Process Control*, 2012, 22(1): 60–71.

[17] X. Y.. Qing, J. Jin, Y. G. Niu, and S. L. Zhao, Time-space coupled learning method for model reduction of distributed parameter systems with encoder-decoder and RNN. *AICHE Journal*, 2020, 66(8): e16251.

[18] L. Ai, J. Z. Gan, X. J. Feng, and X. Q. Chen, SSAE and GRU Based Joint Modeling for Nonlinear Distributed Parameter Systems. *IEEE Access*, 2022, 10(9): 98501–98511.

[19] L. X. Lu, F. Yin, Chang. Liu, and M. H. Huang, Online Spatiotemporal Extreme Learning Machine for Complex Time-Varying Distributed Parameter Systems. *IEEE Transations on Industrial Informatics*, 2017, 13(4): 1753–1762.

[20] K. K. Xu, H. D. Yang, and C. J. Zhu, A novel extreme learning Machine-based Hammerstein-Wiener model for complex nonlinear industrial processes. *Neurocomputing*, 2019, 358(17): 246–254.

[21] C. J. Zhu, H. D. Yang, Y. J. Fan, B. Fan, and K. K. Xu, Online spatiotemporal modeling for time-varying distributed parameter systems using Kernel-based Multilayer Extreme Learning Machine. *Nonlinear Dynamics*, 2022, 107(11): 761–780.

[22] Z. Yan, and J. Wang, Robust Model Predictive Control of Nonlinear Systems With Unmodeled Dynamics and Bounded Uncertainties Based on Neural Networks. *IEEE Transations on Neural Networks and Learning Systems*, 2014, 25(3): 457–469.

[23] G. B. Huang, H. M. Zhou, and X. J. Ding, Extreme Learning Machine for Regression and Multiclass Classification. *IEEE Transactions on Systems, Man, and Cybernetics, Part B*, 2012, 42(6): 513–529.

[24] G. Williams, P. Drews, B. Goldfain, J, M. Rehg, and E. A. Theodorou, Aggressive Driving with Model Predictive Path Integral Control, in *IEEE International Conference on Robotics and Automation (ICRA)*, 2016: 1433–1440.

[25] X. Y. Qing, J. Song, J. Jin, and S. L. Zhao, Nonlinear model predictive control for distributed parameter systems by time–space-coupled model reduction. *AICHE Journal*, 2021, 67(8): e17246.

Proceedings of the 3rd Conference on Fully Actuated System Theory and Applications
May 10-12, 2024, Shenzhen, China

Distributed Fault Detection Scheme for Snake Robot Platoon

Qin Wang[1], Darong Huang[1], Yuhong Na[1], Yunhu Zhou[1,2]

1. School of Artificial Intelligence, Anhui University, Hefei 230601, P. R. China
E-mail: drhuangjs@ahu.edu.cn, wa23301085@stu.ahu.edu.cn

2. R&D Center, Efort Intelligent Equipment Co., Ltd, Wuhu 241007, P. R. China

Abstract: This paper investigates distributed fault detection for snake robot platoons in zero-trust environments, employing a scheme based on $\mathcal{L}_2$ observers to enhance reliability through secure information transmission. The approach defines relative output estimation errors based on communication topologies, then designs a fault detection scheme based on $\mathcal{L}_2$ observers and verifies its stability and conditions for existence. Simulation results confirm the effectiveness of the scheme, demonstrating its potential to improve fault detection accuracy and security in complex robotic systems.

Key Words: Snake robot, Distributed system, Fault detection, $\mathcal{L}_2$ observer, Zero-trust

1 Introduction

With the development of technology, people's comprehensive demand for various intelligent terminals is soaring, including smart cars, aircraft, etc. Among them, snake robots are a kind of flexible robots with multiple degrees of freedom, which can play the role of detection, rescue, maintenance, etc. in special work scenarios. Snake robots are a special kind of mobile robots, which rely on the friction between their own modules and the ground to generate motion. Snake robots have super-redundant degrees of freedom, compared with traditional mobile robots, their motion has strong flexibility, high environmental adaptability, and incomparable advantages. Compared with legged mobile robots and wheeled mobile robots, snake robots have a slender shape, which can enter narrow pipes and gaps; snake robots are also suitable for exploring unknown and harsh areas, and can enter disaster-stricken ruins for search and rescue; snake robots can also complete the extravehicular maintenance and repair of space stations and satellites, acting as mechanical arms [1]. In the field of multi-robot collaboration [2], the complex structure of snake robots also brings challenges to fault detection. Since there are multiple nodes in snake robots, how to timely detect and locate abnormal joints in the formation system, and how to identify different joints of the same robot, are the problems concerned in this paper. The prototype of the multi-snake robot in this article is shown in Figure 1.

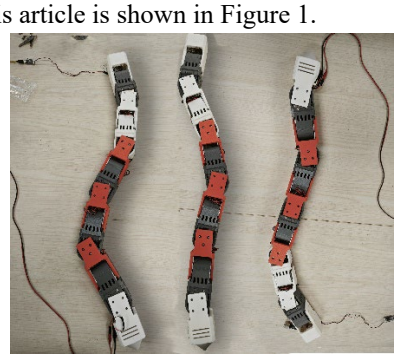

Fig. 1: Prototype of Multi-Snake Robot

As information science advances, an increasing number of entities can interact within their environment. Nonetheless, diverse forms of information exchange carry the risk of network attacks and data breaches, underscoring the critical importance of assessing information reliability. In 2011, Forrester et al. [3] introduced the concept of "zero trust", which is a security paradigm based on distrust and continuous verification. Based on this concept, in [4], an intelligent zero trust architecture is designed to meet the security needs of untrusted infrastructure networks. In [5], the author further improved the integrated process of trust establishment, and proposed a standardized trust evaluation method by comparing and evaluating trust assumptions and zero trust assumptions, laying the foundation for subsequent research. Reference [6] proposed an innovative information sharing solution based on blockchain for IoT devices in zero-trust environments, aiming to achieve anonymity and entity authentication, data privacy and data trustworthiness, participant incentives and fairness. Reference [7] proposed an innovative two-layer access control architecture based on the zero-trust model, which combines with the risk-driven process, supports the migration of existing infrastructure, and prioritizes the identification of network security risk changes. Reference [8] proposed a zero-trust security framework based on the Rich model, which is used for trust verification of SaaS (Software as a Service), and uses machine learning to analyze the multimedia data of service processing behavior, to improve the visibility of service operation and risk. The framework relies on federated learning, extracting features from artificial intelligence processing data of different cloud service users. It can be seen that there is more and more research on zero-trust, especially for ensuring the reliability of information transmission.

Fault detection refers to the process of monitoring the input and output signals of the system during system operation, judging whether there is a fault in the system, and determining the type, location and degree of the fault. The purpose of fault detection is to ensure the safe, reliable and efficient operation of the system, and to provide the basis for

*This work was supported by Department of Education of Anhui Province under Grant KJ2021A0050 and Anhui Provincial Natural Science Foundation under Grant 2308085QF210.

fault diagnosis and fault recovery. For fault detection, there are already some research works, mainly divided into two categories: data-based methods and model-based methods. For example, for the distributed consensus problem of multi-agent systems (MAS) with non-identical unknown nonlinear dynamics and undetectable actuator failures, a robust adaptive fault-tolerant consensus protocol was developed, which can simultaneously compensate for uncertain dynamics/disturbances and time-varying but unpredictable actuator failures [9]. In [10], based on data-driven and statistical framework, two distributed optimal fault detection schemes for large-scale systems were developed. These two are data-driven methods. Reference [11] proposed a distributed fault detection and isolation (FDI) method, which is applicable to heterogeneous multi-agent system networks with different dynamics and orders. In [12], a potential fault diagnosis method based on ADRC was proposed, which effectively separated the potential fault from the interference by treating it as a new state variable. These two are model-based method. These two methods have their own advantages and disadvantages. Data-based methods require a large number of data samples, using machine learning or deep learning techniques, to identify the features or patterns of faults by analyzing the sensor data or image data of the robot. Model-based methods require accurate model information. In [13], a data-driven design for distributed fault detection of dynamic systems using measurements in complex sensor networks was developed, using subspace techniques and average consensus algorithms. Gain scheduling methods were also studied for the analysis and integrated design of different types of complex systems, such as, for the FD system based on observers, an integrated design scheme for affine nonlinear systems combining $\mathcal{L}_2$ stability theory was proposed and applied to study the FD problem of $\mathcal{L}_2$ stable systems [14]. For discrete-time switched systems with uncertainties, FD system design schemes for matching and mismatching periods were proposed respectively [15]. This paper also uses $\mathcal{L}_2$ stability theory to design fault observers.

This paper explores the analysis and design of distributed fault detection for snake robots in zero-trust environments using $\mathcal{L}_2$ observer-based methods. The model-based method is adopted, which models the dynamic model of the snake-like robot, and compares the difference between the actual output and the expected output, to judge whether there is a fault. The subsequent sections of this paper are structured as follows. Section 2 presents the system description. In Section 3, a fault detection scheme utilizing an $\mathcal{L}_2$ observer in a zero-trust environment is elaborated. Section 4 provides an example simulation result to demonstrate the feasibility and effectiveness of the proposed distributed fault detection scheme. Finally, Section 5 presents the conclusions of this paper.

Notations: In this paper, the notations utilized adhere to standard conventions. $\|\cdot\|$denotes the Euclidean norm of a vector. $\mathbb{R}^+ = [0, \infty)$. A function $\gamma: \mathbb{R}^+ \to \mathbb{R}^-$ is considered to be in class $\mathcal{K}$ if it is strictly increasing and satisfies $\gamma(0) = 0$; it belongs to class $\mathcal{K}_\infty$ if $\lim_{k\to\infty} \gamma(k) = \infty$. The $\mathcal{L}_{2,[0,\tau]}$ -norm of $u(k)$ is defined as $\|u_\tau\|_2 = (\sum_{k=0}^{\tau}\|u(k)\|^2)^{1/2}$. The set of real matrices with dimension $m \times n$ is denoted by $\mathbb{R}^{m\times n}$. For a matrix $A \in \mathbb{R}^{n\times n}$, its transpose is denoted by A^T. The symbol $\otimes$ represents the Kronecker product. In a symmetric matrix, $*$ denotes the symmetric elements. $diag$ indicates that the matrix is diagonal.

2 Preliminaries and problem formulation

2.1 System Description

A snake robot consists of N rigid links of length $2l$, connected by $N-1$ motor joints. The model does not consider the width of each link. All N links have the same mass m and moment of inertia $J = \frac{1}{3}ml^2$. The total mass of the snake robot is Nm. The mass of each link is uniformly distributed, so the center of mass of the link is located at the center point (i.e., the point at a distance of l from both ends of the joint). All wheels are passive, all joints are active, passive wheels do not slide sideways, wheels are mounted at the midpoint of the link. l is half the length of each link. θ_i is the direction of link i. ϕ_i is the yaw angle of joint i, defined as $\phi_i = \theta_{i+1} - \theta_i$. Let (x_h, y_h) be the head position. Let $\boldsymbol{x_i}$ be the position vector of the center of link i, expressed as $\boldsymbol{x_i} = [x_h, y_h]^T$. Define $\boldsymbol{x}, \boldsymbol{y} : \boldsymbol{x} = [x_1, \cdots, x_n]^T$, $\boldsymbol{y} = [y_1, \cdots, y_n]^T$, $\boldsymbol{\theta}, \boldsymbol{\phi}$: $\boldsymbol{\theta} = [\theta_1, \cdots, \theta_n]^T$, $\boldsymbol{\phi} = [\phi_1, \cdots, \phi_{n-1}]^T$.

After applying local feedback linearization to the snake robot model, the model is transformed into the standard form of a control affine system [16].

By defining $\boldsymbol{x}_1 = \boldsymbol{q}_a$, $\boldsymbol{x}_2 = \boldsymbol{q}_u$, $\boldsymbol{x}_3 = \dot{\boldsymbol{q}}_a$, $\boldsymbol{x}_4 = \dot{\boldsymbol{q}}_u$ and $\boldsymbol{x} = [\boldsymbol{x}_1^T, \boldsymbol{x}_2^T, \boldsymbol{x}_3^T, \boldsymbol{x}_4^T]^T \in \mathbb{R}^{2N+4}$, where $\boldsymbol{q}_a = [\phi_1, \cdots, \phi_{N-1}]^T \in \mathbb{R}^{N-1}$ represents the driven degrees of freedom, $\boldsymbol{q}_u = [\theta_N, p_x, p_y]^T \in \mathbb{R}^3$ represents the undriven degrees of freedom, $\bar{\boldsymbol{u}} = [\bar{u}_1, \cdots, \bar{u}_{N-1}]^T \in \mathbb{R}^{N-1}$ is a set of new control inputs, rewrite the model into the following standard form of control affine system.

$$\dot{\boldsymbol{x}} = \begin{bmatrix} \dot{\boldsymbol{x}}_1 \\ \dot{\boldsymbol{x}}_2 \\ \dot{\boldsymbol{x}}_3 \\ \dot{\boldsymbol{x}}_4 \end{bmatrix} = \begin{bmatrix} \boldsymbol{x}_3 \\ \boldsymbol{x}_4 \\ \bar{\boldsymbol{u}} \\ \boldsymbol{A}(\boldsymbol{x}) + \boldsymbol{B}(\boldsymbol{x}_1)\bar{\boldsymbol{u}} \end{bmatrix}$$

$$= \boldsymbol{f}(\boldsymbol{x}) + \textstyle\sum_{j=1}^{N-1}(\boldsymbol{g}_j(\boldsymbol{x}_1)\bar{u}_j) \qquad (1)$$

where

$$\boldsymbol{f}(\boldsymbol{x}) = \begin{bmatrix} \boldsymbol{x}_3 \\ \boldsymbol{x}_4 \\ \boldsymbol{0}_{(N-1)\times 1} \\ \boldsymbol{A}(\boldsymbol{x}) \end{bmatrix}, \ \boldsymbol{g}_j(\boldsymbol{x}_1) = \begin{bmatrix} \boldsymbol{0}_{(N-1)\times 1} \\ \boldsymbol{0}_{3\times 1} \\ \boldsymbol{e}_j \\ \boldsymbol{B}_j(\boldsymbol{x}_1) \end{bmatrix} \qquad (2)$$

In the formula, $j \in \{1, \ \ldots, \ N-1\}$, $\boldsymbol{e}_j$ denotes the jth standard basis vector in $\mathbb{R}^{N-1}$ (the jth column of $\boldsymbol{I}_{N-1}$), $\boldsymbol{B}_j(\boldsymbol{x}_1)$ denotes the jth column of $\boldsymbol{B}(\boldsymbol{x}_1)$. Where

$$\boldsymbol{A}(\boldsymbol{x}) = \boldsymbol{A}(\boldsymbol{q}_\phi, \dot{\boldsymbol{q}}_\phi) = -\bar{\boldsymbol{M}}_{22}^{-1}(\bar{\boldsymbol{W}}_2 + \bar{\boldsymbol{G}}_2\boldsymbol{f}_R) \in \mathbb{R}^3$$
$$\boldsymbol{B}(\boldsymbol{x}_1) = \boldsymbol{B}(\boldsymbol{q}_a) = -\bar{\boldsymbol{M}}_{22}^{-1}\bar{\boldsymbol{M}}_{21} \in \mathbb{R}^{3\times(N-1)} \qquad (3)$$

where $\bar{\boldsymbol{M}}(\bar{\boldsymbol{\phi}}) = \begin{bmatrix} \boldsymbol{H}^T\boldsymbol{M}_\theta(\bar{\boldsymbol{\phi}})\boldsymbol{H} & \boldsymbol{0}_{N\times 2} \\ \boldsymbol{0}_{2\times N} & Nm\boldsymbol{I}_2 \end{bmatrix}$, $\bar{\boldsymbol{W}}\left(\bar{\boldsymbol{\phi}}, \dot{\bar{\boldsymbol{\phi}}}\right) = \begin{bmatrix} \boldsymbol{H}^T\boldsymbol{W}(\bar{\boldsymbol{\phi}})\mathrm{diag}(\boldsymbol{H}\dot{\bar{\boldsymbol{\phi}}})\boldsymbol{H}\dot{\bar{\boldsymbol{\phi}}} \\ \boldsymbol{0}_{2\times 1} \end{bmatrix}$, $\bar{\boldsymbol{G}}(\boldsymbol{\phi}) = \begin{bmatrix} -l\boldsymbol{H}^T\boldsymbol{S}_{\boldsymbol{H}\bar{\boldsymbol{\phi}}}\boldsymbol{K} & l\boldsymbol{H}^T\boldsymbol{C}_{\boldsymbol{H}\bar{\boldsymbol{\phi}}}\boldsymbol{K} \\ -\boldsymbol{e}^T & \boldsymbol{0}_{1\times N} \\ \boldsymbol{0}_{1\times N} & -\boldsymbol{e}^T \end{bmatrix}$, $\boldsymbol{q}_\phi = \begin{bmatrix} \bar{\boldsymbol{\phi}} \\ \boldsymbol{p} \end{bmatrix}$, $\bar{\boldsymbol{\phi}} =$

$[\phi_1, \cdots, \phi_{N-1}, \theta_N]^T \in \mathbb{R}^N$ contains the $N-1$ joint angles and the absolute link angle $\theta_N \in \mathbb{R}$ of the head link of the snake robot.

By applying local linearization to $\dot{\boldsymbol{x}}_4 = \boldsymbol{A}(\boldsymbol{x}) + \boldsymbol{B}(\boldsymbol{x}_1)\bar{\boldsymbol{u}}$, we have

$$\boldsymbol{A}(\boldsymbol{x}) + \boldsymbol{B}(\boldsymbol{x}_1)\bar{\boldsymbol{u}} = \bar{\boldsymbol{A}}\boldsymbol{x} + \bar{\boldsymbol{B}}\bar{\boldsymbol{u}}$$

where $\bar{\boldsymbol{B}} = \boldsymbol{B}(\boldsymbol{x}_1)$, $A_i(x) = \bar{a}_i^T x, i = 1,2,\ldots,n$.

After a series of transformations, we obtain

$$\bar{a}_i = \dot{A}_i(x_0) + \frac{A_i(x) - x_0^T \dot{A}_i(x_0)}{\|x_0\|^2} x_0,\ x_0 \neq 0 \tag{4}$$

where $\bar{a}_i^T$ represents the ith row of the matrix $\bar{\boldsymbol{A}}$.

Represent the state vector of the snake robot as $\boldsymbol{x}_i(k) = \left[\theta_N, p_x, p_y\right]^T$, the state output equation as $\boldsymbol{y}_i(k) = [\theta_N, p_x, p_y]^T = \boldsymbol{C}\boldsymbol{x}_i(k)$, then, the overall discrete-time dynamics of the array becomes

$$\begin{cases} \boldsymbol{x}_i(k+1) = \bar{\boldsymbol{A}}\boldsymbol{x}_i(k) + \bar{\boldsymbol{B}}\bar{\boldsymbol{u}}_i(k) \\ \boldsymbol{y}_i(k) = \boldsymbol{C}\boldsymbol{x}_i(k) \end{cases} \tag{5}$$

2.2 Graph Theory

The usage of graph theory in the multi-snake robot system involves describing the communication relationships and topologies among the snake robot systems. A typical graph $\mathcal{G} = (\mathcal{V}, \mathcal{E})$ comprises a node set $\mathcal{V} = \{1,2,\cdots,n\}$ and an edge set $\mathcal{E} = \{e_1, e_2, \cdots, e_n\}$. Each edge $e_{ij} = (i,j)$ links node $i \in \mathcal{V}$ with node $j \in \mathcal{V}$, making nodes i and j adjacent to one another. The edge e_{ij} and these nodes are interconnected. In a directed graph, connections between nodes are typically one-way, like $i \to j$, denoted as (i,j). If connections in an algebraic graph are undirected, such as $(i,j) = (j,i)$, then the graph is termed undirected. Generally, connections between nodes in an undirected graph are bidirectional, resembling a special case of a directed graph. When an edge in graph $\mathcal{G}$ identical points, i.e., $e_{jj} = (j,j)$, it constitutes a self-loop. Since this paper delves into directed graphs, the subsequent section emphasizes directed graphs.

We define a_{ij} as representing the transmission of a message from node i to node j. When a message is delivered, $a_{ij} = 1$, otherwise $a_{ij} = 0$. Therefore, the adjacency matrix $\mathcal{A} = a_{ij} \in \mathbb{R}^{n\times n}$, where its elements are either 0 or 1. Furthermore, we define the out-degree of a node i as

$$d(i) = \sum_{j=1}^{n} a_{ij} \tag{6}$$

The degree matrix $\mathcal{D}$ of the graph $\mathcal{G}$ is defined as follows

$$\mathcal{D} = \mathrm{diag}\{d(1), d(2), \cdots, d(n)\} \tag{7}$$

So the Laplacian matrix of the graph $\mathcal{G}$ is defined as

$$L = \mathcal{D} - \mathcal{A} \tag{8}$$

And we define the self-loop matrix of the graph $\mathcal{G}$ as

$$\mathcal{G} = diag\{g(1), g(2), \cdots, g(n)\} \tag{9}$$

where $g(i)$ indicates whether node i has a self-loop. If a node has a self-loop, then $g(i) = 1$, and otherwise $g(i) = 0$.

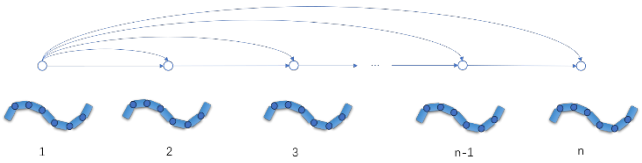

Fig. 2: Leader-predecessor following (LPF) topology

Illustrated in Fig. 2, every snake node functions as a separate entity within a zero-trust setting. Communication topologies in a zero-trust environment typically necessitate treating external nodes as untrusted entities, requiring real-time authorization for all node interactions. The focus of this paper lies in parameterizing the Laplacian matrix under a zero-trust framework and characterizing it through the trust degree matrix

$$L_{zt} = a_{ij} f(a_{ij}) \in \mathbb{R}^{n\times n} \tag{10}$$

this ensures that it integrates the trust level for each node's communication message. The trust level is determined by assessing all messages from that particular node, with values ranging between 0 and 1. A trust level of 0 signifies complete lack of trust in the node, whereas a level of 1 indicates full trustworthiness. Nevertheless, the trust level is subject to fluctuations over time.

2.3 Model-based Fault Detection Scheme

In practical applications, real-time fault detection utilizes a moving window $[t1, t2]$, where the evaluation function is defined as

$$J = \sum_{k=t_1}^{t_2} r^T(k) r(k) \tag{11}$$

and the threshold as

$$J_{th} = \sum_{k=t_1}^{t_2} \gamma^2 \tilde{u}^T(k)\tilde{u}(k) + V\big(0, x(0), \hat{x}(0)\big) \tag{12}$$

When the snake robot system is functioning normally, the residual signal remains below the threshold. However, if a malfunction occurs within the snake robot system, the residual signal exceeds the threshold. The decision logic can be summarized as:

$$\begin{cases} J < J_{th} \Rightarrow \text{fault-free} \\ J \geq J_{th} \Rightarrow \text{alarm for fault} \end{cases} \tag{13}$$

3 Main Results

3.1 Fault Observer With Zero Trust

The focus of this research is on examining distributed fault detection for snake robots operating within a zero-trust environment. We analyze a specific category of systems that involve unknown disturbances.

$$\begin{cases} x_i(k+1) = Ax_i(k) + Bu_i(k) + Fh_i(k) \\ y_i(k) = Cx_i(k) \end{cases} \tag{14}$$

where $x_i(k+1) \in \mathbb{R}^n$, $u_i(k) \in \mathbb{R}^m$, and $y_i(k) \in \mathbb{R}^p$ represent the state, input, and output of the i th agent, respectively. Additionally, $h_i(k) \in \mathbb{R}^d$ denotes the unknown input vector with an $\mathcal{L}_2$ bounded condition, such that $\|h(k)\|^2 \leq \delta_d^2$. Matrices A, B and F are constant real matrices of suitable dimensions. It is assumed that all snake robots are isomorphic. Furthermore, the matrices F are presumed to be full rank, and the pair (A, C) is observable.

The relative observer for the ith node in system (14) is formulated as follows

$$\begin{cases}\hat{x}(k+1) = A\hat{x}(k) + Bu(k) + Ky(k) - K\hat{y}(k) \\ \hat{y}(k) = C\hat{x}(k)\end{cases} \quad (15)$$

where K denotes the observer gain. We define the error vectors for the ith node as follows

$$e_i(k) = x_i(k) - \hat{x}_i(k) \quad (16)$$

By introducing graph theory, we can obtain the following formula

$$\begin{aligned} e_i(k+1) &= x_i(k+1) - \hat{x}_i(k+1) \\ &= Ax_i(k) + Bu_i(k) + Fh_i(k) - A\hat{x}_i(k) - Bu_i(k) \\ &\quad -Kg_i\big(y_i(k) - \hat{y}_i(k)\big) \\ &= Ae_i(k) + Fh_i(k) - K\textstyle\sum_{j\epsilon N_i} l_{ij}\big(y_i(k) - \hat{y}_i(k)\big) \\ &\quad -\Big(-K\textstyle\sum_{j\epsilon N_i} l_{ij}\Big(y_j(k) - \hat{y}_j(k)\Big)\Big) \\ &\quad -Kg_i\big(y_i(k) - \hat{y}_i(k)\big) \\ &= Ae_i(k) + Fh_i(k) \\ &\quad -KC\Big(\textstyle\sum_{j\epsilon N_i} a_{ij}\Big(e_i(k) - e_j(k)\Big) + g_i e_i(k)\Big) \end{aligned} \quad (17)$$

To devise a global fault estimation observer for snake robot system, it is essential to define the following global error vector as follows

$$\begin{aligned} e(k) &= [e_1^T(k), e_2^T(k), \cdots, e_N^T(k)]^T \\ h(k) &= [h_1^T(k), \theta_2^T(k), \cdots, \theta_N^T(k)]^T \end{aligned} \quad (18)$$

Given that all snake robots are interconnected according to the communication topology, the fault estimation observer must take into account the information exchange among nodes. The relative residuals of the ith node are defined as follows

$$\begin{aligned} r(k) = \sum_{j\in N_i} l_{ij}\big(y_i(k) - \hat{y}_i(k)\big) - \Big(y_j(k) - \hat{y}_j(k)\Big) \\ +g_i(y_i(k) - \hat{y}_i(k)) \end{aligned} \quad (19)$$

where l_{ij} and g_i, respectively, are the element of trust degree matrix L_{zt} and loop-graph matrix G.

So $e(k+1)$ can also be represented as

$$\begin{cases} e(k+1) = (I_N \otimes A)e(k) + (I_N \otimes F)h(k) \\ \qquad\quad -(I_N \otimes K)\big((L_{zt} + G) \otimes C\big)e(k) \\ \qquad = (I_N \otimes A - (L_{zt} + G) \otimes KC)e(k) \\ \qquad\quad +(I_N \otimes F)h(k) \\ r(k) = (L_{zt} + G) \otimes Ce(k) \end{cases} \quad (20)$$

So the global error dynamic equation is

$$\begin{cases} e(k+1) = \overline{A}e(k) + \overline{F}h(k) \\ r(k) = \overline{C}e(k) \end{cases} \quad (21)$$

where

$$\overline{A} = I_N \otimes A - (L_{zt} + G) \otimes KC$$

$$\overline{C} = (L_{zt} + G) \otimes C$$

$$\overline{F} = I_N \otimes F$$

3.2 $\mathcal{L}_2$ Reconfigurability

Definition 1[14]: System (14) is called $\mathcal{L}_2$ reconstructible if there exists a system (19), such that $\forall x, \hat{x}$

$$\sum_{k=0}^{\tau} \varphi_1(\|r(k)\|) \le \sum_{k=0}^{\tau} \varphi_2(\|\tilde{u}(k)\|) + \gamma_0(x(0), \hat{x}(0))$$

where $\tilde{u}(k) = [u^T(k) \;\; h^T(k)]^T$. $\varphi_1(\cdot) \in \mathcal{K}$, $\varphi_2(\cdot) \in \mathcal{K}_\infty$, and $\gamma_0(\cdot) \ge 0$ is a finite constant for given $x(0), \hat{x}(0)$.

Theorem 1[14]: Given system (14) and observer-based residual generator (15), if there exist (i) a set of switched Lyapunov functions, $V_{ij}\big(k, x(k), \hat{x}(k)\big), i, j \in \Gamma$, (ii) functions $\varphi_1(\cdot) \in \mathcal{K}$, $\varphi_2(\cdot) \in \mathcal{K}_\infty$, such that $\forall i, j, l, q \in \Gamma$,

$$\begin{aligned} V_{lq}\big(k+1, x(k+1), \hat{x}(k+1)\big) - V_{ij}\big(k, x(k), \hat{x}(k)\big) \\ \le -\varphi_1(\|r(k)\|) + \varphi_2(\|\tilde{u}(k)\|) \end{aligned}$$

then the system (14) is $\mathcal{L}_2$ reconstructible.

In this paper, $\mathcal{L}_2$ reconfigurability is a sufficient condition for the existence and threshold setting of an $\mathcal{L}_2$ observerbased FD system. Then, we have

$$\begin{bmatrix} e(k) \\ h(k) \end{bmatrix}^T \Psi \begin{bmatrix} e(k) \\ h(k) \end{bmatrix} \le 0 \quad (22)$$

where

$$\begin{aligned} \Psi &= \begin{bmatrix} \overline{A}^T \\ \overline{F}^T \end{bmatrix} P \begin{bmatrix} \overline{A} \; \overline{F} \end{bmatrix} + \begin{bmatrix} \overline{C}^T\overline{C} & 0 \\ 0 & 0 \end{bmatrix} - \begin{bmatrix} P & 0 \\ 0 & \gamma^2 I \end{bmatrix} \le 0 \\ &= -\begin{bmatrix} \overline{A}^T \\ \overline{F}^T \end{bmatrix} (-P) \begin{bmatrix} \overline{A} \; \overline{F} \end{bmatrix} + \begin{bmatrix} -P & 0 \\ 0 & -\gamma^2 I \end{bmatrix} + \begin{bmatrix} \overline{C}^T\overline{C} & 0 \\ 0 & 0 \end{bmatrix} \le 0 \end{aligned} \quad (23)$$

where γ^2 is a positive constant.

By applying Schur complement, we can get:

$$\begin{bmatrix} -P & 0 & \overline{A}^T & \overline{C}^T \\ * & -\gamma^2 I & \overline{F}^T & 0 \\ * & * & -P^{-1} & 0 \\ * & * & * & -I \end{bmatrix} \le 0 \quad (24)$$

Note that the inverse of the Lyapunov function matrices P^{-1} is in the third column of the matrix. It leads to the coupling between the system matrix and the Lyapunov function matrix. Consequently, adjusting the congruence of the matrix by $diag\{I, I, P, I\}$ becomes essential in this context.

Based on the congruence transformation, the system is feasible when and only when the following inequality holds

$$\begin{bmatrix} -P & 0 & \overline{A}^T P & \overline{C}^T \\ * & -\gamma^2 I & \overline{F}^T P & 0 \\ * & * & -P^{-1} & 0 \\ * & * & * & -I \end{bmatrix} \le 0 \quad (25)$$

By solving the inequality matrix above, we can derive a solution that ensures the system meets the requirements for $\mathcal{L}_2$ reconfigurability. This establishes the system as both an existential and threshold setting for an $\mathcal{L}_2$ observer-based FD system.

4 An Illustrative Example

This section takes the distributed system model composed of four snake robots as an example.

4.1 System Description

Suppose the communication topology of the snake robot distributed system is shown in Figure 3. According to the communication topology diagram, the adjacency matrix $\mathcal{A}$ and the degree matrix $\mathcal{D}$ can be obtained as

$$\mathcal{A} = \begin{bmatrix} 0 & 0 & 0 & 0 \\ 1 & 0 & 0 & 0 \\ 1 & 1 & 0 & 0 \\ 1 & 0 & 1 & 0 \end{bmatrix}, \mathcal{D} = \begin{bmatrix} 0 & 0 & 0 & 0 \\ 0 & 1 & 0 & 0 \\ 0 & 0 & 2 & 0 \\ 0 & 0 & 0 & 2 \end{bmatrix}.$$

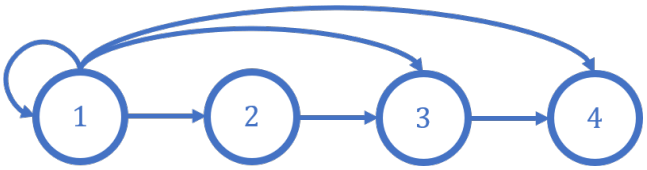

Fig. 3: The communication topology diagram

The first snake robot in the directed graph topology contains a self-loop of the Laplacian matrix and the closed-loop matrix:

$$L = \begin{bmatrix} 0 & 0 & 0 & 0 \\ -1 & 1 & 0 & 0 \\ -1 & -1 & 2 & 0 \\ -1 & 0 & -1 & 2 \end{bmatrix}, \quad G = \begin{bmatrix} 1 & 0 & 0 & 0 \\ 0 & 0 & 0 & 0 \\ 0 & 0 & 0 & 0 \\ 0 & 0 & 0 & 0 \end{bmatrix}.$$

This experiment assumes that the trustworthiness of snake 2 is 0.8, and the trustworthiness of the rest of the snakes is 1, which means complete trust. The real-time update of trustworthiness will be the follow-up work. The trustworthiness matrix L_{zt} obtained from this can be obtained as

$$L_{zt} = \begin{bmatrix} 0 & 0 & 0 & 0 \\ -0.8 & 0.8 & 0 & 0 \\ -1 & -0.8 & 2 & 0 \\ -1 & 0 & -1 & 2 \end{bmatrix}$$

The external disturbance input matrix of the system is set as follows

$$F = \begin{bmatrix} 0.5 & 0 & 0 \\ 0 & 0.5 & 0 \\ 0 & 0 & 0.5 \end{bmatrix}$$

4.2 Existence Condition

Use the LMI toolbox to solve the condition equation (25), and optimize γ^2. The normal number γ^2 is equal to 0.0036, then the fault diagnosis observer gain matrix K can be obtained as

$$K = \begin{bmatrix} -0.0022 & 0.2784 \\ 0.2333 & 3.3892 \\ -0.0777 & -0.0131 \end{bmatrix}$$

and the Lyapunov function matrices P can be obtained as

$$P = \begin{bmatrix} 12.683 & 0.0027 & -6.2978 \\ 0.0027 & 7.7218 & -0.0109 \\ -6.2978 & -0.0109 & 7.9808 \end{bmatrix}$$

So, it shows that the system is stable and $\mathcal{L}_2$ reconstructible.

4.3 Simulation

A snake robot formation simulation diagram was built in Simulink. In the experiment, each snake robot was encapsulated, and each snake robot output the local output estimation error $e_{yi}(t)(i = 1,\ldots,4)$. The Mux module is used to form the global output estimation error vector $e_y(t)$ according to the output of each snake robot, and then feed it to each snake robot module, forming a distributed fault diagnosis observer according to the given communication topology.

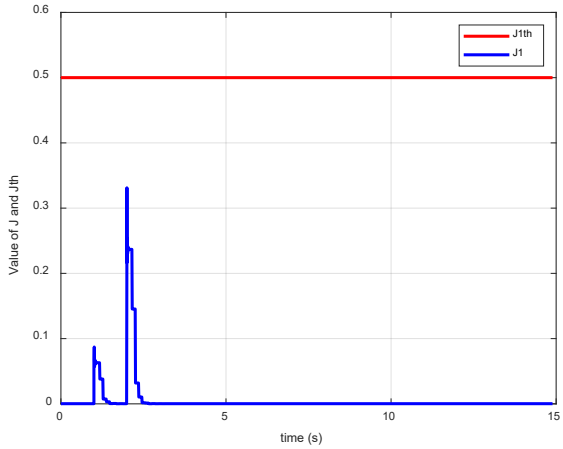

Fig. 4: Simulation results of snake 1

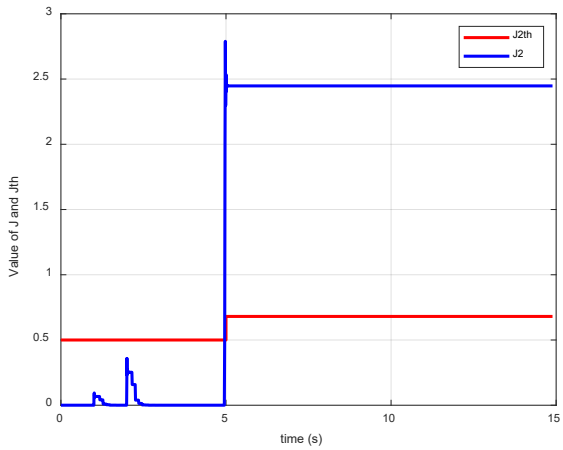

Fig. 5: Simulation results of snake 2

Assuming disturbances occur in snake robot systems 1 and 2 at the 1st and 2nd seconds, and in systems 3 and 4 at the 1st and 4th seconds, with failures occurring in systems 2 and 4 at the 5th and 10th seconds respectively, the simulation results depicted in Figures 4-7 can be obtained. From Figures 4 and 6, it is evident that their systems remain fault-free. Figure 5 demonstrates that the designed fault diagnosis observer accurately detects the fault in snake robot system 2. Likewise, Figure 7 shows that the designed fault diagnosis observer accurately detects the fault in snake robot system 4. Additionally, as the disturbances do not exceed the threshold, they do not affect the normal detection process.

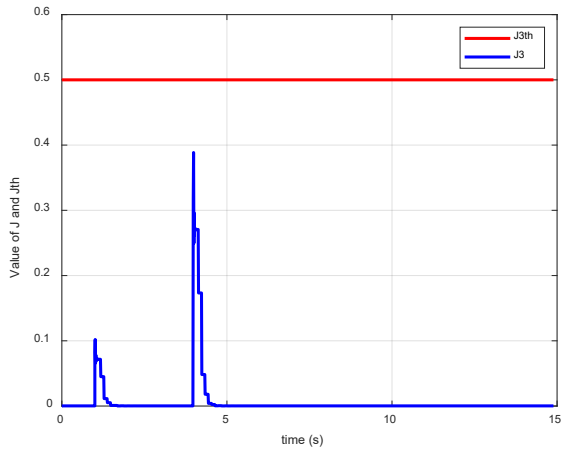

Fig. 6: Simulation results of snake 3

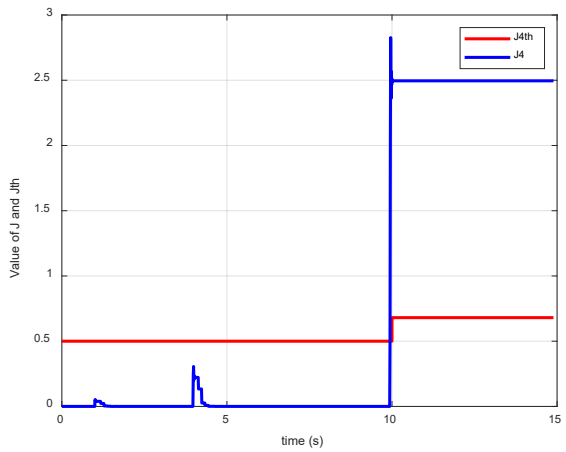

Fig. 7: Simulation results of snake 4

Through the above simulation experiments, it can be seen that the fault can be effectively detected in a zero-trust environment.

5 Conclusions and future works

This paper considers the problem of distributed fault detection for snake robots in a zero-trust environment. It examines the impact of the zero-trust paradigm on fault diagnosis in detail, analyzes the stability and existence conditions of the $\mathcal{L}_2$ observer, and finally verifies the validity of the model analysis results through numerical examples. This article proposes the following advantages for the method: First, adopting a zero-trust architecture enhances the security and defense capability against potential threats. Second, linearizing the nonlinear model of snake robots. If the article's topology can ensure sufficient information flow, the accuracy of fault detection will be improved; otherwise, it may affect the accurate diagnosis of faults. However, the computational burden of this paper is relatively heavy. It provides a detailed mathematical description of the dynamic model of snake robots, requiring complex mathematical derivations and stability analysis. Moreover, since it is targeted at fault detection in real-time systems, all computation and decision-making processes must be completed within a limited time, imposing higher demands on computational resources. Future research can use a more concise snake robot model.

References

[1] J. Liu, Y. Tong, J. Liu, Review of snake robots in constrained environments. *Robotics and Autonomous Systems*, 2021, 141: 103785.

[2] G. J. Lim, S. Kim, J. Cho, Y. Gong, A. Khodaei, Multi-UAV pre-positioning and routing for power network damage assessment. *IEEE Transactions on Smart Grid*, 2016, 9(4): 3643-3651.

[3] M. Shore, S. Zeadally, A. Keshariya, Zero Trust: The What,How,Why,and When *Computer*, 2021,54(11):26-35.

[4] K. Ramezanpour, J. Jagannath, Intelligent zero trust architecture for 5G/6G networks: Principles,challenges, and the role of machine learning in the context of O-RAN. *Computer Networks*, 2022, 217.

[5] A. Wylde, Questions of Trust in Norms of Zero Trust. *Intelligent Computing*, 2022, 508:837-846.

[6] Y. Liu, X. Hao, W. Ren, R. Xiong, T. Zhu, K. R. Choo, G. Min, A Blockchain-Based Decentralized, Fair and Authenticated Information Sharing Scheme in Zero Trust Internet-of-Things. *IEEE Transactions on Computers*, 2023, 72(2):501-512.

[7] F. Federici, D. Martintoni, V. Senni, A Zero-Trust Architecture for Remote Access in Industrial IoT Infrastructures. *Electronics*, 2023, 12(3):566.

[8] M. Saleem, M. R. Warsi, S. Islam, Secure information processing for multimedia forensics using zero-trust security model for large scale data analytics in SaaS cloud computing environment. *Journal of Information Security and Applications*, 2023, 72:2214-2126.

[9] Y. Wang, Y. Song, F. L. Lewis, Robust adaptive fault-tolerant control of multiagent systems with uncertain nonidentical dynamics and undetectable actuation failures. *IEEE Trans. on Autom. Control*, 2015, 62(6): 3978-3988.

[10] L. Li, S. X. Ding, X. Peng, Distributed data-driven optimal fault detection for large-scale systems. *Journal of Process Control*, 2020,96:94-103.

[11] M. R. Davoodi, K. Khorasani, H. A. Talebi and H. R. Momeni, Distributed fault detection and isolation filter design for a network of heterogeneous multiagent systems. *IEEE Trans. on Control Syst. Technol.*, 2014, 22(3): 1061-1069.

[12] D. Huang, X. Hua, B. Mi, Y. Liu, and Z. Zhang, Incipient fault diagnosis on active disturbance rejection control. *Science China-Information Sciences*, 2022,65(9): 199202

[13] C. Cheng, Q. Wang, Y. Nikitin, C. Liu, Y. Zhou, H. Chen, A data-driven distributed fault detection scheme based on subspace identification technique for dynamic systems. *Int J Robust Nonlinear Control*, 2023,33(5):3107-3128.

[14] Y. Yang, S. X. Ding, L. Li, On observer-based fault detection for nonlinear systems. *Systems & Control Letters*, 2015, 82:18-25.

[15] Y. Na, L. Li, S. X. Ding, A. Abdo, A Fault Detection Scheme for Uncertain Switched Systems Under Asynchronous Switching. *IFAC-PapersOnLine*, 2018, 51(24):117-122.

[16] P. Liljeback, K. Y. Pettersen, A. Stavdahl and J. T. *Snake Robots: Modelling, Mechatronics, and Control.* London: Springer, 2013.

Proceedings of the 3rd Conference on Fully Actuated System Theory and Applications
May 10-12, 2024, Shenzhen, China

Distributed Secondary Control for DC Microgrids Leveraging a Fully Actuated System Approach

Xiaoran Dai[1], Guo-Ping Liu[2], Wenshan Hu[1], Zhongcheng Lei[1]. Hong Zhou[1], Jun Zhang[1]
1. School of Electrical Engineering and Automation, Wuhan University, Wuhan 430072, P. R. China
2. Center for Control Science and Technology, Southern University of Science and Technology, Shenzhen 518055, P. R. China
E-mail: liugp@sustech.edu.cn

Abstract: This paper explores the application of a Fully Actuated System (FAS) approach in the secondary control strategy for DC microgrids. Through an in-depth analysis of the microgrid electrical and control architecture, we propose a large-signal model that integrates circuitry and control, with a specific focus on addressing coupling issues among distributed generation units (DGs). Based on this foundation, a distributed FAS-based secondary control strategy is designed, utilizing the FAS theory to tackle coupling and control challenges in DC microgrids. Simulation results demonstrate the effectiveness of our proposed secondary control method in maintaining system stability and economic efficiency.

Key Words: DC microgrids, fully actuated system approach, secondary control

1 Introduction

The escalating global demand for energy, coupled with the imperative to transition towards sustainable solutions, has propelled the significance of renewable energy sources to the forefront of the energy landscape [1]. The conventional reliance on fossil fuels has led to environmental degradation and raised concerns about the long-term viability of our energy systems. In this context, the exploration and integration of new energy sources have become imperative for addressing both the environmental and economic challenges posed by traditional energy models. Microgrids, particularly in the form of DC systems, are emerging as pivotal players in facilitating the seamless assimilation of renewable energy into existing power grids [2–4].

Current microgrid control architectures predominantly employ hierarchical structures to manage the dynamic behavior of distributed energy resources, namely primary control, secondary control and tertiary control [5]. Primary control stabilizes voltage and oversees rough current sharing. Secondary control compensates for voltage drops, ensuring precise current allocation. Tertiary control, operating at the highest level, optimizes performance based on economic or stability considerations, guiding the actions of secondary control. In recent years, several studies have integrated the economic allocation aspect of tertiary control into secondary control [6, 7]. This integration proves valuable as it reduces the impact of temporal scales, allowing for a more seamless coordination between economic considerations and the precision of current allocation facilitated by the secondary control, which is the insterest of our work.

After defining the control objectives, the effective realization of economic sharing in secondary control becomes a focal point. For example, authors in [8] propose a distributed secondary control for voltage regulation and optimal power sharing using the properties of cascade systems and the input-to-state stability theory. Similarly, a distributed periodic optimal sharing control is proposed in [9] for DC microgrids with an event-triggered mechanism. For addressing the communication delay in the economic sharing problems, a networked predictive control strategy is developed in [6].

Most of the aforementioned control approaches are based on simplified multi-agent physical-network models. Moreover, it is well-known that achieving more effective control performances requires accurate models. For addressing the modeling challenges in DC microgrids, authors in [10] propose a generic reduced-order modeling method for DC microgrids under droop control methods. The large-signal stability in microgrids with constant power loads are studied in [11]. Considering the control effect of converters in microgrids, a transient modeling technique is developed in [12] for fault detection, location and isolation.

In recent years, the emerging High-Order Fully Actuated (HOFA) theory has proven effective in addressing the integration challenges between physical models and control [13–15]. It utilizes the derived HOFA model for controller design, ensuring that the closed-loop system of the controller becomes a constant linear system with a desired eigenstructure. This theory's effectiveness has been widely validated in fields such as aerospace and microgrids [16, 17].

Inspired by these concepts, this paper proposes an FAS-based secondary control strategy. Optimal secondary controller design is achieved by establishing the FAS model of the microgrid. This approach effectively addresses the physical coupling among multiple DGs in microgrids and ensures the control performance of the whole system.

2 DC Microgrids Modeling Based on FAS Approach

In this paper, a typical islanded DC microgrid consisting of distributed DGs and power lines is considered as shown in Fig. 1. As seen, secondary control provides the voltage sepoint v_i^n for primary control. Primary control supplies the voltage reference value v_i^{ref} for the inner control of each converter via a droop mechanism. The inner control, a dual-loop control for voltage and current, directly outputs duty cycles to drive the converters. As highlighted in [4], existing works often design secondary controllers based on first-order multi-agent models, potentially leading to inaccuracies in controller design. In contrast, model-based con-

This work is supported by National Natural Science Foundation (NNSF) of China under Grants 62173255 and 62103308.

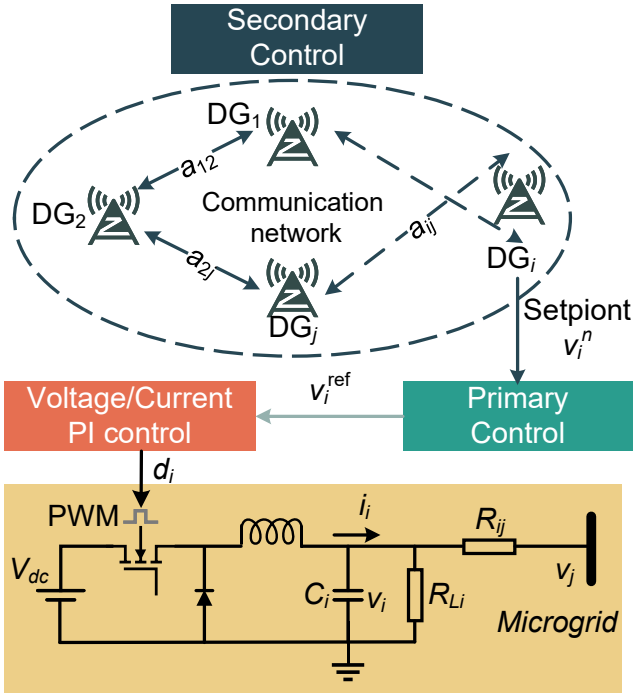

Fig. 1: Typical islanded DC microgrid diagram

troller design offers better assurance of microgrids' control performance.

To address these challenges, it is essential to establish a comprehensive large-signal model that integrates the circuitry and control aspects of the DC microgrid. Commencing with the converter model, leveraging energy storage technologies enables us to regard fluctuating renewable energy generation as a DC voltage source. Through the application of Quasi Stationary Line estimation techniques and Kirchhoff's laws, one can model the converter system in Fig. 1 as follows.

$$\begin{aligned} \dot{v}_i &= \frac{i_i}{C_i} - \frac{v_i}{C_i R_i} + \sum_{j \in N_i^p} \frac{v_j - v_i}{C_i R_{ij}}, \\ \dot{i}_i &= -\frac{v_i}{L_i} - \frac{R_{Li}}{L_i} i_i + \frac{V_{dc} d_i}{L_i}, \end{aligned} \tag{1}$$

where v_i, i_i are the output voltage and current of the ith DG, v_j is the voltage at the port connected to the ith DG, N_i^p is the set of physically adjacent DG units connected to the ith DG, $d_i \in (0,1)$ represents the duty cycle, which is the control input as well. In addition to the above variables, C_i, L_i, R_i are the filter capacitance, the storage inductance, and the local load, respectively, R_{ij} represents the line impedance. Here, we equivalently consider i_i as the output current of the ith DG cause the inductor current often equals the output current under steady-state operation.

Subsequently, we model the hierarchical control strategy based on the converter dynamics. The duty cycle d_i in equation (1) serves as the pivotal link between the circuit model and the control model. It is directly generated by the inner dual-loop PI control, where the specific voltage outer loop and current inner loop control dynamics can be expressed as follows.

$$\begin{aligned} \dot{\theta} &= v_i^{\text{ref}} - v_i, \\ i_i^{\text{ref}} &= k_i^{pv} \left(v_i^{\text{ref}} - v_i \right) + k_i^{iv} \theta, \\ \dot{\vartheta} &= i_i^{\text{ref}} - i_i, \\ d_i &= k_i^{pi} \left(i_i^{\text{ref}} - i_i \right) + k_i^{ii} \vartheta, \end{aligned} \tag{2}$$

where k_i^{pv}, k_i^{iv} and k_i^{pi}, k_i^{ii} are, respectively, the proportional and integral gains for voltage and current PI controllers, v_i^{ref} represents the reference voltage generated by droop control, i_i^{ref} is the reference value of the current loop, θ and ϑ are auxiliary integral variables.

The typical droop mechanism is expressed as follows.

$$v_i^{\text{ref}} = v_i^n - r_i^{\text{vir}} i_i, \tag{3}$$

where v_i^n is the rated voltage. Upon activation of secondary control, v_i^n in equation (3) is provided by the secondary control. Hence, in the following modeling process, we take $v_i^n(t)$ as the control input, $u_i(t)$.

By combining equations (1)-(3), one can derive the large-signal model of the ith DG in the DC microgrid as follows.

$$\dot{x}_i = A_{ii} x_i + \sum_{j \in N_i^p} A_{ij} x_j + B_i u_i, \tag{4}$$

where $x_i(t) = \begin{bmatrix} v_i(t) & i_i(t) & \theta(t) & \vartheta(t) \end{bmatrix}^T$ and $u_i(t) = v_i^n(t)$. The system matrix A_{ii}, A_{ij} can be obtained from (1)-(3), $B_i = \begin{bmatrix} 0 & \frac{k_i^{pv} k_i^{pi} V_{dc}}{L_i} & 1 & k_i^{pv} \end{bmatrix}^T$.

For a DC microgrid, the output of each generation unit is of interest. Therefore, selecting the output current as the system output, denoted as $y_i(t) = h_i(x_i(t)) = C_i x(t)$, where $C_i = \begin{bmatrix} 0 & 1 & 0 & 0 \end{bmatrix}$. From the structure of equation (4), it is evident that a single DG system is a multi-agent system with physical coupling to other DGs. Controllers for such multi-agent systems are often complex due to the need to consider coupling factors. The recent emergence of FAS methods can effectively address this issue.

From the FAS theory perspective, system (4) is considered as an under-actuated system. Deriving the large-signal model (4), one can obtain the following dynamics.

$$\dot{i}_i = L_{F_i} h_i(x_i) = C_i \left(A_{ii} x_i + \sum_{j \in N_i^p} A_{ij} x_j \right) + b_i u_i, \tag{5}$$

where $F_i(t) = \dot{x}_i(t)$, $L_{F_i} h_i(x_i)$ represents the Lie derivative of $h_i(x_i)$ along F_i, and $b_i = C_i B_i = \frac{k_i^{pv} k_i^{pi} V_{dc}}{L_i}$. Therefore, according to the HOFA theory, the FA secondary control protocol can be expressed as

$$u_i = b_i^{-1} \left(-C_i \left(A_{ii} x_i + \sum_{j \in N_i^p} A_{ij} x_j \right) + \mu_i \right), \tag{6}$$

where μ_i represents the auxiliary controller to be designed.

Substituting equation (6) into (5) yields the following DG model.

$$\dot{i}_i = \mu_i \tag{7}$$

According to the dynamics (7), one can achieve the regulation of output currents for each DG through the design

of the auxiliary controller μ_i. Compared to traditional first-order multi-agent microgrid systems, the proposed model, with the introduction of FAS system approach, can consider more underlying circuit and control models, making it more conducive to controller design.

3 Optimal Secondary Controller Design

After completing the modeling based on the FAS approach, this section focuses on achieving cooperative control in DC microgrids with communication delays.

3.1 Control Obejectives under Communication Delays

As mentioned in the Introduction, some research has already discussed the economic dispatch problem of microgrids at a small time scale. This paper adopts a synergizing incremental cost method to achieve economic load sharing. Specifically, the generation cost $J_i(i)$ for each DG can be represented by a quadratic function, as shown below.

$$J_i(i) = a_i i_i^2 + b_i i_i + c_i \tag{8}$$

where a_i, b_i, c_i are the cost coefficients for the respective DG. Using the Lagrange multiplier method, when the incremental costs are equal, the total generation cost for all DGs in the microgrid is minimized. The incremental cost eta can be expressed as:

$$\eta_i = \dot{J}_i = 2a_i i_i + b_i. \tag{9}$$

Therefore, the control objective of the secondary controller in this paper is to ensure that the voltage remains within an allowable range, i.e., $v_i \in [(1-\epsilon)\, v_i^n, (1+\epsilon)\, v_i^n]$, where ϵ is the percentage of voltage deviation required by the power grid (e.g., 7% for 220-V bus). Simultaneously, it ensures uniform incremental costs for each DG, aiming to achieve the minimum overall generation cost for the microgrid system. This requirement can be expressed as:

$$\lim_{t\to\infty} |\eta_i(t) - \eta_j(t)| = 0. \tag{10}$$

3.2 FAS-Based Secondary Controller Design

Firstly, let us consider the critical threshold requirements for the output voltage. According to the description in reference [18], it is reasonable to assume that $v_i = v_i^{\text{ref}}$ cause the inner loop control exhibits a faster response compared to secondary control. To meet the voltage constraints, define the upper and lower bounds of v_i^{ref} as $(1+\epsilon)\, v_i^n$ and $(1-\epsilon)\, v_i^n$.

Subsequently, to meet the economic operational requisites of the entire microgrid system, the consensus problem of incremental costs must be addressed. For this purpose, transmute the output of the system (4) from the output current i_i to the incremental cost η_i, specifically, $y_i(t) = \eta_i(t) = 2a_i i_i(t) + b_i$. Therefore, the secondary control (6) can be converted to the following equation.

$$u_i = b_{\eta i}^{-1}\left(-C_i\left(A_{ii}x_i + \sum_{j\in N_i^p} A_{ij}x_j\right) + \omega_i\right), \tag{11}$$

where $b_{\eta i} = 2a_i \frac{k_i^{pv} k_i^{pi} V_{dc}}{L_i}$, ω_i represents the auxiliary controller for economic sharing. Similar to (7), the dynamics of the incremental cost can be modeled as:

$$\dot{\eta}_i = \omega_i. \tag{12}$$

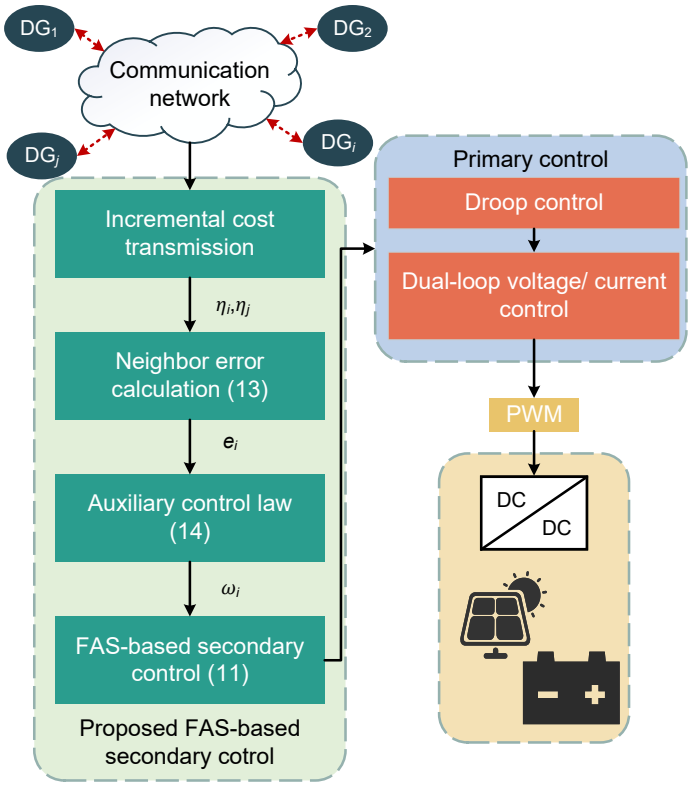

Fig. 2: FAS-based secondary control strategy implemented in a DC microgrid

Drawing from the graph theory, define the neighbor error of the incremental cost as:

$$e_i(t) = \sum_{j\in\mathcal{N}_i} a_{ij}\left(\eta_j(t) - \eta_i(t)\right). \tag{13}$$

where a_{ij} and $\mathcal{N}_i$ are the communication weight and networked neighbor set, respectively.

According to the FAS-based modeling shown in (12), one can regulate the system response via the design of the control law ω_i. In this paper, we employ the subsequent error feedback control:

$$\omega_i(t) = c_i e_i(t), \tag{14}$$

where c_i represents the coupling gain to be designed for ideal control performance.

The actual output of the secondary control can thus be derived from (11). As a result, the overall FAS-based secondary control diagram for each DG is shown in Fig. 2. Specifically, DGs exchange incremental cost information with their neighbors through the communication network. Subsequently, auxiliary control variables ω_i are computed based on equations (13) and (14), and the actual secondary control outputs are further obtained. Ultimately, the DC-DC converters of each DG are controlled through the primary control to regulate their operation.

4 Simulation Results

In order to verify the performance of the developed FAS-based secondary control, a cyber-physical DC microgrid is

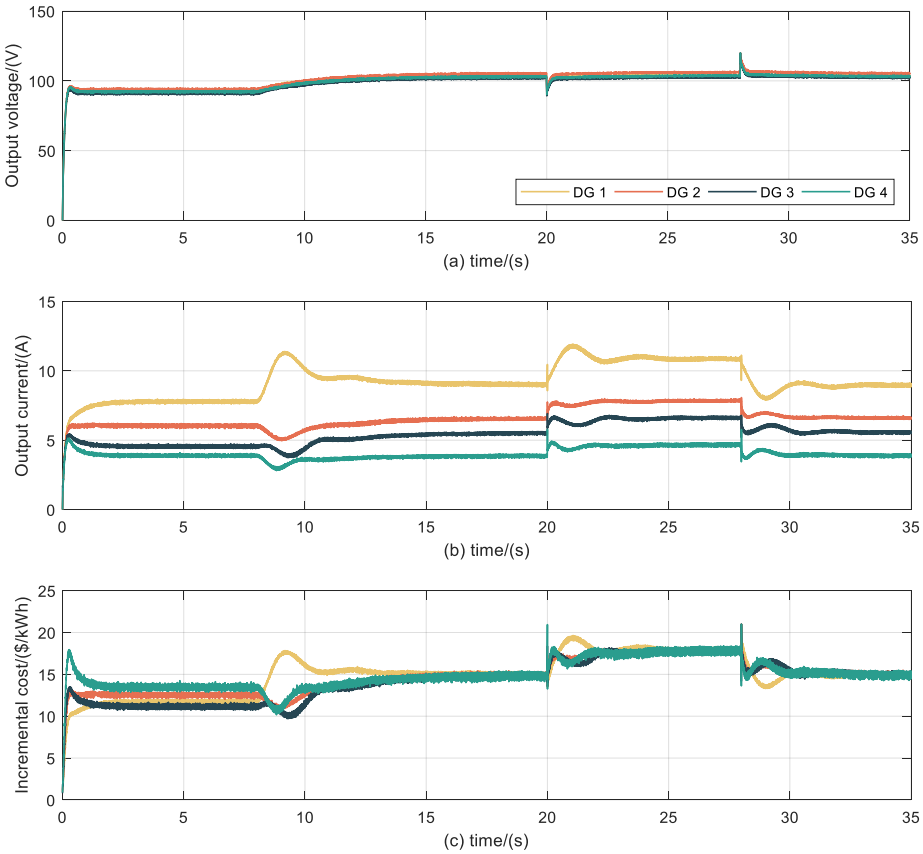

Fig. 3: Performance of the proposed FAS-based secondary controller. (a) Output voltages. (b) Output currents. (c) Incremental costs.

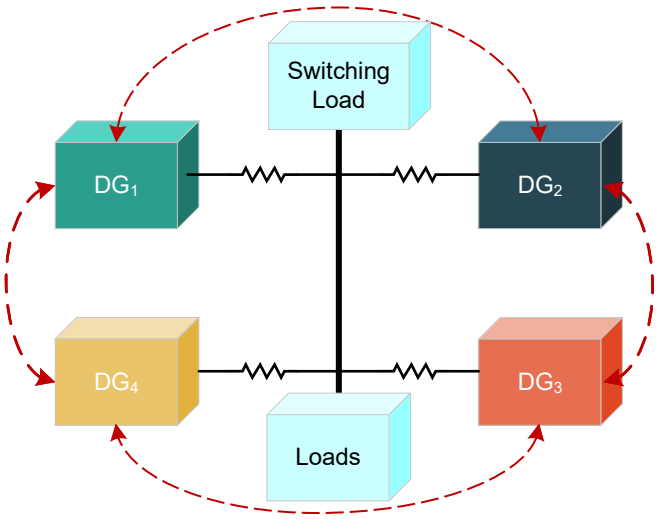

Fig. 4: Detailed schematic of the DC microgrid

Table 1: Parameters of The Test DC Microgrid

Parameters	Value
Desired voltage	100 V
Required voltage deviation	7%
DC source voltage	160 V
Load resistance	4 Ω
Switching load resistance	20 Ω
Storage inductor	2 mH
Filter capacitor	1 mF
Communication weights	$a_{ij} = 1, j \in \mathcal{N}_i$
Virtual resistance	[1, 1, 2, 2]
Voltage loop PI gains	0.008 + 1/s
Current loop PI gains	0.1 + 2/s
Coupling gain	2
Generation cost	a = [0.015, 0.02, 0.025, 0.035] b = [1,1.2,0.8,0.9] c = [1,1.5,1.2,0.9]

built in the MATLAB/SimPowerSystems environment. The electrical and cyber topology is shown in Fig. 4, and the detailed parameters are given in Table 1.

To validate the effectiveness of the proposed FAS-Based secondary control, our simulations primarily follow these steps:

1) 0 to 8 seconds: Microgrid initialization phase with only droop control activated;
2) 8 to 20 seconds: Activation of the proposed secondary control method;
3) 20 to 28 seconds: Addition of a switching load while maintaining secondary control;
4) 28 to 35 seconds: Removal of the load.

The specific simulation results are depicted in Fig. 3. From Fig. 3(a), during the initialization phase, the voltage do not reach the required 100 V due to the influence of droop control. However, after activating our secondary controller, the voltages can recover within the specified range.

Additionally, one can see that the voltages can rapidly recover when the load was switched. The current waveform in Fig. 3(b) shows that, whether in the droop control or secondary control phase, the current distribution cannot follow the 1:1:2:2 ratio. This is attributed to the mechanism of incremental cost, enabling global economic optimization. Finally, from Fig. 3(c), it can be observed that after activating secondary control, the incremental costs for all DGs tend to be consistent, implying global optimal generation cost. Therefore, these results validate the effectiveness and robustness of the proposed control method as presented in this paper.

5 Conclusion

This paper introduces and validates the secondary control strategy for DC microgrids using the FAS approach. By proposing a comprehensive large-signal model that integrates both circuitry and control, the coupling and control challenges among DGs within the microgrid architecture can be addressed. The FAS-based secondary control strategy is proposed using the achieved model for optimal economic operation. Simulation results verify the efficacy of our method, showcasing its ability to ensure system stability and economic efficiency across various scenarios. As we look ahead, the integration of FAS theory presents a promising avenue for advancing the control paradigms in DC microgrids, ensuring their resilience and optimal performance in the face of evolving energy landscapes.

References

[1] M. K. G. Deshmukh, M. Sameeroddin, D. Abdul, and M. Abdul Sattar, "Renewable energy in the 21st century: A review," *Materials Today: Proceedings*, vol. 80, pp. 1756–1759, 2023.

[2] Z. Lei, H. Zhou, X. Dai, W. Hu, and G.-P. Liu, "Digital twin based monitoring and control for dc-dc converters," *Nature Communications*, vol. 14, no. 1, p. 5604, 2023.

[3] S. Chaturvedi, V.-H. Bui, W. Su, and M. Wang, "Reinforcement learning-based integrated control to improve the efficiency of dc microgrids," *IEEE Transactions on Smart Grid*, vol. 15, no. 1, pp. 149–159, 2024.

[4] Y. Yu, G.-P. Liu, Y. Huang, and J. M. Guerrero, "Coordinated predictive secondary control for dc microgrids based on high-order fully actuated system approaches," *IEEE Transactions on Smart Grid*, vol. 15, no. 1, pp. 19–33, 2024.

[5] J. M. Guerrero, J. C. Vasquez, J. Matas, L. G. de Vicuna, and M. Castilla, "Hierarchical control of droop-controlled ac and dc microgrids—a general approach toward standardization," *IEEE Transactions on Industrial Electronics*, vol. 58, no. 1, pp. 158–172, 2011.

[6] X. Dai, G.-P. Liu, W. Hu, Q. Deng, and Z. Lei, "Distributed secondary control for dc microgrids with time-varying communication delays: A networked predictive control scheme," *IEEE Transactions on Power Systems*, pp. 1–14, 2023.

[7] Z. Fan, B. Fan, and W. Liu, "Distributed control of dc microgrids for optimal coordination of conventional and renewable generators," *IEEE Transactions on Smart Grid*, vol. 12, no. 6, pp. 4607–4615, 2021.

[8] Y. Dou, M. Chi, Z.-W. Liu, G. Wen, and Q. Sun, "Distributed secondary control for voltage regulation and optimal power sharing in dc microgrids," *IEEE Transactions on Control Systems Technology*, vol. 30, no. 6, pp. 2561–2572, 2022.

[9] J. Peng, B. Fan, Z. Tu, W. Zhang, and W. Liu, "Distributed periodic event-triggered optimal control of dc microgrids based on virtual incremental cost," *IEEE/CAA Journal of Automatica Sinica*, vol. 9, no. 4, pp. 624–634, 2022.

[10] P. Li, L. Guo, X. Li, H. Wang, L. Zhu, F. Gao, J. Zhu, and C. Wang, "Reduced-order modeling and comparative dynamic analysis of dc voltage control in dc microgrids under different droop methods," *IEEE Transactions on Energy Conversion*, vol. 36, no. 4, pp. 3317–3333, 2021.

[11] Y. Gui, R. Han, J. M. Guerrero, J. C. Vasquez, B. Wei, and W. Kim, "Large-signal stability improvement of dc-dc converters in dc microgrid," *IEEE Transactions on Energy Conversion*, vol. 36, no. 3, pp. 2534–2544, 2021.

[12] L. Kong and H. Nian, "Transient modeling method for faulty dc microgrid considering control effect of dc/ac and dc/dc converters," *IEEE Access*, vol. 8, pp. 150 759–150 772, 2020.

[13] G. Duan, "High-order fully actuated system approaches: Part i. models and basic procedure," *International Journal of Systems Science*, vol. 52, no. 2, pp. 422–435, 2021.

[14] G.-P. Liu, "Coordination of networked nonlinear multi-agents using a high-order fully actuated predictive control strategy," *IEEE/CAA Journal of Automatica Sinica*, vol. 9, no. 4, pp. 615–623, 2022.

[15] P. Li and G. Duan, "High-order fully actuated control approaches of flexible servo systems based on singular perturbation theory," *IEEE/ASME Transactions on Mechatronics*, vol. 28, no. 6, pp. 3386–3397, 2023.

[16] D.-W. Zhang, G.-P. Liu, and L. Cao, "Coordinated control of high-order fully actuated multiagent systems and its application: A predictive control strategy," *IEEE/ASME Transactions on Mechatronics*, vol. 27, no. 6, pp. 4362–4372, 2022.

[17] Y. Yu, G.-P. Liu, Y. Huang, and J. M. Guerrero, "Distributed learning-based secondary control for islanded dc microgrids: A high-order fully actuated system approach," *IEEE Transactions on Industrial Electronics*, vol. 71, no. 3, pp. 2990–3000, 2024.

[18] P. Shafiee, Y. Khayat, Y. Batmani, Q. Shafiee, and J. M. Guerrero, "On the design of event-triggered consensus-based secondary control of dc microgrids," *IEEE Transactions on Power Systems*, vol. 37, no. 5, pp. 3834–3846, 2022.

Proceedings of the 3rd Conference on Fully Actuated System Theory and Applications
May 10-12, 2024, Shenzhen, China

A method for multi-snake-like robot formation control and cooperative obstacle avoidance

Yunbo Pang[1], Darong Huang[1], Yuhong Na[1], Yunhu Zhou[1,2]

1. School of Artificial Intelligence, Anhui University, Hefei 230601, China
E-mail: drhuangjs@ahu.edu.cn, wa23301078@stu.ahu.edu.cn

2. R&D Center, Efort Intelligent Equipment Co., Ltd, Wuhu, 241007, China

Abstract: Snake-like robots are multi-degree-of-freedom, multi-mode unmanned intelligent robots suitable for complex and hazardous environments and research fields. The coordination of multiple snake-like robots expands their capabilities and spatial range for tasks. The paper introduces a method for controlling and coordinating multiple snake-like robots in formation and obstacle avoidance. Multiple snake-like robots are organized into a formation and move forward in a specific configuration or layout, while also coordinating to avoid obstacles. The leader-follower model is utilized for formation control, allowing the robot group to switch to suitable formation configurations based on different scenarios encountered, thereby enhancing the adaptability of the formation. In the context of cooperative obstacle avoidance, the artificial potential field method is employed. It creates repulsive potential fields between snake-like robots and obstacles or other robots, ensuring that the formation can effectively and stably navigate around obstacles while maintaining its overall structure.

Key Words: Snake-like robot, Multiple agents, Formation control, Cooperative obstacle avoidance, Artificial potential field method

1 Introduction

Snake-like robots are a type of biomimetic robot inspired by the movement of snakes. They rely on friction generated by the relative movement between their bodies and the ground to propel themselves forward. Compared to traditional robots, snake-like robots possess greater flexibility and adaptability, enabling them to navigate and perform tasks in various complex environments[1]. In practical applications, compared to single snake-like robots, multiple snake-like robots operating in coordination offer higher task efficiency, stronger adaptability, and robustness. They can handle more complex tasks and environmental demands[2], making them highly promising and versatile in scenarios such as search and rescue, environmental monitoring, and exploration. In the realm of multi-robot cooperation[3], formation control is a complex and critical issue. Effective and rational formations enable multiple robots to achieve efficient collective behavior, adapting to various complex environments and task requirements. Numerous studies have made significant progress in this area, including but not limited to the following aspects: 1) Behavior-based formation control methods[4], which rely on specific behavior patterns or rules for each robot to achieve coordinated actions within the formation. This approach typically does not require global information but instead relies on local perception and decision-making for each robot. 2) Leader-follower methods designate certain robots as leaders within the formation, with the remaining robots following the leaders' movements. Leaders typically handle path planning and decision-making, while followers maintain appropriate distance and relative positions with the leaders through perception and control[5]. 3) Virtual structure-based methods organize multiple robots into a virtual structure, such as a grid, circle, or snake-like formation. By controlling the interactions between robots and the virtual structure, formation control can be achieved[6]. 4) Consensus-based methods involve adjusting the interactions among multiple robots to ensure they maintain consistency or coordination in their actions, aiming to achieve specific objectives[7].

When addressing the multi-robot formation control problem, it's crucial to consider the interaction between robot formations and the environment. This ensures that robots can maintain their formation during motion and adapt to external disturbances and environmental changes[8]. Indeed, multi-robot cooperative obstacle avoidance is another typical challenge, especially in complex environments. Currently, path planning-based obstacle avoidance algorithms are widely used in robot navigation. These algorithms plan obstacle-free paths in known environments, enabling robots to avoid obstacles and reach their destination points. Common path planning-based obstacle avoidance algorithms include Ant Colony Optimization (ACO), Artificial Potential Field (APF) method, A* algorithm, Rapidly-exploring Random Tree (RRT) algorithm, and others[9].

Given the significant importance of multi-snake-like robot coordination in addressing more complex task requirements and adapting to uncertain environments, this paper investigates the technology and methods of multi-snake-like robot formation coordination and obstacle avoidance control. It proposes a method that combines the artificial potential field method with a leader-follower model for multi-snake-like robot formation control and cooperative obstacle avoidance.

*This work was supported by Department of Education of Anhui Province under Grant KJ2021A0050 and Anhui Provincial Natural Science Foundation under Grant 2308085QF210.

Based on this, the structure of this article is as follows: The second part presents Preliminaries, introducing the dynamics equations of snake-like robots. The third part, titled Main Results, constructs formations based on the leader-follower model and employs the artificial potential field method to design dynamic obstacle avoidance schemes. The fourth part demonstrates the effectiveness of the proposed method through simulations. Finally, the fifth part includes Conclusion and outlines potential Future Work.

2 Preliminaries and problem formulation

2.1 problem formulation

Based on this, the structure of this article is as follows: The second part presents Preliminaries, introducing the dynamics equations of snake-like robots. The third part, titled Main Results, constructs formations based on the leader-follower model and employs the artificial potential field method to design dynamic obstacle avoidance schemes. The fourth part demonstrates the effectiveness of the proposed method through simulations. Finally, the fifth part includes Conclusion and outlines potential Future Work.

The design for cooperative obstacle avoidance among multiple snake-like robots is as follows:

- Multiple snake-like robots depart from the same starting point, forming an appropriate formation, and proceed along a predetermined path towards the designated task point for operation.
- The environment between the starting point and the task destination is complex, with obstacles present. When robots detect obstacles, they need to change their direction of movement to avoid collisions with obstacles or other robots.

2.2 The gait pattern lateral undulation of snake-like robots.

The lateral undulation of snakes is a unique locomotion method that enables them to move across various terrains, including flat surfaces, uneven terrain, and even in water. In 1993, Hirose proposed the "serpenoid curve" based on research on biological snakes. He observed specific morphology and movement patterns in snakes during crawling, attempting to describe this motion using mathematical language[10]. Equation (1) gives the expression for the serpenoid curve. The characteristic of the serpenoid curve is that its curvature exhibits a sinusoidal variation during the snake's crawling process. In other words, as the snake crawls, the curvature of its body varies sinusoidally. This variation enables the snake to move efficiently across various terrains.

$$x(s)=\int_0^s cos(\,acos(b\sigma)+c\sigma)\,d\sigma$$
$$y(s)=\int_0^s sin(\,acos(\,b\sigma\,)+c\sigma)\,d\sigma \quad (1)$$

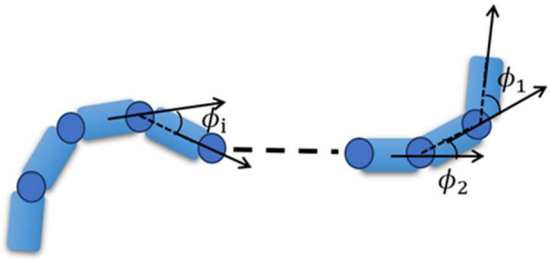

Fig. 1: Planar two-dimensional link snake-like robot

As shown in Figure 1, for a planar two-dimensional snake-like robot consisting of N links and N-1 joints, the serpentine crawling gait pattern can be achieved through the joint movements of the planar snake-like robot represented by Equation (2).

$$\phi_{i,ref}=\alpha\,sin\big(\omega t+\delta(i-1)\big)+\phi_o \quad (2)$$

which $i\in\{1,\cdots,N-1\}$; α and ω represent the amplitude and angular frequency, respectively, of the sinusoidal joint motion; δ denotes the phase shift of the joint angles, ensuring that the joint angles are always out of phase and never entirely equal; ϕ_o represents the joint angle offset, which can be utilized to control the direction of movement. This offset causes the direction of link motion to be asymmetrical with respect to the current orientation of the robot.

2.3 The Line-of-Sight (LOS) guidance law

The LOS guidance law can be used for both straight-line path tracking and curved path tracking. It is commonly employed in the tracking control of surface vessels[11]. The LOS guidance law converts the control of three degrees of freedom of snake-like robots position coordinates $(p_x\,,p_y)$ and forward direction $\bar{\theta}$ into the control of two degrees of freedom: forward velocity $\overline{v_t}$ and forward direction $\bar{\theta}$. The principle of the LOS (Line-of-Sight) algorithm is illustrated in Figure 2. By aligning the heading of the controlled object with the LOS angle, appropriate control can lead the object to its desired position, achieving path tracking.

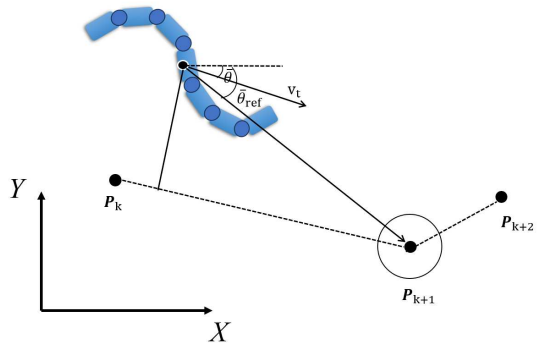

Fig. 2: The LOS algorithm principle

In Figure 2, P_k represents the previously tracked path point, and P_{k+1} represents the current path tracking point. When the snake-like robot approaches a certain range around the path point, it switches to tracking the next path point P_{k+2}. By dividing the tracking path into several path points, the robot can effectively track any desired path.

Define the reference direction angle according to the LOS guidance law:

$$\bar{\theta}_{ref} = -\arctan\left(\frac{p_y}{\Delta}\right) \tag{3}$$

where p_y represents the lateral tracking error, while $\Delta > 0$ stands for the forward distance. Further, design a joint angle offset controller:

$$\phi_o = k_\theta\left(\bar{\theta} - \bar{\theta}_{ref}\right) \tag{4}$$

where k_θ denotes the controller gain and ϕ_o represents the joint angle offset.

3 Main results

3.1 Formation control method for multi-snake-like robots based on leader-follower model

The leader-follower model is a common control strategy in multi-robot formation control, used to coordinate and manage the movement of robot groups. In this model, robots are divided into two categories: leaders and followers. The leaders are typically part of the robot group and are responsible for devising the motion strategy and path planning for the entire formation system. The actions of the leaders have a decisive impact on the motion trajectory of the entire formation. The followers can adjust their speed, direction, and position based on the movements of the leaders to maintain a certain relationship with them, thereby forming the desired configuration of the entire formation system. In the leader-follower model, typically only one robot is designated as the leader, while the rest of the robots act as followers, as depicted in Figure 3.

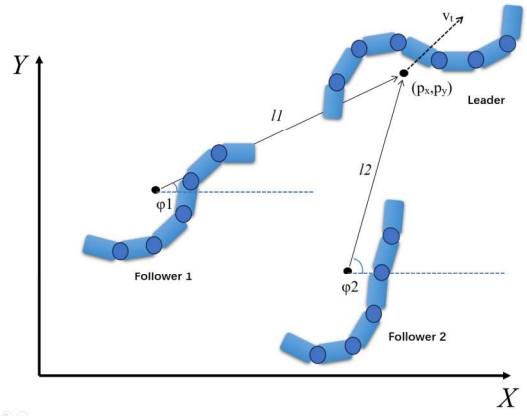

Fig. 3: Leader-follower method schematic diagram

The leader-follower model is relatively simple, easy to understand, and deployable. It can be implemented through straightforward rules and algorithms. As long as the motion state of the leader is predefined, controlling the relative angle and distance of the followers relative to the leader suffices[12]. Considering the use of the LOS algorithm for path tracking in snake-like robots, the followers' path points are set as relative position points to the leader in the desired formation. As the leader continues to move, the followers' path points are continuously updated, thus achieving the goal of maintaining the desired formation.

3.2 Multi-snake-like robot cooperative obstacle avoidance based on artificial potential field method

In the artificial potential field method[13], robots are considered objects subject to two types of forces: attraction and repulsion. The attraction force generated by the target point draws the robot towards it, encouraging it to get as close to the target as possible. The repulsive force generated around obstacles prevents robots from approaching the obstacles, thereby avoiding collisions. The artificial potential field method can be utilized for local path planning of snake-like robots. The snake-like robot formation detects the surrounding environment, including the positions and shapes of obstacles, as well as the locations of other robots, through sensors or other devices. Based on the detected obstacle information, the local potential field around the snake-like robots is computed. The global potential field originates from the path points specified along the given mission path. The snake-like robots select the direction and speed of their next move based on the merged potential field information. It tends to move towards the target point but is influenced by the repulsive force of obstacles to avoid them. Through this approach, robots can intelligently navigate around obstacles in the local environment and move towards the target along the globally planned path, thus accomplishing the task of local path planning.

The definitions of the attraction and repulsion field functions are as follows:

$$U_{att}(q) = \frac{1}{2}k_a\rho^2\left(q, q_{goal}\right)$$

$$U_{rep}(q) = \begin{cases} \frac{1}{2}k_r\left(\frac{1}{\rho(q,q_{obs})} - \frac{1}{\rho_0}\right)^2, \rho(q,q_{obs}) \le \rho_0 \\ 0, \rho(q,q_{obs}) \ge \rho_0 \end{cases} \tag{5}$$

In equation (5), k_a and k_r represent the proportional constants, q represents the centroid coordinates (p_x, p_y) of the robot, while q_{goal} and q_{obs} denote the centroid coordinates of the target point and the obstacle, respectively. $\rho(q, q_{obs})$ and $\rho\left(q, q_{goal}\right)$ represent the distance from the centroid coordinates of the current robot to the obstacle and the target, respectively. ρ_0 represents the effective range of each obstacle potential field.

In order to compute the attraction force F_{att}, repulsion force F_{rep}, and the combined force F exerted on a single snake-like robot, we calculate the negative gradient of the attraction and repulsion fields, as depicted below:

$$F_{att}(q) = k_a\left(q_{goal} - q\right)$$

$$F_{rep}(q) = \begin{cases} k_r\left(\frac{1}{\rho(q,q_{obs})} - \frac{1}{\rho_0}\right)\frac{1}{\rho^2(q,q_{obs})}, \rho(q,q_{obs}) \le 0 \\ 0, \rho(q,q_{obs}) \ge 0 \end{cases} \tag{6}$$

$$F(q) = F_{att}(q) + F_{rep}(q) \tag{7}$$

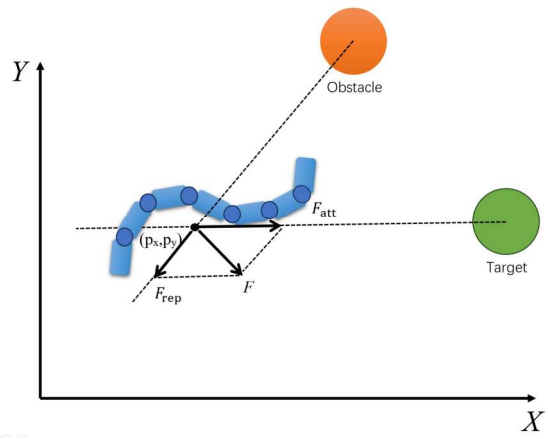

Fig. 4: Diagram illustrating the forces acting on an individual snake-like robot

The force situation of an individual snake-like robot in the potential field is depicted in Figure 4. Analyzing each snake-like robot, the resultant force F obtained from the artificial potential field method is used for local path planning[14], guiding obstacle avoidance behavior.

3.3 Formation shape transformation

The formation transformation of a multi-snake-like robot formation refers to the adjustment of positions and orientations among multiple robots working in coordination to achieve specific formations or layouts. This enables better adaptation of multi-snake-like robots to complex environments and task requirements. Snake-like robots can adopt a wedge formation during environmental perception and detection, enabling comprehensive observation of obstacles from all directions[15]. Considering the geometric characteristics of snake-like robots, where the length in the direction of motion exceeds that in the normal direction, encountering large obstacles or narrow spaces can significantly disrupt the wedge formation. Therefore, adopting an l-shaped formation is necessary.

Here, this paper introduces a formation transformation parameter $\gamma \in \{\gamma_i | i = 0,1\}$ and an expression for the interference error:

$$E = \| \text{current formation} - \text{desired formation} \| = \frac{1}{N}\sum_{n=1}^{N} \| p_i - p_i^d \| \quad (8)$$

Where N represents the number of snake-like robots, $\|\cdot\|$ denotes the Euclidean distance, p_i and p_i^d represent the coordinates of the current position and the expected position point of individual snake-like robots, respectively.

The magnitude of the expression E, which evaluates the interference error of the formation during the formation avoidance process, serves as the basis for formation transformation. Once the interference error E exceeds a certain threshold E_{max}, the formation changes to an l-shaped formation. After completing the avoidance maneuver and moving a certain distance away from the obstacle, the original wedge formation is restored.

The specific formation transformation mode is as follows:

1) During operation, the formation system continuously monitors the interference error E between the current formation and the desired formation. If E is less than the threshold E_{max}, then $\gamma = 0$, and the default wedge formation is maintained.
2) If the interference error E exceeds the threshold E_{max}, then $\gamma = 1$, triggering formation transformation. The formation is changed to an l-shape to address the presence of obstacles.
3) After the formation completes obstacle avoidance and moves a distance D away from the obstacle, the interference error E is checked again to see if it is less than E_{max}.
4) If it is, then $\gamma = 0$ to restore the original formation; otherwise, $\gamma = 1$ to continue maintaining the l-shaped formation.

After introducing formation transformation, the obstacle avoidance process for the entire snake-like robot formation is as follows:

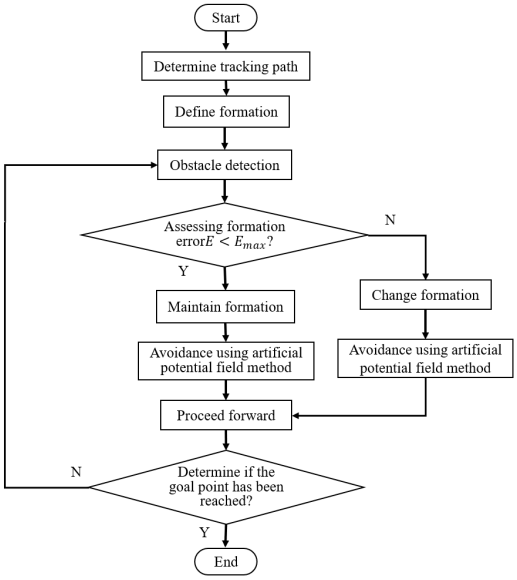

Fig. 5: Flowchart for multi-snake-like robot cooperative obstacle avoidance

4 Simulation results and analysis

4.1 Simulation of multi-snake-like robot formation

To validate the feasibility of the multi-snake-like robot cooperative obstacle avoidance algorithm proposed in this paper, a simulation was conducted using the CoppeliaSim (V-REP) platform. A two-dimensional snake-like robot model was constructed for simulation. The parameters of the snake-like robot were configured as follows: $2l$=0.3，α=0.5，ω=1，δ=50.4。

Table 1: Initial state of the snake-like robot

Snake	$x_0(m)$	$y_0(m)$	$\bar{\theta}$(deg)
Leader	-0.5	0	0
Follower 1	-1.9	0.6	35
Follower 2	-2.2	-1	-15

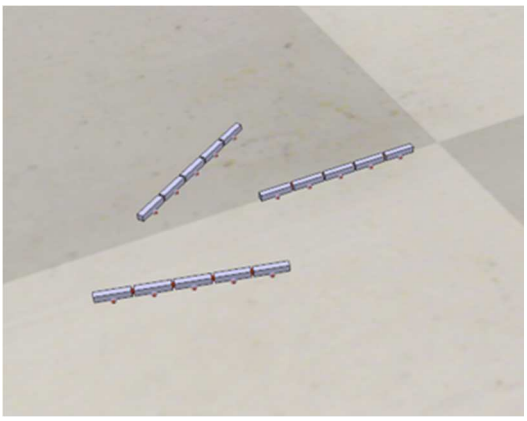

Fig. 6: Initial state of the snake-like robot

In order to enhance the visualization of the model, the results obtained from the CoppeliaSim simulation software (including the centroid coordinate trajectories of each snake-like robot) will be plotted as a graph. Figure 7 shows the motion trajectory of the multi-snake-like robot formation in an ideal environment.

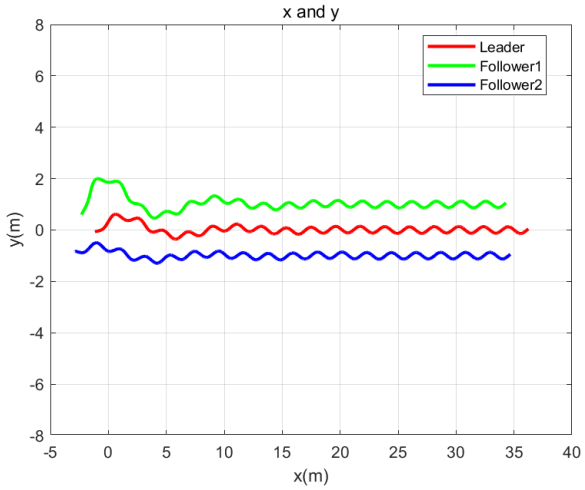

Fig. 7: The motion trajectory of the snake-like robot formation under ideal conditions

It can be observed that the adopted leader-following model effectively maintains the desired formation of the snake-like robot group. The wave-like pattern in the trajectory of the robots in the figure is due to the movement mechanism of the snake-like robots. Snake-like robots propel forward by generating friction with the ground through the back-and-forth twisting of their joints.

4.2 Simulation of multi-snake-like robot formation with obstacle avoidance.

Figure 8 illustrates the collaborative obstacle avoidance effect of the snake-like robot formation with the introduction of formation evaluation function.

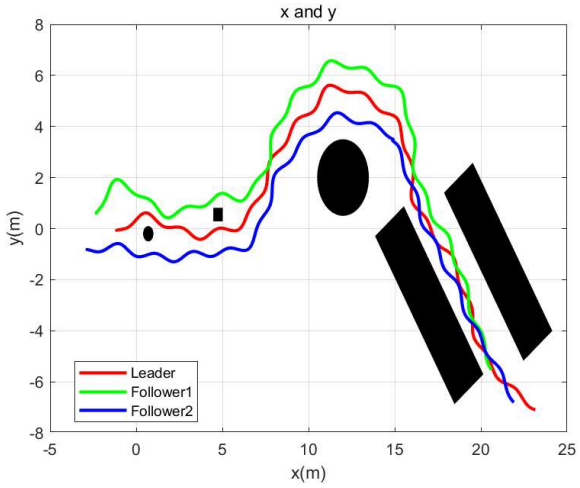

Fig. 8: Motion trajectory of the snake-like robot formation during obstacle avoidance.

It can be observed that with the introduction of the formation evaluation function, the snake-like robot formation switches to a more flexible l-shaped formation when encountering obstacles that significantly affect the formation. The robots initially proceed with wedge formation. Upon detecting small obstacles, they rely on artificial potential field methods for local path planning and adjust the relative positions between robots. This allows them to achieve obstacle avoidance while maintaining the formation as much as possible. When encountering larger obstacles or narrow spaces, the formation evaluation function facilitates a switch to an l-shaped formation to navigate through obstacles, ultimately reaching the task operation point.

5 Conclusion

This paper presents a method for multi-snake-like robot formation coordination and obstacle avoidance, which combines artificial potential field methods and leader-follower models. This method enables a group of multiple snake-like robots, including one leader and several followers, to advance towards the task point in an organized manner according to the desired formation. When obstacles are detected along the path, the snake-like robot group performs obstacle avoidance behavior based on artificial potential field methods while maintaining the formation. Furthermore, an additional formation evaluation function is introduced. During obstacle avoidance, this function can continuously detect the deviation between the current formation and the desired formation. When encountering large obstacles that significantly disrupt the formation, the current formation is disrupted. The robot group can rely on the formation evaluation function to transform the formation into a flexible l-shaped formation, ultimately reaching the task point. Finally, the effectiveness of the proposed method for multi-snake-like robot formation control and obstacle avoidance was verified using CoppeliaSim simulation software. In future work, we plan to implement this method on actual snake-like robot groups.

References

[1] J. Liu, Y. Tong, J. Liu, Review of snake robots in constrained environments. *Robotics and Autonomous Systems*, 2021, 141: 103785.

[2] G. J. Lim, S. Kim, J. Cho, Y. Gong, A. Khodaei, Multi-UAV pre-positioning and routing for power network damage assessment. *IEEE Transactions on Smart Grid*, 2016, 9(4): 3643-3651.

[3] M. Liu, Y. Li, L. Zhu, Y. Guo, B. Liu, Formation Control for Mixed-Order UAVs‐USVs‐UUVs Systems under Cooperative and Optimal Control. *Journal of Marine Science and Engineering*, 2023, 11(4): 704.

[4] J. Wen, J. Yang, Y. Li, J. He, Z. Li, H. Song, Behavior-based formation control digital twin for multi-aug in edge computing. *IEEE Transactions on Network Science and Engineering*, 2022, 10(5): 2791-2801.

[5] Y. Li, J. Zhang and S. Tong, Fuzzy adaptive optimized leader-following formation control for second-order stochastic multiagent systems. *IEEE Transactions on Industrial Informatics*, 2021, 18(9): 6026-6037. M. Shore, S. Zeadally, A. Keshariya, Zero Trust: The What,How,Why,and When Computer, 2021,54(11):26-35.

[6] A. Abbaspour, K. Alipour, H. Z. Jafari, S. A. A. Moosavian, Optimal formation and control of cooperative wheeled mobile robots. *Comptes Rendus Mécanique*, 2015, 343(5-6): 307-321.

[7] W. Ren, Consensus strategies for cooperative control of vehicle formations. *IET Control Theory & Applications*, 2007, 1(2): 505-512.

[8] L. Li, L. Yang, B. Li, Formation control for multiple robots in uncertain environments. In *Proceedings of the 10th World Congress on Intelligent Control and Automation*, 2012, 3607-3610).

[9] S. Lin, A. Liu, J. Wang, X. Kong, A review of path-planning approaches for multiple mobile robots. *Machines*, 2022, 10(9): 773.

[10] S. Hirose, H. Yamada, Snake-like robots machine design of biologically inspired robots. *IEEE Robotics & Automation Magazine*, 2009, 16(1):88-98.

[11] N. Gu, D. Wang, Z. Peng, J. Wang, Q. L. Han, Advances in line-of-sight guidance for path following of autonomous marine vehicles: An overview. *IEEE Transactions on Systems, Man, and Cybernetics: Systems*, 2022, 53(1): 12-28.

[12] T. Liu, M. de Queiroz, Distance+ angle-based control of 2-d rigid formations. *IEEE transactions on cybernetics*, 2020, 51(12): 5969-5978.

[13] X. N. Gao, L. J. Wu, Multi-robot formation control based on the artificial potential field method. *Applied Mechanics and Materials*, 2014, 519: 1360-1363.

[14] D. Li, Z. Zhou, H. Deng, C. Wang, K. Li, C. Wang, P. Teng, 2D obstacle avoidance method for snake robot based on modified artificial potential field. In *2017 IEEE International Conference on Unmanned Systems (ICUS)* 2017, 358-363.

[15] X. Fu, J. Pan, H. Wang, X. Gao, A formation maintenance and reconstruction method of UAV swarm based on distributed control. *Aerospace Science and Technology*, 2020, 104: 105981.

Proceedings of the 3rd Conference on Fully Actuated System Theory and Applications
May 10-12, 2024, Shenzhen, China

Ship Energy Efficiency Prediction Method Based on Data Mining Techniques

Nuo Cheng, Liheng Chen, Depeng Zeng
College of Intelligent Systems Science and Engineering, Harbin Engineering University, Harbin 150001, China.
E-mail: clh114131@gmail.com

Abstract: Intelligent energy efficiency management is a key technology within the "Intelligent Ship Code" system released by the China Classification Society. It drives the smart and green development of ships by automatically monitoring, analyzing, and optimizing ship energy efficiency. Trailing suction hopper dredgers (TSHDs) are vital for tasks like port maintenance but are known for their high energy consumption. This study aims to explore TSHD energy efficiency deeply by utilizing data analysis techniques, including clustering algorithms and neural networks, to establish predictive models. Our goal is to optimize TSHD energy management, enhance operational efficiency, and provide technical support for the intelligent and green development of the maritime industry.

Key Words: TSHD, Clustering, Neural Network, Energy Efficiency Prediction

1 Introduction

In recent years, research in the shipping industry on intelligent energy efficiency optimization for vessels has gradually deepened, and there has been preliminary exploration of big data technology in the field of shipping optimization management[1-3]. Reference [1] explores the construction content of big data for inland vessels, providing methods for acquiring and analyzing vessel big data. Building on this, reference [2] designs a big data monitoring platform for energy efficiency optimization management in vessels, proposing corresponding technical indicators and experimental verification plans. Reference [3] investigates an intelligent optimization method for ship routes, providing optimal route decision-making through the analysis of historical big data on typical routes. Although there have been initial exploratory achievements in the application of big data technology to intelligent optimization management in shipping, the traditional energy efficiency management systems for trailing suction hopper dredgers, being biased toward data collection, currently lack comprehensive analysis and exploration of data features. This disparity results in uncertainty when correlating the energy efficiency of trailing suction hopper dredgers with the operational parameters of the vessels themselves. Therefore, exploring the underlying patterns in dredger operational data to predict energy efficiency more accurately is a worthwhile research question.

With the rapid development of artificial intelligence technology, strategies for evaluating ship energy efficiency levels using intelligent optimization models and algorithms have garnered attention from scholars both domestically and internationally[4-9]. Reference [4] has developed an oil tanker decision-making system based on neural networks to predict energy efficiency during cruise voyages. Furthermore, reference [5] delves deeper into the entire process of fuel consumption, further enhancing prediction accuracy. Reference [6] has established ship performance models under various conditions, enabling accurate prediction of fuel consumption for cruise ships.However, due to the influence of multiple factors during the dredging process, the operation of TSHD exhibits strong nonlinearity. Traditional energy efficiency modeling methods struggle to achieve accurate energy efficiency predictions for TSHDs. Currently, there is no definitive theoretical outcome for the assessment and optimization of TSHD efficiency.

To address the aforementioned issues, this paper first preprocesses the data through clustering algorithms, mining implicit information in the dredger data and clustering the data. Subsequently, using correlation analysis, it selects features with significant correlations to trailing suction hopper dredger (TSHD) energy efficiency as the research focus. By integrating data from various clusters and employing a Backpropagation(BP) neural network, a TSHD energy efficiency prediction model has been established, resulting in accurate energy efficiency forecasts.

2 Research Methods

The dredging process of trailing suction hopper dredgers (TSHDs) exhibits typical characteristics of nonlinearity and time delay, making the relationship between energy efficiency and operational parameters complex and challenging to establish predictive models. Therefore, in this paper, non-working condition data is first removed based on the energy efficiency formula. Subsequently, clustering algorithms are applied to preprocess the data, uncovering hidden relationships within the data and further categorizing it. After dividing the data into different clusters, a correlation analysis is conducted to identify features with significant correlations to energy efficiency as the research focus. A predictive model for TSHD energy efficiency has been developed using BP neural networks, ensuring precise forecasts. The specific methodological process is illustrated in Fig. 1.

This work was supported in part by the National Natural Science Foundation of China (62273114), in part by the Macao Young Scholars Program (AM2022004), in part by the China Postdoctoral Science Foundation (No. 2019M661255, No. 2021T140149).
Corresponding author: Liheng Chen

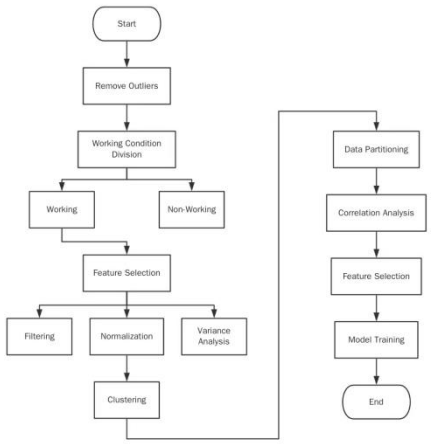

Fig. 1: Overall Process Diagram

2.1 DBSCAN Based on Particle Swarm Optimization Algorithm

The DBSCAN algorithm is a type of density-based clustering algorithm. It defines clusters as the maximal set of density-connected points, allowing the discovery of clusters of arbitrary shapes and identification of noise points in the dataset. Concepts such as Eps, MinPts, core objects, direct density reachability, density reachability, and density connectivity in the DBSCAN algorithm are detailed in reference [10]. The selection of Eps and MinPts parameters in the DBSCAN algorithm is crucial. To address this, the Particle Swarm Optimization (PSO) algorithm is employed to optimize the values of Eps and MinPts, as illustrated in the experimental process diagram in Fig. 2.

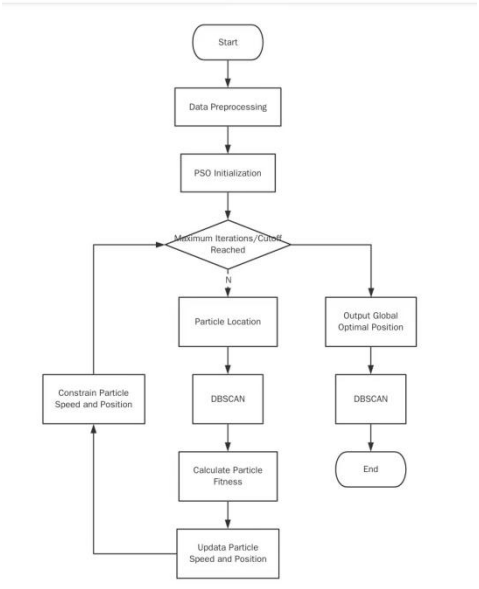

Fig. 2: Clustering Process Diagram

To enhance clustering effectiveness, this paper uses the silhouette coefficient as the evaluation metric for clustering results and employs it as the fitness function in the PSO algorithm. The formula for calculating the silhouette coefficient for all sample points is as follows:

$$S = \frac{1}{N}\sum_{i}\frac{b(i) - a(i)}{\max\{a(i), b(i)\}}$$

In the formula, N represents the total number of samples, a(i) denotes the average distance from sample point i to the other points within the same cluster. If a cluster contains only one sample, this value is 0, indicating the dissimilarity among samples within the cluster. Refer to the specific details in reference [11]. b(i) represents the minimum average distance from sample point i to the points in other clusters, describing the dissimilarity among samples from different clusters. The silhouette coefficient has a range of [-1,1], with values closer to 1 indicating better clustering effectiveness.

2.2 Backpropagation Neural Network

Neural networks can map complex relationships based on system input and output data, constructing intricate nonlinear models through layers of neurons and weighted connections. In this paper, we utilize the Backpropagation (BP) neural network to investigate the issue of predicting the energy efficiency of trailing suction hopper dredgers. The typical structure of a BP neural network is depicted in the diagram below, comprising an input layer, hidden layers, and an output layer reference [12-13].

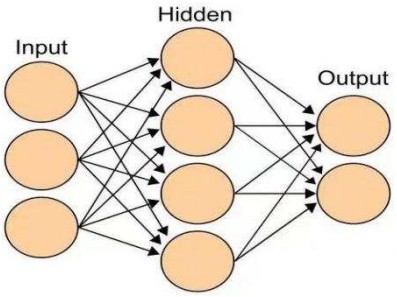

Fig. 3: Diagram of the BP Neural Network Structure

The BP neural network achieves continuous optimization of model parameters through forward signal propagation and backward error propagation. To reduce the complexity of the model and enhance prediction accuracy, prior to constructing and training the model, this paper performs feature selection for the neural network by calculating the correlation between various operational parameters of the trailing suction hopper dredger and its energy efficiency. The correlation calculation is as follows:"

$$\rho_{XY} = \frac{Cov(X,Y)}{\sqrt{D(X)} * \sqrt{D(Y)}}$$

In the formula, X and Y represent two distinct features, Cov(X, Y) denotes the covariance, and D(X) and D(Y) represent the variance of the features.

3 Experimental Analysis

The dataset used in this paper consists of actual ship data from a specific trailing suction hopper dredger, totaling 17,640 samples and including 35 features such as slurry pump concentration, displacement, speed, and flow rate. Due to the energy efficiency formula:

$$\text{Energy Efficiency} = \frac{\text{Power}}{(\text{Concentration} * \text{Density} * \text{Flow Rate})}$$

In the subsequent data preprocessing, four related factors, namely slurry pump power, slurry pump concentration, slurry pump density, and slurry pump flow rate, cannot undergo correlation analysis. As per the formula, during the dredging process, the mud compartment capacity undergoes a significant increase, and the slurry pump speed is in a high-speed state, resulting in a higher slurry pump concentration. In non-working processes, the mud compartment capacity remains relatively stable, the slurry pump speed is close to zero, and the concentration is also close to zero. Therefore, based on the values of slurry pump concentration, the data is divided into two working conditions: working and non-working.

3.1 Clustering

Based on the distribution of slurry pump concentration data for the trailing suction hopper dredger, a concentration threshold of 0.64 is set to classify the dredger data into two working conditions: working and non-working. The focus of this study is on predicting efficiency in the working state. To address the influence of noise in the data, Gaussian filtering is employed for denoising, followed by normalization using the linear normalization method.

By calculating the variance between different features, features with higher variance are selected as input features for clustering. Larger feature variances indicate greater differences among sample points in that feature, making it easier for clustering algorithms to separate samples of different categories. The calculated feature variances range from a minimum of 0.006807 to a maximum of 0.074087. Features with higher variances are selected, and the information is detailed in Table 1.

Table 1: Cluster Feature Variance Table

Feature	Variance
Average Draft	0.059311
Bow Draft Calculation	0.059051
Current Slurry Compartment Liquid Level	0.055694
Current Slurry Compartment Capacity	0.058265
Ship Displacement	0.059068
Tide Level	0.074087

The distribution of the original data is shown in the figure below:

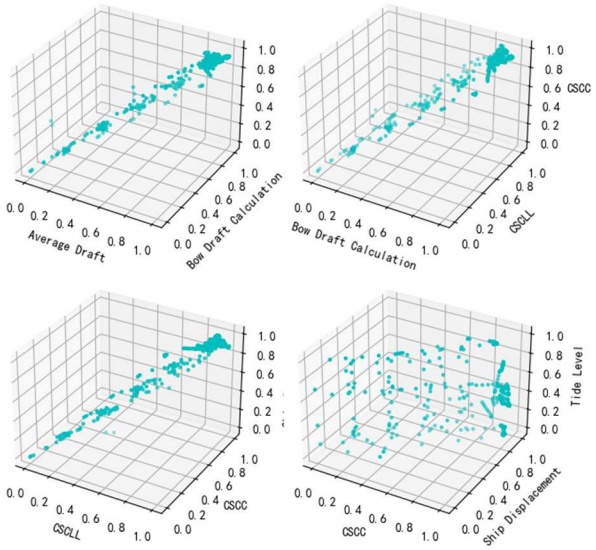

Fig. 4: Graph of the Distribution of Original Data

In this paper, the KMeans clustering algorithm is initially employed, with a hyperparameter k ranging from 2 to 10. The silhouette coefficient is used as the evaluation metric. By iterating through all values of k, the best clustering performance is achieved when k=2, as shown in the clustering results in Fig. 5.

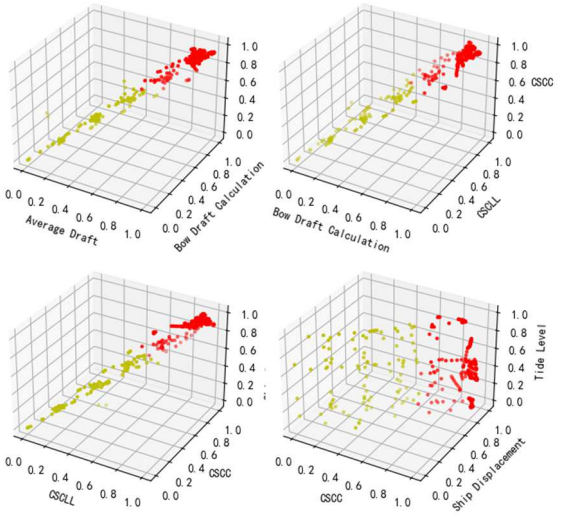

Fig. 5: KMeans Clustering Result Graph

From the distribution of sample data, it is evident that the data does not exhibit a spherical shape, and there are clear linear relationships between some features, causing the data to appear in a bar-like manner in certain feature dimensions. This makes KMeans less suitable. Therefore, in this paper, DBSCAN is used for clustering. The PSO optimization algorithm is applied to optimize the parameters Eps and MinPts in the DBSCAN clustering algorithm. Eps is set within the range of [0.1, 5], and MinPts within the range of [1, 8]. The optimal results are obtained when Eps=0.188 and MinPts=6, with a silhouette coefficient of 0.591. This result

is slightly better than KMeans. The clustering results are shown in Fig. 6.

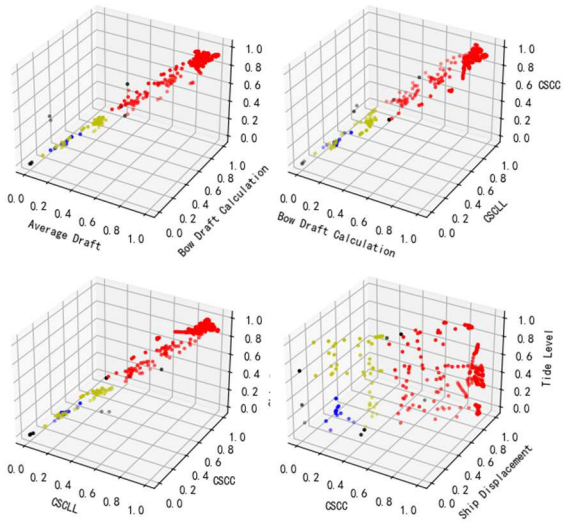

Fig. 6: DBSCAN Clustering Result Graph

3.2 Energy Efficiency Prediction

To improve the accuracy of the prediction model, separate training is conducted on the classified data. Data preprocessing, including Gaussian filtering and normalization, is performed. Feature selection is carried out through correlation analysis. By calculating the correlation coefficients between different features and energy efficiency, features with higher correlation are selected as input parameters for the neural network model. The correlation coefficient values range from -1 to 1, where values closer to 0 indicate lower correlation, values closer to 1 indicate a positive correlation, and values closer to -1 indicate a negative correlation. The results of feature selection are shown in Table 2.

Table 2: Neural Network Input Feature Table

Feature	Correlation Coefficient
Left High Pressure Flush Pump Discharge Pressure Pump Discharge Pressure	0.300213
Left High Pressure Flush Pump Speed	0.331820
Slurry Pump 1 Speed	0.789902
Slurry Pump 1 Flow Rate	-0.368278
Slurry Pump 1 Pressure	0.337156
Slurry Pump 1 Motor Speed	0.789940

The training results of the BP neural network on the training set are shown in Fig. 7, and the testing results on the testing set are presented in Fig. 8. Here, only the performance of the model on data from one cluster is displayed:

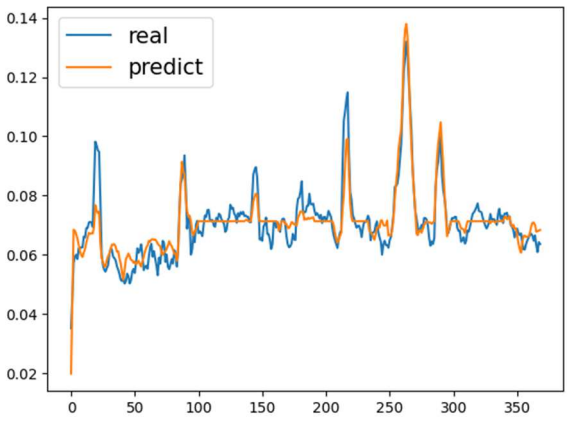

Fig. 7: Training Set Model Prediction Results Graph

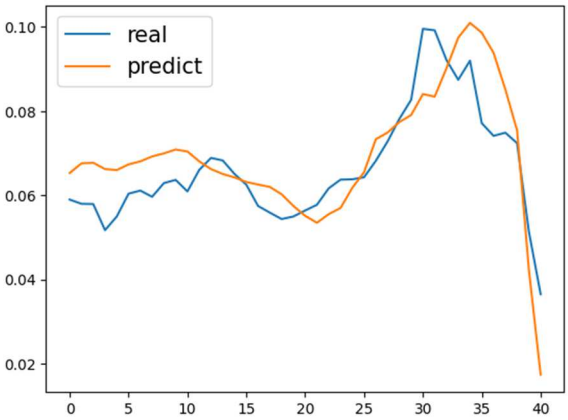

Fig. 8: Testing Set Model Prediction Results Graph

The Mean Absolute Error (MAE) of the BP neural network on the testing set is 0.00723, and the Root Mean Square Error (RMSE) is 0.00899.

4 Conclusion

This paper, initially through variance analysis, selected input features for the clustering algorithm. By observing the distribution of the dataset and comparing KMeans with DBSCAN clustering, the decision was made to use the DBSCAN algorithm for clustering the original dataset. Simultaneously, with the aid of the Particle Swarm Optimization (PSO) algorithm, it optimized the hyperparameters of the DBSCAN algorithm, achieving classification of trailing suction hopper dredger operational data. Subsequently, an analysis was conducted on the classified data. Through Gaussian filtering and correlation analysis, suitable features were selected. Leveraging the powerful nonlinear mapping capability of the BP neural network, a successful nonlinear model between the energy efficiency and operational parameters of the trailing suction hopper dredger was established. This enabled rapid and accurate prediction of the energy efficiency of the dredger.

References

[1] Cao, Mengmeng , and C. Guo . "Key technologies of big data and its development in intelligent ship." International Conference 2017:61-65.

[2] Erto, Pasquale , et al. "A procedure for predicting and controlling the ship fuel consumption: Its implementation and test." Quality and Reliability Engineering 31.7(2015):1177-1184.

[3] Wang, Kai , et al. "Study on route division for ship energy efficiency optimization based on big environment data." International Conference on Transportation Information & Safety IEEE, 2017.

[4] Besikci, E. Bal , et al. "An artificial neural network based decision support system for energy efficient ship operations." Computers & Operations Research 66.FEB.(2016):393-401.

[5] Tillig, Fabian , et al. "Analysis of uncertainties in the prediction of ships' fuel consumption – from early design to operation conditions." Ships and Offshore Structures 13.S1(2018):S13-S24.

[6] Lu, Ruihua , O. Turan , and E. Boulougouris . "Voyage optimisation: Prediction of ship specific fuel consumption for energy efficient shipping." LCS 2013 - 3rd International Conference on Technologies, Operations, Logistics and Modelling for Low Carbon Shipping 2013.

[7] Hou, Yuanhang , et al. "Vessel energy efficiency uncertainty optimization analysis in ice zone considering interval parameters." Ocean engineering 232-Jul.15(2021).

[8] Christos, Spandonidis , et al. "Evaluation of ship energy efficiency predictive and optimization models based on noon reports and condition monitoring datasets." International Conference on Data Analytics 2018.

[9] Theodoropoulos, Panayiotis , et al. "Evaluation of different deep-learning models for the prediction of a ship's propulsion power." Journal of Marine Science and Engineering 9.2(2021):116.

[10] Dafir, Zineb , Y. Lamari , and S. Slaoui . "A survey on parallel clustering algorithms for big data." (2021).

[11] Aranganayagi, S. , and K. Thangavel . "Clustering categorical data using silhouette coefficient as a relocating measure." International Conference on Conference on Computational Intelligence & Multimedia Applications IEEE, 2007:13-17.

[12] Xue, Yang , et al. "Fault detection based on backpropagation neural network for liquid propellant rocket engine." International Symposium on Test and Measurement 2005.

[13] Little, Gordon R. , S. C. Gustafson , and R. A. Senn . "Generalization of the backpropagation neural network learning algorithm to permit complex weights." Applied Optics 29.11(1990):1591-2.

Proceedings of the 3rd Conference on Fully Actuated System Theory and Applications
May 10-12, 2024, Shenzhen, China

Circular Phased Array Ultrasonic Transducer Design for Internal Inspection of Natural Gas Pipeline

ZhongWei Qi[1], Mingyan Liao[1], Li Sheng *[1], Zhongyu Chen[1], Yichun Niu[2]

1. College of Control Science and Engineering, China University of Petroleum (East China), Qingdao 266580, China
E-mail: shengli@upc.edu.cn

2. College of Electrical Engineering and Automation, Shandong University of Science and Technology,Qingdao 266590, China
E-mail: niuyichun123@163.com

Abstract: In the paper, a 256-element circular array ultrasonic transducer is designed to create a controllable and focused 3D cylindrical ultrasound beam for pipeline inspection of natural gas pipelines. First, a localized three-dimensional acoustic modeling of the considered 250-mm-caliber pipeline is constructed by using the k-Wave toolbox. Then, the layout manner of the phased array is given previously, while the active aperture and input signal frequency of the phased array are determined via the experimental method. Finally, the simulation results on the axial-radial and circumferential-radial planes are exhibited to analysis the effectiveness of the proposed method. The results indicate that the piezoelectric transducer array can derive a feasible focused beam, providing a basis for future transducer prototyping.

Key Words: Natural gas pipelines, Circular ultrasonic phased array, Pipeline inspection, K-Wave toolbox

1 Introduction

With the development of ultrasound technology in the field of the non-destructive testing (NDT), there is a growing demand for ultrasound techniques used in the internal inspection of pipes, and the requirements for focused adjustable beam profiles in three-dimensional cylindrical spaces are also increasing[1, 2]. In traditional detection methods, transducer arrays may need to move and deflect to detect three-dimensional cylindrical sound fields. Additionally, the detection sensitivity and resolution of traditional single-element imaging devices are unsatisfactory, despite can detect the circumferential cracks and pinholes[3].

To address the above drawbacks, in recent years, a phased array technology is proposed and widely extended to the field of NDT[4, 5]. Under the phased array technology, various steering or focusing sound beams can be formed by appropriately exciting the phased array through focal law delay elements[6, 7]. Furthermore, in ultrasound testing and power ultrasound, scanning the entire space for NDT can be achieved by controlling the phase of linear or planar phased array excitation signals[8, 9]. Currently, the researches on phased array beam control are mainly focused on linear, planar, spherical, and quasi-spherical focusing arrays, which are well-suited for scanning spherical, sector-shaped, or square spaces[10]. The literature[11] indicates that the scanning sound fields in cylindrical three-dimensional spaces has a certain degree of complexity. It is hoped that by manipulating the focus of the sound field through phased array technology, the entire three-dimensional space of the pipeline can be scanned, thereby addressing internal inspection challenges in pipelines.

Inspired by the discussions above, this paper proposes a circular array ultrasound transducer consisting of 256 rectangular piezoelectric elements for studying the acoustic field distribution of phased array ultrasound in three-dimensional cylindrical space, aiming to enhance internal detection in pipelines. Firstly, by using the k-Wave toolbox, a localized three-dimensional acoustic modeling of the considered 250-mm-caliber pipeline is constructed where the circular array ultrasound transducer concentric with the pipeline. Subsequently, based on the designed delay laws of the phased array ultrasound, the expected focal positions of the ultrasound waves in a non-uniform medium are calculated. An analysis of the axial radial plane (ARP) and circumferential radial plane (CRP) acoustic pressure field distribution is conducted based on the temporal simulation results of the ultrasound waves, determining parameters such as active aperture size and operating frequency. Finally, considering the determined active aperture size and frequency, the impact of the spacing between array elements and the width of array elements on the acoustic field is analyzed. To ensure successful internal detection in pipelines, phase control techniques are employed to manipulate the focal points of the acoustic field and scan the entire pipeline. The main contributions of this paper are as follows:

1) This paper, for the first time, proposes a 256-element circular array ultrasonic transducer.The proposed transducer can create a controllable and focused 3D cylindrical ultrasound beam used for the internal inspection of natural gas pipelines.
2) The proposed design scheme analyzes the arrangement parameters of a circular array of sensors and provides a method for the acoustic field analysis of circular array ultrasound transducers, laying the foundation for the next step in constructing a prototype based on the transducer principles.

2 Sound Field Simulation Theory

When sound waves pass through a medium, some physical quantities may be changed such as pressure, density, temperature, and particle velocity. These changes are explained by a coupled first-order partial differential equations that are based on the conservation of mass, momentum, and energy. The propagation of an acoustic wave with high energy in a non-uniform medium is nonlinear, which can be reflected in

This work is supported by the Postdoctoral Program for Innovative Talents of Shandong Province of China under Grant SDBX2023021.

the following system equation[12]:

$$\begin{cases} \frac{\partial u}{\partial t} = -\frac{1}{\rho_0}\nabla p \\ \frac{\partial \rho}{\partial t} = -\left(2\rho + \rho_0\right)\nabla \cdot u - u \cdot \nabla \rho_0 \\ p = c_0^2\left(\rho + d \cdot \nabla \rho_0 + \frac{B}{2A}\frac{\rho^2}{\rho_0} - L\rho\right) \end{cases} \tag{1}$$

where u is the acoustic particle velocity; ρ_0 is the ambient density; ρ is the acoustic density; d is the acoustic particle displacement; p is the acoustic pressure; t is the time; c_0 is the isentropic sound velocity; B/A is the nonlinearity parameter; L is a linear integral-differential operator which can be expressed as:

$$L = \tau\frac{\partial}{\partial t}\left(-\nabla^2\right)^{y/2-1} + \eta\left(-\nabla^2\right)^{(y+1)/2-1} \tag{2}$$

in which τ is the absorption scaling factor, η is the dispersion scaling factor and y is the power law exponent.

For solving partial differential equations, the traditional finite element and finite difference methods need to employ a large number of grid points for each acoustic wavelength, which makes it difficult to solve them using the regular computer. For this challenge, the spectrum of spatial derivatives is computed by using the k-Wave toolbox, the k-space pseudo-spectral method and fast Fourier transform. In tests, the k-Wave is a effective toolbox on modeling nondestructive experiment environment. To obtain accurate results, only two grid points per wavelength are theoretically required since the basis functions are sinusoidal, which can allow a quick calculation. After discretizing the coupled acoustic equations, we can obtain the following discretized equation:

$$\begin{cases} \frac{\partial}{\partial \xi}p^n = \mathcal{F}^{-1}\left\{ik_\xi \kappa e^{-ik_\xi \nabla\xi/2}\mathcal{F}\left\{p^n\right\}\right\} \\ u_\xi^{n+\frac{1}{2}} = u_\xi^{n-\frac{1}{2}} - \frac{\Delta t}{\rho_0}\frac{\partial}{\partial \xi}p^n + \Delta t S_{F_\xi}^n \\ \frac{\partial}{\partial \xi}u_\xi^{n+\frac{1}{2}} = \mathcal{F}^{-1}\left\{ik_\xi \kappa e^{-ik_\xi \nabla\xi/2}\mathcal{F}\left\{u_\xi^{n+\frac{1}{2}}\right\}\right\} \\ \rho_\xi^{n+1} = \frac{\rho_\xi^n - \Delta t\rho_0 \frac{\partial}{\partial \xi}u_\xi^{n+\frac{1}{2}}}{1+2\Delta t\frac{\partial}{\partial \xi}u_\xi^{n+\frac{1}{2}}} \\ p^{n+1} = c_0^2\left(p^{n+1} + \frac{B}{2A}\frac{1}{\rho_0}\left(\rho^{n+1}\right)^2 - L_d\right) \end{cases} \tag{3}$$

where $\mathcal{F}$ denotes the Fourier transform, i is the imaginary unit, k_ξ denotes the number of waves in the ξ-direction, $\nabla\xi$ denotes the grid spacing in the ξ-direction, $\mathcal{F}^{-1}$ denotes the Fourier inverse transform, $\kappa = \mathrm{sinc}\left(c_{ref}k\Delta t/2\right)$ is the k-space operator, c_{ref} is the reference speed of sound, and ξ is described as $\xi = x \in \mathbb{R}$, $\xi = [x, y]^T \in \mathbb{R}^2$ and $\xi = [x, y, z]^T \in \mathbb{R}^3$ under one, two and three dimensional vector spaces respectively. The density ρ_ξ^{n+1} is decomposed into Cartesian components to introduce anisotropic perfectly matched layer. At each time step, the source values are typically added to appropriate grid points in the computational domain, which can contain a mass or force source. Similarly, the experiment results can be obtained by recording the acoustic variables at specific grid points at each time step.

3 Delay Law for Phased Array and Simulation Model

3.1 Delay law for phased array

The transducer array is retrofitted to the pipe robot and is coaxial with the pipe during pipe work. The schematic diagram of the transducer array, pipeline robot, and pipeline is shown in Fig. 1, N transducer elements are equidistantly spaced at a center distance P, with width W and length l. Ultrasonic waves with a center frequency f are emitted by these elements. The spacing in the thickness of D_w is filled with water. The speed of sound in the water is measured as $c_1 = 1540m/s$, and the speed of sound in the wall of the natural gas pipe is measured as $c_2 = 5890m/s$. The outer diameter of the natural gas pipe is $2R_0$, and the radius of the transducer array is R_T. The thickness of the wall of the pipe is D_{tw}. The specific parameters are shown in Table 1.

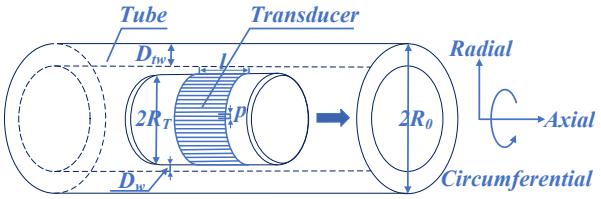

Fig. 1: Schematic diagram of the transducer in the pipeline.

Table 1: Parameters of circular transducer

Symbol	Parameter	Value
N	Element number	64
P	Pitch	2.33mm
W	Element width	2.0mm
l	Element length	10.0mm
R_T	Transducer radius	95mm
f	Central frequency	10MHz
D_w	Coupling agent thickness	25mm
R_0	Tube outer radius	125mm
D_{tw}	Tube wall thickness	5.0mm

When designing the delay law, the following factors need to be considered: (1) the difficulty of detecting defects on the inner and outer walls of a pipeline increases with the acoustic pressure difference between the inner and outer walls of the pipeline; (2) if the sound beam becomes narrower the resolution increases, if the sound pressure increases the detection sensitivity increases. (3) a suitable focusing point needs to be selected to balance the sound beam, sound pressure and acoustic pressure difference, achieving high accuracy, resolution and sensitivity in internal pipe inspection. To verify the delay law and analysis the performance of the acoustic beam during the simulation, a rectangular area of 30 mm × 35 mm is taken as the simulation area in the CRP, which is shown in Fig. 2. The delay times Δt_i are computed by the following equation:

$$\nabla t_i = \left(\frac{D_w}{\cos\alpha_i} - D_w\right)\frac{1}{c_1} + \left(\frac{F}{\cos\beta_i} - F\right)\frac{1}{c_2} \tag{4}$$

where $i = 1, 2, \cdots n$, the number of array elements is n in the active aperture, the thickness of the medium is D_w in me-

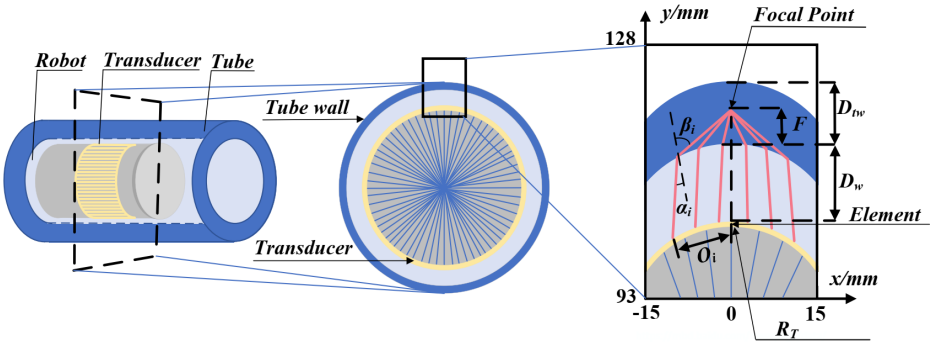

Fig. 2: Sketch of the simulation area.

ters, the angle of ultrasound incidence is α_i at the medium-steel interface in radians, the angle of ultrasound refraction is β_i in radians, the depth of focusing of the pipeline wall is F in meters, c_1 and c_2 are the velocities of the ultrasound waves in the medium and the steel, respectively. α_i and β_i are given by the equations:

$$D_w \tan\alpha_i + F \ \tan\beta_i = R_T \cdot \angle O_i \tag{5}$$

$$\frac{\sin\alpha_i}{\sin\beta_i} = \frac{c_1}{c_2} \tag{6}$$

where R_T stands for the radius of the array in meters; $\angle O_i$ stands for the angle between the midpoint of the i-th array element width and the centerline in radians.

3.2 Simulation model

Based on the selected simulation region, the construction of the acoustic field is carried out in the k-Wave toolbox, which is shown in Fig. 3 (8 elements). Furthermore, six cycles of a 1MHz Gaussian plus windowed sine wave signal is used as an input signal, as displayed in Fig. 4. The array element simulation calculation area for the three-dimensional space($N_x \times N_y \times N_z$) exists the following parameters: the number of grids along the x-direction $N_x = 150$; the number of grids along the y-direction $N_y = 300$; the number of grids along the z-direction $N_z = 350$, $dx = dy = dz = 0.1 \times 10^{-3} m$.

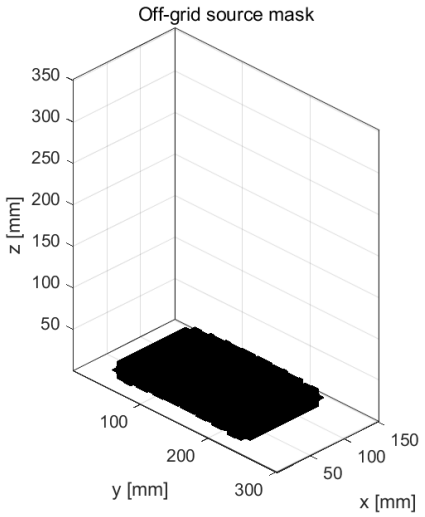

Fig. 3: Sensor array setup in the computational domain.

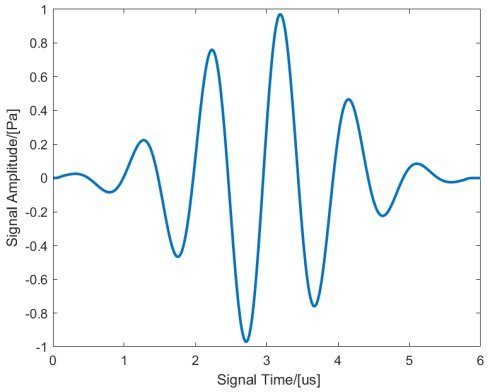

Fig. 4: 6-cycle Gaussian plus windowed 1MHz sine wave.

4 Numerical simulation

The focal point based on the k-Wave toolbox simulation is located in the middle of the tube wall with a focal depth of 2.5 mm. The sound beam is set to fixed and transducers are configured for each grid to record pressure. Considering only the area inside the tube wall is involved in the experiment, the area outside the pipeline wall is set to 0 when displaying the sound pressure distribution.

4.1 Active aperture analysis

The acoustic field is simulated in a designated simulation area, and the ultrasonic acoustic fields are simulated for active apertures with elements of four, six, eight, and ten. The acoustic field in the CRP and ARP for various apertures can be seen in Figs. 5 and 6, and the beam characteristics are detailed in Table 2.

Table 2: Parameters of circular transducer

Element number		4	6	**8**	10
Maximum pressure	Pa	3.60	4.19	**4.11**	4.38
Inner wall pressure	Pa	3.60	4.19	**4.01**	3.67
Outer wall pressure	Pa	2.08	2.97	**3.73**	4.26
$\Delta P = \lvert P_{outer} - P_{inner} \rvert$	Pa	1.52	1.22	**0.28**	0.59
Focal point depth	mm	0	0.1	**2.1**	3.5
Beam width(Circumferential)	mm	4.8	4.6	**4.8**	4.4
Beam width(Axial)	mm	6.4	6.2	**7.4**	8.6

The 4-element aperture, shown in Figs. 5(a) and 6(a), produces an unfocused acoustic beam. The 6-element apertures shown in Figs. 5(b) and 6(b) are more uniformly distributed, but the focus remains near the inner wall of the pipe. The 8-element and 10-element apertures have a focused a-

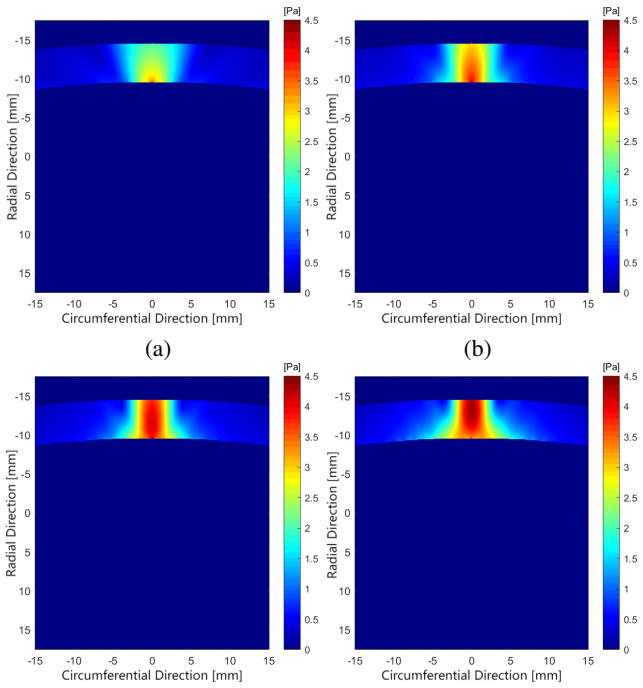

Fig. 5: Normalized beam profile of different apertures (CRP). (a)four-element. (b)six-element. (c)eight-element. (d)ten-element.

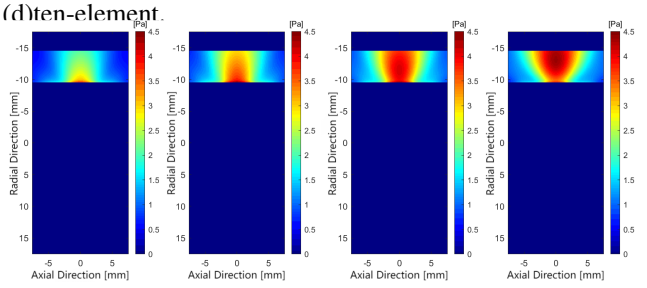

Fig. 6: Normalized beam profile of different apertures (ARP). (a)four-element. (b)six-element. (c)eight-element. (d)ten-element.

coustic field, with beam widths of 4.8 mm and 4.4 mm in the CRP, and 7.4 mm and 8.6 mm in the ARP, respectively, as surveyed by the full width at half maximum (FWHM) method. According to the FWHM method, the 8-element and 10-element apertures are presented as focused acoustic fields, where the beamwidths of 4.8 mm and 4.4 mm for CRP and 7.4 mm and 8.6 mm for ARP, respectively. The results show that the 8-element can derive a smaller side lobe and that its sound field focus is located at a depth of 2.1 mm in the tube wall, which is close to the ideal value. In all four cases, the 8-element aperture possesses the optimal results for the sound field distribution of CRP and ARP.

Analysis of both the CRP and ARP acoustic fields reveals that an aperture size of 8 elements is the most suitable for the detection of the pipe wall when a single array element with a length of 10 mm, width of 2 mm, and an array element center distance of 2.33 mm is used, and the input signal frequency is 1 MHz.

4.2 Input signal analysis

The above simulation determines the optimal active aperture size of the 8-element in the case of a single array element with a length of 10 mm, a width of 2 mm, an array element center distance of 2.33 mm, and a frequency of 1 MHz for the input signal. To determine the optimal frequency of the input signal, the size of the active aperture is set to 8-element, while the rest of the transducer parameters remain unchanged. The acoustic field is simulated using the k-Wave toolbox in the designed simulation area, and the ultrasonic acoustic field is simulated for the input signal with frequencies of 0.8 MHz, 1 MHz, and 1.2 MHz. The results of the simulation of the acoustic field of CRP and ARP at different frequencies are shown in Figs. 7 and 8, and the beam characteristic parameters are listed in Table 3.

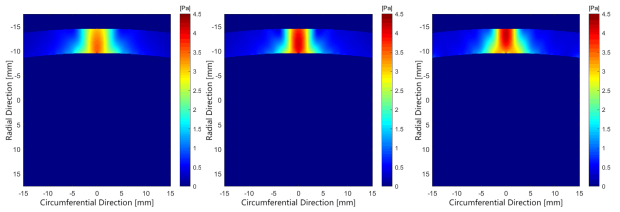

Fig. 7: Normalized beam profile of various frequency signals (CRP). (a)0.8 MHz. (b)1 MHz. (c)1.2 MHz.

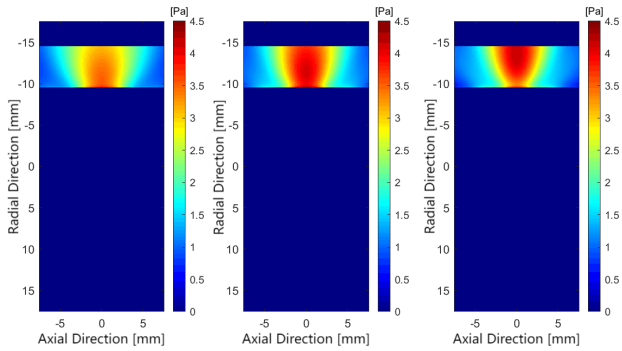

Fig. 8: Normalized beam profile of various frequency signals (ARP). (a)0.8 MHz. (b)1 MHz. (c)1.2 MHz.

Table 3: Characteristic Parameters of Different Input Signal

Transducer operating frequency	MHz	0.8	**1**	1.2
Maximum pressure	Pa	3.75	**4.11**	4.18
Inner wall pressure	Pa	3.75	**4.01**	3.59
Outer wall pressure	Pa	3.08	**3.73**	4.14
$\Delta P = \lvert P_{outer} - P_{inner} \rvert$	Pa	0.67	**0.28**	0.55
Focal point depth	mm	0	**2.1**	3.9
Beam width(Circumferential)	mm	8.6	**4.8**	4.6
Beam width(Axial)	mm	6.8	**7.4**	7.6

The results of the simulation analysis for CRP and ARP sound fields indicate that, when the input frequency is below 1MHz, a downward shift in the acoustic field focus is observed, leading to higher sound pressure near the inner tube wall, smaller overall sound pressure, and a wider sound beam width when measured with the FWHM. When the frequency exceeds 1MHz, a smaller sound beam width is measured with the FWHM, but an upward shift in the focus of the acoustic field occurs, resulting in higher sound pressure near the outer pipe wall and a slight increase in overall acoustic

pressure. At 1MHz, The overall sound pressure difference of the pipe is minimized, and the focus is brought close to the middle of the pipe wall. Consequently, with 8 active aperture sizes, the best sound field distribution for the input signal is achieved at 1 MHz.

4.3 Array spacing analysis

Maintaining the active aperture size of 8-element unchanged, the spacing between the array elements from the original 0.33 mm to 0 mm spacing and the rest of the transducer parameters constant, the use of the k-Wave toolbox in the designed simulation area for the simulation of the acoustic field produces the CRP and ARP acoustic field simulation results shown in Fig. 9, and the acoustic beam characteristic parameters are listed in Table 4.

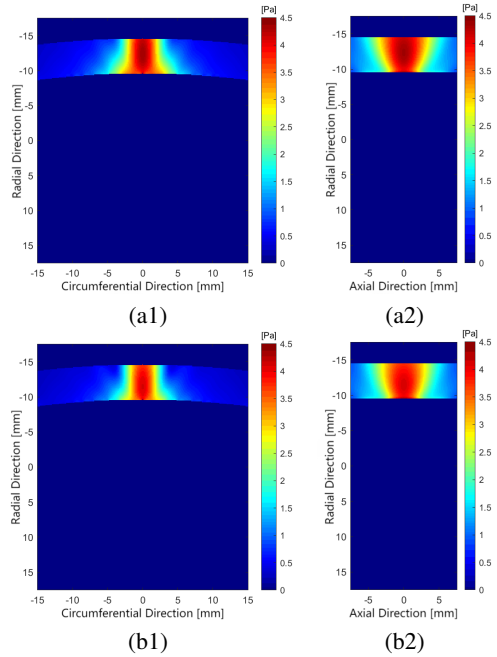

Fig. 9: Normalized beam profile of various array element spacing. (a)$P = 0mm$. (b)$P = 0.33mm$.

Table 4: Characteristic Parameters of Different Input Signal

Array element spacing	mm	0	1
Maximum pressure	Pa	4.34	4.11
Inner wall pressure	Pa	4.08	4.01
Outer wall pressure	Pa	4.16	3.73
$\Delta P = \lvert P_{outer} - P_{inner} \rvert$	Pa	0.08	0.28
Focal point depth	mm	2.7	2.1
Beam width(Circumferential)	mm	5.4	4.8
Beam width(Axial)	mm	8.0	7.4

When the spacing between the array elements is reduced to zero, the sound field shown in Fig. 9(a) exhibits an overall increase in sound pressure, which reduces the pressure difference between the inside and outside of the pipe wall. The focus is closer to the center of the tube wall at 2.7 mm. The beam width on the CRP and ARP is 5.4mm and 8.0mm respectively, slightly larger than before. The analysis shows that reducing the spacing of the array elements increases the effective length of the array, improving its beam focusing ability, increasing the emission area, and resulting in more acoustic energy being radiated and a stronger overall acoustic field.

4.4 Element width analysis

The width of the array element is reduced from 2 mm to 1 mm while keeping the size of the 8-element active aperture unchanged. At the same time, the number of elements is increased to 16. Keeping the rest of the parameters unchanged, the designed simulation area is used to simulate the sound field using k-Wave, and the results are shown in Fig. 10. The acoustic beam characteristics of the parameter are listed in Table 5.

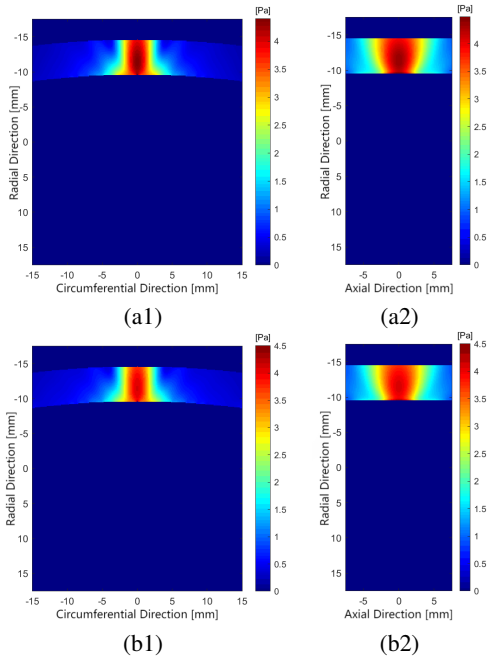

Fig. 10: Normalized beam profile of various array element width and number. (a)$W = 1mm, N = 16$. (b)$W = 2mm, N = 8$.

Table 5: Characteristic Parameters of Different Input Signal

Element number		16	8
Maximum pressure	Pa	4.38	4.11
Inner wall pressure	Pa	4.22	4.01
Outer wall pressure	Pa	3.93	3.73
$\Delta P = \lvert P_{outer} - P_{inner} \rvert$	Pa	0.29	0.28
Focal point depth	mm	2.2	2.1
Beam width(Circumferential)	mm	4.4	4.8
Beam width(Axial)	mm	7.0	7.4

In the CRP and ARP sound field analysis, the width of each array element is 1 mm. Therefore, the sound pressure enhancement in the 16-element sound field is slightly larger compared with the 8-element sound field shown in Fig. 12(a). The focus depth of 2.2mm is closer to the middle of the pipe wall. The CRP and ARP sound fields have narrow beam widths. Reducing the width of the array element and increasing the number of array elements can improve the directionality of the ultrasonic beam, thereby resulting in a narrower main lobe width and a more focused acoustic beam.

5 Conclusion

The paper has presented the design of a 256-element circular array ultrasonic transducer aimed at generating a controllable and focused 3D cylindrical ultrasound beam for the inspection of natural gas pipelines. Initially, a localized

three-dimensional acoustic model of the 250-mm-caliber pipeline under consideration has been constructed using the k-Wave toolbox. Subsequently, the layout of the phased array, along with the determination of the active aperture and input signal frequency, have been outlined earlier, relying on experimental methods. In conclusion, the simulation results on the axial-radial and circumferential-radial planes have been presented to assess the effectiveness of the proposed method. The findings have suggested that the piezoelectric transducer array can be capable of producing a viable focused beam, laying the groundwork for future transducer prototyping.

References

[1] X. Yang, G. Yin, Y. Tian, and J. Guo, Generating an adjustable focused field with an annular shape using a cylindrical acoustic transducer array, *IEEE Transactions on Ultrasonics, Ferroelectrics, and Frequency Control*, 2020, 67(2): 356-364.

[2] Z. Xi, X. Luo, Y. Peng, and X. Wang, Development and validation of independent dual-focusing transducer for internal inspection of tubes, *IEEE Transactions on Ultrasonics, Ferroelectrics, and Frequency Control*, 2021, 68(6): 2227-2237.

[3] H. Wu, M. Ravan, R. Sharma, J. Patel, and R. K. Amineh, Nondestructive testing of non-Metallic concentric pipes using microwave measurements, *2020 IEEE/MTT-S International Microwave Symposium (IMS)*,2020: 369-372.

[4] D. A. Sednev, A. Dmitry, A. I. Soldatov, A. A. Soldatov, M. A. Kostina, D. O. Dolmatov, and D. A. Koneva, Studies of angular resolution for acoustic arc arrays, *Sensors*,2023, 23(13): 6007.

[5] M. J. Ranjbar Naserabadi and S. Sodagar, Application of phased array ultrasonic transducers for guided wave scanning of plates using multi-point focusing technique, *Journal of Nondestructive Evaluation*, 2022,41(2): 38-46.

[6] P. Lukacs, G. Davis, D. Pieris, A. Gachagan, and T. Stratoudaki, Grating lobe suppression through novel, sparse laser induced phased array design, *2022 IEEE International Ultrasonics Symposium (IUS)*,2022:1-4.

[7] T. Y. Park, H. J. Kim, S. H. Park, W. S. Chang, H. Kim, and K. Yoon, Differential evolution method to find optimal location of a single-element transducer for transcranial focused ultrasound therapy,*Computer Methods and Programs in Biomedicine*, 2022, 219: 106777.

[8] Z. Xi, X. Luo, Y. Peng, and X. Wang, Simulation and performance study of circular ultrasonic array for tubes internal inspection, *Ultrasonics*,2021, 116: 106598.

[9] Z. Hu, L. Xu, C. Y. Chien, and Y. Yang, 3-D Transcranial microbubble cavitation localization by four sensors, *IEEE Transactions on Ultrasonics, Ferroelectrics, and Frequency Control*, 2021,68(11): 3336-3346.

[10] Y. Humeida, P. D. Wilcox, M. D. Todd, and B. W. Drinkwater, A probabilistic approach for the optimisation of ultrasonic array inspection techniques, *Ndt & E International*, 2014,68: 43-52.

[11] C. Ennaceur, P. Mudge, B. Bridge, M. Kayous, and T. H. Gan, Application of the time reversal technique to the focusing of long-range ultrasound in pipelines, *Insight - Non-Destructive Testing and Condition Monitoring*, 2007,49(4): 217-223.

[12] B. E. Treeby and B. T. Cox, K-Wave: MATLAB toolbox for the simulation and reconstruction of photoacoustic wave-fields, *Journal of Biomedical Optics*, 2010, 15(2): 021314.

Proceedings of the 3rd Conference on Fully Actuated System Theory and Applications
May 10-12, 2024, Shenzhen, China

Intelligent warehouse multi-robot scheduling system based on improved A* algorithm

Ao Wang

Harbin Engineering University, Harbin 150001, China
E-mail: 15810017526@163.com

Abstract: The multi-robot intelligent dispatch system for warehouse means that in the warehouse system, order processing is carried out by each robot transporting a designated rack to the picking station, and the task allocation and path planning of the robot are particularly important to improve the system efficiency. In this paper, we choose a task allocation algorithm based on market auction, in which the robot combines the cost of the task itself with the associated cost between tasks to optimize the total distance of all robots and the longest running time of robots when bidding. And for multi-robot path planning, the grid method is used to model the map, and an improved A* algorithm is proposed, which combines the traditional A* algorithm with the traffic regulations and the reservation table to realize the optimal path from the start point to the target point. At the end of the paper, we make simulation experiments. The GUI interface is designed to show the task generation, distribution and robot working status in the warehousing environment and the feasibility and effectiveness of the proposed scheme are verified.

Key Words: Warehousing Environment, Multi-robot System, Task Allocation, Path Planning

1 Introduction

In recent years, there has been a significant development in information technology and industrial technology, leading to a global wave of technological advancement centered around artificial intelligence. E-commerce logistics, as one of the fastest-growing industries in China, faces challenges such as a high volume of platform business, diverse products, and high precision requirements. Relying solely on manual operations not only fails to meet efficiency requirements but also increases enterprise costs. Therefore, the complex operation and management of warehousing and logistics systems require greater automation, diversification, informatization and intelligentization.

The introduction of a multi-robot system in warehousing can address problems such as repetitive and heavy workloads, as well as challenging environmental conditions. This can significantly reduce labor costs and improve enterprise efficiency. However, as a multi-agent system, it is crucial to address issues related to task allocation and path planning in such an environment. The primary concern in a warehousing environment is how to allocate tasks and plan paths for a robot cluster at the lowest cost within limited space. The rationality of task allocation algorithms determines the work efficiency of multiple robots—specifically, their ability to quickly and accurately obtain the optimal solution in an environment with few tasks or robots. Meanwhile, the path planning problem directly impacts the practical performance of the system and is closely linked to system robustness and speed[3].Consequently, when designing a multi-robot system, it is necessary to consider critical challenges such as collaboration schemes among robots, timing arrangements for travel, congestion, and collision avoidance in the actual working environment.

Currently, the path planning algorithms commonly utilized in warehousing environments can be categorized into three groups: traditional methods, intelligent methods, and other methods. Traditional methods typically involve finding paths through graph modeling, which can simplify the environment and make the algorithm more straightforward. However, their drawback lies in the difficulty of finding the optimum solution and their impracticality for dynamic environments. Intelligent algorithms primarily make use of environmental learning or heuristic search algorithms, such as the A* algorithm, ant colony algorithm, and genetic algorithm. Other methods include fuzzy control methods and optimal control methods. Among these, intelligent methods like the A* algorithm are relatively mature. Nevertheless, due to the numerous shelves within the warehouse and the narrow movement environment of the robot, using the traditional A* algorithm can lead to severe collisions and deadlocks. Hence, there is a need to enhance the A* algorithm to address these issues.

This paper primarily focuses on the design of a large-scale warehousing multi-robot intelligent scheduling system based on an improved A* algorithm. For the task allocation problem in multi-robot systems, the market auction algorithm is employed to achieve the optimal allocation of tasks to multiple robots. For the path planning problem of multiple robots, an improved A* algorithm based on optimization methods such as traffic regulations and appointment table is proposed to solve congestion issues. Finally, the feasibility of the methods applied in this paper is verified through software simulation.

2 Multi-robot Task allocation in Warehouse Systems

2.1 Overview of Task Allocation Problem

The task allocation in multi-robot systems entails assigning distinct sub-tasks from the global task to individual robots within the system. Upon receiving a task, the robots possess the capability to autonomously conduct path planning and adjust the allocation scheme based on their objectives. They are responsible for orderly extracting goods and completing the task with minimal cost. The objective of task allocation is to effectively utilize resources and maximize resource utilization efficiency. In the context of warehousing, task allocation has the potential to minimize unnecessary costs in subsequent path planning, achieve global optimization, and enhance the operational efficiency of intelligent warehousing.

Given its proficiency in handling dynamic task allocation and similar predicaments, this paper employs the market auction algorithm to tackle the dynamic task allocation problem in multi-robot intelligent warehousing systems. The ultimate aim is to strike a balance between efficiency and accuracy.

2.2 Auction Algorithm

Derived from auction trading, the auction algorithm is a straightforward approach employed for resource allocation in multi-robot systems. The algorithm determines the allocation of tasks based on the bidding prices, specifically the highest and lowest bids. In this context, the robots serve as bidders, while the tasks represent the items up for auction. Pursuant to the predefined objective, the robot with the lowest bid is designated as the winning bidder.

Set performance indicators as follows:

$$\min f\left(c\left(r_1, L_1\right), c\left(r_2, L_2\right), \cdots c\left(r_n, L_n\right)\right) \quad (1)$$

In the formula, r_i represents the robot. $\{L_1,L_2,...,L_n\}$ represents the sequence of tasks assigned to each robot, L_i represents $t_{i1} \rightarrow t_{i2} \rightarrow \ldots \rightarrow t_{ik}$, specifically the sequence of tasks that needs to be completed. Function C represents the total cost for each robot to complete the assigned task, defined as:

$$c\left(r_{i,} L_i\right)=\sum_{p=1}^{k} S\left(t_{ip}\right)+\sum_{p=1}^{k-1} R\left(t_{ip}, t_{i(p+1)}\right) \quad (2)$$

Function f represents the total cost of all robots to complete the task, and describes the total distance required for all robots to complete all the current tasks:

$$\begin{aligned} & f\left(c\left(r_1, L_1\right), c\left(r_2, L_2\right), \cdots c\left(r_n, L_n\right)\right) \\ & =\sum_{p=1}^{n} c\left(r_p, L_p\right) \end{aligned} \quad (3)$$

Define the sequence of tasks assigned to each robot as $\{L_1,L_2,...,L_n\}$, the set of unassigned tasks is defined as T_{wait}. At this time, the robot bids for each unassigned task one round after another. The system selects the smallest bidding price among all bidding prices and assigns tasks to the corresponding robot. For example, suppose that there are 4 robots to assign 5 tasks, the quotation of each robot is shown in Figure 1 below, find the minimum quotation of each robot, and then find the minimum quotation value 10 from these quotations, so the task is assigned to the robot, and then the task is deleted from the T to be assigned, and the next round of quotation is carried out.

Tasks / Roborts	t_1	t_2	t_3	t_4	t_5
r_1	24	(16)	29	21	33
r_2	35	25	(10)	40	28
r_3	(19)	32	23	46	20
r_4	24	30	27	(14)	22

Fig. 1: The robot bidding diagram

3 Multi-robot Path Planning in Warehouse Systems

3.1 Overview of Path Planning Problem

The robot's path planning can be conceptualized as the identification of an optimal route based on predefined objectives, such as minimizing travel time, distance, or task completion. This task entails considering numerous factors, including environmental perception, positioning, and obstacle avoidance. These factors may involve known quantities, unknown variables, or dynamic elements. In complex and dynamic environments that feature obstacles, it becomes critical to efficiently generate obstacle-free paths from the origin to the intended destination while minimizing the overall path cost.Currently, the A* algorithm is widely employed for this purpose, although it necessitates customization and refinement to suit specific application scenarios. With the aim of enhancing its applicability within warehouse settings, this research endeavors to optimize and adapt the A* algorithm for integration into an intelligent scheduling system design.

3.2 Grid-Based Modeling in Warehouse Systems

To facilitate the path planning of multi-robot systems, a commonly used approach is to simplify the steps and express the movement path more intuitively through modeling. A grid map divides the working environment of robots into a series of equally sized square grids, and each grid can be represented by a number indicating its occupancy state. In a warehousing environment, path planning can consider only three modes: from the starting point to the task point, from the

task point to the picking station, and from the picking station back to the task point.

Figure 2 illustrates the use of grid-based modeling with the following specifications in a Cartesian coordinate system:

1. The mobile robot's movement direction is limited to up, down, left, and right, without diagonal driving.

2. The value assigned to each grid point signifies its current state: 0 for unoccupied, 1 for shelf position, 2 for occupied by a robot, and 3 for picking station position.

3. The mobile robot maintains a constant speed while traversing the warehouse, moving one grid per unit of time.

Utilizing a grid map to represent path planning not only simplifies the creation and maintenance processes but also allows for easy scalability. Perhaps its most significant advantage lies in the map's simplification and accurate representation of pertinent information.

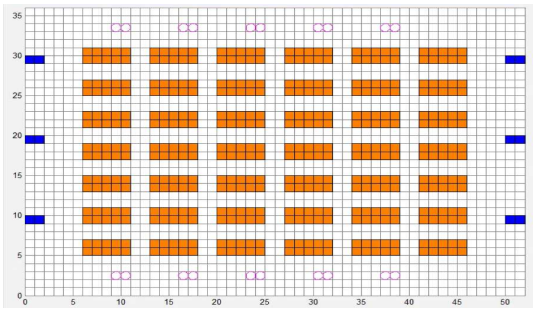

Fig. 2: Grid-based modeling diagram

3.3 Multi-robot Path Planning in Warehouse based on Improved A* Algorithm

3.3.1 A* Algorithm

The A* algorithm is based on the principle of heuristic search to guide the robot's movement in a given space. Its objective is to calculate the shortest path cost from a specific starting node to the destination node. The robot utilizes a heuristic function to estimate the cost required for each neighboring node from the initial node. Based on these estimates, the nodes are ranked, and the node with the lowest estimated cost is automatically chosen as the next move. This process continues iteratively until the robot reaches the destination node.

The heuristic function plays a crucial role in the traditional A* algorithm and is expressed as follows:

$$f(n) = g(n) + h(n) \tag{4}$$

The evaluation function includes the following parameters: n represents the path node to be estimated, g(n) signifies the actual cost from the starting point to the current position, encompassing factors such as the actual path length, required time, and energy consumption. On the other hand, h(n) denotes an estimation of the optimal distance from the current position to the destination. A more intricate h(n) indicates more stringent path conditions, leading to increased time requirements. Conversely, fewer constraints reduce the time needed, but the resulting route may not be optimal. F(n), which combines g(n) and h(n), represents the total estimated cost of reaching the goal node after traversing grid node n from the starting point.

In a finite motion environment, the A* algorithm is guaranteed to discover the shortest path, thus exhibiting strong completeness. However, its limitation lies in its suitability for individual robots only. When multiple robots move simultaneously, issues such as collisions and blockages are prone to arise.

In real warehousing environments where a multitude of robots form a multi-robot system, collisions are likely to occur due to the presence of various obstacles, such as shelves in the cargo hold, when employing the traditional A* algorithm. Therefore, this paper aims to enhance the traditional A* algorithm by implementing traffic and time regulation to bolster operational efficiency.

3.3.2 A* Algorithm base on Traffic Regulations

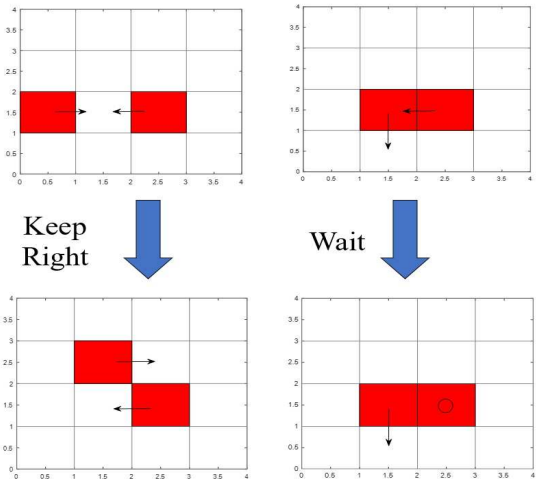

Fig. 3: Traffic regulation diagram

In warehousing environment characterized by a multitude of robots and limited operational space, the occurrence of traffic congestion is highly probable. Adhering to the traditional strategy of waiting and passing for obstacle avoidance would undoubtedly lead to a reduction in actual operational efficiency.

To rectify this problem, a novel rule table tailored specifically to the warehousing environment has been developed, drawing inspiration from real-world traffic regulations governing two-way roads. As illustrated in Figure 2, the previous one-way paths have been replaced with comprehensive two-way roads, each equipped with clearly specified directions of travel. This strategic implementation effectively mitigates the risk of head-on collisions among robots that may cause detrimental traffic blockages during operation. Additionally, predefined locations have been allocated for picking stations and

shelf areas, thereby streamlining the transportation of goods. These well-designed measures significantly reduce the occurrence of deadlock issues, thus optimizing overall workflow efficiency.

3.3.3 A* Algorithm base on Reservation Table

The implementation of traffic regulations serves to minimize the occurrence of collisions in space. However, even with these regulations in place, collisions between robots can still happen when tasks overlap at the same location and execution time. To overcome this, we can establish time rules that assign priorities to robot actions, enabling the implementation of a waiting mechanism to prevent collisions.

col / row	col_1	col_2	···	col_{m-1}	col_m
row_1	0	1	···	1	0
row_2	1	0	···	0	0
···	···	···	···	···	···
row_{n-1}	0	1	···	0	1
row_n	0	0	···	0	0

Fig. 4: Reservation table diagram

To illustrate this concept, Figure 4 demonstrates how the time rules correspond to the two-dimensional coordinates of each unit node within the grid map. The figure displays a reservation table for a specific time . Each occupied grid node is marked with the robot ID currently in operation. By utilizing this time rule table, we gain a clear understanding of the positions of all robots, which aids in making informed decisions for subsequent path planning steps.

Hence, when a robot in motion is about to enter the next grid cell, it performs a check to verify if the corresponding cell position is already occupied. If it is, the robot must wait until the corresponding node becomes unoccupied by other robots before proceeding to enter.

When multiple moving robots want to enter the same node in the map simultaneously, coordination rules among the robots need to be established to ensure that they all pass through the node in a reasonable and orderly manner. Based on different robot states and departure times, different priorities are assigned to the robots to pass through the node in order of priority. The priority rules are as follows:

1. Robots without a load have the lowest priority.

2. When robots are simultaneously loaded, the priority is determined based on their departure time, with earlier departures having higher priority.

3. For the same priority, robots with lower ID numbers pass through first.

By following the above rules, high-priority robots can occupy nodes and pass through them first, achieving orderly collision avoidance.

4 Simulation Experiment and Result Analysis

Previous research has primarily addressed task allocation and path planning problems concerning multiple robots in a warehousing environment. These studies have offered introductory insights and algorithmic designs from a theoretical standpoint. In order to assess the practical applicability of the aforementioned algorithms, our study involved software simulation experiments, accompanied by the development of a graphical user interface (GUI). The GUI was instrumental in visualizing the robots' operational processes within the warehouse setting.

4.1 Simulation Interface Design

The simulated interface mainly includes three parts: storage environment, task pool and the state of the robot executing the task, and the button group. The specific functions are as follows:

1.Warehouse Environment

The warehousing environment consists of a 36×52 grid-based map, including robots, shelves, picking stations, and navigable areas for robots. Among them, the initial positions of the robots are uniformly distributed both horizontally and vertically on the map, totaling 20 robots, represented by pink circles. Shelves are evenly distributed in the central area of the map, represented by orange squares. Each shelf block has a size of 2×5 and contains 10 shelves. There are a total of 6×7 shelf blocks, which gives a total of 420 shelves. Picking stations are placed on the left and right sides of the map, totaling 6, represented by blue squares. The remaining white areas represent the navigable areas for robots. During the operation of the robots, if a robot has not received a task yet, it is represented by a blue outlined circle. When it receives a task but does not transport a shelf, it is represented by a black outlined circle. During the process of transporting a shelf, it is represented by a black outlined square. Shelves can be in two states during the entire operation: being transported or remaining stationary. When a shelf is stationary, it is represented by an orange square. If it is being transported by a robot, the original position is represented by a white space.

2.Task Pool and Robot Task Status

This part is located in the right half of the simulation interface. The task pool is displayed in the form of a list, including all tasks: unfinished and completed. The tasks are represented by coordinates on the map, which are adjacent to the shelves. The status of robots executing tasks is displayed in the list, with a total of 20 robots showing their task sequences. When a task is completed, it is removed from the list. When a new task is added, the task sequence in the list is updated in real-time.

3.Button group

This part includes the functional buttons needed for the operation of the entire system, including the “Open Map” button to open/initialize the entire map, the “Generate Task” button to generate new tasks, and the “Task Assignment” button to allocate tasks. After task allocation is completed, the process of completing tasks will immediately begin.

The GUI interface is shown in Figure 5 below:

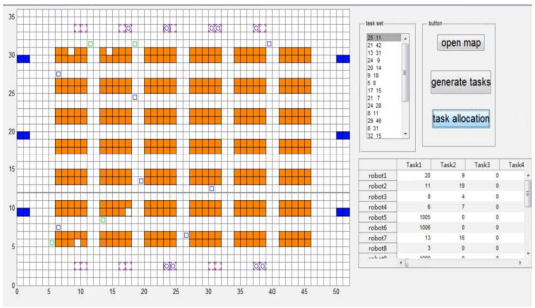

Fig. 5: GUI simulation interface diagram

4.2 Multi-robot System in Warehouse based on Improved A* Algorithm

In the previous section, the warehousing environment of the simulation experiment was modeled based on an improved A* algorithm. Double lanes were added to the original grid map, and the optimized A* algorithm was used for multi-robot path planning. The functional interface is shown in Figure 4. At the initial state, all robots are idle and located at their initial positions, and 20 tasks are randomly generated each time. Now, let's proceed with the simulation experiment:

1. Generating Task Set

The "Generate Task" button can randomly generate 20 tasks.

2. Task Allocation

The Task Allocation button performs a single allocation on the generated task set.

3. Robot Path Planning

After task allocation is completed, the functional interface looks like Figure 6. The robots that receive tasks perform path planning for the tasks in the task sequence in the order they received. The process of executing a task involves going to the task location, carrying the shelf to the picking station, and finally returning to the task location with the shelf. The following diagram shows the path planning of a robot reaching a task location: The initial position of the robot is (3,10), and the coordinates of the task location are (32,44). The length of the robot's path is 63, indicating that this path is the optimal path satisfying the set rules.

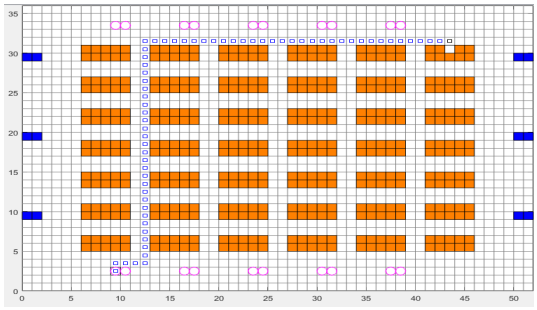

Fig. 6: A single robot's motion trajectory

The above diagram demonstrates that the A* algorithm can achieve optimal path planning for a single robot. However, in a multi-robot system, collisions may occur during robot operations. To avoid such collisions, traffic rules and reservation tables are employed. Next, the collision avoidance capability of the improved system is validated by performing simultaneous path planning for two robots, as illustrated in Figures 7 to 9.

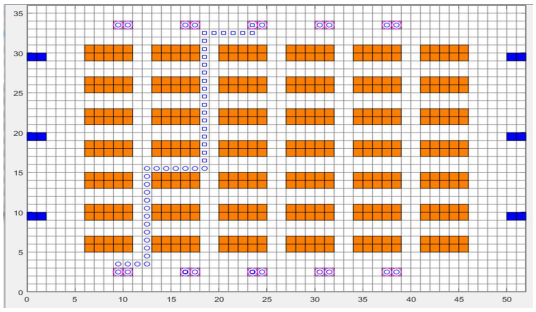

Fig. 7: Collision motion trajectory of two robots

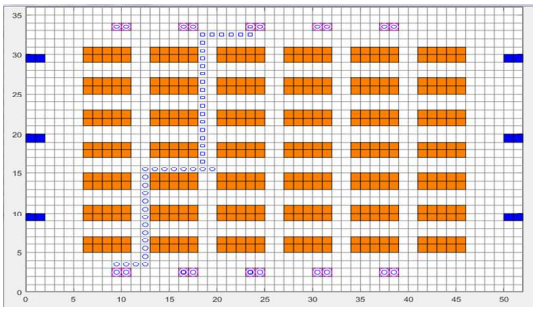

Fig. 8: Robot waiting for another robot to pass

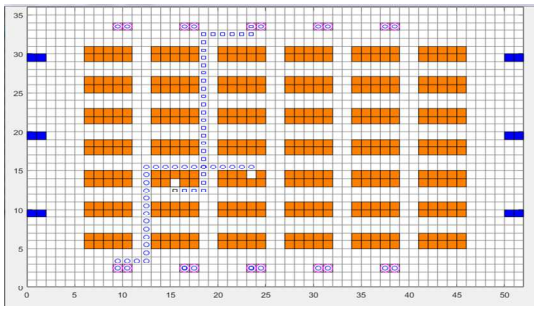

Fig. 9: Two robots resuming normal operation

From Figure 7 to 9, it can be observed that the robots prioritize higher priority robots to pass first at locations where collisions may occur, to prevent collisions from happening.

The following diagram shows the scenario of path planning when there are 20 robots.

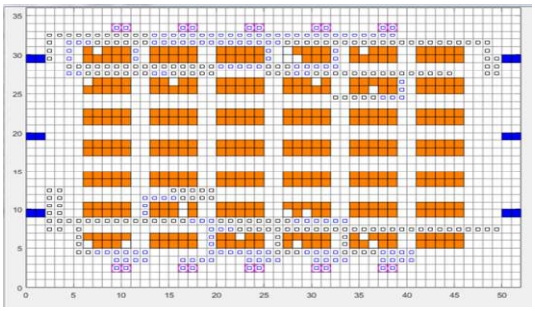

Fig. 10: When 20 robots are running at the same time

4.3 Comparative Analysis of Different Path Planning Methods

For this simulation, we used a combination of the random task sorting with auction algorithm, traditional A* algorithm (Algorithm 1), and optimized A* algorithm using rule table and reservation table (Algorithm 2) as two different path planning methods (as shown in Table 1) for comparison.

As shown in Figure 11, it presents the occurrence of congestion for robots using different path planning algorithms under different numbers of robots. It was observed that the congestion frequency significantly decreases when using Algorithm 2, compared to Algorithm 1, across different numbers of robots.

Table 1: Algorithm correspondence table

Title	Algorithm type
Algorithm 1	A* algorithm
Algorithm 2	Improved A* algorithm using rule table and reservation table

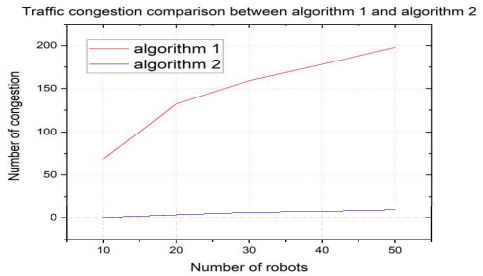

Fig. 11: Simulation results of different algorithm comparisons.

Based on the above results, it can be seen that the proposed A* algorithm combining traffic regulations and reservation table can effectively reduce collisions and achieve the goal of saving travel time for multi-robot systems, thereby improving work efficiency. In this chapter, simulation experiments were conducted to integrate.

5 Conclusion

This paper presents the design of a multi-robot intelligent scheduling system for warehouse environments, which involves the redesign and optimization of conventional algorithms for multi-robot systems. Firstly, a hybrid control method combined with a market auction algorithm is employed to improve task allocation efficiency. Secondly, an innovative approach combining traffic rules and reservation tables is introduced to assist multi-robot systems in path planning, improving the A* algorithm. This fundamentally addresses the issue of traffic congestion in multi-robot systems and reduces the occurrence of collisions, deadlocks, and other problems, thereby enhancing system robustness and overall work efficiency. Finally, software simulation verification is conducted, with a GUI interface displaying task generation, allocation, robot work status, and other related information in the warehouse environment. The proposed solution is verified to effectively improve the work efficiency of multi-robot systems based on intelligent warehousing.

References

[1] A. Khamis, A. Hussein, A. Elmogy, Multi-robot Task Allocation: A Review of the State-of-the-Art, *Studies in Computational Intelligence*, 2015, 604: 31-51.

[2] Gerkey, B., Mataric, M. A framework for studying multi-robot task allocation[C]. *2003 International Workshop on Multi-Robot Systems.* 2003: 15-26.

[3] J. Zhang, P.C.Zhang, Decentralized Multi-robot Collision Avoidance Based on Coordinated Control, *In Proceedings of Automation and Instrumentation*, 2022,37(09):29-31.

[4] M. B. Dias, R. Zlot, N. Kalra and A. Stentz, Market-Based Multirobot Coordination: A Survey and Analysis, *in Proceedings of the IEEE*, 2006, vol. 94, no. 7, pp. 1257-1270.

[5] Chaimowicz, Luiz et al. Dynamic role assignment for cooperative robots, *in Proceedings 2002 IEEE International Conference on Robotics and Automation*, 2002: 293-298.

[6] H. Gao*, Z. Li, X. Yu, and J. Qiu, Hierarchical multi-objective heuristic for PCB assembly optimization in a beam-head surface mounter. *IEEE Transactions on Cybernetics*, 2022: vol. 52, no. 7, pp. 6911-6924.

[7] Zhiguang Feng, Ruibing Li, Naifu Zhang, Ligang Wu. Event-Based Asymptotic Tracking Control for Constrained MIMO Nonlinear Systems via a Single-Parameter Adaptation Method. *IEEE Transactions on Systems, Man, and Cybernetics: Systems*, TSMC.2023.3301189.

[8] Zhiguang Feng, Ruibing Li, Ligang Wu. Adaptive decentralized control for constrained strong interconnected nonlinear systems and its application to inverted pendulum. *IEEE Transactions on Neural Networks and Learning Systems*, TNNLS.2023.3238819.

Proceedings of the 3rd Conference on Fully Actuated System Theory and Applications
May 10-12, 2024, Shenzhen, China

Intention Recognition Algorithm for Multi-agent Systems Based on High-order Fully Actuated System Approach

Qinlong Du[1], Xin Huo[1], Dianle Zhou[2], Kai Zheng[3], Rongmei Li[1]

1. Control and Simulation Center, Harbin Institute of Technology, Harbin 150080, P. R. China
E-mail: huoxin@hit.edu.cn

2. College of Advanced Interdisciplinary Studies, National University of Defence Technology, Changsha 410073, P. R. China
E-mail: lafiiche@163.cn

3. Marine Electrical Engineering College, Dalian Marine University, Dalian 116026, P. R. China
E-mail: kzh@dlmu.edu.cn

Abstract: Intention recognition for multiple agents is an important problem in multi-agent systems (MASs), and is widely used in the field of autonomous driving, human-machine interaction and military. In order to improve the competitive ability in multi-agent confrontation, an intention recognition algorithm for multi-agent systems based on high-order fully actuated (HOFA) system approach is proposed. Due to the uncertainty of the closed-loop system of the agents, the HOFA system approach is introduced to generate a data set with more extensive features, and an algorithm for the data set establishment is proposed. To obtain the intention prediction results, an intention recognition model based on artificial neural networks is proposed. Structures of both convolutional neural networks and recurrent neural networks are introduced to process the time features and spatial features. The intention predictor is trained via the data set based on HOFA system approach and tested on the test set. The simulation results shows that the proposed predictor has a better performance for intention recognition problem.

Key Words: high-order fully actuated system approach, multi-agent systems, intention recognition, artificial neural networks

1 Introduction

With the development of artificial intelligence these days, multi-agent systems (MASs) theory has been widely used in autonomous driving, human-machine interaction and military field [1–3]. Intention recognition, as a popular research topic of MASs, is an important procedure in decision making [4]. The goal of intention recognition is to predict the intention of the rival MASs based on the agent states and other observable information. The intention recognition model for MASs can be applied to computer-assisted command and intelligent equipment, which will play a more important role in the future battlefield environment.

The classic intention recognition models are based on bayesian networks, and the recognition targets are mainly single agent. This method depends on expert knowledge and performs well on single agent problems. Hence the significant breakthrough of artificial neural networks, researches about intention recognition based on deep learning model are also conducted. In [5], a weighted contrastive predictive coding model was proposed to solve complex scenarios and deceptive data problems. In order to achieve intention recognition via uncertain and incomplete information, an information fusion method based on deep learning and fuzzy discount-weighting was proposed in [6]. What's more, an intention recognition method based on bidirectional gated recurrent unit and conditional random field was proposed, and has been verified to have a better performance and interpretability [7].

However, most of the current work about MASs utilizes the first-order state-space method for modeling, which brings great challenges for control design and causes the loss of physical meaning of the system [8]. In order to solve this problem, high-order fully actuated (HOFA) system approach, a novel methodology for control design, was proposed by Duan in [9]. The HOFA model can take fully consider of the physical information of the system and provide a more convenient method for the control design, which has become the focus of research.

With the idea of HOFA system approach, the relationship between the controllability and the fully actuated features was constructed and many correlational methods were proposed [10–13]. As the immense potential of the HOFA system approach, many applications of the HOFA system theory in different fields have also been studied[14]. In [15–17], the HOFA-based predictive control methods were proposed for the cooperative control of the MASs.

In this paper, an intention recognition algorithm is designed to recognize the intention of the rival MASs for the multi-agent confrontation problem. In order to obtain a better data set for model training, a HOFA-MASs model and the corresponding controller are introduced to establish a data set with more extensive features. The intention recognition model is then constructed based on artificial neural networks. In the proposed model, 1d-convolutional layers and gate recurrent unit (GRU) are utilized to process the time features and spatial features separately. The intention predictor is finally trained via the data set based on HOFA system approach.

The rest of the paper is organized as follows. In Section 2, the problems of intention recognition and high-order fully actuated system approach are formulated. In Section 3, the data set based on the HOFA model is established and the intention recognition model based on artificial neural networks is proposed. In Section 4, the HOFA model for the simulation is introduced and the model is tested on the data set and in some typical scenarios. In Section 5, the paper is concluded and the direction of future work is given.

This work was partially supported by the National Natural Science Foundation of China under Grant 62373128, the Science Center Program of National Natural Science Foundation of China under Grant 62188101, and the Heilongjiang Touyan Team Program.

2 Problem Formulation

2.1 Intention Recognition for MASs

In the multi-agent confrontation problem, the intention of the rival MASs is the important information for decision-making. However, it is difficult to observe this information directly in most conditions. Hence, the intention needs to be predicted based on other observable information practically.

In the intention recognition problem, the observable information can be divided into environment characteristics, agent attributes and agent states. The environment characteristics include information that describes the environment, such as terrain information and obstacle information. The agent attributes are the time-invariant information of the agent, such as the model and parameters of the agent. The agent states comprise the time-variant information, such as position and velocity.

In this paper, the intention of rival MASs is divided into "encircle", "intercept", "follow", and "irrelevant". The corresponding formations are shown in Fig 1. The formation of "encircle" intention is a circle centered on self agent, which is shown in Fig 1(a). The target of "intercept" intention is to restrict the capacity of forward motion of self agent, and the rival MASs need to distribute in the area ahead of the self agent. The corresponding formation is shown in Fig 1(b). The target of "follow" intention is to keep the distance between self agent and rival MASs, and the rival MASs need to distribute behind the self agent. The specific formation is shown in and Fig 1(c). The "irrelevant" intention denotes that the motion of the rival MASs is independent from the target, and an example of this intention is shown in Fig 1(d).

Then, the optimization goal of the intention recognition problem is given as follows,

$$J_1 = \frac{1}{T}\sum_{t=0}^{T} \|Y_t - Y_t'\|_2 \tag{1}$$

where J_1 denotes the optimization index of the intention recognition, Y_t and Y_t' denote the vectors related to true intention and the prediction result on time t, T denotes the time for intention recognition. The prediction results can be obtained as follows,

$$Y_t' = \mathrm{model}(S_t, P_t, O_t; w) \tag{2}$$

where $\mathrm{model}(\cdot)$ denotes the intention recognition model, S_t, P_t and O_t denote the agent states, agent attributes and environment characteristics separately, w denotes the parameters of the model, which can be obtained as follows,

$$W = \arg\min_{w} J_1(w) \tag{3}$$

where W is the optimal parameters to be found.

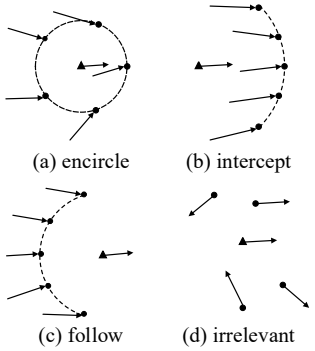

Fig. 1: Intentions of agents

2.2 Fully Actuated System Approach

High-order fully actuated system approach is a methodology which has great potential in multi-agent system control. In this paper, the intention recognition problem for HOFA-MASs is discussed, and the corresponding HOFA-based MASs can be described as follows.

The problem of intention recognition based on HOFA-MASs is shown in Fig 2. The agents in the environment can be divided into rival MASs and self MASs, and each of the agents can be described based on HOFA model. The goal of the intention recognition algorithm is to predict the intention of the rival MASs based on observable information, and the prediction results can be utilized for the plan making.

The interaction of the HOFA-MASs is considered by a directed graph $\mathcal{G} = \{\mathcal{N}, \mathcal{E}, \mathcal{A}\}$, where $\mathcal{N} = \{1, 2, \cdots, N\}$ represents the set of HOFA-MASs, $\mathcal{E} \subset \mathcal{N} \times \mathcal{N}$ represents the edge set of HOFA-MASs, $\mathcal{A} = \{a_{ij}\}$ is an adjacent matrix with $a_{ij} \geq 0$ and $a_{ii} = 0$. The mathematical model of the ith HOFA-agent is given as follows,

$$\begin{cases} x_i^{(m)} = f_i(x_i^{(0\sim m-1)}, \zeta) + g_i(x_i^{(0\sim m-1)}, \zeta_i, u_i), \\ y_i = C_i x_i, \end{cases} \tag{4}$$

where x_i, $u_i \in \mathbb{R}^n$ denote the state vector and control input of the agent, $y_i \in \mathbb{R}^p$ denotes the output vector of the agent, ζ_i denotes a parameters vector, $f_i(\cdot,\cdot)$, $g_i(\cdot,\cdot)$ are given functions, $C_i \in \mathbb{R}^{p\times n}$ is the output matrix, and $\det(g_i(x_i^{(0\sim m-1)}, \zeta_i, u_i)) \neq 0$. Then the corresponding HOFA controller can be obtained as follows,

$$\begin{cases} w_i = -\sum_{j=0}^{m-1} A_{ij} x_i^{(j)} - f_i(x_i^{(0\sim m-1)}, \zeta_i) + v_i, \\ u_i = g_i^{-1}(w_i, x_i^{(0\sim m-1)}, \zeta_i), \end{cases} \tag{5}$$

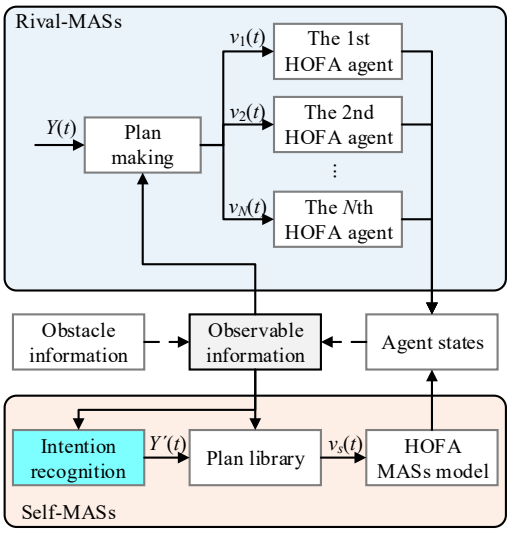

Fig. 2: Problem of intention recognition on HOFA-MASs

where v_i is the external signal of the ith agent, A_{ij} is the parameter matrix, w_i is an intermediate variable. The closed-loop HOFA-agent is realized as follows,

$$x_i^{(m)} + \sum_{j=0}^{m-1} A_{ij} x_i^{(j)} = v_i \tag{6}$$

This paper aims to obtain an intention recognition model to predict the intention of the rival MASs. The agent in the environment can be described by (4), and the optimal goal is to minimize the target in (1).

3 Intention Recognition Algorithm Design

In this paper, an artificial neural network is utilized to predict the intention of the rival MASs, and HOFA-MASs is used to generate corresponding data set for the model training. The main procedures of the intention recognition algorithm design is shown in Fig 3.

3.1 Data Set

In order to obtain sufficient amount of data for the later model training, the HOFA system approach is introduced for the data generating. Hence the high degree of control design freedom of the HOFA system approach, HOFA-MASs can be utilized to establish a data set with more extensive features conveniently. Data with different features can be obtained via choosing different controller parameters. The selected controller parameters need to ensure the stability of the closed-loop system, and the performance of the system should also be considered, which is specifically discussed as follows.

According to [9], the stability of each agent can be committed by selecting a stable matrix $F_i \in \mathbb{R}^{r\times r}$ and a nonsingular matrix $Z_i \in \mathbb{R}^{m\times r}$, where $r = mn$ and the matrices F_i and Z_i satisfy

$$\begin{cases} A_{i(0\sim m-1)} = -Z_i F_i^n V^{-1}(Z_i, F_i) \\ \det V(Z_i, F_i) \neq 0 \end{cases} \tag{7}$$

where $A_{i(0\sim m-1)} = [A_{i0}, A_{i1}, \cdots, A_{i(m-1)}]$ is the parameter matrix, $V(Z_i, F_i)$ is given by

$$V(Z_i, F_i) = \begin{bmatrix} Z_i \\ Z_i F_i \\ \vdots \\ Z_i F_i^{n-1} \end{bmatrix} \tag{8}$$

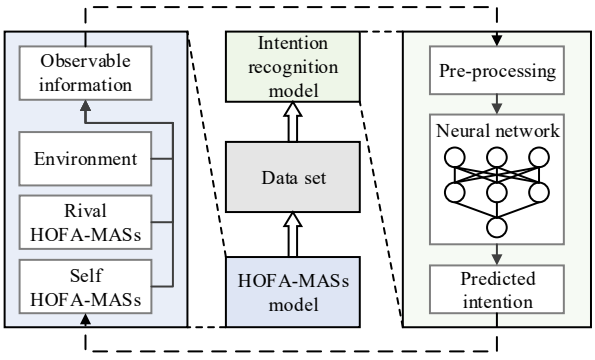

Fig. 3: Procedures of intention recognition model design

In order to ensure the performance of the system, a set of point can be selected as the constraint of the poles of the closed-loop system. Then the feasible parameters can be obtained by solving the following optimal problem via intelligent optimization algorithms,

$$\begin{aligned} &\min \sum_{i=0}^{n}\sum_{k=0}^{m} J_2(p_k; F_i, Z_i) \\ &\text{s.t. } \det V(Z_i, F_i) \neq 0 \end{aligned} \tag{9}$$

where p_k is the kth pole of the closed-loop system and can be determined by F_i and Z_i, $J_2(p_k; F_i, Z_i)$ is the optimization function of the kth pole, which is given by

$$J_2(p_k; F_i, Z_i) = \begin{cases} \|p_k - p_0\| - r_0 & p_k \notin Q \\ 0 & p_k \in Q \end{cases} \tag{10}$$

where $Q = \{p | \|p - p_0\| < r_0\}$ is the selected point set, p_0 and r_0 denote the center and radius of the set separately.

By solving the optimal problem via intelligent optimization algorithm, a data set with more extensive features can be established, and the data set establishing algorithm can be derived as follows.

Algorithm 1 Establishment of Data Set

Given: n_d: the number of the data to be generated
n_o: the maximum number of optimization iterations
Q: the selected point set
T_l: the length limit of the data
while $q \leq n_d$ **do**
1. Randomly initial the parameters of the controllers.
while $j \leq n_o$ and $p_k \in Q$ **do**
2. Solve the optimization problem described by (10).
end while
3. Calculate controller parameters $A_{i(0\sim m-1)}$ for each agents.
4. Randomly initial the obstacle information, states of the agents and intention of the rival MASs.
while $t \leq T_l$ **do**
5. Run the plan making and path planning algorithms of each agents in the environment.
6. Get the controller output of each agents based on HOFA controller described by (5).
end while
7. Save the states of each agents and the obstacle information in the simulation.
end while

3.2 Intention Predictor

In order to realize intention recognition without prior knowledge, an intention recognition model based on artificial neural networks is proposed in this paper. The structure of the model is shown in Fig 4.

The intention recognition model is mainly constructed by data pre-processing and intention classification procedures. The data pre-processing procedure needs to convert the input data into a similar order of magnitude, which can improve the iteration efficiency of model training and the generalization ability of the model.

The data to be processed in this paper can be divided into agents trajectories and obstacle information. The agents trajectories include the positions and angles of each agents,

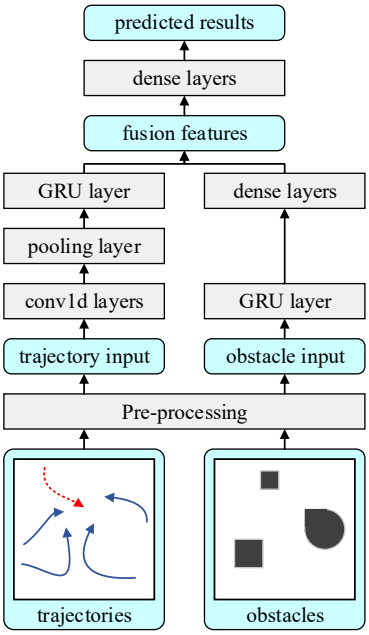

Fig. 4: Structure of intention predictor

which can be processed as follows,

$$\begin{cases} x_t^{i\prime} = \dfrac{x_t^i - s_{\min}}{s_{\max} - s_{\min}} \\ y_t^{i\prime} = \dfrac{y_t^i - s_{\min}}{s_{\max} - s_{\min}} \\ \theta_t^{i\prime} = \dfrac{\theta_t^i}{2\pi} + \pi \end{cases} \tag{11}$$

where x_t^i, y_t^i and θ_t^i denote the x, y coordinates and the facing angle of the ith agent on time t; $x_t^{i\prime}$, $y_t^{i\prime}$ and $\theta_t^{i\prime}$ denote the corresponding data after processing; $s_{\min}$ and $s_{\max}$ denote the minimum and the maximum of the x, y coordinates.

The obstacle information includes the shape, position and size of the obstacles, which can be processed as follows,

$$\begin{cases} x_o^{i\prime} = \dfrac{x_o^i - s_{\min}}{s_{\max} - s_{\min}} \\ y_o^{i\prime} = \dfrac{y_o^i - s_{\min}}{s_{\max} - s_{\min}} \\ r_o^{i\prime} = \dfrac{r_o^i}{s_{\max} - s_{\min}} \end{cases} \tag{12}$$

where x_o^i, y_o^i and r_o^i denote the x, y coordinates and the size of the ith obstacle; $x_o^{i\prime}$, $y_o^{i\prime}$ and $r_o^{i\prime}$ denote the corresponding obstacle information after processing.

After data pre-processing, an intention classification model based on artificial neural networks is constructed. The input features can be divided into trajectory features and obstacle features.

As the trajectory input contains both time and spatial features, 1d-convolutional layers and pooling layers are introduced to process the spatial features, and the recurrent neural network layers are introduced to process the time features. The recurrent unit of the model is selected as GRU [18].

The obstacle input contains only spatial features, but the number of the obstacles is unknown. In order to solve this problem, GRU layers are used to process the obstacle information and dense layers are used to obtain the obstacle feature output. Finally, the feature outputs are fused and the prediction results are obtained by further processing using dense layers.

3.3 Model Training

In order to train the intention prediction model, the data set is divided into three parts for the training and testing of the networks - 60% for the training set, 20% for the validation set and 20% for the test set. The hyperparameters of the model training are shown in Table 1.

Table 1: Hyperparameters for Network Training

Hyperparameters	Value
Learning rate	0.0005
Batch size	16
Maximum epoch	1000
Activate function	Relu
Optimizer	Adam

The training results are shown in Fig 5. The accuracy of the training set and the validation set converges to 97.62% and 96.03%, and the loss values converge to 0.062 and 0.127 separately. The results show that the intention recognition model has a good performance on the data set.

4 Numerical Simulation

4.1 Simulation Set-up

The physical model of the agent in this paper is chosen as vehicle with Mecanum wheels [19], and the structure of the chassis of the vehicle is shown in Fig 6. The coordinate x_gOy_g is the ground coordinate; the coordinate x_bOy_b is the body coordinate; l_a and l_b are the distance between the center of the vehicle and the wheels along the x_b-axis and y_b-axis separately; and θ is the facing angle of the agent.

The input of the agent can be described as follows,

$$\begin{cases} a_{w1} = a_{by} - a_{bx} + \alpha(l_a + l_b) \\ a_{w2} = a_{by} + a_{bx} - \alpha(l_a + l_b) \\ a_{w3} = a_{by} - a_{bx} - \alpha(l_a + l_b) \\ a_{w4} = a_{by} + a_{bx} + \alpha(l_a + l_b) \end{cases} \tag{13}$$

where a_{w1}, a_{w2}, a_{w3} and a_{w4} denote the accelerates of the four wheels separately; a_{bx} and a_{by} denote the accelerates of the vehicle along the body coordinate; α denotes the angular accelerate of the vehicle. Once the states of the vehicle are determined, the control output of the wheels can be

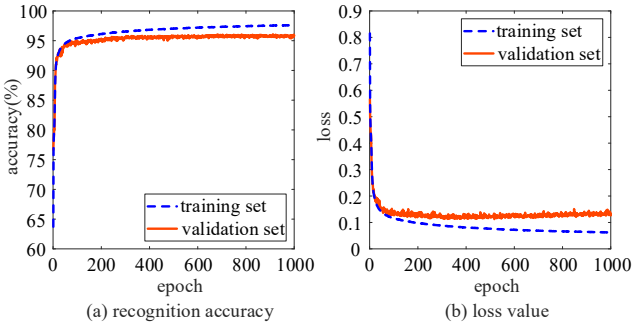

(a) recognition accuracy (b) loss value

Fig. 5: Training results of intention recognition model

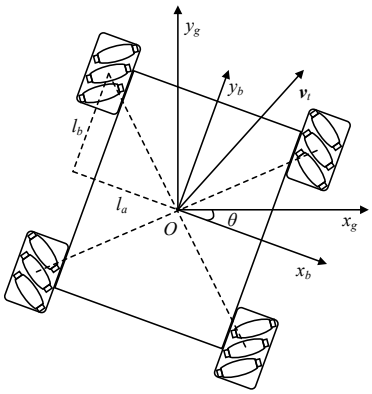

Fig. 6: Chassis of the vehicle with Mecanum wheels

correspondingly obtained. The model of the vehicle can be described as follows,

$$\begin{cases} \dot{x}_g = \dot{x}_b \cos\theta + \dot{y}_b \sin\theta \\ \dot{y}_g = \dot{x}_b \sin\theta + \dot{y}_b \cos\theta \\ \ddot{x}_b = a_{bx} \\ \ddot{y}_b = a_{by} \\ \ddot{\theta} = \alpha \end{cases} \tag{14}$$

which can be further transformed into the following HOFA form,

$$\begin{cases} \ddot{x}_g = -\dot{y}_g\dot{\theta} + a_{bx}\cos\theta + a_{by}\sin\theta \\ \ddot{y}_g = \dot{x}_g\dot{\theta} + a_{bx}\sin\theta - a_{by}\cos\theta \\ \ddot{\theta} = \alpha \end{cases} \tag{15}$$

where x_g, y_g are the coordinates of the vehicle on the ground coordinate; x_b, y_b are the coordinates of the vehicle on the body coordinate.

Then the HOFA controller can be obtained as follows,

$$\begin{cases} u_x = -A_{10}[\dot{x}_g, \dot{y}_g, \dot{\theta}]^T - A_{00}[x_g, y_g, \theta]^T + r_x \\ u_y = -A_{11}[\dot{x}_g, \dot{y}_g, \dot{\theta}]^T - A_{01}[x_g, y_g, \theta]^T + r_y \\ \alpha = -A_{12}[\dot{x}_g, \dot{y}_g, \dot{\theta}]^T - A_{02}[x_g, y_g, \theta]^T + r_\theta \\ a_{bx} = u_x\cos\theta + u_y\sin\theta \\ a_{by} = u_x\sin\theta + u_y\cos\theta \end{cases} \tag{16}$$

where A_{00}, A_{01}, A_{02}, A_{10}, A_{11} and A_{12} are adjustable parameter matrices, $R = [r_x, r_y, r_\theta]^T$ are the references, u_x and u_y are a part of the control outputs.

The simulation is conducted based on the model shown in Fig 6, and the HOFA controller described by (16) is utilized. The data set is established based on Algorithm 1, and the intention predictor is trained based on the data set using the hyperparameters in Table 1.

4.2 Simulation Results and Analysis

The proposed intention recognition model is tested in some typical scenarios to show the performance. In these scenarios, several obstacles with different shapes distribute in the environment, and a model which can not utilize the obstacle information is tested for comparison.

In the scenario shown in Fig 7(a), the motion of the rival agents is not related to the self agent, and the intention is defined as "irrelevant". The prediction results are shown in Fig 7(b). Both of the intention recognition models can obtain the correct intention in the end, and the proposed model has a lower false alarm rate.

In the scenario shown in Fig 8(a), the task of the rival agents is to restrict the motion of the self agent in all directions, and the intention is defined as "encircle". As the prediction results shown in Fig 8(b), both of the models can correctly predict the intention before the formation forms and have similar performance in this scenario.

In the scenario shown in Fig 9(a), the task of the rival agents is to restrict the forward motion of the self agent, and the intention is defined as "intercept". It is shown in Fig 9(b) that both of the models predict correctly in the end. With the consideration of obstacle information, the proposed model can realize the intention faster.

In the scenario shown in Fig 10(a), the task of the rival agents is to restrict the backward motion of the self agent, and the intention is defined as "follow". The prediction results are shown in Fig 10(b), and the proposed model performs well. However, the comparison model can not predict correctly before the formation forms in this scenario.

The proposed predictor is further tested on the test set, and the false alarm rate of the predictor is shown in Table 2. The results show that the model can predict the intention correctly when the features are adequate for intention recognition. The false alarm at the beginning of the intention recognition is mainly caused by the ambiguity of the information.

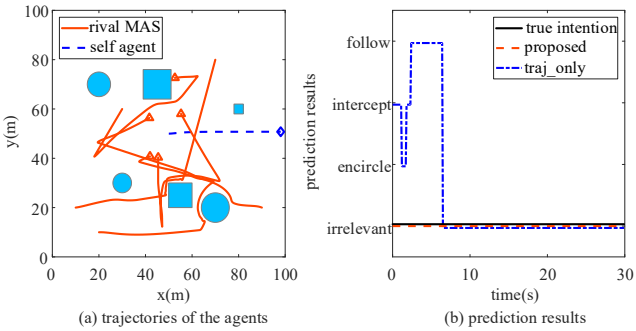

Fig. 7: Trajectory of multiple agents and corresponding output of predictors when intention is "irrelevant"

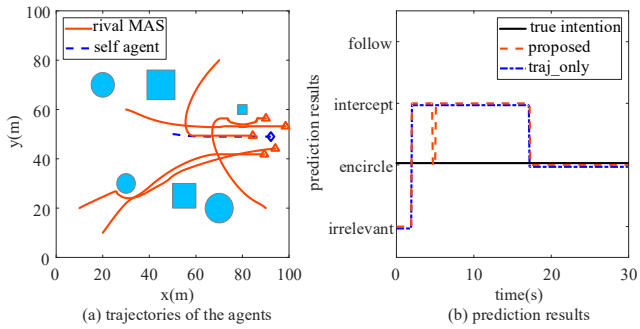

Fig. 8: Trajectory of multiple agents and corresponding output of predictors when intention is "encircle"

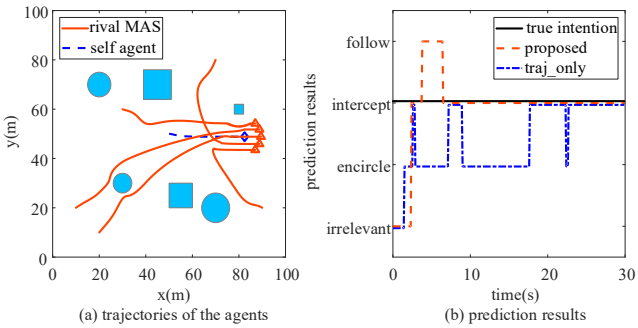

Fig. 9: Trajectory of multiple agents and corresponding output of predictors when intention is "intercept"

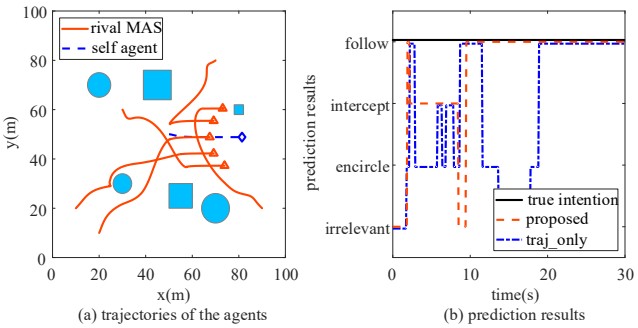

Fig. 10: Trajectory of multiple agents and corresponding output of predictors when intention is "follow"

Table 2: False Alarm Rate of the Proposed Model

Time/s	Intention			
	Encircle	Intercept	Follow	Irrelevant
5	41.0%	72.5%	87.5%	8.0%
10	16.0%	40.0%	43.0%	5.0%
15	15.0%	3.0%	10.5%	0.0%
20	6.5%	0.0%	0.0%	0.0%

5 Conclusion and Future Work

In this paper, the intention recognition problem for rival MASs is considered. The model of MASs is constructed based on the theory of high-order fully actuated systems approach and a data set based on HOFA model with more extensive features is established. Utilizing the data set, an intention recognition model based on artificial neural networks is constructed and trained. In the model, 1d-convolutional layers and recurrent neural networks are introduced to process the time features and spatial features. In order to increase the accuracy, both agent trajectories and obstacle information are utilized in the model training. The predictor is tested on some typical scenarios, and the results show that the proposed predictor has a better performance in the environment with obstacles.

In the future, we will consider more kinds of intentions and apply the HOFA system theory to more fields of the MASs. In order to get better results, we will also further adjust the parameters and the structure of the model.

References

[1] C. Schlenoff, Z. Kootbally, A. Pietromartire, et al, Intention recognition in manufacturing applications, *Robotics and Computer-Integrated manufacturing*, 2015, 33(6): 29-41.

[2] A. A. Nasr, CMSV: a new cloud multi-agents for self-driving vehicles as a services, *Journal of Grid Computing*, 2024, 22(1): 11.

[3] Z. X. Sun, H. Y. Piao, Z. Yang, et al, Multi-agent hierarchical policy gradient for air combat tactics emergence via self-play, *Engineering Application of Artificial Intelligence*, 2021, 98(2): 104112.

[4] Z. Zhang, Y. F. Zheng, W. H. Jiang, et al, Intention recognition for multiple agents, *Information Science*, 2023, 628(5): 360-376.

[5] L. Chen, X. X. Liang, Y. H. Feng, et al, Online intention recognition with incomplete information based on a weighted contrastive predictive coding model in wargame, *IEEE Transactions on Neural Networks and Learning Systems*, 2023, 34(10): 7515-7528.

[6] Z. Zhang, H. F. Wang, J. Geng, et al, An information fusion method based on deep learning and fuzzy discount-weighting for target intention recognition, *Engineering applications of Artificial Intelligence*, 2022, 109(5): 104610.

[7] S. Y. Wang, G. Wang, Q. Fu, et al, STABC-IR: an air target intention recognition method based on bidirectional gated recurrent unit and conditional random field with space-time attention mechanism, *Chinese Journal of Aeronautics*, 2023, 36(3): 316-334.

[8] D. W. Zhang, G. P. Liu and L. Cao, Constrained cooperative control for high-order fully actuated multiagent systems with application to air-bearing spacecraft simulators *IEEE-ASME Transactions on Mechatronics*, 2023, 28(3): 1570-1581.

[9] G. R. Duan, High-order fully actuated system approaches: Part I-Models and basic procedure, *International Journal of Systems Science*, 2021, 52(2): 422-435.

[10] G. R. Duan, High-order fully actuated system approaches: part VII-Controllability, stabilisability and parametric designs, *International Journal of Systems Science*, 2021, 52(14): 3091-3114.

[11] G. R. Duan, High-order fully actuated system approaches: Part III-Robust control and high-order backstepping, *International Journal of Systems Science*, 2021, 52(5): 952-971.

[12] G. R. Duan, High-order fully actuated system approaches: Part IV-Adaptive control and high-order backstepping, *International Journal of Systems Science*, 2021, 52(5): 972-989.

[13] G. R. Duan, High-order fully actuated system approaches: Part V-Robust adaptive control, *International Journal of Systems Science*, 2021, 52(10): 2129-2143.

[14] M. Cai, X. He and D. H. Zhou, An active fault tolerance framework for uncertain nonlinear high-order fully-actuated systems, *Automatica*, 2023, 152: 110969.

[15] G. P. Liu, Coordination of networked nonlinear multi-agents using a high-order fully actuated predictive control strategy, *IEEE-CAA Journal of Automatica Sinica*, 2022, 9(4): 615-623.

[16] D. W. Zhang, G. P. Liu, L. Cao, Coordinated control of high-order fully actuated multiagent systems and its application: a predictive control strategy, *IEEE-ASME Transactions on Mechatronics*, 2022, 27(6): 4362-4372.

[17] G. R. Duan, Proportional integral predictive control of high-order fully actuated networked multiagent systems with communication delays, *IEEE Transactions on Systems, Man, and Cybernetics: Systems*, 2023, 53(2): 801-812.

[18] J. Y. Chung, C. Gulcehre, K. H. Cho and Y. Bengio, Empirical evaluation of gated recurrent neural networks on sequence modeling, *Arxiv*, 2014, DOI: arXiv:1412.3555.

[19] A. Gfrerrer, Geometry and kinematics of the Mecanum wheel, *Computer Aided Geometric Design*, 2008, 25(9): 784-791.

Proceedings of the 3rd Conference on Fully Actuated System Theory and Applications
May 10-12, 2024, Shenzhen, China

Optimization Strategy for Wind-Solar Complementary Energy Storage Capacity Leveraging Photovoltaic Virtual Energy Storage

Jiahua Ni[1], Yuwei Chen[1], Tong Wang[2] Wei Jin[1]

1. Powerchina Huadong Engineering Corporation Limied, Hangzhou 311122, P. R. China

2. School of Information and Electrical Engineering, Hangzhou City University, Hangzhou 311122, P. R. China

Abstract: In this study, we present an integrated optimization model for configuring energy storage capacities in wind-solar energy systems, utilizing an innovative approach of Photovoltaic (PV) Virtual Energy Storage (PV-VES). This model aims to mitigate the high costs associated with conventional electrochemical storage solutions by integrating cost-effective PV components. The proposed optimization framework constructs a cost-minimization objective function, considering the operational characteristics and constraints of wind turbines, PV arrays, and energy storage units. By calculating the optimal installation capacities for both electrochemical and virtual energy storage, the model provides selective cost advantages in investment for renewable energy storage infrastructures. The results demonstrate that PV-VES can enhance the economic feasibility of wind-solar complementary storage systems.

Key Words: capacity optimization, electrochemical storage, PV, virtual energy storage

1 Introduction

As the world strides towards a zero-carbon future, renewable energy emerges as a cornerstone in the global energy transition [1–3]. This shift is not merely a trend but a necessity, driven by the urgent need to mitigate climate change and to establish sustainable energy systems. Within this paradigm, wind turbine and photovoltaic (PV) generation have become pivotal, owing to the abundant and clean nature of wind and solar power [4–6]. According to the report released by the international energy agency (IEA) in January 2024 [7], renewable electricity capacity additions reached an estimated 507 GW in 2023, nearly 50% higher than in 2022, with PV and wind accounting for approximately 95% of it. By 2028, PV and wind turbine capacity additions are expected to more than double compared to 2022, reaching nearly 710 GW.

The integration of a large number of wind turbine and PV generation aids in the economic and social transition to a low-carbon, green model, but it also presents two major challenges to the power grid [8, 9]. Firstly, the power generation of wind turbine and PV generation is subject to environmental impacts, leading to uncertainty and intermittency, which increases the pressure on the grid to mitigate the power fluctuations. Secondly, wind turbine and PV generation are typically connected to the grid through power electronic converters. The influx of a large number of these power electronic devices introduces problems of harmonics and low inertia, gradually deteriorating the quality of electrical energy in the grid. Energy Storage, characterized by its ability to store more electrical energy and release less, becomes an ideal choice to facilitate the absorption of wind turbine and PV generation [10].

The deployment of energy storage faces two main issues: type and capacity. Energy storage systems can be broadly categorized based on their underlying principles: mechanical, chemical, electrical, and thermal [11, 12]. Mechanical storage, exemplified by pumped hydro storage, compressed air storage and flywheels, capitalizes on kinetic or potential energy; it's renowned for its large-scale capacity and long life span but is limited by geographical constraints and high initial costs. Chemical storage, primarily through batteries like lithium-ion, lead-acid, and flow batteries, relies on chemical reactions to store and release energy. While offering high energy density and efficiency, they often face challenges with lifespan, cost, and environmental impact. Electrical storage, such as supercapacitors, stores energy in an electric field. These systems boast rapid charging and discharging capabilities, but their energy density is relatively low compared to other forms. Lastly, thermal storage, including molten salt and ice storage, retains heat or cold for later use. This type is highly efficient and cost-effective for large-scale applications, though its use is typically confined to specific cases like district heating or cooling. However, considering the aspects of technological maturity and safety reliability, the types of storage currently widely applied are still limited to pumped hydro storage and lithium battery storage.

Capacity is closely related to economic viability. The determination of optimal capacity configuration for diverse types of storage systems across various scenarios currently stands as a prominent subject of research interest [13, 14]. Literature [15] investigates the integration of Battery Energy Storage Systems (BESS) with wind power generation, emphasizing the optimization of BESS component sizing to enhance efficiency and reduce costs. Literature [16] presents a novel framework for optimizing the sizing of both thermal and electrical energy storage systems in residential buildings with PV systems. The study demonstrates how combining thermal storage and battery storage can significantly reduce both daily electricity and life cycle costs. Literature [17] introduces a methodology for the optimal design and deployment of large-scale Gravity Energy Storage (GES) systems in hybrid PV-wind power plants. The study demon-

This work is supported by National Key R&D of China (2021YFB2400600)) and Zhejiang Postdoctoral Preferential Funding Project (2022011).

strates that integrating GES with renewable energy sources can effectively balance energy supply and demand, offering a cost-effective and robust alternative to traditional energy storage methods, with a significant advantage in terms of depth of discharge and lifetime compared to battery energy storage. Literature [18] explores the optimization of a hybrid photovoltaic-wind system with battery storage for Net Zero Energy Buildings (NZEBs), focusing on minimizing total energy transfer (TET) to the grid, loss of power supply probability (LPSP), and system cost. This approach leads to more efficient sizing of renewable energy generators and battery storage, contributing to sustainable and reliable energy management in NZEBs. Literature [19] introduces an enhanced methodology for optimally sizing small-scale microgrids, integrating PV systems with hybrid energy storage (batteries and supercapacitors). The approach uniquely factors in battery aging and operational degradation, aiming to improve system longevity and reduce costs, with successful application in case studies from Puerto Carreño, Colombia. In summary, as there are various types of storage, each with different application scenarios, the key and challenge in capacity optimization lies in constructing a reasonable optimization model and solving it using appropriate tools.

Among the numerous types of storage, electrochemical storage represented by lithium batteries is widely applied due to its high energy density, rapid response capability, and flexible, convenient installation. Especially in large-scale storage configurations, lithium battery storage is often the preferred option. However, its drawbacks should not be overlooked. The lifespan of lithium battery storage is shorter compared to the service cycle of wind and PV generation equipment, necessitating replacement during its lifetime. Additionally, due to sustained high demand, the lifecycle cost of lithium battery storage remains high.

1.1 Contribution

In this paper, we introduce a groundbreaking approach to optimizing energy storage in wind-solar systems, notably through the integration of Photovoltaic Virtual Energy Storage (PV-VES). We develop a comprehensive optimization model that intricately balances the cost minimization objective against the operational characteristics and constraints of wind turbines, PV arrays, and energy storage units. Our model is instrumental in demonstrating significant investment cost reductions by optimally configuring both electrochemical and virtual energy storage. Through a practical case study, we validate the model's real-world applicability and its superiority in cost-effectiveness over conventional energy storage methods.

1.2 Organization

The remainder of this paper is organized as follows. Section 2 elaborates the core of the paper, the Optimization Model. This section is subdivided into parts discussing the Objective Function and Constraints, detailing the approach to minimize the system's costs while adhering to operational limitations. Section 3 provides a Case Study, applying the model in a practical scenario and contrasting the proposed PV-VES strategy with traditional ECS methods. The paper is concluded in Section 4.

2 Optimization Model

2.1 Objective function

The objective function generally aims to minimize the system's investment and operational costs. As the service life of PV and electrochemical storage are not equal, the average lifetime of a PV plant is 25 years [20] and a lithium-ion energy storage station is 10 years [21], to equate the costs of PV-VES and ECS, we use the annualized cost of the system to construct the objective function [18]:

$$\min \quad f_{\text{acs}} = C_{\text{acs,pv}} S_{\text{ves}} + C_{\text{acs,ecs}} S_{\text{ecs}} \tag{1}$$

where $S_{\text{ves}}, S_{\text{ecs}}$ are rated capacity of PV-VES and ECS, respectively; $C_{\text{acs,pv}}, C_{\text{acs,ecs}}$ represent the annualized unit capacity costs of PV-VES and ECS, respectively.

The annualized unit capacity costs of PV-VES and ECS are generally composed of three parts: annualized capital cost, annualized replacement cost and annualized operation and maintenance cost. The specific calculation methods for the three are as follows [18]:

(1) Annualized capital cost

The calculation method for both PV and ECS is consistent and can be unified by the following formula:

$$C_{\text{cap}} = C_c \cdot \frac{r \cdot (1+r)^{Y_{\text{com}}}}{(1+r)^{Y_{\text{com}}} - 1} \tag{2}$$

where C_c is the capital cost of the each component, Y_{com} is the component lifespan in year, r is the annual interest rate.

(2) Annualized replacement cost

Since the lifespan of PV modules is longer than that of ECS, this paper measures by the lifecycle of PV modules, with the annualized replacement cost of PV modules being 0. Here, only the annualized replacement cost of ECS is considered, and the calculation formula is as follows:

$$C_{\text{rep,ecs}} = C_r \cdot \frac{r}{(1+r)^{Y_{\text{rep}}} - 1} \tag{3}$$

where C_{r} is the single replacement cost of ECS, Y_{rep} is service life of the ECS in year.

(3) Annualized operation and maintenance costs

The annual operation and maintenance cost per unit component is generally a fixed expense, which can be specifically estimated based on local labor costs and other related factors [22, 23].

(4) Annualized cost of system

Based on the above descriptions of annualized capital cost, replacement costs, and operation and maintenance costs, we can derive the annualized costs for PV-VES and ECS as follows:

$$\begin{aligned} C_{\text{acs,pv}} &= C_{\text{cap,pv}} + C_{\text{om,pv}} \\ C_{\text{acs,ecs}} &= C_{\text{cap,ecs}} + C_{\text{rep,ecs}} + C_{\text{om,ecs}} \end{aligned} \tag{4}$$

where $C_{\text{cap,pv}}$,$C_{\text{cap,ecs}}$ are the annualized capital cost of PV-VES and ECS, calculated according to equation (2), respectively; $C_{\text{om,pv}}$,$C_{\text{om,ecs}}$ are the annualized operation and maintenance cost of PV-VES and ECS, respectively.

2.2 Constraints

The set of constraints ensures the operational feasibility and the technical limits of the energy system components.

These include output capacity limits for generation units, the operational bounds for charging and discharging the electrochemical energy storage, maintaining power supply and demand balance.

(1) Wind turbine, PV, Virtual storage output constraints

These constraints limit the active power output of wind turbines, PV systems, and virtual energy storage units to their respective maximum available power at any given moment. These limits are essential to prevent over-generation and to match the power production with the variable nature of renewable energy sources and storage capabilities.

$$\begin{cases} 0 \le p_{\text{wt}}^k \le P_{\text{max,wt}}^k \\ 0 \le p_{\text{pv}}^k \le P_{\text{max,pv}}^k \\ 0 \le p_{\text{ves}}^k \le P_{\text{max,ves}}^k \end{cases} \tag{5}$$

where p_{wt}^k, p_{pv}^k, and p_{ves}^k represent the active power outputs of the wind turbine, photovoltaic (PV), and virtual energy storage at moment k, respectively; $P_{\text{max,wt}}^k$, $P_{\text{max,pv}}^k$, and $P_{\text{max,ves}}^k$ denote their respective maximum available powers at the same moment, which are influenced by environmental factors such as wind speed and solar irradiance.

The maximum available power of a wind turbine can be estimated based on the wind speed, and its estimation formula is as follows [24]:

$$P_{\text{max, wt}}^k = \begin{cases} 0, & (v^k \le v_{\text{ci}}) \vee (v^k \ge v_{\text{co}}) \\ S_{\text{wt}} \frac{v^k - v_{\text{ci}}}{v_{\text{r}} - v_{\text{ci}}}, & v_{\text{ci}} \le v^k \le v_{\text{r}} \\ S_{\text{wt}}, & v_{\text{r}} \le v^k \le v_{\text{co}} \end{cases} \tag{6}$$

where S_{wt} is the installed capacity of the wind turbine; v^k is the wind speed at moment k; v_{ci} is the cut-in wind speed; v_{co} is the cut-out wind speed; v_{r} is the rated wind speed.

The maximum available power of PV generations and virtual storage can be estimated based on the solar irradiance and ambient temperature, and the estimation formula is as follows [25]:

$$P_{\text{pv}}^k = S_{\text{pv}} \times \frac{G^k}{G_{\text{ref}}} \left[1 + \beta \left((T_{\text{amb}}^k + (0.0256 \times G^k)) - T_{\text{ref}} \right) \right] \tag{7}$$

where P_{pv}^k is the output power of the PV panels at moment k, S_{pv} is the installed capacity of the PV panels, G^k is the solar irradiance (W/m^2) at moment k, G_{ref} is the reference solar irradiance (1000 W/m^2), T_{ref} is the reference temperature (25 °C), β is -3.7×10^{-3} (1/°C) , and T_{amb}^k is the ambient temperature at moment k.

(2) Electrochemical storage output constraints

These constraints define the permissible charging and discharging activities of electrochemical storage systems. They ensure that storage units do not charge and discharge simultaneously and that the charging and discharging power levels do not exceed the system's maximum capacity.

$$\begin{cases} 0 \le \lambda_{\text{c}}^k + \lambda_{\text{d}}^k \le 1 \\ 0 \le p_{\text{ecs,c}}^k \le \lambda_{\text{c}}^k P_{\text{max,ecs}} \\ 0 \le p_{\text{ecs,d}}^k \le \lambda_{\text{d}}^k P_{\text{max,ecs}} \end{cases} \tag{8}$$

where λ_{d}^k and λ_{c}^k represent the binary states of discharging and charging at moment k, respectively; $p_{\text{ecs,c}}^k$ and $p_{\text{ecs,d}}^k$ are the respective charging and discharging powers; $P_{\text{max,ecs}}$ is the rated power capacity of the electrochemical storage.

(3) Electrochemical storage state of charge constraint

This constraint governs the state of charge of the electrochemical storage system, accounting for the energy balance over time. It ensures the energy content of the storage remains within the specified bounds, considering the efficiency of charging and discharging processes and the time interval between the operational moments.

$$\begin{cases} E_{\text{ecs}}^k = E_{\text{ecs}}^{k-1} + \eta_{\text{ecs,c}} p_{\text{ecs,c}}^k \Delta T - \frac{p_{\text{ecs,d}}^k}{\eta_{\text{ecs,d}}} \Delta T \\ S_{\text{ecs}} SOC^{\min} \le E_{\text{ecs}}^k \le S_{\text{ecs}} SOC^{\max} \end{cases} \tag{9}$$

where E_{ecs}^k and E_{ecs}^{k-1} are the energy content of the storage at the current and previous moments; $\eta_{\text{ecs,c}}$ and $\eta_{\text{ecs,d}}$ are the charging and discharging efficiencies; ΔT is the time interval; $SOC^{\min}$ and $SOC^{\max}$ are the minimum and maximum state of charge limits.

(4) Power balance constraint

The power balance constraint ensures that the total power generation matches the load demand at every moment. It is a fundamental requirement for the stable operation of an electrical grid, ensuring that all the power consumed by the load is supplied by the generation units and storage systems.

$$p_{\text{load}}^k = p_{\text{pv}}^k + p_{\text{wt}}^k + \lambda_{\text{d}}^k p_{\text{ecs,d}}^k - \lambda_{\text{c}}^k p_{\text{ecs,c}}^k + p_{\text{ves}}^k \tag{10}$$

where p_{load}^k is the load power at moment k.

3 Case Study

This section endeavors to employ the parameters of a source-grid-load-storage system for the purpose of contrasting the cost expenditures associated with the proposed PV-VES configuration strategy against those of the conventional ECS configuration method.

Table 1: Parameters of PV-VES and ECS

Types	PV-VES	ECS
Capital cost	3582 ¥/kW	1437 ¥/kWh
Replacement cost	/	1060 ¥/kWh
Operation and maintenance cost	7.2 ¥/kW	12.4 ¥/kW
Service lifetime	25 years	10 years
Interest rate	4%	4%

Table 2: Constant Parameters in the Proposed Optimization Model

Types	Value
$C_{\text{acs,pv}}$	236.49
$C_{\text{acs,wt}}$	419.76
$SOC^{\min}$	0.05
$SOC^{\max}$	0.95
$\eta_{\text{ecs,c}}$	0.95
$\eta_{\text{ecs,d}}$	0.95

3.1 Data preparation

The installed capacity of PV and wind turbine are 200MW and 150MW, respectively. Based on the historical data of irradiance, temperature, and wind speed at the site location

for the entire year of 2023, measured on an hourly scale, and according to equations (6) and (7), we obtained the maximum power data for the wind turbine and the PV stations, as shown in Fig. 1 and 2. Moreover, the load power is also based on the historical data of 2023, as plotted in the Fig. 3.

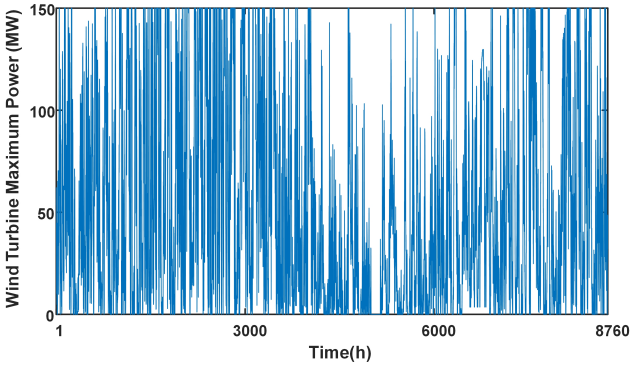

Fig. 1: Hourly maximum power curve of the wind turbine station for the entire year.

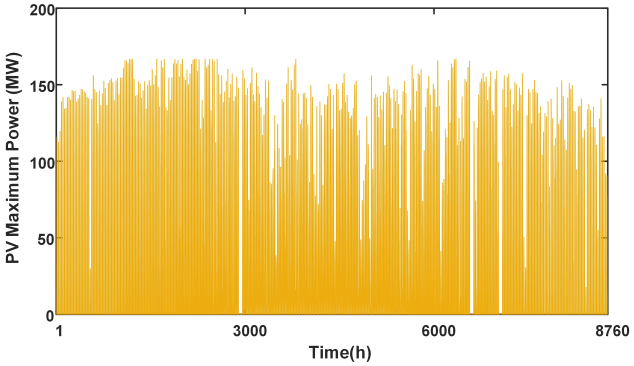

Fig. 2: Hourly maximum power curve of the PV station for the entire year.

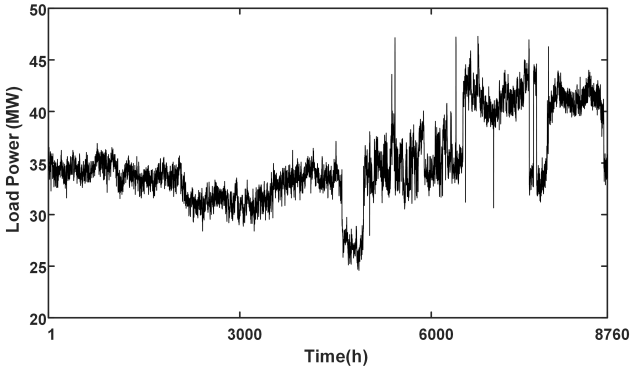

Fig. 3: Hourly load curve for the entire year.

To visually present the monthly resource situation, we have drawn a line graph showing the average monthly power of PV, wind turbines, and load, as illustrated in Fig. 5. Wind resources are more abundant in the spring, summer, and winter seasons, and relatively less in autumn. The distribution of solar resources is relatively even throughout the four seasons, with somewhat lesser availability in winter. Additionally, a distinct characteristic of solar resources is that they

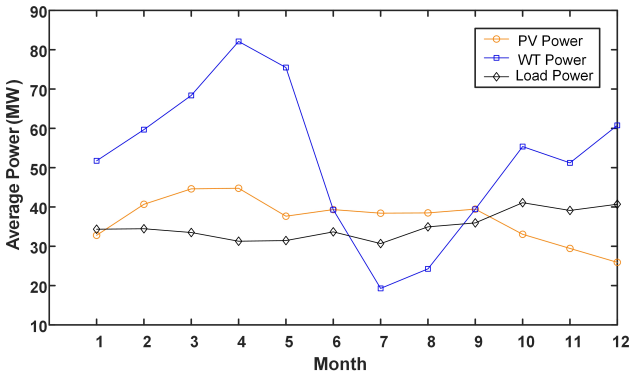

Fig. 4: Monthly average power of PV, wind turbine and load.

drop to zero at night, whereas wind resources fluctuate randomly throughout the day. The demand for load is quite stable, without significant fluctuations daily, although there is an increase in demand during the autumn and winter seasons.

Based on the current engineering construction data, we can obtain the cost-related parameters for PV-VES and ECS, as shown in Tab. 1. Here, the ECS is exemplified by the most commonly used lithium-ion batteries. Then, we can obtain the annualized costs of PV-VES and ECS according to equations (2)-(4), which is 236.49 ¥/kW and 419.76 ¥/kW. In addition, to prevent overcharging and over-discharging of the ECS, we set the maximum and minimum values of SOC to 0.05 and 0.95, respectively. The charge and discharge efficiency can be set to 95% [26]. Thus, the constant parameters in the proposed optimization model can be list in Tab. 2.

3.2 Result and discussion

Given that wind and PV resources display unique seasonal traits, as illustrated in Fig. 1 and 2, our study aims to exhibit the efficacy of the proposed PV-VES configuration approach under varying resource endowments. This objective is pursued by initially conducting monthly capacity optimization solutions, subsequently extending to an annual capacity optimization. The outcomes of these solutions are then juxtaposed with the conventional capacity configuration method, which exclusively incorporates electrochemical storage, exemplified by the use of lithium battery storage.

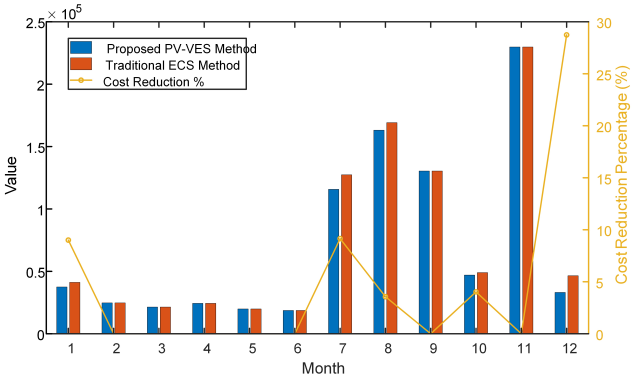

Fig. 5: Monthly annualized cost and cost reduction percentage of the proposed PV-VES method and the traditional ECS method.

Table 3: Results Comparison between Proposed PV-VES Method and Traditional ECS Method

Month	Proposed PV-VES Method			Traditional ECS Method		Cost Reduction (%)
	PV-VES Capacity (MW)	ECS Capacity (MWh)	Annualized Cost ($\times 10^4$)	ECS Capacity (MWh)	Annualized Cost ($\times 10^4$)	
1	69.09	854.48	37 501.63	981.85	41 214.18	9.01
2	0.00	589.53	24 746.21	589.53	24 746.21	0.00
3	0.00	510.24	21 417.93	510.24	21 417.93	0.00
4	0.00	580.75	24 377.95	580.75	24 377.95	0.00
5	0.00	473.93	19 893.96	473.93	19 893.96	0.00
6	0.00	444.66	18 664.95	444.66	18 664.95	0.00
7	428.03	2516.12	115 739.28	3034.96	127 395.39	9.15
8	852.05	3406.84	163 155.84	4030.53	169 185.55	3.56
9	0.00	3107.03	130 421.08	3107.03	130 421.08	0.00
10	24.31	1106.71	47 030.06	1167.43	49 004.00	4.03
11	0.00	5474.80	229 810.17	5474.80	229 810.17	0.00
12	141.42	709.84	33 140.86	1107.94	46 507.07	28.74
1-12	24.31	1106.71	47 030.06	1167.43	49 004.00	4.03

Table 3 illustrates the energy storage capacity optimization results comparison between the proposed PV-VES method and the traditional ECS method. As shown, The cost-reduction effect of the proposed PV-VES algorithm varies monthly, mainly influenced by the relative availability of sunlight resources. From February to June, wind and solar resources are abundant, especially wind resources, which far exceed the load demand. In this period, the proposed algorithm sets the PV virtual storage capacity to zero, not showing any cost reduction advantage. However, during July and August, when wind resources are relatively scarce and solar resources are relatively abundant, the proposed algorithm allocates a larger capacity for PV virtual storage, leading to a significant cost reduction. Looking at the data configuration for the entire year, the proposed PV virtual storage configuration strategy can reduce costs by 4.03%.

4 Conclusion

This study introduces an innovative optimization strategy for enhancing the cost-effectiveness of energy storage in wind-solar energy systems, leveraging the concept of PV-VES. By integrating PV-VES with traditional ECS solutions, the model significantly reduces investment costs for renewable energy storage infrastructures. The optimization framework, with its cost-minimization objective function, adeptly addresses operational characteristics and constraints of wind turbines, PV arrays, and storage units, demonstrating the substantial economic benefits of PV-VES in a comprehensive case study. The results underline the potential of PV-VES in improving the economic feasibility of wind-solar complementary storage systems, thereby contributing to the advancement of sustainable and efficient renewable energy integration into the power grid.

References

[1] Xi Yuan, Chi-Wei Su, Muhammad Umar, Xuefeng Shao, and Oana-Ramona LobonŢ. The race to zero emissions: Can renewable energy be the path to carbon neutrality? *Journal of Environmental Management*, 308:114648, 2022.

[2] Emadul Islam, Asheer Shah, and Tariq A Karim. Role of renewable energy policy in ensuring net-zero carbon emissions and energy sustainability: A bangladesh perspective. In *Moving Toward Net-Zero Carbon Society: Challenges and Opportunities*, pages 59–77. Springer International Publishing Cham, 2023.

[3] Olivier Joseph Abban, Yao Hong Xing, Alina Cristina Nuţă, Florian Marcel Nuţă, Prasad Siba Borah, Charles Ofori, and Yao Jing Jing. Policies for carbon-zero targets: Examining the spillover effects of renewable energy and patent applications on environmental quality in europe. *Energy Economics*, 126:106954, 2023.

[4] X Costoya, M deCastro, David Carvalho, and M Gómez-Gesteira. Assessing the complementarity of future hybrid wind and solar photovoltaic energy resources for north america. *Renewable and Sustainable Energy Reviews*, 173:113101, 2023.

[5] Laibao Liu, Gang He, Mengxi Wu, Gang Liu, Haoran Zhang, Ying Chen, Jiashu Shen, and Shuangcheng Li. Climate change impacts on planned supply–demand match in global wind and solar energy systems. *Nature Energy*, 8(8):870–880, 2023.

[6] Yijing Wang, Rong Wang, Katsumasa Tanaka, Philippe Ciais, Josep Penuelas, Yves Balkanski, Jordi Sardans, Didier Hauglustaine, Wang Liu, Xiaofan Xing, et al. Accelerating the energy transition towards photovoltaic and wind in china. *Nature*, 619(7971):761–767, 2023.

[7] International Energy Agency. Renewables 2023. Technical report, IEA, Paris, 2024. License: CC BY 4.0.

[8] Md Shafiul Alam, Fahad Saleh Al-Ismail, Aboubakr Salem, and Mohammad A Abido. High-level penetration of renewable energy sources into grid utility: Challenges and solutions. *IEEE Access*, 8:190277–190299, 2020.

[9] Jan Shair, Haozhi Li, Jiabing Hu, and Xiaorong Xie. Power system stability issues, classifications and research prospects in the context of high-penetration of renewables and power electronics. *Renewable and Sustainable Energy Reviews*, 145:111111, 2021.

[10] Bruno Cárdenas, Lawrie Swinfen-Styles, James Rouse, Adam Hoskin, Weiqing Xu, and SD Garvey. Energy storage capacity vs. renewable penetration: A study for the uk. *Renewable Energy*, 171:849–867, 2021.

[11] AG Olabi, C Onumaegbu, Tabbi Wilberforce, Mohamad Ramadan, Mohammad Ali Abdelkareem, and Abdul Hai Al-Alami. Critical review of energy storage systems. *Energy*, 214:118987, 2021.

[12] Ahmed Zayed AL Shaqsi, Kamaruzzaman Sopian, and Amer Al-Hinai. Review of energy storage services, applications, limitations, and benefits. *Energy Reports*, 6:288–306, 2020.

[13] MA Hannan, M Faisal, Pin Jern Ker, RA Begum, ZY Dong, and C Zhang. Review of optimal methods and algorithms for sizing energy storage systems to achieve decarbonization in microgrid applications. *Renewable and Sustainable Energy Reviews*, 131:110022, 2020.

[14] Bo Yang, Junting Wang, Yixuan Chen, Danyang Li, Chunyuan Zeng, Yijun Chen, Zhengxun Guo, Hongchun Shu, Xiaoshun Zhang, Tao Yu, et al. Optimal sizing and placement of energy storage system in power grids: A state-of-the-art one-stop handbook. *Journal of Energy Storage*, 32:101814, 2020.

[15] Ye Liu, Xiaogang Wu, Jiuyu Du, Ziyou Song, and Guoliang Wu. Optimal sizing of a wind-energy storage system considering battery life. *Renewable Energy*, 147:2470–2483, 2020.

[16] Ali Baniasadi, Daryoush Habibi, Waleed Al-Saedi, Mohammad AS Masoum, Choton K Das, and Navid Mousavi. Optimal sizing design and operation of electrical and thermal energy storage systems in smart buildings. *Journal of Energy Storage*, 28:101186, 2020.

[17] Anisa Emrani, Asmae Berrada, and Mohamed Bakhouya. Optimal sizing and deployment of gravity energy storage system in hybrid pv-wind power plant. *Renewable Energy*, 183:12–27, 2022.

[18] N Niveditha and MM Rajan Singaravel. Optimal sizing of hybrid pv–wind–battery storage system for net zero energy buildings to reduce grid burden. *Applied Energy*, 324:119713, 2022.

[19] L.M. León, D. Romero-Quete, N. Merchán, and C.A. Cortés. Optimal design of pv and hybrid storage based microgrids for healthcare and government facilities connected to highly intermittent utility grids. *Applied Energy*, 335:120709, 2023.

[20] Rachit Srivastava, AN Tiwari, and VK Giri. An overview on performance of pv plants commissioned at different places in the world. *Energy for Sustainable Development*, 54:51–59, 2020.

[21] Mei Shengwei, Li Jianlin, and Jianquan Zhu. *Energy Storage*. China Machine Press, 2022.

[22] Graciele Rediske, Leandro Michels, Julio Cezar Mairesse Siluk, Paula Donaduzzi Rigo, Carmen Brum Rosa, and Andrei Cunha Lima. A proposed set of indicators for evaluating the performance of the operation and maintenance of photovoltaic plants. *Applied Energy*, 354:122158, 2024.

[23] Ye Jiawen. Research on technical adaptability and benefit evaluation of energy storage system in typical application scenarios. Master's thesis, North China Electric Power University, 2021.

[24] BP Numbi and SJ Malinga. Optimal energy cost and economic analysis of a residential grid-interactive solar pv system-case of ethekwini municipality in south africa. *Applied Energy*, 186:28–45, 2017.

[25] Mohammad Javad Morshed, Jalel Ben Hmida, and Afef Fekih. A probabilistic multi-objective approach for power flow optimization in hybrid wind-pv-pev systems. *Applied energy*, 211:1136–1149, 2018.

[26] Siamak Farhad and Ashkan Nazari. Introducing the energy efficiency map of lithium-ion batteries. *International Journal of Energy Research*, 43(2):931–944, 2019.

Proceedings of the 3rd Conference on Fully Actuated System Theory and Applications
May 10-12, 2024, Shenzhen, China

Optimizing Hybrid Energy Storage in Offshore Wind Farms with a Focus on Extending Storage Life

Yuwei Chen[1], Tong Wang[2], Jiahua Ni[1], Hongke Li[1], Fei Yang[1], Yiheng Wang[3]

1. Renewable Energy Institute, Powerchina Huadong Engineering Corporation, Hangzhou 311122, P. R. China
E-mail: chen_yw2@hdec.com,ni_jh@hdec.com,li_hk@hdec.com,yang_f2@hdec.com

2. School of information and electrical engineering, Hangzhou City University, Hangzhou 310015, P. R. China
E-mail: wangtong@hzcu.edu.cn

3. College of Electrical Engineering, Zhejiang University, Hangzhou 310027, P. R. China
E-mail: 1513323439@qq.com

Abstract: This paper presents an innovative approach to optimizing hybrid energy storage systems (HESS) in offshore wind farms, with a particular focus on extending the storage's lifetime. We introduce a novel optimization model that integrates the complexities of offshore wind energy generation with the dynamic characteristics of multiple energy storage technologies. The model aims to maximize the efficiency and reliability of energy storage by effectively balancing the load between different storage units, thereby mitigating the degradation of storage components and prolonging their operational lifespan.The results demonstrate that our optimized HESS not only improves the overall performance of offshore wind systems but also significantly reduces the long-term operational and maintenance costs by extending the storage units' lifetime.

Key Words: Hybrid Energy Storage Optimization, Offshore Wind Farms, Extending Storage Life

1 Introduction

Offshore wind farms are pivotal in the transition towards sustainable and renewable energy sources[1, 2]. The incorporation of hybrid energy storage systems (HESS) is increasingly recognized as a vital component in enhancing the operational efficiency and reliability of these farms. The variable and unpredictable nature of wind energy necessitates innovative and adaptable solutions in energy storage and management. This challenge has been the focus of numerous recent research efforts, aiming to optimize energy use, reduce waste, and improve system resilience[3–5].

HESS has gained widespread application in renewable energy systems for its versatility and efficiency. A notable contribution by Suvitha et al. (2024) introduces a method for selecting sustainable hydro-power renewable energy sources. This method emphasizes the crucial aspect of choosing efficient and sustainable energy systems in renewable energy projects, which is vital for long-term environmental and economic viability[6]. Hou et al. (2015) extend this discussion by exploring hybrid energy storage and generator control monitoring systems. Their research underscores the need for ongoing technological advancements and system innovations to optimize the performance of renewable energy farms, particularly in the face of evolving energy demands and environmental concerns[7].

Furthermore, Nkwanyana et al. (2023) delve into the complexities of optimizing HESS, addressing critical issues such as durability, charging/discharging efficiency, temperature management, cost-effectiveness, and overall lifespan of the storage systems. Their comprehensive assessment of these factors provides valuable insights into the multifaceted nature of HESS optimization in renewable energy systems[8]. Behera et al. (2024) contribute to this discourse by highlighting the role of hybrid energy storage in effectively managing excess energy during peak generation periods and smoothing out the fluctuations in power output, which is a critical aspect of maintaining grid stability and ensuring consistent energy supply[9].

In the specific context of wind farms, Choi et al. (2016) investigate the application of frequency regulation techniques using pulse-width modulation. Their study offers a nuanced look at how HESS can be effectively integrated to manage frequency variations and enhance the overall efficiency of wind farm operations[10]. Wang et al. (2023) propose the use of zero-phase CARIMA filtering as an innovative approach to integrate hybrid energy storage systems for smoothing wind power fluctuations. This technique represents a significant advancement in optimizing the balance between energy generation and storage, ensuring a more reliable and steady power output from wind farms[11].

Zhang et al. (2023) focus on the strategic allocation of HESS resources using a scenario clustering algorithm. This approach allows for more informed decision-making in the distribution and utilization of energy storage resources, aligning with the dynamic and variable nature of wind energy generation[13]. Chen et al.(2022) propose an innovative method for determining the target power in HESS. Their approach leverages the capabilities of a low-pass filter algorithm to make strategic decisions regarding the distribution of energy within the HESS[12]. Finally, Li et al. (2023) present a novel concept of hybrid electric-methanol energy storage to improve the stability and reliability of power systems. Their research showcases the potential of combining different energy storage technologies to create a more resilient and adaptable energy system, particularly in the context of offshore wind energy generation [14].

These studies collectively emphasize the pivotal role and progressive development of HESS in the realm of renewable energy. The implementation of HESS is instrumental in stabilizing the inherent fluctuations characteristic of renewable energy sources, thereby enhancing the reliability and predictability of power supply. Additionally, integrating technologies such as super-capacitors into these systems can significantly extend the life of batteries, thereby improving the

overall efficiency and sustainability of the energy storage solution.

In power generation systems, energy storage serves three main functions: smoothing the output power curve of wind and solar energy, tracking the load power curve, and peak shaving and valley filling[15, 16]. Depending on the role of energy storage, the system adopts different energy dispatch strategies, and the configuration of energy storage capacity also varies.

In this study, we unveil an innovative optimization algorithm that masterfully integrates the intricacies of offshore wind energy generation with the dynamic functionality of various energy storage technologies. This algorithm is particularly geared towards exploring an effective combined configuration approach for energy storage power stations, tailored to align with the output characteristics of new energy field station clusters. The primary application of this model is in refining the output power curve of wind power generation.

Furthermore, we delve into the potential of advanced control strategies and smart grid technologies to further enhance the performance of HESS. These strategies include real-time monitoring and adaptive control mechanisms that respond dynamically to mitigate the fluctuations of wind energy. By incorporating these technologies, our model not only extends the life of energy storage components but also paves the way for more intelligent and autonomous renewable energy systems.

2 Wind Farm with HESS

Energy storage systems can be classified into two types based on their charging and discharging characteristics: energy-type storage and power-type storage[17]. Energy-type storage, such as batteries, has a high energy density, but frequent charging and discharging can affect its service life. On the other hand, power-type storage, such as flywheels and super-capacitors, has a high power density, short start-stop response time, and minimal impact on lifespan. Currently, using a single type of energy storage cannot cope with the complex fluctuations in renewable energy output. Therefore, a hybrid energy storage system combining energy-type and power-type storage is considered to jointly mitigate these fluctuations. In this paper, the HESS system is composed with the battery and super-capacitor.

In the wind power farm with HESS, the total output of the system can be depicted as

$$P_{Out} = P_{Wind} + P_{HESS} \tag{1}$$

Where P_{Out} is the total output of the system. P_{Wind} represents the power generated by the wind farm. P_{HESS} is the output of the storage system.In this equation, the energy directed to the storage system is considered as negative (indicating charging), whereas energy discharged from the storage system is positive.

Since there are rigid standards for grid-connected power fluctuations of offshore wind farm, the low-pass filter is applied in power distribution of the system. The first-order lower pass filter is shown in 1.

In this filter, according to the relationship of the components, we have

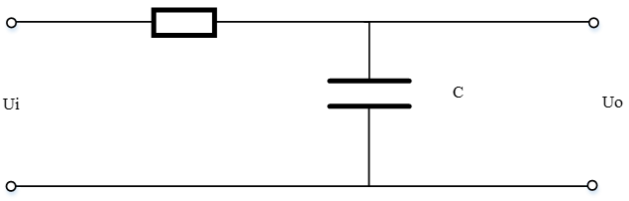

Fig. 1: A first-order lower pass filter

$$RC^* \frac{dU_o}{dt} + U_o = U_i \tag{2}$$

Where $\tau = RC$ is the filter time constant, U_i is the input signal, and U_o is the low-pass filter output signal. Similarly, by applying this algorithm into mitigating the fluctuation, the following equation can be acquired,

$$P_{Out}(t) = (1-a)P_{Out}(t-1) + aP_{Wind}(t) \tag{3}$$

t indicates the sampling time, a is the fluctuation coefficient. Since $a \in (0, 1)$, the bigger a shows deeper influence of the wind fluctuations.

The wind power fluctuation is modelled as

$$a(t) = \begin{cases} \dfrac{\min\{P_{Out}(t-\Delta t) + \gamma P_r - P_{Out}(t-1)\}}{P_{Wind}(t) - P_{Out}(t-1)}, \\ \qquad\qquad P_{Wind}(t) > P_{Out}(t-1) \\ \dfrac{\max\{P_{Out}(t-\Delta t) - \gamma P_r - P_{Out}(t-1)\}}{P_{Wind}(t) - P_{Out}(t-1)}, \\ \qquad\qquad P_{Wind}(t) < P_{Out}(t-1) \\ 1, \\ \qquad\qquad P_{Wind}(t) = P_{Out}(t-1) \end{cases} \tag{4}$$

γ is the fluctuation rate of wind power, Δ_t is the time scale, P_r is the rated power of the wind farm.

With filter coefficient a, P_{Out} and P_{Wind} can be acquired. With equation (1),the combined output of HESS can be calculated.

3 Distribution Power Between Battery and Supercapacitor

With the stabilizing policy proposed in section 2, after incorporating the hybrid energy storage system, the overall real-time smoothing control strategy framework for wind farm power fluctuations is depicted in fig.2 below.

In this figure, the flowchart of management system for wind farm with HESS is depicted. The components and their connections are as follows: "Real-time Output of the wind farm" is the starting point, indicating the immediate energy production from the wind farm. This output goes into a "Fluctuation Stabilizing Policy" which represents the set of procedures or technologies aimed at reducing the variability of the wind energy before it's fed into the system. The output from the fluctuation policy is then directed to the "HESS Control Policy" which will be carefully discussed in this section. Within the HESS, there are two types of storage indicated: "Super-capacitor" and "Battery". Thus how to distribute energy between them is of great importance. Finally, the energy goes to the "Grid-connected Output," which is the energy that is actually fed into the power grid.

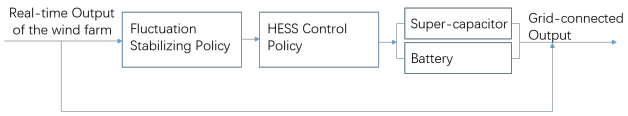

Fig. 2: Control strategy framework for wind farm power fluctuations

During charging and discharging, the power of an energy storage system is limited to ensure its normal operation and prevent damage caused by overcharging or over-discharging. One crucial parameter is the state of charge (SOC), which refers to the ratio of the remaining capacity to the rated capacity of the energy storage system after charging or discharging.

$$SOC = \frac{E_{ini} + \int_0^t \left(\eta_{ch} P_{ch} + \frac{1}{\eta_{dis}} P_{dis}\right) dt}{E_r} \tag{5}$$

Where E_{ini} represents the initial remaining capacity of the energy storage device before charging or discharging, η_{ch} and η_{dis} are the charging and discharging efficiencies of the battery respectively, P_{ch} and P_{dis} are the charging and discharging powers, t is the charging or discharging time, E_r and is the rated capacity of the energy storage device. In this paper, the sampling time for wind power is 1 second, the charging and discharging efficiency of the energy storage battery ranges from 70% to 90%, and the charging and discharging efficiency of the super-capacitor ranges from 90% to 95%. The mathematical model for charging and discharging of the hybrid energy storage system is shown in eq.6. To ensure that both the energy storage battery and the super-capacitor operate under normal conditions and to minimize charging and discharging losses, both should operate within their respective state of charge (SOC) limits.

$$\begin{cases} \mathrm{SOC}_B(t) = \mathrm{SOC}_B(t-1) + P_B(t)\eta_{ch}/E_{B_r} \\ \qquad\qquad (P_B(t) \geq 0) \\ \mathrm{SOC}_B(t) = \mathrm{SOC}_B(t-1) + P_B(t)/\left(E_{B_r}\eta_{\mathrm{dis}}\right) \\ \qquad\qquad (P_B(t) < 0) \end{cases}$$
$$\begin{cases} \mathrm{SOC}_{SC}(t) = \mathrm{SOC}_{SC}(t-1) + P_{SC}(t)\eta_{ch}/E_{SC_r} \\ \qquad\qquad (P_{SC}(t) \geq 0) \\ \mathrm{SOC}_{SC}(t) = \mathrm{SOC}_{SC}(t-1) + P_{SC}(t)/\left(E_{SC_r}\eta^{dis}\right) \\ \qquad\qquad (P_{SC}(t) < 0) \end{cases}$$
$$\begin{cases} SOC_B^{\min} \leq SOC_B(t) \leq SOC_B^{\max} \\ SOC_{SC}^{\min} \leq SOC_{SC}(t) \leq SOC_{SC}^{\max} \end{cases} \tag{6}$$

When P_B and P_{SC} are greater than zero, it indicates the charging process of the storage. When P_B and P_{SC} are smaller than zero, it indicates the discharging process of the storage.

To enhance battery longevity by managing its State of Charge (SOC) and extending its cycle life, we incorporate a coefficient b into our energy distribution strategy. In conjunction with this, an auxiliary variable k is introduced to provide a more nuanced control over the battery's charging and discharging processes. At any specific sampling time, we define k for the battery as the normalized difference between its maximum SOC and its current SOC, expressed mathematically as:

$$k = \frac{|SOC_B^{max} - SOC_B|}{SOC_B^{max} - SOC_B^{min}} \tag{7}$$

This equation serves to scale the SOC within a normalized range of 0 to 1, providing a relative measure of the battery's charge level with respect to its operational bounds.

When k falls below the threshold of 0.1, an indication that the battery is near its maximum or minimum SOC, we define a quadratic relation for the coefficient b to modulate the charging rate and avoid extreme states that could harm the battery:

$$b = k^2 \tag{8}$$

This quadratic relationship reduces the energy allocated to the battery, denoted as $P_B(t)$, to a fraction determined by b, thereby conserving the battery's health and extending its useful life:

$$P_B(t) = b \cdot P_B^{Cal} \tag{9}$$

Conversely, if k exceeds 0.1, suggesting the SOC is within a safer operational range, the coefficient b is set to 1, allowing for normal energy allocation without additional modulation.

The variable P_B^{Cal} represents the calculated power for the battery derived from the HESS using a first-order filter algorithm, which can be expressed as:

$$P_B^{Cal}(t) = (1-c) \cdot P_B(t-1) + c \cdot P_{HESS} \tag{10}$$

Here, the filter coefficient c for the battery is initially defined as 0.9 to prioritize recent data while still accounting for past behaviour, ensuring a smooth response to changing energy demands.

With the calculated value P_B, the power allocated to the super-capacitor P_{SC} can be readily determined using the total power from the HESS completing the energy distribution strategy for the integrated storage system.

$$P_{SC}(t) = P_{HESS}(t) - P_B(t) \tag{11}$$

To ensure the effective operation of the hybrid energy storage system (HESS), it is crucial to monitor the State of Charge (SOC) of the super-capacitor, denoted as SOC_{SC}. The SOC should remain within predefined normal ranges to maintain system stability and integrity.

Upon confirmation that the SOC is within acceptable limits, the energy distribution process for the HESS is deemed complete. However, if the SOC deviates beyond these limits, indicating a potential discrepancy in the current capacity settings of the HESS, the energy distribution is considered unsuccessful. In such instances, it becomes necessary to adjust the filter coefficient to realign the SOC with its desired range. The adjustment is performed according to the following equation:

$$c = (1-k) \cdot c \tag{12}$$

This modification of the filter coefficient c is directly influenced by the variable k, which serves as an indicator of the SOC's proximity to its boundaries. By dynamically tuning c, the system can respond to fluctuations in energy storage and demand, ensuring that the super-capacitor operates within safe and efficient parameters.

This methodical approach to energy management not only stabilizes the energy output from variable renewable sources but also preserves the health of the storage components, ultimately contributing to the resilience and efficiency of the overall power system.

The whole procedure of the hybrid energy storage optimization can be shown in fig.3.

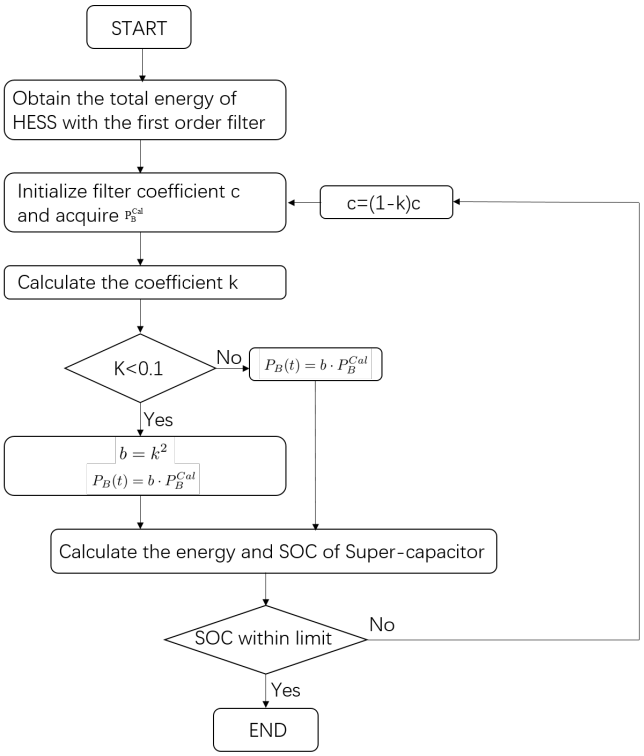

Fig. 3: Procedure of the hybrid energy storage optimization

The flowchart outlines the sequence for managing the power output from HESS. The process begins by capturing the total energy from the HESS using a first-order filter. Next, a filter coefficient c is initialized and a calibrated power value for the battery, denoted as P_{cal}^{B}, is obtained. Subsequently, a coefficient k is calculated, which is pivotal in determining the next steps.

If $k < 0.1$, the power at time t for the battery, expressed as $P_B(t)$, is calculated directly by multiplying a constant b with P_{cal}^{B}. However, if $k \geq 0.1$, the constant b is adjusted to the square of k before being used in the power calculation for $P_B(t)$.

Following the computation of power for the battery, the algorithm proceeds to calculate the energy and the State of Charge SOC of the super-capacitor. The process reaches its end if the SOC is within the predetermined acceptable limits. If SOC of the super-capacitor is out of ranges, the filter coefficient will be updated and re proceed the whole process.

4 Case Study

In a 100MW offshore wind farm, the configuration of parameters of HESS and wind farm are shown in table1.

The original and filtered wind power is shown in fig.4.

The illustration features two distinct areas: the grey region represents the variability of wind power generation, while the blue region indicates the output power that has been modulated by the incorporation of the HESS.

Table 1: Configuration of Parameters

Rated Power of Wind Farm	100MW
Sampling Time	1s
Time Scale	8000s
Fluctuation Rate	5%
Initial SOC Value of Battery	0.5
Initial SOC Value of Super-Capacitor	0.5
Battery SOC Maximum	0.9
Battery SOC Minimum	0.1
Super-capacitor SOC Maximum	0.95
Super-capacitor SOC Minimum	0.05
Charging and Discharging Efficiency of Battery	1
Charging and Discharging Efficiency of Super-capacitor	1
Minimum Charging and Discharging Initial Value of c	0.9

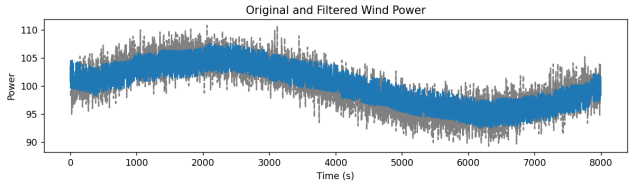

Fig. 4: The original and filtered wind power

The fluctuation rate of wind farm with HESS in one-minute is shown in fig.5.

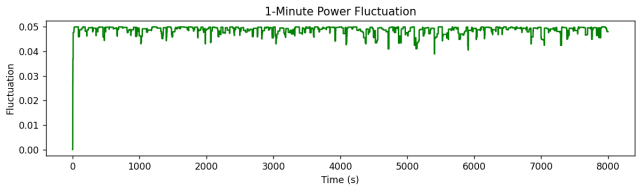

Fig. 5: The fluctuations of wind power in 1-minute

Examining fig.5, it is observable that the implementation of the HESS significantly stabilizes the output of the wind farm over an 8000-second interval, maintaining fluctuations within a narrow margin of 5%. This demonstrates the efficacy of the HESS in dampening the variability of wind energy production.

The requirement of HESS can be calculated with eq.1, thus the total energy requirement from the storage is shown in fig.6.

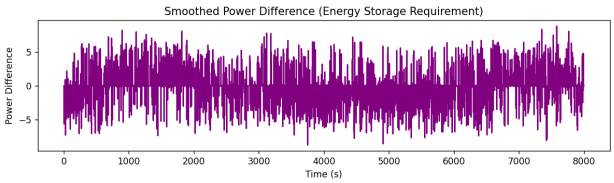

Fig. 6: The smoothed power difference

The smoothed power difference is the input of HESS optimization. With the proposed method and optimization policy, the charging and discharging processes of the battery and super-capacitor are shown in fig.7.

The y label 0 means no charging and discharging of HESS. When the value of y is below zero, it means the

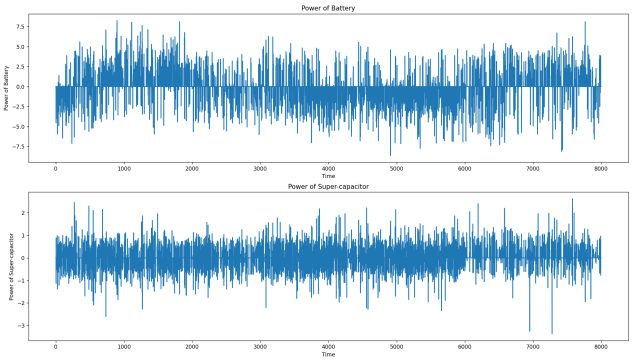

Fig. 7: The charging and discharging process of HESS

discharging process of the storage. When the value of y is greater than zero, it means the charging process of the storage.

The SOC change of battery and capacitor is shown in the fig.8.

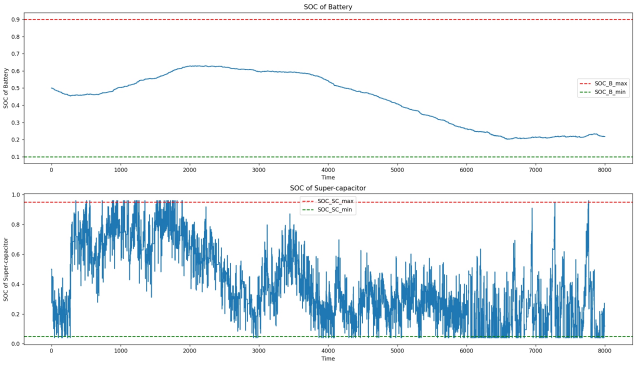

Fig. 8: The SOC change of HESS

As illustrated in fig.8, it is evident that the State of Charge (SOC) for both the battery and the super-capacitor remains within their respective operational limits. This observation underscores the effectiveness of the proposed methodology in managing the energy distribution. By implementing this strategy, we can safeguard the battery against excessive cycling, thereby enhancing its longevity and maintaining optimal performance.

5 Conclusion

This paper presents a strategic optimization policy tailored for the HESS of offshore wind farms. Central to our optimization approach is the meticulous consideration of the SOC of the battery, with the explicit objective of prolonging its life-cycle. We have introduced a coefficient that acts as a regulatory mechanism, imposing strict limits on the battery's SOC to curtail the frequency of charge and discharge cycles. By dynamically updating the filter coefficient in conjunction with the battery's energy levels, we can achieve a timely and efficient distribution of stored energy, ensuring the system operates within the desired parameters for enhanced sustainability and reliability.

References

[1] Gallaher, Adam, et al. Breaking wind: A comparison between US and European approaches in offshore wind energy leadership in the North Atlantic region.*Renewable and Sustainable Energy Reviews*, 2023, 187: 113766.

[2] DeCastro, M., et al. Europe, China and the United States: Three different approaches to the development of offshore wind energy. *Renewable and Sustainable Energy Reviews*, 2019, 109: 55-70.

[3] Panda, Ambarish, et al. Recent advances in the integration of renewable energy sources and storage facilities with hybrid power systems.*Cleaner Engineering and Technology*, 2023: 100598.

[4] Nadeem, Furquan, et al. Comparative review of energy storage systems, their roles, and impacts on future power systems. *IEEE access*, 2018, 7:4555-4585.

[5] Li, Xiangjun, and Shangxing Wang. Energy management and operational control methods for grid battery energy storage systems.*CSEE Journal of Power and Energy Systems*, 2019, 7(5): 1026-1040.

[6] Suvitha, Krishnan, et al. Effective hydropower renewable energy source selection using fuzzy neutrosophic boundary approximate area. *Renewable Energy Focus*, 2024: 100537.

[7] J. Hou, J. Sun and H. Hofmann. Interaction analysis and integrated control of hybrid energy storage and generator control system for electric ship propulsion. *2015 American Control Conference (ACC), Chicago, IL, USA*, 2015, pp. 4988-4993.

[8] Nkwanyana, Thamsanqa B., et al. An assessment of hybrid-energy storage systems in the renewable environments.*Journal of Energy Storage*, 2023:72: 108307.

[9] Behera, Pradyumna Kumar, and Monalisa Pattnaik. Design and real-time implementation of wind–photovoltaic driven low voltage direct current microgrid integrated with hybrid energy storage system. *Journal of Power Sources*, 2024, 595: 234028.

[10] Choi, Jin Woo, Shin Young Heo, and Mun Kyeom Kim. Hybrid operation strategy of wind energy storage system for power grid frequency regulation. *IET Generation, Transmission & Distribution*, 2016, 10(3): 736-749.

[11] W. Wang, P. Chen, G. Ren, J. Liu, F. Fang and Z. Chen. Zero-phase CARIMA filtering and application in wind-storage system sizing and power dispatch optimization. *CSEE Journal of Power and Energy Systems*, doi: 10.17775/CSEE-JPES.2022.06930.

[12] Y. Chen, H. Li, Q. Chen and Q. Yang. Target Power Determination for Real-time Stabilization of Grid-Connected Offshore Wind Power Fluctuation. *2022 21st International Symposium on Distributed Computing and Applications for Business Engineering and Science (DCABES), Chizhou, China*, 2022, pp. 188-191, doi: 10.1109/DCABES57229.2022.00077.

[13] Zhang, J.; Zhang, T.; Cheng, P.; Yang, D.; Yan, J.; Tian, X. Optimal Allocation of Hybrid Energy Storage System Based on Smoothing Wind Power Fluctuation and Improved Scenario Clustering Algorithm. *Processes*, 2023, 11: 3407.

[14] W. Li, F. Bu, K. Zhang, S. Zhang, J. Zhang and C. Hou. Electric-Methanol Hybrid Energy Storage Control Strategy for Smoothing the Fluctuation of New Energy Generation. *2023 Power Electronics and Power System Conference (PEPSC), Hangzhou, China*, 2023, pp. 61-67, doi: 10.1109/PEPSC58749.2023.10395183.

[15] Uddin, Moslem, et al. A novel peak shaving algorithm for islanded microgrid using battery energy storage system. *Energy*, 2020, 196: 117084.

[16] Tan, Kang Miao, et al. Empowering smart grid: A comprehensive review of energy storage technology and application with renewable energy integration.*Journal of Energy Storage*, 2021, 39: 102591.

[17] Abdi, H., Mohammadi-ivatloo, B., Javadi, S., Khodaei, A. R., & Dehnavi, E. Energy storage systems. *Distributed generation systems*, 2017, 7, 333-368.

Proceedings of the 3rd Conference on Fully Actuated System Theory and Applications
May 10-12, 2024, Shenzhen, China

Partially Observed Optimal Control with Correlated Noises

Zhipeng Li[1], Minyue Fu[2], Huanshui Zhang[3] Zhongcai Zhang[1]
1. College of Engineering, Qufu Normal University, Rizhao 276826, China
E-mail: Zhipenglie@sina.com, zhangzc@qfnu.edu.cn
2. SDIM, South University of Science and Technology of China, Shenzhen 518055, China
E-mail: fumy@sustech.edu.cn
3. College of Electrical Engineering and Automation, University of Shandong University of Science and Technology, Qingdao 266590, China
E-mail: hszhang@sdu.edu.cn

Abstract: We derive a minimum principle for a class of partially observed optimal control model, where the system noise and the observation noise are correlated and the performance index is in a form of an exponential of integral. An approximate formula is derived and it allows us to approximate the original forward-backward stochastic partial differential equations appearing in the minimum principle by a singular forward-backward stochastic ordinary differential equations.

Key Words: Stochastic Optimal Control, Variation Method, Nonlinear System, Partial Differential Equation (PDE).

1 Introduction

Partially observed optimal control problem has attracted lots of attention over the past half century, related work may refer to Mortensen [1], Davis & Varaiya [2], Fleming & Pardoux [3], Borkar [4], Beneš & Karatzas [5], Baras, Elliott & Kohlmann [6], Bensoussan [7], Tang [8], Charalambous & Elliott [9], and so on. In this work, we deal with a general model whose signal system contains a system noise and the observation noise, its cost criterion is in a form of an exponential of integral. Our motivation on this model is that these signal systems have been appeared in many works, see [10] or the recent works [11] [12].

We employ the method proposed by Mortenson [1], but to derive the minimum principle of the optimal control problem on the basis of Bensousan's work [7]. The related infinite system corresponding with our model changes to be more complex, reflected in the diffusion term appearing the differential operator. In order to develop the approximate procedure, an orthogonal direct sum decomposition method of Hilbert space is proposed to deal with the estimate and computation problem. Some interesting analysis can be carried out using tools from projection theory of Hilbert space. An approximation formula is obtained, it allows us to recast the original problem as that of solving a singular forward-backward stochastic ordinary differential equations. These are our main innovation.

Notations Let $V = H^1(\mathbb{R}^n)$, $H = L^2(\mathbb{R}^n)$ and denote by V^* the dual of V. We will denote by $\|\cdot\|$, $|\cdot|$ and $|||\cdot|||$ the norms in V, H and V^* respectively; by $<\cdot,\cdot>$ the duality product between V and V^*, and by $((\cdot,\cdot))$ and $(\cdot,\cdot)$ the scalar product in V and H respectively. For a bounded linear operator $\mathscr{F} \in \mathscr{L}(V,H)$, we use $\mathscr{F}^* \in \mathscr{L}(H,V^*)$ to denote its adjoint. Sometimes, M^* also denote the transpose of matrix M. In addition, $\langle\alpha,\beta\rangle$ or $\alpha\cdot\beta$ denotes the scalar product in Euclidean space. Letting X be a norm space, we define: $L^\infty([0,T];X)$ denotes the class of essentially bounded X-valued measurable functions; $C([0,T];X)$ denotes the space of X-valued continuous functions with the uniformly norm; $L^2(\Omega,\mathcal{F},P;X)$ denotes the space of X-valued random objects with the usual L^2-norm of probability measure space $(\Omega,\mathcal{F},P)$.

This work is supported by Youth Foundation of Shandong Natural Science Foundation under Grant ZR2023QF091, as well as the National Natural Science Foundation of China under Grants No. U23A20325, No.62173118 and No.62350710214.

2 Problem Formulation

2.1 A Partially Observed Optimal Control Problem

The dynamics of the object to be controlled is described by

$$\begin{aligned} dx(t) =& f(x(t),u(t),t)dt + g(x(t),t)dv(t) \\ &+ k(x(t),t)dw(t), \end{aligned} \tag{1}$$

where $x \in \mathbb{R}^n$ is the state variable and $u \in U \subset \mathbb{R}^d$ is the control variable. w, v are the standard Wiener processes, independent from each other, on the measure space $(\Omega,\mathcal{F},P^u)$.

The noisy observation of the state is given by

$$dy(t) = h(x(t),t)dt + dv(t). \tag{2}$$

We use $Y_t = \sigma(y(s), 0 \le s \le t)$ to denote the σ-field generated by the history path of y until instant t. The admissible control set U_{ad} is defined as all U-valued square-integrable processes which are adapted to $(Y_t)_t$.

The cost functional to be minimized is

$$\begin{aligned} J(u(\cdot)) =& E^u[\int_0^T l(x(t),u(t),t) \\ &\times \exp(\int_0^t -c(x(s),u(s),s)ds)dt \\ &+ m(x(T),T) \\ &\times \exp(-\int_0^T (c(x(t),u(t),t)dt))], \end{aligned} \tag{3}$$

where E^u denotes the expectation operator defined by measure P^u.

Assumptions

(A1). All functions f, g, k, h, l, c, m are measurable in their respect variables and bounded. f, g, k, h are Lipschitz continuous in the spatial variable x.

(A2) f, l, c have bounded first derivatives in x; g, k have bounded second derivatives in x.

(A3) kk^* is uniformly positive definite, i.e., for any $\xi \in \mathbb{R}^n$, it holds $\xi^* kk^* \xi \geq \epsilon I_n$ for $\forall\, (x,t) \in \mathbb{R}^n \times [0,T]$, $\epsilon > 0$.

(A4) The initial value $x(0)$ is independent of system and observation noises w, v and its density function is in H.

(A5). For any $(u,t) \in U \times [0,T]$, $l(\cdot,u,t) \in H$ and $m(\cdot,t) \in H$. In particular, $|l(\cdot,u,t)| \leq C$, independent of u.

(A6) f, c have bounded and continuous first derivatives in u; l has continuous first derivative in u and $|\partial l(x,u,t)/\partial u| \leq \zeta(x)$, with $\zeta(\cdot) \in H$.

***(P1)**. The partially observed optimal control problem is to minimize the performance index (3) under the admissible control set U_{ad}, subject to the controlled dynamic system (1) and the noisy observation (2).*

2.2 Reduced to Fully Observed Case

Inserting (2) to (1), it leads to

$$\begin{aligned} dx(t) =& [f(x(t),u(t),t) - g(x(t),t)h(x(t),t)]dt \\ &+ g(x(t),t)dy(t) + k(x(t),t)dw(t), \end{aligned} \tag{4}$$

Next, we look for a probability measure under which two processes $\{y(t)\}_{0\leq t\leq T}$ and $\{w(t)\}_{0\leq t\leq T}$ behave like two independent standard Wiener processes. This can be completed by Girsanov's theorem. By defining

$$\begin{aligned} \Lambda^u(t) =& \exp\{\int_0^t \langle h(x(s),s), dy(s)\rangle \\ &- \frac{1}{2}\int_0^t \langle h(x(s),s), h(x(s),s)\rangle ds\}, \end{aligned} \tag{5}$$

then, the measure P defined by $dP^u = \Lambda^u(T)dP$ is the one needed.

Furthermore, denote

$$Z^u(t) = \exp\{\int_0^t -c(x(s),u(s),s)ds\},\ t \in [0,T]. \tag{6}$$

Then the cost functional can be written as

$$\begin{aligned} J(u(\cdot)) =& E[\int_0^T \Lambda^u(t)Z^u(t)l(x(t),u(t),t)dt \\ &+ \Lambda^u(T)Z^u(T)m(x(T),T)] \end{aligned} \tag{7}$$

where the martingale property of $\{\Lambda^u(t)\}_{0\leq t\leq T}$ has been used.

Let

$$q(x,t)dx = E\left[\chi_{x(t)\in dx}(\omega)\Lambda^u(t)Z^u(t)|Y_t\right], \tag{8}$$

Then

$$\begin{aligned} J(u(\cdot)) =& E\int_0^T E\left[\Lambda^u(t)Z^u(t)l(x(t),u(t))\big|Y_t\right]dt \\ &+ E\left[\Lambda^u(T)Z^u(T)m(x(T),T)\big|Y_T\right] \\ =& E\int_0^T (l(u(t)),q(t))dt + E(m(T),q(T)). \end{aligned} \tag{9}$$

We use the following notations throughout this paper.

$$A^u(t)\psi = \sum_i f_i(x,u)\frac{\partial\psi}{\partial x_i} + \frac{1}{2}\sum_{i,j} a_{ij}(x)\frac{\partial^2\psi}{\partial x_i \partial x_j},$$

$$B^k(t)\psi = \sum_i g_{ik}(x)\frac{\partial\psi}{\partial x_i} + h_k(x)\psi;$$

$$A^{u,*}(t)\psi = \sum_{i,j}\frac{\partial}{\partial x_i}(a_{ij}(x)\frac{\partial\psi}{\partial x_j}) + \sum_i \frac{\partial}{\partial x_i}(a^i(x,u)\psi),$$

$$B^{k,*}(t)\psi = g^k(x)\psi - \sum_i g_{ik}(x)\frac{\partial\psi}{\partial x_i};\ \text{with}$$

$$a^i(x,u) = -f_i(x,u) + \sum_j \frac{\partial}{\partial x_j}a_{ij}(x),$$

$$g^k(x) = h_k(x) - \sum_i \frac{\partial}{\partial x_i}g_{ik}(x),$$

$$a = (gg^* + kk^*)/2.$$

Lemma 1 *Suppose $\varphi : \mathbb{R}^n \to \mathbb{R}$ is C^2 function with compact support. Then*

$$\sigma_t(\varphi) = E\left[\varphi(x(t))\Lambda^u(t)Z^u(t)|Y_t\right] \tag{10}$$

satisfies

$$\begin{aligned} \sigma_t(\varphi) =& + \int_0^t \sigma_s(A^{u(s)}(s)\varphi)ds - \int_0^t \sigma_s(c(u)\varphi)ds \\ &+ \sum_k \int_0^t \sigma_s(B^k(s)\varphi)dy_k(s) + \sigma_0(\varphi). \end{aligned} \tag{11}$$

Proof. Use Itô's rule to function $t \mapsto \varphi(x(t))\Lambda^u(t)\phi^u(t)$, and then condition each side on Y_t. Q.E.D

Lemma 2 *If the measure defined by $\sigma_t(\cdot)$ has a density $q(x,t)$ such that*

$$\begin{aligned} \sigma_t(\varphi) &= E[\varphi(x(t))\Lambda^u(t)Z^u(t)|Y_t] \\ &= \int_{\mathbb{R}^n} \varphi(x)q(x,t)dx, \end{aligned} \tag{12}$$

then $q(x,t)$ satisfies

$$\begin{aligned} q(t) =& + \int_0^t A^{u(s),*}(s)q(s)ds - \int_0^t c(u(s))q(s)ds \\ &+ \sum_{k=1}^K \int_0^t B^{k,*}(s)q(s)dy_k(s) + q(0), \\ q(0) =& q_0(x). \end{aligned} \tag{13}$$

***(P2)**. The fully observed optimal control problem is to minimize the performance index (9) under the admissible control set U_{ad}, subject to the controlled dynamic system (13).*

3 Minimum Principle

3.1 Existence and Uniqueness of Solution

Let $L_Y^2([0,T];X)$ denote the space of the X-valued and $(Y_t)_t$-adapted square integral processes. We have

Proposition 1 *Suppose Assumptions 1-6 hold. Then for any admissible control $u(\cdot) \in U_{ad}$, there exists one and only one solution of (13) in $L_Y^2([0,T];V) \cap L^2(\Omega,\mathcal{F},P;C([0,T];H))$.*

Proof. Its proof is omitted in the conference version. Q.E.D.

3.2 Variation Calculation

We shall use the notations below until the end of this paper.

$$\begin{aligned}\mathscr{A}(u;t) &= A^{u,*}(t) - c(x,u,t), \quad \forall\, u \in U,\ \ t \in [0,T];\\ \mathscr{B}^k(t) &= B^{k,*}(t), \quad k = 1,2,..,K.\\ \psi_u^{'}(\check{u}) &= \frac{\partial \psi(u)}{\partial u}\Big|_{u=(\check{u})},\end{aligned}$$

where the last derivative on u can be denoted similarly for functions $f_i(\cdot,u,\cdot)$, $c(\cdot,u,\cdot)$ and $l(\cdot,u,\cdot)$.

Lemma 3 *Suppose Assumptions 1-6 hold. The Gâteaux derivative of the cost functional exists and is*

$$\begin{aligned}&\frac{d}{d\theta}J(u^\star(\cdot)+\theta u(\cdot))\Big|_{\theta=0}\\ =&+E\int_0^T (l(u^\star(t),t),\zeta(t))dt + E(m(T),\zeta(T))\\ &+E\int_0^T (l_u^{'}(u^\star(t))\cdot u(t), q^\star(t))dt,\end{aligned} \tag{14}$$

where $q^\star(\cdot)$ satisfies (13) corresponding to the control $u^\star(\cdot)$, we write it in a differential form, i.e.,

$$\begin{aligned}dq^\star &= \mathscr{A}(u^\star(t);t)q^\star dt + \sum_{k=1}^K \mathscr{B}^k(t)q^\star dy_k(t),\\ q^\star(0) &= q_0.\end{aligned} \tag{15}$$

The random process $\zeta(\cdot)$ satisfies

$$\begin{aligned}&\zeta \in L_Y^2([0,T];V)\cap L^2(\Omega,\mathcal{F},P;C([0,T];H)),\\ d\zeta =&+\mathscr{A}(u^\star(t);t)\zeta dt - c_u^{'}(u^\star(t))\cdot u(t)q^\star dt\\ &-\sum_{i=1}^n \frac{\partial}{\partial x_i}(f_{i,u}^{'}(u^\star(t))\cdot u(t)q^\star)dt\\ &+\sum_{k=1}^K \mathscr{B}^k(t)\zeta dy_k(t), \quad \zeta(0)=0.\end{aligned} \tag{16}$$

Proof. Its proof is omitted for the space limitation. Q.E.D.

3.3 Linear Functional Representation

Given two $(Y_t)_{t\geq 0}$-adapted random processes $\phi \in L_Y^2([0,T];V^*)$ and $\psi \equiv (\psi_1,..,\psi_K) \in (L_Y^2([0,T];H))^K$, we define a stochastic PDE of the type (16) (called variation equation)

$$\begin{aligned}d\lambda =&+(\mathscr{A}^{u(t)}(t)\lambda+\phi(t))dt\\ &+\sum_{k=1}^K(\mathscr{B}^k(t)\lambda+\psi_k(t))dy_k(t), \quad \lambda(0)=0.\end{aligned} \tag{17}$$

From the energy equality, it can be checked that for every $u(\cdot)\in U_{ad}$, (17) defines a linear and continuous mapping

$$\begin{aligned}F_{\phi,\psi}^u : L_Y^2([0,T];V^*)\times(L_Y^2([0,T];H))^K &\to L_Y^2([0,T];V)\\ (\phi(\cdot),\psi(\cdot)) &\mapsto \lambda(\cdot)\end{aligned}$$

In addition, for every $u(\cdot)\in U_{ad}$, it also can be verified that

$$\begin{aligned}F_\lambda^u : L_Y^2([0,T];V) &\longrightarrow \mathbb{R},\\ \lambda(\cdot) &\mapsto E\int_0^T (l(u(t),t),\lambda(t))dt + E(m(T),\lambda(T))\end{aligned}$$

is linear and continuous.

Hence, the composite mapping $F_\lambda^u \circ F_{\phi,\psi}^u$ is a continuous linear functional on $L_Y^2([0,T];V^*)\times(L_Y^2([0,T];H))^K$. From Riesz representation theorem, there is a unique element $(p(\cdot),\gamma(\cdot))\in L_Y^2([0,T];V)\times(L_Y^2([0,T];H))^K$ such that

$$\begin{aligned}&E\int_0^T <\phi,p>dt + \sum_{k=1}^K E\int_0^T (\psi_k,\gamma_k)dt\\ =&E\int_0^T (l(u(t)),\lambda(t))dt + E(m(T),\lambda(T)),\end{aligned} \tag{18}$$

where γ_k is the k-th coordinate of γ.

In particular, take $u^\star(\cdot)\in U_{ad}$ and

$$\begin{cases}\phi^\star(t) = -\sum\limits_i \frac{\partial}{\partial x_i}\left(f_{i,u}^{'}(u^\star(t))\cdot u(t)q^\star\right)\\ \qquad\qquad - c_u^{'}(u^\star(t))\cdot u(t)q^\star,\\ \psi^\star(t)=0,\end{cases} \tag{19}$$

where the corresponding solution of (17) denoted by $\lambda^\star$.

In view of (14) and (16), the linear functional $F_{\lambda^\star}^{u^\star}\circ F_{\phi^\star,\psi^\star}^{u^\star}$ has the following representation

$$\begin{aligned}&-E\int_0^T <\sum_i \frac{\partial}{\partial x_i}(f_{i,u}^{'}(u^\star(t))\cdot u(t)q^\star)\\ &+c_u^{'}(u^\star(t))\cdot u(t)q^\star, p^\star(t)>dt\\ =&E\int_0^T (l(u^\star(t),t),\zeta(t))dt + E(m(T),\zeta(T)),\end{aligned} \tag{20}$$

where $(p^\star(\cdot),\gamma^\star(\cdot))$ is the duality pair, found by Riesz representation theorem, to (19).

Now, (14) can be rewritten as

$$\begin{aligned}&\frac{d}{d\theta}J(u^\star(\cdot)+\theta u(\cdot))\Big|_{\theta=0}\\ =&-E\int_0^T <\sum_i \frac{\partial}{\partial x_i}\left(f_{i,u}^{'}(u^\star(t))\cdot u(t)q^\star\right), p^\star(t)>dt\\ &-E\int_0^T <c_u^{'}(u^\star(t))\cdot u(t)q^\star, p^\star(t)>dt\\ &+E\int_0^T (l_u^{'}(u^\star(t))\cdot u(t), q^\star(t))dt.\end{aligned} \tag{21}$$

Based on the above formula, we have the following result.

Theorem 1 *Suppose Assumptions 1-6 hold and the control set U is convex. Then, if $u^\star(\cdot)$ is an optimal control for problem (**P2**) and $q^\star$ is the corresponding trajectory described by (15). Then there exists $(p^\star,\gamma^\star)\in L_Y^2([0,T];V)\times(L_Y^2([0,T];H))^K$ founded by (20) (its equation will be given later) such that*

$$\begin{aligned}&\langle H_u^{'}(q^\star(x,t),p^\star(x,t),u^\star(t),t),\mu-u^\star(t)\rangle \geq 0,\\ &\qquad\qquad \forall\,\mu\in U,\ a.e.\ t,\ a.s.,\end{aligned} \tag{22}$$

where

$$H(q,p,u,t) = + \int_{\mathbb{R}^n} \langle f(x,u,t), Dp(x,t)\rangle q(x,t)dx + \int_{\mathbb{R}^n} l(x,u,t)q(x,t)dx - \int_{\mathbb{R}^n} c(x,u,t)p(x,t)q(x,t)dx. \tag{23}$$

4 Adjoint Equation

4.1 Approximation for Variation Equation

Let $V_m = \text{span}\{h_1, ..., h_m\}$ be a finite dimension linear subspace of V spanned by $\{h_1, ..., h_m\}$, which is not necessarily orthogonal. We also denoted by H_m the range of the continuous embedding $V_m \hookrightarrow H$ and by V_m^* the normed dual space of V_m.

Now approximate variation equation (17) by

$$d\lambda^m = + (\mathscr{A}_m^{u(t)}(t)\lambda^m + \phi^m)dt + \sum_{k=1}^{K}(\mathscr{B}_m^k(t)\lambda^m + \psi_k^m)dy_k(t), \quad \lambda^m(0) = 0. \tag{24}$$

Here $\mathscr{A}_m^u(t) \in \mathscr{L}(V_m, V_m)$ and $\mathscr{B}_m^k(t) \in \mathscr{L}(V_m, H_m)$, $k = 1, 2, .., K$, are defined by the restrictions of operators to the subspaces marked

$$\begin{aligned} \mathscr{A}_m^u(t) &= \mathscr{A}^u(t)|_{V_m \times V_m}, \\ \mathscr{B}_m^k(t) &= \mathscr{B}^k(t)|_{H_m \times H_m}, \end{aligned} \tag{25}$$

respectively. In addition, $\phi^m \in V_m^*$ and $\psi_k^m \in H_m$, $k = 1, 2, .., K$, are defined similarly as

$$\begin{aligned} \phi^m &= \phi|_{V_m}, \\ \psi_k^m &= \psi_k|_{H_m}. \end{aligned} \tag{26}$$

For each $j \le m$, we may multiply h_j on both sides of (24). By using (25) and (26), it yields another expression of (24)

$$\begin{aligned} (d\lambda^m, h_j) =& + < h_j, \mathscr{A}^{u(t)}(t)\lambda^m + \phi > dt \\ & + \sum_k (h_j, \mathscr{B}^k(t)\lambda^m + \psi_k)dy_k(t), \\ (\lambda^m(0), h_j) =& 0. \end{aligned} \tag{27}$$

We have the following results.

Lemma 4 *Suppose Assumptions 1-6 hold. The following estimate holds*

$$\begin{aligned} & E\int_0^t \|\lambda^m(s)\|^2 ds \vee E(\sup_{0\le s\le t}|\lambda^m(s)|^2) \\ \le & CE\int_0^t (|||\phi^m|||^2 + \sum_k |\psi_k^m|^2)ds, \ \ \forall\, t \in [0,T]. \end{aligned} \tag{28}$$

Proof. Its proof needs a series inequalities and the property of projective operator, we omit here. Q.E.D.

Lemma 5 *Suppose Assumptions 1-6 hold. We have the strong convergence*

$$\lambda^m \to \lambda \ \text{ in } \ L_Y^2([0,T];V) \cap L^2(\Omega, \mathcal{F}, P; C([0,T];H)).$$

Proof. Let $\lambda^m, \lambda^{m'}$ be the solutions of (24) corresponding to (ϕ^m, ψ^m) and $(\phi^{m'}, \psi^{m'})$ respectively. Denoted by $\tilde{\lambda}^{m,m'} \equiv \lambda^m - \lambda^{m'}$, $\tilde{\phi}^{m,m'} \equiv \phi^m - \phi^{m'}$ and $\tilde{\psi}^{m,m'} \equiv \psi^m - \psi^{m'}$ the deviations.

We may check that the state-"control" pair $\tilde{\lambda}^{m,m'}$ and $(\tilde{\phi}^{m,m'}, \tilde{\psi}^{m,m'})$ still satisfies (28), due to the linearity of equation (24), i.e.,

$$\begin{aligned} & E\int_0^T \|\tilde{\lambda}^{m,m'}(t)\|^2 dt \vee E(\sup_{0\le t\le T}|\tilde{\lambda}^{m,m'}(t)|^2) \\ \le & CE\int_0^T (|||\tilde{\phi}^{m,m'}|||^2 + \sum_k |\tilde{\psi}_k^{m,m'}|^2)dt. \end{aligned} \tag{29}$$

Hence, (λ^m) is a Cauchy sequence in $L_Y^2([0,T];V) \cap L^2(\Omega, \mathcal{F}, P; C([0,T];H))$ under the strong topologies induced by the norms on the left hand side of (29). Here, Bessel's inequality is used to show that the right hand side of (29) tenders to zero, as $m, m' \to +\infty$. We only prove the case of $|||\tilde{\phi}^{m,m'}|||$. By the triangle inequality, $|||\tilde{\phi}^{m,m'}||| \le |||\phi^m - \phi||| + |||\phi^{m'} - \phi|||$. Letting B be the closed unit ball of V, we estimate

$$\begin{aligned} |||\phi^m - \phi||| &= \sup_{v\in B} | < v, \phi^m - \phi > | \\ &= \sup_{v\in B} | < \mathscr{P}_{V_m}(v) + \tilde{v}_m, \phi^m - \phi > | \\ &= \sup_{v\in B} | < \tilde{v}_m, \phi^m - \phi > | \\ &\le (|||\phi^m||| + |||\phi|||)\|\tilde{v}_m\|, \end{aligned}$$

where $\tilde{v}_m \equiv v - \mathscr{P}_{V_m}(v) \in V_m^\perp$, with $\mathscr{P}_{V_m}$ being the orthogonal projective operator and $V_m^\perp$ being the orthogonal complement subspace of V_m. Choose an orthonormal basis $\{e_1, .., e_m; e_{m+1}, ..\}$ of V, and represent $\tilde{v}_m = \sum_{j>m}((\tilde{v}_m, e_j))e_j$. Then, $\|\tilde{v}_m\|^2 = \sum_{j>m}|((\tilde{v}_m, e_j))|^2$, which is small for large m by Bessel's inequality. Similarly, $|||\phi^{m'} - \phi|||$ is small for large m'. Hence, the case of $|||\tilde{\phi}^{m,m'}|||$ is completed.

Suppose the strong limit of λ^m is $\breve{\lambda}$, we next verify that it satisfies (17). Due to $E\int_0^T \|\lambda^m(t)\|^2 dt \le C$, there is a subsequence of λ^m, denoted still by λ^m, weakly converges. From Hölder inequality, we have

$$\begin{aligned} & E\int_0^T < \lambda^m - \breve{\lambda}, \varphi > dt \\ \le & (E\int_0^T \|\lambda^m - \breve{\lambda}\|^2 dt)^{\frac{1}{2}} (E\int_0^T |||\varphi|||^2 dt)^{\frac{1}{2}}, \ \ \forall\, \varphi \in V^*. \end{aligned}$$

The above estimate and the Hausdorff property of weak topology imply that the weak limit coincides with the strong one. We then concentrate on finding out the weak limit, this can be finished by using (27).

To overcome passing to the limit of the stochastic integral term, we employed the method mentioned in [7] by marking it by a complex number tag. Let $\beta \in L^\infty([0,T], \mathbb{R}^K)$ be deterministic and consider the complex valued martingale

$$\gamma(t) = \exp\left(i\int_0^t \langle \beta(s), dy(s)\rangle + \frac{1}{2}\int_0^t |\beta(s)|^2 ds\right).$$

Applying Itô rule to the mapping $t \mapsto \gamma(t)(\lambda^m, h_j)$, it yields

$$\begin{aligned} &E[\gamma(t)(\lambda^m(t), h_j)] \\ =&+ E\int_0^t \gamma(s) < h_j, \mathscr{A}^{u(s)}(s)\lambda^m + \phi > ds \\ &+ \sum_{k=1}^K E\int_0^t i\gamma(s)\beta_k(s)(h_j, \mathscr{B}^k(t)\lambda^m + \psi_k)ds, \ \ \forall\, t. \end{aligned}$$

We can take the limit weakly in each term of the preceding equality to get

$$\begin{aligned} &E[\gamma(t)(\breve{\lambda}(t), h_j)] \\ =&+ E\int_0^t \gamma(s) < h_j, \mathscr{A}^{u(s)}(s)\breve{\lambda} + \phi > ds \\ &+ \sum_{k=1}^K E\int_0^t i\gamma(s)\beta_k(s)(h_j, \mathscr{B}^k(s)\breve{\lambda} + \psi_k)ds, \ \ \forall\, t. \end{aligned}$$

By the martingale property of γ, rewrite the above equality as

$$\begin{aligned} &E[\gamma(t)(\breve{\lambda}(t), h_j)] \\ =&+ E[\gamma(t)(\int_0^t < h_j, \mathscr{A}^{u(s)}(s)\breve{\lambda} + \phi > ds \\ &+ \sum_{k=1}^K \int_0^t (h_j, \mathscr{B}^k(s)\breve{\lambda} + \psi_k)dy_k(s))]. \end{aligned}$$

Since β is arbitrary, it implies

$$\begin{aligned} (\breve{\lambda}(t), h_j) =&+ \int_0^t < h_j, \mathscr{A}^{u(s)}(s)\breve{\lambda} + \phi > ds \\ &+ \sum_{k=1}^K \int_0^t (h_j, \mathscr{B}^k(s)\breve{\lambda} + \psi_k)dy_k(s). \end{aligned}$$

Using the separability of V, it follows that $\breve{\lambda}$ satisfies (17) and necessarily $\breve{\lambda} = \lambda$.

Q.E.D

4.1.1 Approximation for Adjoint Equation

Be given $(\phi^m, \psi^m) \in L^2_Y([0,T]; V_m^*) \times (L^2_Y([0,T]; H_m))^K$, we may consider the mapping defined by (24)

$$\begin{aligned} F^{m,u}_{\phi^m,\psi^m} : L^2_Y([0,T]; V_m^*) \times (L^2_Y([0,T]; H_m))^K &\\ \to L^2_Y([0,T]; V_m) &\\ (\phi^m, \psi^m) \quad \mapsto \lambda^m & \end{aligned}$$

and the functional

$$\begin{aligned} F^{m,u}_{\lambda^m} : L^2_Y([0,T]; V_m) &\to \mathbb{R} \\ \lambda^m \mapsto E[\int_0^T (l(u(t)), \lambda^m)dt + (m(T), \lambda^m(T))]. & \end{aligned}$$

As before, there is a unique pair

$$\begin{aligned} &p^m(t) \in L^2_Y([0,T]; V_m), \\ &\gamma^m_k(t) \in L^2_Y([0,T]; H_m), \ \ k = 1, 2, .., K, \end{aligned}$$

such that

$$\begin{aligned} &E\int_0^T [< p^m, \phi^m > + \sum_k (\gamma^m_k, \psi^m_k)]dt \\ =&E\int_0^T (l(u(t)), \lambda^m)dt + E(m(T), \lambda^m(T)). \end{aligned} \tag{30}$$

Lemma 6 *With assumptions as earlier, the strong convergence holds*

$$\begin{aligned} &p^m \to p \ \text{ in } \ L^2_Y([0,T]; V), \\ &\gamma^m \to \gamma \ \text{ in } \ (L^2_Y([0,T]; H))^K, \quad \text{as } \ m \to +\infty. \end{aligned}$$

4.1.2 Equation of Adjoint process

We give the following result but omit its proof.

Lemma 7 *The processes p^m and γ^m of (30) satisfy*

$$\begin{aligned} (h_j, dp^m) =& - [< h_j, \mathscr{A}^{u(t),*}(t)p^m > \\ &+ \sum_k (h_j, \mathscr{B}^{k,*}(t)\gamma^m_k) \\ &+ (h_j, l(u(t))]dt \\ &+ \sum_k (h_j, \gamma^m_k)dy_k(t), \\ (h_j, p^m(T)) =& + (h_j, m(T)), \quad j \le m. \end{aligned} \tag{31}$$

From now on, we may take the limit in (31) in virtue of Lemma 6 and check the limited state (p, γ) satisfies

$$\begin{aligned} dp(t) =& -[A^{u(t)}(t)p(t) - c(u(t))p(t) + l(u(t))]dt \\ &+ \sum_k (\gamma_k dy_k(t) - B^k(t)\gamma_k dt), \ \ p(T) = m(T). \end{aligned}$$

The uniqueness of the solution holds by the uniqueness of the representation of the functional $F^u_\lambda \circ F^u_{\phi,\psi}$ defined in (18).

In particular, evaluating $(\phi^\star, \psi^\star)$ as in (19) and taking $u^\star(\cdot) \in U_{ad}$, the above backward stochastic pde is exactly the one stated in Theorem 1. We state it as follows.

Proposition 2 *The assumptions are those of Theorem 1. The adjoint process $(p^\star(\cdot), \gamma^\star(\cdot)) \in L^2_Y([0,T]; V) \cap L^2(\Omega, \mathcal{F}, P; C([0,T]; H)) \times (L^2_Y([0,T]; H))^K$ founded by (20) satisfies*

$$\begin{aligned} dp^\star =& -[\mathscr{A}^{u^\star(t),*}(t)p^\star(t) + l(u^\star(t))]dt \\ &+ \sum_k (\gamma^\star_k(t)dy_k(t) - B^k(t)\gamma^\star_k(t)dt), \\ p^\star(T) =& \, m(T). \end{aligned} \tag{32}$$

4.2 Approximation Formula

Notice that (15) has the same form as (17). We may approximate it as follows

$$\begin{aligned} (dq^{\star,m}, h_j) =&+ < h_j, \mathscr{A}^{u(t)}(t)q^{\star,m} > dt \\ &+ \sum_k (h_j, \mathscr{B}^k(t)q^{\star,m})dy_k(t), \\ (q^{\star,m}(0), h_j) =&(q_0, h_j), \quad j \le m. \end{aligned} \tag{33}$$

Now, the forward-backward stochastic pdes (15) and (32), involved in Theorem 1, can be approximated by (33) and

(31) respectively. Lemma 5,6 imply that the strong convergence holds.

Assume we approximate the solution of equation (15) and (32) in the form (for brevity, we shall omit the mark $\star$ below)

$$\begin{aligned} q^m(x,t) &= \sum_{i=1}^m \alpha_i^m(t) h_i(x), \\ p^m(x,t) &= \sum_{i=1}^m \beta_i^m(t) h_i(x), \\ \gamma_k^m(x,t) &= \sum_{i=1}^m \eta_{k,i}^m(t) h_i(x), \ \ k=1,2,..,K, \end{aligned} \tag{34}$$

where α_i^m, β_i^m and $\eta_{k,i}^m$ are the Fourier coefficients to be pinned down later.

Inserting the first equality into (33), we get

$$\begin{aligned} \sum_i d\alpha_i^m(t)(h_i,h_j) =& + \sum_i \alpha_i^m(t) < h_j, \mathscr{A}^{u(t)}(t)h_i > dt \\ &+ \sum_{k,i} \alpha_i^m(t)(h_j, \mathscr{B}^k(t)h_i) dy_k(t), \\ \sum_i \alpha_i^m(0)(h_i,h_j) =& (q_0,h_j). \end{aligned}$$

Substituting the last two equalities to (31), we also have

$$\begin{aligned} \sum_i d\beta_i^m(t)(h_j,h_i) =& - [\sum_i \beta_i^m(t) < h_j, \mathscr{A}^{u(t),*}(t)h_i > \\ &+ \sum_{k,i} \eta_{k,i}^m(t)(h_j, \mathscr{B}^{k,*}(t)h_i) \\ &+ (h_j, l(u(t)]dt \\ &+ \sum_{k,i} \eta_{k,i}^m(t)(h_j,h_i) dy_k(t), \\ \sum_i \beta_i^m(T)(h_j,h_i) =& + (h_j, m(T)). \end{aligned}$$

Writing them in a compact form, we obtain the following singular forward-backward stochastic ordinary differential system

$$\begin{aligned} \hbar d\alpha^m(t) =& \mathbf{A}(t)\alpha^m(t)dt + \sum_{k=1}^K \mathbf{B}^k(t)\alpha^m(t)dy_k(t), \\ \hbar d\beta^m(t) =& - [\mathbf{A}^*(t)\beta^m(t) + \sum_{k=1}^K \mathbf{B}^{k,*}(t)\eta_k^m(t) + \iota^m(t)]dt \\ &+ \sum_{k=1}^K \hbar\eta_k^m(t)dy_k(t), \end{aligned}$$

with the boundary conditions

$$\hbar\alpha^m(0) = q_0^m, \quad \hbar\beta^m(T) = (m(T))^m.$$

In the above, we have used the following matrices

$$\begin{aligned} \hbar =& (h_{ij})_{i,j}, \ \ h_{ij} = (h_j,h_i) = h_{ji}, \\ \mathbf{A} =& (A_{ij})_{i,j}, \ \ A_{ij} =< h_j, \mathscr{A}^u(t)h_i >, \\ \mathbf{B}^k =& (B_{ij}^k)_{i,j}, \ \ B_{ij}^k = (h_j, \mathscr{B}^k(t)h_i), \ k=1,..,K, \end{aligned}$$

and vectors

$$\begin{aligned} \iota^m =& (\iota_j^m)_j, \quad \iota_j^m = \int_{\mathbb{R}^n} h_j(x) l(u(t),x)dx, \\ q_0^m =& (q_{0,j}^m)_j, \ \ q_{0,j}^m = \int_{\mathbb{R}^n} h_j(x) q(x,0)dx, \\ (m(T))^m =& ((m(T))_j^m)_j, \ (m(T))_j^m = \int_{\mathbb{R}^n} h_j(x) m(x,T)dx. \end{aligned}$$

Remark 1 *A set of complete basis of $L^2(\mathbb{R}^n)$ to be chosen is the Gaussian density functions*

$$\begin{aligned} & h_j(x) = h_j(x, m_j, \Sigma_j) \\ =& \frac{1}{\sqrt{(2\pi)^n}\det(\Sigma_j)^{1/2}} \exp\{-\frac{1}{2}(x-m_j)^*\Sigma_j^{-1}(x-m_j)\}, \end{aligned}$$

where m_j is the mean and Σ_j is the covariance matrix.

5 Conclusion

We discuss a class of partially observed optimal control problem and recast the original problem as that of solving a singular forward-backward stochastic ordinary differential equations. Based on it, one related fully observable optimal control problem may be constructed. Then, finite element computation can be carried out on the Hamilton-Jacobi-Bellman equation involved in the optimal control problem constructed and others.

References

[1] R.E. Mortensen, Stochastic Optimal Control with Noisy Observations, *Int. J. Control*, 4(4): 455–464, 1966.

[2] M. A. Davis, P. Varaiya, Dynamic programming Conditions for Partially Observable Stochastic Systems, *SIAM J. Control*, 11(2): 455–464, 1973.

[3] W. H. Fleming, E. Pardoux, Optimal control for partially Observated Diffusions, *SIAM J. Control*, 20(2): 261–285, 1982.

[4] Vivek S. Borkar, Existence of optimal controls for partially observed diffusions, *Stochastics*, 11: 103-141, 1983.

[5] V. Beneš , I. Karatzas, On the Relation of Zakai's and Mortensen's Equations, *SIAM J. Control*, 21(3): 472–489, 1983.

[6] J. Baras, R. Elliott, and M. Kohlmann, The partially Observated Stochastic Minmum Principle, *SIAM J. Control*, 27(6): 1279-1292, 1989.

[7] A. Bensouussan, *Stochastic Control of partially Observable systems*, Cambridge University Press, 1992.

[8] S. tang, The maximum Principle for partially Observated Optimal Control of Stochastic Differential Equations, *SIAM J. Control*, 36(65): 1596-1617, 1998.

[9] C. Charalambous and R. Elliott, Certain Nonlinear Partially Observable Stochastic Optimal Control Problems with Explicit Control Laws Equivalent to LEQG/LQG Problems, *IEEE Transactions on Automatic Control*, 42(4): 482-497, 1997.

[10] J. Yong, X. Zhou, Stochastic Controls Hamiltonian Systems and HJB Equations, Springer, 1999.

[11] J. Sun and J. Xiong, Stochastic Linear-Quadratic Optimal Control with Partial Observation, SIAM Journal on Control and Optimization, 61(3): 1231-1247, 2023.

[12] Z. Li, D. Marelli, M. Fu, H. Zhang, LQG differential stackelberg game under nested observation information patterns, IEEE Transactions on Automatic Control 68 (8): 5111-5118, 2023.

Proceedings of the 3rd Conference on Fully Actuated System Theory and Applications
May 10-12, 2024, Shenzhen, China

Adaptive Coverage Path Planning of Marine Vehicles with Multi-Sensor

Zheng Zhang[1], Peng Wang[1]
1. Department of Automation, Shanghai Jiao Tong University, Shanghai 200240, China.
E-mail: zhengzhang1002@gmail.com, wangpeng605@sjtu.edu.cn

Abstract: Recent advancements in autonomous underwater vehicles (AUV) have made ocean exploration a key future frontier. This study addresses the complex challenge of adaptive coverage path planning with multi-sensors (ACPPMS) in marine environments, aiming to optimize AUV's area coverage under strict time and energy constraints. We propose a novel approach that integrates considerations of energy consumption, information acquisition, and spatial coverage, assessing the intricate trade-offs between extending area coverage and enhancing data collection. Our methodology extends traditional adaptive information path planning by incorporating the decision-making dilemma of balancing coverage with information gain, which we tackle through a tree-based sequential decision-making framework, specifically a partially observable Markov decision process. Utilizing an online planning solution, we validate our approach through rigorous simulation in a search and rescue scenario. The results affirm ACPPMS's adaptability and its superior performance in environments with medium to low reward densities, although it falls short in highly rewarding settings compared to conventional full-coverage strategies. Notably, employing multiple sensors not only elevates path efficiency but also contributes to significant energy savings, showcasing the practical benefits of our multi-sensor integration strategy in adaptive maritime exploration.

Key Words: Adaptive Coverage Path Planning, Area Coverage, Partially Observable Markov Decision Process.

1 Introduction

The regional exploration of marine robots equipped with multi-sensors is mainly aimed at resource exploration, search, rescue, and other application environments in unknown deep-sea environments. Agents must collect information in partially observable uncertain environments and accept information about the world by carrying sensors with different detection accuracy. Observation and its energy are both limited. To carry out regional exploration as effectively as possible, we also added the complexity of regional coverage. We call this problem adaptive coverage path planning with multi-sensors (ACPPMS) that requires joint reasoning for perception and motion in three aspects: energy consumption, information acquisition, and area coverage. Amanda et al.[1] presented a similar work—adaptive coverage path planning, but this is an unknown environment for other people to consider, and there are no sensory factors to consider. However, the problem for us to think about is that we have a sensor that covers the automatic passageway, which is partially intelligible. Our goal is to obtain an adaptive strategy that, starting from the starting point, covers all areas of interest as fully as possible with limited energy.

Coverage path planning (CCPP) algorithm[2] is designed to ensure that a robot or unmanned aerial vehicle covers all areas of interest with minimal overlap, aiming to improve efficiency in path length and execution time. These algorithms are critical in applications such as precision agriculture, search and rescue, and surveillance. Existing coverage path planning algorithms are basically divided into three categories: 1. Behavioral coverage-random collision method. The principle of this method is mainly that the robot tentatively covers the work area based on simple movement behaviors. If it encounters obstacles, Then execute the corresponding steering command. The behavior full coverage algorithm has low work efficiency and the path planning strategy is simple. The comparative typical algorithm contains comprehensive cattle arable algorithm[3], decomposing into polygon algorithm [4] and traveling salesman problem based on gird [5]. 2. Region segmentation method. To enable the robot to reduce the calculation amount of the algorithm, Li et al. [6] proposed a method to simplify the given workplace into smaller sub-regions for coverage on the standard map and extend it to special missions [7]. The algorithm that combines navigation and local navigation divides the entire area into several areas for coverage. 3. The neural network method uses self-learning, parallelism, and other characteristics of the neural network to enhance the "intelligence" of the robot and improve coverage efficiency. Inspired by the similarity between the neural network structure and the grid map unit, Canadian scholar Han et al. [8] proposed a neural network method to cover. The neurons of the network correspond one to one, and the real-time path planning for the robot to achieve full coverage is generated by the activity value of the neurons and the previous position of the robot. However, the calculation amount of this method will be extremely large, and the parameters will change according to different environments, so using this method to adapt to different environments is difficult. The existing coverage path planning algorithm may lead to inefficiency in large or complex environments because it requires covering all areas, even if some areas are not important or of low value, which often means longer trips and more Energy consumption. In addition, these methods usually lack the ability to adapt to environmental changes. To this end, we propose an adaptive coverage path planning algorithm that can adapt to most environments. By prioritizing those key areas with high value, prioritizing resource allocation, and improving task performance.

Our key idea is to jointly reason about multimodal per-

This work is supported in part by National Natural Science Foundation of China under Grant 62188101, 62203302, 62273230 and the Oceanic Interdisciplinary Program of Shanghai Jiao Tong University (project number SL2023MS011 and SL2022MS003).
Corresponding author: Peng Wang

ception and motion by formulating the problem as a partially observable Markov decision process (POMDP) [9] and using an online solver to accommodate states, observation spaces, and globally visited nodes. We use an optimal greedy search in an online solver to tailor the strategy while trying to constrain the energy. Through this online POMDP framework, we use the POMCP [10] algorithm to solve the ACPPMS problem online and maintain a global access status to avoid repeated access as much as possible, penalize repeated access, and improve global coverage. The main contributions of this article are as follows:

- We propose an adaptive coverage path planning method, which aims to cover all valuable areas quickly and efficiently, and can be applied in environments with large areas and low reward density such as oceans.
- We separate sensing and action to save energy consumption, and perform joint reasoning from three aspects: information acquisition, energy consumption, and area coverage.
- We have verified our algorithm in different environments, and experiments have proven that the proposed algorithm can effectively solve problems similar to ocean search. The algorithm has fast convergence speed, low repetition rate, and low energy consumption.

The rest of the paper unfolds as follows: Section 2 provides essential background information on partially observable Markov decision processes (POMDPs) and their relevance to coverage path planning. Section 3 defines the problem we aim to solve, setting the stage for our proposed approach detailed in Section 4, which covers the POMDP formulation and online planning tailored to adaptive coverage path planning with multi-sensors (ACPPMS). Section 5 presents a comprehensive set of experiments designed to validate the effectiveness of our approach, including simulations in various scenarios to demonstrate its adaptability and performance. We conclude in Section 6 by summarizing our findings, highlighting the significant advantages of our approach in optimizing area coverage under strict energy and time constraints, and suggesting directions for future research.

2 Background

This part provides background on partially observable Markov decision-making (POMDP), online POMDP solver, and full coverage path planning(CCPP).

2.1 Overview of POMDP

Partially observable Markov decision processes[11] (POMDP) serve as a fundamental framework for decision-making processes where uncertainty is a key factor. These processes are defined by a set of elements: state space (S), action space (A), observation space (O), along with transition (T), observation (Z), and reward (R) functions, and a discount factor γ. In POMDP, the agent's actions are based on a belief about the state, which is not directly observable but inferred from noisy observations. The transition function T defines the probability of transitioning to a new state given a current state and an action. The observation function Z models the likelihood of observing a particular outcome from a state after an action. The reward function R assigns an expected reward for actions in given states, and the discount factor γ is used for problems with an infinite horizon to ensure bounded total expected rewards. The primary goal of POMDP is to develop an optimal policy (π) that maximizes cumulative rewards over time. While exact solutions exist for both finite and infinite horizons, they are generally impractical for complex problems, leading to a focus on approximate solution strategies. Existing methods to solve the POMDP problem are roughly divided into the following categories: 1. Value iteration method: similar to the value iteration in MDP, but uses observed values instead of states to update the value function. This is very computationally intensive. For example, the heuristic search value iteration method of POMDP proposed by Smith et al [12]. 2. Monte Carlo method: approximating the optimal solution through simulation is often more efficient but may not be accurate enough. 3. Approximation methods: such as point-based value iteration [13] or using neural networks to approximate value functions [14]. 4. Online Planning: For example, partially observable Monte-Carlo planning(POMCP) plans in real-time and re-plans every time a decision needs to be made.

2.2 Online POMDP solver

In the context of online POMDP planning, the decision-making process involves selecting actions based on a current belief state and considering possible future belief states within a limited horizon. This adaptive approach allows for real-time decision-making in dynamic environments. Key methodologies in this area include branch-and-bound and forward search strategies. Two notable modern methods in online POMDP planning are the partially observable Monte Carlo planning (POMCP) [15] and the determinized sparse partially observable tree (DESPOT) [16]. POMCP utilizes Monte Carlo tree search combined with upper confidence bounds to guide exploratory actions, while DESPOT employs a sparse approximation of the belief tree. In this research, the simpler POMCP framework is adopted for its adaptability and efficiency, with the potential for modifications to suit various scenarios, including those with continuous action spaces. Recent advancements also include approaches like the Pareto-optimal Monte Carlo tree search, which optimizes the balance between exploration and exploitation, though it does not inherently support multimodal sensing capabilities.

3 Problem definition

We have a location graph $G = (V, R)$, where node V represents the location that all robots can visit, and R represents the reward at each node, that is, the reward that can be generated immediately when the robot performs an action to this node, repeated visits don't get rewards twice. In the initial state, we place the robot at the initial position V_s and need to give the number of iterations, since when the depth of the decision tree constructed by the POMCP algorithm is given, the time required for each iteration can be roughly considered to be the same, so we use the number of iterations to approximate the task execution time. Our task goal is to maximize coverage and reward under the constraints of task time and energy.

There are two actions that an agent can choose: one is movement, and the other is perception. Movement can

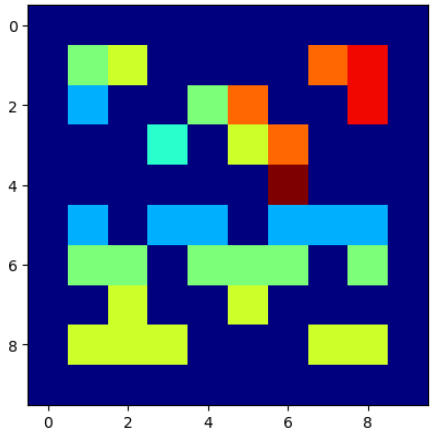

Fig. 1: environment: different colors represent different reward values, when agent arrives at the specified location, the reward can be got immediately.

achieve state transfer and obtain immediate rewards, while perception cannot. However, through perception, the probability of observation can be increased, and from the perspective of the entire historical sequence, Perhaps beneficially, we can use it to make better control decisions for higher returns. Below we will briefly explain this matter in a two-state world.

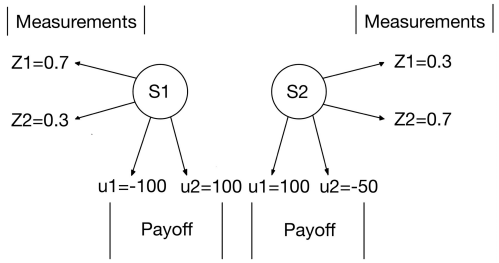

Fig. 2: A two-state environment illustrating confidence space value iteration.

As shown in Fig 2, it is a world with two states. The states are denoted as x_1 and x_2. The robot can choose two different actions u_1 and u_2. Observations are denoted as z_1 and z_2. When the action is performed, they will immediately produce the following rewards: $r(x_1, u_1) = -100$, $r(x_2, u_1) = +100$, $r(x_1, u_2) = +100$, $r(x_2, u_2) = -50$. Without perception:

$$V_1(b) = \max\{-100p_1 + 100(1-p_1), \\ 100p_1 - 50(1-p_1)\}. \tag{1}$$

In the case of perception: Our measurement model is described by the following probability distribution: $p(z_1 \mid x_1) = 0.7$, $p(z_2 \mid x_1) = 0.3$, $p(z_1 \mid x_2) = 0.3$, $p(z_2 \mid x_2) = 0.7$. and p_1' after sensing z_1:

$$p_1' = p(x_1 \mid z) = \frac{p(z_1 \mid x_1)p(x_1)}{p(z_1)} = \frac{0.7p_1}{p(z_1)}, \tag{2}$$

$$p_2' = \frac{0.3(1-p_1)}{p(z_1)}, \tag{3}$$

$$p(z_1) = 0.7p_1 + 0.3(1-p_1) = 0.4p_1 + 0.3, \tag{4}$$

$$\hat{p}_1 = \frac{0.7p_1}{0.4p_1 + 0.3}, \tag{5}$$

$$V_1(b \mid z_1) = \max\{-100 \cdot \frac{0.7p_1}{p(z_1)} + 100 \cdot \frac{0.3(1-p_1)}{p(z_1)}, \\ 100 \cdot \frac{0.7p_1}{p(z_1)} - 50 \cdot \frac{0.3(1-p_1)}{p(z_1)}\}, \tag{6}$$

$$\bar{V}_1(b) = \mathbb{E}_z[V_1(b \mid z)] = \sum_{i=1}^{2} p(z_i)V_1(b \mid z_i), \tag{7}$$

and

$$\begin{aligned} &\bar{V}_1(b) \\ &= \max\{70p_1 + 30(1-p_1), 70p_1 - 15(1-p_1)\} + \\ &\quad \max\{-30p_1 + 70(1-p_1), 30p_1 - 35(1-p_1)\}. \end{aligned} \tag{8}$$

From the comparison between $V_1(b)$ and $\bar{V}_1(b)$, perception ability improves the value function of the entire area to a higher level, so although perception ability does not obtain immediate rewards, it is very meaningful for future control choices.

4 Approach

We inherit all the complexity of the previous IPP problem [17] and add two levels of complexity: multi-modality and coverage.

Our approach is to explicitly develop and solve the ACPPMS challenge within the POMDP framework. This strategy allows for a comprehensive consideration of both movement and the use of various sensing modes. The details of this formulation are presented in Section 4.1, followed by an explanation in Section 4.2 on the application of a specialized online POMDP solver, designed specifically for ACPPMS scenarios

4.1 POMDP FOrmulation

In this section, we redefine AIPPMS within the POMDP framework, as referenced in Section 3. The structure of ACPPMS is a discrete-time, limited-horizon POMDP with constraints. For any given moment t, the state is articulated as $s_t = (v_t, \xi_t, \Delta e_t, X_V)$. Here, v_t indicates the agent's present location in the node network, ξ_t is the aggregate of nodes traversed thus far, and $\Delta e_t = B - \sum_{i=1}^{t-1} C(p_{s_i}, a_i)$ represents the residual budget after costs. These components are all observable. The X_V parameter, which describes the state of the world, is specific to the given problem and remains unobservable. Belief centers on the most likely world state, predominantly within the belief space $B \subset X^{|V|}$, although it's feasible to impose constraints on the joint distribution to maintain computational feasibility; this model is independent of the POMDP solver specifics.

The transition function T is deterministic. If a_t represents a movement action to an adjacent node, then the ensuing state is $s_{t+1} = (v_{t+1}, \xi_{t+1}, \Delta e_{t+1}, X_V)$ where $v_{t+1} = a_t$, $\xi_{t+1} = \xi_t \cup \{v_{t+1}\}$, and $\Delta e_{t+1} = \Delta e_t - C(s_t, a_{t+1})$. For a sensing action, the only change from s_t to s_{t+1} is in $\Delta e_{t+1} = \Delta e_t - C(s_t, a_{t+1})$. The belief state about the world is updated based on the sensor's observation as follows:

We define the belief state at the next time step b_{t+1} by using the state transition function τ, which is based on the current belief state b_t, the observation o_t, and the action σ.

$$b_{t+1} = \tau(b_t, o_t, \sigma). \tag{9}$$

This update reflects how the system adjusts its estimation of the environmental state based on the latest observations and actions.

Then, we consider the specific manner in which the belief state is updated. Given the current observation o_t and the action σ, the new belief state $b_{t+1}(x'_v)$ is proportional to the probability of this observation and also depends on the cumulative effect of all possible states x_v.

$$\begin{aligned} b_{t+1}(x'_v) &\propto P(o_t|x'_v, o_t, b_t)P(x'_v|o_t, b_t) \\ &\propto Z(x'_v, \sigma, o_t) \sum_{x_v} T(\sigma, x_v, x'_v)P(x_v|b_t), \end{aligned} \tag{10}$$

$$b_{t+1}(x'_v) \propto Z(x'_v, \sigma, o_t)b_t(x'_v). \tag{11}$$

The computation of $b_{t+1}(x'_v)$ reflects the conditional probability of the state x'_v occurring given the current observation o_t and action σ. This probability is composed of two parts: one is the observation model Z, which describes the probability of observing o_t given the state and action; the other part is the cumulative calculation through the transition probabilities T from all possible previous states x_v and their probabilities in the previous belief state.

4.2 Online Planning for ACPPMS

In our approach, we adopt the partially observable Monte Carlo planning (POMCP) method as our main online solver. We specifically adapted POMCP to address the challenges of ACPPMS by incorporating two key modifications. First, we formulate a push-out strategy that works effectively with a relevant subset of utility functions. Second, since sensing does not gain immediate rewards, but it is effective in the long run, we borrow the method of Shushman Choudhury et al [18]. A utility function is added for sensing, and the information gain obtained is also expressed as a reward, so that movement and sensing can be considered comprehensively during the simulation. Third, to improve the regional coverage, we maintain a set of exploration nodes. Not only will no rewards be obtained for repeated exploration, but there will also be a penalty for the number of repeated explorations. This adaptive solver is designed to cope more efficiently with the complexity of ACPPMS.

Firstly, since we have to comprehensively consider budget, regional coverage, and reward value, so we design a new utility function here.

$$F = action.V + C_0 \times \text{budget} + C_1 \times ucb(N_h, N_{h_a}). \tag{12}$$

Among them, when the system uses the Monte Carlo tree search for rollout, $action.V$ represents the reward value, $budget$ represents the remaining energy and C_0 represents the weight of the budget. N_h is the total number of visits to the parent node, N_{h_a} is the number of times a specific action is selected, and C_1 is the exploration parameter, which encourages trying actions that have not been completely explored.

Secondly, We add a utility function which is borrowed from the method of Shushman Choudhury et al. [18] to sense, and express the obtained information gain as a reward, so that movement and sensing can be considered comprehensively during the simulation process. This approach integrates an anticipated information gain technique[19] with the understanding that distribution mode can serve as a simplified representation of negative information entropy[20], given that collapsed distributions inherently exhibit higher density concentration.

$$\begin{aligned} IG(a|b) &= \sum_o P(o|b, a) \left[\max_s \tau(b, o, a)(s) - \max_s b(s)\right] \\ &\approx \sum_i \left[\max_s \tau(b, o_i, a)(s) - \max_s b(s)\right]. \end{aligned} \tag{13}$$

Last but not least, we denote the set of all feasible states as $\mathcal{S}$. Then, for any feasible state $s \in \hat{\mathcal{S}}$, the set of feasible actions comprises those that can only lead to another feasible state, i.e. We also defined the global variable trajectory to penalize nodes that are visited repeatedly.

$$\mathcal{A}(s) = \{a \in \mathcal{A} \mid T(s, a, s') > 0 \rightarrow s' \in \mathcal{S}\}. \tag{4}$$

The complete POMCP algorithm is described in Algorithm 1.

5 Experiments

We run all simulations in python language to verify our POMCP customization strategy in the POMDP framework. At the same time, since we introduced a new problem ACPPMS (Adaptive Coverage Path Planning with Multi-Sensors). Table 1 are the parameters we believe may affect the experiment. Our experimental field is the field of search

Table 1: Parameters

γ	Discount Factor
T	The depth of the search tree constructed
density	Bonus Density (Mainly depends on the map built)
σ	sensor

and rescue. The agent is an aircraft with limited energy and carries a variety of different sensors. Different sensors can bring observations with different accuracy. The agent needs to search and rescue a certain amount of information under a certain number of instructions. area survivors. We model the environment simply as a two-dimensional grid, and the density of survivors as instant rewards in the grid.

Result 1 First, we compared the agent coverage when building search trees of different depths, and the number of iterations required for complete coverage.

We model the environment as a 10×10 grid. When the tree depths are 3, 5, and 8 respectively, the coverage when the number of iterations is 100 is as Fig.5.

At the same time, we counted the number of iterations when the agent obtained all rewards in the environment and achieved full coverage. Experimental results show that when the tree is built deeper, it may consider the future more, and can show higher coverage in a limited number of steps. This also results in the loss of local optimality at higher depths, and more iterations are required for complete coverage.

Algorithm 1 POMCP with GCB Rollout for ACPPMS

Global $Trajectory$ = []
Global R = []
Global $Budget$ = []
procedure SIMULATE(s, u, depth)
  if $\gamma^{\text{depth}} < \varepsilon$ **then**
    return 0
  end if
  if $h \notin T$ **then**
    for all $a \in A(s)$ **do**
      $T(ha) \leftarrow (N_{\text{init}}(ha), V_{\text{init}}(ha), \emptyset)$
    end for
    return ROLLOUT(s, h, depth) ▷ This uses ACTION internally
  end if
  $a \leftarrow \arg\max_{b \in A(s)} V(hb) + C_0 * budget + C_1\sqrt{(\log N(h)/N(hb))}$
  $(s', o, r) \sim G_{\text{sim}}(s, a)$
  $R \leftarrow r + \gamma \cdot$ SIMULATE(s', u', depth + 1)
  $B(h) \leftarrow B(h) \cup \{s\}$
  $N(h) \leftarrow N(h) + 1$
  $N(ha) \leftarrow N(ha) + 1$
  $V(ha) \leftarrow V(ha) + (R - V(ha))/N(ha)$
  $Trajectory \leftarrow Trajectory \cup \{s'\}$
  return R
end procedure
procedure ACTION($\pi_{\text{rollout}}, s, h$)
  for all $a \in A(s)$ **do**
    if $a \in V$ **then** ▷ a is for movement
      $U(a) \leftarrow E_b(X_v)[\Delta F(a|s, X_v)]/C(s, a)$
    else
      $U(a) \leftarrow IG(a|b(X_v))/C(a)$
    end if
  end for
  return $a \sim$ SoftMax(U)
end procedure
procedure ROLLOUT(s, h, depth) ▷ Modified for exploration
  $s_{next} \leftarrow s + a \in A(s)$
  while not terminal state and depth < max_depth **do**
    if s_{next} not in $Trajectory$ **then**
      Reward(a) = r
    else
      Reward(a) = num($Trajectory[a]$) * (-1)
    end if
  end while
  return Reward(a)
end procedure

Result 2 We compared the number of iterations required for complete agent coverage in environments with different reward densities. The Table 2 shows the number of iterations required to build search trees of different depths to achieve full coverage in environments of different densities. Experimental results show that for low-density reward environments, the number of iterations required to construct search trees of different depths is roughly the same, but also shows a slight decreasing trend. This may be because when the depth of the constructed search tree is shallower, its local optimality is lost, and different actions lead to the same reward, so the number of iterations to achieve full coverage is slightly more. As the reward density increases, the advantages of constructing a local optimum of a shallower search tree begin to appear, and the number of iterations required will become smaller than that of a deeper search tree.

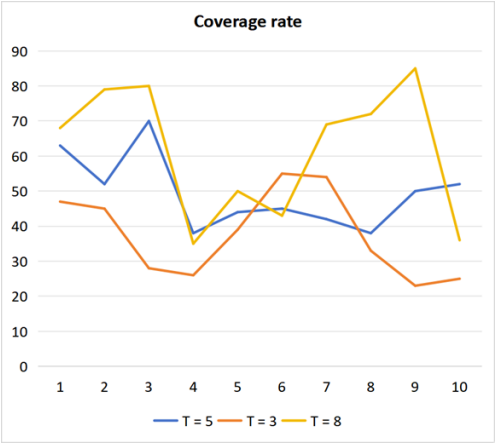

Fig. 3: coverage rate in different T depth.

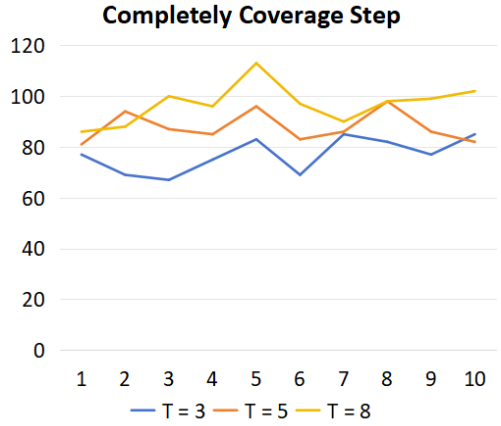

Fig. 4: Number of steps required to completely cover.

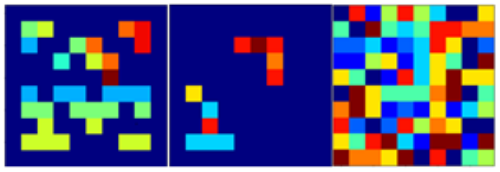

Fig. 5: Environments of different density.

Result 3 We compare the energy savings of carrying multiple sensors compared to a single sensor.

Using multiple sensors can result in significant energy savings compared to using a single sensor. This result demonstrates the efficacy of multi-sensor systems in improving the energy efficiency of autonomous agents in exploration tasks.

These analyses collectively illustrate the robustness and adaptability of the proposed adaptive coverage path planning strategy with multi-sensor integration in marine environments, highlighting its potential for efficient exploration and resource management.

6 Conclusion

In this study, we introduced an innovative approach for adaptive coverage path planning of multi-sensor equipped autonomous underwater vehicles (AUVs), aiming to opti-

Table 2: the number of iterations required for complete agent coverage in environments with different reward densities

	T = 3	T = 5	T = 8
low density	35	33	30
medium density	77	87	98
high density	150	180	250

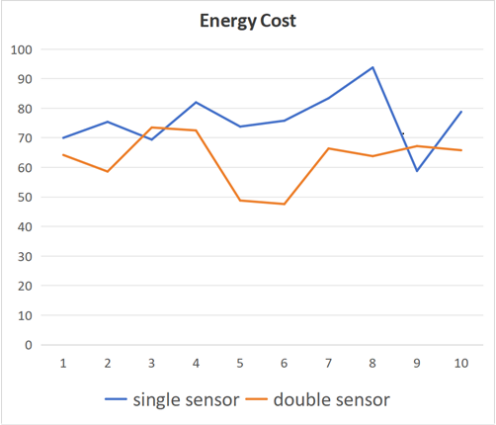

Fig. 6: Single sensor: 0.6 observation probability, 1 energy cost; Double sensor: 0.8 observation probability, 1.2 energy cost and 0.6 observation probability, 1 energy cost.

mize the marine environment under the constraints of limited time and energy. area coverage. By formulating the problem as a partially observable Markov decision process (POMDP) and applying the online partially observable Monte-Carlo planning (POMCP) algorithm, our approach achieved remarkable performance in terms of efficiency and adaptability. Our experiments confirmed that the proposed ACPPMS method effectively balances the trade-off between exploration depth and resource constraints, resulting in more informed decisions in uncertain marine environments. By integrating multi-sensor data and dynamically adjusting planning strategies based on real-time observations, our system achieved excellent area coverage and information acquisition, demonstrating the potential of multi-sensor integration in enhancing AUV capabilities. As we continue to explore the ocean depths, the flexibility and efficiency of our adaptive coverage path planning approach demonstrated the potential of intelligent robotic systems to overcome the challenges of ocean exploration.

Future work will focus on improving the efficiency of the algorithm, exploring the integration of additional sensory modalities, and expanding the application areas of this research to include more complex and diverse marine environments.

References

[1] A. Bouman, J. Ott, S.-K. Kim, K. Chen, M. J. Kochenderfer, B. Lopez, A.-a. Agha-mohammadi, and J. Burdick, "Adaptive coverage path planning for efficient exploration of unknown environments," in *2022 IEEE/RSJ International Conference on Intelligent Robots and Systems (IROS)*, pp. 11916–11923, IEEE, 2022.

[2] E. Galceran and M. Carreras, "A survey on coverage path planning for robotics," *Robotics and Autonomous systems*, vol. 61, no. 12, pp. 1258–1276, 2013.

[3] H. Choset, "Coverage of known spaces: The boustrophedon cellular decomposition," *Autonomous Robots*, vol. 9, pp. 247–253, 2000.

[4] T. Oksanen and A. Visala, "Coverage path planning algorithms for agricultural field machines," *Journal of field robotics*, vol. 26, no. 8, pp. 651–668, 2009.

[5] L. Zeng, S. Chopra, and K. Smilowitz, "The covering path problem on a grid," *Transportation Science*, vol. 53, no. 6, pp. 1656–1672, 2019.

[6] C. Li, Z. Wang, F. Wang, Y. Song, and Y. Li, "A ccpp algorithm based on the standard map for the mobile robot," in *2017 Chinese Automation Congress (CAC)*, pp. 4963–4968, IEEE, 2017.

[7] C. Li, Z. Wang, C. Fang, Z. Liang, Y. Song, and Y. Li, "An integrated algorithm of ccpp task for autonomous mobile robot under special missions," *International Journal of Computational Intelligence Systems*, vol. 11, no. 1, pp. 1357–1368, 2018.

[8] S. X. Yang and C. Luo, "A neural network approach to complete coverage path planning," *IEEE Transactions on Systems, Man, and Cybernetics, Part B (Cybernetics)*, vol. 34, no. 1, pp. 718–724, 2004.

[9] M. T. Spaan and N. Spaan, "A point-based pomdp algorithm for robot planning," in *IEEE International Conference on Robotics and Automation, 2004. Proceedings. ICRA'04. 2004*, vol. 3, pp. 2399–2404, IEEE, 2004.

[10] W. Chen and L. Liu, "Pareto monte carlo tree search for multi-objective informative planning," *arXiv preprint arXiv:2111.01825*, 2021.

[11] M. T. Spaan, "Partially observable markov decision processes," in *Reinforcement learning: State-of-the-art*, pp. 387–414, Springer, 2012.

[12] T. Smith and R. Simmons, "Heuristic search value iteration for pomdps," *arXiv preprint arXiv:1207.4166*, 2012.

[13] J. Pineau, G. Gordon, S. Thrun, *et al.*, "Point-based value iteration: An anytime algorithm for pomdps," in *Ijcai*, vol. 3, pp. 1025–1032, 2003.

[14] Y. Han and P. Gmytrasiewicz, "Ipomdp-net: A deep neural network for partially observable multi-agent planning using interactive pomdps," in *Proceedings of the AAAI Conference on Artificial Intelligence*, vol. 33, pp. 6062–6069, 2019.

[15] D. Silver and J. Veness, "Monte-carlo planning in large pomdps," *Advances in neural information processing systems*, vol. 23, 2010.

[16] A. Somani, N. Ye, D. Hsu, and W. S. Lee, "Despot: Online pomdp planning with regularization," *Advances in neural information processing systems*, vol. 26, 2013.

[17] J. Binney, A. Krause, and G. S. Sukhatme, "Informative path planning for an autonomous underwater vehicle," in *2010 IEEE International Conference on Robotics and Automation*, pp. 4791–4796, IEEE, 2010.

[18] S. Choudhury, N. Gruver, and M. J. Kochenderfer, "Adaptive informative path planning with multimodal sensing," in *Proceedings of the International Conference on Automated Planning and Scheduling*, vol. 30, pp. 57–65, 2020.

[19] C. Stachniss, G. Grisetti, and W. Burgard, "Information gain-based exploration using rao-blackwellized particle filters.," in *Robotics: Science and systems*, vol. 2, pp. 65–72, 2005.

[20] L. Dressel and M. Kochenderfer, "Efficient decision-theoretic target localization," in *Proceedings of the International Conference on Automated Planning and Scheduling*, vol. 27, pp. 70–78, 2017.

Proceedings of the 3rd Conference on Fully Actuated System Theory and Applications
May 10-12, 2024, Shenzhen, China

Pricing Frequency Ancillary Services for Low-Inertia Power Systems under Model Nonconvexity

Zhihao Li[1,2], Yinliang Xu[1]

1. Tsinghua-Berkeley Shenzhen Institute, Shenzhen International Graduate School, Tsinghua University, Shenzhen 518055, China
E-mail: lizhihao21@mails.tsinghua.edu.cn; xu.yinliang@sz.tsinghua.edu.cn

2. Pengcheng Laboratory, Shenzhen 518055, China

Abstract: To enhance the frequency stability in low-inertia power systems, system operators incentivize controllable energy resources to deliver the frequency ancillary service in the wholesale electricity market. In this paper, a pricing scheme for frequency ancillary service is established for low-inertia power systems in the day-ahead electricity market. The distinct response characteristics of thermal generators and wind farms are considered in the modeling of the system frequency response, which then forms frequency security constraints for unit commitment (UC). A convex hull pricing model is proposed to address the research gap related to pricing under the nonconvexity of UC scheduling in the frequency ancillary service market. Numerical results demonstrate the effectiveness of the proposed pricing scheme in incorporating renewable sources and addressing nonconvexity issues.

Key Words: Frequency-constrained unit commitment, ancillary services market, convex hull pricing.

1 Introduction

In recent years, renewable energy sources (RES) have been extensively deployed in power grids to facilitate decarbonization goals. To improve the stability of highly RES-penetrated systems, various converter control techniques have been proposed to harness the fast response capability of RES for frequency support, such as virtual inertia (VI) control [1], droop control, and virtual synchronous machine control [2]. Procuring balancing capabilities from available energy resources is a promising solution for independent system operators (ISOs) to enhance the resilience of the power system. Market mechanisms are needed to assign incentives for energy resources to provide frequency response services. Pricing mechanisms of frequency ancillary services have also been investigated in recent studies [3–7]. The pricing scheme in [3] derives the prices of inertia and frequency response with diverse dynamics. However, the pricing scheme for frequency services of non-synchronous energy resources is not investigated in [3]. In [4], a VI pricing mechanism is proposed based on the Vickrey-Clarke-Groves (VCG) payment rule, which only focuses on the inertia price of electronic-based resources. The work in [5] formulates a joint market to procure energy, reserve and inertia from traditional generators and non-synchronous resources but only considers the inertia requirement on Rate-of-Change-of-Frequency (RoCoF). To incorporate the nonconvex nadir constraint in scheduling, references [6, 7] formulate the frequency nadir constraint as a rotated second-order cone constraint and a set of piecewise linear constraints, respectively. Therefore, constructing a pricing scheme that considers the energy resources with different characteristics and system security requirements is challenging. Due to the nonconvexity of the commitment variables in unit commitment (UC) problems, using locational marginal prices (LMPs) [8–11] may necessitate additional payments to incentivize market participants to comply with the ISO's dispatch. Such payments made to a bidder are not transparent to other participants. Convex hull pricing (CHP) methods have been widely employed to mitigate the impact of model convexities by constructing convex hulls and convex envelopes of the original problems [12, 13]. In the frequency ancillary service market, frequency-related constraints typically do not introduce nonconvexity to the dispatch model because most of them are formulated as linear constraints. However, the procurement of inertia and frequency reserve from traditional generators may lead to the dispatch being out of merit order, affecting pricing rationality. Existing works on frequency ancillary services pricing [3, 5, 6] only discuss on methodologies for convex hull pricing. No instance in this field proposes a pricing scheme to address uplift payments caused by the nonconvex nature of commitment variables.

Aiming to address the modeling and pricing issues discussed above, the main contributions of this paper are summarized as follows:

1) A joint pricing model of energy and frequency ancillary services is proposed for low-inertia power systems. To ensure the predefined frequency security metrics, inertial and droop responses are procured from both thermal units and wind farms. The effects of resources' distinct response speeds and frequency response dead-band are considered in the modeling of the system frequency dynamic model.
2) A convex hull pricing model is proposed for the joint market under nonconvexity. To alleviate the impacts of nonconvexity and ancillary services procurement, the pricing result minimizes the uplift payments, including lost opportunity cost (LOC) and product revenue shortfall (PRS). An extreme-point enumeration method is developed to derive the pricing solution.

2 Problem Formulation

2.1 Modeling on Frequency Responses of Generators

We consider a transmission system, including a set of buses indexed by $i \in \mathcal{B} := \{1, \ldots, |\mathcal{B}|\}$, a set of thermal generators indexed by $g \in \mathcal{G} := \{1, \ldots, |\mathcal{G}|\}$, a set of wind

This work is supported in part by the National Key R&D Program under Grant 2021YFB1507100, in part by the National Nature Science Foundation of China under Grant 52277107, and in part by the Major Key Project of PCL under Grant No. PCL2022A05.

farms indexed by $w \in \mathcal{W} := \{1, \ldots, |\mathcal{W}|\}$, and a set of transmission lines connected with bus i and bus j defined as $l_{ij} \in \mathcal{E} := \{1, \ldots, |\mathcal{E}|\}$, where $j \in \mathcal{B}, j \neq i$. The dispatch intervals of the transmission system is denoted as $t \in \mathcal{T} =: \{1, \ldots, |\mathcal{T}|\}$, and let $|\mathcal{T}| = T$.

Rotational inertia is an inherent feature of traditional generators to prevent the frequency from a drastic decline in the event of a sudden power loss. For a synchronous generator g with generation capacity $P_g^{\max}$ and inertial constant H_g, the inertia capacity of generator g is expressed as:

$$H_{g,t}^G = H_g P_g^{\max} z_{g,t} / f_0, \forall t \in \mathcal{T}, \tag{1}$$

where $z_{g,t}$ is the binary commitment state; f_0 is the system nominal frequency at 50Hz.

On the other hand, power control loops allow a wind turbine to release the kinetic energy from the rotor to emulate inertia. It is assumed that the actual inertia provision $H_{w,t}^W$ of a wind farm is constrained by its maximum available inertia capacity $H_{w,t}^{\max}$, which can be calculated by the energy stored in each wind turbine within the wind farm.

Both synchronous generators and wind turbines can react against the frequency deviation. The primary frequency response (PFR) of a thermal generator is achieved by the droop response of the speed governor, which is delivered at the timescale of seconds. Controllable wind turbines can provide fast frequency response (FFR) at the expense of curtailing power as frequency regulation reserve, which can be operated by power control loops within 1 second. We assume that a disturbance occurs at $\tau = 0$, PFR and FFR are activated at $\tau = t_{\text{DB}}$ when frequency deviation exceeds the deadband Δf_{DB}, and linearly increasing with distinct delivery times T_g and T_w. PFR and FFR models are formulated as:

$$\Delta P_{g,t}^{\text{PFR}}(\tau) = \begin{cases} 0, & \text{if } \tau \leq \tau_{\text{DB}} \\ R_{g,t}^{\text{G}} \frac{\tau - \tau_{\text{DB}}}{T_g}, & \text{if } \tau_{\text{DB}} < \tau < T_g + \tau_{\text{DB}}, \\ R_{g,t}^{\text{G}}, & \text{if } \tau \geq T_g + \tau_{\text{DB}} \end{cases} \tag{2}$$

$$\Delta P_{w,t}^{\text{FFR}}(\tau) = \begin{cases} 0, & \text{if } \tau \leq \tau_{\text{DB}} \\ R_{w,t}^{\text{W}} \frac{\tau - \tau_{\text{DB}}}{T_w}, & \text{if } \tau_{\text{DB}} < \tau < T_w + \tau_{\text{DB}}, \\ R_{w,t}^{\text{W}}, & \text{if } \tau \geq T_w + \tau_{\text{DB}} \end{cases} \tag{3}$$

The maximum power adjustments are dependent on the frequency regulation reserves $R_{g,t}^G$ and $R_{w,t}^W$.

2.2 Modeling on System Frequency Dynamics

For notation simplicity, the system's total inertia capacity, denoted as H_t^{sys}, is calculated as the sum of the inertia capacities of thermal generators and wind farms: $\sum_{g \in \mathcal{G}} H_{g,t}^G + \sum_{w \in \mathcal{W}} H_{w,t}^W$. Similarly, the overall PFR reserve R_t^G and FFR reserve R_t^W are obtained by aggregating the single-unit reserve capacities: $R_t^G := \sum_{g \in \mathcal{G}} R_{g,t}^G$, $R_t^W := \sum_{w \in \mathcal{W}} R_{w,t}^W$.

Incorporating the frequency response of thermal generators and wind farms, the system's frequency dynamic model can be expressed by the swing equation:

$$\begin{aligned} &2H_t^{\text{sys}} \frac{d\Delta f(\tau)}{dt} + DP_t^L \Delta f(\tau) \\ =&\sum_{g \in \mathcal{G}} \Delta P_{g,t}^{\text{PFR}}(\tau) + \sum_{w \in \mathcal{W}} \Delta P_{w,t}^{\text{FFR}}(\tau) - \Delta P_t^d(\tau), \end{aligned} \tag{4}$$

where D and P_t^L are the load damping factor and total load demand at period t; the positive value ΔP_t^d indicates the power loss disturbance.

By substituting (2) and (3) into the swing equation of the system, we can derive the frequency response $\Delta f(\tau)$ of the system, which is a piecewise function. Taking the time derivative of the frequency response $\Delta f(\tau)$, we can derive the nadir time t_{nadir} by solving the differential equation $\Delta \dot{f}(\tau) = 0$. Finally, we can obtain the expression of frequency nadir Δf_{nadir} by substituting τ_n into $\Delta f(\tau)$, which is a nonlinear function about H_t^{sys}, R_t^G and R_t^W.

The maximum Rate-of-Change-of-Frequency occurs at the outset of stepwise disturbance (i.e., $\tau = 0$), dependent on the disturbance and system inertia: $f_t^{\max} = -\Delta P_t^d / (2H_t^{\text{sys}})$. The Quasi-Steady-State frequency deviation is calculated as follows: $\Delta f_t^{\text{qss}} = -(\Delta P_t^d - R_t^G - R_t^W)/(DP_t^L)$.

2.3 Frequency-Constrained Unit Commitment Model

2.3.1 Objective Function

The objective function of the frequency-constrained UC problem is to minimize the operation cost including no-load cost, fuel cost and PFR reserve cost of thermal generators and VI control cost of wind farms:

$$\min \sum_{t \in \mathcal{T}} \sum_{g \in \mathcal{G}} \left(c_g^{\text{nl}} z_{g,t} + c_g P_{g,t}^G + c_g^{\text{FR}} R_{g,t}^G\right) + \sum_{t \in \mathcal{T}} \sum_{w \in \mathcal{W}} c_w^{\text{vi}} H_{w,t}^W, \tag{5}$$

where c_g^{nl}, c_g, c_g^{FR} are cost coefficients of no-load cost, fuel cost and PFR reserve cost of generator g; c_w^{vi} is the virtual inertia control cost of wind farm w. $P_{g,t}^G$ denotes the power output of generator g.

2.3.2 System Power Balance Constraints

The system-wide power balance constraint is expressed as:

$$(\rho_t^e) : \sum_{g \in \mathcal{G}} P_{g,t}^G + \sum_{w \in \mathcal{W}} (P_{w,t}^W - P_{w,t}^{\text{wc}}) = \sum_{i \in \mathcal{B}} P_{i,t}^D, \ \forall t \in \mathcal{T}, \tag{6}$$

where $P_{w,t}^{\text{wc}}$ is the power curtailment of wind farm w and $P_{i,t}^D$ is the power demand on bus i. Note that ρ_t^e and other greek letters in the parentheses hereinafter are the dual multipliers of operational constraints.

2.3.3 Generator Operational Constraints

$$z_{g,t} \in \{0, 1\}, \forall g \in \mathcal{G}, t \in \mathcal{T}, \tag{7a}$$

$$(\nu_{g,t}^{g+}) : P_{g,t}^G + R_{g,t}^G \leq z_{g,t} P_g^{\max}, \forall g \in \mathcal{G}, t \in \mathcal{T}, \tag{7b}$$

$$(\nu_{g,t}^{g-}) : P_{g,t}^G \geq z_{g,t} P_g^{\min}, \forall g \in \mathcal{G}, t \in \mathcal{T}, \tag{7c}$$

$$(\nu_{g,t}^{fr0}, \nu_{g,t}^{fr+}) : 0 \leq R_{g,t}^G \leq z_{g,t} R_g^{G,\max}, \forall g \in \mathcal{G}, t \in \mathcal{T}, \tag{7d}$$

where (7b) and (7c) enforce that the generator output is within its upper bound $P_g^{\max}$ and lower bound $P_g^{\min}$. (7d) regulates the PFR capacity with an upper limit $R_g^{G,\max}$.

2.3.4 Wind Farm Operational Constraints

$$(\nu_{w,t}^{wc}) : P_{w,t}^{\text{wc}} \leq \gamma_w^{\max} P_{w,t}^W, \forall w \in \mathcal{W}, t \in \mathcal{T}, \tag{8a}$$

$$(\nu^{wr0}_{w,t}, \nu^{wr+}_{w,t}) : 0 \leq R^W_{w,t} \leq P^{\text{wc}}_{w,t}, \forall w \in \mathcal{W}, t \in \mathcal{T}, \quad (8b)$$

$$(\nu^{wh0}_{w,t}, \nu^{wh+}_{w,t}) : 0 \leq H^W_{w,t} \leq H^{\max}_{w,t}, \forall w \in \mathcal{W}, t \in \mathcal{T}. \quad (8c)$$

Power curtailment of wind farm w is constrained in (8a) by a curtailment cap $\gamma^{\max}_w P^W_{w,t}$, which is set as 5% of the wind generation. In (8b), the FFR reserve is restricted by the amount of curtailed wind power. Constraint (8c) ensures that the VI capacity is no more than its maximum capacity.

2.3.5 Transmission Line Capacity Constraints

We use a shift-based DC power flow model with the shift factor matrix $\Phi \in \mathbb{R}^{|\mathcal{E}|\times|\mathcal{B}|}$. The power flow across line l_{ij} is expressed by:

$$P^F_{ij,t} = \Phi_{(ij,:)} \left(A^G \boldsymbol{P}^G_t + A^W (\boldsymbol{P}^W_t - \boldsymbol{P}^{\text{wc}}_t) - \boldsymbol{P}^D_t \right), \quad \forall l_{ij} \in \mathcal{E}, t \in \mathcal{T}, \quad (9)$$

where $A^G \in \mathbb{R}^{|\mathcal{B}|\times|\mathcal{G}|}$ and $A^W \in \mathbb{R}^{|\mathcal{B}|\times|\mathcal{W}|}$ are "bus-thermal generator" and "bus-wind farm" incidence matrices. $\boldsymbol{P}^G_t$, $\boldsymbol{P}^W_t$, $\boldsymbol{P}^{\text{wc}}_t$, and $\boldsymbol{P}^D_t$ are vectors of generator outputs, wind power outputs, wind curtailed power and power demand at period t. Transmission line power flows are limited within the capacity bounds $[-L^{\max}_{ij}, L^{\max}_{ij}]$ as follows:

$$(\overline{\rho}_{ij,t}) : P^F_{ij,t} \leq L^{\max}_{ij}, \forall l_{ij} \in \mathcal{E}, t \in \mathcal{T}, \quad (10a)$$

$$(\underline{\rho}_{ij,t}) : P^F_{ij,t} \geq -L^{\max}_{ij}, \forall l_{ij} \in \mathcal{E}, t \in \mathcal{T}, \quad (10b)$$

2.3.6 Frequency Security Constraints under a Power Loss

The frequency security constraints include constraints of nadir (11a), constraint of RoCoF (11b), and constraint of QSS deviation (11c):

$$(\rho^{fn}_t) : \Delta f_{\lim} \leq \beta^H_{t,s} H^{\text{sys}}_t + \beta^G_{t,s} R^G_t + \beta^W_{t,s} R^W_t + \beta^c_{t,s}, \forall s \in \mathcal{S}, t \in \mathcal{T}, \quad (11a)$$

$$(\rho^{fr}_t) : \frac{\Delta P^d_t}{2\dot{f}_{\lim}} \leq H^{\text{sys}}_t, \forall t \in \mathcal{T}, \quad (11b)$$

$$(\rho^{fe}_t) : \Delta f^{\text{qss}}_{\lim} \leq -\frac{\Delta P_{d,t} - R^G_t - R^W_t}{D P^L_t}, \forall t \in \mathcal{T}, \quad (11c)$$

where $\Delta f_{\lim}$, $\dot{f}_{\lim}$ and $\Delta f^{\text{qss}}_{\lim}$ are the security threshold values of frequency deviation, RoCoF and QSS deviation, respectively. Due to the nonlinearity of the frequency nadir expression, we adopt the piecewise linearization method to transform the nonlinear nadir constraint into a series of linear constraints. On each subspace s of the nonlinear hyperspace $\mathcal{S}$, $\beta^H_{t,s}$, $\beta^G_{t,s}$, $\beta^W_{t,s}$, $\beta^c_{t,s}$ represent the linear coefficients of decision variables and the constant term, respectively.

3 Pricing Schemes for Energy and Frequency Regulation

3.1 Marginal Pricing

Most ISOs implement a two-step pricing procedure to derive the LMP, by first deciding the market clearing quantities and then constructing a restricted pricing model. Marginal prices are derived from the dual multipliers of the system-wide constraints to reflect the marginal cost of fulfilling the systems' demands. However, the binary commitment variables of thermal generators make the operational region non-convex. In the marginal pricing scheme, the commitment variables $z_{g,t}$ are fixed at their optimal values $z^*_{g,t}$ to form an economic dispatch (ED) model according to the optimal solution of the UC problem. We can formulate the Lagrangian function $\mathcal{L}$ based on the convex ED model. The marginal prices of energy, inertia, PFR reserve and FFR reserve are derived from the optimal dual multipliers as follows:

$$\pi^e_{i,t} := \rho^{e*}_t - \sum_{l_{ij}\in\mathcal{E}} \Phi_{(ij,:)} (\overline{\rho}^*_{ij,t} - \underline{\rho}^*_{ij,t}), \forall i \in \mathcal{B}, t \in \mathcal{T}, \quad (12)$$

$$\pi^{in}_t =: \beta^{H*}_t \rho^{fn*}_t + \rho^{fr*}_t, \forall t \in \mathcal{T}, \quad (13)$$

$$\pi^{pfr}_t =: \beta^{G*}_t \rho^{fn*}_t + \rho^{fe*}_t, \forall t \in \mathcal{T}, \quad (14)$$

$$\pi^{ffr}_t =: \beta^{W*}_t \rho^{fn*}_t + \rho^{fe*}_t, \forall t \in \mathcal{T}, \quad (15)$$

where the variables in the format of $\rho^{(\cdot)*}_t$ are the optimal solution of dual multipliers. β^{H*}_t, β^{G*}_t, β^{W*}_t are the linear coefficients of the binding frequency nadir constraint in the ED model. Given the prices $\pi^e_{i,t}$, π^{in}_t, π^{pfr}_t, and π^{ffr}_t, the profits of generators and wind farms are calculated as follows:

$$\Pi_{g,t} = \left(\pi^{eg}_{g,t} - c_g\right) P^G_{g,t} + \left(\pi^{pfr}_t - c^{\text{FR}}_g\right) R^G_{g,t} + \pi^{in}_t H^G_{g,t} - c^{\text{nl}}_g z_{g,t}, \forall g \in \mathcal{G}, t \in \mathcal{T}, \quad (16)$$

$$\Pi_{w,t} = \left(\pi^{vi}_t - c^{\text{vi}}_w\right) H^W_{w,t} + \pi^{ffr}_t R^W_{w,t}, \forall w \in \mathcal{W}, t \in \mathcal{T}, \quad (17)$$

where the price of unit g is $\pi^{eg}_{g,t} = [\pi^e_{1,t}, \ldots, \pi^e_{|\mathcal{B}|,t}] A^G_{(:,g)}$.

3.2 Pricing under Nonconvexities

However, the marginal prices obtained through restricted pricing sometimes fail to satisfy the individual rationality of market participants. This pricing mechanism requires ISOs to cover the lost opportunity cost, which accounts for the gap between the maximum profit achievable through participants' self-scheduling and the profit obtained by complying with the ISO's dispatch. Product revenue shortfall [12] is another side-payment resulting from the non-zero Lagrange multipliers associated with nonbinding system-wide constraints, such as transmission capacities and ancillary services in the UC model. Therefore, we propose a convex hull pricing scheme that aims to minimize the uplift payments caused by the nonconvexity of binary commitment variables.

Let $\mathcal{R} = \mathcal{G} \cup \mathcal{W}$ denote the set of all types of energy resources with index r. We consider a compact formulation of the proposed UC problem with the convex hull of the operation region:

$$\min \sum_{t\in\mathcal{T}} \sum_{r\in\mathcal{R}} f_{r,t}(\boldsymbol{x}_{r,t}, z_{r,t}) \quad (18a)$$

$$\text{s.t. } (\boldsymbol{\rho}_t) : \sum_{r\in\mathcal{R}} (\mathbf{A}_{r,t}\boldsymbol{x}_{r,t} + \mathbf{B}_{r,t} z_{r,t}) \geq \mathbf{c}_t, \forall t \in \mathcal{T}, \quad (18b)$$

$$(\boldsymbol{f}_r, \boldsymbol{x}_r, \boldsymbol{z}_r) \in conv(\mathcal{X}_r), \forall r \in \mathcal{R}, \quad (18c)$$

where $f_{r,t}, \boldsymbol{x}_{r,t}, z_{r,t}$ represent the operation cost, decision variables vector and commitment variable ($z_{r,t} = 0$ for

wind farms) of resource r at period t. (18b) represents the system-wide constraints with coefficient matrix $\mathbf{A}_{r,t}$ and vector $\mathbf{B}_{r,t}$ for resource r, along with the constant vector $\mathbf{c}_t$ at period t. The vector $\boldsymbol{\rho}_t$ corresponds to the dual multipliers of system-wide constraints. In constraints (18c), $\boldsymbol{f}_r = [f_{r,1}, \ldots, f_{r,T}]^{\mathrm{T}}, \boldsymbol{x}_r = [\boldsymbol{x}_{r,1}, \ldots, \boldsymbol{x}_{r,T}], \boldsymbol{z}_r = [z_{r,1}, \ldots, z_{r,T}]^{\mathrm{T}}$ represent the operation cost vector, decision variables matrix and commitment variable vector across the dispatch horizon. The original operation region $\mathcal{X}_r$ consisting of local constraints of resource r is nonconvex due to the commitment states $\boldsymbol{z}_r$. Therefore, we use its convex hull $conv(\mathcal{X}_r)$ instead in the operation region (18c) of CHP scheme.

The Lagrange dual problem of the commitment model is represented as:

$$\max_{\boldsymbol{\rho}_t \geq 0} \left(\begin{array}{l} \min\limits_{\boldsymbol{f}_r, \boldsymbol{x}_r, \boldsymbol{z}_r} \sum\limits_{t\in\mathcal{T}} \sum\limits_{r\in\mathcal{R}} f_{r,t} \\ - \sum\limits_{t\in\mathcal{T}} \boldsymbol{\rho}_t^{\mathrm{T}} \left[\sum\limits_{r\in\mathcal{R}} (\mathbf{A}_{r,t}\boldsymbol{x}_{r,t} + \mathbf{B}_{r,t} z_{r,t}) - \mathbf{c}_t \right] \\ \text{s.t. } (\boldsymbol{f}_r, \boldsymbol{x}_r, \boldsymbol{z}_r) \in conv(\mathcal{X}_r), \forall r \in \mathcal{R} \end{array} \right). \tag{19}$$

Next, we introduce constant terms $(f^*_{r,t}, \boldsymbol{x}^*_{r,t}, z^*_{r,t})$ obtained from the optimal solution of UC problem and rearrange the Lagrange dual problem, resulting in the pricing model:

$$\min_{\boldsymbol{\rho}_t \geq \mathbf{0}} \sum_{r\in\mathcal{R}} U_r + \sum_{t\in\mathcal{T}} \boldsymbol{\rho}_t^{\mathrm{T}} \left[\sum_{r\in\mathcal{R}} (\mathbf{A}_{r,t}\boldsymbol{x}^*_{r,t} + \mathbf{B}_{r,t} z^*_{r,t}) - \mathbf{c}_t \right] \tag{20a}$$

$$\pi^x_{r,t} = \boldsymbol{\rho}_t^{\mathrm{T}} \mathbf{A}_{r,t}, \forall r \in \mathcal{R}, t \in \mathcal{T}, \tag{20b}$$

$$\pi^z_{r,t} = \boldsymbol{\rho}_t^{\mathrm{T}} \mathbf{B}_{r,t}, \forall r \in \mathcal{R}, t \in \mathcal{T}, \tag{20c}$$

$$\text{s.t. } U_r \geq \left(\begin{array}{l} \max\limits_{\boldsymbol{f}_r, \boldsymbol{x}_r} \sum\limits_{t\in\mathcal{T}} (\pi^x_{r,t}\boldsymbol{x}_{r,t} + \pi^z_{r,t} z_{r,n,t} - f_{r,t}) \\ \text{s.t. } (\boldsymbol{f}_r, \boldsymbol{x}_r) \in \mathcal{X}_{r,n}, \forall n \in \mathcal{N}_r \end{array} \right) - \sum_{t\in\mathcal{T}} (\pi^x_{r,t}\boldsymbol{x}^*_{r,t} + \pi^z_{r,t} z^*_{r,t} - f^*_{r,t}), \forall r \in \mathcal{R}, t \in \mathcal{T}. \tag{20d}$$

The objective function of (20) elucidates the purpose of the CHP model, which is to minimize the LOC U_r for each energy resource and the PRS simultaneously. Constraints (20b), (20c) define the price expressions $\pi^x_{r,t}$ and $\pi^z_{r,t}$ for decision variables and commitment variables using dual multipliers of system-wide constraints. Note that the nonconvex operation region $\mathcal{X}_r$ can be represented as the union of disjunctive convex subregions $\mathcal{N}_r$ by enumerating the set of commitment variables $z_{r,t} = \{z_{r,1,t}, \ldots, z_{r,|\mathcal{N}_r|,t}\}$: $(\boldsymbol{f}_r, \boldsymbol{x}_r) \in \cup_{n\in\mathcal{N}_r} \mathcal{X}_{r,n}$. According to *Lemma 3* in [14], the optimization problem with $\cup_{n\in\mathcal{N}_r} \mathcal{X}_{r,n}$ is equivalent to the problem with $conv(\mathcal{X}_r)$. Therefore, the maximization problem in LOC constraint (20d) defines the maximum profit that the resource can gain with the given prices.

Inspired by [14], the optimal solution of the profit-maximization problem can be obtained at one of the extreme points of $\mathcal{X}_{r,n}$. Specifically, the possible combinations of maximum profits for thermal units and wind farms can be formulated as follows:

$$\Pi^{\max}_{g,t} = \left\{ \begin{array}{l} 0, \\ \left(\pi^{eg}_{g,t} - c_g\right) P^{\min}_g + \pi^{in}_t H^G_{g,t} - c^{\mathrm{nl}}_g z_{g,t}, \\ \left(\pi^{eg}_{g,t} - c_g\right) P^{\min}_g + \pi^{in}_t H^G_{g,t} \\ + (\pi^{pfr}_t - c^{\mathrm{FR}}_g) R^{G,\max}_g - c^{\mathrm{nl}}_g z_{g,t}, \\ \left(\pi^{eg}_{g,t} - c_g\right) P^{\max}_g + \pi^{in}_t H^G_{g,t} - c^{\mathrm{nl}}_g z_{g,t}, \\ (\pi^{eg}_{g,t} - c_g)(P^{\max}_g - R^{G,\max}_g) + \pi^{in}_t H^G_{g,t} \\ + (\pi^{pfr}_t - c^{\mathrm{FR}}_g) R^{G,\max}_g - c^{\mathrm{nl}}_g z_{g,t}, \end{array} \right. \tag{21}$$
$$\forall g \in \mathcal{G}, t \in \mathcal{T},$$

$$\Pi^{\max}_{w,t} = \left\{ \begin{array}{l} 0, \\ \left(\pi^{in}_t - c^{\mathrm{vi}}_w\right) H^{\max}_{w,t}, \\ \pi^{ffr}_t \gamma^{\max}_w P^W_{w,t}, \\ \left(\pi^{in}_t - c^{\mathrm{vi}}_w\right) H^{\max}_{w,t} + \pi^{ffr}_t \gamma^{\max}_w P^W_{w,t}, \end{array} \right. \tag{22}$$
$$\forall w \in \mathcal{W}, t \in \mathcal{T}.$$

Substituting (21) and (22) into the maximization problem in the LOC constraint (20d), decomposing the nonlinear LOC constraint into combinations of linear constraints at extreme points. Consequently, the resulting convex pricing model can be solved by commercial solvers.

4 Case study

The proposed pricing scheme is validated on a modified IEEE 5-bus power system with 4 thermal generators (G1-G4) and 3 wind farms (WF1-WF3). The power network topology is shown in Fig.1. Detailed parameters of transmission lines, generators, and forecast data are provided in [15]. The auxiliary parameters of the UC problem are listed in Table 1.

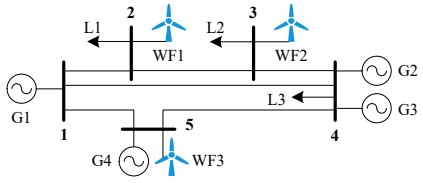

Fig. 1: System topology of the 5-bus power system.

Table 1: Auxiliary system parameters

$\dot{f}_{\max}$	$\Delta f_{\max}$	Δf_{qss}	f_{DB}	D	T_g	T_w	T
0.2 Hz/s	0.5 Hz	0.2 Hz	0.033 Hz	1 %/Hz	10 s	1 s	24

4.1 Effects of wind farms' frequency responses

To assess the impact of procuring frequency responses from wind farms, we examine the pricing results for the following two scenarios: (S1) - frequency responses are procured only from traditional generators; (S2) - wind farms provide both virtual inertia and fast frequency responses. The optimal commitment decisions in S1 and S2 are illustrated in Fig. 2. There are fewer generators online in S2 compared to S1, where the frequency responses from wind farms are procured.

The revenue, cost and profit of these two scenarios are summarized in Table 2. Compared to Scenario 1, the operation costs of thermal units and the whole system in Scenario 2

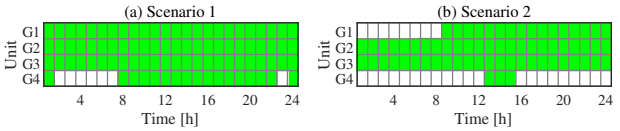

Fig. 2: Commitment decisions in Scenario 1,2 (green-online, white-offline).

decrease by \$5622.5 and \$4352.6, respectively, as the procurement of flexible wind power ancillary services reduces the costs. In terms of profit, the total profit of all market participants increases (from \$18007.41 to \$22060.60), even though the thermal units get less profit. In Scenario 2, wind farms receive more payments for the provision of frequency ancillary services.

Table 2: Revenue, cost, and profit in different pricing scenarios (\$)

	Scenario 1		Scenario 2	
	Gen.	WF	Gen.	WF
Revenue	201066.95	0	192425.81	8341.70
Cost	183059.55	0	177437.01	1269.90
Profit	18007.41	0	14988.80	7071.80

4.2 Pricing results under different wind penetration rates

Next, we investigate the pricing result of the single-period problem with wind power penetration rate changing from 30% to 70%. The inertia price in Fig.3(a) increases from 30% to 40% due to the shutdown of thermal generators. Then, the price decreases again as more virtual inertia becomes available in scenarios with high RES penetration. Similarly, Fig.3(b) indicates that frequency response (FR) reserve prices gradually decline as more wind power accounts for the load demand.

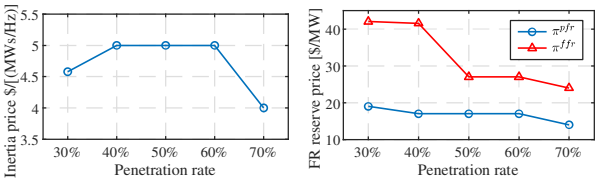

(a) Inertia price (b) FR reserve prices

Fig. 3: Frequency ancillary service prices under different wind power penetration rates

The revenue, cost and profit of frequency ancillary services (FAS) with different wind power profiles are summarized in Table 3. The result of the energy market is not considered in this part as traditional generator accounts for less power in high-RES scenarios. It can be seen that the total FAS cost gradually declines as wind farms provide FAS with lower operation costs. As for the profit, both wind farms and the whole system can receive relatively high payments around the penetration rate of 40%. FAS profit becomes lower due to the low level of inertia and frequency reserve prices as the penetration rate rises.

Table 3: Revenue, cost and profit of frequency ancillary services under different wind power penetration rates (\$)

Penetration rate		30%	40%	50%	60%	70%
Gen.	FAS revenue	521.81	389.58	332.36	332.44	269.82
	FAS cost	401.72	302.58	284.36	255.42	255.42
	FAS profit	120.09	87.00	48.00	77.02	14.40
WF	FAS revenue	287.56	414.35	339.36	339.23	294.25
	FAS cost	27.50	66.89	63.12	59.34	57.28
	FAS profit	260.06	347.46	276.24	279.89	236.97
Total FAS cost		429.22	369.47	347.48	314.76	312.70
Total FAS profit		380.15	434.46	324.24	356.91	251.37

4.3 Effects of convex hull pricing

To investigate the effects of CHP in a nonconvex market, results of restricted pricing and the CHP model (20) are compared in Table 4. Parameters and scheduling of generators for a single-period dispatch are summarized in Table 5. According to the scheduling result, G1 is committed online at a minimum generation of 18 MW, making G3 the marginal unit. There is an uplift payment including the LOC of \$22.22 and PRS of \$0.06 in restricted pricing. Taking the prices derived from the CHP model, the LOC for following the dispatch plan (\$2.63) is lower than that in the restricted pricing method.

Table 4: Comparison of pricing methods under nonconvexity (\$)

	π_g^{eg}	π^{in}	π^{pfr}	π^{ffr}	LOC	PRS
Restricted	27	4.36	17	36.81	22.22	0.06
CHP	27.44	5	17.44	37.77	2.63	0.06

Table 5: Parameters and scheduling of generators

	c_g (\$)	c_g^{FR} (\$)	c_g^{nl} (\$)	$P_g^{\min}/P_g^{\max}$ (MW)	P_g^G (MW)	R_g^G (MW)
G1	29	19	80	18/180	18	0
G2	24	14	60	13/130	117	13
G3	27	17	60	15/150	146.06	0.94
G4	31	20	80	20/200	0	0

5 Conclusion

This paper proposes a pricing scheme for energy and frequency ancillary services considering the nonconvexity of the unit commitment model. The price expressions of energy, inertia and frequency responses for thermal generators and wind farms are derived based on a frequency-constrained UC model. The numerical results show that the inclusion of renewable sources avoids additional commitment of traditional units and saves operation costs. Additionally, the proposed convex hull pricing model minimizes the uplift payment compared to the restricted pricing model. In the future, we aim to establish the pricing scheme under nonconvexities and uncertainties.

References

[1] Z. Chu, U. Markovic, G. Hug, and F. Teng, "Towards optimal system scheduling with synthetic inertia provision from wind

turbines," *IEEE Trans. Power Syst.*, vol. 35, no. 5, pp. 4056–4066, Sep. 2020.

[2] U. Markovic, O. Stanojev, P. Aristidou, E. Vrettos, D. Callaway, and G. Hug, "Understanding small-signal stability of low-inertia systems," *IEEE Trans. Power Syst.*, vol. 36, no. 5, pp. 3997–4017, Sep. 2021.

[3] L. Badesa, F. Teng, and G. Strbac, "Pricing inertia and frequency response with diverse dynamics in a mixed-integer second-order cone programming formulation," *Appl. Energy*, vol. 260, pp. 114 334–114 334, Feb. 2020.

[4] B. K. Poolla, S. Bolognani, N. Li, and F. Dorfler, "A market mechanism for virtual inertia," *IEEE Trans. Smart Grid*, vol. 11, no. 4, pp. 3570–3579, Jul. 2020.

[5] Z. Liang, R. Mieth, and Y. Dvorkin, "Inertia pricing in stochastic electricity markets," *IEEE Trans. Power Syst.*, vol. 38, no. 3, pp. 2071–2084, May 2023.

[6] L. Badesa, C. Matamala, Y. Zhou, and G. Strbac, "Assigning shadow prices to synthetic inertia and frequency response reserves from renewable energy sources," *IEEE Trans. Sustain. Energy*, vol. 14, no. 1, pp. 12–26, Jan. 2023.

[7] K. Li, H. Guo, X. Fang, S. Liu, F. Teng, and Q. Chen, "Market mechanism design of inertia and primary frequency response with consideration of energy market," *IEEE Trans. Power Syst.*, vol. 38, no. 6, pp. 5701–5713, Nov. 2023.

[8] J. M. Morales, A. J. Conejo, K. Liu, and J. Zhong, "Pricing electricity in pools with wind producers," *IEEE Trans. Power Syst.*, vol. 27, no. 3, pp. 1366–1376, Aug. 2012.

[9] J. Kazempour, P. Pinson, and B. F. Hobbs, "A stochastic market design with revenue adequacy and cost recovery by scenario: Benefits and costs," *IEEE Trans. Power Syst.*, vol. 33, no. 4, pp. 3531–3545, Jul. 2018.

[10] X. Fang, B. M. Hodge, E. Du, C. Kang, and F. Li, "Introducing uncertainty components in locational marginal prices for pricing wind power and load uncertainties," *IEEE Trans. Power Syst.*, vol. 34, no. 3, pp. 2013–2024, May 2019.

[11] W. Zhong, K. Xie, Y. Liu, S. Xie, and L. Xie, "Chance constrained scheduling and pricing for multi-service battery energy storage," *IEEE Trans. Smart Grid*, vol. 12, no. 6, pp. 5030–5042, Nov. 2021.

[12] D. A. Schiro, T. Zheng, F. Zhao, and E. Litvinov, "Convex hull pricing in electricity markets: Formulation, analysis, and implementation challenges," *IEEE Trans. Power Syst.*, vol. 31, no. 5, pp. 4068–4075, Sep. 2016.

[13] B. Hua and R. Baldick, "A convex primal formulation for convex hull pricing," *IEEE Trans. Power Syst.*, vol. 32, no. 5, pp. 3814–3823, Sep. 2017.

[14] Z. Yang, T. Zheng, J. Yu, and K. Xie, "A unified approach to pricing under nonconvexity," *IEEE Trans. Power Syst.*, vol. 34, no. 5, pp. 3417–3427, Sep. 2019.

[15] Z. Li, "Test system data," Feb. 2024. [Online]. Available: https://github.com/esterleds/Frequency-Ancillary-Services

Proceedings of the 3rd Conference on Fully Actuated System Theory and Applications
May 10-12, 2024, Shenzhen, China

Neural-Network-Based Nonlinear Model Predictive Control of Suspension Gravity Offload System

Huixing Yan, Hongqian Lu, Hanyu Wang, Zhen Zhang, Xianlin Huang
Control Theory and Guidance Center, Harbin Institute of Technology, Harbin 150001, P. R. China
E-mail: huixing.yan@stu.hit.edu.cn

Abstract: To address the underactuation issue induced by passive dampers in a suspension Gravity offload(SGO) system, this paper introduces the utilization of active control using Pneumatic Artificial Muscles(PAM) to transform it into a fully actuated physical system. However, due to the inherent non-linear characteristics such as flexibility and hysteresis in PAM, achieving precise force control poses challenges. Therefore, this paper proposes a Neural Network-based Nonlinear Model Predictive Control (NMPC) approach. We apply the proposed approach to the constant force control of the SGO system based on PAM. Simulation results demonstrate a marked improvement in control accuracy when compared to the feedforward PID control method.

Key Words: Pneumatic Artificial Muscles, Nonlinear Model Predictive Control, suspension Gravity offload

1 Introduction

For space missions involving extraterrestrial sample collection, survey exploration, astronaut landings, and similar tasks, the complex surface and gravity environments necessitate the use of ground-based micro/low-gravity experimental systems [1, 2]. These systems serve as crucial means for overall mission design and performance testing, with a primary focus on addressing the key challenge of gravity offload [3, 4]. In current ground-based micro/low-gravity experimental systems, the commonly employed setup is the beam-cable structure Suspended Gravity Offload(SGO) platform [5], as depicted in Figure 1. It comprises a two-dimensional gimbal subsystem and a Suspended Constant Force(SCF) subsystem. Due to the susceptibility of cable tension to abrupt fluctuations and the inherent flexibility resulting from relatively low spacecraft stiffness, existing suspended constant-force systems commonly incorporate elastic dampers (such as springs) to mitigate force spikes and minimize force errors. However, the introduction of flexible dampers reduces the system's bandwidth, leading to a diminished disturbance suppression capability of torque motors. Additionally, the incorporation of passive dampers renders the cable-driven suspended system underactuated [6]. This significantly amplifies the difficulty in controlling suspended constant-force systems, posing challenges in simulating precise micro/low-gravity environments.

Currently, extensive research has yielded diverse outcomes regarding the constant tension technique, particularly in its application across different scenarios, involving the combination of rigid driving and elastic buffering. Literature [7] addresses the issue of restricted stiffness in passive elastic components by introducing an active driving source. It employs an electric push rod combined with a buffering spring to form an active elastic component. Literature [8] employs a bypass tensioning constant force mechanism capable of maintaining a nearly constant output force within a specific output stroke range. However, these approaches do not fundamentally resolve the issue of under-driving introduced by passive springs.

This work is supported by National Natural Science Foundation (NNSF) of China under Grant 62203300.

In recent years, Pneumatic Artificial Muscles(PAM) have been extensively applied in aerospace, industrial manufacturing, medical rehabilitation, and various other fields due to their advantages of structural simplicity, lightweight materials, flexibility, and robust safety features [9]. Due to the flexible nature of PAM, which can serve as dampers, and their lightweight property that significantly mitigates issues associated with system parasitic mass, there is potential for them to replace passive springs in suspended constant-force systems. However, the inherent characteristics of pneumatic artificial muscles, such as hysteresis, high nonlinearity, and creep, pose challenges in achieving precise control over them [10].

Some scholars have proposed corresponding control methods to address the uncertainty issues in the PAM model. Jonathon [11] proposed a combined approach of sliding mode control with proportional and integral compensation to endow the control system with sufficient robustness. Mahdi Chavoshian [12] introduced a novel hybrid control approach for PAM position control integrating Dynamic Neural Networks (DNN) and Proportional-Integral-Derivative (PID) methods. These methods offer significant reference value for subsequent research on PAM control, yet there are still some shortcomings.

Model Predictive Control (MPC) empowers the anticipation of future system behaviors within the control framework [13]. The predictive capability and the ability to accommodate rigid constraints render this method highly advantageous in the control of real systems. With the advancement of computer technology and the increasing accessibility of intricate process models across diverse systems, control methods based on MPC are increasingly applied in practical engineering [14, 15]. However, The precision of MPC control highly depends on the accuracy of the prediction model. Therefore, this paper proposes utilizing online neural network models to predict the complex dynamics of PAM, followed by MPC optimization solving to enhance the precision of constant force control.

The main contributions of this paper can be summarized as follows:

1) A control strategy based on PAM-driven buffering is proposed, offering potential solutions to the underactu-

ation issue in suspended gravity offload systems.

2) A complete Neural Network NMPC framework is introduced for a SGO system. The stability of the closed-loop system is guaranteed.

In this paper, Section 2 presents the dynamic model of the SGO Platform and emphasize the issues addressed in this paper. Section 3 illustrates the design process of the proposed control method using the SCF system and its theoretical analysis. Section 4 presents the results of simulation experiments. The conclusions of this paper is in Section 5.

2 System Modelling

2.1 Suspension Gravity offload Platform

The SGO system with commonly used beam structures is an efficient gravity unloading technique, as depicted in Figure 1. The SGO consists of a two-dimensional tracking subsystem and a SCF subsystem.

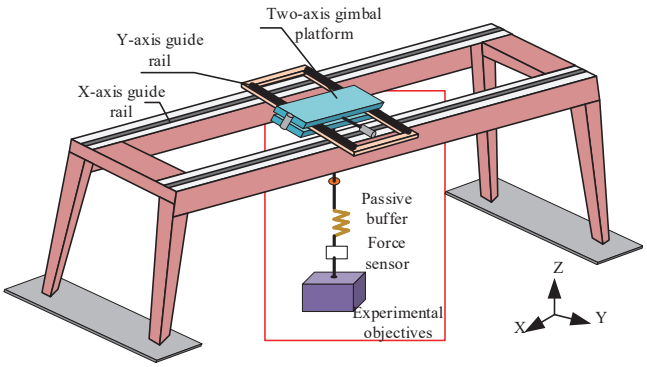

Fig. 1: Structure of SGO system

The two-dimensional tracking subsystem is required to achieve horizontal movement, while the SCF subsystem applies a counter force to the experimental target through suspension, necessitating the maintenance of the stability of this counter force. To suppress force impact and reduce errors in cable tension, passive dampers were introduced. However, this has simultaneously resulted in the issue of underactuated, reducing the system's bandwidth and posing challenges to achieving precise force control.

This note focuses on investigating the SCF subsystem within the SGO system. Figure 2 illustrates the schematic diagram of the SCF subsystem based on PAM proposed by us. Defining the upward retraction of the rope as the positive direction and the downward extension as the negative direction, the initial position of the entire system is considered as zero along the x-axis.

As depicted in Figure 2, The SCF subsystem comprises two actuators: a torque motor and a PAM. The torque motor, facilitated by a reducer, regulates the spatial position within the load space, while the PAM replaces traditional passive dampers and directly maintains constant force control with the load. Additionally, the SCF system incorporates laser displacement sensors and force sensors.

2.2 Mathematical Model

A.Dynamics Analysis of PAM

Several researchers have extensively investigated PAM modeling and analysis. Particularly, the literature [16] introduced a widely adopted three-element model consisting

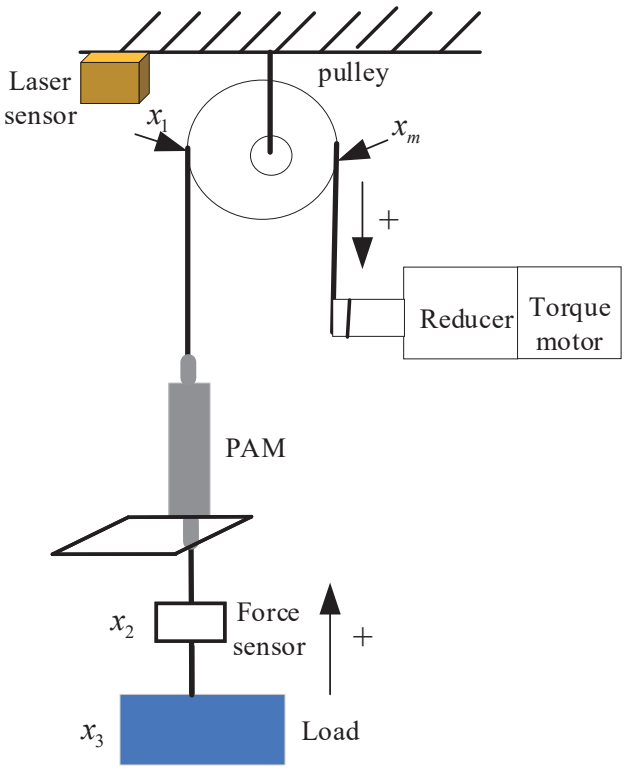

Fig. 2: Structure of SCF

of the contraction force element, spring element, and damping element arranged in parallel. Therefore, our analysis of the dynamics of the SCF system is also based on the three-element model of PAM.

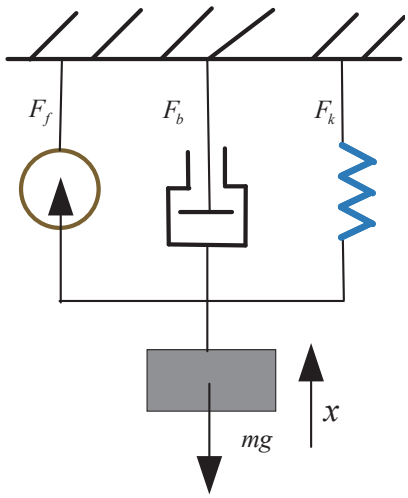

Fig. 3: The three-element model of PAM

The illustration of the PAM's three-element model is depicted in Figure 3, showcasing the PAM oriented vertically, its upper end immobilized, and its lower end affixed to a functional payload. It is posited that the PAM consists of a contraction element, a damping element, and a spring element, configured in parallel. The dynamic representation of the PAM is characterized as

$$F_p = \sum_{k=0}^{n_1} f_k p + \sum_{k=0}^{n_2} b_k p\dot{x} + \sum_{i=1}^{N}\sum_{k=0}^{n_3} k_{ik} p x^i, \quad (1)$$

where $p(t)$ represents the internal pressure, x denotes expansion displacement of PAM, $\sum_{k=0}^{n_1} f_k p$, $\sum_{k=0}^{n_2} b_k p$, and $\sum_{k=0}^{n_3} k_{ik} p$ are the contractile force, the damping coefficient and the spring constant, n_1, n_2, and n_3 are the order of the approximated polynomials, f_k, b_k, and $k_i k$ are the polynomial coefficients.

In general, larger values of n_1, n_2, and n_3 tend to yield more precise models, yet concurrently increase the complexity of the model. In practical applications, simpler models are often chosen for ease of control and management. For example, the model with $n1 = 1$, $n2 = 1$, and $n3 = 3$ is represented by Eq (2).

$$F_p = f(p) + b(p)\dot{x} + \sum_{i=1}^{N} k_i(p) x^i + \tau(x, \dot{x}), \quad (2)$$

where $f(p) = f_0 + f_1 p$, $b(p) = b_0 + b_1 p$, and $k(p) = k_{i0} + k_{i1} p$ represent the contraction force, damping coefficient, and elasticity coefficient, respectively, f_0, f_1, b_0, b_1, k_{i0} and k_{i1} are all unknown constants, and τ denotes the unmodeled characteristics introduced by the simplified model.

B.Dynamics Analysis of SCF

The angular velocity of the pulley can be determined as

$$\dot{\alpha} = \frac{1}{2r}(\ddot{x}_m + \ddot{x}_1), \quad (3)$$

where α denotes the angular velocity of the pulley, r represents the radius of the pulley, x_m signifies the displacement at the motor output, and x_1 signifies the spatial displacement of the rope at the output end of the pulley.

In the scenario where there is no slippage in the rope, thus $x_1 = x_m$, the dynamic equation governing the rotation of the pulley can be derived as follows.

$$T_m - F_p r = \frac{J_w}{r}\ddot{x}_1, \quad (4)$$

where T_m represents the torque output at the reducer, F_p denotes the tensile force of the PAM (Pneumatic Artificial Muscle), and J_w stands for the rotational inertia of the pulley.

The motion equations for simulating the movement of a micro-low-gravity unloading load are as follows.

$$F_p + F_d - m_L g = m_L \ddot{x}_3 + \Delta, \quad (5)$$

where F_d represents the ground reaction force, m_L signifies the mass of the load, x_3 denotes the displacement of the load, and Δ represents an unknown disturbance.

Based on Eq. (4) and Eq. (5), the simplified dynamic model of SCF can be derived as:

$$\begin{aligned} T_m - F_p r &= \frac{J_w}{r}\ddot{x}_1 \\ F_p + F_d - m_L g &= m_L \ddot{x}_3 + \Delta. \end{aligned} \quad (6)$$

The actuating components of the SCF system consist of a torque motor and a PAM. The input control variables are the torque signal u_m and the air pressure signal u_p, while the output variable is the force F_p of the PAM, forming a Multiple-Input Single-Output(MISO) system.

Remark 1 *In the SCF system, achieving the goal of gravity unloading involves two scenarios: contact with the ground and suspended levitation above the ground. Taking the simulation of the moon as an example: 1) When in contact with the ground, $F_p + F_d - m_L g = 0$, where $F_p = 5/6mg$. 2) While suspended above the ground, $F_p - m_L g = m_L \ddot{x}_3$, where $F_p = 5/6mg$. Therefore, the ultimate objective of the constant force control within the SCF system is to attain $F_p = 5/6mg$.*

The output of the Pneumatic Artificial Muscle (PAM) in the SCF system can be obtained from Equations (2) and (6) as:

$$\begin{aligned} F_p = f_0 + f_1 u_p + (b_0 + b_1 u_p)\Delta\dot{x} + (k_{10} + k_{11} u_p)\Delta x \\ + (k_{20} + k_{21} u_p)\Delta x^2 + \tau(\Delta x, \Delta\dot{x}), \end{aligned} \quad (7)$$

where u_p represents the air pressure control signal, $\Delta x = x_1 - x_2$, and x_2 denotes the displacement of the force sensor.

Taking into account the presence of multiple unknown parameters in the PAM model within the SCF system, alongside unmodeled characteristics, this paper proposes utilizing a neural network model to predict the output of the PAM in the SCF system.

3 Neural Network-based Model Predictive Constant Force Control

3.1 Principle Diagram of SCF Control

The control block diagram of the SCF system is illustrated in Figure 4, representing a MISO control system. The actuating components consist of a torque motor and a PAM: the torque motor operates in torque mode to achieve extensive motion control, while the PAM accomplishes precise force-tracking control.

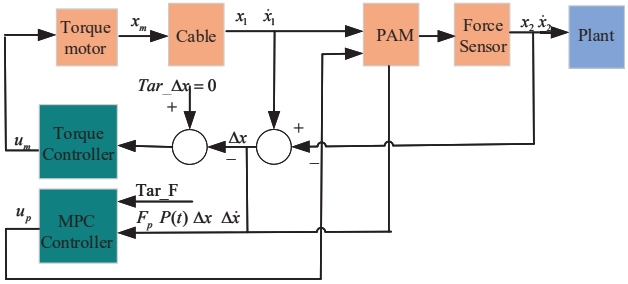

Fig. 4: Principle Diagram of SCF Control

As shown in Figure 4, the SCF control diagram comprises a torque controller and an MPC Controller. The torque controller outputs the control law u_m to govern the torque motor, while the MPC controller outputs the control law u_p to regulate the PAM. The focal point of this study lies in the MPC controller for regulating PAM. It forecasts the subsequent temporal tension force of PAM by utilizing the previous time-domain actual force F_p, actual pressure $P(t)$, displacement Δx, and velocity $\Delta\dot{x}$. Subsequently, it optimizes and solves for the control law u_p.

3.2 Neural Network Prediction Model

According to Eq (7), we consider the predictive form of the PAM model within the SCF system as a nonlinear difference equation.

$$\begin{aligned}\hat{y}_{k+1} = f(&y_k, \cdots, y_{k-n_y}, \Delta x_k, \cdots, \Delta x_{k-n_x}, \\ &\Delta\dot{x}_k, \cdots, \Delta\dot{x}_{k-n_v}, u_k, \cdots, u_{k-n_u}),\end{aligned} \tag{8}$$

where y_k denotes the output of the PAM at time k, Δx_k and $\Delta\dot{x}_k$ represent the position and velocity of the PAM's extension at time k, and u_k signifies the control input of the PAM at time k. n_y, n_x, n_v, and n_u respectively denote the orders of consideration for the output, displacement, velocity, and input delays of the PAM.

In pursuit of a more precise PAM model, we propose employing radial basis function neural networks to describe the nonlinear PAM. A typical three-layer RBF structure is illustrated in Figure 5. The first layer serves as the input layer, the middle layer acts as the hidden layer employing Gaussian basis functions as activation functions, and the third layer represents the output layer. RBF neural networks possess the characteristics of a simple structure and strong generalization ability. Its universal approximation property enables the network's output to fit any nonlinear curve with a fast convergence rate.

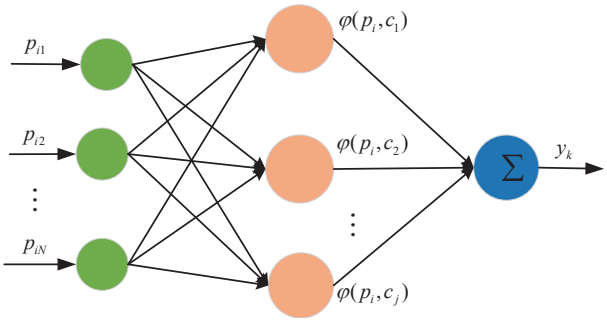

Fig. 5: Single-hidden-layer RBF network

The basis function of a neuron and the complete approximation function is given by

$$\begin{aligned}&\varphi_i(p, c_i) = e^{-\frac{\|p-c_i\|^2}{2\sigma_i^2}} \\ &\theta = [\varphi_1, \varphi_2, \cdots, \varphi_j]^\top \\ &Y = W^\top\theta(p) + B,\end{aligned} \tag{9}$$

where p signifies the input to the RBF NN, and j indicates the neuron count, the function $\varphi_i(p, c_i)$ is identified as the i-th Gaussian kernel function, with c_i marking the nucleus of the i-th kernel, and σ_i specifying the Gaussian kernel's breadth. The term $\|p - c_i\|$ quantifies the Euclidean discrepancy between p and c_i, the kernel's focal point. The neuronal weight is expressed as $W = [\omega_1, \omega_2, \cdots, \omega_j]$, θ is the output of the Gaussian basis function, B is the bias of the neural network, and Y denotes the network output.

In Eq. (8), the nonlinear difference equation for PAM prediction, namely, $\hat{y}_{k+1}$ is approximated by an RBF Neural Network. The input of the RBF Neural Network is defined as

$$\begin{aligned}p = \big[&y_k \cdots, y_{k-n_y}, \Delta x_k, \cdots, \Delta x_{k-n_x} \\ &\Delta\dot{x}_k, \cdots, \Delta\dot{x}_{k-n_v}, u_k, \cdots, u_{k-n_u}\big].\end{aligned} \tag{10}$$

The output of Neural Network Prediction model is

$$\hat{y}_{k+1} = W_k^T\theta_k(p) + b_k. \tag{11}$$

The objective of the RBF training is to minimize

$$\min_{c_i,\sigma_i} J = \sum_{j=1}^{N}(y_j - \hat{y}_j)^2, \tag{12}$$

where y_j represents the actual measured data of the PAM's extension force.

To achieve multi-step prediction, we employed a cascaded structure of neural network prediction models, as depicted in Figure 6.

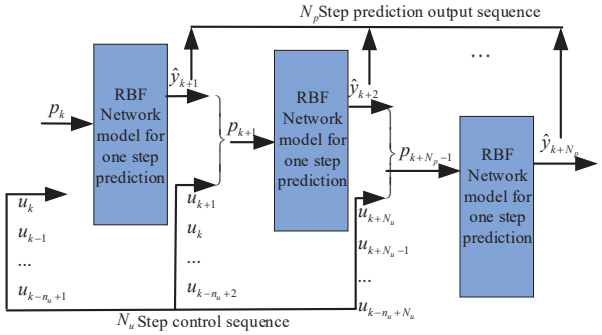

Fig. 6: Cascaded multi-step prediction model

To implement online updating of the RBF neural network prediction model, a buffer for storing input-output data is employed in the control system. Once the buffer stores data for 3000 control cycles, the network is trained to update its parameters. After updating the network parameters, the buffer is cleared to store new data, initiating the training process for the next cycle.

3.3 Neural Network-based Model Predictive Control

The cost function in this paper is formulated as follows

$$\begin{aligned}&\min_{u_k} J = \sum_{j=1}^{N_p} e_{k+j}^2 + \rho \sum_{j=0}^{N_u-1} \Delta u_{k+j}^2 \\ &\textbf{s.t.} \quad e_{k+N_p+j} = 0,\ j = 1, 2, \cdots, N_c \\ &\qquad |\Delta u| \le \Delta u_{max} \\ &\qquad u_{min} \le u_k \le u_{max},\end{aligned} \tag{13}$$

where N_p represents the prediction horizon, N_u signifies the control horizon, and it is essential to ensure that $N_u \le N_p$, ρ stands for the weighting factor, $e_{k+j} = r_k - \hat{y}_{k+j}$ is the tracking error, r_k is the reference signal at time k, $\hat{y}_{k+j}$ is the prediction of future outputs, $\Delta u(k+j) = u(k+j) - u(k+j-1)$, $u(k)$ is the control signal at time k.e_{k+N_p+j} denotes terminal constraints, and N_c stands for constraint horizon.

To improve the disturbance suppression capability of the MPC controller and enhance the precision of constant force control, we have introduced feedback correction. The correction error at time step k, denoted as $e_{c,k}$, is calculated as the difference between the predicted output $\hat{y}_k$ and the measured output y_k, expressed as $e_{c,k} = \hat{y}_k - y_k$.

Subsequently, utilizing $e_{c,k}$, the reference trajectory is adjusted. In the context of N_p step prediction, the reference

output can be corrected to:

$$\begin{cases} r_{c,k+1} = r_{k+1} + \lambda e_{c,k} \\ r_{c,k+2} = r_{k+2} + \lambda e_{c,k} \\ \quad \cdots \\ r_{c,k+N_p} = r_{k+N_p} + \lambda e_{c,k}, \end{cases} \tag{14}$$

where λ denotes correction coefficientsubstitute reference trajectory r_{k+1} with $r_{c,k+1}$ for optimization purposes.

3.4 Stability Analysis

Terminal cost functions and constraint regions constitute a widely employed approach for ensuring the effectiveness of MPC strategies [17]. This study examines the stability of MPC in the presence of terminal constraints. Stability is maintained by ensuring a monotonically nonincreasing cost function $J(\cdot)$ [18].

In Eq. (13), we consider u_k as the optimal control obtained through the optimization process at time k. To illustrate monotonicity, we introduce a suboptimal control u^*_{k+1} at time $k+1$.

$$u^*_{k+1} = [u_{k+1}, \cdots, u_{k+N_u-1}]^\top. \tag{15}$$

The control sequence u^*_{k+1} is generated based on the control derived at time k. Assuming the external disturbance remains constant within the prediction horizon, namely, the prediction $y_{k+i} = y_{k+1+i}$. Consequently, for the suboptimal control $u*_{k+1}$, the cost function can be defined as:

$$minJ^*_{k+1} = \sum_{j=1}^{N_p} e^2_{k+j} + \rho \sum_{j=2}^{N_u} \Delta u^2_{k+j}. \tag{16}$$

The difference between the cost functions $J(k)$ and $J^*(k+1)$ can be defined as:

$$J^*_{k+1} - J_k = e^2_{k+N_p+1} - e^2_k - \rho \Delta u^2_k. \tag{17}$$

Given the set of terminal constraint Eq. (13), it follows that when $e_{k+N_p+1} = 0$, this evidently leads to

$$J^*_{k+1} - J_k = -e^2_k - \rho \Delta u^2_k \leq 0. \tag{18}$$

The analysis of Eq. (15) involves prediction errors beyond the prediction time domain.

$$e_{k+N_p+j} = r_{k+N_p+j} - \hat{y}_{k+N_p+j} \tag{19}$$

$\hat{y}_{k+N_p+j}$ in Eq. (19) is given by Eq.(8).

$$\begin{aligned} \hat{y}_{k+N_p+j} = f(&y_{k+N_p+j-1}, \cdots, y_{k+N_p+j-n_y}, \\ &\Delta x_{k+N_p+j-1}, \cdots, \Delta x_{k+N_p+j-n_x}, \\ &\Delta \dot{x}_{k+N_p+j-1}, \cdots, \Delta \dot{x}_{k+N_p+j-n_v}, \\ &u_{k+N_p+j-1}, \cdots, u_{k+N_p+j-1}). \end{aligned} \tag{20}$$

For all $j \geq 1$, if the following conditions are met, the equality constraint for tracking error holds.

1)if $N_c \geq n_y + 1$, then $n_y \geq n_u + 1 + N_u - N_p$

2)if $N_c \geq n_u + 1 + N_u - N_p$, then $n_y \geq n_u + 1 + N_u - N_p$

Utilizing the above two results, temporal constraints can be formulated

$$N_c = max[n_y + 1, n_u + 1 + N_u - N_p]. \tag{21}$$

A comprehensive analysis indicates that, given $\rho \neq 0$ and the condition for N_c being fulfilled as outlined in Eq. (21), it is possible to derive the expression presented in Eq. (18). Consequently, this substantiates the premise that the nonlinear MPC system, as described by Eq. (13) and leveraging Neural Network-based prediction, achieves asymptotic stability.

4 Simulation Results

4.1 RBF network prediction Experiment

Based on PyTorch, a radial basis function (RBF) was implemented, and an RBF neural network was constructed. The network was trained using the training dataset, and during the training process, it was found that the hidden layer had 32 nodes, resulting in good training performance. To validate the predictive accuracy of the RBF Network Prediction model, the input data from the testing set is utilized as the model input. Subtracting the network model's output $\hat{y}_{k+1}$ from the testing set's y_{k+1} yielded the force error as shown in Figure 7.

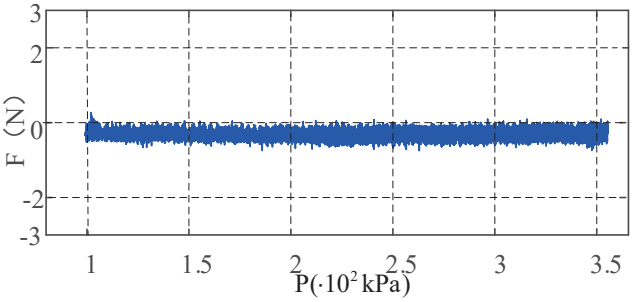

Fig. 7: The error of RBF Network prediction model

Comparing the predicted results of the neural network model to the actual output of the PAM, it is evident that the trained neural network prediction model accurately approximates the nonlinear PAM model.

4.2 Constant Force Experiment

To validate the disturbance-suppressing capability of the PAM-based SCF system, we conducted a comparative analysis between the feed-forward PID controller and the controller proposed in this paper. Two sets of comparative simulations are performed.

(1) To assess the ability of the PAM-based SCF system to suppress step disturbances under constant force conditions.Setting the system to track a 600N step signal, introducing a sustained 1-second step disturbance of 200N at 20 seconds.

(2) To assess the SCF system's ability to suppress sinusoidal disturbances under constant force control. A continuous $F_f = 200sin2\pi t$ sinusoidal disturbance is applied to a 600N constant force system for 1 seconds, starting at 20 seconds.

It is obvious that performance of the proposed Neural Network MPC framework outperforms the feed-forward PID control. From Figures 8 and 9, it can be observed that the proposed control method not only exhibits faster response speed but also suppresses the 200N disturbance to within 10%.

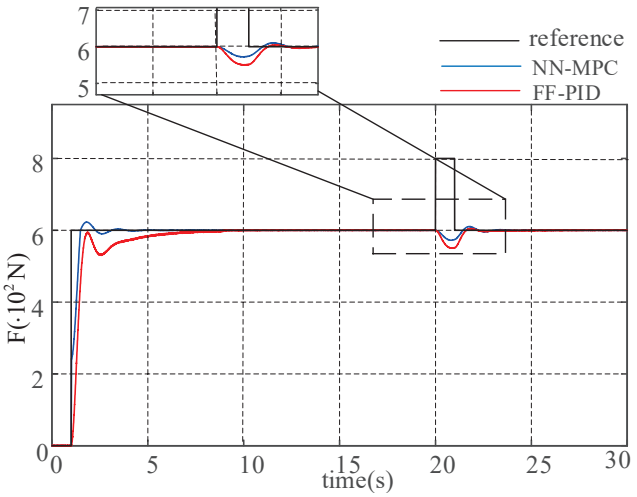

Fig. 8: Comparision diagram of step disturbance suppression

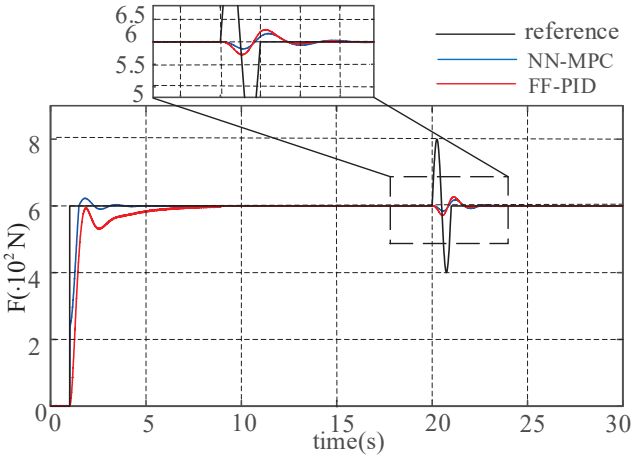

Fig. 9: Comparision diagram of sinusoidal disturbance suppression

5 Conclusion

This paper proposes the utilization of a flexible PAM actuator to address the underactuation issue in the current suspension cable gravity unloading system. Due to the complexity and unmodeled characteristics of the PAM model, achieving precise force control has posed challenges, hence the proposal of the RBF neural network-based predictive control method. Firstly, we train the RBF neural network model to predict the output force of the PAM. Subsequently, we analyze the stability of the proposed neural network model predictive controller presented in this paper.Finally, we conducted simulation experiments. The experiments indicate that the prediction error of the RBF network predictive model is within 1N, and under constant force control, it can suppress a 200N disturbance to within 10%. However, during the experimental process, we also identified certain issues: the MPC optimization solution needs improvement, and there is a slow response phenomenon in driving the PAM.

References

[1] M. Chao, C. Long, and L. Lei, "Development of ultra-quiet gravity unloading for microvibration testing of space precision payloads," *n 2021 IEEE 16th Conference on Industrial Electronics and Applications (ICIEA)*, pp. 1763-1768 *IEEE*, 2021.

[2] O. Sophie, C. James, and R. Jesse, "Effects of walking, running, and skipping under simulated reduced gravity using the nasa active response gravity offload system (argos)," *Acta Astronautica*, 197: 115-125, 2022.

[3] M. Huina, L. G. Pier, and G. Michele, "Deployment of bistable selfdeployable tape spring booms using a gravity offloading system," *Journal of Aerospace Engineering*, 30(4): 04017007, 2017.

[4] K. D. Larry, S. V. Paul, and R. B. Derek, "Active response gravity offload and method," *U.s Patent* No. 9,194,977, 2015.

[5] H. Olyvia, K. David, and K. Scott, "Gravity-off-loading system for large-displacement ground testing of spacecraft mechanisms," *In Proceedings of the 40th aerospace mechanisms symposium*, 2010.

[6] J. Jiao, J. Yingmin, and S. Shihao, "Preliminary design and development of an active suspension gravity compensation system for ground verification," *Mechanism and Machine Theory*, 128: 492-507, 2018.

[7] J. Zhihong, L. Shilong, and L. Hui, "Mechanism design and system control for humanoid space robot movement using a simple gravity-compensation system," *International Journal of Advanced Robotic Systems*, 10(11): 389, 2013.

[8] Z. Meng, F. Shihao, and S. Ruiyang, "Effect of gravity on the mechanical properties of lunar regolith tested using a low gravity simulation device," *Journal of Terramechanics*, 60: 11-22, 2015.

[9] K. Bhaben, L. Alexander, and K. D. Santosha, "A review on the development of pneumatic artificial muscle actuators: Force model and application," *In Actuators*, v. 11, p. 288 *MDPI*, 2022.

[10] C. Yu and H. Jian, "Neural-network-based nonlinear model predictive tracking control of a pneumatic muscle actuator-driven exoskeleton," *IEEE/CAA Journal of Automatica Sinica*, 7(6): 1478-1488, 2020.

[11] E. S. Jonathon and L. N. Mark, "Robust control law for pneumatic artificial muscles," *In Fluid Power Systems Technology*, v. 58332, pp. V001T01A009, *American Society of Mechanical Engineers*, 2017.

[12] C. Mahdi, T. Mostafa, and M. Mahmood, "Hybrid dynamic neural network and pid control of pneumatic artificial muscle using the pso algorithm," *International Journal of Automation and Computing*, 17(3): 428-438, 2020.

[13] K. Basil and C. Mark, "Model predictive control," *Switzerland: Springer International Publishing*, 38, 2016.

[14] H. Honggui, Z. Lu, and H. Ying, "Nonlinear model predictive control based on a self-organizing recurrent neural network," *IEEE transactions on neural networks and learning systems*, 27(2): 402-415, 2015.

[15] W. Daming, J. S. Zheng, and Y. Xin, "Model predictive control using artificial neural network for power converters," *IEEE Transactions on Industrial Electronics*, 69(4): 3689-3699, 2021.

[16] D. zhang, X. Zhao, and J. Han, " Active model-based control for pneumatic artificial muscle," *IEEE Transactions on Industrial Electronics*, 64(2): 1686-1695, 2016.

[17] Q. M. David, B. R. James, and V. R. Christopher, "Constrained model predictive control: Stability and optimality," *Automatica*, 36(6): 789-814, 2000.

[18] P. Krzysztof, "Neural network-based model predictive control: Fault tolerance and stability," *IEEE Transactions on Control Systems Technology*, 23(3): 1147-1155, 2014.

Proceedings of the 3rd Conference on Fully Actuated System Theory and Applications
May 10-12, 2024, Shenzhen, China

Model Predictive Control for Attitude Tracking of Rehabilitation Exoskeleton Robots

Zheming Wang[1], Bin Wang[1], Yuan Zhou[1], Ming Chen[1], Bo Chen[1*], Jiyu Zhang[2]

1. Department of Automation, Zhejiang University of Technology, Hangzhou 310023, P. R. China
E-mail: wangzheming@zjut.edu.cn

2. Harbin Institute of Technology, Harbin 150001, P. R. China
E-mail: 19b901013@stu.hit.edu.cn

Abstract: In this paper, an attitude tracking controller is proposed for lower-limb rehabilitation exoskeleton robots with parameter uncertainties and external disturbances using model predictive control (MPC). Firstly, the exoskeleton dynamics model is converted into a fully-actuated (FA) system model. Then, the above system undergoes discretization through a zero-order hold mechanism. Lastly, a MPC approach is performed to obtain the instantaneous optimal control signal inputs in the sense of FA system with parameter uncertainties and external disturbances, aiming to minimize trajectory error. For comparison, a classical PID controller is designed as the benchmark. A numerical simulation example is designed to evaluate the proposed controller. The results show that the proposed MPC control method exhibits performance improvement, which is reflected in greater tracking precision and tougher robustness compared with the benchmark controller.

Key Words: Fully-actuated system, Model predictive control, Lower-limb rehabilitation exoskeleton, Attitude tracking

1 Introduction

Balance dysfunction resulting from aging and neurological disorders has attracted more and more attention. In the USA, there are approximately 320,000 patients who experience serious falls within one year as a result of stroke [1]. This gives rise to a demand for rehabilitation services that are high-level, high-quality, and diverse, which traditional rehabilitation healthcare services are struggling to meet. Assisting patients with effective methods has become a realistic problem, and lower-limb rehabilitation exoskeleton robots have natural advantages in helping patients with rehabilitation training [2–6].

With the advancements in robotics technology and deep learning, the functionality of lower-limb rehabilitation exoskeletons for rehabilitation training has been gradually improving, leading to their application in the existing literature. MINDWALKER is a lower-limb rehabilitation exoskeleton rehabilitation robot developed by University of Twente in Netherlands designed for paraplegics to regain locomotion capability [7]. ReWalk, developed by an Israeli company, is a powered exoskeleton that can restore independent walking capabilities to patients with thoracic-level motor-complete spinal cord injuries [8]. Twin is a powered exoskeleton developed by the Istituto Italiano di Tecnologia in Italy, which can determine the patients's intension by detecting trunk inclination [9]. However, there are still numerous challenges that need to be addressed to ensure the clinical applicability and viability of such technologies [10].

The design of a control strategy for lower-limb rehabilitation exoskeleton is a crucial factor in the successful implementation of a robotic rehabilitation system. In [11], an adaptive sliding mode variable admittance controller is designed to deal with the attitude tracking problem of lower-limb rehabilitation exoskeleton. The combination of the Kalman filter algorithm is utilized to estimate the patient's torques in [12]. In [13], an optimal impedance control is presented based on the estimation of torque and impedance parameters of the patient during the gait. Model predictive control (MPC) is a model-based method, which can exploit knowledge of the dynamics model of the system [14]. Thanks to significant advancements in the field, MPC methods are now feasible for both linear and nonlinear systems, as well as hybrid model formulations [15–18]. In [19], a MPC method is designed to control an upper-limb rehabilitation robot under disturbance conditions. A feedback MPC is designed to handle the slow update rate associated with the computational restrictions of mobile platforms in [20].

In the literatures mentioned above, the majority of studies deal with the exoskeleton attitude tracking control problem using a linear system model. However, the linearized system does not accurately represent the actual physical background. The fully-actuated (FA) system method is proposed in [21], which can complete the attitude tracking control of the lower-limb rehabilitation exoskeleton while avoiding the linearization of the system.

In this paper, an exoskeleton attitude tracking controller is proposed. The main contribution of the paper lies in 1) an FA model for general dynamics model is firstly proposed; 2) a MPC approach is designed based on the FA system, which allows us to consider state limitations to ensure safety and protect hardware, meanwhile, considering parameter uncertainties and external disturbances in the modeling process; 3) a numerical simulation example is completed to signify the applicability of the established controller. The results show that the designed MPC control method exhibits superior tracking precision and tougher robustness compared with the benchmark PID controller.

The paper is organized as follows: Section 2 presents an FA model for dynamics model of lower-limb rehabilitation exoskeleton. In Section 3, the proposed MPC controller is designed. Meanwhile, a classical PID controller is designed as the benchmark for comparison. Section 4 presents the

This work is supported by National Natural Science Foundation of China (No. 62303416) and Primary Research and Development Plan of Zhejiang Province (No. 2022C03029).

*Corresponding Author: bchen@zjut.edu.cn, bchen@aliyun.com

simulation results with parameter uncertainties and external disturbances through MATLAB and Section 5 presents the conclusion.

2 Modeling and Preliminaries

2.1 Attitude Dynamics Model

This paper considers the motion of human lower-limbs in three-dimensional space as plane motion on the sagittal plane [10]. As the legs exhibit symmetry on the sagittal plane during exercise, this study focuses on a single swinging lower-limb as the research subject. In the dynamics model of the exoskeleton robot, the hip and knee joints are considered as active joints, while the ankle joint is regarded as passive [2].

A 2-Degree of Freedom lower-limb rehabilitation exoskeleton shown in Fig. 1 is taken into consideration. The parameter m_i (i = 1, 2) is the mass of the thigh part or shank segment; I_i (i = 1, 2) is the moment of inertia of the exoskeleton thigh part or shank segment; q_i (i = 1, 2) is the angle of the exoskeleton hip joint or knee joint; l_i (i = 1, 2) is the length of the exoskeleton thigh part or shank segment; and l_{ci} (i = 1, 2) is the distance from the pivotal axes to the centroid of the thigh part or shank segment [2].

The dynamics model of the 2-Degree of Freedom lower-limb rehabilitation exoskeleton is represented as [10]:

$$\mathbf{M}(q(t))\ddot{q}(t)+\mathbf{C}(q(t),\dot{q}(t))\dot{q}(t)+\mathbf{G}(q(t))=\tau(t), \quad (1)$$

where $q(t)$ stands for the generalized position coordinate, $\dot{q}(t)$ stands for velocity, $\ddot{q}(t)$ stands for acceleration of thigh part and shank segment, $\tau(t)$ stands for the vector of the torques. $\mathbf{M}(q(t))$ represents the inertia matrix, $\mathbf{C}(q(t),\dot{q}(t))$ represents the Coriolis and centrifugal force matrix, $\mathbf{G}(q(t))$ represents the gravitational torque vector. $\mathbf{M}(q(t)$, $\mathbf{C}(q(t),\dot{q}(t))$, $\mathbf{G}(q(t))$ are given as

$$\mathbf{M}(q(t))=\begin{bmatrix} M_{11}(q(t)) & M_{12}(q(t)) \\ M_{21}(q(t)) & M_{22} \end{bmatrix},$$

$$\mathbf{C}(q(t),\dot{q}(t))=\begin{bmatrix} C_{11}(q(t),\dot{q}(t)) & C_{12}(q(t),\dot{q}(t)) \\ C_{21}(q(t),\dot{q}(t)) & 0 \end{bmatrix},$$

$$\mathbf{G}(q(t))=\begin{bmatrix} G_1(q(t)) \\ G_2(q(t)) \end{bmatrix},$$

where

$$\begin{aligned} M_{11}(q(t)) &= I_1+m_1l_{c1}^2+m_2l_1^2+I_2+m_2l_{c2}^2 \\ &\quad +2m_2l_1l_{c2}\cos q_2(t), \\ M_{12}(q(t)) &= M_{21}(q(t))=I_2+m_2l_{c2}^2+m_2l_1l_{c2}\cos q_2(t), \\ M_{22} &= I_2+m_2l_{c2}^2, \\ C_{11}(q(t),\dot{q}(t)) &= -2m_2l_1l_{c2}\dot{q}_2(t)\sin q_2(t), \\ C_{12}(q(t),\dot{q}(t)) &= -m_2l_1l_{c2}\dot{q}_2(t)\sin q_2(t), \\ C_{21}(q(t),\dot{q}(t)) &= m_2l_1l_{c2}\dot{q}_1(t)\sin q_2(t), \\ G_1(q(t)) &= -m_1gl_{c1}\sin q_1(t)-m_2gl_1\sin q_1(t) \\ &\quad -m_2gl_{c2}\sin(q_1(t)+q_2(t)), \\ G_2(q(t)) &= -m_2gl_{c2}\sin(q_1(t)+q_2(t)). \end{aligned}$$

Considering a lumped term $\psi(q(t),\dot{q}(t),\ddot{q}(t))$ to denote the existence of parameter uncertainties and external disturbances, which is given by

$$\begin{aligned} \psi(q(t),\dot{q}(t),\ddot{q}(t)) &= \Delta\mathbf{M}(q(t))\ddot{q}(t)+\Delta\mathbf{C}(q(t),\dot{q}(t))\dot{q}(t) \\ &\quad +\Delta\mathbf{G}(q(t))-\tau_d(t), \end{aligned} \quad (2)$$

where $\Delta\mathbf{M}(q(t))$, $\Delta\mathbf{C}(q(t),\dot{q}(t))$ and $\Delta\mathbf{G}(q(t))$ denote uncertain parameters, and $\tau_d(t)\in\Re^{2\times1}$ denotes the external disturbance torque.

The final model can be represented as

$$\begin{aligned} &\mathbf{M}(q(t))\ddot{q}(t)+\mathbf{C}(q(t),\dot{q}(t))\dot{q}(t) \\ &+\mathbf{G}(q(t))+\psi(q(t),\dot{q}(t),\ddot{q}(t))=\tau(t). \end{aligned} \quad (3)$$

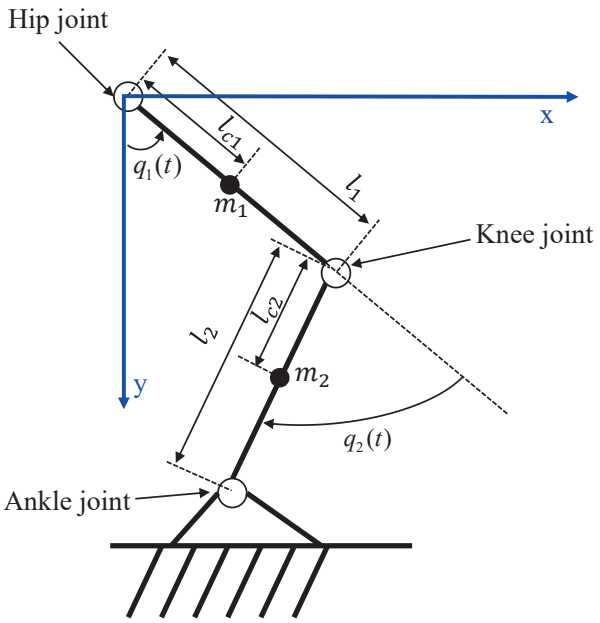

Fig. 1: Schematic representation of the 2-Degree of Freedom lower-limb rehabilitation exoskeleton [2].

2.2 FA System

On the basis of (3), the following uncertain FA system model can be obtained [22, 23]:

$$\begin{aligned} \ddot{q}(t) &= \mu(q(t),\dot{q}(t))-\mathbf{M}^{-1}(q(t))\psi(q(t),\dot{q}(t),\ddot{q}(t)) \\ &\quad +\mathbf{M}^{-1}(q(t))\tau(t), \end{aligned} \quad (4)$$

where

$$\mu(q(t),\dot{q}(t))=-\mathbf{M}^{-1}(q(t))(\mathbf{C}(q(t),\dot{q}(t))\dot{q}(t)+\mathbf{G}(q(t))).$$

For (4), the torque signals $\tau(t)$ is proposed as below:

$$\tau(t)=-\mathbf{M}(q(t))(\mu(q(t),\dot{q}(t))-\mathbf{u}(t)), \quad (5)$$

where $\mathbf{u}(t)=\begin{bmatrix} u_1(t) \\ u_2(t) \end{bmatrix}$ is the control signal inputs vector.

Through (4) and (5), we obtain

$$\ddot{q}(t)=\mathbf{u}(t)-\mathbf{M}^{-1}(q(t))\psi(q(t),\dot{q}(t),\ddot{q}(t)). \quad (6)$$

We define the state vector $\mathbf{x}(t)$ and the vector of parameter uncertainties and external disturbances $\mathbf{d}$(t). $\mathbf{x}(t)$, $\mathbf{d}$(t) are

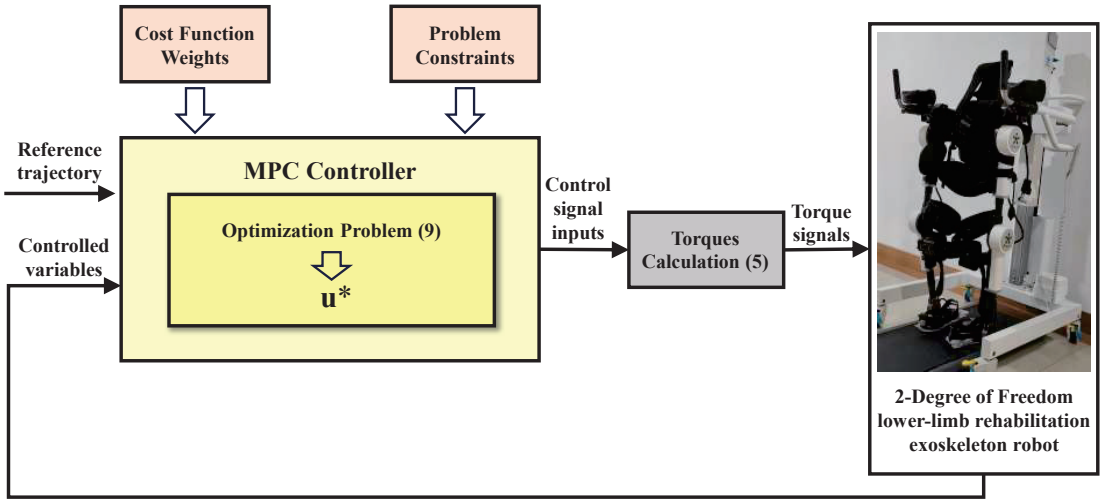

Fig. 2: The block diagram of the MPC control scheme.

given as

$$\mathbf{x}(t) = \begin{bmatrix} q_1(t) & q_2(t) & \dot{q}_1(t) & \dot{q}_2(t) \end{bmatrix}^T,$$
$$\mathbf{d}(t) = \begin{bmatrix} \mathbf{0}_{2\times 1} \\ \mathbf{M}^{-1}(q(t))\psi(q(t),\dot{q}(t),\ddot{q}(t)) \end{bmatrix},$$

where q_i (i = 1, 2) is the angle of the exoskeleton hip joint or knee joint; $\dot{q}_i$ (i = 1, 2) is the velocity of the exoskeleton hip joint or knee joint; $\mathbf{d}(t) \in \Re^{4\times 1}$ are the vector of parameter uncertainties and external disturbances. Then, from (6), we have

$$\dot{\mathbf{x}}(t) = \mathbf{A}\mathbf{x}(t) + \mathbf{B}\mathbf{u}(t) + \mathbf{d}(t), \tag{7}$$

where

$$\mathbf{A} = \begin{bmatrix} \mathbf{0}_{2\times 2} & \mathbf{I}_2 \\ \mathbf{0}_{2\times 2} & \mathbf{0}_{2\times 2} \end{bmatrix}, \mathbf{B} = \begin{bmatrix} \mathbf{0}_{2\times 2} \\ \mathbf{I}_2 \end{bmatrix}.$$

The T is the sampling period. Then, discretizing (7) using a zero-order holder, we have

$$\mathbf{x}(k+1) = \mathbf{A}_c\mathbf{x}(k) + \mathbf{B}_c\mathbf{u}(k) + \mathbf{C}_c\mathbf{d}(k), \tag{8}$$

where

$$\mathbf{A}_c = e^{AT},$$
$$\mathbf{B}_c = \int_0^T e^{A(T-\eta)}Bd\eta,$$
$$\mathbf{C}_c = \int_0^T e^{A(T-\eta)}d\eta.$$

3 Control Design

3.1 MPC controller

The general idea of the control is to accurately track the reference trajectory of the exoskeleton. The general control scheme is shown in Fig. 2. The controlled variables are the joint angles and joint velocities. The control variables are the control signal inputs.

The optimal control signal inputs $\mathbf{u}^*$ is obtained through solving an optimization problem by MPC controller. $\mathbf{u}^*$ are converted into torques applied at each joint through the formula (5) and the actual joint angles and joint velocities are fed back to the MPC controller.

Initially, we define the reference trajectory $\mathbf{x}_r(k)$ as

$$\mathbf{x}_r(k) = [q_{r_1}(k) \quad q_{r_2}(k) \quad \dot{q}_{r_1}(k) \quad \dot{q}_{r_2}(k)]^T,$$

where $q_{r_i}(k)$ (i = 1, 2) is the reference angle of the exoskeleton hip joint or knee joint; $\dot{q}_{r_i}(k)$ (i = 1, 2) is the reference velocity of the exoskeleton hip joint or knee joint.

The goal is to find $\mathbf{u}^*$ to minimize the cost function J in [10]. Therefore, we state the MPC problem as

$$\min_{\mathbf{u}} J = \sum_{k=t}^{t+N-1} ((\mathbf{x}(k) - \mathbf{x}_r(k))^T\mathbf{P}(\mathbf{x}(k) - \mathbf{x}_r(k)) + \mathbf{u}(k)^T\mathbf{R}\mathbf{u}(k). \tag{9}$$

$$\text{s.t.} \quad \mathbf{x}(k+1) = \mathbf{A}_c\mathbf{x}(k) + \mathbf{B}_c\mathbf{u}(k) + \mathbf{C}_c\mathbf{d}(k)$$
$$q_1(k) \in [q_{1\min},\ q_{1\max}],\ q_2(k) \in [q_{2\min},\ q_{2\max}]$$
$$\dot{q}_1(k) \in [\dot{q}_{1\min},\ \dot{q}_{1\max}],\ \dot{q}_2(k) \in [\dot{q}_{2\min},\ \dot{q}_{2\max}]$$
$$\tau_1(k) \in [\tau_{1\min},\ \tau_{1\max}],\ \tau_2(k) \in [\tau_{2\min},\ \tau_{2\max}]$$
$$u_1(k) \in [u_{1\min},\ u_{1\max}],\ u_2(k) \in [u_{2\min},\ u_{2\max}]$$

where

$$\mathbf{P} = \begin{bmatrix} p_1 & 0 & 0 & 0 \\ 0 & p_2 & 0 & 0 \\ 0 & 0 & p_3 & 0 \\ 0 & 0 & 0 & p_4 \end{bmatrix}, \mathbf{R} = \begin{bmatrix} r_1 & 0 \\ 0 & r_2 \end{bmatrix}.$$

The N shows the prediction horizon, and k denotes the kth sample [24]. $\mathbf{P}$ is the tracking weight matrix, affecting joint tracking error cost. And $\mathbf{R}$ is the control signal inputs weight matrix, affecting the lower-limb rehabilitation exoskeleton control signal inputs cost. The range of control signal inputs can be calculated from the range of the torque inputs through the formula (5).

The cost function is solved in real-time using convex programming (CVX) toolkit in MATLAB mathematical simulation platform. CVX based numerical algorithms are widely

and freely available for solving convex optimization problems [25].

A benefit of employing the MPC approach is the ability to seek optimal solutions while considering constraints on the state variables and control signal inputs. Constrained optimization inherently imposes limitations on the range and velocity of joint motion, aiming to mitigate subject discomfort and safeguard the integrity of the hardware system [26].

3.2 PID controller

In order to demonstrate the superiority of the proposed controller, a classical PID control scheme is introduced as the benchmark. Initially, we define the tracking error $e(k)$ as

$$e(k) = \begin{bmatrix} e_1(k) \\ e_2(k) \\ e_3(k) \\ e_4(k) \end{bmatrix} = \begin{bmatrix} q_{r1}(k) - q_1(k) \\ q_{r2}(k) - q_2(k) \\ \dot{q}_{r1}(k) - \dot{q}_1(k) \\ \dot{q}_{r2}(k) - \dot{q}_2(k) \end{bmatrix}.$$

The PID control method input is given as

$$\begin{aligned} \Delta\tau(k) &= K_p(e(k) - e(k-1)) + K_i e(k) \\ &\quad + K_d(e(k) - 2e(k-1) + e(k-2)), \\ \tau(k) &= \Delta\tau(k) + \tau(k-1), \end{aligned} \tag{10}$$

where K_p, K_i, K_d represent proportional, integral and derivative gains, respectively.

4 Simulation Result

The parameters required for the simulation are provided in Tables 1.

Table 1: Parameter Setting

Name	Value
Mass of thigh m_1	6.099kg
Length of thigh l_1	0.460m
Position of thigh centroid l_{c_1}	0.4046m
Inertia of thigh I_1	0.0837kg $\cdot$ m^2
Mass of shank m_2	4.257kg
Length of shank l_2	0.480m
Position of shank centroid l_{c_2}	0.2275m
Inertia of shank I_2	0.5689kg $\cdot$ m^2
Acceleration of gravity g	9.79m/s^2
Prediction horizon N	100
Sampling period T	0.006s

The designed angle tracking weights are $p_1 = 7$, $p_2 = 9$, $p_3 = 0.2$, $p_4 = 0.4$. The designed control signal inputs weights are $r_1 = 0.0001$, $r_2 = 0.0001$. The designed PID weights are $K_p = 500$, $K_i = 1$, $K_d = 10$.

The reference angle of the exoskeleton hip joint $q_{r_1}(k)$ and the reference angle of the exoskeleton knee joint $q_{r_2}(k)$ are given as

$$\begin{aligned} q_{r_1}(k) &= 8.006 + 8.906\sin(3.884k) - 0.471\sin(7.768k) \\ &\quad - 1.373\sin(11.652k) - 18.74\cos(3.884k) \\ &\quad - 4.453\cos(7.768k) - 0.46\cos(11.652k), \end{aligned} \tag{11}$$

$$\begin{aligned} q_{r_2}(k) &= -15.89 - 22.96\sin(3.863k) - 9.482\sin(7.726k) \\ &\quad + 3.612\sin(11.589k) - 5.186\cos(3.863k) \\ &\quad + 12.68\cos(7.726k) + 1.214\cos(11.589k). \end{aligned} \tag{12}$$

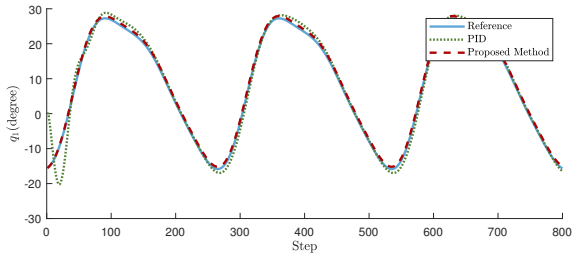

(a)

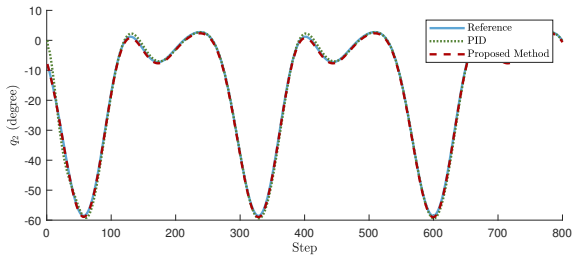

(b)

Fig. 3: Lower-limb rehabilitation exoskeleton angle trajectory. (a) Trajectory of hip joint. (b) Trajectory of knee joint.

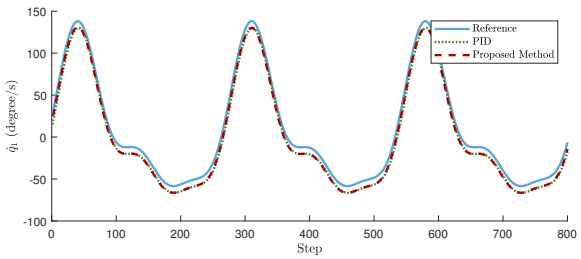

(a)

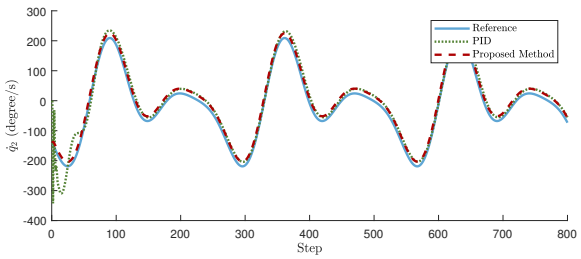

(b)

Fig. 4: Lower-limb rehabilitation exoskeleton velocity trajectory. (a) Trajectory of hip joint. (b) Trajectory of knee joint.

Fig. 3, Fig. 4 show that the attitude of lower-limb rehabilitation exoskeleton can track the reference trajectory fastly. This illustrates that the lower-limb rehabilitation exoskeleton can achieve attitude tracking control based on the proposed controller. Fig. 5, Fig. 6 display the tracking errors of lower-limb rehabilitation exoskeleton.

We can see that the actual angles of the hip joint and knee joint can track the reference trajectories by using proposed method with high precision in the whole process, while the tracking accuracy under the PID control method is obviously lower. In 10 steps, PID control method exhibits difficulty in accurately tracking the reference trajectory, while proposed method is almost unaffected.

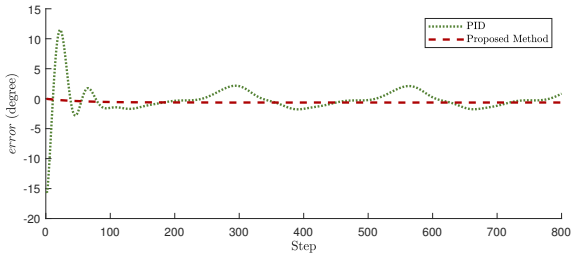

(a)

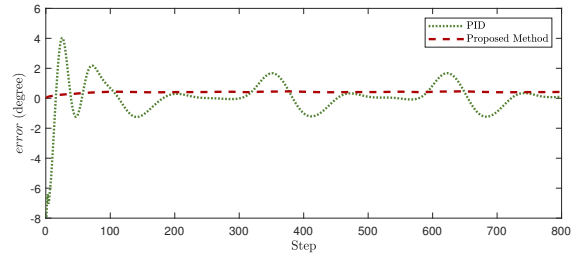

(b)

Fig. 5: Angle tracking errors. (a) Angle tracking error of hip joint. (b) Angle tracking error of knee joint.

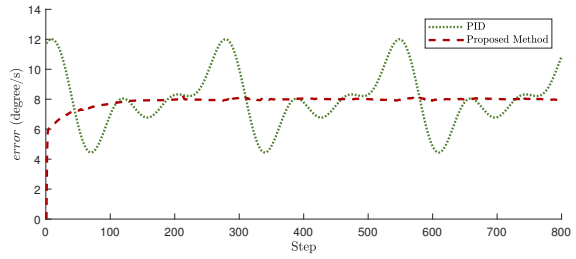

(a)

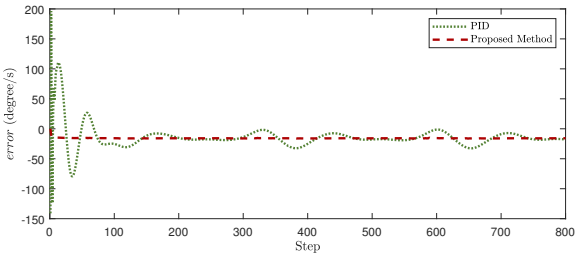

(b)

Fig. 6: Velocity tracking errors. (a) Velocity tracking error of hip joint. (b) Velocity tracking error of knee joint.

Therefore, we can conclude that the proposed method owns superior tracking performance and tougher robustness in dealing with the parameter uncertainties and external disturbances in comparison with the benchmark control method.

5 Conclusion

In this paper, a MPC controller based on an FA system with parameter uncertainties and external disturbances is proposed and investigated for the trajectory tracking control of lower-limb rehabilitation exoskeleton. The proposed method allows us to consider state limitations to ensure safety and protect hardware. Specially, in this paper, the constraint range of the control signal inputs are calculated by the constraint range of the torque signals through the designed FA system. The effectiveness of the proposed method is verified by a numerical simulation example. The results demonstrate that the proposed method can track the given reference trajectory more accurately and better cope with the parameter uncertainties and external disturbances compared with the benchmark controller.

References

[1] S. Zhang, J. Ye, G. Chen, C. Fu, and Y. Leng, An intelligent rehabilitation assessment method for stroke patients based on lower limb exoskeleton robot, *IEEE Transactions on Neural Systems and Rehabilitation Engineering*, 31: 3106–3117, 2023.

[2] Z. Sun, Z. Li, Y. Zhou, and B. Chen, Robust control of a 2-dof lower limb exoskeleton rehabilitation robot using nonsingular terminal sliding mode, in *Proceedings of the 2022 IEEE 17th International Conference on Control & Automation*, 2022: 438–443.

[3] J. Jiang, X. Ma, B. Huo, Y. Zhang, and X. Yu, Recent advances on lower limb exoskeleton rehabilitation robot, *Recent Patents on Engineering*, 11(3): 194–207, 2017.

[4] M. Sanchez, D. Gomez, D. Casas, M. Munera, and C. Cifuentes, Development of a robotic lower-limb exoskeleton for gait rehabilitation: Agora exoskeleton, in *2018 IEEE ANDESCON*, 2018: 1–6.

[5] D. Pinto, D. Torricelli, M. del, F. Aller, K. Mombaur, R. Conti, N. Vitiello, J. C. Moreno, and J. L. Pons, Performance evaluation of lower limb exoskeletons: a systematic review, *IEEE Transactions on Neural Systems and Rehabilitation Engineering*, 28(7): 1573–1583, 2020.

[6] W. Meng, Q. Liu, Z. Zhou, Q. Ai, B. Sheng, and S. Xie, Recent development of mechanisms and control strategies for robot-assisted lower limb rehabilitation, *Mechatronics*, 31: 132–145, 2015.

[7] L. Wang, S. Wang, E. van, and H. van, Actively controlled lateral gait assistance in a lower limb exoskeleton, in *2013 IEEE/RSJ International Conference on Intelligent Robots and Systems*, 2013: 965–970.

[8] M. Talaty, A. Esquenazi, and J. Briceno, Differentiating ability in users of the rewalk tm powered exoskeleton: An analysis of walking kinematics, in *2013 IEEE 13th international conference on rehabilitation robotics*, 2013: 1–5.

[9] R. Iandolo, F. Marini, M. Semprini, M. Laffranchi, M. Mugnosso, A. Cherif, L. Michieli, M. Chiappalone, and J. Zenzeri, Perspectives and challenges in robotic neurorehabilitation, *Applied Sciences*, 9(15): 3183–3212, 2019.

[10] W. Santos, A. Siqueira, Optimal impedance via model predictive control for robot-aided rehabilitation, *Control Engineering Practice*, 93: 104177–104185, 2019.

[11] Y. Tu, A. Zhu, J. Song, H. Shen, Z. Shen, X. Zhang, and G. Cao, An adaptive sliding mode variable admittance control method for lower limb rehabilitation exoskeleton robot, *Applied Sciences*, 10(7): 2536–2557, 2020.

[12] J. Jaimes, A. Siqueira, Preliminary evaluation of disturbance torque estimation approaches for lower-limb robotic rehabilitation, in *2019 IEEE 16th International Conference on Rehabilitation Robotics*, 2019: 715–720.

[13] W. Santos, A. Siqueira, Optimal impedance control for robot-aided rehabilitation of walking based on estimation of patient behavior, in *2016 6th IEEE International Conference on Biomedical Robotics and Biomechatronics*, 2016: 1023–1028.

[14] H. Nguyen, M. Kamel, K. Alexis, and R. Siegwart, Model predictive control for micro aerial vehicles: A survey, in *2021 European Control Conference*, 2021: 1556–1563.

[15] S. Tahamipour, S. Hosseini, M. Akbarzadeh, A. Akbarzadeh, and M. Farajzadeh, Design and implementation of a real-time nonlinear model predictive controller for a lower limb exoskeleton with input saturation, *Iranian Journal of Science and Technology-Transactions of Electrical Engineering*, 45(1): 309–320, 2021.

[16] Y. Ding, L. Wang and Y.Li, Model predictive control and its application in agriculture: A review, *Computers and Electronics in Agriculture*, 151: 104-117, 2018.

[17] S. Tahamipour, S. Sani, A. Akbarzadeh, and I. Kardan, An assistive strategy for compliantly actuated exoskeletons using non-linear model predictive control method, in *Proceedings of 24th Iranian Conference on Electrical Engineering*, 2018: 982–987.

[18] G. Incremona, A. Ferrara, and L. Magni, MPC for robot manipulators with integral sliding modes generation, *IEEE/ASME Transactions on Mechatronics*, 22(3): 1299–1307, 2017.

[19] S. Raza, S. Ahmed, A. Ali, K. Kadir, M. Joyo, S. Khan, and Z. Janin, Model predictive control for upper limb rehabilitation robotic system under noisy condition, in *2018 IEEE 5th International Conference on Smart Instrumentation, Measurement and Application*, 2018: 1–4.

[20] R. Grandia, F. Farshidian, R. Ranftl, and M. Hutter, Feedback mpc for torque-controlled legged robots, in *2019 IEEE/RSJ International Conference on Intelligent Robots and Systems*, 2019: 4730–4737.

[21] D. Gu, S. Wang, A high-order fully actuated system approach for a class of nonlinear systems, *Journal of Systems Science and Complexity*, 35(2): 714–730, 2022.

[22] G. Duan, High-order fully-actuated system approaches: Part vi. disturbance attenuation and decoupling, *International Journal of Systems Science*, 52(10): 2161–2181, 2021.

[23] G. Duan, G. Liu, Attitude and orbit optimal control of combined spacecraft via a fully-actuated system approach, *Journal of Systems Science and Complexity*, 35(2): 623–640, 2022.

[24] J. Egbert, J. Harlaar, and G. Van, Electromechanical delay during knee extensor contractions, *Medicine and science in sports and exercise*, 23(10): 1187–1193, 1991.

[25] W. Wong, J. Zhou, CVX-based algorithms for constructing various optimal regression designs, *Canadian Journal of Statistics*, 47(3): 374–391, 2019.

[26] C. Caulcrick, W. Huo, E. Franco, S. Mohammed, W. Hoult, and R. Vaidyanathan, Model predictive control for human-centred lower limb robotic assistance, *IEEE Transactions on Medical Robotics and Bionics*, 3(4): 980–991, 2021.

Proceedings of the 3rd Conference on Fully Actuated System Theory and Applications
May 10-12, 2024, Shenzhen, China

An Improved Model Predictive Control with Neutral-Point Voltage Balancing and Common-Mode Voltage Suppression for Three-Level T-type Converters

Xiaomin Han[1], Hongliang Zhang[2], Yuying Ma[1], Huiqing Wu[1]

1. Shandong University of Engineering and Vocational Technology, Jinan 250200, China
E-mail: 346086053@qq.com

2. Shandong Aotai Electric Company Ltd., Jinan 250101, China
E-mail: 18660138145@163.com

Abstract: The three-phase three-level T-type converters have been used in many industrial applications. However, the common-mode voltage (CMV) and neutral point (NP) voltage are a coupled issue. In this paper, an improved model predictive control (MPC) method is proposed to solve this problem. Firstly, the CMV is analyzed and vectors with smaller CMV are selected as the candidate vectors. Secondly, the space voltage vector diagram is divided into 12 sectors and in each sector two seven-segment sequences are adopted. By switching them, the NP voltage can be balanced actively and no addition switching occurs. Thirdly, the duty ratios are calculated through the cost function results. Finally, the steady-state and the dynamic simulations are conducted to verify the effectiveness of the proposed MPC method.

Key Words: Three-level T-type converter, CMV suppression, NP voltage balancing, MPC

1 Introduction

Compared with conventional two-level converters, three-level topologies show many advantages in less device voltage stress, smaller *dv*/*dt*, higher quality output current, etc. [1]. They have been applied in many industrial applications such as Photovoltaic (PV) field, wind power generation, etc. Among many existing three-level topologies, the T-type structure has fewer switches and highest efficiency in medium switching frequencies [2]. Therefore, this paper focuses on the three-phase three-level T-type converter.

It is necessary to balance the neutral point (NP) voltage for normally operating the T-type converter. When NP voltage is unbalanced, serious current distortions will occur and the lifespan of the dc-link capacitors will be reduced [3]. Therefore, the NP voltage should be balanced all the time. And when the imbalance NP voltage occur, the program should have the ability to recover it actively. In [4], a zero-voltage injection method is proposed to balance the NP voltage. However, it is difficult to calculate the zero-voltage value.

The common-mode voltage (CMV) is harmful to the system and it will cause leakage currents, electromagnetic interference (EMI), etc. [5]. Therefore, suitable CMV suppression method should be considered and the modified modulation strategy can make it without adding any additional hardware. In [6], only zero and medium vectors are used to track the current. The medium and zero vectors have no CMV, thus it achieves zero CMV. However, using partial vectors will greatly reduce the max modulation index and the dc-link value has to be increased. Besides, the medium vectors can cause imbalanced NP voltage. Although the whole method can achieve the self-balancing NP voltage, it lacks the ability of active recovering. In [7], an LMZSVM method using lager, medium and zero vectors is proposed. It can run within whole modulation index but the absence of small vectors cannot recover the unbalanced NP voltage actively. The conventional method using seven-segment sequences formed by four vectors can balance the NP voltage actively, but the CMV is impossible to be suppressed. Therefore, it is concluded that balancing the NP voltage actively and suppressing the CMV are a coupled issue.

With the rapid development of microprocessors, the model predictive control (MPC) method shows many advantages in multiple objective control, strong robustness, etc. [8]. Compared with conventional proportional-integral (PI) controller, it shows fast response and does not require parameter tuning. The MPC applies a cost function to achieve the multiple objective control. All the variables are taken into the cost function and the smallest one corresponds to the optimal solution. Therefore, it requires weighting factors to achieve this. However, the selection of the weighting factors is a tedious work and there is no certain guideline [9]. Minor differences between the weighting factors may have a significant impact on the control objectives. For the T-type converter, it has to achieve current tracking, NP voltage balancing and CMV suppressing. The three control targets will mislead the selection of the weighting factors.

In this paper, an MPC method is proposed to solve this issue. The proposed method uses four vectors to form a seven-segment sequence. The CMV is limited within the smallest values. The NP voltage can be balanced actively. Besides, when balancing the NP voltage and even switching the sectors, no addition switching occurs. During the whole program, there is no weighting factor which saves the tedious work for searching it.

The rest of the paper is organized as follows. In Section II, the basic operating principle of the T-type converter and the mathematical model of the proposed MPC is built. In Section III, the proposed MPC strategy is given in details. In Section IV, the simulation is conducted to verify the effectiveness of the proposed MPC method. In Section V, a conclusion is drawn.

2 Basic Principle of T-type Converters

2.1 Operating Principle of T-type Converters

The topology of the three-phase T-type converter is shown in Fig. 1. The dc link voltage is V_{dc}. The upper and lower capacitors on dc link are defined as C_p and C_n, and their voltages are V_p and V_n respectively. The neutral point (NP) is O and the current flows out of O is defined as i_o. The output currents are i_a, i_b and i_c. L and R represent the filter and the load respectively. Point n is the common output point.

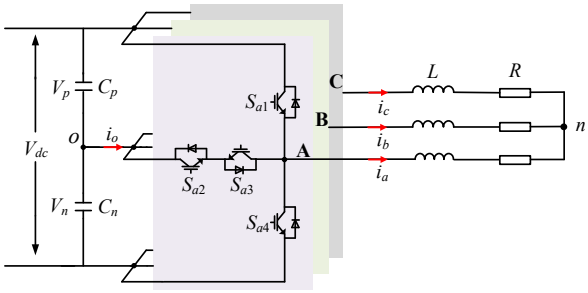

Fig. 1: Topology of the three-phase T-type converter.

For phase A, there are four power devices named S_{a1}, S_{a2}, S_{a3} and S_{a4}. S_{a1}, S_{a3} and S_{a2}, S_{a4} work in a complementary state, which means when S_{a1} is on S_{a3} is off. According to the different working states of the power switch, the T-type converter can generate three different output phase voltages. Their relationship is concluded in Table 1. Therefore, there are totally 27 (3^3) vectors in the space voltage vector diagram as shown in Fig. 2. They can be divided into four types: 12 small vectors, 6 medium vectors, 6 lager vectors and 3 zero vectors as listed in Table 2.

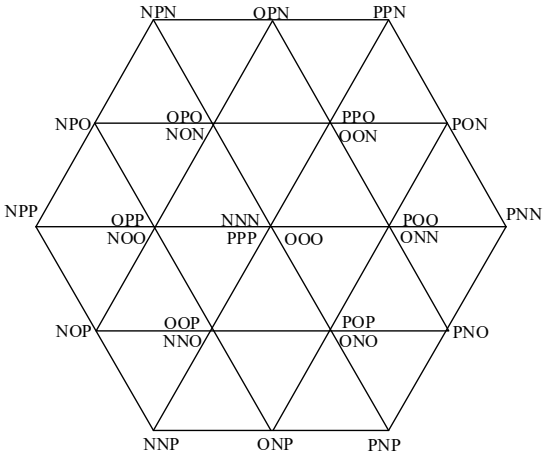

Fig. 2: Space voltage vector diagram of T-type converters.

Table 1: Relationship Between Devices and Phase Voltage

State	Phase voltage	(S_{x1}, S_{x2}, S_{x3}, S_{x4},)
P	$+V_{dc}/2$	(1,1,0,0)
O	0	(0,1,1,0)
N	$-V_{dc}/2$	(0,0,1,1)

Table 2: Classification of 27 Vectors

Type	Name		
Large vector	[PNN]	[PPN]	[NPN]
	[NPP]	[NNP]	[PNP]
Medium vector	[PON]	[OPN]	[NPO]
	[NOP]	[ONP]	[PNO]
Small vector	[POO]	[PPO]	[OPO]
	[ONN]	[OON]	[NON]
	[OPP]	[OOP]	[POP]
	[NOO]	[NNO]	[ONO]
Zero vector	[NNN]	[OOO]	[PPP]

2.2 Mathematical Model of the MPC

According to the Kirchhoff laws, the output voltage is defined as

$$\begin{cases} u_{an} = L\dfrac{\mathrm{d}i_a}{\mathrm{d}t} + Ri_a \\ u_{bn} = L\dfrac{\mathrm{d}i_b}{\mathrm{d}t} + Ri_b \\ u_{cn} = L\dfrac{\mathrm{d}i_c}{\mathrm{d}t} + Ri_c \end{cases} \tag{1}$$

Using forward- Euler principle, (1) in the discrete state is expressed as

$$\begin{cases} u_{an}(k) = (\dfrac{L}{T_s} + R)i_a^*(k+1) - \dfrac{L}{T_s}i_a(k) \\ u_{bn}(k) = (\dfrac{L}{T_s} + R)i_b^*(k+1) - \dfrac{L}{T_s}i_b(k) \\ u_{cn}(k) = (\dfrac{L}{T_s} + R)i_c^*(k+1) - \dfrac{L}{T_s}i_c(k) \end{cases} \tag{2}$$

where $i_x(k)$ and $u_{xn}(k)$ are the output current and voltage at the k instant respectively, and $i^*_x(k+1)$ are the output current reference at the (k+1) instant (x=a, b, c). T_s is the sampling time.

$i^*_x(k+1)$ can be calculated by

$$i_x^*(k+1) = 3i_x^*(k) - 3i_x^*(k-1) + i_x^*(k-2) \quad (x = a,b,c) \tag{3}$$

where $i^*_x(k\text{-}2)$, $i^*_x(k\text{-}1)$ and $i^*_x(k)$ are the output current reference at the (k-2), (k-1) and k instant respectively.

Applying the voltage prediction instead of the current form can help reduce the computational burden. It has been verified that there is only one constant difference between the current form and the voltage form. Using current form will penalize 27 vectors per sampling time while only 19 are calculated in the voltage form.

Except for current tracking, the NP voltage should also be considered for normally operating the converter. The voltage difference between the V_p and V_n in the discrete form is expressed as

$$\Delta V_{pn}(k+1) = V_p(k+1) - V_n(k+1) \tag{4}$$

where $V_p(k+1)$ and $V_n(k+1)$ are the predicted voltages of V_p

and V_n at the (k+1) instant respectively. By specific turning off the power switches, the above predictive calculation can be achieved.

Therefore, the final cost function is expressed as

$$j = \sqrt{\lambda_1 (u^*_{xn}(k) - u_{xn}(k))^2 + \lambda_2 (\Delta V_{pn}(k+1))^2} \quad (x = a, b, c) \tag{5}$$

where $u^*_{xn}(k)$ are the output voltage reference (V_{ref}) at the k instant and it can be obtained based on Table I. λ_1 and λ_2 are the weighting factors for current tracking and NP voltage balancing respectively. As analyzed above, it is always a tedious task for selecting the suitable weighting factors and yet there are no selecting guidelines. They are usually determined through working experience.

3 The Proposed MPC Strategy

3.1 Decoupling of CMV and NP Voltage Balancing

The common-mode voltage (CMV) of three phase topologies is define as

$$CMV = \frac{u_{ao} + u_{bo} + u_{co}}{3} \tag{6}$$

where u_{xo} are the output phase voltage shown in Table 1 (x=a, b, c).

Therefore, the T-type three-level converter totally has 7 different CMV values: $\pm 1/6V_{dc}$, $\pm 2/6V_{dc}$ and 0. Different vectors may gain the different CMV values and they are concluded in Table 3. in order to suppress the CMV, the vectors with smaller CMV values should be considered. For example, only zero vectors consisted of medium and [OOO] vectors are applied in [6]. However, the modulation index is limited and the larger dc-link value is needed for the converter. Also, only large, medium, partial small vectors and [OOO] can be used to suppress the CMV. But the NP voltage cannot be recovered actively.

Table 3: Vectors with Different CMV Values

CMV value	Name		
$-1/2V_{dc}$		[NNN]	
$-1/3V_{dc}$	[ONN]	[NON]	[NNO]
$-1/6V_{dc}$	[PNN]	[NPN]	[NNP]
	[OON]	[NOO]	[ONO]
0		[OOO]	
	[PON]	[OPN]	[NPO]
	[NOP]	[ONP]	[PNO]
$1/6V_{dc}$	[PPN]	[NPP]	[PNP]
	[POO]	[OPO]	[OOP]
$1/3V_{dc}$	[PPO]	[OPP]	[POP]
$1/2V_{dc}$		[PPP]	

In fact, the common way to balance the NP voltage is using the small vectors, just like a seven-segment sequence formed by three nearest vectors (one redundant small vector is considered). However, as observed in Table 3, the CMV values of the small vectors are conflicted with their NP voltage balancing ability. In other words, they are coupled to a certain extent. Besides, the converter is supposed to operate in a lager modulation index. For the existing MPC strategies, few of them have been reported on that issue.

As introduced before, the T-type three-level converters have four types of vectors. Take redundant vector [POO] and [ONN], medium vector [PON], lager vector [PNN] and zero vector [OOO] as an example. As shown in Fig. 3(a), none of the three legs of [PNN] are connected with the NP, thus it has no influence on NP voltage. Although three legs of [OOO] are connected to the NP, no other current are flown into or out of the NP as shown in Fig. 3(e). Therefore, [OOO] has no impact on NP voltage. As analyzed in Fig. 3(b), the medium vector can increase or decrease the NP voltage. It is the reason causing the NP voltage unbalanced. As shown in Fig. 3 (c) and (d), the redundant small vectors have an opposite influence on NP voltages. In details, the P-type vector [POO] can increase the lower capacitor voltage and decrease the upper capacitor voltage, thus it can reduce the NP voltage, and the N-type vector [ONN] vise verse. However, as analyzed above, [ONN] can bring lager CMV values and it should be discarded. Therefore, in this paper, [ONN] is replaced by a different N-type vector and the sectors are redistributed.

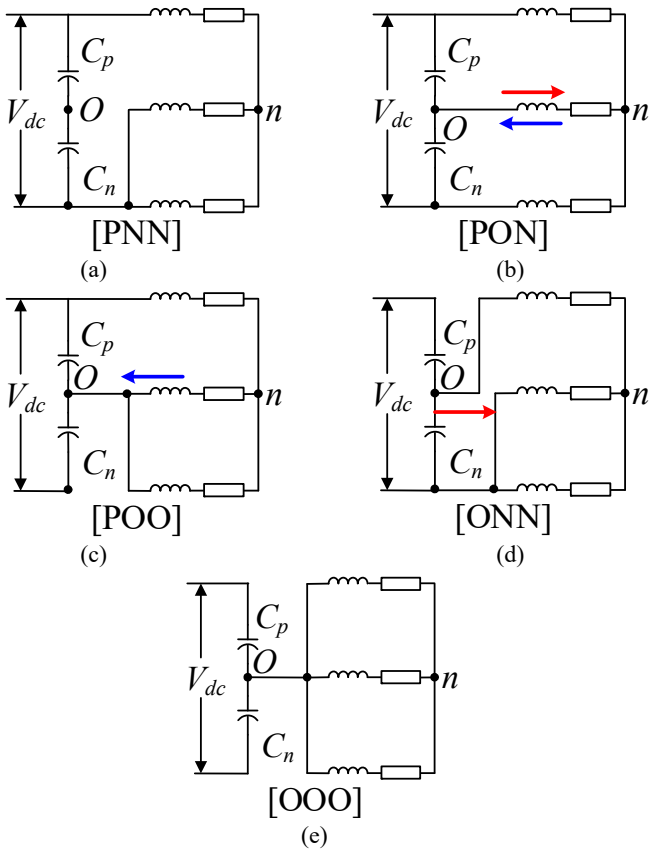

Fig. 3: Impacts on NP voltage of different vectors. (a) Lager vector [PNN]. (b) Medium vector [PON]. (c) Small P-type vector [POO]. (d) Small N-type vector [ONN].

The space voltage vector diagram is divided into 12 sectors as shown Fig. 4. The dividing method is based on the phase angle of the V_{ref}.

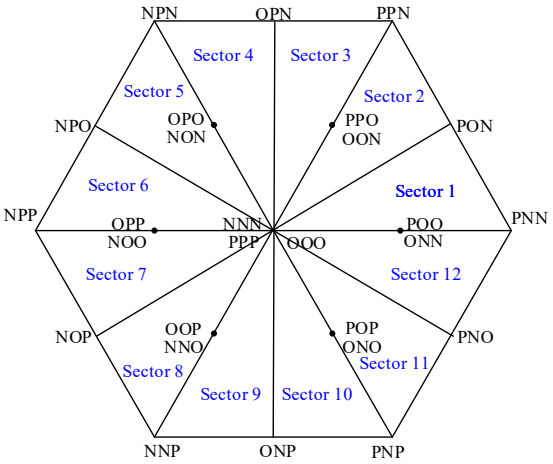

Fig. 4: 12 sectors of the proposed method.

Take sector 1(from 0 degree to 30 degree) as an example. In order to balance the NP voltage, a P-type and an N-type sequences are applied to cover this sector. Then, switching the sequence can actively balance the NP voltage. The P-type seven-segment sequence [OOO]-[POO]-[PON]-[PNN]-[PON]-[POO]-[OOO] formed by four vectors: [OOO], [POO], [PON] and [PNN]. Similarly, the N-type seven-segment sequence [OOO]-[OON]-[PON]-[PNN]-[PON]-[OON]-[OOO] formed by four vectors: [OOO], [OON], [PON] and [PNN]. It can be easily observed that the two sequences cover sector 1, which means the NP voltage can be actively balanced in this sector and the modulation index can reach to the max value. The two seven-segment sequences change only one switching state per phase just like the conventional method. Moreover, there is no switching steps when changing the sequences because both sequences star and end with the same zero vector [OOO]. The CMV values of the two sequences are limited between + and -, which greatly suppress the CMV. All in all, the redesigned sequences can actively balance the NP voltage and suppress the CMV at the same time. According to the above analysis, the sequences in all sectors are concluded in Table. 4. Another conclusion can be drawn that in all sectors all the sequences start and end with the zero vector [OOO]. Therefore, no extra switching changes happen when switching the sectors, which can help reduce the unnecessary switching losses.

Table 4: All Seven-segment Sequences in 12 Sectors.

S	P/N	Seven-segment sequence
1	P	[OOO]-[POO]-[PON]-[PNN]-[PON]-[POO]-[OOO]
	N	[OOO]-[OON]-[PON]-[PNN]-[PON]-[OON]-[OOO]
2	P	[OOO]-[POO]-[PON]-[PPN]-[PON]-[POO]-[OOO]
	N	[OOO]-[OON]-[PON]-[PPN]-[PON]-[OON]-[OOO]
3	P	[OOO]-[OPO]-[OPN]-[PPN]-[OPN]-[OPO]-[OOO]
	N	[OOO]-[OON]-[OPN]-[PPN]-[OPN]-[OON]-[OOO]
4	P	[OOO]-[OPO]-[OPN]-[NPN]-[OPN]-[OPO]-[OOO]
	N	[OOO]-[OON]-[OPN]-[NPN]-[OPN]-[OON]-[OOO]
5	P	[OOO]-[OPO]-[NPO]-[NPN]-[NPO]-[OPO]-[OOO]
	N	[OOO]-[NOO]-[NPO]-[NPN]-[NPO]-[NOO]-[OOO]
6	P	[OOO]-[OPO]-[NPO]-[NPP]-[NPO]-[OPO]-[OOO]
	N	[OOO]-[NOO]-[NPO]-[NPP]-[NPO]-[NOO]-[OOO]
7	P	[OOO]-[OPO]-[NPO]-[NPP]-[NPO]-[OPO]-[OOO]
	N	[OOO]-[NOO]-[NPO]-[NPP]-[NPO]-[NOO]-[OOO]
8	P	[OOO]-[OOP]-[NOP]-[NNP]-[NOP]-[OOP]-[OOO]
	N	[OOO]-[NOO]-[NOP]-[NNP]-[NOP]-[NOO]-[OOO]
9	P	[OOO]-[OOP]-[ONP]-[NNP]-[ONP]-[OOP]-[OOO]
	N	[OOO]-[ONO]-[ONP]-[NNP]-[ONP]-[ONO]-[OOO]
10	P	[OOO]-[OOP]-[ONP]-[PNP]-[ONP]-[OOP]-[OOO]
	N	[OOO]-[ONO]-[ONP]-[PNP]-[ONP]-[ONO]-[OOO]
11	P	[OOO]-[POO]-[PNO]-[PNP]-[PNO]-[POO]-[OOO]
	N	[OOO]-[ONO]-[PNO]-[PNP]-[PNO]-[ONO]-[OOO]
12	P	[OOO]-[POO]-[PNO]-[PNN]-[PNO]-[POO]-[OOO]
	N	[OOO]-[ONO]-[PNO]-[PNN]-[PNO]-[ONO]-[OOO]

3.2 Duty Ratio Calculation

Proper duty ratios should be distributed to obtain better output currents. However, using the convention voltage-second principle cannot solve this issue, because the number of the unknown quantity are more than the equations. In order to calculate the suitable duty ratios, a simple method based on the cost function results of the MPC are proposed. In the above part, the NP voltage is balanced by switching the N- and P-type sequences. Therefore, the item for the NP voltage balancing in cost function j can be removed. The new cost function is only used for current tracking and it is expressed as

$$g = \sqrt{(u_{xn}^{*}(k) - u_{xn}(k))^2} \quad (x = a,b,c) \tag{7}$$

The cost function g represents the distance between the V_{ref} and vectors. Thus, larger the result, farther the distance, which also means the duty ratio of the vector is smaller. Therefore, the duty ratio and the cost function result are inversely proportional and the duty ratios of the four vectors can be calculated by

$$\begin{cases} d_1 = \dfrac{g_2 g_3 g_4}{g_1 g_2 g_3 + g_1 g_2 g_4 + g_2 g_3 g_4 + g_1 g_3 g_4} \\ d_2 = \dfrac{g_1 g_3 g_4}{g_1 g_2 g_3 + g_1 g_2 g_4 + g_2 g_3 g_4 + g_1 g_3 g_4} \\ d_3 = \dfrac{g_1 g_2 g_4}{g_1 g_2 g_3 + g_1 g_2 g_4 + g_2 g_3 g_4 + g_1 g_3 g_4} \\ d_4 = \dfrac{g_1 g_2 g_3}{g_1 g_2 g_3 + g_1 g_2 g_4 + g_2 g_3 g_4 + g_1 g_3 g_4} \end{cases} \tag{8}$$

4 Simulation Verification

The proposed MPC strategy is verified in the Matlab/Simulation. The steady-state and dynamic cases are simulated. The simulated parameters are listed in Table 5.

Table 5: Parameters for Simulation

Parameters/components	Values
DC input voltage (V_{dc})	100 v
Load (R)	6 Ω
Filter (L)	5 mH
Dc-link capacitor ($C_{p,n}$)	3760 μF
Sampling period (T_s)	100 μs
Fundamental frequency	50 Hz
Amplitude of the current reference (i_d)	4A and 8 A

4.1 Steady-state Results

As shown in Fig. 5(a), i_d=4A. The total harmonic distortion (THD) of the output current is 3.75%. The

three-phase currents show a sinusoidal waveform. The CMV is well limited between +1/6V_{dc} (16.6V) and -1/6V_{dc} (-16.6V). The NP voltage is effective balanced around half of the dc-link value (50V). When i_d goes to 8A, the THD is reduced to 1.35% and better output currents are generated. The CMV and NP values are the same with the case when, which indicates that the proposed MPC method performs well in different steady-state cases of effective CMV suppression, NP voltage balance and high quality output currents.

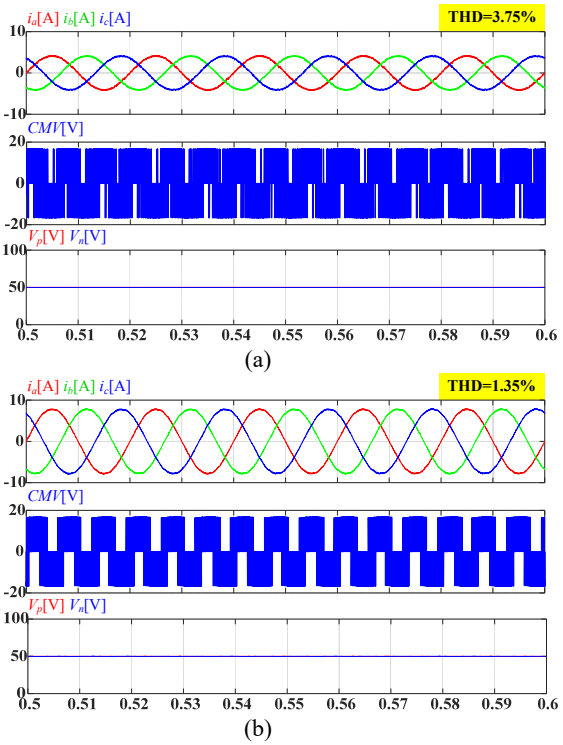

Fig. 5: The steady-state simulation results. (a) i_d=4A. (b) i_d=8A.

4.2 Dynamic Results

When i_d suddenly changes at t=0.55s from 4A to 8A as shown in Fig. 6(a), the output current can quickly track this step, indicating that the proposed MPC method has strong robustness. During the whole response process, the CMV is well suppressed and the NP is effectively balanced.

When setting ΔV_{pn} as 20V as shown in Fig. 6(b), the proposed MPC method can hold this difference until it is set to 0 at t=0.55s. The process of the NP voltage recovering takes about 0.06s. Due to the unbalanced NP voltage, the CMV shows different values. But as soon as the NP voltage is recovered, it is limited between +16.6V and -16.6V. During the dynamic process shown in Fig. 6, the output currents show no significant distortions.

Cost function (7) aims for current tracking only, which means the results of (7) are the optimal vector for current tracking. In other words, it may not the optimal results for both current tracking, NP voltage balancing and CMV suppression in (5). But from the simulated results, the proposed MPC strategy still gains a good output current quality and effective balancing for NP voltages.

The existing research has been proved that adjusting the weighting factors is a tedious work and their different values will greatly influence the control performance. The optimal result from the cost function with weighting factors is a trade-off value for the control targets. The proposed MPC strategy simplify this complex process.

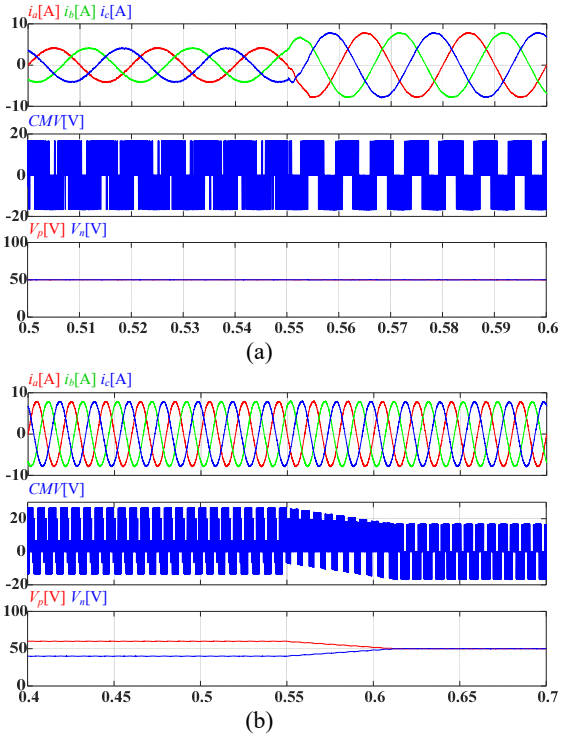

Fig. 6: The dynamic simulation results. (a) Change i_d. (b) Recover NP voltage.

5 Conclusions

In this paper, an improved MPC method is proposed to suppress the CMV and balance the NP voltage actively. Unlike using small vectors for balancing the NP voltage, two different sequences are applied. By switching the sequences in different 12 sectors, the NP voltage can be balanced actively and no other additional switching occurs, even when switching sectors. The two sequences are seven-segment sequences formed by four vectors with the smallest CMV values. Using the conventional voltage-second principle cannot solve the accurate duty ratios, thus in this paper a method based on the cost function results is adopted. Through a simple calculation, the four duty ratios can be solved rapidly. During the whole progress, the weighting factors are removed which saves the tedious work for its selection. Finally, the proposed MPC method is verified simulation, and the results show the proposed MPC method can effectively balance the NP voltage and reduce the CMV values in the steady-state and the dynamic simulation testing.

References

[1] U. -M. Choi, H. -H. Lee and K. -B. Lee, "Simple Neutral-Point Voltage Control for Three-Level Inverters Using a Discontinuous Pulse Width Modulation," *IEEE Transactions on Energy Conver.*, vol. 28, no. 2, pp. 434-443, June 2013.

[2] M. Schweizer and J. W. Kolar, “Design and implementation of a highly ef-ficient 3-level T-type converter for low-voltage applications,” *IEEE. Trans. Power Electron.*, vol. 28, no. 2, pp. 889–907, Feb. 2013.

[3] X. Xing, X. Li, F. Gao, C. Qin and C. Zhang, "Improved Space Vector Modulation Technique for Neutral-Point

Voltage Oscillation and Common-Mode Voltage Reduction in Three-Level Inverter," *IEEE Trans. Ind.Electron*., vol. 34, no. 9, pp. 8697-8714, Sept. 2019.

[4] F. Chen, W. Qiao, H. Wang and L. Qu, "A Simple Zero-Sequence Voltage Injection Method for Carrier-Based Pulsewidth Modulation of the Three-Level NPC Inverter," *IEEE Trans. J. Emerg.Sel. Topics Power Electron.*, vol. 9, no. 4, pp. 4687-4699, Aug. 2021.

[5] C. Liu *et al*., "Leakage Current Suppression of Transformerless 5L-ANPC Inverter With Lower Ripple Model Predictive Control," *IEEE Trans. Ind. Appl.,* vol. 58, no. 5, pp. 6297-6309, Sept.-Oct. 2022.

[6] M. C. Cavalcanti, A. M. Farias, K. C. Oliveira, F. A. S. Neves, and J. L. Afonso, "Eliminating leakage currents in neutral point clamped in- verters for photovoltaic system," *IEEE Trans. Ind. Electron.*, vol. 59, no. 1, pp. 435–443, Jan. 2012.

[7] H.-J. Kim, H.-D. Lee, and S.-K. Sul, "A new PWM strategy for common mode voltage reduction in neutral-point-clamped inverter-fed ac motor drives," *IEEE Trans. Ind. Appl.*, vol. 37, no. 6, pp. 1840–1845, Nov./Dec. 2001.

[8] C. Liu, X. Xing, C. Du, B. Zhang, C. Zhang and F. Blaabjerg, "An Improved Model Predictive Control Method Using Optimized Voltage Vectors for Vienna Rectifier With Fixed Switching Frequency," *IEEE Trans. Power Electron.,* vol. 38, no. 1, pp. 358-371, Jan. 2023.

[9] Y. Yang *et al*., "Computation-Efficient Model Predictive Control With Common-Mode Voltage Elimination for Five-Level ANPC Converters," *IEEE Trans. Transport. Electrific.*, vol. 6, no. 3, pp. 970-984, Sept. 2020.

Proceedings of the 3rd Conference on Fully Actuated System Theory and Applications
May 10-12, 2024, Shenzhen, China

Simplified Double-vector Finite Control Set Model Predictive Control for *LCL*-filtered T-type Inverters with Active Damping

Bei Liu[1], Xiangyang Xing[1], Chang Liu[1]

1. School of Control Science and Engineering, Shandong University, Jinan, Shandong, P. R. China
E-mail: beiliu.sdu@gmail.com

Abstract: The conventional model predictive control (MPC) suffers from high complexity of implementation and large output current ripples. In this article, a simplified double-vector finite control set MPC (FCS-MPC) method with active damping is proposed for three-level T-type ($3LT^2$) inverters with LCL filter. First, the predictive model with active damping method is derived. Second, to reduce computation burden, a phase-to-line voltage coordinate algorithm is adopted. Furthermore, the vector space where reference voltage locates is simplified from three-level space to two-level space. Third, a geometry-based technique is used to select two optimized candidate vectors and calculate duty cycles. The proposed strategy not only enhances the portability of the conventional FCS-MPC method, but also reduces the harmonic components induced by LCL filter. In the end, simulations are performed to validate the effectiveness of the proposed strategy.

Key Words: three level T-type converters, LCL filter, double vector FCS-MPC

1 Introduction

As large scale exploitation of renewable energy continues to domain the power generation landscape, the renewable-based power system has been widely implemented. The grid-connected inverter, which inverts dc power into ac power for the grid integration, is essential for the overall system operation. Among various topologies, three level T-type ($3LT^2$) inverter is one of the most promising candidates with benefits such as low total harmonic distortion (THD), low cost, and higher overall efficiency[1]. Furthermore, in order to fulfill the grid code requirements for $3LT^2$ inverters, LCL filter, which offers good resonance attenuation performance, is now widely applied to interface the inverters to the grid.

Nevertheless, various challenges exist for the LCL-filtered $3LT^2$ inverter. One inherent risk of the potential imbalance of the NP (upper and lower capacitors of dc link) voltage of T-type inverter, which requires specific control. Besides that, LCL filter brings resonance-induced harmonics, which should also be well suppressed[2]. Numerous control strategies have been proposed to tackle related problems. Among them, FCS-MPC is becoming a competitive strategy due to high response speed and control flexibility[3].

Several studies have investigated the implementation of FCS-MPC in three-level converters. An improved FCS-MPC method was first proposed in [4], in which the synthesized vectors are calculated without going through the look up table, but the steady state performance of the proposed method is limited due to the single vector usage in every sampling period. [5] proposed a double-vector MPC (DMPC) method, in which both optimal phase and length vectors are synthesized to suppress current ripples and achieve NP voltage balance. However, the calculation complexity is high, making it hard to implement. In [6], a fast FCS-MPC method was proposed for the $3LT^2$ inverter without weighting factors, which well guaranteed the NP voltage balance and steady-state performance, and reduced the computational burden. [7] and [8] also proposed simplified DMPC methods with reduced complexity. Although these studies revealed the superiority of DMPC methods, few of them discussed simplified DMPC method considering the LCL harmonics damping. Typically, to achieve grid current with low THD, adequate filter design and active damping(AD) strategies are required, as suggested in [9]. Motivated by the above-mentioned, this paper proposes a low harmonic simplified DMPC method for the LCL filtered $3LT^2$ inverter. The main contributions of this article can be summarized as follows:

1) To eliminate harmonics caused by LCL filter, an active damping method using the high-frequency component of filter capacitor voltage is considered and prediction model is derived in this paper.

2) An easy and intuitive DMPC method is proposed in this paper. In the proposed method, a geometric technique for the selection of optimized candidate vectors and calculation of their corresponding duty ratios is adopted. The vector space where reference voltage resides is simplified from three-level space to two-level space, therefore reducing the conventional tedious candidate vector selection procedures.

2 Model of LCL-filtered $3LT^2$ inverter

Fig.1 presents the structure of the three-level T-type inverter with the *LCL* filter, where V_{dc} is the voltage on the dc side, V_p and V_n are dc side capacitor voltages; i_{1a}, i_{1b}, and i_{1c} are the inverter-side currents, i_{2a}, i_{2b}, and i_{2c} the grid-side currents; L_1, L_2, C_f are the inductors and capacitors of the *LCL* filter, R_1, R_2 are the parasitic resistances of the inductors, u_{Cfa}, u_{Cfb}, and u_{Cfc} are the three-phase filter capacitor voltages.

*This work was supported in part by the Science Center Program of National Natural Science of China under Grant 62188101.

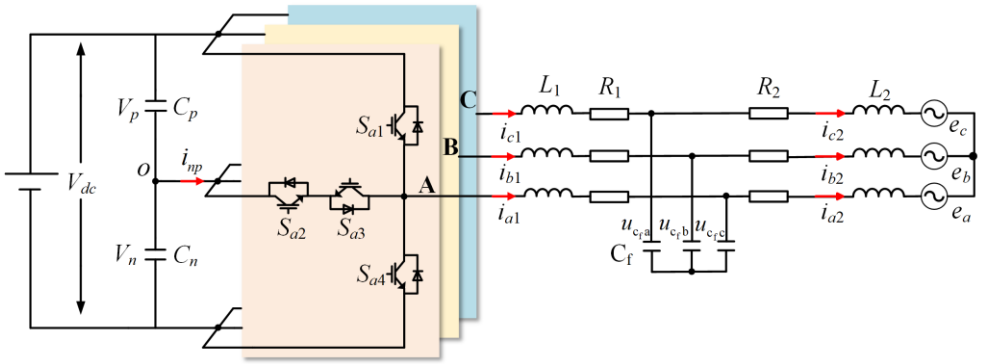

Fig.1: Topology of the LCL-filtered T-type inverter

According to Kirchhoff's voltage Law, the inverter-side voltage balance equation can be derived as:

$$\begin{cases} u_{ao} = L_1 \dfrac{\mathrm{d}i_{1a}}{\mathrm{d}t} + R_1 i_{1a} + u_{c_f a} \\ u_{bo} = L_1 \dfrac{\mathrm{d}i_{1b}}{\mathrm{d}t} + R_1 i_{1b} + u_{c_f b} \\ u_{co} = L_1 \dfrac{\mathrm{d}i_{1c}}{\mathrm{d}t} + R_1 i_{1c} + u_{c_f c} \end{cases} \tag{1}$$

where u_{ao}、u_{bo}、u_{co} are the inverter output voltages.

Using Clark transformation and backward Euler approximation of Eq. (1), we derive

$$\begin{cases} u_{\alpha o}(k+1) = \dfrac{L}{T_s} i_{1\alpha}(k+1) + (R_1 - \dfrac{L}{T_s}) i_{1\alpha}(k) + u_{c_f \alpha}(k+1) \\ u_{\beta o}(k+1) = \dfrac{L}{T_s} i_{1\beta}(k+1) + (R_1 - \dfrac{L}{T_s}) i_{1\beta}(k) + u_{c_f \beta}(k+1) \end{cases} \tag{2}$$

where T_s is the sampling period, $u_{\alpha o}(k+1)$, $u_{\beta o}(k+1)$ are the $(k+1)$th-sampling-instant inverter output voltages, $u_{C f\alpha}(k+1)$ and $u_{C f\beta}(k+1)$ are the $(k+1)$th-sampling-instant capacitor voltages, $i_{1\alpha}(k)$, $i_{1\beta}(k)$ and $i_{1\alpha}(k+1)$, $i_{1\beta}(k+1)$ are the inverter-side currents at the kth and $(k+1)$th sampling instant.

According to Eq. (2), the tracking of inverter reference current $i_1^*(k+1)$ equals to the tracking of reference voltage $u^*(k+1)$. Also as filter capacitor voltage changes at a relatively slow speed, kth-sampling-instant capacitor voltage $u_{C f\alpha}(k)$ and $u_{C f\alpha}(k+1)$ can be considered constant, therefore, the prediction model can be obtained as

$$\begin{cases} u^*_{\alpha o}(k+1) = \dfrac{L}{T_s} i^*_{1\alpha}(k+1) + (R_1 - \dfrac{L}{T_s}) i_{1\alpha}(k) + u_{c_f \alpha}(k) \\ u^*_{\beta o}(k+1) = \dfrac{L}{T_s} i^*_{1\beta}(k+1) + (R_1 - \dfrac{L}{T_s}) i_{1\beta}(k) + u_{c_f \beta}(k) \end{cases} \tag{3}$$

In addition, the cost function g based on inverter output voltage is

$$g = [u^*_\alpha(k+1) - u_\alpha(k+1)]^2 + [u^*_\beta(k+1) - u_\beta(k+1)]^2 \tag{4}$$

To eliminate the the deviation between the given value of reference current and its actual value, the reference current $i_1^*(k+1)$ needs to be obtained by

$$\begin{cases} i^*_{1\alpha}(k+1) = 3i^*_{1\alpha}(k) - 3i^*_{1\alpha}(k-1) + i^*_{1\alpha}(k-2) \\ i^*_{1\beta}(k+1) = 3i^*_{1\beta}(k) - 3i^*_{1\beta}(k-1) + i^*_{1\beta}(k-2) \end{cases} \tag{5}$$

where $i_{1\alpha}(k-1)$, $i_{1\beta}(k-1)$ and $i_{1\alpha}(k-2)$, $i_{1\beta}(k-2)$ are the inverter-side current at the $(k-1)$th and $(k-2)$th sampling instant,

3 Active damping method

Omitting parasitic resistance of filter inductors, the equivalent circuit of Fig.1 and system control block are displayed in Fig.2.

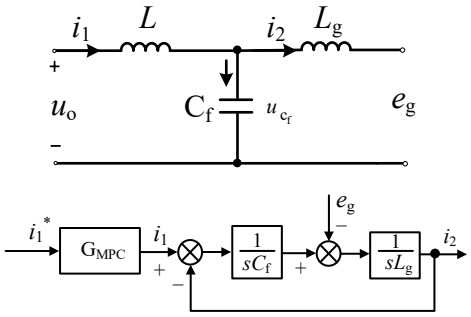

Fig.2: Equivalent circuit and control block of system with no added damping

To provide adequate damping for the system, an active damping method is adopted, displayed in Fig.3.

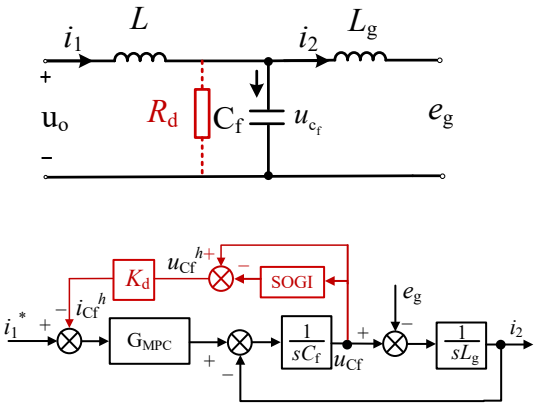

Fig.3: Equivalent circuit and control block of system with active damping

In Fig.3, SOGI (Second Order Generalized Integrator), seen as a low pass filter, is used to obtain the fundamental frequency component of the filter voltage. K_d represents the damping coefficient, usually calculated by

$$K_d = 2\mu\sqrt{\frac{C}{L_2}} \tag{6}$$

where μ is 0.6. Considering the transfer function of MPC is 1, the open loop transfer functions of system in Fig.2 and Fig.3 can be derived, respectively, as G_1 and G_2:

$$\begin{cases} G_1 = \dfrac{1}{s^2 L_g C_f + 1} \\ G_2 = \dfrac{1}{L_g C_f s^2 + K_d L_g s + 1} \end{cases} \tag{7}$$

The comparison of system bode plot is presented in Fig.4, showing that the active damping method can effectively mitigate the resonance peak.

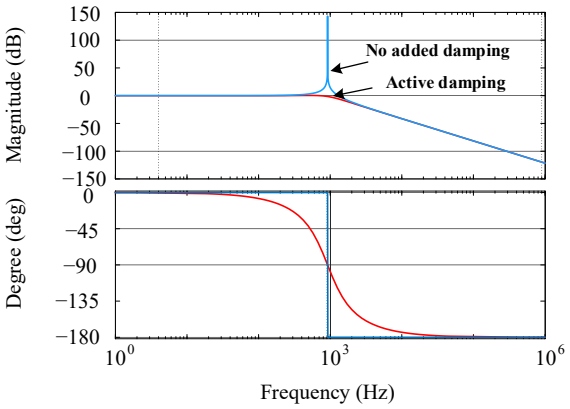

Fig.4: Comparison of system bode plots

Compare the control block diagram transformation after employing the active damping method, it can be concluded that the LCL resonance suppression is achieved by suppressing the high-frequency component of the filter capacitor current. From the perspective of voltage, it can be considered that the full-frequency component of the filter capacitor voltage $u_{Cf}(k)$ involved in the calculation of the prediction equation before can be replaced by the low-frequency component of the capacitor voltage $u_{Cf_l}(k)$, thus the prediction model of the system after the addition of active damping can be re-derived as

$$\begin{cases} u_{\alpha o}^{*}(k+1) = (R_1 - \dfrac{L_1}{T_s}) i_{1\alpha}(k) + \dfrac{L_1}{T_s} i_{1\alpha}^{*}(k+1) + u_{C_f\alpha_l}(k) \\ u_{\beta o}^{*}(k+1) = (R_1 - \dfrac{L_1}{T_s}) i_{1\beta}(k) + \dfrac{L_1}{T_s} i_{1\beta}^{*}(k+1) + u_{C_f\beta_l}(k) \end{cases} \tag{8}$$

Further, the MPC cost function is given as

$$g = [u_\alpha^*(k+1) - u_\alpha(k+1)]^2 + [u_\beta^*(k+1) - u_\beta(k+1)]^2 \tag{9}$$

4 Proposed double-vector FCS-MPC

4.1 Phase/Line-voltage coordinate transformation

Fig.5 displays the space vector diagram of the 3LT^2 inverter in line voltage coordinate. Define the reference voltage vector coordinates as $u_x(k)(x=a, b, c)$ in the abc voltage coordinate system and $u_{xy}(k)(xy=ab, bc, ca)$ in the line voltage coordinate system, then the line voltage coordinates of the any vector can be given as

$$\begin{bmatrix} u_{ab}(k) \\ u_{bc}(k) \\ u_{ca}(k) \end{bmatrix} = \begin{bmatrix} 1 & -1 & 0 \\ 0 & 1 & -1 \\ -1 & 0 & 1 \end{bmatrix} \begin{bmatrix} u_a(k) \\ u_b(k) \\ u_c(k) \end{bmatrix} \tag{10}$$

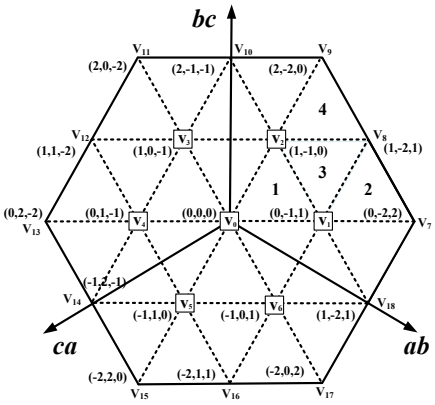

Fig. 5: Space vector diagram under line voltage coordinate

Unlike the traditional algorithms where Clarke transformations are required, the line voltage coordinate system proposed in this section does not require complex coordinate transformations, so it greatly simplifies the vector selection and duty cycle calculation process.

There are two types of triangular sectors in the space vector diagram under the line voltage coordinate system, which can be divided into equilateral and inverted triangular sectors, as shown in Fig.6. The vectors can be selected and their duty cycles calculated according to the different sectors where the reference voltage is located.

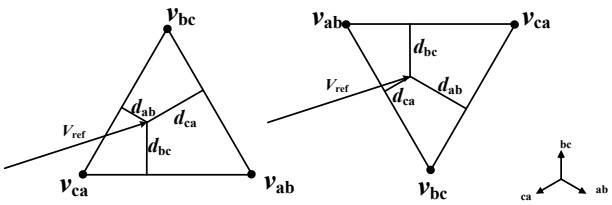

Fig. 6: Equilateral and inverted triangle sectors

In order to determine the sector type as well as calculate duty cycles, first we obtain $u^f_{xy}(k)$ by

$$u^f_{xy}(k) = floor(u_{xy}(k)) \quad (xy=ab,bc,ca) \tag{11}$$

where *floor*() is a function that can round down the real values to the integer values. Since the reference voltage is usually transformed into per unit values beforehand, the height of the triangle sector becomes 1, so the method of determining the type of triangle where the reference vector is located can be expressed as follows:

$$V_{ref} \text{ locates in } \begin{cases} \text{equilateral triangle sector, if } \sum\limits_{xy=ab,bc,ca} u^f_{xy}(k) = -1 \\ \text{inverted triangle sector, if } \sum\limits_{xy=ab,bc,ca} u^f_{xy}(k) \neq -1 \end{cases} \tag{12}$$

The corresponding duty cycles d_{ab}, d_{bc}, d_{ca} for synthesizing vectors v_{ab}, v_{bc}, v_{ca} are denoted as

$$\begin{cases} d_{ab} = u_{ab}(k) - u^{f}_{ab}(k) \\ d_{bc} = u_{bc}(k) - u^{f}_{bc}(k) \\ d_{ca} = u_{ca}(k) - u^{f}_{ca}(k) \end{cases} \text{, if } V_{ref} \text{ in equilateral triangles}$$

$$\begin{cases} d_{ab} = 1 - [u_{ab}(k) - u^{f}_{ab}(k)] \\ d_{bc} = 1 - [u_{bc}(k) - u^{f}_{bc}(k)] \\ d_{ca} = 1 - [u_{ca}(k) - u^{f}_{ca}(k)] \end{cases} \text{, if } V_{ref} \text{ in inverted triangle} \quad (13)$$

4.2 Vector space mapping

To further simplify the calculation, this subsection proposes a mapping method based on the line voltage coordinate system, which reduces the three-level vector space to a two-level space, as shown in Fig.7.

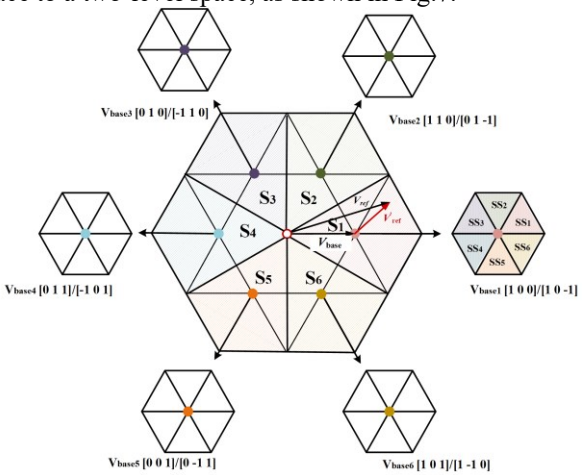

Fig. 7: Vector mapping process

Therein, the three-level space vector map can be regarded as a composition of six two-level space vector maps, and each two-level space vector map contains six small triangular sectors. In order to simplify the calculation, the reference vectors in the three-level space are mapped into the two-level space by subtracting the center voltage vectors V_{base} of the two-level space vector maps:

$$u^{d}_{x}(k) = u_{x}(k) - U_{base} \quad (x=a,b,c) \quad (14)$$

where u^{d}_{x} is the coordinates of the reference vector under the two-level space after mapping, u_x is the coordinates of the reference vector under the three-level space before mapping, and U_{base} is the coordinate of centre voltage vector.

V_{base} can be selected according to the three-level macrosector in which the reference voltage is located:

$$S = \begin{cases} S_1 \ \ if \ u_a(k) > 0, \ u_b(k) < 0, \ u_c(k) < 0 \\ S_2 \ \ if \ u_a(k) > 0, \ u_b(k) > 0, \ u_c(k) < 0 \\ S_3 \ \ if \ u_a(k) < 0, \ u_b(k) > 0, \ u_c(k) < 0 \\ S_4 \ \ if \ u_a(k) < 0, \ u_b(k) > 0, \ u_c(k) > 0 \\ S_5 \ \ if \ u_a(k) < 0, \ u_b(k) < 0, \ u_c(k) > 0 \\ S_6 \ \ if \ u_a(k) > 0, \ u_b(k) < 0, \ u_c(k) > 0 \end{cases} \quad (15)$$

where S_1 to S_6 are the two-level vector space numbers.

Next, to determine the small triangle sector number where the reference voltage is located in the two-level space vector map, we should follow:

$$ss = \begin{cases} ss_1 \ \ if \ u^{d}_{a}(k) > 0, \ u^{d}_{b}(k) > 0, \ u^{d}_{c}(k) < 0 \\ ss_2 \ \ if \ u^{d}_{a}(k) < 0, \ u^{d}_{b}(k) > 0, \ u^{d}_{c}(k) < 0 \\ ss_3 \ \ if \ u^{d}_{a}(k) < 0, \ u^{d}_{b}(k) > 0, \ u^{d}_{c}(k) > 0 \\ ss_4 \ \ if \ u^{d}_{a}(k) < 0, \ u^{d}_{b}(k) < 0, \ u^{d}_{c}(k) > 0 \\ ss_5 \ \ if \ u^{d}_{a}(k) > 0, \ u^{d}_{b}(k) < 0, \ u^{d}_{c}(k) > 0 \\ ss_6 \ \ if \ u^{d}_{a}(k) > 0, \ u^{d}_{b}(k) < 0, \ u^{d}_{c}(k) < 0 \end{cases} \quad (16)$$

Using simple logical judgement of the phase and line voltages, respectively, we can finally obtain the small sector where the reference voltage is located, and then the combination of vector states in the two levels can be obtained. In this process, Eq. (15) determines the section where V_{ref} locates and Eq. (16) determines the sub-section where V'_{ref} stays.

In the same time, the number of candidate vectors is reduced from 27 to 3, so the computational effort is greatly reduced.

Next, the optimal double synthesizing vectors and their optimal duty cycles need to be determined from the chosen combination of two level vector states

4.3 Double vector selection and duty cycle calculation

In the two-level space, there are three candidate vectors in every sector, so we need to select two vectors out of three. Based on experience, the vector with the smallest duty ratio contributes least for the synthesis. Therefore, in order to achieve the minimum current tracking error, the vectors with the largest and second largest duty ratios are considered to be the two optimized vectors in our proposed method.

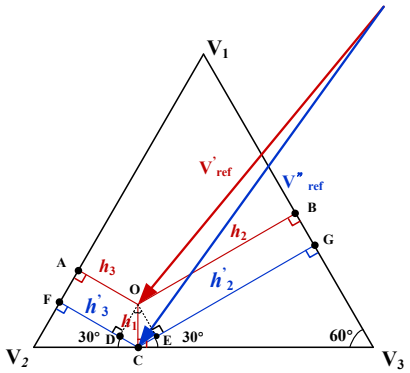

Fig. 8: Duty ratio calculation diagram for double vectors

Fig.8 displays an example of the selection process, in which h_1 is the smallest duty ratio of three, thus we select V_2 and V_3 as the optimized candidate vectors. Using V_2 and V_3, we obtain the synthesized vector V''_{ref}, which has the most approximation to V'_{ref}. It can be observed from Fig.8 that the auxiliary line segment OD forms a 30° angle with both OC and OE, therefore DC and CE both equal to half of OC. Also as DF equals OA, EG equals OB, the duty ratio for V_2 (h'_2/CG) and V_3(h'_3/CF) in synthesizing V''_{ref} are

$$\begin{cases} h'_2 = h_2 + h_1 / 2 \\ h'_3 = h_3 + h_1 / 2 \end{cases} \quad (17)$$

To generalize the calculation, we have

$$
\begin{aligned}
&h_{\min} = \min(h_1, h_2, h_3) \\
&\text{if } h_{\min} = h_1 \\
&\begin{cases} h_{op1} = h_2 + h_1/2 \\ h_{op2} = h_3 + h_1/2 \end{cases}, \ V^d_{op1}=V_2 \ \ V^d_{op2}=V_3 \\
&\text{if } h_{\min} = h_2 \qquad (18) \\
&\begin{cases} h_{op1} = h_1 + h_2/2 \\ h_{op2} = h_3 + h_2/2 \end{cases}, \ V^d_{op1}=V_1 \ \ V^d_{op2}=V_3 \\
&\text{if } h_{\min} = h_3 \\
&\begin{cases} h_{op1} = h_1 + h_3/2 \\ h_{op2} = h_2 + h_3/2 \end{cases}, \ V^d_{op1}=V_1 \ \ V^d_{op2}=V_2
\end{aligned}
$$

Following the above procedures, the optimal two-vector V^d_{op1}、V^d_{op2} in two-level space and their corresponding duty cycles h_{op1}、h_{op2} can be determined, which eventually need to be remapped to the three-level space in order to determine the switching states of the corresponding vectors and output the control signals.

4.4 NP voltage balancing

Using the characteristics of redundant small vectors, the NP voltages on the dc side can be well balanced by switching positive and negative redundant small vectors.

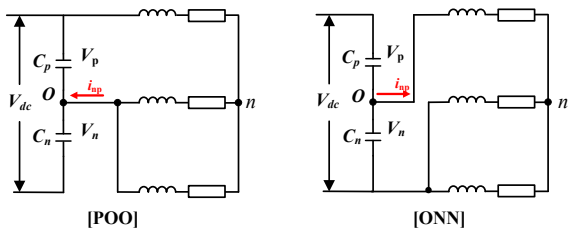

(a) (b)

Fig.9: Impacts on NP voltage of different vectors, (a) Small P-type vector [POO], (b) Small N-type vector [ONN]

Define Δv_{pn} to be the deviation of upper and lower capacitor voltage, and Δv_{pn} can be used to make the switching judgement of redundant small vectors. If $\Delta v_{pn} > 0$, then $v_p > v_n$, then the upper capacitor C_p needs to be discharged, so the positive small vector should be selected; if $\Delta v_{pn} < 0$, then $v_p < v_n$, then the upper capacitor C_p needs to be charged, so the negative small vector should be selected then. The priority of midpoint voltage balance control is ranked after current tracking. In the actual optimal switching vector selection process, when the redundant small vectors participate in the synthesis of the reference voltage, the corresponding redundant small vectors are selected for the midpoint balancing control according to the midpoint voltage, so that the introduction of the weight factor in the value function can be avoided.

5 Simulation Verification

In order to verify the feasibility and advantages of the proposed AD-based DMPC (AD-DMPC) method, simulation is performed using the parameters in Table I.

Table 1: Simulation parameters

Parameters	Values
DC input voltage (V_{dc})	300 v
Dc link capacitor (C_p, C_n)	2000 μF
Inverter-side inductor(L)	3 mH
Grid-side inductor (L_g)	1.5 mH
Filter capacitor (C_f)	20 μF
Parasitic resistor R_1	0.5 Ω
Sampling period (T_s)	100 μs
Output fundamental frequency	50 Hz
Inverter-side reference current $i_{1\ ref}$	15 A/10A

Define Method-1 to be the conventional single-vector FCS-MPC strategy and Method-2 to be the simplified two-vector FCS-MPC with active damping proposed in this paper.

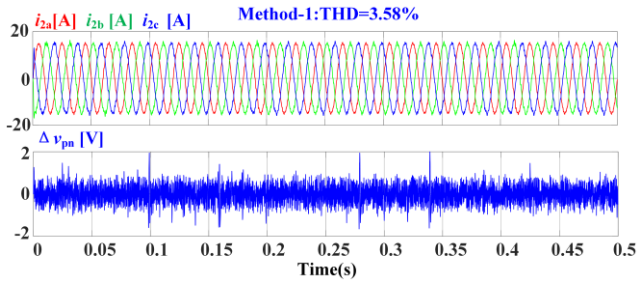

(a) Method-1

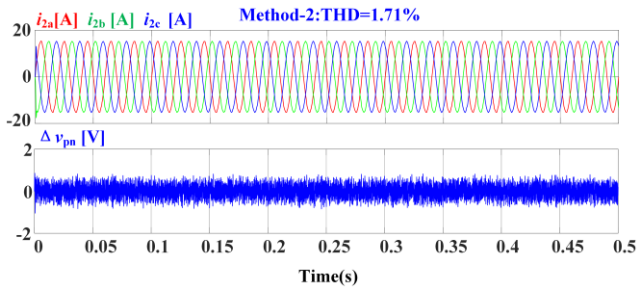

(b) Method-2

Fig.10: The steady-state simulated results of grid-side current and dc link capacitor voltage deviation

It can be observed from Fig.10 that the THD of Method-2 is lower than Method-1. Since two vectors are used to synthesize the reference voltage in each control cycle, the quality of the grid-side current can be improved. In addition, Method-2 not only balances the midpoint voltage, but also facilitates midpoint voltage fluctuation suppression.

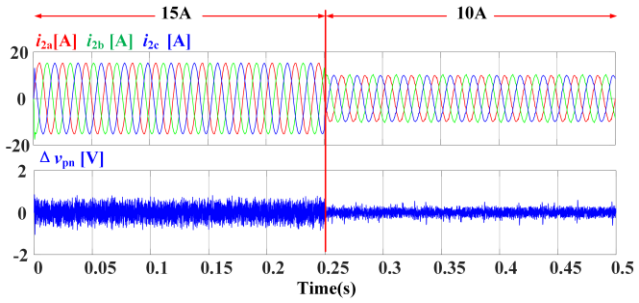

Fig.11: The dynamic simulated results when changing the amplitude of i_{1_ref} with Method-2

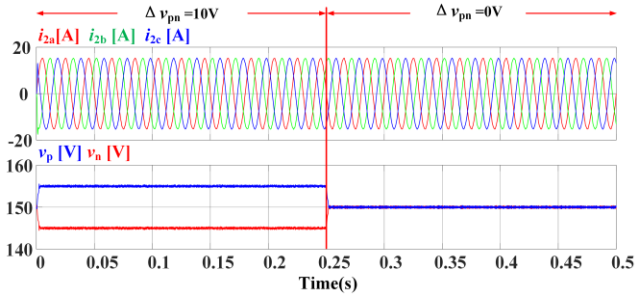

Fig.12: The dynamic simulated results when changing Δv_{pn} with Method-2

It can be seen from Fig.11 that when i_{1_ref} is switched at the moment of t=0.25 sec and the amplitude is switched between 10A and 15A, the grid-side current responds very fast, and it can track up to the amplitude of i_{1_ref} at the instant of t=0.25 sec. In addition, the midpoint voltage is effectively balanced in the process of dynamic change, and no distortion occurs in the grid-side currents.

The midpoint balancing is controlled by switching the redundant small vectors and therefore also has the ability to actively balance the midpoint voltage. As shown in Fig.12, at different given currents, when Δv_{pn} is switched to 0 at 0.25 sec, the midpoint voltage is quickly balanced, and both the upper and lower capacitor voltages on the DC side are maintained at about 150V.

6 Conclusion

Aiming at the problems of low control accuracy and high computational burden of the traditional FCS-MPC method, this paper proposes a simplified dual-vector FCS-MPC algorithm with active damping, which simplifies the implementation of the dual-vector FCS-MPC algorithm while reducing the distortion of the output current. Compared with the traditional methods, the proposed AD-based dual-vector FCS-MPC strategy cleverly reduces the complexity of finite-set candidate vector evaluation using simple logic judgement and geometric principles, which decreases the difficulty in optimal dual-vector selection and duty cycle calculation. Simulations verify the effectiveness of the proposed method in improving the quality of grid-side currents.

References

[1] Wang H, Zhang H. Study on an improve finite-control-set model predictive control (FCS-MPC) strategy for a T-type rectifier with direct power control strategy[J]. *IEEE Transactions on Electrical and Electronic Engineering*, 2023, 18(3): 442-450.

[2] Finite control set model predictive control for LCL-filtered grid-tied inverter with minimum sensors[J]. *IEEE Transactions on Industrial Electronics*, 2020, 67(12): 9980-9990.

[3] Xue C, Zhou D, Li Y. Finite-control-set model predictive control for three-level NPC inverter-fed PMSM drives with LC filter[J]. *IEEE Transactions on Industrial Electronics*, 2020, 68(12): 11980-11991.

[4] J. Lee, J. Lee, H. Moon, and K. Lee, "An improved finite-set model predictive control based on discrete space vector modulation methods for grid-connected three-level voltage source inverter," *IEEE Trans. J. Emerg.Sel. Topics Power Electron.*, vol. 6, no. 4, pp. 1744–1760, Dec. 2018.

[5] Mohapatra S R, Agarwal V. Model predictive controller with reduced complexity for grid-tied multilevel inverters[J]. *IEEE Transactions on Industrial Electronics*, 2018, 66(11): 8851-8855.

[6] Yang Y, Wen H, Fan M, et al. Fast finite-switching-state model predictive control method without weighting factors for T-type three-level three-phase inverters[J]. *IEEE Transactions on Industrial Informatics*, 2018, 15(3): 1298-1310.

[7] Liu T, Chen A, Qin C, et al. Double vector model predictive control to reduce common-mode voltage without weighting factors for three-level inverters[J]. *IEEE Transactions on Industrial Electronics*, 2020, 67(10): 8980-8990.

[8] Zhou H，Huang L，Yang J，et al．Low Complexity Double Vector Model Predictive Control with Minimum Root Mean Square Error for Three-phase Three-Level Inverters[J]．*IEEE Journal of Emerging and Selected Topics in Power Electronics*，2023，11(6)：5809-5819．

[9] Falkowski P, Sikorski A. Finite control set model predictive control for grid-connected AC–DC converters with LCL filter[J]. *IEEE Transactions on Industrial Electronics*, 2017, 65(4): 2844-2852.

Proceedings of the 3rd Conference on Fully Actuated System Theory and Applications
May 10-12, 2024, Shenzhen, China

Fully-actuated Robust Predictive Control for Cascaded Under-actuated Systems

Xiubo Wang[1], Guangren Duan[1,2]

1. Center for Control Theory and Guidance Technology, Harbin Institute of Technology, Harbin, 150001, P. R. China
E-mail: xiubowang@outlook.com

2. Shenzhen Key Laboratory of Control Theory and Intelligent System, Southern University of Science and Technology, Shenzhen, 518055, P. R. China
E-mail: g.r.duan@hit.edu.cn.

Abstract: This study focuses on robust predictive control for cascaded under-actuated systems (UASs) based on fully-actuated system (FAS) approaches. Rooted in the fundamental principles of model mechanics, the dynamic model for a cascade UAS is derived from the Lagrangian equation. A global coordinate transformation is given for the cascaded UAS, which kinetic and potential energy are in general forms, such that the cascade UAS is converted into an equivalent FAS. Meanwhile, considering discretization errors inevitably introduced during the model discretization process, the FAS-RPC control scheme is proposed. The predictive controller is solved through linear matrix inequalities (LMI) and the asymptotical stability of the closed-loop system and minimum of robust performance index can be guaranteed simultaneously. Finally, the effectiveness of the proposed algorithm is verified by the simulation of a cascaded under-actuated dual rotational translational actuator (RTAC) system.

Key Words: Cascaded UASs, FAS approaches, coordinate transformation, discretization errors, robust predictive control.

1 Introduction

In the field of control systems engineering, effectively controlling under-actuated systems (UASs) remains a pivotal challenge, which becomes an important research topic aiming at significant improvement of the behavioural performance and energy efficiency [1]. UASs characterized by having fewer control inputs than degrees of freedom, pose significant challenges due to their inherent complexity and nonlinearity [2]. The burgeoning interest in UASs stems from their extensive applicability, ranging from aerospace engineering to marine manipulators, robotics systems , flexible systems, mobile systems, locomotive systems, etc [3–6].

As benchmarks, some UASs are used to test different control techniques [7–9]. Effective control strategies must not only address the inherent under-actuation but also mitigate impacts arising from system nonlinearities and uncertainties [10]. Control methods for UASs encompass, but are not limited to, feedback linearization, sliding mode control, energy-shaping methods, adaptive control, optimal control, predictive control, intelligent control, and hybrid control. Each method offers unique advantages and is suited for specific scenarios. For instance, feedback linearization simplifies control challenges by linearizing nonlinear system dynamics [11]. A linear auxiliary sliding mode controller is designed to avoid the singularity problem in a UAS [12]. Predictive control is used for unactuated constraints with constraints conversions [13], and energy-shaping methods manipulate the system's energy landscape to achieve control objectives [14].

As mentioned in [15], it is essential to highlight that the most methods outlined above employ the state-space representation of system models for the subsequent controller design. The solution procedure of the nonlinear optimization problem for the first-order state-space model via variable augmentation becomes more and more intractable, and the optimization solutions begin to transition from an offline accurate analytical solution to a numerical online solution. As a methodology, the FAS approach breaks away from traditional thinking, which takes a new perspective on the problem of FASs by starting from the models' mechanics and focusing on control variables [16]. Specifically, the FAS approach, by preserving a full actuation model with physically meaningful or establishing one with mathematically meaningful, fully leverages the attributes of full actuation [17]. This approach also encompasses some foundational works on UASs [16], such as strict feedback system [18], non-holonomic systems, Brockett's examples [19, 20] and some benchmark UASs [17, 21, 22].

However, current research for UASs based on FAS approaches lacks paradigmatic breakthroughs. Drawing inspiration from FAS methodologies, this study embarks on bridging the gap between UASs and FASs, and concurrently explores robust predictive control (RPC) for a type of cascaded UASs. Specifically, we venture to the following aspects in this paper:

1) A novel paradigm for converting a general type cascaded UASs into FASs is proposed. Based on the fundamental principles of the model, a concise form of the Euler-Lagrange equations for cascaded UASs is delineated. Meanwhile, considering that the kinetic and potential energy of each sub-UAS are in general forms, a global coordinate transformation relation is given to transform the cascaded UAS into a FAS.

2) A FAS-RPC control scheme is proposed for digitally implemented discrete-time FAS with discretization error. The inevitable discretization error in the digital implementation of predictive control is regarded as a bounded uncertainty term for comprehensive controller designed.

3) The complexity of predictive control issues in the cascaded UAS is significantly reduced. Based FAS approaches, the optimization problem, originally a multivariable infinite-time domain issue, is transformed into

This work has been partially supported by the Science Center Program of the National Natural Science Foundation of China under grant No. 62188101

several independent, decoupled sub-optimization problem. Each sub-optimization problem focuses on optimizing an upper bound of performance index.

For the sake of convenience, the following notations are frequently used in this paper. In continuous-time cases, for variable vectors $x_i \in \mathbb{R}^m$, as in [16], we denote that

$$x_i^{(j)}\Big|_{j=p\sim q}=\begin{bmatrix} x_i^{(p)} \\ x_i^{(p+1)} \\ \vdots \\ x_i^{(q)} \end{bmatrix}, x_i^{(j)}\Big|_{i=m\sim n, j=p\sim q}=\begin{bmatrix} x_m^{(j)}\Big|_{j=p\sim q} \\ x_{m+1}^{(j)}\Big|_{j=p\sim q} \\ \vdots \\ x_n^{(j)}\Big|_{j=p\sim q} \end{bmatrix}.$$

Parallelly, in discrete-time cases, we use the following ones as [23]:

$$z_i^{(j)}(k)\Big|_{j=p\sim q}=\begin{bmatrix} z^{(p)}(k) \\ z^{(p+1)}(k) \\ \vdots \\ z^{(q)}(k) \end{bmatrix}, z_i^{\lfloor j \rfloor}(k)|_{i=m\sim n, j=p\sim q}=\begin{bmatrix} z_m^{\lfloor j \rfloor}(k) \\ z_{m+1}^{\lfloor j \rfloor}(k) \\ \vdots \\ z_n^{\lfloor j \rfloor}(k) \end{bmatrix},$$

where $z_i^{(j)}(k) = z_i(k+j)$. Meanwhile, $\mathcal{D}\left(x^{(i)}\right)$ presents the discretization operation for the continuous-time derivatives $x^{(i)}$, $\langle X \rangle Y$ presents the the coefficient of X in polynomial Y

2 Cascade UASs

In this section, a type of cascaded UASs is studied from model mechanisms. Based on the Euler Lagrange equation of each sub-UAS, the multi-order UASs model is firstly derived. Then a transformation paradigm from UASs to FASs and its discretization model with uncertainties are given.

2.1 From UASs to FASs

Consider a cascaded UAS with n sub-UASs, the Euler-Lagrange equation for the i-th sub-UAS is given as follows

$$\begin{cases} \dfrac{\mathrm{d}}{\mathrm{d}t}\dfrac{\partial \mathcal{L}_i}{\partial \dot{p}_i} - \dfrac{\partial \mathcal{L}_i}{\partial p_i} = 0 \\ \dfrac{\mathrm{d}}{\mathrm{d}t}\dfrac{\partial \mathcal{L}_i}{\partial \dot{q}_i} - \dfrac{\partial \mathcal{L}_i}{\partial q_i} = \tau_i,\ i = 1, 2, \cdots, n, \end{cases} \tag{1}$$

where $\mathcal{L}_i = K_i - V_i$, and p_i, $q_i \in \mathbb{R}$, $i = 1, 2, \cdots, n$, are states of the i-th under-actuated system, τ_i, $i = 1, 2, \cdots, n$, are generalized forces. And the kinetic energy of the i-th UAS K_i is symmetric, generally presented as

$$\begin{cases} K_i = \dfrac{1}{2}\dot{\rho}_i^{\mathrm{T}} M_i(q_i)\dot{\rho}_i \\ M_i(q_i) = \begin{bmatrix} m_i^{11}(q_i) & m_i^{12}(q_i) \\ m_i^{21}(q_i) & m_i^{22}(q_i) \end{bmatrix}, \end{cases} \tag{2}$$

where $\rho_i = [p_i, q_i]^{\mathrm{T}}$, $M_i(q_i)$, $i = 1, 2, \cdots, n$, are the inertia matrices, $m_i^{11}, m_i^{22} \neq 0$. And the potential energy of the i-th UAS is $V_i(p_i, q_i) = U_i^1(p_i) + U_i^2(q_i)$, where

$$U_i^1(p_i) = \frac{1}{2}K_i^a p_i^2 + K_i^b p_i + K_i^c, \tag{3}$$

K_i^a, K_i^b and K_i^c are constants relative to actual potential energy calculation.

By simple rearrangements, the sub-UAS (1) can be rewritten in the following form

$$\begin{cases} m_i^{11}(q_i)\ddot{p}_i + m_i^{12}(q_i)\ddot{q}_i + h_i^1\left(p_i^{(0\sim 1)}, q_i^{(0\sim 1)}\right) = 0 \\ m_i^{21}(q_i)\ddot{p}_i + m_i^{22}(q_i)\ddot{q}_i + h_i^2\left(p_i^{(0\sim 1)}, q_i^{(0\sim 1)}\right) = \tau_i, \end{cases} \tag{4}$$

where

$$\begin{cases} m_i^{11}(q_i) = \langle \ddot{p}_i \rangle \dfrac{\mathrm{d}}{\mathrm{d}t}\dfrac{\partial K_i}{\partial \dot{p}_i} \\ m_i^{12}(q_i) = \langle \ddot{q}_i \rangle \dfrac{\mathrm{d}}{\mathrm{d}t}\dfrac{\partial K_i}{\partial \dot{p}_i} \\ h_i^1(\cdot) = -\dfrac{\partial \mathcal{L}_i}{\partial p_i} - \left(m_i^{11}(q_i)\right)'\dot{p} - \left(m_i^{12}(q_i)\right)'\dot{q}, \end{cases}$$

and

$$\begin{cases} m_i^{21}(q_i) = \langle \ddot{p}_i \rangle \dfrac{\mathrm{d}}{\mathrm{d}t}\dfrac{\partial K_i}{\partial \dot{q}_i} \\ m_i^{22}(q_i) = \langle \ddot{q}_i \rangle \dfrac{\mathrm{d}}{\mathrm{d}t}\dfrac{\partial K_i}{\partial \dot{q}_i} \\ h_i^2(\cdot) = -\dfrac{\partial \mathcal{L}_i}{\partial q_i} - \left(m_i^{12}(q_i)\right)'\dot{p} - \left(m_i^{22}(q_i)\right)'\dot{q}. \end{cases}$$

From the first sub-equation of (4), one has

$$\ddot{p}_i = -\frac{h_i^1 + m_{12}\ddot{q}_i}{m_{11}}$$

taking above the equation into the second sub-equation of (4), we have $\ddot{p} = u_i$, where

$$u_i = \frac{m_i^{11}(q_i)\tau_i - m_i^{11}(q_i)h_i^2(\cdot) + m_i^{21}(q_i)h_i^1(\cdot)}{m_i^{11}(q_i)m_i^{22}(q_i) - m_i^{21}(\cdot)m_i^{12}(\cdot)}. \tag{5}$$

Since $M_i(q_i) > 0$, the input conversion (5) always exists.

The following assumptions are used in this paper.

Assumption 1 $\det m_i^{11}(q_i) \neq 0, i = 1, 2, \cdots, n, \forall q_i \in \mathbb{R}$.

Assumption 2 *There exist a group of invertible functions* $\gamma_i(\cdot)$, $i = 1, 2, \cdots, n$, *such that* $\mathrm{d}\gamma_i(q_i) = \left(m_i^{11}\right)^{-1} m_i^{12}\mathrm{d}q_i$, $i = 1, 2, \cdots, n$, *where* $\left(m_i^{11}\right)^{-1} m_i^{12}\mathrm{d}q_i$ *are exact one-forms.*

Based on the above preparations, a normal forms FASs can be devoted in the following theorem.

Theorem 1 *Consider the cascaded UAS* (1) *with the input conversion* (5) *satisfies Assumptions* $1 - 2$. *If*
1. $m_i^{11}(q_i)$ *is a constant;*
2. $K_i^{1a} > 0$*;*
3. $\left(\gamma_i^{-1}\right)' \neq 0$*;*

there exist the following global transformation of coordinates

$$z_i = p_i + \gamma_i(q_i),\ i = 1, 2, \cdots, n, \tag{6}$$

such that the cascaded UAS (4) *is transformed into a FAS as follows*

$$\begin{aligned} z_{1\sim n}^{(4)} =& F_{1\sim n}\left(z_i^{(0\sim 3)}\Big|_{i=1\sim n}\right) \\ &+ \hat{B}\left(z_i^{(0\sim 3)}\Big|_{i=1\sim n}\right)u_{1\sim n}, \end{aligned} \tag{7}$$

where

$$\begin{cases} \hat{B}(\cdot) = \operatorname{diag}\left(-\dfrac{1}{M_i(\cdot)},\ i = 1 \sim n\right) \\ F_i(\cdot) = \left(\gamma_i^{-1}\right)''\left(\dfrac{\dot{z}_i}{M_i(\cdot)} - \dfrac{m_i^{11} z_i^{(3)}}{K_i^a M_i(\cdot)}\right) + \left(\gamma_i^{-1}\right)' \dfrac{\ddot{z}_i}{M_i(\cdot)} \\ M_i(\cdot) = \dfrac{\left(\gamma_i^{-1}\right)' m_i^{11}}{K_i^a}. \end{cases}$$

Proof. Then taking the derivative of (6), one has

$$\dot{z}_i = \dot{p}_i + \left(m_i^{11}\right)^{-1} m_i^{12} \dot{q}_i = \frac{1}{m_i^{11}} \frac{\partial K_i}{\partial \dot{p}_i}.$$

According to the first sub-equation in (1), we have

$$\ddot{z}_i = \frac{1}{m_i^{11}} \frac{\partial \mathcal{L}_i}{\partial p_i}. \tag{8}$$

From the kinetic energy given in (2), that $\frac{\partial K_i}{\partial p_i} = 0$, then

$$\begin{aligned} \ddot{z}_i &= -\frac{1}{m_i^{11}} \frac{\partial V_i}{\partial p_i} = \frac{1}{m_i^{11}} \left[K_i^a p_i + K_i^b\right]\Big|_{p_i = z_i - \gamma_i(q_i)} \\ &= \frac{1}{m_i^{11}} \left(K_i^a \left(z_i - \gamma\left(q_i\right)\right) + K_i^b\right). \end{aligned}$$

After simplify rearrangement, one has

$$q_i = \gamma_i^{-1}\left(z_i - \frac{m_i^{11} \ddot{z}_i - K_i^b}{K_i^a}\right),$$

and then taking the second derivative, we have

$$\left(\gamma_i^{-1}\right)''\left(\dot{z}_i - \frac{m_i^{11} z_i^{(3)}}{K_i^a}\right) + \left(\gamma_i^{-1}\right)'\left(\ddot{z}_i - \frac{m_i^{11} z_i^{(4)}}{K_i^a}\right) = u_i,$$

which is equal to (7).

Thus, this proof is completed. ■

Remark 1 *The common potential energy in practical application includes gravitational potential energy, elastic potential energy, electric potential energy, gravitational potential energy, etc. For the elastic potential energy, it can be presented as* $U = \frac{1}{2}kx^2$, *where* k *is the spring constant and* x *is the displacement form the equilibrium position. It is equal to* $K_i^a p_i$ *in* (3). *The gravitational potential energy* $U = mgh$, *where* m *is the mass of the object,* g *is the acceleration due to gravity, and* h *is the height of the object relative to a reference point. For charged particles in an electric field, the electric potential energy can be calculated as* $U = qV$, *where* q *is the charge of the particle and* V *is the electric potential at the particle's position. The type of gravitational potential energy and electric potential energy can be uniformly expressed as* $K_i^b p_i$ *in* (3). *For objects influenced by the gravity of celestial bodies, such as planets or stars, the potential energy is given by* $U = -\frac{Gm_1m_2}{r}$, *where* G *is the gravitational constant,* m_1 *and* m_2 *are the masses of the two objects,* r *is the distance between the centers of the two objects, which generally can be regarded as a constant as* K_i^c *in* (3).

2.2 Discretization

In predictive control, systems are typically represented by discrete-time models. Consequently, We make discretization for the above continuous-time FAS model (7). During this process, the introduction of discretization errors is unavoidable, so we treat the discretization errors as uncertainties that are bounded by the norm related to the state of the system. The discretization results of the FAS (7) is given as follows:

$$\begin{aligned} z_{1\sim n}^{\lfloor 4 \rfloor}(k+1) =& F_{1\sim n}\left(z_i^{\lfloor 0\sim 3 \rfloor}\Big|_{i=1\sim n}(k)\right) \\ &+ \hat{B}\left(z_i^{\lfloor 0\sim 3 \rfloor}\Big|_{i=1\sim n}(k)\right) u_{1\sim n}(k) \\ &+ \Delta f_{1\sim n}\left(z_i^{\lfloor 0\sim 3 \rfloor}\Big|_{i=1\sim n}(k)\right), \end{aligned} \tag{9}$$

where

$$\begin{cases} F_i(\cdot) = \mathcal{D}\left(F_i\left(z_i^{(0\sim 3)}\Big|_{i=1\sim n}\right)\right) + \sum_{j=0}^{3} C_4^j z_i^{\lfloor j \rfloor}(k) \\ \hat{B}(\cdot) = \mathcal{D}\left(\hat{B}\left(z_i^{(0\sim 3)}\Big|_{i=1\sim n}\right)\right), \end{cases}$$

and the uncertainties satisfy the following assumption.

Assumption 3 *There exists a non-negative constant function* $\rho_i\left(z_{1\sim n}^{\lfloor 0\sim 3 \rfloor}\right)$, $i = 1, 2, \cdots, n$, *such that uncertainties satisfy*

$$\|\Delta f_i(\cdot)\|^2 \le \left\|z_i^{\lfloor 0\sim 3 \rfloor}(k)\right\|_{\Phi_i}^2,$$

where $\Phi_i = \rho_i^2(\cdot) I_4$.

And the full-actuation assumption for system (9) is

Assumption 4 *[16]*$\det \hat{B}(\cdot) \neq 0$ *or* ∞, *for* $\forall\, z_i^{(0\sim 3)}|_{i=1\sim n}$.

3 FAS-RPC scheme for FASs

For the discrete-time FAS (9), the FAS-RPC controller is designed in the following form:

$$u_{1\sim n}(k) = B^{-1}(\cdot)\left(-F_{1\sim n}(\cdot) + v_{1\sim n}(k)\right), \tag{10}$$

where

$$v_i(k) = K_i(k)\, z_i^{\lfloor 0\sim 3 \rfloor}(k),\ i = 1, 2, \cdots, n, \tag{11}$$

are robust predictive controllers to be designed.

Consider the system performance, we define the following common receding-horizon optimization index:

$$J_\infty(k) = \sum_{j=0}^{\infty} \left(\begin{array}{l} \left\| z_i^{\lfloor 0\sim 3 \rfloor}(k+j|\,k)\Big|_{i=1\sim n} \right\|_{\bar{Q}}^2 \\ + \| v_i(k+j)|_{i=1\sim n} \|_{\bar{R}}^2 \end{array} \right), \tag{12}$$

where $Q_i,\ R_i > 0,\ i = 1 \sim n$, are predictive weights, compose the following diagonal block matrices

$$\begin{cases} \bar{Q} = \operatorname{diag}(Q_i,\ i = 1, 2, \cdots, n) \\ \bar{R} = \operatorname{diag}(Ri,\ i = 1, 2, \cdots, n). \end{cases}$$

Problem 1 *Consider the discrete-time FAS* (9) *satisfies Assumptions* $1 - 4$, *to design a FAS-RPC controller* (10), *such that there exists the minimum of receding-horizon optimization index* (12), *and the resultant closed-loop system is robust asymptotically stable.*

3.1 Model and optimization problem decoupling

Taking the FAS-RPC controller (10) into the FAS model (9), we have

$$z_i^{\lfloor 3 \rfloor}(k+1) = v_i(k) + \Delta f_i(\cdot),\ i = 1, 2, \cdots, n.$$

Subsequently, the above systems can be decoupled and rewritten into canonical forms, presented as follows:

$$\begin{aligned} z_i^{\lfloor 0\sim 3 \rfloor}(k+1) =& A_i z_i^{\lfloor 0\sim 3 \rfloor}(k) + B_i v_i(k) \\ &+ B_i \Delta f_i(\cdot),\ i = 1, 2, \cdots, n, \end{aligned} \tag{13}$$

where

$$A_i = \left.\begin{bmatrix} 0 & 1 & 0 & \cdots & 0 \\ 0 & 0 & 1 & \cdots & 0 \\ 0 & 0 & 0 & \ddots & \vdots \\ \vdots & \vdots & \vdots & \cdots & 1 \\ 0 & 0 & 0 & \cdots & 0 \end{bmatrix}\right\} i,\ B_i = \left.\begin{bmatrix} 0 \\ 0 \\ \vdots \\ 0 \\ 1 \end{bmatrix}\right\} i. \tag{14}$$

It can be directly observed from the above equations, the FAS (9) is directly decoupled under the controller (10). And the receding-horizon optimization index (12) can be further decoupled as

$$J_\infty(k) = \sum_{i=1}^{n} J_{i_\infty}(k), \tag{15}$$

where

$$J_{i_\infty}(k) = \sum_{j=0}^{\infty} \left(\left\| z_i^{\lfloor 0\sim 3 \rfloor}(k+j|k) \right\|_{Q_i}^2 + \| v_i(k+j) \|_{R_i}^2 \right).$$

3.2 Controller design

For FAS system (9), one can choose the following Lyapunov functions as

$$V(k) = \sum_{i=1}^{n} V_i(k), \tag{16}$$

where

$$V_i(k) = \left\| z_i^{\lfloor 0\sim 3 \rfloor}(k) \right\|_{P_i}^2, \tag{17}$$

and $P_i, i = 1, 2, \cdots, n$, are positive-definite, and impose the stability condition

$$\begin{aligned} & V_i(k+j+1|k) - V_i(k+j|k) \\ \le & -l_i\left(z_i^{\lfloor 0\sim 3 \rfloor}(k+j|k), v_i(k+j|k) \right), \end{aligned} \tag{18}$$

where

$$l_i(\cdot) = \left\| z_i^{\lfloor 0\sim 3 \rfloor}(k+j|k) \right\|_{Q_i}^2 + \| v_i(k+j|k) \|_{R_i}^2.$$

Theorem 2 *Consider the discrete-time FAS* (9) *satisfies Assumptions* 3 *and* 4*, if there exist matrices Y_i, symmetric positive definite matrices G_i, and scalar $\gamma_i > 0$, $i = 1, 2, \cdots, n$, solved by the following optimization problem*

$$\min_{Y_i, G_i, \gamma_i} \gamma_i,\ i = 1, 2, \cdots, n,$$

$$\text{s.t.} \begin{bmatrix} 1 & * \\ z_i^{\lfloor 0\sim 3 \rfloor}(k) & G_i \end{bmatrix} > 0, \tag{19}$$

$$\begin{bmatrix} G_i & * & * & * & * \\ A_i G_i + B_i Y_i & G_i & * & * & * \\ \sqrt{B_i^{\mathrm{T}} B_i}\rho_i G_i & 0 & G_i & * & * \\ \sqrt{Q_i} G_i & 0 & 0 & \gamma_i I_4 & * \\ \sqrt{R_i} Y_i & 0 & 0 & 0 & \gamma_i \end{bmatrix} > 0, \tag{20}$$

where $K_i = Y_i G_i^{-1}$, $G_i = \gamma_i P_i^{-1}$, then:
1. *there exists the FAS-RPC controller given as follows*

$$\begin{cases} u_{1\sim n}(k) = B^{-1}(\cdot)\left(-F_{1\sim n}(\cdot) + v_{1\sim n}(k)\right), \\ v_i(k+j|k) = Y_i G_i^{-1} z_i^{\lfloor 0\sim 3 \rfloor}(k+j|k),\ i = 1, 2, \cdots, n; \end{cases}$$

2. *if the optimization problem is feasible at k instant, then under the above FAS-RPC controller, the resultant closed-loop system is robust asymptotically stable.*

Proof. When the system is asymptotically stable, $V_i(\infty) = z_i(\infty) = 0$. By summing (18) from $j = 0$ to $j = \infty$, we have

$$J_{i\infty}(k) \le V_i(k).$$

Thus optimizing problem of the minimize the index (12) is equivalent to minimizing (16). Let the upper bound of $V_i(k)$ is γ_i, then combing (17), and the Schur complement property, the first inequality (19) is obtained.

For the stability condition (18), using (13) and (11), we have

$$\begin{aligned} & \Delta V_i(k+j|k) + l_i\left(z_p^{\lfloor 0\sim 3 \rfloor}(k+j|k), v_p(k+j|k), j \right) \\ \le & \left\| \left(A_i + B_i Y_i G_i^{-1}\right) z_i^{\lfloor 0\sim 3 \rfloor}(k+j|k) + B_i \Delta f_i(k+j|k) \right\|_{P_i}^2 \\ & - \left\| z_i^{\lfloor 0\sim 3 \rfloor}(k+j|k) \right\|_{P_i}^2 + \left\| z_i^{\lfloor 0\sim 3 \rfloor}(k+j|k) \right\|_{Q_i}^2 \\ & + \left\| z_i^{\lfloor 0\sim 3 \rfloor}(k+j|k) \right\|_{\left(Y_i G_i^{-1}\right)^{\mathrm{T}} R_i Y_i G_i^{-1}}^2 \\ \le & \left\| z_i^{\lfloor 0\sim 3 \rfloor}(k+j|k) \right\|_{\left(A_i + B_i Y_i G_i^{-1}\right)^{\mathrm{T}} P_i \left(A_i + B_i Y_i G_i^{-1}\right)}^2 \\ & + \left\| z_i^{\lfloor 0\sim 3 \rfloor}(k+j|k) \right\|_{Q_i}^2 - \left\| z_i^{\lfloor 0\sim 3 \rfloor}(k+j|k) \right\|_{P_i}^2 \\ & + \left\| z_p^{\lfloor 0\sim 3 \rfloor}(k+j|k) \right\|_{B_i^{\mathrm{T}} B_i \rho_i^2(\cdot) I_4 P_i}^2 \\ & + \left\| z_i^{\lfloor 0\sim 3 \rfloor}(k+j|k) \right\|_{\left(Y_i G_i^{-1}\right)^{\mathrm{T}} R_i Y_i G_i^{-1}}^2. \end{aligned}$$

If

$$\begin{aligned} & \left(A_i + B_i Y_i G_i^{-1}\right)^{\mathrm{T}} P_i \left(A_i + B_i Y_i G_i^{-1}\right) \\ & + B_i^{\mathrm{T}} B_i \rho_i^2(\cdot) I_4 P_i + Q_i + \left(Y_i G_i^{-1}\right)^{\mathrm{T}} R_i Y_i G_i^{-1} - P_i < 0, \end{aligned} \tag{21}$$

the stability condition (18) is hold, the resultant closed-loop system is robust asymptotically stable. Pre- and post-multiplying by G_i, then applying Schur complements, the (21) is equivalent to the second inequality (20). Thus, the whole proof is completed. ■

4 Simulations

Consider the cascaded under-actuated dual rotational translational actuator (RTAC) system as Fig. 1. The kinetic

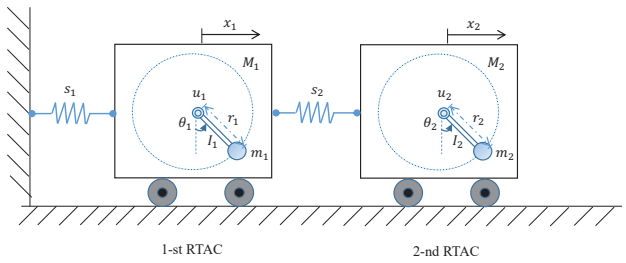

Fig. 1: The simplified model of dual-RTAC system.

and potential energy of each RTAC system in the dual-RTAC system is computed as

$$\begin{cases} K_i = \frac{1}{2}\left((M_i+m_i)\dot{x}_i^2 + 2m_iL_i\dot{x}\dot{\theta}\cos\theta_i + \left(J_i+m_iL_i^2\right)\dot{\theta}_i^2\right) \\ V_i = \frac{1}{2}k_ix_i^2 + m_igL_i\left(1-\cos\theta_i\right), \ i=1,2, \end{cases}$$

where x_i is the i-th cart's horizontal displacement, θ_i denotes the ith rotor's rotational angle with respect to the vertical direction, M_i and m_i denote the mass of the i-th cart and the eccentric ball, J_i represents the moment of inertia of the i-th rotor. k_i represents the stiffness coefficient of the i-th spring. L_i be the rotational radius of the i-th eccentric ball.

It can be observed that the kinetic and potential energy of each RTAC system in the dual-RTAC system are matched with system (1). And the conditions (1) and (2) in Theorem 1 are satisfied. And the dynamical equations of each RTAC system is derived as

$$\begin{cases} (M_i+m_i)\ddot{x}_i + m_iL_i\cos\theta_i\ddot{\theta} = m_iL_i\dot{\theta}^2\sin\theta_i + k_ix_i \\ m_iL_i\cos\theta_i\ddot{x}_i + \left(J_i+m_iL_i^2\right)\ddot{\theta} + mgL_i\sin\theta_i = \tau_i. \end{cases} \quad (22)$$

4.1 Model conversion

Define

$$\mathrm{d}\gamma_i = \frac{m_iL_i\cos\theta_i}{M_i+m_i}\mathrm{d}\theta_i,$$

then we have

$$\gamma_i = \frac{m_iL_i}{M_i+m_i}\sin\theta_i.$$

From (6), the global transformation for each sub-RTAC system is

$$z_i = x_i + \frac{m_iL_i}{M_i+m_i}\sin\theta_i, \ i=1,2. \quad (23)$$

According to Theorem 1 and the forward Euler discretization, under the input transformation

$$u_i = \frac{(M_i+m_i)\tau_i - (M_i+m_i)m_igL_i\sin\theta_i - m_i^2L_i^2\sin\theta_i\cos\theta_i\dot{\theta}_i}{(M_i+m_i)(J_i+m_iL_i^2) - m_i^2l_i^2\cos^2\theta_i}$$

a discrete-time uncertain FAS can be obtained as follows:

$$\begin{aligned} z_{1\sim2}^{\lfloor 4\rfloor}(k) = & F_{1\sim2}\left(z_i^{\lfloor 0\sim 3\rfloor}\Big|_{i=1\sim2}(k)\right) \\ & + \hat{B}_{1\sim2}\left(z_i^{\lfloor 0\sim 3\rfloor}\Big|_{i=1\sim2}(k)\right)u_{1\sim2}(k) \\ & + \Delta f_i\left(z_i^{\lfloor 0\sim 3\rfloor}(k)\right)\Big|_{i=1\sim2}, \end{aligned}$$

where

$$\begin{cases} M_i = \frac{(M_i+m_i)(\gamma_i^{-1})'}{k_i} \\ F_i = \left(\gamma_i^{-1}\right)''\left(\frac{\mathcal{D}(\dot{z})}{M_i} - \frac{(M_i+m_i)\mathcal{D}(z^{(3)})}{M_i}\right) + \left(\gamma_i^{-1}\right)'\left(\frac{\mathcal{D}(\ddot{z})}{M_i}\right) \\ \gamma_i^{-1} = \arcsin\left(z_i - \frac{(M_i+m_i)(z_{k+2}-2z_{k+1}+z_k)}{k_i}\right) \\ \hat{B}(\cdot) = \mathrm{diag}\left(-\frac{1}{M_i}, \ i=1,2\right), \end{cases}$$

and system uncertainties satisfy that

$$\left\|\Delta f_i(\cdot)\right\|^2 \le \rho_i^2(\cdot)\left\|z_i^{\lfloor 0\sim 3\rfloor}(k)\right\|^2, \ i=1,2,$$

where $\rho_1(\cdot) = 0.1$ and $\rho_2(\cdot) = 0.2$. For simulation verification that system uncertainties are selected as $\Delta f_i(\cdot) = 0.01\sin(k)\left\|z_i^{\lfloor 0\sim 3\rfloor}(k)\right\|^2$, $i=1,2$, which satisfy that

$$\left\|\Delta f_i(\cdot)\right\|^2 \le \rho_i^2(\cdot)\left\|z_i^{\lfloor 0\sim 3\rfloor}(k)\right\|^2, \ i=1,2,$$

where $\rho_1(\cdot) = 0.1$ and $\rho_2(\cdot) = 0.2$.

4.2 Simulation Results

Let $m_1 = m_2 = 1$ kg, $k_1 = k_2 = 100$ N/m, $M_1 = M_2 = 5$ kg, $L_1 = L_2 = 0.1$ m, $J_1 = J_2 = 0.02$ kg·m^2.
The initial states of the dual-RTAC system are selected as follows

$$\begin{aligned} & x_1(0) = 0.1, x_1(1) = -0.02, \theta_1(0) = 0.08, \ \theta_1(1) = 0.1, \\ & x_2(0) = -0.1, x_2(1) = 0.02, \theta_2(0) = 0.1, \ \theta_2(1) = 0.07. \end{aligned}$$

Then combing with (8) and (23), the initial states of system (22) are calculated as

$$\begin{aligned} & z_1(0) = 0.1, z_1(1) = -0.018, z_1(2) = 1.53, z_1(3) = -12, \\ & z_2(0) = -0.09, z_2(1) = 0.02, z_2(2) = -1.52, z_2(3) = 12. \end{aligned}$$

The predictive parameters are selected as $Q_1 = Q_2 = 0.9I_4$, $R_1 = R_2 = 0.1$.

The simulation trajectories of the dual-RTAC system are given in Figures 2 and 3.

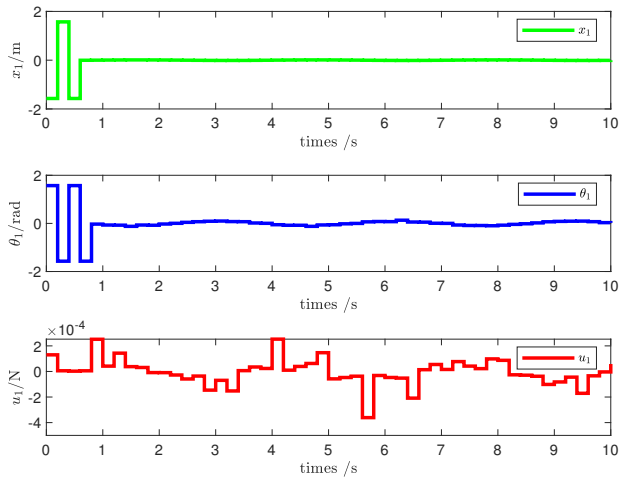

Fig. 2: The responses of the 1-st RTAC system.

It can be easily observed that the displacement and angle of the dual-RTAC system finally converge into bounded

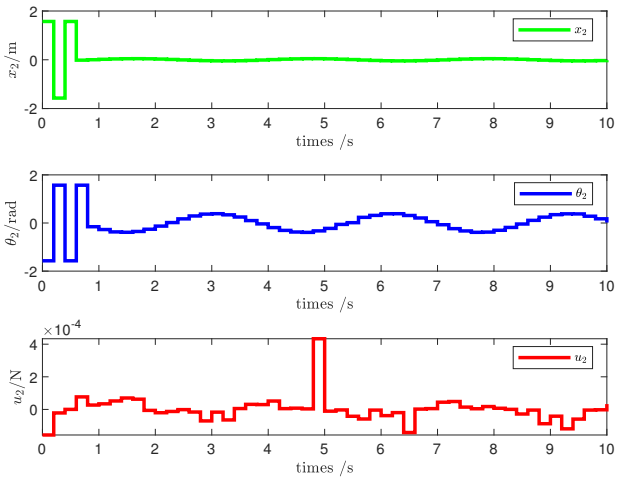

Fig. 3: The responses of the 2-nd RTAC system.

region at the origin. And from the response of states, the proposed FAS-RPC scheme has good time specifications, such as lower setting time, lower overshoot and lower fluctuations.

5 Conclusions

This study presents a paradigm for the transformation of cascaded UASs into FASs, accounting for uncertainties in the model arising from discretization of continuous-time model. A FAS-RPC control scheme for discrete-time uncertain FAS is proposed, demonstrating the existence of a upper bounded of the performance optimization index over an infinite time horizon. This ensures that the resultant closed-loop system maintains robust asymptotic stability. The efficacy of the proposed method is validated using the dual-RTAC system as a benchmark UAS, achieving robust asymptotic stabilization.

References

[1] Soukaina Krafes, Zakaria Chalh, and Abdelmjid Saka. A review on the control of second order underactuated mechanical systems. *Complexity*, 2018:1–17, 2018.

[2] Bin He, Shuai Wang, and Yongjia Liu. Underactuated robotics: a review. *International Journal of Advanced Robotic Systems*, 16(4):1729881419862164, 2019.

[3] Bara J Emran and Homayoun Najjaran. A review of quadrotor: An underactuated mechanical system. *Annual Reviews in Control*, 46:165–180, 2018.

[4] Pengcheng Liu, M Nazmul Huda, Li Sun, and Hongnian Yu. A survey on underactuated robotic systems: bio-inspiration, trajectory planning and control. *Mechatronics*, 72:102443, 2020.

[5] Ying He, Dao Bo Wang, and Zain Anwar Ali. A review of different designs and control models of remotely operated underwater vehicle. *Measurement and Control*, 53(9-10):1561–1570, 2020.

[6] Daniela Rus and Michael T Tolley. Design, fabrication and control of soft robots. *Nature*, 521(7553):467–475, 2015.

[7] Javier Moreno-Valenzuela and Carlos Aguilar-Avelar. *Motion control of underactuated mechanical systems*, volume 1. Springer, 2018.

[8] Yao Zou and Kewei Xia. Robust fault-tolerant control for underactuated takeoff and landing uavs. *IEEE Transactions on Aerospace and Electronic Systems*, 56(5):3545–3555, 2020.

[9] Felix Wiebe, Shivesh Kumar, Lasse J Shala, Shubham Vyas, Mahdi Javadi, and Frank Kirchner. Open source dual-purpose acrobot and pendubot platform: Benchmarking control algorithms for underactuated robotics. *IEEE Robotics & Automation Magazine*, 2023.

[10] Jun Ning, Yifan Ma, Tieshan Li, CL Philip Chen, and Shaocheng Tong. Event-triggered based trajectory tracking control of under-actuated unmanned surface vehicle with state and input quantization. *IEEE Transactions on Intelligent Vehicles*, 2023.

[11] MJ Mahmoodabadi and M Andalib Sahnehsaraei. Parametric uncertainty handling of under-actuated nonlinear systems using an online optimal input–output feedback linearization controller. *Systems Science & Control Engineering*, 9(1):209–218, 2021.

[12] Tieshan Li, Rong Zhao, CL Philip Chen, Liyou Fang, and Cheng Liu. Finite-time formation control of under-actuated ships using nonlinear sliding mode control. *IEEE transactions on cybernetics*, 48(11):3243–3253, 2018.

[13] Meng Zhai, Ning Sun, Tong Yang, and Yongchun Fang. Underactuated mechanical systems with both actuator and actuated/unactuated state constraints: A predictive control-based approach. *IEEE/ASME Transactions on Mechatronics*, 2022.

[14] M Reza J. Harandi, Hamid D Taghirad, Amir Molaei, and Jose Guadalupe Romero. Bounded inputs total energy shaping for a class of underactuated mechanical systems. *International Journal of Robust and Nonlinear Control*, 31(18):9267–9281, 2021.

[15] Xiubo Wang and Guangren Duan. Fully actuated system approaches: Predictive elimination control for discrete-time nonlinear time-varying systems with full state constraints and time-varying delays. *IEEE Trans. Circuits Syst. I Regul. Pap.*, 2023.

[16] Guangren Duan. High-order fully actuated system approaches: Part I. models and basic procedure. *International Journal of Systems Science*, 52(2):422–435, 2021.

[17] Guangren Duan. High-order fully actuated system approaches: part vii. controllability, stabilisability and parametric designs. *International Journal of Systems Science*, 52(14):3091–3114, 2021.

[18] Guangren Duan. High-order fully actuated system approaches: Part II. Generalized strict-feedback systems. *International Journal of Systems Science*, 52(3):437–454, 2021.

[19] Guang-Ren Duan. Brockett's first example: An fas approach treatment. *Journal of Systems Science and Complexity*, 35(2):441–456, 2022.

[20] Guang-Ren Duan. Brockett's second example: A fas approach treatment. *Journal of Systems Science and Complexity*, 36(5):1789–1808, 2023.

[21] Xiubo Wang and Guangren Duan. A subfully actuated system application: Predictive control for multi-rtac systems. In *2023 2nd Conference on Fully Actuated System Theory and Applications (CFASTA)*, pages 948–953. IEEE, 2023.

[22] Xiubo Wang and Guangren Duan. High-order fully actuated system approaches: Model predictive control with applications to under-actuated systems. *J. Franklin Inst.*, 360(10):6953–6975, 2023.

[23] Guangren Duan. High-order fully-actuated system approaches: Part IX. Generalised PID control and model reference tracking. *International Journal of Systems Science*, 53(3):652–674, 2022.

Proceedings of the 3rd Conference on Fully Actuated System Theory and Applications
May 10-12, 2024, Shenzhen, China

A prioritized replay safe soft-actor critic (PR-sSAC) deep reinforcement learning for real-time energy dispatch of integrated energy systems.

Tobi Michael Alabi[1], Zaiyue Yang[2], Lin Lu[3]

1. Centre for Advances in Reliability and Safety (CAiRS), Hong Kong SAR, China
E-mail: tobimichael.alabi@cairs.hk

2. Department of Mechanical and Energy Engineering, Southern University of Science and Technology, Shenzhen, China
E-mail: yangzy3@sustech.edu.cn

3. Department of Building Environment and Energy Engineering, The Hong Kong Polytechnic University, Hong Kong
E-mail: vivien.lu@polyu.edu.hk

Abstract: Integrated energy systems (IES) are complex systems that integrate multiple energy sources, converters, and loads to achieve optimal operation and carbon neutrality. However, conventional optimization methods for IES scheduling face challenges such as nonconvexity, uncertainty, and system dynamics. This paper proposes a novel deep reinforcement learning (DRL) approach for real-time energy dispatch of IES. The approach uses a prioritized replay safe soft-actor critic (PR-sSAC) algorithm that incorporates a safety network and a prioritized experience replay mechanism to improve the performance and reliability of the DRL agent. The safety network ensures that the agent's actions do not violate the physical constraints of the IES components, while the prioritized experience replay mechanism enhances the sampling efficiency and convergence speed of the agent. Simulation experiments are conducted on a case study of an IES model with six components and the approach is compared with other DRL methods and a theoretical optimization model. The results show that the approach achieves near-optimal operation cost and tolerable constraint violation, demonstrating its effectiveness and applicability for IES scheduling.

Key Words: Integrated energy system, deep reinforcement learning, carbon neutrality.

1.1 Introduction

Integrated energy systems (IES) energy management challenges have been widely studied using conventional mathematical modeling to achieve optimal schedule. These methods include different types of math programming, ADMM, game theory, and dealing with uncertainty using stochastic and robust optimization. For instance, a community level MES was modeled with a MILP algorithm in [1]. Trans et al. [2] proposed a distributed control strategy based on ADMM and consensus theory to achieve optimal schedule for IES. A flexible energy management model using a Stackelberg game theory method was developed in [3]. Further, Alabi et al. [4] also proposed a two-stage robust stochastic optimization technique to reduce the cost of IES operation by taking into account the uncertainties of renewable resources and multi-energy demand.

Mathematical model optimization methods have many limitations, such as the requirement of a specific optimization model because of nonconvexity that may lead to nonconvergence solution, challenges in estimating uncertainties accurately, diverse operation constraints, and the system dynamics of energy scheduling problem. Therefore, it is hard to develop a precise model-based optimization method for IES. In this situation, the recent interdisciplinary research between engineering and data science, and the access to big data and ICT technology improvement has made a data-driven method called deep reinforcement learning (DRL) a viable alternative. As a common type of ML algorithms, DRL uses its DNN feature to solve high-dimension optimization problems without any prior knowledge or mathematical information of the environment, this is done by using the experience gained from the constant interaction with the environment to progressively learn the optimal control decisions [5]. Contrast to the conventional model-based optimization, the DRL agent treats the environment technical parameters and mathematical models as a black-box, this lowers the dependence on precise physical models or the need to avoid inaccurate model parameters by using suitable algorithm improvements[6].

Moreover, DRL handles the system uncertainties and adjusts to different state dynamics by using the shared data from the environment effectively during online training. Lastly, a well-trained DRL agent has more flexibility than traditional model-based optimization during real-time execution since its policy can be implemented on milliseconds timescales. Therefore, DRL is regarded as a powerful tool for real-time control applications.

However, physical constraint and security concerns are essential in IES model, any control policy that will be applied in real-time for scheduling task must guarantee that the systems' operation states do not breach the physical constraints. At the same time, the training phase of DRL is an unconstrained optimization problem, the common method to deal with this inevitable issue is to add the constraint violation that is expressed as a penalty term to the reward function [7]. Nevertheless, this approach makes control policy unreliable for large number of constraints. Fewer studies have tackled this issue by suggesting safety DNN network as a key component of DRL[8, 9].

*This work is supported by the Centre for Advances in Reliability and Safety (CAiRS), Hong Kong SAR, China admitted under AIR@InnoHK Research Cluster.

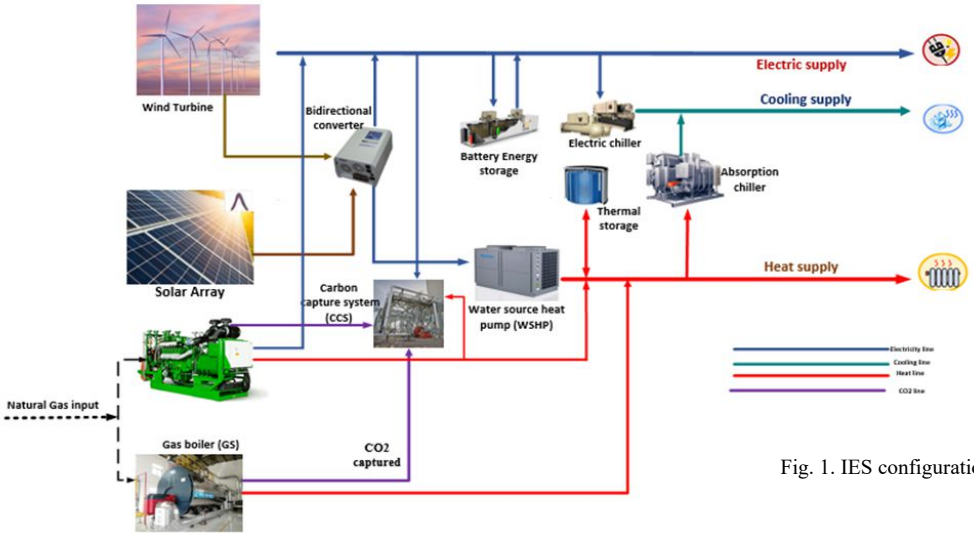

Fig. 1. IES configuration model

1.1 Main contributions

This paper presents a novel DRL approach for real-time energy dispatch of IES components with carbon capture system. This configuration optimizes the trade-off between economic cost and carbon emission reduction while respecting the physical limits of the systems. The approach uses an offline-trained and online-deployed DRL agent that considers the safety impact of its actions through a safety network.

Compared to conventional DRL methods, the optimal policy of the proposed DRL agent is trained with the mindset of its selected actions' safety implication. This is implemented with the introduction of a safety-guided network and contributes to near-optimal performance of the agent in real-time autonomous decision making. Furthermore, the sampling efficiency during the training of agent is improved with prioritized experience replay mechanism and results in low computational cost compared to conventional approach.

1.2 Integrated Energy System model

As Fig. 1 shows, the suggested MES model has six components: (1) electric and heat loads as two types of energy demand; (2) wind and solar power as two sources of renewable energy supply (RES); (3) a natural gas-powered cogeneration unit (CCHP) for combined heat and power production; (4) two kinds of energy storage devices for saving excess energy and supporting the system when RES is low; (5) a water-source heat pump (WSHP) and a gas boiler (GB) as two thermal devices for heating, and (6) a carbon capture technology (CDR) for reducing the CO_2 emissions from CCHP and GB. The system prioritizes using or storing all the energy from wind and solar power to minimize renewable power curtailments. The carbon capture unit (PCC) is attached to the exhaust outlet of CCHP and GB to collect the exhaust gas, separate the CO_2 by adsorption, and release the clean air to the environment. This study does not account for the regeneration of the PCC absorbent after capturing CO_2.

1.3 Energy generation and converters

Aside from renewable energy sources (RES) utilization, CHP is considered as a key component of MES due to its single-input-multi-output characteristics.

$$P_t^{chp} = CAP^{chp} a_t^{chp}, \quad \forall t \in T, \quad 0 \le a_t^{chp} \le 1 \qquad (1)$$

$$g_t^{chp} = P_t^{chp} \Big/ \eta_{chp}^{e} LHV_g, \qquad \forall t \in T \qquad (2)$$

$$Q_t^{chp} = g_t^{chp} \eta_{chp}^{q} LHV_g, \qquad \forall t \in T \qquad (3)$$

GAS boiler model

$$Q_t^{GB} = CAP^{GB} a_t^{GB}, \qquad \forall t \in T, \ 0 \le a_t^{GB} \le 1 \qquad (4)$$

$$g_t^{GB} = Q_t^{GB} \Big/ \eta_{GB} LHV_g, \qquad \forall t \in T \qquad (5)$$

WSHP model

$$Q_t^{HP} = CAP^{HP} a_t^{HP}, \qquad \forall t \in T, \ 0 \le a_t^{HP} \le 1 \qquad (6)$$

$$P_t^{HP} = Q_t^{HP} \Big/ COP_{AC}, \qquad \forall t \in T \qquad (7)$$

Absorption chiller

$$Q_t^{AC} = CAP^{AC} a_t^{AC}, \qquad \forall t \in T, \ 0 \le a_t^{AC} \le 1 \qquad (8)$$

$$q_t^{ac} = Q_t^{AC} \Big/ COP_{AC}, \qquad \forall t \in T \qquad (9)$$

Energy storages

The energy storage devices chosen are BES and TES, which can save energy when there is surplus renewable production or low-cost period and supply energy when needed. The two devices have the same modeling method as shown in (10) – (13). The remaining power in the storage at each time step t is the state of charge (SOC), which is calculated in (10). Eq (11) prevents the SOC from going beyond its capacity limit and the charging power P_t^{ch} is limited by the maximum power and a binary variable ζ_t^{ESS}. The storage is either charging when $\zeta_t^{ESS} = 1$ or discharging or idle when $\zeta_t^{ESS} = 0$, as indicated in (12).

$$S_{t+1}^{EES} = S_t^{EES} + P_t^{ch} \Delta t \eta^{EES} / B^{cap} + P_t^{dch} \Delta t / \eta^{EES} B^{cap} \qquad (10)$$

$$SOC_{min}^{EES} \le S_t^{EES} \le SOC_{max}^{EES} \qquad (11)$$

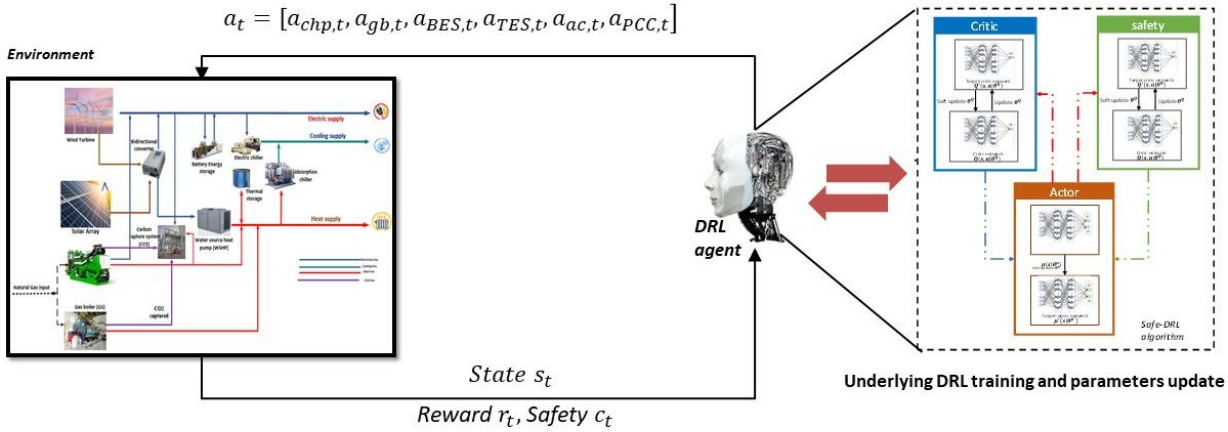

Fig. 2. Proposed DRL interaction with IES environment

$$0 \le P_t^{ch} \le P_{max}\zeta_t^{ESS}, \quad \zeta_t^{ESS} \in \{0,1\} \tag{12}$$
$$0 \le P_t^{dch} \le P_{max}(1-\zeta_t^{ESS}), \quad \forall t \in T \tag{13}$$

Post carbon capture system (PCC)

Eq (14)-eq (16) show the mathematical model of PCCS. The first step is to find the total CO_2 emission from the burning devices (i.e. CHP and GB) using eq (14) where χ^{co_2} is the amount of carbon released by natural gas combustion, which is 0.368 t/MWh [10].

$$CO_{2,t}^{emit} = \chi^{co_2}\left(g_t^{chp} + g_t^{GB}\right), \quad \forall t \in T \tag{14}$$
$$PCC_t^{cap} = CO_{2,t}^{emit} a_t^{pcc}, \quad \forall t \in T, \ 0 \le a_t^{pcc} \le 1 \tag{15}$$
$$PCC_t^{el} = PCC_t^{cap}\kappa_{pcc}^{el}, \quad \forall t \in T \tag{16}$$
$$PCC_t^{q} = PCC_t^{cap}\kappa_{pcc}^{q}, \quad \forall t \in T \tag{17}$$

Finally, the aim of the study is to minimize the associated economic implications of operating energy systems. Thus, the objective function $F(t)$ is described as:

$$F(t) = e_t P_{grid,t}^{+} + g_t\left(g_t^{chp} + g_t^{GB}\right) - e_t P_{grid,t}^{-} \tag{18}$$
$$P_{grid,t}^{+/-} = P_{pv,t} + P_{WT,t} + P_t^{chp} + P_t^{dch} - EL_t - P_t^{HP} - P_t^{ch} - PCC_t^{el} \tag{19}$$

Where, e_t is the electricity price, $P_{grid,t}^{+}$ denotes the electricity export to the grid at time t, $P_{grid,t}^{-}$ is the amount of energy that is required from the grid to balance the on-site demand, g_t is the natural gas price, and EL_t represents the electricity demand by the prosumer at time t

2. Proposed prioritized safe soft-actor critic deep reinforcement learning.

In this section, the energy management scheduling of the proposed IES is formulated as a Markov decision process (MDP). To achieve reliable optimal operation and system constraints, a safety function is introduced following a similar approach of the reward function computation in a conventional DRL method. An improved SAC algorithm is used to solve the scheduling problem, where safety network and prioritized experience replay are introduced to improve its performance. This ensures that the developed DRL agent can make reasonable scheduling decisions while satisfying constraint conditions. Specifically, the improved DRL agent ensures (1) the system does not violate specified constraints and (2) fast learning period by sampling the most crucial data from the pool of experience that are pertinent to the reward and safety optimization during training.

3.1 Markov Decision Process for formulation and Prioritized experience replay.

1) *State space:* The state s_t represents the observed information from the IES environment by the DRL agent, this information include renewable energy (PV_t, PW_t), electricity and cooling demand (ED_t, HD_t), the current State of Charge of BES and TES $(SOCe_t, SOCh_t)$, and the energy price at each time step i.e, electricity and gas price (e_t, g_t). It is expressed as:

$$s_t = [PV_t, PW_t, ED_t, HD_t, e_t, g_t, SOCe_t, SOCh_t] \in S$$

2) *Action space*: The action space A contains the controlled action a_t implemented by the IES agent base on the input state s_t to control the IES components. The control action is a 6-dimensional vector,

$$a_t = \left[a_{chp,t}, a_{gb,t}, a_{hp,t}, a_{BES,t}, a_{TES,t}\right] \in [-1, 1]$$

3) *Reward function*: Considering the cost associated with the IES operation, i.e., the energy exchange with the grid. The designed reward function is:

$$r_t(s_t, a_t) = -[e_t P_{grid,t}^{+} + g_t\left(g_t^{chp} + g_t^{GB}\right) - e_t|P_{grid,t}^{-}|]\ \Delta t \tag{20}$$

4) *Safety function*: The formulation of the safety function is one of the improvements introduced in this study, which is a constraint cost function of the IES components comprising of grid exchange violation and thermal balance constraint. It is expressed as:

$$c_t(s_t, a_t) = -\left|Q_t^{GB} + Q_t^{HP} + Q_t^{chp} + P_t^{TES,dch} - PCC_t^{q} - P_t^{TES,ch} - HD_t\right| - \left|P_{grid,t}^{-/+} - P_{grid}^{max}\right| \tag{21}$$

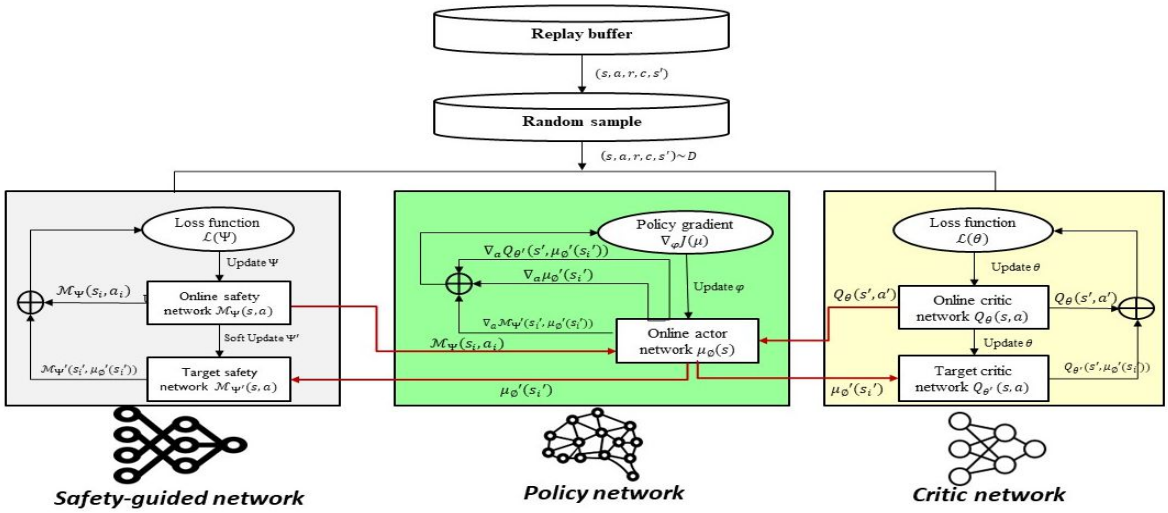

Fig. 2. Proposed safe-DRL training process.

Considering the long-term goal of scheduling problem, a discount factor γ is introduced to weight the immediate and future rewards and safety value as:

$$R(t) = \sum_{\tau=0}^{T} \gamma^{\tau}(t+\tau) \tag{22}$$

Prioritized experience replay (PER)

PER was introduced in this a study for efficient sampling during SAC algorithm training. This is achieved by assigning a priority to the samples that are crucial to the reward and safety. The approach is mathematically expressed as:

$$P_i = (|\delta_i| + \epsilon)^{\alpha} \tag{23}$$

$$P(i) = \frac{p_i^{\alpha}}{\sum_k p_k^{\alpha}} \tag{24}$$

Where P_i is the priority experience of the i-th experience, $|\delta_i|$ denotes the absolute TD error, ϵ is a small positive constant, and α is the hyperparameter for controlling the degree of prioritization. Eq (24) describes the probability of sampling transition i from the experience buffer with cache size k.

Safe Soft actor critic (safe-SAC) deep reinforcement learning model.

In this study, we propose a SAC algorithm that has three networks: the actor network, the critic network, and the safety network. The actor network takes the input state information s_t as input and outputs the controllable action a at the current timestep. The critic network takes the state s_t and the action a from the actor network as input and generates the Q value. The safety network takes the state s and the action a as input and outputs a safety value that is mainly affected by the constraint cost function. Both the Q value and the safety value are used to evaluate the action from the actor network.

Figure 3 illustrates the training process for the three networks. Before the commencement of the training, the network parameters of all the neural networks are initialized. During the training, random action sampling is performed by the network without updating the network parameters, the information is stored in a replay buffer. After storing enough experience, network update is initiated, by sampling from the stored experience using PER to obtain the most crucial experience, the obtained information is then used for gradient descent computation and network updates.

In the conventional DRL methods, the systems constraints are usually described by incorporating a penalty term into the reward function. However, selecting appropriate penalty coefficient is a difficult task and the approach may not generalise across different environment. Thus, a safety network is introduced in the SAC algorithm in this study. The proposed safety guided function is applied to compute the safety of the current policy in the future by estimating the action-value function of the accrued safety $\mathcal{M}_\Psi(s, a)$. The network follows the critic network evaluation procedure by using DNN parameterised by Ψ. The action-value function is computed as shown in eq (25). Given the stochastic policy $\mu_{\emptyset(s)}$, TD learning approach is applied to minimise the loss function during the training process as illustrated in eq (26). Similarly, the network parameter is updated in eq (27) by applying gradient descent on $\mathcal{L}(\Psi)$ while the target safety network parameter is update in eq (28) using soft update.

$$\mathcal{M}_\Psi(s, a) = \mathbb{E}_{s' \sim \varepsilon}\left[c + \gamma \max_{a'} \mathcal{M}_\Psi(s', a')\right] \tag{25}$$

$$\mathcal{L}(\Psi) = \mathbb{E}_{s,a,c,s' \sim D}\,[(c + \gamma \max_{a'} \mathcal{M}_\Psi(s', a')|_{a=\mu_{\emptyset(s)}} - [\mathcal{M}_\Psi(s, a) - \log \pi_\emptyset(\alpha_t|s_t)])^2 \tag{26}$$

$$\psi\Psi_{t+1} \leftarrow \psi\Psi_t - \alpha_c \nabla_\Psi \mathcal{L}(\Psi) \tag{27}$$

$$\bar{\Psi}_{t+1} \leftarrow \kappa\Psi_t + (1-\kappa)\bar{\Psi}_t \tag{28}$$

The proposed safe-SAC is an off-policy DRL algorithm that can update the DNN function parameters using past experiences. Meanwhile, these experiences that are attained from the environment are temporarily correlated. Thus, to break this correlation and stabilise the training performance, an experience replay buffer D of cache size KD is employed. The buffer stores the agent's experience in form of a transition tuple (s, a, r, c, s'). During the training period, a minibatch of H experiences is uniformly sampled from the

buffer $(s, a, r, c, s') \sim D, \forall_i = 1 \ldots . H$ using PER approach in eq (23) and eq (24) to evaluate the online actor network policy gradient $\nabla_{\varphi}\mathcal{L}(\varphi)$, TD error of critic ($\mathcal{L}(\theta)$) and safety network ($\mathcal{L}(\Psi)$), and parameters $(\theta, \varphi, \check{\theta}, \Psi, \check{\Psi})$ soft-update.

3. Simulation results and Analysis

In this section, a simulation experiment on the proposed IES is presented, and the parameters of the IES components and algorithms are presented.

3.1 Parameters settings for the DRL algorithm and IES scheduling

The deep reinforcement learning algorithm introduced in this study is implemented using Pytorch framework and real time multi-energy data, renewable energy, gas and electricity price for analysis [9,10]. The yearly data is split into training and test data by selecting every fifth day for test (73 days in total), while the remaining days (292 days) as the training data. The time interval of 1hr is applied while and the episode length is 24 hours timestep per day. The algorithm hyperparameters setting are presented in Table 1.

Table 1: DRL agent selected hyperparameters.

Hyperparameters	value
Buffer size	60,000
Discount factor γ	0.95
Soft update factor	0.002
Actor learning rate	0.0002
Safety and critic learning rate	0.002
Batch size	32
PER parameters	0.6, 0.4
Neural network size (all networks)	[400, 300]
Training Epochs	30,000

3.2 Analysis of the simulation results

Figure 4 presents the training operation cost curves of all the considered DRL algorithms. All the agents randomly interact with the environment for the first 3000 episodes to obtain enough training experience. After obtaining enough experience, the actual training commences, and the algorithm starts updating the network parameters of all the neural networks. Noticeably, the SAC with safety network converges early to achieve tolerable system physical constraints at 10,000 episodes compared to other algorithms as illustrated in Fig 4b. Besides, other algorithms could not reach tolerable constraints despite converging at 20,000 episodes which indicates the penalty value needed to be tuned. Whereas, safe-SAC does not require penalty value and achieve tolerable constraint, this indicates the efficacy of the proposed method. Another interesting observation is in Fig 4a, proposed algorithm achieved the least operation cost, this is possible with the introduction of PER to sample the most important data for the network update during training.

The training elapsed duration of each DRL agent and the elapsed time to reach convergence is presented in Table 2. Agents with safety network take more training periods to complete the specified training epochs with is due to additional network structure. However, they converged early compared to the conventional SAC due to the introduced PER and reduction on the critic network burden during training. This indicates that lower epochs can be initiated for the proposed agent and contribute to low computational cost with optimal performance. A comparative analysis is conducted to validate the effectiveness of the proposed DRL strategy in achieving optimal energy cost in real-time. The obtained results are shown in Table 3, the proposed improved strategy is benchmarked against theoretical optimization and other existing DRL agents. The proposed model achieved near optimal results and tolerable constraint in relation to theoretical optimization.

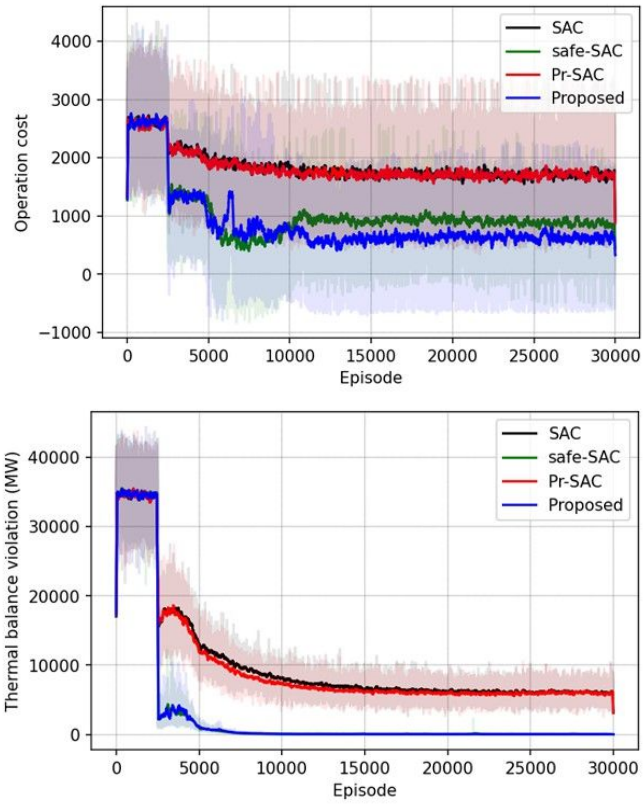

Fig 4. Agents Episodic training curves (a) operation cost (b) thermal balance constraint

Table 2: DRL agents elapsed and training period.

Trained models	Total Training period (h)	Elapsed time to converge (h)
SAC	4.13	3.56
Safe-SAC	5.70	2.45
per-SAC	4.17	3.58
Proposed (PER +safe)	5.86	2.57

Table 3: DRL agents average Optimal cost on the test data.

Trained models	Operation cost (k$)	Grid violation (MW)	Thermal balance violation (MW)
Theoretical Optimization	23.46	0.00	0.00
SAC	28.28	0.00	24.60
Safe-SAC	26.05	0.00	4.57
per-SAC	27.69	0.00	18.54
Proposed (PER +safe)	25.74	0.00	1.12

4. Conclusion

This study presents an improved SAC model for real-time autonomous scheduling of IES components. The improved strategy incorporates PER for efficient sampling from the pool stored experience which contributes to fast convergency of the model. The second strategy is the inclusion of a safety network to handle the physical constraints associated with the system. This approach enables the actor policy network to be constraint conscious in action decision making. Consequently, the proposed strategy achieved near optimal results with tolerable constraints.

4.1 References

[1] M. Yan, M. Shahidehpour, A. Paaso, L. Zhang, A. Alabdulwahab, and A. Abusorrah, "Distribution Network-Constrained Optimization of Peer-to-Peer Transactive Energy Trading Among Multi-Microgrids," *IEEE Transactions on Smart Grid,* vol. 12, no. 2, pp. 1033-1047, 2021, doi: 10.1109/tsg.2020.3032889.

[2] H. N. Tran, T. Narikiyo, M. Kawanishi, S. Kikuchi, and S. Takaba, "Whole-day optimal operation of multiple combined heat and power systems by alternating direction method of multipliers and consensus theory," *Energy Conversion and Management,* vol. 174, pp. 475-488, 2018, doi: 10.1016/j.enconman.2018.08.046.

[3] Ö. Erol and Ü. Başaran Filik, "A Stackelberg game approach for energy sharing management of a microgrid providing flexibility to entities," *Applied Energy,* vol. 316, p. 118944, 2022/06/15/2022,doi:https://doi.org/10.1016/j.apenergy.2022.118944.

[4] T. M. Alabi, L. Lu, and Z. Yang, "Stochastic optimal planning scheme of a zero-carbon multi-energy system (ZC-MES) considering the uncertainties of individual energy demand and renewable resources: An integrated chance-constrained and decomposition algorithm (CC-DA) approach," *Energy,* vol. 232, 2021, doi: 10.1016/j.energy.2021.121000.

[5] A. H. Ganesh and B. Xu, "A review of reinforcement learning based energy management systems for electrified powertrains: Progress, challenge, and potential solution," *Renewable and Sustainable Energy Reviews,* vol. 154, 2022, doi: 10.1016/j.rser.2021.111833.

[6] B. Zhang, W. Hu, D. Cao, Q. Huang, Z. Chen, and F. Blaabjerg, "Deep reinforcement learning–based approach for optimizing energy conversion in integrated electrical and heating system with renewable energy," *Energy Conversion and Management,* vol. 202, 2019, doi: 10.1016/j.enconman.2019.112199.

[7] S. Aslam, H. Herodotou, S. M. Mohsin, N. Javaid, N. Ashraf, and S. Aslam, "A survey on deep learning methods for power load and renewable energy forecasting in smart microgrids," *Renewable and Sustainable Energy Reviews,* vol. 144, 2021, doi: 10.1016/j.rser.2021.110992.

[8] D. Qiu, Z. Dong, X. Zhang, Y. Wang, and G. Strbac, "Safe reinforcement learning for real-time automatic control in a smart energy-hub," *Applied Energy,* vol. 309, 2022, doi: 10.1016/j.apenergy.2021.118403.

[9] A. Daneshvar Garmroodi, F. Nasiri, and F. Haghighat, "Optimal dispatch of an energy hub with compressed air energy storage: A safe reinforcement learning approach," *Journal of Energy Storage,* vol. 57, 2023, doi: 10.1016/j.est.2022.106147.

[10] T. M. Alabi, N. P. Lawrence, L. Lu, Z. Yang, and R. Bhushan Gopaluni, "Automated deep reinforcement learning for real-time scheduling strategy of multi-energy system integrated with post-carbon and direct-air carbon captured system," *Applied Energy,* vol. 333, 2023, doi: 10.1016/j.apenergy.2022.120633

[11] X. Zhang, G. Strbac, N. Shah, F. Teng, and D. Pudjianto, "Whole-system assessment of the benefits of integrated electricity and heat system," *IEEE Transactions on Smart Grid,* vol. 10, no. 1, pp. 1132-1145, 2018

Proceedings of the 3rd Conference on Fully Actuated System Theory and Applications
May 10-12, 2024, Shenzhen, China

Predictive Path-following Control for Tilt-quadrotor UAV based on Fully-actuated System Approaches

Lixue Xu[1], Xiubo Wang[2], Ping He[1], Yan Wang[1]

1. Department of Control Science and Engineering, , Harbin Institute of Technology, Harbin, 150001, P. R. China
E-mail: lixuexu@outlook.com

2. Center for Control Theory and Guidance Technology, Harbin Institute of Technology, Harbin, 150001, P. R. China
E-mail: xiubowang@outlook.com

Abstract: This study focuses on predictive path-following control (PPFC) for a tilt-quadrotor UAV based on fully-actuated system (FAS) approaches. Rooted in the fundamental principle of tilt-quadrotor UAV model mechanics, the dynamic model of the tilt-quadrotor UAV is derived into a FAS model with multiple degree of freedoms. Concurrently, the PPFC-FAS control scheme is proposed for tilt-quadrotor UAV path-following, the path-following problem is transformed into a trajectory tracking problem with the tilt-quadrotor FAS model and parameterized path. If the cost function and the penalty function in the predictive performance index satisfies the certain conditions, the convergence of path-following errors is guaranteed. Finally, the simulation results verify the effectiveness and efficiency of the proposed PPFC-FAS control scheme.

Key Words: Predictive control, fully actuated system approaches, tilt-quadrotor UAV, path-following

1 Introduction

In recent years, the rapid advancement in drone technology has led to an increased interest in autonomous Unmanned Aerial Vehicles (UAVs), particularly in quadrotors, due to their versatility, maneuverability, and robustness[1, 2]. Among the various configurations of quadrotors, the tilt-rotor design has gained significant attention[3, 4]. This design, featuring rotors that can tilt independently, offers enhanced aerodynamic efficiency and superior control over motion, making these UAVs suitable for a wide range of applications, from aerial photography and surveillance to search and rescue operations and package delivery[5, 6].

However, the most literature on tilt-quadrotors focus on trajectory tracking control[4, 7, 8]. It is noteworthy that trajectory tracking mission requires the UAV to track a time-related reference trajectory. This implies a requirement for system response speed, and the tracking error seriously affects the safe performance of the system. If the overshoot of the tracking error is too large to meet the accessibility of the actual system control capability and speed response, such that the UAV will not be able to follow the reference trajectory [9]. The reason for this phenomenon is that the pre-planning offline fixed time reference trajectory does not take into account the actual capabilities of the actual system. Yet not all problems encountered in tilt-quadrotor missions are trajectory-tracking problems, and the accuracy of movement along a trajectory is more important than speed.

One way to overcome this problem is the path-following control, which drive the system along a geometric reference without any pre-specified timing information[10, 11]. There also exists one problem. The sophisticated, multi-variable and coupled dynamics of the tilt-quadrotor for path-following poses substantial challenges in the control system design of the tilt-quadrotor. These challenges are compounded when the UAV is required to follow a predetermined path while maintaining stability and smooth response dynamics.

Predictive control, known for its ability to anticipate future events and take control actions accordingly, emerges as a promising solution to these challenges[12]. Particularly, it is well-suited for managing the multi-variable control problems inherent in tilt-quadrotors due to its optimization-based approach that allows for the consideration of future path-following and constraints. As a methodology, the fully actuated system (FAS) approach breaks away from traditional thinking, which takes a new perspective on the problem of FASs by starting from the models' mechanics and focusing on control variables[13, 14]. Specifically, the FAS approach, by preserving a full actuation model with physically meaningful or establishing one with mathematically meaningful, fully leverages the attributes of full actuation fully-actuated system (FAS) approaches have unique advantages in dealing with the decoupling and optimization of nonlinear and multi-variable systems [15–17].

This study focuses on predictive path-following control (PPFC) for a tilt-quadrotor UAV based on FAS approaches, which propose PPFC-FAS control scheme to achieve path following. The contribution of this paper is given as follows.

1) The nonlinear coupled tilt-quadrotor system into a FAS system with control degrees of freedom.
2) Predictive control provides the tilt-quadrotor inputs and the path-following inputs, which provided by minimizing the performance index.

2 Modeling

In this section, a type of cascaded UASs is studied from model mechanisms. Based on the Euler Lagrange equation of each sub-UAS, the multi-order UASs model is firstly derived. Then a transformation paradigm from UASs to FASs and its discretization model with uncertainties are given.

For a tilt-quadrotor UAV, its structure is shown in Figure 1. The symbols in tilt-quadrotor model used in the following section are listed in Table 1.

The transformation matrix, from the frame $\mathcal{B}$ to the frame $\mathcal{W}$, denotes as $R_{\mathcal{B}/\mathcal{W}}$. It is calculated by a rotation sequence

Table 1: Symbols description in tilt-quadrotor system.

symbols	Meaning
$\mathcal{B}$	body-fixed frame
$\mathcal{W}$	world frame
m	mass of quadrotor
g	gravitation acceleration
I	moment of inertia matrix
k_f, k_m	constants of force and moment
(x, y, z)	position in $\mathcal{W}$ coordinates
(ϕ, θ, ψ)	yaw, pitch and roll angles
$\theta_i,\ i = 1 \sim 4$	tilted angle of ith rotors
$\omega_i,\ i = 1 \sim 4$	angular velocity of ith rotor

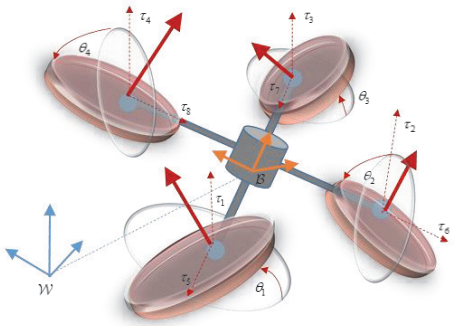

Fig. 1: The structure of the tilt-quadrotor.

along axis of X, Y and Z in sequence as follows

$$R_{\mathcal{B}/\mathcal{W}}=\begin{bmatrix} c\psi c\theta & c\psi s\theta s\phi - s\psi c\phi & c\psi s\theta c\phi + s\psi s\phi \\ s\psi c\theta & s\psi s\theta s\phi + c\psi c\phi & \sin\psi s\theta c\phi - c\psi s\phi \\ -s\theta & c\theta s\phi & c\theta c \end{bmatrix}.$$

where c and s denote $\cos(\cdot)$ and $\sin(\cdot)$, respectively.

Using the Newton-Euler method, the equations of motion in world-frame is given as:

$$\begin{bmatrix} \ddot{x} \\ \ddot{y} \\ \ddot{z} \end{bmatrix} = -\begin{bmatrix} 0 \\ 0 \\ g \end{bmatrix} + \frac{R_{\mathcal{B}/\mathcal{W}}}{m}\begin{bmatrix} \tau_6 + \tau_8 \\ -\tau_5 - \tau_7 \\ \tau_1 + \tau_2 + \tau_3 + \tau_4 \end{bmatrix}, \quad (1)$$

$$\begin{bmatrix} \dot{p} \\ \dot{q} \\ \dot{r} \end{bmatrix} = I^{-1}\begin{bmatrix} l(\tau_2 - \tau_4) + \frac{k_m}{k_f^2}(\tau_6 + \tau_8) \\ l(\tau_3 - \tau_1) + \frac{k_m}{k_f^2}(\tau_7 + \tau_5) \\ \begin{pmatrix} l(-\tau_5 - \tau_6 + \tau_7 + \tau_8) \\ -\frac{k_m}{k_f^2}(\tau_1 - \tau_2 + \tau_3 - \tau_4) \end{pmatrix} \end{bmatrix} - I^{-1}\begin{bmatrix} p \\ q \\ r \end{bmatrix} \times I \begin{bmatrix} p \\ q \\ r \end{bmatrix}, \quad (2)$$

$$\begin{bmatrix} \dot{\phi} \\ \dot{\theta} \\ \dot{\psi} \end{bmatrix} = R^{-1}\begin{bmatrix} p \\ q \\ r \end{bmatrix}, \quad (3)$$

where

$$R = \begin{bmatrix} 1 & 0 & -\sin\theta \\ 0 & \cos\phi & \cos\theta\sin\phi \\ 0 & -\sin\phi & \cos\theta\cos\phi \end{bmatrix},$$

$$R^{-1} = \begin{bmatrix} 1 & \sin\phi\frac{\sin\theta}{\cos\theta} & \cos\phi\frac{\sin\theta}{\cos\theta} \\ 0 & \cos\phi & -\sin\phi \\ 0 & \frac{\sin\phi}{\cos\theta} & \frac{\cos\phi}{\cos\theta} \end{bmatrix},$$

and the assigned control inputs τ_i, $i = 1 \sim 8$, are given as

$$\tau_i = k_f\omega_i^2\cos\theta_i,\ i = 1, 2, 3, 4,$$

$$\tau_j = k_f\omega_i^2\sin\theta_i,\ j = 5, 6, 7, 8.$$

Taking the derivative on the both side of (3), then by simple rearrangement, one has

$$\begin{bmatrix} \ddot{\theta} \\ \ddot{\theta} \\ \ddot{\psi} \end{bmatrix} = -R^{-2}\dot{R}\begin{bmatrix} p \\ q \\ r \end{bmatrix} + R^{-1}\begin{bmatrix} \dot{p} \\ \dot{q} \\ \dot{r} \end{bmatrix}. \quad (4)$$

Further, from (3), one can be obtained

$$\begin{bmatrix} p \\ q \\ r \end{bmatrix} = R\begin{bmatrix} \dot{\phi} \\ \dot{\theta} \\ \dot{\psi} \end{bmatrix}, \quad (5)$$

taking equations (2) and (5) into (4), we have

$$\begin{bmatrix} \ddot{\phi} \\ \ddot{\theta} \\ \ddot{\psi} \end{bmatrix} = -R^{-2}\dot{R}R\begin{bmatrix} \dot{\phi} \\ \dot{\theta} \\ \dot{\psi} \end{bmatrix} - R^{-1}I^{-1}R\begin{bmatrix} \dot{\phi} \\ \dot{\theta} \\ \dot{\psi} \end{bmatrix} \times IR\begin{bmatrix} \dot{\phi} \\ \dot{\theta} \\ \dot{\psi} \end{bmatrix} + R^{-1}I^{-1}\begin{bmatrix} l(\tau_2 - \tau_4) + \frac{k_m}{k_f^2}(\tau_6 + \tau_8) \\ l(\tau_3 - \tau_1) + \frac{k_m}{k_f^2}(\tau_7 + \tau_5) \\ \begin{pmatrix} l(-\tau_5 - \tau_6 + \tau_7 + \tau_8) \\ -\frac{k_m}{k_f^2}(\tau_1 - \tau_2 + \tau_3 - \tau_4) \end{pmatrix} \end{bmatrix}. \quad (6)\ (7)$$

Let $\eta = [x, y, z, \phi, \theta, \psi]^{\mathrm{T}}$, combing (1) and (7), the dynamics of the tilt-quadrotor UAV can be cased into the following form:

$$\ddot{\eta} = f_{1\sim 2}\left(\eta^{(0\sim 1)}\right) + b\left(\eta^{(0\sim 1)}\right)\tau_{1\sim 8}, \quad (8)$$

where

$$b(\cdot) = \mathrm{diag}\left(\frac{R_{B/E}}{m}, R^{-1}I^{-1}\right) \times \begin{bmatrix} 0 & 0 & 0 & 0 & 0 & 1 & 0 & 1 \\ 0 & 0 & 0 & 0 & -1 & 0 & -1 & 0 \\ 1 & 1 & 1 & 1 & 0 & 0 & 0 & 0 \\ 0 & l & 0 & -l & 0 & \frac{k_m}{k_f^2} & 0 & \frac{k_m}{k_f^2} \\ -l & 0 & l & 0 & \frac{k_m}{k_f^2} & 0 & \frac{k_m}{k_f^2} & 0 \\ -\frac{k_m}{k_f^2} & \frac{k_m}{k_f^2} & -\frac{k_m}{k_f^2} & \frac{k_m}{k_f^2} & -l & -l & l & l \end{bmatrix},$$

and

$$\begin{cases} f_1(\cdot) = -\begin{bmatrix} 0 \\ 0 \\ g \end{bmatrix} \\ f_2(\cdot) = -R^{-2}\dot{R}R\begin{bmatrix} \dot{\phi} \\ \dot{\theta} \\ \dot{\psi} \end{bmatrix} - R^{-1}I^{-1}R\begin{bmatrix} \dot{\phi} \\ \dot{\theta} \\ \dot{\psi} \end{bmatrix} \\ \quad \times IR\begin{bmatrix} \dot{\phi} \\ \dot{\theta} \\ \dot{\psi} \end{bmatrix}. \end{cases} \tag{9}$$

and η is the state vector, and $\tau_i \in \mathcal{T}_i \subseteq \mathbb{R}$, $i = 1 \sim 8$, denote the compact set of input constraints. It can easily observed that $\text{rank}(b(\cdot)) = 6$.

3 Control scheme design

Building upon the foregoing modeling, we further consider the path-following problem for the tilt-quadrotor UAV system based on FAS system approach. In this section, we first make FAS control allocation, and then give the PPFC-FAS control scheme.

3.1 FAS control allocation

Inspired by FAS approaches and the nonlinear tilt-quadrotor model (8), selecting the controller in the following form

$$\begin{aligned} \tau_{1\sim 8} =& B^{+}(\cdot)\left[A_0\eta + A_1\eta^{\lfloor 1 \rfloor} + B_0 u_{1\sim 6} - F(\cdot)\right] \\ &+ Y - B^{+}BY, \end{aligned} \tag{10}$$

where $F = f_{1\sim 2}(\cdot), B = b(\cdot)$ given in (8), A_0, A_1, $\bar{B}$ and Y are matrices to be selected with appropriate dimensions. Then the tilt-quadrotor model can be cased in the following linear over-actuated system

$$\ddot{\eta} = A_1\dot{\eta} + A_0\eta + B_0 u_{1\sim 6}, \tag{11}$$

which can be further transformed into the following state-space form:

$$\dot{\eta}^{(0\sim 1)} = \bar{A}\eta^{(0\sim 1)} + \bar{B}u_{1\sim 6}, \tag{12}$$

where

$$\bar{A} = \begin{bmatrix} 0_6 & I_6 \\ A_0 & A_1 \end{bmatrix}, \ \bar{B} = \begin{bmatrix} 0_{6\times 6} \\ B_0 \end{bmatrix}.$$

Condition 1 *By selecting matrices A_0, A_1, Y and B_0, such that the following conditions are satisfied*

1) *the pair $\left(\bar{A}, \bar{B}\right)$ is controllable;*
2) *the pair $\left(\bar{A}, C\right)$ is observable;*
3) *Y provides extra DOFs for the constraints requirment of $\tau_{1\sim 8}$.*

The parameterized reference path is

$$\mathcal{Y}_r = \left\{ y_r \in \mathbb{R}^6 \middle| \left[\rho_{\text{start}}, \rho_{\text{end}}\right] \ni \rho \mapsto y_r = r_{pf}(\rho) \right\}, \tag{13}$$

where $r_{pf}(\kappa) : \mathbb{R} \mapsto \mathbb{R}^6$. And the path-following error is defined as

$$e_{pf} = \eta - \eta_r.$$

The control object is summarized as follows.

Problem 1 *Consider the tile-quadrotor system* (12) *with the parameter path* (13)*, to design the FAS allocation control in following form* (10)*, such that:*

1) *the path convergence is achieved, i.e. $\lim_{t\to\infty} \|e_{pf}(t)\| = 0$;*
2) *the reference path-following system motions keep forward, i.e. $\dot{\rho} \geq 0$ and $\lim_{t\to\infty} \rho(t) = \rho_{\text{end}}$;*
3) *the constraints always hold, i.e. $\tau_i(t) \in \mathcal{T}_i$, $i = 1 \sim 8$, $\forall t \geq 0$.*

Remark 1 *The selection of matrices A_0, A_1, B_0 and Y provide a certain degrees of freedom. These degrees of freedom acting on the input channel can adjust the input performance of the tilt-quadrotor UAV, such as amplitude, energy, constraints, etc. Due to the limitation of the space, the selection of matrices A_0, A_1, B_0 and Y are not reported in this paper. For simplification, let $A_0 = A_1 = 0_6$, $B_0 = I_6$ and $Y = 0_6$ in the following section. And the input constraints alway hold by selecting matrix Y.*

3.2 Predictive path-following control

We design the following virtual reference system as follows

$$\ddot{\rho} = v, \tag{14}$$

where v is the virtual reference input to be designed, such that the reference states constraint $\rho^{(0\sim 1)} \in \mathcal{P}$ holds, where $\mathcal{P} = \left\{ \rho^{(0\sim 1)} \in \mathbb{R}^2 \middle| \rho \in \left[\rho_{\text{start}}, \rho_{\text{end}}\right], \ \dot{\rho} \geq 0 \right\}$.

Let $e = \eta - r_{pf}(\rho)$, combing (11) and (14), we have

$$\dot{e}^{(0\sim 1)} = Ae^{(0\sim 1)} + BU, \tag{15}$$

where

$$U = u_{1\sim 6} - \frac{\partial^2 r_{pf}(\rho)}{\partial \rho^2}\dot{\rho} + \frac{\partial r_{pf}(\rho)}{\partial \rho}v,$$

then the path-following problem is converted into trajectory tracking problem. And the common horizon performance index is given as follows

$$\begin{aligned} &J_{pf}\left(\eta^{(0\sim 1)}(t_k), \rho^{(0\sim 1)}(t_k), v(t_k), U(t_k)\right) \\ &= \int_{t_k}^{t_k+T} L\left(e^{(0\sim 1)}(s), \rho^{(0\sim 1)}(s), v(s), U(s)\right) \mathrm{d}s \\ &\quad + E_{pf}\left(e^{(0\sim 1)}(t_k + T), \rho^{(0\sim 1)}(t_k + T)\right), \end{aligned}$$

where $L(\cdot)$ is the path-following error continous continuous function, and $E_{pf}(\cdot) \in \mathcal{C}^1$ is the end penalty positive semi-definite function.

Then the optimization problem in the predictive path-following control can be stated as

$$\begin{aligned} \min_{U,v} \quad & J_{pf}(\cdot) \\ \text{s.t.} \quad & (14), (15), \\ & \rho^{(0\sim 1)} \in \mathcal{P}. \end{aligned} \tag{16}$$

Building upon the foregoing analysis, the following results with simplified proof can be given.

Theorem 1 *Consider the tilt-quadrotor system* (12) *satisfies condition* (1) *with the parameter path 13 and the performance index* (3.2)*. Suppose that the following conditions hold*

1) $L\left(e^{(0\sim1)},\rho^{(0\sim1)},v,U\right) \geq \Gamma\left(\left\|e_{pf},\rho-\rho_{end}\right\|^{\mathrm{T}}\right)$, *where* Γ *is the* $\mathcal{K}$ *function;*

2) $E_{pf}\left(e^{(0\sim1)},\rho^{(0\sim1)}\right)\geq 0$ *is* $\mathcal{C}^1$;

3) there exist a scalar $0<\delta\leq\epsilon$, *such that*

$$\begin{aligned}&\frac{\mathrm{d}}{\mathrm{d}s}\left(E_{pf}\left(e^{(0\sim1)}(s),\rho^{(0\sim1)}(s)\right)\right)+\\&\quad L\left(e^{(0\sim1)}(s),\rho^{(0\sim1)}(s),v(s),U(s)\right)\leq 0,\\&\quad \forall s\in[t,t+\delta],\ t\geq 0 \text{ and } \rho^{(0\sim1)}(0)\in\mathcal{P};\end{aligned}$$

4) the optimal control problem (16) *is feasible for* $t=0$; *then the Problem 1 is solved, that is, the* (16) *is recursively feasible and the path-following error* $e_{pf}(t)$ *converges to zero under the following PPFC-FAS controller*

$$\begin{cases}\tau_{1\sim8}=B^{+}(\cdot)\left[A_0\eta+A_1\eta^{\lfloor1\rfloor}+B_0u_{1\sim6}-F(\cdot)\right]\\\qquad\quad +Y-B^{+}BY\\u_{1\sim6}=U+\dfrac{\partial^2r_{pf}(\rho)}{\partial\rho^2}\dot{\rho}-\dfrac{\partial r_{pf}(\rho)}{\partial\rho}v,\end{cases}$$

where U *and* v *are solved by* (16).

Proof. Select the following value function $V(t_k)=J_{pf}(t_k)$ with optimization solution U^* and v^*, and $V(t_k)\geq 0$. At $t_k+\delta$ instant, the performance index with feasible states U and v is

$$\begin{aligned}&J_{pf}(t_k+\delta)\\=&\int_{t_k+\delta}^{t_k+T}L\left(e^{(0\sim1)}(s),\rho^{(0\sim1)}(s),v(s),U(s)\right)\mathrm{d}s\\&+\int_{t_k+T}^{t_k+\delta+T}L\left(e^{(0\sim1)}(s),\rho^{(0\sim1)}(s),v(s),U(s)\right)\mathrm{d}s\\&+E_{pf}\left(e^{(0\sim1)}(t_k+\delta+T),\rho^{(0\sim1)}(t_k+\delta+T)\right).\end{aligned}$$

Since $V(t_k+\delta)\leq J_{pf}(t_k+\delta)$, then we have

$$\begin{aligned}&V(t_k+\delta)-V(t_k)\\\leq&-\int_{t_k}^{t_k+\delta}L\left(e^{(0\sim1)}(s),\rho^{(0\sim1)}(s),v(s),U(s)\right)\mathrm{d}s\\&+\int_{t_k+T}^{t_k+\delta+T}L\left(e^{(0\sim1)}(s),\rho^{(0\sim1)}(s),v(s),U(s)\right)\mathrm{d}s\\&+E_{pf}\left(e^{(0\sim1)}(t_k+\delta+T),\rho^{(0\sim1)}(t_k+\delta+T)\right)\\&-E_{pf}\left(e^{(0\sim1)}(t_k+T),\rho^{(0\sim1)}(t_k+T)\right).\end{aligned}$$

According to condition 3, the aforementioned inequality holds

$$\begin{aligned}&E_{pf}\left(e^{(0\sim1)}(t_k+\delta+T),\rho^{(0\sim1)}(t_k+\delta+T)\right)\\&-E_{pf}\left(e^{(0\sim1)}(t_k+T),\rho^{(0\sim1)}(t_k+T)\right)\\\leq&-\int_{t_k+T}^{t_k+\delta+T}L\left(e^{(0\sim1)}(s),\rho^{(0\sim1)}(s),v(s),U(s)\right)\mathrm{d}s.\end{aligned}$$

Then it can conclude that $V(\cdot)$ is a monotonically decreasing positive function, the path-following errors will converge to zero as time increase. Thus the whole proof is completed. ■

4 Simulations

To validate the proposed controller, a numerical simulation of tilt-quadrotor UAV is given in this section.

The values of physical parameters in the tilt-quadrotor model are are selected as $m=1$ kg, $g=9.8$ kg/m^2, $k_f=3\times10^{-6}$, $k_m=1.2\times10^{-7}$, and

$$I=\begin{bmatrix}2.95\times10^{-3}&0&0\\0&2.95\times10^{-3}&0\\0&0&5.9\times10^{-3}\end{bmatrix}.$$

The initial state vector is selected as $\eta^{(0\sim1)}(0)=[1,-2,1,0,0,0,-0.1,-0.8,-0.05,-1.05,0.2,-0.28]^{\mathrm{T}}$.

The parameters in parameterized path are selected as $\rho^{(0\sim1)}(0)=[0,0]^{\mathrm{T}}$, $\rho_{\text{start}}=0$, $\rho_{\text{end}}=9990$, and

$$r_{pf}(\rho)=\begin{bmatrix}\sin(0.001\rho)\\\cos(0.001\rho+\pi/2)\\0.001\rho\\0_3\end{bmatrix}^{\mathrm{T}}.$$

The cost and the end penalty functions are selected as

$$L(\cdot)=\left\|\begin{bmatrix}\eta^{(0\sim1)}\\\rho^{(0\sim1)}\end{bmatrix}\right\|_Q^2+\left\|\begin{bmatrix}U\\v\end{bmatrix}\right\|_R^2,$$

where $Q=10^5I_{14}$, $R=10^{-3}I_7$, and $E_{pf}(\cdot)=0$.

The simulation results of the tilt-quadrotor system are given in Figures 2-5. It can be easily observed that the position and the attitude of the tilt-quadrotor system finally converge into the path-following trajectory. And from the response of states, the proposed PPFC-FAS control scheme has good time specifications, such as lower setting time, lower overshoot and lower fluctuations.

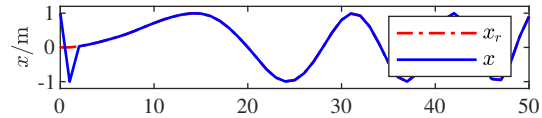

(a) The response curve of x

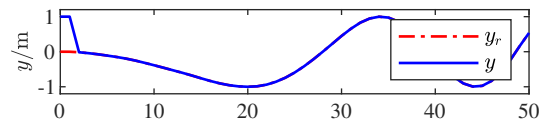

(b) The response curve of y

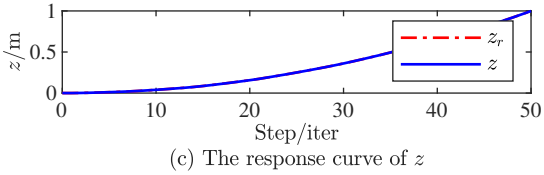

(c) The response curve of z

Fig. 2: The position results of the tilt-quadrotor UAV system.

5 Conclusions

This paper effectively solves the path-following problem of the tilt-quadrotor UAV in practical applications by integrating FAS system approaches and predictive control strategy. The study starts from the system model, transforming

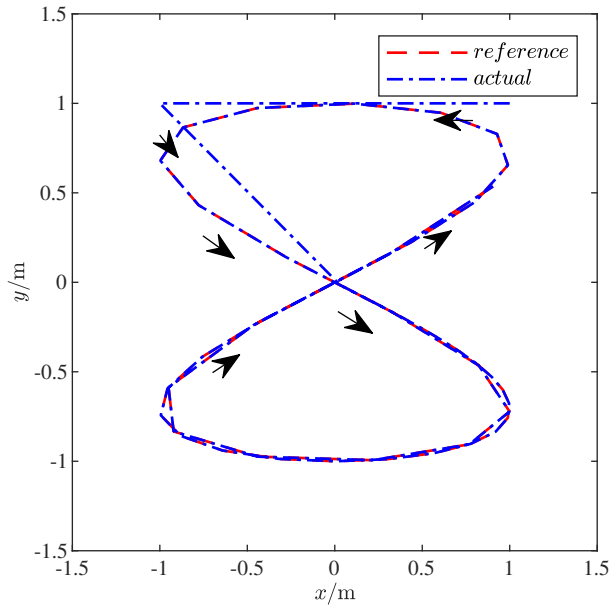

Fig. 3: The path following convergence in the $x-y$ space.

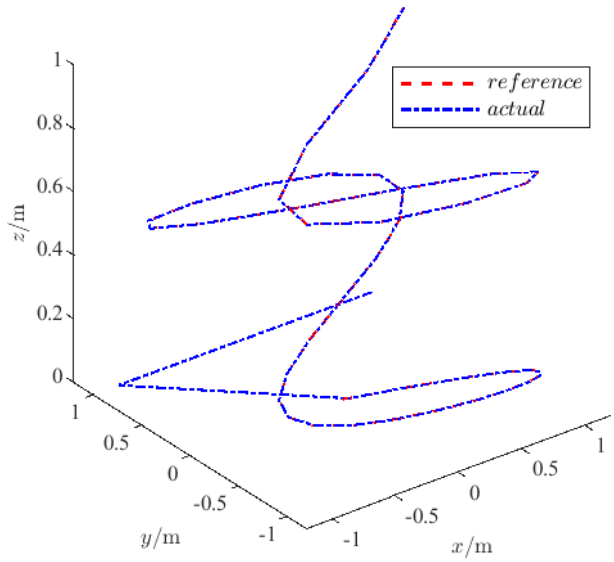

Fig. 4: The trajectory results of the tilt-quadrotor UAV system.

the tilt-quadrotor system into a FAS with input DOF, and further converts the path-following problem into a more manageable trajectory tracking problem. Then, in conjunction with the predictive control strategy, it not only achieves the design of the UAV controller with the minimum optimization index but also obtains virtual inputs for adjusting path-following. The comprehensive application of this method not only enhances the accuracy and reliability of the quadrotor UAV's path-following but also provides an innovative solution to control problems of complex dynamic systems. In summary, the results of this research enrich the theoretical field of FASs and predictive control, and are also expected to provide strong support for the development of path-following technologies for quadrotor UAVs in practice.

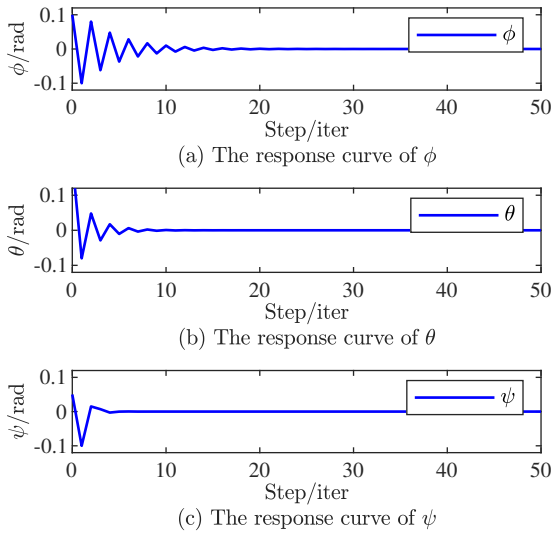

(a) The response curve of ϕ

(b) The response curve of θ

(c) The response curve of ψ

Fig. 5: The response of attitude of the tilt-quadrotor UAV system.

References

[1] Davide Falanga, Kevin Kleber, Stefano Mintchev, Dario Floreano, and Davide Scaramuzza. The foldable drone: A morphing quadrotor that can squeeze and fly. *IEEE Robotics and Automation Letters*, 4(2):209–216, 2018.

[2] Xiubo Wang and Guangren Duan. Comprehensive reconstructions and predictive control for quadrotor uav information gathering tracking missions based on fully actuated system approaches. *ISA transactions*, 2024.

[3] Zong-Yang Lv, Yuhu Wu, Qing Zhao, and Xi-Ming Sun. Design and control of a novel coaxial tilt-rotor uav. *IEEE Transactions on Industrial Electronics*, 69(4):3810–3821, 2021.

[4] Leonard Bauersfeld, Lukas Spannagl, Guillaume JJ Ducard, and Christopher H Onder. Mpc flight control for a tilt-rotor vtol aircraft. *IEEE Transactions on Aerospace and Electronic Systems*, 57(4):2395–2409, 2021.

[5] Ruihang Ji, Jie Ma, and Shuzhi Sam Ge. Modeling and control of a tilting quadcopter. *IEEE Transactions on Aerospace and Electronic Systems*, 56(4):2823–2834, 2019.

[6] Daniel N Cardoso, Sergio Esteban, and Guilherme V Raffo. A new robust adaptive mixing control for trajectory tracking with improved forward flight of a tilt-rotor uav. *ISA transactions*, 110:86–104, 2021.

[7] Jiesong Yang, Zhihao Cai, Jiang Zhao, Zexin Wang, Yongfei Ding, and Yingxun Wang. Indi-based aggressive quadrotor flight control with position and attitude constraints. *Robotics and Autonomous Systems*, 159:104292, 2023.

[8] Ismail Al-Ali, Yahya Zweiri, Nawaf AMoosa, Tarek Taha, Jorge Dias, and Lakmal Senevirtane. State of the art in tilt-quadrotors, modelling, control and fault recovery. *Proceedings of the Institution of Mechanical Engineers, Part C: Journal of Mechanical Engineering Science*, 234(2):474–486, 2020.

[9] Ningyuan Guo, Xudong Zhang, Yuan Zou, Basilio Lenzo, and Tao Zhang. A computationally efficient path-following control strategy of autonomous electric vehicles with yaw motion stabilization. *IEEE Transactions on Transportation Electrification*, 6(2):728–739, 2020.

[10] Bartomeu Rubí, Ramon Pérez, and Bernardo Morcego. A survey of path following control strategies for uavs focused

on quadrotors. *Journal of Intelligent & Robotic Systems*, 98(2):241–265, 2020.

[11] Chao Shen, Yang Shi, and Brad Buckham. Path-following control of an auv: A multiobjective model predictive control approach. *IEEE Transactions on Control Systems Technology*, 27(3):1334–1342, 2018.

[12] Max Schwenzer, Muzaffer Ay, Thomas Bergs, and Dirk Abel. Review on model predictive control: An engineering perspective. *The International Journal of Advanced Manufacturing Technology*, 117(5-6):1327–1349, 2021.

[13] Guangren Duan. High-order fully actuated system approaches: Part I. models and basic procedure. *International Journal of Systems Science*, 52(2):422–435, 2021.

[14] Guangren Duan. High-order fully actuated system approaches: Part II. Generalized strict-feedback systems. *International Journal of Systems Science*, 52(3):437–454, 2021.

[15] Guangren Duan. High-order fully actuated system approaches: Part VIII. Optimal control with application in spacecraft attitude stabilisation. *International Journal of Systems Science*, 53(1):54–73, 2022.

[16] Xiubo Wang and Guangren Duan. High-order fully actuated system approaches: Model predictive control with applications to under-actuated systems. *J. Franklin Inst.*, 360(10):6953–6975, 2023.

[17] Xiubo Wang and Guangren Duan. Fully actuated system approaches: Predictive elimination control for discrete-time nonlinear time-varying systems with full state constraints and time-varying delays. *IEEE Trans. Circuits Syst. I Regul. Pap.*, 2023.

Proceedings of the 3rd Conference on Fully Actuated System Theory and Applications
May 10-12, 2024, Shenzhen, China

Robust Model Predictive Control for Trajectory Tracking of Robotic Manipulators Based on Fully Actuated System Approach

Yi Heng Yang[1], Kai Zhang[1,2], Zhi Hua Chen[3], Bin Li[1]

1. Department of Aeronautics and Astronautics, Sichuan University, Chengdu 610065, China
E-mail: yangyh@scu.edu.cn, zhangkaihit@gmail.com (Corresponding author), bin.li@scu.edu.cn

2. Robotic Satellite Key Laboratory of Sichuan Province, Sichuan University, Chengdu 610065, China

3. Beijing Institute of Control Engineering, Beijing 100190, China
E-mail: chenzhihuahit@126.com

Abstract: Multi-degree-of-freedom (DOF) manipulators demonstrate vast application potential in aerospace, medical, and agricultural domains. In this paper, the robust model predictive control (MPC) scheme based on fully actuated system approach (FASA) is proposed for trajectory tracking problem of robotic manipulators with state constraints on joint angle, angular velocity and control torque. First, to handle with the coupled dynamics nonlinearity, a FASA-based controller is adopted. Fortunately, the obtained closed-loop system is linear and concise, brings all the design degrees of freedom, which can be further optimized to satisfy the trajectory tracking performance and state constraints. Furthermore, in addressing the system uncertainties and state constraints, the robust model control scheme is proposed to optimize the FASA-based controller, and the optimization problem is transformed into a quadratic programming (QP) problem. Finally, numercial simulation is carried out to verify the effectiveness of proposed method.

Key Words: Robotic Manipulators, State Constraints, Fully Actuated System Approach, Robust Model Predictive Control

1 Introduction

In recent years, propelled by the ongoing progress in science and technology, robotic manipulators have exhibited considerable potential across diverse fields, serving as viable substitutes for humans in a myriad of tasks. The use of robotic manipulators has substantially elevated efficiency and precision, concomitantly reducing risks and labor costs. This burgeoning trend has instigated comprehensive research in the realm of control technology for robotic manipulators. Owing to the intricate nonlinear characteristics inherent in manipulators, advanced nonlinear control methods have been developed, such as sliding mode control [1], backstepping control [2], feedback linearization [3] and so on.

Recently, the theory and application of fully actuated system approach (FASA) are currently experiencing a phase of robust development. Pioneering works in literature [5–13] introduced the concept of the fully actuated system, employing innovative perspectives to address control challenges inherent in high-order systems. Different from the modern control approach developed on the first-order system within the state space, the FASA inherits the benefits of general high order fully actuated (HOFA) model, and gives a concise design method for the control law of pratical nonlinear system [4, 14, 15]. Subsequently, scholars have conducted extensive research in this domain. In [16], a three-channel joint optimal attitude control method for roll, yaw, and pitch was devised based on the aircraft's fully actuated model. Contribution in [17] established a necessary and sufficient condition for the controllability of a linear discrete periodic system within the framework of high-order full drive. Additionally, [18] transformed the Rodriguez parameter model of spacecraft attitude into a high-order full drive model, designing a robust controller to ensure the convergence of the system state to any ellipsoid region. [19] utilized the fully actuated system to formulate the dynamics of network control, achieving an optimal control scheme based on Nash equilibrium through a prediction model completed by the Diophantine equation. Furthermore, [20] introduced a proportional integral predictive controller to enhance collaborative performance in high-order fully driven multi-agent systems with communication delays. Utilizing the FASA, [21] developed a sliding mode-based adaptive tube model predictive control for robotic manipulators with model uncertainty and state constraints. Under the framework of FASA, once the HOFA models are given, we can immediately obtain the controllers, which provide all the design degrees of freedom to be further utilised to achieve additional system requirements [12]. However, the FASA has less discussions on the state constraints problem.

Upon scrutinizing the dynamic model of robotic manipulators with multi-degree-of-freedom, although the model is a highly coupled multi-input multi-ouput nonlinear system, it becomes evident that it manifests as a typical second-order fully actuated system, which fits well for the application of FASA. In addition, in the pratical situation, the joint angle, angular velocity and control torque of manipulator are always limited, correspondingly model predictive control (MPC) scheme is one of the mostly used strategies to deal with constraints. With the FASA, the obatained closed-loop system is linear and stable, it can be directly constructed as predictive model. Importantly, FASA-based controller provide the design degrees of freedom, which can be optimized in the MPC scheme to satisfy the state constraints, be aganist uncertainties and improve the trajectory tracking performance.

Motivated by the above discussions, this paper aims to develop a control scheme taking advantage of the FASA and MPC method, in order to deal with the highly coupled dy-

This work is supported by National Natural Science Foundation (NNSF) of China under Grant 62273245, Sichuan Science and Technology Program under Grant 24NSFSC3005, the Opening Project of Robotic Satellite Key Laboratory of Sichuan Province and National Natural Science Foundation (NNSF) of China under Grant 62173033.

namic nonlinearity and guarantee the satisfication of state constraints and system performance. First, to handle with the coupled dynamics nonlinearity, a FASA-based controller is adopted. The obtained closed-loop system is linear and stable, it is constructed as the preditve model. Furthermore, in addressing the system uncertainties and state constraints, the robust model control scheme is proposed to optimize the FASA-based controller, and the optimization problem is transformed into a quadratic programming (QP) problem. The main contributions are stated as follows.

1) A novel FASA-based robust MPC scheme is proposed to deal with the trajectory trakcing control problem of robotic manipulators with complicated nonlinearites, state constraints on joint angle, angular velocity and control torque under uncertain conditions.

2) By using the mean information of uncertainty to formulate the objective function in the form of first-order statistical moments and employing the freezing strategy, the optimization problem is transformed into a quadratic programming (QP) problem, which can effectively reduce computational complexity.

The structure of remaining paper is organized as follows. Chapter 2 initiates with the Lagrangian dynamics model of the multi-degree-of-freedom manipulator. It proceeds to derive the error dynamics system based on reference information and concludes with the design of the FASA-based controller. Chapter 3 focuses on the linear steady system model post-compensation by the actuated controller. The optimization of control inputs is achieved through the design of the objective function and constraints within the framework of robust model predictive control. Chapter 4 utilizes the tracking of a two-degree-of-freedom manipulator in a practical scenario as a case study to accomplish all tasks. The paper culminates in the simulation verification of the designed control inputs.

2 Fully Actuated System Approach Based Controller

In this paper, the trajectory tracking control problem of robotic manipulators is considered. Let $\bar{q}, \dot{\bar{q}}, \ddot{\bar{q}}$ represent the desired joint angle, angular velocity and angular acceleration respectively, the state error dynamic model of robotic manipulators with n-DOF can be described by the following Lagrangian equation

$$M\left(q_e\right)\ddot{q}_e + C\left(q_e, \dot{q}_e\right)\dot{q}_e + \Psi\left(q_e, \dot{q}_e\right) = u \tag{1}$$

where $q, \dot{q}, \ddot{q} \in R^n$ represent the actual state of joint angle, angular velocity and angular acceleration respectively, $q_e = q - \bar{q}, \dot{q}_e = \dot{q} - \dot{\bar{q}}, \ddot{q}_e = \ddot{q} - \ddot{\bar{q}} \in R^n$ denote the state error, $u \in R^n$ is the joint control torque, $\Psi\left(q_e, \dot{q}_e\right) = G\left(q_e\right) + M\left(q_e\right)\ddot{\bar{q}} + C\left(q_e, \dot{q}_e\right)\dot{\bar{q}}$, $M(q_e) \in R^{n\times n}$ is the inertia matrix, $C(q_e, \dot{q}_e) \in R^{n\times n}$ is the centrifugal force and coriolis force matrix, $G(q_e) \in R^n$ is the earth's gravitational term.

Obviously, the state error dynamic model (1) satisfies the standard type required of second-order fully actuated system. Therefore, according to [9, 10], we can immediately obtain the following FASA-based controller

$$\begin{aligned} &u = u_c + u_f \\ &u_c = \Psi\left(q_e, \dot{q}_e\right) \\ &u_f = K_0(q_e, \dot{q}_e)q_e + K_1(q_e, \dot{q}_e)\dot{q}_e + v \end{aligned} \tag{2}$$

where $v \in R^n$ is the part of control input to be designed, $K_0(q_e, \dot{q}_e), K_1(q_e, \dot{q}_e) \in R^{n\times n}$ are the feedback gain matrices given by

$$\begin{aligned} &\begin{bmatrix} K_0(q_e, \dot{q}_e) & K_1(q_e, \dot{q}_e), \end{bmatrix} = WP^{-1}, \\ &P = P(Z, F) = \begin{bmatrix} Z \\ ZF \end{bmatrix}, \\ &W = M(q_e)ZF^2 + C(q_e, \dot{q}_e)ZF \end{aligned} \tag{3}$$

with $F \in R^{2n\times 2n}$ being the Jordan canonical form and its eigenvalues lieing in the left-half open complex plane, the parameter matrix $Z \in R^{n\times 2n}$ satisfying

$$\det \begin{bmatrix} Z \\ ZF \end{bmatrix} \neq 0 \tag{4}$$

It is noted that in the FASA-based controller, the parameter matrices Z, F provide the freedom of design, they can be determined by solving the following optimization problem with close-loop eigenvalue sensitivities index

$$\begin{aligned} \min_{Z} \quad & \left\| \begin{bmatrix} Z \\ ZF \end{bmatrix} \right\| \cdot \left\| \begin{bmatrix} Z \\ ZF \end{bmatrix}^{-1} \right\| \\ \text{s.t.} \quad & \det \begin{bmatrix} Z \\ ZF \end{bmatrix} \neq 0 \end{aligned} \tag{5}$$

where F is the pre-selected Jordan canonical form with its eigenvalues in the left-half open complex plane.

Based on the results of FASA in [9, 10], we can obtain the following model of (1) with controller (2)

$$\begin{aligned} &\dot{y} = \bar{A}y + Dv \\ &y = \begin{bmatrix} q_e \\ \dot{q}_e \end{bmatrix}, \quad \bar{A} = PFP^{-1}, \quad D = \begin{bmatrix} 0 \\ M^{-1} \end{bmatrix} \end{aligned} \tag{6}$$

where A is a linear time-invariant matrix and possess stability in the Lyapunov sense, the control input v can be further utilised to acheive additional performance requriment of manipulator motion control system. However, in the pratical situation, there always exist the state constraints on the joint angle, angular velocity and control torque. In the folllowing procedure, in order to satisfy physical constraints and improve the anti-disturbance capability of FASA-based controller, the robust MPC scheme is proposed to optimize the control input v online.

3 Robust Model Predictive Control Scheme of FASA-based Controller

By formulating the entire uncertainties, such as environmental noise and modeling errors, as a additive random disturbance variable ω, the model (6) can be rewritten as follows

$$\dot{y}(t) = \bar{A}y(t) + D(t)v(t) + H\omega(t) \tag{7}$$

where $H \in R^{2n\times 2n}$ is the weight matrix of the disturbance, $\omega(t) \in R^{2n}$ is only dependent of the t, $E(\omega) = \mu, |\omega_i| \leq \zeta_i, i = 1, 2\cdots 2n$, its mean value μ and boundary value ζ are known, while variance value $\aleph$ is not required.

Suppose that the sampling period T_s is small enough, the continuous model (7) will be discretized by utilizing Shannon's sampling theorem. Let $t = kT_s$, yielding the following

expression

$$\begin{aligned}\dot{y}(kT_s) &= \lim_{T_s\to 0}\frac{y[(k+1)T_s]-y(kT_s)}{T_s}\\ &\approx \frac{y[(k+1)T_s]-y(kT_s)}{T_s}\end{aligned} \tag{8}$$

Combining with (8), the model (7) can be approximately discretized as

$$y(k+1) = A_d y(k) + D_d(k)v(k) + H_d\omega(k) \tag{9}$$

where $A_d = T_s\bar{A} + I_{2n}, D_d(k) = T_s D(k), H_d = T_s H$.

For an actual manipulator, there exist physical constraints on joint angle, angular velocity and control torque, which can be expressed in the following form

$$\begin{aligned}&q_{\min} \le q(k) \le q_{\max},\ \dot{q}_{\min} \le \dot{q}(k) \le \dot{q}_{\max}\\ &u_{\min} \le u(k) \le u_{\max}\end{aligned} \tag{10}$$

where $q_{\min}, q_{\max}, \dot{q}_{\min}, \dot{q}_{\max}, u_{\min}, u_{\max}$ are known constants.

Following the approach in [22], the objective function based on the first-order statistical moment, as depicted below, is employed

$$\min_{\widetilde{\mathbf{v}}} J(\widetilde{\mathbf{v}}) = E\left\{\widetilde{\mathbf{y}}^\top \mathbf{Q}\widetilde{\mathbf{y}} + \widetilde{\mathbf{v}}^\top \mathbf{R}\widetilde{\mathbf{v}}\right\} \tag{11}$$

where the prediction time domain is N, the weight matrices $\mathbf{Q} \in R^{(2n.N)\times(2n.N)}$ and $\mathbf{R} \in R^{(n.N)\times(n.N)}$ are positive definite and symmetric, the state $\widetilde{\mathbf{v}}, \widetilde{\mathbf{y}}$ is given by

$$\widetilde{\mathbf{y}} = \begin{bmatrix} y(k+1)\\ \vdots\\ y(k+N)\end{bmatrix}, \widetilde{\mathbf{v}} = \begin{bmatrix} v(k)\\ \vdots\\ v(k+N-1)\end{bmatrix} \tag{12}$$

Combining with (9),(10) and (11), the robust MPC problem P1 for FASA-based controller (2) is described as

$$\begin{aligned}\min_{\widetilde{\mathbf{v}}} J(\widetilde{\mathbf{v}}) &= E\left\{\widetilde{\mathbf{y}}^\top \mathbf{Q}\widetilde{\mathbf{y}} + \widetilde{\mathbf{v}}^\top \mathbf{R}\widetilde{\mathbf{v}}\right\}\\ \text{s.t.}\quad & y(k+l+1) = A_d y(k+l)\\ &\quad + D_d(k+l)v(k+l) + H_d\omega(k+l)\\ & u(k+l) = \Psi(q_e,\dot{q}_e) + K_0(q_e,\dot{q}_e)q_e\\ &\quad + K_1(q_e,\dot{q}_e)\dot{q}_e + v\\ & q_{\min} \le q(k+l+1) \le q_{\max}\\ & \dot{q}_{\min} \le \dot{q}(k+l+1) \le \dot{q}_{\max}\\ & u_{\min} \le u(k+l) \le u_{\max}\end{aligned} \tag{13}$$

where $l = 0, \cdots, N-1$, $y(k)$ is updated by the actual state of manipulator. By solving the optimal problem online to obatine the FASA-based controller (2), we can guarantee the satisfaction of state constraints and improve the tracking performance of controller.

In the following, the optimization problem P1 (13) will be transformed into a QP problem. During the forward prediction, a freezing strategy is employed. The expansion matrix in the prediction time domain is expressed concisely as follows

$$\widetilde{\omega} = \begin{bmatrix}\omega(k)\\ \omega(k+1)\\ \vdots\\ \omega(k+N-1)\end{bmatrix}, \widetilde{\mathbf{A}} = \begin{bmatrix} A_d\\ \vdots\\ A_d^N\end{bmatrix},$$

$$\widetilde{\mathbf{D}} = \begin{bmatrix} D_d & 0 & \cdots & 0\\ A_dD_d & H_d & \cdots & 0\\ \vdots & \vdots & \vdots & \vdots\\ A_d^{N-1}D_d & A_d^{N-2}D_d & \cdots & D_d\end{bmatrix}, \tag{14}$$

$$\widetilde{\mathbf{H}} = \begin{bmatrix} H_d & 0 & \cdots & 0\\ A_dH_d & H_d & \cdots & 0\\ \vdots & \vdots & \vdots & \vdots\\ A_d^{N-1}H_d & A_d^{N-2}H_d & \cdots & H_d\end{bmatrix}$$

Then combining with (12) and(14), in the prediction time domain N, the discrete model (9) of manipulator is rewritten as the following compact form

$$\widetilde{\mathbf{y}} = \widetilde{\mathbf{A}}y(k) + \widetilde{\mathbf{D}}\widetilde{\mathbf{v}} + \widetilde{\mathbf{H}}\widetilde{\omega} \tag{15}$$

To reformulate the objective function (11) into the tractable form, the lemma from [23] is stated as follows.

Lemma 1 *Assuming λ is a symmetric matrix, when $\bar{\vartheta} = E(\vartheta), \Sigma = E\left[(\vartheta-\bar{\vartheta})^\top(\vartheta-\bar{\vartheta})\right]$, we have*

$$E\left\{\vartheta^\top\lambda\vartheta\right\} = \mathrm{tr}\{\lambda\Sigma\} + \bar{\vartheta}^\top\lambda\bar{\vartheta} \tag{16}$$

where $\mathrm{tr}\{\cdot\}$ *represents the trace of a matrix*

According to Lemma 1, Substituting (15) into (11), we obtain

$$\begin{aligned}J(\widetilde{\mathbf{v}}) =& 2y^\top(k)\widetilde{\mathbf{A}}^\top\mathbf{Q}\widetilde{\mathbf{D}}\widetilde{\mathbf{v}} + 2\boldsymbol{\mu}^\top\widetilde{\mathbf{H}}^\top\widetilde{\mathbf{Q}}\widetilde{\mathbf{D}}\widetilde{\mathbf{v}}\\ &+ \widetilde{\mathbf{v}}^\top\widetilde{\mathbf{D}}^\top\widetilde{\mathbf{Q}}\widetilde{\mathbf{D}}\widetilde{\mathbf{v}} + \widetilde{\mathbf{v}}^\top\widetilde{\mathbf{R}}\widetilde{\mathbf{v}} + \boldsymbol{\Lambda}\\ \boldsymbol{\Lambda} =& y^\top(k)\widetilde{\mathbf{A}}^\top\widetilde{\mathbf{Q}}\widetilde{\mathbf{A}}y(k) + 2y^\top(k)\widetilde{\mathbf{A}}^\top\widetilde{\mathbf{Q}}\widetilde{\mathbf{H}}\boldsymbol{\mu}\\ &+ \mathrm{tr}\left\{\widetilde{\mathbf{H}}^\top\widetilde{\mathbf{Q}}\widetilde{\mathbf{H}}\aleph\right\} + \boldsymbol{\mu}^\top\widetilde{\mathbf{H}}^\top\widetilde{\mathbf{Q}}\widetilde{\mathbf{H}}\boldsymbol{\mu}\end{aligned} \tag{17}$$

where $\boldsymbol{\mu} = I_N \otimes \mu$, $\otimes$ stands for the Kronecker product, I_N denotes the unit matrix of order N, $\boldsymbol{\Lambda}$ is an item that has nothing to do with the decision vector $\widetilde{\mathbf{v}}$. $\widetilde{\mathbf{v}}$ has no dependency on $\aleph$, therefore, it can be treated as a constant term in the ongoing optimization process. Easily, the objective function (17) can be rewritten as the following quadratic form

$$J(\widetilde{\mathbf{v}}) = \widetilde{\mathbf{v}}^\top\mathbf{L}\widetilde{\mathbf{v}} + \mathbf{S}\widetilde{\mathbf{v}} + \boldsymbol{\Lambda} \tag{18}$$

where

$$\begin{aligned}\mathbf{S} &= 2y(k)^\top\widetilde{\mathbf{A}}^\top\mathbf{Q}\widetilde{\mathbf{D}} + 2\boldsymbol{\mu}^\top\widetilde{\mathbf{H}}^\top\widetilde{\mathbf{Q}}\widetilde{\mathbf{D}}\\ \mathbf{L} &= \widetilde{\mathbf{D}}^\top\widetilde{\mathbf{Q}}\widetilde{\mathbf{D}} + \widetilde{\mathbf{R}}\end{aligned} \tag{19}$$

Since $\bar{x} = [\bar{q} \quad \dot{\bar{q}}]^\top$, all state constraints (10) can be expressed as

$$y + \bar{x} \in \mathcal{X}, u_c(k) + u_f(k) + v \in \mathcal{U} \tag{20}$$

where $\mathcal{X}$,$\mathcal{U}$ represent feasible regions of the convex polyhedron of corresponding dimensions. Considering (15), the

state constraints (20), incorporating terms of stochastic disturbance in the prediction time domain, can be formulated as follows

$$\begin{aligned}&\widetilde{\mathbf{A}}y(k)+\widetilde{\mathbf{D}}\widetilde{\mathbf{v}}+\bar{\mathbf{X}}\pm\widetilde{\mathbf{H}}\widetilde{\omega}_{opt}\in\mathcal{X}\\&\mathbf{u}_0+\widetilde{\mathbf{v}}\in\mathcal{U}\\&\bar{\mathbf{X}}=[\bar{x}(k+1),\bar{x}(k+2)\cdots\bar{x}(k+N)]^\top\end{aligned}\tag{21}$$

where $\mathbf{u}_0=I_N\otimes(u_c+u_f)$, $\widetilde{\omega}_{opt}$ can be determined by solving the following optimization problem offline in advance

$$\begin{aligned}\max_{\widetilde{\omega}_{opt}}\quad&(\widetilde{\mathbf{H}}\widetilde{\omega}_{opt})^\top\widetilde{\mathbf{H}}\widetilde{\omega}_{opt}\\\text{s.t.}\quad&\widetilde{\omega}_{opt}\in\mathcal{W}\end{aligned}\tag{22}$$

with convex polyhedron $\mathcal{W}$ being composed of $\pm\zeta_i, i=1,2,\cdots,2n$.

As $\widetilde{\mathbf{H}}$ is a fixed lower triangular matrix, $\widetilde{\mathbf{H}}^\top\widetilde{\mathbf{H}}$ results in a positive definite symmetric matrix. Consequently, the objective function becomes a pure quadratic form, and $\widetilde{\omega}_{opt}$ resides within the convex polyhedron. Therefor, the simulated annealing algorithm is well-suited for finding the global optimal solution.

Finally, comprehensively considering equations (18), (20) and (21), the robust MPC problem P1 (2) for FASA-based controller is reformulated as follows

$$\begin{aligned}\min_{\widetilde{\mathbf{v}}}\ &J(\widetilde{\mathbf{v}})=\widetilde{\mathbf{v}}^\top\mathbf{L}\widetilde{\mathbf{v}}+\mathbf{S}\widetilde{\mathbf{v}}+\mathbf{\Lambda}\\&\text{s.t.}\quad\widetilde{\mathbf{A}}y(k)+\widetilde{\mathbf{D}}\widetilde{\mathbf{v}}+\bar{\mathbf{X}}\pm\widetilde{\mathbf{H}}\widetilde{\omega}_{opt}\in\mathcal{X}\\&\quad\quad\{u_c(k)+u_f(k)\}\mathbf{1}_N+\widetilde{\mathbf{v}}\in\mathcal{U}\end{aligned}\tag{23}$$

which can be solved using the Quadprog solver. By online solving the optimization problem (23) to generate $v(k)$, substituting $v(k)$ into FASA-based controller (2), we can obtain the control torque $u(k)$, which is applied into the motion control system of each manipulator joint.

4 Numercial Simulation

In order to verify the feasibility and control effect of the proposed manipulator control method, a two-link rigid manipulator is taken as an example to conduct simulation verification of the robust model predictive controller based on FASA. At the same time, the physical parameter settings of the manipulator are shown in Tables 1 and 2.

Table 1: Model Parameters

Symbol	Value	Symbol	Value
m_1	2kg	m_2	2kg
l_1	0.5m	l_2	0.5m
I_1	0.125kg.m^2	I_2	0.125kg.m^2

Table 2: State Constraints

Symbol	Value	Symbol	Value
$u_{\min}$	-20 N.m	$u_{\max}$	20 N.m
$q_{\min}$	-4 rad	$q_{\max}$	4 rad
$\dot{q}_{\min}$	-1 rad/s	$\dot{q}_{\max}$	1 rad/s

The calculation of the manipulator's inertia matrix in (1) is given as follows

$$\begin{aligned}M(q_e)=&\begin{bmatrix}M_{11}(q_e)&M_{12}(q_e)\\M_{21}(q_e)&M_{22}(q_e)\end{bmatrix}\\M_{11}(q_e)=&m_2l_1^2+\frac{1}{4}m_2l_2^2+\frac{1}{4}m_1l_1^2+I_1+I_2\\&+m_2l_1l_2\cos(q_{e2}+\bar{q}_2)\\M_{12}(q_e)=&M_{21}(q_e)=\frac{1}{4}m_2l_2^2+I_2\\&+\frac{1}{2}m_2l_1l_2\cos(q_{e2}+\bar{q}_2)\\M_{22}(q_e)=&\frac{1}{4}m_2l_2^2+I_2\end{aligned}\tag{24}$$

Coriolis force matrix is given as follows

$$\begin{aligned}C(q_e,\dot{q}_e)=&\begin{bmatrix}C_{11}(q_e,\dot{q}_e)&C_{12}(q_e,\dot{q}_e)\\C_{21}(q_e,\dot{q}_e)&C_{22}(q_e,\dot{q}_e)\end{bmatrix}\\C_{11}(q_e,\dot{q}_e)=&-\frac{1}{2}m_2l_1l_2\sin(q_{e2}+\bar{q}_2)(\dot{q}_{e2}+\dot{\bar{q}}_2)\\C_{12}(q_e,\dot{q}_e)=&-\frac{1}{2}m_2l_1l_2\sin(q_{e2}+\bar{q}_2)\\&*(\dot{q}_{e1}+\dot{\bar{q}}_1+\dot{q}_{e2}+\dot{\bar{q}}_2)\\C_{21}(q_e,\dot{q}_e)=&\frac{1}{2}m_2l_1l_2\sin(q_{e2}+\bar{q}_2)(\dot{q}_{e1}+\dot{\bar{q}}_1)\\C_{22}(q_e,\dot{q}_e)=&0\end{aligned}\tag{25}$$

Gravity matrix is given as follows

$$\begin{aligned}G(q_e)=&\begin{bmatrix}G_1(q_e)\\G_2(q_e)\end{bmatrix}\\G_1(q_e)=&\left(\frac{1}{2}m_1+m_2\right)gl_1\cos(q_{e1}+\bar{q}_1)\\&+\frac{1}{2}m_2gl_2\cos(q_{e1}+\bar{q}_1+q_{e2}+\bar{q}_2)\\G_2(q_e)=&\frac{1}{2}m_2gl_2\cos(q_{e1}+\bar{q}_1+q_{e2}+\bar{q}_2)\end{aligned}\tag{26}$$

where gravity coefficient$g$ is 9.8 N/kg.

Combined with the state information during the actual movement of manipulators, the mean of stochastic disturbance ω is designed as $\mu=[0,0,0,0]$, the variance is designed to be less than 10 orders of magnitude of the state quantity, that is, $\aleph=[0.01,0.01,0.01,0.01]$, and the boundary ω_b is designed to be of the same order of magnitude as the state quantity, that is, $\zeta=[0.1,0.1,0.1,0.1]$.

For the preset matrix F in robust model predictive controller based on FASA, it is taken as $F=\text{blockdiag}([\begin{smallmatrix}-1&1\\-1&-1\end{smallmatrix}],-3,-4)$, then $\lambda(F)=(-1\pm j,-3,-4)$. Eigenvalues are located in the left semi-open complex plane, so the system state will not diverge. By solving the optimization problem (5), Z is obtained as follows

$$Z=\begin{bmatrix}1.4947&-0.0842&0.8128&0.0463\\-0.0882&1.5055&0.0094&0.6331\end{bmatrix}\tag{27}$$

The weight matrix $\mathbf{Q}$ is $I_N\otimes\text{diag}[10,10,1,1]$, $\mathbf{R}$ is $I_N\otimes\text{diag}[0.01,0.01]$, the prediction time domain N is 10,

the number of simulation steps is 1000, and the sampling interval is 0.1 s.

The initial joint angle q_0 of the manipulator is set to be $[0, 0]$, the joint angular velocity $\dot{q}_0$ is set to be $[0, 0]$, the joint angular acceleration $\ddot{q}_0$ is set to be $[0, 0]$. The reference trajectory is set to be a circular trajectory with the center coordinate located at $[0.3, 0.3]$, and the radius is set to 0.2 m. Since the disturbance has stochastic characteristics, the experiment will conduct Monte Carlo simulation of 1000 times. The tracking results of the fully actuated controller FA and the FASA-based robust model predictive controllerFA-RMPC are obtained through MATLAB's parallel calculation as shown below.

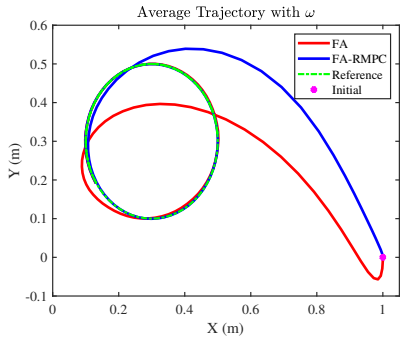

Fig. 1: End effector tracking with uncertainty

Figure 1 shows the position tracking results of the circular trajectory. The results of FA and FA-RMPC under 1000 Monte Carlo simulations are averaged. It can be seen that both control algorithms can achieve tracking of the reference trajectory, and FA-RMPC can achieve faster convergence.

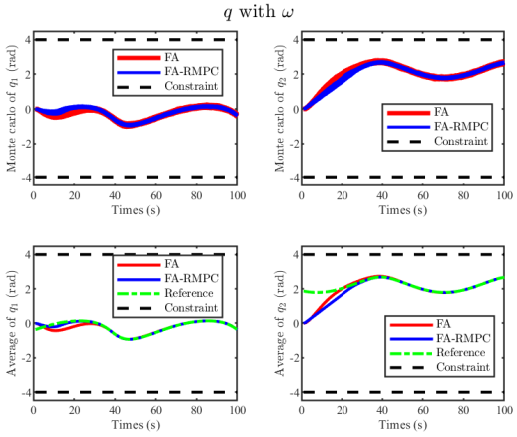

Fig. 2: Joint angle tracking with uncertainty

Figure 2 shows the tracking results of the joint angle. It can be seen that both FA and FA-RMPC controllers can track the reference angle trajectory, but for unknown external disturbances, FA-RMPC has a smaller fluctuation range and better anti-disturbance ability.

Figure 3 shows the tracking results of the joint angular velocity. It can be seen that although the FA controller can complete the tracking of the reference angular velocity trajectory, it is difficult to meet the constraint requirements, while the FA-RMPC method can complete the reference angular velocity trajectory tracking while satisfying the constraints.

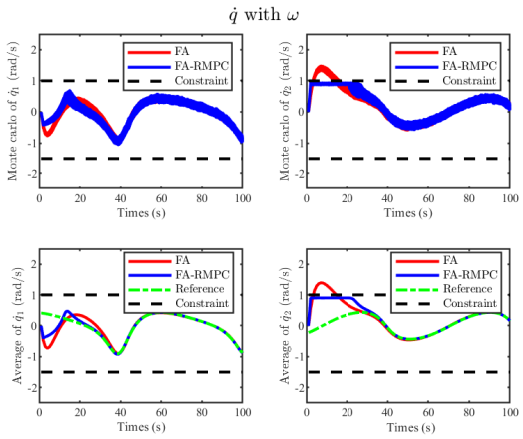

Fig. 3: Joint velocity tracking with uncertainty

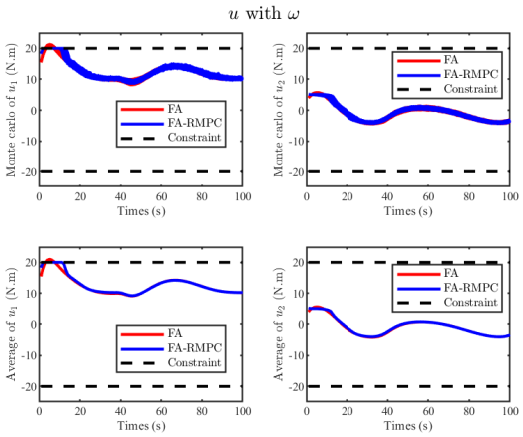

Fig. 4: Control torque of tracking with uncertainty

Figure 4 shows the joint torque during the tracking process. It can be seen from the figure that FA-RMPC can obtain an optimal control quantity that satisfies the constraints in the prediction time domain through optimization solution, which is better than the state feedback FA control rate that is difficult to satisfy the constraints.

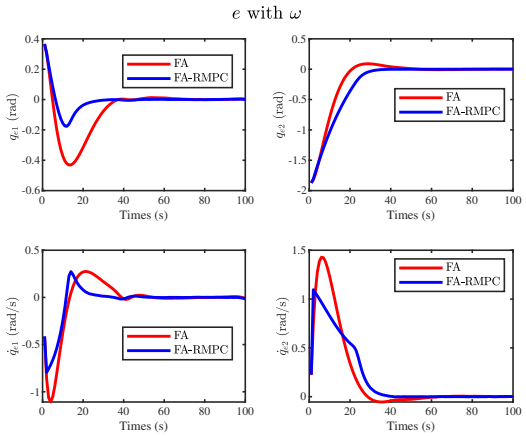

Fig. 5: State error of tracking with uncertainty

Figure 5 shows the state error during the tracking process. It can be seen that FA-RMPC can converge to the predetermined state at a faster speed and with a smaller overshoot than FA.

Based on the above simulation results, it can be concluded that the proposed FASA-based robust model predictive control method is significantly better than the state feedback fully actuated control in the manipulator tracking control with environmental interference, system uncertainty and state constraints.

5 Conclusion

Aiming at the time-varying trajectory tracking problem of multi-degree-of-freedom manipulators in complex environments, a FASA-based robust model predictive control method is proposed. After converting the pseudo-linear system of the manipulator into a linear steady system by applying the FASA-based controller, Shannon sampling is used for discretization to construct the predictive model. By constructing the objective function of the first-order statistical moment, the disturbance term can be preprocessed offline, and then robust model predictive control shceme is used to optimize the FASA-based controller online, finally the optimization problem is transformed into a QP problem. This method proposes a feasible solution to the tracking control problem of the manipulator under uncertainty, and is superior to the state feedback fully actuated control method in terms of tracking accuracy and constraint satisfaction. In the further work, the research will focus on the parameter optimal problem of FASA-based controller and the combination of FASA and distributionally robust model predictive control method.

References

[1] Su J, Yang J and Li S. Finite-time Disturbance Rejection Control for Robotic Manipulators Based on Sliding Mode Differentiator. Chinese Control and Decision Conference, 2013: 3844-3849.

[2] Hsiao Y Y, Tu P H, Hung J W and Lin J S. Sliding Backstepping Control Design for Robotic Manipulator Systems with Motor Dynamics. IEEE International Conference on Control and Automation, 2014: 667-672.

[3] Miranda A B and Forner-Cordero A. Upper Limb Exoskeleton Control Based on Sliding Mode Control and Feedback Linearization. ISSNIP Biosignals and Biorobotics Conference: Biosignals and Robotics for Better and Safer Living (BRC), 2013: 1-6.

[4] Chen H, Liu B, Qu Y and Zhou X. Low speed control for PMSM based on reduced-order adaptive Kalman filter. Proceedings of the 33rd Chinese Control Conference, 2014: 7959-7963.

[5] Duan G R. Direct Parametric Approach for Cascaded Systems with Application in Robot Control. 2014 14th International Conference on Control, Automation and Systems, 2014: 29-35.

[6] Duan G R. Quaternion-Based Satellite Attitude Control—a Direct Parametric Approach. 2014 14th International Conference on Control, Automation and Systems, 2014: 935-941.

[7] Duan G R. Substability and Substabilization: Control of Subfully Actuated Systems. IEEE Transactions on Cybernetics, 2023, 53(11): 7309-7322.

[8] Duan G R. Stabilization via Fully Actuated System Approach: A Case Study. Journal of Systems Science & Complexity, 2022, 35(3): 731-747.

[9] Duan G R. High-order Fully Actuated System Approaches: Part I. Models and basic procedure. International Journal of Systems Science, 2021, 52(2): 422–435.

[10] Duan G R. Direct parametric control of fully-actuated second-order nonlinear systems—The normal case. Proceedings of the 33rd Chinese Control Conference, Nanjing, China, 2014: 2406-2413.

[11] Duan G R. Cooperative Spacecraft Rendezvous—a Direct Parametric Control Approach. Proceeding of the 11th World Congress on Intelligent Control and Automation, Shenyang, China, 2014: 4589-4595.

[12] Duan G R. High-order fully actuated system approaches: part II. Generalized strict-feedback systems. International Journal of Systems Science, 2021, 52(3): 437–454.

[13] Duan G. R. A FAS Approach for Stabilization of Generalized Chained Forms: Part I. Discontinuous Control Laws. Science China-Information Sciences, 2023, doi: 10.1007/s11432-022-3730-8.

[14] Duan, G. R. High-order System Approaches – I. Fully Actuated Systems and Parametric Designs. Acta Automatica Sinica, 2020, 46(7): 1333–1345. (in Chinese)

[15] Duan, G. R. High-order System Approaches – II. Controllability and Full-actuation. Acta Automatica Sinica, 2020, 46(8): 1571–1581. (in Chinese)

[16] Liu X, Hao M, Fan Y, Zhen Y and Zhuang Y. Aircraft Attitude Control on High-order Fully Actuated System Theory. 2023 2nd Conference on Fully Actuated System Theory and Applications, 2023: 687-692.

[17] Lv L and Li Z. Controllability of linear discrete periodic systems based on fully-actuated system approaches. 2023 2nd Conference on Fully Actuated System Theory and Applications, 2023: 42-48.

[18] Jin D, Jia S, Wang T and Qiu J. Spacecraft Attitude Tracking Control Based On High-Order Fully Actuated System Approach. 2023 2nd Conference on Fully Actuated System Theory and Applications, 2023: 1040-1044.

[19] Zhang D W and Liu G P. Game-Based Control of Systems Under Network Constraints via a High-Order Fully Actuated Predictive Control. 2023 9th International Conference on Control Science and Systems Engineering, 2023: 338-343.

[20] Zhang D W, Liu G P and Cao L. Proportional Integral Predictive Control of High-Order Fully Actuated Networked Multiagent Systems With Communication Delays. IEEE Transactions on Systems, Man, and Cybernetics: Systems, 2022, 53(2): 801-812.

[21] Kang E, Liu Y and Qiao H. Sliding Mode-based Adaptive Tube Model Predictive Control for Robotic Manipulators with Model Uncertainty and State Constraints. Control Theory and Technology, 2023, 21: 334–351.

[22] Farina M, Giulioni L, Magni L, and Scattolini R. An approach to output-feedback MPC of stochastic linear discrete-time systems. Automatica, 2015, 55: 140-149.

[23] Petersen K B and Pedersen, M. S. Matrix Cookbook. Technical University of Denmark, 2008.

Proceedings of the 3rd Conference on Fully Actuated System Theory and Applications
May 10-12, 2024, Shenzhen, China

Fixed-time Attitude Control and Active Vibration Suppression for Flexible Spacecraft based on the Fully-actuated System Approach

Kerun Liu[1], Ming Liu[2], Huayi Li[2]

1. School of Future Technology, Harbin Institute of Technology, Harbin 150001, P. R. China
E-mail: Ericlkr@outlook.com

2. School of Astronautics, Harbin Institute of Technology, Harbin 150001, P. R. China
E-mail: mingliu23@hit.edu.cn, lihuayi@hit.edu.cn

Abstract: This paper investigates attitude control with high accuracy and active vibration suppression for flexible spacecraft with external disturbances and inertia uncertainty. A novel control scheme is technically proposed based on the fully-actuated system approach. Firstly, based on the 3-dimensional Special Orthogonal Group, a second-order fully-actuated system described by exponential coordinates is constructed and then converted into a constant linear system with an arbitrarily eigenstructure. After that, a fixed-time sliding mode control scheme is proposed to ensure the fixed-time convergence of the error exponential coordinates and the flexible mode simultaneously. By using Lyapunov approach, the stability of the closed-loop system is analysed. Finally, a numerical simulation is carried out to vindicate the effectiveness of the controller.

Key Words: Fully-actuated system, Attitude control, Active vibration suppression, Fixed-time control, Exponential coordinates

1 Introduction

For many current spacecrafts, it is common to carry large flexible accessories such as solar sail and truss antenna, which would largely intensify vibration during attitude maneuvers. In the meantime, spacecrafts would usually suffer from external disturbances due to various conditions in practice such as atmospheric drag, earth geomagnetic, solar radiation pressure, etc. And the inertia uncertainty is also a common situation in actual space missions. Thus, it is increasingly important to design a new control scheme to ensure precision of spacecraft attitude control and also deal with the obstacles above.

Lots of control techniques for flexible spacecraft attitude control have been presented previously including adaptive robust control [1, 2], finite-time control [3], active disturbance rejection control [4], fuzzy control [5], etc. However, most of the control systems in previous works are nonlinear, which has perceptible drawbacks including complex calculation and inflexibility of design process. More recently, a novel proposed methodology called the fully-actuated system(FAS) approach [6–11] has been proved to be more effective in addressing the nonlinear control problems by converting the original nonlinear fully-actuated system into a constant linear system with an arbitrarily assignable eigenstructure. Despite the benefits of the FAS approach, it is not enough to deal with uncertainties caused by large external disturbance, unknown inertia and flexible vibration because the implementation of the FAS approach requires detailed information of system dynamics. This may result in degradation of control performance or even instability of the close-loop system. So it is necessary to combine the FAS approach with other methods in the process of control law design.

Apart from that, although previous control schemes have high robustness and are able to suppress the flexible vibration, it is hard to achieve highly effective performance of vibration control. Piezoelectric material is a kind of intelligent material that is able to change the characteristics of the structure through active control. Many control schemes for vibration suppression have been developed based on piezoelectric actuators [12]. Xu et al. [13] developed a novel vibration suppression control law with piezoelectric actuators by using the adaptive sliding mode control. Zhang et al. [14] studied an active prescribed vibration suppression control for a flexible spacecraft by using active vibration suppression controller for piezoelectric actuators. And in [15] and [16], active vibration suppression technique is also applied in the processes of controller design to deal with flexible vibration. By using piezoelectric actuators, the flexible mode could be taken into consideration as state variables while applying the FAS approach, which could largely reduce the flexible vibration effect to attitude control and also actively suppress the vibration.

Inspired by all aforementioned methodology, this paper would concentrate on the design of a novel scheme for flexible spacecraft attitude control and active vibration suppression. To this end, control input of the piezoelectric actuators is added in the attitude dynamics of flexible spacecraft. And the 3-dimensional Special Orthogonal Group has been introduced to describe the error attitude kinematics, which is combined with the attitude dynamics to construct a second-order fully-actuated system based on exponential coordinates without the problem of singularity. By applying the FAS approach, the nonlinearities would be eliminated and the nonlinear system is converted in to a constant linear one with a designable eigenstructure. Then the control law of the system is designed via the fixed-time terminal sliding mode control scheme. Under this control strategy, the error exponential coordinates and the flexible mode would be all

This work is supported by the Science Center Program of National Natural Science Foundation of China (Grant No.62188101), the National Natural Science Foundation of China (Grant No.61690212), the Heilongjiang Touyan Team, the Guangdong Major Project of Basic and Applied Basic Research (Grant No.2019B030302001), and the grant of SiYuan collaborative innovation alliance of artificial intelligence science and technology (Grant No.HTKJ2023SY502003).

guaranteed to converge to a region around the equilibrium.

2 Problem Formulation and Preliminaries

Notations: $sign(\cdot)$ represents the standard sign function; $\mathbb{SO}(3)$ denotes the 3-dimensional Special Orthogonal Group, which is also the Lie Group, and the Lie algebra associated with it is denoted by $\mathfrak{so}(3)$; $(\cdot)^{\times}$ stands for the cartesian mapping: $\mathbb{R}^3 \to \mathfrak{so}(3)$; $\boldsymbol{I}_n$ denotes the identity matrix of $n \times n$ and $|\cdot|$ stands for the absolute value of a scalar; $\|\cdot\|$ is the standard Euclidean norm of a vector; For any $\boldsymbol{x} = [x_1, \ldots, x_n]^{\mathrm{T}} \in \mathbb{R}^n$, $\mathrm{diag}(\boldsymbol{x}) = \mathrm{diag}(x_1, \ldots, x_n)$ is a diagonal matrix and $sig^r(\boldsymbol{x}) = [sig^r(x_1), \ldots, sig^r(x_n)]^{\mathrm{T}}$ with $sig^r(x_i) = |x_i|^r sign(x_i)$.

2.1 Attitude Dynamics and Kinematics

The attitude dynamics of a flexible spacecraft with active vibration suppression using piezoelectric smart materials is described as follows[17, 18]:

$$\begin{cases} J\dot{\boldsymbol{\omega}} + \boldsymbol{\omega}^{\times} J\boldsymbol{\omega} + B\ddot{\boldsymbol{\eta}} = \boldsymbol{T} + \boldsymbol{d} \\ \ddot{\boldsymbol{\eta}} + 2\xi\Lambda\dot{\boldsymbol{\eta}} + \Lambda^2\boldsymbol{\eta} + B^{\mathrm{T}}\dot{\boldsymbol{\omega}} = \Delta\boldsymbol{u}_p \end{cases} \tag{1}$$

where $\boldsymbol{\omega} \in \mathbb{R}^3$ is the angular velocity; $J \in \mathbb{R}^{3\times3}$ is the inertia matrix of the rigid spacecraft and $J = J_0 + \delta J$ with J_0 and δJ being the nominal part and the uncertain part of the inertia matrix; $\boldsymbol{T} \in \mathbb{R}^3$ represents the control torque and $\boldsymbol{d} \in \mathbb{R}^3$ stands for the external disturbance torque; $\boldsymbol{\eta} \in \mathbb{R}^n$ is the flexible mode coordinates with n being the number of flexible modes; $\xi \in \mathbb{R}^{n\times n}$ and $\Lambda \in \mathbb{R}^{n\times n}$ are the modal damping and modal frequency coefficients; $B \in \mathbb{R}^{3\times n}$ is the coupling matrix between the flexible structures and the rigid body; $\Delta \in \mathbb{R}^{n\times n}$ is the coupling matrix between the piezoelectric actuators and the flexible structures and $\boldsymbol{u}_p \in \mathbb{R}^n$ denotes the control voltage input of the piezoelectric actuators.

Due to the fact that in most practical projects the number of the flexible modes is no more than 3, in this paper we let $n = 3$ for analysing purpose. Let $\boldsymbol{T} = \boldsymbol{\omega}^{\times} J_0\boldsymbol{\omega} + \boldsymbol{u}_c$ and $\boldsymbol{d}' = \boldsymbol{d} - \delta J\dot{\boldsymbol{\omega}} - \boldsymbol{\omega}^{\times}\delta J\boldsymbol{\omega}$, then we have:

$$\begin{cases} J_0\dot{\boldsymbol{\omega}} + B\ddot{\boldsymbol{\eta}} = \boldsymbol{u}_c + \boldsymbol{d}' \\ \ddot{\boldsymbol{\eta}} + 2\xi\Lambda\dot{\boldsymbol{\eta}} + \Lambda^2\boldsymbol{\eta} + B^{\mathrm{T}}\dot{\boldsymbol{\omega}} = \Delta\boldsymbol{u}_p \end{cases} \tag{2}$$

And the kinematics of the spacecraft is given as follows:

$$\dot{R} = R\boldsymbol{\omega}^{\times} \tag{3}$$

where $R \in \mathbb{SO}(3)$ is the direction cosine matrix from the body-fixed frame $\mathcal{B}$ to the inertia reference frame $\mathcal{I}$.

Before further proceeding, it is necessary to make a mild assumption as follows.

Assumption 1. The disturbance $\boldsymbol{d}$ and the second part of the inertia δJ are unknown, but we suppose that $\boldsymbol{d}, \delta J, \boldsymbol{\omega}$ and $\dot{\boldsymbol{\omega}}$ are all bounded, thus $\boldsymbol{d}'$ is also bounded and satisfies $\|\boldsymbol{d}'\| \leq d_m$, where $d_m > 0$ is an unknown constant.

Assumption 2. In most practical cases, the basic parameter matrices of the flexible spacecrafts would satisfy

$$\det(\xi) \neq 0,\ \det(\Lambda) \neq 0,\ \det(B) \neq 0$$
$$\text{and } \det\left(I_3 - B^{\mathrm{T}}J_0^{-1}B\right) \neq 0$$

2.2 Definitions and Lemmas

Definition 1. For any $\boldsymbol{\psi}^{\times} \in \mathfrak{so}(3)$, the exponential mapping $exp(\cdot)$: $\mathfrak{so}(3) \to \mathbb{SO}(3)$ is defined as:

$$\exp\left(\boldsymbol{\psi}^{\times}\right) = I_3 + \frac{\sin\|\boldsymbol{\psi}\|}{\|\boldsymbol{\psi}\|}\boldsymbol{\psi}^{\times} + \frac{1-\cos\|\boldsymbol{\psi}\|}{\|\boldsymbol{\psi}\|^2}\boldsymbol{\psi}^{\times}\boldsymbol{\psi}^{\times} \tag{4}$$

And for any $R \in \mathbb{SO}(3)$, while $tr(R) \neq 1$, the inverse map of the exponential mapping is logarithmic mapping $log(\cdot)$: $\mathbb{SO}(3) \to \mathfrak{so}(3)$, which is defined as follows:

$$\boldsymbol{\psi}^{\times} = \log(R) = \frac{\varphi}{2\sin\varphi}\left(R - R^{\mathrm{T}}\right) \tag{5}$$

where $\cos(\varphi) = 0.5(\mathrm{tr}(R) - 1), |\varphi| \leq \pi$. $\log(R) = \pm\pi\boldsymbol{\mu}^{\times}$ while $tr(R) = 1$, $\boldsymbol{\mu}$ is the unit eigenvector associated with characteristic value 1 in R. $\boldsymbol{\psi}$ is the exponential coordinate of R.

Definition 2. ([19]) For any $\boldsymbol{a} \in \mathbb{R}^6$ and $r > 0$, we define $\boldsymbol{\chi}^r_{(a)} = [\chi^r_{(a_1)}, \chi^r_{(a_2)}, \chi^r_{(a_3)}, \chi^r_{(a_4)}, \chi^r_{(a_5)}, \chi^r_{(a_6)}]^{\mathrm{T}}$ with $\chi^r_{(a_i)}$ being

$$\chi^r_{(a_i)} = \begin{cases} sig^r(a_i), & |a_i| > \epsilon \\ (2-r)\,\epsilon^{r-1}a_i + (r-1)\,\epsilon^{r-2}sig^2(a_i), & |a_i| \leq \epsilon \end{cases} \tag{6}$$

where $i = 1, 2, 3, 4, 5, 6$ and ϵ is a small positive constant selected as 0.0001 in this paper. And the time derivation of $\chi^r_{(a_i)}$ is defined as

$$\dot{\chi}^r_{(a_i)} = \begin{cases} r\,|a_i|^{r-1}\,\dot{a}_i, & |a_i| > \epsilon \\ (2-r)\,\epsilon^{r-1}\dot{a}_i + 2\,(r-1)\,\epsilon^{r-2}\,|a_i|\,\dot{a}_i, & |a_i| \leq \epsilon \end{cases} \tag{7}$$

Lemma 1 ([20])**.** *Consider the following nonlinear system:*

$$\dot{\boldsymbol{x}} = \boldsymbol{f}(\boldsymbol{x}(t)), \quad \boldsymbol{x}(0) = 0, \quad \boldsymbol{f}(0) = 0 \tag{8}$$

where $\boldsymbol{x} \in \mathbb{R}^N$. If there exist a Lyapunov function $V(\boldsymbol{x})$ and scalars $\alpha > 0, \beta > 0, 0 < p < 1, q > 1$ and $0 < \vartheta < \infty$, satisfying that

$$\dot{V}(\boldsymbol{x}) \leq -\alpha V(\boldsymbol{x})^p - \beta V(\boldsymbol{x})^p + \vartheta \tag{9}$$

then the trajectory of this system is practical fixed-time stable and the residual set of the solution of the system can be given by

$$\left\{\boldsymbol{x} \mid V(\boldsymbol{x}) \leq \min\left\{\alpha^{-\frac{1}{p}}\left(\frac{\vartheta}{1-\theta}\right)^{\frac{1}{p}}, \beta^{-\frac{1}{q}}\left(\frac{\vartheta}{1-\theta}\right)^{\frac{1}{q}}\right\}\right\}$$

where θ is a scalar and satisfy $0 < \theta \leq 1$. And the time needed to reach the residual set is bounded as

$$T \leq \frac{1}{\alpha\theta(q-1)} + \frac{1}{\beta\theta(1-p)} \tag{10}$$

Lemma 2 ([21])**.** *Let $\rho_1, \rho_2, \ldots, \rho_N \geq 0$, then*

$$\sum_{i=1}^{N}\rho_i^p \geq \left(\sum_{i=1}^{N}\rho_i\right)^p \quad if \quad 0 < p < 1$$
$$\sum_{i=1}^{N}\rho_i^p \geq N^{1-p}\left(\sum_{i=1}^{N}\rho_i\right)^p \quad if \quad 1 \leq p < \infty$$

2.3 Second-order Fully Actuated System

According to Definition 1, we let $\boldsymbol{\psi}_e^{\times} = \log(\boldsymbol{R}_e)$ and rewrite the error attitude kinematics using exponential coordinates as follows:

$$\dot{\boldsymbol{\psi}}_e = E(\boldsymbol{\psi}_e)\boldsymbol{\omega} \tag{11}$$

where

$$E(\boldsymbol{\psi}_e) = I_3 + \frac{1}{2}\boldsymbol{\psi}_e^{\times} + \frac{1 - \frac{\|\boldsymbol{\psi}_e\|}{2}\cot\left(\frac{\|\boldsymbol{\psi}_{e2}\|}{2}\right)}{\|\boldsymbol{\psi}_e\|^2}\boldsymbol{\psi}_e^{\times}\boldsymbol{\psi}_e^{\times} \tag{12}$$

and $E(\boldsymbol{\psi}_e)$ is simplified as E for brevity.

Remark 1. Note that the determinant value of E can be calculated by the following formular:

$$\det(E) = \frac{\|\boldsymbol{\psi}_e\|^2}{4} + \frac{\|\boldsymbol{\psi}_e\|^2}{4}\cot^2\left(\frac{\|\boldsymbol{\psi}_e\|}{2}\right)$$

And also $\lim_{\|\boldsymbol{\psi}_e\|\to 0} E(\boldsymbol{\psi}_e) = I_3$. Thus $E(\boldsymbol{\psi}_e)$ is invertible.

After some simple calculations, we can get:

$$\dot{\boldsymbol{\omega}} = E^{-1}\ddot{\boldsymbol{\psi}}_e + \dot{E}^{-1}\dot{\boldsymbol{\psi}}_e \tag{13}$$

By substituting (13) into (2) and letting $\boldsymbol{x}_e = \begin{bmatrix} \boldsymbol{\psi}_e \\ \boldsymbol{\eta} \end{bmatrix}$ and $\boldsymbol{u} = \begin{bmatrix} \boldsymbol{u}_c \\ \boldsymbol{u}_p \end{bmatrix}$, we can further transform the system into a Lagrange-like form as follows:

$$M(\boldsymbol{\psi}_e)\ddot{\boldsymbol{x}}_e + C(\boldsymbol{\psi_e}, \dot{\boldsymbol{\psi}}_{\boldsymbol{e}})\dot{\boldsymbol{x}}_e + N\boldsymbol{x}_e = P\boldsymbol{u} + Q\boldsymbol{d}^{'} \tag{14}$$

with

$$M(\boldsymbol{\psi}_e) = \begin{bmatrix} J_0E^{-1} & B \\ B^{\mathrm{T}}E^{-1} & I_3 \end{bmatrix}, C(\boldsymbol{\psi_e}, \dot{\boldsymbol{\psi}}_{\boldsymbol{e}}) = \begin{bmatrix} J_0\dot{E}^{-1} & \boldsymbol{0} \\ B^{\mathrm{T}}\dot{E}^{-1} & 2\xi\Lambda \end{bmatrix}$$

$$N = \begin{bmatrix} \boldsymbol{0} & \boldsymbol{0} \\ \boldsymbol{0} & \Lambda^2 \end{bmatrix}, \quad P = \begin{bmatrix} I_3 & \boldsymbol{0} \\ \boldsymbol{0} & \Delta \end{bmatrix}, \quad Q = \begin{bmatrix} I_3 \\ \boldsymbol{0} \end{bmatrix}$$

Remark 2. Examining (14), note that $M(\boldsymbol{\psi}_e)$ and P are invertible according to Assumption 2. And $M(\boldsymbol{\psi}_e), C(\boldsymbol{\psi_e}, \dot{\boldsymbol{\psi}}_{\boldsymbol{e}})$ will be simplified as M, C for brevity.

Consider the fully-actuated system described by (14) and the following control input

$$\boldsymbol{u} = \begin{bmatrix} K_0\left(\boldsymbol{\psi_e}, \dot{\boldsymbol{\psi}}_{\boldsymbol{e}}\right) & K_1\left(\boldsymbol{\psi_e}, \dot{\boldsymbol{\psi}}_{\boldsymbol{e}}\right) \end{bmatrix} \begin{bmatrix} \boldsymbol{x}_e \\ \dot{\boldsymbol{x}}_e \end{bmatrix} + \boldsymbol{v} \tag{15}$$

with

$$\begin{cases} \begin{bmatrix} K_0\left(\boldsymbol{\psi_e}, \dot{\boldsymbol{\psi}}_{\boldsymbol{e}}\right) & K_1\left(\boldsymbol{\psi_e}, \dot{\boldsymbol{\psi}}_{\boldsymbol{e}}\right) \end{bmatrix} = P^{-1}WV^{-1} & \text{(16a)} \\ W = MZF^2 + CZF + NZ & \text{(16b)} \\ V = \begin{bmatrix} Z \\ ZF \end{bmatrix} & \text{(16c)} \end{cases}$$

where $K_0\left(\boldsymbol{\psi_e}, \dot{\boldsymbol{\psi}}_{\boldsymbol{e}}\right), K_1\left(\boldsymbol{\psi_e}, \dot{\boldsymbol{\psi}}_{\boldsymbol{e}}\right) \in \mathbb{R}^{6\times 6}$ are the time-varying feedback gain matrices simplified as K_0, K_1. And $Z \in \mathbb{R}^{6\times 12}$, $F \in \mathbb{R}^{12\times 12}$ are two constant matrixes to be designed.

Then, by letting $\boldsymbol{X}_e = [\boldsymbol{x}_e^{\mathrm{T}}, \dot{\boldsymbol{x}}_e^{\mathrm{T}}]^{\mathrm{T}}$, $A_{cl} = -M^{-1}(N - PK_0)$ and $A_{cr} = -M^{-1}(C - PK_1)$, the second-order system (14) could be transformed into a linear augmented form as follows:

$$\dot{\boldsymbol{X}}_e = A_c\boldsymbol{X}_e + P_c\boldsymbol{v} + Q_c\boldsymbol{d}^{'} \tag{17}$$

with

$$\begin{cases} A_c = \begin{bmatrix} 0 & I_6 \\ A_{cl} & A_{cr} \end{bmatrix} & \text{(18a)} \\ P_c = \begin{bmatrix} 0 \\ M^{-1}P \end{bmatrix} & \text{(18b)} \\ Q_c = \begin{bmatrix} 0 \\ M^{-1}Q \end{bmatrix} & \text{(18c)} \end{cases}$$

where $\boldsymbol{v}$ is the control law of the system (17) to be designed.

Furthermore, combining (16), it can be derived easily that

$$\begin{aligned} & V^{-1}A_cV \\ =& V^{-1}\begin{bmatrix} ZF \\ M^{-1}\left(P\begin{bmatrix} K_0 & K_1 \end{bmatrix}V - CZF - NZ\right) \end{bmatrix} \\ =& V^{-1}\begin{bmatrix} ZF \\ ZF^2 \end{bmatrix} \\ =& V^{-1}VF = F \end{aligned} \tag{19}$$

then $A_c = VFV^{-1}$ is a constant matrix and similar to F. And Z, F should satisfy that [22]

1) $F \in \mathbb{R}^{12\times 12}$ is a Hurwitz matrix;
2) $\exists Z \in \mathbb{R}^{6\times 12}$ such that $\det V(Z, F) \neq 0$.

3 Main Result

In what follows, a fixed-time terminal sliding mode surface is applied in the process of control law design. And an adaptive law is also designed to deal with the external disturbance and the inertia uncertainty. Finally, we analyse the stability of control system under the designed control law using Lyapunov approach.

3.1 Control Law Design

Let $\boldsymbol{X}_e = [\boldsymbol{X}_{e1}^{\mathrm{T}}, \boldsymbol{X}_{e2}^{\mathrm{T}}]^{\mathrm{T}}$, then the system (17) can be rewritten in the following form:

$$\begin{cases} \dot{\boldsymbol{X}}_{e1} = \boldsymbol{X}_{e2} \\ \dot{\boldsymbol{X}}_{e2} = A_{cl}\boldsymbol{X}_{e1} + A_{cr}\boldsymbol{X}_{e2} + M^{-1}P\boldsymbol{v} + M^{-1}Q\boldsymbol{d'} \end{cases} \tag{20}$$

Then a terminal sliding mode surface is selected as follows:

$$\boldsymbol{s} = \dot{\boldsymbol{X}}_{e1} + \alpha_1\boldsymbol{\chi}_{(\boldsymbol{X}_{e1})}^{p_1} + \beta_1\boldsymbol{\chi}_{(\boldsymbol{X}_{e1})}^{q_1} \tag{21}$$

where $\alpha_1 > 0, \beta_1 > 0, 0 < p_1 < 1$ and $q_1 > 1$ are all constant parameters to be designed.

Evaluating the time derivative of s, it gives:

$$\dot{\boldsymbol{s}} = \dot{\boldsymbol{X}}_{e2} + \alpha_1\dot{\boldsymbol{\chi}}_{(\boldsymbol{X}_{e1})}^{p_1} + \beta_1\dot{\boldsymbol{\chi}}_{(\boldsymbol{X}_{e1})}^{q_1} \tag{22}$$

The control law and the adaptive law are designed as:

$$\begin{aligned} \boldsymbol{v} =& P^{-1}M\Big[- A_{cl}\boldsymbol{X}_{e1} - A_{cr}\boldsymbol{X}_{e1} - \alpha_1\dot{\boldsymbol{\chi}}_{(\boldsymbol{X}_{e1})}^{p_1} - \beta_1\dot{\boldsymbol{\chi}}_{(\boldsymbol{X}_{e1})}^{q_1} \\ & - \alpha_2 sig^{p_2}(\boldsymbol{s}) - \beta_2 sig^{q_2}(\boldsymbol{s}) - \frac{\hat{\gamma}\boldsymbol{s}}{2\varepsilon^2}\Big] \end{aligned} \tag{23}$$

$$\dot{\hat{\gamma}} = k_1\left(\frac{\|\boldsymbol{s}\|^2}{2\varepsilon^2} - k_2\hat{\gamma}\right) \tag{24}$$

where $\alpha_2 > 0, \beta_2 > 0, 0 < p_2 < 1, q_2 > 1, k_1 > 0, k_2 > 0$ and $\varepsilon > 0$ are all constant parameters to be designed; $\hat{\gamma}$ is the estimation of γ, which is defined in the following Remark.

Remark 3. Since $\boldsymbol{d}^{'}$ is bounded, we define $\gamma > 0$ as an unknown constant satisfying $\gamma \geq \|M^{-1}Q\boldsymbol{d}^{'}\|^2$. And the initial value of $\hat{\gamma}$ should be set as $\hat{\gamma}(0) \geq 0$ to ensure $\hat{\gamma}(t) \geq 0$ all the time. Additionally, in the proposed control law, the following terms would accelerate the convergence rate:

$$\alpha_2 sig^{p_2}(\boldsymbol{s}) + \beta_2 sig^{q_2}(\boldsymbol{s}) \tag{25}$$

In detail, while the system states are larger than 1, the first term in (25) has a dominant effect on the convergence rate as $q_2 > 1$; and while the system states are less than 1, the second term in (25) has a dominant effect on the convergence rate because $0 < p_2 < 1$.

Then by (15), we could get the control input:

$$\boldsymbol{u} = \begin{bmatrix} K_0 & K_1 \end{bmatrix} \boldsymbol{X}_e + \boldsymbol{v} \tag{26}$$

with

$$\begin{cases} [K_0\ K_1] = P^{-1}WV^{-1} \\ W = MZF^2 + CZF + NZ \\ V = \begin{bmatrix} Z \\ ZF \end{bmatrix} \end{cases}$$

where M, C, N and P are all consistent with the definitions in (14); Z, F are parameter matrices to be designed. As $\boldsymbol{u} = [\boldsymbol{u}_c^{\mathrm{T}},\ \boldsymbol{u}_p^{\mathrm{T}}]^{\mathrm{T}}$, we could get $\boldsymbol{u}_c$ and $\boldsymbol{u}_p$ separately, and the control torque $\boldsymbol{T} = \boldsymbol{\omega}^{\times} J_0 \boldsymbol{\omega} + \boldsymbol{u}_c$ can be calculated.

3.2 Stability Analysis

In this section, we are ready to present the primary results of this paper, which is given in theorem 1.

Theorem 1. *Consider the flexible spacecraft attitude system* (1) *and* (3)*, under the proposed controller* (26)*, the error exponential coordinates $\boldsymbol{\psi}_e$ will converge to a small region around the equilibrium and meanwhile the flexible mode η will converge to a small region around 0 within fixed time while Z, F satisfy that*

1) $F \in \mathbb{R}^{12\times 12}$ is a Hurwitz matrix;
2) $\exists Z \in \mathbb{R}^{6\times 12}$ such that $\det V(Z,F) \neq 0$.

Proof. Construct the following Lyapunov function for the system (14):

$$V = \frac{1}{2}\boldsymbol{s}^{\mathrm{T}}\boldsymbol{s} + \frac{1}{2k_1}\tilde{\gamma}^2 \tag{28}$$

where $\tilde{\gamma} = \gamma - \hat{\gamma}$ is the estimation error of $\hat{\gamma}$.

Evaluating the time derivative of V along the trajectories of the system leads to:

$$\dot{V} = \boldsymbol{s}^{\mathrm{T}}\dot{\boldsymbol{s}} - \frac{1}{k_1}\tilde{\gamma}\dot{\hat{\gamma}} \tag{29}$$

By substituting (22) and (24) into (29), also combining (20), it can get:

$$\begin{aligned} \dot{V} =& \boldsymbol{s}^{\mathrm{T}}(A_{cl}\boldsymbol{X}_{e1} + A_{cr}\boldsymbol{X}_{e2} + M^{-1}P\boldsymbol{v} + M^{-1}Q\boldsymbol{d}' \\ &+ \alpha_1 \dot{\boldsymbol{\chi}}_{(\boldsymbol{X}_{e1})}^{p_1} + \beta_1 \dot{\boldsymbol{\chi}}_{(\boldsymbol{X}_{e1})}^{q_1}) - \tilde{\gamma}(\frac{\|\boldsymbol{s}\|^2}{2\varepsilon^2} - k_2\hat{\gamma}) \end{aligned} \tag{30}$$

Then we substitute the control law (23) into (30), it follows:

$$\begin{aligned} \dot{V} =& -\alpha_2 \boldsymbol{s}^{\mathrm{T}} sig^{p_2}(\boldsymbol{s}) - \beta_2 \boldsymbol{s}^{\mathrm{T}} sig^{q_2}(\boldsymbol{s}) + \boldsymbol{s}^{\mathrm{T}} M^{-1} Q \boldsymbol{d}^{'} \\ &+ k_2\tilde{\gamma}\hat{\gamma} - \frac{\gamma\|\boldsymbol{s}\|^2}{2\varepsilon^2} \end{aligned} \tag{31}$$

By some simple calculation, we could get

$$\begin{aligned} \boldsymbol{s}^{\mathrm{T}} M^{-1} Q \boldsymbol{d}^{'} \leq& \|\boldsymbol{s}\| \cdot \|M^{-1}Q\boldsymbol{d}^{'}\| \\ \leq& \frac{\gamma\|\boldsymbol{s}\|^2}{2\varepsilon^2} + \frac{\varepsilon^2}{2} \end{aligned} \tag{32}$$

Additionally, by using the inequation $\gamma\tilde{\gamma} \leq \frac{1}{2}\gamma^2 + \frac{1}{2}\tilde{\gamma}^2$, it can give

$$\begin{aligned} k_2\tilde{\gamma}\hat{\gamma} =& -k_2\tilde{\gamma}^2 + k_2\tilde{\gamma}\gamma \\ \leq& -\frac{k_2}{2}\tilde{\gamma}^2 + \frac{k_2}{2}\gamma^2 \end{aligned} \tag{33}$$

Incorporating (32) and (33) into (31), it gives

$$\dot{V} \leq -\alpha_2 \sum_{i=1}^{6} (s_i^2)^{\frac{p_2+1}{2}} - \beta_2 \sum_{i=1}^{6} (s_i^2)^{\frac{q_2+1}{2}} - \frac{k_2}{2}\tilde{\gamma}^2 + \frac{\varepsilon^2}{2} + \frac{k_2}{2}\gamma^2 \tag{34}$$

Then by Lemma 2, we could get

$$\begin{aligned} \dot{V} \leq& -\alpha_2(\boldsymbol{s}^{\mathrm{T}}\boldsymbol{s})^{\frac{p_2+1}{2}} - 6^{\frac{1-q_2}{2}}\beta_2(\boldsymbol{s}^{\mathrm{T}}\boldsymbol{s})^{\frac{q_2+1}{2}} - \alpha_2(\frac{\tilde{\gamma}^2}{k_1})^{\frac{p_2+1}{2}} \\ &- 6^{\frac{1-q_2}{2}}\beta_2(\frac{\tilde{\gamma}^2}{k_1})^{\frac{q_2+1}{2}} + \alpha_2(\frac{\tilde{\gamma}^2}{k_1})^{\frac{p_2+1}{2}} + 6^{\frac{1-q_2}{2}}\beta_2(\frac{\tilde{\gamma}^2}{k_1})^{\frac{q_2+1}{2}} \\ &- \frac{k_2}{2}\tilde{\gamma}^2 + \frac{\varepsilon^2}{2} + \frac{k_2}{2}\gamma^2 \\ \leq& -\alpha_2(2V)^{\frac{p_2+1}{2}} - 12^{\frac{1-q_2}{2}}\beta_2(2V)^{\frac{q_2+1}{2}} - \frac{k_2}{2}\tilde{\gamma}^2 \\ &+ \alpha_2(\frac{\tilde{\gamma}^2}{k_1})^{\frac{p_2+1}{2}} + 6^{\frac{1-q_2}{2}}\beta_2(\frac{\tilde{\gamma}^2}{k_1})^{\frac{q_2+1}{2}} + \frac{\varepsilon^2}{2} + \frac{k_2}{2}\gamma^2 \end{aligned} \tag{35}$$

Due to $\tilde{\gamma} = \gamma - \hat{\gamma}$ and $\hat{\gamma} \geq 0$, $\gamma \geq \tilde{\gamma}$ is always satisfied. Then we let $\kappa = \gamma^2 - \tilde{\gamma}^2$, and it follows:

$$\dot{V} \leq -\lambda_1(V)^{\frac{p_2+1}{2}} - \lambda_2(V)^{\frac{q_2+1}{2}} + \phi \tag{36}$$

with

$$\begin{cases} \lambda_1 = 2^{\frac{p_2+1}{2}}\alpha_2 \\ \lambda_2 = 2 \times 6^{\frac{1-q_2}{2}}\beta_2 \\ \phi = \alpha_2(\frac{\tilde{\gamma}^2}{k_1})^{\frac{p_2+1}{2}} + 6^{\frac{1-q_2}{2}}\beta_2(\frac{\tilde{\gamma}^2}{k_1})^{\frac{q_2+1}{2}} + \frac{\varepsilon^2}{2} + \frac{k_2}{2}\kappa \end{cases}$$

From Lemma 1, the trajectory of the system tends to be practical fixed-time stable. Moreover, the residual set D is calculated as $D = \{\boldsymbol{s} \mid V \leq \min\{[\frac{\phi}{\lambda_1(1-\theta)}]^{\frac{2}{p_2+1}}, [\frac{\phi}{\lambda_2(1-\theta)}]^{\frac{2}{q_2+1}}\}\}$ and the settling time T_s is given by $T_s \leq \frac{1}{\lambda_1\theta(\frac{q_2+1}{2}-1)} + \frac{1}{\lambda_2\theta(1-\frac{p_2+1}{2})}$. Hence, the proof is completed. □

4 Simulation Results

In this section, we carry out a numerical simulation to vindicate the controller designed above. The simulation parameters are selected as follows. The nominal part of the inertia is chosen as $J_0 = \mathrm{diag}(500, 400, 450)(\mathrm{Kg}\cdot\mathrm{m}^2)$ with

the uncertain part of the inertia matrix selected as $\delta J = 0.3\sin(0.5t)J_0$; The modal damping and modal frequency coefficients are chosen as $\xi = \mathrm{diag}(0.005, 0.002, 0.008)$ and $\Lambda = 2\pi \times \mathrm{diag}(0.15, 0.25, 0.2)$; The coupling matrix between the piezoelectric actuators and the flexible structures is $\Delta = \mathrm{diag}(0.02, -0.004, 0.07)$. The coupling matrix between flexible structures and the rigid body is selected as:

$$B = \begin{bmatrix} 6.4564 & -4.2562 & 8.1169 \\ 1.2781 & -1.9176 & 4.4890 \\ 2.1563 & -1.6728 & -4.8368 \end{bmatrix}$$

The initial attitude quaternions are $\boldsymbol{Q} = [-0.8155, 0.1, 0.35, -0.45]^{\mathrm{T}}$ and the initial angular velocity is 0; The desired attitude quaternions are $\boldsymbol{Q}_d = [-0.6982, 0.3, 0.25, -0.6]^{\mathrm{T}}$; The initial value of the flexible mode and its derivation are both 0; The external disturbance $\boldsymbol{d}\,(\mathrm{N}\cdot\mathrm{m})$ is given as follows:

$$\boldsymbol{d} = 10^{-3} \times \begin{bmatrix} 3\cos(0.1t) + 4\sin(0.03t) - 1 \\ -1.5\cos(0.02t) - 3\sin(0.05t) + 1.5 \\ 2\sin(0.1t) - 1.5\sin(0.04t) + 1 \end{bmatrix}$$

The control torque is limited with $|T_{i,\max}| \leq 1\,(\mathrm{N}\cdot\mathrm{m})$ with $i = 1, 2, 3$. And the control voltage of the piezoelectric actuators is limited with $|u_{pi,\max}| \leq 10\,(\mathrm{V})$ with $i = 1, 2, 3$.

Select the parameter matrices $Z = [I_6\ I_6]$, and $F = \mathrm{diag}(-0.2, -0.2, -0.2, -0.3, -0.3, -0.3, -0.1, -0.1, -0.1, -0.15, -0.15, -0.15)$. Then by Z and F, we can calculate V and $A_c = VFV^{-1}$. Other parameters are chosen as $\alpha_1 = 0.05, \alpha_2 = 0.05, \beta_1 = 0.1, \beta_2 = 0.1, p_1 = 0.8, q_1 = 8, p_2 = 0.8, q_2 = 8$ and $\varepsilon = 0.05, k_1 = 0.001, k_2 = 0.8$. And the initial value of $\hat{\gamma}$ is set as 0.

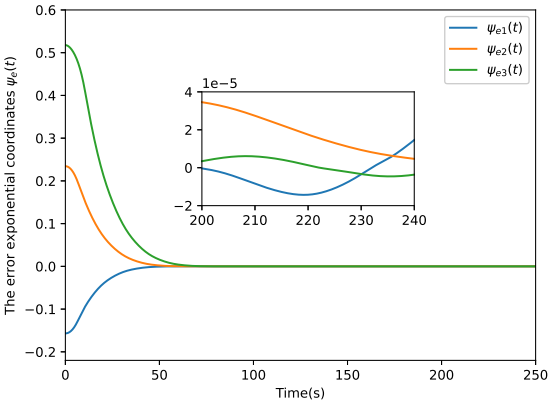

Fig. 1: Time responses of the error exponential coordinates $\boldsymbol{\psi}_e$.

The trajectories of the error exponential coordinates $\boldsymbol{\psi}_e$, the angular velocity $\boldsymbol{\omega}$ and the flexible mode $\boldsymbol{\eta}$ are shown in Fig.1, Fig.2 and Fig.4, demonstrating that all state errors are guaranteed to converge to small regions in fixed-time and the stability of the system is realized. Fig.3 and Fig.5 illustrate the control torque $\boldsymbol{T}$ and the control voltage of the piezoelectric actuators $\boldsymbol{u}_p$. And time responses of the adaptive parameter $\hat{\gamma}$ is plotted in Fig.6, which shows the effectiveness of uncertainty estimation.

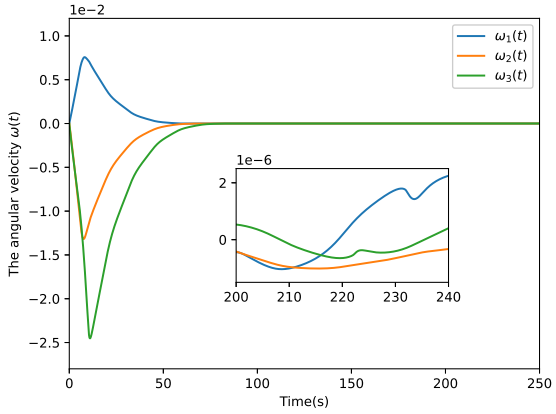

Fig. 2: Time responses of the angular velocity $\boldsymbol{\omega}\ (\mathrm{rad}\cdot\mathrm{s}^{-1})$.

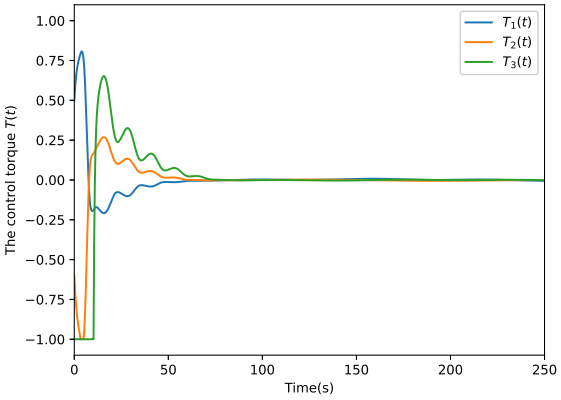

Fig. 3: Time responses of the control torque $\boldsymbol{T}\ (\mathrm{N}\cdot\mathrm{m})$.

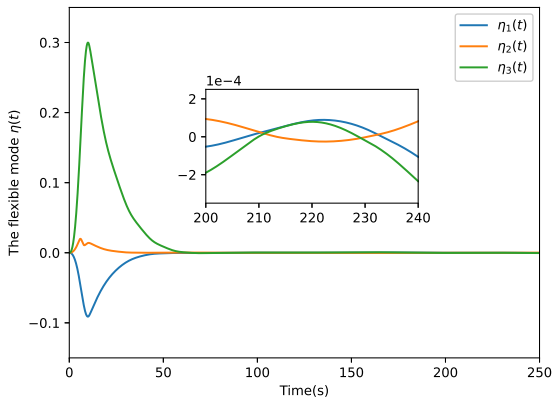

Fig. 4: Time responses of the flexible mode coordinates $\boldsymbol{\eta}$.

5 Conclusion

In this article, we have presented a attitude control scheme and active vibration suppression method for a flexible spacecraft subject to inertia uncertainty and external disturbances. The main feature of this controller is that a second-order fully-actuated system expressed by the error exponential coordinates and the flexible mode coordinates has been constructed based on the Lie algebra of $\mathbb{SO}(3)$, which would

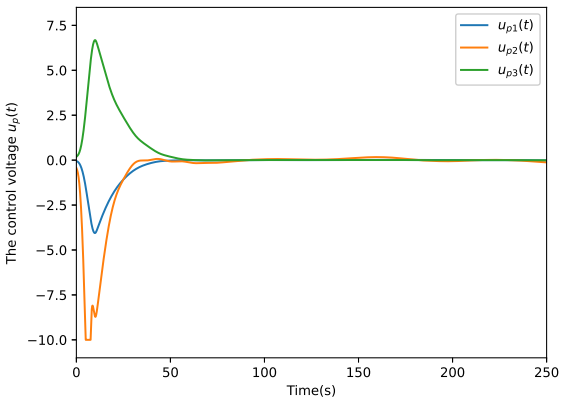

Fig. 5: Time responses of the control voltage $\boldsymbol{u}_p$ (V).

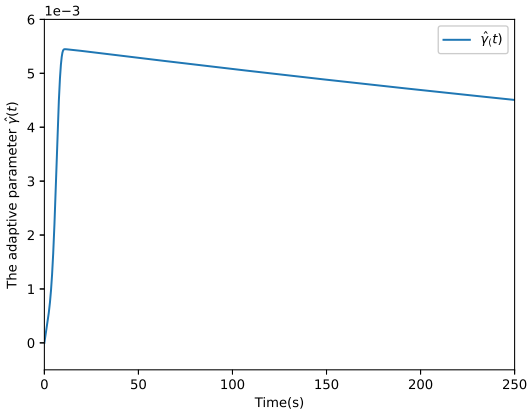

Fig. 6: Time responses of the adaptive parameter $\hat{\gamma}$.

avoid singularity in the system. And by adopting a direct parametric approach for fully-actuated systems, the nonlinear system would be converted into a linear constant system with a desired eigenstructure. Then a fixed-time terminal sliding mode control law has been designed to guarantee that the closed-loop system achieves fixed-time stability without singularity theoretically. The stability of the system has been analyzed by Lyapunov approaches, and a numerical simulation verified the effectiveness of the proposed controller.

References

[1] Z. Yu, Y. Guo, L. Wang, Y. Wu, and J. Guo, "Desired compensation adaptive robust active vibration control of flexible spacecraft," *Zhendong yu Chongji/Journal of Vibration and Shock*, vol. 36, pp. 230–236, 12 2017.

[2] G.-P. Yuan, X.-P. Shi, and L. Li, "Adaptive robust attitude maneuver control of a flexible spacecraft with active vibration suppression," *Zhendong yu Chongji/Journal of Vibration and Shock*, vol. 32, pp. 110–115, 06 2013.

[3] W. Lu, G. Yu, and W. Yi-Fei, "Finite-time adaptive robust control for sgcmgs-based flexible spacecraft," *Acta Automatica Sinica*, vol. 47, no. 3, pp. 641–651, 2021.

[4] S. Zhong, Y. Huang, and J. Hu, "Active disturbance rejection control for attitude control of deep space explorer," *Control Theory & Applications*, vol. 36, no. 12, pp. 2028–2034, 2019.

[5] F. Liu, X. Chen, Y. Jia, and C. Liu, "Application of fuzzy auto disturbance rejection controller in flexible spacecraft vibration suppression," *Journal of Vibration and Shock*, vol. 34, no. 9, pp. 9–14, 2015.

[6] G. Duan, "High-order fully actuated system approaches: Part viii. optimal control with application in spacecraft attitude stabilisation," *International Journal of Systems Science*, vol. 53, no. 1, pp. 54–73, 2022.

[7] D. Guang-Ren, "Direct parametric control of fully-actuated second-order nonlinear systems—the normal case," in *Proceedings of the 33rd Chinese Control Conference*. IEEE, 2014, pp. 2406–2413.

[8] G. Duan, "High-order fully actuated system approaches: Part i. models and basic procedure," *International Journal of Systems Science*, vol. 52, no. 2, pp. 422–435, 2021.

[9] ——, "High-order fully actuated system approaches: Part ii. generalized strict-feedback systems," *International Journal of Systems Science*, vol. 52, no. 3, pp. 437–454, 2021.

[10] ——, "High-order fully actuated system approaches: Part iv. adaptive control and high-order backstepping," *International Journal of Systems Science*, vol. 52, no. 5, pp. 972–989, 2021.

[11] ——, "High-order fully-actuated system approaches: Part vi. disturbance attenuation and decoupling," *International Journal of Systems Science*, vol. 52, no. 10, pp. 2161–2181, 2021.

[12] X. Wang, V. Pommier-Budinger, A. Reysset, and Y. Gourinat, "Simultaneous compensation of hysteresis and creep in a single piezoelectric actuator by open-loop control for quasi-static space active optics applications," *Control Engineering Practice*, vol. 33, pp. 48–62, 2014.

[13] S. Xu, N. Cui, Y. Fan, and Y. Guan, "Flexible satellite attitude maneuver via adaptive sliding mode control and active vibration suppression," *AIAA Journal*, vol. 56, pp. 1–8, 06 2018.

[14] C. Zhang, G. Ma, Y. Sun, and C. Li, "Prescribed performance adaptive attitude tracking control for flexible spacecraft with active vibration suppression," *Nonlinear Dynamics*, vol. 96, 05 2019.

[15] D. L. ZHANG Xiuyun, ZONG Qun, "Active vibration suppression and attitude control for flexible spacecraft," *Acta Aeronautica et Astronautica Sinica*, vol. 4, 2019.

[16] W. Zhu, Q. Zong, B. Tian, and W. Liu, "Disturbance observer-based active vibration suppression and attitude control for flexible spacecraft," *IEEE Transactions on Systems, Man, and Cybernetics: Systems*, vol. 52, no. 2, pp. 893–901, 2022.

[17] G.-P. Yuan, X.-P. Shi, and L. Li, "Adaptive robust attitude maneuver control of a flexible spacecraft with active vibration suppression," *Zhendong yu Chongji/Journal of Vibration and Shock*, vol. 32, pp. 110–115, 06 2013.

[18] G.-R. D. Tianyi ZHAO, "Fully actuated system approach to attitude control of flexiblespacecraft with nonlinear time-varying inertia," *SCIENCE CHINA Information Sciences*, vol. 65, no. 11, pp. 212 201–, 2022.

[19] S. Shao, Q. Zong, B. Tian, and F. Wang, "Finite-time sliding mode attitude control for rigid spacecraft without angular velocity measurement," *Journal of the Franklin Institute*, vol. 354, no. 12, pp. 4656–4674, 2017.

[20] B. Jiang, Q. Hu, and M. I. Friswell, "Fixed-time attitude control for rigid spacecraft with actuator saturation and faults," *IEEE Transactions on Control Systems Technology*, vol. 24, no. 5, pp. 1892–1898, 2016.

[21] Z. Zuo and L. Tie, "A new class of finite-time nonlinear consensus protocols for multi-agent systems," *International Journal of Control*, vol. 87, no. 2, pp. 363–370, 2014.

[22] G. Liu, K. Zhang, and B. Li, "Fully-actuated system approach based optimal attitude tracking control of rigid spacecraft with actuator saturation," *Journal of Systems Science and Complexity*, vol. 35, pp. 688–702, 04 2022.

Proceedings of the 3rd Conference on Fully Actuated System Theory and Applications
May 10-12, 2024, Shenzhen, China

Active Disturbance Rejection Controller with Variable Control Gain for Aero-Engine

Shuheng Liu, Liang Yu, Zhongyang Fei, Wenbo Zhang

School of Control Science and Engineering, Dalian University of Technology, Dalian, 116000, China
E-mail: Michellp411@mail.dlut.edu.cn; dlut_yl@dlut.edu.cn; zhongyangfei@dlut.edu.cn; zwb@mail.dlut.edu.cn

Abstract: The working environment for aero-engine is highly demanding, and stringent performance standards must be met. Consequently, a robust active disturbance rejection controller is essential for effective control. However, several issues are associated with the classical active disturbance rejection control technique used in aero engines. These issues include:(1) The system control gain changes with the operating conditions, making the parameter b_0 difficult to tune; (2) Gain of extended state observer is too high due to high-frequency components in the unmodeled dynamics. Therefore, an improved active disturbance rejection control technique with variable control gain is proposed in this paper. Firstly, for the aero-engine speed model, the Gram–Schmidt algorithm is used to identify the control gain offline under various operating conditions. Secondly, by incorporating the concept of gain scheduling, the switching of parameter b_0 is implemented, and the unmodeled dynamics identification value $\hat{f}(k)$ is calculated and used to compensate for improving the classical active disturbance rejection controller. Lastly, a complete simulation experiment was conducted. The simulation results indicate that the proposed method is effective in regulating the aero-engine working process during the transition state, which can quickly tune the parameter b_0 and effectively reduce the bandwidth of the observer under the premise of ensuring the performance.

Keywords: adaptive disturbance rejection control, aero-engine, system identification, gain scheduling

1. Introduction

The aero-engine control system has undergone several stages of development and has now evolved into a full authority digital electronic control system (FADEC) for gas turbine engines. Since then, aero-engine technology worldwide has exhibited a notable trend of accelerated development. It is expected to progress towards achieving high thrust-to-weight ratios, high speeds, wide usability, enhanced reliability and applicability, reduced fuel consumption, minimized noise emissions, decreased environmental pollution, and enhanced economic efficiency. The high-performance engine needs and high-intensity mission requirements will eventually cause the control system's operating environment to deteriorate progressively [1]. Hence, it is crucial for the control technology employed in aero-engine fuel systems to be robust. Active Disturbance Rejection Control (ADRC), which consists of real-time estimation of total disturbance and dynamic compensated linearization, is being applied to the design of fuel control for aero-engine during the transition state.

In the 1990s, the famous control scholar Han Jingqing deeply considered the difference between model theory and cybernetics [2], overcame traditional PID control technique's shortcomings, and proposed the Active Disturbance Rejection Control(ADRC) technique. ADRC reduces the impact of unmodeled dynamics and external disturbance by treating them as total system disturbance. It then estimates the total disturbance and compensates for it within the system, effectively transforming the system into integral series system so that we can use the error feedback law to control [3,4]. To simplify the ADRC parameter tuning process and promote wider adoption of the ADRC technique, Gao [5] proposed the Linear Active Disturbance Rejection Control (LADRC), which relates the ADRC parameters to the frequency of the controller and observer. The problem of parameter tuning is transformed into the issue of bandwidth adjustment, and the workload of parameter tuning is greatly reduced.

In recent years, ADRC has been used in the field of aero-engine control many times. Zhang et al. [6] integrated the ADRC algorithm and an augmented LQR method to control the aftereffect transition state of the aero-engine, which could better coordinate the aftereffect fuel supply and nozzle opening and had little influence on the work of the core engine during the whole transition state. Wang et al. [7] applied ADRC to the design of a limit protection controller, which can effectively transform the out-of-limit deviation into the correction of the main loop instruction, and the comprehensive control system has a fast response speed and achieves the purpose of limit protection. Li et al. [8] implemented a multivariable control framework based on ADRC, and the proposed controller can not only decouple the two control loops but also keep the turbine outlet temperature within the specified limit. Qian et al. [9] proposed an intake pressure control method based on linear active disturbance rejection control. This method can effectively control the intake pressure without engine information, has high versatility and excellent inference immunity, and can greatly improve the adjustment quality of the intake system in the transition state test.

ADRC has strong robustness and inference immunity, but its performance depends on the parameter tuning. Many scholars have explored and studied the parameter tuning of LADRC. Chen et al. [10] proposed a tuning method in which all the parameters except the parameter b_0 can be calculated on the premise of known settling time, while the parameter b_0 can only be obtained by stepwise trial. The trial-and-error method means a huge time cost caused by repeated tests, and the feasibility of this method is greatly reduced due to the high cost and risk of aero-engine experiments. In [11,12], the control gain b of the system is identified directly to complete the tuning of the parameter b_0. In [12], the successive approximation [13] is used to identify the control gain b online. However, the above identification methods need to

know the system's structural terms and are unsuitable for the aero-engine with strong nonlinearity and uncertainty. The parameter b_0 in LADRC is called the compensation factor and affects the compensation performance of the total disturbance in the controller. Reference [14] points out that better control performances can be achieved when the relative error between compensation factor b_0 and control gain b is within 30%. Therefore, the accurate identification of the system control gain b is the key to tuning the parameter b_0 when the structural terms of the aero-engine model are unknown.

ADRC technique regards the unmodeled dynamics and external disturbance in the aero-engine model as the total system disturbance, which is estimated by the extended state observer and compensated into the system. Due to the existence of high-frequency disturbance, high-gain observer is needed to achieve accurate estimation. However, due to measurement noise, using a high-gain observer requires a tradeoff between fast state reconstruction and reasonable state estimation error [15]. Therefore, using a low-gain observer to achieve better estimation is another key in the design of ADRC for aero-engine.

The purpose of this paper is to improve the classical adaptive disturbance rejection control technique using system identification and gain scheduling, where the improved control technique not only allows for fast parameterization but also achieves the same observational performance using a smaller observer bandwidth.

2. Problem Formulation

2.1 Fuel Control of Aero-Engine in Transition State

In this paper, the main fuel flow control is carried out for the working process of the aero-engine during the transition state. The transition state test of the aero-engine is a vital examination content to test the maneuverability and other indicators of the engine, including inertial starting and thrust transient. The main fuel flow delivered to the actuator is comprehensively determined by multiple control loops, including steady-state control, acceleration-and-deceleration control, starting, and ignition. The main fuel flow comprehensive control logic is shown in Fig. 1.

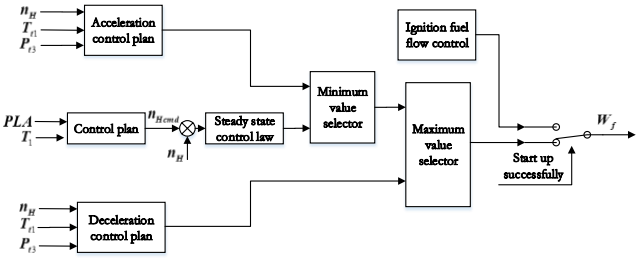

Fig. 1: Main fuel flow comprehensive control logic

Considering the order, nonlinearity and uncertainty of the aero-engine speed model, the model can be established as follows based on LADRC:

$$\ddot{N}_2 = \tilde{b}u + f(N_2, \dot{N}_2, w) \tag{1}$$

where N_2 is the engine's high-pressure rotor speed, u is the main fuel flow, $\tilde{b}$ is variable control gain, w is the external disturbance, and $f(N_2, \dot{N}_2, w)$ is unmodeled system dynamics.

2.2 Active Disturbance Rejection Control of Fuel Flow

When the control gain is unknown and variable, the control gain can only be approximated by tuning the compensation factor b_0. In this case, (1) should be expressed as follows:

$$\ddot{N}_2 = b_0 u + (\tilde{b} - b_0)u + f(N_2, \dot{N}_2, w) \tag{2}$$

According to the framework of LADRC, we can set $x_1 = N_2, x_2 = \dot{N}_2, x_3 = (\tilde{b} - b_0)u + f(N_2, \dot{N}_2, w)$. In this case, (2) can be transformed into the state space expression form:

$$\begin{cases} \dot{x}_1(t) = x_1(t) \\ \dot{x}_2(t) = x_2(t) + b_0 u(t) \\ \dot{x}_3(t) = h(t) \end{cases} \tag{3}$$

According to (3), LESO can be designed as follows:

$$\begin{cases} \dot{z}_1(t) = z_2(t) + \beta_1(y(t) - z_1(t)) \\ \dot{z}_2(t) = z_3(t) + b_0 u(t) + \beta_2(y(t) - z_1(t)) \\ \dot{z}_3(t) = \beta_3(y(t) - z_1(t)) \\ y(t) = x_1(t) + v(t) \end{cases} \tag{4}$$

where z_1, z_2, z_3 are the estimated values of x_1, x_2, x_3, respectively, $\beta_1, \beta_2, \beta_3$ are observer gain of different channels, and v is measurement noise. Based on the bandwidth method proposed in [5], the characteristic polynomial of the error dynamic equation of the observation system can be obtained by using (3) and (4) as follows:

$$s^3 + \beta_3 s^2 + \beta_2 s + \beta_1 = (s + \omega_0)^3 \tag{5}$$

It can be seen that $\beta_1 = 3\omega_o, \beta_2 = 3\omega_0^2, \beta_3 = \omega_o^3$, where ω_o is the bandwidth of the observer, the performance of the observer can be adjusted only by tuning ω_o.

Assuming that the reference speed of the system is N_{2r}, the designed control law is:

$$\begin{cases} u = \dfrac{u_0 - z_3}{b_0} \\ u_0 = k_p(N_{2r} - z_1) + k_d(\dot{N}_{2r} - z_2) \end{cases} \tag{6}$$

Through (2) and (6), the following can be obtained:

$$\ddot{N}_{2r} = k_p(N_{2r} - y) + k_d(\dot{N}_{2r} - \dot{y}) \tag{7}$$

Therefore, the characteristic polynomial of (7) is as follows:

$$s^2 + k_p s + k_d = (s + \omega_c)^2 \tag{8}$$

It can be seen that $k_p = 2\omega_c, k_d = \omega_c^2$, where ω_c is the controller bandwidth, only ω_c needs to be adjusted to make the engine meet the excellent tracking performance.

At this point, we need to clarify two problems that still exist when LADRC is applied to control aero-engine. Firstly, the control gain of the fuel system in the aero-engine changes with the operating condition. If using the trial-and-error method simply, it will cause great costs. If we choose a compensation factor b_0 with large deviation from the control gain $\tilde{b}$, it may cause overtemperature and overrotation and then damage the engine. Therefore, the tuning of the parameter b_0 is the first difficulty. Secondly, the aero-engine is highly nonlinear and uncertain and contains high-frequency thermal-mechanical dynamics. LESO is employed in LADRC to uniformly estimate the system's unmodeled dynamics and external disturbances. Due to high-frequency dynamics, we need to use a high-gain observer, which will increase the influence of measurement noise. Therefore, decreasing the observer gain while ensuring the observation performance is the second difficulty. In the following parts of this paper, the classical ADRC will be improved by system identification and gain scheduling to solve the above two problems.

3. Design of Controller

The design idea of the controller is as follows: Firstly, the control gain b and the unmodeled dynamics f of the aero-engine speed model are identified in a single operating condition by the system identification method. Secondly, the identification value of control gain $\hat{b}$ during different operating conditions of the speed models are obtained using the above identification method. By switching control gain $\hat{b}$ according to the aero engine speed N_2, the tuning of parameter b_0 is completed. The tracking problem for variable control gain $\tilde{b}$ is translated into an interpolation problem for control gains at different operating conditions. Finally, the identification value of unmodeled system dynamics $\hat{f}(k)$ and the estimated total disturbance z_3 under different control gains are used as feedforward terms to compensate the observer and the control law, hoping to eliminate the influence of the total disturbance. The improved extended state observer and control law constitute an improved LADRC technique with variable control gain for aero-engine. In this chapter, we first introduce the system identification method for the aero-engine speed model, then introduce the parameter tuning method for different operating conditions, and finally improve LADRC by using the identification results of the unmodeled dynamics and the control gain of the system.

3.1 Control Gain and System Unmodeled Dynamics Identification of The Speed Model

The aero-engine speed model is a nonlinear system with unknown time-varying parameters. Considering that the structure term of the speed model is unknown, a nonlinear discrete model is used for fitting. In this paper, the NARMAX(Nonlinear Auto Regressive Moving Average with Exogenous Inputs) model is selected, which is an input-output description of nonlinear systems and can characterize the dynamic characteristics of nonlinear systems [16].

Equation (1) is transformed into the following using forward difference:

$$N_2(k) = T^2 bu(k-2) + T^2 f(k-2) + 2N_2(k-1) - N_2(k-2) \quad (9)$$

where T is the sampling period. Thus, the identification of the control gain b and the unmodeled dynamics f of the system is transformed into the identification of b and $f(k-2)$ in (9).

In this paper, the RMGS [17,18] algorithm is used to identify the above two terms. The RMGS algorithm employs a selection of principal elements strategy, adjusts the order of orthogonalization, and utilizes orthogonal least squares and forward stepwise regression to complete the integrated identification of structures and parameters. The linear parameter model corresponding to NARMAX is constructed as follows:

$$y(t) = \sum_{i=1}^{M} \phi_i(t)\theta_i + e(t) \quad (10)$$

where $y(t)$ is the model output, $\phi_i(t)$ is the model structure term, θ_i is the parameter corresponding to the model structure term, $e(t)$ is the model error, and M is the number of model structure terms.

Using the input and output data of the model in a certain period, the matrix form of the linear parameter model can be obtained:

$$Y = \Phi\Theta + E \quad (11)$$

where $Y = [y(t_1), y(t_2), \dots, y(t_N)]^T$, $\Phi = [\Phi_1, \Phi_2, \dots, \Phi_M]$, $\Phi_i = [\phi_i(t_1), \phi_i(t_2), \dots, \phi_i(t_N)]^T$, $E = [e(t_1), e(t_2), \dots, e(t_N)]^T$, $\Theta = [\theta_1, \theta_2, \dots, \theta_M]^T$, $N \geq M$.

Then, the RMGS algorithm is carried out, and the iterative process is as follows:

Algorithm 1 RMGS algorithm

QR Decomposition:

$Y = \Phi\Theta + E = QR\Theta + E = QG + E, G = D^{-1}Q^T, D = Q^TQ$

Iterative Calculation:

Set $I_1 = \{1,2,\dots,M\}$;
for $i = 1$ *to* M
  $q_i = \phi_i$;
  $ERR_i = \frac{g_i^2 < q_i, q_i >}{< Y, Y >}; g_i = \frac{< q_i, Y >}{< q_i, q_i >}$;
  $r_{11} = 1$;
end for
$l_1 = arg \ \ max_{i \in I_1}\{ERR_i\}$;
$q_1^0 = q_{l_1}; g_1^0 = \frac{< q_1^0, Y >}{< q_1^0, q_1^0 >}; Y = Y - g_1^0 q_1^0$;
for $j = 2$ *to* M
  $I_j = I_{j-1} \backslash \{l_{j-1}\}$;
  for *all* $i \in I_j$
    $q_i = \phi_i - \sum_{k=1}^{j-1} \frac{< \phi_i, q_k^0 >}{< q_k^0, q_k^0 >} q_k^0$;
    $ERR_i = \frac{g_i^2 < q_i, q_i >}{< Y, Y >}, g_i = \frac{< q_i, Y >}{< q_i, q_i >}$;
  end for
  $l_j = arg \ \ max_{i \in I_j}\{ERR_i\}$;
  $q_j^0 = q_{l_j}; r_{jj} = 1; g_j^0 = \frac{< q_j^0, Y >}{< q_j^0, q_j^0 >}; Y = Y - g_j^0 q_j^0$;
  for $k = 1$ *to* $j-1$
    $r_{kj} = \frac{< q_k^0, \phi_{lj} >}{< q_k^0, q_k^0 >}$;
  end for
end for

Parameters Calculation:

$R = [r_{ij}]_{M \times M}; G = [g_1^0, \cdots, g_M^0]^T$;
$R\Theta = G \rightarrow \Theta = [\theta_1, \theta_2, \dots, \theta_M]^T$;

For making the RMGS applicable to identification, (9) is assumed in advance to be a second-order system with both input and output delays equal to 3, and the model structure term is set to$\{u(k-1), \dots, u(k-3), N_2(k-1), \dots, N_2(k-3), u(k-1)^2, \dots, u(k-1)u(k-3), \dots, u(k-3)^2, N_2(k-1)^2, \dots, N_2(k-1)N_2(k-1), \dots, N_2(k-3)^2, u(k-1)N_2(k-1), \dots, u(k-3)N_2(k-3)\}$.

Since model structure item $u(k-2)$ corresponds to parameter θ_2, thus we can get:

$$b = \frac{\theta_2}{T^2} \quad (12)$$

$$f(k-2) = \frac{N_2(k) - 2N_2(k-1) + N_2(k-2)}{T^2} - bu(k-2) \quad (13)$$

Therefore, the identification of control gain b and unmodeled dynamics f are completed.

3.2 Control Gain Switching at Different Operating Conditions

For the steady-state control of the aero-engine speed model at a single operating condition, the system identification method proposed in Section 3.1 can be used for integrated identification of the control gain b and the unmodeled dynamics f of the system, and the identification results can be used to complete the tuning of parameter b_0 and the compensation of the unmodeled dynamics f. However, the limitation of linearization design is that the controller can only be designed to work in a certain domain at a single operating condition. Considering the diverse operating conditions in the transition state of the aero-engine working process, it is essential to note that the corresponding control gain may vary accordingly. Therefore, the linearized design method for the single operating condition is not suitable for the working process during the transition state.

Gain scheduling can extend the effectiveness of the linearization method to several operating conditions. In many cases, the dynamic characteristics of the system with its operating condition are known, and the operating condition can be described by one or more variables as parameters, which are called allocation variables. In this way, the system can be linearized at several operating conditions, a linear feedback controller can be designed for each operating condition, and a set of linear controllers can be executed as one controller. Its parameters can be changed by monitoring allocation variables. Such a controller is called a gain scheduling controller [19,20].

In this paper, the system identification method described in Section 3.1 is used to identify the control gain in different operating conditions offline. We establish the control gain interpolation table, and gain scheduling is performed based on the actual speed of the aero-engine. This facilitates the online tuning of parameter b_0.

3.3 Improvement of Control Law and Observer

By using the system identification method described in Section 3.1, the identification values of the control gain $\hat{b}$ and the identification value of unmodeled system dynamics $\hat{f}(k)$ in the aero-engine speed model can be obtained. Because LADRC performs better when the parameter b_0 is close to b, we can set b_0 to $\hat{b}$ or fine-tune it near $\hat{b}$. $\hat{f}(k)$ is the identification value of the unmodeled dynamics f of the system and therefore contains information about the high-frequency components of f. If $\hat{f}(k)$ is added to LESO, the total disturbance will contain no or fewer high-frequency dynamics and the low-gain LESO can be used to estimate the total disturbance accurately and reduce the influence of measurement noise.

Let $x_1 = N_2$, $x_2 = \dot{N}_2$, $x_3 = (b - b_0)u + [f(N_2, \dot{N}_2, w) - \hat{f}(k)]$, then the system dynamic equation is:

$$\begin{cases} \dot{x}_1(t) = x_2(t) \\ \dot{x}_2(t) = x_3(t) + \hat{f}(k) + b_0 u(t) \\ \dot{x}_3(t) = h(t) \end{cases} \tag{14}$$

Therefore, the improved LESO(ILESO) is:

$$\begin{cases} \dot{z}_1(t) = z_2(t) + \beta_1(y(t) - z_1(t)) \\ \dot{z}_2(t) = z_3(t) + \beta_2(y(t) - z_1(t)) + \hat{f}(k) + b_0 u(t) \\ \dot{z}_3(t) = \beta_3(y(t) - z_1(t)) \\ k = int(\frac{t}{T}) \end{cases} \tag{15}$$

where z_1, z_2, z_3 are the estimates of x_1, x_2, x_3, respectively, and $int(\cdot)$ is the integer operator. Since the identification value $\hat{f}(k)$ is introduced into ILESO, z_3 is the estimated value of $(b - b_0)u + [f - \hat{f}(k)]$. To eliminate the influence of the total disturbance, the improved control law is:

$$\begin{cases} u = \frac{u_0 - z_3 - \hat{f}(k)}{b_0} \\ u_0 = k_p(N_{2r} - z_1) + k_d(\dot{N}_{2r} - z_2) \end{cases} \tag{16}$$

Combined with (16), (1) can be approximated as:

$$\ddot{N}_2 = \tilde{b}\frac{u_0 - z_3 - \hat{f}(k)}{b_0} + f \approx u_0 \tag{17}$$

It can be seen that the unmodeled dynamics in the aero-engine speed model have been compensated, and only the parameters k_p and k_d need to be adjusted to ensure excellent tracking performance.

4. Simulation

This paper conducts numerical simulation based on MATLAB/Simulink. The dual-rotor turbofan engine in the simulation system is built with real data, which can effectively replicate the behavior of a real engine, enabling researchers to analyze its performance under different conditions and scenarios. The input of the engine model is the main fuel flow, and the output is the relative converted speed. The relative converted speed N_2 of the high-pressure rotor can be calculated by the following formula:

$$N_2 = \frac{N_{cur}}{N_{max-des}} \times 100\% \tag{18}$$

where N_{cur} is current speed, $N_{max-des}$ is the maximum design speed.

In the simulation system, the reference speed is mapped using the throttle lever angle. Specifically, we utilize the changing process of the throttle lever angle as shown in Fig. 2 to simulate the engine's operation under various operating conditions. The control gain corresponding to different operating conditions needs to be identified offline in advance and switched according to the actual speed during the working process.

Firstly, the offline identification of the control gain is carried out, the working process is set up with the engine in a starting stage, and reference speeds are stable at different values. The given value of the main fuel flow of the actuator is used as the identification input, and the relative converted speed of the high-pressure rotor of the engine is used as the identification output. The integrated identification of the control gain b and the unmodeled dynamics f of the system is carried out using the method proposed in Section 3.1. The identification results of control gain at different operating conditions are shown in Table 1.

According to the concept of gain scheduling proposed in Section 3.2 and the established control gain interpolation table, the parameter b_0 is dynamically switched online according to the actual speed of the aero-engine during operation.

Further tuning of the controller bandwidth ω_c and observer bandwidth ω_o is required. The tuning of the

controller bandwidth ω_c needs to balance the problem between tracking error, overshoot, and oscillation, while tuning the observer bandwidth ω_o also needs to balance the problem between estimation error and the influence of measurement noise. Based on practical control performances, the controller bandwidth ω_c is set to 9, and the observer bandwidth ω_o is set to 5. The controller parameters are chosen as $k_p = \omega_c^2$ and $k_d = 2\omega_c$. The observer gains are chosen as $\beta_1 = 3\omega_o$, $\beta_2 = 3\omega_0^2$, and $\beta_3 = \omega_o^3$.

Fig. 3 shows the comprehensive control curve of the main fuel flow. It can be seen that the output of the ILADRC steady-state control law has some over-limits, and the actual output of the main fuel flow is the output of the ILADRC steady-state control processed by the comprehensive control logic. Fig. 4 shows the speed tracking performance controlled by ILADRC. It can be seen that the actual speed can follow the reference speed during the transition state.

Table 1: Control gain interpolation table

PLA	N_2Dem	N_2Real	$\hat{b}$
60	99.98	98.14	0.0027
55	98.64	98.15	0.0024
50	96.69	96.69	0.0022
45	94.13	94.13	0.0024
40	92.09	92.09	0.0029
35	87.93	87.93	0.0057
30	85.95	85.95	0.0069
25	82.44	82.44	0.0225
20	76.22	76.22	0.0060
15	70.00	70.00	0.0041

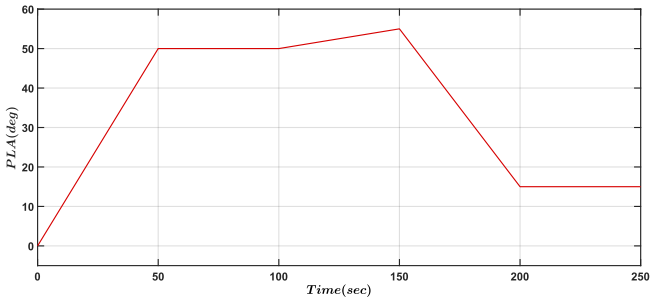

Fig. 2: Throttle lever angle

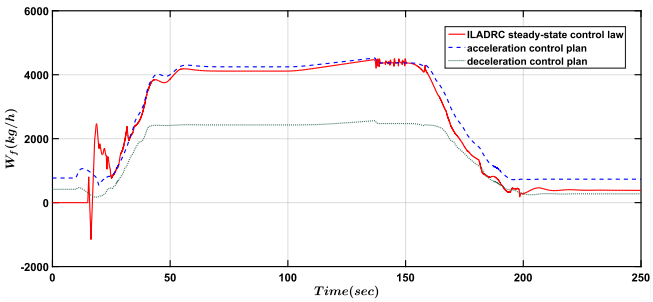

Fig. 3: Main fuel flow comprehensive control curve

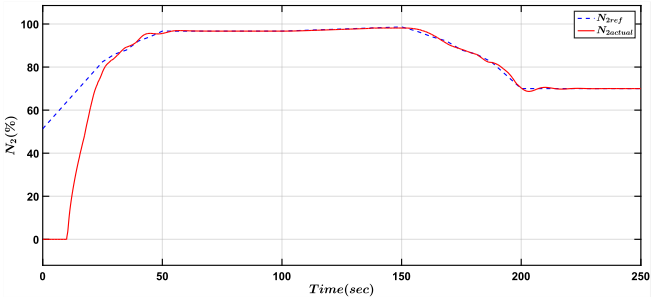

Fig. 4: Speed tracking performance

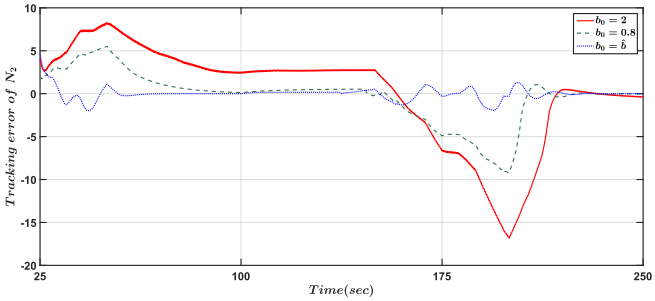

Fig. 5: Speed tracking error with different parameter b_0

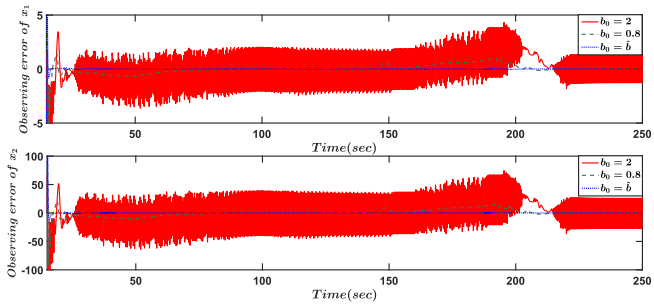

Fig. 6: Observing errors with different parameter b_0

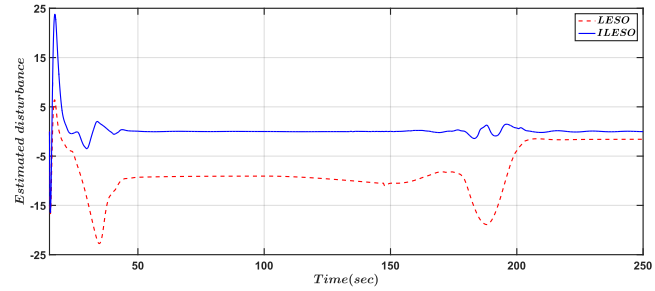

Fig. 7: Estimated disturbance z_3 of LESO and ILESO

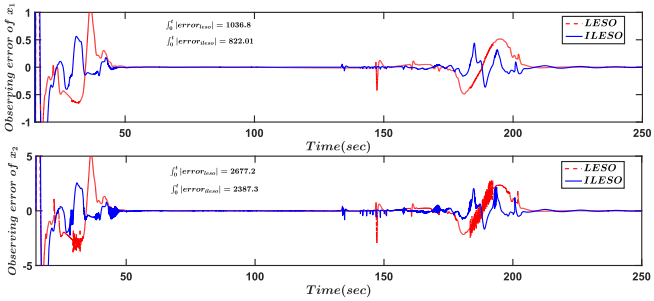

Fig. 8: Observing errors of LESO and ILESO

Fig. 5 and Fig. 6 show the speed tracking error, observation error of x_1 and observation error of x_2 with different parameter b_0 respectively. Compared with the

system tuning b_0 by trial-and-error method, the speed tracking error, observation error of x_1 and observation error of x_2 of the system tuning b_0 by gain scheduling are smaller overall.

Fig. 7 shows the estimated disturbance values before and after compensation of the unmodeled dynamics identification value $\hat{f}(k)$, which shows that the estimated disturbance of ILESO is much smaller than that of LESO. After compensation, most high-frequency components are removed from the total disturbance estimated by ILESO, which can reduce the observer bandwidth and the influence of measurement noise. Therefore, ILESO's estimating performance will surpass LESO's when the same observer bandwidth is used. Fig. 8 shows the observation errors of LESO and ILESO, and it can be seen that integral absolute errors of observation errors of ILESO are smaller than those of LESO when using the same observer bandwidth.

5. Conclusion

LADRC used in aero-engine has the problems that the parameter b_0 is difficult to tune, and the gain of extended state observer is too high. An improved LADRC with variable control gain is proposed in this paper, which can quickly tune the parameter b_0 during the transition state and compensate for the unmodeled dynamics $\hat{f}(k)$ in real-time through system identification and gain scheduling, reducing the observer bandwidth to ensure performance. Finally, the performance of the improved LADRC with variable control gain is verified by simulation.

References

[1] H. Yao, Development Trend of Aircraft Engine Control Technology, *Aeronautical Science & Technology*, 2012, 6: 1-6.

[2] J. Han, Control theory - model theory or cybernetics, *Journal of Systems Science and Mathematical Sciences*, 1989, 4: 328-335.

[3] J. Han, Adaptive disturbance rejection controller and its application, *Control and Decision*, 1998, 1: 19-23.

[4] J. Han, From PID Technique to Active Disturbance Rejection Control Technique, *Control Engineering of China*, 2002, 3: 13-18.

[5] Z. Gao, Scaling and bandwidth-parameterization based controller tuning, *Proceedings of the 2003 American Control Conference*, 2003: 4989-4996.

[6] H. Zhang and J. Sun, Application of active disturbance rejection control method in afterburning transition state control, *Journal of Propulsion Technology*, 2010, 31(2): 219-225.

[7] Y. Wang, Q. Li, and X. Huang, Controller design for limit protection of aero-engine based on ADRC, *Journal of Beijing University of Aeronautics and Astronautics*, 2012, 9: 1154-1157.

[8] Y. Li, X. Du, X. Sun, A. Dai and J. Chen, Multivariable Control for Aero-Engine Based on Active Disturbance Rejection Control, *2019 Chinese Control Conference (CCC)*, 2019: 773-778.

[9] Q. Qian, Z. Dan, S. Zhang, X. Pei and X. Wang, Linear active disturbance rejection control method for intake pressure control in aero-engine transient test, *Journal of Aerospace Power*, 2019, 34(10): 2271-2279.

[10] X. Chen, D. Li, Z. Gao, and C. Wang, Tuning method for second-order active disturbance rejection control, *Proceedings of the 30th Chinese Control Conference*, 2011: 6322-6327.

[11] Q. Liang, C. Wang, J. Pan, Y. Wei, and Y. Wang, Parameter identification of b_0 and parameter tuning law in linear active disturbance rejection control, *Control and Decision*, 2015, 30(9): 1691-1695.

[12] Z. Chen, Q. Gao, Modified extended state observer: analysis and implementation, *Control Theory & Applications*, 2018, 35(8): 1199-1206.

[13] R. Zhang, J. Han, Parameter Identification by Model Compensation Auto Disturbance Rejection Controller, *Control Theory & Applications*, 2000, 1: 79-81.

[14] J. Han, *Active Disturbance Rejection Control Technique - the technique for estimating and compensating the uncertainties*, National Defense Industry Press, 2008.

[15] A. A. Prasov and H. K. Khalil, A Nonlinear High-Gain Observer for Systems with Measurement Noise in a Feedback Control Framework, *IEEE Transactions on Automatic Control*, 2013, 58(3): 569-580.

[16] I. J. Leontaritis and S. A. Billings, Input-output parametric models for non-linear systems Part I: deterministic non-linear systems, *International Journal of Control*, 1985, 41(2): 303-328.

[17] W. Jia, J. Peng, S. Xie, Y. Liu, T. Li and D. He, Nonlinear polynomial model's structure and parameter integration identification, *Journal of Beijing University of Aeronautics and Astronautics*, 2018, 44(6): 1303-1311.

[18] H. Wei, S. A. Billings, J. Liu, Term and variable selection for non-linear system identification, *International Journal of Control*, 2004, 77(1): 86-110.

[19] J. R. Wilson, S. S. Jeff, Research on gain scheduling, *Automatica*, 2000, 36(10): 1401-1425.

[20] H. K. Khalil, *Nonlinear Systems (3rd Ed.)*, Prentice Hall, 2002.

Proceedings of the 3rd Conference on Fully Actuated System Theory and Applications
May 10-12, 2024, Shenzhen, China

Multi-Spacecraft adaptive tracking control with collision avoidance based on fully actuated system approach

Xiaoxiang Zhang[1], Yunhai Geng[1], Baolin Wu[1]
1. Research Center of Satellite Technology, Harbin Institute of Technology, Harbin 150001, China
E-mail: wuba0001@e.ntu.edu.sg

Abstract: In this paper, an adaptive tracking control problem of a constrained multi-spacecraft system in observation mission for a rotating target is investigated. Based on the integrated spacecraft attitude-orbit kinematic described on Lie group SE(3) and a positive definite configuration error function, a second-order fully actuated system model for error configuration is derived. Considering collision avoidance problem, a collision avoidance scheme based on the collision detection algebraic condition is established, which considers the interaction of relative attitude and geometric shapes of two spacecraft. In view of the influence of external disturbance, an adaptive controller based on the fully actuated system theory is further designed. According to Lyapunov stability theory, it is proved that the resulting closed-loop system is ultimately uniformly bounded. The simulation results prove the effectiveness of the proposed control strategy.

Key Words: Spacecraft pose tracking control, Lie group SE(3), Fully actuated system approach, Collision avoidance

1 Introduction

With the development of space technology, there is a need for on-orbit monitoring of a failed high-value spacecraft to extract some characteristic information for subsequent capture and maintenance missions [1]. Compared with one-to-one on-orbit service, utilizing mass-produced small spacecraft for operations in close range [2] has the advantage of cost reduction and efficiency improvement. However, once multiple spacecraft simultaneously perform proximity operations for target, this poses a challenge for collision avoidance between spacecraft. Therefore, it is necessary to address the safety control problem in multi-spacecraft observation mission of failed target under collision avoidance constraint.

When considering spacecraft collision avoidance, there are roughly two approaches to modeling collision avoidance constraint from the perspective of the geometric shape of the chaser spacecraft. One is to treat the chaser as a point mass and depict the envelope for target spacecraft as accurately as possible, such as safety path constraint [3], spherical forbidden zone [4], Superquadratics curved surface envelope [5]. The second is to consider the envelope of chaser as a simple sphere. As in [6, 7], a composite envelope combined a sphere and an ellipsoid is designed for target, while the envelope of chaser is a standard sphere. However, if chasers are equipped with large sails or accessories, using ellipsoidal envelope to describe its shape can further reduce the conservatism of constraint modeling. The collision avoidance constraint modeling methods mentioned above consider chaser as a point mass or an attitude independent sphere, which is not applicable to the collision avoidance problem with considering the geometric shapes of all chasers simultaneously.

In order to achieve high-precision on-orbit monitoring and other close range operation missions, Lie group SE(3) is used to describe the integrated coupled attitude-orbit model. Based on Lie group SE(3), the formation spacecraft attitude-orbit integrated control problem [8, 9] and multi-agent formation control problem [10] are addressed. The spacecraft attitude orbit integration model based on Lie group SE(3) is more precise and concise, and it is convenient for the design of attitude-orbit integrated controller. However, due to the strong non-linearity of the spacecraft system, the introduction of nonlinear control algorithms leads to complicated controller design processes and strict stability conditions.

In recent years, the fully actuated system approach(FASA) proposed by Duan has gradually received attention from scholars due to its simplicity and effectiveness in designing nonlinear control systems [11–13]. The pose control problems of single spacecraft and combined spacecraft are solved in [14, 15] by combining the parameterized design method of FASA with prescribed performance control method, respectively. In [16], an attitude obstacle avoidance control method based on FASA under attitude constraints is designed. An adaptive tracking control problem for a class of uncertain fully actuated systems with actuator faults and full state constraints is studied in [17]. However, the above research focuses on the pose control problem of a single spacecraft. There is currently limited research on multi-spacecraft pose tracking control based on FASA under safety constraint.

Based on the above analysis, this paper proposes a robust adaptive pose controller based on FASA and the potential function in the presence of collision avoidance and external disturbance. Firstly, according to the pose kinematic model described on the Lie group SE(3) and spacecraft dynamics equation, a second-order fully actuated system model for error configuration is established. Meanwhile, to meet the safety requirements during observation mission, this paper describes the geometric shape of all spacecraft as ellipsoids, and then algebraic condition is used to derive the collision avoidance scheme between chaser spacecraft. Next, to address the external disturbance, an adaptive controller is proposed based on FASA. According to the Lyapunov method, it is proven that the second-order fully actuated system of pose error is ultimately uniformly bounded. The simulation results show that the multi-spacecraft system accomplishes fly-around mission without collision, which illustrates the effectiveness of the proposed control strategy.

This work is supported by National Natural Science Foundation (NNSF) of China under Grant 62188101, and in part by the Heilongjiang Touyan Team Program.

2 Preliminaries

For $\forall n \in N_+$, $E_n \in \mathbb{R}^{n\times n}$ represents an identity matrix. Given a set $\mathcal{A}$, its interior is denoted by $\mathring{\mathcal{A}}$. A smooth function $\sigma(x)$ is defined as $\sigma(x)=0$, if $x \leq 0$, $\sigma(x)=e^{-\frac{1}{x}}$, if $x>0$. The detailed definitions of mapping $(\cdot)^{\wedge}: \mathbb{R}^6 \mapsto \mathfrak{se}(3)$.

Proposition 1 [18]: Consider cubic polynomial equations with constant coefficients $f(\lambda) = a_3\lambda^3 + a_2\lambda^2 + a_1\lambda^1 + a_0 = 0$, $a_i \in \mathbb{R}$, $\forall i \in \{0...3\}$ and roots λ_1, λ_2, λ_3. Then the discriminant of $f(\lambda)$ is given as $\Delta = (a_3)^4 \prod (\lambda_i - \lambda_j)^2, i \in \{1,2\}, j \in \{i+1,...,3\}$. The following statements then hold

1) $\Delta = 0 \Leftrightarrow$ at least two roots are equal.
2) $\Delta > 0 \Leftrightarrow$ all three roots are real and distinct.

Proposition 2 [18]: Consider two planar ellipsoids $\mathcal{A} = \left\{z \in \mathbb{R}^3 \text{ s.t. } z^{\mathrm{T}} A(t) z \leq 0\right\}$, $\mathcal{B} = \left\{z \in \mathbb{R}^3 \text{ s.t. } z^{\mathrm{T}} B(t) z \leq 0\right\}$, where $z = [x^{\mathrm{T}}, 1]^{\mathrm{T}}$, $x \in \mathbb{R}^2$. A, $B \in \mathbb{R}^{3\times3}$ describe the motion of $\mathcal{A}$ and $\mathcal{B}$ in the plane, respectively. The characteristic polynomial between two ellipsoids is given as $f(\lambda) = \det(\lambda A - B)$, then the following statements hold

1) $\exists \lambda^* > 0$ s.t. $f(\lambda^*) = 0$, which implies one of the roots of $f(\lambda)$ is always positive.
2) $\mathcal{A} \cap \mathcal{B} = \emptyset \Leftrightarrow f(\lambda)$ has two distinct negative roots.
3) $\mathcal{A} \cap \mathcal{B} \neq \emptyset$ with $\mathring{\mathcal{A}} \cap \mathring{\mathcal{B}} = \emptyset \Leftrightarrow f(\lambda) = 0$ has a negative double root, which means $\mathcal{A}$ touches $\mathcal{B}$ externally.

Assumption 1 [19]: $\left\|\varphi_d^k - \widehat{\varphi}_d^k\right\| \leq \delta_0$, $\left\|\dot{\varphi}_d^k - \dot{\widehat{\varphi}}_d^k\right\| \leq \delta_1$, δ_0 and δ_1 are non-negative constants.

Lemma 1 [19]: Let $\hat{\varphi}_d^k$ be the estimation of the unknown disturbance φ_d^k, and define

$$\begin{aligned} \tilde{\varphi}_d^k &= \varphi_d^k - \hat{\varphi}_d^k \\ \tilde{\varphi}_{de}^k &= \hat{\varphi}_d^k - \widehat{\varphi}_d^k \\ \tilde{\varphi}_{dr}^k &= \varphi_d^k - \widehat{\varphi}_d^k \end{aligned} \tag{1}$$

then, on the basis of Assumption 1, the following relations hold:

$$\begin{aligned} \tilde{\varphi}_d^k &= \tilde{\varphi}_{dr}^k - \tilde{\varphi}_{de}^k \\ \left(\tilde{\varphi}_{dr}^k\right)^T \tilde{\varphi}_d^k &\leq \frac{1}{2}\left(\delta_0^2 + \left\|\tilde{\varphi}_d^k\right\|^2\right) \\ \left(\dot{\tilde{\varphi}}_{dr}^k\right)^T \tilde{\varphi}_d^k &\leq \frac{1}{2}\left(\delta_1^2 + \left\|\tilde{\varphi}_d^k\right\|^2\right) \end{aligned} \tag{2}$$

3 Second-order Fully Actuated System Modeling

According to the the basics of Lie group SE(3) defined in [10], spacecraft pose kinematic equation can be expressed in a compact manner as

$$\dot{g}_{kI} = g_{kI}\left(\xi_k^k\right)^{\wedge} \tag{3}$$

where $g_{kI} = \begin{bmatrix} R_{Ik} & p_k^I \\ 0_{1\times3}^{\mathrm{T}} & 1 \end{bmatrix} \in \mathrm{SE}(3)$ denote spacecraft configuration in $\mathcal{F}_I$, R_{Ik} is a rotation matrix from to $\mathcal{F}_k$ to $\mathcal{F}_I$, p_k^I is the position of kth chaser in $\mathcal{F}_I$. $\xi_k^k = \left[\omega_k^k; v_k^k\right] \in \mathbb{R}^6$ denotes motion velocity. ω_k^k and v_k^k denote the angular velocity and translational velocity of kth chaser in $\mathcal{F}_k$, respectively. $\left(\xi_k^k\right)^{\wedge}$ is defined as $\left(\xi_k^k\right)^{\wedge} = \begin{bmatrix} {\omega_k^k}^{\times} & v_k^k \\ 0_{1\times3} & 0 \end{bmatrix} \in \mathbb{R}^{4\times4}$.

Taking the time derivative of ξ_k^k and after deducing, the spacecraft dynamics equation expressed in frame $\mathcal{F}_k$ is obtained

$$\dot{\xi}_k^k = \bar{\Xi}_k^{-1} \mathrm{ad}_{\xi_k}^T \bar{\Xi}_k \xi_k^k + \bar{\Xi}_k^{-1}\left(\varphi_c^k + \bar{\varphi}_g^k + \varphi_d^k\right) \tag{4}$$

where $\Xi_k = \mathrm{blockdiag}(J_k, m_k E_3) \in \mathbb{R}^{6\times6}$ denotes inertial matrix of kth chaser. Here, J_k and m_k denote moment of inertia matrix and mass, respectively. $\varphi_c^k = \left[\tau_c^k; u_c^k\right] \in \mathbb{R}^6$, τ_c^k and u_c^k are control torque and control force, respectively. $\bar{\varphi}_g^k$ denotes the nominal gravity force. $\varphi_d^k \in \mathbb{R}^6$ denotes external disturbance. The adjoint operator $\mathrm{ad}_{(\cdot)}$ is defined as

$$\mathrm{ad}_{\xi_k^k} = \begin{bmatrix} \left(\omega_k^k\right)^{\times} & 0_{3\times3} \\ \left(v_k^k\right)^{\times} & \left(\omega_k^k\right)^{\times} \end{bmatrix} \in \mathbb{R}^{6\times6}$$

The desired pose of kth chaser is set as g_{dI}. Then, the configuration tracking error of kth chaser can be calculated by $g_{kd} = g_{dI}^{-1} g_{kI}$. For the convenience of controller design, the following positive definite Morse potential function is introduced to evaluate the configuration tracking error

$$\begin{aligned} \psi(g_{kd}) &= \psi^R(R_{dk}) + \psi^p\left(p_{kd}^d\right) \\ &= 2 - \sqrt{1 + \mathrm{tr}(R_{kd})} + \frac{1}{2}\left(p_{kd}^d\right)^T p_{kd}^d \end{aligned} \tag{5}$$

where R_{dk}, p_{kd}^d are the attitude and position tracking errors, respectively. Taking the time derivative of (9), configuration error vector is obtained

$$e_k = \begin{bmatrix} e_k^R \\ e_k^p \end{bmatrix} = \begin{bmatrix} \frac{1}{2\sqrt{1+\mathrm{tr}(R_{dk})}}\left(R_{dk} - R_{dk}^T\right)^{\vee} \\ R_{dk}^T p_{kd}^d \end{bmatrix} \tag{6}$$

Taking time derivative of (6), and then pose error kinematic and dynamic equations are derived as

$$\dot{e}_k = F_{kd}\xi_{kd}^k \tag{7}$$

where

$$F_{kd} = \begin{bmatrix} F_a & 0_{3\times3} \\ \left(R_{dk}^T p_{kd}^d\right)^{\times} & E_3 \end{bmatrix}$$

$$F_a = \frac{1}{2\sqrt{1+\mathrm{tr}(R_{dk})}}\left(\mathrm{tr}(R_{dk})E_3 - R_{dk}^T + 2e_k^R\left(e_k^R\right)^T\right)$$

Taking the time derivative of (6) yields

$$\ddot{e}_k = \dot{F}_{kd}\xi_{kd}^k + F_{kd}\dot{\xi}_{kd}^k \tag{8}$$

where $\dot{F}_{kd}$ denotes the derivative of F_{kd}, the expression of $\dot{\xi}_{kd}^k$ is given as

$$\dot{\xi}_{kd}^k = \dot{\xi}_k^k - \mathrm{Ad}_{g_{kd}^{-1}}\dot{\xi}_d^d - \frac{\mathrm{dAd}_{g_{kd}^{-1}}}{\mathrm{d}t}\xi_d^d \tag{9}$$

where

$$\mathrm{Ad}_{g_{kd}^{-1}} = \begin{bmatrix} R_{dk}^T & 0_{3\times3} \\ -R_{dk}^T\left(p_{kd}^d\right)^{\times} & R_{dk}^T \end{bmatrix} \in \mathbb{R}^{6\times6}$$

$$\frac{\mathrm{dAd}_{g_{kd}^{-1}}}{\mathrm{d}t} = -\mathrm{ad}_{\xi_{kd}^k}\mathrm{Ad}_{g_{kd}^{-1}}$$

Combining (4) with the derivative of (7), the following pose error dynamic equation can be obtained

$$\begin{aligned}\ddot{e}_k =& F_{kd}\bar{\Xi}_k^{-1}\left(\mathrm{ad}_{\xi_k}^T\bar{\Xi}_k\mathrm{Ad}_{g_{kd}^{-1}}\xi_k^k+\bar{\varphi}_{kg}^k+\varphi_c^k+\varphi_d^k\right)\\&+F_{kd}\left(\mathrm{ad}_{\xi_{kd}^k}\mathrm{Ad}_{g_{kd}^{-1}}\xi_d^d-\mathrm{Ad}_{g_{kd}^{-1}}\dot{\xi}_d^d+\Delta f_k\right)\\&+\dot{F}_{kd}\xi_{kd}^k\end{aligned}\tag{10}$$

As long as $\det\left(F_{kd}\bar{\Xi}_k^{-1}\right)\neq 0$ is met, the system (10) is a second-order fully actuated system.

4 Collision avoidance scheme

Define a set of ellipsoidal spacecraft systems $\mathcal{N}=\{1,...,N\}$, including N chasers. Each spacecraft can be described by ellipsoid $\mathcal{A}_i\left(g_i\right)=\left\{y\in\mathbb{R}^4:y^{\mathrm{T}}A_i\left(g_i\right)y\leq 0\right\}$, $i\in\mathcal{N}$, $g_i=g_{Ik}$. $A_i\left(g_i\right)=g_i^{-\mathrm{T}}\hat{A}_ig_i^{-1}$, where $\hat{A}_i=\mathrm{diag}\left\{a_i^{-2},b_i^{-2},c_i^{-2},-1\right\}$.

For $\mathcal{A}_i,i\in\mathcal{N}$, its projections on the planes can be denoted as $\mathcal{A}_i^s\left(g_i\right)=\left\{y\in\mathbb{R}^3\,\mathrm{s.t.}\,y^{\mathrm{T}}A_i^s\left(g_i\right)y\leq 0\right\}$, $\forall s\in\{xy,xz,yz\}$. There are three states between chasers: Separating, Overlapping, and Touching. If $\mathcal{A}_i$ and $\mathcal{A}_j,j\in\mathcal{N},j\neq i$ collide each other, then the projections of the two ellipsoids on the three planes must also collide, such that for all $s\in\{xy,xz,yz\}$

$$\mathcal{A}_i^s\left(g_i\right)\cap\mathcal{A}_j^s\left(g_j\right)\neq\emptyset\tag{11}$$

Thus, $\mathcal{A}_i$ does not collide with $\mathcal{A}_j$ if and only if $\mathcal{A}_i^s\left(g_i\right)\cap\mathcal{A}_j^s\left(g_j\right)=\emptyset$ for at least one $s\in\{xy,xz,yz\}$.

Whereas the relevant properties given in *Proposition 2*, which indicates for at least one $s\in\{xy,xz,yz\}$ characteristic equation $f_{i,j}^s\left(\lambda\right)=\det\left(\lambda A_i^s\left(g_i\right)-A_j^s\left(g_j\right)\right)=0$ must always have two distinct negative and one positive roots. The discriminant of $f_{i,j}^s\left(\lambda\right)=0$ is abbreviated as $\Delta_{i,j}^s$. It can be seen that $\Delta_{i,j}^s>0$ must always be satisfied for at least one $s\in\{xy,xz,yz\}$ from *Proposition 1*, because $\forall s\in\{xy,xz,yz\}$, $\Delta_{i,j}^s=0$ implies a collision between ellipsoids .

In summary, $\Delta_{i,j}^s=0\Leftrightarrow\sigma\left(\Delta_{i,j}^s\right)=0$, $\forall s\in\{xy,xz,yz\}$, if planar ellipsoid $\mathcal{A}_i$ collides with $\mathcal{A}_j$, $\sigma\left(\Delta_{i,j}^{xy}\right)+\sigma\left(\Delta_{i,j}^{xz}\right)+\sigma\left(\Delta_{i,j}^{yz}\right)>0$ if and only if $\mathcal{A}_i$ does not collide with $\mathcal{A}_j$. Here, the equivalent condition for collision avoidance have been established. Therefore, a continuously differentiable safety index function for all $k\in\mathcal{N}$ is defined as

$$\Delta_{kj}=\sigma\left(\Delta_{k,j}^{xy}\right)+\sigma\left(\Delta_{k,j}^{xz}\right)+\sigma\left(\Delta_{k,j}^{yz}\right)\,j\in\mathcal{N},j\neq k\tag{12}$$

To save computational resources for the multi-spacecraft systems, safety radius of chaser is incorporated in the collision avoidance scheme. Let $\bar{\Delta}_{kj}=\Delta_{kj}^{xy}+\Delta_{kj}^{xz}+\Delta_{kj}^{yz}$, for the same safety radius, different relative attitude corresponds to different $\bar{\Delta}_{kj}$. The lower bound of $\bar{\Delta}_{kj}$ corresponding to the safety radius between chasers is defined as follows

$$\widehat{\Delta}_{kj}=\inf_{(g_k,g_j)}\left\{\bar{\Delta}_{kj}\,\mathrm{s.t.}\left\|p_{kt}^t-p_{jt}^t\right\|\leq\min\left\{d_{sr,k},d_{sr,j}\right\}\right\}\tag{13}$$

where $p_{jt}^t=R_{tk}((p_{kj}^k)^T+p_{kt}^k)$, p_{kj}^k can be obtained by relative pose measurement device. $d_{sr,k}$, $d_{sr,j}$ are safety radius of kth chaser and jth chaser, respectively. Since $\forall k,j\in\mathcal{N},k\neq j$, $d_{sr,k}>\max\{a_k,b_k,c_k\}+\max\{a_j,b_j,c_j\}+\varpi$, where ϖ is a positive constant, there exists a positive constant $\tilde{\Delta}_{kj}$ such that $\widehat{\Delta}_{kj}\geq\tilde{\Delta}_{kj}>0$. Subsequently, the safety index function is defined for all $k\in\mathcal{N}$ as follows

$$\rho_k=\min_{\substack{j\in\mathcal{N}\\j\neq k}}\rho_{kj}=\min_{\substack{j\in\mathcal{N}\\j\neq k}}\left\{\frac{\Delta_{kj}}{\Delta_{kj}+\sigma\left(\tilde{\Delta}_{kj}-\bar{\Delta}_{kj}\right)}\right\}>0\tag{14}$$

Only if $\rho_{ks}>0$ implies that kth chaser has not collided with other chasers.

$$V_r=\sum_{j\in\mathcal{N},j\neq k}\frac{1}{\left(n_{kj}\rho_{kj}\right)^{\kappa_{kj}}}\tag{15}$$

where n_{kj} and κ_{kj} are positive constants. According to (15), when $\rho_{kj}\to 0$, $V_b\to\infty$, it means that external contact will occur between spacecraft. If $\rho_{ks}>0$ is satisfied at the beginning, as long as a suitable control law is designed, then V_b is always bounded.

5 Controller Design

This section proposes a 6-DOF pose tracking controller based on APF, which is used to ensure that each spacecraft reaches desired states with collision avoidance constraint being satisfied.

Define a sliding surface as follow

$$s=\dot{e}_k+\left(k_aV_a+k_p\right)e_k\tag{16}$$

where k_p and γ are positive constants.

Then, for the second-order fully actuated system model of error configuration, the following controller is proposed

$$\varphi_c^k=\varphi_{c1}^k+\varphi_{c2}^k\tag{17}$$

$$\begin{aligned}\varphi_{c1}^k=&-\bar{\Xi}_k\left(\mathrm{ad}_{\xi_{kd}^k}\mathrm{Ad}_{g_{kd}^{-1}}\xi_d^d-\mathrm{Ad}_{g_{kd}^{-1}}\dot{\xi}_d^d\right)\\&-\bar{\Xi}_kF_{kd}^{-1}\dot{F}_{kd}\xi_{kd}^k-\mathrm{ad}_{\xi_k}^{\mathrm{T}}\bar{\Xi}_k\xi_k^k-\bar{\varphi}_{kg}^k\end{aligned}\tag{18}$$

$$\varphi_{c2}^k=\bar{\Xi}_kF_{kd}^{-1}\left(-k_ss-k_p\dot{e}_k-k_aV_a\dot{e}_k-k_a\dot{V}_ae_k-\hat{\varphi}_d^k\right)\tag{19}$$

where k_s is a positive constant. $\hat{\varphi}_d^k$ is updated from the following adaptive law

$$\dot{\hat{\varphi}}_d^k=\bar{\Xi}_k^{-T}F_{kd}s-\left(2k_s+1\right)\left(\hat{\varphi}_d^k-\bar{\varphi}_d^k\right)-\dot{\bar{\varphi}}_d^k\tag{20}$$

Theorem 1: Consider spacecraft pose error second-order fully actuated system (10) with the proposed control strategy (17). If assumption 1 holds, the resulting closed-loop system is ultimately uniformly bounded, and the pose error vector e_k and its derivative $\dot{e}_k$ can converge exponentially to the ellipse $\pi_{(\kappa_1,c)}\left(0\right)=\left\{s^Ts+\left(\tilde{\varphi}_d^k\right)^T\tilde{\varphi}_d^k\leq 2\kappa_1/c\right\}$, where $\kappa_1=\frac{1}{2}\left(\delta_1^2+\left(2k_s+1\right)\delta_0^2\right)$. Meanwhile, the collision avoidance constraint (14) always holds.

proof: Define Lyapunov candidate function as follows

$$V=\frac{1}{2}s^Ts+\frac{1}{2}\left(\tilde{\varphi}_d^k\right)^T\tilde{\varphi}_d^k\tag{21}$$

Taking the derivative of (21) yields

$$\dot{V} = s^T \left(\ddot{e}_k + k_a \dot{V}_a e_k + \left(k_a V_a + k_p \right) \dot{e}_k \right) + \left(\tilde{\varphi}_d^k \right)^T \dot{\tilde{\varphi}}_d^k \tag{22}$$

Substituting (10) and (17) into (22) yields

$$\begin{aligned} \dot{V} =& s^T \left(F_{kd} \bar{\Xi}_k^{-1} \varphi_d^k - F_{kd} \bar{\Xi}_k^{-1} \hat{\varphi}_d^k - k_s s \right) + \left(\tilde{\varphi}_d^k \right)^T \dot{\tilde{\varphi}}_d^k \\ =& - k_s s^T s - k_s \left(\tilde{\varphi}_d^k \right)^T \tilde{\varphi}_d^k + k_s \left(\tilde{\varphi}_d^k \right)^T \tilde{\varphi}_d^k \\ & + \left(\tilde{\varphi}_d^k \right)^T \dot{\tilde{\varphi}}_d^k + s^T F_{kd} \bar{\Xi}_k^{-1} \tilde{\varphi}_d^k \\ =& - 2 k_s V + V_n \end{aligned} \tag{23}$$

where,

$$V_n = k_s \left(\tilde{\varphi}_d^k \right)^T \tilde{\varphi}_d^k + s^T F_{kd} \bar{\Xi}_k^{-1} \tilde{\varphi}_d^k + \left(\tilde{\varphi}_d^k \right)^T \dot{\tilde{\varphi}}_d^k \tag{24}$$

According to Lemma 1, $\eta_k = \tilde{\varphi}_{dr}^k - \tilde{\varphi}_{de}^k - \tilde{\varphi}_d^k = 0$. Then, V_n can be written as

$$\begin{aligned} V_n =& \left(k_s \tilde{\varphi}_d^k + \bar{\Xi}_k^{-T} F_{kd} s + \dot{\tilde{\varphi}}_d^k \right)^T \tilde{\varphi}_d^k + \left(2k_s + 1 \right) \eta_k^T \tilde{\varphi}_d^k \\ =& \left(\bar{\Xi}_k^{-T} F_{kd} s - \dot{\tilde{\varphi}}_{de}^k - \left(2k_s + 1 \right) \tilde{\varphi}_{de}^k \right)^T \tilde{\varphi}_d^k + \left(\dot{\tilde{\varphi}}_{dr}^k \right)^T \tilde{\varphi}_d^k \\ & + \left(2k_s + 1 \right) \left(\tilde{\varphi}_{dr}^k \right)^T \tilde{\varphi}_d^k - \left(k_s + 1 \right) \left(\tilde{\varphi}_d^k \right)^T \tilde{\varphi}_d^k \end{aligned} \tag{25}$$

Substituting the adaptive law (20) into (25) obtains

$$\begin{aligned} V_n =& \left(\dot{\tilde{\varphi}}_{dr}^k \right)^T \tilde{\varphi}_d^k + \left(2k_s + 1 \right) \left(\tilde{\varphi}_{dr}^k \right)^T \tilde{\varphi}_d^k \\ & - \left(k_s + 1 \right) \left(\tilde{\varphi}_d^k \right)^T \tilde{\varphi}_d^k \\ \leq & \frac{1}{2} \left(\delta_1^2 + \left\| \tilde{\varphi}_d^k \right\|^2 \right) - \left(k_s + 1 \right) \left\| \tilde{\varphi}_d^k \right\|^2 \\ & + \frac{2k_s + 1}{2} \left(\delta_0^2 + \left\| \tilde{\varphi}_d^k \right\|^2 \right) \\ =& \frac{1}{2} \left(\delta_1^2 + \left(2k_s + 1 \right) \delta_0^2 \right) \end{aligned} \tag{26}$$

Substituting (26) into (23) yields

$$\dot{V} \leq -cV + \kappa_1 \tag{27}$$

where $c = 2k_s$, $\kappa_1 = \frac{1}{2} \left(\delta_1^2 + \left(2k_s + 1 \right) \delta_0^2 \right)$. Consider a closed region $\prod = \left\{ \left(s, \tilde{\varphi}_d^k \right) : V \leq \rho_0, \forall \rho_0 > 0 \right\}$, and the control parameter can be selected as $c \geq \kappa_1 / \rho_0$. If $V(0) \leq \rho_0$, V will always stay in the region $\prod$ because $\dot{V} \leq -\left(\kappa_1 / \rho_0 \right) \rho_0 + \kappa_1 = 0$. Solving (27) obtains

$$0 \leq V \leq \frac{\kappa_1}{c} + \left(V(0) - \frac{\kappa_1}{c} \right) e^{-ct}, \forall t > 0 \tag{28}$$

According to equation (28), $\lim_{t \to \infty} V = \kappa_1 / c$. Therefore, s and $\tilde{\varphi}_d^k$ remain bounded and will eventually converge to the following ellipse

$$\pi_{(\kappa_1, c)}(0) = \left\{ s^{\mathrm{T}} s + \left(\tilde{\varphi}_d^k \right)^T \tilde{\varphi}_d^k \leq 2\kappa_1 / c \right\} \tag{29}$$

Combining (16) with (29), it is known that the configuration error vector e_k and its derivative $\dot{e}_k$ will also converge exponentially to $\pi_{(\kappa_1, c)}(0)$. Therefore, the second-order fully actuated system (10) is ultimately uniformly bounded under control law (17), which also means that the collision avoidance constraint (14) is satisfied all the time.

6 Simulation Results

To achieve on-orbit observation of space rotating target by multi-spacecraft system, the desired motion of spacecraft is to fly around the target in LVLH frame. The desired radius and period of fly-around are 30m and 400s. The desired attitude is to maintain accurate pointing to the target during the flying around. The initial attitude and velocity of each spacecraft are consistent with target.

Initial states of target are $\omega_t = (0, 0.01, 0.01)\mathrm{rad/s}$, $(6878140, 0.01, 30^\circ, 45^\circ, 120^\circ, 90^\circ)$, $R_t^I = E_3$. Mass is chosen as $m_k = 25\mathrm{kg}$. Moment of inertia is set as

$$J_k = \begin{bmatrix} 7.9 & 0.7 & 0.4 \\ 0.7 & 8.8 & 0.9 \\ 0.4 & 0.9 & 10.1 \end{bmatrix} \mathrm{kg \cdot m^2}$$

The geometric shape of spacecraft is chosen as $L_{s1} = 1\mathrm{m}, \mathrm{W_{s1}} = 2\mathrm{m}$, $L_{s2} = 4\mathrm{m}$, $W_{s2} = 1\mathrm{m}$, according to minimum envelope ellipse defined in [20]. The relative position between spacecraft and target are given as $p_{1t}^l = [13; 20; 19]\,\mathrm{m}$, $p_{2t}^l = [-6; 15; -6]\,\mathrm{m}$, $p_{3t}^l = [-10; 10; 13]\,\mathrm{m}$. $\alpha_1 = (0^\circ, -60^\circ, -50^\circ), \alpha_2 = (0^\circ, 0^\circ, 0^\circ), \alpha_3 = (0^\circ, 120^\circ, 50^\circ)$ denote the rotation angle from LVLH frame to flying coordinate system by '3-2-1' rotation sequence, respectively. $\bar{\varphi}_d^k = (1.2, 1.2, 1.2, 4, 4, 4) \times 10^{-3}\,(\mathrm{Nm, N})$, $\hat{\varphi}_d^k = 0_{6\times 1}$, $\zeta = 0.001$, $n_{kj} = 1$, $\kappa_{kj} = 1.5$. $k_s = 0.1$, $k_p = \mathrm{blkdiag}(0.4E_3, 0.3E_3)$. $u_{c\max}^k = 1\mathrm{Nm}$, $\tau_{c\max}^k = 8\mathrm{N}$.

$$\varphi_d^k = \begin{bmatrix} 1.2 + \sin(0.03t + 1) \\ 1 + \sin(0.048t + 1) \\ 1.5 + \cos(0.05t + 1) \\ 4 + 5\sin(2\pi n t) \\ 4.5 + 4\cos(2\pi n t) \\ 3 + 2.5\sin(2\pi n t + \frac{\pi}{3}) \end{bmatrix} \times 10^{-3}\,(\mathrm{Nm, N})$$

Fig. 1 and Fig. 2 show attitude and position tracking errors. Fig. 3 and Fig. 4 show attitude and position tracking errors.

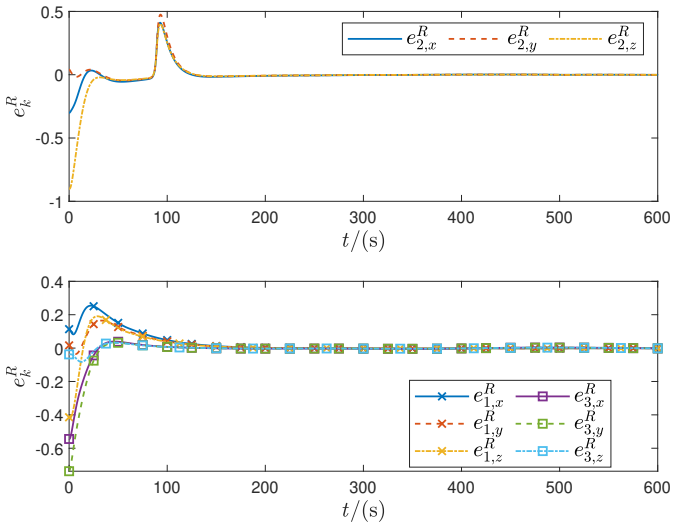

Fig. 1: Attitude tracking errors e_k^R

All spacecraft can converge to the desired pose to perform fly-around observation mission. Because of consideration of collision avoidance, it can be observed that state of 2th spacecraft have a significant fluctuation near t=100s. From the change of the state, it is clear that not only position and

velocity, but also attitude and angular velocity fluctuate. This is due to the attitude-orbit coupling is considered in the collision avoidance scheme.

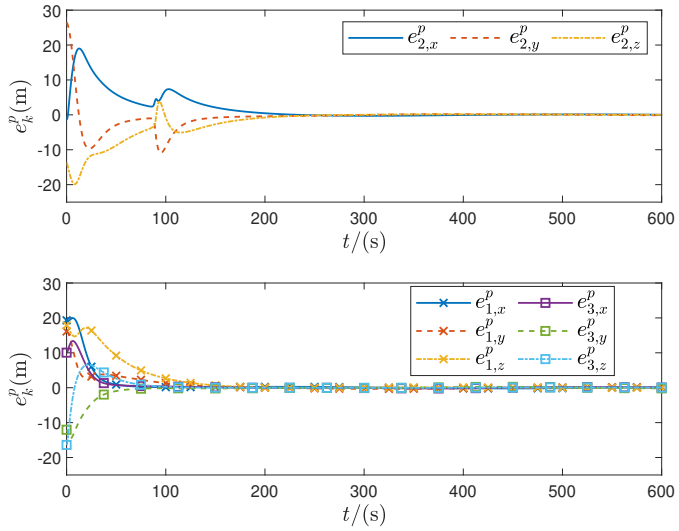

Fig. 2: Position tracking errors e^p_k

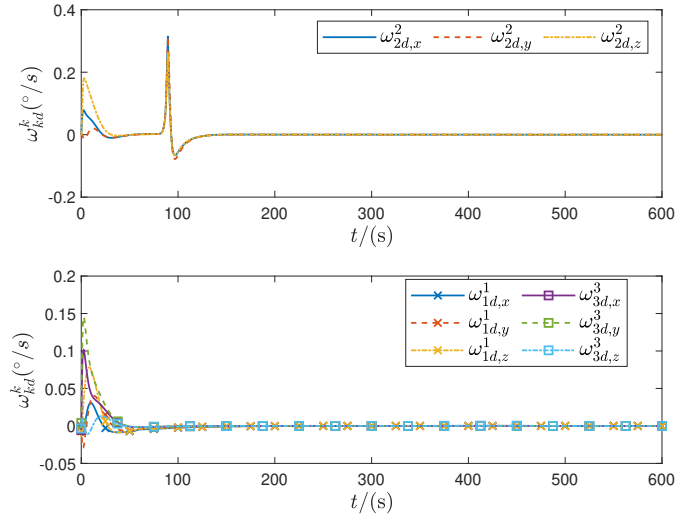

Fig. 3: Angular velocity tracking errors ω^k_{kd}

The norm of control torque and force are given in Fig. 5, as mentioned above, control torque and control force sudden increase simultaneously. Values of safety index function are given in Fig. 6, when the collision avoidance constraint is not considered, 2th chaser collides with 3th chaser. 3D trajectory of 2th chaser and 3th chaser in frame $\mathcal{F}_t$ are shown in Fig. 7(a) and Fig. 7(b), which correspond to the safety index function in Fig. 6. From the comparison results in Fig. 7, it is clear that collision between spacecraft can be avoided under the proposed control scheme.

7 Conclusion

This paper investigates the problem of fly-around control of tumbling target by a multi-spacecraft system in the presence of safety constraint and external disturbance. Firstly, the second-order fully actuated system model of error configuration is derived by combining the attitude-orbit kinematic equation on SE(3). Then, a collision avoidance mech-

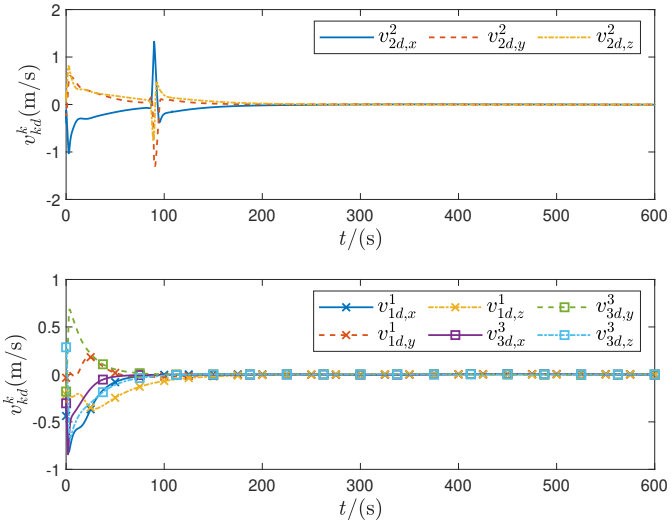

Fig. 4: Velocity tracking errors v^k_{kd}

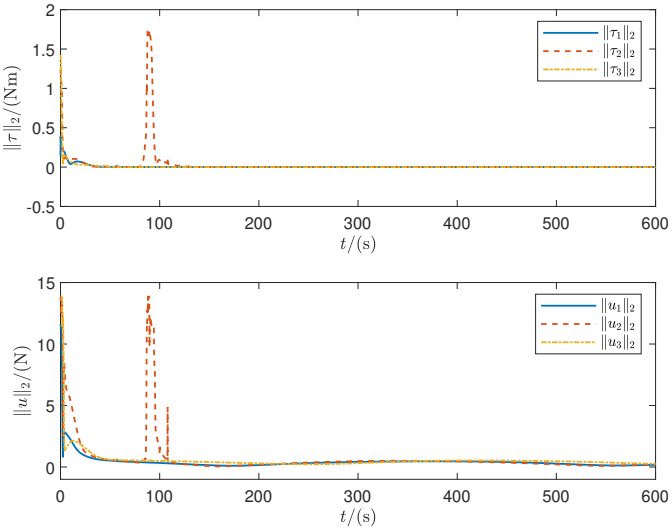

Fig. 5: Control input

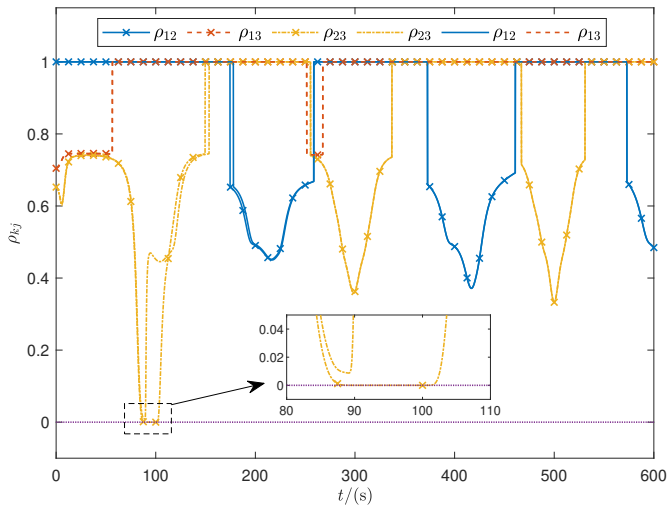

Fig. 6: Safety index function:marked trajectories without collision constraint / unmarked trajectories with collision constraint

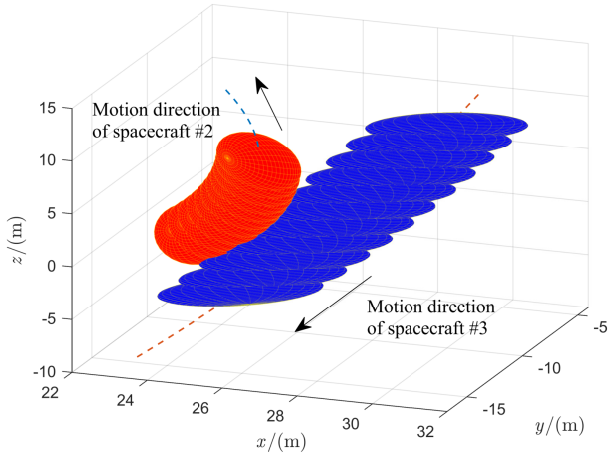

(a) without collision avoidance constraint (t=87.5-112.5s)

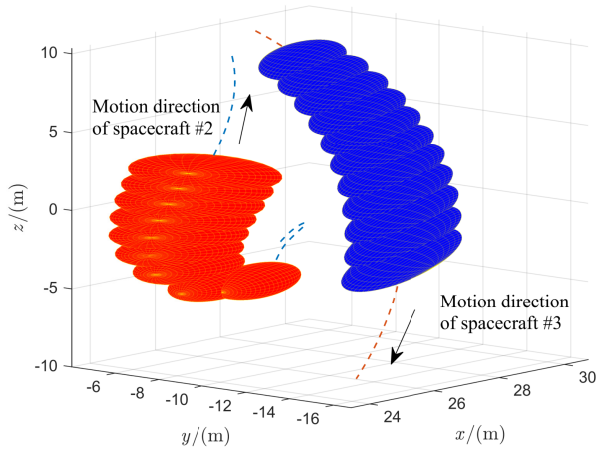

(b) with collision avoidance constraint (t=87.5-112.5s)

Fig. 7: 3D trajectory in frame $\mathcal{F}_t$ (Enlarged view)

anism is established for multi-spacecraft system based on collision detection algebraic conditions. Finally, an adaptive controller is proposed based on FASA adaptive technology. The simulation results show that the proposed control strategy can enable each spacecraft in multi- spacecraft system to safely fly-around target and maintain accurate attitude pointing. This work can implement collision avoidance between spacecraft with attitude and geometric coupling in 3D sense with analytical control law.

References

[1] W.-J. Li, D.-Y. Cheng, X.-G. Liu *et al.*, "On-orbit service (oos) of spacecraft: A review of engineering developments," *Progress in Aerospace Sciences*, vol. 108, pp. 32–120, 2019.

[2] Y. Liu, P. Huang, F. Zhang, and Y. Zhao, "Distributed formation control using artificial potentials and neural network for constrained multiagent systems," *IEEE Transactions on Control Systems Technology*, vol. 28, no. 2, pp. 697–704, 2020.

[3] K. Dong, J. Luo, Z. Dang, and L. Wei, "Tube-based robust output feedback model predictive control for autonomous rendezvous and docking with a tumbling target," *Advances in Space Research*, vol. 65, no. 4, pp. 1158–1181, 2020.

[4] Q. Li, J. Yuan, and H. Wang, "Sliding mode control for autonomous spacecraft rendezvous with collision avoidance," *Acta Astronautica*, vol. 151, pp. 743–751, 2018.

[5] Q. Li, S. Song, C. Sun, Q. Gou, and Z. Niu, "Robust output-feedback control for spacecraft proximity operations with forbidden zone," *IEEE Transactions on Aerospace and Electronic Systems*, vol. 58, no. 1, pp. 96–107, 2021.

[6] X. Chu, J. Zhang, S. Lu, Y. Zhang, and Y. Sun, "Optimised collision avoidance for an ultra-close rendezvous with a failed satellite based on the gauss pseudospectral method," *Acta Astronautica*, vol. 128, pp. 363–376, 2016.

[7] D. Zhou, Y. Zhang, and S. Li, "Receding horizon guidance and control using sequential convex programming for spacecraft 6-dof close proximity," *Aerospace Science and Technology*, vol. 87, pp. 459–477, 2019.

[8] D. Lee, A. K. Sanyal, and E. A. Butcher, "Asymptotic tracking control for spacecraft formation flying with decentralized collision avoidance," *Journal of Guidance, Control, and Dynamics*, vol. 38, no. 4, pp. 587–600, 2015.

[9] H. Zhang, D. Ye, Y. Xiao, and Z. Sun, "Adaptive control on se (3) for spacecraft pose tracking with harmonic disturbance and input saturation," *IEEE Transactions on Aerospace and Electronic Systems*, vol. 58, no. 5, pp. 4578–4594, 2022.

[10] K. Ghasemi, J. Ghaisari, and F. Abdollahi, "Robust formation control of multiagent systems on the lie group se (3)," *International Journal of Robust and Nonlinear Control*, vol. 30, no. 3, pp. 966–998, 2020.

[11] Z. Gao, Y. Zhang, and G. Guo, "Fixed-time leader-following formation control of fully-actuated underwater vehicles without velocity measurements," *Journal of Systems Science and Complexity*, vol. 35, no. 2, pp. 559–585, 2022.

[12] F.-Z. Xiao and L.-Q. Chen, "Fully actuated systems in terms of quaternions for spacecraft attitude control," *Acta Astronautica*, vol. 209, pp. 1–5, 2023.

[13] G. Liu, K. Zhang, and B. Li, "Fully-actuated system approach based optimal attitude tracking control of rigid spacecraft with actuator saturation," *Journal of Systems Science and Complexity*, vol. 35, no. 2, pp. 688–702, 2022.

[14] M. Liu, R. Fan, s. Qiu, and X. Cao, "Spacecraft attitude-orbit prescribed performance control based on fully actuated system approach," *Acta Aeronautica et Astronautica Sinica*, no. 1-16.

[15] G. Duan and G. Liu, "Adaptive prescribed performance control for position and attitude of combined spacecraft based on fully actuated system approach," *Acta Aeronautica et Astronautica Sinica*, no. 1-10.

[16] M. Lu, X. Chen, F. Wu, and X. Cao, "Attitude maneuver control of spacecraft based on second-order fully actuated system under attitude constraints," *Acta Aeronautica et Astronautica Sinica*, no. 1-9.

[17] R. Dong, C. Hua, K. Li, and R. Meng, "Adaptive fault-tolerant control for high-order fully actuated system with full-state constraints," *Journal of the Franklin Institute*, 2023.

[18] Y.-K. Choi, W. Wang, Y. Liu, and M.-S. Kim, "Continuous collision detection for two moving elliptic disks," *IEEE Transactions on Robotics*, vol. 22, no. 2, pp. 213–224, 2006.

[19] G. Duan, "High-order fully actuated system approaches: Part v. robust adaptive control," *International Journal of Systems Science*, vol. 52, no. 10, pp. 2129–2143, 2021.

[20] J. Wang, R. Chen, Z. Chen, Y. Zhao, Y. Bai, and X. Chen, "Trajectory planning for complex shaped spacecraft proximity based on critical safety curve and disturbed fluid," *IEEE Transactions on Aerospace and Electronic Systems*, 2023.

Proceedings of the 3rd Conference on Fully Actuated System Theory and Applications
May 10-12, 2024, Shenzhen, China

Unwinding-Free Attitude Control via Fully Actuated System Approach

Fu-Zheng Xiao[1], Li-Qun Chen[1]
1. School of Science, Harbin Institute of Technology, Shenzhen 518055, P. R. China
E-mail: fuzshaw@yeah.net, chenliqun@hit.edu.cn

Abstract: Quaternion representation is widely used to describe the attitude motions of rigid bodies because it provides a global representation and is free from singularities. Nevertheless, the double cover property of the representation can result in the unwinding phenomenon, where the rotation angles exceed π radians. The present work proposes a fundamental attitude control law via the fully actuated system approach. The fundamental control law, without the need for additional operations, can avoid the unwinding phenomenon. Based on the fundamental control law, external disturbances and input saturation are considered. Consequently, an unwinding-free controller is proposed for the attitude control of rigid bodies. Lyapunov's direct method is used to verify the stability of the system. Numerical simulations demonstrate the validity of both the fundamental control law and the proposed controller.

Key Words: Attitude Control, Unwinding Phenomenon, Fully Actuated System approach, Second-Order Quaternion

1 Introduction

The attitude of rigid bodies expressed in quaternions (Euler parameters) has attractive advantages such as global representation and singularity-free [1]. Nevertheless, the inherent ambiguity from the double cover property of the quaternion representation would lead to the rotation angles of rigid bodies being larger than π radians when the rigid bodies perform attitude motions, which is known as the unwinding phenomenon [2].

The property offers two sets of quaternions to describe a given physical orientation of rigid bodies. Hence, the corresponding physical equilibrium point is also represented by two sets of quaternions $Q_{+1}(+1,\ 0,\ 0,\ 0)$ and $Q_{-1}(-1,\ 0,\ 0,\ 0)$. Ordinary attitude controllers only consider Q_{+1} as the equilibrium point even if the present attitude is near Q_{-1} [3], which leads to the occurrence of the unwinding phenomenon.

Many scholars have come up with effective methods for the unwinding phenomenon. Dong et al. [4] combined a sliding mode technology with a switching function to address the unwinding phenomenon. Tan et al. [5] utilized the rotation matrix to represent attitude, and then the rotation matrix-based controller is naturally without the unwinding phenomenon. Su et al. [6] used modified Rodrigues parameters to describe the attitude of spacecraft, and then a nonlinear sliding surface was introduced to obtain the anti-unwinding property. Huang and Meng [7] presented a hybrid distributed observer to avoid the unwinding phenomenon. Hu et al. [8] proposed a novel attitude error function to realize the unwinding-free performance. Su et al. [9] employed a unified auxiliary variable to avoid the unwinding phenomenon.

The above controllers are mainly designed based on the state-space models. There are novel models named the fully actuated system models [10, 11]. The present work finds a fundamental control law designed based on the fully actuated system models capable of achieving unwinding-free performance. The fundamental control law prevents the occurrence of the unwinding phenomenon without the need for additional operations. Based on the unwinding-free control law, the present work addresses attitude control issues such as external disturbances and input saturation.

The remainder of the manuscript is presented as follows: **Section 2** shows a deduction process of a quaternion-based fully actuated system. **Section 3** proposes an unwinding-free control law, designs an observer-based controller, and proves the stability of the controlled system. **Section 4** employs numerical simulations to confirm the validity of the proposed controllers. **Section 5** provides some conclusion remarks to end the manuscript.

2 Quaternion-Based Fully Actuated System

Consider an attitude system of a rigid body. $\boldsymbol{J} \in \mathbb{R}^{3\times 3}$ is the inertia matrix of the rigid body. The attitude is expressed in unit quaternion $\boldsymbol{Q} \triangleq \left[q_0\ \boldsymbol{q}^{\mathrm{T}}\right]^{\mathrm{T}} = [q_0\ q_1\ q_2\ q_3]^{\mathrm{T}} \in \mathbb{R}^4$, where q_0 is a scalar and $\boldsymbol{q} \in \mathbb{R}^3$ is a vector. $\boldsymbol{\omega} = [\omega_1\ \omega_2\ \omega_3]^{\mathrm{T}} \in \mathbb{R}^3$ denotes the angular velocity. An input torque $\boldsymbol{u} = [u_1\ u_2\ u_3]^{\mathrm{T}} \in \mathbb{R}^3$ adjusts the attitude. Moreover, there are disturbances $\boldsymbol{d} = [d_1\ d_2\ d_3]^{\mathrm{T}} \in \mathbb{R}^3$ affecting the system. Then, the attitude systems are presented as follows:

$$\dot{\boldsymbol{Q}} = \frac{1}{2}\boldsymbol{Q} \circ \boldsymbol{\Omega}, \tag{1}$$

$$\boldsymbol{J}\dot{\boldsymbol{\omega}} + \boldsymbol{\omega}^{\times}\boldsymbol{J}\boldsymbol{\omega} = \boldsymbol{d} + \boldsymbol{u}, \tag{2}$$

where $\boldsymbol{\Omega} \triangleq \left[\omega_0\ \boldsymbol{\omega}^{\mathrm{T}}\right]^{\mathrm{T}} \in \mathbb{R}^4$ is a pure quaternion, and "$\circ$" represents the quaternion multiplication rule.

Symbol "$\times$" converts a 3D vector to its skew-symmetric matrix, such as

$$\boldsymbol{\omega}^{\times} = \begin{bmatrix} 0 & -\omega_3 & \omega_2 \\ \omega_3 & 0 & -\omega_1 \\ -\omega_2 & \omega_1 & 0 \end{bmatrix}. \tag{3}$$

A desired attitude $\boldsymbol{Q}_d \triangleq \left[q_{d,0}\ \boldsymbol{q}_d^{\mathrm{T}}\right]^{\mathrm{T}} = [q_{d,0}\ \ q_{d,1}\ \ q_{d,2}\ \ q_{d,3}]^{\mathrm{T}} \in \mathbb{R}^4$ and a desired angular velocity $\boldsymbol{\omega}_d \in \mathbb{R}^3$ are introduced to construct the error dynamic systems. The error quaternion

This work is supported by National Natural Science Foundation (NNSF) of China under Grant Nos. 62188101 and 12132002.

Corresponding author: Li-Qun Chen (E-mail: chenliqun@hit.edu.cn).

$\boldsymbol{Q}_e \triangleq \left[q_{e,0}\ \boldsymbol{q}_e^{\mathrm{T}}\right]^{\mathrm{T}} = [q_{e,0}\ q_{e,1}\ q_{e,2}\ q_{e,3}]^{\mathrm{T}} \in \mathbb{R}^4$ and error angular velocity $\boldsymbol{\omega}_e \in \mathbb{R}^3$ both used to represent the relative motion are obtained [12]:

$$\begin{aligned} \boldsymbol{q}_e &= q_{d,0}\boldsymbol{q} - q_0\boldsymbol{q}_d + \boldsymbol{q}^{\times}\boldsymbol{q}_d, \\ q_{e,0} &= q_{d,0}q_0 + \boldsymbol{q}\cdot\boldsymbol{q}_d, \end{aligned} \tag{4}$$

$$\boldsymbol{\omega}_e = \boldsymbol{\omega} - \tilde{\boldsymbol{C}}_e\boldsymbol{\omega}_d, \tag{5}$$

where

$$\tilde{\boldsymbol{C}}_e = \left(q_{e,0}^2 - \boldsymbol{q}_e^{\mathrm{T}}\boldsymbol{q}_e\right)\boldsymbol{I} + 2\boldsymbol{q}_e\boldsymbol{q}_e^{\mathrm{T}} - 2q_{e,0}\boldsymbol{q}_e^{\times}, \tag{6}$$

and $\boldsymbol{I}$ denotes an identity matrix.

Then, the error dynamic systems are presented as follows:

$$\dot{\boldsymbol{Q}}_e = \frac{1}{2}\boldsymbol{Q}_e \circ \boldsymbol{\Omega}_e, \tag{7}$$

$$\begin{aligned} \boldsymbol{J}\dot{\boldsymbol{\omega}}_e = &-\left(\boldsymbol{\omega}_e + \tilde{\boldsymbol{C}}_e\boldsymbol{\omega}_d\right)^{\times}\boldsymbol{J}\left(\boldsymbol{\omega}_e + \tilde{\boldsymbol{C}}_e\boldsymbol{\omega}_d\right) + \boldsymbol{u} + \boldsymbol{d} \\ &+ \boldsymbol{J}\boldsymbol{\omega}_e^{\times}\tilde{\boldsymbol{C}}_e\boldsymbol{\omega}_d - \boldsymbol{J}\tilde{\boldsymbol{C}}_e\dot{\boldsymbol{\omega}}_d. \end{aligned} \tag{8}$$

The following equation can be yielded by Eq. (7):

$$\frac{1}{2}\boldsymbol{\Omega}_e = \tilde{\boldsymbol{Q}}_e \circ \dot{\boldsymbol{Q}}_e, \tag{9}$$

where $\boldsymbol{\Omega}_e \triangleq \left[0\ \boldsymbol{\omega}_e^{\mathrm{T}}\right]^{\mathrm{T}} \in \mathbb{R}^4$, and $\tilde{\boldsymbol{Q}}_e \in \mathbb{R}^4 \triangleq \left[q_{e,0}\ -\boldsymbol{q}_e^{\mathrm{T}}\right]^{\mathrm{T}}$.

The following equation is employed to replace $\boldsymbol{\omega}_e$:

$$\boldsymbol{\omega}_e = \boldsymbol{G}^{-1}\dot{\boldsymbol{q}}_{\boldsymbol{e}}, \tag{10}$$

where

$$\boldsymbol{G} = \frac{1}{2}\begin{bmatrix} q_{e,0} & -q_{e,3} & q_{e,2} \\ q_{e,3} & q_{e,0} & -q_{e,1} \\ -q_{e,2} & q_{e,1} & q_{e,0} \end{bmatrix}. \tag{11}$$

Base on Eq. (10), Eq. (8) is updated as follows:

$$\begin{aligned} \boldsymbol{J}\dot{\boldsymbol{\omega}}_e = &-\left(\boldsymbol{G}^{-1}\dot{\boldsymbol{q}}_{\boldsymbol{e}} + \tilde{\boldsymbol{C}}_e\boldsymbol{\omega}_d\right)^{\times}\boldsymbol{J}\left(\boldsymbol{G}^{-1}\dot{\boldsymbol{q}}_{\boldsymbol{e}} + \tilde{\boldsymbol{C}}_e\boldsymbol{\omega}_d\right) \\ &+ \boldsymbol{J}\left(\left(\boldsymbol{G}^{-1}\dot{\boldsymbol{q}}_{\boldsymbol{e}}\right)^{\times}\tilde{\boldsymbol{C}}_e\boldsymbol{\omega}_d - \tilde{\boldsymbol{C}}_e\dot{\boldsymbol{\omega}}_d\right) + \boldsymbol{u} + \boldsymbol{d}. \end{aligned} \tag{12}$$

Eq. (12) can be rewritten as follows:

$$\dot{\boldsymbol{\omega}}_e = \boldsymbol{f} + \boldsymbol{f}_d + \boldsymbol{J}^{-1}\boldsymbol{u}, \tag{13}$$

where

$$\begin{aligned} \boldsymbol{f} = &-\boldsymbol{J}^{-1}\left(\boldsymbol{G}^{-1}\dot{\boldsymbol{q}}_{\boldsymbol{e}} + \tilde{\boldsymbol{C}}_e\boldsymbol{\omega}_d\right)^{\times}\boldsymbol{J}\left(\boldsymbol{G}^{-1}\dot{\boldsymbol{q}}_{\boldsymbol{e}} + \tilde{\boldsymbol{C}}_e\boldsymbol{\omega}_d\right) \\ &+ \left(\boldsymbol{G}^{-1}\dot{\boldsymbol{q}}_{\boldsymbol{e}}\right)^{\times}\tilde{\boldsymbol{C}}_e\boldsymbol{\omega}_d - \tilde{\boldsymbol{C}}_e\dot{\boldsymbol{\omega}}_d, \end{aligned} \tag{14}$$

and

$$\boldsymbol{f}_d = \boldsymbol{J}^{-1}\boldsymbol{d}. \tag{15}$$

Define some pure quaternions: $\boldsymbol{F} \triangleq \left[0\ \boldsymbol{f}^{\mathrm{T}}\right]^{\mathrm{T}}$, $\boldsymbol{F}_d \triangleq \left[0\ \boldsymbol{f}_d^{\mathrm{T}}\right]^{\mathrm{T}}$, and $\boldsymbol{U} \triangleq \left[0\ \left(\boldsymbol{J}^{-1}\boldsymbol{u}\right)^{\mathrm{T}}\right]^{\mathrm{T}}$, then Eq. (13) is rewritten as the following equation:

$$\dot{\boldsymbol{\Omega}}_e = \boldsymbol{F} + \boldsymbol{F}_d + \boldsymbol{U}. \tag{16}$$

Taking the derivative of Eq. (7) yields

$$\ddot{\boldsymbol{Q}}_e = \dot{\boldsymbol{Q}}_e \circ \frac{1}{2}\boldsymbol{\Omega}_e + \frac{1}{2}\boldsymbol{Q}_e \circ \dot{\boldsymbol{\Omega}}_e. \tag{17}$$

Using Eqs. (9) and (16) to replace $\boldsymbol{\Omega}_e$ and $\dot{\boldsymbol{\Omega}}_e$ obtains the final system [10, 11]:

$$\ddot{\boldsymbol{Q}}_e = \dot{\boldsymbol{Q}}_e \circ (\tilde{\boldsymbol{Q}}_e \circ \dot{\boldsymbol{Q}}_e) + \frac{1}{2}\boldsymbol{Q}_e \circ (\boldsymbol{F} + \boldsymbol{F}_d + \boldsymbol{U}), \tag{18}$$

which is named the quaternion-based fully actuated system in [13] and differs from the Lagrange form of [14].

3 Controller Design

3.1 Unwinding-Free Control Law

The quaternion-based fully actuated system has three vector subsystems and a scalar subsystem [13], the vector subsystems are generally employed:

$$\ddot{\boldsymbol{q}}_e = \boldsymbol{g} + \boldsymbol{g}_d + \boldsymbol{B}\boldsymbol{u}, \tag{19}$$

where $\boldsymbol{g} = \dot{\boldsymbol{G}}\boldsymbol{G}^{-1}\dot{\boldsymbol{q}}_e + \boldsymbol{G}\boldsymbol{f}$, $\boldsymbol{g}_d = \boldsymbol{G}\boldsymbol{f}_d$, and $\boldsymbol{B} = \boldsymbol{G}\boldsymbol{J}^{-1}$.

A fundamental control law provided by the fully actuated system approach is presented as follows [11]:

$$\boldsymbol{u} = -\boldsymbol{B}^{-1}\left(\boldsymbol{g} + \boldsymbol{g}_d + \boldsymbol{A}_{0\sim1}\boldsymbol{q}_e^{(0\sim1)} + \sum_{i=1}^{n}\boldsymbol{v}_i\right), \tag{20}$$

$$\boldsymbol{A}_{0\sim1} = \begin{bmatrix} \boldsymbol{A}_0 & \boldsymbol{A}_1 \end{bmatrix}, \tag{21}$$

$$\boldsymbol{q}_e^{(0\sim1)} = \begin{bmatrix} \boldsymbol{q}_e \\ \dot{\boldsymbol{q}}_e \end{bmatrix}, \tag{22}$$

where $\boldsymbol{A}_0 \in \mathbb{R}^{3\times3}$ and $\boldsymbol{A}_1 \in \mathbb{R}^{3\times3}$ are parameter matrices. $\boldsymbol{v}_i \in \mathbb{R}^3$, $i = 1 \sim n$ are additional vector functions.

While $\det \boldsymbol{B} \neq 0$, the fundamental control law exists. Because $\boldsymbol{J}$ is a symmetric positive matrix, condition $\det \boldsymbol{B} \neq 0$ is equivalent to

$$\det \boldsymbol{G} = q_{e,0} \neq 0. \tag{23}$$

The equilibrium point of system (18) is represented by two sets of quaternions: $\boldsymbol{Q}_{+1}(+1,\ 0,\ 0,\ 0)$ and $\boldsymbol{Q}_{-1}(+1,\ 0,\ 0,\ 0)$. Most controllers only consider $\boldsymbol{Q}_{+1}$ as the equilibrium point, even if the current attitude is close to $\boldsymbol{Q}_{-1}$ [15]. Then, the rotation angles will be larger than π radians, this is known as the unwinding phenomenon [16].

The phenomenon means that $q_{e,0}$ will equal zero, but $q_{e,0} = 0$ means that the fundamental control law does not exist. Thus, the control law and the phenomenon cannot coexist. Because $q_{e,0} = 0$ is avoidable, the following work will provide two ways to hold $q_{e,0} \neq 0$.

3.2 Disturbance Estimation

Eq. (20) is an ideal control law. Unfortunately $\boldsymbol{g}_d$ is unknown. Thus, an assumption and an observer are introduced to estimate $\boldsymbol{g}_d$.

Assumption 1 *$\boldsymbol{g}_d$ is Lipschitz. In other words, there is a positive real number d_1 such that $\dot{\boldsymbol{g}}_d^{\mathrm{T}}\dot{\boldsymbol{g}}_d \leqslant d_1$.*

Then, the following nonlinear disturbance observer is employed [17]:

$$\dot{\boldsymbol{s}} = -k\boldsymbol{s} - k\left(\boldsymbol{g} + \boldsymbol{B}\boldsymbol{u} + k\dot{\boldsymbol{q}}_e\right), \tag{24}$$

$$\hat{\boldsymbol{g}}_d = \boldsymbol{s} + k\dot{\boldsymbol{q}}_e, \tag{25}$$

where $\boldsymbol{s} \in \mathbb{R}^3$ is the state of the nonlinear disturbance observer, $\hat{\boldsymbol{g}}_d \in \mathbb{R}^3$ is used to observe $\boldsymbol{g}_d$, $k = \frac{1+\mu}{2}$, and μ is a scalar parameter.

Based on Eqs. (24) and (25), Eq. (20) is updated:

$$\boldsymbol{u} = -\boldsymbol{B}^{-1}\left(\boldsymbol{g} + \hat{\boldsymbol{g}}_d + \boldsymbol{A}_{0\sim1}\boldsymbol{q}_e^{(0\sim1)} + \sum_{i=1}^{n}\boldsymbol{v}_i\right). \tag{26}$$

3.3 Design of Additional Function $\boldsymbol{v}_i$

This subsection deals with the estimated error between the observed and the actual values of $\boldsymbol{g}_d$, and then the saturation effects are considered. Thus, Eq. (19) is updated as follows:

$$\ddot{\boldsymbol{q}}_e = \boldsymbol{g} + \boldsymbol{g}_d + \boldsymbol{B}\boldsymbol{u} + \boldsymbol{B}\Delta\boldsymbol{u}, \tag{27}$$

where $\Delta\boldsymbol{u} = \mathrm{sat}(\boldsymbol{u}) - \boldsymbol{u}$,

$$\mathrm{sat}(\boldsymbol{u}) = \left[\begin{array}{ccc} \mathrm{sat}(u_1) & \mathrm{sat}(u_2) & \mathrm{sat}(u_3) \end{array}\right]^{\mathrm{T}}, \tag{28}$$

and

$$\mathrm{sat}(u_i) = \begin{cases} u_{max} & u_i \geqslant u_{max}, \\ u_i & -u_{max} < u_i < u_{max},\ i = 1 \sim 3, \\ -u_{max} & u_i \leqslant -u_{max}. \end{cases} \tag{29}$$

To deal with the error between the estimated and the actual values of $\boldsymbol{g}_d$, an assumption and an adaptive system are employed [18, 19].

Assumption 2 *There exist two positive real numbers δ_0 and δ_1 such that $\| \boldsymbol{e}_{gd} \| \leqslant \delta_0$ and $\| \dot{\boldsymbol{e}}_{gd} \| \leqslant \delta_1, \forall\, t \geqslant 0$, where $\boldsymbol{e}_{gd} = \boldsymbol{g}_d - \hat{\boldsymbol{g}}_d$.*

$$\dot{\hat{\boldsymbol{\delta}}} = -2k\hat{\boldsymbol{\delta}} + P_L^{\mathrm{T}}\boldsymbol{q}_e^{(0\sim1)}, \tag{30}$$

where $\boldsymbol{P}_L \in \mathbb{R}^{6\times3}$ is a designed matrix, and $\hat{\boldsymbol{\delta}} \in \mathbb{R}^3$ is the state of the adaptive system.

Furthermore, input saturation is inevitable. An auxiliary system is designed to mitigate the saturation effects [20]:

$$\dot{\boldsymbol{\xi}} = \begin{cases} -k\boldsymbol{\xi} - \boldsymbol{K}^{\mathrm{T}}\boldsymbol{P}_L^{\mathrm{T}}\boldsymbol{q}_e^{(0\sim1)} \\ -\dfrac{f_q + f_\Delta}{\| \boldsymbol{\xi} \|^2}\boldsymbol{\xi} + \boldsymbol{B}\Delta\boldsymbol{u}, \quad \Delta\boldsymbol{u} \neq 0 \\ \boldsymbol{0}, \qquad\qquad\qquad\quad \|\boldsymbol{\xi}\| < \vartheta\ \&\ \Delta\boldsymbol{u} = 0 \end{cases} \tag{31}$$

where $f_q = \left|\boldsymbol{q}_e^{(0\sim1)^{\mathrm{T}}}\boldsymbol{P}_L\boldsymbol{B}\Delta\boldsymbol{u}\right|$, $f_\Delta = \frac{1}{2}\| \boldsymbol{B}\Delta\boldsymbol{u} \|^2$, $\boldsymbol{\xi} \in \mathbb{R}^3$ is the state of the auxiliary system, ϑ is a positive real number, $\boldsymbol{K} \in \mathbb{R}^{3\times3}$ is a parameter matrix.

Based on adaptive system (30) and auxiliary system (31), Eq. (26) is updated again:

$$\boldsymbol{u} = -\boldsymbol{B}^{-1}\left(\boldsymbol{g} + \hat{\boldsymbol{g}}_d + \boldsymbol{A}_{0\sim1}\boldsymbol{q}_e^{(0\sim1)} + \sum_{i=1}^{2}\boldsymbol{v}_i\right), \tag{32}$$

where

$$\boldsymbol{v}_1 = \hat{\boldsymbol{\delta}}, \tag{33}$$

$$\boldsymbol{v}_2 = -\boldsymbol{K}\boldsymbol{\xi}. \tag{34}$$

The nonlinear disturbance observer is also updated as follows:

$$\dot{\boldsymbol{s}} = -k\boldsymbol{s} - k\left(\boldsymbol{g} + \boldsymbol{B}\mathrm{sat}(\boldsymbol{u}) + k\dot{\boldsymbol{q}}_e\right). \tag{35}$$

Substituting Eqs. (32), (33), and (34) into Eq. (27) yields

$$\ddot{\boldsymbol{q}}_e + \boldsymbol{A}_{0\sim1}\boldsymbol{q}_e^{(0\sim1)} = \boldsymbol{e}_\delta + \boldsymbol{K}\boldsymbol{\xi} + \boldsymbol{B}\Delta\boldsymbol{u}, \tag{36}$$

where $\boldsymbol{e}_\delta = \boldsymbol{e}_{gd} - \hat{\boldsymbol{\delta}}$.

Eq. (36) is rewritten as the following form:

$$\dot{\boldsymbol{q}}_e^{(0\sim1)} = \boldsymbol{\Phi}(\boldsymbol{A}_{0\sim1})\boldsymbol{q}_e^{(0\sim1)} + \left[\begin{array}{c} \boldsymbol{0} \\ \boldsymbol{I} \end{array}\right]\left(\boldsymbol{e}_\delta + \boldsymbol{K}\boldsymbol{\xi} + \boldsymbol{B}\Delta\boldsymbol{u}\right), \tag{37}$$

where

$$\boldsymbol{\Phi}(\boldsymbol{A}_{0\sim1}) = \left[\begin{array}{cc} \boldsymbol{0} & \boldsymbol{I} \\ -\boldsymbol{A}_0 & -\boldsymbol{A}_1 \end{array}\right]. \tag{38}$$

3.4 System Analysis

Some lemmas used for system analysis are presented as follows:

Lemma 1 *[18, 19]: The following condition can be held by assigning the values of $\boldsymbol{A}_i \in \mathbb{R}^{r\times r}$:*

$$\mathrm{Re}\,\lambda_i(\boldsymbol{\Phi}(\boldsymbol{A}_{0\sim n-1})) \leqslant -\frac{\mu}{2}, \quad i = 1, 2, \ldots, n. \tag{39}$$

where $\mu > 0$ is a scalar parameter,

$$\boldsymbol{\Phi}(\boldsymbol{A}_{0\sim n-1}) = \left[\begin{array}{cccc} \boldsymbol{0} & \boldsymbol{I} & & \\ & & \ddots & \\ & & & \boldsymbol{I} \\ -\boldsymbol{A}_0 & -\boldsymbol{A}_1 & \cdots & -\boldsymbol{A}_{n-1} \end{array}\right], \tag{40}$$

and $\boldsymbol{0}$ is a zero matrix.

Thus, there is a positive definite matrix satisfying

$$\begin{aligned} &\boldsymbol{\Phi}^{\mathrm{T}}(\boldsymbol{A}_{0\sim n-1})\boldsymbol{P}(\boldsymbol{A}_{0\sim n-1}) + \boldsymbol{P}(\boldsymbol{A}_{0\sim n-1})\boldsymbol{\Phi}(\boldsymbol{A}_{0\sim n-1}) \\ &\leqslant -\mu\boldsymbol{P}(\boldsymbol{A}_{0\sim n-1}). \end{aligned} \tag{41}$$

Lemma 2 *For any two vectors $\boldsymbol{a}$ and $\boldsymbol{b}$, there holds*

$$\boldsymbol{a}^{\mathrm{T}}\boldsymbol{b} \leqslant \frac{1}{2}\boldsymbol{a}^{\mathrm{T}}\boldsymbol{a} + \frac{1}{2}\boldsymbol{b}^{\mathrm{T}}\boldsymbol{b}. \tag{42}$$

The system analysis including two cases are presented as follows.

Case 1: Saturated case:

A Lyapunov function is defined as follows:

$$V = V_1 + V_2, \tag{43}$$

where

$$V_1 = \frac{1}{2}\left(\boldsymbol{q}_e^{(0\sim1)}\right)^{\mathrm{T}}\boldsymbol{P}(\boldsymbol{A}_{0\sim1})\boldsymbol{q}_e^{(0\sim1)}, \tag{44}$$

$$V_2 = \frac{1}{2}\boldsymbol{e}_{gd}^{\mathrm{T}}\boldsymbol{e}_{gd} + \frac{1}{2}\boldsymbol{e}_\delta^{\mathrm{T}}\boldsymbol{e}_\delta + \frac{1}{2}\boldsymbol{\xi}^{\mathrm{T}}\boldsymbol{\xi}. \tag{45}$$

Taking the derivative of Eq. (44) yields

$$\begin{aligned} \dot{V}_1 =& \frac{1}{2}\left(\dot{\boldsymbol{q}}_e^{(0\sim1)}\right)^{\mathrm{T}}\boldsymbol{P}\boldsymbol{q}_e^{(0\sim1)} + \frac{1}{2}\left(\boldsymbol{q}_e^{(0\sim1)}\right)^{\mathrm{T}}\boldsymbol{P}\dot{\boldsymbol{q}}_e^{(0\sim1)} \\ =& \frac{1}{2}\left(\boldsymbol{\Phi}\boldsymbol{q}_e^{(0\sim1)} + \left[\begin{array}{c} \boldsymbol{0} \\ \boldsymbol{e}_\delta + \boldsymbol{K}\boldsymbol{\xi} + \boldsymbol{B}\Delta\boldsymbol{u} \end{array}\right]\right)^{\mathrm{T}}\boldsymbol{P}\boldsymbol{q}_e^{(0\sim1)} \\ &+ \frac{1}{2}\boldsymbol{q}_e^{(0\sim1)^{\mathrm{T}}}\boldsymbol{P}\left(\boldsymbol{\Phi}\boldsymbol{q}_e^{(0\sim1)} + \left[\begin{array}{c} \boldsymbol{0} \\ \boldsymbol{e}_\delta + \boldsymbol{K}\boldsymbol{\xi} + \boldsymbol{B}\Delta\boldsymbol{u} \end{array}\right]\right) \\ \leqslant& -\frac{\mu}{2}\boldsymbol{q}_e^{(0\sim1)^{\mathrm{T}}}\boldsymbol{P}\boldsymbol{q}_e^{(0\sim1)} + \boldsymbol{q}_e^{(0\sim1)^{\mathrm{T}}}\boldsymbol{P}_L\left(\boldsymbol{e}_\delta + \boldsymbol{K}\boldsymbol{\xi} + \boldsymbol{B}\Delta\boldsymbol{u}\right) \\ =& -\mu V_1 + \boldsymbol{q}_e^{(0\sim1)^{\mathrm{T}}}\boldsymbol{P}_L\left(\boldsymbol{e}_\delta + \boldsymbol{K}\boldsymbol{\xi} + \boldsymbol{B}\Delta\boldsymbol{u}\right). \end{aligned} \tag{46}$$

where $\boldsymbol{P}$ is a parameter matrix satisfying **Lemma 1**, and $\boldsymbol{P}_L = \boldsymbol{P}\left[\boldsymbol{0}\ \boldsymbol{I}\right]^{\mathrm{T}}$.

Differentiating Eq. (45) obtains

$$\dot{V}_2 = \dot{\boldsymbol{e}}_{gd}^{\mathrm{T}}\boldsymbol{e}_{gd} + \boldsymbol{e}_{\delta}^{\mathrm{T}}\dot{\boldsymbol{e}}_{\delta} + \dot{\boldsymbol{\xi}}^{\mathrm{T}}\boldsymbol{\xi}. \tag{47}$$

Substituting Eqs. (44) and (45) into the first derivative of Eq. (43) yields the following inequality:

$$\begin{aligned}\dot{V} \leqslant & -\mu V_1 + \boldsymbol{q}_e^{(0\sim1)^{\mathrm{T}}}\boldsymbol{P}_L\left(\boldsymbol{e}_{\delta} + \boldsymbol{K}\boldsymbol{\xi} + \boldsymbol{B}\Delta\boldsymbol{u}\right) \\ & + \boldsymbol{e}_{\delta}^{\mathrm{T}}\dot{\boldsymbol{e}}_{\delta} + \dot{\boldsymbol{\xi}}^{\mathrm{T}}\boldsymbol{\xi} + \dot{\boldsymbol{e}}_{gd}^{\mathrm{T}}\boldsymbol{e}_{gd} \\ = & -\mu V + \dot{V}_{\delta} + \dot{V}_{\xi} + \dot{V}_{gd},\end{aligned} \tag{48}$$

where

$$\dot{V}_{\delta} = \boldsymbol{q}_e^{(0\sim1)^{\mathrm{T}}}\boldsymbol{P}_L\boldsymbol{e}_{\delta} + \boldsymbol{e}_{\delta}^{\mathrm{T}}\dot{\boldsymbol{e}}_{\delta} + \frac{\mu}{2}\boldsymbol{e}_{\delta}^{\mathrm{T}}\boldsymbol{e}_{\delta}, \tag{49}$$

$$\dot{V}_{\xi} = \boldsymbol{q}_e^{(0\sim1)^{\mathrm{T}}}\boldsymbol{P}_L\left(\boldsymbol{K}\boldsymbol{\xi} + \boldsymbol{B}\Delta\boldsymbol{u}\right) + \dot{\boldsymbol{\xi}}^{\mathrm{T}}\boldsymbol{\xi} + \frac{\mu}{2}\boldsymbol{\xi}^{\mathrm{T}}\boldsymbol{\xi}, \tag{50}$$

$$\dot{V}_{gd} = \dot{\boldsymbol{e}}_{gd}^{\mathrm{T}}\boldsymbol{e}_{gd} + \frac{\mu}{2}{\boldsymbol{e}_{gd}}^{\mathrm{T}}\boldsymbol{e}_{gd}. \tag{51}$$

Substituting Eq. (35) into Eq.(51) yields

$$\begin{aligned}\dot{V}_{gd} = & \boldsymbol{e}_{gd}^{\mathrm{T}}\dot{\boldsymbol{g}}_d - \boldsymbol{e}_{gd}^{\mathrm{T}}\dot{\hat{\boldsymbol{g}}}_d + \frac{2k+1}{2}\boldsymbol{e}_{gd}^{\mathrm{T}}\boldsymbol{e}_{gd} \\ = & \boldsymbol{e}_{gd}^{\mathrm{T}}\dot{\boldsymbol{g}}_d - \boldsymbol{e}_{gd}^{\mathrm{T}}\left(\dot{\boldsymbol{s}} + k\ddot{\boldsymbol{q}}_e\right) + \frac{2k+1}{2}\boldsymbol{e}_{gd}^{\mathrm{T}}\boldsymbol{e}_{gd} \\ = & k\boldsymbol{e}_{gd}^{\mathrm{T}}\left(\boldsymbol{s} + \boldsymbol{B}\mathrm{sat}(\boldsymbol{u}) + \boldsymbol{g} + k\dot{\boldsymbol{q}}_e - \ddot{\boldsymbol{q}}_e\right) \\ & + \boldsymbol{e}_{gd}^{\mathrm{T}}\dot{\boldsymbol{g}}_d + \frac{2k+1}{2}\boldsymbol{e}_{gd}^{\mathrm{T}}\boldsymbol{e}_{gd} \\ = & \boldsymbol{e}_{gd}^{\mathrm{T}}\dot{\boldsymbol{g}}_d + \frac{1}{2}\boldsymbol{e}_{gd}^{\mathrm{T}}\left(\boldsymbol{s} + k\dot{\boldsymbol{q}}_e - \boldsymbol{g}_d\right) \\ = & \boldsymbol{e}_{gd}^{\mathrm{T}}\dot{\boldsymbol{g}}_d - \frac{1}{2}\boldsymbol{e}_{gd}^{\mathrm{T}}\boldsymbol{e}_{gd}.\end{aligned} \tag{52}$$

According to **Lemma 2** and **Assumption 2**, the following inequality is obtained:

$$\dot{V}_{gd} \leqslant \frac{1}{2}\dot{\boldsymbol{g}}_d^{\mathrm{T}}\dot{\boldsymbol{g}}_d \leqslant \frac{d_1}{2}. \tag{53}$$

Substituting Eq. (31) into Eq.(50) obtains

$$\begin{aligned}\dot{V}_{\xi} = & \boldsymbol{q}_e^{(0\sim1)^{\mathrm{T}}}\boldsymbol{P}_L\left(\boldsymbol{K}\boldsymbol{\xi} + \boldsymbol{B}\Delta\boldsymbol{u}\right) - \frac{1}{2}\boldsymbol{\xi}^{\mathrm{T}}\boldsymbol{\xi} - \boldsymbol{f}_q \\ & - \frac{1}{2}\parallel\boldsymbol{B}\Delta\boldsymbol{u}\parallel^2 + \boldsymbol{\xi}^{\mathrm{T}}B\Delta\boldsymbol{u} - \boldsymbol{\xi}^{\mathrm{T}}\boldsymbol{K}^{\mathrm{T}}\boldsymbol{P}_L^{\mathrm{T}}\boldsymbol{q}_e^{(0\sim1)} \\ \leqslant & -\frac{1}{2}\boldsymbol{\xi}^{\mathrm{T}}\boldsymbol{\xi} - \frac{1}{2}\parallel\boldsymbol{B}\Delta\boldsymbol{u}\parallel^2 + \boldsymbol{\xi}^{\mathrm{T}}\boldsymbol{B}\Delta\boldsymbol{u}.\end{aligned} \tag{54}$$

On the basis of **Lemma 2**, the following inequality holds

$$\begin{aligned}\dot{V}_{\xi} \leqslant & -\frac{1}{2}\boldsymbol{\xi}^{\mathrm{T}}\boldsymbol{\xi} - \frac{1}{2}\parallel\boldsymbol{B}\Delta\boldsymbol{u}\parallel^2 + \frac{1}{2}\boldsymbol{\xi}^{\mathrm{T}}\boldsymbol{\xi} + \frac{1}{2}\parallel\boldsymbol{B}\Delta\boldsymbol{u}\parallel^2 \\ = & 0.\end{aligned} \tag{55}$$

A variable is employed $\boldsymbol{\kappa} = \boldsymbol{e}_{gd} - \hat{\boldsymbol{\delta}} - \boldsymbol{e}_{\delta}$, and subsequently there is

$$\begin{aligned}\dot{V}_{\delta} = & \boldsymbol{e}_{\delta}^{\mathrm{T}}\boldsymbol{P}_L^{\mathrm{T}}\boldsymbol{q}_e^{(0\sim1)} + \boldsymbol{e}_{\delta}^{\mathrm{T}}\dot{\boldsymbol{e}}_{\delta} + \frac{2k+1}{2}\boldsymbol{e}_{\delta}^{\mathrm{T}}\boldsymbol{e}_{\delta} \\ = & \boldsymbol{e}_{\delta}^{\mathrm{T}}\left(\boldsymbol{q}_e^{(0\sim1)^{\mathrm{T}}}\boldsymbol{P}_L + \dot{\boldsymbol{e}}_{\delta}\right) + \frac{2k+1}{2}\boldsymbol{e}_{\delta}^{\mathrm{T}}\boldsymbol{e}_{\delta} + 2k\boldsymbol{\kappa}^{\mathrm{T}}\boldsymbol{e}_{\delta} \\ = & \boldsymbol{e}_{\delta}^{\mathrm{T}}\left(\boldsymbol{P}_L^{\mathrm{T}}\boldsymbol{q}_e^{(0\sim1)} - \dot{\hat{\boldsymbol{\delta}}} + \dot{\boldsymbol{e}}_{gd}\right) + \frac{2k+1}{2}\boldsymbol{e}_{\delta}^{\mathrm{T}}\boldsymbol{e}_{\delta} \\ & + 2k\boldsymbol{\kappa}^{\mathrm{T}}\boldsymbol{e}_{\delta} \\ = & \boldsymbol{e}_{\delta}^{\mathrm{T}}\left(\boldsymbol{P}_L^{\mathrm{T}}\boldsymbol{q}_e^{(0\sim1)} - \dot{\hat{\boldsymbol{\delta}}} - 2k\hat{\boldsymbol{\delta}}\right) + \dot{\boldsymbol{e}}_{gd}^{\mathrm{T}}\boldsymbol{e}_{\delta} \\ & + \frac{2k+1}{2}\boldsymbol{e}_{\delta}^{\mathrm{T}}\boldsymbol{e}_{\delta} + 2k(\boldsymbol{e}_{gd}^{\mathrm{T}} - \boldsymbol{e}_{\delta}^{\mathrm{T}})\boldsymbol{e}_{\delta}.\end{aligned} \tag{56}$$

Substituting Eq. (30) into Eq. (56) obtains the following equation:

$$\dot{V}_{\delta} = \dot{\boldsymbol{e}}_{gd}^{\mathrm{T}}\boldsymbol{e}_{\delta} + \frac{2k+1}{2}\boldsymbol{e}_{\delta}^{\mathrm{T}}\boldsymbol{e}_{\delta} + 2k(\boldsymbol{e}_{gd}^{\mathrm{T}} - \boldsymbol{e}_{\delta}^{\mathrm{T}})\boldsymbol{e}_{\delta}. \tag{57}$$

Based on **Lemma 2** and **Assumption 2**, the following inequality holds

$$\dot{V}_{\delta} \leqslant \frac{\delta_1^2 + 2k\delta_0^2}{2}. \tag{58}$$

According to Eqs. (48), (53), (55), and (58), there is

$$\dot{V} \leqslant -\mu V + \epsilon, \tag{59}$$

where $\epsilon = \frac{\delta_1^2 + 2k\delta_0^2 + d_1}{2}$.

Based on the comparison theorem [19], there holds

$$V \leqslant V(0)\exp(-\mu t) + \frac{\epsilon}{\mu}\left(1 - \exp(-\mu t)\right), \tag{60}$$

then,

$$V \leqslant \left(V(0) - \frac{\epsilon}{\mu}\right)\exp(-\mu t) + \frac{\epsilon}{\mu} \to \frac{\epsilon}{\mu},\ t \to \infty. \tag{61}$$

Based on Eq. (61), the states of the controlled system eventually stabilize within the following ellipsoid:

$$\begin{aligned}\Theta_{\mu,\varepsilon}(0) = \{&\boldsymbol{q}_e,\ \boldsymbol{e}_{\delta},\ \boldsymbol{e}_{gd},\ \boldsymbol{\xi} \\ & \left| \boldsymbol{q}_e^{\mathrm{T}}\boldsymbol{P}\left(\boldsymbol{A}\right)\boldsymbol{q}_e + \boldsymbol{e}_{gd}^{\mathrm{T}}\boldsymbol{e}_{gd} + \boldsymbol{e}_{\delta}^{\mathrm{T}}\boldsymbol{e}_{\delta} + \boldsymbol{\xi}^{\mathrm{T}}\boldsymbol{\xi} \leqslant \frac{2\epsilon}{\mu}\right\}.\end{aligned} \tag{62}$$

Case 2: Unsaturated case:

The proof process is similar to the saturated case.

Unwinding-free condition:

According to (61), increasing μ or decreasing ε ensures that V is monotonically decreasing, which leads to the monotone increasing of $q_{e,0}^2$. Hence the unwinding phenomenon can be avoided.

4 Numerical Simulations

The physical parameters, controller parameters, and initial values are shown in Tabs. 1, 2, and 3, respectively.

Figs. 1 and 2 are the time responses of attitude. Although the default target is Q_d, controller (32) still drives the current attitude to the closer one $-Q_d$, which means that controller (32) can avoid the unwinding phenomenon. Fig. 3 shows the time responses of angular velocity. Fig. 4 is about the control

Table 1: Physical Parameters

Quantity	Value
$\boldsymbol{J}$	$\begin{bmatrix} 8.542 & -0.065 & 0.136 \\ -0.065 & 10.767 & -0.198 \\ 0.136 & -0.198 & 8.727 \end{bmatrix}$ kg·m^2
u_{max}	0.2 N·m
$\boldsymbol{d}$	$0.005 \cdot [\sin(0.5t)\ \sin(t)\ \cos(0.5t + \frac{\pi}{3})]^{\mathrm{T}}$ N·m

Table 2: Controller Parameters

Quantity	Value
$\boldsymbol{A}_0$	diag(0.2, 0.2, 0.2)
$\boldsymbol{A}_1$	diag(0.8, 0.8, 0.8)
$\boldsymbol{Q}_d$	(0.3772, 0.4329, -0.6645, -0.4783)
$\boldsymbol{\omega}_d$	(0, 0, 0) rad·s^{-1}
μ	0.7
ϑ	10^{-5}
$\boldsymbol{K}$	diag(0.1, 0.1, 0.1)

Table 3: Initial Values

Quantity	Value
$\boldsymbol{Q}(0)$	(-0.7500, -0.6300, 0.1800, 0.0906)
$\boldsymbol{\omega}(0)$	(0, 0, 0) rad·s^{-1}
$\boldsymbol{s}(0)$	(0, 0, 0)
$\boldsymbol{\xi}(0)$	$(0.5,\ -0.5,\ 0)$
$\hat{\boldsymbol{\delta}}(0)$	(0, 0, 0)

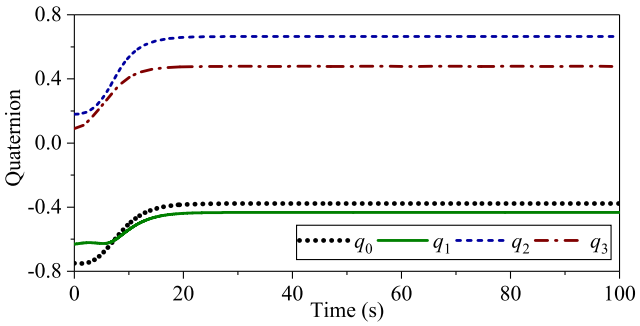

Fig. 1: Time responses of quaternions

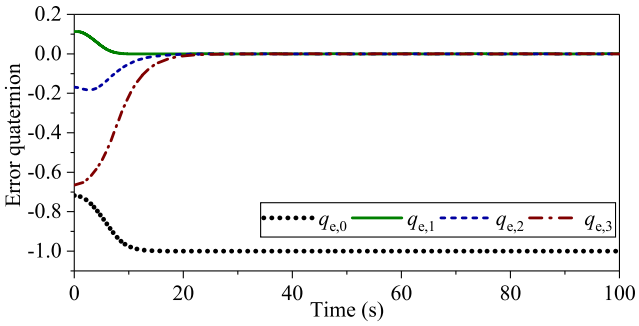

Fig. 2: Time responses of error quaternions

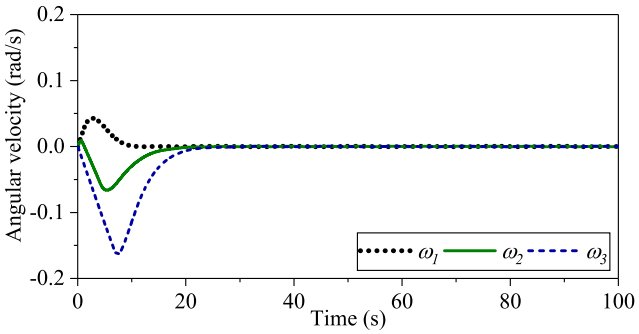

Fig. 3: Time responses of angular velocities

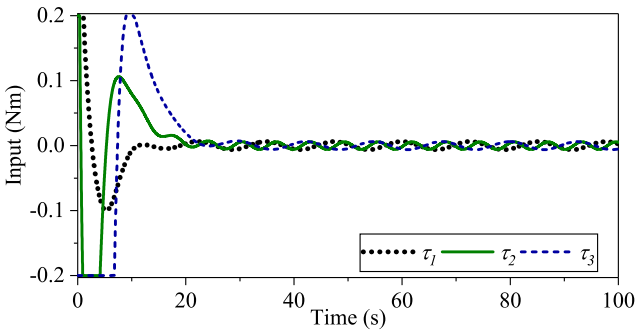

Fig. 4: Torque of control inputs

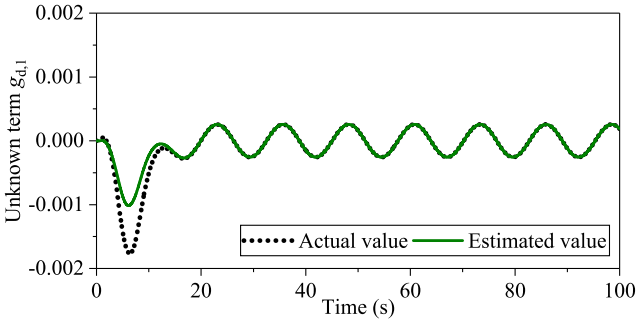

Fig. 5: Actual and estimated values of $g_{d,1}$

input, where the input saturation duration is 10.40 seconds. Figs. 5, 6, and 7 present the actual and estimated values of $\boldsymbol{g}_d$. It is clear that the observer (35) can accurately estimate $\boldsymbol{g}_d$. Fig. 8 is the time responses of the adaptive state. Fig. 9 is the time responses of the auxiliary system state, illustrating that the run time (28.06 seconds) of the auxiliary system (31) far exceeds the saturation duration (10.40 seconds).

5 Conclusion

This work presents an unwinding-free control law and designs an attitude controller for rigid bodies with external disturbances and input saturation. Based on the Lyapunov stability theory and numerical simulations, the present study obtains the following conclusions:

- The fundamental control law realizes unwinding-free performance without the need for additional operations.
- The proposed controller based on the fundamental control law can be unwinding-free even in the presence of

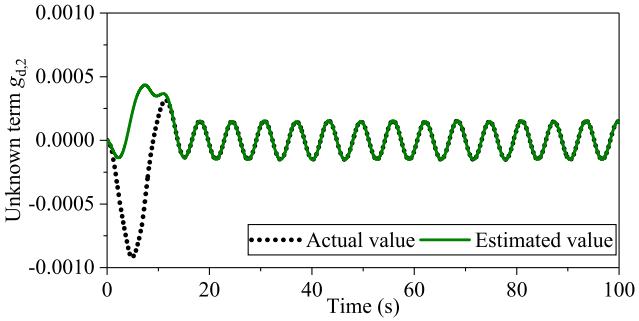

Fig. 6: Actual and estimated values of $g_{d,2}$

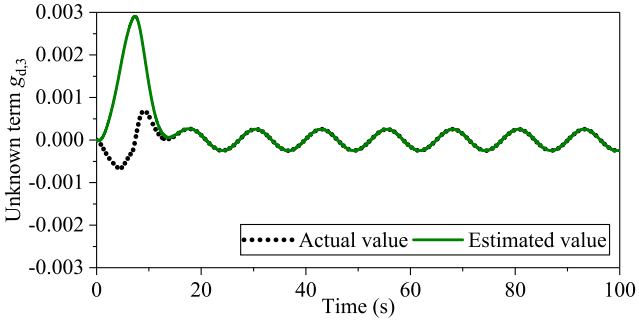

Fig. 7: Actual and estimated values of $g_{d,3}$

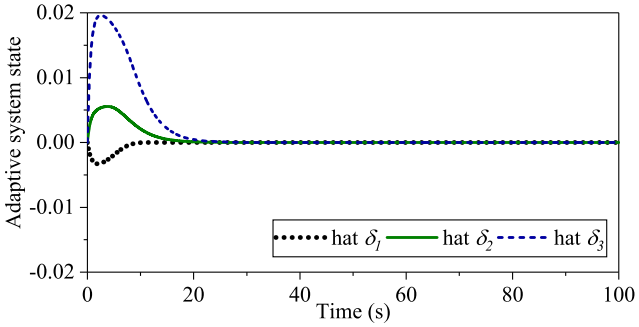

Fig. 8: Time responses of adaptive system states

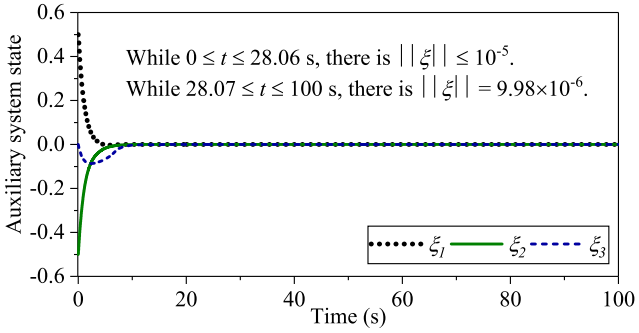

Fig. 9: Time responses of auxiliary system states

external disturbances and input saturation.

References

[1] M. D. Shuster, A survey of attitude representations, *Journal of The Astronautical Sciences*, 41, 439–517, 1993.

[2] S. P. Bhat, and D. S. Bernstein, A topological obstruction to continuous global stabilization of rotational motion and the unwinding phenomenon, *Systems Control Letter*, 39(1): 63–70, 2000.

[3] M. N. Hasan, M. Haris, and S. Qin, Fault-tolerant spacecraft attitude control: A critical assessment, *Progress in Aerospace Sciences*, 130: 100806, 2022.

[4] R. Q. Dong, R. Nagamune, and A. G. Wu, Anti-unwinding nonsingular terminal sliding mode control with attitude maneuver planning for flexible spacecraft, *International Journal of Robust and Nonlinear Control*, 33(3): 2090–2112, 2023.

[5] C. Tan, G. Xu, L. Dong, Y. Xie, Y. He, Y. Hao, and F. Han, Rotation matrix-based finite-time attitude coordinated control for spacecraft, *Advances in Space Research*, 69(2): 976–988, 2022.

[6] Y. Su, Y. Yang, X. Yang, and X. Zhang, Anti-unwinding adaptive super-twisting attitude control for spacecraft, *International Journal of Control*, 2023.

[7] Y. Huang and Z. Meng, Global distributed attitude tracking control of multiple rigid bodies via quaternion-based hybrid feedback, *IEEE Transactions on Control of Network Systems*, 8(1): 367–378, 2021.

[8] Q. Hu, L. Li, and M. I. Friswell, Spacecraft anti-unwinding attitude control with actuator nonlinearities and velocity limit. *Journal of Guidance, Control, and Dynamics*, 38(10): 2042–2050, 2015.

[9] Z. Su, X. Lin, B. Huang, D. Zhao, and H. Sun, Improved dynamic event-triggered anti-unwinding control for autonomous underwater vehicles, *Ocean Engineering*, 272: 113619, 2023.

[10] G. R. Duan, High-order fully actuated system approaches: Part I. Models and basic procedure, *International Journal of Systems Science*, 52(2): 422–435, 2021.

[11] G. R. Duan, High-order fully actuated system approaches: Part II. Generalized strict-feedback systems, *International Journal of Systems Science*, 52(3): 437–454, 2021.

[12] K. K. Zhang, B. Zhou, H. Jiang, and G. R. Duan, Finite-time control of a class of nonlinear underactuated systems with application to underactuated axisymmetric spacecraft, *IEEE Transactions on Aerospace and Electronic Systems*, 59(5): 7061–7071, 2023.

[13] F. Z. Xiao and L. Q. Chen, Fully actuated systems in terms of quaternions for spacecraft attitude control, *Acta Astronautica*, 209: 1–5, 2023.

[14] K. K. Zhang, B. Zhou, and G. R. Duan, Prescribed-time input-to-state stabilization of normal nonlinear systems by bounded time-varying feedback, *IEEE Transactions on Circuits and Systems I: Regular Papers*, 69(9): 3715–3725, 2022.

[15] S. M. Amrr, M. Nabi, and P. M. Tiwari, A fault-tolerant attitude tracking control of spacecraft using an anti-unwinding robust nonlinear disturbance observer, *Proceedings of the Institution of Mechanical Engineers, Part G: Journal of Aerospace Engineering*. 233(16): 6005–6018, 2019.

[16] X. Shao, Q. Hu, D. Li, Y. Shi, and B. Yi, Composite adaptive control for anti-unwinding attitude maneuvers: An exponential stability result without persistent excitation, *IEEE Transactions on Aerospace and Electronic Systems*, 59(2): 1051–1066, 2023.

[17] L. Sun and Z. Zheng, Disturbance-observer-based robust backstepping attitude stabilization of spacecraft under input saturation and measurement uncertainty, *IEEE Transactions on Industrial Electronics*, 64(10): 7994–8002, 2017.

[18] G. R. Duan, High-order fully actuated system approaches: Part IV. Adaptive control and high-order backstepping, *International Journal of Systems Science*, 52(5): 972–989, 2021.

[19] G. R. Duan, High-order fully actuated system approaches: Part V. Robust adaptive control, *International Journal of Systems Science*, 52(10): 2129–2143, 2021.

[20] F. Z. Xiao and L. Q. Chen, Saturated adaptive control for high-order fully actuated systems with an extended state, *International Journal of Systems Science*, 2024 (Online).

Proceedings of the 3rd Conference on Fully Actuated System Theory and Applications
May 10-12, 2024, Shenzhen, China

Reinforcement learning-based three-dimensional cooperative guidance law

Zhen Gu[1], Zeqi Zhang[1], Honglong Kang[1], Jianfeng Li[1], Keyuan Yue[2*], Shenmin Song[1]

1. Center for Control Theory and Guidance Technology, Harbin Institute of Technology, Harbin 150001, China
E-mail: guzhen@stu.hit.edu.cn, 1412979100@qq.com, kanghonglong@stu.hit.edu.cn, 20B904036@stu.hit.edu.cn, songshenmin@hit.edu.cn

2. Science and Technology on Complex System Control and Intelligent Agent Cooperation Laboratory，Beijing 100074，China
E-mail: yuekeyuan@buaa.edu.cn

Abstract: An innovative three-dimensional cooperative guidance law for striking stationary target, based on proximal policy optimization (PPO), is introduced. This novel guidance law directly correlates engagement state information with the navigation ratio of proportional navigation guidance (PNG). Initially, the cooperative homing guidance problem is transformed into a Markov decision process, and the reward function incorporates considerations for the zero-effort-miss (ZEM) and the consensus error of time-to-go. Subsequently, the cooperative homing guidance problem is transposed into the framework of reinforcement learning (RL). Ultimately, the effectiveness of the cooperative homing guidance solution is validated through numerical simulations, encompassing agent model training and Monte Carlo cases.

Key Words: Reinforcement learning, Cooperative guidance law, Three dimensional

1 Introduction

In the practical design of missile guidance laws, proportional navigation guidance (PNG) plays a pivotal role in targeting to achieve ZEM. In recent years, there has been a growing emphasis on guidance laws addressing impact angle constraint and impact time constraint. The inclusion of impact time constraint enables saturation attacks against air defense systems, while incorporating impact angle constraint enhances overall attack effectiveness.

The objective of Proportional Navigation Guidance (PNG) is to minimize the rate of change of line-of-sight (LOS) between the missile and the target. Extensive research efforts have been dedicated to PNG for engaging both stationary and maneuvering targets. To address the impact time constraint problem, an effective approach is to incorporate time-to-go considerations into the guidance law design. This strategy has led to the development of a diverse range of guidance laws. In[1], a 3D cooperative guidance law, integrating PNG with a time-biased feedback, was introduced to address the impact time constraint problem. In[2], a guidance law that incorporates PNG and a time error feedback term was employed to achieve coordinated attacks involving multiple missiles. In addition to guidance laws relying on time-to-go estimation, the impact time constraint (ITC) can also be addressed through the missile state profile [3].

Beyond these PNG-based guidance laws, significant efforts have been devoted to addressing ITC through advanced control techniques [4]. Optimal guidance is also widely utilized for ITC. In [5], an optimal guidance law based on time-to-go was introduced. Utilizing the state-dependent Riccati equation (SDRE) technique, [6] and [7] proposed suboptimal Impact Angle Control Guidance laws. Through the estimation of time-to-go, [8] introduced a nonsingular sliding-mode guidance law to solve ITC. In [9] and [10], impact time control guidance was presented based on Lyapunov, providing an exact closed-form solution for impact time guidance. Finite-time stability of multi-agent consensus error was designed in [11] for cooperative interception. Additionally, [12] proposed a new sliding surface that does not require the estimation of time-to-go.

As a prominent branch of intelligent control, Artificial Intelligence (AI) algorithms, particularly those represented by Reinforcement Learning (RL), have found extensive applications in the field of homing guidance. To showcase the potential of RL, [13] proposed an intelligent guidance algorithm based on the reward of miss distance, energy, and time. Subsequently, an impact angle guidance law considering a field-of-view constraint was developed in [14] based on RL. This guidance law comprises PNG and two bias terms generated by agents. A Deep Deterministic Policy Gradients (DDPG)-based guidance law was introduced in [15] to intercept maneuvering targets, with this method mapping the states to the acceleration of the missile. In [16], a novel 3D guidance law, considering the field-of-view, was developed to address ITC by training hyperparameters based on RL to optimize energy.

The aforementioned investigations highlight the need for further exploration of reinforcement learning applications in homing guidance. To the best of our knowledge, there have been no papers designed to develop three-dimensional centralized cooperative guidance laws based on RL without resorting to numerical iterations and hyperparameter selection. Consequently, this paper introduces a novel centralized cooperative guidance law with the framework of RL.

The main contributions of this paper are summarized as follows. Firstly, the proposed guidance law establishes a framework for addressing ITC using RL. The problem considered in this paper represents an end-to-end mapping challenge, as the essence of the cooperative guidance law

*This work is supported by Aeronautical Science Foundation of China under Grant 20170112012, 20180112003.

using PNG is to adjust the navigation ratio to maintain consistent time-to-go. Secondly, the trained agent model can be easily applied to any other scenarios without the need for retraining the model or fine-tuning hyperparameters, thanks to the fact that the states of the agent involve relative parameters in the homing guidance process.

The subsequent sections of this paper are organized as follows: Section 2 presents the three-dimensional engagement model and provides some preliminaries. In Section 3, the guidance objectives are outlined, and the Proximal Policy Optimization (PPO) agent for cooperative homing guidance is introduced. Section 4 details the training process of the guidance law and presents the results of numerical simulations to validate the performance of the proposed guidance law. The paper concludes with Section 5, summarizing the findings and presenting conclusions.

2 Problem formulation and Preliminary

2.1 Three-Dimensional Engagement Model

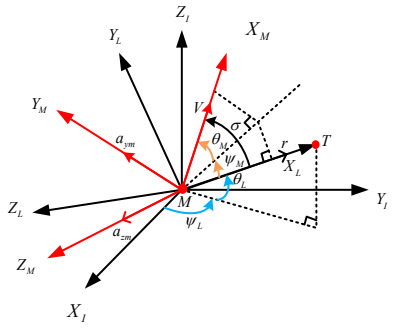

Fig. 1: Three-dimensional engagement geometry

The equation of motion for the missile and a stationary target in three-dimensional relative kinematics can be formulated as follows:

$$\dot{r}_i = -V_{M_i}\cos\theta_{M_i}\cos\psi_{M_i} \tag{1}$$

$$r_i\dot{\theta}_{L_i} = -V_{M_i}\sin\theta_{M_i} \tag{2}$$

$$r_i\cos\theta_{L_i}\dot{\psi}_{L_i} = -V_{M_i}\cos\theta_{M_i}\sin\psi_{M_i} \tag{3}$$

$$\dot{\theta}_{M_i} = \frac{a_{zm_i}}{V_{M_i}} - \dot{\theta}_{L_i}\cos\psi_{M_i} - \dot{\psi}_{L_i}\sin\theta_{L_i}\sin\psi_{M_i} \tag{4}$$

$$\dot{\psi}_{M_i} = \frac{a_{ym_i}}{V_{M_i}\cos\theta_{M_i}} - \dot{\theta}_{L_i}\sin\psi_{M_i}\tan\theta_{M_i} - \dot{\psi}_{L_i}\cos\theta_{L_i} + \dot{\psi}_{L_i}\sin\theta_{L_i}\cos\psi_{M_i}\tan\theta_{M_i} \tag{5}$$

where i represents the ith missile. The velocity of the ith missile is denoted as V_{M_i}, which is supposed to be constant. The relative distance between the ith missile and the target is denoted by r_i. The inertial frame, LOS frame and velocity frame are represented by $X_IY_IZ_I$, $X_LY_LZ_L$ and $X_MY_MZ_M$, respectively. The a_{ym_i} and a_{zm_i} denote the guidance command along MY_M and MZ_M axes, respectively. The θ_{L_i} and ψ_{L_i} represent the elevation and azimuth LOS angles. The leading angles in pitch and yaw directions and the total leading angle are represented by θ_{M_i}, ψ_{M_i} and σ_i, respectively.

The geometric relation between θ_{M_i}, ψ_{M_i} and σ_i can be formulated as

$$\cos\sigma_i = \cos\theta_{M_i}\cos\psi_{M_i} \tag{6}$$

2.2 Reinforcement Learning

Reinforcement learning is a framework for mapping agent states to actions. The interaction between the environment and the agent is often modeled as a Markov decision process (MDP), which is composed of the state space S, the action space A, and the reward $R: S\times A\to R$.

Reinforcement learning algorithms are generally categorized into value function and policy gradient approaches. PPO belongs to the policy gradient category and utilizes an actor-critic structure. This structure comprises an actor and a critic. PPO, as a deep reinforcement learning method based on the policy gradient algorithm, is well-suited for the cooperative guidance law in this paper due to its excellent performance and fast convergence. The architecture of PPO is illustrated in Fig. 2.

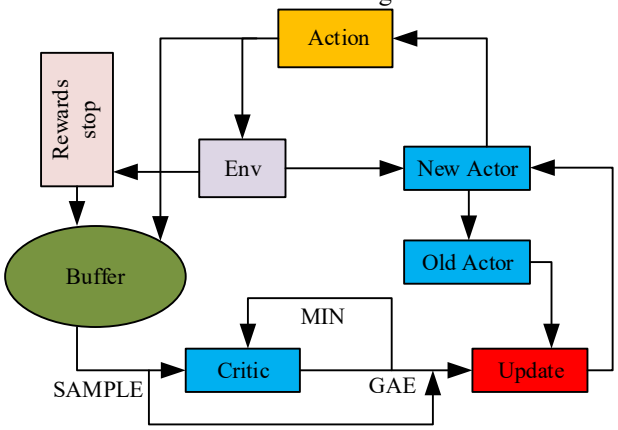

Fig. 2: Framework of PPO

The PPO algorithm employs an 'advantage' function to assess the relative advantage of taking an action in a state that yields high returns. The 'advantage' function is defined as follows:

$$A(s_t,a_t) = Q(s_t,a_t) - V(s_t) \tag{7}$$

where $Q(s_t,a_t)$ represents the action value function for taking action a_t in state s_t, signifying the expected benefit derived from that action a_t. Meanwhile, $V(s_t)$ represents the state value function in state s_t, reflecting the anticipated benefit in the current state s_t. The 'advantage' function

gauges the benefit of choosing the current action in the present state relative to other potential actions. A positive value for $A(s_t,a_t)$ implies that adopting the current action a_t is more advantageous. In this paper, the assessment of the 'advantage' function is conducted through temporal difference error, calculated as:

$$A(s_t,a_t)=r_t+\gamma V^{\pi}(s_{t+1})-V^{\pi}(s_t) \tag{8}$$

where $V^{\pi}(s_{t+1})$ and $V^{\pi}(s_t)$ are computed by the critic network, while r_t represents the reward function.

The update of the critic network is the same as the traditional Actor-Critic (AC) algorithm, but the actor network adopts new ideas for parameter updating. The PPO algorithm introduces a ratio to describe the difference between the old and new strategies, as expressed in:

$$r_t(\theta)=\frac{\pi_\theta(a_t|s_t)}{\pi_{\theta k}(a_t|s_t)} \tag{9}$$

Then, θ is to update to maximize the following equation:

$$J^{PPO}(\theta)=\hat{E}_t\left[\min\left(r_t(\theta)\hat{A}_t,clip\left(r_t(\theta),1-\varepsilon,1+\varepsilon\right)\hat{A}_t\right)\right] \tag{10}$$

where θ is policy parameter, $r_t(\theta)$ is the probability ratio of new policy to the previous policy, $\hat{A}_t$ is an "advantage" function at time t, ε is hyperparameter and $\hat{E}_t$ is empirical expectation.

2.3 Explanation of time-to-go

Under the assumption that $\sin\sigma=\sigma+O(\sigma^3)$, $\cos\sigma=1-\sigma^2/2+O(\sigma^4)$, a widely adopted formulation for calculating the time-to-go in PNG is expressed as follow:

$$t_{go}=\frac{r}{V_M}\left(1+\frac{\sigma^2}{2(2N-1)}\right) \tag{11}$$

where N is navigation ratio.

3 RL Homing Guidance Law

3.1 Objective of design

Assuming that n missiles exchange coordinate variables with each other to attack the target simultaneously, the time-to-go is considered as a coordinate variable for designing the law.

$$t_{go_i}=\frac{r_i}{V_{M_i}}\left(1+\frac{\sigma_i^2}{2(2N_i-1)}\right) \tag{12}$$

In (12), i represents the ith missile. The consensus error of the ith missile is defined as follows:

$$\xi_i=\sum_{j=1}^{n}a_{ij}\left(t_{go_j}-t_{go_i}\right),i=1,2,\cdots,n \tag{13}$$

Next the objective of designing the cooperative guidance is to develop a guidance law that ensures

$$\xi_i\to 0,r_i\to 0 \tag{14}$$

Then, n missiles will simultaneously attack the target.

3.2 PPO for cooperative homing guidance

3.2.1 Learning strategy

The command of the guidance law is structured as

$$a_{ym_i}=-\bar{N}_i\frac{V_{m_i}^2}{r_i}\sin\psi_{m_i} \tag{15}$$

$$a_{zm_i}=-\bar{N}_i\frac{V_{m_i}^2}{r_i}\sin\theta_{m_i}\cos\psi_{m_i} \tag{16}$$

where $\bar{N}_i$ is the navigation ratio of PNG, $\bar{N}_i$ will be designed using RL.

3.2.2 MDP for cooperative homing guidance

The cooperative homing guidance process involving the missile and the target is modeled as a MDP. We use the variables r_i, σ_i, and tgo_i to define the state space, which can be expressed as:

$$S=\left[r_1,\sigma_1,tgo_1,r_2,\sigma_2,tgo_2,r_3,\sigma_3,tgo_3\right] \tag{17}$$

where we set n to 3, indicating the design of cooperative homing guidance for coordinating the attack of 3 missiles on a target simultaneously. S represents the state space in the RL problem we design. Additionally, we normalize the state space S by dividing it by the initial value.

$$S=\left[\frac{r_1}{r_{1_0}},\frac{\sigma_1}{\sigma_{1_0}},\frac{tgo_1}{tgo_{1_0}},\frac{r_2}{r_{2_0}},\frac{\sigma_2}{\sigma_{2_0}},\frac{tgo_2}{tgo_{2_0}},\frac{r_3}{r_{3_0}},\frac{\sigma_3}{\sigma_{3_0}},\frac{tgo_3}{tgo_{3_0}}\right] \tag{18}$$

The PPO algorithm is highly effective in addressing continuous action problems. Since the control mode of the missile is continuous, the action space in the MDP is also continuous. In PNG, the trajectory becomes curved as the navigation ratio increases, and more curved as the navigation ratio decreases. By adjusting the navigation ratio, it is possible to coordinate multiple missiles to attack the target simultaneously. Therefore, we utilize PPO to obtain the navigation ratios for three missiles. The output of PPO consists of three action values mapped by each state, as shown in the following equation:

$$A=\left[N_1,N_2,N_3\right],N_1,N_2,N_3\in\left\{-N_{\max},N_{\max}\right\} \tag{19}$$

where, N_1,N_2 and N_3 represent the navigation ratios of PNG for the three missiles.

The design of the reward function is crucial in RL problems. In the design of RL action spaces, the range of the navigation ratio is from negative six to positive six. Therefore, both the consensus error and the miss distance should be taken into account. The reward function is designed as follows:

During interception, a smaller relative distance corresponds to a reduced ZEM. The reward is designed as follows:

$$reward_r_i=\begin{cases}-(\bar{r}_i)^{0.3}, & if\ r_i>1\\ -(\bar{r}_i)^{0.3}+10, & else\end{cases} \tag{20}$$

where $\bar{r}_i=r_i/r_{i0}$, r_{i0} is the initial value of r_i.

To ensure simultaneous attacks on the target, a consensus error reward is necessary. Specifically, it is expressed as:

$$reward_\xi_i=\begin{cases}-10\xi_i, & if\ \xi_i>0.02\\ -10\xi_i+10, & else\end{cases} \tag{21}$$

To sum up, the total reward is as follows:

$$reward = \sum_{i=1}^{3}\left(reward_r_i + reward_\xi_i\right) \tag{22}$$

4 Simulation and Analysis

Measurement errors are not considered in agent training. The equations of motion are solved using the Runge-Kutta method with a fourth order, and the simulation step is set to 0.001s. The simulations are terminated when the distance between the missile and target is less than 1m. The simulation results include agent training, agent validation, and Monte Carlo experiments. Following each simulation result, a detailed analysis is provided.

4.1 Parameter setup

Table 1: Initial conditions of missiles and target

Missile	V_M (m/s)	r (km)	θ_L $(\deg)$	ψ_L $(\deg)$	θ_M $(\deg)$	ψ_M $(\deg)$
1	330	10	-50	-60	20	30
2	320	10	-80	-10	15	40
3	310	10	-10	-20	40	10

Table 2: Architecture of the actor network

Layers	Size	Activation functions
Input of state	9	\
Hidden layer 1	128	Relu
Output	3	Tanh

Table 3: Architecture of the critic network

Layers	Size	Activation functions
Input of state	9	\
Hidden layer 1	128	Relu
Output	3	Tanh

Table 4: The hyperparameters of PPO

Hyperparameter	Parameter value
Maximum iterations	700
Discount factor	0.2
Coefficient of soft update	0.9
Reward coefficient	1,1
Noise attenuation rate	0.01
Value network learning rate	0.0001
Policy network learning rate	0.005

The position of the target is set to $(0,0,0)$, and the initial conditions of the three missiles are provided in Table 1. The maximum lateral accelerations are set to 20g, where g represents the acceleration due to gravity.

The PyTorch framework is utilized for constructing the PPO network. The actor and critic of PPO are implemented using fully connected neural networks. Tables 2 and 3 provide the network structure for the actor and critic. The parameters play a crucial role in agent training, and if they are not set appropriately, the agent is hard to converge. Table 4 summarizes the parameters for PPO agent training.

4.2 Training Simulation

The simulations in this paper were conducted using a computer equipped with a GeForce RTX 3050 GPU and a 3.3GHz CPU. The Python version used is 3.9, and PyTorch version 2.0 was employed for algorithm implementation. Training the agent model for 700 episodes took approximately 1.6 hours.

The changes in reward during agent training are depicted in Fig. 3. The horizontal axis represents the training episodes, and the vertical axis represents the total and average rewards. The solid blue curve in the figure represents the cumulative reward without smoothing, while the dotted red curve depicts the average reward over every 40 episodes. As observed from Fig. 3, the maximum cumulative reward is achieved in the 150th episode. In the early episodes, the reward gradually increases. After 150 iterations, the cumulative reward stabilizes around the maximum value, indicating that the agent has converged.

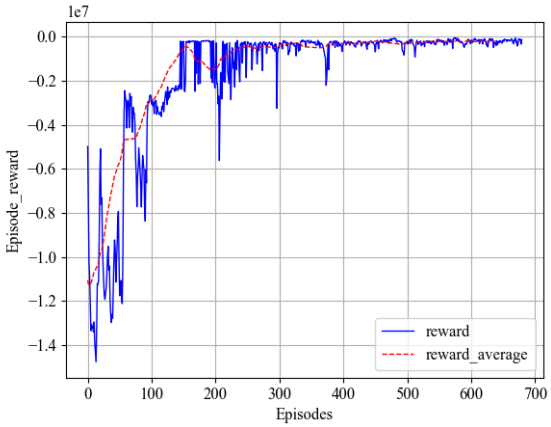

Fig. 3: PPO cumulative reward change

4.3 Test Analysis

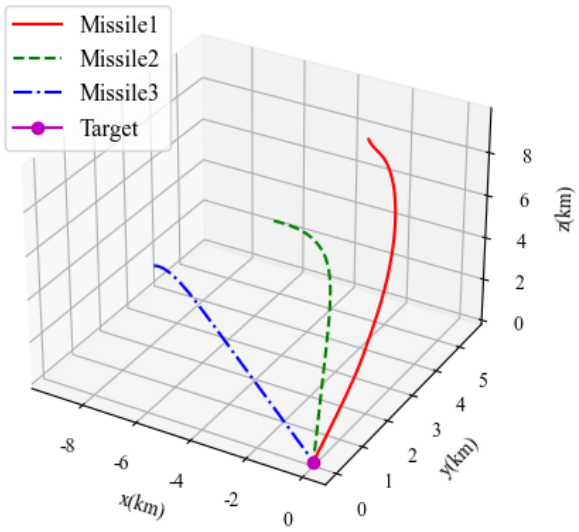

(a) Trajectories

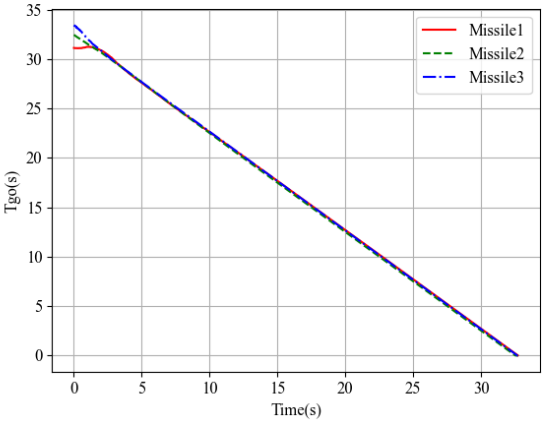

(b) Estimated time to go

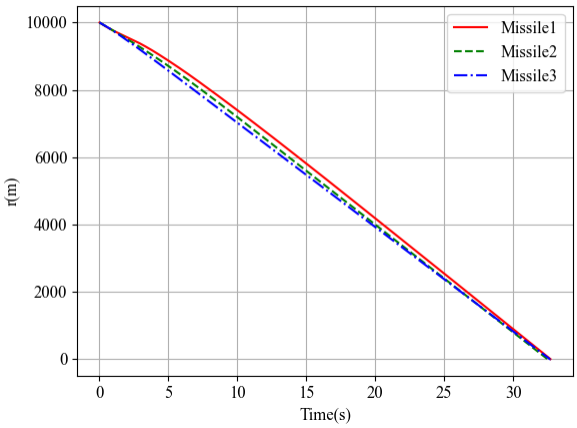

(c) Relative distance between missile and target

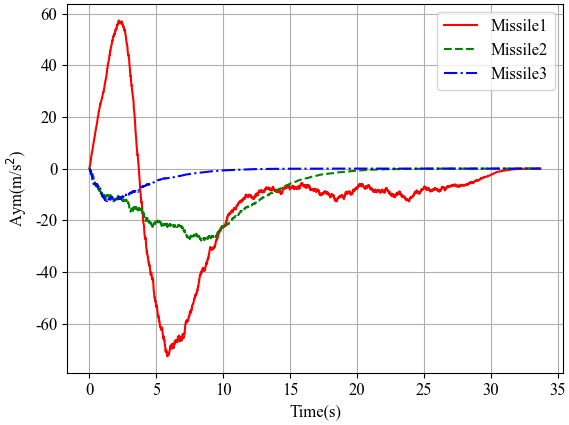

(d) Azimuth command

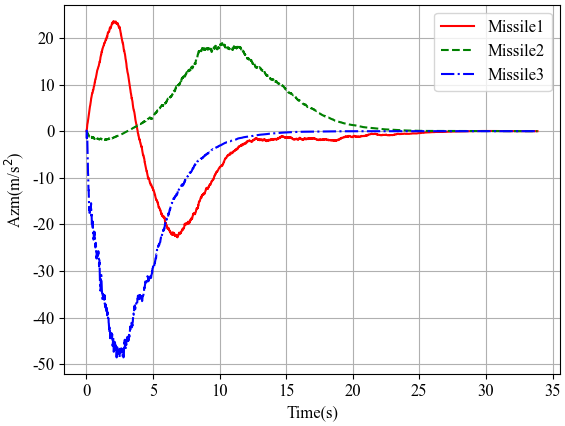

(e) Elevation command

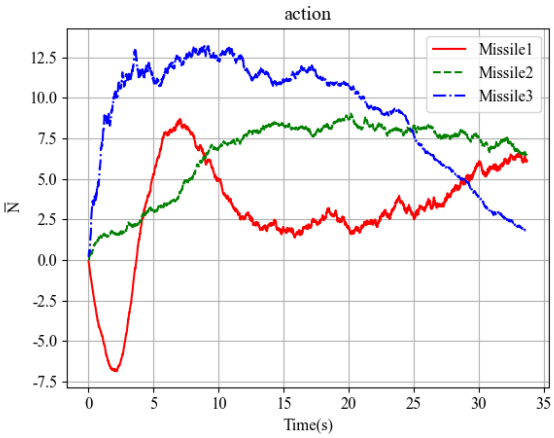

(f) Actions of agent

Fig. 4: PPO simulation results for the same scenario as training

Numerical simulations are conducted to assess the effectiveness of cooperative guidance control using the trained agent. The simulation results are presented in Fig. 4. The terminal miss distance and the time needed to attack are provided in Table 5. Figure 4a illustrates the trajectory curves of the missiles, showing that missile 1 has the most curved trajectory. Figure 4b indicates that the remaining flight time tgo_i remains consistent at around 3 seconds, demonstrating time synchronization among the three missiles. Additionally, Figure 4c displays the relative distance between the missiles and the target, showing that the relative distances reach the same value at almost the same time. Figures 4d and 4e depict the corresponding acceleration curves of the cooperative guidance laws. It's noteworthy that the proposed guidance law can cause the terminal accelerations to converge to zero. Figure 4f illustrates the corresponding navigation ratio curves of the three missiles, indicating that in the initial 10 seconds, the navigation ratio $\bar{N}$ change drastically and stabilize gradually.

Table 5 presents the results of the numerical simulation. The first column indicates the missile number, and the subsequent two columns display the miss distance and running time, respectively. The values of miss distance are all less than 1 meter, indicating successful interceptions. The

maximum consensus error for the three missiles is 0.23 seconds, affirming the success of coordinated attacks.

Table 5: Miss distance and time needed to attack

Missile	r_f (m)	time(s)
1	0.93	32.69
2	0.86	32.46
3	0.95	32.63

4.4 Robustness Against Uncertainties

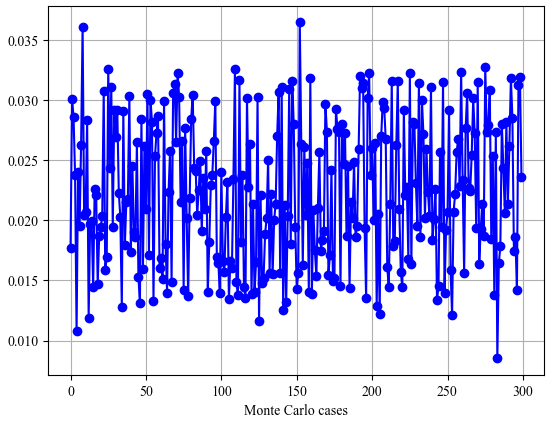

Fig. 5: Maximum consensus error

In this scenario, the robustness of the proposed cooperative guidance law is validated through three hundred Monte Carlo simulations, taking into account autopilot lag and initial errors. A significant advantage of the cooperative guidance law based on reinforcement learning is the adaptability of the trained agent model to any scenario without requiring retraining or adjusting hyperparameters. Leveraging this advantage, the trained agent model is applied to assess its capability to adapt to unfamiliar scenarios.

In these simulations, the autopilot lag is set to 0.2 seconds. Additionally, the initial condition errors are assumed to follow Gaussian distributions with standard deviations of $[-5°, 5°]$ for the initial values of LOS angles, $[-200, 200]$ m for the initial relative range, and $[-10, 10]$ m/s for the missile velocity. The terminal maximum consensus errors of 300 Monte Carlo runs are depicted in Fig. 5.

Figure 5 illustrates that, despite the scenarios differing significantly from the training scenarios, three missiles successfully attack the target simultaneously under the proposed cooperative guidance law. Note that, it is observed that the maximum consensus errors are within 0.038s, meeting the practical implementation requirements.

5 Conclusion

This paper proposes a PPO-based three-dimensional cooperative guidance law designed for stationary targets. The study aims to develop a novel guidance framework based on RL to address time constraints. Numerical simulation results indicate that the trained agent model exhibits excellent performance. Furthermore, Monte Carlo simulation results demonstrate the effectiveness and robustness of the cooperative guidance law.

References

[1] H. L. Kang, P. Y. Wang, S. M. Song. A generalized three-dimensional cooperative guidance law for various communication topologies with field-of-view constraint[J]. Proceedings of the Institution of Mechanical Engineers, Part G: Journal of Aerospace Engineering, 2023: 09544100231153265.

[2] I. S. Jeon, J. I. Lee, M. J. Tahk. Impact-time-control guidance law for anti-ship missiles[J]. IEEE Transactions on control systems technology, 2006, 14(2): 260-266.

[3] M. Snyder, Z. H. Qu, R. Hull, R. Prazenica. Quad-segment polynomial trajectory guidance for impact-time control of precision-munition strike[J]. IEEE Transactions on Aerospace and Electronic Systems, 2016, 52(6): 3008-3023.

[4] H. L. Kang, P. Y. Wang, S. H. Wei, S. M. Song. Three-Dimensional Impact-Time-Constrained Proportional Navigation Guidance Using Range-Varying Gain[J]. Aerospace Science and Technology, 2023: 108419.

[5] C. K. Ryoo, H. Cho, M. J. Tahk. Time-to-go weighted optimal guidance with impact angle constraints[J]. IEEE Transactions on control systems technology, 2006, 14(3): 483-492.

[6] A. Ratnoo, D. Ghose. State-dependent Riccati-equation-based guidance law for impact-angle-constrained trajectories[J]. Journal of Guidance, Control, and Dynamics, 2009, 32(1): 320-326.

[7] C. Y. Wang, W. Dong, J. N. Wang, J. Y. Shan. Nonlinear suboptimal guidance law with impact angle constraint: An SDRE-based approach[J]. IEEE Transactions on Aerospace and Electronic Systems, 2020, 56(6): 4831-4840.

[8] D. Cho, H. J. Kim, M. J. Tank. Nonsingular Sliding Mode Guidance for Impact Time Control[J]. Journal of Guidance Control and Dynamics, 2016, 39(1):1-8.

[9] A. Saleem, A. Ratnoo. Lyapunov-Based Guidance Law for Impact Time Control and Simultaneous Arrival[J]. Journal of Guidance Control Dynamics, 2016, 39(1):1-9.

[10] M. Kim, B. Jung, B. Han, S. Lee and Y. Kim, Lyapunov-based impact time control guidance laws against stationary targets, IEEE Transactions on Aerospace and Electronic Systems, 2015, 51(2): 1111-1122.

[11] J. H. Song, S. M. Song, S. L. Xu. Three-dimensional cooperative guidance law for multiple missiles with finite-time convergence[J]. Aerospace Science and Technology, 2017, 67:193-205.

[12] X. T. Chen, J. Z. Wang. Nonsingular sliding-mode control for field-of-view constrained impact time guidance[J]. Journal of Guidance, Control, and Dynamics, 2018, 41(5): 1214-1222.

[13] S. M. He, H. S. Shin, A. Tsourdos. Computational Missile Guidance: A Deep Reinforcement Learning Approach[J]. Journal of Aerospace Information Systems, 2021(8): 1-12.

[14] S. M. Lee, Y. J. Lee, Y. D. Kim. Impact Angle Control Guidance Considering Seeker's Field-of-View Limit Based on Reinforcement Learning[J]. Journal of Guidance, Control, and Dynamics, 2023: 1-15.

[15] Y. G. Liang, J. Tang, Z. H. Bai. Homing Guidance Law Design against Maneuvering Targets Based on DDPG[J]. International Journal of Aerospace Engineering, 2023.

[16] N. Y. Wang, X. G. Wang, N. G. Cui. Deep reinforcement learning-based impact time control guidance law with constraints on the field-of-view[J]. Aerospace Science and Technology, 2022, 128: 107765.

Proceedings of the 3rd Conference on Fully Actuated System Theory and Applications
May 10-12, 2024, Shenzhen, China

Optimal Control Method for Deployment and Retrieval of Transverse Formation Satellite-Sail Systems

Yini Zhong[1], Minglang Tan[1], Qian Zhang[1], Wenbin Wu[1], Ronghao Yuan[1]

1. Aerospace System Engineering Shanghai, Shanghai 201109
E-mail: iriszhong1999@163.com

Abstract: One of the crucial applications of tether systems is formation flying. In recent research endeavors aimed at meeting the requirements of remote sensing satellites for interferometric measurements of ground targets, a new type of tethered solar sail spacecraft has been proposed. This spacecraft replaces the subsatellites of traditional tethered satellites with solar sail spacecraft, forming a distinctive formation configuration. Specifically, the main satellite is positioned in a sun-synchronous orbit, while the sub solar sail is in a suspended orbit. If the solar sail assumes an appropriate orientation, the main satellite and the solar sail spacecraft, linked by a metallic tether, can move side by side. Consequently, this formation system is termed the "transverse formation." The inter-satellite baseline in this transverse formation system is perpendicular to the satellite's ground track, effectively addressing the periodic trigonometric variations observed in the inter-satellite baseline of traditional flyby formations. This paper delves into the control laws for the deployment and retrieval of tethered solar sails by constructing and resolving an optimal control problem.

Key Words: Flight control; transverse formation; formation deployment; tethered satellite-sail system; solar sail

1 Introduction

Since the concept of satellite formation flying was introduced in the 1990s, it has become a focal point of research in the development of space technology in the 21st century [1]. Currently, satellite formation flying plays a crucial role in space missions such as satellite remote sensing, electronic reconnaissance, and deep space exploration [2].Satellite formation flying involves two or more small satellites maintaining a certain distance while in flight, forming a system with a specific configuration and larger scale. Previous researches extensively studied flyby formations through analysis and numerical methods [3,6]. However, the inter-satellite baseline in such flyby formations exhibits periodic trigonometric variations, which are not conducive to the requirements of Earth observation and other applications of formation flying.

To address this issue, recent research has proposed a novel type of dual-satellite formation flying. Solar sail spacecraft, continuously influenced by solar radiation pressure, could move along specific suspended orbits. Ref. [7] investigates this new type of solar sail system composed of satellites in sun-synchronous orbits and solar sails on parallel-displacement orbits.As shown in Fig. 1, if the solar sail is in the appropriate orientation, the main satellite and the solar sail spacecraft could move side by side. Consequently, this formation system is referred to as the "Transverse Formation." The inter-satellite baseline in this transverse formation system is perpendicular to the satellite's ground track, effectively addressing the problem of periodic trigonometric variations in the inter-satellite baseline observed in traditional flyby formations.

However, due to the typically lightweight nature of solar sails, a single solar sail is usually incapable of carrying a substantial payload. Addressing this issue, [7] delves into a further discussion. Taking inspiration from the structure of tethered satellites, the main satellite is connected to the solar sail using a metallic tether. The primary payload needed for the mission could be carried on the main satellite, and the electrical power required for the camera on the sail could be transmitted through the conductive tether.

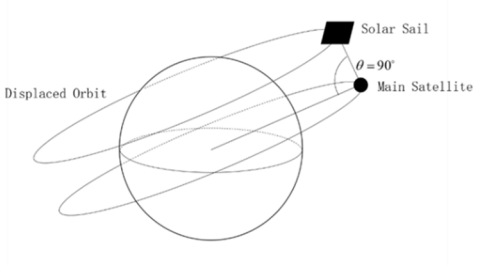

Fig. 1:Transverse formation

Numerous control strategies, including tether length control [8], tether velocity control [9], tension control [10,11], and optimal control [12,13,14], have been designed for tethered satellite deployment and retrieval.Addressing the deployment and retrieval challenges specific to tethered solar sail systems, Ref. [15] proposed a sliding mode controller with a saturation function and discussed deployment strategies for tethered solar sail spacecraft. Ref. [16] introduced an alternative attitude angle definition for system modeling and described a tether velocity control law, discussing deployment and retrieval strategies for tethered solar sail systems.In the study of the deployment and retrieval processes of this novel spacecraft, the design of control laws is subject to various constraints influenced by practical considerations. This paper delves into the control laws for the deployment and retrieval of tethered solar sails under these limiting factors. Treating these practical constraints as constraints in an optimal planning problem,

the paper will construct and resolve an optimal control problem.

2 Dynamics

This paper assumes that the spacecraft operates on a circular sun-synchronous orbit at an altitude of 1000 km. The descending node time is set at 18:00 (i.e., a dawn-dusk orbit). The solar rays are approximated to be nearly perpendicular to the orbital plane, allowing the satellite to continually receive usable solar radiation pressure. Additionally, a tether length of 1000 m is selected for close-range formation and imaging tasks.

2.1 Definition of coordinate systems

The primary coordinate systems defined in this paper are as follows:

1. Inertial Coordinate System (Si):

- Origin Oi coincides with the Earth's center.

- Axis Definition: The xi-axis points from the Earth toward the ascending node of the satellite's orbit, the zi-axis is perpendicular to the orbital plane, and the yi-axis lies within the orbital plane in accordance with the right-hand rule.

2. Orbital Coordinate System (So):

- Origin Oo coincides with the main satellite.

- Axis Definition: The xo-axis points along the Earth toward the main star, the zo-axis aligns with the orbital velocity vector, and the yo-axis follows the right-hand rule.

3. Tethered Solar Sail System Body Coordinate System (Sb):

- Origin Ob coincides with the main satellite.

- The three axes are oriented as shown in Fig.3.

The coordinate transformation relationships between Sb and So are as follows:

$$S_o \xrightarrow{R_y(\alpha)} \bullet \xrightarrow{R_x(\beta)} S_b \tag{1}$$

Finally, to better describe the attitude of the solar sail, a coordinate system is defined for the solar sail body.

Solar Sail Body Coordinate System (Sd):

- Origin Od coincides with the center of the solar sail.

- The zd-axis is opposite to the direction of sunlight incidence on the solar sail. Since the satellite operates in a sun-synchronous orbit, and the Earth-Sun distance is much greater than the orbital radius, the direction of sunlight incidence could be considered parallel to the orbital plane.

- The xd-axis and yd-axis are parallel to the xo-axis and yo-axis, respectively.

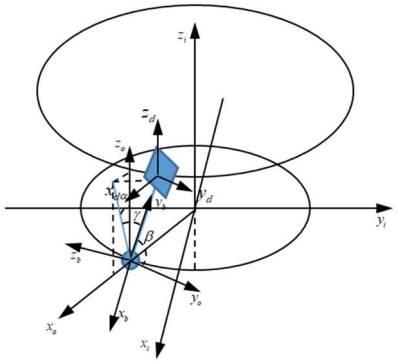

Fig. 2: Definition of coordinate systems for traverse formation

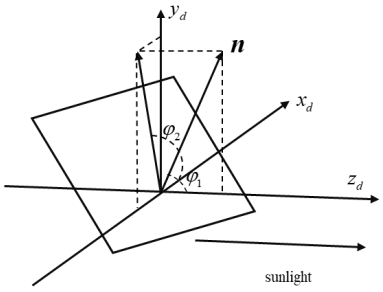

Fig. 3: Solar sail body coordinate system

2.2 Dynamical Model

Assuming a stable deployment process where the solar sail is fully deployed and the tether is fully extended, the control forces in this scenario include solar radiation pressure and tether tension. Due to the minimal impact of the attitude motions of the main satellite and the solar sail on the dynamic effects of tether release, they could be treated as point masses in the dynamic model.

Ref. [16] derived and provided the dynamic equations for the tethered solar sail system. The resulting dynamic equations for each channel in a circular orbit were obtained:

$$\begin{aligned} \ddot{l} = &\left[\left(-\omega_o \cos\beta\cos\alpha + \sin\beta\dot{\alpha}\right)^2\right. \\ &\left.+\left(-\omega_o \sin\alpha + \dot{\beta}\right)^2 + \omega_o^2\left(3\sin^2\beta\sin^2\alpha - 1\right)\right] l + \frac{Q_l}{\bar{m}} \end{aligned} \tag{2}$$

$$\ddot{\alpha} = -2\frac{\cos\beta}{\sin\beta}\dot{\alpha}\dot{\beta} - 2\omega_o\dot{\beta}\cos\alpha + 4\omega_o^2\sin\alpha\cos\alpha - 2\dot{l}l^{-1}\left(-\frac{\cos\alpha\cos\beta}{\sin\beta}\omega_o + \dot{\alpha}\right) + \frac{Q_\alpha}{\bar{m}l^2\sin^2\beta} \tag{3}$$

$$\ddot{\beta} = 2\omega_o\sin^2\beta\cos\alpha\dot{\alpha} - 2\dot{l}l^{-1}\left(-\omega_o\sin\alpha + \dot{\beta}\right) + \sin\beta\cos\beta\left(\dot{\alpha}\right)^2 + \left(4\sin^2\alpha - 1\right)\omega_o^2\sin\beta\cos\beta + \frac{Q_\beta}{\bar{m}l^2} \tag{4}$$

where α, β are attitude angles for satellite-sail system, l is length of tether, ω_o is orbit angular velocity. Q_l, Q_α, and Q_β represent the generalized forces corresponding to each variable.

In the general case, where the mass of the main satellite is much greater than that of the solar sail, i.e., $m_1 \gg m_2$, it could be approximated as $\bar{m} \approx m_2$.

The control forces in the system consist of solar radiation pressure Fs and tether tension Tl. The relationship between generalized forces and control forces is as follows:

$$\begin{cases} Q_l = -T_l + \left[F_s\right]_{yb} \\ Q_\alpha = \left[F_s\right]_{xb} l\sin\beta \\ Q_\beta = \left[F_s\right]_{zb} l \end{cases} \tag{5}$$

In the equations, $\left[F_s\right]_{xb}$, $\left[F_s\right]_{yb}$, $\left[F_s\right]_{zb}$ are the projected components of solar radiation pressure along the axes of the solar sail body coordinate system (Sb), and T_l represents the tension in the tether.

According to Eq. (5), the direct control input variables for the dynamics of the tethered solar sail system are solar radiation pressure and tether tension. However, the precise control of the magnitude of solar radiation pressure on the spacecraft is challenging. The solar sail could change its attitude angles to alter the distribution of solar radiation pressure on its surface. Therefore, the system could be indirectly controlled by manipulating the attitude angles of the solar sail.

To thoroughly investigate the characteristics of solar radiation pressure, in Section 2.1, the solar sail attitude coordinate system $\boldsymbol{S}_d$ was defined. The solar sail attitude angles φ_1, φ_2 are defined as shown in Fig. 3. According to geometric relationships, the normal direction of the sail in the coordinate system $\boldsymbol{S}_d$ could be expressed as:

$$\boldsymbol{n} = \left[\sin\varphi_1\cos\varphi_2 \quad \sin\varphi_1\sin\varphi_2 \quad \cos\varphi_1\right]^{\mathrm{T}} \tag{6}$$

The expression for solar radiation pressure is:

$$\boldsymbol{F}_s = m_2\xi\frac{\mu_s}{r_{sd}^2}\cos^2\varphi_1\boldsymbol{n} \tag{7}$$

In the Eq. (7), μ_s is the solar gravitational constant, and r_{sd} is the distance between the Sun and the sail.

Eq. (7) describes the ideal solar sail model with perfect specular reflection. In reality, considering the effects of diffuse reflection and wrinkles in the solar sail membrane, it is necessary to multiply by an optical efficiency factor κ to study the actual radiation pressure on the solar sail under non-ideal conditions. The expression for solar radiation pressure under non-ideal conditions is:

$$\boldsymbol{F}_s = \kappa m_2\xi\frac{\mu_s}{r_{sd}^2}\cos^2\varphi_1\boldsymbol{n} \tag{8}$$

Due to the much greater distance between the Earth and the Sun (rse) compared to the satellite's orbital radius and the relative distance between the main satellite and the solar sail, $r_{sd} \approx r_{se}$. ξ is the areal density ratio of the solar sail, which is a constant for a specific solar sail. According to Ref. [5], to maintain the displacement of the sun-synchronous orbit, the required solar radiation pressure acceleration magnitude for the solar sail is given by:

$$a_{req} = \bar{\omega}^2 h\left(1 + \left(\frac{\rho}{h}\right)^2\left(1 - \frac{\omega^2}{\bar{\omega}^2}\right)^2\right)^{\frac{3}{2}} \tag{9}$$

In the Eq. (9): $\bar{\omega}=\sqrt{\mu_e / r_d^3}$ is the angular velocity of the solar sail's rotation around the Earth, μ_e is the Earth's gravitational constant, r_d is the distance between the Earth and the solar sail, h is the displacement height, ρ is the orbital radius. From geometric relationships, $r_d = \sqrt{\rho^2 + h^2}$. Considering that $\rho \gg h$, in the study, it could be approximated as $\bar{\omega} \approx \omega_o$.

Eq. (9) describes a solar sail planetary floating orbit influenced solely by planetary gravity and solar radiation pressure. Once the required orbital radius and h are determined, the solar radiation pressure coefficient ξ is also determined. However, for the tether solar sail studied in this paper, the solar sail is additionally affected by tether tension. Therefore, in the study of the tether solar sail system, it is not necessary to design the solar sail coefficient solely based on Eq. (9). In this paper, the selected solar radiation pressure is $F_s = 3\omega_o^2 l_0$ In this case, $\xi = 0.4993$ is required, corresponding to an areal density ratio of $3.0641\mathrm{g/m}^2$.

The coordinate transformation matrix from *Sb* to *Sd* is defined as follows:

$$\boldsymbol{A}_{bd} = \boldsymbol{A}_{bo} \tag{10}$$

Therefore, it follows that:

$$\left[\boldsymbol{F}_s\right]_d = \boldsymbol{A}_{bd}\left[\boldsymbol{F}_s\right]_b \tag{11}$$

That is:

$$\kappa m_2 \xi \frac{\mu_s}{r_{sd}^2}\begin{bmatrix}\cos^2\varphi_1\sin\varphi_1\cos\varphi_2\\ \cos^2\varphi_1\sin\varphi_1\sin\varphi_2\\ \cos^3\varphi_1\end{bmatrix} = \boldsymbol{A}_{ob}\begin{bmatrix}\left[F_s\right]_{xb}\\ \left[F_s\right]_{yb}\\ \left[F_s\right]_{zb}\end{bmatrix} \tag{12}$$

According to the Ref. [7], Eq. (12) could be considered as a nonlinear system of equations. Solving the nonlinear system of equations (12) will yield the required attitude angles for the solar sail. Following the methods in Ref. [7], [15], and [16], this paper utilizes the Newton iteration method to solve the nonlinear system of equations.

3 Design of Control Law

This section will provide corresponding strategies by transforming the deployment and retrieval problem of the tethered solar sail spacecraft into an optimal control problem. Ensuring that the tension in the tether remains positive, i.e., considering $F_{te} > 0$, is treated as a control constraint in the optimal control problem. By solving this optimal control problem, optimal deployment and retrieval trajectories are obtained. These optimal trajectories are then applied as reference tether length trajectories for the deployment and retrieval of the tethered solar sail spacecraft. In general, the continuous form model of an optimal control problem is as follows:

$$J = \Phi\left(\boldsymbol{x}(t_0), t_0, \boldsymbol{x}(t_f), t_f\right) + \int_{t_0}^{t_f} \boldsymbol{f}\left[\boldsymbol{x}(t), \boldsymbol{u}(t), t\right] dt \tag{13}$$

$$\dot{\boldsymbol{x}}(t) = \boldsymbol{g}\left(\boldsymbol{x}(t), \boldsymbol{u}(t), t\right) \tag{14}$$

$$\sigma_{\min} \le \sigma\left(\boldsymbol{x}(t_0), t_0, \boldsymbol{x}(t_f), t_f\right) \le \sigma_{\max} \tag{15}$$

$$\boldsymbol{\gamma}_{\min} \le \boldsymbol{\gamma}\left(\boldsymbol{x}(t), \boldsymbol{u}(t), t\right) \le \boldsymbol{\gamma}_{\max} \tag{16}$$

Where $\boldsymbol{x}$ is the state variable, $\boldsymbol{u}$ is the control variable. Eq. (13) represents the value function of the optimization problem, (14) is the dynamic constraint, (15) is the boundary constraint, and (16) is the path constraint. The above equations are also known as the continuous Bolza problem for optimal control.

The objective function is formulated as follows:

$$J = k_1\dot{\alpha}_f^2 + k_2\dot{\beta}_f^2 + k_3\dot{l}_f^2 \tag{17}$$

The state variables are represented by $\boldsymbol{x}$, and the control variables are denoted by $\boldsymbol{u}$. The dynamic constraints of the system are given by:

$$\begin{cases}
\ddot{l} = \dfrac{m^*}{\tilde{m}}\Big[\left(-\omega_o\cos\beta\cos\alpha + \sin\beta\dot{\alpha}\right)^2 + \left(-\omega_o\sin\alpha + \dot{\beta}\right)^2 \\
\quad + \omega_o^2\left(3\sin^2\beta\sin^2\alpha - 1\right)\Big] l - \dfrac{(2m_1 - m)m_t}{m\tilde{m}}\dfrac{\dot{l}^2}{l}\dfrac{Q_l}{\tilde{m}} \\
\ddot{\alpha} = -2\dfrac{\cos\beta}{\sin\beta}\dot{\alpha}\dot{\beta} - 2\omega_o\dot{\beta}\cos\alpha + 4\omega_o^2\sin\alpha\cos\alpha \\
\quad - 2\dfrac{m_1(m_2 + 0.5m_t)}{mm^*}\dot{l}l^{-1}\left(-\dfrac{\cos\alpha\cos\beta}{\sin\beta}\omega_o + \dot{\alpha}\right) \\
\quad + \dfrac{Q_\alpha}{m^* l^2\sin^2\beta} \\
\ddot{\beta} = 2\omega_o\sin^2\beta\cos\alpha\dot{\alpha} - 2\dfrac{m_1(m_2 + 0.5m_t)}{mm^*}\dot{l}l^{-1}\left(-\omega_o\sin\alpha + \dot{\beta}\right) \\
\quad + \sin\beta\cos\beta\left(\dot{\alpha}\right)^2 + \left(4\sin^2\alpha - 1\right)\omega_o^2\sin\beta\cos\beta + \dfrac{Q_\beta}{m^* l^2}
\end{cases} \tag{18}$$

The relationship between Q_l, Q_α, and Q_β, and the control variable is given by Eq. (6).

$$\begin{bmatrix}\left[F_s\right]_{xb}\\ \left[F_s\right]_{yb}\\ \left[F_s\right]_{zb}\end{bmatrix} = \boldsymbol{A}_{ob} m_2 \xi \frac{\mu_s}{r_{sd}^2}\begin{bmatrix}\cos^2\varphi_1\sin\varphi_1\cos\varphi_2\\ \cos^2\varphi_1\sin\varphi_1\sin\varphi_2\\ \cos^3\varphi_1\end{bmatrix} \tag{19}$$

The state constraints during the deployment process are as follows:

$$\begin{aligned}
&0 \le l \le 1000\text{m}, 0 \le \alpha \le \frac{\pi}{9}, 0 \le \beta \le \frac{\pi}{9} \\
&-0.6 \le \dot{l} \le 0.6\ \text{m/s}, -\frac{\pi}{30} \le \dot{\alpha} \le \frac{\pi}{30}, -\frac{\pi}{30} \le \dot{\beta} \le \frac{\pi}{30}
\end{aligned} \tag{20}$$

The control constraints are as follows

$$0 \le F_{te} \le 1N, -\frac{5\pi}{180} \le \varphi_1, \varphi_2 \le \frac{5\pi}{180} \tag{21}$$

where $l_0 = 8m$, $\dot{l}_0 = 0m/s$, $\alpha_0 = \beta_0 = \frac{\pi}{9}$, $\dot{\alpha}_0 = \dot{\beta}_0 = 0$, $\dot{\alpha}_0 = \dot{\beta}_0 = 0$.

The state constraints for the retrieval process are as follows:

$$\begin{aligned}
&0 \le l \le 1000\text{m}, 0 \le \alpha \le \frac{\pi}{180}, 0 \le \beta \le \frac{\pi}{180} \\
&-0.6 \le l \le 0.6\ \text{m/s}, -\frac{\pi}{1800} \le \dot{\alpha} \le \frac{\pi}{1800}, -\frac{\pi}{1800} \le \dot{\beta} \le \frac{\pi}{1800}
\end{aligned} \tag{22}$$

The initial and final values of the states are: $l_0 = 1000\text{m}$, $\dot{l}_0 = 0\text{m/s}$, $\alpha_0 = \beta_0 = \frac{\pi}{180}$, $\dot{\alpha}_0 = \dot{\beta}_0 = 0$, $\alpha_f = \beta_f = 0$.

4 Simulation and Results

The optimal control problem in this study will be solved using the GPOPS toolbox, an open-source MATLAB optimization package developed by Professor Anil V. Rao's team at the Vehicle Dynamics and Optimization Laboratory (VDOL) at the University of Florida. The GPOPS toolbox is a widely used software package for solving optimal control problems using the pseudospectral method.

The procedure involves first using the GPOPS software to solve the optimal deployment control trajectory designed in this section. The computed trajectory is then utilized as the reference trajectory for tethervelocity deployment, and closed-loop control is applied to the dynamical model. The results of the optimal tethervelocity trajectory and the actual simulation of state changes are compared, as shown in Fig.4 to 5. The simulation results demonstrate that the GPOPS software successfully solved the corresponding optimal problem, and the simulation of the actual model ran smoothly, with the tether being successfully deployed. The corresponding control quantities are shown in the Fig.6 and Fig.7, indicating that limiting tension as a constraint in the optimal planning problem ensures the non-negativity of the tether tension.

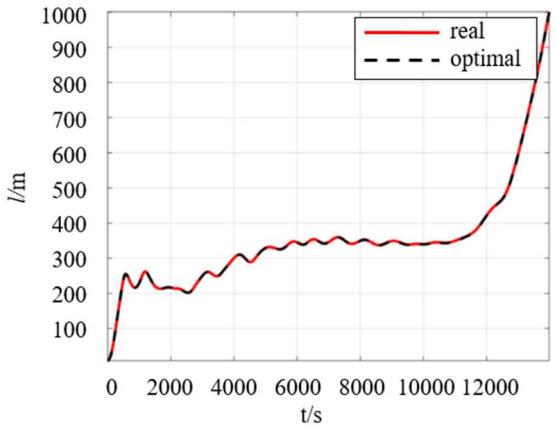

Fig.4:States trajectory during the deployment of a satellite-sail system (length)

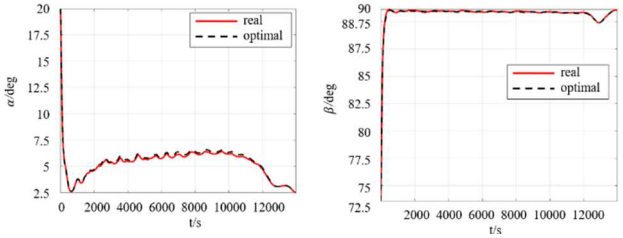

Fig.5:States trajectory during the deployment of a satellite-sail system

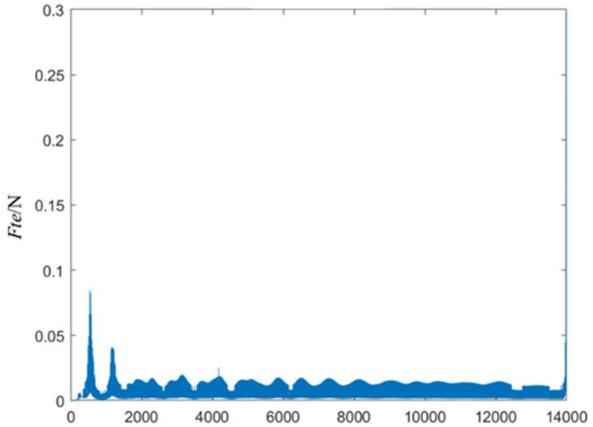

Fig.6:Control inputs trajectory during the deployment of a satellite-sail system (Tension)

The same approach is applied for the retrieval process. GPOPS software is used to solve the optimal retrieval trajectory designed in this section. The computed trajectory is then utilized as the reference trajectory for tethervelocity retrieval, and closed-loop control is applied to the simulation model.

The results of the optimal tethervelocity trajectory and the actual simulation of state changes are compared in Fig.8 to Fig.9. The simulation results demonstrate that the GPOPS software successfully solved the optimal retrieval problem, and the simulation of the actual model ran smoothly, with some angular channel errors within the permissible range for engineering.The tether was successfully retrieved, and the tension in the tether was ensured to be non-negative in Fig.10 and Fig.11, as indicated by the control quantities.

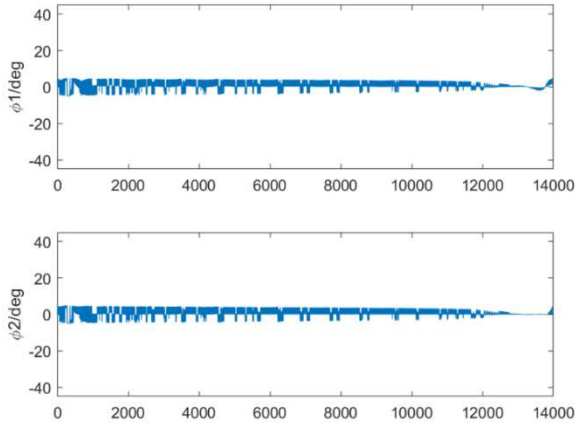

Fig.7:Control inputs trajectory during the deployment of a satellite-sail system (Angle of Solar Sail)

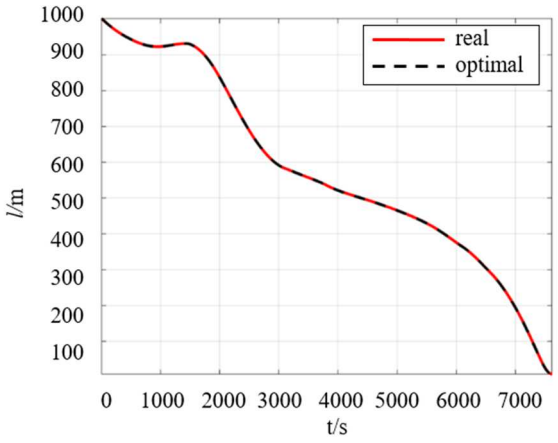

Fig.8:States trajectory during the retrieval of a satellite-sail system (length)

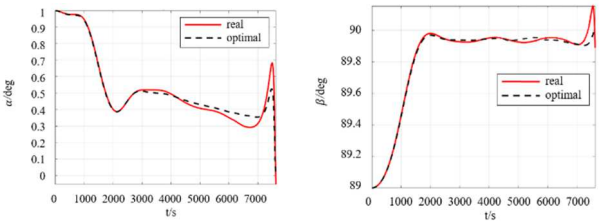

Fig.9:States trajectory during the retrieval of a satellite-sail system

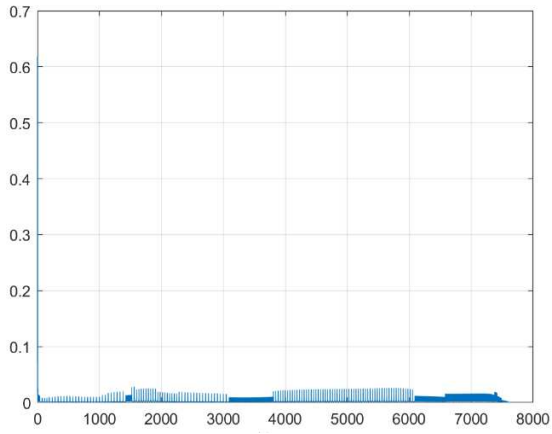

Fig.10:Control inputs trajectory during the retrieval of a satellite-sail system (Tension)

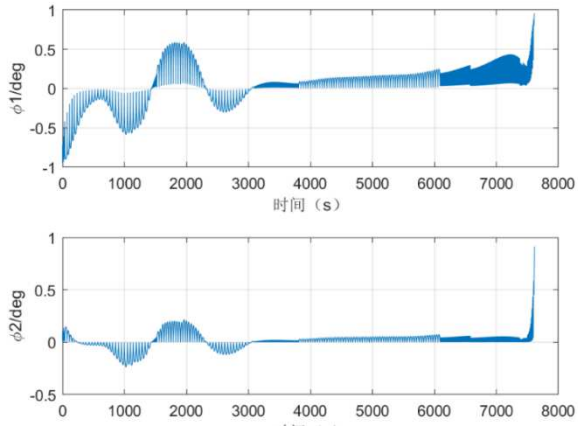

Fig.11:Control inputs trajectory during the retrieval of a satellite-sail system (Angle of Solar Sail)

5 Conclusions

This paper discusses the deployment and retrieval issues of a novel concept spacecraft, the tether-controlled solar sail system. Considering the characteristic that the tethercould only withstand tension and not compression, the goal is to successfully achieve deployment and retrieval under the constraint of limited inputs. In light of this, a tether velocity deployment control law is designed, taking into account the characteristics of the actuation system used in the deployment and retrieval control process of space tether systems. The optimal control method is employed, appropriate optimization criteria are selected, and the constraint of limited inputs is formulated as a constraint in the optimal planning problem. The control method for the deployment and retrieval of the tether-controlled solar sail spacecraft is investigated. Simulation results demonstrate that the spacecraft could successfully and stably deploy and retrieve to the target tether length and configuration, indicating the effectiveness of the proposed control law.

References

[1] K. 6, S. R.Vadali, P.Gurfil, et al.,*Spacecraft formation flying: Dynamics, control and navigation.* Elsevier, 2009.

[2] N. J. Murray, D. A. Keith, L. M. Bland, et al., The role of satellite remote sensing in structured ecosystem risk assessments. *Science of the Total Environment*, 2018, s619-620:249-257.

[3] H. Schaub, K. T.Alfriend, J2 invariant relative orbits for spacecraft formations. *Celestial Mechanics and Dynamical Astronomy*, 2001, 79(2): 77-95.

[4] F. A. Abd El-Salam, I. A. El-Tohamy, M. K. Ahmed, et al, Invariant relative orbits for satellite constellations: A second order theory,*Applied mathematics and computation*, 2006, 181(1): 6-20.

[5] M. Xu, Y. Wang, S. Xu, On the existence of J2 invariant relative orbits from the dynamical system point of view,*Celestial Mechanics and Dynamical Astronomy*, 2012, 112(4): 427-444.

[6] M. Xu, S Xu, J2 invariant relative orbits via differential correction algorithm,*Acta MechanicaSinica*, 2007, 23(5): 585-595.

[7] X. Pan, M. Xu, Y. Dong, et al, Relative Dynamics and Station-Keeping Strategy of Satellite–Sail Transverse Formation,*Journal of Guidance, Control, and Dynamics,* 2020, 43(11): 2156-2164.

[8] A. E. Zakrzhevskii, Method of deployment of a space tethered system aligned to the local vertical,*The Journal of the Astronautical Sciences*, 2016, 63(3): 221-236.

[9] S. Yu, Tethered satellite system analysis (1)—Two-dimensional case and regular dynamics,*Acta Astronautica*, 2000, 47(12): 849-858.

[10] C. C. Rupp, A tether tension control law for tethered subsatellites deployed along local vertical,*NASA STI/Recon Technical Report N*, 1975, 76: 11194.

[11] R. Zhong, S. Xu, Simple tension control strategy for variable length tethered satellite system,*Chinese Space Science and Technology*, 2009, 6.

[12] K. D. Kumar, T.Yasaka, Rotation formation flying of three satellites using tethers,*Journal of Spacecraft and Rockets*, 2004, 41(6): 973-985.

[13] A. Steindl, H. Troger, Optimal control of deployment of a tethered subsatellite, *Nonlinear dynamics,* 2003, 31(3): 257-274.

[14] P. Williams, Optimal deployment/retrieval of tethered satellites,*Journal of Spacecraft and Rockets,* 2008, 45(2): 324-343.

[15] X. Zuo, X. Pan, M. Xu, et al., Deployment strategy for satellite-sail transverse formation,*Acta Astronautica*, 2021.

[16] Y. Zhong, R. Zhong, Dynamics, Deployment and Retrieval Strategy for Satellite-Sail Transverse Formation with Model Inaccuracy,*Aerospace*, 2022, 9(10): 602.

[17] M. A. Patterson, A. V. Rao, GPOPS-II: A MATLAB Software for Solving Multiple-Phase Optimal Control Problems Using Hp-Adaptive Gaussian Quadrature Collocation Methods and Sparse Nonlinear Programming,*ACM Transactions on Mathematical Software (TOMS)*, 2014, 41(1): 1-37.

Proceedings of the 3rd Conference on Fully Actuated System Theory and Applications
May 10-12, 2024, Shenzhen, China

Research on Algorithm Design and Code Automatic Generation for Satellite Attitude Planning

Zhouhuai Luo, Ronghao Yuan, Xiaokun Liu, QianZhang, Yang Jin

Aerospace System Engineering Shanghai, Shanghai 201109, China
E-mail: luozhouhuai@nuaa.edu.cn

Abstract: This article proposes a satellite attitude planning algorithm based on potential function to meet the requirements of satellite attitude constraints on ground stations. The algorithm dynamically adjusts the satellite attitude by designing attractive and repulsive potential functions and adjusting their corresponding weight values, enabling the satellite to avoid optical and radar stations in the same area. In addition, a design approach based on Model-Based Design (MBD) was adopted, combining MBD technology with practical engineering. Through soft-ware digital design processes such as model rule checking, model coverage testing, automatic code generation, code checking, and semi physical simulation testing, algorithm design, modeling and simulation, and automatic code generation were integrated, greatly improving development efficiency, Promoted the process of project development from the traditional document centered development model to the digital development model.

Key Words: Attitude planning; Potential function; MBD technology; Code generation

1 Introduction

During the process of satellite attitude maneuvering, it often encounters constraints on attitude orientation, which can generally be categorized into attitude pointing constraints and attitude avoidance constraints. The issue of attitude maneuvering under pointing constraints has gradually become a focal point in the field of spacecraft attitude control. At the same time, accelerating the advancement of digitalization in the aerospace sector and enhancing operational efficiency through digital means are also key developmental priorities in the current stage.

With the continuous enrichment of in-orbit missions for spacecraft, practical needs such as sunlit observation and telemetry control support pose higher demands on attitude planning. The geometric approach, by establishing a relationship between the current and desired attitudes, enables the rapid derivation of analytical maneuver paths. Duan[1] proposed a two-step tangent maneuver path based on Euler axis-angles, achieving the avoidance of forbidden pointing regions for a single line of sight axis. Xu[2] proposed a solution to the effective path discrimination problem under multiple cone constraints based on the reduction of pointing vector dimensions. However, geometric methods face challenges in adapting to problems involving multiple axes and constraints. In contrast, the potential function approach, guided by gradient principles, dynamically plans trajectories and exhibits excellent performance in scenarios with multiple constraints and real-time calculations. Guo[3] established the premise of the repulsive potential function and investigated a backstepping tracking controller, achieving adaptive adjustment of control amplitudes. Shen[4] utilized normalized quaternions to construct a quadratic potential function, enabling flexible appendage satellites to avoid forbidden pointing regions. Feng[5] rapidly accomplished attitude planning and maneuvering processes while ensuring sensor sun avoidance and antenna-to-ground communication based on a logarithmic potential function.

The MBD method is the mainstream implementation approach for the digital development of control algorithms and software, gradually gaining application in the aerospace and automotive industries. In the design of spacecraft control systems, engine control systems, and avionics systems, the MBD software development mode has been adopted by renowned companies such as NASA, Boeing, Airbus, Honeywell, and others. The Asia-Pacific Center of Trane Technology[6] has applied the MBD design pattern to the development of air conditioning control software. Compared to traditional software development models, this approach has significantly improved development efficiency. The Xi'an Aeronautical Computing Technology Research Institute[7] has applied Model-Based Systems Engineering (MBSE) technology to the research and development of aircraft power control systems, completing model-based design and development. The Beijing Telemetry Technology Research Institute[8] has applied MBSE technology to the modeling of telemetry and control subsystems, transitioning from a traditional document-based development mode to a model-based development approach. This transformation has effectively enhanced development efficiency. The China Aerospace Standardization Research Institute[9] has conducted research on the development of aerospace enterprises in the context of digital transformation. The study analyzes the current status of digital transformation in aerospace enterprises and the necessity of digitizing transformation for the aerospace industry.

This article proposes a satellite attitude planning algorithm based on potential functions, which achieves the avoidance of optical and radar stations by the satellite. Simultaneously, leveraging a software-driven digital design process, it integrates algorithm design, modeling simulation, and code generation seamlessly. by combining digital

methods with practical engineering, it promotes the digital transformation process in the aerospace field.

2 Satellite Attitude Planning Algorithms Design

2.1 Background

Satellites simultaneously avoid a designated area within the same orbit, which includes both a radar station and an optical station. A potential function algorithm is designed to ensure that the satellite's desired reference attitude aligns the weakest region of the satellite's Radar Cross Section (RCS) with the radar station. Building upon this, fine adjustments to the satellite's attitude are made to prevent sunlight reflected off the satellite's solar panels from entering the optical station.

2.2 Metrics

Radar Station: When the satellite passes over the radar station, the angle between a specific pointing axis (weakest region of RCS) in the satellite's body frame and the line connecting to the ground station remains consistently below 15°.

Optical Station: When the satellite passes over the optical station, the angle between the line connecting to the ground station and the sunlight vector, after reflection off the satellite's solar panels, consistently remains greater than 15°. This ensures that the reflected sunlight does not enter the optical station.

2.3 Potential Function Algorithm Design

The potential function includes attractive and repulsive components. In this paper, the attractive potential function V_a is designed as a function of the quaternion error:

$$V_a = k_1 \left\| \boldsymbol{e}^2 \right\| \tag{1}$$

The expression of V_a reveals that V_a has only one local minimum, denoted as $\boldsymbol{e} = [0 \ 0 \ 0]^T$, indicating alignment between the current attitude and the desired attitude, at which V_a=0. The desired attitude corresponds to pointing the low RCS region towards the ground radar station.

Next, we provide the definition of the repulsive potential function V_r:

$$V_r = \frac{k_o}{m - \tilde{\boldsymbol{e}}^T \bar{\boldsymbol{A}} \tilde{\boldsymbol{e}}} \tag{2}$$

Equation (2) represents the forbidden attitude region between the sunlight reflection and the ground optical station, preventing strong light from entering the optical station. $k_o > 0$ is the weight of the forbidden attitude region in the entire repulsive potential function.

The value of k_o follows a three-segment distribution, as shown in the following equation:

$$k_o = \begin{cases} k\left(\dfrac{1}{q} - \dfrac{1}{q_{od}}\right) & q < q_{od} \\ 0 & q > q_{od} \end{cases} \tag{3}$$

Where q represents the angles between various connecting vectors, q_{od} is the field of view of the optical station, and k is the gain weighting factor. When $q < q_{od}$, the closer the current attitude is to the forbidden attitude region, the greater the repulsive force generated.

Based on the above content, we construct the potential function V_p as follows[10]:

$$V_p = V_a + V_r \tag{4}$$

The constructed potential function is smooth and convex for all forms of quaternion error-based quadratic functions, and it globally attains its minimum at the quaternion $\tilde{\boldsymbol{e}} = [0 \ 0 \ 0 \ 1]^T$. Incorporating the designed potential function into the spacecraft attitude control process enables the satellite to simultaneously avoid both the optical station and the radar station.

2.4 Building Simulation Models Based on MBD

MBD (Model-Based Design) software design tool includes a model library, model rule library, code rule library, code auto-generation tool, model rule checking tool, code rule checking tool, and report auto-generation tool, covering all requirements from model establishment to code auto-generation. MBD software design platform is illustrated in the following Fig.1:

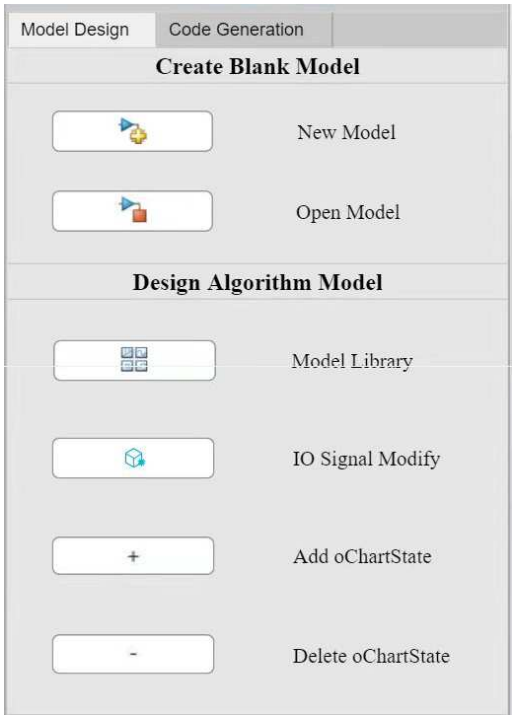

Fig. 1: MBD Software Design Platform

3 Simulation Validation

In this section, simulation validation is conducted to verify whether the aforementioned algorithm meets the requirements for satellite attitude avoidance.

Assuming that a region includes an optical station and a radar station simultaneously. The simulation parameters are as shown in Table 1:

Table 1: Simulation Parameters

Parameters	Values
Epoch Time	2023-12-08 15:10:00.000
Semi-Major Axis (km)	6928.137000
Eccentricity	0
Inclination	97.687°
Right Ascension of Ascending Node	48.167°
Argument of Perigee	0°
True Anomaly	34.886°
Geographical Coordinates of the Region	$(120^{\circ}E, 30^{\circ}N)$
Coordinates of the Weakest RCS Reflection Region on the Satellite (m) (In the satellite body frame)	[0.3; 0.4; 0.8]

The angle between the line connecting the reflected sunlight and the optical station is shown in Fig. 2.

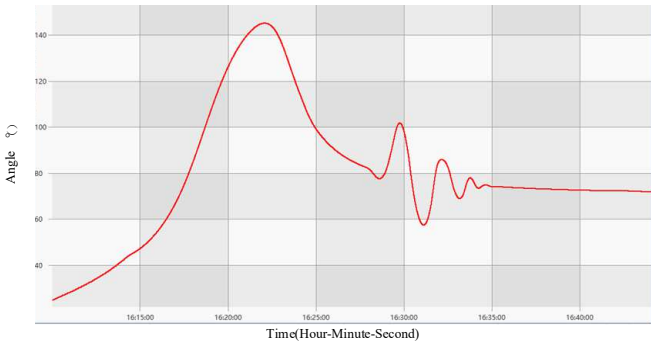

Fig. 2: Angle between the line to the ground station and the sunlight-reflected light when the satellite passes over the optical station

According to the above simulation results, it can be observed that:

(1) When the satellite passes over the radar station, the angle between the pointing axis and the line to the ground station consistently remains below 3°, ensuring that the weakest RCS reflection region always points towards the radar station, thereby achieving avoidance of the radar station by the satellite;
(2) When the satellite passes over the optical station, the angle between the sunlight-reflected light and the line to the ground station consistently remains above 20°. This ensures that the sunlight vector, after reflection off the satellite's solar panels, never enters the ground optical station, thereby achieving avoidance of the optical station by the satellite.

4 Automatic Generation of On-board Code

The design and modeling simulation of satellite attitude planning algorithm based on MBD have been completed in the previous text. According to the MBD software development process, it is also necessary to complete steps such as model rule checking, model coverage testing, automatic code generation, code rule checking, model code consistency testing, and semi physical simulation testing to ensure that the software meets the requirements of the on-board code.

4.1 Model Rule Check

The MBD software design platform integrates model specification checking function for automated specification checking and inspection item management, as shown in Fig. 3.

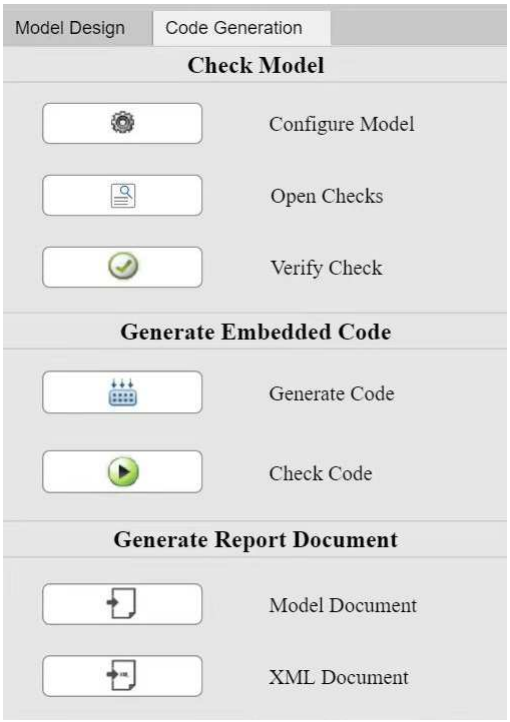

Fig. 3: Model Rule Check

Among them, the model rule check items mainly include:

- Domain model checking rules, used in conjunction with modeling standards used in domain model libraries;
- High security rules, used for specifications related to high security code generation;
- Consistency check rules, relevant rules for verifying the consistency of project code models;
- Run a specification check tool, select the model or model directory to be checked, perform automated specification checks on the model, and generate an inspection report.

4.2 Model Coverage Testing

According to software design specifications, development work requires sufficient dynamic and static testing of software (models) and performance. The static testing methods at the model level are model rule checking and code checking, which are completed:

- Design compliance of the model under safety and reliability constraints;
- Consistency between code and model

The typical method of dynamic testing is model coverage testing, while meeting the requirements of code coverage testing through use case reuse. In the MIDE software system, coverage testing is a tool and a test case. Use cases are generated manually and automatically, provided that the tester has a thorough understanding of the design requirements of the tested model.

4.3 Code Generation

The MBD software design platform integrates automatic code generation function, which is used to generate high-quality C code from the model, as shown in Figure 5. After the model has passed the model rule check, click the auto generate code start button. The software calls the compiler at the bottom level for code generation, and using a highly reliable and secure model environment configuration can ensure that the code generated by the model conforms to high reliability and high security, thus achieving the transformation from model to code.

The automatically generated part of the code corresponding to the model in this project is shown in Fig. 4.

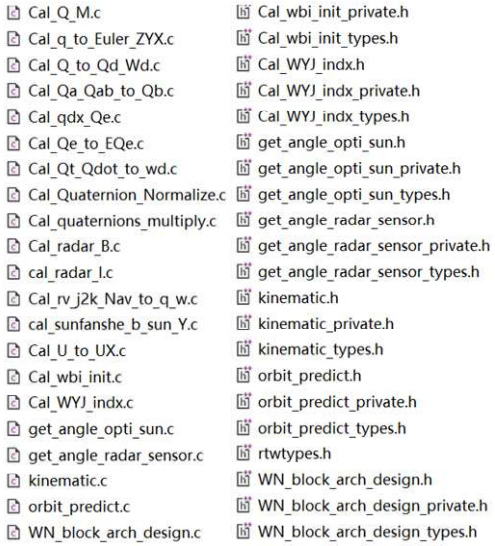

Fig. 4: Partial automatic code generation

4.4 Code Rule Check

The MBD software design platform integrates code checking function. Clicking on the code checking option directly on the generated code can complete the current code check. This check is mainly used to check whether the model and code are structurally consistent. Code rules are checked separately for automatically generated code.

According to the code inspection results, it can be seen that the structure of the code and the model are consistent.

4.5 Model Code Consistency Testing

Code model consistency testing is a test that ensures complete functional consistency between the code and the model. This tool uses the SIL test method. Setting SIL in the model is mainly based on the Ref Model method, that is, in the same model, the model and the code generated by the model are synchronously simulated and compared to verify the functional consistency of the generated code.

4.6 Semi Physical Simulation Testing

Semi physical simulation is the most realistic test that reflects the actual satellite in orbit environment. The automatically generated code is embedded into the onboard computer and subjected to semi physical simulation testing.

Telemetry the results of the onboard computer (single precision) to the ground and compare them with the ground simulation results, as shown in Fig. 5.

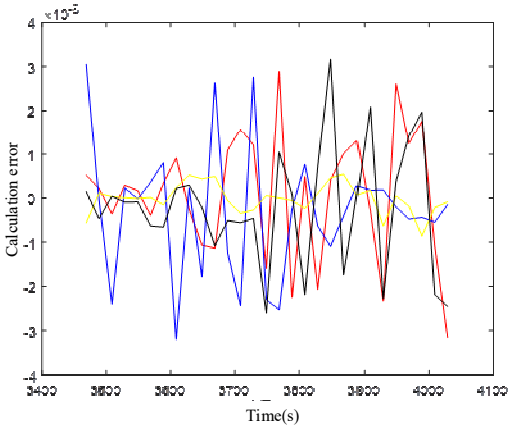

Fig. 5: Comparison error of attitude planning results

From the above figure, it can be seen that the results of the on-board computer running automatic code generation are consistent with the ground simulation results.

4.7 Brief Summary

Through steps such as model rule checking, model coverage testing, automatic code generation, code rule checking, model code consistency testing, and semi physical simulation testing, the transition from model to code has been achieved.

5 Summarize

This article designs target pointing and potential function algorithms based on the requirements of satellite avoidance of ground radar stations and optical stations. Modeling and mathematical simulation of algorithms based on MBD software design tools. At the same time, model rule checking, model coverage testing, code automatic generation, code rule checking, model code consistency testing, and semi physical simulation testing were carried out, achieving the integration of algorithm design, modeling and simulation, and code automatic generation.

References

[1] DUAN C, HU Q L, ZHANG Y M, et al. Constrained single-axis path planning of underactuated spacecraft[J]. Aerospace Science and Technology, 2020,107:106345.

[2] XU R, GENG Z Y, ZHU S Y. Spherical geometric planning method for spacecraft attitude maneuver under complex constraints [J]. Journal of Astronautics, 2021, 42(3):359-366 (In Chinese).

[3] GUO Y L, LI C J, MA G F. Autonomous attitude maneuver control of spacecraft based on potential function method [J]. Chinese Journal of Aeronautics,2011,32(3):457-464(In Chinese).

[4] SHEN Q, YUE C F, GOH C H. Velocity-free attitude reorientation of a flexible spacecraft with attitude constraints[J]. Journal of Guidance, Control, and Dynamics, 2017,40(5):1289-1295.

[5] FENG Z Y, GUO J G, ZHOU J. Multi constraint attitude maneuver planning method for micro satellites [J]. Journal of Astronautics, 2019, 40(10): 1205-1211(In Chinese).

[6] LIU H J, D J, S P. A modeling design method of small satellite TT&C subsystem based on MBSE[J]. Journal of Telemetry, 2022, 43(3), 54-61.

[7] YANG H. Development Practices of HVAC Controller Software Design Based on MBD[J]. FORUM, 2021, 11-16.

[8] SHI P Y, Yu Z T, Liao X Y. Application of MBSE in Aircraft Power Control System[J]. ELECTRONICS WORLD, 2022, 200-202.

[9] CAN Z C, Yang T J, Li X L. Research on Development Strategies of Aerospace Enterprises under the Back-ground of Digital Transformation[J]. Research Re-view, 2022, 5(463), 26-29.

[10] HUANG C H, Wen H, Che Y. Research on improved RBF network algorithm based on potential function clustering[J]. Journal of Yanbian University, 2020, 46(2), 145-149.

Proceedings of the 3rd Conference on Fully Actuated System Theory and Applications
May 10-12, 2024, Shenzhen, China

Non-Cooperative Target Approach Strategy Design Based on Bearing-only Measurement

Yinkang Li[1], Weixing Liu[1], Xiaokun Liu[1], Xiaoran Chen[1], Yang Jin[1]

1. Aerospace System Engineering Shanghai, Shanghai 201109, China
E-mail: liyinkang96@nuaa.edu.cn

Abstract: In view of the challenge in obtaining accurate relative navigation information during the close-range guidance phase of space non-cooperative target approaching missions, making it difficult to achieve high-precision rapid approach control, this paper proposes an approaching control strategy for close-range guidance based on bearing-only measurement for non-cooperative target approaching. Firstly, the relative orbital motion dynamic model between the mission satellite and the non-cooperative target is established, and the mission scenario is defined. Subsequently, a close-range guidance control strategy is designed based on bearing-only measurement. The lateral control law of the mission satellite is devised through the deviation of the target's elevation and azimuth angles. Moreover, the course control law is designed based on the initial and desired position relative to the target, thereby achieving rapid linear approach control of the target. Finally, a comparative simulation is conducted with traditional methods involving bearing-only navigation combined with real-time closed-loop control. The simulation results demonstrate that the proposed approach outperforms traditional methods in terms of energy consumption, accuracy, and transfer time, validating the superiority and practical value of the method in engineering applications.

Key Words: Bearing-only measurement, Non-Cooperative target, Fast approaching control

1 Introduction

With the continuous development of human spaceflight technology, spacecraft are gradually becoming lighter and smaller. Micro spacecraft are increasingly replacing traditional large spacecraft in tasks such as space debris removal and in-orbit maintenance of non-cooperative targets. Micro spacecraft are typically released into orbit by a mother spacecraft and then autonomously approach non-cooperative targets to perform tasks such as debris removal and in-orbit maintenance. This paper focuses on the guidance and control strategy during the approach phase.

The approach task to a non-cooperative target can be divided into the near-range guidance phase, the flyby observation phase, and the high-precision ultra-close range approach phase. The near-range guidance phase involves approaching the target from a position several kilometers away to within a few hundred meters, allowing for more precise measurements and facilitating tasks such as hovering and flyby observation in high-precision relative orbital motion control. Control methods for the near-range guidance phase are typically classified into continuous low-thrust, impulse thrust, and relay-type thrust control.

Continuous low-thrust methods mainly involve electric propulsion techniques, but the thrust is usually low, making it unsuitable for rapid approaches. Impulse thrust is commonly used in CW guidance control strategies. For example, Yang et al. addressed the uncertainty in elliptical orbit maneuvering under J2 perturbation using a nonlinear uncertainty analysis method based on the state transition matrix tensor[1]. Hablani H et al. tackled the problem of autonomous approach to a target spacecraft operating on a circular orbit and derived a guidance method for an exponential slip orbit. This method ensures that the approaching spacecraft's flight process conforms to a certain changing pattern[2]. Li studied control methods under pulse maneuvers [3]. However, on one hand, the control error of CW guidance control makes it not suitable for high-precision control. On the other hand, CW guidance control methods require high-quality relative position and velocity information about the target. Therefore, it is typically used in cooperative target rendezvous missions. For non-cooperative targets, it is often impractical to accurately obtain the relative motion information of the target, leading to the ineffectiveness of CW guidance control methods.

In non-cooperative target approach scenarios, relay-type thrust control is commonly employed. Relay-type thrust involves constant thrust magnitude with toggleable on-off thrust. Zhang proposed an adaptive control law and studied the relative position tracking problem of non-cooperative target spacecraft using line-of-sight relative motion dynamics in the presence of external disturbances, unmodeled dynamics, and thrust saturation[4]. Xing designed a control law to minimize relative velocity during the spacecraft approaching phase[5]. Wang introduced control in the direction of the line connecting the spacecraft and the target based on classical proportional guidance to address challenges in non-cooperative targets, such as missing self-information, difficulties in measurement, and communication[6]. However, the mentioned studies assume accurate measurement of the target's relative motion information. For kilometer-level non-cooperative targets, typically only bearing measurements are available, without distance information. Therefore, the practical applicability of the above methods is limited in engineering.

*This work is supported by National Natural Science Foundation (NNSF) of China under Grant 00000000.

For non-cooperative targets with only bearing measurements, the typical approach for achieving approach control is to use bearing-only navigation combined with optimal guidance control. However, relying solely on bearing information in non-cooperative relative navigation can lead to the problem of unobservable states. Currently, methods such as camera biasing, complex dynamics methods, and orbital maneuvering are employed to enhance the observability of states. Camera biasing, despite its simplicity, has the drawback of being limited to applicable distances[7]. Complex dynamics methods can address the unobservability issue but are susceptible to noise interference and may not be suitable for close encounters[8]. Orbital maneuvering introduces increased fuel consumption and makes navigation and guidance performance directly influenced by the encounter trajectory[9]. Therefore, the method of using bearing-only navigation combined with optimal guidance control also has certain limitations.

In response to the challenge of low accuracy in relative navigation information during the close-range guidance phase, hindering the achievement of high-precision approach control, this paper proposes a strategy for close-range guidance of non-cooperative targets based on bearing-only measurements. By establishing the mapping relationship between the target line-of-sight pointing deviation and lateral position deviation, a lateral control law is designed. By controlling the lateral position of the spacecraft, the line-of-sight axis of the spacecraft is kept pointing towards the target. Subsequently, open-loop control is applied in the course direction, with the course velocity given at the initial moment and deceleration applied when approaching, thereby achieving high-precision and rapid approach control in the close-range guidance phase with bearing-only measurement.

2 Dynamics and Mission Scenario definition

In the inertial frame, the orbital motion equations for the target and the chaser are given by:

$$\begin{cases} \ddot{\boldsymbol{r}}_t = -\dfrac{\mu}{r_t^3}\boldsymbol{r}_t \\ \ddot{\boldsymbol{r}}_c = -\dfrac{\mu}{r_c^3}\boldsymbol{r}_c \end{cases} \tag{1}$$

This paper adopts the CW equations as the relative dynamics model for space rendezvous[11], which can be expressed as:

$$\begin{cases} \ddot{x} - 2\omega\dot{z} = f_x \\ \ddot{y} + \omega^2 y = f_y \\ \ddot{z} + 2\omega\dot{x} - 3\omega^2 z = f_z \end{cases} \tag{2}$$

The mission scenario is defined as follows: at the initial moment, the chaser and the target are located in the same circular orbital plane, and the chaser has already performed a CW orbital transfer to hover 5 km behind the target, as shown in Fig. 1.

3 Approaching control strategy

3.1 Traditional control strategy

For the space non-cooperative target approach control with bearing-only measurement, traditional methods generally adopt the approach of bearing-only navigation combined with optimal guidance control. Since this paper focuses on the design of control strategies, and the bearing-only navigation method has been detailed in the reference [10], it will not be reiterated here. Taking the LQG control

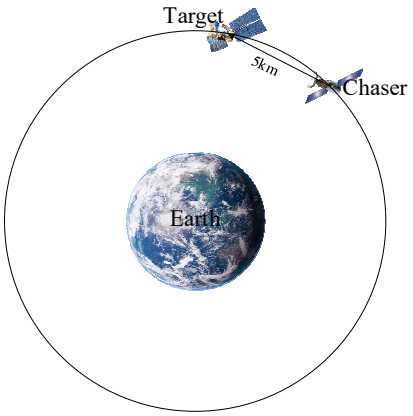

Fig. 1: Mission Scenario Definition

method as an example, the controller design is briefly introduced as follows:

The control acceleration acting on the spacecraft body-axis system is given by:

$$\begin{cases} u_S = (R_{T/S_b})^T (u_K + \Delta u_G - u_L) \\ u_L = -u_{l_{T/S}^d} - \Delta u_g \\ u_{l_{T/S}^d} = -\begin{bmatrix} \dot{\theta}_T^2 & \ddot{\theta}_T & 0 \\ -\ddot{\theta}_T & \dot{\theta}_T^2 & 0 \\ 0 & 0 & 0 \end{bmatrix}\begin{bmatrix} l_x \\ l_y \\ l_z \end{bmatrix} - 2\begin{bmatrix} 0 & \dot{\theta}_T & 0 \\ -\dot{\theta}_T & 0 & 0 \\ 0 & 0 & 0 \end{bmatrix}\begin{bmatrix} \dot{l}_x \\ \dot{l}_y \\ \dot{l}_z \end{bmatrix} + \begin{bmatrix} \ddot{l}_x \\ \ddot{l}_y \\ \ddot{l}_z \end{bmatrix} \\ \Delta u_G = (\dfrac{\mu}{\|r_T\|^3})^{\frac{1}{2}} \begin{bmatrix} 2 & 0 & 0 \\ 0 & -1 & 0 \\ 0 & 0 & -1 \end{bmatrix}\begin{bmatrix} x \\ y \\ z \end{bmatrix} \\ \Delta u_g = (\dfrac{\mu}{r_S^3}\begin{bmatrix} r_T + l_x + x \\ l_y + y \\ l_z + z \end{bmatrix} - \dfrac{\mu}{r_T^3}\begin{bmatrix} r_T \\ 0 \\ 0 \end{bmatrix}) \\ u_K = -K\hat{X}_K \end{cases} \tag{3}$$

where r_T is the distance from the target spacecraft to the center of the Earth; r_S is the distance from the spacecraft to the center of the Earth; $l_{T/S}^d = \begin{bmatrix} l_x, & l_y, & l_z \end{bmatrix}^T$ is the formation vector, which can be obtained through cubic polynomial interpolation algorithm; $\Delta r_{T/S} = \begin{bmatrix} x, & y, & z \end{bmatrix}^T$ is

the relative position vector in the target spacecraft's orbital coordinate system; $\dot{\theta}_T$ is the first derivative of the true anomaly change with respect to time; $\ddot{\theta}_T$ is the second derivative of the true anomaly change with respect to time; R_{T/S_b} is the direction cosine matrix from the spacecraft body-axis coordinate system to the target spacecraft's orbital coordinate system; μ is the gravitational constant of the Earth. The state feedback gain matrix K is obtained by solving the Riccati equation based on the performance objective function; the estimated relative state quantity $\hat{X}_K$ is provided by the navigation system.

For discrete control systems, we need to find the optimal state feedback control law:

$$u_k = -KX_k \tag{4}$$

To minimize the quadratic cost function:

$$J = \sum_{n=1}^{\infty} [X_k^T Q X_k + u_k^T R u_k + 2X_k^T N u_k] \tag{5}$$

When there are no cross terms in the cost function J, $N = 0$. Here, Q and R are weighted matrices for state and control variables, respectively. According to the extremum principle, the state feedback gain matrix for optimal control in discrete quadratic form can be derived.

$$K = (\Gamma^T S \Gamma + R)^{-1} (\Gamma^T S \Phi + N^T) \tag{6}$$

where the matrix S must satisfy the Riccati equation of discrete system.

3.2 Approach Control Strategy Design Based on Bearing-only Measurement

The lateral control law is designed as follows:

When the attitude of the chaser is oriented towards the Earth, the line of sight axis always points to the positive +X-axis direction in the VVLH frame. Therefore, adjusting the positions in the Y-axis and Z-axis directions can achieve adjustments in the elevation and azimuth angles of the target in the chaser body frame, as shown in Fig. 2. When the chaser is behind the target, to control the elevation and azimuth angles and keep the line of sight axis pointing to the target, the desired azimuth angle is 0°, and the desired elevation angle can be calculated using the following equation:

$$\alpha_d = \frac{1}{2} \arccos\left(\frac{2R^2 - d^2}{2R^2}\right) \tag{7}$$

Where d is the relative distance between the two stars, and R is the orbital radius.

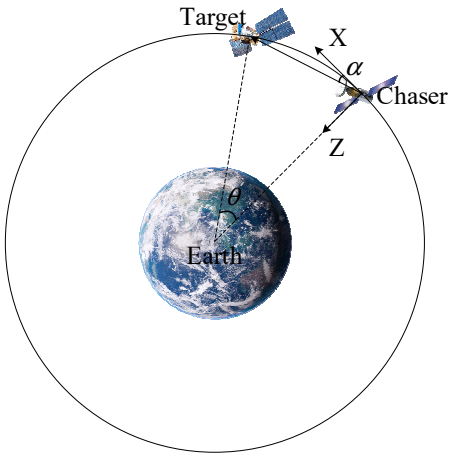

Fig. 2: Diagram of the desired elevation angle

After obtaining the desired elevation and azimuth angles, it is necessary to design lateral control laws to achieve control over these angles. As shown in Fig. 2, elevation angle control is primarily achieved by adjusting the Z-axis position in VVLH frame, while azimuth angle control is achieved by adjusting the Y-axis position. Therefore, the lateral control laws can be designed as follows:

$$\begin{aligned} F_y &= k_{py}\beta(k) + k_{dy}\dot{\beta}(k) \\ F_z &= -k_{pz}\alpha(k) - k_{dz}\dot{\alpha}(k) \end{aligned} \tag{8}$$

where k_{py}, k_{dy} and k_{pz}, k_{dz} are the PD control parameters of Y-axis and Z-axis, respectively.

The course control law is designed as follows:

When the attitude of the chaser is directed towards the Earth, we expect to first accelerate to the given speed in the course direction. Subsequently, the thruster is turned off. When the chaser flies to a certain distance behind the target, the thruster needs to apply reverse thrust to decelerate. This is to prevent the chaser from being unable to decelerate in a timely manner when reaching the distance range where range information can be obtained due to excessive speed. This could lead to the chaser being too far from the hover observation distance, or even directly colliding or flying over the target.

According to the above analysis, we set the thruster to a constant thrust of 0.01 m/s² for 300 seconds, accelerating the chaser to a relative course speed of about 3 m/s. The thruster is then turned off. The chaser flies for about 1300 seconds with a relative speed of approximately 3 m/s. Afterward, the thruster applies a -0.01 m/s² thrust in the opposite direction for 250 seconds, decelerating to about 0.5 m/s. It then continues to fly until it reaches a distance within 100 meters of the target. The entire control process is illustrated in Fig. 3.

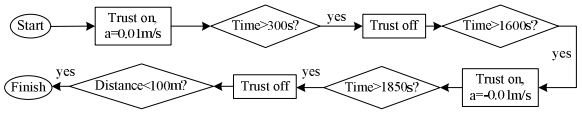

Fig. 3: Flowchart of the course control

4 Simulation and Analysis

Simulations were conducted to compare the method proposed in this paper with the approach of using bearing-only navigation combined with real-time closed-loop control.

The task scenario was set as follows: 1) The target's orbit was a circular orbit with an altitude of 550 km and an inclination angle of 53°; 2) The chaser was in the same orbit as the target, initially positioned 5 km behind the target. The initial mass of the chaser was set to 5 kg, and control parameters were chosen as $k_{py} = k_{pz} = 0.5543$, $k_{dy} = k_{dz} = 2.9779$. For the real-time closed-loop control method, the task time was set to 53 minutes. The simulation results are shown in Fig. 4-11.

Fig. 4-6 shows the simulation results obtained using the method proposed in this paper. Fig. 4 and 5 depict the three-axis relative positions of the chaser in the target VVLH frame and an enlarged view of the X-axis relative position, respectively. Fig. 6 illustrates the variation in elevation and azimuth angles of the target relative to the chaser during the approach process. From Fig. 4 and 5, it can be observed that the entire approach process takes about 2650 seconds, with a final X-axis direction control error of approximately 8 meters. The relative positions in the Y and Z-axis directions are both oscillatory and convergent, with the amplitude of the Z-axis being much larger than the Y-axis. This is because applying thrust in the X-axis direction will inevitably cause a change in orbital altitude, resulting in a change in the Z-axis direction position of the chaser in the target VVLH frame.

From Fig. 6, it can be seen that during the approach process, the elevation angle can be controlled within the range of ±2°, while the azimuth angle can be controlled within ±0.1°. This is because the elevation angle reflects the position deviation in the Z-axis direction, while the azimuth angle reflects the position deviation in the Y-axis direction, and as seen from Fig. 4, the Z-axis direction position deviation is much larger than the Y-axis, reflecting in the elevation and azimuth angle as well.

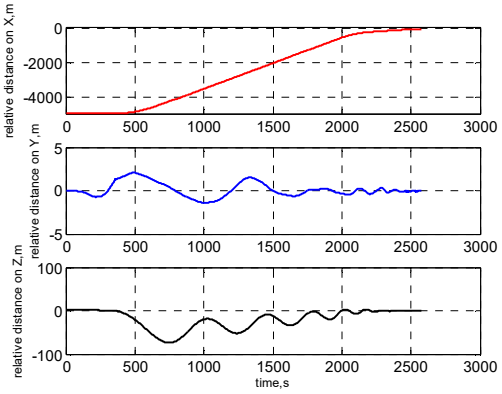

Fig. 4: Relative distance between target and chaser

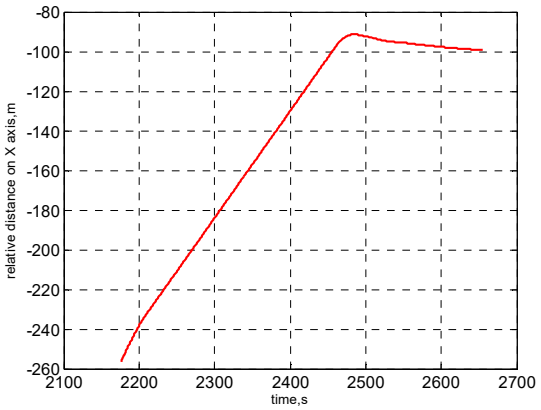

Fig. 5: Relative distance on the X axis at the end

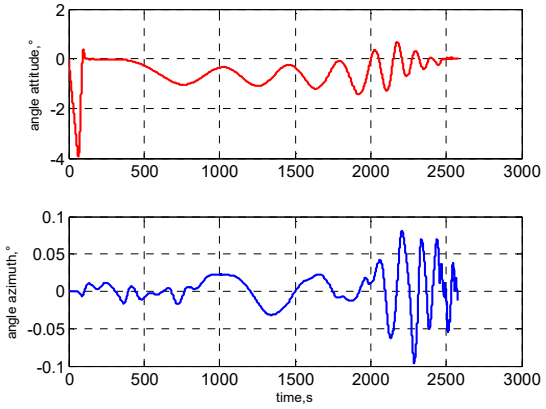

Fig. 6: The elevation and azimuth angle

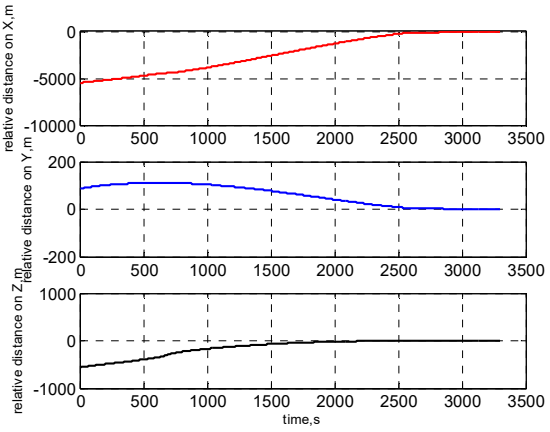

Fig. 7: Relative distance between target and chaser

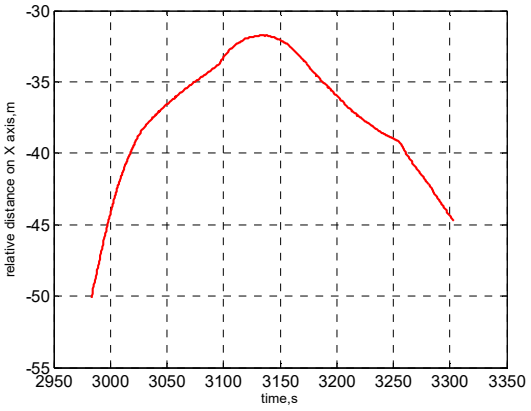

Fig. 8 Relative distance on the X axis at the end

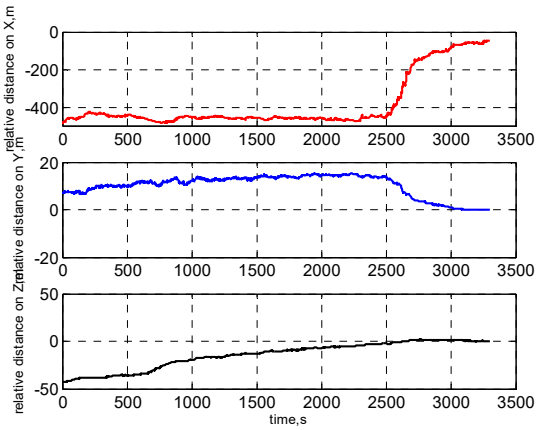

Fig. 9 The error of bearing-only navigation

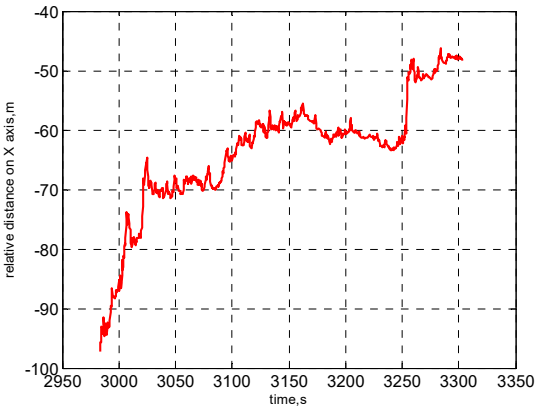

Fig. 10: The navigation error on the X axis at the end

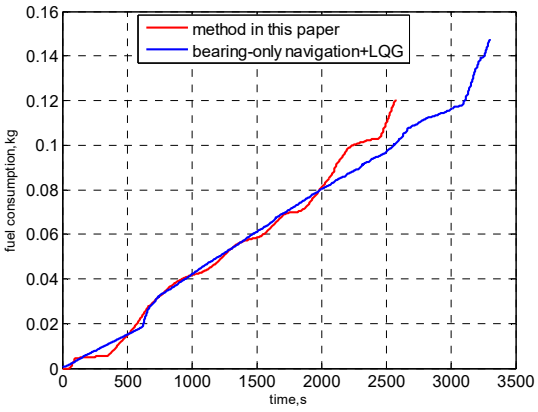

Fig. 11: The comparison of fuel consumption

Fig. 7-10 show the results obtained using the bearing-only navigation combined with real-time closed-loop control method. Fig. 7 and 8 depict the three-axis relative positions of the chaser in the target VVLH frame and an enlarged view of the X-axis relative position, respectively. Fig. 9 and 10 show the three-axis relative error of bearing-only navigation and an enlarged view of the X-axis at the end. From Fig. 7 and 8, it can be observed that the entire approach process takes about 3300 seconds, with a final X-axis direction control error of approximately 70 meters. From Fig. 9 and 10, it can be seen that the bear-only navigation error in the X-axis direction is much larger than that in the Y and Z-axis directions. The initial navigation error is about -450 meters, and even after convergence, there is still an error of about -50 meters near the end of the approach. This results in a significant control error in the X-axis direction for the real-time closed-loop control method, which cannot meet the requirements for further tasks such as flying around and observing after the approach.

Fig. 11 compares the fuel consumption of the two methods. It can be seen from the figure that the method proposed in this paper saves about 20% of fuel consumption compared to the traditional method. In summary, the method proposed in this paper is superior to the traditional method in terms of approach time, control accuracy, and fuel consumption.

5 Conclusion

The paper proposes a non-cooperative target approach strategy based on bearing-only measurement. Based on bearing-only measurement, the method achieves closed-loop control of the lateral position error of the chaser and designs control logic based on the time axis for the course direction. Simulation results demonstrate that the proposed method significantly outperforms traditional bearing-only navigation combined with real-time closed-loop control approach, in terms of fuel consumption, approach time, and end-point control. The method shows promising prospects for practical engineering applications.

References

[1] Yang Z, Luo Y Z, Lappas V, et al. Nonlinear Analytical Uncertainty Propagation for Relative Motion near J2-Perturbed Elliptic Orbits[J]. Journal of Guidance Control and Dynamics, 2017:1-16.

[2] D Dana-Bashian, Hablani H, Tapper M. Guidance algorithms for autonomous rendezvous of spacecraft with a target vehicle in circular orbit[C]// Aiaa Guidance, Navigation, & Control Conference & Exhibit. 2001(1).

[3] Li Z, Yang X, Gao H. Autonomous Impulsive Rendezvous for Spacecraft under Orbital Uncertainty and Thruster Faults[J]. Journal of the Franklin Institute, 2013, 350(9): 2455-2473.

[4] Zhang K, Qin N, Sun Y. Adaptive spacecraft relative position tracking control for non-cooperative target with thrust saturation[C]// 2019 14th IEEE Conference on Industrial Electronics and Applications (ICIEA). IEEE, 2019.

[5] Xing J, Ju J. On the sub-low contact velocity control of rendezvous docking for smart world[J]. Cluster Computing, 2019, 22(11-12).

[6] Wang W. Mission Plan of Active Debris Removal and Design of Guidance and Control Techniques Applying Space Maneuver Vehicle[D]. National University of Defense Technology, 2017.

[7] Geller D K, Klein I. Angles-only navigation state observability during orbital proximity operations[J]. Journal of Guidance, Control and Dynamics, 2014, 37(6): 1976-1983.

[8] Kaufman E, Lovell T A, Lee T. Nonlinear observability for relative orbit determination with angles-only measurements[J]. Journal of the Astronautical Sciences, 2016, 63(1): 60-80.

[9] Grzymisch J, Fichier W. Observability criteria and unobservable maneuvers for in-orbit bearings-only navigation[J]. Journal of Guidance, Control and Dynamics, 2014, 37(4): 1 -10.

[10] Luo J, Lv D, Gong B, et al. Closed Loop Optimal Guidance for Multi Constrained Rendezvous with Angles Only Navigation[J]. Journal of Astronautics, 2017, 38(9): 956.

[11] Clohessy W H, Wiltshire R S. Terminal guidance system for satellite proximity operations using Tschauner-Hempel equations[J]. Journal of Astronautical Sciences, 1960, 27 (9): 653-678.

Proceedings of the 3rd Conference on Fully Actuated System Theory and Applications
May 10-12, 2024, Shenzhen, China

An Status-deformation Cooperative Control for Morphing Vehicle

Wenquan Zheng[1], Ye Tian[1], Saixian Ye[1], Yihuan Jin[1], Lu Liu[1]

1. Department of Flight Control, Shanghai Aerospace Control Technology Institute, Shanghai 201109, China
E-mail: zhengwenquan0803@163.com

Abstract: Morphing vehicles achieve optimal flight performance by changing shape under different flight conditions and missions to meet different mission requirements. In this paper, the variable span vehicle is studied, and the status-deformation cooperative control of the morphing vehicle is developed. The structural deformation of the vehicle is treated as the control input, and the status-deformation cooperative control model is established. Then, a virtual adaptive sliding mode control law is designed and assigned to the actual control inputs by solving the optimization problem. Simulations show that the control algorithm achieves status-deformation cooperative control, Compared to conventional vehicles, morphing vehicle can achieve desired cost function optimization by actively changing the wingspan at different flight phases, reducing fuel or rudder deflection requirements.

Key Words: morphing vehicle, variable span vehicle, adaptive sliding mode, control allocation

1 Introduction

Morphing vehicles, as a new concept, have been one of the research hotspots in the aerospace field in recent years. Compared to conventional vehicles, variant vehicles can have greater range and greater environmental suitability by morphing [1].

Since the concept of a morphing vehicle was proposed, scholars have investigated multiple ways of morphing. In general, variant vehicles can be divided into three categories by the size of the deformation scale [2]: The first is small-scale deformation, such as local deformation such as ballooning; The second is medium-scale deformation, such as wing camber, thickness changes; The third is large-scale deformation, including variable span, variable wing area and wing surface shape, variable sweep.

A deformable structure is a prerequisite for a morphing vehicle to be able to achieve deformation, and current morphing vehicles can perform structural deformation by some mechanical construction and drive components or distributed drive systems [3]. However, the ideal deformation mechanism still needs further research and breakthrough, such as simple, lightweight, reliable and other requirements can not be achieved.

Changes in aerodynamic characteristics, center of gravity, and moment of inertia of the vehicle due to deformation bring many difficulties to the design of the control system. Overall, there are currently two main research ideas for the relationship between the deformation process of the morphing vehicle and its control system. The first is to treat the deformation as an external given command, and the vehicle deforms over time according to the given command, on which the control system is then designed. The second is to treat the structural deformation as an input to the control system, and the deformation is coupled and affected by the flight state.

Variant vehicle control applies more methods of robust adaptive control, control based on backstepping, sliding mode control and so on. Reference [4] gives the different regions of the vehicle sweep range, then gives the solution conditions for the system to satisfy the robust H_∞ performance according to the different control objectives in the different regions, and designs the corresponding controllers. Ligang GONG [5] et al. established a non-linear model of the vehicle's motion, using the backstepping method to design controllers such that all signals in the closed-loop system are bounded and the vehicle altitude tracking error eventually tends to a stable smaller value. An adaptive super twisted sliding mode controller is proposed in reference [6]. the simulation results show that the proposed algorithm has good tracking performance and robust performance. All of the above control methods treat structural deformation of the variant vehicle as an externally given command.Cunyu Bao[7] et al. investigated an integrated approach to control and guidance for hypersonic missiles with variable span assist control. Simulations showed that the variable span missile had a smaller miss distance and flight time than conventional missiles, and the end fall angle was closer to the design value.

In this paper, the status-deformation cooperative control algorithm of variable span vehicle is designed. The simulation results show that the status-deformation cooperative control algorithm designed can make the vehicle actively change its wingspan in different flight phases to achieve the desired cost function optimization, reducing fuel or rudder deflection requirements compared to conventional vehicles

2 Dynamics modeling of status-deformation cooperative control for morphing vehicles

2.1 Model of aerodynamic parameters varying with span

The variable span vehicle discussed in this article is capable of autonomously varying the length of the wing during flight, with the wingspan on either side being lengthened or shortened symmetrically. The change in span is described by the span deformation ratio ξ, defined as follows [8]:

*This work is supported by Shanghai Aerospace Control Technology Institute.

$$\xi = \frac{b - b_{\min}}{b_{\max} - b_{\min}} \tag{1}$$

where b is the actual span and $b_{\min}, b_{\max}$ is the shortest and longest span, respectively, and it is clear that the span deformation ratio ξ varies with the vehicle's span, taking values in the range [0,1].

Morphing vehicle longitudinal aerodynamic forces and moments are defined as:

$$\begin{cases} L = QS_w C_L \\ D = QS_w C_D \\ M = QS_w c_A C_m \end{cases} \tag{2}$$

where $Q = 0.5\rho V^2$ is the dynamic pressure, ρ is the atmospheric density, S_w, c_A is the wing reference area and characteristic length, respectively, C_L, C_D, C_m are the lift coefficient, drag coefficient, and pitch moment coefficient, respectively, which are functions of the span deformation rate. Aerodynamic parameter C_L, C_D, C_m can be fitted as a polynomial as follows:

$$\begin{cases} C_L = C_{L_{\alpha=0}} + C_{L_\alpha}\alpha + C_{L_{\delta_e}}\delta_e + C_{L_q}\dfrac{c_A}{2V}q \\ C_D = C_{D_{\alpha=0}} + C_{D_\alpha}\alpha + C_{D_{\alpha^2}}\alpha^2 \\ C_m = C_{m_{\alpha=0}} + C_{m_\alpha}\alpha + C_{m_{\delta_e}}\delta_e + C_{m_q}\dfrac{c_A}{2V}q \end{cases} \tag{3}$$

where α is the angle of attack and δ_e is the rudder deflection in radians. $C_{L_{\alpha=0}}, C_{D_{\alpha=0}}, C_{m_{\alpha=0}}$ are the lift coefficient, drag coefficient, and pitch moment coefficient at zero angle of attack, respectively. $C_{L_{\delta e}}, C_{D_{\delta e}}, C_{m_{\delta e}}$ are the aerodynamic derivatives of lift, drag and pitching moment with respect to elevator deflection, respectively. $C_{L_\alpha}, C_{D_\alpha}, C_{m_\alpha}$ are lift, drag and pitching moment with respect to angle of attack, $C_{D_{\alpha^2}}$ is the secondary aerodynamic derivative of drag with respect to angle of attack, and C_{L_q}, C_{m_q} are the aerodynamic derivatives of lift and pitching moment with respect to pitch angle velocity, respectively.

The above aerodynamic derivatives are functions of flight altitude h, Ma, and span deformation rate ξ.

$$\begin{aligned} C_{L_{\alpha=0}}(Ma,\xi) &= 0.0098Ma + 0.4890\xi + 0.3340 \\ C_{L_\alpha}(h,Ma,\xi) &= -0.0001h - 1.0957Ma + 6.0872\xi + 5.9792 \\ C_{L_{\delta_e}}(h,Ma) &= -0.0013h + 0.0316Ma + 0.4099 \\ C_{L_q}(Ma,\xi) &= 0.8710Ma + 5.1386\xi + 9.6995 \end{aligned} \tag{4}$$

$$\begin{aligned} C_{D_{\alpha=0}}(h,Ma,\xi) &= 0.0005h - 0.0277Ma + 0.0142\xi + 0.0288 \\ C_{D_\alpha}(h,Ma,\xi) &= 0.0001h + 0.0325Ma + 0.0906\xi + 0.1883 \\ C_{D_{\alpha^2}}(h,Ma,\xi) &= -0.0011h - 1.2434Ma + 0.1408\xi + 2.1775 \end{aligned} \tag{5}$$

$$\begin{aligned} C_{m_{\alpha=0}}(h,Ma,\xi) &= -0.0001h + 0.0031Ma - 0.2436\xi + 0.0121 \\ C_{m_\alpha}(h,Ma,\xi) &= -0.0001h - 0.0922Ma - 1.4954\xi - 1.6444 \\ C_{m_{\delta_e}}(h,Ma) &= 0.0030h - 0.1256Ma - 0.9766 \\ C_{m_q}(Ma,\xi) &= -0.6857Ma - 1.0762\xi - 18.1012 \end{aligned} \tag{6}$$

where h is in km, $C_{D_{\alpha^2}}$ is in rad^{-2}, and other aerodynamic derivatives are in rad.

Further, the aerodynamic parameters (4)-(6) are organized into matrix forms for height, Mach and span deformation correlation.

$$\begin{aligned} &\left[C_{L_{\alpha=0}}, C_{L_\alpha}, C_{L_q}, C_{D_{\alpha=0}}, C_{D_\alpha}, C_{D_{\alpha^2}}, C_{m_{\alpha=0}}, C_{m_\alpha}, C_{m_q}, C_{L_{\delta_e}}, C_{m_{\delta_e}}\right]^{\mathrm{T}} \\ &= C\left[h, Ma, \xi, 1\right]^{\mathrm{T}} \end{aligned} \tag{7}$$

where the coefficient matrix

$$C = \begin{bmatrix} 0 & 0.0098 & 0.4890 & 0.3340 \\ -0.0001 & -1.0597 & 6.0872 & 5.9792 \\ 0 & 0.8710 & 5.1386 & 9.6995 \\ 0.0005 & -0.0277 & 0.0142 & 0.0288 \\ 0.0001 & 0.0325 & 0.0906 & 0.1883 \\ -0.0011 & -1.2434 & 0.1408 & 2.1775 \\ -0.0001 & 0.0031 & -0.2436 & 0.0121 \\ -0.0001 & -0.0922 & -1.4954 & -1.6444 \\ 0 & -0.6857 & -1.0762 & -18.1012 \\ -0.0013 & 0.0316 & 0 & 0.4099 \\ 0.0030 & -0.1256 & 0 & -0.9766 \end{bmatrix} \tag{8}$$

2.2 Status-deformation cooperative control model

With reference to the conventional vehicle dynamics modeling process, the longitudinal dynamics equation for a variable span vehicle is

$$\begin{cases} \dot{V} = \dfrac{T\cos\alpha}{m} - \dfrac{D(\xi_1)}{m} - g\sin(\vartheta - \alpha) \\ \dot{\alpha} = q - \dfrac{T\sin\alpha}{mV} - \dfrac{L(\xi_1)}{mV} + \dfrac{g\cos(\vartheta - \alpha)}{V} \\ \dot{\vartheta} = q \\ \dot{q} = \dfrac{M(\xi_1)}{I_y} \\ \dot{h} = V\sin(\vartheta - \alpha) \end{cases} \tag{9}$$

where m is the mass, V is the velocity, $L(\xi), D(\xi), T$ are lift, drag, and thrust respectively, $\alpha, \theta, \vartheta$ are the angle of attack, ballistic inclination, and pitch angle respectively, I_y is the component of the vehicle's moment of inertia with respect to the z axis of the body coordinate system, q is the component of the angular velocity of rotation of the body frame relative to the ground frame on the axis of body frame z, and $M(\xi)$ is the pitching moment. Both aerodynamic forces and aerodynamic moment $L(\xi), D(\xi), M(\xi)$ are related to the span deformation rate, see previous article for specific expressions.

Additionally, vehicle thrust is described using a linear relationship

$$T = T_{\delta_t}\delta_t \tag{10}$$

where $T_{\delta_t} = 85.2\text{N}/\%$ is the engine thrust coefficient and δ_t is the engine throttle opening.

Further, the structural deformation of the morphing vehicle is treated as a system control input, and the dynamic model of state deformation coordinated control of the variant vehicle is established as follows.

$$\dot{x} = f_m(x,\xi) + g_m(x,\xi)u_m + d \tag{11}$$

where $x = [V \quad \alpha \quad \vartheta \quad q \quad h]^{\mathrm{T}}$ is the state vector, $u_m = [\delta_e \quad \delta_t \quad \xi]^{\mathrm{T}}$ is the input vector, d is the compound interference vector, and the system function $f_m(x,\xi)$ is

$$f_m(x,\xi) = [f_{m1}, f_{m2}, f_{m3}, f_{m4}, f_{m5}]^{\mathrm{T}} \tag{12}$$

where

$$\begin{cases} f_{m1} = -\dfrac{\rho V^2 S_w}{2m}\begin{bmatrix}(C_{41}h + C_{42}Ma + C_{44}) + (C_{51}h + C_{52}Ma + C_{54})\alpha \\ +(C_{61}h + C_{62}Ma + C_{64})\alpha^2\end{bmatrix} \\ \qquad -g\sin(\vartheta - \alpha) \\ f_{m2} = -\dfrac{\rho V S_w}{2m}\begin{bmatrix}(C_{11}h + C_{12}Ma + C_{14}) + (C_{21}h + C_{22}Ma + C_{24})\alpha \\ +(C_{31}h + C_{32}Ma + C_{34})\dfrac{c_A}{2V}q\end{bmatrix} \\ \qquad +q + \dfrac{g\cos(\vartheta - \alpha)}{V} \\ f_{m3} = q \\ f_{m4} = \dfrac{\rho V^2 S_w c_A}{2I_y}\begin{bmatrix}(C_{71}h + C_{72}Ma + C_{74}) + (C_{81}h + C_{82}Ma + C_{84})\alpha \\ +(C_{91}h + C_{92}Ma + C_{94})\dfrac{c_A}{2V}q\end{bmatrix} \\ f_{m5} = V\sin(\vartheta - \alpha) \end{cases}$$

The system function $g_m(x,\xi)$ is

$$g_m(x,\xi) = [g_{m1}(x,\xi) \quad g_{m2}(x,\xi) \quad g_{m3}(x,\xi)] \tag{13}$$

where,

$$g_{mi}(x,\xi) = [g_{mi1} \quad g_{mi2} \quad g_{mi3} \quad g_{mi4} \quad g_{mi5}]^{\mathrm{T}}, i = 1,2,3$$

$$\begin{cases} g_{m11} = 0 \\ g_{m12} = -0.5\rho V S_w(C_{10,1}h + C_{10,2}Ma + C_{10,4}) \\ g_{m13} = 0 \\ g_{m14} = 0.5\rho V^2 S_w c_A(C_{11,1}h + C_{11,2}Ma + C_{11,4})/I_y \\ g_{m15} = 0 \end{cases}$$

$$\begin{cases} g_{m21} = T_{\delta_t}\cos\alpha / m \\ g_{m22} = -T_{\delta_t}\sin\alpha/(mV) \\ g_{m23} = 0 \\ g_{m24} = 0 \\ g_{m25} = 0 \end{cases}$$

$$\begin{cases} g_{m31} = -\dfrac{1}{2m}\rho V^2 S_w(C_{43} + C_{53}\alpha + C_{53}\alpha^2) \\ g_{m32} = -\dfrac{1}{2m}\rho V S_w\left(C_{13} + C_{23}\alpha + C_{33}\dfrac{c_A}{2V}q\right) \\ g_{m33} = 0 \\ g_{m34} = \dfrac{1}{2I_y}\rho V^2 S_w c_A\left(C_{73} + C_{83}\alpha + C_{93}\dfrac{c_A}{2V}q\right) \\ g_{m35} = 0 \end{cases}$$

3 Design of state deformation cooperative control algorithm for morphing vehicle

3.1 Design of adaptive sliding mode control algorithm

In this section, the adaptive sliding mode control algorithm is designed according to the morphing vehicle status-deformation cooperative control model. The velocity subsystem and attitude subsystem are extracted, and an adaptive sliding mode control law with preset adjustment time is designed for the two subsystems, respectively, to enable the velocity and attitude (obtained from the desired altitude) of the system to track the command signal within the specified time.

The variable span vehicle status-deformation cooperative control model (11) is broken down into two subsystems:

$$\dot{V} = f_{m1} + [g_{m11} \quad g_{m21} \quad g_{m31}]u_m + d_1 \tag{14}$$

$$\ddot{\vartheta} = f_{m4} + [g_{m14} \quad g_{m24} \quad g_{m34}]u_m + d_4 \tag{15}$$

Denote $v_{c1} = f_{m1} + [g_{m11} \quad g_{m21} \quad g_{m31}]u_m$ and $v_{c2} = f_{m4} + [g_{m14} \quad g_{m24} \quad g_{m34}]u_m$

$$\dot{V} = v_{c1} + d_1 \tag{16}$$

$$\ddot{\vartheta} = v_{c2} + d_4 \tag{17}$$

Furthermore, the proposed adaptive sliding mode control algorithm is designed as follows:

$$\begin{cases} f_1 = 0, g_1 = 1 \\ e_1 = V - V_d \\ s_1 = e - \eta_1 \\ w_1 = \dot{\eta}_1 \\ \dot{\hat{d}}_1 = \begin{cases} \mu_1 |s_1|, & |s_1| > \varepsilon_1 \\ 0, & |s_1| \le \varepsilon_1 \end{cases}, \hat{d}_1(0) = 0 \\ v_{c1} = g_1^{-1}\left(-f_1 - \text{sat}\left(\frac{s_1}{\varepsilon_1}\right)\hat{d}_1 + w_1 - \text{sat}\left(\frac{s_1}{\varepsilon_1}\right)k_1 \right) \end{cases} \tag{18}$$

$$\begin{cases} f_2 = 0 \\ g_2 = 1 \\ e_2 = \vartheta - \vartheta_d \\ z_2 = e_2 - \eta_2 \\ s_2 = \dot{z}_2 + C_2 z_2 \\ w_2 = \ddot{\vartheta}_d + \ddot{\eta}_2 - C_2(\dot{\vartheta} - \dot{\vartheta}_d - \dot{\eta}_2) \\ \dot{\hat{d}}_4 = \begin{cases} \mu_2 |s_2|, & |s_2| > \varepsilon_2 \\ 0, & |s_2| \le \varepsilon_2 \end{cases}, \hat{d}_4(0) = 0 \\ v_{c2} = g_2^{-1}\left(-f_2 - \text{sat}\left(\frac{s_2}{\varepsilon_2}\right)\hat{d}_4 + w_2 - \text{sat}\left(\frac{s_2}{\varepsilon_2}\right)k_2 \right) \end{cases} \tag{19}$$

where $e_i\,(i=1,2)$ is the system tracking error, $\eta_i\,(i=1,2)$ is the designed expected error curve, $s_i\,(i=1,2)$ is the designed sliding surface, and $\hat{d}_i\,(i=1,4)$ is the estimate of the unknown bounded parameter $d_i\,(i=1,4)$, which is updated by the following adaptive law:

$$\text{sat}\left(\frac{s_i}{\varepsilon_i}\right) = \begin{cases} -1, & s_i < -\varepsilon_i \\ \dfrac{s_i}{\varepsilon_i}, & -\varepsilon \le s_i \le \varepsilon_i \\ 1, & s_i > \varepsilon_i \end{cases} \tag{20}$$

where sat(.) represents the saturation function, ε_i satisfies the inequality $0 < \varepsilon_i < \frac{1}{\sqrt{2}} C_i \delta_i$, δ_i is the steady-state tracking accuracy,. $C_i\,(i=1,2)$, $\mu_i\,(i=1,2)$, $k_i\,(i=1,2)$ are the design parameters.

Lemma 1 [9]: For system (14)-(15), when the reference command signal V_d, ϑ_d has a second order continuous derivative and is bounded, the proposed adaptive sliding mode control algorithm (18)-(19) can realize that:

(1) $V, \dot{V}, \vartheta, \dot{\vartheta}$ are all bounded;

(2) When $t \to \infty$, $\hat{d}_i(t) \to \hat{d}_{i,\infty}\,(i=1,4)$, where $\hat{d}_{i,\infty}$ is a constant;

(3) For the preset settling time $T_f > 0$ and steady-state tracking accuracy $\delta_i > 0$, if the design parameters are chosen such that $\mu_i \ge \frac{\overline{d}_i^2}{\varepsilon_i^2}$, then, when $t \ge T_f$, the system state V, ϑ satisfies that: $|V - V_d| \le \delta_1$, $|\vartheta - \vartheta_d| \le \delta_2$.

3.2 Control Input Assignment

This section assigns the two virtually control designed previously to the three actual control inputs, rudder deflection, throttle opening, and span deformation rate

An expression entered by the virtual control gives:

$$\begin{bmatrix} f_{m1} \\ f_{m4} \end{bmatrix} + \begin{bmatrix} g_{m11} & g_{m21} & g_{m31} \\ g_{m14} & g_{m24} & g_{m34} \end{bmatrix} u_m = \begin{bmatrix} v_{c1} \\ v_{c2} \end{bmatrix} \tag{21}$$

Further, make $A = \begin{bmatrix} f_{m1} \\ f_{m4} \end{bmatrix}, B = \begin{bmatrix} g_{m11} & g_{m21} & g_{m31} \\ g_{m14} & g_{m24} & g_{m34} \end{bmatrix}$, $v = v_c - A$, Then the formula above translates to:

$$Bu_m = v \tag{22}$$

Therefore, the problem is transformed into solving the actual control law u_m by the above equation.

In making control allocation, the control inputs are considered to be as close to the initial equilibrium state of the system as possible, while the rate of change of the control inputs is as small as possible, so the above control allocation problem is represented as an optimization problem as shown below

$$\begin{aligned} &\min_{u_m} \left\{ \left\| W_1 (u_m - u_{m0}) \right\|_2 + \left\| W_2 (u_m - u_m(t-T)) \right\|_2 \right\} \\ &s.t. \quad Bu_m = v \end{aligned} \tag{23}$$

where u_{m0} is the control input in the initial equilibrium state of the system and T is the sampling time of the system.

Two lemmas are introduced below to solve the above optimization problem.

Lemma 2 [10]: an optimization problem

$$\min_x \left\{ \left\| W_1 (x - x_1) \right\|_2 + \left\| W_2 (x - x_2) \right\|_2 \right\} \tag{24}$$

is equivalent to:

$$\min_x \left\{ \left\| W (x - x_0) \right\|_2 \right\} \tag{25}$$

where $W = \left(W_1^2 + W_2^2\right)^{1/2}$, $x_0 = W^{-2}\left(W_1^2 x_1 + W_2^2 x_2\right)$.

Lemma 3 [10]: For the optimization problem:

$$\begin{aligned} &\min_x \left\{ \left\| W (x - x_0) \right\|_2 \right\} \\ &s.t. \quad y = Ax \end{aligned} \tag{26}$$

there are the following solution:

$$x = Fx_0 + Gy \tag{27}$$

where $F = I - GA, G = W^{-1}\left(AW^{-1}\right)^{-1}$.

Note that since AW^{-1} is not a square matrix, here $\left(AW^{-1}\right)^{-1}$ represents the pseudoinverse of AW^{-1}, and the specific solution expression is:

$$\left(AW^{-1}\right)^{-1} = \left(AW^{-1}\right)^{\mathrm{T}}\left[\left(AW^{-1}\right)\left(AW^{-1}\right)^{\mathrm{T}}\right]^{-1} \quad (28)$$

Finally, from the above two lemmas, the solution of the optimization problem (24) can be obtained as

$$u_m = Fu_1 + Gv \quad (29)$$

where:

$$F = I - GB, G = W^{-1}\left(BW^{-1}\right)^{-1}, W = \left(W_1^2 + W_2^2\right)^{1/2}$$

$$u_1 = W^{-2}\left(W_1^2 u_0 + W_2^2 u\left(t - T\right)\right)$$

So far, the control law of state deformation coordinated control for variable span vehicles is obtained. In which, the wingspan deformation rate is adjusted as control input according to the state of the system, achieving the flight status-deformation cooperative control of the morphing vehicle. In addition, by adjusting the weight matrix, the approach degree of the three inputs to the initial equilibrium point and the rate of change of the three inputs can be controlled, so the problems such as the controller saturation control quantity changing violently can be solved to some extent.

4 Simulation results

In this section, the advantages of the morphing vehicle over conventional vehicles and the effectiveness of the proposed adaptive sliding mode control algorithm are verified through a numerical simulation.

4.1 Simulation condition

The control task is to use the proposed control algorithm such that: the speed increases from 100 m/s to 150 m/s in 50s and remains thereafter, and altitude remains at a level of 2km in the first 50s and climbs to 2.5 km from 50s to 80s, remains at a level of 2.5km from 80 to 140s, decreases to 2 km from 140 to 170s, and remains at a level of 2 km thereafter. The thrust optimization is expected in the flat flight phase, and the rudder deflection and rudder rate optimization are expected in the maneuvering phase.

The parameters are set as:

$$S_w = 17.09, c_A = 1.74, I_y = 4067.5, T_{\delta_t} = 85.2, g = 9.8$$

$$m = 1247, k_1 = 3, \varepsilon_1 = 0.8, T_{f1} = 50, \mu_1 = 15, k_2 = 10$$

$$\varepsilon_2 = 0.05, T_{f2} = 0.2, \mu_2 = 13$$

Cruise flight segment

$$W_1 = \mathrm{diag}\left(\left[1 \quad 0.1 \quad 10\right]\right), W_2 = \mathrm{diag}\left(\left[200 \quad 0.1 \quad 10\right]\right)$$

Maneuvering flight segment

$$W_1 = \mathrm{diag}\left(\left[100 \quad 0.1 \quad 10\right]\right), W_2 = \mathrm{diag}\left(\left[200 \quad 0.1 \quad 10\right]\right)$$

4.2 Simulation results and analysis

The simulation results are shown in fig:

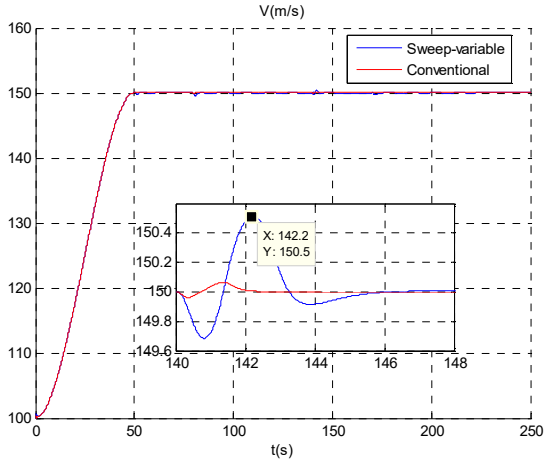

Fig. 1: Flight speed curve

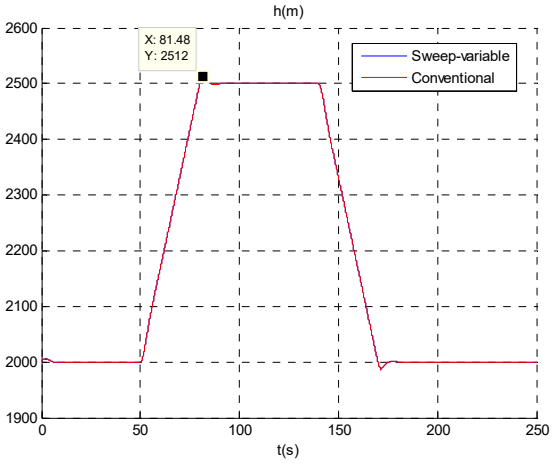

Fig. 2: Flight altitude curve

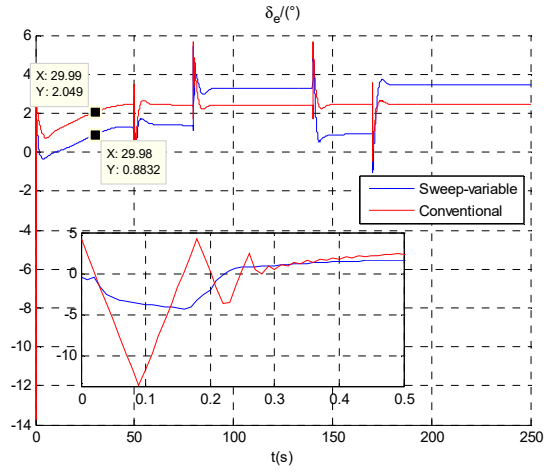

Fig. 3: Rudder deflection curve

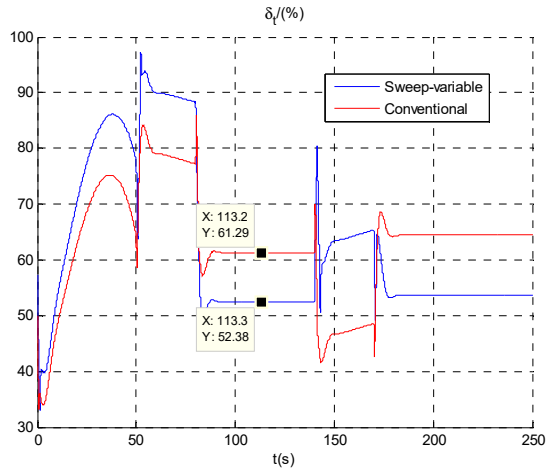

Fig. 4: Throttle opening curve

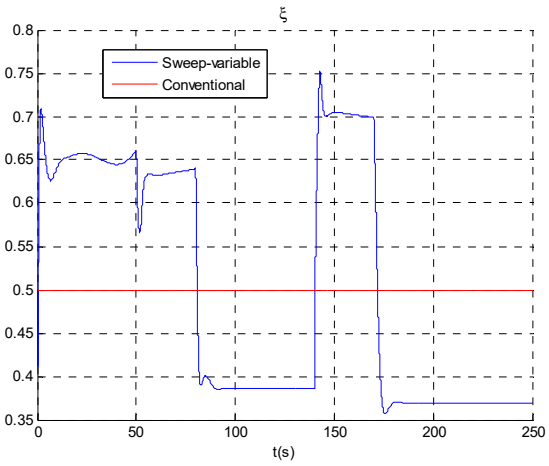

Fig. 5: Span deformation rate curve

From Figure 1, both conventional and variable span vehicles are capable of reaching a specified speed in 50 s, without overshoot, and without steady state error. Variable span vehicles have minor (within 0.5 m/s) fluctuations in velocity near steady state values at the moment of span change

From Figure 2, both conventional and variable span vehicles are capable of the assigned altitude mission, with essentially no difference between the dynamic and steady-state processes, with a steady state error of 0 and an overshoot of 0.5%.

From Figure 3, in the vehicle maneuvering phase (0~80s, 140~170s), the variable span vehicle rudder deflection requirements are significantly smaller than for conventional vehicles (more than 57%). In the initial start control phase, both rudder deflection and angular velocity requirements are large for conventional vehicles, with rudder deflection requirements around 14 ° and rudder deflection velocity reaching a limiting amplitude (350 °/s), while variable span vehicles reduce both rudder deflection and angular velocity requirements through span changes, with maximum rudder deflection within 5 ° and rudder deflection velocity significantly reduced.

From Figure 4, in the level flight phase (80-140s, 170-250s), a variable span vehicle changes aerodynamics through span deformation, reducing thrust requirements by more than 14.5% for the same mission.

From Figure 5, the conventional vehicle wingspan deformation rate maintains an initial wingspan of 0.5, while the variable span vehicle changes the wingspan according to mission requirements, thereby achieving different optimization goals for different phases of flight.

5 Conclusion

In this paper, the span deformation is regarded as the control input of a variable span vehicle, and the vehicle status-deformation cooperative control dynamics model is established; An adaptive sliding mode method with preset adjustment time is applied, which ensures the vehicle state under compound jamming converges in a specified time. The simulation results show that the state deformation coordinated control has little difference from the conventional vehicle in state tracking accuracy and dynamic process. However, compared to conventional vehicles, the state deformation coordinated control of variant vehicles can change the wingspan and reduce thrust or rudder deflection requirements by adjusting the control gain allocation matrix.

References

[1] Kudva J N. Overview of the DARPA smart wing project[J]. Journal of Intelligent Material Systems and Structures, 2004, 15(4): 261-267.

[2] Barbarino S, Bilgen O, Ajaj R M, et al. A review of morphing aircraft[J]. Journal of Intelligent Material Systems and Structures, 2011, 22(9): 823-877.

[3] Reich G W, Sanders B, Joo J J. Development of skins for morphing aircraft applications via topology optimization[R]. Reston, VA, USA: American Institute of Aeronautics and Astronautics, 2007.

[4] He Y, Li C, Zhang W, et al. Switching LPV control design with MDADT and its application to a morphing aircraft[J]. Kybernetika -Praha-, 2016, 52(6):967-987.

[5] Ligang GONG, Qing WANG, Changhua HU, et al. Switching control of morphing aircraft based on Q-learning [J]. Chinese Journal of Aeronautics, 2020, 33(2):672-687.

[6] Yan B, Dai P, Liu R, et al. Adaptive super-twisting sliding mode control of variable sweep morphing aircraft[J]. Aerospace Science and Technology,2019, 92(SEP.):198-210.

[7] Bao C, Wang P, Tang G. Integrated Guidance and Control for Hypersonic Morphing Missile Based on Variable Span Auxiliary Control[J]. International Journal of Aerospace Engineering, 2019, 2019(PT.2):1-20.

[8] Yin Ming, Lu Yu Ping, Xu Liang, He Zhen. Sliding mode disturbance observer-based gain-scheduled control for telescopic-wing aircraft in morphing flight[J]. ICIC Express Letters, Part B: Applications, 2015, 6(11): 2943-2950.

[9] Hou M, Tan F, Han F, et al. Adaptive sliding mode control of uncertain nonlinear systems with preassigned settling time and its applications[J]. International Journal of Robust and Nonlinear Control, 2019(3): 1-25.

[10] O Härkegård. Backstepping and control allocation with applications to flight control[J]. Linkpings Universitet, 2003.

Proceedings of the 3rd Conference on Fully Actuated System Theory and Applications
May 10-12, 2024, Shenzhen, China

A Method of Lunar Autonomous Driving Perception Planning Based on Hybrid A*

Tao Hu[1,2,3], Tao Cao[1,2,3], Bo Zheng[1,2,3], Zhouyuan Qian[1,2,3], Fei Han[1,2,3], Liang He[4],

1. Shanghai Institute of Spaceflight Control Technology, Shanghai 201109, China
E-mail: nuaa__ht@163.com

2. Shanghai Key Laboratory of Intelligent Control Technology, Shanghai 201109, China

3. Shanghai Manned Lunar Exploration Fusion and Innovation Center, Shanghai 201109, China

4. College of Software, Northwestern Polytechnical University, Xian 710129, China

Abstract: As humans continue to deepen their exploration of space, lunar autonomous driving technology has gradually become a research hotspot. This article conducts a comprehensive and in-depth study of lunar autonomous driving technology, aiming to provide technical support for future lunar exploration missions. First, the background and significance of lunar autonomous driving technology are introduced, and the characteristics of the lunar environment and the importance of autonomous driving in lunar exploration are explained. This paper proposes a lunar surface autonomous driving method based on hybrid A*. This method detects obstacles and 3D targets through pre-fusion of radar and images, thereby constructing a passable grid map, and then uses the hybrid A* algorithm as a During the global planning period, the path is planned in real time, control instructions are output, and automatic detection and avoidance of obstacles are realized. At the same time, combined with the Lidar vision inertial fusion odometer algorithm, autonomous navigation of lunar vehicles is achieved. Finally, the feasibility and effectiveness of the proposed method were verified through experiments. The research results of this article will provide important technical support for future lunar exploration missions and help promote the further development of lunar surface autonomous driving technology.

Key Words: Lunar surface exploration, autonomous driving, hybrid A*, unstructured paths, lunar surface environment perception

1 Introduction

As terrestrial autonomous driving technology becomes more and more mature, and the craze for manned lunar landings is promoted, some countries and institutions are actively combining terrestrial autonomous driving technology to carry out research and exploration of lunar autonomous driving[1] . For example, NASA and the private company SpaceX are both developing lunar autonomous driving technology.

In the future, humans will need to establish bases and facilities on the moon. By using autonomous driving technology, lunar surface construction and base construction can be carried out more quickly and efficiently, providing more support and guarantee for human survival and development in space. And the moon contains abundant resources, including water, oxygen, helium-3, etc. By using autonomous driving technology, these resources can be developed and utilized more quickly and efficiently, providing more support and guarantee for human survival and development in space[2] . In addition to applications on the moon, lunar autonomous driving technology can also be applied to other deep space exploration missions, such as exploration missions to Mars, Venus and other planets.

Ground autonomous driving mainly relies on advanced sensors, computer vision, artificial intelligence and machine learning technologies to perceive, analyze and make decisions on the road environment, thereby achieving autonomous navigation and control of the vehicle. The computing resources for autonomous driving on the lunar surface are relatively demanding, and special problems such as complex lunar terrain, communication delays, and energy supply need to be solved.

Terrestrial autonomous driving usually relies on the global positioning system for positioning. On the lunar surface, due to the lack of communication systems on the earth, other methods need to be used for positioning, such as using lunar maps and odometry.

In terms of application scenarios, ground autonomous driving is mainly used in road scenarios such as urban roads and highways. Complex traffic environments and factors such as road signs and signals need to be considered. Autonomous driving on the lunar surface is mainly used in the rugged lunar terrain and special environments without an atmosphere. It needs to solve problems such as lunar terrain identification and obstacle avoidance. However, autonomous driving on the lunar surface is also divided into three parts: perception, planning and control, as shown in the figure below.

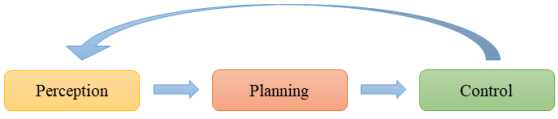

Fig. 1: Schematic diagram of the lunar autonomous driving process

Among them, helping astronauts realize automatic perception planning on the lunar surface has the following advantages:

(1) It can improve mission efficiency: the environment on the lunar surface is complex and harsh, including uneven

*This work is supported by Shanghai Sailing Program(22YF1447200).

terrain and lack of atmospheric protection. Autonomous driving technology can help lunar probes or vehicles navigate and avoid obstacles autonomously, thereby improving mission execution efficiency.

(2) Reduce human errors: Astronauts are prone to errors when operating in complex and harsh environments, and autonomous driving technology can use algorithms and sensors to perceive the environment and make decisions, reducing risks caused by human errors.

(3) Achieve remote operation: Due to the long distance between the moon and the earth, communication delay is an important issue. Autonomous driving technology can reduce reliance on real-time communications, allowing lunar probes or vehicles to perform tasks autonomously without real-time instructions.

(4) Cost reduction: Autonomous driving technology can reduce the operating costs of lunar missions because it reduces the need for expensive human resources and allows for more efficient use of resources.

With the deepening of research on planning algorithms, reinforcement learning is increasingly used to train agents and output control instructions end-to-end. R. U. Sonsalla et al[3] address a solution to access and map a lunar lava tube with a semi-autonomous heterogenous team of exploration rovers. Yu X et al[4] designed an end-to-end path planning algorithm based on deep reinforcement learning methods, including state space, action space, network structure, reward function that considers slip behavior, and a training method based on proximal policy optimization. However, this innovative method lacks safety when operating on the lunar surface and is limited by the training constraint function. Among traditional algorithms, S. Sedighi et al[5] present an innovative and computationally efficient approach of fusing the well-known Hybrid A-star search engine with the Visibility Diagram planning to find the shortest possible non-holonomic path in a hybrid (continuous-discrete) environment for valet parking. Similar to the A* algorithm, Hybrid A* planning is based on raster maps. The difference is that A* does not consider the kinematic constraints of the moving body (robot or vehicle) when searching for surrounding nodes, while Hybrid A* considers this constraint and limits the direction of progress when expanding the node, so its output trajectory is certain. is passable.

Therefore, this article uses sensors such as lidar, cameras, and IMUs to perceive the lunar surface environment, uses the LVI-SAM[6] algorithm to provide positioning information and perform three-dimensional mapping, and uses the octree algorithm to convert the surrounding environment information into a voxel grid and then perform secondary processing. Dimensional projection is used as the global two-dimensional grid map input of the planning algorithm, and the hybrid A-star algorithm is used as the global planner to carry out path planning and conduct actual experimental tests. The success rate of path planning can reach more than 90%.

2 Perception Method of Lunar Surface Autonomous Driving

The lunar surface scene mainly consists of undulating terrain such as craters. There are no unique ground objects such as trees and buildings. It lacks significant visual texture and geometric features. Conventional SLAM solutions using a single sensor face huge challenges. In addition, the lunar scene also presents many challenges due to the undulating terrain, bumps during the robot's exploration, sudden changes in posture, and dramatic changes in lunar illumination. Therefore, this article uses LVI-SAM multi-sensor fusion to obtain visual, laser, and inertial multi-modal data. Different modal data complement each other's advantages and significantly improve the robustness to environmental challenges. In order to achieve reliable autonomous positioning of the patrol vehicle, special attention is paid to autonomous positioning in degraded scenarios, which is the basis for autonomous driving on the lunar surface.

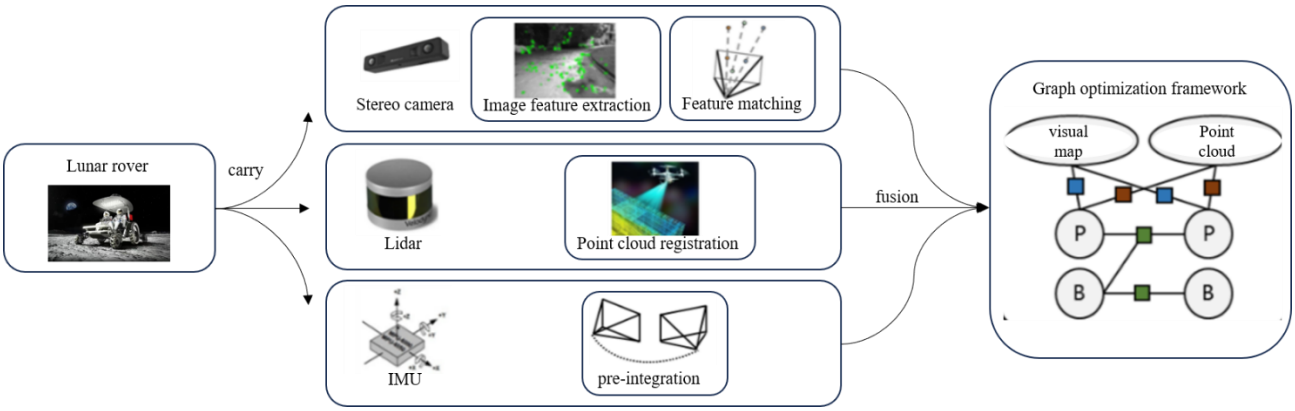

Fig. 2: Lidar vision-inertia fusion positioning algorithm flow chart

As shown in the figure, the IMU odometry node is added to the laser odometry and visual odometry threads, and with the IMU as the central node, the lidar, IMU, and camera are integrated to perform motion recovery in a coarse-to-precision manner. The visual inertial odometry establishes a reprojection error for factor graph optimization. The error factors include visual reprojection error, IMU pre-integration error, marginalization error and a priori pose error provided by the IMU odometry. Laser inertial odometry, based on the extraction of point, line and surface features in the laser point cloud, uses the prior pose of the IMU to determine the area where the point, line and surface features to be matched in the laser point cloud are located, and uses the dynamic octree algorithm to perform laser The

addition of new points and the removal of old points in the point cloud, as well as the search for feature points. Use linearity, flatness and curvature to establish point-point, point-line, point-surface measurement error functions, and add the error factors in the laser inertial odometry together with the IMU pre-integration error and the IMU prior pose error.

The visual inertial odometry subsystem and the laser inertial odometry subsystem provide pose estimation to constrain the IMU's bias, establish the IMU pre-integration factor, and update the IMU pre-integration result. After this, two different residuals are obtained, different weights are given to the two residuals, and the IMU residual factor calculation is performed using the reliability of the observation environment. Finally, motion prediction is implemented in the IMU odometry node.

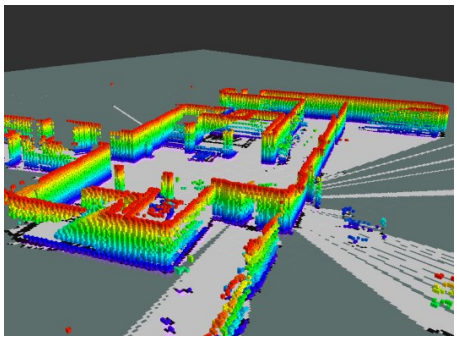

Fig. 3: Octree map of experimental scene

At the same time, after the slam algorithm establishes a point cloud map, the point cloud map needs to be processed to meet navigation planning requirements. Two-dimensional raster maps and octree maps can be used directly for planning, while octree maps are sparse, structured, and indirect coordinate index queries, which can reduce memory consumption. Therefore, laser point clouds are used for constructing octree maps, the octree uses probability to describe the occupancy of nodes. Given lidar measurements $z_{1:t}$, the probability $P\left(n\middle|z_{1:t}\right)$ that a leaf node n is occupied is calculated as:

$$P\left(n\middle|\ z_{1:t}\right)=\left[1+\frac{1-P\left(n\middle|\ z_t\right)}{P\left(n\middle|\ z_t\right)}\frac{1-P\left(n\middle|\ z_{1:t-1}\right)}{P\left(n\middle|\ z_{1:t-1}\right)}\frac{P(n)}{1-P(n)}\right]^{-1} \quad (1)$$

The above equation depends on the current measurement z_t, the prior probability $P(n)$ and the previous estimate $P\left(n\middle|z_{1:t-1}\right)$. $P\left(n\middle|z_t\right)$ represents the probability that voxel n is occupied given the measurement of z_t, this value is specific to the lidar that generated z_t, and then stores the logit value of the probability $P\left(n\middle|z_{1:t}\right)$, where:

$$\mathrm{L}(n)=\log\left[\frac{P(n)}{1-P(n)}\right] \quad (2)$$

The updated formula after Logit transformation is as follows:

$$\mathrm{L}\left(n\middle|\ z_{1:t}\right)=\mathrm{L}\left(n\middle|\ z_{1:t-1}\right)+\mathrm{L}\left(n\middle|\ z_t\right) \quad (3)$$

Then map the octree map, set the threshold of the z-axis of the point cloud map, fine-tune the minimum value of the z-axis to just filter out the ground information, characterize the obstacle information higher than the ground, and obtain a two-dimensional raster map Used for subsequent path planning algorithms, as shown in the figure below, an area is divided into many small grids, and then a binary value (0 or 1, 0 means free; 1 means occupied) is placed in each grid. As shown below, a two-dimensional raster map with a resolution of 0.05m:

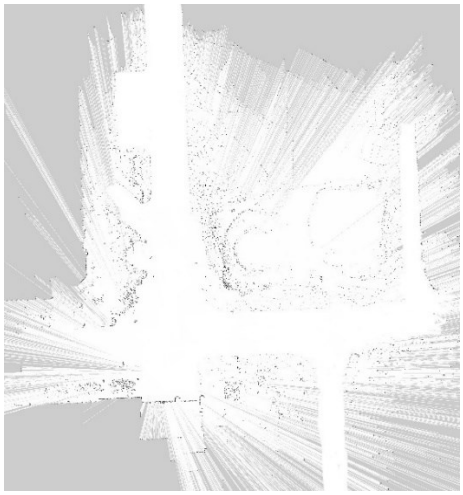

Fig. 4: 2D raster map of the experimental scene

3 Method of Path Planning Based on Hybrid A*

At present, a variety of planning algorithms have been proposed in the field of mobile robots. They can be roughly divided into two categories: global path planning algorithms and local path planning algorithms based on their application problem scenarios. Global path planning can usually plan an optimal path, but it requires Accurate information about the environment is known in advance. At the same time, because the planned map space is large, it is generally difficult to consider kinematic constraints to ensure completeness and solution efficiency. Local path planning focuses on considering the current local environment information of the robot, and it relies on the sensors carried by the robot. Dynamically obtain local environment information around the robot, and change it in real time as the environment changes. Compared with global path planning, local path planning has higher real-time performance due to smaller planning space, and can also satisfy kinematics and dynamics. constraints, but global optimality is difficult to guarantee. Considering that the environmental information may be unknown or incomplete when the lunar rover performs special tasks such as autonomous driving and scientific exploration, the solution that combines global path planning and local path planning algorithms is more suitable for autonomous driving on the lunar surface.

This paper uses the hybrid A* algorithm as the global path planner. The hybrid A* algorithm is an algorithm for path planning in a continuous state space, which combines the traditional A algorithm and the vehicle dynamics model. Through the combination of discretized state space and continuous dynamics model, this algorithm can find the optimal path while considering vehicle constraints. First, we need to define the map and related parameters of the target

area. Assume that the target area is a rectangular area. The three-dimensional octree map is obtained by the positioning and mapping algorithm introduced in Section 2, and then converted into a two-dimensional raster map, where, 0 represents the drivable area and 1 represents the obstacle area. Additionally, we need to define the coordinates of the starting and target points.

The lunar rover is different from the Ackermann steering structure like a car, and may have a unique mechanism type. This article assumes that the lunar rover's kinematic model is:

$$\dot{x} = v\sin(\theta) \tag{4}$$

$$\dot{y} = v\cos(\theta) \tag{5}$$

$$\dot{\theta} = \omega \tag{6}$$

Vehicle motion satisfies the following conditions:

$$\dot{x}\cos(\theta) - \dot{y}\sin(\theta) = 0 \tag{7}$$

The Hybrid A* algorithm structure is very similar to the A* algorithm process. The core difference lies in (1) generation of child nodes (2) heuristic function design.

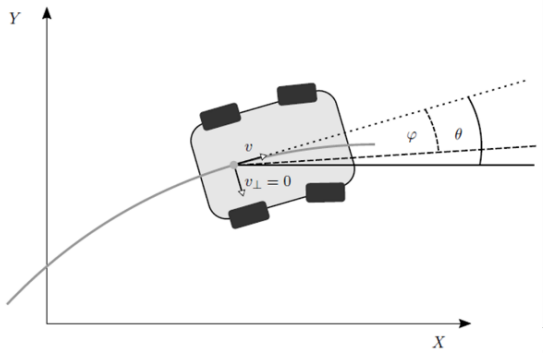

Fig. 5: Car body movement diagram

Node expansion mainly uses different turning angles to generate different short-distance nodes. First, it is decided whether to evaluate the node based on whether the local trajectory collides. If there is no collision, the arc length of the generated node can be used to determine the cost. Of course, the cost caused by steering and the cost of changes in the traveling direction can also be considered.

For each child node, consider the grid that the node reaches：

(1) If the node reaches the grid and the grid is not in the closed set, it means that the grid has not been expanded, then continue to expand the evaluation.

(2) If the grid is not in the open set (indicating that this grid has not been extended by any previous node) and if the cost-so-far of the parent node plus the cost of extending the child node to the current grid is less than the cost-so- of the current node far, the new node is considered to be a child node of the parent node, and the g function is updated at the same time, and the heuristic function is used to estimate the cost-to-come, and the child node is added to the open set.

Two heuristic functions are used in Hybrid A*: constrained heuristic and unconstrained heuristic, which represent different node expansion methods.

Constrained heuristic considers vehicle imperfections and ignores environmental obstacles. This heuristic function considers the current heading and turning radius of the vehicle in order to maintain the correct posture when the vehicle approaches the target node. Commonly used heuristic function values can use Dubins and Reeps-Shepp curves to calculate the shortest distance between two points, so the heuristic function formula is acceptable.

Unconstrained heuristic only considers obstacles and ignores vehicle incomplete restrictions. This heuristic function can be calculated entirely based on the shortest path distance from the current point to the target point. Commonly used heuristic functions can use Euclidean distance, etc., so this heuristic function is also acceptable.

Since both heuristic functions are acceptable, we only need to go to the maximum value between the two as the final heuristic function value.

$$h_c(x) = \max\left\{l(x), d(x, x_g)\right\} \tag{8}$$

In the formula, $l(x)$ is the extended node distance function, and $d(x, x_g)$ is the function between the current node and the target node.

Although the path planned by Hybrid A* is executable, there are some unnecessary turning operations, so the path smoothing of the Hybrid A* planning result is required to obtain a smoother and safer path. By using a gradient descent smoother, its objective function can be expressed as

$$P = \omega_{obs}P_{obs} + \omega_{cur}P_{cur} + \omega_{smo}P_{smo} + \omega_{vor}P_{vor} \tag{9}$$

P_{obs} is Defined as an obstacle term that penalizes collisions with objects. Assume that x_i is each point on the path, for the point that satisfies $|x_i - o_i| \le d_{obs}$, where o_i is the nearest obstacle from x_i, d_{obs} is the maximum threshold of collision risk, the penalty between the two can be expressed by a quadratic function, that is $\left(|x_i - o_i| - d_{obs}\right)^2$.

$$P_{obs} = \sum_{i=0}^{N} \sigma_{obs}\left(|x_i - o_i| - d_{obs}\right) \tag{10}$$

Among them, σ_{obs} is the quadratic penalty function, when $|x_i - o_i| > d_{obs}$ is 0. P_{cur} is defined as the curvature term. for $\frac{\Delta\Phi_i}{|\Delta x_i|} > \kappa_{\max}$ punishment,

$$P_{cur} = \sum_{i=1}^{N-1} \sigma_{cur}\left(\frac{\Delta\Phi_i}{|\Delta x_i|} - \kappa_{\max}\right) \tag{11}$$

Among them, σ_{cur} is defined as the quadratic penalty function, and $\Delta\Phi_i = \arccos\frac{x_i x_{i+1}}{|x_i||x_{i+1}|}$ is the change of the tangent angle between the point i and the adjacent point. $\Delta x_i = x_i - x_{i-1}$ is the vector difference between point i and its adjacent points. The displacement vector between vertices is evaluated for the smoothing term P_{smo}, which can be defined as,

$$P_{smo} = \sum_{i=1}^{N-1} \left(\Delta x_{i+1} - \Delta x_i \right)^2 \quad (12)$$

P_{vor} can make the path away from obstacles. This definition uses the voronoi field function, which is simply expressed as

$$P_{vor} = \sum_{i=1}^{N} \rho V \left(x_i, o_i \right) \quad (13)$$

4 Experiments

4.1 Structured Park Experiment

We use the unmanned vehicle platform system to organize field tests on the perception planning method proposed above. The hardware mainly includes AutoBots-Pro - a modular and highly intelligent wire-controlled chassis with strong load capacity (Full load mass 1700KG) and passing capacity are suitable for a variety of application scenarios. It supports manual remote control driving and automatic driving, and reserves multi-sensor wiring harness interfaces for automatic driving. It can be equipped with sensors and intelligent devices such as lidar, positioning module RTK-GNSS, and cameras, making it convenient for developers to apply various automatic driving scenarios.



Fig. 6: Experimental platform and sensors

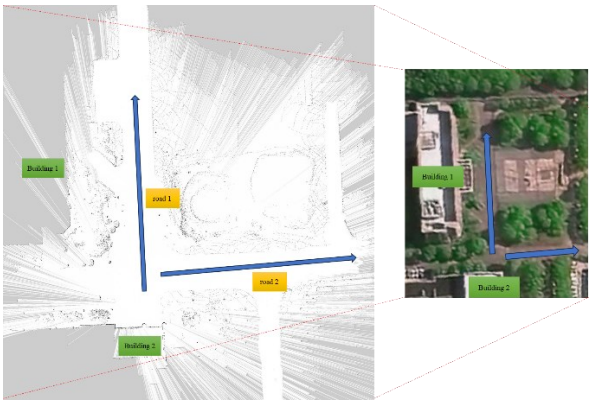

Fig. 7: Comparison of environmental maps and satellite maps

Table 1: Test parameter table

project	parameter
Length*width*height (mm)	3250*1675*660
suspension solution	Front and rear double wishbone independent suspension
Minimum turning radius (m)	⩽3.2
Communication Interface	CAN 2.0B
control mode	Remote control/computer command control
camera	Flir 41c6c
lidar	Ch128X1
IMU	Yesense 510A
On-board computer	NVIDIA AGX Xavier

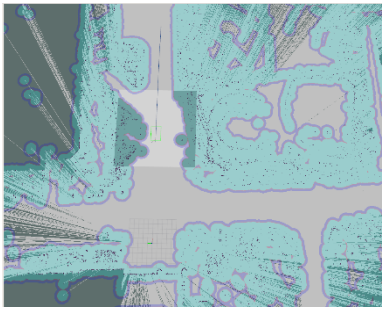

（a）

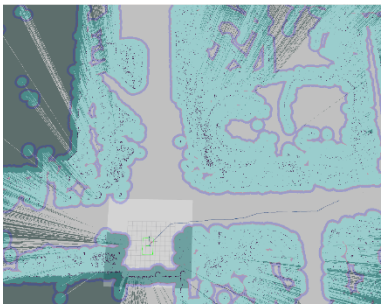

（b）

Fig. 6: Structured park experimental path planning results

In the structured park test site, our global path planning technical framework based on this complex map is shown in Figure 8. First, the hybrid A* algorithm is used to perform path planning on a low-precision environmental data model. Subsequently, the obtained path is segmented, and the starting point and end point of each segmented path are re-planned using the direction-guided path search method. Finally, the segmented paths are connected to form the final global path. This method aims to improve the computational efficiency of the algorithm while reducing the length cost of path planning.

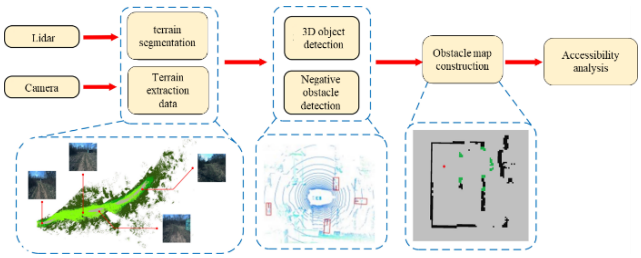

Fig. 8: Autonomous driving test flow chart

4.2 Unstructured Lunar Terrain Simulation Experiment

In addition, we conducted autonomous driving tests in an unstructured simulated lunar scene. The venue is as shown

below. After determining the absolute coordinate system, vehicle body coordinate system, and odometer coordinate system, we continuously solved the vehicle body motion through sensor data. position to provide positioning information. At the same time, lidar and cameras sense the area ahead, represent it with an octree map, and then map it into a two-dimensional grid map, which is provided to the hybrid A* global planner to plan a safe path to the target location. . Since there are no dynamic obstacles on the lunar surface, dynamic local obstacle avoidance is not considered for the time being. The planning results are shown in Figure 10.



Fig. 9: Unstructured experimental site

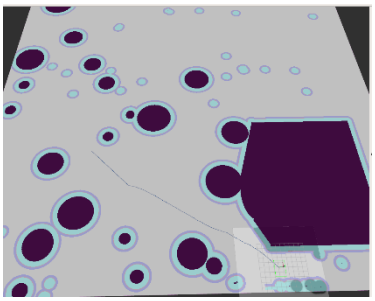

（a）

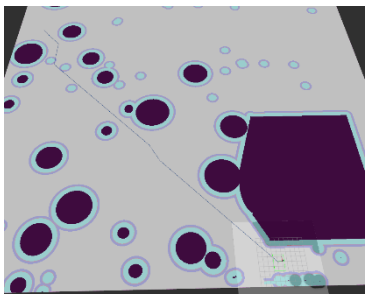

（b）

Fig. 10: Experimental results of unstructured simulated lunar terrain path planning

5 Conclusion

In response to the demand for global path planning technology in complex terrain, the research team plans to conduct research on overcoming the limitations of low computational efficiency in long-distance cross-country path planning. This study combines the characteristics of off-road path planning that are not restricted by road network traffic and the theory of the straight-line shortest path between two points, proposes a direction-based search guidance path planning method, and performs path segmentation optimization to improve path quality and improve Computational efficiency.

Through forward fusion of radar vision, negative obstacle detection and 3D target detection are performed to construct a passable grid map. Improving the lunar rover's scene understanding and cognitive capabilities will help the lunar rover better plan its autonomous movements in complex terrain environments.

References

[1] J. Thangavelautham, A. Chandra and E. Jensen, "Autonomous Robot Teams for Lunar Mining Base Construction and Operation," 2020 IEEE Aerospace Conference, Big Sky, MT, USA, 2020, pp. 1-16, doi: 10.1109/AERO47225.2020.9172811.

[2] M. Allan et al., "Planetary Rover Simulation for Lunar Exploration Missions," 2019 IEEE Aerospace Conference, Big Sky, MT, USA, 2019, pp. 1-19, doi: 10.1109/AERO.2019.8741780.

[3] R. U. Sonsalla et al., "Towards a Semi-Autonomous Robotic Exploration of a Lunar Skylight Cavity," 2022 IEEE Aerospace Conference (AERO), Big Sky, MT, USA, 2022, pp. 1-20, doi: 10.1109/AERO53065.2022.9843610.

[4] Yu X, Wang P, Zhang Z. Learning-Based End-to-End Path Planning for Lunar Rovers with Safety Constraints. Sensors. 2021; 21(3):796. https://doi.org/10.3390/s21030796

[5] S. Sedighi, D. -V. Nguyen and K. -D. Kuhnert, "Guided Hybrid A-star Path Planning Algorithm for Valet Parking Applications," 2019 5th International Conference on Control, Automation and Robotics (ICCAR), Beijing, China, 2019, pp. 570-575, doi: 10.1109/ICCAR.2019.8813752.

[6] T. Shan, B. Englot, C. Ratti and D. Rus, "LVI-SAM: Tightly-coupled Lidar-Visual-Inertial Odometry via Smoothing and Mapping," 2021 IEEE International Conference on Robotics and Automation (ICRA), Xi'an, China, 2021, pp. 5692-5698, doi: 10.1109/ICRA48506.2021.9561996.

Proceedings of the 3rd Conference on Fully Actuated System Theory and Applications
May 10-12, 2024, Shenzhen, China

Robust Tracking Control for A Type of Combined Spacecraft: A Discrete-Time FAS Approach

Kai-Xin Cui [1], Guang-Ren Duan [1,2]

1. Center for Control Theory and Guidance Technology, Harbin Institute of Technology, Harbin 150001, P. R. China
E-mail: 19b904071@stu.hit.edu.cn

2. Center for Control Science and Technology, Southern University of Science and Technology, Shenzhen 518055, P. R. China
E-mail: g.r.duan@hit.edu.cn

Abstract: In this paper, the robust tracking control of a combined spacecraft simulator (CSS) system is investigated based on the discrete-time fully actuated system (FAS) approach. Firstly, the CSS system is modeled as a discrete-time uncertain second-order FAS model and generalized to general discrete-time high-order fully actuated systems (HOFASs) with nonlinear uncertainties. Secondly, for the proposed tracking control problem, a sufficient condition to solve it is given by designing a discrete-time HOFA robust controller, followed by a stability analysis. Further, the designed controller generates a closed-loop system with an arbitrary assignable eigenstructure in which the design degrees of freedom can be exploited further. Finally, the proposed control technique is used to solve the robust tracking control of CSS, and the simulation results demonstrate the effectiveness and practicality of the proposed method.

Key Words: Discrete-time HOFASs, combined spacecraft simulator, step backward uncertain HOFA models, robust tracking control, parametric design.

1 Introduction

Robust control is used to deal with uncertainties in the system, and its related research has always been a research hotspot in the field of control theory and application. Especially in recent years, for the robust control of discrete-time systems, many scholars have combined robust control with some advanced control methods, giving birth to many theoretical and practical research results. Such as, based on the robust output regulation theory, literature [1] investigated the optimal output tracking problem for linear discrete-time systems with unknown dynamics. While a observer based robust tracking predictive controller for discrete-time nonlinear affine systems was developed in [2]. And literature [3] studied the problem of static output feedback preview tracking control for discrete-time systems with time-varying parameters. Also for practical applications, literature [4] presented the design of a robust observer based on discrete-time formulation of uncertainty and disturbance estimators for controlling robotic manipulators. And for multi-input multi-output uncertain discrete-time systems, a systematic method to design robust tracking controllers, including mechatronics applications, was developed in [5].

Besides, in recent years, with the rapid development of the world's aerospace science and technology, the increasing complexity of aerospace vehicle structure and control tasks, as well as the increasingly high system performance requirements, the uncertainty problems in aerospace vehicle systems have become more complex and diversified. Accordingly, the application of relevant methods based on robust control in aerospace vehicles has burst into new vigor. Based on the nonlinear disturbance observer control technique, literature [6] investigated the robust control of attitude tracking system between two rigid spacecraft, and subsequently, the authors also proposed a composed control approach by combining a nonlinear disturbance observer and an asymptotic tracking control for spacecraft formation flying system [7], while the robust cooperative tracking and application for heterogeneous spacecraft systems were addressed in [8]. And in [9], the problem of robust output-feedback motion tracking control for spacecraft close-range proximity maneuvers was considered. Also, for robust attitude tracking control of spacecraft, see [10, 11] and their associated studies.

One thing to note is that most of the research on robust control, including the above, has been carried out in the first-order state-space framework. The state-space approach can still be effective in dealing with linear systems containing uncertainties, but it is often impotent when faced with uncertain systems containing complex nonlinearities. Fortunately, the fully actuated system (FAS) method has brought a new light to deal with complex nonlinear problems [12, 13]. Since its inception, it has demonstrated strong superiority and capability in both continuous and discrete-time systems, including adaptive control [14], fault tolerance control [15] predictive control [16], model reference tracking control [17], etc. Especially the robust control of continuous systems has been deeply discussed in [18].

This paper further investigates the robust tracking control of a combined spacecraft simulator (CSS) system based on the discrete-time high-order fully actuated system (HOFAS) approach framework established in [19], which is of great significance for studying the tracking control of postcapture combined spacecraft in space.

2 Problem description

In this paper, I_n represents the identity matrix, $\det(A)$, A^{-1} and $\|A\|_2$ are the determinant, inverse and 2-norm of matrix A, respectively. For $K_i \in \mathbb{R}^{m\times m}$, $i = 1, 2, \cdots, n$, define $K_{0\sim n} = \begin{bmatrix} K_0 & K_1 & \cdots & K_n \end{bmatrix}$ and

$$\Psi(K_{0\sim n}) = \begin{bmatrix} K_0 & K_1 & \cdots & K_n \\ I & & & \\ & \ddots & & \\ & & I & 0 \end{bmatrix}.$$

This work was supported by the Science Center Program of National Natural Science Foundation of China (62188101).

For $x(k)$, there is $x_p(k)|_{p=1\sim\eta}=\left[x_1^{\mathrm{T}}(k)\, x_2^{\mathrm{T}}(k)\cdots x_\eta^{\mathrm{T}}(k)\right]^{\mathrm{T}}$, and let q^{-1} be the one-step backward operator, i.e., $x^{\lceil i\rceil}(k)=q^{-i}x(k)=x(k-i)$. For $n_0,n_i\in\mathbb{N}$, $n_0<n_i$, $i=1,2,\ldots,n$,

$$x^{\lceil n_0\sim n_i\rceil}(k)=\begin{bmatrix} x^{\lceil n_0\rceil}(k)\\ x^{\lceil n_0+1\rceil}(k)\\ \vdots\\ x^{\lceil n_i\rceil}(k)\end{bmatrix},\qquad x_p^{\lceil n_0\sim n_p\rceil}(k)|_{p=i\sim j}=x_{i\sim j}^{\lceil n_0\sim n_p\rceil}(k)=\begin{bmatrix} x_i^{\lceil n_0\sim n_i\rceil}(k)\\ x_{i+1}^{\lceil n_0\sim n_{i+1}\rceil}(k)\\ \vdots\\ x_j^{\lceil n_0\sim n_p\rceil}(k)\end{bmatrix}.$$

2.1 Discrete-time FAS modeling for the CSS system

As shown in Fig. 1, the CSS consists of two air-bearing spacecraft simulators (ABSSs) with three degrees of freedom and a robotic arm. ABSS 1 and ABSS 2 respectively represent the service spacecraft and the target spacecraft of postcapture combined spacecraft, which are suspended with the aid of air feet and are moved by the hollow cup propellers controlled by the "on-board controller". In this paper, we consider the robust tracking control of CSS in the case of power failure of the target spacecraft (for more details see [17]). The parameters of CSS are listed in Table 1.

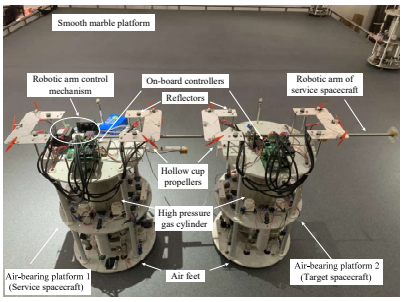

Fig. 1: The combined spacecraft simulator

Table 1: Related parameters of the CSS

Parameter	Notation	Value
Mass of the CSS	M_c	35.4kg
Distance between two centroids	L	0.776 m
Moment of inertia of the CSS	J_c	5.758kg $\cdot$ m^2
Sampling time	T_s	0.2s
Maximum thrust	\	0.2N

Consider the following step backward second-order FAS model of CSS system with uncertainties

$$\begin{cases} x_c(k+1)=2x_c(k)-x_c^{[1]}(k)+T_s^2\frac{1}{M_c}F_x(k)+T_s^2\eta sin(x_c(k))\\ y_c(k+1)=2y_c(k)-y_c^{[1]}(k)+T_s^2\frac{1}{M_c}F_y(k)+T_s^2\eta sin(y_c(k))\\ \varphi_c(k+1)=2\varphi_c(k)-\varphi_c^{[1]}(k)+T_s^2\frac{1}{J_c}F_\varphi(k)+T_s^2\frac{L}{2}\eta sin(\varphi_c(k)),\end{cases} \tag{1}$$

and noting that $x_1(k)=x_c(k)$, $x_2(k)=y_c(k)$, $x_3(k)=\varphi_c(k)$, (1) can be rewritten into a more compact form

$$x_{1\sim3}(k+1)=2x_{1\sim3}(k)-x_{1\sim3}^{[1]}(k)+\breve{B}u^*(k)+\Delta\breve{f}(x_{1\sim3}(k),k), \tag{2}$$

where $x_{1\sim3}(k)=\left[x_1(k)\, x_2(k)\, x_3(k)\right]^{\mathrm{T}}$ represents the state vector, $u^*(k)=\left[F_x(k)\, F_y(k)\, F_\varphi\right]^{\mathrm{T}}$ denotes the control vector, $\breve{B}=T_s^2\mathrm{diag}\{1/M_c,1/M_c,1/J_c\}$ apparently satisfies the full-actuation $\det\breve{B}\neq0$, and $\Delta\breve{f}(x_{1\sim3}(k),k)=T_s^2\mathrm{diag}\{\eta sin(x_1(k)),\eta sin(x_2(k)),\frac{L}{2}\eta sin(x_3(k))\}$ is the unknown uncertainty of CSS system.

Remark 1. *In (1), uncertainties $\eta sin(x_c(k))$, $\eta sin(y_c(k))$ and $\eta sin(\varphi_c(k))$ represent the effects of external airflow and subtle differences in the leveling of the marble platform at different locations on the states of the CSS system.*

Combined with the experimental setting of the practical CSS, the control objective for the second-order FAS (2) is given as: by designing a second-order fully actuated robust controller $u^*(k)$, the state $x_{1\sim3}(k)$ of FAS (2) is able to track a given reference signal $\bar{x}_{1\sim3}(k)$ under certain conditions satisfied by the uncertainty.

2.2 General step backward uncertain HOFASs

Without loss of generality, the second-order FAS (2) can be generalized to general discrete-time step backward HOFASs subject to uncertainties, following the basic framework of discrete-time HOFAS established in [19],

$$\begin{aligned} x_p(k+1)|_{p=1\sim\eta}=&f\left(x_p^{\lceil0\sim\mu_p-1\rceil}(k)\Big|_{p=1\sim\eta},k\right)+\Delta f(\cdot,k)\\ &+B\left(x_p^{\lceil0\sim\mu_p-1\rceil}(k)\Big|_{p=1\sim\eta},k\right)u(k),\end{aligned} \tag{3}$$

where $f(\cdot,k)=\left[f_1^{\mathrm{T}}(\cdot,k)\, f_2^{\mathrm{T}}(\cdot,k)\cdots f_\eta^{\mathrm{T}}(\cdot,k)\right]^{\mathrm{T}}$ and $\Delta f(\cdot,k)=\left[\Delta f_1^{\mathrm{T}}(\cdot,k)\,\Delta f_2^{\mathrm{T}}(\cdot,k)\cdots\Delta f_\eta^{\mathrm{T}}(\cdot,k)\right]^{\mathrm{T}}$ are nonlinear vector function and unknown nonlinear uncertainty, respectively, $u(k)\in\mathbb{R}^r$ is the control input vector, $x_p\in\mathbb{R}^{r_p}$, $p=1,2,\ldots,\eta$, is a set of state vectors, μ_p and r_p are given positive integers satisfying

$$r_1+r_2+\cdots+r_\eta=r, \tag{4}$$

and $B(\cdot,k)\in\mathbb{R}^{r\times r}$ satisfies the fully actuated condition $\det B(\cdot,k)\neq0$. Also, the nonlinear uncertainty satisfies

Assumption 1. *There exists a non-negative scalar γ such that the nonlinear uncertainty $\Delta f(\cdot,k)$ satisfies*

$$\|\Delta f(\cdot,k)\|_2\le\gamma\left\|x_{1\sim\eta}^{\lceil0\sim\mu_p-1\rceil}(k)\right\|_2, \tag{5}$$

where γ is the positive real number to be found.

Problem 1. *Consider the discrete-time HOFAS (3) subject to uncertainties, and let $\bar{x}(k)$ be a given discrete-time reference signal to be tracked by the state $x(k)$. To obtain a HOFA robust controller $u(k)$ such that the state of HOFAS (3) is able to track the given reference signal $\bar{x}(k)$ under the condition (5) satisfied by nonlinear uncertainty.*

3 Main results

For the proposed Problem 1, this section gives the main results of solving for it.

3.1 HOFA robust controller design and stability analysis

Denote

$$\xi(k)=x(k)-\bar{x}(k), \tag{6}$$

there are

$$\begin{cases}\xi_p^{\lceil0\sim\mu_p-1\rceil}(k)=x_p^{\lceil0\sim\mu_p-1\rceil}(k)-\bar{x}_p^{\lceil0\sim\mu_p-1\rceil}(k)\\ \xi_p(k+1)=x_p(k+1)-\bar{x}_p(k+1),p=1,\cdots,\eta,\end{cases}$$

and $f\left(x_{1\sim\eta}^{\lceil 0\sim\mu_p-1\rceil}(k),k\right)$, $\Delta f\left(x_{1\sim\eta}^{\lceil 0\sim\mu_p-1\rceil}(k),k\right)$ and $B\left(x_{1\sim\eta}^{\lceil 0\sim\mu_p-1\rceil}(k),k\right)$ can be converted accordingly with respect to $\xi(k)$

$$\begin{cases} f\left(x_{1\sim\eta}^{\lceil 0\sim\mu_p-1\rceil}(k),k\right)=f\left(\xi_{1\sim\eta}^{\lceil 0\sim\mu_p-1\rceil}(k),k\right) \\ \Delta f\left(x_{1\sim\eta}^{\lceil 0\sim\mu_p-1\rceil}(k),k\right)=\Delta f\left(\xi_{1\sim\eta}^{\lceil 0\sim\mu_p-1\rceil}(k),k\right) \\ B\left(x_{1\sim\eta}^{\lceil 0\sim\mu_p-1\rceil}(k),k\right)=B\left(\xi_{1\sim\eta}^{\lceil 0\sim\mu_p-1\rceil}(k),k\right). \end{cases}$$

Further, the HOFAS (3) can be transformed into

$$\begin{aligned}\xi_{1\sim\eta}(k+1)=&f\left(\xi_{1\sim\eta}^{\lceil 0\sim\mu_p-1\rceil}(k),k\right)+\Delta f\left(\xi_{1\sim\eta}^{\lceil 0\sim\mu_p-1\rceil}(k),k\right)\\&+B\left(\xi_{1\sim\eta}^{\lceil 0\sim\mu_p-1\rceil}(k),k\right)u(k)-\bar{x}_{1\sim\eta}(k+1).\end{aligned} \tag{7}$$

Apparently, the tracking control of HOFAS (3) can be equivalently converted to the stabilization control of above system (7). And a HOFA robust stabilization controller for system (7) can be given as

$$\begin{cases} u(k)=B^{-1}(\cdot,k)\left[-f\left(\xi_p^{\lceil 0\sim\mu_p-1\rceil}(k)\Big|_{p=1\sim\eta},k\right)+v(k)\right] \\ v(k)=\begin{bmatrix}[K_1]_{0\sim\omega_1-1}\xi_1^{\lceil 0\sim\omega_1-1\rceil}(k)\\ [K_2]_{0\sim\omega_2-1}\xi_2^{\lceil 0\sim\omega_2-1\rceil}(k)\\ \vdots\\ [K_\eta]_{0\sim\omega_\eta-1}\xi_\eta^{\lceil 0\sim\omega_\eta-1\rceil}(k)\end{bmatrix}+\bar{x}_{1\sim\eta}(k+1), \end{cases} \tag{8}$$

where $[K_p]_{0\sim\omega_p-1}=\left[\begin{array}{cccc}K_{p,0} & K_{p,1} & \cdots & K_{p,\omega_p-1}\end{array}\right]\in\mathbb{R}^{r_p\times\omega_p r_p}$, $p=1,2,\ldots,\eta$, are a set of feedback gain matrices to be determined, and ω_p, $p=1,2,\ldots,\eta$, are a set of integers satisfying $\omega_p\geq 1$. Under the control law (8), the following series of closed-loop systems containing nonlinear uncertainties can be obtained

$$\begin{aligned}\xi_p(k+1)=&[K_p]_{0\sim\omega_p-1}\xi_p^{\lceil 0\sim\omega_p-1\rceil}(k)\\&+\Delta f_p\left(\xi_{1\sim\eta}^{\lceil 0\sim\mu_p-1\rceil}(k),k\right),p=1,2,\ldots,\eta.\end{aligned} \tag{9}$$

And, if written in state-space form, the closed-loop system (9) can be represented as, according to the preceding notation,

$$\begin{aligned}\xi_p^{\lceil 0\sim\omega_p-1\rceil}(k+1)=&\Psi\left([K_p]_{0\sim\omega_p-1}\right)\xi_p^{\lceil 0\sim\omega_p-1\rceil}(k)\\&+\begin{bmatrix}\Delta f_p\left(\xi_{1\sim\eta}^{\lceil 0\sim\mu_p-1\rceil}(k),k\right)\\ 0_{(\omega_p-1)r_p\times r_p}\end{bmatrix},p=1,2,\ldots,\eta.\end{aligned} \tag{10}$$

Furthermore, denote

$$K_E=\text{blockdiag}\left\{[K_p]_{0\sim\omega_p-1},p=1,2,\ldots,\eta\right\}, \tag{11}$$

$$\Psi(K_E)=\text{blockdiag}\left\{\Psi\left([K_p]_{0\sim\omega_p-1}\right),p=1,2,\ldots,\eta\right\} \tag{12}$$

and

$$\Delta f_H(\cdot,k)=\left.\begin{bmatrix}\Delta f_p\left(\xi_{1\sim\eta}^{\lceil 0\sim\mu_p-1\rceil}(k),k\right)\\ 0_{(\omega_p-1)r_p\times r_p}\end{bmatrix}\right|_{p=1\sim\eta}. \tag{13}$$

Then, obviously, the closed-loop system (10) has a more compact form as

$$\begin{aligned}\xi_p^{\lceil 0\sim\omega_p-1\rceil}(k+1)\Big|_{p=1\sim\eta}=&\Psi(K_E)\,\xi_p^{\lceil 0\sim\omega_p-1\rceil}(k)\Big|_{p=1\sim\eta}\\&+\Delta f_H(\cdot,k).\end{aligned} \tag{14}$$

It is easy to see that the matrix $\Psi(K_E)$ can be made Schur stable by finding $[K_p]_{0\sim\omega_p-1}=\left[\begin{array}{cccc}K_{p,0} & K_{p,1} & \cdots & K_{p,\omega_p-1}\end{array}\right]$, $p=1,2,\ldots,\eta$. Further, there is the following well-known lemma.

Lemma 1. *For a Schur matrix $\Psi(K_E)$, there exists a positive definite symmetric matrix $P(K_E)$ that satisfies the following discrete-time Lyapunov matrix equation*

$$\Psi^{\mathrm{T}}(K_E)P(K_E)\Psi(K_E)-P(K_E)=-2I. \tag{15}$$

It is already known that the asymptotic stabilization of system (14) means that the state of HOFAS (3) is eventually able to track the reference signal $\bar{x}(k)$. Then, according to the Lyapunov theories of discrete-time systems, the sufficient condition regarding the asymptotic stabilization of the HOFAS (14) is as follows.

Theorem 1. *The state of HOFAS (3) can ultimately track the reference signal $\bar{x}(k)$ under the transformation (6) and the control law (8), if for a matrix $P(K_E)$ satisfying Lyapunov matrix equation (15), the uncertainty bound γ in condition (5) is given by*

$$\gamma=\frac{\Theta-\left\|\Psi^{\mathrm{T}}(K_E)P(K_E)\right\|_2}{\|P(K_E)\|_2}, \tag{16}$$

where $\Theta=\sqrt{\|\Psi^{\mathrm{T}}(K_E)P(K_E)\|_2^2+2\|P(K_E)\|_2}$.

Proof. For derivation convenience, denote

$$\Xi(k)=\xi_{1\sim\eta}^{\lceil 0\sim\omega_p-1\rceil}(k).$$

Then, choose the Lyapunov function

$$V(\Xi(k))=\Xi^{\mathrm{T}}(k)P(K_E)\Xi(k). \tag{17}$$

The increment of Lyapunov function (17) along system (14) can be expressed as

$$\begin{aligned}\Delta V=&V(\Xi(k+1))-V(\Xi(k))\\=&\left(\Psi(K_E)\Xi(k)+\Delta f_H(\cdot,k)\right)^{\mathrm{T}}P(K_E)\\&\times\left(\Psi(K_E)\Xi(k)+\Delta f_H(\cdot,k)\right)-\Xi^{\mathrm{T}}(k)P(K_E)\Xi(k)\\=&\Xi^{\mathrm{T}}(k)\left(\Psi^{\mathrm{T}}(K_E)P(K_E)\Psi(K_E)-P(K_E)\right)\Xi(k)\\&+2\Xi^{\mathrm{T}}(k)\Psi^{\mathrm{T}}(K_E)P(K_E)\Delta f_H(\cdot,k)\\&+\Delta f_H^{\mathrm{T}}(\cdot,k)P(K_E)\Delta f_H(\cdot,k).\end{aligned} \tag{18}$$

Substituting (15) into (18) gives

$$\begin{aligned}\Delta V=&-2\Xi^{\mathrm{T}}(k)\Xi(k)+2\Xi^{\mathrm{T}}(k)\Psi^{\mathrm{T}}(K_E)P(K_E)\Delta f_H(\cdot,k)\\&+\Delta f_H^{\mathrm{T}}(\cdot,k)P(K_E)\Delta f_H(\cdot,k).\end{aligned} \tag{19}$$

It is not difficult to determine that if the following inequality holds

$$-2\|\Xi(k)\|_2^2+2\|\Xi(k)\|_2\left\|\Psi^{\mathrm{T}}(K_E)P(K_E)\right\|_2\|\Delta f_H(\cdot,k)\|_2$$

$$+\|P(K_E)\|_2\|\Delta f_H(\cdot,k)\|_2^2<0, \tag{20}$$

then we have, for the above equation (19),

$$\Delta V<0.$$

Dividing both sides of the inequality (20) by $\|P(K_E)\|_2\|\Xi(k)\|_2^2$ simultaneously, gives

$$\begin{aligned}&\frac{-2}{\|P\|_2}+2\frac{\left\|\Psi^{\mathrm{T}}P\right\|_2}{\|P\|_2}\frac{\|\Delta f_H(\cdot,k)\|_2}{\|\Xi(k)\|_2}+\frac{\|\Delta f_H(\cdot,k)\|_2^2}{\|\Xi(k)\|_2^2}<0\\ \Leftrightarrow&\left(\frac{\|\Delta f_H(\cdot,k)\|_2}{\|\Xi(k)\|_2}+\frac{\left\|\Psi^{\mathrm{T}}P\right\|_2+\sqrt{\|\Psi^{\mathrm{T}}P\|_2^2+2\|P\|_2}}{\|P\|_2}\right)\\ &\times\left(\frac{\|\Delta f_H(\cdot,k)\|_2}{\|\Xi(k)\|_2}+\frac{\left\|\Psi^{\mathrm{T}}P\right\|_2-\sqrt{\|\Psi^{\mathrm{T}}P\|_2^2+2\|P\|_2}}{\|P\|_2}\right)<0,\end{aligned} \tag{21}$$

where $\Psi(K_E)$ and $P(K_E)$ are abbreviated as Ψ and P, respectively, for clarity of presentation. It follows from the above inequality that if

$$\left(\frac{\|\Delta f_H(\cdot,k)\|_2}{\|\Xi(k)\|_2}+\frac{\left\|\Psi^{\mathrm{T}}P\right\|_2-\sqrt{\|\Psi^{\mathrm{T}}P\|_2^2+2\|P\|_2}}{\|P\|_2}\right)<0, \tag{22}$$

holds, then the inequality (20) holds, which implies $\Delta V<0$. And the above inequality (22) leads naturally to expression (16) in Theorem 1. □

Remark 2. *Theorem 1 gives a sufficient condition for the state of HOFAS (3) to achieve asymptotic tracking in the presence of specific uncertainties. For a certain uncertainty, combined with Lyapunov equation (15), it can be seen that the key to achieving this condition is to find a suitable Schur matrix $\Psi(K_E)$ such that the relation (5) holds with γ derived from (16).*

3.2 Parameterization of the control law

For the Schur matrix $\Psi(K_E)\in\mathbb{R}^{\varpi\times\varpi}$, $\varpi=\sum_{p=1}^{\eta}r_p\omega_p$, to be determined in (14), combining the previous notations and (11)-(12), there is

$$\Psi(K_E)=\Psi_0+\digamma_H K_E, \tag{23}$$

where

$$\begin{aligned}\Psi_0=&\mathrm{blockdiag}\left\{\Psi_{0p},\ p=1,2,\ldots,\eta\right\},\\ \digamma_H=&\mathrm{blockdiag}\left\{\digamma_p,\ p=1,2,\ldots,\eta\right\},\\ \Psi_{0p}=&\begin{bmatrix}0&0&\cdots&0\\ I_{r_p}&\cdots&0&0\\ \vdots&\ddots&\vdots&\vdots\\ 0&\cdots&I_{r_p}&0\end{bmatrix},\ \digamma_p=\begin{bmatrix}I_{r_p}\\0\\\vdots\\0\end{bmatrix}.\end{aligned}$$

It is not difficult to determine the matrix pair $(\Psi_0,\digamma_H)$ is controllable. Apparently, for matrix $\Psi(K_E)$, the corresponding eigenvector matrix $\mathscr{V}\in\mathbb{R}^{\varpi\times\varpi}$ and the expected Jordan standard type $\mathscr{F}\in\mathbb{R}^{\varpi\times\varpi}$ can be determined by the following Sylvester equation

$$(\Psi_0+\digamma_H K_E)\mathscr{V}=\mathscr{V}\mathscr{F}, \tag{24}$$

where the eigenvector matrix $\mathscr{V}$ satisfies

$$\det\mathscr{V}\neq 0. \tag{25}$$

The solution of (24) can be converted into a standard eigenstructure assignment problem, that is, given the expected Jordan standard type $\mathscr{F}$ of $\Psi(K_E)$, find the eigenvector matrix $\mathscr{V}$ and configuration matrix K_E, such that (24) and (25) hold. Based on the basic scheme of parametric design in [13, 20], the following Algorithm 1 is built to solve it, which also includes the process of solving for γ in (16).

Algorithm 1 Compute the matrix K_E and γ in (16)

Input $\Psi_0,\digamma_H$

Output K_E,γ

1) Solve a pair of right coprime polynomial matrices $\mathscr{N}(s)$ and $\mathscr{D}(s)$ satisfying
$$(sI-\Psi_0)^{-1}\digamma_H=\mathscr{N}(s)\mathscr{D}^{-1}(s).$$
2) Denote $\mathscr{D}(s)=[d_{ij}(s)]_{r\times r}$, and $\alpha=\max\{\deg(d_{ij}(s)),\ i,j=1,2,\ldots,r\}$, such that
$$\mathscr{N}(s)=\sum_{i=0}^{\alpha}\mathscr{N}_i s^i,\ \mathscr{N}_i\in\mathbb{R}^{\varpi\times r}$$
$$\mathscr{D}(s)=\sum_{i=0}^{\alpha}\mathscr{D}_i s^i,\ \mathscr{D}_i\in\mathbb{R}^{r\times r}.$$
3) Choose a Schur matrix $\mathscr{F}$ and an arbitrary matrix $\mathscr{Z}$ to compute two parameter matrices $\mathscr{V}$ and $\mathscr{W}$
$$\mathscr{V}=\mathscr{N}_0\mathscr{Z}+\mathscr{N}_1\mathscr{Z}\mathscr{F}+\cdots+\mathscr{N}_\alpha\mathscr{Z}\mathscr{F}^\alpha,$$
$$\mathscr{W}=\mathscr{D}_0\mathscr{Z}+\mathscr{D}_1\mathscr{Z}\mathscr{F}+\cdots+\mathscr{D}_\alpha\mathscr{Z}\mathscr{F}^\alpha.$$
4) **If** (25) holds, compute K_E via $K_E=\mathscr{W}\mathscr{V}^{-1}$. **Else**, return to Step 3) to recompute matrices $\mathscr{V}$ and $\mathscr{W}$.
5) Use the resulting K_E to obtain the compound matrix $\Psi(K_E)$ following (23).
6) Solve for $P(K_E)$ by substituting $\Psi(K_E)$ obtained in Step 5) into Lyapunov equation (15).
7) Acquire γ by substituting $\Psi(K_E)$ and $P(K_E)$ obtained in Step 5) and Step 6), respectively, into (16).

Remark 3. *In Algorithm 1, the sufficient design freedom due to the arbitrariness of $\mathscr{F}$ and $\mathscr{Z}$ can be further exploited, see literature [17] for details.*

4 Application to the CSS system

First, applying the transformation (6), the second-order FAS (2) can be rewritten as

$$\begin{aligned}\xi_{1\sim3}(k+1)=&2(\xi_{1\sim3}(k)+\bar{x}_{1\sim3}(k))-(\xi_{1\sim3}^{[1]}(k)+\bar{x}_{1\sim3}^{[1]}(k))\\ &+\breve{B}u^*(k)+\Delta\breve{f}(\xi_{1\sim3}(k),k)-\bar{x}_{1\sim3}(k+1),\end{aligned} \tag{26}$$

Then, on the basis of Theorem 1, for the above system (26), the second-order fully actuated robust tracking controller can

be designed as

$$u^*(k) = \breve{B}^{-1}\left(\begin{bmatrix} [K_1]_{0\sim1}\xi_1^{\lceil 0\sim1\rceil}(k) \\ [K_2]_{0\sim1}\xi_2^{\lceil 0\sim1\rceil}(k) \\ [K_3]_{0\sim1}\xi_3^{\lceil 0\sim1\rceil}(k) \end{bmatrix} + \bar{x}_{1\sim3}(k+1) + \bar{x}_{1\sim3}^{\lceil 1\rceil}(k) - 2\bar{x}_{1\sim3}(k)\right) \tag{27}$$

where, without loss of generality, the reference signal $\bar{x}_{1\sim3}(k)$ to be tracked is set to $\bar{x}_{1\sim3}(k) = \left[\, 0.5sin(2\pi k/100)\ 0.5sin(2\pi k/100)\ 0.3sin(2\pi k/100) \,\right]^{\mathrm{T}}$. Further, the following closed-loop system can be obtained

$$\xi_{1\sim3}(k+1) = 2\xi_{1\sim3}(k) - \xi_{1\sim3}^{\lceil 1\rceil}(k) + \Delta\breve{f}(\xi_{1\sim3}(k),k) + \begin{bmatrix} [K_1]_{0\sim1}\xi_1^{\lceil 0\sim1\rceil}(k) \\ [K_2]_{0\sim1}\xi_2^{\lceil 0\sim1\rceil}(k) \\ [K_3]_{0\sim1}\xi_3^{\lceil 0\sim1\rceil}(k) \end{bmatrix}$$

with $\Delta\breve{f}(\xi_{1\sim3}(k),k)$ being

$$\Delta\breve{f}(\xi_{1\sim3}(k),k) = T_s^2\mathrm{diag}\{\eta sin\left(\xi_1(k)+\bar{x}_1(k)\right), \eta sin\left(\xi_2(k)+\bar{x}_2(k)\right), \frac{L}{2}\eta sin\left(\xi_3(k)+\bar{x}_3(k)\right)\},$$

where $\eta = 0.01$ in conjunction with the actual experimental setting.

In addition, the expected Jordan standard type $\mathscr{F}$ is set to be the diagonal matrix formed by real numbers within the unit circle of the z-plane, namely

$$\mathscr{F} = \mathrm{diag}\left\{0.674, 0.720, 0.718, 0.674, 0.444, 0.4909\right\},$$

and the free matrix $\mathscr{Z}$ is selected as

$$\mathscr{Z} = \begin{bmatrix} 6.243 & 7.195 & 0 & 0 & 0 & 0 \\ 0 & 0 & -4.491 & 4.533 & 0 & 0 \\ 0 & 0 & 0 & 0 & 7.133 & 6.299 \end{bmatrix},$$

and the other parameters are shown earlier.

Then, by solving the program in Algorithm 1, we get

$$K_E = \mathrm{blockdiag}\left\{\begin{bmatrix} -0.606 \\ 0.515 \end{bmatrix}^{\mathrm{T}}, \begin{bmatrix} -0.608 \\ 0.516 \end{bmatrix}^{\mathrm{T}}, \begin{bmatrix} -1.065 \\ 0.782 \end{bmatrix}^{\mathrm{T}}\right\},$$

$$\Psi(K_E) = \mathrm{blockdiag}\left\{\begin{bmatrix} 1.394 & -0.486 \\ 1 & 0 \end{bmatrix}, \begin{bmatrix} 1.392 & -0.484 \\ 1 & 0 \end{bmatrix}, \begin{bmatrix} 0.935 & -0.218 \\ 1 & 0 \end{bmatrix}\right\},$$

$$P(K_E) = \mathrm{blockdiag}\left\{\begin{bmatrix} 43.987 & -20.046 \\ -20.046 & 12.369 \end{bmatrix}, \begin{bmatrix} 43.493 & -19.744 \\ -19.744 & 12.186 \end{bmatrix}, \begin{bmatrix} 10.216 & -1.708 \\ -1.708 & 2.485 \end{bmatrix}\right\},$$

and $\gamma = 0.020$. Eventually, based on the simulation results, it can be verified easily that

$$\frac{\left\|\Delta\breve{f}_H(\xi_{1\sim3}(k),k)\right\|_2}{\left\|\xi_{1\sim3}^{\lceil 0\sim1\rceil}(k)\right\|_2} = 0.014 < \gamma,$$

which implies the inequality relation (5) holds.

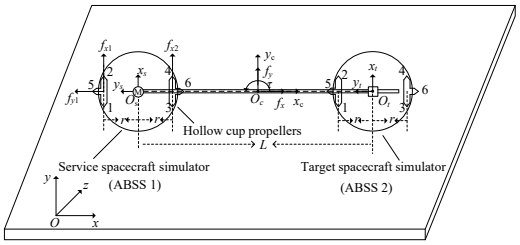

Fig. 2: The top view of the CSS

Before giving the simulation results, for better understanding of the thrust distribution of CSS, a top view of the CSS is given here as shown in Fig. 2. Therein, the inertial frame O-xyz is fixed to the marble platform on which the CSS moves. O_s-x_sy_s, O_t-x_ty_t and O_c-x_cy_c represent the body frames of ABSS 1, ABSS 2 and CSS, respectively. The propellers numbered 1–4 and 5–6 on ABSS 1 represent the tangential and radial propellers, respectively, with the corresponding thrusts being denoted as $f_{11}, \cdots, f_{16}$. And let

$$f_{x1} = f_{11} - f_{12},\ f_{x2} = f_{13} - f_{14},\ f_{y1} = f_{16} - f_{15}$$

represent the equivalent thrusts along the 1–2, 3–4 and 5–6 thrust directions, respectively. The corresponding simulation results are shown in Fig. 3–Fig. 6.

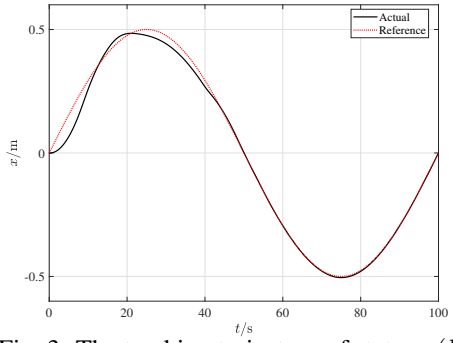

Fig. 3: The tracking trajectory of state $x_c(k)$

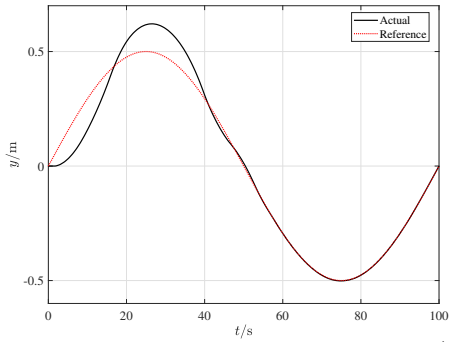

Fig. 4: The tracking trajectory of state $y_c(k)$

As can be seen from the tracking trajectories of states $x_c(k)$ and $y_c(k)$ shown in Figs. 3 and 4, the tracking trajectories of the two states have certain tracking errors in the first 40 s, but then they keep tracking the reference signals. On the contrary, the yaw angle shown in Fig. 5 shows good tracking performance throughout the tracking process. It can be said that our tracking objective for the CSS proposed in Subsection 2.1 has been successfully achieved.

In addition, from the equivalent thrusts results of the CSS shown in Fig. 6, it can be seen that during the period when

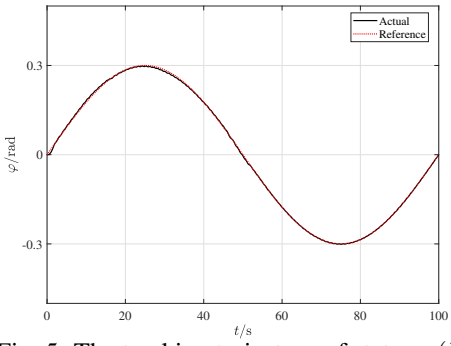

Fig. 5: The tracking trajectory of state $\varphi_c(k)$

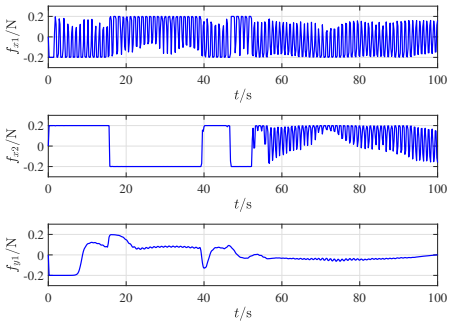

Fig. 6: The equivalent thrusts f_{x1}, f_{x2} and f_{y1} in different directions

there are significant tracking errors in the state trajectories, i.e., within approximately the first $40\,\mathrm{s}$, the thrust outputs in all three directions are close to or even at the saturated value of $0.2\,\mathrm{N}$. After all states tracked up to the reference signals, the outputs of all thrusts are significantly reduced as compared to the previous ones.

5 Conclusion

In this paper, the HOFA robust tracking control of a class of CSS systems with nonlinear uncertainties is investigated. The discrete-time HOFA controller designed for the proposed tracking control problem not only gives sufficient conditions for the existence of the solution, but also well eliminates the nonlinear terms in the system. In addition, the eigenstructure of the closed-loop system can be configured arbitrarily through the control law parameterization process. The entire process of controller design and parameter solving is simple enough, easily solvable and the numerical results are stable. Finally, the proposed technique successfully solves the robust tracking control problem of the CSS system and obtains satisfactory tracking results.

In the following research, a more complex dynamic scenario of the CSS system, i.e., the system with both nonlinear uncertainties and unknown parameters, will be considered, and discrete-time robust adaptive control based on the FAS method will be investigated in this case.

References

[1] C. Chen, L. H. Xie, Y. Jiang, K. Xie and S. L. Xie, Robust output regulation and reinforcement learning-based output tracking design for unknown linear discrete-time systems. *IEEE Transactions on Automatic Control*, 2023, 68(4): 2391–2398.

[2] A. Zamani and H. Bolandi, Robust MPC for tracking changing setpoints in discrete-time non-linear systems with non-additive unknown disturbance. *IET Control Theory and Applications*, 2022, 16(9): 846–860.

[3] L. Li and F. C. Liao, Output feedback preview tracking control for discrete-time polytopic time-varying systems. *International Journal of Control*, 2019, 92(12): 2979–2989.

[4] R. Padmanabhan, M. Shetty and T. S. Chandar, Discrete robust control of robot manipulators using an uncertainty and disturbance estimator. *Journal of Dynamic Systems Measurement and Control-Transactions of the Asme*, 2023, 145(5): 051002.

[5] L. Celentano and M. V. Basin, A robust tracking method for MIMO uncertain discrete-time systems: mechatronic applications. *IEEE Access*, 2020, 8: 33113–33124.

[6] D. Lee, Nonlinear disturbance observer-based robust control of attitude tracking of rigid spacecraft. *Nonlinear Dynamics*, 2017, 88(2): 1317–1328.

[7] D. Lee, Nonlinear disturbance observer-based robust control for spacecraft formation flying. *Aerospace Science and Technology*, 2018, 76: 82–90.

[8] B. H. Wang, W. S. Chen, B. Zhang, P. Shi and H. Y. Zhang, A nonlinear observer-based approach to robust cooperative tracking for heterogeneous spacecraft attitude control and formation applications. *IEEE Transactions on Automatic Control*, 2023, 68(1): 400–407.

[9] Q. Li, S. Song, C. Sun, Q. X. Gou and Z. Q. Mu, Robust output-feedback control for spacecraft proximity operations with forbidden zone. *IEEE Transactions on Aerospace and Electronic Systems*, 2022, 58(1): 96–107.

[10] Q. Cao, H. Y. Li, Q. X. Jia, C. Ma and Y. C. Zhang, Multi-observer approach for tracking control of flexible spacecraft using exponential mapping of SE(3). *Nonlinear Dynamics*, 2023, 111(6): 5329–5343.

[11] Q. J. Yao, Robust attitude tracking control of spacecraft under unified actuator dynamics. *International Journal of Control*, 2023, 96(6): 1514–1528.

[12] G. R. Duan, High-order fully actuated system approaches: Part I. Models and basic procedure. *International Journal of Systems Science*, 2021, 52(2), 422–435.

[13] G. R. Duan, High-order system approaches: I. Fully actuated systems and parametric designs. *Acta Automatica Sinica*, 2020, 46(02), 1333–1345.

[14] G. R. Duan, High-order fully actuated system approaches: Part IV. Adaptive control and high-order backstepping. *International Journal of Systems Science*, 2021, 52(05), 972–989.

[15] M. Cai, X. He and D. H. Zhou, An active fault tolerance framework for uncertain nonlinear high-order fully-actuated systems. *Automatica*, 2023, 152: 110969.

[16] D. W. Zhang, G. P. Liu, and L. Cao, Proportional integral predictive control of high-order fully actuated networked multi-agent systems with communication delays. *IEEE Transactions on Systems, Man, and Cybernetics: Systems*, 2023, 53(2), 801–812.

[17] K. X. Cui, G. R. Duan and M. Z. Hou, Discrete-time model reference tracking control for a class of combined spacecraft: A high-order fully actuated system approach. *IEEE Transactions on Automation Science and Engineering*, 2023, DOI: 10.1109/TASE.2023.3335106.

[18] G. R. Duan, High-order fully actuated system approaches: Part III. Robust control and high-order backstepping. *International Journal of Systems Science*, 2021, 52(05), 952–971.

[19] G. R. Duan, High-order fully actuated system approaches: Part X. Basics of discrete-time systems. *International Journal of Systems Science*, 2022, 53(4), 810–832.

[20] G. R. Duan, Parametric approaches for eigenstructure assignment in high-order descriptor linear systems. *International Journal of Control Automation & Systems*, 2005, 3(3), 419-429.

Proceedings of the 3rd Conference on Fully Actuated System Theory and Applications
May 10-12, 2024, Shenzhen, China

Sliding-Mode Disturbance Observer-Based HOFA Predictive Control of Spacecraft Flying-Around

Da-Wei Zhang[1], Guo-Ping Liu[1,2]

1. Center for Control Theory and Guidance Technology, Harbin Institute of Technology, Harbin 150001, P. R. China
E-mail: zhangdawei@stu.hit.edu.cn, cldya@163.com

2. Cente for Control Science and Technology, Southern University of Science and Technology, Shenzhen 518055, P. R. China
E-mail: liugp@sustech.edu.cn

Abstract: On the basis of high-order fully actuated (HOFA) system theory, this research is devoted to a flying-around problem of spacecraft with lumped disturbances under a sight coordinate system, where the lumped disturbances are used to represent the total impacts of the model uncertainties and external disturbances. Following the HOFA system theory, a nonlinear HOFA system model is exploited to establish the relative dynamical model of spacecraft flying-around under the sight coordinate system, such that the flying-around mission can be equivalent to a tracking control problem. A sliding-mode disturbance observer-based HOFA (SMDOB-HOFA) predictive control method is proposed to handle this problem. Specifically, a HOFA sliding-mode disturbance observer is designed to estimate and compensate for the lumped disturbances. Then, an incremental HOFA prediction model including the errors of disturbance estimation is developed with the help of Diophantine Equation to construct the multi-step ahead predictions. Based on these predictions, an objective function involving the tracking control performance can be minimized to obtain an optimal tracking controller for the realization of flying-around mission. The capability of SMDOB-HOFA predictive control is verified via a flying-around experiment of air-bearing spacecraft (ABS) simulator in a desired circular orbit.

Key Words: Spacecraft Flying-Around, Lumped Disturbances, Sliding-Mode Disturbance Observer, HOFA Predictive Control, Experimental Verification via ABS simulator

1 Introduction

Because of less prior knowledge of non-cooperative target spacecraft, it is hard to obtain its related characteristics for correspondingly service and maintenance in orbit. To cope with this problem, spacecraft flying-around is studied as an important task to monitor the status of non-cooperative target, such that the comprehensive characteristics of spacecraft can be obtained to achieve the subsequent service and maintenance in orbit. Thus, many scholars focus on this field and have obtained a string of results (see [1–3] and the references therein). During the flying-around mission, the disturbances are always present to damage the control performances due to complex space scenarios, so that a number of representative approaches have been proposed to consider this problem, such as fixed-time terminal sliding-mode control [4], finite-time fault-tolerant control [5], appointed-time safety-guaranteed control [6], etc.. Among so many methods, the disturbance observer-based control has become one the most widely used ways in the spacecraft control, which can realize the active compensation of disturbances to raise the control performances (see [7, 8] and their associated literature).

A shortcoming of the above is that they still utilize a traditional first-order state space model to describe the attitude and orbit dynamics of spacecraft. In fact, the dynamic model of spacecraft control is almost always second-order fully actuated. When using a traditional state space model, the original dynamics of spacecraft have to be converted into a first-order form, such that the physical meanings of original systems are lost and some drawbacks are caused during the process of model reduction. Following this framework, the design and computation complexities are obviously increased.

This work was supported in part by the National Natural Science Foundation of China under Grants 62173255 and 62188101, and in part by the Shenzhen Key Laboratory of Control Theory and Intelligent Systems under Grant ZDSYS20220330161800001.

To address this problem, HOFA system theory is recently created in [9], which involves the combination of modeling, analysis, design and applications of control systems. In this theory, a HOFA system model is applied to describe the considered original systems, so that the full actuation characteristic is guaranteed to reduce the difficulties of design process. In the control design based on HOFA system theory, predictive control plays a significant role and has obtained a string of reults on the related work of this study (see [10–13]). Concretely, [10, 11] designed a HOFA disturbance observer to estimate both external disturbances generated by exogenous system and slowly time-variant lumped disturbances, respectively, and then combined with a HOFA predictive control to realize the tracking control. [12] transformed the spacecraft flying-around problem into a tracking control one of nonlinear HOFA systems, and then developed a HOFA predictive control to deal with this problem. Following [12], [13] further used the HOFA predictive control to address the communication constraints in the flying-around task. The results in [10–13] gave a solid basis for the realization of spacecraft flying-around under lumped disturbances in this study.

This paper considers a SMDOB-HOFA predictive control to implement the spacecraft flying-around under lumped disturbances, where a nonlinear HOFA system model is adopted to describe the relative dynamics of spacecraft flying-around in a sight coordinate system. Based on this idea, the flying-around task can be equivalent to a tracking control problem. To solve this problem, a HOFA sliding-mode disturbance observer is to estimate and compensate for the lumped disturbances. Then, an incremental HOFA prediction model containing the errors of disturbance estimation is established by applying a Diophantine Equation to generate the multi-step ahead predictions, so that an object function including the tracking control performance is optimized to obtain an optimal tracking controller for achieving the flying-around mis-

sion. Further, a flying-around experiment of ABS simulator is taken to demonstrate the practicality of SMDOB-HOFA predictive control. The advantages of this paper are summarized in three aspects.

1) By using the HOFA system model, full actuation characteristic can be ensured to eliminate the nonlinearities for simplifying the design process.
2) A sliding-mode disturbance observer in HOFA form is designed to estimate the lumped disturbance, which relaxes the constraint that lumped disturbance is slowly time-variant.
3) An incremental HOFA prediction model is established to replace a first-order prediction model, so that the design and representation of predictive control are completed in the perspective of HOFA system theory.

Notation. N_x and N_v are the prediction horizons for state and control vectors, and $N_x \geq N_v$. z is time operator satisfying $\varrho(t+\mu) = z^{\mu}\varrho(t)$, $\mu \in \mathbb{Z}$, where $\varrho(t)$ is an arbitrary signal. Δ represents a difference operator satisfying $\Delta = 1-z^{-1}$ so that $\Delta\varrho(t) = \varrho(t)-\varrho(t-1)$ is an increment of $\varrho(t)$. $\hat{\varrho}(t+\mu|t)$ denotes the μ-th ahead prediction of $\varrho(t)$ based on t time. T indicates the sampling period.

2 Problem Formulation

2.1 Fully actuated model for spacecraft flying-around

A flying-around problem that servicing spacecraft points to the target one is studied here, whose sketch and its associated coordinate systems are provided in Fig. 1. Concretely,

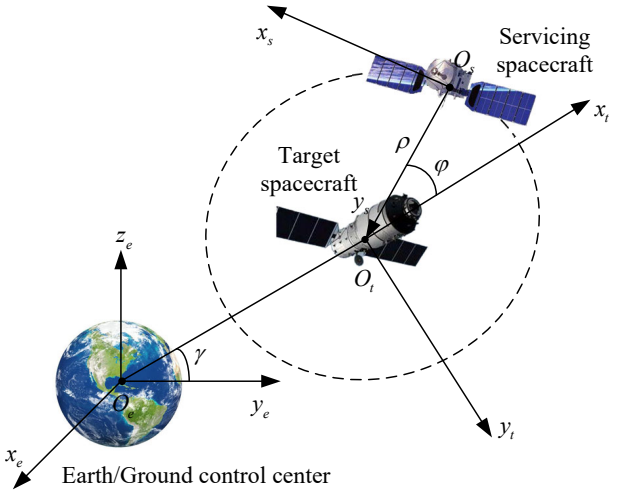

Fig. 1: The sketch of flying-around of servicing spacecraft and its associated coordinate systems.

$O_s{-}x_sy_sz_s$, $O_t{-}x_ty_tz_t$ and $O_e{-}x_ey_ez_e$ represent the sight, orbit and centered inertial coordinate systems. According to [1], the relative orbit dynamic model of spacecraft flying-around in the $O_s - x_sy_sz_s$ coordinate system is given as

$$\begin{aligned} \ddot{\rho} - \rho\dot{\varphi}^2 + 2\omega_{ts}\rho\dot{\varphi} - 3\rho\omega_{ts}^2\sin^2(\varphi) &= u_\rho, \\ \rho\ddot{\varphi} + 2\dot{\rho}\dot{\varphi} - 2\omega_{ts}\dot{\rho} - \frac{3}{2}\rho\omega_{ts}^2\sin(2\varphi) &= u_\varphi, \end{aligned} \tag{1}$$

where ρ and φ denote the relative distance and the sight angle, u_ρ and u_φ represent the associated control inputs, and ω_{ts} is the orbital angular velocity of target spacecraft. Denote $x(t) = \left[\begin{array}{cc} \rho(t) & \varphi(t) \end{array}\right]^{\mathrm{T}}$, $u(t) = \left[\begin{array}{cc} u_\rho(t) & u_\varphi(t) \end{array}\right]^{\mathrm{T}}$, and then adopt a forward difference operator $\dot{x}(t) = \frac{x(t+1)-x(t)}{T}$ to realize the discretization of system (1), it is yielded that

$$x(t+2) = f(x(t), x(t+1)) + g(x(t), x(t+1))u(t) + \zeta(t), \tag{2}$$

where $f(x(t), x(t+1))$ and $g(x(t), x(t+1))$ indicate the known nonlinear vector and matrix functions, and $\zeta(t)$ denotes a bounded disturbance. In detail, they are defined as

$$\begin{aligned} f(x(t), x(t+1)) &= \left[\begin{array}{c} f_1(x(t), x(t+1)) \\ f_2(x(t), x(t+1)) \end{array}\right], \\ g(x(t), x(t+1)) &= \left[\begin{array}{cc} T^2 & 0 \\ 0 & T^2/\rho(t) \end{array}\right], \\ \zeta(t) &= \left[\begin{array}{c} 3T^2\rho(t)\omega_{ts}^2\sin^2(\varphi(t)) \\ \frac{3}{2}T^2\omega_{ts}^2\sin(2\varphi(t)) \end{array}\right], \end{aligned}$$

with $f_1(x(t), x(t+1)) = 2\rho(t+1) + (\varphi^2(t+1) - 2\varphi(t+1)\varphi(t) + \varphi^2(t) - 1)\rho(t) - 2T\omega_{ts}\rho(t)(\varphi(t+1) - \varphi(t))$, $f_2(x(t), x(t+1)) = 2\varphi(t+1) - \varphi(t) + 2T\omega_{ts}(\rho(t+1)/\rho(t) - 1) - 2(\varphi(t+1) - \varphi(t))(\rho(t+1)/\rho(t) - 1)$. From [14], system (2) is a discrete-time nonlinear second-order fully actuated one. In this paper, system (2) and its general promotion expression will be deeply considered.

Based on [12, 13], the flying-around mission in the $O_s - x_sy_sz_s$ coordinate system can be realized if and only if the following tracking control target is achieved, that is,

$$x(t) = \left[\begin{array}{c} \rho(t) \\ \varphi(t) \end{array}\right] \to x^\star(t) = \left[\begin{array}{c} \rho^\star(t) \\ \varphi^\star(t) \end{array}\right], t \to \infty, \tag{3}$$

where $\rho^\star(t)$ is a desired relative distance between target and servicing spacecraft, $\varphi^\star(t)$ is a desired sight angle that is set as a periodic function with $\varphi^\star(t) \in [0, 2\pi]$. Summarizing the above shows that the purpose of this paper is to propose a $u(t)$ for system (2), such that condition (3) is held.

2.2 Problem statement

Based on the extension of system (2), a class of discrete-time nonlinear HOFA systems is investigated as

$$\begin{aligned} x(t+n) =& f\left(x^{\lfloor 0,n-1\rfloor}(t), u^{\lceil p,1\rceil}(t)\right) \\ &+ g\left(x^{\lfloor 0,n-1\rfloor}(t), u^{\lceil p,1\rceil}(t)\right)u(t) + \zeta(t), \\ x(t) =& x_0(t),\ u(t) = u_0(t),\ t \leq 0, \end{aligned} \tag{4}$$

with

$$\begin{aligned} x^{\lfloor 0,n-1\rfloor}(t) :=& \{x(t), x(t+1), \cdots, x(t+n-1)\}, \\ u^{\lceil p,1\rceil}(t) :=& \{u(t-p), u(t-p+1), \cdots, u(t-1)\}, \end{aligned}$$

where $x(t) \in \mathbb{R}^{\tilde{n}}$ and $u(t) \in \mathbb{R}^{\tilde{n}}$ represent the state and control vectors, $x_0(t) \in \mathbb{R}^{\tilde{n}}$ and $u_0(t) \in \mathbb{R}^{\tilde{n}}$ are the related initial values of $x(t)$ and $u(t)$. n and p indicate the highest order of state vector and the lowest order of control vector, respectively. $f\left(x^{\lfloor 0,n-1\rfloor}(t), u^{\lceil p,1\rceil}(t)\right) \in \mathbb{R}^{\tilde{n}}$ and $g\left(x^{\lfloor 0,n-1\rfloor}(t), u^{\lceil p,1\rceil}(t)\right) \in \mathbb{R}^{\tilde{n}\times\tilde{n}}$ are the known nonlinear vector and matrix functions, which are denoted by $f(\cdot)$ and $g(\cdot)$. $\zeta(t) \in \mathbb{R}^{\tilde{n}}$ is a lumped disturbance including the model uncertainties and external disturbances.

Assumption 1. *1)* $\forall t \geq 0$, $\det(g(\cdot)) \neq 0$ or ∞, *2) The state vector of system* (4) *is available, 3)* $\zeta(t)$ *is unknown but bounded, which satisfies* $\|\Delta\zeta(t+1)\| \leq \zeta_{\max}$.

Remark 1. *In some researches, such as [11, 15], the lumped disturbances are required to be slowly time-varying, that is,* $\Delta\zeta(t+1) \approx 0$*, but it is almost impossible in practice. Hence, the lumped disturbances can not be effectively estimated and compensated, which seriously affect the control performances. This paper uses* $\|\Delta\zeta(t+1)\| \leq \zeta_{\max}$ *to replace* $\Delta\zeta(t+1) \approx 0$*, which relaxes the constraint of lumped disturbances and is more applicable to actual applications.*

For nonlinear HOFA system (4), a SMDOB-HOFA predictive control is designed as

$$u(t) = g^{-1}(\cdot)\left(\Upsilon(A_{0\sim n-1}, x(t)) - f(\cdot) - \hat{\zeta}(t|t-1) + v(t)\right), \tag{5}$$

where $\Upsilon(A_{0\sim n-1}, x(t)) = \sum_{\mu=0}^{n-1} A_\mu x(t+\mu) \in \mathbb{R}^{\tilde{n}}$ aims to realize the adjustment of closed-loop system performances and $A_\mu \in \mathbb{R}^{\tilde{n}\times\tilde{n}}$ represents the coefficient matrix to be determined, $-f(\cdot)$ is used to eliminate the system nonlinearities, $\hat{\zeta}(t|t-1) \in \mathbb{R}^{\tilde{n}}$ is the disturbance estimation generated by a sliding-mode disturbance observer, and $v(t) \in \mathbb{R}^{\tilde{n}}$ is a tracking control item designed by HOFA predictive control. By applying (5), a closed-loop form of nonlinear HOFA system (4) is achieved as

$$\begin{aligned} x(t+n) =& \Upsilon(A_{0\sim n-1}, x(t)) + e_\zeta(t) + v(t) \\ =& \sum_{\mu=0}^{n-1} A_\mu x(t+\mu) + e_\zeta(t) + v(t), \end{aligned} \tag{6}$$

where $e_\zeta(t) = \zeta(t) - \hat{\zeta}(t|t-1)$ is the estimation error. For the tracking control, an objective function $\mathcal{J}(t)$ is given as

$$\mathcal{J}(t) = \left\|\hat{X}(t+N_x|t) - R(t+N_x)\right\|_{W_1}^2 + \left\|\Delta\hat{V}(t+N_v|t)\right\|_{W_2}^2, \tag{7}$$

with

$$\begin{aligned} \hat{X}(t+N_x|t) &= \left[\begin{array}{cccc} \hat{x}^{\mathrm{T}}(t+N_x|t) & \cdots & \hat{x}^{\mathrm{T}}(t+1|t) \end{array}\right]^{\mathrm{T}}, \\ \Delta\hat{V}(t+N_v|t) &= \left[\begin{array}{cccc} \Delta\hat{v}^{\mathrm{T}}(t+N_v|t) & \cdots & \Delta\hat{v}^{\mathrm{T}}(t|t) \end{array}\right]^{\mathrm{T}}, \\ R(t+N_x) &= \left[\begin{array}{cccc} r^{\mathrm{T}}(t+N_x) & \cdots & r^{\mathrm{T}}(t+1) \end{array}\right]^{\mathrm{T}}, \end{aligned}$$

where $\hat{x}(t+\mu|t)$, $\mu = 1, 2, \ldots, N_x$, and $\Delta\hat{v}(t+\mu|t)$, $\mu = 0, 1, \ldots, N_v$, indicate the μ-th ahead predictions of state $x(t)$ and tracking control increment $\Delta v(t)$. $r(t)$ represents a known reference input, W_1 and W_2 are the positive definite weighted coefficient matrices. In (7), the first part considers the implementation of tracking control by measuring the differences of reference input and state predictions. The second part proposes a constraint of changing rate and amplitude for $\Delta v(t)$ in the view of algorithm design, which is benefit for physical implementation of controller.

Problem 1. *For nonlinear HOFA systems* (4) *with Assumption 1, a SMDOB-HOFA predictive control* (5) *is proposed by optimizing* (7) *to ensure the stability and tracking control performance of closed-loop system* (6)*, such that Conditions C1–C2 below can be satisfied.*

C1 $\forall t \geq 0$, $\|y(t)\| < \infty$ *with* $\|r(t)\| < \infty$,

C2 $\lim_{t\to\infty}\|y(t) - r(t)\| = 0$.

3 Main Results

3.1 Design of sliding-mode disturbance observer

By utilizing the z operator, system (4) can be equivalently converted as

$$x(t+1) = \tilde{f}(\cdot) + \tilde{g}(\cdot)u(t) + \tilde{\zeta}(t), \tag{8}$$

with $\tilde{f}(\cdot) = z^{1-n}f(\cdot)$, $\tilde{g}(\cdot) = z^{1-n}g(\cdot)$, $\tilde{\zeta}(t) = z^{1-n}\zeta(t)$. In this case, Assumption 1–3) should be revised as $\|\Delta\tilde{\zeta}(t+1)\| \leq \zeta_{\max}$, and the estimation error is redefined as $e_{\tilde{\zeta}}(t) = \tilde{\zeta}(t) - \hat{\tilde{\zeta}}(t|t-1) = z^{1-n}e_\zeta(t)$. Meanwhile, the vector form of system (8) is given as

$$x_i(t+1) = \tilde{f}_i(\cdot) + \tilde{g}_i(\cdot)u(t) + \tilde{\zeta}_i(t), \tag{9}$$

where $i = 1, 2, \ldots, \tilde{n}$, and

$$\begin{aligned} x(t) &= \left[\begin{array}{c} x_1(t) \\ \vdots \\ x_{\tilde{n}}(t) \end{array}\right], \ \tilde{f}(\cdot) = \left[\begin{array}{c} \tilde{f}_1(\cdot) \\ \vdots \\ \tilde{f}_{\tilde{n}}(\cdot) \end{array}\right], \\ \tilde{g}(\cdot) &= \left[\begin{array}{c} \tilde{g}_1(\cdot) \\ \vdots \\ \tilde{g}_{\tilde{n}}(\cdot) \end{array}\right], \ \tilde{\zeta}(t) = \left[\begin{array}{c} \tilde{\zeta}_1(t) \\ \vdots \\ \tilde{\zeta}_{\tilde{n}}(t) \end{array}\right]. \end{aligned}$$

For system (9), an auxiliary system is constructed as

$$\begin{aligned} s_i(t) =& x_i(t) - \hat{x}_i(t|t-1), \\ \hat{x}_i(t+1|t) =& \tilde{f}_i(\cdot) + \tilde{g}_i(\cdot)u(t) + \hat{\tilde{\zeta}}_i(t|t-1) - \kappa_{i,1}\mathrm{sgn}(s_i(t)), \end{aligned} \tag{10}$$

where $\kappa_{i,1} > 0$ is a parameter to be designed. By using (9) and (10), it is yielded that

$$s_i(t+1) = e_{\tilde{\zeta},i}(t) + \kappa_{i,1}\mathrm{sgn}(s_i(t)), \tag{11}$$

where $e_{\tilde{\zeta},i}(t)$ is the i-th element of $e_{\tilde{\zeta}}(t)$. Then, a sliding-mode disturbance observer is presented as

$$\begin{aligned} \hat{\tilde{\zeta}}_i(t|t-1) =& \kappa_{i,2}(s_i(t) - \varepsilon_i(t)), \\ \varepsilon_i(t+1) =& -\frac{1}{\kappa_{i,2}}\hat{\tilde{\zeta}}_i(t|t-1) + \kappa_{i,1}\mathrm{sgn}(s_i(t)), \end{aligned} \tag{12}$$

where $\kappa_{i,2} > 0$ is also a parameter to be designed. Combining (11) with (12) derives that $\hat{\tilde{\zeta}}_i(t+1|t) = \hat{\tilde{\zeta}}_i(t|t-1) + \kappa_{i,2}e_{\tilde{\zeta},i}(t)$, and

$$e_{\tilde{\zeta},i}(t+1) = \Delta\tilde{\zeta}_i(t+1) + (1-\kappa_{i,2})e_{\tilde{\zeta},i}(t), \tag{13}$$

with $|\Delta\tilde{\zeta}_i(t+1)| \leq \zeta_{\max,i}$. Then, Theorem 1 is provided to obtain the sliding-mode disturbance observer (12)

Theorem 1. *For nonlinear HOFA system* (9) *and sliding-mode disturbance observer* (12)*, the estimation error* $e_{\tilde{\zeta},i}(t)$ *is uniformly bounded if there exist three parameters* $\kappa_{i,1} > 0$*,* $\kappa_{i,2} > 0$ *and* $\kappa_{i,3} > 0$ *such that* $\Omega_{i,1} > 0$ *and* $\Omega_{i,2} > 0$*, where*

$$\begin{aligned} \Omega_{i,1} =& 1 - 2\kappa_{i,2}^2 - (1-\kappa_{i,2})^2 - \kappa_{i,3}(1-\kappa_{i,2})^2, \\ \Omega_{i,2} =& 2\kappa_{i,2}^2\kappa_{i,1}^2 + \zeta_{\max,i}^2 + \frac{\zeta_{\max,i}^2}{\kappa_{i,3}}. \end{aligned} \tag{14}$$

Proof. From (11), it is obtained that $s_i^2(k+1) \leq 2e_{\tilde{\zeta},i}^2(t) + 2\kappa_{i,1}^2$. Based on (13), it is yield that $e_{\tilde{\zeta},i}^2(t+1) \leq \zeta_{\max,i}^2 + (1-\kappa_{i,2})^2 e_{\tilde{\zeta},i}^2(t) + \frac{\zeta_{\max,i}^2}{\kappa_{i,3}} + \kappa_{i,3}(1-\kappa_{i,2})^2 e_{\tilde{\zeta},i}^2(t)$. Then, a Lyapunov function for systems (10) and (13) is designed as

$$\mathscr{V}_i(t) = \kappa_{i,2}^2 s_i^2(t) + e_{\tilde{\zeta},i}^2(t),$$

so that $\Delta\mathscr{V}_i(t+1) = \mathscr{V}_i(t+1) - \mathscr{V}_i(t)$, that is,

$$\begin{aligned}
&\Delta\mathscr{V}_i(t+1)\\
&\quad= \kappa_{i,2}^2 s_i^2(t+1) + e_{\tilde{\zeta},i}^2(t+1) - \kappa_{i,2}^2 s_i^2(t) - e_{\tilde{\zeta},i}^2(t)\\
&\quad\le 2\kappa_{i,2}^2 e_{\tilde{\zeta},i}^2(t) + 2\kappa_{i,2}^2\kappa_{i,1}^2 + \zeta_{\max,i}^2 + (1-\kappa_{i,2})^2 e_{\tilde{\zeta},i}^2(t)\\
&\qquad+ \frac{\zeta_{\max,i}^2}{\kappa_{i,3}} + \kappa_{i,3}(1-\kappa_{i,2})^2 e_{\tilde{\zeta},i}^2(t) - \kappa_{i,2}^2 s_i^2(t) - e_{\tilde{\zeta},i}^2(t)\\
&\quad= -(1 - 2\kappa_{i,2}^2 - (1-\kappa_{i,2})^2 - \kappa_{i,3}(1-\kappa_{i,2})^2) e_{\tilde{\zeta},i}^2(t)\\
&\qquad- \kappa_{i,2}^2 s_i^2(t) + 2\kappa_{i,2}^2\kappa_{i,1}^2 + \zeta_{\max,i}^2 + \frac{\zeta_{\max,i}^2}{\kappa_{i,3}}\\
&\quad= -\Omega_{i,1} e_{\tilde{\zeta},i}^2(t) - \kappa_{i,2}^2 s_i^2(t) + \Omega_{i,2}\\
&\quad\le -\Omega_{i,1} e_{\tilde{\zeta},i}^2(t) + \Omega_{i,2},
\end{aligned}$$

where $\Omega_{i,1}$ and $\Omega_{i,2}$ are given in (14). When $|e_{\tilde{\zeta},i}| > \sqrt{\frac{\Omega_{i,2}}{\Omega_{i,1}}}$, $\Delta\mathscr{V}_i(t+1) < 0$. Thus, the estimation error $e_{\tilde{\zeta},i}(t)$ is uniformly bounded, and its corresponding convergence radius is $\sqrt{\frac{\Omega_{i,2}}{\Omega_{i,1}}}$. By properly adjusting the $\kappa_{i,1}$, $\kappa_{i,2}$ and $\kappa_{i,3}$, the estimation errors can be become small enough.

This completes the proof. □

3.2 Design of SMDOB-HOFA predictive control

By applying the z operator, system (6) is transformed as

$$\mathcal{A}(z^{-1})x(t) = \mathcal{B}(z^{-1})v(t-1) + \mathcal{B}_e e_\zeta(t), \qquad (15)$$

with $\mathcal{A}(z^{-1}) = I - \sum_{\mu=0}^{n-1} A_\mu z^{-n+\mu}$, $\mathcal{B}(z^{-1}) = z^{-n+1}$ and $\mathcal{B}_e(z^{-1}) = z^{-1}\mathcal{B}(z^{-1})$. From [10], a Diophantine Equation in relation to system (15) is shown as

$$\mathcal{E}_\mu(z^{-1})\mathcal{A}(z^{-1})\Delta + z^{-\mu}\mathcal{F}_u(z^{-1}) = I,$$

where $\mathcal{E}_\mu(z^{-1})$ and $\mathcal{F}_\mu(z^{-1})$ are two polynomial matrices that are decided by the prediction horizon μ and the system polynomial matrix $\mathcal{A}(z^{-1})$. Concretely, they are shown as $\mathcal{E}_\mu(z^{-1}) = \sum_{\eta=0}^{\mu-1} \mathrm{e}_{\mu,\eta} z^{-\eta}$ and $\mathcal{F}_\mu(z^{-1}) = \sum_{\eta=0}^{n} \mathrm{f}_{\mu,\eta} z^{-\eta}$. Then, multiplying $\mathcal{E}_\mu\Delta z^\mu$ at (15) obtains that

$$\mathcal{E}_\mu\mathcal{A}\Delta x(x+\mu) = \mathcal{E}_\mu\mathcal{B}\Delta v(t+\mu-1) + z^\mu\mathcal{E}_\mu\mathcal{B}_e\Delta e_\zeta(t).$$

Substituting the Diophantine Equation into the above establishes an incremental HOFA prediction model as

$$x(t+\mu) = \mathcal{F}_\mu x(t) + \mathcal{G}_\mu\Delta e_\zeta(t) + \mathcal{L}_\mu\Delta v(t+\mu-1), \quad (16)$$

where $\mathcal{G}_\mu(z^{-1}) = z^\mu\mathcal{E}_\mu(z^{-1})\mathcal{B}_e(z^{-1})$ and $\mathcal{L}_\mu(z^{-1}) = \mathcal{E}_\mu(z^{-1})\mathcal{B}(z^{-1})$.

For $\mu = 1, 2, \ldots, N_x$, the multi-step ahead predictions by using (16) are derived as

$$\begin{aligned}
\hat{x}(t+1|t) =& \mathcal{F}_1 x(t) + \mathcal{G}_1\Delta e_\zeta(t) + \mathcal{L}_1\Delta\hat{v}(t|t),\\
&\vdots\\
\hat{x}(t+N_x|t) =& \mathcal{F}_{N_x} x(t) + \mathcal{G}_{N_x}\Delta e_\zeta(t) + \mathcal{L}_{N_x}\Delta\hat{v}(t+N_x-1|t),
\end{aligned}$$

for $\mu = N_v+1, N_v+2, \ldots, N_x$, $\hat{v}(t+N_v|t) = \hat{v}(t+\mu|t)$ so that $\Delta\hat{v}(t+\mu|t) = 0$, hence the above can be concluded as

$$\hat{X}(t+N_x|t) = P_1 x(t) + P_2\Delta e_\zeta(t) + P_3\Delta\hat{V}(t+N_v|t), \quad (17)$$

with

$$P_1 = \begin{bmatrix} \mathcal{F}_{N_x} \\ \vdots \\ \mathcal{F}_1 \end{bmatrix},\ P_2 = \begin{bmatrix} \mathcal{G}_{N_x} \\ \vdots \\ \mathcal{G}_1 \end{bmatrix},$$

$$P_3 = \begin{bmatrix} \mathcal{L}_{N_x} & 0 & \cdots & 0 \\ \vdots & \vdots & \cdots & \vdots \\ \mathcal{L}_{N_v+1} & 0 & \cdots & 0 \\ 0 & \mathcal{L}_{N_v} & \ddots & \vdots \\ \vdots & \ddots & \ddots & 0 \\ 0 & \cdots & 0 & \mathcal{L}_1 \end{bmatrix}.$$

Meanwhile, a stair-like incremental limitation about predictive control is introduced as

$$\Delta\hat{v}(t+\mu|t) = \gamma\Delta\hat{v}(t+\mu-1|t) = \cdots = \gamma^\mu\Delta\hat{v}(t|t),$$

where $\mu = 1, 2, \ldots, N_v$, and $\gamma > 0$ is a weighting factor and $\Gamma = \mathrm{Blockdiag}\{\gamma^{N_v} I, \ldots, \gamma I, I\}$ indicated a stair-like factor matrix.Thus, P_3 is converted as $P_4 = P_3\Gamma$.

In order to solve the optimal predictive control increment, let $\frac{\partial\mathcal{J}(t)}{\Delta\hat{V}(t+N_v|t)} = 0$, taking (17) into the above yields that

$$\begin{aligned}
P_4^{\mathrm{T}} W_1 \big(&P_1 x(t) + P_2\Delta e_\zeta(t) + P_4\Delta\hat{V}(t+N_v|t)\\
&- R(t+N_x)) + W_2\Delta\hat{V}(t+N_v|t) = 0,
\end{aligned}$$

which can be summarized as

$$\begin{aligned}
\Delta\hat{V}(t+N_v|t) =& M_1^{-1} M_2 x(t) + M_1^{-1} M_3\Delta e_\zeta(t)\\
&+ M_1^{-1} M_4 R(t+N_x),
\end{aligned}$$

with $M_1 = P_4^{\mathrm{T}} W_1 P_4 + W_2$, $M_2 = -P_4^{\mathrm{T}} W_1 P_1$, $M_3 = -P_4^{\mathrm{T}} W_1 P_2$, $M_4 = P_4^{\mathrm{T}} W_1$. Thus, the optimal predictive control increment $\Delta v(t)$ is defined as $\Delta v(t) = \Delta\hat{v}(t|t) = H\Delta\hat{V}(t+N_v|t)$ with $H = \begin{bmatrix} 0 & \cdots & 0 & I \end{bmatrix}$, which can be given as

$$\begin{aligned}
\Delta v(t) =& H M_1^{-1} M_2 x(t) + H M_1^{-1} M_3\Delta e_\zeta(t)\\
&+ H M_1^{-1} M_4 R(t+N_x).
\end{aligned} \qquad (18)$$

Remark 2. *In this paper, $\Upsilon(A_{0\sim n-1}, x(t))$ in* (5) *is used to stabilize the system $x(t+n) = \sum_{\mu=0}^{n-1} A_\mu x(t+\mu)$. On the one hand, it can improve the accuracy of incremental HOFA prediction model* (16) *via feedback correction. On the other hand, it can adjust the tracking control performance. An effective way for obtaining the coefficient matrices A_μ of $\Upsilon(A_{0\sim n-1}, x(t))$ is to construct a matrix $\Phi(A_{0\sim n-1})$ that is similar to a Schur matrix with*

$$\Phi(A_{0\sim n-1}) = \begin{bmatrix} 0 & I & & \\ \vdots & & \ddots & \\ 0 & & & I \\ A_0 & A_1 & \cdots & A_{n-1} \end{bmatrix}.$$

In this view, the coefficient matrices A_μ can be obtained by utilizing the eigenstructure assignment method (refer to the Remark 3.2 in [12]). The paper length prevents that the details are not discussed here.

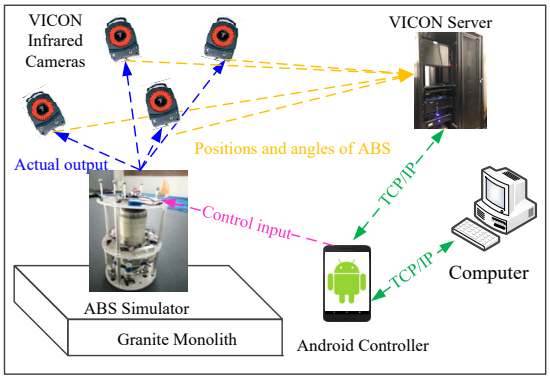

Fig. 2: The sketch of semi-physical simulation platform.

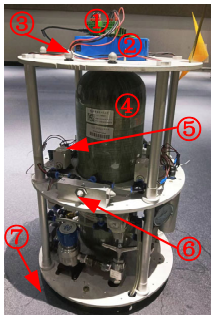

① Wireless actuator
② Battery
③ Optical markers
④ Air bank
⑤ Relays
⑥ Thrusters
⑦ Planar air bearings

Fig. 3: The hardware of ABS simulator.

4 Experimental Verification

A semi-physical simulation platform of spacecraft control is shown in Fig. 2, where ABS simulator in Fig. 3 is regarded as a frequently-used equipment to simulate the ground experiment of spacecraft control under micro-gravity site, such as [10, 12, 13]. In this platform, ABS simulator has three degrees of freedom to be considered, involving the positions in xoy plane (x and y) and the angle rotating the z-axis (ψ), such that ABS simulator can satisfy the requirement of the proposed flying-around mission in Fig. 1. Table 1 offer the basic parameters of ABS simulator. Based on [12], the dynamic model of ABS simulator is given as

Table 1: Basic parameters of ABS simulator.

Parameter	Notation	Value
Mass	M	19.4 kg
Moment of inertia	J	0.239 kg $\cdot$ m^2
Radius	r	0.18 m

$$M(\ddot{x}-\dot{y}\dot{\psi})=F_x,\ M(\ddot{y}-\dot{x}\dot{\psi})=F_y,\ J\ddot{\psi}=F_T, \quad (19)$$

where F_x, F_y, F_T are the thrusts and torque of ABS simulator. By using a forward difference operation, the discrete-time form of system (19) is expressed as

$$Mx(t+2)=f_x(\cdot)+T^2F_x(t)+\zeta_x(t), \quad (20a)$$
$$My(t+2)=f_y(\cdot)+T^2F_y(t)+\zeta_y(t), \quad (20b)$$
$$J\psi(t+2)=f_\psi(\cdot)+T^2F_T(t), \quad (20c)$$

where $f_x(\cdot)=2Mx(k+1)-Mx(k)$, $\zeta_x(t)=M\Delta y(k+1)\Delta\psi(k+1)$, $f_y(\cdot)=2My(k+1)-My(k)$, $\zeta_y(t)=M\Delta x(k+1)\Delta\psi(k+1)$ and $f_\psi(\cdot)=2J\psi(k+1)-J\psi(k)$.

A flying-around experiment in circular orbit is carried out to illustrate the capability of SMDOB-HOFA predictive control, the desired orbit parameters are set that the center of orbit is (0, 1.5)m and its radius is 0.5m. In this case, condition (3) is set as $\rho^\star=0.5$m and $\varphi^\star(t)=\pi+\pi\sin(\frac{\pi}{50}t)$rad.

For systems (20a) and (20b), a SMDOB-HOFA predictive control in the form of (5) is presented as

$$F_x(t)=\frac{\Upsilon(A_{x,0\sim n-1},x(t))-f_x(\cdot)-\hat{\zeta}_x(t|t-1)+v_x(t)}{T^2},$$
$$F_y(t)=\frac{\Upsilon(A_{y,0\sim n-1},y(t))-f_y(\cdot)-\hat{\zeta}_y(t|t-1)+v_y(t)}{T^2}, \quad (21)$$

where $\Upsilon(A_{x,0\sim1},x(t))=19.4x(t+1)-0.3802x(t)$ and $\Upsilon(A_{y,0\sim1},y(t))=19.4y(t+1)-0.3802y(t)$. Meanwhile $\hat{\zeta}_x(t|t-1)$ and $\hat{\zeta}_y(t|t-1)$ are estimated by adopting the sliding-mode disturbance observer in the form of (10)–(12) with $\kappa_{x,1}=1$, $\kappa_{x,2}=0.2$, $\kappa_{x,3}=0.4$ and $\kappa_{y,1}=1$, $\kappa_{y,2}=0.5$, $\kappa_{y,3}=0.8$. For system (20c), it is only required to realize the stabilization. Then, a stabilization control in the form of (5) without tracking control and estimation items is presented as

$$F_T(t)=\frac{\Upsilon(A_{\psi,0\sim1},\psi(k)-f_\psi(\cdot)}{T^2}, \quad (22)$$

with $\Upsilon(A_{\psi,0\sim1},\psi(t))=0.2629\psi(t+1)-0.0717\psi(t)$. For predictive control part, let $N_x=5$, $N_v=3$, $W_1=I$, $W_2=5I$, $\gamma=2$. By utilizing the control laws (21) and (22), the experimental results are shown in Fig. 4.

Figs. 4a and 4b implies that x- and y-axes responses of ABS simulator can realize the desired tracking control performance within allowable errors, and Fig. 4c shows the shortcoming that there exist the vibrations of ψ-axis response of ABS simulator during the steady process. The reasons are that the presented controller does not consider the reaction forces of thrusters and the the airflow around experimental environment. In Fig. 4d, the estimation errors of sliding-mode disturbance observer can be converged to 0 by choosing the proper parameters, so that the feasibility of sliding-mode disturbance observer can be ensured. The practical trajectory of ABS simulator is provided in Fig. 4e, which means that ABS simulator can reach the desired circular orbit and continue to perform the flying-around mission. The control inputs are plotted in Fig. 4f. According to the experimental results in Fig. 4, the capability and practicality of SMDOB-HOFA predictive control can be fully verified, which provides the theoretical support and experimental basis for further application and promotion of SMDOB-HOFA predictive control in actual spacecraft control.

5 Conclusions

In this study, a flying-around problem of spacecraft with lumped disturbances in the sight coordinate system has been investigated under the framework of HOFA system theory. A nonlinear HOFA system model has been applied to describe the relative orbital dynamics for flying-around mission of spacecraft with lumped disturbances. A sliding-mode disturbance observer in HOFA form has been designed to realize the estimation of lumped disturbances. Then, an incremental HOFA prediction model with estimation errors has

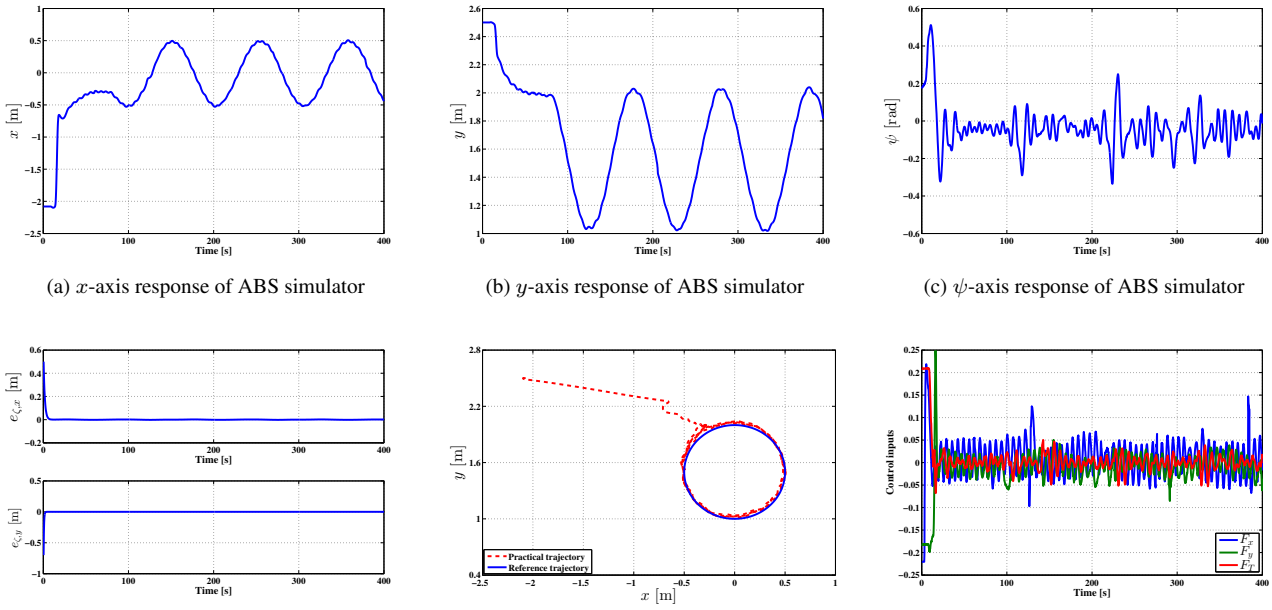

(a) x-axis response of ABS simulator (b) y-axis response of ABS simulator (c) ψ-axis response of ABS simulator

(d) Estimation errors (e) Practical trajectory of ABS simulator (f) Control inputs

Fig. 4: The experimental results for flying-around in circular orbit of ABS simulator by using (21) and (22).

been developed in HOFA form with the help of Diophantine Equation, so that multi-step ahead predictions have been constructed to optimize an objective function involving the tracking control performance. By adopting this result, an optimal tracking controller has been established to achieve the desired flying-around mission. An experimental verification on flying-around in circular orbit of ABS simulator has been taken to verify the capability and practicality of SMODB-HOFA predictive control. A drawback of this study is that the errors of disturbance estimation are only bounded, it is hard to obtain a result that the errors converge to 0. The future work will continue to improve this result by designing a new disturbance observer and to consider the more complex flying-around missions, including input constraints, pointing constraints, non-holonomic constraints and other situations.

References

[1] D. W. Zhang and G. P. Liu. Output feedback predictive control for discrete quasilinear systems with application to spacecraft flying-around. *Asian Journal of Control*, 24(4):1846–1861, 2022.

[2] Y. Su, Y. Yang, X. Yang, and W. Ye. Attitude tracking control for observation spacecraft flying around the target spacecraft. *IET Control Theory & Applications*, 15(14):1868–1881, 2021.

[3] S. Liang, Y. Zhang, W. Wang, and L. Jia. Fly-around control of space tumbling target under multiple constraints. *IEEE Access*, 10:70174–70186, 2022.

[4] Y. Huang and Y. Jia. Adaptive fixed-time six-DOF tracking control for noncooperative spacecraft fly-around mission. *IEEE Transactions on Control Systems Technology*, 27(4):1796–1804, 2019.

[5] S. Liang and Y. Zhang. Intelligent attitude fault-tolerant control of space tumbling target fly-around based on RBF neural network. *IEEE Access*, 11:6610–6622, 2023.

[6] Y. Xing, Z. Yin, and C. Wei. Appointed-time safety-guaranteed control for spacecraft flying around non-cooperative target based on fully actuated system theory. *International Journal of Systems Science*, 2024. DOI: 10.1080/00207721.2024.2313648.

[7] M. Golestani, W. Zhang, Y. Yang, and N. Xuan-Mung. Disturbance observer-based constrained attitude control for flexible spacecraft. *IEEE Transactions on Aerospace and Electronic Systems*, 59(2):963–972, 2023.

[8] H. Teng, Z. Wang, Y. Zhu, X. Yao, and L. Guo. Adaptive fixed-time disturbance observer-based proximity control for spacecrafts with dynamic obstacle constraints. *IEEE Transactions on Aerospace and Electronic Systems*, 59(6):8521–8534, 2023.

[9] G. R. Duan. High-order fully actuated systems approaches: Part I. Models and basic procedure. *International Journal of Systems Science*, 52(2):422–435, 2021.

[10] D. W. Zhang and G. P. Liu. Predictive control for networked high-order fully actuated systems subject to communication delays and external disturbances. *ISA Transactions*, 139:425–435, 2023.

[11] D. W. Zhang and G. P. Liu. Disturbance observer-based predictive tracking control of uncertain HOFA cyber-physical systems. *IEEE/CAA Journal of Automatica Sinica*, 2023. DOI: 10.1109/JAS.2023.124080.

[12] D. W. Zhang and G. P. Liu. A high-order fully actuated predictive control approach for spacecraft flying-around. *International Journal of Systems Science*, 2024. DOI: 10.1080/00207721.2024.2315223.

[13] D. W. Zhang and G. P. Liu. A high-order fully actuated predictive control approach of spacecraft flying-around under time-variant communication constraints (in Chinese). *Acta Aeronautica et Astronautica Sinica*, 45(1):628633, 2024.

[14] G. R. Duan. High-order fully actuated systems approaches: Part X. Basics of discrete-time systems. *International Journal of Systems Science*, 53(4):810–832, 2022.

[15] Liu Zhang, Quan Zhi Liu, Guo Wei Fan, Xue Ying Lv, Yu Gao, and Yang Xiao. Parametric control for flexible spacecraft attitude maneuver based on disturbance observer. *Aerospace Science and Technology*, 130:107952, 2022.

Proceedings of the 3rd Conference on Fully Actuated System Theory and Applications
May 10-12, 2024, Shenzhen, China

Safety-Critical Control in Multi-Spacecraft Specific Tracking of Rotating Target Based on Fully Actuated System Models

Zijie Lin[1], Baolin Wu[1], Junyu Chen[1], Zhaobo Sun[1]

1. Research Center of Satellite Technology, Harbin Institute of Technology, Harbin 150080, P. R. China
E-mail: 21b918079@stu.hit.edu.cn, wubaolin@hit.edu.cn, 22s018114@stu.hit.edu.cn, 22b918090@stu.hit.edu.cn

Abstract: This paper addresses the close-proximity multi-spacecraft mission of tracking a tumbling space object under safety constraints. The six-degree-of-freedom control objectives of spacecraft include: 1) hovering at a specific area above the target, and 2) maintaining a line of sight that continuously points toward the target. During the control process, motion constraints for both position and attitude are considered: 1) position constraints ensure collision avoidance among multiple spacecraft and the target, and 2) attitude constraints require the sensor's optical axis to avoid direct sunlight. To achieve these goals, a high-order fully actuated system is established for specific tracking, and the direct parametric method is used to design control law based on fully actuated theory. Subsequently, the backup control barrier function method with quadratic programming (CBF-QP) is introduced to the fully actuated system. This safety-critical control framework transforms the tracking control inputs, initially not considering safety, into guaranteed-safe control inputs that satisfy motion constraints. Finally, a numerical simulation of multi-satellite hovering observation is conducted to validate the effectiveness of the proposed algorithm.

Key Words: Safety-Critical Control, Spacecraft Specific Tracking, Control Barrier Function, Fully Actuated System

1 Introduction

On-orbit servicing (OOS) has garnered widespread attention, generally including refueling, maintenance, space debris removal and asteroid sampling return [1]. Traditional large service spacecraft has the drawbacks, such as high construction costs, long development cycles and single-point failure. Thus, low-cost and more redundant microsatellite clusters have been employed in OOS. For instance, satellite swarms are utilized for takeover control [2], cooperative observation [3], and debris dragging [4]. However, the precise and un-simplified attitude and orbital dynamics are both nonlinear. There is coupled behavior between attitude and orbit in six-degree-of-freedom (6-DOF) control. When operating at close distances, various constraints must also be considered. These factors make the control for multiple spacecraft in OOS a great challenge.

Duan [5] firstly proposes a general method to design control law for nonlinear systems. The fully actuated (FA) system can be controlled as a desired closed-loop system through a direct parametric method, thereby achieving the desired performance. For an ordinary spacecraft, both its translational motion and attitude motion are second-order fully actuated (SOFA) system. Thus, the fully actuated theory provide a new approach to design a 6-DOF tracking controller. Numerous controller design studies have already employed the FA theory for dynamics control tasks, such as formation flying [6], attitude control [7], manipulator [9], and so on. However, there has been no prior study to incorporate FA into the tracking mission of tumbling target by multiple satellites, especially under safety motion constraints.

During the multi-spacecraft tracking process, position and attitude constraints need to be considered. The former refers to maintaining a minimal distance between the chasers and the target or among chasers themselves, preventing physical collisions that could lead to mission failure. The latter refers to avoid the direct sunlight for chasers equipped with optical sensor, preventing burnt out image plane.

Currently, studies primarily address motion constraints through methods of path planning (PP), model predictive control (MPC), and the artificial potential field (APF) [10]. PP and MPC fall under trajectory optimization, which consume excessive onboard computational resources. APF is a physically meaningful and computationally simple controller with an explicit solution, but it faces issues of unsmooth movement and excessively large commands at the obstacles' boundaries.

Based on the theories of invariance set and control Lyapunov function, [11] has developed a novel safety-critical control framework named control barrier function (CBF) with quadratic program (QP). By solving a convex QP problem for an unsafe control command, a sufficiently safe control command is obtained. Under this control command, the motion state can always be guaranteed within a well-designed invariant set. Compared to MPC, which optimizes the control commands over multiple steps in one horizon, CBF-QP only optimizes the current control command. Although CBF-QP also operates within an optimization framework, the single-step convex programming significantly reduces computational complexity.

CBF-QP is a universal safety-critical control framework that separates the constrained control objective into two processes: one for designing a controller that disregards safety momentarily but achieves stability, and the other for designing the CBF with constraints. Then, the QP relates these two in one framework. It has been gradually studied in robotics [13] and manipulators [14]. Existing applications of CBF in spacecraft control are limited to simple tasks such as one-on-one rendezvous and docking [15], attitude control [16], and flybys of asteroid [17]. This paper considers a more complex mission of 6-DOF control problem described by nonlinear SOFA systems. This safety-critical control framework addresses both multiple objects collision avoidance and light avoidance constraints simultaneously.

Inspired by the aforementioned discussion, this paper con-

This work is supported by National Natural Science Foundation (NNSF) of China under Grant 62188101 and in part by the Heilongjiang Touyan Team Program. (*Corresponding author: Baolin Wu*)

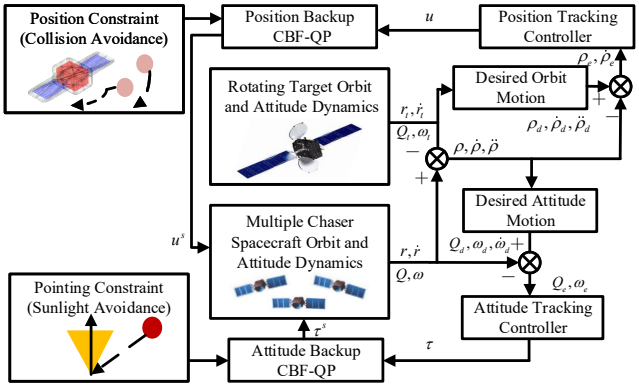

Fig. 1: Structure of safety-critical control for multi-spacecraft specific tracking.

siders the control problem of multiple chasers tracking mission. The relative motion control system and attitude control system are complex systems characterized by strong nonlinearity and multivariate coupling. Particularly, with the introduction of various motion constraints, achieving control objectives becomes a challenging task. We introduce a safety-critical control framework into such fully-actuated systems. The main contributions of this paper involves:

- The SOFA systems are derived for spacecraft attitude and orbital dynamics and their error systems. For objective of hovering and observation, the desired motion is established. The direct parametric method based on fully actuated system is utilized to design 6-DOF tracking controller.

- Considering the collision avoidance and sunlight avoidance, the forbidden zone of motion constraints are established by superquadric sphere and cone, respectively. Then, the safety-critical framework, named backup CBF-QP is introduced to addresses these established constraints. So, the unsafe 6-DOF tracking controller can be transformed into a guaranteed-safe one to keep motion states in safe invariant set.

The structure of control scheme proposed by this paper is illustrated in Fig. 1. Each one module will correspond to a section to be explained.

2 Spacecraft Dynamic Modeling

In this section, coordinate frames are described firstly. Then relative orbit and attitude dynamics are derived to establish second order fully actuated system.

2.1 Coordinate Frames

This paper considers five coordinate frames, illustrated in Fig. 1. Inertial frame, local vertical horizontal frame [10] are denoted by $O_I X_I Y_I Z_I$ and $O_L X_L Y_L Z_L$, respectively. Body-fixed coordinate frames of target and i-th chaser are denoted by $O_T X_T Y_T Z_T$ and $O_{C_i} X_{C_i} Y_{C_i} Z_{C_i}$, respectively. The desired body-fixed coordinate frame of chaser is represented by $O_{D_i} X_{D_i} Y_{D_i} Z_{D_i}$. In the subsequent sections, the coordinate frames will be abbreviated as $\{I, L, T, C_i, D_i\}$.

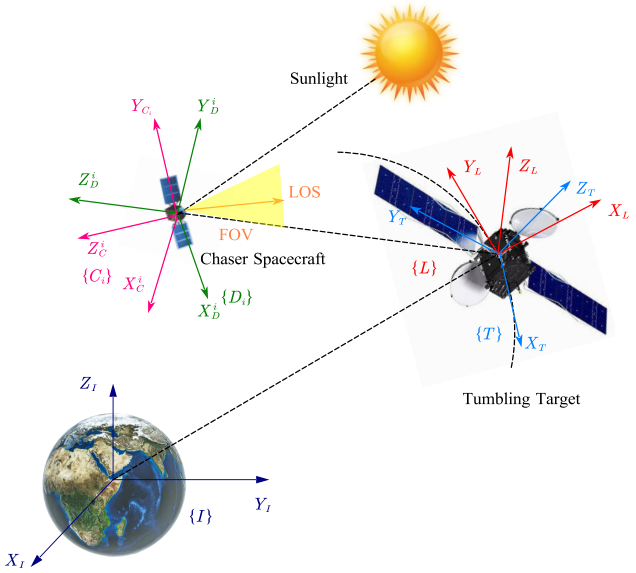

Fig. 2: Scenario and coordinate frames.

2.2 Relative Orbit Dynamics

The translational motion in $\{I\}$ of i-th chaser spacecraft and uncontrolled target are described by

$$\ddot{r}_i + \frac{\mu}{l_i^3} r_i = f_i \qquad \ddot{r}_t + \frac{\mu}{l_t^3} r_t = 0 \tag{1}$$

where r_i, r_t denote the position vectors from earth to spacecraft or target respectively, expressed in $\{I\}$; $l_i = \|r_i\|$, $l_t = \|r_t\|$ denote the distance from earth to spacecraft or target respectively. u_i denotes the control force unit mass of chaser spacecraft; $\mu = 3986004418 \times 10^{14}\ \mathrm{m^3/s^2}$ is the gravitational constant.

Define relative position between chaser and target as $\rho_i = r_i - r_t = [x_i, y_i, z_i]$, expressed in $\{L\}$. Relative motion kinematics is gotten by [10]

$$\ddot{\rho} = \begin{bmatrix} \ddot{x}_i + 2\dot{f}\left(\dot{y}_i - y_i \dot{l}_t / l_t - \dot{f}^2 x_i\right) \\ \ddot{y}_i - 2\dot{f}\left(\dot{x}_i - x_i \dot{l}_t / l_t - \dot{f}^2 y_i\right) \\ \ddot{z}_i \end{bmatrix} \tag{2}$$

where $\dot{f}$ represent the orbital angular velocity of target, caculated by [10]. Then the relative motion dynamics yields

$$\ddot{\rho}_i + A\dot{\rho}_i + B_i \rho_i + C_i = u_i \tag{3}$$

where

$$A = \begin{bmatrix} 0 & -2\dot{f} & 0 \\ 2\dot{f} & 0 & 0 \\ 0 & 0 & 0 \end{bmatrix} \quad B_i = \begin{bmatrix} \mu/l_i^3 - \dot{f}^2 & 2\dot{f}\dot{l}_t/l_t & 0 \\ -2\dot{f}\dot{l}_t/l_t & \mu/l_i^3 - \dot{f}^2 & 0 \\ 0 & 0 & \mu/l_i^3 \end{bmatrix}$$

$C_i = \left[\mu(l_t/l_i^3 - 1/l_i^2), 0, 0\right]$; u_i represent the control force unit mass expressed in $\{L\}$. Obviously, both ranks of control input u_i and state ρ_i are three, so relative motion dynamics in (3) is a typical SOFA system.

If the desired relative position, velocity, acceleration are ρ_{di}, $\dot{\rho}_{di}$, $\ddot{\rho}_{di}$, then error states are defined as

$$\rho_{ei} = \rho_{di} - \rho_i \qquad \dot{\rho}_{ei} = \dot{\rho}_{di} - \dot{\rho}_i \qquad \ddot{\rho}_{ei} = \ddot{\rho}_{di} - \ddot{\rho}_i \tag{4}$$

Then the SOFA error system is gotten from (3) as follows

$$\ddot{\rho}_{ei} + A\dot{\rho}_{ei} + B_i\rho_{ei} - L_i + u_i = 0 \tag{5}$$

where $L_i = \ddot{\rho}_{di} + A\dot{\rho}_{di} + B_i\rho_{di} + C_i$. Only if both $\dot{\rho}_{ei}$ and ρ_{ei} are asymptotically converge to zero, $\rho_i \to \rho_{di}$ and $\dot{\rho}_i \to \dot{\rho}_{di}$ can be obtained.

2.3 Attitude Dynamics

The attitude kinematics in quaternion of i-th chaser is represented by

$$\dot{q}_{0i} = -\frac{1}{2}q_{vi}^T\omega_i \qquad \dot{q}_{vi} = \frac{1}{2}\left(q_{0i}I + q_{vi}^{\times}\right)\omega_i \tag{6}$$

where $Q_i = [q_{0i}, q_{vi}]$ is unit quaternion, q_{0i} represent the scalar part of quaternion and q_{vi} represent the vector part of quaternion; ω_i denote the body angular velocity with respect to inertial frame expressed in body-fixed frame; I represents identity matrix and $(\cdot)^{\times}$ is cross-product matrix, with expression as

$$a^{\times} = \begin{bmatrix} 0 & -a_3 & a_2 \\ a_3 & 0 & -a_1 \\ -a_2 & a_1 & 0 \end{bmatrix} \tag{7}$$

Neglecting flexible parts and liquid sloshing, the attitude dynamics of rigid spacecraft expressed in $\{C_i\}$is

$$J_i\dot{\omega}_i + \omega_i^{\times}J_i\omega_i = \tau_i \tag{8}$$

where J_i is inertia matrix and τ_i is control torque to be designed. Target's attitude motion can be described by (6) and (8) when subscript i is replaced by t.

The error quaternion is defined by quaternion product

$$Q_{ei} = Q_i \otimes Q_{di}^{-1} \tag{9}$$

where Q_{ei} is error quaternion, Q_{di} is desired quaternion; $\otimes$ denote the product of quaternion; "-1" denotes the inverse of quaternion here. The error system of attitude yields [2]

$$\begin{aligned} \dot{q}_{e0i} &= -\frac{1}{2}q_{evi}^T\omega_{ei} \quad \dot{q}_{evi} = \frac{1}{2}\left(q_{e0i}I + q_{evi}^{\times}\right)\omega_{ei} \\ J_i\dot{\omega}_{ei} &= -\omega_i^{\times}J_i\omega_i + J_i\left(\omega_{ei}^{\times}R_{ei}\omega_{di} - R_{ei}\dot{\omega}_{di}\right) + \tau_i \end{aligned} \tag{10}$$

where $\omega_{ei} = \omega_i - R_{ei}\omega_{di}$ is error angular velocity expressed in $\{C_i\}$; ω_{di} is desired velocity expressed in $\{D_i\}$; $R_{ei} = R_{D_i}^{C_i}$ is the rotation matrix from $\{D_i\}$ to $\{C_i\}$, gotten by Q_{ei}, expressed by

$$R_{D_i}^{C_i} = \left(q_{e0i}^2 - q_{evi}^Tq_{evi}\right)I + 2q_{evi}q_{evi}^T - 2q_{e0i}q_{evi}^{\times} \tag{11}$$

Only if both q_{vei} and ω_{ei} are asymptotically converge to zero, $Q_i \to Q_{di}$ and $\omega_i \to \omega_{di}$ can be obtained.

Obviously, (10) is a nonlinear dynamics but strict feedback system, so SOFA system is also can be derived [8]. According to the second equation of (10), it follows that

$$\omega_{ei} = 2G_i(Q_{ei})\dot{q}_{evi} \tag{12}$$

where $G_i = \left(q_{e0i}I + q_{evi}^{\times}\right)^{-1}$. Then taking the second derivative of q_{evi} yields SOFA system as follows

$$2G_i\ddot{q}_{evi} + \bar{A}_i\dot{q}_{evi} = J_i^{-1}\tau_i + \bar{L}_i \tag{13}$$

where $\bar{A}_i = -2G_i\left(\dot{q}_{e0i}I + \dot{q}_{evi}^{\times}\right)G_i$

$$\bar{L}_i = -J_i^{-1}\omega_i^{\times}J_i\omega_i + \omega_{ei}^{\times}R_{ei}\omega_{di} - R_{ei}\dot{\omega}_{di}$$

Thus, the control objective in SOFA is to $q_{vei} \to 0$ and $\dot{q}_{vei} \to 0$.

3 Relative Motion and Attitude Tracking Controller Design Based on SOFA Systems

Here, the 6-DOF tracking controller is designed based on direct parametric method. Safety constraints are temporarily not considered, but will be addressed in section 4.

3.1 Establishment of Desired Motion

3.1.1 Desired Position Motion

The desired input for hovering position is usually described in $\{T\}$, represented by d_i, which is determined by observation mission. It should be transformed to ρ_{di}, $\dot{\rho}_{di}$, $\ddot{\rho}_{di}$ in $\{L\}$, corresponding to (5).

The transformation matrix from $\{L\}$ to $\{I\}$ is

$$R_L^I = \begin{bmatrix} {}^IX_L & {}^IY_L & {}^IZ_L \end{bmatrix} \tag{14}$$

where $X_L = r_t/\|r_t\|$, $Z_L = r_t^{\times}\dot{r}_t/\|r_t^{\times}\dot{r}_t\|$, which denote the direction of orbital radius and normal of target, respectively. $Y_L = {Z_L}^{\times}X_L$.

Then, desired hovering position, velocity and acceleration in $\{L\}$ is obtained as

$$\begin{aligned} \rho_{di} &= R_T^L \qquad \dot{\rho}_{di} = R_T^L\omega_{tl}^{\times}d_i \\ \ddot{\rho}_{di} &= R_T^L\omega_{tl}^{\times}\omega_{tl}^{\times}d_i + R_T^L\dot{\omega}_{tl}^{\times}d_i \end{aligned} \tag{15}$$

where ω_{tl} and $\dot{\omega}_{tl}$ denote the orbit-attitude coupling angular velocity of target, expressed by

$$\omega_{tl} = \omega_t - R_L^T\omega_l \quad \dot{\omega}_{tl} = \dot{\omega}_t + \omega_{tl}^{\times}R_L^T\omega_l - R_L^T\dot{\omega}_l \tag{16}$$

where ω_t and ω_l denote the angular and the orbital velocities, respectively.

3.1.2 Desired Attitude Motion

The desired attitude motion is coupled with motion of position, due to the requirement of align the LOS toward the target. As illustrated by Fig. 2, the sensor axis is fixed on axis $-Z_{Ci}$. So the following equation expressed in $\{L\}$ should be satisfied $\rho/\|\rho\| = Z_{Ci}$. Similar to (14), the transformation matrix from $\{D_i\}$ to $\{L\}$ can be established by

$$R_{D_i}^L = \begin{bmatrix} {}^LX_{D_i} & {}^LY_{D_i} & {}^LZ_{D_i} \end{bmatrix} \tag{17}$$

where $X_{D_i} = \rho_i^{\times}\dot{\rho}_i/\|\rho_i^{\times}\dot{\rho}_i\|$, $Z_{D_i} = \rho_i/\|\rho_i\|$, $Y_{D_i} = {Z_{D_i}}^{\times}X_{D_i}$. Then, desired attitude is derived by

$$R_I^{D_i} = R_L^{D_i}R_I^L \tag{18}$$

Through the conversion between quaternions and rotation matrix, we caculated desired quaternion Q_{di} from $R_I^{D_i}$. Next, desired angular velocity and acceleration are given by

$$\begin{aligned} \omega_{di} &= \omega_{dli} + R_L^{D_i}\omega_l \\ \dot{\omega}_{di} &= \dot{\omega}_{dli} - \omega_{dli}^{\times}R_L^{D_i}\omega_l + R_L^{D_i}\dot{\omega}_l \end{aligned} \tag{19}$$

where

$$\omega_{dli} = \begin{bmatrix} -Y_{D_i}\cdot\dot{Z}_{D_i} \\ X_{D_i}\cdot\dot{Z}_{D_i} \\ Y_{D_i}\cdot\dot{X}_{D_i} \end{bmatrix} \quad \dot{\omega}_{dli} = \begin{bmatrix} -\dot{Y}_{D_i}\cdot\dot{Z}_{D_i} - Y_{D_i}\cdot\ddot{Z}_{D_i} \\ \dot{X}_{D_i}\cdot\dot{Z}_{D_i} + X_{D_i}\cdot\ddot{Z}_{D_i} \\ \dot{Y}_{D_i}\cdot\dot{X}_{D_i} + Y_{D_i}\cdot\ddot{X}_{D_i} \end{bmatrix} \tag{20}$$

3.2 Tracking Controller Design for SOFA system

3.2.1 Position Tracking Controller

According to [5], for a quasi-linear SOFA system, a normal control law in (5) for i-th chaser can be designed as

$$u_i = L_i + (K_{1i} - A)\dot{\rho}_{ei} + (K_{0i} - B_i)\rho_{ei} \tag{21}$$

where K_{i1} and K_{i0} are given matrices. Substituting (21) into (5) yields

$$\ddot{\rho}_{ei} + K_{1i}\dot{\rho}_{ei} + K_{0i}\rho_{ei} = 0 \tag{22}$$

In order to obtain a closed-loop system with expected performance, we only need to be appropriately select K_{1i} and K_{0i}. The direct parametric method is introduced [8]. We rewrite (22) in a first order form as

$$\dot{\mathcal{X}}_i = \mathcal{A}_i\mathcal{X}_i \tag{23}$$

where $\mathcal{X}_i = \begin{bmatrix}\rho_{ei} & \dot{\rho}_{ei}\end{bmatrix}^T$ and $\mathcal{A}_i = \begin{bmatrix}0 & I; & -K_{0i} & -K_{1i}\end{bmatrix}$

Given a constant matrix $\mathcal{F}_i$ of whom all eigenvalues have negative real parts, e.g., Hurwitz matrix. To ensure stability of (23), the K_{0i} and K_{1i} should satisfy as $\mathcal{A}_i\mathcal{V}_i = \mathcal{V}_i\mathcal{F}_i$, where $\mathcal{V}_i$ denotes eigenvector matrix. According to [8], $\mathcal{V}_i$ can be chosen by $\mathcal{V}_i = \begin{bmatrix}\mathcal{Z}_i & \mathcal{Z}_i\mathcal{F}_i\end{bmatrix}^T$ where $\mathcal{Z}_i$ is an arbitrary matrix. Then, the gain matrices are obtained as below

$$\begin{bmatrix}K_{0i} & K_{1i}\end{bmatrix} = -\mathcal{Z}_i\mathcal{F}_i^2 \tag{24}$$

3.2.2 Attitude Tracking Controller

For quasi-linear SOFA system in (13), the control torque can be designed as

$$\tau_i = -J_i\bar{L}_i + \left(J_i\bar{A}_i - \bar{K}_{1i}\right)\dot{q}_{evi} - \bar{K}_{0i}q_{evi} \tag{25}$$

where $\bar{K}_{1i}$ and $\bar{K}_{0i}$ are gain matrices. The same direct parametric method for selecting gain matrices can be applied in the attitude controller. Substituting (25) into (13) yields

$$\dot{\bar{\mathcal{X}}}_i = \bar{\mathcal{A}}_i\bar{\mathcal{X}}_i \tag{26}$$

where $\bar{\mathcal{X}}_i = \begin{bmatrix}q_{vei} & \dot{q}_{evi}\end{bmatrix}^T$ and $\bar{\mathcal{A}}_i = \begin{bmatrix}0 & I; & -E_{0i}^{-1}\bar{K}_{0i} & -E_{1i}^{-1}\bar{K}_{1i}\end{bmatrix}$ Similar to algorithm from Section 3.2.1, if $\bar{\mathcal{Z}}_i$ is arbitrary matrix, $\bar{\mathcal{F}}_i$ is Hurwitz matrix, the gain matrices are

$$\begin{bmatrix}\bar{K}_{0i} & \bar{K}_{1i}\end{bmatrix} = -2G_i\bar{\mathcal{Z}}_i\bar{\mathcal{F}}_i^2 \tag{27}$$

4 Safety-Critical Control Framework Based on Backup CBF-QP

In this section, the constraints for position and pointing forbidden zones are modeling [10]. Then, the safety-critical control framework based on backup CBF-QP will be used to transform unsafe controller designed in (21) and (25) to a safe-enough one.

4.1 Constraint Modeling

4.1.1 Position Forbidden Zone

The forbidden zone is to describe the collision envelope among chasers and target. It includes the collision between two chasers and collision between chaser and target.

For the former type of collision, the superquadric surface is employed to describe the envelope of the tumbling target, serving as a restricted region for the chasers' maneuvering trajectories. Its mathematical expression is given by

$$h_{ki}\left(\rho_i\right) = \left(\frac{{}^T\rho_{xi}}{a_k}\right)^{\frac{2}{m_k}} + \left(\frac{{}^T\rho_{xi}}{b_k}\right)^{\frac{2}{m_k}} + \left(\frac{{}^T\rho_{xi}}{c_k}\right)^{\frac{2}{m_k}} - 1 \tag{28}$$

where subscript k, i denotes the k-th parts of target should not collide with i-th chaser; $a_k, b_k, c_k > 0$ and $0 < m_k \leq 1$ are parameters; ${}^T\rho_i = R_L^T\rho_i$ denotes the relative position of i-th chaser expressed in $\{T\}$. Only if $h_{ki} > 0$ is satisfied, the chaser is out of envelope of target for safety. As analyzed by [10], with the decrease of m_k, h_{ki} becomes more similar to a cuboid with more sharpened edges. In this paper, h_{1i} and h_{2i} represent the envelope of central main body and solar array wings, respectively.

For the second type of collision, chasers are seemed as spheres. So the collision discrimination function can be

$$l_{ji}\left(\rho_i, \rho_j\right) = \left(\rho_i - \rho_j\right)^T\left(\rho_i - \rho_j\right) - r_s^2 \tag{29}$$

where r_s are the safe distance for two chasers. $l_{ji} > 0$ should be ensured without collision among chaser spacecraft.

4.1.2 Attitude Forbidden Zone

The chaser spacecraft is equipped with an optical camera. To enhance image quality or protect the image plane from being burnt, the sunlight vector should be outside the cone formed by the field of view (FOV), as illustrated in Fig. 2. The attitude exclusion zones are utilized to depict scenarios of sunlight avoidance.

Assuming that the line of sight (LOS) is fixed along $-Z_{C_i}$, the discrimination function for pointing forbidden is defined as follows

$$g_i\left(Q_i\right) = \cos\theta - Z_{C_i}^T R_I^{C_i} S_o \tag{30}$$

where θ represent the half-angle of FOV, S_o is the sunlight vector expressed in $\{I\}$. Compared with orbit motion, change of sunlight vector is slower, so S_o can be considered constant, $R_{C_i}^T$ denotes the transform matrix from $\{I\}$ to $\{C_i\}$, caculated from quaternions as follows

$$R_I^{C_i} = \left(q_{0i}^2 - q_{vi}^T q_{vi}\right) I + 2q_{vi}q_{vi}^T - 2q_{0i}q_{vi}^{\times} \tag{31}$$

Only if $g_i > 0$ is ensured, the safety of attitude motion is maintained.

4.2 Backup CBF-QP

We begin with the brief review of CBF theory. For an affine system $\dot{x} = f(x, u)$, the state and control input is x, u. Given a function $H(x)$ satisfies

$$\begin{aligned}&\forall x \in \mathcal{X}_0, H(x) \geq 0 \qquad \forall x \in \mathcal{X}_d, H(x) < 0\\ &\forall x \in \mathcal{C}, \exists u \in \mathcal{U}\ \dot{H} + \alpha(H) \geq 0\end{aligned} \tag{32}$$

where $\mathcal{X}_0$ and $\mathcal{X}_d$ are the initial set and danger set, respectively. $\mathcal{C} = \{x \mid H(x) \geq 0\}$ is named safe set. $\alpha(\cdot)$ is a class-$\mathcal{K}$ function. Then H is named the CBF. For any legacy control input u^0, CBF is combined with QP optimization as follows [11]

$$\begin{aligned}u^* = &\arg\min_{u \in \mathcal{U}} \left\|u - u^0\right\|^2\\ &\text{s.t.} \nabla H \cdot f\left(x, u\right) + \alpha\left(H\right) \geq 0,\end{aligned} \tag{33}$$

where u^* is the guaranteed-safe control input from an unsafe control input u^0. In this paper, x represents Q_i or ρ_i, u^0 represents the unsafe input given in (21) and (25), u represents the safe control law. H is set as h_{ki}, l_{ji} and g_i.

However, such general CBF-QP has two limitations and is not suitable for our SOFA system of position and attitude motion. The first limitation is that the existence of control set $\mathcal{U}$ may cause QP infeasible. The second limitation is that due to the second-order character, the optimization conditions in (33) do not explicitly contain u after taking first derivative. One method to address these issues is backup CBF [13]. If a backup policy is defined as $\pi_b(x)$, then recurrent state over time t for initial x is $\Phi_b^t(x)$, expressed as

$$\Phi_b^t(x) = x + \int_0^t f(x, \pi_b(x))dt \tag{34}$$

As basic idea for backup CBF, a suitable safe set $\mathcal{C}$ is hard to obtain when considering various constraints, but a small and apparent safe set $\mathcal{C}_b$ named backup safe set can be determined easily. The state under $\pi_b(x)$ is forward invariant in $\mathcal{C}_b$. Using $\Phi_b^t(x)$, the small $\mathcal{C}_0$ can be enlarged to $\mathcal{C}_s$, so that $\mathcal{C}_b \subseteq \mathcal{C}_s \subseteq \mathcal{C}$. The backup safe set is described by backup CBF as $\mathcal{C}_b = \{x \mid G(x) > 0\}$. With the increasing horizon, the $\mathcal{C}_s$ is larger. The $\mathcal{C}_s$ is formed by

$$\mathcal{C}_s = \left\{x \mid \Phi_b^t \in \mathcal{C}, \Phi_b^T \in \mathcal{C}_b\right\} \tag{35}$$

In this paper, backup policy ϕ_b is chosen by quick brake of chaser spacecraft. The backup CBF is set as the small domain of zero for position and angular velocity [13].

According to above explanation, the backup CBF-QP safety-critical control is given by

$$\begin{aligned} u^* = &\arg\min_{u\in\mathcal{U}} \left\|u - u^0\right\|^2 \\ \text{s.t.} &\nabla H(\Phi_b^t)\cdot D^t(x)\cdot f(x,u) + \alpha\left(H\left(\Phi_b^t\right)\right) \geq 0 \\ &\nabla G(\Phi_b^T)\cdot D^T(x)\cdot f(x,u) + \alpha\left(G\left(\Phi_b^T\right)\right) \geq 0 \end{aligned} \tag{36}$$

where t is divided by horizon T into $t = [t_0, t_1, \cdots, T]$, $D^t(x) = \partial\Phi_b^t(x)/\partial x$ is the sensitivity matrix. As analyzed in [13], the optimization problem is feasible. And, the constraint in backup CBF-QP framework in (36) is a sufficient condition for $\dot{H} + \alpha(H) \geq 0$ corresponding to normal CBF-QP in (33).

5 Numerical Simulation

Here is a simulation provided for the tracking of a tumbling target to validate the proposed control strategy. The target is orbiting at an altitude of 600 km with an eccentricity of 0.001, an inclination of 50°, a perigee argument of 193°, a right ascension of the ascending node at 315°, and a true anomaly at perigee of 140°. The target's inertia is represented by diag(500, 500, 1000) kgm^2, and its mass is 1500 kg. The chaser's inertia is diag(12, 23, 45) kgm^2, with a mass of 20 kg. The chaser's initial positions in $\{T\}$ are [-10, -20, -30] m, [-10, 12, 8] m, [-15, -7, 15] m, [10, -15, 7] m, respectively. The initial velocities in $\{T\}$ are [0, 0, 0] m/s. The desired hover positions for the chaser are [0, 5, 2] m, [-10, -10, 2] m, [15, -7, 15] m, and [0, 10, 6] m, respectively. The target's angular velocity is [1, 1, 1]°/s, with an initial quaternion [1, 0, 0, 0]. Each of chaser's angular velocity is [0, 0, 0.1]°/s, with an initial quaternion [0.2706, 0.6533, 0.2706, 0.6533].

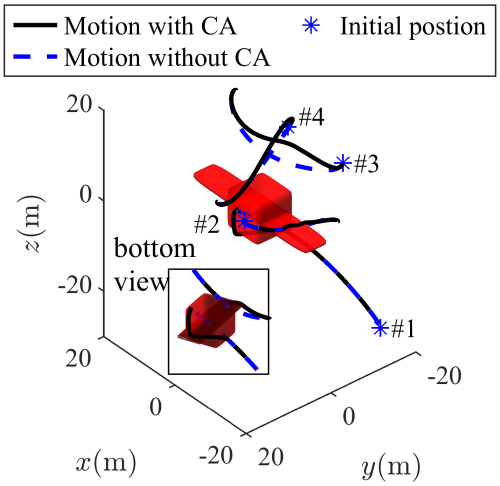

Fig. 3: The trajectories of position for four chasers in $\{T\}$.

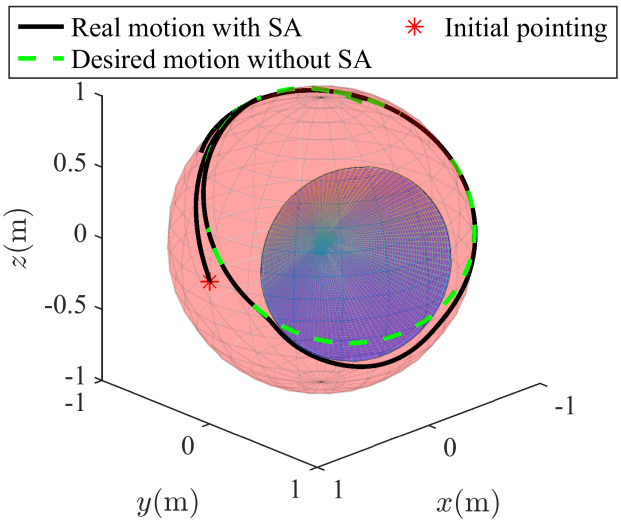

Fig. 4: The trajectory of pointing for Chaser 3 in $\{I\}$.

The simulation results are illustrated in Figs. 3 to 7. Fig. 3 depicts the trajectories of the four chaser spacecraft in the $\{T\}$ frame, comparing scenarios with and without considering collision avoidance (CA). The dashed lines represent trajectories without CA, where Chaser 1 and Chaser 2 intersect with the main body and solar wings (red surfaces) of the target spacecraft. However, with CA strategies, the chasers bypass the designed restricted zones to ensure safety. Fig. 5 represent the indices for Chaser 1 and Chaser 2, respectively, ensuring that the safety condition $h_{11}, h_{22} > 0$ is consistently maintained; otherwise, they would intersect the zero line. The trajectories of Chaser 3 and 4 do not exhibit prominent CA in Fig. 3, but in Fig. 5, a noticeable safety transition of l_{34} from < 0 to > 0 is apparent. Fig. 4 illustrates the sunlight avoidance (SA) simulation results for Chaser 3. Without the introduction of the safety-critical framework, the expected motion of the optical axis passes through the conical restricted area (purple region), where sunlight invades the FOV directly. Introducing SA strategies successfully steers the optical axis around the designated forbidden region. Fig.

5 also demonstrates the consistent maintenance of $g_3 > 0$. Figs. 6 and 7 present the relative position deviation and attitude deviation, with final steady-state deviations of 0.01 m and 0.1°, respectively. In comparison to scenarios without considering CA and SA, the state deviations increase when bypassing restricted zones to ensure safety, so that they converge slower to relax the stability for safety.

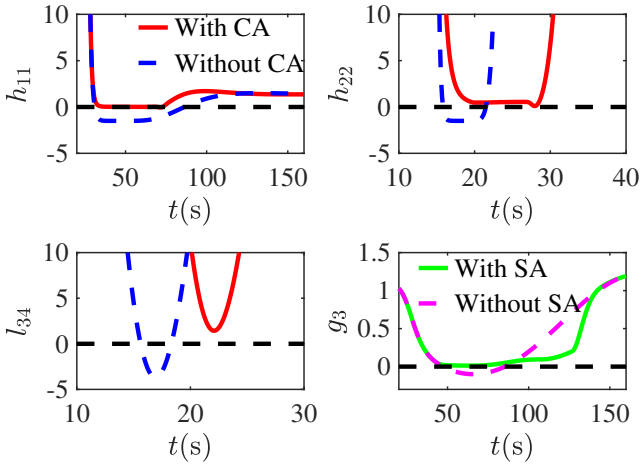

Fig. 5: Safety discrimination function of h_{ki}, l_{ji} and g_i.

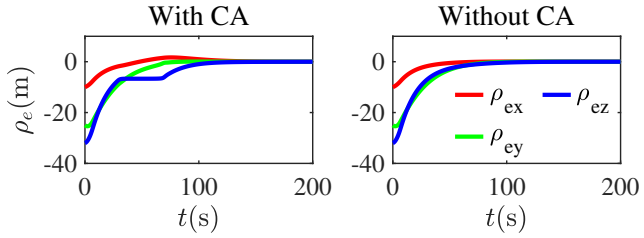

Fig. 6: Relative position error for Chaser 1.

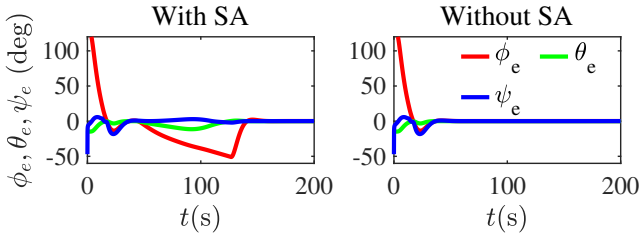

Fig. 7: Attitude error of for Chaser 3.

6 Conclusion

This paper addresses the control problem of multiple spacecraft tracking a tumbling space object under safe motion constraints. Firstly, second-order fully actuated systems are derived to describe the 6-DOF motion of chasers. Then, based on the fully actuated theory, the direct parametric method is used to design a tracking controller to achieve the desired performance of closed-loop systems. Then, safety-critical control framework, named backup control barrier function with quadratic program is introduced to convert unsafe control law into a guaranteed-safe one. Simulation validates the proposed controller in a multi-satellite observation mission. When chasers move to desired pose, the collision avoidance and sunlight avoidance can be achieved. Future work will combine both light avoidance and collision avoidance into coupling desired motion.

References

[1] W. J. Li, D. Yi. Cheng, X. G. Liu, Y. B. Wang, *et al.*, On-orbit service (OOS) of spacecraft: A review of engineering developments. *Progress in Aerospace Sciences*, 2019, 108:23-120.

[2] M. L. Wang, Y. H. Geng, B. L. Wu, D. W. Wang, Distributed adaptive attitude takeover control of failed spacecraft with parameters identification. *IEEE Transactions on Control Systems Technology*, 2023, 31(2):897-904.

[3] Y. K. Nakka, W. Honig, C. Choi, A. Harvard, *et al.*, Information-based guidance and control architecture for multi-spacecraft on-orbit inspection.*Journal of Guidance, Control, and Dynamics*, 2022, 45(7):1184-1201.

[4] C. Bonnal, D. McKnight, C. Phipps, C. Dupont, *et al.*, Just in time collision avoidance-A review. *Acta Astronautica*, 2020, 170:637-651.

[5] G. R. Duan, High-order fully actuated system approaches: Part I. Models and basic procedure. *International Journal of Systems Science*, 2021, 52(2):422-435.

[6] Z. Gao, Y. Zhang, G. Guo, Fixed-time leader-following formation control of fully-actuated underwater vehicles without velocity measurements. *Journal of Systems Science and Complexity*, 2022, 35(2):559-585.

[7] T. Zhao, G. R. Duan, Fully actuated system approach to attitude control of flexible spacecraft with nonlinear time-varying inertia. *Science China Information Sciences*, 2022, 65(11):212201.

[8] G. R. Duan, Quaternion-based satellite attitude control—A direct parametric approach, in *Proceedings of 14th International Conference on Control, Automation and Systems*, 2014:935-941.

[9] H. Sun, L. Huang, L. He, Research on the trajectory tracking control of a 6-DOF manipulator based on fully-actuated system models. *Journal of Systems Science and Complexity*, 2022, 35(2):641-659.

[10] Z. J. Lin, B. L. Wu and D. W. Wang, Specific Tracking Control of Rotating Target Spacecraft Under Safe Motion Constraints, *IEEE Transactions on Aerospace and Electronic Systems*, 2023, 59(3):2422-2438.

[11] A. D. Ames, X. Xu, J. W. Grizzle, P. Tabuada, Control barrier function based quadratic programs for safety critical systems. *IEEE Transactions on Automatic Control*, 2016, 62(8):3861-3876.

[12] L. Wang, A. D. Ames, M. Egerstedt, Safety barrier certificates for collisions-free multirobot systems. *IEEE Transactions on Robotics*, 2017, 33(3):661-674.

[13] Y. Chen, A. Singletary, A. D. Ames, Guaranteed obstacle avoidance for multi-robot operations with limited actuation: A control barrier function approach. *IEEE Control Systems Letters*, 2020, 5(1): 127-132.

[14] A. Singletary, S. Kolathaya, A. D. Ames. Safety-critical kinematic control of robotic systems. *IEEE Control Systems Letters*, 2021, 6:139-144.

[15] J. Breeden, D. Panagou, Guaranteed safe spacecraft docking with control barrier functions. *IEEE Control Systems Letters*, 2021, 6:2000-2005.

[16] Y. Y. Wu, H. J. Sun. Attitude tracking control with constraints for rigid spacecraft based on control barrier Lyapunov functions. *IEEE Transactions on Aerospace and Electronic Systems*, 2021, 58(3):2053-2062.

[17] J. Breeden, D. Panagou. Quadratic programs for high relative degree spatial constraints and spatiotemporal specifications with spacecraft applications, in *2020 59th IEEE Conference on Decision and Control (CDC)*, 2020:1496-1502.

Proceedings of the 3rd Conference on Fully Actuated System Theory and Applications
May 10-12, 2024, Shenzhen, China

Longitudinal Active Load Relief Control of Launcher based on Fully-Actuated System Approach

Feng Zhang[1], Haipeng Chen[1], Shengbao Wu[1]

1. Research and Development Center, China Academy of Launch Vehicle Technology, Beijing, 100076
E-mail: jimmyzf2004@126.com (Correspongding author: Feng Zhang)

Abstract: This paper tackles the longitudinal load relief control problem of launcher during ascent phase. By doing so, the longitudinal control equation in the load feedback framework is firstly formulated and then transformed to a classical Sylvester equation. Due to fully characterized freedoms of the closed-loop system via the parameterized approach in fully-actuated system approach, the feedback gains can be optimized to simultaneously satisfy multiple control objectives involving closed-loop stabilization, load relief and low sensitivity of closed-loop poles. Finally, a numerical example is given to verify the proposed control method.

Key Words: Launcher, Active Load Relief Control, Fully-Actuated System Theory

1 Introduction

Load relief control is to reduce the wind impact on a flying launcher during its ascent phase, ensuring its reliable flight in case of wind disturbances.

There are mainly two methods enabling load relief in practice. One is the passive strategy, which mainly utilizes the measurement of wind to modify the trajectory before launch. Based on pre-compensation philosophy, the load relief can be achieved by flying along the resulting multiple modified trajectories. The other method is the active load relief control, which introduces angle-of-attack or load signals into the control loop enabling load relief in real time. By comparison, the latter one is able to reduce the dependence on the meteorological measurement and meanwhile guarantee the real-time control performance, especially in case of wind disturbance, thereby drawing a wide of attentions[1-4].

Initial studies focusing on the active load relief control mainly introduce angle-of-attack sensors and directly use the synthesized angle-of-attack to construct feedback law for load attenuation[3]. However, it is hard to ensure a satisfactory configuration and specification of angle-of-attack sensors, and thus hard to use in practice. Alternatively, the signals of accelerator are often used to enable load relief control by indirectly introducing angle-of-attack into the control-loop[4]. This forms the background of the present study.

This paper deals with the active load relief control problem by introducing the parameterized approach in the fully-actuated system (FAS) theory[5-7]. To this end, the traditional longitudinal control equation in the load feedback framework is firstly transformed to the Sylvester equation. Then, due to fully characterized freedoms of the closed-loop system by using the parameterized approach, the feedback gains can be optimized such that multiple control objectives can be achieved, including closed-loop stabilization, minimized load relief and minimized sensitivity of closed-loop poles. Finally, a numerical example is given to verify the proposed control method.

2 System Modeling and Control Problem

2.1 Modeling

The longitudinal model of a launcher during ascent phase can be described by [1-4]

$$\begin{cases} \Delta\ddot{\varphi} + b_1\Delta\dot{\varphi} + b_2\Delta\alpha + b_3\Delta\delta_\varphi = -b_2\alpha_w + M_{bz} \\ \Delta\dot{\theta} = c_1\Delta\alpha + c_2\Delta\theta + c_3\Delta\delta_\varphi + c_1'\alpha_w + F_{BY} \\ \Delta\alpha = \Delta\varphi - \Delta\theta \end{cases} \tag{1}$$

where $\Delta\varphi$ denotes the pitch angle error, $\Delta\alpha$ denotes the angle-of-attack error, $\Delta\delta_\varphi$ denotes the control deflection, $\Delta\theta$ denotes the trajectory inclination angle error, M_{bz}, F_{BY} are the disturbance torque and force for the longitudinal channel, b_1 is the longitudinal aerodynamic damping torque coefficient, b_2 is the longitudinal aerodynamic stabilizing torque coefficient, b_3 is the control torque coefficient, c_1 is the longitudinal aerodynamic force coefficient, c_1' is the longitudinal aerodynamic damping force coefficient, c_2 is the longitudinal gravitational force coefficient, c_3 is the longitudinal control force coefficient, α_w denotes the angle-of-attack causing by wind.

The load relief control problem is mainly to reduce the wind impact on the pitch motion and meanwhile ensure the longitudinal closed-loop stability. In the light of this, the timescale of translational motion of a launcher is larger than that of rotational motion, so the $\Delta\theta$ -dynamics can be omitted such that

$$\Delta\ddot{\varphi} + b_1\Delta\dot{\varphi} + b_2\Delta\varphi = -b_3\Delta\delta_\varphi - b_2\alpha_w + M_{bz} \tag{2}$$

Traditional PD control only stabilizes the above system, but hard to reduce the wind impact. To overcome this problem, angle-of-attack would be a good choice but void due to its immeasurability. Instead, the load feedback control introducing accelerator signals is often utilized in practice, yielding

$$\Delta\delta_\varphi = a_0\Delta\varphi + a_1\Delta\dot{\varphi} + g_2\Delta\dot{W}_\varphi \tag{3}$$

*This work is supported by National Natural Science Foundation (NNSF) of China under Grant 61703437, Grant 61690210, Grant 61690212, Grant 62173301 and the Youth Talent Support Program of CASC.

where a_0, a_1 are PD feedback gains, g_2 denotes the load relief gain, and $\Delta\dot{W}_\varphi$ is the accelerator signal governed by

$$\Delta\dot{W}_\varphi = k_2(\Delta\alpha + \alpha_w) + l_a\Delta\ddot{\varphi} + k_3\delta_\varphi \tag{4}$$

where k_2, k_3 are the dynamic and control force coefficients, respectively, and l_a denotes the distance between the mass center and the accelerator.

Integrating Eq. (3) and (4) gives that

$$\Delta\delta_\varphi = \frac{1}{1-g_2k_3}\left(a_0^\varphi\Delta\varphi + a_1^\varphi\Delta\dot{\varphi} + g_2k_2(\Delta\alpha+\alpha_w) + g_2l_a\Delta\ddot{\varphi}\right) \tag{5}$$

by which, the longitudinal closed-loop pitch dynamics can be obtained from (2) as

$$\begin{aligned}&\left(1-g_2(k_3-b_3l_a)\right)\Delta\ddot{\varphi} + \left(b_1 - g_2k_3b_1 + b_3a_1^\varphi\right)\Delta\dot{\varphi}\\ &\quad + \left(b_3a_0^\varphi + b_2 - g_2(k_3b_2 - k_2b_3)\right)\Delta\varphi\\ &= -\left(b_2 - g_2(k_3b_2 - k_2b_3)\right)\alpha_w + (1-g_2k_3)M_{bz}\end{aligned} \tag{6}$$

2.2 Control Problem

The load relief control problem can be described as follows.

Control Problem: for system (6), design control gains a_0, a_1, g_2 such that the closed-loop poles are stable while the disturbance α_w has a minimum impact on the pitch motion.

3 Control Scheme

3.1 Load Relief Gain Design

Let

$$x = \begin{bmatrix} x_1 \\ x_2 \end{bmatrix} = \begin{bmatrix} \Delta\varphi \\ \Delta\dot{\varphi} \end{bmatrix}, \tag{6}$$

and the system in Eq. (6) can be re-written as

$$\dot{\boldsymbol{x}} = (\boldsymbol{A} + \boldsymbol{BK})\boldsymbol{x} + \boldsymbol{H}_w\alpha_w + \boldsymbol{H}_dM_{bz} \tag{7}$$

where

$$\begin{aligned}\boldsymbol{B} &= -\frac{b_3}{1-g_2(k_3-b_3l_a)}\begin{bmatrix}0\\1\end{bmatrix},\\ \boldsymbol{K} &= \begin{bmatrix}a_0^\varphi & a_1^\varphi\end{bmatrix},\\ \boldsymbol{H}_w &= -\frac{b_2 - g_2(k_3b_2 - k_2b_3)}{1-g_2(k_3-b_3l_a)}\begin{bmatrix}0\\1\end{bmatrix},\\ \boldsymbol{H}_d &= \frac{1-g_2k_3}{1-g_2(k_3-b_3l_a)}\begin{bmatrix}0\\1\end{bmatrix},\end{aligned}$$

In practice, to minimize the impact of wind, one often choose that

$$b_2 - g_2(k_3b_2 - k_2b_3) = 0 \tag{8}$$

which obtains the gain g_2 as

$$g_2 = \frac{b_2}{k_3b_2 - k_2b_3} \tag{9}$$

and one has

$$\boldsymbol{A} = \begin{bmatrix}0 & 1\\ 0 & -\dfrac{b_1 - g_2k_3b_1}{1-g_2(k_3-b_3l_a)}\end{bmatrix}, \quad \boldsymbol{H}_w = 0 \tag{10}$$

3.2 Control Feedback Gains Design

Since the load relief gain is given, the impact from disturbance M_{bz} on the pitch motion is almost determined, but we can reduce the sensitivity of the closed-loop poles besides the basic stable requirement.

To do so, the parameterized design method from FAS approach [5-7] is utilized to find appropriate control feedback gains.

Let the closed-loop matrix be the following Hurwitz matrix

$$\boldsymbol{F}_c = \begin{bmatrix} s_a & s_b \\ -s_b & s_a \end{bmatrix} \tag{11}$$

where s_a, s_b are scalars to be adjusted, satisfying

$$s_a < 0 \tag{12}$$

Then, according to FAS theory [5-7], the whole solutions of the following matrix equation

$$\boldsymbol{AV} + \boldsymbol{BW} = \boldsymbol{VF}_c \tag{13}$$

can be described by

$$\begin{aligned}\boldsymbol{V} &= \boldsymbol{N}_0\boldsymbol{Z} + \boldsymbol{N}_1\boldsymbol{ZF}_c + \boldsymbol{N}_2\boldsymbol{ZF}_c^2\\ \boldsymbol{W} &= D_0\boldsymbol{Z} + D_1\boldsymbol{ZF}_c + D_2\boldsymbol{ZF}_c^2\end{aligned} \tag{14}$$

where $\boldsymbol{Z} = [z_a \;\; z_b] \in \mathbb{R}^{1\times 2}$ are arbitrary matrix and

$$\begin{aligned}\boldsymbol{N}_2 &= \begin{bmatrix}0\\0\end{bmatrix}, \quad \boldsymbol{N}_1 = -\frac{b_3}{1-g_2(k_3-b_3l_a)}\begin{bmatrix}0\\1\end{bmatrix},\\ \boldsymbol{N}_0 &= -\frac{b_3}{1-g_2(k_3-b_3l_a)}\begin{bmatrix}1\\0\end{bmatrix},\\ D_2 &= 1, \quad D_1 = \frac{b_1 - g_2k_3b_1}{1-g_2(k_3-b_3l_a)}, \quad D_0 = 0\end{aligned} \tag{15}$$

At last the control gains can be obtained by

$$\begin{bmatrix}a_0 & a_1\end{bmatrix} = \boldsymbol{K} = \boldsymbol{WV}^{-1} \tag{16}$$

3.3 Solution to Control Feedback Gains

According to the requirements of control feedback gains, three main issues are taken into account and mathematically characterized to choose the values of s_a s_b and the matrix $\boldsymbol{Z}$:

- System stability: i.e., Eq. (12)
- The sensitivity of closed-loop poles:

$$J_1 = \sum\nolimits_{i=1}^{2}\left|e_i^T\boldsymbol{V}^{-1}(\boldsymbol{A}_\delta + \boldsymbol{B}_\delta\boldsymbol{K})\boldsymbol{V}e_i\right| \tag{17}$$

- Control efforts

$$J_2 = \left\| \boldsymbol{W} \boldsymbol{V}^{-1} \right\| \tag{18}$$

where

$$\boldsymbol{A}_\delta = \begin{bmatrix} 0 & 0 \\ 0 & -\dfrac{b_1 - g_2 k_3 b_1}{1 - g_2 (k_3 - b_3 l_a)} \end{bmatrix}, \boldsymbol{B}_\delta = -\frac{b_3}{1 - g_2 (k_3 - b_3 l_a)} \begin{bmatrix} 0 \\ 1 \end{bmatrix}$$

$$\boldsymbol{V}^{-1} = \frac{1}{b_0 s_b (s_a^2 + s_b^2)(z_A^2 + z_b^2)} \cdot \begin{bmatrix} -s_a z_b - s_b z_a & z_b s_a^2 + 2 z_a s_a s_b - z_b s_b^2 \\ -s_b z_b + s_a z_a & -z_a s_a^2 + 2 z_b s_a s_b + z_a s_b^2 \end{bmatrix}$$

Then, by introducing a weight scalar η to balance the above two indices, once the optimization problem is solved

$$\begin{aligned} \min_{Z,F} \quad & J = \eta J_1 + (1-\eta) J_2 \\ \text{s.t.} \quad & s_a < 0 \end{aligned} \tag{19}$$

the control gains can be hence solved by using Eq. (16).

4 Numerical Examples

To verify the proposed method, a characteristic ascent flight point of a launch vehicle is considered, where the wind gives a higher impact.

By using Eq. (9), one can obtain that $g_2 = 0.0217$, and the system matrices are set as

$$\boldsymbol{A} = \begin{bmatrix} 0 & 1 \\ 0 & -0.0538 \end{bmatrix}, \boldsymbol{B} = \begin{bmatrix} 0 \\ -0.5308 \end{bmatrix}$$

Thus the component $\boldsymbol{N}_i$ and D_i can be obtained as

$$\boldsymbol{N}_2 = \begin{bmatrix} 0 \\ 0 \end{bmatrix}, \boldsymbol{N}_1 = \begin{bmatrix} 0 \\ -0.5308 \end{bmatrix}, \boldsymbol{N}_0 = \begin{bmatrix} -0.5308 \\ 0 \end{bmatrix},$$
$$D_2 = 1, \quad D_1 = 0.5308, \quad D_0 = 0$$

Select $\eta = 0.8$, and solve the optimization problem in Eq. (19), one can obtain that

$$J = 0.1753$$
$$\boldsymbol{F}_c = \begin{bmatrix} -0.1 & 0.045 \\ -0.045 & -0.1 \end{bmatrix}$$
$$\boldsymbol{Z} = \begin{bmatrix} 0.9618 & 1.0639 \end{bmatrix}$$

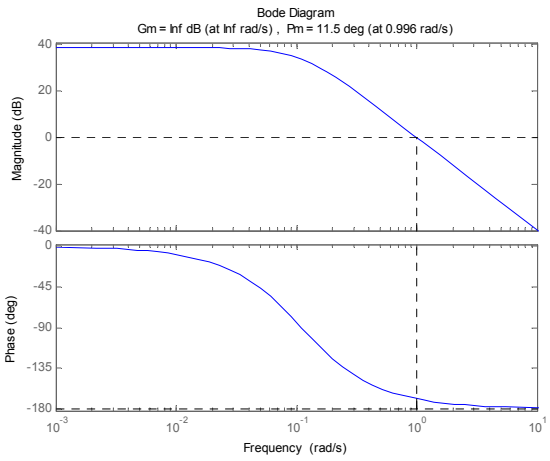

Fig. 1: Closed-loop system margins (no perturbation)

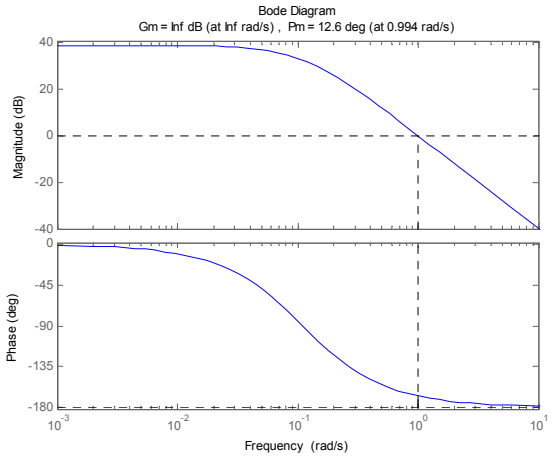

Fig. 2: Closed-loop system margins (+10% perturbation)

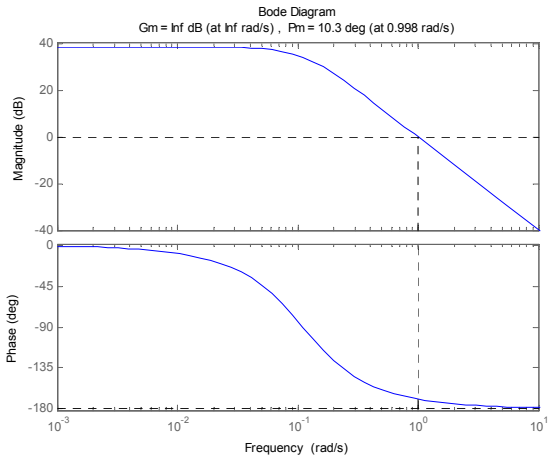

Fig. 3: Closed-loop system margins (-10% perturbation)

and the corresponding gains and closed-loop poles are

$$\begin{cases} s_1 = -0.1 + 0.045\mathrm{i} \\ s_2 = -0.1 - 0.045\mathrm{i} \end{cases}, \begin{cases} a_0 = 0.0227 \\ a_1 = 0.2754 \end{cases}$$

Figs. 1-3 show the margin results of the closed-loop system in case of no perturbation, +10% perturbations and -10% perturbations. The results indicate that the proposed method ensure a robust gain and phase margins of the closed-loop system.

5 Conclusions

This paper deals with the longitudinal load relief control problem of launcher during ascent phase. To do so, the control equation in the load feedback framework is firstly formulated and then transformed to a classical Sylvester equation. By making full use of design freedoms of the closed-loop system provided by the parameterized approach in fully-actuated system approach, the feedback gains can be optimized to simultaneously satisfy multiple control objectives involving closed-loop stabilization, load relief and low sensitivity of closed-loop poles. Finally, a numerical example is given to verify the proposed control method.

References

[1] Z.Y. Song, Load control technology in launch vehicle, *Aerospace Control,* 2013, 31(5): 3-9.

[2] W.D. Zhang, C. Y. He, J. Zhou, and, K. Wu, The In-Flight Load Relief of Launch Vehicles Based on the Signal Identification, *Aerospace Control,* 2018, 36(3): 3-14.

[3] Gyeongtaek Oh, Jongho Park, Jeongha Park, et al., Load relief control of launch vehicle using aerodynamic angle estimation, *Proceedings of Institution of Mechanical Engineers, Part G: Journal of Aerospace Engineering*, 2018, 232(8): 1598-1605.

[4] W. Yang, S, Tang, and Z. Xu, Control enhance and parameterized load relief technology for a launch vehicle, AIAA Modeling and Simulation Technologies Conference, 22-26 June 2015, Dallas, USA.

[5] G. R. Duan, High-order system approaches: I. Fully-actuated systems and parametric designs, *Acta Automatica Sinica*, 2020, 46(7): 333-1345.

[6] G. R. Duan, High-order fully actuated system approaches: Part VI. Disturbance attenuation and decoupling, *International Journal of Systems Science*, 2021, 52(10) 2161-2181.

[7] G. R. Duan, High-order fully actuated system approaches: Part VII. Controllability, stabilizability and parametric designs, *International Journal of Systems Science*, 2021, 52(14) 3091-3114.

Proceedings of the 3rd Conference on Fully Actuated System Theory and Applications
May 10-12, 2024, Shenzhen, China

Predefined-time based Tracking and Formation Control for Hypersonic Flight Vehicles

Dinghua Wang[1,2,3], Jie Wang[1,2,3], Jicheng Yuan[1,2,3]

1. School of Intelligence Science and Technology, University of Science and Technology Beijing
E-mail: M202210587@xs.ustb.edu.cn

2. Institute of Artificial Intelligence, University of Science and Technology Beijing
E-mail: wang_jie@ustb.edu.cn

3. Key Laboratory of Intelligent Bionic Unmanned Systems, Ministry of Education, University of Science and Technology Beijing, Beijing 100083, China
E-mail: D202310390@xs.ustb.edu.cn

Abstract: In this paper, the hypersonic flight vehicle(HFV) is taken as the research object. The problems of tracking control and formation control are studied. A predefined time control method is proposed to ensure the stability of the system in the expected time. Considering the complexity of the model, firstly, the hypersonic flight vehicle model is decoupled. Secondly, the desired value tracking control is realized for a single HFV. Next, on the basis, it is extended to multiple HFVs system to realize formation control. Then, the stability is proved according to Lyapunov stability theory. Finally, the effectiveness of the proposed control methods is verified by simulation results.

Key Words: Hypersonic Flight Vehicles, Predefined-time control, Tracking Control, Formation Control

1 Introduction

In recent years, with the increasing number of flight tasks, the increasingly complex flight environment and the continuous expansion of activity range in flight operations, the research on aircraft has become more and more in-depth, covering the aviation area, orbit to deep space and near space. The near space plays an irreplaceable strategic role in long-range strike, navigation and positioning, comprehensive early warning, reconnaissance and surveillance, and electronic countermeasures[1], so it has been widely concerned and favored by researchers at home and abroad. Hypersonic flight vehicle (HFV) is one of the main aircrafts flying in this region. Because of its advantages of long-range rapid response and large range maneuvering penetration, it has become a hot spot and difficulty in the development of aerospace field. In order to ensure the control accuracy, there are many intelligent control methods, such as robust control[2, 3] and quantitative learning control[4].

The above research methods have achieved some well control effect, most of them study the situation of a single aircraft. Reference [5] completes the tracking problem of two different HFVs by planning different maneuvering trajectories. And the reference [6] proposes an anti-interference composite control solution based on additive state decomposition (ASD) theory, which uses feedback linearization method to transform complex nonlinear problems into linear problems and realize control problems.

Considering the changes of the flight environment, multi-vehicle formation has a huge advantage that a single aircraft cannot match, and can complete more functions, more complex and more difficult tasks in many fields, which is the direction of future development of aircraft system technology[7]. For example, in reference [8], according to the state and output of the system, corresponding control commands are obtained to make each member move along the reference trajectory to achieve and maintain the desired geometry. In reference [9], a distributed time cooperative guidance method based on finite time control theory is proposed for multi-hypersonic vehicles system.

Given that the convergence rate is very important for formation flight, the fixed time theory is proposed based on the finite time theory. The convergence time of the fixed-time theory no longer depends on the initial conditions. The distributed formation control of multiple hypersonic flight vehicles is studied in reference [10]. Based on multi-HFVs formation flight frame, a global fixed-time formation control scheme is proposed. In addition, the global fixed time distributed formation control protocol with guaranteed tracking behavior is proposed in reference [11] to realize collision-free formation tracking of multiple hypersonic vehicles.

However, the relationship between system parameters and convergence time is not clear in fixed time theory, so it is challenging to determine the convergence time in predefined time[12]. The predefined time theory can overcome the above shortcomings and ensure that the convergence time can be arbitrarily selected by the system adjustable parameters[13]. Therefore, how to make the upper bound of the system convergence time independent of the initial state, simple in form and predefined by the obvious control parameters[14], that is, to achieve convergence within the settling time , is a problem worth studying.

The present study focuses on the glide phase of the HFVs, specifically referring to the power-off and thrust-free stage. In the second section, the preparatory knowledge including the graph theory, the predefined time theory and the model description are given. In the third section, the concrete form of control law is given and the stability of system is proved. The fourth section is the simulation results, and the fifth section is the summary of this paper.

This work is supported by the National Natural Science Foundation of China (Nos. 61703134, 62022060, 62073234, 62003236, 61972040). The China Postdoctoral Science Foundation under Grant 2019M650874. Open Fund of Complex System Cognition and Decision Lab, Institute of Automation, Chinese Academy of Sciences E2T0X4D803.

2 Preliminaries

2.1 Graph Theory

The graph theory is used to represent the communication between individuals in a system. An undirected graph can be represented as $G = (\upsilon, \epsilon, A)$, where $\upsilon = \{\upsilon_1, \upsilon_2, ..., \upsilon_N\}$ is a node set, $\epsilon \subseteq \upsilon \times \upsilon$ is an edge set, and $A = [a_{ij}] \in R^{N\times N}$ is a weighted adjacency matrix. In an undirected graph, it is known that $(\upsilon_i, \upsilon_j) \subseteq \epsilon \Leftrightarrow (\upsilon_j, \upsilon_i) \subseteq \epsilon, a_{ij} = a_{ji}$. An edge $(\upsilon_i, \upsilon_j) \subseteq \epsilon$ means that υ_i and υ_j can communicate with each other, and the adjacency matrix coefficients meet $a_{ij} > 0$. On the contrary, communication is not available, and $a_{ij} = 0$ is satisfied. $D = \mathrm{diag}\{d_1, d_2, ..., d_N\}$ is the degree matrix with $d_i = \sum_{j=1}^{N} a_{ij}$. So, the Laplacian matrix can be written as $L = D - A = [l_{ij}] \in R^{N\times N}$. In addition, if there is a path between any two nodes, the undirected graph is called connected.

2.2 Hypersonic Flight Vehicles Model Description

The HFVs possess a vast flight envelope, characterized by highly complex and nonlinearly coupled dynamics. Therefore, when constructing the control-oriented model, certain secondary factors should be disregarded in accordance with the actual flight environment. When studying formation flight, they can be regarded as particles. Assume that the Earth is a uniform sphere and ignore its rotation. The three degrees of freedom model of HFV can be obtained in the following form

$$\begin{aligned}
\dot{x}_i =& V_i \cos\theta_i \cos\psi_i \\
\dot{y}_i =& V_i \sin\theta_i \\
\dot{z}_i =& V_i \cos\theta_i \sin\psi_i \\
\dot{V}_i =& -D_i - g\sin\theta_i \\
\dot{\theta}_i =& \frac{L_i \cos\gamma_{\mathrm{v}_i} - g\cos\theta_i}{V_i} \\
\dot{\psi}_i =& \frac{L_i \sin\gamma_{\mathrm{v}_i}}{V_i \cos\theta_i}
\end{aligned} \tag{1}$$

where V_i, θ_i, ψ_i and γ_{v_i} respectively represent the velocity, the flight path angle, heading angle and the bank angle of the i-th HFV. L_i and D_i represent the lift and resistance of the HFV, which are expressed as follows

$$\begin{aligned}
L_i =& \frac{1}{2m}\rho_i {V_i}^2 S(c_y^{\alpha}\alpha_i + c_y^{\beta}\beta_i) \\
D_i =& \frac{1}{2m}\rho_i {V_i}^2 S(c_{x0} + c_x^{\alpha}|\alpha_i| + c_x^{\beta}|\beta_i|)
\end{aligned} \tag{2}$$

where α is the angle of attack, and β is the side slip angle. m and S represent the mass and reference area of the aircraft, ρ_i is the air density, and its specific expression is $\rho_i = 1.2258e^{-1.3785\times10^{-4}y}$. Considering the specific flight environment, the aerodynamic parameters are fitted and the specific values are $c_y^{\alpha} = 57.16$, $c_y^{\beta} = -0.08$, $c_{x0} = 0.32$, $c_x^{\alpha} = 0.21$, $c_x^{\beta} = 0.19$. Therefore, the above lift and drag forces can be fully expressed.

2.3 Predefined-time Stability

Consider the following autonomous system

$$\dot{x} = f(x(t), \varphi), \quad x(0) = x_0 \tag{3}$$

where $x \in R^n$ is the state variable and $x_0 = x(0)$ is the initial value of the system. φ is a tunable parameter of the system. $f : R^n \to R^n$ is a nonlinear function. The solution of the system (3) is assumed to be $\Phi(t, x_0)$, while the origin serves as the equilibrium.

Definition 1. The origin of system is globally finite-time stable if the origin of system (3) is globally asymptotically stable and $\Phi(t, x_0)$ reaches the equilibrium point within a finite time. In conclusion, it can be expressed as $\Phi(t, x_0) = 0, \forall t \geq T(x_0)$. $T(x_0) : R^n \to R^+ \setminus \{0\}$ is the convergence time function.

Definition 2. Assuming that the convergence time function $T(x_0)$ of system (3) is bounded, that is, $\exists T_{\max} > 0 : \forall x_0 \in R^n : T(x_0) \leq T_{\max}$, then the origin of system has fixed time stability.

Definition 3. Assuming that the system (3) is fixed time stable, and there are parameter φ and settling time $T(\varphi)$ satisfying $\forall x_0 \in R^n : T(x_0) \leq T(\varphi)$. Therefore, the origin of system has predefined time stability, where $T(\varphi)$ is the predefined convergence time.

Lemma 1[15]. The requirement for system (3) is the existence of a radially unbounded and positive definite Lyapunov function $V(x)$ that satisfies the following relation:

$$\dot{V} \leq -\frac{4}{T_c M(1-\mu)}(MV + NV^{\frac{1+\mu}{2}} + KV^{\frac{3-\mu}{2}}) \tag{4}$$

where $M, N, K > 0$, $4NK = M^2$ and $0 < \mu < 1$. Therefore, the system is predefined time stable. The settling time is T_c, which depends on the system parameters.

Proof. Considering the properties of differential inequalities, equation (4) is transformed into:

$$\mathrm{d}t \leq \frac{\mathrm{d}V}{-\frac{4}{T_c M(1-\mu)}(MV + NV^{\frac{1+\mu}{2}} + KV^{\frac{3-\mu}{2}})} \tag{5}$$

Suppose that the initial condition $V_0 > 0$ of the Lyapunov function converges to $V_r = 0$ in time $T(x_0)$. Therefore, provided that both sides of equation (5) are integrated simultaneously, the settling time $T(x_0)$ can be satisfied

$$\begin{aligned}
T(x_0) \leq& -\int_{V_0}^{V_r} \frac{T_c M(1-\mu)}{4} \frac{\mathrm{d}V}{MV + NV^{\frac{1+\mu}{2}} + KV^{\frac{3-\mu}{2}}} \\
=& \frac{T_c\sqrt{NK}(\mu-1)}{2} \int_{V_0}^{V_r} \frac{\mathrm{d}V}{V^{\frac{1+\mu}{2}}(\sqrt{N} + \sqrt{K}V^{\frac{1-\mu}{2}})^2} \\
=& -T_c\sqrt{NK} \int_{V_0}^{V_r} \frac{\mathrm{d}(V^{\frac{1-\mu}{2}})}{(\sqrt{N} + \sqrt{K}V^{\frac{1-\mu}{2}})^2} \\
=& \frac{T_c\sqrt{N}}{\sqrt{N} + \sqrt{K}V^{\frac{1-\mu}{2}}}\Bigg|_{V_0}^{V_r} \\
=& T_c(1 - \frac{\sqrt{N}}{\sqrt{N} + \sqrt{K}V_0^{\frac{1-\mu}{2}}}) \\
\leq& T_c
\end{aligned} \tag{6}$$

Therefore, the proof of Lemma 1 is complete.

2.4 Control objective

Considering the system given by (1), in order to facilitate the design of formation control law, the x and y direction control is considered in this paper. Given the desired relative distance, a sliding mode controller based on predefined time is constructed to make the HFVs reach the desired position and realize the formation configuration.

3 Predefined-time sliding mode control law

Since the HFV dynamic model is complex and has a strong coupling, the following method is used to achieve system decoupling while realizing the desired formation control performance. Assuming the control inputs u and v, the system model can be expressed as

$$\begin{aligned} \dot{x}_i =& u_i \\ \dot{y}_i =& v_i \end{aligned} \tag{7}$$

where $u_i = V_i \cos\theta_i \cos\psi_i$ and $v_i = V_i \sin\theta_i$.

Assuming the desired trajectory of the formation are x_d and y_d, and the relative distance between the i-th HFV and the expected trajectory is δ_{xi} and δ_{yi}, the formation error can be expressed as

$$\begin{aligned} e_{xi} =& \sum_{j=1}^{N} a_{ij}(\tilde{x_i} - \tilde{x_j}) + b_i\tilde{x_i} \\ e_{yi} =& \sum_{j=1}^{N} a_{ij}(\tilde{y_i} - \tilde{y_j}) + b_i\tilde{y_i} \end{aligned} \tag{8}$$

where $\tilde{x_i} = x_i - x_d - \delta_{xi}$ and $\tilde{y_i} = y_i - y_d - \delta_{yi}$. The formation error is selected as sliding mode function. Therefore, the horizontal direction control law designed according to the predefined time theory is as follows

$$u_i = \frac{1}{(l_{ii} + b_i)}(-a_1 e_{xi} - b_1 {e_{xi}}^{\frac{p}{q}} - c_1 {e_{xi}}^{2-\frac{p}{q}}) + \dot{x}_d \tag{9}$$

where $a_1, b_1, c_1 > 0$, p, q are positive odd numbers and satisfy $p < q$. Similarly, the control law of the longitudinal plane is designed as

$$v_i = \frac{1}{(l_{ii} + b_i)}(-a_2 e_{yi} - b_2 {e_{yi}}^{\frac{p}{q}} - c_2 {e_{yi}}^{2-\frac{p}{q}}) + \dot{y}_d \tag{10}$$

where $a_2, b_2, c_2 > 0$ are the control gains. Thus, using the above control inputs can ensure that the system realize the desired formation and meet the desired relative distance requirements.

Theorem 1. Consider the system shown in (7), assuming that the communication graph of the system is connected. The control law (9) and (10) can ensure that the system converges in a predefined time T_c, that is, the desired formation is achieved.

Proof. According to the basic knowledge of graph theory, the formation error (8) is transformed into the form of vector

$$\begin{aligned} e_x =& (L + B)\tilde{x} \\ e_y =& (L + B)\tilde{y} \end{aligned} \tag{11}$$

where $\tilde{x} = [\tilde{x}_1, \tilde{x}_2, ...\tilde{x}_N] \in R^N$, $\tilde{y} = [\tilde{y}_1, \tilde{y}_2, ...\tilde{y}_N] \in R^N$ and $e_x = [e_{x1}, e_{x2}, ...e_{xN}]^T \in R^N$. Both L and B are matrices of order N. Supposing there is a matrix $I = [1, 1, ..., 1]_N{}^T$, the control law can be expressed as

$$\begin{aligned} u &= (L + B)^{-1}(-a_1 e_x - b_1 {e_x}^{\frac{p}{q}} - c_1 {e_x}^{2-\frac{p}{q}}) + I\dot{x}_d \\ v &= (L + B)^{-1}(-a_2 e_y - b_2 {e_y}^{\frac{p}{q}} - c_2 {e_y}^{2-\frac{p}{q}}) + I\dot{y}_d \end{aligned} \tag{12}$$

Select system parameters in the same way as above. Considering the stability proof in the horizontal direction, the Lyapunov function is chosen as

$$V_1 = \frac{1}{2} e_x^T e_x \tag{13}$$

The matrix is inherently positive definite, and its derivative can be derived

$$\begin{aligned} \dot{V}_1 =& e_x^T \dot{e}_x \\ =& e_x^T (u - I\dot{x}_d) \\ =& e_x^T (L + B)(u - I\dot{x}_d) \\ =& e_x^T (-a_1 e_x - b_1 {e_x}^{\frac{p}{q}} - c_1 {e_x}^{2-\frac{p}{q}}) \\ =& -a_1^{'} V_1 - b_1^{'} V_1^{\frac{1+p/q}{2}} - c_1^{'} V_1^{\frac{3-p/q}{2}} \\ =& -(a_1^{'} V_1 + b_1^{'} V_1^{\frac{1+p/q}{2}} + c_1^{'} V_1^{\frac{3-p/q}{2}}) \end{aligned} \tag{14}$$

According to Lemma 1, the selection of parameters obtained by comparing (4) and (14) should satisfy the following conditions

$$\begin{aligned} a_1^{'} \geq& \frac{4}{T_{c1}(1 - p/q)} \\ b_1^{'} \geq& \frac{2\sqrt{N}}{T_{c1}\sqrt{K}(1 - p/q)} \\ c_1^{'} \geq& \frac{2\sqrt{K}}{T_{c1}\sqrt{N}(1 - p/q)} \end{aligned} \tag{15}$$

Therefore, let $p/q = \mu$ and $0 < \mu < 1$, the Lyapunov function can be rewritten as

$$\dot{V}_1 \leq -\frac{4}{T_{c1} M(1 - \mu)}(MV_1 + NV_1^{\frac{1+\mu}{2}} + KV_1^{\frac{3-\mu}{2}}) \tag{16}$$

Similarly, we can select the Lyapunov function as $V_2 = \frac{1}{2} e_y^T e_y$ in the longitudinal plane which satisfies the above conditions. Hence, the designed control law ensures that the system converges in the predefined time T_{c1}, and Theorem 1 is proved completely.

The expected heading angle and the flight path angle can be inversely determined based on the expressions of u_i and v_i. So the specific expressions are as follows

$$\begin{aligned} \psi_{id} =& \arccos(\frac{u_i}{V_i \cos\theta_i}) \\ \theta_{id} =& \arcsin(\frac{v_i}{V_i}) \end{aligned} \tag{17}$$

Thus, the tracking error is defined as

$$\begin{aligned} e_{\psi i} =& \psi_i - \psi_{id} \\ e_{\theta i} =& \theta_i - \theta_{id} \end{aligned} \tag{18}$$

The real control inputs of this system are the bank angle γ_{v_i} and the attack angle α_i, so according to the above errors, the control law can be designed as:

$$\begin{aligned}(L_i\sin(\gamma_{v_i}))_d =& V_i\cos\theta_i(u_{\psi_i}+\dot{\psi}_{id})\\ (L_i\cos(\gamma_{v_i}))_d =& V_i(v_{\theta_i}+\dot{\theta}_{id})+g\cos\theta_i\end{aligned} \tag{19}$$

and

$$\begin{aligned}u_{\psi_i} =& (-a_3e_{\psi i}-b_3e_{\psi i}^{\frac{p}{q}}-c_3e_{\psi i}^{2-\frac{p}{q}})\\ v_{\theta_i} =& (-a_4e_{\theta i}-b_4e_{\theta i}^{\frac{p}{q}}-c_4e_{\theta i}^{2-\frac{p}{q}})\end{aligned} \tag{20}$$

where $a_3,b_3,c_3>0$, $a_4,b_4,c_4>0$, p,q are positive odd numbers and satisfy $p<q$.

Therefore, the following equations can be obtained

$$\begin{aligned}\Omega &= \mathrm{sign}((L_i\cos(\gamma_{v_i}))_d)\\ L_i &= \Omega\sqrt{(L_i\cos(\gamma_{v_i}))_d{}^2+(L_i\sin(\gamma_{v_i}))_d{}^2}\\ \gamma_{v_i} &= \arctan(\frac{(L_i\sin(\gamma_{v_i}))_d}{(L_i\cos(\gamma_{v_i}))_d})\\ \alpha_i &= \frac{2L_im}{\rho_iV_i^2Sc_y^{\alpha}}\end{aligned} \tag{21}$$

The HFVs system formation control laws are designed.

Theorem 2. Taking the model represented by (1) as the research object, the expressions of the real control law γ_{v_i} and α_i shown in (20) and (21) can ensure that the system achieves the desired formation.

Proof. The Lyapunov functions are designed as $V_3=\frac{1}{2}e_{\psi i}^2$ and $V_4=\frac{1}{2}e_{\theta i}^2$. Taking the derivative of V_3, the result is as follows

$$\begin{aligned}\dot{V}_3 =& e_{\psi i}\dot{e}_{\psi i}\\ =& e_{\psi i}(\dot{\psi}_i-\dot{\psi}_{id})\\ =& e_{\psi i}(\frac{V_i\cos\theta_i(u_{\psi_i}+\dot{\psi}_{id})}{V_i\cos\theta_i}-\dot{\psi}_{id})\\ =& e_{\psi i}(-a_3e_{\psi i}-b_3e_{\psi i}^{\frac{p}{q}}-c_3e_{\psi i}^{2-\frac{p}{q}})\\ =& -a_3e_{\psi i}^2-b_3e_{\psi i}^{\frac{p+q}{q}}-c_3e_{\psi i}^{\frac{3q-p}{q}}\\ =& -(a_3^{'}V_3+b_3^{'}V_3^{\frac{1+p/q}{2}}+c_3^{'}V_3^{\frac{3-p/q}{2}})\end{aligned} \tag{22}$$

If the parameters $a_3^{'},b_3^{'},c_3^{'}$ are selected in the same way as (15), there is

$$\dot{V}_3\le-\frac{4}{T_{c2}M(1-\mu)}(MV_3+NV_3^{\frac{1+\mu}{2}}+KV_3^{\frac{3-\mu}{2}}) \tag{23}$$

The above form can also be obtained by taking the derivative of V_4 in the same way. Theorem 2 is proved. Because the convergence rate of the control inner ring is greater than that of the control outer ring, the HFVs system can be guaranteed to be stable in the predefined time $T_c=T_{c1}(T_{c2}<T_{c1})$.

4 Simulations

4.1 Single HFV tracking control

In this section, the tracking control problem of a single aircraft is studied. The initial values of x and y directions are $x_0=1000m$ and $y_0=34000m$ respectively. The expected value is set to $x_d=200m$ and $y_d=33300m$, and the predefined time is selected to $T_c=6.5s$. The specific simulation results are shown in the Fig.1 and Fig.2.

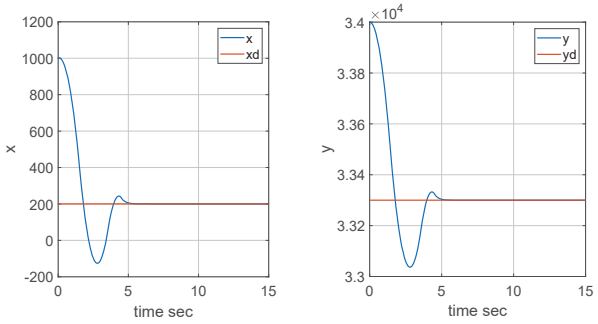

Fig. 1: Tracking control performances

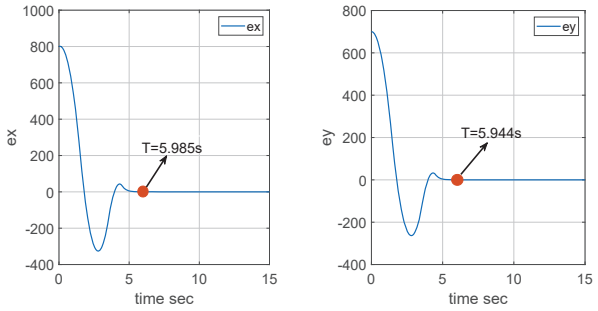

Fig. 2: Tracking control errors

By analyzing the above simulation results, it can be concluded that: Fig.1 shows that the state variables of the horizontal and vertical planes can eventually track the expected values, making the system stable. Fig.2 shows the tracking errors, which can be guaranteed to converge within T_c to achieve predefined time tracking control.

4.2 Multiple HFVs formation control

A multi-aircraft system consisting of three HFVs is considered based on a single HFV. Multiple aircrafts in the system start from the same initial position, and the expected relative distances in the horizontal and the longitudinal direction are $\delta_x=[0;-2500;2500]$ and $\delta_y=[0;1000;1000]$, respectively, to form the expected triangular formation. Supposing the HFVs can communicate with each other. The predefined time is designed as $T_c=13s$, and the specific simulation results are as follows.

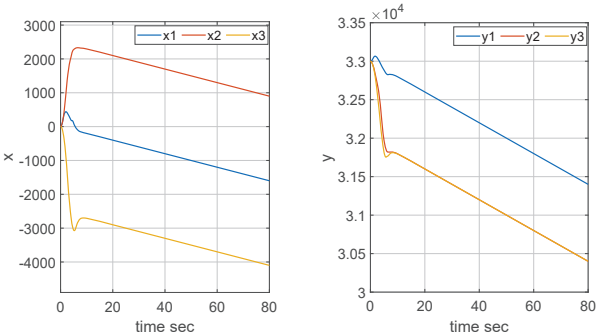

Fig. 3: Formation control performances

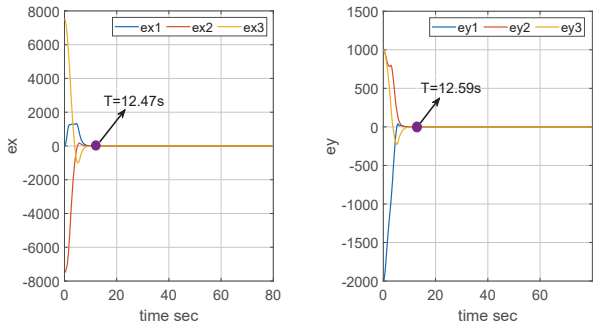

Fig. 4: Formation control errors

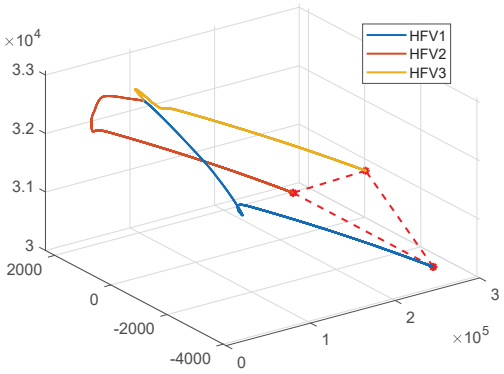

Fig. 5: Three-dimensional formation

According to the above simulations, it can be seen from Fig.3 that the positions can guarantee the expected relative distance values. Fig.4 indicates that the errors reach zero at the predefined time, that is, the system can be stable within T_c. Fig.5 gives the three-dimensional formation, which eventually formes a triangular formation.

5 Conclusions

The purpose of this paper is to design the predefined time control law for the HFVs control. In order to solve the problem of high coupling, a virtual control input is introduced to transform the complex model into a first-order system. Then the actual control law is designed by inverting the expected value. The Lyapunov function is utilized to demonstrate the stability of both the internal and external rings within the system, and the simulations show that the system can reach the expected values and stabilize in a settling time.

References

[1] H. Stephens, Air Force Magazine. *Near-space*, 2005, 88(7): 36–40.

[2] J. Li, Y, Liu, J. Yu, A new result on semi-synchronous event-triggered backstepping robust control for a class of non-Lipschitzian networked systems. *Applied Mathematics and Computation*, 2022, 424(6): 127027.

[3] S. Liang, B. Xu, Kalman-filter-based robust control for hypersonic flight vehicle with measurement noises. *Aerospace Science and Technology*, 2021, 112:106566.

[4] Y. Shi, X. Shao, W. Zhang, Quantized learning control for flexible air-breathing hypersonic vehicle with limited actuator bandwidth and prescribed performance. *Aerospace Science and Technology*, 2020, 97: 105629.

[5] Z. Liang, J. Yu, Z, Ren, Trajectory planning for cooperative flight of two hypersonic entry vehicles, in *21st AIAA International Space Planes and Hypersonics Technologies Conference*, 2017: 1-14.

[6] B. Hang, R. Ren, B. Xu, Robust anti-disturbance tracking control method for hypersonic flight vehicles. *Flight Dynamics*, 2023, 41(4): 67-73+87.

[7] L. Cheng, F. Jiang, Z. Wang, Multiconstrained real-time entry guidance using deep neural networks. *IEEE Transactions on Aerospace and Electronic Systems*, 2021, 57(1): 325-340.

[8] P. Yang, A. Zhang, W. Bi, Cooperative group formation control for multiple quadrotors system with finite- and fixed-time convergence. *ISA transactions*, 2023: n. pag.

[9] K. An, Z. Guo, W. Huang, A cooperative guidance approach based on the finite-time control theory for hypersonic vehicles. *International Journal of Aeronautical and Space Sciences*, 2022, 23: 169-179.

[10] Y. Zhang, X. Wang, S. Tang, A globally fixed-time solution of distributed formation control for multiple hypersonic gliding vehicles. *Aerospace Science and Technology*, 2020, 98: 105643.

[11] X. Wu, C. Wei, T. Chen, On novel distributed fixed-time formation tracking of multiple hypersonic flight vehicles with collision avoidance. *Aerospace Science and Technology*, 2023, 141: 108517.

[12] J.D. Sánchez-Torres, G. David, A class of predefined-time stable dynamical systems. *IMA Journal of Mathematical Control and Information*, 2017, 35: n. pag.

[13] E. Jiménez-Rodríguez, A lyapunov-like characterization of predefined-time stability. *IEEE Transactions on Automatic Control*, 2020, 65(11): 4922-4927.

[14] S. Xu, Y. Guan, J. Pu, Predefined-time sliding mode control for VTHL launch vehicle in reentry phase. *Acta Aeronautica et Astronautica Sinica*, 2023, 44(7): 326857.

[15] H.B. Xue, X.H. Liu, A novel fast terminal sliding mode with predefined-time synchronization. *Chaos, Solitons and Fractals*, 2023, 175: 114049.

Proceedings of the 3rd Conference on Fully Actuated System Theory and Applications
May 10-12, 2024, Shenzhen, China

Disturbance Separation-Based Antidisturbance Attitude Control for Flexible Liquid-Filled Spacecrafts

Baopeng Zhu[1], Hao Teng[2], Yan Meng[2], Yukai Zhu[3]

1. School of Automation, Southeast University, Nanjing 210096, China
E-mail: zbpneu@gmail.com

2. School of Automation Science and Electrical Engineering, Beihang University, Beijing 100191, China
E-mail: hteng@buaa.edu.cn; mengyan102@buaa.edu.cn

3. School of Astronautics, Beihang University, Beijing 100191, China
E-mail: ykzhubuaa@126.com

Abstract: Tightly coupled disturbances such as flexible vibration and liquid sloshing reduce the attitude control accuracy and stability of spacecrafts. The separation and thereby compensation of tightly coupled disturbances are crucial for improving attitude control performance. This paper investigates disturbance separation-based antidisturbance attitude control for flexible liquid-filled spacecrafts. First, based on the rigid-flexible-liquid interaction mechanism of spacecrafts, the flexible vibration disturbance and liquid sloshing disturbance are finely characterized, and a tightly coupled attitude dynamics model of a flexible liquid-filled spacecraft is established. Then, a disturbance separability criterion is established and two disturbance separability observers are designed to estimate the flexible vibration disturbance and the liquid shaking disturbance, respectively. Furthermore, a tightly coupled antidisturbance attitude control law is designed to accurately compensate for the flexible vibration disturbance and the liquid sloshing disturbance, thereby improving the attitude control accuracy and stability of spacecrafts. Finally, a numerical simulation is given to verify the validity of the proposed methodology.

Key Words: Flexible liquid-filled spacecrafts, disturbance separation, tightly coupled disturbances, disturbance observer-based control (DOBC)

1 Introduction

With the development of space technology, high-precision space missions, such as in-orbit communications and Earth observation, have placed rigorous requirements on the precision and stability of spacecraft control. However, in the microgravity environment of space, factors such as satellite manoeuvres and changes in environment temperature can excite the continuous vibration of the satellite's flexible appendages and generate multi-modal rigid-flexible coupling disturbances, which reduces the accuracy and stability of attitude control. In addition, during satellite manoeuvring, the sloshing of a large amount of fuel carried on the spacecraft will cause oscillations in the satellite attitude. In particular, the tight coupling between the flexible vibration and the liquid fuel sloshing will seriously affect the attitude control accuracy of the satellite. Therefore, the accurate estimation and the compensation of flexible vibration disturbance and liquid sloshing disturbance in flexible liquid-filled satellites is crucial to the attitude control performance of rigid-flexible-liquid satellites.

For the anti-disturbance attitude control problem of flexible liquid-filled satellites, various robust control methods have been widely studied, such as H_∞ control, sliding mode control, etc [1–3]. These robust control methods attribute disturbances such as flexible vibration and liquid sloshing to the norm-bounded uncertainty, and use the robust characteristics of control methods itself to suppress disturbances. Compared with robust control methods that utilize robust characteristics to suppress disturbances with limited performance, disturbance compensation based methods are an effective anti-disturbance control method. By estimating the disturbance using the disturbance observer and then compensating for it, the system's anti-disturbance ability is improved [4–9]. [5] revealed the uniqueness of active disturbance rejection control (ADRC) for dealing with the uncertainties. In [7], a nonlinear ADRC is designed to ensure the semiglobal and global convergence for the general nonlinear systems. [10] presented an ADRC strategy to estimates and compensates for internal dynamic changes in the drive axis of micro-electro-mechanical systems gyroscope.

However, it is worth noting that the above method is a direct estimation of the disturbance and does not make use of the information of the disturbance, which leads to a large conservatism in disturbance rejection. In contrast, disturbance observer based control (DOBC) method achieves accurate estimation of disturbance compensation by utilizing partial information of disturbances [11, 12]. In practical engineering, the disturbance is multi-source rather than single. The performance of anti-disturbance can be effectively improved by the fine estimation of multiple disturbances. In particular, the composite hierarchical antidisturbance control (CHADC) with "disturbance observer + robust control" first proposed by Guo and Chen can simultaneously attenuate and reject the multiple disturbances and has been widely applied in various fields [13–17].

Although abundant results have been obtained on spacecraft attitude control, it is worth noting that the applicability of disturbance estimation is limited by the fact that the above mentioned disturbance estimation methods only deal with single type disturbance or all heterogeneous disturbances is classified as lumped disturbance for ease of handling. However, by classifying heterogeneous and isomeric disturbances as the lumped disturbance to estimate disturbances reduces the accuracy of the disturbance estimation, which leads to more conservative. Therefore, how to achieve separation es-

This work was supported in part by Beijing Natural Science Foundation under Grant 4232048, in part by the Fundamental Research Funds for the Central Universities. (Corresponding author: Yukai Zhu).

timation of multiples tight-coupling disturbances by analyzing different disturbances with heterogeneous property is a critical challenge.

In this paper, disturbance separation-based antidisturbance attitude control for flexible liquid-filled spacecrafts subject to flexible vibration disturbance and liquid sloshing disturbance. First, based on the constructed tightly coupled attitude dynamic model, the definition and criterion for the disturbance separability are given to ensure that the tightly coupled disturbances are refined estimated. Then, two disturbance observer are designed to estimate flexible vibration disturbance and liquid sloshing disturbance, respectively. Finally, a tightly coupled antidisturbance attitude control law is designed to accurately compensate for the flexible vibration disturbance and the liquid sloshing disturbance.

The remainder of this paper is organized as follows. The tightly coupled dynamics model is introduced in Section 2. In Section 3, the definition and criterion for the disturbance separability are given and two disturbance observers are designed. Section 4 presents antidisturbancc attitude control law designed and stability proof. A numerical simulation is given in Section 5. Finally, Section 6 concludes this paper.

2 Problem Formulation

Consider a flexible liquid-filled spacecraft, whose attitude kinematics equations based on Euler angles in a small-angle case are described as

$$\omega_1 = \dot{\varphi} - \omega_0\psi,\ \ \omega_2 = \dot{\theta} - \omega_0,\ \ \omega_3 = \dot{\psi} + \omega_0\varphi \quad (1)$$

where $\varphi \in \mathbb{R}$, $\theta \in \mathbb{R}$ and $\psi \in \mathbb{R}$ are roll, pitch, and yaw angles, respectively. $\omega_1 \in \mathbb{R}$, $\omega_2 \in \mathbb{R}$ and $\omega_3 \in \mathbb{R}$ are the angular velocities of the roll, pitch, and yaw channels, respectively. The constant $\omega_0 \in \mathbb{R}$ stands for the orbit angular velocity.

The attitude dynamics model of the flexible liquid-filled spacecraft is conducted as

$$J\dot{\omega} + \omega^{\times}J\omega + \delta_0\ddot{\eta} + \delta_1\ddot{q} = u \quad (2)$$

$$\ddot{\eta} + D_0\dot{\eta} + K_0\eta + \delta_0^T\dot{\omega} = O_{n\times 1} \quad (3)$$

$$\ddot{q} + K_1 q + \delta_2\dot{\omega} + \delta_3\Theta = O_{m\times 1} \quad (4)$$

where $J \in \mathbb{R}^{3\times 3}$ is spacecraft inertia matrix. $\omega = [\omega_1\ \omega_2\ \omega_3]^T \in \mathbb{R}^3$ is the angular velocity vector composed of ω_1, ω_2, and ω_3. $\Theta = [\varphi\ \theta\ \psi]^T \in \mathbb{R}^3$ is the attitude angle vector. $\delta_0 \in \mathbb{R}^{3\times n}$ denotes the rigid-flexible coupling matrix. $\delta_1 \in \mathbb{R}^{3\times m}, \delta_2 \in \mathbb{R}^{m\times 3}$ and $\delta_3 \in \mathbb{R}^{m\times 3}$ are constant matrices related to the rigid-liquid coupling. $u \in \mathbb{R}^{3\times 1}$ is the tightly coupled anti-jamming attitude control law. $\eta \in \mathcal{R}^n$ is the modal displacement vector of flexible appendage. $D_0 = \text{diag}\{2\varsigma_1\varpi_1, 2\varsigma_2\varpi_2, \cdots, 2\varsigma_n\varpi_n\} \in \mathbb{R}^{n\times n}$ and $K_0 = \text{diag}\{\varpi_1^2, \varpi_2^2, \cdots, \varpi_n^2\} \in \mathbb{R}^{n\times n}$ are the damping matrix and the stiffness matrix, respectively. $\varsigma_i \in \mathbb{R}(i = 1, 2, \cdots, n)$ and ϖ_i are the damping ratio and the modal frequency, respectively. $q \in \mathcal{R}^m$ denotes the modal displacement of the liquid sloshing disturbance. K_1 represents the modal frequency matrix of liquid sloshing disturbance. $\omega^{\times}$ is a skew-symmetric matrix denoted as

$$\omega^{\times} = \begin{bmatrix} 0 & -\omega_3 & \omega_2 \\ \omega_3 & 0 & -\omega_1 \\ -\omega_2 & \omega_1 & 0 \end{bmatrix}.$$

Let $w_1 = \eta$ and $w_2 = \dot{\eta}$. From (2)–(4), the dynamic of flexible vibration disturbance is obtained as

$$\begin{cases} \dot{w} = W_0 w + H_0(u + d_s + \delta_1\delta_3\Theta - \omega^{\times}J\omega) \\ d_v = V_0 w \end{cases} \quad (5)$$

where $w = [w_1^T\ w_2^T]^T \in \mathbb{R}^{2n}$. $d_s = \delta_1 K_1 q$ is the liquid shaking disturbance, $J_0 = J - \delta_0\delta_0^T - \delta_1\delta_2$ is a known constant matrix. The coefficient matrices $W_0 \in \mathbb{R}^{2n\times 2n}$, $H_0 \in \mathbb{R}^{2n\times 3}$, and $V_0 \in \mathbb{R}^{3\times 2n}$ are given as

$$W_0 = \begin{bmatrix} O_{n\times n} & I_{n\times n} \\ -(I_{n\times n} + \delta_0^T J_0^{-1}\delta_0)K_0 & -(I_{n\times n} + \delta_0^T J_0^{-1}\delta_0)D_0 \end{bmatrix},$$

$$H_0 = \begin{bmatrix} O_{n\times 3} \\ -\delta_0^T J_0^{-1} \end{bmatrix}, V_0 = \begin{bmatrix} \delta_0 K_0 & \delta_0 D_0 \end{bmatrix}.$$

Similarly, let $\xi_1 = q$ and $\xi_2 = \dot{q}$. The dynamic of liquid sloshing disturbance is represented as

$$\begin{cases} \dot{\xi} = W_1\xi + H_1(u + d_v + \delta_1\delta_3\Theta - \omega^{\times}J\omega) + H_2 \\ d_s = V_1\xi \end{cases} \quad (6)$$

where $\xi = [\xi_1^T\ \xi_2^T]^T \in \mathbb{R}^{2m}$, and the coefficient matrices $W_1 \in \mathbb{R}^{2m\times 2m}$, $H_1 \in \mathbb{R}^{2m\times 3}$, $H_2 \in \mathbb{R}^{2m}$, and $V_1 \in \mathbb{R}^{3\times 2m}$ are given as

$$W_1 = \begin{bmatrix} O_{m\times m} & I_{m\times m} \\ -(I_{m\times m} + \delta_2^T J_0^{-1}\delta_1)K_1 & O_{m\times m} \end{bmatrix},$$

$$H_1 = \begin{bmatrix} O_{m\times 3} \\ -\delta_2 J_0^{-1} \end{bmatrix}, H_2 = \begin{bmatrix} O_{m\times 1} \\ -\delta_3\Theta \end{bmatrix}, V_1 = \begin{bmatrix} \delta_1 K_1 & O_{m\times m} \end{bmatrix}.$$

Combining the attitude dynamics model (2)–(4), the flexible vibration disturbance model (5) and the liquid sloshing disturbance model (6), the deep-coupled model can be established as

$$\begin{bmatrix} \dot{\omega} \\ \dot{w} \\ \dot{\xi} \end{bmatrix} = A_s \begin{bmatrix} \omega \\ w \\ \xi \end{bmatrix} + B_s(u + \delta_1\delta_3\Theta - \omega^{\times}J\omega) + D_s \quad (7)$$

where $A_s = \begin{bmatrix} O_{3\times 3} & J_0^{-1}V_0 & J_0^{-1}V_1 \\ O_{2n\times 3} & W_0 & H_0V_1 \\ O_{2m\times 3} & H_1V_0 & W_1 \end{bmatrix}$, $B_s = \begin{bmatrix} J_0^{-1} \\ H_0 \\ H_1 \end{bmatrix}$, and $D_s = \begin{bmatrix} O_3 \\ O_{2n} \\ H_2 \end{bmatrix}$.

Remark 1 *In this paper, different from the existing works ([10, 11, 18]), the dynamic of flexible vibration disturbance d_v and liquid slosh disturbance d_s are described by an exogenous model, which utilize the partially known disturbance information. Especially the disturbance between d_v and the disturbance d_s are mutually contained, resulting in a tightly coupled disturbance. Furthermore, the deep-coupled mode is established based on attitude dynamics model and two disturbance models. In addition, this deep-coupled model will provide important support for the subsequent discussion on the separability of disturbance.*

3 Disturbance Separability and Estimation

3.1 Disturbance separability

In order to obtain accurate estimation of multiple disturbances, it is necessary to ensure that the multiple disturbances have separability, that is, each disturbance can be

independently estimated. Inspired by the disturbance estimatability in [17], the definition of disturbance separability is given as follows.

Definition 1 *For a given initial time instant $t_0 \in T_s$, if there exist a finite time $t_f \in T_s(t_f > t_0)$, such that the disturbance initial states $w(t_0)$ and $\xi(t_0)$ can be uniquely determined based on the system output $y(t)$ during time interval $[t_0, t_f]$. Hence, the disturbance states $w(t_0)$ and $\xi(t_0)$ can be independently estimated. If for any time instant $t \in T_s$, the disturbance states can be independently estimated, the disturbance d_v and d_s are said to be separable.*

The angular velocity tracking error ω can be regarded as the system output, then a sufficient condition for disturbance separability criterion can be given as

$$\text{Rank}(\begin{bmatrix} C_s \\ C_s A_s \\ \cdots \\ C_s A_s^{2m+2n+2} \end{bmatrix}) = 2m + 2n + 3, \tag{8}$$

where A_s has been given in (7), $C_s = [I_{3\times3}\ O_{3\times2n}\ O_{3\times2m}]$.

Remark 2 *In order to ensure the separation of tightly coupled disturbances, it is only necessary to ensure that each type of disturbance in tightly coupled model can be accurately estimated, that is, to ensure the estimatability of disturbance. Therefore, the definition of disturbance separability is reasonable. By utilizing the observability of the deep coupling model (7), the disturbance d_v and d_s can be refined estimated, which indicates that the tightly coupled disturbance has separability.*

3.2 Separation estimation of multiple disturbances

In order to obtain the flexible vibration disturbance described in (5), the disturbance observer is designed as

$$\begin{cases} \hat{d}_v = V_0 \hat{w}, \ \ \hat{w} = \zeta_0 + L_0 J_0 \omega \\ \dot{\zeta}_0 = (W_0 - L_0 V_0)\hat{w} + (H_0 - L_0)(u + \hat{d}_s + \delta_1\delta_3\Theta - \omega^\times J\omega) \end{cases} \tag{9}$$

where $\hat{d}_v$ and $\hat{w}$ are estimation of d_v and w, respectively. ζ_0 is the auxiliary variable. L_0 is the observer gain matrix.

Similarly, the disturbance observer for estimating liquid sloshing disturbance in (6) is designed as

$$\begin{cases} \hat{d}_s = V_1 \hat{\xi}, \ \ \hat{\xi} = \zeta_1 + L_1 J_0 \omega \\ \dot{\zeta}_1 = (W_1 - L_1 V_1)\hat{\xi} + (H_1 - L_1)(u + \hat{d}_v + \delta_1\delta_3\Theta - \omega^\times J\omega) + H_2 \end{cases} \tag{10}$$

where $\hat{d}_s$ and $\hat{\xi}$ are estimation of d_s and ξ, respectively. ζ_1 is the auxiliary variable. L_1 is the observer gain matrix.

Define the estimation error of (9) and (10) as $\tilde{w} = w - \hat{w}$ and $\tilde{\xi} = \xi - \hat{\xi}$, respectively. Thus, we have

$$\begin{bmatrix} \dot{\tilde{w}} \\ \dot{\tilde{\xi}} \end{bmatrix} = W_\xi \begin{bmatrix} \tilde{w} \\ \tilde{\xi} \end{bmatrix} \tag{11}$$

where $W_\xi = \begin{bmatrix} W_0 - L_0 V_0 & (H_0 - L_0 V_1) \\ (H_1 - L_1)V_0 & W_1 - L_1 V_1 \end{bmatrix}$.

Therefore, in order to ensure the convergence of disturbance estimation errors $\tilde{w}$ and $\tilde{\xi}$, the disturbance observer gain matrices L_0 and L_1 are selected to ensure that all poles of matrix W_ξ have negative real parts by pole placement method.

Remark 3 *Due to the disturbance d_v and d_s are in the same channel, namely, tightly coupled disturbance, it is impossible to separate the tightly coupled disturbance by using traditional methods. However, due to the heterogeneity between d_v and d_s, the disturbances exhibit different characteristics. Especially, locally known disturbance information provides support conditions for tightly coupled disturbances. Two designed disturbance observers can refined estimate the tightly coupled disturbances by locally known disturbance information, such as the damping ratio and the modal frequency. In addition, the deep-coupled model (7) provides conditions for the estimatability of disturbances, that is, system observability, which decides the disturbance separability.*

4 Anti-Disturbance Controller Design

Based on satellite attitude kinematics, the expected attitude angular velocity is defined as $\omega^* = -k_0\Theta - \begin{bmatrix} \omega_0\psi \\ \omega_0 \\ -\omega_0\varphi \end{bmatrix}$, where k_0 is a positive constant.

Theorem 1 *Consider the attitude control system (1)–(2) and the disturbance estimation (9)–(10). The attitude angle vector of the spacecraft asymptotically converges to the equilibrium point, if the anti-disturbance control law u is designed as*

$$u = -k_1(\omega - \omega^*) + \omega^\times J\omega - \delta_1\delta_3\Theta + J_0\dot{\omega}^* - \hat{d}_v - \hat{d}_s \tag{12}$$

where $k_1 > 1$. $\dot{\omega}^*$ is obtained by calculation based on the definition of ω^*, (2) and (7).

Proof 1 *Choose the Lyapunov function*

$$V = \begin{bmatrix} \tilde{w} \\ \tilde{\xi} \end{bmatrix}^T P \begin{bmatrix} \tilde{w} \\ \tilde{\xi} \end{bmatrix} + \frac{1}{2}(\omega - \omega^*)^T J_0 (\omega - \omega^*). \tag{13}$$

The time derivative of $V(t)$ is calculated as

$$\begin{aligned} \dot{V}(t) &= \begin{bmatrix} \dot{\tilde{w}} \\ \dot{\tilde{\xi}} \end{bmatrix}^T P \begin{bmatrix} \tilde{w} \\ \tilde{\xi} \end{bmatrix} + \begin{bmatrix} \tilde{w} \\ \tilde{\xi} \end{bmatrix}^T P \begin{bmatrix} \dot{\tilde{w}} \\ \dot{\tilde{\xi}} \end{bmatrix} + (\omega - \omega^*)^T J_0 (\dot{\omega} - \dot{\omega}^*) \\ &= \begin{bmatrix} \tilde{w} \\ \tilde{\xi} \end{bmatrix}^T (W_\xi^T P + P W_\xi) \begin{bmatrix} \tilde{w} \\ \tilde{\xi} \end{bmatrix} + (\omega - \omega^*)^T (u + d_v + d_s \\ &\quad + \delta_1\delta_3\Theta - \omega^\times J\omega - J_0\dot{\omega}^*). \end{aligned} \tag{14}$$

Substituting the control law (12) into (14), we get

$$\begin{aligned} \dot{V}(t) &= \begin{bmatrix} \tilde{w} \\ \tilde{\xi} \end{bmatrix}^T (W_\xi^T P + P W_\xi) \begin{bmatrix} \tilde{w} \\ \tilde{\xi} \end{bmatrix} - k_1 \|\omega - \omega^*\|^2 \\ &\quad + (\omega - \omega^*)^T (\tilde{d}_v + \tilde{d}_s). \end{aligned} \tag{15}$$

Note that the following inequalities hold:

$$(\omega - \omega^*)^T \tilde{d}_v \le \frac{1}{2}\|\omega - \omega^*\|^2 + \frac{1}{2}\|\tilde{d}_v\|^2, \tag{16}$$

$$(\omega - \omega^*)^T \tilde{d}_s \le \frac{1}{2}\|\omega - \omega^*\|^2 + \frac{1}{2}\|\tilde{d}_s\|^2. \tag{17}$$

It is obvious that inequalities $\|\tilde{d}_v\| \le V_0\|\tilde{w}\|$ *and* $\|\tilde{d}_s\| \le V_1\|\tilde{\xi}\|$ *hold. Substituting (16)–(17) into (15), we get*

$$\begin{aligned}\dot{V}(t) \le & \begin{bmatrix}\tilde{w}\\ \tilde{\xi}\end{bmatrix}^T (W_\xi^T P + P W_\xi)\begin{bmatrix}\tilde{w}\\ \tilde{\xi}\end{bmatrix} - (k_1-1)\|\omega-\omega^*\|^2 \\ & + \frac{1}{2}\max\{\|V_0\|^2, \|V_1\|^2\}(\|\tilde{w}\|^2 + \|\xi\|^2) \\ = & \begin{bmatrix}\tilde{w}\\ \tilde{\xi}\end{bmatrix}^T (W_\xi^T P + P W_\xi + \frac{1}{2}\max\{\|V_0\|^2, \|V_1\|^2\} I)\begin{bmatrix}\tilde{w}\\ \tilde{\xi}\end{bmatrix} \\ & - (k_1-1)\|\omega-\omega^*\|^2. \end{aligned} \tag{18}$$

Furthermore, there is a positive parameter α *satisfying the following inequality*

$$W_\xi^T P + P W_\xi + \frac{1}{2}\max\{\|V_0\|^2, \|V_1\|^2\} I < -\alpha I. \tag{19}$$

Therefore, (18) can be further transformed into

$$\begin{aligned}\dot{V}_2 \le & -\alpha(\|\tilde{w}\|^2 + \|\xi\|^2) - (k_1-1)\|\omega-\omega^*\|^2 \\ \le & -\min\{\alpha, k_1-1\}(\|\tilde{w}\|^2 + \|\xi\|^2 + \|\omega-\omega^*\|^2) \\ \le & -\beta V, \end{aligned} \tag{20}$$

where $\beta = \frac{\min\{\alpha, k_1-1\}}{\max\{\lambda_P, \frac{1}{2}\|J_0\|\}}$ *and* $\lambda_{\max}(P)$ *denotes the maximum eigenvalue of* P.

Furthermore, we have

$$V_2 \le V(0)e^{-\beta t}. \tag{21}$$

Therefore, the attitude angle vector of the spacecraft asymptotically converges to the equilibrium point. The proof is completed.

Remark 4 *The designed composite attitude anti-disturbance controller contains a feedback control part* $-k_1(\omega-\omega^*) + \omega^\times J\omega - \delta_1\delta_3\Theta + J_0\dot{\omega}^*$ *and a disturbance compensation part* $-\hat{d}_v - \hat{d}_s$. *Compared with traditional compensation methods for the lumped disturbance, this paper considers some prior information of tightly coupled disturbances, such as the flexible vibration frequency, damping ratio, liquid fuel oscillation frequency and so on. By separating tightly coupled disturbances based on the criterion of disturbance separability (8), the estimation accuracy of disturbances based on (9)–(10) is improved, thereby enhancing the anti-disturbance ability of the composite controller (12). Therefore, the proposed composite controller is suitable for control systems subject to tightly coupled disturbances.*

5 Numerical Simulation

In this section, the numerical simulation is given to verify the effectiveness of proposed methods. The inertia matrix of the spacecraft is $J = \text{diag}\{50, 50, 50\}\text{kgm}^2$. The orbital angular velocity is $\omega_0 = 0.0011$rad/s. For the flexible appendage of the spacecraft, the modal frequencies and damping ratios are given as $\varpi_1 = 1.85$rad/s, $\varpi_2 = 2.25$rad/s, $\varpi_3 = 3.45$rad/s, and $\varsigma_1 = \varsigma_2 = \varsigma_3 = 0.0001$. The rigid-flexible coupling matrix δ_0 is selected as $0.2 \times \begin{bmatrix} 1.25 & 0.15 & 0.12 \\ -1.30 & 0.20 & 0.05 \\ 1.20 & -0.15 & 0.02 \end{bmatrix}$. For the liquid-slosh of the spacecraft, the relevant parameters are set as follows: $\delta_1 = \begin{bmatrix} 0 & -2.6281 \\ 2.6281 & 0 \\ 0 & 0 \end{bmatrix}$, $K_1 = 10^{-1} \times \begin{bmatrix} 1.0589 & 0 \\ 0 & 1.0589 \end{bmatrix}$, $\delta_2 = \begin{bmatrix} 0 & 0.6174 & 0 \\ -0.6174 & 0 & 0 \end{bmatrix}$, $\delta_3 = 10^{-3} \times \begin{bmatrix} 0 & 4.37 & 0 \\ 4.37 & 0 & 0 \end{bmatrix}$.

Due to $\text{rank}([C_s \; C_sA_s \; \cdots \; C_sA_s^{12}]^T) = 13$, the multiple disturbances is separable. By pole placement method, the observer gains of the disturbance observer (9) and (10) are chosen as

$$L_1 = \begin{bmatrix} -6.4930 & 29.5976 & 27.6492 \\ -9.8791 & 15.6704 & 20.3825 \\ -0.8705 & 3.1476 & 3.1296 \\ -0.3976 & 1.1446 & 1.2176 \end{bmatrix},$$

$$L_0 = \begin{bmatrix} -7.6892 & 16.8900 & 27.6355 \\ 1.1385 & -2.4987 & -4.3669 \\ 0.7720 & -0.8244 & 0.3050 \\ -0.5335 & 0.8483 & -0.8180 \\ 10.7525 & -23.4151 & -38.1542 \\ -19.0163 & 41.7845 & 68.7963 \end{bmatrix}.$$

First, the disturbance separation estimation is verified by the disturbance separation observer. Fig.1 shows the flexible vibration disturbance and its estimated value. Fig.2 represents liquid fuel slosh disturbance of spacecraft. From which it can be seen that the flexible disturbance and liquid slosh disturbance are well estimated, which verifies the rationality of disturbances separability criterion. Fig.3 exposes the response of the attitude angular velocity. The actual attitude angular velocity ω can well track the desired attitude angular velocity ω^*. Fig. 4 exhibits the attitude angle Θ, which implies that although the spacecraft is affected by multiple disturbances, the attitude angle Θ can still maintain convergence. Fig.5 depicts the control input u. These results show that the multiple disturbances can be accurately estimated based on the disturbance separability criterion, thereby achieving good angular velocity tracking performance.

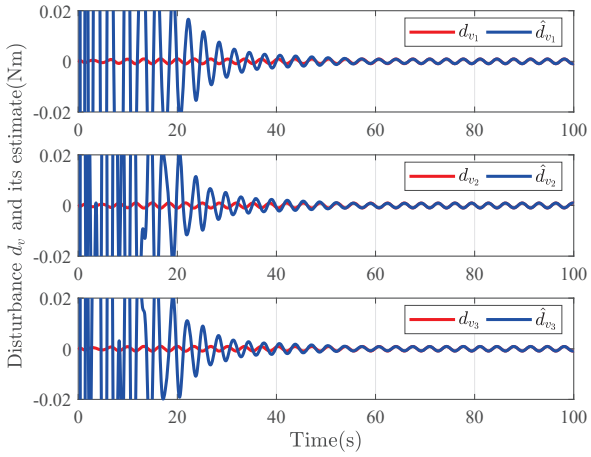

Fig. 1: Response of the flexible disturbance and its estimate

6 Conclusion

This paper has studied the antidisturbance attitude control for flexible liquid-filled spacecrafts subject to the flexible vi-

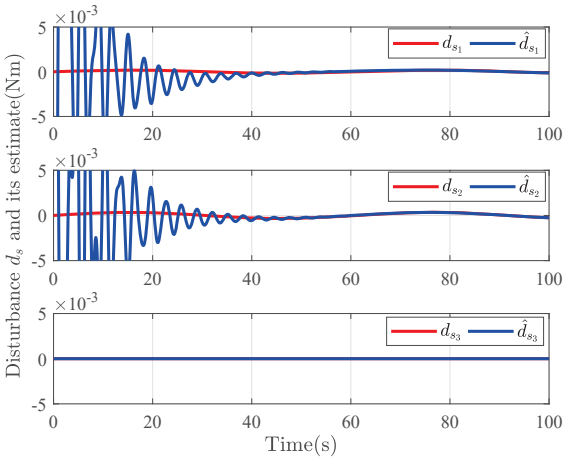

Fig. 2: Response of liquid slosh disturbance and its estimate

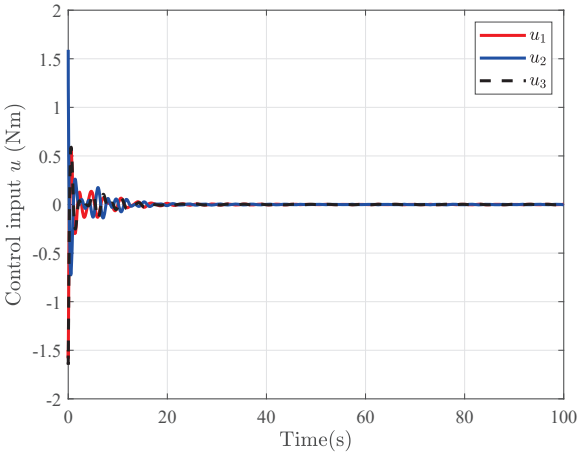

Fig. 5: Response of the control input

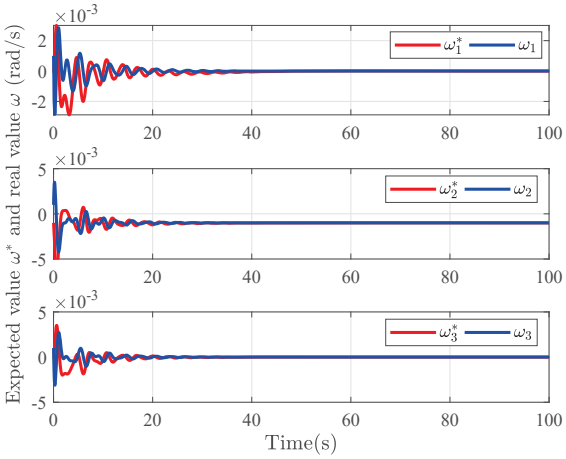

Fig. 3: Response of ideal and actual angular velocity

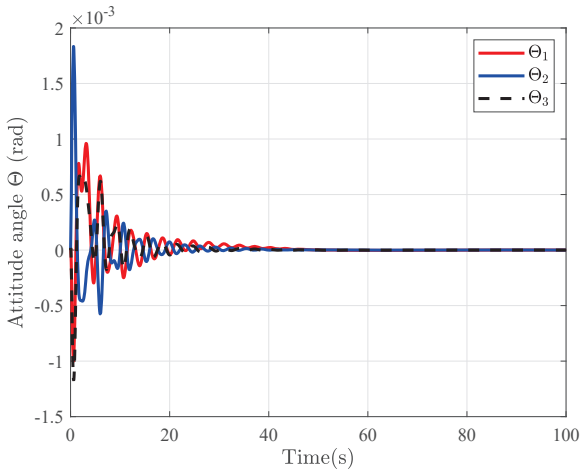

Fig. 4: Response of attitude angles

bration disturbance and liquid sloshing disturbance. A tightly coupled attitude dynamics model of a flexible liquid-filled spacecraft has been established. The definition and criterion of disturbance separability have been given, and two disturbance separability observers have been designed to estimate tightly coupled disturbances. Furthermore, the attitude control law has been proposed. Finally, the numerical simulation has shown the effectiveness of the proposed method.

References

[1] Z. Zhang, Y. Shi and W. Yan, "A novel attitude-tracking control for spacecraft networks with input delays," *IEEE Transactions on Control Systems Technology*, 2021, 29(3): 1035–1047.

[2] B. Xiao, Q. Hu and Y. Zhang, "Adaptive sliding mode fault tolerant attitude tracking control for flexible spacecraft under actuator saturation," *IEEE Transactions on Control Systems Technology*, 2012, 20(6): 1605–1612.

[3] Y. Ma, H. Ren, G. Tao and B. Jiang, "Adaptive compensation for actuation sign faults of flexible spacecraft," *IEEE Transactions on Aerospace and Electronic Systems*, 2021, 57(2): 1288–1300.

[4] J. Han, "From PID to active disturbance rejection control," *IEEE Transactions on Industrial Electronics*, 2009, 56(3): 900–906.

[5] Y. Huang and W. Xue, "Active disturbance rejection control: Methodology and theoretical analysis," *ISA Transactions*, 2014, 53(4): 963–976.

[6] W. Xue, W. Bai, S. Yang, K. Song, Y. Huang and H. Xie, "ADRC with adaptive extended state observer and its application to air-fuel ratio control in gasoline engines," *IEEE Transactions on Industrial Electronics*, 2015, 62(9): 5847–5857.

[7] B. Guo and Z. Zhao, "On convergence of the nonlinear active disturbance rejection control for MIMO systems," *SIAM Journal on Control and Optimization*, 2013, 51(2): 1727–1757.

[8] Y. Wang, B. Zhu, H. Zhang, W. X. Zheng, "Functional observer-based finite-time adaptive ISMC for continuous systems with unknown nonlinear function," *Automatica*, 2021, 125: 109468.

[9] S. Li and Z. Liu, "Adaptive speed control for permanent-magnet synchronous motor system with variations of load inertia," *IEEE Transactions on Industrial Electronics*, 2009, 56(8): 3050–3059.

[10] Q. Zheng, L. Dong, D. H. Lee and Z. Gao, "Active disturbance rejection control for MEMS Gyroscopes," *IEEE Transactions on Control Systems Technology*, 2009, 17(6): 1432–1438.

[11] W. -H. Chen, J. Yang, L. Guo and S. Li, "Disturbance-observer-based control and related methods-an overview," *IEEE Transactions on Industrial Electronics*, 2016, 63(2): 1083–1095.

[12] L. Sun and Z. Zheng, "Disturbance observer-based robust saturated control for spacecraft proximity maneuvers," *IEEE*

Transactions on Control Systems Technology, 2018, 26(2): 684–692.

[13] L. Guo and W. H. Chen, "Disturbance attenuation and rejection for systems with nonlinearity via DOBC approach," *International Journal of Robust and Nonlinear Control*, 2005, 15(3): 109–125.

[14] B. Zhu, Y. Xu and Y. Zhu, "Functional observer-based asynchronous composite anti-disturbance control for markov jump systems with multiple disturbances," *Journal of the Franklin Institute*, 2023, 360(7): 4548–4571.

[15] Y. Zhu, J. Qiao and L. Guo, "Adaptive sliding mode disturbance observer-based composite control with prescribed performance of space manipulators for target capturing," *IEEE Transactions on Industrial Electronics*, 2019, 66(3): 1973–1983.

[16] J. Qiao, Z. Li, J. Xu and X. Yu, "Composite nonsingular terminal sliding mode attitude controller for spacecraft with actuator dynamics under matched and mismatched disturbances," *IEEE Transactions on Industrial Informatics*, 2020, 16(2): 1153–1162.

[17] X. Yu, Y. Zhu, J. Qiao and L. Guo, "Antidisturbance controllability analysis and enhanced antidisturbance controller design with application to flexible spacecraft," *IEEE Transactions on Aerospace and Electronic Systems*, 2021, 57(5): 3393–3404.

[18] Y. Zhu, Z. Bao, H. Teng, Y. Yang and Y. Cui, "Disturbance separation-based enhanced antidisturbance attitude control for flexible spacecrafts with composite disturbances," *IEEE Transactions on Industrial Electronics*, 2024. doi: 10.1109/TIE.2023.3344849.

Proceedings of the 3rd Conference on Fully Actuated System Theory and Applications
May 10-12, 2024, Shenzhen, China

Research on Fixed-Time Convergence of Multi-Missile Cooperative Terminal Guidance Law

Jiakuo Lin[1], Pengfei CHENG[2], Yu-jie Si[3*], Changqing Wang[1], Yong Guo[1]

1. School of Automation, Northwestern Polytechnical University, Xi'an Shaanxi 710072, China

2. Xi'an Modern Control Technology Research Institute, Xi'an Shaanxi 710065, China

3. Beijing Institute of Electronic Engineering, Beijing 100039, China
E-mail:siyujiehit@126.com

Abstract: This paper investigates the problem of cooperative guidance strategies for multiple missiles attacking a maneuvering target. Based on the consistency theory and algebraic graph, a fixed-time cooperative guidance law with a terminal line-of-sight (LOS) angle constraint is proposed. Initially, the maneuvers of target in the LOS direction and normal to the LOS are considered as disturbances affecting the missiles. A two-dimensional guidance encompassing three degrees of freedom model is formulated based on the missile-target kinematics. Next, the guidance law design is divided into two parts. Along the LOS, a disturbance observer estimates the disturbances, and a fixed-time convergent, time-coordinated guidance law is formulated, integrating a consensus protocol to handle these disturbances. In the LOS normal direction, an adaptive estimation method is utilized to estimate the upper bound of disturbance. A non-singular fast terminal sliding mode control method is employed to generate LOS normal acceleration commands while ensuring convergence to the sliding surface within a fixed time. Lastly, a scenario with three missiles engaging a maneuvering target is designed, and saturation limits are applied on the acceleration commands in both directions. The simulations validate the proposed cooperative guidance law's accuracy and efficacy for multiple missiles with a LOS angle constraint.

Key Words: Cooperative Guidance Law, Consensus Theory, Non-singular Terminal Fast Sliding Mode, Adaptive Control.

1 Introduction

Multi-Missile Cooperative Guidance (MMCG) is an advanced guidance technique applied in missile systems. As a crucial component of cooperative guidance technology, MMCG law has been extensively studied for cooperative engagement against stationary and slow-moving targets. References [1] and [2] present studies on cooperative guidance laws for engaging against stationary targets with multi missiles. Reference [3] modified the proportional guidance law's coefficient according to the remaining time to target. However, these cooperative guidance laws are not applicable when the target is maneuvering. Obtaining target maneuvering information in combat environment is challenging. To address this problem**,** someone utilized adaptive estimation to estimate the upper bound of target's acceleration disturbance along the LOS direction in reference [4]. When dealing with the maneuvering information of a target, the target's maneuver can be regarded as a disturbance to the system, which can be estimated in the form of an observer. In reference [5], scholars have considered the system's disturbance as a new state and used an extended state observer (ESO) to observe the disturbance experienced by the system.

The most critical issue in multi-missile collaborative attack on a target is the problem of time coordination, which can be achieved through three main approaches. The first method involves presetting the attack time for all missiles before attacking the target, as described in reference [6] and [7], so that all missiles attack on a target simultaneously. However, this method does not leverage the dynamic information from other missiles. The second method involves utilizing a centralized cooperative guidance architecture, with a typical example being the master slave cooperative guidance architecture. By tracking the remaining attack time of the lead missile, the slave missiles achieve time coordination within the entire missile group, as described in references [8] and [9]. However, this type of cooperative architecture leads to significant computational burden on the central coordinating unit. The final method involves employing a distributed, two layers cooperative architecture for inter-missile communication. The distributed communication method within the missile group enables each missile to promptly adjust its control inputs through inter-missile communication, thereby achieving consistent remaining attack times. In reference [10], a distributed time coordination guidance law with finite-time convergence is designed using sliding mode control and first-order consensus protocols.

In the majority of research literature, the design of cooperative guidance law is typically predicated on the assumption of a constant missile velocity. However, during the terminal guidance phase, the missile actually generates acceleration along its velocity vector. In light of this, the present study re-evaluates the construction of a missile-target guidance model within a two-dimensional plane. This model lays the groundwork for subsequent research on saturation control of acceleration in the LOS direction within a three-dimensional space. The work of this paper are as follows: Under the premise of **Assumption 1**, a missile-target guidance model is established and a cooperative guidance law along the LOS and normal to LOS directions is designed. Theoretical proof is provided to demonstrate that this cooperative guidance law can direct all missiles to simultaneously engage a maneuvering target with a desired

*This paper was supported by the National Natural Science Foundation of China (Grant No.62273277), Key Research and Development Program of Shaanxi (Grant No. 2023-GHZD-32), and the Aeronautical Science Foundation of China (No.201901053004).

LOS angle within a fixed time. Finally, the effectiveness of this cooperative guidance law is proved through simulations.

2 Fundamental Knowledge

2.1 The Establishment of Model

Considering the guidance problem of a missile intercepting a maneuvering target, we can obtain the relative motion relationship between the missile and the target in the plane. As shown in the Fig. 1, M represents the center of mass of the missile, and T represents the center of mass of the target. r represents the relative distance between the missile and the target. V_t and V_m represent the velocity of the target and missile. q represents the LOS angel between the target and missile. The velocity heading angle of the target and missile are denoted by φ_t and φ_m, respectively. a_{mr} and a_{mq} represent the acceleration along the velocity direction and the acceleration along the velocity normal direction of missile. And a_{mr} is generated by the thrust of the missile's engine. According to Fig. 1, it can be obtained the relative motion equation between the missile and the target:

$$\dot{r} = V_t \cos(q-\varphi_t) - V_m \cos(q-\varphi_m) \tag{1}$$

$$r\dot{q} = -V_t \sin(q-\varphi_t) + V_m \sin(q-\varphi_m) \tag{2}$$

$$\dot{\varphi}_t = a_{tq} / V_t \tag{3}$$

$$\dot{\varphi}_m = a_{mq} / V_m \tag{4}$$

$$\dot{V}_m = a_{mr} \tag{5}$$

Furthermore, the derivative of the equation (1) can be obtained:

$$\begin{aligned}\ddot{r} = &-V_t\dot{q}\sin(q-\varphi_t) + V_m\dot{q}\sin(q-\varphi_m) + a_{tq}\sin(q-\varphi_t) \\ &- a_{mr}\cos(q-\varphi_m) - a_{mq}\sin(q-\varphi_m)\end{aligned} \tag{6}$$

Assumption 1. In the terminal guidance phase, the velocity leading angle between the LOS and the velocity vector is very small, that means $(q-\varphi_m)$ is very small.

Remark 1. The guidance law designed herein is intended solely for the terminal guidance phase. During this phase, the target has been acquired by the seeker and is within the seeker's line of sight, making the aforementioned assumptions reasonable.

Next, the first-order derivative of equation (2) is:

$$\begin{aligned}\dot{r}\dot{q} + r\ddot{q} = &-V_t\cos(q-\varphi_t)(\dot{q}-\dot{\varphi}_t) + a_{mr}\sin(q-\varphi_m) \\ &+V_m\cos(q-\varphi_m)(\dot{q}-\dot{\varphi}_m)\end{aligned} \tag{7}$$

Simplifying the Equation (7), this yields:

$$\begin{aligned}\ddot{q} = &-\frac{2\dot{r}\dot{q}}{r} + \frac{a_{tq}\cos(q-\varphi_t)}{r} + \frac{a_{mq}\cos(q-\varphi_m)}{r} \\ &\frac{a_{mr}\sin(q-\varphi_m)}{r}\end{aligned} \tag{8}$$

Finally, the dynamic equations between the missile and target are expressed as

$$\begin{aligned}\ddot{r} &= r\dot{q}^2 - u_r + w_r \\ \ddot{q} &= -\frac{2\dot{r}\dot{q}}{r} - \frac{u_q}{r} + \frac{w_q}{r}\end{aligned} \tag{9}$$

where, $u_r = a_{mr}\cos(q-\varphi_m) + a_{mq}\sin(q-\varphi_m)$ and it represents the acceleration component along the direction of LOS. $u_r = a_{mr}\sin(q-\varphi_m) + a_{mq}\cos(q-\varphi_m)$, and it represents the acceleration component along the LOS normal direction. $w_r = a_t\sin(q-\varphi_t)$ represents the projection of the target's acceleration in the LOS direction, and $w_r = a_t\cos(q-\varphi_t)$ represents the projection of the target's acceleration in the LOS normal direction.

These state variables are defined in the following paper: $x_1 = r$, $x_2 = \dot{r}$, $x_3 = q - q_d$, $x_4 = \dot{q}$, where q_d is the desired angle of the LOS. It can be obtained that the state space equation between the missile and the target:

$$\begin{cases}\dot{x}_1 = x_2 \\ \dot{x}_2 = x_1x_4^2 - u_r + w_r \\ \dot{x}_3 = x_4 \\ \dot{x}_4 = -\dfrac{2x_2}{x_1}x_4 - \dfrac{u_q}{x_1} + \dfrac{w_q}{x_1}\end{cases} \tag{10}$$

It can be obtained that the motion relationship between a single missile and a moving target in Fig. 1.

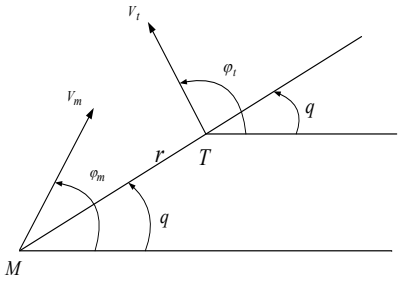

Fig. 1: Missile-target engagement geometry

To design cooperative guidance law that enable all missiles to attack a target simultaneously, introducing a new variable: t_{go} to represent the remaining attack time between the missiles and target. Using the following formula to estimate the remaining time to impact between the missiles and target:

$$t_{go} = -\frac{r}{\dot{r}} \tag{11}$$

This yields the first-order derivative of equation (11):

$$\dot{t}_{go} = -1 + \frac{x_1^2x_4^2}{x_2^2} - \frac{x_1}{x_2^2}u_r + \frac{x_1}{x_2^2}w_r \tag{12}$$

Fig. 2 describes the motion relationship of multiple missiles intercepting a target simultaneously during the terminal guidance phase. In order to ensure the consistency of the remaining time for all missiles to attack, it is necessary for every missile to communicate with the others, to ensure the consistency of t_{go}. To differentiate between different missiles, the state of each missile is represented by the subscript $i(i = 1,2,3...)$.

Treating the impact time of missiles for each missile as a new state variable. It can be obtained that a new state space equation:

$$\begin{cases} \dot{t}_{goi} = -1 + \dfrac{x_{1i}^2 x_{4i}^2}{x_{2i}^2} - \dfrac{x_{1i}}{x_{2i}^2} u_{ri} + \dfrac{x_{1i}}{x_{2i}^2} w_{ri} \\ \dot{x}_{3i} = x_{4i} \\ \dot{x}_{4i} = -\dfrac{2x_{2i}}{x_{1i}} x_{4i} - \dfrac{u_{qi}}{x_{1i}} + \dfrac{w_{qi}}{x_{1i}} \end{cases} \tag{13}$$

Define a new control input variable:

$$\tilde{u}_{ri} = \frac{x_{1i}^2 x_{4i}^2}{x_{2i}^2} - \frac{x_{1i}}{x_{2i}^2} u_{ri} \tag{14}$$

Substituting equation (14) into equation (13), it follows that:

$$\begin{cases} \dot{t}_{goi} = -1 + \tilde{u}_{ri} + d_{ri} \\ \dot{x}_{3i} = x_{4i} \\ \dot{x}_{4i} = -\dfrac{-2x_{2i}}{x_{1i}} x_{4i} - \dfrac{u_{qi}}{x_{1i}} + d_{qi} \end{cases} \tag{15}$$

where $d_{ri} = \dfrac{x_{1i}}{x_{2i}^2} w_{ri}$, and $d_{qi} = \dfrac{w_{qi}}{x_{1i}}$.

Assumption 2. Treating the projection of the target's acceleration in the LOS frame: d_{ri} and d_{qi}, as the disturbance to the system. And they satisfy the following inequalities: $|d_{ri}| \le \Delta_{ri}$ and $|d_{qi}| \le D_{qi}$, where Δ_{ri} and D_{qi} are positive constants.

Based on the analysis of the model mentioned above, we can design the following two components to achieve the two major control objectives: three missiles attack the target simultaneously, and every missile satisfy the desired LOS angle constraints. Firstly, designing the time-coordinated guidance law along the LOS direction. Treating the component of the target's acceleration along the LOS as disturbance, design the time-coordinated guidance law: u_{ri}, to enable all the missiles to attack the target simultaneously. Secondly, design a guidance law: u_{qi}, which can converge the LOS angle between missiles and the target to the desired LOS angle.

Remark 2. Because all the missiles are in the terminal guidance phase, $(q - \varphi_m)$ is very small, the acceleration along the LOS direction is primarily provided by thrust of engine. Therefore, in the final simulation stage of this study, we will use a saturation function to limit u_{ri} to be greater than or equal to zero.

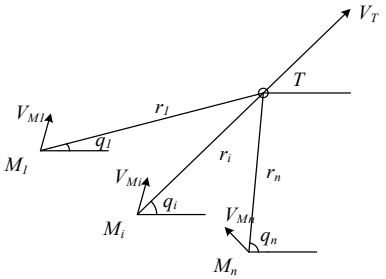

Fig. 2: Multi-missiles interception a maneuvering target

2.2 Foundational Knowledge

Fixed-time stability refers to the property where the system state converges to the equilibrium point within a fixed time, and the convergence time is independent of the initial state. For the convenience of subsequent stability proofs of control laws, the following definition and lemma are provided.

Consider a nonlinear system:

$$\dot{x}(t) = f(x(t)) \tag{16}$$

where, $f(0) = 0$, $t_0 = 0$, $x_0 \triangleq x(0)$, $x(t) \in R^n$ is the state of the system. $f : U \to R^n$ is domain that includes origin. $0 \in R^n$ represents the zero vector. x_0 represents the initial state of the system.

Definition 1[11]: If system (16) converges in finite time and the upper bound of convergence is independent of the initial conditions, then the system is fixed-time stable.

Lemma 1[11]: For system (16), if there exists a positive definite and continuous function $V(x)$ defined on the domain U that satisfies the following inequality:

$$\dot{V}(x) \le -\alpha V(x)^p - \beta V(x)^g \tag{17}$$

where, $x \in U \setminus \{0\}$, α, β, p and g are positive constants, p and g satisfy: $p < 1$, $g > 1$, the system can stabilize within a fixed time, the upper bound of convergence time is:

$$T_r < \frac{1}{\alpha(1-p)} + \frac{1}{\beta(g-1)}$$

Lemma 2[12]: $x_i \in R$, $i = 1, 2, \cdots, n$, v is a positive constant.

If $v \in (0,1]$, then

$$\left(\sum_{i=1}^{n} |x_i|\right)^v \le \sum_{i=1}^{n} |x_i|^v \tag{18}$$

When $v > 1$, then

$$\left(\sum_{i=1}^{n} |x_i|\right)^v \le n^{v-1} \left(\sum_{i=1}^{n} |x_i|^v\right) \tag{19}$$

Lemma 3[13]: Let us consider $L \in R^{N \times N}$ as the Laplacian matrix of the graph G, then we can obtain the following conclusion:

(1) If the matrix L is positive semi-definite and has exactly one zero eigenvalue, then when the communication topology graph G is undirected and connected, all the other eigenvalues of the Laplacian matrix are positive real numbers.

(2) If graph G is undirected and connected, it can be obtained that:

$$x^T L x = \frac{1}{2} \sum_{i=1}^{N} \sum_{i=1}^{N} a_{ij} (x_j - x_i)^2 \tag{20}$$

Lemma 4[13]: There is a Laplacian matrix L of the undirected graph G. The second smallest eigenvalue of the matrix L satisfies the following inequality:

$$\lambda_2(L) = \min_{\|x\| \ne 0, 1_N^T x = 0} \frac{x^T L x}{\|x\|^2} > 0 \tag{21}$$

If $\sum_{i=1}^{N} x_i = 0$, then

$$x^T L x \ge \lambda_2(L) x^T x \tag{22}$$

3 The Design of Cooperative Guidance Laws

3.1 Time-coordinated guidance law with convergence within a fixed time.

First, from equation (11), we can obtain the remaining time t_{goi} to target for each missile. Therefore, we can determine the time from the missile launch to the moment each missile reaches the target's position based on the remaining time to target:

$$t_{fi} = t + t_{goi} \tag{23}$$

where, t_{fi} represents the moment when the ith missile attacks the target.

Take the derivative of the above equation and substitute equations (12) and (14):

$$\begin{aligned} \dot{t}_{fi} &= \tilde{u}_{ri} + d_{ri} \\ &= \frac{x_{1i}^2 x_{4i}^2}{x_{2i}^2} - \frac{x_{1i}}{x_{2i}^2} u_{ri} + d_{ri} \end{aligned} \tag{24}$$

where, u_{ri} is the acceleration along the LOS, and $\tilde{u}_{ri}$ is consistency protocol.

This part aims to achieve:

$$\lim_{t \to T_r} (t_{fj} - t_{fi}) = \lim_{t \to T_r} (t_{goj} - t_{goi}) = 0 \tag{25}$$

Based on consensus control protocol and equation (21), it follows that the guidance law u_{ri}:

$$u_{ri} = -\frac{x_{2i}^2}{x1i} \tilde{u}_{ri} + x_{1i} x_{4i}^2 \tag{26}$$

And the consensus control protocol $\tilde{u}_{ri}$ is:

$$\begin{aligned} \tilde{u}_{ri} &= \sum_{j=1}^{N} \varphi_{ij} (t_{goj} - t_{goi}) \\ \varphi_{ij} &= a_{ij} [sig^{\alpha_1} (t_{goj} - t_{goi}) + sig^{\beta_1} (t_{goj} - t_{goi}) \\ &\quad + \bar{d} sign(t_{goj} - t_{goi})] \end{aligned} \tag{27}$$

where, $0 < \alpha_1 < 1$, $\beta_1 > 1$, $\bar{d} = \sqrt{2} \Delta_{ri} N^{1/2} / \sqrt{\lambda_2(L)}$. N represents the numbers of missiles. $\lambda_2(L)$ represents the second smallest eigenvalue of the matrix L.

It can be obtained that the upper bound of convergence time:

$$T_1 < T_{\max} = \frac{1}{\bar{\alpha}(1-p)} + \frac{1}{\bar{\beta}(q-1)} \tag{28}$$

where, $\bar{\alpha} = 2^{2p-1} \lambda_2^p (L_{\alpha_1})$, $\bar{\beta} = 2^{2q-1} \lambda_2^q (L_{\beta_1})$, $p = \frac{\alpha_1 + 1}{2}$, $q = \frac{\beta_1 + 1}{2}$.

Stability proof

First, let $\bar{t}_f = \frac{1}{N} \sum_{j=1}^{N} t_{goj}$ and $e_i = t_{goi} - \bar{t}_{go}$, where, e_i and $\bar{t}_f$ represent the error between the remaining attack time of the ith missile and the average remaining attack time of all missiles. The following equation obviously holds: $\varphi_{ij}(t_{goj} - t_{goi}) = -\varphi_{ji}(t_{goi} - t_{goj})$ and $e_j - e_i = t_{goj} - t_{goi}$.

Taking the derivative of e_i with respect to time, this yields:

$$\begin{aligned} \dot{e}_i &= \tilde{u}_{ri} + d_{ri} - \frac{1}{N} \sum_{j=1}^{N} (\tilde{u}_{rj} + d_{rj}) \\ &= \sum_{j=1}^{N} \varphi_{ij} (t_{goj} - t_{goi}) + d_{ri} - \frac{1}{N} \sum_{j=1}^{N} \sum_{i=1} \varphi_{ji} (t_{goi} - t_{goj}) - \frac{1}{N} \sum_{j=1}^{N} d_{rj} \end{aligned} \tag{29}$$

It can be obtained that the following relationship:

$$\sum_{i=1}^{N} \sum_{j=1}^{N} \varphi_{ij} (t_{goj} - t_{goi}) = 0 \tag{30}$$

Then, substituting equation (28) into equation (27), this yields:

$$\dot{e}_i = \sum_{j=1}^{N} \varphi_{ij} (t_{goj} - t_{goi}) + d_{ri} - \frac{1}{N} \sum_{j=1}^{N} d_{ri} \tag{31}$$

Construct the Lyapunov function in the following form:

$$V(e) = \frac{1}{2} \sum_{i=1}^{N} e_i^2 \tag{32}$$

Furthermore, it can be obtained that:

$$\dot{V} = \sum_{i=1}^{N} e_i \dot{e}_i = \sum_{i=1}^{N} e_i \sum_{j=1}^{N} \varphi_{ij} (t_{goj} - t_{goi}) + \sum_{i=1}^{N} e_i (d_{ri} - \frac{1}{N} \sum_{j=1}^{N} d_{rj}) \tag{33}$$

For $\sum_{i=1}^{N} e_i = 0$, we can obtain $\sum_{i=1}^{N} e_i \frac{1}{N} \sum_{j=1}^{N} d_{rj} = 0$. The above equation (33) can be rewritten as

$$\begin{aligned} \dot{V} &= \sum_{i=1}^{N} e_i \sum_{j=1}^{N} \varphi_{ij} (t_{goj} - t_{goi}) + \sum_{i=1}^{N} e_i d_{ri} \\ &= -\frac{1}{2} \sum_{i=1}^{N} \sum_{j=1}^{N} (e_j - e_i) \varphi_{ij} (e_j - e_i) + \sum_{i=1}^{N} e_i d_{ri} \\ &\le -\frac{1}{2} \sum_{i=1}^{N} \sum_{j=1}^{N} a_{ij} (|e_j - e_i|^{\alpha_1 + 1} + |e_j - e_i|^{\beta_1 + 1}) \\ &\quad -\frac{1}{2} \bar{d} \sum_{i=1}^{N} \sum_{j=1}^{N} a_{ij} |e_j - e_i| + \Delta_{ri} \sum_{i=1}^{N} |e_i| \end{aligned} \tag{34}$$

Based on **Lemma 2** and **Lemma 3**, it can be obtained that:

$$\sum_{j=1}^{N} a_{ij} |e_j - e_i|^{\alpha_1 + 1} \ge (\sum_{j=1}^{N} a_{ij}^{\frac{2}{\alpha_1 + 1}} (e_j - e_i)^2)^{\frac{\alpha_1 + 1}{2}} \tag{35}$$

$$\sum_{j=1}^{N} a_{ij} |e_j - e_i|^{\beta_1 + 1} \ge N^{\frac{1 - \beta_1}{2}} (\sum_{j=1}^{N} a_{ij}^{\frac{2}{\beta_1 + 1}} (e_j - e_i)^2)^{\frac{\beta_1 + 1}{2}} \tag{36}$$

$$\sum_{j=1}^{N} a_{ij} |e_j - e_i| \ge (\sum_{j=1}^{N} a_{ij}^2 (e_j - e_i)^2)^{\frac{1}{2}} \tag{37}$$

$$\sum_{i=1}^{N} |e_i| \le N^{\frac{1}{2}} (\sum_{i=1}^{N} e_i^2)^{\frac{1}{2}} \tag{38}$$

Based on **Lemma 4**, it can be obtained that:

$$\begin{aligned} \sum_{i=1, j=1}^{N} a_{ij}^{\frac{2}{\alpha_1 + 1}} (e_j - e_i)^2 &= 2 e^T L_{\alpha_1} e \\ &\ge 2 \lambda_2 (L_{\alpha_1}) e^T e \\ &= 4 \lambda_2 (L_{\alpha_1}) V(e) \end{aligned} \tag{40}$$

$$\sum_{i=1, j=1}^{N} a_{ij}^{\frac{2}{\beta_1 + 1}} (e_j - e_i)^2 \ge 4 \lambda_2 (L_{\beta_1}) V(e) \tag{41}$$

$$\sum_{i=1, j=1}^{N} a_{ij}^2 (e_j - e_i)^2 \ge 4 \lambda_2 (L_{\infty}) V(e) \tag{42}$$

Substituting equations (40) ~ (42) into equation (34), this yields:

$$\begin{aligned}\dot{V}(e) &\le -2^{\alpha_1}\lambda_2^{\frac{\alpha_1+1}{2}}(L_\alpha)V^{\frac{\alpha_1+1}{2}} - 2^{\beta_1}N^{\frac{1-\beta_1}{2}}(L_\beta)V^{\frac{\beta_1+1}{2}} \\ &= -\bar{\alpha}V^p - \bar{\beta}V^q\end{aligned} \tag{43}$$

According to **Lemma 2**, the system state will stabilize within a fixed time. **Proof completed.**

Lemma 5[14]: Using FxTDO to estimate the disturbance value. In the design of the cooperative guidance law, the observed values from FxTDO are incorporated into the design of the control law (For the proof of convergence of FxTDO, refer to Ref[14]). z_2 is estimation value of the d_{ri}. $|d_i - z_2|$ will converge to a stable state within a fixed time.

$$\begin{cases}\dot{z}_1 = k_1\phi_1(\dfrac{x_i - z_1}{\delta}) + z_2 + a + bu \\ \dot{z}_2 = \dfrac{k_2}{\delta}\phi_2(\dfrac{x_i - z_1}{\delta})\end{cases} \tag{44}$$

where, $k_1, k_2 > 0$, $k_1 > \sqrt{k_2}$, $0 < \delta < 1$, $0.5 < \alpha' < 1$, $1 < \beta' < 1.5$. $\phi_1(\bullet)$ and $\phi_2(\bullet)$ are correction terms defined as follow:

$$\phi_1(x) = sig^{\alpha'}(x) + sig^{\beta'}(x) \tag{45}$$

$$\phi_2(x) = sig^{2\alpha'-1}(x) + sig^{2\beta'-1}(x) \tag{46}$$

The purpose of introducing the FxTDO is to avoid excessive control gains, which could lead to control chattering phenomena. Based on **Lemma 5,** the specific form of the FxTDO adopted is as follows:

$$\begin{cases}\dot{z}_{1i} = k_1\phi_1(\dfrac{x_i - z_{1i}}{\delta}) + z_{2i} + \tilde{u}_{ri} \\ \dot{z}_{2i} = \dfrac{k_2}{\delta}\phi_2(\dfrac{x_i - z_{1i}}{\delta})\end{cases} \tag{47}$$

Based on FxTDO, transform the $\bar{d} = \sqrt{2}\Delta_{ri}N^{1/2}/\sqrt{\lambda_2(L)}$ to $\bar{d} = \sqrt{2}\,|z_{2i}|\,N^{1/2}/\sqrt{\lambda_2(L)}$.

3.2 Design of u_{qi} satisfying terminal angle constraints.

Through equation (13), it can be obtained that:

$$\begin{cases}\dot{x}_{3i} = x_{4i} \\ \dot{x}_{4i} = -\dfrac{2x_{2i}}{x_{1i}}x_{4i} - \dfrac{u_{qi}}{x_{1i}} + d_{qi}\end{cases} \tag{48}$$

Construct a non-singular terminal sliding surface:

$$s_i = x_{3i} + \alpha_1 sig^{\lambda_1}(x_{3i}) + \beta_1 sig^{\lambda_2}(x_{4i}) \tag{49}$$

where $sig^{\lambda}(\bullet) = |\bullet|^{\lambda}\, sign(\bullet)$, $1 < \lambda_2 < 2$, $\lambda_1 > \lambda_2$, $\alpha_1 > 0$, $\beta_1 > 0$.

Select the following approximation law:

$$\dot{s}_i = -\alpha_2 sig^{\gamma_1}(s_i) - \beta_2 sig^{\gamma_2}(s_i) - \sigma_i\hat{D}_{qi}sign(s_i) \tag{50}$$

where $\alpha_2 > 0$, $\beta_2 > 0$, $0 < \gamma_1 < 1$, $\gamma_2 > 1$, $\sigma_i > 1$ .Combining equations (48), (49), and (50), we construct the control law and adaptive law:

$$\begin{aligned}u_{qi} = x_{1i}(&-\frac{2x_{2i}}{x_{1i}}x_{4i} + \beta_1^{-1}\lambda_2^{-1}sig^{2-\lambda_2}(x_{4i})(1 + \alpha_1\lambda_1|x_{3i}|^{\lambda_1-1}) \\ &+\alpha_2 sig^{\gamma_1}(s_i) + \beta_2 sig^{\gamma_2}(s_i) + \sigma_i\hat{D}_{qi}sign(s_i))\end{aligned} \tag{51}$$

where, $\sigma_i > 1$, $\hat{D}_{qi}$ represents the estimate of D_{qi}. Adaptive law:

$$\dot{\hat{D}} = \sigma_i\beta_1\lambda_2|x_{4i}|^{\lambda_2-1}|s_i| \tag{52}$$

Stability proof

Constructing a Lyapunov function:

$$V_1 = \frac{1}{2}s_i^2 + \frac{1}{2}\tilde{D}_{qi}^2 \tag{53}$$

where, $\tilde{D}_{qi} = D_{qi} - \hat{D}_{qi}$ represents the difference between the upper bound of disturbance and the estimated value. To differentiate equation (51), substitute it into equations (49) and (50), it can be obtained that:

$$\begin{aligned}\dot{V}_1 &= s_i[\beta_1\lambda_2|x_{4i}|^{\lambda_2-1}(-\alpha_2 sig^{\gamma_1}(s_i) - \beta_2 sig^{\gamma_2}(s_i) \\ &\quad - \sigma_i\hat{D}_{qi}sign(s_i) + d_{qi})] - \tilde{D}(\sigma_i\beta_1\lambda_2|x_{4i}|^{\lambda_2-1}|s_i|) \\ &\le -\beta_1\lambda_2|x_{4i}|^{\lambda_2-1}\alpha_2|s_i|^{1+\gamma_1} - \beta_1\lambda_2|x_{4i}|^{\lambda_2-1}\beta_2|s_i|^{1+\gamma_2}\end{aligned} \tag{54}$$

where $1 < \lambda_2 < 2$, $\beta_1 > 0$, $\alpha_2 > 0$, $\beta_2 > 0$, Therefore, we can draw the following conclusion: $\dot{V} < 0$, equation (54) indicates that both s_i and $\tilde{D}_{qi}$ are bounded. Further construct the following Lyapunov function:

$$V_2 = \frac{1}{2}s_i^2 \tag{55}$$

Taking the derivative of (53) and substituting (49) and (50), it can be obtained that:

$$\begin{aligned}\dot{V}_2 = s_i\dot{s}_i &\le (D_{qi} - \hat{D}_{qi}\sigma_i)|s| \\ &\quad - \beta_1\lambda_2|x_{4i}|^{\lambda_2-1}\alpha_2|s_i|^{1+\gamma_1} \\ &\quad - \beta_1\lambda_2|x_{4i}|^{\lambda_2-1}\beta_2|s_i|^{1+\gamma_2}\end{aligned} \tag{56}$$

where, $\hat{D}_{qi}(0) > 0$. Through (52), it can be obtained that $\hat{D}_{qi} \ge \hat{D}_{qi}(0) > 0$, Let $\hat{D}_{qi}(0)$ be as large as possible. Let the following inequalities hold:

$$\sigma_i \ge \frac{\sqrt{s_i^2(0) + \hat{D}_{qi}(0)^2}}{\hat{D}_{qi}(0)} + 1 \tag{57}$$

Therefore, the following inequalities hold:

$$\begin{aligned}D_{qi} - \hat{D}_{qi}\sigma_i &\le D_{qi} - \sqrt{s_i^2(0) + \hat{D}_{qi}^2(0)} - \hat{D}_{qi}(0) \\ &\le |\tilde{D}_{qi}(0)| - \sqrt{s_i^2(0) + \hat{D}_{qi}^2(0)} \\ &\le |\hat{D}_{qi}(0)| - \sqrt{s_i^2(0) + \hat{D}_{qi}^2(0)} \\ &\le 0\end{aligned} \tag{58}$$

This yields that:

$$\begin{aligned}\dot{V}_2 &\le -\beta_1\lambda_2|x_{4i}|^{\lambda_2-1}\alpha_2|s_i|^{1+\gamma_1} - \beta_1\lambda_2|x_{4i}|^{\lambda_2-1}\beta_2|s_i|^{1+\gamma_2} \\ &= -2^{\frac{1+\gamma_1}{2}}\beta_1\lambda_2|x_{4i}|^{\lambda_2-1}\alpha_2V_2^{\frac{1+\gamma_1}{2}} - 2^{\frac{1+\gamma_2}{2}}\beta_1\lambda_2|x_{4i}|^{\lambda_2-1}\beta_2V_2^{\frac{1+\gamma_2}{2}}\end{aligned} \tag{59}$$

It can conclude that under the action of this control law, the sliding surface can converge to the sliding surface $s_i = 0$ from any initial value within a fixed time. According to the finite-time convergence property on the nonsingular terminal sliding surface, the system state can converge to zero within a finite time. **Proof complete**.

4 Simulation Analysis

Design the following combat scenario: three missiles simultaneously attack a moving target. The communication topology among the three missiles is shown in the following

Fig. 3. The initial position of the target is set at $(0\,m, 0\,m)$, the initial heading angle is 0°. The magnitude of the velocity is $300m/s$. Next, the following table is provided to illustrate the initial position coordinates, initial velocity, initial heading angle, initial LOS angle, and terminal LOS angle constraints for the three missiles. Finally, considering saturation of control inputs, the following constraints are imposed on the LOS direction and the magnitude of the LOS normal acceleration for the missile-target scenario: u_{ri} is constrained in $0 \sim 30g$, u_{qi} is constrained in $-30g \sim 30g$, where $g = 9.8m/s^2$.

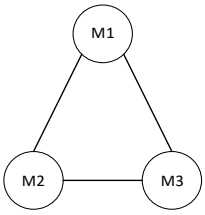

Fig. 3: The communication topology among the three missiles

Table 1: Initial condition for three missiles

Missile	Initial position (/ m)	Initial heading angle (/deg)	Initial velocity (/ $m \cdot s^{-1}$)	Desired LOS angle (/deg)
Missile1	(-3200, 2098)	-30	600	-20
Missile2	(-4098, -2680)	35	600	15
Missile3	(-2708, -2090)	40	600	20

The parameters used in equations (27) and (44) are: $\alpha_1 = 0.5$, $\beta_1 = 1.5$, $\alpha' = 0.75$, $\beta' = 1.25$, $k_1 = 3$, $k_2 = 1$, $\delta = 0.5$. The parameters used in equations (51) are: $\alpha_1 = 1$, $\beta_1 = 1$, $\alpha_2 = 1$, $\beta_2 = 1$, $\lambda_1 = 2$, $\lambda_2 = 1.5$, $\gamma_1 = 0.75$, $\gamma_2 = 1.2$. To prevent the occurrence of chattering phenomenon in the controller, a saturation function is used to replace the sign function in the controller.

Using an asymmetric saturation constraint function to handle u_{ri}, the specific mathematical form is as follows:

$$g_u(v) = \begin{cases} v & |v_{jm}| < u_{dis} - \dfrac{1}{4\varepsilon_u} \\ u_{mid} + sign(v_{jm})\{u_{dis} - \varepsilon_u \\ [v - sign(v_{jm})(u_{dis} + \dfrac{1}{4\varepsilon_u}) - u_{mid}]^2\} & u_{dis} - \dfrac{1}{4\varepsilon_u} \le |v_{jm}| \le u_{dis} + \dfrac{1}{4\varepsilon_u} \\ u_{mid} + sign(v_{jm})u_{dis} & |v_{jm}| > u_{dis} + \dfrac{1}{4\varepsilon_u} \end{cases}$$

where, $v_{jm} = v - u_{mid}$, ε_u is a positive constant, which is used to adjust the error between the smooth saturation function and the $sat()$ function. $u_{mid} = (\overline{u} + \underline{u})/2$, $u_{dis} = (\overline{u} - \underline{u})/2$, $\overline{u}$ and $\underline{u}$ are the upper and lower saturation bounds.

Using $sat()$ function to handle u_{qi}:

$$sat(s) = \begin{cases} 1 & s > \Delta \\ ks & |s| \le \Delta. \quad k = 1/\Delta \\ -1 & s < -\Delta \end{cases}$$

To demonstrate the good anti-disturbance characteristics of the guidance law, we consider two types of target motion: non-maneuvering and cosine maneuvering. The acceleration of target is: $a_t = 5g\cos(t)$, The simulation results are shown in the following figures. Fig. 4 (a) to (g) illustrate the simulation results for the non-maneuvering target scenario, while Fig. 5 (a) to (g) depict the simulation results for the pre-maneuvering target scenario.

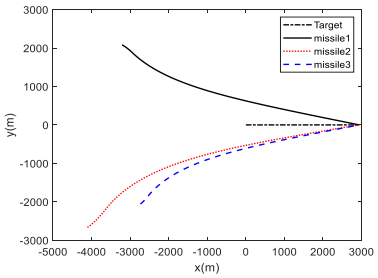

(a). Missile-target trajectory plot

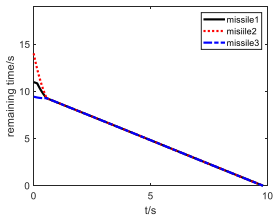

(b). The remaining attack time

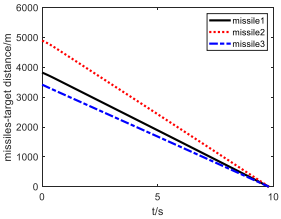

(c). The remaining attack distance

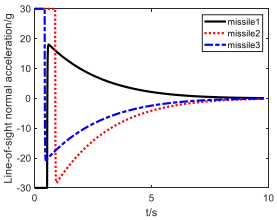

(d). LOS normal acceleration

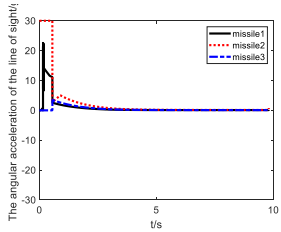

(e). The angular acceleration of the LOS

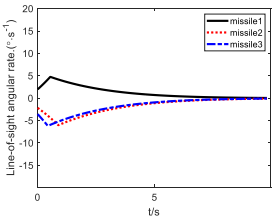

(f). LOS angular rate

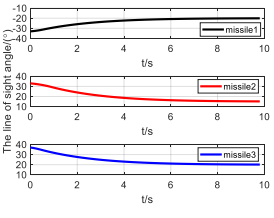

(g). LOS angle

Fig. 4: Simulation results under the condition of non-maneuvering target

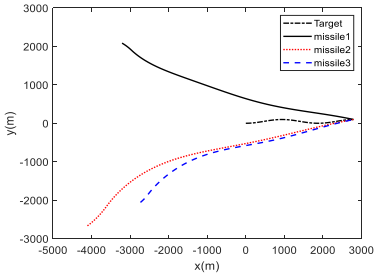

(a). Missile-target trajectory plot

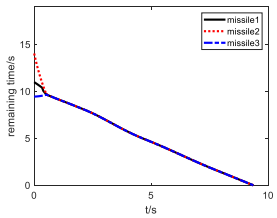

(b). The remaining attack time

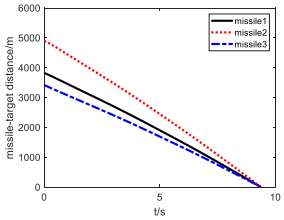

(c). The remaining attack distance

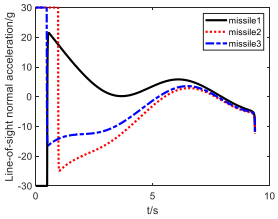

(d). LOS normal acceleration

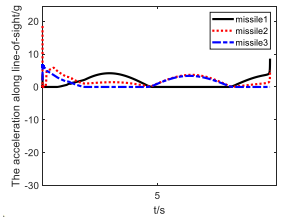

(e). The angular acceleration of the LOS

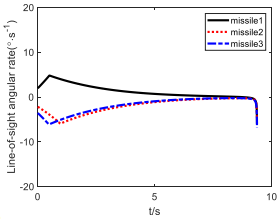

(f). LOS angular rate

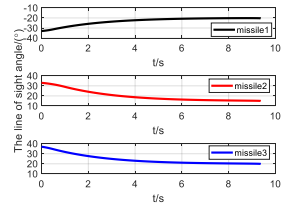

(g). LOS angle

Fig. 5: Simulation results under the condition of cosine maneuvering target

Table 2: Miss distances, interception time and LOS angle errors

Types of target maneuvers	missile	Miss distance ($/m \cdot s^{-1}$)	Interception time(/s)	LOS angle error(/deg)
Non-maneuvering	Missile1	0.351	9.805	0.080
	Missile2	0.451	9.805	0.150
	Missile3	0.312	9.805	0.117
Cosine maneuvering	Missile1	0.122	9.377	-0.430
	Missile2	0.156	9.377	0.048
	Missile3	0.107	9.377	0.193

5 Conclusion

This paper studies the combat scenario where three missiles intercept a maneuvering target simultaneously with the expected LOS angle, the fixed-time cooperative guidance laws are designed. The main conclusions are listed as follows:

(1). A distributed cooperative guidance law with fixed time convergence characteristics is designed based consistency theory and algebraic graph, to address the problem of impacting time consistency.

(2). To enable every missile to attack the target with the desired LOS angle, a guidance law based on nonsingular fast terminal sliding mode control is proposed, with fixed time convergence characteristics.

(3). Through simulating two types of target maneuvers, results have shown the effectiveness and high precision guidance performance of both guidance laws with input saturation.

This paper explores the design of cooperative guidance laws within a two-dimensional plane, but we don't consider the problem of cooperative guidance law design in three-dimensional space. Furthermore, the paper does not delve into the control stability under conditions of input saturation. Future research will focus on developing more efficient cooperative guidance law in three-dimensional space, particularly considering the case of input saturation.

References

[1] Wang X, Lu X. Three-dimensional impact angle constrained distributed guidance law design for cooperative attacks[J]. ISA transactions, 2018, 73: 79-90.

[2] Chen Y, Wang J, Shan J, et al. Cooperative guidance for multiple powered missiles with constrained impact and bounded speed[J]. Journal of Guidance, Control, and Dynamics, 2021, 44(4): 825-841.

[3] Jeon I S, Lee J I, Tahk M J. Homing guidance law for cooperative attack of multiple missiles[J]. Journal of guidance, control, and dynamics, 2010, 33(1): 275-280.

[4] Song J, Song S, Xu S. Three-dimensional cooperative guidance law for multiple missiles with finite-time convergence[J]. Aerospace Science and Technology, 2017, 67: 193-205.

[5] Sun Z, Simo J, Gong S. Satellite attitude identification and prediction based on neural network compensation[J]. Space: Science & Technology, 2023, 3: 0009.

[6] Lee J I, Jeon I S, Tahk M J. Guidance law to control impact time and angle[J]. IEEE Transactions on Aerospace and Electronic Systems, 2007, 43(1): 301-310.

[7] Zhao S Y, Zhou R, Wei C. Design and feasibility analysis of a closed-form guidance law with both impact angle and time constraints[J]. Journal of Astronautics, 2009, 30(3): 1064-1085.

[8] Li G, Wu Y. Adaptive cooperative guidance with seeker-less followers: A position coordination-based framework[J]. ISA transactions, 2023, 143: 168-176. Wang Z, Fu W, Fang Y, et al.

[9] Prescribed-time cooperative guidance law against maneuvering target based on leader-following strategy[J]. ISA transactions, 2022, 129: 257-270.

[10] You H, Chang X, Zhao J, et al. Three-dimensional impact-angle-constrained cooperative guidance strategy against maneuvering target[J]. ISA transactions, 2023.

[11] Polyakov A. Nonlinear feedback design for fixed-time stabilization of linear control systems[J]. IEEE transactions on Automatic Control, 2011, 57(8): 2106-2110.

[12] Qian C, Lin W. A continuous feedback approach to global strong stabilization of nonlinear systems[J]. IEEE Transactions on Automatic Control, 2001, 46(7): 1061-1079.

[13] Olfati-Saber R, Murray R M. Consensus problems in networks of agents with switching topology and time-delays[J]. IEEE Transactions on automatic control, 2004, 49(9): 1520-1533.

[14] Wu R, Wei C, Yang F, et al. FxTDO-based non-singular terminal sliding mode control for second-order uncertain systems[J]. IET Control Theory & Applications, 2018, 12(18): 2459-2467.

Proceedings of the 3rd Conference on Fully Actuated System Theory and Applications
May 10-12, 2024, Shenzhen, China

Data-driven control design for UAV autolanding: a pitch-only case study

Qiuyang Tian[1], Weiwen Chen[1], Zelin Wang[1], Mingxuan Sun[3], Bo Zhu[1*], Laibing Jia[4], Tianjiang Hu[1,2*]

1. School of Aeronautics and Astronautics, Sun Yat-Sen University, Shenzhen 518107, China
E-mail: { tianqy3, chenww59, wangzlin25, zhubo5, hutj3} @mail2.sysu.edu.cn

2. School of Artificial Intelligence, Sun Yat-Sen University, Zhuhai 519000, China

3. College of Information Engineering, Zhejiang University of Technology, Hangzhou 310023, China
E-mail: mxsun@zjtu.edu.cn

4. Department of Naval Architecture, Ocean and Marine Engineering, University of Strathclyde, UK
Email: l.jia@strath.ac.uk

Abstract: This paper aims at exploring a new-type mode for autolanding control of fixed-wing unmanned aerial vehicles (UAVs). A discrete-time data-driven control scheme is tentatively proposed and developed with its pitch-only channel as a case study. Eventually, data-driven controllers inspired by attracting laws are introduced for a series of difference models. Numerical simulation for pitch-only dynamics is demonstrated to validate and compare performances of proposed DDC laws. Simulation results indicate that DDC laws can achieve the desired performance by altering data-driven models with different orders.

Key Words: Data-driven control, characteristic model, attracting laws (ALs)

1 Introduction

Fixed-wing unmanned aerial vehicles (UAVs) have numerous applications in fields including agriculture, traffic surveillance, industrial accident monitoring, crime prevention, assessment and restoration of nature reserve areas [1-5], etc. Compared with unmanned helicopters, multi-rotor aircraft, flapping-wing aircraft, and other aircraft, fixed-wing UAVs have advantages such as large payload, high speed, low energy consumption, long range, and high safety [6-7]. The increasing demand for tasks such as aerial reconnaissance, communication relays, resource exploration, and border surveillance, combined with the rapid advancements in technologies such as structural engineering, flight control algorithms, and power systems, are driving the development of fixed-wing UAVs toward greater autonomy and intelligence capabilities [8-9]. As the utilization of fixed-wing becomes more widespread, an increasing number of incidents of varying severity are being reported. Particularly, almost half of these UAV accidents occur in landing scenarios. This trend emphasizes developing more robust and adaptable control strategies to counteract modeling uncertainties and external disturbances that may arise during autolanding [10-11].

Typical landing trajectories usually involve three phases: approach, glide, and flare [12-13]. Numerous studies have demonstrated the possibility of developing autolanding algorithms using decoupled longitudinal and lateral models [14-16], but linear model-based approaches are practical only within narrow ranges surrounding operation points. To overcome this limitation, the gain scheduling method is introduced to widen operational ranges by adjusting pre-designed control parameters for varying operation points. The following challenge is that interpolated parameters generated by gain scheduling cannot always guarantee the stability of the closed-loop system [17]. In addition, numerous nonlinear control techniques have been researched for autolanding. However, their effectiveness still depends significantly on the complexity and accuracy of nonlinear dynamic models [18-19].

In this context, data-driven control approaches, which do not rely on complicated dynamics, have gained more and more interest [21-26]. DDC methods aim to use only input/output (I/O) data to design control laws. For fixed-wing UAVs, uncertainties arising from model errors and environmental influences, such as wind disturbances and aerodynamic changes, cannot be neglected. DDC methods adapt well to model uncertainties because they utilize full historical data, including those from disturbed conditions. The concept of data-driven modeling originated from the characteristic modeling approach [24]. The data-driven modeling method represents nonlinear systems as linear models with a single lumped, unmodeled term instead of various time-varying coefficients. DDC laws can be obtained from different data-driven models with similar structures, which means that few modifications are required to adapt controllers to new application scenarios.

This paper discusses the application of DDC methods in UAV autolanding. Motivated by attracting laws, DDC laws are derived with guaranteed stability and error bounds from models of different orders. The main contributions of this study include: 1) the longitudinal motion of fixed-wing UAVs is introduced and analyzed, and the data-driven modeling on pitch-only dynamics is derived; 2) DDC laws are designed for data-driven models with different orders; 3) a numerical simulation is performed to demonstrate the application of DDC laws for tracking desired trajectories.

2 Data-driven modeling for pitch-only dynamics of one fixed-wing UAV

This section presents data-driven modeling for the pitch-only dynamics. The physical model of a fixed-wing aircraft comprises several coupled non-linear equations. When the fixed-wing UAV is in steady-state flight, many coupled terms can be sufficiently small. As a result, the dynamic model of a fixed-wing can be decomposed into

*This work is supported by National Natural Science Foundation of China under Grant 61973327 and the Royal Society's International Exchanges 2021 Cost Share NSFC.

longitudinal and lateral motions. Our study focuses on the longitudinal dynamics of a fixed-wing UAV, specifically its pitch-only model, which describes vertical rotation during the autolanding procedure.

The longitudinal autopilot for autolanding typically uses the throttle for airspeed and the elevator for pitch control. The inertial and body frames, represented by O_I and O_B, mentioned in this section are illustrated in Fig. 1. When the airspeed reaches the desired value, for example, in a trimmed condition, the elevator δ_e is utilized to adjust the pitch angle θ and pitch rate q. Consider a pitch-only longitudinal motion, the equation of pitch angle is expressed as follows:

$$\begin{cases} \dot{\theta} = q \\ \dot{q} = \mathrm{M} \ / J_{yy} \end{cases} \tag{1}$$

where J_{yy} is the moment of inertia, and M is the pitch moment that is shown as follows:

$$\begin{aligned} \mathrm{M} &= \frac{1}{2}\rho_{air} V_a{}^2 Sc \\ &\times \left(C_{\mathrm{M}_0} + C_{\mathrm{M}_\alpha}\alpha + C_{\mathrm{M}_q}\frac{c}{2V_a}q + C_{\mathrm{M}_{\delta_e}}\delta_e \right) \end{aligned} \tag{2}$$

where C_{M_0}, C_{M_α}, and C_{M_q} are aerodynamic coefficients; α is the angle of attack; ρ_{air} is the air density; S is the planform area and c is the mean chord of the fixed-wing, respectively. By combining Eq.(1) and Eq.(2), the equation for pitch-only dynamics can be derived as follows:

$$\begin{aligned} \ddot{\theta} &= \frac{\rho_{air} V_a{}^2 Sc}{2J_{yy}} \left(C_{\mathrm{M}_q}\frac{c}{2V_a}\dot{\theta} + C_{\mathrm{M}_{\delta_e}}\delta_e \right) \\ &+ \frac{\rho_{air} V_a{}^2 Sc}{2J_{yy}} \left(C_{\mathrm{M}_0} + C_{\mathrm{M}_\alpha}\alpha \right) \end{aligned} \tag{3}$$

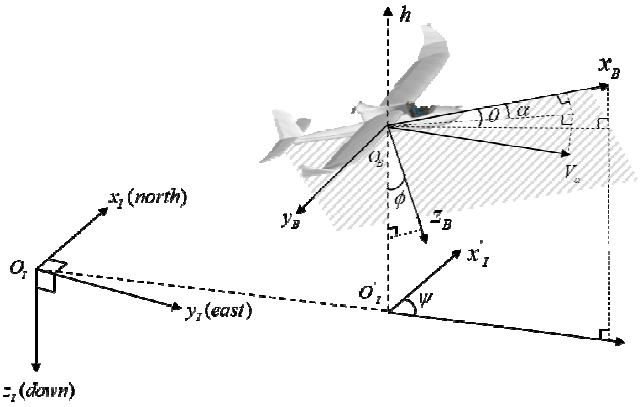

Fig. 1. Illustration of frames and state variables

To derive a discrete-time model for pitch-only dynamics, the following backward differences representation is defined:

$$\begin{aligned} \dot{\theta} &= \theta(k) - \theta(k-1)/h \\ \ddot{\theta} &= \left(\theta(k+1) - 2\theta(k) + \theta(k-1)\right)/h^2 \end{aligned} \tag{4}$$

where k is the discrete time instance; h is the sampling period. The data-driven model for pitch-only dynamics can be expressed as

$$\begin{aligned} \theta(k+1) &= f_{\theta,1}\theta(k) + f_{\theta,2}\theta(k-1) \\ &+ g_\theta \delta_e(k) + \varepsilon_\theta(k) \end{aligned} \tag{5}$$

where $\varepsilon_\theta(k)$ is the unmodeled term; $f_{\theta,1}$, $f_{\theta,2}$ and g_θ are constant parameters:

$$f_{\theta,1} = 2 + \frac{\rho_{air} V_a{}^2 Sc^2 C_{\mathrm{M}_q}}{4J_{yy}V_a}h$$

$$f_{\theta,2} = -1 - \frac{\rho_{air} V_a{}^2 Sc^2 C_{\mathrm{M}_q}}{4J_{yy}V_a}h$$

$$g_\theta = \frac{\rho_{air} V_a{}^2 Sc C_{\mathrm{M}_{\delta_e}}}{2J_{yy}}h^2$$

Similarly, backward first-order and second-order differences of the unmodeled term $\varepsilon_\theta(k)$ can be represented by:

$$\begin{aligned} \nabla\varepsilon_\theta(k) &= \varepsilon_\theta(k) - \varepsilon_\theta(k-1) \\ &= h\varepsilon_\theta^1(t_k) \\ \nabla^2\varepsilon_\theta(k) &= \nabla\varepsilon_\theta(k) - \nabla\varepsilon_\theta(k-1) \\ &= h^2\varepsilon_\theta^2(t_k) \end{aligned} \tag{6}$$

where $\varepsilon_\theta^1(t_k)$ and $\varepsilon_\theta^2(t_k)$ are derivatives lie within sampling points. Eq.(6) indicates that backward differences are bounded if respective derivatives are bounded. If the disturbance signal $\varepsilon_\theta(k)$ is a polynomial function of time, its derivatives can be seen as signals that change slowly over time. For example, it is seen that $\nabla\varepsilon_\theta = 0$, when ε_θ is a constant signal; $\nabla^2\varepsilon_\theta = 0$, as ε_θ is a ramp signal. It is easier to estimate slow-varying signals than fast-varying ones, which indicates that higher-order models are more practical in most scenarios. For pitch-only dynamics of the fixed-wing, first-order and second-order models, can be derived by transforming Eq.(5) into difference equations:

$$\begin{aligned} \nabla\theta(k+1) &= f_{\theta,1}\nabla\theta(k) + f_{\theta,2}\nabla\theta(k-1) \\ &+ g_\theta\nabla\delta_e(k) + \nabla\varepsilon_\theta(k) \\ \nabla^2\theta(k+1) &= f_{\theta,1}\nabla^2\theta(k) + f_{\theta,2}\nabla^2\theta(k-1) \\ &+ g_\theta\nabla^2\delta_e(k) + \nabla^2\varepsilon_\theta(k) \end{aligned} \tag{7}$$

3 Control design based on data-driven models

This section presents a design methodology for DDC based on data-driven models. The primary objective of the pitch-only controller is to accurately follow the desired pitch angle produced by the outer-loop autopilot. By applying the attracting law, the discrete-time dynamic of the tracking error can be designed as

$$e(k+1)=(1-\rho)e(k) \tag{8}$$

where $e(k)=\theta_d(k)-\theta(k)$ is the tracking error of pitch angle; $\theta_d(k)$ represents the desired pitch angle; $\rho\in(0,1)$ is a tunable parameter. According to Eq.(8), the relationship between $e(k+1)$ and $e(k)$ satisfies $|e(k+1)|<|e(k)|$, which indicates that the tracking error $e(k)$ decreases as time steps increase. Combining Eq.(5) and Eq.(8), we have

$$\begin{aligned} e(k+1)&=\theta_d(k+1)-\theta(k+1)\\ &=\theta_d(k+1)-f_{\theta,1}\theta(k)+f_{\theta,2}\theta(k-1)\\ &\quad+g_\theta\delta_e(k)+\varepsilon_\theta(k)\\ &=(1-\rho)e(k) \end{aligned} \tag{9}$$

The ideal data-driven control law $\bar{\delta}_e(k)$ can be derived from Eq.(9):

$$\begin{aligned} \bar{\delta}_e(k)=\frac{1}{g_\theta}\big[&-(1-\rho)e(k)+\theta_d(k+1)\\ &-f_{\theta,1}\theta(k)-f_{\theta,2}\theta(k-1)-\varepsilon_\theta(k)\big] \end{aligned} \tag{10}$$

However, the ideal control law Eq.(10) is not realizable because the disturbance $\varepsilon_\theta(k)$ is unknown. A simple estimation $\hat{\varepsilon}_\theta(k)$ of the disturbance signal $\varepsilon_\theta(k)$ is its time-delay signal $\varepsilon_\theta(k-1)$ which yields:

$$\begin{aligned} \hat{\varepsilon}_\theta(k)=\theta(k)&-f_{\theta,1}\theta(k-1)\\ &-f_{\theta,2}\theta(k-2)-g_\theta\delta_e(k-1) \end{aligned} \tag{11}$$

Thus, the practical data-driven control law $\delta_e(k)$ is given as follows:

$$\begin{aligned} \delta_e(k)=\frac{1}{g_\theta}\big[&-(1-\rho)e(k)+\theta_d(k+1)\\ &-f_{\theta,1}\theta(k)-f_{\theta,2}\theta(k-1)-\hat{\varepsilon}_\theta(k)\big] \end{aligned} \tag{12}$$

According to Eq.(6), if the first-order difference $\nabla\varepsilon_\theta(k)$ is bounded, the maximum norm of $\nabla\varepsilon_\theta(k)$ can be noted by $\nabla\varepsilon_{\theta_{\max}}$. The closed-loop system Eq.(5) governed by DDC law is stable, and the upper limit of tracking error is bounded:

$$\overline{\lim_{k\to\infty}}|e(k)|\le\frac{\nabla\varepsilon_{\theta_{\max}}}{\rho} \tag{13}$$

For data-driven models Eq.(7) with higher-order differences, the 1-order DDC and 2-order DDC can be designed as:

$$\begin{aligned} \delta_e(k)=\delta_e(k-1)&+\frac{1}{g_\theta}\\ &\times\big[-(1-\rho)e(k)+\theta_d(k+1)-\theta(k)\\ &-f_{\theta,1}\nabla\theta(k)-f_{\theta,2}\nabla\theta(k-1)-\nabla\hat{\varepsilon}_\theta(k)\big] \end{aligned} \tag{14}$$

and

$$\begin{aligned} \delta_e(k)=\delta_e(k-1)+\nabla\delta_e(k-1)&+\frac{1}{g_\theta}\\ &\times\big[-(1-\rho)e(k)+\theta_d(k+1)-\theta(k)-\nabla\theta(k)\\ &-f_{\theta,1}\nabla^2\theta(k)-f_{\theta,2}\nabla^2\theta(k-1)-\nabla^2\hat{\varepsilon}_\theta(k)\big] \end{aligned} \tag{15}$$

where estimations for $\nabla\varepsilon_\theta(k)$ and $\nabla^2\varepsilon_\theta(k)$ are given by:

$$\begin{aligned} \nabla\hat{\varepsilon}_\theta(k)&=\nabla\theta(k)-f_{\theta,1}\nabla\theta(k-1)\\ &\quad-f_{\theta,2}\nabla\theta(k-2)-g_\theta\nabla\delta_e(k-1)\\ \nabla^2\hat{\varepsilon}_\theta(k)&=\nabla^2\theta(k)-f_{\theta,1}\nabla^2\theta(k-1)\\ &\quad-f_{\theta,2}\nabla^2\theta(k-2)-g_\theta\nabla^2\delta_e(k-1) \end{aligned} \tag{16}$$

4 Numerical Simulation

This section presents the results from numerical simulation to demonstrate the properties and effectiveness of the data-driven controllers. For the scenario of UAV autolanding, consider the pitch-only dynamics Eq.(3) with following parameters：

$$\begin{aligned} &m=1\,\text{kg},\ g=9.81\,\text{m/s}^2,\ \rho_{air}=1.29\,\text{kg/m}^3\\ &S=0.123\,\text{m}^2,\ c=0.1\,\text{m},\ J=0.0092\,\text{m}\times\text{kg}^2\\ &C_{\text{M}_0}=0.0026,\ C_{\text{M}_q}=-0.0003,\ C_{\text{M}_{\delta_e}}=-0.0051 \end{aligned}$$

The airspeed is set to 20 m/s , and the sampling time h is chosen as 0.001 s . As a consequence, constant parameters given by Eq.(5) can be computed as follows:

$$f_{\theta,1}=1.999997,\ f_{\theta,2}=-0.999997,\ g_\theta=-0.008862$$

The desired pitch trajectory is set as a constant signal $\theta_d=0.15$ rad , while the disturbance $\varepsilon_\theta(k)$ is assumed to be a sine wave signal $\varepsilon_\theta(k)=0.05*\sin(20\pi k\Delta t)$ rad . The initial states and control input for numerical simulation are assumed as follows:

$$\theta(0)=0.1\ \text{rad},\nabla\theta(0)=\nabla^2\theta(0)=0\ \text{rad},$$
$$\delta_e(0)=\nabla\delta_e(0)=\nabla^2\delta_e(0)=0\ \text{rad},$$

To achieve a clear comparison, the 0-order,1-order, and 2-order DDC laws use the same tunable parameter ρ , which is set to 0.5.

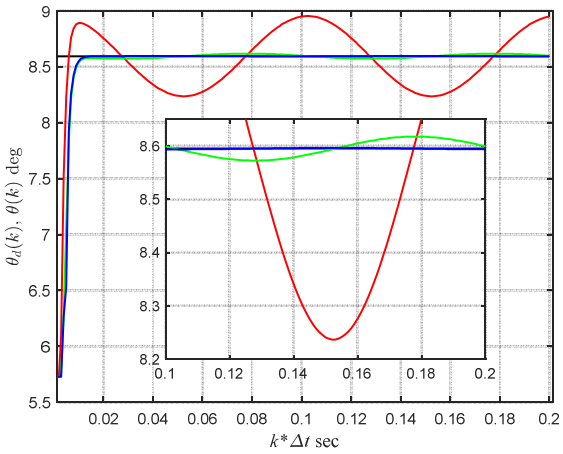

Fig. 2. Desired pitch angle $\theta_d(k)$ (black) and tracking trajectories $\theta(k)$ by using 0-order (red), 1-order (green) and 2-order (blue) DDC laws

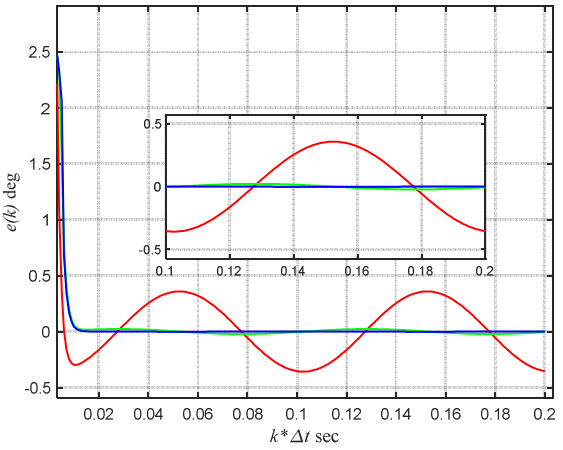

Fig. 3. Tracking errors $e(k)$ by using 0-order (red), 1-order (green) and 2-order (blue) DDC laws

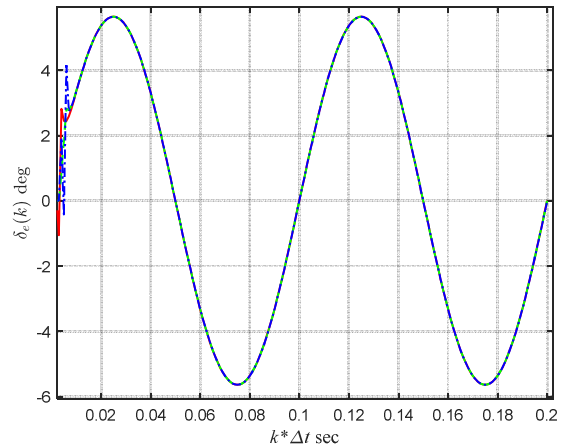

Fig. 4. Control inputs $\delta_e(k)$ of 0-order (red solid), 1-order (green dashed) and 2-order (blue dash-dot) DDC laws

According to numerical simulation results presented in Figs. 2-3, all tracking errors decrease rapidly within a short period of time. The 1-order DDC law yields better results than the 0-order DDC law while obtaining the similar performance as the 2-order DDC law. The tracking error of the 0-order DDC law is significantly influenced by the maximum absolute value of $\varepsilon_\theta(k)$ that can be approximated by $\nabla\varepsilon_{\theta_{\max}}/\rho$. Recorded data from numerical simulation indicates that absolute values of unmodeled terms with different differences satisfy $\varepsilon_{\theta_{\max}} > \nabla\varepsilon_{\theta_{\max}} > \nabla^2\varepsilon_{\theta_{\max}}$. It means that the upper limit of the tracking error gets smaller when a higher order data-driven model is chosen.

5 Conclusions

In this paper, a data-driven control (DDC) design method is tentatively proposed and developed for the autolanding of fixed-wing UAVs. The longitudinal pitch-only channel of UAV flights is concentrated on as a case study. Three DDC laws based on different difference models have been explored. Optimizing DDC laws can be achieved by selecting different models, while parameter tuning is simple with only one parameter. Numerical simulation shows that DDC laws can effectively govern pitch-only dynamics for closed-loop tracking with predictable error bounds. For practical implementation, it is suggested to use a lower order difference model that balances the performance of tracking error and system band. Further study is required to explore DDC schemes on UAV autolanding for lateral control loops and coupled systems.

References

[1] Yuan, Huali, et al. Design and testing of a crop growth sensor aboard a fixed-wing unmanned aerial vehicle[J]. *Computers and Electronics in Agriculture.* 2022. 194: 106762.

[2] Wang, Liang, Fangliang Chen, and Huiming Yin. Detecting and tracking vehicles in traffic by unmanned aerial vehicles[J]. *Automation in construction*. 2016, 72: 294-308.

[3] Hu, Shuyan, et al. Disguised tailing and video surveillance with solar-powered fixed-wing unmanned aerial vehicle[J]. *IEEE Transactions on Vehicular Technology*. 2022 71(5): 5507-5518.

[4] El Tin, Fares, Inna Sharf, and Meyer Nahon. Fire Monitoring with a Fixed-wing Unmanned Aerial Vehicle[J]. *IEEE 2022 International Conference on Unmanned Aircraft Systems* (ICUAS). pp. 1350-1358.

[5] Yuan, Xin, et al. Deep Reinforcement Learning-Driven Reconfigurable Intelligent Surface-Assisted Radio Surveillance with A Fixed-Wing UAV[J]. *IEEE Transactions on Information Forensics and Security*. 2023, 18: 4546-4560.

[6] Trittler, Martin, Thomas Rothermel, and Walter Fichter. Autopilot for landing small fixed-wing unmanned aerial vehicles with optical sensors[J]. *Journal of Guidance, Control, and Dynamics.* 2016,39(9): 2011-2021.

[7] Lungu, Mihai. Backstepping and dynamic inversion combined controller for auto-landing of fixed wing UAVs[J]. *Aerospace Science and Technology*. 2020, 96: 105526.

[8] Thurrowgood, Saul, et al. A biologically inspired, vision-based guidance system for automatic landing of a fixed- wing aircraft[J]. *Journal of Field Robotics*. 2014, 31(4): 699-727.

[9] Ambati, Pradeep R., and Radhakant Padhi. Robust auto-landing of fixed-wing UAVs using neuro-adaptive design[J]. *Control Engineering Practice*. 2017, (6): 218-232.

[10] Zhao, Shulong, et al. A novel data-driven control for fixed-wing UAV path following[C]. *IEEE 2015 International Conference on Information and Automation*. pp. 3051-3056.

[11] Liang, Shaojun, et al. Data-driven fault diagnosis of FW-UAVs with consideration of multiple operation conditions[J]. *ISA transactions*, 2022, 126: 472-485.

[12] Wu, H., Hu, J. Theory, Methods and Applications of Characteristic Modeling, in Chinese[M]. *National Defense Industry Press*, Beijing, 2019.

[13] Warren, Michael, et al. An Automated Emergency Landing System for Fixed - Wing Aircraft: Planning and Control[J]. *Journal of Field Robotics*. 2015, 32(8): 1114-1140.

[14] Ahsan, Mansoor, et al. Performance comparison of two altitude-control algorithms for a fixed-wing UAV[C]. *2013 3rd IEEE International Conference on Computer, Control and Communication (IC4)*. IEEE, 2013.

[15] Anjali, B. S., A. Vivek, and J. L. Nandagopal. Simulation and analysis of integral LQR controller for inner control loop design of a fixed wing micro aerial vehicle (MAV)[J]. *Procedia Technology* 25 (2016): 76-83.

[16] Sedlmair, Nicolas, Julian Theis, and Frank Thielecke. Flight testing automatic landing control for unmanned aircraft including curved approaches[J]. *Journal of Guidance, Control, and Dynamics* 45.4 (2022): 726-739.

[17] Rugh, Wilson J., and Jeff S. Shamma. Research on gain scheduling[J]. *Automatica.* 36.10 (2000): 1401-1425.

[18] Zhang, Qingrui, and Hugh HT Liu. Robust nonlinear close formation control of multiple fixed-wing aircraft[J]. *Journal of Guidance, Control, and Dynamics* 44.3 (2021): 572-586.

[19] Li, Yu, et al. A cascaded nonlinear fault-tolerant control for fixed-wing aircraft with wing asymmetric damage[J]. *ISA transactions* 136 (2023): 503-524.

[20] Reinhardt, Dirk, and Tor Arne Johansen. Control of fixed-wing uav attitude and speed based on embedded nonlinear model predictive control[J]. *IFAC-PapersOnLine* 54.6 (2021): 91-98.

[21] Baldi, S., Sun, D., Xia, X., Zhou, G., & Liu, D. (2022). ArduPilot-based adaptive autopilot: architecture and software-in-the-loop experiments[J]. *IEEE Transactions on Aerospace and Electronic Systems*, 58(5), 4473-4485

[22] Hashjin, Saeid Aghaei, et al. Data-driven model-free adaptive current control of a wound rotor synchronous machine drive system[J]. *IEEE Transactions on Transportation Electrification* 6.3 (2020): 1146-1156.

[23] Gao, Han, et al. Forecasting-based data-driven model-free adaptive sliding mode attitude control of combined spacecraft[J]. *Aerospace Science and Technology* 86 (2019): 364-374.

[24] Wu, H., Hu, J., & Xie, Y. Characteristic model-based all-coefficient adaptive control method and its applications[J]. *IEEE Transactions on Systems, Man, and Cybernetics, Part C (Applications and Reviews)*. 2007, 37(2), 213-221. Doi: 10.1109/TSMCC.2006.887004

[25] Sun, M., Wu, L., Hu, Y., & Zhou, W. (2017). Digital control strategies with attractiveness and invariance specifications[J]. *IEEE Transactions on Control Systems Technology*, 26(4), 1272-1284.

[26] Sun, M., Li, W., & Wu, L. (2021). Dead-beat terminal sliding-mode control: A guaranteed attractiveness approach[J]. *Automatica*, 129, 109609.

Proceedings of the 3rd Conference on Fully Actuated System Theory and Applications
May 10-12, 2024, Shenzhen, China

Sliding Mode Control for Helicopter Systems Based on Fully Actuated Method

Yankai Li[1], Jinyu Xu[1], Xiaohui Xue[1], Dongping Li[2], Yingmin Yi[1], Shuyi Shao[3]

1. School of Automation and Information Engineering, Xi'an University of Technology, Xi`an, 710048
E-mail: liyankai@xaut.edu.cn, jelly_xujinyu@163.com, xuexhgj@163.com, yiym@xaut.edu.cn
2. School of Sciences, Xi'an Technological University, Xi'an 710021
E-mail: li_dongping@126.com
3. College of Automation Engineering, Nanjing University of Aeronautics and Astronautics, Nanjing 211106,
E-mail: shaosy@nuaa.edu.cn

Abstract: Based on fully actuated technology, a sliding mode control approach is suggested for helicopter systems with all degrees of freedom. First, the degree of nonlinearity and coupling is lessened by applying the feedback linearization technique. And the helicopter systems transform into fully actuated systems. Secondly, a sliding mode controller is built with the assumption of system stability in order to achieve the intended tracking task. Third, the reliability of complete closed-loop structures is investigated using Lyapunov theory. Finally, this work presents simulation data to validate the effectiveness of the designed control technique.

Key Words: Helicopter systems, Feedback linearization, Sliding mode control, Fully actuated method.

1 Introduction

Because of unique advantages of helicopter, such as the vertical takeoff and landing, air hovering, flexible flight, helicopters could be used to search, rescue, inspection and so many applications. Therefore, in recent years, helicopter systems have become extensively developed and used in both the military and the civilian sectors [1-2]. The significant nonlinearity, high order, and strong coupling of helicopter systems make them underdriven systems that are challenging to regulate [3-4]. For this reason, creating a sturdy controller is essential to improving helicopter flight quality. At present, a large number of domestic and foreign scholars have proposed various control methods in the application of helicopters, and achieved many excellent results.

In the early days, the flight control issues have been studied for helicopters, and the linear flight control methods are the most commonly control schemes. The attitude controller in [5] was designed using output feedback linear quadratic regulator (LQR) technology, taking into account helicopters in a hovering condition. In [6], in order to obtain good control efficacy, the PID approach is utilized to improve the traditional controller, which was built using the inner and outer loop control structure as the basis for design. In [7], for the purpose of controlling the attitude of the helicopter, a robust controller made up of a robust compensator and PI controller was created. Although the linear control development is more complete and has the characteristics of convenient in controller design and stability analysis, it has large limitations. It is suitable for control tasks with low control accuracy.

Helicopter control performance is impacted by a variety of disturbances that the control system experiences during actual flight. Numerous nonlinear control techniques have been presented by researchers to address the issue. In [8], the attitude robust control issues were discussed for ship-based unmanned helicopters. In [9], a finite-time tolerant of faults control technique was introduced for systems with quadrotors and actuator faults. In [10], the anti-disturbance flight control technique for helicopters was examined in combination with the neural network control and active disturbance rejection control methods. In [11], for 3-DOF model aircraft systems, the adaptive neural fault-tolerant control technique was recommended. In our earlier results [12], Using the anti-disturbance stochastic flight control approach, the position and elevation helicopter systems were managed under random disturbances.

This study will comprehensively consider the coupling of the helicopter systems with full degrees of freedom, based on the aforementioned research. The full-degree-of-freedom aircraft control method combines the sliding mode control method with input and output feedback linearization. The helicopter model and mathematical preparation are given Section II. In Section III, the system will be modified using the feedback linearization approach and the sliding mode control method will be developed. The effectiveness of the control system is verified and the outcomes of the helicopter tracking simulation are displayed in Section IV. The paper is finally summarized in Section V.

2 Helicopter Model and Mathematical Preparation

The two right-handed coordinate systems used to model the helicopter system are the body coordinate system (O_b, x_b, y_b, z_b) and the inertial coordinate system (O_i, x_i, y_i, z_i), where O_b is the helicopter's center of gravity, x_b, y_b, z_b are its unit vectors, x_b points to the helicopter's head, and z_b points to its underneath; O_i is a fixed point on the ground, x_i points to the north, and z_i points to the earth's center. The forces and moments of the helicopter are analyzed under above two coordinate systems, the helicopter systems are presented as follow [13]:

* The National Natural Science Foundation of China (Grants 62103327 and 12101481), the Shaanxi-Provincial Education Department's Scientific Research Program (Grant 23JY053), the Key Research and Development Plan of Shaanxi Province (Grant 2024GX-YBXM-298), and the Science Center Program of the National Natural Science Foundation of China (Grant 62188101) provided partial funding for this work.

$$
\begin{aligned}
&\dot{P}_x(t) = V_x(t),\\
&\dot{P}_y(t) = V_y(t),\\
&\dot{P}_z(t) = V_z(t),\\
&\dot{V}_x(t) = -\frac{T_m}{m}(C_\phi S_\theta C_\psi + S_\phi S_\psi),\\
&\dot{V}_y(t) = -\frac{T_m}{m}(C_\phi S_\theta S_\psi - S_\phi C_\psi),\\
&\dot{V}_z(t) = -g - \frac{T_m}{m} C_\phi S_\theta,\\
&\dot{\phi}(t) = p(t) + \frac{S_\phi S_\theta}{C_\theta} q(t) + \frac{C_\phi S_\theta}{C_\theta} r(t),\\
&\dot{\theta}(t) = C_\phi q(t) - S_\phi r(t),\\
&\dot{\psi}(t) = \frac{S_\phi}{C_\theta} q(t) + \frac{C_\phi}{C_\theta} r(t),\\
&J_{xx}\dot{p}(t) = (J_{yy} - J_{zz}) q(t) r(t) - T_m L_y + (C_m + T_m L_z) b - T_t H_z,\\
&J_{yy}\dot{q}(t) = -(J_{xx} - J_{zz}) p(t) r(t) - T_m L_x + (C_m + T_m L_z) a,\\
&J_{zz}\dot{r}(t) = (J_{xx} - J_{yy}) p(t) q(t) - Q_m + T_t H_x,
\end{aligned} \tag{1}
$$

where g is the acceleration caused by gravity, m is the helicopter's mass, J_{xx} is the rolling moment of inertia, J_{yy} is the pitch moment of inertia, and J_{zz} is the yaw moment of inertia; P_x, P_y, P_z are the position, and V_x, V_y, V_z is the velocity in the inertial coordinate system; T_m and T_t represent the moments generated by the main and tail rotors, respectively; the main rotor's lateral and longitudinal flapping angles are represented by a and b; $\phi(t)$ is the roll angle, $\theta(t)$ is the pitch angle, $\psi(t)$ is the yaw angle; $Q_m(t) = C_k T_m^{1.5}(t) + D_k$; $C_m, L_z, H_z, L_y, L_x, H_x$ and D_k are known constants;

The model (1) is organized such that $\boldsymbol{P}(t) = (P_x(t)\ P_y(t)\ P_z(t))^{\mathrm{T}}$ and $\boldsymbol{V}(t) = (V_x(t)\ V_y(t)\ V_z(t))^{\mathrm{T}}$, Where $\boldsymbol{P}(t), \boldsymbol{V}(t)$ stand for position and velocity vector in the inertial coordinate system.; $\boldsymbol{\Omega}(t) = (\phi(t)\ \theta(t)\ \psi(t))^{\mathrm{T}}$ is the attitude angle vector of the helicopter; $\boldsymbol{W}(t) = (p(t)\ q(t)\ r(t))^{\mathrm{T}}$ is the attitude angular velocity vector; $\boldsymbol{e}_3 = (0\ 0\ 1)^{\mathrm{T}}$; $\boldsymbol{J} = \mathrm{diag}\{J_{xx}, J_{yy}, J_{zz}\}$ is the helicopter's inertia matrix; $\boldsymbol{R}(t)$ is the matrix of rotations between the body and inertial coordinates:

$$
\boldsymbol{R}(t) = \begin{pmatrix}
C_\theta C_\psi & S_\phi S_\theta C_\psi - C_\phi S_\psi & C_\phi S_\theta C_\psi + S_\phi S_\psi \\
C_\theta S_\psi & S_\phi S_\theta S_\psi + C_\phi C_\psi & C_\phi S_\theta S_\psi - S_\phi C_\psi \\
-S_\theta & S_\phi C_\theta & C_\phi S_\theta
\end{pmatrix},
$$

where $C*$ and $S*$ denote respectively as $\cos(*)$ and $\sin(*)$, $*$ denote $\phi(t), \theta(t)$ or $\psi(t)$. The attitude kinematic matrix $\boldsymbol{H}(t)$ is showed as follows:

$$
\boldsymbol{H}(t) = \begin{pmatrix}
1 & \frac{S_\phi S_\theta}{C_\theta} & \frac{C_\phi S_\theta}{C_\theta} \\
0 & C_\phi & -S_\phi \\
0 & \frac{S_\phi}{C_\theta} & \frac{C_\phi}{C_\theta}
\end{pmatrix}.
$$

The cross-product operator matrix, denoted as $\boldsymbol{W}(t)^\times$, is provided as follows:

$$
\boldsymbol{W}(t)^\times = \begin{pmatrix}
0 & -r(t) & q(t) \\
r(t) & 0 & -p(t) \\
-q(t) & p(t) & 0
\end{pmatrix}.
$$

Moreover, the force produced by the main rotor of a helicopter is expressed as $\boldsymbol{f}(t) = (0\ 0\ -T_m(t))^{\mathrm{T}}$; while the moments from the main and tail rotors are expressed as $\boldsymbol{\tau}(t)$, which are expressed as

$$
\boldsymbol{\tau}(t) = \begin{pmatrix}
-T_m L_y + (C_m + T_m L_z) b - T_t H_z \\
-T_m L_x + (C_m + T_m L_z) a \\
-Q_m + T_t H_x
\end{pmatrix},
$$

The following helicopter model (2) was obtained through the above organization [14]:

$$
\begin{aligned}
&\dot{\boldsymbol{P}}(t) = \boldsymbol{V}(t),\\
&\dot{\boldsymbol{V}}(t) = -g\boldsymbol{e}_3 + \frac{1}{m}\boldsymbol{R}(t)\boldsymbol{f}(t),\\
&\dot{\boldsymbol{\Omega}}(t) = \boldsymbol{H}(t)\boldsymbol{W}(t),\\
&\boldsymbol{J}\dot{\boldsymbol{W}}(t) = -\boldsymbol{W}(t)^\times \boldsymbol{J}\boldsymbol{W}(t) + \boldsymbol{\tau}(t),
\end{aligned} \tag{2}
$$

In this paper, a robust control method will be designed for the helicopter system (2) to ensure that the helicopter track to the desired position $\boldsymbol{P}_d(t)$ and yaw angle $\psi_d(t)$.

To make the controller design and stability analysis simpler, the ensuing Lemmas and Premises are presented:

Assumption 1 [15]: During helicopter flight process, roll angle $\phi(t)$ and pitch angle $\theta(t)$ satisfy respectively $\phi(t) \in \left(-\frac{\pi}{2}, \frac{\pi}{2}\right)$ and $\theta(t) \in \left(-\frac{\pi}{2}, \frac{\pi}{2}\right)$.

Assumption 2 [16]: For $t > 0$, there exist positive constants $\delta_i (i = 1, 2, 3, 4)$ which are not known in such a way that $\| x_d^{(i)} \| \leqslant \delta_i$.

Lemma 1 [17]: $\boldsymbol{V}(t)$ is a continuous function. When $\forall t \in R^+$, $V(t) \geqslant 0$, and $V(0)$ are bounded, $V(t)$ is asymptotically stable if the inequality $\dot{V} < 0$ holds.

3 Controller Design for Helicopter Systems

This section describes a flight controller that uses sliding mode control to make sure the helicopter systems track to the intended yaw angle $\psi_d(t)$ and position $\boldsymbol{P}_d(t)$. Initially the nonlinear and tightly coupled problems of helicopter systems are treated using the input and output feedback linearity method. The tracking signals $\boldsymbol{P}_d(t)$ and $\psi_d(t)$ are then combined to develop the helicopter systems' basic tracking fault nonlinear model. Then, a flight controller that can guarantee the required control performances is designed using the sliding mode control method. Fig. 1 depicts the flight controller's design process:

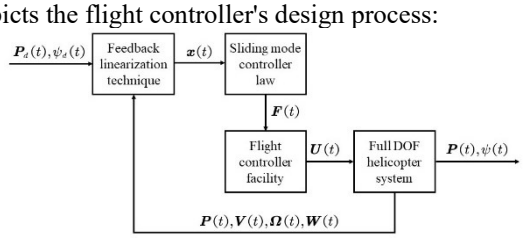

Fig. 1: The flight controller designed process block diagram

3.1 System transformation based on input-output feedback linearization

It is evident that the helicopter systems' control input consists solely of 4-dimensional variables. During the actual flight, the helicopters not only need to track to the desired position $\boldsymbol{P}_d(t)$ and yaw angle $\psi_d(t)$, but also need to control the six degrees of freedom. Therefore, the helicopters are a typical underdriven nonlinear control system. Because of this, the input and output feedback linearization approach will be used to create a system that is comparable to system (2), and the controller for flight will be constructed using the new system in this section.

The expanded system is generated by adding two extra variables, ensuring that the helicopters can be linearized via the input-output feedback linearization technique, $T_{1m}(t)$ and $T_{2m}(t)$, as shown in [18]:

$$\begin{aligned}
&\dot{\boldsymbol{P}}(t) = V(t),\\
&\dot{\boldsymbol{V}}(t) = -g\boldsymbol{e}_3 - \frac{1}{m}\boldsymbol{R}(t)\boldsymbol{f}(t),\\
&\dot{T}_m(t) = T_{1m}(t),\\
&\dot{T}_{1m}(t) = T_{2m}(t),\\
&\dot{\boldsymbol{\Omega}}(t) = \boldsymbol{H}(t)\boldsymbol{W}(t),\\
&\boldsymbol{J}\dot{\boldsymbol{W}}(t) = -\boldsymbol{W}(t)^{\times}\boldsymbol{J}\boldsymbol{W}(t) + \boldsymbol{\tau}(t).
\end{aligned} \tag{3}$$

Select system (2) with $T_{2m}(t)$ and $\boldsymbol{\tau}(t)$ as inputs, $\boldsymbol{P}(t)$ and $\psi(t)$ as outputs. The system's overall relative order $R_T = 14$, The dimensions of the system $R_n = 14$, namely, $R_T = R_n$. Thus, there exists a diffeomorphism that enables the system to be transformed from the original system to a new system. The following variables were selected for the new system:

$$\begin{aligned}
&\boldsymbol{x}_1(t) = \boldsymbol{P}(t) - \boldsymbol{P}_d(t),\\
&\boldsymbol{x}_2(t) = \boldsymbol{V}(t) - \dot{\boldsymbol{P}}_d(t),\\
&\boldsymbol{x}_3(t) = -g\boldsymbol{e}_3 - \frac{T_m}{m}\boldsymbol{R}(t)\boldsymbol{e}_3 - \ddot{\boldsymbol{P}}_d(t),\\
&\boldsymbol{x}_4(t) = -\frac{\dot{T}_m}{m}\boldsymbol{R}(t)\boldsymbol{e}_3 - \frac{T_m}{m}\boldsymbol{R}(t)\boldsymbol{W}^{\times}(t)\boldsymbol{e}_3 - \dddot{\boldsymbol{P}}_d(t),\\
&x_5(t) = \psi(t) - \psi_d(t),\\
&x_6(t) = \boldsymbol{\beta}_1(t)\boldsymbol{W}(t) - \dot{\psi}_d(t),
\end{aligned} \tag{4}$$

where $\boldsymbol{\beta}_1(t) = (0 \ \sin\phi(t)\sec\theta(t) \ \cos\phi(t)\sec\theta(t))$.

Since there exists a diffeomorphism for system (2), there is a bijection between its state variable $\boldsymbol{\Gamma}(t) = (\boldsymbol{P}(t) \ \boldsymbol{V}(t) \ T_m(t) \ T_{1m}(t) \ \boldsymbol{\Omega}(t) \ \boldsymbol{W}(t))^{\mathrm{T}}$ and the state variable $\boldsymbol{x}(t) = (\boldsymbol{x}_1^{\mathrm{T}}(t) \ \boldsymbol{x}_2^{\mathrm{T}}(t) \ \boldsymbol{x}_3^{\mathrm{T}}(t) \ \boldsymbol{x}_4^{\mathrm{T}}(t) \ x_5^{\mathrm{T}}(t) \ x_6^{\mathrm{T}}(t))^{\mathrm{T}}$ of system (4). As a result, system (4) is obtained as follows:

$$\begin{aligned}
&\dot{\boldsymbol{x}}_1(t) = \boldsymbol{x}_2(t),\\
&\dot{\boldsymbol{x}}_2(t) = \boldsymbol{x}_3(t),\\
&\dot{\boldsymbol{x}}_3(t) = \boldsymbol{x}_4(t),\\
&\dot{\boldsymbol{x}}_4(t) = \boldsymbol{F}_1(t),\\
&\dot{x}_5(t) = x_6(t),\\
&\dot{x}_6(t) = F_2(t),
\end{aligned} \tag{5}$$

where $\boldsymbol{F}(t) = \boldsymbol{A}(t) + \boldsymbol{B}(t)\boldsymbol{U}(t)$,

$$\boldsymbol{A}(t) = \begin{pmatrix}\boldsymbol{\Gamma}_1(t)\\ \Gamma_2(t)\end{pmatrix},\ \boldsymbol{U}(t) = \begin{pmatrix}T_{2m}(t)\\ \boldsymbol{\tau}(t)\end{pmatrix},\ \boldsymbol{F}(t) = \begin{pmatrix}\boldsymbol{F}_1(t)\\ F_2(t)\end{pmatrix}$$

$$\boldsymbol{B}(t) = \begin{pmatrix}-\frac{1}{m}\boldsymbol{R}(t)\boldsymbol{e}_3 & -\frac{T_m}{m}\boldsymbol{R}(t)\boldsymbol{\alpha}_1\boldsymbol{J}^{-1}\\ 0 & \boldsymbol{\beta}_1(t)\boldsymbol{J}^{-1}\end{pmatrix},\ \boldsymbol{\alpha}_1 = \begin{pmatrix}0 & 1 & 0\\ -1 & 0 & 0\\ 0 & 0 & 0\end{pmatrix},$$

$$\boldsymbol{\Gamma}_1(t) = -\frac{\ddot{T}_m}{m}\boldsymbol{R}(t)\boldsymbol{e}_3 - \frac{2\dot{T}_m}{m}\boldsymbol{R}(t)\boldsymbol{W}^{\times}(t)\boldsymbol{e}_3 - \frac{T_m}{m}\boldsymbol{R}(t)\boldsymbol{W}^{\times}(t)\boldsymbol{W}^{\times}(t)\boldsymbol{e}_3 - \dddot{\boldsymbol{P}}_d(t),$$

$$\begin{aligned}
\Gamma_2(t) = &-\boldsymbol{\beta}_1(t)\boldsymbol{J}^{-1}\boldsymbol{W}(t)^{\times}\boldsymbol{J}\boldsymbol{W}(t) - \ddot{\psi}_d(t)\\
&+\left[\cos\phi(t)\sec\theta(t)\dot{\phi}(t) + \sin\phi(t)\sec\theta(t)\tan\theta(t)\dot{\theta}(t)\right]q(t)\cdot\\
&-\left[\sin\phi(t)\sec\theta(t)\dot{\phi}(t) - \cos\phi(t)\sec\theta(t)\tan\theta(t)\dot{\theta}(t)\right]r(t)
\end{aligned}$$

In system (5), $\boldsymbol{F}_1(t)$ and $F_2(t)$ are the control inputs. $\boldsymbol{x}_1(t)$ is the helicopters' position tracking error, $\boldsymbol{x}_2(t)$ is the velocity tracking error, $\boldsymbol{x}_3(t)$ is the acceleration produced by the helicopter's controllable combined force, $\boldsymbol{x}_4(t)$ is the force variability, The helicopters' yaw angle tracking inaccuracy is represented by $x_5(t)$, and $x_6(t)$ is the yaw angle rate tracking error. In order for the helicopters to do the intended tracking task, the control rule will be designed in this work using the sliding mode control approach.

3.2 Sliding mode controller design

The system (5) can be considered as two subsystems, a fourth-order position subsystem and a second-order yaw angle subsystem. Thus, the position tracking error of the helicopters $\boldsymbol{x}_1(t)$ is controlled by a fourth-order system, and the yaw angle tracking error $x_5(t)$ is controlled by a second-order system. To ensure that the tracking error approaches to zero, the controller for flight in the following is designed using the sliding mode control approach.

For a fourth-order system which controls $\boldsymbol{x}_1(t)$, defining the tracking error $\boldsymbol{e}_1$ as

$$\boldsymbol{e}_1 = \boldsymbol{x}_1 - \boldsymbol{x}_{1d} \tag{6}$$

where $\boldsymbol{x}_{1d}$ is the desired tracking error of $\boldsymbol{x}_1$.

Create a sliding modal surface that is

$$\boldsymbol{s}_1 = \boldsymbol{K}_1\boldsymbol{e}_1 + \boldsymbol{K}_2\dot{\boldsymbol{e}}_1 + \boldsymbol{K}_3\ddot{\boldsymbol{e}}_1 + \dddot{\boldsymbol{e}}_1 \tag{7}$$

where, $\boldsymbol{s}_1 = (s_{1\phi} \ s_{1\theta} \ s_{1\psi})^{\mathrm{T}}$, $\boldsymbol{K}_1 = \mathrm{diag}(K_{1x} \ K_{1y} \ K_{1z}) > 0$, $\boldsymbol{K}_2 = \mathrm{diag}(K_{2x} \ K_{2y} \ K_{2z}) > 0$ and $\boldsymbol{K}_3 = \mathrm{diag}(K_{3x} \ K_{3y} \ K_{3z}) > 0$.

Differentiating (7) yields

$$\begin{aligned}
\dot{\boldsymbol{s}}_1 &= \boldsymbol{K}_1\dot{\boldsymbol{e}}_1 + \boldsymbol{K}_2\ddot{\boldsymbol{e}}_1 + \boldsymbol{K}_3\dddot{\boldsymbol{e}}_1 + \ddddot{\boldsymbol{e}}_1\\
&= \boldsymbol{K}_1\dot{\boldsymbol{e}}_1 + \boldsymbol{K}_2\ddot{\boldsymbol{e}}_1 + \boldsymbol{K}_3\dddot{\boldsymbol{e}}_1 + \boldsymbol{F}_1(t) - \ddddot{\boldsymbol{x}}_{1d}
\end{aligned} \tag{8}$$

The designed control law is

$$\boldsymbol{F}_1(t) = -\boldsymbol{K}_1\dot{\boldsymbol{e}}_1 - \boldsymbol{K}_2\ddot{\boldsymbol{e}}_1 - \boldsymbol{K}_3\dddot{\boldsymbol{e}}_1 + \ddddot{\boldsymbol{x}}_{1d} - \boldsymbol{m}_1\boldsymbol{s}_1 - \boldsymbol{n}_1\mathrm{sign}(\boldsymbol{s}_1) \tag{9}$$

where $\boldsymbol{m}_1 = \mathrm{diag}\{m_1, m_1, m_1\}$, $\boldsymbol{n}_1 = \mathrm{diag}\{n_1, n_1, n_1\}$.

Invoking (8) yields

$$\begin{aligned}\boldsymbol{s}_1^{\mathrm{T}}\dot{\boldsymbol{s}}_1 &= \boldsymbol{s}_1^{\mathrm{T}}(-m_1\boldsymbol{s}_1 - n_1\mathrm{sign}(\boldsymbol{s}_1)) \\ &= -m_1\boldsymbol{s}_1^{\mathrm{T}}\boldsymbol{s}_1 - n_1\boldsymbol{s}_1^{\mathrm{T}}\mathrm{sign}(\boldsymbol{s}_1) \\ &= -m_1(s_{1\phi}^2 + s_{1\theta}^2 + s_{1\psi}^2) - n_1(|s_{1\phi}| + |s_{1\theta}| + |s_{1\psi}|)\end{aligned} \tag{10}$$

For a second-order system which controls $x_5(t)$, defining the tracking error

$$e_2 = x_5 - x_{5d} \tag{11}$$

Create a sliding modal surface that is

$$s_2 = k_4 e_2 + \dot{e}_2 \tag{12}$$

where k_4 is a positive constant.

Differentiating (12) yields

$$\begin{aligned}\dot{s}_2 &= k_4\dot{e}_2 + \ddot{e}_2 \\ &= k_4\dot{e}_2 + F_2(t) - \ddot{x}_{5d}\end{aligned} \tag{13}$$

The designed control law is

$$F_2(t) = -k_4\dot{e}_2 + \ddot{x}_{5d} - m_2 s_2 - n_2\mathrm{sign}(s_2) \tag{14}$$

Invoking (15) and (16) yields

$$\dot{s}_2 = -m_2 s_2 - n_2\mathrm{sign}(s_2) \tag{15}$$

Theorem 1: Think about the helicopters (5). The tracking error has converged under the sliding mode control strategy, and each closed-loop signal is consistently controlled.

Select the Lyapunov function as proof.

$$V = \frac{1}{2}\boldsymbol{s}_1^{\mathrm{T}}\boldsymbol{s}_1 + \frac{1}{2}s_2^2 \tag{16}$$

Considering (10) and (15), the time derivative of V is

$$\begin{aligned}\dot{V} &= \boldsymbol{s}_1^{\mathrm{T}}\dot{\boldsymbol{s}}_1 + s_2\dot{s}_2 \\ &= -m_1(s_{1\phi}^2 + s_{1\theta}^2 + s_{1\psi}^2) - n_1(|s_{1\phi}| + |s_{1\theta}| + |s_{1\psi}|) \\ &\quad - m_2 s_2^2 - n_2|s_2| \\ &< 0\end{aligned} \tag{17}$$

Lemma 1 provides asymptotically stabilization of the function, as demonstrated by (17), so guaranteeing the stability of the systems constructed by this research. The closed-loop signals all came together. The goal of control was achieved.

4 Simulation Study

This section employs data from [19] helicopters that have the following relevant attributes in order to confirm the efficacy of the control system that is presented in this paper:

$$m = 800kg, g = 9m/s^2, C_k = 30mm/N^{\frac{1}{2}}, C_m = 52N/rad,$$

$$\boldsymbol{J} = \mathrm{diag}\{358.4\ 777.9\ 601.4\}kg\cdot m^2,$$

$$L_x = 0mm, L_y = 0mm, L_z = 2100mm, D_k = 4.4N\cdot m,$$

$$H_x = 400mm, H_z = 70mm.$$

The helicopters need to use the controller that this study suggests in order to track the appropriate location and yaw degree. Default tracking signal configuration is as follows:

$$\boldsymbol{P}_d(t) = \begin{bmatrix} 50\cos(0.1t) \\ 0.2t \\ -50\sin(0.1t) \end{bmatrix}, \psi_d(t) = 0.1.$$

The initial values are set as $\boldsymbol{P}(0) = [51\ 1\ 21]^{\mathrm{T}}$ and $\psi(0) = 1.1rad$.

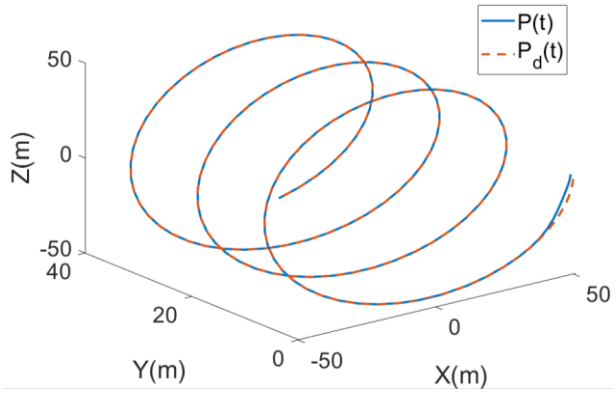

Fig. 2: The position trajectories of helicopter system

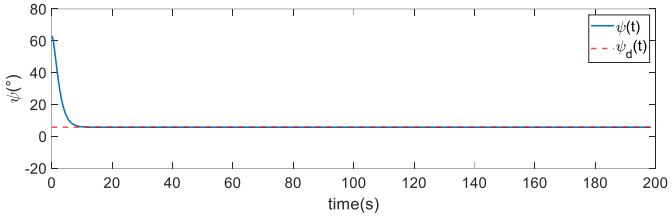

Fig. 3: The tracking error of yaw angle ψ of helicopter systems

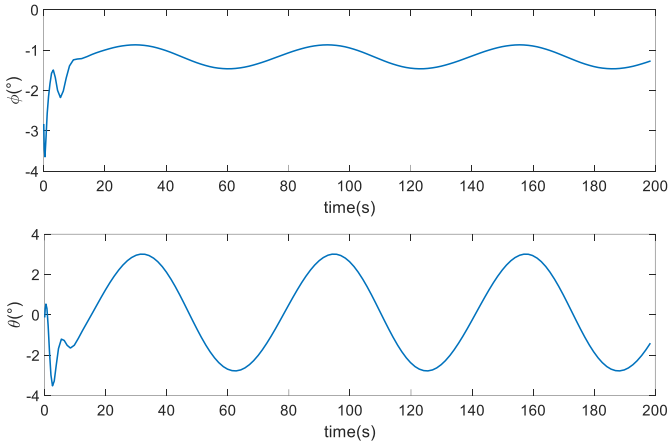

Fig. 4: The helicopter system's roll angle ϕ and pitch angle θ .

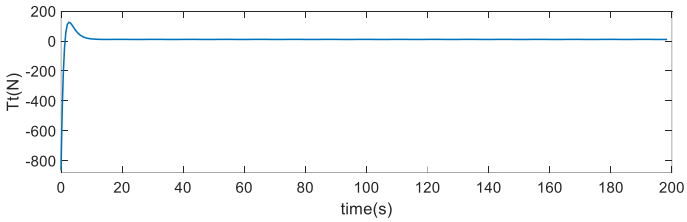

Fig. 5: The helicopter tail rotor's thrust

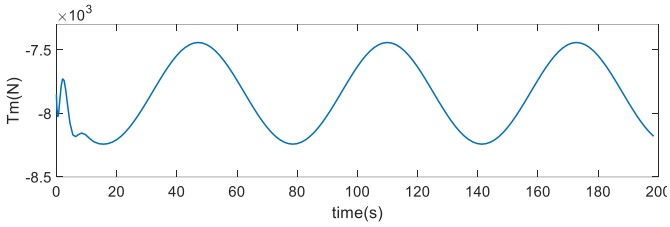

Fig. 6: The main rotor thrust of a helicopter

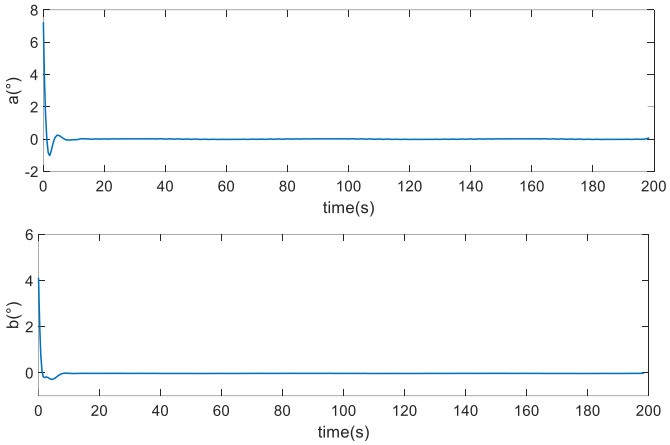

Fig. 7: The main rotor of a helicopter's waving angles

The helicopter's position tracking trajectory is displayed in Fig. 2. After making a small adjustment, the helicopter may swiftly track the intended course under the guidance of the specified flight controller. Fig. 3 shows the desired yaw angle and tracking curve of helicopter, from which it can be seen that the yaw angle of helicopter tracks on the desired value after 8s. Figure 4 shows the helicopter's roll and pitch angles, which varies within $(-5°, 5°)$, indicating that there is no capsizing and overturning caused by excessive roll angle and pitch angle during the flight. The helicopter's control inputs are depicted in Figures 5, 6, and 7, and all simulation values fall within a suitable range. Consequently, the helicopter can be efficiently controlled by the sliding mode controller that this study has designed.

5 Conclusion

This work tackled the flight control problem of the full-degree-of-freedom chopper system. During the flight controller design phase, both the input and the output loop linearity method is applied to reduce the coupling and nonlinearity of the helicopter systems. Next, a nonlinear flight regulator is constructed using the sliding mode control methodology. The reliability of the system is then shown using the Lyapunov technique. Ultimately, simulation confirms that the controller developed in this study is capable of enabling the helicopter to track the intended signal.

References

[1] J. Luo and Z. Wang, A review of development and application of UAV detection and counter technology. *Control and Decision*, 2022, 37(3): 530-544.

[2] Y. Huang and J. Xu, Target localization system of unmanned helicopter. *Journal of Nanjing University of Aeronautics & Astronautics*, 2018, 50(2): 251-257.

[3] S. Pan, T. Wang, H. Zhang and T. Li, Reference model tracking control for unmanned aerial helicopters based on adaptive disturbance observer. *Journal of Nanjing University of Aeronautics & Astronautics*, 2023, 55(6): 977-987.

[4] H. Wang and L. Zhou, Design of a backstepping integral adaptive controller for QUAV. *Acta Armamentarii*, 2021, 42(6): 1283-1289.

[5] Y. Liu, X. Wang, X. Yu, Design and simulation of hovering control law for a helicopter based on LQR. *Computer Measurement & Control*, 2008, 16(5): 670-672.

[6] P. Xue, G. Zeng, F. Yan, J. Zu and Y. Huang, Position control technology of hover and low-speed flight for small unmanned helicopter. *Computer Measurement & Control*, 2012, 20(4): 966-969.

[7] X. Wang, Y. Chen, G. Lu and Y. Zhong, Robust attitude tracking control of small-scale unmanned helicopter. *International Journal of Systems Science*, 2015, 46(8): 1472-1485.

[8] Z. Yao, J. Zu, X. Ye and S. Liu, Design of robust attitude controller for unmanned helicopter carrier take-off and landing. *Machinery & Electronics*, 2023, 41(12): 74-80.

[9] S. Zhang, H. Wu and X. Zheng, Finite-time fault tolerant control of quadrotor UAV with actuator faults. *Control Theory & Applications*, 2023, 40(7): 1270-1276.

[10] S. Shen and J. Xu, Adaptive neural network-based active disturbance rejection flight control of an unmanned helicopter, *Aerospace Science and Technology*, 2021, 119: 107062.

[11] M. Chen, P. Shi and C. -C. Lim, Adaptive neural fault-tolerant control of a 3-DOF model helicopter system. *IEEE Transactions on Systems, Man, and Cybernetics: Systems*, 2016, 46(2): 260-270.

[12] Y. Li, M. Chen, S. S. Ge and D. Li, Anti-disturbance control for attitude and altitude Systems of the Helicopter under Random Disturbances. *Aerospace Science and Technology*, 2019, 96: 105561.

[13] B. Ren, S. S. Ge, C. Chen, C. H. Fua and T. H. Lee, *Modeling, control and coordination of helicopter systems*. New York: Springer, 2012, chapter 2.

[14] Y. Li, Y. Huang, D. Li, Y. Sun, H. Liu and Y. Jin, Flight Tracking Control for Helicopter Attitude and Altitude Systems Using Output Feedback Method under Full State Constraints. *Aerospace*, 2023,10(8): 696.

[15] K. Yan, Q. Wu and M. Chen, Robust adaptive backstepping control for unmanned autonomous helicopter with flapping dynamics. *The 13th IEEE International Conference on Control & Automation*, 2017: 1027-1032.

[16] M. Chen, S. S. Ge and B.B. Ren, Adaptive tracking control of uncertain MIMO nonlinear systems with input constraints. *Automatica*, 2011, 47(3): 452-465.

[17] B. Liu and W. Tang, *Modern control theory*. Beijing: China Machine Press, 2011, chapter 4.

[18] Y. Li, M. Chen, P. Shi and T. Li, Stochastic Anti-Disturbance Flight Control for Helicopter Systems with Switching Disturbances Under Markovian Parameters. *IEEE Transactions on Aerospace and Electronic Systems*, 2023, 59(3): 2933-2946.

[19] K. Yan, Q. Wu and M. Chen, Robust adaptive backstepping control for unmanned autonomous helicopter with flapping dynamics. *The 13th IEEE International Conference on Control & Automation*, 2017: 1027-1032.

Proceedings of the 3rd Conference on Fully Actuated System Theory and Applications
May 10-12, 2024, Shenzhen, China

Attitude Control of Hypersonic Vehicle based on Reinforcement Learning

Jingwen Liu[1], Hongdong Fan [1], Yonghua Fan[2], Guangbin Cai[1]

1. Rocket Force University of Engineering，Xi'an 710025, China
E-mail: liujw5525@163.com

2. Northwestern Polytechnical University, Xi'an 710072, China
E-mail: fyhlixin@163.com

Abstract: In this paper, the attitude control problem of hypersonic vehicle is studied. The DDQN (double deep Q network) algorithm is used to realize the online adaptive adjustment of the control parameters of the PID (proportional-integral-derivative) controller. Firstly, the dynamic model of hypersonic vehicle is established. Then, the implementation process of parameter adjustment using DDQN algorithm is described. By building two neural networks, the main network is used to determine the action to be performed, and the target network is used to determine the action value, so as to realize the adaptive adjustment of the control parameters. Finally, the effectiveness of the proposed method is verified by simulation experiments.

Key Words: hypersonic vehicle, intelligent control, attitude control, DDQN

1 Introduction

Hypersonic vehicle itself has the characteristics of strong coupling, strong nonlinearity and strong uncertainty. Concurrently, the flight environment is subject to various external disturbances. The span of flight altitudes and Mach numbers is extensive, the flight environment is intricate, the aerodynamic characteristics undergo drastic changes, and there are numerous flight constraints[1]. These factors impose higher requirements on the attitude control system of high-speed vehicle. To fulfill the control demands of strong stability and high precision, the design of the flight control methods needs to embody rapid response, accuracy, and robustness. Designing an attitude control method for high-speed vehicle that meets these stringent control requirements remains a focal point of research [2-4].

At present, a multitude of methods have been employed in the domain of hypersonic vehicle attitude control. With advancements in control theory and intelligent technology, novel approaches continue to emerge, including control theories such as backstepping control[5], sliding mode control[6], and performance preset control[7], as well as the integration of disturbance observer, state observer, and combining BP neural network, RBF neural network with control theory[8][9]. Reference[10] introduces a predictive sliding mode control method founded on trajectory linearization and an extended Kalman filter, designed to facilitate rapid tracking control of a hypersonic vehicle's attitude amid parameter random perturbations and nonlinear disturbances. Reference [11] presents a nonsingular fast terminal sliding mode fault-tolerant control approach that considers prescribed performance for addressing the attitude control challenge of hypersonic vehicles affected by model uncertainty, external disturbances, and actuator faults. LU[12] proposes a nonlinear control approach drawing upon the backstepping method. Reference [13] proposes a fuzzy Q-learning algorithm for the parameter tuning of active disturbance rejection control in attitude systems of hypersonic vehicles. Reference [14] designs an intelligent attitude control algorithm by integrating deep reinforcement learning with the dynamic surface control method to address the control challenges of hypersonic vehicles. Reinforcement learning is a control method to obtain the maximum long-term return. It has the characteristics of autonomously exploring the system environment and improving the control performance, and has been widely used in various fields. Moreover, it does not require a model and is suitable for the control problem of hypersonic vehicles[15].

In this paper, the reinforcement learning framework is used to explore the intelligent adjustment strategy of PID controller parameters by using the double deep Q Network (DDQN) algorithm. The goal is to design an adaptive attitude controller for hypersonic vehicle, which can dynamically adjust PID control parameters according to different flight conditions. The organizational structure of this paper is described as follows: In section 2, the motion model of vehicle attitude control is established, which lays a foundation for the design of subsequent controllers. The third section describes the construction of the control system based on DDQN algorithm, and describes the training process of the algorithm. In section 4, simulation studies are carried out to evaluate the effectiveness of the proposed controller. Finally, the thesis is summarized in section 5, which summarizes the main findings and contributions of this study.

2 Hypersonic vehicle model establishment

Without losing generality, the earth is regarded as a sphere with uniform mass, ignoring the influence of the earth's oblateness and tangential gravitational acceleration, and ignoring the influence of the earth's rotation[16]. Based on the above assumptions, the force analysis of the vehicle is carried out in the longitudinal plane, and the force diagram is shown in Figure 1.

* This work is supported by the National Natural Science Foundation of China under Grant 61773387.

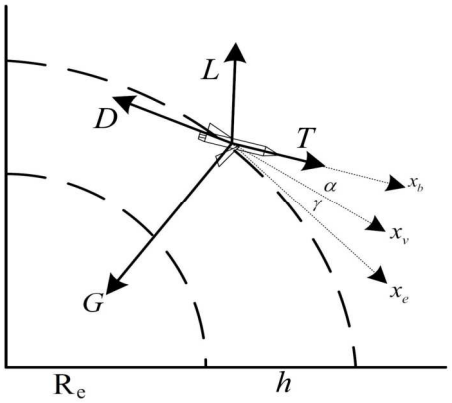

Fig. 1: Hypersonic vehicle force diagram

Based on the above assumptions, the following pitch dynamics model is considered:

$$\begin{cases} \dot{x} = v\cos\theta\left(\dfrac{\mathrm{R_e}}{\mathrm{R_e}+y}\right) \\ \dot{y} = v\sin\theta \\ \dot{z} = -v\cos\theta\left(\dfrac{\mathrm{R_e}}{\mathrm{R_e}+y}\right) \\ \dot{v} = \dfrac{T\cos - D}{m} - g\sin\theta \\ \dot{\theta} = \dfrac{T\sin\alpha + L}{mv} + \cos\left(\dfrac{v}{\mathrm{R_e}+y} - \dfrac{g}{v}\right) \\ \dot{\omega}_z = \dfrac{M_z}{I_z} \\ \dot{\vartheta} = \omega_z \\ \alpha = \vartheta - \theta \\ \dot{m} = -m_c \\ \delta_{e_u} = f(\cdot) \end{cases} \tag{1}$$

Among them, v is the speed of the vehicle, θ is the trajectory angle, α is the angle of attack, ϑ is the pitch angle, ω_z is the pitch angle velocity, x is the flight distance, y is the flight height, m is the mass, m_c is the fuel consumption rate, M_z is the pitching moment, I_z is the pitching moment of inertia, R_e is the radius of the earth, g is the acceleration of gravity, δ_{e_u} is the elevator drive voltage, and the real elevator Angle is δ_e, T is the thrust, D is the resistance, L is the lift, The calculation expression is as follows:

$$\begin{aligned} T &= qSC_T \\ D &= qSC_D \\ L &= qSC_L \\ q &= 0.5\rho v^2 \end{aligned} \tag{2}$$

where C_L, C_D, and C_T are the lift coefficient, drag coefficient and thrust coefficient of the vehicle, respectively. S is the reference area of the vehicle, q is dynamic pressure ; ρ is the atmospheric density; The dynamic equation of elevator steering gear is:

$$\begin{cases} M_z = m_z qSL_c \\ m_z = m_{z_0} + 2m_{z_{\delta_e}} + m_{zz}\dfrac{\omega_z L_c}{2V} \end{cases} \tag{3}$$

In Eq. (3), q is the dynamic pressure, S is the area, L_c is the longitudinal reference length, m_z , $m_{z_{\delta_e}}$, m_{zz} is the function of angle of attack, Mach number and elevator.

Next, the controller design based on reinforcement learning will be carried out based on the above model.

3 Controller Design

Hypersonic vehicles are the epitome of a class of control objects, which are full of considerable uncertainty and significant nonlinearity. The traditional manual tuning method of PID parameters mainly depends on the iterative trial and error method, which depends heavily on the professional knowledge and subjective judgment of the tuning personnel. This method not only takes a long time, but also often fails to achieve the high-precision tracking performance required for hypersonic flight control.

In order to cope with the complex challenges faced by such vehicle control systems, this study introduces a PID parameter tuning framework based on the principle of deep reinforcement learning (DRL). This method can automatically adjust the PID parameters in real time by receiving information related to the current flight state of the hypersonic vehicle. By using DRL, the adjustment strategy transcends the limitations of manual adjustment and is expected to improve the adaptability and accuracy of the control system in rapidly changing and unpredictable hypersonic flight dynamics.

The double deep Q network enhances the standard deep Q network (DQN) by using a dual neural network architecture. This design reduces the overestimation bias inherent in the original DQN, where a single network is responsible for both action selection and value estimation. In DDQN, action selection is performed by a main network, and a separate target network evaluates the selected actions to provide more stable and reliable action value estimation.

DDQN algorithm is a kind of deep reinforcement learning based on value function. Through trial and error, the optimal action value function $Q(s_t, a_t)$ is learned and trained, which is expressed as

$$Q(s_t, a_t) = E\left(R_t + \gamma \cdot Q(S_{t+1}, A_{t+1})\right) \tag{4}$$

In Eq. (4), γ is the discount factor, E is expectation. Solving the optimal action value function is to give the state S_{t+1} in the learning, and select the action A_{t+1} to meet the Q maximization, that is,

$$\begin{cases} A_{t+1} = \arg\max\limits_a Q(S_{t+1}, a) \\ Q(S_{t+1}, A_{t+1}) = \max\limits_a Q(S_{t+1}, a) \end{cases} \tag{5}$$

can be obtained

$$Q(S_{t+1}, A_{t+1}) = E\left[R_t + \gamma \cdot \max_a Q(S_{t+1}, a)\right] \tag{6}$$

The Monte Carlo approximation of the above equation can be obtained

$$E\left[R_t+\gamma\cdot\max_a Q(S_{t+1},a)\right]\approx r_t+\gamma\cdot\max_a Q(S_{t+1},a) \quad (7)$$

Among them, r_t represents the reward received at the current time, and $\gamma\cdot\max_a Q(S_{t+1},a)$ is the TD target. Since the TD target includes both the current real reward and the predicted reward value, the TD target is more accurate than the predicted value Q. Through continuous updating, the Q is close to the TD target, and the iterative process of the Q value is as follows:

$$Q(\mathrm{s}_t,\mathrm{a}_t)\leftarrow Q(\mathrm{s}_t,\mathrm{a}_t)+\tau\left[r_t+\gamma\cdot\max_a Q(S_{t+1},a)-Q(\mathrm{s}_t,\mathrm{a}_t)\right] \quad (8)$$

The target value of DDQN

$$Y_t^{DoubleDQN}=R_{t+1}+\gamma Q\left(S_{t+1},\arg\max_{a'}Q(S_{t+1},a';\theta_t),\theta^-\right) \quad (9)$$

As the iteration progresses, the loss function is the current moment reward minus the reward value that can be obtained by taking action in the existing state. The mean square error of the estimated Q value of the current main network and the Q value of the target network is defined as the loss function.

$$L(\theta_t)=E\left[\frac{1}{2}\left(r_t+\gamma\max_{a'}Q(S_{t+1},a';\theta^-)-Q(S_t,a;\theta_t)\right)^2\right] \quad (10)$$

When the neural network is used to approximate the function, the update of the merit function is actually to update the parameter θ_t in the neural network. The update method is the gradient descent method：

$$\theta_{t+1}=\theta_t+\tau\left[r_t+\gamma\cdot\max_a Q(S_{t+1},a)-Q(\mathrm{s}_t,a)\right]\nabla Q(\mathrm{s}_t,a;\theta_t) \quad (11)$$

The control goal is to design a PID controller for the pitch attitude, so that the pitch angle can track the relevant command signal.

$$\delta_e(k)=k_p e_q(k)+k_i\sum e_q(k)+k_d\frac{e_q(k)-e_q(k-1)}{\Delta t} \quad (12)$$

The DDQN algorithm training agent is shown in the fig.2, and the detailed steps are as follows:

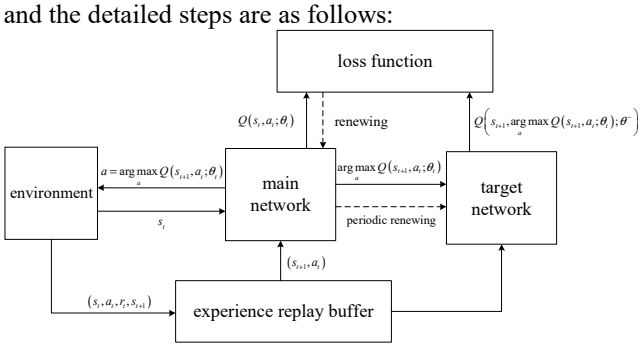

Fig. 2: DDQN network training model

Step 1) Initialize the main network and target network parameters;

Step 2) The attitude control problem is transformed into the state features needed to train the agent;

step 3) Use the current state s_t as the main network input to obtain the corresponding Q value output of the deep Q network for all actions. According to the ' ε-greedy ' strategy, the action a with the largest Q value is selected with a probability of 1-ε;

step 4) Perform an action a under the state s_t, get a new state s_{t+1} and a reward r, and put the experience (s, a, r, s_{t+1}) generated this time into the experience replay buffer;

step 5) Sample m samples from the experience replay buffer, calculate the target Q value and the main network Q value, and use the loss function to update the main network parameters through the gradient back propagation of the neural network;

step 6) Assign the main network parameters to the target network parameters every constant episode;

step 7) Check whether s_{t+1} is the termination state. If yes, determine whether the set number of training is reached, if not, the current episode ends and jumps to step 2, otherwise the algorithm training ends. If not, let $s_t=s_{t+1}$, skip to step 3.

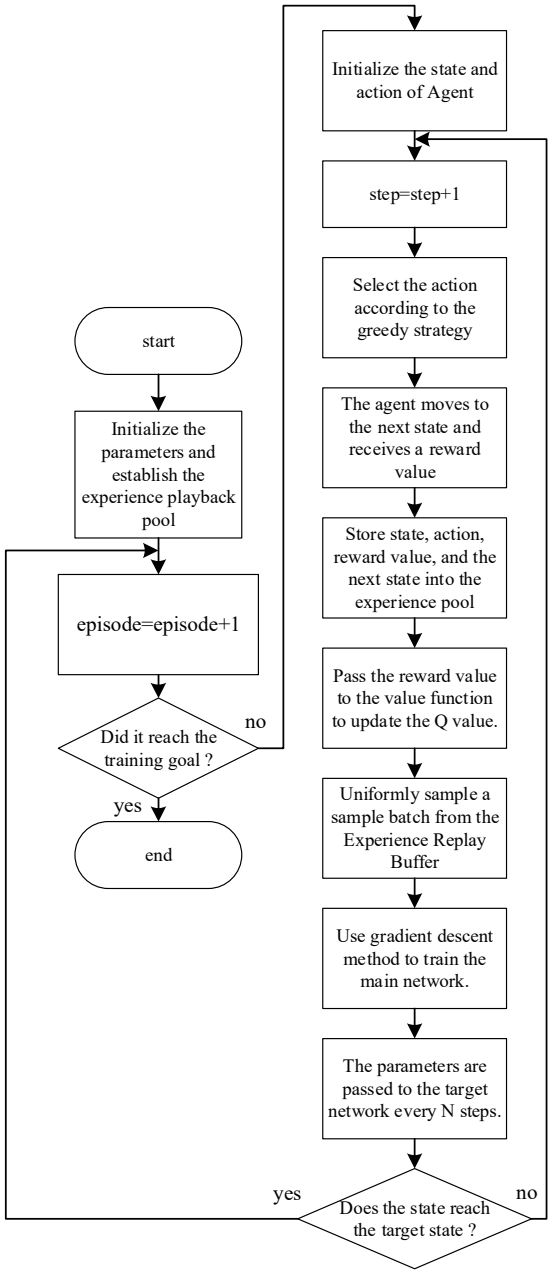

Fig. 3: The flow chart of DDQN algorithm training

4 Simulation and Experiment Results

This section will verify the effectiveness of the proposed algorithm through the simulation of the Winged-Cone model. For simplicity, direct hypothesis. The number of hidden layer nodes of the two neural networks is 20, and the network weight adopts the random distribution number between (0,1). The initial value of the learning step size of the two networks is $l(0) = l_{\text{target}}(0) = 0.04$, and finally gradually reduced to 0.005, forgetting factor $\eta = 0.95$, weight factor $\lambda = 5$ and $\mu = 70$. The parameter settings of the algorithm training are shown in Table 1.

Table 1: DDQN Parameter setting table

parameter	numerical value
forgetting factor	0.95
initial value of learning step size	0.05
final value of the learning step size	0.005
update frequency of the target network	500
size of the experience replay buffer	100000
number of samples taken each time	256
discount factor	0.99
learning rate	0.0001
initial exploration rate	0.99

The output curve of the pitch angle is shown in Fig.4. It shows the tracking of the pitch angle to the given signal, which shows the effectiveness of the algorithm. From the simulation image, it can be seen that the aircraft can achieve stable control of the pitch angle at about 300 steps, and achieve stable tracking of the target signal.

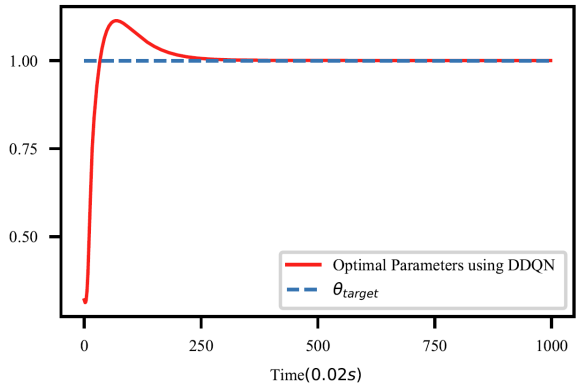

Fig. 4: pitch angle

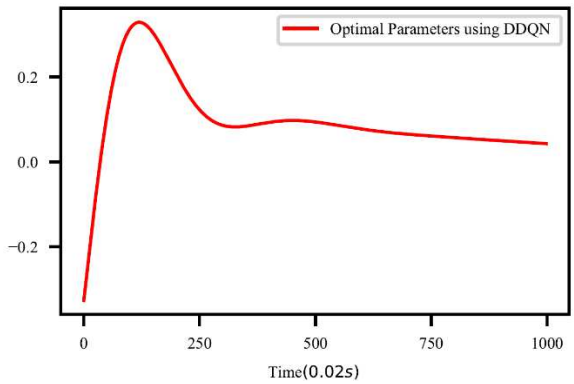

Fig. 5: attack angle

Fig.5 shows the change of angle of attack in the process of signal tracking. As shown in the figure, the state and control quantity of the angle of attack curve are stable.

5 Conclusion

In this paper, the attitude control problem of hypersonic vehicle is addressed and an attitude controller based on deep reinforcement learning is designed. Based on the traditional PID control, the DDQN algorithm is used to realize the autonomous adjustment of the control parameters to adapt to the complex flight environment in the near space, and the control effect that meets the control requirements is achieved. The simulation results show that the proposed control algorithm can make the hypersonic vehicle obtain the ideal control state.

References

[1] Y. Ding, X. Yue, and G. Chen, etc. Review of control and guidance technology on hypersonic vehicle. *Chinese Journal of Aeronautics*. 35(7): 1-18, 2022.

[2] Y. Zhang, X. Huang, and K. Lu, etc. Research progress and prospect of the hypersonic flight vehicle control technology. *Journal of Astronautics*. 43(7): 866-879, 2022.

[3] C. Mu, Y. Zhang, and Y. Yu, etc. An overview on robust control of aviation and aerospace aircraft based on adaptive dynamic programming. *Aerospace Control and Application*. 45(4): 71-79, 2019.

[4] D. Zhao, Z. Hu, and Z. Xia, etc. Full-range adaptive cruise control based on supervised adaptive dynamic programming. *Neurocomputing*. 125: 57-67, 2014.

[5] Y. Meng, B. Jiang, and R. Qi. Adaptive fault-tolerant attitude tracking control of hypersonic vehicle subject to unexpected centroid-shift and state constraints. *Aerospace Science and Technology*. 95, 2019.

[6] X. Yu, P. Li, and Z. Zhang. Fixed time actuator fault accommodation applied to hypersonic gliding vehicles. *IEEE Transactions on Automation Science and Engineering*. 18(3): 1429-1440, 2020.

[7] H. Li, J. Wei, and D. Fang, etc. Prescribed performance control for hypersonic vehicle considering input constraint. *Journal of National University of Defense Technology*. 45(2): 27-36, 2023.

[8] J. Liu, M. Hao, and M. Sun, etc. PID attitude controller tuning for aerodynamic missile based on reinforcement learning. *Tactical missile technology*, 5: 58-63, 2019.

[9] X. Luo, Y. Chen, and J. Si, etc. Longitudinal control of hypersonic vehicles based on direct heuristic dynamic programming using ANFIS. *IEEE International Joint Conference on Neural Networks*. New York: IEEE . 3685-3692, 2014.

[10] Z. Liu, L. Zhou, and R. Zhang. Attitude control of hypersonic vehicle with random parameter perturbations. *Systems Engineering and Electronics.* 1-13, 2023.
[11] Z. Wang, Y. Liao, and C. Wei. Fast terminal sliding mode fault-tolerant control of hypersonic vehicle with guaranteed performance. *Acta Aeronautica et Astronautica Sinica*, 44 (24): 162-175, 2023.
[12] Y. Lu, X. Liu, and K. Lu. An attitude control method for non-affine hypersonic flight vehicles. *Journal of Astronautics*, 42(1): 132-140, 2021.
[13] Q. Gao, X. Li, and Y. Ge, etc. Research on active disturbance rejection control of hypersonic vehicle based on Q-learning. *Control Engineering of China*. 43(7): 1-6, 2024.
[14] B. Xu, C. Zhao, and L. Li, etc. Dynamic surface control method for hypersonic vehicle based on deep reinforcement learning. *Flight control and detection*. 6(1): 15-23, 2023.
[15] H, Hui, G, Cai, and C, Mu, etc. Analytical reentry guidance framework based on swarm intelligence optimization and altitude-energy profile. *Chinese Journal of Aeronautics.* 36(12): 336-348, 2023.
[16] S. Keshmiri, R. Colgren, and M. Mirmirani. Six-DOF modeling and simulation of a generic hypersonic vehicle, for control and navigation purposes. *AIAA guidance, navigation, and control conference and exhibit*. 6694, 2006.

Proceedings of the 3rd Conference on Fully Actuated System Theory and Applications
May 10-12, 2024, Shenzhen, China

Global Stabilization of Circular Orbit Rendezvous by Bounded Linear Feedback

Weiwei Luo[1], Wenbo Fu[1], Song Zhu[1] Chuanchuan Xu[2]

1. School of Mathematics, Jiangsu Center for Applied Mathematics (CUMT), China University of Mining and Technology, Xuzhou, 221116, China.
E-mail: weiweiluo@cumt.edu.cn

2. Nanjing Research Institute of Electronic Engineering, Nanjing, China.

Abstract: The global stabilization problem is revisited for the circular orbit spacecraft rendezvous system with actuator saturation. The linearized relative motion equation transformed into its Luenberger canonical form. It is noted that the system decomposed into a cascade of neutral stable linear systems, and bounded linear state feedback controllers for subsystems are designed respectively based on the absolute stability theory. The global stability of the closed-loop system is proved by providing explicit conditions on the parameters in the feedback gains. Optimal feedback gains are also discussed. Simulation results are given to show the effectiveness of the presented approaches.

Key Words: Bounded linear feedback, Global stabilization, Spacecraft rendezvous

1 Introduction

The completion of spacecraft rendezvous is the necessary prerequisite for many space missions such as repair, preservation, interception, docking, and satellite networking [15]. During the last few decades, the spacecraft rendezvous control problem has been widely discussed and many design methods have been devised, see, [4–6, 23], and the references therein. Assuming the target spacecraft is running on an approximately circular orbit, while another chasing spacecraft is flying near it. The relative motion between the chaser spacecraft and the target spacecraft can be represented by second-order nonlinear differential equations. As a basic tool of the spacecraft rendezvous control systems, C-W equations, which were proposed by Clohessey and Wiltshire in [3], have been widely investigated in the literature. With the development of control theory and practical purpose, numerous useful methods have been proposed to solve the rendezvous control problem. For example, [7] proffers a robust state-feedback controller design method for spacecraft rendezvous, [20] investigates the sampled-data control problem.

Saturation nonlinearity is always unavoidable in every practical control system, because of the boundedness of the output of physical actuators [13, 16, 18, 21]. If the actuator saturation is ignored in controller design, it will significantly reduce control performance and may even lead to instability of the closed-loop system [14]. Control systems subject to actuator saturation has been widely analysis and design in the literature. To mention a few, containment control for double-integrator discrete-time multi-agent systems was investigated with input and velocity constraints in [19]. The global finite-gain stabilization problem for neutrally stable systems by saturated linear feedback was investigated in [10]. There are further results on the related problems, see [16], [17], and references therein.

As a typical practical control system, there is an actuator saturation problem in spacecraft rendezvous control systems, mainly due to the limited acceleration provided by the thrust configured on the chasing spacecraft [25]. Therefore, the boundedness of control signals should be considered in spacecraft rendezvous systems. In the past few years, the stabilization problem of spacecraft rendezvous with thrust saturation has received much attention(see, [2], [6], [8], [9]). The optimal power limitation problem of spacecraft rendezvous systems with thrust constraints was studied in [2]. The bounded, low-thrust, fixed-time, fuel-optimal constrained terminal approach direction rendezvous using the relative linearized equations of motion is investigated in [8]. The fixed time minimum fuel solution is obtained by using a C-W linearized kinetic model and the optimal finite time solution is by minimizing the problem involving both fuel consumption and final time [9]. Recently, Zhou et al. proposed saturated linear feedback controllers based on the Lyapunov equation for circular orbit spacecraft rendezvous[13, 22, 23, 25]. Based on absolute stability theory, a class of saturated linear state feedback controller was proposed to stabilize globally the C-W equations [25].

Motivated by the existing results on this topic, we consider the global stabilization problem for the circular orbit spacecraft rendezvous system with actuator saturation. The linearized relative motion equations can be transformed to a set of coupled single-input subsystems that are neutral stable by Luenberger canonical form.

This work was supported in part by the National Natural Science Foundation of China under grant number 62303466, and by the PhD Program of Mass Entrepreneurship and Innovation Talents of Jiangsu Province under grant numbers JSSCBS20211216.

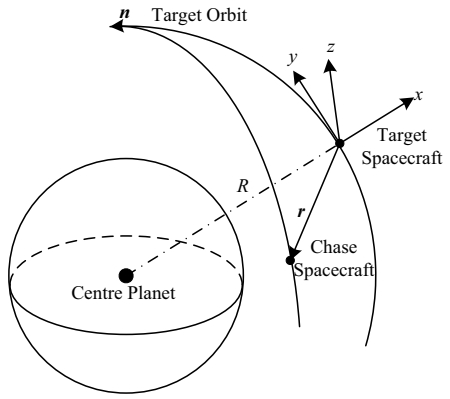

Fig. 1: Circular orbit and coordinate system

Bounded linear state feedback controllers for subsystems are designed respectively by utilizing Lyapunov functions that contain positive (semi)definite quadratic term and integral terms. The global stability of the closed-loop system is proved by providing explicit conditions on the parameters in the feedback gains. The determination of the optimal gain parameters are also obtained. Numerical simulations show the effectiveness of the proposed approaches.

The remainder of this paper is organized as follows. In Section 2, the model of the spacecraft circular orbit rendezvous control system is introduced. The main results regarding global stabilization of the relative motion are proposed in Section 3. A numerical simulation is given to demonstrate the effectiveness of the proposed control law in Section 4. Finally, Section 5 concludes the paper.

2 Equation of Relative Motion

Assume that the target spacecraft is in a circular orbit whose radius is R (see in fig. 1). Let the right-handed coordinate system (rotating coordinate system) (x, y, z) be fixed at the center of mass of the target, where the x-axis is along the radial direction, the y-axis is along the flight direction of the target, and the z-axis is out of the orbit plane, respectively. Denote the gravitational parameter $\mu = GM$ where M is the mass of the center planet and G is the gravitational constant. Then the orbit rate of the target orbit is given by $n = \mu^{1/2}/R^{3/2}$. The relative motion model between the target and chaser can be described by Newton's equations [1]

$$\begin{cases} \ddot{x}(t) = 2n\dot{y}(t) + n^2(R + x(t)) - \varphi\mu(R + x(t)) \\ \qquad\quad + \sigma_{\delta_1}(a_x(t)), \\ \ddot{y}(t) = -2n\dot{x}(t) + n^2 y(t) - \varphi\mu y(t) + \sigma_{\delta_2}(a_y(t)), \\ \ddot{z}(t) = -\varphi\mu z(t) + \sigma_{\delta_3}(a_z(t)), \end{cases} \tag{1}$$

where $\varphi = ((R + x(t))^2 + y^2(t) + z^2(t))^{-\frac{3}{2}}$, and

$$a(t) = \left[\begin{array}{ccc} a_x(t) & a_y(t) & a_z(t) \end{array}\right]^{\mathrm{T}}, \tag{2}$$

is the acceleration vector due to thrust forces on the chaser, in which δ_1, δ_2 and δ_3 are three given nonnegative scalars representing the saturation levels on the thrust, namely, δ_1, δ_2 and δ_3 are respectively the maximal accelerations that the thrusts can generate in the three directions. Here $\sigma_\delta(\cdot) : \mathbf{R} \to [-\delta, \delta]$ defined as

$$\sigma_\delta(x) = \begin{cases} x, & |x| \le \delta, \\ \delta \mathrm{sign}(x), & |x| > \delta, \end{cases}$$

is the saturation function and $\sigma_1(x)$ will be denoted by $\sigma(x)$ for short. The linearized equation of (1) is given by

$$\begin{cases} \ddot{x}(t) = 2n\dot{y}(t) + 3n^2 x(t) + \sigma_{\delta_1}(a_x(t)), \\ \ddot{y}(t) = -2n\dot{x}(t) + \sigma_{\delta_2}(a_y(t)), \\ \ddot{z}(t) = -n^2 z(t) + \sigma_{\delta_3}(a_z(t)), \end{cases} \tag{3}$$

which is known as the Hill's equation or Clohessy-Wiltshire equation [3] when $a = 0$.

The whole rendezvous process can be described by the transformation of state vectors $\phi = [x, y, z, \dot{x}, \dot{y}, \dot{z}]^{\mathrm{T}}$ from nonzero initial states $\phi(t_0)$ to the terminal state $\phi(t_f) = 0$, where t_f is the rendezvous time (settling time). In this paper, saturated linear feedback laws will be established to achieve the rendezvous mission in the presence of actuator saturation.

3 Global Stabilization of Spacecraft Rendezvous

In this section we only consider the global stabilizing controllers design for the in-plane motion.

By choosing the state vector X and control vector u as

$$\begin{aligned} X &= \left[\begin{array}{cccc} x & y & \dot{x} & \dot{y} \end{array}\right]^{\mathrm{T}}, \\ u &= \left[\begin{array}{cc} \frac{1}{\delta_1}a_x & \frac{1}{\delta_2}a_y \end{array}\right]^{\mathrm{T}}, \end{aligned} \tag{4}$$

the in-plane motion involving the variables $x(t)$ and $y(t)$ in the C-W equation (3) can be expressed as

$$\dot{X} = AX + B\sigma(u), \tag{5}$$

where A and B are constant matrices given by

$$\begin{aligned} A &= \left[\begin{array}{cccc} 0 & 0 & 1 & 0 \\ 0 & 0 & 0 & 1 \\ 3n^2 & 0 & 0 & 2n \\ 0 & 0 & -2n & 0 \end{array}\right], \\ B &= \left[\begin{array}{cc} 0 & 0 \\ 0 & 0 \\ \delta_1 & 0 \\ 0 & \delta_2 \end{array}\right] = \left[\begin{array}{cc} b_1 & b_2 \end{array}\right]. \end{aligned} \tag{6}$$

Here the identity $\sigma_\delta(a) = \delta\sigma\left(\frac{a}{\delta}\right)$ has been used.

It is well known that a linear system could be stabilized globally by bounded controls if and only if the

system is asymptotically null controllable with bounded controls (ANCBC), namely, it is stabilizable in the ordinary sense and all the eigenvalues of A are on the closed-left half plane [17]. It is noted that

$$\det\left[\begin{array}{cccc} b_2 & Ab_2 & A^2b_2 & A^3b_2 \end{array}\right] = 12\delta^4 n^4 \quad (7)$$

which is nonzero, namely, (A, b_2) is controllable. On the other hand, we can compute

$$\lambda(A) = \{0, 0, \pm n\mathrm{i}\},$$

which implies that all the eigenvalues of A are on the imaginary axis. Hence (A, B) (actually, (A, b_2)) is ANCBC. Therefore, there is a globally stabilizing controller for system (5).

Existing results show that a linear global stabilizing controller can be designed if A is neutral stable, namely, all the eigenvalues of A are simple. However, this is not satisfied for system (5) since A possesses a zero eigenvalue with multiplicity two. In fact, the Jordan form J_A of A is given by

$$J_A = \left[\begin{array}{cccc} 0 & 1 & & \\ & 0 & & \\ & & n\mathrm{i} & \\ & & & -n\mathrm{i} \end{array}\right].$$

As a result, global stabilizing linear bounded controller can not be proposed by using positive definite solutions to Lyapunov equations associated with the open-loop system [12, 24]. Then, the system (5) can be transformed into its Luenberger canonical form [11]. We choose the nonsingular matrix

$$L = \begin{bmatrix} 0 & \delta_1 & 0 & 0 \\ 0 & 0 & -2n\delta_1 & 0 \\ \delta_1 & 0 & -n^2\delta_1 & 0 \\ 0 & -2n\delta_1 & 0 & \delta_2 \end{bmatrix}, \quad (8)$$

and consider the transformation

$$Y = [y_1, y_2]^{\mathrm{T}} = L^{-1}X,$$

where $y_1 \in \mathbf{R}^3$ and $y_2 \in \mathbf{R}$. As a result, we obtain

$$\dot{Y} = \begin{bmatrix} A_1 & A_{12} \\ 0_{1\times 3} & A_2 \end{bmatrix} Y + \begin{bmatrix} d_1 & 0 \\ 0 & d_2 \end{bmatrix} \sigma(u), \quad (9)$$

where the coefficient matrices $A_1 \in \mathbf{R}^{3\times 3}, A_2, A_{12}, d_2$ and $d_1 \in \mathbf{R}^{3\times 1}$ are given by

$$\begin{bmatrix} A_1 & A_{12} \\ 0_{1\times 3} & A_2 \end{bmatrix} = \begin{bmatrix} 0 & 0 & 0 & \frac{3n\delta_2}{2\delta_1} \\ 1 & 0 & -n^2 & 0 \\ 0 & 1 & 0 & -\frac{\delta_2}{2n\delta_1} \\ 0 & 0 & 0 & 0 \end{bmatrix},$$

$$\begin{bmatrix} d_1 & 0 \\ 0 & d_2 \end{bmatrix} = \begin{bmatrix} 1 & 0 \\ 0 & 0 \\ 0 & 0 \\ 0 & 1 \end{bmatrix}.$$

It is easy to see that $\lambda(A_1) = \{0, \pm ni\}$. Hence A_1 is neutral stable (or stable in the Lyapunov sense). The linear state feedback controllers for the A_2 subsystem and A_1 subsystem can be proposed respectively by using positive definite solutions to Lyapunov equations associated with the open-loop system [13].

Different from [13], we will propose global stabilizing controllers for the A_2 subsystem and A_1 subsystem based on the absolute stability theory. Then we have the following result.

Theorem 1 *The linear system (5) with input saturation can be globally stabilized by the linear state feedback*

$$u = FX,$$
$$F = \begin{bmatrix} f_{11} & \frac{n^2k_1}{2\delta_1} & -\frac{n(k_1+k_3)}{\delta_1} & f_{14} \\ -\frac{2n}{\delta_2}k_4 & 0 & 0 & -\frac{k_4}{\delta_2} \end{bmatrix}, \quad (10)$$

in which $k_i, i = 1, 3, 4 > 0, k_2 \geq 0$ and

$$f_{11} = -\frac{n^2\left(3k_1 + 3k_1k_4^2 + k_2k_4^3 + 4k_3k_4^2 - 3k_2k_4\right)}{k_4\left(k_4^2+1\right)\delta_1},$$
$$f_{14} = -\frac{n\left(4k_2k_4 - 3k_1k_4^2 - 4k_3k_4^2 - 3k_1\right)}{2k_4\left(k_4^2+1\right)\delta_1}.$$

Moreover, the linearized closed-loop system possesses the eigenvalue set

$$\Gamma = \{-nk_4\} \cup \lambda\left(n\begin{bmatrix} -k_1 & -k_2 & -k_3 \\ 0 & 0 & 1 \\ -k_1 & -k_2-1 & -k_3 \end{bmatrix}\right). \quad (11)$$

In the following, the determination of the gain parameters $k_i, i = 1, 2, 3, 4$ will be discussed. Since the closed-loop system consisting of (5) and (10) will operate in linear region after finite time, one may want to find a suitable F to the following min–max problem:

$$J_0 = \min_{k_j, j\in\{1,2,3,4\}} \max_{i=1,2,3,4} \mathrm{Re}\{\lambda_i(A + BF)\}.$$

We can see from (11) that the above min–max optimization problem is independent of n. Denote the matrix A_k as

$$A_k = \begin{bmatrix} -k_1 & -k_2 & -k_3 \\ 0 & 0 & 1 \\ -k_1 & -1-k_2 & -k_3 \end{bmatrix}, \quad (12)$$

whose characteristic equation is given by

$$|\lambda I_3 - A_k| = \lambda^3 + (k_1+k_3)\lambda^2 + (1+k_2)\lambda + k_1. \quad (13)$$

It follows that the zeros of $|\lambda I_3 - A_k| = 0$ cannot arbitrarily assigned by choosing k_1, k_2 and k_3. To find the optimal $k_i, i = 1, 2, 3$ such that the maximal real part of the zeros of $|\lambda I_3 - A_k| = 0$ is minimized, we have the following result.

Theorem 2 *Let A_k be given by (12). The optimal solution k_* satisfies $k_* \in K^*$ with*

$$K^* = \Big\{ k : k_1 = a_*^3 > 0, k_2 = 3a_*^2 - 1 \geq 0, \\ k_3 = 3a_* - a_*^3 > 0 \Big\}, \tag{14}$$

where $a_* > 0$. Then

$$\min_{k_j, j\in\{1,3\}} \max_{i=1,2,3} \mathrm{Re}\left\{\lambda_i\left(A_k\right)\right\} = -a_*. \tag{15}$$

4 Simulation

Simulation will be carried out on the nonlinear model (1). Assume that $\delta_1 = \delta_2 = 8 \times 10^{-3}\mathrm{m/s}^2$ and $\delta_3 = 6 \times 10^{-3}\mathrm{m/s}^2$. Hence $\eta = 1$. Assume also that the target spacecraft is in a circular orbit with the Earth as the centre planet and the orbital height is $500\mathrm{km}$. Hence, the radius of the target orbit is $R = 6.8781 \times 10^6\mathrm{m}$ and the gravitational parameter is $\mu = 3.9860 \times 10^{14}\mathrm{m}^3/\mathrm{s}^2$. For simulation purpose, the initial conditions are chosen as

$$\begin{bmatrix} x & y & z & \dot{x} & \dot{y} & \dot{z} \end{bmatrix} \\ = \begin{bmatrix} 8000 & 10000 & -15000 & 4 & -8 & 5 \end{bmatrix}. \tag{16}$$

For the out-of-plane motion, we use the controller (42) in [25] where $f_1 = f_2 = 5$ which is such that $\lambda\left(\Phi_0 + \Psi_0 H_0\right) = \{-2, -3\}$. For the in-plane motion, the system decomposition cased controller (10) where $k_1 = 1$, $k_2 = 2$, $k_3 = 2$(i.e. $a_* = 1$ in (15)) and $k_4 = 1$. The state trajectories and control signals of the closed-loop system are leads to respectively recorded in Figs. 2 and 3. It follows that the closed-loop systems are asymptotically stable with these parameters, say, the rendezvous mission is accomplished.

5 Conclusion

This paper revisited the global stabilization problem for the circular orbit spacecraft rendezvous system with actuator saturation. The linearized relative motion equation could be decomposed into a cascade of neutral stable linear systems, bounded linear state feedback controllers for subsystems were designed by using the absolute stability theory. The global stability of the closed-loop system was proved, and optimal linear feedback gains were also obtained.

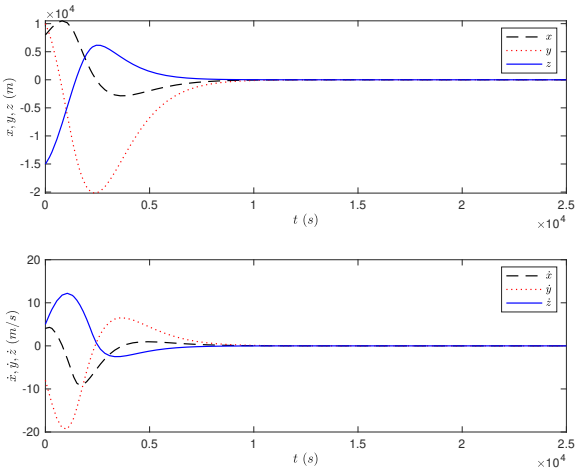

Fig. 2: State response of system (1) by saturated linear feedback (10) and (42) in [25].

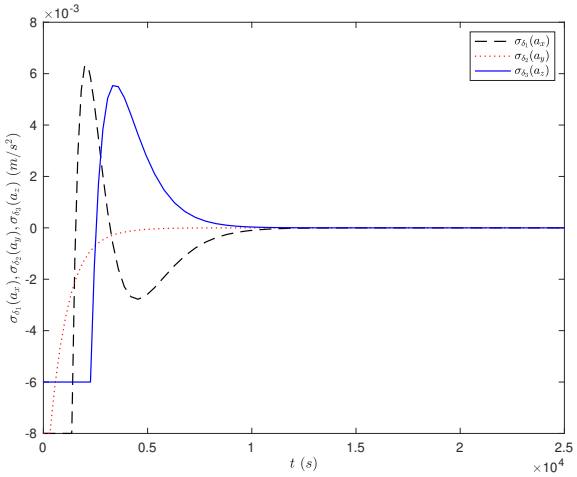

Fig. 3: Control signals for system (1) by saturated linear feedback (10) and (42) in [25].

References

[1] T. E. Carter, State transition matrices for terminal rendezvous studies: Brief survey and new example, *Journal of Guidance, Control, and Dynamics*, Vol. 21, No. 1, pp. 148-155, 1998.

[2] T. E. Carter and C. J. Pardis, Optimal power-limited rendezvous with upper and lower bounds on thrust. *Journal of Guidance, Control, and Dynamics*, Vol. 19, No. 5, pp. 1124-1133, 1996.

[3] W. H. Clohessy and R. S. Wiltshire, Terminal guidance system for satellite rendezvous, *Journal of the Aeronautical Sciences*, Vol. 27, No. 9, pp. 653-658, 1960.

[4] H. Cai and J. Huang, Leader-following adaptive consensus of multiple uncertain rigid spacecraft systems, *SCIENCE CHINA Information Sciences*, Vol. 59, 010201:1-010201:13, 2016.

[5] L. Cao, and X. Chen, Minimum sliding mode error feedback control for inner-formation satellite system with J_2 and small eccentricity, *SCIENCE CHINA Information Sciences*, Vol. 59, 072203:1-072203:18, 2016.

[6] T. N. Edelbaum, Optimum low-thrust rendezvous and station keeping, *AIAA Journal*, Vol. 2, No. 7, pp. 1196-1201, 1964.

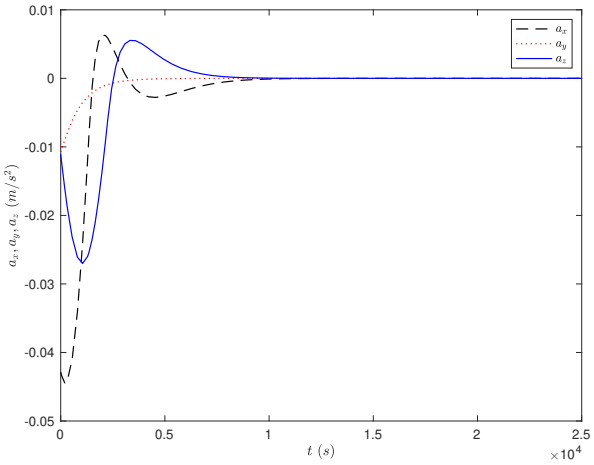

Fig. 4: Control signals for system (1) by the unbounded controller.

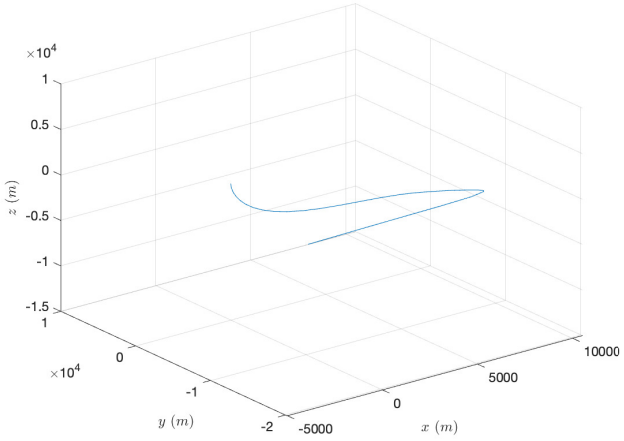

Fig. 5: Spatial relative position in the rendezvous process with input saturations.

[7] H. Gao, X. Yang and P. Shi, Multi-objective robust H_∞ control of spacecraft rendezvous, *IEEE Transactions on Control Systems Technology*, Vol. 17, No. 4, pp. 794-802, 2009.

[8] M. Guelman and M. Aleshin, Optimal bounded low-thrust rendezvous with fixed terminal-approach direction, *Journal of Guidance, Control, and Dynamics,* Vol. 24, No. 2, pp. 378-385, 2001.

[9] C. A. Lembeck and J. E. Prussing, Optimal impulsive intercept with low-thrust rendezvous return, *Journal of Guidance, Control, and Dynamics*, Vol. 16, No. 3, pp. 426-433, 1993.

[10] W. Liu, Y. Chitour, and E. Sontag, On finite-gain stabilizability of linear systems subject to input saturation, *SIAM Journal on Control and Optimization*, Vol. 34, No. 4, pp. 1190–1219, 1996.

[11] D. G. Luenberger, Canonical forms for linear multivariable systems, *IEEE Transactions on Automatic Control*, Vol. 12, No. 3, pp. 290-293, 1967.

[12] W. Luo and B. Zhou, Magnetic attitude control of bias momentum spacecraft by bounded linear feedback, *Aerospace Science and Technology*, Vol. 70, pp. 419-427, 2017.

[13] W. Luo, B. Zhou, L. He and G.-R. Duan, Global stabilization of the spacecraft rendezvous system by delayed and bounded linear feedback. *IEEE Transactions on Systems, Man, and Cybernetics: Systems*, Vol. 52, No.3, pp. 1373-1384, 2022.

[14] S. Mitani and H. Yamakawa, Satisficing nonlinear rendezvous approach under control magnitude and direction constraints, *Journal of Guidance, Control, and Dynamics*, Vol. 37, No. 2, pp. 497-512, 2014.

[15] M. E. Polites, Technology of automated rendezvous and capture in space, *Journal of Spacecraft and Rockets*, Vol. 36, No. 2, pp. 280-291, 1999.

[16] A. Saberi, Anton A. Stoorvogel, and P. Sannuti, *Internal and External Stabilization of Linear Systems with Constraints*, Birkhauser, 2012.

[17] G. J. Sussmann, E. D. Sontag and Y. Yang, A general result on the stabilization of linear systems using bounded controls, *IEEE Transactions on Automatic Control,* Vol. 39, No. 12, pp. 2411-2425, 1994.

[18] B. Xiao, Q. Hu and P. Shi, Attitude stabilization of spacecrafts under actuator saturation and partial loss of control effectiveness, *IEEE Transactions on Control Systems Technology*, Vol. 21, No. 6, pp. 2251-2263, 2013.

[19] J. Xu, P. Lin, L. Cheng, H. Dong, Containment control with input and velocity constraints, *Automatica*, Vol. 142, 110417, 2022.

[20] X. Yang, X. Cao, and H. Gao, Sampled-data control for relative position holding of spacecraft rendezvous with thrust nonlinearity, *IEEE Transactions on Industrial Electronics*, Vol. 59, No. 2, pp. 1146-1153, 2012.

[21] B. Zhang, Y. Jia, J. Du and J. Zhang, Finite-time synchronous control for multiple manipulators with sensor saturations and a constant reference, *IEEE Transactions on Control Systems Technology*, Vol. 22, No. 3, pp. 1159-1165, 2014.

[22] B. Zhou, Q. Wang, Z. Lin and G. Duan, Gain scheduled control of linear systems subject to actuator saturation with application to spacecraft rendezvous, *IEEE Transactions on Control Systems Technology*, Vol. 22, No. 5, pp. 2031-2038, 2014.

[23] B. Zhou and Z. Y. Li, Truncated predictor feedback for periodic linear systems with input delays with applications to the elliptical spacecraft rendezvous, *IEEE Transactions on Control Systems Technology*, Vol. 23, No. 6, pp. 2238-2250, 2015.

[24] B. Zhou, Global stabilization of periodic linear systems by bounded controls with applications to spacecraft magnetic attitude control, *Automatica*, Vol. 60, pp. 145-154, 2015.

[25] B. Zhou and J. Lam, Global stabilization of linearized spacecraft rendezvous system by saturated linear feedback, *IEEE Transactions on Control Systems Technology*, Vol. 26, No. 6, pp. 2185-2193, 2017.

Proceedings of the 3rd Conference on Fully Actuated System Theory and Applications
May 10-12, 2024, Shenzhen, China

Fault-tolerant attitude tracking control of combined spacecraft with actuator saturation based on fully-actuated system approach

Xiuwei Huang[1], Peng Yang[1], Zhen Liu[1,2], Li An[1], Hao Wang[1]
1. Ji Hua Laboratory, Foshan 528000, P. R. China
E-mail: huangxiuwei_hit@163.com
2. Key Labratory of Modern Acoustics, MOE, Nanjing University, Nanjing 210023, P. R. China

Abstract: In this article, the attitude tracking control problem of combined spacecraft actuated by three reaction wheels under actuator fault, actuator saturation, and external disturbance is investigated. Based on the fully-actuated system approach, a new fault-tolerant attitude tracking scheme is developed by incorporating the Nussbaum gain technique, time-delay estimation (TDE) method, and adaptive method. Firstly, the attitude tracking kinematic and dynamic equation with actuator fault and actuator saturation is transformed into a fully-actuated system model, where a smooth function is used to approximate the actuator torque. After estimating the lumped uncertainty which contains actuator fault, inertia uncertainty, and external disturbance by a TDE method, a new control scheme is designed, where Nussbaum gain is introduced to address the time-varying actuator gain arising from actuator saturation, an adaptive law is adopted to suppress the estimation error. Furthermore, the convergence of the attitude tracking error and angular velocity tracking error is strictly proven by Lyapunov method. Simulation results demonstrate the effectiveness of the proposed control method.

Key Words: Fully-actuated system approach, Attitude tracking control, Combined spacecraft, Actuator fault, Actuator saturation, Time-delay estimation method

1 Introduction

With the increasing abundance of space missions, such as the construction of space station, space debris removal operations and on-orbit servicing (OOS) missions, combined spacecrafts which are constructed after an active spacecraft capturing another space target exist widely[1]. The inertia properties of the combined spacecraft are hard to obtain accurately for the large change of the configuration after capture. Besides, the control ability of the combined spacecraft will be strictly limited because no maneuver ability exists in the noncooperative target. Thus, the attitude takeover control of the combined spacecraft is an urgent and tough problem.

Despite the above difficulties, many scholars have made some achievements in this field. In [2], Jiang et al. proposed an approximated iteration method for the combined spacecraft with noncooperative target such that a prescribed convergence rate was guaranteed. Huang et al. [3] proposed a dynamic surface method incorporating a robust dynamic control allocation strategy for attitude control of a combined chaser-target system. Under measurement uncertainties, a novel practical prescribed time attitude control method for post-capture combined spacecraft for attitude and angular velocity was developed in [4]. Without model information, data-driven model-free adaptive control (MFAC) strategies were developed for attitude stabilization of a combined spacecraft in [5] and [6]. However, a nonlinear closed-loop system will be obtained by the above methods, which do not provide much convenience for the control problem. Recently, fully actuated system (FAS) approach has been developed by Duan [7], by which a controller can be immediately designed to make the closed-loop system a constant linear one with a desired eigenvalue. The FAS approach has obtain fully developed and been applied into many fields, such as spacecraft attitude control [8], manipulator systems [9], flexible servo systems [10] and etc.

As one important application of the FAS approach, spacecraft control has gain much attentions [11], [12], [13], [14], [15], [16], [17], [18]. Among these works, the attitude or orbit control problems of the spacecraft with inertia uncertainty, external disturbance or input saturation were considered and the lumped uncertainties was estimated by extended state observer (ESO). Particularly, for the combined spacecraft, Duan and Cui [19], [20], [21] investigated the attitude tracking control problem based on fully-actuated system approach with prescribed performance or adaptive disturbance observer. However, the spacecraft system control performance will be seriously affected by actuator faults which has not been considered in the existing FAS approach based spacecraft control work. To simply and effectively address the actuator fault problem and other uncertainties, the time-delay estimation (TDE) algorithm [22] is adapted in this paper. Compared with ESO, TDE has less turning parameters and calculation burden. And to reduce the estimation error, an adaptive law is contained in the controller to achieve better performance. To reduce the effect of the actuator saturation, a smooth function is used to approximate the saturated actuator. Besides, inspired by [15], a Nussbum-type function is contained in the control scheme to tackle the nonlinearity arising from actuator saturation.

In this paper, a FAS approach-based attitude tracking control problem of combined spacecraft with actuator fault and actuator saturation is investigated. The main contributions of this article are stated as follows:

1) The attitude tracking problem of the combined spacecraft with actuator faults and actuator saturation is firstly ad-

This work is supported in part by the National Nature Science Foundation of China under Grant 62103164 and Grant 62273245, Fundamental Research Funds for the Central Universities (grants No. 020414380195), and Guang Dong Basic and Applied Basic Research Foundation (No.2023A1515011537).

dressed based on fully-actuated system approach, which is a direct linearization method.

2) A time-delay estimation method is adapted to estimate the lumped disturbance with less adjusted parameters and an adaptive law is combined to eliminate the estimation error where more precisely estimated result can be obtained.

3) A smooth function is used to appropriate the saturated actuator and a Nussbum-type function is contained in the controller to effectively address the nonlinear term come from actuator, which achieves a high performance in the system.

The structure of this paper is stated as follows. Section 2 gives the problem formulation, including attitude tracking kinematics and dynamics of the combined spacecraft with actuator faults, actuator saturation and control objects. The control scheme with time-delay estimation, Nussbum-type function and adaptive law is developed in Section 3. Section 4 demonstrates the effectiveness of the control scheme. Section 5 concludes.

2 Problem Formulation

2.1 Attitude tracking kinematics and dynamics of the combined spacecraft

This paper investigates a combined spacecraft comprised of a rigid service spacecraft, a rigid space manuscript and a rigid target spacecraft, where three reaction wheels are mounted on the service spacecraft. Based on the analysis in [23], the kinematic and dynamic equation of the combined spacecraft is stated as:

$$\begin{cases} \dot{\sigma} = G(\sigma)\omega \\ J\dot{\omega} = -\omega^{\times}(J\omega + C_\omega J_\omega \Omega_\omega) - C_\omega J_\omega \tau + u_g + d \end{cases} \tag{1}$$

where $\sigma = [\sigma_1, \sigma_2, \sigma_3]^{\mathrm{T}}$ is Modified Rodrigues Parameters (MRPs) vector, $\omega = [\omega_1, \omega_2, \omega_3]^{\mathrm{T}}$ is the angular velocity, $\omega^{\times}$ represents its skew-symmetric matrix, in which

$$\omega^{\times} = \begin{bmatrix} 0 & -\omega_3 & \omega_2 \\ \omega_3 & 0 & -\omega_1 \\ -\omega_2 & \omega_1 & 0 \end{bmatrix}$$

And $J \in \mathbb{R}^{3\times3}$ is the inertia matrix of the combined spacecraft, $J_\omega \in \mathbb{R}^{3\times3}$ is the inertia matrix of the whole reaction wheels, $C_\omega \in \mathbb{R}^{3\times3}$ is the reaction wheel's configuration matrix expressed in the body frame of the combined spacecraft, $\Omega_\omega \in \mathbb{R}^3$ is the angular velocity of reaction wheels, $\tau = \dot{\Omega}_\omega \in \mathbb{R}^3$ is the control torque, $u_g \in \mathbb{R}^3$ denotes the gravity gradient torque and is expressed as

$$u_g = 3\omega_0^2 R_3^{\times}(\sigma) J R_3(\sigma)$$

with the orbit velocity ω_0 and $R_3(\sigma)$ is denoted as

$$R_3(\sigma) = \begin{bmatrix} \frac{8\sigma_3\sigma_1 - 4\sigma_2(1-\sigma^{\mathrm{T}}\sigma)}{1+\sigma^{\mathrm{T}}\sigma} \\ \frac{8\sigma_3\sigma_2 + 4\sigma_1(1-\sigma^{\mathrm{T}}\sigma)}{1+\sigma^{\mathrm{T}}\sigma} \\ \frac{4(\sigma_3^2 - \sigma_2^2 - \sigma_1^2) + (1-\sigma^{\mathrm{T}}\sigma)^2}{1+\sigma^{\mathrm{T}}\sigma} \end{bmatrix}$$

and $G(\sigma)$ is denoted as $G(\sigma) = \frac{(1-\sigma^{\mathrm{T}}\sigma)I_3}{4} + \frac{\sigma^{\times}}{2} + \frac{\sigma\sigma^{\mathrm{T}}}{2}$ and $d \in \mathbb{R}^3$ denotes the external disturbance.

Denote the desired attitude and angular velocity as σ_d and ω_d, then the attitude and angular velocity tracking error is defined as

$$\begin{cases} \sigma_e = \frac{\sigma_d(\sigma^{\mathrm{T}}\sigma - 1) + \sigma(1 - \sigma_d^{\mathrm{T}}\sigma_d) - 2\sigma_d^{\times}\sigma}{1 + \sigma^{\mathrm{T}}\sigma\sigma_d^{\mathrm{T}}\sigma_d + 2\sigma_d^{\mathrm{T}}\sigma} \\ \omega_e = \omega - R(\sigma_e)\omega_d \end{cases}$$

with the rotation matrix $R(\sigma_e)$ denotes as

$$R(\sigma_e) = I_3 - \frac{4\sigma_e^{\times}(1 - \sigma_e^{\mathrm{T}}\sigma_e)}{(1 + \sigma_e^{\mathrm{T}}\sigma_e)^2} + \frac{8(\sigma_e^{\times})^2}{(1 + \sigma_e^{\mathrm{T}}\sigma_e)^2}$$

Then, the kinematics and dynamics of the combined spacecraft's attitude tracking system is expressed as

$$\begin{cases} \dot{\sigma}_e = G(\sigma_e)\omega_e \\ J\dot{\omega}_e = -\omega^{\times}(J\omega + C_\omega J_\omega \Omega_\omega) + J\omega_e^{\times} R(\sigma_e)\omega_d \\ \qquad -JR(\sigma_e)\dot{\omega}_d - C_\omega J_\omega \tau + u_g + d \end{cases} \tag{2}$$

Due to the configuration of the combined spacecraft has changed after capturing the target, it is hard to estimate the inertia property of the combined spacecraft precisely. Thus, there exists a certain deviation between the actual inertia matrix and the estimated one. The actual inertia matrix J can be denoted as

$$J = J_0 + \Delta J \tag{3}$$

where J_0 is the nominal inertia matrix and ΔJ denotes the diviation between J and J_0. With equation (3), the error system (2) can be represented as

$$\begin{cases} \dot{\sigma}_e = G(\sigma_e)\omega_e \\ \dot{\omega}_e = -J_0^{-1}\omega^{\times}(J_0\omega + C_\omega J_\omega \Omega_\omega) + \omega_e^{\times} R(\sigma_e)\omega_d \\ \qquad -R(\sigma_e)\dot{\omega}_d - J_0^{-1} C_\omega J_\omega \tau + J_0^{-1} u_{g0} + d_1 \end{cases} \tag{4}$$

where

$$u_{g0} = 3\omega_0^2 R_3^{\times}(\sigma) J_0 R_3(\sigma)$$

$$d_1 = -\Delta J_n \omega^{\times}(J\omega + C_\omega J_\omega \Omega_\omega) - J_0^{-1}\omega^{\times}\Delta J\omega - \Delta J_n C_\omega J_\omega \tau + \Delta J_n u_g + 3\omega_0^2 J_0^{-1} R_3^{\times}(\sigma)\Delta J R_3(\sigma) + J^{-1} d$$

with

$$\Delta J_n = J^{-1} - J_0^{-1}$$

2.2 Actuator faults

According to the analysis in [23] and [24], a fault or failure may occur in several components of the reaction wheels. The actual control torque generated by the reaction wheels can be written as:

$$\tau = \tau_c + B(t, T_{fault})(\Lambda(t) - I_3)\tau_c + \bar{\tau}_c \tag{5}$$

where τ_c is the input torque vector of the actuators, $\Lambda(t) = \mathrm{diag}\{\Lambda_1, \Lambda_2, \Lambda_3\}$ denotes the effectiveness matrix of the reaction wheels and $\Lambda_i \in (0, 1]$, $\bar{\tau}_c \in \mathbb{R}^3$, $B(t, T_{fault}) = \mathrm{diag}\{b_{1,T_1}, b_{2,T_2}, b_{3,T_3}\}$ denotes the time schedule when the ith wheel fault occurs, i.e.,

$$b_{i,T_i} = \begin{cases} 1 - e^{-a_i(t-T_i)} & \text{if } t \geq T_i \\ 0 & \text{if } t < T_i \end{cases}$$

with $a_i > 0 (i = 1, 2, 3)$ and $T_i \geq 0 (i = 1, 2, 3)$. Then, based on the actuator fault model (5), the attitude tracking system (4) can be represented as

$$\begin{cases} \dot{\sigma}_e = G(\sigma_e)\omega_e \\ \dot{\omega}_e = -J_0^{-1}\omega^{\times}(J_0\omega + C_\omega J_\omega \Omega_\omega) + \omega_e^{\times} R(\sigma_e)\omega_d \\ \qquad -R(\sigma_e)\dot{\omega}_d - J_0^{-1} C_\omega J_\omega \tau_c + J_0^{-1} u_{g0} + d_2 \end{cases} \tag{6}$$

with

$$d_2 = d_1 - J_0^{-1} C_\omega J_\omega (B(t, T_{fault})(\Lambda(t) - I_3)\tau_c + \bar{\tau}_c)$$

2.3 Actuator saturation

Due to the physical limitation, the constraints on the actuators should also be taken into account. The saturation on the actuator $\tau_c(u) = [\tau_{c1}(u_1), \tau_{c2}(u_2), \tau_{c3}(u_3)]^{\mathrm{T}}$ can be expressed as

$$\tau_{ci}(u_i) = \begin{cases} \tau_{\max,i}, & u_i > \tau_{\max,i} \\ u_i, & \tau_{\min,i} \le \tau_{ci} \le \tau_{\max,i} \\ \tau_{\min,i}, & u_i < \tau_{\min,i} \end{cases}, i = 1,2,3 \quad (7)$$

Then according to the analysis in [22], a smooth function is introduced to approximate the actuator and then the actuator $\tau_c(u)$ can be expressed as

$$\tau_c(u) = \Pi(u, \vartheta) + \Delta\tau_c \quad (8)$$

where $\Pi(u, \vartheta) = [\Pi_1(u_1, \vartheta_1), \Pi_2(u_2, \vartheta_2), \Pi_3(u_3, \vartheta_3)]^{\mathrm{T}}$ with

$$\Pi_i(u_i, \vartheta_i) = \begin{cases} \vartheta_i\tau_{\max,i} + \bar{\tau}_{\max,i}, & u_i > \vartheta_i\tau_{\max,i} \\ u_i, & \vartheta_i\tau_{\min,i} \le u_i \le \vartheta_i\tau_{\max,i} \\ \vartheta_i\tau_{\min,i} + \bar{\tau}_{\min,i}, & u_i < \vartheta_i\tau_{\min,i} \end{cases}$$

and

$$\bar{\tau}_{\max,i} = (1-\vartheta_i)\tau_{\max,i}\tanh\left(\frac{u_i - \vartheta_i\tau_{\max,i}}{(1-\vartheta_i)\tau_{\max,i}}\right)$$

for $i = 1,2,3$. It shoud be noted that the discrepancy $\Delta\tau_c$ will vanish when the actuator $\tau_c(u)$ does not exceed the value interval $[\vartheta \odot \tau_{\min}, \vartheta \odot \tau_{\max}]$ and be effectively reduced by increasing ϑ when the actuator $\tau_c(u)$ exceeds the above interval. Thus, there exists a positive constant D_τ satisfying $\|\Delta\tau_c\| \le D_\tau$. Now define $\Phi = \mathrm{diag}(\phi_1, \phi_2, \phi_3)$ with $\phi_i = \Pi_i(u_i, \vartheta_i)/u_i$ where $\phi_i = 1$ when $u_i = 0 (i = 1,2,3)$, then ϕ_i satisfies $\phi_i \in (0, 1]$. Thus, the actuator (8) can be rewritten as

$$\tau_c(u) = \Phi u + \Delta\tau_c \quad (9)$$

2.4 Control object

Now, both consider the actuator fault (5) and actuator saturation (8), the attitude tracking error system of the combined spacecraft (4) can be given as

$$\begin{cases} \dot{\sigma}_e = G(\sigma_e)\omega_e \\ \dot{\omega}_e = F - J_0^{-1}C_\omega J_\omega \Phi u + d_3 \end{cases} \quad (10)$$

with $d_3 = -J_0^{-1}C_\omega J_\omega \Delta\tau_c + d_2$ and

$$F = -J_0^{-1}\omega^{\times}(J_0\omega + C_\omega J_\omega \Omega_\omega) + \omega_e^{\times}R(\sigma_e)\omega_d - R(\sigma_e)\dot{\omega}_d + J_0^{-1}u_{g0}$$

By some simple derivations, the error system (10) can be further written as

$$M\ddot{\sigma}_e + C\dot{\sigma}_e + g = B\Phi u + D \quad (11)$$

where

$$\begin{aligned} M &= G^{-\mathrm{T}}J_0G, \\ C &= -M\dot{G}G^{-1} + G^{-\mathrm{T}}(G^{-1}\dot{\sigma}_e)^{\times}J_0G^{-1} \\ g &= G^{-\mathrm{T}}\omega^{\times}C_\omega J_\omega\Omega_\omega - G^{-\mathrm{T}}J_0\omega_e^{\times}R(\sigma_e)\omega_d \\ &\quad + G^{-\mathrm{T}}J_0R(\sigma_e)\dot{\omega}_d - G^{-\mathrm{T}}u_{g0} \\ B &= -G^{-\mathrm{T}}C_\omega J_\omega \\ D &= G^{-\mathrm{T}}J_0d_3 \end{aligned}$$

And it is easy to obtain that $\det(M) > 0$ and $\det(B\Phi) \neq 0$ for any σ_e and $\dot{\sigma}_e$.

The object of this paper is stated as follows: for the attitude tracking system of the combined spacecraft (11) with actuator fault, actuator saturation and external disturbance, the goal is to develope a control scheme such that the error MRPs σ_e and the angular velocity error ω_e converge to a small region abound equilibrium.

2.5 Preliminary definitions and lemmas

In order to facilitate the design of fully-actuated fault-tolerant control law under actuator saturation, the following definitions and lemmas are introduced.

Definition 1 *[25]For a continuously differentiable function $h(\chi) : [0,\infty) \mapsto (-\infty,\infty)$ is called a Nussbaum function if the following equalities holds:*

$$\limsup_{T\to\infty}\frac{1}{T}\int_0^{\mathrm{T}} h(\chi)d\chi = \infty$$
$$\liminf_{T\to\infty}\frac{1}{T}\int_0^{\mathrm{T}} h(\chi)d\chi = -\infty$$

In this article, $h(\chi)$ is selected as

$$h(\chi) = 1 + e^{\chi^2/2}(\chi^2 + 2)\sin(\chi)$$

Lemma 2 *[26]Let $V(t)$ and $\chi_i(t) (i = 1,2,\cdots,N)$ be smooth functions defined on $[0, t_f)$ with $V(t) \ge 0$ and $\chi_i(0) = 0$. Also, let $h(\chi)$ be Nussbaum function. Then if the following inequality holds:*

$$V(t) \le c_0 + e^{-c_1 t}\sum_{i=1}^{N}\int_0^t (-g_i(\iota)N(\chi_i(\iota)) + 1)\dot{\chi}_i(\iota)e^{c_1\iota}d\iota \quad (12)$$

where c_0 is a bounded constant, $c_1 > 0$, $g_i(t)$ is a time-varying parameter that takes value in the unknown set $I : [g^-, g^+]$ with $0 \notin I$ and all $g_i(t) (i = 1,2,\cdots,n)$ have the same sign, then $V(t), \chi_i(t)$ and $\sum_{i=1}^{N}\int_0^t g_i(\iota)N(\chi_i(\iota))\dot{\chi}_i(\iota)d\iota$ are bounded on $[0, t_f)$.

Lemma 3 *[27]For $h, V : [0,\infty) \mapsto \mathbb{R}$ and $t_0 \in (0, t)$, the following result can be conducted:*

$$V(t) \le e^{-\alpha(t-t_0)}V(t_0) + \int_0^t e^{-\alpha(t-\tau)}h(\tau)d\tau \quad (13)$$

if $\dot{V} \le -\alpha V + \tau$ with $\alpha > 0$ is satisfied.

Lemma 4 *[28]Consider the following second-order fully-actuated system:*

$$A_2(x,\dot{x})\ddot{x} + A_1(x,\dot{x})\dot{x} + A_0(x,\dot{x})x + \xi(x,\dot{x}) = B(x,\dot{x})u \quad (14)$$

where $x \in \mathbb{R}^n$ is the state vector, $u \in \mathbb{R}^n$ is the controller, $\det A_2(x,\dot{x}) \neq 0$ and $\det B(x,\dot{x}) \neq 0$, the dimensions of the other vectors and matrices match the above equality, by designing the following controller

$$u = u_c + u_f$$

where

$$\begin{aligned} u_c &= B^{-1}(x,\dot{x})\xi(x,\dot{x}) \\ u_f &= K_0(x,\dot{x})x + K_1(x,\dot{x})\dot{x} \end{aligned}$$

with

$$[K_0(x,\dot{x}), K_1(x,\dot{x})] = B^{-1}(x,\dot{x})WV^{-1}$$

and

$$V = \begin{bmatrix} Z \\ ZF \end{bmatrix}$$
$$W = A_2(x,\dot{x})ZF^2 + A_1(x,\dot{x})ZF + A_0(x,\dot{x})Z$$

and F and Z satisfy

$$F \in F = \{F | F \in \mathbb{R}^{2n\times 2n},\ and\ \exists Z \in \mathbb{R}^{n\times 2n}\ s.t.\ \det\begin{bmatrix} Z \\ ZF \end{bmatrix} \neq 0\}$$

and

$$\det\begin{bmatrix} Z \\ ZF \end{bmatrix} \neq 0$$

the system (14) can be turned into the following constant linear system

$$\dot{X} = VFV^{-1}X$$

where $X = [x, \dot{x}]^{\mathrm{T}}$. *Furthermore, the second-order fully-actuated system (14) is globally stable if and only if F is a Hurwitz matrix.*

3 Main result

In this section, for the attitude tracking system with actuator saturation and actuator fault (11), based on the recently developed fully-actuated system approach, a new controller will be designed, where the lumped disturbance is compensated by time-delay estimation (TDE) method and the actuator saturation effect is tackled by Nussbaum function. Besides, two new adaptive laws are added in the control scheme, where one is used to generate the Nussbaum function, and the other one is used to suppress the compensation error including the TDE error and improve the system robustness.

In order to estimate the lumped uncertainty D in system (11) accurately and efficiently, TDE method is used. Based on the analysis about TDE method in [22], the lumped uncertainty $D(t)$ is estimated as

$$\begin{aligned}\hat{D} = D(t-T_s) &= M\ddot{\sigma}_e(t-T_s) + C\dot{\sigma}_e(t-T_s) \\ &+ g(t-T_s) - B\Phi(t-T_s)u(t-T_s)\end{aligned} \tag{15}$$

where T_s is the sampling time period. Now define $\epsilon = D(t) - \hat{D}$ as the estimation error, then according to the analysis in [29] and [30], $\hat{D}$ can effectively estimate the $D(t)$ when sampling time period T_s is sufficiently small and the following result holds.

Lemma 5 *[29],[30],[22]There exists a positive constant* $\bar{\epsilon}$ *such that the following inequality holds*

$$\|\epsilon\| \leq \bar{\epsilon}$$

For the system (11), to achieve the tracking object, define $X = [\sigma_e^{\mathrm{T}}, \dot{\sigma}_e^{\mathrm{T}}]^{\mathrm{T}} \in \mathbb{R}^6$ and the controller is designed as

$$u = h_N(\chi)U_s \tag{16}$$

with

$$U_s = u_1 + u_2 + u_3 \tag{17}$$

where u_1 is the fully-actuated system approach-based controller, u_2 is used to compente the lumped disturbance and u_3 is used to suppress the estimation error:

$$\begin{aligned} u_1 &= B^{-1}g + KX, \\ u_2 &= B^{-1}\hat{D} \\ u_3 &= -\hat{\epsilon}B^{-1}N^*\|N\|\,\mathrm{sgn}(X)\end{aligned}$$

with

$$\begin{aligned} K &= B^{-1}WV^{-1}, \\ W &= MZF^2 + CZF, \\ V &= [Z^{\mathrm{T}}, (ZF)^{\mathrm{T}}]^{\mathrm{T}},\end{aligned}$$

and

$$\begin{aligned} N &= P\begin{bmatrix} 0_{3\times 3} \\ M^{-1} \end{bmatrix} \in \mathbb{R}^{6\times 3} \\ N^* &= N^{\mathrm{T}}(NN^{\mathrm{T}})^{-1} \in \mathbb{R}^{3\times 6} \\ \|N\| &= \sqrt{\left\|NN^{\mathrm{T}}\right\|} \in \mathbb{R}\end{aligned}$$

and $h_N(\chi) = \mathrm{diag}(h_1(\chi_1), h_2(\chi_2), h_3(\chi_3))$ with $h_i(\chi_i)(i = 1,2,3)$ being Nussbaum function. And $\chi = [\chi_1, \chi_2, \chi_3]^{\mathrm{T}}$ is defined by the following adaptive law:

$$\dot{\chi} = -\alpha\mathrm{diag}(s)U_s, \chi(0) = 0 \tag{18}$$

where $\alpha > 0$ and $\mathrm{diag}(s) = \mathrm{diag}(s_1, s_2, s_3)$ with

$$s = [s_1, s_2, s_2] = X^{\mathrm{T}}NB$$

where P is a positive matrix defined later. Besides, $\hat{\epsilon}$ is used to estimate the upper bound $\bar{\epsilon}$ and defined by the following law:

$$\dot{\hat{\epsilon}} = \Gamma(\|N\|\,\|X\| - \delta\hat{\epsilon}) \tag{19}$$

where $\Gamma, \delta > 0$.

The main result of this paper is conducted in the following theorem.

Theorem 6 *Consider the combined spacecraft attitude tracking control system (11) with actuator fault (5) and actuator saturation (8), the proposed controller (16) with the TDE (15), the updating law (18) and the adaptive law (19) can ensure the attitude error* σ_e *and the angular velocity error* ω_e *converge to a small region around the equilibrium if the controller parameters* $\alpha, \Gamma, \delta > 0$ *and there exists a positive definite matrix* $P > 0$ *such that*

$$PA + A^{\mathrm{T}}P < 0 \tag{20}$$

where $A = VFV^{-1}$.

Proof 7 *Construct the following Lyapunov function for the attitude tracking system (11)*

$$V = \frac{1}{2}X^{\mathrm{T}}PX + \frac{1}{2\Gamma}\tilde{\epsilon}^2$$

where Γ *is a positive constant,* $P > 0$ *is a positive definite matrix and* $\tilde{\epsilon} = \bar{\epsilon} - \hat{\epsilon}$. *Now, taking the time derivative of V, it*

can be obtained that

$$\begin{aligned}\dot{V} &= X^{\mathrm{T}}P\dot{X} + \frac{1}{\Gamma}\tilde{\epsilon}\dot{\tilde{\epsilon}} \\ &= X^{\mathrm{T}}P\begin{bmatrix} \dot{\sigma}_e \\ -M^{-1}C\dot{\sigma}_e - M^{-1}g + M^{-1}BU_s \end{bmatrix} \\ &+ X^{\mathrm{T}}P\begin{bmatrix} 0_{3\times3} \\ M^{-1}D \end{bmatrix} + X^{\mathrm{T}}P\begin{bmatrix} 0_{3\times3} \\ M^{-1}B \end{bmatrix}(\Phi u - U_s) \\ &- \frac{1}{\Gamma}\tilde{\epsilon}\dot{\hat{\epsilon}} \end{aligned} \tag{21}$$

Then, substitute (17) into (21), based on Lemma 4 and the adaptive law (19), we have

$$\begin{aligned}\dot{V} &= X^{\mathrm{T}}P\begin{bmatrix} \dot{\sigma}_e \\ -M^{-1}C\dot{\sigma}_e - M^{-1}g + M^{-1}Bu_1 \end{bmatrix} \\ &+ X^{\mathrm{T}}P\begin{bmatrix} 0_{3\times3} \\ M^{-1}Bu_2 \end{bmatrix} + X^{\mathrm{T}}P\begin{bmatrix} 0_{3\times3} \\ M^{-1}Bu_3 \end{bmatrix} \\ &+ X^{\mathrm{T}}P\begin{bmatrix} 0_{3\times3} \\ M^{-1}D \end{bmatrix} + X^{\mathrm{T}}P\begin{bmatrix} 0_{3\times3} \\ M^{-1}B \end{bmatrix}(\Phi u - U_s) \\ &- \frac{1}{\Gamma}\tilde{\epsilon}\dot{\hat{\epsilon}} \\ &= X^{\mathrm{T}}PAX + X^{\mathrm{T}}N\epsilon - \hat{\epsilon}X^{\mathrm{T}}NN^{*}\,\|N\|\,sgn(X) \\ &+ s(\Phi h_N(\chi)U_s - U_s) - \tilde{\epsilon}(\|N\|\,\|X\| - \delta)\hat{\epsilon} \\ &= \frac{1}{2}X^{\mathrm{T}}(PA + A^{\mathrm{T}}P)X + s(\Phi h_N(\chi)U_s - U_s) \\ &+ \|X\|\,\|N\|\,(\|\epsilon\| - \bar{\epsilon}) + \delta\tilde{\epsilon}\hat{\epsilon} \end{aligned} \tag{22}$$

with $A = VFV^{-1}$, then based on Lemma 5, $\|\epsilon\| - \bar{\epsilon} \le 0$ is satisfied, then the above inequality (22) can be written as

$$\dot{V} \le \frac{1}{2}X^{\mathrm{T}}(PA + A^{\mathrm{T}}P)X + s(\Phi h_N(\chi)U_s - U_s) + \delta\tilde{\epsilon}\hat{\epsilon} \tag{23}$$

Considering the updating law (18), we have

$$\begin{aligned} & s(\Phi h_N(\chi)U_s - U_s) \\ &= s(\Phi h_N(\chi) - I_3)U_s \\ &= -\frac{1}{\alpha}s(\Phi h_N(\chi) - I_3)(dig(s))^{-1}\dot{\chi} \\ &= -\frac{1}{\alpha}\sum_{i=1}^{3}(\phi_i h_i(\chi) - 1)\dot{\chi}_i \end{aligned} \tag{24}$$

And for the term $\delta\tilde{\epsilon}\hat{\epsilon}$, with the help of Yong's inequality, we have

$$\delta\tilde{\epsilon}\hat{\epsilon} = \delta\tilde{\epsilon}(\bar{\epsilon} - \tilde{\epsilon}) = -\delta\tilde{\epsilon}^2 + \delta\tilde{\epsilon}\bar{\epsilon} \le -\frac{\delta\tilde{\epsilon}^2}{2} + \frac{\delta\bar{\epsilon}^2}{2} \tag{25}$$

Then combined (24) and (25), (23) can be written as

$$\begin{aligned}\dot{V} &\le \frac{1}{2}X^{\mathrm{T}}(PA + A^{\mathrm{T}}P)X - \frac{1}{\alpha}\sum_{i=1}^{3}(\phi_i h_i(\chi) - 1)\dot{\chi}_i - \frac{\delta\tilde{\epsilon}^2}{2} + \frac{\delta\bar{\epsilon}^2}{2} \\ &\le -\beta_1\frac{1}{2}X^{\mathrm{T}}PX - \delta\Gamma\frac{1}{2\Gamma}\tilde{\epsilon}^2 - \frac{1}{\alpha}\sum_{i=1}^{3}(\phi_i h_i(\chi) - 1)\dot{\chi}_i + \frac{\delta\bar{\epsilon}^2}{2} \end{aligned} \tag{26}$$

where

$$\begin{aligned}\beta_1 &= -\max\lambda(A + P^{-1}A^{\mathrm{T}}P), \\ \beta_2 &= \frac{\delta\bar{\epsilon}^2}{2}, \end{aligned}$$

For equation (20) is satisfied,

$$A + P^{-1}A^{\mathrm{T}}P < 0$$

is satisfied. Then, it can be conducted that $\beta_1 > 0$. Now define $\beta_* = \min\{\beta_1, \delta\Gamma\}$, then (26) can be written as

$$\dot{V} \le -\beta_* V + \beta_2 - \frac{1}{\alpha}\sum_{i=1}^{3}(\phi_i h_i(\chi) - 1)\dot{\chi}_i$$

Based on Lemma 3, the inequality (26) can deduce

$$\begin{aligned}V(t) &\le e^{-\beta_* t}V(0) + \int_0^t e^{-\beta_*(t-\tau)}\left(\beta_2 - \frac{1}{\alpha}\sum_{i=1}^{3}(\phi_i h_i(\chi) - 1)\dot{\chi}_i\right)d\tau \\ &= e^{-\beta_* t}V(0) + \frac{\beta_2}{\beta_*}(1 - e^{-\beta_* t}) \\ &- e^{\beta_* t}\sum_{i=1}^{3}\int_0^t \frac{1}{\alpha}(\phi_i h_i(\chi) - 1)\dot{\chi}_i e^{\beta_*\tau}d\tau \end{aligned} \tag{27}$$

Because $e^{-\beta_* t}V(0) + \frac{\beta_2}{\beta_*}(1 - e^{-\beta_* t})$ are bounded on $[0, t_f)$ and $\phi_i \in (0, 1]$ is bounded, according to Lemma 2, we can obtain that $V(t), \chi_i(t)$ and $\sum_{i=1}^{N}\int_0^t g_i(\iota)N(\chi_i(\iota))\dot{\chi}_i(\iota)d\iota$ are bounded on $[0, t_f)$. Denote $V_{\max}$ as the upper bound of $V(t)$,then it can be deduced that

$$\begin{aligned}\|X\| &\le \sqrt{\frac{2V_{\max}}{\lambda_{\min}(P)}} \\ \|\tilde{\epsilon}\| &\le \sqrt{2V_{\max}\Gamma} \end{aligned}$$

According to the proof analysis in Theorem 1 of reference [23], $2 \le \left\|G^{-1}(\sigma_e)\right\| \le 4$, then based on (10), it can be obtained that

$$\begin{aligned}\|\omega_e\| &= \left\|G^{-1}(\sigma_e)\dot{\sigma}_e\right\| \le \left\|G^{-1}(\sigma_e)\right\|\|\dot{\sigma}_e\| \\ &\le \left\|G^{-1}(\sigma_e)\right\|\|X\| \le 4\|X\| \end{aligned}$$

Therefore, σ_e and $\dot{\sigma}_e$ will ultimately converge to the residual set

$$\Omega_1 = \left\{X = [\sigma_e^{\mathrm{T}}, \dot{\sigma}_e^{\mathrm{T}}]^{\mathrm{T}} | \,\|X\| \le \sqrt{\frac{2V_{\max}}{\lambda_{\min}(P)}}\right\}$$

the angular velocity error ω_e will ultimately converge to the residual set

$$\Omega_2 = \left\{\omega_e | \,\|\omega_e\| \le 4\sqrt{\frac{2V_{\max}}{\lambda_{\min}(P)}}\right\}$$

and the estimation error of the upper bound $\tilde{\epsilon}$ will ultimately converge to a residual set

$$\Omega_3 = \left\{\tilde{\epsilon} | \,\|\tilde{\epsilon}\| \le \sqrt{2V_{\max}\Gamma}\right\}$$

4 Simulation Result

In this section, a combined spacecraft described in [23] is used to demonstrate the effectiveness of the proposed control scheme. The simulation time is set as 50 seconds and the sampling time is set as 0.01. The inertia matrix of the combined spacecraft is set $J = \mathrm{diag}\{12, 14, 18\}$ kg·m^2, the inertia matrix of the whole reaction wheels is

$J_\omega = \text{diag}\{0.338, 0.338, 0.338\}\text{kg}\cdot\text{m}^2$, the orbit velocity $\omega_0 = 7.292115 \times 10^{-5}$, the configuration matrix is set as

$$C_\omega = \begin{bmatrix} 0.9992 & -0.0300 & -0.0256 \\ -0.0394 & 0.7455 & 0.6653 \\ 0.0009 & -0.6658 & 0.7461 \end{bmatrix}$$

and the actuator control torque $\tau_c(u)$ is bounded by $\tau_{\max,i} = 35$ rad/s^2 and $\tau_{\min,i} = -35$ rad/s^2. The faults acted on the actuator are set as $\Lambda(t) = \text{diag}\{0.8, 0.8, 1\}$, $\bar{\tau}_c = [0.5, 0, -0.5]$, and these faults occur at time $T_1 = 5$, $T_2 = 10$, $T_3 = 5$ and the fault evolution rate $a_i = 1 (i = 1, 2, 3)$. The external disturbance is $d(t) = 10^{-3} \times [5\cos(0.02t), -5\cos(0.025t), 6\cos(0.04t)]^T$. The initial attitude and angular velocity is set as $\sigma(0) = [0.323, -0.194, -0.388]^T$ and $\omega(0) = [-0.01, 0.02, -0.03]^T$, the desired attitude and angular velocity is set as $\sigma_d(0) = [0.217, -0.109, -0.163]^T$ and $\omega_d(0) = [-0.02\cos(t/100), -0.01\sin(t/100), -0.03\cos(t/100)]^T$ rad/s. To achieve the attitude tracking goal, the parameters of the controller is set as $Z = [I_3, I_3]$, $F = \text{diag}\{-2, -2, -2, -1.5, -1.5, -1.5\}$ and P is selected as

$$P = \begin{bmatrix} 3.877 & 0 & 0 & 0.5596 & 0 & 0 \\ 0 & 3.877 & 0 & 0 & 0.5596 & 0 \\ 0 & 0 & 3.877 & 0 & 0 & 0.5596 \\ 0.5596 & 0 & 0 & 0.6395 & 0 & 0 \\ 0 & 0.5596 & 0 & 0 & 0.6395 & 0 \\ 0 & 0 & 0.5596 & 0 & 0 & 0.6395 \end{bmatrix}$$

which satisfies inequality (20). And other parameters are set as $\alpha = 0.001, \Gamma = 1$ and $\delta = 1$.

The trajectories of attitude tracking error $\sigma_e(t)$, angular velocity error $\omega_e(t)$, and actuator torque τ are shown in Fig. 1-3 respectively. From Fig. 1 and 2, it can be seen that both all the state errors are convergent to a small neighborhood of zero and thus the stability of the closed-loop system is guaranteed. And the amplitude of the control torque are constrained in the saturation from Fig. 3. The trajectory of adaptive parameter state are shown in Fig. 4, it can be seen that each element of χ is convergent to a constant value.

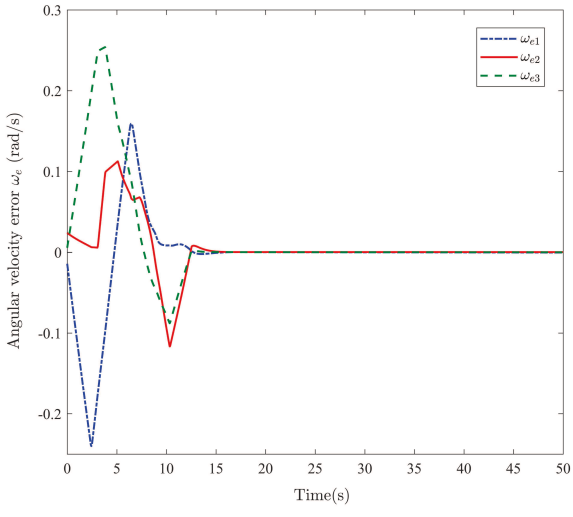

Fig. 1: Trajectory of the angular velocity error ω_e

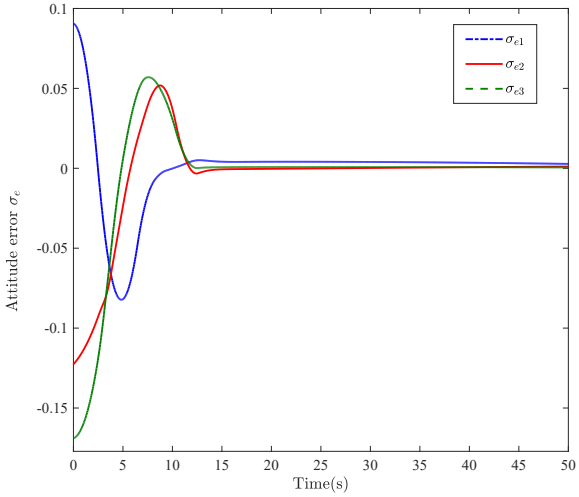

Fig. 2: Trajectory of the attitude error σ_e

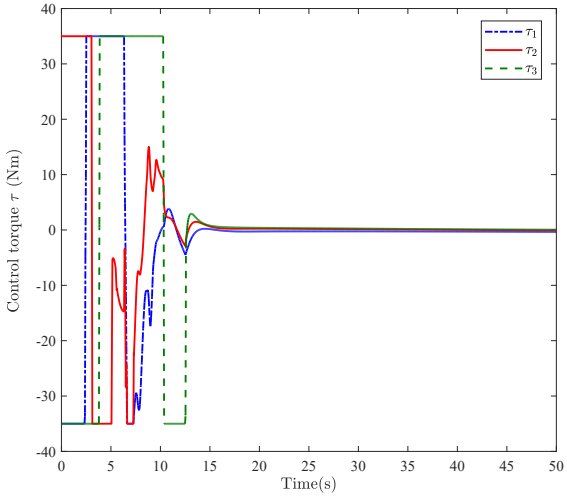

Fig. 3: Trajectory of the control torque τ

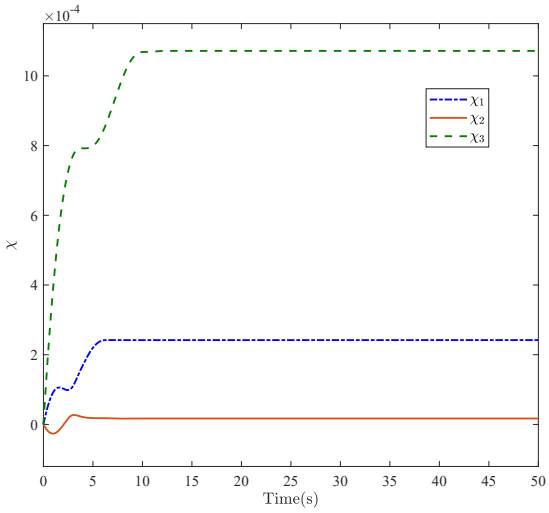

Fig. 4: Trajectory of the adaptive parameter χ

5 Conclusion

This article has developed a fault-tolerant attitude tracking control scheme for combined spacecraft with actuator fault. The major characteristic of this controller was that the direct parameter approach was adapted in the fully-actuated system. Besides, a Nubbaum gain with an updating law was introduced to tackle the influence caused by actuator saturation. Furthermore, a time-delay estimate method was adapted to compensate the lumped uncertainty and an adaptive law is used to suppress the estimation error. A simulation result was shown to illustrate the effectiveness of developed control scheme. In the future, the flexible spacecraft system will be investigated with the proposed method.

6 Simulation Result

References

[1] S. Li and Y. She, Recent advances in contact dynamics and post-capture control for combined spacecraft, *Progress in Aerospace Sciences*, 2021, 120:100678.

[2] H. Jiang, B. Zhou, D. Li, and G. R. Duan, Data-driven–based attitude control ofcombined spacecraft with noncooperative target. *International Journal of Robust and Nonlinear Control*, 2018: 1-19.

[3] X. Huang, James D. Biggs, and G. R. Duan, Post-capture attitude control with prescribed performance. *Aerospace Science and Technology*, 2020, 96: 105572.

[4] X. Guo and Z. Meng, Practical prescribed time attitude stabilization of combined spacecraft with measurement uncertainties, *Advances in Space Research*, 2023, 72(4): 1399-1411.

[5] H. Gao, G. Ma, Y. Lyu, and Y. Guo, Data-driven model-free adaptive attitude control of partially constrained combined spacecraft with external disturbances and input saturation. *Chinese Journal of Aeronautics*, 2019, 32(5): 1281-1293.

[6] X. Huang, Z. Dong, F. Zhang, and L. Zhang, Model-free adaptive attitude control for combined spacecraft with input saturation and prescribed performance. *in 2022 IEEE 11th Data Driven Control and Learning Systems Conference (DDCLS)*, 2022: 65-70.

[7] G. R. Duan, High-order fully actuated system approaches: Part I. Models and basic procedure. *International Journal of Systems Science*, 2021, 52(2): 422-435.

[8] F. Z. Xiao and L. Q. Chen, Fully actuated systems in terms of quaternions for spacecraft attitude control. *Acta Astronautica*, 2023, 209: 1-5.

[9] H. Sun, L. Huang, and L. He, Research on the trajectory tracking control of a 6-DOF manipulator based on fully-actuated system models. *Journal Of Systems Science and Complexity*, 2022, 35: 641-659.

[10] P. Li and G. Duan, High-order fully actuated control approaches of flexible servo systems based on singular perturbation theory. *IEEE/ASME Transactions on Mechatronics*, 2023, 28(6): 3386-3397.

[11] G. Duan, High-order fully actuated system approaches: Part VIII. Optimal control with application in spacecraft attitude stabilisation. *International Journal of Systems Science*, 2021, 53(1): 54-73.

[12] G. Liu, K. Zhang and B. Li, Fully-actuated system approach based optimal attitude tracking control of rigid spacecraft with actuator saturation. *Journal of Systems Science and Complexity*, 2022, 35(2): 688-702.

[13] Q. Zhao and G. R. Duan, Fully actuated system approach for 6DOF spacecraft control based on extended state observer. *Journal of Systems Science and Complexity*, 2022, 35(2): 604-622.

[14] T. Zhao and G. R. Duan, Fully actuated system approach to attitude control of flexible spacecraft with nonlinear time-varying inertia. *Science China Information Sciences*, 2022, 65: 212201.

[15] Z. Feng, M. Liu, and X. Cao, A fully-actuated system approach for spacecraft attitude control with input saturation. *in Proceedings of the 2nd Conference on Fully Actuated System Theory and Applications*, 2023: 705-710.

[16] D. Jin, S. Jia, T. Wang, and J. Qiu, Spacecraft attitude tracking control based on high-order fully actuated system approach. *in Proceedings of the 2nd Conference on Fully Actuated System Theory and Applications*, 2023: 1040-1044.

[17] Q. Z. Liu, G. W. Fan, X. Y. Lv, Y. Gao, Y. Xiao, and Y. Son, Attitude tracking control of rigid spacecraft based on fully actuated system models. *in Proceedings of the 2nd Conference on Fully Actuated System Theory and Applications*, 2023: 998-1003.

[18] D. Wang, Y. Wu, X. Chen, Y. Zhang, S. Liu, and Y. Mao, Fully actuated system based spacecraft attitude finite time control. *in Proceedings of the 2nd Conference on Fully Actuated System Theory and Applications*, 2023: 100-105.

[19] G. Q. Duan, G. Liu, and Y. Fu, Combined spacecraft attitude tracking control with prescribed performance via a fully actuated system approach, *in 2023 42nd Chinese Control Conference (CCC)*, 2023: 5253-5257.

[20] G. Q. Duan and G. Liu, Fully actuated system game-based attitude control for combined spacecraft, *in 2023 2nd Conference on Fully Actuated System Theory and Applications (CFASTA)*, 2023: 983-986.

[21] K. Cui and G. R. Duan, Adaptive disturbance observer design for discrete-time high-order fully actuated systems based on LMI and its application to combined spacecrafts, *in 2023 2nd Conference on Fully Actuated System Theory and Applications (CFASTA)*, 2023: 12-17.

[22] X. Huang, Z. Dong, P. Yang, and L. Zhang, Model-free adaptive trajectory tracking control of robotic manipulators with practical prescribed-time performance, *Nonlinear Dynamics*, 2023, 111: 20015–20039.

[23] X. Huang X and G. R. Duan, Fault-tolerant attitude tracking control of combined spacecraft with reaction wheels under prescribed performance. *ISA transactions*, 2020, 98: 161-172.

[24] D. Ran, X. Chen, A. de Ruiter, and B. Xiao, Adaptive extended-state observer based fault tolerant attitude control for spacecraft with reaction wheels. *Acta Astronaut*, 2018, 145: 501-14.

[25] Z. Chen, Nussbaum functions in adaptive control with time-varying unknown control coefficients, *Automatica*, 2019, 102: 72-79.

[26] Q. Hu, X. Shao, and L. Guo, Adaptive fault-tolerant attitude tracking control of spacecraft with prescribed performance, *IEEE/ASME Transactions On Mechatronics*, 2017, 23(1): 331-341.

[27] P. A Ioannou and J. Sun, Robust adaptive control. Prentice-Hall: Upper Saddle River, NJ, USA, 1996.

[28] G. R. Duan, Quasi-linear system approaches for aerocraft control: Part 2. Methods and prospects, *Journal of Astronautics*, 2020, 41(7): 839-849.

[29] G. Cho, P. Chang, S. Park, and et al, Robust tracking under nonlinear friction using time-delay control with internal model, *IEEE Transactions on Control Systems Technology*, 2009, 17(6): 1406-1414.

[30] M. Jin, J. Lee, P. Chang, and et al, Practical nonsingular terminal sliding-mode control of robot manipulators for high-accuracy tracking control, *IEEE Transactions on Industrial Electronics*, 2009, 56(9): 3593-3601.

Proceedings of the 3rd Conference on Fully Actuated System Theory and Applications
May 10-12, 2024, Shenzhen, China

A Novel Rolling Takeoff Flight Control for Fixed-Wing Unmanned Aerial Vehicle

Wangkui Liu[1,2], Xiangyu Wang[1,2], Zunshi Shui[1,2], Zhihua Chen[3], Huabing Qiu[1,2], Xuefei Yang[4]

1. Beijing Institute of Aerospace Technology, Beijing 100074, China
2. National Key Laboratory of Aerospace Flight Technology, Beijing 100074, China
3. Beijing Institute of Control Engineering, Beijing 100190, China
4. Harbin Institute of Technology, Harbin 150001, China
E-mail: liuwangkui@126.com

Abstract: A new rolling takeoff flight control method for fixed-wing unmanned aerial vehicle(UAV) which launched obliquely and powered by propeller is proposed. The fixed-wing UAV has the characteristics of low launch velocity, insufficient control ability of aileron, and strong reaction torque caused by propeller, which leads to insufficient control ability in rolling channel during initial takeoff phase. Different from the traditional flight control system, the reaction torque is utilized as a part of control torque to make the UAV roll 360deg with the direction of reaction torque in the initial phase. With the control ability of aileron increasing and the reaction torque decreasing, the aileron is used to restrict the influence of reaction torque and stabilize the roll angle of UAV at 0deg. The effectiveness of the proposed flight control strategy is illustrated by numerical simulation results.

Key Words: Unmanned Aerial Vehicle, Rolling Takeoff, Flight Control, Reaction Torque

1 Introduction

As a special of aircraft, the unmanned aerial vehicle (UAV) can execute flight mission autonomously without pilot onboard. Originally, UAVs were used to perform military missions in dirty or dangerous environment for pilot[1]. With the rapid development of UAVs, UAVs play an important role in more civil application scenarios, such as aerial photography or mapping, modern agriculture, forest fire monitoring[2] and infrastructure patrol. Although UAVs are designed with various different configuration, the UAV can be classified into two categories: multi-rotor configuration and fixed-wing configuration[3-5]. The multi-rotor configuration UAV utilizes rotary wings to produce aerodynamic forces for flight. The aerodynamic forces of fixed-wing UAV are generated by wings and control surfaces. It is well known that the aerodynamical efficiency of fixed-wing UAV is higher than multi-rotor UAV. The fixed-wing configuration has many advantages compared to multi-rotor configuration, such as larger flight range, longer flight time, higher speed and heavier mission load. Due to the advantages such as low cost, portable deployment and flight concealment, small fixed-wing UAVs (usually less than 20 kg) have been widely used in recent years. For instance, Switchblade UAV and Zala Lancet have been well-known in Russo-Ukrainian War.

In recent decades, various control methods have been used in fixed-wing UAV flight control[1], such as backstepping control[6], sliding mode control[7-9], nonlinear model predictive control[10,11] and linear quadratic Gaussian control[12]. To improve the performance of flight control system and flight quality of UAV, it is unavoidable to reduce the adverse influence of disturbance. Thus, disturbance rejection is an important issue in UAV control. Based on wind tunnel experiment to acquire linear dynamic models of UAV, model predictive controller has been designed in [10] to enhance the disturbance rejection. In many studies, kinds of disturbance observers have been widely used for UAV fight control to estimate the external disturbance[13-16], and satisfactory control performance have been obtained by compensating the estimation of disturbance.

The authors focus on a small fixed-wing UAV which similar to Switchblade recently. The UAV is launched obliquely on rail type launcher and powered by propeller motor. The pitch and roll channel of UAV are manipulated simultaneously by a single pair of control surface. Due to the length of launcher, structural strength of UAV and measurement capacity of MEMS accelerometer, the acceleration and acceleration distance of UAV on the launcher are constrained which leads to the low launching velocity of UAV. Besides, the pitch channel of UAV is statically unstable and the thrust direction of the propeller motor is coincided with body axis due to the structure and equipment installation. Several experiment results show that an reaction torque with large peak is generated by propeller motor in roll channel when the propeller rotate with high speed. The reaction torque has adverse influence on the stability of roll channel which was treated as disturbance in many studies. It is obvious that the velocity of UAV is reduced firstly in the initial flight phase since the thrust generated by propeller motor is hysteresis than thrust command. As a result, the dynamic pressure and the control efficiency of control surfaces are low. Considering the physical limitation on deflection angle of control surface and a part of control surface is necessary to control the statically unstable pitch channel, the deflection angle of control surface and the maximum control torque can be used in roll channel is limited. As a result, the control torque for roll channel have no advantage to the reaction torque and disturbance caused by other factors in initial flight phase. In conclusion, the influence of reaction torque in roll channel must be considered in the design of control system to ensure the stability of roll channel, such that satisfactory flight quality and flight safety of UAV can be achieved.

*This work is supported by National Natural Science Foundation of China(Grant No. U2141229,62003271,62173033 and 61903102), National Defense Basic Scientific Research Program of China under Grant JCKY2020204B044, and the Fundamental Research Funds for the Central Universities under Grant HIT.OCEF.2023007.

Unlike the preceding studies, the reaction torque which is generated by the propeller motor is considered in this paper. Compared with normal disturbances, the reaction torque disturbance can easily get close to or even large than the operational torque of roll channel in the initial flight phase. Therefore, the reaction torque should be considered particularly rather than treated as uncertainties to compensate. Motivated by previous discussion, a new rolling takeoff flight control method for fixed-wing UAV is presented to deal with the reaction torque in roll channel. The reaction torque is utilized to control the attitude of UAV such that the UAV can execute a 360-degree roll promptly. With the improved control capability of roll channel, normal flight control strategy is adopted subsequently. The numerical simulation results illustrate the efficiency of the proposed flight control strategy.

2 Dynamic Model and Problem Formulation

In this section, the dynamic model for fixed-wing UAV with aerodynamic force and moment model are introduced firstly. After that, the dynamic characteristic of propeller motor and the control objective of this thesis are presented.

2.1 Dynamic Model Description of Fixed-Wing UAV

Following [17,18], the orientational dynamics of fixed-wing UAV can be expressed as

$$\begin{cases} \dfrac{d\vartheta}{dt} = \omega_y \sin\gamma + \omega_z \cos\gamma \\ \dfrac{d\psi}{dt} = (\omega_y \cos\gamma - \omega_z \sin\gamma)/\cos\vartheta \\ \dfrac{d\gamma}{dt} = \omega_x - \tan\vartheta(\omega_y \cos\gamma - \omega_z \sin\gamma) \end{cases} \tag{1}$$

$$\begin{cases} J_x \dfrac{d\omega_x}{dt} + \left(J_z - J_y\right)\omega_z\omega_y = M_x \\ J_y \dfrac{d\omega_y}{dt} + \left(J_x - J_z\right)\omega_x\omega_z = M_y \\ J_z \dfrac{d\omega_z}{dt} + \left(J_y - J_x\right)\omega_y\omega_x = M_z \end{cases} \tag{2}$$

where ϑ, ψ and γ are pitch angle, yaw angle and roll angle, respectively; ω_x, ω_y and ω_z denote roll, yaw and pitch angular rates, respectively; J_x, J_y and J_z represent the moment of inertia around corresponding axis; M_x, M_y and M_z are roll, yaw and pitch moment, respectively.

The translational dynamics of fixed-wing UAV are given as:

$$\begin{cases} \dfrac{dx}{dt} = V\cos\theta\cos\psi_V \\ \dfrac{dy}{dt} = V\sin\theta \\ \dfrac{dz}{dt} = -V\cos\theta\sin\psi_V \end{cases} \tag{3}$$

$$\begin{cases} m\dfrac{dV}{dt} = P\cos\alpha\cos\beta - F_D - mg\sin\theta \\ mV\dfrac{d\theta}{dt} = P(\sin\alpha\cos\gamma_V - \cos\alpha\sin\beta\sin\gamma_V) \\ \qquad + F_L\cos\gamma_V - F_Z\sin\gamma_V - mg\cos\theta \\ -mV\cos\theta\dfrac{d\psi_V}{dt} = P(\sin\alpha\sin\gamma_V - \cos\alpha\sin\beta\cos\gamma_V) \\ \qquad + F_L\sin\gamma_V + F_Z\cos\gamma_V \end{cases} \tag{4}$$

where x, y and z denote the 3-D position of the UAV in the inertial coordinate frame; m and V are the mass and airspeed of the UAV, respectively; α, β, θ, ψ_V and γ_V denote the angle of attack, side-slip angle, flight path angle, heading angle and velocity bank angel, respectively; F_D, F_L, F_Z and P denote the drag, lift , side force and thrust generated by propeller, respectively; g represents the acceleration of gravity.

The aerodynamic force, aerodynamic moment and thrust of UAV can be modeled as follows:

$$\begin{cases} F_k = \dfrac{1}{2}\rho V^2 s c_k\left(\alpha,\beta,V,\delta_i\right) + \Delta F_k,\ k = D,L,Z, i = x,z \\ M_i = \dfrac{1}{2}\rho V^2 s l m_i\left(\alpha,\beta,V,\delta_i\right) + \Delta M_k,\ i = x,z \\ P = T\left(\phi,V\right) + \Delta P \end{cases} \tag{5}$$

where the non-dimensional aerodynamic coefficients c_i and m_i are nonlinear functions of airspeed, angle of attack, side-slip angle and the deflections of control surfaces; δ_x and δ_z denote the deflections of the aileron and the elevator, respectively; ϕ, ρ, s and l denote the throttle command, air density, the reference area and length of UAV, respectively; T is nonlinear functions of throttle command and airspeed. ΔF_k、ΔM_i and ΔP represent the uncertainties of aerodynamic forces, aerodynamic moments and thrust, respectively, which are caused by external disturbance, parametric uncertainty and unmodeled dynamics.

2.2 Problem Formulation

In this subsection, the dynamic characteristic of propeller motor is presented. Based on the analysis of the control dynamic of UAV in the initial flight phase, the control objective of this thesis is summarized.

Based on the wind tunnel experiments, we got the thrust and reaction torque data of propeller motor. The size of propeller is 13*6.5 inch, and the available range of throttle command is 0.1 to 1. The thrust generated by propeller motor with different wind velocity is presented in Fig. 1. Fig. 2 shows the curves of normalized thrust and reaction torque under step throttle command. Fig.3 shows the curves of trim angle of aileron for reaction torque with different angle of attack and velocities.

From these figures, it is obvious that the thrust generated by propeller motor is increased by the throttle command, and decreased with the velocity. Moreover, when the flight velocity of UAV is 20m/s, the throttle command should be larger than 0.5 such that the thrust of propeller motor is positive. Compared with throttle command, the thrust generated by the propeller is hysteretic and the lag time is larger than 0.5s as shown in figure 2. Besides, reaction torque increased obviously then became decreased, and the peak of reaction torque occurs earlier than the thrust. It is obvious that the trim angle of aileron is decreased with the velocity, and the minimum trim angle is 24deg with the velocity of 18m/s.

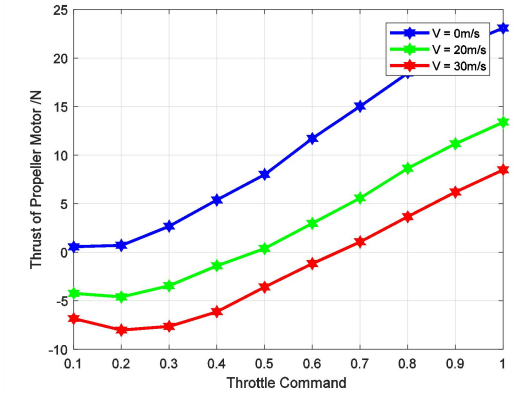

Fig. 1: The curves of thrust with different velocity

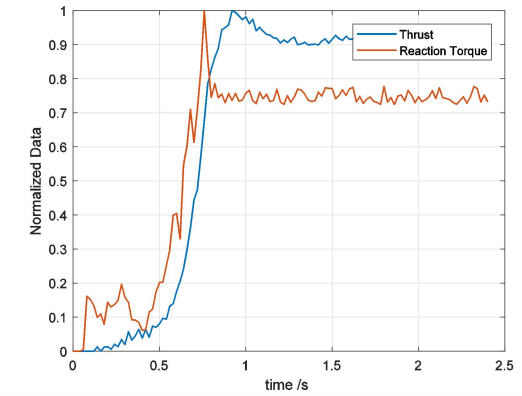

Fig. 2: The curves of normalized thrust and reaction torque

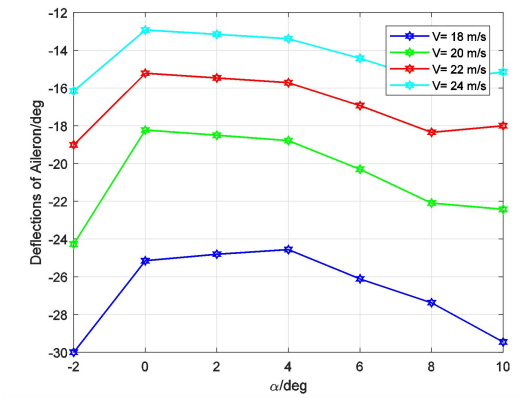

Fig. 3: The trim angle of aileron for reaction torque

Based on above analysis, we can know that the control ability of aileron is insufficient to restrain the reaction torque when the velocity of UAV is low in the initial flight phase. The roll angle of UAV is unable to stabilise at 0deg and the lifting of UAV loss seriously. As a result, the height of UAV will decrease quickly and the flight safety of UAV can not be guaranteed. In conclusion, the flight control problem of fix-wing UAV in initial flight phase with both strong disturbance and insufficient control ability in rolling channel should be taken into account.

3 Rolling Takeoff Flight Control System Design

In contrary to the traditional flight control method which tread the reaction torque as disturbance, the reaction torque is used as control torque for rolling channel in the initial phase in this paper. After the reaction torque decreased and the control ability of aileron increases rapidly with the increase of velocity, the aileron is used to restrict the influence of reaction torque and other disturbance. In this paper, the proportional–integral–derivative (PID) control method is adopted to design the attitude controller of UAV due to its simplicity and low computational intensity.

Based on PID control structure, the control signals for the roll and pitch channel are calculated as follows:

$$\delta_x = k_{px}\left(\gamma-\gamma_{cmd}\right)+k_{dx}\omega_x+k_{ix}\int\left(\gamma-\gamma_{cmd}\right)dt+\delta_{fx} \quad (6)$$

$$\delta_z = k_{pz}\left(\vartheta-\vartheta_{cmd}\right)+k_{dz}\omega_z+k_{iz}\int\left(\vartheta-\vartheta_{cmd}\right)dt \quad (7)$$

where ϑ_{cmd} and γ_{cmd} are pitch angle command and roll angle command, respectively. k_{pz}, k_{dz}, k_{iz}, k_{px}, k_{dx} and k_{ix} are control parameters, δ_{fx} is the feedforward compensation.

The pitch angle command and roll angle command are proposed as follows:

$$\vartheta_{cmd}=\begin{cases}\vartheta_{ini}\left(1-\Phi_0^{t_\vartheta}(t)\right)+\vartheta_{trans}\Phi_0^{t_\vartheta}(t), t\le t_{trans}\\ k_{ph}\left(H-H_{cmd}\right)+k_{dh}\left(V_y-V_{ycmd}\right)+k_{ih}\int\left(H-H_{cmd}\right)dt, else\end{cases} \quad (8)$$

$$\gamma_{cmd}=\begin{cases}-180, t\le t_R\\ -180\left(1-\Phi_0^{t_\gamma}(t)\right), else\end{cases} \quad (9)$$

where ϑ_{ini}, H_{cmd} and V_{ycmd} are the initial pitch angle, height command and vertical velocity command, respectively. k_{ph}, k_{dh} and k_{ih} are control parameters. t_{trans} and t_R are end time of constant pitch angle climb phase and roll flight, respectively. t_ϑ and t_γ are transition time of pitch angle and roll angle, respectively. The transition function $\Phi_{x_1}^{x_2}(x)$ is defined as follows:

$$\Phi_{x_1}^{x_2}(x)=\begin{cases}0, & if\left(x<x_1\right)\\ \frac{1}{2}\left(\sin\left(\frac{x-x_1}{x_2-x_1}-\frac{1}{2}\right)\pi+1\right), & if\left(x_1\le x<x_2\right)\\ 1, & if\left(x_2\le x\right)\end{cases} \quad (10)$$

The velocity control for the fixed-wing UAV is proposed as follow:

$$\phi = 1 - k_{p\phi}\left(V - V_{cmd}\right) + k_{i\phi}\int\left(V - V_{cmd}\right)dt \qquad (11)$$

where $k_{p\phi}$ and $k_{i\phi}$ are control parameters for velocity, and V_{cmd} is the cruising velocity of UAV.

Remark 1. The novel rolling takeoff flight control strategy for small fixed-wing UAV can be segmented into two stages. In the first stage, in view of the reaction torque is larger and the control ability of aileron is insufficient, the control objective of roll channel is to control the UAV roll 360deg by utilizing the reaction torque as control torque. With the reaction torque decreasing and the control ability of aileron increasing, the control objective of roll channel is to stabilize the roll angle of the UAV at 0deg by treating the reaction torque as disturbance in the second control stage. It is obvious that the transition time between the first stage and the second stage is the key point which influence the flight performance.The transition time is determined by the characteristics of reaction torque and control ability of aileron.

4 Numerical Simulation

To demonstrate the effectiveness of the proposed rolling takeoff flight control algorithm, the full six degrees of freedom model simulation experiments are carried out in this section. The specifications and initial states of the UAV are described in Table 1. Parts of controller components in the rolling takeoff flight control are shown in Table 2. Meanwhile, the flight controller operates at a sampling time of 5ms, and the measure data transmission delay is considered as 40ms.

Table 1: Physical parameters of the UAV

Parameter	Value
Reference area	0.064m^2
Reference length	0.08m
Mass	3kg
Moment of inertia	$I_{xx} = 0.02\text{kg/m}^2$ $I_{yy} = 0.12\text{kg/m}^2$ $I_{zz} = 0.1\text{kg/m}^2$
Launch Velocity	21m/s
Pitch angle	29.5deg
Roll angle	2.5deg
Height	500m

Table 2: Controller components

Parameter	Value
V_{cmd}	30m/s
ϑ_{cmd}	15deg
H_{cmd}	600m
$t_{trans}, t_R, t_\vartheta, t_\gamma$	10s, 1s, 6s, 2s

Besides, the control signals of aileron, elevator and throttle command should satisfy the following constraints:

$$\delta_x \in [-25,25], \delta_x \in [-25,25], \phi \in [0.5,1]$$

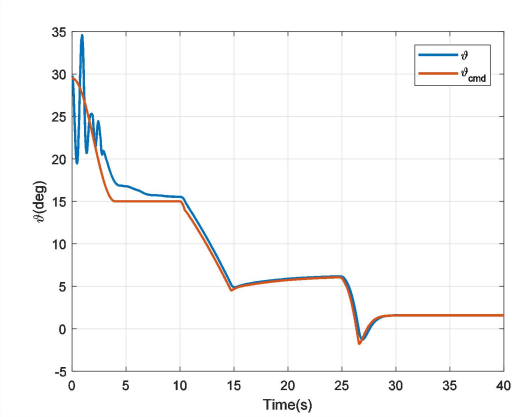

Fig. 4: The curves of pitch angle

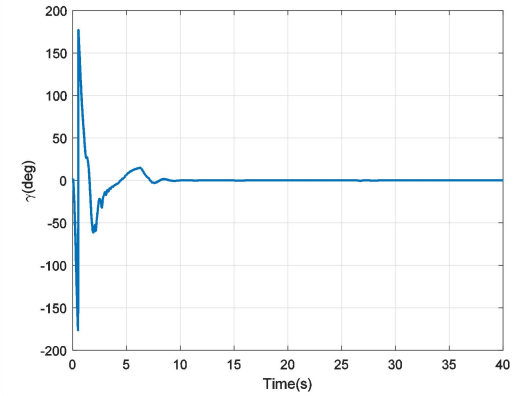

Fig. 5: The curve of roll angle

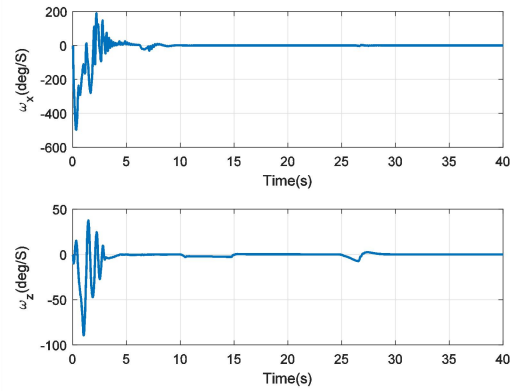

Fig. 6: The cures of angular velocity

As shown in Figure 4, the pitch angle can tracking the pitch angle command accurately and quickly. The Figure 5 shows the curve of roll angle, it is apparent that the UAV roll 360deg in 1.6s and then stabilize at 0deg quickly. Figure 6 and 7 show the curves of angular velocity and control command, respectively. Follows that, we can conclude that the attitude of the UAV is stable and the control objective of rolling channel have been achieved. The curve of height, velocity and throttle command of UAV are shown in Figure

8, 9 and 10, respectively. The height of UAV increase firstly and then decreases slightly, after that the UAV climb to the cruise height at 15s. The minimum velocity of UAV is 17.48m/s at 0.875s, and the UAV accelerate to cruise velocity 30m/s in 8.5s. Figure 11 shows the flight trajectory of UAV in 3D. Based on the analysis of simulation results, we can conclude that the proposed novel rolling takeoff flight control strategy is effective to deal with the influence of reaction torque, and satisfactory flight performance have been achieved by utilizing the proposed control scheme.

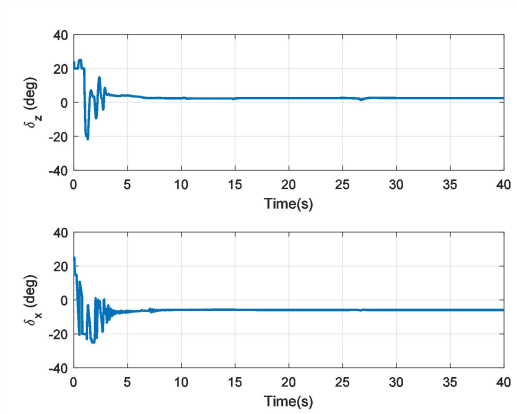

Fig. 7: The cures of control input

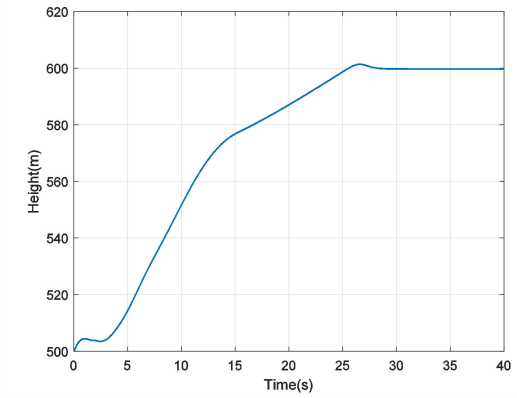

Fig. 8: The cure of height

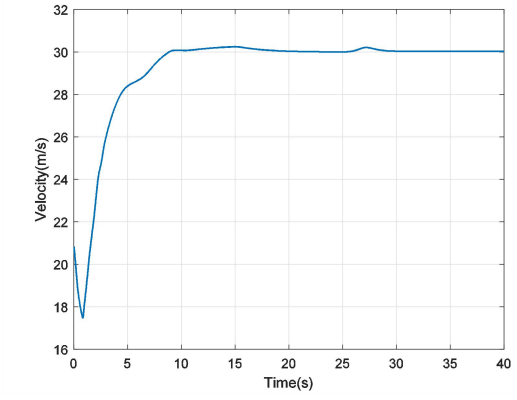

Fig. 9: The cure of velocity

5 Conclusion

In this paper, a new rolling takeoff flight control scheme for fixed-wing UAV which launched obliquely and powered by propeller was proposed. The fixed-wing UAV has the characteristics of low launch speed, insufficient control ability of aileron, and strong reaction torque caused by propeller, which leads to insufficient control ability in rolling channel during initial takeoff phase. By analyzing the characteristics of rolling channel disturbance torque, a novel takeoff flight control method is proposed. In the direction of reaction torque, a 360-degree roll was executed by the UAV in initial launched phase.With the established of dynamic pressure and the improved control capability of aileron, traditional flight control method was adopted. Different from the traditional anti-disturbance control method, the reaction torque in rolling channel was firstly utilized to control the attitude of UAV in this article. The effectiveness of the proposed scheme was verified by the numerical simulation results.

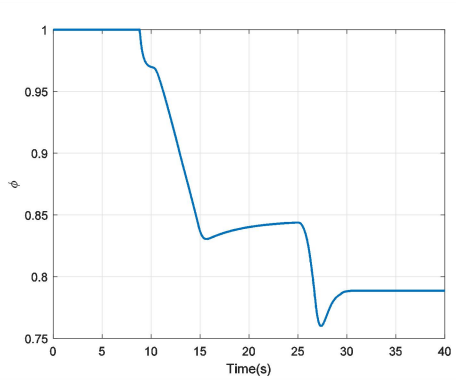

Fig. 10: The cure of throttle command

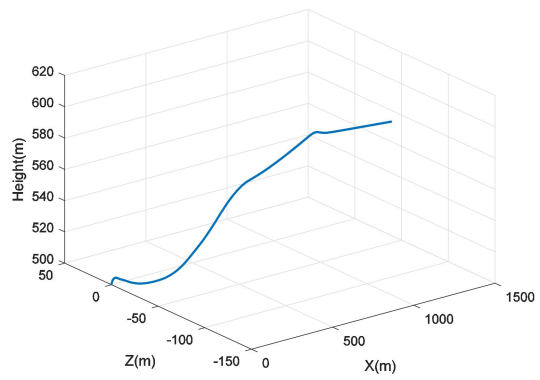

Fig. 11: The flight trajectory of UAV

References

[1] Zuo Z, Liu C, Han Q L, et al. Unmanned aerial vehicles: Control methods and future challenges, *IEEE/CAA Journal of Automatica Sinica*, 9(4): 601-614, 2022.

[2] C. Yuan, Y. Zhang, and Z. Liu, A survey on technologies for automatic forest fire monitoring, detection, and fighting using unmanned aerial vehicles and remote sensing techniques, *Canadian Journal of Forest Research*,45(7):783-792, 2015.

[3] Boon M A, Drijfhout A P, Tesfamichael S. Comparison of a fixed-wing and multi-rotor UAV for environmental mapping applications: A case study, *The International Archives of the Photogrammetry, Remote Sensing and Spatial Information Sciences*, 42: 47-54, 2017.

[4] Thamm F P, Brieger N, Neitzke K P, et al. SONGBIRD-an innovative UAS combining the advantages of fixed wing and multi rotor UAS, *The International Archives of the Photogrammetry, Remote Sensing and Spatial Information Sciences*, 40: 345-349, 2015.

[5] Yang X, Zhou B, Lam J, Stabilisation of quadrotor aircraft with constrained controls, *International Journal of Systems Science*, 53(6): 1245-1259, 2022.

[6] Tan J, Guo S, Backstepping control with fixed-time prescribed performance for fixed wing UAV under model uncertainties and external disturbances, *International Journal of Control*, 95(4): 934-951, 2022.
[7] Bao C, Guo Y, Luo L, et al, Design of a fixed-wing UAV controller based on adaptive backstepping sliding mode control method, *IEEE Access*, 9: 157825-157841, 2021.
[8] Zhang C, Zhang G, Dong Q, Multi-variable finite-time observer-based adaptive-gain sliding mode control for fixed-wing UAV, *IET control theory & applications*, 15(2): 223-247, 2021.
[9] Guo Y, Luo L, Bao C, Design of a fixed-wing UAV controller combined fuzzy adaptive method and sliding mode control, *Mathematical Problems in Engineering*, 2022, 2022.
[10] Kang Y, Hedrick J K, Linear tracking for a fixed-wing UAV using nonlinear model predictive control, IEEE Transactions on Control Systems Technology, 17(5): 1202-1210, 2009.
[11] Zhang B, Sun X, Liu S, et al, Adaptive model predictive control with extended state observer for multi-UAV formation flight, *International Journal of Adaptive Control and Signal Processing*, 34(10): 1341-1358, 2020.
[12] Xiong S, Liu H H T. Low-altitude fixed-wing robust and optimal control using a barrier penalty function method, *Journal of Guidance, Control, and Dynamics*, 46(11): 2218-2223, 2023.
[13] Cao S, Wang X, Yu H, Incremental adaptive fixed-wing unmanned aerial vehicle maneuver control with nonlinear disturbance observer: A finite-time approach, *Asian Journal of Control*, 25(6): 4302-4318, 2023.
[14] Smith J, Su J, Liu C, et al, Disturbance observer based control with anti-windup applied to a small fixed wing UAV for disturbance rejection, *Journal of Intelligent & Robotic Systems*, 88: 329-346, 2017.
[15] Nguyen N P, Oh H, Moon J, et al, Multivariable Disturbance Observer-Based Finite-Time Sliding Mode Attitude Control for Fixed-Wing UAVs under Matched and Mismatched Disturbances, *IEEE Control Systems Letters*, 2023.
[16] Yan D, Zhang W, Chen H, et al, Robust control strategy for multi-UAVs system using MPC combined with Kalman-consensus filter and disturbance observer, *ISA transactions*, 135: 35-51, 2023.
[17] Beard RW, McLain TW, Small unmanned aircraft: theory and practice, *Princeton University Press*, 2012.
[18] Yang W, Shi Z, Zhong Y, Robust adaptive three-dimensional trajectory tracking control scheme design for small fixed-wing UAVs, *ISA transactions*, 141: 377-391, 2023.

Proceedings of the 3rd Conference on Fully Actuated System Theory and Applications
May 10-12, 2024, Shenzhen, China

Input saturation control of manipulator based on fully actuated system approach

Yongqiang Xiao[1], Guangbin Cai[1*], Mingzhe Hou[2]

1. Department of Missile Engineering, Rocket Force University of Engineering, Xi'an 710025, China
E-mail: cgb0712@163.com
2. Center for Control Theory and Guidance Technology, Harbin Institute of Technology, Harbin 150001, China

Abstract: A control strategy based on fully actuated system approach is proposed for the manipulator system with input saturation. By introducing a smooth hyperbolic tangent function to approximate the saturation function, the original system is transformed into a smooth system. The complex differential operation is converted into algebraic operation by introducing a first-order low-pass filter. By designing an adaptive law, the uncertainty of the system model is effectively estimated. Based on fully actuated system approach, the controller for the manipulator system is directly designed, which eliminates the step of converting the original second-order strict feedback system into a first-order strict feedback system, reduces the steps of controller design, lowers the complexity of algorithm design, and effectively avoids the "differential explosion" problem. The Lyapunov stability theory is used to prove that all signals in the closed-loop system are uniformly ultimately bounded. Finally, numerical simulations of the manipulator system are performed to verify the effectiveness of the proposed method.

Key Words: Manipulator system, Fully actuated system approach, Input saturation, Smooth function

1 Introduction

The manipulator system, with its advantages of flexibility and versatility, has been widely used in various fields such as industrial production, aerospace, and military applications. However, the physical characteristics, structural limitations, and operating environment of the mechanical arm system components inevitably lead to saturation nonlinearity. Ignoring this issue can result in degraded control performance and even instability of the system. Therefore, it is necessary to consider the design of input saturation controllers to achieve high-precision control of the mechanical arm system under input saturation conditions. Researchers have proposed strategies based on the backstepping/dynamic surface control methods, combined with approximations of the input saturation function using smooth functions, to effectively address this problem[1][2].

However, the model of the manipulator system is typically a cascade of two second-order subsystems, and the backstepping method is commonly used to design controllers for it. However, when using this method to design controllers, the model needs to be transformed into four first-order cascaded systems. This not only disrupts the full-actuation characteristics of the system but also increases the complexity of controller design. It is well-known that when there are many steps in the backstepping design process, the problem of "differential explosion" can occur. Therefore, reducing the steps in the design of the manipulator control system and designing a simple and efficient controller while ensuring control accuracy is currently a challenge[3][4][5][6].

Recently, the fully actuated system approach has shown significant advantages in the analysis and design of nonlinear systems. This method employs the idea of elimination in the process of establishing the physical model, simplifying the control instruction design steps while ensuring model accuracy. By eliminating the open-loop system characteristics, the closed-loop system can be stabilized and linearized, and all degrees of freedom in the system model can be configured to meet the system control requirements[7][8]. In particular, for higher-order cascade systems, the fully actuated system approach allows for direct controller design without the need to transform the high-order strict-feedback system into a first-order strict-feedback system. This eliminates the conversion process and reduces the design steps, effectively mitigating the problem of "differential explosion" associated with the backstepping method[9]. Based on this approach, researchers have proposed high-order backstepping methods, high-order dynamic surface control methods, and high-order command filtering control methods, which have achieved significant research results. Following this line of thinking, in order to effectively control the manipulator system under the influence of input saturation, simplify the design steps, and mitigate the "differential explosion" problem, this paper designs the controller for the manipulator system based on the fully actuated system approach[10]-[18].

First, let's define the relevant symbols for the input saturation controller of the manipulator system.

$\lambda_{\min}(P_i)$ and $\lambda_{\max}(P_i)$ represent the smallest and largest eigenvalues of matrix P_i, and $P_i > 0$ denotes that the matrix P_i is a positive-definite symmetric matrix. Moreover,

$$x^{(0\sim n)} = \begin{bmatrix} x \\ \dot{x} \\ \vdots \\ x^{(n)} \end{bmatrix}, x_{i\sim j}^{(0\sim n)} = \begin{bmatrix} x_i^{(0\sim n)} \\ x_{i+1}^{(0\sim n)} \\ \vdots \\ x_j^{(0\sim n)} \end{bmatrix}, j \geq i,$$

$$A^{0\sim n-1} = \begin{bmatrix} A_0 & A_1 & \cdots & A_{n-1} \end{bmatrix},$$

*This work is supported by National Natural Science Foundation of China under Grant 62188101、61773387.

$$\Phi\left(A^{0\sim n-1}\right)=\begin{bmatrix} 0 & I & & \\ & & \ddots & \\ & & & I \\ -A_0 & -A_1 & \cdots & -A_{n-1} \end{bmatrix}.$$

2 Problem Formulation

Consider the manipulator system with input saturation, as shown in equation (1):

$$\begin{cases} ML^2\ddot{q}+MgL\sin q+F(\dot{q})+Kq=Kq_m, \\ J\ddot{q}_m+B\dot{q}_m+K\left(q_m-q\right)=u(v), \end{cases} \tag{1}$$

where, q and q_m are the angular positions of the link and the motor, M and L are the mass and length of the link, g is the acceleration of gravity, K represents the equivalent spring elasticity coefficient, J is the rotational inertia of the motor, B is the buffer coefficient, $F(\dot{q})=B_1Mg\cos\alpha\tanh\dot{q}$ represents the friction term, B_1 is friction coefficient, $u(v)$ is the motor control torque affected by saturation.

By defining $x_1=q$, $x_2=q_m$, and $u(v)$ the control input, the manipulator system can be represented as

$$\begin{cases} \dot{x}_1 = f_{1,0}\left(x_1,\dot{x}_1\right)+f_1\left(x_1,\dot{x}_1\right)\theta_1+g_1\left(x_1,\dot{x}_1\right)x_2, \\ \dot{x}_2 = f_{2,0}\left(x_{1\sim2}^{(0\sim1)}\right)+f_2\left(x_{1\sim2}^{(0\sim1)}\right)\theta_2+g_2\left(x_{1\sim2}^{(0\sim1)}\right)u(v), \end{cases} \tag{2}$$

where, $f_1=-\sin x_1$, $f_{1,0}=-\dfrac{F\left(\dot{x}_1\right)}{ML^2}-\dfrac{Kx_1}{ML^2}$, $g_1=\dfrac{K}{ML^2}$, $f_2=-\dot{x}_2$, $f_{2,0}=\dfrac{K}{J}\left(x_1-x_2\right)$ and $g_2=\dfrac{1}{J}$. θ_1=B and $\theta_2=\dfrac{B}{J}$ are uncertain system parameters. $u(v)$ is the motor control torque affected by saturation, and can be represented as follows:

$$u(v)=sat(v)=\begin{cases} sign(v)u_M, & |v|\ge u_M \\ v, & |v|<u_M \end{cases} \tag{3}$$

where, v is the control input that needs to be designed, $u(v)$ is the input affected by saturation, and u_M is the maximum amplitude of $u(v)$. At point $|v|=u_M$, $u(v)$ is not smooth, and cannot be directly designed with the backstepping control method. To address this issue, a smooth hyperbolic tangent function $g(v)$ is employed to approximate $u(v)$:

$$g(v)=u_M\times\tanh(\frac{v}{u_M})=u_M\frac{e^{v/u_M}-e^{-v/u_M}}{e^{v/u_M}+e^{-v/u_M}} \tag{4}$$

Combining equations (3) and (4), $sat(v)$ can be represented as:

$$sat(v)=g(v)+d(v) \tag{5}$$

where, $d(v)$ is the approximation error, and its upper bound is

$$\left|d(v)\right|=\left|sat(v)-g(v)\right|\le u_M\left(1-\tanh(1)\right)=d_m \tag{6}$$

Let $h(v)=\dfrac{\partial g(v)}{\partial v}$, by the properties of the hyperbolic tangent function, we can get that

$$0<h(v)=\frac{4}{\left(e^{v/u_M}+e^{-v/u_M}\right)^2}\le 1 \tag{7}$$

The manipulator system can be further transformed as

$$\begin{cases} \dot{x}_1 = f_{10}\left(x_1,\dot{x}_1\right)+f_1\left(x_1,\dot{x}_1\right)\theta_1+g_1\left(x_1,\dot{x}_1\right)x_2, \\ \dot{x}_2 = f_{20}\left(x_{1\sim2}^{(0\sim1)}\right)+f_2\left(x_{1\sim2}^{(0\sim1)}\right)\theta_2 \\ \quad +g_2\left(x_{1\sim2}^{(0\sim1)}\right)(g(v)+d(v)), \\ \dot{v}=-cv+w, \end{cases} \tag{8}$$

where, $c>0$ is a constant, and w is the auxiliary signal to be designed.

The control objective of this paper is to design an input saturation controller that enables the system output $y=x_1$ to effectively track the desired reference signal y_d. In the closed-loop system, all signals are uniformly ultimately bounded, and the tracking error converges to a sufficiently small neighborhood around zero.

To achieve the control objectives of this paper, the following assumptions and lemmas are given:

Assumption 1: $g_j(x_i^{(0\sim1)}|_{i=1\sim2})\ne 0,\ j=1,2$.

Assumption 2: The desired output tracking trajectory is smooth, available, and satisfies $y_d,\dot{y}_d,y_d^{(2)},y_d^{(3)}\in\Omega_0=$

$$\left[y_d \quad \dot{y}_d \quad y_d^{(2)} \quad y_d^{(3)}\right]^{\mathrm{T}}\,|\,y_d^2+\dot{y}_d^2+(y_d^{(2)})^2+(y_d^{(3)})^2\le r_0^2,$$

where r_0 is a constant.

Assumption 3: The system is input-to-state stable (ISS).

Lemma 1. For any $\mu>0$, there exists a vector $A^{0\sim n-1}$ such that

$$\lambda_{\min}\left[\Phi\left(A^{0\sim n-1}\right)\right]<-\frac{\mu}{2} \tag{9}$$

Furthermore, it can be derived that there exists a positive definite symmetric matrix $A^{0\sim n-1}$ such that

$$\begin{aligned} &\Phi^{\mathrm{T}}\left(A^{0\sim n-1}\right)P\left(A^{0\sim n-1}\right)+P\left(A^{0\sim n-1}\right)\Phi\left(A^{0\sim n-1}\right) \\ &<-\mu P\left(A^{0\sim n-1}\right) \end{aligned} \tag{10}$$

Lemma 2. $V(\bullet)$ and $\chi(\bullet)$ are both smooth functions defined on the interval $\left[0,\ t_f\right)$. Moreover, $\forall t\in\left[0,\ t_f\right)$, $V(t)\ge 0$ holds, where $N(\chi)$ is the Nussbaum gain function. If inequality (11) holds, then the functions $V(\bullet)$ and $\chi(\bullet)$ must be bounded on the interval $\left[0,\ t_f\right)$.

$$V\le V(0)e^{-\gamma t}+\frac{\varepsilon}{\gamma}\left(1-e^{-\gamma t}\right)+\frac{e^{-\gamma t}}{\gamma_\chi}\int_0^t\left(hN(\chi)\dot{\chi}-\dot{\chi}\right)e^{\gamma\tau}\mathrm{d}\tau \tag{11}$$

where, ε, γ, $\gamma_\chi>0$ are all constants, and h is a positive variable.

Lemma 3: Let a, b be two real numbers, and $b>0$. Then the following relation holds:

$$a-\frac{a^2}{4b}\le b \tag{12}$$

3 Controller design

3.1 Input saturation control algorithm

For the transformed system (8), the main steps for designing an input saturation controller are as follows:

Step 1 Define

$$z_1=x_1-x_{1c} \tag{13}$$

and

$$z_2=x_2-x_{2c} \tag{14}$$

where, z_1 is the tracking error, z_2 is the virtual error, and $x_{1c}=y_d$, y_d is the desired tracking signal. x_{2d} is the virtual control to be designed, and x_{2c} is obtained by x_{2d} through two first-order low-pass filters:

$$\alpha_{2,i}\dot{\omega}_{2,i}+\omega_{2,i}=\omega_{2,(i-1)},\ i=1,2 \tag{15}$$

where $\omega_{2,0}=x_{2d}$, $\omega_{2,1}=x_{2c}$,the filter parameters $\alpha_{2,i}>0, i=1,2$ are constants, and the initial parameters satisfy $\omega_{2,i}(0)=\omega_{2,(i-1)}(0),\ i=1,2$.

Define filtering errors as:

$$s_{2,i}=\omega_{2,i}-\omega_{2,(i-1)},\ i=1,2 \tag{16}$$

Then it follows that

$$x_2=x_{2d}+z_2+\sum_{i=1}^{2}s_{2,i} \tag{17}$$

and

$$\begin{cases}\dot{s}_{2,1}=-\dfrac{1}{\alpha_{2,1}}s_{2,1}-\dot{x}_{2d}\\ \dot{s}_{2,2}=-\dfrac{1}{\alpha_{2,2}}s_{2,2}+\dfrac{1}{\alpha_{2,1}}s_{2,1}\end{cases} \tag{18}$$

Define $\hat{\theta}_1$ as the estimate of θ_1 .We then define the estimation error as

$$\tilde{\theta}_1=\hat{\theta}_1-\theta_1 \tag{19}$$

Then it follows that

$$\dot{\tilde{\theta}}_1=\dot{\hat{\theta}}_1 \tag{20}$$

and

$$z_1^{(2)}=x_1^{(2)}-x_{1c}^{(2)}=$$
$$f_{1,0}+f_1\theta_1+g_1\left(x_{2d}+z_2+\sum_{i=1}^{2}s_{2,i}\right)-x_{1c}^{(2)} \tag{21}$$

Select the virtual control law as

$$x_{2d}=\frac{1}{g_1}\left(-f_{1,0}-f_1\hat{\theta}_1-A_1^{0\sim1}z_1^{(0\sim1)}+x_{1c}^{(2)}\right) \tag{22}$$

where, $A_1^{0\sim1}$ is the design parameter.

$$z_1^{(2)}+A_1^{0\sim1}z_1^{(0\sim1)}=g_1\left(z_2+\sum_{i=1}^{2}s_{2i}\right)-f_1\tilde{\theta}_1 \tag{23}$$

Define

$$V_{z1}=\left(z_1^{(0\sim1)}\right)^{\mathrm{T}}P_1z_1^{(0\sim1)} \tag{24}$$

We can get

$$\dot{V}_{z1}\le-\mu_1\left(z_1^{(0\sim1)}\right)^{\mathrm{T}}P_1z_1^{(0\sim1)}-2\left(z_1^{(0\sim1)}\right)^{\mathrm{T}}P_{1L}f_1\tilde{\theta}_1$$
$$+2\left(z_1^{(0\sim1)}\right)^{\mathrm{T}}P_1\begin{bmatrix}0\\g_1\end{bmatrix}\left(z_2+\sum_{i=1}^{2}s_{2i}\right) \tag{25}$$

where, P_{1L} is the last column of matrix P_1.

Define

$$V_{\theta_1}=\tilde{\theta}_1^{\mathrm{T}}\tilde{\theta}_1 \tag{26}$$

$$V_1=V_{z1}+V_{\theta1} \tag{27}$$

Select the adaptive law as

$$\dot{\hat{\theta}}_1=\left(z_1^{(0\sim1)}\right)^{\mathrm{T}}P_{1L}f_1-\gamma_1\hat{\theta}_1 \tag{28}$$

where, $\gamma_1>0$ is the design parameter, and we can get

$$\dot{V}_1\le-\mu_1\left(z_1^{(0\sim1)}\right)^{\mathrm{T}}P_1z_1^{(0\sim1)}-2\gamma_1\tilde{\theta}_1^{\mathrm{T}}\hat{\theta}_1$$
$$+2\left(z_1^{(0\sim1)}\right)^{\mathrm{T}}P_1\begin{bmatrix}0\\g_1\end{bmatrix}\left(z_2+\sum_{i=1}^{2}s_{2i}\right) \tag{29}$$

Step 2 Define

$$z_3=g(v)-x_{3c} \tag{30}$$

where, x_{3d} is the virtual control to be designed, and x_{3c} is obtained by x_{3d} through a first-order low-pass filter.

$$\alpha_{3,1}\dot{x}_{3c}+x_{3c}=x_{3d} \tag{31}$$

where, the filter parameter $\alpha_{3,1}>0$ is a constant, and the initial parameter satisfies $x_{3c}(0)=x_{3d}(0)$. Define the filtering error as

$$s_{3,1}=x_{3c}-x_{3d} \tag{32}$$

Then we can get

$$g(v)=x_{3d}+z_3+s_{3,1} \tag{33}$$

and

$$z_2^{(2)}=x_2^{(2)}-x_{2c}^{(2)}=$$
$$f_{2,0}+f_2\theta_2+g_2\left(x_{3d}+z_3+s_{3,1}+d(v)\right)-x_{2c}^{(2)} \tag{34}$$

Define $\hat{\theta}_2$ as the estimate of θ_2 .We then define the estimation error as:

$$\tilde{\theta}_2=\hat{\theta}_2-\theta_2 \tag{35}$$

then we can get

$$\dot{\tilde{\theta}}_2=\dot{\hat{\theta}}_2 \tag{36}$$

Construct the virtual control law as

$$x_{3d}=\frac{1}{g_2}\left(-f_{2,0}-f_2\hat{\theta}_2+x_{2c}^{(2)}-A_2^{0\sim1}z_2^{(0\sim1)}-\frac{1}{4\sigma}g_2^2d_m^2P_{2L}^{\mathrm{T}}z_2^{(0\sim1)}\right) \tag{37}$$

where, $\sigma>0$ is a constant, P_{2L} is the last column of matrix P_2.

Then we can get

$$z_2^{(2)}+A_2^{0\sim1}z_2^{(0\sim1)}=-f_2\tilde{\theta}_2+g_2\left(z_3+s_{3,1}\right)+\phi \tag{38}$$

$$\phi=-\frac{1}{4\sigma}g_2^2d_m^2P_{2L}^{\mathrm{T}}z_2^{(0\sim1)}+g_2d(v) \tag{39}$$

Define

$$V_{z_2} = \left(z_2^{(0\sim1)}\right)^{\mathrm{T}} P_2 z_2^{(0\sim1)} \tag{40}$$

Then, we can get

$$\begin{aligned}\dot{V}_{z2} \le & -\mu_n \left(z_2^{(0\sim1)}\right)^{\mathrm{T}} P_2 z_2^{(0\sim1)} - 2\left(z_2^{(0\sim1)}\right)^{\mathrm{T}} P_{2L} f_2 \tilde{\theta}_2 \\ & +2\left(z_2^{(0\sim1)}\right)^{\mathrm{T}} P_{2L}\phi + 2\left(z_2^{(0\sim1)}\right)^{\mathrm{T}} P_{2L} g_2 \left(z_3 + s_{3,1}\right)\end{aligned} \tag{41}$$

Based on Lemma 3, we can get

$$\begin{aligned}\dot{V}_{z2} \le & -\mu_2 \left(z_2^{(0\sim1)}\right)^{\mathrm{T}} P_2 z_2^{(0\sim1)} - 2\left(z_2^{(0\sim1)}\right)^{\mathrm{T}} P_{2L} f_2 \tilde{\theta}_2 \\ & + 2\left(z_2^{(0\sim1)}\right)^{\mathrm{T}} P_{2L} g_2 \left(z_3 + s_{3,1}\right) + 2\sigma\end{aligned} \tag{42}$$

Define

$$V_{\theta_2} = \tilde{\theta}_2^{\mathrm{T}} \tilde{\theta}_2 \tag{43}$$

$$V_2 = V_{z_2} + V_{\theta_2} \tag{44}$$

Construct the adaptive law as

$$\dot{\hat{\theta}}_2 = \left(z_2^{(0\sim1)}\right)^{\mathrm{T}} P_{2L} f_2 - \gamma_2 \hat{\theta}_2 \tag{45}$$

and we can get

$$\begin{aligned}\dot{V}_2 \le & -\mu_2 \left(z_2^{(0\sim1)}\right)^{\mathrm{T}} P_2 z_2^{(0\sim1)} - 2\gamma_2 \tilde{\theta}_2^{\mathrm{T}} \hat{\theta}_2 \\ & + 2\left(z_2^{(0\sim1)}\right)^{\mathrm{T}} P_{2L} g_2 \left(z_3 + s_{3,1}\right) + 2\sigma\end{aligned} \tag{46}$$

Step 3 Construct

$$w = N(\chi)\bar{w} \tag{47}$$

$$\bar{w} = -c_3 z_3 - 2(z_2^{0\sim1})^{\mathrm{T}} P_{2L} g_2 + h(v)cv + \dot{x}_{3c} \tag{48}$$

$$N(\chi) = \chi^2 \cos\chi \tag{49}$$

and

$$\dot{\chi} = \gamma_\chi \bar{w} z_3 \tag{50}$$

where, $\gamma_\chi > 0$ and $c_3 > 0$ are design parameters, and $N(\chi)$ is a Nussbaum type function.

Define

$$V_3 = \frac{1}{2} z_3^2 \tag{51}$$

and

$$\begin{aligned}\dot{V}_3 = z_3 \dot{z}_3 = & -c_3 z_3^2 - 2(z_2^{0\sim1})^{\mathrm{T}} P_{2L} g_2 z_3 \\ & + \frac{1}{\gamma_\chi}(h(v)N(\chi) - 1)\dot{\chi}\end{aligned} \tag{52}$$

4 Stability analysis

Theorem 1. For the system (1), the input saturation controller created by combining the virtual control law in Equations (22) and (37), the control law in Equations (48)-(51), and the adaptive law in Equations (28) and (46), achieves uniform ultimate boundedness of all signals in the closed-loop system and effective tracking of the desired reference signal even when the system is subject to input saturation.

Proof. It follows that

$$\begin{aligned}\sum_{i=1}^{3}\dot{V}_i \le & -\sum_{i=1}^{2}\mu_i \left(z_i^{(0\sim1)}\right)^{\mathrm{T}} P_i z_i^{(0\sim1)} - c_3 z_3^2 - \sum_{i=1}^{2} 2\gamma_i \tilde{\theta}_i^{\mathrm{T}} \hat{\theta}_i \\ & +2\left(z_1^{(0\sim1)}\right)^{\mathrm{T}} P_{1L} g_1 \left(z_2 + \sum_{j=1}^{2} s_{2j}\right) \\ & +2\left(z_2^{(0\sim1)}\right)^{\mathrm{T}} P_{2L} g_2 s_{3,1} + 2\sigma + \frac{1}{\gamma_\chi}(h(v)N(\chi) - 1)\dot{\chi}\end{aligned} \tag{53}$$

Define

$$V_{s2} = \frac{1}{2}\sum_{j=1}^{2} s_{2j}^2 \tag{54}$$

$$V_{s3} = \frac{1}{2} s_{3,1}^2 \tag{55}$$

then we can get

$$\begin{aligned}\dot{V}_{s2} = & -\frac{1}{\alpha_{2,1}} s_{2,1}^2 - s_{2,1}\dot{x}_{2d} - \frac{1}{\alpha_{2,2}} s_{2,2}^2 + \frac{1}{\alpha_{2,1}} s_{2,1} s_{2,2} \\ \le & -\frac{1}{2\alpha_{2,1}} s_{2,1}^2 - \left(\frac{1}{\alpha_{2,2}} - \frac{1}{2\alpha_{2,1}}\right) s_{2,2}^2 - s_{2,1}\dot{x}_{2d}\end{aligned} \tag{56}$$

and

$$\dot{V}_{s3} = s_{3,1}\dot{s}_{3,1} = -\frac{1}{\alpha_{3,1}} s_{3,1}^2 - s_{3,1}\dot{x}_{3d} \tag{57}$$

Define

$$V = \sum_{i=1}^{3} V_i + \sum_{i=2}^{3} V_{si} \tag{58}$$

then we can get

$$\begin{aligned}\dot{V} \le & -\sum_{i=1}^{2}\mu_i \left(z_i^{(0\sim1)}\right)^{\mathrm{T}} P_i z_i^{(0\sim1)} - c_3 z_3^2 - \sum_{i=1}^{2}\gamma_i \tilde{\theta}_i^{\mathrm{T}} \tilde{\theta}_i + \sum_{i=1}^{2}\gamma_i \theta_i^{\mathrm{T}} \theta_i \\ & +2\left(z_1^{(0\sim1)}\right)^{\mathrm{T}} P_{1L} g_1 \left(z_2 + \sum_{j=1}^{2} s_{2j}\right) \\ & +2\left(z_2^{(0\sim1)}\right)^{\mathrm{T}} P_{2L} g_2 s_{3,1} + 2\sigma + \frac{1}{\gamma_\chi}(h(v)N(\chi) - 1)\dot{\chi} \\ & -\frac{1}{2\alpha_{2,1}} s_{2,1}^2 - \left(\frac{1}{\alpha_{2,2}} - \frac{1}{2\alpha_{2,1}}\right) s_{2,2}^2 - \frac{1}{\alpha_{3,1}} s_{3,1}^2 - \sum_{i=2}^{3} s_{i1}\dot{x}_{id}\end{aligned} \tag{59}$$

It is obvious that $\dot{x}_{id}$, $i = 1,2$ is a function of the variables z_i, $z_1^{(0\sim1)}$, $y_d^{(0\sim3)}$, $\hat{\theta}_i$, $i = 1,2$, z_3 and $x_{ic}^{(2)}$, $f_{i,0}$, f_i, $i = 1,2$, $\dot{x}_{3c}$ and the parameters $A_i^{(0\sim1)}$, $i = 1,2$. Thus, there exists a non-negative continuous function η_i, which is a function of the aforementioned variables and depends on the design parameters mentioned above, such that $|\dot{x}_{id}| \le \eta_i$. For any $V(0) > 0$, the set

$$\Omega = \left\{ z_i, z_1^{(0\sim1)}, s_{2,1}, s_{2,2}, \tilde{\theta}_i, i = 1,2, z_3, s_{3,1} \middle| \; V \le V(0) \right\} \tag{60}$$

is a compact. Note that $\left[y_d \;\; \dot{y}_d \;\; y_d^{(2)} \;\; y_d^{(3)} \right]^{\mathrm{T}} \in \Omega_0$. Therefore, $\eta_i, \forall i \in \{1,2\}$ has a maximum value on $\Omega \times \Omega_0$ denoted by $\bar{\eta}_i$. Therefore, on Ω, we can get

$$\begin{aligned}\dot{V} \le & -\sum_{i=1}^{2}\mu_i\left(z_i^{(0\sim1)}\right)^{\mathrm{T}}P_i z_i^{(0\sim1)}-c_3 z_3^2-\sum_{i=1}^{2}\gamma_i\tilde{\theta}_i^{\mathrm{T}}\tilde{\theta}_i+\sum_{i=1}^{2}\gamma_i\theta_i^{\mathrm{T}}\theta_i\\ & +2\left(z_1^{(0\sim1)}\right)^{\mathrm{T}}P_{1L}g_1\left(z_2+\sum_{j=1}^{2}s_{2j}\right)\\ & +2\left(z_2^{(0\sim1)}\right)^{\mathrm{T}}P_{2L}g_2 s_{3,1}+2\sigma+\frac{1}{\gamma_\chi}(h(v)N(\chi)-1)\dot{\chi}\\ & -\frac{1}{2\alpha_{2,1}}s_{2,1}^2-\left(\frac{1}{\alpha_{2,2}}-\frac{1}{2\alpha_{2,1}}\right)s_{2,2}^2-\frac{1}{\alpha_{3,1}}s_{3,1}^2+\sum_{i=2}^{3}|s_{i1}|\bar{\eta}_i\end{aligned} \tag{61}$$

Because

$$\sum_{i=2}^{3}|s_{i1}|\bar{\eta}_i=\sum_{i=2}^{3}\frac{\bar{\eta}_i^2}{4\tilde{\sigma}}s_{i1}^2+2\tilde{\sigma} \tag{62}$$

where, $\tilde{\sigma}>0$ is a constant.

And we can get

$$\begin{aligned}\dot{V} \le & -(\mu_1-3)\left(z_1^{(0\sim1)}\right)^{\mathrm{T}}P_1 z_1^{(0\sim1)}\\ & -\left(\mu_2-\frac{\lambda_{\max}(P_1)}{\lambda_{\min}(P_2)}g_1^2-1\right)\left(z_2^{(0\sim1)}\right)^{\mathrm{T}}P_2 z_2^{(0\sim1)}\\ & -c_3 z_3^2-\left(\frac{1}{2\alpha_{2,1}}-\frac{\bar{\eta}_2^{\,2}}{4\tilde{\sigma}}-\lambda_{\max}(P_1)g_1^2\right)s_{2,1}^2\\ & -\left(\frac{1}{\alpha_{2,2}}-\frac{1}{2\alpha_{2,1}}-\lambda_{\max}(P_1)g_1^2\right)s_{2,2}^2\\ & -\left(\frac{1}{\alpha_{3,1}}-\lambda_{\max}(P_2)g_2^2-\frac{\bar{\eta}_3^{\,2}}{4\tilde{\sigma}}\right)s_{3,1}^2-\sum_{i=1}^{2}\gamma_i\tilde{\theta}_i^{\mathrm{T}}\tilde{\theta}_i\\ & +\sum_{i=1}^{2}\gamma_i\theta_i^{\mathrm{T}}\theta_i+2\sigma+2\tilde{\sigma}+\frac{1}{\gamma_\chi}(h(v)N(\chi)-1)\dot{\chi}\end{aligned} \tag{63}$$

Therefore, if the design parameters meet:

$$\begin{cases}\mu_1-3\ge\gamma\\ \mu_2-\dfrac{\lambda_{\max}(P_1)}{\lambda_{\min}(P_2)}g_1^2-1\ge\gamma\\ c_3\ge\gamma\\ \dfrac{1}{2\alpha_{2,1}}-\dfrac{\bar{\eta}_2^{\,2}}{4\tilde{\sigma}}-\lambda_{\max}(P_1)g_1^2\ge\gamma\\ \dfrac{1}{\alpha_{2,2}}-\dfrac{1}{2\alpha_{2,1}}-\lambda_{\max}(P_1)g_1^2\ge\gamma\\ \dfrac{1}{\alpha_{3,1}}-\lambda_{\max}(P_2)g_2^2-\dfrac{\bar{\eta}_3^{\,2}}{4\tilde{\sigma}}\ge\gamma\\ \gamma_i\ge\gamma\ ,i=1,2\end{cases} \tag{64}$$

where γ is an arbitrarily given positive number.

Define

$$\varepsilon=\sum_{i=1}^{2}\gamma_i\theta_i^{\mathrm{T}}\theta_i+2\sigma+2\tilde{\sigma} \tag{65}$$

Then, we can get

$$\dot{V}\le-\gamma V+\varepsilon+\frac{1}{\gamma_\chi}(h(v)N(\chi)-1)\dot{\chi} \tag{66}$$

By integrating Equation (70), we obtain

$$\begin{aligned}V\le & V(0)\mathrm{e}^{-\gamma t}+\frac{\varepsilon}{\gamma}(1-\mathrm{e}^{-\gamma t})\\ & +\frac{\mathrm{e}^{-\gamma t}}{\gamma_\chi}\int_0^t(h(v)N(\chi)\dot{\chi}-\dot{\chi})\mathrm{e}^{\gamma\tau}\mathrm{d}\tau\end{aligned} \tag{67}$$

Therefore, we can conclude from Lemma 2 that V and χ are bounded. Furthermore, it follows that all signals in the closed-loop system are bounded. Theorem 1 is thus proved.■

5 Illustrative simulation

To validate the effectiveness of the proposed algorithm, simulations were conducted by selecting the parameters for the manipulator system: $M=0.25\,\mathrm{kg}$, $L=1\,\mathrm{m}$, $g=9.8\ \mathrm{m\cdot s^{-2}}$, $K=2\,\mathrm{N\cdot m\cdot rad^{-1}}$, $B=0.6$, $B_1=0.01$, $J=0.001\ \mathrm{m\cdot s^{-2}}$ and $\alpha=\dfrac{\pi}{36}$. θ_1 and θ_2 are uncertain system parameters, and their real values are $\theta_1=9.8$ and $\theta_2=600$, respectively.

The tracking reference signal is set to $y_d=0.5(\sin(t)+\sin(0.5t))$. The relevant parameters selected for the simulation are $\hat{\theta}_1(0)=9$, $\hat{\theta}_2(0)=590$, $x_1(0)=0.1$, $\dot{x}_1(0)=0.2$, $x_2(0)=0.5$, $\dot{x}_2(0)=0.5$ and $u_M=2$.

The results are shown in Figs.1–5.

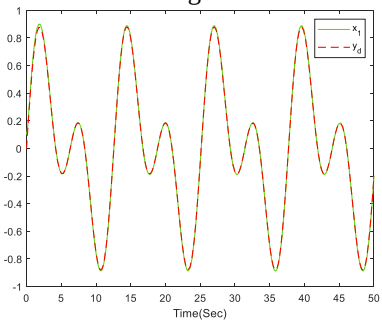

Fig. 1: The output $x_1(t)$ and the desired trajectory $y_d(t)$

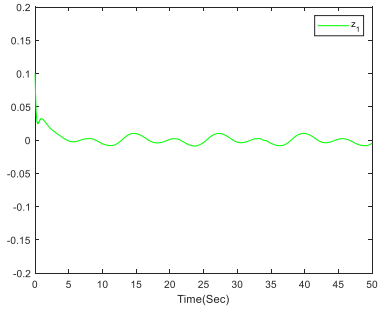

Fig. 2: Tracking error $z_1(t)$

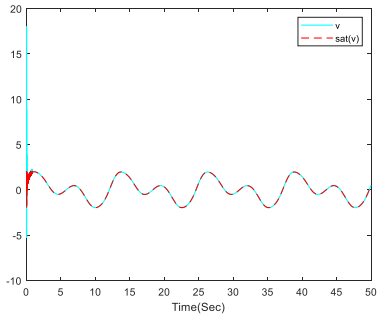

Figure 3: control input v and saturated control input $sat(v)$.

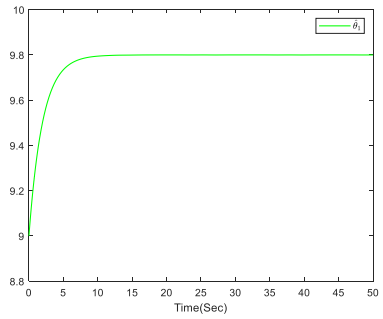

Figure 4: parameter estimation $\hat{\theta}_1$

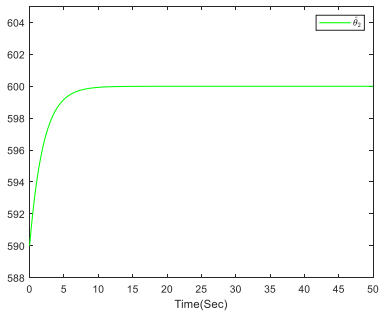

Figure 5: parameter estimation $\hat{\theta}_2$

In the above simulation results, Figures 1 and 2 show the system output tracking results and tracking error. Figure 3 shows the system control input v and saturated control input $sat(v)$. It can be observed that, when considering input saturation constraints, the actual control input remains within the constraint range except for experiencing input saturation during the transient phase. Figures 4 and 5 display the system's uncertain parameter estimation results, which indicate that the proposed method can accurately converge the parameter estimation to the true value of the parameters.

5. Conclusion

In this paper, a control strategy based on the fully actuated system approach is designed for a second-order cascaded manipulator system (1) with input saturation. The proposed controller is developed directly using the fully actuated system approach, eliminating the need for transforming the original second-order strict feedback system into a first-order strict feedback system. Smooth functions and Nussbaum functions were employed to address the input saturation issue. The Lyapunov stability theory is employed to prove that all signals of the closed-loop system are uniformly ultimately bounded. Numerical simulations of the manipulator system are performed to verify the effectiveness of the proposed method.

References

[1] Chen Z S, Wang X S, and Chen Y H. Continuous non-singular fast terminal sliding mode control of robotic manipulators considering disturbance and input saturation [J]. *Control and Decision* (In Chinese), 2022,37(04):903-912.

[2] Ling X M. Adaptive control of single-link manipulator with saturated input by compound filtering [J]. J*ournal of Yuxi Normal University* (In Chinese), 2022,38(03):16-20.

[3] Wen C Y, Zhou J, Liu Z T, et al. Robust adaptive control of uncertain nonlinear systems in the presence of input saturation and external disturbance [J].*IEEE Transactions on Automatic Control*, 2011, 56(7): 1672-1678.

[4] Li Y, Wei S. Adaptive asymptotic tracking of uncertain nonlinear systems with input saturation. *Control and Decision* (In Chinese). 2023; 38(8): 2326–2334.

[5] Wang L, Shi Q, Liu J, et al. Backstepping control of flexible joint manipulator based on hyperbolic tangent function with control input and rate constraints[J]. *Asian Journal of Control*, 2020, 22(3): 1268-1279.

[6] Ling S, Wang H, Liu P X. Adaptive fuzzy dynamic surface control of flexible-joint robot systems with input saturation[J]. *IEEE/CAA Journal of Automatica Sinica*, 2019, 6(1): 97-107.

[7] Duan G R. High-order system approaches: I. Fully-actuated systems and parametric designs[J]. *Acta Automatica Sinica*, 2020, 46(7): 1333-1345. (In Chinese)

[8] Duan G. High-order fully actuated system approaches: Part I. Models and basic procedure[J]. *International Journal of Systems Science*, 2021, 52(2): 422-435.

[9] Duan G. High-order fully actuated system approaches: Part II. Generalized strict-feedback systems[J]. *International Journal of Systems Science*, 2021, 52(3): 437-454.

[10] Duan G. High-order fully actuated system approaches: Part III. Robust control and high-order backstepping[J]. *International Journal of Systems Science*, 2021, 52(5): 952-971.

[11] Duan G. High-order fully actuated system approaches: Part IV. Adaptive control and high-order backstepping[J]. *International Journal of Systems Science*, 2021, 52(5): 972-989.

[12] Hou M, Shi W, Fang L, et al. Adaptive dynamic surface control of high-order strict feedback nonlinear systems with parameter estimations[J]. *Science China Information Sciences*, 2023, 66(5): 159203.

[13] Liu W, Duan G, Hou M. High-order robust command filtered backstepping design for strict-feedback systems: A high-order fully actuated system approach[J]. *International Journal of Robust and Nonlinear Control*, 2022, 32(18): 10251-10270.

[14] Xiao Y, Cai G, Duan G. High-order adaptive dynamic surface control for output-constrained non-linear systems based on fully actuated system approach[J]. *International Journal of Systems Science*, 2024, 55(3): 482-498.

[15] Cai G, Xiao Y, Wei H, et al. Robust adaptive dynamic surface control of high-order strict feedback systems based on fully actuated system approach[J]. *International Journal of Systems Science*, 2024: 1-14.

[16] Xiao Y, Cai G, Hou M, et al. High-order robust dynamic surface control for uncertain nonlinear systems based on fully actuated system approach[C]//*2023 2nd Conference on Fully Actuated System Theory and Applications (CFASTA). IEEE*, 2023: 728-733.

[17] Cai Guang-Bin, Xiao Yong-Qiang, Hu Chang-Hua, Yang Xiao-Gang, Fan Yong-Hua. Time-varying output constraint control of high-order strict-feedback systems based on fully actuated system approach. *Acta Automatica Sinica*, 2024: 1−14, (early access).

[18] Zhang H Y, Wang W and Chen S. W. Integrated guidance and control design based on fully actuated system method [J]. *Acta Aeronautica et Astronautica Sinica* (In Chinese),2023,1-15.

[19] Khalil, H. K. Nonlinear Systems, 3rd Edition [M]. *Prentice Hall*, Upper Saddle River, 2002.

Proceedings of the 3rd Conference on Fully Actuated System Theory and Applications
May 10-12, 2024, Shenzhen, China

Adaptive Attitude Tracking Control of Spacecraft Based on High-Order Fully Actuated System Approach

Dongyan Jin, Mingyu Hou, Tong Wang, Jianbin Qiu

Research Institute of Intelligent Control and Systems, Harbin Institute of Technology, Harbin 150001, China
E-mail: 22S104176@stu.hit.edu.cn; 120L011616@stu.hit.edu.cn; twang@hit.edu.cn; jbqiu@hit.edu.cn

Abstract: In this paper, the adaptive attitude tracking control of spacecraft with unknown time-varying disturbances is studied. Firstly, the attitude model is established using modified Rodriguez parameters, which is transformed into a high-order fully actuated (HOFA) system model with unknown time-varying parameters. Then, a novel adaptive attitude tracking control strategy based on the HOFA system approach is proposed. With the proposed control strategy, the unknown time-varying disturbances are estimated and compensated. The system stability of spacecraft attitude is guaranteed via Lyapunov theory. Finally, the effectiveness of the proposed control strategy is verified through numerical simulations.

Key Words: Adaptive control, high-order fully actuated system approach, spacecraft attitude control, modified Rodrigues parameters.

1 Introduction

Alongside the advancement of the space industry, there is an increasing demand for diverse space missions, which imposes higher requirements on the attitude control of spacecrafts. For the attitude control of spacecrafts, it is essential to consider the nonlinear characteristics of its attitude model and the impact of unknown time-varying disturbances. These factors make the attitude control of spacecrafts more complex and crucial.

Consequently, the attitude control of spacecrafts has recently gained significant attention during the past decades and has been studied by proposing different control strategies in [1–3]. It is necessary to highlight that most research findings concerning attitude control of spacecrafts are grounded in the foundational framework of the state space model.

Recently, inspired by the concept of fully actuation of actual engineering systems, the high-order fully actuated (HOFA) system approach was suggested for the first time in [4]. Unlike most of the traditional control strategies, a novel control strategy utilizing the HOFA system approach was thus introduced. As a result of the fully actuation property, the known nonlinear functions can be completely compensated, which facilitates the controller design process [4]. Furthermore, the aforementioned results were extended to the cases of robust control, adaptive control, and generalized PID control in [5–8].

It should be noted that the HOFA systems can be derived from numerous different types of systems through transformation, including strict-feedback systems, feedback linearizable systems, and controllable linear and nonlinear systems. Moreover, controlled plants based on the law of momentum, Lagrangian equations, and Kirchhoff's laws can also be transformed into HOFA systems. Recently, based on the HOFA system approach, the attitude tracking control strategy for a rigid body spacecraft by using the modified Rodrigues parameters was presented in [9]. The linear quadratic regulator control and the adaptive control for a combined spacecraft by using Euler angles and the C-W equation were studied in [10, 11], respectively. Then, the rigid body spacecraft attitude control using quaternions was investigated in [12]. However, limited findings were reported for the attitude tracking control of spacecraft via the adaptive HOFA system approach by using the modified Rodrigues parameters.

Therefore, inspired by [7], a novel adaptive attitude tracking control strategy of a rigid body spacecraft derived from the adaptive HOFA system approach is designed. The unknown time-varying disturbances can be effectively estimated based on the proposed control strategy, enabling the successful control of spacecraft attitude.

The main contribution of this paper is to propose a novel attitude tracking control strategy, which ensures the stability of the spacecraft system. It successfully addresses the impact of unknown time-varying disturbances while compensating for system nonlinearities.

The notations employed in this paper are

$$x^{(0\sim n)} = \begin{bmatrix} x \\ \dot{x} \\ \vdots \\ x^{(n)} \end{bmatrix},$$

$$A^{0\sim n-1} = \begin{bmatrix} A_0 & A_1 & \cdots & A_{n-1} \end{bmatrix},$$

$$\Phi\left(A^{0\sim n-1}\right) = \begin{bmatrix} 0 & I & & \\ & & \ddots & \\ & & & I \\ -A_0 & -A_1 & & -A_{n-1} \end{bmatrix}.$$

The subsequent structure of this paper is outlined below. In Section 2, the kinematic and dynamic attitude models are established based on the modified Rodriguez parameters. Then, it is converted into a HOFA system model with unknown time-varying parameters. A novel adaptive control strategy is designed, and the system stability is proved in Section 3. The effectiveness of the proposed control strategy is validated through numerical simulations in Section 4. Section 5 concludes this paper.

This work was supported by the National Natural Science Foundation of China (U21B6001, 62273121).

2 Problem Formulation

Several different attitude models are presented in this section to show the superiority of the modified Rodriguez parameters modeling technique. Then, the attitude error model is transformed into a HOFA model with time-varying unknown parameters. Finally, the control objective of this paper is presented.

Euler angles, quaternions, and modified Rodriguez parameters are commonly used to describe the attitude of spacecraft. These methods have their own advantages and disadvantages. Euler angles and modified Rodriguez parameters are the least parameterized modelling methods. However, they both have the disadvantage of singularity. In addition, if Euler angles are used to describe the attitude model, a significant amount of trigonometric calculations are required, which increases the computational burden. Quaternions are globally non-singular subject to unit constraints. Therefore, based on the above analysis, modified Rodriguez parameters are chosen as the modelling tool for the spacecraft attitude in this paper.

The kinematics and dynamics based on the modified Rodrigues parameters are given as

$$\dot{q}_e = \Pi(q_e)\omega_e, \tag{1}$$

$$\begin{aligned} J\dot{\omega}_e =& -(\omega_e + C\omega_d)^{\times} J(\omega_e + C\omega_d) \\ & - J\left(C\dot{\omega}_d - \omega_e^{\times} C\omega_d\right) + u + d(t) \end{aligned} \tag{2}$$

where $q_e = [q_{e1}, q_{e2}, q_{e3}]^{\mathrm{T}}$ is the error of modified Rodriguez parameters, $J \in R^{3\times 3}$ is the moment of inertia matrix of spacecraft, $u = [u_1, u_2, u_3]^{\mathrm{T}}$ is the control torque, and $d(t) = [d_1(t), d_2(t), d_3(t)]^{\mathrm{T}}$ is the unknown time-varying disturbances torque caused by factors including solar radiation atmospheric drag, and other factors. $\omega_e = [\omega_{e1}, \omega_{e2}, \omega_{e3}]^{\mathrm{T}}$ and $\omega_d = [\omega_{d1}, \omega_{d2}, \omega_{d3}]^{\mathrm{T}}$ are the error and desired angular velocity of the spacecraft, respectively. $\omega_e^{\times}$ is defined as

$$\omega_e^{\times} = \begin{bmatrix} 0 & -\omega_{e3} & \omega_{e2} \\ \omega_{e3} & 0 & -\omega_{e1} \\ -\omega_{e2} & \omega_{e1} & 0 \end{bmatrix}. \tag{3}$$

C is the attitude transformation matrix, satisfying

$$C = I_3 + \frac{8(q_e^{\times})^2 - 4(1 - q_e^{\mathrm{T}} q_e) q_e^{\times}}{(1 + q_e^{\mathrm{T}} q_e)^2}. \tag{4}$$

where I_3 is a 3x3 identity matrix.

$\Pi(q_e)$ is given as

$$\Pi(q_e) = \frac{1}{2}\left(\frac{1 - q_e^{\mathrm{T}} q_e}{2} I_3 + q_e^{\times} + q_e q_e^{\mathrm{T}}\right). \tag{5}$$

Assumption 1: The $d(t)$ is differentiable and bounded. Let the pre-estimate of $d(t)$ as $d_0(t)$, which satisfies

$$\|d(t) - d_0(t)\| \le \delta_0, \forall t \ge 0, \tag{6}$$

$$\left\|\dot{d}(t) - \dot{d}_0(t)\right\| \le \delta_1, \forall t \ge 0 \tag{7}$$

where δ_0 and δ_1 are non-negative real numbers representing the estimation error and derivative estimation error of $d(t)$, respectively.

Then, the kinematics and dynamics of spacecraft attitude error (1) and (2) will be converted into a HOFA system model.

Calculating the time derivative of (1) and substituting (2) into it, the following expression is obtained.

$$\begin{aligned} \ddot{q}_e =& \dot{\Pi}(q_e)\Pi^{-1}(q_e)\dot{q}_e \\ & - \Pi(q_e) J^{-1}\left(\Pi^{-1}(q_e)\dot{q}_e \right. \\ & \left. + C\omega_d\right)^{\times} J\left(\Pi^{-1}(q_e)\dot{q}_e + C\omega_d\right) \\ & - \Pi(q_e)\left(C\dot{\omega}_d - \left(\Pi^{-1}(q_e)\dot{q}_e\right)^{\times} C\omega_d\right) \\ & + \Pi(q_e) J^{-1} u + \Pi(q_e) J^{-1} d(t). \end{aligned} \tag{8}$$

Based on the properties of the modified Rodrigues parameters, the following equation holds.

$$\Pi^{-1}(q_e) = \frac{16}{(1 + q_e^T q_e)^2}\Pi^{\mathrm{T}}(q_e). \tag{9}$$

Therefore, it always satisfies

$$\det \Pi(q_e) J^{-1} \ne 0. \tag{10}$$

Based on (10), it is concluded that (8) is a HOFA system model. Furthermore, by considering unknown time-varying disturbances, (8) can be regarded as a HOFA system model with uncertain time-varying parameters proposed in [7]

$$\begin{aligned} x^{(n)} =& f\left(x^{(0\sim n-1)}\right) + H^{\mathrm{T}}\left(x^{(0\sim n-1)}\right)\theta \\ & + L\left(x^{(0\sim n-1)}\right) u \end{aligned} \tag{11}$$

where x and u represent the system state vector and control input, respectively. $f\left(x^{(0\sim n-1)}\right)$, $H\left(x^{(0\sim n-1)}\right)$ and $L\left(x^{(0\sim n-1)}\right)$ are continuous functions of the system states. θ represents the unknown time-varying parameter.

Our previous results in [13] have introduced the detailed derivation process of (8). Therefore, this paper directly presents the final attitude error HOFA spacecraft model (8) omitting the intermediate derivation process.

This paper aims to develop an adaptive control strategy building upon the HOFA system approach, ensuring bounded estimation error of unknown time-varying disturbances and system stability.

3 Control Strategy Design

The following Lemmas are introduced before designing the adaptive control strategy based on the HOFA system approach.

3.1 Lemma Description

Let the estimation value of $d(t)$ as $\hat{d}(t)$, and the following equations hold

$$\tilde{d}(t) = d(t) - \hat{d}(t), \tag{12}$$

$$\tilde{d}_{e0}(t) = \hat{d}(t) - d_0(t), \tag{13}$$

$$\tilde{d}_{r0}(t) = d(t) - d_0(t). \tag{14}$$

Lemma 1 ([7]) According to (12)-(14), and under assumption 1, we have

$$\tilde{d}(t) = \tilde{d}_{r0}(t) - \tilde{d}_{e0}(t), \tag{15}$$

$$\tilde{d}_{r0}^{\mathrm{T}}(t)\tilde{d}(t) \leq \frac{1}{2}\left(\delta_0^2 + \|\tilde{d}(t)\|^2\right), \tag{16}$$

$$\dot{\tilde{d}}_{r0}^{\mathrm{T}}(t)\tilde{d}(t) \leq \frac{1}{2}\left(\delta_1^2 + \|\tilde{d}(t)\|^2\right). \tag{17}$$

Lemma 2 ([7]) For any $\mu > 0$, matrices $A_i \in \mathbb{R}^{r\times r}, i = 0, 1, \ldots, n-1$ exist, such that

$$\operatorname{Re}\lambda_i\left(\Phi\left(A^{0\sim n-1}\right)\right) < -\frac{\mu}{2}, \quad i = 1, 2, \ldots, nr. \tag{18}$$

Lemma 3 ([7]) If Lemma 2 holds, there exist a positive definite matrix $P\left(A^{0\sim n-1}\right)$ defined as

$$P\left(A^{0\sim n-1}\right) = \left[\begin{array}{cccc} P_1 & P_2 & \cdots & P_n \end{array}\right], P_i \in \mathbb{R}^{nr\times r}. \tag{19}$$

Then, we have

$$\begin{aligned}&\Phi^{\mathrm{T}}\left(A^{0\sim n-1}\right)P\left(A^{0\sim n-1}\right) + P\left(A^{0\sim n-1}\right)\Phi\left(A^{0\sim n-1}\right)\\ &\quad\leq -\mu P\left(A^{0\sim n-1}\right)\end{aligned} \tag{20}$$

Denote

$$P_L\left(A^{0\sim n-1}\right) = P_n. \tag{21}$$

Lemma 4 ([7]) For any matrix $F \in R^{nr\times nr}$, $A^{0\sim n-1}$ and V hold as

$$\Phi\left(A^{0\sim n-1}\right) = VFV^{-1}$$

in which

$$A^{0\sim n-1} = -ZF^nV^{-1}(Z, F)$$

$$V = V(Z, F) = \left[\begin{array}{c} Z \\ ZF \\ \vdots \\ ZF^{n-1} \end{array}\right]$$

where $Z \in R^{r\times nr}$ satisfies

$$\det V(Z, F) \neq 0.$$

3.2 Controller Design

The control strategy is designed as

$$\left\{\begin{array}{l} u = -J_0\Pi^{-1}(q_e)\left(A^{0\sim1}q_e^{(0\sim1)} + u_0 + u_1\right)\\ u_0 = \dot{\Pi}(q_e)\Pi^{-1}(q_e)\dot{q}_e\\ \qquad -\Pi(q_e)J^{-1}\left(\Pi^{-1}(q_e)\dot{q}_e\right.\\ \qquad \left.+C\omega_d\right)^{\times}J\left(\Pi^{-1}(q_e)\dot{q}_e + C\omega_d\right)\\ \qquad -\Pi(q_e)\left(C\dot{\omega}_d - \left(\Pi^{-1}(q_e)\dot{q}_e\right)^{\times}C\omega_d\right)\\ u_1 = \Pi(q_e)J^{-1}\hat{d}(t)\end{array}\right. \tag{22}$$

in which $\hat{d}(t)$ satisfies

$$\begin{aligned}\dot{\hat{d}}(t) = &\left(\Pi(q_e)J^{-1}\right)^{\mathrm{T}}P_L^{\mathrm{T}}\left(A^{0\sim n-1}\right)q_e^{(0\sim1)}\\ &-(\mu+1)\left(\hat{d}(t) - d_0(t)\right) + \dot{d}_0(t).\end{aligned} \tag{23}$$

Theorem 1: The states of the system and the estimation error of unknown time-varying disturbance converge to the following ellipsoidal domain under the proposed control strategy (22)-(23).

$$\begin{aligned}&\Theta_{(\mu,\delta)}(0)\\ &= \left\{\left[\begin{array}{c} q_e^{(0\sim1)} \\ \tilde{d}(t) \end{array}\right] \middle| \left\|q_e^{(0\sim1)}\right\|_P^2 + \|\tilde{d}(t)\|^2 \leq 2\frac{\delta}{\mu}\right\}\end{aligned} \tag{24}$$

where $\delta = \frac{1}{2}\left(\delta_1^2 + (\mu+1)\delta_0^2\right)$.

Proof.

Substituting (22) into (8) yields

$$\ddot{q}_e = A^{0\sim n-1}q_e^{(0\sim1)} + \Pi(q_e)J^{-1}\tilde{d}(t). \tag{25}$$

Then, it can be transformed into

$$\dot{q_e}^{(0\sim1)} = \Phi\left(A^{0\sim1}\right)q_e^{(0\sim1)} + \left[\begin{array}{c} 0_{3\times1} \\ d^* \end{array}\right] \tag{26}$$

where $d^* = \Pi(q_e)J^{-1}\tilde{d}(t)$.

Design the Lyapunov function as

$$V = \frac{1}{2}\left(q_e^{(0\sim1)}\right)^{\mathrm{T}}P\left(A^{0\sim1}\right)q_e^{(0\sim1)} + \frac{1}{2}\tilde{d}^{\mathrm{T}}(t)\tilde{d}(t). \tag{27}$$

Differentiating equation (27) with respect to time results in

$$\begin{aligned}\dot{V} =&\frac{1}{2}\left(\dot{q_e}^{(0\sim1)}\right)^{\mathrm{T}}P\left(A^{0\sim1}\right)q_e^{(0\sim1)}\\ &+\frac{1}{2}\left(q_e^{(0\sim1)}\right)^{\mathrm{T}}P\left(A^{0\sim1}\right)\dot{q_e}^{(0\sim1)}\\ &+\frac{1}{2}\dot{\tilde{d}}^{\mathrm{T}}(t)\tilde{d}(t) + \frac{1}{2}\tilde{d}^{\mathrm{T}}(t)\dot{\tilde{d}}(t)\\ =&\frac{1}{2}\left(\Phi\left(A^{0\sim1}\right)q_e^{(0\sim1)}\right.\\ &\left.+\left[\begin{array}{c} 0_{3\times1} \\ d^* \end{array}\right]\right)^{\mathrm{T}}P\left(A^{0\sim1}\right)q_e^{(0\sim1)}\\ &+\frac{1}{2}\left(q_e^{(0\sim1)}\right)^{\mathrm{T}}P\left(A^{0\sim1}\right)\left(\Phi\left(A^{0\sim1}\right)q_e^{(0\sim1)}\right.\\ &\left.+\left[\begin{array}{c} 0_{3\times1} \\ d^* \end{array}\right]\right) + \dot{\tilde{d}}^{\mathrm{T}}(t)\tilde{d}(t)\\ =&\frac{1}{2}\left(q_e^{(0\sim1)}\right)^{\mathrm{T}}\left(\Phi\left(A^{0\sim1}\right)^{\mathrm{T}}P\left(A^{0\sim1}\right)\right.\\ &\left.+P\left(A^{0\sim1}\right)\Phi\left(A^{0\sim1}\right)\right)q_e^{(0\sim1)}\\ &+\left(q_e^{(0\sim1)}\right)^{\mathrm{T}}P\left(A^{0\sim1}\right)\left[\begin{array}{c} 0_{3\times1} \\ d^* \end{array}\right] + \dot{\tilde{d}}^{\mathrm{T}}(t)\tilde{d}(t).\end{aligned} \tag{28}$$

From Lemmas 1 and 3, it can be concluded that

$$\begin{aligned}
\dot{V} \leq & -\frac{\mu}{2}\left(q_e^{(0\sim1)}\right)^{\mathrm{T}} P\left(A^{0\sim1}\right) q_e^{(0\sim1)} \\
& + \left(q_e^{(0\sim1)}\right)^{\mathrm{T}} P_L\left(A^{0\sim1}\right) d^* + \dot{\tilde{d}}^{\mathrm{T}}(t)\tilde{d}(t) \\
= & -\mu V + \frac{\mu}{2}\tilde{d}^{\mathrm{T}}(t)\tilde{d}(t) \\
& + \left(q_e^{(0\sim1)}\right)^{\mathrm{T}} P_L\left(A^{0\sim1}\right) d^* + \dot{\tilde{d}}^{\mathrm{T}}(t)\tilde{d}(t) \\
= & -\mu V + \frac{\mu}{2}\tilde{d}^{\mathrm{T}}(t)\tilde{d}(t) \\
& + \left(\left(q_e^{(0\sim1)}\right)^{\mathrm{T}} P_L\left(A^{0\sim1}\right)\Pi(q_e)J^{-1} + \dot{\tilde{d}}^{\mathrm{T}}(t)\right)\tilde{d}(t) \\
= & -\mu V + \frac{\mu}{2}\tilde{d}^{\mathrm{T}}(t)\tilde{d}(t) \\
& + \Bigg(\left(q_e^{(0\sim1)}\right)^{\mathrm{T}} P_L\left(A^{0\sim1}\right)\Pi(q_e)J^{-1} \\
& - \dot{\tilde{d}}_{e0}^{\mathrm{T}}(t) + \dot{\tilde{d}}_{r0}^{\mathrm{T}}(t)\Bigg)\tilde{d}(t) \\
& + (\mu+1)\left(-\tilde{d}_{e0}^{\mathrm{T}}(t) + \tilde{d}_{r0}^{\mathrm{T}}(t) - \tilde{d}^{\mathrm{T}}(t)\right)\tilde{d}(t) \\
= & -\mu V + \frac{\mu}{2}\tilde{d}^{\mathrm{T}}(t)\tilde{d}(t) \\
& + \Bigg(\left(q_e^{(0\sim1)}\right)^{\mathrm{T}} P_L\left(A^{0\sim1}\right)\Pi(q_e)J^{-1} \\
& - \dot{\tilde{d}}_{e0}^{\mathrm{T}}(t)\Bigg)\tilde{d}(t) + \dot{\tilde{d}}_{r0}^{\mathrm{T}}(t)\tilde{d}(t) \\
& - (\mu+1)\tilde{d}_{e0}^{\mathrm{T}}(t)\tilde{d}(t) + (\mu+1)\left(\tilde{d}_{r0}^{\mathrm{T}}(t) - \tilde{d}^{\mathrm{T}}(t)\right)\tilde{d}(t) \\
= & \Bigg(\left(q_e^{(0\sim1)}\right)^{\mathrm{T}} P_L\left(A^{0\sim1}\right)\Pi(q_e)J^{-1} \\
& - \dot{\tilde{d}}_{e0}^{\mathrm{T}}(t) - (\mu+1)\tilde{d}_{e0}^{\mathrm{T}}(t)\Bigg)\tilde{d}(t) + \dot{\tilde{d}}_{r0}^{\mathrm{T}}(t)\tilde{d}(t) \\
& - \mu V + (\mu+1)\tilde{d}_{r0}^{\mathrm{T}}(t)\tilde{d}(t) - \frac{\mu+2}{2}\tilde{d}^{\mathrm{T}}(t)\tilde{d}(t).
\end{aligned} \tag{29}$$

From Lemma 3 and (23), we have

$$\begin{aligned}
\dot{V} \leq & -\mu V + \dot{\tilde{d}}_{r0}^{\mathrm{T}}(t)\tilde{d}(t) + (\mu+1)\tilde{d}_{r0}^{\mathrm{T}}(t)\tilde{d}(t) \\
& - \frac{\mu+2}{2}\tilde{d}^{\mathrm{T}}(t)\tilde{d}(t) \\
\leq & -\mu V + \frac{1}{2}\left(\delta_1^2 + \|\tilde{d}(t)\|^2\right) \\
& + \frac{(\mu+1)}{2}\left(\delta_0^2 + \|\tilde{d}(t)\|^2\right) - \frac{\mu+2}{2}\|\tilde{d}(t)\|^2 \\
= & -\mu V + \frac{1}{2}\left(\delta_1^2 + (\mu+1)\delta_0^2\right) \\
= & -\mu V + \delta
\end{aligned} \tag{30}$$

Based on the Comparison Theorem, the states of the system and the estimation error of unknown time-variance disturbance will eventually converge to the ellipsoid region (24). Thus, Theorem 1 is proved. □

The parameter matrices designed in this paper are given as

$$F = -\begin{bmatrix} 2 & 0 & 0 & 0 & 0 & 0 \\ 0 & 2 & 0 & 0 & 0 & 0 \\ 0 & 0 & 2 & 0 & 0 & 0 \\ 0 & 0 & 0 & 6 & 0 & 0 \\ 0 & 0 & 0 & 0 & 6 & 0 \\ 0 & 0 & 0 & 0 & 0 & 6 \end{bmatrix} * 0.1, \tag{31}$$

$$Z = \begin{bmatrix} 1 & 0 & 0 & 1 & 0 & 0 \\ 0 & 1 & 0 & 0 & 1 & 0 \\ 0 & 0 & 1 & 0 & 0 & 1 \end{bmatrix}. \tag{32}$$

Based on Lemma 4, V becomes

$$\begin{aligned}
V &= \begin{bmatrix} Z \\ ZF \end{bmatrix} \\
&= -\begin{bmatrix} -1 & 0 & 0 & -1 & 0 & 0 \\ 0 & -1 & 0 & 0 & -1 & 0 \\ 0 & 0 & -1 & 0 & 0 & -1 \\ 0.2 & 0 & 0 & 0.6 & 0 & 0 \\ 0 & 0.2 & 0 & 0 & 0.6 & 0 \\ 0 & 0 & 0.2 & 0 & 0 & 0.6 \end{bmatrix}
\end{aligned} \tag{33}$$

which guarantees $\det V \neq 0$.

Then, we have

$$\begin{aligned}
A^{0\sim1} &= -ZF^2V^{-1} \\
&= \begin{bmatrix} 0.12 & 0 & 0 & 0.8 & 0 & 0 \\ 0 & 0.12 & 0 & 0 & 0.8 & 0 \\ 0 & 0 & 0.12 & 0 & 0 & 0.8 \end{bmatrix},
\end{aligned} \tag{34}$$

$$\begin{aligned}
&\Phi\left(A^{0\sim1}\right) = VFV^{-1} \\
&= -\begin{bmatrix} 0 & 0 & 0 & -1 & 0 & 0 \\ 0 & 0 & 0 & 0 & -1 & 0 \\ 0 & 0 & 0 & 0 & 0 & -1 \\ 0.12 & 0 & 0 & 0.8 & 0 & 0 \\ 0 & 0.12 & 0 & 0 & 0.8 & 0 \\ 0 & 0 & 0.12 & 0 & 0 & 0.8 \end{bmatrix}.
\end{aligned} \tag{35}$$

Considering Lemma 3, it holds that

$$\begin{aligned}
&\left(\Phi\left(A^{0\sim1}\right) + 0.1I\right)^{\mathrm{T}} P\left(A^{0\sim1}\right) \\
&+ P\left(A^{0\sim1}\right)\left(\Phi\left(A^{0\sim1}\right) + 0.1I\right) = -0.001I.
\end{aligned} \tag{36}$$

From (36), we have

$$\begin{aligned}
&\Phi^{\mathrm{T}}\left(A^{0\sim1}\right) P\left(A^{0\sim1}\right) + P\left(A^{0\sim1}\right)\Phi\left(A^{0\sim1}\right) \\
&\leq -0.2P.
\end{aligned} \tag{37}$$

Therefore, $P_L\left(A^{0\sim1}\right)$ can be derived as

$$P_L\left(A^{0\sim1}\right) = \begin{bmatrix} 0.0119 & 0 & 0 \\ 0 & 0.0119 & 0 \\ 0 & 0 & 0.0119 \\ 0.0177 & 0 & 0 \\ 0 & 0.0177 & 0 \\ 0 & 0 & 0.0177 \end{bmatrix}. \tag{38}$$

4 Simulation

The validity of the developed control strategy (22)-(23) will be demonstrated through numerical simulations.

The inertia matrix is $J = \mathrm{diag}(40, 40, 40)\mathrm{kg}\cdot\mathrm{m}^2$, the desired angular velocity is specified as $\omega_d = [\sin(t), 2\cos(t), -\sin(t)]^{\mathrm{T}} * 0.001$, and the initial errors in attitude and angular velocity are $q_{e0} = [0.3, 0.2, -0.1]^{\mathrm{T}}$ and $\omega_e = [0, 0, 0]^{\mathrm{T}}$, respectively. The disturbances is $d(t) = [0.11 + 0.01\sin(t), 0.1 - 0.01\sin(t), 0.09 + 0.01\cos(t)]^{\mathrm{T}}$, and their pre-estimated values are chosen as $\hat{d}_0(t) = [0.1, 0.1, 0.1]^{\mathrm{T}}$.

Based on the above designed parameters and initial values, simulation results are depicted in Figs. 1-4, respectively.

According to Figs. 1-4, the control objective has been successfully achieved.

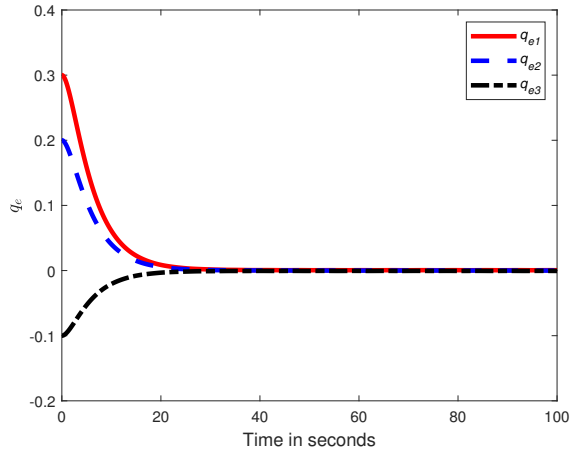

Fig. 1: The trajectories of attitude tracking errors

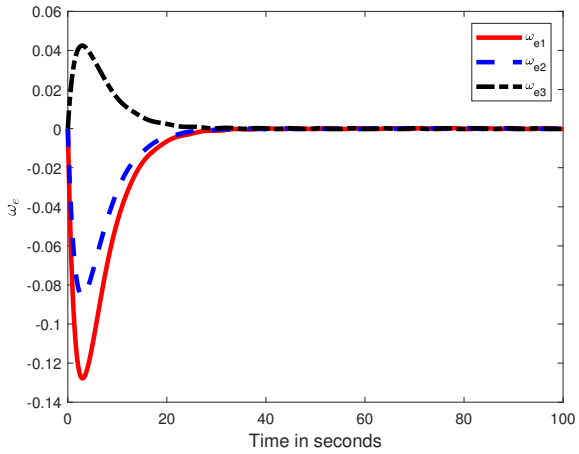

Fig. 2: The trajectories of angular velocity tracking errors

5 Conclusion

A novel spacecraft attitude adaptive tracking control strategy based on adaptive HOFA system approach is proposed in this paper. The system stability and the boundedness of the estimation errors for time-varying disturbances are guaranteed with the developed control strategy. It successfully addresses the impact of unknown time-varying disturbances while compensating for system nonlinearities, fully demonstrating its advantages.

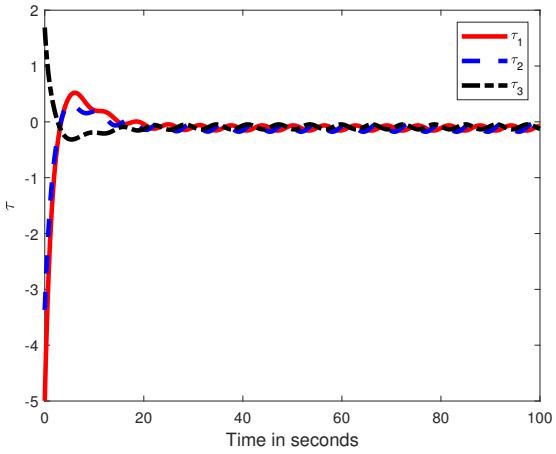

Fig. 3: The trajectories of control torque

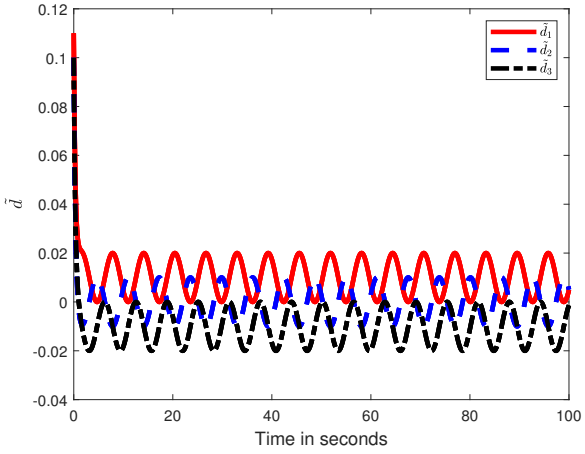

Fig. 4: The trajectories of estimation errors

References

[1] B. Jiang, Q. Hu, and Friswell M I, Fixed-time attitude control for rigid spacecraft with actuator saturation and faults, *IEEE Transactions on Control Systems Technology*, 24(5): 1892-1898, 2016.

[2] B. Wu and X. Cao, Robust Attitude Tracking Control for Spacecraft with Quantized Torques, *IEEE Transactions on Aerospace and Electronic Systems*, 54(2): 1020-1028, 2018.

[3] Q. Hu, Y. Shi, and X. Shao, Adaptive fault-tolerant attitude control for satellite reorientation under input saturation, *Aerospace Science and Technology*, 78:171-182, 2018.

[4] G. Duan, High-order system approaches-I. Fully-actuated systems and parametric designs, *Acta Automatica Sinica*, 46(7): 1333-1345, 2020.

[5] G. Duan, High-order fully actuated system approaches: Part III. Robust control and high-order backstepping, *International Journal of Systems Science*, 52(5): 952-971, 2021.

[6] G. Duan, High-order fully actuated system approaches:Part IV. Adaptive control and high-order backstepping, *International Journal of Systems Science*, 52(5): 972-989, 2021.

[7] G. Duan, High-order fully actuated system approaches: Part

V. Robust adaptive control, *International Journal of Systems Science*, 52(10): 2129-2143, 2021.

[8] G. Duan. High-order fully actuated system approaches: Part IX. Generalized PID control and model reference tracking. *International Journal of Systems Science*, 53(3): 652-674, 2022.

[9] G. Liu, K. Zhang, and B. Li, Fully-actuated system approach based optimal attitude tracking control of rigid spacecraft with actuator saturation, *Journal of Systems Science and Complexity*, 35(2): 688-702, 2022

[10] G. Duan and G. Liu, Attitude and Orbit Optimal Control of Combined Spacecraft via a Fully-Actuated System Approach, *Journal of Systems Science and Complexity*, 35(2): 623-640, 2022.

[11] G. Duan and G. Liu, Adaptive prescribed performance control for position and attitude of combined spacecraft based on fully actuated system approach. *Acta Aeronautica et Astronautica Sinica*, doi: 10.7527/S1000- 6893.2023.28837(in Chinese).

[12] F. Xiao and L. Chen, Attitude control of spherical liquid-filled spacecraft based on high-order fully actuated system approaches, *Journal of Systems Science and Complexity*, 35(2): 471-480, 2022.

[13] D. Jin, S. Jia, T. Wang and J. Qiu, Spacecraft Attitude Tracking Control Based On High-Order Fully Actuated System Approach, in *2023 2nd Conference on Fully Actuated System Theory and Applications (CFASTA),* 2023: 1040-1044.

[14] H. Gao, Z. Li, X. Yu, and J. Qiu, Hierarchical Multiobjective Heuristic for PCB Assembly Optimization in a Beam-Head Surface Mounter, *IEEE Transactions on Cybernetics,* 52(7): 6911-6924, 2022.

Proceedings of the 3rd Conference on Fully Actuated System Theory and Applications
May 10-12, 2024, Shenzhen, China

Robust Attitude Control of a Tilt Trirotor in VTOL mode

Zemin Lin[1], Shikang Lian[1], Wei Meng[1]
1. School of Automation, Guangdong University of Technology, Guangzhou 510006
E-mail: Ablen@mail2.gdut.edu.cn

Abstract: This paper introduces a novel Fast Nonsingular Terminal Sliding Mode with Integral (FNTSM-I) attitude controller tailored for tilt trirotor aircraft operating in Vertical Take-off and Landing (VTOL) mode. The proposed controller incorporates an integral component designed to guide the attitude error towards convergence within a finite timeframe, even in the presence of wind disturbances. Furthermore, to mitigate the risk of gimbal lock during large angle flight maneuvers, the motion representation of the tilt trirotor utilizes quaternions instead of Euler angles. Moreover, this study integrates angular tracking into the controller architecture to ensure both rapid response times and precise control accuracy. Additionally, comprehensive guidelines for the selection of controller parameters are provided. Simulation results demonstrate that the proposed controller significantly reduces overshoot and enhances the tracking response speed of tilt trirotor Unmanned Aerial Vehicles (UAVs), thereby augmenting overall system robustness.

Key Words: Attitude control, Finite time control, Tilt Trirotor, Sliding Mode Control (SMC), Unmanned Aerial Vehicles (UAV)

1 INTRODUCTION

The tilt-rotor Unmanned Aerial Vehicle (UAV) represents a specialized aerial platform endowed with the capability to seamlessly transition between high-speed cruise flight mode and Vertical Take-off and Landing (VTOL) flight mode[1]. This unique versatility renders it indispensable across diverse domains such as offshore wind power inspection, post-disaster search and rescue operations, remote traffic management, and other environments characterized by complexity. Within these multifaceted environments, precise hovering and secure control in VTOL mode are imperative, particularly amidst external disturbances stemming from airflow dynamics, variable payloads, and uncertain system parameters. The attitude controller constitutes the fundamental underpinning of the position controller[2]. However, tilt-rotor Unmanned Aerial Vehicles (UAVs) manifest heightened vulnerability to disturbances stemming from turbulent airflow, a consequence of their aerodynamic profile, surpassing that encountered by traditional multi-rotor UAVs. Consequently, the imperative emerges to engineer an attitude tracking controller endowed with rapid responsiveness, precision, and robustness tailored specifically for tilt-rotor UAVs operating in Vertical Take-off and Landing (VTOL) flight mode.

The field of attitude control for tilt-rotor Unmanned Aerial Vehicles (UAVs) has garnered considerable attention among researchers, resulting in the proposition of various control methodologies such as Proportional-Integral-Derivative (PID)[3], Sliding Mode Control (SMC),H_∞, Linear Quadratic Regulator (LQR), state observer-based algorithms[4], and optimal preview control techniques[5]. For instance, in the work [6], a novel tilt-rotor octocopter is introduced, wherein both inner-loop attitude control and outer-loop position control are established using PID controllers, albeit without consideration for interference, leading to suboptimal performance in the presence of gust disturbances. Conversely, the study in [2] presents a fixed-time SMC strategy aimed at addressing the challenge of fixed-time attitude stabilization for tilt-rotor UAVs amidst parameter uncertainties and external disturbances. Nonetheless, the utilization of Newton-Euler equations to model UAV rotation introduces the issue of gimbal lock. Another innovative approach, proposed in [7], is the Constraint-based Adaptive Robust Prescribed Performance Control (CARPPC), which exhibits promising performance during transitional states. However, this method is yet to be optimized specifically for attitude control objectives. Meanwhile, [8] advocates for Model Predictive Control (MPC) in the context of a tilt quadrotor, although its computational demands render it impractical for applications necessitating high control frequencies, thereby limiting its suitability for attitude control tasks. In another study in [9], a Fuzzy Backstepping Control with an Extended-State Observer (FBS-ESO) is introduced to mitigate the effects of internal and external disturbances during full-flight operations, demonstrating effectiveness against external wind disturbances but lacking optimization for convergence time. Lastly, [10] proposes a fixed-time convergence attitude tracking controller employing actor-critic neural networks to estimate modeling uncertainties. However, the varying nature of modeling uncertainties across tasks remains a challenge yet to be fully addressed.

Sliding mode control (SMC) is widely recognized for its robustness and rapid convergence rate, rendering it extensively applied across various domains including linear motor positioners[12], underwater vehicles[13], robot manipulators[14], and quadrotor UAVs[15]. Traditional SMC approaches asymptotically drive the system status to stationary points, which, however, fall short of meeting the high-speed response demands characteristic of tilt-trirotor operation in VTOL mode. To address this limitation, terminal sliding mode (TSM) control has been introduced, ensuring that tracking error diminishes to zero within a finite duration propelled by a nonlinear hyperplane on the sliding surface[16]. Nonetheless, this method entails unbounded control output when the tracking error hovers around zero. To mitigate this deficiency, nonsingular terminal sliding mode (NTSM) control has been devised[17]. However, the abrupt variation in control gain of the discontinuous operator at the reaching control component leads to pronounced chattering, potentially jeopardizing the actuator and overriding the response bandwidth. Consequently, a plethora of strategies have been explored, including second-order sliding

mode[18], adaptive SMC[19], and fractional-order sliding mode[20]. Additionally, fast nonsingular terminal sliding mode (FNTSM) control has been proposed to dampen chattering by altering the switching mechanism in the reaching control law, albeit at the expense of tracking precision. An adaptive fast nonsingular terminal sliding mode (AFNTSM) control, incorporating integral elements, has been developed as a refinement; however, it falls short of completely eliminating chattering[21].

Motivated by the aforementioned discussions, FNTSM-I control is proposed to further improve control of [21] by introducing angular velocity control and integral for extent disturbance and uncertainties parameters. The contribution of the developed method are showed as follow.

1) In this article, a fast nonsingular terminal sliding function with integral element is presented, which is able to improve the attitude control error tracking accuracy under the interference of wind.
2) Angular velocity as an important element is introduced into attitude control to smooth system state, reducing the chattering without compromising response speed and control accuracy.

The rest of this article is organized as follows. Section 2 presents the kinematics model of tilt trirotor in VTOL mode. The method of FNTSM-I controller is developed in Section 3, in which the stability analysis and control parameters are discussed in details. In section 4, simulation results are presented. Finally, Section 5 concludes this article.

2 MODELING

Before the design of attitude controller for a tilt trirotor aircraft, two coordinate systems are defined as Fig.1, where $\mathbf{E}_b = O_b\{x_b, y_b, z_b\}$ denotes the body frame and $\mathbf{E}_n = O_n\{x_n, y_n, z_n\}$ denotes the navigation frame. A unit quaternion $\mathbf{q}$ is used to present the rotation from navigation frame to body frame, which is

$$\mathbf{q} = \begin{bmatrix} q_0 \\ \mathbf{q}_v \end{bmatrix}, \tag{1}$$

while $\mathbf{q}_v = [q_1, q_2, q_3]^T$ and $\|\mathbf{q}\| = q_0^2 + q_1^2 + q_2^2 + q_3^2 = 1$. And $\mathbf{q}$ is differential to be as

$$\dot{\mathbf{q}} = \frac{1}{2}\mathbf{q} \otimes \begin{bmatrix} 0 \\ \mathbf{\Omega}_b \end{bmatrix}, \tag{2}$$

where $\mathbf{\Omega}_b \in \mathbb{R}^3$ is angular velocity respect to body frame and $\otimes$ is quaternion operation,

$$\mathbf{q}_a \otimes \mathbf{q}_b = \begin{bmatrix} q_{a,0}q_{b,0} - \mathbf{q}_{a,v}^T\mathbf{q}_{b,v} \\ \mathbf{q}_{a,v} \times \mathbf{q}_{b,v} + q_{a,0}\mathbf{q}_{b,v} + q_{b,0}\mathbf{q}_{a,v} \end{bmatrix}, \tag{3}$$

and both $\mathbf{q}_a$ and $\mathbf{q}_b$ are unit quaternions. $\dot{\mathbf{q}}$ is rewritten as

$$\begin{cases} \dot{q_0} = -\frac{1}{2}\mathbf{q}_v^T\mathbf{\Omega}_b \\ \dot{\mathbf{q}}_v = \frac{1}{2}\left([\mathbf{q}_v]^\times + q_0\mathbf{I}\right)\mathbf{\Omega}_b \end{cases}, \tag{4}$$

where $[\mathbf{b}]^\times$ is defined as

$$[\mathbf{b}]^\times = \begin{bmatrix} 0 & -b_3 & b_2 \\ b_3 & 0 & -b_1 \\ -b_2 & b_1 & 0 \end{bmatrix} \tag{5}$$

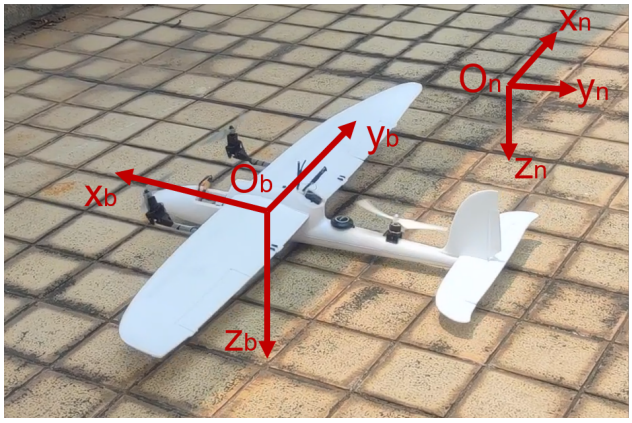

Fig. 1: Body frame and navigation frame.

and $\mathbf{b} = [b_1, b_2, b_3]^T \in \mathbb{R}^3$. So the kinematics model is

$$\mathbf{J}\dot{\mathbf{\Omega}}_b = -\mathbf{\Omega}_b \times (\mathbf{J}\mathbf{\Omega}_b) + \mathbf{M} + \mathbf{d}, \tag{6}$$

where $\mathbf{J} = \mathrm{diag}\,(J_{xx}, J_{yy}, J_{zz})$ denotes the moment of inertia of drone, $\mathbf{M} = [\tau_x, \tau_y, \tau_z]^T$ and $\mathbf{d} = [d_1, d_2, d_3]^T$ denotes the bounded interference.

3 CONTROL DESIGN

In this section, a FNTSM-I controller is designed to ensure the tilt trirotor UAVs can track the desired attitude under the wind disturbances with bound. Besides, the stability of the controller has been proven by Lyapunov functions. Finally, parameter tuning is discussed.

3.1 Attitude control

The desired attitude is defined as

$$\mathbf{q}_{des} = \mathbf{q} \otimes \mathbf{q}_e, \tag{7}$$

where $\mathbf{q}_e$ denotes the error of attitude. So the $\mathbf{q}_e$ is

$$\mathbf{q}_e = \mathbf{q}^{-1} \otimes \mathbf{q}_{des}. \tag{8}$$

The differentials, $\dot{\mathbf{q}}_{des}$ and $\dot{\mathbf{q}}_e$, are

$$\begin{cases} \dot{q}_{des,0} = -\frac{1}{2}\mathbf{q}_{des,v}^T\mathbf{\Omega}_{des} \\ \dot{\mathbf{q}}_{des,v} = \frac{1}{2}\left([\mathbf{q}_{des,v}]^\times + q_{des,0}\mathbf{I}\right)\mathbf{\Omega}_{des} \end{cases} \tag{9}$$

and

$$\begin{cases} \dot{q}_{e,0} = -\frac{1}{2}\mathbf{q}_{e,v}^T\mathbf{\Omega}_e \\ \dot{\mathbf{q}}_{e,v} = \frac{1}{2}\left([\mathbf{q}_{e,v}]^\times + q_{e,0}\mathbf{I}\right)\mathbf{\Omega}_e \end{cases}, \tag{10}$$

where $\mathbf{\Omega}_{des} = -\boldsymbol{\alpha}_a q_{e,0}\mathbf{q}_{e,v}$ denotes the desired angular respect to body frame. And $\boldsymbol{\alpha}_a$ is a positive diagonal parameter matrix. And $\mathbf{E}_q = 2q_{e,0}\mathbf{q}_{e,v}$ denotes the angle error respect to body frame. $\mathbf{\Omega}_e$ denotes the angular error velocity respect to body frame, which can calculated by

$$\mathbf{\Omega}_e = \mathbf{\Omega}_b - \mathbf{\Omega}_{des}. \tag{11}$$

In addition, (6) can be rewritten as

$$\begin{aligned} \mathbf{J}\dot{\mathbf{\Omega}}_e = & \ \mathbf{J}\left(\dot{\mathbf{\Omega}}_b - \dot{\mathbf{\Omega}}_{des}\right) \\ = & \ -\mathbf{\Omega}_b \times (\mathbf{J}\mathbf{\Omega}_b) + \mathbf{M} + \mathbf{d} - \mathbf{J}\dot{\mathbf{\Omega}}_{des} \end{aligned}. \tag{12}$$

A terminal sliding mode function $\mathbf{S}$ is define as

$$\mathbf{S} = \boldsymbol{\Omega}_e + \alpha_1 \mathbf{E}_q + \alpha_2 \int_{t_0}^{t} \Upsilon(\mathbf{E}_q, \beta_0) d\tau, \tag{13}$$

where α_1 and α_2 are positive values, and $\beta_0 > 1$ is the controller parameter in sliding function. The sliding variable satisfy $\mathbf{S} = [S_1, S_2, S_3]^T \in \mathbb{R}^3$ The function $\Upsilon(\mathbf{v}, \rho)$ is defined as

$$\Upsilon(\mathbf{v}, \rho) = \begin{bmatrix} |v_1|^\rho \operatorname{sgn}(v_1) \\ |v_2|^\rho \operatorname{sgn}(v_2) \\ |v_3|^\rho \operatorname{sgn}(v_3) \end{bmatrix}, \tag{14}$$

where $\mathbf{v} = [v_1, v_2, v_3]^T \in \mathbb{R}^3$ is any vector and ρ is nonnegative.

$\mathbf{S}$ takes the derivative of time to be

$$\dot{\mathbf{S}} = \dot{\boldsymbol{\Omega}}_e + \alpha_1 \dot{\mathbf{E}}_q + \alpha_2 \Upsilon(\mathbf{E}_q, \beta_0), \tag{15}$$

where

$$\dot{\mathbf{E}}_q = -\mathbf{q}_{e,v}^T \boldsymbol{\Omega}_e \mathbf{q}_{e,v} + q_{e,0} \left([\mathbf{q}_{e,v}]^\times + q_{e,0} \mathbf{I}_3 \right) \boldsymbol{\Omega}_e. \tag{16}$$

Based on the equivalent control input method, let the sliding mode variable satisfy $\dot{\mathbf{S}} = 0$. And substituting (12) into (15), removing the uncertain disturbance terms, the equivalent control input $\boldsymbol{\tau}_0$ is

$$\begin{aligned} \boldsymbol{\tau}_0 = \quad & -\mathbf{J} \left[\alpha_1 \dot{\mathbf{E}}_q + \alpha_2 \Upsilon(\mathbf{E}_q, \beta_0) \right] \\ & + \boldsymbol{\Omega}_b \times (\mathbf{J}\boldsymbol{\Omega}_b) + \mathbf{J}\dot{\boldsymbol{\Omega}}_{des} \end{aligned}. \tag{17}$$

And the reaching control input is designed as

$$\boldsymbol{\tau}_1 = -\mathbf{J} \left[\alpha_3 \mathbf{S} + \alpha_4 \Upsilon(\mathbf{S}, \beta_1) + D \operatorname{sgn}(\mathbf{S}) \right], \tag{18}$$

where α_3 and α_4 are positive values, and $\beta_1 \in (0, 1)$ is the reaching law parameter. D is positive scalars, $\operatorname{sgn}(\mathbf{S}) = [\operatorname{sgn}(S_1), \operatorname{sgn}(S_2), \operatorname{sgn}(S_3),]^T$ and $|D\operatorname{sgn}(\mathbf{S})| \geq \left|\mathbf{J}^{-1}\mathbf{d}\right|$. Hence, the control input can be combined as

$$\boldsymbol{\tau} = \boldsymbol{\tau}_0 + \boldsymbol{\tau}_1. \tag{19}$$

3.2 Stability Analysis

To improve the stability of FNTSM-I, a Lyapunov function is defined as

$$V_1 = \frac{1}{2} \mathbf{S}^T \mathbf{S}, \tag{20}$$

which the derivative of V_1 is

$$\dot{V}_1 = \mathbf{S}^T \dot{\mathbf{S}}. \tag{21}$$

Based on (13)-(19) and the system (12), the derivative of sliding variable $\dot{S}$ is able to be reconstructed as

$$\dot{\mathbf{S}} = -\left[\alpha_3 \mathbf{S} + \alpha_4 \Upsilon(\mathbf{S}, \beta_1) + D \operatorname{sgn}(\mathbf{S}) \right] + \mathbf{J}^{-1}\mathbf{d}. \tag{22}$$

Therefore, the derivative of $\dot{V}_1$ can be rewritten as

$$\begin{aligned} & \dot{V}_1 = -\mathbf{S}^T \left[\alpha_3 \mathbf{S} + \alpha_4 \Upsilon(\mathbf{S}, \beta_1) + D \operatorname{sgn}(\mathbf{S}) - \mathbf{J}^{-1}\mathbf{d} \right] \\ & = -\alpha_3 \mathbf{S}^T \mathbf{S} - \alpha_4 \mathbf{S}^T \Upsilon(\mathbf{S}, \beta_1) - \mathbf{S}^T D \operatorname{sgn}(\mathbf{S}) + \mathbf{S}^T \mathbf{J}^{-1}\mathbf{d} \\ & \leq -\alpha_3 \mathbf{S}^T \mathbf{S} - \alpha_4 \mathbf{S}^T \Upsilon(\mathbf{S}, \beta_1) - \left| \mathbf{S}^T D \operatorname{sgn}(\mathbf{S}) \right| + \left| \mathbf{S}^T \mathbf{J}^{-1}\mathbf{d} \right| \\ & = -\alpha_3 \mathbf{S}^T \mathbf{S} - \alpha_4 \mathbf{S}^T \Upsilon(\mathbf{S}, \beta_1) - \left| \mathbf{S}^T \right| \left(|D \operatorname{sgn}(\mathbf{S})| - \left| \mathbf{J}^{-1}\mathbf{d} \right| \right) \\ & \leq -\alpha_3 \mathbf{S}^T \mathbf{S} - \alpha_4 \mathbf{S}^T \Upsilon(\mathbf{S}, \beta_1) \\ & = -\alpha_3 \mathbf{S}^T \mathbf{S} - \alpha_4 |\mathbf{S}|^T |\mathbf{S}|^{\beta_1} \\ & = -\alpha_3 \mathbf{S}^T \mathbf{S} - \alpha_4 \left(|S_1|^{1+\beta_1} + |S_2|^{1+\beta_1} + |S_3|^{1+\beta_1} \right), \end{aligned} \tag{23}$$

where $|D\operatorname{sgn}(\mathbf{S})| \geq \left|\mathbf{J}^{-1}\mathbf{d}\right|$. According to [22],

$$\begin{aligned} \dot{V}_1 & \leq -\alpha_3 \mathbf{S}^T \mathbf{S} - \alpha_4 \left(|S_1|^2 + |S_2|^2 + |S_3|^2 \right)^{\frac{1+\beta_1}{2}} \\ & = -2\alpha_3 V_1 - \alpha_4 (2V_1)^{\frac{1+\beta_1}{2}} \\ & = -2\alpha_3 V_1 - 2^{\frac{1+\beta_1}{2}} \alpha_4 (V_1)^{\frac{1+\beta_1}{2}} \end{aligned}. \tag{24}$$

For any initial condition $V_1(\mathbf{S}(0)) = V_1(0)$, the system moves to sliding surface $\mathbf{S}(T_s) = 0$ in a finite time by [23], which is

$$T_s \leq \frac{1}{\alpha_3 (1 - \beta_1)} \ln \left[1 + \frac{\alpha_3 V_1^{\frac{1-\beta_1}{2}}(0)}{2^{\frac{\beta_1 - 1}{2}} \alpha_4} \right]. \tag{25}$$

Furthermore, in order to certify that the attitude error will be driven to zero in a finite time, a Lyapunov function is defined as

$$V_2 = \mathbf{q}_{e,v}^T \mathbf{q}_{e,v}. \tag{26}$$

Follow the rule of unit quaternion, V_2 can be rewritten as

$$V_2 = 1 - q_{e,0}^2 \tag{27}$$

So combining (10), the derivative of V_2 is

$$\begin{aligned} \dot{V}_2 & = -2 q_{e,0} \dot{q_{e,0}} \\ & = q_{e,0} \mathbf{q}_{e,v}^T \boldsymbol{\Omega}_e \end{aligned} \tag{28}$$

The sliding surface reaches zero after T_s, and at this point $\mathbf{S}(T_s) = 0$, so (13) can be rewritten as

$$\boldsymbol{\Omega}_e = -\alpha_1 \mathbf{E}_q - \alpha_2 \int_{t_0}^{t} \Upsilon(\mathbf{E}_q, \beta_0) d\tau \tag{29}$$

. Substituting it into $\dot{V}_2$, the result is

$$\begin{aligned} \dot{V}_2 & = -q_{e,0} \mathbf{q}_{e,0}^T \left(\alpha_1 \mathbf{E}_q + \alpha_2 \int_{t_0}^{t} \Upsilon(\mathbf{E}_q, \beta_0) d\tau \right) \\ & = -2\alpha_1 q_{e,0}^2 \mathbf{q}_{e,v}^T \mathbf{q}_{e,v} - \alpha_2 q_{e,0} \mathbf{q}_{e,v}^T \int_{t_0}^{t} \Upsilon(\mathbf{E}_q, \beta_0) d\tau \end{aligned}. \tag{30}$$

A operator is extracted from (30), which is

$$\begin{aligned} & \varepsilon_{\alpha 2} q_{e,0} \mathbf{q}_{e,v}^T \int_{t_0}^{t} \Upsilon(\boldsymbol{\alpha}_s \mathbf{E}_q, \beta_0) d\tau \\ & = \varepsilon_{\alpha 2} q_{e,0} \left| \mathbf{q}_{e,v}^T \right| \mathbf{M}_s \int_{t_0}^{t} \Upsilon(\boldsymbol{\alpha}_s \mathbf{E}_q, \beta_0) d\tau \\ & = \varepsilon_{\alpha 2} q_{e,0} \left| \mathbf{q}_{e,v}^T \right| \int_{t_0}^{t} \left| \Upsilon(\boldsymbol{\alpha}_s \mathbf{E}_q, \beta_0) \right| d\tau \\ & \geq 0 \end{aligned}. \tag{31}$$

So the (30) can be written as

$$\begin{aligned} \dot{V}_2 & \leq -2\alpha_1 q_{e,0}^2 \mathbf{q}_{e,v}^T \mathbf{q}_{e,v} \\ & = -2\alpha_1 q_{e,0}^2 V_2 \\ & = -\varrho V_2^{\frac{1}{2}} \end{aligned}, \tag{32}$$

where $\varrho = 2\alpha_1 q_{e,0}^2 V_2^{\frac{1}{2}} > 0$ when $V_2 \neq 0$. According to [23], for any initial condition of $\mathbf{q}_{e,v}(0)$ and $\boldsymbol{\Omega}(0)$, $\mathbf{q}_{e,v}$ would approach to zeros at a finite time T_q, which is

$$T_q \leq \frac{2 V_2^{\frac{1}{2}}(0)}{\varrho}. \tag{33}$$

Therefore, the attitude error reaches to $\mathbf{q}_e^T = [1, 0, 0, 0]^T$, which takes the finite time $T_r = T_s + T_q$ for any command attitude angle $\mathbf{q}_c$. In a word, system state approaches sliding surface in finite time T_r driven, and the angular velocity respect to body frame would also converge to command angular $\boldsymbol{\Omega}_c$, which drives attitude $\mathbf{q}$ to command attitude $\mathbf{q}_c$ at the same time. At this point, the proof is completed.

3.3 Parameters Tuning

In addition to uncertain interferences and sensor noise, the control performances of tilt trirotor in VTOL mode would also be affected by the control parameters, so it is significant to choose appropriate parameters. In this subsection, some suggestions are given about the choice of control parameters.

3.3.1 Selection of α_1, α_2 and β_0

α_1, α_2 and β_0 effect the convergence rate of attitude error to $[1, 0, 0, 0]^T$. But they also lead to chattering near by point, due to their large control output. However, due to their large control output, they can also cause chatter near the stagnation point. To balance the control rapidity and precision, they are $\alpha_1 = 8.8$, $\alpha_2 = 12.5$ and $\beta_0 = 4.2$.

3.3.2 Selection of α_3, α_4 and β_1

According equation (25), it is showed that these parameters determine the reach time T_s in which sliding surface value $\mathbf{S}$ converges to zero. Larger values α_3 and α_4 can reinforce the robust of system and β_1 give it a stronger and smoother output. Thus, they are $\alpha_3 = 18$, $\alpha_4 = 15$ and $\beta_1 = 0.10$ in our simulation.

3.3.3 Selection of α_a and D

$\boldsymbol{\alpha}_a$ is a gain matrix that effects the system state convergence rate. Different from roll and pitch, yaw control of tilt trirotor has a lower activity bounds. Therefore, it is best to choose a smaller yaw gain. And D is the upper bound of uncertain disturbance, where the large one would also cause chattering. At last, they are $\alpha_a = \mathrm{diag}(8.4, 8.4, 8.4)$ and $D = 0.032$.

4 SIMULATION RESULTS

Simulations on MATLAB are carried out to certify the improvement of proposed attitude controller for tilt trirotor in VOTL mode. Here, simulations of this article include attitude tracking responses and hover accuracy experience under wind interferences.

Comparisons include convention SMC and FNTSM, where the reach control input of SMC is $\tau_i = -k_{i,1}S_i - k_{i,2}\mathrm{sig}\,(S_i)$ and FNTSM is $\tau_i = -k_{i,1}S_i - k_{i,2}\mathrm{sig}^{\beta_i}\,(S_i)$. And control parameters for detail are list in Table 1. On the tracking response task, the roll, pitch and yaw are moved from 0° to 10°, where the system state would transform from quaternion to Euler angle to show characteristics in different control method. The performance of attitude tracking is show in Fig.2. It is obvious that convergence time of FNTSM-I is much shorter than the other two controller in this simulation.

To prove the disturbance rejection performance of the three controllers mentioned, accidental wind disturbance is introduced into the simulation in which their bounds are set as 0.0225 N·m lasting from 1s to 2s. Their detailed performances is shown in Fig.3. It is clear that the FNTSM-I controller can quickly return its stable state after being disturbed, benefiting from its integral element of sliding surface and introducing the angular velocity into control input.

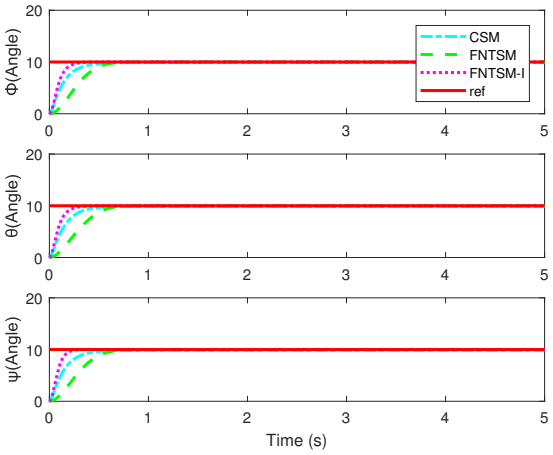

Fig. 2: Attitude tracking responses to step reference.

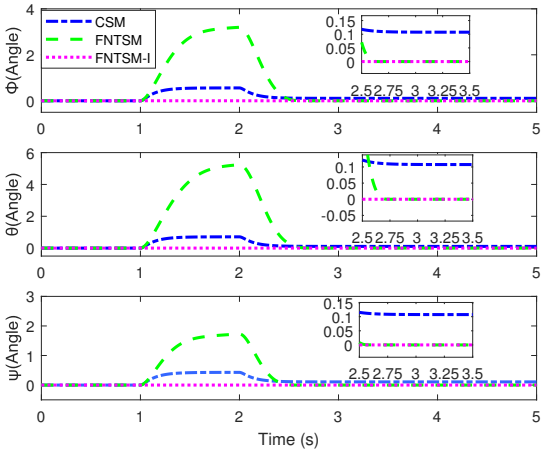

Fig. 3: Wind disturbance rejection of three control methods.

Table 1: Control Parameters in the Simulations.

Controllers	Control parameters	Roll	Pitch	Yaw
FNTSM-I	$\boldsymbol{\alpha}_a$	8.4	8.4	8.4
	α_1	8.8	8.8	8.8
	α_2	12.5	12.5	12.5
	α_3	18	18	18
	α_4	15	15	15
	β_0	4.2	4.2	4.2
	β_1	0.10	0.10	0.10
	D	0.032	0.032	0.032
FNTSM	β	1.3	1.3	1.3
	λ	0.16	0.16	0.16
	ρ	0.6	0.6	0.6
	k_1	1.2	1.2	1.2
	k_2	10	10	10
CSM	λ	50	50	50
	k_1	10	10	10
	k_2	0.8	0.8	0.8

5 CONCLUSIONS

In this article, a FNTSM-I attitude controller is presented for tilt trirotor in VTOL mode, in which the integral element drives the attitude error to convergence point in a finite time under the wind disturbance. And the motion description of tilt trirotor is modelled by using quaternion instead of Euler angle avoiding the gimbal lock on large angle flight task. Furthermore, an angular tracking is introduced into the controller, which can achieve rapid response speed while ensuring accuracy. In addition, some suggestions about selections of controller parameters are submitted. Finally, the results of simulation show that the proposed controller reduces the overshoot and improves tracking response speed of tilt trirotor UAVs, enhancing system robustness.

References

[1] Z. Liu, Y. He, L. Yang, and J. Han, "Control techniques of tilt rotor unmanned aerial vehicle systems: A review," *Chinese Journal of Aeronautics*, vol. 30, no. 1, pp. 135–148, 2017.

[2] L. Yu, G. He, X. Wang, and S. Zhao, "Robust fixed-time sliding mode attitude control of tilt trirotor uav in helicopter mode," *IEEE Transactions on Industrial Electronics*, vol. 69, DOI 10.1109/TIE.2021.3118556, no. 10, pp. 10 322–10 332, 2022.

[3] C. Papachristos, K. Alexis, and A. Tzes, "Design and experimental attitude control of an unmanned tilt-rotor aerial vehicle," in *2011 15th International Conference on Advanced Robotics (ICAR)*, DOI 10.1109/ICAR.2011.6088631, pp. 465–470, 2011.

[4] S. Song, W. Wang, K. Lu, and L. Sun, "Nonlinear attitude control using extended state observer for tilt-rotor aircraft," in *The 27th Chinese Control and Decision Conference (2015 CCDC)*, pp. 852–857. IEEE, 2015.

[5] P. Huangzhong, Z. Ziyang, and G. Chen, "Tiltrotor aircraft attitude control in conversion mode based on optimal preview control," in *Proceedings of 2014 IEEE Chinese Guidance, Navigation and Control Conference*, pp. 1544–1548. IEEE, 2014.

[6] Z. Qin, J. Wei, M. Cao, B. Chen, K. Li, and K. Liu, "Design and flight control of a novel tilt-rotor octocopter using passive hinges," *IEEE Robotics and Automation Letters*, vol. 9, DOI 10.1109/LRA.2023.3320008, no. 1, pp. 199–206, 2024.

[7] H. Liu, N. Wang, Z. Zhang, and H. Yin, "Agile and precise attitude control of tiltrotor aircraft in transition flight," *IEEE Transactions on Intelligent Vehicles*, 2023.

[8] L. Bauersfeld, L. Spannagl, G. J. Ducard, and C. H. Onder, "Mpc flight control for a tilt-rotor vtol aircraft," *IEEE Transactions on Aerospace and Electronic Systems*, vol. 57, no. 4, pp. 2395–2409, 2021.

[9] S. Shen, J. Xu, and Q. Xia, "A fuzzy backstepping attitude control based on an extended state observer for a tilt-rotor uav," *Aerospace*, vol. 9, no. 11, p. 724, 2022.

[10] T. Xie, B. Xian, and X. Gu, "Fixed-time convergence attitude control for a tilt trirotor unmanned aerial vehicle based on reinforcement learning," *ISA transactions*, vol. 132, pp. 477–489, 2023.

[11] L. Yu, G. He, S. Zhao, X. Wang, and L. Shen, "Immersion and invariance-based sliding mode attitude control of tilt tri-rotor uav in helicopter mode," *International Journal of Control, Automation and Systems*, vol. 19, pp. 722–735, 2021.

[12] K. Shao, J. Zheng, K. Huang, H. Wang, Z. Man, and M. Fu, "Finite-time control of a linear motor positioner using adaptive recursive terminal sliding mode," *IEEE Transactions on Industrial Electronics*, vol. 67, DOI 10.1109/TIE.2019.2937062, no. 8, pp. 6659–6668, 2020.

[13] R. Cristi, F. Papoulias, and A. Healey, "Adaptive sliding mode control of autonomous underwater vehicles in the dive plane," *IEEE Journal of Oceanic Engineering*, vol. 15, DOI 10.1109/48.107143, no. 3, pp. 152–160, 1990.

[14] S. Islam and X. P. Liu, "Robust sliding mode control for robot manipulators," *IEEE Transactions on Industrial Electronics*, vol. 58, DOI 10.1109/TIE.2010.2062472, no. 6, pp. 2444–2453, 2011.

[15] L. Besnard, Y. B. Shtessel, and B. Landrum, "Quadrotor vehicle control via sliding mode controller driven by sliding mode disturbance observer," *Journal of the Franklin Institute*, vol. 349, no. 2, pp. 658–684, 2012.

[16] M. Zhihong and X. H. Yu, "Terminal sliding mode control of mimo linear systems," *IEEE Transactions on Circuits and Systems I: Fundamental Theory and Applications*, vol. 44, DOI 10.1109/81.641769, no. 11, pp. 1065–1070, 1997.

[17] L. Yang and J. Yang, "Nonsingular fast terminal sliding-mode control for nonlinear dynamical systems," *International Journal of Robust and Nonlinear Control*, vol. 21, no. 16, pp. 1865–1879, 2011.

[18] E.-H. Zheng, J.-J. Xiong, and J.-L. Luo, "Second order sliding mode control for a quadrotor uav," *ISA transactions*, vol. 53, no. 4, pp. 1350–1356, 2014.

[19] H. Bouadi, S. Simoes Cunha, A. Drouin, and F. Mora-Camino, "Adaptive sliding mode control for quadrotor attitude stabilization and altitude tracking," in *2011 IEEE 12th International Symposium on Computational Intelligence and Informatics (CINTI)*, DOI 10.1109/CINTI.2011.6108547, pp. 449–455, 2011.

[20] M. Vahdanipour and M. Khodabandeh, "Adaptive fractional order sliding mode control for a quadrotor with a varying load," *Aerospace Science and Technology*, vol. 86, pp. 737–747, 2019.

[21] S. Lian, W. Meng, Z. Lin, K. Shao, J. Zheng, H. Li, and R. Lu, "Adaptive attitude control of a quadrotor using fast nonsingular terminal sliding mode," *IEEE Transactions on Industrial Electronics*, vol. 69, DOI 10.1109/TIE.2021.3057015, no. 2, pp. 1597–1607, 2022.

[22] H. Du, S. Li, and C. Qian, "Finite-time attitude tracking control of spacecraft with application to attitude synchronization," *IEEE Transactions on Automatic Control*, vol. 56, no. 11, pp. 2711–2717, 2011.

[23] S. Yu, X. Yu, B. Shirinzadeh, and Z. Man, "Continuous finite-time control for robotic manipulators with terminal sliding mode," *Automatica*, vol. 41, no. 11, pp. 1957–1964, 2005.

Proceedings of the 3rd Conference on Fully Actuated System Theory and Applications
May 10-12, 2024, Shenzhen, China

High-order Fully-actuated System Approach Based Fault-tolerant Attitude Tracking Control via Extended State Observer

Shixiang Jia[1], Yang Jin[2], Tong Wang[1], Jianbin Qiu[1]

1. Research Institute of Intelligent Control and Systems, Harbin Institute of Technology, Harbin 150001, P. R. China
E-mail: 23S004037@stu.hit.edu.cn; twang@hit.edu.cn; jbqiu@hit.edu.cn

2. Areospace System Engineering Shanghai, Shanghai 201109, P. R. China
E-mail: 634103718@qq.com

Abstract: This paper addresses the attitude fault-tolerant control of a rigid spacecraft subject to multiple actuator faults, uncertain inertia, unknown disturbances, and unknown system state variables. A high-order fully-actuated (HOFA) model is derived based on the state-space representation by using variable elimination method. The extended state observer (ESO) is employed to estimate the unknown state variables and their derivatives, as well as the generalized disturbances, which include uncertain inertia, external disturbances, and bias fault. The assumption that the system states are known, which is required in the HOFA approach, is relaxed. The controller designed based on the HOFA approach ensures a linear closed-loop system and incorporates ESO for compensating the total disturbances. The tracking error is guaranteed to converge to a small neighborhood of the origin and the closed-loop system is proved to be bounded. Numerical simulations are conducted to demonstrate the effectiveness of the proposed control law.

Key Words: Fault-tolerant control, High-order fully-actuated system approach, Attitude tracking, Extended state observer

1 Introduction

Attitude control of a spacecraft is one of the most fundamental issues, which are usually utilized in spacecraft operations such as on-orbit service, space circumnavigation mission, etc. Due to the severe operating environment, spacecrafts are often subjected to different external disturbances and uncertainties [1]. The inertia of the spacecraft is uncertain due to various factors, such as fuel consumption, payload deployment, etc. Therefore, it is essential to enhance the robustness of the controller. In response to this issue, a sliding mode control strategy was presented in [2]. Furthermore, an adaptive backstepping control scheme was proposed for attitude tracking of non-rigid spacecraft by considering external disturbances and inertia uncertainties [3].

The aforementioned methods show their robustness in dealing with external disturbances and uncertainties. However, they did not show their ability in addressing the fault-tolerant control problem with actuators faults. During the spacecraft operations, the occurrence of various actuator faults is inevitable, which may result in potential satellite damages and different active and passive fault-tolerant control strategies were proposed in [4–9]. In this paper, a passive fault-tolerant control strategy was proposed due to its simplicity in structure and excellent real-time performance [7]. Then, by combining with traditional control methods such as backstepping control and sliding mode control, a considerable number of fault-tolerant control strategies have been proposed to cope with actuator faults.

However, the aforementioned methods are all based on state-space models, which bring challenges when dealing with nonlinear systems [2–10]. For instance, most of the traditional control strategies can only achieve local stability, but not global stability. Moreover, these methods are often utilized for some specific system forms or under some certain conditions. Recently, a novel method named HOFA system approach was proposed in [11], whose ability is to construct a closed-loop linear system. It has demonstrated significant strengths in addressing various aspects, such as adaptive control [12], robust control [13], and optimal control [14].

Nevertheless, the HOFA system approach requires the knowledge of the system states and higher-order states, which may be uncertain in practical systems. Additionally, it heavily relies on the actuators. It poses significant challenges for the application of this theory that actuators have multiplicative or additive faults. Motivated by the aforementioned challenges, this paper proposes an extended-observer HOFA system approach for fault-tolerant attitude tracking control. The main contributions of this paper are summarized as follows:

1) The utilization of ESO relaxed the assumption that the system states are measurable.
2) The proposed fault-tolerant control strategy effectively addresses actuator faults, disturbances, and uncertain inertia.
3) The HOFA system approach based fault-tolerant control strategy offers standardized and parametric controller structure, along with semi-global uniformly bounded stability results.

Notations: $\omega_{e,f}^{(g)}$ represents the angular velocity of $\mathcal{O}_f$ relative to $\mathcal{O}_e$ expressed in $\mathcal{O}_g$. R_e^f indicates the rotation matrix from $\mathcal{O}_e$ to $\mathcal{O}_f$. $\|\cdot\|$ denotes the 2-norm of vectors and the induced 2-norm of matrices. The maximum and minimum eigenvalues of a matrix are represented by $\lambda_{max}(\cdot)$ and $\lambda_{min}(\cdot)$, respectively. $S(f)$ stands for the anti-symmetric matrix for any $f \in \mathbb{R}^3$. $Re(\cdot)$ is the real part of complex numbers. $diag[f_1, f_2, f_3]$ denotes the diagonal matrix with f_1, f_2, f_3 as its diagonal elements. $x^{(0\sim n-1)}$

This work was supported by the National Natural Science Foundation of China (U21B6001, 62273121).

denotes $\begin{bmatrix} x & \dot{x} & \dots & x^{(n-1)} \end{bmatrix}^T$. For a set of matrices $A_j \in \mathbb{R}^{m\times m}, j = 0, 1, \dots, n-1$, we use the following definitions:

$$A_{0\sim n-1} = \begin{bmatrix} A_0 & A_1 & \cdots A_{n-1} \end{bmatrix}, \bar{A}_{0\sim n-1} = A_{0\sim n-1}^T,$$

$$\Phi(A_{0\sim n-1}) = \begin{bmatrix} 0 & I & & \\ & & \ddots & \\ & & & I \\ -A_0 & -A_1 & \dots & -A_{n-1} \end{bmatrix},$$

$$\Psi(A_{0\sim n-1}) = \begin{bmatrix} -A_{n-1} & I & & \\ \vdots & & \ddots & \\ -A_1 & & & I \\ -A_0 & & & 0 \end{bmatrix}, \bar{I} = \begin{bmatrix} & & & 1 \\ & & \iddots & \\ & 1 & & \\ 1 & & & \end{bmatrix}.$$

2 Problem Formulation and Preliminaries

In order to describe the relative attitude of a spacecraft, we define the Earth-Centered Inertial (ECI) frame as $\mathcal{O}_i$. The body frame, denoted as $\mathcal{O}_b$, is established by placing the origin at the center of mass of the spacecraft. Furthermore, the reference frame $\mathcal{O}_r$ is defined with its origin and orientation specified based on the desired attitude of the spacecraft.

2.1 Attitude Dynamics for Rigid Spacecraft

The relative attitude between $\mathcal{O}_b$ and $\mathcal{O}_r$ denoted in $\mathcal{O}_b$ can be represented by the modified Rodrigues parameters (MRPs) $\sigma = \begin{bmatrix} \sigma_1 & \sigma_2 & \sigma_3 \end{bmatrix}^T$. According to [15], the relative attitude dynamics are expressed as

$$\begin{cases} \dot{\sigma} = G(\sigma)\omega, \\ J\dot{\omega} + C_r\omega + n_r = \tau + \tau_d, \end{cases} \tag{1}$$

where $\omega = \omega_{i,b}^{(b)} - R_r^b\omega_{i,r}^{(r)}$ represents the relative angular velocity with rotation matrix provided by $R_r^b = I_3 - 4(1-\sigma^T\sigma)S(\sigma)/(1+\sigma^T\sigma)^2 + 8S^2(\sigma)/(1+\sigma^T\sigma)^2$, $G(\sigma) = \frac{1}{4}[(1-\sigma^T\sigma)I_3 + 2S(\sigma) + 2\sigma\sigma^T]$, J denotes the inertia matrix of the spacecraft, $C_r = JS(R_r^b\omega_{i,r}^{(r)}) + S(R_r^b\omega_{i,r}^{(r)})J - S(J(\omega + R_r^b\omega_{i,r}^{(r)}))$ is an anti-symmetric matrix, $n_r = S(R_r^b\omega_{i,r}^{(r)})JR_r^b\omega_{i,r}^{(r)} + JR_r^b\dot{\omega}_{i,r}^{(r)}$ represents a nonlinear vector, and the control torque is denoted as τ while the disturbance torque is represented as τ_d.

Considering the actuators faults, τ in (1) is represented as

$$\tau = \rho v(t) + \delta(t), \tag{2}$$

where $\rho = diag[\rho_1, \rho_2, \rho_3] \in \mathbb{R}^{3\times3}$ with $0 < \rho_i \leq 1 (i = 1, 2, 3)$ is the control effectiveness matrix, $v(t) \in \mathbb{R}^3$ represents the ideal control input to be designed and $\delta(t) \in \mathbb{R}^3$ is the bias fault.

Considering the practical situation, the spacecraft subjects to the following assumptions.

Assumption 1. The angular velocity ω is unmeasurable.

MRPs possess the following proposition [16], making it relatively easy to obtain the HOFA model.

Proposition 1. The matrix $G(\sigma)$ is non-singular, which satisfies

$$G^T(\sigma)G(\sigma) = \frac{1}{16}(1+\sigma^T\sigma)^2 I_3,$$

and $G^{-1}(\sigma)$ is

$$G^{-1}(\sigma) = \frac{16G^T(\sigma)}{(1+\sigma^T\sigma)^2}.$$

2.2 HOFA Model

The state space model (1) can be converted into the HOFA model through taking multiple derivatives [11]. Based on the first equation in (1), ω can be represented as

$$\omega = G^{-1}(\sigma)\dot{\sigma}. \tag{3}$$

By differentiating equation (3) with respect to time and taking into account the second equation in (1), we can obtain the following equation

$$\begin{aligned} \dot{\omega} &= \frac{dG^{-1}(\sigma)}{dt}\dot{\sigma} + G^{-1}(\sigma)\ddot{\sigma} \\ &= J^{-1}(-C_r\omega - n_r + \tau + \tau_d), \end{aligned} \tag{4}$$

where

$$\begin{aligned} \frac{dG^{-1}(\sigma)}{dt} =& \frac{4}{(1+\sigma^T\sigma)^2}[-2\sigma^T\dot{\sigma}I_3 - 2S(\dot{\sigma}) + \dot{\sigma}\sigma^T + \sigma\dot{\sigma}^T] \\ &- \frac{64}{(1+\sigma^T\sigma)^3}G^T(\sigma)(\sigma^T\dot{\sigma}). \end{aligned}$$

Furthermore, the attitude dynamics (1) can be transformed into the following second-order model

$$\ddot{\sigma} = F(\sigma^{(0\sim1)}(t)) + G(\sigma(t))J^{-1}(\tau + \tau_d) \tag{5}$$

where

$$\begin{aligned} F(\sigma^{(0\sim1)}(t)) =& -[G(\sigma)\frac{dG^{-1}(\sigma)}{dt} + G(\sigma)J^{-1}C_rG^{-1}(\sigma)]\dot{\sigma} \\ &- G(\sigma)J^{-1}n_r. \end{aligned}$$

Assumption 2. The J can be decomposed as $J = J_0 + \Delta J$, where J_0 is the known nominal value, and ΔJ is the bounded uncertainty.

The inertia matrix J is invertible and the subsequent equation holds

$$J^{-1} = (J_0 + \Delta J)^{-1} = J_0^{-1} + \Delta\widetilde{J} \tag{6}$$

where $\Delta\widetilde{J} = -J_0^{-1}\Delta J(I_3 + J_0^{-1}\Delta J)^{-1}J_0^{-1}$. Considering the uncertainty in the inertia matrix and bias fault in the actuators, (5) can be represented as

$$\ddot{\sigma} = -G(\sigma)J_0^{-1}n_{r0} + \bar{F}(\sigma^{(0\sim1)}(t), \tau_d, \delta(t)) + G_1(\sigma)\rho v(t) \tag{7}$$

where

$$n_{r0} = S(R_r^b\omega_{i,r}^{(r)})J_0R_r^b\omega_{i,r}^{(r)} + J_0R_r^b\dot{\omega}_{i,r}^{(r)},$$

$$\begin{aligned} \bar{F}(\sigma^{(0\sim1)}(t), \tau_d, \delta(t)) =& S(R_r^b\omega_{i,r}^{(r)})\Delta JR_r^b\omega_{i,r}^{(r)} + \Delta JR_r^b\dot{\omega}_{i,r}^{(r)} \\ &- G(\sigma)\Delta\widetilde{J}n_r + G[J_0^{-1}\delta(t) + \Delta\widetilde{J}(\rho v(t) + \delta(t))] \\ &- \left[G(\sigma)\frac{dG^{-1}(\sigma)}{dt} + G(\sigma)J^{-1}C_rG^{-1}(\sigma)\right]\dot{\sigma} + G(\sigma)J^{-1}\tau_d, \end{aligned}$$

and $G_1(\sigma) = G(\sigma)J_0^{-1}$. $\bar{F}$ is the generalized disturbance, encompassing all unmeasurable variables, which fulfills the following assumption.

Assumption 3. [17] The generalized disturbance $\bar{F} \in \mathcal{C}^1$ satisfies $\|\dot{\bar{F}}\| \leq \bar{g}$, where $\bar{g}$ is a positive constant.

Taking into account Proposition 1 and reversibility of the matrix J_0, $G_1(\sigma)$ is invertible. Hence, according to the definition in [11], it can be concluded that the system described by equation (7) is fully actuated.

Before presenting the main results, it is necessary to provide the following Lemmas.

Lemma 1. *[18] Let $A \in \mathbb{R}^{n\times n}$ satisfy*

$$Re(\lambda_j(A)) \leq -\frac{\gamma}{2}, \quad j = 1, 2, \ldots, n \tag{8}$$

where $\gamma > 0$, then there exits a positive definite matrix $P \in \mathbb{R}^{n\times n}$ such that

$$A^T P + PA \leq -\gamma P. \tag{9}$$

Lemma 2. *[18] For any $\mu, \mu^* > 0$, there exist a series of $A_j, A_j^* \in \mathbb{R}^{n\times n}, j = 0, 1, \ldots, n-1$, such that*

$$Re(\lambda_j(\Phi(A_{0\sim n-1}))) \leq -\frac{\mu}{2}, \tag{10}$$

$$Re(\lambda_j(\Psi(A^*_{0\sim n-1}))) \leq -\frac{\mu^*}{2}. \tag{11}$$

3 Fault-tolerant Control Design Based on ESO

3.1 ESO Design

In this section, the fault-tolerant control strategy based on an ESO is introduced.

Denote

$$\begin{cases} z_1 = \sigma, \\ z_2 = \dot{\sigma}. \end{cases} \tag{12}$$

Then, (7) can be reformulated in the following form

$$\begin{cases} \dot{z}_1 = & z_2, \\ \dot{z}_2 = & -G(z_1)J_0^{-1}n_{r0} + \bar{F}(z^{(0\sim1)}(t), \tau_d, \delta(t)) \\ & +G_1(z_1)\rho v(t). \end{cases} \tag{13}$$

By introducing the ESO design technique, we define $z_3 = \bar{F}(z^{0\sim1}(t), \tau_d, \delta(t))$ and $\dot{z}_3 = g(t)$. Based on Assumption 3, $g(t)$ is unknown and bounded. Hence, (13) can be rewritten as

$$\begin{cases} \dot{z}_1 = z_2, \\ \dot{z}_2 = -G(z_1)J_0^{-1}n_{r0} + z_3 + G_1(z_1)\rho v(t), \\ \dot{z}_3 = g(t). \end{cases} \tag{14}$$

Let $e_1 = \hat{z}_1 - z_1$, and the ESO can be designed as

$$\begin{cases} \dot{\hat{z}}_1 = \hat{z}_2 - A_2^* e_1, \\ \dot{\hat{z}}_2 = -G(z_1)J_0^{-1}n_{r0} + \hat{z}_3 + G_1(z_1)\rho v(t) - A_1^* e_1, \\ \dot{\hat{z}}_3 = -A_0^* e_1, \end{cases} \tag{15}$$

where $\hat{z}_1, \hat{z}_2$ and $\hat{z}_3$ are the estimations of z_1, z_2 and z_3, respectively. $A_0^*, A_1^*, A_2^* \in \mathbb{R}^{3\times3}$ are the matrices to be designed. Defining the observer error vector as $e = \begin{bmatrix} e_1^T & e_2^T & e_3^T \end{bmatrix}^T$, where $e_2 = \hat{z}_2 - z_2$ and $e_3 = \hat{z}_3 - z_3$.

Lemma 3. *[19] Consider the system (7) with Assumptions 2-3. Let μ^* be an arbitrarily positive number and $A_j^*, j = 0, 1, 2$ be a series of matrices satisfying (11), there exists a positive definite matrix $P^*(A^*_{0\sim2})$ satisfying (9). Therefore, ESO (15) for the uncertain system (7) ensures that the observation errors converge to an ellipsoid of the origin as follows:*

$$\Theta_{\xi,\kappa}(0) = \left\{ e | e^T P^*(A^*_{0\sim2}) e \leq \frac{\xi}{\kappa} \right\} \tag{16}$$

where ξ and κ can be appropriately designed to guarantee that the errors are small enough.

3.2 Control Law Design

In accordance with the HOFA system approach and the above ESO (15), the controller can be formulated as follows.

Let μ be a positive number and $A_0, A_1 \in \mathbb{R}^{3\times3}$ be the matrices that satisfy (10), then the control law is given by

$$\begin{cases} v(t) = -G_1^{-1}(\sigma)(v_0(t) + v_1(t)), \\ v_0(t) = A_1\hat{z}_2 + A_0\hat{z}_1 - G(\sigma)J_0^{-1}n_{r0} + \hat{z}_3, \\ v_1(t) = \frac{1}{4\epsilon}P_L^T(A_{0\sim1})\hat{z}^{(0\sim1)}. \end{cases} \tag{17}$$

where the nonlinear control law $v_0(t)$ converts the high-order nonlinear system into a linear time-invariant system, while the control law $v_1(t)$ counteracts the effects of faults. It is reasonably assumed that the control law is bounded.

Theorem 1. *For the system (7), the control law (17) with the ESO (15) ensures that the states $\sigma^{(0\sim1)}$ converge to an ellipsoid of the origin as follows:*

$$\Theta_{\epsilon_m,\mu} = \left\{ \sigma^{(0\sim1)} | (\sigma^{(0\sim1)})^T P(A_{0\sim1})\sigma^{(0\sim1)} \leq 2\frac{\epsilon_m}{\mu} \right\}, \tag{18}$$

where ϵ_m and μ are provided in the subsequent proof.

Proof. For the HOFA model (7), the controller (17) produces the following linear system

$$\ddot{\sigma} + A_1\dot{\sigma} + A_0\sigma = \overline{\omega} - v_1(t) - G_1(\sigma)(I_3 - \rho)v(t), \tag{19}$$

where $\overline{\omega} = -A_1e_2 - A_0e_1 - e_3$. The state-space form of (19) is

$$\begin{aligned} \dot{\sigma}^{(0\sim1)} =& \Phi(A_{0\sim1})\sigma^{(0\sim1)} \\ &+ \begin{bmatrix} 0 \\ \overline{\omega} - v_1(t) - G_1(\sigma)(I_3 - \rho)v(t) \end{bmatrix} \end{aligned} \tag{20}$$

where $\Phi(A_{0\sim1})$ satisfies (10).

Then, $v_1(t)$ can be rewritten as

$$\begin{aligned} v_1(t) =& \frac{1}{4\epsilon}P_L^T(A_{0\sim1})\hat{z}^{(0\sim1)} - \frac{1}{4\epsilon}P_L^T(A_{0\sim1})\sigma^{(0\sim1)} \\ &+ \frac{1}{4\epsilon}P_L^T(A_{0\sim1})\sigma^{(0\sim1)} \\ =& \frac{1}{4\epsilon}P_L^T(A_{0\sim1})\begin{bmatrix} e_1 \\ e_2 \end{bmatrix} + \frac{1}{4\epsilon}P_L^T(A_{0\sim1})\sigma^{(0\sim1)}. \end{aligned} \tag{21}$$

Furthermore, (20) can be expressed as

$$\dot{\sigma}^{(0\sim1)} = \Phi(A_{0\sim1})\sigma^{(0\sim1)} + \begin{bmatrix} 0 \\ \psi \end{bmatrix}, \tag{22}$$

where

$$\psi = \overline{\omega}_n - G_1(\sigma)(I_3 - \rho)v(t) - \frac{1}{4\epsilon}P_L^T(A_{0\sim1})\sigma^{(0\sim1)}, \quad (23)$$

with

$$\overline{\omega}_n = \overline{\omega} - \frac{1}{4\epsilon}P_L^T(A_{0\sim1})\begin{bmatrix}e_1\\ e_2\end{bmatrix}. \quad (24)$$

$\overline{\omega}_n$ denotes the effect of observation error on the system, which is assumed to be bounded.

According to Lemma 1, there exists a positive matrix $P(A_{0\sim1})$ satisfying (9). Consider the following Lyapunov function:

$$V = \frac{1}{2}(\sigma^{(0\sim1)})^T P(A_{0\sim1})\sigma^{(0\sim1)}. \quad (25)$$

We define

$$P = P(A_{0\sim1}), \Phi = \Phi(A_{0\sim1}), G_1 = G_1(\sigma),$$
$$P_L = P_L(A_{0\sim1}) = P\begin{bmatrix}0_3\\ I_3\end{bmatrix},$$

The time-derivative of V is

$$\begin{aligned}\dot{V} =& \frac{1}{2}(\dot{\sigma}^{(0\sim1)})^T P\sigma^{(0\sim1)} + \frac{1}{2}(\sigma^{(0\sim1)})^T P\dot{\sigma}^{(0\sim1)}\\ =& \frac{1}{2}(\Phi\sigma^{(0\sim1)} + \begin{bmatrix}0\\ \psi\end{bmatrix})^T P\sigma^{(0\sim1)}\\ &+ \frac{1}{2}(\sigma^{(0\sim1)})^T P(\Phi\sigma^{(0\sim1)} + \begin{bmatrix}0\\ \psi\end{bmatrix})\\ =& \frac{1}{2}(\sigma^{(0\sim1)})^T(\Phi^T P + P\Phi)\sigma^{(0\sim1)}\\ &+ (\sigma^{(0\sim1)})^T P\begin{bmatrix}0\\ \psi\end{bmatrix}\\ \leq& -\frac{\mu}{2}(\sigma^{(0\sim1)})^T P\sigma^{(0\sim1)} + (\sigma^{(0\sim1)})^T P\begin{bmatrix}0\\ \psi\end{bmatrix}\\ =& -\mu V + V_1\end{aligned} \quad (26)$$

where

$$V_1 = (\sigma^{(0\sim1)})^T P\begin{bmatrix}0\\ \psi\end{bmatrix} = (\sigma^{(0\sim1)})^T P_L\psi. \quad (27)$$

From equations (17) and (23), we have

$$\begin{aligned}V_1 =& (\sigma^{(0\sim1)})^T P_L\\ &[\overline{\omega}_n - G_1(I_3 - \rho)v(t) - \frac{1}{4\epsilon}P_L^T\sigma^{(0\sim1)}]\\ =& -\frac{1}{4\epsilon}[(\sigma^{(0\sim1)})^T P_L P_L^T\sigma^{(0\sim1)}]\\ &+ (\sigma^{(0\sim1)})^T P_L[\overline{\omega}_n - G_1(I_3 - \rho)v(t)]\\ \leq& -\frac{1}{4\epsilon}\|P_L^T\sigma^{(0\sim1)}\|^2\\ &+ \|\overline{\omega}_n - G_1(I_3 - \rho)v(t)\|\|P_L^T\sigma^{(0\sim1)}\|.\end{aligned} \quad (28)$$

Taking into account the boundedness of $\overline{\omega}_n, \sigma$, and the control law v, there exists a positive constant v_m such that the following inequality holds

$$\|\overline{\omega}_n - G_1(I_3 - \rho)v(t)\| \leq v_m. \quad (29)$$

Thus, the inequality (28) is represented as

$$\begin{aligned}V_1 \leq& -\frac{1}{4\epsilon}\|P_L^T\sigma^{(0\sim1)}\|^2 + v_m\|P_L^T\sigma^{(0\sim1)}\|\\ \leq& \epsilon v_m^2 = \epsilon_m\end{aligned} \quad (30)$$

The combination of (26) and (30) leads to the following expression

$$\dot{V} \leq -\mu V + \epsilon_m. \quad (31)$$

Consequently, according to the comparison lemma, it is concluded that

$$\begin{aligned}V \leq& V(0)e^{-\mu t} + \frac{\epsilon_m}{\mu}(1 - e^{-\mu t})\\ =& \left[V(0) - \frac{\epsilon_m}{\mu}\right]e^{-\mu t} + \frac{\epsilon_m}{\mu}\\ \rightarrow& \frac{\epsilon_m}{\mu}(t \rightarrow \infty).\end{aligned} \quad (32)$$

Hence, the state $\sigma^{(0\sim1)}$ will ultimately converge to the ellipsoid $\Theta_{\epsilon_m,\mu}$. It is evident that by appropriately choosing parameters ϵ and μ, the upper bound of the overall errors are minimized. The proof is completed. □

3.3 Parametric Solutions of $A_{0\sim n-1}$ and $A^*_{0\sim n-1}$

For HOFA closed-loop system, appropriate parameter matrices are designed based on different circumstances. The parametric solutions of $A_{0\sim n-1}$ and $A^*_{0\sim n-1}$ are given in the following.

Lemma 4. *[11, 20] For a given matrix $F \in \mathbb{R}^{nm\times nm}$, appropriate choice of a matrix $A_{0\sim n-1}$ and a nonsingular matrix $V \in \mathbb{R}^{nm\times nm}$ satisfy the following conditions*

$$\begin{aligned}&\Phi(A_{0\sim n-1}) = VFV^{-1},\\ &A_{0\sim n-1} = -ZF^nV^{-1}(Z,F),\\ &V = V(Z,F) = \begin{bmatrix}Z\\ ZF\\ \vdots\\ ZF^{n-1}\end{bmatrix}\end{aligned} \quad (33)$$

where $Z \in \mathbb{R}^{m\times nm}$ is an arbitrarily designed matrix satisfying $\det V(Z,F) \neq 0$.

Lemma 5. *[19] For a given matrix $\bar{F} \in \mathbb{R}^{nm\times nm}$, appropriate choice of a matrix $\bar{A}^*_{0\sim n-1}$ and a nonsingular matrix $\bar{V} \in \mathbb{R}^{nm\times nm}$ satisfy the following conditions*

$$\begin{aligned}&\Psi(A^*_{0\sim n-1}) = \bar{V}\bar{F}\bar{V}^{-1},\\ &\bar{A}^*_{0\sim n-1} = -(\bar{I}\bar{V})\bar{F}^n\bar{Z},\\ &\bar{V} = \bar{V}(\bar{Z},\bar{F}) = \bar{I}\begin{bmatrix}\bar{Z} & \bar{F}\bar{Z} & \cdots & \bar{F}^{n-1}\bar{Z}\end{bmatrix}^{-1}\end{aligned} \quad (34)$$

where $\bar{Z} \in \mathbb{R}^{nm\times m}$ is an arbitrarily designed matrix satisfying $\det\begin{bmatrix}\bar{Z} & \bar{F}\bar{Z} & \cdots & \bar{F}^{n-1}\bar{Z}\end{bmatrix} \neq 0$.

4 Simulation Studies

In this section, a numerical simulation example is provided to show the effectiveness of the proposed fault-tolerant control strategy. The simulation is conducted under similar

conditions as described in [19]. The nominal value of the spacecraft's inertia matrix is given as:

$$J_0 = \begin{bmatrix} 2500 & 50 & 30 \\ 50 & 1500 & 40 \\ 30 & 40 & 3500 \end{bmatrix} kg \cdot m^2$$

and the corresponding actual value is given as $J = 1.1J_0$. The desired attitude is set as

$$(\sigma_{i,r}^{(r)})^T = \begin{bmatrix} 0 & 0 & 0 \end{bmatrix}, \quad (\omega_{i,r}^{(r)})^T = \begin{bmatrix} 0 & 0 & \omega_0 \end{bmatrix}$$

where $\omega_0 = 0.00117 rad/s$ represents the orbital angular velocity. For the periodic influences from other objects [21], the spacecraft subjects to an external disturbance described as:

$$\tau_d = b_0 + b_1 sin(\omega_0 t) + b_2 cos(\omega_0 t)$$

where

$$(b_0)^T = \begin{bmatrix} 0.09 & 0.06 & 0.07 \end{bmatrix},$$
$$(b_1)^T = \begin{bmatrix} -0.08 & -0.06 & 0.05 \end{bmatrix},$$
$$(b_2)^T = \begin{bmatrix} 0.03 & -0.02 & 0.01 \end{bmatrix}.$$

The relative attitude and relative angular velocity are given as:

$$(\sigma(0))^T = \begin{bmatrix} -0.3152 & 0.4516 & 0.3461 \end{bmatrix},$$
$$(\omega(0))^T = \begin{bmatrix} 0.02 & -0.01 & 0.02 \end{bmatrix} rad/s.$$

At $t = 30s$, the actuators failure occurs with the following form

$$\tau = diag[\rho_1, \rho_2, \rho_3] v(t) + \delta(t),$$

$$\rho_1 = \begin{cases} 1, t \le 30, \\ 0.6 + 0.4e^{-t+30}, t > 30, \end{cases}$$

$$\rho_2 = \begin{cases} 1, t \le 30, \\ 0.7 + 0.3e^{-t+30}, t > 30, \end{cases}$$

$$\rho_3 = \begin{cases} 1, t \le 30, \\ 0.5 + 0.5e^{-t+30}, t > 30, \end{cases}$$

$$\delta(t) = \begin{bmatrix} 6 + 6e^{-t+30} sin(10t) \\ 5 + 5e^{-t+30} sin(15t) \\ 3 + 3e^{-t+30} sin(20t) \end{bmatrix}.$$

The parameter matrices $A_{0\sim1}$ of the fault-tolerant controller (17) are given as

$$A_0 = 0.0002 I_3, A_1 = 0.03 I_3,$$

and the parameter matrices $A_{0\sim2}^*$ of the ESO (15) are given as

$$A_0^* = 6 \times 10^{-5} I_3, A_1^* = 0.0047 I_3, A_2^* = 0.12 I_3.$$

The simulation results are presented in Figs. 1-5. The observer errors are defined as $e_i = \begin{bmatrix} e_i(1) & e_i(2) & e_i(3) \end{bmatrix}^T$, $i = 1, 2, 3$. The time responses of the ESO (15) errors are shown in Fig. 1. The states $\sigma, \dot{\sigma}$ and the generalized disturbance $\bar{F}$ are well estimated. The designed control law enables that the relative attitude and relative angular velocity converge to zero, as presented in Figs. 2 and 3, respectively. Figs. 4 and 5 illustrate time responses of the control torque and the ideal control inputs, respectively. At the beginning, control torque of relatively large value drives the spacecraft

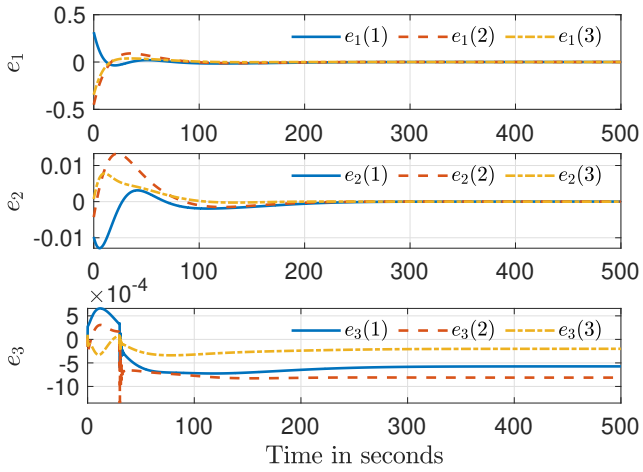

Fig. 1: Time responses of observation errors e_1, e_2, e_3.

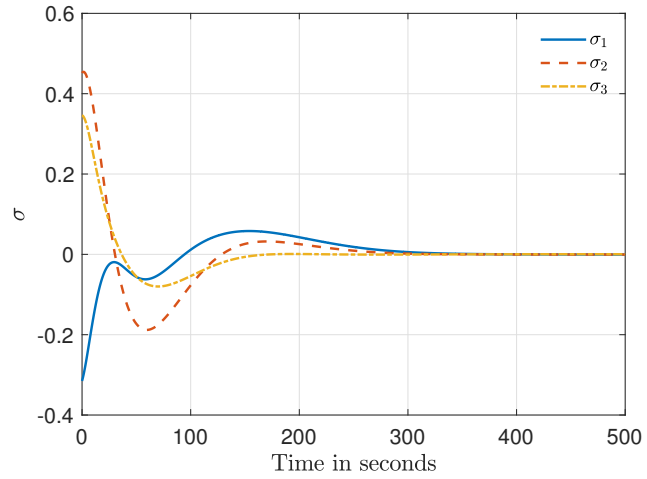

Fig. 2: Time responses of relative attitude.

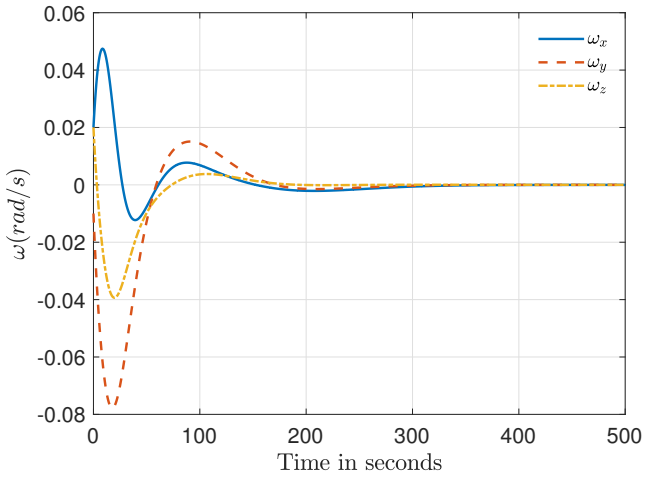

Fig. 3: Time responses of relative angular velocity.

towards the desired attitude. Afterwards, the magnitude of the control torque rapidly decays to a small value to maintain the spacecraft attitude. The actuators fail at $t = 30s$, resulting in small jump in the control torque. In order to compensate the effect of the generalized disturbance $\bar{F}$, the ideal control inputs do not converge to zero, as shown in Fig. 5. The simulation results demonstrate that the proposed con-

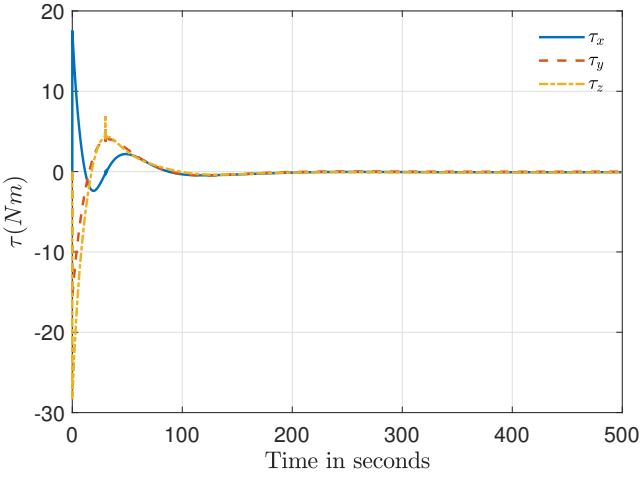

Fig. 4: Time responses of control torque.

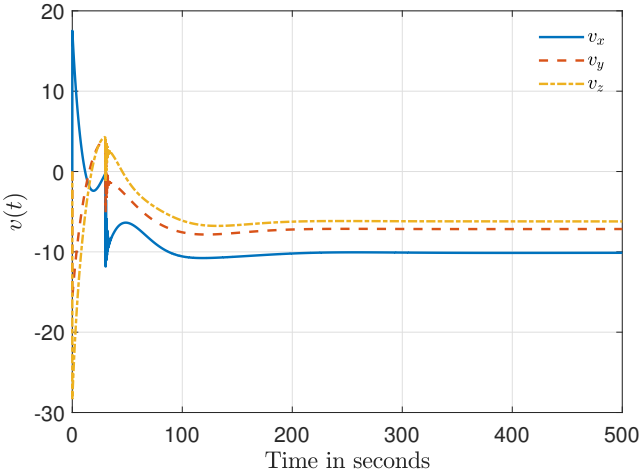

Fig. 5: Time responses of ideal control inputs.

trol scheme is able to handle imprecise inertia parameters, actuator failures, external disturbance and unknown state information $\dot{\sigma}$.

5 Conclusion

In this paper, a fault-tolerant control scheme is proposed to effectively address the challenges posed by spacecraft with uncertain inertia, external disturbances, actuator faults, and unknown state information. By employing the ESO, the assumption that the system states should be known is relaxed. The nonlinearity is compensated by the proposed control strategy. The designed fault-tolerant controller exhibits excellent capability in handling actuator faults. By appropriately selecting parameter matrices, the linear closed-loop system achieves satisfactory performance, which is a significant advantage of the HOFA system approach. The numerical simulation results show the effectiveness of the control scheme.

References

[1] X. Yu, Y. Zhu, J. Qiao, L. Guo, Antidisturbance controllability analysis and enhanced antidisturbance controller design with application to flexible spacecraft, *IEEE Transactions on Aerospace and Electronic Systems*, 2021, 57(5): 3393–3404.

[2] K. Lu, Y. Xia, Adaptive attitude tracking control for rigid spacecraft with finite-time convergence, *Automatica*, 2013, 49(12): 3591–3599.

[3] Y. Li, F. Yang, Robust adaptive attitude control for non-rigid spacecraft with quantized control input, *IEEE/CAA Journal of Automatica Sinica*, 2020, 7(2): 472–481.

[4] S. Murugesan, P. S. Goel, Fault-tolerant spacecraft attitude control system, *Sadhana*, 1987, 11(1): 233–261.

[5] J. Zhang, G. Yang, Robust adaptive fault-tolerant control for a class of unknown nonlinear systems, *IEEE Transactions on Industrial Electronics*, 2016, 64(1): 585–594.

[6] N. Ji, J. Liu, Adaptive actuator fault-tolerant control for a three-dimensional Euler-Bernoulli beam with output constraints and uncertain end load, *Journal of the Franklin Institute*, 2019, 356(7): 3869–3898.

[7] Q. Hu, X. Shao, L. Guo, Adaptive fault-tolerant attitude tracking control of spacecraft with prescribed performance, *IEEE/ASME Transactions on Mechatronics*, 2017, 23(1), 331–341.

[8] Q. Shen, C. Yue, C. H. Goh, B. Wu, D. Wang, Rigid-body attitude tracking control under actuator faults and angular velocity constraints, *IEEE/ASME Transactions on Mechatronics*, 2018, 23(3): 1338–1349.

[9] W. Cai, X. H. Liao, Y. D. Song, Indirect robust adaptive fault-tolerant control for attitude tracking of spacecraft, *Journal of Guidance, Control, and Dynamics*, 2008, 31(5): 1456–1463.

[10] H. Gao, Z. Li, X. Yu, J. Qiu, Hierarchical multiobjective heuristic for PCB assembly optimization in a beam-head surface mounter, *IEEE Transactions on Cybernetics*, 2022, 52(7): 6911-6924.

[11] G. Duan, High-order system approaches: I. Fully-actuated systems and parametric designs, *Acta Automatica Sinica*, 2020, 46(7): 1333–1345.

[12] G. Duan, High-order fully actuated system approaches: Part IV. Adaptive control and high-order backstepping, *International Journal of Systems Science*, 2021, 52(5): 972–989.

[13] G. Duan, High-order fully-actuated system approaches: Part VI. Disturbance attenuation and decoupling, *International Journal of Systems Science*, 2021, 52(10): 2161–2181.

[14] G. Duan, High-order fully actuated system approaches: Part VIII. Optimal control with application in spacecraft attitude stabilisation, *International Journal of Systems Science*, 2022, 53(1): 54–73.

[15] R. Kristiansen, E. I. Grtli, P. J. Nicklasson, J. T. Gravdahl, A model of relative translation and rotation in leader-follower spacecraft formations, *Modeling, Identification and Control*, 2007, 28(1): 3–13.

[16] Q. Li, J. Yuan, B. Zhang, Extended state observer based output control for spacecraft rendezvous and docking with actuator saturation, *ISA Transactions*, 2019, 88: 37–49.

[17] B. Z. Guo, Z. L. Zhao, On the convergence of an extended state observer for nonlinear systems with uncertainty, *Systems & Control Letters*, 2011, 60(6): 420–430.

[18] G. Duan, High-order fully actuated system approaches: Part III. Robust control and high-order backstepping, *International Journal of Systems Science*, 2021, 52(5): 952–971.

[19] Q. Zhao, G. Duan, Fully actuated system approach for 6DOF spacecraft control based on extended state observer, *Journal of Systems Science and Complexity*, 2022, 35(18): 604–622.

[20] G. Duan, High-order fully actuated system approaches: Part V. Robust adaptive control, *International Journal of Systems Science*, 2021, 52(10): 2129-2143.

[21] J. R. Wertz, W. J. Larson, *Space Mission Analysis and Design*, Torrance: Springer Dordrecht, 1999.

Proceedings of the 3rd Conference on Fully Actuated System Theory and Applications
May 10-12, 2024, Shenzhen, China

Fully Actuated Control for Directional Accuracy in Multiaxis Antennas utilizing Sliding Mode and STESO Observers

Feng Gao, Jiayang Li, Heng Deng, Guanghui Sun
Harbin Institute of Technology, Harbin 150001, P. R. China
E-mail: guanghuisun@hit.edu.cn

Abstract: This study presents an innovative control strategy designed to substantially improve directional accuracy in multiaxis antenna systems. It achieves this by integrating sliding mode control (SMC) with fully actuated (FA) theory, further augmented by a super twisting extended state observer (STESO). Initially, a control-oriented dynamics model was developed, serving as a crucial foundation for the design and execution of the algorithm. This model, derived through an analytical methodology employing both general and quasi-coordinate Lagrangian formulations, accurately defines the kinematics and dynamics that are unique to multiaxis antennas. Subsequently, FA theory was applied to transform the dynamic model into a fully actuated configuration, streamlining the control of antenna movements and avoiding the complexities inherent to manipulating the original system. The subsequent integration of SMC with this transformed model, complemented by the deployment of a STESO, effectively mitigates uncertainties in the system model, thereby significantly enhancing control precision. Simulation experiments conducted using a multiaxis antenna system demonstrate the efficacy of the proposed method and show a substantial improvement in directional accuracy.

Key Words: Fully Actuated Theory, Sliding Mode Control, Super Twisting Extended State Observer, Control-Oriented Dynamics Model, Multiaxis Antennas, Directional Accuracy

1 Introduction

In the rapidly evolving field of wireless communication and radar systems, precise control over the direction of antenna beams is essential [1]. Multiaxis antennas, known for their enhanced maneuverability and exceptional targeting accuracy, play a critical role in applications such as satellite communication, air traffic control, and mobile telephony, where precise positioning and orientation directly impact performance and reliability [2–4].

However, the inherent complexities of multiaxis systems, coupled with external disturbances and system uncertainties, pose significant challenges to achieving optimal directional accuracy. Extensive research has been conducted to develop advanced control strategies capable of overcoming these challenges. For instance, Kang et al. demonstrated the use of passive magnetic pointing for CubeSats, simplifying orientation control by aligning with Earth's magnetic field [5, 6]. While cost-effective and reducing complexity, this method lacks the dynamic responsiveness required in non-static magnetic environments, highlighting a gap in adaptability under variable conditions. Mahbubul Alam's development of an automated satellite tracking system ensures precise alignment with satellites [7]. However, this system's reliance on static predefined parameters makes it less effective in dealing with real-time dynamic disturbances or unforeseen changes in satellite orientation. Hadi Aliakbarian's digitally beam-steerable antenna array improves error rates and power efficiency [8], but the complexity and cost of the hardware limit its widespread application and adaptability in economically constrained projects. Lita's control system using spherical coordinates for accurate antenna orientation is user-friendly [9], yet it struggles with rapid, real-time adjustments necessary in fast-changing operational environments. Finally, Ahn's employment of reinforcement learning to optimize satellite antenna profiles, although adaptive, requires significant computational resources and extensive data, rendering it impractical in limited-resource settings or where quick deployment is critical [10].

Recognizing these gaps, the study introduces a novel control strategy that leverages the high-order fully actuated (HOFA) theory, initially proposed by Duan [11–13]. HOFA simplifies the control of complex systems by transforming underactuated systems into a linear form, allowing for strategic pole placement to ensure system stability—an improvement over traditional methods [14–16]. The approach integrates the precision of fully actuated theory with the resilience of sliding mode control (SMC) and the robustness of a super twisting extended state observer (STESO), addressing both the nonlinear dynamics and external disturbances effectively. Key contributions of the research include the development of a control-oriented dynamics model tailored for multiaxis antennas and the innovative application of STESO for enhanced state estimation and disturbance rejection. The results from simulation experiments suggest significant improvements in directional accuracy, potentially influencing future developments in the field and enhancing the robustness and reliability of communication networks.

2 Kinematics and Dynamics of the Multiaxis Antenna System

This section describes the kinematic and dynamic framework of the multiaxis antenna system as shown in Fig.1. Simplifying assumptions are made by neglecting the effects of elastic deformation and gravity on the structure. The architecture of the system comprises a main satellite body, denoted as B_0, which is flanked by a pair of solar wings, each connected through a rotary joint with a single degree of freedom. The structure also includes two serially connected segments of a mechanical arm, terminating in a large antenna. Each component, indexed by i, is assumed to be a rigid body, where B_i represents the ith body link. The kinematic and

This work is supported by National Natural Science Foundation (NNSF) of China under Grant 62173107.

dynamic equations of motion are established in relation to a local coordinate system C_i affixed to each segment, ensuring precise control over the directional movement of the antenna.

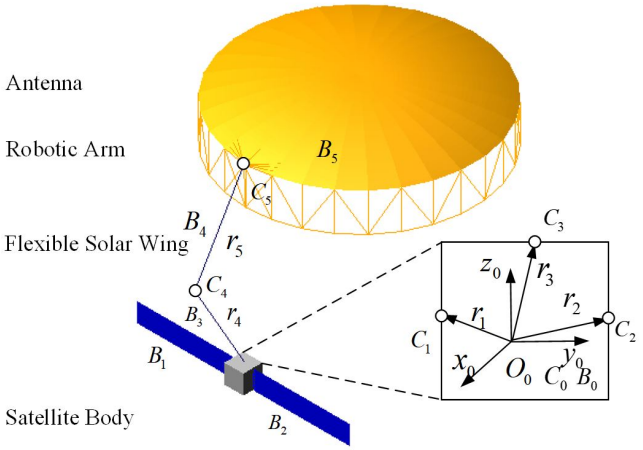

Fig. 1: Multiaxis Antenna System

The kinetic energy for the ith component is expressed as follows

$$T_i = \frac{1}{2}\begin{bmatrix}\boldsymbol{v}_i \\ \boldsymbol{\omega}_i\end{bmatrix}^{\mathrm{T}}\begin{bmatrix}m_i\boldsymbol{I} & \boldsymbol{P}_i \\ \boldsymbol{P}_i^{\mathrm{T}} & \boldsymbol{I}_i\end{bmatrix}\begin{bmatrix}\boldsymbol{v}_i \\ \boldsymbol{\omega}_i\end{bmatrix} \tag{1}$$

where $i = 0, 1, \ldots, N$. $\boldsymbol{I}_i$ and $\boldsymbol{P}_i$ represent the 3×3 inertia tensor and the first moment of mass about its body fixed frame C_i, respectively. The term m_i denotes the mass, and $\boldsymbol{I}$ is the 3×3 identity matrix. The variables $\boldsymbol{v}_i$ and $\boldsymbol{\omega}_i$ are the linear and angular velocities with respect to the inertial frame, and are represented as vectors.

The velocity constraint between the ith component B_i and B_{i-1} is given by the following

$$\begin{bmatrix}\boldsymbol{v}_i \\ \boldsymbol{\omega}_i\end{bmatrix} = \begin{bmatrix}\boldsymbol{0} \\ \dot{q}_i\boldsymbol{z}_i\end{bmatrix} + \begin{bmatrix}\boldsymbol{rot}_z(q_i) & \boldsymbol{0} \\ \boldsymbol{0} & \boldsymbol{rot}_z(q_i)\end{bmatrix}\begin{bmatrix}\boldsymbol{C}_{i-1} & \boldsymbol{C}_{i-1}\tilde{\boldsymbol{r}}_{i-1}^{\mathrm{T}} \\ \boldsymbol{0} & \boldsymbol{C}_{i-1}\end{bmatrix}\begin{bmatrix}\boldsymbol{v}_{i-1} \\ \boldsymbol{\omega}_{i-1}\end{bmatrix} \tag{2}$$

and

$$\boldsymbol{rot}_z(q_i) = \begin{bmatrix}\cos(q_i) & \sin(q_i) & 0 \\ -\sin(q_i) & \cos(q_i) & 0 \\ 0 & 0 & 1\end{bmatrix} \tag{3}$$

where $\boldsymbol{z}_i$ is the unit z-dimensional vector of the frame C_i and q_i is the corresponding joint angle. $\boldsymbol{C}_{i-1}$ is the rotation matrix with respect to the frame C_{i-1}, and $\tilde{\boldsymbol{r}}_i$ is the 3×3 skew-symmetric matrix associated with the vector $\boldsymbol{r}_i$.

Define $\boldsymbol{S}_i$ and $\boldsymbol{R}_i(q_i)$ as

$$\boldsymbol{S}_i = \begin{bmatrix}\boldsymbol{0} & \boldsymbol{0} \\ \boldsymbol{0} & \mathrm{diag}(0,0,1)\end{bmatrix}$$

$$\boldsymbol{R}_i(q_i) = \begin{bmatrix}\boldsymbol{rot}_z(q_i) & \boldsymbol{0} \\ \boldsymbol{0} & \boldsymbol{rot}_z(q_i)\end{bmatrix}\begin{bmatrix}\boldsymbol{C}_{i-1} & \boldsymbol{C}_{i-1}\tilde{\boldsymbol{r}}_{i-1}^{\mathrm{T}} \\ \boldsymbol{0} & \boldsymbol{C}_{i-1}\end{bmatrix} \tag{4}$$

where $\mathrm{diag}(0,0,1)$ denotes the diagonal matrix.

For the kth component, the kinematic equations of motion can be assembled as follows

$$\begin{bmatrix}\boldsymbol{v}_k \\ \boldsymbol{\omega}_k\end{bmatrix} = \left(\prod_{i=1}^{k}\boldsymbol{R}_i(q_i)\right)\begin{bmatrix}\boldsymbol{v}_0 \\ \boldsymbol{\omega}_0\end{bmatrix} + \sum_{j=1}^{k-1}\left(\prod_{i=j+1}^{k}\boldsymbol{R}_i(q_i)\right)\boldsymbol{S}_j\dot{q}_j + \boldsymbol{S}_k\dot{q}_k \tag{5}$$

Consequently, all of the intermediate terms can be combined and written in a more compact form as follows

$$\begin{aligned}\boldsymbol{\Phi}_{k0}(q) &= \left(\prod_{i=1}^{k}\boldsymbol{R}_i(q_i)\right) \\ \boldsymbol{\Phi}_{kj}(q) &= \prod_{i=j+1}^{k}\boldsymbol{R}_i(q_i)\,\boldsymbol{S}_j \qquad j = 1, 2, \ldots, k-1 \\ \boldsymbol{\Phi}_{kk}(q) &= \boldsymbol{S}_k\end{aligned} \tag{6}$$

Thus, the equation above can be rewritten as follows

$$\begin{bmatrix}\boldsymbol{v}_k \\ \boldsymbol{\omega}_k\end{bmatrix} = \boldsymbol{\Phi}_{k0}(q)\begin{bmatrix}\boldsymbol{v}_0 \\ \boldsymbol{\omega}_0\end{bmatrix} + \begin{bmatrix}\boldsymbol{\Phi}_{k1}(q) & \boldsymbol{\Phi}_{k2}(q) & \ldots & \boldsymbol{\Phi}_{kk}(q)\end{bmatrix}\dot{q}_{1\sim k} \tag{7}$$

where $\dot{\boldsymbol{q}}_{1\sim k} = [\dot{q}_1, \dot{q}_2, \ldots, \dot{q}_k]^{\mathrm{T}}$.

Therefore, the total kinetic energy of the multiaxis antenna system is as follows

$$\begin{aligned}T &= T_0 + \sum_{i=1}^{n} T_i \\ &= \frac{1}{2}\begin{bmatrix}\boldsymbol{v}_0 \\ \boldsymbol{\omega}_0\end{bmatrix}^{\mathrm{T}}\boldsymbol{M}_0\begin{bmatrix}\boldsymbol{v}_0 \\ \boldsymbol{\omega}_0\end{bmatrix} \\ &\quad + \frac{1}{2}\sum_{i=1}^{n}\begin{bmatrix}\boldsymbol{v}_0 \\ \boldsymbol{\omega}_0 \\ \dot{\boldsymbol{q}}_i\end{bmatrix}^{\mathrm{T}}\boldsymbol{M}_i(\boldsymbol{q}_i)\begin{bmatrix}\boldsymbol{v}_0 \\ \boldsymbol{\omega}_0 \\ \dot{\boldsymbol{q}}_i\end{bmatrix} \\ &= \begin{bmatrix}\boldsymbol{v}_0 \\ \boldsymbol{\omega}_0 \\ \dot{\boldsymbol{q}}_i\end{bmatrix}^{\mathrm{T}}\boldsymbol{M}(\boldsymbol{q})\begin{bmatrix}\boldsymbol{v}_0 \\ \boldsymbol{\omega}_0 \\ \dot{\boldsymbol{q}}_i\end{bmatrix}\end{aligned} \tag{8}$$

where $\boldsymbol{M}(\boldsymbol{q})$ is the generalized inertia matrix,

$$\boldsymbol{M}(\boldsymbol{q})) = \frac{1}{2}\begin{bmatrix}\boldsymbol{M}_0 + \sum_{i=1}^{n}\boldsymbol{M}_{00}(q_i) & \boldsymbol{M}_{0q}(q_1) & \boldsymbol{M}_{0q}(q_2) & \cdots & \boldsymbol{M}_{0q}(q_n) \\ \boldsymbol{M}_{q0}(q_1) & \boldsymbol{M}_{qq}(q_1) & \boldsymbol{0} & \cdots & \boldsymbol{0} \\ \boldsymbol{M}_{q0}(q_2) & \boldsymbol{0} & \boldsymbol{M}_{qq}(q_2) & \cdots & \boldsymbol{0} \\ \vdots & \vdots & \vdots & \ddots & \vdots \\ \boldsymbol{M}_{q0}(q_n) & \boldsymbol{0} & \boldsymbol{0} & \cdots & \boldsymbol{M}_{qq}(q_n)\end{bmatrix}$$

It is important to note that the angular velocity ω_0 of the base is not considered a generalized coordinate because the attitude angle of the base cannot be directly obtained by integrating the angular velocity. As a result, employing the classical Lagrangian formulation, which is based on generalized coordinates, to directly derive the rotational motion of the multiaxis antenna base, is particularly challenging. To address this challenge, a quasi-Lagrangian approach is preferred for describing the base motion, since it allows for a more manageable and direct representation of the system's dynamics.

The governing equations of motion derived from this formulation can be represented as follows

$$\frac{\mathrm{d}}{\mathrm{d}t}\frac{\partial T}{\partial \dot{\boldsymbol{q}}} - \frac{\partial T}{\partial \boldsymbol{q}} = \boldsymbol{\tau} \tag{9}$$

where $\boldsymbol{\tau}$ represents the generalized forces acting on the system. Additionally, for the rotational motion of the base, the modified equation takes the following form

$$\left(\frac{\mathrm{d}}{\mathrm{d}t} + \tilde{\boldsymbol{\omega}}_0\right)\frac{\partial T}{\partial \boldsymbol{\omega}} + \begin{bmatrix}\boldsymbol{0} \\ \tilde{\boldsymbol{v}}_0\frac{\partial T}{\partial \boldsymbol{v}_0}\end{bmatrix} = \begin{bmatrix}\boldsymbol{F}_0 \\ \boldsymbol{T}_0\end{bmatrix} \tag{10}$$

where $\tilde{\boldsymbol{\omega}}_0$ and $\tilde{\boldsymbol{v}}_0$ denote the skew-symmetric matrices corresponding to the angular and linear velocities of the base,

respectively, and $\boldsymbol{F_0}$ and $\boldsymbol{T_0}$ represent the external forces and torques, respectively.

The dynamics model of the multiaxis antenna system can be succinctly represented by the following equation

$$\begin{aligned}\boldsymbol{M}\dot{\boldsymbol{\rho}}+\frac{\mathrm{d}\boldsymbol{M}}{\mathrm{d}t}\boldsymbol{\rho}+\operatorname{diag}\left(\tilde{\boldsymbol{\omega}}_0,\tilde{\boldsymbol{\omega}}_0\right)\begin{bmatrix}\tilde{\boldsymbol{M}}_0\\ \mathbf{0}\end{bmatrix}\boldsymbol{\rho}\\ -\frac{1}{2}\begin{bmatrix}\mathbf{0}\\ \boldsymbol{\rho}^{\mathrm{T}}\frac{\partial \boldsymbol{M}}{\partial q_1}\boldsymbol{\rho}\\ \boldsymbol{\rho}^{\mathrm{T}}\frac{\partial \boldsymbol{M}}{\partial q_2}\boldsymbol{\rho}\\ \cdots\end{bmatrix}^{\mathrm{T}}+\begin{bmatrix}\mathbf{0}\\ \tilde{\boldsymbol{v}}_0\begin{bmatrix}\boldsymbol{I} & \mathbf{0}\end{bmatrix}\boldsymbol{M}_0\boldsymbol{\rho}\\ \mathbf{0}\end{bmatrix}=\boldsymbol{T}\end{aligned} \tag{11}$$

where $\boldsymbol{\rho}=[\boldsymbol{v}_0,\boldsymbol{\omega}_0,\boldsymbol{q}]^{\mathrm{T}}$ describes the state variables of the system, including the linear and angular velocities of the base and the joint positions. The matrix $\tilde{\boldsymbol{M}}_0=[\boldsymbol{M}_{00},\boldsymbol{M}_{q0}]$ represents the inertial properties. The total forces and torques acting on the system, $\boldsymbol{T}$, are represented as $\boldsymbol{T}=[\boldsymbol{F}_0,\boldsymbol{T}_0,\tau_1,\tau_2,\ldots,\tau_n]^{\mathrm{T}}$, and τ_i denotes the joint torque.

To facilitate the derivation of the control method, the compact form of the dynamics model is expressed as follows

$$\boldsymbol{H}(\boldsymbol{q})\dot{\boldsymbol{\rho}}+\boldsymbol{C}\left(\boldsymbol{v}_0,\boldsymbol{\omega}_0,\boldsymbol{q},\dot{\boldsymbol{q}}\right)=\boldsymbol{T} \tag{12}$$

To effectively distinguish between the dynamics of the base and the antennas within the system, the comprehensive variable $\boldsymbol{\rho}$ may be segregated into $\boldsymbol{x}_b$ and $\boldsymbol{q}$, where $\boldsymbol{x}_b$ represents the position and attitude of the base and is characterized by the velocity and angular velocity vectors . By incorporating the external forces and moments acting on the antennas and following a partitioned approach, Equation (29) can be further delineated as follows

$$\begin{bmatrix}\boldsymbol{H}_b & \boldsymbol{H}_{bm}\\ \boldsymbol{H}_{bm}^{\mathrm{T}} & \boldsymbol{H}_m\end{bmatrix}\begin{bmatrix}\ddot{\boldsymbol{x}}_b\\ \ddot{\boldsymbol{q}}\end{bmatrix}+\begin{bmatrix}\boldsymbol{c}_b\\ \boldsymbol{c}_m\end{bmatrix}=\begin{bmatrix}\boldsymbol{F}_b\\ \boldsymbol{\tau}\end{bmatrix}+\begin{bmatrix}\boldsymbol{J}_b^{\mathrm{T}}\\ \boldsymbol{J}_m^{\mathrm{T}}\end{bmatrix}\boldsymbol{F}_h, \tag{13}$$

Subsequently, this can be compactly expressed as follows

$$\boldsymbol{H}^*\ddot{\boldsymbol{q}}+\boldsymbol{c}^*=\boldsymbol{\tau}+\boldsymbol{J}_b^*\boldsymbol{F}_b+\boldsymbol{J}_h^*\boldsymbol{F}_h, \tag{14}$$

where the modified terms $\boldsymbol{H}^*$, $\boldsymbol{c}^*$, $\boldsymbol{J}_b^*$, and $\boldsymbol{J}_h^*$ describe the dynamic interrelations and external influences on the system, thereby streamlining the dynamics model for more efficient analysis and control strategy development.

For the purposes of tracking control and formulating an effective control strategy, an error dynamics equation is pivotal. By defining the tracking error $\boldsymbol{e}_q$ as the difference between the reference trajectory $\boldsymbol{q}_r$ and the current position $\boldsymbol{q}$, we quantify the deviation of the control objective from the current state of the system. Subsequently, by modeling the acceleration of this error $\ddot{\boldsymbol{e}}_q$, we determine the response of the system to external forces and control inputs, thereby facilitating a deeper understanding of the dynamics of the system and aiding in the development of robust control laws. The error dynamics equation can be established as follows

$$\boldsymbol{e}_q=\boldsymbol{q}_r-\boldsymbol{q} \tag{15}$$

$$\ddot{\boldsymbol{e}}_q=\ddot{\boldsymbol{q}}_r-(\boldsymbol{\tau}+\boldsymbol{J}_b^*\boldsymbol{F}_b+\boldsymbol{J}_h^*\boldsymbol{F}_h-\boldsymbol{c}^*)\boldsymbol{H}^{*^{-1}} \tag{16}$$

where $\boldsymbol{e}_q$ denotes the tracking error, $\boldsymbol{q}_r$ is the reference trajectory, $\boldsymbol{q}$ is the current state, $\ddot{\boldsymbol{q}}_r$ is the acceleration of the reference trajectory, $\boldsymbol{\tau}$ is the control input, $\boldsymbol{J}_b^*\boldsymbol{F}_b$ and $\boldsymbol{J}_h^*\boldsymbol{F}_h$ account for the external forces acting on the system, $\boldsymbol{c}^*$ describes the inherent dynamic properties of the system, and $\boldsymbol{H}^{*^{-1}}$ is the inverse of the modified system inertia matrix. This formulation provides a solid foundation for the derivation and implementation of tracking control algorithms.

3 Main Results

3.1 Traditional Fully Actuated Control Approach

The traditional fully actuated control approach leverages a strategy of element reduction and order escalation, effectively converting a lower-order underactuated system into a higher-order fully actuated system. This transformation mitigates the nonlinear dynamics inherent to the system, producing a linear, fully actuated structure amenable to stabilization control via pole placement techniques. As outlined in the "Kinematics and Dynamics of the Multiaxis Antenna System" section, the model developed herein has been conceptualized as a fully actuated system, thereby permitting the utilization of this theoretical framework to negate the nonlinear components within each control channel.

Drawing from the foundational Equations (15) and (16), the resulting controllers can be meticulously designed as follows

$$\boldsymbol{\tau}_A=(-\boldsymbol{J}_b^*\boldsymbol{F}_b-\boldsymbol{J}_h^*\boldsymbol{F}_h+\boldsymbol{c}^*)+\boldsymbol{H}^*\ddot{\boldsymbol{q}}_r+\boldsymbol{H}^*\boldsymbol{k}_0\boldsymbol{q}+\boldsymbol{H}^*\boldsymbol{k}_1\dot{\boldsymbol{q}} \tag{17}$$

where $\boldsymbol{k}_0$ and $\boldsymbol{k}_1$ are instrumental in modulating the pole positions for both the position control channel and the synchronization control channel. This preceding segment is appropriately tailored to abate known and nonlinear aspects of the model, thereby facilitating an optimal pole configuration setup. The stability and response characteristics of a control system are fundamentally influenced by the locations of its system poles. This capability to modify pole positions by altering $\boldsymbol{k}_0$ and $\boldsymbol{k}_1$ provides a powerful tool for designing and optimizing control systems, ensuring that they achieve the desired level of performance across a wide range of operating conditions.

3.2 Fully Actuated Sliding Mode Control Approach

By leveraging the principles of FA control, the system is transformed into an FA linear system. This transformation underscores the adaptability and effectiveness of FA control in achieving precise pole placement for system stabilization. However, the application of control theory to FA systems may encounter challenges, such as an excessively high system order, which could exacerbate model uncertainty and amplify noise levels. To mitigate these issues, SMC provides a viable solution to reduce the order of a system, thereby enhancing system robustness against uncertainties and noise.

In the context of a second-order control system(18), the adoption of SMC augments convergence speed. Notably, the linear SMC approach and the FA control method share equivalency in terms of pole configuration, demonstrating the versatility of SMC in achieving desired dynamic behaviors. The original system structure can be expressed as follows

$$\ddot{\boldsymbol{x}}+\boldsymbol{k}_1\dot{\boldsymbol{x}}+\boldsymbol{k}_0\boldsymbol{x}=\boldsymbol{b}\boldsymbol{u}_{smc} \tag{18}$$

where $\boldsymbol{u}_{smc}$ represents the sliding mode control input. To implement SMC effectively, a sliding mode variable for this

linear system is introduced as follows:

$$\boldsymbol{s} = \boldsymbol{C}_x \boldsymbol{x} + \dot{\boldsymbol{x}} \tag{19}$$

which facilitates dynamic behavior to ensure system stability and rapid convergence. By selecting appropriate parameters, it can be shown that

$$\dot{\boldsymbol{s}} + \boldsymbol{\eta}\boldsymbol{s} = \ddot{\boldsymbol{x}} + (\boldsymbol{C}_x + \boldsymbol{\eta})\dot{\boldsymbol{x}} + \boldsymbol{C}_x \boldsymbol{\eta}\boldsymbol{x} \tag{20}$$

This provides a direct analogy to the dynamics of a system under SMC. If the parameters satisfy the relationship as follows

$$\boldsymbol{k}_1 = \boldsymbol{C}_x + \boldsymbol{\eta} \tag{21}$$

$$\boldsymbol{k}_0 = \boldsymbol{C}_x \boldsymbol{\eta} \tag{22}$$

the dynamic equation on the sliding surface can be made equivalent to the original dynamics of the control system, provided that appropriate choices of $\boldsymbol{C}_x$ and $\boldsymbol{\eta}$ are made.

In order to accelerate the convergence speed, the control law is designed to ensure that the unique states of the subsystem converge to zero. Specifically, when $s = 0$, the state variable $\boldsymbol{x}$ is engineered to exponentially converge to zero. The control law is expressed as follows

$$\boldsymbol{\tau}_{smc} = \frac{\boldsymbol{\eta}}{b}\boldsymbol{s} - \boldsymbol{k}\left(|\boldsymbol{s}|^{\frac{1}{2}} + \boldsymbol{k}_s\right)\operatorname{sgn}(\boldsymbol{s}) - r\boldsymbol{s} \tag{23}$$

This leverages the HOFA theory effectively reconfiguring the poles to a stable state. This approach enables the transformation of the original system into one with an FA linear configuration(24)

$$\ddot{\boldsymbol{e}}_y + \boldsymbol{k}_1 \dot{\boldsymbol{e}}_y + \boldsymbol{k}_0 \boldsymbol{e}_y = b_c \boldsymbol{\tau}_s \tag{24}$$

Ultimately, by integrating Equations (17) and (23), the final control action is obtained as follows

$$\boldsymbol{\tau} = \boldsymbol{\tau}_A + \boldsymbol{\tau}_{smc} \tag{25}$$

highlighting the synergistic integration of control strategies required to optimize system performance.

3.3 Compensating for system disturbances and unmodeled dynamics using STESO

In order to compensate for the uncertainties inherent in most real-world scenarios, where model parameters are subject to significant perturbations leading to external disturbances, a STESO may be applied. STESOs are widely utilized for estimating system states and disturbances, including those arising from model uncertainties and external variations, thereby enhancing the robustness of control strategies.

The observation error signal is calculated as follows

$$e_o = x - z \tag{26}$$

where x is the actual state and z is the state estimated using STESO.

For the linear system under consideration, the sliding manifold is designed as follows

$$\sigma = c_1 e_1 + c_2 e_2 + \cdots + c_{n-1} e_{n-1} + e_n \tag{27}$$

which is instrumental in delineating the system's response to disturbances.

To circumvent the residual estimation errors typical of the linear extended state observer (LESO), the STESO is designed with the following structure:

$$\begin{aligned}
\dot{z}_1 &= z_2 + \beta_1 e_1, \\
\dot{z}_2 &= z_3 + \beta_2 e_1, \\
&\vdots \\
\dot{z}_n &= z_{n+1} + u_a + bu, \\
\dot{z}_{n+1} &= k_3 \operatorname{sgn}(\sigma) + k_4 \sigma
\end{aligned}$$

where u_a is an auxiliary error feedback designed to address the bounded total disturbance, with k_3 and k_4 being parameters that can be tuned to ensure the asymptotic convergence of the STESO. The parameter $k_4\sigma$ is tailored for this purpose.

The estimation error dynamics of STESO are then represented as follows:

$$\begin{aligned}
\dot{e}_1 &= e_2 - \beta_1 e_1, \\
\dot{e}_2 &= e_3 - \beta_2 e_1, \\
&\vdots \\
\dot{e}_n &= e_{n+1} - u_a, \\
\dot{e}_{n+1} &= h - k_3 \operatorname{sgn}(\sigma) - k_4 \sigma
\end{aligned}$$

Based on the super-twisting algorithm, u_a is designed as follows

$$\begin{aligned}
u_a = c_1 e_2 + c_2 e_3 + \cdots + c_{n-1} e_n + k_1 |\sigma|^{\frac{1}{2}} \operatorname{sgn}(\sigma) + k_2 \sigma \\
- \left(c_1 \beta_1 + c_2 \beta_2 + \cdots + c_{n-1} \beta_{n-1}\right) e_1,
\end{aligned} \tag{28}$$

Then, the derivative of σ can be presented as follows

$$\dot{\sigma} = -k_1 |\sigma|^{\frac{1}{2}} \operatorname{sgn}(\sigma) - k_2 \sigma + e_{n+1} \tag{29}$$

$$\dot{e}_{n+1} = -k_3 \operatorname{sgn}(\sigma) - k_4 \sigma + h \tag{30}$$

where u_a serves as an auxiliary error feedback designed to counteract the total bounded disturbance, in which k_1, k_2, k_3, and k_4 are tunable parameters that facilitate control, thereby ensuring the robustness and effectiveness of the control strategy under the influence of uncertainties and disturbances.

In the analysis of the system's stability, a Lyapunov function approach is employed to demonstrate the system's local finite-time stability. Consider the system in (29), and suppose there exists a Lyapunov function $V(\boldsymbol{\eta})$ defined within the neighborhood $U \in \mathbb{R}^n$ of the origin. If

$$\dot{V}(\boldsymbol{\eta}) \leq -\beta_1 V^{\alpha_1}(\boldsymbol{\eta}) \tag{31}$$

for all $\boldsymbol{\eta} \in U \setminus \{0\}$, with $0 < \alpha_1 < 1$ and $\beta_1 > 0$, then the system exhibits local finite-time stability. Furthermore, the time T required for the system to reach $V(\boldsymbol{\eta}) = 0$ is bounded by the following:

$$T \leq \frac{1}{\beta_1(1-\alpha_1)} |V(\boldsymbol{\eta}(0))|^{1-\alpha_1} \tag{32}$$

where $\boldsymbol{\eta}(0)$ represents the initial state of the system.

4 Results

This study focuses on a multiaxis antenna system, which is primarily evaluated based on its capability to accurately track five separate rotational axes. Each axis represents a distinct rotational degree of freedom for the antenna, with tracking performance measured in degrees to reflect its precision in angular positioning.

The components of the system include a satellite body, modeled as a rigid body with a mass of 100 kg and triaxial moments of inertia, each at 100 kg m^2. The system also features robotic arms, each weighing 50 kg, with moments of inertia $I_{xx} = I_{yy} = 100\,\text{kg}\,\text{m}^2$ and $I_{zz} = 5\,\text{kg}\,\text{m}^2$. Flexible elements such as the solar wings and antennas were initially modeled using Nastran finite element software and later integrated into Adams with modal neutral files up to the 12th modal frequency for dynamic simulation.

The simulation involved applying a step signal with a 1° amplitude to assess the system's control precision across its five axes. These axes include rotational angles q_1 and q_2 for solar wing articulation, q_3 for the connection from the satellite body to the first robotic arm, q_4 between the robotic arms, and q_5 for the final connection to the antenna. An S-shaped speed profile was used to test the system's adaptability to dynamic conditions, highlighting the control challenges inherent in managing complex mechanical linkages. This S-shaped curve is particularly suited for such applications as it provides a smooth acceleration and deceleration, minimizing mechanical stress and potential overshooting during angle adjustments. This choice is reflected in the tracking performance where the control methods strive to follow this profile, thus explaining the similar curve types across all tests.

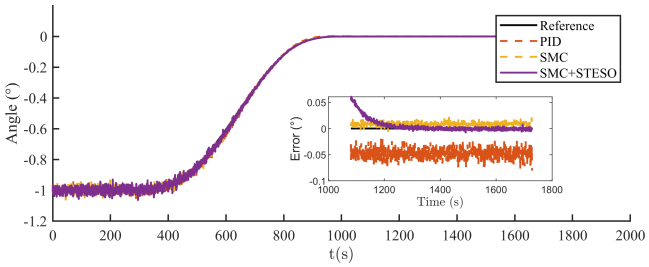

Fig. 2: Axis $q1$ tracking with PID, SMC, and SMC+STESO.

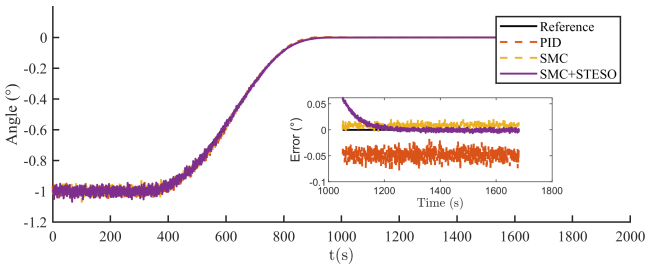

Fig. 3: Axis $q2$ tracking with PID, SMC, and SMC+STESO.

The simulation results, presented in Figs. 2–6, compare the tracking performance of three control methods: PID, SMC, and SMC+STESO. The evaluation criteria focus on the angular tracking error for each of the five axes in the system. From the perspectives of rise time and overshoot, the three control methods exhibited similar rise times with no overshoot observed. In terms of tracking error, a comprehensive assessment of the five figures reveals that the static error is significantly lower when using the SMC+STESO controller. For instance, as shown in Fig. 2, the static error for the PID controller is approximately $0.05°$, while for the SMC controller it is around $0.01°$. However, the use of the SMC+STESO controller reduces the static error to approximately $0.006°$. Moreover, it is observable that SMC method exhibits strong chattering due to the sign function in its control law, whereas, in comparison, the SMC+STESO control method alleviates some of the chattering issues inherent in SMC control, resulting in smaller errors. Overall, SMC+STESO offers a significant advantage in terms of positioning accuracy over the traditional PID and SMC.

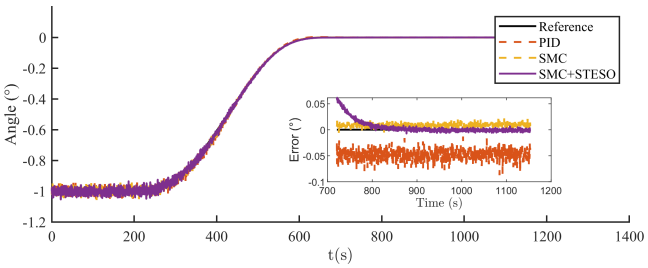

Fig. 4: Axis $q3$ tracking with PID, SMC, and SMC+STESO.

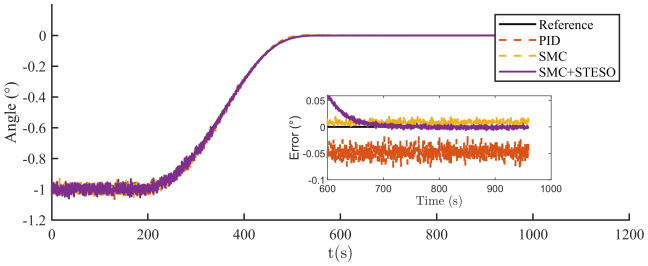

Fig. 5: Axis $q4$ tracking with PID, SMC, and SMC+STESO.

5 Conclusion

This study introduces an innovative control strategy that significantly enhances directional accuracy in multiaxis antenna systems by integrating sliding mode control with fully actuated theory and a super twisting extended state observer. Through the development of a control-oriented dynamics model based on analytical methodologies and the application of FA theory, the study transforms the dynamic model into a fully actuated configuration, simplifying control over antenna movements. The integration of SMC with this model, augmented by a STESO, effectively addresses system uncer-

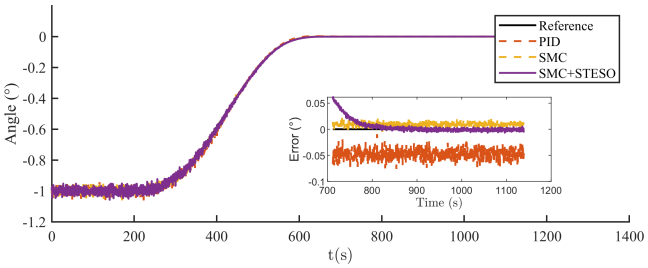

Fig. 6: Axis $q5$ tracking with PID, SMC, and SMC+STESO.

tainties, leading to improved control precision. Simulation results confirm the superiority of the SMC+STESO method over traditional PID and SMC in terms of positioning accuracy, demonstrating a significant reduction in static error and alleviation of chattering issues. This advancement lays a foundational framework for future developments in antenna control systems, offering substantial benefits for satellite communication, air traffic control, and mobile telephony networks.

Looking forward, there are several avenues to explore that could further enhance the robustness and efficiency of control systems for multiaxis antennas. Particularly, the incorporation of advanced models that account for the mechanical flexibility of antenna structures and the dynamic effects of robotic arms could lead to even more precise control. Mechanical flexibility, often observed in the long, slender components of antennas and solar panels, introduces additional dynamic challenges due to the modal responses of these structures. Addressing these challenges requires the development of control strategies that can effectively dampen oscillations and manage the micro-vibrations induced by environmental factors and operational maneuvers.

Additionally, considering the integration of adaptive control algorithms could further refine the responsiveness of the system to unforeseen disturbances and model inaccuracies. These algorithms could dynamically adjust control parameters in real-time, based on continuous system identification processes that detect changes in the system's dynamic characteristics. This approach would be particularly beneficial in scenarios involving prolonged space missions where environmental conditions and system properties may vary significantly over time.

References

[1] H. Huang, "Flexible wireless antenna sensor: A review," *IEEE Sensors Journal*, vol. 13, no. 10, pp. 3865–3872, 2013.

[2] X. Wu, G. Eleftheriades, and T. van Deventer-Perkins, "Design and characterization of single- and multiple-beam mm-wave circularly polarized substrate lens antennas for wireless communications," *IEEE Transactions on Microwave Theory and Techniques*, vol. 49, no. 3, pp. 431–441, 2001.

[3] S. X. Ta, H. Choo, I. Park, and R. W. Ziolkowski, "Multi-band, wide-beam, circularly polarized, crossed, asymmetrically barbed dipole antennas for gps applications," *IEEE Transactions on Antennas and Propagation*, vol. 61, no. 11, pp. 5771–5775, 2013.

[4] C. Waldschmidt and W. Wiesbeck, "Compact wide-band multimode antennas for mimo and diversity," *IEEE Transactions on Antennas and Propagation*, vol. 52, no. 8, pp. 1963–1969, 2004.

[5] J. S. Kang, J. T. King, C. R. Anderson, and M. H. Sanders, "Performance analysis of passive magnetic pointing method for implementation of directional antennas on cubesats," *Int. J. Aeronaut. Space Sci.*, vol. 23, no. 4, pp. 734–745, 2022.

[6] J. S. Kang, J. T. King, C. R. Anderson, and M. Sanders, "Passively pointing directional satellite antenna by leveraging earth's magnetic field," in *2021 IEEE Aerospace Conference*, pp. 1–9, 2021.

[7] M. M. Alam, M. M. Islam, and A. T. Mansoor, *Fully automated satellite tracking system for directional antenna*. PhD thesis, BRAC University, 2018. Available online at http://dspace.bracu.ac.bd/xmlui/handle/10361/10932.

[8] H. Aliakbarian *et al.*, "A digitally beam-steerable antenna array system for positioning-based tracking applications," *IEEE Antennas and Propagation Magazine*, vol. 55, no. 6, pp. 35–49, 2013.

[9] I. Lita and D. A. Visan, "Spherical coordinates control system for accurate orientation of directional antennas," in *2012 IEEE 18th International Symposium for Design and Technology in Electronic Packaging (SIITME)*, pp. 233–236, 2012.

[10] H.-S. Ahn, O. Jung, S. Choi, J.-H. Son, D. Chung, and G. Kim, "An optimal satellite antenna profile using reinforcement learning," *IEEE Transactions on Systems, Man, and Cybernetics, Part C (Applications and Reviews)*, vol. 41, no. 3, pp. 393–406, 2010.

[11] G. Duan, "High-order system approaches: I. fully-actuated systems and parametric designs," *Acta Automatica Sinica*, vol. 46, no. 7, pp. 1333–1345, 2020.

[12] G. Duan, "High-order system approaches: Ii. controllability and full-actuation," *Acta Automatica Sinica*, vol. 46, no. 8, pp. 1571–1581, 2020.

[13] G. Duan, "High-order system approaches: Iii. observability and observer design," *Acta Automatica Sinica*, vol. 46, no. 9, pp. 1885–1895, 2020.

[14] G. Duan, "High-order fully actuated system approaches: Part i. models and basic procedure," *International Journal of Systems Science*, vol. 52, no. 2, pp. 422–435, 2021.

[15] G. Duan, "High-order fully actuated system approaches: Part ii. generalized strict-feedback systems," *International Journal of Systems Science*, vol. 52, no. 3, pp. 437–454, 2021.

[16] G. Duan, "High-order fully actuated system approaches: Part vi. disturbance attenuation and decoupling," *International Journal of Systems Science*, vol. 52, no. 10, pp. 2161–2181, 2021.

Proceedings of the 3rd Conference on Fully Actuated System Theory and Applications
May 10-12, 2024, Shenzhen, China

High-order Fully Actuated System Approach for a 3-DOF Quadrotor Control Based on Extended State Observers

Shi Lu, Konstantinos Tsakalis, Yan Chen*

Arizona State University, Tempe, AZ 85281, United States
E-mail: shilu@asu.edu; tsakalis@asu.edu; yanchen@asu.edu

Abstract: This paper focuses on position tracking control of a 3-DOF quadrotor under practical disturbances. High-order terms of system states, inputs, and disturbances are generated after the highly coupled underactuated quadrotor system is converted into two high-order fully actuated (HOFA) systems. To observe high-order terms for control design, which were not previously discussed in other approaches, as well as disturbances rejection in control, we developed extended state observers (ESOs) of the HOFA systems for the 3-DOF quadrotor. The convergence of ESOs is rigorously proven using the Lyapunov stability theory. Furthermore, we present the simulation results to verify the proposed observer and control design for the HOFA models of the 3-DOF quadrotor.

Key Words: High-order fully actuated system approach, Quadrotor control, Extended state observer.

1 Introduction

In recent decades, unmanned aerial vehicles (UAVs) have garnered significant attention due to their wide-ranging applications in education, commerce, industry, and the military [1]. Among rotorcraft UAVs, quadrotors offer distinct advantages over fixed-wing UAVs, including the ability to hover in place, execute vertical takeoffs and landings, and perform agile maneuvers. Their unique design sets quadrotors apart, which eliminates the need for complex mechanical linkages found in other rotorcraft, such as helicopters and tiltrotors. Quadrotors are characterized as highly coupled, under-actuated systems with four rotor inputs (used for roll, pitch, yaw, and throttle control) and six outputs (comprising 3-DOF translational position and 3-DOF orientation). Typically, flight controllers focus on tracking the 3-DOF translational parts and yaw angle of a quadrotor with respect to the Earth frame. Achieving independent control of roll and pitch angles with just four inputs presents a notable challenge.

In pursuit of optimal quadrotor flight performance, the hierarchical architecture is a commonly adopted approach for segregating control tasks based on distinct time scales: the rapid inner loop control governing attitude and the more gradual outer loop control overseeing position. Nevertheless, in the case of hierarchical controllers utilizing first-order state space representations, the performance of position tracking may prove unsatisfactory if the quadrotor cannot rapidly and accurately follow the desired attitude. Recently, a novel system modeling technique known as the high-order fully actuated (HOFA) model [3], aimed at eliminating nonlinear terms through complete actuation, has emerged. By removing nonlinearities, globally stabilized linear (sub)systems in controllable forms can be obtained. Subsequently, controllers for the (sub)systems can be readily formulated. Ultimately, the closed-loop system comprises several independent linear time-invariant (LTI) (sub)systems, allowing for flexible eigenstructures. Applying the HOFA approach to the quadrotor platform [7] offers advantages over the conventional hierarchical designs in the literature.

Nevertheless, the HOFA approach introduces high-order unmeasurable terms, such as jerk and derivatives of system inputs [7], which have a considerable impact on the quadrotor's tracking performance. In [11, 12], the jerk dynamic model and other general high-order terms were based on a statistical model driven solely by white random processes. The obtained estimator actually has no intrinsic difference from a second-order low-pass filter. Furthermore, jerk was computed based on the differential flatness of an ideal quadrotor model [9, 10], highlighting its close relationship with angular velocity and acceleration. However, the input derivatives were neglected, which also played a substantial role in jerk dynamics. Hence, a suitable observer is needed for the quadrotor model in the HOFA form due to the introduced high-order terms of inputs. A systematic observer design method for high-order systems was proposed in [4]. However, a specific form was required to accomplish the complete cancellation of nonlinear terms, which is not applicable to the quadrotor model.

Moreover, the HOFA approach also introduces derivatives of disturbances, creating significant uncertainties that inevitably affect the performance of the closed-loop system. To address these uncertainties, the extended state observer (ESO) proves to be an effective method, requiring minimal model information. A nonlinear ESO applied to HOFA systems for the 6DOF motion of spacecraft was presented in [13]. The convergence proof was grounded in a rigorous Lyapunov analysis, ensuring that the estimation error converges within a neighborhood of the origin. However, it is essential to emphasize that the proof relies on the complete cancellation of nonlinear terms, and it assumes that only the lowest-order variables are measurable—a condition that does exist for the quadrotor model.

Inspired by [13], an observation scheme is proposed in this paper to address all high-order terms, including system states, input derivatives, and disturbance derivatives, in the quadrotor model. This approach is based on the modified HOFA approach discussed in [7]. The choice of the 3-DOF planar quadrotor model is particularly apt, as it represents a typical non-minimum phase dynamical system that has been

*Corresponding author: Yan Chen

extensively featured in the literature on acrobatic robots. To illustrate the effectiveness of the ESO design, we opt to employ the 3-DOF planar quadrotor model. Following a similar structure as presented in [5, 7], we divide the quadrotor model into two subsystems, each with its respective ESO design and convergence proof.

The paper is structured as follows. The quadrotor HOFA model and the problem formulation are proposed in Section II. The extended observer designed for HOFA with convergence proof is presented in Section III. Simulation results are presented in Section IV, and the paper is concluded in Section V.

2 HOFA Model and Problem Formulation

This section introduces modeling and control of 3-ODF quadrotor HOFA systems based on [7] with disturbance compensation. For $x \in \mathbb{R}^n, A_i \in \mathbb{R}^{n\times n}$ $(i = 1,2,\cdots,m)$ and $, A_{j,k} \in \mathbb{R}^{n\times n}$ $(j = 1,2,3$ and $k = 1,2,\cdots,m_1)$, frequently used symbols in this paper are defined as follows,

$$\begin{aligned} x^{(0\sim m)} &\triangleq \begin{bmatrix} x \\ \dot{x} \\ \vdots \\ x^{(m)} \end{bmatrix} \\ A_{0\sim m} &\triangleq [A_0 \quad A_1 \quad \cdots \quad A_m] \\ A_{j,1\sim m_1} &\triangleq [A_{j,1} \quad A_{j,2} \quad \cdots \quad A_{j,m_1}] \end{aligned} \tag{1}$$

2.1 3-DOF Quadrotor Model

The 3-DOF planar quadrotor system is depicted in Fig. 1. This quadrotor is limited to motion within the x-z plane, and its mathematical model with disturbances is presented below.

$$\begin{cases} \ddot{x} = \dfrac{f_1 + f_2}{m}\sin\theta + d_1 \\ \ddot{z} = \dfrac{f_1 + f_2}{m}\cos\theta - g + d_2 \\ \ddot{\theta} = \dfrac{f_2 - f_1}{J} + d_3 \end{cases} \tag{2}$$

where θ is the pitch angle, f_1, f_2 are rotor thrusts, m is the quadrotor mass, J is the yaw moment of inertia, and g is the gravity acceleration. d_1, d_2 and d_3 denote disturbances along the x axis, z axis, and the rotation y axis.

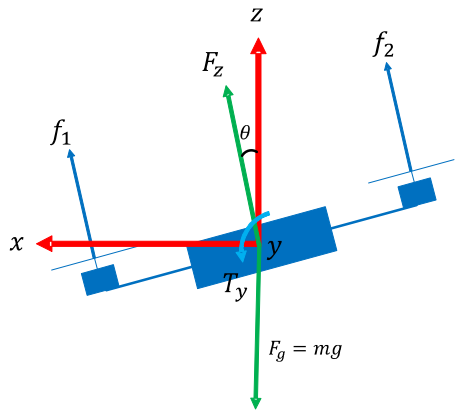

Fig. 1: 3-DOF quadrotor for a planar motion

To control the positions of x and z with the modified HOFA approach [7], we select the system inputs as $u_1 = \frac{f_1+f_2}{m}$, $u_2 = \frac{f_2-f_1}{J}$. We have

$$\begin{cases} \ddot{x} = u_1\sin\theta + d_1 \\ \ddot{z} = u_1\cos\theta - g + d_2 \\ \ddot{\theta} = u_2 + d_3 \end{cases} \tag{3}$$

This system can be reformulated into two subsystems using the HOFA approach.

2.2 HOFA Control with Disturbance Rejection

The first subsystem is

$$\ddot{z} = u_1\cos\theta - g + d_2 \tag{4}$$

which is already a HOFA system. It is trivial to have

$$u_1 = \frac{g - A_{0\sim1}^z z^{(0\sim1)} + v_1}{\cos\theta} \tag{5}$$

and results in the following closed-loop system

$$\ddot{z} + A_{0\sim1}^z z^{(0\sim1)} = v_1 + d_2 \tag{6}$$

Then, we can take the 2nd order derivative of the first equation in (3) yields,

$$\begin{aligned} x^{(4)} = {} & \ddot{u}_1\sin\theta + 2\dot{u}_1\dot{\theta}\cos\theta \\ & -\dot{\theta}^2 u_1\sin\theta + \ddot{\theta}u_1\cos\theta + \ddot{d}_1 \end{aligned} \tag{7}$$

Substituting the third equation from (3), we have the second HOFA subsystem

$$\begin{aligned} x^{(4)} = {} & \ddot{u}_1\sin\theta + 2\dot{u}_1\dot{\theta}\cos\theta - \dot{\theta}^2 u_1\sin\theta \\ & + u_2 u_1\cos\theta + d_3 u_1\cos\theta + \ddot{d}_1 \end{aligned} \tag{8}$$

and we can design u_2 as,

$$\begin{aligned} u_2 = {} & \frac{u_2^* + A_{0\sim3}^x x^{(0\sim3)} - v_2}{u_1\cos\theta}, u_2^* = -\ddot{u}_1\sin\theta \\ & -2\dot{u}_1\dot{\theta}\cos\theta + \dot{\theta}^2 u_1\sin\theta \end{aligned} \tag{9}$$

which gives the following closed-loop system

$$\begin{aligned} x^{(4)} + A_{0\sim3}^x x^{(0\sim3)} = {} & v_2 \\ & + d_3 u_1\cos\theta + \ddot{d}_1 \end{aligned} \tag{10}$$

$A_{0\sim3}^x \in \mathbb{R}^{1\times4}, A_{0\sim1}^z \in \mathbb{R}^{1\times2}$ and v_1, v_2 are external signals containing the commanding trajectory and observed disturbance information. Since (8) does not match the specific form in [4], the following assumption is made for the above two subsystems.

Assumption 1: Regarding the second-order derivative of input u_1 and the disturbance terms $\ddot{d}_1, d_2, d_3$ arising from external factors such as wind and ground effects in (4) and (8), it is reasonable to assume that the high-order derivatives of these terms are bounded and differentiable. There exists

$$\begin{cases} d_1^{(3)} = g_1(t) \\ \dot{d}_2 = g_2(t) \\ \dot{d}_3 = g_3(t) \\ u_1^{(3)} = g_u(t) \end{cases}, \quad \begin{cases} |g_1(t)| \le \bar{g}_1 \\ |g_2(t)| \le \bar{g}_2 \\ |g_3(t)| \le \bar{g}_3 \\ |g_u(t)| \le \bar{g}_u \end{cases} \tag{11}$$

$\bar{g}_1, \bar{g}_2, \bar{g}_3$ and $\bar{g}_u$ are positive scalars.

Remark 1: Different from the measurement condition in [13], in the real quadrotor applications, $x^{(0\sim1)}, z^{(0\sim1)}$ can be measured from the motion capture system (MOCAP) or the onboard visual-inertial odometry device (VIO). $\ddot{x}, \ddot{z}$ and $\theta^{(0\sim1)}$ can be measured from the IMU on the onboard flight

controller. For aggressive motions, θ measurement sometimes relies on MOCAP or VIO.

Thus, in this paper, we aim to design an extended state observer containing the rest of the unmeasurable terms $u_1^{(1\sim2)}, x^{(3)}$ and the disturbance terms $\dot{d}_1, d_2, d_3$.

3 ESO for the HOFA approach

In this section, ESOs for the subsystems mentioned above are designed to estimate external disturbance uncertainties and unmeasurable terms. Before presenting the main results, we provide some preliminary information as follows.

3.1 Preliminaries

Lemma 1 [14]: Let $A \in \mathbb{R}^{n\times n}$ satisfy

$$\mathrm{Re}\lambda_i(A) \le -\frac{\gamma}{2}, \qquad i = 1,2,\cdots n \tag{12}$$

Where γ >0, then there exists a positive definite matrix $P \in \mathbb{R}^{n\times n}$ satisfying

$$A^T P + PA \le -\gamma P \tag{13}$$

Proposition 1: Given a HOFA system in the following form

$$x^{(m)} = f\left(x^{(0\sim m-1)}, u\right) + d \tag{14}$$

If the system states $x^{(0\sim m)}$ are all measurable and u is known, we can directly acquire d with

$$d = f\left(x^{(0\sim m-1)}, u\right) - x^{(m)} \tag{15}$$

This condition could arise within specific subsystems.

3.2 ESO and Control of Subsystem 1

Denote $z_{1,1} = z, z_{1,2} = \dot{z}$ and $z_{1,3} = d_2$, then (4) can be written in the following form based on Assumption 1

$$\begin{cases} \dot{z}_{1,1} = z_{1,2} \\ \dot{z}_{1,2} = u_1\cos\theta - g + z_{1,3} \\ \dot{z}_{1,3} = g_2(t) \end{cases} \tag{16}$$

Note that $z_{1,1}, z_{1,2}, \theta$ and $\ddot{z}$ are measurable. Following proposition 1, we can acquire $z_{1,3}$ with

$$z_{1,3} = \ddot{z} - u_1\cos\theta + g \tag{17}$$

Let

$$\begin{aligned} e_1 &= \left[e_{1,1\sim3}\right]^T, i = 1,2,3 \\ e_{1,i} &= \hat{z}_{1,i} - z_{1,i} \end{aligned} \tag{18}$$

and we can design the following ESO

$$\begin{cases} \dot{\hat{z}}_{1,1} = \hat{z}_{1,2} - a_{1,1}e_{1,1} \\ \dot{\hat{z}}_{1,2} = u_1\cos\theta - g + \hat{z}_{1,3} - a_{1,2}e_{1,2} \\ \dot{\hat{z}}_{1,3} = -a_{1,3}e_{1,3} \end{cases} \tag{19}$$

where $\hat{z}_{1,1}, \hat{z}_{1,2}$ and $\hat{z}_{1,3}$ represent the estimates of $z_{1,1}, z_{1,2}$ and $z_{1,3}$, respectively. $a_{1,1}, a_{1,2}$ and $a_{1,3}$ are positive scalars. Then, based on (16) and (19), the error dynamics is

$$\dot{e}_1 = \underbrace{\begin{bmatrix} -a_{1,1} & 1 & 0 \\ 0 & -a_{1,2} & 1 \\ 0 & 0 & -a_{1,3} \end{bmatrix}}_{\Phi_1} + \begin{bmatrix} 0_{2\times1} \\ -g_2(t) \end{bmatrix} \tag{20}$$

Obviously, Φ_1 is a negative definite matrix.

Theorem 1: Given a system such as (**20**) in the following state-space form

$$\dot{e} = \Phi e + g(t) \tag{21}$$

where $e \in \mathbb{R}^n$, Φ is a negative definite matrix satisfying the condition in lemma 1, and $\|g(t)\| \le \bar{g}$ ($\bar{g}$ is a positive scalar). Then e will converge to the following ellipsoid centered at the origin

$$\Theta_{\varepsilon,\kappa}(0) = \left\{e \middle| \frac{1}{2}e^T e \le \frac{\varepsilon}{\kappa}\right\} \tag{22}$$

where ε and κ are given in the following proof.

Proof: The following Lyapunov function can be chosen for the system (22) as

$$V = \frac{1}{2}e^T e \tag{23}$$

Based on lemma 1, we have (ξ, η are positive numbers) the time derivative of V along (23)

$$\begin{aligned} \dot{V} &= \frac{1}{2}\dot{e}^T e + \frac{1}{2}e^T\dot{e} = \frac{1}{2}\left(\Phi e + g(t)\right)^T e + \\ &+ \frac{1}{2}e^T\left(\Phi e + g(t)\right) = \frac{1}{2}e^T(\Phi^T + \Phi)e + \\ &g^T(t)e \le -\frac{\xi}{2}e^T e + e^T g(t) \le -\frac{\xi}{2}e^T e + \\ &-\frac{\xi}{2}e^T e + \frac{\eta}{2}\|e\|^2 + \frac{1}{2\eta}\|g(t)\|^2 \le \\ &-\left(\frac{\xi}{2} - \frac{\eta}{2}\right)\|e\|^2 + \frac{1}{2\eta}\bar{g}^2 = -\kappa V + \varepsilon \end{aligned} \tag{24}$$

where

$$\kappa = \frac{\xi}{2} - \frac{\eta}{2}, \qquad \varepsilon = \frac{1}{2\eta}\bar{g}^2 \tag{25}$$

By selecting appropriate ξ, η, we can have $\kappa > 0$. Finally,

$$V \le \left(V(0) - \frac{\varepsilon}{\kappa}\right)e^{-\kappa t} + \frac{\varepsilon}{\kappa} \to \frac{\varepsilon}{\kappa}, t \to \infty \tag{26}$$

Thus, e eventually converges into the ellipsoid $\Theta_{\varepsilon,\kappa}(0)$. The proof is completed.

the observer states error e_1 eventually converges into the ellipsoid $\Theta_{\varepsilon_1,\kappa_1}(0)$ with (ξ_1, η_1 are appropriate positive numbers)

$$\kappa_1 = \frac{\xi_1}{2} - \frac{\eta_1}{2}, \qquad \varepsilon_1 = \frac{1}{2\eta_1}\bar{g}_1^2 \tag{27}$$

Proposition 2: the following controller of the subsystem 1 is

$$\begin{aligned} u_1 &= \frac{g - A_{0\sim1}^z\hat{z}^{(0\sim1)} + v_1}{\cos\theta} \\ v_1 &= -\hat{z}_{1,3} + v_{c,1} \end{aligned} \tag{28}$$

and produces the following linear system

$$\ddot{z} + A_{0\sim1}^z z^{(0\sim1)} = v_{c,1} \tag{29}$$

where $v_{\mathrm{ref},1}$ contains commanding trajectory and disturbance information.

3.3 ESO and Control of Subsystem 2

Denote $z_{2,1} = x, z_{2,2} = \dot{x}, z_{2,3} = \ddot{x}, z_{2,4} = x^{(3)}$ and $z_{2,5} = \dot{d}_1$, then (8) can be written in the following form based on assumption 1

$$\begin{cases} \dot{z}_{2,1} = z_{2,2} \\ \dot{z}_{2,2} = z_{2,3} \\ \dot{z}_{2,3} = z_{2,4} \\ \dot{z}_{2,4} = f\left(\theta^{(0\sim1)}, u_1^{(0\sim2)}, d_3\right) + u_2 u_1 \cos\theta + z_{2,5} \\ \dot{z}_{2,5} = g_1(t) \end{cases} \quad (30)$$

$$f(\cdot) = \ddot{u}_1 \sin\theta + 2\dot{u}_1\dot{\theta}\cos\theta - \dot{\theta}^2 u_1 \sin\theta + d_3 u_1 \cos\theta$$

Note that $z_{2,1}, z_{2,2}, z_{2,3}$ and θ are measurable. Let

$$e_2 = \left[e_{2,1\sim5}\right]^T, i = 1,2,\cdots 5 \quad (31)$$
$$e_{2,i} = \hat{z}_{2,i} - z_{2,3}$$

and we can design the following ESO

$$\begin{cases} \dot{\hat{z}}_{2,1} = \hat{z}_{2,2} - a_{2,1}e_{2,1} \\ \dot{\hat{z}}_{2,2} = \hat{z}_{2,3} - a_{2,2}e_{2,2} \\ \dot{\hat{z}}_{2,3} = \hat{z}_{2,4} - a_{2,3}e_{2,3} \\ \dot{\hat{z}}_{2,4} = \hat{f}(\cdot) + \hat{z}_{2,4} + u_2 u_1 \cos\theta - a_{2,4}e_{2,3} \\ \dot{\hat{z}}_{2,5} = -a_{2,5}e_{2,3} \end{cases} \quad (32)$$

where $\hat{z}_{2,i}$ represents the estimate of $z_{2,i}$ and $a_{2,i}$ is a positive scalar ($i = 1,2,\cdots,5$). Then, the error dynamics is

$$\dot{e}_1 = \underbrace{\begin{bmatrix} -a_{2,1} & 1 & 0 & 0 & 0 \\ 0 & -a_{2,2} & 1 & 0 & 0 \\ 0 & 0 & -a_{2,3} & 1 & 0 \\ 0 & 0 & -a_{2,4} & 0 & 1 \\ 0 & 0 & -a_{2,5} & 0 & 0 \end{bmatrix}}_{\Phi_2} + \begin{bmatrix} 0_{3\times1} \\ \hat{f}(\cdot) - f(\cdot) \\ -g_1(t) \end{bmatrix} \quad (33)$$

Clearly, Φ_1 is a negative definite matrix. Nevertheless, we must ensure $\left|\hat{f}(\cdot) - f(\cdot)\right|$ is bounded, as per theorem 1. Denote

$$\begin{aligned} z_{3,1} &= \left[z_{3,1,1}, z_{3,1,2}\right]^T = [u_1, \theta]^T \\ z_{3,2} &= \left[z_{3,2,1}, z_{3,2,2}\right]^T = \left[\dot{u}_1, \dot{\theta}\right]^T \\ z_{3,3} &= \left[z_{3,3,1}, z_{3,3,2}\right]^T = [\ddot{u}_1, d_3]^T \end{aligned} \quad (34)$$

and we have the prerequisite system model based on (3) and assumption 1

$$\begin{cases} \dot{z}_{3,1} = z_{3,2} \\ \dot{z}_{3,2} = z_{3,3} + [0, u_2]^T \\ \dot{z}_{3,3} = [g_u(t), g_3(t)]^T \end{cases} \quad (35)$$

Let $e_3 = \left[e_{3,1\sim3}\right]^T$ with

$$\begin{aligned} e_{3,i} &= \left[e_{3,i,1}, e_{3,i,2}\right] = \\ &\left[\hat{z}_{3,i,1} - z_{3,i,1}, \hat{z}_{3,i,2} - z_{3,i,2}\right]^T, i = 1,2,3 \\ A_{3,i} &= \mathrm{diag}\left\{a_{3,i,1}, a_{3,i,2}\right\} \end{aligned} \quad (36)$$

$a_{3,i,1}, a_{3,i,2}$ are positive scalars, and we can design the following ESO

$$\begin{cases} \dot{\hat{z}}_{3,1} = \hat{z}_{3,2} - A_{3,1}e_{1,1} \\ \dot{\hat{z}}_{3,2} = \hat{z}_{3,3} + [0, u_2]^T - A_{3,2}\begin{bmatrix} \hat{z}_{3,1,1} - z_{3,1,1} \\ \hat{z}_{3,2,2} - z_{3,2,2} \end{bmatrix} \\ \dot{\hat{z}}_{3,3} = -A_{3,3}\begin{bmatrix} \hat{z}_{3,1,1} - z_{3,1,1} \\ \hat{z}_{3,2,2} - z_{3,2,2} \end{bmatrix} \end{cases} \quad (37)$$

where $\hat{z}_{3,1}, \hat{z}_{3,2}$ and $\hat{z}_{3,3}$ represent the estimates of $z_{3,1}, z_{3,2}$ and $z_{3,3}$, respectively. Then, based on (35) and (37), the error dynamics is

$$\dot{e}_3 = \Phi_3 e_3 + [0_{4\times1}, g_3(t), g_u(t)]^T$$

$$\Phi_3 = \begin{bmatrix} -a_{3,1,1} & 0 & 1 & 0 & 0 & 0 \\ 0 & -a_{3,1,2} & 0 & 1 & 0 & 0 \\ -a_{3,2,1} & 0 & 0 & 0 & 1 & 0 \\ 0 & 0 & 0 & -a_{3,2,2} & 0 & 1 \\ -a_{3,3,1} & 0 & 0 & 0 & 0 & 0 \\ 0 & 0 & 0 & -a_{3,3,2} & 0 & 0 \end{bmatrix} \quad (38)$$

Φ_3 is also a negative definite matrix. Following theorem 1, the observer states error e_3 eventually converges into the ellipsoid $\Theta_{\varepsilon_3,\kappa_3}(0)$ with (ξ_3, η_3 are appropriate positive numbers)

$$\kappa_3 = \frac{\xi_3}{2} - \frac{\eta_3}{2}, \qquad \varepsilon_3 = \frac{1}{2\eta_3}(\bar{g}_3^2 + \bar{g}_u^2) \quad (39)$$

Considering $\theta, \dot{\theta}$ are measurable and u_1 is known, per (30), (34), and (36), we can have

$$\begin{aligned} \hat{f}(\cdot) - f(\cdot) = e_{3,3,1}\sin\theta + 2e_{3,2,1}\dot{\theta}\cos\theta \\ + e_{3,3,2}u_1\cos\theta \end{aligned} \quad (40)$$

Remark 2: With u_1 saturated, it is straightforward to find $e_{3,3,1}\sin\theta$ and $e_{3,3,2}u_1\cos\theta$ remain bounded. Considering the robustness property of HOFA control leading to bounded $\dot{\theta}$ and selection of high gains in (37) to small $e_{3,2,1}$, it is also evident that $2e_{3,2,1}\dot{\theta}\cos\theta$ can also be bounded. Consequently, we can establish that $\left|\hat{f}(\cdot) - f(\cdot)\right| \le \bar{g}_f$ (where $\bar{g}_f$ is a positive scalar).

Following theorem 1 and (33), the observer state error e_2 eventually converges into the ellipsoid $\Theta_{\varepsilon_2,\kappa_2}(0)$ with (ξ_2, η_2 are appropriate positive numbers)

$$\kappa_2 = \frac{\xi_2}{2} - \frac{\eta_2}{2}, \qquad \varepsilon_2 = \frac{1}{2\eta_2}\left(\bar{g}_1^2 + \bar{g}_f^2\right) \quad (41)$$

Proposition 3: the following controller of the subsystem 2 is

$$\begin{aligned} u_2 = \frac{u_2^* - A_{0\sim3}^x \hat{x}^{(0\sim3)} + v_2}{u_1\cos\theta}, u_2^* = -\hat{z}_{3,3,1}\sin\theta \\ -2\hat{z}_{3,2,1}\dot{\theta}\cos\theta + \dot{\theta}^2 u_1 \sin\theta \\ v_2 = -\hat{z}_{3,3,2}u_1\cos\theta - \hat{z}_{2,5} + v_{c,2} \end{aligned} \quad (42)$$

and produces the following linear system

$$x^{(4)} + A_{0\sim3}^x x^{(0\sim3)} = v_{c,2} \quad (43)$$

where $v_{\mathrm{ref},2}$ contains commanding trajectory and disturbance information.

4 Simulation Results

This section presents simulation results in MATLAB to validate the proposed ESO for the HOFA approach to control the 3-DOF planar quadrotor. The quadrotor parameters are set as $m = 1.0$ kg, $J = 0.01\mathrm{kg}\cdot\mathrm{m}^2$ and $g = 9.8$ m/s.

4.1 Results of Subsystem 1

The control and observation parameters are

Picking

$$A_{0\sim1}^{z} = [20,14]$$
$$v_1 = [20,14]z_{\text{ref}}^{(0\sim1)} \quad (44)$$
$$a_{2,1\sim5} = [40,40,20]$$

$$\bar{g}_1 = 4, \xi_1 = 90, \eta_1 = 10$$
$$\frac{\varepsilon_1}{\kappa_1} = \bar{g}_1^2/(\xi_1\eta_1 - \eta_1^2) = 0.02 \quad (45)$$

the commanding and disturbances signals are

$$z_{\text{ref}} = \sin\left(\pi/_5\, t\right) \text{ m/s}$$
$$d_2 = 4\sin\left(\pi/_5\, t\right) + d_{2,s} \text{ m/s}^2 \quad (46)$$
$$d_{2,s} = \begin{cases} 0, & t < 10s \\ -8, & t \geq 10s \end{cases}$$

Observation results and errors are depicted in Fig. 2 and Fig. 3, respectively.

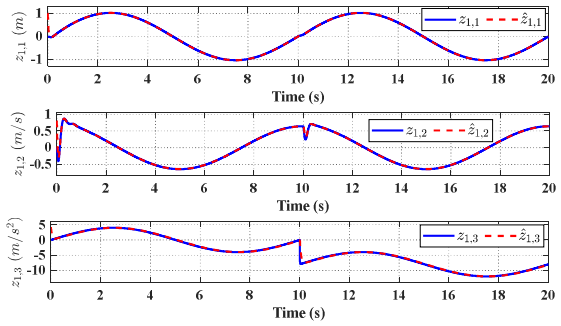

Fig. 2: Subsystem 1 Observation Results

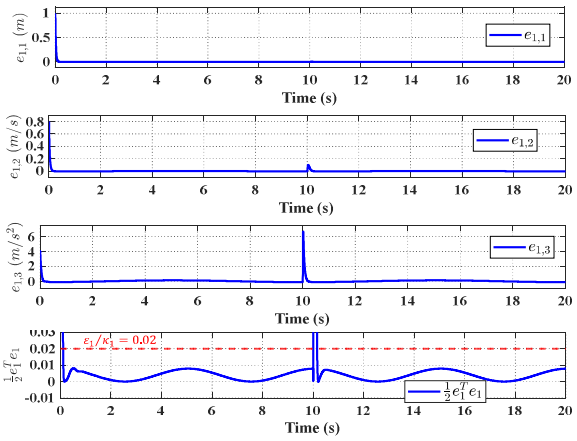

Fig. 3: Subsystem 1 Observation Error

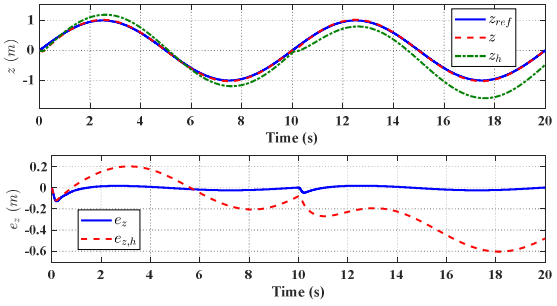

Fig. 4: Subsystem 1 Tracking Results

It is evident that all the observed values converge to the actual values, ultimately resulting in $\frac{1}{2}e_1^T e_1 \leq \varepsilon_1/\kappa_1$ as indicated by (26). Tracking results are illustrated in Fig. 4. z_h represents the tracking results without $\hat{z}_{1,3}$ in (28) for comparison. It is clear that z tracking exhibits smaller tracking errors compared to z_h, demonstrating the robustness of the proposed design.

4.2 Results of Subsystem 2

For the prerequisite system (35), observation parameters are

$$A_{3,1} = \text{diag}\{60,100\}, A_{3,2} = \text{diag}\{180,100\}$$
$$A_{3,3} = \text{diag}\{480,400\}, \quad (47)$$

Picking

$$d_3 = \sin\left(\pi/_5\, t\right) + d_{3,s} \text{ rad/s}^2$$
$$d_{3,s} = \begin{cases} 0, & t < 10s \\ -2, & t \geq 10s \end{cases} \quad (48)$$
$$\bar{g}_3 = 1, \xi_3 = 4.61, \eta_3 = 3.2$$
$$\frac{\varepsilon_3}{\kappa_3} = \bar{g}_3^2/(\xi_3\eta_3 - \eta_3^2) = 0.04$$

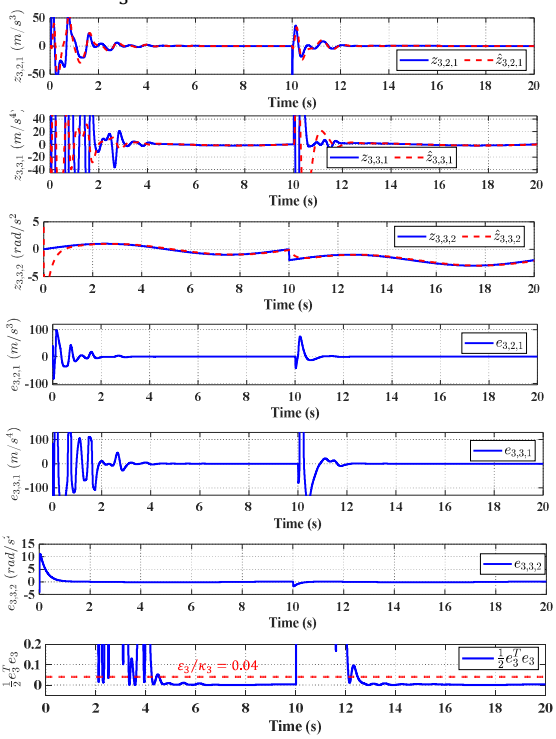

Fig. 5: Prerequisite System Observation Results

Observation results (including observation error) of $z_{3,2,1}, z_{3,3,1}, z_{3,3,2}$, and $\frac{1}{2}e_3^T e_3$ are depicted in Fig. 5. It is evident that the shown observed values converge to the actual values, ultimately resulting in $\frac{1}{2}e_3^T e_3 \leq \varepsilon_3/\kappa_3$ as indicated by (26). For subsystem 2, the control and observation parameters are

$$A_{0\sim3}^{x} = [280,256,96,6]$$
$$v_2 = [280,250,85,5]z_{\text{ref}}^{(0\sim1)} \quad (49)$$
$$a_{2,1\sim5} = [60,60,60,300,900]$$

Picking

the commanding and disturbances signals are

$$\bar{g}_1 = 1.414, \xi_2 = 23.46, \eta_2 = 5.61$$
$$\frac{\varepsilon_2}{\kappa_2} = \bar{g}_1^2/(\xi_2\eta_2 - \eta_2^2) = 0.02 \quad (50)$$

$$x_{\text{ref}} = \sin\left(\pi/5\, t\right) \text{ m/s}$$
$$d_2 = \sin\left(\pi/5\, t\right) + d_{2,s} \text{ m/s}^2 \quad (51)$$
$$d_{2,s} = \begin{cases} 0, & t < 10s \\ -2, & t \geq 10s \end{cases}$$

Observation results and errors of unmeasurable terms $z_{2,4}, z_{2,5}$ and $\frac{1}{2}e_2^T e_2$ are depicted in Fig. 6.

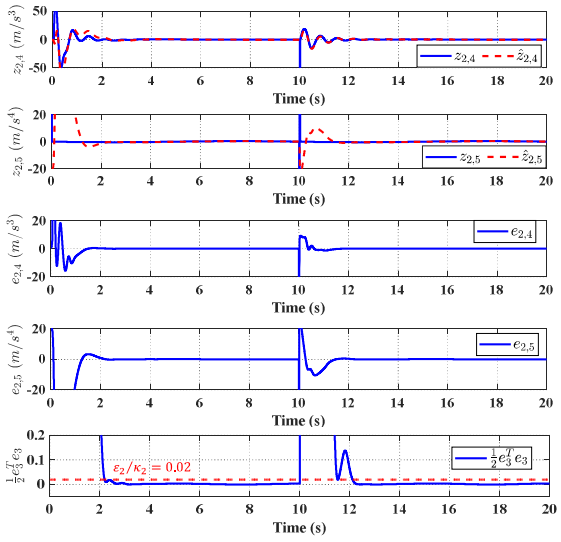

Fig. 6: Subsystem 2 Observation Results

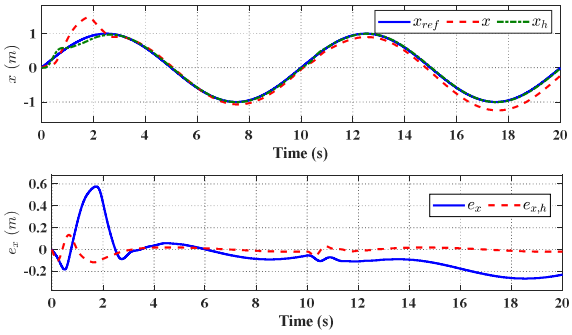

Fig. 7: Subsystem 2 Tracking Results

The results demonstrate the observer's convergence, ultimately leading to $\frac{1}{2}e_2^T e_2 \leq \varepsilon_2/\kappa_2$, even though $\frac{1}{2}e_2^T e_2$ is large at $t = 10\sim12$s due to the step disturbance. Tracking results are illustrated in Fig. 7. x_h represents the tracking results without disturbance compensation in (28)(42) for comparison. It is clear that x tracking exhibits smaller tracking errors compared to x_h, demonstrating the effectiveness of the proposed design.

5 Conclusions

The HOFA approach introduces high-order derivatives of system state, inputs, and disturbances, resulting in substantial uncertainties that inevitably affect the performance of the closed-loop system. Employing the ESO technique enables us to estimate all unmeasurable terms and incorporate them into the HOFA controller with disturbance compensation. Theoretical development and simulation results collectively demonstrate the effectiveness of our proposed approach.

References

[1] V. Kumar and N. Michael, "Opportunities and challenges with autonomous micro aerial vehicles." *The International Journal of Robotics*, vol. 31, no. 11, pp. 1279–1291, 2012.

[2] S. Lu, A. Rodriguez, K. Tsakalis and Y. Chen, "Design and characteristics of a new transformable UAV with both coplanar and omnidirectional features," *2022 International Conference on Unmanned Aircraft Systems (ICUAS)*, pp. 831-838, 2022.

[3] G. Duan, "High-order system approaches – I. Fully-actuated systems and parametric designs," *Acta Automatica Sinica*, vol. 46, no. 7, pp. 1333-1345, 2020.

[4] G. Duan, "High-order system approaches – III. Observability and observer design," *Acta Automatica Sinica*, vol. 46, no. 9, pp. 1885-1895, 2020.

[5] G. Duan, "High-order fully actuated system approaches: Part I. Models and basic procedure," *International Journal of Systems Science*, vol. 52, no. 2, pp. 422-435, 2022.

[6] G. Duan, "High-order fully actuated system approaches: Part II. Generalized strict-feedback systems," *International Journal of Systems Science*, vol. 52, no. 3, pp. 437-454, 2021.

[7] S. Lu, K. Tsakalis and Y. Chen, "Development and application of a novel high-order fully actuated system approach: Part I. 3-DOF quadrotor control," *IEEE Control Systems Letters*, vol. 7, pp. 1177-1182, 2023.

[8] S. Lu, K. Tsakalis and Y. Chen, "Development and application of a novel high-order fully actuated system approach: Part II. 6-DOF quadrotor control," *2023 American Control Conference (ACC)*, pp. 661-666, 2023.

[9] E. Tal and S. Karaman, "Accurate tracking of aggressive quadrotor trajectories using incremental nonlinear dynamic inversion and differential flatness," *IEEE Transactions on Control Systems Technology*, vol. 29, no. 3, pp. 1203-1218, 2021.

[10] J. Medrano, F. Yumbla, S. Jeong, I. Choi, Y. Park, E. Auh and H. Moon, " Jerk estimation for quadrotor based on differential flatness," *2020 17th International Conference on Ubiquitous Robots (UR)*, pp. 99-104, 2020.

[11] S. Nakazawa, I. Tadashi and I. Hikaru, "Real-time algorithms for estimating jerk signals from noisy acceleration data," *International Journal of Applied Electromagnetics and Mechanics*, vol. 18, no. 1-3, pp. 149-163, 2003.

[12] W. Xu, D. He, Y. Cai and F. Zhang, "Robots' state estimation and observability analysis based on statistical motion models," *IEEE Transactions on Control Systems Technology*, vol. 30, no. 5, pp. 2030-2045, 2022.

[13] Z. Qin and G. Duan, "Fully actuated system approach for 6DOF spacecraft control based on extended state observer," *Journal of systems science and complexity*, vol. 35, no. 2, pp. 604-622, 2022.

[14] G. Duan, "High-order fully actuated system approaches: Part III. Robust control and high-order backstepping," *International Journal of Systems Science*, vol. 52, no. 5, pp. 952-971, 2021

Proceedings of the 3rd Conference on Fully Actuated System Theory and Applications
May 10-12, 2024, Shenzhen, China

A Practical Method for Quadrotor Modeling and Parameter Identification

Tianwei Liang, Rui Li, Qiang Geng, Yingjing Shi
School of Automation Engineering, University of Electronic Science and Technology of China, Chengdu 611731, P. R. China
E-mail: lirui@uestc.edu.cn

Abstract: This article introduces a methodology for modeling and parameter identification of the quadrotor systems, which obviates the need for external devices. The model parameters and inherent system disturbances can be identified via flight data acquisition through closed-loop system flight testing of an unmanned aerial vehicle (UAV). This study initially simplifies the model for each axis into second-order systems with disturbances, which necessitates the identification of only three characteristic parameters, thereby alleviating the complexity of the identification process. Subsequently, the identification of optimal model parameters is achieved via closed-loop measurement data. The subsequent physical experiment validates that the accurancy of Normalized Mean Square Error (NMSE) for the three-axis angles and angular velocities exceeds 90%. The proposed algorithm constructs an inner-loop controlled object model for quadrotor systems, facilitating the design of closed-loop control system for both angular velocity and outer loops.

1 Introduction

Quadrotors serve as practical platforms extensively employed across various domains, including military, agricultural, educational, and scientific applications. Research in this field spans mapping, localization, path planning, and control, among other areas. To achieve true autonomy, it is crucial to develop an effective flight control system, as this significantly influences the performance of advanced applications. In the realm of control systems, the primary emphasis is on model establishment and controller design. The model encapsulates the quadrotor's physical properties, and the controller is tasked with guiding the quadrotor to its intended state. While model-free control strategies, such as PID and ADRC, exist, models remain essential for the precise tuning of controller parameters. System modeling entails two fundamental aspects: the structure of the model and the determination of its parameters.

Quadrotors are typically modeled as six-degree-of-freedom (6-DOF) rigid bodies, where torque and total thrust serve as input controls, and attitude and position represent the system states[1–4].The advantage of such modeling approach is that the primary measured parameters include the three-axis principal moments of inertia and the drone's mass, which are straightforward to ascertain. However, the disadvantage is that the true input for quadrotors is motor throttle, not torque and total thrust. Furthermore, the literature frequently fails to explicitly delineate the relationship between torque/total thrust and throttle. Moreover, the six-degree-of-freedom rigid body model neglects some characteristics of quadrotors, such as the relationship between motor speed and throttle, the relationship between propeller thrust and speed, and motor dynamic processes, potentially compromising the model's accuracy.

To enhance the accuracy of the quadrotor model, some studies have modeled its components individually, including the battery, motors, electronic speed controllers (ESCs), and propellers, which supplements the transformation relationship between the throttle and torque[5, 6]. Meanwhile, certain studies concentrate on the process of propeller thrust generation and the identification of relevant parameters, achieved by formulating optimization problems[7–9]. Ultimately, the approximated model is derived, depicting motor speed and throttle as a first-order inertial system with steady-state speed linearly related to throttle input. The lift generated by the propeller is observed to be proportional to the square of the propeller speed. All coefficients are empirically fitted using measured data. When combined with the six-degree-of-freedom rigid body model, this approach yields a comprehensive quadrotor model. The advantages of such model include its ability to reflect the physical properties of quadrotors and to provide parameters with clear physical interpretations. However, it has several drawbacks: specialized equipment may be required for measurement, and cumulative errors may arise due to the successive multiplication of parameters.

In the mentioned mechanism modeling, installation discrepancies are frequently disregarded. For example, the four motors may not align on the exact same horizontal plane, and the differential responses among the four motors and four propellers are often not taken into account. Nonetheless, in practice, such an assumption proves invalid and may introduce persistent errors into the system. Omitting these factors can lead to steady-state inaccuracies in the control system.

Besides acquiring quadrotor models via mechanistic modeling, system identification represents another pivotal approach[10–12]. System identification entails selecting a suitable model structure followed by estimating the model parameters from input-output data. The advantage of system identification is that its capacity to derive system models without delving into intricate internal dynamics. However, there are several disadvantages. Firstly, when there exists a weak relationship between inputs and outputs, such as employing throttle as input and axis as output, it becomes difficult to establish robust models. Secondly, the selection of model structure is subjective, and model parameters generally lack physical interpretation. Higher-order systems may offer improved fit, but this may lead to overfitting. Further-

[0]This work is supported in part by National Natural Science Foundation (NNSF) of China under Grant 61973055 and the Fundamental Research Funds for the Central Universities under Grant 2023NSFSC0511.

more, system identification typically deals with stable systems. Quadrotor models, however, are inherently unstable due to the integral relationship between throttle input and measurable angular velocities, rendering direct application of system identification less suitable.

To leverage the advantages of both mechanistic modeling and system identification, these methods are frequently integrated to create a more precise quadrotor model. In the design of quadrotor controllers, angular velocity, attitude, velocity, and position are typically selected as states, thereby constructing a closed-loop feedback system. Among these, angular velocity is frequently designated as the inner loop and forms the foundation for the closed-loop structure. Therefore, establishing a clear relationship between motor throttle input and angular velocity is particularly important, a focus that is central to the objectives of this paper.

The structure of this paper is arranged as follows: In Section 2, the quadrotor model is established and linearized, with throttle increment as the input and angular velocity as the output, yielding a standard second-order system transfer function.Section 3 introduces a closed-loop structure, identifies model parameters, and examines the effects of varying closed-loop design and battery voltage on the model. Actual flight data are employed to resolve the issue and to finalize the parameter identification. Section 4 utilizes the identified model to redesign the controller, aiming to enhance control performance, and compares real output data with model predictions to assess the model's accuracy.

2 Modeling

A quadrotor's control inputs consist of throttle commands for its four motors, with outputs typically encompassing angular velocity, attitude, velocity, and position. In practical design, angular velocity is often considered as the first set of measurable states and serves as the foundation for the initial closed-loop design in controller design. Therefore, in this section, a model relating angular velocity to throttle commands is developed and subsequently linearized to yield a typical second-order system.

Firstly, the steady-state speed of the motor is linearly related to the voltage on both sides

$$\varpi_{i,ss} = kv_i + b \quad (i = 1, 2, 3, 4) \tag{1}$$

wherein, v_i represents the voltage across the ith motor, normalized to the range of $v_i \in [0, 1]$; $\varpi_{i,ss}$ represents the steady-state speed of the ith motor under voltage v_i, in $[rad/s]$; k is the proportionality coefficient; b is the intercept coefficient.

The voltage across the motor terminals is the product of the battery voltage and the throttle command.

$$v_i = U_{bat}\sigma_i \quad (i = 1, 2, 3, 4) \tag{2}$$

wherein, U_{bat} represents the normalized battery voltage, and σ_i represents the normalized motor throttle.

The motor can be approximated as a first-order inertial system

$$T_m\dot{\varpi}_i + \varpi_i = \varpi_{i,ss} \quad (i = 1, 2, 3, 4) \tag{3}$$

Wherein, T_m represents the motor time constant. A smaller T_m implies a faster motor response, reaching steady-state values more quickly.

Therefore, the dynamic model of the motor can be written as

$$T_m\dot{\varpi}_i + \varpi_i = kv_i + b \quad (i = 1, 2, 3, 4) \tag{4}$$

The lift generated by the propeller is proportional to the square of the motor speed

$$F_i = c_T\varpi_i^2 \quad (i = 1, 2, 3, 4) \tag{5}$$

Wherein, c_T represents the lift coefficient, in units of $\left[N/(rad/s)^2\right]$. Due to the imbalance in lift among the four propellers, torque is generated along the axes of the aircraft. For the following layout of the quadrotor, establishing the body coordinate system, it is easy to determine the torques generated along each axis

$$\begin{aligned} \tau_x &= \frac{\sqrt{2}}{2}dc_T(-\varpi_1^2 + \varpi_2^2 + \varpi_3^2 - \varpi_4^2) \\ \tau_y &= \frac{\sqrt{2}}{2}dc_T(\varpi_1^2 + \varpi_2^2 - \varpi_3^2 - \varpi_4^2) \\ \tau_z &= c_M(\varpi_1^2 - \varpi_2^2 + \varpi_3^2 - \varpi_4^2) \end{aligned} \tag{6}$$

Wherein, d represents the horizontal distance from the motor to the origin of the body coordinate system, in units of $[m]$; c_M represents the coefficient of counter-torque, in units of $\left[N \cdot m/(rad/s)^2\right]$.

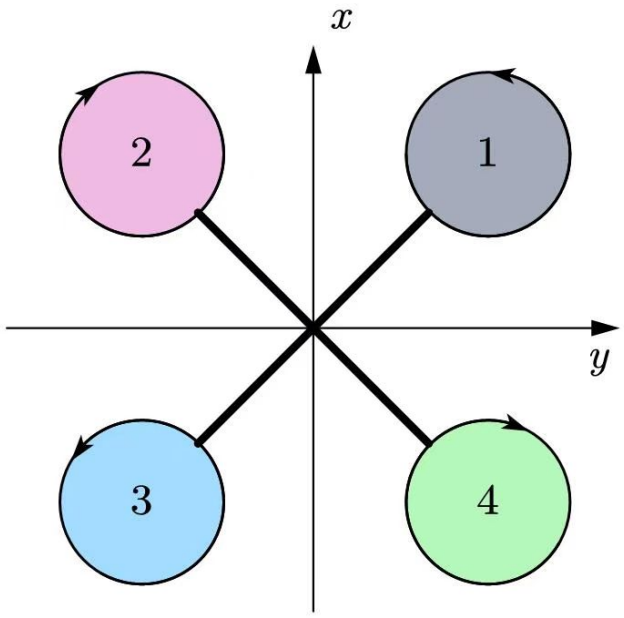

Fig. 1: Quadcopter motor steering schematic

Given the torques along the three axes, according to Euler's dynamics equation, we obtain

$$J\dot{\omega} + \omega \times (J\omega) = \tau \tag{7}$$

Where, $J \in R^{3\times3}$ is the moment of inertia matrix; $\omega = (\omega_x, \omega_y, \omega_z)^T$ is the angular velocity vector; $\tau = (\tau_x, \tau_y, \tau_z)^T$ is the torque vector along the three axes in the body coordinate system.

Due to the symmetry of the quadrotor structure, the inertia products relative to the principal moments of inertia are

negligible. Therefore, we take $J = diag(J_x, J_y, J_z)$. In this case

$$\begin{aligned} J_x\dot{\omega}_x &= (J_y - J_z)\omega_y\omega_z + \tau_x \\ J_y\dot{\omega}_y &= (J_z - J_x)\omega_z\omega_x + \tau_y \\ J_z\dot{\omega}_z &= (J_x - J_y)\omega_x\omega_y + \tau_z \end{aligned} \tag{8}$$

The relationship between Euler angles and body angular velocities is as follows

$$\begin{bmatrix} \dot{\phi} \\ \dot{\theta} \\ \dot{\psi} \end{bmatrix} = \begin{bmatrix} 1 & tan\theta sin\phi & tan\theta cos\phi \\ 0 & cos\phi & -sin\phi \\ 0 & sin\phi/cos\theta & cos\phi/cos\theta \end{bmatrix} \begin{bmatrix} \omega_x \\ \omega_y \\ \omega_z \end{bmatrix} \tag{9}$$

Where ϕ, θ, and ψ are respectively the roll angle, pitch angle, and yaw angle.

The above model is nonlinear, which complicates system analysis and controller design. By making reasonable assumptions, the nonlinear model can be linearized. Below is the linearized model of the controlled object

$$\begin{aligned} G_x &= \frac{K_x}{s(T_x s+1)} \quad K_x = \frac{4\sqrt{2}kdc_T(kv_0+b)}{J_x} \\ G_y &= \frac{K_y}{s(T_y s+1)} \quad K_y = \frac{4\sqrt{2}kdc_T(kv_0+b)}{J_y} \\ G_z &= \frac{K_z}{s(T_z s+1)} \quad K_z = \frac{8kc_M(kv_0+b)}{J_z} \end{aligned} \tag{10}$$

3 Parameter Identification

3.1 Principle of Parameter Identification

Given the necessity to collect data from actual drone flights, it is essential to design a closed-loop system that facilitates takeoff. For simplicity, a cascaded proportional controller is used. The diagram of the closed-loop system for roll angle control is presented as follows. Note that the angle loop is designed for ease of flight implementation, and only angular velocity loop data is used for the identification process.

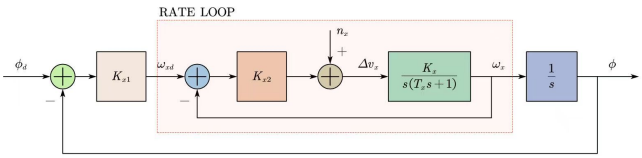

Fig. 2: Block diagram of closed-loop system for roll angle

where $\phi_d\,[rad]$ is the desired roll angle, $\phi\,[rad]$ is the measured roll angle, $\omega_{xd}\,[rad/s]$ is the desired roll angle angular velocity, and $\omega_x\,[rad/s]$ is the Measured roll angle angular velocity; $\Delta\sigma_x$ is the incremental throttle input, the throttle is normalized between $[0, 1]$, and the hover throttle is approximately 0.5, so the range of values Δv_x is $[-0.5, 0.5]$; d_x is constant external perturbation brought about by the installation of the four motors and the incomplete agreement of the propeller model. The parameters to be recognized in the whole system are n_x,K_x,T_x.

In theory, parameters K_x,T_x could be identified based on the system input Δv_x and output ω_x. However, due to the instability of the system being identified, low identification accuracy, and the inability to identify disturbances n_x , a stable system constructed by the desired angular velocity $\omega_x d$ and the measured angular velocity ω_x is used as the system to be identified.

The actual control output is a digital signal, which is equivalent to sampling the continuous output and then passing it through a zero-order hold. Its equivalent structure is as follows

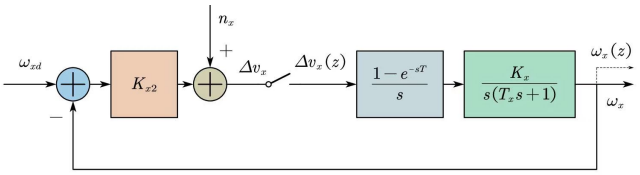

Fig. 3: Discrete block diagram of a closed-loop system

The discrete closed-loop transfer function from input ω_{xd} to output ω_x is given by

$$\Phi_{\omega x}(z) = \frac{b_1' z^{-1} + b_0' z^{-2}}{1 + a_1' z^{-1} + a_0' z^{-2}} \tag{11}$$

The closed-loop transfer function from the perturbation n_x to the output $\omega_x d$is given by

$$\Phi_{nx}(z) = \frac{b_1 z^{-1} + b_0 z^{-2}}{1 + a_1' z^{-1} + a_0' z^{-2}} \tag{12}$$

Among them

$$\begin{cases} b_1 = K_x(T_x e^{-T/T_x} + T - T_x), \\ b_0 = -K_x(Te^{-T/T_x} + T_x e^{-T/T_x} - T_x), \\ a_1 = -(1 + e^{-T/T_x}), \\ a_0 = e^{-T/T_x} \end{cases} \tag{13}$$

$$\begin{cases} b_1' = K_{x2} b_1, \\ b_0' = K_{x2} b_0, \\ a_1' = a_1 + K_{x2} b_1, \\ a_0' = a_0 + K_{x2} b_0 \end{cases} \tag{14}$$

According to the Z-transform results, it is easy to write the recursive formula for the output sequence $\hat{\omega}_x[k]$ in terms of the input sequence $\omega_{xd}[k]$ and the disturbance sequence $n[k]$

$$\begin{aligned} \hat{\omega}_x[k] = &- a_1'\hat{\omega}_x[k-1] - a_0'\hat{\omega}_x[k-2] + b_1'\hat{\omega}_{xd}[k-1] \\ &+ b_0'\hat{\omega}_{xd}[k-2] + b_1 n[k-1] + b_0 n[k-2] \end{aligned} \tag{15}$$

The actual measured output sequence is denoted as $\omega_x[k]$.

Therefore, we aim for the sequence $\hat{\omega}_x[k]$ calculated according to the recursive formula to closely match the actual output sequence $\omega_x[k]$, minimizing the cost function.

$$min \qquad J(K_x, T_x, d) = \sum_{k=1}^{n} (\hat{\omega}_x[k] - \omega_x[k])^2 \tag{16}$$

Due to the complexity of the equations, this paper employs the Particle Swarm Optimization (PSO) algorithm, renowned for its global optimization capabilities, for solving.

3.2 Flight Data Acquisition

The experiment employs a 450mm wheelbase frame, JFRC U2814 KV900 motors, Hobbywing Platinum 30A ESCs, a 5300mAh 30C battery, and APC MR 1045 propellers. We utilize a self-developed flight controller, with a total drone mass of 2.16kg.



Fig. 4: Flight data acquisition platform

The flight controller's sensors include an Inertial Measurement Unit (IMU) and a magnetometer. The gyroscope in the IMU supplies the craft's angular velocity, and an Extended Kalman Filter (EKF) fuses data from the IMU and magnetometer to estimate the drone's attitude. The body's angular velocity and attitude serve as feedback states in the controller. The desired attitude and hover throttle are provided by the remote controller, while the desired angular velocity is determined by the attitude controller's output.

For data recording, the flight controller is equipped with wireless telemetry, which is linked to a personal computer via a ground station. Data are recorded at a frequency of 500 Hz.

3.3 Parameter Identification Results

- Comparison of Roll Angle Recognition Output

In the experiments, $K_{x1} = 5$, K_{x2} are selected as 0.6, 0.8, 1.0 three sets of parameters, respectively, and five sets of experiments are conducted, and each experiment selects 10s of data are used to recognize the parameters. The results of trajectory following are as follows

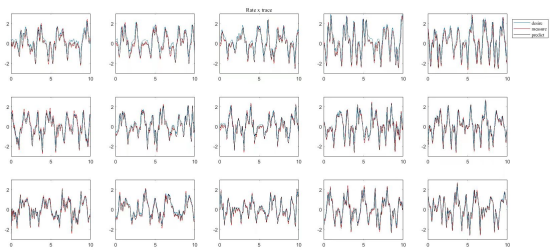

Fig. 5: Trajectory following results

It can be observed that the output obtained from the identification system is quite close to the real output, without any signs of divergence or significant deviation. In 15 experiments, the angular velocity errors are as shown in the following graph:

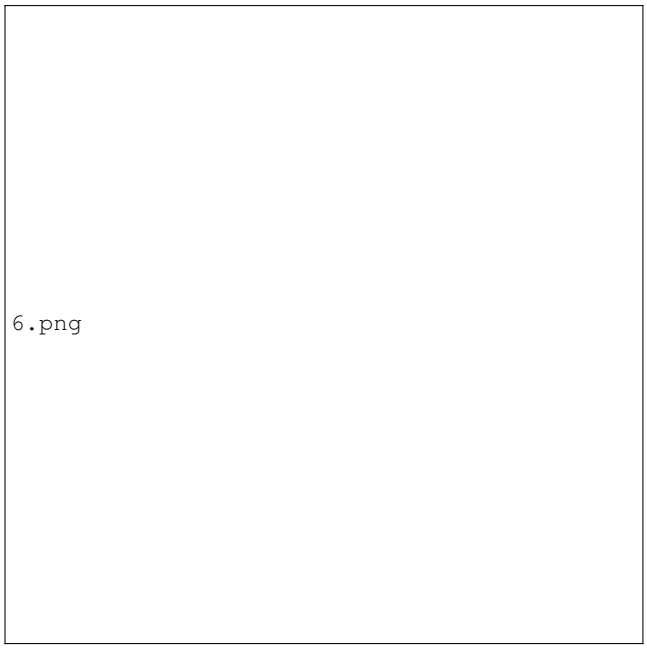

Fig. 6: Experimental results of angular velocity error

Except for the 6th experiment, the median error is around 0 rad/s, with 50% of the errors within 0.1 rad/s, and all angular velocity errors are within 0.7 rad/s. It can be seen that the identified system closely matches the real system with high accuracy.

- Roll Angle Parameter Identification Results

As shown in the figure, the battery used in the experiment has a maximum voltage of 16.8V and a minimum voltage of 14.8V, which is 88.1% of the maximum voltage. Assuming the battery voltage remains constant is referred to as Case A, while considering battery voltage variations is referred to as Case B. The measured parameter results are shown in the following figure

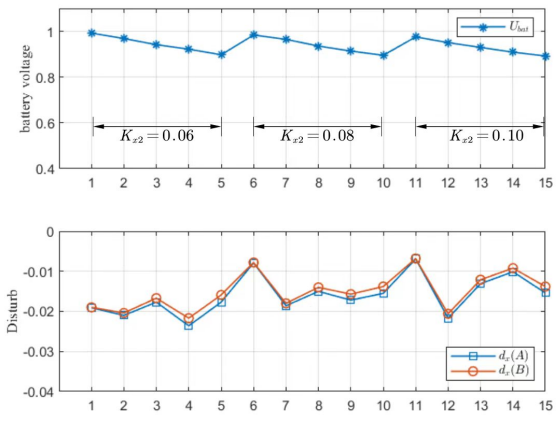

Fig. 7: Battery voltage and disturbance

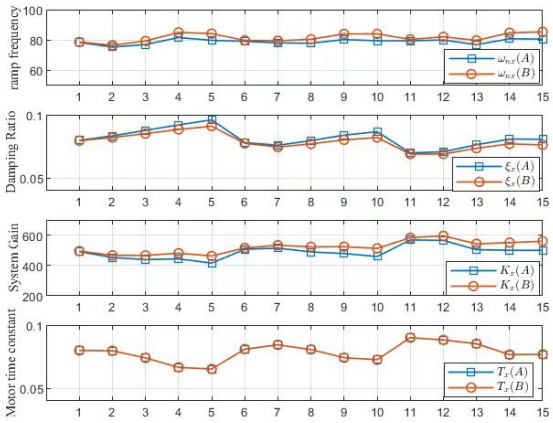

Fig. 8: Parameter identification results

Table 1: Parameter identification results and error range

	K_x	T_x	ω_{nx}	ξ_x	d_x
Situation A	488.4	0.0783	78.99	0.0814	-0.016
Error Range(%)	[-15.0, 16.4]	[-16.7, 14.9]	[-4.6, 3.4]	[-14.2, 18.0]	[-47.0, 56.8]
Situation B	520.57	0.0784	81.60	0.0788	-0.0150
Error Range(%)	[-11.1, 14.2]	[-16.7, 14.9]	[-6.2, 4.6]	[-12.4, 15.5]	[-44.6, 55.0]

1. From the figure, it can be seen that the variation in battery voltage has almost no effect on the undamped natural oscillation frequency ω_n. When not considering voltage changes, the system's ω_{nx} is 78.98 rad/s. Considering voltage changes, since the battery voltage is not greater than 1, the obtained ω_{nx} slightly increases to 81.60 rad/s.

2. The battery voltage will change the damping ratio ξ_x to some extent; as the voltage decreases, the damping ratio increases. This is mainly because when the battery voltage is lower, the hover throttle will slightly increase, and since the motor speed is not entirely linear with the throttle, it leads to an error.

3. Considering the variation in battery voltage, the open-loop gain of the system almost does not change with battery voltage variation, but it slightly increases with the increase of controller parameters.

4. The motor time constant will slightly decrease with the decrease in voltage. This is mainly because when the battery voltage is lower, the hover throttle slightly increases, leading to a slight change in the system's equilibrium point.

5. The mean of the disturbance in the system is -0.015, but its range varies greatly. This is mainly due to external factors such as wind force, changes in hover throttle, and nonlinearities during motion.

It can be seen that the variation in battery voltage has a minimal effect on the system. Therefore, it is assumed that the battery voltage remains constant.

- Roll, Pitch and Yaw Results

Using the same method as for the roll angle, and for simplicity, only 3 sets of data are used instead of 15. The parameters for pitch and yaw angles identified are as follows

Table 2: Three-axis parameters for roll, pitch and yaw

	ω_n	ξ	K	T	d
roll	78.99	0.0814	488.4	0.0783	-0.016
pitch	81.92	0.0883	466.2	0.0701	-0.021
yaw	-	-	31.94	0.0000	-0.033

It can be observed that the results for the pitch angle loop are essentially similar to those for the roll angle loop. The differences mainly arise from the incomplete symmetry of the quadrotor. For example, if the battery is placed in the y-direction, it may result in the moment of inertia about the y-axis being slightly larger than that about the x-axis, leading to a decrease in the corresponding open-loop gain.

The open-loop gain for the yaw angle loop is smaller by an order of magnitude compared to the horizontal attitude angles. The motor time constant is close to 0, primarily because the yaw response is slow, and the motor response time can be neglected. The entire system approaches an integrator system. In this case, the undamped natural oscillation frequency and the damping ratio approach infinity, which do not have practical physical significance.

4 Model Validation

4.1 Controller Design

To verify the accuracy of the model, the controller is designed to ensure the UAV can fly well, facilitating comparison between the model output and actual measured values.

The angular velocity loop utilizes velocity feedback and proportional control, while the angular loop employs proportional control. The controller diagram is shown below

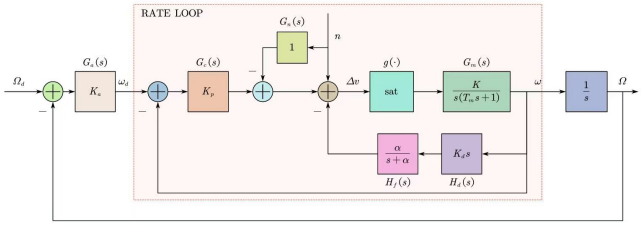

Fig. 9: Controller block diagram

where $\Omega_d[rad]$ is the desired angle; $\Omega[rad]$ is the measured roll angle; $\omega_d[rad/s]$ is the desired angular velocity; $\omega[rad/s]$ is the measured roll angle angular velocity; and Δv is the throttle increment input.

$H_d(s) = K_d s$ provides negative feedback on its derivative, enhancing the dynamic performance of the system.

The $H_f(s) = \frac{\alpha}{s+\alpha}$ link realizes the low-pass filtering of the differential signal, and the cutoff frequency of this first-order filter is $\alpha[rad/s]$.This link on the one hand can effectively reduce the interference of noise, can effectively solve with the control frequency increases, the noise "amplification" phenomenon, on the other hand, makes the differential signal physically achievable, not exceeding the maximum throttle can provide.

$G_c(s) = K_p$ link changes the open-loop gain of the system, which is used to regulate the response speed of the system. When K_p is small, the system response is slow, and there is no overshoot or small overshoot; when K_p is large, the system response is fast, and the overshoot is big.

$G_n(s) = 1$ link is a feedforward control by disturbance, which is used to minimize the effect of the disturbance on the system, e.g., to reduce the steady-state error. This feedforward is also ultimately negative feedback and the disturbance needs to be subtracted to eliminate it.

$g(\cdot)$ is a limiter to avoid system instability caused by too large a physically unrealizable input or by the system entering the nonlinear region.

$G_a(s) = K_a$ adjusts the angular loop gain, and K_a is smaller for a slower system response and larger for a faster system response, but may result in overshooting.

The controller parameters are shown in the table below

Table 3: Controller parameters

controller parameters	roll-loop parameters	pitch-loop parameters	yaw-loop parameters
K_a	6.0	6.0	6.0
K_p	0.12	0.12	0.12
K_d	0.003	0.003	0
α	50	50	0
limit amplitude	± 0.15	± 0.15	± 0.1

As battery voltage variation is not considered, the real input for the four motors is the sum of the hover throttle and throttle increment. Here, the throttle increment is represented by the outputs of the angular velocity loop controller $\Delta\sigma_x$,$\Delta\sigma_y$,$\Delta\sigma_z$. The hover throttle σ_0 is directly provided by the throttle channel of the remote controller

$$\begin{bmatrix} \sigma_1 \\ \sigma_2 \\ \sigma_3 \\ \sigma_4 \end{bmatrix} = \begin{bmatrix} 1 & 1 & 1 & 1 \\ -1 & 1 & -1 & 1 \\ -1 & -1 & 1 & 1 \\ 1 & -1 & -1 & 1 \end{bmatrix} \begin{bmatrix} \Delta\sigma_x \\ \Delta\sigma_y \\ \Delta\sigma_z \\ \sigma_0 \end{bmatrix} \tag{17}$$

4.2 Comparison of Results

The controller described above was designed and implemented in the flight controller to control the UAV. The remote controller signal was used as the reference signal. Roll, pitch, and yaw attitudes along with angular velocity data were collected. The desired attitude was loaded into the simulation environment, and the differences between simulation output and real output were compared. As shown in the figure below, both the angles and angular velocities can effectively track the reference signals, and the simulation output closely matches the real output.

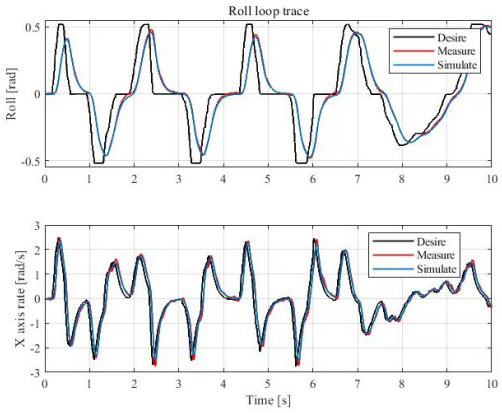

Fig. 10: attitude and angular velocity data of roll angular

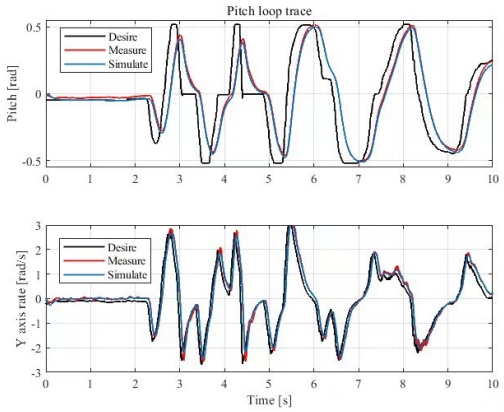

Fig. 11: attitude and angular velocity data of pitch angular

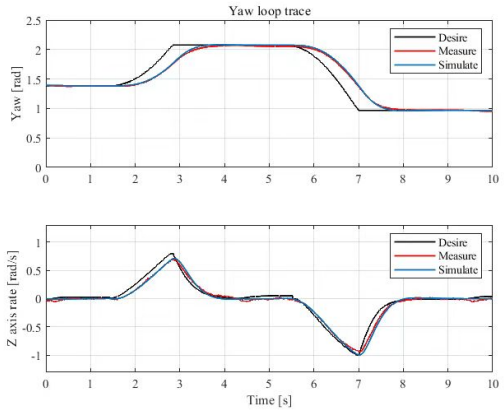

Fig. 12: attitude and angular velocity data of raw angular

The error curves and error distributions between simulation and real output are depicted in the following figures.The roll angle error is mostly within the range $[-0.02, 0.02]\,rad$. The pitch angle error is mostly within the range $[-0.04, 0]\,rad$, with a non-zero mean value, mainly due to inaccurate estimation of external disturbances. The yaw angle error is mostly within the range $[-0.04, 0.04]\,rad$. Compared to the horizontal attitude angles, the yaw angle error is slightly larger, primarily due to the slightly lower model accuracy.

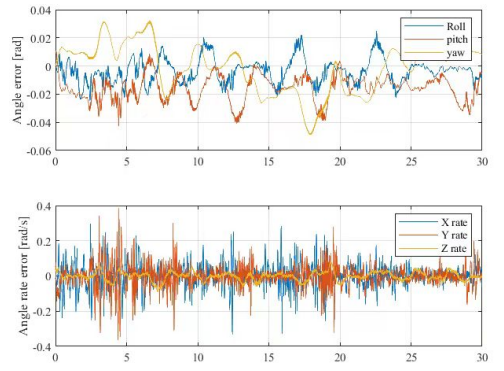

Fig. 13: Error curves between simulated and real outputs

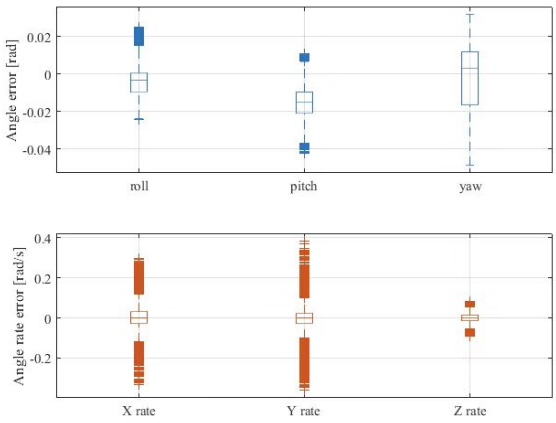

Fig. 14: Error distribution between simulated and real outputs

The mean and variance of the errors are as follows

Table 4: Mean and variance of attitude angle error

	Roll	Pitch	Yaw
$\mu_e[rad]$	-3.634×10^{-3}	-1.565×10^{-2}	-5.334×10^{-4}
$\sigma_e^2 t[rad]$	8.510×10^{-3}	9.406×10^{-3}	1.796×10^{-2}
NRMSE	96.62%	92.09%	97.08%

Table 5: Mean and variance of angular velocity error

	X rate	Y rate	Z rate
$\mu[rad/s]$	4.765×10^{-4}	-1.044×10^{-3}	-1.808×10^{-3}
$\sigma_e^2[rad/s]$	6.449×10^{-2}	5.889×10^{-2}	2.433×10^{-2}
NRMSE	92.78%	92.93%	92.19%

From the above results, it can be seen that for the angle prediction, the error between the model output and the measured output has a mean value of 1° and the variance is less than 2°; for the angular velocity prediction, the error between the model output and the measured output has a mean value of 0.6°/s and the variance is less than 3.8°/s; this verifies the accuracy of the model and the parameter identification. The fitting accuracy is evaluated here using the normalized mean square error (NRMSE), which is defined as

$$c = (1 - \frac{\|y - \hat{y}\|}{\|y - \overline{y}\|}) \times 100\% \tag{18}$$

where y is the measurement sequence, $\overline{y}$ is the mean value of the sequence y, $\hat{y}$ is the model output sequence, $\|\cdot\|$ is the vector paradigm, and c is the NRMSE value. The value of c ranges from $(-\infty, 1]$. If the model output is the same as the measurement output, i.e., $\hat{y} = y$, then $c = 1$, otherwise $c < 1$, and a larger value of c indicates a more accurate model.

The accuracy of NRMSE did not reach 100%, mainly due to two reasons: firstly, the model is not entirely accurate, and secondly, there is some level of noise in the measurement data.

5 Conclusions

This paper models the quadrotor by treating throttle increment as the input and angular velocity as the output, converting the controlled object of the angular velocity loop into a second-order system, and identifying model parameters through closed-loop design. Based on this model, controllers for both the angular velocity and attitude loops are developed and experimentally validated, with an accuracy of over 90% in terms of NRMSE..

In future work, we aim to extend the closed-loop model to incorporate quadrotor velocity and position control. Additionally, we plan to design innovative controllers, based on the identified model, to enhance control performance.

References

[1] J. Lin, Y. Wang, Z. Miao, H. Zhong and R. Fierro, Low-Complexity Control for Vision-Based Landing of Quadrotor UAV on Unknown Moving Platform, in IEEE Transactions on Industrial Informatics, vol. 18, no. 8, pp. 5348-5358, Aug. 2022, doi: 10.1109/TII.2021.3129486.

[2] D. Mellinger and V. Kumar, Minimum snap trajectory generation and control for quadrotors, 2011 IEEE International Conference on Robotics and Automation, 2011, pp. 2520-2525, doi: 10.1109/ICRA.2011.5980409.

[3] P. Foehn and D. Scaramuzza, Onboard State Dependent LQR for Agile Quadrotors, 2018 IEEE International Conference on Robotics and Automation (ICRA), 2018, pp. 6566-6572, doi: 10.1109/ICRA.2018.8460885.

[4] X. Zhang, Y. Wang, G. Zhu, X. Chen and C. -Y. Su, Discrete-Time Adaptive Neural Tracking Control and Its Experiments for Quadrotor Unmanned Aerial Vehicle Systems, in IEEE/ASME Transactions on Mechatronics, doi: 10.1109/TMECH.2021.3112470.

[5] D. Shi, X. Dai, X. Zhang and Q. Quan, A Practical Performance Evaluation Method for Electric Multicopters, in IEEE/ASME Transactions on Mechatronics, vol. 22, no. 3, pp. 1337-1348, June 2017, doi: 10.1109/TMECH.2017.2675913.

[6] P. Pillay and R. Krishnan, Modeling, simulation, and analysis of permanent-magnet motor drives PartII: The brushless DC motor drive, in IEEE Transactions on Industry Applications, vol. 25, no. 2, pp. 274-279, 1989, doi: 10.1109/28.25542.

[7] A. S. Sanca, P. J. Alsina and J. d. J. F. Cerqueira, Dynamic Modelling of a Quadrotor Aerial Vehicle with Nonlinear Inputs, 2008 IEEE Latin American Robotic Symposium, 2008, pp. 143-148, doi: 10.1109/LARS.2008.17.

[8] D. Sartori and W. Yu. Experimental Characterization of a Propulsion System for Multi-rotor UAVs, Journal of Intelligent & Robotic Systems, 2019.

[9] A. Letalenet and P. Morin, Identification and evaluation of a force model for multirotor UAVs, 2020 IEEE International Conference on Robotics and Automation (ICRA), 2020, pp. 4280-4286, doi: 10.1109/ICRA40945.2020.9197317.

[10] Ö. Elbir, A. U. Batmaz and C. Kasnakoğlu, Improving quadrotor 3-axes stabilization results using empirical results and system identification, 2013 9th Asian Control Conference (ASCC), 2013, pp. 1-5, doi: 10.1109/ASCC.2013.6606281.

[11] J. -C. Liu and L. -H. Geng, Attitude model identification of a quadrotor using the subspace identification method, 2020 39th Chinese Control Conference (CCC), 2020, pp. 1227-1232, doi: 10.23919/CCC50068.2020.9188994.

[12] E. Ekawati, A. Widyotriatmo and I. Askandari, Quadrotor position control based on model identification and proportional-derivative algorithm, 2014 2nd International Conference on Technology, Informatics, Management, Engineering & Environment, 2014, pp. 169-173, doi: 10.1109/TIME-E.2014.7011612.

Proceedings of the 3rd Conference on Fully Actuated System Theory and Applications
May 10-12, 2024, Shenzhen, China

High-order Fully-actuated Controller Design for a Dual-Quadrotor Suspension System

Zhipeng Jiang[1], Xianwei Li[1,2,3]
E-mail: jiangzhipeng@sjtu.edu.cn; xianwei.li@sjtu.edu.cn
1. Department of Automation, Shanghai Jiao Tong University, Shanghai 200240, P. R. China
2. Key Laboratory of System Control and Information Processing, Ministry of Education of China, Shanghai 200240, P. R. China
3. Shanghai Engineering Research Center of Intelligent Control and Management, Shanghai 200240, P. R. China

Abstract: In this paper, the mathematical model of dual-quadrotor suspension system is established, and the high-order fully-actuated (HOFA) model of the system is derived. Then the direct parametric control method of HOFA nonlinear systems is used to design a controller of the dual-quadrotor suspension system. Simulation results about tracking a circle of the suspension system are presented, which show that HOFA controller have good control effects with relatively smaller tracking errors, while the thrusts of the two quadrotors are within a reasonable range. Compared with a benchmark PD controller in [1], the HOFA controller designed in this paper can mitigate the drastic oscillation in positions of the quadrotor and the load, while the fluctuation of the load attitudes are maintained within a reasonable range.

Key Words: Dual quadrotors, suspension systems, high-order fully-actuated (HOFA) method

1 Introduction

Quadrotors are a type of unmanned aerial vehicles, and they are being used in an increasingly wide range of applications. Quadrotors have the ability to take off and land vertically, which gives them a high degree of flexibility to perform services such as aerial inspection [2], surveillance [3] and mapping [4]. Quadrotors have the potential to play a huge role in a variety of industries and services such as agriculture, disaster relief, search and rescue, parcel delivery, inspection and surveillance.

A quadrotor suspension system is a system for transporting items by hanging them from a drone. It typically consists of one or more drones with ropes or robotic arms that can be remotely controlled or pre-programmed to hang items down for transportation. Quadrotor suspension system can be used in many areas such as logistics and transportation, firefighting, search and rescue, and building and construction, such as Amazon's emerging package delivery system service using quadrotors. Advantages of using quadrotors for load transportation include high flexibility, fast response, and low operating cost.

The control objective of a quadrotor suspension system is generally to make part of the system states track a reference command and stabilize the rest of the states. PID controllers are the most typical linear controllers commonly used for position and attitude control. The performance of PID controllers can be optimized by tuning the feedback gain, and is robust to disturbance such as the adjustment of a payload mass. The PID controller is often used in combination with other control methods as a basic controller, or as the reference controller to compare the performance of other controllers in simulation. The paper [5] uses a PID controller to stabilize the position and attitude of a quadrotor suspension system.

Linear controllers can only deal with a simplified model of the quadrotor suspension system and have a limited scope of application. Because the system model is nonlinear, nonlinear control methods need to be used in actual flight to ensure global stability. Feedback linearization has the advantages of simple structure and easy stability analysis, and is widely used in the quadrotor suspension system. The paper [6, 7] use feedback linearization to achieve finite time control of quadrotor's takeoff and trajectory tracking, and extend feedback linearization to the quadrotor suspension system. The research [8] decomposes the control input into the horizontal and vertical components of the quadrotor suspension system, where the horizontal component is controlled using feedback linearization.

If the system has too many degrees of freedom, it is difficult to write the system in non-cascade form for controller design and stability analysis, and sometimes the system model is transformed into cascade form using backstepping method for design. In the study of a single quadrotor suspension system, the controller in the paper [9] is designed through Lyapunov and backstepping techniques, and the control laws for the thrust and angular velocity are presented, which guarantee the closed-loop system to be asymptotically stable. The work [1] considers a system composed of a bar tethered to two aerial vehicles, and develop a backstepping controller for the position and attitude tracking. The first control step is to provide an input and a state transformations which convert the system vector field into one that highlights the cascaded structure of the problem. Then this paper designs a controller for the transformed system by exploring that cascaded structure.The research in [10] has similar results, but its stability analysis does not use the traditional Lyapunov asymptotic stability theorem, but first proves that its Lyapunov function is bounded, and then derives the asymptotic stability of the state error based on the relationship of each state in the system model equation.

Due to the physical laws such as Newton's laws, there are many fully-actuated systems in the physical world, and many of them can be modeled as second-order or higher-order models compounded from second-order models. How-

This work was supported by the Science Center Program of National Natural Science Foundation of China under Grant 62188101, the Natural Science Foundation of China under Grants 62273227, 92367203, and the Natural Science Foundation of Shanghai under Grant 21ZR1430500.

ever, in past studies, the state-space method has been commonly used to study these models by generalizing them into augmented first-order systems. Although the first-order system approach has played a great role in the development of control system science, and is a good way to deal with problems such as state response analysis and observer design of control systems, it does not provide any convenience in solving the control problems of dynamic systems. Converting a high-order system into a first-order system, when the system is nonlinear, it is not guaranteed that the controller of the system can be definitely obtained. Even if it can be obtained, the global stability of the closed-loop system may not be guaranteed. At the same time, modeling the system as a first order system description destroys the fully-actuated property of the system [11], and the property can allow us to eliminate all the dynamics of the open-loop system no matter the system is linear or nonlinear, while establishing completely new ideal closed-loop dynamics. This approach provides an ideal constant linear closed-loop system even in the case of nonlinear systems. Considering the above characteristics, we use the high-order fully-actuated(HOFA) controller in the research of the dual-quadrotor suspension system.

2 System Description

2.1 Notation

The map $S(x)$ yields a skew-symmetric matrix as

$$S(x) = \begin{bmatrix} 0 & -x_3 & x_2 \\ x_3 & 0 & -x_1 \\ -x_2 & x_1 & 0 \end{bmatrix}$$

for $x = [x_1; x_2; x_3]$, which can be shown to satisfy $S(a)b = a \times b$, for any $a, b \in R^3$. $S^2 = \left\{x \in R^3 : x^T x = 1\right\}$ denotes the set of unit vectors in R^3.

2.2 System Modeling

The considered dual-quadrotor suspension system follows the same as the one in [1]. For convenience and completeness, we briefly describe the system model in this section. Consider the schematic diagram of a system of dual quadrotors with a slung load shown in Fig. 1, where two quadrotors are connected, by ropes, to the ends of a load that is abstracted as a bar-like object. The motion of the quadrotors causes the load to move in position and attitude. In order to facilitate the analysis of the system model, the slung load is simplified to be a homogeneous rod, and the slung rope is regarded as a massless, inelastic, and flexible rope that is rigidly connected to the quadrotors. In addition, since this paper is concerned with the stabilization of the system, we ignore external environmental perturbations. Physical quantities are shown in the figure. The symbol $u_i \in R^3$ represents the input thrust of the ith quadrotor. Define the state variables of the dual-quadrotor slung system as

$$z = (z_k, z_d) = (p, n, p_1, p_2, v, \omega, v_1, v_2). \tag{1}$$

In the above equation, $z_k = (p, n, p_1, p_2)$ corresponds to the kinematic variables and $z_d = (v, \omega, v_1, v_2)$ corresponds to the dynamic variables. The state variable p denotes the load position, and n denotes the load attitude. p_1 denotes the position of the first quadrotor, and p_2 denotes the position of the second quadrotor. v denotes the speed of load translation, and ω denotes the angular velocity of load rotation. v_1 denotes the flight speed of the first quadrotor, and v_2 denotes the flight speed of the second quadrotor. The meaning of other physical quantities in Fig. 1 is given in Table 1.

Table 1: Names and meanings of quantities in Fig. 1

Quantity	Meaning
m	mass of the load
m_1	mass of the first quadrotor
m_2	mass of the second quadrotor
l_1	length of the first rope
l_2	length of the second rope
T_1	tension of the first rope
T_2	tension of the second rope
d_1	distance from load's center to one end
d_2	distance from load's center to the other end
J	moment of inertia of the load
g	acceleration of gravity
e_1	unit vector $(1, 0, 0)$
e_2	unit vector $(0, 1, 0)$
e_3	unit vector $(0, 0, 1)$

Define unit vectors associated with the ropes:

$$n_i(z_k) = \frac{p_i - (p + d_i n)}{\|p_i - (p + d_i n)\|} = \frac{p_i - (p + d_i n)}{l_i} \in S^2,$$

which means the unit vector in which the ith rope is located. From the kinematic analysis we can get

$$\dot{z}_k = \begin{bmatrix} \dot{p} \\ \dot{n} \\ \dot{p}_1 \\ \dot{p}_2 \end{bmatrix} = \begin{bmatrix} v \\ -S(n)\omega \\ v_1 \\ v_2 \end{bmatrix}, \tag{2a}$$

and from the kinetic analysis we can get

$$\dot{z}_d = \begin{bmatrix} \dot{v} \\ \dot{\omega} \\ \dot{v}_1 \\ \dot{v}_2 \end{bmatrix} = \begin{bmatrix} \sum_{i=1}^{2} \frac{T_i(z,u)}{m} n_i(z_k) - g e_3 \\ \sum_{i=1}^{2} \frac{T_i(z,u)}{J} S(d_i n) n_i(z_k) \\ \frac{u_1}{m_1} - \frac{T_1(z,u)}{m_1} n_1(z_k) - g e_3 \\ \frac{u_2}{m_2} - \frac{T_2(z,u)}{m_2} n_2(z_k) - g e_3 \end{bmatrix}. \tag{2b}$$

In the above equation, g represents the acceleration of gravity, $u = [u_1; u_2]$ represents the input of the system, $T_i(z, u)$ represents the tension in the ith rope, and $e_3 = (0, 0, 1)$ represents the Z-axis in the Earth fixed coordinate system. $T_1(z, u)$ and $T_2(z, u)$ constitute the internal forces of the ropes whose expressions cannot be obtained by the Newton-Euler equations of motion. However, the state locus is constrained to the state set z in Eq.(1), forcing the vector field $\dot{z}_k$ and $\dot{z}_d$ in Eq.(2a) and Eq.(2b) to be in the tangent set of the state set. This constraint uniquely defines the tension on the cable [1]

$$\begin{bmatrix} T_1(z,u) \\ T_2(z,u) \end{bmatrix} = M_T(z_k) u + \begin{bmatrix} T_1(z, 0_6) \\ T_2(z, 0_6) \end{bmatrix}, \tag{3}$$

where, with $a = S(n)n_1(z_k)$, $b = S(n)n_2(z_k)$ and $c =$

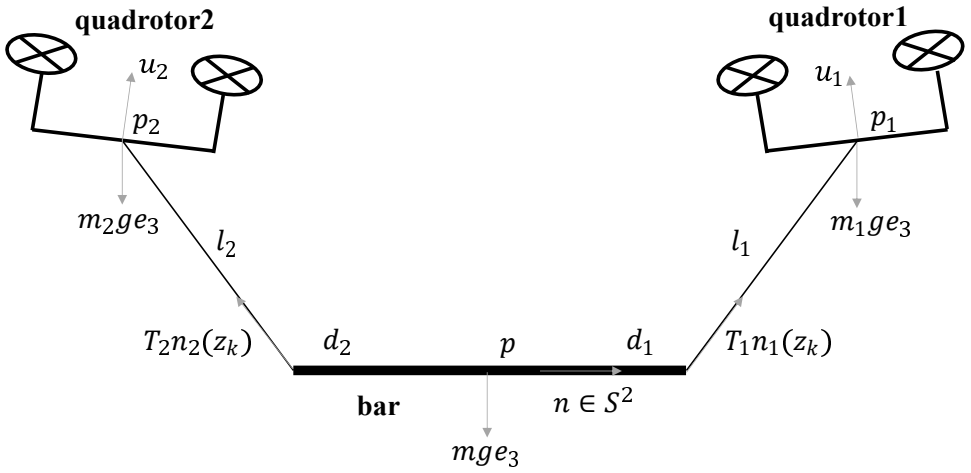

Fig. 1: Dual quadrotors with a slung load

$n_1(z_k)^{\mathrm{T}} n_2(z_k)$, $M_T(z_k)$ is a 2×6 matrix satisfying

$$\begin{aligned} & M_T(z_k)\, u \\ &= \begin{bmatrix} 1+\frac{m}{m_1}+\frac{md_1^2}{J}\|a\|^2 & c+\frac{md_1d_2}{d^{\mathrm{T}}b}b \\ c+\frac{md_1d_2}{J}a^{\mathrm{T}}b & 1+\frac{m}{m_2}+\frac{md_2^2}{J}\|b\|^2 \end{bmatrix}^{-1} \\ &\quad \times \begin{bmatrix} \frac{mn_1(z_k)^{\mathrm{T}}u_1}{m_1} \\ \frac{mn_2(z_k)^{\mathrm{T}}u_2}{m_2} \end{bmatrix}, \end{aligned}$$

and $T_1(z, 0_6)$ and $T_2(z, 0_6)$ are some terms that are determined by the system state but independent of the input u_i:

$$\begin{aligned} & \begin{bmatrix} T_1(z,0_6) \\ T_2(z,0_6) \end{bmatrix} \\ &= \begin{bmatrix} 1+\frac{m}{m_1}+\frac{md_1^2}{J}\|a\|^2 & c+\frac{md_1d_2}{d^{\mathrm{T}}b}b \\ c+\frac{md_1d_2}{J}a^{\mathrm{T}}b & 1+\frac{m}{m_2}+\frac{md_2^2}{J}\|b\|^2 \end{bmatrix}^{-1} \\ &\quad \times \left(m \begin{bmatrix} \frac{\|v_1-(v+d_1S(\omega)n)\|^2}{l_1} \\ \frac{\|v_2-(v+d_2S(\omega)n)\|^2}{l_2} \end{bmatrix} + m\|\omega\|^2 \begin{bmatrix} d_1n^{\mathrm{T}}n_1(z_k) \\ d_2n^{\mathrm{T}}n_2(z_k) \end{bmatrix} \right) \end{aligned}$$

2.3 An HOFA Model of the Dual Quadrotors

From (2a) and (2b), the relationship between quadrotors' position and input is

$$\begin{cases} m_1\ddot{p}_1 + T_1(z,u)n_1(z_k) + m_1ge_3 = u_1, \\ m_2\ddot{p}_2 + T_2(z,u)n_2(z_k) + m_2ge_3 = u_2. \end{cases} \tag{4}$$

In order to obtain an HOFA dynamic model of p_1 and p_2 versus u_1 and u_2 for control design, substituting (3) into (4) yields

$$\begin{aligned} & m_1\ddot{p}_1 + \frac{T_1(z,0_6)}{l_1}p_1 - \frac{T_1(z,0_6)(p+d_1n)}{l_1} + m_1ge_3 \\ &= ([I_3 \quad 0_{3\times3}] - \frac{p_1-(p+d_1n)}{l_1}[1 \quad 0]\, M_T(z_k))u, \\ & m_2\ddot{p}_2 + \frac{T_2(z,0_6)}{l_2}p_2 - \frac{T_2(z,0_6)(p+d_2n)}{l_2} + m_2ge_3 \\ &= ([0_{3\times3} \quad I_3] - \frac{p_2-(p+d_2n)}{l_2}[0 \quad 1]\, M_T(z_k))u. \end{aligned}$$

Then a second-order fully-actuated model of the system can be obtained as

$$\begin{aligned} & \begin{bmatrix} m_1I_3 & 0_{3\times3} \\ 0_{3\times3} & m_2I_3 \end{bmatrix} \ddot{p}_{12} + \begin{bmatrix} \frac{T_1(z,0_6)}{l_1}I_3 & 0_{3\times3} \\ 0_{3\times3} & \frac{T_2(z,0_6)}{l_2}I_3 \end{bmatrix} p_{12} \\ &\quad - \begin{bmatrix} \frac{T_1(z,0_6)(p+d_1n)}{l_1} + m_1ge_3 \\ \frac{T_2(z,0_6)(p+d_2n)}{l_2} + m_2ge_3 \end{bmatrix} \\ &= \left(I_6 - \begin{bmatrix} \frac{p_1-(p+d_1n)}{l_1} & 0_{3\times1} \\ 0_{3\times1} & \frac{p_2-(p+d_2n)}{l_2} \end{bmatrix} M_T(z_k) \right) u, \end{aligned} \tag{5}$$

where

$$p_{12} = \begin{bmatrix} p_1 \\ p_2 \end{bmatrix}.$$

To simplify the presentation of the control law design in the next section, (5) can be rewritten in a compact form of

$$A_2\ddot{p}_{12} + A_0p_{12} - \xi = Bu, \tag{6}$$

where A_2, A_0 and B are some 6×6 matrices and ξ is a 6×1 vector associated with the forces due to the earth gravity and the rope tension. Note that A_2 and B are reversible matrices.

3 Control Law Design

For the second-order fully-actuated system Eq.(6), we design a control law consisting of two parts

$$u = u_c + u_f,$$

where u_c compensates for ξ

$$u_c = -B^{-1}\xi;$$

while u_f is the state feedback

$$u_f = K_0p_{12} + K_1\dot{p}_{12} + v_{ref} = \begin{bmatrix} K_0 & K_1 \end{bmatrix} \begin{bmatrix} p_{12} \\ \dot{p}_{12} \end{bmatrix} + v_{ref}.$$

$K_0, K_1 \in \mathbb{R}^{6\times6}$ is the feedback gain to be designed and v_{ref} is the external signal. Applying this controller to the second-order fully-actuated system Eq.(6) yields the following closed-loop system

$$A_2\ddot{p}_{12} + A_1^c\dot{p}_{12} + A_0^cp_{12} = Bv_{ref}, \tag{7}$$

where

$$\begin{cases} A_0^c = A_0 - BK_0, \\ A_1^c = -BK_1. \end{cases}$$

Define

$$P = \begin{bmatrix} p_{12} \\ \dot{p}_{12} \end{bmatrix},$$

the closed-loop system Eq.(7) is transformed into the following form

$$\dot{P} = A_c P + B_c v_{ref},$$

with

$$\begin{aligned} A_c &= \begin{bmatrix} 0 & I_6 \\ -A_2^{-1}A_0^c & -A_2^{-1}A_1^c \end{bmatrix}, \\ B_c &= \begin{bmatrix} 0 \\ A_2^{-1}B \end{bmatrix}. \end{aligned}$$

According to the research [12, Theorem 1], for a chosen matrix $F \in \mathbb{R}^{12\times12}$, there exists a constant matrix $Z \in \mathbb{R}^{6\times12}$ and a pair of gain matrices $K_0 \in \mathbb{R}^{6\times6}$ and $K_1 \in \mathbb{R}^{6\times6}$, such that

$$\begin{bmatrix} Z \\ ZF \end{bmatrix}^{-1} A_c \begin{bmatrix} Z \\ ZF \end{bmatrix} = F,$$

while

$$\begin{vmatrix} Z \\ ZF \end{vmatrix} \neq 0.$$

At the same time, K_0 and K_1 can be represented by Z, F and other matrices about the system

$$[K_0 \quad K_1] = B^{-1}(A_2ZF^2 + A_1ZF + A_0Z) \begin{bmatrix} Z \\ ZF \end{bmatrix}^{-1}.$$

We only need to choose the appropriate matrices Z and F to complete the controller design, and the choice of matrices turns out to be very broad [12]. Since matrix F is similar to matrix A_c, in order to stabilize the system, the eigenvalues of matrix F should be less than 0. The selection of matrix Z only needs to satisfy that the determinant of matrix $[Z; ZF]$ is not equal to 0. At the same time, we can further design matrix F and Z according to the requirement of control objective such as rapidity.

4 Simulation

The dual-quadrotor suspension system is modeled in MATLAB. Consider the system with parameters $m = 0.15kg$, $m_1 = m_2 = 0.18kg$, $d_1 = -d_2 = 0.3m$, $l_1 = l_2 = 0.5m$. In the initial state, the center position of the load is $(-4, 0, 0)$, the attitude of the load is $(0, 1, 0)$, and the positions of the two quadrotors are $(-2, 1, 1.4)$ and $(-2, -1, 1.4)$. The task is to move the dual-quadrotor suspension system along a circle in the (x, y) plane with the load's attitude tangent to the circle. The center of the circle is located at the position $(-4, 0, 0)$ and the radius is $4m$. The system is controlled by the high-order fully-actuated controller designed in this paper. The parameters of the controller are selected as $Z = [I_6\ I_6]$ and $F = diag([-2, -3, -4, -5, -6, -7, -8, -9, -10, -11, -12, -13])$. The 3D trajectory is plotted as Fig. 2, where the red solid line is the trajectory of the load and the red dashed line is the desired trajectory.

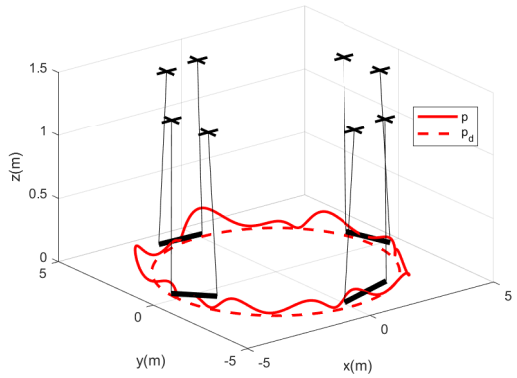

Fig. 2: The three-dimensional trajectory of the system

Trajectories of the two quadrotors' position are obtained as Fig. 3(a) and Fig. 3(b). The solid line represents the components of the actual quadrotor trajectory in the three coordinate axes, and the dashed line represents the corresponding desired trajectory.

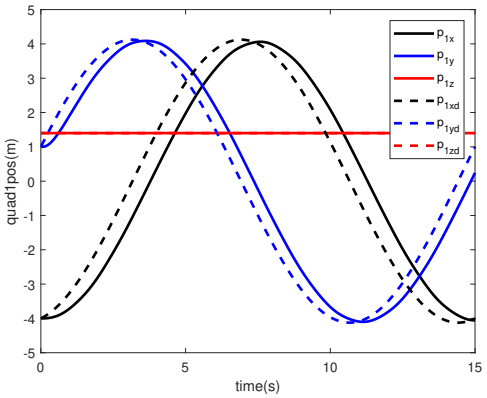

(a) Position of quadrotor 1

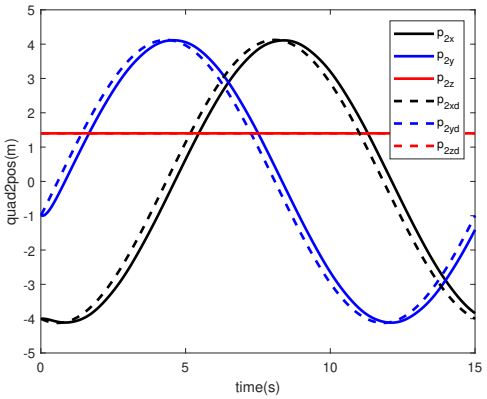

(b) Position of quadrotor 2

Fig. 3: Position of two quadrotors under HOFA control

From Fig. 3(a) and Fig. 3(b) we can see that the two quadrotors are able to track the desired trajectory very well. In actual flight, it is required that quadrotors' thrust should be within its own capability and avoid sudden changes in thrust as much as possible. The magnitude of thrust of the two quadrotors is plotted as Fig. 4.

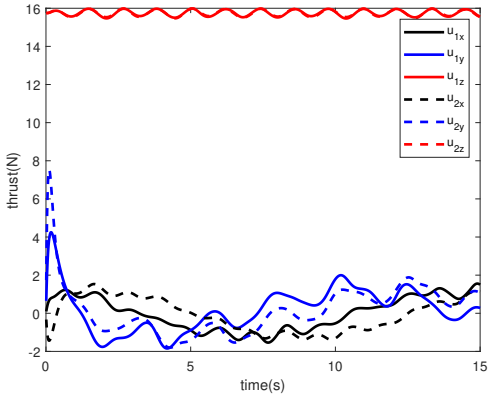

Fig. 4: Two quadrotors' thrust under HOFA control

From Fig. 4 we can see that the x-axis and y-axis components of the two quadrotors' thrust fluctuate between $-2N$ and $2N$ after about one second, while the z-axis component stays at about $16N$. Overall, the thrust does not fluctuate greatly and is within the capability of the quadrotor, which can meet the requirements of practical use.

We plot the trajectory of load's position and attitude as shown in Fig. 5(a) and Fig. 5(b). In order to visualize the load's attitude more intuitively in Fig. 5(b), we use two angles ψ and θ to measure the change of the load's attitude. Where ψ denotes the angle of load's rotation in the (x, y) plane and θ denotes the angle between the load and (x, y) plane.

We can see from Fig. 5(a) and Fig. 5(b) that the load is able to track on the desired trajectory of position and attitude. The simulation shows that high-order fully-actuated controller can be applied to the trajectory tracking of the dual-quadrotor suspension system with less tracking error.

For comparison, we conduct the same simulation experiment using the PD controller designed in literature [5] for the dual-quadrotor suspension system. The control law is defined as

$$u = u^{\star} + \left({u_1}^{pd},\ {u_2}^{pd}\right),$$

where $u^{\star}$ represents the input when the system is in equilibrium:

$$u^{\star} = \left(\left(m_1 + \frac{md_2}{d_2 - d_1}\right) ge_3, \left(m_2 + \frac{md_1}{d_1 - d_2}\right) ge_3\right),$$

and ${u_i}^{pd}$ are as follows $(i = 1,\ 2)$:

$$u_i^{pd} = \begin{bmatrix} m_i \left(k_{p,x} e_1^{\mathrm{T}} \left(p_i - p_i^{\star}\right) + k_{d,x} e_1^{\mathrm{T}} v_i\right) \\ m_i \left(k_{p,y} e_2^{\mathrm{T}} \left(p_i - p_i^{\star}\right) + k_{d,y} e_2^{\mathrm{T}} v_i\right) \\ \left(m_i + \frac{m}{2}\right) \left(k_{p,z} e_3^{\mathrm{T}} \left(p_i - p_i^{\star}\right) + k_{d,z} e_3^{\mathrm{T}} v_i\right) \end{bmatrix}.$$

The PD controllers' parameters in this simulation are $k_{i_{x,p}} = 2.9$, $k_{i_{x,d}} = 2.4$, $k_{i_{y,p}} = 2.9$, $k_{i_{y,d}} = 2.4$, $k_{i_{z,p}} = 1.0$, $k_{i_{z,d}} = 1.2$. Trajectories of the two quadrotors' position are obtained as Fig. 6(a) and Fig. 6(b), and trajectories of load's position and attitude are shown in Fig. 7(a) and Fig. 7(b).

Comparing Fig. 3(a) - Fig. 3(b) and Fig. 6(a) - Fig. 6(b), we can see that the high-order fully-actuated controller for the dual-quadrotor suspension system can achieve better control effect of quadrotors' position than the PD controller

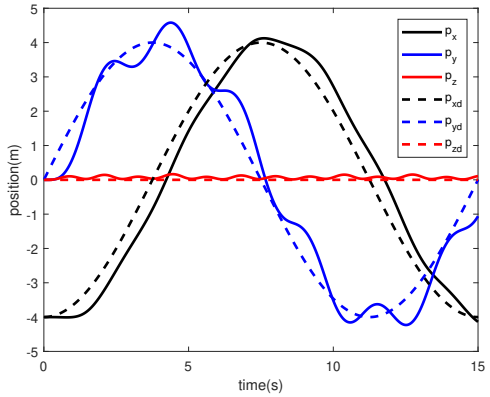

(a) Trajectory of the load's position

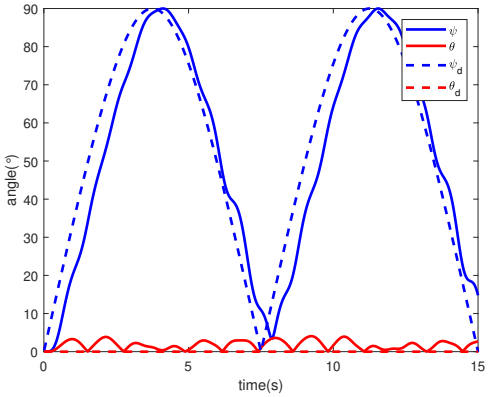

(b) Trajectory of the load's attitude

Fig. 5: Trajectory of the load under HOFA control

designed in literature [5] with less tracking error. Comparing Fig. 5(a) - Fig. 5(b) and Fig. 7(a) - Fig. 7(b), we can see that the high-order fully-actuated controller can obtain better tracking result of load's position than the PD controller while the attitude trajectories are not much different.

5 Conclusion

We can conclude that the high-order fully-actuated controller can achieve better tracking effect than the PD controller for the dual-quadrotor suspension system, while avoiding the difficulty of tuning parameters of the PD controller. The high-order fully-actuated controller has better control effect than the PD controller is because the high-order fully-actuated controller is designed according to the kinematics and dynamics of the system, instead of relying only on the position and velocity information of two quadrotors, which is the case of the PD controller. However, the high-order fully-actuated controller designed in this paper requires the position and attitude information of the load, which are difficult to obtain in real scenarios. How to solve this problem is subject to further research in the future.

References

[1] P. O. Pereira and D. V. Dimarogonas, "Nonlinear pose tracking controller for bar tethered to two aerial vehicles with bounded linear and angular accelerations," in *2017 IEEE 56th Annual Conference on Decision and Control (CDC)*, (Mel-

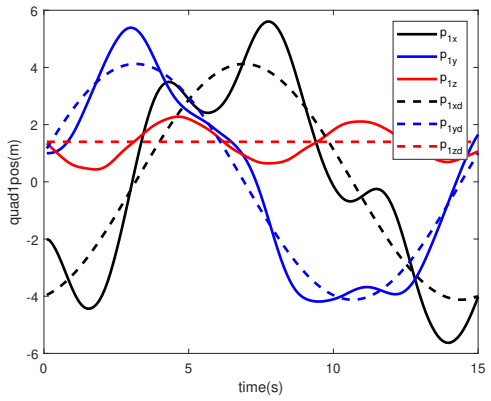

(a) Position of quadrotor 1

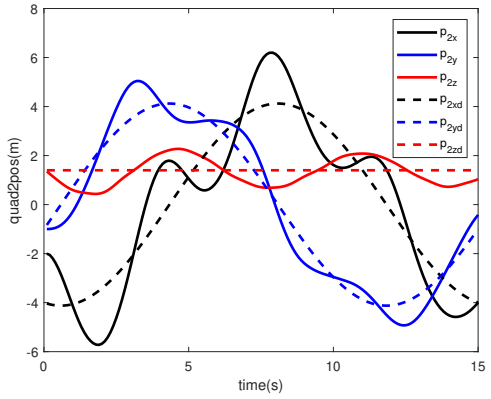

(b) Position of quadrotor 2

Fig. 6: Position of two quadrotors under PD control

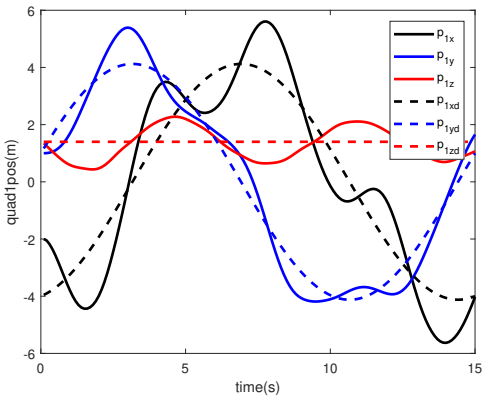

(a) Trajectory of the load's position

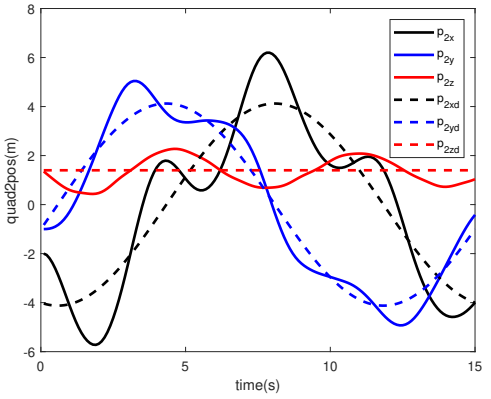

(b) rajectory of the load's attitude

Fig. 7: Trajectory of the load under PD control

bourne, Australia), pp. 4260–4265, IEEE, Dec. 2017. (document), 1, 2.2, 2.2

[2] L. F. Luque-Vega, B. Castillo-Toledo, A. Loukianov, and L. E. Gonzalez-Jimenez, "Power line inspection via an unmanned aerial system based on the quadrotor helicopter," in *MELECON 2014-2014 17th IEEE Mediterranean Electrotechnical Conference*, pp. 393–397, IEEE, 2014. 1

[3] S. Zhang, H. Wang, S. He, C. Zhang, and J. Liu, "An autonomous air-ground cooperative field surveillance system with quadrotor UAV and unmanned ATV robots," in *2018 IEEE 8th Annual International Conference on CYBER Technology in Automation, Control, and Intelligent Systems (CYBER)*, pp. 1527–1532, IEEE, 2018. 1

[4] B. Renardi, E. Khosasi, Y. Y. Nazaruddin, and E. Juliastuti, "Using Multi-Quadrotor System for Effective Road Mapping," in *2019 6th International Conference on Electric Vehicular Technology (ICEVT)*, pp. 246–252, IEEE, 2019. 1

[5] P. O. Pereira and D. V. Dimarogonas, "Collaborative transportation of a bar by two aerial vehicles with attitude inner loop and experimental validation," in *2017 IEEE 56th Annual Conference on Decision and Control (CDC)*, (Melbourne, Australia), pp. 1815–1820, IEEE, Dec. 2017. 1, 4, 4

[6] M. Algabri, H. Mathkour, M. A. Mekhtiche, M. A. Bencherif, M. Alsulaiman, M. A. Arafah, and H. Ghaleb, "Wireless vision-based fuzzy controllers for moving object tracking using a quadcopter," *International Journal of Distributed Sensor Networks*, vol. 13, no. 4, p. 1550147717705549, 2017. Publisher: SAGE Publications Sage UK: London, England. 1

[7] M. H. Amoozgar, A. Chamseddine, and Y. Zhang, "Fault-tolerant fuzzy gain-scheduled PID for a quadrotor helicopter testbed in the presence of actuator faults," *IFAC Proceedings Volumes*, vol. 45, no. 3, pp. 282–287, 2012. Publisher: Elsevier. 1

[8] H. Yang, L. Cheng, Y. Xia, and Y. Yuan, "Active disturbance rejection attitude control for a dual closed-loop quadrotor under gust wind," *IEEE Transactions on Control Systems Technology*, vol. 26, no. 4, pp. 1400–1405, 2017. 1

[9] G. Yu, D. Cabecinhas, R. Cunha, and C. Silvestre, "Nonlinear Backstepping Control of a Quadrotor-Slung Load System," *IEEE/ASME Transactions on Mechatronics*, vol. 24, pp. 2304–2315, Oct. 2019. 1

[10] G. V. Raffo, M. G. Ortega, and F. R. Rubio, "Backstepping/nonlinear H control for path tracking of a quadrotor unmanned aerial vehicle," in *2008 American Control Conference*, pp. 3356–3361, IEEE, 2008. 1

[11] G.-R. DUAN, "High-order system approaches: I. fully-actuated systems and parametric designs," *Acta Automatica Sinica*, vol. 46, no. 7, pp. 1333–1345, 2020. 1

[12] G.-R. DUAN, "Direct Parametric Control of Fully-actuated Second-order Nonlinear Systems—The Normal Case," in *Proceedings of the 33rd Chinese Control Conference*, (Nanjing, China), pp. 2406–2413, IEEE, July 2014. 3

Proceedings of the 3rd Conference on Fully Actuated System Theory and Applications
May 10-12, 2024, Shenzhen, China

Terminal Angle Constrained Three-Dimensional Disturbance Rejection Guidance via an Incremental Twisting Algorithm

Jintao Hu[1], Qinglei Hu[1,3,4], Tuo Han*[2,3,4]

1. School of Automation Science and Electric Engineering, Beihang University, Beijing 100191, China
E-mail: huql_buaa@buaa.edu.cn

2. School of Aeronautic Science and Engineering, Beihang University, Beijing 100191, China
E-mail: hantuo@buaa.edu.cn

3. Hangzhou International Innovation Institute, Beihang University, Hangzhou 311115, China

4. Tianmushan Laboratory, Hangzhou 311115, China

Abstract: This paper proposes an incremental terminal angle constrained guidance law for the interception of maneuvering targets. The guidance commands are first derived based on the nonlinear PD-like twisting control as a base-line. Then, an incremental guidance law of the baseline command is presented based on the incremental twisting algorithm such that the robustness can be further enhanced. The incremental twisting guidance law has a simple structure and exploits the latest guidance information as closed-loop feedback to the system. Numerical simulations are carried out against various maneuvering targets with different terminal angle constraints. Simulation results show that the constructed guidance scheme is effective in achieving desired terminal angles while capturing maneuvering targets.

Key Words: Incremental guidance, homing guidance, terminal angle constraint

1 Introduction

Proportional navigation guidance (PNG) is generally applied in the tactical guided missiles' trajectory generation task [1]. Research on PNG has long been a hot topic since its first conception during the World War II, and one early study example of PNG was reported [2]. Soon after the war, the first missile to use PNG, named Lark missile, was tested [3]. As a matter of fact, PNG is proved to be optimal in certain cases [4]. With the increased mission requirement, some scenarios that PNG law has limited capability promote the development of advanced guidance laws. An instance can be referred to the impact angle constraint. This requirement has a crucial meaning, e.g., threats like well-armed warships and tanks can hardly be destroyed by normal tactical missiles unless being hit with a specific angle from its side or top, respectively [5, 6].

One early work proposing a guidance law with impact angle constraints was presented in [7], where a guidance law for ballistic re-entry vehicles was derived using linear quadratic optimization. Then, the optimal guidance laws with terminal angle requirements were investigated in [5, 8, 9, 10]. This approach is also known as the optimal guidance. In [5], the terminal angle guidance was solved by using the optimal control to adjust the terminal maneuver acceleration. C. Ryoo generalized the optimal guidance with specified impact angle [8]. In [9], an optimal terminal angle guidance law was presented, and the field-of-view (FOV) constraint was also considered. L. Hou developed a time and angle constraint guidance law, where the optimal control is also used[10]. Another nature way comes from modifying the origin PNG. This makes the guidance format like the PNG, and is able to handle impact angle or other constraints [11, 12, 13, 14]. For example, a variable gain PNG law was developed in [11]. The desired terminal angle was achieved by higher navigation gain at a closer stage. By adding the impact angle error as a feedback term to PNG law, an impact angle guidance law was presented in [12]. Another well-known guidance method based on PNG to address this issue is called biased proportional navigational guidance law [13, 14]. In [13], the PNG law was modified using the trajectory shaping approach. The terminal angle constraint was achieved by a time-varying PNG scheme [14].

The terminal angle constraint becomes challenge to be achieved when facing maneuvering targets and complex perturbation such as measuring errors and noises. As a robust control method, sliding mode control (SMC) aims to eliminate the terminal angle error by enforcing an error-varied sliding surface to the origin using the sign function. In [15], an impact angle guidance was developed using SMC and virtual target technics. L. Bai proposed a 3-D SMC guidance law with terminal angle constraint, and the FOV limit was also considered [16]. A sliding mode impact angle guidance was proposed against maneuvering targets in [17]. In [18], an impact angle guidance was developed with finite time convergence. A SMC-based guidance was presented against constant moving and maneuvering targets in [19]. In [20], the authors proposed a multivariable twisting control-based terminal angle guidance law against various target motions. The twisting guidance method shows good performance with strong robustness and simple structure that is feasible in intercepting maneuvering targets. Note that the guidance law parameter selection for robustness depends on the perturbation to be rejected.

*Corresponding author: Tuo Han.

This work was supported by the National Natural Science Foundation of China under Grant 62203031 and Grant 61960206011; in part by the Zhejiang Provincial Natural Science Foundation of China under Grant LD22E050004 and LY24F030002; in part by the Beijing Natural Science Foundation under Grant 4242041; in part by the Fundamental Research Funds for the Central Universities; in part by the China Postdoctoral Science Foundation (2022M710312); and in part by the fellowship of China National Postdoctoral Program for Innovative Talents (BX20220370).

Higher perturbation bounds would require a greater guidance gain that has risks for causing chattering issue in practice. Another issue is that the guidance performance is affected by the measuring errors and noises in practice. How to avoid using full guidance information in generating guidance commands becomes crucial for reliability maintenance under complex & harsh working conditions. Therefore, it is meaningful to provide solutions for enhancing the guidance robustness while reducing the guidance gains and relying not on all guidance information, especially coupled line-of-sight (LOS) dynamics.

Considering the above points, this paper aims to design an incremental 3-D twisting guidance law for disturbance rejection with terminal angle constraints. It is an incremental version of the conventional twisting guidance law that has good performance in eliminating both the LOS errors and rates. Theoretical design and simulations for both guidance laws are provided for comparison.

The paper is organized as follows. Sec. 2 describes the problem and LOS dynamics. Sec. 3 presents the guidance law design. In Sec. 4, simulations are conducted, and the conclusions are remarked in Sec. 5.

Notions:

$\|\bullet\|$ denotes the 2-norm of a vector in Euclidean space.

2 Model Description

2.1 Engagement geometry

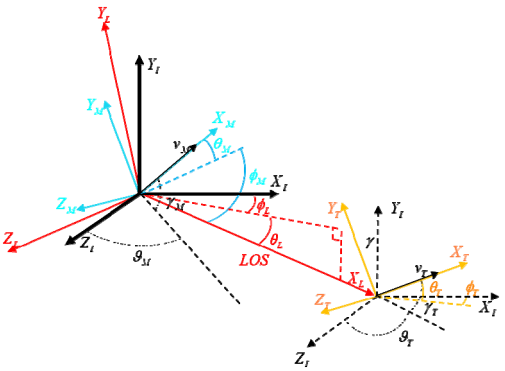

Fig. 1. Guidance geometry

Considering a missile (M) and a target (T) engaged in 3-D space, as is depicted in Fig. 1. Both vehicles can be regarded as points of mass, thus the attitude dynamics is ignored. $OX_IY_IZ_I$ stands for the inertial ground reference frame, $OX_LY_LZ_L$ is for the LOS reference frame, where OX is the LOS direction measured from the missile. $OX_MY_MZ_M$ and $OX_TY_TZ_T$ are the body coordinates of missile and target, respectively. As stated previously, the motion of attitude is not considered, then the OX axis of the body coordinate coincides with the velocity direction. θ_L and ϕ_L are the elevation and azimuth angle of LOS, respectively. $\boldsymbol{r}$ is the range vector, and $R=\|\boldsymbol{r}\|$ is the distance. $\boldsymbol{v}_M$ and $\boldsymbol{v}_T$ are the missile and target velocity, and their magnitudes are defined as $V_M=\|\boldsymbol{v}_M\|$, $V_T=\|\boldsymbol{v}_T\|$. γ_M, ϑ_M are the flight path angles, and θ_M, ϕ_M are the lead angles. The missile and target lateral acceleration are denoted as a_{yM}, a_{zM} and a_{yT}, a_{zT}.

2.2 The 3-D coupled LOS dynamics

Given the above 3-D guidance model, the LOS dynamics is given as

$$\begin{aligned} R\ddot{\theta}_L =& -2\dot{R}\dot{\theta}_L + a_{yT}\cos\theta_T - a_{yM}\cos\theta_M \\ & -R\dot{\phi}_L^2\sin\theta_L\cos\theta_L \end{aligned} \tag{1}$$

$$\begin{aligned} R\ddot{\phi}_L =& -2\dot{R}\dot{\phi}_L + \frac{\sin\theta_M\sin\phi_M}{\cos\theta_L}a_{zM} \\ & -\frac{\cos\phi_M}{\cos\theta_L}a_{yM} - \frac{\sin\theta_T\sin\phi_T}{\cos\theta_L}a_{zT} \\ & +\frac{\cos\phi_T}{\cos\theta_L}a_{yT} + 2R\dot{\phi}_L\dot{\theta}_L\tan\theta_L \end{aligned} \tag{2}$$

The derivation of $\dot{\theta}_L$ and $\dot{\phi}_L$ contains couplings, which hinders the coupled guidance law design in both the longitude and lateral plane.

3 Three-Dimensional Disturbance Rejection Guidance Law Design

To enhance the robustness, a 3-D terminal angle guidance law using the twisting algorithm[20] is presented for disturbance rejection. First, the problem is tackled by scaling the errors between expected terminal angles and the real ones. Then, the guidance law is constructed via the single variable twisting algorithm. To further enhance the robustness and guidance performance against maneuvering targets with reduced guidance information, an incremental twisting algorithm-based guidance law is designed.

3.1 Preparation

The approaching LOS angles are defined as

$$\theta_{LAppr} = \lim_{t\to t_f}\theta_L$$

$$\phi_{LAppr} = \lim_{t\to t_f}\phi_L$$

where t_f is the time of collision. $R_f=\lim R$ is the miss distance, or the final relative distance. It is the destination for a guidance law to meet the target as close as possible, thus $R_f\to 0$ is the basic goal. For a guidance law with terminal angle demands, there will be a set of expected final LOS angles θ_{Lf} and ϕ_{Lf}, and the approaching angles should be close to them. Hence, the guidance law is to meet

$$\begin{cases} R_f \to 0 \\ \theta_{LAppr}\to\theta_{Lf}, \phi_{LAppr}\to\phi_{Lf} \end{cases} \tag{3}$$

3.2 Twisting algorithm-based guidance law

The acceleration command in longitude plane is first considered. Let $\alpha=\theta_L-\theta_{Lf}$, then $\dot{\alpha}=\dot{\theta}_L$, because θ_{Lf} is a constant. Thus, the requirement $\theta_{LAppr}\to\theta_{Lf}$ in (3) becomes $\alpha\to 0$. Considering (1), the LOS angular acceleration dynamics in the pitch plane can be given by

$$\ddot{\alpha} = c_1(\mathrm{t}) - \frac{\cos\theta_M}{R}a_{yM} + d_1(\mathrm{t}) \tag{4}$$

where $c_1(\mathrm{t})=-2\dot{R}\dot{\alpha}/R-\dot{\phi}_L^2\sin(\theta_L)\cos(\theta_L)$ is known, $d_1(\mathrm{t})=a_{yT}\cos\theta_T/R+dis_1$ contains unknown terms including the target maneuver, and dis_1 is the external disturbance. Design the guidance command in the plane as

$$a_{yM} = a_{yeq} + a_{yd} \tag{5}$$

where $a_{yeq}=Rc_1/\cos\theta_M$ is the elimination term. a_{yd} is designed using twisting algorithm as follows

$$a_{yd} = \frac{p_1\,\mathrm{sgn}\,\alpha + p_2\,\mathrm{sgn}\,\dot{\alpha}}{\cos\theta_M}R \tag{6}$$

where sgn is the sign function, $p_1 > 0$, $p_2 > 0$. Substituting the designed two terms into (5) yields

$$\begin{aligned} a_{yM} &= a_{yeq} + a_{yd} \\ &= -\frac{2\dot{R}\dot{\alpha} + R\dot{\phi}_L^2 \sin(\theta_L)\cos(\theta_L)}{\cos\theta_M} \\ &\quad + \frac{p_1 \operatorname{sgn}\alpha + p_2 \operatorname{sgn}\dot{\alpha}}{\cos\theta_M} R \end{aligned} \tag{7}$$

Therefore, the dynamics in the pitch plane is

$$\ddot{\alpha} = d_1 - p_1 \operatorname{sgn}\alpha - p_2 \operatorname{sgn}\dot{\alpha} \tag{8}$$

Assume dis_1 is bounded, and consider that the target maneuver is limited, then the unknown term d_1 is bounded. Under these conditions, the dynamics with the form of (8) can converge to the origin [21]. In other words, it can be guaranteed that $\alpha \to 0$ and $\dot{\alpha} \to 0$ given the designed guidance command with appropriate parameter selection.

Accordingly, the guidance command in the yaw plane can be designed by eliminating an error named $\beta = \phi_L - \phi_{Lf}$. Specifically,

$$\ddot{\beta} = c_2(\mathrm{t}) - \frac{\cos\phi_M}{R\cos\theta_L} a_{zM} + d_2(\mathrm{t}) \tag{9}$$

where

$$c_2(\mathrm{t}) = -\frac{2\dot{R}\dot{\phi}_L}{R} + 2\dot{\phi}_L\dot{\theta}_L \tan\theta_L + \frac{\sin\theta_M \sin\phi_M}{R\cos\theta_L} a_{yM} ,$$

$$d_2(\mathrm{t}) = -\frac{\sin\theta_T \sin\phi_T}{R\cos\theta_L} a_{yT} + \frac{\cos\phi_T}{R\cos\theta_L} a_{zT} + dis_2$$

Therein, dis_2 stands for the external disturbance. Similarly, the guidance command in the yaw plane is consisted of two parts, the elimination term $a_{zeq} = Rc_2(\mathrm{t})\cos\theta_L / \cos\phi_M$, and the twisting term a_{zd} , presented as follows

$$\begin{aligned} a_{zM} &= a_{zeq} + a_{zd} \\ &= \frac{-2\dot{R}\dot{\phi}_L \cos\theta_L + 2R\dot{\phi}_L\dot{\theta}_L \sin\theta_L + a_{yM}\sin\theta_M \sin\phi_M}{\cos\phi_M} \\ &\quad + \frac{q_1 \operatorname{sgn}\beta + q_2 \operatorname{sgn}\dot{\beta}}{\cos\phi_M} R\cos\theta_L \end{aligned} \tag{10}$$

where $q_1 > 0$, and $q_2 > 0$ are design parameters.

On the basis of assuming the boundness of dis_2 and the target maneuver, it can be known that $\beta \to 0$ and $\dot{\beta} \to 0$ with the guidance command (10) for the LOS angular acceleration dynamics (9).

3.3 Incremental twisting-based guidance design

To further enhance robustness, the twisting guidance will be extended to an incremental version via the incremental guidance concept [21, 22]. Rewrite the formula (4) in its incremental form by Taylor expansion:

$$\ddot{\alpha} = \ddot{\alpha}_0 - \frac{\cos\theta_{M_0}}{R_0} \Delta a_{yM} + \Delta d_1(\mathrm{t}) \tag{11}$$

where $\Delta d_1(\mathrm{t})$ is the change of external disturbance in a sampling step, the subscript "0" denotes the last recorded value at the latest sampling time, and in particular, t_0 is the last recorded sampling time. $\Delta a_{yM} = a_{yM} - a_{yM0}$, $\Delta t = t - t_0$ is the time change from t_0 to t , i.e., the sampling step. $\ddot{\alpha}_0$, R_0 and θ_{M_0} is the value of $\ddot{\alpha}$, R and θ_M at time t_0 , respectively. Note that the term $\ddot{\alpha}_0$ contains unmeasurable terms, which can be real-time estimated using a certain observer [23].

Then, the incremental twisting guidance law in the pitch plane (defined as Δa_{yM}) can be designed as

$$\Delta a_{yM} = \Delta a_{Iyeq} + \Delta a_{Iytw} \tag{12}$$

where the subscript I refers to the incremental design, $\Delta a_{Iyeq} = R_0\hat{\ddot{\alpha}}_0 / \cos\theta_{M_0}$ is the elimination term, and the incremental twisting term is

$$\Delta a_{Iytw} = \frac{m_1 \operatorname{sgn}\alpha + m_2 \operatorname{sgn}\dot{\alpha}}{\cos\theta_{M_0}} R_0 \tag{13}$$

where $m_1 > 0$, and $m_2 > 0$.

The complete incremental guidance law (defined as a_{IyM}) in the pitch plane can be presented as

$$\begin{aligned} a_{IyM} &= a_{IyM0} + \Delta a_{yM} \\ &= a_{IyM0} + \frac{R_0\ddot{\alpha}_0}{\cos\theta_{M_0}} \\ &\quad + \frac{m_1 \operatorname{sgn}\alpha + m_2 \operatorname{sgn}\dot{\alpha}}{\cos\theta_{M_0}} R_0 \end{aligned} \tag{14}$$

Substituting (14)into dynamics (11)yields:

$$\ddot{\alpha} = \Delta d_1(\mathrm{t}) - m_1 \operatorname{sgn}\alpha - m_2 \operatorname{sgn}\dot{\alpha} \tag{15}$$

Note that the system dynamics is similar to the form as (8), and thus the convergence can be guaranteed.

As for the incremental guidance law design for the yaw plane, rewriting (9) in an incremental form by Taylor expansion as

$$\ddot{\beta} = \ddot{\beta}_0 + f_y - \frac{\cos\phi_{M_0}}{R_0\cos\theta_{L_0}} \Delta a_{zM} + \Delta d_2(\mathrm{t}) \tag{16}$$

The incremental guidance law in the yaw plane is designed as

$$\begin{aligned} a_{IzM} &= a_{IzM0} + \Delta a_{zM} \\ &= a_{IzM0} + \frac{R_0\cos\theta_{L_0}}{\cos\phi_{M_0}} \left(\ddot{\beta}_0 + f_y\right) \\ &\quad + \frac{R_0\cos\theta_{L_0}}{\cos\phi_{M_0}} \left(n_1 \operatorname{sgn}\beta + n_2 \operatorname{sgn}\dot{\beta}\right) \end{aligned} \tag{17}$$

where $f_y = \sin\theta_{M_0} \sin\phi_{M_0} \Delta a_{yM} / R_0 / \cos\theta_{L_0}$ is known in each step, $n_1 > 0$, and $n_2 > 0$ are design parameters.

Substituting Δa_{zM} into (16) yields:

$$\ddot{\beta} = \Delta d_2(\mathrm{t}) - n_1 \operatorname{sgn}\beta - n_2 \operatorname{sgn}\dot{\beta} \tag{18}$$

Similarly, the incremental guidance law in the yaw plane can also ensure that $\beta \to 0$ and $\dot{\beta} \to 0$.

Notably, it can be observed from the guidance dynamics (8) and (15) for the pitch plane (the same analysis for the yaw plane) that the disturbance to be rejected in the incremental guidance law is the incremental value of the disturbance. This is usually smaller than the disturbance itself, especially in a small sampling period. Therefore, the guidance parameter selection for the incremental twisting guidance will be more feasible (smaller and easy-tuning) for chattering avoidance than the twisting one, and will be more robust because: 1) the latest LOS angular acceleration and guidance command that reflect the real condition is included; 2) the coupled information c_1 and c_2 are not required in the incremental guidance law.

4 Numerical Simulation

The twisting control-based impact angle guidance (TCIAG) and incremental twisting control based-impact angle guidance (ITCIAG) are compared for intercepting

both constant moving and maneuvering targets via conducting extensive simulations. The initial conditions are listed in Table 1, and the simulation runs at 1ms per step, the guidance period is 20ms. The well-known PNG takes N=4 as navigation ratio. The designed guidance parameters are : $p_1 = 0.02$, $p_2 = 0.03$, $q_1 = 0.02$, $q_2 = 0.03$ for the TCIAG, and $m_1 = 0.004$, $m_2 = 0.0038$, $n_1 = 0.004$, $n_2 = 0.0038$ for the ITCIAG.

4.1 Simulation against constant moving target

Table 1: Initial configurations

Missile position/m	(10000,0,10000)
Target position/m	(0,10000,0)
Missile speed/(m/s)	500
Target speed/(m/s)	300
Missile flight path angle/°	$(\gamma_M, \vartheta_M) = (-30, -60)$
Target flight path angle/°	$(\gamma_T, \vartheta_T) = (0, -90)$

First, four different expected terminal LOS angle cases are tested against a constant moving target in Fig. 2. The constraint settings are in Table 2.

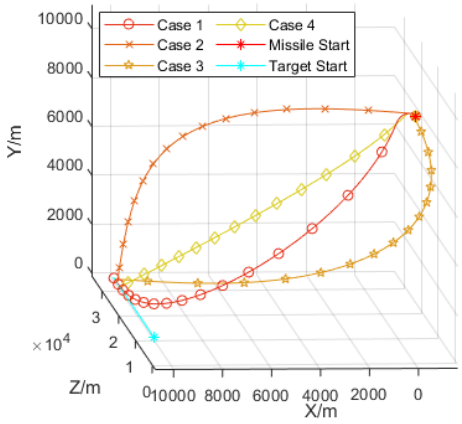

Fig. 2: Trajectories with various terminal angles against a constant moving target

Table 2: Constraint settings

Case	θ_{Lf} /rad	ϕ_{Lf} /rad
1	0	$-\pi/2$
2	$-\pi/3$	$-\pi/2$
3	0	0
4	$-\pi/6$	$-\pi/3$

The achieved LOS angles under different methods are given in Fig. 3. The comparison results show that both guidance can enforce the LOS angles to the expected ones.

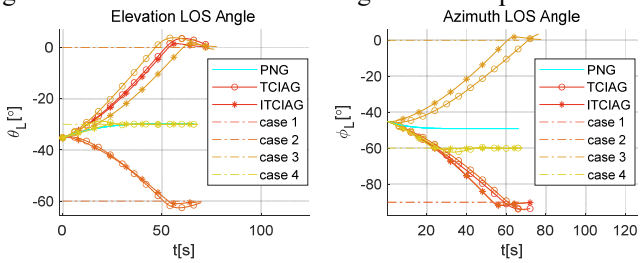

Fig. 3: LOS angle variation under various constraints against a constant moving target

4.2 Simulation against a maneuvering target

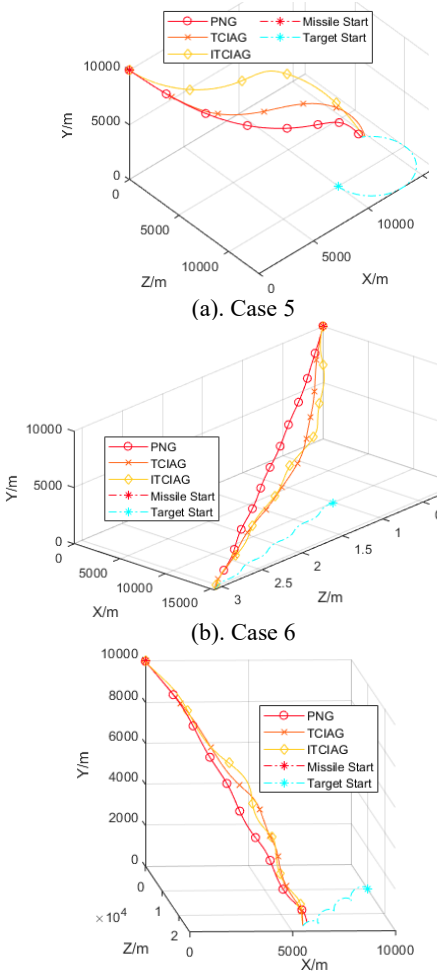

(a). Case 5

(b). Case 6

(c). Case 7

Fig. 4: Trajectories under different guidance laws against maneuvering targets

The terminal angle is set as $(\theta_{Lf}, \phi_{Lf}) = (-\pi/6, -\pi/3)$ against maneuvering targets under the following cases:

Case 5: $a_{yT} = 0, a_{zT} = -3g$

Case 6: $a_{yT} = 0, a_{zT} = -3g\sin(\pi t/8)$

Case 7: $a_{yT} = 3g\sin(\pi t/8 + \pi/2), a_{zT} = 3g\sin(\pi t/8)$

The 3-D interception trajectories are shown in Fig. 4, the guidance law can create feasible trajectories for capturing the target from specified approach direction (terminal angle). The LOS angles and guidance commands are shown in Fig. 5 and Fig. 6, respectively. Both the TCIAG and ITCIAG can achieve the terminal angle constraints with feasible guidance commands. In addition, it is noteworthy that the design parameters of the ITCIAG are smaller than the TCIAG, this is because the perturbation to be rejected is an incremental value of the disturbance.

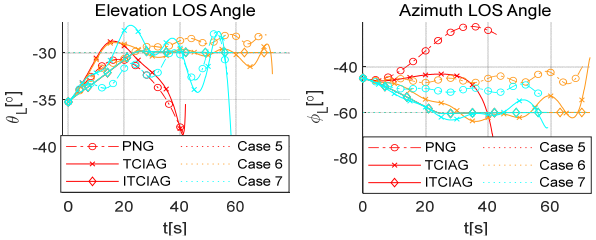

Fig. 5: LOS angle variation under various constraints against maneuvering targets

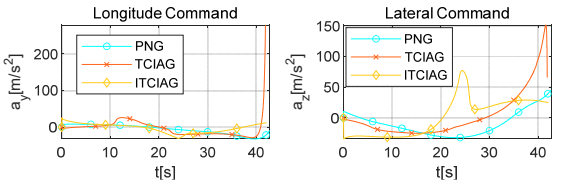

(a) Case 5

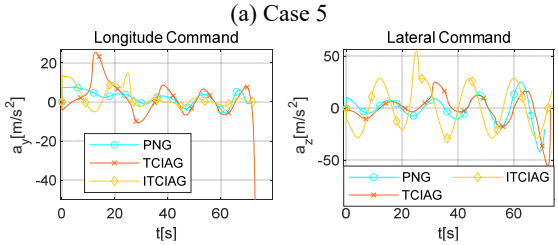

(b) Case 6

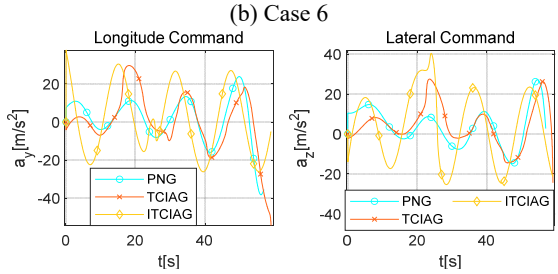

(c) Case 7

Fig. 6: Guidance commands against maneuvering targets

5 Conclusion

In this paper, an incremental twisting algorithm-based terminal angle guidance is investigated in the 3-D space. The nonlinear PD-like twisting algorithm utilizes the angle errors and LOS rate information, and can guarantee the convergence in finite time. Its incremental extension with application to the guidance law design also shows the simple guidance structure and enhanced robustness. Future work would be the online observation of LOS angular acceleration and the influences of the noises on the incremental guidance scheme.

References

[1] P. Zarchan, *Tactical and Strategic Missile Guidance, 6th ed.* Reston: AIAA, 2012, pp. 108-133.

[2] L. Yuan, Homing and navigational courses of automatic target-seeking devices, *Journal of Applied Physics*, 19(12): 1122-1128, 1948.

[3] F. William, and P. Zarchan, A new look at classical vs modern homing missile guidance, *Journal of Guidance Control & Dynamics*, 1981.

[4] A. Bryson, and Y. Ho, *Applied Optimal Control.* Washington, D.C.: Hemisphere, 1975.

[5] Y. Lee, C. Ryoo and E. Kim, Optimal guidance with constraints on impact angle and terminal acceleration in *AIAA Guidance, Navigation, and Control Conference and Exhibit*, 2003.

[6] H. Shin, J. Lee, H. Cho, and A. Tsourdos, Trajectory modulation guidance law for anti-ship missiles in *AIAA Guidance, Navigation, and Control Conference*. 2011.

[7] M. Kim, and K. Grider, Terminal guidance for impact attitude angle constrained flight trajectories, *IEEE Transactions on Aerospace and Electronic Systems*, 9(6): 852-859, 1973.

[8] C. Ryoo, H. Cho, and M. Tahk, Optimal guidance laws with terminal impact angle constraint, *Journal of Guidance Control & Dynamics*, 28(4):724-732, 2005.

[9] Y. Chen, S. Wu, and X. Wang, Impact time and angle control optimal guidance with field-of-view constraint, *Journal of Guidance, Control, and Dynamics*, 45(12): 2369-2378, 2022.

[10] L. Hou, H. Luo, H. Shi, H. Shin, and S. He, An optimal geometrical guidance law for impact time and angle control, *IEEE Trans on Aerospace and Electronic Systems*, 59(6): 9821-9830, 2023.

[11] A. Ratnoo, and D. Ghose, Impact angle constrained interception of stationary targets, *Journal of Guidance, Control, and Dynamics*, 31(6): 1817–1822, 2008.

[12] C. Lee, T. Kim, and M. Tahk, Interception angle control guidance using proportional navigation with error feedback, *Journal of Guidance, Control, and Dynamics*, 36(5): 1556–1561, 2013.

[13] P. Zarchan, *Tactical and Strategic Missile Guidance, 6th ed.* Reston: AIAA, 2012, pp. 575-576.

[14] B. Kim, J. Lee, and H. Han, Biased PNG law for impact with angular constraint, *IEEE Transactions on Aerospace and Electronic Systems*, 34(1): 277-288, 1998.

[15] G. Li, Q. Yang, and X. Huang, Virtual Target Based Terminal Guidance Law for Cruise Projectile Considering Impact Angle Constraint in *42nd Chinese Control Conference*, 2023.

[16] L. Bai, Y. Wang, E. Wang, C. Wang, and J. Qiao, Three-dimensional anti-disturbance guidance for impact angle control with field-of-view constraint in *42nd Chinese Control Conference*, 2023.

[17] K. Majumder, and S. Kumar, Prescribed performance terminal sliding mode based guidance with impact angle constraints in *AIAA SCITECH 2023 Forum*, 2023.

[18] S. Kumar, S. Rao, and D. Ghose, Nonsingular terminal sliding mode guidance with impact angle constraints, *Journal of Guidance, Control, and Dynamics*, 37(4): 1114-1130, 2014.

[19] X. Wang, Y. Zhang, and H. Wu, Sliding mode control based impact angle control guidance considering the seeker's field-of-view constraint, *ISA Transactions*, 61: 49-59, 2016.

[20] Q. Hu, T. Han, and M. Xin, Three-dimensional guidance for various target motions with terminal angle constraints using twisting control, *IEEE Transactions on Industrial Electronics*, 67(2): 1242-1253, 2020.

[21] A. Polyakov, and A. Poznyak, Lyapunov function design for finite-time convergence analysis: "Twisting" controller for second-order sliding mode realization, *Automatica*, 45(2): 444-448, 2009.

[22] T. Han, Q. Hu, H. Shin, A. Tsourdos, and M. Xin, Sensor-based robust incremental three-dimensional guidance law with terminal angle constraint, *Journal of Guidance, Control, and Dynamics*, 44(11): 2016-2030, 2021.

[23] T. Han, H. Shin, and Q. Hu, Differentiator-based incremental three-dimensional terminal angle guidance with enhanced robustness, *IEEE Transactions on Aerospace and Electronic Systems*, 58(5): 4020-4032, 2022.

Proceedings of the 3rd Conference on Fully Actuated System Theory and Applications
May 10-12, 2024, Shenzhen, China

Predefined time sliding mode attitude tracking control for rigid spacecraft based on fully actuated system method

Yin Zheng[1], He Zhang[1], Yan Wang[1]
1. School of Astronautics, Harbin Institute of Technology, Heilongjiang 150001, P. R. China
E-mail: zhengyinhit@163.com,hezhanghit@163.com,yanw@hit.edu.cn

Abstract: Based on the control theory of the fully actuated system method, this paper proposes a method of attitude-tracking control for rigid spacecraft by using a predefined time terminal sliding mode scheme. First, we establish the fully-actuated system model for the spacecraft by using the attitude dynamics and kinematics equation, then in order to improve the control efficiency, a new predefined time controller is designed by combining the fully actuated system method and the nonsingular terminal sliding mode control method. Finally, the effectiveness of the designed controller is verified by numerical simulation.

Key Words: Fully actuated system method, Attitude tracking, Predefined time stability, Terminal sliding mode

1 Introduction

In recent years, spacecraft attitude control has received extensive attention due to its wide application in space exploration, satellite communication, interactive docking and other space missions [1, 2]. The purpose of designing the attitude controller is to ensure that the spacecraft attitude can remain stable and still be able to complete the task of tracking the target attitude when the spacecraft has unknown external disturbances, parameter uncertainties, sensor failures, and so on.

In order to solve these control problems that may exist in aerospace missions, researchers have proposed sliding mode control methods [3, 4] backstepping control methods [5, 6] and other robust control methods for nonlinear systems, and applied these methods to spacecraft attitude control. The reference [4] designed a sliding mode attitude controller to solve the attitude tracking problem of spacecraft systems with inertial uncertainties and external disturbances. In [5], a robust controller based on the backstepping control method is proposed to solve the attitude control problem of spacecraft with external disturbance, parameter uncertainty, and input saturation. Hu proposed a finite-time observer and a linear finite-time terminal sliding mode controller to solve the attitude tracking problem [7]. In [8], an adaptive fixed-time terminal sliding mode attitude control law for rigid spacecraft.

Moreover, most of the above works are the research of asymptotic convergence, finite time convergence, and fixed time convergence, comparison with the above control method, The predefined time convergence system has the advantages of a fast convergence rate, high control accuracy, and the upper bound of convergence time is decidable. As a research hotspot in recent years, predefined time has received extensive attention. In [9], a nonsingular predefined-time controller was developed for attitude stabilization of rigid spacecraft. It is worth noting that the above research is based on the state space model. In [10], a continuous precise predefined-time attitude tracking control law was proposed for a rigid spacecraft. In [11], the time-varying technique was applied to design a predefinedtime output-feedback controller for second-order nonlinear systems.

Duan first proposed a new control method, fully actuated system method, in 2021 [12]. Compared with the state space method, the fully actuated system theory can compensate the dynamic characteristics of the system without considering the complexity of the nonlinear term of the system while keeping the physical environment unchanged. Since the fully actuated system was proposed, recent research on the control theory and application of the fully actuated system has gradually increase. Duan proposed the framework of the fully actuated system method under the conditions like full state feedback systems [13], robust control systems [14], adaptive control systems[15], adaptive robust control systems[16], discrete-time systems [17]. With the development of the fully actuated system theory, more and more researchers have applied the fully actuated system theory to practical engineering. In [18], Duan proposed the application of generalized PID control in tracking system under the theory of fully actuated system. In Reference [19], duan proposed an optimal control method in fully actuated system for spacecraft attitude stability. In [20] proposed high order fully actuated proportional integral predictive control to achieve cooperative control and compensate for fixed communication delays.In [21], a high order fully actuated predictive sliding mode control method is designed to realize the cooperative control of multi-agent systems. Although the full drive system has been studied for a period of time, there are relatively few research results on predefined time control based on fully actuated system considering external disturbances. Therefore, this paper studies a scheduled time spacecraft attitude problem based on the fully actuated system method.

The main contribution of this paper is to establish the attitude system of the spacecraft based on the fully actuated system method, and a new nonsingular terminal sliding mode controller is proposed to complete the attitude tracking control of the system.

2 Preliminaries

2.1 The fully actuated Attitude Kinematics and Dynamics model for spacecraft

The attitude model of the spacecraft is shown in Fig.1. The origin of the coordinate system is the center of the spacecraft, the z-axis is the direction from the center of the spacecraft to the center of the earth, the x-axis is consistent with

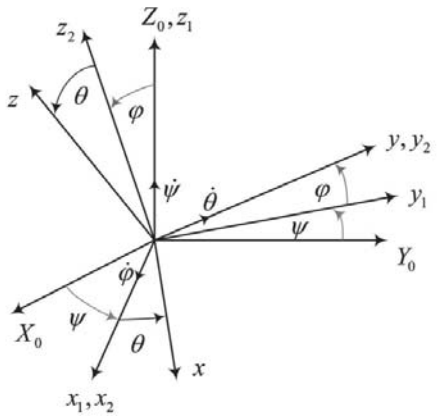

Fig. 1: Coordinate system transformation

the flight direction of the spacecraft, and the y-axis is determined by the right-handed coordinate system. It is denoted by $\sigma = [\varphi, \theta, \psi]^T$, where φ, θ, and ψ are the roll angle, pitch angle, and yaw angle. If the rotation of the coordinate system is $Z(\psi) \to Z(\varphi) \to Z(\theta)$ the spacecraft coordinate transformation matrix from ω to $\dot{\sigma}$ is defined as

$$G = \begin{bmatrix} -\sin\theta/\cos\theta & 0 & \cos\theta/\cos\varphi \\ \cos\theta & 0 & \sin\theta \\ -\sin\varphi\sin\theta/\cos\theta & 1 & -\cos\theta\sin\varphi/\cos\varphi \end{bmatrix} \tag{1}$$

As normal, the attitude kinematic and dynamic equation of the rigid spacecraft with the external disturbance is defined as

$$\dot{\sigma} = G(\sigma)\omega \tag{2}$$

$$J\dot{\omega} = -\omega^{\times} J\omega + u + d \tag{3}$$

where J is the inertia matrix, ω is the angular velocity, u is the control torque, d is the external disturbance. $\omega^{\times}$ is the skew-symmetric matrix, which is defined as

$$\omega^{\times} = \begin{bmatrix} 0 & -\omega_3 & \omega_2 \\ \omega_3 & 0 & -\omega_1 \\ -\omega_2 & \omega_1 & 0 \end{bmatrix} \tag{4}$$

From (2), there have

$$\begin{aligned} &\ddot{\sigma} = \dot{G}(\sigma)\omega + G(\sigma)\dot{\omega} \\ &= \dot{G}(\sigma)G^{-1}(\sigma)\dot{\sigma} + G(\sigma)[J^{-1}(G^{-1}(\sigma)\dot{\sigma})^{\times} \cdot J(G^{-1}(\sigma)\dot{\sigma})] \\ &+G(\sigma)J^{-1}u + G(\sigma)J^{-1}d \end{aligned} \tag{5}$$

define $f(\sigma, \dot{\sigma}) = \dot{G}(\sigma)G^{-1}(\sigma)\dot{\sigma} + G(\sigma)[J^{-1}(G^{-1}(\sigma)\dot{\sigma})^{\times} \cdot J(G^{-1}(\sigma)\dot{\sigma})]$, $B(\sigma) = G(\sigma)J^{-1}$ and $\det B(\sigma) \neq 0$.
The system satisfies the form of high order fully actuated in literature (Duan, 2021).

$$\ddot{\sigma} = f(\sigma, \dot{\sigma}) + \Delta f(\sigma, \dot{\sigma}) + B(\sigma)u \tag{6}$$

where $f(\sigma, \dot{\sigma}) = -M^{-1}(\sigma)D(\sigma, \dot{\sigma})\dot{\sigma} - M^{-1}(\sigma)\xi(\sigma, \dot{\sigma})$, $B(\sigma) = M^{-1}(\sigma)$ and $\det B(\sigma) \neq 0$

2.2 Definition and Lemma

Definition [17]: Consider the following matrix second-order system

$$x^{(n)} = f(x^{(0\sim n-1)}) + \Delta f(x^{(0\sim n-1)}) + L(x^{(0\sim n-1)})u \tag{7}$$

where x is the system state and u is the control vector, $f(x^{(0\sim n-1)})$ is a continuous vector function, $L(x^{(0\sim n-1)})$ is continuous matrix functions, and satisfies $\det L(x^{(0\sim n-1)}) \neq 0$.
Lemma 1 [17]: A stabilizing controller for the above system is defined by

$$u = u_0 + u_1 \tag{8}$$

where $u_0 = -L^{-1}[A^{(0\sim n-1)}x^{(0\sim n-1)} + \Delta f(x^{(0\sim n-1)}) + f(x^{(0\sim n-1)})]$ is the basic part, which aims to assign the linear term $A^{(0\sim n-1)}x^{(0\sim n-1)}$ to the closed-loop system, u_1 is the auxiliary controller to make the system achieve improved dynamic performance such as the predefined time convergence of the state.
Lemma 2 : consider the continuous nonlinear system $\dot{x}(t) = z(x,t)$, $z(0) = 0$ suppose there is an unbounded Lyapunov function V and $0 < \eta < 1$, such that $V > 0$ for any nonzero x, the following inequality can be satisfied

$$\dot{V} \leq -\frac{2}{t_p\eta}(2V + V^{\frac{1+\eta}{2}} + V^{\frac{3-\eta}{2}}) \tag{9}$$

Hence, the system is predefined time stability, and the settling time depends on the predefined time parameter t_p, and the settling time $t_c < t_p$.
proof: since the Lyapunov function with an initial condition $V_0 > 0$ converges to $V_f > 0$ in the time t_c, the equation can be expressed as

$$\begin{aligned} &\dot{V} \leq -\tfrac{2}{t_p\eta}(2V + V^{\frac{1+\eta}{2}} + V^{\frac{3-\eta}{2}}) \\ &t_c \leq -\tfrac{t_p\eta}{2}\int_{V_0}^{V_f} \frac{1}{2V+V^{\frac{1+\eta}{2}}+V^{\frac{3-\eta}{2}}}dV \\ &= -\tfrac{t_p\eta}{2}\int_{V_0}^{V_f} \frac{1}{V^{\frac{1+\eta}{2}}(V^{\frac{1-\eta}{2}}+2+V^{1-\eta})}dV \\ &= -\tfrac{t_p\eta}{2}\int_{V_0}^{V_f} \frac{1}{V^{\frac{1+\eta}{2}}(1+V^{\frac{1-\eta}{2}})^2}dV \\ &= -\tfrac{t_p\eta}{2}\int_{V_0}^{V_f} \frac{1}{V^{\frac{1+\eta}{2}}(1+V^{\frac{1-\eta}{2}})^2}dV \\ &= -t_p\int_{V_0}^{V_f} \frac{1}{(1+V^{\frac{1-\eta}{2}})^2}dV^{\frac{1-\eta}{2}} \\ &= t_p(1 - \frac{1}{1+V_0^{\frac{1-\eta}{2}}}) \leq t_p \end{aligned} \tag{10}$$

This completes the proof

3 The design of PTNTSM controller

Denote σ_d is the desired attitude, define the tracking error

$$\begin{cases} e_1 = \sigma - \sigma_d \\ e_2 = \dot{\sigma} - \dot{\sigma}_d \end{cases} \tag{11}$$

Assumption1: the leader spacecraft σ_d, $\dot{\sigma}_d$, $\ddot{\sigma}_d$ and the disturbance d is bounded.
A novel nonsingular terminal sliding surface proposed

$$s = \dot{e}_1 + \frac{2}{t_p\eta}(k_0 e_1 + k_1 sig^{\frac{\alpha}{\beta}}(e_1) + k_2 sig^{2-\frac{\alpha}{\beta}}(e_1) + k_3 sign(e_1)) \tag{12}$$

where s and e_1 are the sliding mode function and attitude velocity tracking error of spacecraft, respectively, and the parameter $\alpha > 0$, $\beta > 0$, $k_i > 0$ $i = 0, 1, 2, 3$ are positive constant and $\alpha < \beta$, $\eta = \frac{\alpha}{\beta}$ when $s = 0$ there have

$$\dot{e}_1 = \frac{2}{t_p\eta}(-k_0 e_1 - k_1 sig^{\frac{\alpha}{\beta}}(e_1) - k_2 sig^{2-\frac{\alpha}{\beta}}(e_1) - k_3 sign(e_1)) \tag{13}$$

construct a Lyapunov function

$$V_1 = \frac{1}{2}e_1^2 \tag{14}$$

taking the derivative of

$$\begin{aligned}
&\dot{V}_1 = e_1\dot{e}_1 = e_1(\tfrac{2}{t_p\eta}(-k_0e_1 - k_1 sig^{\frac{\alpha}{\beta}}(e_1) - k_2 sig^{2-\frac{\alpha}{\beta}}(e_1) \\
&-k_3 sign(e_1))) \\
&= \tfrac{2}{t_p\eta}(-e_1(k_0e_1 + k_1 sign(e_1)|e_1|^{\frac{\alpha}{\beta}} + k_2 sign(e_1)|e_1|^{2-\frac{\alpha}{\beta}} \\
&+k_3 sign(e_1))) \\
&= \tfrac{2}{t_p\eta}(-k_0e_1^2 - k_1|e_1|^{\frac{\alpha+\beta}{\beta}} - k_2|e_1|^{\frac{3\beta-\alpha}{\beta}} - k_3\,|e_1|) \\
&\leq -\tfrac{2}{t_p\eta}(k_0e_1^2 - k_1|e_1|^{\frac{\alpha+\beta}{\beta}} - k_2|e_1|^{\frac{3\beta-\alpha}{\beta}}) \\
&\leq -\tfrac{2}{t_p\mu}(2V_1 + V_1^{\frac{1+\mu}{2}} + V_1^{\frac{3-\mu}{2}})
\end{aligned} \tag{15}$$

Then, the sliding mode reaching law can be defined as:

$$\dot{s} = l_0 s + \frac{2}{t_p\eta}(l_1 sig^{\frac{p}{q}}(s) + l_2 sig^{2-\frac{p}{q}}(s) + l_3 sign(s)) \tag{16}$$

taking the derivative of s

$$\begin{aligned}
&\dot{s} = \dot{e}_2 + \\
&\tfrac{2}{t_p\eta}(k_0e_2 + k_1\tfrac{\alpha}{\beta}|e_1|^{\frac{\alpha}{\beta}-1}e_2 + k_2\tfrac{2\beta-\alpha}{\beta}|e_1|^{\frac{\alpha}{\beta}-1}e_2 + k_3\,|e_1|\,e_2)
\end{aligned} \tag{17}$$

moreover, the singularity problem will occur if $e_1 = 0$ and $\dot{e}_1 \neq 0$, when the term $\frac{\alpha}{\beta} - 1 < 0$. so, saturation function is addressed by the literature [21] to solve the singularity problem.
To limit the amplitude of the singularity term $e_1^{\frac{\alpha}{\beta}-1}$, saturation function is applied in the controller and it is defined as:

$$sat(m,n) = \begin{cases} m, n > |m| \\ nsign(m), |n| \leq m \end{cases} \tag{18}$$

According to the lemma 1, for the spacecraft attitude fully actuated system model (5), the following controller is proposed in this paper.

$$u = -L^{-1}(x^{(0-1)})(A^{(0-1)}\sigma^{(0-1)} + u_s) \tag{19}$$

and the u_1 is given as

$$\begin{aligned}
&u_s = \dot{G}(\sigma)G^{-1}(\sigma)\dot{\sigma} + G(\sigma)[J^{-1}(G^{-1}(\sigma)\dot{\sigma})^{\times} \cdot J(G^{-1}(\sigma)\dot{\sigma})] \\
&-\ddot{\sigma}_d + G(\sigma)J^{-1}d + \tfrac{2}{t_p\eta}(k_0e_1 + sat(k_1\tfrac{\alpha}{\beta}sig^{\frac{\alpha}{\beta}-1}(e_1)e_2, h) \\
&+k_2\tfrac{2\beta-\alpha}{\beta}sig^{1-\frac{\alpha}{\beta}}(e_1)e_2 + k_3 sign(e_1)e_2 - l_0 s - l_1 sig^{\frac{p}{q}}(s) \\
&-l_2 sig^{2-\frac{p}{q}}(s) - l_3 sign(s))
\end{aligned} \tag{20}$$

where u_0 is the linear state feedback based on the fully actuated system, u_s is a nonsingular terminal sliding mode controller for nonlinear dynamic compensation to achieve predefined time convergence control.

4 Simulation

In order to verify the effectiveness of the designed control method, considering the tracking system composed of a leader spacecraft and a follower spacecraft, the simulation parameters are defined as follows:
The inertia matrix of the spacecraft is defined as $J = [5.86, 0, 0; 0, 2.56, 0; 0, 0, 6.88]$.
The sine wave disturbance $d = 0.1[\sin(0.1t), \cos(0.2t), \sin(0.3t)]^T$ of the spacecraft is randomly added.
The initial attitude and initial angular velocity of the target spacecraft are $\sigma_d = [0, 0, 0]^T$.
The initial attitude and initial angular velocity of the following spacecraft is $\sigma = [0.5825; 0. - 5225; 0.1825]^T$, $\omega = [0, 0, 0]^T$. The predefined time $t_p = 10s$, it is means the attitude tracking error will converge to a small region in 10s.
The controller parameters are given by $k_0 = l_0 = 5$,$k_1 = k_2 = l_1 = l_2 = 10$, $k_3 = l_3 = 3$,$\alpha = 7$, $\beta = 9$, $p = 5$, $q = 9$, $h = 100$, $A_0 = diag[-8, -5, -6]$, $A_1 = diag[-7, -12, -3]$ and the minimum and maximum control inputs are set to $u_{\min} = -5N/m$, $u_{\max} = 5N/m$.

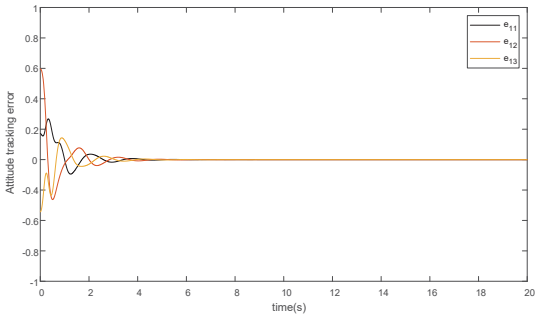

Fig. 2: Attitude tracking error under the controller (20)

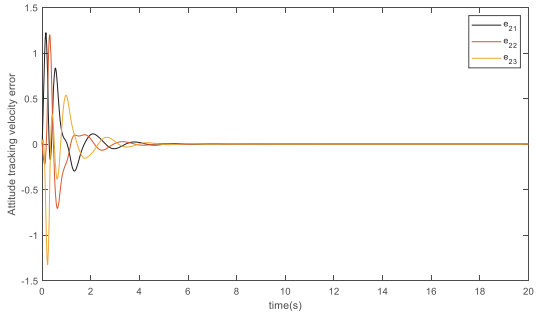

Fig. 3: Attitude tracking error velocity error under the controller (20)

Attitude tracking error (e1) and attitude tracking velocity error (e2) under the controller (20) is shown in fig.2 and fig.3, from the figures, it can be observed that all tracking errors are guaranteed to converge to small regions within the predefined time 10s. The results show that the proposed control scheme can achieve attitude tracking even if there are disturbances. The curve of sliding mode and control input are presented in fig.4 and fig.5, it is evident to see that no chattering occurs and the control inputs are continuous. The sliding mode surface converges to within 10s.

In order to prove the superiority of the fully actuated system method, this paper applies the controller without the fully actuated method as a comparison, and we use u_2 as the controller.

$$u_2 = B(\sigma)u_s \tag{21}$$

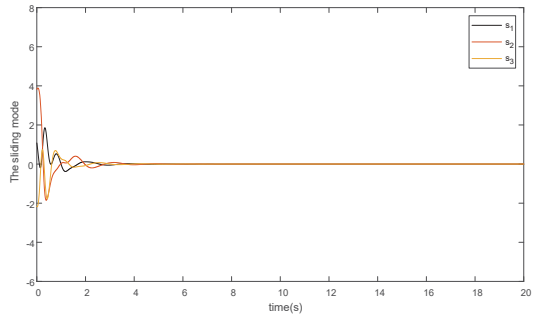

Fig. 4: Response of the sliding mode under the controller (20)

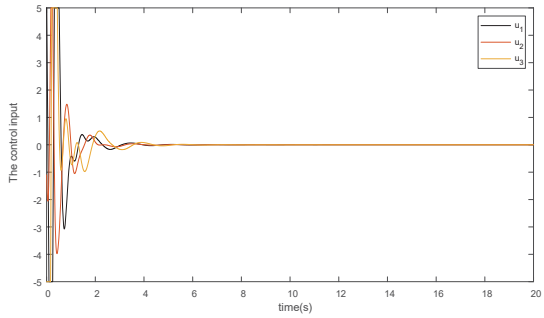

Fig. 5: Response of the controller (20)

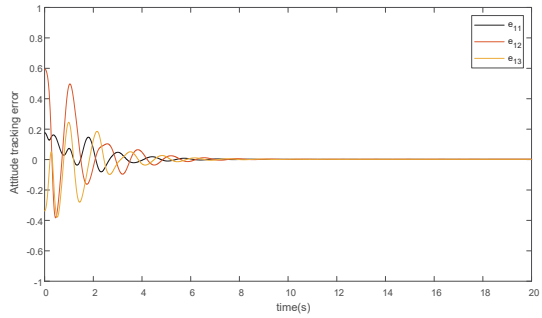

Fig. 6: Attitude tracking error under the controller (21)

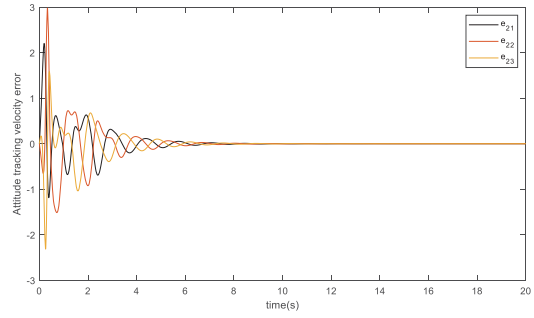

Fig. 7: Attitude tracking velocity error under the controller (21)

the simulation are shown in fig.6 and fig.7, one can see that the system can converge to a small regions in the predifined time 10s. But the control performance is not as good as the controller (20).

Therefore, the method designed in this paper is effective and can enable the spacecraft system to complete the attitude tracking task in a predefined time, which can be applied in actual working conditions because its upper bound of convergence time is decidable.

5 Conclusion

In this paper, the predefined time terminal sliding mode method and fully actuated system method are used to successfully accomplish the attitude tracking of the spacecraft in a predefined time. On this basis, the non-singular terminal sliding mode surface is used to design the control law, which ensures the predefined time convergence of the attitude tracking error in the presence of external disturbances and the effectiveness of the control scheme is verified by numerical simulation.

References

[1] Dong R Q, Wu A G, Zhang Y, et al., Anti-unwinding sliding mode attitude control via two modified Rodrigues parameter sets for spacecraft, Automatica, 2021, 129: 109642.

[2] Su Q Y and Huang Y, Su, Qiya, and Yi Huang. "Observability analysis and navigation algorithm for distributed satellites system using relative range measurements." Journal of Systems Science and Complexity 31.5 (2018): 1206-1226.

[3] Cao Q, Wei DQ. Dynamic surface sliding mode control of chaos in the fourth-order power system. Chaos, Solitons Fractals 2023;170. https://doi.org/10.1016/j.chaos.2023.113420.

[4] Xia Y, Zhu Z, Fu M, et al., Attitude tracking of rigid spacecraft with bounded disturbances, IEEE Transactions on Industrial Electronics, 2011, 58(2): 647–659.

[5] Sun L and Zheng Z W, Disturbance-observer-based robust backstepping attitude stabilization of spacecraft under input saturation and measurement uncertainty, IEEE Transactions on Industrial Electronics, 2017, 64(10): 7994–8002.

[6] Zou A M, Kumar K D, and Ruiter A H, Fixed-time attitude tracking control for rigid spacecraft, Automatica, 2020, 113: 108792.

[7] Hu Q, Jiang B and Zhang Y (2017) Observer-based output feedback attitude stabilization for spacecraft with finite time convergence. IEEE Transactions on Control Systems Technology 27(2): 781–789.

[8] Zou AM and Fan Z (2020) Distributed fixed-time attitude coordination control for multiple rigid spacecraft. International Journal of Robust and Nonlinear Control 30(1): 266–281.

[9] D. Ye, A.M. Zou, Z.W. Sun, Predefined-time predefined-bounded attitude tracking control for rigid spacecraft, IEEE Trans. Aerosp. Electron. Syst. 58 (1) (2022) 464–472.

[10] W.C. Wang, M.S. Hou, Y.K. Fu, B.J. Liu, Continuous precise predefined-time attitude tracking control for a rigid spacecraft, Int. J. Control (2022), https://doi.org/10.1080/00207179.2021.2021290, early access.

[11] J. Ni, L. Liu, Y. Tang, and C. Liu, "Predefined-time consensus tracking of second-order multiagent systems," IEEE Trans. Syst., Man, Cybern., Syst., vol. 51, no. 4, pp. 2550–2560, Apr. 2021.

[12] G. Duan. High-Order Fully Actuated System Approaches:Part I. Models and Basic Procedure. International Journal of Systems Science, 2021, 52(2): 422-435.
[13] G. Duan. High-Order Fully Actuated System Approaches: Part II. Generalized Strict-Feedback Systems. International Journal of Systems Science, 2021, 52(3): 437-454.
[14] G. Duan. High-Order Fully Actuated System Approaches: Part III. Robust Control and High-Order Backstepping. International Journal of Systems Science, 2021, 52(5): 952-971.
[15] G. Duan. High-Order Fully Actuated System Approaches: Part IV. Adaptive Control and High-Order Backstepping. International Journal of Systems Science, 2021, 52(5): 972-989.
[16] G. Duan. High-Order Fully Actuated System Approaches: part VII. Controllability, Stabilization and Parametric Designs. International Journal of Systems Science, 2021, 52(14): 3091-3114.
[17] G. Duan. High-Order Fully Actuated System Approaches: Part X. Basics of Discrete-Time Systems. International Journal of Systems Science, 2022, 53(4): 810-832.
[18] G. Duan. High-Order Fully Actuated System Approaches: Part IX. Generalized PID control and Model Reference Tracking. International Journal of Systems Science, 2022, 53(3): 652-674.
[19] G. Duan. High-Order Fully Actuated System Approaches:Part VIII. Optimal Control with Application in Spacecraft Attitude Stabilization. International Journal of Systems Science, 2022, 53(1): 54-73.
[20] Zhang DW, Liu GP, Cao L. Proportional integral predictive control of high-order fully actuated networked multiagent systems with communication delays. IEEE Trans Syst, Man, Cybern: Syst 2023;53(2):801–12.
[21] Zhang DW, Liu GP. Predictive sliding-mode control for networked high-order fully actuated multiagents under random deception attacks. IEEE Trans Syst, Man, Cybern: Syst 2023. URL: https://doi.org/10.1109/TSMC.2023.3311438.
[22] Ni J, Liu L, Liu C, Hu X and Li S (2016) Fast fixed-time nonsingular terminal sliding mode control and its application to chaos suppression in power system. IEEE Transactions on Circuits and Systems II: Express Briefs 64(2): 151–155.

Author Index

A

AI Ling ... 1271
ALABI Tobi ... 1376
AN Li ... 1513
AN Tianjiao ... 1089

B

BAI Xiaoshan ... 577
BAN Xiao Jun ... 1164
BAO Feng ... 110
BAO Jie ... 632
BI Cong ... 426
BIAN Hanlin ... 885

C

CAI Chenxiao ... 644
CAI Guang-Bin ... 1503
... 1526
CAI He ... 389
CAI Miao ... 529
CAI Yu ... 1164
CAO Tao ... 1447
CAO Yipeng ... 962
CHANG Chenxu ... 552
CHANG Le ... 993
CHEN Anlong ... 482
CHEN Bo ... 460
CHEN Bo ... 1352
CHEN Cai ... 319
CHEN Haipeng ... 1471
CHEN Jian ... 337
CHEN Jianliang ... 638
CHEN Junyu ... 1465
CHEN Kai ... 770
CHEN Li-Qun ... 1412
CHEN Liangming ... 1216
CHEN Liheng ... 1222
... 1228
... 1294
CHEN Ming ... 1352
CHEN Qihong ... 254
CHEN Shiwei ... 249
CHEN ShouYan ... 620
CHEN Siyuan ... 308
CHEN Weifang ... 1152
CHEN Xiang ... 1035
CHEN Xiaoran ... 1435
CHEN Yan ... 1555
CHEN Yue ... 401
CHEN Yunqi ... 158
CHEN Yuwei ... 1317
... 1323
CHEN Zhang ... 885
CHEN Zhang ... 701
CHEN Zhihua ... 1388
... 1520
CHEN Zhijun ... 48
CHEN Zhongyu ... 25
... 1299
CHENG Nie ... 595
CHENG Nuo ... 1294
CHENG Peng ... 644
CHENG Pengfei ... 1486
CHENG Wen ... 595
CHENG Yu ... 638
CHI Kun ... 319
CHU Hongchun ... 319
CONG Yirui ... 775
CUI En-Yuan ... 216
CUI Hailong ... 359
CUI Kaixin ... 1453
CUI Yang ... 127
... 134

D

DAI Dongyan ... 271
DAI Wei ... 208
DAI Xiaoran ... 1283
DENG Heng ... 1549
DENG Jibao ... 614
DENG Yaoming ... 395
DIAO Huineng ... 804
DING Dong ... 837
DING Ning ... 1265
DING Shengsi ... 296
DING Yuanpeng ... 19
DONG Bo ... 1089
DONG Tianshu ... 798
DOU Jinzhou ... 650
DU Haibo ... 1259
DU Junjun ... 110
DU Qinlong ... 1311
DUAN Guang-Ren ... 103
... 986
... 1193
DUAN Guangren ... 48
... 72
... 86
... 92
... 152
... 158
... 571
... 668
... 674
... 974
... 1061
... 1066
... 1370
... 1453

F

FAN Debao ... 915
FAN Hongdong ... 1503
FAN Jun-fang ... 249
FAN ShiXiong ... 897
FAN Yong Hua ... 1503
FAN Yu ... 938
FAN Yuan ... 837
... 897
... 1187
FANG Jing ... 1084
FEI Han ... 903
FEI Zhongyang ... 1400
FENG Haolong ... 438

FENG Huijuan 1216
FENG Jun-e 13
..... 19
FENG Yongxing 546
FENG Yuxin 680
FENG Zhiguang 749
..... 764
FU Cheng 993
FU Minyue 1328
FU Wenbo 1508
FU Yanran 831

G

GAO Fangzheng 1050
GAO Feng 1222
GAO Feng 1549
GAO Huanli 389
GAO Qing 1253
GAO Sheng 609
GAO Xiangyu 482
GAO Xinglong 879
GAO Yabin 488
..... 707
GAO Yang 1046
GAO Yuan 815
GAO Yuan 815
..... 809
GAO Zhe 13
GAO Zifan 691
GE Fengying 66
GENG Guangchao 78
..... 110
..... 1123
GENG Hang 770
GENG Shiyao 494
GENG Yunhai 1406
GOLESTANI Mehdi 103
..... 152
GONG Mengtong 540
GONG Yi 494
..... 500
GOU Xuan 770
GU Dake 171
GU Yaxin 325
GU Zhen 1418
GUAN Bin 854
GUAN Yichun 494
GUO Cheng 868
GUO Haihua 426
GUO Jing 737
GUO Jing 804
GUO Qingzheng 764
GUO Xiaomeng 171
GUO Yong 1486
GUO Zhenwei 383
GUOWEI Zhao 749

H

HAN Chunyan 60
..... 66
..... 97
HAN Fei 438
..... 1447
HAN Liangheng 873
HAN Lincong 1113
HAN Tuo 656
..... 1574
HAN Xiaomin 1358
HAN Xinyu 552
HAN Zhimin 455
HAO Jun 183
HAO Liming 1084
HAO Mengjuan 831
HAO Mingrui 938
HE Liang 1447
HE Ping 1382
HE Qiang 466
HE Qiyong 265
HE Xiao 529
HE Zhaoshui 680
HE Zhenyu 1242
HE Ziqi 259
HONG Junjie 873
HONG Xiao 1123
HOU Bowen 798
HOU Mingyu 1532
HOU Mingzhe 1055
..... 1526
HOU Nan 271
HOU Qimin 488
HU Jinfei 296
HU Jintao 1574
HU Jun 603
..... 758
HU Liyao 674
HU Qinglei 656
..... 1574
HU Tao 1447
HU Tianjiang 1493
HU Wenshan 1283
HU Xinjue 1234
HU Yanmei 343
HU Zhihuan 1041
HU Zhiyu 891
HUA Changchun 31
..... 141
..... 926
..... 932
..... 945
..... 957
HUA Shan 879
HUANG Darong 1277
..... 1288
HUANG Jiacai 1050
HUANG Jian 546
HUANG Jiazhu 432
..... 443
HUANG Likun 222
HUANG Ling 737
..... 743
HUANG Peng 1046
HUANG Xianlin 1346
HUANG Xin 552
HUANG Xiuwei 1513
HUANG Zixin 222
HUCHENG Jiang 1089
HUO Xin 1199
..... 1311
HUO Yingning 1123

J

JI Wenqiang 302

JI Yi 249
JIA Chaoqing 319
JIA Shixiang 1543
JIAHUA Ni 1317
JIALING Zhou 432
..... 443
JIANG Bin 534
..... 565
..... 583
..... 662
JIANG Hao 1095
JIANG Hong 72
JIANG Huaiyuan 1140
JIANG Quanyuan 78
JIANG Shihui 1084
JIANG Wu 1023
JIANG Yanna 331
JIANG Yongchao 259
JIANG Yue 1247
JIANG Zhipeng 1568
JIANG Zhong-Ping 511
JIAO Xiaohong 42
JIN Dongyan 1532
JIN Wei 1317
JIN Yan 165
JIN Yang 1430
..... 1435
..... 1543
JIN Yihuan 1441
JIYUAN Kuang 488
JUN Zhang 1283

K

KANG Honglong 1418
KE Yang 1107
KOMADA Satoshi 314
KONG He 103
..... 152
..... 571
..... 1066
KUMAR Lalitesh 337

L

LAI Jun 775
LAN Weiyao 1204
..... 1210
LANG Hongfei 110
LEI Tao 319
LEI Zhongcheng 1283
LI Aoshen 577
LI Bin 1029
..... 1388
LI Bing 743
LI Cheng 707
LI Fanbiao 701
LI Fangyuan 707
LI Fuxing 226
LI Gang 1017
LI Gonghe 226
LI Guodong 909
LI Hao 141
LI Haoran 383
LI Hongyi 680
LI Huayi 1394
LI Jianfeng 1418
LI Jiangang 891
LI Jiangrong 517
..... 1265
LI Jiayang 1549
LI Jing 1017
LI Jingsui 885
LI Jisen 254
LI Li 31
..... 962
LI Linlin 626
LI Mengjie 731
LI Peng 407
..... 1011
LI Ping 1061
..... 1193
LI Qingxue 1123
LI Rongmei 1199
..... 1311
LI Rui 290
..... 1561
LI Runkun 753
LI Shaoyuan 343
LI Shijie 1234
LI Shilun 1176
LI Shunli 974
LI Siquan 1050
LI Wangyan 632
LI Wei 389
LI Weijian 271
LI Weikang 546
LI Xianwei 1568
LI Xiaolei 1078
LI Xiaolei 349
LI Xing 420
LI Xinyu 337
LI Xiuxian 265
LI Xuefang 1107
..... 1170
LI Yan 432
..... 443
LI Yang 1234
LI Yankai 1498
LI Yanqiu 460
LI Yibin 1017
LI Yinkang 1435
LI Yuan 725
LI Yuanlong 998
LI Yuntao 903
LI Zhaoyang 25
LI Zhihao 1340
LI Zhipeng 1328
LI Zhiqiang 680
LI Zhongliang 337
LI Zijing 54
LI Zixuan 614
LI Zuan 903
LIAN Shikang 1538
LIAO MingYan 1299
LIJUN Gao 731
LIN Honglei 786
LIN Jiakuo 1486
LIN Mengying 222
LIN Na 758
LIN Wei 650
LIN Xiaohan 1176

LIN Xiaojie 331
LIN Xinpo 707
LIN Yanjun 466
..... 471
LIN Zemin 1538
LIN Zhiyun 455
LIN Zijie 1465
LING Tianwei 1561
LIU Aoqiang 897
..... 1187
LIU Bei 1364
LIU Chang 1364
LIU Chao 962
LIU Cheng-Lin 365
..... 371
LIU Chenguang 1253
LIU Da-Yan 957
LIU Derong 1182
LIU Fuqiang 577
LIU Guangxin 707
LIU Guopin 926
..... 945
LIU Guoping 1283
..... 1459
LIU Jason Jinrong 644
LIU Jialun 1234
LIU Jianxing 325
..... 707
..... 713
LIU Jiarui 517
LIU Jiawei 1078
LIU Jinfang 809
LIU Jing 552
LIU Jingwen 1503
LIU Jingyue 200
LIU Kerun 1394
LIU Li 254
LIU Li 1129
LIU Lin 92
LIU Lu 1441
LIU Meiqin 449
LIU Ming 819
..... 1394
LIU Qiang 786
LIU Shaojie 1216
LIU ShengYang 438
LIU Shuheng 1400
LIU Tengteng 511
LIU Wangkui 1520
LIU Wanquan 189
LIU Weixing 1435
LIU Weizhen 103
..... 152
..... 1199
LIU Xiaohan 97
LIU Xiaomin 226
LIU Xing 1084
LIU Xinxin 325
LIU Xinyu 938
LIU Xueqing 523
LIU Yang 680
LIU Yang 1146
LIU Yang 37
LIU Yanling 951
LIU YiMin 476
..... 595
..... 614
LIU Yin-Dong 171
LIU Yongchao 284
LIU Zhen 1513
LIU Zhihao 1011
LIU Zhijie 1066
LU Hongqian 1346
LU Jinhu 1253
LU Jinhui 1041
LU Jun-Guo 1
LU Lingxia 449
LU Ruitao 909
LU Shi 1555
LUAN Fan 471
LUO Cheng 577
LUO Lu 932
LUO Weiwei 1508
LUO Zhouhuai 1430
LUO Zongjie 271
LV Lingling 685
LV Yuezu 432
..... 443
LV Zhengyang 609

M

MA Baihe 331
MA Bing 1089
MA Chenglong 1035
MA Dan 968
MA Dazhong 1158
MA Guangfu 506
MA Jianwei 1265
MA Siteng 603
MA Siyuan 609
MA Song 1004
MA Xin 1017
MA Yonghao 534
MA Yuying 1358
MAI Junpeng 1216
MAO Songheng 837
..... 897
MAO Xujing 1050
MEI Jie 506
MENG Deshan 177
MENG Fan-wei 1029
MENG Min 265
MENG Wei 1538
MENG Yan 1480
MENG Yanan 831
MIAO Linlong 494
MIAO Qiyang 565
MING Wu 414
MO Zhibin 189

N

NA Tuopu 1035
NA Yuhong 1277
..... 1288
NCUBE Sisindisiwe Nomalanga 577
NING Lei 1035
NING Pengju 141
NIU Yichun 25
..... 1299

NIU Yugang 701

P

PAN Chengqi 1023
PAN Qi 1072
PANG Yujing 831
PANG Yunbo 1288
PEI Chao 885
PENG Kai 1247
PENG Xiafu 1204
PENG Xiuhui 1072

Q

QI Lin 1210
QI Ruiyun 558
QI Wenhai 753
QI Wenjuan 238
QI Wennian 195
QI ZhongWei 1299
QIAN Mengmeng 897
QIAN Zhouyuan 1447
QIANG Jiaping 962
QIN Ao 13
QIN CunFu 1101
QIN XuJie 775
QING Jiansong 466
QIU Feihang 804
QIU Huabing 1520
QIU Jianbin 1532
..... 1543
QIU Ming 389
QU ChuanKun 1176
QU Menghao 731
QUAN Fangyi 249

R

RAN Chenjian 243
REN Weijie 314
..... 571
REN Yueru 873

S

SANG Yingli 1118
SHAN JINJUN 420
SHANG Hanjun 488
SHANG Yanling 1050
SHAO Hanzhao 1216
SHAO Shuyi 1498
SHAO Xiangyu 200
SHE Xingjing 770
SHEN Dong 1095
SHEN Junyu 1041
SHEN Xiaoning 707
SHENG Li 25
..... 523
..... 540
..... 1299
SHI Xiasheng 355
SHI Yankui 695
SHI Ying Jing 290
..... 1561
SHIWEI Chen 110
SHUI Zunshi 1520
SI YuJIe 1486
SONG Jian 632
SONG Lei 259
SONG Shenmin 1418
SONG Ting 438
SONG Yangyi 238
SU Hanguang 1158
SU Xiaojie 325
SUI Tianju 355
SUN Anping 552
SUN Guanghui 1549
SUN Hui-Jie 177
..... 189
SUN Li 879
SUN Liying 921
SUN Shuli 815
SUN Wei 7
SUN Wei 980
SUN Wendi 938
SUN Xiaowei 1123
SUN Xunhong 1259
SUN Yingbing 951
SUN Yougang 1242
SUN Zhaobo 1465
SUO Jinghui 414

T

TAN Feng 1055
TAN Lining 177
TAN Minglang 825
..... 1424
TAN Zhao 951
TANG Feilong 1078
TAO Guili 780
TAO Wenguang 909
TENG Hao 1480
TEO Kok Lay 1271
TIAN Congcong 506
TIAN Guangtai 103
..... 152
TIAN Ye 1441
TONG Ruizhi 695
TONG Wang 1317
TONG Zhang 349
TONG Zheyu 1152
TSAKALIS Konstantinos ... 1555

W

WAN Jianjun 466
WAN Muchun 110
WAN Xiongbo 589
WANG Ao 1305
WANG Baohua 879
WANG Bin 1352
WANG Bo 455
WANG Changqing 1486
WANG Chenggang 259
WANG Chenqi 279
..... 725
WANG Chunxiao 1129
WANG Dayi 798
WANG Dian 1004
WANG Dinghua 1475
WANG Guopeng 903
WANG Hanyu 1346
WANG HAOQIAN 860
WANG Hao 1513
WANG Heng 78
WANG Hongxia 1247
WANG Jian-Qiao 482

WANG Jiange 349
WANG Jianqi 780
WANG Jie 1475
WANG Jiongqi 798
WANG Jun 1176
WANG Jun 546
WANG Kehao 843
WANG Limin 620
WANG Lipeng 1023
WANG Lou 31
WANG Peng 932
WANG Peng 1334
WANG Ping 986
WANG Qian 165
WANG Qin 1277
WANG Qingxiang 749
WANG Rui 1158
WANG Runze 695
WANG Shaoquan 854
WANG Shujia 232
WANG Tingrui 691
WANG Tong 1532
..... 1543
WANG Wei 222
WANG Wei 1253
WANG Xiangke 775
WANG Xiangyu 1520
WANG Xianlian 879
WANG Xiao 1101
WANG Xiaotian 909
WANG Xinyuan 165
WANG Xiubo 1370
..... 1382
WANG Xu 331
WANG Xuemei 780
WANG Xueyan 1072
WANG Yan 1382
..... 1579
WANG Yanan 662
WANG Yang 308
WANG YanHai 957
WANG Yiyang 279
WANG Yu 183
WANG Yujue 383
WANG Yunfei 743
WANG Yuzhong 349
WANG Yuzhong 1061
..... 1193
WANG Zheming 1352
WANG Zhenhuan 488
WANG Zhentao 743
WANG Zhixiao 879
WANG Ziqian 589
WANG Ziyi 302
WANG ZunHeng 873
WEI Caisheng 1152
WEI Jiayu 552
WEI Muheng 1234
WEI Yan-Qiao 349
..... 957
WEI Yeqi 200
WEN Guilin 951
WU Aiguo 195
WU Aijing 1199
WU Baolin 1406
..... 1465
WU Chang Mao 1228
WU Hao 1123
WU Huiqing 1358
WU Jiameng 371
WU Jie 719
WU Jing 1134
WU Shengbao 1471
WU Songtai 438
WU Wenbin 825
..... 1424
WU Xiang 116
..... 121
WU Xueqi 7
WU Yifan 831
WU Yue 308
WU Yunhua 1004
WU Yuqiang 1046
WU Yuyao 177
..... 189
WU Zhihui 603

X

XIA Jianwei 980
XIA Jingping 565
XIA Lin 1123
XIA Qing 819
XIANG Zhihua 1078
XIAO Fu-Zheng 1412
XIAO Yongqiang 1526
XIAO YuShan 792
XIAOKUN Liu 1430
..... 1435
XIE Linbo 420
XIE Wei 1041
XIN Liu 208
XING Lantao 1134
XING Xiangyang 1364
XING Yang 476
XINPENG Di 903
XIONG Liang 903
XU Chuanchuan 1140
..... 1508
XU Jianfeng 583
XU Jiang 1204
XU Jing 701
XU Jingwen 265
XU Jinyu 1498
XU Juncheng 891
XU Linke 200
XU Lixue 1382
XU Xiang 426
XU Xiangdong 455
XU Yang 1271
XU Yinliang 1340
XU Yuhang 583
XU Zhihao 1247
XU Zixin 500
XUE Hao Liang 377
XUE Xiaohui 1498
XUEQIN Chen 1271

Y

YAN Chengyuan 980
YAN Fei 713
YAN Haoyu 1089

YAN Huixing 1346
YAN Tian 909
YAN Xiaoming 1146
YAN Xunliang 1526
YAN Yuchao 903
YANG Chunshan 780
YANG Chunyu 226
YANG Delong 685
YANG Hai 208
YANG Hua 1152
YANG Jinhong 1084
YANG Lin 998
YANG Meng 401
YANG Peng 1513
YANG Rongni 719
YANG Ruirui 314
YANG Ruohan 302
YANG Shu 1187
YANG Tianle 116
..... 121
YANG Xin 365
YANG Xin-Rong 147
YANG Xuefei 1140
..... 1520
YANG Yana 926
..... 945
YANG Yi Heng 1388
YANG Zaiyue 395
..... 1376
YANG Zhenrong 792
YANQIN Wang 271
YAO Fuxing 1066
YASHIRO Daisuke 314
YAXIN An 284
YE Saixian 1441
YE Yueyao 915
YI Yingmin 1498
YIN Mali 1170
YIN Rongji 1041
YINGWEI Chen 1271
YU Boyuan 494
..... 500
YU Hui 603
YU Jiangbo 1129
YU Liang 1400
YU Miao 1055
YU Qianxiang 626
YU Tianze 603
YU Xiao 1204
YU Xiao 1129
YU Yao 1041
YU Yongyuan 19
YUAN Jicheng 1475
YUAN Linsong 650
YUAN Ronghao 825
..... 1424
..... 1430
YUBAI Kazuhiro 314
YUE Keyuan 1418
YUEBIN Qiu 116
..... 121
YUXIN Weng 78

Z

ZENG Chujian 1182
ZENG Depeng 873
..... 1294
ZENG Deyu 620
ZENG Qingjie 909
ZENG Rijie 1041
ZENG Yi 695
ZHAI Xiangping 54
ZHAN Lei 1210
ZHANG Bi 1193
ZHANG Changzhu 296
ZHANG Chaoyue 656
ZHANG Cui-Hua 31
..... 962
ZHANG Da-Wei 1459
ZHANG Dandan 343
ZHANG Dawei 232
..... 691
ZHANG Feng 1471
ZHANG Guanguan 993
ZHANG Guoshan 854
ZHANG Haili 626
ZHANG Hang 449
ZHANG Hao 843
ZHANG He 1579
ZHANG Hongliang 1358
ZHANG Hongwei 54
ZHANG Hongxu 758
ZHANG Huanshui 1328
ZHANG Hui 848
ZHANG Hui 116
..... 121
ZHANG Jialong 951
ZHANG Jiaming 37
ZHANG Jie 195
ZHANG Jin-Xi 216
ZHANG Jing 121
ZHANG Jiyu 1352
ZHANG Kai 650
ZHANG Kai 308
..... 1388
ZHANG Kangkang 1140
ZHANG Ke 534
..... 565
..... 662
ZHANG Kun 873
ZHANG Liming 455
ZHANG Lizong 466
ZHANG Luhan 31
ZHANG Menghua 1113
ZHANG Qian 825
..... 1424
..... 1430
ZHANG Qinghao 1
ZHANG Senlin 449
ZHANG Shanfeng 308
ZHANG Shaojie 200
ZHANG Shijie 116
..... 121
ZHANG Shiyu 48
..... 668
ZHANG Sixing 249
ZHANG Siyuan 552
ZHANG Tao 860
ZHANG Weidong 1041
ZHANG Wenbo 1400

ZHANG Xianfu 915
ZHANG Xiaobo 407
ZHANG Xiaoxiang 1406
ZHANG Xing 792
ZHANG Xinyu 243
ZHANG Xinyu 183
ZHANG Xirui 511
ZHANG Xu 804
ZHANG Xuenan 809
ZHANG Xujie 86
ZHANG Ya 848
ZHANG Yabo 921
ZHANG Yahui 42
..... 951
ZHANG Yanhui 1152
ZHANG Yi 279
..... 725
ZHANG Yi Fan 1152
ZHANG Ying 31
ZHANG Yu 945
ZHANG Yu 1029
ZHANG Yuan Zhuo 1216
ZHANG Yue 494
..... 500
ZHANG Zeqi 1418
ZHANG Zeyi 1095
ZHANG Zhen 1346
ZHANG Zheng 1334
ZHANG Zhengqiang 1118
ZHANG Zhongcai 1046
..... 1328
ZHANG Zicheng 993
ZHAO Bo 1035
ZHAO Bo 1182
ZHAO Dongqi 254
ZHAO Guanglei 359
..... 932
ZHAO Haohan 42
..... 951
ZHAO Haotian 819
ZHAO Huarong 420
ZHAO Ping 1101
ZHAO Qinglun 60
ZHAO Qingyi 134
ZHAO Runchen 1259
ZHAO Weiyi 325
ZHAO Xiaoning 1242
ZHAO Yan 1129
ZHAO Ying 780
ZHAO Yu 377
ZHAO Yue 713
ZHAO Yuzhuo 968
ZHAO Zhiliang 511
ZHEN Wei 466
ZHEN Yan 938
ZHENG Baifu 809
ZHENG Bo 1447
ZHENG Haibin 383
ZHENG Kai 1311
ZHENG Liu 780
ZHENG Ronghao 449
ZHENG Sen 127
ZHENG Wenquan 1441
ZHENG Yin 1579
ZHI Gan 1158
ZHIQIANG Xu 1242
ZHONG Yini 825
..... 1424
ZHONG Zefeng 147
ZHOU Aozhan 758
ZHOU Chen 290
ZHOU Chengbao 1164
ZHOU Dianle 1311
ZHOU Dongcheng 466
ZHOU Donghua 523
..... 529
ZHOU Donghua 540
ZHOU Hong 1283
ZHOU Linna 226
ZHOU Shisen 589
ZHOU Xiaoshuang 926
ZHOU Yirong 558
ZHOU Yuan 377
ZHOU Yuan 1352
ZHOU Yunhu 1277
..... 1288
ZHOU Zhicheng 848
ZHU Baopeng 1480
ZHU Fuxing 713
ZHU Jiajian 383
ZHU Jiming 517
ZHU Jing 54
ZHU Jingjuan 831
ZHU Shuqian 232
ZHU Song 1508
ZHU Wei 460
..... 885
ZHU Wenwu 1259
ZHU Yukai 1480
ZHUANG Guangming 831
ZHUANG Liu 488
..... 713
ZOU Chenyang 609
ZOU Die 222
ZOU Xiangxiang 177
ZUO Xiaozhong 609
ZUO YuXin 500
ZUO Zhiyuan 758